MODERN

MAGNETIC RESONANCE

EDITOR: GRAHAM A. WEBB

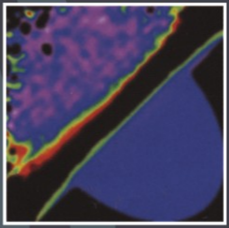

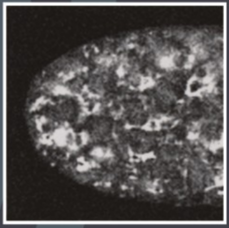

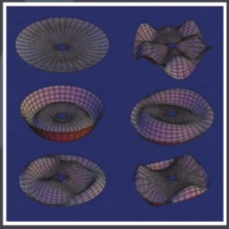

3

Applications in Materials Science and Food Science

Springer

Modern Magnetic Resonance

Part 1

Part 1: Applications in Chemistry, Biological and Marine Sciences
Part 2: Applications in Medical and Pharmaceutical Sciences
Part 3: Applications in Materials Science and Food Science

Modern Magnetic Resonance

Part 1: Applications in Chemistry, Biological and Marine Sciences

Graham A. Webb (Ed.)
Royal Society of Chemistry, London, UK

Springer

A C.I.P. Catalogue record for this book is available from the Library of Congress.

ISBN 978-1-4020-3894-5 (HB)
ISBN 978-1-4020-3910-2 (e-book)

Published by Springer,
P.O. Box 17, 3300 AA Dordrecht, The Netherlands.

www.springer.com

Printed on acid-free paper

First published in 2006
Reprinted with corrections in 2008

All rights reserved.
© 2008 Springer
No part of this work may be reproduced, stored in a retrieval system, or transmitted in any form or by any means, electronic, mechanical, photocopying, microfilming, recording or otherwise, without written permission from the Publisher, with the exception of any material supplied specifically for the purpose of being entered and executed on a computer system, for exclusive use by the purchaser of the work.

Contents

List of Section Editors XI
Preface XIII
Color Plate Section XV

APPLICATIONS IN CHEMISTRY

Foreword 3
Abbreviations 5
Amyloids 9

- **Kinetics of Amyloid Fibril Formation of Human Calcitonin,** *Miya Kamihira, Hazime Saitô, and Akira Naito* 11
- **Polymorphism of Alzheimer's Aβ Amyloid Fibrils,** *Oleg N. Antzutkin* 19

Chemical Shifts and Spin-Couplings 29

- **^{13}C, ^{15}N, ^{1}H, ^{2}H, and ^{17}O NMR Chemical Shift NMR for Hydrogen Bonds,** *Shigeki Kuroki* 31
- **NMR Chemical Shift Map,** *Isao Ando and Tetsuo Asakura* 37
- **NMR Chemical Shifts Based on Band Theory,** *Hiromichi Kurosu and Takeshi Yamanobe* 43
- **Modeling NMR Chemical Shifts,** *Julio C. Facelli* 53
- ***Ab Initio* Calculation of NMR Shielding Constants,** *Peter B. Karadakov* 63
- **Crystal Structure Refinement Using Chemical Shifts,** *Ulrich Sternberg, Raiker Witter, and Anne S. Ulrich* 71
- **The Theory of Nuclear Spin–Spin Couplings,** *Hiroyuki Fukui* 79

Fibrous Proteins 85

- **Investigation of Collagen Dynamics by Solid-State NMR Spectroscopy,** *Göran Zernia and Daniel Huster* 87
- **Solid-State NMR Studies of Elastin and Elastin Peptides,** *Kristin K. Kumashiro* 93
- **Structural Analysis of Silk Fibroins using NMR,** *Tetsuo Asakura and Yasumoto Nakazawa* 101

Field Gradient NMR 107

- **NMR Diffusometry,** *William S. Price* 109
- **Field Gradient NMR of Liquid Crystals,** *István Furó and Sergey V. Dvinskikh* 117
- **Field Gradient NMR for Polymer Systems with Cavities,** *Yuji Yamane and Sunmi Kim* 123
- **NMR Measurements Using Field Gradients and Spatial Information,** *Shingo Matsukawa* 129
- **Theory and Application of NMR Diffusion Studies,** *Torsten Brand, Eurico J. Cabrita, and Stefan Berger* 135

Host–Guest Chemistry 145

- **Solid-State NMR in Host–Guest Chemistry,** *John A. Ripmeester and Christopher I. Ratcliffe* 147

Imaging 155

- **Mapping of Flow and Acceleration with NMR Microscopy Techniques,** *Elke Kossel, Bogdan Buhai, and Rainer Kimmich* 157
- **Industrial Application of *In situ* NMR Imaging Experiments to Steel-Making Process,** *Koji Saito* 163
- **Biomedical NMR Spectroscopy and Imaging,** *Toshiro Inubushi and Sigehiro Morikawa* 173

Electron Spin Resonance Imaging in Polymer Research, *Shulamith Schlick* 179
NMR Imaging: Monitoring of Swelling of Environmental Sensitive Hydrogels, *Karl-Friedrich Arndt, Manfred Knörgen, Sven Richter, and Thomas Schmidt* 187

Inorganic Materials and Catalysis 195

Exploiting $^1H \rightarrow ^{29}Si$ Cross-Polarization Features for Structural Characterization of Inorganic Materials, *Piotr Tekely* 197
Solid State NMR Characterization of Solid Surface of Heterogeneous Catalysts, *Feng Deng, Jun Yang, and Chaohui Ye* 205

Isotope Labeling 213

Recent Developments in Stable-Isotope-Aided Methods for Protein NMR Spectroscopy, *Shin-ya Ohki and Masatsune Kainosho* 215
Structural Glycobiology by Stable-isotope-assisted NMR Spectroscopy, *Yoshiki Yamaguchi and Koichi Kato* 223

Lipid Bilayer and Bicelle 231

Development and Application of Bicelles for Use in Biological NMR and Other Biophysical Studies, *Charles R. Sanders* 233
Nuclear Magnetic Resonance of Oriented Bilayer Systems, *Akira Naito, Shuichi Toraya, and Katsuyuki Nishimura* 241
Solid-State Deuterium NMR Spectroscopy of Membranes, *Michael F. Brown, Silvia Lope-Piedrafita, Gray V. Martinez, and Horia I. Petrache* 249
Solid State ^{19}F-NMR Analysis of Oriented Biomembranes, *Anne S. Ulrich* 261

Membrane-Associated Peptides 269

Solid-State NMR Studies of the Interactions and Structure of Antimicrobial Peptides in Model Membranes, *Marise Ouellet and Michèle Auger* 271
Anisotropic Chemical Shift Perturbation Induced by Ions in Conducting Channels, *Jun Hu, Eduard Chekmenev, and Timothy A. Cross* 279
NMR Studies of Ion-Transporting Biological Channels, *James F. Hinton* 285

Membrane Proteins 289

Site-Directed NMR Studies on Membrane Proteins, *Hazime Saitô* 291
Structure of Membrane-Binding Proteins Revealed by Solid-State NMR, *Satoru Tuzi, Naoko Uekama, Masashi Okada, and Hitoshi Yagisawa* 299
Solid-State NMR of Membrane-Active Proteins and Peptides, *John D. Gehman and Frances Separovic* .. 305
Magnetic Resonance Spectroscopic Studies of the Integral Membrane Protein Phospholamban, *Gary A. Lorigan* 313
NMR Studies of the Interactions Between Ligands and Membrane-Embedded Receptors: New Methods for Drug Discovery, *David A. Middleton* 319
Photosynthetic Antennae and Reaction Centers, *H.J.M. de Groot* 327
Insight into Membrane Protein Structure from High-Resolution NMR, *Philip L. Yeagle and Arlene Albert*. 335

New Developments 345

Fast Multidimensional NMR: New Ways to Explore Evolution Space, *Ray Freeman and Eriks Kupče* 347
High-Sensitivity NMR Probe Systems, *P.J.M. van Bentum and A.P.M. Kentgens* 353
CRAMPS, *B.C. Gerstein and H. Kimura* 363
Mobile NMR, *B. Blümich and F. Casanova* 373
Rheo-NMR, *Paul T Callaghan* 383
Analytical Aspects of Solid-State NMR Spectroscopy, *Cecil Dybowski* 389

^{3}H NMR and Its Application, *John R. Jones and Shui-Yu Lu* 395
On-line SEC–NMR, *Tatsuki Kitayama and Koichi Ute* 399

NOE and Chemical Exchange 407

The Nuclear Overhauser Effect, *Mike P Williamson* 409
Solute–Solvent Interactions Examined by the Nuclear Overhauser Effect, *J.T. Gerig* 413
Chemical Exchange, *Alex D Bain* 421

NQR & ESR 429

Separated Detection of H-Transfer Motions in Multi-H-Bonded Systems Studied by Combined ^{1}H NMR and ^{35}Cl NQR Measurements, *Ryuichi Ikeda* 431
EPR: Principles, *Bruce R. McGarvey* 439
Zero Field NMR: NMR and NQR in Zero Magnetic Field, *David B. Zax* 445

Organo Metallic Chemistry 453

Organoboron Chemistry, *Bernd Wrackmeyer* 455
Organogermanium Chemistry, *Bernd Wrackmeyer* 459
Organotin Chemistry, *Bernd Wrackmeyer* 461

Paramagnetic Effects 465

^{1}H and ^{13}C High-Resolution Solid-State NMR of Paramagnetic Compounds Under Very Fast Magic Angle Spinning, *Yoshitaka Ishii and Nalinda P. Wickramasinghe* 467
Paramagnetic Effects of Dioxygen in Solution NMR—Studies of Membrane Immersion Depth, Protein Topology, and Protein Interactions, *R.S. Prosser and F. Evanics* 475

Protein Structure 485

TROSY NMR for Studies of Large Biological Macromolecules in Solution, *César Fernández, Gerhard Wider* 487
NMR Insight of Structural Stability and Folding of Calcium-Binding Lysozyme, *Makoto Demura* 497
NMR Investigation of Calmodulin, *Tapas K. Mal and Mitsuhiko Ikura* 503
Analytical Framework for Protein Structure Determination by Solid-State NMR of Aligned Samples, *Alexander A. Nevzorov and Stanley J. Opella* 517
Determining Protein 3D Structure by Magic Angle Spinning NMR, *Ovidiu C. Andronesi, Henrike Heise, and Marc Baldus* 527
^{19}F NMR Study of *b*-Type Haemoproteins, *Yasuhiko Yamamoto, Satoshi Nagao, and Akihiro Suzuki* 531

Polymer Structure 539

NMR in Dry or Swollen Temporary or Permanent Networks, *Jean-Pierre Cohen Addad* 541
Crystalline Structure of Ethylene Copolymers and Its Relation to the Comonomer Content, *Qun Chen* 545
Isomorphism in Bacterially Synthesized Biodegradable Copolyesters, *Naoko Yoshie and Yoshio Inoue* ... 551
Two-Dimensional NMR Analysis of Stereoregularity of Polymers, *A.S. Brar and Gurmeet Singh* 557
Quantitative Analysis of Conformations in Disordered Polymers by Solid-State Multiple-Quantum NMR, *Hironori Kaji* 563
Polymer Microstructure: The Conformational Connection to NMR, *Alan E. Tonelli* 567
Solid-State NMR Characterization of Polymer Interfaces, *Peter A. Mirau* 575
The Structure of Polymer Networks, *Andrew K. Whittaker* 583
^{1}H CRAMPS NMR of Polypeptides in the Solid State, *Akira Shoji* 591

Polymer Dynamics 605

Dynamics of Amorphous Polymers, *Fumitaka Horii* 607
Molecular Motions of Crystalline Polymers by Solid-State MAS NMR, *Toshikazu Miyoshi* 615

Dynamics in Polypeptides by Solid State ^{2}H NMR, *Toshifumi Hiraoki* 621

Polymer Blends 629

Polymer Blends, *Atsushi Asano* 631
Configurational Entropy and Polymer Miscibility: New Experimental Insights From Solid-State NMR, *Jeffery L. White* 637

Quantum Information Processing 645

Quantum Information Processing as Studied by Molecule-Based Pulsed ENDOR Spectroscopy, *Robabeh Rahimi, Kazunobu Sato, Daisuke Shiomi, and Takeji Takui* 647

Residual Dipolar Couplings and Nucleic Acids 655

New Applications for Residual Dipolar Couplings: Extending the Range of NMR in Structural Biology, *Rebecca S. Lipsitz and Nico Tjandra* 657
Refinement of Nucleic Acid Structures with Residual Dipolar Coupling Restraints in Cartesian Coordinate Space, *Nikolai B. Ulyanov, Zhihua Du, and Thomas L. James* 665
Conformational Analysis of DNA and RNA, *Gota Kawai* 671

Solid-State NMR Technique 677

Analytical and Numerical Tools for Experiment Design in Solid-State NMR Spectroscopy, *Niels Chr. Nielsen, Thomas Vosegaard, and Anders Malmendal* 679
Homonuclear Shift-Correlation Experiment in Solids, *K. Takegoshi* 689
Two-Dimensional ^{17}O Multiple-Quantum Magic-Angle Spinning NMR of Organic Solids, *Gang Wu* 695
A Family of PISEMA Experiments for Structural Studies of Biological Solids, *Ayyalusamy Ramamoorthy and Kazutoshi Yamamoto* 703

Structural Constraints in Solids 711

Rotational-Echo, Double-Resonance NMR, *Terry Gullion* 713
REDOR in Multiple Spin System, *Katsuyuki Nishimura and Akira Naito* 719
Torsion Angle Determination by Solid-State NMR, *Mei Hong* 727
Secondary Structure Analysis of Proteins from Angle-Dependent Interactions, *Toshimichi Fujiwara and Hideo Akutsu* 735

Telomeric DNA Complexes 741

Comparison of DNA-Binding Activities Between hTRF2 and hTRF1 with hTRF2 Mutants, *Shingo Hanaoka, Aritaka Nagadoi, and Yoshifumi Nishimura* 743

APPLICATIONS IN BIOLOGICAL SCIENCES

Abbreviations 755

Optimization of MRI Contrast for Pre-Clinical Studies at High Magnetic Field, *Yu-Ting Kuo, Amy H. Herlihy* 759
The Application of *In Vivo* MRI and MRS in Phenomic Studies of Murine Models of Disease, *Po-Wah So and Jimmy D. Bell* 769
Experimental Models of Brain Disease: MRI Contrast Mechanisms for the Assessment of Pathophysiological Status, *David L. Thomas, Louise van der Weerd, Mark F. Lythgoe, and John S. Thornton* 787
Experimental Models of Brain Disease: MRI Studies, *Louise van der Weerd, David Thomas, John Thornton Mankin choy, and Mark F. Lythgoe* 801
Application of MRS in Cancer in Pre-clinical Models, *Y.-L. Chung, M. Stubbs, and J.R. Griffiths* 823
Experimental Cardiovascular MR in Small Animals, *Jürgen E. Schneider and Stefan Neubauer* 835

Application of Pharmacological MRI to Preclinical Drug Discovery and Development, *Matthew D. Ireland and Steven C.R. Williams* 855
Application of MRI to Cell Tracking, *Kishore Bhakoo, Catherine Chapon, Johanna Jackson, and William Jones* 879

APPLICATIONS IN MARINE SCIENCE

Foreword 893
Abbreviations 895

Comprehensive Compositional Analysis of Fish Feed by Time Domain NMR, *Emil Veliyulin, Karl Østerhus, Wolfgang Burk, Trond Singstad, and Tore Skjetne* 897
Low Field NMR Studies of Atlantic Salmon (*Salmo salar*), *Ida Grong Aursand, Emil Veliyulin, and Ulf Erikson* 905
Water Distribution and Mobility in Fish Products in Relation to Quality, *Bo M. Jørgensen and Kristina N. Jensen* 915
Proton NMR of Fish Oils and Lipids, *R. Sacchi, M. Savarese, L. Falcigno, I. Giudicianni, and L. Paolillo* .. 919
Determination of Fatty Acid Composition and Oxidation in Fish Oils by High Resolution Nuclear Magnetic Resonance Spectroscopy, *Rosario Zamora and Francisco J. Hidalgo* 925
Resonance Spectroscopy to Study Lipid Oxidation in Fish and Fish Products, *E. Falch and M. Aursand* 933
Omega-3 Fatty Acid Content of Intact Muscle of Farmed Atlantic Salmon (*Salmo Salar*) Examined by ^{1}H MAS NMR Spectroscopy, *M. Aursand, I.S. Gribbestad, and I. Martinez* 941
HR MAS NMR Spectroscopy of Marine Microalgae, Part 1: Classification and Metabolite Composition from HR MAS ^{1}H NMR Spectra and Multivariate Analysis, *Matilde Skogen Chauton and Trond Røvik Størseth* 947
HR MAS NMR Spectroscopy of Marine Microalgae, Part 2: ^{13}C and ^{13}C HR MAS NMR Analysis Used to Study Fatty Acid Composition and Polysaccharide Structure, *Trond Røvik Størseth, Matilde S. Chauton, and Jostein Krane* 953
Post-mortem Studies of Fish Using Magnetic Resonance Imaging, *Emil Veliyulin, Alv Borge, Trond Singstad, Ingrid Gribbestad, and Ulf Erikson* 959
How is the Fish Meat Affected by Technological Processes?, *Loïc Foucat, Ragni Ofstad, and Jean-Pierre Renou* 967

Author Index
Subject Index

List of Section Editors

Subject	Name	Type of Editor
	Graham A. Webb	Editor-In-Chief
Chemistry	Hazime Saitô Himeji Institute of Technology and QuLiS, Hiroshima University Japan e-mail: hsaito@siren.ocn.ne.jp	Section Editors
	Isao Ando Department of Chemistry and Materials Science Tokyo Institute of Technology, Ookayama, Meguro-ku Tokyo 152-0033 Japan e-mail: iando@polymer.titech.ac.jp	
	Tetsuo Asakura Department of Biotechnology Tokyo University of Agriculture and Technology Koganei, Tokyo 184-8588 Japan e-mail: asakura@cc.tuat.ac.jp	
Biological Sciences	Jimmy D. Bell Molecular Imaging Group, MRC Clinical Sciences Centre Hammersmith Hospital Campus, Imperial College London London, W12 OHS UK e-mail: jimmy.bell@csc.mrc.ac.uk	Section Editor
Marine Science	M. Aursand SINTEF Fisheries and Aquaculture Ltd N-7465 Trondheim Norway e-mail: marit.aursand@sintef.no	Section Editor
Medical Science	Carolyn Mountford Institute for Magnetic Resonance Research, and Department of Magnetic Resonance in Medicine University of Sydney, PO Box 148, St Leopards, 1590, NSW Australia email: caro@imrr.usyd.edu.au	Section Editor
	Uwe Himmelreich, PhD Max-Planck-Institute for Neurological Research In vivo NMR Group, Gleueler Str 50, Cologne, D-50931 Germany email: himmelreich@mpin-koeln.mpg.de	
	Deborah Edward Pageturner (Editing & Research Services)	Assistant Editor

Subject	Name	Type of Editor
Pharmaceutical Science	David Craik Institute for Molecular Bioscience University of Queensland Brisbane 4072, Queensland Australia e-mail: d.craik@imb.uq.edu.au	Section Editor
Materials Science	Marcel Utz University of Connecticut, 97 N Eagleville Rd Storrs CT 06269-3136 e-mail: marcel.utz@uconn.edu	Section Editor
Food Science	Peter Belton School of Chemical Sciences and Pharmacy University of East Anglia Norwich NR4 7TJ, UK e-mail: p.belton@uea.ac.uk	Section Editor

Preface

It is a great pleasure for me to Introduce the handbook of Modern Magnetic Resonance, MMR. The various techniques which comprise MMR derive essentially from three sources, all of which were produced by physicists. Today they are widely used by scientists working in many diverse areas such as chemistry, biology, materials, food, medicine and healthcare, pharmacy and marine studies.

The first source of MMR studies is nuclear magnetic resonance, NMR. This provides details on the relative positions of nuclei, i.e. atoms, in a molecule. Consequently NMR provides structural information on samples which may be in the solid, liquid or gaseous state. Nuclear relaxation data yield dynamic information on the sample and the topology of the dynamic processes if the sample is undergoing a molecular change. Thus high and low resolution NMR studies provide information on all interesting aspects of molecular science. The protean nature of NMR is reflected in its many applications in chemistry, biology and physics which explore and characterize chemical reactions, molecular conformations, biochemical pathways and solid state materials, to name a few examples.

Magnetic resonance imaging, MRI, is the second source of MMR data. MRI provides a three-dimensional image of a substance, and is consequently widely employed to assess materials both *in vitro* and *in vivo*. The importance of MRI studies in many areas of science and medicine is shown by the recent award of the Nobel Prize to Lauterbur and Mansfield.

The third source of MMR results is due to electron spin resonance, ESR. This is a technique for detecting unpaired electrons and their interactions with nuclear spins in a given sample. Thus ESR data are often used to complement the results of NMR experiments.

Taken together NMR, MRI and ESR comprise the field of MMR, recent years have witnessed the fecundity of these techniques in many scientific areas. The present three volumes cover applications in most of these areas. Part 1 deals with Chemical Applications, Biological and Marine Sciences. Medical and Pharmaceutical Sciences are covered in Part 2. Part 3 provides examples of recent work in the Materials Science and Food Science.

I wish to express my gratitude to all of the Section Editors and their many contributors for their hard work and dedication in the creation of MMR. My thanks also go to Emma Roberts and the production staff at Springer, London, for their assistance in the realization of these volumes.

Royal Society of Chemistry
Burlington House
Piccadilly
London, W1J OBA

G.A.WEBB
February 2005

Please note that authors used either British or American English spelling depending on the language of their choice for individual papers.

Graham A. Webb (ed.), Modern Magnetic Resonance, XIII.
© 2008 *Springer.*

Color Plate Section

Part I

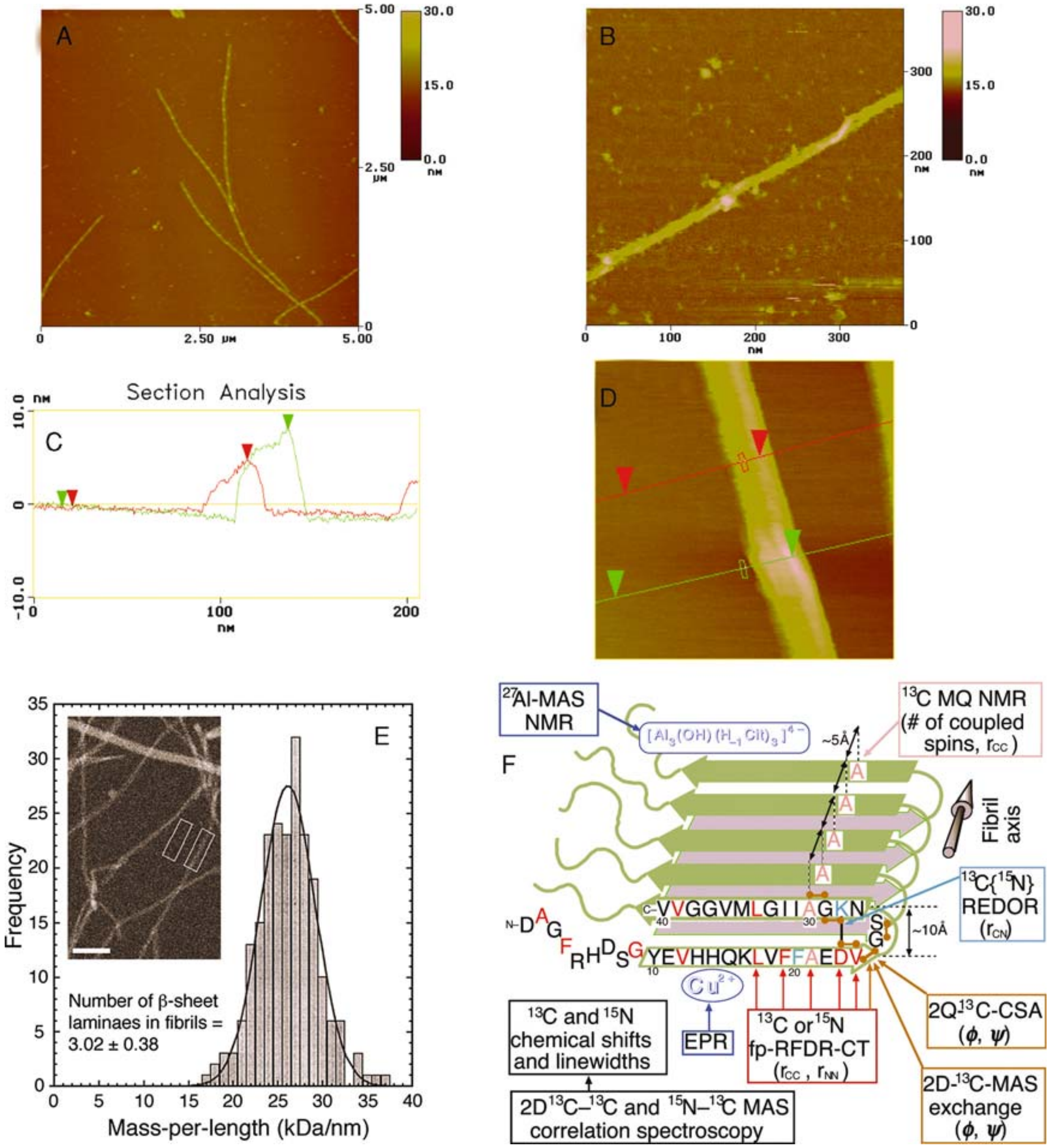

Plate 1. See also Figure 1 on page 21.

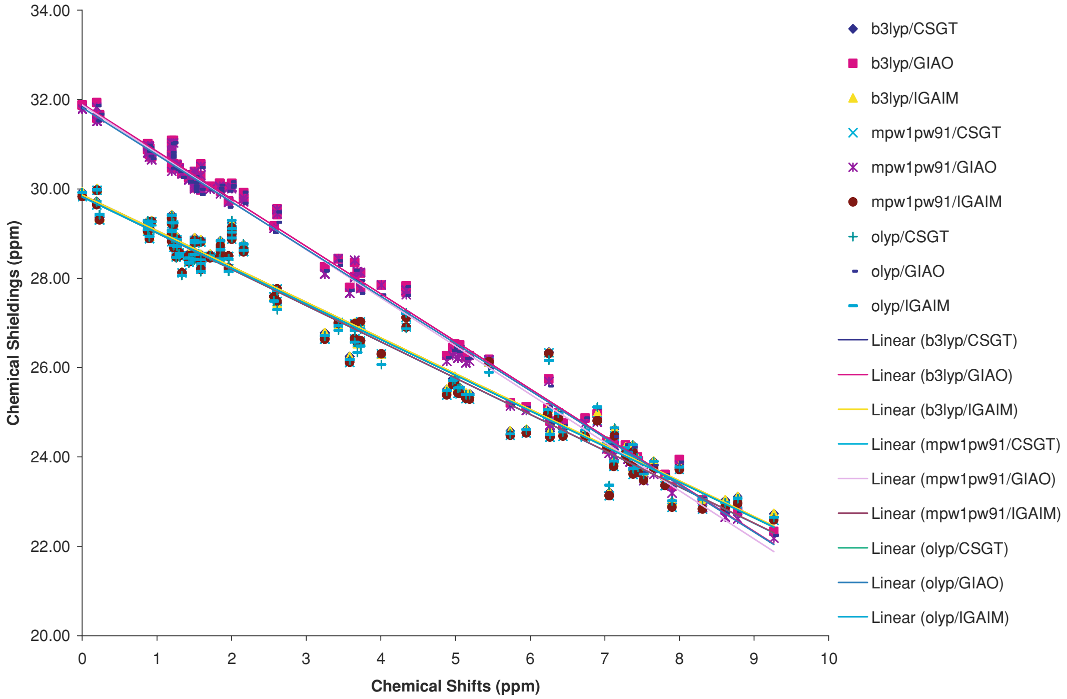

Plate 2. See also Figure 2 on page 57.

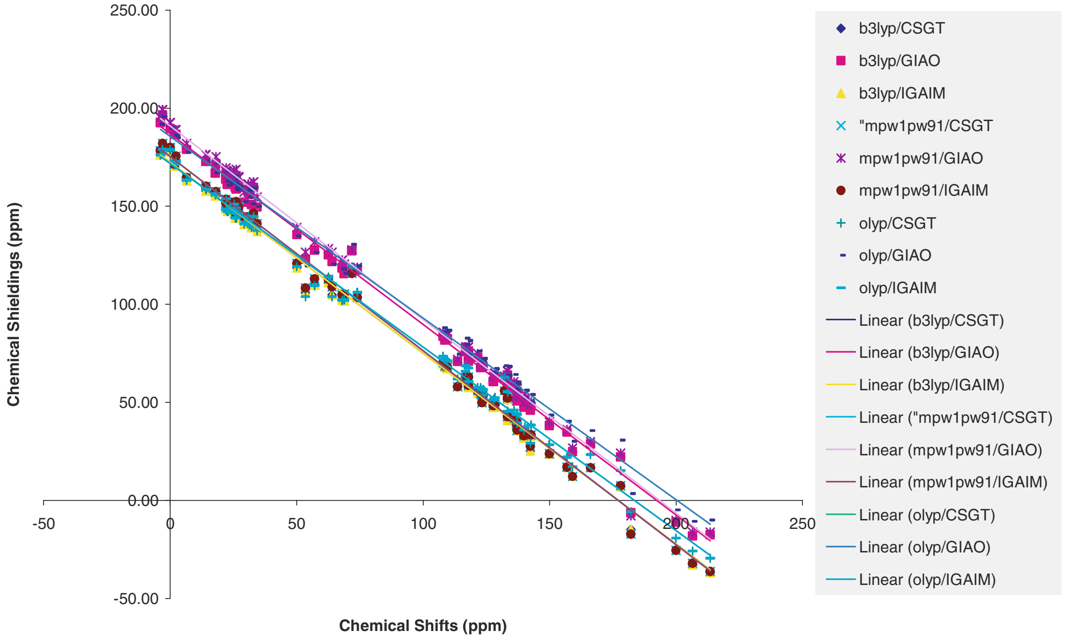

Plate 3. See also Figure 3 on page 58.

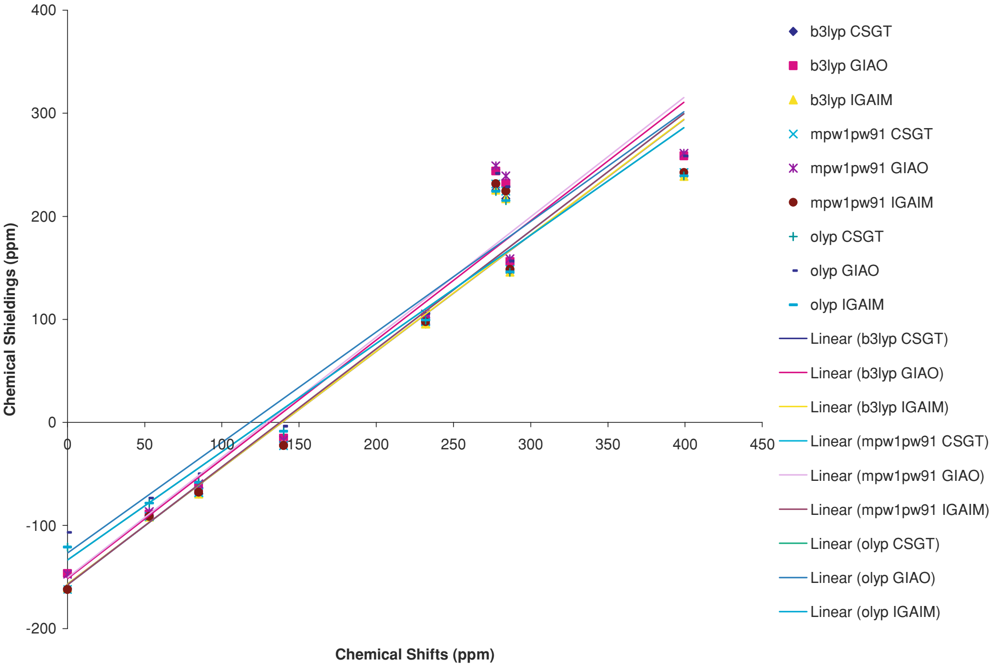

Plate 4. See also Figure 4 on page 59.

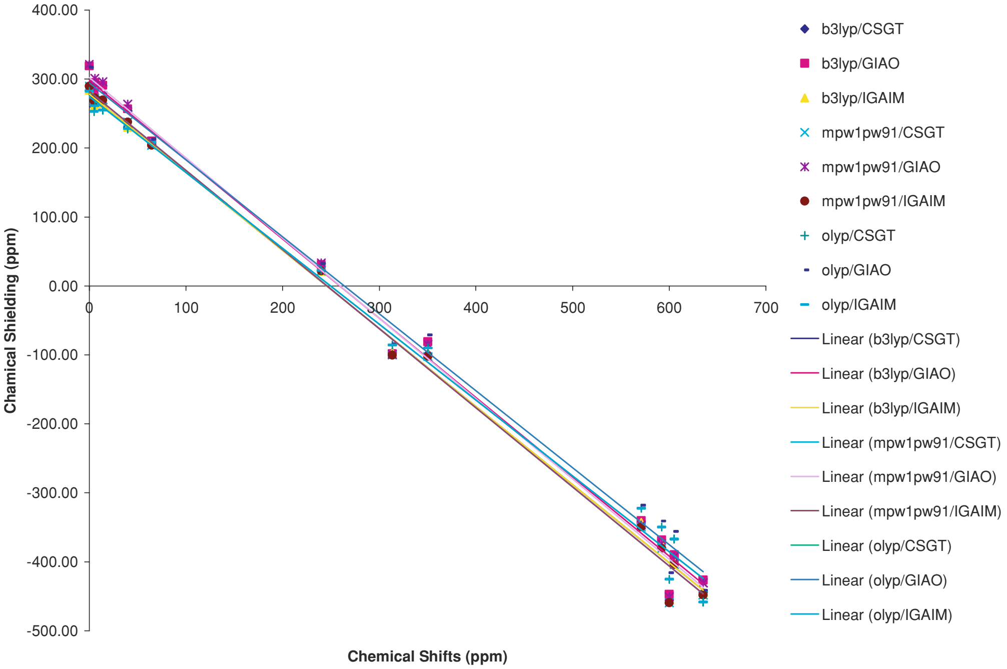

Plate 5. See also Figure 5 on page 60.

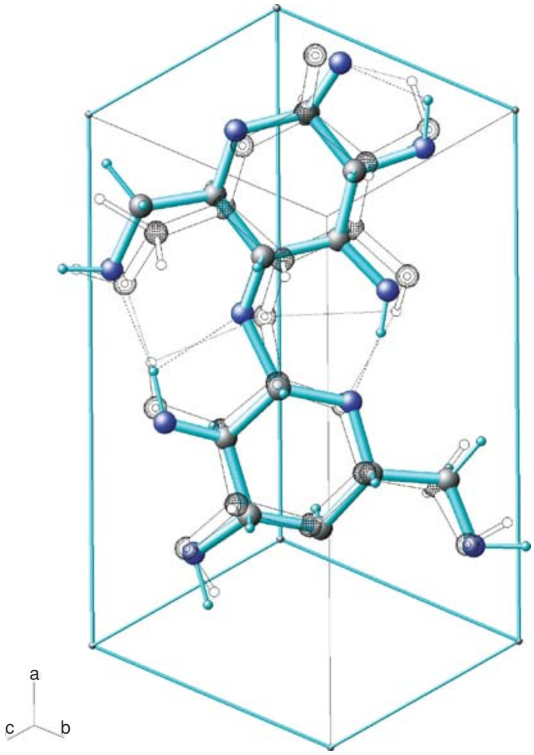

Plate 6. See also Figure 2 on page 76.

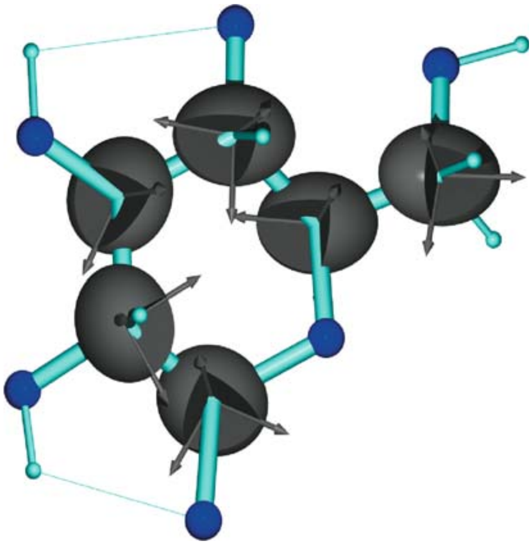

Plate 7. See also Figure 4 on page 77.

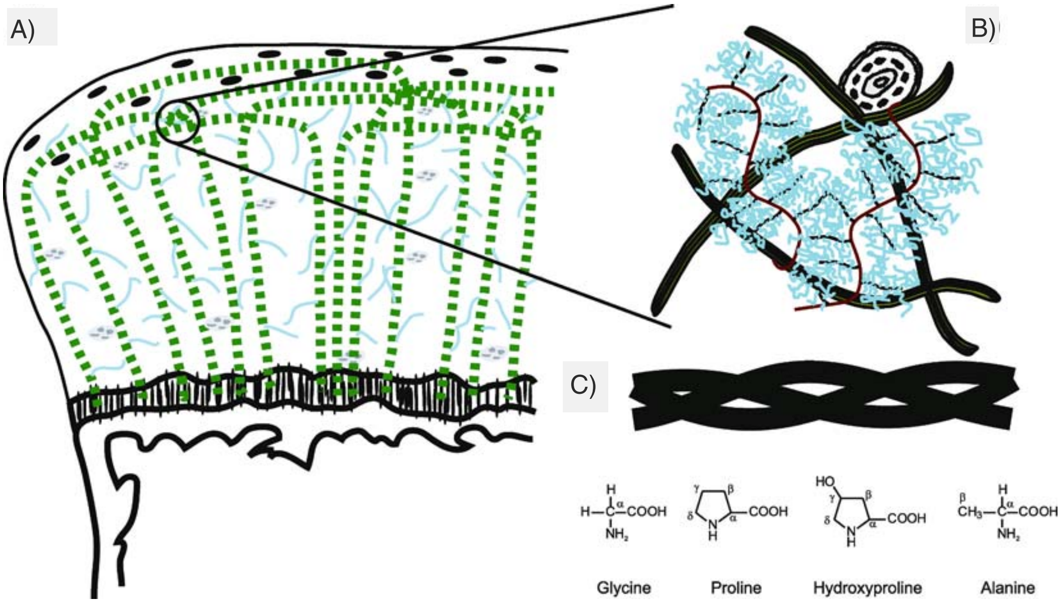
A)
B)
C)
Glycine
Proline
Hydroxyproline
Alanine

Plate 8. See also Figure 1 on page 88.

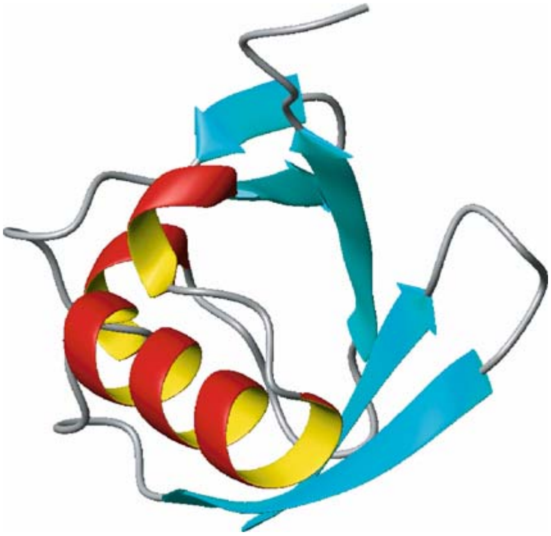

Plate 9. See also Figure 4 on page 138.

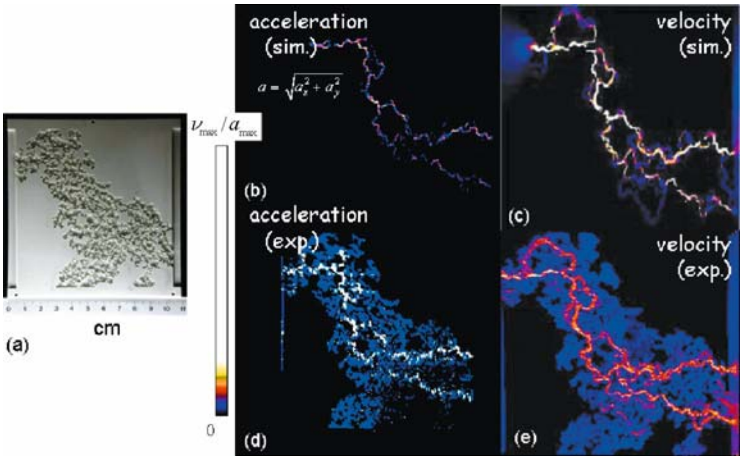

Plate 10. See also Figure 3 on page 161.

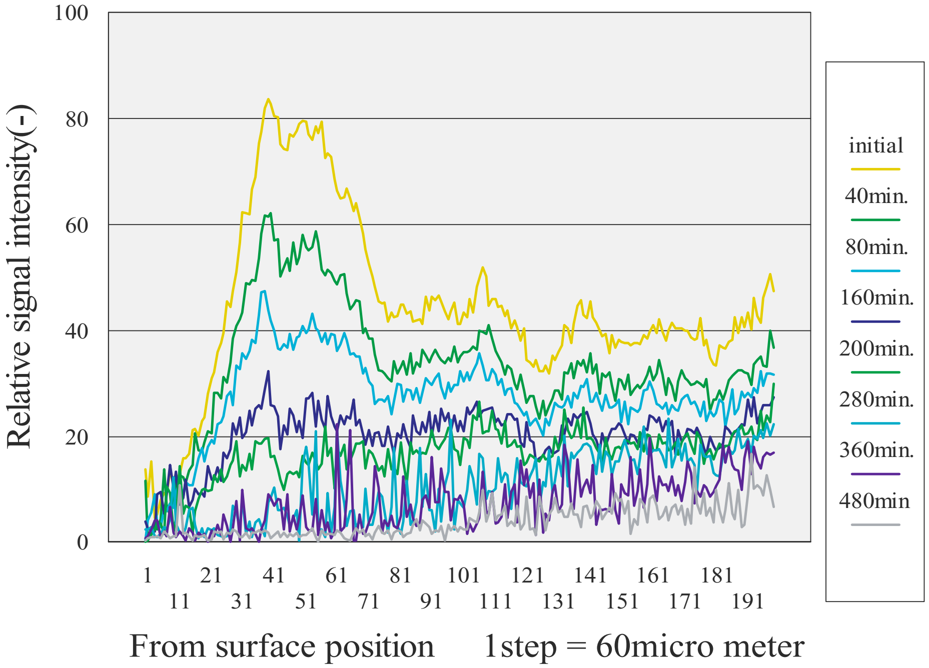

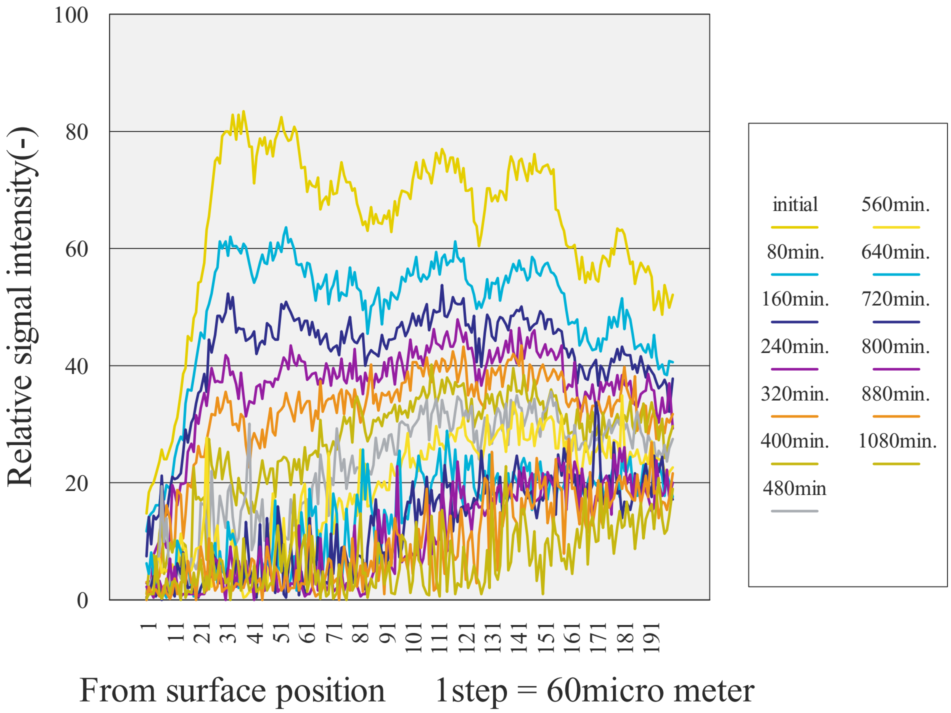

Plate 11. See also Figure 1 on page 164.

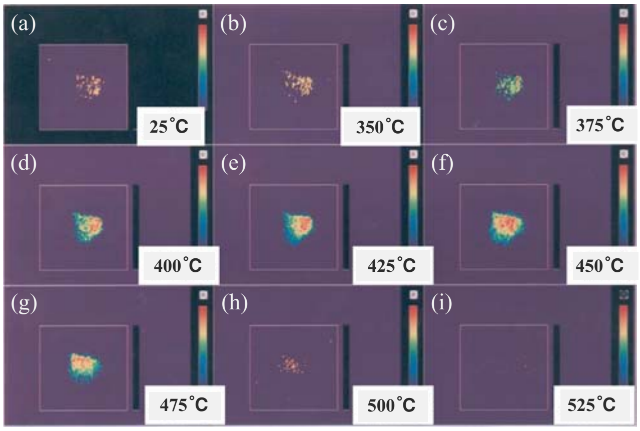
(a)
25°C
(b)
350°C
(c)
375°C
(d)
400°C
(e)
425°C
(f)
450°C
(g)
475°C
(h)
500°C
(i)
525°C

Plate 12. See also Figure 7 on page 170.

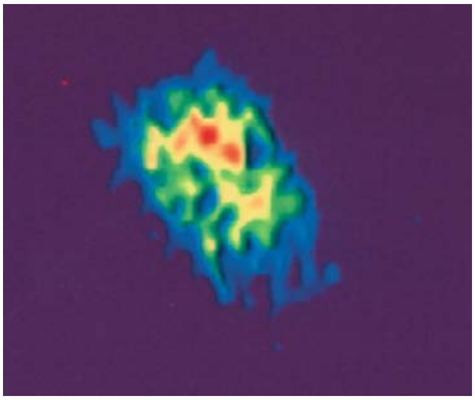

Plate 13. See also Figure 8 on page 170.

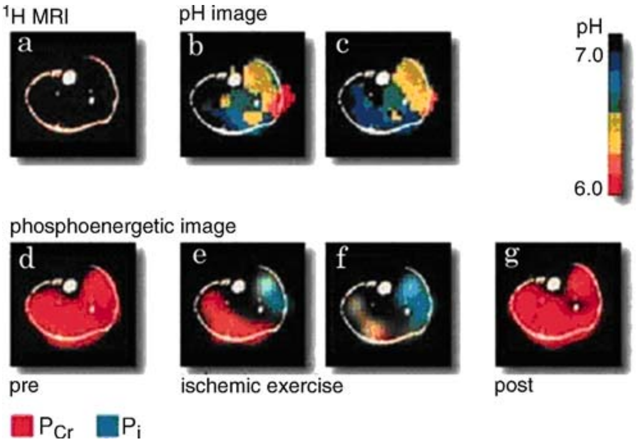
^{1}H MRI
pH image
a
b
c
pH
7.0
6.0
phosphoenergetic image
d
e
f
g
pre
ischemic exercise
post
🟥 P_{Cr} 🟦 P_i

Plate 14. See also Figure 2 on page 175.

Plate 15. See also Figure 3 on page 176.

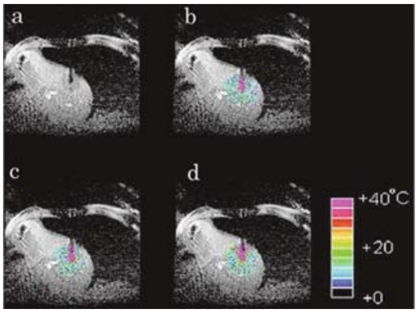

Plate 16. See also Figure 5 on page 177.

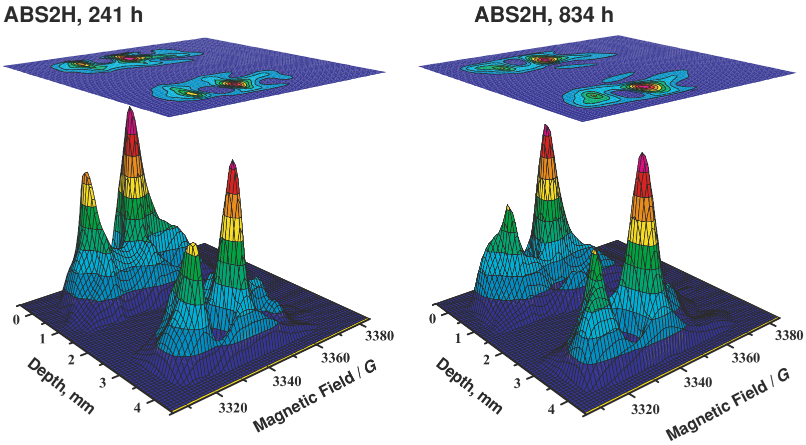

Plate 17. See also Figure 4 on page 184.

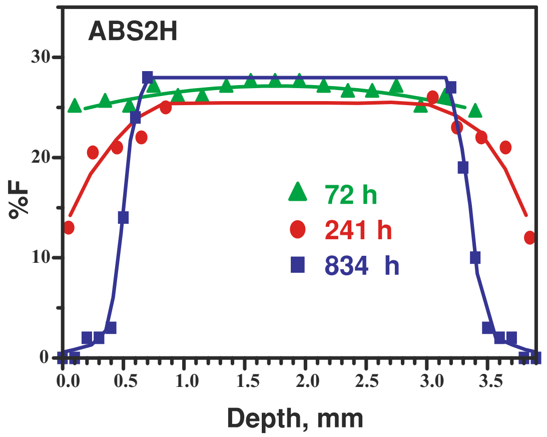

Plate 18. See also Figure 5 on page 184.

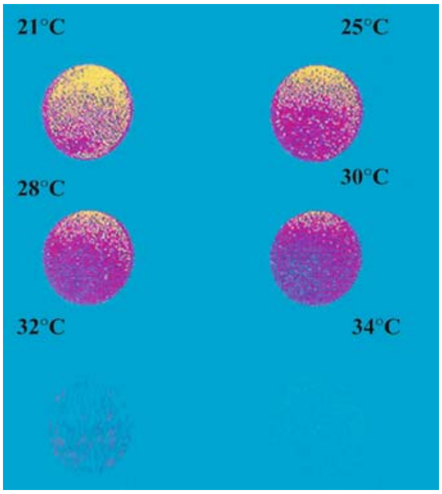
21°C
25°C
28°C
30°C
32°C
34°C

Plate 19. See also Figure 4 on page 190.

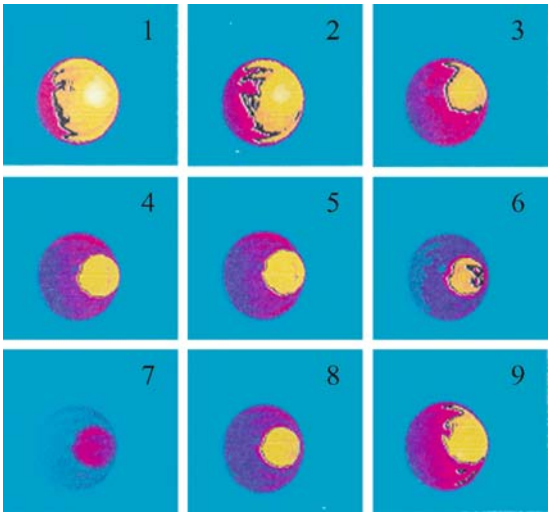

Plate 20. See also Figure 5 on page 190.

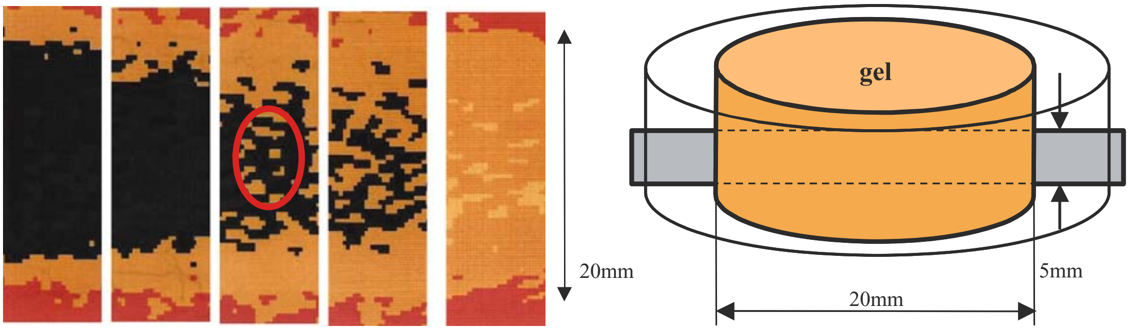
20mm
gel
5mm
20mm

Plate 21. See also Figure 6 on page 191.

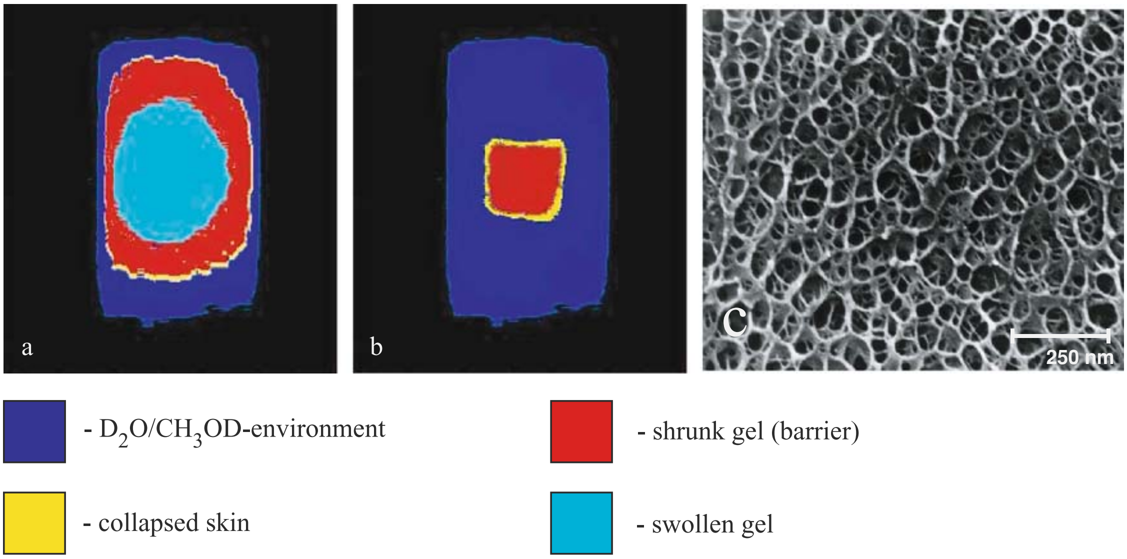
a
b
c
250 nm
🟦 - D_2O/CH_3OD-environment
🟥 - shrunk gel (barrier)
🟨 - collapsed skin
🟦 - swollen gel

Plate 22. See also Figure 7 on page 192.

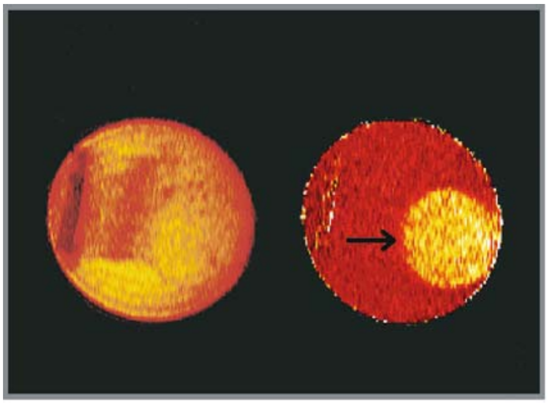

Plate 23. See also Figure 8 on page 192.

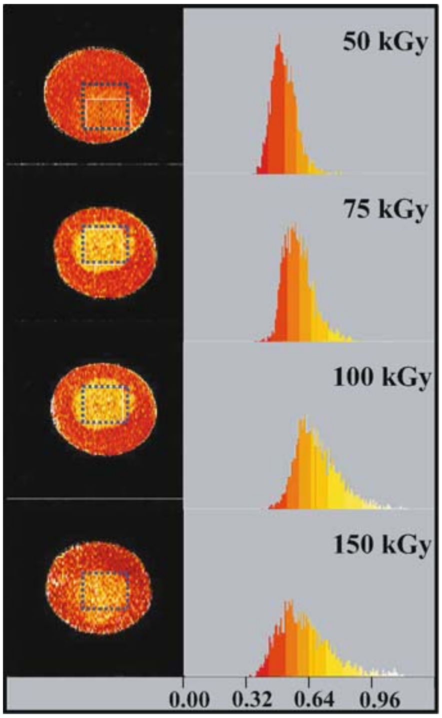

Plate 24. See also Figure 9 on page 193.

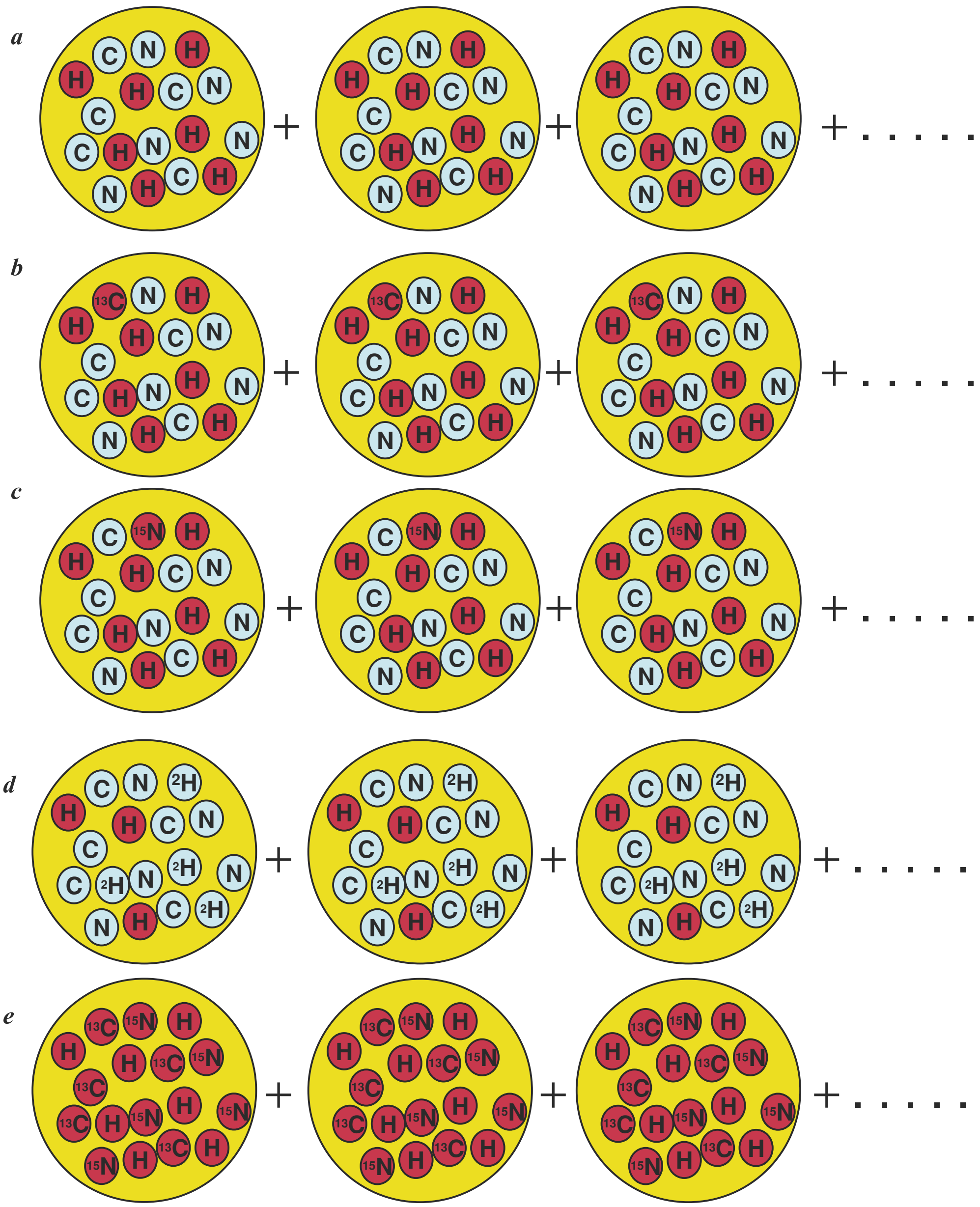

Plate 25. See also Figure 1 on page 216.

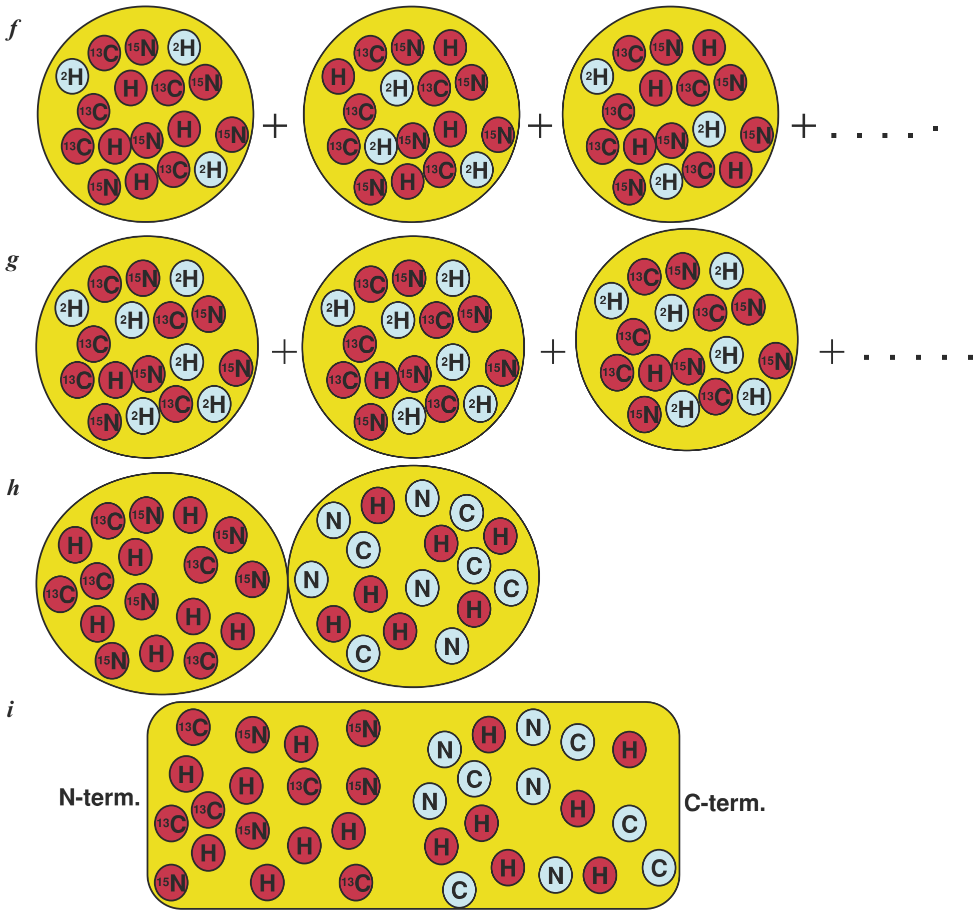
f
+ . . . . .
g
+ . . . . .
h
i
N-term.
C-term.

Plate 25. (*Continued*) See also Figure 1 on page 217.

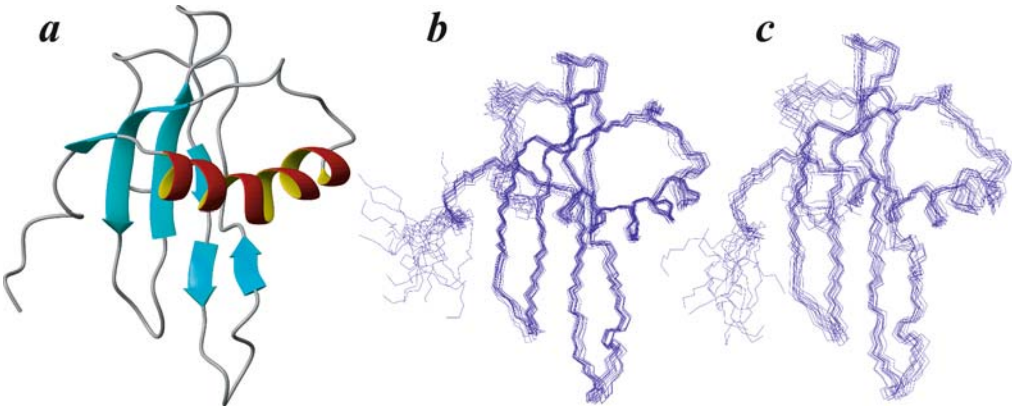

Plate 26. See also Figure 4 on page 221.

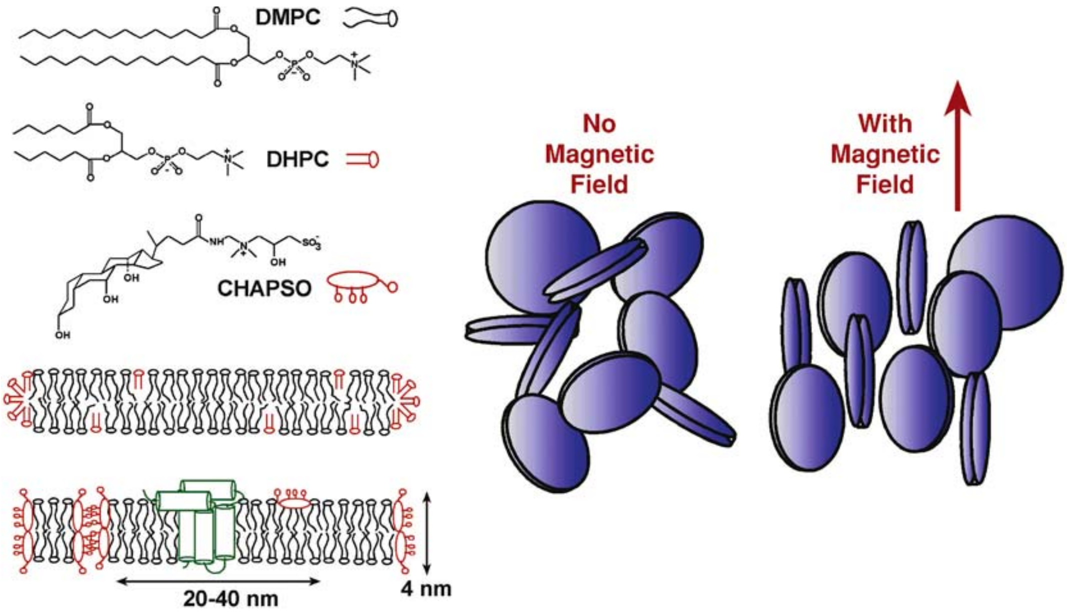
DMPC
DHPC
CHAPSO
20-40 nm
4 nm
No Magnetic Field
With Magnetic Field

Plate 27. See also Figure 1 on page 234.

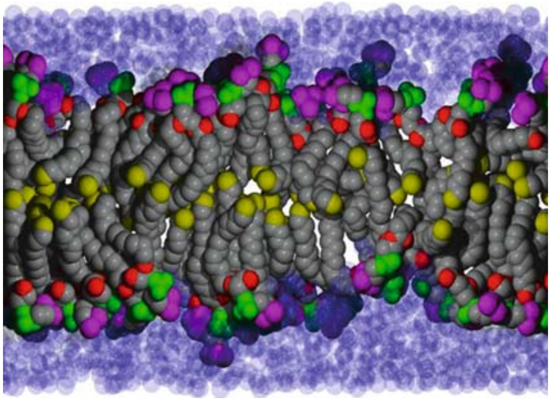

Plate 28. See also Figure 1 on page 250.

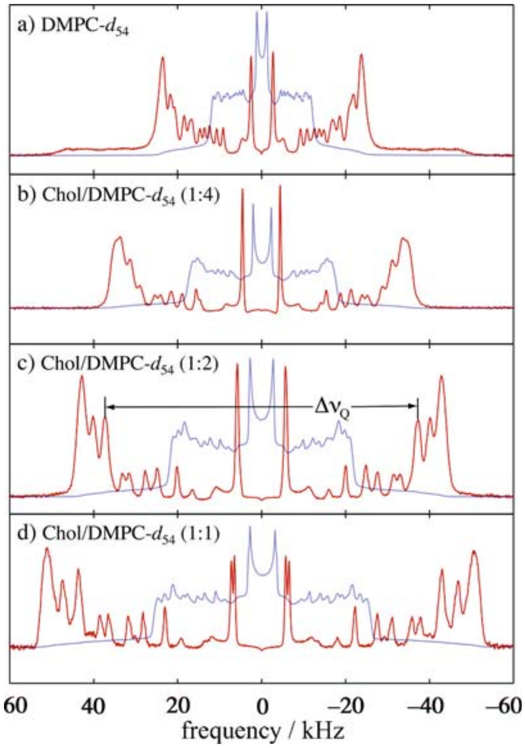

Plate 29. See also Figure 4 on page 253.

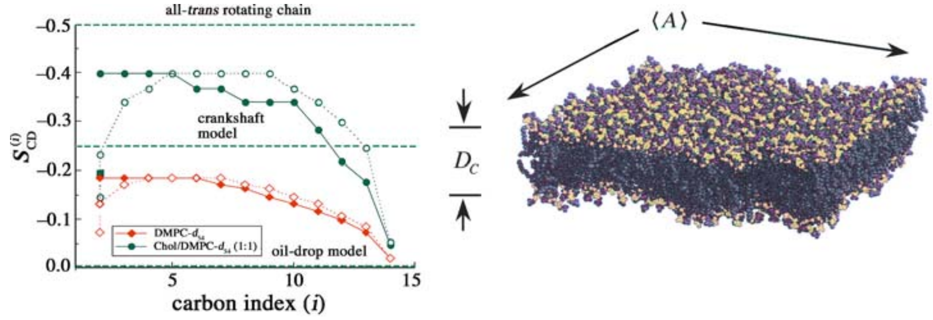

Plate 30. See also Figure 5 on page 254.

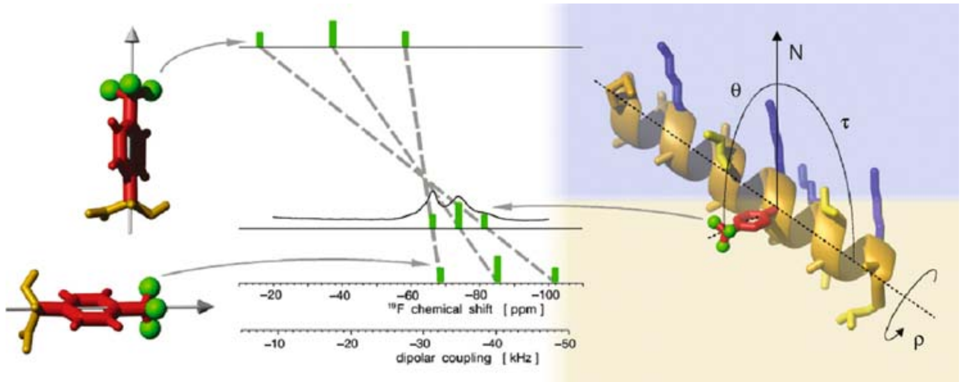
N
θ
τ
ρ
–20
–40
–60
–80
–100
¹⁹F chemical shift [ppm]
–10
–20
–30
–40
–50
dipolar coupling [kHz]

Plate 31. See also Figure 1 on page 262.

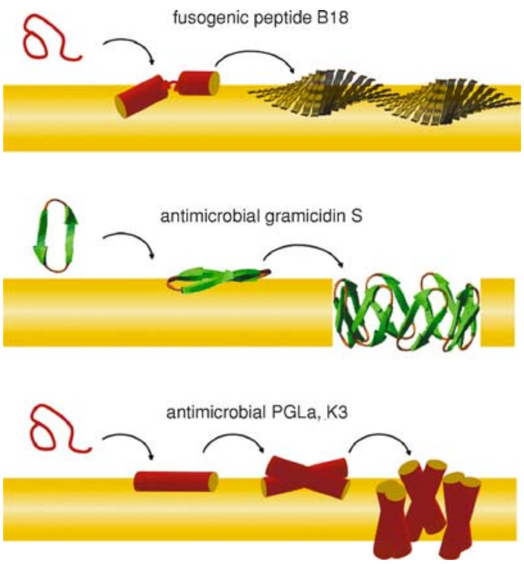
fusogenic peptide B18
antimicrobial gramicidin S
antimicrobial PGLa, K3

Plate 32. See also Figure 2 on page 265.

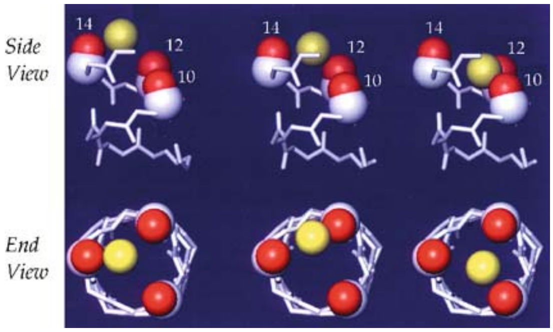
Side View
End View
14
12
10
14
12
10
14
12
10

Plate 33. See also Figure 2 on page 280.

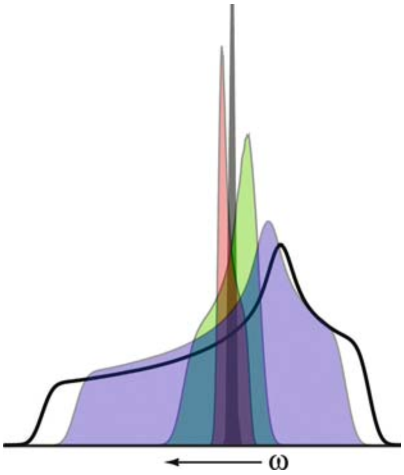

Plate 34. See also Figure 1 on page 307.

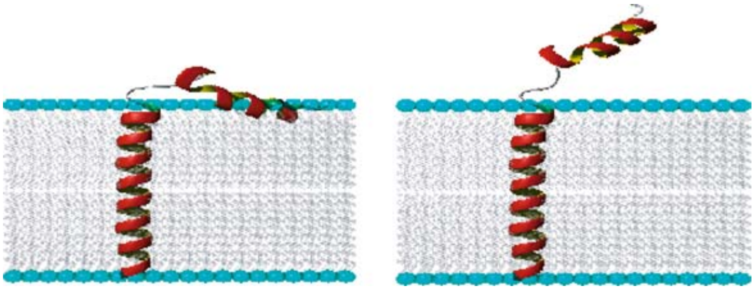

Plate 35. See also Figure 1 on page 314.

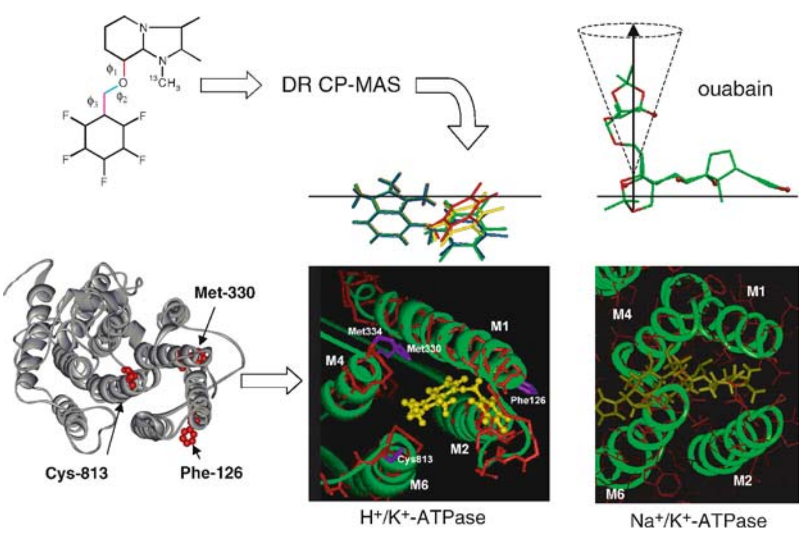
N
$φ_1$
O
$^{13}CH_3$
$φ_3$
$φ_2$
F
F
F
F
F
DR CP-MAS
ouabain
Met-330
Cys-813
Phe-126
M1
Met334
Met330
M4
Phe126
M2
Cys813
M6
H+/K+-ATPase
M1
M4
M2
M6
Na+/K+-ATPase

Plate 36. See also Figure 3 on page 324.

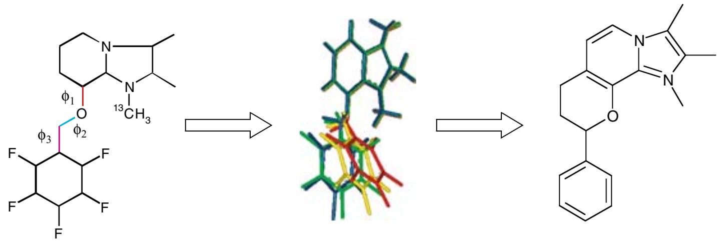
N
N
$^{13}CH_3$
φ1
O
φ2
φ3
F
F
F
F
F
N
N
O

flexible, IC_{50} = 10 µM NMR conformation Constrained, IC_{50} = 100 nM

Plate 37. See also Figure 4 on page 325.

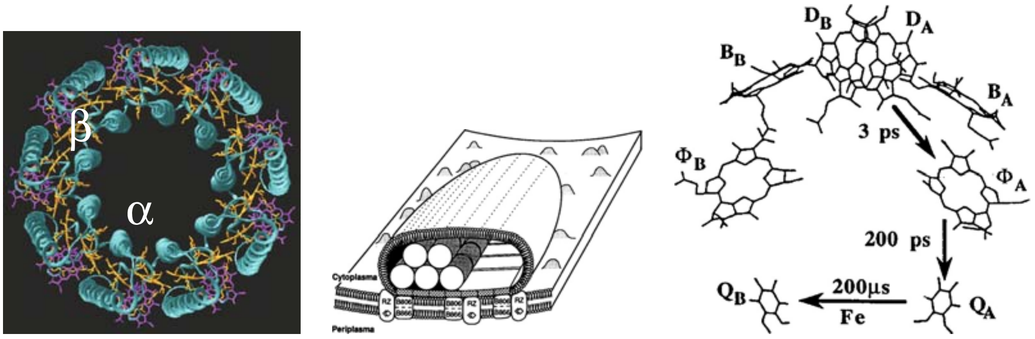
β
α
Cytoplasma
Periplasma
D_B
D_A
B_B
B_A
3 ps
Φ_B
Φ_A
200 ps
Q_B
200µs
Fe
Q_A

Plate 38. See also Figure 1 on page 328.

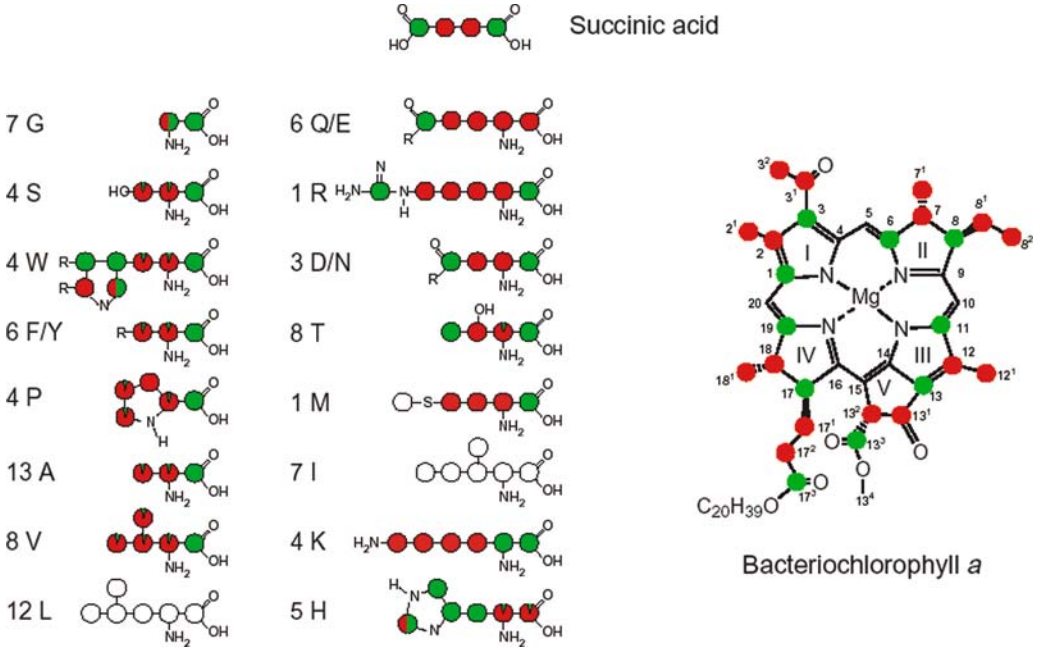
Succinic acid
HO
OH
7 G
4 S
4 W
6 F/Y
4 P
13 A
8 V
12 L
6 Q/E
1 R
3 D/N
8 T
1 M
7 I
4 K
5 H
NH_2
OH
R
HO
N
H
H_2N
S
Mg
I
II
III
IV
V
$C_{20}H_{39}O$
Bacteriochlorophyll *a*

Plate 39. See also Figure 4 on page 331.

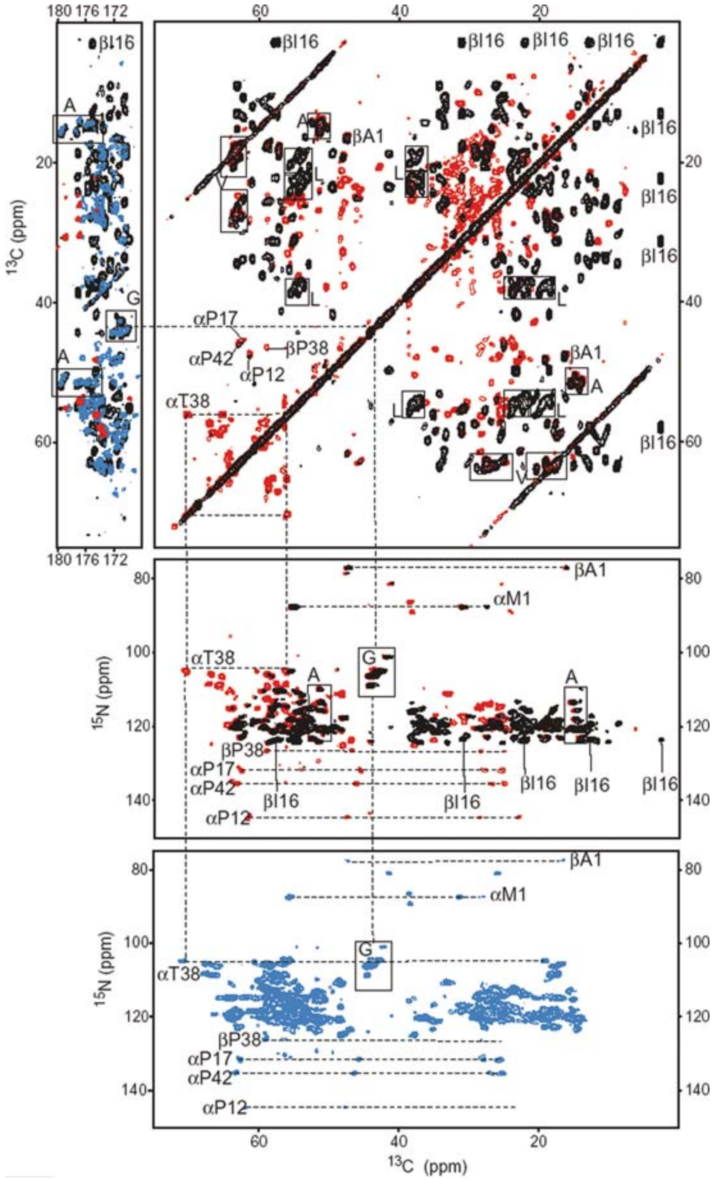

Plate 40. See also Figure 5 on page 332.

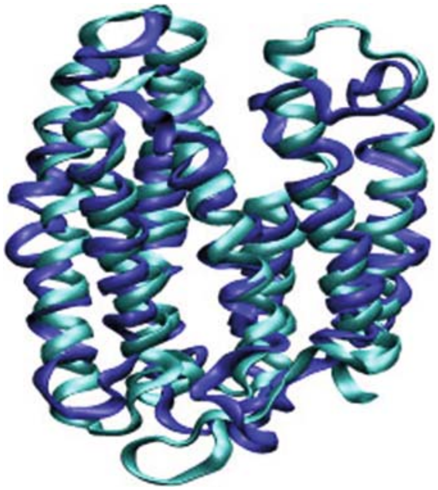

Plate 41. See also Figure 2 on page 340.

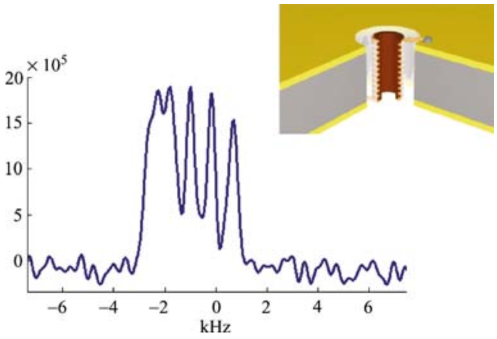

Plate 42. See also Figure 5 on page 358.

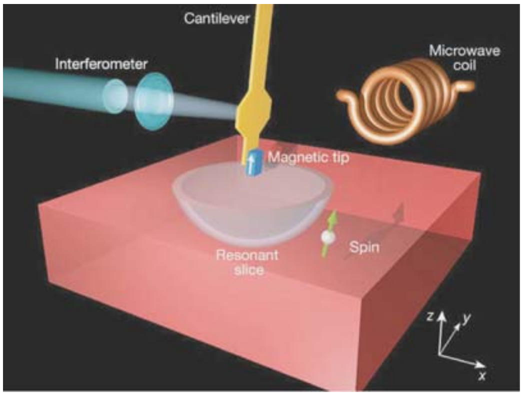
Cantilever
Interferometer
Microwave coil
Magnetic tip
Resonant slice
Spin
z
y
x

Plate 43. See also Figure 7 on page 360.

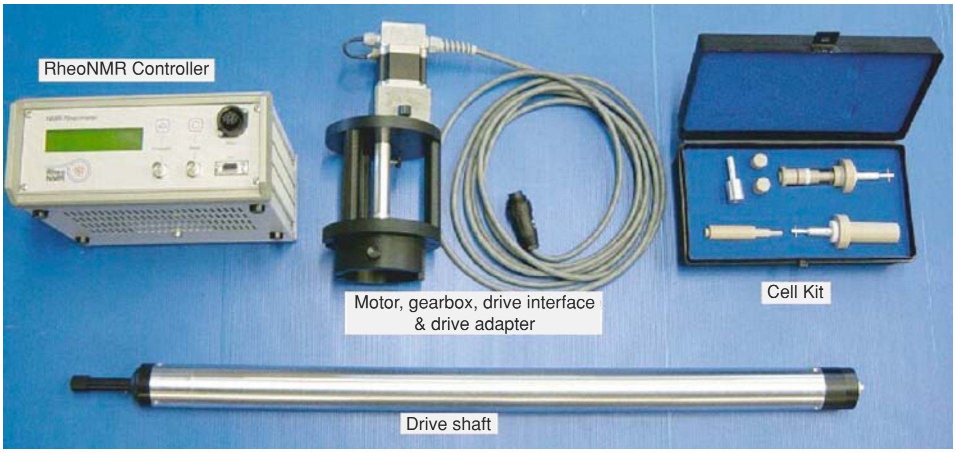
RheoNMR Controller
Motor, gearbox, drive interface & drive adapter
Cell Kit
Drive shaft

Plate 44. See also Figure 2 on page 384.

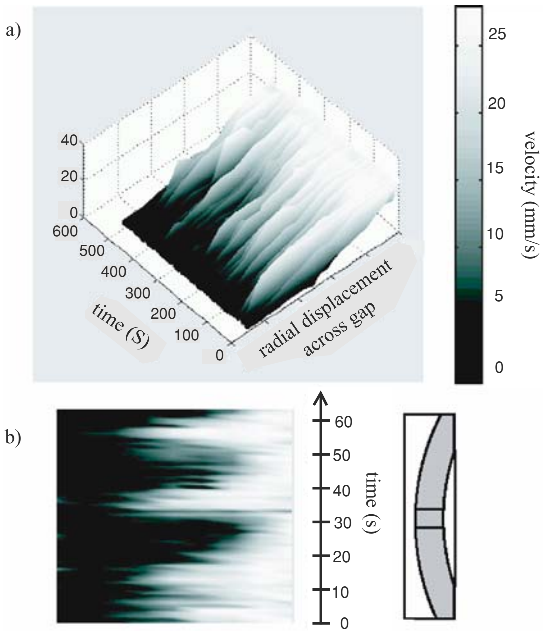

Plate 45. See also Figure 4 on page 385.

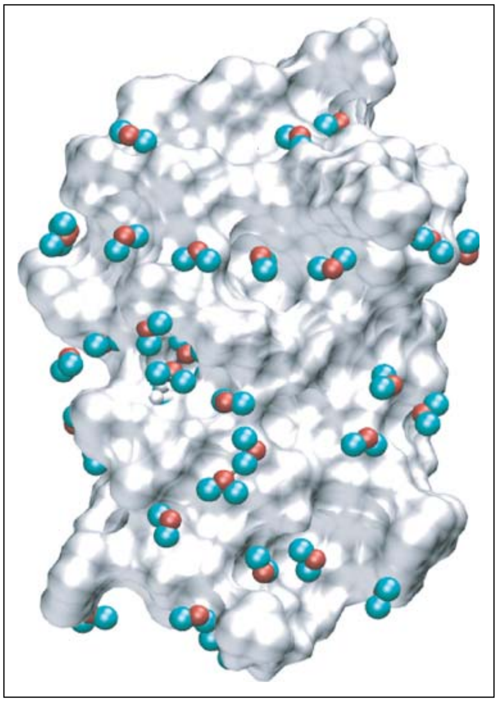

Plate 47. See also Figure 3 on page 419.

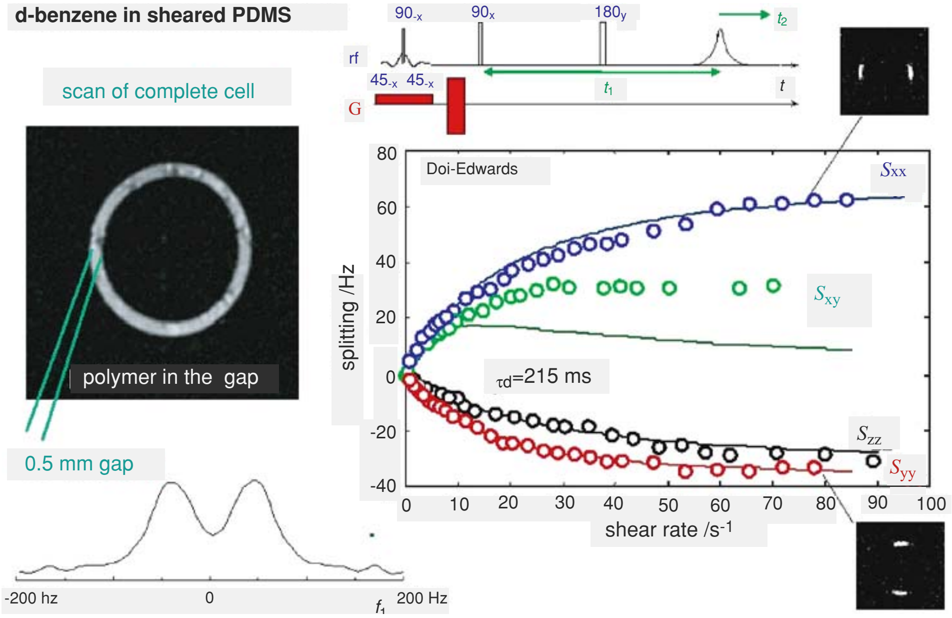

Plate 46. See also Figure 6 on page 387.

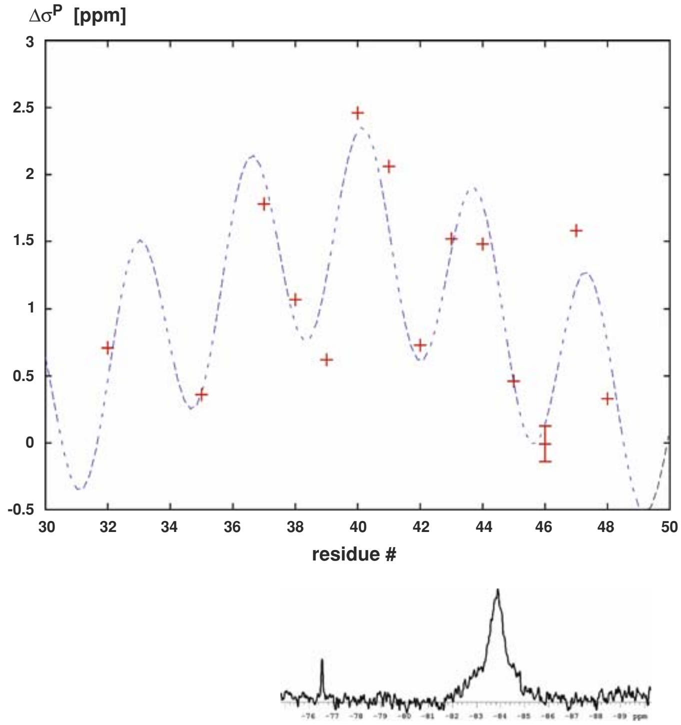

Plate 48. See also Figure 4 on page 480.

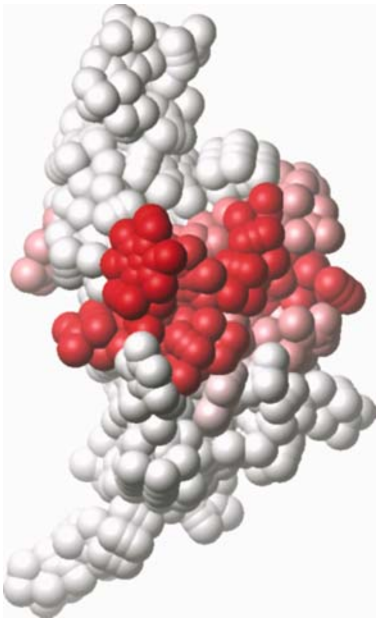

Plate 49. See also Figure 6 on page 482.

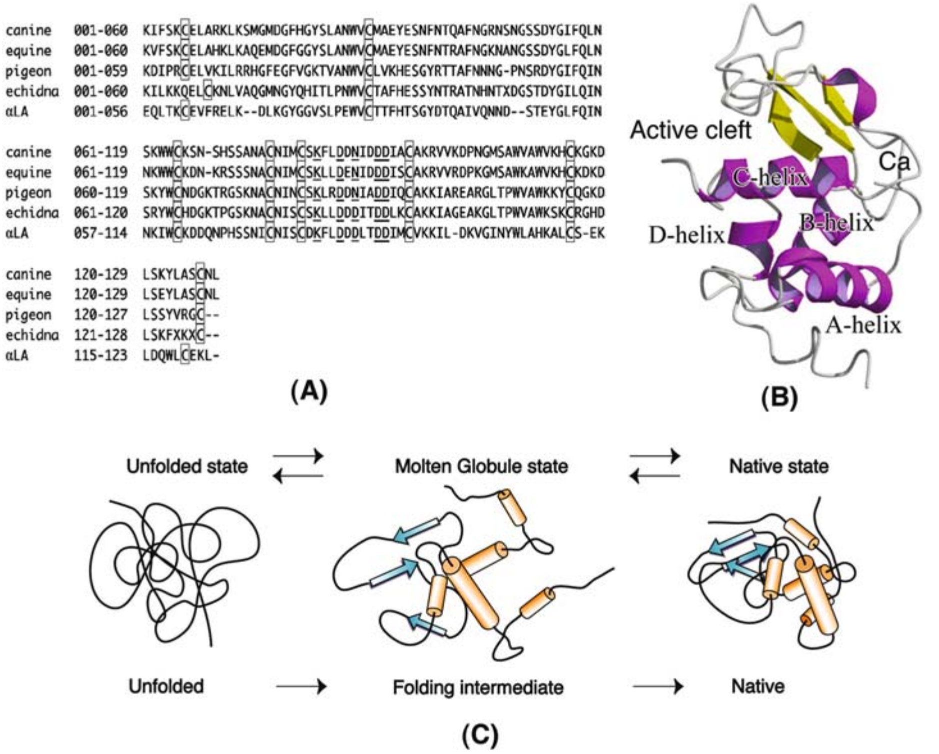

```
canine   001-060  KIFSKCELARKLKSMGMDGFHGYSLANWVCMAEYESNFNTQAFNGRNSNGSSDYGIFQLN
equine   001-060  KVFSKCELAHKLKAQEMDGFGGYSLANWVCMAEYESNFNTRAFNGKNANGSSDYGLFQLN
pigeon   001-059  KDIPRCELVKILRRHGFEGFVGKTVANWVCLVKHESGYRTTAFNNNG-PNSRDYGIFQIN
echidna  001-060  KILKKQELCKNLVAQGMNGYQHITLPNWVCTAFHESSYNTRATNHNTXDGSTDYGILQIN
αLA      001-056  EQLTKCEVFRELK--DLKGYGGVSLPEWVCTTFHTSGYDTQAIVQNND--STEYGLFQIN

canine   061-119  SKWWCKSN-SHSSANACNIMCSKFLDDNIDDDIACAKRVVKDPNGMSAWVAWVKHCKGKD
equine   061-119  NKWWCKDN-KRSSSNACNIMCSKLLDENIDDDISCAKRVVRDPKGMSAWKAWVKHCKDKD
pigeon   060-119  SKYWCNDGKTRGSKNACNINCSKLRDDNIADDIQCAKKIAREARGLTPWVAWKKYCQGKD
echidna  061-120  SRYWCHDGKTPGSKNACNISCSKLLDDDITDDLKCAKKIAGEAKGLTPWVAWKSKCRGHD
αLA      057-114  NKIWCKDDQNPHSSNICNISCDKFLDDDLTDDIMCVKKIL-DKVGINYWLAHKALCS-EK

canine   120-129  LSKYLASCNL
equine   120-129  LSEYLASCNL
pigeon   120-127  LSSYVRGC--
echidna  121-128  LSKFXKXC--
αLA      115-123  LDQWLCEKL-
```

(A)
Active cleft
Ca
C-helix
B-helix
D-helix
A-helix
(B)
Unfolded state
Molten Globule state
Native state
Unfolded
Folding intermediate
Native
(C)

Plate 50. See also Figure 1 on page 498.

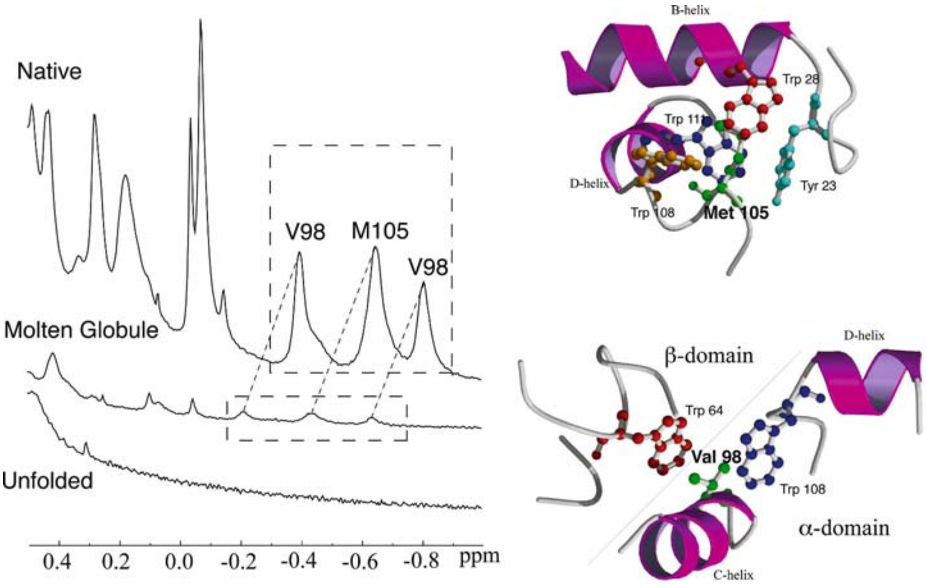

Plate 51. See also Figure 2 on page 499.

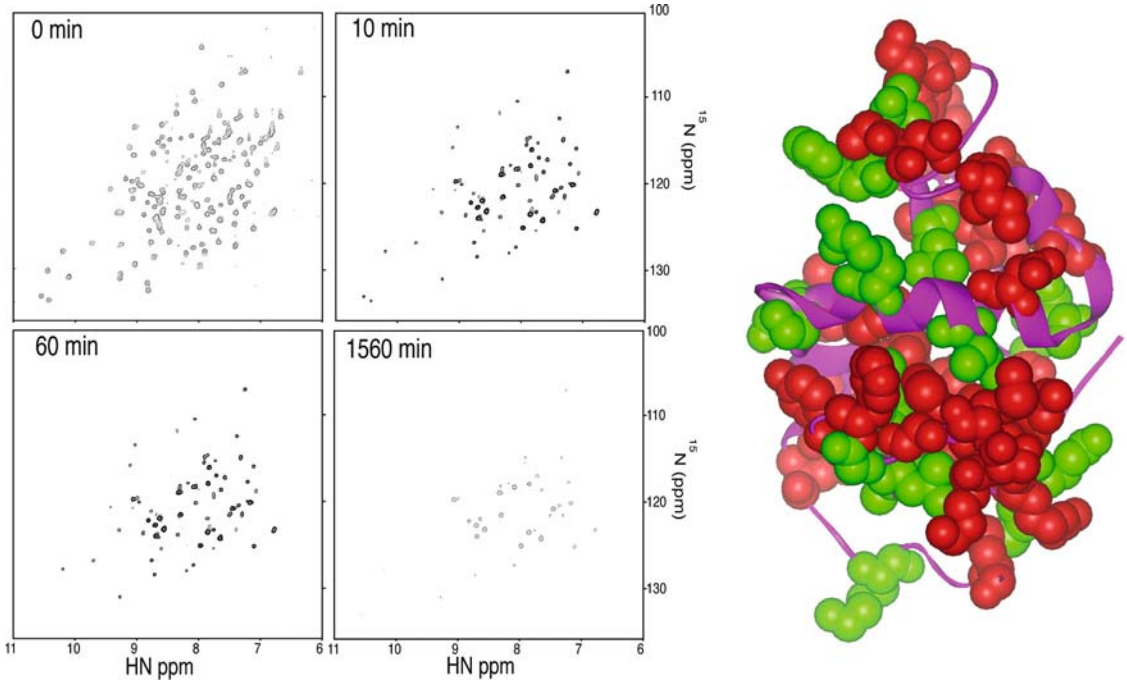

Plate 52. See also Figure 3 on page 500.

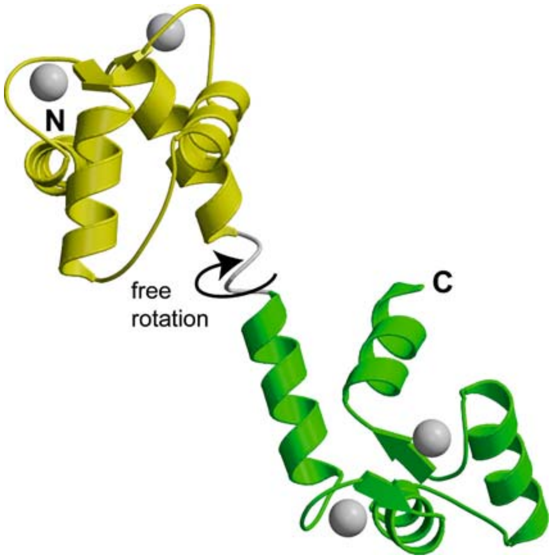
N
C
free rotation

Plate 53. See also Figure 1 on page 504.

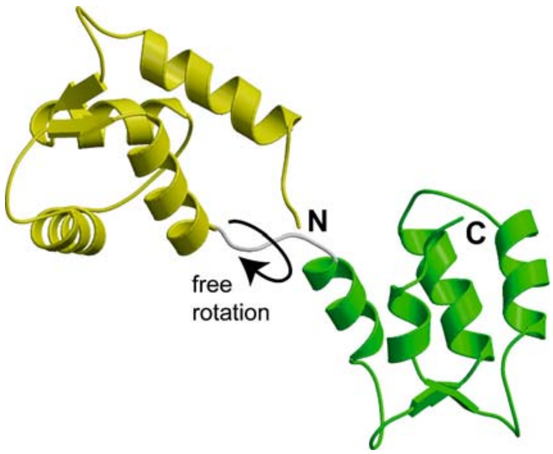
N
C
free rotation

Plate 54. See also Figure 3 on page 508.

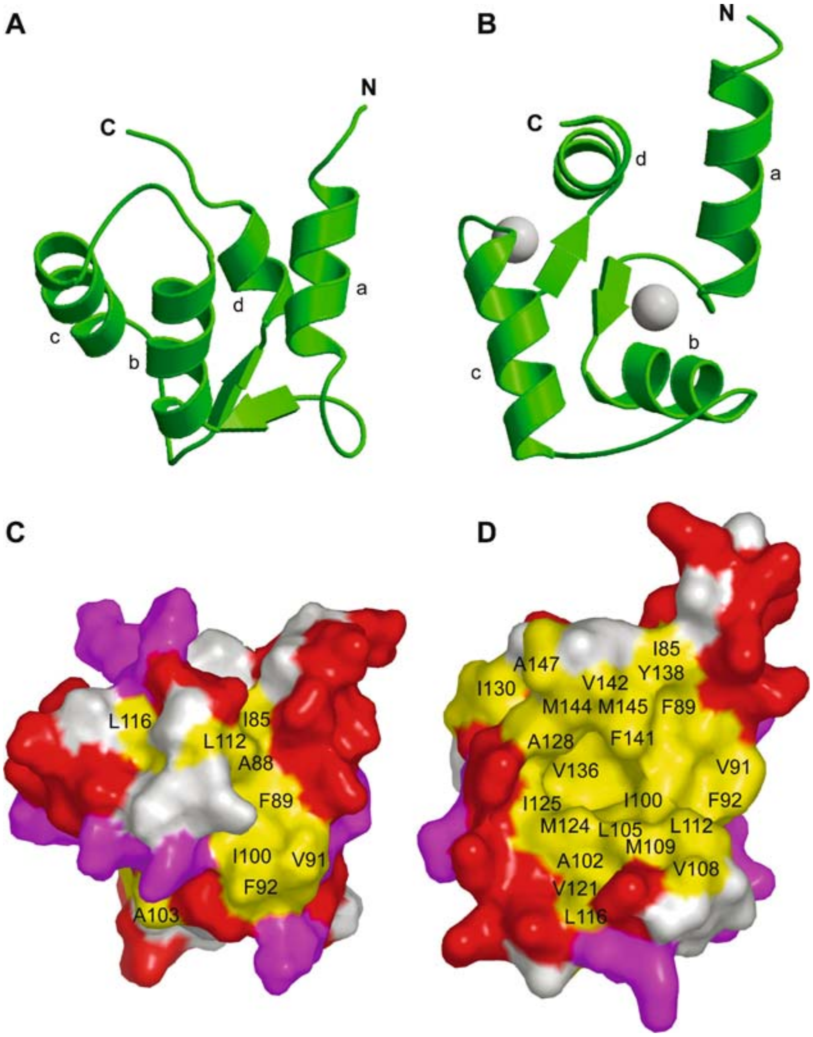
A
N
C
a
b
c
d
B
N
C
a
b
c
d
C
L116
I85
L112
A88
F89
I100
V91
F92
A103
D
I85
A147
Y138
I130
V142
M144
M145
F89
A128
F141
V91
V136
I100
F92
I125
M124
L105
L112
M109
A102
V108
V121
L116

Plate 55. See also Figure 4 on page 509.

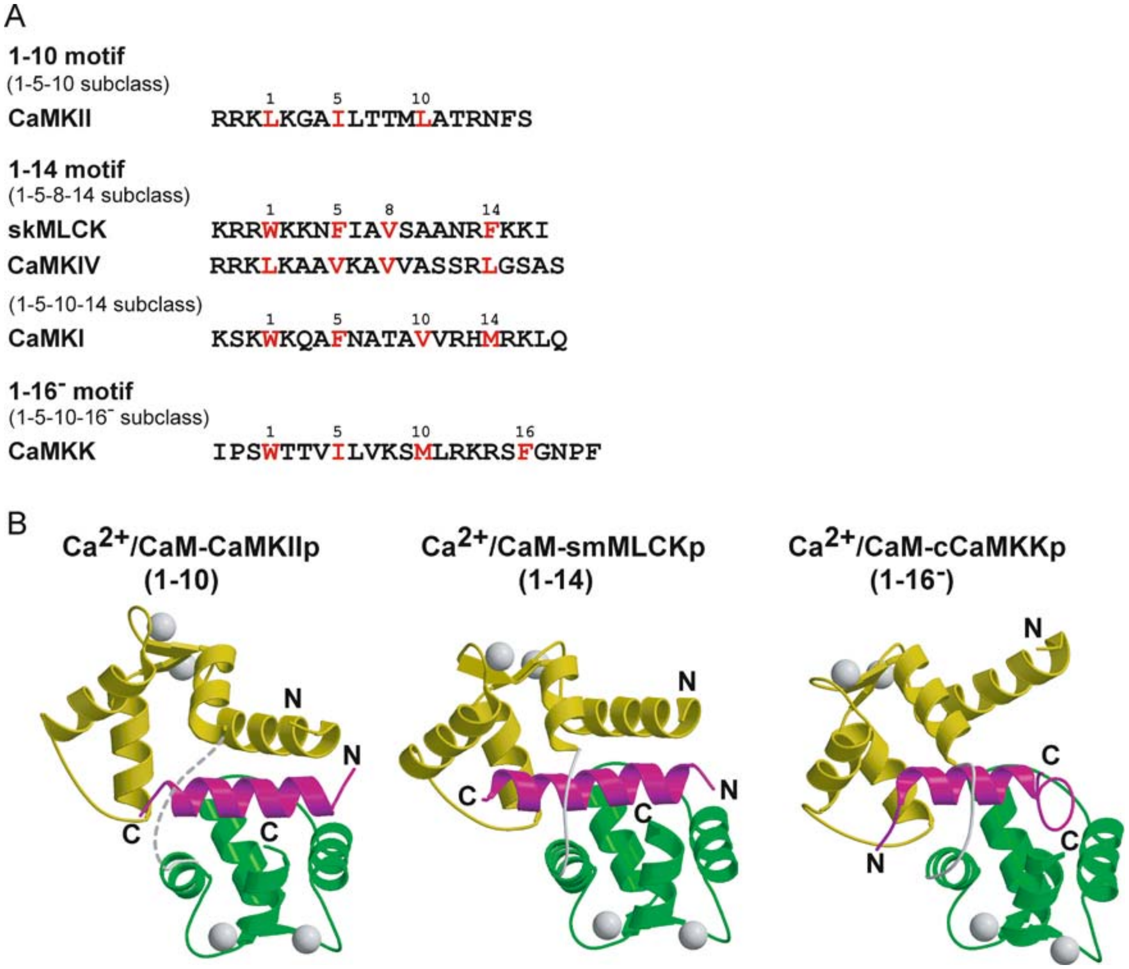
A
1-10 motif
(1-5-10 subclass)
1 5 10
CaMKII RRKLKGAILTTMLATRNFS
1-14 motif
(1-5-8-14 subclass)
1 5 8 14
skMLCK KRRWKKNFIAVSAANRFKKI
CaMKIV RRKLKAAVKAVVASSRLGSAS
(1-5-10-14 subclass)
1 5 10 14
CaMKI KSKWKQAFNATAVVRHMRKLQ
1-16⁻ motif
(1-5-10-16⁻ subclass)
1 5 10 16
CaMKK IPSWTTVILVKSMLRKRSFGNPF
B
Ca2+/CaM-CaMKIIp (1-10)
Ca2+/CaM-smMLCKp (1-14)
Ca2+/CaM-cCaMKKp (1-16⁻)
N
N
C
C
N
N
C
C
N
C
N
C

Plate 56. See also Figure 5 on page 510.

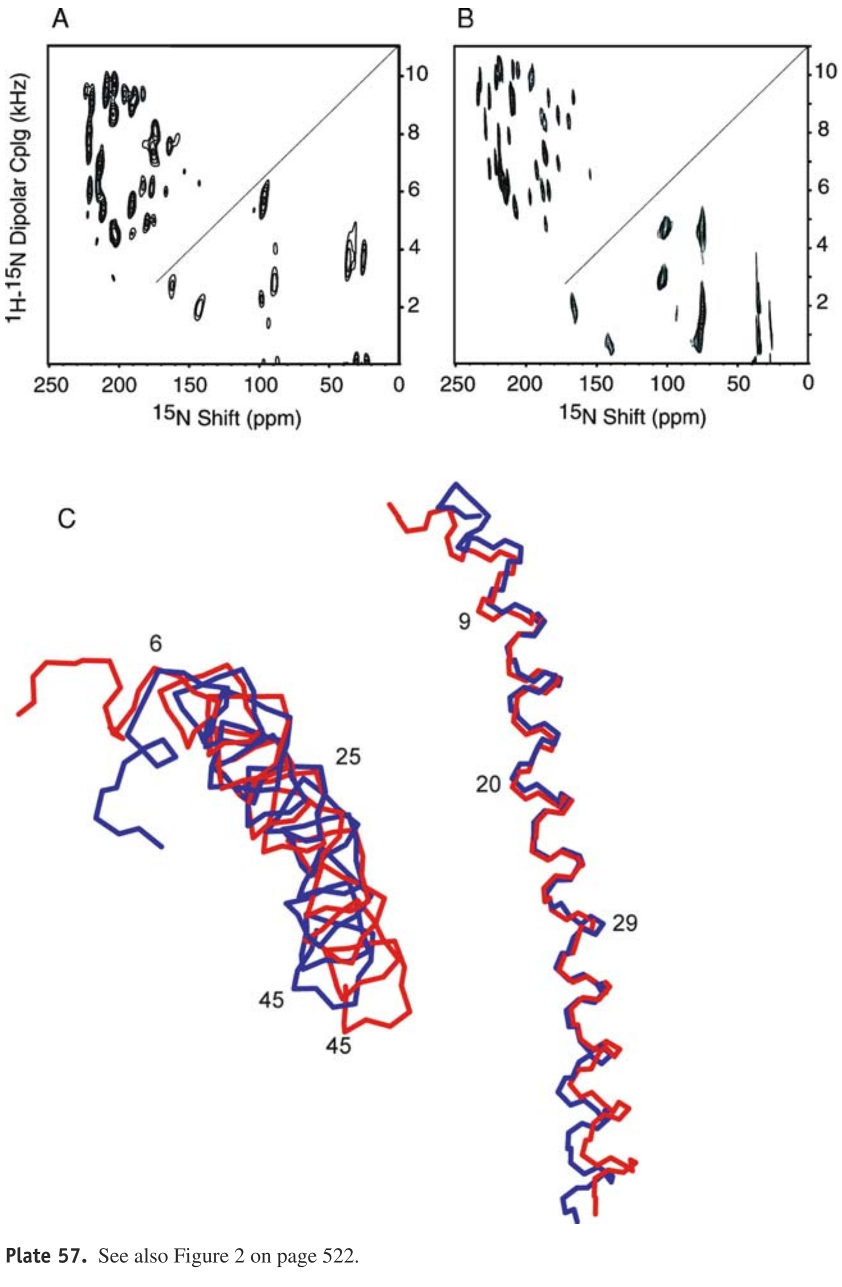

Plate 57. See also Figure 2 on page 522.

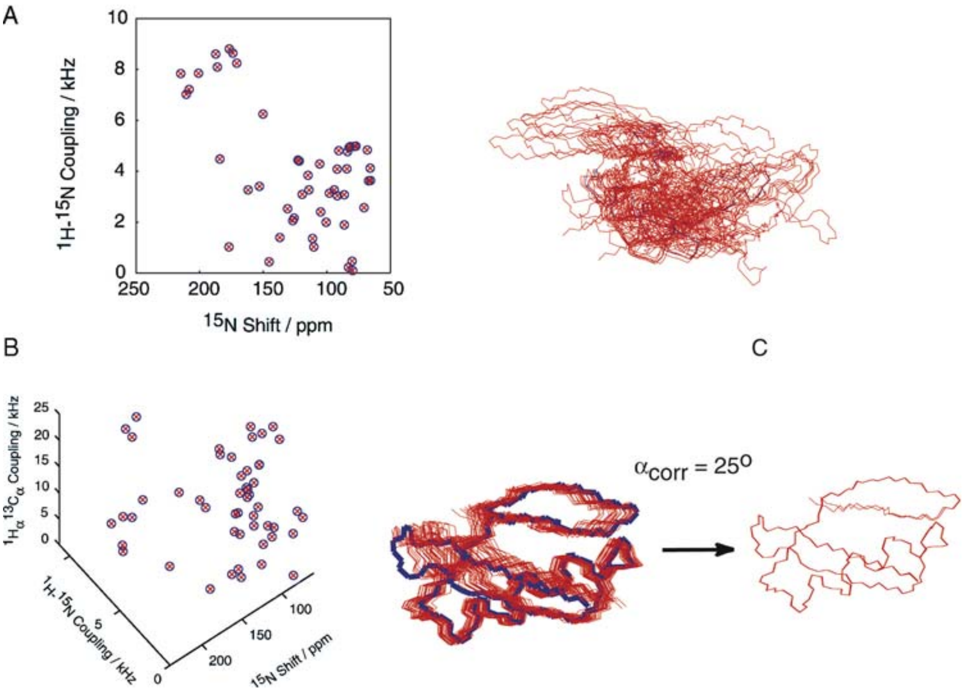

Plate 58. See also Figure 3 on page 523.

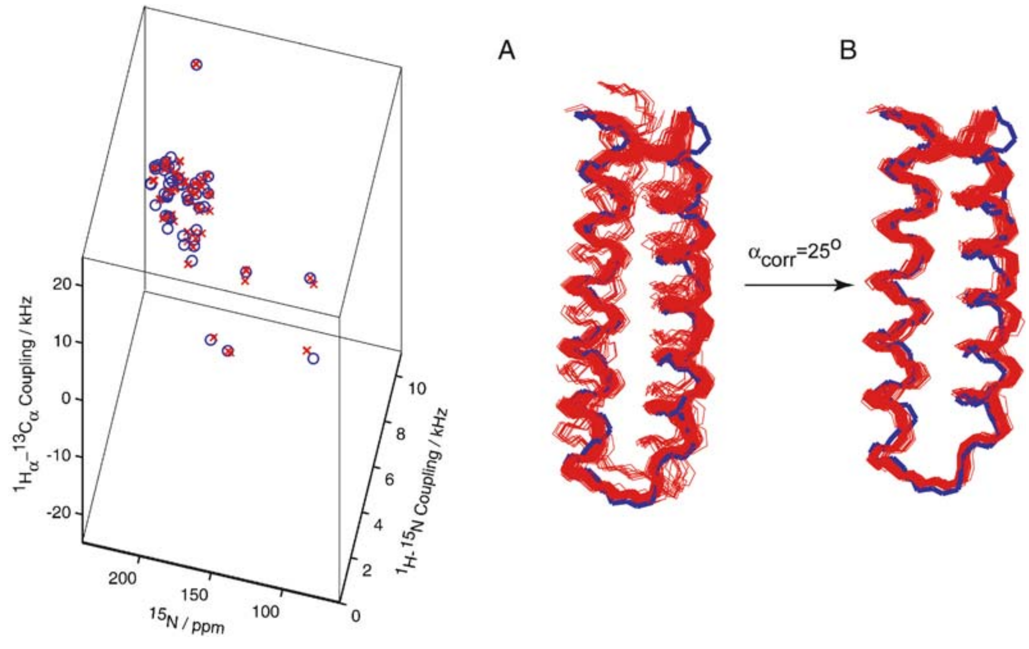

Plate 59. See also Figure 4 on page 524.

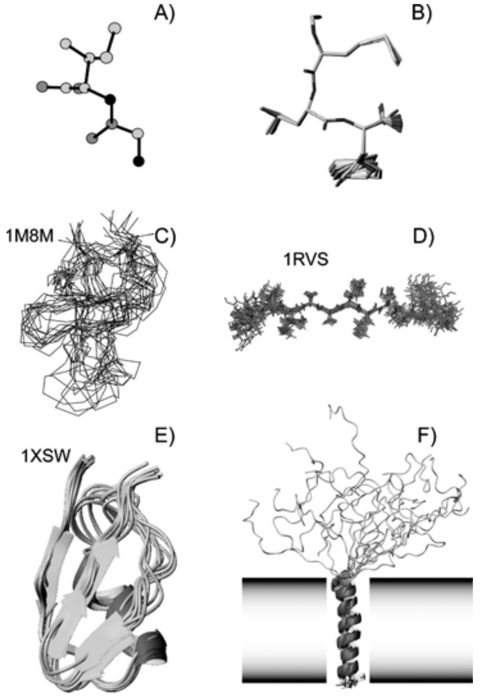
A)
B)
1M8M
C)
D)
1RVS
E)
1XSW
F)

Plate 60. See also Figure 2 on page 529.

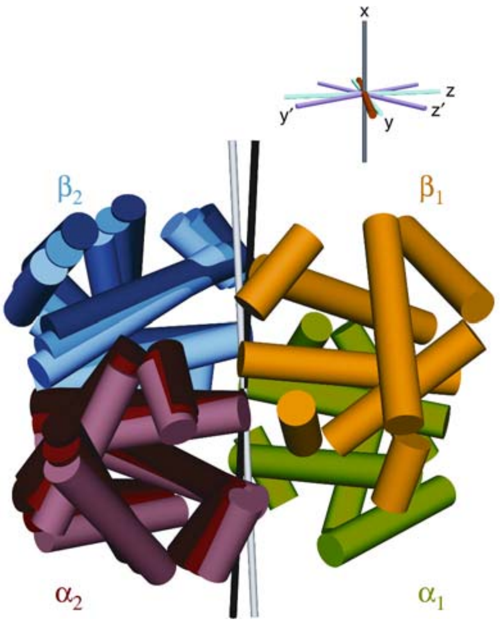
x
z
z'
y'
y
β2
β1
α2
α1

Plate 61. See also Figure 1 on page 659.

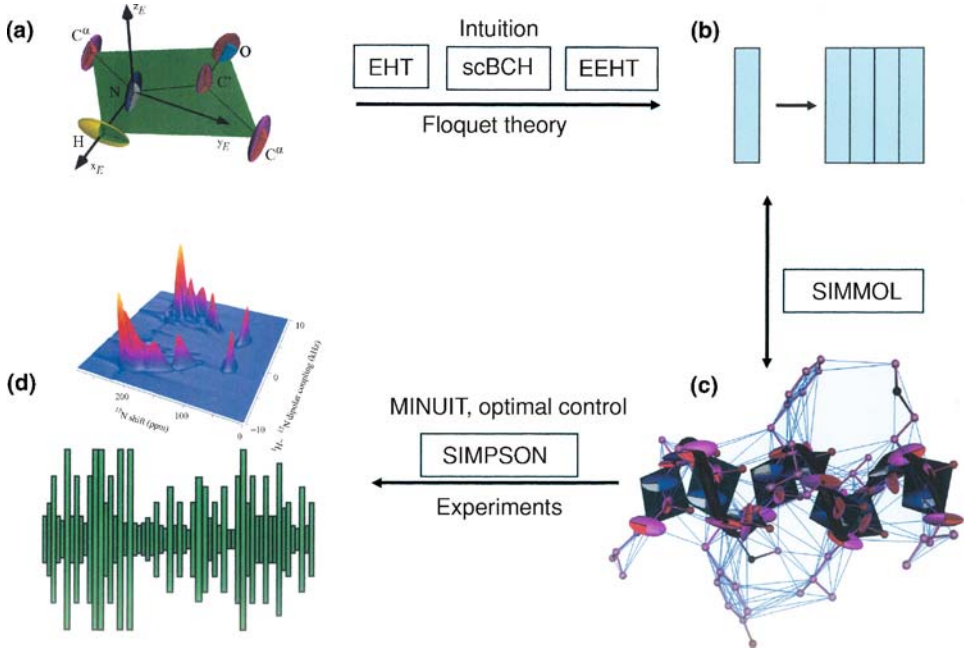
(a)
zE
Cα
O
N
C'
H
yE
xE
Cα
Intuition
EHT
scBCH
EEHT
Floquet theory
(b)
SIMMOL
(c)
(d)
200
100
0
10
0
-10
15N shift (ppm)
1H-15N dipolar coupling (kHz)
MINUIT, optimal control
SIMPSON
Experiments

Plate 62. See also Figure 1 on page 680.

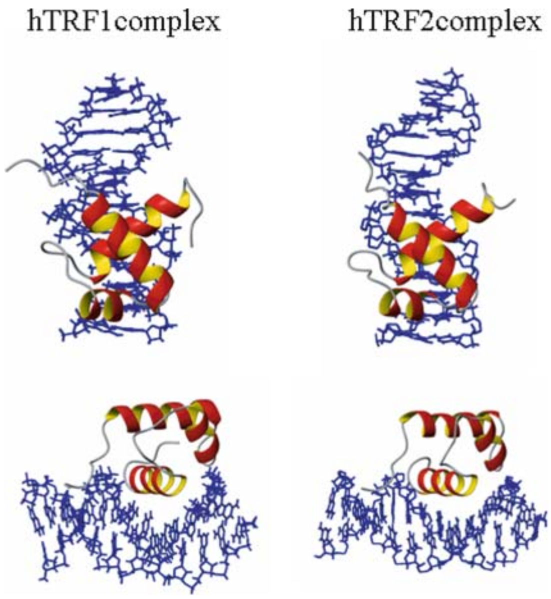
hTRF1complex
hTRF2complex

Plate 63. See also Figure 1 on page 744.

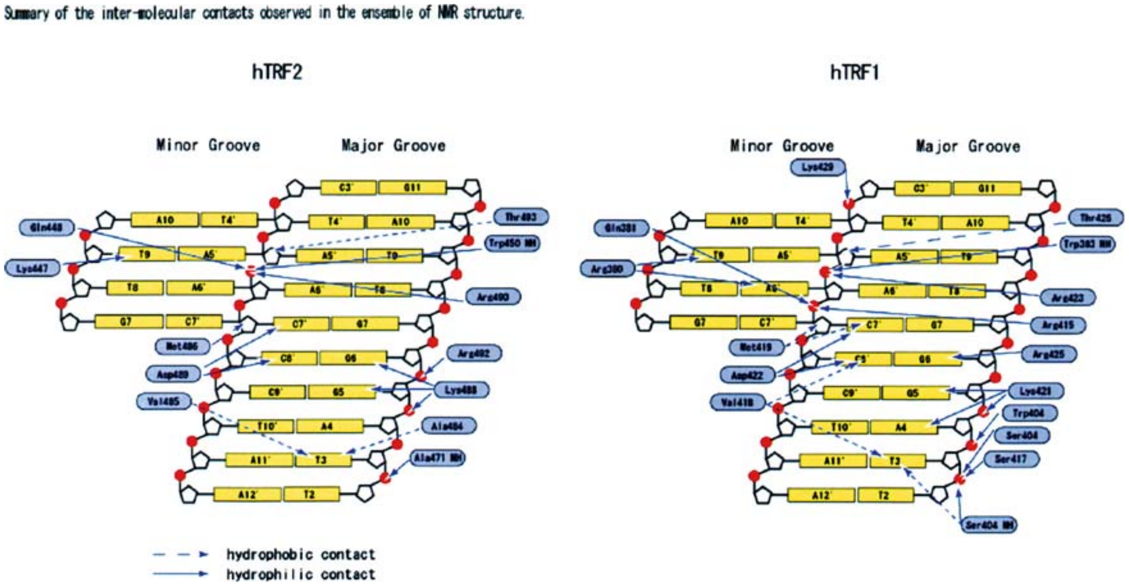
Summary of the inter-molecular contacts observed in the ensemble of NMR structure.

hTRF2
Minor Groove
Major Groove
C3'
G11
A10
T4'
T4'
A10
T9
A5'
A5'
T9
T8
A6'
A6'
T8
G7
C7'
C7'
G7
C8'
G6
C9'
G5
T10'
A4
A11'
T3
A12'
T2
Gln448
Lys447
Thr493
Trp450 NH
Arg490
Met486
Asp489
Val485
Arg492
Lys488
Ala484
Ala471 NH
hydrophobic contact
hydrophilic contact
hTRF1
Minor Groove
Major Groove
Lys429
Gln381
Arg380
Thr426
Trp383 NH
Arg423
Arg415
Met419
Asp422
Val418
Arg425
Lys421
Trp404
Ser404
Ser417
Ser404 NH

Plate 64. See also Figure 2 on page 744.

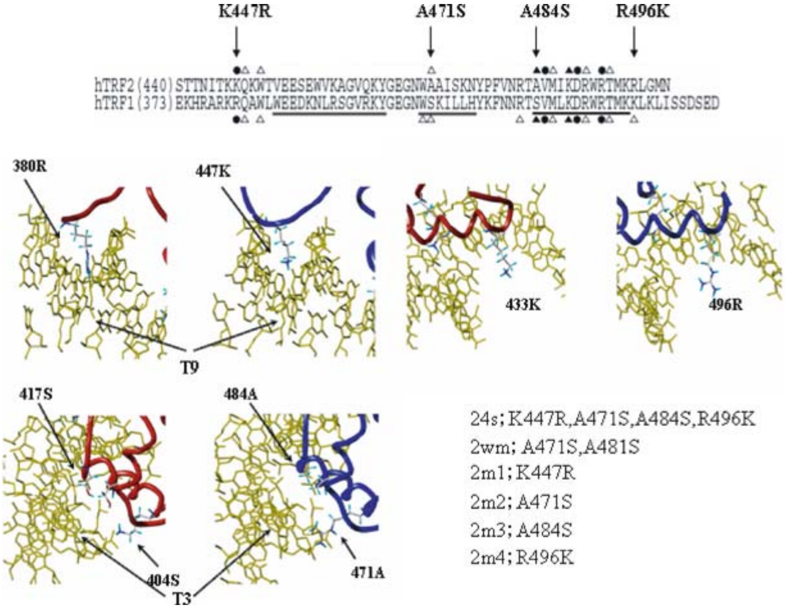
K447R
A471S
A484S
R496K
hTRF2 (440) STTNITKKQKWTVEESEWVKAGVQKYGEGNWAAISKNYPFVNRTAVMIKDRWRTMKRLGMN
hTRF1 (373) EKHRARKRQAWLWEEDKNLRSGVRKYGEGNWSKILLHYKFNNRTSVMLKDRWRTMKKLKLISSDSED
380R
447K
433K
496R
T9
417S
484A
404S
T3
471A
24s; K447R, A471S, A484S, R496K
2wm; A471S, A481S
2m1; K447R
2m2; A471S
2m3; A484S
2m4; R496K

Plate 65. See also Figure 3 on page 745.

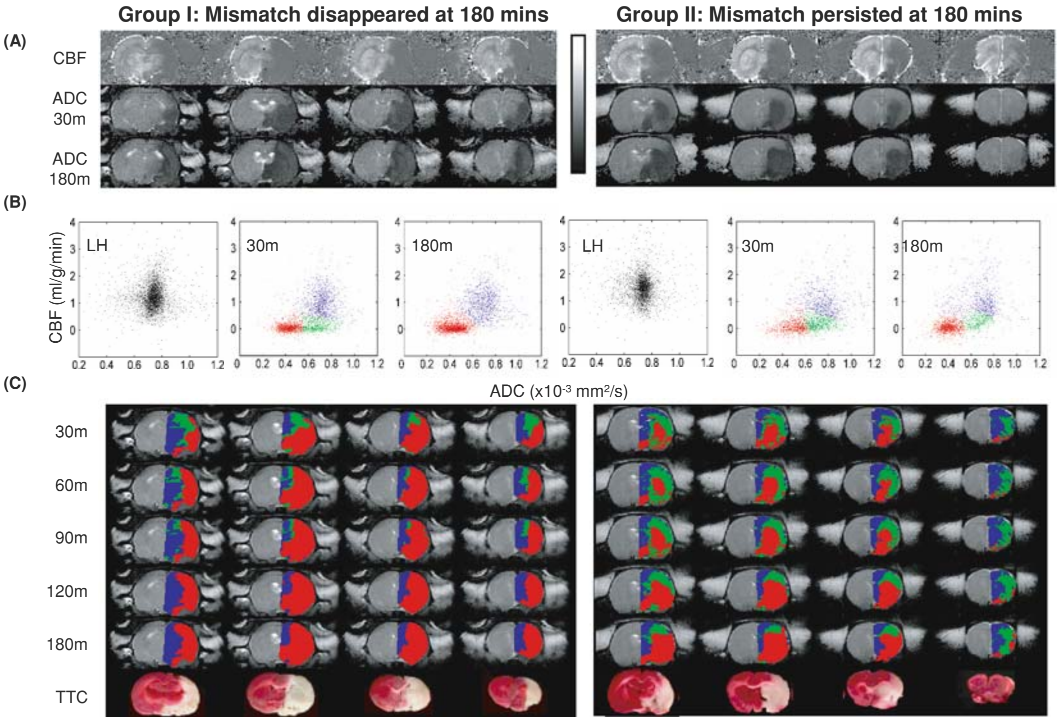
Group I: Mismatch disappeared at 180 mins
Group II: Mismatch persisted at 180 mins
(A)
CBF
ADC 30m
ADC 180m
(B)
CBF (ml/g/min)
LH
30m
180m
LH
30m
180m
ADC (x10-3 mm2/s)
(C)
30m
60m
90m
120m
180m
TTC

Plate 66. See also Figure 2 on page 806.

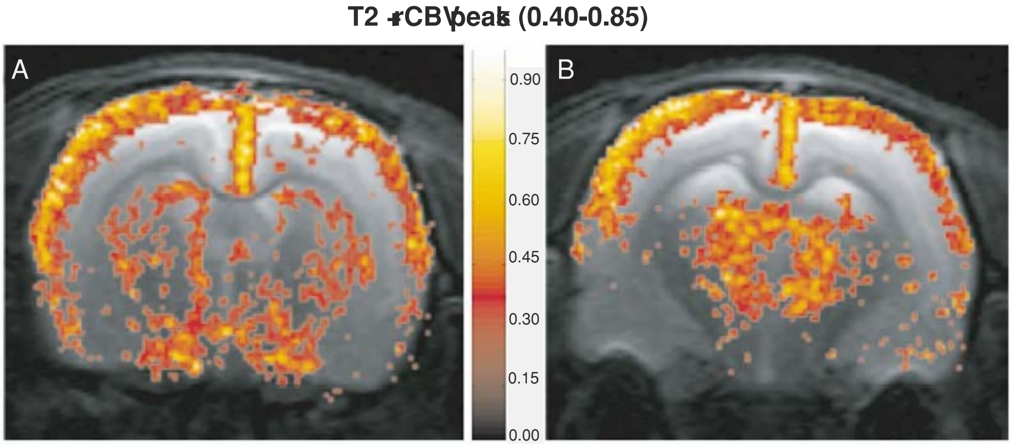
T2 + rCBVpeak (0.40-0.85)
A
B
0.90
0.75
0.60
0.45
0.30
0.15
0.00

Plate 67. See also Figure 3 on page 809.

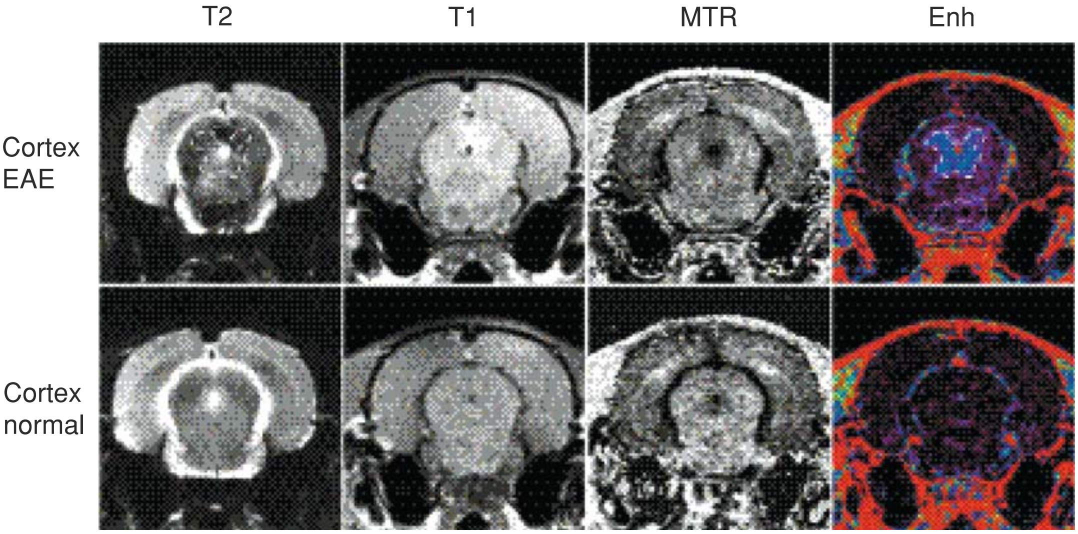
T2
T1
MTR
Enh
Cortex EAE
Cortex normal

Plate 68. See also Figure 4 on page 812.

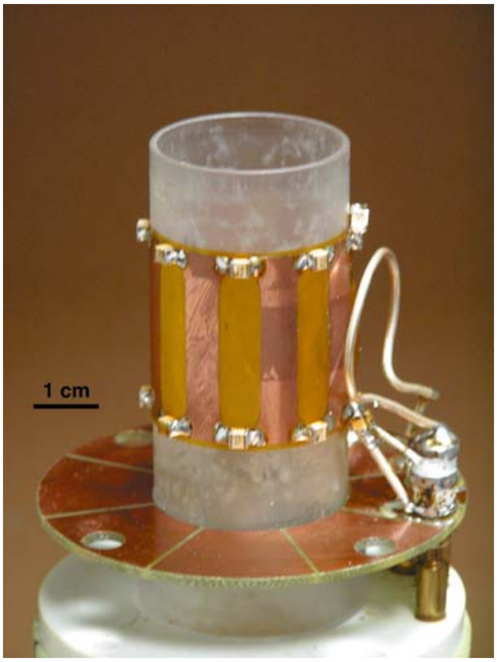

Plate 69. See also Figure 1 on page 836.

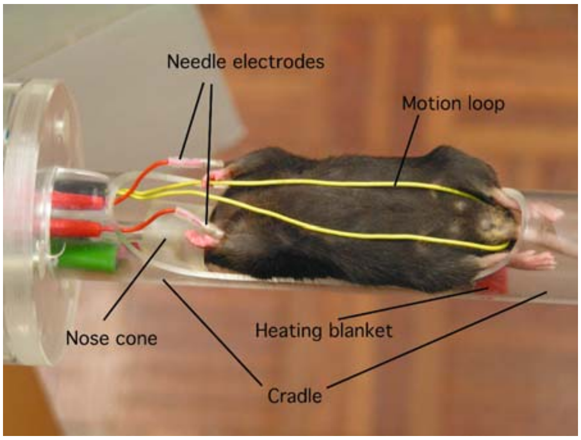
Needle electrodes
Motion loop
Nose cone
Heating blanket
Cradle

Plate 70. See also Figure 2 on page 837.

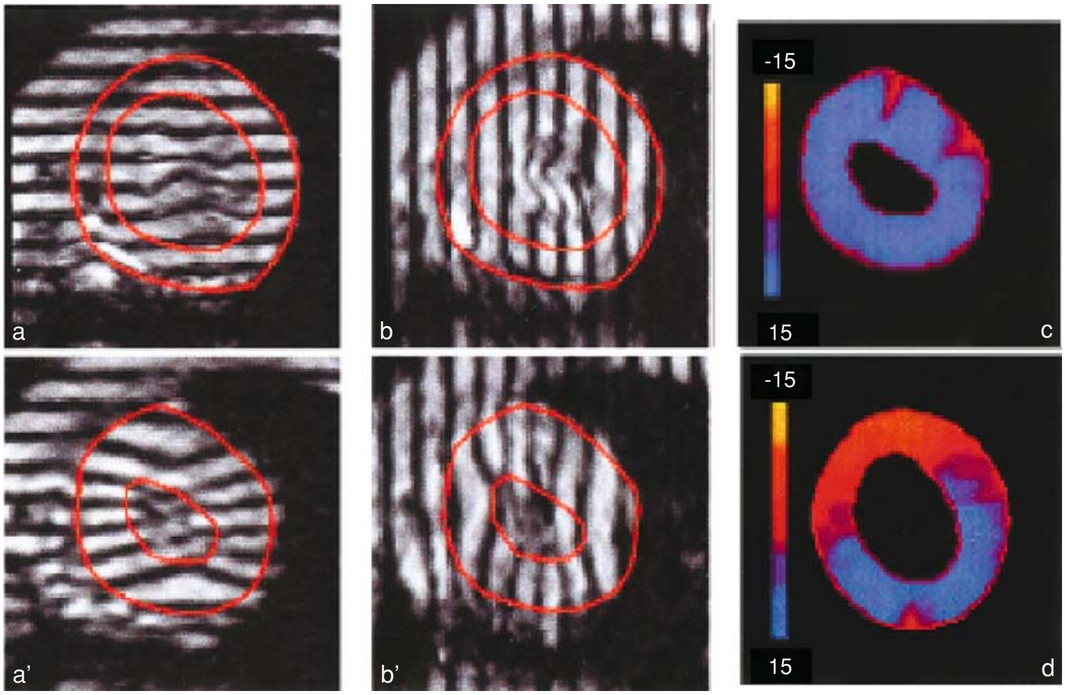
a
b
-15
15
c
a'
b'
-15
15
d

Plate 71. See also Figure 9 on page 843.

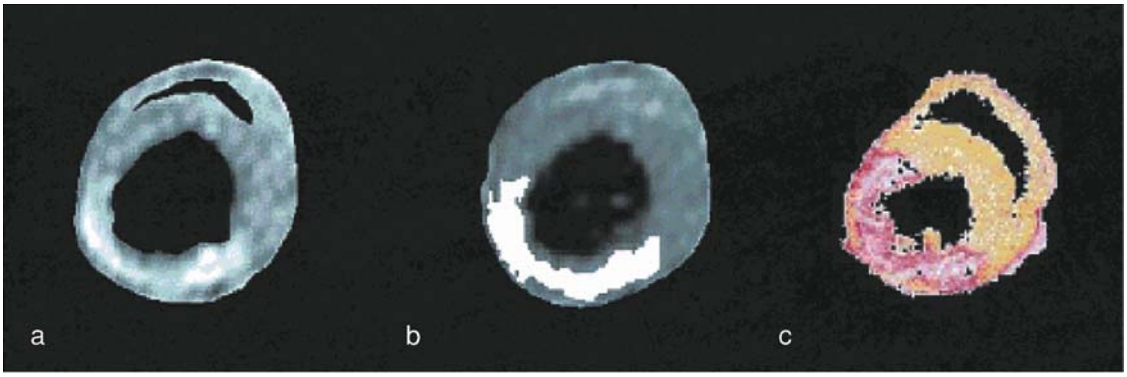

Plate 72. See also Figure 12 on page 848.

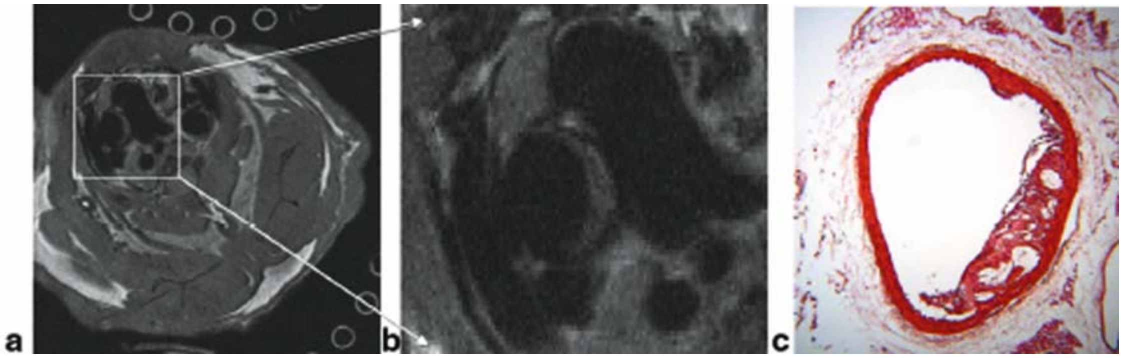

Plate 73. See also Figure 13 on page 849.

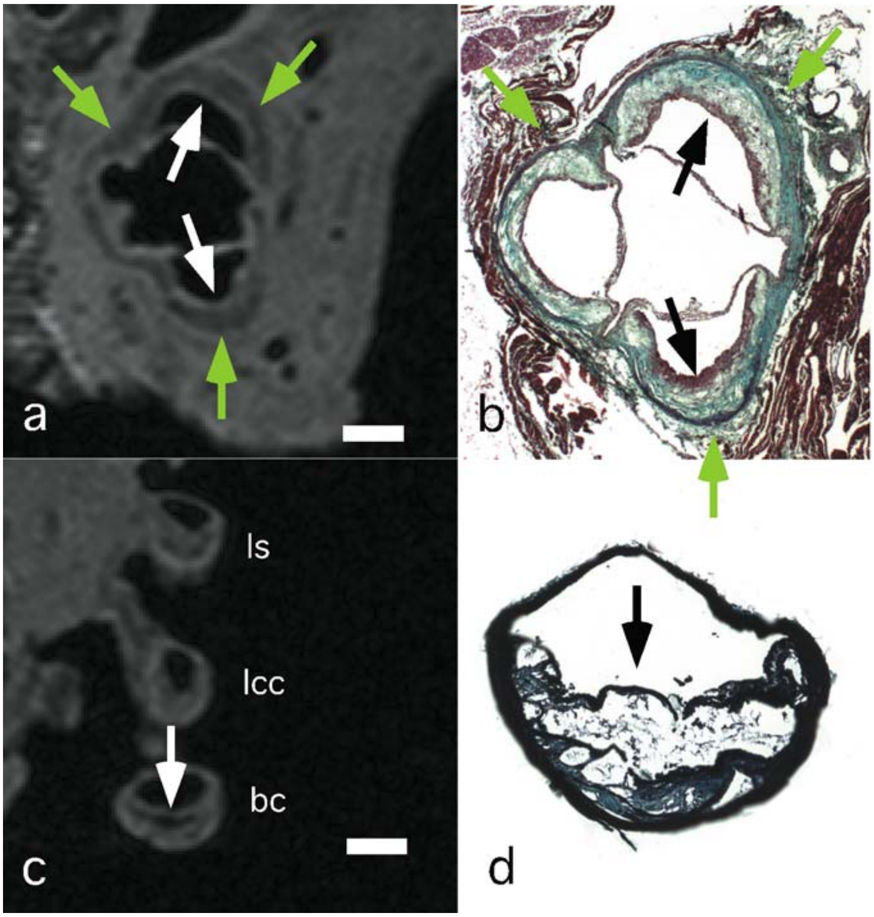
a
b
ls
lcc
bc
c
d

Plate 74. See also Figure 14 on page 850.

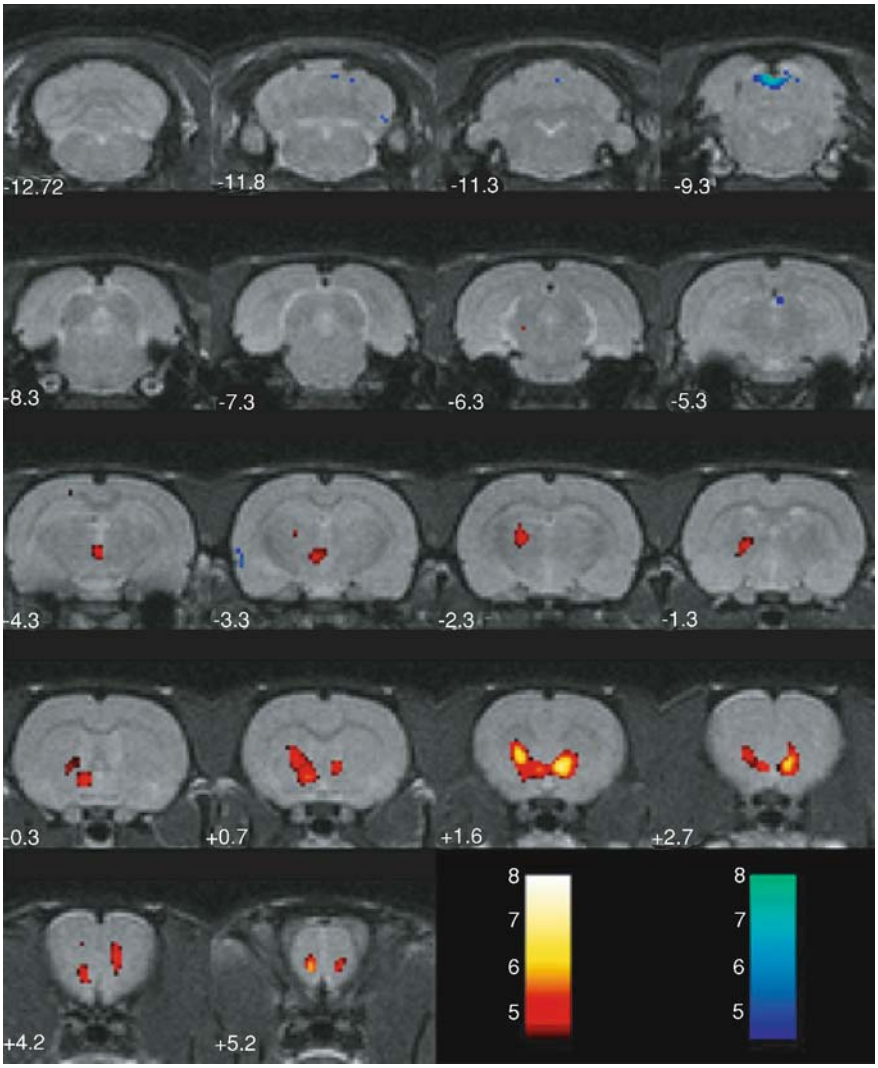
-12.72
-11.8
-11.3
-9.3
-8.3
-7.3
-6.3
-5.3
-4.3
-3.3
-2.3
-1.3
-0.3
+0.7
+1.6
+2.7
+4.2
+5.2
8
7
6
5
8
7
6
5

Plate 75. See also Figure 1 on page 866.

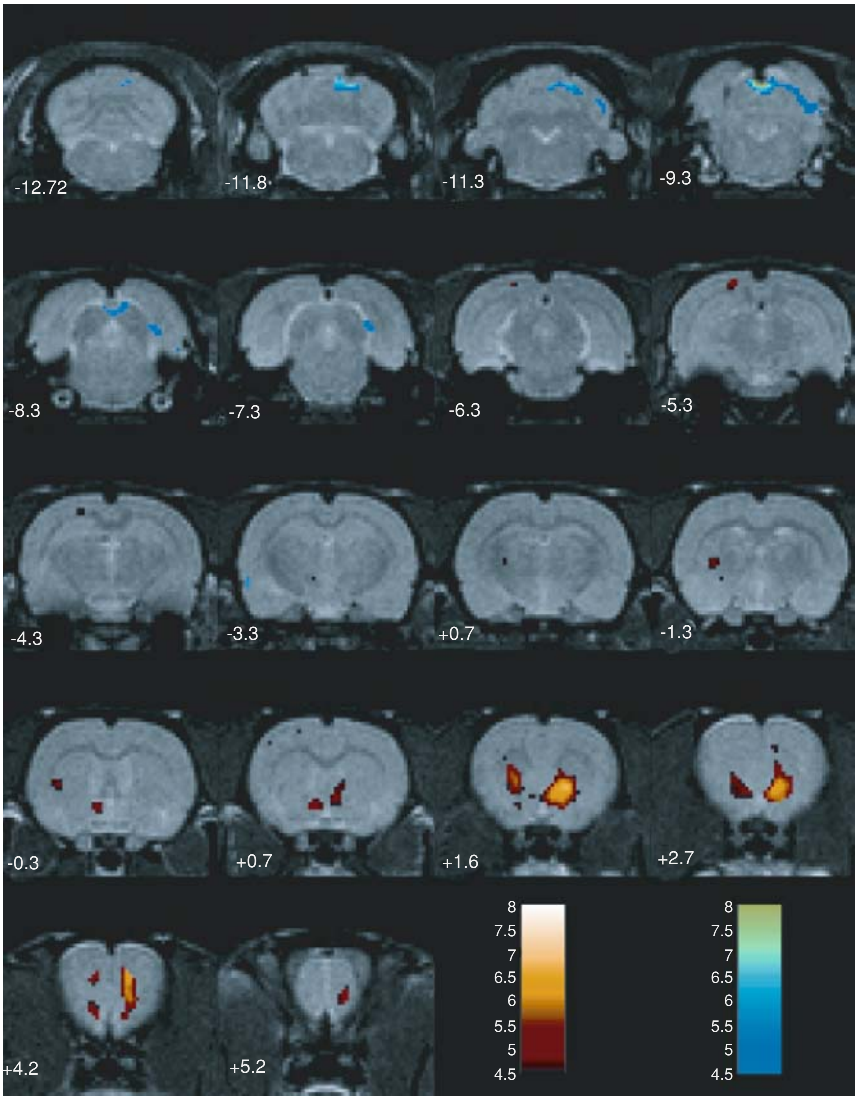
-12.72
-11.8
-11.3
-9.3
-8.3
-7.3
-6.3
-5.3
-4.3
-3.3
+0.7
-1.3
-0.3
+0.7
+1.6
+2.7
+4.2
+5.2
8
7.5
7
6.5
6
5.5
5
4.5
8
7.5
7
6.5
6
5.5
5
4.5

Plate 76. See also Figure 3 on page 868.

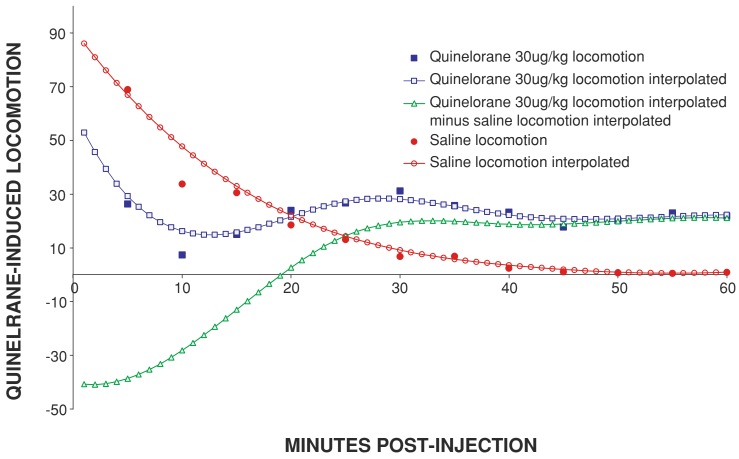

Plate 77. See also Figure 4 on page 869.

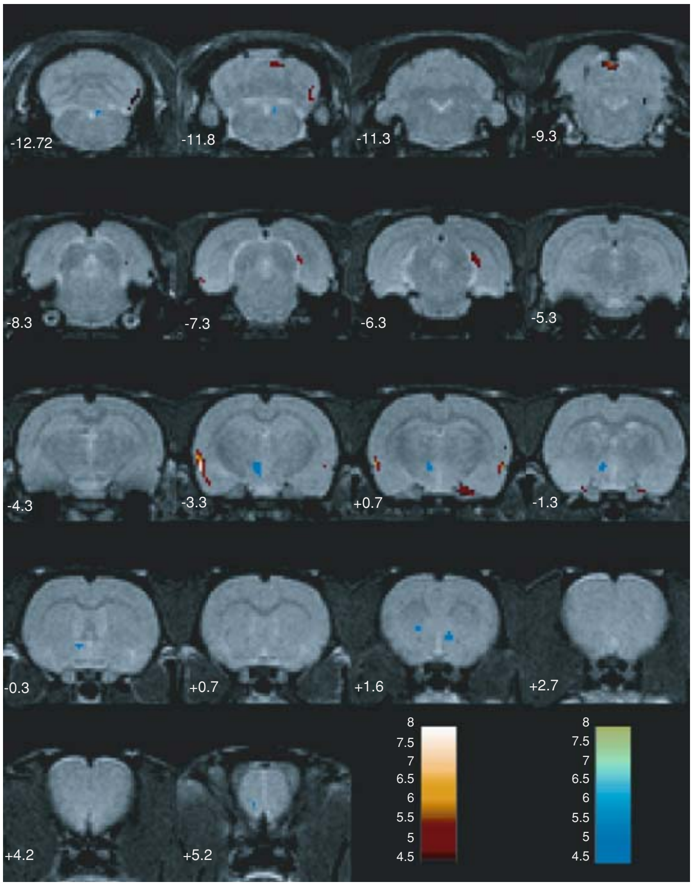
-12.72
-11.8
-11.3
-9.3
-8.3
-7.3
-6.3
-5.3
-4.3
-3.3
+0.7
-1.3
-0.3
+0.7
+1.6
+2.7
+4.2
+5.2
8
7.5
7
6.5
6
5.5
5
4.5
8
7.5
7
6.5
6
5.5
5
4.5

Plate 78. See also Figure 5 on page 870.

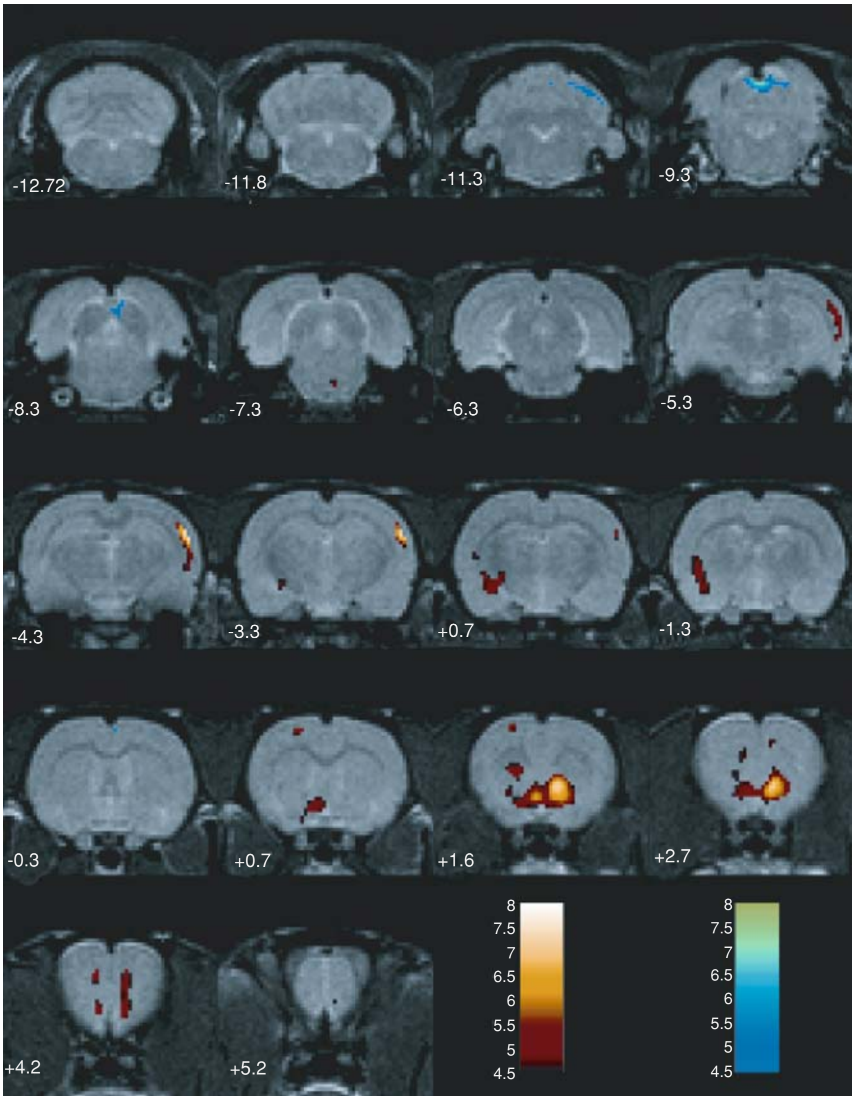
-12.72
-11.8
-11.3
-9.3
-8.3
-7.3
-6.3
-5.3
-4.3
-3.3
+0.7
-1.3
-0.3
+0.7
+1.6
+2.7
+4.2
+5.2
8
7.5
7
6.5
6
5.5
5
4.5
8
7.5
7
6.5
6
5.5
5
4.5

Plate 79. See also Figure 6 on page 871.

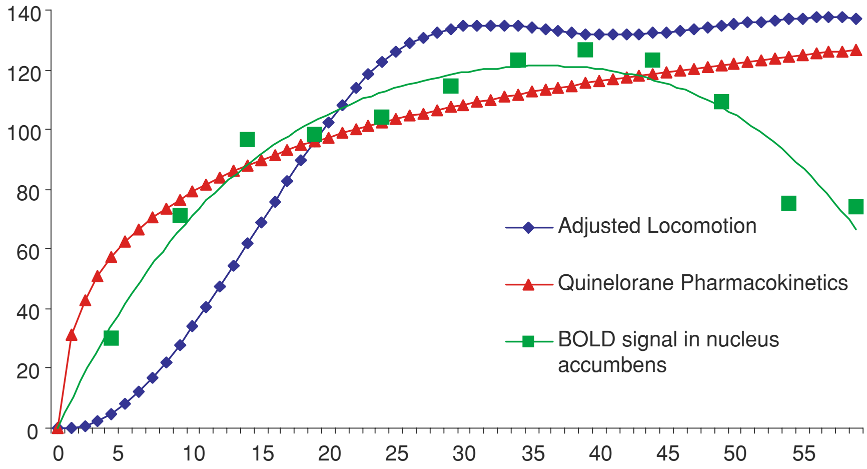

Plate 80. See also Figure 7 on page 872.

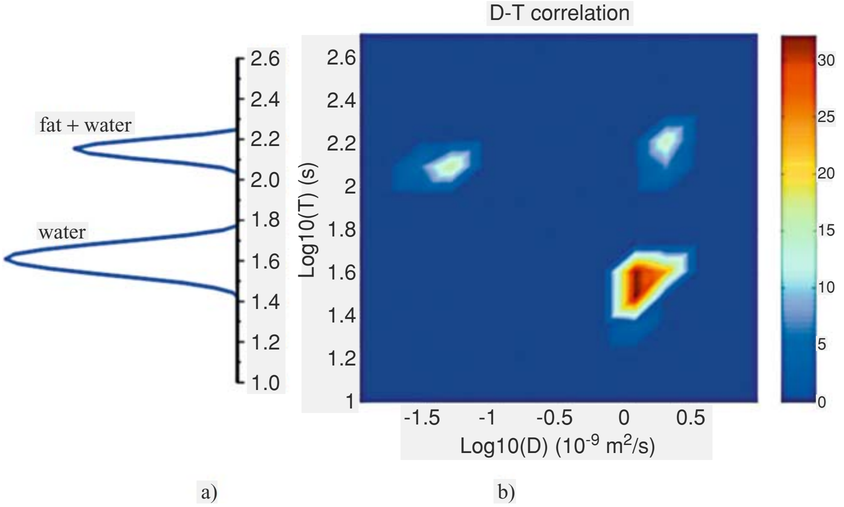

Plate 81. See also Figure 8 on page 912.

Part I, Section 1: Applications in Chemistry

Foreword to Application in Chemistry

Magnetic resonance has continued to be an emerging technique, to be applied to almost all fields of pure and applied sciences, including chemistry, physics, biology, materials science, medicine, etc. during past 60 years since its discovery. The applications in chemistry of this volume covers advanced studies on chemical aspect of magnetic resonance spectroscopy and imaging dealing with the state-of-the-art developments of new techniques together with those of basic concepts and techniques, consisting of 93 articles which are grouped to 25 chapters. They are alphabetically arranged for convenience of readers: amyloids, chemical shifts and spin coupling constants, fibrous proteins, field gradient NMR, host-guest chemistry, imaging, inorganic materials and catalysis, lipid bilayers and bicelles, membrane-associated peptides, membrane proteins, new developments, NOE and chemical exchange, NQR and ESR, organometallic chemistry, paramagnetic effects, protein structures, polymer structure, polymer dynamics, polymer blends, quantum information processing, residual dipolar couplings and nucleic acids, solid state NMR techniques, structural constraints in solids, and telomeric DNA complexes. The section editors are grateful to contributors to this section for their fine contributions.

Tetsuo Asakura, Hazime Saitô and Isao Ando

Abbreviations

AFM: atomic force microscopy

AHT: average Hamiltonian theory

Bicelle: bilayered micelles

BPPLED: bipolar pulse longitudinal eddy current

BPT: bond polarization theory

CC: coupled cluster

CD: circular dichroism

CHF: coupled Hartree-Fock

CNDO: complete neglect of differential overlap

CP-MAS: cross polarization-magic angle spinning

CODEX: centerband-only detection of exchange

COSY: correlated spectroscopy

CPMG: Carr-Purcell-Meiboom-Gill

CRAMPS: combined rotation and multiple pulse spectroscopy

CRINEPT: cross-correlated relaxation-enhanced polarization transfer

CRIPT: cross-correlated relaxation induced polarization transfer

CS: chemical shift

CSA: chemical shift anisotropy

CSI: chemical shift imaging

CTDQFD: constant-time double-quantum filter

CTOCD: continuous transformation of the current density

DARR: dipolar-assisted rotational resonance

DAS: dynamic angle spinning

DEPT: distortionless enhancement by polarization transfer

DD-MAS: dipolar decoupled-magic angle spinning

DECORDER: direction exchange with correlation for orientation-distribution evaluation and reconstruction

DFS: double frequency sweep

DFT: density functional theory

DIPSHIFT: dipolar chemical shift

DNMR: dynamic NMR

DNP: dynamic nuclear polarization

DOQSY: double quantum spectroscopy

DOR: double rotation

DOSY: diffusion-ordered NMR spectroscopy

DPMAS: direct polarization magic angle spinning

DQ: double quantum

DQDRAW: double quantum, dipolar recovery with windowless sequence

DRAW: dipolar recovery with windowless sequence

DSO: diamagnetic spin orbital

EFG: electric field gradient

EEHT: exact effective Hamiltonian theory

EHT: effective Hamiltonian theory

ENDOR: electron nuclear double resonance

EPSI: echo planar spectroscopic imaging

EPR: electron paramagnetic resonance

ESRI: electron spin resonance imaging

Et-NOESY: exchange transferred nuclear Overhauser effect spectroscopy

EXSY: exchange spectroscopy

FDR: frequency selective dipolar recoupling

FOV: field of view

FPT: finite perturbation theory

FC: Fermi contact

GE-HMQC: gradient enhanced-heternuclear multiple quantum coherence

GIAO-CHF: gauge-independent atomic-orbitals coupled Hartree-Fock

GC: gas chromatograph

HETCOR: heteronuclear correlation

HMBC: heteronuclear multiple bond correlation

HMQC: heteronuclear multiple quantum correlation

HOHAHA: homonuclear Hartmann Hahn

HSQC: heteronuclear single quantum correlation

HPDEC: high power decoupling

IGLO: individual gauge for localized orbitals

INADEQUATE: incredible natural abundance double quatum transfer experiment

INDO: intermediate neglect of differential overlap

INEPT: insensitive nuclei enhancement by polarization transfer

LC-NMR: liquid chromatography-NMR

LDA: local density approximation

LDBS: locally dense basis set

LORG: localized orbitals local origin

LG-CP: Lee Goldburg-cross polarization

MAOSS: magic angle oriented sample spinning

MAS: magic angle spinning

MCSCF: multi-configurational self-consistent field

MD: molecular dynamics

MI: molecular imaging

MOVS: magnetically oriented vesicle systems

MQMAS: multiple quantum magic angle spinning

MREV-8: Mansfield-Rhim-Elleman-Vaughan 8 cycle

MRI: magnetic resonance imaging

MRFM: magnetic resonance force microscopy

MSREDOR: multi spin REDOR

NMR: nuclear magnetic resonance

NMR-MOUSE: NMR-mobile universal surface explorer

NOE: nuclear Overhauser enhancement

NOESY: nuclear overhauser and exchange spectroscopy

NQR: nuclear quadrupole resonance

ODF: order-director fluctuation

ONIOM: Our own n-layered integrated molecular Orbital + molecular mechanics

ONP: optical nuclear polarization

PET: positron emission tomography

PFG: pulsed field-gradient

PGSE: pulsed gradient-field spin echo

Photo-CIDNP: photochemically induced dynamic nuclear polarization

PISA: polarity index slant angle

PISEMA: polarization inversion spin exchange at magic angle

PM5: parametric method 5

PSO: paramagnetic spin orbital

QC: quantum computation

QEDOR: quadrupole echo double resonance

QED: quantum electrodynamics

QCPMG: quadrupolar Carr-Purcell-Meiboom-Gill refocusing pulse

QIP: quantum information processing

QM/MM: quantum mechanics/molecular mechanics

QRI: quantum resonance interferometry

PFG: pulse field gradient

RACO: relayed anisotropy correlation

RDC: residual dipolar coupling

REAPDOR: rotational echo adiabatic passage double resonance

REDOR: rotational echo double resonance

RFDR: radio frequency driven resonance

RMSD: root mean-square deviation

ROCSA: recoupling of chemical shift anisotropy

ROCSA-LG: recoupling of chemical shift anisotropy-Lee Goldburg

ROE: rotating frame Overhauser experiment

RR: rotational resonance

SAIL: stereo-array-isotope-labelling

SASS: switching angle sample spinning

scBCH: semi-continuous Baker-Campbell-Hausdorff

SDC: superdense coding

SEC-NMR: size exclusion chromatography-NMR

SEDOR: spin echo double resonance

SELFIDOQ: separated-local-field double quantum

SFAM: simultaneous frequency amplitude modulation

SOPPA: second order polarization propagator approximation

SOS: sum-over-states method

SQ: single quantum

SQUID: superconducting quantum interference device

SSNMR: solid state NMR

STD: saturation transfer difference spectroscopy

STRAFI: stray field magnetic resonance imaging

STO: Slater-type orbital

TB MO: tight-binding molecular-orbital

TOCSY: total correlation spectroscopy

TORQUE: T one rho quenching

TRAPDOR: transfer of populations in double resonance

TPPM: two pulse phase modulation

TROSY: transverse relaxation optimized spectroscopy

VFMAS: very fast magic angle spinning

water LOGSY: water-ligand observation by gradient spectroscopy

WISE: wide-line separation

XRD: x-ray diffraction

ZQ: zero-quantum

Amyloids

Part I

Kinetics of Amyloid Fibril Formation of Human Calcitonin

Miya Kamihira[1], Hazime Saitô[1], and Akira Naito[2]
[1]Department of Life Science, Himeji Institute of Technology, Harima Science Garden City, Kamigori, Hyogo 678-1297, Japan; and
[2]Department of Engineering, Yokohama National University, Hodogaya, Yokohama 240-8501, Japan

Introduction

Amyloid fibril formation is one of the common phenomena associated with many serious diseases such as Alzheimer's disease, Parkinson's, bovine spongiform encephalopathy (BSE), scrapie, and so on. Independent of the constituent polypeptides, the amyloid fibrils exhibit highly organized filamentous structures which are typically ∼100 Å in diameter, as revealed by electron microscopy and atomic force microscopy. Mechanism of the amyloid fibril formation has been extensively studied by various spectroscopic techniques, related to misfolding of proteins. Especially, solid-state NMR spectroscopy has made a great contribution to determine the structures of the fibrils from several peptides/proteins at the molecular level. For example, Alzheimer's β-amyloid peptides, which consist of 40–42 amino acid residues, have gained insights into the three-dimensional (3D) structures in the fibrils as a double-layered cross-β structure with parallel β-sheets by accumulating the local and spatial conformational restraints [1–3]. Also, an 11-residue fragment of human transthyretin (TTR) in its fibrillar form which *in vivo* is allied with familial amyloid polyneuropathy and senile systemic amyloidosis, was revealed the complete 3D structures of the extended β-strand conformation, by establishing dihedral angles of the backbone and ^{13}C–^{15}N distances [4,5]. These results indicate that solid-state NMR spectroscopy is a powerful tool to determine the non-crystal, non-soluble, fibrillar structures.

In this chapter, a solid-state NMR application on the kinetics analyses of the amyloid fibril formation is described. Human calcitonin (hCT) is a thyroid hormone which regulates the mineral metabolism in the bones [6–8]. hCT contains 32 amino acid residues and its sequence is CGNLSTCMLGTYTQDFNKFHTFPQTAIGVGAP-NH_2 with a disulfide bond between Cys^1 and Cys^7 and a C-terminus amide. In a high concentrated solution, however, it is known to form the amyloid fibrils, which are typically 80 Å in diameter [9,10].

Properties of Fibril Formation of hCT

For concentrations above 15 mg/ml hCT, the solution changes in time into a turbid gel as the end fibrillated state, while for the concentrations below and around 1 mg/ml, the equilibrium state consists of a clear solution containing punctuate aggregates which may precipitate [11]. Long fibrils were observed from the gel (pH 3.3, 80 mg/ml) and short fibril aggregates were seen in the precipitates from a diluted solution (1.5 mg/ml, pH 7.5) [12]. Turbidity measurement showed absorption of the hCT solution increased gradually after a lag time which was dependent on the hCT concentrations [11]. As mentioned later, from the results, the kinetics of hCT fibrillation was proposed to be a double nucleation mechanism [11,13–15]. The fibrillation is also temperature-dependent and an apparent activation enthalpy for the reaction was obtained to be 20 kcal/mol at 10 mg/ml (pH 7.4) [11]. Also the rate of the fibril formation was found to be largely pH-dependent and in acidic solution it is much slower than that in neutral pH [11,12]. Solution NMR studies on hCT (80 mg/ml, pH 2.9) showed a gradual broadening of the peptide peaks, followed by a rapid broadening and subsequent disappearance of the NMR signals [16]. The phenomenon was not seen simultaneously and the peaks from the residues in the N-terminal (Cys^1-Cys^7) and in the central (Met^8-Pro^{23}) regions broadened and disappeared faster than those in the C-terminal region (Gln^{24}-Pro^{32}). Furthermore the peaks of Cys^1, Leu^{4,9}, Met^8, Tyr^{12}, Asp^{15}, and Phe^{16,19,22} disappeared faster than the others [16]. These results together with hydrogen–deuterium exchange of amide protons indicate that the amphiphilicity of hCT in the central region might cause a formation of α-helical bundles leading to the fibril formation [16].

Conformational Changes of hCT

To determine the fibrillation process further, the solid-state NMR methods were applied. For this purpose the conformation-dependent ^{13}C chemical shifts are efficient means to determine the secondary structures around the ^{13}C sites straightaway [17–21], especially in the case where the state changes as elapsed time. ^{13}C CP-MAS spectra of the hCT fibrils formed in 15 mM acetic acid solution (80 mg/ml) showed much narrower signals than those before dissolved in the solution (lyophilized powder) (Figure 1), suggesting that the fibril is conformationally more homogeneous than the lyophilized powder. Also

Graham A. Webb (ed.), Modern Magnetic Resonance, 11–17.
© 2008 *Springer.*

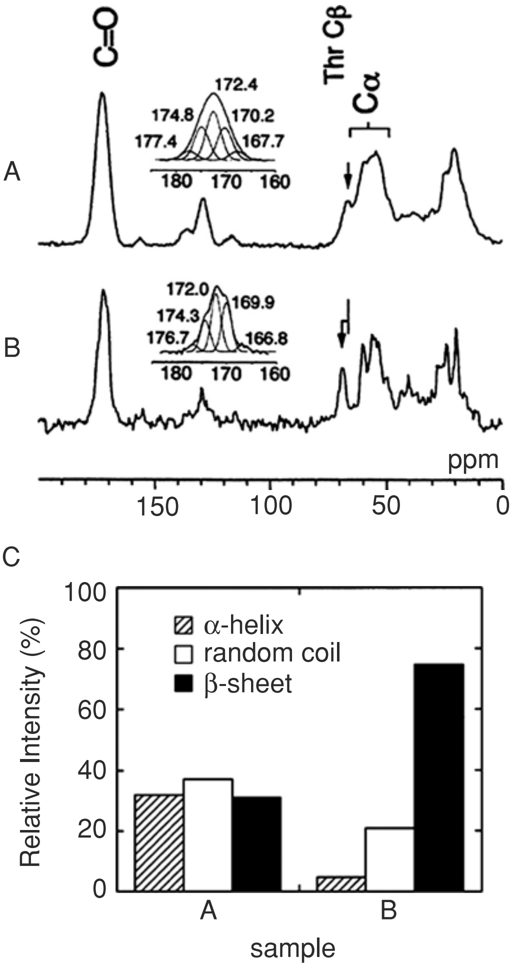

Fig. 1. ^{13}C CP-MAS spectra of lyophilized powder of hCT (Ciba-Geigy, Japan) (A) and the hCT fibrils obtained after 48 h from dissolution in 15 mM acetic acid solution (80 mg/ml) (B). The spectra were recorded on a Chemagnetics CMX 400 NMR spectrometer at the resonance frequency of 100.6 MHz (^{13}C). Insets show deconvoluted spectra of the carbonyl resonances using Peak Fit (SPSS Inc., Chicago, USA). The deconvoluted signals were assigned to be β-sheet (lower frequency than 172.2 ppm; black bars), random coil (172.2–174.5 ppm; open bars), and α-helix (higher frequency than 174.5 ppm; hatched bars) respectively (C).

it is noted that the peak positions have shifted. Deconvolution of the carbonyl signals clearly indicated that the β-sheet conformation gained largely during the fibril formation (Figure 1C). The signals which could be assigned to Thr C_β marked by arrows were also shifted from 65.7 (assigned to random coil) to 67.8 ppm (β-sheet) [18] (Figure 1A and B). Local conformations were examined using site-specifically ^{13}C labeled hCTs [12]. DD-MAS (single 90^o pulse excitation with a proton decoupling under magic angle spinning) and CP-MAS (cross-polarization with a proton decoupling under magic angle spinning) spectra were recorded, since in the CP-MAS spectra a fibril component was detected, while in the DD-MAS spectrum the solution component was mainly observed, especially for the carbonyl carbons in view of the long spin–lattice relaxation time compared with the recycle delay. During the fibrillation at pH 3.3, it was clarified that conformational transitions occur from an α-helix (in the solution) to a β-sheet structure (in the fibril), and from a random coil to a β-sheet structure in the central region, around Gly^{10} and Phe^{22}, respectively [12]. The C-terminus region (around Ala^{26} and Ala^{31}) also changed the conformation partially from a random coil to a β-sheet structure [12]. Further the existence of polymorphs of the fibrils was clearly shown in molecular level, depending on the pH (3.3, 4.1, and 7.5) in the solution [12,22]. It is suggested that at pH 7.5 hCT forms the antiparallel β-sheet by a favorable electrostatic interaction between Asp^{15}(−) and Lys^{18}(+), in addition to the hydrophobic interaction among the amphiphilic helices [12]. The fibrils at pH 3.3 may be a mixture of antiparallel and parallel β-sheet structures, because no attractive ionic interaction to fix the unique direction for the molecular association is present in this case to result in the presence of two conformations up to the C-terminus region [12]. Whereas the β-sheet formed at pH 4.1 is shorter than the others, suggesting probable ionic interactions of the side chain of Asp^{15} with the amino group of the N-terminus (Cys^{1}), rather than with the side chains of Lys^{18}(+) or His^{20}(+) [22]. Accordingly, it was demonstrated that the charged residues existing in hCT (amide nitrogen, Asp^{15}, His^{18}, and Lys^{20}) play a central role for determination of the molecular alignment of the hCT monomers. Indeed absence of the negative charge at Asp^{15} (mutated to Asn^{15}: D15N-hCT) did not make any differences in the local conformations of the fibrils from neutral and acidic solution [23].

Kinetic Analysis of hCT Fibrillation

When hCT solution was dissolved in 15 mM acetic acid solution (80 mg/ml, pH 3.3), it became a turbid, viscous gel in 2–3 days. Time course of the ^{13}C DD- and CP-MAS NMR spectra accumulated repeatedly, showed gradual increase of the CP-MAS signals, synchronously with decrease of the DD-MAS signals, after a certain time (Figure 2A). Although a MAS frequency of 4000 Hz was applied to the sample in a 5-mm o.d. rotor in a 400 MHz spectrometer, the observed increases in the CP-MAS signals were corresponding to the increases in turbidity and

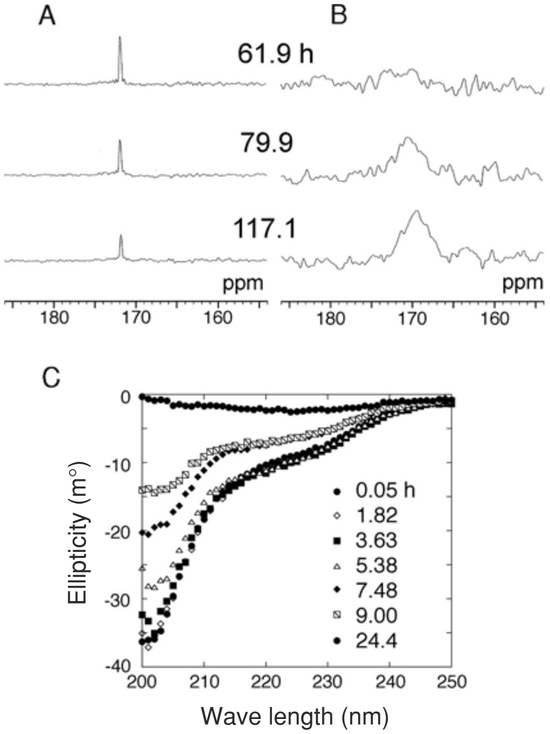

Fig. 2. Time course of ^{13}C DD- (A) and CP-MAS (B) NMR spectra of hCT monomers and fibrils, respectively [pH 3.3, 80 mg/ml (23.4 mM)] at 20 °C. The number of accumulations for the DD- and CP-MAS signals was 1000 and 2000, respectively. Magic angle spinning frequency of 4000 Hz was applied. Stacked CD spectra measured on an AVIV model 62DS using quartz cuvettes with path length of 0.02 cm (B). Sample concentration was 0.2 mg/ml (58.5 μM) in 20 mM phosphate buffer (pH 7.5). Temperature was controlled to 25 °C. The time when hCT was dissolved was regarded as 0.

viscosity by visual observation of the rest of the same solution located outside the magnet. The changes of the peak intensities in the DD- and CP-MAS spectra (Figures 2B and 3A) show a two-step reaction process: for the case of [1-^{13}C]Gly^{10}-hCT, the first and the second step may occur at ∼60 and 60–118 h, respectively. The chained changes in the DD- and CP-MAS spectra and the presence of the lag time suggest that this hCT fibrillation process could be explained by the two-step autocatalytic reaction mechanism, in which the first reaction is a homogeneous nucleation step and the second one is a heterogeneous fibrillation process to elongate and to mature the fibrils. Here, the components of hCT molecules observed by the DD- and CP-MAS experiments are defined as A and B forms, respectively. For an early stage, it is proposed that a formation of micelles which corresponds to the α-helical bundle [16], are reversibly formed from monomers with the same aggregation number $n_0(A_{n_0})$, as shown in Reaction (1) (Figure 4A and B),

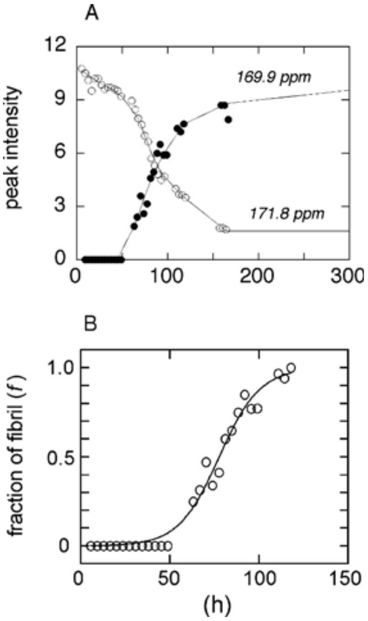

Fig. 3. A plot of [1-^{13}C]Gly^{10} peak heights in ^{13}C DD- (open circle) and CP-MAS (closed circle) of hCT (pH 3.3, 80 mg/ml) against the elapsed time (A). The time of dissolution was taken as 0. Acquisition was started 6 h after dissolution. The intensity of the CP-MAS signals was normalized as that observed at 119 h after dissolution as unity (B). The line in (B) shows the best fit to Equation (7) representing the two-step reaction mechanism.

$$n_0\text{A(monomers)} \leftrightarrow A_{n_0}\text{(micelle)}. \qquad (1)$$

Here, the hCT molecules in the monomer and the micelle states are supposed to give the same DD-MAS NMR signals as the other signals were not appeared. We consider the case where the total hCT concentration of A form ($[\mathrm{A_T}] = n_0[A_{n_0}] + c^*$) is always much higher than the critical micellar concentration c^*, then $[\mathrm{A}_{n_0}]$ can be expressed as $[\mathrm{A_T}]/n_0$. Under these conditions, the first reaction step is given by,

$$\mathrm{A}_{n_0} \xrightarrow{k_1} \mathrm{B}_{n_0}, \qquad (2)$$

where k_1 is the rate constant of Reaction (2) and B_{n_0} is the nucleus of fibril consisting of n_0 number of hCT. If f is defined as the fraction of the B form (fibril) in the system,

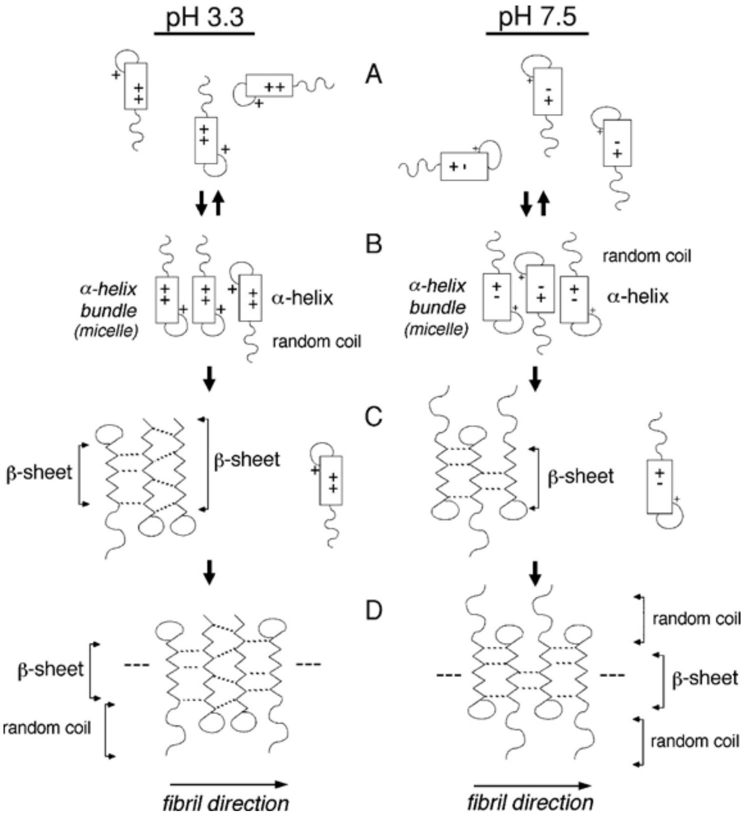
pH 3.3
pH 7.5
A
B
α-helix bundle (micelle)
α-helix
random coil
α-helix bundle (micelle)
random coil
α-helix
C
β-sheet
β-sheet
β-sheet
D
β-sheet
random coil
random coil
β-sheet
random coil
fibril direction
fibril direction

Fig. 4. Schematic representation of a proposed model for the fibril formation. hCT monomers in solution (A) make a homogeneous association to form α-helical bundles (micelles) (B) and simultaneously they change conformations to form β-sheet (C) which could be nuclei of the fibril for heterogeneous fibrillation process to grow the fibril (D).

the kinetic equation of Reaction (2) can be given by

$$\left(\frac{\mathrm{d}f}{\mathrm{d}t}\right)_1 = k_1(1-f). \tag{3}$$

The second autocatalytic fibrillation process can be given by

$$\mathrm{A} + \mathrm{B}_n \xrightarrow{k_2} \mathrm{B}_n + 1, \tag{4}$$

where k_2 is the rate constant of the Reaction (4) and B_n and B_{n+1} are the elongated fibrils with n and $n+1$ numbers of hCT molecules, respectively. In this process, each hCT molecule in B_n is assumed to act as catalytic sites to accelerate the change from A to B forms. Thus $[\mathrm{B}_n]$ can be replaced by

$$\begin{aligned}[\mathrm{B}] &= n_0[\mathrm{B}_{n_0}] + (n_0+1)[\mathrm{B}_{n_0}+1] + \cdots + n[B_n] + \cdots \\ &= af\end{aligned}$$

in the kinetic equation where a is the initial concentration of hCT in the solution. Although micelles are formed, individual hCT molecules (A form) could also react with B_n in the second autocatalytic step. As a consequence of the Reaction (4), $[\mathrm{A_T}] = a(1-f)$ can be used as [A], and [B] increases stepwise after a certain delay time. The relevant differential equation is given by

$$\left(\frac{\mathrm{d}f}{\mathrm{d}t}\right)_2 = k_2 af(1-f). \tag{5}$$

Then the overall kinetic equation for the two-step autocatalytic reaction may be expressed as

$$\frac{\mathrm{d}f}{\mathrm{d}t} = \left(\frac{\mathrm{d}f}{\mathrm{d}t}\right)_1 + \left(\frac{\mathrm{d}f}{\mathrm{d}t}\right)_2 = k_1(1-f) + k_2 af(1-f). \tag{6}$$

The differential equation can be integrated to provide

$$f = \frac{\rho\,\{\exp\left[(1+\rho)\,kt\right] - 1\}}{1 + \rho\exp\left[(1+\rho)\,kt\right]}, \tag{7}$$

Table 1: Kinetic parameters for the fibril formation of hCTs in various pH solution

Sample pH	Method (observed signal)	Concentration (mM)	k_1 (s^{-1})	k_2 ($s^{-1}M^{-1}$)	ak_2 (s^{-1})
hCT					
pH 3.3*	NMR (Gly^{10} C=O)	23.4	$2.71(\pm0.11) \times 10^{-8}$	$9.01(\pm0.81) \times 10^{-4}$	$2.11(\pm0.19) \times 10^{-5}$
pH 4.1	NMR (Gly^{10} C=O)	23.4	$3.86(\pm1.79) \times 10^{-6}$	$5.89(\pm2.94) \times 10^{-4}$	$1.38(\pm0.69) \times 10^{-5}$
pH 7.5*	CD (205 nm)	0.0585	$2.79(\pm0.04) \times 10^{-6}$	$2.29(\pm0.14)$	$1.34(\pm0.08) \times 10^{-4}$
pH 7.5*	CD (205 nm)	0.439	$6.44(\pm0.29) \times 10^{-8}$	$2.78(\pm0.19)$	$1.22(\pm0.08) \times 10^{-3}$
DFNKF†					
pH 7.5	NMR ($Phe^{2(16)}$ C=O)	23.4	$1.02(\pm0.35) \times 10^{-7}$	$7.28(\pm1.54) \times 10^{-3}$	$1.70(\pm0.36) \times 10^{-4}$

*Taken from Ref. [12].

†Taken from Ref. [22].

under the boundary condition of $t = 0$ and $f = 0$, where $\rho = k_1/k$ represents the dimensionless value to describe the ratio of k_1 to k and $k = ak_2$ is an effective rate constant of Reaction (4). After the peak height observed in the CP-MAS spectra was normalized as that observed at 119 h after dissolution as unity (Figure 3B), fitting of the data to the Equation (7) yielded the rate constants, k_1 and k_2, separately (Table 1). Almost the same values were obtained from increase of the intensities in the methyl signals in the ^{13}C CP-MAS signals as well [12] or from analysis of the decrease of the DD-MAS signals (data not shown). A proposed fibrillation process is illustrated in Figure 4. Similarly the rate constants for the fibrillation at pH 4.1 were obtained [22]. The fibrillation of hCT at pH 7.5 was examined using CD spectroscopy instead of NMR at low peptide concentrations (0.2 and 1.5 mg/ml), because the solution becomes a gel in a short time. Decrease of the intensity was observed as elapsed time (Figure 2B) and the same reaction mechanism was applied to it too (Table 1) [12]. Although the effective rate constant, ak_2, is affected by different initial concentrations, it is considered that the reaction rates should be compared as the rate constants, k_1 and k_2. This fact was justified by observing that the comparable k_2 values were determined in the two different initial concentrations (at pH 7.5; Table 1).

The most striking feature was that in the case of fibril formation of hCT the k_1 values were a couple of orders smaller than the k_2 and ak_2 values (Table 1). This suggests that the first homogeneous nucleation process is much slower than the second heterogeneous fibrillation step. Simulation of the Equation (7) reveals that if $k_1 \geq k_2$, the lag time disappears and as k_1 becomes longer the lag time increases gradually (Figure 5A). Basically, $ak_2(k)$ and the ratio of k_1 and $k(\rho)$ determine the reaction effectively. On the other hand, it became clear that if $k_2(k)$ increases by one order, the reaction attains to $f = 1$ by ~10 times faster (Figure 5B), while 10 times larger k_1 does not provide such big differences (Figure 5A). Accordingly,

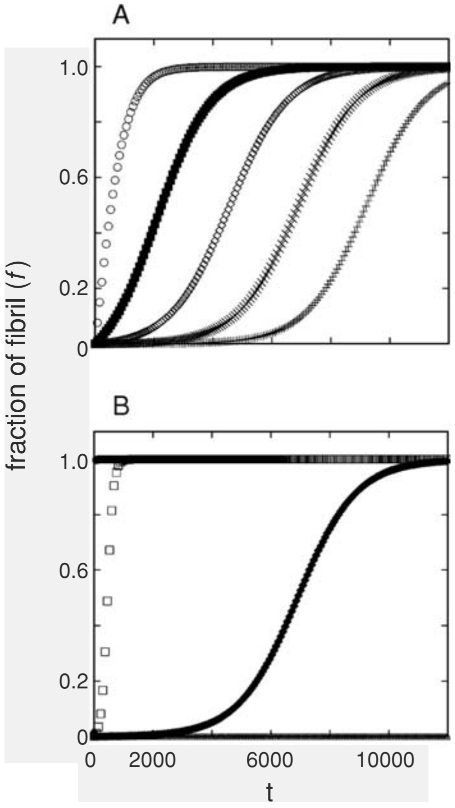

Fig. 5. A computational simulation of kinetics of the two-step autocatalytic reaction. The plot (A) shows at $k = 10^{-2}$ and ρ is varied for 10 (open circle), 1 (closed square), 10^{-1} (open diamond), 10^{-2} (×), and 10^{-3} (+) respectively, representing the effect of k_1 under fixed k_2 on the plot. Whereas the plot (B) shows the variation of k and ρ at the same time to demonstrate the effect of k_2 under fixed k_1: closed circle; 10^{-1}, open square; 10^{-2}, closed diamond; 10^{-3}, cross; 10^{-4}.

reflecting the large difference in the lag time, clear difference in the k_2 values appeared among the samples at pH 3.3 (and 4.1) and 7.5 (Table 1). Thus it is important to determine the rate constants for the first and the second reaction steps separately. The separation of k_1 from k_2 is also important to discuss the factor of fibrillation mechanism in the first step separately from that in the second step.

Mechanism of Fibril Formation

Recently many models have been proposed for the mechanism of amyloid fibril formations from several peptides/proteins [24]. The *double nucleation mechanism* explains the fibril formation starts with a homogeneous nucleation step from hCT monomers and afterward fibrillation continues with development of new fibrils from existing ones [11,13–15]. Formation of peptide micelles above a certain critical peptide concentration has been proposed in the *nucleated polymerization model* in which fibrils nucleate within these micelles or on existing nuclei (seeds) heterogeneously, following fibrils grow by irreversible binding of monomers to the fibrils ends [25–27]. Then the *nucleated conformational conversion model* describes that structurally fluid oligomeric complexes accumulate into nuclei or associate with existing ones where conformational conversion takes place as a rate-determining step [28]. The autocatalytic reaction mechanism we proposed, however, explains the conformational changes occurred together and the rate-limiting step that is characteristic to the amyloid fibril formation clearly. In the solution state, there also exist several different models. It has been proposed for the amyloidosis of β_2-microglobulin that there should be a monomeric amyloidogenic intermediate from a native monomer to assemble each other to form an early assembly intermediate, following it changes to a nucleus where the monomeric intermediates make an interaction together to elongate the fibril [29,30]. On the contrary, in a *mathematical model*, a rapid, irreversible commitment occurs to form either stable monomer/dimer or unstable intermediate, only which associates cooperatively into a multimeric nucleus (filament) [31]. Further, elongation of the filament may occur via addition of the unstable intermediate and by end-to-end association of the filaments [31]. We have also considered that many other fast reactions may exist during the process of a large fibril formation. However, the secondary structure and the chemical environments of the components observed in the DD- and CP-MAS spectra did not change throughout this process, and no additional peaks were observed (Figure 2A). These findings in ^{13}C NMR experiments imply that it is sufficient to consider the two-step reaction for the fibrillation kinetics of peptides.

Then what is the direct force to cause the molecular interaction among the monomers, to form a nucleus (at the first step) or to make an interaction of a monomer with a nucleus (at the second step)? Generally, it has been claimed that the hydrophobic and the electrostatic interaction might be necessary for the fibril formation since the “core region” which is essential to form a fibril, contains (a) cluster(s) of those amino acid residues. In the case of hCT, there exists only one negatively charged residue (Asp^{15}) in it, together with three positively charged group/side chains (NH_3^+, Lys^{18}, and His^{20}). And the results used D15N-hCT demonstrated that the negative charge at Asp^{15} does not increase the rate of fibrillation [22,23]. Instead larger positive net charges around Lys^{18} and His^{20} could cause decrease of the reaction rates, because the side chains of them locate on the same side of the β-strand which might destabilize the structure and disturb elongation of the fibrils [23]. On the other hand, a hCT fragment DFNKF (15–19) which is the shortest one to form a fibril in hCT [32] and is determined to be important for *in vivo* bioactivity too [33], gave 300 times smaller k_2 values at pH 7.5 compared with those of hCT at pH 7.5 (Table 1) [22]. Further, the loss of aromatic rings in the central region was observed to cause the delay in the second step of the fibrillation (Kamihira *et al.*, manuscript in preparation). These results could be a clue to the elucidation of the molecular association to lead to fibril formation.

Conclusion

It was clearly demonstrated that the use of solid-state NMR spectroscopy is very efficient to determine the local conformational changes during the amyloid fibril formation of hCT. Especially the analysis of the signal intensities enabled to examine the kinetic property of hCT fibrillation as a two-step autocatalytic reaction. Further determination using this method could clarify the mechanism of amyloid fibril formations more in detail.

Acknowledgment

We thank Dr. Atsuko Y. Nosaka for helpful discussions.

References

1. Tycko R. Curr. Opin. Chem. Biol. 2000;4:500.
2. Tycko R. Methods Enzymol. 2001;339:390.
3. Tycko R. Curr. Opin. Struct. Biol. 2004;14:96.
4. Jaroniec CP, MacPhee CE, Bajaj VS, McMahon MT, Dobson CM, Griffin RG. Proc. Natl. Acad. Sci. U.S.A. 2004;101:711.
5. Jaroniec CP, MacPhee CE, Astrof NS, Dobson CM, Griffin RG. Proc. Natl. Acad. Sci. U.S.A. 2002;99:16748.

6. Copp DH, Cameron EC, Cheney BA, Davidson AGF, Henze KG. Endocrinology. 1962;70:638.
7. Kumar MA, Foster GV, MacIntyre I. Lancet. 1963;2:480.
8. Austin LA, Heath HD. N. Engl. J. Med. 1981;304:269.
9. Sieber P, Riniker B, Brugger M, Kamber B, Rittel W. Helv. Chim. Acta. 1970;53:2135.
10. Bauer HH, Aebi U, Haner M, Hermann R, Muller M, Merkle HP. J. Struct. Biol. 1995;115:1.
11. Arvinte T, Cudd A, Drake AF. J. Biol. Chem. 1993;268:6415.
12. Kamihira M, Naito A, Tuzi S, Nosaka YA, Saito H. Protein Sci. 2000;9:867.
13. Ferrone FA, Hofrichter J, Eaton WA. J. Mol. Biol. 1985;183:591.
14. Ferrone FA, Hofrichter J, Sunshine HR, Eaton WA. Biophys. J. 1980;32:361.
15. Samuel RE, Salmon ED, Briehl RW. Nature. 1990;345:833.
16. Kanaori K, Nosaka AY. Biochemistry. 1995;34:12138.
17. Saito H. Magn. Reson. Chem. 1986;24:835.
18. Saito H, Ando I. Annu. Rep. NMR Spectrosc. 1989;36:209.
19. Saito H, Tuzi S, Naito A. Annu. Rep. NMR Spectrosc. 1998;36:79.
20. Wishart DS, Sykes BD. Methods Enzymol. 1994;239:363.
21. Wishart DS, Sykes BD, Richards FM. J. Mol. Biol. 1991;222:311.
22. Naito A, Kamihira M, Inoue R, Saito H. Magn. Reson. Chem. 2004;42:247.
23. Kamihira M, Oshiro Y, Tuzi S, Nosaka YA, Saito H, Naito A. J. Biol. Chem. 2003;278:2859.
24. Zerovnik E. Eur. J. Biochem. 2002;269:3362.
25. Lomakin A, Chung DS, Benedek GB, Kirechner DA, Teplow DB. Proc. Natl. Acad. Sci. U.S.A. 1996;93:1125.
26. Lomakin A, Teplow DB, Kirschner DA, Benedek GB. Proc. Natl. Acad. Sci. U.S.A. 1997;94:7942.
27. Walsh DM, *et al*. J. Biol. Chem. 1999;274:25945.
28. Serio TR, Cashikar AG, Kowal AS, Sawicki GJ, Moslehi JJ, Serpell L, Arnsdorf MF, Lindquist SL. Science. 2000;289:1317.
29. McParland VJ, Kalverda AP, Homans SW, Radford SE. Nat. Struct. Biol. 2002;9:326.
30. Hoshino M, Katou H, Hagihara Y, Hasegawa K, Naiki H, Goto Y. Nat. Struct. Biol. 2002;9:332.
31. Pallitto MM, Murphy RM. Biophys. J. 2001;81:1805.
32. Reches M, Porat Y, Gazit E. J. Biol. Chem. 2002;277:35475.
33. Kazantzis A, Waldner M, Taylor JW, Kapurniotu A. Eur. J. Biochem. 2002;269:780.

Polymorphism of Alzheimer's Aβ Amyloid Fibrils

Oleg N. Antzutkin

Division of Chemistry, Luleå University of Technology, S-971 87 Luleå, Sweden

Abstract

An overview of the strategy and experimental solid-state NMR, STEM, and AFM methods useful for obtaining structural constraints on Alzheimer's amyloid-β peptide fibrils is presented. Polymorphism of amyloid fibrils and the relevance to neurotoxicity is discussed.

Abbreviations: STEM, scanning transmission electron microscopy; AFM, atomic force microscopy.

Alzheimer's disease (AD) is a form of senile dementia, which affects ca. 40 million senior citizens worldwide [1]. AD is one of the most expensive diseases because an intense daycare of patients is needed over many years. For example, direct and indirect costs of AD and other forms of dementia in Sweden alone (ca. 160,000 patients, a half of them with AD) amount to more than 5400 million euro in 2004 [2]. To this day, a microscopic diagnosis of AD is made on the invariable presence of the two primary criteria: (i) the presence of extracellular senile amyloid plaques surrounded by dead or severely damaged nerve cells in certain regions of the cerebral cortex, such as the hippocampus, amygdala, and other regions of the brain important for memory, learning, and judgment and (ii) dense bundles of abnormal fibers, neurofibrillar tangles, formed by another normally occurring neuronal protein, tau-protein, in the cytoplasm of certain degenerating neurons [3]. In addition, the pathology of AD was found to involve marked decreases in acetylcholine, the chemical used by nerve cells to transmit signals.

In 1984 Glenner and Wong [4,5] and later Masters *et al.* [6] found that amyloid isolated from blood vessels in the meninges and from Alzheimer's amyloid plaques consist of ca. 90% of amyloid-β-peptides (Aβ), 39–43 amino acid residue peptides with the principal components Aβ$_{(1-40)}$ and Aβ$_{(1-42)}$: DAEFRHDSGY$_{10}$ EVHHQKLVFF$_{20}$AEDVGSNKGA$_{30}$IIGLMVGGVV$_{40}$IA [4–8]. Transmission electron microscopy of amyloid plaques revealed numerous unbranched Aβ amyloid fibrils with diameter 6–12 nm, surrounded by the amorphous aggregates, diffuse amyloid.

Despite an imperfect correlation between amyloid deposits and dementia [9–11], recent reports from various research groups all tend to implicate Aβ, rather than tau-protein, as triggering a long cascade of biochemical reactions finally leading to neurodegeneration [12–14]. Early onsets of AD have been connected to the following genetic factors: (i) mutations in proteins Presenilin I and Presenilin II (putatively assigned to γ-secretases [12]) which lead to elevated plasma concentrations of Aβ$_{(1-42)}$, a more hydrophobic and neurotoxic form of human Aβ; (ii) point mutations in human Aβ$_{(1-40)}$ (and Aβ$_{(1-42)}$), Aβ$_{(1-40)}$(A21G) "Flemish" [15], Aβ$_{(1-40)}$(E22Q) "Dutch" [16], Aβ$_{(1-40)}$(E22K) "Italian" [17], Aβ$_{(1-40)}$(E22G) "Arctic" [18], and Aβ$_{(1-40)}$(D23N) "Iowa" [19]. Remarkably, these mutants aggregate faster and at lower critical concentrations compared with the wild type Aβ$_{(1-40)}$ [20]. Also, it has been found that the "Arctic" mutant found in Northern Swedish families with an early onset of AD (54–61 years), Aβ$_{(1-40)}$(E22G), forms a larger relative amount of smaller aggregates and proto-fibrils [18] as well as the peptide shows a high degree of polymorphism of amyloid fibrils grown in TRIS buffer solution at pH 7.4 (two non-coiled and three coiled types of fibrils) [21,22].

The sequence of Aβ includes the first 28 residues (mainly hydrophilic) of the extracellular domain and 11–15 residues (mainly hydrophobic) of the transmembrane region of a 695-residue amyloid precursor protein (APP), whose function is not fully understood [7]. It is believed that putatively incorrect processing [23] or abnormal post-translational modifications of APP [24] give rise to the extracellular neurotoxic Aβ. Moreover, it has been observed *in vitro* that significant levels of peptide aggregation into a structural fibrillar form are always associated with significant Aβ-induced neurotoxicity [25–27]. The exact mechanism of the Aβ neurotoxicity is still unknown, though recent reports suggest that Aβ$_{(1-40)}$ and Aβ$_{(1-42)}$ amyloid fibrils with distinct different morphologies and different supramolecular structures show remarkably different toxicity *in vitro* for cell cultures of hippocampal neurons obtained from rat embryos [28,29]. Even small but putatively structured Aβ oligomers have been found toxic for nerve cell cultures both *in vitro* [13] and *in vivo* [14]. These make structural studies on Alzheimer's amyloid fibers and oligomers significant neuropathologically.

It has been reported in a fair number of studies that both synthetic Aβ and its fragments [30–46], as well as isolated Alzheimer's senile plaque proteins [47,48],

Graham A. Webb (ed.), Modern Magnetic Resonance, 19–27.
© 2008 *Springer.*

spontaneously assemble into the typical 60–120 Å amyloid fibers that exibit a β-pleated sheet conformation and other properties consistent with native AD Aβ-peptides. Morphology and macroscopic features of the amyloid fibrils (shape, left or right handed twist, pitch, maximum and minimum heights) can be readily studied by AFM (see Figures 1A and B) or/and TEM (not shown). AFM is advantageous over TEM, because AFM allows very fine measurements of height and, therefore, all dimensions of coiled amyloid fibrils can be precisely elucidated (see Figure 1C and D). The latter is crucial in distinguishing of different types of fibril morphology, which may correlate with different neurotoxicity as discussed above. Polymorphism of Alzheimer's Aβ$_{(1-40)}$ (two types of amyloid fibrils [28]) and Aβ$_{(1-40)}$E22G ("Arctic" mutant, five different types of fibrils [21,22]) has been recently investigated in detail.

Structural features of amyloid fibrils can be further investigated by scanning transmission electron microscopy (STEM) [28,49,50] (mass-per-length measurements, Figure 1E) using the methods developed in the earlier works [51–54]. By STEM mass-per-length of different polymorphs of amyloid fibrils can be measured by recording intensity of the dark-field STEM image across an amyloid fibril, correcting it on image background and further normalizing to intensity of the signal across a calibrant, tobacco mosaic virus (TMV) with mass-per-length 131 kDa/nm known from single crystal X-ray diffraction data. Additional information that Alzheimer's amyloid fibrils adopt a cross-β-sheet structure with multiple folded or stacked β-sheet laminae, comes from X-ray diffraction data on oriented amyloid fibrils [32]. A cross-β-sheet structure is characterized by two typical reflections, which correspond to ca. 4.9 Å spacing (i.e. intermolecular hydrogen bonding) perpendicular to ∼10 Å spacing (interlaminae spacing filled with side groups of amino acid residues forming structures stabilized by van der Waals and electrostatic interactions). Therefore, mass-per-length statistics of amyloid fibrils can be readily recalculated into a number of β-sheet laminae folded and packed into fibrils, provided that molecular weight of peptide molecules is known (for example, MW(Aβ$_{(1-40)}$) ≈4329 a.u.). Fibrils with different morphology may be composed of different number of laminae: two, three or four, depending on the peptide sequence and on the preparation procedure (acidic or neutral pH, type of buffer, incubation with or without agitation [21,28,49]. For example, Alzheimer's amyloid fibrils of Aβ$_{(1-40)}$(R5G, Y10F, H13R), called as "rat" or "rodent" sequence, prepared at pH 7.25 in non-buffered solution and without additional agitation, consist of three folded laminae (see statistics in Figure 1E). Human Aβ$_{(1-40)}$ fibrils prepared in vertical dialysis tubes in an unstirred bath of phosphate buffer solution at pH 7.45 also consist of three laminae. In contrast, a gentle circular agitation of 0.1–1.0 mM Aβ$_{(1-40)}$ solutions (buffered or non-buffered, pH 7.4, room temperature, 1–10 weeks of incubation) in polypropylene tubes gives rise to fibrils with either two or four β-sheet laminae and with remarkably lower neurotoxicity compared with the quiescent three-laminated fibrils [28]. Interestingly, Aβ$_{(1-42)}$, which is more amyloidogenic peptide, and a shorter peptide, Aβ$_{(10-35)}$, usually used as a convenient model system [55–58], also form amyloid fibrils with either two or four β-sheet laminae when prepared in non-buffered solutions at either pH 3.8 or 7.4 with additional agitation [49].

However, mass-per-length STEM measurements combined with X-ray diffraction data on oriented amyloid fibrils provide only information about a number of β-sheet laminae packed and propagating along the long axis of fibrils. Pertinent questions about more detailed supramolecular structure of fibrils and their properties are: (i) Which fragments of peptide molecules form parallel or antiparallel β-sheets? (ii) Are any fragments of molecules, which do not adopt a β-sheet secondary structure? (i.e. forming α-helices, turns or random coils) (iii)What are precise structural parameters of these non-β-sheet structural fragments? (iv) Do certain side groups of amino acid residues form salt bridges? (v) Which side groups are packed together forming hydrophobic clusters? (vi) How a single β-sheet lamina is folded, "upwards" or "downwards", exposing side groups of different amino acid residues to the surrounding solution? (vii) What are these amino acid residues, which side groups form outer surfaces of amyloid fibrils and which may, therefore, induce neurotoxicity or can be accessed by "attacking" inhibitors or proteases of amyloid fibrils *in vivo*? (viii) How two (or three, or four) different β-sheet laminae are folded and packed together giving rise to a "ready" amyloid fibril? (ix) Where are binding sites either for metal ions that can stabilize certain structures of Aβ oligomers and fibrils (Cu^{2+}, Zn^{2+}, Fe^{3+}, and Al^{3+} found in Alzheimer's amyloid plaques) or for highly soluble metal–ligand complexes that can easily penetrate brain-blood-barrier (for example, alumninum citrates, $[Al_3(OH)(H_{-1}Cit)_3]^{4-}$ or $[Al_3(OH)_4(H_{-1}Cit)_3]^{7-}$)? (x) How different known pathologic point mutations in the peptide sequence affect the supramolecular structure, polymorphism, aggregation kinetics, and neurotoxicity of amyloid fibrils? (xi) Is the structure of aggregation intermediates (small oligomers, spherical bodies or protofilaments, which are also believed to be neurotoxic [13,14]) similar to structural fragments of amyloid fibrils or structural transitions do occur in the course of the aggregation cascade? (xii) How the assembly of amyloid fibrils proceeds, either by single molecules or by small oligomeric domains?

Solid-state NMR spectroscopy combined with either selective or uniform ^{13}C, ^{15}N isotopic labeling of Alzheimer's β-amyloid peptides were found as useful methods for answering on some of aforementioned questions about supramolecular structure of amyloid fibrils

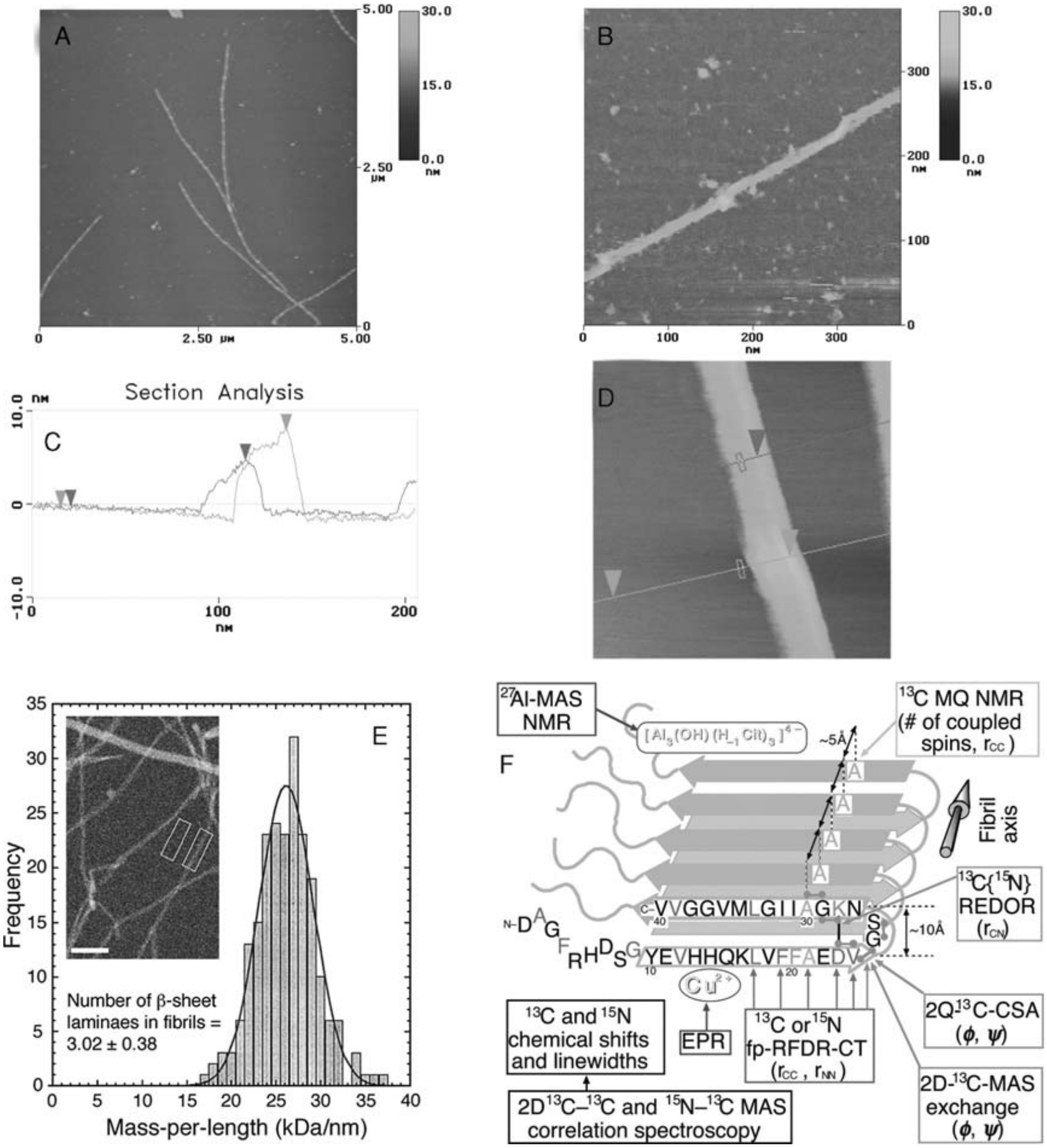

Fig. 1. (A–D) Tapping mode AFM images of A$\beta_{(1-40)}$ preparations on mica. A$\beta_{(1-40)}$ was incubated at 50 µM in TRIS buffer (10 mM TRIS, 0.5 mM EDTA, 10 mM KCl and 0.01wt% NaN_3, pH 7.4 adjusted with NaOH) in plastic tubes without additional agitation for 8 days. Images were obtained by M. Hellberg and N. Norlin (MSc thesis, Luleå University of Technology, 2003). Heights (C) can be readily measured across the fibril (D). (E) Mass-per-length of A$\beta_{(1-40)}$(R5G, Y10F, H13R), "rat"-sequence fibrils (incubated at pH 7.25 for 4 months without additional agitation) as determined by STEM. Fibrils appear as narrow structures of uniform intensity. Images were recorded at a dose of approximately 10^3 e/nm^2 and a pixel size of 1 nm. White boxes show typical regions from which the integrated signal in a 100 nm segment of fibril and background film were measured; the TMV was used as a calibrant (seen as wide fibrillar structures). Scale bar is 50 nm. Mass-per-length values of 215 individual fibril segments pooled into

(*Continued overleaf*)

(see Figure 1F) [21,59–61]. Recently, useful structural constraints on Alzheimer's amyloid fibrils were obtained from solid-state NMR and new structural models for A$\beta_{(10-35)}$ and A$\beta_{(1-40)}$ fibril polymorphs with either two or four β-sheet laminae have been developed [49,62]. The model for A$\beta_{(1-40)}$ fibrils was based on: (i) a few tens of distance and torsion angle constraints on singly and doubly ^{13}C-labeled Aβ-peptides aggregated in fibrils, obtained from specific novel solid-state NMR experiments, ^{13}C-MQ-NMR [63,64], CT-fp-RFDR [65,66], 2D-exchange-MAS [67–69], 2Q-CSA [69,70] (see Figure 1F); (ii) from about 180 ^{13}C and ^{15}N chemical shifts and line widths of resonance lines obtained from 2D correlation MAS NMR experiments on four A$\beta_{(1-40)}$ fibril samples with a small number (five, six, or seven) of selectively chosen and uniformly ^{13}C/^{15}N-labeled amino acid residues [28,62]; and (iii) from mass-per-length data for fibrils obtained from STEM [28,49].

For molecular structure determination local structural features of molecules can be elucidated by measuring either interspin distances or torsion angles in selectively ^{13}C- or ^{13}C/^{15}N- labeled parts of the peptide sequence. α-helix, β-sheet secondary structures can be estimated from chemical shifts and chemical shift anisotropies. Interspin distances can be measured using both homonuclear and heteronuclear dipole–dipole recoupling sequences, such as constant-time finite-pulse RFDR (fp-RFDR-CT) and REDOR, respectively, and using other analogous methods. Peptide torsion angles, ϕ and ψ can be measured, for example, by correlating ^{13}C chemical shift tensors of carbonyl carbons in $^{13}C_2$-labeled peptides (two consecutive amino acid residues) by means of either spin-diffusion (2D-^{13}C MAS exchange in Figure 1F) or by excitation of double-quantum coherences (2Q-^{13}C-CSA, see Figure 1F) or in combination with fp-RFDR-CT, which sets constraint on the interspin distance, r_{CC}, and, therefore, on the peptide angle ϕ. Structural domains of aggregated peptides and the geometry of spin clusters can be tested by "spin-counting" techniques, such as ^{13}C multiple-quantum NMR spectroscopy [63,71,72]. These methods are particularly useful for testing supramolecular organization of singly ^{13}C-labeled Aβ-peptides that form either parallel or antiparallel β-sheet secondary structures. For an in-register parallel β-sheet organization ^{13}C spins form an infinite "in-register" cluster of spins with interspin distance of ~5 Å that are coupled by the homonuclear dipole–dipole interaction of ca. 70 Hz (see pink labels in Figure 1F). In this particular situation a number of coherent spin states can be excited by a specific pulse sequence, and the highest order of the excited multiple-quantum coherence would be roughly the "count" of the number of coupled spins in the cluster.

The aforementioned solid-state NMR methods were used in obtaining structural constraints and developing structural models for Alzheimer's amyloid fibrils. The most important results are given below:

(i) Y_{10}EVHHQKLVFFAEDV$_{24}$ and A_{30}IIGLMVG-GVV$_{40}$ segments of A$\beta_{(1-40)}$ (fibrils prepared at pH 7.4) form *parallel* in-register β-sheets [64,66];

(ii) V_{24}GSNKGA$_{30}$ fragment of A$\beta_{(1-40)}$ forms a "loop" in fibrils since (ϕ, ψ) angles deviate considerably from those in β-sheet structures [62,69]. However, this is not a true β-hairpin structure, since hydrogen bonding between these amino acid residues is *intermolecular* rather than *intramolecular*. Therefore, a "loop" is a "fold" of the A$\beta_{(1-40)}$ laminate [62].

(iii) The D_1AEFRHDSG$_9$ segment is predominantly in a random coil conformation as was concluded from both ^{13}C chemical shifts and line widths of resonance lines in two-dimensional ^{13}C-^{13}C and ^{15}N-^{13}C MAS

Fig. 1. (*Continued*)
a histogram which was fitted with a single Gaussian curve to give an average mass-per-length of 26.15 kDa/nm with an s.d. of 3.29 kDa/nm. Images and the histogram were obtained from RD Leapman. (F) Putative model for a single A$\beta_{(1-40)}$ folded laminate with selective amino acid isotope labeling scheme shown in color (each label corresponds to a separate sample prepared for solid state NMR measurements): singly ^{13}C labeled carbonyl (*red F4, V12, L17, F20, V24, L34 and V39*) or methyl (*pink A2, A21 and A30*) sites in amino acid residues for ^{13}C fp-RFDR-CT (measurements of r_{cc} interspin intermolecular distances) or ^{13}C MQ NMR for elucidation of either a parallel or an antiparallel β-sheet supramolecular structures; ^{15}N labeled sites (*blue*) for frequency selective ^{13}C{^{15}N}-REDOR measurements of salt bridges (*black link D23-K28*) between the negatively charged side chain carboxylate carbon of Asp23 and the positively charged side chain amino nitrogen of Lys28 (uniformly ^{13}C and ^{15}N labeled amino acid residues); doubly ^{13}C labeled samples at carbonyl carbons of two consecutive amino acid residues (*orange links D23-V24, V24-G25, G25-S26, K28-G29 and G29-A30*) for ϕ and ψ peptide angle measurements using a combination of methods, 2Q-^{13}C-CSA, 2D-^{13}C-MAS exchange and ^{13}C fp-RFDR-CT NMR. ^{13}C and ^{15}N chemical shifts, line widths and sequential assignment were extracted from 2D ^{13}C-^{13}C and ^{15}N-^{13}C MAS NMR correlation spectra on A$\beta_{(1-40)}$ fibril samples with a few (five, six or seven) ^{15}N, ^{13} C uniformly labeled amino acid residues scattered across the peptide sequence. Binding of Cu^{+2} ions or Al-citrate complexes to A$\beta_{(1-40)}$ fibrils was tested by either Electron Paramagnetic Resonance or by ^{27}Al MAS NMR (after incubation, samples were dialyzed in 1 kDa cut-off dialysis tubes to remove unbound ions or complexes). (See also Plate 1 on page XVII in the Color Plate Section.)

correlation spectra of uniformly labeled amino acid residues scattered across the peptide sequence [62].

(iv) Two short fragments of Aβ, Ac-$A\beta_{(16-22)}$-NH_2 (Ac-K_{16}LVFFAE_{22}-NH_2) and $A\beta_{(11-25)}$ also form amyloid fibrils at pH 7.4. However, $A\beta_{(16-22)}$ or $A\beta_{(11-25)}$ molecules are organized in in-register *anti-parallel* β-sheets which are stabilized by electrostatic interactions (for example, Lys16 and Glu22) as well as by hydrophobic interactions between side-groups of amino acid residues in the central region of the peptide, LVFFA [68,73].

(v) Peptide molecules in $A\beta_{(1-42)}$-fibrils form *parallel* in-register β-sheets as concluded from ^{13}C fp-RFDR-CT and $^{13}C\{^{15}N\}$-REDOR measurements on a single sample of $A\beta_{(1-42)}$ ^{13}C-labeled in Ala21 ($^{13}CH_3$) and Leu34(^{13}CO) positions and ^{15}N-labeled in Val40 [49].

(vi) $A\beta_{(10-35)}$ (NH_2-Y_{10}EVHHQKLVFFAEDVGS-NKGAIIGLM_{35}-NH_2) fibrils also form a *parallel* in-register β-sheet structure as has been earlier suggested by Meredith, Lynn, and Botto on the basis of 2Q-DRAWS solid-state NMR measurements [55–58]. Our fp-RFDR-CT, REDOR, and ^{13}C-MQ NMR data have confirmed this conclusion [49]. However, we suggest that the $A\beta_{(10-35)}$ laminates are folded between V24 and A30 amino acid residues (similar to $A\beta_{(1-40)}$ fibrils) [49] instead of an extended β-sheet structure originally proposed by Lynn, Meredith, and co-workers [74]. The folded structure does not contradict with 2Q-DRAWS and other solid-state NMR measurements since molecules build two parallel in-register β-sheets, while it also fits well with fibril dimensions estimated from TEM and to STEM mass-per-length measurements consistent with only two or four laminates in fibrils prepared at pH 3.8 and 7.4, respectively [49].

It is important to note that the central, mostly hydrophobic, region of Alzheimer's amyloid peptides is of particular importance for the formation and stability of amyloid fibrils [75]. Therefore, it can be appreciated that all point mutations found so far in $A\beta_{(1-40)}$ which are associated with an early-onset of dementia are either at amino acid residues next to the central hydrophobic region of the peptide, LVFFA or those replacing negatively charged Glu22 or Asp23 residues on neutral (E22Q, D23N), hydrophobic (E22G), or positively charged (E22K) residues. All these mutations would change the net charge of the peptide, changing its solubility at neutral pH, make the "folding" region of the peptide molecule more flexible (as in the "Arctic" mutation, E22G) or enlarge the central hydrophobic region of the peptide, which will additionally stabilize β-sheet secondary structure in amyloid fibrils.

Figure 1F also shows that another NMR active isotope, such as ^{27}Al ($I = 5/2$, 100% natural abundance) can be useful in studies of binding of various biologically relevant soluble aluminum complexes (for example, aluminum citrate species, which may pass the brain-blood-barrier [76]) to Aβ-oligomers and fibrils. It is well known in biochemistry and medicine that aluminum ions are highly toxic. A link between aluminum and AD has been extensively discussed since beginning of the 1980s when high concentrations of aluminum were detected for the first time in Alzheimer's neurofibrillary tangles and later also in amyloid plaquies [77,78]. However, exact mechanism, binding sites for aluminum ions and Al complexes on Aβ-peptides and other important features of Al–Aβ-interaction are still unknown. For example, different Al-citrate complexes at low concentrations can either accelerate or retard the aggregation kinetics of $A\beta_{(1-40)}$ and also stabilize certain polymorphs of Aβ fibrils [79].

Binding of Cu(II) ions to $A\beta_{(1-28)}$, $A\beta_{(1-40),}$ and $A\beta_{(1-42)}$ molecules [80,81] has been studied by another magnetic resonance method, electron spin resonance (ESR). Due to its high sensitivity, ESR is a very useful method in studies of metal-ion binding to Aβ. The effects of metal ions on $A\beta_{(1-40)}$ aggregation are currently widely discussed after the observation of co-localization of high concentrations of Al(III), Zn(II), Cu(II), and Fe(III) at the center of the core of Alzheimer's amyloid plaques [82]. These metal ions accelerate Aβ aggregation kinetics, may stabilize amyloid fibrils and also increase neurotoxic effects of Aβ peptides [83,84]. It has been also suggested by Bush and co-workers that Cu(II) and Zn(II) may induce Aβ to form allosterically ordered oligomers that can penetrate lipid membranes [80]: Cu(II) ion initially coordinates His6, His13, His14, and Tyr10 in one Aβ molecule (see Figure 1F) but subsequently can coordinate two peptide molecules stabilizing a dimer and facilitating further aggregation of Aβ. Coordination of Cu(II) with His13 and His14 in two neighboring $A\beta_{(1-40)}$ molecules would facilitate propagation and stabilization of amyloid fibrils with in-register parallel β-sheet arrangement as found in all known polymorphs of $A\beta_{(1-40)}$ fibrils by recent solid state NMR measurements discussed above. Thus, studies of complexation of metal ions with Aβ are important in the search for the causes of and potential treatments for AD.

In order to answer the questions formulated in this article more efforts must be directed towards determining the structure of different polymorphs of Aβ-fibrils and oligomers, the effects of point mutations, metal ions, and metal complexes on the aggregation kinetics of Aβ-peptides, the search for potential inhibitors [85] and finally neurotoxicity tests on nerve cells cultures. Solid-state NMR has been already proven as a powerful tool in structural studies on other amyloidogenic peptides [86,87].

Acknowledgments

O.N.A. acknowledges financial support from the Foundation to the memory of J.C. and Seth M. Kempe, the Swedish Foundation of International Cooperation in Research and Higher Education (STINT), the Swedish Research Council and the Swedish Alzheimer's Fund. Collaboration on these projects with R. Tycko, R.D. Leapman, J.J. Balbach, Y. Ishii, A. Petkova, N.W. Rizzo, N.A. Oyler, D.J. Gordon, S.C. Meredith, J. Reed, F. Dyda, F. Delaglio in the U.S.A., with M. Lindberg, N. Almqvist, M. Hellberg, N. Norlin, P. Eriksson, G. Gröbner, A. Filippov, A. Lund in Sweden, I. Tóth in Hungary, and R. Dupree, M. Smith, and A. Kukol in the U.K. are greatly acknowledged.

References

1. Alzheimer A. On a distinctive disease of the cerebral cortex. *Z. Psychiatry* 1907;64:146–148.
2. http://www.alzheimerforeningen.nu.
3. Selkoe DJ. Amyloid protein and Alzheimer's disease. Sci. Am. 1991;November:68–78.
4. Glenner GG, Wong CW. Alzheimer's disease: initial report of the purification and characterization of a novel cerebrovascular amyloid protein. Biochem. Biophys. Res. Commun. 1984;120:885–889.
5. Glenner GG, Wong CW. Alzheimer's disease and Down's syndrome: sharing of a unique cerebrovascular amyloid fibril protein. Biochem. Biophys. Res. Commun. 1984;122:1131–1135.
6. Masters CL, Multhaup G, Simms G, Pottgiesser J, Martins RN, Beyreuther K. Neuronal origin of a cerebral amyloid: neurofibrillary tangles of Alzheimer's disease contain the same protein as the amyloid of plaque cores and blood vessels. EMBO J. 1985;4:2757–2763.
7. Kang J, Lemaire H-G, Unterbeck A, Salbaum JM, Masters CL, Grzeschik K-H, Multhaup G, Beyreuther K, Müller-Hill B. The precursor of Alzheimer's disease amyloid A4 protein resembles a cell-surface receptor. Nature (London) 1987;325:733–736.
8. Shivers BD, Hilbich C, Multhaup G, Salbaum M, Beyreuther K, Seeburg PH. Alzheimer's disease amiloidogenic glycoprotein: expression pattern in rat brain suggests a role in cell contact. EMBO J. 1988;7(5):1365–1370.
9. Marx J. Alzheimer's debate boils over. Science 1992; 257: 1336–1338.
10. Dickson DW, Yen SH. Beta-amyloid deposition and paired filament formation: Which histopathological feature is more significant in Alzheimer's disease? Neurobiol. Aging 1989;10:402–404.
11. Terry RD, Masliah E, Salmon DP, Butters N, deTeresa R, Hill R, Katzman R. Physical basis of cognitive alterations in Alzheimer's disease: synapse loss is the major correlate of cognitive impairment. Ann. Neurol. 1991;30:572–580.
12. Selkoe DJ. Deciphering Alzheimer's disease: molecular genetics and cell biology yield major clues. J. NIH Res. 1995;April 7:57–64.
13. Kayed R, Head E, Thompson JL, McIntire TM, Milton SC, Cotman CW, Glabe ChG. Common structure of soluble amyloid oligomers implies common mechanism of pathogenesis. Science 2003;300:486–489.
14. Walsh DM, Klyubin I, Fadeeva JV, Cullen WK, Anwyl R, Wolfe MS, Rowan MJ, Selkoe DJ. Naturally secreted oligomers of amyloid β protein potently inhibit hippocampal long-term potentiation in vivo. Nature 2002;416:535–539.
15. Hendriks L, van Duijn CM, Cras P, Cruts M, Hul WV, van Harskamp F, Warren A, McInnis MG, Antonarakis SE, Martin J-J, Hofman A, Broeckhoven CV. Presenile dementia and cerebral haemorrhage linked to a mutation at codon 692 of the β-amyloid precursor protein gene. Nat. Genet. 1992;1:218–221.
16. Levy E, Carman MD, Fernandez-Madrid IJ, Power MD, Lieberburg I, van Duinen SG, Bots GthAM, Luyendijk W, Frangione B. Mutation of the Alzheimer's disease amyloid gene in hereditary cerebral hemorrhage, Dutch type. Science 1990;248:1124–1126.
17. Tagliavini F, Rossi G, Padovani A, Magoni M, Andora G, Sgarzi M, Bizzi A, Savoiardo M, Carella F, Morbin M, Giaccone G, Bugiani O. A new βPP mutation related to hereditary cerebral haemorrhage. Alz. Report 1999;2:S28.
18. Nilsberth C, Westlind-Danielsson A, Eckman ChB, Condron MM, Axelman K, Forsell Ch, Stenh Ch, Luthman J, Teplow DB, Yonkin SG, Näslund J, Lannfelt L. The 'Arctic' APP mutation (E693G) causes Alzheimer's disease by enhanced Aβ protofibril formation. Nature Neurosc. 2001;4(9):887–893.
19. Grabowski TJ, Cho HS, Vonsattel JPG, Rebeck GW, Greenberg SM. Novel amyloid precursor protein mutation in an Iowa family with dementia and severe cerebral amyloid angiopathy. Ann. Neurol. 2001;49:697–705.
20. Kirkitadze MD, Condron MM, Teplow DB. Identification and characterization of key kinetic intermediates in amyloid β-protein fibrillogenesis. J. Mol. Biol. 2001;312:1103–1119.
21. Antzutkin ON. Amyloidosis of Alzheimer's Aβ-peptides: solid-state nuclear magnetic resonance, electron paramagnetic resonance, transmission electron microscopy, scanning transmission electron microscopy and atomic force microscopy studies. Magn. Reson. Chem. 2004;42:231–246.
22. Hellberg M, Norlin N, Antzutkin ON, Almqvist N. Morphology and Growth Kinetics of Alzheimer's Amyloid β-peptides, $A\beta_{(1-40)}$ and the Arctic Mutation $A\beta_{(1-40)}$ (E22G): In Situ Atomic Force Microscopy Study. In: G Grateau, RA Kyle, M Skinner (Eds). Amyloid and Amyloidosis. CRC Press, Boca Raton, Florida, 2005, pp 408–410.
23. Sisodia SS, Koo EH, Beyreuther K, Unterbeck A, Price DL. Evidence that β-amyloid protein in Alzheimer's disease is not derived by normal processing. Science 1990;248:492–495.
24. Buxbaum JD, Gandy SE, Ciccetti P, Ehrlich ME, Czernik AJ, Fracasso RP, Ramabhadran TV, Unterbeck AJ, Greengard P. Processing of Alzheimer β/A4 amyloid precursor protein: modulation by agents that regulate protein phosphorylation. Proc. Natl. Acad. Sci. U.S.A. 1990;87:6003–6006.
25. Pike ChJ, Burdick D, Walencewicz AJ, Glabe GCh, Cotman CW. Neurodegeneration induced by β-amyloid peptides *in vitro*: the role of peptide assembly state. J. Neurosc. 1993;13(4):1676–1687.

26. Lorenzo A, Yankner B. β-amyloid neurotoxicity requires fibril formation and is inhibited by Congo red. Proc. Natl. Acad. Sci. U.S.A. 1994; 91: 12243–12247.
27. Howlett DR, Jennings KH, Lee DC, Clark MS, Brown F, Wetzel R, Wood SJ, Camilleri P, Roberts GW. Aggregation state and neurotoxic properties of Alzheimer beta-amyloid peptide. Neurodegeneration 1995;4:23–32.
28. Petkova AT, Leapman RD, Guo Z, Yau W-M, Mattson MP, Tycko R. Self-propagating, molecular-level polymorphism in Alzheimer's β-amyloid fibrils. Science 2005;307:262–265.
29. Seilheimer B, Bohrmann B, Bondolfi L, Müller F, Stüber D, Döbeli H. The toxicity of the Alzheimer's β-amyloid peptide correlates with a distinct fiber morphology. J. Struct. Biol. 1997;119:59–71.
30. Castaño EM, Ghiso J, Prelli F, Gorevic PD, Migheli A, Frangione B. *In vitro* formation of amyloid fibrils from two synthetic peptides of different lengths homologous to Alzheimer's disease β-protein. Biochem. Biophys. Res. Commun. 1986;141:782–789.
31. Gorevic PC, Castaño EM, Sarma R, Frangione B. Ten to fourteen residue peptides of Alzheimer's disease protein are sufficient for amyloid fibril formation and its characteristic X-ray diffraction pattern. Biochem. Biophys. Res. Commun. 1987;147:854–862.
32. Kirschner DA, Inouye H, Duffy LK, Sinclair A, Lind M, Selkoe DJ. Synthetic peptide homologous to β protein from Alzheimer disease forms amyloid-like fibers *in vitro*. Proc. Nat. Acad. Sci. U.S.A. 1987;84:6953–6957.
33. Halverson K, Fraser P, Kirschner DA, Lansbury PT Jr. Molecular determinants of amyloid deposition in Alzheimer's disease: conformational studies of synthetic β-protein fragments. *Biochemistry* 1990;29:2639–2644.
34. Fraser PE, Duffy LK, O'Malley MB, Nguyen JT, Inouye H, Kirschner DA. Morphology and antibody recognition of synthetic beta-amyloid peptides. J. Neurosci. Res. 1991;28:474–485.
35. Fraser PE, Nguyen JT, Surewicz WK, Kirschner DA. pH-dependent structural transitions of Alzheimer amyloid β/A4 peptides. Biophys. J. 1991;60:1190–1201.
36. Fraser PE, McLachlan DR, Surewicz WK, Mizzen CA, Snow AD, Nguyen JT, Kirschner DA. Conformation and fibrillogenesis of Alzheimer Aβ peptides with selected substitution of charged residues. J. Mol. Biol. 1994;244:64–73.
37. Hilbich C, Kisters-Woike B, Reed J, Masters CL, Beyreuthers K. Aggregation and secondary structure of synthetic amyloid βA4 peptides of Alzheimer's disease. J. Mol. Biol. 1991;218:149–163.
38. Hilbich C, Kisters-Woike B, Reed J, Masters CL, Beyreuthers K. Human and rodent sequence analogs of Alzheimer's amyloid βA4 share similar properties and can be solubilized in buffers of pH 7.4. Eur. J. Biochem. 1991;201:61–69.
39. Hilbich C, Kisters-Woike B, Reed J, Masters CL, Beyreuthers K. Substitutions of hydrophobic amino acids reduce the amyloidogenicity of Alzheimer's disease βA4 peptides. J. Mol. Biol. 1992;228:460–473.
40. Barrow CJ, Zagorski MG. Solution structures of β peptide and its constituent fragments: relation to amyloid deposition. Science 1991;253:179–182.
41. Barrow CJ, Yasuda A, Kenny PTM, Zagorski MG. Solution conformations and aggregational properties of synthetic amyloid β-peptides of Alzheimer's disease. Analysis of circular dichroism spectra. J. Mol. Biol. 1992;225:1075–1093.
42. Burdick D, Soreghan B, Kwon M, Kosmoski J, Knauer M, Henschen A, Yates J, Cotman C, Glabe C. Assembly and aggregation properties of synthetic Alzheimer's A4/β amyloid peptide analogs. J. Biol. Chem. 1992;267:546–554.
43. Malinchik SB, Inouye H, Szumowski KE, Kirschner DA. Structural analysis of Alzheimer's β(1–40) amyloid: protofilament assembly of tubular fibrils. Biophys. J. 1998; 74:537–545.
44. Serpell LC, Blake CCF, Fraser PE. Molecular structure of a fibrillar Alzheimer's Aβ fragment. Biochemistry 2000;39: 13269–13275.
45. Serpell LC, Smith JM. Direct visualization of the β-sheet structure of synthetic Alzheimer's amyloid. J. Mol. Biol. 2000;299:225–231.
46. Lansbury PT, Costa PR, Griffiths JM, Simon EJ, Auger M, Halverson KJ, Kocisko DA, Hendsch ZS, Ashburn TT, Spencer RGS, Tidor B, Griffin RG. Structural model for the β-amyloid fibril based on interstrand alignment of an antiparallel-sheet comprising a C-terminal peptide. Nat. Struct. Biol. 1995;2:990–998.
47. Kirschner DA, Abraham CR, Selkoe DJ. X-ray diffraction from intraneuronal paired helical filaments and extraneuronal amyloid fibers in Alzheimer disease indicated cross-β conformation. Proc. Nat. Acad. Sci. U.S.A. 1987;83:503–507.
48. Roher AE, Lowenson JD, Clarke S, Woods AS, Cotter RJ, Gowing E, Ball MJ. β-Amyloid-(1–42) is a major component of cerebrovascular amyloid deposits: implications for the pathology of Alzheimer disease. Proc. Nat. Acad. Sci. U.S.A. 1993;90:10836–10840.
49. Antzutkin ON, Leapman RD, Rizzo NW, Balbach JJ, Tycko R. Supramolecular structural constraints on Alzheimers β-amyloid fibrils from electron microscopy and solid state nuclear magnetic resonance. Biochemistry 2002;41:15436–15450.
50. Goldsbury CS, Wirtz S, Müller SA, Sunderji S, Wicki P, Aebi U, Frey P. Studies on the in vitro assembly of $A\beta_{(1-40)}$: Implications for the search for Aβ fibril formation inhibitors. J. Struc. Biol. 2000;130:217–231.
51. Engel A, Baumeister W, Saxton WO. Mass mapping of a protein complex with the scanning transmission electron microscope. Proc. Natl. Acad. Sci. U.S.A. 1982;79:4050–4054.
52. Wall JS, Hainfeld JF. Mass mapping with the scanning transmission electron microscope. Ann. Rev. Biophys. Biophys. Chem. 1986;15:355–376.
53. Müller SA, Goldie KN, Burki R, Haring R, Engel A. Factors influencing the precision of quantitative scanning transmission electron microscopy. Ultramicroscopy 1992;46:317–334.
54. Thomas D, Schultz P, Steven AC, Wall JS. Mass analysis of biological macromolecular complexes by STEM. Biol. Cell 1994;80:181–192.
55. Benzinger TLS, Gregory DM, Burkoth TS, Miller-Auer H, Lynn DG, Botto RE, Meredith SC. Propagating structure

of Alzheimer's β-amyloid$_{(10-35)}$ is parallel β-sheet with residues in exact register. Proc. Natl. Acad. Sci. U.S.A. 1998;95:13407–13412.

56. Gregory DM, Benzinger TLS, Burkoth TS, Miller-Auer H, Lynn DG, Meredith SC, Botto RE. Dipolar recoupling NMR of biomolecular self-assemblies: determining inter- and intrastrand distances in fibrilized Alzheimer's β-amyloid peptide. Solid State Nucl. Magn. Reson. 1998;13:149–166.
57. Burkoth TS, Benzinger TLS, Urban V, Morgan DM, Gregory DM, Thiyagarajan P, Botto RE, Meredith SC, Lynn DG. Structure of the β-amyloid(10–35) fibril. J. Am. Chem. Soc. 2000;122:7883–7889.
58. Benzinger TLS, Gregory DM, Burkoth TS, Miller-Auer H, Lynn DG, Botto RE, Meredith SC. Two-dimensional structure of β-amyloid(10–35) fibrils. Biochemistry 2000;39:3491–3499.
59. Antzutkin ON. Molecular structure determination: Applications in biology. In: MJ Duer (Ed). Solid State Nuclear Magnetic Resonance Spectroscopy, Principles and Application, Blackwell Science: Oxford, 2002, pp 280–390.
60. Tycko R. Insight into amyloid folding problem from solid-state NMR. Biochemistry 2003;42(11):3151–3159.
61. Tycko R. Application of Solid State NMR to the Structural Characterization of Amyloid Fibrils: Methods and Results. Prog. Nucl. Magn. Reson. Spectr. 2003; 42:53–68.
62. Petkova AT, Ishii Y, Balbach JJ, Antzutkin ON, Leapman RD, Delaglio F, Tycko R. A structural model for Alzheimer's β-amyloid fibrils based on experimental constraints from solid state NMR. Proc. Nat. Acad. Sci. U.S.A. 2002;99(2):16742–16747.
63. Antzutkin ON, Tycko R. High-order multiple quantum excitation in ^{13}C nuclear magnetic resonance spectroscopy of organic solids. J. Chem. Phys. 1999;110(6):2749–2752.
64. Antzutkin ON, Balbach JJ, Leapman RD, Rizzo NW, Reed J, Tycko R. Multiple quantum solid state NMR indicates a parallel, not antiparallel, organization of β-sheets in Alzheimer's β-amyloid fibrils. Proc. Nat. Acad. Sci. U.S.A. 2000;97(24):13045–13050.
65. Ishii Y, Balbach JJ, Tycko R. Measurement of dipole-coupled lineshapes in a many-spin system by constant-time two-dimensional solid state NMR with high-speed magic-angle-spinning. Chem. Phys. 2001;266:231–236.
66. Balbach JJ, Petkova AT, Oyler NA, Antzutkin ON, Gordon DJ, Meredith SC, Tycko R. Supramolecular structure in full-length of Alzheimer's β-amyloid fibrils: Evidence for a parallel β-sheet organization from solid state Nuclear Magnetic Resonance. Biophys. J. 2002;83(2):1205–1216.
67. Weliky DP, Tycko R. Determination of peptide conformations by two-dimensional magic angle spinning NMR exchange spectroscopy with rotor synchronization. J. Am. Chem. Soc. 1996;118:8487–8488.
68. Balbach JJ, Ishii Y, Antzutkin ON, Leapman RD, Rizzo NW, Dyda F, Reed J, Tycko R. Amyloid fibril formation by Aβ$_{(16-22)}$, a seven-residue fragment of the Alzheimer's β-amyloid peptide, and structural characterization by solid state NMR. Biochemistry 2000;39(45):13748–13759.
69. Antzutkin ON, Balbach JJ, Tycko R. Site-specific identification of non-β-strand conformations in Alzheimer's β-amyloid fibrils by solid state NMR. Biophys. J. 2003;84(5):3326–3335.
70. Blanco FJ, Tycko R. Determination of peptide backbone dihedral angles in solid-state NMR by double quantum ^{13}C chemical shift anisotropy measurements. J. Magn. Reson. 2001;149:131–138.
71. Tycko R. Selection rules for multiple quantum NMR excitation in solids: derivation from time-reversal symmetry and comparisons with simulations and ^{13}C NMR experiments. J. Magn. Reson. 1999;139:302–307.
72. Oyler NA, Tycko R. Multiple quantum ^{13}C NMR spectroscopy in solids under high-speed magic-angle-spinning. J. Phys. Chem. B 2002;106:8382–8389.
73. Petkova AT, Buntkowsky G, Dyda F, Leapman RD, Yau W-M, Tycko R. Solid state NMR reveals a pH-dependent antiparallel β-sheet registry in fibrils formed by a β-amyloid peptide. J. Mol. Biol. 2004;335:247–260.
74. Lynn DG, Meredith SC. Review: model peptides and the physicochemical approach to β-amyloids. J. Struc. Biol. 2000;130:153–173.
75. Tjernberg LO, Näslund J, Lindqvist F, Johansson J, Karlström AR, Thyberg J, Terenius L, Nordstedt C. Arrest of β-amyloid fibril formation by a pentapeptide ligand. J. Biol. Chem. 1996;271(15):8545–8548.
76. Slanina P, Falkeborn Y, Frech W, Cedergren A. Aluminium concentrations in the brain and bone of rats fed citric acid, aluminium citrate or aluminium hydroxide. Fd. Chem. Toxic. 1984;22:391–397.
77. Exley Ch. The aluminium-amyloid cascade hypothesis and alzheimer's disease. In R Harris, F Fahrenholz (Eds). Alzheimer's Disease: Cellular and Molecular Aspects of Amyloid beta, Series: Subcellular Biochemistry, Vol. 38, 225–234.
78. Exley Ch, Korchazhkina O. The association of aluminium and β amyloid in Alzheimer's disease. In: Ch Exley (Ed). Aluminium and Alzheimer's disease. The science that describes the link. Elsevier Science B. V., Amsterdam, The Netherlands, 2001, pp 421–433.
79. Antzutkin ON, Norlin N, Hellberg M, Eriksson P, Almqvist N, Leapman RD, Tycko R, Petkova AT, Tóth I, Howes AP, Dupree R. Binding of aluminium(III)-citrate complexes, $[Al_3(H_{-1}Cit)_3(OH)]^{-4}$ and $[Al_3(H_{-1}Cit)_3(OH)_4]^{-7}$, to alzheimer's Aβ peptides: In situ atomic force, electron microscopy and solid state ^{13}C and ^{27}Al MAS NMR studies. Sixth Keele Meeting "Aluminium, Lithosphere to Biosphere (and Back)", Buçaco, Portugal, February 26 to March 2, 2005.
80. Curtain CC, Ali FE, Volitakis I, Cherny RA, Norton RS, Beyreuther K, Barrow CJ, Masters CL, Bush AI, Barnham KJ. Alzheimer's disease amyloid-β binds copper and zinc to generate an allosterically ordered membrane-penetrating structure containing superoxide dismutase-like subunits. J. Biol. Chem. 2001;276(23):20466–20473.
81. Curtain CC, Ali FE, Smith DG, Bush AI, Masters CL, Barnham KJ. Metal ions, pH, and cholesterol regulate the interactions of Alzheimer's disease amyloid-β peptide with membrane lipid. J. Biol. Chem. 2003;278(5):2977–2982.
82. Lovell MA, Robertson JD, Teesdale WJ, Campbell JL, Markesbery WR. Copper, iron and zinc in Alzheimer's disease senile plaques. J. Neurol. Sci. 1998;158:47–52.

83. Mantyh PW, Ghilardi JR, Rogers S, DeMaster E, Allen CJ, Stimson ER, Maggio JE. Aluminium, iron, and zinc ions promote aggregation of physiological concentrations of beta-amyloid peptide. J. Neurochem. 1993;61:1171–1174.
84. Atwood CS, Moir RD, Huang X, Scarpa RC, Bacarra NME, Romano DM, Hartshorn MA, Tanzi RE, Bush AI. Dramatic aggregation of Alzheimer Aβ by Cu(II) is induced by conditions representing physiological acidosis. J. Biol. Chem. 1998;273:12817–112826.
85. Gordon DJ, Meredith SC. Probing the role of backbone hydrogen bonding in β-amyloid fibrils with inhibitor peptides containing ester bonds at alternate positions. Biochemistry 2003;42:475–485.
86. Naito A, Kamihira M, Inoue R, Saitô H. Structural diversity of amyloid fibril formed in human calcitonin as revealed by site-directed ^{13}C solid-state NMR spectroscopy. Magn. Reson. Chem. 2004;42:247–257.
87. Jaroniec CP, MacPhee CE, Bajaj VS, McMahon MT, Dobson CM, Griffin RG. High-resolution molecular structure of a peptide in an amyloid fibril determined by magic angle spinning NMR spectroscopy. Proc. Natl. Acad. Sci. U.S.A. 2004;101:711.

Chemical Shifts and Spin-Couplings

^{13}C, ^{15}N, ^{1}H, ^{2}H, and ^{17}O NMR Chemical Shift NMR for Hydrogen Bonds

Shigeki Kuroki
Department of Chemistry and Materials Science, Tokyo Institute of Technology, Ookayama, Meguro-ku, Tokyo 152-8552, Japan

Introduction

Hydrogen bonding plays an important role in forming higher-order structures of peptides, polypeptides and proteins. Accordingly, the nature of the hydrogen bond has been widely studied by various spectroscopic methods. High-resolution NMR spectroscopy has been used as one of the most powerful methods for obtaining useful information on the details of the hydrogen-bonded structure.

NMR chemical shifts are one of the most important parameters for providing information about molecular structure. Since the electronic structure around the carbonyl-carbon and oxygen, amide-nitrogen and hydrogen atoms in peptides and polypeptides is greatly affected by the nature of the hydrogen bond, the NMR chemical shifts for these atoms are sensitive to the spatial arrangement of the nuclei comprising the hydrogen bond. Also the electritic gradient (*eq*), which determined by the NMR spectrum of quadrupdan nucleus, is greatly affected by the electronic structure around the hydrogen bond.

Here, recent studies on the hydrogen-bonded structures of peptides and polypeptides in the solid state are presented through the observation of ^{13}C, ^{15}N, ^{1}H, ^{2}H, and ^{17}O NMR chemical shifts and theoretical calculations of nuclear shielding with a view to find a deeper understanding of the nature and inference of hydrogen bonds.

Hydrogen-bonded Structure and ^{13}C Chemical Shift [1–4]

Hydrogen-Bond Length and the ^{13}C Isotropic Chemical Shift (δ_{iso}) of the Carbonyl-Carbon in Several Amino Acids

At first, the relationship between the isotropic ^{13}C chemical shifts of carbonyl-carbons and the hydrogen-bonded structure is discussed. Figure 1 shows the plot of the observed isotropic ^{13}C chemical shifts (δ_{iso}) for the carbonyl-carbon in Gly, L-Ala, L-Val, D,L-Leu, and L-Asp residues in peptides against the $\mathrm{N}\cdots\mathrm{O}$ hydrogen-bond length($R_{\mathrm{N}\ldots\mathrm{O}}$). It is found that a decrease in $R_{\mathrm{N}\ldots\mathrm{O}}$ leads to a higher frequency shift, and there exists approximately a linear relationship between the ^{13}C chemical shift and $R_{\mathrm{N}\ldots\mathrm{O}}$. It is noted that not only in oligopeptides (dimer or trimer) but also in polypeptides, the carbonyl-carbon chemical shifts give a similar hydrogen-bond length dependence. This suggests that the ^{13}C chemical shifts of the carbonyl-carbon taking the hydrogen-bond, which is formed between the amide >C=O and amide >N–H, are predominantly determined by the hydrogen-bond length. The slope of this linear relationship is quite characteristic of individual amino acid residues.

Hydrogen-Bond Length and the Principal Values(δ_{11}, δ_{22} and δ_{33}) of the Carbonyl-Carbon

It is expected that the principal values of the ^{13}C chemical shift tensors (δ_{11}, δ_{22} and δ_{33}, from higher to lower frequency) are, in principle, more sensitive as parameters for obtaining detailed information on hydrogen-bonding to be related with electronic structure, than will the isotropic ^{13}C chemical shift ($\delta_{\mathrm{iso}} = (\delta_{11} + \delta_{22} + \delta_{33})/3$). It is well known that δ_{11} is in the amide sp^2 plane and lies along the direction normal to the C=O bond, the δ_{22} component lies almost along the amide C=O bond, and the δ_{33} component is aligned perpendicular to the amide sp^2 plane.

From the plots of the observed principal values of the ^{13}C chemical shift tensors such as δ_{11}, δ_{22} and δ_{33} for Gly, L-Ala, L-Val, D, L-Leu, and L-Asp residues in peptides against the $\mathrm{N}\cdots\mathrm{O}$ hydrogen-bond length ($R_{\mathrm{N}\ldots\mathrm{O}}$), it is found that the experimental δ_{22} values are the most sensitive to $R_{\mathrm{N}\ldots\mathrm{O}}$, and the δ_{22} values move linearly to high frequency with a decrease of $R_{\mathrm{N}\ldots\mathrm{O}}$. The δ_{22} component lies almost along the amide C=O bond, so the δ_{22} values are the most sensitive to a changing in $R_{\mathrm{N}\ldots\mathrm{O}}$. The slope and intercept of the variation of the plot ofδ_{22} against $R_{\mathrm{N}\ldots\mathrm{O}}$ varies depending on the amino acid residues. The δ_{11} and δ_{33} values are insensitive to a change in $R_{\mathrm{N}\ldots\mathrm{O}}$, but it seems that the δ_{11} and δ_{33} values move slightly to low and to high frequencies with a decrease in $R_{\mathrm{N}\ldots\mathrm{O}}$, respectively. Therefore, it can be said that the large high-frequency shift in δ_{iso}, with a decrease in $R_{\mathrm{N}\ldots\mathrm{O}}$, is predominantly governed by a decrease in δ_{22}. To understand the relationship between the ^{13}C chemical shifts and hydrogen-bond length, some theoretical MO calculations on the

Graham A. Webb (ed.), Modern Magnetic Resonance, 31–35.
© 2008 *Springer.*

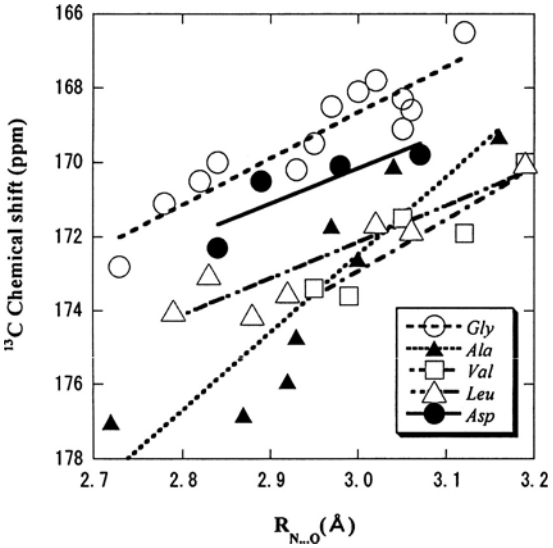

Fig. 1. Plots of the observed isotropic ^{13}C chemical shifts (δ_{iso}) for the carbonyl-carbon in Gly, L-Ala, L-Val, D, L-Leu, and L-Asp residues in peptides against the N *cdots* O hydrogen-bond length($R_{N...O}$).

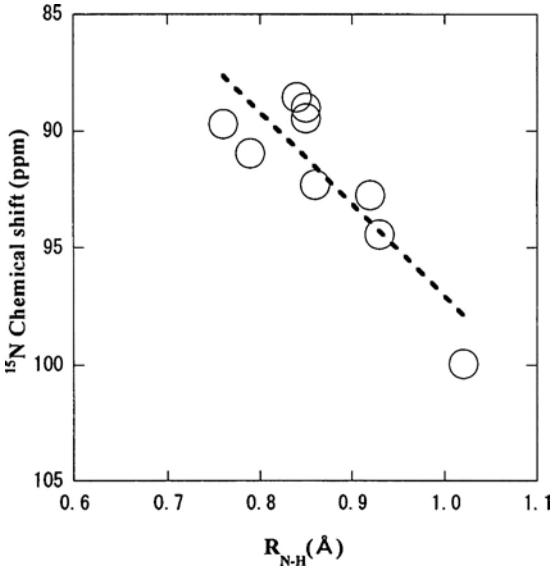

Fig. 2. Plot of the observed ^{15}N chemical shifts of the glycine residue in X-Gly-Gly against the N–H bond length (R_{N-H}) associated with a hydrogen bond.

^{13}C shielding tensors of model peptides have been carried out. From the calculations, it is found that δ_{22} is the most sensitive to a change of $R_{N...O}$ and moves linearly to high-frequency with a decrease in $R_{N...O}$. Correspondingly, δ_{11} increases with a decrease in $R_{N...O}$, whereas δ_{33} is insensitive to changes in $R_{N...O}$. The results of the theoretical calculations agree well with the experimental results. Such an agreement indicates that the ^{13}C chemical shift changes originate predominately from the change of the electronic state of the amino carbonyl groups caused by the hydrogen-bond length variation. Further, it can be said that the amino acid residue dependence of the calculated tensor components is similar to the experimental one.

Hydrogen-bonded Structure and ^{15}N NMR Chemical Shift

High-resolution ^{15}N NMR spectroscopy has been increasingly applied to the investigation of peptides, polypeptides and proteins in the solid state[5,6]. It is expected that a similar hydrogen-bond length dependence of the ^{13}C-carbonyl-carbon chemical shifts will aply to the amide nitrogen ^{15}N chemical shifts. But, there is no clear relationship between the observed ^{15}N chemical shifts of the Gly NH of peptides against the N$\cdots$O hydrogen-bond length ($R_{N...O}$).

The plot of the observed ^{15}N chemical shifts of the glycine residue in X-Gly-Gly against the N–H bond length (R_{N-H}) associated with a hydrogen bond is shown as in Figure 2. It is found that there is a clear relationship between these parameters and the decrease of R_{N-H} leads to a linear increase in shielding. Amide ^{15}N chemical shifts are closely related to the length of the N–H bond but are not related to $R_{N...O}$ distance. This implies that the ^{15}N chemical shift value gives useful information about the length of N–H bonds. It seems that the hydrogen bond angle ($\angle$N–H$\cdots$O) is also related to the ^{15}N chemical shift.

Theoretical calculations of ^{15}N chemical shift shows that a decrease of R_{N-H} leads to an increase of the calculated ^{15}N isotropic shielding which agrees with the experimental results. Therefore, such a relationship suggests that the isotropic ^{15}N chemical shift value can be used in the estimation of R_{N-H}. Combined with the carbonyl ^{13}C chemical shifts we can get very useful information about the hydrogen-bonded structure.

Hydrogen-bonded Structure and ^{1}H NMR Chemical Shift

The chemical shift of a ^{1}H nucleus has been widely applied to many works on the hydrogen bonding studies of peptides and proteins in the solution state.[7,8] However, in the solution state, the ^{1}H chemical shifts of peptides with rotational isomers are often the averaged values for all isomers because of rapid inversion by rotation about bonds and further are strongly influenced by solvent, pH, etc. Therefore, it is not easy to separate only the hydrogen-bonding effect on the ^{1}H chemical shift. In the solid state, chemical shifts provide information on fixed conformations and of hydrogen-bonded structures. But, in the solid state there are few studies on the high-resolution ^{1}H NMR of amide protons in peptides and polypeptides. One of the main reasons is the very large dipolar interaction of ^{1}H nuclei, which leads to a large broadening of the spectral line.

The problem is how to eliminate these dipolar interactions. The most popular method is combined rotational and multi-pulse spectroscopy (CRAMPS) with magic angle spinning (MAS).[9] One of the typical homo-nuclear dipolar decoupling sequence to be used in the CRAMPS experiments is br24. Although the conventional CRAMPS experiments have been made with a relatively low spinning rate of ∼3 kHz, this MAS rate is not always enough for the removal of dipolar couplings between protons and other nuclei. This is true for the amide proton of peptides and polypeptides bonded directly to the ^{14}N nucleus considered under here.

It is possible to eliminate this dipolar interaction between the amide ^{1}H bonded directly to the ^{14}N nucleus by high speed MAS such as 30 kHz and the observation at a high frequency such as 800 MHz. This procedure permits one to obtain, very high-resolution, ^{1}H spectra of peptides and polypeptides.

Figure 3 shows the observed amide proton chemical shifts plotted against the hydrogen-bond length between the amide nitrogen and oxygen atoms ($R_{N...O}$). It is shown that the ^{1}H chemical shift values move to high frequency with a decrease in $R_{N...O}$. This means that the observation of the amide proton ^{1}H chemical shift value leads to the determination of $R_{N...O}$. From neutron diffraction and *ab initio* MO studies it is shown that the reduction of $R_{N...O}$ leads to a decrease in the hydrogen-bond length ($R_{H...O}$) between the amide proton and the carbonyl oxygen. Thus, it can be said that the ^{1}H chemical shift values move to high frequency with a decrease in $R_{H...O}$.

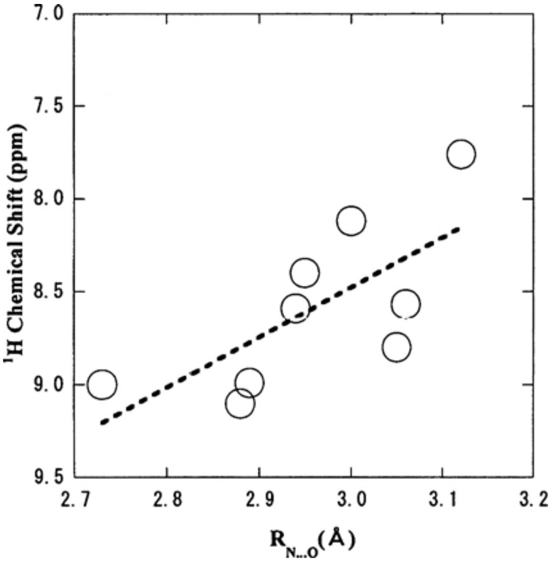

Fig. 3. Plot of the observed amide ^{1}H chemical shifts against the N · · · O hydrogen-bond length($R_{N...O}$).

Hydrogen-bonded Structure and ^{17}O NMR Quadrupolar Coupling Constant and Chemical Shift[10−13]

The oxygen atom is also one of the most important one forming hydrogen-bonded structures in peptides and polypeptides. Nevertheless, solid-state ^{17}O NMR studies of peptides and polypeptides have not been carried out due to the very weak sensitivity of the solid-state ^{17}O NMR measurements which arises from the fact that the ^{17}O nucleus has a very low natural abundance of 0.037 %, and that the ^{17}O nuclear spin quantum number (I) is 5/2, thus the nucleus is quadrupolar, and the ^{17}O signal is broadened by nuclear quadrupolar effects in the solid. Solid-state ^{17}O NMR spectra of Poly(Gly) form I (PG I),Poly(Gly) form II (PG II), glycylglycine (GlyGly) and glycylglycine nitrate(GlyGly·HNO_3) are discussed with a view to understand the relationship between the hydrogen-bonded structure and the ^{17}O NMR parameters.

Figure 4(a) shows a plot of the observed quadrupolar coupling constant (e^2qQ/h) values against the hydrogen bond length ($R_{N...O}$). The e^2qQ/h values decrease linearly with a decrease of $R_{N...O}$ between the amide nitrogen and oxygen atoms. This change comes from a change of the q values which are the largest component of the electric gradient tensor. This experimental result shows that the decrease in the hydrogen bond length leads to a decrease in the electric field gradient. The q value seems to be very sensitive to the hydrogen-bonding length change. The results of theoretical MO calculations agree well with these experimental results.

Figure 4(b) shows the plot of the observed isotropic ^{17}O chemical shift (δ_{iso}) values against the hydrogen bond length ($R_{N...O}$). The isotropic ^{17}O chemical shift (δ_{iso}) values in both peptides and polypeptides move to low frequencies with a decrease in the hydrogen bond length ($R_{N...O}$). The difference of the chemical shifts between peptides and polypeptides comes from the geometrical location of the amide group and the carbonyl group which forms hydrogen-bonding. From the plots of the observed principal values (δ_{11}, δ_{22} and δ_{33}, from higher to lower

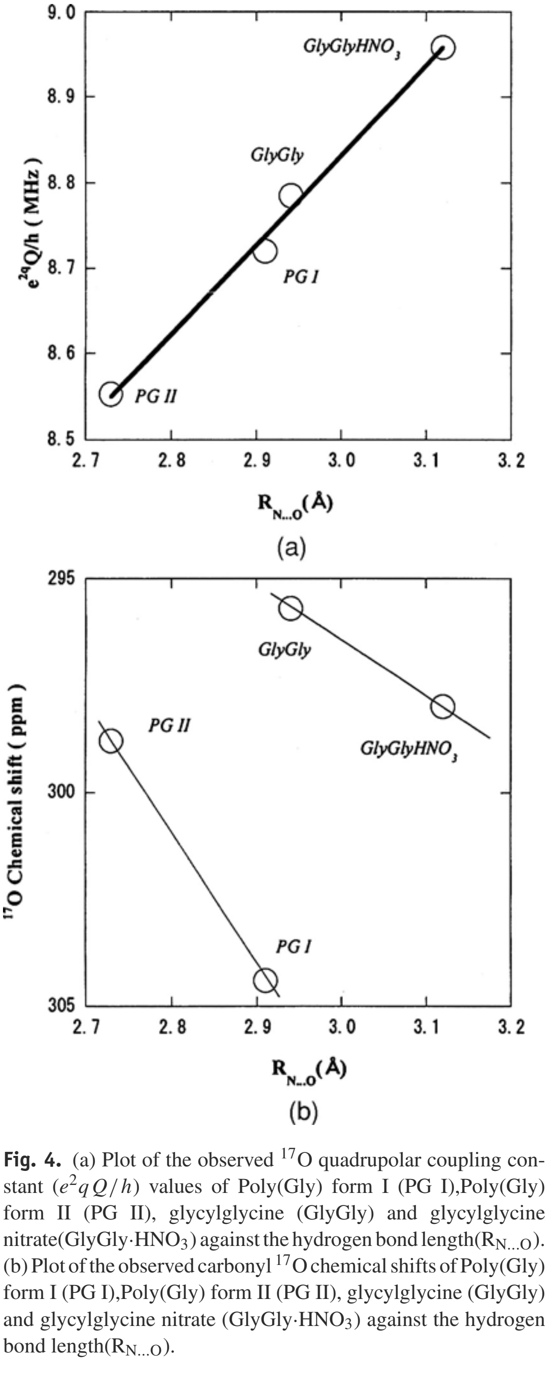

(a)

(b)

Fig. 4. (a) Plot of the observed ^{17}O quadrupolar coupling constant (e^2qQ/h) values of Poly(Gly) form I (PG I),Poly(Gly) form II (PG II), glycylglycine (GlyGly) and glycylglycine nitrate(GlyGly·HNO_3) against the hydrogen bond length($R_{N...O}$). (b) Plot of the observed carbonyl ^{17}O chemical shifts of Poly(Gly) form I (PG I),Poly(Gly) form II (PG II), glycylglycine (GlyGly) and glycylglycine nitrate (GlyGly·HNO_3) against the hydrogen bond length($R_{N...O}$).

frequency) of the ^{17}O chemical shifts against the hydrogen bond length ($R_{N...O}$), every principal value in both the peptides and polypeptides moves to low-frequency with a decrease in the hydrogen bond length ($R_{N...O}$). The hydrogen bond length dependence of the calculated isotropic chemical shielding (δ_{iso}) of the Gly carbonyl oxygen in the model molecule system shows that the ^{17}O chemical shift moves largely to low-frequency with an increase in $R_{N...O}$. This explains qualitatively the experimental trend as mentioned above.

Hydrogen-bonded Structure and ^{2}H Quadrupolar Coupling Constant[13]

The ^{2}H nucleus of an amide group in which ^{1}H is substituted by ^{2}H is one of the most important nuclei involved in a hydrogen-bonded structure in peptides and polypeptides.

In Figure 5, the plots of the observed e^2qQ/h values for ^{2}H against the hydrogen bond length ($R_{N...O}$) are shown. The e^2qQ/h value decreases with a decrease in $R_{N...O}$. The experimental result shows that the reduction of the hydrogen-bond length leads to a linear decrease in electritic field gradient (eq). The eq value is very sensitive to change in the hydrogen bond length. This experimental finding is consistent with the experimental results

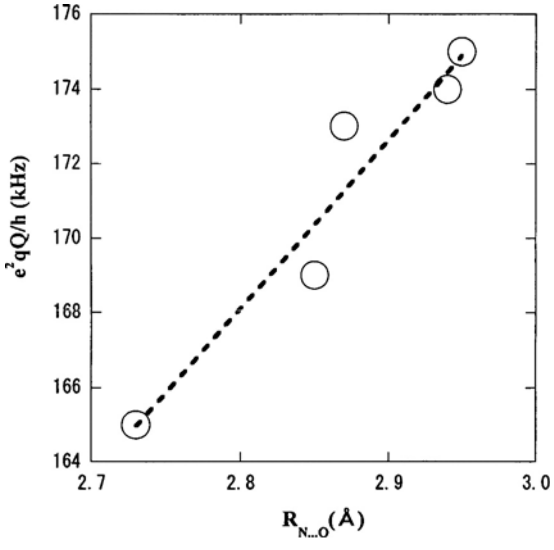

Fig. 5. Plots of the observed ^{2}H quadrupolar coupling constant e^2qQ/h values against the hydrogen bond length ($R_{N...O}$).

of the hydrogen-bonded amide ^{17}O nucleus of peptides and polypeptides and of other deuterium containing compounds. From this relationship, it is apparent that useful information about the hydrogen-bond length in peptides and polypeptides can be obtained by observation of the e^2qQ/h value.

Conclusion

As discussed, it is concluded that solid state ^{13}C, ^{15}N, ^{1}H, ^{2}H, and ^{17}O NMR spectroscopy combined with theoretical MO calculations is a very useful methodology for elucidating the hydrogen-bonded structures of peptides and polypeptides in the solid state.

References

1. Ando S, Ando I, Shoji A, Ozaki T, J. Am. Chem. Soc. 1988; 110:3380.
2. Asakawa N, Kuroki S, Kurosu H, Ando I, Shoji A, Ozaki T, J. Am. Chem. Soc. 1992;114:3261.
3. Tsuchiya K, Takahashi A, Takeda N, Asakawa N, Kuroki S, Ando I, Shoji A, Ozaki T, J. Mol. Struct. 1995;350:233.
4. Kameda T, Takeda N, Kuroki S, Kurosu H, Ando I, Shoji A, Ozaki T, J. Mol. Struct. 1995;384:178.
5. Kuroki S, Ando S, Ando I, Shoji A, Ozaki T, Webb GA, J. Mol. Struct. 1990; 240: 19.
6. Kuroki S, Asakawa N, Ando S, Ando I, Shoji A, Ozaki T, J. Mol. Struct. 1991;245:69.
7. Yamauchi K, Kuroki S, Fujii K, Ando I, Chem. Phys. Lett. 2000;324:435.
8. Hori S, Yamauchi K, Kuroki S, Ando I. Inter. J. Mol. Sci. 2002;1:8.
9. Shoji A, Kimura H, Ozaki T, Sugisawa H, Deguchi K, Am. Chem. Soc. 1996;118:7604.
10. Kuroki S, Takahashi A, Ando I, Shoji A, Ozaki T, J. Mol. Struct. 1994;323:197.
11. Takahashi A, Kuroki S, Ando I, Ozaki T, Shoji A, J. Mol. Struct. 1998;422:195.
12. Yamauchi K, Kuroki S, Ando I, Ozaki T, Shoji A, Chem. Phys. Lett. 1999;302:331.
13. Yamauchi K. Kuroki S, Ando I, J. Mol. Struct. 2002;602–603:171.
14. Ono S, Taguma T, Kuroki S, Ando I, Kimura H, Yamauchi K, J. Mol. Struct. 2002;602–603:49.

NMR Chemical Shift Map

Isao Ando[1] and Tetsuo Asakura[2]
[1]Department of Chemistry and Materials Science, Tokyo Institute of Technology, Ookayama, Meguro-ku, Tokyo 152-0033, Japan; and
[2] Department of Biotechnology, Tokyo University of Agriculture and Technology, Koganei, Tokyo 184-8588, Japan

Most recently, the concept of an NMR chemical shift map has been used to characterize the conformation of synthetic polypeptides and the conformation of any specified amino acid residues of proteins. Here, we are concerned with the chemical shift map as established by a theoretical approach and experimental approach. The amino acid residues except for the proline amino acid residue have the freedom of internal rotation about the two consecutive bonds, NH–C_αHR and C_αHR–CO bonds, where R is the side chain. These torsional angles are defined by Φ and Ψ, respectively. It is very convenient to represent the chemical shift of the amino acid residue as a function of the torsional angles (Φ, Ψ), because the conformation-dependent chemical shift can be obtained and then the conformation can be determined through the chemical shift value. This is the so-called "chemical shift contour map" or "chemical shift map." This has similar significance to the Ramachandran map for the conformational energy of amino acid residues.

First, we are concerned with the theoretical approach for establishing the concept of an NMR chemical shift map. In the crystalline state polymer chains assume a fixed conformation. In this case, the structural information obtained from the chemical shift corresponds to the fixed conformation [1]. The calculation of ^{13}C chemical shifts for dipeptide fragments (N-acetyl-N′-methyl-L-alanine amide) [Ac-L-Ala-NHMe] of poly (L-alanine) and the L-alanine residue containing proteins has been attempted using the finite perturbation theory (FPT) method for chemical shift within the semi-empirical MO framework [2] in order to understand and predict the ^{13}C chemical shift behavior of polypeptides associated with the secondary structures such as the α-helix form, the β-sheet form, etc., and the determination of secondary structure through the observation of the ^{13}C chemical shift [1]. The observed ^{13}C chemical shifts of the C_β carbon of the L-Ala residue in various peptides and polypeptides vary significantly depending on the conformation, which may be the right-handed α-helix form, β-sheet form, or another form. Such sizeable displacements of the ^{13}C chemical shifts can be characterized by variations in the electronic structures of the local conformation as defined by the torsion angles (Φ, Ψ). The chemical shift maps for the C_β and C_α carbons have been made on the basis of the calculated data. From these maps, we can estimate semi-quantitatively the ^{13}C shielding for any specified conformation. This is a very useful representation of the chemical shift behavior resulting from changing the dihedral angles as in a Ramachandran energy map. It has been demonstrated from comparisons of the experimental data and the predicted values given by this chemical shift map that the map successfully predicts the ^{13}C chemical shifts of L-alanine residues in polypeptides and proteins [1–5].

More sophisticated *ab initio* calculations for the NMR chemical shifts have become available for medium-size molecules as a consequence of the remarkable advances in performance of workstations, personal computers, and supercomputers [3–5]. This leads to a quantitative discussion of the chemical shift behavior. From such a situation, the ^{13}C chemical shift map was made by *ab initio* MO calculations with the 4-31G basis set using the GIAO-CHF (gauge-independent atomic-orbital coupled Hartree–Fock) method on N-acetyl-N′-methyl-L-alanine amide as shown in Figure 1 [3], which is the same model molecule as used in the case of the above FPT calculations. All the geometrical parameters are energy-optimized. The isotropic ^{13}C chemical shift map of the C_β carbon as a function of the torsion angles was calculated as shown in Figure 1, where the positive sign indicates an increase in shielding and the calculated ^{13}C shielding of methane is 207.2 ppm and the observed ^{13}C chemical shift is −2.1 ppm relative to TMS. The overall trend of this map is similar to that obtained by the FPT method. The calculated isotropic shielding constant (σ) for the C_β carbon is 186.4 ppm for the torsion angles (Φ, Ψ), corresponding to the anti-parallel β (β_A)-sheet form, 189.4 ppm for the right-handed α(α_R)-helix form, 189.6 ppm for the left-handed α(α_L)-helix form as shown in Figure 1 (In Table 1 the calculated shieldings are converted to chemical shifts relative to TMS. Thus, the chemical shift values for the β_A-sheet form, the α_R-helix form, and the α_L-helix form become 18.74, 15.72, and 15.4 ppm, respectively.). On the other hand, the observed isotropic chemical shifts (δ) are 21.0 ppm for the β_A-sheet form, 15.5 ppm for the α_R-helix form, and 15.9 ppm for the α_L-helix form (Table 2). Such an experimental chemical shift behavior is well explained

Graham A. Webb (ed.), Modern Magnetic Resonance, 37–42.
© 2008 *Springer.*

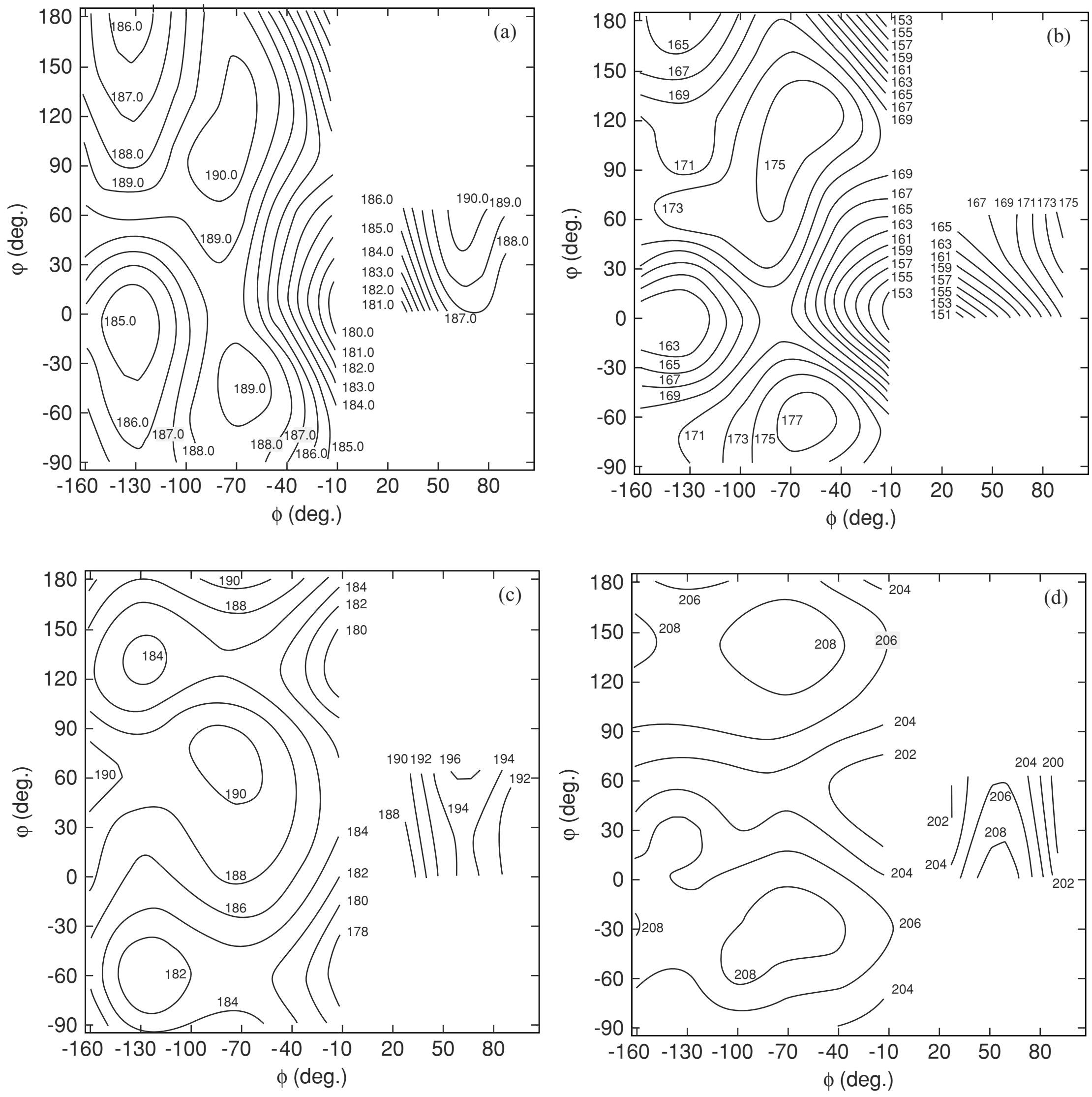

Fig. 1. The calculated ^{13}C chemical shift map of the C$_\beta$ and carbons of N-acetyl-N′-methyl-L-alanine amide by using the GIAO-CHF method with 4-31G *ab initio* MO basis sets. The 4-31G optimized geometries for the peptide were employed. (a) isotropic; (b) σ_{11}; (c) σ_{22} and (d) σ_{33} for the C$_\beta$ carbon(in ppm), and (e) isotropic; (f) σ_{11}; (g) σ_{22} and (h) σ_{33} for the C$_\alpha$ carbon(in ppm).

by the calculated behavior. It is found that the change of the torsion angle dominates the isotropic chemical shift behavior of the L-alanine residue C$_\beta$ carbon.

The principal values of the chemical shift tensor give information about the three dimensional electronic state of a molecule. However, in order to understand the behavior of the principal values, one should obtain information about the orientation of the principal axis system of the chemical shift tensor with respect to the molecular fixed frame. The orientations of the principal axis systems of the chemical shift tensors of the L-alanine C$_\beta$-carbons in some peptides can be theoretically determined [4], whose L-alanine moieties have different main chain torsion angles, $(\Phi, \Psi) = (-57.4°, -47.5°)$ [α_R-helix form],

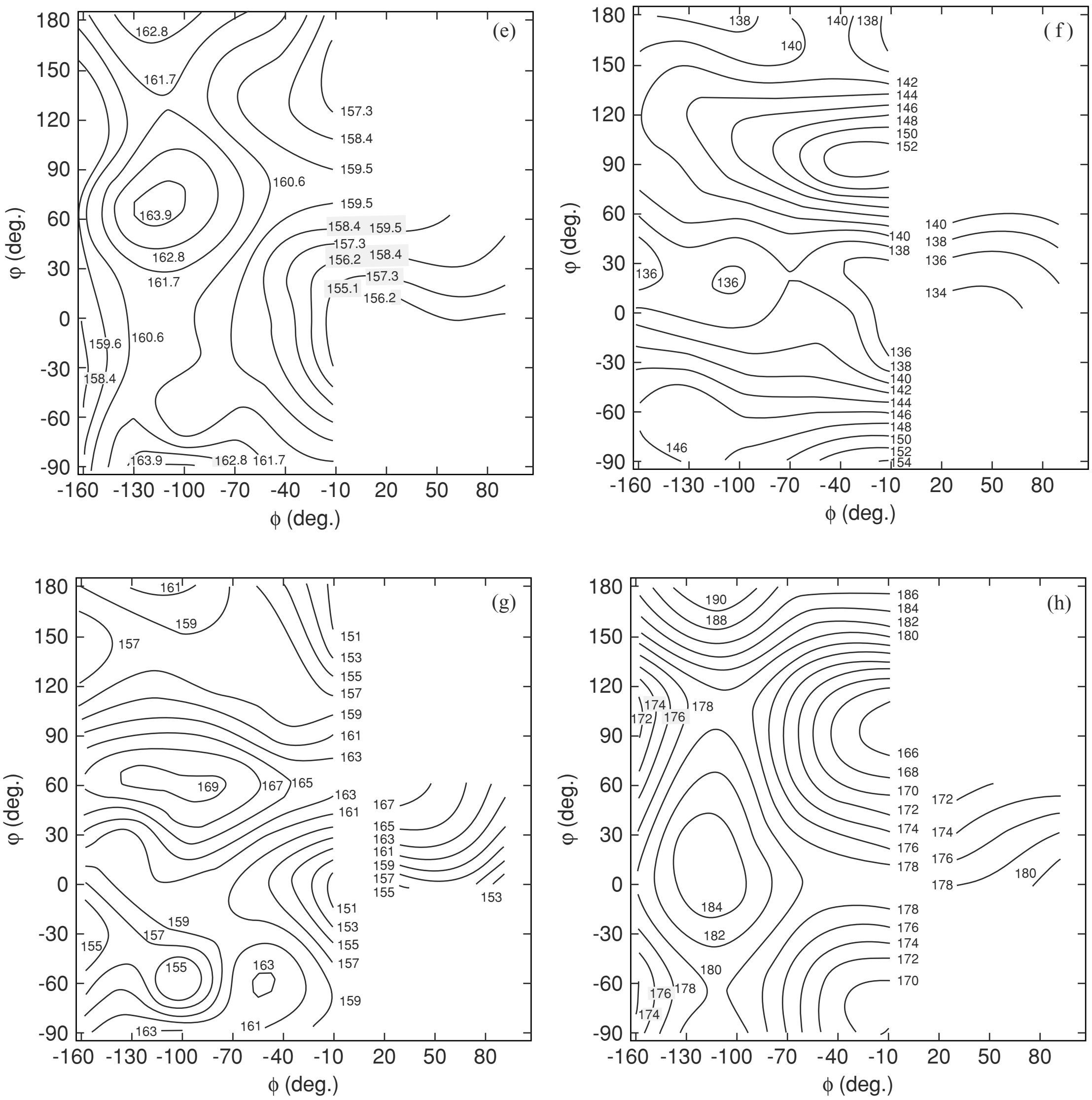

Fig. 1. (*Continued*)

(−138.8°, 134.7°) [β_A-sheet form], (−66.3°, −24.1°) [$3_{10}{}^{R}$-helix form], and (−84.3°, 159.0°) [3_1-helix form]. The σ_{33} component nearly lies along the $C_\alpha - C_\beta$ bond for all the peptides considered here, and also the σ_{11} is nearly perpendicular to the plane defined by the C_β, the C_α, and the N atoms in the L-alanine residue; on the other hand, σ_{22} is parallel to the plane. These results agree with the experimentally determined direction of σ_{33} of the C_β carbon in L-Ala amino acid by Naito *et al.* [7]. The σ_{11} component for the dihedral angles corresponding to the β_A-sheet form is 37.06 ppm. This shows a high frequency shift of about 9 ppm with respect to that for the α_R-helix form. This result means that the σ_{11} dominates the high frequency shift on the isotropic chemical shift of the C_β carbon for the β_A-sheet form. Since the σ_{11} value does not orient along a specified chemical bond, it is not easy to comprehend intuitively the chemical shift tensor behavior of the C_β carbon. However, it is obvious that the

Table 1: Calculated ^{13}C chemical shifts (ppm) of L-alanine residue C_α- and C_β-carbons by the 4-31G–GIAO-CHF method

Sample	C_α				C_β			
	σ_{iso}	σ_{11}	σ_{22}	σ_{33}	σ_{iso}	σ_{11}	σ_{22}	σ_{33}
Ac-Ala-NHMe	43.62	65.79	46.46	18.91	15.94	33.80	17.97	−3.49
	—	—	—	—	—	—	—	—*
Boc-Ala-Aib-OH	45.71	64.74	55.04	26.37	15.84	32.47	19.03	−4.00
Boc-Ala-Pro-OH	—	—	—	—	—	—	—	—*
Poly (Ala)†	45.52	61.93	43.69	30.93	15.72	28.16	22.14	−3.16
Poly (Ala)‡	44.73	62.02	47.53	24.64	18.74	37.06	21.70	−2.53

*The chemical shifts could not be calculated because of SCF failures.
†With the α^R-helix conformation.
‡With the β_A-helix conformation.

through-space interaction between the C_β methyl group and its surroundings might be important for understanding the σ_{11} behavior.

For all the torsion angles employed in the calculations, the σ_{33} component of the chemical shift tensor of the L-alanine C_α-carbons always lies along the C_α–C′ bond. However, for the α_R-helix, the 3_{10}^{R}-helix, and the 3_1-helix forms, the σ_{11} component lies in a slightly deviated direction from the C_α–C_β bond: and for the β_A-sheet form, the σ_{11} component is along this direction. The tensor component which is nearly along the C_α–C_β bond is 47.53 ppm for the β_A-sheet form, 61.93 ppm for the α_R-helix form, 64.74 ppm for the 3_{10}^{R}-helix form, and 65.79 ppm for the 3_1-helix form. The change of the dihedral angles causes the large deviation of the chemical shift tensor component which is along the C_α–C_β bond. Moreover, since σ_{33} depends on changes from one torsion angle to another, it is obvious that there exists the explicit torsion angle dependence on σ_{33}. It is thought that if the carbonyl group in the L-Ala residue forms a hydrogen bond, σ_{33} will be probably affected [6].

Next, we are concerned about the preparation of isotropic NMR chemical shift maps for the C_α and C_β carbons in proteins from an empirical database [8]. It seems to be important to assemble a larger database of ^{13}C shifts in proteins of known structure, to enable us to study the effect of protein conformation and sequence on C_α and C_β chemical shifts experimentally. The database which contains 3,796 $^{13}C_\alpha$ and 2,794 $^{13}C_\beta$ chemical shifts from 40 different proteins are used for the preparation of the chemical shift maps. All the proteins have high-resolution crystal structures, and NMR studies have indicated that the

Table 2: Observed ^{13}C chemical shifts of L-alanine residue C_α- and C_β-carbons for peptides including L-alanine residues in the solid state, as determined by ^{13}C CP-MAS NMR, and their geometrical parameters

Sample	^{13}C chemical shift (ppm)		Dihedral angle (deg)		
	C_α	C_β	Φ	Ψ	ω
Ac-Ala-NHMe	49.3, 50.4	18.8, 21.1	−84.3	159.0	173.3
			−87.6	154.8	171.9
Boc-Ala-Aib-OH	52.3	17.4	−66.3	−24.1	171.8
Boc-Ala-Pro-OH	49.2	17.2	−95.4	153.6	179.9
Poly (Ala)*	53.0	15.5	−57.4	−47.5	−179.8
Poly (Ala)†	48.7	21.0	−138.8	134.7	−178.5

*With the α^R-helix conformation.
†With the β_A-helix conformation.

solution conformation of the protein is essentially identical to that in the crystal. There is no systematic effect of temperature, reference compound, or pH on the reported shifts, but there appear to be differences in the reported shifts arising from referencing differences of up to 4.2 ppm. The major factor affecting chemical shifts is the backbone geometry, which causes differences of *ca.* 4 ppm between typical α-helix and β-sheet geometries for C_α, and of *ca.* 2 ppm for C_β. The side chain dihedral angle χ_1 has an effect of up to 0.5 ppm on the C_α shift, particularly for amino acids with branched side chains at C_β. Hydrogen bonding to main chain atoms has an effect of up to 0.9 ppm, which depends on the main chain conformation. The sequence of the protein and ring-current shifts from aromatic rings has an insignificant effect (except for residues following proline). There are significant differences between different amino acid types in the backbone geometry dependence; the amino acids can be grouped together into five different groups with different (Φ, Ψ) shielding surfaces. The overall fit of individual residues to a single non-residue-specific surface, incorporating the effects of hydrogen bonding and χ_1 angle, is 0.96 ppm for both C_α and C_β.

As examples, the chemical shift maps prepared for the C_α and C_β carbons of Ala residues are shown in Figure 2a and b, respectively, as functions of the torsion angles (Φ, Ψ) [9]. Here only the regions $(-180^\circ < \Phi < 0^\circ, -180^\circ < \Psi < 180^\circ)$ are shown. Data are only shown for areas with enough data points to give reliable chemical shift predictions, in which the density function is greater than 1. There is a clear conformation dependence in the chemical shifts, for example, the chemical shift in the

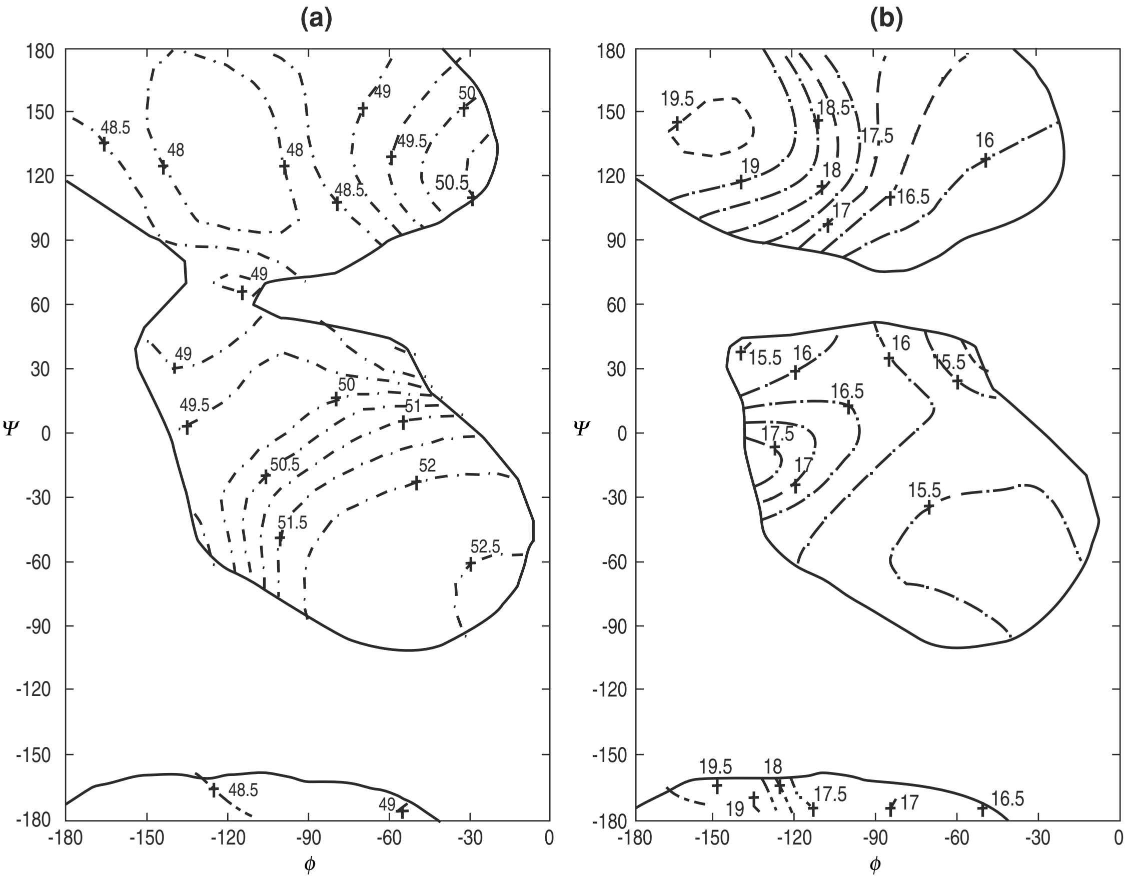

Fig. 2. Contour plots of the conformation-dependent chemical shifts (in ppm) of C_α(a) and C_β(b) carbons of Ala residues in 40 proteins. Chemical shift values in the region $(-180^\circ < \Phi < 0^\circ, -180^\circ < \Psi < 180^\circ)$ are shown, where the density function is more than 1. Random coil chemical shifts are 50.0 ppm for Ala C_α carbon and 16.6 ppm for Ala C_β carbon.

α-helix region is predicted at lower frequency for C_α than the chemical shift in the β-sheet region, but at higher frequency for the C_β. These chemical shift maps in turn will help to guide efforts in protein structure refinement using ^{13}C chemical shifts.

References

1. Saito H, Ando I. Ann. Rep. NMR Spectrosc. 1989;21:209.
2. Ando I, Saito H, Tabeta R, Shoji A, Ozaki T. Macromolecules. 1984;17:457.
3. Asakawa N, Kurosu H, Ando I. J. Mol. Struct. 1994;323:279.
4. Asakawa N, Kurosu H, Ando I, Shoji A, Ozaki T. J. Mol. Struct. 1994;317:119.
5. Ando I, Kuroki S, Kurosu H, Yamanobe T. Prog. NMR Spectrosc. 2001;39:79.
6. Asakawa N, Kameda T, Kuroki S, Kurosu H, Ando S, Ando I, Shoji A. Ann. Rep. NMR Spectrosc. 1995;35:233.
7. Naito A, Ganapathy S, Akasaka K, McDowell CA. J. Chem. Phys. 1981;90:679.
8. Iwadate M, Asakura T, Williamson MP. J. Biomol. NMR 1999;13:199.
9. Asakura T, Iwadate M, Demura M, Williamson MP. Int. J. Biol. Macromol. 1999;24:167.

NMR Chemical Shifts Based on Band Theory

Hiromichi Kurosu[1] and Takeshi Yamanobe[2]
[1]*School of Natural Science and Ecological Awareness, Graduate School of Humanities and Science, Nara Women's University, Kitauoya-Nishimachi, Nara 630-8506, Japan*
[2]*Department of Chemistry, Gunma University, 1-5-1 Tenjin-cho, Kiryu, Gunma 376-8515, Japan*

Introduction

Nuclear shielding offers microscopic information about the stereochemical and crystal structures of polymers which in turn are important factors in understanding physical properties. Details of electronic structure can also be deduced from nuclear shielding data, and this is also important in controlling physical properties [1]. In order to obtain the information about the electronic structure of polymers from nuclear shielding, it is necessary to use a theoretical approach in addition to an experimental one.

In general, there are two possibilities to obtain such information by theoretical methods. One is to use a fragment of a polymer such as a dimer, trimer, etc. for theoretical calculations. Such an approach is useful because the nuclear shielding is sometimes governed by the local electronic structure. However, there is doubt whether the electronic structure obtained from the model compound appropriately reproduces that of the polymer chain. Another approach is to employ directly an infinite polymer chain with periodic structure. This leads to the application of the tight-binding (TB) molecular orbital approximation, which was developed in the field of solid-state physics [2]. Its advantages are that it treats the polymer directly and that relatively long-range interactions such as hydrogen bonding in the α-helix form of the polypeptide may be included.

In using the model compound approach, the electronic structure of large chains can be visualized by drawing the orbital energies associated with chains of increasing length. On the other hand, for an infinite polymer chain, the energy levels are built up as a continuous band structure. As rotation about the bond is strongly restricted in solid polymers, the periodicity of a polymer chain is retained. From the point of view of calculating nuclear shielding, use of the TB model for the calculation of the electronic structure of polymers has been successful. Herein we described the basic ideas for deducing the electronic structure and the nuclear shielding of solid polymers by the TB approximation.

Theoretical Aspects of Electronic State and Nuclear Shielding in Solid Polymers

Polymers can be characterized by a possible periodicity in their conformational structure and a large number of electrons. In this system, the potential energy that an electron experiences is periodic. Periodic systems have the advantage of translational symmetry when compared with aperiodic systems. It is possible to exploit this symmetry in order to reduce to reasonable proportions the formidable task of computing the electronic states of an extended system. The TB molecular orbital model is employed to describe the electronic structure of linear periodic polymers within the framework of a "linear combination of atomic orbitals" approximation for electronic eigenfunctions. By means of Bloch's theory [3], the eigenfunction $\Phi_n(k)$ for an electron at position r, belonging to the nth crystal orbital is given by

$$\Phi_n(k) = N^{-(1/2)} \sum_{j=-(N-1)/2}^{(N-1)/2} \sum_{\nu=1}^{s} e^{ijkb} C_{\nu n}(k) \phi_\nu(r - jb) \qquad (1)$$

where k is the wave number, ν is an orbital index for the jth cell, s is the total number of atomic orbitals in a given cell, N is the total number of cells considered, and b is the unit vector of translational symmetry. In equation (1), $\phi_\nu(r - jb)$ represents the ν atomic orbital in the jth cell and $C_{\nu n}$ (k) its expansion coefficient in the linear combination of atomic orbitals. The limits of k, within a given Brillouin zone, are $-\pi/2$ and $\pi/2$. Using Equation (1), the total energy E of the polymer can be expressed as

$$E(k) = \sum_{n}^{\mathrm{occ}} \left\langle \Psi_n(k) \left| \hat{H} \right| \Psi_n(k) \right\rangle \qquad (2)$$

where $\Psi_n(k)$ is the Slater determinant composed of $\Phi_n(k)$. $\hat{H}$ is the Hamiltonian, consisting of terms representing the kinetic energy, the potential energy of the electronic field

Graham A. Webb (ed.), Modern Magnetic Resonance, 43–52.
© 2008 *Springer.*

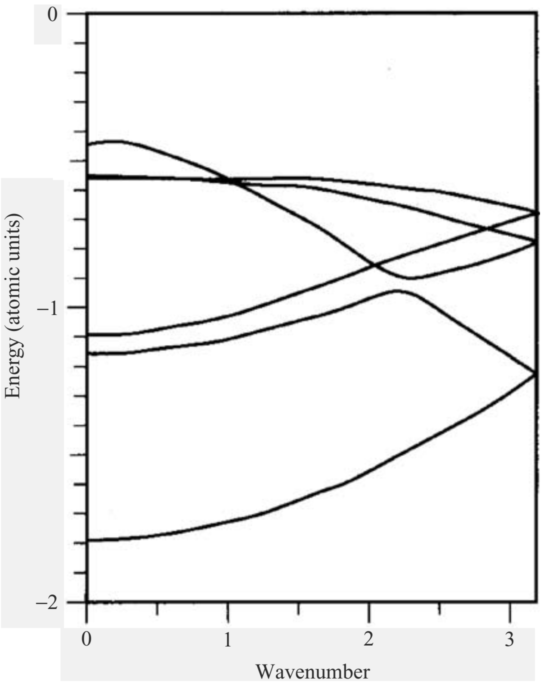

Fig. 1. Electronic band structure of polyethylene with trans zigzag conformation calculated using CNDO/2 TB MO.

of the polymer, and the electron repulsion energy. The advantage of Equation (1) is that calculation of the electronic structure of an infinite polymer can be reduced to the calculation for a unit cell (monomer unit) interacting with all other unit cells, using the periodicity of the polymer.

By solving the Fock matrix, the expansion coefficients in Equation (1) can be obtained. These expansion coefficients and energies are dependent on k, which leads to a band structure for a polymer chain. Figure 1 shows the calculated band structure of polyethylene with a trans zigzag conformation.

As only six valence electrons in a monomer unit cell are included in the calculation, the corresponding six valence bands can be seen in Figure 1. Calculations with model compounds give discrete energy levels. In a series of homogeneous molecules, the number of energy levels increases with the molecular size, and correspondingly the separation between these energy levels decreases. For an infinite polymer chains, the energy level is the continuous band structure as shown in Figure 1. The electronic structure of solid polymers is characterized by this band structure, with a dependence of energy level on k.

The nuclear shielding for the various nuclei in a given macromolecule can be calculated from the obtained electronic band structure, $C_{\nu n}(k)$ and $E_n(k)$. In general, a nuclear shielding can be written as [1]

$$\sigma = \sigma^{\mathrm{d}} + \sigma^{\mathrm{p}} + \sigma' \tag{3}$$

where σ^{d} and σ^{p} are the diamagnetic and paramagnetic contributions, respectively, σ' is the contribution from neighboring atoms. For a carbon atom, σ' is much smaller than 1 ppm and can be considered to be negligible. Thus, σ can be estimated by the sum of σ^{d} and σ^{p}. Based on the TB MO theory, $\sigma^{\mathrm{d}}$and σ^{p} are obtained by a sum-over-states (SOS) method as follows [4–6]:

$$\sigma^{\mathrm{d}}_{\mathrm{A}}(k) = \frac{\mu_0 e^2}{6\pi m_{\mathrm{e}}^2} \sum_{\nu}^{\mathrm{A}} \sum_{\nu'}^{\mathrm{A}} P_{\nu\nu'}(k) \left\langle \phi_\nu(r) \left| r^{-1} \right| \phi'_\nu(r) \right\rangle \tag{4}$$

$$\begin{aligned}\sigma^{\mathrm{p}}_{\mathrm{A},\alpha\beta}(k) = {} & \frac{-\mu_0 h^2 e^2}{4\pi m_{\mathrm{e}}^2} \sum_{m}^{\mathrm{occ}} \sum_{n}^{\mathrm{unocc}} \sum_{j}^{\mathrm{A}} \langle r^{-3} \rangle_{2\mathrm{p}} \left({}^1E_m^n - {}^1E_0 \right)^{-1} \\ & \times \sum_{j}^{\mathrm{B}} \sum_{l}^{\mathrm{B}} [X(j, m, n, \beta, \gamma) X(l, n, m, \gamma, \alpha) \\ & - Y(j, m, n, \beta, \gamma) Y(l, n, m, \gamma, \alpha) \\ & + X(j, m, n, \gamma, \alpha) X(l, n, m, \beta, \gamma) \\ & - Y(j, m, n, \gamma, \alpha) Y(l, n, m, \beta, \gamma)]\end{aligned} \tag{5}$$

Here e is the charge and m_{e} the mass of the electron, μ_0 is the permeability of free space,

$$P_{\nu\nu'}(k) = \sum_{m}^{\mathrm{occ}} C^*_{\nu m}(k) C_{\nu' m}(k) \tag{6}$$

where m refers to the number of occupied crystal orbitals and n to those that are unoccupied, E_0 is the electronic energy of the ground state and E_m^n is the energy of the state created by promoting an electron from orbital m to orbital n. j and l are atomic orbitals on centers A and B, respectively, and

$$\begin{aligned} X(j, m, n, \beta, \gamma) = {} & C^{\mathrm{R}\beta}_{jm} C^{\mathrm{I}\gamma}_{jn} + C^{\mathrm{R}\beta}_{jn} C^{\mathrm{I}\gamma}_{jm} \\ & - C^{\mathrm{R}\gamma}_{jn} C^{\mathrm{I}\beta}_{jm} - C^{\mathrm{R}\gamma}_{jm} C^{\mathrm{I}\beta}_{jn} \end{aligned} \tag{7}$$

$$\begin{aligned} Y(j, m, n, \beta, \gamma) = {} & C^{\mathrm{R}\beta}_{jm} C^{\mathrm{R}\gamma}_{jn} - C^{\mathrm{R}\gamma}_{jm} C^{\mathrm{R}\beta}_{jn} \\ & + C^{\mathrm{I}\beta}_{jm} C^{\mathrm{I}\gamma}_{jn} - C^{\mathrm{I}\gamma}_{jm} C^{\mathrm{I}\beta}_{jn} \end{aligned} \tag{8}$$

where α, β, and γ refer to the x, y, and z components of the shielding tensor in cyclic order and R and I indicate the real and imaginary parts of the coefficients

$C_{vn}(k)$. As shown by Equations (4) and (5), the nuclear shielding is calculated as a function of k. In order to be able to compare the calculated and experimental values of the nuclear shielding, it is necessary to average the calculated data over k, within the first Brillouin zone, as given by

$$\sigma = \int_{-(\pi/b)}^{\pi/b} \sigma(k) D(k) dk \tag{9}$$

where $D(k)$ is the density of state, namely the number of states per unit amount of energy. Thus, the nuclear shielding can be obtained through the electronic band structure of a polymer, especially a solid polymer.

The quantities calculated using Equations (4) and (5) are the nuclear shielding, σ, and so the negative sign means deshielding. On the other hand, a negative sign of the observed chemical shift, δ, means an increase in shielding. Hereinafter, calculated and observed data are expressed as the nuclear shielding and chemical shift, respectively. The absolute value of the calculated shielding should be compared directly with the observed chemical shift.

Furthermore, the formalism for calculating the NMR shieldings of infinite polymer chains with a three-dimensional (3D) periodicity in the crystalline state by *ab initio* TB MO theory has been developed [7]. For the calculations on a 3D system, the program code CRYSTALS88 [8,9] which is available for a crystal orbital calculation of 3D systems was used for calculating the electronic states and a program for calculating the shielding constant[4,5,10,11] using the SOS method was added to CRYSTAL88.

Interpretation of Nuclear Shielding by the TB Method

^{13}C shielding reflects the magnetic environment of the atom considered, and this depends on the conformation, configuration, and crystal structure in the case of polymers. In order to understand ^{13}C shielding, examples illustrating the applications of TB MO methods to some polymers will be described.

Conformation

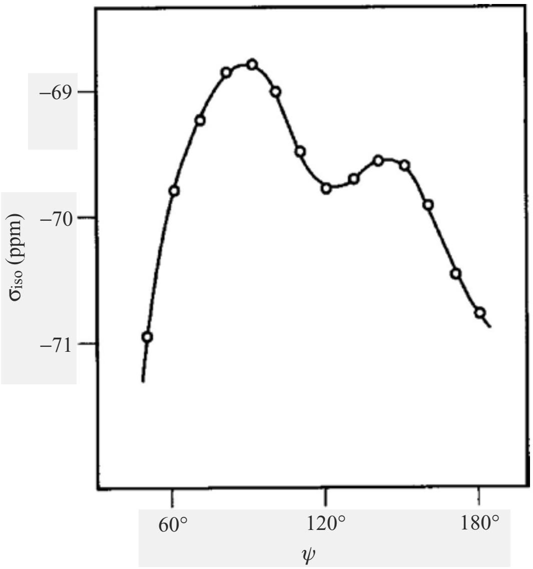

Fig. 2. Dependence of the calculated ^{13}C NMR shielding of polyoxymethylene on dihedral angle ψ.

It is known from an X-ray diffraction study that a polyoxymethylene chain in the crystalline region takes an all-gauche conformation with a 9/5 helix [12]. However, in the non-crystalline region the structure is not yet determined exactly, because of the complicated conformation of the chain. It has been reported that the observed ^{13}C chemical shifts of polyoxymethylene in the crystalline and non-crystalline regions appear at 88.5 and 89.5 ppm, respectively [13]. Figure 2 shows the dependence of the calculated isotropic ^{13}C shielding on the dihedral angles (ψ) within the framework of the CNDO/2 TB MO method.

The isotropic ^{13}C shielding increases as ψ is increased from 50° to 90°, and the shielding decreases through a minimum value as ψ is increased from 90° to 180°. The values of 60° and 180°, for ψ correspond to the all-gauche and all-trans conformations, respectively. The calculated isotropic ^{13}C shielding of the all-gauche conformation appears at lower frequency by about 1 ppm than that of the all-trans conformation. Dividing the difference of ^{13}C shielding between the all-gauche and all-trans conformations, for the diamagnetic term, the difference between the all-gauche and all-trans conformations is 0.1 ppm, and for the paramagnetic term the corresponding difference is 0.9 ppm. Thus, the contribution to the relative ^{13}C shielding is due mainly to a change in the paramagnetic term. The diamagnetic term is determined only by the ground state, whereas the paramagnetic term involves interactions between the ground and excited states, as seen from Equations(4) and (5). Thus, the observed chemical shift difference between the crystalline and non-crystalline regions comes from a variable interaction due to a conformational change. Therefore, it can be argued that the calculated value confirms well the experimental finding that the ^{13}C shielding for the crystalline region is greater by about 1 ppm than that for the non-crystalline region.

Calculated results of $\Delta\sigma (= \sigma_{yy} - \sigma_{zz}$; spectrum breadth) for the all-gauche and all-trans conformations are 37.7 and 1.8 ppm, respectively. $\Delta\sigma$ for the all-gauche conformation is much larger than that for the all-trans conformation. On the other hand, the experimental values of $\Delta\delta$ for the crystalline and non-crystalline regions are about 35 and 7–10 ppm, respectively [13]. The calculated and experimental values agree relatively well with each other. The fact that the calculated value of $\Delta\sigma$ for the all-trans conformation is rather small suggests that the electronic environment around the carbon nucleus considered here is relatively symmetric. The small value of $\Delta\delta$ may be due mainly to the high symmetry of the electronic environment in addition to the averaging of the ^{13}C shielding anisotropy by molecular motion. Further, we are concerned with the behavior of δ_{22}, whose value is obtained from the apex of the tent-like powder pattern. In the experimental data, δ_{22} for the crystalline region appears at about 5 ppm to low frequency when compared with that for the non-crystalline region. However, the calculated value of σ_{xx} for the all-gauche conformation appears at lower frequency by about 2.5 ppm when compared with that for the all-trans conformation. Thus the calculation explains the experimental observation reasonably, despite the rough assumption of an all-trans conformation for the non-crystalline region.

Table 1 shows the calculated and observed ^{13}C shieldings of a polyglycine chain with forms I and II [14]. The observed carbonyl ^{13}C signal for form I is shielded by about 4 ppm compared with that for form II. The calculated ^{13}C shielding for form I is larger by about 11 ppm than that for form II, which matches the experimental finding. There is no significant difference between the methylene ^{13}C chemical shifts for forms I and II within experimental error. At this stage, it cannot be determined whether the methylene shielding for form I or that for form II is the larger. The calculated shielding of ^{13}C for form I is smaller by about 3 ppm than that for II, so the calculation predicts the existence of a shielding difference (about 3 ppm) between forms I and II. It appears that the calculated shieldings are somewhat exaggerated compared with the observed values. Nevertheless, the observed trend that the ^{13}C chemical shift difference for the methylene carbon is very small when compared with that for the carbonyl carbon is reproduced qualitatively by the calculation.

Table 1: Observed and calculated ^{13}C chemical shifts and shieldings of an isolated polyglycine chain

	δ_{obs}(ppm)*		σ_{calc}(ppm)†	
	Form I	Form II	Form I	Form II
CH$_2$	43.5	43.5	−127.2	−124.4
C=O	168.4	172.3	−236.7	−248.1

*From TMS. The positive sign means deshielding.

†The negative sign means deshielding.

Configuration

Polyacetylene (PA) is the simplest conjugated polyene and has two configurations (cis and trans). It is reported that the ^{13}C shielding of *cis*-PA appears at a lower frequency by about 10 ppm than that of *trans*-PA [15]. Calculations of the ^{13}C shielding of PAs are carried out based on the use of CNDO/2 TB MO and INDO/S TB MO methods. The differences in the isotropic ^{13}C shielding between the *cis*- and *trans*-PAs, calculated by the CNDO/2 and INDO/S TB MO methods, are about 2.0 and 3.5 ppm, respectively [16], i.e. the results differ by a factor of about 2. As the observed difference is about 10 ppm, both types of calculation somewhat underestimate the real value in this case.

Figure 3 shows the observed [17] and calculated components of the ^{13}C shielding tensors of *cis*- and *trans*-PAs. As is seen, the absolute values of Φ_{zz} and Φ_{xx} calculated using the INDO/S TB MO method are smaller by about 40 ppm than those obtained by the CNDO/2 TB MO method. The value of σ_{yy} calculated by the INDO/S TB MO method is larger by about 10 ppm than that obtained using CNDO/2 TB MO procedure. Consequently, the separation between the values of σ_{xx} and σ_{yy} calculated using the INDO/S TB MO is much larger than that obtained by CNDO/2 TB MO's. Further, it is shown that in going from the calculation using CNDO/2 method to that using INDO/S the values of σ_{zz} and σ_{xx} are changed considerably. The most remarkable difference is in the estimation of the π–π overlap integral. The values of σ_{zz} and σ_{xx} are affected by the distribution of π electrons.

The electronic band structures of a PA consist of five valence bands within the framework of the semiempirical methods. The highest occupied band has π symmetry. Comparing the electronic band structures calculated by CNDO/2 TB MO with that of INDO/S TB MO, the energies of the three high-energy bands increase, in particular that of the highest occupied band. As can be seen from Equation (3), σ^{p} contains a term proportional to the inverse of the excitation energy. The increase in the energies of the three high-energy bands is one of the factors leading to the deshielding of σ_{zz} and σ_{xx}, which implies a lower excitation energy. In fact, the band gaps (the energy difference between the highest occupied and the lowest

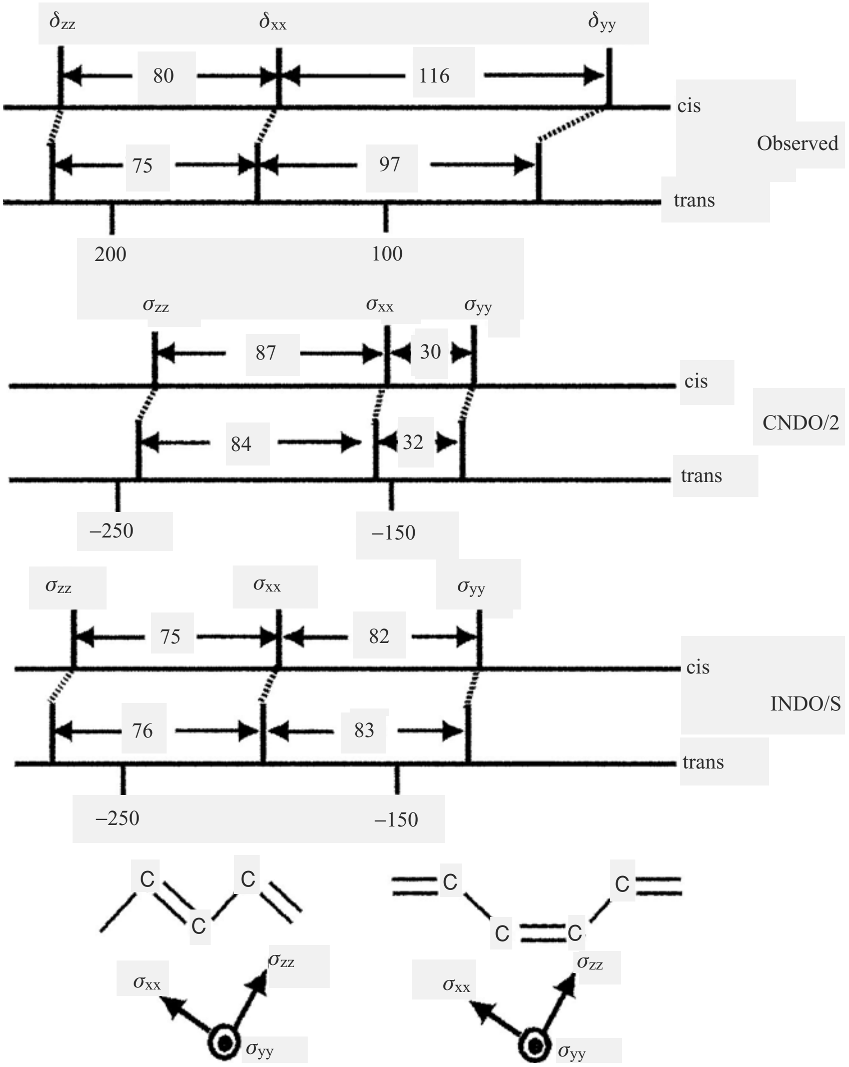
δzz
δxx
δyy
80
116
cis
Observed
75
97
trans
200
100
σzz
σxx
σyy
87
30
cis
CNDO/2
84
32
trans
–250
–150
σzz
σxx
σyy
75
82
cis
INDO/S
76
83
trans
–250
–150
C
C
C
C
C
C
σxx
σzz
σyy
σxx
σzz
σyy

Fig. 3. Observed and calculated components of ^{13}C NMR shielding tensors of *cis*- and *trans*-PAs. The directions of the principal axes are indicated at the bottom.

unoccupied bands) for *trans*-PA, calculated using the CNDO/2 and INDO/S TB MO methods, are about 8.0 and 4.2 eV, respectively. The observed band gap for *trans*-PA is about 1.9 eV. Thus, the description of the contributions of these high energy bands to σ_{xx} and σ_{zz} is remarkably improved in going from the CNDO/2 to the INDO/S TB MO procedure.

It is clear from Figure 3 that the reason why the calculated difference in isotropic shielding of ^{13}C between the *cis*- and *trans*-PAs is underestimated is that the difference in σ_{yy} cannot be reasonably reproduced. In order to reproduce more reasonably the observed difference in σ_{yy} between the *cis*- and *trans*-PAs, it may be necessary to use MOs that can properly describe band structures that have σ symmetry.

Polypyrrole is one of a series of heterocyclic polymers that has attracted much attention because of its characteristic electric and electronic properties. Fundamental structural formulae have been proposed for undoped and doped polypyrroles, where the aromatic form

Table 2: Calculated ^{15}N shieldings and band gaps for aromatic and quinoid polypyrrole models using INDO/S TB MO

Structure	Calculated shielding σ_{iso}(ppm)	Band gap (eV)
Aromatic	−223.50	5.12
Quinoid	−232.21	2.86

corresponds to the undoped state and the quinoid form to the doped state. From analysis of the high-resolution solid-state ^{15}N NMR, it is known that the ^{15}N chemical shift for the quinoid form appears to high frequency of that for the aromatic form. In order to obtain information about the ^{15}N chemical shift, and electronic band structures of an infinite polypyrrole chain with aromatic or quinoid forms, calculations were carried out using the INDO/S TB MO's [18].

As listed in Table 2, the calculated shielding of ^{15}N for the quinoid form appears to high frequency compared with that for the aromatic form. The calculated results agree with the observed ones, suggesting that the electronic band structure has been properly estimated. From the calculated electronic band structure, the band gaps for the aromatic and quinoid forms are 5.1 and 2.9 eV, respectively. This result implies that the electrical conductivity of the quinoid form is larger than that of the aromatic form. Therefore, it can be expected that if the amount of the quinoid form is increased, polypyrrole with a higher electric conductivity can be obtained.

Crystal Structure

The crystal structure in the solid state, which describes how molecules condense, is an important factor when discussing physical properties. The effect of crystal structure on the nuclear shielding in principle, can be separated from the effect of conformation and configuration within the limitation of a given quantum chemical method.

Experimentally, it is reported that the ^{13}C chemical shifts of the CH_2 carbon for the n-paraffins, cyclic paraffins, and polyethylene with a trans zigzag conformation in the orthorhombic and triclinic forms are about 33 and 34 ppm, respectively [19,20]. As the conformation is the same in each case, the difference of about 1 ppm may be due to a local change in intermolecular interactions resulting from the change of the orthorhombic to the triclinic form. Paraffins can be considered as models for the crystallographic form of polyethylene. The result of X-ray diffraction studies suggests that the trans zigzag plane of any specified chain in the orthorhombic and triclinic forms is, respectively, perpendicular and parallel to those of the neighboring chains. The ^{13}C chemical shift of polyethylene with a monoclinic form appears at higher frequency by 1.4 ppm compared with that of polyethylene with the orthorhombic form. The orientation of the trans zigzag plane in the monoclinic form is very close to that in the triclinic form [21]. Thus, the solid-state ^{13}C NMR chemical shift depends on the orientation of the C–C–C plane in trans zigzag chains.

Since the chains lie periodically in the solid state, calculations of the chemical shifts should be employed that take account of the 3D structure, including interactions between chains. In order to take into account interchain interaction, a "seven-polyethylene-chains model" has been used to compute the ^{13}C shielding [10]. Figure 4 shows models for polyethylenes with an orthorhombic form and a monoclinic form. The setting angle ψ for the orthorhombic polyethylene is not clearly determined. Figure 5 shows the ψ dependence of difference in shielding of the ^{13}C between orthorhombic and monoclinic polyethylenes ($\sigma_{\text{orth}} - \sigma_{\text{mono}}$) calculated using the INDO/S TB MO method.

As can be seen, the calculated difference in the shielding of the ^{13}C between these forms is positive in the case of $\psi = 25°–42°$, and negative in the case of $\psi = 20°–25°$ and $\psi = 42°–55°$. The largest difference occurs at $\psi = 35°$. From these results, the angle of $\psi = 25°–42°$ is good for the setting angle of orthorhombic polyethylene, and can reasonably reproduce the observed data. This result shows that the difference in chemical shift between the orthorhombic and monoclinic forms is caused by the difference in interchain interactions through the electronic band structure.

In order to elucidate the intermolecular interaction effect on the NMR chemical shift of PA crystal, the 3D *ab initio* TB MO calculations were carried out [22]. Before going to the 3D PA crystal, it is significant to employ a single PA chain, because the intermolecular interaction effect on the electronic structure and NMR chemical shift behavior is clear. In Table 3, the total energy per monomer unit and NMR chemical shielding for a single *cis*- and *trans*-PA chain are shown as calculated by using the *ab initio* TB MO method within the framework of the STO-3G minimal basis set. It is shown that, the total energy per monomer unit for *trans*-PA is lower by 0.0069 a.u. than that for *cis*-PA. This means that the trans-form is more stable than the cis-form. The tendency of the calculated results qualitatively explains the experimental results that, undoped trans-PA is thermally more stable than *cis*-PA. Experimentally, the ^{13}C chemical shift for the cis-form appears at a lower frequency by 10 ppm than that of the trans-form [17]. On the other hand, the calculation shows that the ^{13}C chemical shift of

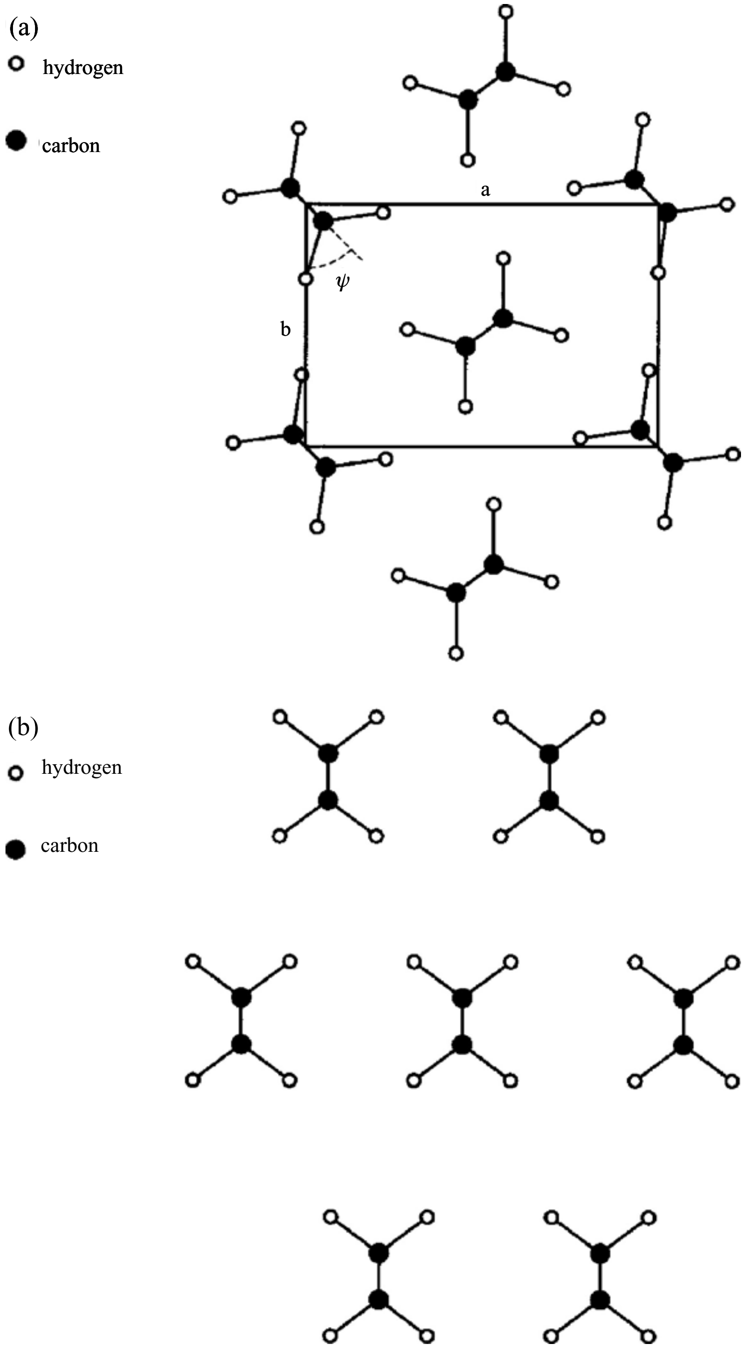
(a)
hydrogen
carbon
a
ψ
b
(b)
hydrogen
carbon

Fig. 4. The “seven-polyethylene-chains” model: (a) Orthorhombic form; (b) Monoclinic form.

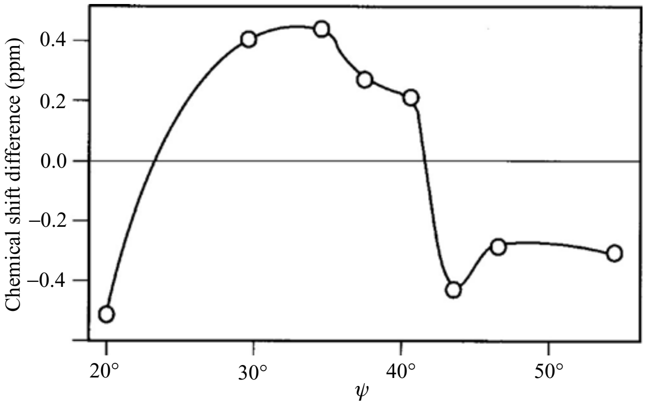

Fig. 5. The ^{13}C NMR chemical shift difference between the orthorhombic and monoclinic polyethylene chains calculated using the seven-chains model, as a function of the setting angle ψ.

the cis-form appears at a slightly lower frequency by 0.1 ppm than that of the trans-form. Comparing with the experimental results, the chemical shift difference between the cis- and trans-forms, is very small. This means that, the single chain model is insufficient to reasonably explain the experimental results. Therefore, it can be said that the interchain interactions should be taken into account by the 3D polymer crystal. The electronic structures and NMR chemical shieldings of the 3D infinite *cis*- and *trans*-PA chains with orthorhombic crystallographic form were calculated using the *ab initio* TB MO method within the framework of the STO-3G minimal basis set. The total energies per monomer unit and chemical shieldings, along with the experimental chemical shift values are listed in Table 3. The total energy per monomer unit for the trans-form is lower by 0.0024 a.u. than that for the cis-form. The trans-form is thus more stable than the cis-form. This explains reasonably the experimental thermal stability of the trans-form in the PA crystal over the cis-form.

As seen from Table 3, the ^{13}C chemical shift for the cis-form in a the PA crystal appears at a lower frequency by 1.0 ppm than that for the trans-form, calculated using the experimental lattice parameters (Case A). The calculated results approach the experimental ones more closely, compared to the single chain model. This shows that the intermolecular interaction plays an important role towards the ^{13}C chemical shift behavior. What is the ^{13}C chemical shift behavior if the intermolecular interaction is increased in the 3D PA crystal model? When the lattice

Table 3: Total energies, band gaps, and NMR chemical shieldings for a single chain of *cis*- and *trans*-polyacetylenes and for a 3D crystal of *cis*- and *trans*-polyacetylenes as calculated by *ab initio* TB MO method within the framework of STO-3G minimal basis set

	A single chain		Three-dimensional crystal			
				^{13}C chemical shielding[‡] (ppm)		
Polyacetylene form	Total energy[†] (a.u.)	^{13}C chemical shielding[‡] (ppm)	Total energy[†] (a.u.)	Case A[§]	Case B[§]	Experimental ^{13}C chemical shift[*] δ (ppm)
Cis-form	−75.9368	−121.6	−75.9430	−117.7	−114.7	127.3
Trans-form	−75.9437	−121.7	−75.9454	−118.7	−119.2	137.3
		Δ[¶] = 0.1		Δ[¶] = 1.0	4.5	

[*] Relative to TMS. The positive sign means deshielding. This is opposite to the calculation.

[†] Per monomer unit.

[‡] The calculated ^{13}C chemical shielding indicates that the negative sign means deshielding.

[§] *Case A*: by using experimental lattice parameters and *Case B*: using reduced interchain distance (reduce lattice parameter $b = 5.0$ A. This means that the reduced interchain distance leads to increase intermolecular interaction).

[¶] Chemical shift difference between cis- and trans-forms.

Fig. 6. The plots of the ^{13}C chemical shieldings for a 3D crystal of *cis*- and *trans*-PAs, as calculated by the *ab initio* TB MO method within the framework of STO-3G minimal basis set against the length of the lattice parameter *a*.

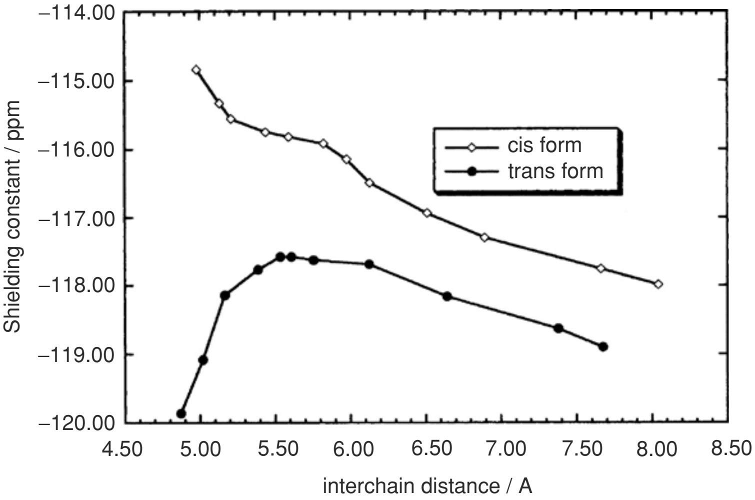

parameter *a* is reduced to 5 A(this means an increase in the intermolecular interaction) (Case B), the ^{13}C chemical shift difference between the cis- and trans-forms becomes 4.5 ppm. This approaches the experimental results more closely.

Therefore, in order to clarify the interchain distance effect of the ^{13}C chemical shift for the cis- and trans-forms, their ^{13}C chemical shieldings were calculated, with a change in the length of the lattice parameter *a* using the *ab initio* TB MO method, within the framework of the STO-3G minimal basis set. The calculated chemical shieldings are plotted against the length of the lattice parameter *a* as shown in Figure 6. It is seen that the ^{13}C chemical shift for the cis-form moves slowly to low frequency, as the length of the lattice parameter *a* decreases from 8 to 5 A, that is, the intermolecular interaction increases. On the other hand, for the trans-form, the ^{13}C chemical shift, moves slowly to low frequency, as the length of the lattice parameter *a* decreases from 7.7 to 5.6 A, and moves largely to high frequency as the length of the lattice parameter *a* decreases from 5.6 to 4.9 A. With a decrease in the length of the lattice parameter *a* below 5.5 A, the chemical shift difference becomes large and quantitatively approaches the experimental result. As predicted from Figure 6, the calculated chemical shift difference becomes 10 ppm (the experimental value) when the length of the lattice parameter *a* is about 4.7 A. The calculation with a shorter length of the lattice parameter *a* agrees with the experimental result. This may come from the approximations implied with the low level MO minimal basis set such as STO-3G, which is used in the calculation. If a higher level minimal basis set is used, the situation may be modified. Nevertheless, it can be said that the present calculation explains well the experiment, and the chemical shift is very sensitive to intermolecular interactions. This means that the ^{13}C chemical shift is a very sensitive measure for use in investigating intermolecular interactions in a polymer crystal.

References

1. Ando I, Webb GA. Theory of NMR Parameters. Academic Press: London, 1983.
2. Imamura A. J. Chem. Phys. 1970;52:3168.
3. Bloch F. Z. Phys. 1928;52:555.
4. Yamanobe T, Ando I. J. Chem. Phys. 1985;85:3154.
5. Yamanobe T, Chujo R, Ando I. Mol. Phys. 1983;50:123.
6. Yamanobe T, Ando I, Saito H, Tabeta R, Shoji A, Ozaki T. Bull. Chem. Soc. Jpn. 1985;58:23.
7. Uchida M, Toida Y, Kurosu H, Ando I. J. Mol. Struct. 1999;508:181.
8. Dovesi R, Pisani C, Roetti C, Causa M, Saunders VR. Quantum Chemistry Program Exchange, Department of Chemistry, Indiana University, IN 47405, Program No. 577.
9. Pisani C, Dovesi R, Roetti C. In: G Berthier, MJS Dewar, H Fischer, K Fukui, GG Hall, J Hinze, HH Jaffe, J Jortner, W Kutzellnig, K Ruedenberg, J Tomasi (Eds). Lecture Notes in Chemistry, Vol. 48. Springer: Berlin, 1988.
10. Kurosu H, Ando I, Yamanobe T. J. Mol. Struct. 1989;201:239.
11. Ishii T, Kurosu H, Yamanobe T, Ando I. J. Chem. Phys. 1988;89:7315.
12. Tadokoro H, Kobayashi M, Kawaguchi Y, Kobayashi A, Murashashi S. J. Chem. Phys. 1963;38:703.
13. Kurosu H, Yamanobe T, Komoto T, Ando I. J. Chem. Phys. 1987;116:391.

14. Yamanobe T, Ando I, Saito H, Tabeta R, Shoji A, Ozaki T. Bull. Chem. Soc. Jpn. 1985;58:23.
15. Maricq MM, Waugh JS, MacDiarmid AG, Shirakawa H, Heeger AT. J. Am. Chem. Soc. 1978;100:7729.
16. Yamanobe T, Ando I, Webb GA. J. Mol. Struct. 1987;151:191.
17. Terao T, Maeda S, Yamabe T, Akagi K, Shirakawa H. Chem. Phys. Lett. 1984;103:347.
18. Kikuchi M, Kurosu H, Ando I. J. Mol. Struct. 1992;29: 193.
19. Yamanobe T, Sorita T, Komoto T, Ando I, Sato H. J. Mol. Struct. 1985;131:267.
20. VanderHart DL. J. Magn. Reson. 1981;44:117.
21. VanderHart DL, Khoury F, Polymer 1984;25:1589.
22. Fujii K, Kuroki S, Uchida M, Kurosu H, Ando I. J. Mol. Struct. 2002;602–603:3.

Modeling NMR Chemical Shifts

Julio C. Facelli
Center for High Performance Computing, University of Utah, Salt Lake City, UT 84112-0190, USA

Abstract

This article presents a discussion of the origin of the chemical shieldings, which is followed by a discussion on how they are calculated using state-of-the-art electronic structure methods. Several examples of quantum chemical calculations of chemical shieldings in common nuclei are presented to provide the reader with a general overview of the reliability of these calculations. The shortcomings of the current methods are finally discussed.

Introduction

Perhaps the most important discovery after the successful detection of the NMR signal has been the observation that the nuclear spin resonance frequencies depend on the chemical or electronic environment of the nuclei [1,2], or as Norman Ramsey states in his landmark papers [3,4] of 1950: "In measurements of nuclear magnetic moments, a correction must be made for the magnetic field arising from the motions of the molecular electrons which are induced by the externally applied field." Ramsey realized that corrections using only Lamb's diamagnetic theory were inadequate for molecules because there are additional shielding contributions arising from the second-order paramagnetism. To address this problem, he developed the necessary theoretical framework to explain and eventually to calculate the "chemical effect," that would become the chemical shift commonly used in our days for structural elucidation. The calculation of chemical shieldings has been a challenge to theoreticians and computational chemists for more than 50 years. Great impetus for this theoretical and modeling work has been provided by the extraordinary sensitivity of the chemical shielding to electronic and molecular structure and environment which can only be unraveled by computational modeling.

It should be noted that the chemical shieldings are tensor properties, i.e. the shift of the resonance frequency depends on the molecular orientation with respect to the external magnetic field, but the brevity of this article precludes any discussion of the tensor properties of the chemical shieldings [5]. In this chapter, as customary in the literature, we will refer to the isotropic component of the chemical shielding tensor as the chemical shielding.

There is considerable confusion in the literature about the use of the terms "chemical shift" and "chemical shielding." The chemical shielding is the tensor that describes the relative change in the local magnetic field at the nucleus position relative to the external magnetic field. This change in the local magnetic field, which is originated in the interaction of the electron cloud with the external magnetic field, can produce shielding or de-shielding of the nucleus. In the first case, the local magnetic field is increased with respect to the external field, while in the second case the local field is decreased. In general, shielding effects are associated with diamagnetic effects from spherical charge distributions, while de-shielding effects are associated with the nonspherical charge distribution originating from *p* or higher angular momentum electrons. When experiments are performed at a constant magnetic field, as it is normally done in modern NMR spectrometers, a shielding effect results on a shift of the resonance to a higher frequency, while a de-shielding effect will result in a lower resonance frequency. In practice, NMR experiments do not measure the chemical shielding directly, instead the common practice is to measure the chemical shifts as the change of resonance frequency of a nucleus relative to a given standard. Moreover, for historic reasons it is customary to reverse the frequency scale, i.e. nuclei more shielded than the standard are considered to have lower chemical shifts and those less shielded larger ones. The formal relation between the chemical shift and chemical shielding tensors is given by

$$\boldsymbol{\delta} = \mathbf{1}\sigma_{\text{iso}} - \boldsymbol{\sigma}. \tag{1}$$

where $\boldsymbol{\delta}$ is the chemical shift tensor, $\boldsymbol{\sigma}$ is the chemical shielding tensor, $\mathbf{1}$ is the unit matrix and σ_{iso} is the isotropic value or trace of the chemical shielding of the standard reference used in the NMR experiments. The determination of the value of σ_{iso}, usually known as absolute chemical shift, is quite difficult. It involves the estimation of the paramagnetic contribution to the chemical shielding in the center of mass of the molecule using its relationship with the spin rotational constant and the calculation of the corresponding diamagnetic part using quantum mechanical methods. The procedure for selecting primary and secondary reference compounds has been extensively discussed by Mason [6].

Graham A. Webb (ed.), Modern Magnetic Resonance, 53–62.
© 2008 *Springer.*

The material presented in this chapter is restricted to the chemical shifts and shielding calculations in diamagnetic molecules. When the molecular electronic ground state is not a singlet, i.e. there are unpaired electrons present in the sample, additional mechanisms contributing to the chemical shielding are present [7].

Theory of the Chemical Shieldings

The theory and modeling of the chemical shifts have been described in numerous publications [8–36]. To obtain exact expressions for the calculation of chemical shieldings using the non-relativistic Born–Oppenheimer approximation [37], it is necessary to include the vector potential representing the external magnetic field and the dipolar field from the magnetic moment of the nucleus into the electronic Hamiltonian. In the gauge of Coulomb, the final expressions for the diamagnetic and paramagnetic contributions are given by

$$\sigma^{d}_{\alpha\beta}(\mathrm{O}) = \frac{1}{2c^2}\left\langle \psi_0 \left| \left(r_k r_{Nk} \delta_{\alpha\beta} - r_{k_\alpha} r_{Nk_\beta} \right) r_{Nk}^{-3} \right| \psi_0 \right\rangle, \tag{2}$$

$$\begin{aligned} \sigma^{p}_{\alpha\beta}(\mathrm{O}) = \frac{-1}{2c^2} \sum_n \frac{1}{E_n - E_0} \left\langle \psi_0 \left| L_{k_\alpha} \right| \psi_n \right\rangle \\ \times \left\langle \psi_n \left| L_{Nk_\beta} r_{Nk}^{-3} \right| \psi_0 \right\rangle + C.C. \end{aligned} \tag{3}$$

Following the derivation in reference [11], we have indicated explicitly that Eqs. [2] and [3] are valid when the origin of the vector potential is at the position O. The sum in Eq. [3] is over all the exited states of the molecule. It is important to understand the behavior of the diamagnetic, Eq. [2], and paramagnetic, Eq. [3], terms under a translation of the origin of coordinates. Both terms exhibit an explicit dependence on the origin of coordinates used in the calculations, but as demonstrated elsewhere for exact and variational wave functions in a complete space, these dependences cancel each other making the total chemical shielding independent of the origin of coordinates. Unfortunately, this is not true for a finite expansion of the wave function. Serious complications arise in chemical shielding calculations as a consequence of the imperfect cancelation of origin-dependent terms in the diamagnetic and paramagnetic components.

Several methods have been proposed to mitigate the gauge problem and to make the results formally gauge invariant for incomplete basis sets and hopefully to produce better results when using moderate size basis sets. The most common approach is to use London or Gauge Invariant (or including) Atomic Orbitals or GIAOs in the atomic expansion of the molecular orbitals [17,20,21]. Other popular methods are individual gauge for localized orbitals (IGLO) [30,31,38], localized orbitals local origin (LORG) [39,40], individual gauges for atoms in molecules (IGAIM) [41], and continuous gauge transformation (CSGT) [42]. While the methods mentioned above take different approaches to mitigate the gauge problem, all of them are exact and converge to the same chemical shielding values in the limit of very large basis [33]. Of course, the converged values are identical to those obtained with the common origin method when the same extended basis is used in the calculations. But what is more important for practical applications is that these methods produce better results when using somehow modest basis sets.

Modeling Chemical Shieldings

The calculation of the diamagnetic part, Eq. [2], presents no serious complications and can be evaluated for any kind of wave function or electronic density. This calculation requires only the computation of one electron integrals of the type 1/r, $1/r^3$, and xy/r^3, which are readily available for almost any approximation used to calculate the electron density in most quantum chemical codes. The more complex paramagnetic term, Eq. [3], requires, in principle, the knowledge of all the exited electronic states of the molecule, in which case direct evaluation of Eq. [3] would be immediate. Unfortunately, this is not the case and a great deal of effort is necessary to obtain reliable values of the paramagnetic contribution. It is always important, if possible, to calculate the paramagnetic contribution with the same accuracy as the diamagnetic contribution to achieve the greatest possible gauge invariance of the numerical results. Unfortunately, this may increase the computational complexity beyond practical limits, therefore making the evaluation of the paramagnetic contribution the limiting factor in the calculations of chemical shieldings.

Today, there are two major approaches to the calculation of the paramagnetic component of the shielding, which are based on the two predominant types of electronic structure methods in use. Those based in the Hartree–Fock theory and its systematic improvements using perturbation methods to include the electronic correlation [37], which we will label "traditional *ab initio* methods" and those based on the Density Functional Theory (DFT) [43]. The reader is referred to the recent reviews by Gauss and Stanton [44] and by Wilson [45] for up-to-date comprehensive reviews of these two complementary methodologies. The first approach is preferred because it provides a systematic path to improve the calculated results, but this systematic improvement arrives with a considerable increase in the computational cost of the calculations. Therefore, in practice these highly precise calculations of chemical shieldings using traditional *ab initio* methods are restricted to small molecules of relative minor interest to practitioner chemists. In the fourth column of Table 1, we present a compilation of the best

Table 1: Comparison of the calculated chemical shieldings using the KT1, KT2, and KT3 exchange-correlation functionals with those from other electronic structure methods. The calculations were performed using the experimental geometries of the compounds. Data from references [46–49] in ppm, referenced to the bare nucleus (i.e. absolute shieldings).

		Exp.	*Ab initio*	HF	LDA	B3LYP	KT1	KT2	KT3
Stdv.			11.3	52.8	36.4	30.1	14.3	16.0	17.4
Slope			1.00	1.04	1.09	1.05	1.01	1.01	1.01
Interc.			−3.5	−39.4	−48.8	−43.7	−6.2	−10.3	−10.2
c.c.			0.9993	0.9875	0.9945	0.9959	0.9989	0.9987	0.9985
HF	^{19}F	419.7	418.6	414.3	416.2	411.1	412	412.4	411.3
H_2O	^{17}O	357.6	337.9	328.6	334.8	327.7	330.7	329.6	327.5
CH_4	^{13}C	198.4	198.9	195.1	193.1	188.7	196.4	195.2	192.8
CO	^{13}C	2.8	5.6	−23.7	−20.3	−19	10.4	7.4	5.8
	^{17}O	−36.7	−52.9	−84.3	−87.5	−81.1	−56.1	−57.1	−55.1
N_2	^{15}N	−59.6	−58.1	−110.2	−91.4	−92.3	−55.8	−59.7	−61.3
F_2	^{19}F	−192.8	−186.5	−166.2	−284.2	−250.4	−193.6	−211	−225.4
PN	^{31}P	53	86	−77.3	−73.7	−50.7	46.6	47.1	47.2
	^{15}N	−349	−341	−483.7	−414.9	−431.3	−358.8	−361.5	−355.3
H_2S	^{33}S	752	754.6	719.9	733.9	705.2	741.5	735.7	730.2
NH_3	^{15}N	273.3	270.7	262.2	266.3	259.9	265.9	264.5	261.8
HCN	^{13}C	82.1	86.3	71.9	65.3	69.1	87.2	86	85.9
	^{15}N	−20.4	−13.6	−48.5	−56.7	−49.5	−18.6	−19.4	−17.9
C_2H_2	^{13}C	117.2	121.8	115.7	100.8	106.9	120.5	120.4	121.1
C_2H_4	^{13}C	64.5	71.2	59.8	40.9	47.2	64.3	63.2	63.4
H_2CO	^{13}C	−4.4	4.7	−6	−40	−24.5	−3	−4.7	−3.5
	^{17}O	−375	−383.1	−436.8	−493.5	−452.4	−383.8	−379.6	−370
N′ON	$^{15}N'$	99.5	100.5	63.9	87.7	81.9	106.8	102.1	101.5
	^{15}N	11.3	5.3	−32.4	−2.3	−11.4	14.2	12.2	13.7
	^{17}O	200.5	198.8	175.4	179	173.1	184.1	177.5	175.2
CO_2	^{13}C	58.8	63.5	51.9	50	48.9	65	63.7	63.8
	^{17}O	243.4	236.4	223.3	209.7	213.5	224.5	221.6	220.9
OF_2	^{17}O	−473.1	−465.5	−439.5	−667.5	−583.1	−516.7	−534	−544.5
H_2CNN'	^{13}C	164.5	171.9	164.7	164.5	160	170.1	167.4	165
	^{15}N	−43.4	−31.6	−11.4	−61.5	−60.1	−37.5	−41.7	−42.3
	^{15}N	−149	−142.4	−299.2	−166.4	−192.8	−128.3	−138.4	−142
HCl	^{35}Cl	952	962.3	950.7	959.5	936.5	961.3	958.6	955.5
SO_2	^{33}S	−126	−134.2	−321.9	−242.9	−262	−149.5	−156.8	−134.4
	^{17}O	−205	−170.4	−284.9	−282	−287.8	−244.6	−251.8	−247.8
PH_3	^{31}P	599.9	594	587.9	583.1	564.5	600.5	596	591.9

calculations available using traditional *ab initio* methods for a representative set of small molecules with shieldings spanning over 1500 ppm. The agreement between theory and experiment is quite impressive; the observed standard deviation of 11.3 ppm corresponds to a relative error of 0.7%. Also, it is remarkable that the slope of the correlation is almost exactly one, indicating that for this level of calculation there is no need for any *ad hoc* scaling of the calculated results. For medium size and large molecules, the computational limitations of the traditional *ab initio* methods make those based on DFT, with their relatively low computational cost and increasingly improved performance, highly competitive. As a result, DFT methods have become the dominant approach for modeling chemical shieldings for medium-to-large molecules. While DFT does not provide a systematic way to improve the results, recently introduced exchange-correlation functionals designed to reproduce chemical shifts (KT1, KT2, and KT3) [46–49] are able to provide results that are quite comparable to those from the best electronic structure calculations. An example of these results is given in Table 1 and Figure 1, where the KT*n* results are compared with the

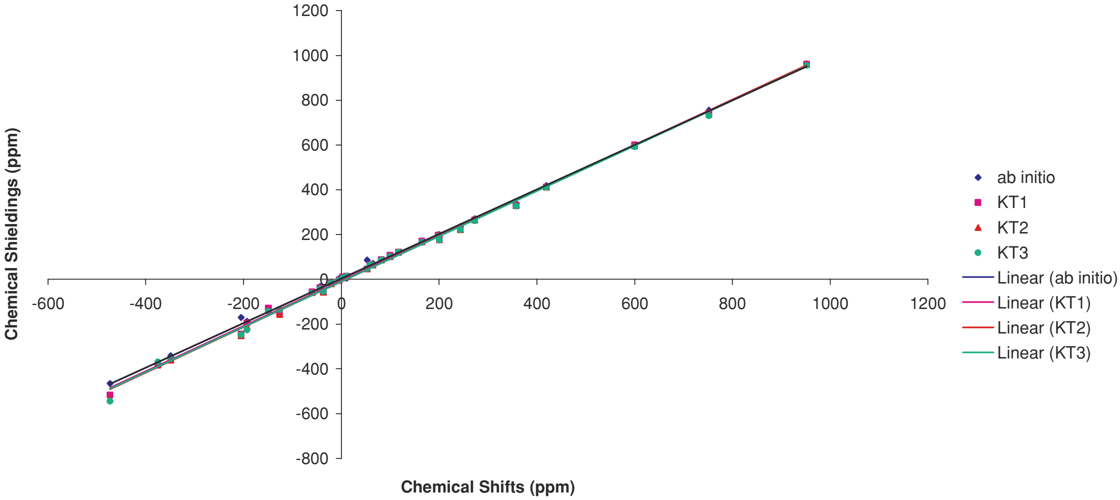

Fig. 1. Comparison of the linear correlation between calculated and experimental chemical shieldings for DFT calculations using the KT1, KT2, and KT3 exchange-correlation functional with those from the best traditional *ab inito* electron correlated calculations. All calculations were performed using the experimental structures of the molecules. Data from references [46–49].

best traditional *ab inito* (electron correlated calculations), Hartree–Fock and DFT calculations using the LDA (local density approximation) [43] and the hybrid B3LYP [50] exchange-correlation functional. In this set of small molecules, the performance of the KT*n* functionals is quite impressive. While not achieving the level of the best *ab inito,* electron correlated calculation, the KT*n* results show relative errors of only 1.1–0.9% compared with 2% for B3LYP, 2.4% for LDA, and 3.5% for the Hartree–Fock calculations. It should be noted that the scaling of the KT*n* results is only a 1% correction in the slope of the correlation, while this correction is 5% for B3LYP, 9% for LDA, and 4% for Hartree–Fock.

While the results presented above demonstrate that the KT*n* exchange-correlation functionals outperform most other DFT methods in this set of small molecules, there have not been calculations, using these functionals, reported for larger molecules. In the following, we provide a general overview of the quality of results that can be obtained routinely when using the popular B3LYP [50], MPW1PW91 [51], and OLYP [52] exchange-correlation functionals for shielding calculations in medium size organic molecules from the G2 and G3 standard sets [53,54]. The calculations were done with the popular Gaussian system for molecular modeling [55], using the GIAO [56], CSGT [42], and IGAIM [41] approaches to enforce the gauge invariance and the Dunning's d95** basis sets [57]. In all cases, the calculations were performed using the optimized (mp2(full)/6-31g*) geometries that are available for the molecules in the G2 and G3 data sets (http://chemistry.anl.gov/compmat/comptherm.htm). From the molecules selected for the shielding calculations, we have included for the analysis presented here 244 ^{1}H chemical shieldings, 133 ^{13}C chemical shieldings, 18 ^{15}N chemical shieldings, and 26 ^{17}O chemical shieldings.

Figures 2–5 and Tables 2–5 depict the correlation between the calculated and their corresponding experimental chemical shifts. In the tables the slope, intercept, and standard deviation of the linear fits are given. Deviations of the values of the slopes from the ideal value of –1 (except for ^{15}N where it is one) provide an estimate of the systematic errors in the calculations that are usually attributed to the deficiencies in the way that the electron correlation is taken into account. In general, the values of the intercept are less informative because it is widely accepted that there are large uncertainties in determining absolute shieldings of reference compounds. Finally, for practical applications it is important to use the standard deviation to estimate the relative accuracy of the calculations, which gives an indication on how successful the method is in discriminating the resonances of nuclei with similar chemical environments.

The methods considered here are able to predict the ^{1}H chemical shifts with relative accuracies of 2–3%. The slopes, that vary from 10% (GIAO) to 20% (IGAIM and CSGT), are independent of the exchange-correlation functional used. For ^{13}C the results also are quite satisfactory, providing relative accuracies of 1.4–1.9% and slopes different than -1 by less than 6%. A more

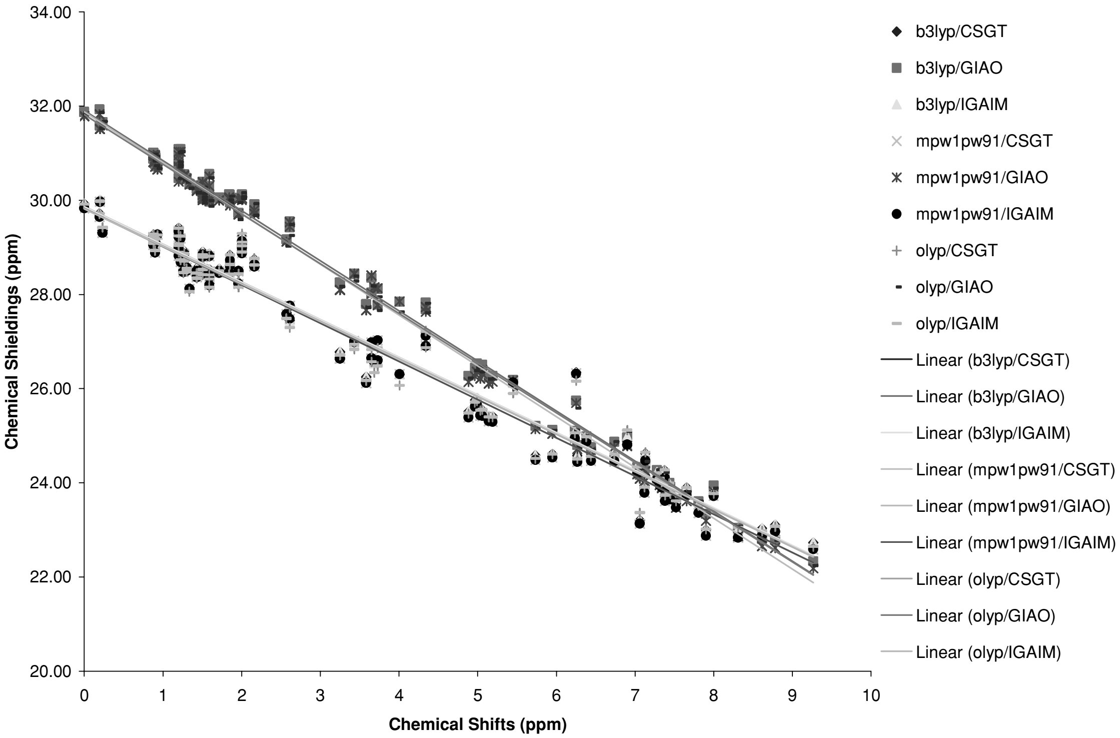

Fig. 2. Calculated ^{1}H chemical shift using different exchange-correlation functionals with the GIAO, CSGT, and IGAIM approaches for selected molecules in the G2 and G3 set of molecules. (See also Plate 2 on page XVIII in the Color Plate Section.)

clear indication of deficiencies of these methods becomes apparent for ^{15}N and ^{17}O chemical shieldings, where the standard deviations reach ~10% and ~14%, respectively. Also significantly larger deviations in the slopes are observed for these nuclei, up to 20% for ^{15}N and up to 8% for ^{17}O. However, in these cases the agreement can be also reduced by well known medium effects on these experimental chemical shifts [6], that are not taken into account in the calculations. The results presented here to illustrate the agreement between calculated and experimental isotropic chemical shifts represent a best case scenario because it has been recently documented that fortuitous cancelation of errors in the individual tensor components of the calculated chemical shieldings can lead to artificially high agreement in the isotropic chemical shifts [58].

In spite of the success of the chemical shielding calculations demonstrated above, there are several limitations in the current methods that should be considered. These limitations can be broadly divided as those inherent to the approximations used in the calculations and those due to the lack of knowledge of the molecular or crystalline structure.

Table 2: Parameters defining the linear correlation between calculated ^{1}H chemical shieldings and measured chemical shifts in selected molecules from the G2 and G3 sets.

	B3LYP			MPW1PW91			OLYP		
	CSGT	GIAO	IGAIM	CSGT	GIAO	IGAIM	CSGT	GIAO	IGAIM
Stdv.	0.3414	0.1950	0.3402	0.3423	0.2032	0.3411	0.3530	0.2017	0.3520
Slope	−1.21	−0.93	−1.21	−1.19	−0.92	−1.20	−1.21	−0.94	−1.21
Intercept	36.4	29.8	36.4	35.8	29.4	35.8	36.4	30.0	36.4

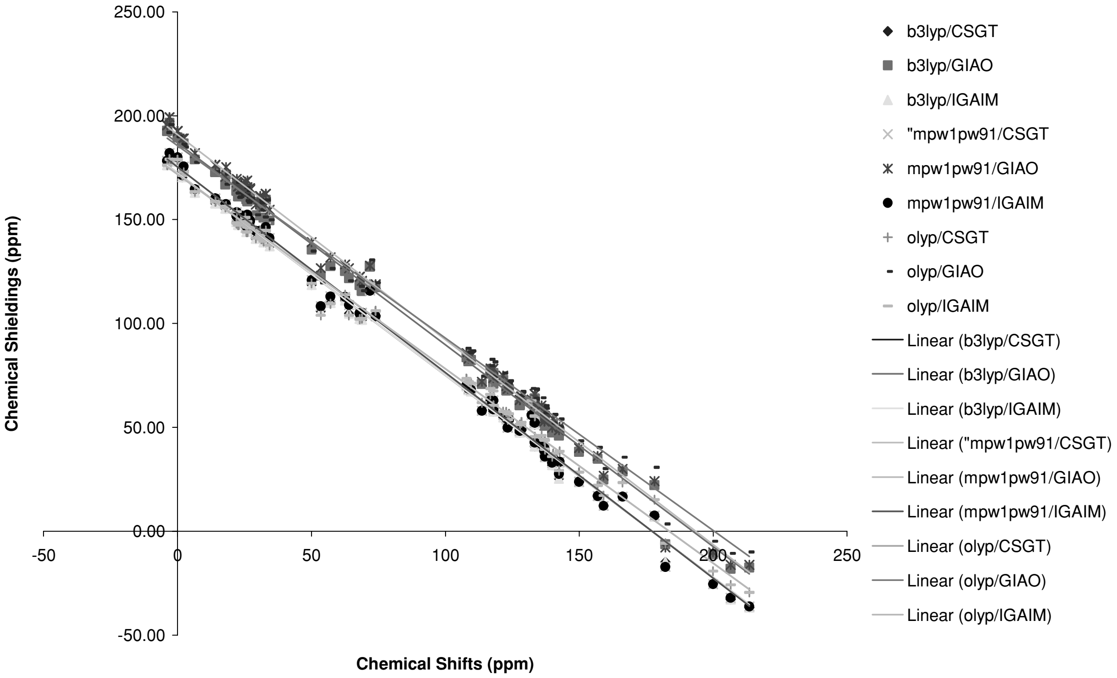

Fig. 3. Calculated ^{13}C chemical shift using different exchange-correlation functionals with the GIAO, CSGT, and IGAIM approaches for selected molecules in the G2 and G3 set of molecules. (See also Plate 3 on page XVIII in the Color Plate Section.)

In the first category, the greatest deficiency of the current methods is the neglect of relativistic corrections. This is of minor consequence when dealing with molecules including first or second row atoms but becomes a significant problem when the molecule includes atoms beyond the third row of the periodic table. There is a great deal of literature dealing with relativistic effects on chemical shielding calculations but there are no well-established methods that can be used routinely. Moreover, the most common approximations to take into account these effects have not been implemented in the most popular software used for chemical shielding calculations. The calculation of chemical shieldings in molecules containing heavy atoms remains mostly the realm of very specialized research groups [59], a situation that may change with the recent implementation of shielding calculations using the ZORA [60,61] approach in the ADF (http://www.scm.com/) package.

The second methodological challenge in the calculation of NMR chemical shielding is associated with the uncertainties in the molecular or crystalline geometry and the effects that the lattice may have on the NMR chemical shieldings. The first problem is a consequence of the great sensitivity of the chemical shieldings to the molecular geometry, a fact that has been known for some time [62,63]. This sensitivity has been instrumental in using

Table 3: Parameters defining the linear correlation between calculated ^{13}C chemical shieldings and measured chemical shifts in selected molecules from the G2 and G3 sets.

	B3LYP			MPW1PW91			OLYP		
	CSGT	GIAO	IGAIM	CSGT	GIAO	IGAIM	CSGT	GIAO	IGAIM
Stdv.	4.1056	3.6650	4.1091	3.7800	3.3856	3.7829	4.5959	4.1226	4.5994
Slope	−1.02	−1.02	−1.02	−1.00	−1.00	−1.00	−1.06	−1.07	−1.06
Intercept	176.7	191.9	176.7	176.7	193.1	176.7	182.8	199.6	182.8

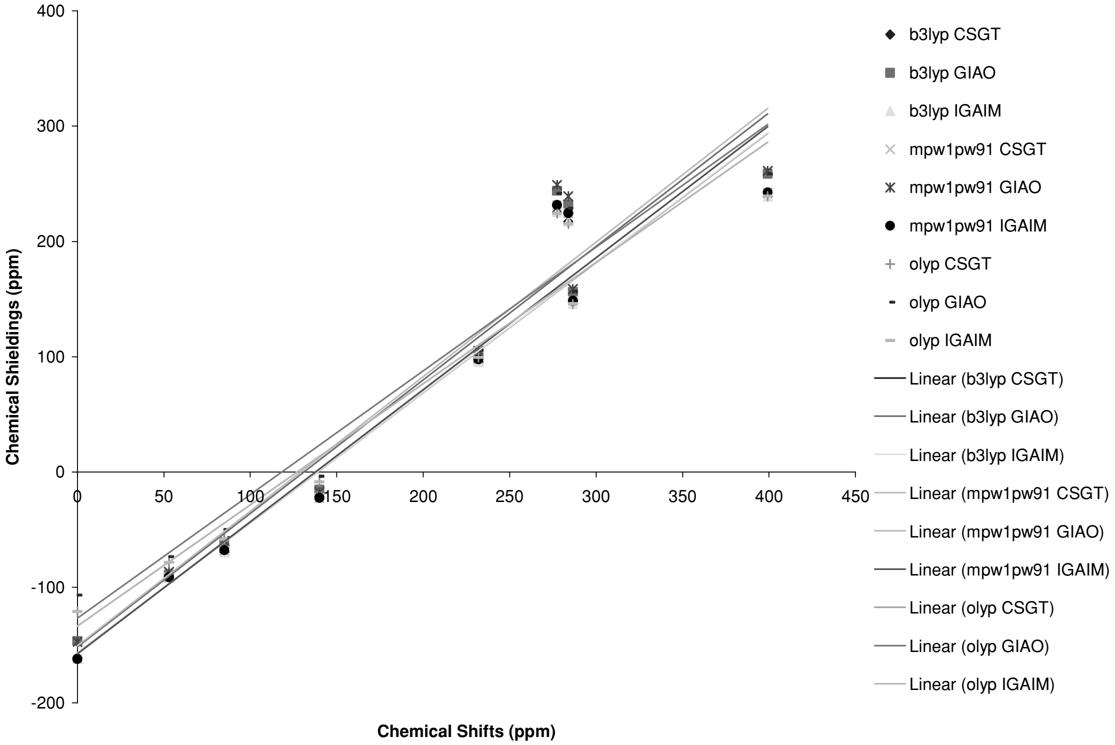

Fig. 4. Calculated ^{15}N chemical shift using different exchange-correlation functionals with the GIAO, CSGT, and IGAIM approaches for selected molecules in the G2 and G3 set of molecules. (See also Plate 4 on page XIX in the Color Plate Section.)

NMR chemical shift information to elucidate structural problems [64], but at the same time it can lead to unacceptable large errors in the calculated chemical shieldings due to the uncertainties in the position of hydrogen atoms determined by common structural methods such as X-ray. It has become a common practice to optimize the position of the hydrogen atoms, determined by X-ray structures before performing shielding calculations. Unfortunately, the practice of using optimized or partially optimized structures to calculate NMR chemical shieldings leads to significant questions about possible cancelation of errors between the method used to optimize the geometry and the one used to calculate the NMR chemical shieldings. It is conceivable that good agreement could be achieved due to the use of a optimized geometry that underestimates the interatomic bond distances, in conjunction with a method to calculate NMR chemical shieldings that also underestimates the shieldings or vice versa. Note that almost always the derivative of the chemical shielding with respect to the interatomic bond distances is negative, $\frac{\delta\sigma}{\delta r} \leq 0$ [65].

Table 4: Parameters defining the linear correlation between calculated ^{15}N chemical shieldings and measured chemical shifts in selected molecules from the G2 and G3 sets.

	B3LYP			MPW1PW91			OLYP		
	CSGT	GIAO	IGAIM	CSGT	GIAO	IGAIM	CSGT	GIAO	IGAIM
Stdv.	38.4057	40.1664	38.4026	40.3231	41.8324	40.3200	36.6648	38.4835	36.6598
Slope	0.83	0.81	0.83	0.81	0.80	0.81	0.89	0.87	0.89
Intercept	141.4	134.1	141.4	140.5	132.6	140.5	130.5	122.4	130.5

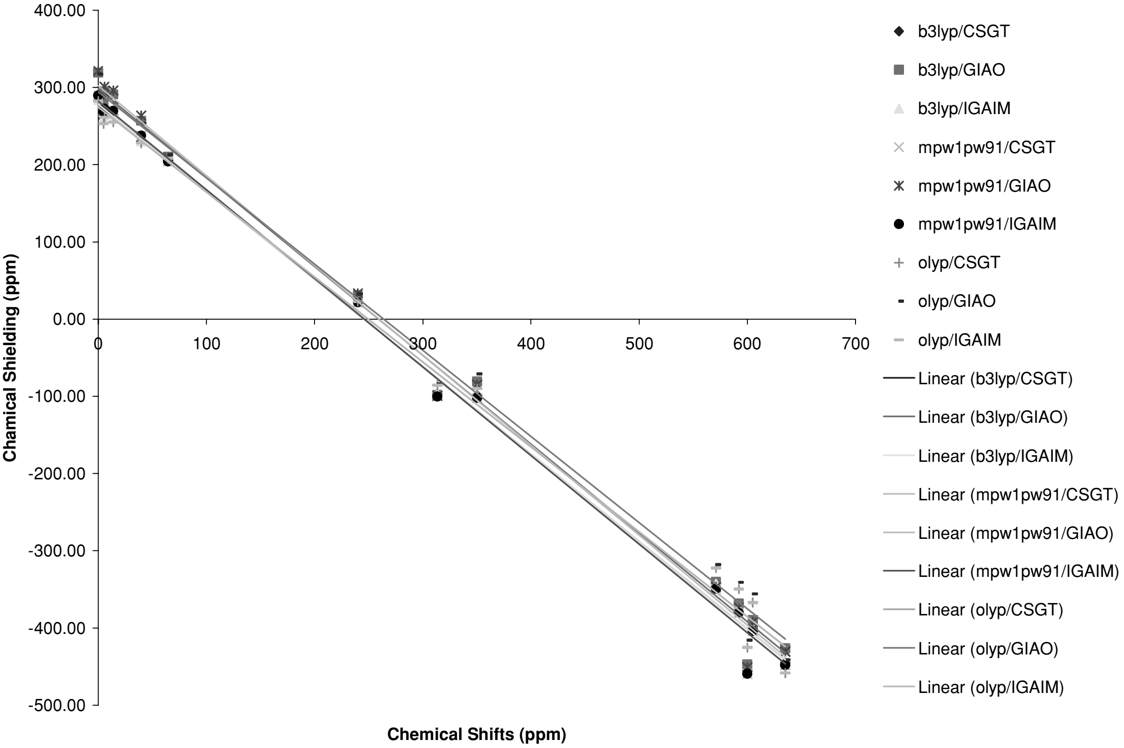

Fig. 5. Calculated ^{17}O chemical shift using different exchange-correlation functionals with the GIAO, CSGT, and IGAIM approaches for selected molecules in the G2 and G3 set of molecules. (See also Plate 5 on page XIX in the Color Plate Section.)

This situation has been recently discussed in the case of the calculations of the ^{15}N chemical shifts of $^{15}NO_2$ in aminonitropyridines, aminonitropyrimidines, and their *N*-oxides [66]. Comprehensive studies, including intermolecular effects (see below) and vibrational corrections are needed to fully understand the interplay between geometry optimization and chemical shielding calculations.

The inclusion of intermolecular effects in the calculation of chemical shieldings has attracted a great deal of attention over the years [8,16,34,67–69] but no "off the shelf" methods are available to take into account these effects in solid or in liquid phase. Unfortunately, in many cases the intermolecular interactions cannot be neglected without losing the quantitative agreement between experimental and calculated results. In these situations, it is necessary to exercise care and complement the standard methods available to calculate chemical shieldings with appropriate ways to take into account the intermolecular effects.

Table 5: Parameters defining the linear correlation between calculated ^{15}N chemical shieldings and measured chemical shifts in selected molecules from the G2 and G3 sets.

	B3LYP			MPW1PW91			OLYP		
	CSGT	GIAO	IGAIM	CSGT	GIAO	IGAIM	CSGT	GIAO	IGAIM
Stdv.	91.7201	90.3712	91.7200	92.2539	91.4189	92.2538	89.5895	88.0658	89.5893
Slope	−0.96	−0.94	−0.96	−0.94	−0.92	−0.94	−1.02	−0.99	−1.02
Intercept	219.7	237.7	219.8	221.9	239.7	221.9	227.7	246.5	227.7

Acknowledgments

Support from the National Science Foundation, The National Institutes of Health, and the Office of Science of the Department of Energy, which over the years have provided funding for the NMR program at Utah, is gratefully acknowledged. The calculations presented here were performed at the CHPC Arches Metacluster, which was partially funded by grant 1 S10 RR17214-01 from the NIH National Center for Research Resources.

References

1. Purcell EM. Phys. Rev. 1949;76:1262.
2. Anderson HL. Phys. Rev. 1949;76:1460.
3. Ramsey NF. Phys. Rev. 1950;77:567.
4. Ramsey NF. Phys. Rev. 1950;78:699.
5. Grant DM. Chemical shift tensors. In: DM Grant, RK Harris (Eds). Encyclopedia of Nuclear Magnetic Resonance. Wiley & Sons: London, 1996, p 1298.
6. Mason J. Multinuclear NMR. Plenum Press: New York, 1987.
7. Berini I, Luchiant C, Parigu G. Solution NMR of Paramagnetic Molecules. Elsevier: Amsterdam, 2001.
8. Jameson CJ, de Dios AC. Theoretical and physical aspects of nuclear shielding. In: GA Webb (Ed). Specialist Periodical Reports on Nuclear Magnetic Resonance. Royal Society: London, 2004, p 47.
9. Webb GA. Shielding: overview of theoretical methods. In: DM Grant, RK Harris (Eds). Encyclopedia of Nuclear Magnetic Resonance. John Wiley & Sons: London, 1996, p 4307.
10. Facelli JC. Shielding calculations. In: DM Grant and RK Harris (Eds). Encyclopedia of Nuclear Magnetic Resonance. John Wiley & Sons: London, 2002, p 323.
11. Facelli JC. Concepts Magn. Reson. 2004;20A:42.
12. Facelli JC, De Dios AC. Modeling NMR chemical shifts: gaining insights into structure and environment. ACS Symp. Ser. 1999;732.
13. Facelli JC. Shielding calculations: perturbation methods. In: DM Grant and RK Harris (Eds). Encyclopedia of Nuclear Magnetic Resonance. John Wiley & Sons: London, 1996, p 4299.
14. Facelli JC. Shielding tensor calculations. In: DM Grant, RK Harris (Eds). Encyclopedia of Nuclear Magnetic Resonance. John Wiley & Sons: London, 1996, p 4327.
15. de Dios AC, Jameson CJ. Annu. Rep. NMR Spectrosc. 1994;29:1.
16. de Dios AC, Oldfield E. Solid State Nucl. Magn. Reson. 1996;6:101.
17. Pulay P, Hinton JF. Shielding theory: GIAO method. In: DM Grant, RK Harris (Eds). Encyclopedia of Nuclear Magnetic Resonance. John Wiley & Sons: London, 1996, p 4334.
18. Lazzeretti P, Malagoli M, Zanasi R. Shielding in small molecules. In: DM Grant and RK Harris (Eds). Encyclopedia of Nuclear Magnetic Resonance. John Wiley & Sons: London, 1996, p 4318.
19. Buhl M, Kaupp M, Malkina OL, Malkin VG. J. Comput. Chem. 1999;20:91.
20. Cheeseman JR, Trucks GW, Keith TA, Frisch MJ. J. Chem. Phys. 1996;104:5497.
21. Ditchfield R. Mol. Phys. 1974;27:789.
22. Fukui H. Prog. Nucl. Magn. Reson. Spectrosc. 1997;31:317.
23. Geertsen J. Chem. Phys. Lett. 1991;179:479.
24. Hansen AE, Bilde M. Shielding calculations: LORG and SOLO approaches. In: DM Grant, RK Harris (Eds). Encyclopedia of Nuclear Magnetic Resonance. John Wiley & Sons: London, 1996, p 4292.
25. Malkin VG, Malkina OL, Salahub DR. Chem. Phys. Lett. 1994;221:91.
26. Malkin VG, Malkina OL, Eriksson LA, Salahub DR. The calculation of NMR and ESR spectroscopy parameters using density functional theory. In: JM Seminario, P. Politzer (Eds). Modern Density Functional Theory. Elsevier Science: Amsterdam, 1995, p 273.
27. Chesnut DB. Annu. Rep. NMR Spectrosc. 1989;21:51.
28. Chesnut DB. Annu. Rep. NMR Spectrosc. 1994;29:71.
29. Chesnut DB. The ab initio computation of nuclear magnetic resonance chemical shielding. In: KB Lipkowitz, DB Boyd (Eds). Reviews in Computational Chemistry. VCH Publishers: New York, 1996, p 245.
30. Kutzelnigg W, Fleischer U, Schindler M. NMR Basic Principles and Progress 1990;23:165.
31. Kutzelnigg W, Fleischer U, van Wüllen C. Shielding calculations: IGLO Method. In: DM Grant, RK Harris (Eds). Encyclopedia of Nuclear Magnetic Resonance. John Wiley & Sons: London, 4284, p 4284.
32. Fleischer U, van Wüllen C, Kutzelnigg W. NMR chemical shift computation: ab initio. In: P von Ragué Schleyer (Ed). Encyclopedia of Computational Chemistry. John Wiley & Sons: London, 1998, p 1827.
33. Schreckenbach G. Theor. Chim. Acta 2002;108:246.
34. Helgaker T, Jaszunski M, Ruud K. Chem. Rev. 1999;99: 293.
35. Mauri F, Pfrommer BG, Louie SG. Phys. Rev. Lett. 1996;77:5300.
36. Sebastiani D, Goward G, Schnell I, Parrinello M. Comput. Phys. Communications 2002;147:707.
37. Simons J, Nichols J. Quantum Mechanics in Chemistry. Oxford University Press: New York, 1997.
38. Kutzelnigg W. Isr. J. Chem. 1980;19:193.
39. Hansen AE, Bilde M. Shielding calculations: LORG and SOLO approaches. In: DM Grant, RK Harris (Eds**). Encyclopedia of Nuclear Magnetic Resonance. John Wiley & Sons: London, 1996, p 4292.
40. Facelli JC, Grant DM, Bouman TD, Hansen AE. J. Comput. Chem. 1990;11:32.
41. Keith TA, Bader RFW. Chem. Phys. Lett. 1992;194:1.
42. Keith TA, Bader RFW. Chem. Phys. Lett. 1993;210:223.
43. Parr RG, Yang W. Density-Functional Theory of Atoms and Molecules. Oxford University Press: Oxford, 1989.
44. Gauss J, Stanton JF. Electron-correlated approaches for calculation of chemical shifts. In: I Prigogine, SA Rice (Eds). Advances in Chemical Physics. John Wiley & Sons, Inc., Somerset, NJ08875, 2002, p 355.
45. Wilson PJ. Annu. Rep. NMR Spectrosc. 2003;49:118.
46. Keal TW, Tozer DJ. J. Chem. Phys. 2003;119:3015.
47. Keal TW, Tozer DJ. J. Chem. Phys. 2004;121:5654.
48. Keal TW, Tozer DJ, Helgaker T. Chem. Phys. Lett. 2004;391:374.

49. Allen MJ, Keal TW, Tozer DJ. Chem. Phys. Lett. 2003;380:70.
50. Becke AD. J. Chem. Phys. 1993;98:5648.
51. Adamo C, Barone V. Chem. Phys. Lett. 1997;274:242.
52. Handy NC, Cohen AJ. Mol. Phys. 2001;99:403.
53. Curtiss LA, Raghavachari K, Redfern PC, Rassolov V, Pople JA. J. Chem. Phys. 1998;109:7746.
54. Curtiss LA, Raghavachari K, Trucks GW, Pople JA. J. Chem. Phys. 1991;94:7221.
55. Frisch MJ, Trucks GW, Schlegel HB, *et al*. Gaussian, Inc.: Pittsburgh, PA, 2003. Gaussian 03 Software System for Molecular Modeling, http://www.gaussian.com.
56. Wolinski K, Hinton JF, Pulay P. J. Am. Chem. Soc. 1990;112:8251.
57. Dunning TH, Jr. J. Chem. Phys. 1989;90:1007.
58. Sefzik T, Turco D, Iuliucci RJ, Facelli JC. J. Chem. Phys. 2005;109:1180.
59. Melo JI, Ruiz de Azua MC, Giribet CG, Aucar GA, Romero RH. J. Chem. Phys. 2003;118:471.
60. Autschbach J, Ziegler T. Relativistic computation of NMR shieldings and spin–spin coupling constants. In: DM Grant and RK Harris (Eds). Encyclopedia of Nuclear Magnetic Resonance, Supplementary Volume. John Wiley & Sons: London, 2002, p 306. Author: Please replace "Supplementary Volume" with correct volume number, if available for reference number 60.
61. Autschbach J. The calculation of NMR parameters in transition metal complexes. In: N Kaltsoyannis, JE McGrady (Eds). Principles and Applications of Density Functional Theory in Inorganic Chemistry. Springer-Verlag GmbH: Berlin, 2004, p 1.
62. Facelli JC, Grant DM. Nature. 1993;365:325.
63. Grant DM, Liu F, Iuliucci RJ, Phung CG, Facelli JC, Alderman DW. Acta Crystallogr. B1995;51:540.
64. Harper JK, Facelli JC, Barich DH, McGeorge G, Mulgrew AE, Grant DM. J. Am. Chem. Soc. 2002;124:10589.
65. Jameson CJ, Osten HJ. Annu. Rep. NMR Spectrosc. 1986;17:1.
66. Anderson KL, Merwin LH, Wilson WS, Facelli JC. Int. J. Mol. Sci. 2002;3:858.
67. Jameson CJ, Jameson AK, Parker H, Cohen SM, Lee C-L. J. Chem. Phys. 1978;68:2861.
68. Besley NA, Hirst JD. J. Am. Chem. Soc. 1999;121:8559.
69. Chalmet S, Ruiz-Lopez MF. J. Chem. Phys. 1999;111:1117.

Ab Initio Calculation of NMR Shielding Constants

Peter B. Karadakov
Department of Chemistry, University of York, Heslington, York YO10 5DD, UK

Introduction

The *ab initio* calculation of NMR shielding constants is one of the "hot" areas in contemporary theoretical chemistry. The reasons for this follow from the extremely high popularity of NMR as an experimental approach and from the fact that, while in many other areas the existing quantum chemical methodology and codes promise much but frequently deliver less than what is required by the practicing chemist, the *ab initio* theoretical NMR results even at this stage reproduce many experimental measurements to a high degree of accuracy.

The aim of the present text is to provide a concise account of the quantum chemical methods for calculating NMR shielding constants, placing the emphasis on the approaches that already are, or are very likely to become available to the research community through implementations in widely available *ab initio* program packages. Although this choice will inevitably lead to certain omissions, it should be emphasized that there is no shortage of detailed review articles covering a wide range of topics within the area. Central place amongst these is taken by the very comprehensive account of the *ab initio* methods for the calculation of NMR shielding and indirect spin–spin coupling constants presented by Helgaker *et al.*[1] Various aspects of the theory and its applications have been discussed by Gauss,[2,3] Jameson,[4] de Dios,[5] Fukui,[6] Bühl *et al.*[7] The *Encyclopedia of NMR*[8] contains a wealth of information on pre-1996 work.

In the next section, we have given a brief overview of the theoretical background. This is followed, in the third section, by an overview of the *ab initio* program packages capable of evaluating NMR shielding tensors. The concluding section discusses the methods suitable for the calculation of NMR shielding tensors in large molecules.

Overview of the Theoretical Background

The electronic Hamiltonian which describes a molecule in the presence of a uniform magnetic field **B** and the field of fixed nuclear magnetic moments $\{\mathbf{m}_J\}$ at positions R_J can be written as[9] (in atomic units)

$$\begin{aligned}\hat{H}(\mathbf{B},\{\mathbf{m}_J\}) &= \sum_j \hat{h}_j(\mathbf{B},\{\mathbf{m}_J\}) + \frac{1}{2}\sum_{j\neq k} r_{jk}^{-1} \\ &= \hat{H}_1(\mathbf{B},\{\mathbf{m}_J\}) + \hat{H}_2, \qquad (1)\end{aligned}$$

where all differences from the standard non-relativistic time-independent many electron Hamiltonian are confined to the modified one-electron operator

$$\begin{aligned}\hat{h}_j(\mathbf{B},\{\mathbf{m}_J\}) &= \frac{1}{2}\left[-i\nabla_j + c^{-1}\mathbf{A}(\mathbf{r}_j-\mathbf{R})\right]^2 \\ &\quad -\sum_J Z_J r_{jJ}^{-1}. \qquad (2)\end{aligned}$$

In these expressions c is the velocity of light, Z_J stands for the charge of nucleus J, and r_{jJ} and r_{jk} are the distances between electron j and nucleus J, and between electrons j and k, respectively. The vector potential at electron j

$$\mathbf{A}(\mathbf{r}_j-\mathbf{R}) = \frac{1}{2}\mathbf{B}\times(\mathbf{r}_j-\mathbf{R}) + \sum_J(\mathbf{m}_J\times\mathbf{R}_{jJ})\,r_{jJ}^{-3}, \qquad (3)$$

depends on the gauge origin **R** which can be chosen arbitrarily. Physical intuition suggests that the energy spectrum of $\hat{H}(\mathbf{B},\{\mathbf{m}_J\})$, as well as all other electronic properties of the molecule should be independent of the choice of **R**. A rigorous proof of the gauge invariance of properties calculated with the exact eigenfunctions of $\hat{H}(\mathbf{B},\{\mathbf{m}_J\})$ has been provided by Hameka.[10] As shown by Epstein,[11] variational methods employing approximate wavefunctions made of orbitals, such as the Hartree–Fock (HF) approach and multiconfigurational self-consistent field (MCSCF) theory, also produce gauge-invariant results, if the orbitals are expanded in a complete basis. By implication, the same is assumed for results obtained using complete-basis-set non-variational approximate wavefunctions, for example, second-order and fourth-order Møller–Plesset (MP2 and MP4) constructions and coupled–cluster (CC) theory.

Graham A. Webb (ed.), Modern Magnetic Resonance, 63–70.
© 2008 *Springer.*

Calculations with finite basis sets based on the Hamiltonian (1) produce results which, as a rule, are gauge-dependent. One way to minimize the associated errors is to use larger basis sets which is computationally inefficient, especially for larger molecules. Another possibility is to employ techniques that introduce local gauge origins to define the vector potential of the external magnetic field.

Two approaches of this type have become particularly popular: the first of these uses London's gauge-including atomic orbitals (GIAOs), while the second one, individual gauge for localized orbitals (IGLOs) associates an individual gauge origin with each of the localized molecular orbitals (MOs) in a molecular system. Both approaches exist in HF, as well as in post-HF implementations, based on multi-configuration self-consistent field (MCSCF) wavefunctions (MC-IGLO[12] and MCSCF-GIAO[13]), second- and higher-order MP perturbation theory expansions (MP2-GIAO,[14,15] MP3-GIAO[16] and MP4-GIAO[17]), CC constructions (CCSD-GIAO[18] and CCSD(T)-GIAO[19]). Density functional theory (DFT) incarnations of the IGLO and GIAO ideas are also available (DFT-IGLO[20,21] and DFT-GIAO[22]).

In the GIAO scheme, which was first applied to NMR shielding calculations by Ditchfield,[23] the MOs for a molecule in a magnetic field are constructed from basis functions that depend on the field explicitly

$$\chi_p(\mathbf{B}) = \exp\left\{-\frac{i}{2c}[\mathbf{B}\times(\mathbf{R}_p-\mathbf{R})]\cdot\mathbf{r}\right\}\chi_p(\mathbf{0}), \qquad (4)$$

where $\chi_p(\mathbf{0})$ is the usual field-independent AO associated with the atomic centre at $\mathbf{R}_p$. Each GIAO has its own local gauge origin placed at its centre. The GIAO approach became very popular after Wolinski *et al.* developed a highly efficient HF-level implementation[24] incorporating computational techniques similar to those used in the calculation of analytical gradients. In a GIAO calculation, in addition to the two-electron integrals over the original basis functions $\chi_p(\mathbf{0})$, one needs to evaluate two-electron integrals over an extended basis involving the original basis functions $\chi_p(\mathbf{0})$ and their products with x, y and z. Integrals of this type are calculated by the analytic gradients routines present in most standard *ab initio* packages. This has much facilitated the provision of HF and post-HF GIAO-based approaches within large *ab initio* codes: the HF-GIAO implementation in TEXAS90[24] (based on Pulay's TEXAS[25]) was soon followed by similar developments in GAUSSIAN94 (the current version of the GAUSSIAN suite is GAUSSIAN03, see Ref. 26), ACES II[27] and TURBOMOLE.[28]

The IGLO approach[29] takes an alternative route and assumes that the local gauge origins are associated with localized MOs, rather than AOs. The wavefunction in the presence of a magnetic field is constructed in terms of field-dependent MOs defined similar to Equation (4),

$$\phi_j(\mathbf{B}) = \exp\left\{-\frac{i}{2c}[\mathbf{B}\times(\mathbf{R}_j-\mathbf{R})]\cdot\mathbf{r}\right\}\phi_j(\mathbf{0}), \qquad (5)$$

where $\phi_j(\mathbf{0})$ is a localized occupied MO in the zero-field wavefunction and $\mathbf{R}_j$ is usually chosen as the corresponding orbital centroid,

$$\mathbf{R}_j = \langle\phi_j(\mathbf{0})|\mathbf{r}|\phi_j(\mathbf{0})\rangle. \qquad (6)$$

From a computational viewpoint, the main difference between the GIAO and IGLO methods is that IGLO avoids calculating the additional two-electron integrals required by GIAO by means of a completeness insertion. This approximation is well-justified when using MOs, but would not work for AOs (that is, in the GIAO case). As a result, an IGLO calculation can be much cheaper computationally than a corresponding GIAO calculation, especially for large molecules. Despite this advantage, the IGLO scheme is currently less popular than its GIAO counterpart which is related to the lower availability of IGLO-based codes and the absence of MPn-IGLO (especially MP2-IGLO) approaches.

The elements of the NMR chemical shielding tensor of a nucleus J can be expressed as the second partial derivative of the molecular energy in the presence of an external magnetic field $\mathbf{B}$ with respect to the components of the nuclear magnetic moment $\mathbf{m}_J$ and $\mathbf{B}$ (in the following expression $\alpha, \beta \in \{x, y, z\}$):

$$\sigma_{J,\alpha\beta} = \left.\frac{\partial^2 E}{\partial m_{J,\alpha}\,\partial \boldsymbol{B}_\beta}\right|_{\mathbf{B}=\mathbf{0},\forall\mathbf{m}_J=0}. \qquad (7)$$

σ_J is a second-rank tensor, which can be written as the sum of three tensors of ranks zero, one and two, respectively,[30]

$$\boldsymbol{\sigma}_J = \sigma_{J,\,\mathrm{iso}}\begin{pmatrix}1&0&0\\0&1&0\\0&0&1\end{pmatrix} + \begin{pmatrix}0&\sigma^{\mathrm{A}}_{J,xy}&\sigma^{\mathrm{A}}_{J,xz}\\-\sigma^{\mathrm{A}}_{J,xy}&0&\sigma^{\mathrm{A}}_{J,yz}\\-\sigma^{\mathrm{A}}_{J,xz}&\sigma^{\mathrm{A}}_{J,yz}&0\end{pmatrix}$$
$$+\begin{pmatrix}d_{J,xx}&d_{J,xy}&d_{J,xz}\\d_{J,xy}&d_{J,yy}&d_{J,yz}\\d_{J,xz}&d_{J,yz}&d_{J,zz}\end{pmatrix} \qquad (8)$$

where $\sigma_{J,\mathrm{iso}}$ is the isotropic shielding

$$\sigma_{J,\mathrm{iso}} = \tfrac{1}{3}(\sigma_{J,xx}+\sigma_{J,yy}+\sigma_{J,zz}), \qquad (9)$$

$\sigma^{\mathrm{A}}_{J,\alpha\beta}$ stands for the antisymmetry parameter

$$\sigma^{\mathrm{A}}_{J,\alpha\beta} = \tfrac{1}{2}(\sigma_{J,\alpha\beta} - \sigma_{J,\beta\alpha}), \tag{10}$$

and the quantities $d_{J,\alpha\beta}$ are given by

$$d_{J,\alpha\beta} = \tfrac{1}{2}(\sigma_{J,\alpha\beta} + \sigma_{J,\beta\alpha} - 2\sigma_{J,\mathrm{iso}}). \tag{11}$$

As a rule, shielding tensors are quoted in the principal axis system (PAS), in which the second-rank tensor with elements $d_{J,\alpha\beta}$ in Eq. (8) is diagonal (and so is the symmetrized shielding tensor $\boldsymbol{\sigma}^{\mathrm{S}}_J = \frac{1}{2}(\boldsymbol{\sigma}_J + \boldsymbol{\sigma}^{\mathrm{T}}_J)$, where $\boldsymbol{\sigma}^{\mathrm{T}}_J$ is the transpose of $\boldsymbol{\sigma}_J$). It is usual to assume that the PAS shielding tensor is diagonal, which amounts to discarding the first-rank tensor involving the antisymmetry parameters in Eq. (8),

$$\boldsymbol{\sigma}^{\mathrm{PAS}}_J = \sigma_{J,\mathrm{iso}} \begin{pmatrix} 1 & 0 & 0 \\ 0 & 1 & 0 \\ 0 & 0 & 1 \end{pmatrix} + \begin{pmatrix} d^{\mathrm{PAS}}_{J,xx} & 0 & 0 \\ 0 & d^{\mathrm{PAS}}_{J,yy} & 0 \\ 0 & 0 & d^{\mathrm{PAS}}_{J,zz} \end{pmatrix}. \tag{12}$$

The shielding anisotropy, $\triangle\sigma_J$, and asymmetry, η_J, are defined as

$$\triangle\sigma_J = \sigma^{\mathrm{PAS}}_{J,11} - \tfrac{1}{2}(\sigma^{\mathrm{PAS}}_{J,22} + \sigma^{\mathrm{PAS}}_{J,33}) \tag{13}$$

and

$$\eta_J = \left(\sigma^{\mathrm{PAS}}_{J,22} - \sigma^{\mathrm{PAS}}_{J,11}\right) \Big/ \left(\sigma^{\mathrm{PAS}}_{J,33} - \sigma^{\mathrm{PAS}}_{J,11}\right) \tag{14}$$

where it is assumed that $\sigma^{\mathrm{PAS}}_{J,33} \geq \sigma^{\mathrm{PAS}}_{J,22} \geq \sigma^{\mathrm{PAS}}_{J,11}$. Other quantities that can be used to characterize the shielding tensor are the span, Ω_J, and the skew, κ_j,[31]

$$\Omega_J = \sigma^{\mathrm{PAS}}_{J,33} - \sigma^{\mathrm{PAS}}_{J,11} \tag{15}$$

and

$$\kappa_J = 3\left(\sigma_{J,\mathrm{iso}} - \sigma^{\mathrm{PAS}}_{J,22}\right) \Big/ \left(\sigma^{\mathrm{PAS}}_{J,33} - \sigma^{\mathrm{PAS}}_{J,11}\right). \tag{16}$$

Theoretical values for NMR chemical shifts can be obtained through the expression

$$\begin{aligned} \delta_J &= (\sigma_{J,\mathrm{iso,ref}} - \sigma_{J,\mathrm{iso}})/(1 - \sigma_{J,\mathrm{iso,ref}}) \\ &\approx \sigma_{J,\mathrm{iso,ref}} - \sigma_{J,\mathrm{iso}} \quad \text{when } |\sigma_{J,\mathrm{iso,ref}}| \ll 1, \end{aligned} \tag{17}$$

where $\sigma_{J,\mathrm{iso,ref}}$ is the (absolute) isotropic shielding of nucleus J in a reference molecule.

The energy expectation value of the Hamiltonian (1) for an arbitrary wavefunction constructed from MOs expanded in a GIAO basis can be represented in terms of the elements of the one- and two-electron density matrices in the GIAO basis, P_{pq} $(\mathbf{B})$ and $\Pi_{pq,rs}$ $(\mathbf{B})$, in analogy to a well-known expression for the $\mathbf{B} = \mathbf{0}$ case,[32] as

$$\begin{aligned} E(\mathbf{B}, \{\mathbf{m}_J\}) = &\sum_{p,q} P_{pq}(\mathbf{B}) \langle \chi_q(\mathbf{B}) | \hat{h}(\mathbf{B}, \{\mathbf{m}_J\}) | \chi_p(\mathbf{B}) \rangle \\ &+ \frac{1}{2} \sum_{p,q,r,s} \Pi_{pq,rs}(\mathbf{B}) \langle \chi_r(\mathbf{B}) \chi_s(\mathbf{B}) \\ &\times | r_{12}^{-1} | \chi_p(\mathbf{B}) \chi_q(\mathbf{B}) \rangle. \end{aligned} \tag{18}$$

In view of the fact that the terms dependent on the nuclear magnetic moments are just those involving the matrix elements of $\hat{h}(\mathbf{B}, \{\mathbf{m}_J\})$, it is convenient to start the derivation of the expression for the elements of the shielding tensor (7) based on Equation (18) with the derivative (see Ref. 17)

$$\frac{\partial E}{\partial m_{J,\alpha}} = \sum_{p,q} P_{pq}(\mathbf{B}) \frac{\partial h_{qp}(\mathbf{B}, \{\mathbf{m}_J\})}{\partial m_{J,\alpha}} \tag{19}$$

where $h_{qp}(\mathbf{B}, \{\mathbf{m}_J\}) = \langle \chi_q(\mathbf{B}) | \hat{h}(\mathbf{B}, \mathbf{m}_1, \mathbf{m}_2, \ldots) | \chi_p(\mathbf{B}) \rangle$. A second derivation differentiation, with respect to the elements of $\mathbf{B}$, yields

$$\begin{aligned} \sigma_{J,\alpha\beta} = &\sum_{p,q} P_{pq}(\mathbf{0}) \left. \frac{\partial^2 h_{qp}(\mathbf{B}, \{\mathbf{m}_J\})}{\partial m_{J,\alpha} \partial B_\beta} \right|_{\mathbf{B}=\mathbf{0}, \forall \mathbf{m}_J=0} \\ &+ \sum_{p,q} \left. \frac{\partial P_{pq}(\mathbf{B})}{\partial B_\beta} \right|_{\mathbf{B}=\mathbf{0}} \left. \frac{\partial h_{qp}(\mathbf{B}, \{\mathbf{m}_J\})}{\partial m_{J,\alpha}} \right|_{\mathbf{B}=\mathbf{0}, \forall \mathbf{m}_J=0}. \end{aligned} \tag{20}$$

This equation provides a convenient starting point for the calculation of NMR shielding tensors by means of GIAO approaches utilizing different wavefunction constructions (see e.g., Refs. 17, 33). Detailed expressions for the derivatives of the matrix elements of the one-electron operator $\hat{h}(\mathbf{B}, \{m_J\})$ have been reported by Gauss.[33] The derivatives of the one-electron density matrix with respect to the magnetic field are evaluated using linear response theory which, in the case of a HF wavefunction, is well-known as the coupled-perturbed HF (CPHF) approach.

An alternative expression for the elements of the NMR shielding tensor can be obtained through direct differentiation of the expectation value of the Hamiltonian $\hat{H}(\mathbf{B}, \{\mathbf{m}_J\})$ [see Equation (2)] with respect to a field-dependent wavefunction $\Psi(\mathbf{B})$ as follows:

$$\begin{aligned}
&\frac{\partial}{\partial m_{J,\alpha}}\left\langle \Psi(\mathbf{B}) \middle| \hat{H}(\mathbf{B},\{\mathbf{m}_J\}) \middle| \Psi(\mathbf{B}) \right\rangle \\
&\qquad = \left\langle \Psi(\mathbf{B}) \middle| \frac{\partial \hat{H}_1(\mathbf{B},\{\mathbf{m}_J\})}{\partial m_{J,\alpha}} \middle| \Psi(\mathbf{B}) \right\rangle, \\
&\sigma_{J,\alpha\beta} = \left[\left\langle \Psi(\mathbf{B}) \middle| \frac{\partial^2 \hat{H}_1(\mathbf{B},\{\mathbf{m}_J\})}{\partial m_{J,\alpha}\partial B_\beta} \middle| \Psi(\mathbf{B}) \right\rangle \right. \\
&\qquad \left. \left. + 2\,\mathrm{Re}\left\langle \frac{\partial \Psi(\mathbf{B})}{\partial B_\beta} \middle| \frac{\partial \hat{H}_1(\mathbf{B},\{\mathbf{m}_J\})}{\partial m_{J,\alpha}} \middle| \Psi(\mathbf{B}) \right\rangle \right] \right|_{\mathbf{B}=\mathbf{0},\forall \mathbf{m}_J=0} .
\end{aligned} \tag{21}$$

When dealing with complicated wavefunction constructions, it may prove simpler and more straightforward to evaluate the first derivatives of the wavefunction with respect to the elements of the magnetic field, rather than the corresponding derivatives of the elements of the one-electron density matrix required by Equation (20).

Ab Initio Program Packages Capable of Calculating NMR Chemical Shielding Tensors

There are several general-purpose *ab initio* program packages which incorporate modules for calculating NMR chemical shielding tensors. Apart from these packages, most of which are commercial, there are other codes with similar or even better functionality, developed in different research groups, which are less readily available to the scientific community. The focus in this section will be on the first group of packages, as their features and functionality are much better documented.

The GAUSSIAN suite (see *http://www.gaussian.com*) is probably the most widely used general-purpose *ab initio* package. It has been capable of computing NMR chemical shielding tensors since the 1994 version, GAUSSIAN94, which introduced implementations of the GIAO, continuous set of gauge transformations (CSGT), individual gauges for atoms in molecules (IGAIM) and single origin approaches at the HF and DFT levels of theory. GAUSSIAN94 and later versions of the package can also calculate HF and DFT-level magnetic susceptibilities with the CSGT, IGAIM and single origin approaches. GAUSSIAN98 extended the NMR-related capabilities of the package through the addition of an MP2-GIAO module. In addition to this, the current version, GAUSSIAN03,[26] allows the calculation of indirect spin–spin coupling constants using HF and DFT wavefunctions, as well as the calculation of NMR properties in the presence of a solvent.

The DFT functionals in the GAUSSIAN suite do not include magnetic field dependent terms, which may be one of the reasons why the DFT-level NMR results are not systematically better than their HF-level counterparts. However, it should be pointed out that the results of Lee *et al.*[34] indicate that the use of a local exchange-correlation functional, which depends on both the electron density and the paramagnetic current density in the DFT-GIAO framework leads only to a slight deshielding effect. There is computational evidence (see Ref. 35) showing that extension of the basis set in DFT-GIAO calculations performed using GAUSSIAN can lead to poorer-quality NMR shielding constants. This suggests that although the DFT-GIAO approach is one attractive way of including correlation effects in shielding calculations on large molecules, the results should be treated with care.

The HF-GIAO and DFT-GIAO codes incorporated into the GAUSSIAN suite are reasonably fast and have relatively modest memory and disk space requirements, especially when use is made of the direct routines which recompute all integrals as required instead of storing them after the initial evaluation. The GAUSSIAN MP2-GIAO module is much slower, uses the conventional procedure of storing integrals to disk and, as a result, needs large amounts of temporary disk space. It can treat systems involving more than 255 basis functions (up to 361 on a 32-bit computer system), although the disk space requirements can become prohibitive: a calculation with a large locally dense basis set on hexafluorobenzene (90 electrons, 270 basis functions) produces a read–write file of over 52 Gb. This is well beyond the capabilities of 32-bit computer systems, which cannot handle files larger than 16 Gb.

The ACES II[27] package (see *http://www.qtp.ufl.edu/Aces2/*) can calculate NMR chemical shielding tensors at the HF-GIAO and MP2-GIAO levels of theory. The HF-GIAO and MP2-GIAO codes in this package were contributed by J. Gauss and realize the theory presented in Ref. 15. The memory requirements for an MP2-GIAO calculation in ACES II are about $2n^2N^2/h$ double (eight-byte) words, where n and N denote the numbers of occupied and virtual orbitals, respectively, and h stands for the order of the molecular point group. The MP2-GIAO code in ACES II uses the conventional procedure of storing integrals to disk, and the size of each of the three largest temporary files, associated with the perturbations corresponding to the elements of $\mathbf{B}$, is about $1.5M^4/(4h)$ double words, where M stands for the number of basis functions. The program can treat the perturbations caused by the three magnetic field components separately, which can lead to a substantial reduction in the disk space requirements at the expense of some loss of efficiency. The maximum number of basis functions in a MP2-GIAO calculation performed within ACES II is 255.

Turbomole[28] (see *http://www.ipc.uni-karlsruhe.de/tch/tch1/index.de.html*) is another *ab initio* package that can computes NMR chemical shieldings within the GIAO ansatz at the HF and MP2 levels of theory. The MPSHIFT module of Turbomole implements the direct MP2-GIAO approach developed by Kollwitz and Gauss[36], which allows calculations on large molecules using machines with limited amounts of memory and disk space. For example, the largest MP2-GIAO calculation reported by Kollwitz and Gauss,[36] on the anthracenium cation (94 electrons, 288 basis functions), was carried out on a workstation with just 128 Mb RAM and 2 Gb of scratch disk space. The most recent version of this code makes full use of molecular point group symmetry, including non-Abelian point groups,[37] and has been used in calculations on highly symmetric molecules involving more than 600 basis functions.[37]

DALTON[38] (see *http://www.kjemi.uio.no/software/dalton/dalton.html*) is an *ab initio* package that can calculate a very wide range of molecular properties at different levels of theory. Gauge origin independent nuclear shieldings and magnetizabilities can be obtained through the use of GIAOs, or through the continuous transformation of the origin of the current density (CTOCD) approach,[39] in its CTOCD-DZ form.[40] Dalton allows the use of GIAOs with HF and MCSCF wavefunctions, while the CTOCD-DZ technique can be combined with the second order polarization propagator approximation (SOPPA), and with SOPPA with CCSD amplitudes. Dalton can also calculate indirect spin–spin coupling constants using the triplet linear response function.

deMon (Density of Montréal)[41] (see *http://www.demon-software.com*) is a DFT package that incorporates the deMon-NMR code written by Malkin *et al.* deMon-NMR can calculate chemical shifts, coupling constants and electron pair resonance quantities. It implements the sum-over-states-density functional perturbation theory (SOS-DFPT) approach[21,42] in combination with the IGLO choice of gauge origins and in many cases produce more accurate results than the standard DFT-GIAO and DFT-IGLO methods, and the more common HF-GIAO and HF-IGLO approaches. The reasonable accuracy and lower computational costs of the SOS-DPFT-IGLO method makes it an attractive alternative to MP2-GIAO in shielding calculations on larger molecular systems (for example, biosystems or transition metal complexes), which require inclusion of correlation effects.

DGauss (see *http://www.cachesoftware.com/cache/dgauss/index.shtml*) is another DFT code for calculating NMR shielding constants, which is also largely based on theory developed by Malkin *et al.*[20,43] DGauss uses DFT in combination with the IGLO and LORG (localized orbital/local origin) techniques.

The Cambridge analytic derivatives package (CADPAC) (see *http://www-theor.ch.cam.ac.uk/software/cadpac.html*) incorporates HF-LORG and DFT-LORG modules for calculating NMR shielding constants.

The RPAC molecular properties package developed mainly by Bouman and Hansen[44] (e-mail address for enquiries concerning RPAC: *aaeh@rpac.ki.ku.dk*) is a post-SCF code that can work with the US version of GAMESS[45] or with GAUSSIAN. It calculates electronic excitation and response properties employing first-order (random-phase approximation/coupled HF) and second-order (SOPPA/second-order LORG (SOLO)) linear response theory. In addition to a number of other electronic ground state response properties, RPAC can calculate NMR shielding tensors with the inclusion of electron correlation effects in the case of the SOLO approach.

Ab Initio Calculation of NMR Chemical Shielding Tensors for Large Molecules

In recent years, the calculation of NMR chemical shielding constants of large molecules, using a variety of theoretical methods, has become largely a routine task. However, the computational cost scales with at least the fourth power of the number of basis functions and the calculations can quickly become prohibitively expensive in terms of the computational resources required, particularly when electron correlation is included. The demand on resources can be reduced by taking into account the fact that nuclear shielding is predominantly governed by local effects. This idea is behind the locally dense basis set (LDBS) technique suggested by Chesnut and Moore[46] in which the atoms of interest are described using larger basis sets, while a smaller basis set is employed for the rest of the molecule. All *ab initio* packages discussed in the previous section allow straightforward specification of different basis set for different atoms, which has made the use of LDBS constructions the most popular way of reducing the computational effort associated with NMR shielding tensor calculations. A now classic example of the advantage of LDBS involves the study of a cluster of 17 H_2O molecules,[47] in which the results obtained using a 6-311G(d,p) basis on the central H_2O molecule and its two-nearest hydrogen-bonded partners were found to be virtually identical to those obtained using the larger basis throughout, but were produced in just one-sixth of the time required for the larger calculation.

The treatment of very large molecular systems may require more drastic approximations. In one approach, advanced by de Dios *et al*, distant parts of the molecular system, solvent molecules, etc., are modeled by partial point charges, creating a classical electrostatic field. In spite of its simplicity, this idea has been demonstrated to work very well for the ^{13}C shielding tensors in crystals of L-tyrosine and L-threonine.[48] This idea was taken further by Cui and Karplus,[49] who suggested a general approach to chemical shielding calculations within the quantum mechanics/molecular mechanics (QM/MM) framework, in which the most important region of a molecule is described by a QM wavefunction, while its surroundings are described using MM. These authors showed that the MM atoms, which polarize the wavefunction of the QM region as point charges, make a two-fold contribution to the elements of the NMR shielding tensor in Equation (20): firstly, the charges on the MM atoms modify the one-electron density matrix P_{pq} ($\mathbf{0}$) and, secondly, these atoms influence the derivatives of the density matrix, $\partial P_{pq}(\mathbf{B})/\partial B_\beta|_{\mathbf{B}=\mathbf{0}}$. As a consequence, the correct treatment of the effects due to the charges on the MM atoms requires a modified variant of linear response theory. The results of Cui and Karplus show that their QM/MM approach, with an appropriate QM/MM partitioning, allows a good description of the environmental effects on the chemical shifts. The typical errors relative to full QM calculations within the same basis set were found to be about 1–2 ppm for distances between QM and MM atoms greater than 2.5 Å. At shorter distances, such as those corresponding to hydrogen bonds, the deviations from the full QM results become more significant as the QM/MM model does not account for the Pauli repulsion and the magnetic susceptibility of the environment. One way to correct for this is to extend the QM region so that it includes all atoms that interact directly with the atom of interest.

The fact that it is possible to perform higher level calculations on the nuclei of interest in a large molecule, as long as their local chemical environment is adequately described, without having to use the same level of theory for the whole system, is fully exploited in the ONIOM-NMR approach,[50] which is quickly gaining popularity (for example, see Refs. 51, 52).

The ONIOM approach involves splitting the system into two or more layers that can be described using different levels of theory and/or basis sets (for an in-depth discussion of the theory behind the ONIOM, our own n-layer integrated molecular orbital and molecular mechanics, approach see, e.g., Refs. 53, 54). A two-layer ONIOM-NMR construction requires the performance of three NMR calculations in order to obtain the shielding of each of the nuclei of interest. First, the shieldings for the whole system must be calculated at the selected lower level of theory, and then those for the molecular fragment surrounding the nucleus of interest have to be evaluated at both the selected higher and lower levels of theory. The expression for the elements of the NMR chemical shielding tensor for nucleus J in the two-layer ONIOM-NMR approach is given by

$$\begin{aligned}&\sigma_{J,\alpha\beta}[\text{ONIOM2(H-GIAO}:\text{L-GIAO)}]\\&\quad=\sigma_{J,\alpha\beta}(\text{H-GIAO, model})\\&\quad+\sigma_{J,\alpha\beta}(\text{L-GIAO, real})-\sigma_{J,\alpha\beta}(\text{L-GIAO, model}),\end{aligned}\tag{22}$$

where ‘H’ and ‘L’ represent the higher and lower levels of theory, respectively, both of which would normally

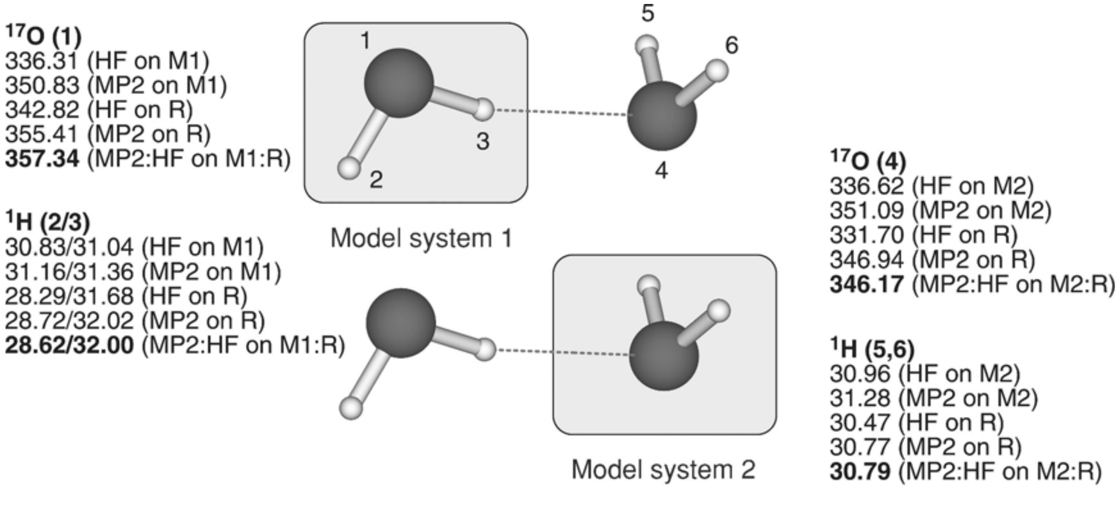

Fig. 1. Application of the ONIOM2(MP2-GIAO:HF-GIAO) approach to the water dimer (MP2//6-31G** geometry of C_s symmetry). Abbreviations in the shielding descriptions: HE = HF-GIAO/6-31G**, MP2 = MP2-GIAO/6-31G**, MP2:HF = ONIOM2(MP2-GIAO/6-31G**:HF-GIAO/6-31G**), Ml = model system 1 (left water molecule), M2 = model system 2 (right water molecule), R = real system (the whole dimer). All shieldings in ppm.

be GIAO-based approaches. The 'model' system corresponds to the inner layer formed by nucleus *J* and its local environment, and the 'real' system represents the entire molecule. One important advantage of the ONIOM-NMR approach is that the expression (21) can be evaluated using any *ab initio* package that implements the 'H-GIAO' and 'L-GIAO' methods, without any need for additional programing.

The choice of suitable molecular fragments is a very important aspect of the use of the ONIOM-NMR approach. In most cases, when calculating the shielding of a particular nucleus, inclusion of its nearest neighbours in the "model" system is sufficient to achieve an adequate description of its local environment. Usually, the definition of the "model" system requires breaking of chemical bonds, and within the ONIOM approach the resulting "free valencies" are saturated through the addition of terminal hydrogen atoms. The ONIOM-NMR approach works particularly well for hydrogen-bonded systems, as illustrated by Figure 1, which shows the results of its application to the water dimer.[50]

Due to the local nature of the NMR shielding tensor, local-correlation treatments (see *e.g.* ref. 55) should be a suitable way of reducing the computational effort associated with post-HF shielding calculations on large molecules. Gauss and Werner have developed a LMP2-GIAO scheme,[56] which has been shown to be comparable in accuracy to the standard MP2-GIAO approach. However, the limited data available at the moment does not allow an estimate of the potential computational savings associated with the use of this local-correlation treatment.

References

1. Helgaker T, Jaszuński M, Ruud K, Chem. Rev. 1999;99:293.
2. Gauss J, Ber. Bunsenges. Phys. Chem. 1995;99:1001.
3. Gauss J In: Grotendorst J (Ed). Modern Methods and Algorithms of Quantum Chemistry, Proceedings, Second Edition, NIC Series, Vol. 3, John von Neumann Institute for Computing, Jülich, 2000, p. 541.
4. Jameson CJ, Ann. Rev. Phys. Chem. 1996;47:135.
5. de Dios AC, Progr. Nucl. Magn. Res. Spectr. 1996;26:229.
6. Fukui H, Progr: Nucl. Magn. Res. Spectr. 1997;31:317.
7. Bühl M, Kaupp M, Malkina OL, Malkin VG, J. Comput. Chem. 1999;20:21.
8. Grant DM, Harris RK (Eds). Encyclopedia of NMR, Wiley: NY, 1996.
9. Ditchfield R, J. Chem. Phys. 1972;56:5688.
10. Hameka HF, Rev. Mod. Phys. 1962;34:87.
11. Epstein ST, J. Chem. Phys. 1964;42:2897.
12. van Wüllen C, Kutzelnigg W, Chem. Phys. Lett. 1993; 205:563.
13. Ruud K, Helgaker T, Kobayashi R, Jørgensen P, Bak K, Jensen H, J. Chem. Phys. 1994;100:8178.
14. Vauthier EC, Comenau M, Odiot S, Eliszar S, Can. J. Chem. 1988;66:1781.
15. Gauss J, Chem. Phys. Lett. 1992;191:614.
16. Fukui H, Baba T, Matsuda H, Miura K, J. Chem. Phys. 1994;100:6608.
17. Gauss J, Chem. Phys. Lett. 1994;229:198.
18. Gauss J, Stanton J, J. Chem. Phys. 1995;103:3561.
19. Gauss J. Stanton J, J. Chem. Phys. 1996;104:2574.
20. Malkin VG, Malkina OL, Salahub DR, Chem. Phys. Lett. 1993;204:87.
21. Malkin VG, Malkina OL, Casida ME, Salahub DR, J. Am. Chem. Soc. 1994;116:5898.
22. Cheeseman J, Trucks GW, Keith TA, Frisch M, J. Chem. Phys. 1996;104:5497.
23. Ditchfield R, Mol. Phys. 1974;27:789.
24. Wolinski K, Hinton JF, Pulay P, J. Am. Chem. Soc. 1990;112:8251.
25. Pulay P, Theor. Chim. Acta. 1979;50:299.
26. Frisch MJ, Trucks GW, Schlegel HB, Scuseria GE, Robb MA, Cheeseman JR, Montgomery JA, Jr, Vreven T, Kudin KN, Burant JC, Millam JM, Iyengar SS, Tomasi J, Barone V, Mennucci B, Cossi M, Scalmani G, Rega N, Petersson GA, Nakatsuji H, Hada M, Ehara M, Toyota K, Fukuda R, Hasegawa J, Ishida M, Nakajima T, Honda Y, Kitao O, Nakai H, Klene M, Li X, Knox JE, Hratchian HP, Cross JB, Bakken V, Adamo C, Jaramillo J, Gomperts R, Stratmann RE, Yazyev O, Austin AJ, Cammi R, Pomelli C, Ochterski JW, Ayala PY, Morokuma K, Voth GA, Salvador E, Dannenberg JJ, Zakrzewski VG, Dapprich S, Daniels AD, Strain MC, Farkas O, Malick DK, Rabuck AD, Raghavachari K, Foresman JB, Ortiz JV, Cui Q, Baboul AG, Clifford S, Cioslowski J, Stefanov BB, Liu G, Liashenko A, Piskorz P, Komaromi I, Martin Rl, Fox DJ, Keith T, Al-Laham MA, Peng CY, Nanayakkara A, Challacombe M, Gill PMW, Johnson B, Chen W, Wong MW, Gonzalez C, Pople JA, Gaussian 03, Revision C.02, Gaussian, Inc., Wallingford, CT, 2004.
27. Stanton JF, Gauss J, Watts JD, Nooijen M, Oliphant N, Perera SA, Szalay PG, Lauderdale WJ, Kucharski SA, Gwaltney SR, Beck S, Balková A, Bernholdt DE, Baeck KK, Rozyczko P, Sekino H, Hober C, Bartlett RJ, ACES II, An Ab Initio Program System, Release 2.0, Quantum Theory Project, Departments of Chemistry and Physics, University of Florida, Gainesville, 1997.
28. Ahlrichs R, Bär M, Baron H-P, Bauernschmitt R, Böcker S, Ehrig M, Eichkorn K, Elliott S, Furche F, Haase F, Häser M, Horn H, Huber C, Huniar U, Kollwitz CKM, Ochsenfeld C, Öhm H, Schäfer A, Schneider U, Treutler O, von Arnim M, Weigend F, Weis P, Weiss H, TURBOMOLE, Program Package for ab initio Electronic Structure Calculations, Version 5.1, Quantum Chemistry Group, University of Karlsruhe, Karlsruhe, 1999.
29. Kutzelnigg W, Isr. J. Chem. 1980;19:193.
30. Smith SA, Palke WE, Gerig JT, Cont. Magn. Reson. 1992;4:107.
31. Mason J, Solid State Nut. Magn. Reson. 1993;2:285.
32. McWeeny R, Methods of Molecular Quantum Mechanics, London: Academic Press, 1992.
33. Gauss J, J. Chem. Phys. 1993;99:3629.
34. Lee AM, Handy AC, Colwell SM, J. Chem. Phys. 1995;103:10095.
35. Karadakov PB, Webb GA, England JE, ACS Symp. Series, 1999;732:115.
36. Kollwitz M, Gauss J, Chem. Phys. Lett. 1996;260:639.

37. Kollwitz M, Häser M, Gauss J, J. Chem. Phys. 1998;108:8295.
38. Angeli C, Bak KL, Bakken V, Christiansen O, Cimiraglia R, Coriani S, Dahle P, Dalskov EK, Enevoldsen T, Fernandez B, Hättig C, Hald K, Halkier A, Heiberg H, Helgaker T, Hettema H, Jensen HJA, Jonsson D, Jørgensen P, Kirpekar S, Klopper W, Kobayashi R, Koch H, Ligabue A, Lutnæs OB, Mikkelsen KV, Norman P, Olsen J, Packer MJ, Pedersen TB, Rinkevicius Z, Rudberg E, Ruden TA, Ruud K, Satek P, de Meras AS, Saue T, Sauer SPA, Schimmelpfennig B, Sylvester-Hvid KO, Taylor PR, Vahtras O, Wilson DJ, Ågren H, DALTON Release 2 Program Manual, 2005.
39. Lazzeretti P, Malagoli M, Zanasi R, Chem. Phys. Lett. 1994;220:299.
40. Ligabue A, Sauer SPA, Lazzeretti P, J. Chem. Phys. 2003;118:6830.
41. Köster AM, Calaminici P, Escalante S, Flores-Moreno R, Goursot A, Patchkovskii S, Reveles JU, Salahub DR, Vela A, Heine T, The deMon User's Guide, Version 1.0.3, 2003–2004, deMon Software, 2004.
42. Malkin VG, Malkina OL, Eriksson LA, Salahub DR, In: Seminario J, Politzer P (Eds), Theoretical and Computational Chemistry, vol. 2, Modern Density Functional Theory: A Tool For Chemistry, Amsterdam: Elsevier, 1995, p. 273.
43. Malkin VG, Zhidomirov GM, Zh. Strukt. Khim. 1988;29:32.
44. Bouman TD, Hansen AE, Chem. Phys. Lett. 1990;175:292.
45. Schmidt MW, Baldridge KK, Boatz JA, Elbert ST, Gordon MS, Jensen JH, Koseki S, Matsunaga N, Nguyen KA, Su SJ, Windus Tl, Dupuis M, Montgomery JA, J. Comput. Chem. 1993;14:1347.
46. Chesnut DB, Moore KD, J. Comput. Chem. 1989;10:648.
47. Hinton JE, Guthrie P, Pulay P, Wolinski k, J. Am. Chem. Soc. 1992;114:1604.
48. de Dios AC, Laws DD, Oldfield E, J. Am. Chem. Soc. 1994;116:7784.
49. Cui Q, Karplus M, J. Phys. Chem. B. 2000;104:3721.
50. Karadakov PB, Morokuma K, Chem. Phys. Lett. 2000;317:589.
51. Molina PA, Jensen JH, J. Phys. Chem. B. 2003;107:6226.
52. Markwick PRL, Sattler M, J. Am. Chem. Soc. 2004;126:11424.
53. Svensson M, Humbel S, Froese RDJ, Matsubara T, Sieber S, Morokuma K, J. Phys. Chem. 1996;100:19357.
54. Humbel S, Sieber S, Morokuma K, J. Chem. Phys. 1996;105:1959.
55. Saebø S, Pulay P, Ann. Rev. Phys. Chem. 1993;44:213.
56. Gauss J, Werner H-J, Phys. Chem. Chem. Phys. 2000;2:2083.

Crystal Structure Refinement Using Chemical Shifts

Ulrich Sternberg[1], Raiker Witter[1], and Anne S. Ulrich[1,2]
[1]*Institute of Biological Interfaces, Forschungszentrum Karlsruhe, POB 3640 D-76021 Karlsruhe, Germany; and*
[2]*Institute of Organic Chemistry, University of Karlsruhe, Fritz-Haber-Weg 6, D-76131 Karlsruhe, Germany*

Introduction

The NMR chemical shift is available from practically every conventional NMR experiment. In contrast to X-ray diffraction it is mainly caused by the density distribution of the valence electrons, hence it contains genuine information about the valence structure of the molecular system. High-resolution solid-state investigations on crystalline systems revealed a considerable dependence of the chemical shift on the 3D arrangement of the atoms and on their packing within the unit cell [1]. In many cases, an asymmetric content of the unit cell could be deduced from NMR line splittings. The point group symmetry of the molecule under study is frequently reflected within the NMR spectra and especially within the chemical shift tensors [2]. It was demonstrated by Taulelle [3] that even the complete space group could be deduced from NMR results.

The success of diffraction methods originates from the direct dependence of the measured intensities on the coordinate of the scattering particles. NMR structure analysis is more complex, but the better we understand how chemical shifts change with the 3D arrangement of atoms, the more reliably we can construct molecular models from our experiments. In the case of chemical shifts, this connection is far from simple and requires quantum chemical computations. In some cases, the molecular packing could be directly deduced by calculating chemical shifts induced by intermolecular interactions [4]. These effects become dominant with increasing polarity of the lattice. In *ab initio* chemical shift calculations molecules are embedded into point charge lattices to simulate the crystallographic surrounding [5]. These computations are highly demanding and for many solid state problems prohibitive. The quest for simple empirical and semi-empirical approaches to structure analysis using chemical shifts has been recently reviewed by Sternberg *et al.* [6]. The ultimate goal will be to perform an accurate chemical shift calculation coupled to a 3D structure refinement. In many cases, *ab initio* CS calculations are used to supplement NMR investigations to extract aspects of the spatial arrangement, but for complete structure refinement a number of severe problems still have to be solved. Chemical shift calculations often require extended basis sets or correlation corrections that may easily lead to multiples of the original computational time. If refinements are to be performed in addition to the chemical shift calculation, their derivatives with respect to the molecular coordinates need to be evaluated. This is again much more demanding than the chemical shift calculations alone. We believe that the success story of liquid state NMR in protein structure elucidation is going to continue in the solid state once chemical shifts can be successfully exploited.

In many cases, the chemical shift will be only one parameter amongst many others that can yield constraints for structure calculation. In solution, we can measure Nuclear Overhauser Enhancements (NOEs), J-couplings, and residual dipolar couplings, and for these parameters there exist well-established relationships to aspects of the molecular structure. In solid-state investigations, we face the situation that up to now there is no general protocol for structure calculations from NMR data. Direct dipolar couplings are often used as distance constraints, provided that the interaction between two spins can be singled out. Likewise, anisotropic chemical shift information is highly useful to determine orientational constraints in macroscopically oriented samples such as membranes or fibers. For solid-state NMR protein structure analysis there exist a number of excellent reviews covering most aspects of chemical shift approaches [7–10].

To solve crystal structures by NMR or to at least augment diffraction studies, the following computational requirements have to be fulfilled: (i) the energy of a unit cell including the influence of the lattice has to be calculated, (ii) extremely fast methods are required for calculating chemical shifts, and (iii) the chemical shift derivatives with respect to the atomic coordinates need to be evaluated. The following paragraphs will give a short introduction into the appropriate methods, before several applications will be presented.

Computational Methods

Bond Polarization Theory for Chemical Shifts

In principle, chemical shielding calculations are performed by investigating the perturbation of a molecular wave function due to the presence of an external field B_Z

Graham A. Webb (ed.), Modern Magnetic Resonance, 71–78.
© 2008 *Springer.*

and magnetic moments caused by the nuclei. Within the context of the Hartree-Fock (HF) theory we have to solve perturbed HF equations. Even if more powerful computers will be available in the future and *ab initio* nuclear shielding calculations are sped up further [11], the calculations will still be very computationally demanding. In many cases, the HF level is not sufficient for reliable results. Correlated methods, such as coupled clusters, have to be applied. However, for MD calculations of crystal lattices these methods are far too time consuming. Therefore, we have to apply a highly efficient method that concentrates on the key points of quantum mechanical chemical shift calculations.

The first key point is that chemical shift is a local quantity, which depends mainly on the first sphere of chemical bonds around the nucleus under consideration. Therefore, bond orbitals are best suited for our task. Bond orbitals can be constructed from the geometry of the system, provided that their occupation numbers and polarity parameters are known.

Secondly, we account for polarization by invoking anti-bonds as excited configurations. Instead of parametrizing the Hamiltonian matrix like other semi-empirical methods the expectation value for the chemical shift is parametrized directly. The complete wave function is not needed, because we are only interested in the change of a local quantity and rather than its absolute value.

Finally, we arrive at an expression were two (in the tensorial case 6) linear empirical parameters per bond type have to be determined. Within the bond polarization theory BPT approach [12, 13] the chemical shift tensor is expressed by

$$\left\langle \Psi_0 | \hat{\delta}_{\alpha\beta} | \Psi_0 \right\rangle = \sum_{i}^{i \in A} \sum_{\alpha'\beta'} D^{i}_{\alpha\alpha'} D^{i}_{\beta\beta'} \left(n_i \delta_i^{\alpha'\beta'} + n_i^2 A_i^{\alpha'\beta'} \right. \\ \left. \times \left[\langle \chi_{\mathrm{A}}^{i} \,|\, \hat{V} \,|\, \chi_{\mathrm{A}}^{i} \rangle - \langle \chi_{\mathrm{B}}^{i} \,|\, \hat{V} \,|\, \chi_{\mathrm{B}}^{i} \rangle \right] \right). \quad (1)$$

The matrix elements $D_{\alpha\alpha'}$ describe the coordinate transformation from the bond orbital frame to the reference frame. The first sum runs over all bond contributions of atom A. The bond polarization matrix elements are given (in atomic units) by

$$\left\langle \chi_\lambda \,|\, \hat{V} \,|\, \chi_\lambda \right\rangle = \sum_{x}^{\text{charges}} \sum_{k} h_k^2 \int \phi_k^\lambda(r) \\ \times \frac{Q_x}{|R_x - r|} \phi_k^\lambda(r) \mathrm{d}r^3, \quad (2)$$

with the charges Q_x at position R_x, the Slater type orbitals [14] $\phi_k^\lambda(r)$, and the bond coefficients h_k. The first sum runs over all polarizing atomic charges. The bond tensor increments $\delta_i^{\alpha\beta}$ and polarization tensor parameters $A_i^{\alpha\beta}$ (in ppm/Hartree) are obtained by calibration procedures, [15]. A collection of crystal structures and single crystal chemical shift measurements has been used to establish a set of linear equations for the parameters [16][17], and in some cases we also included *ab initio* results.

The correlation coefficient obtained from the parameter calibration is $R = 0.994$ with a standard deviation of $\mathrm{SD} = 7.2$ ppm. Once the bond increments $\delta_i^{\alpha\beta}$ and polarization parameters$A_i^{\alpha\beta}$ are determined, only the matrix elements $\langle \chi_\lambda^i | \hat{V} | \chi_\lambda^i \rangle$ and the occupation numbers n_i (from valences [18]), have to be calculated. Introducing point charges in the expression for the potential $\hat{V}$ leads to compact analytic expressions for the integrals, hence calculations within the BPT approach are highly efficient. In Equation (1) there are two sums, which run over all bond contributions of the atom under consideration and over all polarizing charges of the potential $\hat{V}$. If the charge distribution is known, the computational cost for a chemical shift calculation is thus proportional to the number of atoms N.

BPT Calculation of Atomic Charges

As can be seen from Equation (2), accurate atomic charges, Q_x, are also prerequisite of BPT chemical shift calculations. The chemical shifts in this theory are proportional to bond polarization integrals that account for the change of the chemical shift caused by surrounding charge distributions. Since semi-empirical polarization parameters are introduced into the chemical shift calculations, the absolute values of the charges are not of concern. The polarization parameters $A_i^{\alpha\beta}$, on the other hand, will depend on the type of *ab initio* calculation and on the procedure for the population analysis. The atomic charges can be calculated within the BPT approach in a manner analogous to Equation (1) [19]:

$$Q_{\mathrm{A}} = \sum_{i}^{i \in A} \left(n_i q_i + n_i^2 A_i^q \left[\left\langle \chi_{\mathrm{A}}^i \left| \frac{Q_x}{|R_x - r|} \right| \chi_{\mathrm{A}}^i \right\rangle \right. \right. \\ \left. \left. - \left\langle \chi_{\mathrm{B}}^i \left| \frac{Q_x}{|R_x - r|} \right| \chi_{\mathrm{B}}^i \right\rangle \right] \right). \quad (3)$$

Overlap contributions are omitted when calculating the bond polarization integrals. By investigating the charge equations, it is obvious that the charge on atom A, Q_{A}, has to be estimated from all other charges Q_x. By taking the Q_x as factors out of the integrals, we end up with a system of linear equations for the Q_x and Q_{A} with the sum over $n_i q_i$ as inhomogeneities. The parameters q_i and A_i^q have been calibrated against atomic charges of a set of 175 structures consisting of H, C, N, O, F, Si, P, S, Cl, and Zn atoms [20]. The calculations were performed using the 6-31G(d, p) basis set, and the atomic charges are obtained by a natural population analysis (NPA) of the *ab initio* charge distributions. BPT and *ab initio* charges of small molecules correlate regularly with $R = 0.996$. For details of the parametrization and the formalism see Witter [20].

Molecular Force Fields and Chemical Shift Pseudo-Forces

For a complete solid-state NMR structure determination the most desirable approach would be to calculate the energy, the chemical shifts and their derivatives using *ab initio* methods. Even on fast computers this does not seem to be feasible for systems with much more than 10 heavy atoms. With the advent of DFT calculations the situation improved, but a breakthrough in chemical shift calculations was not achieved. One of the most promising developments is the combination of quantum mechanical *ab initio* methods with molecular mechanics calculations (QM/MM). Cui and Karplus [21] combined the empirical CHARMM force field [22] with HF and DFT calculations. In this framework, the chemical shielding calculations can be performed on the GIAO-DFT, -HF or -MP2 level in the QM part of the system under the influence of a larger MM surrounding. The electrostatic perturbations of all relevant matrix elements are treated by a point charge distribution from the MM part of the system, and their influence on the chemical shielding can be studied. Even with the limitations on the size of the QM part this method will be of great value, especially in the treatment of reaction centers in large molecules.

Traditional methods for the treatment of large molecular systems using NMR constraints are molecular mechanics force fields like DYANA [23]. It was demonstrated that such empirical force field reproduce the 3D structures rather well and can compete in this aspect with elaborate *ab initio* calculations. The limitations of molecular mechanics in system size are due to the calculation of the intermolecular energy terms, which scale with the second power of the number of atoms. Hundreds or even thousands of atoms are no real problem for molecular mechanics force field calculations. The most popular method for the search of global minima in NMR force field calculations is to run MD simulations at elevated temperatures, to surmount most conformational barriers and populate extended areas of the configurational space. A larger number of coordinate snapshots is then cooled down in the so-called simulated annealing procedure, or the energy minimum is determined by geometry optimization. The latter method has the advantage that we can weight every structure by its minimum energy. A combination of simulated annealing and geometry optimization is preferred in some investigations to avoid side minima.

The problem of all previous molecular mechanics force field methods is that electronic properties cannot be calculated without wave functions or electron distributions. Even atomic charges are mostly fixed parameters of the force field, and polarizations of the electron distribution are excluded. One possibility to overcome the limitations of the traditional molecular mechanics is the combination of the BPT with a force field. Within the COSMOS force field [24, 25] two-center bond orbitals are constructed for every bond defined in the force field. If the hybridization coefficients and the bond occupation numbers n_i are calculated from the geometry, only the bond polarities are left as free parameters. Within the framework of the BPT, bond polarities or atomic charges can be readily calculated. Therefore, this force field works with charges that depend in the same way on the 3D structure of the molecular systems as the *ab initio* charge values that were used in the parametrization. For σ-bonds the occupation numbers n_i are set to two, and for conjugated π-bonds the value is estimated from the bond distance[25].

Using the COSMOS force field it is possible to divide the molecular system into an MM part and a BPT-QM part, which considers only the polarizations caused by the point charges of the MM part. BPT calculations are very fast and scale with the number of atoms multiplied by the number of bonds. Nevertheless, the BPT atomic charge calculation is the most time consuming step in the force field cycle, hence cutoffs or smaller QM parts help to run efficient simulations. Since all polarizations can be included into the Coulomb energy, the COSMOS force field can be used to study interactions of highly charged systems as for instance ions and peptides [25].

To apply molecular mechanics calculations to crystal structures, the force field has to represent the influence of the crystal lattice in an adequate way. This is achieved by surrounding a central unit cell by one or two shells of translationally created images of itself. The number of shells depends on the electrostatic cutoff radius in relation to the size of the unit cell. In most molecular crystal structures some of the bonds span the borders of the unit cell, therefore, one also has to account for these periodic intramolecular contributions besides the intermolecular energy. To perform realistic crystal structure simulations, the force field has to maintain strict lattice periodicity throughout the calculations:

$$\vec{F}(\vec{r}) = \vec{F}(\vec{r} + i\vec{a} + j\vec{b} + k\vec{c}), \{i, j, k\} = 0, \pm1, \pm2. \tag{4}$$

For every part of a molecule that is not within the unit cell, a code is stored to update the positions of the atoms, forces, and charges from the central unit cell (analogous to

Equation 4). Therefore, all energies and forces are only-calculated only for the central unit cell, but under the influence of one or two shells of neighboring cells. Space group symmetry was not enforced, but the chemical shift constraints conserve the symmetry relations within the unit cell if two or more sites display the same chemical shift value.

Given the COSMOS force filed, NMR parameters are now introduced as constraints in the energy calculations. When searching for the most probable structure of a polyatomic molecule like a peptide, one has to find an energy minimum on a hypersurface possessing a vast multitude of minima. Every experimental constraint will limit the free configurational space and drive the system toward the genuine structure. Even with a large number of constraints we have to search for a global minimum on a multidimensional energy hypersurface. It is important to realize that the minimum structure will not be the most probable structure, because this will depend on Gibbs free energy, ΔG, containing not only the enthalpy but also the entropy. Broad shallow minima may thus be preferred because of the entropic term. Our NMR constraints, on the other hand, will contain an average over the most probable structures in solution or the solid state. Therefore, in most cases the experimental constraints will drive our molecular system energetically uphill.

BPT Pseudo-Forces

In order to obtain energetic corrections, the contribution of the bonds around nucleus A to the polarization energy has to be calculated [20]. The total energy can be approximated by

$$E = \sum_{\mathrm{A}} \sum_{i}^{i\in A} \left(2n_i E_0^i + n_i^2 \frac{\langle \chi_{\mathrm{A}}^i | \hat{V} | \chi_{\mathrm{A}}^i \rangle - \langle \chi_{\mathrm{B}}^i | \hat{V} | \chi_{\mathrm{B}}^i \rangle}{E_0 - E_{i*}} \right). \tag{5}$$

E_0^i are the energies of un-polarized bond contributions, E_0 is the total ground state energy of the molecular system, E_{i*} is the excited state energy for the polarized bond contribution i, and n_i is the occupation number. In a force field approach, we are only interested in relative energies and disregard the constant contributions, hence we introduce the molecular polarization energy E^{P} as well as the atomic polarization energy $E_{\mathrm{A}}^{\mathrm{P}}$

$$E^{\mathrm{P}} = \sum_{\mathrm{A}} \sum_{i}^{i\in A} n_i^2 \frac{\langle \chi_{\mathrm{A}}^i | \hat{V} | \chi_{\mathrm{A}}^i \rangle - \langle \chi_{\mathrm{B}}^i | \hat{V} | \chi_{\mathrm{B}}^i \rangle}{E_0 - E_{i*}} = \sum_{\mathrm{A}} E_{\mathrm{A}}^{\mathrm{P}} \tag{6}$$

The chemical shift can be expressed in terms of the atomic polarization energy [20]. By expanding it with respect to the chemical shift tensor $\delta_{\alpha\beta}^{\mathrm{theo}}$ around the experimental value $\delta_{\alpha\beta}^{\mathrm{exp}}$ and evaluating the gradient, the BPT pseudo-force can be deduced (for isotropic chemical shifts) as:

$$F_j = k^{\mathrm{CS}} (\delta^{theo} - \delta^{\mathrm{exp}}) \frac{\partial \delta^{theo}}{\partial x_j}. \tag{7}$$

The chemical shift derivatives can be calculated within the BTP approach mainly from the derivatives of the polarization energy integrals (see Equation 2). In this case, the force constant becomes

$$k^{CS} = \sum_{\mathrm{A}} \sum_{i}^{i\in A} \frac{2A_i^q}{n_i^2 (A_i^\delta)^2}. \tag{8}$$

The computational cost depends, to a first degree, on the charge calculation, which is proportional to the cube of the number of atoms, N^3. Calculations on systems of about 10^4 atoms are feasible within a day on current standard GHz machines.

Applications in Crystal Structure Refinement

Refinement of Proton Positions

The first application of the COSMOS–NMR force field to a crystallographic problem was the refinement of proton positions from ^{13}C chemical shifts [26]. Accurate proton positions are not so readily determined by X-ray diffraction, especially for large molecules, because protons have no core electrons. Even if there are good X-ray data available, the refinement of the proton sites using NMR chemical shifts will lead to better-defined structures, and can provide valuable insights into the formation of hydrogen bonds. In our first example of β-D-mannitol, both the high-resolution X-ray structure and the solid-state ^{13}C chemical shifts were known. The BPT calculations of the chemical shifts from the X-ray atomic positions gave a mean deviation from the experimental NMR data of 1.7 ppm, with a maximum difference of 2.7 ppm. A force field optimization of the protons, while keeping the positions of the heavy atoms unchanged, lead to a structure with an even larger mean deviation of 2.5 ppm for the calculated ^{13}C chemical shifts from their experimental values. Next, ^{13}C chemical shift pseudo-forces were switched on, to act only on the proton positions. Even though ^{13}C chemical shifts are used as target parameters, this does not mean that the pseudo-forces act only on the carbons. All atoms that contribute to the polarization of a carbon bond acquire pseudo-forces and can thus be influenced by the geometry optimization. The pseudo-forces were scaled in a range starting from 10^{-3} up to 10^3. Significant changes started

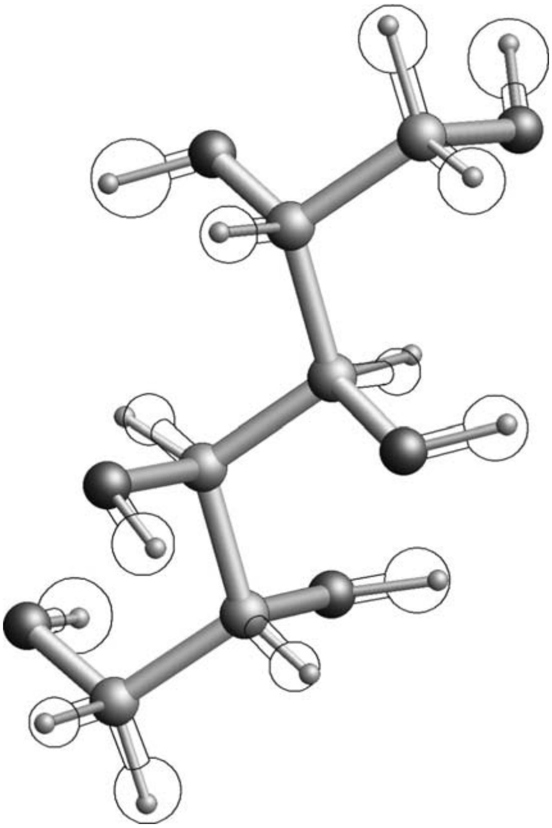

Fig. 1. Superposition of the X-ray structure of D-mannitol with its refinement from ^{13}C NMR chemical shifts. The 50% probability spheres of the protons from the X-ray investigation are shown for comparison.

to show up around 10^{-1}, and at for a scaling constant of 10^2 a lower limit of 0.02 ppm for the chemical shift difference is reached. Notably, the refined proton positions do not violate the limits of the X-ray diffraction, even if the pseudo-forces exceed all other force field energies. The average proton displacement parameter derived from the temperature factor is about 0.2 Å. The standard deviation of the NMR-refined structure with respect to the X-ray structure is only about 0.13 Å [26].

In Figure 1, the superposition of the X-ray and the porton-refined structure (scaling factor 1000) is shown. The spheres at the proton positions are the isotropic 50% probability ellipsoids. It is thus possible to refine crystal structures using chemical shifts as target functions, and thereby resolve structural features such as proton positions that are not well represented in diffraction investigations.

Structure of Cellulose Polymorphs from ^{13}C Chemical Shifts

The lack of crystalline order in polymers such as cellulose or silk fibers significantly reduces the number of interference spots in diffraction investigations, hence the patterns often cannot be analyzed unambiguously. In these cases, a crystal structure refinement using NMR chemical shifts will be of great value, because it does not require long-range crystalline order.

For cellulose three major polymorphs are known, namely natural occurring cellulose I_α and I_β, as well as regenerated cellulose II. When starting our investigations, good crystal structures had been published for cellulose II, while for the other polymorphs only preliminary models based on electron diffraction were available. Optimizations with ^{13}C chemical shift target functions succeeded to produce structures that fulfill the requirements of both the NMR and diffraction data [27]. It was thus demonstrated that some inner-chain hydrogen bonds induce geometry changes of the glycosidic linkage, which cause the C4 resonance to shift from an amorphous value of typically 75 ppm to the observed crystalline value of about 88 ppm. Since this chemical shift value is observed in all cellulose I and II polymorphs, it was concluded that their hydrogen bond patterns have to be similar. The chemical shift of the C4 carbon site can thus be taken as indicator of crystallinity for all three cellulose polymorphs [27].

Recently, native cellulose structures was re-investigated by Nishiyama *et al.* [28], using X-ray and neutron diffraction experiments. For the first time, data concerning the hydrogen bond network could be extracted, hence it was of interest to compare the diffraction results with newly refined NMR structures. 2D NMR investigations on ^{13}C-enriched bacterial cellulose made it possible to assign all six resonances of the glucose units, and moreover to obtain chemical shift anisotropy data [29]. Nishiyama *et al.* [28] had discussed two possible schemes of how the hydroxyl groups could form two alternative hydrogen bond networks. These two networks were proposed to coexist within the cellulose crystallites, and the authors presented occupation numbers for the alternative deuteron positions.

We used these two sets of data to derive two alternative structural models (A and B) with the COSMOS–NMR force field. There are furthermore two possibilities of assigning the two simultaneously observed sets of chemical shifts to the two glucose rings in the unit cell (designated with I and II), hence four sets of MD calculations had to be performed (see Table 1). To assess the stability of the hydrogen bond schemes and to clarify the glucose assignments, we ran 100 ps crystal dynamics simulations on each model, in which the coordinates and atomic charges were recalculated every 0.5 femtoseconds. The simulations

Table 1: Energy contributions and chemical shift differences of the original and chemical shift refined cellulose Iα structures

Structure and method	Hydrogen bond scheme	NMR assignment of glucose units	Van der Waals energy (kJ/mol)	Electrostatic energy (kJ/mol)	Pseudo-energy (kJ/mol)	Total energy (kJ/mol)	RMSD of CS values (ppm)
Neutron diffraction	A	I	40.4	−622.6	2970.4	161.8	5.4
		II			2991.0		5.4
CS optimized	A	I	67.0	−1369.1	71.0	−1111.6	0.83
		II	93.8	−1557.6	323.0	−1249.7	1.77
Neutron diffraction	B	I	71.1	65.2	3677.3	876.4	6.0
		II			3705.1		6.0
CS optimized	B	I	139.6	−1389.7	389.0	−1061.7	1.93
		II	77.9	−1624.8	702.8	−1294.6	2.61

were performed at 293 K to create structures near all minima that could be populated at room temperature. A total of 200 coordinate snapshots were sampled for geometry optimizations with ^{13}C isotropic chemical shifts as target functions. First, all structures were geometry optimized, and in a second step the chemical shift pseudo-forces were switched on.

The results of the optimization procedures are given in Table 1. The first remarkable observation is that for both hydrogen bond schemes, A and B, deep minima for the electrostatic and total energies are obtained, which makes a spontaneous conversion of the two forms at room temperature very unlikely. Since in most cases the chemical shift pseudo-forces drive the structures energetically uphill, we selected the most preferable structure according to the sum of the total and pseudo energies. The most favorable structural model thus corresponds to hydrogen bond scheme A and assignment I (A-I). This structure is moreover in 6th best position of all optimized MD conformations with respect to the total energy, and it has the lowest RMS deviation between the calculated and observed chemical shifts (see Table 1).

The drop in total energy in all cases where chemical shift pseudo-energies are applied, is a clear indication that the calculated chemical shifts are of high quality. After optimization we reach minima with small pseudo-energies and with chemical shift values that lie within the error range of the NMR experiment. The pseudo-energy of 71 kJ/mol is only about 5% of the electrostatic energy in the case of the A-I structure. To test the reliability of the chemical shift refined structured, a least-squares superposition of structure A-I onto the original neutron diffraction coordinates was performed. The RMSD of the two cellulose chain fragments is 0.51Å for all atoms, and this difference drops to 0.37 Å if only heavy atoms are considered (see Figure 2). Most atomic positions fall clearly within the error bounds of the fiber diffraction analysis.

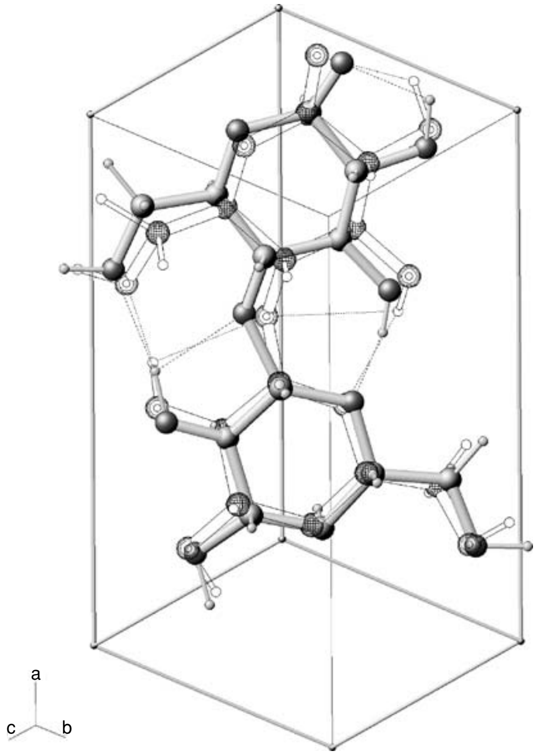

Fig. 2. Least-squares superposition of the cellulose I_α coordinates from neutron diffraction by Nishiyama *et al.* [28] (transparent model) together with the NMR-refined structure A-I (hydrogen bond scheme A and chemical shift assignment I, see Table 1) that was optimized according to chemical shift restraints. The RMSD for all atoms is 0.51 Å, and 0.37 Å for the carbon and oxygen atoms. (See also Plate 6 on page XX in the Color Plate Section.)

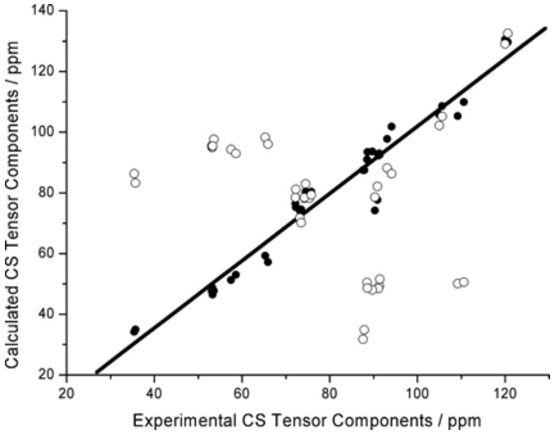

Fig. 3. Calculated principal ^{13}C chemical shift tensor components (δ_{11}, δ_{22}, δ_{33}) of cellulose I_α, plotted against the experimental values. The values after optimization with chemical shift-pseudo-forces are displayed as filled circles, while the result evaluated from the original (non-optimized) diffraction structure are open circles.

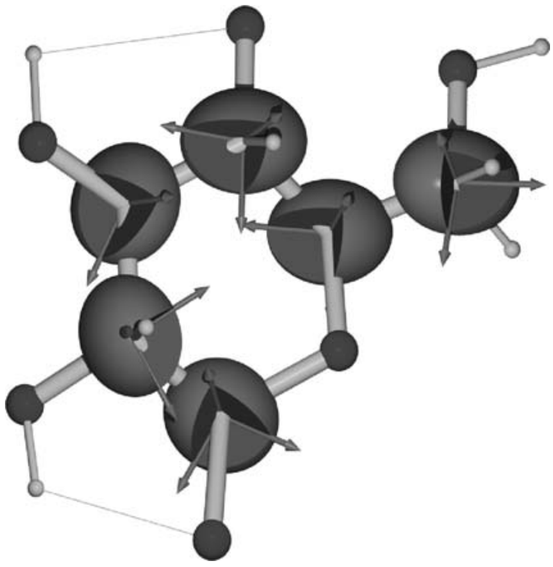

Fig. 4. Orientation of the ^{13}C chemical shift tensors in a glucose ring, calculated from a structure obtained by a geometry optimization with chemical shift boundary conditions. The δ_{33} principal axis components of the tensors (calculated by BPT) are nearly parallel with the C–O bond directions. In the case of carbon C1 with two neighboring oxygen atoms, the δ_{22} component lies on the bisector of the O–C–O angle. (See also Plate 7 on page XX in the Color Plate Section.)

Figure 3 shows an excellent correlation between the observed and calculated principal CS tensor components of all 12 carbons in the unit cell (filled circles). Notably, the chemical shift components derived from the original diffraction coordinates gave no correlation at all (open circles). This must be regarded as strong evidence for the validity of the new NMR-refined structure (see Figure 2). It has moreover been possible for the first time to derive the orientations of the individual chemical shift tensors in the molecular framework of the glucose rings, as illustrated in Figure 4.

Based on these chemical shift calculations, some characteristic rules for CS tensors in carbohydrates can be tested. As discussed by Koch *et al.* [30], for carbons carrying a hydroxyl group the principal component δ_{33} should be oriented along the C–O bond. As seen from Figure 4, the δ_{33} directions deviate only by a few degrees from the respective C–O bond directions. In the case of C1, which is bound to two oxygen atoms, the δ_{33} component lies within the O1–C1–O5 plane, and the δ_{22} direction is aligned with the bisector of the angle formed by the three atoms.

References

1. Brown SP, Spiess HW. Chem. Rev. 2001;101:4125.
2. Klaus E, Sebald A. Magn. Reson. Chem. 1994;32:679.
3. Taulelle F. Solid State Sci. 2004;6:1053.
4. Ochsenfeld C, Brown SP, Schnell I, Gauss J, Spiess HW. J. Am. Chem. Soc. 2001;123:2597.
5. de Dios AC, Laws DD, Oldfield E. J. Am. Chem. Soc. 1994;116: 7784.
6. Sternberg U, Witter R, Ulrich AS. Annu. Rep. NMR Spectrosc. 2004;52:53.
7. Case DA, Dyson HJ, Wright PE. Methods Enzymol. 1994; 239:392.
8. Szilagyi L. Prog. Nucl. Magn. Reson. Spectrosc. 1995;27: 325.
9. Williamson MP, Asakura T. Methods Mol. Biol. 1997;60: 53.
10. Wishart DS, Sykes BD. Methods Enzymol. 1994;239:363.
11. Ochsenfeld C, Kussmann J, Koziol F. Angew. Chem. Int. Ed. 2004;43:4485.
12. Sternberg U. J. Mol. Phys. 1988;63:249.
13. Sternberg U. Priess W. J. Magn. Reson. 1997;125:8.
14. Slater JC. Phys. Rev. 1930;36:57.
15. Priess W, Sternberg U. J. Mol. Struct. (Theochem) 2001; 544:181.
16. Veeman WS. Prog. NMR Spectrosc. 1984;20:193.
17. Sherwood MH, Alderman DW, Grant MG. J. Magn. Reson. 1989;84:466.
18. O'Keefe M, Brese NE. J. Am. Chem. Soc. 1991;113:3226.
19. Koch F-T, Möllhoff M, Sternberg U. J. Comp. Chem. 1994; 15:524.
20. Witter R. *Three Dimensional Structure Elucidation with the COSMOS-NMR Force Field*, thesis, 2003, www.dissertation.de.

21. Cui Q, Karplus M. J.Phys. Chem. B. 2000;104:3721.
22. Cui Q, Karplus M. J. Chem. Phys. 2000;112:1133.
23. Güntert P. Q. Rev. Biophys. 1998;31:145.
24. Möllhoff M, Sternberg U. J. Mol. Model. 2001;7:90.
25. Sternberg U, Koch F-Th, Bräuer M, Kunert M, Anders E. J. Mol. Model. 2001;7:54.
26. Witter R, Prieß W, Sternberg U. J. Comp. Chem. 2002;23: 289.
27. Sternberg U, Koch F-Th, Prieß W, Witter R. Cellulose. 2003;10:189.
28. Nishiyama Y, Sugiyamam J, Chanzy H, Langan P. J. Am. Chem. Soc. 2003;125:14300.
29. Witter R, Sternberg U, Hesse S, Kondo T, Koch F-Th, Ulrich AS. Macromolecules 2006: in press.
30. Koch F-Th, Prieß W, Witter R, Sternberg U. Macromol. Chem. Phys. 2000;201:1930.

The Theory of Nuclear Spin–Spin Couplings

Hiroyuki Fukui
Kitami Institute of Technology, Kitami, Hokkaido, Japan

Introduction

One of the reasons for difficulties in explaining indirect nuclear spin–spin coupling constants is that this phenomenon has no analogs in classical physics. The main driving force for inducing nuclear spin–spin couplings in molecules is not electromagnetic interactions but the Pauli's exclusion principle, operating between electrons with the same spin. It was demonstrated that Fermi correlation, due to the Pauli's exclusion principle, can be considered to be the mechanism whereby distant atoms communicate with each other [1]. The indirect nuclear spin–spin coupling is described by the form of $J_{MN}\vec{I}_M \cdot \vec{I}_N$ in which $\vec{I}_M$ and $\vec{I}_N$ are the nondimensional nuclear spin vectors, and J_{MN} is called an isotropic nuclear spin–spin coupling constant [2,3]. J_{MN} has the units of hertz (2π rad/s) Unlike the direct interaction of magnetic dipoles, an energy of this sort of nuclear spin–spin coupling does not average out to zero when the molecules are rotating, so its effect still remains in the spectra of liquids. This fact indicates that the indirect nuclear spin–spin coupling comes from an indirect coupling mechanism via the electrons in the molecule. The indirect coupling mechanism between nuclear spins will be considered in the next section.

Origin of the Indirect Nuclear Spin–Spin Coupling Interaction

A full and successful theory of the indirect nuclear spin–spin coupling based on the complete Hamiltonian for electron–nuclear interactions was first outlined by Ramsey and Purcell [4] and developed in more detail in a later paper by Ramsey [5]. We will describe the origin of the indirect nuclear spin–spin coupling interaction below.

The electron–nuclear magnetic interactions come from the interactions between nuclear spins and electronic motions or electronic spins. The magnetic interactions in an electronic system are well described with the use of the relativistic Dirac equation [6,7]. Let us consider an electronic system consisting of one electron and two hypothetical nuclear spins which have the nuclear magnetogyric ratios, γ_M and γ_N, respectively, but do not possess nuclear charges. The time-independent Dirac equation for the electron is then given by

$$\begin{aligned}\Bigg\{\begin{bmatrix}0 & c\vec{\sigma}\\ c\vec{\sigma} & 0\end{bmatrix}\cdot\Big[&-i\hbar\vec{\nabla}+(\mu_0/4\pi)e\hbar\gamma_M r_M^{-3}\vec{I}_M\\ &\times\vec{r}_M+(\mu_0/4\pi)e\hbar\gamma_N r_N^{-3}\vec{I}_N\times\vec{r}_N\Big]\\ &+m_\mathrm{e}c^2\begin{bmatrix}0 & 0\\ 0 & -2\end{bmatrix}\Bigg\}\psi=E\psi,\end{aligned}\tag{1}$$

where $\vec{\sigma}$ is the 2×2 Pauli spin matrix vector. The three components of the $\vec{\sigma}$ vector are given by

$$\sigma_x=\begin{bmatrix}0 & 1\\ 1 & 0\end{bmatrix},\ \sigma_y=\begin{bmatrix}0 & -i\\ i & 0\end{bmatrix},\ \sigma_z=\begin{bmatrix}1 & 0\\ 0 & -1\end{bmatrix}.\tag{2}$$

$\vec{\sigma}$ is the double of the electronic spin vector $\vec{s}$, i.e. $\vec{\sigma} = 2\vec{s}\cdot$ μ_0 is the permeability of the vacuum, c is the velocity of light, and m_e and $-e$ are the rest mass and electronic charge of the electron, respectively. $\vec{r}_M$ and $\vec{r}_N$ are defined by $\vec{r}_M = \vec{r} - \vec{R}_M$ and $\vec{r}_N = \vec{r} - \vec{R}_N$, respectively, with the electronic position $\vec{r}$ and the nuclear positions, $\vec{R}_M$ and $\vec{R}_N$. The wave function ψ has four components, i.e. large two-component spinor ϕ_L (the first and second components of ψ) and small two-component spinor ϕ_S (the third and fourth components of ψ). Equation (1) is decomposed into the two component equations:

$$c\vec{\sigma}\cdot\vec{\pi}\phi_\mathrm{S}=E\phi_\mathrm{L}\tag{3}$$

and

$$c\vec{\sigma}\cdot\vec{\pi}\phi_\mathrm{L}-2m_\mathrm{e}c^2\phi_\mathrm{S}=E\phi_\mathrm{S},\tag{4}$$

where

$$\begin{aligned}\vec{\pi}&=-i\hbar\vec{\nabla}+(\mu_0/4\pi)e\hbar\gamma_M r_M^{-3}\vec{I}_M\times\vec{r}_M\\ &\quad+(\mu_0/4\pi)e\hbar\gamma_N r_N^{-3}\vec{I}_N\times\vec{r}_N.\end{aligned}\tag{5}$$

π is called the mechanical momentum of the electron.

In order to eliminate the small component ϕ_S, we solve Equation (4) for ϕ_S and obtain

$$\phi_\mathrm{S}=(2m_\mathrm{e}c^2+E)^{-1}c\vec{\sigma}\cdot\vec{\pi}\phi_\mathrm{L}.\tag{6}$$

Graham A. Webb (ed.), Modern Magnetic Resonance, 79–83.
© 2008 *Springer.*

We substitute Equation (6) into Equation.(3) and get

$$\left[\left(2m_{\mathrm{e}}c^2 + E\right)^{-1} c^2 \left(\vec{\sigma} \cdot \vec{\pi}\right)^2 - E\right]\phi_{\mathrm{L}} = 0. \tag{7}$$

Equation (7) gives us the energy of the system

$$E_{\pm} = -m_{\mathrm{e}}c^2 \pm \left[m_{\mathrm{e}}^2 c^4 + c^2(\vec{\sigma} \cdot \vec{\pi})^2\right]^{1/2}. \tag{8}$$

We are usually interested in the positive energy of the system. So we discard the negative energy E_- and keep the positive energy E_+ alone. We expand the positive energy E_+ in terms of a power series of the reciprocal velocity of light c^{-1}.

$$E_+ = (\vec{\sigma} \cdot \vec{\pi})^2/2m_{\mathrm{e}} - (\vec{\sigma} \cdot \vec{\pi})^4/8m_{\mathrm{e}}^3c^2 + O(c^{-4}) + \cdots. \tag{9}$$

The first term is the nonrelativistic energy of the system. The second term proportional to c^{-2} is the lowest order of relativistic correction to the energy. In this chapter, we consider only the nonrelativistic term and ignore the relativistic corrections to the energy.

Using the identity [6,7]

$$(\vec{\sigma} \cdot \vec{\pi})^2 = \vec{\pi}^{\,2} + i\vec{\sigma} \cdot \vec{\pi} \times \vec{\pi}, \tag{10}$$

we obtain

$$\begin{aligned} E_+ &= (\vec{\sigma} \cdot \vec{\pi})^2/2m_{\mathrm{e}} = -(\hbar^2/2m_{\mathrm{e}})\Delta \\ &\quad + (e^2/2m_{\mathrm{e}})(\vec{A}_M^2 + \vec{A}_N^2) + h_{MN}^{\mathrm{DSO}} + h_M^{\mathrm{PSO}} \\ &\quad + h_N^{\mathrm{PSO}} + h_M^{\mathrm{FC}} + h_N^{\mathrm{FC}} + h_M^{\mathrm{SD}} + h_N^{\mathrm{SD}}, \end{aligned} \tag{11}$$

where

$$\vec{A}_a = (\mu_0/4\pi)\hbar\gamma_a r_a^{-3}\vec{I}_a \times \vec{r}_a, \quad a = M \; or \; N, \tag{12}$$

$$\begin{aligned} h_{MN}^{\mathrm{DSO}} &= (\mu_0/4\pi)^2 \left(e^2\hbar^2/m_{\mathrm{e}}\right) \gamma_M \gamma_N r_M^{-3} r_N^{-3} \\ &\quad \times \left[\left(\vec{I}_M \cdot \vec{I}_N\right)\left(\vec{r}_M \cdot \vec{r}_N\right) - \left(\vec{I}_M \cdot \vec{r}_N\right)\left(\vec{I}_N \cdot \vec{r}_M\right)\right], \end{aligned} \tag{13}$$

$$\begin{aligned} h_a^{\mathrm{PSO}} &= 2(\mu_0/4\pi)\mu_{\mathrm{B}}\gamma_a r_a^{-3}\vec{I}_a \cdot \vec{l}_a, l_a = -i\hbar\vec{r}_a \times \vec{\nabla}, \\ a &= M \text{or} \; N, \end{aligned} \tag{14}$$

$$\begin{aligned} h_a^{\mathrm{FC}} &= (8\pi/3)(\mu_0/4\pi)\mu_{\mathrm{B}}\hbar\gamma_a\delta(\vec{r}_a)\vec{\sigma} \cdot \vec{I}_a, \\ a &= M \text{ or } N, \end{aligned} \tag{15}$$

$$\begin{aligned} h_a^{\mathrm{SD}} &= (\mu_0/4\pi)\mu_{\mathrm{B}}\hbar\,\gamma_a \Big[-r_a^{-3}\vec{\sigma} \cdot \vec{I}_a \\ &\quad + 3r_a^{-5}\left(\vec{\sigma} \cdot \vec{r}_a\right)\left(\vec{I}_a \cdot \vec{r}_a\right)\Big], \quad a = M \text{ or } N \end{aligned} \tag{16}$$

and

$$\mu_{\mathrm{B}} = e\hbar/2m_{\mathrm{e}}. \tag{17}$$

h^{DSO} and h^{PSO} are the diamagnetic spin orbital (DSO) and paramagnetic spin orbital (PSO) interactions, respectively. h^{FC} and h^{SD} are the Fermi contact (FC) and spin dipole (SD) interactions, respectively. μ_{B} is the Bohr magneton. In the calculation of $\vec{\pi} \times \vec{\pi}$ in Equation (10), we used the identity [7]

$$\begin{aligned} \nabla_u(r_u/r^3) &= (4\pi/3)\delta(\vec{r})\delta_{uv} + \delta_{uv}/r^3 - 3r_u r_v/r^5, \\ &(u, v \in \{x, y, z\}). \end{aligned} \tag{18}$$

The field-independent splitting of NMR lines, usually described in hertz, is due to the isotropic part J_{MN} of the indirect nuclear spin–spin coupling tensor $\hat{J}_{MN}$. The nuclear spin–spin coupling energy is written as $\sum_{uv} J_{MN,uv} I_{Mu} I_{Nv} (u, v \in x, y, z)$. The (u,v) component $J_{MN,uv}(u, v \in \{x, y, z\})$ of the tensor $\hat{J}_{MN}$ has five different contributions [5], all of which result from electron-coupled interactions between the two nuclear spin components, I_{Mu} and I_{Nv}. Four of these contributions are due to second-order perturbations and depend on the first-order wave function, whereas one contribution is due to a first-order perturbation type and can be expressed using only the zeroth-order wave function. Four of these contributions can be expressed as a sum-over-states (SOS) formula [8]

$$\begin{aligned} J_{MN,uv}^{\mathrm{AB}} &= h^{-1} \sum_{m>0} \left[\frac{\langle 0 \,|H_{M,u}^{\mathrm{A}}|\, m\rangle\langle m \,|H_{N,v}^{\mathrm{B}}|\, 0\rangle}{E_0 - E_m} \right. \\ &\quad \left. +(1 - \delta_{\mathrm{AB}})\frac{\langle 0 \,|H_{M,u}^{\mathrm{B}}|\, m\rangle\langle m \,|H_{N,v}^{\mathrm{A}}|\, 0\rangle}{E_0 - E_m} \right] + \mathrm{C.C.}, \end{aligned} \tag{19}$$

where $|0\rangle$ and $|m\rangle$ represent the many-electron ground and excited states of the unperturbed system, respectively. C.C. means the complex conjugate of the former term. A and B represent the type of interaction Hamiltonians, that is, the PSO, FC, and SD interactions whose one-electron interaction operators are given by Equations (14)–(16). The isotropic part J_{MN} is equal to the diagonal average of the tensor, i.e. $(J_{MN,xx} + J_{MN,yy} + J_{MN,zz})/3$. The FC and SD interactions have matrix elements between the singlet ground state and the triplet excited states, whereas the PSO term has matrix elements between the singlet ground and excited states. So we have the four possible combinations of FC–FC, SD–SD, FC–SD, and PSO–PSO contributing to $J_{MN,uv}$. The FC–FC contribution is fully isotropic, namely, all the diagonal elements of the FC–FC contribution are equal to each other, and all the off-diagonal elements of it are zero. On the other hand, the FC–SD contribution is fully anisotropic and makes no contributions to the isotropic part. The other two combinations, SD–SD and PSO–PSO, yield both isotropic and anisotropic contributions. The last contribution to the tensor component $J_{MN,uv}$ is the DSO term, which is of a different form, being an average value in the ground state of the interaction Hamiltonian $H^{\mathrm{DSO}}_{MN,uv}$ whose one-electron interaction operator is given by Equation (13).

Quantum electrodynamics (QED) [9] tells us that the electronic spin magnetic moment should be changed from $-\mu_{\mathrm{B}}\vec{\sigma}$ to the $-g_{\mathrm{e}}\mu_{\mathrm{B}}\vec{s}$ [7], where g_{e} is called the electronic g factor. The Dirac equation gives us a g_{e} value of exactly 2. However, the QED corrected g_{e} value is

$$\begin{aligned} g_{\mathrm{e}} &= 2 + (\alpha/\pi) - 0.65696(\alpha/\pi)^2 + 1.49(\alpha/\pi)^3 \\ &\quad + O((\alpha/\pi)^4) + \ldots = 2.02319, \end{aligned} \tag{20}$$

where

$$\alpha = e^2/4\pi\varepsilon_0\hbar c = 1/137.0359895. \tag{21}$$

The nondimensional constant α is called the fine structure constant. The four kinds of one-electron interaction operators can be easily written using Equations (13)–(16). The nonrelativistic unperturbed Hamiltonian H_0 is written as

$$H_0 = \sum_k h^{(0)}(k) + \sum_{k<1} \left(e^2/4\pi\varepsilon_0 r_{kl}\right), \tag{22}$$

where

$$h^{(0)}(k) = -\left(\hbar^2/2m_{\mathrm{e}}\right)\Delta_k - \sum_{\mathrm{A}} \left(Z_{\mathrm{A}} e^2/4\pi\varepsilon_0 r_{\mathrm{A}k}\right). \tag{23}$$

Z_{A} is the atomic number of nucleus A. For simplicity, atomic units (au) are used from now, that is,

$$e = 1,\ \hbar = 1,\ m_{\mathrm{e}} = 1,\ 4\pi\varepsilon_0 = 1,\ \mu_0/4\pi = \alpha^2. \tag{24}$$

Coupled Hartree–Fock Approximation

It was stated in the previous section that the nuclear spin–spin coupling tensor components $J_{MN,uv}$ are generally given as the sum of the five different contributions. The calculation of the DSO contribution of the first-order perturbation type is trivial. It can be straightforwardly evaluated following the numerical integration method by Matsuoka and Aoyama [10]. On the other hand, the calculation of the other four contributions of the second-order perturbation type is not easy. So most efforts at calculating the nuclear spin–spin couplings have been devoted to computation of the four contributions of the second-order type, especially to the evaluation of the FC contribution. It is well known that the FC term predominates in the isotropic coupling constants of H–H and C–H in most organic compounds [11,12]. However, the FC contribution to the nuclear spin–spin couplings is one of the most difficult quantities to be evaluated in quantum chemistry because the electronic behavior at the nuclear positions is not described well by most commonly used approximate molecular wave functions based on Gaussian basis sets. In this section, the coupled Hartree–Fock (CHF) method is introduced to calculate the four contributions of the second-order type at the Hartree–Fock (HF) level.

The M–N nuclear spin–spin coupling tensor element $J^{\mathrm{AB}}_{MN,uv}$ due to the A–B type interaction is given by

$$\begin{aligned} J^{\mathrm{AB}}_{MN,uv} = h^{-1} \Bigg\{ & \left[\frac{\partial^2 \left\langle 0 \left| H(\lambda_{\mathrm{A}} H^{\mathrm{A}}_{M,u}, \lambda_{\mathrm{B}} H^{\mathrm{B}}_{N,v}) \right| 0 \right\rangle}{\partial\lambda_{\mathrm{A}}\partial\lambda_{\mathrm{B}}} \right]_{\lambda_{\mathrm{A}}=0,\lambda_{\mathrm{B}}=0} \\ & + (1-\delta_{\mathrm{AB}}) \left[\frac{\partial^2 \langle 0 |\, H(\lambda_{\mathrm{B}} H^{\mathrm{B}}_{M,u}, \lambda_{\mathrm{A}} H^{\mathrm{A}}_{N,v})\, | 0 \rangle}{\partial\lambda_{\mathrm{A}}\partial\lambda_{\mathrm{B}}} \right]_{\lambda_{\mathrm{A}}=0,\lambda_{\mathrm{B}}=0} \Bigg\}, \end{aligned} \tag{25}$$

where λ_{A} and λ_{B} are the nondimensional perturbation parameters. Here,

$$H\left(\lambda_{\mathrm{A}} H^{\mathrm{A}}_{M,u}, \lambda_{\mathrm{B}} H^{\mathrm{B}}_{N,v}\right) = H_0 + \lambda_{\mathrm{A}} H^{\mathrm{A}}_{M,u} + \lambda_{\mathrm{B}} H^{\mathrm{B}}_{N,v}, \tag{26}$$

In the condition that the molecular spin orbitals are determined variationally, the Hellmann–Feynman theorem reduces Equation (25) to a simpler form

$$\begin{aligned} J^{\mathrm{AB}}_{MN,uv} = h^{-1} \Bigg\{ & \left[\frac{\partial}{\partial\lambda_{\mathrm{B}}} \left\langle 0 \left| H^{\mathrm{A}}_{M,u} \right| 0 \right\rangle \right]_{\lambda_{\mathrm{B}}=0} \\ & + (1-\delta_{\mathrm{AB}}) \left[\frac{\partial}{\partial\lambda_{\mathrm{B}}} \right] \left\langle 0 \left| H^{\mathrm{A}}_{N,v} \right| 0 \right\rangle_{\lambda_{\mathrm{B}}=0} \Bigg\}, \end{aligned} \tag{27}$$

where $|0\rangle$ is the single Slater determinant for the ground state of the perturbed Hamiltonian, $H = H_0 + \lambda_{\mathrm{B}} H^{\mathrm{B}}_{N,v}$ or $H = H_0 + \lambda_{\mathrm{B}} H^{\mathrm{B}}_{M,u}$. The perturbed self-consistent field (SCF) spin orbitals $\psi(\lambda_{\mathrm{B}})(p = 1, 2, \ldots)$ are the eigenfunctions of the perturbed Fock operator $\hat{f}(\lambda_{\mathrm{B}})$ for the system whose Hamiltonian is $H_0 + \lambda_{\mathrm{B}} H^{\mathrm{B}}_{N,v}$ or $H_0 + \lambda_{\mathrm{B}} H^{\mathrm{B}}_{M,u}$. The perturbed occupied spin orbitals $\psi_i(\lambda_{\mathrm{B}})(i = 1, 2, \ldots, K)$ can be expanded as

$$\begin{aligned} \psi_i(\lambda_{\mathrm{B}}) = \psi_i^{(0)} + \lambda_{\mathrm{B}} \psi^{(1)}_{i,\mathrm{B}} = \psi_i^{(0)} \\ + \lambda_{\mathrm{B}} \sum_a^{\mathrm{unocc}} d^{\mathrm{B}}_{ai} \psi_a^{(0)}, \quad (i = 1, 2, \ldots, K), \end{aligned} \tag{28}$$

where K is the number of electrons in the system. K must be even here. $\psi_a^{(0)}(a = K+1, K+2, \ldots)$ are the unperturbed unoccupied spin orbitals. Using the unperturbed orbital energies $\varepsilon^{(0)}$, the coefficients d_{ai}^{B} can be determined by

$$\left(\varepsilon_a^{(0)} - \varepsilon_i^{(0)}\right) d_{ai}^{\mathrm{B}} + \sum_{j=1}^{K} \sum_{b=K+1}^{L} \times\left[\langle aj \,||\, ib\rangle\, d_{bj}^{\mathrm{B}} + \langle ab|\,|ij\rangle\, d_{bj}^{\mathrm{B}*}\right] = -\left\langle \psi_a^{(0)} \left|h^{\mathrm{B}}\right| \psi_i^{(0)}\right\rangle, \quad (i = 1, 2, \ldots, K), \tag{29}$$

where h^{B} is $h_{N,v}^{\mathrm{B}}$ or $h_{M,u}^{\mathrm{B}}$, and L is equal to the double of the number of used basis functions. The CHF formula for the tensor component $J_{MN,uv}^{\mathrm{AB}}$ is given by

$$J_{MN,uv}^{\mathrm{AB}} = h^{-1} \sum_{i=1}^{K} \sum_{a=N+1}^{L} \left[\left\langle \psi_i^{(0)} \left|h_{M,u}^{\mathrm{A}}\right| \psi_a^{(0)}\right\rangle d_{ai}^{\mathrm{B}}(N, v) + (1 - \delta_{\mathrm{AB}})\left\langle \psi_i^{(0)} \left|h_{N,v}^{\mathrm{A}}\right| \psi_a^{(0)}\right\rangle d_{ai}^{\mathrm{B}}(M, u)\right] + \mathrm{C.C.} \tag{30}$$

Triplet Instability of Coupled Hartree–Fock Calculation

It is noted that the PSO interaction operator is imaginary and spin independent, the FC one is real and spin dependent, and the SD one is complex and spin dependent. The expansion coefficients $d_{ai}^{\mathrm{B}}(N, v)$s have the same property as the type B interaction operator $h_{N,v}^{\mathrm{B}}$. Therefore, we obtain for example

$$d_{ai}^{\mathrm{B}\alpha} = d_{ai}^{\mathrm{B}\beta} = -d_{ai}^{\mathrm{B}\alpha*} = -d_{ai}^{\mathrm{B}\beta*} \text{ for B } = \text{PSO} \tag{31a}$$

$$d_{ai}^{\mathrm{B}\alpha} = -d_{ai}^{\mathrm{B}\beta} = d_{ai}^{\mathrm{B}\alpha*} = -d_{ai}^{\mathrm{B}\beta*} \quad \text{for } v = z \text{ when B} = \text{FC}. \tag{31b}$$

The diagonal elements of the coefficient matrix (the coefficient of $d_{ai}^{\mathrm{B}\alpha}$) for the simultaneous equations Equation (29) for $h_{N,z}^{\mathrm{FC}}$ are given by $\Delta_{ia}(\mathrm{FC}) = \left[\varepsilon_a^{(0)} - \varepsilon_i^{(0)} - (aa|ii) - (ai|ai)\right]$ where

$$(pq|rs) = \int \psi_p^{(0)*}(1)\psi_q^{(0)}(1)r_{12}^{-1}\psi_r^{(0)*}(2)\psi_s^{(0)}(2)\mathrm{d}\tau_1\, \mathrm{d}\tau_2. \tag{32}$$

It is well known that $\Delta_{ia}(\mathrm{FC})$ yields a triplet excitation energy which is too small, especially for molecules having multiple bonds such as C_2H_4, C_2H_2, etc. Sometimes $\Delta_{ia}(\mathrm{FC})$ becomes negative and the CHF calculation gives us meaningless results [13]. This phenomenon is called the "triplet instability."

Electron Correlation Effects

The triplet instability is due to the lack of electron correlation effects in the HF level calculations. It is known that the electron correlation effects for overcoming the triplet instability are introduced by the multiconfigurational self-consistent field (MCSCF) theory [14] or the coupled-cluster (CC) approach [15–19]. One of the most powerful methods for overcoming the triplet instability is the MCSCF calculation for the FC and SD terms. The first MCSCF calculation of the FC contribution to nuclear spin–spin couplings was performed by Laaksonen *et al.* [20] with the finite perturbation theory (FPT) in which the second-order derivatives of the electronic energy are evaluated numerically. The analytical differentiation of the MCSCF energy is carried out with the use of multiconfigurational self-consistent field linear response (MCLR) theory [14]. The linear response theory is called the propagator theory [21]. For interaction operators P and Q, the linear response function may be written as

$$\langle\langle p; q\rangle\rangle E = [P_1, P_2] \times \begin{bmatrix} ES - A & E\Delta - B \\ -E\Delta^* - B & -ES^* - A^* \end{bmatrix}^{-1} \begin{bmatrix} Q_1 \\ Q_2 \end{bmatrix}. \tag{33}$$

If we define two operators $q_v^+ = a_r^+ a_s$ and $K_n^+ = |n\rangle\,\langle 0|$ for the condition of $r > s$ and $n > 0$,

$$(P_1)_{vn} = \left[\langle 0 \left|\left[P, q_v^+\right]\right| 0\rangle \langle 0 \left|\left[P, K_n^+\right]\right| 0\rangle\right], \tag{34a}$$

$$(P_2)_{vn} = \left[\langle 0 \left|[P, q_v]\right| 0\rangle\; \langle 0 \left|[P, K_n]\right| 0\rangle\right], \tag{34b}$$

$$(Q_1)_{vn} = \begin{bmatrix} \langle 0|[q_v, Q]|0\rangle \\ \langle 0|[K_n, Q]|0\rangle \end{bmatrix},$$

$$(Q_2)_{vn} = \begin{bmatrix} \langle 0|[q_v^+, Q]|0\rangle \\ \langle 0|[K_n^+, Q]|0\rangle \end{bmatrix}, \tag{35}$$

$$(S)_{vn,v'n'} = \begin{bmatrix} \left\langle 0\middle|\left[q_v, q_{v'}^+\right]\middle|0\right\rangle & \left\langle 0\middle|\left[q_v, K_{n'}^+\right]\middle|0\right\rangle \\ \left\langle 0\middle|\left[K_n, q_{v'}^+\right]\middle|0\right\rangle & \left\langle 0\middle|\left[K_n, K_{n'}\right]\middle|0\right\rangle \end{bmatrix}, \tag{36}$$

$$(\Delta)_{vn,v'n'} = \begin{bmatrix} \langle 0|[q_v, q_{v'}]|0\rangle & \langle 0|[q_v, K_{n'}]|0\rangle \\ \langle 0|[K_n, q_{v'}]|0\rangle & \langle 0|[K_n, K_{n'}]|0\rangle \end{bmatrix}, \tag{37}$$

$$(A)_{vn,v'n'} = \begin{bmatrix} \left\langle 0\middle|\left[q_v, \left[H_0, q_{v'}^+\right]\right]\middle|0\right\rangle & \left\langle 0\middle|\left[\left[q_v, H_0\right], K_{n'}^+\right]\middle|0\right\rangle \\ \left\langle 0\middle|\left[K_n, \left[H_0, q_{v'}^+\right]\right]\middle|0\right\rangle & \left\langle 0\middle|\left[K_n, \left[H_0, K_{n'}^+\right]\right]\middle|0\right\rangle \end{bmatrix}, \tag{38}$$

and

$$(B)_{\nu n,\nu' n'} = \begin{bmatrix} \langle 0|[q_\nu, [H_0, q_{\nu'}]]|0\rangle & \langle 0|[[q_\nu, H_0], K_{n'}]|0\rangle \\ \langle 0|[K_n, [H_0, q_{\nu'}]]|0\rangle & \langle 0|[K_n, [H_0, K_{n'}]]|0\rangle \end{bmatrix}. \quad (39)$$

The CC method is an attempt to introduce interactions among electrons within a cluster and to permit the wave function to contain all possible "disjoint couplings" among the clusters. The second-order correction to the wave function due to quadruply excited configurations arises as products of doubly excited configurations. This is an example of disjoint couplings among the two-electron clusters. We write the exact ground state wave function $|0\rangle$ of the system Hamiltonian H as

$$|0\rangle = e^T |\phi_0\rangle , \quad (40)$$

where T is called a cluster operator and $|\phi_0\rangle$ is the normalized HF wave function. It is now assumed that the wave function $|0\rangle$ satisfies the intermediate normalization condition, $\langle\phi_0|0\rangle = 1$. For a system containing an even number of electrons $2n$, the cluster operator T generates one-, two-, ..., $2n$ electron clusters:

$$T = T_1 + T_2 + \cdots + T_{2n}, \quad (41)$$

where T_k is the k-electron cluster. The CC energy E of the ground state is determined by the Schrödinger equation

$$He^T |\phi_0\rangle = Ee^T |\phi_0\rangle , \quad (42)$$

from which the system energy is given by

$$E = \left\langle 0 \left| e^{-T} He^T \right| \phi_0 \right\rangle , \quad (43)$$

or

$$E = \left\langle \phi_0 \left| He^T \right| \phi_0 \right\rangle . \quad (44)$$

An analytical differentiation of the CC energy E is obtained by using the equation-of-motion coupled-cluster (EOM-CC) method [22] or the coupled-cluster polarization propagator (CCPPA) method [23]. As the start of the EMO-CC approach, Perera *et al.* [22] assumed that

$$\langle 0| = \langle\phi_0| (e^T)^\dagger = \langle\phi_0| (1 + \Lambda), \quad (45)$$

where Λ is the de-excitation operator. It is assumed that the energy functional

$$E = \langle\phi_0| (1 + \Lambda)e^{-T} He^T |\phi_0\rangle \quad (46)$$

is variational under the condition that

$$\langle\phi_0 |(1 + \Lambda)| \phi_0\rangle = 1.$$

The operator Λ is expanded as $\Lambda = \Lambda_1 + \Lambda_2 + \cdots + \Lambda_{2n}$. The operator Λ is determined variationally using the stationary condition of E. The CCPPA uses the linear response function in the framework of perturbation theory at the level of CC approximation. The detail is shown elsewhere [24].

References

1. Bader RFW, Streitwieser A, Neuhaus A, Laidig KE, Speers P. J. Am. Chem. Soc. 1996;118:4959.
2. Gutowsky HS, McCall DW, Slichter CP. Phys. Rev. 1951;84: 589.
3. Hahn EL, Maxwell DE. Phys. Rev. 1951;84 :1286.
4. Ramsey NF, Purcell EM. Phys. Rev. 1952;85:143.
5. Ramsey NF. Phys. Rev. 1953;91:303.
6. Schiff LI. Quantum Mechanics (Chapter 13), 3rd ed. McGraw Hill: New York, 1968.
7. Moss RE. Advanced Molecular Quantum Mechanics. Chapman and Hall: London, 1973.
8. Fukui H, Miura K, Matsuda H, Baba T. J. Chem. Phys. 1992; 97:2299.
9. Berestetskii VB, Lifshitz EM, Pitaevskii LP. Quantum Electrodynamics, 2nd ed. Pergamon: New York, 1982.
10. Matsuoka O, Aoyama T. J. Chem. Phys. 1980;73:5718.
11. Pople JA, Schneider WG, Bernstein HJ. High-Resolution Nuclear Magnetic Resonance. McGraw Hill: New York, 1959.
12. Pople JA, Beveridge DL. Approximate Molecular Orbital Theory. McGraw Hill: New York, 1970.
13. Guest MF, Saunders VR, Overill RE. Mol. Phys. 1978;35:427.
14. Dalgaad E. J. Chem. Phys. 1980;72:816.
15. Coester F. Nucl. Phys. 1958;7:421.
16. Cizek J, Paldus J. Int. J. Quant. Chem. 1971;5:359.
17. Harris FE. Int. J. Quant. Chem. 1977;S11:403.
18. Harris FE, Phariseau P, Scheive L (Eds). Electrons in Finite and Infinite Structures. Plenum Press: New York, 1977.
19. Bartlett RJ, Purvis GP. Int. J. Quant. Chem. 1978;16:561.
20. Laaksonen A, Kowalewski J, Saunders VR. Chem. Phys. 1983;80:221.
21. Jørgensen P, Simons J. Second Quantitization-Based Methods in Quantum Chemistry. Academic Press: New York, 1981.
22. Perera SA, Nooijen M, Bartlett RJ. J. Chem. Phys. 1996;104: 3290.
23. Geertsen J, Oddershede J. J. Chem. Phys. 1986;85:2112.
24. Fukui H. Prog. Nucl. Magn. Reson. Spectrosc. 1999;35:267.

Fibrous Proteins

Investigation of Collagen Dynamics by Solid-State NMR Spectroscopy

Göran Zernia and Daniel Huster
Junior Research Group “Solid-State NMR Studies of Membrane-Associated Proteins”, Biotechnological Biomedical Centre, Institute of Medical Physics and Biophysics, University of Leipzig, D-04107 Leipzig, Germany

Introduction

Collagen is the most abundant protein on the earth. It is found in many different tissues of animals and humans. The major property of collagen is to provide tensile strength to tissues such as tendons, ligaments, skin, cartilage, blood vessels, and bone [1].

The remarkable tensile strength of collagen can be understood from its unique secondary structure. The polypeptide chain of collagen forms a slightly twisted left-handed helix with three amino acids per turn. Three collagen chains are coiled together to form the three-stranded collagen triple helix. In the amino acid sequence of each polypeptide chain, every third residue is glycine (Gly). In the triple helix, the Gly residues of two chains come in close proximity to form a hydrogen bond. This structural arrangement is too dense to allow a larger side chain explaining the high Gly content of collagen. Further, collagen consists of approximately 21% proline (Pro) and hydroxyproline (HyPro). These amino acids impart rigidity and stability to the structure, especially by hydrogen bonds between the hydroxyl groups of HyPro. Together with 9% alanine (Ala) and 5% glutamic acid (Glu), these five amino acids account for about 70% of all the residues in collagen. Collagen forms fibrils, which are superstructures of collagen triple helices. The individual structure of this arrangement determines the tensile strength of collagen. The collagen triple helices are linked by covalent lysine–hydroxylysine bridges [1,2].

There are about 30 structural variants of collagen depending on the function of the respective tissue. The most relevant species are collagen type I (as found in bone, tendon, or ligament) and type II (as found in cartilage). Each collagen type has a slightly different amino acid sequence [1].

A characteristic feature of many biological tissues are the viscoelastic properties. Tendons, ligaments, or cartilage must respond quickly, robustly, and reversibly to deformations caused by mechanical load or dynamic stresses [3]. These elastic properties of many biological tissues are a consequence of the structural arrangement of fibrillar collagen and proteoglycans. The versatile molecular dynamics of these different macromolecules, the osmotic pressure, and the flow of aqueous tissue fluids represent the physical basis of the unique viscoelasticity of these tissues. Therefore, to cope with the various compressive stresses, acting on the tissue, these molecules undergo dynamic reorientations of very different geometries within a broad time window [3]. A sketch of the molecular organization in articular cartilage is given in Figure 1.

NMR techniques have been successfully applied to investigate the macromolecular species in tissues and to describe their dynamic properties. This short review focuses on the application of solid-state NMR methods to investigate the dynamical properties of isolated and tissue collagen. Solid-state NMR methods have to be applied since collagen is largely rigid due to its fibrillar structure and large molecular weight. Therefore, the anisotropic NMR interactions such as the chemical shift anisotropy and dipolar couplings are not averaged out by motions and the NMR spectra show the characteristic orientation dependence of the NMR frequency that is observed for solid materials. Solid-state NMR spectroscopy has unique capabilities for studying the molecular dynamics with correlation times from picoseconds to seconds by relaxation time measurements, lineshape analysis, or exchange methods [4,5]. All molecular motions are studied in the absence of an overall tumbling of the molecules that is present in solution NMR and might interfere with the motional analysis [6].

In this chapter, we will discuss static and magic angle spinning (MAS) solid-state NMR methods that have been applied to investigate the dynamics of tissue collagen. Further, recent data of our ongoing research on the dynamics of cartilage collagen will be discussed.

Investigation of Collagen Dynamics by Static Solid-State NMR

First NMR studies on collagen have been published by Torchia and co-workers [7,8]. Because of the rigidity of collagen fibrils, solution NMR fails to resolve their signals and solid-state NMR methods are most appropriate to

Graham A. Webb (ed.), Modern Magnetic Resonance, 87–92.
© 2008 *Springer.*

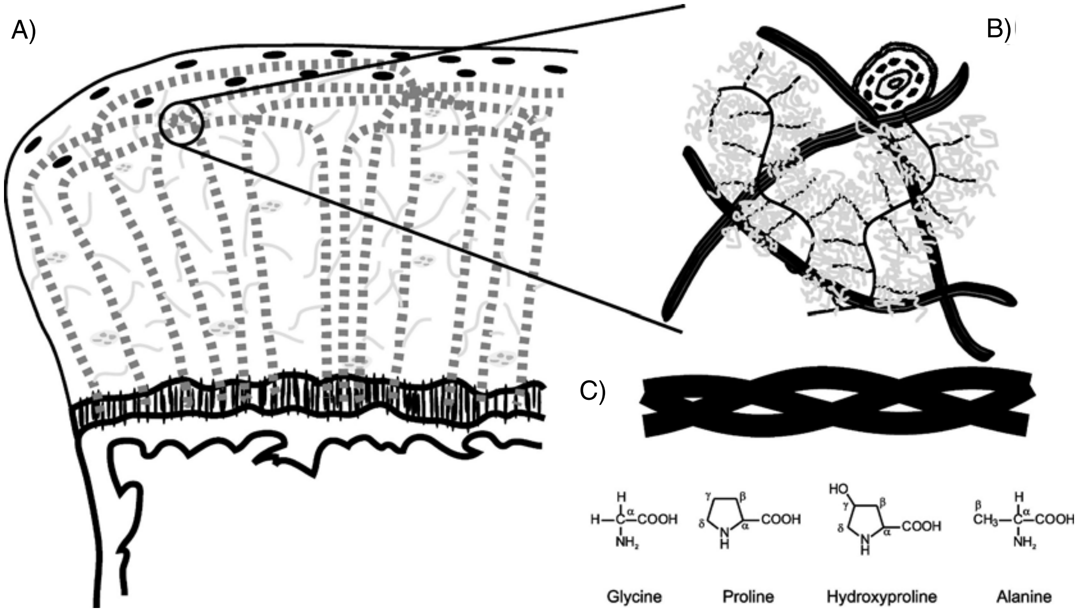

Fig. 1. (A) Schematic structure of articular cartilage with collagen molecules (green) and proteoglycans. (B) Proteoglycans consist of a strand of hyaluronic acid (red), to which a core protein (black) is attached. On the core protein, glycosaminoglycans (blue) such as chondroitin sulfate and keratan sulfate are covalently bound in a bottle-brush fashion. (C) The typical triple helix structure of collagen molecules and the chemical structure of the major amino acids in collagen are depicted. (See also Plate 8 on page XX in the Color Plate Section.)

study these molecules. Typically, solid-state NMR spectra of large molecules consist of a superposition of many broad anisotropic lineshapes that cannot be resolved in one dimension. Therefore, selective isotopic labeling is a prerequisite for any further analysis of the NMR spectra. To this end, collagen fibrils were labeled in animal tissue cultures. ^{2}H-, ^{13}C-, ^{15}N-, or ^{19}F-labeled amino acids were fed or injected to rats, chicken, or rabbits [9]. Thus, isotopically labeled collagen was produced and isolated from tendon, calvaria, tail, or sternum of those animals.

Besides structural data, the static solid-state NMR lineshapes contain information about the dynamics of a respective site. Since molecular motions decrease the strength of anisotropic interactions, they partially or fully abolish the orientation dependence of the NMR frequency. Therefore, lineshape measurements are sensitive both to the amplitude and to the correlation time of the molecular motions. Consequently, the presence of fast motions leads to a reduction of the width of the anisotropic spectrum.

Amplitudes and correlation times of motions can be determined from ^{2}H NMR spectra. The deuterium electric field gradient tensor is axially symmetric along the C–D bond, which simplifies the analysis. For the analysis, experimental ^{2}H NMR spectra are compared to simulated spectra that are calculated by applying a specific motional model. In particular, side chain motions have been studied by ^{2}H NMR spectroscopy. Using collagen molecules with ^{2}H-labeled Ala, leucine (Leu), Pro, or methionine (Met), these spectra showed typical features of motionally averaged lineshapes at ambient temperature [10–13]. Only at low temperature, the characteristic Pake spectra with the full quadrupolar splitting were detected. Application of a two-site jump hop for the Ala side chains in chick calvaria collagen revealed fast reorientations of the Cα–Cβ bond vector over an angle of $\sim 30^\circ$ with a correlation time $\sim 10^{-7}$ s [11,13]. Fast two-site exchange with an amplitude of $\sim 55^\circ$ and a correlation time of 8×10^{-7} s were also found for Leu side chains [10]. For Pro and HyPro puckering motions have been identified from the ^{2}H NMR spectra with root mean square amplitudes in the 11°–30° range [12]. A typical example of static ^{2}H NMR lineshapes for [^{2}H$_{10}$] Leu-labeled collagen as a function of temperature is given in Figure 2.

The backbone motions of collagen molecules have been investigated by static ^{13}C solid-state NMR methods using ^{13}CO Gly-labeled collagen. Similar to ^{2}H NMR lineshapes, anisotropic ^{13}C NMR spectra contain information about motional amplitudes and provide at least an upper limit for the correlation times. Root mean square amplitudes of 41°, 33°, and 14° were calculated for the backbone motions in uncross-linked, cross-linked, and mineralized collagen, respectively [14]. These findings

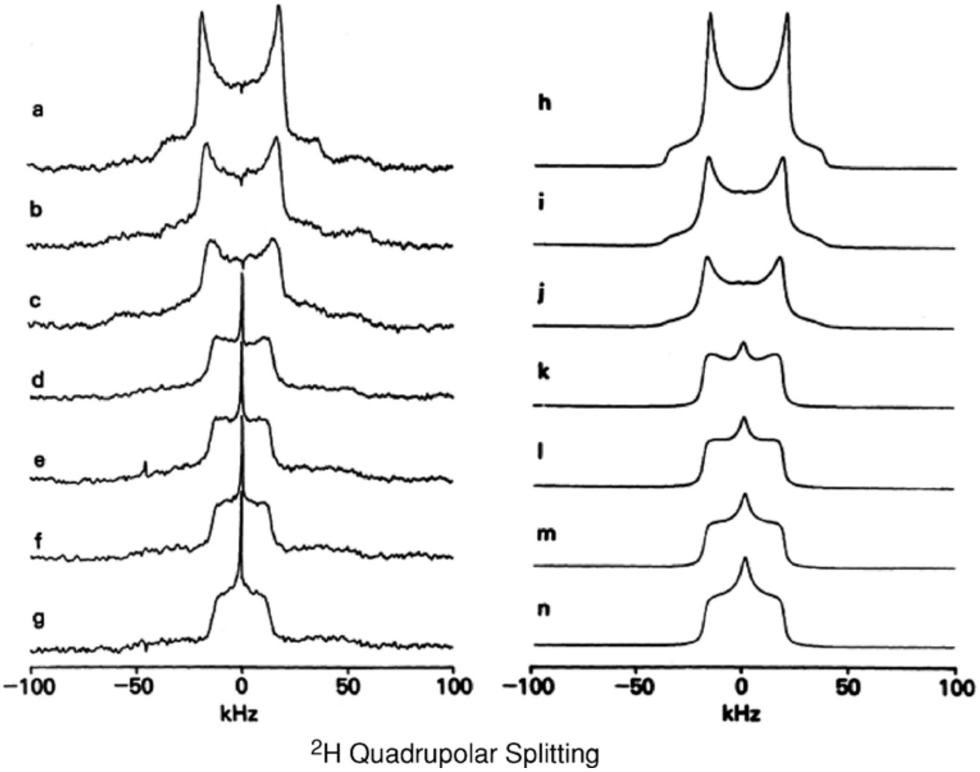

Fig. 2. Static ^{2}H NMR lineshapes of collagen to determine side chain mobility in [$^2H_{10}$] Leu-labeled collagen. The left column shows 38.5 MHz ^{2}H NMR spectra of [$^2H_{10}$] Leu-labeled collagen at various temperatures (a, −85 °C; b, −43 °C; c, −18 °C; d, −6 °C; e, +1 °C; f, +15 °C; g, +30°C). In the right column, lineshape simulations of the experimental spectra are displayed. These simulations assume a two-site hop model in which the Cγ–Cδ bond axes are assumed to hop between two sites separated by 108°–112° and κ defines the hopping rate (h, $\kappa \leq 6 \times 10^3$ rad/s; i, $\kappa = 1.9 \times 10^4$ rad/s; j, $\kappa = 3.1 \times 10^4$ rad/s; k, $\kappa = 3.7 \times 10^5$ rad/s; l, $\kappa = 6.3 \times 10^5$ rad/s; m, $\kappa = 8.7 \times 10^5$ rad/s; n, $\kappa = 1.2 \times 10^6$ rad/s). Reproduced with permission from Ref. [10].

were derived from the anisotropic carbonyl chemical shift tensor measurements indicating that the upper limit for the correlation times of these motions is 10^{-4} s. In addition to these somewhat slower motions, relaxation studies on collagen labeled with ^{13}Cα Gly revealed fast motions with correlation times in the 1–5 ns range exhibiting small amplitudes of 10°, 9°, and 5.5° uncross-linked, cross-linked, and mineralized collagen, respectively [15]. Because of their very fast correlation times, these motions must be segmental. While there is an obvious dependence of the backbone motion on the degree of cross-linking and mineralization, the side chain motions are only slightly affected by mineralization of collagen [12].

Recently, the static NMR data from the Torchia group have been reanalyzed and interpreted in terms of a librational rod model [16]. This analysis revealed that the ^{2}H NMR data are also consistent with small-angle librations about internal bond directions.

Application of CP MAS Methods to Study the Molecular Properties of Collagen

While static solid-state NMR spectra are broad and typically signals of only one or very few sites can be resolved in one dimension, MAS methods allow to resolve many relatively sharp signals at once. The first applications of cross-polarization (CP) MAS solid-state NMR methods have been demonstrated by the groups of Schaefer [17] and Saitô [18,19]. By application of MAS, the spectral intensity of the broad anisotropic solid-state NMR spectra is collected into a sharp central band of a line width on the order of one or a few ppm and a series of spinning sidebands. The number and intensity of spinning sidebands depends on the MAS frequency and the Larmor frequency of the NMR spectrometer. Thus, relatively well-resolved ^{13}C NMR spectra from isolated collagen samples have been obtained at natural abundance. The NMR signals of

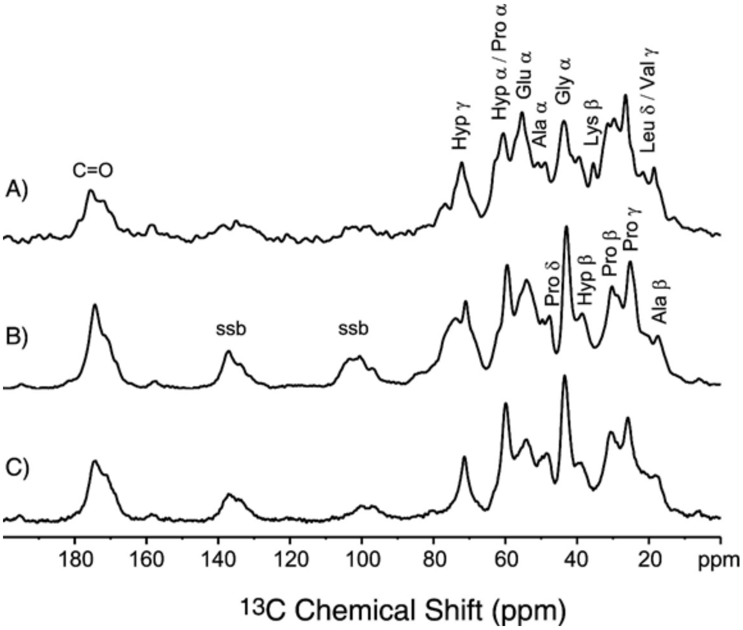

Fig. 3. Proton decoupled 188.6 MHz ^{13}C CP MAS spectra of fully hydrated porcine articular cartilage (A), dried porcine articular cartilage (B), and dry collagen type II (C) at a MAS frequency of 7 kHz and a temperature of 37 °C. The amino acid assignment is given. Spectra were externally calibrated with respect to TMS.

^{13}C CP MAS spectra could be assigned to the most abundant amino acids in collagen (Gly, Ala, Pro, HyPro, and Glu) [18]. Further, in comparison to dry collagen spectra, sharper lines have been detected in hydrated collagen indicating the presence of fast motions [19]. Thus, besides cross-linking and the degree of mineralization, the level of hydration seems to be a determining factor for the molecular mobility of collagen in tissue. This is also consistent with the static NMR spectra that indicated that the collagen dynamics is dependent on the state of the surrounding water [16].

Therefore, a systematic investigation of collagen mobility as a function of hydration has been carried out by ^{13}C CP MAS techniques [20]. While anisotropic NMR lineshapes contain information about the molecular dynamics, the anisotropic contributions to the NMR spectra need to be reintroduced by slow spinning [21] or recoupling methods [22–24] to exploit these quantities to obtain information about molecular dynamics. If carried out as a separated local field experiment [25], these techniques provide comprehensive dynamical information about all resolved signals in one experiment. For instance, in a separated local field experiment, a motional amplitude for each site that provides a resolved signal in the MAS spectrum can be determined.

For the study of collagen mobility as a function of hydration [20], the ^{1}H–^{13}C dipolar couplings have been measured in a DIPSHIFT experiment [26–28]. Thus, the dipolar coupling of each resolved collagen signal could be determined. Fast motions average out dipolar couplings, the amplitude of these motions can be described by a molecular order parameter, which is calculated as the ratio of motionally averaged and full dipolar coupling. Generally, motional amplitudes were found to be larger in the side chains compared to the backbone of collagen underlying the importance of hydration for the molecular dynamics of collagen. Further, with increasing hydration level, a decrease in the order parameters has been observed. The upper limit for the correlation times of motion calculated from motionally averaged ^{1}H–^{13}C dipolar couplings is on the order of 4×10^{-5} s.

With the recent introduction of high field magnets, it is now possible to study collagen in native tissues such as cartilage [29]. This is particularly remarkable since cartilage consists of ~82 wt% water, ~6 wt% proteoglycans, and only ~12 wt% collagen [30–32]. Due to this high water and ion content, the sample volumes have to be restricted to avoid sample heating by the application of high power decoupling fields. This means that only milligram quantities of collagen can be investigated, which calls for extremely sensitive instrumentations. Figure 3A shows a 188.6 MHz ^{13}C CP MAS spectrum of porcine articular cartilage obtained on approximately 15 mg cartilage tissue at natural abundance. While still relatively noisy, the signals of the main amino acid of collagen could be identified and assigned. For comparison, the ^{13}C CP MAS spectra of dried porcine articular cartilage and isolated collagen type II are shown in Figure 3B and C, respectively.

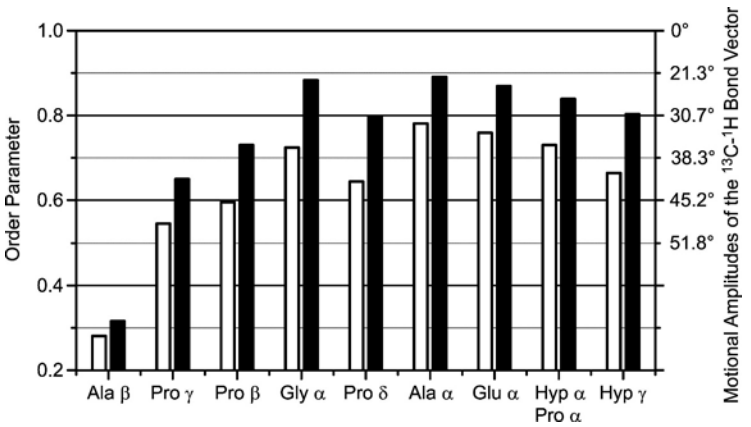

Fig. 4. ^{1}H–^{13}C order parameters of collagen in native (fully hydrated, open bars) and dried porcine articular cartilage (filled bars) at a temperature of 37 °C. Order parameters were determined from DIPSHIFT experiments carried out at a MAS rotational frequency of 7 kHz.

This indicates that almost exclusively collagen signals are detected in ^{13}C CP MAS spectra of articular cartilage. In addition, signals from rigid proteoglycans of cartilage (mostly hyaluronan) can be detected in the ^{13}C CP MAS spectrum of cartilage. These signals are assigned to the ring carbons of the proteoglycans with typical chemical shifts between 65 and 80 ppm [33–35]. In fully hydrated cartilage, these signals are strongly attenuated in ^{13}C CP MAS spectra because of their high mobility, but contribute significantly to the NMR spectrum of dried cartilage.

Figure 4 shows typical order parameters of collagen in dried and native porcine articular cartilage. In the dry sample, the backbone signals exhibit order parameters between 0.9 and 0.94 in agreement with the rigid molecular structure. For the side chains, order parameters between 0.64 and 0.87 indicate motions with root mean square amplitudes between 42.5° and 24.4°. In contrast, much smaller order parameters have been observed in fully hydrated cartilage. For the backbone, order parameters between 0.73 and 0.78 are consistent with motions of amplitudes in the range of 36.1°–32.3°. Even larger amplitudes of 48.6°–41.1° are observed in the side chains of collagen in fully hydrated cartilage with order parameters of 0.55–0.66. For Ala Cβ, order parameters < 0.33 are obtained, characteristic for the fast rotation of methyl groups about the Cα–Cβ bond.

What Has Been Learned from Solid-State NMR Studies of Collagen?

Solid-state NMR techniques have strongly contributed to our understanding of the molecular dynamics in isolated and tissue collagen. The first interesting observation was that even dry collagen is not entirely rigid. The amplitude of collagen motions is not greatly influenced by cross-linking, however, mineralization reduces collagen flexibility in bone. The amino acids in collagen undergo fast segmental reorientations that can be described by root mean square amplitude fluctuations. Very small amplitudes are observed for the collagen backbone, while the motional amplitudes increase into the side chains of the amino acids. For Pro and HyPro, puckering motions of the entire ring structure have been identified. The methyl groups of amino acid side chains undergo fast rotations about the C–C bond axis.

In hydrated collagen, a more versatile molecular dynamics was found. While the segmental motions of dry collagen occur on a fast timescale of the order of a few nanoseconds, in hydrated collagen also slower motions with correlation times of the order of 10^{-4} s have been observed. The motional amplitudes of hydrated collagen are significantly increased in comparison to dry collagen.

Tissue collagen of fully hydrated articular cartilage shows the largest motional amplitudes. This is mostly due to the high water content. Different types of collagen do not show any dynamical diversity as concluded from comparison of collagens I and II. Although most amino acids in collagen are uncharged, there are several polar groups in the backbone and the side chains that represent water binding sites. In particular, the hydroxyl groups of HyPro have been identified as water binding sites according to X-ray studies since they have both hydrogen bond donor and acceptor properties [36]. It has been suggested that the collagen triple helices acquire extra hydrogen bonding capacity by prolyl hydroxylation [37].

The possible functional significance of the collagen mobility has already been suggested [15]. Due to their high tensile strength, collagen fibers provide mechanical stability to connective tissues. When tension is applied, collagen molecules are able to make rapid conformational changes. Thus, stress is distributed uniformly and the mechanical energy can be dissipated and adsorbed by the segmentally flexible molecules. The motions that have been identified so far occur on a sub-microsecond timescale. However, the stress that is exerted on connective tissues by our daily tasks such as walking, climbing the stairs, or exercising stresses the connective tissue on a slower timescale of tens to hundreds of milliseconds. Therefore, motions with these correlation times may also be relevant for collagen. At the moment, only preliminary data for collagen motions in that time window are available [20]. However, several newly developed solid-state NMR methods will allow to investigate such motions in collagen as well [38].

Besides understanding of the basic properties of collagen in regard to the viscoelasticity of biological tissue, recent tissue engineering developments have led to an increasing interest in the quantitative characterization of artificial tissues. For various applications in regenerative medicine (stem) cells are seeded into organic or inorganic scaffolds to produce extracellular matrix *in vitro*. The monitoring and quality control of the engineered tissues represents a major challenge to produce high quality replacements. NMR spectroscopy is very well suited to contribute to this field. Artificially grown tissues need to exhibit very similar properties as the natural tissue in order to be built into cartilage, bone, or other defects. The methods described in this chapter may be used to characterize artificial tissue and compare its properties with those of natural specimen. Thus, the optimal procedures for tissue engineering may be determined aided by a comprehensive monitoring of the dynamical properties of the tissue macromolecules as a prerequisite for a successful implantation.

Acknowledgments

This research has been funded by the European Funds for Regional Development (EFRE, Project #: 4212/03-12). D.H. would like to thank Jan Keller for help in preparing the figures.

References

1. Nelson D, Cox M. Lehninger Biochemie. Springer-Verlag: New York, 2001.
2. Creighton TE. Proteins: Structures and Molecular properties. W. H. Freeman and Company: New York, 1993.
3. Scott JE. J. Physiol. 2003;553:335.
4. Palmer AG III, Williams J, McDermott A. J. Phys. Chem. 1996;100:13293.
5. Tycko R. In: R Tycko (Ed). Nuclear Magnetic Resonance Probes of Molecular Dynamics. Kluwer Academic Publishers: Dodrecht, 1994, p 1.
6. Opella SJ. Methods Enzymol. 1986;131:327.
7. Torchia DA. Methods Enzymol. 1982;82:174.
8. Torchia DA. Annu. Rev. Biophys. Bioeng. 1984;13:125.
9. Jelinski LW, Torchia DA. J. Mol. Biol. 1979;133:45.
10. Batchelder LS, Sullivan CE, Jelinski LW, Torchia DA. Proc. Natl. Acad. Sci. U.S.A. 1982;79:386.
11. Jelinski LW, Sullivan CE, Torchia DA. Nature. 1980;284:531.
12. Sarkar SK, Hiyama Y, Niu CH, Young PE, Gerig JT, Torchia DA. Biochemistry. 1987;26:6793.
13. Jelinski LW, Sullivan CE, Batchelder LS, Torchia DA. Biophys. J. 1980;32:515.
14. Sarkar SK, Sullivan CE, Torchia DA. J. Biol. Chem. 1983;258:9762.
15. Sarkar SK, Sullivan CE, Torchia DA. Biochemistry. 1985;24:2348.
16. Aliev AE, Chem. Phys. Lett. 2004;398:522.
17. Stejskal EO, Schaefer J. J. Am. Chem. Soc. 1976;98:1031.
18. Saitô H, Tabeta R, Shoji A, Ozaki T, Ando I, Miyata T. Biopolymers. 1984;23:2279.
19. Saitô H, Yokoi M. J. Biochem. (Tokyo). 1992;111:376.
20. Reichert D, Pascui O, deAzevedo ER, Bonagamba TJ, Arnold K, Huster D. Magn. Reson. Chem. 2004;42:276.
21. Antzutkin ON. Prog. Nucl. Magn. Reson. Spectrosc. 1999;35:203.
22. Griffin RG. Nat. Struct. Biol. 1998;5:508.
23. Bennett AE, Griffin RG, Vega S. In: NMR Basic Principles and Progress. Springer Verlag: Berlin Heidelberg, 1994, p 3.
24. Dusold S, Sebald A. Annu. Rep. NMR Spectrosc. 2000;41:185.
25. Waugh JS. Proc. Natl. Acad. Sci. U.S.A. 1976;73:1394.
26. Munowitz MG, Griffin RG, Bodenhausen G, Huang TH. J. Am. Chem. Soc. 1981;103:2529.
27. Schaefer J, Stejskal EO, McKay RA, Dixon WT. J. Magn Reson. 1983;52:123.
28. Hong M, Gross JD, Griffin RG. J. Phys. Chem. 1997;101:5869.
29. Huster D, Schiller J, Arnold K. Magn. Reson. Med. 2002;48:624.
30. Maroudas A. In: MAR Freeman (Ed). Adult Articular Cartilage. Pitman Medical: Tunbridge Wells, 1973, p 131.
31. Maroudas A. In: A Maroudas, K. Kuetter (Eds). Methods in Cartilage Research. Academic Press: London, 1990, p 211.
32. Ratcliffe A, Mow VC. In: WD Comper (Ed). Extracellular Matrix, Volume 1, Tissue Function. Harwood Academic Publishers GmbH: Amsterdam, 1996, p 234.
33. Brewer CF, Keiser H. Proc. Natl. Acad. Sci. U.S.A. 1975;72:3421.
34. Torchia DA, Hasson MA, Hascall VC. J. Biol. Chem. 1977;252:3617.
35. Naji L, Kaufmann J, Huster D, Schiller J, Arnold K. Carbohydr. Res. 2000;327:439.
36. Bella J, Eaton M, Brodsky B, Berman HM. Science. 1994;266:75.
37. Bella J, Brodsky B, Berman HM. Structure. 1995;3:893.
38. Luz Z, Tekely P, Reichert D. Prog. Nucl. Magn. Reson. Spectrosc. 2002;41:83.

Solid-State NMR Studies of Elastin and Elastin Peptides

Kristin K. Kumashiro
Department of Chemistry, University of Hawaii at Manoa, Honolulu, Hawaii 96822, USA

Introduction

The skin and blood vessels of a vertebrate have a uniquely resilient and elastic quality to them. These properties are traced to *elastin*, the principal protein component of the fibers that comprise a large portion of these elastic tissues. Numerous reviews have been written on the biology and chemistry of this unique protein [1–3]. Briefly, the elastin gene encodes tropoelastin, which is crosslinked in post-translational modification to form insoluble elastin or, simply, *elastin*. The molecular weight of tropoelastin is large, with molecular weights ranging from 70 to 80 kDa, and its high-resolution structure is not yet solved. Generally, tropoelastin and insoluble elastin are considered to have two "domains," namely, hydrophobic and crosslinking. Much attention has been focused on the hydrophobic regions that are dominated with the small nonpolar amino acids, glycine, alanine, proline, and valine. A number of repeating polypeptide sequences are found in this domain. Among them are $(\mathrm{VPGVG})_n$ and $(\mathrm{PGVGVA})_n$. The crosslinking domain is rich with alanines, with a typical repeat sequence of $(\mathrm{KAAK})_n$ or $(\mathrm{KAAAK})_n$. In portions of tropoelastin, the hydrophobic and crosslinking domains alternate. Figure 1 illustrates several domains of rat tropoelastin, as reported by Pierce *et al.* [4].

To date, there is limited information on the three-dimensional structure of insoluble elastin. If one were to consider the size and nature of tropoelastin, then it would be easy to see why this problem is so difficult. That is, the predominance of the small hydrophobic residues and the presence of the crosslinks are the root causes for the insolubility of amorphous, or "mature," elastin in all but the harshest conditions. Hence, solution nuclear magnetic resonance (NMR) and X-ray crystallography are virtually useless for high-resolution structure determination. Indeed, elastin has more in common with synthetic organic polymers than with many proteins characterized thus far with NMR spectroscopy.

In the past, numerous models have emerged to explain the elasticity of elastin [5–8]. They range from the most disordered and globular to ones with significant degrees of order. As examples of the former, Hoeve and Flory used thermodynamic measurements to suggest that elastin was much like rubber, with long hydrophobic chains interspersed randomly with crosslinks [5]. In contrast, the "oiled coils" from predictive methods [6] and the "β-spiral" from structural studies of elastin-based peptides [7–10] suggest that this polymer has a much greater degree of order. More recent computational studies on the elastin peptides have provided some new insights [11,12]. It is generally accepted, though, that the Ala-rich crosslinking domains are mostly α-helical, whereas the hydrophobic domain's organization is much less clear. Again, the lack of site-, residue-, and sequence-specific data, such as those obtained by solution and solid-state NMR spectroscopy, has greatly hampered the understanding of the native protein's structure–function relationships.

Two basic approaches have emerged as viable ways to characterize this intriguing protein by solid-state NMR spectroscopy. One focuses on the native (or nativelike) elastin, while the other uses smaller model peptides.

Studies of the native protein would be most physiologically relevant, when drawing conclusions regarding structure–function relationships. The preparation of elastin from connective tissue is straightforward [13–15], and large quantities are easily obtained. With purified elastin samples, various groups [13,16–22] have characterized the natural-abundance ^{13}C populations present in the native protein, complete, in most cases, with the waters of hydration. To complement this approach, methods for isotopic enrichment of a given residue type have also emerged [23–25]. These labeling schemes are essential for NMR studies targeting key amino acid types in elastin, and the power of solid-state NMR as a high-resolution structural tool is becoming more evident as these findings are reported.

Alternatively, now-classic approaches in elastin biochemistry have focused on mimetics, most notably, the repeating polypenta and hexapeptides, as studied by Urry [7–10,26] and Tamburro [27–29]. The use of these smaller peptides circumvents the problems associated with the polymeric nature and insolubility of elastin. Typically, the rationale for using these peptides is based on the fact that the hydrophobic regions of elastin have an abundance of these somewhat unusual repeating motifs, and elasticity has been assumed to originate from this domain. In addition, the repeating polypeptides possess properties similar to the native tropoelastin, such as coacervation, and can

Graham A. Webb (ed.), Modern Magnetic Resonance, 93–99.
© 2008 *Springer.*

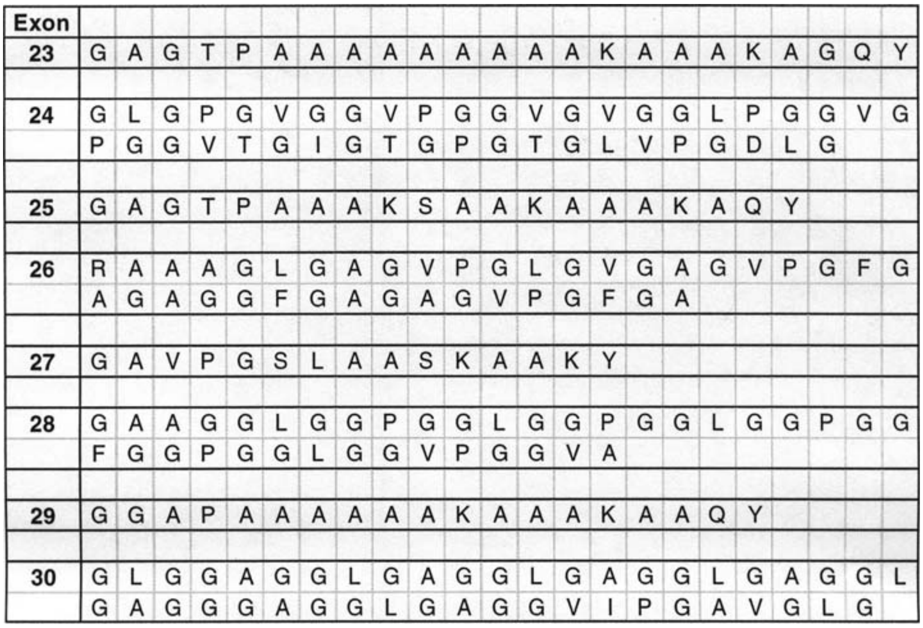

Exon																						
23	G	A	G	T	P	A	A	A	A	A	A	A	A	A	K	A	A	A	K	A	G	Q	Y
24	G	L	G	P	G	V	G	G	V	P	G	G	V	G	V	G	G	L	P	G	G	V	G
	P	G	G	V	T	G	I	G	T	G	P	G	T	G	L	V	P	G	D	L	G		
25	G	A	G	T	P	A	A	A	K	S	A	A	K	A	A	A	K	A	Q	Y			
26	R	A	A	A	G	L	G	A	G	V	P	G	L	G	V	G	A	G	V	P	G	F	G
	A	G	A	G	G	F	G	A	G	A	G	V	P	G	F	G	A						
27	G	A	V	P	G	S	L	A	A	S	K	A	A	K	Y								
28	G	A	A	G	G	L	G	G	P	G	G	L	G	G	P	G	G	L	G	G	P	G	G
	F	G	G	P	G	G	L	G	G	V	P	G	G	V	A								
29	G	G	A	P	A	A	A	A	A	A	K	A	A	A	K	A	A	Q	Y				
30	G	L	G	G	A	G	G	L	G	A	G	G	L	G	A	G	G	L	G	A	G	G	L
	G	A	G	G	G	A	G	G	L	G	A	G	G	V	I	P	G	A	V	G	L	G	

Fig. 1. Amino acid sequence of rat tropoelastin as encoded by exons 23–30, as reported by Pierce *et al*. [4]. Exons 23, 25, 27, and 29 are the Ala-rich crosslinking domains. Exons 24, 26, 28, and 30 are the hydrophobic domains, dominated by small hydrophobic residues, such as glycines.

also be crosslinked by reaction with oxidizing reagents or by exposure to γ-irradiation. Modern approaches, such as those based on recombinant methods, has facilitated the synthesis of biopolymers with elastinlike subunits for solid-state NMR characterization. In comparison to the task of labeling native elastin, the isotopic enrichment strategies for the elastin-based peptides or mimetics, whether by synthesis or bacterial expression, tend to be more straightforward. However, by virtue of the inherent simplicity of these systems, one may wonder about the relevance of the repeating polypeptides to the questions surrounding elastin's elasticity. One major and valid concern focuses on the fact that many of the model peptides reported thus far do not contain the Ala-rich crosslinking domains.

In this chapter, we focus on recently reported and current work using solid-state NMR spectroscopy to characterize elastin and elastin peptides. After a short review with a description of important results obtained over two decades ago, recent work by this author's lab and others will be described. Many of these studies are based on techniques in "high-resolution solid-state NMR," utilizing cross-polarization magic-angle-spinning (CPMAS) as a cornerstone, although some projects incorporate non-spinning methods. It will also be shown that the unusual nature of elastin requires new and creative approaches for the continued use of NMR spectroscopy as a powerful tool for characterizing the structure and dynamics of one of nature's most novel and unique elastomers.

Studies of Native Elastin Focus Mainly on the Natural-Abundance ^{13}C Populations

In the 1970s and early 1980s, Torchia and co-workers reported a series of studies using NMR to characterize elastin [16,17,23,24]. Their earliest work [16] used ^{13}C NMR to examine calf ligamentum nuchae, which is rich in elastin. Their results indicated that elastin, unlike collagen, was comprised of "highly mobile chains." A subsequent study [17] provided a more quantitative picture of this unusual mobility in elastin with relaxation data, including T_1 and NOE determinations, for elastin swollen in various solvent environments. With this data, they again concluded that there was significant and unusually high mobility in this amorphous protein, although molecular motion was slightly more restricted in the Ala-rich regions.

Other groups made additional contributions to this early picture of elastin. Urry and Mitchell reported a ^{13}C NMR study of α-elastin and fibrous elastin [30], with most of their focus on qualitative comparisons of the various protein samples with each other and with the elastin polypentapeptide. Ellis and Packer also contributed to this early picture with their ^{2}H relaxation measurements of hydrated elastin [18]. Their work identified the existence of three types of water in these samples. To close out this era, Kricheldorf and Muller reported the ^{13}C chemical shifts for a sample of commercially available elastin [19]. To assist with their interpretation of the elastin spectra, they also looked at the ^{13}C chemical shifts of several Pro-rich polypeptides. Their analysis focused particularly on the backbone carbonyl population. It was concluded that ~25% of the protein was α-helical, another population was "helical segments of unknown pitch," and a third was simply described as an "amorphous phase." Furthermore, they emphasized that elastin's structure possessed no long-range order, although local segments were structured.

In the years since Torchia, Kricheldorf, and others first reported their compelling findings on elastin, the area of biological solid-state NMR has greatly evolved. From the development of progressively higher-field instrumentation and other hardware to the boom in new pulse sequences for defining, e.g. progressively more refined structural data, solid-state NMR spectroscopy has seen a tremendous growth. Furthermore, the tools of molecular biology for protein expression are much more accessible. As a result, many more questions surrounding protein structure and function may be addressed in this day and age.

To begin our review of more recent results, the effects of temperature and hydration on the structure and dynamics of elastin are first discussed [13]. In this study, ^{13}C solid-state NMR experiments were applied to samples of bovine nuchal ligament elastin that were purified using the cyanogen bromide (CNBr) method [13–15]. Samples of elastin at various hydration levels at four different temperatures were first characterized. ^{13}C CPMAS data showed that elastin with little or no water (0–30% hydration) had similar profiles; i.e. in the lyophilized and drier samples, chemical shifts were identified for the center-of-mass of the backbone carbonyl, the aromatic, and 8–9 resolved aliphatic peaks. In contrast, spectra of wetter samples (40–100% hydration) at physiological and room temperatures were observed with markedly lower signal-to-noise than the drier samples. Only the 53 ppm peak was clearly resolved with relatively high signal-to-noise in the C$_\alpha$ region, and several peaks were noted in the upfield region of ca. 10–30 ppm. The differences between the profiles of the wetter and drier samples were negligible as the sample temperature is lowered to $-20\,^{\circ}$C. To further examine the nature of elastin, a number of additional experiments were conducted. For instance, the CPMAS spectrum of the hydrated sample was compared to DPMAS data, as shown in Figure 2. With DPMAS, all sites are observed. In contrast, CPMAS data reflect marked differences for the backbone carbonyl carbons, as well as selected carbons in the aliphatic region. With regards to the latter, the lack of much ^{13}C$_\alpha$-Gly signal is striking. This simple experiment highlighted the heterogeneous nature of elastin; i.e. some segments of elastin, particularly those that are Gly-rich, are so mobile that CP efficiency is greatly compromised. In addition, static experiments showed the presence of unusually narrow lines in the spectrum of the wet sample, clearly unusual for a typical solid. These qualitative measurements were complemented by T$_1$ experiments, which again showed portions of the hydrated sample at 37 °C to have almost *liqidlike mobility* —a term first used by Torchia and coworkers in their examination of elastin in the 1970s [24]. While the drier samples tended to behave more like typical peptides in the solid state, the hydrated samples tended to exhibit more heterogeneity, particularly in terms of their dynamics.

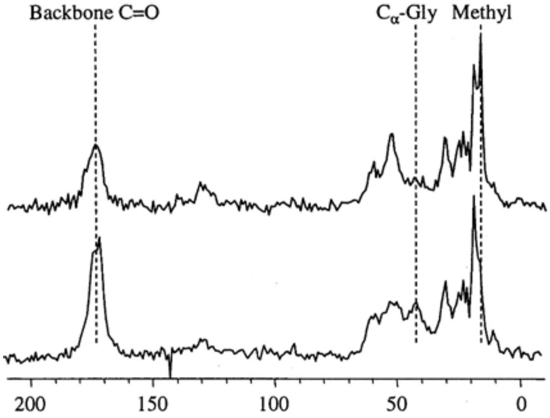

Fig. 2. CPMAS (top) and DPMAS (bottom) spectra of hydrated elastin at 37 °C, as originally reported by Perry *et al.* [13]. Major differences are identified for the backbone carbonyl and in selected regions of the aliphatic carbons, such as the C$_\alpha$-Gly and methyls.

Another recent solid-state NMR study of unenriched elastin samples purified from tissue was also reported by Pometun *et al.* [20]. In their study, solid-state NMR methods were employed to characterize "elastin fibers" obtained from a commercial source. A number of techniques were employed to characterize these samples. First, ^{2}H and ^{17}O NMR were used to identify the dynamics of the exchangeable backbone amides, as well as the waters of hydration. The data showed that there was no evidence for the tightly bound waters of hydration, unlike the work of Ellis and Packer [18]. The ^{2}H spectra were also used to conclude that the entire protein was mobile, whereby typical powder patterns found for most solid peptides were not observed in these conditions. Two-dimensional spectra of dry and hydrated elastin yielded small ^{13}C shielding anisotropies of the resolved carbons in hydrated elastin. The order parameter S (<0.1) was similarly characteristic of high mobility. To explore the structure of this hydrated sample further, ^{13}C chemical shifts were also measured at a carbon resonance frequency of ~200 MHz and with a sample temperature of 75 °C. It was noted that the sample remained elastic at this arguably high temperature for the duration of the experiment. The chemical shifts of all resolved features were assigned to the major amino acids of elastin, and all were identified as having values similar to those of a random coil at this elevated temperature. Finally, a novel method for preparing stretched samples for NMR was reported. This innovation anchored an elastin fiber by its top and bottom, and then the sample could be stretched by means of a captured screw. When the sample of the elastin was stretched, the peaks of the static ^{13}C spectrum broadened. Interestingly, a similar suggestion to that of Kricheldorf and Muller [19] was made, namely, that the high-proline content is a key factor in understanding the structure (or its lack thereof) and dynamics of elastin.

Most of the work in the recent and past literature had focused on elastin obtained from normal tissue. However, two published studies used solid-state ^{13}C NMR to identify structural differences between normal and abnormal elastin. Tarnawski *et al.*, characterized samples of elastin from normal and atherosclerotic human aorta, using 1D methods in ^{13}C NMR [21]. Chemical shifts and the ^{1}H $T_{1\rho}$ reflected very little differences, if any. However, ^{13}C $T_{1\rho}$ measurements reflected subtle differences in the aliphatic region with the accumulation of lipid and calcium deposits. The 43 ppm peak in the atherosclerotic elastin, for example, had a higher ^{13}C $T_{1\rho}$ than normal, whereas the peaks at 32 and 23 ppm had lower values. This result suggested that the latter sites have some type of hydrophobic interaction with the additional lipids found in the affected tissue.

More recently, this author's group published a study of the α-elastin obtained from normal and undercrosslinked pig aorta [22]. The crosslinking in normal vertebrate systems occurs by means of post-translational modification *via* the copper-dependent enzyme lysyl oxidase. If the animal is deprived of copper in its diet, then fewer crosslinks form, and aortic rupture typically results. α-Elastin is prepared by solubilizing elastin with oxalic acid [31,32]. In contrast to other methods of obtaining soluble elastin peptides from the amorphous protein, this scheme retains peptides of significant molecular weight (>10 kDa). Also, α-elastin retains properties of the native system, such as coacervation.

As with the above-described study of the normal versus atherosclerotic elastin [21], there were no discernible differences in ^{13}C chemical shift for the normal versus undercrosslinked [22]. (Indeed, it has been shown that the chemical shifts of the key amino acid types have nearly identical chemical shifts over a broad range of samples.) However, it was noted that the differences in peak intensities of the two samples did not correspond to the simple change in composition, i.e. fewer desmosine and isodesmosine crosslinks and more underivatized lysines. Few differences were observed for the two types of samples based on ^{13}C T_1 and ^{1}H $T_{1\rho}$ measurements. However, ^{13}C $T_{1\rho}$ values indicated that motion on the kHz scale was slowed in the undercrosslinked sample, leading to the arguably counterintuitive conclusion that some mobility is lost with fewer crosslinks. As with the study on the elastin from atherosclerotic tissue, impaired function of the elastic fiber is correlated with a change in dynamics, again lending support to the idea that mobility of the protein is a salient feature of its elasticity.

A New Approach for Production of Isotopically Labeled Elastin Utilizes a Mammalian Cell Culture

This section begins with a description of the earliest successful attempts of isotopic enrichment of elastin, as established by Torchia and co-workers [23,24]. In these early experiments, chick aorta was cultured with media containing the isotopic label. First, ^{14}C-labeled glycine or alanine was used to show that isotopic scrambling was relatively low (>10%) and also to provide a basis for estimating incorporation (10–20%) [23]. Subsequently, results were reported for chick aortic elastin that was labeled at the carbonyl carbons of Ala, Val, and Lys. Incorporation of the ^{13}C label was modest, with 6.4, 10.5, and 19.5% enrichment for [1-^{13}C]Ala, [1-^{13}C]Val, and [1-^{13}C]Lys, respectively. However, these levels were enough to observe these key amino acids. As with their natural-abundance results on the nuchal ligament, Torchia and co-workers obtained T_1, linewidth, and NOE values for the various residue types. In addition, the CP efficiency and the effect of dipolar decoupling were also observed to obtain a model that was slightly more refined than the ones obtained previously. Specifically, these experiments indicated that all of the Val, ~75% of the Ala, and ~40% of the Lys residues (and its derivatives) were found in very mobile regions. The remaining Ala and Lys residues were attributed to the crosslinking domains that were "motionally restricted." Linewidth and NOE data were also recorded as a function of temperature.

More recently, this author's lab has shown that a cell line well-known in cardiovascular biology could be successfully exploited for isotopic labeling and, hence, NMR spectroscopy [25]. The neonatal rat smooth muscle cell (NRSMC) line had been well-documented as a viable means of studying elastin synthesis [33,34]. These primary cultures are grown in a mixture of standard growth medium components that have been supplemented with the appropriate isotopically enriched amino acid. The label is introduced upon seeding of the cells. Normally, after 6–8 weeks of growth, the cells and the elastin-rich matrix are harvested, and insoluble elastin is purified from the mixture using the CNBr method. To assay incorporation, we followed the example of Meier and co-workers in their study of isotopically enriched spider silk [35]; acid hydrolysis followed by solution NMR spectroscopy was used to determine the amount of stable isotope that had been incorporated into the protein. For samples of [1-^{13}C]Gly, [2-^{13}C]Gly, and [^{15}N]Gly NRSMC elastin, the product of the acid hydrolysis was dissolved in D_2O and then observed using ^{13}C NMR spectroscopy. Typically, the analysis focused on C_α-Gly peak and the doublets that would result for the enriched sites. Using this approach, 30–40% incorporation of labeled Gly into elastin was confirmed. Solution NMR data were also used to show that isotopic scrambling is minimal. Analysis of other labeled elastin samples is done by an analogous method (unpublished data).

Early NMR results of the elastin samples enriched at the glycines are promising [25]. The ^{13}C CPMAS data tend to be significantly lower in signal intensity than typically seen with samples of this mass and incorporation level, and DPMAS data yield extremely narrow lines for a polymer with the complexity of elastin. Short T_1 values are also consistent with our earlier observations of the natural-abundance ^{13}C populations of hydrated elastin [13]. In addition to earlier work [25], Figure 3 illustrates the ^{2}H spectrum of NRSMC elastin with enrichment at the glycines. The detailed analysis of this sample is forthcoming. However, again we note the remarkably narrow lines observed for this amorphous protein. Finally, we note that this approach has also proven to be feasible for enrichment at the alanines and valines (unpublished data). With the protocols for labeling elastin well in hand, a number of experiments targeting the key amino acids of elastin are underway.

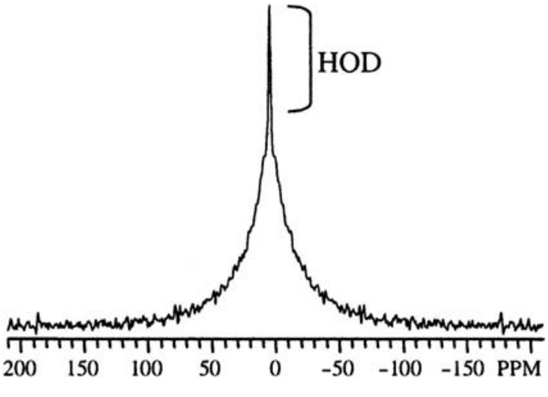

Fig. 3. ^{2}H spectrum of hydrated [2,2-$^2H_2$]Gly NRSMC elastin at 37 °C, swollen in ^{2}H-depleted water.

Information on the Hydrophobic Domain of Elastin is Gleaned from Repeating Polypeptides

As noted above, the hydrophobic domains of elastin are rich with repeating polypeptides. Most well-known are the polypentapeptides $(VPGVG)_n$ [9,10,36]. Much attention has been drawn to Urry's model [7,8], in which each (VPGVG) subunit has the structure of a type II, β-turn and the repeating polypentapeptide, hence, forms a "β-spiral."

Recent solid-state NMR results, however, show little support for such a regular and highly ordered structure. Rather, an inhomogeneous structure seems more likely, even for a simplified repeat like $(VPGVG)_n$. A collaborative study between the Asakura and Kumashiro groups [37], for example, used solid-state spectral editing techniques [38] in combination with 2D spin diffusion under off-magic-angle-spinning conditions to provide another structural picture of the (VPGVG) subunit, as it is found in novel, recombinant silk-elastinlike peptides. These results showed that distorted β structures are predominant in the protein, with significant structural disorder about the central glycine residue in the (VPGVG) subunits. Hong and co-workers also reported a number of studies on elastin mimetics that incorporated the (VPGVG) subunit [39–42]. Their earliest report focused on the central glycine residue found in each of the pentapeptidyl subunits of the 81-kDa elastin-mimetic peptide $[(VPGVG)_4(VPGKG)]_{39}$ [39]. This paper utilized a new technique for selective detection of a residue pair to identify the chemical shift anisotropy of a site that is poorly resolved in the 1D spectra. At the end of this article, they concluded that the Gly_3 CSA is consistent with type I and II β-turn structures. A subsequent study [40] found that the type II β-turn was predominant at the Pro–Gly pair of each subunit, based on Pro ^{15}N and ^{13}C chemical shift measurements. The most recent work on this same pair in $(VPGVG)_3$, however, identified a "bimodal structure distribution" of an "extended and distorted β-strand" and a turn, either as a β-turn or a "previously unidentified turn" as its major and minor forms, respectively [41]. The relative populations of the two general types of conformers are 65 and 35%, which is roughly 2:1, consistent with an earlier report for the 1D ^{13}C CPMAS of $(LGGVG)_n$[43] (described below). It appears that the structural studies by Hong and co-workers have evolved to the same general conclusions as those obtained with the silk-elastinlike peptides [37], namely, that the β-spiral model of regular, repeating β-turns is not supported by solid-state NMR studies of peptides incorporating the (VPGVG) motif.

As a final, interesting note, the work from Hong and co-workers [42] also demonstrated that the dynamics of the $[(VPGVG)_4(VPGKG)]_{39}$ peptide were similar to those of the native elastin [13], underscoring the fact that these simplified systems yield results, in terms of structure, relaxation, and mobility, that are reasonably consistent with those of the more complicated biopolymer found in nature.

Other elastin repeats are good candidates for characterization with solid-state NMR spectroscopy. In collaboration with Martino and Tamburro, this author's lab used a series of ^{13}C CPMAS NMR experiments to characterize poly(LGGVG), a repeating motif found in elastin [43]. Martino *et al*. had earlier reported that the solution structure of this peptide is best described as a "conformational ensemble" that includes both type I and type II β-turns, in addition to some unstructured regions [28]. Solid-state spectral editing techniques were employed to assist in making tentative peak assignments [38]; 1D CPMAS spectra showed clearly that two peaks are observed for the C_β-Val carbon. The features at 32.7 and 29.2 ppm are present in the ratio of 2:1, implying that the conformation(s) corresponding to the downfield peak is dominant. Clearly, this simple result eliminates from consideration the possibility that each subunit may fold into only one type of structure. Furthermore, the nature of the backbone carbonyl lineshape supported this picture; i.e. simple deconvolution subroutines found that the backbone carbonyl peak did not yield results that would support a model such as the β-spiral. Finally, it was noted that, although the T_1's obtained were similar to other lyophilized peptides, we found that they tended to be on the shorter end of the range. That is, even though the peptides are lyophilized, simplified mimetics of the native protein, they tend to mirror the characteristics that set elastin apart from other proteins in the solid-state. Namely, they tend towards structurally heterogeneous samples with dynamics that reflect unusually fast motion.

Concluding Remarks

Studies by Torchia and co-workers, among several others, provided the first glimpse of the unusual nature of the structure and dynamics of elastin, using solid-state NMR spectroscopy. Since then, the field has evolved to utilize a wealth of newer approaches, combining techniques like cell culture and recombinant methods with sophisticated ways to manipulate samples and spins. Overall, it appears that the diverse range of philosophies and approaches are leading to a convergence of themes, to some extent. From the relatively straightforward measurement of T_1's and other relaxation parameters to the multidimensional methods for measuring residual anisotropies, it is clear that the molecular dynamics of elastin is unlike most other proteins in the solid-state. Furthermore, the solid-state NMR studies to-date have all but eliminated any structural model with long-range order. Instead, it appears that even the simplest repeating polypeptides based on the amino acid sequence of elastin have structural parameters that call for a "structure distribution" [41] or "conformational ensemble" [1,28] in proposing a three-dimensional model for this protein. In future years, we can expect that the discrepancies that exist amongst the various results will be reconciled with additional NMR experiments and with the growing number of elastin and elastinlike peptides.

Acknowledgments

Various portions of the work presented in this chapter were supported by the NSF, NIH, and the Hawaii Community Foundation. Current and former members of this author's research laboratory and Dr. W.P. Niemczura (NMR facility, University of Hawaii) are also acknowledged for their participation in this ongoing project.

References

1. Debelle L, Tamburro AM. Int. J. Biochem. Cell Biol. 1999;31:261.
2. Rosenbloom J, Abrams WR, Mecham R. FASEB J. 1993;7:1208.
3. Sandberg LB. Int. Rev. Connect. Tissue Res. 1976;7:160.
4. Pierce RA, Deak SB, Stolle CA, Boyd CD. Biochemistry. 1990;29:9677.
5. Hoeve CAJ, Flory PJ. Biopolymers. 1974;13:677.
6. Gray WR, Sandberg LB, Foster JA. Nature. 1973;246: 461.
7. Urry DW. Adv. Exp. Med. Biol. 1974;43:211.
8. Urry DW, Long MM. Adv. Exp. Med. Biol. 1977;79:685.
9. Venkatachalam CM, Urry DW. Macromolecules. 1981;14:1225.
10. Chang DK, Venkatachalam CM, Prasad KU, Urry DW. J. Biomol. Struct. Dyn. 1989;6:851.
11. Li B, Alonso DOV, Bennion BJ, Daggett V. J. Am. Chem. Soc. 2001;123:11991.
12. Li B, Alonso DOV, Daggett V. J. Mol. Biol. 2001;305:581.
13. Perry A, Stypa MP, Tenn BK, Kumashiro KK. Biophys. J. 2002;82:1086.
14. Starcher BC, Galione MJ. Anal. Biochem. 1976;74:441.
15. Rasmussen BL, Bruenger E, Sandberg LB. Anal. Biochem. 1975;64:255.
16. Torchia DA, Piez KA. J. Mol. Biol. 1973;76:419.
17. Lyerla JR, Torchia DA. Biochemistry. 1975;14:5175.
18. Ellis GE, Packer KJ. Biopolymers. 1976;15:813.
19. Kricheldorf HR, Muller D. Int. J. Biol. Macromol. 1984;6:145.
20. Pometun MS, Chekmenev EY, Wittebort RJ. J. Biol. Chem. 2004;279:7982.
21. Tarnawski R, Tarnawski R, Grobelny J. Atherosclerosis. 1995;115:27.

22. Kumashiro KK, Kim MS, Kaczmarek SE, Sandberg LB, Boyd CD. Biopolymers. 2001;59:266.
23. Torchia DA, Sullivan CE. Adv. Exp. Med. Biol. 1977;79:655.
24. Fleming WW, Sullivan CE, Torchia DA. Biopolymers. 1980;19:597.
25. Perry A, Stypa MP, Foster JA, Kumashiro KK. J. Am. Chem. Soc. 2002;124:6832.
26. Luan C-H, Krishna NR, Urry DW. Int. J. Quantum Chem.: Quantum Biol. Symp. 1990;17:145.
27. Tamburro AM, Guantieri V, Gordini DD. J. Biomol. Struct. Dyn. 1992;10:441.
28. Martino M, Coviello A, Tamburro AM. Int. J. Biol. Macromol. 2000;27:59.
29. Martino M, Tamburro AM. Biopolymers. 2001;59:29.
30. Urry DW, Mitchell LW. Biochem. Biophys. Res. Commun. 1976;68:1153.
31. Partridge SM, Davis HF, Adair GS. Biochem. J. 1955;61:11.
32. Partridge SM, Davis HF. Biochem. J. 1955;61:21.
33. Jones PA, Scott-Burden T, Gevers W. Proc. Natl. Acad. Sci. U.S.A. 1979;76:353.
34. Barone LM, Faris B, Chipman SD, Toselli P, Oakes BW, Franzblau C. Biochim. Biophys. Acta. 1985;840: 245.
35. Kummerlen J, vanBeek JD, Vollrath F, Meier BH. Macromolecules. 1996;29:2920.
36. Urry DW, Trapane TL, Sugano H, Prasad KU. J. Am. Chem. Soc. 1981;103:2080.
37. Ohgo K, Kurano TL, Kumashiro KK, Asakura T. Biomacromolecules. 2004;5:744.
38. Kumashiro KK, Niemczura WP, Kim MS, Sandberg LB. J. Biomol. NMR. 2000;18:139.
39. Hong M, McMillan RA, Conticello VP. J. Biomol. NMR. 2002;22:175.
40. Hong M, Isailovic D, McMillan RA, Conticello VP. Biopolymers. 2003;70:158.
41. Yao XL, Hong M. J. Am. Chem. Soc. 2004;126:4199.
42. Yao XL, Conticello VP, Hong M. Magn. Reson. Chem. 2004;42:267.
43. Kumashiro KK, Kurano TL, Niemczura WP, Martino M, Tamburro AM. Biopolymers. 2003;70:221.

Structural Analysis of Silk Fibroins using NMR

Tetsuo Asakura and Yasumoto Nakazawa

Department of Biotechnology, Tokyo University of Agriculture and Technology, Koganei, Tokyo 184-8488, Japan

Introduction

Recently, much attention has been paid to silks from textile engineers to polymer chemists and biomedical scientists. The silk fibers produced by silkworms or spiders are the nature's most highly engineered structural materials with combinations of strength and toughness not found in today's man-made materials [1]. In addition, there are many kinds of silks from silkworms and spiders with different structures and properties.

The silk fibroin from the domesticated silkworm, *Bombyx mori*, is a well-known fibrous protein whose amino acid composition (in mol%) is 42.9 Gly, 30.0 Ala, 12.2 Ser, 4.8 Tyr, and 2.5 Val. The fibroin consists mostly of the sequence (Ala-Gly-Ser-Gly-Ala-Gly)$_n$ and comes in silk I (the structure before spinning) and silk II (the structure after spinning) structural forms. Despite a long history of studying silk I, the structure remains poorly understood because any attempt to induce a macroscopic orientation of the sample for X-ray diffraction, electron diffraction, or solid-state NMR, readily causes a conversion of the silk I form to the silk II form. Employing several high-resolution solid-state NMR techniques and analyzing ^{13}C CP/MAS NMR chemical shifts quantitatively, in conjunction with molecular simulations, we proposed a repeated β-turn type II structure stabilized by intra-molecular hydrogen bond for the silk I form.

On the other hand, the structure of silk II has been proposed as a regular array of anti-parallel β-sheet firstly by Marsh *et al.* about half century ago, based on a fiber diffraction study of native *B. mori* silk fibroin fiber [1]. Later, Fraser *et al.*, Lotz *et al.*, and Takahashi *et al.* pointed out some intrinsic structural disorder in the silk II structure although they essentially supported the general features of this anti-parallel β-sheet model [2,3]. The solid-state NMR techniques that have been successfully used for the structure of silk I were also used for the detailed structural determination of silk II.

The primary structure of *Samia cynthia ricini* silk fibroin is considerably different from that of *B. mori* silk fibroin [4]. The basic repeat sequence is made of alternating (Ala)$_{12\text{–}13}$ regions and the Gly-rich regions which is similar to the sequence of spider dragline silk (major ampullate) although the length of polyalanine is shorter (Ala)$_{5\text{–}6}$ in the latter case. The use of appropriate stable isotope-labeled model peptides for the repeated sequences of *S. c. ricini* silk fibroin and spider dragline silks coupled with the use of solid-state NMR methods have applied to determination of the precise local structure.

In this chapter, we overview our recent studies on the structural determination of these silks with solid-state NMR.

Structure of *B. mori* Silk Fibroin Before Spinning (Silk I)

The structural features of *B. mori* silk fibroin are conveniently studied using synthetic peptide (AG)$_{15}$, as a model for crystalline region because the lack of Ser in the model peptide (AG)$_{15}$ does not make any difference in the ^{13}C CP/MAS NMR chemical shifts of the Ala and Gly residues in the repeated sequence (AGSGAG)$_n$ of native silk fibroin [5–7]. By combining several solid-state NMR techniques, we have determined the conformation of the model peptide (AG)$_{15}$ in the silk I form: The torsion angles of Ala and Gly residues were ($-60° \pm 5°$, $130° \pm 5°$) and ($70° \pm 5°$, $30° \pm 5°$), respectively. 2D spin-diffusion NMR was used to determine the torsion angles. Figure 1A and B show the observed 2D spin-diffusion NMR spectrum (only the carbonyl region was expanded) of (AG)$_6$A-[1-^{13}C]G^{14}[1-^{13}C]A^{15}G(AG)$_7$ and the spectrum calculated by assuming the torsion angles, $(\phi, \psi) = (-60°, 130°)$, for Ala residue, respectively. Similarly, Figure 1C shows the experimental 2D spin-diffusion NMR spectrum of (AG)$_6$[1-^{13}C]A^{13}[1-^{13}C]G^{14}(AG)$_8$ together with the spectrum D calculated with the torsion angles, $(\phi, \psi) = (70°, 30°)$, for Gly residue. In both cases, the observed spectra could be reproduced well with the calculated spectra. With these torsion angles of Ala and Gly residues determined here, the structural model of an (AG)$_{15}$ chain with silk I form was prepared and shown in Figure 2. This can be called as a repeated β-turn type II structure. In order to confirm this model, REDOR experiments were performed. Namely, the atomic distance between the ^{13}C = O carbon atom of the 14th Gly residue and the ^{15}N nitrogen atom of the 17th Ala residue of (AG)$_{15}$ was determined precisely as shown in Figure 3. The distance was determined to be 4.0 ± 0.1 Å independent of the dilution with unlabeled (AG)$_{15}$ peptide which agrees very well

Graham A. Webb (ed.), Modern Magnetic Resonance, 101–106.
© 2008 *Springer.*

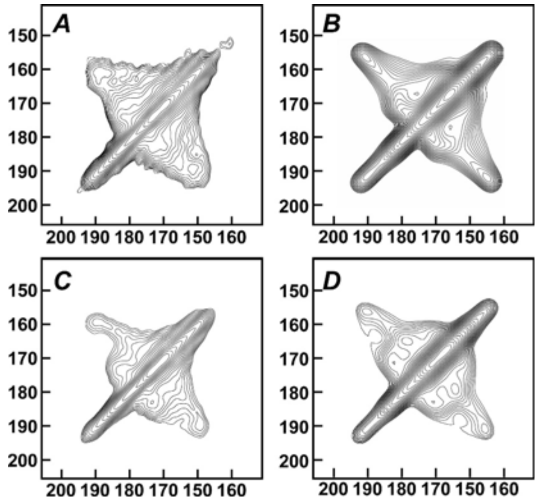

Fig. 1. The (A) experimental and (B) simulated 2D spin-diffusion NMR spectra of $(AG)_6A[1\text{-}^{13}C]G_{14}[1\text{-}^{13}C]A_{15}G(AG)_7$ and the (C) experimental and (D) simulated spectra of $(AG)_6[1\text{-}^{13}C]A_{13}[1\text{-}^{13}C]G_{14}(AG)_8$. The torsion angles of Ala_{15} residue used for the simulation of former spectrum were $(\phi, \psi) = (-60°, 130°)$, while the torsion angles of Gly_{14} residue were $(\phi, \psi) = (70°, 30°)$.

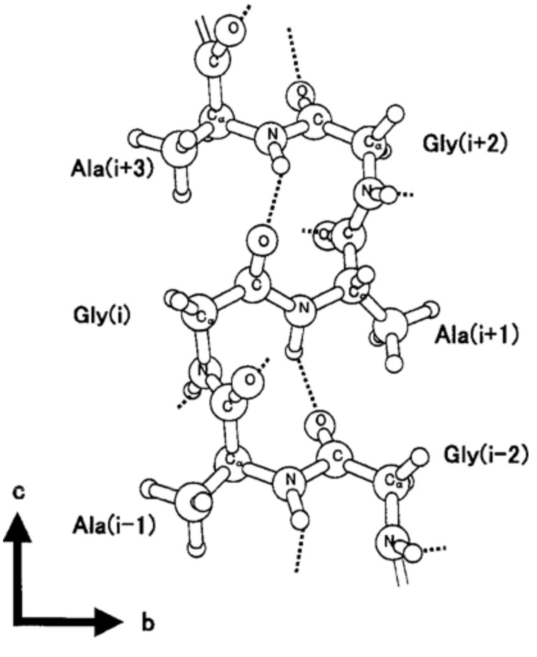

Fig. 2. The conformation of a repeated β-turn type II-like molecule as a model for silk I. There are intra-molecular hydrogen bonds between the carbonyl oxygen atom of the ith Gly residue and the amide hydrogen atom of the $(i + 3)$th Ala residue.

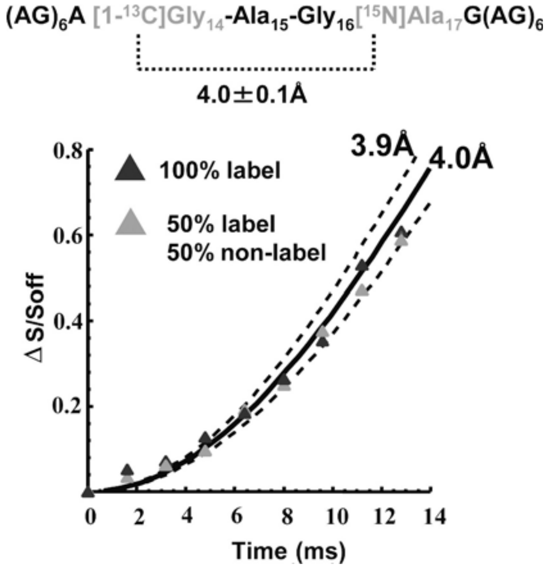

Fig. 3. Observed plots of $\Delta S/S_0 (= 1 - S/S_0)$ values against the corresponding NcTr values for REDOR experiments of $(AG)_6A[1\text{-}^{13}C]GAG[^{15}N]AG(AG)_6$ for the determination of distance between the $^{13}C = O$ carbon of the 14th Gly residue and the ^{15}N nitrogen of the 17th Ala residue. Solid and dotted lines show the theoretical dephasing curves corresponding to the designated distances. The data marked by ○ are observed for the isotope-labeled compound without dilution of natural abundance $(AG)_{15}$ and those by Δ, for a mixture of equivalent amount of the isotope-labeled compound and natural abundance $(AG)_{15}$. By comparing the REDOR data and the theoretical dephasing curve, the ^{13}C–^{15}N inter-atomic distance was determined to be 4.0 ± 0.1 Å, which agrees with the 4.0 Å calculated for intra-molecular hydrogen bond for the repeated β-turn type II-like structure.

with the distance, 4.0 Å, calculated for the corresponding atomic distance of the intra-molecular hydrogen bonding site in the repeated β-turn type II-like structure. This supports the structural model proposed here (Figure 2). By adding X-ray diffraction data of poly(Ala-Gly) in the silk I form to the solid-state NMR data, a more precise model with intra- and inter-molecular hydrogen bond formations alternatively was proposed for the structure in the solid state [8].

Structure of *B. mori* Silk Fibroin After Spinning (Silk II)

As mentioned in the section "Introduction", although Lotz *et al.* [3] and Fraser *et al.*[2] generally supported the anti-parallel β-sheet model proposed by Marsh *et al.* [1], the former researchers also pointed out the presence of an irregular structure in the silk fibers. More recently,

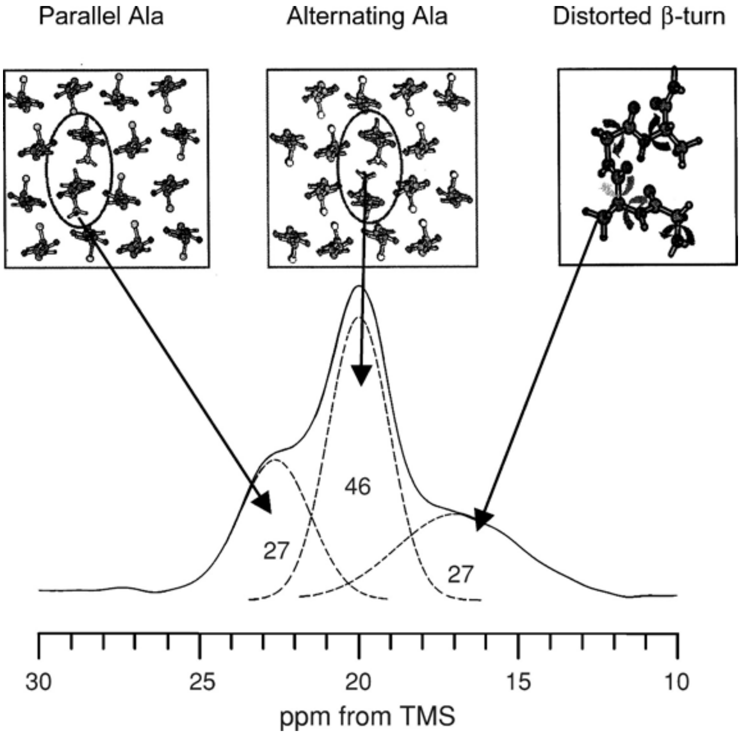

Fig. 4. Expanded Ala C$_\beta$ peak of (AG)$_{15}$ in silk II form, model peptide of the crystalline fraction of *B. mori* silk fibroin fibers. Shown as dotted lines underneath are the spectral deconvolutions with Gaussian peaks.

Takahashi *et al.* [9] proposed that each crystal site of *B. mori* silk fiber is statistically occupied by two anti-parallel β-sheet chains with different relative orientations.

Actually, we recently found out that the Ala C$_\beta$ peak in the ^{13}C CP/MAS NMR spectrum of *B. mori* silk fiber in the silk II form is broad and asymmetric, reflecting the heterogeneous structure of the silk fiber [6,7]. The Ala C$_\beta$ peak of the model peptide (AG)$_{15}$ in silk II form was also asymmetric which consists of three peaks with isotropic chemical shifts of 22.2 (27%), 19.6 (46%), and 16.7 (27%) ppm, respectively (Figure 4). The broad peak at the highest field has essentially the same chemical shift as the sharp Ala C$_\beta$ peak at 16.7 ppm of silk I [7]. Therefore, the broad component at 16.7 ppm in Figure 4 was assigned to distorted β-turn where the averaged ϕ, ψ angles are the same as those of β-turn type II-like structure, but the distribution of the ϕ, ψ angles is larger [10]. The other two components with the chemical shifts of 19.6 and 22.2 ppm can be assigned to anti-parallel β-sheet conformation [7,10,11]. Actually, the 2D spin-diffusion NMR study indicates that the conformation of (AG)$_{15}$ in silk II form is mainly an anti-parallel β-sheet with the torsion angles $(\phi, \psi) = (-150^\circ, 150^\circ)$ of the Ala residue. Since the Ala C$_\beta$ methyl groups are located outside of the protein backbone, the occurrence of two peaks suggests that there is a difference in the mode of side chain packing: The 19.6 ppm peak is assigned to the Ala C$_\beta$ carbons which point in the same direction, while 22.2 ppm peak to the Ala C$_\beta$ carbons which alternately point in opposite directions as shown in Figure 4. The relative peak intensities at 22.2 and 19.6 ppm are approximately 1:2, which is in good agreement with the ratio of different packing modes suggested from X-ray diffraction analysis of *B. mori* silk fiber [9].

Structure of Silk Fibroin from *S. c. ricini* Before Spinning

The ^{13}C CP/MAS NMR chemical shifts of Ala residue clearly indicate that the silk fibroin prepared from the silk gland of *S. c. ricini* and then dried mildly, take a typical α-helix structure and that the structure changed to β-sheet after spinning. This was also supported using the 2D DOQSY (double-quantum single-quantum correlation experiment) NMR measurements [12]. In order to obtain more precise structural information for the sequence of the poly-Ala region, several stable isotope-labeled peptides with the sequence, GGAGGGYGGDGG(A)$_{12}$GGAGDGYGAG, were synthesized. The torsion angles of the central Ala residue, Ala$_{19}$, in the peptide, GGAGGGYGGDGG (A)$_5$-[1-^{13}C]

$A^{18}[1\text{-}^{13}C]A^{19}(A)_5$GGAGDGYGAG were determined using 2D spin-diffusion NMR after TFA treatment. The angles were determined to be $(\phi, \psi) = (-59^\circ, -48^\circ)$ which are typical angles of α-helical structures [13,14]. The torsion angles of the N- and C-terminal Gly residues adjacent to poly-Ala region were also determined using the 2D spin-diffusion NMR method for two model peptides, GGAGGGYGGD$[1\text{-}^{13}C]G^{11}[1\text{-}^{13}C]G^{12}(A)_{12}$GGAGDGYGAG and GGAGGGYGGDG-$G(A)_{11}[1\text{-}^{13}C]A^{24}[1\text{-}^{13}C]G^{25}$GAGDGYGAG. From the error analysis of the observed and calculated spin-diffusion NMR spectra [14], the torsion angles of the Gly^{12} and Gly^{25} residues were determined to be $(\phi, \psi) = (-70^\circ, -30^\circ)$ and $(\phi, \psi) = (-66^\circ, -22^\circ)$, respectively. In order to obtain further structural information on the C-terminal region, REDOR experiments were performed for GGAGGGYGGDGG $(A)_8[1\text{-}^{13}C]A^{21}$-AAA$[^{15}N]G^{25}$GAGDGYGAG. The ^{13}C–^{15}N inter-atomic distance of the stable isotope-labeled site was determined to be 4.8 ± 0.1 Å. When the torsion angles of Ala^{22} residue are $(\phi, \psi) = (-59^\circ, -48^\circ)$ and those of the other two Ala residues, Ala^{23} and Ala^{24}, are $(\phi, \psi) = (-66^\circ, -22^\circ)$, the atomic distance between the $[1\text{-}^{13}C]A^{21}$ and $[^{15}N]G^{25}$atoms was calculated to be 4.8 Å. The similar REDOR method was applied to determination of the local structure at the N-terminal region. With the torsion angles determined here, the structure of the model peptide, GGAGGGYGGDGG$(A)_{12}$GGAGDGYGAG, was proposed in Figure 5. As shown in the left side, the local structure of N- and C-terminal residues besides the α-helical poly-Ala chain is more strongly wound than those found in a typical α-helix. Namely, at the terminals of the helical region, five residues, Gly^{12}, Ala^{21}, Ala^{22}, Ala^{23}, and Ala^{24} contribute to the formation of $i \rightarrow i + 3$ hydrogen bonding (see right side in Figure 5), suggesting that there are mechanisms to stabilize the α-helix structure of poly-Ala region of the silk fibroin in *S. c. ricini* silkworm.

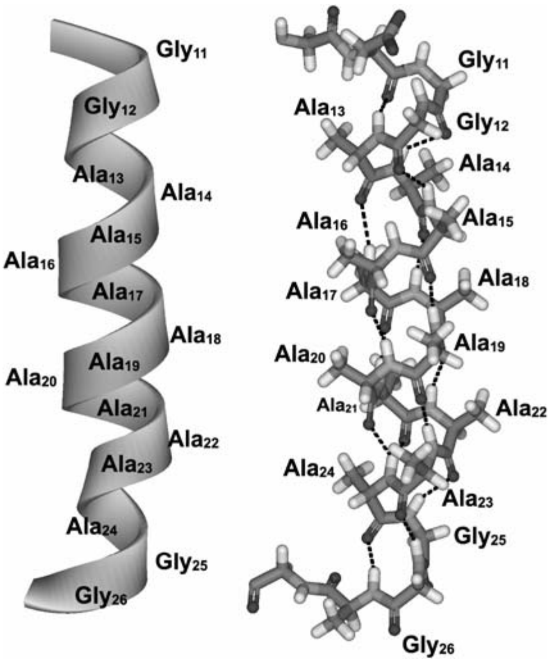

Fig. 5. The structure of poly (L-alanine) region of the model peptide, GGAGGGYGGDGG$(A)_{12}$GGAGDGYGAG of polyalanine region of *S. c. ricini* silk fibroin before spinning. Both structures are the same, but different presentation. The left side presentation shows that α-helix structure of polyalanine region tend to be winded strongly at the both terminal ends. The right side presentation shows the corresponding intra-molecular hydrogen bonding pattern by broken lines.

Structure of *Nephila clavipes* Dragline Silk (MaSp1)

The dragline filaments produced by orb weaving spiders have been the focus of numerous recent studies because they are the toughest protein fibers known [15–17]. The dragline silk of the golden orb web spider *N. clavipes* contains two structural proteins, designated spidroin 1 (MaSp1) and spidroin 2 (MaSp2) [18,19]. The dominant MaSpl protein can be described as a block copolymer consisting of poly-Ala and Gly-rich regions, which is similar to the primary structure of *S. c. ricini* silk fibroin.

Several kinds of solid-state NMR [20–30] and X-ray diffraction methods [31,32] have been applied to clarify the structure and dynamics of native spider silk fibers. It has been shown that silk fibroins undergo substantial structural change from gland silk to native dragline silk. In particular, it has been shown using conformation-dependent ^{13}C chemical shifts of Ala residues that the poly-Ala region in dragline silk fiber adopts a β-sheet structure [21–25]. In contrast, the Gly-rich region in the final silk has been described as: rubber-like [33] or amorphous [31], or recently as mainly 3_1-helical as shown by 2D spin diffusion [22] and by DOQSY and DECODER (direction exchange with correlation for orientation-distribution evaluation and reconstruction) solid-state NMR techniques [27]. However, it is still difficult to judge their precise local structure by solid-state NMR, because heterogeneity in the repeated sequences and resulting large variations in structural distributions must also be taken into account. To avoid the large variations in structural distributions resulting from the heterogeneity in the primary structure, we prepared both a non-labeled peptide with a sequence containing

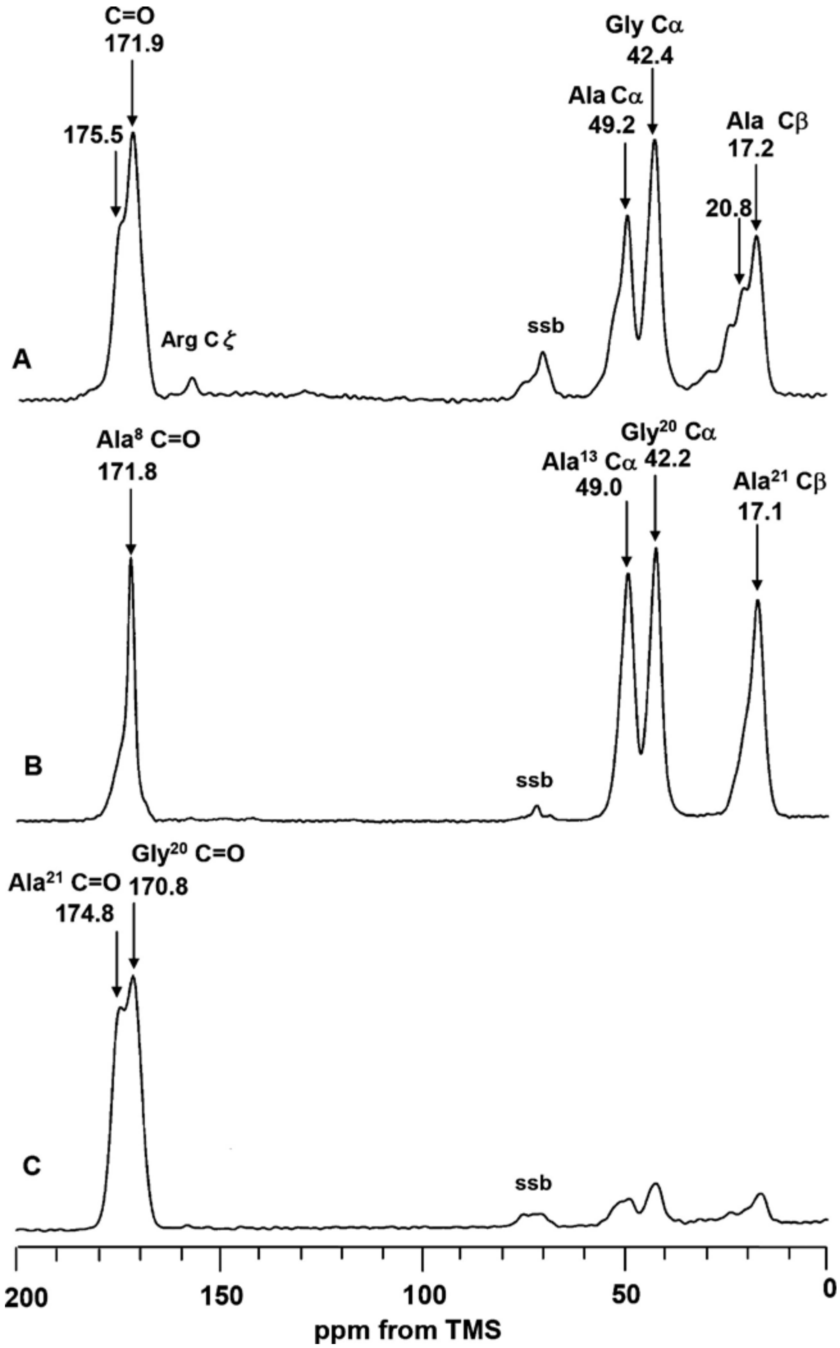

Fig. 6. ^{13}C CP/MAS NMR spectra of I (A), Ia (B), and II (C) after dissolving these peptides in 9 M LiBr and then dialyzing against water (ssb means spinning side band).

both the polyalanine and the repeated GGA regions, QGAG(A)$_6$GGAGA(GGA)$_3$GAGRGGLGG (I), and the ^{13}C-labeled peptides, QGAGAAA[1-^{13}C]A^{8}AAGG[2-^{13}C]A^{13}GAGGAG[2-^{13}C]G^{20}[3-^{13}C]A^{21}GGAGAGRG-GLGG (Ia) and QGAGAAAAAAGGAGAGGAG[1-^{13}C]G^{20}[1-^{13}C]A^{21}GGAGAGRG-GLGG (II), as a local structural model of MaSpl protein. Solvent treatments prior to the NMR measurements induce structural change of these model peptides and provide a model to reproduce the structure of the silk fiber. Conformation-dependent ^{13}C NMR chemical shifts were mainly used to determine the local structure, including the evaluation of the fraction of several conformations. As shown in Figure 6, the characteristic structure; 65% β-sheet for Ala^8 residue in poly-Ala region, and 70% 3_1-helix for Ala^{21} residue and mainly 3_1-helix for Gly^{20} residue in the GG^{20}A^{21} sequence was observed after dissolving the peptides (Ia) and (II) in 9 M LiBr followed by dialysis against water. The 2D spin-diffusion ^{13}C solid-state NMR spectrum of the Ala^{21} residue of the peptide (II) after this treatment was also reproduced by 70% 3_1-helix ($\phi, \varphi = -90^\circ, 120^\circ$) and 30% β-sheet structure ($\phi, \varphi = -150^\circ, 150^\circ$). However, the Ala C$_\beta$ peak assigned to 3_1-helix in the spectrum of (Ia) is broad, implying that the torsion angles of Ala^{21} residue are distributed, but with an average that corresponds approximately to the torsion angles of the 3_1-helix. Increase in the fraction of β-sheet in both poly-Ala and GG^{20}A^{21} regions was observed for (Ia) after dissolving it in formic acid and then drying in air. Moreover, after dissolving (Ia) in formic acid and then precipitating it in methanol, the spectrum showed a tightly packed β-sheet structure with further increase in the fraction of β-sheet although 15% 3_1-helix still remained in the GG^{20}A^{21} region. The β-sheet structure of poly-Ala region, and both 3_1-helix and β-sheet structures in the repeated GGA sequence is in agreement with the structural model for the native spider dragline silk fiber from *N. clavipes* from a previous NMR study. On the other hand, α-helical conformation was found to be dominant for the peptide treated with trifluoroacetic acid together with a significant contribution from other structures. The fraction of the other structures was 20–40% depending on the position of ^{13}C-labeled Ala residue.

References

1. Marsh RE, Corey RB, Pauling L. Biochem. Biophys. Acta. 1955;16:1.
2. Fraser RD, MacRae TP, Stewart FH. J. Mol. Biol. 1966;19: 580.
3. Lotz B, Brack A, Spach G. J. Mol. Biol. 1974;87:193.
4. Asakura T, and Nakazawa Y. Macromol. Biosci. 2004;4:175.
5. Asakura T, Ashida J, Yamane T, Kameda T, Nakazawa Y, Ohgo K, Komatsu K. J. Mol. Biol. 2001;306:291.
6. Asakura T, Yao J, Yamane T, Umemura K, Ulrich AS. J. Am. Chem. Soc. 2002;124:8794.
7. Asakura T, Yao J. Protein Sci. 2002;11:2706.
8. Asakura T., Ohgo K., Komatsu K., Kanenari M., Okuyama K. Macromolecules 2005;38:7397.
9. Takahashi Y, Gehoh M, Yuzuriha K. Int. J. Biol. Macromol. 1999;24:127.
10. Asakura T, Kuzuhara A, Tabeta R, Saito H. Macromolecules. 1985;18:1841.
11. Ishida M, Asakura T, Yokoi M, Saito H. Macromolecules. 1990;23:88.
12. van Beek JD, Beaulieu L, Schafer H, Demura M, Asakura T, Meier BH. Nature. 2000;405:1077.
13. Nakazawa Y, Bamba M, Nishio S, Asakura T. Protein Sci. 2003;12:666.
14. Nakazawa Y, Asakura T. J. Am. Chem. Soc. 2003;125: 7230.
15. O'Brien J, Fahnestock S, Termonia Y, Gardner K. Adv. Mater. 1998;10:1185.
16. Gosline JM, Guerette PA, Ortlepp CS, Savage KN. J. Exp. Biol. 1999;202:3295.
17. Vollrath F, Knight DP. Nature. 2001;410:541.
18. Xu M, Lewis RV. Proc. Natl. Acad. Sci. U.S.A. 1990;87:7120.
19. Hinman MB, Lewis RV. J. Biol. Chem. 1992;267:19320.
20. Simmons A.H., Ray E.D., Jelinski L.W. Macromolecules 1994;27:5235.
21. Simmons A.H., Michal, C.A., Jelinski, L.W. Science 1996;271:84
22. Kümmerlen J., Van Beek J.D., Vollrath F., Meier B.H. Macromolecules 1996;29:2920.
23. Michal C.A., Jelinski L.W. J. Biol. NMR. 1998; 12:231.
24. van Beek J.D., Kümmerlen J., Vollrath F., Meier B.H. Int. J. Biol. Macromol. 1999;24:173
25. Seidel A., Liivak O., Calve S., Adaska J., Ji G., Yang Z., Grubb D., Zax D.B., Jelinski L.W. Macromolecules 2000;33:775.
26. Yang Z., Liivak O., Seidel A., Laverda G., Zax D.B., Jelinski L.W. J. Am. Chem. Soc. 2000;122:9019
27. van Beek J.D., Hess S., Vollrath F., Meier B.H., Proc. Natl. Acad. Sci. USA 2002;99:10266.
28. Eles P.T., Michal C.A. Biomacromolecules 2004;5:661.
29. Eles P.T., Michal C.A. Macromolecules 2004;37:1342.
30. Holland G.P., Lewis R.V., Yarger J.L. J. Am. Chem. Soc. 2004;126:5867.
31. Grubb D.T. and Jelinski L.W. Macromolecules 1997;30:2860.
32. Riekel C., Bränden C., Craig C., Ferrero C., Heidelbach F., Müller M. Int. J. Biol. Macromol. 1999;24:179.
33. Gosline J.M., Denny M.W., DeMont M.E. Nature 1984;309:551.

Field Gradient NMR

NMR Diffusometry

William S. Price
Nanoscale Organization and Dynamics Group, College of Science, Technology and Environment,
University of Western Sydney, Penrith South, NSW 1797, Australia

Diffusion as a Probe

Translational diffusion is inherently important in the chemical and biological world since it constitutes the most basic form of transport. But its study is also important by virtue of the translational motion of a species being affected by molecular interactions (e.g. binding) or restricted diffusion by physical barriers (e.g. within a pore). Thus, the diffusion of a species provides a rich source of information regarding the interactions of a species with other molecules and its environment. NMR provides a conceptually simple but direct and extremely powerful method for measuring diffusion down to about 10^{-14} m^2/s. In contrast to traditional methods, and of particular significance since the species of interest is likely to be a small molecule or ion, the NMR method (generally) does not require labeling and is effectively non-invasive. This chapter provides a brief introduction to the Pulsed Gradient Spin-Echo (PGSE) NMR method (also commonly referred to as Affinity NMR, DOSY, or PFG NMR) for measuring diffusion and its application to solution dynamics and probing porous media.

Already a very large literature exists on NMR diffusometry and applications, and thus the literature cited here is only as an example and is in no way comprehensive. A number of reviews have already appeared including of a general nature [1–8] and specializing in supramolecular and combinatorial chemistry [9], polymer gels [10], proteins [11], transport and binding [12–14], and surfactants [15,16].

Gradient-Based Diffusion Measurements

Although technically difficult the concept underlying the PGSE technique is breathtakingly simple. All PGSE sequences are, as the name suggests, based on some form of spin-echo sequence. We will illustrate the operation of the PGSE sequence with the simplest case, that of a Hahn spin-echo based sequence. From the earliest days of NMR it was realized that the refocusing of the echo in the Hahn sequence could be compromised by the effect of magnetic field gradients. Since should a spin move to a region with a different magnetic field during the sequence, the phase change acquired during the first τ period would not be counteracted by that experienced in the second τ period (recall that the effect of the π pulse is to reverse the sign of the phase change that has accumulated prior to its application). Theoretical modeling of this attenuation of the echo due to spins experiencing different magnetic fields is facilitated if the applied magnetic gradient is constant (often mistakenly referred to as "linear").

The imposition of a magnetic field gradient during the rf pulses and acquisition is deleterious: much stronger rf pulses are required to overcome the gradient induced spreading of the spectrum and chemical shift information is lost during acquisition. Further, it would also result in the timescale of the diffusion measurement being tied to τ. A much better, albeit technically more demanding solution, is to apply the magnetic gradient in the form of two equal pulses of length δ and magnitude and direction $\mathbf{g}$ as depicted in Figure 1. The area of such gradient pulses (i.e. $\delta\mathbf{g}$) leads to the definition of the reciprocal space vector

$$\mathbf{q} = (2\pi)^{-1}\,\gamma\mathbf{g}\delta\left(\mathrm{m}^{-1}\right). \tag{1}$$

It is easily imagined that an infinitely short gradient pulse (SGP) (i.e. $\delta \to 0$ and $|\mathbf{g}| \to \infty$ while $\delta\mathbf{g}$ remains finite) with $\mathbf{g}$ directed along the long axis of a cylindrical sample would wind (i.e. spatially encode) the transverse magnetization into a helix with pitch q^{-1} (m). If instead the pulse had finite duration, the effect of translational diffusion during the pulse would corrupt the helix formation.

Assuming the SGP condition so that motion during the gradient pulse can be neglected, but accounting for motion during the period Δ between the first gradient pulse and the second (i.e. spatially decoding) gradient pulse leads to the SGP relation for the spin-echo attenuation [17]

$$E = \iint \rho(\mathbf{r}_0)\; P(\mathbf{r}_0, \mathbf{r}_1, \Delta)\, \mathrm{e}^{\mathrm{i}2\pi\mathbf{q}(\mathbf{r}_1-\mathbf{r}_0)}\, \mathrm{d}\mathbf{r}_0\, \mathrm{d}\mathbf{r}_1 \tag{2}$$

where $\rho(\mathbf{r}_0)$ is the equilibrium spin-density and $P(\mathbf{r}_0, \mathbf{r}_1, \Delta)$ is the diffusion propagator [18] (or Green function [19]) derived using appropriate boundary conditions and a delta function initial condition. The integral

Graham A. Webb (ed.), Modern Magnetic Resonance, 109–115.
© 2008 *Springer.*

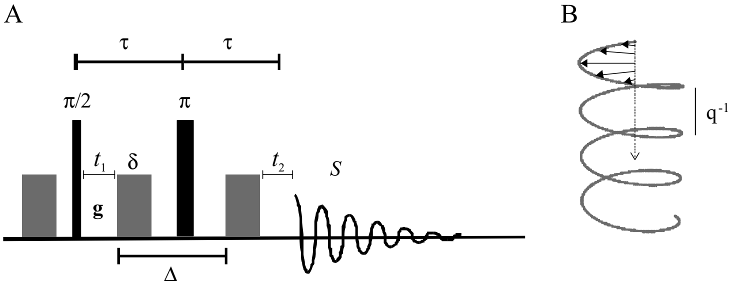

Fig. 1. (A) A PGSE sequence based on a Hahn-spin echo where two equal gradient pulses of duration δ and magnitude **g** are inserted into each τ period. Typically δ is in the range of 1–10 ms, whilst the separation Δ between the leading edges of the gradient pulses is normally in the range of 10 ms to 1 s. The second half of the echo is used as the NMR signal. Normally the echo attenuation, defined by $E(\mathbf{g}) = S(\mathbf{g})/S(\mathbf{g} = 0)$, is used to determine the diffusion coefficient as it allows the effects of spin relaxation to be normalized out. A gradient pre-pulse is included before the $\pi/2$ rf pulse to reduce eddy current and gradient mismatch effects. (B) An example of a magnetization helix (the arrows represent nuclear spins and the spiral curve is a guide for the eye), with pitch q^{-1} that would be formed by applying a gradient pulse along the long axis of a cylindrical sample. Any imperfection in gradient constancy or motion during the pulse results in a distorted helix.

is taken over all starting ($\mathbf{r}_0$) and finishing ($\mathbf{r}_1$) positions. Equation (2) states that the echo attenuation is given by the Fourier transform of the diffusion propagator with respect to q. In the case of free diffusion, Equation (2) leads to

$$E = \exp\left(-4\pi^2 q^2 D\Delta\right). \tag{3}$$

Importantly, diffusion is measured along the direction of the gradient. Equation (3) states that the echo attenuation for the simple case of free diffusion is given by a single exponential. Despite the relative simplicity of the SGP approximation, apart from free isotropic diffusion, solutions to Equation (2) are only available for simple symmetrical geometries, such as between reflecting planes separated by a distance a, viz [17].

$$\begin{aligned} E = {} & \frac{2[1-\cos(2\pi q a)]}{(2\pi q a)^2} + 4(2\pi q a)^2 \\ & \times \sum_{n=1}^{\infty} \exp\left(-\frac{n^2\pi^2 D\Delta}{a^2}\right) \frac{1-(-1)^n\cos(2\pi q a)}{\left[(2\pi q a)^2-(n\pi)^2\right]^2} \end{aligned} \tag{4}$$

At long Δ, the second term in Equation (4) disappears leaving the long-time diffractive behavior with diffractive minima, which arise from the first term, appearing at $q = n/a\,(n = 1, 2, 3, \ldots)$.

In cases where $P(\mathbf{r}_0, \mathbf{r}_1, \Delta)$ is unknown, expansion of Equation (2) reveals that for small q with respect to the characteristic distance of the restricting geometry, R, the echo attenuation is given by,

$$E\left(\mathbf{q} \ll R^{-1}, \Delta\right) \approx 1 - \frac{(2\pi q)^2 \left\langle z^2(\Delta)\right\rangle}{2} \tag{5}$$

where $\left\langle z^2(\Delta)\right\rangle$ is the mean squared-displacement along the direction of the gradient (i.e. taken to be along the z-axis) and in such cases the PGSE data can be analyzed on the basis of an effective diffusivity [20,21]

$$D_{\mathrm{eff}}(\Delta) = \frac{\left\langle z^2(\Delta)\right\rangle}{2\Delta}. \tag{6}$$

Experimental Complications

Here we consider some experimental complications peculiar to PGSE NMR measurements. In almost all cases experimental imperfections lead to faster "apparent" diffusion coefficients.

Finite Gradient Pulses

Experimentally, the SGP approximation is never completely justified and including its effect in the theoretical analysis is difficult. For example, the analytical solution obtained from solving the Bloch equations is [22,23]

$$E = \exp\left(-\gamma^2 g^2 D(\Delta - \delta/3)\right). \tag{7}$$

Comparison with Equation (3) reveals that the $\delta/3$ term is a correction for the finite length of the gradient pulses. In general, analytical solutions are impossible and numerical approaches are indicated [24,25].

Background Gradients

Due to magnetic susceptibility differences resulting from sample heterogeneity and sample interfaces, the presence of background magnetic gradients is unavoidable. And their effects are insidious on the PGSE measurement [26]. Assuming a simple case of a constant background gradient through the sample of direction and magnitude $\mathbf{g}_0$, the analytical solution starting from the Bloch equations is [22,27]

$$E(g, g_0) = \exp\left(-\gamma^2\left[\underbrace{g^2 D\delta^2(\Delta - \delta/3)}_{\mathbf{g}\ \text{term}} + \underbrace{\mathbf{g}\cdot\mathbf{g}_0 D\delta\left[t_1^2 + t_2^2 + \delta(t_1 + t_2) + \frac{2}{3}\delta^2 - 2\tau^2\right]}_{\mathbf{g}\cdot\mathbf{g}_0\ \text{cross terms}}\right]\right) \tag{8}$$

where the delays t_1 and t_2 are defined in Figure 1A. The difference between Equations (7) and (8) is that the inclusion of the $\mathbf{g}\cdot\mathbf{g}_0$ cross terms results in the attenuation being no longer described by a single exponential. The presence of background gradients can be detected by reversing the sign of the applied gradient and thus the cross term. Consequently, sequences incorporating bipolar pulses have been devised to ameliorate PGSE measurements in the presence of background gradients [28–30].

Radiation Damping

In samples with a high concentration of spins (e.g. a sample of water), a feedback loop can arise in which the precessing spin magnetization generates an oscillating current in the receiver coil, which in turn generates an oscillating magnetic field, which rotates the magnetization back to its equilibrium position—generally much more rapidly than that would occur due to longitudinal relaxation. The effect increases with the strength of the static magnetic field. In the PGSE experiment, radiation damping is active in the periods in which the magnetization is not spatially encoded (i.e. during the periods t_1 and t_2 in the sequence as depicted in Figure 1A). Radiation damping complicates the performing of diffusion measurements of strong NMR resonances and can cause effects similar to those caused by background gradients except that the non-exponential behavior is insensitive to the polarity of the applied gradient [26]. Apart from using a very small sample, the only three practicable and generally applicable means by which accurate PGSE experiments can be conducted in conditions that radiation damping will occur are: (1) by keeping all transverse magnetization spatially encoded during as much of the sequence as possible, (2) allowing part of the magnetization to (reproducibly) decay before starting the diffusion part of the sequence or (3) to use Q-switching [31].

Convection

In PGSE measurements of low viscosity samples away from ambient temperature, convective motion can have particularly deleterious effects [32,33]. Importantly, whereas the diffusion coefficient depends on molecular size, the (convective) flow velocity is common to all of the species in the sample. Whereas a net flow of spins along the direction of the gradient is clearly indicated by the resulting net phase change in the PGSE spectra, convection currents do not produce a phase change since the flow of the spins along the direction of the gradient is exactly matched by the flow in the anti-parallel direction [34,35]. Convection causes a cosine modulation of the PGSE signal attenuation (for a single diffusing species). But due to the similarity between the cosine and Gaussian functions, the PGSE data appears to be well described by an exponential [e.g. Equation (3)] but with an apparent diffusion coefficient that increases with Δ. Apart from improving the temperature regulation to decrease any temperature gradients modifying the sample holder to limit flow, convection can also be minimized by using specialized pulse sequences (e.g. Ref. [36]).

Gradient Constancy

Small deviations from constancy of the applied gradient throughout the sample volume do not generally cause serious errors [37]. Nevertheless, as gradient coils only produce a constant gradient over a small volume, to ensure reasonable constancy, the NMR active volume of the sample must be restricted. Often the effective sample volume will be sufficiently restricted by virtue of the size of the rf coils. More generally it is necessary to physically limit the sample volume (although care must be taken not to introduce background gradients) or by including a slice selective element in the PGSE sequence (e.g. Ref. [38]).

Eddy Currents and Gradient Mismatch

Eddy currents in the surrounding conducting surfaces around the gradient coils (e.g. probe housing, etc.) arise from the rapid rise and fall of the gradient pulses and their severity increases with the speed of the rise time and the strength of the gradient pulses. The advent of shielded gradient coils has greatly decreased their effects, but they can still be significant when using large rapidly rising and falling gradient pulses. The decay time of the eddy currents (and their associated magnetic fields) determine the minimum delay required between the end of the gradient pulse and the start of spectral acquisition. Eddy currents can result in: (i) gradient induced broadening of the observed spectrum, (ii) phase changes and anomalous changes in the attenuation, and (iii) time-dependent but spatially invariant B_0 shift effects (which appears as "ringing" in the spectrum).

Gradient pulse mismatch can produce similar artifacts to eddy currents [39]. Even extremely small mismatches can cause a severe loss in echo signal intensity due to the resulting phase twist. If the mismatch increases as a function of gradient strength it has the potential to produce artifactual "diffraction" peaks. The presence of such phase-based artifacts is verified, for example, by performing measurements on a freely diffusing sample with a very small diffusion coefficient (e.g. large polymer).

Apart from the obvious solution of better gradient generation, the easiest means for removing eddy current and gradient mismatch effects is to use shaped gradient pulses [40] or prefixing a number of Δ-spaced gradient prepulses (see Figure 1A) [41]. In the case of gradient mismatch it is also possible, although considerably less convenient, to empirically match the gradient pulse pairs, or, at the expense of chemical shift information, use the imaging-based MASSEY sequence approach [42].

Diffusion in Complex Systems

In the absence of restriction, the diffusion coefficient of a species reports directly on its size, geometry, and the medium in which it is diffusing. This connection is conveniently formulated using the Stokes–Einstein equation, which is derived assuming that the solute sees the solvent as a continuum (e.g. see Ref. [43]),

$$D^0 = \frac{kT}{f} \tag{9}$$

where D^0 is the diffusion coefficient of the solute at infinite dilution (hence the superscript 0), k is the Boltzmann constant, and T is temperature. For the particularly simple case of a sphere under stick boundary conditions the friction coefficient, f is given by (Stokes law)

$$f = 6\pi\eta R \tag{10}$$

where R is the effective hydrodynamic (or Stokes) radius, η is the solvent viscosity. Since f is determined by the overall dimensions of the diffusing species (which may include the effects of solvation and rugosity), few species are well described by a simple geometry. Consequently, f must normally be determined numerically (e.g. Ref. [44])—indeed exact solutions are only known for some simple geometries (e.g. see Table 1 in Ref. [45]). When NMR diffusion measurements are used to separate mixtures on the basis of diffusion differences, it is often referred to as DOSY NMR [7] with the resulting data presented in a two-dimensional format with the diffusion coefficient on one axis and the chemical shift on the other. Some examples of the applications of diffusion measurements are given in the following subsections.

Solution Dynamics and Surfactants

NMR diffusometry finds particular application in studying solution dynamics—especially since it is capable of determining the diffusion behavior of many of the species in a solution simultaneously. For example, the diffusion coefficient of all species in an ethanol–water solution are given in Figure 2. Such detailed data allows inferences to

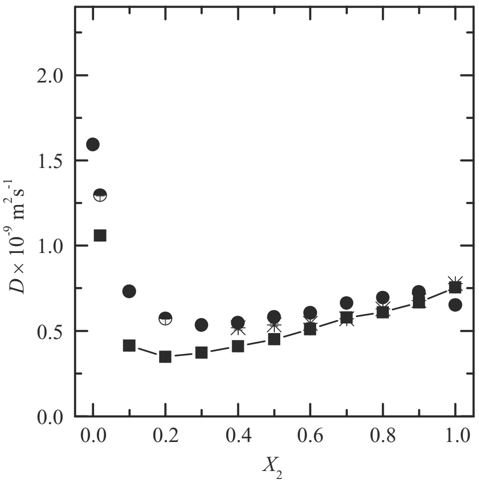

Fig. 2. Diffusion coefficients of the alkyl (■), hydroxyl (∗), water (●), and water-hydroxyl (◑) groups at 285 K at various ethanol mole fractions, X_A, in the ethanol–water system.

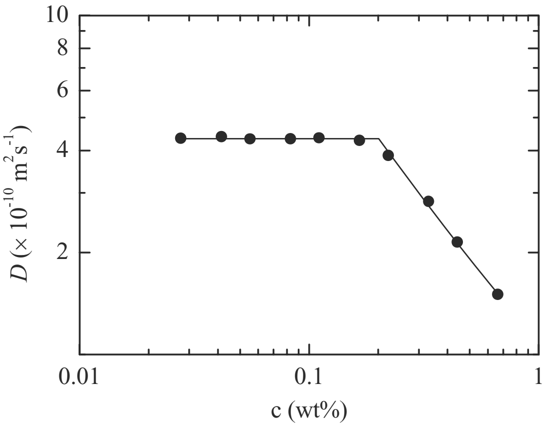

Fig. 3. Determination of the cmc of SDS in D_2O from NMR diffusion measurements as a function of surfactant concentration. The break in the data at $C_t = 0.2$ wt% represents the cmc (modified from Ref. [48]).

be drawn regarding the complicated solution chemistry of this system [46].

Since the diffusion coefficient directly reflects molecular size, diffusion measurements have been used to great effect in determining the critical micellar concentration (cmc) of surfactants. Typically the associating surfactant solution is modeled using a two-site exchange model, in which the observed diffusion coefficient is expressed as a population weighted average between "free" and "bound" (i.e. surfactants in micelles) surfactant [47]:

$$D = D_\mathrm{f}\frac{C_\mathrm{f}}{C_\mathrm{t}} + D_\mathrm{b}\left(1 - \frac{C_\mathrm{f}}{C_\mathrm{t}}\right) \tag{11}$$

where $D_\mathrm{f,b}$ are the diffusion coefficients of free and micellized surfactants, respectively. $C_\mathrm{f,t}$ is the concentration of free and total concentration of surfactant (NB C_f/C_t is the free population), respectively. An example of determining the cmc from diffusion data is given in Figure 3.

Ligand Binding and Aggregation

Since diffusion is an excellent probe of molecular size and mobility, NMR diffusometry is becoming an increasingly important tool in drug development where it is sometimes referred to as "affinity NMR" [49].

As an illustration, consider the simple two site system where a drug (i.e. ligand, L) exchanges between being in free solution to any one of n equivalent binding sites on the protein (P) with a dissociation constant K_d (i.e. $\mathrm{PL} \overset{K_\mathrm{d}}{\rightleftharpoons} \mathrm{P} + \mathrm{L}$). The coupled differential equations describing the echo signal intensities at the free and bound sites are (e.g. see [21,39–41]),

$$\begin{aligned}\frac{\mathrm{d}S_\mathrm{f}}{\mathrm{d}t} &= -\gamma^2 g^2 D_\mathrm{f}\delta^2 S_\mathrm{f} - \frac{S_\mathrm{f}}{\tau_\mathrm{f}} + \frac{S_\mathrm{b}}{\tau_\mathrm{b}}\\ \frac{\mathrm{d}S_\mathrm{b}}{\mathrm{d}t} &= -\gamma^2 g^2 D_\mathrm{b}\delta^2 S_\mathrm{b} - \frac{S_\mathrm{b}}{\tau_\mathrm{b}} + \frac{S_\mathrm{f}}{\tau_\mathrm{f}}\end{aligned} \tag{12}$$

where τ_f and τ_b are the lifetimes in the free and bound sites, respectively. The initial conditions are given by $S_\mathrm{f}\,|_{t=0} = P_\mathrm{f} = (1 - P_\mathrm{b})$ and $S_\mathrm{b}\,|_{t=0} = P_\mathrm{b}$ where P_f and P_b are the populations in the free and bound sites, respectively. At $t = \Delta$ and in the case of fast exchange, this reduces to the particularly simple single exponential form,

$$E = S_\mathrm{b} + S_\mathrm{f} = \exp\left(-\gamma^2 g^2 D_\mathrm{obs}\delta^2\Delta\right) \tag{13}$$

where

$$D_\mathrm{obs} = (1 - P_\mathrm{b})\,D_\mathrm{f} + P_\mathrm{b}D_\mathrm{b} \tag{14}$$

is the population-weighted average diffusion coefficient. In the case of this simple two-site model, the bound population is given by

$$P_\mathrm{b} = \alpha - \sqrt{\alpha^2 - \beta} \tag{15}$$

and

$$\alpha = \frac{(C_\mathrm{L} + nC_\mathrm{P} + K_\mathrm{d})}{2C_\mathrm{L}} \quad \text{and} \quad \beta = \frac{nC_\mathrm{P}}{C_\mathrm{L}} \tag{16}$$

where C_L and C_P are the total concentrations of drug and protein, respectively. D_f can be determined by measuring the diffusion of the drug in protein-free solution, and D_b can normally be taken as equal to the protein diffusion coefficient since the binding of the drug should have negligible effect on the diffusion coefficient of the (much larger) protein molecule. An example of an NMR diffusometry study of drug binding is given in Figure 4.

Restricted Diffusion

As noted above, when diffusion occurs within a restricting geometry, the geometrical restrictions result in characteristic echo attenuation curves. Thus, diffusion measurements provide a powerful means of probing porous materials. An example of probing a simple pore in which water is diffusing between two parallel planes is given in Figure 5.

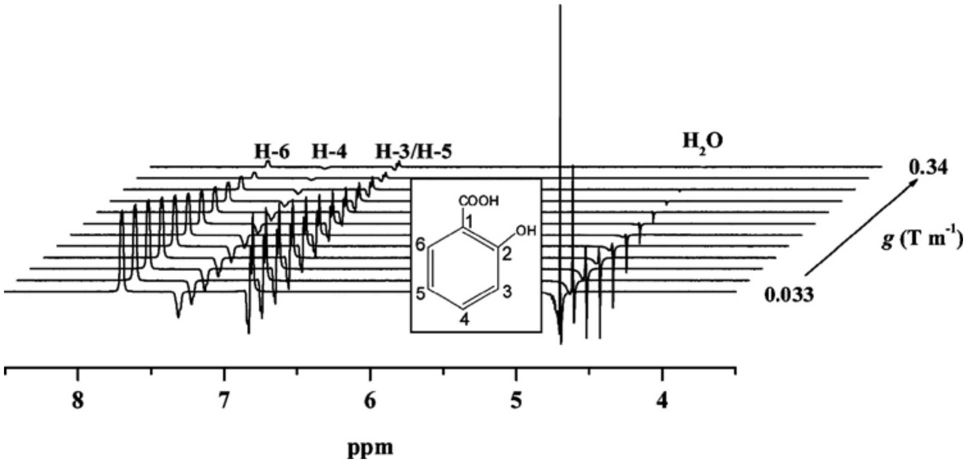

Fig. 4. An example of an NMR diffusion measurement for studying drug binding: A 500 MHz ^{1}H PGSE-WATERGATE spectra of 80 mM salicylate and 0.5 mM bovine serum albumin in water at 298 K. The (residual) water resonance gives rise to the peak at 4.7 ppm and the three peaks to the left originate from salicylate (from left to right: H-6, H-4, H-3/H-5; also see inset) (modified from Price *et al*. [50]).

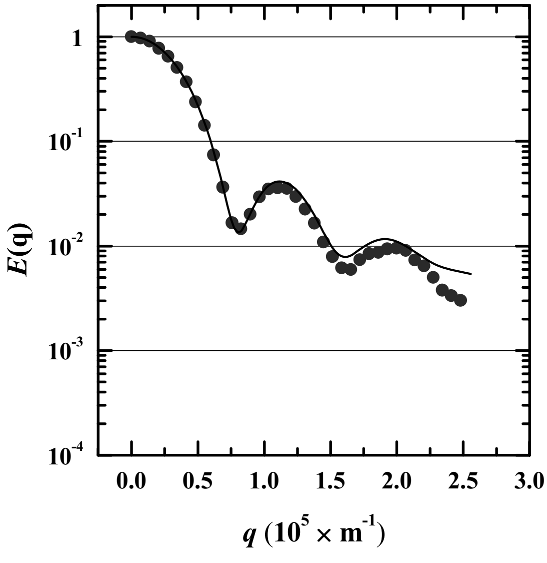

Fig. 5. ^{1}H PGSE NMR attenuation profile for water diffusing between planes separated by distance $a = 128$ μm at 318 K. The gradient is directed perpendicular to the planes. The experimental parameters were $\Delta = 2$ s and $\delta = 2$ ms. The solid black line denotes the result of fitting the data with the SGP formula [Equation (4)]. The diffractive minima appear at $q = n/a (n = 1, 2, 3, \ldots)$ (modified from Ref. [51]).

Acknowledgment

The NSW State Government is acknowledged for support through a BioFirst award.

References

1. Callaghan PT. Aust. J. Phys. 1984;37:359.
2. Stilbs P. Prog. NMR Spectrosc. 1987;19:1.
3. Kärger J, Pfeifer H, Heink W. Adv. Magn. Reson. 1988; 12:1.
4. Callaghan PT. Principles of Nuclear Magnetic Resonance Microscopy. Clarendon Press: Oxford, 1991.
5. Price WS, In: GA Webb (Ed). Annual Reports on NMR Spectroscopy. Academic Press: London, 1996, p. 51.
6. Kimmich R. NMR: Tomography, Diffusometry, Relaxometry. Springer Verlag: Berlin, 1997.
7. Johnson CS Jr. Prog. NMR Spectrosc. 1999;34:203.
8. Stilbs P. In: JC Lindon, GE Tranter, JL Holmes (Eds). Encyclopedia of Spectroscopy and Spectrometry. London, 2000, p. 369.
9. Cohen Y, Avram L, Frish L. Angew. Chem. Int. Ed. 2005;44:520.
10. Matsukawa S, Yasunaga H, Zhao C, Kuroki S, Kurosu H, Ando I. Prog. Polym. Sci. 1999;24:995.
11. Price WS. In: GA Webb (Ed). Annual Reports on the Progress in Chemistry Section C. Royal Society of Chemistry: London, 2000, p. 3.
12. Waldeck AR, Kuchel PW, Lennon AJ, Chapman BE. Prog. NMR Spectrosc. 1997;30:39.

13. Fielding L. Tetrahedron. 2000;56:6151.
14. Price WS. In: DM Grant, RK Harris (Eds). Encyclopedia of Nuclear Magnetic Resonance. Wiley: New York, 2002, p. 364.
15. Söderman O, Stilbs P. Prog. NMR Spectrosc. 1994;26:445.
16. Furó I. J. Mol. Liquids. 2005;117:117.
17. Tanner JE, Stejskal EO. J. Chem. Phys. 1968;49:1768.
18. Kärger J, Heink W. J. Magn. Reson. 1983;51:1.
19. Duffy DG. Green's Functions with Applications. CRC: Boca Raton, 2001.
20. Kärger J, Fleischer G, Roland U. In: J Kärger, P Heitjans, R Haberlandt (Eds). Diffusion in Condensed Matter. Vieweg: Braunschweig, 1998, p. 144.
21. Ben-Avraham D, Havlin S. Diffusion and Reactions in Fractals and Disordered Systems. Cambridge University Press: Cambridge, 2000.
22. Stejskal EO, Tanner JE. J. Chem. Phys. 1965;42:288.
23. Price WS. Concepts Magn. Reson. 1997;9:299.
24. Callaghan PT. J. Magn. Reson. 1997;129:74.
25. Price WS, Söderman O. Isr. J. Chem. 2003;43:25.
26. Price WS, Stilbs P, Jönsson B, Söderman O. J. Magn. Reson. 2001;150:49.
27. Price WS. Concepts Magn. Reson. 1998;10:197.
28. Cotts RM, Hoch MJR, Sun T, Markert JT. J. Magn. Reson. 1989;83:252.
29. Wu D, Chen A, Johnson CS Jr. J. Magn. Reson. A. 1995;115:260.
30. Seland JG, Sørland GH, Zick K, Hafskjold B. J. Magn. Reson. 2000;146:14.
31. Price WS, Wälchli M. Magn. Reson. Chem. 2002;40;S128.
32. Hedin N, Furó I. J. Magn. Reson. 1998;131:126.
33. Hedin N, Yu TY, Furó I. Langmuir. 2000;16:7548.
34. Jerschow A. J. Magn. Reson. 2000;145:125.
35. Mohoric A, Stepišnik J. Phys. Rev. E. 2000;62:6628.
36. Jerschow A, Müller N. J. Magn. Reson. 1997;125:372.
37. Håkansson B, Jönsson B, Linse P, Söderman O. J. Magn. Reson. 1997;124:343.
38. Xia Y. Concepts Magn. Reson. 1996;8:205.
39. Price WS, Hayamizu K, Ide H, Arata Y. J. Magn. Reson. 1999;139:205.
40. Price WS, Kuchel PW. J. Magn. Reson. 1991;94:133.
41. von Meerwall E, Kamat M. J. Magn. Reson. 1989;83:309.
42. Callaghan PT. J. Magn. Reson. 1990;88:493.
43. Tyrrell HJV, Harris KR. Diffusion in Liquids: A Theoretical and Experimental Study. Butterworths: London, 1984.
44. García de la Torre J, Huertas ML, Carrasco B. Biophys. J. 2000;78:719.
45. Price WS. In: Atta-Ur-Rahman (Ed). New Advances in Analytical Chemistry. Harwood Academic Publishers: Amsterdam, 2000, p. 31.
46. Price WS, Ide H, Arata Y. J. Phys. Chem. A. 2003;107:4784.
47. Söderman O, Stilbs P. Prog. Nucl. Magn. Reson. Spectrosc. 1994;26:445.
48. Pettersson E, Topgaard D, Stilbs P, Söderman O. Langmuir 2004;20:1138.
49. Lin M, Shapiro MJ, Wareing JR. J. Org. Chem. 1997;62:8930.
50. Price WS, Elwinger F, Vigouroux C, Stilbs P. Magn. Reson. Chem. 2002;40:391.
51. Price WS, Stilbs P, Söderman O. J. Magn. Reson. 2003;160:139.

Field Gradient NMR of Liquid Crystals

István Furó[1] and Sergey V. Dvinskikh[2]
[1]Department of Chemistry, Division of Physical Chemistry, Royal Institute of Technology; and
[2]Physical Chemistry, Stockholm University, Stockholm, Sweden

Abstract

Field-gradient NMR applications in liquid crystals (LCs) are dominantly experiments that detect the translational self-diffusion of the various structural units of the liquid crystalline phases. The anisotropy of LCs often leads to line broadening effects that must typically be suppressed in order to accommodate sufficient gradient dephasing of the nuclear spins. Having dealt with this problem, diffusion studies provide important insights into both lyotropic and thermotropic liquid crystal systems.

Introduction

Liquid crystals (LCs), although anisotropic, consist of highly mobile molecules just like "usual" isotropic liquids. Hence, all NMR methods that are used for extracting molecular information in isotropic liquids could, in principle, furnish the same type of information in LCs, with one important difference: anisotropy of LCs results in tensor instead of scalar properties. Thus, for example, translational self-diffusion, characterized by a scalar diffusion coefficient D in the isotropic case, becomes instead dependent in LCs on a diffusion tensor $\mathbf{D}$ [1–5]. By diagonalizing $\mathbf{D}$, one can in general extract three pieces of information, represented by the principal components $D_{\alpha\alpha}$, $D_{\beta\beta}$, and $D_{\gamma\gamma}$ of $\mathbf{D}$ [4,6]. Of these three components, two are equal for LCs with a symmetry axis of higher than threefold symmetry.

Here, we intend to provide a brief survey, with representative examples and directions to relevant reviews, of magnetic-field-gradient-based NMR investigations of LCs. Most of the involved studies aimed at measuring self-diffusion in those materials and therefore diffusion studies dominate here, with a few other gradient applications mentioned at the end. Our survey is not chronological and, with over 10^3 relevant publications, cannot be comprehensive. Neither can we elaborate upon related issues, such as the large and still emerging area of diffusion tensor imaging [4,7–10].

With very few exceptions (such as lyotropic cubic phases), LCs [11] are formed by anisomeric objects, often called mesogenic units. Liquid crystalline ordering stems from the anisotropic pair potential among those objects [12]. In thermotropics, one of the two broad classes of LCs, the mesogenic units are typically elongated or flat molecules with no other principal system component. A typical example is 4-pentyl-4′-cyanobiphenyl (5CB) where a rigid central biphenyl group lends the molecule an elongated shape. The other broad LC class contains the lyotropic systems where the common element is a solvent (typically water) that embeds the mesogenic units that can be multi-molecular aggregates but also single molecules. Typical example for the former are lyotropic LCs formed by elongated (e.g. in hexagonal phases) or flat (e.g. in lamellar phases) aggregates of amphiphilic molecules, either surfactants or lipids. Lipid-based LCs, akin to lipid bilayer [13] structures of cells, have a clear biological relevance.

NMR Methods and Diffusion in LCs

Since LCs are anisotropic, their NMR properties depend on the orientation with respect to the applied magnetic field [1,2,4,5,14]. Moreover, anisotropic spin couplings, such as the dipole–dipole or quadrupole interactions, are not averaged by molecular motions to zero but to a residual value. Often, the relation between the instantaneous and residual couplings is simply defined by a scalar order parameter S of the LC phase while in some phases, such as in biaxial ones, this relation may take instead a more complex form [2]. In some LCs, with cubic phases as an example, the residual coupling may vanish by symmetry and the spectra containing narrow lines become similar to those recorded in isotropic liquids.

The manifestation of non-vanishing residual couplings depends on the macroscopic orientational order within the sample. For simplicity, we exemplify this with a uniaxial LC phase where the average orientation of molecules in a given spatial region is defined by a unique direction, the LC director $\mathbf{d}$. The NMR signal given by those molecules depends on the orientation of $\mathbf{d}$ with respect to the applied static magnetic field $\mathbf{B_0}$. Some LCs can be prepared, either through mechanic [15–18] or electromagnetic [19–25] interactions, in a homogeneous state with the same $\mathbf{d}$ all over the sample volume. Such macroscopically oriented LCs are contrasted to "powder" samples with $\mathbf{d}$ that varies randomly from domain-to-domain: if the domain

Graham A. Webb (ed.), Modern Magnetic Resonance, 117–122.
© 2008 *Springer.*

size is small, on the experimental time scale translational diffusion may average the residual coupling to zero.

The appearance of the spectra also depends on the involved spin couplings. The pairwise dipole–dipole interaction typically acts in LCs among a manifold of nuclei. Hence, static spectral splitting typically renders the spectra of dipole–dipole coupled ^{1}H nuclei wide and featureless, even in macroscopically oriented samples, because it consists of many overlapping lines. The only exception is having the director of a macroscopically oriented sample at the "magic angle" to $\mathbf{B_0}$, where all static splitting vanishes. In contrast to the dipole–dipole case, single-spin quadrupole interactions for spin $I > 1/2$ nuclei in a macroscopically oriented LC may result in spectra split into $(2I + 1)$ sharp lines. Powder samples exhibit large static broadening, both for the dipole–dipole and quadrupole cases but often with a discernible "powder pattern" line shape [26] for the latter one.

Spectral broadening translates into a quick decay of spin coherences in the time domain that has a direct bearing on field-gradient NMR experiments for diffusion [27–31]. Irrespective of the specific experiment (pulsed-field-gradient spin or stimulated echo and variations, the former ones often abbreviated as PGSE and PGSTE), NMR detects displacement via gradient-assisted de- and re-phasing of spin coherences. In the absence of motion, all de-phased magnetization can be recovered. Random diffusive displacement of individual molecules introduces random re-phasing errors that manifest themselves in an increasing signal loss upon increasing de-phasing ($\sim\gamma g\delta$, where g and δ are the strength and the length of the applied gradient pulses, respectively and γ is the gyromagnetic ratio), diffusion time Δ, and diffusion coefficient D. In isotropic liquids, the result is described by the well-known Stejskal-Tanner [32–34] expression

$$I(g, \delta, \Delta) \sim \exp[-D\gamma^2 g^2 \delta^2(\Delta - \delta/3)], \qquad (1)$$

whose Gaussian appearance is a direct consequence of the Gaussian spatial propagator for translational self-diffusion. In anisotropic systems this expression is straightforwardly modified to accommodate for the anisotropy of the system as [1,2,4,33]

$$I(\mathbf{g}, \delta, \Delta) \propto \exp[-(\gamma\delta)^2(\Delta - \delta/3)\mathbf{gDg}]; \qquad (2)$$

note that the relative orientation of the gradient vector $\mathbf{g}$ ($g = \sqrt{\mathbf{g}^2}$) and the principal axes of the diffusion tensor $\mathbf{D}$ affects the experimental outcome. Clearly, diffusion can be measured only if the spins can be sufficiently de-phased which is strongly limited in LCs with quick decays of spin coherences. For the same reason, most diffusion experiments were performed in nuclei with large γ (such as ^{1}H and ^{19}F).

The presented solutions suppress the spectral broadening effects by residual spin couplings and involve either the mechanical manipulation of the sample orientation or the radiofrequency (rf) manipulation of the involved spins or both. The simplest and earliest [35–37] method in the former class involves preparation of a homogeneously oriented sample which is then placed by its director at the magic angle with respect to $\mathbf{B}_0$ which often results in a sufficient reduction of the static line broadening [1,38,39]. The disadvantage with the technique is its demand on homogeneous orientation that must be both settable and sustainable at the magic angle. An offspring of this technique is a diffusion experiment performed under MAS conditions [40–43] with the gradient field set along the spinning axis. The other broad option involves various decoupling or echo-based refocusing techniques applied under the de-phasing and re-phasing periods of a diffusion experiment [44–52]. The difficulty with those experiments is to maintain the performance of the selected rf pulse sequences under the far-offset conditions set by the simultaneous application of the field gradient. Slice selection, although at the cost of signal-to-noise ratio, is a straightforward option [45–52]. Spatial slice selection and decoupling can also be replaced by spectral slice selection by long selective pulses [53]. Finally, we note that instead of suppressing line broadening one may try to use stronger field gradients; one way of obtaining such is to use static instead of pulsed ones [54,55]. The disadvantage of that technique is the additional line broadening and connected reduction in signal-to-noise ratio caused by the static gradient.

In whichever case, a full characterization of the diffusion tensor $\mathbf{D}$ requires experiments performed at several relative gradient orientations. This can be achieved on two principally different ways. First, in a homogeneously oriented sample several experiments can be performed with different gradient directions [56–58] with respect to the sample. Conventionally, $D_{||}$ and $D_{\perp}$ denote diffusion along and perpendicular to $\mathbf{d}$. Our examples, shown in Figure 1, are taken from such type of studies. The other option, applicable in unoriented powder samples, exploits the spectral broadening itself by anisotropic spin interactions. In favorable cases, those interactions provide correspondence between the spectral frequency and domain orientation. Hence, differential decay of powder spectra (either by quadrupole interaction [59] or by chemical shift anisotropy [48,60]) for just one gradient direction reveals the complete diffusion tensor $\mathbf{D}$.

If diffusion within individual domains of unoriented powder samples cannot be orientationally assigned (as is typical for ^{1}H nuclei), the diffusional decay becomes the composite of decays for different gradient orientations [4,62–66]. If the orientational distribution is completely random and other effects, such as restricted diffusion, do not complicate the evaluation, the diffusion tensor can also

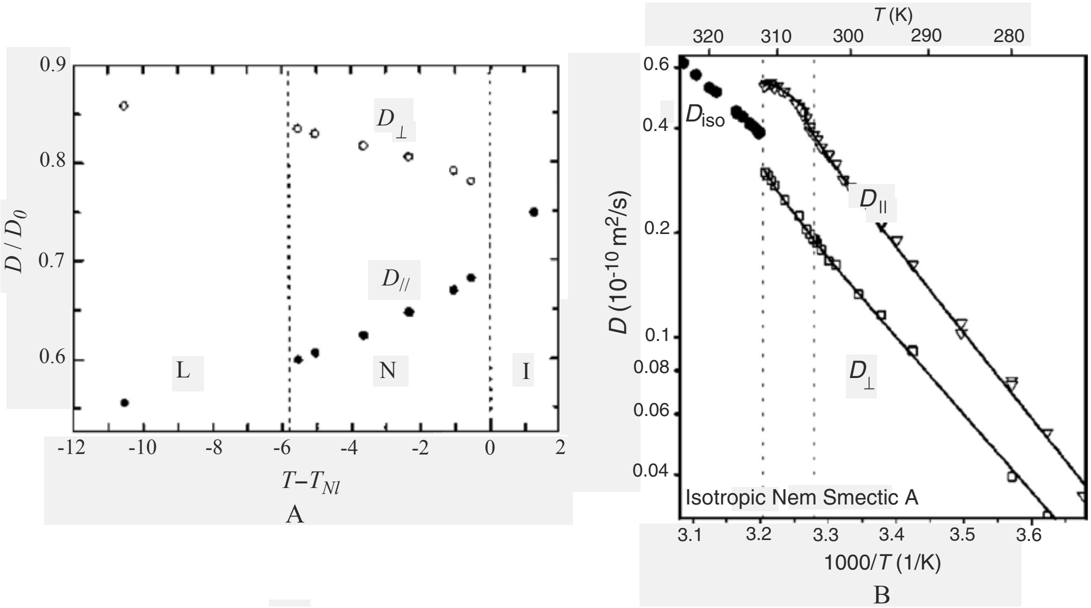

Fig. 1. (A) Temperature dependence of anisotropic diffusion across several lyotropic, [61] and (B) thermotropic [51] phases, measured by pulsed-field-gradient spin-echo-type experiments. In (A), ^{2}H pulsed-field-gradient quadrupole-echo experiment is applied to heavy water in its mixture with cesium perfluorooctanoate (CsPFO). This fluorinated surfactant forms in water flat aggregates, which exhibit nematic order (with their short axis along the field direction) upon cooling below the isotropic–nematic transition temperature T_{NI}. Upon further cooling, the system enters into a lamellar phase (L) consisting of defective CsPFO-bilayers. In (B), the diffusion of the mesogenic unit 4-octyl-4′-cyanobiphenyl (8CB) is followed by ^{2}H pulsed-field-gradient stimulated-echo experiments performed under simultaneous decoupling. Reproduced with permission. © American Physical Society, 1996, 2002.

be extracted either from the composite decay [4,62–66] or from more advanced diffusion–diffusion correlation (or exchange) experiments [67–69].

Lyotropic Applications

Although some molecular lyotropic phases have been investigated by NMR, here we restrict ourselves to systems where the mesogenic units are aggregates of simple surfactants and/or lipids (and thereby also exclude discussion of, e.g. block-copolymer-based lyotropic materials [64,65,70]). The corresponding isotropic phase, typically termed as micellar, has a liquid-like orientational order of the aggregates; diffusion NMR in micellar or related systems has been extensively studied and reviewed [71–74]. Among the LC phases, there exist many different symmetries with an underlying variation of aggregate geometry [24,75–81]. Irrespective of that, the NMR properties of the two main system components, water (solvent) and amphiphile differ: if any, the residual coupling and thereby the static broadening/splitting of water is typically small. Hence, water diffusion is accessible by conventional diffusion experiments, modified if necessary to ascertain refocusing in presence of static dipole or quadrupole splitting [61]. The same is also frequently the case for hydrophobic solubilizates within the amphiphile phase [82,83]. On the other hand, the broadening by residual coupling for the amphiphiles is typically large and must be suppressed in a diffusion experiment. The only exception is formed by cubic phases that, although crystalline, exhibit no static broadening. Hence, most amphiphile diffusion data are from cubic systems [1,3]; those ones from bicontinuous phases where curved amphiphile bilayers separate water- and oil-rich regions are relevant for and representative of bilayer diffusion in lamellar phases, too. Diffusion experiments were also carried out on some surfactant counterion species.

As concerning anisotropic lyotropic LCs, we discuss below nematic phases that consist of orientationally ordered anisomeric micelles, hexagonal phases where elongated aggregates (or water channels in the inverse versions) arrange themselves in a 2D hexagonal lattice, and lamellar phases where flat amphiphilic bilayers exhibit a 1D translational order. In all those systems, there are two issues that have decisive influence on the obtained diffusion data. First, D varies with the molecular environment and molecules exchange quickly among those; therefore, the observed diffusion coefficient is typically a population average. For water, the two environments are the bulk (fast diffusion) and the amphiphilic headgroup region (slow diffusion), while for the amphiphile there exists a small population of quickly diffusing monomers and a large population of slowly diffusing aggregates. The second consideration is topological [84–86]. Pathways for diffusion of water, for example, are obstructed from the hydrophobic interior the aggregates and therefore the spatial average of the diffusion coefficient is lower than the bulk value. If the obstruction is topologically enclosing (or directionally limiting) a region, the diffusion there becomes restricted that may result in very low average diffusion coefficient and/or to a composite diffusional decay.

In nematic lyotropics that consist of closed (finite) aggregates, diffusion in the hydrophobic domain [66], although informative, is less representative of the phase and aggregate structure (except in the region of phase transition into continuous aggregate topologies). Instead, water diffusion can be used to report on these issues but to draw quantitative conclusions require very high accuracy and precision (see data example in Figure 1A) [56]. In the CsPFO/water mixture, large obstruction by flattened aggregates for diffusion parallel to their axis has been used to calculate average aggregate size and the orientational order of the aggregates as function of temperature [61]. The same system forms, upon cooling, a lamellar phase where the bilayer structural unit is pierced by water-filled defects; similar structures appear in lipid-based systems, where amphiphile lateral diffusion becomes indicative of the defects [66,87]. Water diffusion along the defective lamellar phase director (and therefore across the bilayers) is much higher [61,66,86,88–92] than in defect-free lamellar phases [58,93]. In the latter systems, lateral diffusion of the amphiphilic molecules along the bilayers has been addressed by several different methods [1,3,4,36–38,60,94–96] yielding liquid-like mobilities and activation energies where the latter is often dominated by the strong headgroup–headgroup interactions. In contrast to lamellar phases, defects in hexagonal lyotropic LCs break the continuity of the aggregate [82,97]. Since the aggregate shape in hexagonal phases is elongated, obstruction to water diffusion [84,85,98] is weaker than in systems consisting of flattened aggregates.

Thermotropic Applications

Diffusion in thermotropic LCs [11] has been addressed by a broad range of NMR techniques [4,99,100]. These include combining pulse-field-gradients with (i) "nematic" echo [101–103], (ii) multiple pulse decoupling [45–52,104–106], magic-angle sample orientation [25,35,57,102,107–112], (iii) deuterium stimulated (alignment) echo [50], (iv) soft-pulse excitation [53], and (v) multiple quantum NMR [51,113,114]. Besides, static field gradient techniques have also been used [115,116].

Most experiments have been performed in nematic phases that lack translational but possess orientational order. Nematic phases were also frequent choices for development and testing of new techniques for self-diffusion LCs: the nematic phase of 5CB is a benchmark compound. Recently, diffusion data in 5CB obtained by several methods, including also non-NMR techniques, have been compared [49]. While earlier results strongly disagree, obviously due to methodological problems, more recent studies [49,53,115] by advanced NMR techniques demonstrate a better agreement: the diffusion coefficient in 5CB ranges from 10^{-9} to 10^{-10} m^2/s, depending on temperature and diffusion directions. The diffusion anisotropy, $D_{||}/D_{\perp}$ decreases from 2.7 to 1.5 toward the nematic–isotropic transition and, hence, it reflects the decrease of molecular orientational order; the elongated mesogenic units diffuse easier along the director than across it. In the isotropic–nematic transition region, the average diffusion coefficient matches the diffusion coefficient in the isotropic phase, with similar (~30 kJ/mol) activation energies. Clearly, diffusional transport in the nematic phase is liquid-like and broadly consistent with some available diffusion models [49,51]. Conventional PGSE NMR measurements performed on the isotropic side of the isotropic–nematic phase transition indicate the formation of locally ordered nematic clusters [117,118].

The temperature dependencies of the principal components of diffusion tensors were also reported for homologous series of alkoxy–azoxy benzenes and nOCB [111,112]. Characteristic alternation of diffusion coefficients and activation energies as functions of the number of chain segments, i.e. the familiar odd–even effect, has been observed. In a cholesteric–nematic phase [119], PGSTE NMR has detected diffusion anisotropy ($D_{||}/D_{\perp} \approx 1.7$) similar to that in 5CB but $\mathbf{D}$ was strongly dependent on the diffusion time.

Since smectic phases have layered structures with 2D liquid-like order within the layers, their diffusion anisotropy typically becomes $D_{||}/D_{\perp} < 1$ [99], opposite to that in nematics. Exceptions are smectics that exhibit a significant temperature range of a nematic phase: for them $D_{||}/D_{\perp} > 1$ may occasionally be found in the vicinity of the nematic region [51,108] and upon cooling deeper into the smectic phase the diffusion anisotropy changes sense [102]. As concerning activation energies, the relation $E_{||} \geq E_{\perp}$ is always fulfilled in smectics. At the nematic–smectic phase transition $D_{\perp}$ changes nearly continuously, while $D_{||}$ and/or its activation energy may jump, in accordance to the layer-like smectic structure with liquid-like in-layer diffusion and solid-like jumps between adjacent layers [51,99,116]. In contrast to conventional thermotropics built by elongated mesogenic units, discotic materials are formed by flat molecules. In a columnar (smectic) phase of those, ^{2}H PGSE NMR detected very slow ($\sim 10^{-14}$ m^2/s) diffusion with a large activation energy (115 kJ/mol) that suggest solid-like or, perhaps, collective diffusion mechanisms in discotics [52].

Thermotropic LC behavior can also be found for polymeric molecules. Hence, anisotropic diffusion with $D_{||} > D_{\perp}$ relative to α-helical chain axis has been observed in LC phase formed by rod-like polypeptides [120–123], with activation energies recorded as function of the main-chain length [122]. In the polymeric LC formed by the less rigid poly(diethysiloxane), the diffusion was found faster than that in the isotropic phase: this interesting effect was attributed to more entanglements between the polymer chains in the isotropic phase [124].

Due to much lower orientational order, small organic solute molecules in LCs exhibit long decays of spin coherences. Hence, conventional PSGE experiments are typically sufficient to access the diffusion coefficients of solutes [99,125]. In nematic phases, the solute diffusion is fast and the diffusion anisotropy is small [99,100]. This contrasts the strong diffusion anisotropy $D_{||}/D_{\perp} \ll 1$ observed in smectic phases [99]. A particularly interesting and simple solute is the noble gas ^{129}Xe, whose diffusional behavior was studied in detail [126–130]. While no diffusion anisotropy ($D_{||}/D_{\perp} \sim 1$) was detected in a nematic phase [126], weak anisotropy with $D_{||}/D_{\perp} > 1$ has been observed in a related mixture [127]. This contrasts the $D_{||}/D_{\perp} \ll 1$ found in smectic phases of ferroelectric LCs [128,129].

Other Applications of Field Gradients

Magnetic field gradients are useful in high-resolution NMR for selecting and filtering coherence transfer pathways and may advantageously replace or be combined with phase cycling [131]. Hence, magnetic-field-gradient pulses have been used for various multidimensional [42,132,133] and multiple-quantum experiments [134,135] in LCs and for selective suppression of, e.g. water signals in ^{1}H HR-MAS NMR in lipid membrane samples [136]. As another tool for improving spectral quality, field-gradient pulses have been applied in combination with frequency-selective rf pulses to limit the sensitive volume in liquid-crystalline sample in multiple-pulse decoupling PGSE experiments [45,46,48–52,60].

There are also examples of NMR imaging experiments applied to LCs. Velocity imaging of liquid crystalline polymers flowing through an abrupt contraction was performed by pulsed-field-gradient NMR techniques [137]. Magnetic-field-gradient pulses were also incorporated in rheo-NMR experiments on various LC samples as reviewed by Callaghan [138].

References

1. Lindblom G, Orädd G. Progr. Nucl. Magn. Reson. Spectrosc. 1994;26:483.
2. Dong RY, Nuclear Magnetic Resonance of Liquid Crystals. Springer: New York, 1994.
3. Lindblom G, Orädd G. In: DM Grant, RK Harris (Eds). Encyclopedia of Nuclear Magnetic Resonance, Vol. 4. Wiley: Chichester, 1996, p. 2760.
4. Furó I, Dvinskikh SV. Magn. Reson. Chem. 2002;40:S3.
5. Burnell EE, de Lange CA (Eds). NMR of Ordered Liquids, Kluwer: Dordrecht, 2003.
6. Glicksman ME. Diffusion in Solids. Wiley: New York, 2000.
7. Basser PJ *et al.* Biophys. J. 1994;66:259.
8. Basser PJ. NMR Biomed. 1995;8:333.
9. Basser PJ, Pierpaoli CJ. Magn. Reson. B 1996;111:209.
10. Gabrieli J *et al.* (Eds). White Matter in the Cognitive Neurosciences: Advances in Diffusion Tensor Imaging and Its Applications. New York Academy of Sciences: New York, 2005.
11. Demus D *et al.* (Eds). Handbook of Liquid Crystals, Vol. 1–4. Wiley-VCH: Weinheim, 1998.
12. de Gennes PG, Prost J. The Physics of Liquid Crystals, Clarendon: Oxford, 1993.
13. Katsaras J, Gutberlet T (Eds). Lipid Bilayers. Springer: Berlin, 2000.
14. Halle B, Furó I. In: P Tolédano, AM Figueiredo (Eds). Phase Transitions in Complex Fluids, World Scientific: Singapore, 1998, p. 81.
15. Safinya CR *et al.* Science 1993;261:588.
16. Imperor-Clerc M *et al.* Macromolecules 2001;34:3503.
17. Lukaschek M *et al.* Langmuir 1995;11:3590.
18. Lukaschek M *et al.* Colloid Polym. Sci. 1996;274:1.
19. Diehl P, Khetrapal CL. In: P Diehl *et al.* (Eds). NMR Basic Principles and Progress, Vol. 1. Springer: Berlin, 1969, p. 1.
20. Forrest BJ, Reeves LW. Chem. Rev. 1981;81:1.
21. Amaral L. Mol. Cryst. Liq. Cryst. 1983;100:85.
22. Furó I *et al.* J. Phys. Chem. 1990;94:2600.
23. Quist PO *et al.* J. Chem. Phys. 1991;95:6945.
24. Stegemeyer H (Ed.) Lyotrope Flüssigkristalle, Steinkopff: Darmstadt, 1999.
25. Holstein P *et al.* J. Magn. Reson. 2000;143:427.
26. Spiess HW In: P Diehl *et al.* (Eds). Dynamic NMR Spectroscopy, Vol. 15. Springer: Berlin, 1979, p 55.
27. Stilbs P. Prog. Nucl. Magn. Reson. Spectrosc. 1987;19:1.
28. Kärger J *et al.* Adv. Magn. Reson. 1988;12:1.
29. Callaghan PT, Principles of Nuclear Magnetic Resonance Microscopy. Clarendon Press: Oxford, 1991.
30. Price WS, Concepts Magn. Reson. 1997;9:299.
31. Price WS, Concepts Magn. Reson. 1998;10:197.
32. Stejskal EO, Tanner JE. J. Chem. Phys. 1965;42:288.
33. Stejskal EO. J. Chem. Phys. 1965;43:3597.
34. Tanner JE. J. Chem. Phys. 1970;52:2523.
35. Krüger GJ *et al.* Phys. Lett. A. 1975;51:295.

36. Roeder SBW *et al.* J. Chem. Phys. 1976;64:1848.
37. Lindblom G, Wennerström H. Biophys. Chem. 1977;6:167.
38. Ukleja P *et al.* Liquid Cryst. 1991;9:359.
39. Orädd G, Lindblom G. In: EE Burnell, CA de Lange (Eds). NMR of Ordered Liquids, Kluwer: Dordrecht, 2003, p 399.
40. Maas WE *et al.* J. Magn. Reson. 1999;141:29.
41. Pampel A *et al.*, Chem. Phys. Lett. 2002;357:131.
42. Gaede HC, Gawrisch K. Magn. Reson. Chem. 2004;42:115.
43. Polozov IV, Gawrisch K. Biophys. J. 2004;87:1741.
44. Zhang W, Cory DG. Phys. Rev. Lett. 1998;80:1324.
45. Dvinskikh SV *et al.* J. Magn. Reson. 2000;142:102.
46. Dvinskikh SV, Furó I. J. Magn. Reson. 2000;144:142.
47. Dvinskikh SV, Furó I J. Magn. Reson. 2000;146:283.
48. Dvinskikh SV, Furó I. J. Magn. Reson. 2001;148:73.
49. Dvinskikh SV, Furó I. J. Chem. Phys. 2001;115:1946.
50. Dvinskikh SV *et al.* J. Magn. Reson. 2001;153:83.
51. Dvinskikh SV *et al.* Phys. Rev. E. 2002;65:061701.
52. Dvinskikh SV *et al.* Phys. Rev. E. 2002;65:050702.
53. Kim MJ *et al.* J. Chem. Phys. 2004;120:11327.
54. Kimmich R *et al.* J. Magn. Reson. 1991;91:136.
55. Karakatsanis P, Bayerl TM. Phys. Rev. E 1996;54:1785.
56. Furó I, Jóhannesson H. J. Magn. Reson. A. 1996;119:15.
57. Oishi O, Miyajima S. J. Magn. Reson. A. 1996;123:64.
58. Wästerby P *et al.* J. Magn. Reson. 2002;157:156.
59. Callaghan PT *et al.* J. Chem. Phys. 1983;79:6372.
60. Kadi M *et al.* Langmuir 2002;18:5015.
61. Jóhannesson H *et al.* Phys. Rev. E 1996;53:4904.
62. Callaghan PT, Söderman O. J. Phys. Chem. 1983;87:1737.
63. Blum FD *et al.* Langmuir 1985;1:127.
64. Fleischer G *et al.* J. Chem. Phys. 1999;111:2789.
65. F. Rittig *et al.*, Macromolecules 1999;32:5872.
66. Gaemers S, Bax A. J. Am. Chem. Soc. 2001;123:12343.
67. Callaghan PT, Komlosh ME. Magn. Reson. Chem. 2002; 40:S15.
68. Callaghan PT *et al.* Magn. Reson. Imag. 2003;21:243.
69. Callaghan PT, Furó I. J. Chem. Phys. 2004;120:4032.
70. Rittig F *et al.* Macromolecules 2001;34:868.
71. Söderman O, Stilbs P. Prog. Nucl. Magn. Reson. Spectrosc. 1994;26:445.
72. Söderman O, Olsson U. In: DM Grant, RK Harris (Eds). Encyclopedia of Nuclear Magnetic Resonance, Vol. 4. Wiley: Chichester, 1996, p. 3046.
73. Söderman O, Olsson U. Curr. Opinion Colloid Interf. Sci. 1997;2:131.
74. Furó I. J. Mol. Liq. 2005;117:117.
75. Sonin AS. Sov. Phys. Usp. 1987;30:875.
76. Larsson K. J. Phys. Chem. 1989;93:7304.
77. Seddon JM, Templer RH. Phil. Trans. Roy. Soc. London A. 1993;344:377.
78. Laughlin RG. The Aqueous Phase Behavior of Surfactants. Academic Press: London, 1994.
79. Gelbart WM *et al.* (Eds). Micelles, Membranes, Microemulsions, and Monolayers. Springer: New York, 1994.
80. Seddon JM. Ber. Bunsenges. Phys. Chem. 1996;100:380.
81. Tolédano P, Figueiredo Neto AM (Eds). Phase Transitions in Complex Fluids. World Scientific: Singapore, 1998.
82. Joabsson F *et al.* J. Phys. Chem. B 1997;101:9710.
83. Jeong SW *et al.* Langmuir 2002;18:1073.
84. Jönsson B *et al.* Colloid Polym. Sci. 1986;264:77.
85. Jóhannesson H, Halle B. J. Chem. Phys. 1996;104:6807.
86. Celebre G *et al.* Gazz. Chim. Italiana 1996;126:489.
87. Soong R, Macdonald PM. Biophys. J. 2005;88:255.
88. Chidichimo G *et al.* Chem. Phys. Lett. 1985;117:514.
89. Chidichimo G *et al.* Mol. Cryst. Liq. Cryst. 1986;135:223.
90. Chidichimo G *et al.* Mol. Cryst. Liq. Cryst. 1987;150b: 221.
91. Chidichimo G *et al.*, Chem. Phys. Lett. 1988;145:85.
92. Holmes MC *et al.* Langmuir 1995;11:356.
93. Wassall SR. Biophys. J. 1996;71:2724.
94. Ukleja P, Doane JW. In: SK Sinha (Ed). Ordering in Two Dimensions. North-Holland: Amsterdam, 1980, p. 427.
95. G. Lindblom *et al.* Biochemistry 1981;20:2204.
96. Filippov *et al.*, Biophys. J. 2004;86:891.
97. Coppola L *et al.* Langmuir 2000;16:4180.
98. Coppola L *et al.* Langmuir 2003;19:1990.
99. Krüger GJ. Phys. Rep. 1982;82:229.
100. Noack F. In: D Demus *et al.* (Eds). Handbook of Liquid Crystals. Wiley-VCH: Weinheim, 1998, p. 582.
101. Krüger GJ, Spiesecke H. Z. Naturforsch. 1973;28a:964.
102. Krüger GJ *et al.* Mol. Cryst. Liq. Cryst. 1977;40:103.
103. Krüger GJ, Weiss R. J. Phys. (Paris) 1977;38:353.
104. Blinc R *et al.* Phys. Rev. Lett. 1973;30:546.
105. Blinc R *et al.* Phys. Rev. Lett. 1974;33:1192.
106. Zupancic I *et al.* Solid State Comm. 1974;15:227.
107. Krüger GJ *et al.* J. Phys. Colloque (Paris) 1976;37:123.
108. Miyajima S *et al.* Chem. Phys. Lett. 1993;212:277.
109. Oishi O, Miyajima S. J. Phys. Soc. Jpn. 2002;71:2373.
110. Oishi O, Miyajima S. J. Magn. Reson. 2003;160:74.
111. Noack F *et al.* Annu. Rep. NMR Spectrosc. 1997;33:1.
112. Noack F. Mol. Cryst. Liq. Cryst. 1984;113:247.
113. Martin JF *et al.* J. Chem. Phys. 1982;76:2632.
114. Zax D, Pines A. J. Chem. Phys. 1983;78:6333.
115. Vilfan M *et al.* Magn.Reson.Imag. 2001;19:433.
116. Cifelli M *et al.* Phys. Chem. Chem. Phys. 2004;6:4701.
117. Kashirin NV *et al.* Colloid J. 2000;62:68.
118. Gasilova ER *et al.* Liq. Cryst. 2000;27:573.
119. Blinc R *et al.* Phys. Rev. Lett. 1985;54:438.
120. Ando I *et al.* In: DM Grant, RK Harris (Eds). Encyclopedia of Nuclear Magnetic Resonance, Vol. 9. Wiley: Chichester, 2002, p. 770.
121. Yin YG *et al.* J. Chem. Phys. 2000;113:7635.
122. Yin Y *et al.* Macromolecules 2002;35:2335.
123. Yin YG *et al.* Macromolecules 2002;35:5910.
124. Kanesaka S *et al.* Macromolecules 2004;37:453.
125. Moseley ME, Loewenstein A. Mol. Cryst. Liq. Cryst. 1982;90:117.
126. Long HW *et al.* J. Phys. Chem. 1995;99:11989.
127. Ruohonen J, Jokisaari J. Phys. Chem. Chem. Phys. 2001;3:3208.
128. Ruohonen J *et al.* Mol. Phys. 2001;99:711.
129. Cifelli M *et al.* J. Phys. Chem. A 2004;108:3973.
130. Jokisaari J. In EE Burnell, CA de Lange (Eds). NMR of Ordered Fluids, Kluwer: Dordrecht, 2003, p 109.
131. Zhu J-M, Smith CP, Concepts Magn.Reson. 1995;7:281.
132. Lafon O *et al.* J. Magn. Reson. 2004;171:135.
133. Soubias O *et al.* J. Magn. Reson. 2003;165:303.
134. Field LD. In: EE Burnell, CA de Lange (Eds). NMR of Ordered Fluids, Kluwer: Dordrecht, 2003, p. 67.
135. Ramadan SA *et al.* Molec. Phys. 2003;101:1813.
136. Chen JH *et al.* J. Magn. Reson. 2004;171:143.
137. Gentzler M *et al.* Rheol. Acta 2000;39:1.
138. Callaghan PT. Rep. Prog. Phys. 1999;62:599.

Field Gradient NMR for Polymer Systems with Cavities

Yuji Yamane and Sunmi Kim
Department of Chemistry and Materials Science, Tokyo Institute of Technology, 2-12-1 Ookayama, Meguro-ku, Tokyo 152-8552, Japan

Introduction

Pulse field gradient (PFG) NMR method has become a useful technique for studying self-diffusion of probe molecules in polymer systems. Recently, high field-gradient NMR system with a maximum strength of more than 1,000 G/cm and new pulse sequences are possible to measure the diffusion coefficient (D) with the order of 1–10^{-11} cm^2/s in polymer systems. It is expected that the use of this system leads to sophisticated knowledge on nature of polymer systems as well as diffusional behavior of probe molecules in polymer systems. A number of papers, reviews, and monographs in this field have appeared [1–7]. In this section, some of most recent topics especially characterization of the polymer systems such as polymer gels and polymer media with controlled cavity through the diffusion experiments rather than principle of PFG NMR system and diffusional behavior of polymer chains have been described.

Diffusion in Polymer Gel Systems

Probe Diffusion in Polymer Gel Systems

Polymer gel systems consist of network polymer chains, solvents, and probe molecules, and also apply to many industrial fields. These functionalities are closely associated with diffusional behavior of solvents and probe molecules, and intermolecular interactions between networked polymer chains and probe molecules. Matsukawa, *et al.* have studied the diffusional behavior of water and poly(ethylene glycol) (PEG) in chemically cross-linked hydrogels. The D values of HDO ($D_{(\mathrm{HDO})}$) in gels are well explained by modified free volume theory in a wide range of the degree of swelling ($Q = M_{\mathrm{swollen}}/M_{\mathrm{dry}}$) [1], and the D_{PEG} values in gels are followed by $D/D^0_{\mathrm{PEG}} = \exp(-\kappa R)$, the dynamical screening length κ^{-1} is proportional to $c^{-0.71}$. The value of -0.71 is close to that proposed theoretically by de Gennes [8,9].

Masaro, *et al.* have studied the diffusional behavior of PEG in aqueous poly(vinyl alcohol) solution and gels as functions of the polymer concentration and molecular size of the diffusant. Several theoretical models based on different physical concepts have been used to fit the experimental data [10,11], and intermolecular interactions of probe molecules with networked polymer chains have been elucidated from the diffusion data [12–15]. Further, they have studied the effect of shapes of the diffusant on the diffusional behavior in gels [16–18]. Most recently, some groups have measured the D values of ^{7}Li and ^{19}F ions in polyelectrolyte gels to understand deeply the mechanism of ionic conduction [19–23].

Characterization of the Inhomogeneities in Polymer Gels

Polymer gels have generally inhomogeneity of the network size, and then properties of polymer gels depend on their spatial inhomogeneity. The existence of spatial inhomogeneity has been studied by light scattering as speckles [24,25]. One of the clearest manifestations of the inhomogeneity is an appearance of speckle pattern. As for chemically-crosslinked polymer gels, the relationship between speckles and spatial inhomogeneity has been elucidated [26]. Nevertheless, some problems on intermolecular interactions between the network and probe molecules associated with inhomogeneity of the network size in polymer gels remain. The measurement of D by PFG NMR has emerged as a powerful method for detecting inhomogeneities in gels. The method is based on the interpretation of the dependence of D on the time Δ ("diffusing time" or "observation time") between the two gradient pulses in the pulse sequences. The time dependens and the distribution of D are observed in gels [27] and other heterogeneous systems [28,29].

For convenience, we consider a probe molecule in a gel with homogeneous network size distribution (homogeneous gel) and with inhomogeneous network size distribution (inhomogeneous gel). As for probe molecules diffusing within a network cell in both of the gels the D value depends on Δ. If a probe molecule is diffusing through sufficiently many network cells in the homogeneous gel, the diffusion component is a single and the D value is independent of Δ, but in inhomogeneous gel the diffusion components are two or more and then the D value is dependent of Δ. When observed over longer times, the diffusion component becomes a single because the D values that comes from the distribution of the network size

Graham A. Webb (ed.), Modern Magnetic Resonance, 123–127.
© 2008 *Springer.*

are averaged out, and are independent of Δ. Therefore, if appropriate Δ in the PFG experiments is selected, useful information on the inhomogeneous network size distribution of gels can be obtained.

The inhomogeneity of polymer gels such as polystyrene (PS) gel and cross-linked ethoxylate acrylate (CLEAR) gel with deuterium dimethylformamide (DMF-d_7) as solvent has been characterized by using time-dependent diffusion NMR [30]. From the experimental results on the D values of probe amino acid, *tert*-butyloxylcarbonyl-L-phenylalanine (Boc-Phe), in the gels, it is cleared that in the short diffusion time range the amino acid in the gels has two components in diffusion as influenced by the distribution of network size, but in the long diffusion time range has a single component in diffusion. Here, we focus on the diffusing time Δ that the diffusion changes from the two components to the single component in diffusion. This specified Δ value is named as the "specific" diffusion time (S_{time}). Then, the diffusion distance is $d = \sqrt{2D\Delta}$ and the "specific" diffusion distance (S_{distance}) is defined as $S_{\mathrm{distance}} = \sqrt{2DS_{\mathrm{time}}}$. Figure 1 shows the Δ dependence of the fraction of the slow diffusion component (f_{slow}) value for Boc-Phe in $\mathrm{PS}_{(2)}$ gels, $\mathrm{PS}_{(1)}$ gels and CLEAR gels with DMF-d_7 as solvent at 30 °C, where $\mathrm{PS}_{(2)}$ and $\mathrm{PS}_{(1)}$ gels are cross-linked by 1 and 2% divinylbenzene (DVB), respectively, and the Boc-Phe concentration is 10 wt%. As seen from this figure, the f_{slow} value increases with an increase in Δ and changes from the two components to the single component at larger Δ. The S_{time} as estimated from these plots for Boc-Phe in $\mathrm{PS}_{(2)}$ gels, $\mathrm{PS}_{(1)}$ gels, and CLEAR gels are 20, 40, and 30 ms, respectively. It is found that the S_{time} depends on the kinds of gels. As for Boc-Phe in $\mathrm{PS}_{(2)}$ gels, $\mathrm{PS1}_{(1)}$ gels and CLEAR gels at 30 °C, the S_{distance} are 1.1, 1.7, and 2.7 μm, respectively. It can be said that the S_{distance} depends on the kind of gels, and that the S_{distance} of Boc-Phe in CLEAR gels is much larger than that of Boc-Phe in PS gels. The cross-linker of PS gels is DVB, and the cross-linker of CLEAR gels is acrylate.

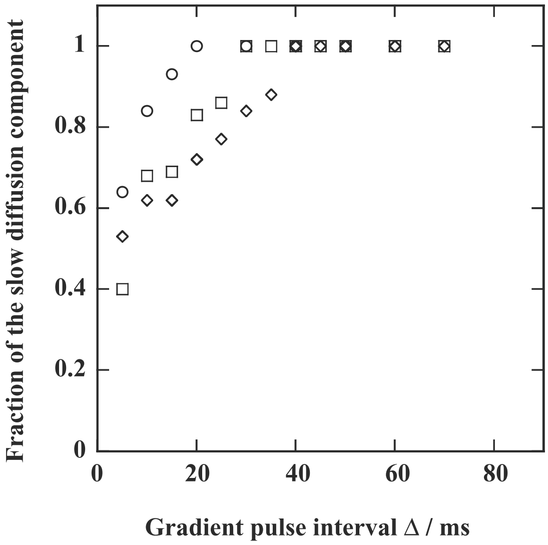

Fig. 1. Dependence of the fraction of the slow diffusion component of Boc-Phe in $\mathrm{PS}_{(2)}$ gels (◯), in $\mathrm{PS}_{(1)}$ gels (◇) and CLEAR gels (□) with DMF-d_7 as solvent at 30 °C on the gradient pulse interval Δ.

One of the goals of this study is to detect inhomogeneities in polymer gels differing in their degree of cross-linking [31]. Then, the networks are prepared at 70 °C by simultaneous polymerization and cross-linking of a mixture of acrylic acid (AA), sodium carbonate, cross-linker (1,4-butanedioldiacrylate), and the redox couple sodium persulfate/sodium isoascorbate as the initiator. Two types of networks are prepared, using the same monomer and sodium carbonate concentrations, but different amounts of the cross-linker, 1.1 and 0.5 wt%, respectively, in the monomer mixture. The corresponding notations are $\mathrm{PAA}_{(1.1)}$ and $\mathrm{PAA}_{(0.5)}$, respectively. Detection of inhomogeneities is based on measuring the D of the probe molecule PEG by time-dependent diffusion NMR. Diffusion measurements are performed as a function of the degree of swelling, $Q = M_{\mathrm{swollen}}/M_{\mathrm{dry}}$, with Q in the range 2.8–10.0.

The different diffusional behavior of the two gel systems emerged as their degree of swelling is varied. For $\mathrm{PAA}_{(1.1)}$ gel with $Q = 10.0$ and 5.2, and for $\mathrm{PAA}_{(0.5)}$ gel with $Q = 10.0$, 5.1, and 4.5, only single diffusion component is detected, independent on the Δ in the range 30–500 ms. For less swollen gels (Q in the range 2.9–4.5 for $\mathrm{PAA}_{(1.1)}$ gel and 2.8–3.9 for $\mathrm{PAA}_{(0.5)}$ gel), two diffusion components (D_{fast} and D_{slow}) are detected as influenced by the distribution of network size, and both of the D_{fast} and D_{slow} values depend on Δ. Here, for all gels, The d_{fast} and d_{slow}, f_{fast}, and f_{slow} values are calculated as a function of Δ. A useful parameter in the interpretation of results is the "specific" degree of swelling (S_{Q}) above which the diffusion of the probe in the two gel systems changed from single to two components. A larger value of S_{Q} in $\mathrm{PAA}_{(1.1)}$ gel is taken as an indicator of a more inhomogeneous gel. Analysis of the effect of Δ on the D, d, and f of the slow and fast diffusion components indicates that both of the gels form a highly cross-linked region in a narrow Q range. In this Q range, the polymer chains interact and form a highly restricted diffusion region. The density and distribution of the cross-links form different restricted diffusion regions in $\mathrm{PAA}_{(1.1)}$ and $\mathrm{PAA}_{(0.5)}$ gel systems, and the heterogeneity in terms of the network size distribution and corresponding populations is higher in the gel with the higher degree of cross-linking.

Characterization of Smart Gels with Regular Structure

Recently, it is necessary to prepare and characterize the smart gel with regular structure, and PFG NMR is more powerful tool for characterizing the soft materials such as gels. It has been reported that highly-oriented poly(γ-benzyl L-gultamate) (PBLG) gel is prepared by cross-linking reaction of highly-oriented PBLG chains in 1,4-dioxane with cross-linker in the magnetic field of an NMR magnet, by monitoring the orientation of the PBLG chains with solid-state static ^{13}C NMR by using the relationship between the observed ^{13}C chemical shift of the main-chain carbonyl carbon in PBLG [32], and then solvents and rod-like molecules in the PBLG gel are anisotropically diffusing in the direction parallel and perpendicular to the α-helix axis by PFG NMR [32,33]. The degree of orientation is 0.81, and the D of 1,4-dioxane molecule in the direction parallel to the α-helical PBLG axis($D_{||}$) to be 5.4×10^{-6} cm^2/s is larger than that perpendicular to the α-helical PBLG axis($D_\perp$) to be 4.5×10^{-6} cm^2/s and the $D_{||}/D_\perp$ value is 1.20. This shows that there exist long channels with small diameter of 15–20 Å (the interchain distances between the nearest-neighboring two PBLG chains determined by the wide angle X-ray diffraction pattern) in the highly-oriented PBLG gel, and that the diffusional behavior of solvents and probe molecules is significantly influenced by the microstructure of network polypeptide chains in gels.

Further, highly-oriented PBLG gels having channel cavities with μm-scale diameters due to phase separation in cross-linking reaction process have been prepared and characterized the structure of the polypeptide gels by PFG NMR and three-dimensional (3D) NMR imaging [34,35]. PBLG gel with channel cavity has two regions consisting of long channel cavity (with μm-scale diameters) region and the remaining gel matrix region without long channel cavity. In the PFG ^{1}H NMR experiments, spin echo signals coming from solvent molecules in the corresponding two regions are observed. In the PBLG gel matrix region, the $D_{||}/D_\perp$ value is 1.29. This shows that the PBLG gel matrix region has anisotropic channel cavity in a nm-scale, and that nm-scale structure of the PBLG gel matrix region in PBLG gel with channel cavity is similar to nm-scale structure of highly-oriented PBLG gel with no μm-scale channels. While, in μm-scale channel cavities of PBLG gel, the 1,4-dioxane molecules may be trapped in channel cavities or may permeate partially and slowly from the channel cavity region to the gel matrix region and from the gel matrix region to the channel cavity region through network of the wall of the channel cavity because the network density near the wall of the channel cavity as formed by cross-linking reaction with phase separation may be higher than that in the PBLG gel matrix region. Thus, if 1,4-dioxan in channel cavity is trapped and mainly diffuse in channel, this reflecting model on diffusion in the space between two infinitely large perfectly reflecting parallel planes (separation $2R$) [36–40] may be approximately used to analyze the diffusion behavior of 1,4-dioxane in the channel cavity of the PBLG gel. The plots of PFG spin echo attenuation $E(q, \Delta = 5$ ms) for diffusion of 1,4-dioxane in PBLG gels with channel cavities against “tunable” parameter $q(= (2\pi)^{-1}\gamma g\delta)$ show the two diffraction minima (not shown) [33]. Here, γ is the gyromagnetic ratio of proton, g is the strength of the field gradient pulse and length δ. When the probe molecules are trapped in restricted space, the diffraction minima corresponding to the size scale of restricted space are often observed as seen from Equation(1).

$$E\,(q,\,\Delta = \infty) = \frac{2\,[1 - \cos{(4\pi q R)}]}{(4\pi q R)^2} \qquad (1)$$

The tendencies for the simulated curves ($2R = 50$ and 60 μm) and the experimental plots are very similar to each other. The slight difference between the experimental and simulated curves may come from the fact that solvent molecules may permeate partially. From this, it can be said that the simulated results do not conflict with the experimental results and thus the mode diameter of the long channel cavities may be estimated to be about 50–60 μm. This is very close to the result by 3D NMR imaging (about 70 μm). Further, it can be said that most of the 1,4-dioxane molecules is reflected at the surface of the wall of channel cavities.

Characterization of the Polymer Media with Nano Cavities

Polymer media with nano cavities has potential as smart membrane, and we need to understand deeply the diffusional behavior of probe molecules and property of cavities. Kärger, *et al.* have shown that PFG experiments gives useful information on zeolites, the molecular dynamics simulations have reasonably explained with the experimental results on self-diffusivity for a binary mixture adsorbed inside zeolite [41–44] and for zeolite and porous media [45,46]. In this section, characterization of the media with controlled nano cavities has been briefly described. The channels in poly(p-biphenylene terephthalate) with long n-dodecyl side chains(PBpT-O12) have been characterized in order to elucidate the nature of the inside of the cylindrical channel cavities as studied by PFG NMR [47]. PBpT-O12 forms the hexagonal columnar phase, and honeycombed network is formed and then has cylindrical cavity channels with diameter of about 3 nm. They aim to prepare PBpT-O12 charged methane and ethane molecules into the cylindrical channel cavities in the hexagonal columnar phase, to measure the D values of the gas in the directions perpendicular ($D_{\perp}$) and parallel ($D_{||}$) to the channel cavity axis.

Methane and ethane molecules in the cylindrical channel cavities have a single diffusion component in the Δ used here. The $D_{||(\mathrm{ethane})}$ value in the cylindrical channel cavities at $\Delta = 6$ ms is determined to be 2.9×10^{-7} cm^2/s. This D value is extremely much smaller than that of ethane gas (0.22 cm^2/s). This means that the diffusion of the ethane molecules is strongly restricted by the nature of the inside of cylindrical channel cavity by intermolecular interactions between the ethane molecules and, especially, long n-dodecyl side chains of the polyester. While, $D_{\perp(\mathrm{ethane})}$ value in the cylindrical channel cavities at $\Delta = 6$ ms is determined to be 9.5×10^{-9} cm^2/s. This D value is extremely much smaller than that of the $D_{||(\mathrm{ethane})}$ value, and also shows that the ethane molecules are not trapped, but diffuse through the wall of the cylindrical channel cavity to the neighboring cylindrical channel cavities. By using $D_{\perp} = 9.5 \times 10^{-9}$ cm^2/s, $\Delta = 6$ ms, we can estimate the d to be 107 nm. Therefore, it can be said that the wall of cylindrical channel cavity has some defects and the ethane molecules are possible to pass through these defects, and that the furthermore ethane molecules in the cylindrical channel cavities are clearly moving through the wall of the cylindrical channel cavity to neighboring cylindrical channel cavities in the direction perpendicular to the cylindrical channel cavity axis in a rod piece of oriented PBpT-O12 polyester media with a diameter of 0.6 mm ($=6.0 \times 10^5$ nm). The ratio of $D_{||(\mathrm{ethane})}/D_{\perp(\mathrm{ethane})}$ is 31, thus, it can be said that the inside of cylindrical cannel cavity is anisotropic field for gas diffusion.

As compared with the $D_{(\mathrm{methane})}$ values in the channel cavities, the $D_{||(\mathrm{ethane})}$ and $D_{\perp(\mathrm{ethane})}$ values are much smaller than those of methane($D_{||(\mathrm{methane})} = 4.2 \times 10^{-7}$ cm^2/s and $D_{\perp(\mathrm{methane})} = 6.5 \times 10^{-8}$ cm^2/s), and then the ratio of $D_{||(\mathrm{ethane})}/D_{\perp(\mathrm{ethane})}$ for ethane is much larger than that for methane($D_{||(\mathrm{methane})}/D_{\perp(\mathrm{methane})} = 6.5$). This means that the cylindrical cannel cavities of PBpT-O12 have high anisotropy in diffusion and the ability for the recognition of the molecular size.

Diffusional Behavior of Linear Molecules in Channels

In general, the inclusion compound is defined as a chemical substance consisting of a lattice of one type of molecule (host) trapping and containing a second type of molecule (guest). The host molecules form a cavity such as a crystal lattice containing spaces with long tunnels or channels in a crystal. According to many kinds of pairs between host and guest molecules, many kinds of inclusion compounds can be formed. Urea usually forms tetragonal structure in the crystalline state. However, in the case of urea adducts, the structure of urea changes to the hexagonal form that is a parallel channel with diameter of about 5.5 Å by strong hydrogen-bonds between urea molecules and n-paraffin molecules are included in the channel. When the host molecule is urea, the inclusion compounds are often called “urea adducts” instead of “urea inclusion compounds.” As a consequence of the requirement for the size and shape compatibilities between the guest molecules and the host channels, typical guest molecules for the urea channel structure are linear molecules such as higher n-alcohols and n-paraffins (with six or more carbon atoms), some n-olefines, n-carboxylic acids, ketones, and esters. The structure and dynamics of urea adduct which has n-paraffin molecules as a guest molecule has been widely studied by various methods such as X-ray diffraction, neutron scattering, Raman, IR, solid-state NMR, molecular dynamics calculation, etc. However, there is little work for elucidating whether guest molecule diffuses in urea channels or not. It is very interesting to think that if guest molecules diffuse in urea channels, how is diffusional behavior? Most recently, the phenomenon that n-paraffins diffuse in urea channels has been successfully detected. It is found that n-paraffin molecules are diffusing in long urea channels and has the two diffusion components such as the fast diffusion component ($D = 10^{-6}$ cm^2/s) and the slow diffusion component ($D = 10^{-7}$ cm^2/s) by using PFG NMR [48]. According to the single-file diffusion model applied in case that molecules cannot pass each other, it can be explained that the two diffusion components such as D_{fast} and D_{slow} are correspond to n-paraffin molecules in the two external regions near the ends of the urea channel and n-paraffin molecules in the central inner region of the urea channel. Furthermore, D of the fast and slow diffusion components of n-paraffin molecules in urea channel are greatly decreased as the carbon number is increased from 8 to 21, but the diffusion coefficients D are slowly decreased as the carbon number is increased from 21 to 32, and from the activation energy of self-diffusion, they say intermolecular interactions between n-paraffin chains and urea channels wall are very smaller than those between n-paraffin chains in the rotator phase [49]. From the diffusing-time (Δ) dependence of the diffusion coefficients, it is cleared that n-paraffin molecules are diffusing colliding with molecules on sides within urea channel. Consequently, the diffusion process of n-paraffins in urea channels is cooperative diffusion such as single file diffusion from the time-dependent diffusion NMR by compared the results of the simulation [50] of the relationships between single file diffusion and diffusion experiments.

Conclusion Remarks

It is demonstrated that PFG experiments gives useful information on the characterization of the polymer systems as well as probe diffusion, and also will have a great potentiality for applications to characterization of smart media with controlled cavities [51,52], aggregation process, lattice-forming process, phase separation systems, and heterogeneous systems [53] as well as gels. Especially, it is important to consider the diffusing time, if so, information about the structure of polymer system and nature of diffusant can be derived from PFG experiments.

References

1. Hahn EL. Phys. Rev. 1950;80:580.
2. Stejskal EO, Tanner JE. J. Chem. Phys. 1965;42:288.
3. Nose T. Ann. Rep. NMR Spectrosc. 1993;27:217.
4. Price WS. Ann. Rep. NMR Spectrosc. 1996;32:51.
5. Callaghan PT, Principles of Nuclear Magnetic Resonance Microscopy. Claredon Press: Oxford, England, 1991.
6. Kimmich R, NMR: Tomography, Diffusiometry, Relaxometry. Springer: Berlin, 1997.
7. Ando I, Kobayashi M, Zhao C, Yin Y, Kuroki S. Encyclopedia of NMR, Vol. 19. Interscience: New York, 2002, p. 770.
8. Matsukawa S, Ando I. Macromolecules. 1996;29:7136.
9. de Gennes PG. Macromolecules. 1976;9:594.
10. Masaro L, Zhu XX, Macdonald PM. Macromolecules. 1998;31:3880.
11. Masaro L, Zhu XX, Macdonald PM. J. Polym. Sci. Polym. Phys. Ed. 1999;37:2396.
12. Matsukawa S, Ando I. Macromolecules. 1997;30:8310.
13. Matsukawa S, Ando I. Macromolecules. 1999;32:1865.
14. Masaro L, Zhu XX. Langmuir 1999;15:8356.
15. Kwak S, Lafleur M. Macromolecules 2003;36:3189.
16. Masaro L, Zhu XX. Macromolecules. 1999;32:5383.
17. Baille WE, Malveau C, Zhu XX, Kim YH, Ford WT. Macromolecules. 2003;36:839.
18. Baille WE, Zhu XX, Fomine S. Macromolecules. 2004;37:8569.
19. Saito Y, Kataoka H, Stephan AM. Macromolecules. 2001;34:6955.
20. Hayamizu K, Aihara Y, Arai S, Price WS. Electrochem. Acta. 2000;45:1313.
21. Ward IM, Williamson MJ, Hubbard HVSt.A, Southall JP, Davies GR. J. Power Sources. 1999;81–82:700.
22. Forsyth M, Sun J, Zhou F, MacFarlane DR. Electrochem. Acta. 2003;48:2129.
23. Darwish MIM, van der Maarel JRC, Zitha PLJ. Macromolecules. 2004;37:2307.
24. Pusey NP, van Megen W. Physica A. 1989;157:705.
25. Ikkai F, Shibayama M. Phys. Rev. E. 1997;56:R51.
26. Mallam S, Horkay F, Hecht AM, and Geissler E. Macromolecules. 1989;22:3356.
27. Rosén O, Boström M, Nydén M, Piculell L. J. Phys. Chem. B. 2003;107:4074.
28. Cicerone MT, Wagner PA, Ediger MD. J. Phys. Chem. B. 1997;101:8727.
29. Lin G, Zhang J, Cao H, Jones AA. J. Phys. Chem. B 2003;107:6179.
30. Yamane Y, Matsui M, Kimura H, Kuroki S, Ando I. Macromolecules. 2003;36:5655.
31. Yamane Y, Ando I, Buchholz FL, Reinhardt AR, Schlick S. Macromolecules. 2004;37:9841.
32. Zhao C, Zhang H, Yamanobe T, Kuorki S, Ando I. Macromolecules. 1999;32:3389.
33. Zhao C, Kuorki S, Ando I. Macromolecules. 2000;33:4486.
34. Yamane Y, Kanekiyo M, Koizumi S, Zhao C, Kuroki S, Ando I. J. Appl. Polym. Sci. 2004;92:1053.
35. Yamane Y, Koizumi S, Kuroki S, Ando I. J. Mol. Struct. 2005;739:137.
36. Price WS. Ann. Rep. NMR Spectrosc. 1996;32:51.
37. Mitra PP, Sen PN. Phys. Rev. B. 1992;45:143.
38. Snaar JEM, Van As H. J. Magn. Reson. A. 1993;102:318.
39. Mitra PP, Sen PN, Schwartz LM. Phys. Rev. B. 1993;47:8565.
40. Callachan PT. J. Magn. Reson. A. 1995;113:53.
41. McDaniel PL, Coe CG, Kärger J, Moyer JD. J. Phys. Chem. 1996;100:16263.
42. Snurr RQ, Kärger J. J. Phys. Chem. B. 1997;101:6469.
43. Heink W, Kärger J, Naylor T, Winkler U. Chem. Commun. 1999;57–58:57.
44. Geier O, Snurr RQ, Stallmach F, Kärger J. J. Chem. Phys. 2004;120:367.
45. Rittig F, Coe CG, and Zielinski JM. J. Am. Chem. Soc. 2002;124:5264.
46. Mair RW, Hürlimann MD, Sen PN, Schwartz LM, Patz S, Walsworth RL. Magn. Reson. Imaging. 2002;19:345.
47. Matsui M, Yamane Y, Kuroki S, Ando I, Fu K, Watanabe J. J. Mol. Struct. 2005;739:131.
48. Kim S, Kimura H, Kuroki S, Ando I. Chem. Phys. Lett. 2003;367:581.
49. Yamakawa H, Matsukawa S, Kuroki S, Kurosu H, Ando I. J. Chem. Phys. 1999;111:5129.
50. Aslangul C. Europhys. Lett. 1998;44:284.
51. Appel M, Fleischer G, Kärger J, Dieng AC, G. Riess. Macromolecules 1995;28:2345.
52. Challa V, Kuta K, Lopina S, Cheung HM, von Meerwall E. Langmuir 2003;19:4154.
53. Seland JG, Ottaviani M, Hafskjold B. J. Colloid Interface Sci. 2001;239:168.

NMR Measurements Using Field Gradients and Spatial Information

Shingo Matsukawa
Department of Food Science and Technology, Tokyo University of Marine Science and Technology,
Minato-ku, Tokyo 108-8477, Japan

Introduction

An application of field gradient attaches a spatial information in NMR signal, therefore, it can produce a spatial distribution of nuclei, that is, NMR imaging [1,2]. When two field gradients for the diphase and rephrase applied, the NMR signal decays due to the displacement of nucleus during the time between two field gradients [3,4]. This gives the diffusion coefficient for Fickian diffusion in free space and the space size for a spatially restricted diffusion [5]. Recently, the field gradient is used for the selection of desired coherence pathway by rephasing the desired coherence and dephasing the undesired coherence [6]. In this chapter, these three important uses of field gradient are described.

Diffusion Coefficient Measurements

The Larmor precession frequency depends on the magnetic field experienced by the nucleus, therefore, it has a spatial dependence under the field gradient. The spatial dependent Larmor frequency $\omega(\mathbf{r})$ at the position $\mathbf{r}$ under a spatially linear field gradient $\mathbf{g}$ is expressed as follows

$$\omega(\mathbf{r}) = \gamma(H_0 + \mathbf{gr}) = \omega_0 + \gamma\mathbf{gr} \tag{1}$$

where H_0 is the externally applied magnetic field and $\mathbf{gr} = 0$ at the position of $\mathbf{r} = 0$. When the duration time of the gradient is δ, the difference of the phase angle at r from that at r = 0 is

$$\phi(\mathbf{r}) = \gamma\mathbf{gr}\delta \tag{2}$$

The distance in the direction of $\mathbf{g}$ where $\phi(\mathrm{r}) = 2\pi$ is

$$q^{-1} = 2\pi/\gamma g\delta \tag{3}$$

q^{-1} is the scale of *length* with the gradient. For example, q^{-1} becomes 235 μm for $g = 10$ G/cm with $\delta = 1$ ms. When the sample size, or the size of detection area, is several times larger than q^{-1}, the total signal intensity vanishes because of the dephasing. For the diffusion coefficient measurements, a second gradient is applied in order to rephase the dephased magnetization. Figure 1 shows a typical pulse sequence with two pulsed field gradients (PFG) with rectangular shape along the z-axis, and the dephasing and rephasing behavior of the magnetization when the individual nucleus did not change their positions in the interval Δ between the two PFG. In Figure 1 (a) The magnetizations are aligned along the y-axis by an rf $\pi/2$ pulse. (b) Under the first PFG, the magnetizations precess at the angular velocity of $\gamma\mathbf{gr}$ corresponding to the z coordinate. (c) At the end of the first PFG, the magnetizations are spirally twisted at a pitch of q^{-1}. (d) The application of an rf π pulse along the y-axis rotates the individual magnetizations along the y-axis through 180°, which makes the mirror-symmetrical arrangement of the magnetizations with respect to the y–z plane. (e) Under the second PFG, the individual magnetizations precess at the same angular velocity with that under the first PFG. (f) At the end of the second PFG, the magnetizations are aligned along the y-axis. When the nucleus has a displacement of Δz in the z direction during Δ, it has a phase angular shift

$$\phi(\Delta z) = 2\pi\frac{\Delta z}{q^{-1}} = \gamma g d\Delta \mathrm{z} \tag{4}$$

The echo signal intensity $I(2\tau, g\delta)$ at 2τ is proportional to the vector sum of magnetizations in the sample, therefore, expressed as follows

$$I(2\tau, g\delta) = I(2\tau, 0)\iint \cos(\phi(\Delta z)) \times\rho(\mathbf{r})\, p(\mathbf{r}, \Delta z)\, \mathrm{d}\mathbf{r}\, \mathrm{d}\Delta z \tag{5}$$

where $\rho(\mathbf{r})$ is the density of the nucleus and is constant for homogeneous sample, $p(\mathbf{r}, \Delta z)$ is the probability of the displacement during Δ for the nucleus at $\mathbf{r}$ and $I(2\tau, 0)$ is the total signal intensity without PFG and expressed as follows

$$I(2\tau, 0) = I(0, 0)\exp(-2\tau/T_2) \tag{6}$$

where $I(0,0)$ is the initial signal intensity just after the rf $\pi/2$ pulse. For the free diffusion in an isotropic medium,

Graham A. Webb (ed.), Modern Magnetic Resonance, 129–134.
© 2008 *Springer.*

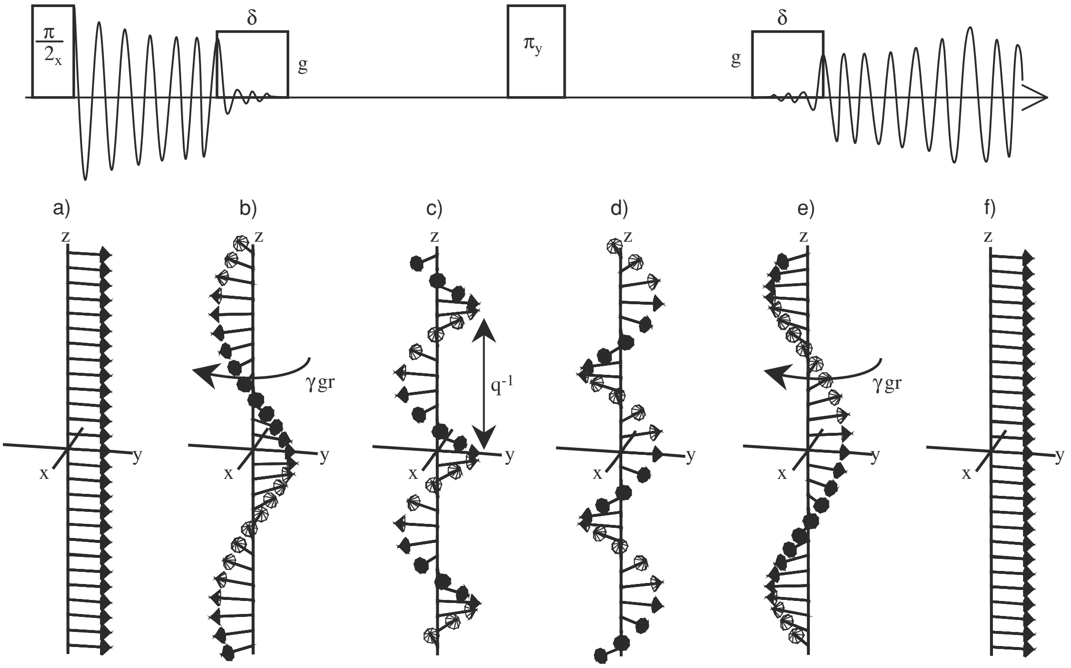

Fig. 1. A typical pulse sequence with two PFG of rectangular shape and the dephasing and rephasing behavior of the magnetization. (a) The magnetizations are aligned along the y-axis by an rf $\pi/2$ pulse. (b) Under the first PFG, the magnetizations precess at the angular velocity of $\gamma\mathbf{gr}$ corresponding to the z coordinate. (c) At the end of the first PFG, the magnetizations are spirally twisted at a pitch of q^{-1}. (d) An rf π pulse along the y-axis rotates the individual magnetizations along the y-axis through 180 degree. (e) Under the second PFG, the individual magnetizations precess at the same angular velocity with that under the first PFG. (f) At the end of the second PFG, the magnetizations are aligned along the y-axis.

$p(\mathbf{r},\Delta z)$ becomes the Gaussian distribution

$$p\,(r,\,\Delta z) = (4\pi\,D\Delta)^{-1/2}\exp\left(-\frac{\Delta z^2}{4D\Delta}\right) \tag{7}$$

where D is the diffusion coefficient. Taking the diffusion during δ into account, Equation (5) is rewritten as follows

$$I(2\tau,g\delta) = I(0,0)\exp\left(-\frac{2\tau}{T_2} - (\gamma g\delta)^2\,D\left(\Delta - \frac{\delta}{3}\right)\right) \tag{8}$$

In common measurements of the free diffusion, $g\delta$ is varied under constant Δ.

For the diffusion in restricted space, the D value obtained by applying Equation (8) is an apparent diffusion constant

$$D_{\text{app}}\,(\Delta) = \frac{\left\langle\Delta z^2\right\rangle(\Delta)}{2\Delta} \tag{9}$$

where $\langle\Delta z^2\rangle(\Delta)$ is the mean square of Δz^2 during Δ. $\langle\Delta z^2\rangle(\Delta)$ is proportional to Δ for the free diffusion, however, becomes smaller than the proportional value due to the spatial restriction, which gives the information of the space size of the restriction.

The signal decay by the displacement under the field gradient can be used to remove peaks for small molecules from the mixture spectrum of small and large molecules. Conversely, the spectrum of peaks for small molecules can be obtained by the subtraction of the decayed spectrum for large molecules from the mixture spectrum. The mixture spectrum is composed of the peaks contained in different molecules that exponentially decay with the square of $\gamma g\delta$ according to individual diffusivity. By changing Equation (8) into a sum of each component, the intensity at each frequency in the mixture spectrum is expressed as follows,

$$I(2\tau,\,g\delta) = I(0,0) \times \sum_i f_i\exp\left(-\frac{2\tau}{T_{2,i}} - (\gamma g\delta)^2\,D_i\left(\Delta - \frac{\delta}{3}\right)\right) \tag{10}$$

where f_i and $T_{2,i}$ are fraction and T_2 for the component with the diffusion coefficient D_i. By using the T_2 weighted fraction of i-th component

$$F_i(2\tau) = f_i \exp(-2\tau/T_{2,i}) \tag{11}$$

Equation (10) is rewritten as follows,

$$I(2\tau, g\delta) = I(0,0) \times \sum_i F_i \exp\left(-(\gamma g\delta)^2 D_i\left(\Delta - \frac{\delta}{3}\right)\right) \tag{12}$$

When F is expressed as a continuos function of D, Equation (12) is rewritten as follows,

$$I(2\tau, g\delta) = I(0,0)\int F(D_i)\exp(-KD)\mathrm{d}D \tag{13}$$

where $K = (\gamma g\delta)^2(\Delta\text{-}\delta/3)$. $F(D)$ is a T_2 enhanced distribution of D. Equation (13) shows that $I(2\tau, g\delta)$ is the Laplace transformation of $F(D)$, therefore, an inverse Laplace transformation of $\mathrm{I}(2\tau, g\delta)$ will give $F(D)$. The 2D spectrum with dimensions of frequency and D, diffusion-ordered NMR spectroscopy (DOSY), gives separated spectrum for each species in the mixture on the diffusivity and the distribution of the diffusivity for each species [7].

NMR Imaging

An application of field gradient along one direction gives one-dimensional profile of spin density. The use of gradients along three direction of x, y and z gives a three dimensional NMR imaging. Figure 2 shows a typical pulse sequence with field gradients of g_x, g_y and g_z along x, y and z, respectively. The g_z applied during rf pulse selects the layer where the Larmor frequency $\omega(\mathbf{r})$ expressed by Equation (1) is equal to the rf frequency. The rf pulse is shaped into sine form $(\mathrm{Sin}(t/d)/(t/d))$ which has a rectangular shape in the frequency domain, which is a Fourier transform of the rf pulse in time domain, and slices the selected layer sharply (Figure 3). The thickness of the layer d is inverse to the rf duration, therefore, a weak rf pulse with long duration is applied for a thin slice of the layer. The g_z causes the phase shift corresponding to the excess magnetic field at $\mathbf{r}$, therefore, a reversed gradient is set after the $\pi/2$ rf pulse in order to rephase the phase shift. The phase shift during the first half of g_z at the π pulse is rephased during the latter half of the period. The pairs of the dephasing and rephasing followed by the slice selection gradient are represented as shadowed portions with upper right and left in Figure 2.

The g_x is applied when the magnetizations are aligned along the y-axis. At the end of the gradient, the magnetization has a phase shift depending on the position along the x-axis, which is given by the rewriting Equation (2) as follows,

$$\phi(x) = \gamma g_x x t_x = 2\pi k_x x \tag{14}$$

where $k_x = \gamma g_x t_x/2\pi$. Then the signal intensity is

$$I(k) = I(0)\int \rho(x)\exp(-2\pi ikx)\mathrm{d}x \tag{15}$$

where, $I(0)$ is the signal intensity without the gradient of g_x and $\rho(x)$ is the projection of the spin density along x-axis in the slice. Equation (15) indicates that $I(k)$ is the Fourier transform of $\rho(x)$, therefore, an inverse Fourier transformation on a series of measured data varying k value (usually varying g_x) gives $\rho(x)$. Figure 4 illustrates the phase shift of magnetization under various g_x. The

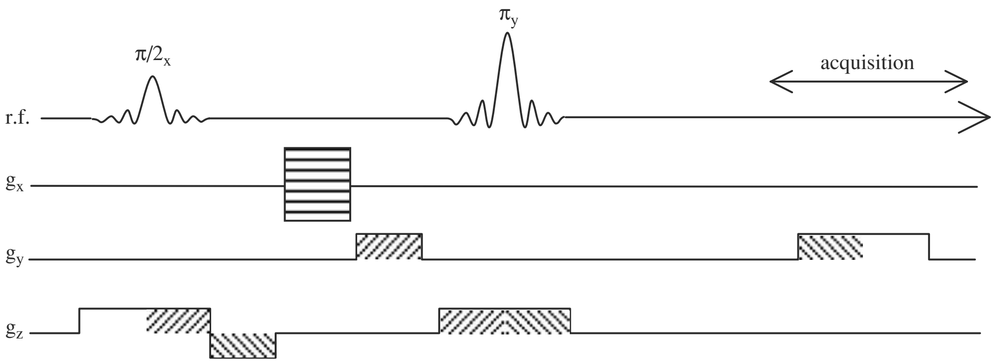

Fig. 2. A typical pulse sequence for three dimensional NMR imaging.

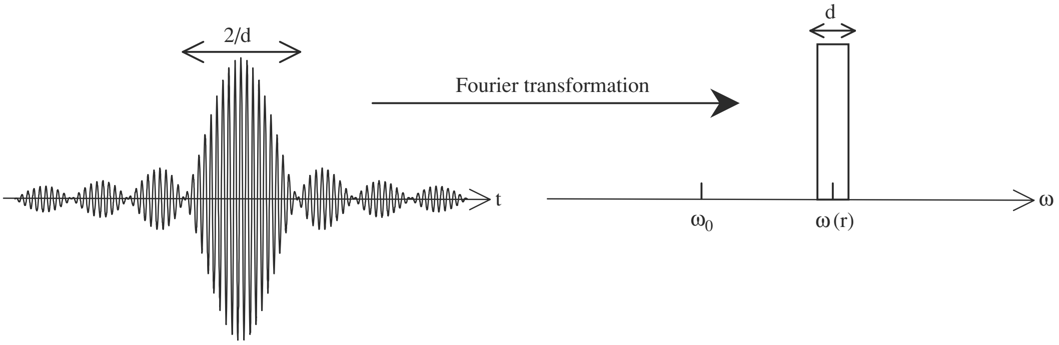

Fig. 3. The rf pulse with the shape of sinc form $(\mathrm{Sin}(t/d)/(t/d))$ and its Fourier transform which has a rectangular shape in the frequency domain.

magnetization without the gradient has an intensity profile corresponding to the projection of the spin density along x-axis in the slice. The application of g_x induces the excessive magnetic field with the strength of $g_x x$ at the x coordinate, which is indicated by gray arrow in Figure 4. The excessive magnetic field rotates each magnetization at the individual rate of $\gamma g_x x$ and the magnetization has the phase shift corresponding to the x coordinate. The pitch of the phase shift k^{-1} is decreased with increasing g_x, and the total magnetization under each g_x is a Fourier component of $\rho(x)$ at k.

The application of g_y during the acquisition period gives each magnetization the difference of precession rate corresponding to the y coordinate, which is reflected in the frequency in spectrum. Therefore, the spectrum obtained by the Fourier transformation of the echo signal is the projection of the spin density along y-axis $\rho(y)$ in the slice. The echo signal $S(k, t)$ is a Fourier component of $\rho(x)$ at k, therefore, the two-dimensional Fourier transform of $S(k, t)$ gives the spin density $\rho(x, y)$ in the slice.

When there are nuclei in different environments, the effect of the excessive magnetic field induced by the field gradient coexist with the shielding effect of surrounding electron clouds, which is the origin of the chemical shift in spectra without field gradients. By using a chemical shift selective pulse, it is possible to obtain NMR imaging of desired nuclei at the chemical shift. It is also possible to remove the undesired signal by a presaturation of the nuclei.

Selection of Coherence

The field gradient is used for the selection of coherence pathways. The coherence selection also achieved by phase cycling, which causes a subtraction of undesired peaks. On the other hand, the field gradient method is based on a spin echo method, which rephases desired peaks and dephases undesired peaks, needs only one scan for a spectrum or an increment in multidimensional measurements.

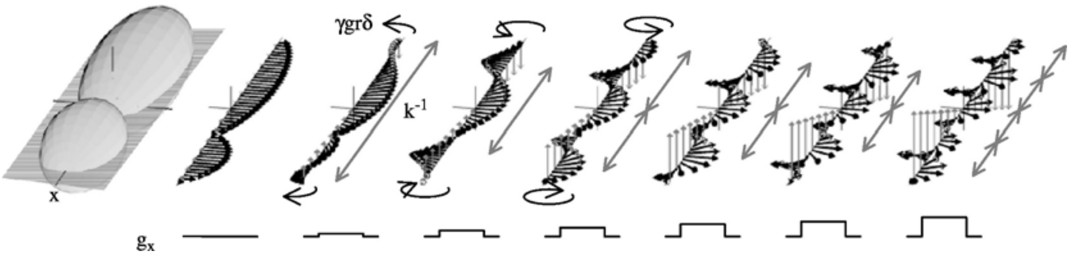

Fig. 4. The phase shift of magnetization under various g_x. The magnetization without the gradient has an intensity profile corresponding to the projection of the spin density along x-axis in the slice. The application of g_x induces the excessive magnetic field with the strength of $g_x x$ (gray arrows), which rotates each magnetization at the individual rate of $\gamma g_x x$ and induces the phase shift corresponding to the x coordinate. The pitch of the phase shift k^{-1} is decreased with increasing g_x.

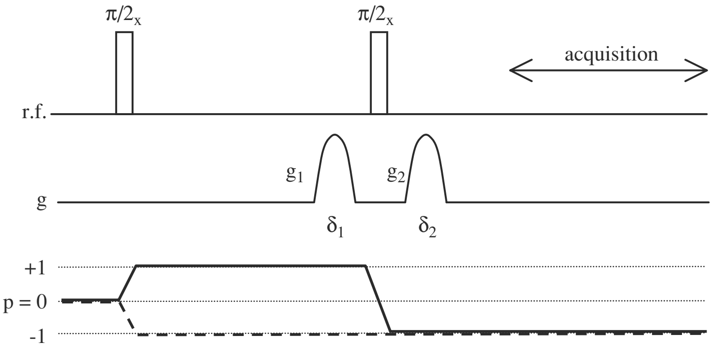

Fig. 5. A pulse sequence for Gradient Selected COSY in magnitude mode. The solid line and dotted line indicate coherence pathways that have the coherence order of –1 at the acquisition period. The former is rephased and the latter remains a phase shift when the gradients are set as $g_1\delta_1 = \gamma_2\delta_2$.

Further, three is no problem of the residue for undesired peaks caused by imperfection of the subtraction in the phase cycling method. Because of this, the application of the gradient gives remarkable improvement for many measurements developed on the basis of the phase cycling method. The gradient method takes advantage of the fact that the space dependent phase shift caused by the gradient depends on the coherence order p. The phase shift is expressed by Equation (2) when $p = 1$. For general orders of p, the phase shift is expressed as follows,

$$\phi(\mathrm{r}) = p\gamma \mathbf{gr}\delta \tag{16}$$

In a homonuclear spin system, the final phase shift after the gradient pulses becomes

$$\phi(\mathrm{r}) = \gamma \sum_{i}^{n} p_i g_i \delta_i r \tag{17}$$

Therefore, the desired coherence pathway corresponding a set of coherence orders $p_1, p_2, \ldots p_i, \ldots p_n$ is rephased by using the set of gradients $g_1\delta_1$, $g_2\delta_2, \ldots g_i\delta_i, \ldots g_n\delta_n$, which satisfies $\phi(\mathrm{r}) = 0$. Other pathways remain the dephase expressed by Equation (17). Figure 5 shows a pulse sequence for *gs* (Gradient Selected)-COSY in magnitude

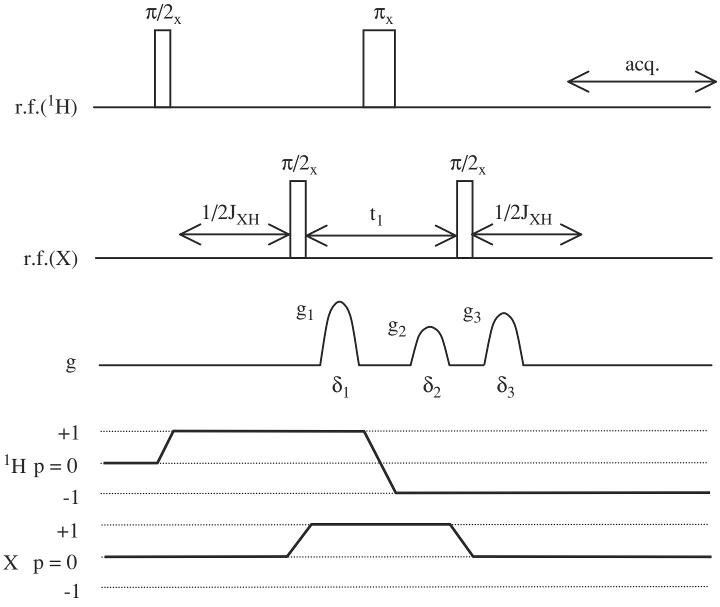

Fig. 6. A pulse sequence for Gradient Selected HMQC. The coherence pathway of solid line is selected when $(\gamma_{\mathrm{H}} + \gamma_{\mathrm{X}})\gamma_1\delta_1 + (-\gamma_{\mathrm{H}} + \gamma_{\mathrm{X}})\gamma_2\delta_2 - \gamma_{\mathrm{H}}\gamma_3\delta_3 = 0$.

mode. The interval of gradients should be short in order to reduce the decay of the signal for the desired pathway by the molecular diffusion. The sinusoidal shaped gradients are used in order to reduce the effect of the eddy current induced by the gradient on the rf pulses. The solid line and dotted line in Figure 5 indicate two coherence pathways that have the coherence order of –1 at the acquisition period. When the gradients are set as $g_1\delta_1 = g_2\delta_2$, $\phi(\mathrm{r}) = 0$ for the coherence pathway of the solid line, on the other hand, $\phi(\mathrm{r}) = 2\gamma g_1\delta_1\mathbf{r}$ for that of the dotted line. Consequently, the former pathway is selected. In a homonuclear spin system, the final phase shift after the gradient pulses becomes

$$\phi(\mathbf{r}) = \sum_{i}^{n}\sum_{j}\gamma_j p_{i,j} g_i \delta_i \mathbf{r} \qquad (18)$$

Figure 6 shows a pulse sequence for gs-HMQC. For the selection of coherence pathway indicated the solid line, the gradients is set as satisfies the equation

$$(\gamma_H + \gamma_X)g_1\delta_1 + (-\gamma_H + \gamma_X)g_2\delta_2 - \gamma_H g_3\delta_3 = 0 \qquad (19)$$

When the nuclear X is $^{13}\mathrm{C}$, $\gamma_{13\mathrm{C}}/\gamma_{\mathrm{H}} \fallingdotseq 0.25$. By using same duration time for each gradient, Equation (19) becomes

$$1.25g_1 - 0.75g_2 - g_3 = 0 \qquad (20)$$

For example, Equation (20) is satisfied when $g_1{:}g_2{:}g_3 = 2{:}2{:}1$, 5:3:4 or 3:5:0. The ^{1}H signals of other pathways such as ^{1}H attached to ^{12}C, which gives a main peak in usual measurements, remains the phase shift and vanishes.

References

1. Callaghan PT, Principles of Nuclear Magnetic Resonance Microscopy, Clarendon Press Oxford, 1991, p. 93.
2. Yasunaga H, Kobayashi M, Matuskawa S, Kurosu H and Ando I, In: GA Webb and I Ando (Eds), Annual Reports on NMR Spectroscopy, Vol. 34, Academic Press: London, 1997, p. 39.
3. Stejskal EO, and Tanner JE. J. Chem. Phys. 1965;42:288.
4. Karger J, Pfeifer H, Heink W. Adv. Magn. Reson. 1988;12:1.
5. (a) Matsukawa S, Ando I. Macromolecules 1996;29:7136; (b) 1997;30:8310; (c) 1999;32:1865; (d) Matsukawa S, Yasunaga H, Zhao C, Kuroki S, Kurosu H, Ando I. Prog. Polym. Sci. 1999;24:995.
6. Claridge TDW. High-Resolution NMR Techniques in Organic Chemistry, Elsevier Science Ltd: Oxford, 1999, Chapter 5.
7. Johnson Jr. CS. Progress in Nuclear Magnetic Resonance Spectroscopy 1999;34:203.

Theory and Application of NMR Diffusion Studies

Torsten Brand[1], Eurico J. Cabrita[2], and Stefan Berger[1]
[1]*Institut für Analytische Chemie, Universität Leipzig, Johannisallee 29, 04103 Leipzig, Germany; and*
[2]*REQUIMTE/CQFB, Department de Química, Faculdade de Ciências e Tecnologia,*
Universidade Nova de Lisboa, 2829-516 Caparica, Portugal

Theoretical Aspects

Concepts of diffusion

Self-diffusion is the random translational motion of molecules driven by their internal kinetic energy [1]. Translational diffusion and rotational diffusion can be distinguished.

Diffusion is related to molecular size, as becomes apparent from the Stokes–Einstein equation:

$$D = k_B T/f \tag{1}$$

where D is the diffusion coefficient, k_B is the Boltzmann constant, T is the temperature, and f is the friction coefficient. If the solute is considered to be a spherical particle with an effective hydrodynamic radius (i.e. Stokes radius) r_S in a solution of viscosity η, then the friction coefficient is given by:

$$f = 6\pi \eta r_S \tag{2}$$

Pulse Sequences for PFG NMR Diffusion Measurements

Using the pulsed-field gradient (PFG) method, motion is measured by evaluating the attenuation of a spin echo signal [2]. The attenuation is achieved by the dephasing of nuclear spins due to the combination of the translational motion and the imposition of gradient pulses. In contrast to relaxation methods, no assumptions concerning the relaxation mechanism(s) are necessary.

The PFG NMR sequence (Figure 1) is the simplest for measuring diffusion [2].

During application of the gradient, which is along the direction of the static, spectrometer field, B_0, the effective magnetic field for each spin is dependent on its position. Therefore, the precession frequency is also position dependent which leads to the development of position dependent phase angles. The 180° pulse changes the direction of the precession. Hence, the second gradient of equal magnitude will cancel the effects of the first and refocus all spins, provided that no change of position, with respect to the direction of the gradient, has occurred. If there is a change of position, the refocusing will not be complete. This results in a remaining dephasing which is proportional to the displacement during the period Δ between the two gradients. Since diffusion is a random motion, there is a distribution of gradient-induced phase angles. These random phase shifts are averaged over the ensemble of spins contributing to the observed NMR signal. Hence, this signal is not phase shifted but attenuated, with the degree of attenuation depending on the displacement. In Ref. [1], this phenomenon is explained in more detail.

It is shown in Ref. [1] that the signal intensity $S(2\tau)$ after the total echo time 2τ is given by:

$$\begin{aligned} S(2\tau) &= S(0)\exp\left(-\frac{2\tau}{T_2}\right)\exp\left(-\gamma^2 g^2 D\delta^2\left(\Delta-\frac{\delta}{3}\right)\right) \\ &= S(2\tau)_{g=0}\exp\left(-\gamma^2 g^2 D\delta^2\left(\Delta-\frac{\delta}{3}\right)\right) \end{aligned} \tag{3}$$

where $S(0)$ is the signal intensity immediately after the 90° pulse, T_2 is the spin–spin relaxation time of the species, γ is the gyromagnetic ratio of the observed nucleus, g is the strength of the applied gradient, and δ and Δ are the length of the rectangular gradient pulses and the separation between them, respectively. Typically, δ is in the range of 0–10 ms, the diffusion time Δ is in the range of milliseconds to seconds, and g is up to 20 T/m [1].

To determine diffusion coefficients, a series of experiments is performed in which either g, δ, or Δ is varied while keeping τ constant to achieve identical attenuation due to relaxation. Normally, the gradient strength g is incremented in subsequent experiments. Non-linear regression of the experimental data can be used for the determination of D.

Nowadays, the BPPLED pulse sequence (see Figure 2) is most often used for measuring diffusion since it allows eddy currents to decay and uses bipolar gradients which enables double effective strength as well as compensation for imperfections. This sequence is not affected by spin–spin coupling since it is based on the stimulated echo sequence.

Graham A. Webb (ed.), Modern Magnetic Resonance, 135–143.
© 2008 *Springer.*

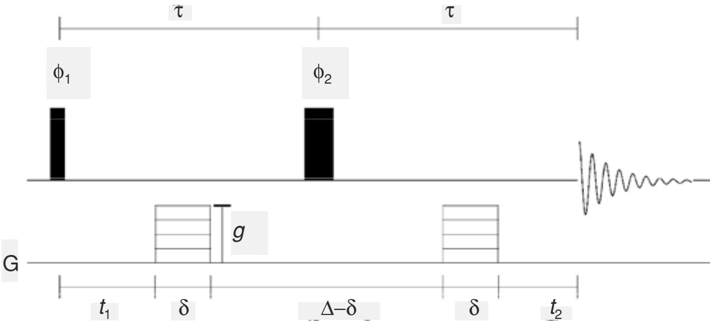

Fig. 1. The Stejskal and Tanner pulsed-field gradient NMR sequence. Narrow and wide filled bars correspond to 90° and 180° pulses, respectively. Open bars with horizontal stripes correspond to pulsed-field gradients whose strength is varied during the experiment. The pulse phases are $\phi_1 = x$ and $\phi_2 = y$. Phase cycling can be included to remove spectrometer artifacts.

The signal intensity of the BPPLED sequence is given by:

$$S = S_{g=0} \exp\left(-\gamma^2 g^2 D \delta^2 \left(\Delta - \frac{\delta}{3} - \frac{\tau_g}{2}\right)\right) \qquad (4)$$

Processing of Diffusion Data

In the chemical shift dimension(s), Fourier transformation (FT) is applied as usual. For each frequency ν, the signal can (in general) have contributions from several components $(1, \ldots n)$ which individually decay with their respective diffusion coefficient:

$$S(g, \nu) = \sum_{i=1}^{n} S_i(0, \nu) \exp\left(-\gamma^2 g^2 D_i \delta^2 \left(\Delta - \frac{\delta}{3}\right)\right) \qquad (5)$$

The individual diffusion coefficients D_i and the signal intensities $S_i(0, \nu)$ have to be extracted in order to construct the diffusion spectra. The name DOSY (diffusion ordered spectroscopy) refers to the presentation of the data obtained in PFG NMR measurements where the chemical shift is plotted in one (or two) dimension and the diffusion coefficient in the other dimension. This presentation allows the identification of signals belonging to one component (or at least to components showing the same diffusion coefficient). Because of this separation, DOSY can be considered as "non-invasive chromatography" [4].

Applications of Diffusion NMR

In PFG spin echo NMR experiments, the interesting observable variable is the diffusion coefficient, therefore, in principle, any phenomena that affects the diffusion coefficient can be studied with this technique. The concept behind the application to the study of molecular interactions is very simple and is based on the fact that the diffusion coefficient of a molecule is altered upon addition of another molecule if there is an interaction between them.

Diffusion NMR has been applied to the study of intermolecular interactions both qualitatively, to identify compounds that bind to a specific receptor in NMR screening

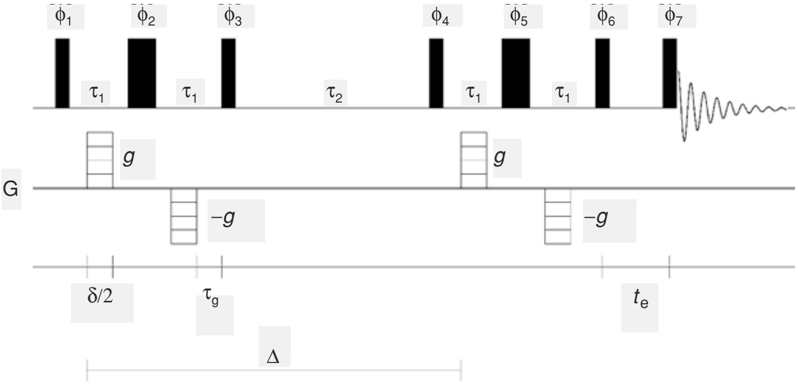

Fig. 2. The LED pulse sequence using bipolar gradients [3]. Narrow and wide filled bars correspond to 90° and 180° pulses, respectively. Phase cycling: $\phi_1 = \phi_2 = \phi_5 = x$; $\phi_3 = 2(x), 2(-x)$, $\phi_4 = \phi_7 = 4(x), 4(-x), 4(y), 4(-y)$; $\phi_6 = x, -x, x, 2(-x), x, -x, x, y, -y, y, 2(-y), y, (-y), y$.

or in studies related to host–guest chemistry [5–8], and quantitatively, in the determination of association constants [9–12] and complex or aggregate sizes [13–18].

For binding and screening studies it is usually sufficient to identify compounds that bind to a certain receptor from a mixture of non-binding compounds, or to establish a relative binding affinity, but the determination of association constants or size requires quantitative determination of the diffusion coefficients with precision and accuracy. A very comprehensive work about the factors that affect data quality in PFG spin echo NMR methods for chemical mixture analysis was published recently by Antalek [19], both data acquisition (including a discussion about experimental conditions and available pulse programs) and data analysis were considered in detail by the author. This chapter complements well the previous work of Price on the experimental aspects of PFG spin echo NMR [2]. After completing this article, an outstanding and comprehensive review on NMR diffusion experiments by Cohen *et al.* has been published [20].

Size and Shape Determination by Diffusion Measurements

Since diffusion NMR allows spectral resolution by size or shape, and this resolution being especially visible in DOSY experiments, it is not surprising that the qualitative or semi-quantitative application of DOSY to the distinction of compounds according to their size is one of the most popular [21]. Examples of this type of application of DOSY can be found in many diverse areas such as in the characterization of polymer additives [22], hydrocarbon mixtures [23], in food chemistry [24,25], or carbohydrate mixture analysis [26,27], just to name a few examples. If some cautions are taken, the experimental diffusion coefficients can be used to obtain quantitative information about the size and shape of a molecule or a particular assembly.

As was already mentioned, the connection between the diffusion coefficient (D) and structural properties arises because diffusion coefficients depend on friction factors (f) which are associated with the molecular size and the viscosity of the solution. The Stokes–Einstein equation [Equation (1)] relates the translational self-diffusion coefficient at infinite dilution of a spherical particle to its hydrodynamic radius r_S, and in spite of the difficulty to justify this equation at a molecular level [28], its simplicity and success in relating experimental diffusion coefficients to molecular radii is the basis for its extensive use in the literature. Examples of the application of experimental diffusion coefficients and the Stokes–Einstein equation for size determination can be found in fields ranging from organometallic chemistry to biochemistry. This relation is usually also the starting point for the development of other models that connect the diffusion coefficient with shapes different from spherical and to expressions related to the molecular weight of the diffusing species.

A simple but very elucidative example is the characterization of THF solvated n-butyllithium aggregates by DOSY [29]. Diffusion ordered spectroscopy was used to distinguish the tetrasolvated dimeric and tetrasolvated tetrameric aggregates (see Figure 3) in THF solution. Theoretical diffusion values for the dimer and tetramer, calculated from the Stokes–Einstein equation, predict measurable differences in diffusion coefficients. For the calculation of the theoretical diffusion the viscosity of neat THF was used, and the hydrodynamic radii were determined from molecular volumes based on crystal structures and gas-phase minimized structures. A good agreement between experimental diffusion coefficients and theoretical values was obtained [29].

As was shown by Waldeck *et al.* [30], by considering the relation between the Stokes radius of a molecule (r_S), its experimentally determinable partial specific volume, V, and its molecular weight, M, a useful expression relating diffusion to molecular weight can be derived:

$$\frac{D_1}{D_2} = \sqrt[3]{\frac{M_2}{M_1}} \tag{6}$$

This general relationship shows that for "ideal" spherical models there is a reciprocal cube dependence of the diffusion coefficient on molecular weight and this allows the calculation of a set of theoretical diffusion coefficients using a reference diffusion (experimental) value. It is therefore worth considering when accounting for the effect of molecular association on the apparent diffusion coefficient, expected to be measured in an experiment.

Another impressive example of the applicability of the Stokes–Einstein equation is found in a study dealing

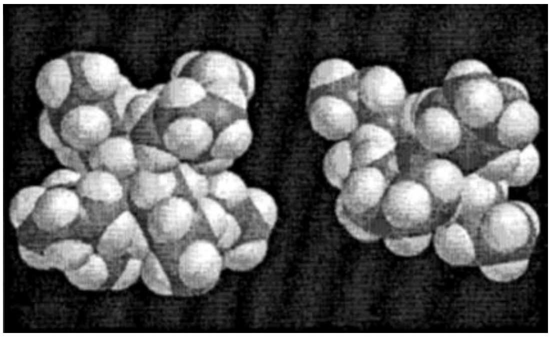

Fig. 3. PM3 optimized structures of $[n\text{-BuLi}]_4{\cdot}\text{THF}_4$ and $[n\text{-BuLi}]_2{\cdot}\text{THF}_4$. Reprinted with permission from Ref. [29]. Copyright (2000) American Chemical Society.

with ubiquitin [32]. The hydrodynamic radius of this protein was calculated from its diffusion coefficient determined by DOSY-HSQC experiments using an accurately calibrated temperature and the viscosity calculated for this temperature. Using Equations (1) and (2) yielded $r_S = 15.8$ Å. Furthermore, the NMR structure of ubiquitin [33] was used for the calculation of its size, which was then converted to $r_S = 16.3$ Å, which is in reasonably good agreement with the value found in DOSY experiments. Thus, the numerical factor 6 given in Equation (2) also holds true for complex situations such as a protein in aqueous solution. This demonstrates that the assumption of a spherical solute moving in a continuous solvent is fulfilled fairly well in this case, which can be verified by inspecting Figure 4.

The field of organometallic chemistry provides several examples of the application of diffusion measurements for size determination, since this is one of the fields where the use of diffusion NMR is becoming more and more popular. Pregosin is among the leaders in the application of PFG diffusion methods in organometallic chemistry and his contributions and perspectives about the technique as well as the most important applications in this field have been the subject of several publications [34].

^{13}C detected DOSY was used by Schlörer *et al.* to study the unstable intermediate **(2)** in the reaction of CO_2 with $[Cp_2Zr(Cl)H]$ **(1)** (see Scheme 1) which was impossible to characterize by other means [35]. $^{13}CO_2$ was used for the reaction which was observed *in situ* by ^{13}C NMR. Following the formation of sufficient amounts of **2**, the mixture has been cooled to −78°C, and ^{13}C INEPT DOSY spectra were recorded. The intermediate **2** was shown to have a smaller diffusion coefficient than the mononuclear complex **3** (see Figure 5) and was therefore proven to be binuclear. Furthermore, its hydrodynamic radius calculated from the experimental results was found to be in good agreement with an estimation based on a minimized gas-phase structure.

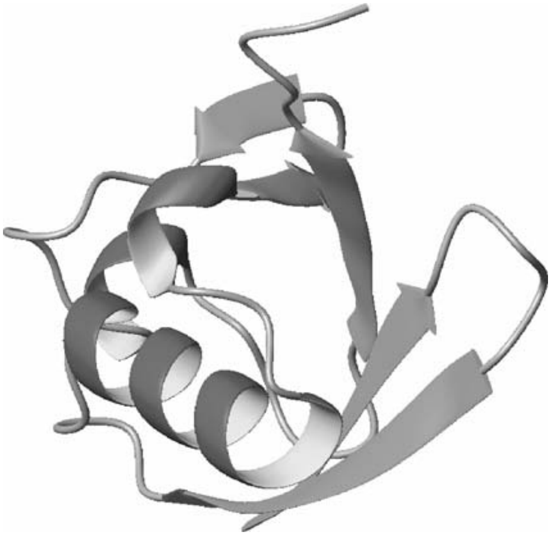

Fig. 4. Schematic representation of the three dimensional structure of ubiquitin. The structure presented here is taken from the data set “1D3Z” [33] in the pdb data bank [31]. (See also Plate 9 on page XXI in the Color Plate Section.)

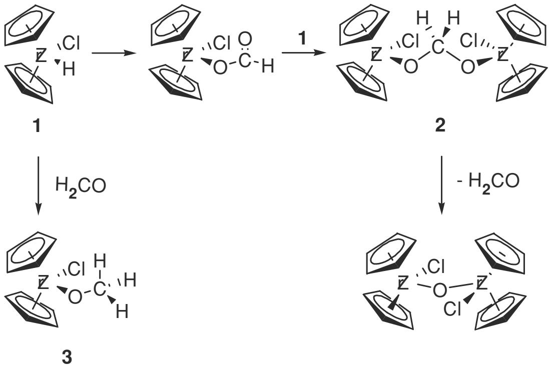

Scheme 1. The reaction of $[Cp_2Zr(Cl)H]$ **(1)** with CO_2 [35].

Still in the field of ionic interactions, a very recent paper from the group of Pregosin explored the application of PGSE NMR studies within the context of chiral cation/anion recognition [36]. According to the authors, this is the first reported example that shows that the diffusion data are sensitive enough to recognize a subtle diastereomeric structural effect on ion translation. The work investigated the dependence of the diffusion value on the diastereomeric structure of the ion pair for chiral organic salts (see Scheme 2). Investigated were the pairs of diastereomers formed between two novel chiral hexacoordinate phosphate anions, known to induce efficient NMR chiral-shifts, and chiral quaternary ammonium cations. Diffusion constants were determined for the salts [**6**][Δ**-4**], [**6**][Δ**-5**], [**6**][PF_6], [**7**][Δ**-4**], [**7**][Δ**-5**], and [**7**][PF_6] at different concentrations and in chloroform, dichloromethane, acetone, and methanol. To facilitate the comparison of results, hydrodynamic radii derived from the Stokes–Einstein equation, using the viscosity of the non-deuterated solvents, were calculated. The methanol data were employed to estimate the size of solvated and independently moving anions and cations. For the cations in methanol, the r_S values were found to be independent of the anion (5.2–5.3 Å for **6** and 5.0 Å for **7**). The values for the anion Δ**-5** are 7.0 Å both in [**6**][Δ**-5**] and [**7**][Δ**-5**], whereas for PF_6^- the values are 2.7 Å in [**6**][PF_6^-] and 2.6 Å in [**7**][PF_6^-] in agreement with previous results for other salts of PF_6^- from the same group [37,38].

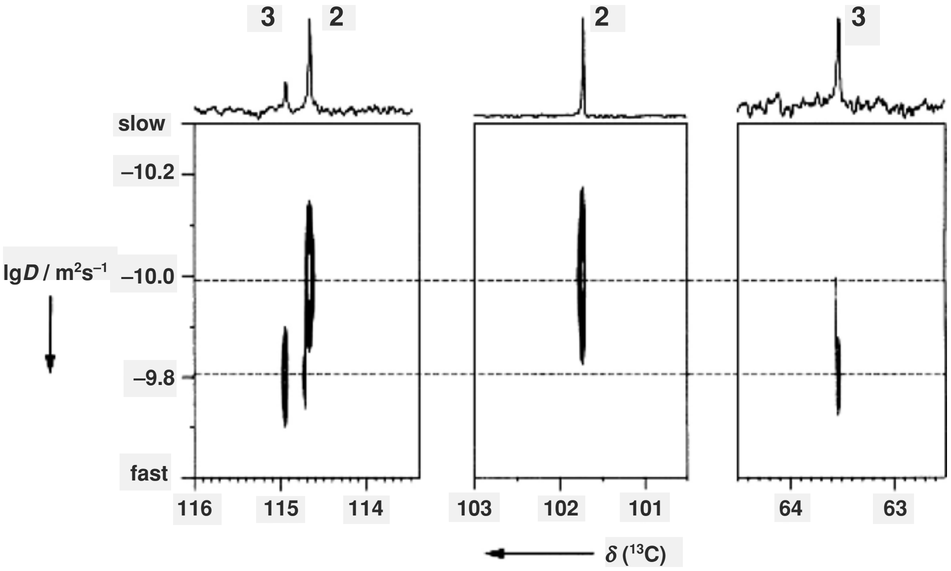

Fig. 5. 100 MHz ^{13}C INEPT DOSY spectrum obtained during the reaction of **1** with $^{13}CO_2$ at –78 °C in [D_8] THF. The sections show the signals of **2** (δ_C = 114.6 ppm (Cp) and 101.7 ppm (CH_2)) and **3** (δ_C = 114.9 ppm (Cp) and 63.5 ppm (OCH_3)). See Scheme 1 for the chemical structure of **1**, **2**, and **3**. Figure taken from Ref. [35]. Reproduced with permission of John Wiley & Sons Limited.

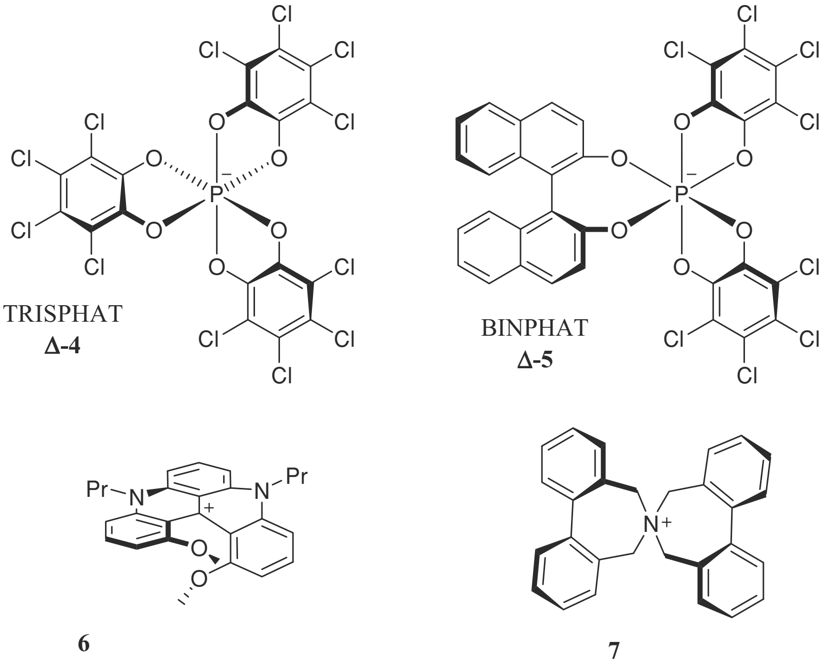

Scheme 2. Chiral anions and cations investigated by Pregosin and coworkers [36].

Internal Standards for Diffusion Measurements

The direct determination of hydrodynamic radii, and thus size, through the Stokes–Einstein equation requires a knowledge of the solution viscosity at the measurement temperature. Additionally, in order to have accurate information about size in studies related to molecular interactions where the comparison of diffusion coefficients obtained in different conditions is usual, it is crucial to be able to separate contributions due to changes in viscosity and effective changes in hydrodynamic radii.

In PFG NMR, two major approaches are frequently used to avoid additional experimental work to measure the viscosity of the solution. The simplest approach is to consider that the viscosity of the solution is approximately the same as the viscosity of the pure non-deuterated solvent. This approximation has been shown to be legitimate in a number of cases, especially when considering pure solvents and diluted solutions and some examples have already been mentioned above for the determination of hydrodynamic radii of, *n*-butyllithium aggregates [29] and solvated anions and cations [36] but many more can be found in the literature. In complex solutions it may be more difficult to obtain a value for the viscosity of the exact solvent mixture, and in these cases the interpretation of size or molecular mass derived from diffusion data has to take into account the validity of the approximations made and the possibility of under/over valuating the viscosity.

The other solution to the problem is the back calculation of the solution viscosity, through the Stokes–Einstein equation, by using the diffusion measured for a non-interacting reference compound of known hydrodynamic radius. This internal probe should be of similar size with respect to the molecules of interest so that it experiences a similar microscopic environment and can act as an internal viscosity standard. The use of such a standard allows the estimation of size even in complex solution mixtures and the comparison of diffusion coefficients in series of experiments where the composition of the solution is altered, a situation that commonly arises in studies related to molecular interactions. The use of a diffusion standard allows one also to separate the contributions due to changes in viscosity and effective changes in hydrodynamic radii even if the hydrodynamic radius of the standard is not known. In fact, the ratio of the diffusion of a particular solute and the reference compound will be independent of the viscosity ($D/D_{\text{ref}} = r_{\text{Sref}}/r_{\text{S}}$) and relative information about changes in hydrodynamic radius can be obtained when comparing ratios measured in different conditions.

This procedure is well exemplified in a study by Cabrita *et al.* where tetramethylsilane (TMS) was used as a standard for the diffusion measurements to account for viscosity changes, and was proposed as a reference for the study of intermolecular interactions involving hydrogen bonds in organic solutions [14]. Kapur *et al.* [39] have shown that DOSY can be a useful technique for the qualitative study of the relative strengths of hydrogen bonds in solution. Since the formation of an intermolecular H-bond leads to a decrease of the diffusion coefficient of a certain molecule, the relative decrease in the diffusion coefficient of a particular molecule in a mixture of molecules, interacting by H-bond with a common H-bond acceptor or donor, was interpreted in terms of the tendency for the molecules in the mixture to be involved in association by H-bonds with the H-bond donor or acceptor. As an example, it was shown that when dimethylsulfoxide (DMSO), a strong H-bond acceptor, is added to a solution containing phenol **(8)** and cyclohexanol **(9)**, two molecules with a similar shape, a higher relative decrease in the diffusion coefficient of phenol was observed. This different behavior was attributed to the greater tendency of phenol to be involved in H-bonding with DMSO, since phenol is more acidic than cyclohexanol [39].

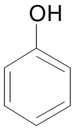

8

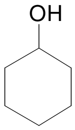

9

Binding, Screening, and Determination of Association Constants

In the previous section, we have shown examples of applications that explore the relation between size and diffusion coefficient primary as a source of information on molecular size. However, this relation can be explored in a different way in order to get information about the strength of intermolecular interactions. The majority of the reports on the application of diffusion NMR to the study of intermolecular interactions deal with the alteration of the diffusion coefficient due to binding phenomena in solution. In fact, when a small molecule binds to a large receptor, its diffusion coefficient may decrease more than one order of magnitude. This means that at least for some time the small molecule will have the diffusion coefficient of the large receptor, and if we consider the fast exchange limit, its observed diffusion coefficient (D_{obs}) is described by:

$$D_{\text{obs}} = f_{\text{free}} D_{\text{free}} + f_{\text{bound}} D_{\text{bound}} \tag{7}$$

where f and D denote the molecular fractions and diffusion coefficients of the free and bound molecule. If the difference in size is large enough, it can be assumed that the diffusion coefficient of the receptor or host (D_{H}) is not greatly modified and that D_{bound} is the same as the D_{H} alone. This relation is the starting point for the majority of the diffusion NMR-related binding studies.

In this field two main lines of application can be identified, one more qualitative, related to the screening of complex mixtures or individual molecules, usually with the aim of identifying potential new drug compounds, and another, more quantitative, concerned with the determination of association constants.

A recent example of the first type of application mentioned above is the binding of cholchicine **10** to α/β tubulines, which is of large interest in cancer-related studies.

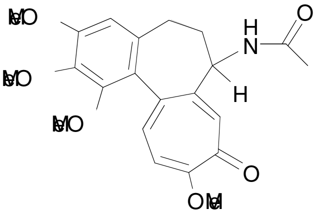

10

For this reason, a model peptide containing the 12 C-terminal residues of α-tubulin (VEGEGEEEGEEY) was investigated with respect to the pH dependence of the binding to **10** [40]. Although binding studies on this system have only been computational using docking programs, it was shown in the diffusion studies that the model peptide adopts different conformations depending on the pH, this being reflected by different observed diffusion constants. In this work, NOE data have also been used, but only for determining the conformation of the single peptide.

The determination of association constants (K_a) from NMR data has been recently reviewed by Fielding [9] with a section dedicated to diffusion experiments. The starting point for the determination of the association constant is Equation (7) and the mathematical treatment to get K_a from D_{obs} is exactly the same as for any other NMR observable, such as δ_{obs}. As Fielding points out in his review, the advantage of measuring D_{obs} instead of δ_{obs} is that the diffusion coefficient of the host–guest complex can be assumed to be the same as that of the non-complexed host molecule, thus reducing one unknown in Equation (7). In principle, this allows one to determine K_a within a single experiment and without the need of titrations, as exemplified below. The formation of a host–guest complex of stoichiometry 1:1 is described by:

$$K_a = \frac{[HG]}{[H]\,[G]} \tag{8}$$

$$D_{obs} = f_G D_G + f_{HG} D_{HG} \tag{9}$$

where [HG], [H], and [G] are the equilibrium concentrations of the host–guest complex, host, and guest, respectively and f_G and f_{HG} are the molar fractions of non-complexed guest and complex, respectively. From Equation (9) it follows that:

$$f_{HG} = \frac{D_G - D_{obs}}{D_G - D_{HG}} \tag{10}$$

If, as it was mentioned earlier, D_{HG} is assumed to be the same as the measurable diffusion coefficient of the host (D_H), then f_{HG} can easily be determined. Accounting for mass balance and combining Equations (8) with (10), we arrive to the expression for the association constant:

$$K_a = \frac{f_{HG}}{(1 - f_{HG})([H]_0 - f_{HG}[G]_0)} \tag{11}$$

where $[H]_0$ and $[G]_0$ represent the total concentrations of host and guest, respectively.

The procedure before is straightforward and examples of its application can be found in recent literature related to host–guest chemistry studies [12,41]. Rather than exemplifying the examples in detail here, we prefer to take a closer look at the limitations of the approximation that $D_{HG} = D_H$.

The assumption that $D_{HG} = D_H$ is valid for the majority of studies involving small molecules binding to macromolecules (typically biological), but may not necessarily be true for smaller host molecules usually employed in host–guest chemistry studies. To test the assumption that $D_{HG} = D_H$ for a typical medium-sized host molecule, Cameron *et al.* [10] have studied the β-cyclodextrin **(11)** complexes of cyclohexylacetic acid **(12)** and cholic acid **(13)**. They have shown that caution should be taken when determining the association constant by the single experiment method, and have employed a data treatment which takes into account the diffusion of all species. With this treatment, the ^{1}H NMR chemical shift titration method and the diffusion coefficient method give the same results for K_a.

Simova and Berger presented a comparison of DOSY experiments and chemical shift titrations with respect to the determination of association constants [42]. The authors investigated camphor and cyclodextrins (CD) in D_2O. They showed that precise association constants are more easily determined by chemical shift titration. Diffusion measurements using HR-DOSY allow easy determination of the complex composition at different concentration ratios and an estimation of the binding energy if a viscosity reference, in this case tetramethylammonium bromide, is present. Linear dependence of the diffusion coefficients on the molecular mass of free and associated CD has been observed (see Figure 6). The solution structures of α- and β-CD complexes of camphor in D_2O were deduced from intermolecular cross-relaxation data obtained by using the ROESY sequence. Different preferential orientation in the 2:1 α-CD and 1:1 β–CD species have been derived in contrast to the weak 1:1 complex

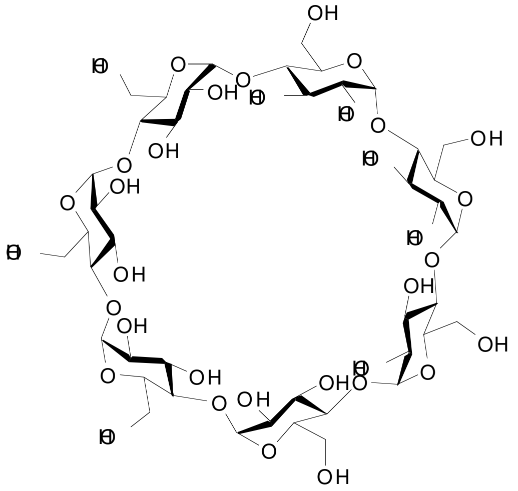

11

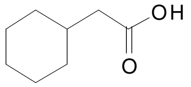

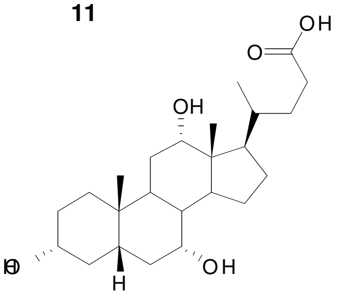

12

13

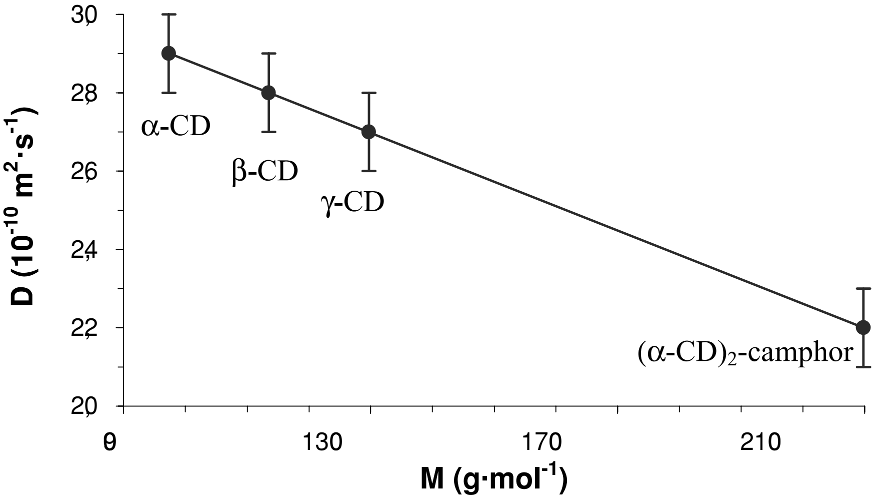

Fig. 6. Dependence of the diffusion coefficients of cyclodextrins and the α-CD complex of camphor on the molecular mass [42].

with γ-CD. Proton NMR chemical shift values proved to be much more sensitive to diastereomeric complex formation than are diffusion coefficients.

References

1. Price WS. Concepts Magn. Reson. 1997;9:299.
2. Price WS. Concepts Magn. Reson. 1998;10:197.
3. Wu D, Chen A, Johnson CS Jr. J. Magn. Reson. A. 1995;115:260.
4. Huo R, Wehrens R, van Duynhoven J, Buydens LMC. Anal. Chim. Acta. 2003;490:231.
5. Meyer B, Peters T. Angew. Chem. Int. Ed. 2003;42:864.
6. Shapiro MJ, Wareing JR. Curr. Opin. Drug Discov. Devel. 1999;2:396.
7. Avram L, Cohen Y. Org. Lett. 2002;4:4365.
8. Avram L, Cohen Y. J. Am. Chem. Soc. 2002;124:15148.
9. Fielding L. Tetrahedron. 2000;56:6151.
10. Cameron KS, Fielding L. J. Org. Chem. 2001;66:6891.
11. Wimmer R, Aachmann FL, Larsen KL, Petersen SB. Carbohydr. Res. 2002;337:841.
12. Avram L, Cohen Y. J. Org. Chem. 2002;67:2639.
13. Price WS, Tsuchiya F, Arata Y. J. Am. Chem. Soc. 1999;121:11503; and references therein as an example of the application to the study of protein aggregation.
14. Cabrita EJ, Berger S. Magn. Reson. Chem. 2001;39: S142.
15. Cameron KS, Fielding L. J. Org. Chem. 2001;66:6891.
16. Valentini M, Pregosin PS, Rüegger H. Organometallics. 2000;19:2551.
17. Zuccaccia C, Bellachioma G, Cardaci G, Macchioni A. Organometallics. 2000;19:4663.
18. Timmerman P, Weidmann J-L, Jolliffe KA, Prins LJ, Reinhoudt DN, Shinkai S, Frish L, Cohen Y. J. Chem. Soc. Perkin Trans. 2000;2:2077.
19. Antalek B. Concepts Magn. Reson. 2002;14:225.
20. Cohen Y, Avram L, Frish L. Angew. Chem. 2005;117: 524.
21. Johnson CS Jr. Prog. NMR Spectrosc. 1999;34:203.
22. Jayawickrama DA, Larive CK, McCord EF, Roe DC. Magn. Reson. Chem. 1998;36:755.
23. Kapur GS, Findeisen M, Berger S. Fuel. 2000;79:1347.
24. Gil AM, Duarte I, Cabrita E, Goodfellow BJ, Spraul M, Kerssebaum R. Anal. Chim. Acta. 2004;506:215.
25. Nilsson M, Duarte IF, Almeida C, Delgadillo I, Goodfellow BJ, Gil AM, Morris GA. J. Agric. Food Chem. 2004;52:3736.
26. Schraml J, Blechta V, Soukupová L, Petráková E. J. Carbohydr. Chem. 2001;20:87.
27. Diaz MD, Berger S. Carbohydr. Res. 2000;329:1.
28. Walser R, Mark AE, van Gunsteren WF. Chem. Phys. Lett. 1999;303:583.
29. Keresztes I, Williard PG. J. Am. Chem. Soc. 2000;122: 10228.
30. Waldeck AR, Kuchel PW, Lennon AJ, Capman BE. Prog. NMR Spectrosc. 1997;30:39.
31. Berman HM, Westbrook J, Feng Z, Gilliland G, Bhat TN, Weissig H, Shindyalov IN, Bourne PE. Nucleic Acids Res. 2000;28:235.
32. Brand T, Cabrita EJ, Morris GA, Berger S. (in preparation).
33. Cornilescu G, Marquardt JL, Ottiger M, Bax A. J. Am. Chem. Soc. 1998;120:6836.
34. Valentini M, Rüegger H, Pregosin PS. Helv. Chim. Acta. 2001;84:2833; and references therein.
35. Schlörer NE, Cabrita EJ, Berger S. Angew. Chem. Int. Ed. 2002;41:107.
36. Martínez-Viviente E, Pregosin PS, Vial L, Herse C, Lancour J. Chem. Eur. J. 2004;10:2912.
37. Kumar PGA, Pregosin PS, Goicoechea JM, Whittlesey MK. Organometallics. 2003;22:2956.
38. Martínez-Viviente E, Pregosin PS. Inorg. Chem. 2003;42: 2209.
39. Kapur GS, Cabrita EJ, Berger S. Tetrahedron Lett. 2000;41: 7181.
40. Pal D, Mahapatra P, Manna T, Chakrabarti P, Bhattacharyya B, Banerjee A, Basu G, Roy S. Biochemistry. 2001;40:512.
41. Frish L, Sansone F, Casnati A, Ungaro R, Cohen Y. J. Org. Chem. 2000;65:5026.
42. Simova S, Berger S. Journal of Inclusion Phenomena and Macrocyclic Chemistry. J. Incl. Phenom. (in press).

Host–Guest Chemistry

Part I

Solid-State NMR in Host–Guest Chemistry

John A. Ripmeester and Christopher I. Ratcliffe
Steacie Institute for Molecular Sciences, National Research Council Canada, Ottawa, ON, Canada K1A 0R6

Introduction

This contribution will focus on the use of NMR spectroscopy to study host–guest chemistry in the solid state. NMR spectroscopy already is a well-established approach for the study of complex formation in solution, for instance, for measurement of equilibrium constants and stoichiometry. In the solid state, guest–host chemistry is a rather more complex issue, as the materials in question range from molecular receptor–guest complexes that have crystallized, to extended framework materials that have cavities, channels, and interlamellar void space which may or may not be easily accessible to guest species. Examples of the first instance are crown ether and cyclodextrin complexes. For the latter, many diverse organic and metal-organic materials have been constructed using the principles of supramolecular chemistry and crystal engineering to assemble frameworks out of building blocks. On the inorganic side, there are zeolites, clathrate hydrates, clathrasils and zeosils, aluminum phosphates (ALPOs), metal cyanides and oxides, clays, carbons (graphite, nanotubes), and mesoporous materials such as the siliceous MCMs, and related materials. Details on all these different kinds of host–guest materials can be found in the series Comprehensive Supramolecular Chemistry [1]. NMR spectroscopy can contribute a great deal to understanding the structure and properties of such host–guest materials, as also reviewed in a chapter in Vol. 8 of the aforementioned series and references therein [2]. The topic of host–guest materials is a very broad area with an extensive literature, and for this reason and the limited length of this chapter we have chosen to illustrate with examples largely from our own work and to refer the interested reader to more extensive reviews.

In the study of solid-state host–guest chemistry, the problems that stand out are the accurate determination of the host structure, the location and orientation of the guest, and the understanding of specific interactions that lead to molecular recognition and selective adsorption or inclusion. This also includes the understanding of the electronic structure as obtainable from the chemical shift. Applications include gas separation and storage, shape-selective catalysis, molecular sensing, drug delivery, and a variety of systems have been developed that are meant to mimic processes in biology in their entirety or in part, for instance, biocatalysis involving enzymes, ion channels, etc. [1,2].

The Solid-State Spectrum

The main interactions that dominate the NMR lineshape in the solid state include the nuclear dipolar interaction, giving information on the distance between magnetic nuclei (up to ~0.8 nm), chemical shielding, giving information on the electronic structure, and the quadrupolar interaction, which is determined by the interaction of the nuclear electric quadrupole with the electric field gradient at the nucleus [3]. Occasionally J-coupling also has an influence. In many if not most cases, several or all of these interactions are present simultaneously. Since all have a spatial dependence (interactions described by second rank tensors), the solid-state NMR lineshape in powdered materials is broad and complex. Most materials have a number of inequivalent atoms, so the selective elimination of some of the interactions in order to obtain high-resolution spectra was a major focus in the NMR spectroscopy of solids for many years. The most commonly used techniques include high power decoupling (HPDEC), generally to eliminate dipolar couplings to abundant spins such as protons, magic angle spinning (MAS), which can reduce dipolar couplings as well as the anisotropic chemical shift [4], and combinations of pulse schemes and spinning to separate chemical shifts and quadrupolar couplings (MQMAS) [5]. Recently, much effort has been expended into re-introducing dipolar couplings into high-resolution spectra to make use of these to measure a variety of internuclear distances [6].

Unfortunately, the spectroscopy of the ubiquitous ^{1}H is rather difficult, as its chemical shift scale is small and homonuclear dipolar couplings dominate the resonance lines which are often very broad. A number of multiple pulse schemes have been developed to give a measure of high resolution [7], and the more recent developments in fast MAS have proved to be particularly powerful [8]. Especially in soft materials such as polymers and biosolids the use of fast MAS has allowed applications of many of the techniques that are routinely used in solution NMR to derive information on structure in the solid state [9].

Graham A. Webb (ed.), Modern Magnetic Resonance, 147–154.
© 2008 *Springer.*

As the design of organic and metal-organic guest–host systems is a heavily researched topic today, many applications deal with the use of ^{13}C NMR spectroscopy in the solid state, which is easily accessible to most researchers, and the interpretation of the spectrum is relatively straightforward. The approaches used are similar to those applied to a number of other spin $^{1}/_{2}$ nuclei (^{15}N, ^{31}P, ^{29}Si), as in all of these cases dipolar couplings are mainly heteronuclear, often to ^{1}H, and can be removed by HPDEC. The use of 2D techniques such as HETCOR and WISE are able to provide information on H atoms that are attached to the above spin $^{1}/_{2}$ nuclei with a measure of resolution that can be considerably greater than the ^{1}H spectrum itself.

General Characterization

One of the first things to realize is that some very simple NMR experiments can provide a great deal of information in the characterization of a host–guest material. For example ^{13}C cross-polarization (CP) and MAS are frequently used to determine which guests are taken up by the host and HPDEC/MAS can be used to quantify the relative amounts of host and guest by comparing intensities of distinct lines (This can also be done with CP provided the CP behavior is calibrated for different resonances). Quite often the question with new materials is simply whether the guest is indeed included, and this can be confirmed by CP/MAS since it detects only material in the solid state, even in the presence of excess gaseous or liquid guest, which is sometimes necessarily present to keep the complex stable. The presence of dynamics can also be established using the dipolar dephasing CP/MAS experiment, since, while only quaternary carbons should appear in this spectrum, non-quaternaries will appear with reduced intensity if their C–H dipolar interactions are considerably reduced by dynamics. ^{13}C chemical shifts have been used to determine conformations, e.g. in crown ethers the methylene shifts relate to torsional angles [10]. Chemical shifts can also be used to identify products in "ship-in-a-bottle" type synthesis, e.g. ^{31}P NMR of P_4S_n ($n = 3 - 7$) synthesized inside zeolites [11] and ^{13}C of organics in zeolites, or to show the existence of unusual or unstable species which are stabilized by inclusion, e.g. a novel P_4S_4 isomer in zeolite [11], Na^- and diamagnetic metal clusters in zeolites [12]. The NMR of metal nuclei such as ^{113}Cd and ^{63}Cu has been used to determine local environments and connectivities in metal cyanide host lattices [13,14], e.g. ^{113}Cd shifts reflect the numbers of C and N atoms attached to tetrahedrally coordinated Cd, with CdC_4 to low field ranging to CdN_4 at high field; quadrupolar effects on ^{63}Cu lineshapes indicate whether its environment is strictly tetrahedral (isotropic line), or slightly distorted CuC_4 (2nd order lineshape) or very distorted CuC_3N (too broad to detect); J-couplings can show connectivities, e.g. ^{63}Cu–$^{13}C_4$ or ^{67}Zn–$^{15}N_4$. Chemical shift and quadrupolar lineshapes (and corresponding asymmetry parameters) also reflect the local crystal symmetry, providing another link to structure, e.g. ^{77}Se NMR of H_2Se clathrate hydrate distinguishes between H_2Se in the small spherical cage (isotropic line) and the oblate larger cage (axially anisotropic line), Figure 1 [15]. Chemical shifts can also be sensitive to the presence of other guests in the same or in neighboring cavities, e.g. ^{129}Xe in Dianin's compound [16]. Similarly, quadrupolar nuclei can be particularly sensitive to loss of local crystal symmetry when guests are removed from neighboring cages, e.g. ^{23}Na in the cages of silicon clathrates [17].

Structural Information from Spin $^{1}/_{2}$ Nuclei

Organic and Metal-Organic Hosts

NMR spectroscopy is primarily a local order technique, which makes it a particularly strong ally to X-ray crystallography, which is a technique that depends on the presence of long-range order. However, the ^{13}C spectrum is sensitive not only to the presence of chemical inequivalence, but also to crystallographic inequivalence. For most materials, the ^{13}C NMR spectrum should confirm the asymmetric unit as determined by diffraction. Hence, in many cases ^{13}C NMR spectroscopy provides a rapid way of detecting structural similarities or differences in guest–host materials with a common host lattice: the spectrum gives a quick assessment of the content of the asymmetric unit, a very useful piece of information before attempting a complete structural determination [18]. This is also particularly useful when dealing with issues of polymorphism or pseudo-polymorphism [19].

In the presence of disorder, which may be dynamic, there may be disagreements between diffraction and NMR, usually with more line splittings in the NMR spectrum than one would expect based on the determined asymmetric unit. This means that either locally, or even on a larger scale, the symmetry of the lattice is lower than expected. For instance, in Dianin's compound with *p*-xylene as guest there are many more splittings than one would expect from the X-ray symmetry, from which the cavity where the *p*-xylene resides has three-fold symmetry and an inversion center [20]. However, the *p*-xylene is statically disordered so that each cage has lost its three-fold axis and inversion center. Since the disorder is not correlated throughout the lattice, it is spatially averaged, which gives a high symmetry in X-ray diffraction, and NMR sees the local symmetry, which is far lower. A different situation exists for the compound of calixarene

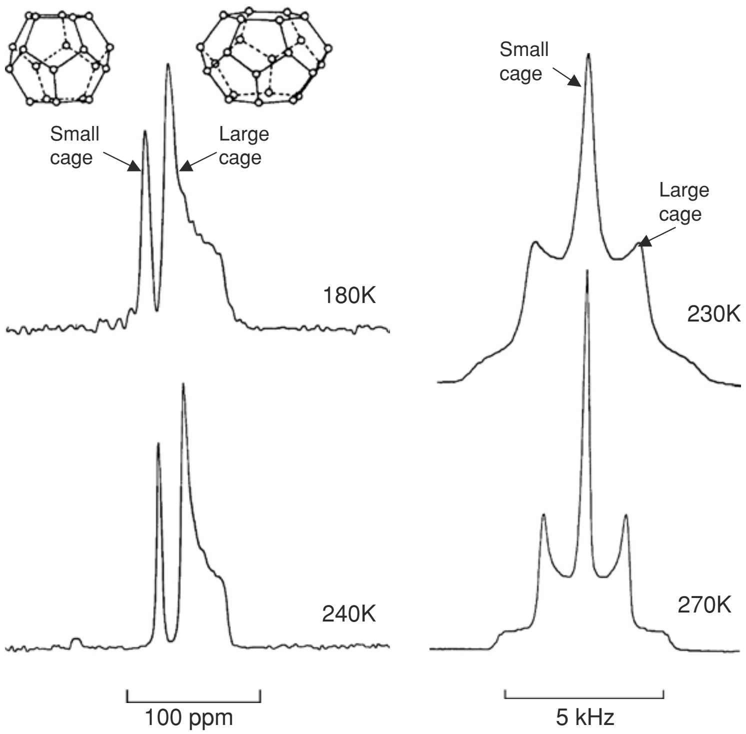

Fig. 1. Symmetry and dynamics in hydrogen selenide structure I clathrate hydrate: ^{77}Se NMR of $H_2Se/7H_2O$ (left) and ^{2}H NMR of $D_2Se/7D_2O$ (right). The spherical small cage gives rise to isotropic lineshapes, whereas the oblate large cage gives axially symmetric ^{77}Se chemical shift anisotropy and ^{2}H quadrupolar lineshapes. The intensities of the two components give the relative cage occupancies. The lines are considerably narrower than the static lineshapes due to rapid reorientation of the guest molecule. The broadening and reduced sharpness of the features, especially of the ^{2}H lineshape, as temperature decreases is due to freezing out of the host–water reorientational motions.

with toluene [21]. NMR spectroscopy shows a symmetry lowering transition to occur at ∼250 K, which is not seen by X-ray diffraction (Cu radiation), Figure 2. However, when shorter wavelength Mo radiation is used, the lower symmetry phase is indeed observed. This can be understood in terms of the volume over which the ordered lattice is coherent. Cu radiation requires a larger volume than Mo, so when using the longer wavelength the spatial averaging inherent in diffraction again shows the lattice to be of higher symmetry than it actually is [22].

As in solution, in the solid state it is possible to use complexation-induced shifts. For instance, guest nuclei that deeply penetrate into the cavity of calix[4]arene are deshielded by ring current effects from four aromatic rings, which can give ^{13}C methyl resonances a high field shift of up to ∼6 ppm [21]. Of course, these may be modified by dynamic processes that involve exchange of methyl groups over different sites. The fact that the toluene methyl has a much larger shift than pentane methyls (with the methyls equivalent) suggests that the pentane molecule can invert itself in the cavity. The X-ray structure shows that there are two positions for the methyl groups of the pentane that are quite different (one in–one out), so that the two methyl groups indeed must exchange between the two positions. This approach has allowed the determination of the order of preference of a variety of moieties for occupancy of the deep cavity in calix[4]arene; generally methyls, methylenes, methines, and hydroxyls are preferred over halogens [23].

Inorganic Hosts

Some of the best-known inorganic host materials are the zeolites. In this case, ^{29}Si NMR spectroscopy has allowed the measurement of the distribution of Si and Al in the lattice, as Si with 0–4 Al nearest neighbors are easily distinguished [24]. Since Al is a quadrupolar nucleus, the Si lines are rather broad, so that further distinctions of inequivalence are not possible. However, on going to an all Si lattice it becomes possible to obtain extremely high resolution spectra, where it is possible to measure through-bond connectivity (COSY), as well as all inter-Si distances less than ∼0.7 nm [25]. A recent example, using a symmetry-based dipolar recoupling scheme has shown that complete three-dimensional structures can be traced out [26].

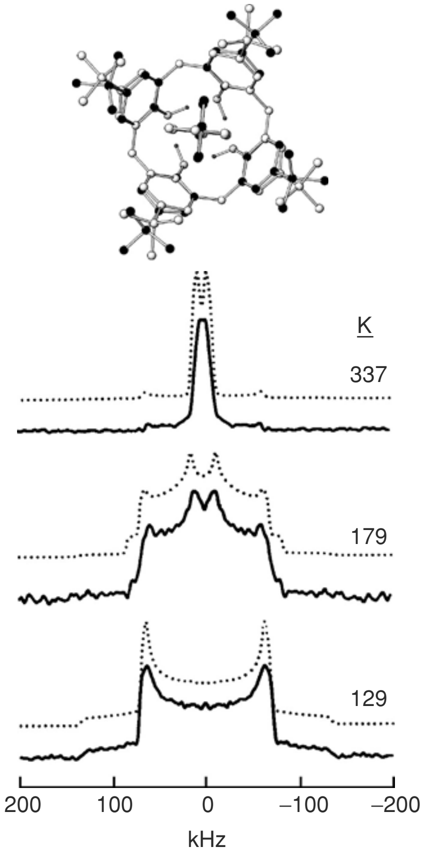

Fig. 2. ^{2}H NMR lineshapes of toluene-d_5 in *t*-butylcalix[4]arene. At 129 K the toluene is static, at 179 K it is undergoing rapid 180° rotations about the molecular axis, and at 337 K it has rapid four-fold reorientation. The weak broader line visible in the 337 K spectrum is from the para-deuteron, which lies along the axis and is largely unaffected by the motion. The switch from two-fold to four-fold motion of the guest is associated with a phase transition at 248 K. In the low temperature phase, the calix host is locked into a two-fold symmetry, but in the higher temperature phase it alternates dynamically between two two-fold structures at 90° to each other.

Distance Measurements

Other methods for measuring distances that give significant information on conformations of the host, or guest–host distances are techniques such as spin-echo double resonance (SEDOR), which is a low-resolution method, and the spinning version, REDOR, which gives high-resolution information. This approach uses the time evolution of the difference in the magnetization for the observed nucleus that arises when it is observed with or without dipolar coupling to one or more nearby heteronuclei. The difference, known as the REDOR fraction, can be modeled in terms of the internuclear distances, e.g. as for the guest–host compound of *p*-*t*-butylcalix[4]arene with Cs [27]. However, an added complication in many guest–host systems would be the presence of molecular motion, giving a distance that is averaged [28]. REAPDOR [29], TRAPDOR, and QUEDOR [30] all are versions related to the SEDOR/REDOR family of experiments but that involve quadrupolar nuclei.

Spin Counting

Spin-counting, a technique that measures the order of the multiple quantum coherence that can be generated, can be used to measure the number of nuclei coupled by dipolar interactions. This can be used to probe the size of clusters of atoms or molecules, which may or may not be bound together, or that fill a cavity in a host material. With increased time, longer distances can be probed, so that intercluster distances can be obtained as well. ^{1}H spin counting in solids was first demonstrated by Munowitz and Pines [31]. One application to host–guest materials was a study of the numbers of protons present in “Si clusters,” and their precursors, formed inside the large cage of Y zeolite [32]. The ^{1}H spin count for the precursor, consisting of Si_2H_6 molecules and Si_2H_5 groups attached to the framework, reaches a plateau at 38 spins corresponding to the number in the cluster held within one cavity, and the final Si-cluster was found to contain 5 H atoms. This evidence helped to show that the clusters must be rather smaller than had been suggested previously.

Probing Pore Spaces

The last two decades have seen the growth of ^{129}Xe NMR [33], and more recently of hyperpolarized (HP) Xe [34,35], as a valuable tool for probing the pore space of host–guest materials. Early work on clathrate hydrates and a number of organic clathrates [36] established a relationship between the size and shape of a closed cavity and the Xe chemical shift and its anisotropy: smaller pores give larger shifts, and anisotropy reflects whether the cavity is spherical (zero anisotropy), oblate (positive anisotropy or skew), prolate (negative anisotropy or skew), or nonaxial. More recently a broad correlation between ^{129}Xe shifts and pore sizes in mesoporous silicas has been determined [37]. The observed Xe lineshape is a dynamic average over all the space accessible to the Xe over the timeframe of the experiment, and in open pore systems this can lead to loading dependent shifts and lineshapes [38]. In some materials incomplete filling leads to signals corresponding to cages with different numbers of Xe [39].

2D EXSY experiments can then be used to follow the exchange of Xe between cages with different occupancies, e.g. in NaA and AgA zeolites [39,40]. Thus Xe can be used to determine the interconnectivity of different pores and the exchange barriers. A recent example is a study of organic aerogels where the hierarchy of exchange between micro and mesopore spaces and the gas phase could be determined [41]. HP Xe is particularly useful due to its enormously enhanced sensitivity. This allows the use of very low Xe concentrations and thus removes the effects caused by Xe–Xe interactions, probing only the Xe–host interaction [42]. Another example is the void space access test, as illustrated in Figure 3 for a low density phase of *p*-*t*-butylcalix[4]arene [42]. HP Xe also makes it possible to follow real time processes, such as the formation/decomposition of gas hydrates [43]. Another important use has been in the study of structural transformations and competitive exchange between Xe and another guest in a metal-organic framework [44]. In recent work on dipeptides, Xe NMR spectroscopy has demonstrated both a new type of material (biozeolites) [45] and experimental and modeling calculations illustrating an application to biomaterials [46]. ^{131}Xe studies have revealed some interesting effects where the quadrupolar interaction probes longer range order/disorder compared to the chemical shift [47].

MRI

While MRI has very broad application in the medical arena, it is finding increasing uses in studies of materials, particularly of porous host–guest systems [48]. This is particularly true of porous host–guest systems where the long T_2 of the guest (as gas or liquid) makes imaging feasible. There has been some use of HP ^{129}Xe as the probe nucleus, but the easiest nucleus is ^{1}H and this is present in many guests, e.g. organic gases or liquids. MRI can be used to study diffusion of a guest into a host, both by direct imaging as a function of time and by MRI spectroscopy [49], and to probe whether the distribution of pore space in a material is homogeneous [41]. HP Xe chemical shift imaging can be used to probe composites of different porous materials [50]. By monitoring the disappearance of the signal from the water as it solidifies into the host framework, ^{1}H MRI was used to establish that growth of gas hydrate from small droplets was not continuous, but had a random component [51].

Dynamics

NMR is the technique par excellence for the detailed study of dynamics in solids (c.f. neutron scattering, dielectric relaxation, and torsional/librational spectroscopy), and dynamics plays a large role in the behavior of host–guest materials [2]: The generally weak interaction between host and guest means that in many instances the guest rotates even at very low temperatures, and is often free to roam about the pore spaces (rotational and translational freedom). This creates problems for structure determination due to dynamic disorder. In many instances the symmetry of the guest does not mesh with the symmetry of the cavity, and the result is an accommodation

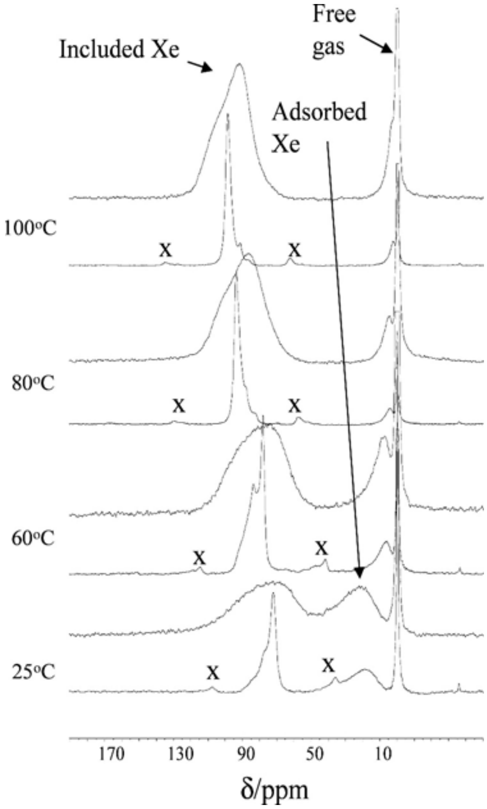

Fig. 3. Void space access test with hyperpolarized ^{129}Xe NMR. The sample, a low density phase of *p*-*t*-butylcalix[4]arene without obvious channels, was exposed to a flow of HP Xe gas at various temperatures in the NMR probe. Static and MAS spectra are shown at each temperature. X marks spinning side bands. At room temperature, the HP Xe signals correspond to adsorbed, or interparticle gas, and included gas. At high temperature much more gas is included, and it has the shape typical of an approximately axial tensor. One can see that the MAS spectrum in intermediate temperature regions consists of two signals. This means that there are two phases, one transforming to the other with increased temperature. The transition is not sharp, as the transition temperature depends on the degree of loading.

with the guest fitting into several possible positions to create a pseudo-symmetry. From the diffraction point of view this disorder can be either static, resulting from spatial averaging over many unit cells, or dynamic, as the molecule hops between the various positions, and NMR can be used to distinguish the two [20,21]. A number of NMR techniques are used to probe dynamics: lineshapes, linewidths, relaxation times, 2D-exchange, dipolar fadeout, etc. The earliest works on host–guest materials used the traditional low field methods of ^{1}H lineshapes, second moments and T_1 vs. temperature to obtain motional models, correlation times and activation energies (E_a), mainly of guests but sometimes of host, as in the case of clathrate hydrates. ^{2}H NMR, however, has perhaps been the greatest tool available for studying reorientational dynamics [52,53] (though it does have the disadvantage of not probing translational motion), and in the process it also sometimes yields geometrical information. As temperature is increased the motion initially distorts the lineshapes which go through a series of changes resulting in a narrowed lineshape in the fast motion limit. The static or fast motion limit lineshapes are readily analyzed to give the three components of the effective quadrupolar coupling tensor, and from these it is usually possible to determine a unique dynamic model. Once a model is determined the lineshapes at different jump rates can be calculated and matched with experiment. A plot of log(rate) vs. temperature then yields an E_a, e.g. 18-crown-6 in its complexes [54]. NMR has shown how surprisingly easy it can sometimes be for rather large molecules, such as 18-crown-6, to reorient in the solid. A guest molecule in cages with different symmetry can have quite different dynamics, resulting in different ^{2}H and chemical shift lineshapes, e.g. H_2Se clathrate hydrate described above [15], and cyclohexane-d_{12} in different metal cyanide frameworks [2]. This sensitivity to symmetry also frequently shows as sudden changes in the dynamic lineshapes of guests at phase transitions [21]. ^{2}H NMR has also been used to study the diffusion of organic molecules as they jump between adsorption sites inside zeolites, e.g. benzene-d_6 in H-SAPO-37 [55]. The analysis of dynamics can lead to a separate determination of the orientation of the guest with respect to crystal axes, and this can help in developing structural models for X-ray refinement, e.g. pyridine-d_5 in *t*-butyl-calix[4]arene [56].

More recently a few cases of dynamics involving non-integer quadrupolar nuclei have come to light, e.g. ^{131}Xe in xenon clathrate hydrate is sensitive to the motion of the framework water molecules [47], and ^{17}O in the water of THF hydrate [57].

NMR and diffraction constitute the two primary tools for the study of structure and dynamics in host–guest materials, and, as will be evident from this brief review, their roles are very much complementary. On the other hand, NMR truly comes into its own when used to provide insight into host–guest materials for which suitable single crystals are not available, or which by their very nature are not crystalline. NMR has a long and bright future in this very diverse and expanding field of chemistry.

References

1. Atwood JL, Davies JED, MacNicol DD, Vogtle F, Lehn JM (Eds). Comprehensive Supramolecular Chemistry, Vols. 1–11. Elsevier: Oxford, 1996.
2. Ripmeester JA, Ratcliffe CI. Solid-State NMR Spectroscopy: Applications to Supramolecular Chemistry. In: JL Atwood, JED Davies, DD MacNicol, F Vogtle, JM Lehn (Eds). Comprehensive Supramolecular Chemistry, Physical Methods, Vol. 8. Elsevier: Oxford, 1996, p 323.
3. Fyfe CA. Solid State NMR for Chemists. CFC Press: Guelph, 1983.
4. Bryce DL, Bernard GM, Gee M, Lumsden MD, Eichele K, Wasylishen RE. Practical aspects of modern routine solid-state multinuclear magnetic resonance spectroscopy: one-dimensional experiments. Can. J. Anal. Sci. Spectrosc. 2001;46:46.
5. Medek A, Harwood JS, Frydman L. Multiple-Quantum Magic-Angle Spinning NMR: A New Method for the Study of Quadrupolar Nuclei in Solids. J. Am. Chem. Soc. 1995;117:12779.
6. Duer MJ (Ed). Solid State NMR Spectroscopy Principles and Applications. Blackwell Science: Oxford, 2002.
7. Gerstein BC, Dybowski CR. Transient Techniques in NMR of Solids. Academic press: London, 1985, p 213.
8. Brown SP, Spiess HW. Advanced Solid-State NMR Methods for the Elucidation of Structure and Dynamics of Molecular, Macromolecular, and Supramolecular Systems. Chem. Rev. 2001;101:4125.
9. Pawsey S, McCormick M, De Paul S, Graf R, Lee YS, Reven L, Spiess HW. ^{1}H Fast MAS NMR Studies of Hydrogen-Bonding Interactions in Self-Assembled Monolayers. J. Am. Chem. Soc. 2003;125:4174.
10. Buchanan GW. Nuclear Magnetic Resonance Studies of Crown Ethers. Prog. NMR Spectrosc. 1999;34:327.
11. Lee GSH, Ratcliffe CI, Ripmeester JA. A Solid State ^{31}P NMR Study of the Synthesis of Phosphorus Sulfides from PCl_3 and H_2S in Microporous Materials. Can. J. Chem. 1998;76: 1660.
12. Nakayama H, Klug DD, Ratcliffe CI, Ripmeester JA. ^{23}Na MAS NMR Evidence for New Sodium Species in Metal-loaded Zeolites. J. Am. Chem. Soc. 1994;116:9777.
13. Nishikori S, Ratcliffe CI, Ripmeester JA. ^{113}Cd NMR Studies of Hofmann Type Clathrates and Related Compounds: Evidence for Two Room Temperature Orientational Glasses. Can. J. Chem. 1990;68:2270.
14. Curtis RD, Ratcliffe CI, Ripmeester JA. Structure and Ordering in Metal Cyanide Lattices: the Use of Doubly Labelled Cyanide (^{13}C-^{15}N) to Simplify the ^{13}C MAS NMR Spectrum. J. Chem. Soc. Chem. Commun. 1992:1800.
15. Collins MJ, Ratcliffe CI, Ripmeester JA. NMR Studies of Guest Species in Clathrate Hydrates: Lineshape Anisotropies, Chemical Shifts and the Determination of

Cage Occupancy Ratios and Hydration Numbers. J. Phys. Chem. 1990;94:157.

16. Lee F, Gabe E, Tse JS, Ripmeester JA. Crystal structure, CP/MAS ^{129}Xe and ^{13}C NMR of local ordering in Dianins compound clathrates. J. Am. Chem. Soc. 1988;110: 6014.
17. He J, Klug DD, Uehara K, Preston KF, Ratcliffe CI, Tse JS. NMR and X-ray Spectroscopy of Sodium-Silicon Clathrates. J. Phys. Chem. B. 2001;105:3475.
18. Sidhu PS, Enright GD, Udachin KA, Ripmeester JA. Structure and polymorphism in a pentamorphic guest-host material: a tris (5-acetyl-3-thienyl) methane (TATM) inclusion compound with 1,3-dichloropropane. Cryst. Growth Des. 2004;4:1240.
19. Soldatov DV, Enright GD, Ripmeester JA. Polymorphism and pseudopolymorphism of the [Ni(4-Methylpyridine)4(NCS)2] Werner complex, the compound that led to the concept of “Organic Zeolites”. Cryst. Growth Des. 2004;4:1185.
20. Enright GD, Ratcliffe CI, Ripmeester JA. Crystal Structure and ^{13}C CP/MAS NMR of the p-Xylene Clathrate of Dianin’s Compound. Mol. Phys. 1999;97:1193.
21. Brouwer EB, Enright GD, Ratcliffe CI, Ripmeester JA. Dynamic Molecular Recognition in Solids: a Synoptic Approach to Structure Determination in t-Butylcalix[4]arene-Toluene. Supramol. Chem. 1996;7:79.
22. Enright GD, Brouwer EB, Udachin KA, Ratcliffe CI, Ripmeester JA. A re-examination of the low temperature crystal structure of the p-*tert*-butylcalix[4]arene toluene inclusion compound: Differences in spatial averaging with Cu and Mo K radiation. Acta Crystallogr. B. 2002;58: 1032.
23. Brouwer EB, Ripmeester JA. Structural and Dynamic Properties of Solid Calixarenes. Adv. Supramol. Chem. 1998;5:121.
24. Engelhardt G, Michel D. High-Resolution Solid-State NMR of Silicates and Zeolites. John Wiley & Sons: New York, 1987.
25. Fyfe CA, Grondey H, Feng Y, Kokotailo GT. Natural-abundance two-dimensional silicon-29 MAS NMR investigation of the three-dimensional bonding connectivities in the zeolite catalyst ZSM-5. J. Am. Chem. Soc. 1990;112:8812.
26. Brouwer DH, Kristiansen PE, Fyfe CA, Levitt MH. Symmetry-Based ^{29}Si Dipolar Recoupling Magic Angle Spinning NMR Spectroscopy: A New Method for Investigating Three-Dimensional Structures of Zeolite Frameworks. J. Am. Chem. Soc. 2005;127:542.
27. Hughes E., Jordan J, Gullion T. J. Structural Characterization of the [Cs(p-*trt*-butylcalix[4]arene -H)(MeCN)] Guest-Host System by ^{13}C-^{133}Cs REDOR NMR. J. Phys. Chem. B2001;105:5887.
28. Brouwer EB, Gougeon RDM, Hirschinger J, Udachin KA, Harris RK, Ripmeester JA. Intermolecular distance measurements in supramolecular solids: ^{13}C-^{19}F REDOR NMR spectroscopy of p-tert-butylcalix[4]arene-fluorobenzene. Phys. Chem. Chem. Phys. 1999;1:4043.
29. Ba Y, Ratcliffe CI, Ripmeester JA. Double Resonance NMR Echo Spectroscopy: New Tools for Materials Characterization. Adv. Mater. 2000;12:603.
30. Tulk CA, Ba Y, Klug DD, McLaurin G, Ripmeester JA. Evidence for phase separation during crystallization of hyperquenched glassy clathrate hydrate forming solutions. J. Chem. Phys. 1999;110:6475.
31. Munowitz M, Pines A. Multiple-Quantum Nuclear Magnetic Resonance Spectroscopy. Science 1986;233:525.
32. He J, Ba Y, Ratcliffe CI, Ripmeester JA, Klug DD, Tse JS, Preston KF. Encapsulated Silicon Nanoclusters in Zeolite Y. J. Am. Chem. Soc. 1998;120:10697.
33. Ratcliffe CI. Xenon NMR In: G. A. Webb (Ed). Annual Reports on NMR Spectroscopy, Vol. 36. Academic Press: London, 1998, p 123.
34. Pietrass T. Optically Polarized ^{129}Xe in Magnetic Resonance Techniques. Magn. Reson. Rev. 2000;17:263.
35. Cherubini A, Bifone A. Hyperpolarised Xenon in Biology. Prog. NMR Spectrosc. 2003;42:1.
36. Ripmeester JA, Ratcliffe CI, Tse JS. The NMR of ^{129}Xe trapped in Clathrates and some other Solids. J. Chem. Soc. Farad Trans. I. 1988;84:3731.
37. Terskikh VV, Moudrakovskii IL, Breeze SR, Lang S, Ratcliffe CI, Ripmeester JA, Sayari A. A General Correlation for the ^{129}Xe NMR Chemical Shift—Pore Size Relationship in Porous Silica Based Materials. Langmuir 2002;18: 5653.
38. Ripmeester JA, Ratcliffe CI. The Anisotropic Chemical Shift of ^{129}Xe NMR in the Molecular Sieve AlPO-11: A Dynamic Averaging Model. J. Phys. Chem. 1995;99:619.
39. Chmelka BF, Raftery D, McCormick AV, Menorval LC, Levine RD, Pines A. Measurement of Xenon Distribution Statistics in Na-A Zeolite Cavities. Phys. Rev. Lett. 1991;66:580.
40. Moudrakovski IL, Ratcliffe CI, Ripmeester JA. ^{129}Xe NMR Study of Adsorption and Dynamics of Xenon in AgA Zeolite. J. Am. Chem. Soc. 1998;120:3123.
41. Moudrakovski IL, Wang L-Q, Baumann T, Exarhos GJ, Ratcliffe CI, Ripmeester JA. Probing the Geometry and Interconnectivity of Pores in Organic Aerogels Using Hyperpolarized ^{129}Xe NMR Spectroscopy. J. Am. Chem. Soc. 2004;126:5052.
42. Moudrakovski IL, Nossov A, Lang S, Breeze SR, Ratcliffe CI, Simard B, Santyr G, Ripmeester JA. Continuous Flow NMR with Hyperpolarized Xenon for the Characterization of Materials and Processes. Chem. Mater. 2000;12:1181; Enright GD, Udachin KA, Moudrakovski IL, Ripmeester JA. J. Am. Chem. Soc. 2003;125:9896.
43. Moudrakovski IL, Sanchez AA, Ratcliffe CI, Ripmeester JA. Nucleation and Growth of Hydrates on Ice Surfaces: New Insights from ^{129}Xe NMR Experiments with Hyperpolarized Xenon. J. Phys. Chem. B. 2003;105:12338.
44. Nossov AV, Soldatov DV, Ripmeester JA. In situ switching of sorbent functionality as monitored with hyperpolarized ^{129}Xe NMR spectroscopy. J. Am. Chem. Soc. 2001;123:3563.
45. Soldatov DV, Moudrakovski IL Ripmeester JA. Peptides as Microporous Materials. Angew. Chem. Int. Ed. 2004;43:6308.
46. Moudrakovski IL, Soldatov DV, Ripmeester JA. Sears DN, Jameson CJ. Xe NMR lineshapes in channels of peptide molecular crystals. Proc. Natl Acad. Sci. 2004;101: 17924.
47. Moudrakovski IL, Ratcliffe CI, Ripmeester JA. ^{131}Xe, a New NMR Probe of Void Space in Solids. J. Am. Chem. Soc. 2001;123:2066.

48. Kaiser LG, Meersmann T, Logan JW, Pines A. Visualization of gas flow and diffusion in porous media. Proc. Natl Acad. Sci. USA. 2000;97:2414.
49. Moudrakovski IL, Sanchez A, Ratcliffe CI, Ripmeester JA. Applications of Hyper-Polarized Xenon to Diffusion in Vycor Porous Glass. J. Phys. Chem. B. 2000;104:7306.
50. Moudrakovski IL, Lang S, Ratcliffe CI, Simard B, Santyr G, Ripmeester JA. Chemical Shift Imaging with Continuously Flowing Hyperpolarized Xenon for the Characterization of Materials. J. Magn. Reson. 2000;144:372.
51. Moudrakovski IL, McLaurin GE, Ratcliffe CI, Ripmeester JA. Methane and Carbon Dioxide Hydrate Formation in Water Droplets: Spatially Resolved Measurements from Magnetic Resonance Microimaging. J. Phys. Chem. B. 2004;108:17591.
52. Hoatson GL, Vold RL. ^{2}H-NMR Spectroscopy of Solids and Liquid Crystals. NMR Basic Principles and Progress. 1994;32:1.
53. Vold RR. Deuterium NMR Studies of Dynamics in Solids and Liquid Crystals. In: R Tycko (Ed). Nuclear Magnetic Resonance Probes of Molecular Dynamics. Kluwer Academic: Dordrecht, 1994, Chap 2, p 27.
54. Ratcliffe CI, Ripmeester JA, Buchanan GW, Denike JK. A Molecular Merry-Go-Round: Motion of the Large Macrocyclic Molecule 18-Crown-6 in its Solid Complexes Studied by ^{2}H NMR. J. Am. Chem. Soc. 1992;114:3294.
55. Bull LM, Cheetham AK, Powell BM, Ripmeester JA, Ratcliffe CI. The Interaction of Sorbates with Acid Sites in Zeolite Catalysts: a Powder Neutron Diffraction and ^{2}H NMR Study of Benzene in H-SAPO-37. J. Am. Chem. Soc. 1995;117: 4328.
56. Brouwer EB, Enright GD, Facey GA, Ratcliffe CI, Ripmeester JA. Weak Intermolecular Interactions: Structure and Dynamics of the Benzene and Pyridine p-tert-Butylcalix[4]arene Inclusions. J. Phys. Chem. B. 1999;103:10604.
57. Ba Y, Ratcliffe CI, Ripmeester JA. Kinetics of Water Molecular Reorientation in Ice and THF (Tetrahydrofuran) Clathrate Hydrate from Line Shape Analysis of ^{17}O Spin-Echo NMR Spectra, in preparation.

Part I

Imaging

Mapping of Flow and Acceleration with NMR Microscopy Techniques

Elke Kossel, Bogdan Buhai, and Rainer Kimmich
Universität Ulm, Albert-Einstein-Allee 11, 89069 Ulm, Germany

Introduction

In this contribution, radio frequency and field gradient pulse sequences for the encoding of position, velocity, and acceleration will be described and explained. The applicability of the techniques will be demonstrated by presenting experimentally obtained velocity and acceleration maps of fluid flow in artificial pore spaces. Porous model objects fabricated on the basis of random percolation clusters are taken as a paradigm for networks in any sort of natural or technical pores or channel complexes. Numerically obtained velocity and acceleration maps will be compared to the experimental data to test the reliability of the methods.

Encoding Principles and Pulse Sequences

Spatial resolution in NMR experiments can be achieved by superimposing a constant field gradient of strength $\hat{G}$ to the external magnetic flux density B_0 during data acquisition. In the presence of the gradient, the Larmor frequency depends linearly on the position of the spins along the axis defined by the gradient. If the gradient is assumed along the x-direction, the resulting Larmor frequencies are given by

$$\omega(x) = \gamma \left(B_0 + \hat{G}_x x\right). \tag{1}$$

As long as the frequency shifts caused by the external field gradient are much larger than chemical shielding or susceptibility-induced shifts, the frequency encoded information of the signal can directly be transformed into spatial information. The "field of view" (FOV) is defined as the spatial window, which can unambiguously be sampled by the pulse sequence:

$$-\frac{\pi}{\gamma \Delta t \hat{G}_x} < x < \frac{\pi}{\gamma \Delta t \hat{G}_x} \tag{2}$$

Here, γ denotes the gyromagnetic ratio of the nuclei and Δt stands for the dwell time of the data acquisition. Contributions from spins outside this window will be folded into the FOV and distort the image. The spatial resolution depends on the FOV and the number of data points N:

$$\Delta x = \frac{2\pi}{\gamma \Delta t \hat{G}_x N} = \frac{x_{\max} - x_{\min}}{N}, \tag{3}$$

where $x_{\max} - x_{\min}$ is the FOV.

Spatial information cannot only be encoded in the frequency of the signal but also in its Larmor precession phase. This can be done by inserting a field gradient pulse of duration τ in the pulse sequence. During the interval τ, the Larmor frequencies along the direction of the gradient, e.g. the y-axis, differ according to Equation (1). After the gradient is switched off, the spins continue to precess with the frequency $\omega = \gamma B_0$, but have gained a position-dependent phase shift given by

$$\varphi(y) = \omega(y)\tau = \int_0^{\tau} \gamma \hat{G}_y y(t) \mathrm{d}t. \tag{4}$$

If the nuclei are displaced by hydrodynamic flow, their positions on the gradient axis become time-dependent:

$$y(t) = y_0 + v_{y_0} t + \frac{1}{2} a_{y_0} t^2 + \cdots. \tag{5}$$

That is, the phase shift depends on the initial position y_0, the initial velocity v_{y_0}, and the initial acceleration a_{y_0}. Higher order terms vanish if the flow field is stationary on the timescale of the NMR experiment (i.e. time-dependent accelerations at a given position do not occur in this case). For a gradient pulse of duration τ and strength $\hat{G}_y$ the total phase shift is consequently

$$\begin{aligned} \varphi &= \gamma \hat{G}_y \left(y_0 \tau + \frac{1}{2} v_{y_0} \tau^2 + \frac{1}{6} a_{y_0} \tau^3 \right) \\ &= \varphi(y_0) + \varphi\left(v_{y_0}\right) + \varphi\left(a_{y_0}\right). \end{aligned} \tag{6}$$

In order to distinguish the three quantities y_0, v_{y_0}, and a_{y_0}, more sophisticated gradient pulse sequences have been designed resulting in phase shifts that essentially depend only on a single parameter or a selection of parameters.

Graham A. Webb (ed.), Modern Magnetic Resonance, 157–162.
© 2008 *Springer.*

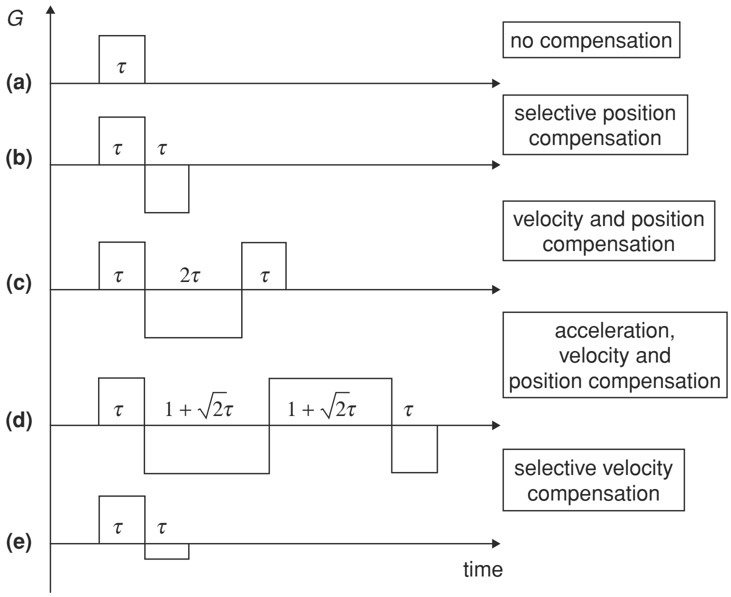
G
(a)
τ
no compensation
(b)
τ
τ
selective position compensation
(c)
τ
2τ
τ
velocity and position compensation
(d)
τ
$1+\sqrt{2}\tau$
$1+\sqrt{2}\tau$
τ
acceleration, velocity and position compensation
(e)
τ
τ
selective velocity compensation
time

Fig. 1. Gradient pulse trains for (a) position encoding in the absence of flow, (b) position-compensated velocity encoding, (c) position- and velocity-compensated acceleration encoding, (d) position, velocity, and acceleration compensation, (e) velocity-compensated position encoding.

For many systems and flow situations, the position-dependent term dominates the phase shift while the velocity-dependent term is still significantly larger than the acceleration-dependent term. As a direct consequence, terms with a higher order of τ than the term including the parameter to be evaluated may often be neglected while terms with a lower order of τ have to be compensated by the gradient pulse sequence. On the other hand, if the magnitude of higher order terms is comparable to that of the term of interest, the maps are disturbed by motion artifacts. In this case, the pulse sequence has to compensate for contributions of higher order terms too.

Figure 1a–e shows typical gradient lobe trains suitable for the compensation of phase shifts due to any of the above quantities. If an intermittent 180° RF pulse is used (such as in the Hahn echo sequences shown in Figure 2), the gradient lobes after the 180° pulse must be inverted relative to the lobes before the 180° pulse.

If no flow is present or if the phase shifts due to velocity and acceleration can be neglected, a single gradient of duration τ (Figure 1a) can be used for the encoding of *spatial information* on the morphology of the sample. It causes a phase shift $\varphi(y) = \gamma \hat{G}_y y \tau$. The Fourier space (also called reciprocal space or k-space) is sampled by repeating the experiment with different strengths of the gradient $\hat{G}_y$. After performing a Fourier transform of the data, the FOV is given by:

$$-\frac{\pi}{\gamma \tau \Delta \hat{G}_y} < y < \frac{\pi}{\gamma \tau \Delta \hat{G}_y}, \tag{7}$$

where $\Delta \hat{G}_y$ denotes the increment of the gradient between two successive experiments. The resolution can be calculated by dividing the FOV by N, the number of experiments with different gradient strengths:

$$\Delta y = \frac{2\pi}{\gamma \tau \hat{G}_y} = \frac{2\pi}{\gamma \tau \Delta \hat{G}_y N} = \frac{y_{\max} - y_{\min}}{N}, \tag{8}$$

where $y_{\max} - y_{\min}$ is the FOV in the y-direction.

The bipolar gradient pulse in Figure 1b compensates phase shifts due to the position, but produces phase shifts by *velocity* and *acceleration* components along the gradient direction: Two gradient pulses of duration τ and of the same magnitude of the amplitude $\hat{G}_y$ but with opposite sign are applied. The position-dependent term of the phase shift vanishes, whereas the velocity-dependent term provides a finite phase shift proportional to the velocity component:

$$\begin{aligned} \varphi(y_0) = 0;\ \varphi\left(v_{y_0}\right) &= \frac{1}{2}\gamma \hat{G}_y v_{y_0}\left(2\tau^2 - 4\tau^2\right) \\ &= -\gamma \hat{G}_y v_{y_0} \tau^2. \end{aligned} \tag{9}$$

Often, this gradient sequence is modified by a delay $\Delta\tau$ between the two gradient lobes, as indicated in Figure 2b. The position-dependent term is not affected by the additional interval, whereas the velocity-dependent term then results in

$$\varphi\left(v_{y_0}\right) = -\hat{G}_y \gamma \left(\tau^2 + \tau \Delta\tau\right) v_{y_0}. \tag{10}$$

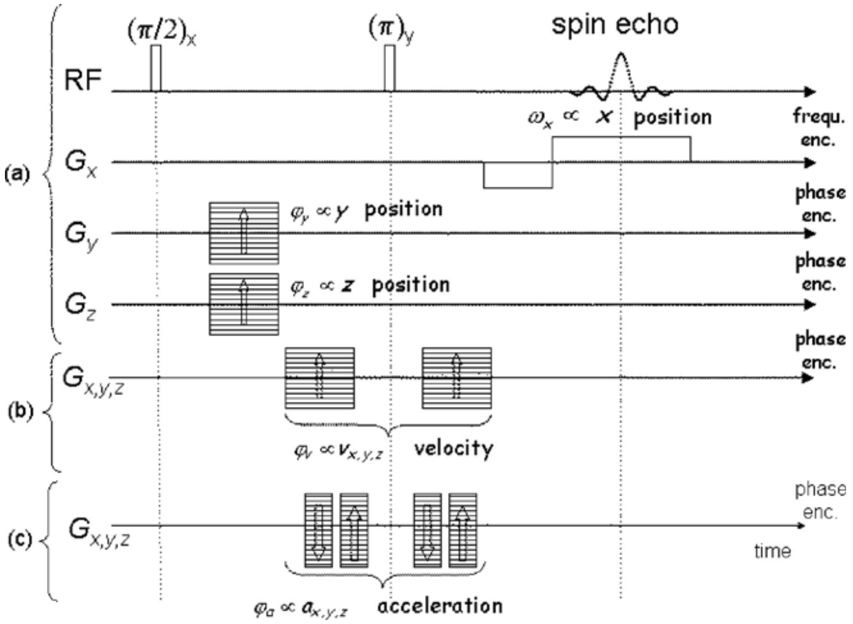

Fig. 2. (a) Complete three-dimensional RF and gradient pulse sequence for spin density mapping, (b) supplement for sequence (a) that allows for velocity mapping, (c) supplement for sequence (a) that allows for acceleration mapping.

Referring to Eq. (9), the velocity "FOV" and the digital resolution are given by

$$-\frac{\pi}{\gamma\tau^2\Delta\hat{G}_y} < v_y < \frac{\pi}{\gamma\tau^2\Delta\hat{G}_y} \tag{11}$$

and

$$\Delta v_y = \frac{\pi}{\gamma\tau^2\hat{G}_y}, \tag{12}$$

respectively.

The gradient pulse variant in Figure 1c compensates phase shifts due to the *position* and to the *velocity* component, but generates phase shifts by the *acceleration* component. The first and the third lobe of this gradient pulse train have the same sign, duration, and amplitude, whereas the second lobe has the same amplitude, an opposite sign, and twice the duration of the first pulse. The induced phase shift can be calculated as

$$\begin{aligned} \varphi(y_0) &= \varphi\left(v_{y_0}\right) = 0; \\ \varphi\left(a_{y_0}\right) &= 2\gamma\hat{G}_y a_{y_0}\tau^3. \end{aligned} \tag{13}$$

The acceleration FOV and the resolution are given by the expressions

$$-\frac{\pi}{2\gamma\tau^3\Delta\hat{G}_y} < a_y < \frac{\pi}{2\gamma\tau^3\Delta\hat{G}_y} \tag{14}$$

and

$$\Delta a_y = \frac{\pi}{2\gamma\tau^3\hat{G}_y}, \tag{15}$$

respectively. The phase shifts caused by gradient pulses, which are separated by time delays (such as shown in Figure 2c) are represented by more complex expressions as published in Ref. [1].

Phase encoding of higher order terms (locally time-dependent accelerations) is feasible in principle according to pulse trains such as the example shown in Figure 1d. However, the relatively long acquisition times of NMR parameter maps conflict with "snapshot" records that would be needed for such maps. Anyway, in Ref. [2], fast imaging techniques are described and discussed that could be employed for moderate versions of "snapshot" experiments.

If an ordinary image or a *spin density map* is to be recorded in the presence of a relatively fast stationary flow with constant velocities, a spatial phase encoding gradient pulse like in Figure 1a should be replaced by the "velocity-compensated" gradient pulse shown in Figure 1e. Otherwise, flow artifacts will arise. This gradient pulse provides spatial phase encoding according to

$$\varphi(y) = \frac{2}{3}\gamma \hat{G}_y \tau y; \quad \varphi\left(v_{y0}\right) = 0, \tag{16}$$

whereas there is no phase shift by the flow velocity.

An appropriate combination of the phase encoding pulse trains given in Figure 1 (modified for an intermittent 180° RF pulse) provides gradient pulse sequences for three-dimensional spin density mapping, as shown in Figure 2a, *velocity component mapping sequences* as given by a combination of Figure 2a and b, or *acceleration component mapping sequences* as given by Figure 2a and c.

In the preceding paragraphs, only the digital resolution of the maps has been discussed. Often, this theoretical resolution cannot be achieved experimentally. Susceptibility differences at material boundaries within the sample, for example, lead to distortions and resolution losses in the frequency encoded spatial direction. These distortions can be avoided by employing phase encoding for all spatial dimensions. But phase encoding, too, may not provide the predicted resolution: High spatial resolution comes along with small voxel sizes and a small number of spins that contribute to the signal that originates from one particular voxel. This small signal is further decreased by diffusion losses in the presence of field gradients and relaxation. In the case of velocity encoding with a bipolar gradient pair like the one shown in Figure 1b, the signal amplitude is decreased due to diffusion by the factor [3]

$$A_{\mathrm{Diff}} = e^{-2/3\gamma^2 \hat{G}^2 D \tau^3},$$

where D is the diffusion coefficient in the liquid.

Pulse sequences that require long gradient pulse trains for parameter encoding suffer substantially from this attenuation. Taking into account the different dependencies of the velocity-induced phase shift ($\propto \tau^2 \hat{G}$) and the diffusive attenuation ($\propto \exp[-(\frac{2}{3})\gamma^2 \hat{G}^2 D \tau^3]$) on the gradient strength and length, it is possible to optimize these two parameters for a given resolution. But especially for experiments with high spatial resolution and a large velocity range to be mapped, this may not be sufficient to retain a satisfactory signal-to-noise ratio. In this case, a number of sub-maps can be recorded and combined to a map that covers the full parameter range but has no equidistant data resolution [4].

Velocity mapping is restricted mainly by two effects: Slow velocities are masked by diffusion and large velocities cause a spin to leave its designated voxel in the time between encoding and signal readout. A flow experiment should be set up in a way that the largest detectable velocity present in the sample is covered by the corresponding velocity FOV. This avoids distortions by back-folding of velocities into the experimental velocity scale. But the larger the FOV is, the longer and stronger gradients are required to maintain the required resolution and the larger is the attenuation by diffusion. Therefore, instead of performing one experiment with a large number of gradient steps, the entire range should better be covered by at least two experiments with a significantly smaller number of gradient steps ('two-step strategy').

The first experiment has a velocity FOV that covers the entire velocity range in a small number of steps. The velocity map is not distorted but small velocities are identified as "zero" due to the coarse resolution.

The second experiment covers the velocity range between the minimum measurable velocity and the minimum velocity detected by the first experiment. It is distorted because of back-folding of high velocities into the spectrum, but it properly shows the small velocities. All voxels from the first map, which show zero velocity can now be compared to the corresponding voxels of the second map. If those show a finite velocity, the value can be transferred to the first map. The combination of the two maps is then a map, which covers the full velocity range and includes small velocities, but has a fine resolution at low velocities and a coarse resolution at high velocities. With this technique, a substantial decrease of the diffusive attenuation of the signal can be achieved.

Experiments

Figures 3 and 4 represent velocity and acceleration mapping experiments carried out in percolation model objects and the corresponding numerical simulations. The template used for the fabrication of the model objects was computer generated based on a two-dimensional site percolation model [5–7] and is shown in Figure 4a. Patterns of this sort were either mechanically milled into polystyrene sheets (photograph in Figure 3a) [8]or etched into 1 mm thick PMMA sheets by Deep X-ray Lithography (photograph in Figure 4b) [9,10].

Experimental results comparing velocity and acceleration maps are shown in Figure 3. The data were measured with the $10 \times 10\ \mathrm{cm}^2$ sample (smallest pore size 400 μm) shown in Figure 3a. Velocity mapping and acceleration mapping experiments were carried out with a Bruker 4.7 T magnet with a 40 cm horizontal bore. The maximum applied field gradient was 50 mT/m. A detailed discussion of the effect of gradient ramps on the phase encoding and of the four pulse gradient sequence (Figure 2c) that was used for acceleration encoding can be found in Ref. [1].

Figures 3b and c show numerically obtained acceleration and velocity maps, whereas the experimental results are presented in Figure 3d and e. The simulations were done with the FLUENT 5.5 (FLUENT Inc., Lebanon, NH, USA) finite-element software package. The positions

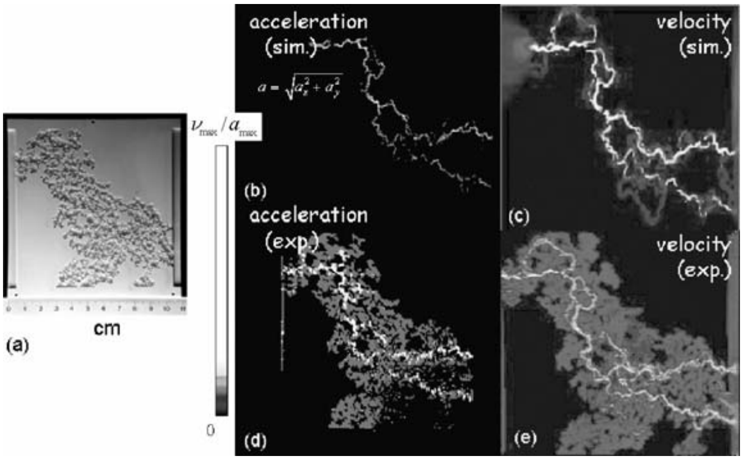

Fig. 3. (a) Photograph of a 10 × 10 cm^2 percolation model object milled into a polystyrene sheet with a depth of 2 mm. (b) Simulated acceleration magnitude map. (c) Simulated velocity magnitude map. (d) Experimental acceleration magnitude map. (e) Experimental velocity magnitude map. (See also Plate 10 on page XXI in the Color Plate Section.)

where the acceleration is finite (i.e. above the experimental resolution) are obviously localized spots in contrast to the more continuous flow patterns visible in the velocity map. That is, acceleration maps specifically reveal the distribution of flow bottlenecks and changes of the flow resistance. Note, that experimentally obtainable velocity maps are too crude to deliver an acceleration map by derivation of the flow field. A distinct method for the direct measurement of acceleration is therefore essential.

Figure 4 refers to the much smaller lithography objects. Three different realizations of the structure are shown in the photographs Figure 4b. Their sizes are 15 × 15, 18 × 18, and 24 × 24 mm^2. The smallest pore sizes within the samples are 50, 60, and 80 μm, respectively. In Figure 4c, a part of a numerically achieved map of the flow velocities (left hand side) is compared to the same part of an experimentally obtained map of flow velocities of $CuSO_4$-doped water (right hand side) [4]. The velocity FOV of the two experiments was chosen to be $\pm{-9.6}$ mm/s for the first experiment and $\pm{-2.4}$ mm/s for the second. Each single measurement had as few as six velocity encoding gradient steps. Zero-filling to 16 steps was applied afterward. The digital spatial resolution was 26.3 × 36.7 μm, whereas the smallest pore size within the sample was 60 × 60 μm^2. The spectrometer used was a BRUKER DSX 400 spectrometer with a microimaging gradient unit. Gradients of up to 0.8 T/m were used for the experiment.

Concluding Remarks

The NMR velocity and acceleration mapping methods described above are suitable to gain insight into flow distributions and flow properties. Since we are dealing with non-invasive and non-optical techniques, any opaque or transparent, non-metallic system can be examined on this basis in the velocity and acceleration fields of view outlined above and with some restriction with respect to the time resolution.

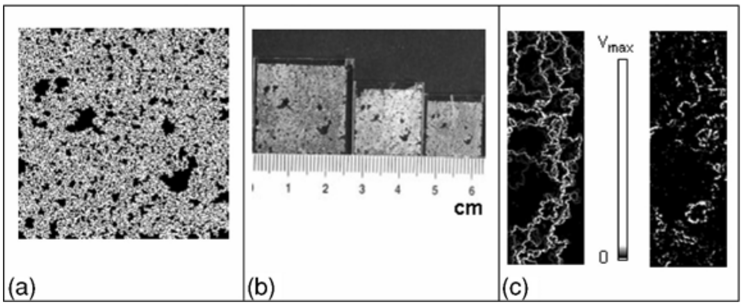

Fig. 4. (a) Computer generated pore space structure that served as template for sample fabrication and as matrix for numerical simulations. (b) Photograph of model objects etched 1 mm deep into PMMA sheets with X-ray lithography. (c) Cut-outs of flow velocity magnitude maps. Left hand side: numerically derived map; right hand side: experimentally obtained map. The size of the displayed section is 6 × 18 mm^2, which is 1/3 of the total sample size.

As a well-defined paradigm for complex pore spaces we have considered random-site percolation clusters that were generated on a computer. Fabricating model objects on this basis provides samples the pore space structures of which are known quantitatively in all details. This in turn permits finite-element or finite-volume computational fluid dynamics studies which in combination with the experimental NMR results provide an unsurpassed conclusiveness concerning the relationship of the pore space structure and the transport properties.

Fundamental investigations with "known" porous media are suitable to reveal the laws needed to understand transport on microscopic length scales. Knowledge elaborated on this basis is expected to trigger studies also of interest for chemical engineering and microsystem technology applications.

Finally, it should be mentioned that hydrodynamic flow is not the only transport phenomenon that can be studied by magnetic resonance microscopy techniques. There are other, more specialized transport quantities that can be examined on this basis as well. Examples are electric current, diffusion, and heat. Corresponding applications to the same sort of percolation model objects reported in this chapter can be found in Refs. [11–13].

References

1. Buhai B, Hakimov A, Ardelean, I, Kimmich R. J. Magn. Reson. 2004;168:175–185.
2. Mantle MD, Sederman AJ. Prog. NMR Spectrosc. 2003;43:3–60.
3. Kimmich R. NMR Tomography, Diffusometry, Relaxometry. Springer: Berlin, 1997.
4. Kossel E, Kimmich R. Magn. Reson. Imaging. 2005;23:397–400.
5. Stauffer D, Aharony A. Introduction to Percolation Theory. Taylor & Francis: London, 1992.
6. Sahimi M. Application of Percolation Theory. Taylor & Francis: London, 1993.
7. Bunde A, Havlin S (Eds). Fractals and Disordered Systems. Springer-Verlag: Berlin, 1996.
8. Klemm S, Kimmich R, Weber M. Phys. Rev. E 2001;63:041514-1–041514-8.
9. Kossel E, Weber M, Kimmich R. Solid State NMR 2004;25:28–34.
10. Madou M. Fundamentals of Microfabrication. CRC Press, Boca Raton, FL, 1997.
11. Weber M, Kimmich R. Phys. Rev. E 2002;66:026306-1–026306-9.
12. Klemm A, Metzler R, Kimmich, R. Phys. Rev. E 2002;65: 021112-1–021112-11.
13. Weber M, Kimmich R. Phys. Rev. E 2002;66:056301-1–056301-13.

Industrial Application of *In situ* NMR Imaging Experiments to Steel-Making Process

Koji Saito
Nippon Steel Corporation, Advanced Technology Research Laboratories, 20-1 Shintomi Futtsu City, Chiba 293-8511, Japan

The biggest advantage of NMR is that is non-destructive. This means that *in situ* experiments are not difficult, when several conditions are established in the experimental scheme and probe. There are many applications of *in situ* NMR which strongly contribute to the solution of industrial problems and clarify complicated phenomena in the science and technology fields. For example, catalysis reactions, chemical reactions, ion or gas or liquid flow, phase transition, etc. In this chapter, I would like to explain mainly two results [1,2] of *in situ* NMR experiments which are very helpful and useful to solve real problems in industries.

NMR imaging is a powerful tool that is widely and successfully used in medical applications. At the same time, its potential to solve materials science problems has been recognized only more recently. NMR imaging of solids is still a challenge despite significant achievements in this field [3]. NMR microscopy allows one to study the macroscopic transport of liquids in materials by monitoring the transformation of the spatial distribution of liquid content in time [4]. Another important process that involves mass transport in materials is drying [5–9]. The conventional approach utilizes the evaluation of the total amount of losses of liquid vs. time (drying curves), e.g. by sample weighing, while its distribution within the porous object is determined using a gravimetric method based on sample sectioning.

It is well known that the presence of water and water transport play key roles in determining the pore structure and long term durability of cementitious mortar materials. In real life, some problems, e.g. hydrogen-explosion, can occur because of poor drying conditions. To date, however, a severely limiting factor has been that resonance line widths in cements are very broad. Consequently, only the most mobile water in the largest capillaries, cracks, and voids has been observed. Only more recently have STRAFI imaging techniques [10] been examined. Surface relaxivity has been exploited by McDonald and Newling [11] using the complementary technique of magnetic resonance relaxometry. These authors show that the initial ^{1}H spin–spin relaxation time (T_2) of water in a dried 0.5 water to cement (w/c) ratio mortar paste varies according to water content, indicating that the rapid exchange model of relaxation can be applied to determine the pore surface area to volume ratio. This paper presents the results of a STRAFI imaging study of the hydration and drying of mortar pastes and of subsequent water transport in dried material. This process may also be performed in underwater environments, and such cases were also studied. The objective is to correlate the bulk relaxation analysis of samples sealed during cure, which are assumed to be spatially uniform, with the structure of the paste based on traditional understanding. Quantitative STRAFI imaging is then used to observe deviations from this model in the case of samples dried open or underwater where spatial heterogeneity is expected. Also, knowledge of the mechanism of the drying of these refractory mortars will permit the optimization of the drying using modern solid state NMR techniques [^{27}Al M(3 and 5)QMAS and ^{1}H–^{27}Al CP/3QMAS in Ref. 12] in the real steel-making process.

Typical refractory mortar samples are prepared as sample 1 (sample 3 + surface active agents) and sample 3(Al_2O_3: 92%, MgO: 7%, CaO: 1%). For most of the studies, mortar samples were cast in glass pots and NMR tubes from real industrial materials using a food processor to mix the water and mortar powder and a vibration table to remove incorporated air. The tubes and pots were sealed. For the measurements made during the cure, the samples were examined *in situ* (50 °C).

Representative STRAFI echo train profiles recorded at 50 °C every 40 min from samples 1 and 3 of drying refractory mortar are shown in Figure 1. In the case of sample 3, a drying time of around 18.3 h is required, whilst sample 1 requires less than half this drying time (8 h) due to the effect of the surface active agent. The STRAFI *in situ* experiments produced a large number of water content profiles. The details of the front shape are distorted by the finite time required to record the profile. Details of the front shape are better determined in a time of flight experiment in which the signal intensity is recorded at a fixed location as the front passes. Because data acquisition is considerably more rapid, the distortion is much less. The analysis discussed below uses a combination of time of flight and profile data. The drying of the sample proceeds from the surface, so that close to the surface the free water ratio decreases with proximity to the surface. However,

Graham A. Webb (ed.), Modern Magnetic Resonance, 163–171.
© 2008 *Springer.*

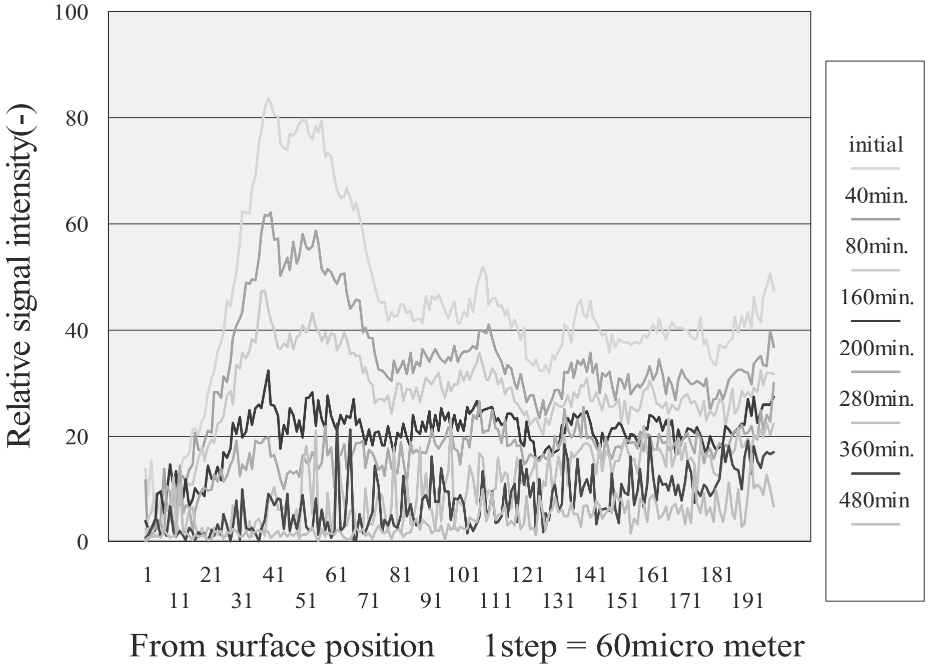

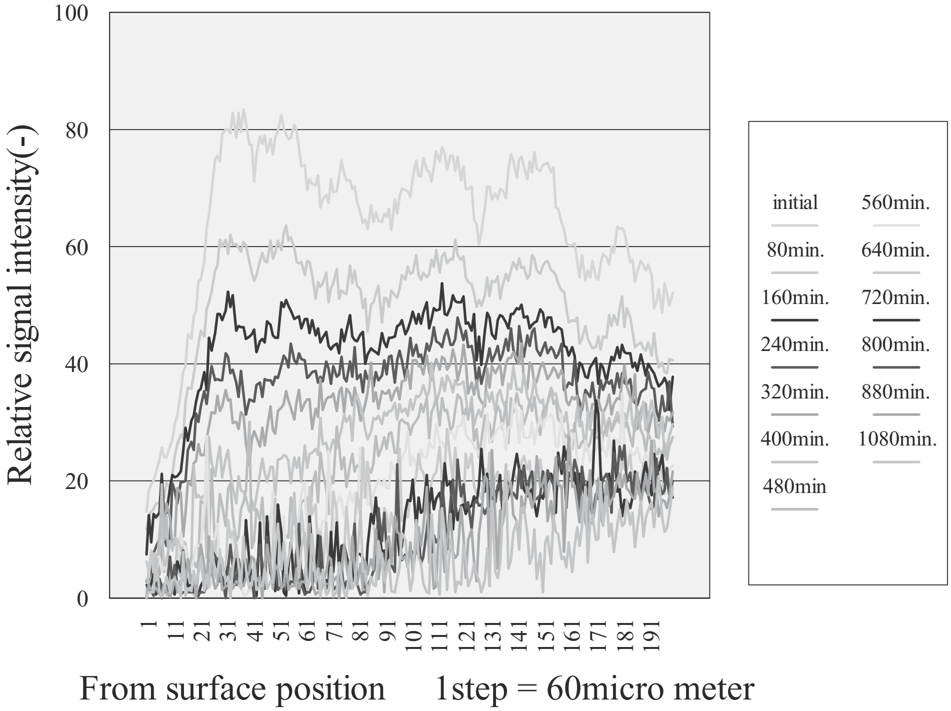

Fig. 1. The typical results of STRAFI experiments of sample 1 (upper) and sample 3 (bottom). (See also Plate 11 on page XXII in the Color Plate Section.)

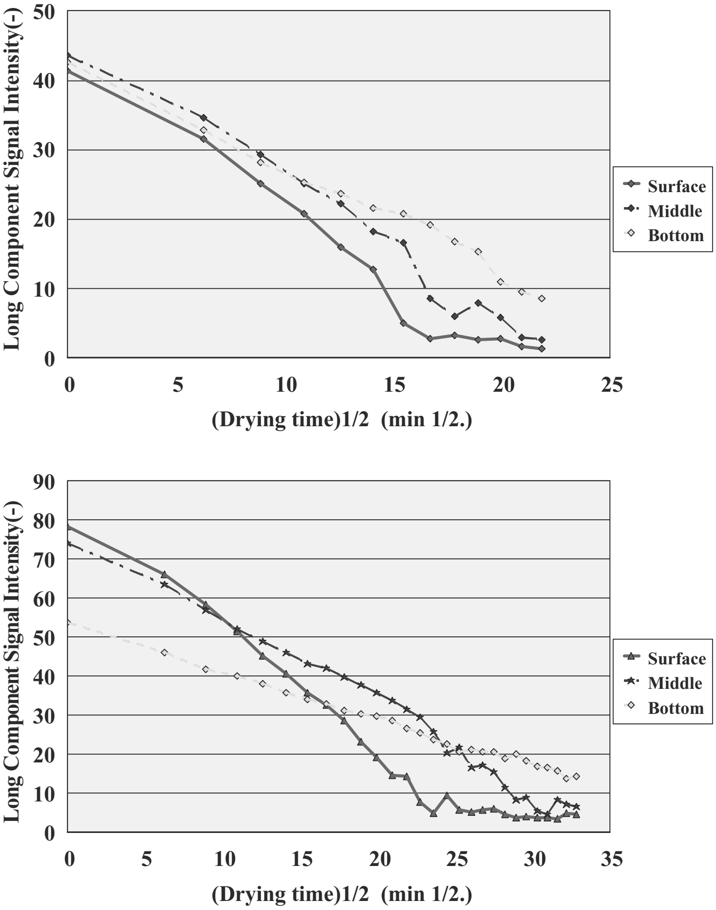

Fig. 2. At the each three position long component of signal intensities as a function of root *t* for a selection of typical drying experiments in the case of sample 1 (upper) and sample 3 (bottom).

behind this initial region the ratio is maintained constant throughout the remaining sample as water diffuses more rapidly from the lower regions. In order to test whether or not the observed STRAFI profiles are due to Fickian diffusion, we plot the diffusing front position as a function of root time, where t is the time. In the case of Fickian diffusion, such a plot will appear linear so long as the front does not approach the far end of the sample. We define the front position as the position where the front reaches half the maximum concentration. The front position is measured relative to the original sample surface whose position is established from a profile measured before the drying.

Figure 2 shows the three positions (surface, middle, bottom) from the surface front as a function of root t for a selection of typical drying experiments for sample 3 and sample 1, respectively. The data in the case of capillary water are all well approximated with linear fits, indicating that Fickian diffusion is taking place. In addition the slopes of all positions are almost identical for sample 1, indicating that the drying is homogeneous. On the other hand, the slope at the bottom position in the case of sample 3 is different from the others. It is likely that inhomogeneous drying is going on. We can obtain a "characteristic" diffusion coefficient D, from these plots since we know that the characteristic diffusion length is given by $(D_{\text{av}}\ t)^{1/2}$ which can be equated to the front position. D_{av} is simply the slope of the front position vs. the $t^{1/2}$ plot. This measure will be used frequently in the subsequent discussion since it is a robust and straightforward way of parametrizing the profile position data and is related to the magnitude of the mutual diffusion coefficient.

The average diffusion coefficient of free water for the drying of sample 3 at 50 °C was found to be $6.1–8.7 \times 10^{-5}$ cm^2/s. For instance, moisture diffusivity in brick and clay is in the range $10^{-5} - 10^{-3}$ cm^2/s for various moisture

Fig. 3. At the each three position short component of signal intensities as a function of root *t* for a selection of typical drying experiments in the case of sample 1 (upper) and sample 3 (bottom).

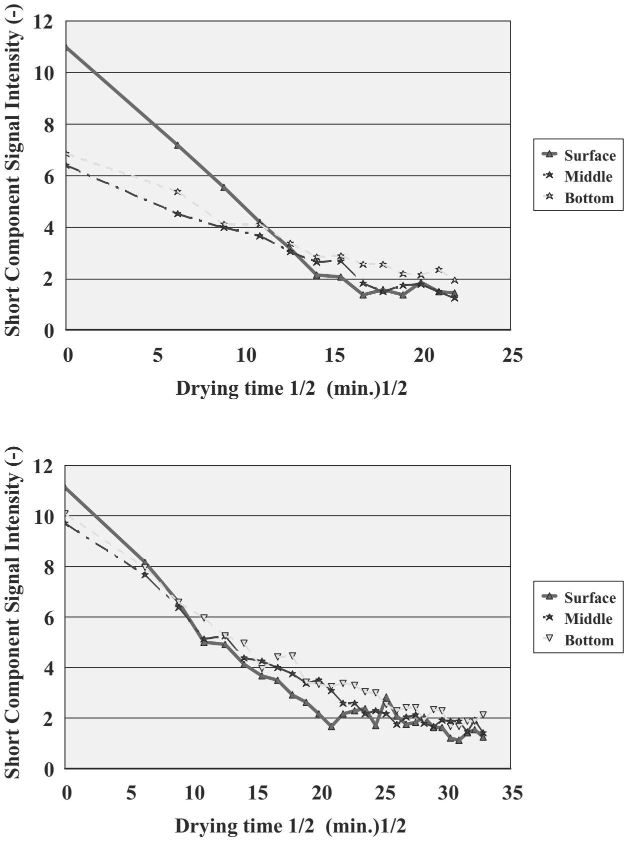

contents in the materials, while the self-diffusion coefficient for water is only 2.1 × 10^{-5} cm^2/s. In the case of sample 1, the average diffusion coefficient for the drying at 50 °C was found to be 9.7 × 10^{-5} cm^2/s. Although the total drying time was quite different between sample 3 (1080 min) and sample 1 (480 min), it is surprising that the average diffusion coefficient of free water is almost the same for both samples.

On the other hand, what about bounded water behavior? Stray-field imaging is a very powerful tool to monitor all capillary water (long T_2, component) and bounded water (short T_2, component). It is found that the recorded quadrature echoes, which in the case of combined water reflect a degree of line narrowing and in the case of mobile water are strongly diffusion attenuated, can be well represented by two-component exponential decays, with the relative amplitudes of the components corresponding to the proportions of capillary water and chemically combined water, respectively. Figure 3 shows profiles of bound water for samples 1 and 3, respectively. A feature of generalized Fickian diffusion is that the water front should advance as $t^{1/2}$. We note that this is the case in the experiments reported here. While it is possible that this is due to the additional drying damaging the delicate gel structure of the mortar, we believe that the result is significant and reflects the different uptake characteristics of refractory mortar to capillary and to bounded water. Based on the fits, the diffusion coefficient for bounded water of sample 1 is calculated to be $D(\text{c}) = (3.4 - 6.2) \times 10^{-5}$ cm^2/s except for the surface position. On the other hand, the diffusion coefficient for combined capillary water of sample 3 is difficult to confirm as Fickian diffusion because of bad linearity of Figure 4. Thus it appears that Case II type diffusion is occurring in the case of bounded water for sample 3.

To clarify chemical reasons we have carried out the measurements of ^{27}Al M(3 and 5)QMAS. Figure 4 shows ^{27}Al 5QMAS spectra for the before drying and after drying of sample 1, respectively. ^{27}Al 5QMAS shows there are mainly four chemical structures (two 4-coordinate type and two 6-coordinate type). Table 1 shows the quantitative analysis of these chemical structures for samples 1

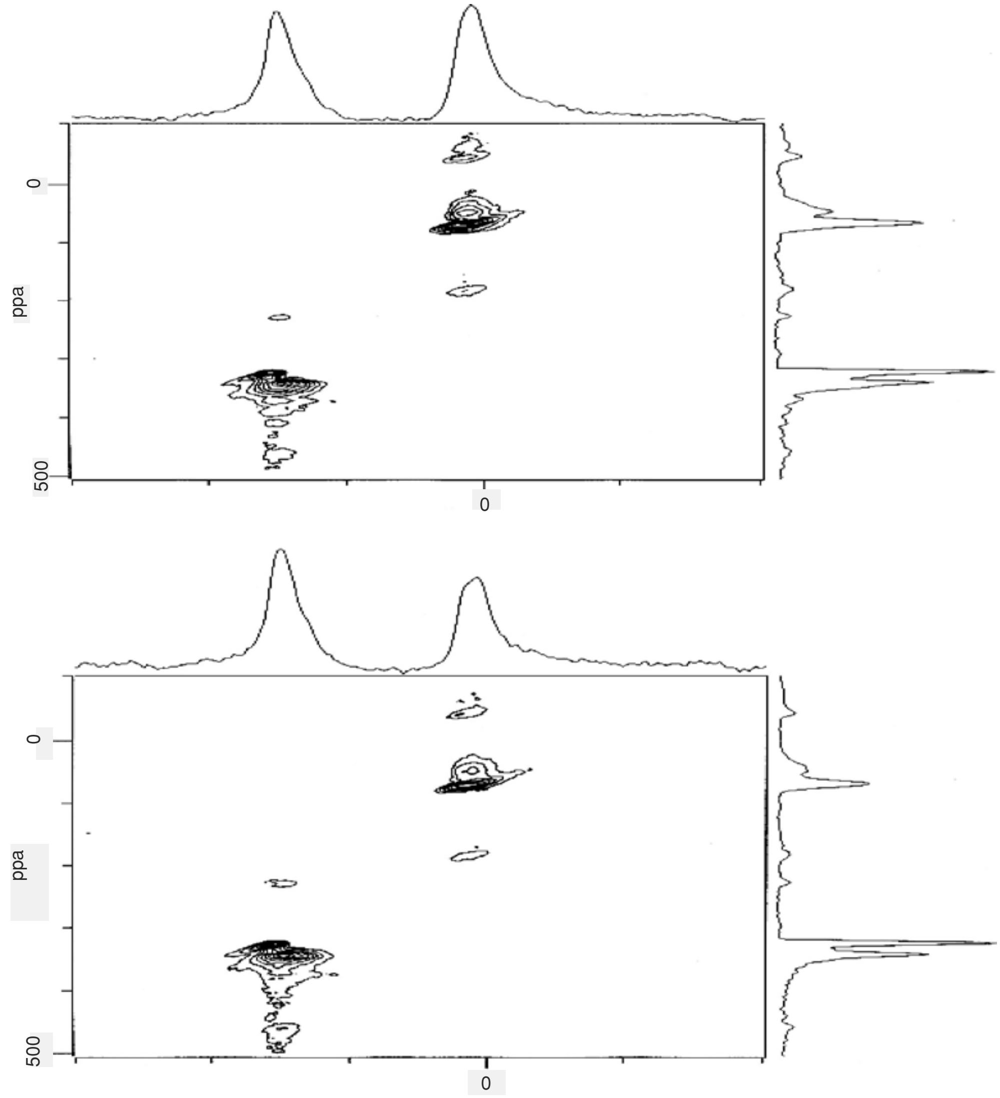

Fig. 4. ^{27}Al 5QMAS spectra for the before drying (upper) and after drying (bottom) of sample 1.

and 3 after drying. It is clear that sample 3 has $Al(OH)_3$ and a 6-coordinate type structure as compared to sample 1, since sample 1 has the surface active agent. On drying, the 6-coordinate type structures change to 4-coordinate type structures because of water loss. It is very difficult to precisely determine the chemical structure because of the high complexity of the mixture, but the effect of quite different proportions of these chemical structures are one of the reasons for the difference of relaxation profiles between samples 1 and 3. These results show the surface active agent is very effective and helpful in optimizing the drying condition for refractory mortar in the real process.

It has been shown that the amplitudes of a simple two-component T_2 analysis of mortar pastes correlate well with the expected fractional volumes of chemically combined and capillary water. It has further been shown that stray-field imaging can quantify all the water. The techniques allow a detailed quantitative study of the effects of drying regimes that result in non-uniform drying and the effects of surface active agents in the water. Differences

Table 1: The quantitative analysis of these chemical structures between sample 1 and 3 after drying obtained by CRAMPS and MQMAS spectra

	Sample 1	Sample 3
CRAMPS study		
H_2O	100*	100*
$Al(OH)_3$	15	31
MQMAS study		
6-coordinate	100†	100†
4-coordinate	50	20

*Integrated signal of H_2O is 100 (standard).

†Integrated signal of the sum of two 6-coordinate is 100 (standard).

between the uptake of capillary water and that of combined capillary water have been observed and quantified. In addition, solid state NMR [^{1}H-CRAMPS and ^{27}Al M(3 and 5)QMAS] studies were performed to clarify the change of chemical structure by drying treatment. It is clear that imaging and solid state NMR give useful information to enable the optimization of the drying conditions. These results are very useful to optimize the drying conditions in the real steel-making process.

Coal [13] is considered to be a heterogeneous organic rock and is typically black, although, deposits can range in color from brown to brownish red. At the same time, it is no doubt that energy 13 is an important commodity because it affects our lives in many ways. Coal is playing a very important role in energy fields. Because total world resources of coal are 1×10^{12} tons; total world production is estimated to be 4.0×10^9 tons/year. The importance of the resource is that, despite having greater problems with production, transportation and utilization compared with oil and gas, it represents a vast resource to meet energy demands well into the future (for more than 1000 years). From the viewpoint of energy resources, coal is a very important material for human and also NMR techniques have many advantage points compared to other methods in order to analyze coal structures.

Thermally induced changes in coals are interesting from the standpoints of both fundamental and applied research for the steel-making process. Furthermore, for very inhomogeneous coals, there is a fascination in the study of the influence of thermal dynamical changes. To monitor the dynamic changes in coals with temperature, an *in situ* method must be used, because it is well-known that the properties of coals change dramatically in high temperature ranges (from 350 to 550 °C) [14–19]. However, the main problem with standard empirical tests, such as the Gieseler plastometer and Audibert-Arnu dilatometer to study the properties of coal changes, is that they have no relationship with the actually occurring structural changes. High temperature ^{1}H-NMR is a powerful technique for the *in situ* investigation of molecular motions in coals during carbonization. The ^{1}H-NMR spectra obtained for coals basically comprise contributions from a mobile and an immobile (rigid) component. The technique was shown by Sanada and coworkers [20] in the late 1970s to clarify fluid materials from coal during early carbonization stages. However, the *in situ* ^{1}H-NMR spectroscopy investigations are limited to the average data for heterogeneous coals which lack information about the distribution of the mobile component and its variations in the specimen due to chemical change by the heating process. We have carried out the first systematic *in situ* variable temperature NMR microimaging study of coals between 25 and 600 °C with our newly developed high temperature microimaging probe and systems in order to clarify the behavior of the mobile component at high temperature in heterogeneous coal specimens. The main specifications of our developed probe are

1. maximum sample temperature is 600 °C,
2. maximum field gradient strength is 250 G/cm,
3. maximum current is 50 A

These specifications can be completely achieved by adopting a rectangular enameled wire for the coil producing the field gradient, using a cooling system by water and alcohol mixture, a coil molding technique, and a very efficient heating system in the probe. The rectangular wire has an extremely high space-factor (over 95% is available), so it is possible to get a high total current density, and it has also good heat dissipation. A Founer–Bessel expansion method [21] was used for optimal coil design. Following this design, the coil was wound as stand alone type coils. Moreover these coils are cooled by a closed circulation cooling system. These coils and cooling pipes are molded by resin for heat dissipation and for preventing coil vibration. Figure 5 shows our variable temperature probe. It has very long spiral heating wire, and the path of the heated N_2 gas is a very close to this heating wire, so that high efficiency of heat exchange is achieved. We have tried the SPI and SPRITE methods at 500 °C using this probe. Both of those two methods are very tolerant of gradient-switching time. For example we applied large pulsed field gradients up to 250 G/cm to this probe, which made the gradient-switching time as long as 150 µs. But the fixed phase-encoding time tp can be shorten as short as 64 µs (method: SPI, FOV: 5 mm, points). So, the combination of high temperature and the SPI or SPRITE method is very effective for coal science. The 2D-SPI sequence for *in situ* experiments was applied in order to observe the distribution of the mobile component in coals using a variable encoding time, because T_2^* of the mobile component for coals is changeable from 100 µs 1 ms with increasing

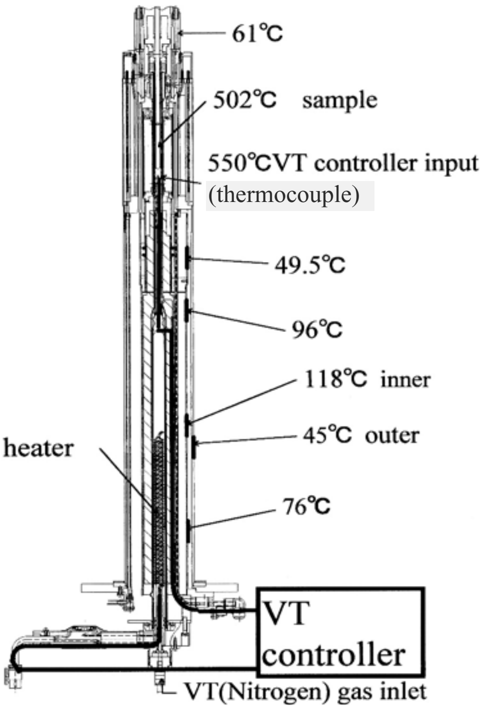

Fig. 5. The developed high temperature imaging probe.

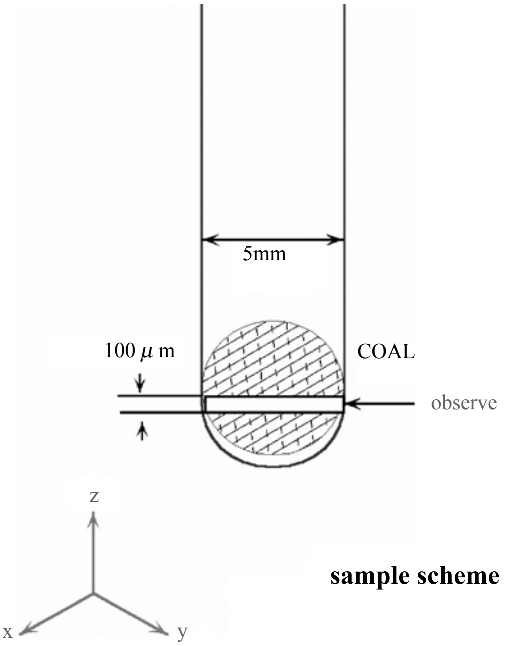

Fig. 6. Experimental sample scheme.

temperature. To avoid the contribution of an immobile component, a variable encoding time at each temperature was optimized. The data matrix size was 128 × 128 (the digital resolution: 50 μm), and the number of signals accumulated was 16. The data acquisition required about 8 min. The experimental sample scheme is shown in Figure 6. The rate of heating was 3 °C /min. which is the same as that of the industrial coking process. This means that the sample temperature was increased by about 24 °C (8 min × 3 °C/min.) during the NMR microimaging measurements.

According to the properties of both coals, the data of Goonyella obtained from Gieselar plastometer and Ro (vitrinite refraction rate %) which are common methods for estimating the properties of coals is better than those of Witbank for coking. It is well-known that coals start to soften and melt at about 400 °C and then, to cake and carbonize at more than 450 °C. The solid echo pulse sequence with a refocusing of 4 μs was used to minimize the loss of signal due to the dead time of the NMR coil. Figure 7A shows NMR image of Goonyella coal at 25 °C and it was found that the distribution of the mobile component was very heterogeneous like the distribution of *macerals* about the coal which was cut with a thickness of 100 μm. As the temperature became higher, the mobile component increased but remained heterogeneity (Figure 7B and C). The images of Figure 7D–F shows that the distribution of the mobile component became more homogeneous. This means that the coal starts to soften and melt, and then the existent rate of the mobile component increases dramatically. It is likely that these areas which are easy to soften and melt are fixed initially, because there are rich areas of the mobile component on the right side of Figure 7A at 25 °C. It is very interesting that the softening and melting areas are moving from the right side to the left side in these images slightly like diffusion phenomena. According to the half-width of the mobile component at 400 °C (where 400 °C means average data from 400 to 425 °C during the measurement, as the temperature increases at the rate of 3 °C/min), compared to other materials measured at the same frequency, the mobility of the mobile component indicates a similarity to gels, rather than liquids. Therefore, it is likely that the stretching of the mobile component occurs since an immobile component can change to a mobile component by heating. At the same time some mobile component parts which have good fluidity initially can melt at first and move with slow diffusion to other areas. As the optimized variable encoding time at each temperature was used in order to avoid the contribution of immobile components in these experiments, it is noted that all results show the behavior of a mobile component only. When the temperature was

Fig. 7. (A) NMR image of Goonyella coal at 25 °C, (B) at 350 °C, (C) at 375 °C, (D) at 400 °C, (e) at 425 °C, (F) at 450 °C, (G) at 475 °C, and (H) at 500 °C. (See also Plate 12 on page XXIII in the Color Plate Section.)

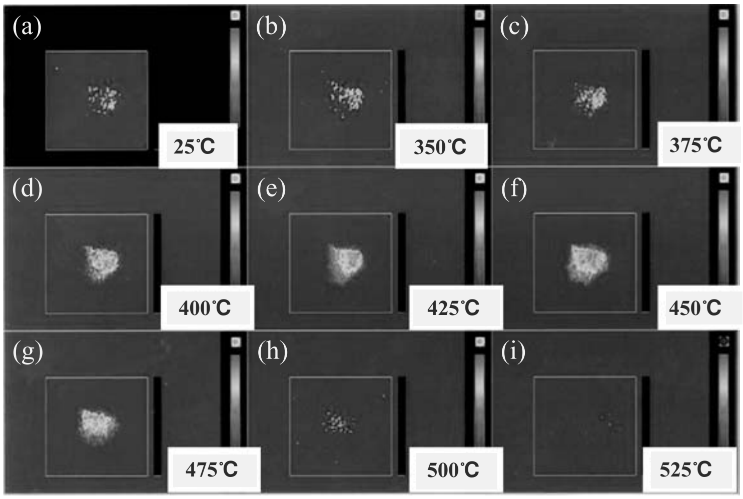

over 450 °C, he resolidification starts and then the mobile component decreased (Figure 7G) and at last, there are a few mobile parts at 500 °C (Figure 7H), because of resolidification this means that a mobile component converts to an immobile component and the carbonization means that the number of protons in coal decreases extremely. On the other hand, Figure 8 shows the image of Witbank coal at 425 °C which indicates the maximum mobility. It is surprising that it shows low mobility areas and retains an unsoftened area, corresponding to an inert area, in spite of the maximum mobility for Witbank. It is likely that low rank coals for coking like Witbank has an inert area which is difficult to soften and melt at its maximum mobility temperature and to move to other areas with diffusion.

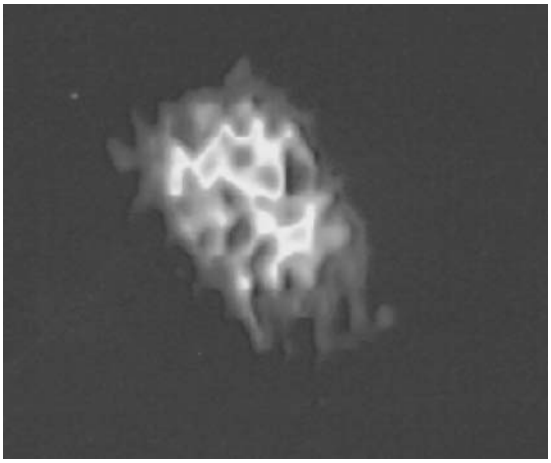

Fig. 8. The image of Witbank coal at 425 °C. (See also Plate 13 on page XXIII in the Color Plate Section.)

Thermally induced changes in coals are interesting from the standpoints of both fundamental and applied research for the iron-making process. Furthermore, for very inhomogeneous coals, there is a fascination in the study about the influence of thermal dynamic changes. To monitor the dynamic changes in coals with temperature, an *in situ* method must be used, because it is well-known that the properties of coals change dramatically in the high temperature range (from 350 to 550 °C). Therefore, we have carried out the first systematic *in situ* high temperature NMR microimaging study of coals between 25 and 550 °C with our newly developed high temperature microimaging probe with systems to clarify the behavior of the mobile component at high temperature in coal specimens. Finally, we have demonstrated the application of recent NMR techniques to new coking process development in the 21st century [22]. It is clear that coal is very inhomogeneous and complex, and at the same time, from the viewpoint of energy coal is very important. But we believe NMR is very powerful, effective and the best tool in order to not only characterize coal structures and clarify the behavior at high temperature but also develop new processes.

References

1. Saito K, Kanehashi K, Saito Y, Godward J. Appl. Magn. Reson. 2002;22:257–68.
2. Saito K, Kanehashi K, Komaki I. Annu. Rep. NMR spectrosc. 2001;44:23–74.

3. Bluemich B, Kuhn W (Eds). In "Magnetic Resonance Microscopy". VCR: Weinheim, 1992.
4. Bluemich B, Bluemler P, Saito K. In "Solid State NMR of Polymers". Elseiver: Amsterdam, 1998, pp 123–61.
5. Gummerson RJ, Hall C, Hoff WD, Hawkes R, Holland GN, Moore WS. Nature. 1999;281:56–7.
6. Papavassiliou G, Milia F, Fardis M, Rumm R, Laganas E. J. Am. Ceram. Soc. 1993;76:2109–11.
7. Kaufmann J, Studer W. Mat. Struct. 1995;28:115–23.
8. Fordham EJ, Roberts TPL, Carpenter TA, Hall LD, Maitland GC, Hall C. AIChE J. 1991;37:1895–99.
9. Nunes T, Randall EW, Samoilenk FG. J. Phys. D Appl. Phys. 1996;29:805–8.
10. McDonald PJ, Perry KP, Roberts SP. Meas. Sci. Technol. 1993;4:896–8.
11. McDonald PJ, Newling B. Rep. Prog. Phys. 1998;61:1441–50.
12. Frydman L, Harwood JS. J. Am. Chem. Soc. 1995;117:5367–70.
13. Retcofsky HL, Link TA. In "Analytical Method for Coal and Coal Products", Vol. 2, Chap. 24. Academic: San Diego, 1978.
14. Saito K, Komaki I, Hasegawa K, Tsuno H. Fuel. 2000;79:405.
15. Saito K, Shinohara M, Hasegawa K, Tsuno H. Bull. Magn. Reson. 1995;18:154.
16. Saito K, Hatakeyama M, Matsuura M, Komaki I. Tetsu-to-Hagane. 1999;85:111.
17. Winans E, Crelling JC. Am. Chem. Ser., No. 252. American Chemical Society: Washington, DC, 1984.
18. van Krevelen W. "Coal", 3rd revised ed. Elseiver: Amsterdam, 1993; Chap. 23, 24.
19. Gerstein C, Murphy PD, Ryan LM. In: RA Meyers (ed). "Coal Structure", Chap. 4. Academic: New York, 1982.
20. Miyazawa K, Yokono T, Sanada Y. Carbon. 1979;17:223.
21. Turner R, Bowley RM. J. Phys. E. 1986;19:876.
22. Saito K, Hatakeyama M, Matsuura M, Komaki I. Tetsu-to-Hagane. 2000;86:79.

Biomedical NMR Spectroscopy and Imaging

Toshiro Inubushi and Sigehiro Morikawa
Biomedical MR Science Center, Shiga University of Medical Science, Seta, Otsu, Shiga 520-2192, Japan

Introduction

An application of NMR spectroscopy for biomedical area is most clearly embodied as MRI, a diagnostic imaging tool, where the information obtained by NMR is presented in a visualized image. Signal intensity, more often, T_1 and T_2, of H_2O signal in ^1H NMR is utilized for the construction of image in 2-dimensional space, as the so-called slice. To acquire data along the direction of chemical shift, it requires further elaborated time in addition to the measurement of MRI data. This is the major reason why the MR spectroscopic imaging is not widely accepted in clinical situation. Furthermore, MR images are sometimes obscured with overlapping images generated by separated signals, so-called "chemical shift artifact." In order to circumvent this bias, it is necessary to employ a technique to enhance the sensitivity of the detection of NMR signal and also to shorten the measurement time by a fast scan technique in MRI. In this section a unique, however, an important area of NMR application, which will lead to the future NMR technology, the so called, molecular imaging (MI) in the near future is discussed.

Tracking of Metabolites: *In Vivo* ^{13}C NMR Images with H-1 Detection

Among many nuclei utilized *in vivo* NMR spectroscopy, a ^{13}C tracer has been widely used for investigating the mechanisms of chemical reactions occurring in biological systems. Despite the difficulties inherent in directly observing ^{13}C NMR signals *in vivo* [1,2], a number of applications have been used ^{13}C tracers to analyze the metabolic pathway in rats [3–5] and humans [6,7].

Various innovative methods have been devised so far, such as hetero nuclear decoupling [8] and cross polarization [9,10], for efficient detection of low sensitive nuclei *in vivo*. One successful method was hetero nuclear editing to select protons coupled with ^{13}C nuclei, which has been extensively applied to studies of ^{13}C-labeled metabolites in animals by Shulman and his colleagues [11,12]. Another approach utilizes the selection of multiple quantum coherence (HMQC) created by the interaction between ^1H and other nuclei having low gyromagnetic ratios, such as ^{13}C and ^{15}N. In the environment of biological NMR, selecting the coherence has been further advanced by employing field gradient pulses (GE-HMQC) [13–16], which can relieve the burden on the NMR instrument by eliminating complicated and eventually time-consuming phase cycling of the RF pulses. Another advantage that accompanies this technique is the removal of unwanted solvent peaks, typically that of H_2O in *in vivo* ^1H NMR spectra, which is forced to diffuse out by the applied field gradient pulses to select the coherence, if the gradient pulses are strong enough. Therefore, it is not necessary to apply a strong RF power on the solvent signal to suppress it. This is particularly beneficial in working with living tissues, in which the ^1H NMR spectrum is dominated by a large H_2O signal. In addition to this, echo planar spectroscopic imaging (EPSI) method was combined to HMQC, which remarkably improved the temporal resolution of spectroscopic imaging [17]. Here the combined technique to observe ^{13}C NMR tracers by ^1H is applied to investigate the metabolic process of 1-^{13}C-glucose in the animal brain [18].

1-^{13}C-glucose data sets were consecutively observed every 35 min. Representative ^{13}C glucose images and the extracted spectra from 10 × 12 voxels of 32 × 32, corresponding to the brain region, are shown in Figure 1A. The glucose images were constructed by summing up the doublet ^1H peaks split by $J^{13}C$-^1H coupling at 1-^{13}C -glucose. These signals were obtained with the ^{13}C frequency selective pulses which excite only the ^{13}C signal at the l-C position of glucose.

Representative serial ^{13}C metabolite images and the extracted spectra in one rat are shown in Figure 1. First, baseline data of 1-^{13}C-glucose and 3/4-^{13}C-Glu/Gln were collected by applying frequency-selective pulses onto 1-^{13}C-glucose and 3/4-^{13}C -Glu/Gln, respectively. Subsequently, 1-^{13}C-glucose infusion was commenced, and acquisition of glucose data was started immediately. After one data set of glucose was collected, the ^{13}C frequency was switched to that of 3/4-Glu/Gln (30 ppm). Thereafter, the data collections of Glu/Gln were repeated.

High ^{13}C-glucose signals in the brain region were detected in the first data set after ^{13}C-glucose infusion, however, then disappeared rapidly. Next, 3/4-^{13}C-Glu/Gln data sets were consecutively observed (Figure 1). The 3/4-Glu/Gln images were constructed from either peak 1 or 2 of the 3/4-^{13}C-Glu/Gln spectra separately, because

Graham A. Webb (ed.), Modern Magnetic Resonance, 173–178.
© 2008 *Springer.*

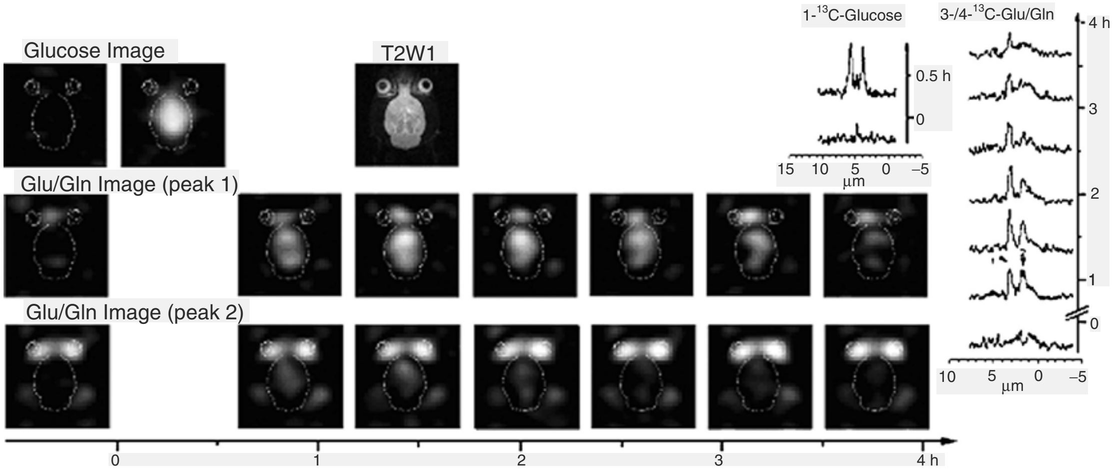

Fig. 1. ^{1}H-detected C-13 Metabolic map of rat brain derived from 1-^{13}C-Glucose. The ^{13}C NMR signals were indirectly detected *via* ^{1}H signals coupled with ^{13}C. The inserted spectra were extracted from 10 × 12 voxels of 32 × 32 CSI data. The images for 1-^{13}C-glucose and for 3-/4-^{13}C glutamate/glutamine were superimposed onto regular ^{1}H images. A measurement of the metabolic map took approximately 20 min. The peak 1 and peak 2 for 3-/4-^{13}C glutamate/glutamine were split by J-coupling with ^{1}H, which were combined to construct the Glu/Gln images.

prominent natural abundant fat CH_2 signals in the orbita also appeared on the peak 2 image. The 3/4-^{13}C-Glu/Gln signals in the brain were minimal in the first data set after ^{13}C-glucose infusion. These signals were maximal in the second and then gradually decreased therefore.

GE-HMQC method possesses several advantages. The GE-HMQC method, in principle, does not require phase cycling, which makes it less sensitive to errors caused by movement of the animal or by hardware instability during high-speed gradient switching. The prominent water signal can be dephased only by the gradient pulses for HMQC selection without water suppression pulses, which enabled us to detect the glucose signal in the brain. The clinically applicable lower magnetic field strength, less expensive tracer, tolerance to movement or hardware performance, and the detection of glucose uptake into the brain might be beneficial for human studies in the future. Thus, the combination of the signal enhancement technique with a rapid acquisition technique enables to obtain chemical shift selective images for living systems.

Physiological Properties: pH

Phosphorus-31 NMR spectroscopy enables the evaluation of the relative concentrations of phosphoenergetic constituents and measurement of intra-cellular pH *in vivo*. The measurement of pH in the living tissues is important to analyze the viability of tissue, since pH change depends upon the oxygen stress. This is clearly demonstrated in an exercised skeletal muscle described below.

The three parameters (height, width, and center frequency) of Pi and PCr peaks in the NMR spectra of 32 × 32 voxels were extracted by specifying the region of each peak with an automatic line-fitting routine to a Lorenzian line shape. Referring to the chemical shift imaging constructed by Pi, we determined the threshold level of Pi signal intensity for pH calculation. The data from the voxels in which the signal intensities of Pi were below that threshold were discarded. Then the pH values in the selected voxels were calculated from the difference (Δ) between the chemical shifts of the two peaks according to the following equation [19].

$$\mathrm{pH} = 6.75 + \log(\Delta - 3.27/5.69 - \Delta) \qquad (1)$$

The calculated pH data were converted to image size 32 × 32 and superimposed onto MRI and/or CSI data [20].

The pH images of human calf muscle after ischemic exercise [21] are shown in Figure 2. Immediately after exercise, ischemic acidosis was severe in the peroneus muscles, moderate in the tibialis anterior muscle and minimal in the triceps muscle of the calf. The severity of acidosis showed good correlation to that of the decrease in phosphoenergetic level. These heterogeneous changes should be caused by the applied workload and heterogenous muscle fiber components. Ten minutes after exercise, the acidosis in either region did not progress further although

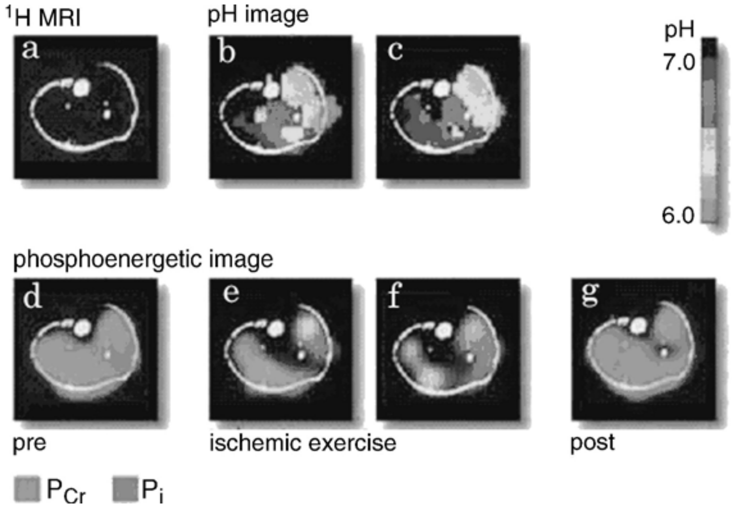

Fig. 2. Metabolic and pH changes in human calf muscle by exercise. ^{1}H MRI image (a) and ^{31}P chemical shift image (d) of human calf muscle in the resting state. A pH image (b) and a chemical shift image (e) during 4 min exercise. (c) and (f) were taken immediately after the exercise. (g) is a chemical shift image obtained 10 min after the exercise. All data were obtained by a clinical MR scanner at 1.5 T. (See also Plate 14 on page XXIII in the Color Plate Section.)

the phosphoenergetic level further decreased during this period. These results suggest that the acidosis is mainly caused not by the ischemia without workload, but by the lactate formed during exercise.

Heterogeneous phosphoenergetic and pH changes in each human calf muscle caused by ischemic exercise are demonstrated as 2D metabolic images using an 1.5 T standard clinical NMR machine and a custom-built volume coil. The spatial and temporal resolution of the images was satisfactory. This non-invasive procedure should be useful in the fields of sports medicine and clinical medicine for peripheral vascular diseases.

Temperature Image and Navigation Surgery Under MRI Guidance

Temperature is also an important parameter to monitor the activity of the living system. Especially in a clinical field, an accurate measurement of the therapeutic area in thermotherapy is essential to carry out appropriate treatment. The use of a thermo coupler or of glass fiber based probe penetrated into the vicinity of the lesion is the only method to monitor the temperature in the treatment. This requires further invasion into a patient other than the surgical invasion. Since there is no reliable method to detect body temperature especially for deeply berried organs in human body at the present time, the temperature image by MRI is the only useful information for the therapeutic response. Temperature image by MRI is based on the temperature dependence of MRI parameters, such as relaxation time T_1, the diffusion coefficient (D) and the hydrogen-bonding shift of tissue water.

Of these parameters, the ^{1}H chemical shift of water has been practically used for temperature mapping. In MRI, chemical shift is calculated from the phase in gradient-echo images

$$\Phi(T) = \gamma\sigma(T)T_\mathrm{E}B_0 \tag{2}$$

where Φ is the phase, γ is the gyromagnetic ratio of the observed nucleus (^{1}H), σ is chemical shift, and T_E is the echo time. In practical, phase shift is measured at given temperature as compared with the phase at reference temperature, and the temperature difference is given as

$$\Delta T = T - T_\mathrm{ref} = [\Phi(T) - \Phi(T_\mathrm{ref})]/\alpha\gamma T_\mathrm{E}B_0 \tag{3}$$

where α is a constant for the temperature dependence of water chemical shift in ppm/°C. Since the constant α is very small at particularly low field and the phase is susceptible to subtle distortion of magnetic field due to body movement of patient, it is important to maintain a stable environment to measure temperature with MRI.

Particularly MRI is advantageous in guiding thermotherapy, since MRI allows not only temperature mapping but can be also used as for target delineation and immediate judgment of therapeutic efficacy during the surgical procedure. We have incorporated the temperature monitoring procedure into intra-operative MRI system introduced at Shiga University of Medical Science.

Temperature monitoring with MRI is undoubtedly a potential tool for the real-time evaluation of the therapeutic effects of thermal ablation. From the viewpoint of electromagnetic interference in the MR images, usage of 2.45 GHz microwave band for ablation is more favorable than the radiofrequency of 500 KHz band for regular ablation. In fact, with radiofrequency ablation, a switching circuit for time sharing is required to reduce the noise in the

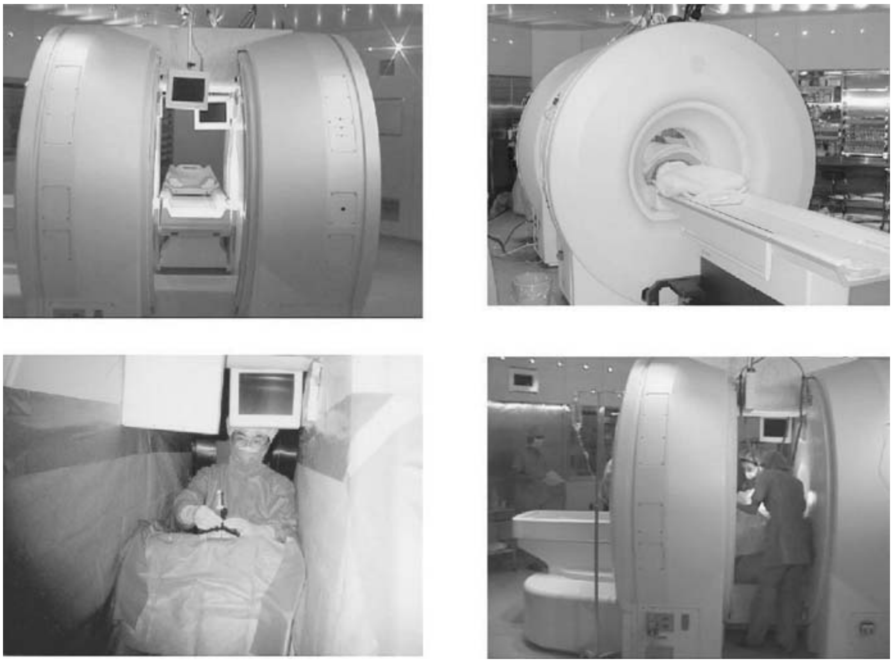

Fig. 3. Photographs of 0.5 Tesla intra-operative MRI instrument (ioMRI). Front (top left) and side (top right) view of the uniquely shaped superconducting magnet having 54 cm vertical gap. Bottom left photo shows that a physician carries out operation over a patient in the MRI magnet, referring to the real time MR images displayed on the monitor placed in the magnet. Supporting staffs also penetrate into the strong magnetic field for patient care (bottom right). (See also Plate 15 on page XXIV in the Color Plate Section.)

MR images [22]. Therefore, we incorporated microwave ablation into MR guidance surgery [23]. Actually, good and reasonable results could be obtained with phantoms or excised tissues. In clinical cases with liver tumors (Figure 4), however, many difficulties should be overcome when using MR temperature monitoring (Figure 5). Because temperature changes are calculated by very small sifts of the water proton resonance frequency form baseline conditions, this technique is highly susceptible to the movement of the liver. This is mainly due to the low-static magnetic field of clinical MR system. Movement of the surgeons and surgical instruments even affects the static magnetic field around the target and results in enormous errors in calculated temperature. From the technical aspect with this MR system, the complicated process and required time for the parameter setting of temperature monitoring were also problems when applying this technique to clinical cases. The improvement of easy and quick parameter setting with our new application was an important step in using temperature monitoring as a useful clinical tool for the evaluation of the therapeutic effects.

The interventional microwave thermocoagulation therapy has regularly been carried out under the guidance of ultrasonography. Actually, ultrasonograpy is an easy, handy, and cost-effective instrument, however, it has serious limitations. The ribs and air space disturb the visibility of ultrasonography and the possible puncture routes are limited. It is sometimes difficult to detect the lesions in the deep parts of the liver. Microbubbles formed by the ablations also perturb the visibility and hampers repeated ablations. The use of MR guidance should be especially beneficial for cases in which ablation therapy is difficult to perform under the guidance of ultrasonography.

Cellular Tracking

Molecular imaging is a newly emerging field of biomedical imaging in which the modern tools of molecular and cellular biology are merged to state-of-art technology for non-invasive imaging. The ultimate goal of this field is to develop technology to investigate molecular and cellular events in living systems. This approach is hoped to lead to better methods for understanding biological processes as well as diagnosing diseases. NMR is one of the key technologies, among positron emission tomography (PET), optical imaging and CT, since NMR is naturally endowed with the ability to operate non-invasive manner.

A technique that can continuously and non-invasively monitor grafted cells in the living system is crucial to

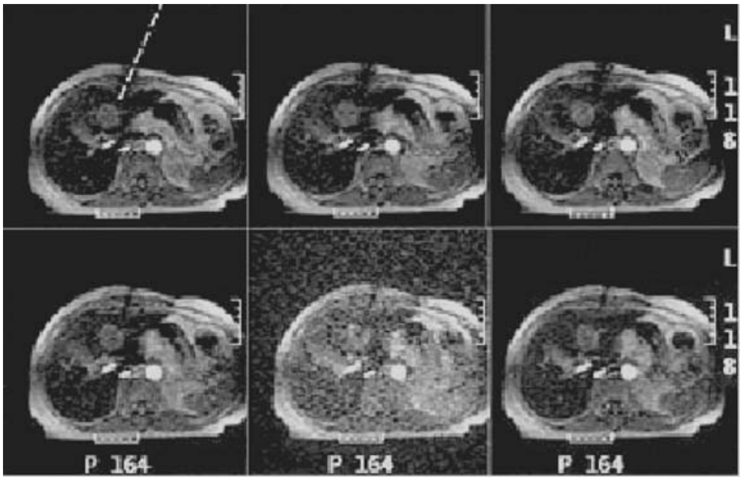

Fig. 4. Microwave ablation therapy for liver tumor under MRI guidance. A surgeon advances a needle to a targeted tumor under the guidance (A) of real time ^{1}H NMR images displayed on a monitor placed inside a magnet. The image for needle was observed as a dark line (B, C). Once the guide needle reached the target, the needle is replace with a microwave antenna (D) and ablation is started (E). During thermal ablation some noises are intruded into a real-time MRI (E). However, the treated area is not distinguished in a regular MRI (F). Therefore, a temperature image is essential for this procedure.

guide further advances in cell transplantation therapy, especially in regenerative medicine using stem cells. So far, various methods have been reported employing available techniques. However, most of these studies have utilized histological techniques, including cytochemistry and imunocytochemistry. These are *ex vivo* techniques, which are limited to apply on postmortem samples and to require corroborative image evidence in order to correlate with *in vivo* data. Recently optical tracking has been developed using luminescent proteins, such as GFP and luciferase. Although these optical methods are operative *in vivo*, a resolution of image is limited and remains difficulty to investigate on a deeply buried organ inside animal body.

Recently, a commercial available MR contrast reagent, dextran-coated superparamagnetic iron oxide (SPIO), was found to be deliverable into several cells, such as, lymphocyte, oligodendrocyte, and HeLa cells with the use of regular lipofection agent, superFect (QIAGEN GmbH, Hilden, Germany) [24]. These magnetically labeled cells on cultured medium showed signal reduction in MRI. More recently ultra small SPIO (USPIO) was incorporated into embryonic stem (ES) cells with lipofection agent, FuGENE (Roche Diagnostics, a division of F. Hoffmann-La Roche Ltd, Basel, Switzerland) and the labeled ES cells were traced by MRI after grafted into rat brain [25]. We have developed a novel method to deliver magnetic labels into cells with an aid of hemagglutinating virus of Japan (HVJ) liposome vehicle, an effective gene transfer vector [26], and also serves as a drag delivery system.

This cell-labeling technique is applicable for many categories of cells, ES cells, neuronal progenitor cells, astrocytes, and PC12 cells. PC12 cells were established from rat adrenal pheochromocytoma, which are described to synthesize catecholamines, such as dopamine and norepinephrine, in response to nerve growth factor. Figure 6 shows the MRI of rat brain received the tagged PC12 cells. MRIs were measured at point to point after the surgical transplantation of the tagged cells up to 2 months. In this period, the implanted cells were well distinguished against the background images in rat brain. The areas of the contrast induced by the grafted cells were observed as long as 2 months, however, they were gradually decreased toward the end of the period, without changing the position.

The efficacy of endosomal labeling of cells and the ability of tracking of the labeled cells is the key factor for

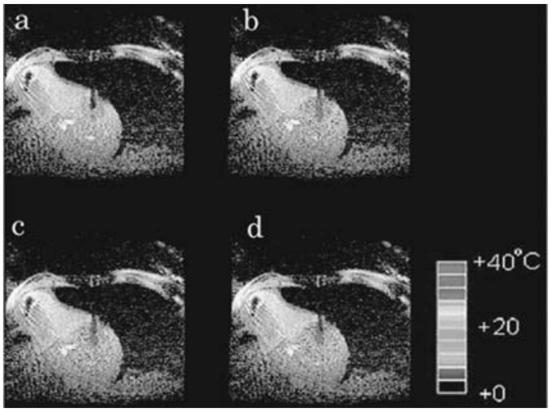

Fig. 5. NMR temperature images obtained during thermotherapy applied for human liver tumor. These figures show that the temperature rises by the microwave ablation. A regular ^{1}H NMR image (A) is superimposed with MR temperature images to display the region treated the thermotherapy. Repetition of ablation brings gradual increase of temperature in the order of (B), (C), and (D) and expands the area reached to the highest temperature. The images (B), (C), and (D) are the display presented to a surgeon during the therapy. (See also Plate 16 on page XXIV in the Color Plate Section.)

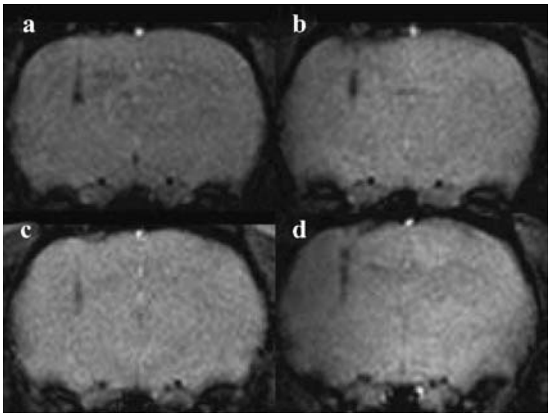

Fig. 6. Coronal views of T_2*-weighted MRI for rat brains received magnetically labeled PC-12 cells. (a) MR image obtained for the rat brain received approximately 2500 labeled cells at day 4 after the transplantation surgery and (b) at day 11 for the same rat as in (a). (c) MR image obtained for the rat brain received approximately 1250 labeled cells at day 4 and (d) at day 11 for the same rat as in (c). Note that the hypo-intensity areas indicating the location of the labeled PC12 cells. The reduction of signal intensity is due to the strong susceptibility effect by the SPIO-based contrast agent Feridex incorporated into the PC12 cells.

the monitoring in cell treatment. The above approach may offer convenient method for studying the distribution and migration of grafted cells in the living system. We expect that MRI tracking of transplanted cells may become a valuable tool for understanding the cellular functions that are key to successful utilization of differentiated stem cells in cell therapy.

Concluding Remarks

Molecular imaging in the future will not merely report on the success or failure of therapy several months after it has been initiated but will play a crucial role in detecting lesions based upon their molecular signatures, will characterize lesions *in situ* to aid in treatment decisions, and will help define successful therapeutic drug levels on an individual basis. The chemical aspect of NMR imaging technology reviewed here shows examples of physiological probes and some example clinical-use paradigms for their implementation into practice. Treatment and screening approaches of number of cancers may benefit in the near future from these tools. In combination with newly emerged bioluminescence and fluorescence imaging techniques targeting specific molecule, an NMR technique, in no doubt, continues to serve as a diagnostic imaging tool in biomedical field.

References

1. Meuller S, Beckmann N. Magn. Reson. Med. 1989;12:400–406.
2. Beckmann N, Meuller N. J. Magn. Reson. 1991;93:186–194.
3. Mason GF, Rothman DL, Behar KL, Shulman RG. J. Cereb. Blood Flow Metab. 1992;12:434–447.
4. Mason GF, Rothman DL, Behar KL, Shulman RG. J. Cereb. Blood Flow Metab. 1992;12:448–455.
5. Cerdan S, Keunnecke B, Seelig J. J. Biol. Chem. 1990;265: 12916–12926.
6. Beckmann N, Turkalj I, Seelig J, Keller U. Biochemistry. 1991;30:6362–6366.
7. Gruetter R, Novotny EJ, Boulware SD, Rothman DL, Mason GF, Shulman RG. Proc. Natl. Acad. Sci. U.S.A. 1992;89:1109–1112.
8. Bottomley PA, Hardy CJ, Roemer PB, Mueller OM. Magn. Reson. Med. 1989;12:348–363.
9. Yeung HN, Swanson SD. J. Magn. Reson. 1989;83:183–189.
10. Beckman N, Meuller S. J. Magn. Reson. 1991;93:299–318.
11. Rothman DL, Behar KL, Hetherington HP, den Hollander JA, Bendall MR, Petrodd OAC, Shulman RG. Proc. Natl. Acad. Sci. U.S.A. 1985;82:1633–1637.
12. Fitzpatrick SM, Hetherington HP, Behar KL, Shulman RG. J. Cereb. Blood Flow Metab. 1990;10:170–179.
13. Knuettel A, Spohn K-H, Kimmich R. J. Magn. Reson. 1990;86:542–548.
14. Hurd RE, John BK. J. Magn. Reson. 1991;91:648–653.
15. van Zijl PCM, Ruiz-Cabello J, Moonen CTW, Cohen JS. Abstract of the 10th SMRM Annual Meeting, 1991, p 1082.
16. Inubushi T, Morikawa S, Kito K, Arai T. Biochem. Biophys. Res. Com. 1993;191:866–872.
17. Morikawa S, Inubushi T, Ishii H, Nakasu Y. Magn. Reson. Med. 1999;42:895–902.
18. Morikawa S, Inubushi TJ. J. Magn. Reson. Imaging. 2001; 13:787–791.
19. Taylor DJ, Styles PM, Matthews DA, Arnold DA, Gadian DG, Bore P, Radda G. Magn. Reson. Med. 1986;3:44–54.
20. Morikawa S, Inubushi T, Kito K, Kido C. Magn. Reson. Med. 1993;29:249–251.
21. Morikawa S, Inubushi T, Kito K, Tabata R. Magn. Reson. Imaging. 1994;12:1121–1126.
22. Morikawa S, Inubushi T, Kurumi Y *et al.* Jpn. J. Magn. Reson. Med. 2001;21:79–84.
23. Zhang Q, Chung YC, Lewin JS, Duerk JL. J. Magn. Reson. Imaging. 1998;8:110–114.
24. Frank JA, Zywicke H, Jordan EK, Mitchell J, Lewis BK, Miller B, Bryant LH Jr, Bulte JW. Acad. Radiol. 2002;9:S484–S487.
25. Hoehn M, Kustermann E, Blunk J, Wiedermann D, Trapp T, Wecker S, Focking M, Arnold H, Hescheler J, Fleischmann BK, Schwindt W, Buhrle C. Proc. Natl. Acad. Sci. U.S.A. 2002;99:16267–16272.
26. Toyoda Y, Tooyama I, Kato M, Sato H, Morikawa S, Hisa Y, Inubushi T. Neuroreport. 2004 Mar;15(4):589–593.

Electron Spin Resonance Imaging in Polymer Research

Shulamith Schlick

Department of Chemistry and Biochemistry, University of Detroit Mercy, Detroit, Michigan 48221-3038, USA

Introduction

In 1973 Paul Lauterbur proposed the use of magnetic field gradients in order to "tell exactly where an NMR signal came from" [1]. The name he coined for the technique, *zeutmatography*, is derived from the Greek word for "joining together": to join the magnetic field gradient and the corresponding radiofrequency in a nuclear magnetic resonance (NMR) experiment. This connection allowed the encoding of spatial information in NMR spectra. The use of magnetic field gradients to separate the resonant frequencies corresponding to different spatial slices led to the development of NMR imaging (NMRI) or, in current language, magnetic resonance imaging (MRI). In the last 25 years, NMRI has blossomed into an essential diagnostic procedure in medicine that provides clear images of previously hidden anatomic parts. Applications of NMRI to Materials Science and other important disciplines, although not as dramatic as the medical applications, are steadily developing [2]. The wonderful story on the discovery of NMRI has been told recently [3].

Imaging based on magnetic field gradients has also been applied to imaging of unpaired electron spins via electron spin resonance (ESR) spectroscopy. The advantages of ESR imaging (ESRI) are the specificity for the detection of paramagnetic species, and the high sensitivity. Papers describing the feasibility of ESRI started to appear in the late 1970s and continue to this day. Early instrumentation, software, and applications of ESRI have been described in a 1991 monograph [4]. Numerous challenges stand in the application of the Lauterbur method to ESRI: First, higher gradients are needed compared to NMRI, usually 100–1000 times larger. Second, ESR spectra are often complex and contain hyperfine splittings that complicate the ESRI experiments. Third, most systems do not contain stable paramagnetic species on which imaging is based; contrast in ESRI is usually provided by radicals produced by irradiation, paramagnetic transition metal ions, or stable nitroxide radicals as dopants.

As seen in the 1991 monograph, the early efforts laid the foundation for the hardware necessary for ESRI and the software necessary for image reconstruction in 1D (spatial) and 2D (spectral-spatial and spatial-spatial). These studies also investigated the feasibility of ESRI experiments in a variety of "phantom" samples, and discussed and estimated the spatial resolution. Typical resolution in ESRI experiments is of the order of 50–80 μm, but can vary widely, depending on the ESR line shapes and line widths.

Information on the spatial distribution of paramagnetic molecules deduced from ESRI experiments has been used successfully for measuring translational diffusion. Diffusion coefficients of paramagnetic diffusants can be deduced from an analysis of the time dependence of concentration profiles along the diffusion direction. Determination of diffusion coefficients for spin probes in liquid crystals and model membranes, and the effect of polymer and probe polydispersity, have been described in a series of papers by Freed and coworkers [5]. These papers represented an effort to move beyond phantoms, and to extract quantitative information from ESRI experiments.

The ability to perform ESRI is restricted to a small number of groups worldwide. While most groups study biological applications of ESRI [6–8], a small number of studies on polymeric materials have appeared: Diffusion coefficients of guests in ion-containing polymers, polymer solutions, crosslinked polymers swollen by solvents, and in self-assembled polymeric surfactants have been determined by 1D ESRI [9–12]. Lucarini *et al.* have determined by 1D ESRI the distribution of the nitroxide radicals in UV-irradiated polypropylene (PP) containing a hindered amine stabilizer (HAS) [13,14]. Ahn *et al.* have deduced the concentration profile of heat-induced radicals in a polyimide resin [15]. *In vitro* degradation of poly(ortho esters) containing 30 mol% lactic acid has been studied by 1D and 2D spectral-spatial ESRI, based on pH-sensitive nitroxide spin probes [16]. Spatially resolved degradation in heterophasic polymer systems, such as poly(acrylonitrile-butadiene-styrene) (ABS) and heterophasic ethylene-propylene copolymers (HPEC), has been described in a series of recent papers [17–25]; details on some of these studies will be described in Section 3 of this Chapter.

ESR Spectra in the Presence of Field Gradients

ESR spectroscopy can be transformed into an imaging method for samples containing unpaired electron spins, if ESR spectra are measured in the presence of magnetic field gradients. In an ESRI experiment the microwave

Graham A. Webb (ed.), Modern Magnetic Resonance, 179–185.

© 2008 *Springer.*

power is absorbed by the unpaired electrons located at coordinate x when the resonance condition, Equation (1), is fulfilled.

$$\nu = (g\beta_e/h)(H_{\text{res}} + xG_x) \qquad (1)$$

In Equation (1) G_x is the linear magnetic field gradient (in G/cm) at x. As in NMRI, the field gradients produce a correspondence between the location x and the resonant magnetic field H_{res}. For a sample consisting of two capillary tubes, the distance between the tubes along the gradient direction can be deduced if the field gradient is known [14b].

The spatial resolution, Δx, is an important parameter in imaging, and can de defined in various ways, as discussed recently [26];the resolution depends on the line width and line shape. Most commonly Δx is expressed as the ratio of the line width to the field gradient, $\Delta H/G_x$; this definition implies that two signals separated by one line width due to the field gradient can be resolved.

An ESRI system can be built with small modifications of commercial spectrometers: gradient coils fixed on the poles of the spectrometer magnet, regulated DC power supplies, and required computer connections. In most systems the software for image reconstruction in 1D and 2D ESRI experiments must be developed on site. Bruker Biospin Inc. has recently commercialized X- and L-band ESR imagers.

Intensity Profiling from 1D ESRI

In the general case, the sample contains a distribution of paramagnetic centers along a given direction, for example x. The ESR spectrum in the presence of the magnetic field gradient is a superposition of signals from paramagnetic centers located at different positions. In 1D ESRI experiments, the intensity profile is obtained from two ESR spectra: $F_0(H)$ measured in the absence of magnetic field gradient, and $F(H)$ measured in the presence of the gradient (the "1D image"). Figure 1 presents the ESR spectrum at 340 K of a nitroxide radical in a HPEC plaque of thickness ≈3 mm: in the absence (top) and in the presence (bottom) of a magnetic field gradient. The intensity (concentration) profile is then determined by deconvolution, as described below.

Mathematically, $F(H)$ is a convolution of $F_0(H)$ with the distribution function of the paramagnetic centers [4,24], Equation (2),

$$F(H) = \int_{-\infty}^{\infty} F_0(H - H^*)\,C(H^*)\,\mathrm{d}H^*, \qquad (2)$$

where $H^* = H_0 - xG$, $H_0 = \mathrm{h}\nu/g\beta_e$, and $C(H^*)$ is the intensity distribution (profile) of the paramagnetic centers along the gradient direction. The convolution expressed in Equation (2) is correct only if the ESR line shape *has no spatial dependence.* This requirement has dictated the conditions for data acquisition in the 1D ESRI study of degradation processes described in Section 3 [17–22].

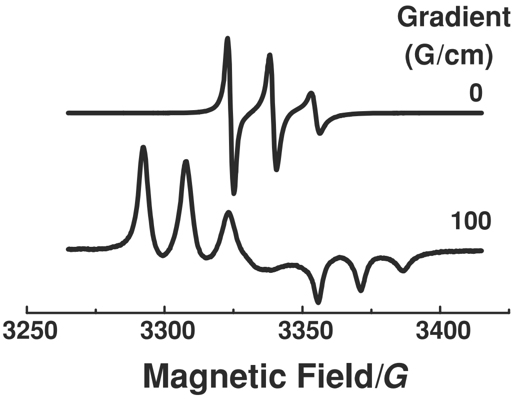

Fig. 1. X-band ESR spectrum at 340 K of HAS-derived nitroxide radicals in a HPEC plaque of thickness ≈3 mm: in the absence (top) and in the presence (bottom) of a magnetic field gradient.

Various optimization methods are viable alternatives to deconvolution. The process starts by assuming an initial distribution, which can be described by a set of parameters. In diffusion studies, for example, the initial distribution is calculated as a function of the diffusion coefficient, diffusion time, and other parameters that define sample configuration [9–12]. Optimization methods use the convolution of this initial distribution function with the experimental spectrum in the absence of magnetic field gradient in order to calculate the spectrum in the presence of the gradient. The deviation between the calculated and the experimental spectra is then minimized by an optimization procedure. In our initial ESRI studies, the concentration profiles of the radicals were deduced by Fourier transform followed by optimization with the Monte Carlo (MC) procedure [13,14,17–20]. The disadvantage of this method is the high-frequency noise present in the optimized profiles. In following publications, the intensity profile was fitted by analytical functions and convoluted with the ESR spectrum measured in the absence of the field gradient in order to simulate the 1D image. The best fit was obtained by variation of the type and parameters of the analytical functions chosen (Gauss or Boltzmann, for example) in order to obtain good agreement with the 1D image, and selected by visual inspection [21,22,24]. Lately the genetic algorithm (GA) for minimization of the difference between simulated and experimental 1D images was implemented; this procedure allowed the best fit to be chosen automatically [23,25]. A typical GA consists of creation of the initial population, calculation of the fit to experimental data, selection of the couples, crossover (reproduction) and mutation. The approach and terminology are adopted from biology and resemble fundamental steps in evolution.

Line Shape Profiling from 2D Spectral-Spatial ESRI

Each 2D image is reconstructed from a complete set of projections, collected as a function of the magnetic field gradient, using a convoluted back-projection algorithm [24]. The number of points for each projection (usually 1024) is kept constant. The maximum experimentally accessible projection angle, $\alpha_{\max}$, depends on the maximum gradient $G_{\max}$ according to $\tan\alpha_{\max} = (L/\Delta H)\, G_{\max}$, where L is the sample length, and ΔH is the spectral width. The maximum sweep width is $\mathrm{SW}_{\max} = \sqrt{2\Delta H/\cos\alpha_{\max}}$. For a width $\Delta H \approx 65$ G (which is typical for the slow-motional component of a nitroxide radical), a sample depth of 3–4 mm, and a maximum field gradient of 250 G/cm along the vertical axis, $\alpha_{\max} = 57^{\circ}$ and $\mathrm{SW}_{\max} = 169$ G. A complete set of data for one image consists of 64–128 projections, taken for gradients corresponding to equally spaced increments of α in the range -90–$+90^{\circ}$; of these projections, typically 41 or 43 (out of 64) are experimentally accessible projections and the rest are projections at missing angles (for α in the intervals 60–90°, and -60° to -90°). The projections at the missing angles can be assumed to be the same as those at the maximum experimentally accessible angle $\alpha_{\max}$, or determined by the projection slice algorithm (PSA) with several iterations [4,17–26].

Spatially-Resolved Degradation from ESRI Experiments

Oxidative degradation of polymeric materials can be viewed on the molecular level as a cascade of events triggered by chemically reactive molecules such as free radicals (R, RO,·and ROO·), and hydroperoxides (ROOH). Modification of polymer properties due to exposure to environmental factors is both on the molecular and macroscopic levels: change of the chemical structure (double bonds formation, chain scission, and crosslinking), and deterioration of mechanical properties. Accelerated degradation is often performed in the laboratory, and the results are interpreted in terms of polymer lifetimes in actual applications [27,28].

Recent advances in the understanding of degradation processes are anchored on the finding that polymer degradation is often spatially heterogeneous. When the rate of oxygen diffusion is not sufficient to supply all the oxygen that can be consumed, only outside layers in contact with oxygen are degraded, whereas the sample interior is protected: this is the diffusion-limited oxidation (DLO) regime [29]. The DLO concept implies that in order to understand degradation and predict lifetimes of polymeric materials in different environments, it is necessary to develop spatially resolved methods for the study of the extent of degradation within sample depth.

Recent studies of photo- and thermal degradation in ABS (Chart 1) and HPEC have demonstrated that one-dimensional (1D) and two-dimensional (2D)

Chart 1

(a) Repeat Units in ABS Polymer

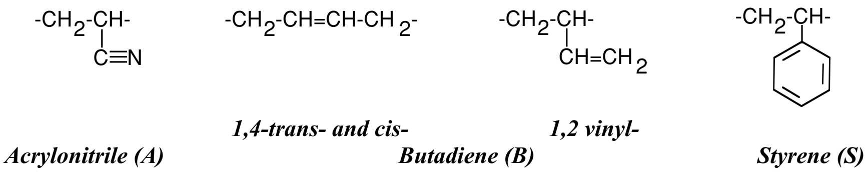

(b) Hindered Amine Stabilizer (HAS): Tinuvin 770

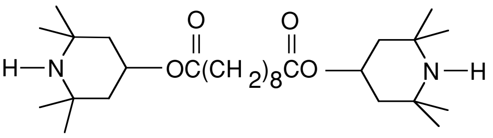

Chart 1. (A) Repeat units in ABS polymer. (B) Hindered amine stabilizer (HAS): Tinuvin 770.

spectral-spatial ESRI can provide details on the extent of degradation as a function of depth and in different morphological domains [14b,17–25]. This approach will be illustrated here for thermally treated ABS [21,22].

ABS polymers are complex, multiphase materials consisting of a butadiene (B) core to which a copolymer of styrene (S) and acrylonitrile (AN) has been grafted [30,31]. The SAN-rich phase is normally continuous, and the size of the B-rich ("rubber") domains is ≤ 1 μm in emulsion polymerization, and 0.5–5 μm in mass polymerization. The ESRI approach was applied to ABS because it represents a polymer that is exceptionally important in technological applications, yet is also vulnerable to thermal and photodegradation, and can be used only in the presence of protecting additives. Hindered amine stabilizers (HAS), for instance bis(2,2,6,6-tetramethyl-4-piperidinyl) sebacate (Tinuvin 770, Chart 1), are added for stabilization of polymeric materials [32,33]. The HAS-derived nitroxides are thermally stable, but can react with free radicals (as scavengers) to yield diamagnetic species; the hydroxylamines can regenerate the original amine, thus resulting in an efficient protective effect. Scheme 1 presents some of the chemical processes involving HAS during exposure to radiation and oxygen.

The HAS-derived nitroxides in the ABS and in the HPEC studied by ESRI perform, however, a triple role. First, they provide the contrast necessary in imaging experiments; second, they probe the morphology of the system, in terms of glass transition characteristics and dynamics; and third, they reflect the degradation process. Once ESRI data are collected and transformed into intensity profile (from 1D ESRI) and spectra as a function of sample depth (from 2D ESRI), the remaining challenge is to translate information extracted from ESRI into details on degradation kinetics and mechanism. Nitroxide radicals reflect not only the spatial extent of degradation, but also events that occur in different morphological domains: In recent studies of ABS polymers, 1D and 2D spectral-spatial ESRI images have enabled the visualization of the selective damage, along the sample depth, in B-rich domains, compared to acrylonitrile/styrene (SAN)-rich domains. Most ESRI experiments were performed on ABS containing ≈10 %B (Magnum 342 EZ, from Dow Chemical Company), doped with 2% wt Tinuvin 770 (Chart 1).

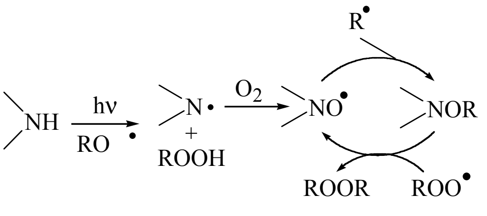

Scheme 1. The Chemistry of Hindered amine stabilizer.

The notation is ABS2H. After treatment, cylindrical samples 3–4 mm in diameter were cut from the plaques; the samples were placed vertically in the ESR resonator, with the symmetry axis along the field gradient.

Typical X-band ESR spectrum at 300 K of HAS-NO in ABS thermally treated at 393 K is presented in Figure 2, and consists of a superposition of two components, from nitroxide radicals differing in their mobility: a "fast" component (F, width ≈32 G), and a "slow" component (S, width ≈64 G). These spectra indicated the presence of HAS-NO radicals in two different environments, and were assigned to nitroxides located respectively in low-T_g domains dominated by B sequences ($T_g \approx 200$ K), and in high-T_g domains dominated by S ($T_g \approx 370$ K) or AN sequences ($T_g \approx 360$ K). By simulation of the fast component and subtraction from the composite spectrum it was possible to reproduce all composite spectra and to determine the relative concentration of the F and S components. The decrease of the relative intensity of F with irradiation or heating time was explained by the consumption of the HAS-derived nitroxide radicals located in B-rich domains of the polymer, which are more vulnerable to degradation [17–20].

The presence of the two spectral components, F and S, is due to the heterophasic nature of ABS. The variation of the F/S ratio with treatment time is, however, due to chemical reactions; in this way a connection was established between the concentration and ESR line shapes of the nitroxides, and the degradation process.

The concentration profiles for the indicated time of thermal treatment at 393 K are shown in Figure 3; the profiles were deduced by simulation of 1D ESR images measured at 240 K. All profiles on the right side are presented with the same maximum height; the profiles on the left are given for one side of the samples (because of symmetry), and normalized by the nitroxide concentration measured

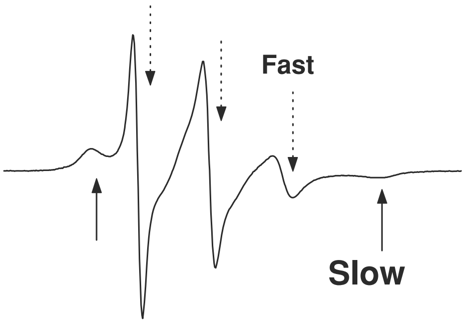

Fig. 2. X-band ESR spectrum at 300 K of HAS-derived nitroxide radicals in heterophasic ABS. Fast and slow components are indicated (see text). The extreme separation of the S component is ≈64 G.

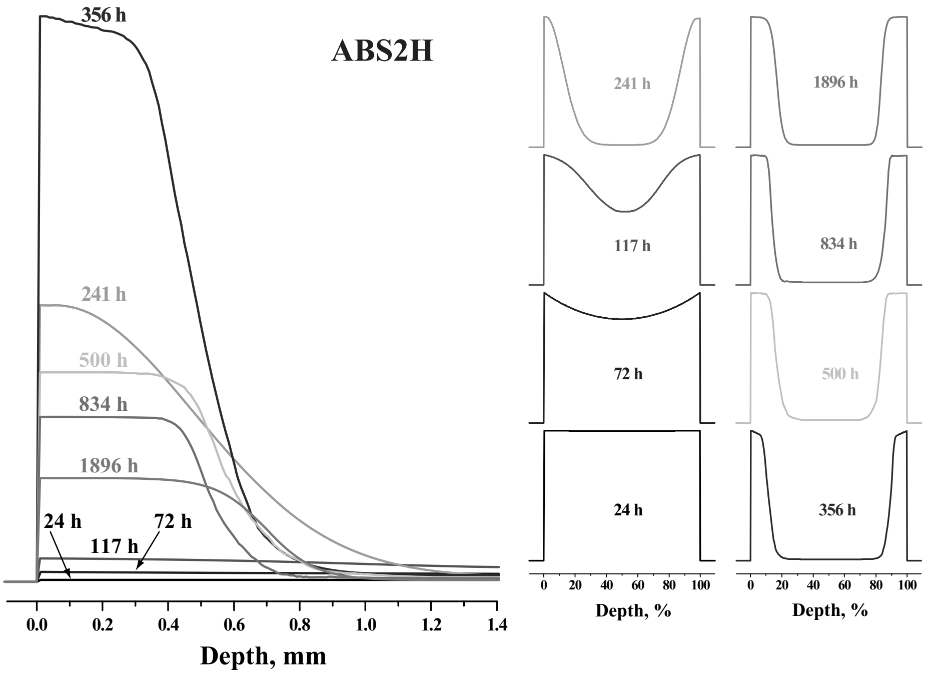

Fig. 3. Right: 1D concentration profiles in ABS2H for the indicated treatment time at 393 K. Left: 1D concentration profiles normalized to the measured total nitroxide concentration; only one side of each (symmetrical) profile is shown (see text).

in whole samples. The evolution from flat profiles in the initial stages of thermal ageing to spatially heterogeneous profiles due to DLO is clearly seen in Figure 3. The 1D profiles indicate that the HAS-derived nitroxides are located at the two sample extremities, in regions of widths is 500–600 μm in ABS2H.

Figure 4 presents 2D spectral-spatial perspective and contour images of nitroxide radicals in ABS2H that has been thermally treated at 393 K for 241 h (left) and 834 h (right). The ESR intensity is presented in absorption mode. Corresponding "virtual" spectral slices obtained nondestructively allowed the determination of the F component (in the B-rich phase) at different depths of the sample: the spectral profile. Figure 5 presents spectral profiles deduced from 2D spectral-spatial ESRI. The evolution of %F along the sample depth is shown as a function of treatment time ($t = 72$, 241 and 834 h), and reflects the nitroxide radicals located in the B-rich domains. The profiles presented in Figure 5 can also be considered as *elastomer profiles*: a look into spatial changes in the elastomeric properties of ABS as degradation progresses. Conclusions from the ESRI experiments were substantiated by attenuated total reflectance (ATR) FTIR spectroscopy of microtomed samples of the polymer [34].

In conclusion, results from ESR imaging, together with the determination of the nitroxide concentration, allowed the mapping of the temporal and spatial variation of the nitroxides, depending on the time and temperature of the treatment. Moreover, the nondestructive ESRI method is sensitive to early stages in the degradation process, and is expected to be complementary to existing profiling methods, for instance FTIR, which are normally applied to more advanced stages of degradation. Finally, the ESRI is of special interest for the study of polymers with phase-separated morphologies. In ABS and HPEC systems, ESRI studies have demonstrated a hierarchical variation of the HAS-derived nitroxide concentration: within the sample depth on the scale of mm, and within morphological domains on the scale of a few μm.

Acknowledgments

ESR and ESRI studies at UDM are supported by the Polymers and International Programs of NSF and by a University Research Grant from The Ford Motor Company. The recent contributions of UDM graduate students S-C Kweon, JG Bokria, and B Varghese; and of J Pilar

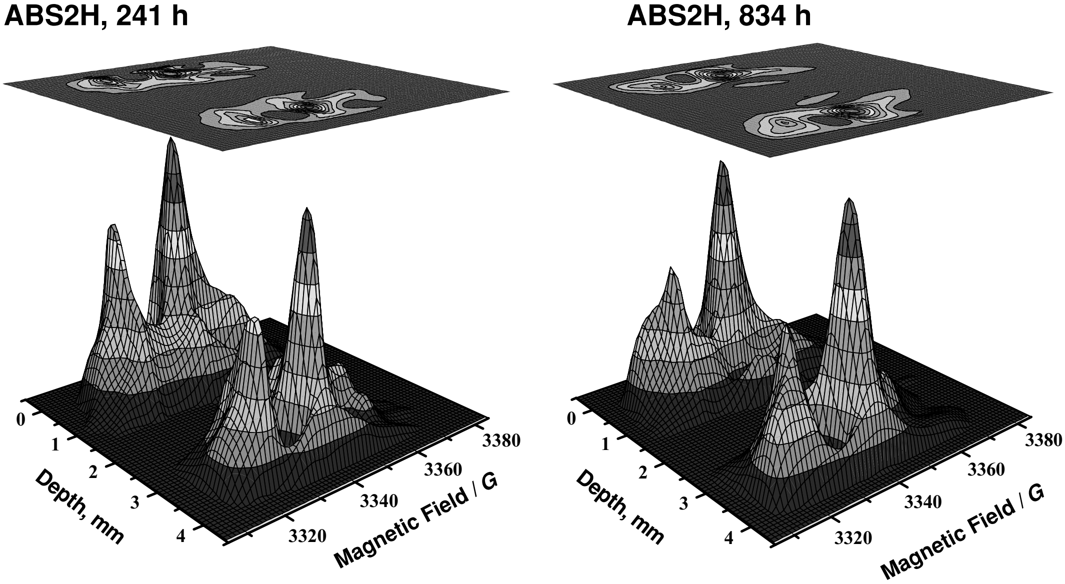

Fig. 4. 2D spectral-spatial contour and perspective plots of HAS-derived nitroxides in ABS2H after 241 h (left) and 834 h (right) of thermal treatment at 393 K, presented in absorption. (See also Plate 17 on page XXIV in the Color Plate Section.)

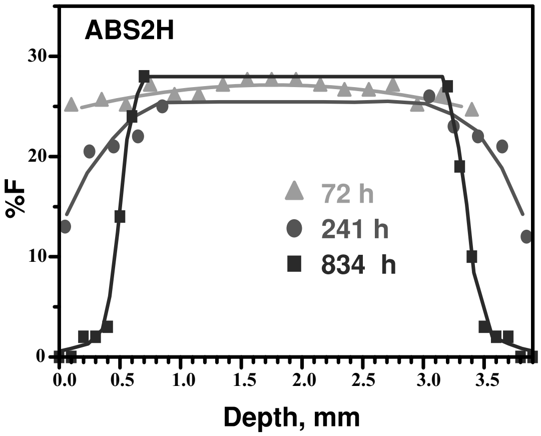

Fig. 5. Spectral profiling, %F as a function of sample depth for ABS2H for the indicated time of thermal treatment at 393 K. Data points were deduced from 200 μm-thick virtual slices in the corresponding 2D spectral-spatial ESR images. (See also Plate 18 on page XXV in the Color Plate Section.)

and A Marek (Prague, Czech Republic), K Kruczala, T Spalek and Z Sojka (Cracow, Poland), and MV Motyakin (Moscow, Russia) have been essential for progress in ESRI methods.

References

1. Lauterbur P, Nature 1973;242:190–191.
2. Blümler P, Blümich B, Botto R, Fukushima E, (Eds). Spatially Resolved Magnetic Resonance: Methods, Materials, Medicine, Biology, Rheology, Ecology, Hardware. Wiley-VCH: Weinheim, Germany, 1998.
3. Kevles BH. Naked to the Bone: Medical Imaging in the Twentieth Century. Rutgers University Press: New Brunswick, N.J., 1997, Chap. 8, pp 173–200.
4. Eaton GR, Eaton SS, Ohno K (Eds). EPR Imaging and in Vivo EPR. CRC Press: Boca Raton, Fla., 1991.
5. Xu D, Hall E, Ober CK, Moscicki JK, Freed JH. J. Phys. Chem. 1996;100:15856–15866, and references therein.
6. Halpern HJ, Chandramouli GVR, Barth ED, Williams BB, Galtsev VE. Curr. Top. Biophys. 1999;23:5–10.
7. Zweier JL, Kuppusamy P, in Ref. 2, Chap. 34, pp 373–388.
8. Oikawa K, Ogata T, Togashi H, Yokoyama H, Ohya-Nishiguchi H, Kamada H. Appl. Radiat. Isot. 1996;47:1605–1609.
9. Degtyarev EN, Schlick S. Langmuir 1999;15:5040–5047.
10. Pilar J, Labsky J, Marek A, Konak C, Schlick S. Macromolecules 1999;32:8230–8233.
11. Schlick S, Eagle P, Kruczala K, Pilar J, in Ref. 2, Chap. 17, pp 221–234.
12. Marek A, Labsky J, Konak C, Pilar J, Schlick S. Macromolecules 2002;35:5517–5528.
13. Lucarini M, Pedulli GF, Borzatta V, Lelli N. Res. Chem. (a) Intermed. 1996;22:581–591; (b) Polym. Degrad. Stab. 1996;53:9–17.

14. (a) Lucarini M, Pedulli GF. Angew. Makromol. Chem. 1997;252:179–193; (b) Lucarini M, Pedulli GF, Motyakin MV, Schlick S. Prog. Polym. Sci. 2003;28: 331–340.
15. Ahn MK, Eaton SS, Eaton GR, Meador MAB. Macromolecules 1997;30:8318–8321.
16. Capancioni S, Abdellaoui KS, Kloeti W, Herrmann W, Brosig H, Borchert H-H, Heller J, Gurny R. Macromolecules 2003;36:6135–6141.
17. Motyakin MV, Gerlock JL, Schlick S. Macromolecules 1999;32:5463–5467.
18. Kruczala K, Motyakin MV, Schlick S. J. Phys. Chem. B 2000;104:3387–3392.
19. Motyakin MV, Schlick S. Macromolecules 2001;34:2854–2864.
20. Schlick S, Kruczala K, Motyakin MV, Gerlock JL. Polym. Degrad. Stab. 2001;73(3): 471–475.
21. Motyakin MV, Schlick S. Polym. Degrad. Stab. 2002;76:25–36.
22. Motyakin MV, Schlick S. Macromolecules 2002;35:3984–3992.
23. Kruczala K, Bokria JG, Schlick S. Macromolecules 2003;36:1909–1919.
24. Motyakin MV, Schlick S. In: CJ Bender, LJ Berliner (Eds). Instrumental Methods in Electron Magnetic Resonance, Biological Magnetic Resonance. Vol. 21, Kluwer Academic/Plenum Publishing Corp.: New York, 2004, pp 349–384.
25. Kruczala K, Aris W, Schlick S. Macromolecules 2005;38: 6979–6987.
26. Van Kienlin M. Pohmann R, in Ref. 2, Chap. 1, pp 3–20.
27. Clough RL, Billingham NC, Gillen KT (Eds). Polymer Durability: Degradation, Stabilization and Lifetime Prediction Adv. Chem. Series 249, American Chemical Society: Washington, DC, 1996.
28. Billingham NC. In G Scott (Ed.), Atmospheric Oxidation and Antioxidants. Vol. II, Elsevier: Amsterdam, 1993, Chap. 4, pp 219–277.
29. Wise J, Gillen KT, Clough RL. Radiat. Phys. Chem. 1997;49:565–573.
30. Kulich DM, Gagger SK. in Ref. 27, Chap. 31, pp 483–501.
31. Aoki Y, Hatano A, Tanaka T, Watanabe H. Macromolecules 2001;34:3100–3107.
32. Pospisil J. Adv. Polym. Sci. 1995;124:87–189.
33. Gerlock JL, Bauer DR, Briggs LM. Polym. Degrad. Stab. 1986;14:53–71; (b) Gerlock JL, Riley T, Bauer DR. Polym. Degrad. Stab. 73–84; (C) Gerlock JL, Bauer DR. Polym. Degrad. Stab. 97–112; Gerlock JL, Kucherov AV, Smith CA. Polym. Degrad. Stab. 2001;73:201–210, and references therein.
34. Bokria JG, Schlick S. Polymer 2003;43:3239–3246.

NMR Imaging: Monitoring of Swelling of Environmental Sensitive Hydrogels

Karl-Friedrich Arndt[1], Manfred Knörgen[2], Sven Richter[1], and Thomas Schmidt[1]
[1] *Institut für Physikalische Chemie und Elektrochemie der Technischen Universität Dresden, D-01062 Dresden, Germany; and*
[2] *Universitätsklinik für Diagnostische Radiologie der Martin-Luther-Universität Halle-Wittenberg, D-06120 Halle, Germany*

Hydrogels

Cross-linked hydrophilic polymers immersed in water can uptake the water. They swell and form hydrogels. The improved performance of hydrogels in biological systems is strongly associated with the water content in the polymeric system. The swelling process is critical to technology areas such as chemical industry (separation matrices), medicine and medical care (gels for cell culture, soft contact lenses, and drug delivery), sanitary products (superabsorbent gels), farming and agriculture (superabsorbend polymer—mixed soil), electric and electronic industries (electrolyte gel), and sensors (fixation of enzymes onto gel) [1]. The kinetic of swelling determines time-constants of the processes using the uptake or loss of swelling agent. The water transport mechanism into the polymer is particularly important for assessing the suitability of hydrogels as drug delivery and drug release systems, as the amount of released drug is dependent on the rate and the transport mechanism of water diffusing into the gel.

Environmental sensitive or "smart" hydrogels are able to change their volume by more than one magnitude in response to different sensitivities such as temperature, pH value, light, ion, and substance concentrations. Therefore, an enormous importance for many technological and scientific applications was expected [2]. The swelling/shrinking of an environmental (or stimuli) sensitive hydrogel starts, if conditions for a volume phase transition, e.g. volume phase transition temperature, mixing ratio of water with a hydrophobic agent like organic solvents, are fulfilled. The swelling/shrinking is connected with a strange change in mobility of the net chains.

Swelling Process

The kinetics of diffusion in polymers ranges from simple Fickian diffusion to high-order diffusion. As proposed by Alfrey *et al*. [3], three models based on the relative rates of penetrant diffusion and relaxation of polymer chain can describe it. In the Fickian (or case I) diffusion, the diffusion is significantly slower than the rate of relaxation of the polymer chains. If the rate of penetrant diffusion is higher than the relaxation rate of the polymer chains a case II diffusion occurs. In a case III or anomalous diffusion, the rates of penetrant diffusion and chain relaxation are comparable.

A variety of techniques to monitor the swelling/shrinking process are known. The easiest and most utilized are based on the determination of the degree of swelling in dependence of time. A partial differential equation describes the swelling for a given geometry [4]. D_{coop}, an apparent cooperative diffusion coefficient associated with long-range diffusion processes involving the cooperative motion of several solute molecules, determines the swelling time. By dynamic light scattering on a swollen gel, it is possible to measure D_{coop} directly [5]. However, since such measurements were performed at a macroscopic level, only little information has been obtained relating to properties of solvent inside the polymeric matrix and the mechanisms of the processes that control the diffusion. Mostly, a network shows varied types of non-regular structures, e.g. distribution of cross-linking density, which influence swelling degree and swell kinetic.

Advantages of NMR Imaging and Application on Network Characterization

NMR methods are a powerful tool for investigation of structure and dynamic in polymer gels [6,7]. NMR relaxation, esp. the dipolar relaxation in fluctuating fields of neighboring spin moments, and model calculations give information about cross-linking density and net chain mobility [8]. NMR spectroscopy and NMR relaxation can be performed as imaging measurements (NMR imaging, NMR microscopy).

This allows a lot of further possibilities, like visualization of non-homogeneities, anisotropy effects, and surface and interface effects [9]. The application of NMR imaging techniques to solid materials have been most rapid in the field of elastomers because of their high chain mobility at moderate temperatures (see review [10]). In the past years, a lot of research work was done concerning the application of NMR imaging on swollen polymers. It can be used to monitor the transport of solvent into

Graham A. Webb (ed.), Modern Magnetic Resonance, 187–193.
© 2008 *Springer.*

solid systems in real time [11], e.g. the shrinking of a poly(methacrylic acid) (PMAA) gel under the application of a d.c. field [12]. It provides information relating to the nature of the diffusion process into a gel on a spatially resolved level with a lateral resolution of about 10–100 μm. An instantaneous diffusion coefficient can be calculated from a single image taken at a specific time. The spatial distributions of low molecular weight components throughout the gel, e.g. profiles of water concentration within different cross-linked hydrogels [13], e.g. distributions of water molecules in PMAA gel under an a.c. field [14], are measurable.

The swelling degree is strongly connected with the cross-linking density. Non-homogeneity in cross-linking density is detectable by measuring a spatial resolved swelling degree within a gel. Some of the water swellable polymers have a low glass transition temperature T_g. By sorption of a solvent, in this case the solvent acts as a plasticizer, T_g decreases. This gives the possibility to monitor the transport of a solvent during swelling by following the change in mobility of the net chain at different places inside the sample.

Combining of NMR imaging with NMR spectroscopic techniques allows both, a quantitative description of the kinetics and mechanism of swelling process and also an insight into the nature of water–polymer interaction. The last could be of great interest in case of application of hydrogels as drug release and drug delivery systems. Fundamental research on hydrogels by means of NMR techniques has been reviewed in reference [15]. Summarizing, NMR imaging gives possibilities to follow time and space resolved a change in concentration of diffused species and, therefore, to collect data to calculate diffusion coefficients, to measure influences on the net chain mobility, and to detect changes in chemical composition due to transport processes. NMR techniques are powerful means of studying dynamics of complicated systems with mobile components such as smart gels and their response process by an application of environmental stimulus.

Experimental

An image delivering MR-measurement consists of two steps in principle: At first the desired effect or contrast (e.g. self-diffusion or relaxation) will be prepared. In a second step, the frequency axis (Larmor frequency) is converted into the space axis by application of an additional gradient field G in direction of the desired profile. For a three dimensional spatial resolution, it can be done in each local dimension x, y, and z:

$$\omega_{\mathrm{L}x(y,z)} = \gamma(B_0 + G_{x(y,z)}) \tag{1}$$

where B_0 is the static magnetic field, γ is the gyromagnetic ratio, and $\omega_{\mathrm{L}x}$ is the resonance frequency of the spin at place x [16].

The spatial resolution Δr depends on the gradient power and the width of the NMR resonance line $\Delta\omega$ of the observed system:

$$\Delta r = \frac{\Delta\omega}{\gamma\,|G_x|} \tag{2}$$

Cross-linked macromolecules show line widths of 0.1–2.0 kHz in dependence on the degree of swelling, solvent molecules of only a few Hz. At a gradient power of 500 mT/m this gives a resolution of about 50 μm, in the case of restricted diffusion of a few μm.

The self-diffusion can be prepared by the Stejskal–Tanner experiment [17]. During the echo time (T_E) of a spin echo two additional magnetic field gradients of strength g and duration δ are switched on at t and $t + \Delta$. Besides the spin-lattice relaxation the displacements of molecules caused by diffusion (D) during Δ lead to an incomplete refocusing of the magnetization of the observed nuclei and an attenuation of the echo S (for details see Figure 1)

$$S(g, \Delta, D) = S_0 \exp\{-\gamma^2 g^2 \delta^2 (\Delta - \delta/3) D\} \tag{3}$$

Higher rates of diffusion strongly weaken the signals. So it is possible to investigate diffusion indirectly by a multiple measurement of echoes influenced by a series of growing/decreasing field gradients.

A further example of the imaging effect is the T_2-contrast of swelling experiments, which can be encoded by a series of spin-echoes with different echo times (Figure 2). The contrast roughly scales the microscopic molecular mobility [18].

Not in any case the echo decay is an (one-) exponential decay. Very often a non-exponential part at the beginning of the relaxation curve can be observed, providing important information on the material, like the anisotropy of molecular motion, which can be a measure for the cross-linking density of a polymer [8].

The spatial information is detected in the second part of the imaging experiment by using a field gradient additionally to the static field B_0. The item “second part” does not mean that the spatial resolution is detected after the contrast preparation in any case. In practice, very often the pulse sequences detect the contrast and the local features during the same echo cycle.

Three-dimensional spatial resolution is done by using three orthogonal gradients, a 2D or 1D (profile imaging) by two or one gradient(s), respectively.

Two basic principles of sampling the spatial information are used:

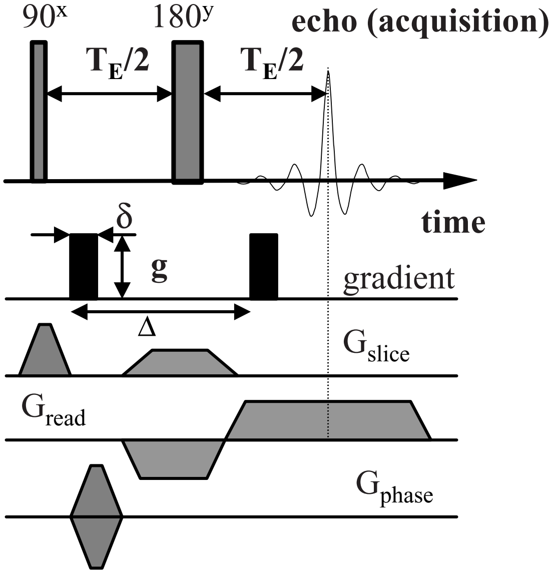

Fig. 1. NMR sequence for diffusion weighted imaging. The upper part agrees with the pulsed experiment of Stejskal and Tanner. The amplitude of the signal is coded in dependence on the diffusion coefficient by two gradients (δ, g) in a time difference Δ because only stationary spins refocus with the original echo amplitude. The lower part shows the magnetic field gradients for coding the coordinates in space (Fourier imaging). $G_{(\mathrm{index})}$ are different field gradients. The read out-, phase-, and slice-gradients normally match the x-, y-, and z-direction of the object.

- Fourier imaging (FI) with a Cartesian sampling of the k-space ($k = 2\pi/\lambda$) and
- (filtered) Back Projection (fBP) with a spherical sampling of the k-space.

The advantage of the FI is the simple calculation of the images by Fourier-transformation. The disadvantage may show up in the higher demands on the technical realization, including gradient rising times of only 1–3 μs, which are needed for the measurement of systems with very short relaxation times, typical of more solid like systems like strongly cross-linked macromolecules.

In opposite to the FI, the gradients of fBP-sequence stay constant during the whole echo pulse sequence until the next projection angle. However, fBP-sequences have more difficulties in the image calculation. The filtering process and the transformation from spherical to Cartesian coordinates are very sensitive to artifacts.

All discussed experiments were done with a VARIAN unity 200 MHz (wide bore) equipped with a homemade imaging probe of following features:

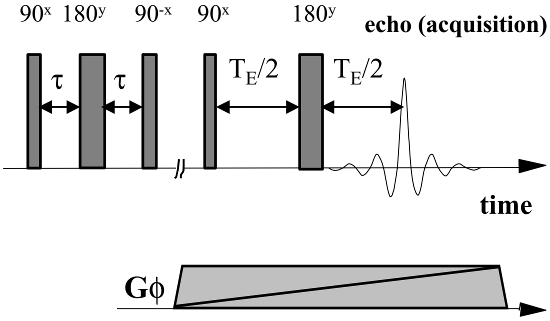

Fig. 2. Spin echo sequence with variable echo time τ for determination of T_2 relaxation curve. The angle of the field-gradient direction with respect to the x-axis is given by $\phi = \arctan(G_y/G_x)$ and is stepped within $0 < \phi < 180°$.

Active shielded design, gradient power up to 50 A (giving a maximum gradient of 5 mT/cm), inner diameter 30 mm, temperature control between 0° and 120°C. Rf-part: resonance frequency 200 MHz (protons) or 67 MHz (deuterium), saddle coil or solenoid (different inner diameters: 5 mm, 7 mm, and 26 mm for the deuterium coil). In case of moderate cross-linked elastomers and gels the resolution is better than 50 μm for ^{1}H-imaging.

The experimental set-up for measurements of concentration profiles along a swelling gel (1D-measurements) are shown in Figure 3a and c. In this case the experiments were done without slice selection, giving a high signal-to-noise ratio in a very short time (<1 min). 2D-measurements with a slice thickness of less than 1 mm

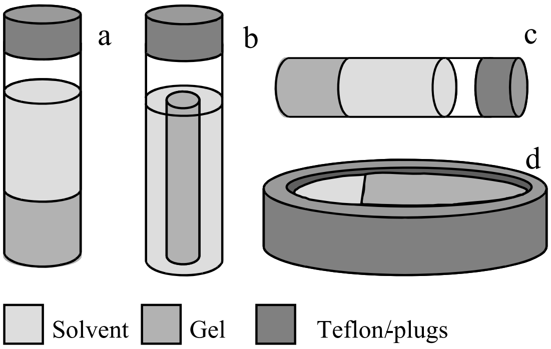

Fig. 3. Experimental set-up for swelling and diffusion experiments on gels. a: vertical arrangement, restricted solvent contact (^{1}H; saddle coil; inner diameter: 7 mm), b: vertical arrangement (^{1}H; saddle coil; inner diameter: 7 mm), c: horizontal arrangement (^{1}H; solenoid; inner diameter: 5 mm), d: vertical arrangement, restricted solvent contact (^{2}D; saddle coil; outer diameter: 30 mm).

are made by an arrangement of the slices perpendicular to the symmetry axis of the coil.

Volume Phase Transition, Net Chain Mobility, and T-Stimulus

An often-investigated T-sensitive polymer is poly(*N*-isopropylacrylamide) (PNIPA). A PNIPA gel undergoes a volume phase transition during heating at about 33 °C, the volume phase transition temperature T_{vpt}. A two-step mechanism is discussed for this transition (isochore conditions). At T_{vpt} the net chains in the swollen gel tend to collapse. They form a macro-network, i.e. bundles of aggregated and stretched polymer chains very fast. A following of this is the reduced mobility of the net chains. Figure 4 shows the 2D Fourier images of PNIPA swollen in D_2O during heating. The signals result from the protons of the net chain. The processes at T_{vpt} causes a reduced T_2 relaxation time and therefore a signal reduction (the color represents the chain mobility), even at a high content of water.

The swelling degree in the first step of the transition process is constant. In a second step the de-swelling starts. The time-constant τ_{swell} to reach the new equilibrium degree of swelling depends on the cooperative diffusion coefficient ($D_{\text{coop}} \approx 10^{-7}$ cm^2/s) and the square of a dimension characterizing the geometry of the gel d^2 (in case of homogeneous gels their macroscopic dimension), $\tau_{\text{swell}} \sim d^2/D_{\text{coop}}$. To follow the whole process of volume phase transition, we investigated the PNIPA gel swollen in H_2O (Figure 5). At $T < T_{\text{vpt}}$ the image contrast represents the T_2-weighted spin density of ^{1}H of the net chains and the self-diffusion and T_2-weighted spin density of ^{1}H of H_2O. At $T > T_{\text{vpt}}$ it represents only the signals of H_2O inside and outside the gel.

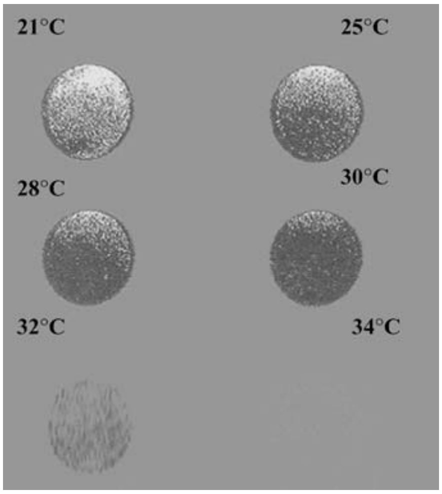

Fig. 4. 2D-^{1}H-Fourier images of PNIPA gel swollen in D_2O at different temperatures. Cross-sections of cylindrical samples (experimental set-up: Figure 3b), contrast from the protons of polymer matrix (T_2-weighted), resolution ca. (30 μm)^2. (See also Plate 19 on page XXV in the Color Plate Section.)

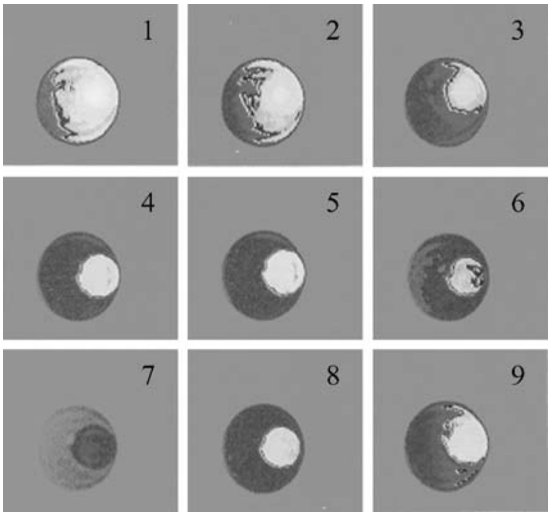

Fig. 5. 2D-^{1}H-Fourier images of PNIPA gel swollen in H_2O at different temperatures and times. 1: 22 °C/0 min, 2: 25 °C/6 min, 3: 30 °C/13 min, 4: 32 °C/16 min, 5: 34 °C/20 min, 6: 40 °C/25 min, 7: 50 °C/50 min, 8: 40 °C/57 min, 9: 30 °C/67 min. The pictures show cross-sections (experimental set-up: Figure 3b) of the immobilized water (contrast mainly from the water protons) inside the polymer matrix (clearly seen as yellow circles in 4, 5, and 8) and of the surrounding free water. 1–4: The signals outside the gel attenuate due to convection during heating. 5: The macro-network formation at T_{vpt} does not influence the signals (as it does at D_2O measurements!). 6: At higher *T* and at longer times structural changes yield to signal attenuation (shortening of T_2, interactions between polymer matrix and water). 7: Polymer matrix is homogeneous. 8,9: Cooling the sample. (See also Plate 20 on page XXV in the Color Plate Section.)

Diffusion of Low Molecular Weight Compounds

Different diffusion processes can occur in a swollen gel. An exchange of the swelling agent inside and outside of the gel is possible. Figure 6 shows the transport of D_2O into a water swollen PNIPA gel ($T < T_{\text{vpt}}$). The signal represents the concentration of D_2O inside the gel in dependence on time.

Under isothermal conditions, the volume phase transition can be achieved by adding an organic solvent to the swelling agent in the surrounding of the gel. The

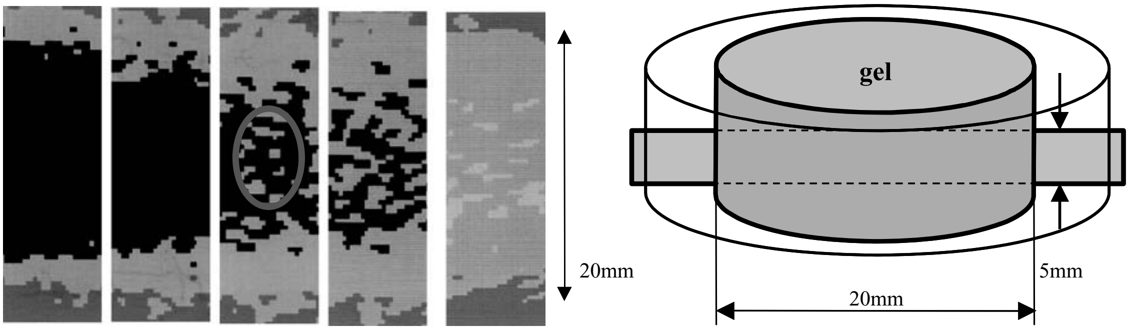

Fig. 6. Diffusion of D_2O into a water swollen PNIPA gel cylinder. Deuterium flash imaging at 20 °C of a thin vertical (5 mm) layer (right); the cylindrical gel (15.5 mm high) is immersed in D_2O. The gel was cross-linked with a high concentration of cross-linker. This results in a non-homogeneous (porous) gel structure, notice the diffusion channels (red ellipse). Time after immersion into D_2O (from left): 2 min, 82 min, 162 min, 212 min, 24 h. (See also Plate 21 on page XXV in the Color Plate Section.)

organic solvent (here methanol) diffuses into the gel. The volume phase transition appears at a given concentration of methanol in the gel (for PNIPA: 20 vol% of methanol in water). The shrinking, which is determined by the cooperative diffusion, starts. The diffusion of partially deuterated methanol (CH_3OD) into the D_2O swollen gel is followed by measuring the change of magnetization in a layer inside the gel of 60 μm thickness at a given distance to the surface [19]. From the time lag between starting the diffusion to the increase of signal due to the raise of CH_3OD D_{MeOD} can be calculated (1D experiment, exp. set-up: Figure 3a). Under the used experimental conditions $D_{MeOD} = (1.8-3.9)\ 10^{-5}$ cm^2/s in dependence of CH_3OD concentration was determined. The same experiment can be performed with H_2O. In this case the self-diffusion coefficient of water inside the gel can be measured ($D_{\text{self}} = 2.3\ 10^{-5}$ cm^2/s).

Distribution of Water Inside the Gel

NMR techniques enable us not only to follow transport processes, but also to visualize the distribution of components inside a gel. Figure 7 gives an example of measuring the distribution of swelling agent, here a mixture of water and partially deuterated methanol, in a gel. The water-swollen gel was immersed in a D_2O/CH_3OD-mixture with such a methanol content (40 vol%) that the volume phase transition occurs. Because the condition for volume phase transition is fulfilled the net chains collapse. A dense layer on the gel surface is formed. This happens at either temperature or solvent induced transitions. In case of a homogeneous gel the layer is thin (skin effect, Figure 7a) and further diffusion is not hindered. But in case of a porous gel a thicker layer of collapsed net chains is formed. It acts as a barrier and prevent shrinking processes (shrinkage barrier [19]). The skin formation is a time-distance problem of different diffusion processes that happen simultaneously: D_{coop} and the typical dimension of the gel determine the time constant for de-swelling. In case of a homogeneous structure, the typical dimension is given by the geometry of the gel. The dimension determining the diffusion in a sponge-like gel (Figure 7c) depends on the geometry of the pores. Now, the shrinking process is faster in comparison with the diffusion of the low molecular weight component.

The shrinkage barrier separates the inner part of the gel from the outer part and prevents a further de-swelling (Figure 7b).

Diffusion Coefficients Inside the Gel—Structure of Non-homogeneous Networks

The diffusion of the swelling agent is influenced by the structure of the gel matrix. An image of the diffusion coefficients inside the gel gives information about the homogeneity of the gel. The Tanner-Stejskal sequence (Figure 1) with different echo-times yields to a series of diffusion weighted images (Figure 8, left shows one image). Using of Equation (3), a reciprocal diffusion coefficient for each pixel can be calculated (Figure 8, right). The signals of the surrounded water are influenced by thermal fluctuation and do not represent a diffusion coefficient.

The temperature-sensitive poly(vinyl methyl ether) (PVME) can be cross-linked by high-energy radiation. A non-homogeneous network is formed at e-beam irradiation of high concentrated aqueous solution [20,21]. Due to absorption of energy the aqueous polymer solution is heated, the volume phase separation occurs and the phase-separated structure is fixed by cross-linking. The gels are sponge-like and show a high response on heating/cooling (the same situation is given, if PNIPA is cross-linked with

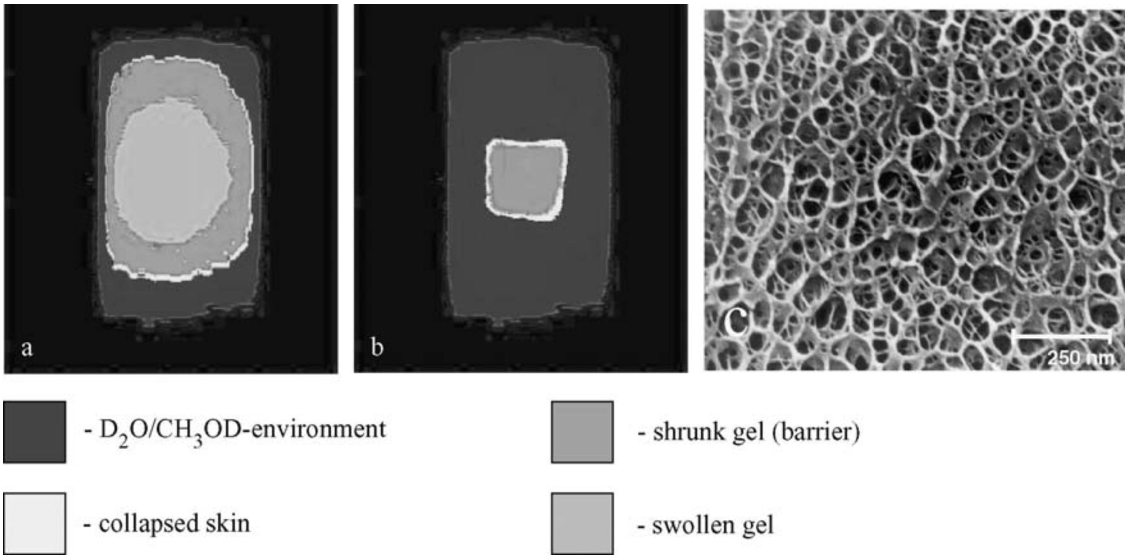

Fig. 7. Distribution of water in collapsed PNIPA gel, de-swelling induced by methanol. Fourier images (slice selection, T_2-weighted) of a vertical plane of PNIPA gels. (a) sponge-like gel after 3 days in D_2O/CH_3OD; (b) homogeneous gel; (c) The FESEM micrograph shows the sponge-like structure of gel b (scale bar: 250 nm). (See also Plate 22 on page XXVI in the Color Plate Section.)

a high concentration of cross-linker, sample Figure 7b). A characterization of such networks with rheological methods is difficult because of its porosity.

The diffusion coefficient of the swelling agent is influenced by the structure of the surrounded gel matrix. The distribution of D (here water) can act as an indirect measure for structural non-homogeneities. Figure 9 shows diffusion images of different PVME gels. The brightness is correlated with a fit parameter d ($\sim 1/D$). The figures illustrate changes in a distribution of d ($\sim 1/D$) with the radiation dose.

With increasing dose the cross-linking density increases and the D decreases. At a dose of 100 kGy the D shows a minimum (Table 1). As mentioned above, at

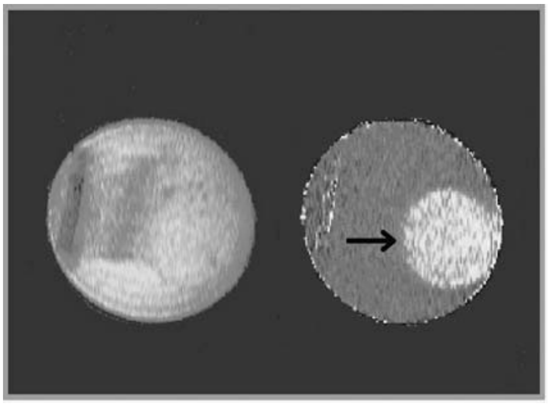

Fig. 8. Determination of diffusion coefficient of water inside a gel. Cross sections of a glass tube (7 mm diameter) containing the cylindrical PNIPA gel (3 mm diameter). Besides the dark strip on the left side (which arises from a piece of Teflon used to fix the gel) no further details can be seen in the diffusion weighted image (left). In the diffusion image (right), the hindered diffusion of water in the gel gives a good contrast to the water outside. Notice, the diffusion is depicted with inverse intensity giving brighter pixels to the gel. A surface layer of stronger diffusion (~0.5 mm) can be observed also (arrow). (See also Plate 23 on page XXVI in the Color Plate Section.)

Table 1: Water diffusion coefficient inside PVME gels with different cross-linking densities (irradiation doses). A calibration of the signal (Figure 9) is necessary to calculate absolute values of D. This was done by means of measurements with pure water at different temperatures

Dose (kGy)	50	75	100	150
$D(H_2O)$ (10^{-5} cm^2/s)	2.1	1.7	1.25	1.65

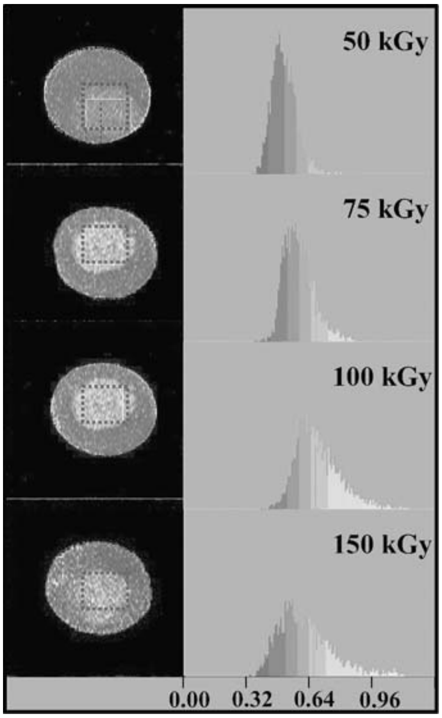

Fig. 9. Influence of cross-linking on D of water and its distribution. Diffusion images (left) of e-beam cross-linked (different doses in kGy) PVME swollen to equilibrium in water at room temperature. To match the Stejskal–Tanner equation (Equation (3)) an one-exponential fit, $I = I_0 \exp(-g^2/d)$, of each data point from at least six diffusion-weighted images of different gradient strength g was performed. The figures show the fit-parameter d. $1/d = \gamma^2\delta^2\left(\Delta - \delta/3\right)D$ (See also Plate 24 on page XXVI in the Color Plate Section.)

higher values of dose due to energy absorption the gels get a sponge-like structure. This results in an increase of *D* and a broader distribution of *D*.

Acknowledgment

The work was partially granted by the Deutsche Forschungsgemeinschaft (DFG), within SFB 287 “Reactive Polymers.” The authors thank R. Reichelt (Westfälische Universität Münster) for the FESEM-micrograph.

References

1. Osada Y, Kajiwara Y (Eds). Gels Handbook, Part 3. Academic Press: San Diego, 2001.
2. English AE, Edelman ER, Tanaka T. Polymer hydrogel phase transitions. In: T Tanaka (Ed). Experimental Methods in Polymer Science: Modern Methods in Polymer Research and Technology. Academic Press: New York, 2000, p 547.
3. Alfrey T, Gurnee EF, Lloyd WG. J. Polym. Sci. C. 1966;12: 249.
4. Tanaka T, Hocker L, Benedek GB. J. Chem. Phys. 1973;59: 5151.
5. Geissler E. Dynamic light scattering from polymer gels. In: W Brown (Ed). Dynamic Light Scattering: The Method and Application. Clarendon Press: Oxford, 1993, p 471.
6. Callaghan PT. Principles of Nuclear Magnetic Resonance Microscopy. Oxford University Press: Oxford, 1991.
7. Blümich B. NMR Imaging of Materials. Clarendon Press: Oxford, 2000.
8. Knörgen M, Heuert U, Schneider H, Heinrich G. J. Macromol. Sci. Phys. 1999;B38(||5 and 6):1009–22.
9. Knörgen M, Heuert U, Schneider H, Barth P, Kuhn W. Polym. Bull. 1997;38:101.
10. Blümich B, Blümler P. Makromolekulare Chem. 1993;194: 2133.
    Blümler P, Blümich B. Rubber Chem. Technol. 1997;70: 468.
11. Fyfe CA, Blazek AI. Macromolecules. 1997;30:6230.
12. Hotta Y, Ando I. J. Mol. Struct. 2002;||602–3:165.
13. George KA, Wentrup-Byrne E, Hill DJT, Whittaker AK. Biomacromolecules. 2004;5:1194.
14. Hotta Y, Shibuya T, Yasunaga H, Kurosu H, Ando I. Polym. Gels Netw. 1998;6:1.
15. Yasunaga H, Kobayashi M, Matsukawa S, Kurosu H, Ando I. Annu. Rep. NMR Spectrosc. 1997;34:39.
16. Lauterbur PC. Nature. 1973;242:190.
17. Stejskal EO, Tanner JE. J. Chem. Phys. 1965;42:288.
18. Knörgen M, Heuert U, Schneider H, Kuckling D, Richter S, Arndt K-F. Macromol. Symp. 1999;145:83.
19. Knörgen M, Arndt K-F, Richter S, Kuckling D, Schneider H. J. Mol. Struct. 2000;554:69.
20. Schmidt T, Querner C, Arndt, K-F. Nucl. Instrum. Methods Phys. Res. B (NIMB) 2003;208:331.
21. Richter S. Colloid Polym. Sci. 2004;282:1213.

Part I

Inorganic Materials and Catalysis

Exploiting $^1H\longrightarrow{}^{29}Si$ Cross-Polarization Features for Structural Characterization of Inorganic Materials

Piotr Tekely
UMR CNRS 7565, Université Henri Poincaré, Nancy I, Vandoeuvre-lès-Nancy, France

Introduction

High-resolution solid state ^{29}Si NMR spectroscopy was frequently used during the last 25 years in structural studies of inorganic materials including zeolites [1–3], minerals [1–3], glasses [3], and cement-based systems [4]. Its important place in structure determination of these materials relies on the fact that ^{29}Si NMR spectra permit a precise determination of the ^{29}Si isotropic chemical shift in different silicon environments of powdered samples. Indeed, for materials with silicon in tetrahedral coordination, the isotropic position of resonance signal provides immediately the degree of condensation of SiO_4 terahedra ($Q^{(n)}$, with $n = 0, 1, 2, 3, 4$) and informs about Si–O–Si bond angles and Si–O bond lengths [1–3]. Although the easiest way to record the quantitative ^{29}Si NMR spectrum is a direct excitation by a single pulse, this cannot be reasonably applied in most cases due to extremely long ^{29}Si longitudinal relaxation times. To avoid this inconvenience, one can take advantage of magnetization transfer from protons to ^{29}Si spins.

In spite of the fact, that when using cross-polarization (CP) procedure, the quantitative proportions of chemically or crystallographically inequivalent sites cannot be reached as with single pulse excitation, an extremely valuable structural and dynamic information can be obtained in this manner. However, to access such information, some basic precautions have to be taken. Indeed, when recording the CP spectra under MAS at spinning frequencies of the same order of magnitude as the dipolar coupling interaction involved in polarization transfer, two complications immediately arise. First, the Hartmann–Hahn (H–H) matching condition is split into several sideband-matching positions (Figure 1a–d).

Consequently, $^1H\rightarrow{}^{29}Si$ CP occurs effectively only when the generalized H–H matching condition $\omega_{1\mathrm{H}} = n\omega_r + \omega_{1\mathrm{Si}}$ with $n = 1, 2, \ldots$ is satisfied. As it is difficult to achieve stable and reproducible results using mismatched H–H CP, because even very small (<0.1%) instability of rf fields may lead to an important loss of intensity of the NMR signal, it may be necessary to render the CP less sensitive to exact matching of the applied radio-frequency field strengths, especially upon higher spinning speeds. The matching condition can be indeed substantially broadened by 180° phase shifts (Figure 1e) or variable-amplitude rf field CP transfer (Figure 1f) and can even trim down the burden of finding and maintaining an exact CP match (Figure 1g). This may be very useful in any experiment involving $^1H\rightarrow{}^{29}Si$ polarization transfer even at modest spinning speed of a few kHz.

Second complication arises from the fact that the CP transfer time may be quite long and even longer than the relaxation time in the rotating frame of protons. This fact must be clearly recognized to avoid a false structural image of investigated materials. In the following, we will first show how one can check the actual CP regime and how the CP dynamics can be exploited to provide subtle structural details including the geometry of strongly hydrogen-bonded silanols.

$^1H\longrightarrow{}^{29}$ Si CP Dynamics: Basic Features and Pitfalls

The CP transfer of magnetization between the abundant I and the rare S spins can be described by the simplified thermodynamic model [5,6] when the average I–I homonuclear dipolar interaction is larger than the I–S heteronuclear dipolar interaction. Assuming that there is no relaxation of the S spins, the NMR signal of these spins, as a function of contact time t_{CP}, can be described by the well-known relationship [6]

$$M_{\mathrm{S}}\left(t_{\mathrm{CP}}\right) = M_{\mathrm{S}}^{\infty}\alpha\frac{\gamma_{\mathrm{I}}}{\gamma_{\mathrm{S}}}\frac{1}{1-\dfrac{T^{\mathrm{IS}}}{T_{1\rho}^{\mathrm{I}}}} \times\left(\exp\left(-\frac{t_{\mathrm{CP}}}{T_{1\rho}^{\mathrm{I}}}\right)-\exp\left(-\frac{t_{\mathrm{CP}}}{T^{\mathrm{IS}}}\right)\right) \quad (1)$$

where M_{S}^{∞} is the equilibrium magnetization of spins S; $\alpha = \omega_{1\mathrm{I}}/\omega_{1\mathrm{S}} = (\gamma_{\mathrm{I}}H_{1\mathrm{I}})/(\gamma_{\mathrm{S}}H_{1\mathrm{S}})$ is the ratio of the radio-frequency fields at the I and S frequencies (the Hartman–Hahn mismatch parameter); $1/T^{\mathrm{IS}}$ is the CP rate, which increases dramatically with the strength of the

Graham A. Webb (ed.), Modern Magnetic Resonance, 197–203.
© 2008 *Springer.*

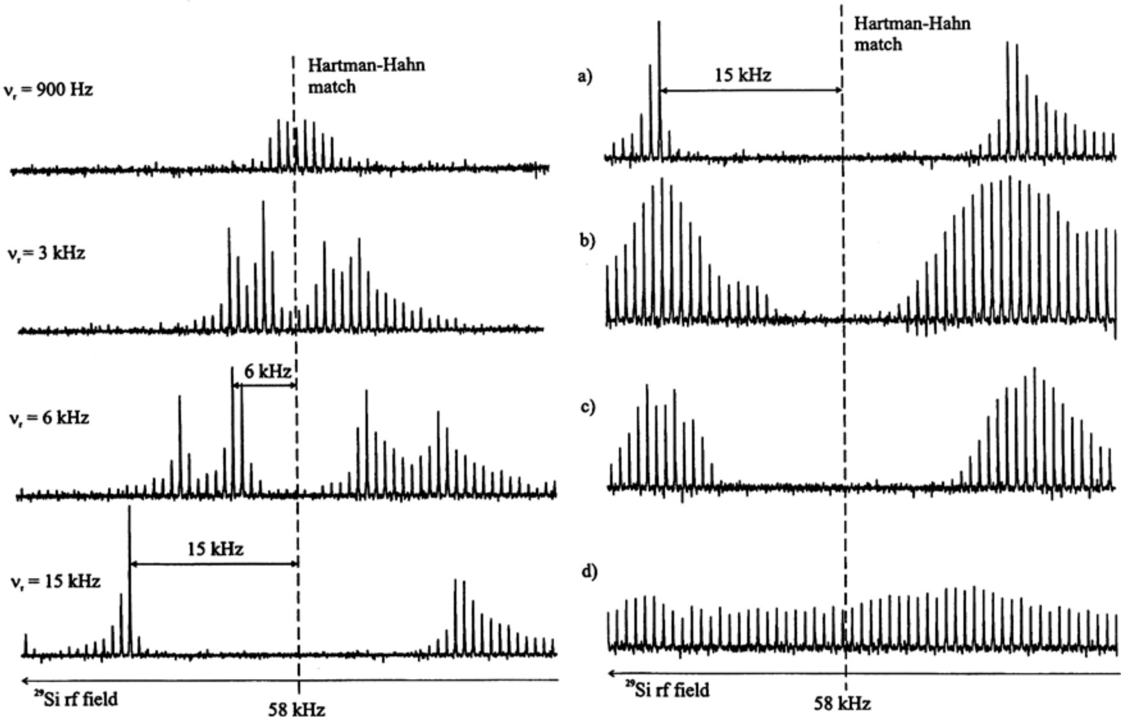

Fig. 1. Hartmann–Hahn (H–H) matching curves for $Q^{(3)}$ site in a layered hydrous silicate at different spinning speeds (left) and at 15 kHz (right). (a) standard CP transfer; (b) phase-inverted (π phase shift every rotor period) ^{29}Si rf irradiation during CP; (c, d) variable-amplitude CP using 15 amplitudes of ^{29} Si rf field increased in steps changing in the range 0.9–1.0 and 0.58–1.0, respectively. The total contact time period was 1 ms in each case.

heteronuclear I–S dipolar interaction but also depends in a complex way on the strength of the homonuclear I–I dipolar interaction, on the correlation time of molecular motions and on the experimental parameters; $T_{1\rho}^{\mathrm{I}}$ is the relaxation time in the rotating frame of the I spins. According to Equation (1), the CP build-up curves are inherently sensitive to internuclear distances via T^{IS} and the presence of mid-kHz motions via $T_{1\rho}^{\mathrm{I}}$, this makes that the dynamics of CP transfer still remain one of the most attractive NMR tools for structural and motional investigation of solids.

As has been pointed out recently [7], the expression (1) is valid not only when $T^{\mathrm{IS}} < T_{1\rho}^{\mathrm{I}}$, the usual condition (fast CP regime), but also holds whatever the ratio $T^{\mathrm{IS}}/T_{1\rho}^{\mathrm{I}}$. NMR CP measurements are usually analyzed assuming that the CP time T^{IS} of magnetization transfer is shorter than the relaxation time $T_{1\rho}^{\mathrm{I}}$. However, the reverse situation (i.e. $T^{\mathrm{IS}} > T_{1\rho}^{\mathrm{I}}$, slow CP regime) can be frequently encountered, especially in inorganic solids where protons are more remote from rare nuclei than in organic systems. In this case, the S spin magnetization will as well begin to rise but this increase cannot proceed further when the I spin system is rapidly depleted by the $T_{1\rho}^{\mathrm{I}}$ relaxation. Consequently, the transfer of magnetization is stopped at a time close to $T_{1\rho}^{\mathrm{I}}$ and there is a reverse flow from the S to I spin system which remains depleted by the faster $T_{1\rho}^{\mathrm{I}}$ relaxation. This reverse flow from the S to the I reservoir occurs, as does the forward one, at the CP rate $1/T^{\mathrm{IS}}$. In such a situation, when analyzing the experimental data under the usual fast CP assumption, an interpretation of both dynamic parameters will be strongly in error. In fact, it is impossible to know from the CP curve alone, whether $T^{\mathrm{IS}} < T_{1\rho}^{\mathrm{I}}$, or $T^{\mathrm{IS}} > T_{1\rho}^{\mathrm{I}}$. This is the consequence of the fact that apart from the intensity factor, Equation (1) is fully symmetrical with respect to the interchange of T^{IS} and $T_{1\rho}^{\mathrm{I}}$.

Contrary to the standard variable-contact CP experiment, a direct visualization of the ratio $T^{\mathrm{IS}}/T_{1\rho}^{\mathrm{I}}$ is easily accessible by using the TORQUE experiment [8]. This experiment has been originally designed with the aim of quenching the I spin $T_{1\rho}^{\mathrm{I}}$ dependence (**T** **O**ne **R**ho **QUE**nching) when studying polarization transfer in solids with $T^{\mathrm{IS}} < T_{1\rho}^{\mathrm{I}}$. It uses a spin lock period on spin I of duration t_{SL} followed by the CP transfer of variable duration t_{CP}, the total time $T_{TORQUE} = t_{CP} + t_{SL}$ being kept constant. The TORQUE signal grows as a function of t_{CP} according to

$$M_S^{TORQUE}(t_{CP}) = \exp\left(-T_{TORQUE}/T^{I}_{1\rho}\right) \times \left(\frac{1 - \exp\left(-(1-\lambda)(t_{CP}/T^{IS})\right)}{(1-\lambda)}\right) \quad (2)$$

with $\lambda = T^{IS}/T^{I}_{1\rho}$. Figure 2 shows the simulations of the temporal evolution of S spin magnetization in a standard CP experiment and in the TORQUE experiment, both in three different situations: (i) $T^{IS} < T^{I}_{1\rho}$; (ii) $T^{IS} > T^{I}_{1\rho}$; (iii) a simple combination of (i) and (ii) cases.

As expected, in the standard CP experiment, beside the differences in the absolute intensity, very similar temporal evolution of magnetization is observed in each case. However, dramatic differences in the curvature of the TORQUE temporal evolution are visible. This allows an unambiguous recognition of the $T^{IS}/T^{I}_{1\rho}$ ratio and assures the proper analysis of dynamic CP parameters in terms of structural and/or motional features. A couple of illustrative examples of such analysis in silica gels and layered hydrous sodium silicates are shown below.

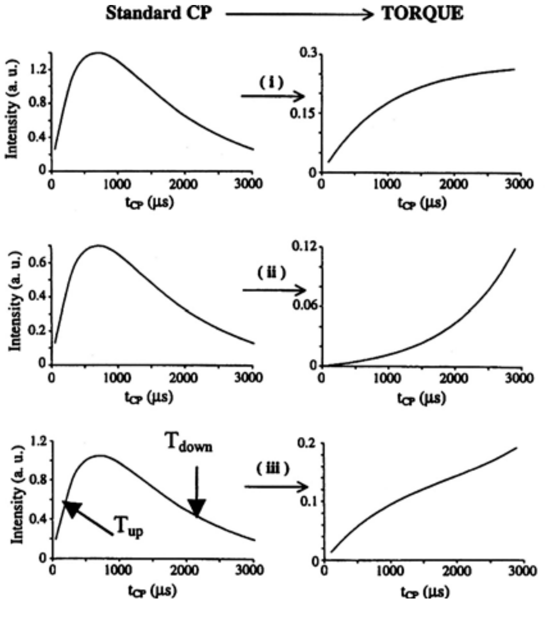

Fig. 2. Magnetization transfer time dependence in standard CP (left) and TORQUE (right) experiments calculated using Equations (1) and (2) with (i) $T^{IS} = 0.5$ ms, $T^{I}_{1\rho} = 1.0$ ms; (ii) $T^{IS} = 1.0$ ms, $T^{I}_{1\rho} = 0.5$ ms; (iii) equally weighted (i) plus (ii) conditions.

Silica Gels

Silica gels are highly porous materials which play an important role in numerous applications such as catalysis or chromatographic separation and have been the subject of much NMR investigations for several years [9]. The high-resolution solid state ^{29}Si CP/MAS NMR spectra of silica gel show three peaks at −91.5, −101, and −110 ppm assigned, respectively, to three $Q^{(2)}$, $Q^{(3)}$, and $Q^{(4)}$ types of silicon environments. The results from the CP, and TORQUE experiments on a Fisher S-157 silica gel sample are presented in Figure 3.

Assuming a simple monoexponential polarization transfer, the results of a fit of three CP curves using Equation (1) are T_{UP} = [2.3, 2.6, 10.3] ms and T_{DOWN} = [10.3, 13.4, 30] ms, for [$Q^{(2)}$, $Q^{(3)}$, $Q^{(4)}$] silicons, respectively. It is also observed that the $T_{1\rho}(^1H)$ relaxation curves are

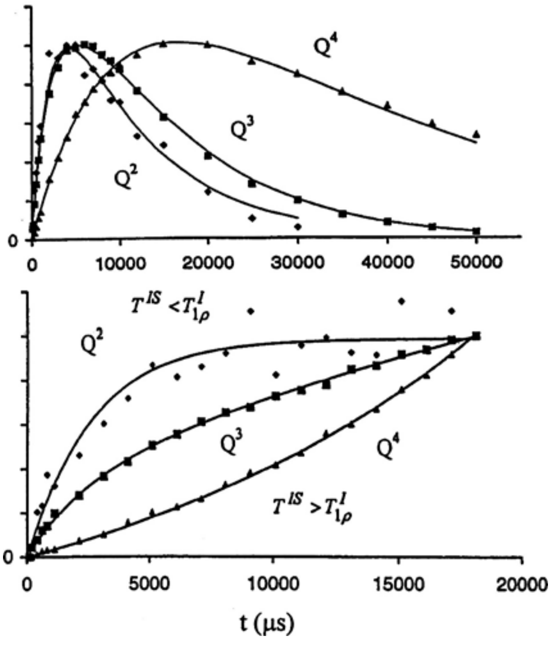

Fig. 3. Time dependence of ^{29}Si magnetization for Q^2 (◆), Q^3 (■), and Q^4 (s) sites of silica gel in the (A) indirect $T_{1\rho}(^1H)$ measurements; (B) TORQUE experiment with a total constant time of 20 ms; (c) standard cross-polarization $^1H \rightarrow ^{29}Si$ experiment. Insert: ^{29}Si CP/MAS spectrum of a silica gel sample (Fisher S-157) showing three peaks assigned to three types of silicon environment.

identical for protons involved in the CP process and give the unique value $T_{1\rho}(^1H) = 10.3 \pm 0.5$ ms. This clearly indicates that the differences observed in the decreasing part of the CP curves do not correspond to different $T_{1\rho}$ of protons involved in the CP transfer on different sites. The value of 10.3 ms is equal to T_{DOWN} for $Q^{(2)}$ and to T_{UP} for $Q^{(4)}$. This suggests that $T^{IS} < T^{I}_{1\rho}$ for $Q^{(2)}$ whereas $T^{IS} > T^{I}_{1\rho}$ holds for $Q^{(4)}$. For $Q^{(2)}$ and $Q^{(4)}$ silicons, these two diametrically opposite situations are visualized immediately by the opposite curvatures of the TORQUE temporal dependence. For $Q^{(3)}$ site, the shape of the TORQUE curve proves the existence of at least two different $Q^{(3)}$ species, first one having $T^{IS} < T^{I}_{1\rho}$, the second one with $T^{IS} > T^{I}_{1\rho}$.

Layered Sodium Hydrous Silicates

This class of materials, available only in microcrystalline form, has a two-dimensional layered structure, the negative charge of the silicate layer being compensated by sodium ions that are coordinated by the oxygen atoms of the intercalated water molecules. Hydrated sodium silicates are of rapidly growing industrial interest due to their high ion- or proton-exchange properties and new applications in catalysis and in the synthesis of composite mesoporous materials. Magadiite, the most frequently researched, has the idealized formula $Na_2Si_{14}O_{29} \cdot nH_2O$ ($n = 8$–10). ^{29}Si MAS NMR studies show the presence of $Q^{(3)}$ and $Q^{(4)}$ silicons in its basic layer structure. The experimental build-up curves obtained from standard CP and TORQUE experiments for $Q^{(3)}$ and Na^+ are shown in Figure 4.

Assuming as usual that $T^{IS} < T^{I}_{1\rho}$, the standard CP curves can be fitted according to Equation (1), each of them being described by two pairs of time constants T_{up} and T_{down} for their rising and decreasing parts, respectively. A simple model for which each site is characterized by a single set of T_{up} and T_{down} values was found to be inadequate. However, the observed curvature in the TORQUE temporal dependence makes it immediately evident that it is essentially the $T^{IS} > T^{I}_{1\rho}$ situation which takes place for $Q^{(3)}$ sites. For Na^+ ions, the situation is even more complex, the TORQUE curve exhibits a pronounced S-shape form which means that both the fast and the slow CP regime are equally relevant for this CP dynamics. From the independent measurements of relaxation in the rotating frames two distinct $T^{I}_{1\rho}$ values have been obtained for protons appearing at 3.8 and 15.2 ppm, respectively. It turns out that these two relaxation times are equal neither to T_{down} nor to T_{up} found in the fitting procedure of CP build-up curves when assuming $T^{IS} < T^{I}_{1\rho}$. As the $T^{I}_{1\rho}$ values reflect two different proton environments existing in magadiite, a realistic model should include both relaxation parameters and assume at least two types of $Q^{(3)}$ as well as sodium sites being differently coupled to hydrogen species. Consequently, the CP and TORQUE build-up curves are each the weighted sums of two different contributions, each one given by Equations (1) and (2) for CP and TORQUE, respectively. A good agreement between experimental and calculated CP and TORQUE temporal dependencies is indeed observed for both species under such assumptions. The fitted T^{IS} and corresponding proportions are given and discussed in structural terms elsewhere [10].

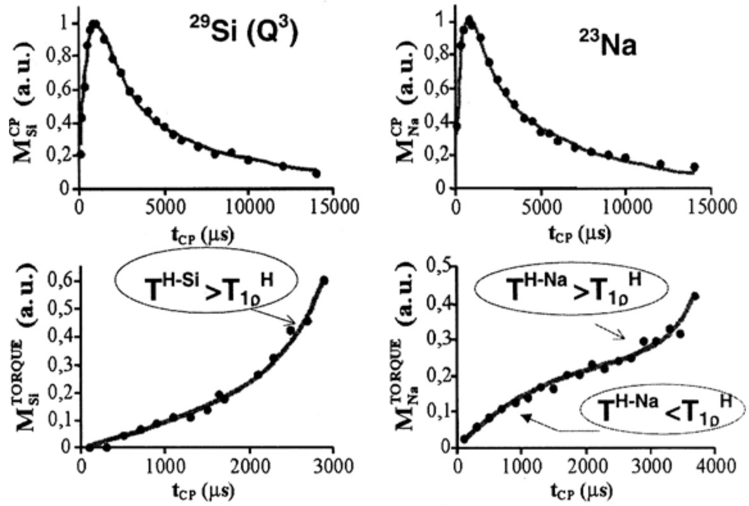

Fig. 4. Temporal evolution of ^{29}Si (left) and ^{23}Na (right) magnetization in the standard CP (top) and TORQUE (bottom) experiments for $Q^{(3)}$ and Na^+ sites of magadiite spinning at 3 kHz. Solid lines correspond to the fitted curves.

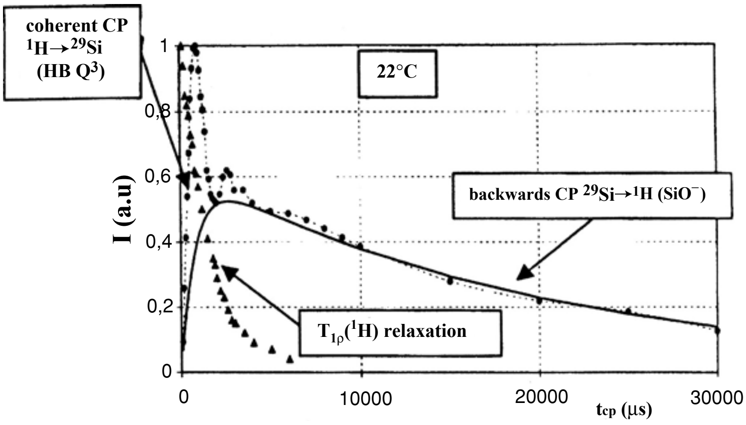

Fig. 5. Temporal evolution of ^{29}Si magnetization for the $Q^{(3)}$ signal during CP and $T_{1\rho}(^1H)$ experiments. All experiments were run with $\omega_{1S} = \omega_{1H} - \omega_r$ Hartmann–Hahn condition and at a spinning frequency of 2.5 kHz. The proton rf power was 62.5 kHz and its carrier frequency was exactly that of hydrogen-bonded protons at 15.98 ppm, though the proton offset corresponding to the water resonance at 3.8 ppm does not lead to any changes in CP dynamics of the nonoscillating component.

The ensemble of fitted dynamic parameters brings evidence that the long time decays of magnetization in the standard CP experiments result from the back flow of magnetization to the proton system.

Very similar situation occurs in the case of layered sodium hydrated octosilicate [11] with the idealized formula $Na_8\{Si_{32}O_{64}(OH)_8\}\cdot 32H_2O$. The experimental CP and indirect $T_{1\rho}(^1H)$ curves of $Q^{(3)}$-type resonance peak are shown in Figure 5.

In this case, an initial CP rapid growth, with an oscillating behavior is followed by long time decay. However, the independent $T_{1\rho}(^1H)$ measurements show a rate of magnetization decay at least one order higher than the observed long time decay. This clearly indicates once again that the observed long time decrease of CP curves is not due to $T^{I}_{1\rho}$ relaxation. Although a single, isotropic $Q^{(3)}$ resonance signal is observed, it is obvious that the CP curves must be interpreted as composed principally of two types of contributions, an oscillating and a nonoscillating component, the first one cross-polarizing under fast CP regime (i.e. $T^{IS} < T^{I}_{1\rho}$), the second evolving under the slow CP regime (i.e. $T^{IS} > T^{I}_{1\rho}$. This implies that, in analogy to magadiite, octosilicate contains two types of structurally different $Q^{(3)}$ silicones present in hydrogen-bonded –Si–O—-H···O–Si– and –Si–O$^-$– type sites having dramatically different abilities to cross-polarize and being sensitive to different mobilities of neighboring hydrous species. In fact, the direct proton $T_{1\rho}$ measurements show that the oscillating component relaxes with the rate of proton signal representing hydrogen-bonded silanols, while the nonoscillating component is mainly influenced by much more rapidly relaxing water molecules. Consequently, the final decrease of the CP curves in Figure 5 can only result from the backwards $^{29}Si \rightarrow ^1H$ flow of the magnetization to the proton reservoir. Unambiguous experimental proof of this is provided by the TORQUE experiment (Figure 6).

Indeed, the TORQUE curve exhibits a clear S-shaped character which according to the discussion above makes it immediately evident that some of $Q^{(3)}$ silicons are coupled to one species of protons under $T^{IS} < T^{I}_{1\rho}$, the others to a second type of protons under $T^{IS} > T^{I}_{1\rho}$. This proves that hydrogen-bonded –Si–O—H···O–Si– and –Si–O$^-$– type sites evolve, respectively, under fast and slow CP regimes.

Finally, it is also worth pointing out that a single set of CSA principal values characterizes both types of $Q^{(3)}$ sites. This means that the ^{29}Si shielding tensor is mainly related to the Si–O bond character (including the lengths and interbond angle differences between terminal and bridging oxygens) in the SiO_4 tetrahedron and is rather insensitive to the presence of protons in the second sphere of coordination.

Probing the Geometry of Strongly Hydrogen-Bonded Silanols

Hydrogen bonds are the most important of all directional intermolecular interactions and play a central role in determining molecular conformation and aggregation, as well as the function and dynamics of a great number of systems ranging from inorganic to biological chemistry. In order to understand the physical and chemical properties of layered microporous materials as well as the role of hydrogen bonds in the aggregation and ordering of silicate layers, the correlation of such contacts with the spectroscopic response is highly desired. In sodium hydrous silicates, the nature of strong hydrogen bonding having an O···O distance of less than 2.60 Å and present at room or higher temperature remains indeed the subject of considerable controversy. Both inter- and intralayer hydrogen bonding involving the silanol or water protons have been proposed. As the intercalation of polar molecules in

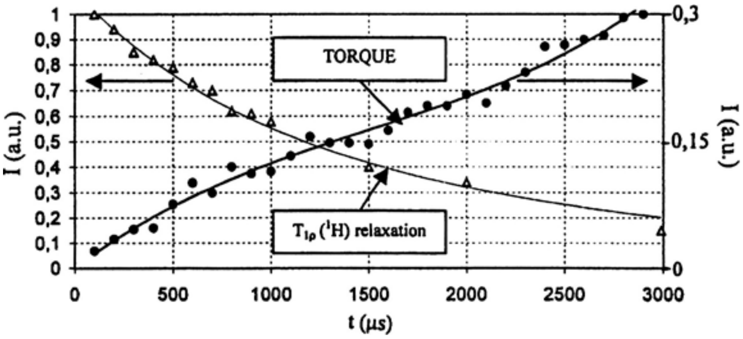

Fig. 6. Experimental time dependence of ^{29}Si magnetization for the $Q^{(3)}$ signal during TORQUE and $T_{1\rho}(^1\text{H})$ experiments. Solid lines correspond to the fitted curves with two components (i) and (ii) having following time constants: for the TORQUE experiment: (i) $T^{\text{IS}} = 0.7$ ms, $T^{\text{I}}_{1\rho} = 2.54$ ms; (ii) $T^{\text{SI}} = 20.0$ ms, $T^{\text{I}}_{1\rho} = 0.8$ ms; for the $T_{1\rho}$ experiment: (i) $T^{\text{I}}_{1\rho} = 0.8$ ms; (ii) $T^{\text{I}}_{1\rho} = 2.54$ ms.

layered materials can be dramatically controlled by the existence of interlayer hydrogen bonds, the appropriate recognition of the extent and the nature of hydrogen bonding present in these materials is of prime importance. To get this local geometric information, one can determine the internuclear Si···H distances and the orientation of the ^{29}Si chemical shift tensor in the hydrogen-bonded $Q^{(3)}$-type units by exploiting a simple experiment based on the CP inversion of the ^{29}Si spin magnetization used as a modulation of the slow magic-angle spinning chemical shift spectrum [12]. The experiment starts with the classical CP procedure followed by a period during which the contact between protons and silicons is maintained but the phase of proton spin-locking irradiation is inverted. As shown in Figure 7, this leads to non-uniform dipolar modulation of the ^{29}Si CSA spinning sidebands recorded under high power proton decoupling.

Such an effect gives evidence for largely coherent magnetization transfer within the silanol groups having a pronounced inhomogeneous character of the dipolar

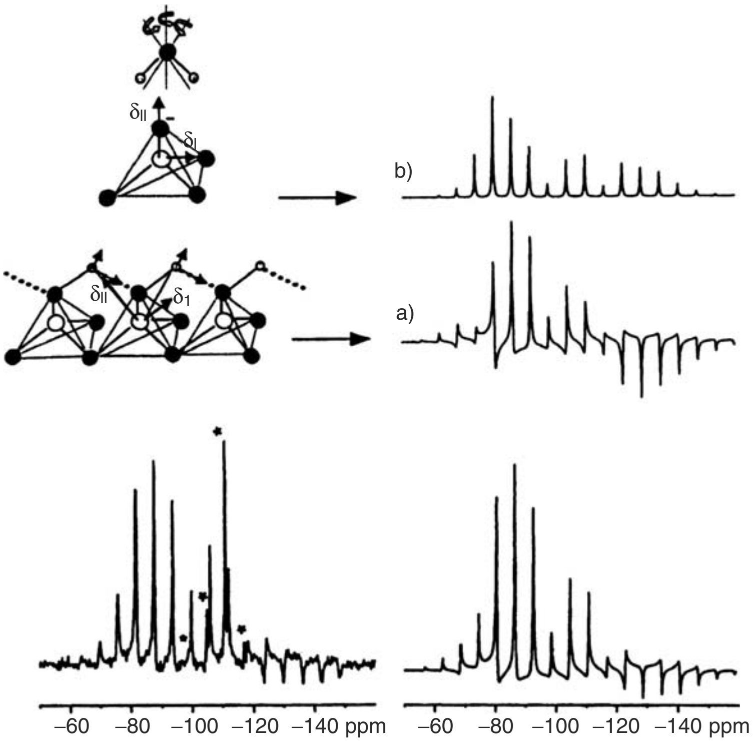

Fig. 7. Dipolar modulated ($t_1 = 400$ μs), natural abundance ^{29}Si NMR spectrum of slowly magic-angle spinning ($\nu_r = 357$ Hz) octosilicate (left bottom). Asterisks indicate the spinning sidebands of $Q^{(4)}$ sites. Fitted spectrum of $Q^{(3)}$ sites along with its individual components (right bottom). Dipolar modulated subspectrum (a) represents as indicated the hydrogen-bonded $Q^{(3)}$ sites, the subspectrum (b) comes from Si–O$^-$ $Q^{(3)}$ type sites cross-polarizing from the water molecules.

system, the observed difference in the dipolar oscillation frequency of different spinning sidebands resulting from variation of the orientation-dependent dipolar coupling. More interesting in the context of this work, the dipolar modulated spinning sidebands contain all the desired information on the hereronuclear distance as well as the magnitude and orientation of the principal elements of the chemical shielding tensor in the molecular frame.

In order to reproduce the observed dipolar modulated envelope of $Q^{(3)}$ spinning sidebands in Figure 6, the presence of two different components representing two types of $Q^{(3)}$ sites has to be assumed. Indeed, as discussed above, although a single isotropic $Q^{(3)}$ resonance signal is observed, two types of $Q^{(3)}$ tetrahedra, hydrogen-bonded silanols and $Si–O^-$ type sites need to be distinguished by their different abilities to cross-polarize. As can be seen in Figure 7, the calculated spectrum is in excellent agreement with the experimental envelope and phase features of the $Q^{(3)}$ family of spinning sidebands. The simulations show that dipolar modulated envelope of spinning sidebands is very sensitive to small changes of $r_{Si...H}$ distances and of their polar coordinates in the chemical shielding principal axis frame [11]. The results clearly support the intralayer character of strongly hydrogen-bonded silanol groups in a bridging albeit not symmetric position between neighboring tetrahedra.

Conclusions

The CP measurements are usually analyzed assuming that the CP time T^{IS} of magnetization transfer from the abundant I spins to the rare S spins is shorter than the relaxation time $T_{1\rho}$ in the rotating frame of the I spins (fast CP regime). Here, it was shown that the reverse situation ($T^{IS} >> T^{I}_{1\rho}$, slow CP regime) frequently occurs for the $^{1}H \rightarrow ^{29}Si$ transfer in commonly encountered inorganic materials. This fact must be clearly recognized to avoid a false structural image of investigated materials. The efficiency of the TORQUE experiment in visualizing the real CP regime or its possible mixed character has been underlined.

The proper exploitation of the proton–silicon polarization transfer spin dynamics in fast and slow magic-angle spinning experiments permits a deeper insight into structural and motional features of silicon-containing materials. The analysis of the dipolar modulated ^{29}Si CSA spectrum yields straightforward geometric information on the hydrogen-bonded silanols, including the orientation of ^{29}Si CSA tensor in the molecular frame. The CP methods employed to obtain such information take advantage of a weakly dipolar coupled proton–proton network, largely disconnected from the heteronuclear dipolar couplings within the silanol groups. This leads to significant truncation of weak dipolar couplings from neighboring protons by the largely dominant flip-flop coupling term of the heteronuclear spin pairs. This in turn makes it possible to exploit the coherent magnetization exchange without applying homonuclear decoupling which itself eliminates any uncertainty about the heteronuclear scaling factor inherently connected with homonuclear decoupling. The presented strategy may be useful to obtain structural information in the related layered alkali metal silicates, silica gels, calcium silicate hydrates as well as in other classes of microporous materials.

References

1. Fyfe CA, Solid State NMR for Chemists. C. F. C. Press: Canada, 1983.
2. Engelhardt G, Michel D. High-Resolution Solid-State NMR of Silicates and Zeolites. John Wiley & Sons: Berlin, 1987.
3. Eckert H. Prog. Nucl. Magn. Reson. Spectrosc. 1992;24:159.
4. Colombet P, Grimmer AR, Zanni H, Sozzani P (Eds). Nuclear Magnetic Resonance Spectroscopy of Cement-Based Materials. Springer-Verlag: Berlin, 1998.
5. McArthur D, Hahn EL, Waldstaet RE. Phys. Rev. 1969;188:609.
6. Mehring M. High-Resolution NMR in Solids. NMR Basic Principles and Progress. Springer-Verlag: Berlin, 1983.
7. Klur I, Jacquinot JF, Brunet F, Charpentier T, Virlet J, Schneider C, Tekely P. J. Phys. Chem. B 2000;104:10162.
8. Tekely P, Gérardy V, Palmas P, Canet D, Retournard A. Solid State NMR 1995;4:361.
9. Maciel GE. In: DM Grant, RK Harris (Eds). Encyclopedia of Nuclear Magnetic Resonance. John Wiley & Sons: Chichester, UK, 1996, p 4370.
10. Gardiennet C, Tekely P. J. Phys. Chem. B 2002;106, 8928.
11. Gardiennet C, Marica F, Fyfe CA, Tekely P. J. Chem. Phys. 2005;122:054705.
12. Gardiennet C, Marica F, Assfeld X, Tekely P. Angew. Chem. Int. Ed. 2004;43:3565.

Solid State NMR Characterization of Solid Surface of Heterogeneous Catalysts

Feng Deng, Jun Yang, and Chaohui Ye
State Key Laboratory of Magnetic Resonance and Atomic and Molecular Physics,
Wuhan Institute of Physics and Mathematics, the Chinese Academy of Science, Wuhan 430071, P. R. China

Solid state NMR spectroscopy has become a powerful tool for investigation of the solid surface of various heterogeneous catalysts [1–4], such as zeolite, metal oxide, and solid heteropoly acid, which are widely used in petrochemical industry. Identification and characterization of the active centers, reaction intermediates, and products are essential for understanding reaction mechanisms occurring on the surface of heterogeneous catalysts. Compared to X-ray diffraction (XRD) which is determined by long-range orderings and periodicities, solid state NMR is more sensitive to local orderings and geometries, thus providing a more detailed description of the local structure, especially for powder samples. Multinuclear magic angle spinning (MAS) NMR, especially ^{1}H MAS NMR, probe molecule techniques, double-resonance techniques as well as two dimension correlation techniques have been employed to reveal the detailed structure of the active sites on heterogeneous catalysts. In addition, *in situ* MAS NMR technique [3,4] has been developed as an indispensable tool for investigation of the heterogeneous catalytic reaction mechanisms. Although many surface properties of heterogeneous catalysts can be investigated by solid state NMR spectroscopy, two main topics will be discussed in this section: surface acidity and catalytic reaction of heterogeneous catalysts.

Surface Acidity of Heterogeneous Catalysts

The surface acidity is described by the following three properties: (1) the type of acid sites (Brönsted or Lewis site); (2) the acid strength, which can be defined, for a Brönsted site, as the ability of the surface hydroxyl groups to protonate an adsorbed molecule; (3) the concentration of acid sites accessible to probe molecules. ^{1}H MAS NMR can resolve various hydroxyl groups that may acts as proton donators (Brönsted acid sites) on the surface of heterogeneous catalysts. In the case of zeolites [1,2], ^{1}H MAS NMR signals consist of non-acidic SiOH groups at chemical shifts of $\delta = 1.2$–2.2 ppm, extra-framework AlOH groups at $\delta \approx 3$ ppm, acidic bridging SiOHAl groups at $\delta = 3.6$–5.2 ppm, and residual ammonium ions at $\delta = 6.5$–7.0 ppm. For an ammonium-free zeolite, adsorption of a small amount of water molecules on Lewis acid site also gives rise to a ^{1}H signal at ca. 7.0 ppm. Hydrogen bonds of the surface OH groups with neighboring oxygen atoms or probe molecules will leads to a downfield shift of 1–20 ppm. For example, in a layered sodium disilicate material [5], isolated SiOH groups gives rise to ^{1}H resonances at 0–3 ppm, while inter-layer hydrogen-bonded SiOH groups correspond to a ^{1}H signal at 14 ppm, and strongly hydrogen-bonded silanols with the proton bonded to non-bridging oxygen at the same silicon atom shift the resonance position to 18.7 ppm. The advantage of ^{1}H MAS NMR over IR spectroscopy lies in the quantitative measurement of signal intensities, allowing an accurate determination of the OH concentrations [1]. Besides, some double resonance methods, such as ^{1}H/^{27}Al Transfer of Populations in Double Resonance (TRAPDOR) NMR technique [6], can correlate the various hydroxyl groups with the neighboring Al spins, while a spin echo pulse sequence is applied to proton and ^{27}Al is irradiated simultaneously during one of the echo period in the experiment. Under the ^{27}Al irradiation, the signals of protons that are strongly coupled with aluminum spins will be significantly suppressed while those that are not coupled with aluminum atoms remain unaffected. Therefore, the heteronuclear dipolar interactions between the two spins and the ^{1}H/^{27}Al internuclear distances can thus be extracted. As an example, Figure 1 shows the ^{1}H/^{27}Al TRAPDOR NMR of the ultrastable Y, the 2.2 ppm signal, which is due to non-acidic SiOH groups at the framework defects, is almost unaffected under ^{27}Al irradiation, while the signals at 4.3 and 5.2 ppm due to two types of the bridging OH groups and the signal at 3.0 ppm arising extra-framework AlOH groups that are all close to the Al atoms are significantly reduced [7].

Using various probe molecules, the surface acidity of heterogeneous catalysts can be well characterized. ^{15}N-enriched pyridine [8] and trimethylphosphine (TMP) [9] are two extensively used probe molecules for discriminating Brönsted and Lewis acid sites and quantitatively determining their concentrations. Both of the probe molecules give rise to large ^{15}N and ^{31}P chemical shift ranges of 100

Graham A. Webb (ed.), Modern Magnetic Resonance, 205–211.
© 2008 *Springer.*

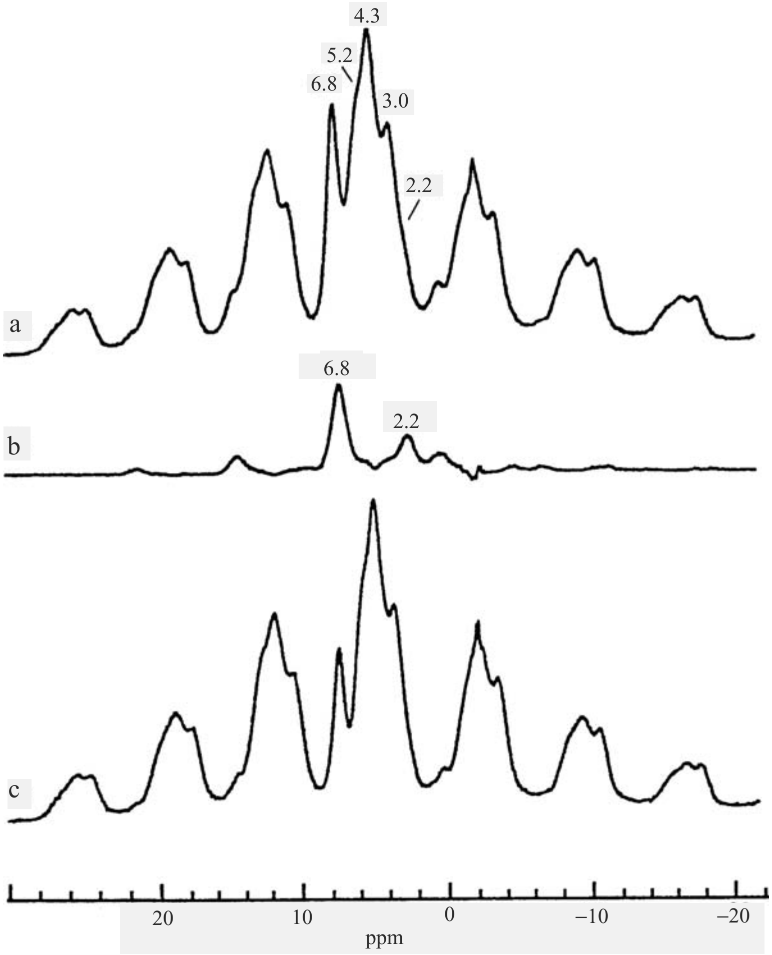

Fig. 1. $^{1}H/^{27}Al$ TRAPDOR NMR spectra of ultrastable HY. (a) without ^{27}Al irraiation, (b) with ^{27}Al irradiation. (c) the different spectrum of (a) and (b) [7].

and 60 ppm, respectively. One important advantage of the TMP over pyridine is the relatively high NMR sensitivity of ^{31}P, which is very useful in the cases where the concentration of the acid sites is very low. When Brönsted or Lewis acid sites are present in zeolites, protonated adduct, $TMPH^{+}$, or Lewis-bound TMP complex are confirmed. The $TMPH^{+}$ is characterized by a ^{31}P resonance at ca. -4 ppm and a J_{P-H} coupling of approximately 500 Hz for zeolites, while the Lewis-bound TMP complexes give rise to resonances in the shift range from -32 to -58 ppm, and the physisorbed or weakly bound TMP has a resonance at ca. –60 ppm. $^{27}Al/^{31}P$ and $^{27}Al/^{1}H$ rotational echo double-resonance (REDOR) NMR methods [10] have been applied to measure Al-P and Al-H_B (H_B is the Brönsted acidic proton) distances in zeolite HY for the acid site-TMP complex of 3.95 and 2.8–3.1 Å, respectively. A P–H_B distance of 1.40 Å was obtained by fitting the spinning sidebands in the ^{1}H MAS spectrum. As shown in Figure 2, combining the NMR results with *ab initio* calculations provides a more detailed description of the exact structure of TMP-Brönsted acid site complex formed in the zeolite.

Various probe molecules are used for determination of the acid strength of surface OH groups. Deuterated pyridine [11] is one of probe molecules for this purpose. The formation of a hydrogen bond between pyridine and non-acidic silanol group (SiOH) shifts the ^{1}H MAS NMR signal position from 2 to ca. 10 ppm. In the case of acidic OH groups (Brönsted acid sites), the adsorption of pyridine results in ^{1}H NMR signals at chemical shifts in the

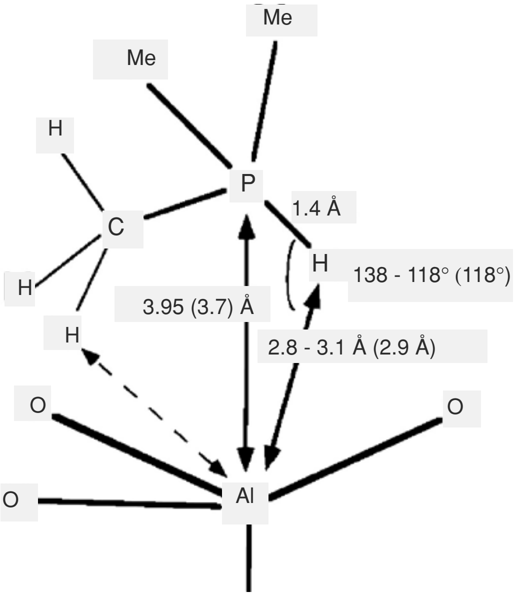

Fig. 2. Comparison of the NMR experimental and calculated distances. Calculated distances and angles obtained for the $TMPH^{+}$-Z_2^{-} cluster are given in parentheses. The dashed line indicates that an interaction between the two spins was observed experimentally, but the distance was not quantified [10].

range 12–19 ppm. The down-field signals result from a proton transfer to the probe molecule, forming pyridine ions. However, no quantitative correlation has been established between the acid strengths and the down-field shift of the ^{1}H signal. A more precise measurement of the acid strength of Brönsted and Lewis sites can be achieved with the aid of the ^{13}C chemical shift of the carbonyl atom of adsorbed 2-^{13}C-acetone [12,13]. The different degrees of interaction between the carbonyl oxygen of adsorbed acetone and the acid site result in different ^{13}C downfield shifts of the carbonyl carbon. By comparing the chemical shifts of 2-^{13}C-acetone adsorbed on various solid catalysts with the resonance position of the molecule in 100% H_2SO_4 solution, Haw *et al.* [13] proposed that the solid acid strengths scale with the ^{13}C NMR isotopic chemical shift of adsorbed 2-^{13}C-acetone (Table 1). According to the scale, the acid strength of the bridging hydroxyl groups in zeolite HZSM-5 corresponds to that of 80% H_2SO_4 solution.

Catalytic Reaction on the Surface of Heterogeneous Catalysts

In situ solid state NMR spectroscopy has been demonstrated to be a very powerful method to study the heterogeneously catalyzed reactions [3, 4, 13–15]. The detection of the change of both active sites on the catalysts and species (such as reactants, products, and intermediates) adsorbed on the surface of catalyst in the process of the reaction can provide more direct information about what happens on the catalyst surface than that obtained by using off-line techniques, such as gas chromatograph (GC) and mass spectroscopy (MS). The large chemical shift of ^{13}C MAS spectra (more than 300 ppm) enables differentiation of various organic species by their characteristic resonances. For example, in the study of methanol to gasoline (MTG) reaction [16], Klinowski *et al.* had (i) identified 29 different adsorbed organic species and monitored their fate during the reaction; (ii) directly observed various kinds of shape selectivity in zeolite ZSM-5; (iii) discriminated mobile species from attached species. These results will assist in the design of shape-selective catalysts and provide a better understanding of the catalytic reaction. *In situ* ^{13}C NMR technique was also employed to study methane dehydroaromatization on Mo/HZSM-5 catalyst. Not only the products, such as benzene, ethane, and ethylene, but also the active phase Mo_2C were directly observed by ^{13}C NMR spectroscopy (Figure 3). The NMR results support the following reaction mechanism [17]:

Table 1: ^{13}C MAS NMR isotopic chemical shift (in ppm) of carbonyl carbon of 2-^{13}C-acetone on (or in) different solid (or liquid) acids [12]

Acetone	208
SAPO-34	217
$CF_3CH(OH)OCF_3$	221
HZSM-5	223
$MgCl_2$	221
$ZnCl_2$	230
$AlBr_3$	243
100%H_2SO_4	244
$AlCl_3$	245
SbF_5	250

(1) During induction period

$$MoO_3 + CH_4 \rightarrow Mo_2C + CO + CO_2 + H_2O + H_2$$

(2) Formation of C_2(Mo_2C species as active center)

$$CH_4 \rightarrow C_2H_4 + C_2H_6$$

(3) Production of benzene (Brönsted acid sites as active center)

$$C_2H_4 \rightarrow C_6H_6 + H_2$$

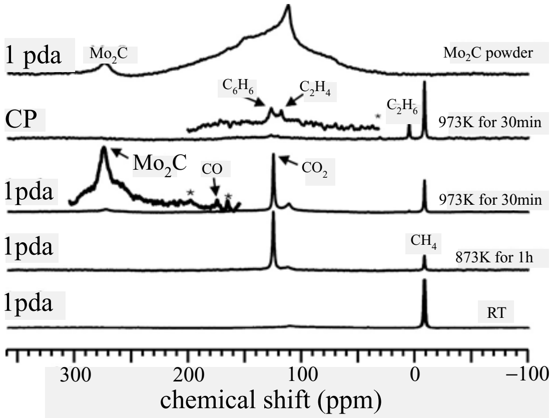

Fig. 3. ^{13}C MAS NMR spectra of methane (^{13}C, 99%) reaction on 6Mo/HZSM-5 at different temperatures, which were acquired at room temperature using one pulse with ^{1}H decoupling (1pda) or ^{1}H–^{13}C cross polarization (CP). For comparison, ^{13}C MAS NMR spectrum of molybdenum carbide powder was also shown. Asterisks denote spinning sidebands. The signal at 112 ppm is due to background of spinning module [17].

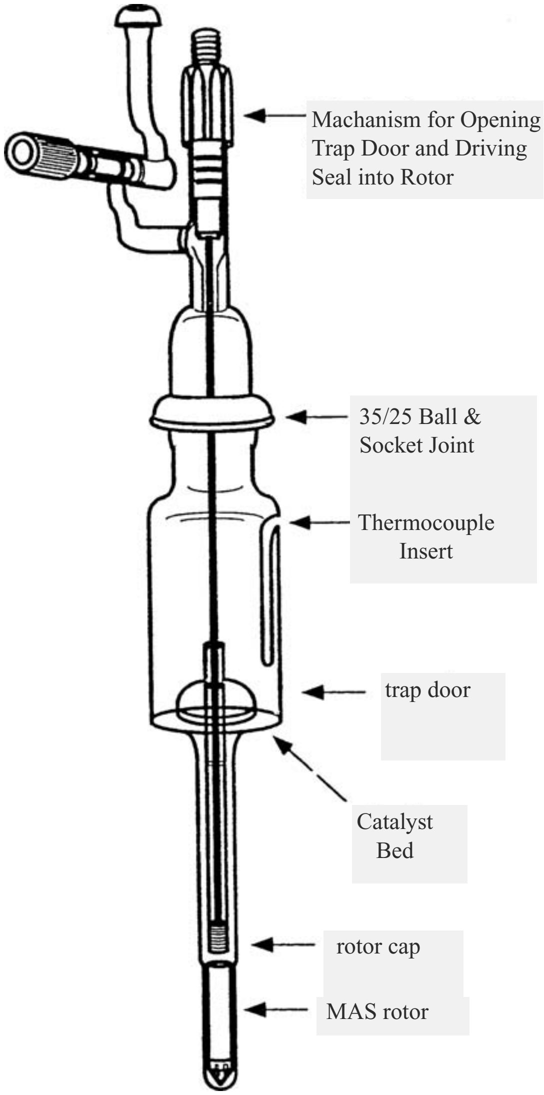
Machanism for Opening Trap Door and Driving Seal into Rotor
35/25 Ball & Socket Joint
Thermocouple Insert
trap door
Catalyst Bed
rotor cap
MAS rotor

Fig. 4. Schematic drawing of a CAVERN device for the sample preparation of *in situ* MAS NMR measurement [13].

Since NMR is a quantitative method, the concentration of the adsorbed species on the surface of catalysts can thus be directly obtained, which is very helpful for investigation of the reaction mechanism. The sensitivity of natural abundance ^{13}C surface species is usually not enough for ^{13}C MAS NMR detection. Although ^{1}H–^{13}C cross polarization experiment can be used to enhance the sensitivity of ^{13}C MAS spectra, ^{13}C isotope-enriched reactants are usually required for the *in situ* NMR study. In some cases, selectively labeled reactants are very much useful to identify the catalytic reaction pathway by monitoring the fate of the labeled atoms at specific sites in the process of the reaction [18].

In the earlier studies, *in situ* MAS NMR experiments were usually carried out under batch condition. The simple and very commonly used method employs a particularly symmetrical glass ampoule [19], which fits well into MAS rotor in order to achieve a stable high magic angle spinning rate at about 3–4 kHz. For the sample preparation of *in situ* MAS NMR measurements, the catalyst is packed into the glass ampoule and activated under a vacuum line at a specified temperature. A known amount of reactant in gas or liquid state is introduced onto the catalyst by freezing with liquid N_2, and then the ampoule is carefully sealed by flame. The reaction is allowed to occur in an oven at a specified temperature for a period of time and quenched with liquid N_2, and then the sealed ampoule is transferred to MAS rotor for NMR observation. Another method for sample preparation employs a specially designed device named CAVERN (CAVERN: cryogenic adsorption vessel enabling rotor nestling, Figure 4)[13], which allows the sample preparation in the MAS rotor with a gas-tight sealed cap. This device can be connected to a vacuum line. Activation of catalysts, adsorption of ^{13}C-enriched reactants, transfer of the loaded catalysts into the MAS rotor, and sealing of the MAS rotor are all carried out in this device,

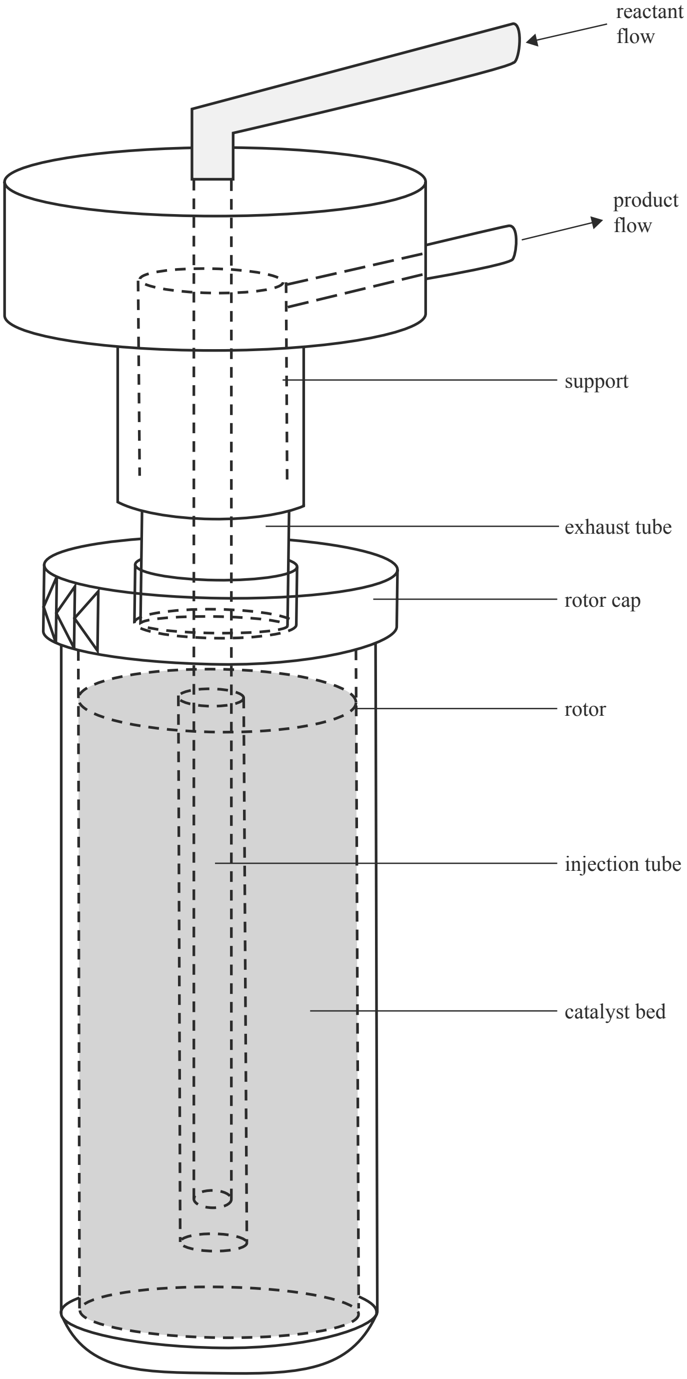
reactant flow
product flow
support
exhaust tube
rotor cap
rotor
injection tube
catalyst bed

Fig. 5. Schematic drawing of a MAS NMR rotor reactor with an injection equipment applied for *in situ* MAS NMR experiments under flow condition [14].

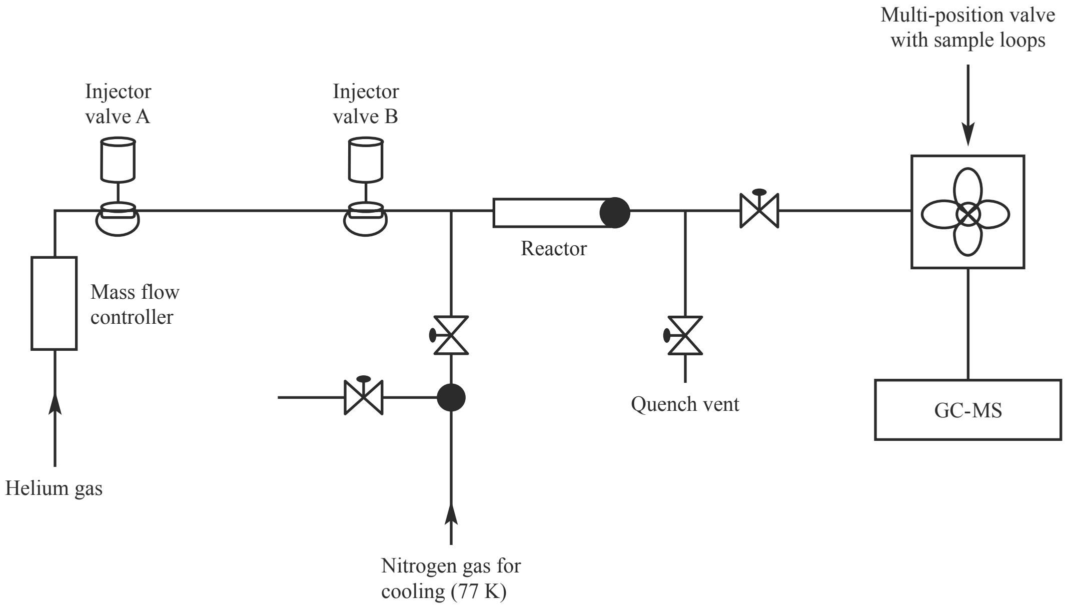

Fig. 6. Schematic drawing of pulse-quench reactor coupled with GC and MS for *in situ* MAS NMR experiments under flow condition [24].

preventing the samples from the exposure of atmosphere. The sealed MAS rotor can be transferred into NMR probe. The reaction is allowed to take place at a specified temperature in NMR magnet for a period of time and then the temperature is allowed to return to room temperature for the *in situ* ^{13}C MAS measurement. This apparatus is suitable for the study of reaction that begins to occur at low temperature. For example, since ethylene is very active on HZSM-5 zeolite at the room temperature, the CAVERN device can realize the adsorption and transfer of the sample at the liquid N_2 temperature, and the ^{13}C MAS NMR observation of the reaction from 77 to ca. 600 K in NMR magnet. The Haw's group has done a large number of *in situ* ^{13}C MAS NMR studies with this device [13]. It is well known that heterogeneously catalyzed reactions are usually operated under the flow condition and the reaction products under the batch condition are different from those under the flow condition. Several groups attempt to develop *in situ* MAS NMR techniques for flow condition measurement [20–25]. Hunger *et al.* [14, 25] reported a device for real continuous-flow MAS measurement (Figure 5). In their device, the activated catalyst bed is pressed as a hollow cylinder in the MAS rotor and an injection tube is inserted into the hollow catalyst via a hole on the cap of rotor, which allows a continuous-flow introduction of reactants into the catalyst during the NMR experiment. The reaction products leave the MAS NMR rotor continuously through an annular gap in the rotor cap. It is possible to couple the *in situ* MAS device directly with an on-line GC [4]. Another *in situ* MAS NMR technique introduced by the Haw's group for the flow condition measurement includes a quench-reactor device coupled with GC and MS (Figure 6) [24]. A significant feature of the apparatus lies in that catalytic reactions can be quenched with cryogenically cooled nitrogen within a few hundred milliseconds. The catalyst loaded with reactants and products is then transferred to the NMR rotor in a glove box at room temperature prior to ^{13}C MAS NMR measurement. Figure 7 shows the pulse-quench ^{13}C NMR spectra [26] of ethylene on HZSM-5 zeolite at 623 K with the reaction time varying from 0.5 to 16 s. The most prominent peaks in the spectrum obtained for the 0.5 s reaction are all almost due to cyclopentenyl cation. As the catalyst ages for 2–4 s, signals from the carbenium ion decrease with a commensurate increase in the signals due to toluene. With further aging in the flow reactor, signals due to toluene and other organic species diminish, and after 16 s only a modest amount of the carbenium ion remains in the catalyst bed. A semilog fit of the decrease of the cyclopentenyl cation over time yielded an approximate half-life time of 6 s at 623 K.

In the last two decades, various catalytic reactions have been studied by *in situ* MAS NMR spectroscopy.

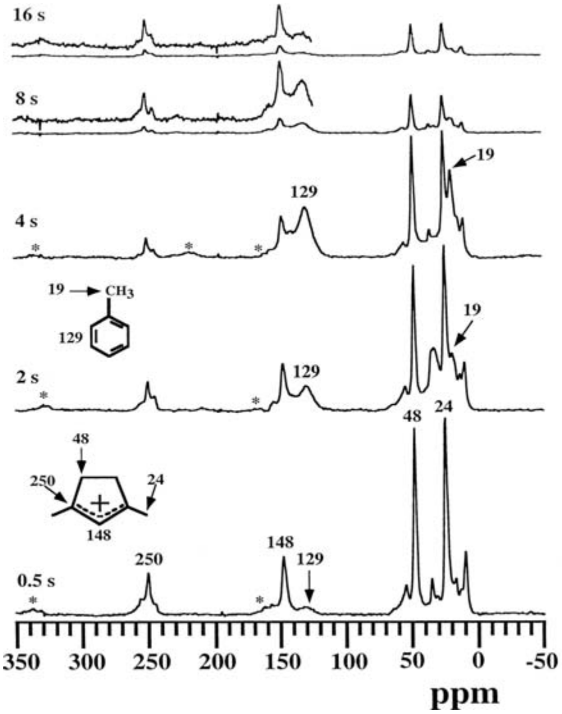

Fig. 7. ^{13}C MAS NMR spectra of ethylene-$^{13}C_2$ adsorbed on zeolite HZSM-5 at 623 K for various reaction time [26].

The formation of alkoxy species, such as methoxy groups ($\delta = 58$ ppm), ethoxy groups ($\delta = 68$ ppm), and isopropoxy groups ($\delta = 87$ ppm), have been observed by ^{13}C NAS NMR following the adsorptions of the olefines and alcohols onto acidic H-ZSM-5 and H–Y zeolites. These species are confirmed to act as reactive components that play an important role in the course of the reaction [4]. Methanol to hydrocabon conversion has been extensively investigated by *in situ* MAS NMR under either batch or flow condition, and the experimental results shed insight on the mechanism of reaction [26,27]. In the reaction of ethylene, methanol, acetone on acidic zeolite, alkyl-substituted, cyclic structure carbenium ion have been observed under batch /flow condition by *in situ* ^{13}C MAS NMR [13, 26], and it was proposed that these carbenium ions and related neutral species might function as reaction centers (hydrocarbon pool species) for the conversion of methanol to hydrocarbon.

References

1. Pfeifer H, Ernst H. Annu. Rep. NMR spectrosc. 1993;28: 91.
2. Hunger M. Catal. Rev. -Sci. Eng., 1997;39:345.
3. Haw JF (Ed.). *In-situ* Spectroscopy in Heterogeneous Catalysis, Wiley/VCH: Weinheim, 2002.
4. Hunger M, Weitkamp J. Angew. Chem. Int. Ed. 2001;40: 2954.
5. Ai X, Deng F, Dong J, Chen L, Ye C. J. Phys. Chem. B. 2002;106:9237.
6. Grey CP, Vega AJ. J. Am. Chem. Soc. 1995;117:8232.
7. Deng F, Yue Y, C Ye C. Solid State NMR. 1998;10:151.
8. Haw JF, Chuang S, Hawkins BL, Maciel GE, J. Am. Chem. Soc. 105, 7206 (1983).
9. Lunsford JH, Rothwell WP, Shen W, J. Am. Chem. Soc. 1985;107:1540.
10. Kao H-M, Liu H, Jiang J-C, Lin S, Grey CP. J. Phys. Chem. Bio. 2000;104:4923.
11. Hunger M. Solid State NMR 1996;6:1.
12. Biaglow AI, Gorte RJ, White D. J. Catal. 1994;148:779; Barich DH, Nicholas JB, Xu T, Haw JF. J. Am. Chem. Soc. 1998;120:12342.
13. Haw JF, Nicholas JB, Xu T, Beck LW, Ferguson DB. Acc. Chem. Res. 1996;29:259.
14. Hunger M. Catal. Today 2004;97:3.
15. Derouane EG, He H, Derouane SB, Lambert D, Ivanova I. J. Mol. Catal. A. 2000;158:5.
16. Anderson MW, Klinowski J, Nature 1989;339:200; Anderson MW, Klinowski J, J. Am. Chem. Soc. 1990;112:10.
17. Yang J, Ma D, Deng F, Luo Q, Zhang M, Bao X, Ye C. Chem. Commun. 2002;24:3046.
18. Ivanova II, Brunel D, Nagy JB, Derouane EG. J. Mol. Catal. A. 1995;95:243.
19. Carpenter TA, Klinowski J, Tennakoon DTB, Smith CJ, Edwards DC. J. Magn. Reson. 1986;68:561.
20. Haddix GW, Reimer JA, Bell AT. J. Catal. 1987;106:111.
21. Ernst H, Freude T, Mildner T. Chem. Phys. Lett. 1994;229: 291.
22. Ferguson DB, Haw JF. Anal. Chem. 1995;67:3342.
23. Haake M, Pines A, Reimer JA, Seydoux R. J. Am. Chem. Soc. 1997;119:11712.
24. Haw JF, Goguen PW, Xu T, Skloss TW, Song W, Wang Z, Angew. Chem. 1998;110:993; Angew. Chem. Int. Ed. 1998;37:948.
25. Hunger M, Horvath T. J. Chem. Soc. Chem. Commun. 1995;14:1423.
26. Haw JF, Nicholas JB, Song WG, Deng F, Wang ZK, Xu T, Heneghan CS. J. Am. Chem. Soc. 2000;122:4763.
27. Seiler M, Schenk U, Hunger M. Catal. Lett. 1999;62:139.

Isotope Labeling

Recent Developments in Stable-Isotope-Aided Methods for Protein NMR Spectroscopy

Shin-ya Ohki[1] and Masatsune Kainosho[2]

[1]Japan Advanced Institute of Science and Technology (JAIST), Ishikawa 923-1292, Japan; and
[2]CREST-JST and Department of Chemistry, Graduate School of Science, Tokyo Metropolitan University, Tokyo 192-0397, Japan

Introduction

The existence of stable isotopes, such as ^{2}H, ^{13}C, and ^{15}N, is a blessing from nature for protein NMR spectroscopy, because protons, carbons, and nitrogens are the major components of proteins. Thus, protein NMR has deeply benefited from these stable isotopes. Since their natural abundance is very low, selective enrichment and/or depletion of these nuclei for incorporation into proteins have/has been desired. These skills are called stable isotope labeling, which is an old technique that is undergoing renewal in protein NMR spectroscopy. Various stable-isotope-labeling methods are illustrated in Figure 1.

Labeling methods can be generally classified into *positive* and *negative*. The former methods use NMR active nuclei, such as ^{13}C and ^{15}N, meaning that this labeling enables the monitoring of only the labeled sites in molecules [1]. The most famous example of the latter category is deuteration. The replacement of ^{1}H by ^{2}H can erase undesired peaks in the ^{1}H NMR spectra [2,3]. Thus, in other words, positive and negative mean “visible” and “invisible,” respectively, for NMR spectroscopy. Such labeling methods were already proposed even in earlier one-dimensional (1D) NMR studies, before the strategy for the three-dimensional (3D) structure determination of proteins was established.

In another context, the labeling methods can be classified as *selective* and *uniform*. Examples of the former are the introduction of ^{13}C and/or ^{15}N into certain site(s) in protein samples. The latter labeling strategy, “uniform labeling,” is the preparation of protein samples in which all of the carbon and nitrogen atoms are labeled with stable isotopes, ^{13}C and ^{15}N, respectively. Then, all of the carbon, nitrogen, and proton atoms in the proteins become visible in NMR experiments. This was first reported with the adoption of new pulse sequences for the separation of peaks into multiple dimensions [4,5]. Nowadays, uniform labeling and multidimensional NMR measurements are standard for the structure determination of proteins smaller than ∼20 kDa.

The demands for NMR have become more complicated lately: structure determination of large molecules, quick structure determinations of proteins with moderate molecular weights, determination of protein structures at higher resolution with high accuracy and precision, identification of ligand-binding sites on the surface of proteins, detailed studies of molecular dynamics, structural transitions, etc. To satisfy these requests, numerous stable isotope techniques have been proposed as an extension of the methods mentioned above. For all of the cases, the key is how ^{2}H, ^{13}C, and ^{15}N are placed in the protein samples, and their concepts can simply be characterized using combinations of the four words: *positive, negative, selective*, and *uniform*. In this chapter, the stable isotope techniques developed in the past several years will be reviewed, and a novel labeling approach of the post-genomic era will be described.

Positive Labeling (Use of ^{13}C and ^{15}N)

About 20 years ago, the strategy to determine the 3D structures of proteins by solution NMR was established [6]. With parallel progress in homonuclear ^{1}H two-dimensional (2D) experimental techniques and computational algorithms, the structure determination of small polypeptides in solution became routine. For proteins larger than ∼10 kDa, however, the cross peaks are crowded in the 2D ^{1}H NMR spectra, so their structures are extremely difficult to determine. To investigate larger molecules, a new labeling technique was proposed in 1990 [4,5]. In that method, all of the carbon and nitrogen atoms in the protein sample are labeled with NMR active stable isotopes by a method called uniform labeling or ^{13}C, ^{15}N-double labeling. Then, all of the proton, carbon, and nitrogen atoms in the uniformly labeled protein become detectable with NMR.

The employment of ^{1}H, ^{13}C, and ^{15}N enables the use of heteronuclear one-bond or two-bond spin–spin couplings in pulse sequences, and thus their through-bond correlations can be monitored. These experimental data

Graham A. Webb (ed.), Modern Magnetic Resonance, 215–222.
© 2008 *Springer.*

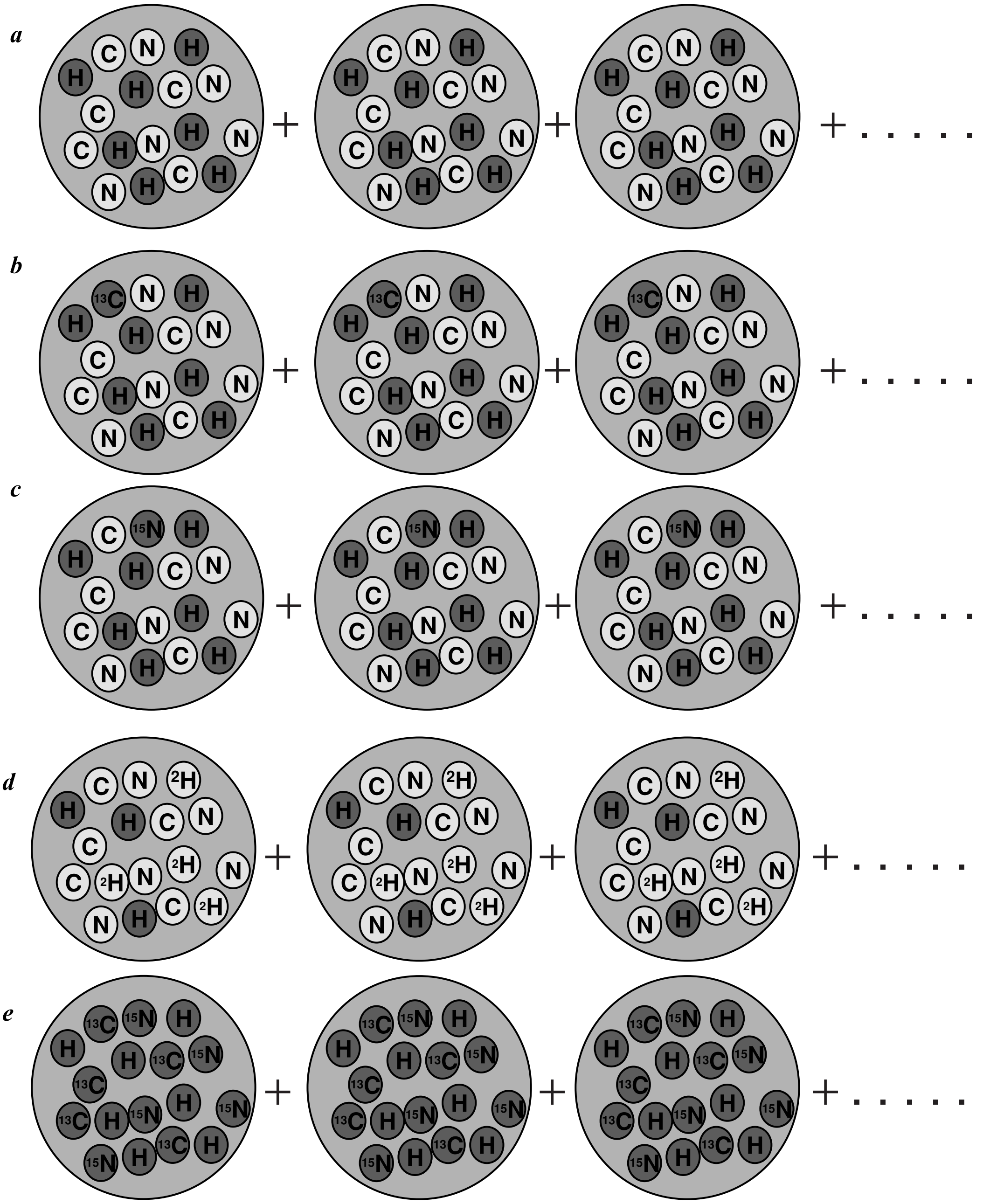

Fig. 1. Cartoons showing protein molecules with various stable-isotope-labeling patterns. Each yellow circle indicates a protein molecule. The small circles labeled H, C, and N indicate atoms. NMR observable and unobservable atoms are colored red and cyan, respectively. (a) Unlabeled, (b) selectively positive-labeled with ^{13}C, (c) selectively positive-labeled with ^{15}N, (d) selectively negative-labeled with ^{2}H, (e) uniformly ^{13}C, ^{15}N-labeled, (f) random-fractionally uniformly deuterated, and uniformly ^{13}C, ^{15}N-labeled, (g) site-specifically protonated, but otherwise uniformly ^{2}H, ^{13}C, ^{15}N-labeled, (h) protein–protein complex (uniformly labeled monomer and unlabeled one), and (i) segmental labeling (N-terminal half of the protein labeled with ^{13}C and ^{15}N). (See also Plate 25 on page XXVII in the Color Plate Section.)

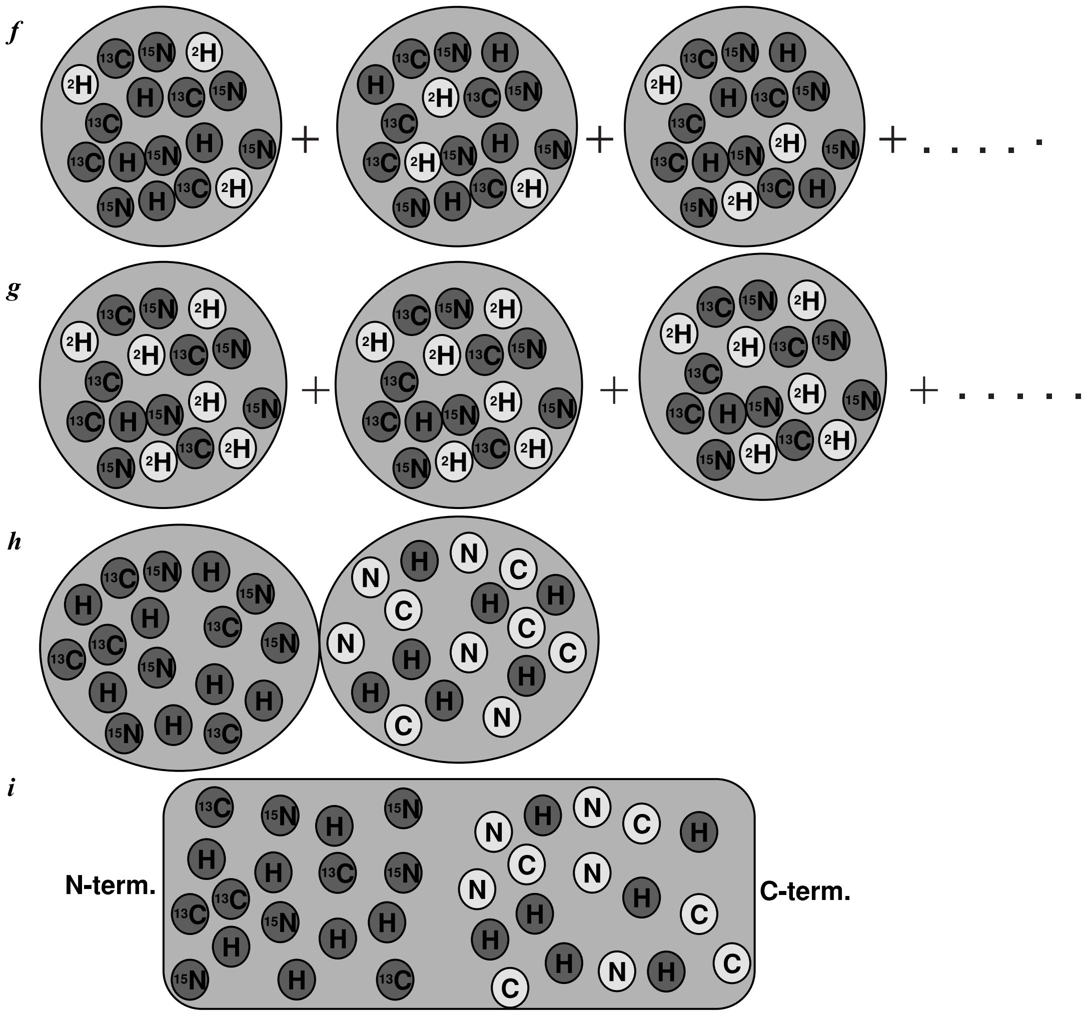

Fig. 1. (*Continued*) (See also Plate 25 on page XXVIII in the Color Plate Section.)

can provide the chemical shifts for all of the ^{1}H, ^{13}C, and ^{15}N in proteins unambiguously. Various *J* coupling constants are also obtainable with such samples, and they provide angle information for the protein backbone and side chains. Furthermore, the novel pulse sequences using ^{13}C or ^{15}N can separate crowded ^{1}H 2D NOESY spectra into several planes with the chemical shifts of the hetero nuclei attached to ^{1}H, thus enabling the identification of numerous NOE peaks for structure calculation. The strategy has expanded the possibility of NMR structure determination for proteins smaller than ~20 kDa.

Uniform labeling has also been adapted to protein complexes. Several labeling approaches have been proposed to study protein-protein complexes and symmetrical oligomers. The most popular method is mixing labeled and unlabeled components, which yields a complex in which one subunit is labeled with ^{13}C and ^{15}N, and the other is unlabeled. The binding surface is identified by intermolecular NOEs using isotope-filtered NMR experiments [7].

In the early 1990s, experimental methods in molecular biology were widely adopted by NMR laboratories, and uniform labeling instantly become a standard technique.

Various vectors and cells are commercially available today, and thus it has become routine to prepare expression systems for proteins from a wide variety of sources. Commonly, bacteria, *Phicia pastoris*, and insect or mammalian cells are used for NMR sample preparation. The uniform labeling is generally achieved by the addition of labeled chemicals into the growth medium. For the ^{13}C-precursors, ^{13}C-labeled glucose, ^{13}C-acetic acid, or ^{13}C-methanol is frequently used, with ^{15}N-labeled NH_4Cl or NH_4SO_4 as the ^{15}N-precursors. In an alternative method, a ^{13}C, ^{15}N-labeled amino acid mixture can be included in the medium.

Amino acid type selective labeling to simplify NMR spectra has been used as a powerful tool to study local conformations. This method can be applied to large proteins, and thus it is still useful in current research. For this case, ^{13}C and ^{15}N are employed as labels, and an expression or chemical synthesis method is needed to prepare the protein samples. When we use *Escherichia coli* to express the NMR samples, it is easy to label the Ile, Leu, Val, Phe, and Tyr residues. However, for several amino acids including Glu, Gln, Asp, and Asn, the selective labeling is not achieved with standard *E. coli* strain such as BL21, because of isotope scrambling and dilution during expression. To overcome these problems, a new set of genetically engineered *E. coli* strains with lesions in the biosynthetic pathways of certain amino acids has been developed [8]. The use of these extraordinary *E. coli* systems is one of the solutions to achieve amino acid type selective labeling. Another choice for sample preparation is to use cell-free protein synthesis. A cell-free system has the potential for robust isotope labeling without isotope scrambling and dilution [9]. The system can also be used for toxic proteins and membrane proteins [10], which are difficult to express in bacteria, and it can be extended to incorporate non-natural amino acids containing spin or fluorescent labels [11].

For large proteins, an attractive labeling method, segmental labeling, has been proposed. This method is used to prepare a protein in which a part is labeled, and is based on peptide splicing reactions with inteins. Inteins are inserted amino acid sequences that splice themselves out after translation [12]. In the first demonstration, the isotopic-labeled N-terminal (or C-terminal) half of a protein was ligated to the unlabeled C-terminal (or N-terminal) half [13]. As a modification of the original method, labeling at the central region of a protein is also possible [14].

Negative Labeling (Use of ^{2}H)

The application of multidimensional NMR experiments for larger proteins (> 20 kDa) often yields poor NMR spectra, due to two factors. One is severe line broadening and the other is overlapping of numerous peaks. The former is caused by the shorter spin–spin relaxation time (T_2) and the latter is due to the number of protons. In the past decade, great progress has been made to overcome these problems. The breakthrough was achieved with new pulse sequences based on the transverse relaxation-optimized spectroscopy (TROSY) technique and a combination of ^{2}H negative labeling and ^{13}C, ^{15}N positive labeling.

The TROSY principle was originally found as a modification of ^{1}H–^{15}N HSQC (heteronuclear single quantum coherence spectroscopy) on biomolecules. The critical feature of TROSY is that heteronuclear one-bond ^{1}H–X ($X = {}^{13}$C, ^{15}N) splitting should not be decoupled. Then, each peak is split into four in the 2Dplane. The line widths of the doublet components in both dimensions are different, because they have different relaxation mechanisms. In the original TROSY experiment, only the sharpest component, which shows the longest T_2, was observed by a phase cycling scheme that cancels the three broader peaks of the multiplet [15,16]. The higher field magnets (800–900 MHz) that are currently available are suitable for obtaining the maximum TROSY effect, and thus the NH detection period in many triple resonance pulse sequences has been rewritten, based on the TROSY technique, for larger proteins [17].

Negative labeling, using of ^{2}H, has been employed to reduce the number of peaks in ^{1}H NMR spectra. This was recognized as a powerful technique even in earlier 1D NMR [2,3]. Moreover, the use of ^{2}H yields another benefit, in that it strengthens and sharpens the signals in NMR spectra. Since ^{2}H has a significantly lower gyromagnetic ratio as compared with ^{1}H ($\gamma[^2\mathrm{H}]/\gamma[^1\mathrm{H}] = 0.15$), the use of ^{2}H can contribute toward eliminating the ^{1}H–^{1}H dipolar and ^{1}H–X ($X = {}^{13}$C, ^{15}N) heteronuclear spin relaxation pathways, resulting in a longer T_2. The first experiments using ^{2}H labeling combined with triple resonance multidimensional NMR experiments were reported in 1993 [18]. The effect of ^{2}H in ^{13}C, ^{15}N-labeled proteins is very successful, and thus many applications using this labeling scheme have been published [19–21]. A recent study has shown that the triple labeling method coupled with TROSY-based NMR analysis can work even for a 900 kDa protein complex [22].

In earlier application of triple-resonance multidimensional experiments with ^{2}H decoupling, the uniformly random fractional incorporation of ^{2}H into the non-exchangeable ^{1}H sites in proteins was employed. In general, the degree of the ^{2}H labeling level affects the quality of the NMR spectra, so a higher level of random uniform ^{2}H labeling yields sharper signals and thus is better for main chain assignments. However, the absence of ^{1}H at non-exchangeable sites is disadvantageous to side chain analysis, especially for the observation of ^{1}H–^{1}H NOEs for structure determination. Thus, 50–90% uniformly

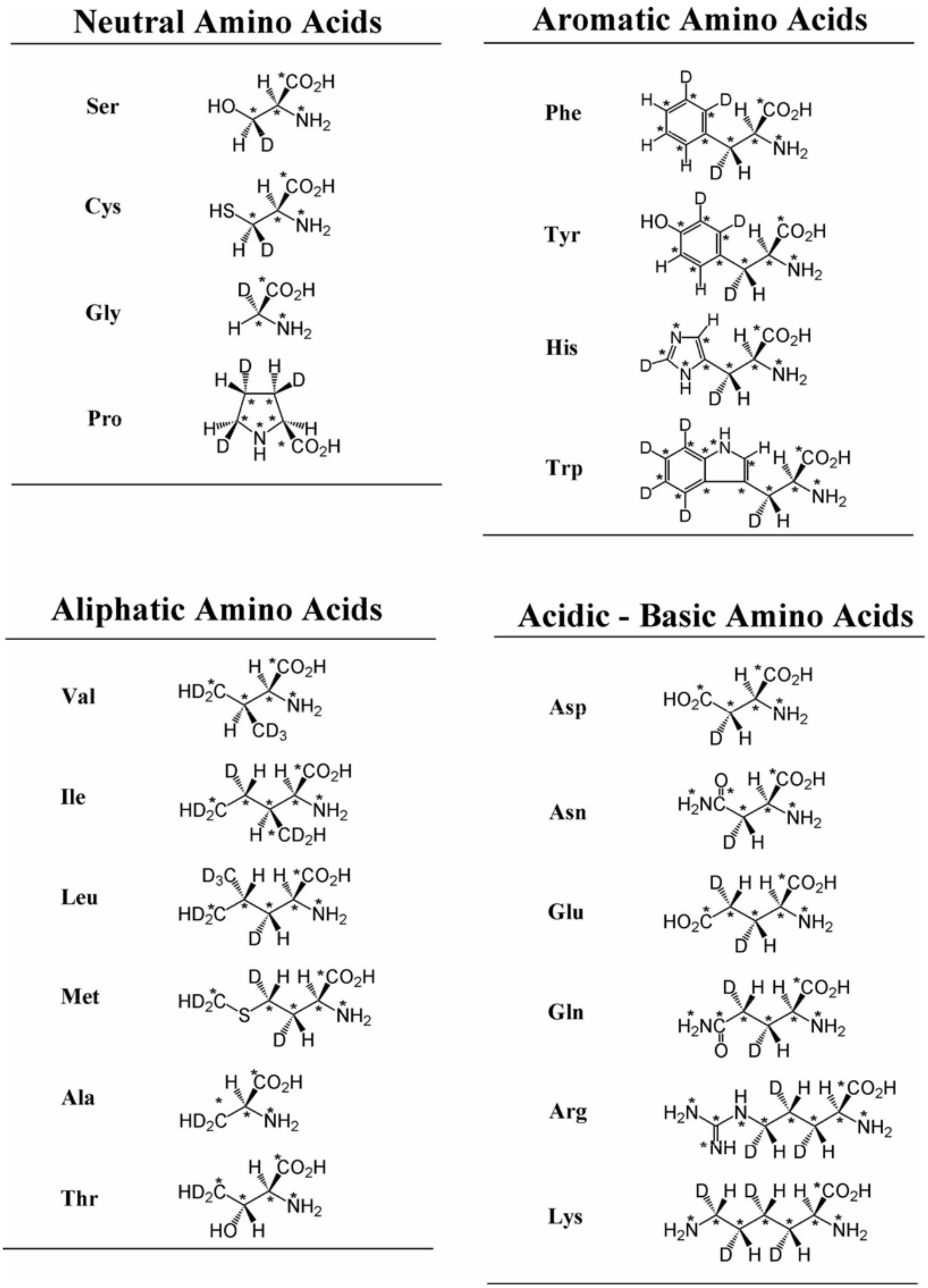
Neutral Amino Acids
Ser
Cys
Gly
Pro
Aromatic Amino Acids
Phe
Tyr
His
Trp
Aliphatic Amino Acids
Val
Ile
Leu
Met
Ala
Thr
Acidic - Basic Amino Acids
Asp
Asn
Glu
Gln
Arg
Lys

Fig. 2. A typical structure of each stereo-arrayed-isotope-labeled (SAIL) amino acid. There are various other isotopomers, which may be useful for NMR applications.

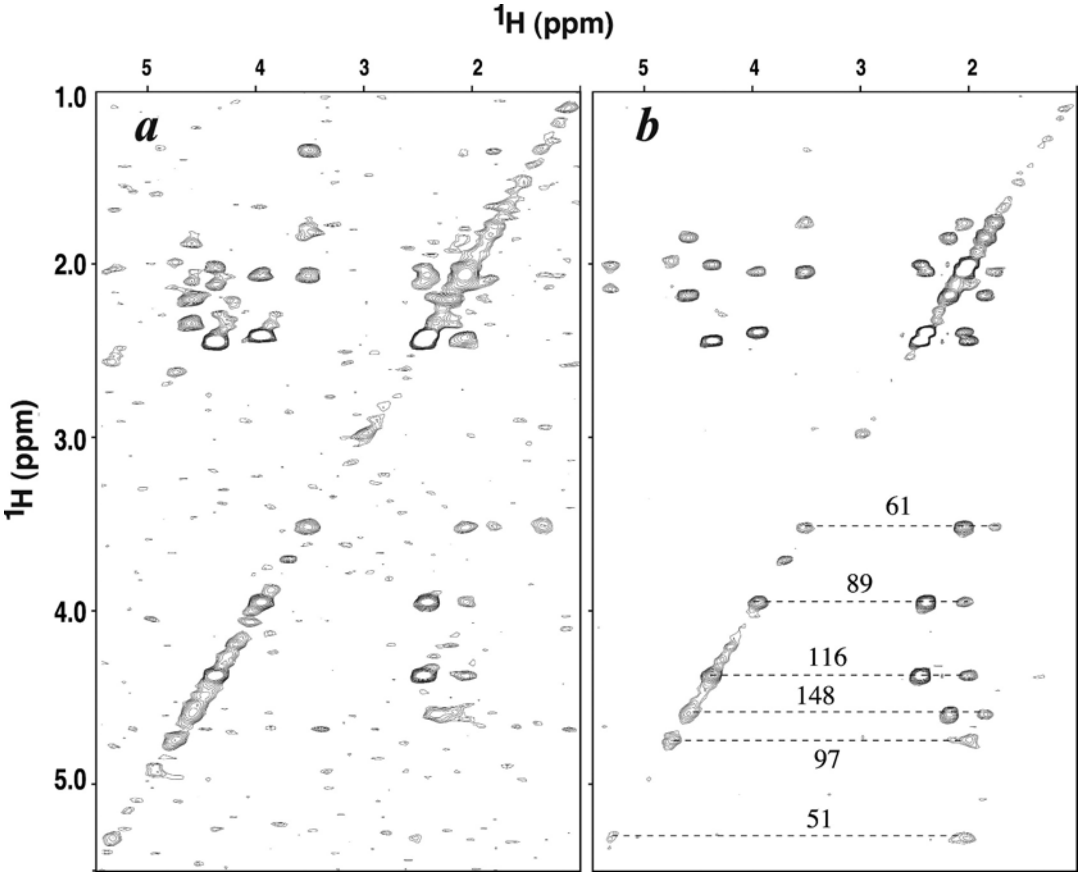

Fig. 3. Two-dimensional HCCH-TOCSY of an 18.2 kDa protein, EPPIb (S. Ohki, T. Hayano, T. Terauchi, M. Kainosho, unpublished data). The sample contains with uniformly ^{13}C, ^{15}N-labeled Gln, [ul-^{13}C,^{15}N]-Gln, (a) and SAIL-Gln (b), respectively. The intra-residue connectivity for each residue is shown by a dotted line with the residue number.

random fractional ^{2}H labeling is frequently employed for analysis, but this has considerable problems related to isotopomers. For example, each methyl group of Ala, Leu, Ile, Val, and Met contains isotopomers, i.e. CH_3, CH_2D, CHD_2, and CD_3. Three of the four isotopomers give NMR signals, and they appear at slightly different chemical shifts due to the isotope shift. Then, the methyl region signals become crowded, which hinders extensive analysis. However, the methyl group is interesting as a probe for protein dynamics. In some cases, $^{13}CH_2D$ is monitored, but the topic of protein dynamics is beyond the scope of this review. Although an optimized sample preparation method and pulse sequences to observe one isotopomer in the sample solution have been reported [23], the signal intensity is lower than expected, because the actual number of detectable molecules is much less than the total sample concentration. If one obtains fine filtered NMR spectra using such pulse techniques, then the number of ^{1}H to be analyzed increases with the molecular weight, and thus the amount of effort is never reduced.

To improve the spectral complexity, alternative labeling methods have been proposed by using ^{2}H, ^{13}C, and ^{15}N. The method is amino acid type selective labeling in deuterated proteins. In other words, the method is selective protonation. In an earlier report of this strategy, the labeled protein sample was expressed in minimal medium containing 95% D_2O, ^{2}H-labeled glucose, $^{15}NH_4SO_4$, and $^{1}H/^{13}C/^{15}N$-{Ile, Leu, Val} amino acids [24]. The samples gave very clear ^{1}H–^{13}C HSQC and NOESY for these hydrophobic residues. The aliphatic–aliphatic NOEs combined with the ^{1}HN–^{1}HN NOEs can

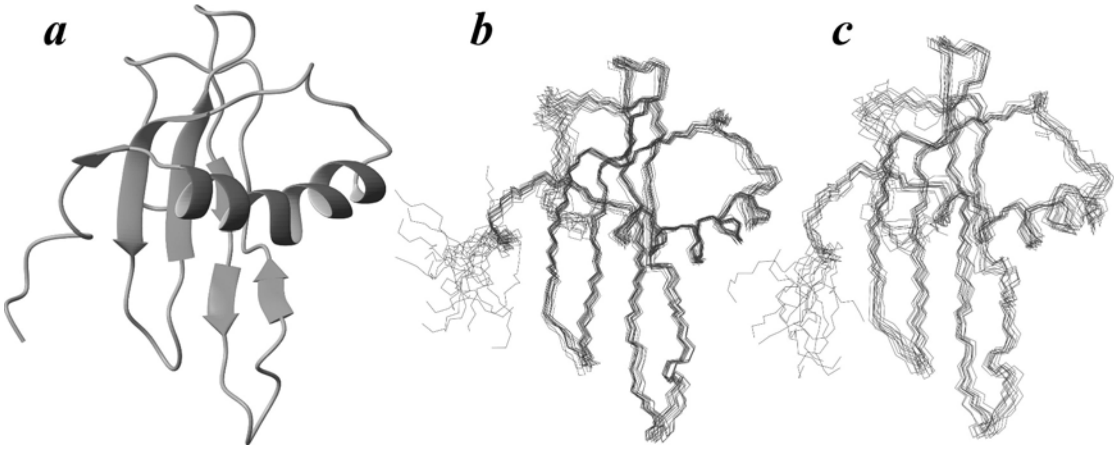

Fig. 4. Simulation of structure determination for proteins labeled with SAIL amino acids (S. Ohki, M. Kainosho, unpublished data). (a) Ribbon model of cystatin A (PDB code; 1CYV) determined by NMR experiments. Structures (b) and (c) were simulated based on the coordinate. (b) Structures using all NOEs theoretically observed, and (c) structures using NOEs expected for the SAILed protein. (See also Plate 26 on page XXVIII in the Color Plate Section.)

be subjected to structure calculations; however, only the global fold is available. Although several ^{13}C precursors, such as ^{13}C pyruvate [23,25,26] or [2-^{13}C]glycerol [27], were examined for the selective labeling, further structural information, such as residual dipolar couplings (RDC), was needed to determine the high-resolution NMR structures of large proteins [28].

Recently, a novel labeling method termed stereo-arrayed isotope labeling (SAIL) has been developed [29]. In this labeling method, the ^{2}H labeling sites and the occupancy are controlled at an extremely high level. The arrayed deuteration sites in proteins are designed to suppress redundant structural information [30]. The SAIL amino acids, shown in Figure 2, are chemically and enzymatically synthesized. Then, these amino acid compounds are incorporated into the cell-free synthesis system for sample protein preparation. The SAILed proteins have ~50% protons as compared to fully protonated proteins, and the SAILed protein molecules in the sample solution represent only one isotopomer. Thus, the NMR spectra are simplified, with very narrow signals. Figure 3 indicates an example of the NMR data. In both samples, only Gln residues were labeled with uniformly [ul-^{13}C, ^{15}N]-Gln (Figure 3a) or SAIL-Gln (Figure 3b). Obviously, the SAIL method gives much better NMR spectrum. Furthermore, a simulation of the structure calculation indicates that obtainable NOEs must be sufficient to solve the structure at high resolution and accuracy (Figure 4). The application of SAIL method promises to relieve the limitation of molecular weight for NMR analyses and to contribute to high-throughput structure determination in the post-genomic era.

Concluding Remarks

The recent progress in stable-isotope-labeling strategies has provided opportunities for NMR studies of a wide range of proteins and their complexes. The advance of methodologies for sample preparation, including conventional expression systems, cell-free systems, and chemical synthesis, will continuously propose various labeling strategies. In concert with improved instruments, novel experimental techniques, and faster computing, the stable-isotope-labeling will become increasingly significant for studying larger biological systems by NMR in the future.

Acknowledgment

The SAIL method that was briefly introduced in this chapter has been developed in the CREST project supported by JST.

References

1. Jardetzky O, Roberts GCK. NMR in Molecular Biology. Academic Press: New York, 1981.
2. Butter TB. Proton magnetic resonance fully deuterated except for ^{1}H-leucine side chains. Science. 1968;161:795–98.
3. Markley JL, Putter I, Jardetzky O. High-resolution nuclear magnetic resonance spectra of selectively deuterated staphylococcal nuclease. Science. 1968;161:1249–51.
4. Kay LE, Ikura M, Tschudin R, Bax A. Three-dimensional triple-resonance NMR spectroscopy of isotopically enriched proteins. J. Magn. Reson. 1990;89:496–514.

5. Ikura M, Kay LE, Bax A. A novel approach for sequential assignment of ^{1}H, ^{13}C, and ^{15}N spectra of proteins: heteronuclear triple-resonance three-dimensional NMR spectroscopy: application to calmodulin. Biochemistry. 1990;29:4659–67.
6. Wüthrich K. NMR of Proteins and Nucleic Acids. John Wiley & Sons: New York, 1986.
7. Folkers PJM, Folmer RHA, Konings RNH, Hilbers CW. Overcoming the ambiguity problem encountered in the analysis of nuclear Overhauser magnetic resonance spectra of symmetric dimer proteins. J. Am. Chem. Soc. 1993;115:3798–99.
8. Waugh DS. Genetic tools for selective labeling of proteins with $\alpha-^{15}N$-labeled amino acids. J. Biomol. NMR. 1996;8:184–192.
9. Torizawa T, Shimizu M, Taoka M, Miyano H, Kainosho M. Efficient production of isotopically labeled proteins by cell-free synthesis: A practical protocol. J. Biomol. NMR. 2004;30:311–25; and references cited therein.
10. Berrier C, Park KH, Abes S, Bibonne A, Betton JM, Ghazi A. Cell-free synthesis of a functional ion channnel in the absence of a membrane and in the presence of detergent. Biochemistry. 2004;43:12585–91.
11. Rothschild KJ, Gite S. t-RNA-mediated protein engineering. Curr. Opin. Biotechnol. 1999;10:64–70.
12. Perler FB. Protein splicing of inteins and hedgehog autoproteolysis: structure, function, and evolution. Cell. 1998;92:1–4.
13. Yamazaki T, Otomo T, Oda N, Kyogoku Y, Uegaki K, Ito N, Ishino Y, Nakamura H. Segmental isotope labeling for protein NMR using peptide splicing. J. Am. Chem. Soc. 1998;120:5591–92.
14. Otomo T, Ito N, Kyogoku Y, Yamazaki T. NMR observation of selected segments in a larger protein: central-segment isotope labeling through intein-mediated ligation. Biochemistry. 1999;38:16040–44.
15. Pervushin K, Riek R, Wider G, Wüthrich K. Attenuated T2 relaxation by mutual cancellation of dipole–dipole coupling and chemical shift anisotropy indicates an avenue to NMR structures of large biological macromolecules in solution. Proc. Natl. Acad. Sci. U.S.A. 1997;94:12366–71.
16. Pervushin K, Riek R, Wider G Wüthrich K. Transverse relaxation-optimized spectroscopy (TROSY) for NMR studies of aromatic spin systems in ^{13}C-labeled proteins. J. Am. Chem. Soc. 1998;120:6394–400.
17. Salzmann M, Pervusin K, Wider G, Senn H, Wüthrich K. TROSY in triple-resonance experiments: new perspectives for sequential NMR assignment of large proteins. Proc. Natl. Acad. Sci. U.S.A. 1998;95:13585–90.
18. Grzesiek S, Anglister J, Ren H, Bax A. ^{13}C line narrowing by ^{2}H decoupling in $^{2}H/^{13}C/^{15}N$-enriched proteins—application to triple-resonance 4D J-connectivity of sequential amides. J. Am. Chem. Soc. 1993;115:4369–70.
19. Yamazaki T, Lee W, Arrowsmith CH, Muhandiram DR, Kay LE. A suite of triple-resonance NMR experiments for backbone assignment of ^{15}N, ^{13}C, ^{2}H-labeled proteins with high-sensitivity. J. Am. Chem. Soc. 1994;116:11655–66.
20. Shan X, Gardner KH, Muhandiram DR, Rao NS, Arrowsmith CH, Kay LE. Assignment of ^{15}N, $^{13}C\alpha$, $^{13}C\beta$, and HN resonances in an ^{15}N, ^{13}C, ^{2}H labeled 64 kDa trp repressor–operator complex using triple-resonance NMR spectroscopy and ^{2}H-decoupling. J. Am. Chem. Soc. 1996;118;6570–79.
21. Garrett DS, Seok YJ, Liao DI, Peterkofsky A, Gronenborn AM, Clore GM. Solution structure of the 30 kDa N-terminal domain of enzyme I of the *Escherichia coli* phosphoenolpyruvate: sugar phosphotransferase system by multidimensional NMR. Biochemistry. 1997;36;2517–30.
22. Flaux J, Bertelsen EB, Horwich AL, Wüthrich K. NMR analysis of a 900K GroEL–GroES complex. Nature. 2002;418:207–11.
23. Ishima R, Louis JM, Torchia DA. Optimized labeling of $^{13}CHD_2$ methyl isotopomers in perdeuterated proteins: potential advantages for ^{13}C relaxation studies of methyl dynamics of larger proteins. J. Biomol. NMR. 2001;21:167–71.
24. Metzler WJ, Wittekind M, Goldfarb V, Mueller L, Farmer II BT. Incorporation of $^{1}H/^{13}C/^{15}N$-$\{$Ile, Leu, Val$\}$ into a perdeuterated, ^{15}N-labeled protein: potential in structure determination of large proteins by NMR. J. Am. Chem. Soc. 1996;118:6800–1.
25. Rosen MK, Gardner KH, Willis RC, Parris WE, Pawson T, Kay LE. Selective methyl group protonation of perdeuterated proteins. J. Mol. Biol. 1996;263:627–36.
26. Lee AL, Urbauer JL, Wand AJ. Improved labeling strategy for ^{13}C relaxation measurements of methyl groups in proteins. J. Biomol. NMR. 1997;9:437–40.
27. LeMaster DM, Kushlan DM. Dynamical mapping of *E. coli* thioredoxin via ^{13}C NMR relaxation analysis. J. Am. Chem. Soc. 1995;118:9255–64.
28. Delaglio F, Kontaxis G, Bax A. Protein structure determination using molecular fragment replacement and NMR dipolar couplings. J. Am. Chem. Soc. 2000;122:2142–43.
29. Kainosho M. The SAIL method for protein NMR spectroscopy. XXIst ICMRBS, Hyderabad, India, 2005. p 46.
30. Terauchi T, Ohki, S, Kainosho M. Developing a new approach for high-throughput, high-accuracy NMR structural analyses of genomic proteins. Protein nucleic acid enzyme. 1998;47:1045–51.

Structural Glycobiology by Stable-isotope-assisted NMR Spectroscopy

Yoshiki Yamaguchi[1,2] and Koichi Kato[1,2,3,4]
[1]*Nagoya City University, Nagoya, Japan;*
[2]*CREST/JST, Saitama, Japan;*
[3]*Institute for Molecular Science, Okazaki, Japan; and*
[4]*Genomic Sciences Center, RIKEN Yokohama Institute, Yokohama, Japan*

Introduction

Recent advances in structural biology have made possible the high-throughput structural determination of proteins, which is reflected in the very rapid growth of Protein Data Bank content. In structural proteomics, recombinant proteins used for structural determination by NMR spectroscopy and X-ray crystallography are conventionally produced by use of bacterial expression systems or recently by cell-free protein expression systems and therefore do not possess carbohydrate moieties. However, many of the proteins in the living systems are covalently linked to carbohydrate moieties, which mediate molecular recognition involved in cell–cell communication, contribute to solubility and structural integrity of proteins, and determine the fates of glycoproteins in cells, i.e. folding, transport, and degradation via interactions with a variety of intra-cellular lectins [1,2].

Although the biological importance of glycans expressed on proteins has been widely recognized, little is known about their specific roles from the structural aspect. This deficiency in our knowledge is largely due to the lack of an appropriate methodology to deal with glycoproteins as targets of structural biology. The carbohydrate moieties of glycoproteins generally exhibit microheterogeneities and possess a significant degree of freedom in internal motion, which hampers crystallization or interpretation of electron density [3,4]. NMR spectroscopy can potentially provide us with information on structure and dynamics of glycoproteins in solution. However, there are few reports of structural determination of glycoproteins by NMR spectroscopy [5–7]. The desirable methods for NMR structural biology of glycoproteins and carbohydrate–protein interactions are

1) Production of a large amount of isotopically labeled glycoprotein by appropriate expression systems.
2) Determination of a covalent structure of target glycoprotein including carbohydrate moieties.
3) Preparation of a large amount of isotopically labeled oligosaccharides that can be used as ligands.

Three-Dimensional HPLC Mapping

Prior to NMR analyses of glycoproteins, it is essential to obtain information concerning the covalent structures of their carbohydrate moieties. Takahashi and coworkers have established a method to identify asparagine-linked oligosaccharides rapidly on inspection of HPLC elution profiles of their pyridylamino (PA)-derivatives [8]. On the basis of the combination of the retention time data on the three kinds of HPLC columns, i.e. anion exchange, ODS, and amide–silica columns, the elution map of the 500 different PA-oligosaccharides has been established. Based on this three-dimensional HPLC map combined with mass spectrometric data, we have recently made GALAXY (http://www.glycoanalysis.info/), a web application that greatly facilitates NMR structural biology of glycoproteins [9]. The HPLC method is also useful for isolation of PA-oligosaccharides discriminating isomeric structures [10], which can be used as ligand for NMR analyses of carbohydrate–protein interactions.

Stable Isotope Labeling of Glycoproteins

The authors have been developing a systematic method for isotope labeling of glycoproteins for NMR analyses using immunoglobulin G (IgG) as model system [11,12]. The Fc portion of IgG possesses one conserved glycosylation site at Asn-297 in each of the two heavy chains, where biantennary complex-type oligosaccharides (Figure 1) are expressed. These carbohydrate chains are essential for the binding to effector molecules such as Fcγ rceptors [13,14]. The carbohydrate chains exhibit microheterogeneities resulting from the presence or absence of the non-reducing terminal galactose (Gal), core fucose (Fuc), and bisecting *N*-acetylglucosamine (GlcNAc)

Graham A. Webb (ed.), Modern Magnetic Resonance, 223–229.
© 2008 *Springer.*

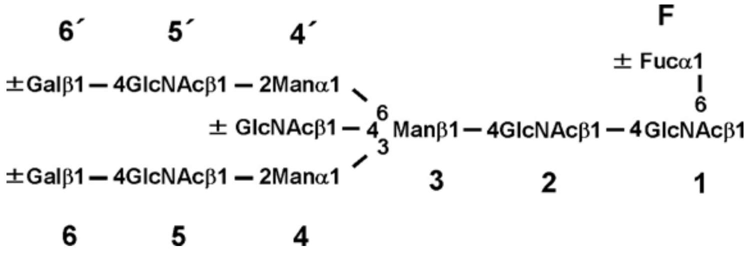
6´
5´
4´
F
± Fucα1
6
±Galβ1 — 4GlcNAcβ1 — 2Manα1
6
± GlcNAcβ1 — 4
3
Manβ1 — 4GlcNAcβ1 — 4GlcNAcβ1
±Galβ1 — 4GlcNAcβ1 — 2Manα1
3
2
1
6
5
4

Fig. 1. The structures of the glycans attached to the Fc portion of IgG.

residues depending upon physiological and pathological states [15,16]. For example, agalacosylation of serum IgG is associated with a variety of diseases such as rheumatoid arthritis [17].

Figure 2 illustrates the scheme of strategy for stable isotope labeling of the Fc glycans. For incorporation of the labeled precursors into the glycoprotein, we use two alternative methods. One is metabolic labeling via biosynthesis pathway of mammalian cells. The other is *in vitro* labeling by use of enzymatic glycosylation onto isolated glycoproteins.

In vitro Labeling of Sugar Chains

Enzymatic attachment of isotopically labeled sugar onto the carbohydrate moiety is a conventional method of selective isotope labeling of the non-reducing terminal sugar

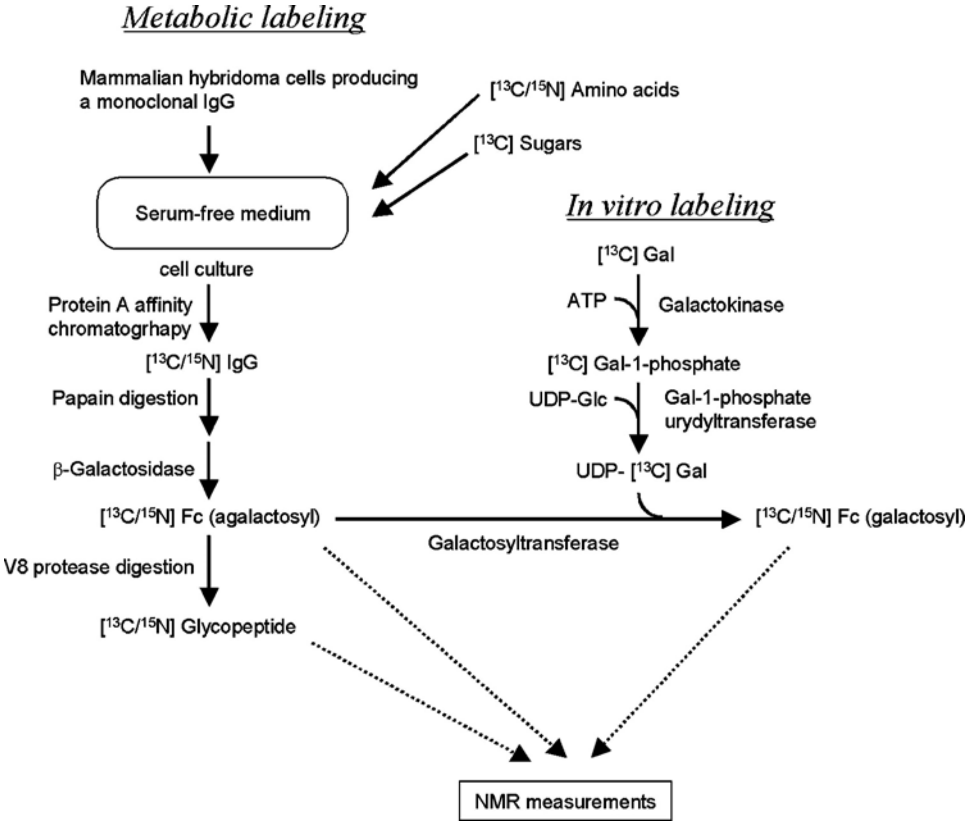
Metabolic labeling
Mammalian hybridoma cells producing a monoclonal IgG
[13C/15N] Amino acids
[13C] Sugars
Serum-free medium
cell culture
Protein A affinity chromatogrhapy
[13C/15N] IgG
Papain digestion
β-Galactosidase
[13C/15N] Fc (agalactosyl)
V8 protease digestion
[13C/15N] Glycopeptide
In vitro labeling
[13C] Gal
ATP
Galactokinase
[13C] Gal-1-phosphate
UDP-Glc
Gal-1-phosphate urydyltransferase
UDP- [13C] Gal
Galactosyltransferase
[13C/15N] Fc (galactosyl)
NMR measurements

Fig. 2. The scheme of stable isotope labeling of the Fc glycoprotein and the glycopeptide derived therefrom.

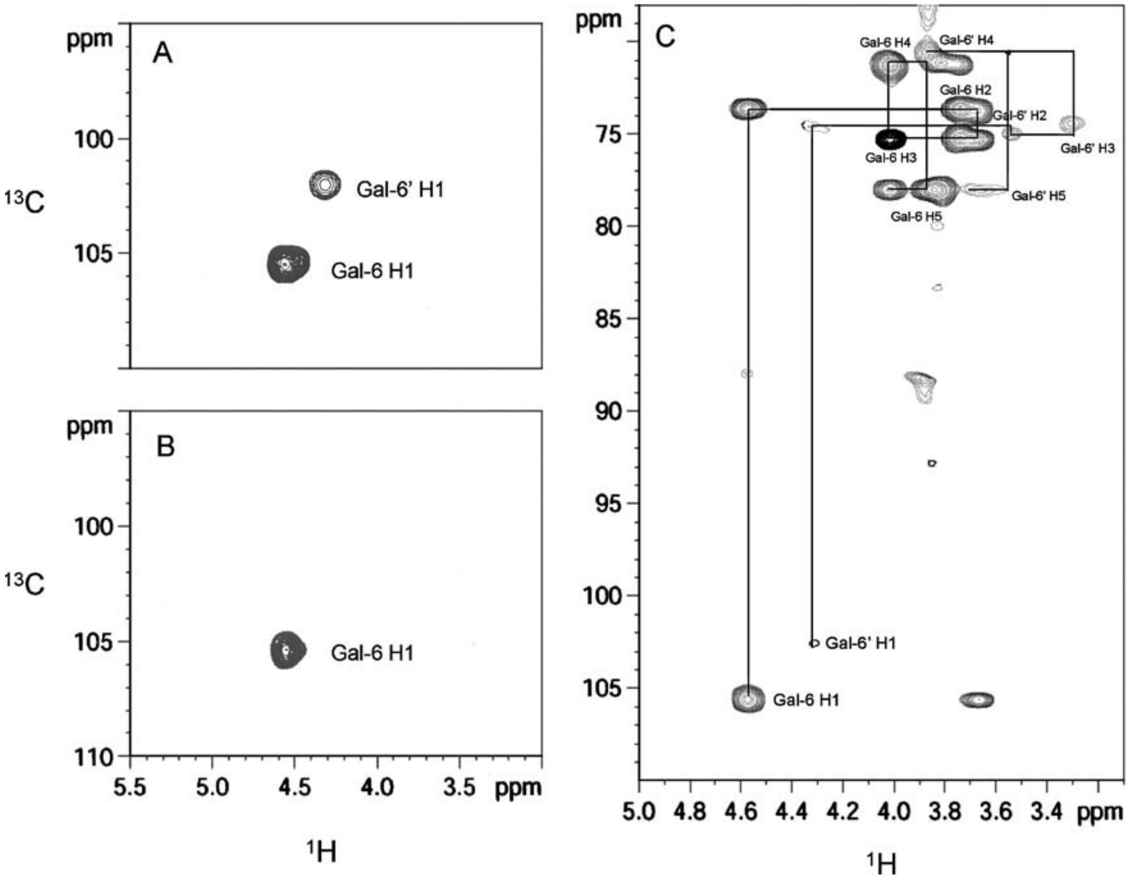

Fig. 3 ^{1}H–^{13}C HSQC of galactosyl Fc in which the Gal residues are fully (A) or partially (B) labeled with ^{13}C by using UDP-[1-^{13}C]Gal and (C) 2D HCCH-COSY spectrum of galactosyl Fc in which the Gal residues are fully labeled with ^{13}C by using UDP-[u-$^{13}C_6$]Gal.

residues such as Gal and sialic acids. Figure 2 shows the scheme of *in vitro* labeling of the terminal Gal residues [12,18]. [1-^{13}C]Gal can be converted to UDP-[1-^{13}C]Gal through the successive enzymatic reactions using galactokinase and galactose-1-phosphate uridyl transferase and then attached by using galactosyltransferase onto the non-reducing ends of the Fc carbohydrate chains, which are degalactosylated in advance. The Fc preparation gave two HSQC peaks originating from the anomeric groups of the terminal Gal residues, i.e. Gal-6 and Gal-6′ (Figure 3A). Under the mild reaction condition using small amount of unlabeled UDP-Gal, galactosylation occurs fully and partially at the mannose (Man) α1-6 and Manα1-3 branches, respectively. The unoccupied Manα1-3 branches of this Fc preparation can be fully galacosylated by use of enough amount of UDP-[^{13}C]Gal, giving rise to Fc labeled with ^{13}C exclusively at Gal-6′. HSQC spectrum of this Fc preparation gave a single anomeric peak originating from Gal-6 (Figure 3B) and therefore led us to assign the peaks shown in Figure 3A to each of the Gal residues. Starting from the anomeric peaks thus assigned, intra-residue scalar connectivities were identified by HCCH-COSY spectrum of the isotopically labeled Fc prepared by using UDP-[1-$^{13}C_6$]Gal (Figure 3C).

It should be noted that the peaks originating from Gal-6 gave much narrower peak than those from Gal-6′, indicating that Gal-6 is much more mobile than Gal-6′. This is consistent with the crystallographic data of Fc, which shows that Gal-6 makes contacts with an inner surface of the C_H2 domain, while the Manα1-3 branch protrude to a space between the C_H2 domains [19]. Hence, ^{13}C resonances can be useful probes to provide us with information

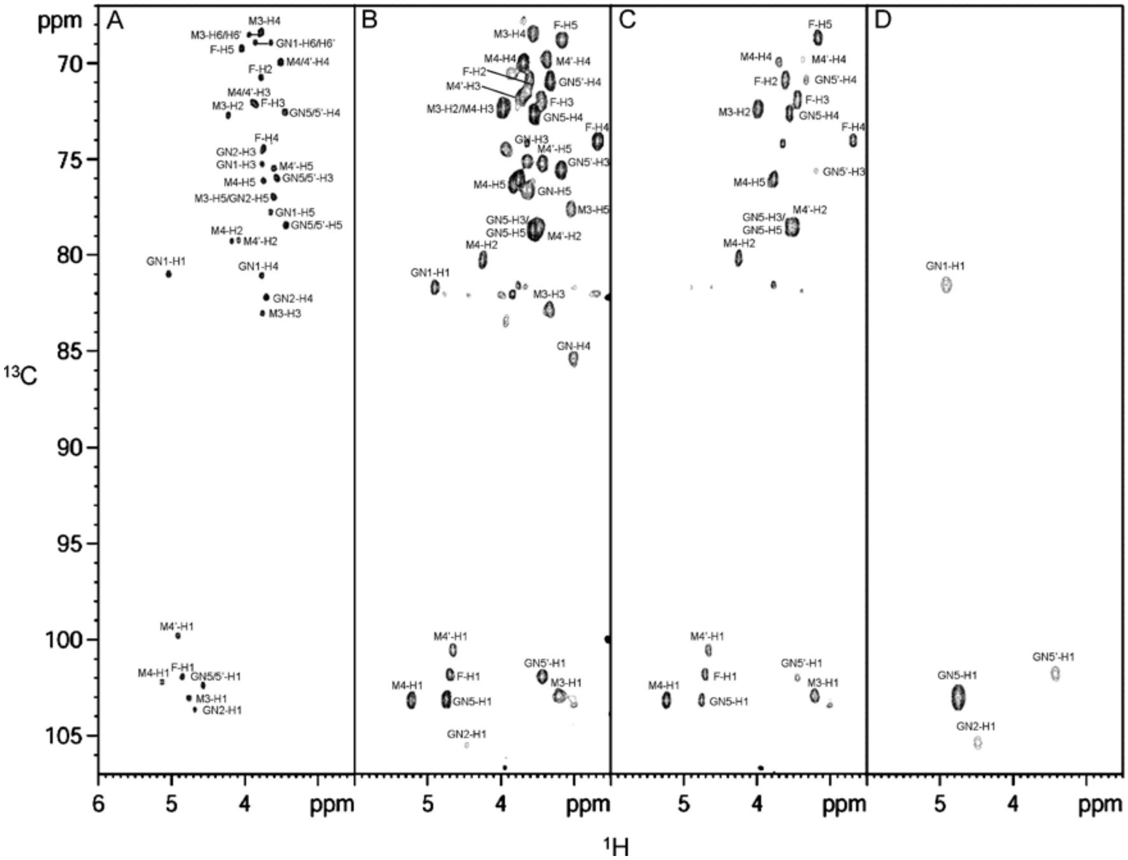

Fig. 4 ^{1}H–^{13}C ct-HSQC spectrum observed for the glycopeptide metabolically labeled with [u-$^{13}C_6$]Glc (A) and ^{1}H–^{13}C HSQC spectra of agalactosyl Fc metabolically labeled with [u-$^{13}C_6$]Glc (B), [u-$^{13}C_6$, $^2H_7$]Glc (C), and [1-^{13}C]GlcN (D). F, fucose; GN, *N*-acetylglucosamine; M, mannose.

on dynamics of the carbohydrate moieties of glycoproteins at atomic resolution. Similar technique can be applied for isotope labeling of the terminal sialic acid residue on galactosylated ovalbumin [20].

Metabolic Labeling of Sugar Chains

The major drawback of *in vitro* labeling method is that it can only be applied to the NMR analyses of nonreducing terminal residues of glycans in glycoproteins. By contrast, metabolic labeling can be applicable for the observation of NMR signals originating from all the sugar residues. For expression of isotopically labeled glycoproteins subjected to NMR analyses, mammalian [5,21], plant [22], yeast [23,24], insect cells [25], and cellular slime mold [26] have so far been available. The authors have developed protocols of metabolic labeling of IgG glycoproteins by cultivating hybridoma cells in a serum-free medium that contains isotopically labeled amino acids and/or sugars [12,27].

Since glucose can be metabolically converted to all of the sugar residues in biosynthetic pathways, isotope labeling using [u-$^{13}C_6$]glucose (Glc) as a metabolic precursor results in uniform ^{13}C labeling of their carbohydrate moieties of glycoproteins. Figures 4A and B compare a part of an HSQC spectrum of uniformly ^{13}C-labeled Fc (agalactosyl form) thus prepared with that of a glycopeptide derived from it by V8 protease digestion. In this spectral region, the peaks originating from the CH groups of carbohydrate moieties are observed. The HSQC peaks originating from the glycopeptide can be unambiguously assigned since their ^{1}H and ^{13}C chemical shifts are in agreement with those of isolated oligosaccharides [28]. On the other hand, significant differences were observed in the chemical shifts of most of the peaks between Fc and the isolated glycopeptide, indicating that the glycans are surrounded by a different environment when they are built in Fc. Especially, two anomeric peaks exhibit pronounced low frequency ^{1}H chemical shift values (<3.5 ppm).

To classify the peaks for Fc in a residue-specific manner, selective isotope labeling techniques are quite useful. Yamaguchi *et al*. have demonstrated advantage of metabolic labeling by using [u-$^{13}C_6$, $^2H_7$]Glc for residue-specific resonance assignments of the peaks originating from carbohydrate moieties of the Fc glycoproteins [11]. In the ^{1}H–^{13}C HSQC spectra of the Fc preparation metabolically labeled by using [u-$^{13}C_6$, $^2H_7$]Glc as a metabolic precursor, peaks originating from part of the CH groups of the carbohydrate moieties are partially observed (Figure 4C) because hydrogen from the medium is incorporated into the CH groups of the sugar residues during the metabolic conversion of [u-$^{13}C_6$, $^2H_7$]Glc to GlcNAc, Man, and Fuc residues of the Fc glycans. The degree of the proton incorporation varies for the different positions of sugar ring and different types of sugar residues. In this example, ^{2}H to ^{1}H exchange ratio at the C1 position of the GlcNAc residues was approximately 20% while those of the Man and Fuc residues were approximately 80%, which was estimated based on relative intensities of the unambiguously assigned HSQC peaks from the glycopeptide derived from the same Fc preparation. Therefore, the peaks originating from those anomeric groups of the Fuc and Man residues are observed with higher intensities than those from the GlcNAc residues. On detailed inspection of relative peak intensities in comparison with those observed for Fc labeled with [u-$^{13}C_6$]Glc, one can achieve residue- (and position-) specific resonance assignments.

Residue- and position-selective ^{13}C labeling of the carbohydrate chains also facilitates spectral assignments of glycoproteins [12]. Figure 4D shows a ^{1}H–^{13}C HSQC spectrum of an Fc that was prepared by cultivating the hybridoma cells in the medium containing D-[1-^{13}C]glucosamine (GlcN). Since GlcN is converted to the GlcNAc residues of glycans, only peaks originating from the four GlcNAc residues are observed. Spectral comparison allows us to identify the GlcNAc peaks. Reversely, metabolic labeling using a medium containing [u-$^{13}C_6$]Glc and unlabeled GlcN results in selective disappearance of the GlcNAc resonances from the spectrum.

Based on the residues-specific resonance assignments and intra-residue scalar connectivities, sequence-specific resonance assignments can be achieved by identification of the inter-residue sequential NOE connectivities.

Carbohydrate–Protein Interactions

Stable isotope labeling of sugar chains is also useful for NMR analyses of carbohydrate–protein interactions. Chemically or enzymatically ^{13}C-labeled oligosaccharides have been used for NMR analyses of interactions of oligosaccharides with their cognate proteins [7,29–31]. The authors used glycopeptides derived from isotopically labeled Fc glycoproteins as ligands. The Fc fragment metabolically labeled with [u-$^{13}C_6$]Glc was digested by V8 protease and trypsin and the isolated glycopeptide was subjected to galactosidase and hexosaminidase treatments for trimming of its carbohydrate moiety giving rise to Manα1-6(Manα1-3)Manβ1-4GlcNAcβ1-4(Fucα1-6)GlcNAcβ1-peptide.

Figure 5 shows HMQC-NOESY spectrum of the ^{13}C-labeled glycopeptide in association with the sugar-binding domain (SBD) of Fbs1, a substrate-binding component of sugar-recognizing ubiquitin ligase SCF$^{\text{Fbs1}}$ [32,33]. Intermolecular NOE connectivities between the anomeric proton of the innermost GlcNAc residue and the aromatic ring of Tyr-279 as well as inter-residue NOE connectivity within the carbohydrate moiety were observed in the spectrum. These data provide us with information of conformation and binding mode of the glycan in association with the SBD of Fbs1.

Concluding Remarks

Conformational analyses of carbohydrate moieties covalently attached to or non-covalently interacting with a protein are very important for obtaining unique knowledge that has never been possible with liberated oligosaccharides and provide information regarding the structural basis of functions of glycans and of rational design of sugar mimics. By stable isotope labeling of glycans, it becomes feasible to elucidate the conformation and dynamics of glycans attached to proteins based on NMR parameters, i.e. chemical shifts, NOEs, or relaxation rates. At higher magnetic field, it becomes possible to observe residual dipolar couplings of isotopically labeled glycoprotein molecules weakly oriented in the presence of ordering media [34,35].

Structural glycobiology is an unexplored field beyond structural genomics. Stable-isotope-assisted NMR spectroscopy will open up a new avenue in this field and greatly contribute to decoding the glycocodes.

Acknowledgments

We wish to acknowledge Dr. Yoji Arata and Dr. Ichio Shimada and colleagues (The University of Tokyo) for the project of NMR analyses of IgG. We acknowledge our fruitful collaboration with the laboratory of Dr. Keiji Tanaka and Dr. Yukiko Yoshida (Tokyo Metropolitan Institute of Medical Science) on Fbs1. This work was supported in part by CREST/JST, by Research on Health

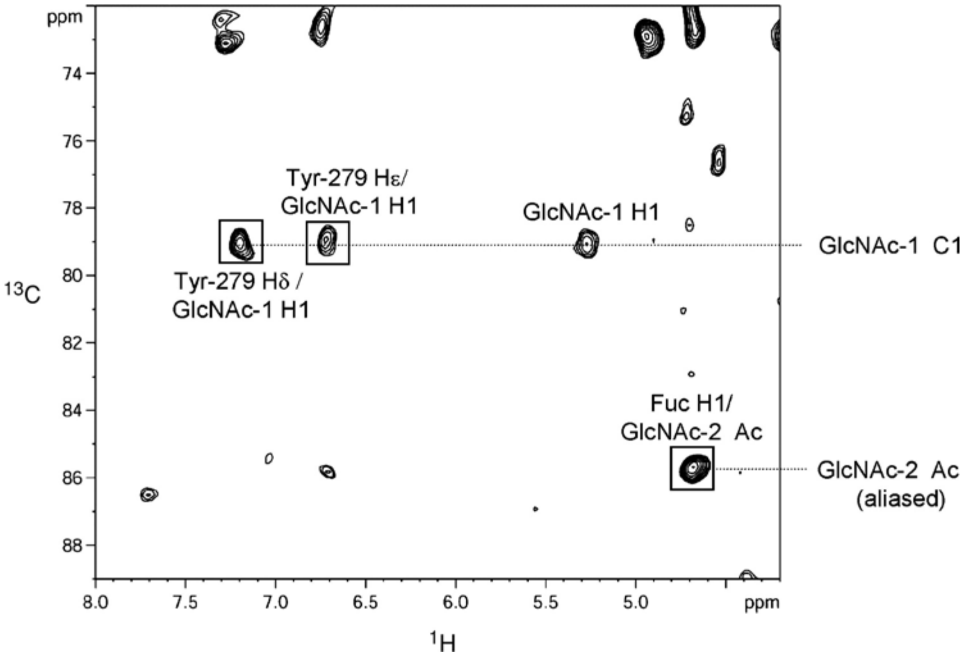

Fig. 5. ^{1}H–^{13}C HMQC-NOESY spectrum of the ^{13}C-labeled glycopeptide complexed with Fbs1-SBD with a molecular mass of 20 kDa (Hirao *et al*., unpublished data).

Sciences focusing on Drug Innovation from the Japan Health Sciences Foundation, and by Grants-in-Aid (15014228, 15032249, 16790037, 17046017 and 17028047) from the Ministry of Education, Culture, Sports, Science and Technology of Japan.

References

1. Helenius A, Aebi M. Annu. Rev. Biochem. 2004;73:1019.
2. Dwek RA. Chem. Rev. 1996;96:683.
3. Petrescu AJ, Petrescu SM, Dwek RA, Wormald MR. Glycobiology. 1999;9:343.
4. Wormald MR, Petrescu AJ, Pao YL, Glithero A, Elliott T, Dwek RA. Chem. Rev. 2002;102:371.
5. Weller CT, Lustbader J, Seshadri K, Brown JM, Chadwick CA, Kolthoff CE, Ramnarain S, Pollak S, Canfield R, Homans SW. Biochemistry. 1996;35:8815.
6. Wyss DF, Choi JS, Li J, Knoppers MH, Willis KJ, Arulanandam AR, Smolyar A, Reinherz EL, Wagner G. Science. 1995;269:1273.
7. Erbel PJ, Karimi-Nejad Y, van Kuik JA, Boelens R, Kamerling JP, Vliegenthart JF. Biochemistry. 2000;39:6012.
8. Tomiya N, Kurono M, Ishihara H, Tejima S, Endo S, Arata Y, Takahashi N. Anal. Biochem. 1987;163:489.
9. Takahashi N, Kato K. Trends Glycosci. Glycotechnol. 2003;84:235.
10. Kato K, Yamaguchi Y, Takahashi N, Nishimura M, Iwamoto S, Sekiya S, Tanaka K. J. Mass Spectrom. Soc. Jpn. 2004;52:284.
11. Yamaguchi Y, Takizawa T, Kato K, Arata Y, Shimada I. J. Biomol. NMR. 2000;18:357.
12. Yamaguchi Y, Kato K, Shindo M, Aoki S, Furusho K, Koga K, Takahashi N, Arata Y, Shimada I. J. Biomol. NMR. 1998;12:385.
13. Tao MH, Morrison SL. J. Immunol. 1989;143:2595.
14. Nose M, Wigzell H. Proc. Natl. Acad. Sci. U.S.A. 1983;80:6632.
15. Rademacher TW, Jaques A, Williams PJ. Abnormalities of IgG Glycosylation and Immunological Disorders. John Wiley & Sons, Inc.: Chichester, 1996, p. 1.
16. Holland M, Takada K, Okumoto T, Takahashi N, Kato K, Adu D, Ben-Smith A, Harper L, Savage CO, Jefferis R. Clin. Exp. Immunol. 2002;129:183.
17. Parekh RB, Dwek RA, Sutton BJ, Fernandes DL, Leung A, Stanworth D, Rademacher TW, Mizuochi T, Taniguchi T, Matsuta K, et al. Nature. 1985;316:452.
18. Gilhespy-Muskett AM, Partridge J, Jefferis R, Homans SW. Glycobiology. 1994;4:485.
19. Deisenhofer J. Biochemistry. 1981;20:2361.
20. Miyazaki T, Sato H, Sakakibara T, Kajihara Y. J. Am. Chem. Soc. 2000;122:5678.
21. Lustbader JW, Birken S, Pollak S, Pound A, Chait BT, Mirza UA, Ramnarain S, Canfield RE, Brown JM. J. Biomol. NMR. 1996;7:295.

22. Ippel JH, Pouvreau L, Kroef T, Gruppen H, Versteeg G, van den Putten P, Struik PC, van Mierlo CP. Proteomics. 2004;4:226.
23. Pickford AR, O'Leary JM. Methods Mol. Biol. 2004;278: 17.
24. Wood MJ, Komives EA. J. Biomol. NMR. 1999;13: 149.
25. Walton WJ, Kasprzak AJ, Logan TM. Glycobiology. 2004;14:1204.
26. Cubeddu L, Moss CX, Swarbrick JD, Gooley AA, Williams KL, Curmi PM, Slade MB, Mabbutt BC. Protein Expr. Purif. 2000;19:335.
27. Kato K, Matsunaga C, Igarashi T, Kim H, Odaka A, Shimada I, Arata Y. Biochemistry. 1991;30:270.
28. Lu J, van Halbeek H. Carbohydr. Res. 1996;296: 1.
29. Low DG, Probert MA, Embleton, Seshadri K, Field RA, Homans SW, Windust J, Davis PJ. Glycobiology. 1997;7:373.
30. Di Virgilio S, Glushka J, Moremen K, Pierce M. Glycobiology. 1999;9:353.
31. Shimizu H, Field RA, Homans SW, Donohue-Rolfe A. Biochemistry. 1998;37:11078.
32. Mizushima T, Hirao T, Yoshida Y, Lee SJ, Chiba T, Iwai K, Yamaguchi Y, Kato K, Tsukihara T, Tanaka K. Nat. Struct. Mol. Biol. 2004;11:365.
33. Yoshida Y, Chiba T, Tokunaga F, Kawasaki H, Iwai K, Suzuki T, Ito Y, Matsuoka K, Yoshida M, Tanaka K, Tai T. Nature. 2002;418:438.
34. Kiddle GR, Homans SW. FEBS Lett. 1998;436:128.
35. Jain NU, Noble S, Prestegard JH. J. Mol. Biol. 2003;328: 451.

Lipid Bilayer and Bicelle

Development and Application of Bicelles for Use in Biological NMR and Other Biophysical Studies

Charles R. Sanders

Department of Biochemistry and Center for Structural Biology, Vanderbilt University, Nashville, TN 37232-8725, U.S.A.

The term "bicelles" was first proposed in 1995 to describe aqueous assemblies of detergent and lipid that were believed to be "**bi**nary, **bi**layered mixed mic**elles** bearing a resemblance to the classical model for **bi**le salt-phosphatidylcholine aggregates" [1]. At that time, bicellar mixtures had already been in use for several years as magnetically alignable model membranes in solid-state NMR studies of membrane-associated molecules (Figure 1). Since 1995, there have been dramatic advances both in the applications of bicelles and in our understanding that bicellar mixtures are morphologically more complex than originally thought. Here, we trace the development and application of bicelles from their initial development in the late 1980s. Other reviews of bicelles and related developments in NMR and sample alignment methods are also available [2–10].

Bicelle Roots

That phospholipid/detergent mixtures believed to form discoidal bilayered mixed micelles can be aligned in a high magnetic field was first demonstrated in the lab of James Prestegard at Yale University. Preetha Ram, a graduate student, observed magnetic alignment of anionic bile salt-phosphatidylcholine mixtures in 1988 [11]. Leading to this achievement were earlier developments in disparate fields:

1. It was known that phospholipid vesicles could be aligned using a strong magnetic field in a way that distorted the (ideally) spherical vesicles to permit a large fraction of the lipid bilayers present to be preferentially aligned with the magnetic field (with bilayer normals orthogonal to the magnetic field) [12–16]. In other words, it was already established that lipid bilayers have significant anisotropy of diamagnetic susceptibility. The magnetic susceptibility tensor of hydrocarbon-based phospholipids is aligned within the molecular frame such that lipids prefer to align with their long axes orthogonal to the direction of the applied magnetic field. Lipid bilayers, therefore, prefer to be uniaxially aligned such that bilayer normals are perpendicular to the field.
2. Through many years of effort by membrane biophysicists, it was already believed that lipids sometimes form discoidal aggregates with detergents of the digestive system (bile salts) [17–19] and with certain amphipathic proteins [20–24]. Thus, bicelles were already known entities, although these systems had not been exploited as model membrane media or subjected to magnetic alignment.
3. By 1988 there were already a number of abiological aqueous lyotropic and nematic liquid crystals that were believed to be either bilayered-discoidal or tubular in morphology and that were known to align in the presence of a strong magnetic field [25–28]. For those believed to be disk-like, systems were available that aligned either with their bilayer normals orthogonal or parallel to the applied field. Several papers were published in the late 1980s in which some of these systems were used as model membrane media for NMR studies of biomolecules trapped in the aligned phases [29–31].
4. The utility of using aligned samples to facilitate measurement of solid-state NMR spectra was already well established (c.f. [32, 32–38]). However, there were limitations and drawbacks associated with existing methods of alignment, providing impetus for bicelle development.
5. The need for methods to attain weak magnetic alignment of molecules for NMR was already manifest. It had been demonstrated in the 1960s that even for highly mobile molecules yielding sharp line widths, induction of too high a degree of molecular alignment leads to NMR spectra of almost unfathomable complexity [39,40]. Later, Bothner-By and co-workers demonstrated the marginal unimolecular alignment of small molecules by very high magnetic fields [41], while MacLean had explored the use of electric fields for the same purpose [42]. Under conditions of marginal alignment, spectral complexity is manageable, so that structurally useful anisotropic parameters such as dipolar couplings can easily be measured. This set the stage not so much for initial bicelle development as for the later application of bicelles as a matrix for soluble protein alignment introduced in 1997 by Tjandra and Bax (see below).

Graham A. Webb (ed.), Modern Magnetic Resonance, 233–239.
© 2008 *Springer.*

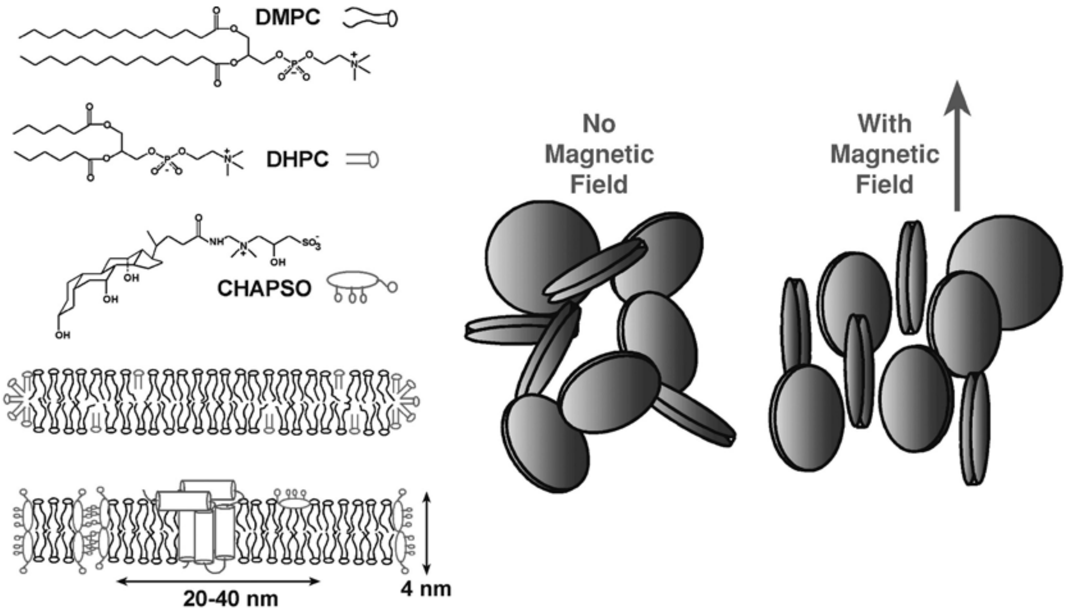

Fig. 1. Classical model for bicellar DMPC-CHAPSO and DMPC-DHPC assemblies (left) and for magnetic alignment of bicelles (right). This figure is reprinted from Sanders CR, Prosser RS. *Structure*. 1998;6:1227–1234 [6] with permission from Elsevier. (See also Plate 27 on page XXIX in the Color Plate Section.)

Early 1990s

Following the original report of bicelle alignment, anionic bile salts were replaced with a mild zwitterionic bile salt derivative, CHAPSO, to yield CHAPSO-dimyristoylphosphatidylcholine (DMPC) mixtures that were observed to be magnetically alignable over a wide range of compositions and temperatures [43]. Moreover CHAPSO-DMPC mixtures were non-denaturing toward soluble proteins. This system was soon employed as a model membrane medium in studies of a number of lipids [44–49]. It was also observed that the usual 90° orientation of CHAPSO-DMPC bicelles in a magnetic field could be flipped to align the bilayer normals with the field by adding certain amphiphilic aromatic hydrocarbons [50].

In 1992, the nascent Sanders lab at Case Western Reserve University introduced bicelles in which bile salt derivatives used in the original bicelle system were replaced by dihexanoyl-PC (DHPC) [51]. Part of the motivation for developing DHPC/DMPC bicelles arose from the fact that the NMR facilities then present at Case were 1970s-vintage. The bicelle project was among the most interesting NMR projects the author could think of that was feasible using such out-of-date instrumentation! This work built upon previous characterization of short-chain phosphatidylcholine micelles and their interactions with phospholipids carried out by the lab of Mary Roberts in Boston [52–55]. DHPC/DMPC mixtures were observed to undergo magnetic alignment over a wide range of compositions. Similar to CHAPSO/DMPC bicelles, alignment was observed to occur only above the gel-to-liquid crystalline phase transition of DMPC—below this temperature both CHAPSO/DMPC and DHPC/DMPC bicelles become isotropic.

^{31}P, ^{13}C, and ^{2}H NMR studies indicated that the dynamics and conformations of the phosphatidylcholine molecules present in the bilayered domain of aligned bicelles are quite similar to those present in bilayered L_α-phase vesicles [56]. It was also demonstrated that the activity of an integral membrane enzyme, diacylglycerol kinase (DAGK), could be supported when this protein was reconstituted into bicelles [1,57]. Most of the DAGK molecule is bilayer-embedded and one of its substrates is a lipid. Moreover, its active site is believed to lie at the water-membrane interface. Therefore, DAGK's functional reconstitution provided a strong biochemical validation of the use of bicelles as model membranes.

In the mid-/late 1990s, the first reports of membrane protein alignment using bicelles were reported for surface-associated membrane proteins [1,58–61] as well as for integral membrane proteins [1,62]. For surface-associating membrane proteins, motion, and orientational disorder are often quite high, such that NMR spectra of very high quality (narrow lines) have been obtained. For transmembrane proteins, the number of spectra reported using aligned bicelles of both the conventional and flipped (see below) variety remains fairly small (cf. [63–65]), although there seems to be renewed interest in exploring the potential of bicelles as a medium for solid-state NMR studies of transmembrane proteins [66].

Late 1990s

Vold, Prosser, and and co-workers made two seminal contributions to bicelle development in the late 1990s. First, they introduced the use of paramagnetic lanthanide ions to induce a change in sign of the anisotropy of magnetic susceptibility of bicelles, such that magnetic alignment takes place with bilayer normals parallel to the field direction [67]. This was an important development because it provided a means by which oriented-sample spectra could be obtained from bicelle-associated molecules even in the absence of rapid rotation around the bilayer normal. Not only was it shown that lanthanide ions confer parallel alignment, but ion-chelating lipids were developed in order to sequester the bicelle-associated ions to prevent unwanted free radical or oxidative chemistry that might damage bicellar molecules [68,69]. A second important contribution of Vold and Prosser was to explore and advocate the use of isotropic bicelles as a medium for solution state NMR of membrane proteins [59,70], which continues to be an area of interest [71]. Isotropic bicelles form below the gel-to-liquid crystalline phase transition of the lipid component of bicelles and at relatively high detergent-to-lipid ratios.

By 1997, it had been demonstrated that biomacromolecules could be magnetically aligned to a degree which allowed many small dipolar couplings to be measured [72–75], heralding the now widespread acquisition and utilization of residual dipolar couplings in solution NMR-based structural analyses. However, unimolecular alignment required both that very high magnetic fields be employed and (usually) that the protein of interest must contain a tightly associated paramagnet in order to provide sufficient magnetic susceptibility. It was therefore a very important development in the field of biomolecular NMR when Bax and Tjandra showed that bicelles could be used as an alignment matrix for water soluble biomolecules [75,76]. Not only was this method widely applicable, it also provided a means by which the degree of alignment could be tuned by varying bicelle/buffer composition. Following this breakthrough were several developments: (1) Classical bicelle mixtures were improved by extending their temperature range and enhancing their chemical and morphological stability [77–83]. (2) The use of additives to bicelles was investigated for a variety of purposes [67–69, 84–93]. For example, by varying bicelle surface charge it is sometimes possible to vary the alignment tensor of the guest proteins, a great advantage for downstream structural calculations. (3) The use of various membranes and liquid crystals has been explored or re-explored, leading to the introduction of alternative membrane-like systems for achieving magnetic alignment of biomolecules [78,84,93–98]. (4) Radically different methods for attaining molecular alignment were developed [95,99–109] such as the use of magnetically aligned phage particles and the use of strained polyacrylamide gels. These methods have been particularly significant for those biomolecules that interact with bicelles and related systems in such a manner that the degree of molecular alignment is too high for solution NMR. Alternative methods of alignment are also welcome in cases where the bicelle matrices are disrupted by the biomolecular solute, or where the structure of the solute of interest is perturbed by bicelles.

2000–2005

The past few years have seen three particularly interesting developments. First, bicelles have been employed in biostructural studies extending beyond the realm of NMR spectroscopy. Lorigan and co-workers have embarked upon a continuing exploration of bicelles as a medium in which to conduct EPR spectroscopy [110–118]. Moreover, James Bowie's lab has shown that polytopic membrane proteins can be crystallized from bicellar mixtures, leading to high-resolution X-ray crystal structures of polytopic integral membrane proteins [119]. The bicelle crystallization approach offers a distinct alternative to crystallization using classical detergent or lipidic cubic phases as the host model membrane medium for the membrane protein of interest. It will be extremely interesting to see whether a range of membrane proteins can be crystallized from bicelles or whether only a few membrane proteins prove to be susceptible to this approach.

A second innovation associated with bicelles is the exploration by several labs of the potential of combining the use of bicelles with rapid sample spinning methods at various sample rotation angles with respect to the magnetic field [120–127]. This work builds upon previous work by a number of labs in which the physics and spectroscopy of liquid crystals under conditions of rapid sample spinning have been explored [128]. The use of rapid sample spinning methods in conjunction with bicelles offers exciting possibilities for manipulating sample orientation and effective orientational order in conjunction with the application of sophisticated solid-state NMR pulse technology.

The other major development in the years leading to 2005 is that the classical "bilayered-disk" model for bicelle aggregate morphology has been challenged. Early characterization of bicelles was almost exclusively NMR in nature. An "Occam's razor" approach was used to argue that the bilayered-disk model (Figure 1) was the most reasonable model that could account for the available NMR data for magnetically alignable bicelles (review in [6,9]). However, the bilayered-disk model could not easily explain the very high viscosity of bicelle mixtures under conditions where magnetic alignment can take place. It was also hard to explain why, for a given bicelle composition, aligned bicelle order remains fairly constant over a wide range of total lipid + detergent content (5–40%, by weight).

Based on more recent, often non-NMR data, from the labs of Katsaras and others it now appears clear that the bilayered-disk model is inadequate to describe all of the detergent-lipid assemblies that fall within compositions typically described as being bicellar—particularly for compositions and temperatures at which magnetic alignment can take place [71,129–137]. While this work is ongoing, it appears that at higher lipid-to-detergent ratios, bicelle morphology can be likened to that of Swiss cheese-like perforated bilayered-lipid sheets. As the detergent-to-lipid ratio is increased, the sheets most likely break up into interconnected bilayered tape-like strands. Continuing to increase detergent content then leads to discoidal bilayer fragments and, finally, to classical mixed micelles (Figure 2).

Recently, Sligar and co-workers have developed bilayered-discoidal aggregates referred to as "nanodiscs" that are composed of mixtures of lipids with amphipathic lipoprotein mimetics [138–140]. These aggregates appear to conform quite closely to the classical bicelle morphology over a wide temperature range. To our knowledge, the potential that nanodisc mixtures can be magnetically aligned has yet to be tested.

Conclusion: How Good are Bicelles as Model Membranes?

The above emerging model for bicelles in which several different morphologies are possible, depending on exact composition and temperature, is very tentative. It will take much time and effort to use multiple techniques to systematically explore the very wide range of temperature and composition space that is inhabited by mixtures falling within the "bicelle" regime. In the meantime, it is likely that bicelles will continue to be employed as model membranes for biophysical studies of membrane-associated molecules. For any class of model membrane, it is reasonable to consider to what extent "native membrane" conditions are reflected by the model system. This question can be experimentally addressed in four ways. First, for a molecule of interest, structural measurements may be repeated in more than one type of bicelle [141]. If the same structural conclusion is reached in multiple systems, the notion that structure is native-like is supported. Second,

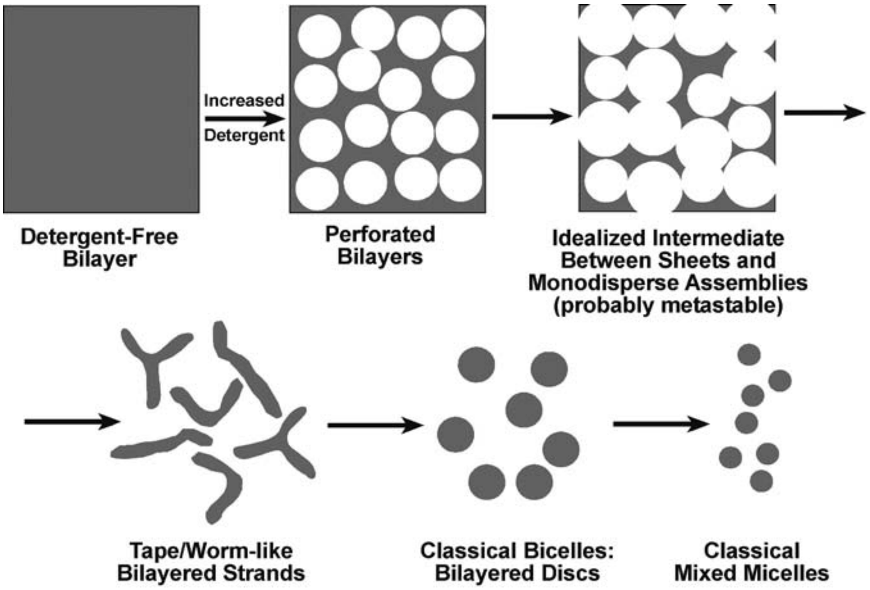
Increased
Detergent
Detergent-Free Bilayer
Perforated Bilayers
Idealized Intermediate Between Sheets and Monodisperse Assemblies (probably metastable)
Tape/Worm-like Bilayered Strands
Classical Bicelles: Bilayered Discs
Classical Mixed Micelles

Fig. 2. Emerging model for morphological transitions occurring in bicelle mixtures as detergent is added to a fixed amount of lipid. The view is looking down onto the bilayer surface. The highly tentative nature of this model is emphasized.

measurements may be repeated as the lipid:detergent ratio is increased [1,141]. By extrapolating anisotropic parameters to a detergent-free limit, it is possible to estimate structural parameters for the solute of interest in lipid bilayers in the absence of detergent. Third, if a solute has an assayable function, a test for native-like function may be carried out under bicellar conditions [57]. Finally, direct verification that a bicelle-derived structure is the same as the structure solved under non-bicellar conditions may sometimes be possible [119]. The limited data generated thus far from these types of control experiments are extremely encouraging in affirming that bicelles typically maintain the native-like structure and dynamics of guest molecules.

Acknowledgment

This review was supported by US NIH grant RO1 GM47485. I thank Dr. Chuck Ellis for proofreading and comments.

References

1. Sanders CR, Landis GC. Biochemistry. 1995;34:4030.
2. Bax A. Prot. Sci. 2003;12:1.
3. Lipsitz RS, Tjandra N. Ann. Rev. Biophys. Biomol. Struct. 2004;33:387.
4. Prestegard JH, Al Hashimi HM, Tolman JR. Q. Rev. Biophys. 2000;33:371.
5. Prestegard JH, Kishore AI. Curr. Opin. Chem. Biol. 2001;5:584.
6. Sanders CR, Prosser RS. Structure. 1998;6:1227.
7. Sanders CR, Hoffmann AK, Grayn DN, Keyes MH, Ellis CD. Chembiochem. 2004;5:423.
8. Whiles JA, Deems R, Vold RR, Dennis EA. Bioorg. Chem. 2002;30:431.
9. Sanders CR, Hare BJ, Howard KP, Prestegard JH. Prog. Nucl. Magn. Reson. Spectrosc. 1994;26:421.
10. Fleming K, Matthews S. Methods Mol. Biol. 2004;278:79.
11. Ram P, Prestegard JH. Biochim. Biophys. Acta. 1988;940:289.
12. Maret G, Dransfeld K. Physica B & C. 1977;86:1077.
13. Sakurai I, Kawamura Y, Ikegami A, Iwayanagi S. Proc. Natl. Acad. Sci. U.S.A. 1980;77:7232.
14. Scholz F, Boroske E, Helfrich W. Biophys. J. 1984;45:589.
15. Seelig J, Borle F, Cross TA. Biochim. Biophys. Acta. 1985;814:195.
16. Speyer JB, Sripada PK, Das Gupta SK, Shipley GG, Griffin RG. Biophys. J. 1987;51:687.
17. Mazer NA, Benedek GB, Carey MC. Biochemistry. 1980;19:601.
18. Muller K. Biochemistry. 1981;20:404.
19. Small DM. Gastroenterology. 1967;52:607.
20. Dempsey CE. Biochim. Biophys. Acta. 1990;1031:143.
21. Andrews AL, Atkinson D, Barratt MD, Finer EG, Hauser H, Henry R, Leslie RB, Owens NL, Phillips MC, Robertson RN. Eur. J. Biochem. 1976;64:549.
22. Brouillette CG, Jones JL, Ng TC, Kercret H, Chung BH, Segrest JP. Biochemistry. 1984;23:359.
23. Dufourcq J, Faucon JF, Fourche G, Dasseux JL, Le Maire M, Gulik-Krzywicki T. Biochim. Biophys. Acta. 1986;859:33.
24. Venkatachalapathi YV, Phillips MC, Epand RM, Epand RF, Tytler EM, Segrest JP, Anantharamaiah GM. Proteins. 1993;15:349.
25. Forrest BJ, Reeves LW. Chem. Rev. 1981;81:1.
26. Boden N, Clements J, Dawson KA, Jolley KW, Parker D. Phys. Rev. Lett. 1991;66:2883.
27. Boden N, Corne SA, Jolley KW. J. Phys. Chem. 1987;91:4092.
28. Boidart M, Hochapfel A, Laurent M. Mol. Crystallogr. Liquid Crystallogr. 1988;154:61.
29. Ram P, Prestegard JH. J. Am. Chem. Soc. 1988;110:2383.
30. Ram P, Mazzola L, Prestegard JH. J. Am. Chem. Soc. 1989;111:3176.
31. Davis JH. Biochemistry. 1988;27:428.
32. Cross TA, Opella SJ. J. Mol. Biol. 1985;182:367.
33. Engelsberg M, Dowd SR, Simplaceanu V, Cook BW, Ho C. Biochemistry. 1982;21:6985.
34. Griffin RG, Powers L, Pershan PS. Biochemistry. 1978;17:2718.
35. Jarrell HC, Jovall PA, Giziewicz JB, Turner LA, Smith IC. Biochemistry. 1987;26:1805.
36. McLaughlin AC, Herbette L, Blasie JK, Wang CT, Hymel L, Fleischer S. Biochim. Biophys. Acta. 1981;643:1.
37. Nall BT, Rothwell WP, Waugh JS, Rupprecht A. Biochemistry. 1981;20:1881.
38. Cross TA, Tsang P, Opella SJ. Biochemistry. 1983;22:721.
39. Emsley JW, Lindon JC. NMR Spectrscopy Using Liquid Crystal Solvents. Pergamon: Oxford, 1975.
40. Khetrapal CL, Kunwar AC, Tracey AS, Diehl P. NMR Basic Princ. Prog. 1975;9:1.
41. Bastiaan EW, Maclean C, Van Zijl PCM, Bothner-By AA. Ann. Rep. NMR Spectrosc. 1987;19:35.
42. Vanzijl PCM, Ruessink BH, Bulthuis J, Maclean C. Acc. Chem. Res. 1984;17:172.
43. Sanders CR, Prestegard JH. Biophys. J. 1990;58:447.
44. Aubin Y, Prestegard JH. Biochemistry. 1993;32:3422.
45. Howard KP, Prestegard JH. J. Am. Chem. Soc. 1995;117:5031.
46. Howard KP, Prestegard JH. Biophys. J. 1996;71:2573.
47. Hare BJ, Rise F, Aubin Y, Prestegard JH. Biochemistry. 1994;33:10137.
48. Sanders CR, Prestegard JH. J. Am. Chem. Soc. 1992;114:7096.
49. Salvatore BA, Ghose R, Prestegard JH. J. Am. Chem. Soc. 1996;118:4001.
50. Sanders CR, Schaff JE, Prestegard JH. Biophys. J. 1993;64:1069.
51. Sanders CR, Schwonek JP. Biochemistry. 1992;31:8898.
52. Lin TL, Chen SH, Gabriel NE, Roberts MF. J. Am. Chem. Soc. 1986;108:3499.
53. Bian JR, Roberts MF. Biochemistry. 1990;29:7928.
54. Gabriel NE, Roberts MF. Biochemistry. 1986;25:2812.
55. Gabriel NE, Roberts MF. Biochemistry. 1987;26:2432.
56. Sanders CR. Biophys. J. 1993;64:171.
57. Czerski L, Sanders CR. Anal. Biochem. 2000;284:327.
58. Sanders CR, Landis GC. J. Am. Chem. Soc. 1994;116:6470.
59. Vold RR, Prosser RS, Deese AJ. J. Biomol. NMR. 1997;9:329.

60. Hauer JA, Struppe J, Taylor SS, Vold RR. FASEB J. 1997;11:A1089.
61. Struppe J, Komives EA, Taylor SS, Vold RR. Biochemistry. 1998;37:15523.
62. Howard KP, Opella SJ. J. Magn Reson. B. 1996;112:91.
63. Glover KJ, Whiles JA, Wood MJ, Melacini G, Komives EA, Vold RR. Biochemistry. 2001;40:13137.
64. Whiles JA, Glover KJ, Vold RR, Komives EA. J. Magn. Reson. 2002;158:149.
65. Biverstahl H, Andersson A, Graslund A, Maler L. Biochemistry. 2004;43:14940.
66. De Angelis AA, Nevzorov AA, Park SH, Howell SC, Mrse AA, Opella SJ. J. Am. Chem. Soc. 2004;126:15340.
67. Prosser RS, Hunt SA, DiNatale JA, Vold RR. J. Am. Chem. Soc. 1996;118:269.
68. Prosser RS, Volkov VB, Shiyanovskaya IV. Biophys. J. 1998;75:2163.
69. Prosser RS, Bryant H, Bryant RG, Vold RR. J. Magn. Reson. 1999;141:256.
70. Vold RR, Prosser RS. J. Magn. Reson. B. 1996;113:267.
71. Chou JJ, Baber JL, Bax A. J. Biomol. NMR, 2004;29:299.
72. Banci L, Bertini I, Huber JG, Luchinat C, Rosato A. J. Am. Chem. Soc. 1998;120:12903.
73. Beger RD, Marathias VM, Volkman BF, Bolton PH. J. Magn. Reson. 1998;135:256.
74. Tolman JR, Flanagan JM, Kennedy MA, Prestegard JH. Proc. Natl. Acad. Sci. U.S.A. 1995;92:9279.
75. Tjandra N, Bax A. Science. 1997;278:1111.
76. Bax A, Tjandra N. J. Biomol. NMR. 1997;10:289.
77. Wang H, Eberstadt M, Olejniczak ET, Meadows RP, Fesik SW. J. Biomol. NMR. 1998;12:443.
78. Tiburu EK, Moton DM, Lorigan GA. Biochim. Biophys. Acta. 2001;1512:206.
79. Ottiger M, Bax A. J. Biomol. NMR. 1998;12:361.
80. Ottiger M, Bax A. J. Biomol. NMR. 1999;13:187.
81. Losonczi JA, Prestegard JH. J. Biomol. NMR. 1998;12:447.
82. Cavagnero S, Dyson HJ, Wright PE. J. Biomol. NMR. 1999;13:387.
83. Aussenac F, Lavigne B, Dubernet O, Raffard G, Dufourc EJ. Biophys. J. 2001;80:333A.
84. Tan CB, Fung BM, Cho GJ. J. Am. Chem. Soc. 2002;124:11827.
85. Struppe J, Whiles JA, Vold RR. Biophys. J. 2000;78:281.
86. Sasaki H, Fukuzawa S, Kikuchi J, Yokoyama S, Hirota H, Tachibana K. Langmuir. 2003;19:9841.
87. Guo J, Pavlopoulos S, Tian X, Lu D, Nikas SP, Yang DP, Makriyannis A. J. Med. Chem. 2003;46:4838.
88. Prosser RS, Shiyanovskaya IV. Concepts Magn. Reson. 2001;13:19.
89. Lu JX, Caporini MA, Lorigan GA. J. Magn. Reson. 2004;168:18.
90. Li XX, Goodson BM. Langmuir. 2004;20:8437.
91. King V, Parker M, Howard KP. J. Magn. Reson. 2000;142:177.
92. Crowell KJ, Macdonald PM. Biophys. J. 2001;81:255.
93. Cho GJ, Fung BM, Reddy VB. J. Am. Chem. Soc. 2001;123:1537.
94. Zweckstetter M, Hummer G, Bax A. Biophys. J., 2004;86:3444.
95. Sass HJ, Musco G, Stahl SJ, Wingfield PT, Grzesiek S. J. Biomol. NMR. 2000;18:303.
96. Prosser RS, Losonczi JA, Shiyanovskaya IV. J. Am. Chem. Soc. 1998;120:11010.
97. Minto RE, Adhikari PR, Lorigan GA. Chem. Phys. Lipids. 2004;132:55.
98. Barrientos LG, Dolan C, Gronenborn AM. J. Biomol. NMR. 2000;16:329.
99. Clore GM, Starich MR, Gronenborn AM. J. Am. Chem. Soc. 1998;120:10571.
100. Barrientos LG, Louis JM, Gronenborn AM. J. Magn. Reson. 2001;149:154.
101. Cierpicki T, Bushweller JH. J. Am. Chem. Soc. 2004;126:16259.
102. Hansen MR, Mueller L, Pardi A. Nat. Struct. Biol. 1998;5:1065.
103. Hansen MR, Hanson P, Pardi A. Methods Enzymol. 2000;317:220.
104. Ishii Y, Markus MA, Tycko R. J. Biomol. NMR. 2001;21:141.
105. Jones DH, Opella SJ. J. Magn. Reson. 2004;171:258.
106. Meier S, Haussinger D, Grzesiek S. J. Biomol. NMR. 2002;24:351.
107. Trempe JF, Morin FG, Xia Z, Marchessault RH, Gehring K. J. Biomol. NMR. 2002;22:83.
108. Zweckstetter M, Bax A. J. Biomol. NMR. 2001;20:365.
109. Fleming K, Gray D, Prasannan S, Matthews S. J. Am. Chem. Soc. 2000;122:5224.
110. Garber SM, Lorigan GA, Howard KP. J. Am. Chem. Soc. 1999;121:3240.
111. Caporini MA, Padmanabhan A, Cardon TB, Lorigan GA. Biochim. Biophys. Acta. 2003;1612:52.
112. Cardon TB, Tiburu EK, Lorigan GA. J. Magn. Reson. 2003;161:77.
113. Fanucci GE, Lee JY, Cafiso DS. J. Am. Chem. Soc. 2003;125:13932.
114. Lorigan GA, Cardon TB. Biophys. J. 2002;82:159A.
115. Lu JX, Caporini MA, Lorigan GA. J. Magn. Reson. 2004;168:18.
116. Mangels ML, Cardon TB, Harper AC, Howard KP, Lorigan GA. J. Am. Chem. Soc. 2000;122:7052.
117. Mangels ML, Harper AC, Smirnov AI, Howard KP, Lorigan GA. J. Magn. Reson. 2001;151:253.
118. Nusair NA, Tiburu EK, Dave PC, Lorigan GA. J. Magn. Reson. 2004;168:228.
119. Faham S, Bowie JU. J. Mol. Biol. 2002;316:1.
120. Kimura A, Takamoto K, Fujiwara H. J. Am. Chem. Soc. 1998;120:9656.
121. Carlotti C, Aussenac F, Dufourc EJ. Biochim. Biophys. Acta. 2002;1564:156.
122. Kurita J, Shimahara H, Utsunomiya-Tate N, Tate S. J. Magn. Reson. 2003;163:163.
123. Lancelot N, Elbayed K, Bianco A, Piotto M. J. Biomol. NMR. 2004;29:259.
124. Tian F, Losonczi JA, Fischer MW, Prestegard JH. J. Biomol. NMR. 1999;15:145.
125. Yu K, Kang S, Kim SD, Ryu PD, Kim Y. J. Biomol. Struct. Dyn. 2001;18:595.
126. Zandomeneghi G, Tomaselli M, Williamson PTF, Meier BH. J. Biomol. NMR. 2003;25:113.
127. Zandomeneghi G, Williamson PTF, Hunkeler A, Meier BH. J. Biomol. NMR. 2003;25:125.

128. Courtieu J, Bayle JP, Fung BM. Prog. Nucl. Magn. Reson. Spectrosc. 1994;26:141.
129. Luchette PA, Vetman TN, Prosser RS, Hancock REW, Nieh MP, Glinka CJ, Krueger S, Katsaras J. Biochim. Biophys. Acta. 2001;1513:83.
130. Nieh MP, Glinka CJ, Krueger S, Prosser RS, Katsaras J. Biophys. J. 2002;82:2487.
131. Nieh MP, Raghunathan VA, Wang H, Katsaras J. Langmuir. 2003;19:6936.
132. Nieh MP, Raghunathan VA, Glinka CJ, Harroun TA, Pabst G, Katsaras J. Langmuir. 2004;20:7893.
133. Rowe BA, Neal SL. Langmuir. 2003;19:2039.
134. Triba MN, Warschawski DE, Devaux PF. Biophys. J. 2005;88:1887.
135. van Dam L, Karlsson G, Edwards K. Biochim. Biophys. Acta. 2004;1664:241.
136. Harroun TA, Koslowsky M, Nieh MP, de Lannoy CF, Raghunathan VA, Katsaras J. Langmuir. 2005;21:5356.
137. Gaemers S, Bax A. J. Am. Chem. Soc. 2001;123:12343.
138. Bayburt TH, Grinkova YV, Sligar SG. Nano Lett. 2002;2:853.
139. Bayburt TH, Sligar SG. Prot. Sci. 2003;12:2476.
140. Bayburt TH, Sligar SG. Proc. Nat. Acad. Sci. U.S.A. 2002;99:6725.
141. Sanders CR. Chem. Phys. Lipids. 1994;72:41.

Nuclear Magnetic Resonance of Oriented Bilayer Systems

Akira Naito, Shuichi Toraya, and Katsuyuki Nishimura
Graduate School of Engineering, Yokohama National University, Hodogaya-ku, Yokohama 240-8501, Japan

Introduction

It is important to elucidate the membrane bound structure of biologically active molecules such as membrane associated peptides and membrane proteins. It is also realized that not only the structure but also the orientations are important factors to understand the biological activity of the molecules. To obtain the information of structure and orientation for the biomolecules bound to membrane, it is useful to uniformly align the membrane in the NMR spectrometer related to the magnetic field direction. Because a number of peptides and membrane proteins are strongly bound to membrane, these biomolecules can also be aligned to the magnetic field provided that the lipid bilayers are aligned to the magnetic field.

The ordering of the lipid bilayers with respect to the magnetic field can be achieved in one of two ways as shown in Figure 1. First, lipid can be macroscopically oriented by pressing lipid–water dispersions between flat glass plates, thus orienting the membrane microdomains by mechanical shearing forces [1–3]. This method has advantages to change the direction of alignment by rotating the supporting glass plate in the magnetic field. This is important because the resolution in the sample is largely depending on the orientation. Second, lipid molecules themselves can be aligned spontaneously to the magnetic field because of their diamagnetic anisotropy [4,5]. This spontaneously magnetically oriented bilayer system has advantages over the mechanically oriented bilayer systems because they show a highly hydrated state compared with the mechanically oriented bilayer systems. Since spontaneously oriented system does not need to use glass plate, it has large filling factor in the receiver coil of the probe and hence higher sensitivity can be expected over the mechanically oriented systems.

Magnetically Oriented Bilayer Systems

Magnetic ordering of lipid bilayers has been reported for pure and mixed phosphatidylcholine bilayers [6–8], including melittin-phospholipid systems [9–12]. Subsequently, such magnetic ordering has been reported in a detergent/lipid mixture called a bicelle [13–15], which was shown to be oriented in the magnetic field by the negative magnetic anisotropy of the lipid acyl chain [16]. Therefore, acyl chain tends to orient perpendicular to the magnetic field if a large number of lipid molecules are ordered in the liquid crystalline phase to possess a sufficient degree of magnetic anisotropy to align the lipid bilayers along the magnetic field.

Principle of Spontaneous Magnetic Orientation

Because small molecules usually have diamagnetic anisotropy, they have different magnetic moments depending on the molecular orientation with respect to the strong magnetic field. Thus, molecules in the magnetic field have a preferential orientation in the magnetic field. However, magnetic alignment of the small molecule cannot be observed because the orientation of the molecule can be easily disturbed by much larger thermal energy.

The interaction of the diamagnetic anisotropy with the magnetic field is given by

$$F = -\left(\frac{1}{2}\right) H_0^2 \left\{\chi_\perp + (\chi_{||} - \chi_\perp)\cos^2\theta\right\}, \tag{1}$$

where F is the interaction energy, and $\chi_\perp$ and $\chi_{||}$ are the perpendicular and parallel components of the magnetic susceptibility, respectively. θ is the angle between the $\chi_{||}$ and the magnetic field. Therefore, orientation energy of the lipid bilayer with N number of lipids is expressed as

$$N\Delta F = -\left(\frac{1}{2}\right) N\Delta\chi H_0^2, \tag{2}$$

where, $\Delta F = F(\theta = 0^\circ) - F(\theta = 90^\circ)$ and $\Delta\chi = \chi_{||} - \chi_\perp$. In the case of phospholipid molecule, negative value, $\Delta\chi = -2 \times 10^{-6}\mathrm{erg/G^2/mol^2}$, is reported [16]. Therefore, lipid molecule tend to be oriented with the unique molecular axis perpendicular to the magnetic field, namely parallel to the bilayer normal because $\Delta\chi$ has negative value for phospholipids. If N is a small number, the orientation energy is again not strong enough to align the macrodomain of lipid bilayer because the thermal energy, kT, tend to disturb the alignment of molecules. In the case of phospholipid bilayers at room temperature,

Graham A. Webb (ed.), Modern Magnetic Resonance, 241–247.
© 2008 *Springer.*

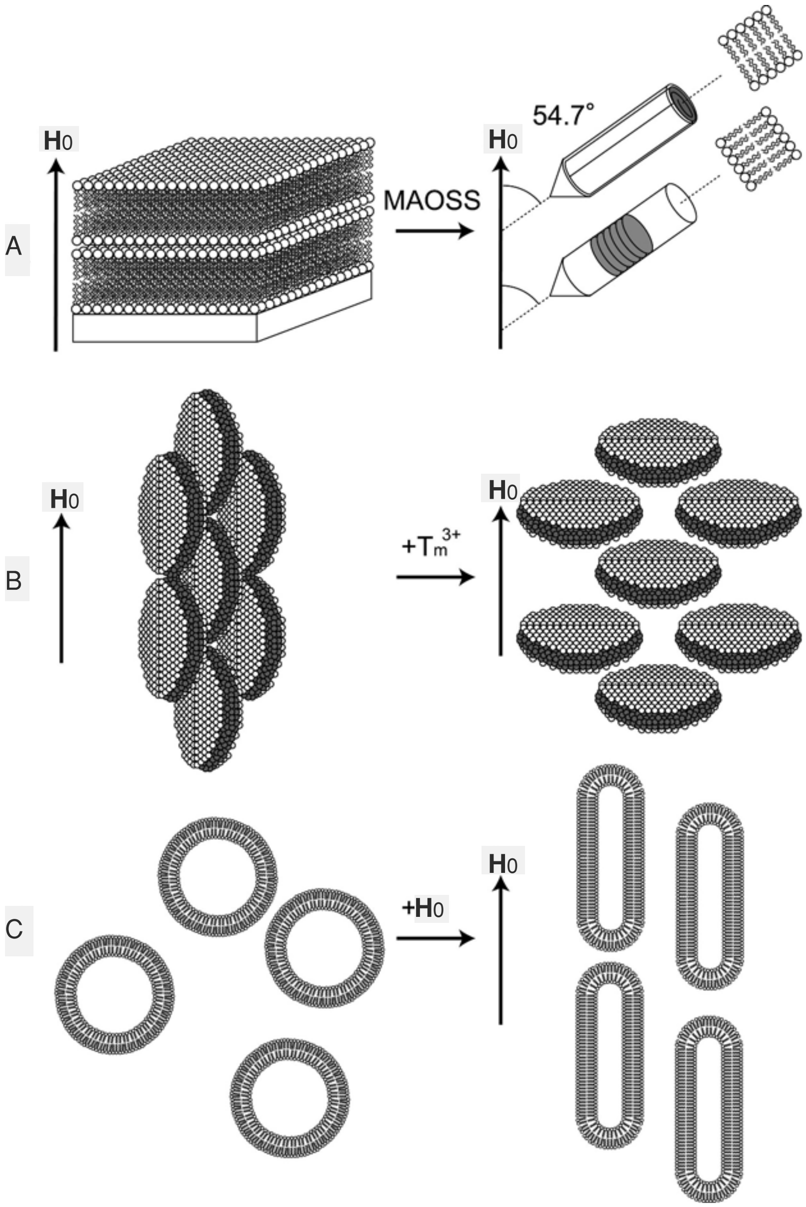

Fig. 1. Mechanically and magnetically oriented bilayers. A(left): Lipid bilayers are stacked on the glass plate. A(right): Two types of magic-angle spinning of oriented samples (MAOSS). B(left): Magnetically oriented bicelles. B(right): After adding T_m^{3+} C: Magnetically oriented vesicle systems (MOVS).

macrodomain of lipid containing 10^6 number of lipid molecules can be spontaneously aligned to the magnetic field. Because orientation energy is proportional to the square of magnetic field, one can expect that a higher-order alignment can be achieved in the very strong magnetic field. This fact is very promising for getting better alignment of the magnetically oriented system because a strong magnetic field is now demanding.

Bicelle

When phospholipid was mixed with a kind of detergent, CHAPSO (3-((3-cholamidopropyl)dimethylammonio)-2-hydroxyl-propane sulfonate) or phospholipid with short acyl chain, dihexanoylphosphatidylcholine (DHPC) with the range of molar ratios from 2:1 to 5:1, edges of bilayers are surrounded by CHPSO [13] or DHPC [14] to form discoidal shape of particle called bicelle [15]. The bicelle is known to be aligned spontaneously to the magnetic field [13,14]. The diameter of the biclelle is about 400 Å, and hence 5000–10,000 of lipid molecules consist of the bicelle [17]. Thus, one bicelle particle has no sufficient orientational energy to be aligned to the magnetic field. It is reported that bicelle particles are stacked each other as disclosed from the small angle X-ray scattering experiments [18]. In this case, if more than 100 bicelles are associated with each other, whole body of bicelle aggregates can have a sufficient orientational energy and the bilayer planes are oriented parallel to the magnetic field (Figure 1B). The degree of magnetic ordering of the bicelle is known to be independent of their concentration in the diluted bicelle media [19] because the associated aggregate is formed even in the diluted solution [18].

When the lanthanide ions, Eu^{3+}, Er^{3+}, Tm^{3+}, or Yb^{3+}, are mixed in the bicelle systems, orientation of bicelle altered 90° to the magnetic field because the magnetic anisotropy of the lanthanide metal has positive and much larger than the diamagnetic anisotropy. This metal is associated with the phosphate group of lipid molecule to cause the positive anisotropy in the bicelle particle leading to the 90° alternation of the orientation as shown in Figure 1B [20,21].

Magnetically Oriented Vesicle Systems

Spontaneous magnetic orientation of lipid bilayer to the external magnetic field has been observed in pure phosphatidylcholine and mixed phophatidylcholine systems [4–8]. In these systems, partly extended vesicles are formed as shown in Figure 1C and the long axis is aligned parallel to the magnetic field [16]. ^{31}P NMR spectra clearly show that in the moderately high concentration of melittin incorporated into the dimyristoylphosphatidylcholine (DMPC) bilayer (DMPC/melittin = 10:1 molar ratio), the bilayer shows lysis and fusion at temperatures lower and higher than the T_c. Above the T_c, giant vesicles were observed for the melittin-DMPC bilayer systems [12]. This lipid bilayer systems shows the very high magnetic ordering at a temperature higher than the T_c. Therefore, it is suggested that elongated bilayer vesicles rather than discoidal bilayers are formed above the T_c in the case of the melittin-DMPC bilayer systems, in which most of the surface area of the bilayers is oriented parallel to the magnetic field, as shown in schematically in Figure1 C. Thus, a large magnetic anisotropy can be induced because most of the phospholipids, which have negative magnetic anisotropy along the acyl chain axes, are aligned perpendicular to the magnetic field by forming elongated vesicles. Since the sizes of the vesicles are the diameter of 20 μm, one vesicle can have enough orientational energy, in contrast to the case of bicelles.

This kind of magnetically oriented system is also formed in DMPC-dynorphin bilayer systems [22]. The line shape of the elongated vesicle for the DMPC-dynorphin has been analyzed by looking at the line shape of the ^{31}P NMR spectra of the elongated vesicle. Line shape of the ^{31}P NMR spectra clearly indicates that the long axis of the elongated vesicle is at least 5 times longer than the short axis.

It is important to point out that the process of lysis and fusion is a prerequisite to allow the orientation of lipid bilayers to the magnetic field. It is also found that membrane surface in the DMPC-melittin system is flexible near at T_c, indicating that the vesicle shape can be reformed to the elongated shape in the magnetic field [23].

Mechanically Oriented Bilayer Systems

Oriented Bilayer on the Glass Plates

Mechanically aligned lipid bilayer system, which is established by casting the lipid bilayer on the glass plate followed by hydrated under high humidity environment [1–3,24]. In this system acyl chain can be aligned perpendicular to the glass plate (Figure 1A). The protein–lipid mixture can be prepared by reconstituting the purified protein or peptide either in an organic solvent followed by solvent removal. The protein–lipid mixture are deposited on the glass slides to form a thin film of sample material, and the solvent is subsequently evaporated. Typically, 10–40 slides are then stacked on top of each other to achieve the required amounts needed for NMR experiments. On hydration and annealing under an atmosphere of controlled humidity, typically several thousands of oriented bilayers form between each pair of slides. Finally, prior to performing the solid-state NMR experiments, the sample is sealed to maintain the hydration levels of the lipid bilayers during experimentation. It is advantageous to use this mechanically aligned lipid bilayer system, because it is possible to align the lipid bilayer surface in any orientation with respect to the magnetic field. Disadvantage of this bilayer system is a low filling factor because of the presence of glass plate in the NMR coil leading a low sensitivity for obtaining NMR signals.

Magic Angle-Oriented Sample Spinning Experiment

Mechanically oriented sample can be prepared on circular plate and can be mounted inside a rotor [25]. Bilayers can also be spread on polymer sheets and rolled up with their central axis collinear with the spinning axis at the magic axis (Figure 1A) [26]. When magic-angle spinning (MAS) is applied to these oriented samples (magic angle-oriented sample spinning, MAOSS), the spinning side band intensities are sensitive to partial or complete ordering within the samples [25]. This technique is useful to investigate the alignment and membrane interactions of phospholipids, peptides, or proteins within oriented bilayer samples [27–29]. Due to the suppression by the support of membrane undulation that occur on a slow timescale, the spectral line width of these samples is considerably reduced and resolution concomitantly improved.

Orientation Dependence of Chemical Shift Interaction

Orientation of peptides bound to the magnetically aligned lipid bilayer can be discussed by looking at the chemical shift anisotropy of the carbonyl carbon in the backbone in the peptide chain. Chemical shift tensors of the carbonyl carbons are well characterized as shown in Figure 2. When the peptide is completely rigid, 150 ppm of anisotropy will be observed in low-temperature experiment. On the other hand, when the temperature is increased to T_c, molecules have large amplitude motion about the bilayer normal. In this case, axially symmetric powder pattern is seen as shown in Figure 2b. Since bilayers tend to align to the magnetic field, slow MAS experiment can be applied to give an axially symmetric powder pattern. It turned out that the molecule actually reorientational motion about the bilayer normal because the axially symmetric pattern was seen in the DMPC-melittin bilayer systems [12]. When the spinning was stopped, lipid bilayer will be spontaneously oriented to the magnetic field and the membrane bound molecule also align to the magnetic field. In most case, membrane bound biomolecule rotates about the membrane normal because of the lateral diffusion of the lipid molecule in the liquid crystalline phase. In the case of melittin, entire molecule form α-helix in the membrane bound state and the helix axis is rotated about the bilayer normal with the tilt angle of ζ and the phase angle γ. Under this dynamic state, the chemical shift anisotropy, $\Delta\delta = \delta_{||} - \delta_{\perp}$ can be expressed as [30]

$$\Delta\delta = \frac{3}{2}\sin^2\varsigma\left(\delta_{11}\cos^2\gamma + \delta_{33}\sin^2\gamma - \delta_{22}\right) + \left(\delta_{22} - \frac{\delta_{11}+\delta_{33}}{2}\right). \qquad (3)$$

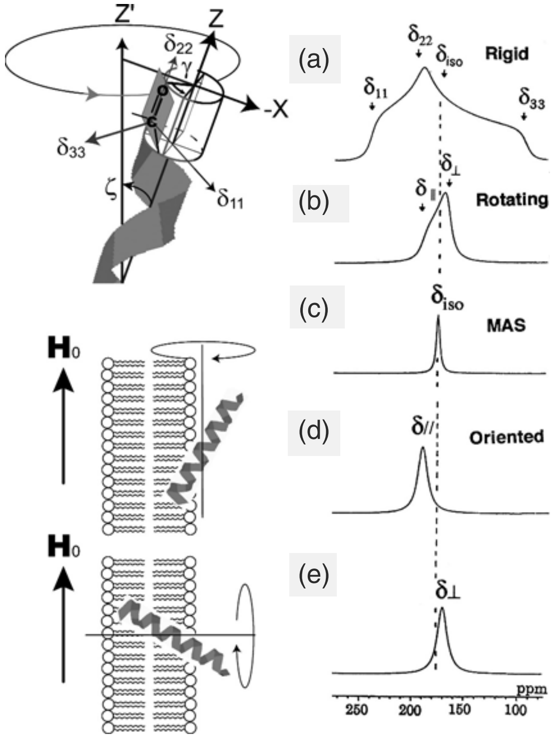

Fig. 2. Direction of the principal axis of the ^{13}C chemical shift tensor of the C = O group, the helical axis, and the static magnetic field (H_0), and ^{13}C NMR spectral patterns of the C = O carbons corresponding to the orientation of the α-helix with respect to the surface of the magnetically oriented lipid bilayers. Simulated spectra were calculated using $\delta_{11} = 241$, $\delta_{22} = 189$, and $\delta_{33} = 96$ ppm for the rigid case (a), rotation about the unique axis (slow MAS) (b), magic-angle spinning (c), magnetic field parallel to the unique axis (d), and magnetic field perpendicular to the magnetic field (e).

In this equation, $\Delta\delta$ values oscillate in the function of γ with the oscillation amplitude of (3/2) $\sin^2\zeta$, that is referred to the chemical shift oscillation [30]. When the α-helical peptide has a large tilt angle, $\Delta\delta$ value changes a large extent as shown in Figure 3. Using this property of $\Delta\delta$, the tilt angle of the α-helix with respect to the bilayer normal can be determined by comparing the anisotropic patterns of carbonyl carbons of consecutive amino acid residues which form α-helix, with the chemical shift values of the corresponding magnetically aligned state (Figure 4). When the peptide is formed an ideal α-helix structure, it can be assumed that the inter-peptide plane angle for consecutive peptide planes is 100°. This tilt angle can be accurately obtained by taking root mean-square deviation (RMSD) values between the observed

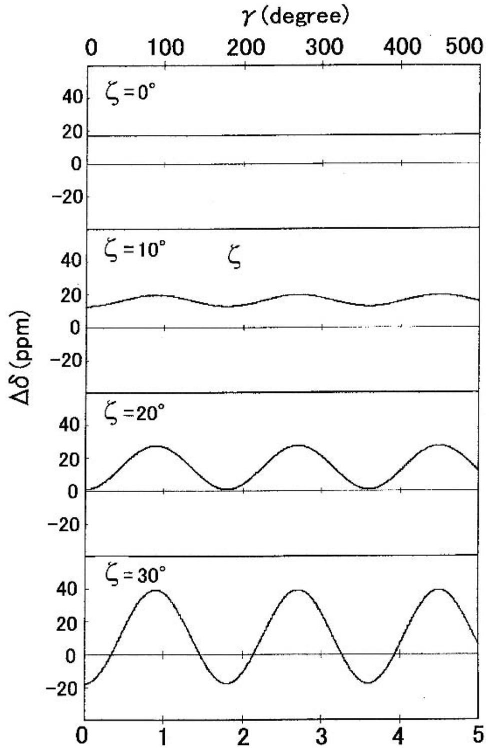

Fig. 3. Plot of chemical shift anisotropy, $\Delta\delta = \delta_{\|} - \delta_{\perp}$ against the phase angle, γ, of the peptide plane for the consecutive amino acid residues as a function of the tilt angles, ζ.

and calculated a chemical shift anisotropy as given by

$$\mathrm{RMSD} = \left[\sum_{i=1}^{N} \left\{ (\Delta\delta_{\mathrm{obs}})_i - (\Delta\delta_{\mathrm{cal}})_i \right\}^2 \Big/ N \right]^{1/2}. \tag{4}$$

Actually, the tilt angles were determined to be −33° and −36° for the N-terminals and 21° and 25° for the C-terminals in the melittin molecule bound to dilauroylphosphatidylchpline (DLPC) and dipalmitoylphosphatidylcholine (DPPC) vesicles (Figure 4) [30].

Orientation Dependence of Dipolar Interaction

Similar information can be obtained by looking at ^{15}N–^{1}H dipolar interaction of the peptide backbone. Polarization Inversion Spin Exchange at the Magic Angle (PISEMA) experiment is a kind of separated local field 2D NMR experiment and gives the excellent resolution for the dipolar dimension in the correlation spectra between ^{15}N chemical shift values and ^{15}N–^{1}H dipolar interaction [31]. It is of interest to note that a characteristic circle pattern, called Polarity Index Slant Angle (PISA) wheels, is seen when α-helix is formed in the membrane and the shape of wheel is sensitive to the tilting angle of the α-helix with respect to the bilayer normal [32–34]. When one observes this PISA wheel, one can evaluate the amino acid residues involved in the α-helix even if amino acid sequence is not known.

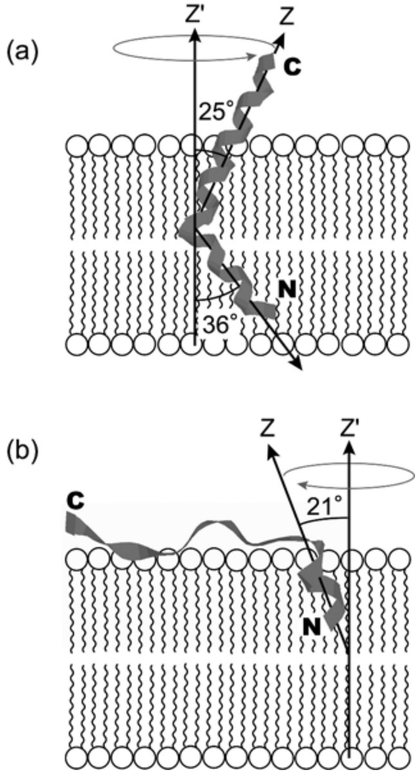

Fig. 4. Schematic representation of the structures and orientations of melittin (a) and dynorphin (b) bound to lipid bilayers. The N- and C-terminal helices are inserted into the bilayers with the tilt angles of (36° and 33°) and (25° and 21°), respectively for melittin. The N-terminal helix inserted into the lipid bilayer with the tilt angle of 21° and the center to the C-terminal show disordered and lies on the surface of the lipid bilayers.

Membrane bound form of the coat protein possesses two distinct domains, a TM helix as well as an amphipathic helix lying on the membrane surface [35]. In contrast, when embedded in the phage particle, the protein forms a single, almost straight α-helix. To solve the assignment problem inherent to the uniformly ^{15}N-labeled samples used for this study, a “shotgun” approach was employed [36]. By analyzing a spectra with a small number of labeled sites from protein samples, which were sparsely ^{15}N-labeled in only one type of amino acid, the complete assignment of PISEMA spectra from uniformly ^{15}N-labeled samples became accessible. This is possible because secondary structure elements, such as α-helices, are mapped to characteristic patterns in the PISEMA spectrum, and a few connectivities between these two representations of the protein structure are sufficient to correlate both. In the case of the filamentous coat protein, the concept of dipolar waves was used to characterize the details in the helix structure. By plotting the ^{15}N–^{1}H dipolar coupling as a function of residue number, an oscillatory pattern becomes apparent. The amplitude, pitch, and offset of these dipolar waves characterize the local structure of helix segments, and regions with different orientation as well as a small helix could be identified.

Structure Determination of Membrane Associated Peptides in the Magnetically Oriented Systems

Dynamic structure of melittin bound to the MOVS consisting of DPPC and DLPC were investigated by analyzing the ^{13}C anisotropic and isotropic chemical shifts of selectively ^{13}C-labelled carbonyl carbons of melittin under the static and MAS conditions [30]. These results indicate that melittin molecules adopt an α-helix structure and laterally diffuse to rotate rapidly around the membrane normal with tilt angles of the N-terminal helix being -33° and -36° and those of the C-terminal helix being 21° and 25° for DLPC and DPPC vesicles, respectively Figure 4a. Although RMSD method successfully determined the tilt angle, ζ and $-\zeta$ cannot be distinguished because of the symmetry relation of Equation (3). Then the rotational echo double resonance method was used to measure the interatomic distance between [1-^{13}C]Val^{8} and [^{15}N]Leu^{13} to further identify the bending α-helical structure of melittin to posses the interhelical angle of 126° and 119° in DLPC and DPPC membranes, respectively. These analyses further lead to the conclusion that α-helices of melittin molecule penetrate the hydrophobic core of the bilayers incompletely as a pseudo-transmembrane structure and indicate fusion and disruption of vesicles.

Secondary structure and orientation of dynorphin bound to DMPC bilayer systems were investigated by solid-state ^{13}C NMR spectroscopy [37]. For this purpose, ^{13}C NMR spectra of the site-specifically ^{13}C-labeled dynorphin were measured in the membrane bound state under static, MAS and slow MAS conditions. It was found that dynorphin adopts an α-helical structure in the N-terminus from Gly^{2} to Leu^{5} by analysis of the isotropic chemical shift obtained from the MAS experiments. In contrast, it adopts disordered conformations from the center to the C-terminus and is located on the membrane surface. The static ^{13}C NMR spectra indicated that MOVS-bound dynorphin was oriented to the magnetic field and rotated rapidly about the bilayer normal. Subsequently, the ^{13}C chemical shift tensor of carbonyl carbons in the peptide backbone was considered by the rotational motion of the N-terminal α-helix. It was revealed that the N-terminal α-helix is inserted into the membrane with the tilt angle of 21° to the bilayer normal as shown in Figure 4b. This structure suggests a possibility that dynorphin interacts with the extracellular loop II of the k-receptor through a helix–helix interaction.

Dynorphin-DMPC MOVS was used as a oriented media to gain insight into the orientation of a transmembrane peptide [1-^{13}C]Ala^{14}-labeled A(6–34) of bacteriorhodopsin. It was found from the ^{13}C NMR spectra that the helical axis of A(6–34) is oriented parallel to the bilayer normal irrespective of the presence and absence of reorientational motion about the helical axis at temperatures above and below the gel to liquid crystalline phase transition temperature [38].

The membrane-disruptive antimicrobial peptide PGLa is found to change its orientation in a DMPC bilayer when its concentration is increased to biologically active levels [39]. The alignment of the α-helix was determined by observing ^{19}F dipolar couplings on CF$_3$-labeled side chains in ^{19}F solid-state NMR, and supported by a non-perturbing ^{15}N label. At a low peptide lipid ratio of 1:200, the amphiphilic peptide resides on the membrane surface in the so-called S-state. However, at high peptide concentration (>1:50 molar ratio) the helix axis changes its tilt angle from about 95° to approximately 125°, with the C-terminus pointing toward the bilayer interior. This tilted "T-state" represents a novel feature of antimicrobial peptides, which is distinct from a membrane inserted I-state. At intermediate concentration, PGLa is in exchange between the S- and T-states in the timescale of the NMR experiment. In both states the peptide molecules undergo fast rotation around the membrane normal in liquid crystalline bilayers, hence large peptide aggregates do not form. Very likely the obliquely tilted T-state represents an antiparallel dimmer of PGLa that is formed in the membrane at increasing concentration.

Conclusions

It is clearly demonstrated that oriented bilayer media can give useful information on structure, orientation, and dynamics of biologically active peptides which are strongly bound to the membranes. Spontaneously oriented bilayer system such as MOVS is shown to be an excellent media to study membrane associated peptides because they show excellent magnetic alignments of molecules bound to the membranes if one carefully prepare the sample. Since the magnetic field will be going higher by the development of higher field magnet, the magnetic alignment of molecule bound to membrane will be much promising in the future. Mechanically aligned bilayer system will be a very good media since one can adjust the orientation to get more information on the membrane bound molecules. The combination of glass aligned sample with the MAS provide high-resolution signals in the oriented systems to provide more information of the structure of membrane associated biologically active molecules.

References

1. Cornall BA, Separovic F, Baldassi AT, Smith R. Biophys. J. 1988;53:67.
2. Ketchem RR, Hu W, Cross TA. Science. 1993;261:1457.
3. Marassi FM, Ramamoothy A, Opella SJ. Proc. Natl. Acad. Sci. U.S.A. 1997;94:8551.
4. Qin X, Miran PA, Pidgeon C. Biochim. Biophys. Acta. 1993;1147:59.
5. Seelig F, Borle F, Cross TA. Biochim Biophys. Acta 1985;814:195.
6. Scholz F, Helfrich W. Biophys. J. 1984;45:589.
7. Spyer JB, Spipada PK, Das Gupta SK, Shipley GG, Griffin RG. Biophys. J. 1987;51:687.
8. Brumm T, Möps C, Dolainsky C, Brückner S, Bayerl TM. Biophys. J. 1992;61:1018.
9. Dempsey CE, Watts A. Biochemistry. 1987;26:5803.
10. Dempsey CE, Sternberg B. Biochim. Biophys. Acta. 1991;1061:175.
11. Pott T, Dufourc EJ. Biophys. J. 1995;68:965.
12. Naito A, Nagao T, Norisada K, Mizuno T, Tuzi S, Saitô H. Biophys. J. 2000;78:2405.
13. Sanders CR, Prestegard JH. Biophys. J. 1990;58:447.
14. Sanders CR, Schwonek JP. Biochemistry. 1992;31:8898.
15. Sanders CA, Landis GC. Biochemistry. 1995;34:4030.
16. Boroske E, Helfrich W. Biophys. J. 1978;24:863.
17. Volt RR, Prosser RS. J. Magn. Reson. 1996;B113:267.
18. Bolze T, Fujisara T, Nagao T, Norisada K, Saitô H, Naito A. Chem. Phys. Lett. 2000;329:215.
19. Bax A, Tjandra N. J. Biomol. NMR. 1997;10:289.
20. Prosser RS, Hunt SA, DiNatale JA, Volt RR. J. Am. Chem. Soc. 1996;118:269.
21. Prosser RS, Hwang JS, Vold RR. Biophys. J. 1998;74:2405.
22. Naito A, Nagao T, Obata M, Sindo Y, Okamoto M, Yokoyama S, Tuzi S, Saitô H. Biochim. Biophys. Acta. 2002;1558: 34.
23. Toraya S, Nagao T, Obata M, Izumi S, Tuzi S, Saito H, Naito A. Biophys. J. 2005;89:3214.
24. Marassi FM. Concepts Magn. Reson. 2002;14:212.
25. Glaubitz C, Watts A. J. Magn. Reson. 1998;130:305.
26. Sizun C, Bechinger B. J. Am. Chem. Soc. 2002;124:1146.
27. Glaubitz C, Burnett IJ, Gröbner G, Mason AJ, Watts A. J. Am. Chem. Soc. 1999;121:5787.
28. Middleton DA, Ahmed A, Glaubitz C, Watts A. J. Magn. Reson. 2000;147:366.
29. Mason AJ, Grage SL, Straus SK, Glaubitz C, Watts A. Biophys. J. 2004;86:1610.
30. Toraya S, Nishimura K, Naito A. Biophys. J. 2004;87:3323.
31. Wu CH, Ramamoothy A, Opella SJ. J. Magn. Reson. 1994;A109:270.
32. Marassi FM, Opella SJ. J. Magn. Reson. 2000;144:150.
33. Marassi FM, Ma C, Gesell JJ, Opella SJ. J. Magn. Reson. 2000;144:156.
34. Wang J, Denny J, Tian C, Kim S, Mo Y, Kovacs F, Song Z, Nishimura K, Gan Z, Fu R, Quine JR, Cross TA. J. Magn. Reson. 2000;144:162.
35. Marassi FM, Opella SJ. Protein Sci. 2003;12:403.
36. Zeri AC, Mesleh MF, Nevzorov AA, Opella SJ. Proc. Natl. Acad. Sci. 2003;100:6458.
37. Uezono T, Toraya S, Obata M, Nishimura K, Tuzi S, Saitô H, Naito A. J. Mol. Struct. 2005;749:13.
38. Kimura S, Naito A, Tuzi S, Saitô H. Biopolymers. 2002;63:122.
39. Glaser RW, Sachse C, Durr UH, Wadhwani P, Afonin S, Strandberg E, Ulrich A. Biophys. J. 2005;88:3392.

Solid-State Deuterium NMR Spectroscopy of Membranes

Michael F. Brown[1,2], Silvia Lope-Piedrafita[3], Gary V. Martinez[1], and Horia I. Petrache[4]
[1]Department of Chemistry, University of Arizona, Tucson, AZ 85721, USA;
[2]Department of Physics, University of Arizona, Tucson, AZ 85721, USA;
[3]Department of Radiology, University of Arizona, Tucson, AZ 85724, USA; and
[4]Laboratory of Physical and Structural Biology, National Institutes of Health, NICHD, Bethesda, MD 20892, USA

Solid-state NMR spectroscopy is widely applicable to the investigation of non-crystalline or amorphous materials, e.g. polymers, glasses, protein precipitates, and membrane proteins. Rather than being mainly an alternative to X-ray crystallography, solid-state NMR is virtually unique among current analytical and spectroscopic methodologies in that it provides both structural and dynamical information at an atomically resolved level. In solid-state NMR, the structural information is obtained from the static or motionally averaged coupling tensors due to dipolar, chemical shift, or quadrupolar interactions [1,2]. Corresponding dynamical information is acquired from the tensor fluctuations, which depend on the mean-squared amplitudes and rates of the motions and affect the NMR lineshapes and relaxation times. For these reasons, solid-state NMR is finding increasing applicability in the chemistry of materials, structural biology, and genomics research, and this trend can be expected to continue well into the future.

One area of solid-state NMR spectroscopy that has proven fruitful with regard to the investigation of membranes is ^{2}H NMR spectroscopy. Previous detailed reviews of ^{2}H NMR as applied to membrane lipids are available [3–7]. Recently, ^{2}H NMR has been used to investigate raft-like lipid mixtures implicated in membrane signaling functions [8–10], and moreover ^{2}H NMR studies of membrane proteins [11–15] and DNA fibers [16] have also been conducted. The present chapter is focused on the liquid-crystalline state of membrane lipids as investigated from combined ^{2}H NMR lineshape and relaxation studies. A related aspect entails the correspondence of ^{2}H NMR studies to molecular dynamics simulations [17]. The salient aspects of ^{2}H NMR are that it enables both membrane lipids and membrane proteins to be studied by substitution of ^{2}H for ^{1}H; the structural data are highly complementary to X-ray [18–21] and neutron diffraction studies [22,23], and virtually unique information regarding the functional dynamics of membrane constituents can be acquired.

Equilibrium and Dynamical Properties of Membrane Lipids are Studied by Solid-State Deuterium NMR

Phospholipid bilayers are classified as smectic A lyotropic liquid crystals, and an illustration of the liquid-crystalline lamellar phase is shown in Figure 1. The hydrophobic effect leads to a sequestering of the nonpolar acyl chains within the bilayer interior, whereas the polar head groups interact with water at the membrane surface. The nanostructure of a membrane lipid aggregate is the result of a delicate balance of forces acting at the level of the polar head groups and hydrocarbon regions of the membrane [24–27]. Representative glycerophospholipids are depicted in Figure 2, in which the polar head groups differ in their size, capacity for hydrogen bonding, and charge, whereas the nonpolar acyl chains vary in their length and degree of unsaturation. The phase equilibria of phosphatidylcholines in excess water include three regions as temperature increases, a lamellar gel phase with tiled chains ($L_{\beta}{}'$), an intermediate ripple phase ($P_{\beta}{}'$), and a lamellar liquid-crystalline phase (L_{α}) [25]. Other types of phospholipid nanostructures are possible, for instance unsaturated phosphatidylethanolamines form the reverse hexagonal (H_{II}) phase, and cubic phases can also be present [25]. Moreover, when cholesterol is present lipid mixtures can form condensed complexes [28], microdomains [29], or undergo phase separation [30] which may be associated with rafts and caveloae in cellular membranes [31].

An important feature of ^{2}H NMR spectroscopy is that one introduces site-specific ^{2}H labels, corresponding to the individual C–^{2}H bonds, and in this way obtains atomically resolved information for liquid-crystalline systems. In liquid-crystalline membranes, the residual quadrupolar couplings correspond to the segmental order parameters of the flexible molecules—they can be directly measured as experimental observables. Moreover, the nuclear spin relaxation rates can be determined, e.g. the relaxation of

Graham A. Webb (ed.), Modern Magnetic Resonance, 249–260.
© 2008 Springer.

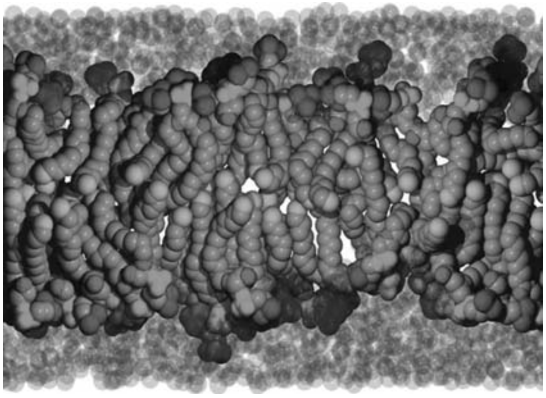

Fig. 1. Nanostructure of a lipid bilayer in the fluid, liquid-crystalline (L_α) phase. Reprinted with permission from Ref. [54]. © 2002 American Chemical Society. (See also Plate 28 on page XXIX in the Color Plate Section.)

Zeeman order (R_{1Z}) or quadrupolar order (R_{1Q}), which depend on the molecular mobility. By combining ^{2}H NMR order parameter measurements with relaxation studies, one can probe the structural fluctuations of fluid membrane lipids that give rise to averaging of the coupling tensors in solid-state NMR spectroscopy.

Deuterium NMR Spectroscopy Allows Direct Observation of Coupling Tensors Related to Molecular Structure and Dynamics

Besides the Zeeman interaction of the nuclear spin with the external magnetic field, additional perturbations are due to magnetic interactions (dipolar coupling, chemical shift) and electric interactions (quadrupolar coupling). These couplings provide a wealth of information regarding both the structure and dynamics of biomolecular systems. Generally speaking the principal values and principal axis systems (PAS) of the various coupling tensors yield structural knowledge, whereas their fluctuations give rise to spectral transitions, and are related to the dynamics of the system of interest.

Deuterium NMR spectroscopy is particularly valuable as an illustration of the principles of solid-state NMR as applied to molecular solids, liquid crystals, and biomembranes [32]. This is because a single coupling is very large—the electric quadrupolar interaction dominates over the magnetic dipolar couplings of the ^{2}H and ^{1}H nuclei, as well as the ^{2}H chemical shifts. The ^{2}H nucleus has a spin of $I = 1$, and hence there are three Zeeman energy levels corresponding to the projection of the nuclear spin angular momentum, with eigenstates $|m>=|0\rangle, |\pm1\rangle$ given by the Hamiltonian $\hat{H}_Z$. According to quantum mechanics, transitions between the adjacent spin energy levels are allowed giving two single-quantum nuclear spin transitions. In ^{2}H NMR the degeneracy is removed due to the coupling of the quadrupole moment of the ^{2}H nucleus with the electric field gradient (EFG) of the C–^{2}H bond, as given by the Hamiltonian $\hat{H}_Q$. (An electric quadrupole interacts with an EFG analogously to the interaction of an electric dipole with an electric field.) This is illustrated in Figure 3, part (a), together with a representative ^{2}H NMR spectrum of a solid polymer, PMMA-d_8, as shown in part (b) which will be discussed subsequently.

A general prescription for calculating the ^{2}H NMR transition frequencies and spectral lineshapes is the

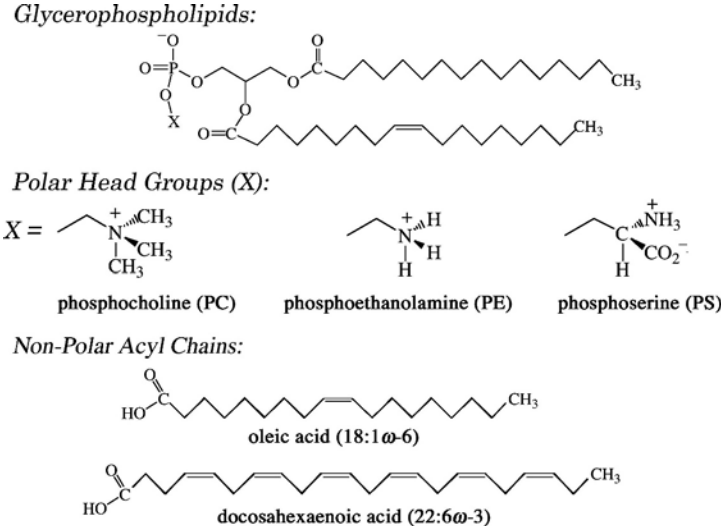

Fig. 2. Chemical structures of representative glycerophospholipids. The polar head groups vary in their size, capacity for hydrogen bonding, and charge. Representative examples are indicated for the zwitterionic head groups phosphocholine (PC) and phosphethanolamine (PE), and the anionic head group phosphoserine (PS). The non-polar acyl chains vary in their length and degree and position of unsaturation.

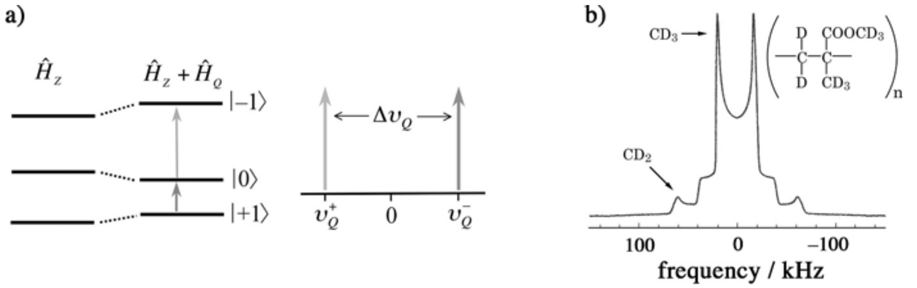

Fig. 3. (a) Energy levels and resonance lines in ^{2}H NMR spectroscopy. The Zeeman Hamiltonian $\hat{H}_Z$ is perturbed by the quadrupolar Hamiltonian $\hat{H}_Q$ giving an unequal spacing of the nuclear spin energy levels, indicated by $|m\rangle$ where $m = 0, \pm 1$. The quadrupolar splitting $\Delta\nu_Q$ is the difference in the frequencies ($\nu_Q^{\pm}$) of the single-quantum transitions, and is due to the perturbing interaction of the ^{2}H nuclear quadrupole moment with the EFG of the C–^{2}H bond. (b) Representative ^{2}H NMR spectrum of an unoriented powder sample of deuterated plexiglass, PMMA-d_8. The contributions from the C^{2}H$_2$ groups differ from those of the C^{2}H$_3$ groups, which undergo rapid threefold motion on the NMR timescale (cf. the text).

following. First one starts with the perturbing Hamiltonian; next Schrödinger's equation is solved to obtain the energy levels; and lastly one introduces the spectroscopic selection rules to calculate the frequencies of the spectral lines. This gives as a final result for the quadrupolar frequencies ($\nu_Q^{\pm}$) that

$$\nu_Q^{\pm} = \pm\frac{3}{4}\chi_Q\left\{D_{00}^{(2)}(\Omega_{PL}) - \frac{\eta_Q}{\sqrt{6}}\left[D_{-20}^{(2)}(\Omega_{PL}) + D_{20}^{(2)}(\Omega_{PL})\right]\right\}. \quad (1)$$

Here $\chi_Q \equiv e^2qQ/h$ is the *static* quadrupolar coupling constant, η_Q is the corresponding asymmetry parameter of the EFG tensor, and $\Omega_{PL} \equiv (\alpha_{PL}, \beta_{PL}, \gamma_{PL})$ are the Euler angles relating the PAS of the EFG tensor (P) and the laboratory frame (L). The experimentally observed ^{2}H NMR quadrupolar splitting (Figure 3) is then given by the difference in the frequencies of the spectral lines, $\Delta\nu_Q \equiv \nu_Q^+ - \nu_Q^-$. One should note that the development is also applicable to other second-rank tensors; for instance the magnetic dipolar interaction and the chemical shift [1,2,32].

Molecular Structures and Motions are Revealed by Deuterium NMR Lineshapes

Measurement of the deuterium (^{2}H) NMR lineshapes yields knowledge of the average structure through the principal values of the coupling tensor, as well as the PAS. For the sake of illustration, let us first consider a static oriented sample, e.g. a single crystal in the absence of motions. The crystal can be rotated with respect to the laboratory frame, giving discontinuities in the NMR spectrum, which correspond to the main external magnetic field aligned along each of the three principal axes of the coupling tensor. The case of an aligned dispersion of phospholipid bilayers deposited on a planar surface is exactly analogous. Here one has a residual or effective coupling tensor, which is pre-averaged by the motions of the flexible lipid molecules in the L_α state, but otherwise the transformation under rotations is identical. In either case, the principal axes and principal values of the static coupling tensor, or the residual tensor in the presence of motions, can be obtained from the rotation pattern according to Equation (1). But often one has a polycrystalline sample with a random or spherical distribution of the various C–^{2}H bond orientations. A powder (or powder-type) spectrum is then obtained, from which one can "read off" the principal values of the coupling tensor directly from the spectral discontinuities [1]. In this case a drawback is that the orientation of the PAS of the coupling tensor within the crystal frame is unavailable, since the spectral discontinuities correspond to the laboratory system.

Returning to Figure 3, an experimental ^{2}H NMR spectrum of a randomly oriented, powder-type sample of deuterated plexiglass, PMMA-d_8, is shown in part (b). Here the outer splitting (±60 kHz) of the powder pattern is due to the C^{2}H$_2$ groups of PMMA-d_8. For the C^{2}H$_2$ groups, motion is essentially absent on the ^{2}H NMR timescale, and the *static* coupling tensor is observed. The experimental ^{2}H NMR splitting (due to the large peaks) represents the $\theta = 90^\circ$ orientation, for which $-3\chi_Q/4 = -127.5$ kHz in the case of immobile methylene groups. (Weaker shoulders are also evident, corresponding to the $\theta = 0^\circ$ orientation with a splitting of $3\chi_Q/2 = 255$ kHz.) On the other hand, the central component (±20 kHz) of the

^{2}H NMR spectrum is due to the methyl groups, which are rapidly rotating in the solid state. The threefold rotation about the methyl axes means that the static coupling tensor is averaged to yield a *residual* coupling tensor, which is axially symmetric ($\eta_Q^{\text{eff}} = 0$), and whose largest principal value (χ_Q^{eff}) is correspondingly reduced by a factor of $-1/3$. Hence, for the $\theta = 90^\circ$ orientation, the C^{2}H$_3$ splitting is $(-3\chi_Q/4)(-1/3) = 42.5$ kHz in good agreement with the experimental spectrum. (The weaker shoulders correspond to the $\theta = 0^\circ$ orientation with a splitting of $\chi_Q/2 = -85.0$ kHz.) According to this example, one can essentially "read off" the coupling parameters, and hence the types of motions, directly from the experimental ^{2}H NMR spectrum [1].

In passing, we note that rather different, uniaxial powder-pattern lineshapes are observed for certain membrane proteins, such as bacteriorhodopsin [13,33] or rhodopsin [15], and also for nucleic acid fibers [16]. From such ^{2}H NMR lineshape investigations, one is able to extract information about the molecular structure, as well as the disorder of the sample in terms of the appropriate distribution functions [15,34].

Our next example involves the case of membrane lipid bilayers, where rapid axial averaging occurs about the normal to the membrane film surface, referred to as the director axis. For membranes in the fluid state, the quadrupolar splittings are due to the orientational order parameters of the individual C–^{2}H-labeled groups, leading to a profile as a function of acyl position. The segmental order parameter S_{CD} describes the amplitudes of the angular excursions of the C–^{2}H-labeled groups and is given by [6]:

$$S_{\text{CD}} \equiv \left\langle D_{00}^{(2)}(0, \beta_{\text{PD}}, 0) \right\rangle = \langle P_2(\cos\beta_{\text{PD}}) \rangle, \qquad (2a)$$

$$= \frac{1}{2}\left\langle 3\cos^2\beta_{\text{PD}} - 1 \right\rangle. \qquad (2b)$$

In the above formula, $D_{00}^{(2)}(\Omega_{\text{PD}})$ is a Wigner rotation matrix element, $P_2(x)$ is the second Legendre polynomial where $x \equiv \cos\beta_{\text{PD}}$, and β_{PD} is the time-dependent angle between the C–^{2}H bond axis and the director axis (perpendicular to the surface of the membrane). The angular brackets mean an average over all the motions faster than the inverse of the anisotropy in the static quadrupolar coupling ($<10^{-5}$ s). The observed quadrupolar splitting then reads

$$\Delta\nu_Q = \frac{3}{2}\chi_Q S_{\text{CD}} \frac{3\cos^2\beta_{\text{DL}} - 1}{2}, \qquad (3)$$

where β_{DL} is the angle between the bilayer normal (director) and the main external magnetic field direction. The segmental order parameters constitute experimental obervables and are related to the equilibrium properties and average structure of the system.

Deuterium NMR Provides Order Parameters Related to Average Membrane Properties

^{2}H NMR spectra of phospholipids in water allow the quadrupolar couplings of the C–^{2}H-labeled segments to be observed directly, e.g. as in the case of the acyl chains [3,5,21,35,36] and head groups [37,38]. What can be learned about the micro- and nanostructures of membrane lipids from ^{2}H NMR spectroscopy? First we note that the ^{2}H NMR spectra of multilamellar dispersions of randomly oriented phospholipids reveal weak singularities arising from the $\theta = 90^\circ$ orientation of the bilayer normal (director axis) relative to the main magnetic field, whereas the weaker shoulders are due to $\theta = 0^\circ$. A characteristic profile of residual quadrupolar couplings is evident for phospholipids having either specifically deuterated [3,39,40] or perdeuterated [4,5,21,27,41–47] acyl chains in the liquid-crystalline (L_α) phase. The largest values correspond to the segments close to the lipid polar head groups, with a progressive reduction along the lipid acyl chains [6]. Comparison of the residual quadrupolar splittings to the static coupling constant (see above) indicates that the acyl groups are considerably disordered in the liquid-crystalline state.

In Figure 4, we show representative ^{2}H NMR spectra for mixtures of a representative acyl (chain) perdeuterated phospholipid, 1,2-diperdeuteriomyristoyl-*sn*-glycero-3-phosphocholine, abbreviated DMPC-d_{54}, at $T = 44\,^\circ$C containing cholesterol. For acyl chain perdeuterated phospholipids, one can deconvolute or de-Pake the powder-type spectra of random multilamellar dispersions to obtain more highly resolved subspectra corresponding to the $\theta = 0^\circ$ orientation [4,48,49]. Upon de-Pakeing, the majority of the acyl C^{2}H$_2$ and C^{2}H$_3$ groups give resolvable signals, and it can be seen that a progressive increase in the splittings occurs with increasing mole fraction of cholesterol. Interaction with the rigid sterol frame leads to a substantial reduction of the number of degrees of freedom of the flexible phospholipids, as evinced by the larger residual quadrupolar splittings, Figure 4.

Now according to Equation (3) the observed residual quadrupolar coupling $\Delta\nu_Q$ is directly related to the segmental order parameter S_{CD}. The residual quadrupolar couplings vary substantially, giving a profile of the segmental order parameters $|S_{\text{CD}}^{(i)}|$ as a function of chain position (index i). This inequivalence arises from the effects of the bilayer packing on the *trans*(t)–*gauche*(g) isomerizations of the acyl groups. Figure 5 shows that the splittings can be expressed in terms of the segmental order parameters $S_{\text{CD}}^{(i)}$, which are plotted as a function of the acyl position (index i) for DMPC-d_{54} alone and

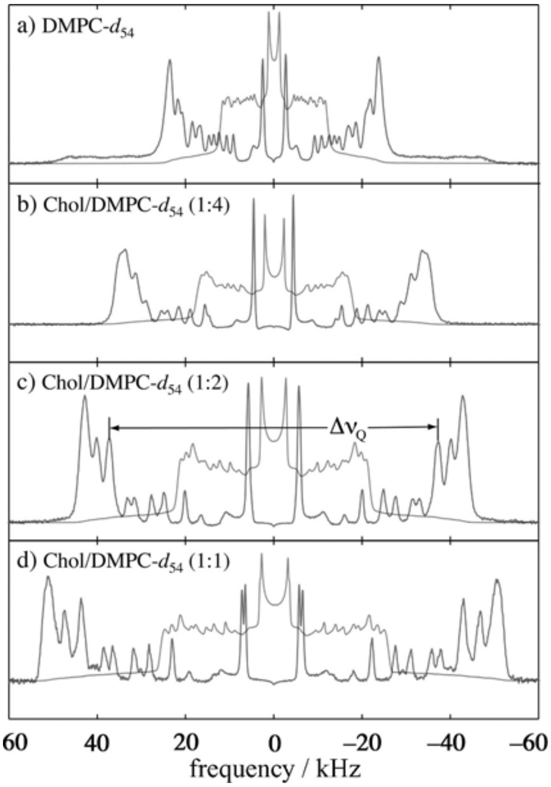

Fig. 4. Representative solid-state ^{2}H NMR spectra for (a) DMPC-d_{54} in the L_α phase and (b)–(d) DMPC-d_{54} containing increasing mole fractions of cholesterol in the liquid-ordered phase. The samples contained 50 wt% $^1\mathrm{H}_2 0$ at 44 °C and the data were acquired at 76.8 MHz (magnetic field strength of 11.7 T). Powder-type spectra (light blue) of randomly oriented multilamellar dispersions were numerically inverted (de-Paked) (dark red). Note that a distribution of residual quadrupolar couplings is evident. (See also Plate 29 on page XXIX in the Color Plate Section.)

DMPC-d_{54} in the presence of cholesterol (1:1). Knowing the assignments from studies of specifically deuterated systems [50], essentially complete order profiles can be obtained. This disorder manifests *trans–gauche* rotational isomerizations of the acyl groups, together with the effects of molecular motions or whole bilayer collective motions.

Referring to Figure 5, the plateau in the order profiles can be explained in terms of preferred configurations of the acyl chains parallel to the membrane normal. For DMPC-d_{54} in the presence of cholesterol (1:1), the segmental order parameters approach the limiting value of $S_{\mathrm{CD}} = -1/2$ expected for an all-*trans* rotating polymethylene chain. The additional disorder can be due to internal degrees of freedom of the acyl chains, e.g. rotational isomerizations, molecular motions, or thermal disturbances of the bilayer lipids. In the absence of cholesterol, the smaller $|S_{\mathrm{CD}}^{(i)}|$ values for DMPC-d_{54} manifest additional degrees of freedom. For a simple crank shaft model, consideration of 3-site jumps together with the statistical weights gives $\langle S_{\mathrm{CD}}\rangle = -1/3$ for a mix of kink ($tg^{\pm}\ tg^{\mp}$) and jog ($tttg^{\pm}\ tttg^{\mp}$) conformations, whereas $\langle S_{\mathrm{CD}}\rangle = -1/4$ for kinks only. Assuming the disorder of the DMPC- d_{54} bilayer is due mainly to rotational isomerism, the acyl chains fall somewhere between a limiting crankshaft model with $\langle S_{\mathrm{CD}}\rangle = -1/4$ and the classical oil-drop model having $\langle S_{\mathrm{CD}}\rangle = 0$. Lastly, for DMPC-$d_{54}$ both in the presence and absence of cholesterol, the increased disorder toward the chain ends must involve further acyl configurations. Within the hydrocarbon core the chains are more disordered to occupy the free volume due to chain terminations, approaching the "oil-drop" limit for very long acyl chain lengths. Note that the presence of an order profile suggests that variations in the degree of chain entanglement are likely as a function of depth in the bilayer.

Now in the lamellar state of membrane lipids, the structural properties include the average thickness $\langle L\rangle$ of the bilayer hydrocarbon region together with the mean interfacial area $\langle A\rangle$ [6,19,27,51,52], which plays a key role in molecular dynamics simulations of lipid bilayers and membranes [53–55]. Starting with the experimental $|S_{\mathrm{CD}}^{(i)}|$ order profiles, one can calculate the bilayer structural parameters using a mean-torque model for the acyl chain distributions [21,27,46]. By interpreting the ^{2}H NMR spectra in terms of the distribution functions for the segment orientations, one is able to gain insight into the intermolecular interactions governing the nanostructures of various membrane lipids. Very briefly, the mean-torque model relates the experimental order parameters to the moments $\langle\cos\beta\rangle$ and $\langle\cos^2\beta\rangle$ [27]. For a disaturated phospholipid such as DMPC-d_{54}, the mean area per molecule at the aqueous interface is given by $\langle A\rangle = 4V_{\mathrm{CH2}}q/D_{\mathrm{M}}$, where $q \equiv \langle 1/\cos\beta\rangle \approx 3 - 3\langle\cos\beta\rangle + \langle\cos^2\beta\rangle$. Here β is the angle between the vector connecting the two neighboring carbons of the ith methylene segment of a saturated acyl chain and the bilayer normal, V_{CH2} is the volume per methylene group, and D_{M} is the projected length along the all-*trans* reference axis (2.54 Å). The volumetric thickness of the bilayer is then given by $D_{\mathrm{C}} = 2V_{\mathrm{C}}/\langle A\rangle$ where V_{C} is the hydrocarbon chain volume. Chain packing profiles can also be obtained which describe the accumulated segmental projections along the membrane normal, proceeding from the midpoint of the bilayer toward the aqueous interface [27].

The above ^{2}H NMR approach has been applied to a homologous series of various phosphatidylcholines, in which both or one of the acyl chains at the *sn*-1 and *sn*-2 positions of the glycerol backbone has been ^{2}H-labeled

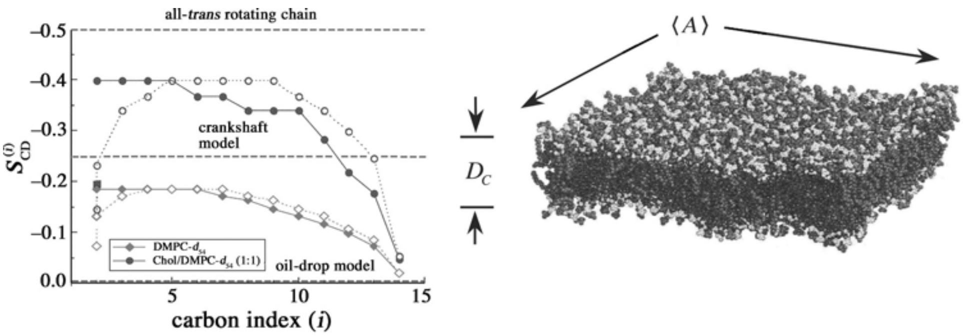

Fig. 5. Profiles of segmental order parameters $S_{\mathrm{CD}}^{(i)}$ as a function of acyl chain position (i) for (♦,◊) DMPC-d_{54} and (●,○) DMPC-d_{54}/cholesterol (1:1) at 44 °C. Filled and open symbols refer to the inequivalent *sn*-1 and *sn*-2 acyl chains, respectively. Reference values of the order parameters for the limiting cases of an oil drop-model ($\langle S_{\mathrm{CD}}\rangle = 0$), a crankshaft model ($\langle S_{\mathrm{CD}}\rangle = -1/4$), and an all-*trans* rotating chain ($S_{\mathrm{CD}} = -1/2$) are indicated for comparison. Bilayer dimensions are described in terms of $\langle A\rangle$, the interfacial or cross sectional area per lipid molecule, and D_{C}, the volumetric thickness of the bilayer (cf. the text). (See also Plate 30 on page XXX in the Color Plate Section.)

by perdeuteration [27]. The main effect of increasing the acyl chain length is an increase in the bilayer hydrocarbon thickness rather than the area per lipid at the aqueous interface. The homologous series of phosphatidylcholines exhibits a universal chain packing profile differing from that of phosphatidylethanolamines. With increasing acyl length the lipid area becomes smaller at a given temperature, reflecting stronger van der Waals attractions for longer lipid chains. Studies of the lateral compressibility of phospholipid bilayers have also been carried out using ^{2}H NMR methods [35]. Additional comparative investigations have focused on a homologous series of mixed chain, saturated–polyunsaturated phosphatidylcholines [21,41–43,45,46]. Highly polyunsaturated acyl chains yield significant disordering of the bilayer, increasing the cross-sectional area per lipid head group relative to disaturated lipid bilayers. The resulting spontaneous curvature (or equivalently the lateral pressure profile) may affect the conformational energetics of membrane proteins such as rhodopsin [56]. Lipids in non-lamellar phases have also been investigated with ^{2}H NMR, including the hexagonal (H_{I}) and reverse hexagonal (H_{II}) phases [57–59], which are implicated in protein-mediated functions of biomembranes [56].

Deuterium Spin–Lattice Relaxation Times Reveal Dynamical Properties of Lipid Membranes

Turning next to the topic of nuclear spin relaxation, for membranes in the liquid-crystalline state a complex hierarchy of motions is to be expected. How can NMR relaxation help to disentangle the various types of motions that account for the statistically averaged membrane properties? Generally speaking, one can separate the motions into broad classes with characteristic mean-squared amplitudes and timescales, which may be related to the material or biological properties of the system of interest. Examples of fast segmental motions include *trans–gauche* isomerizations of the flexible phospholipids in the liquid-crystalline state, whereas slower motions may be due to non-collective rotational diffusion of the lipid molecules or collective disturbances and excitations of the bilayer itself [6,60–65].

The mechanism of NMR relaxation originates from fluctuations of the coupling Hamiltonian arising from the various possible motions of the lipid molecules within the bilayer. In applying ^{2}H NMR spectroscopy to membrane lipids, one is often interested in the relaxation of the Zeeman order ($R_{1\mathrm{Z}}$) or the quadrupolar order ($R_{1\mathrm{Q}}$). Experimentally, the spin–lattice relaxation rates $R_{1\mathrm{Z}}$ and $R_{1\mathrm{Q}}$ are measured by a pulse sequence designed to perturb the magnetization away from the equilibrium value—effectively we can think of these as "magnetization jump" experiments. The subsequent return to equilibrium can then be followed by "reading out" the remaining magnetization as a transverse coherence, which is detected as an oscillating NMR signal and picked up by the radio frequency coil of the spectrometer probe.

An example is provided in Figure 6, which depicts an inversion-recovery measurement of the $R_{1\mathrm{Z}}$ values for a random dispersion of DMPC-d_{54}/cholesterol (1:1) in the liquid-ordered phase. The partially relaxed ^{2}H NMR spectra in part (a) correspond to superposition of Pake doublets due to the various motionally inequivalent C–^{2}H bonds (*vide supra*). Following the inverting π pulse, the z-magnetization appears negative and gradually recovers to equilibrium as the delay increases. In part (b) of Figure 6, the various partially relaxed ^{2}H NMR spectra have

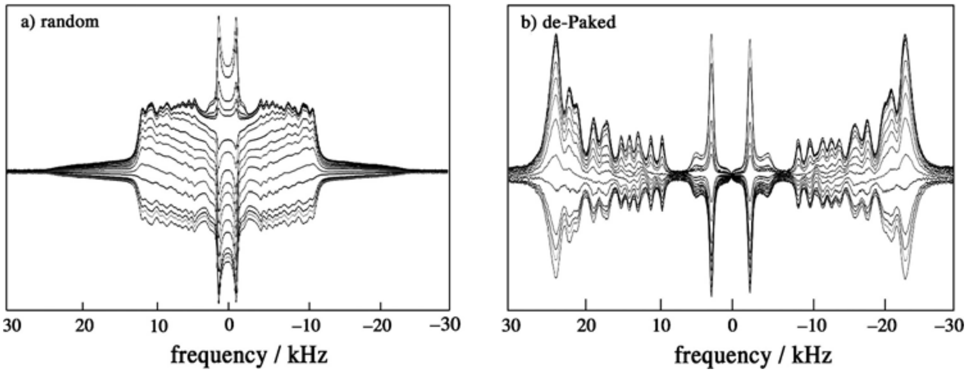

Fig. 6. Example of partially relaxed ^{2}H NMR spectra of DMPC-d_{54} multilamellar dispersion in the liquid-crystalline (L_α) state at 44 °C. Panel (a) shows the experimental ^{2}H NMR spectra, and panel (b) the numerically inverted (de-Paked) ^{2}H NMR spectra ($\theta = 0°$) as a function of the variable delay between the inversion pulse and the spectral acquisition. Data were obtained at 76.8 MHz (magnetic field strength of 11.7 T) using an inversion-recovery pulse sequence, $(\pi\text{p})_x - t_1 - (\pi/2)_x - \tau_1 - (\pi/2)_{\pm y} - \tau_2$ – acquire, with the variable delay t_1 ranging from 5 ms to 3 s [87].

been numerically inverted (de-Paked) to yield the spectra corresponding to the $\theta = 0°$ orientation. The increased resolution allows a more accurate determination of the R_{1Z} rates. It can be seen that the magnetization recovery becomes progressively faster as the residual quadrupolar splittings increase. This behavior points to the influences of order fluctuations, in which the pre-averaged or residual coupling tensor remaining from the local segmental motions is modulated by slower membrane motions, e.g. due to molecular fluctuations or whole bilayer disturbances (*vide infra*).

According to time-dependent perturbation theory, the relaxation is due to orientational fluctuations of the individual C–^{2}H bonds, which induce transitions between the various energy levels of the ^{2}H nuclear spin system. The observable relaxation rates are related to the spectral densities of the various motions within the laboratory frame. According to theory, the R_{1Z} and R_{1Q} rates are given to second order by:

$$R_{1Z} \equiv \frac{1}{T_{1Z}} = \frac{3}{4}\pi^2 \chi_Q^2 [J_1(\omega_D) + 4J_2(2\omega_D)], \quad (4)$$

$$R_{1Q} \equiv \frac{1}{T_{1Q}} = \frac{9}{4}\pi^2 \chi_Q^2 J_1(\omega_D). \quad (5)$$

In these formulas R_{1Z} is the spin–lattice (longitudinal) relaxation rate, where T_{1Z} is the corresponding spin–lattice relaxation time; and R_{1Q} is the spin–lattice relaxation rate for the decay of quadrupolar order, in which T_{1Q} is the quadrupolar order relaxation time. The symbols $J_m(\omega)$ denote irreducible spectral densities of motion, where $m = 1, 2$ and ω_D is the deuteron Larmor (resonance) frequency.

The spectral densities $J_m(\omega)$ express the power spectrum of the motions as a function of frequency ω. They correspond to the fluctuations of the individual Wigner rotation matrix elements which transform the coupling (EFG) tensor from its PAS to the laboratory frame, and are given by the Fourier–Laplace transform:

$$J_m(\omega) = \mathrm{Re} \int_{-\infty}^{\infty} G_m(t) e^{-i\omega t}\, \mathrm{d}t, \quad (6)$$

The autocorrelation functions $G_m(t)$ depend explicitly on time and characterize the C–^{2}H bond fluctuations; they read

$$G_m(t) = \left\langle D_{0m}^{(2)^*}(\Omega_{\mathrm{PL}}; 0) D_{0m}^{(2)}(\Omega_{\mathrm{PL}}; t) \right\rangle - \left| \left\langle D_{0m}^{(2)}(\Omega_{\mathrm{PL}}) \right\rangle \right|^2, \quad (7)$$

where $D_{0m}^{(2)}(\Omega_{\mathrm{PL}})$ denotes a Wigner matrix element (rank 2). Here the symbol Ω_{PL} indicates the three Euler angles [66] (α_{PL}, β_{PL}, γ_{PL}) which rotate the PAS of the EFG coupling tensor to the laboratory frame [6]. Note that the temporal decay of the correlation function is due to the angular reorientations of the C–^{2}H-labeled molecular segments, whereas the long-time values correspond to the average bilayer properties.

Model-Free Analysis Suggests that Collective Membrane Motions Govern the Relaxation

Let us next turn to consider those aspects of the relaxation that are independent of a specific motional model.

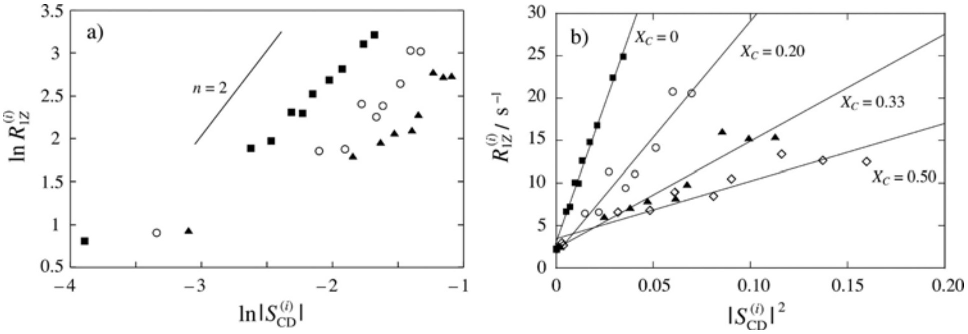

Fig. 7. Dependence of relaxation rate $R_{1Z}^{(i)}$ and order parameter $|S_{CD}^{(i)}|$ profiles for DMPC-d_{54}/cholesterol mixtures at 44 °C. Data for randomly oriented (powder-type) samples were acquired at 76.8 MHz (magnetic field strength of 11.7 T) and numerically inverted (de-Paked). In panel (a) logarithmic plots are shown for three different cholesterol mole fractions X_C . The data are compared to the slope of $n = 2$ predicted for order fluctuations in the limit of a small constant contribution. Panel (b) assumes a square-law functionality of the corresponding relaxation and order profiles for the different values of X_C. Reprinted with permission from Ref. [86]. © 2002 American Physical Society.

We would like to identify the major features of the dynamics in a more or less coarse-grained fashion, leaving the details for subsequent atomistic computer simulations [53–55,67]. We naturally make recourse to relatively fast and relatively slow motions, which successively yield further averaging of the coupling interaction on down to the final residual value. The segmental order parameters clearly depend on the amplitudes of the C–^{2}H bond fluctuations, whereas the relaxation rates depend on both the orientational amplitudes and the rates of the C–^{2}H bond fluctuations. As a result, the ordering and rate of motion must be distinguished in explaining the relaxation of lipid bilayers [68].

Recall that in ^{2}H NMR of membranes, the spectroscopic observables essentially comprise the order parameter and the relaxation rate profiles—thus it is useful to inquire as to the existence and nature of their functional dependence [60]. According to the foregoing development, Equations (4)–(7), the interaction strength (the matrix element) is squared in the transition probabilities that govern the relaxation rates (Fermi's golden rule). Now the fast or local motions modulate the *static* coupling constant, in which case the relaxation profile along the chains is governed essentially by the motional rates [39]. But for slow motions, the *residual* coupling tensor varies along the chains due to the pre-averaging by the faster segmental motions, giving a profile of the interaction strength. If the slow motions affect the lipid molecules to nearly the same extent, e.g. due to molecular rotations or whole bilayer lipid excitations (called order-director fluctuations, ODF), then the relaxation rates depend on the local order parameter squared.

In Figure 7 representative examples of such a square-law dependence of the relaxation and order parameter functions from ^{2}H NMR spectroscopy of fluid lipid bilayers are depicted. In part (a) double-logarithmic plots of $R_{1Z}^{(i)}$ against $|S_{CD}^{(i)}|$ are summarized for different molar ratios of the DMPC-d_{54}/cholesterol bilayers. (Note that the individual acyl positions are not distinguished.) The approximately linear region has a slope of nearly $n = 2$, consistent with a simple square-law functional dependence of $R_{1Z}^{(i)}$ on $|S_{CD}^{(i)}|$. Part (b) of Figure 7 shows the corresponding square-law plots for the multilamellar dispersions of DMPC-d_{54}/cholesterol having different molar ratios of the two lipid components. It can be seen that a square-law functional dependence of the $R_{1Z}^{(i)}$ rates vs. the order parameters $|S_{CD}^{(i)}|$ along the entire acyl chain is indeed observed [60]. Moreover, as the cholesterol mole fraction X_C increases, the slopes of the plots are systematically reduced, paralleling the macroscopic stiffening action of cholesterol [5,69].

Spectral Densities and Correlation Functions are Derived for Simplified Models in Closed Form

The next question we can ask is: what are the slow motions that yield the order fluctuations and produce the square-law functional dependence? First we can consider a simple non-collective model as a description of the effective rotations of the flexible phospholipids in the liquid-crystalline state [60,70,71]. In the case of phospholipids, rapid motions of the flexible molecules yield a reduced moment of inertia tensor, whose principal axes and principal values correspond to the off-axial and axial diffusion constants $D_\perp$ and $D_\parallel$. Modulation of the average or residual coupling tensor by rotations of the "average molecule" about its average principal axes would then produce the relaxation. For such a *non-collective molecular model*, the spectral densities then read

$$J_m^{\mathrm{mol}}(\omega) = \left|\left\langle D_{00}^{(2)}(\Omega_{\mathrm{PI}})\right\rangle\right|^2 \sum_q \sum_n \left| D_{0g}^{(2)}(\Omega_{\mathrm{IM}}) - \frac{\eta_{\mathrm{Q}}^{\mathrm{eff}}}{\sqrt{6}}\left[D_{-2q}^{(2)}(\Omega_{\mathrm{IM}}) + D_{2q}^{(2)}(\Omega_{\mathrm{IM}})\right]\right|^2 \left[\left\langle\left|D_{qn}^{(2)}(\Omega_{\mathrm{MD}})\right|^2\right\rangle - \left|\left\langle D_{qn}^{(2)}(\Omega_{\mathrm{MD}})\right\rangle\right|^2 \delta_{q0}\delta_{n0}\right] j_{qn}^{(2)}(\Omega_{\mathrm{MD}};\omega)\left|D_{nm}^{(2)}(\Omega_{\mathrm{DL}})\right|^2. \tag{8}$$

where $\eta_{\mathrm{Q}}^{\mathrm{eff}}$ is the effective asymmetry parameter of the residual EFG tensor due to averaging by the faster segmental motions. In Equation (8) the Euler angles Ω_{PI}, Ω_{IM}, Ω_{MD}, and Ω_{DL} denote transformation from the PAS (P) of the EFG tensor to an intermediate frame (I), from the intermediate frame to the molecular frame (M), from the molecular system to the director frame (D), and lastly from the director to the laboratory axes system (L) [65]. The symbols $j_{qn}^{(2)}(\Omega_{\mathrm{MD}};\,\omega)$ indicate Lorentzian reduced spectral densities, whose correlation times τ_{qn} depend on the principal values of the rotational diffusion tensor, viz. $D_\perp$ and $D_\parallel$ [72].

Note that in Equation (8) the spectral densities are pre-multiplied by the quantity $|\langle D_{00}^{(2)}(\Omega_{\mathrm{PI}})\rangle|^2$, where Ω_{PI} has to do with only the fast motions. This is merely the square of the fast order parameter $S_{\mathrm{f}}^{(2)}$—hence a squared dependence on the order parameter is predicted in agreement with the experimental finding (Figure 7). However, a molecular rotational diffusion model alone does not describe the NMR relaxation in the MHz range for phospholipids in the liquid-crystalline state, since the distribution of correlation times is not sufficiently wide [60]. Rather a significant contribution from slow motions such as vesicle tumbling is also needed, as obtained from the ^{2}H NMR spectral line width [71].

Yet another possibility is to model the relatively slow order fluctuations in terms of collective thermal disturbances of the bilayer arising from the ensemble of interacting molecules [60]. The bilayer is approximated as a continuous material, and the relaxation is assumed to be due to a distribution of modes, each undergoing overdamped or viscous relaxation. Within this framework, the spectral densities $J_m^{\mathrm{col}}(\omega)$ due to collective excitations of the bilayer are given by [73]

$$J_m^{\mathrm{col}}(\omega) = \frac{5}{2}\left|\left\langle D_{00}^{(2)}(\Omega_{\mathrm{PD}})\right\rangle\right|^2 D\omega^{-(2-d/2)}\left[\left|D_{-1m}^{(2)}(\Omega_{\mathrm{DL}})\right|^2 + \left|D_{1m}^{(2)}(\Omega_{\mathrm{DL}})\right|^2\right], \tag{9}$$

where D is a viscoelastic constant that depends on the elasticity, viscosity, and temperature of the bilayer, and d is the dimensionality of the bilayer thermal excitations. Here the Euler angles Ω_{PD} rotate the PAS of the C–^{2}H bond to the director frame, and the angles Ω_{DL} transform from the bilayer director to the laboratory system. According to Equations (2) and (9) the spectral densities $J_m(\omega)$ depend on the square of the observed order parameter S_{CD}, and the slope of the square-law plot is inversely related to the softness of the membrane.

For such collective bilayer excitations, one can distinguish between two possible limits, depending on the wavelengths of the fluctuations relative to the membrane thickness and the interlamellar separation. Collective order fluctuations in 2-D are described by a *flexible surface model*, e.g. in analogy with smectic liquid crystals, where the finite thickness of the membrane bilayer is neglected. In keeping with Equation (9), for $d = 2$ the spectral densities $J_m^{\mathrm{col}}(\omega)$ have an ω^{-1} frequency dependence [64,74,75]. Alternatively, 3-D order fluctuations are described by a *collective membrane deformation model*, where the bilayer is modeled analogously to a nematic liquid crystal. Equation (9) then predicts an $\omega^{-1/2}$ dependence of the spectral densities $J_m^{\mathrm{col}}(\omega)$ ($d = 3$). Although a 3-D director fluctuation model adequately describes the frequency dispersion of the ^{2}H $R_{1\mathrm{Z}}$ rates for DMPC vesicles [73,76], by itself it does not explain the orientation dependence of the ^{2}H $R_{1\mathrm{Z}}$ and $R_{1\mathrm{Q}}$ relaxation data [77].

How can one simultaneously account for both the orientational anisotropy of the relaxation and the frequency dependence of lipid bilayers in the fluid state? Here we are struck by the fact that the collective membrane deformation model explains the frequency dependence, whereas the non-collective molecular model best explains the angular anisotropy. We are naturally led to consider a composite membrane deformation model, in which collective axial rotations of the flexible phospholipid molecules are superimposed onto the collective bilayer excitations in the liquid-crystalline state [78]. For such a composite process, the laboratory frame spectral densities read

$$J_m(\omega) = J_m^{\mathrm{mol}}(\omega) + J_m^{\mathrm{col}}(\omega) + J_m^{\mathrm{mol-col}}(\omega) \tag{10}$$

in which the small contribution from segmental motions is neglected and the spectral densities $J_m^{\mathrm{mol}}(\omega)$ and $J_m^{\mathrm{col}}(\omega)$ are given above, Equations (8) and (9). The cross-term $J_m^{\mathrm{mol-col}}(\omega)$ is geometrical in origin [78] and cross-correlations between the molecular fluctuations and the collective fluctuations are neglected as a simplifying approximation. Current data indicate that such a composite model can explain the angular and frequency dependencies of the NMR relaxation for lipid bilayers in the fluid phase [78].

In Figure 8 the frequency dispersion of the R_{1Z} rates is shown for vesicles of DMPC in the liquid-crystalline state, comprising a total of 12 different magnetic field strengths. Note that the R_{1Z} values depend on frequency over the entire range from 2.5 to 95.3 MHz—there is no plateau value at either low frequency or high frequency. One cannot identify a regime where a single type of effective motion dominates the relaxation. The non-collective molecular model does not fit the low frequency end of the relaxation dispersion, even if an extreme value of the diffusion tensor anisotropy ($\eta \equiv D_{\|}/D_{\perp}$) is assumed [79]. Consequently an additional contribution from the vesicle tumbling is needed to explain the lower frequency data [71]. The 2-D flexible surface model is characterized by an ω^{-1} dependence and provides a rather poor fit to the data; it is probably most appropriate for interpreting the relaxation at very low frequencies in terms of collective undulations [70]. By contrast the 3-D collective membrane deformation model fits the frequency-dependent R_{1Z} data within the MHz range by an $\omega^{-1/2}$ dependence. Moreover, one can extend the effective frequency range by considering the relaxation of the ^{13}C nucleus, which has a larger magnetogyric ratio than ^{2}H [80]. In the case of ^{13}C NMR the relaxation is due to the magnetic dipolar interaction of the nucleus with its directly bonded hydrogen. The combined frequency-dependent data are described by a simple relaxation law of the form $R_{1Z}^{(i)} = A\tau_{\mathrm{f}} + B|S_{\mathrm{CD}}^{(i)}|^2$, where τ_{f} is the fast correlation time and A and B are constants, which is characteristic of ODF [81].

It follows that NMR results for soft membrane bilayers, involving flexible lipid molecules with many degrees of freedom, can be interpreted using fairly simple concepts inspired by the physics of materials. The small contribution from internal motions of the acyl chains matches the frequency independent relaxation rates of liquid *n*-alkanes [81] and agrees with more recent molecular dynamics simulations [82]. Thus the bilayer microviscosity, where a bulk viscosity cannot be measured, is comparable to an *n*-paraffin such as *n*-hexadecane [81]. The reason why the relaxation is governed by collective order fluctuations is that the local segmental motions of the lipids are very fast ($\tau_{\mathrm{f}} \approx 10$ ps), with spectral densities extending to very high frequencies. Basically the membrane lipids are tethered to the aqueous interface via their polar head groups, and the bilayer interior is essentially liquid hydrocarbon. The experimental findings imply that quasi-coherent order fluctuations are already present in lipid bilayers involving lengths on the order of approximately the bilayer thickness and even less, i.e. the mesoscopic length scale, as illustrated in Figure 9.

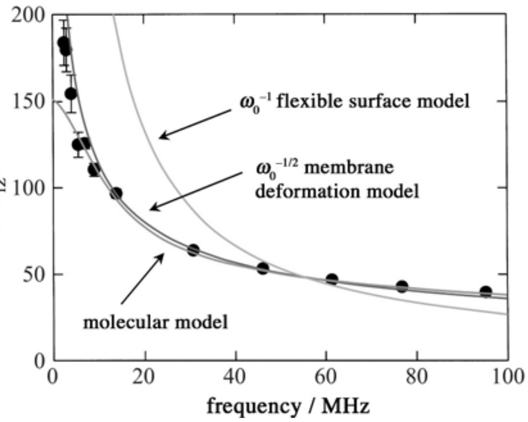

Fig. 8. Experimental ^{2}H R_{1Z} relaxation rates plotted as a function of frequency for vesicles of DMPC deuterated at the C_3 acyl segment in the liquid-crystalline state at 30 °C. Data were acquired at 12 different frequencies (magnetic field strengths) and are shown together with theoretical fits to various motional models (cf. the text) [73].

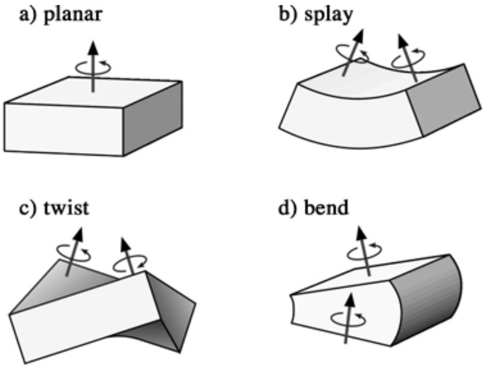

Fig. 9. Examples of collective membrane deformations within a continuum elastic approximation. (a) Planar bilayer, (b) splay, (c) twist, and (d) bend deformations, together with axial rotations about the local director [81,85].

Deuterium NMR Relaxation Allows Detailed Comparison of the Structural and Dynamical Properties of Membranes

Clearly an illuminating new aspect of the work described above is the extension of the concept of membrane elasticity to relatively short distances. This work provides striking evidence that membrane deformational fluctuations occur over a wide range of length and timescales, which depend on the bilayer lipid composition. Indeed, the current results give evidence for a connection between emerger properties on the mesoscopic scale, as studied by NMR relaxation, and macroscopic properties of the bulk material. According to the foregoing development, by combining the ^{2}H NMR relaxation data with the order parameters, we obtain a more comprehensive picture of the biophysical properties of membrane lipids than would be otherwise the case. Using ^{2}H NMR relaxation, the influences of the acyl length (bilayer thickness), polyunsaturation, lipid polar head groups (interfacial area per molecule), addition of a cosurfactant, and incorporation of sterols have been studied and interpreted in terms of the bilayer viscoelastic properties [21,83–87]. The rotational dynamics of the phospholipid and cholesterol components in binary mixtures have also been studied as a probe of their intermolecular interactions [79,88–92]. A scale of bilayer softness is evident, ranging from highly deformable, surfactant or polyunsaturated bilayer systems, to systems containing phosphatidylethanolamine with an increased bilayer stiffness, and ultimately the very rigid yet fluid bilayers containing cholesterol [85]. The theoretical interpretation of the NMR relaxation data correlates well with previous macroscopic studies of membrane bending deformations. Future applications of ^{2}H NMR spectroscopy include studies of membrane lipid nanostructures and lipid-protein interactions, as well as investigations of the structure and dynamics of membrane proteins in relation to their characteristic biological modes of action.

Acknowledgments

This work was supported by the United States National Institutes of Health and the United States National Aeronautics and Space Administration. We are particularly grateful to members of the group and to our collaborators for many fruitful discussions and contributions to the work described.

References

1. Häberlen U. High Resolution NMR in Solids: Selective Averaging. Adv. Magn. Reson. Suppl. 1. Academic Press: New York, 1976.
2. Spiess HW. In: P Diehl, E Fluck, R Kosfeld (Eds). NMR Basic Principles and Progress, Vol. 15. Springer-Verlag: Heidelberg, 1978.
3. Seelig J. Q. Rev. Biophys. 1977;10:353.
4. Davis JH. Biochim. Biophys. Acta. 1983;737:117.
5. Bloom M, Evans E, Mouritsen OG. Q. Rev. Biophys. 1991;24:293.
6. Brown MF. In: K Merz Jr, B Roux (Eds). Biological Membranes. A Molecular Perspective from Computation and Experiment. Birkhäuser: Basel, 1996, p 175.
7. Brown MF, Nevzorov AA. Colloids Surf. A. 1999;158:281.
8. Vist MR, Davis JH. Biochemistry. 1990;29:451.
9. Wassall SR, Brzustowicz MR, Shaikh SR, Cherezov V, Caffrey M, Stillwell W. Chem. Phys. Lipids. 2004;132:79.
10. Veatch SL, Polozov IV, Gawrisch K, Keller SL. Biophys. J. 2004;86:2910.
11. Ketchem RR, Hu W, Cross TA. Science. 1993;261:1457.
12. Copié V, McDermott AE, Beshah K, Williams JC, Spyker-Assink M, Gebhard RT, Lugtenberg J, Herzfeld J, Griffin RG. Biochemistry. 1994;33:3280.
13. Moltke S, Nevzorov AA, Sakai N, Wallat I, Job C, Nakanishi K, Heyn MP, Brown MF. Biochemistry. 1998;37:11821.
14. Gröbner G, Burnett IJ, Glaubitz C, Choi G, Mason AJ, Watts A. Nature (Lond.). 2000;405:810.
15. Salgado GFJ, Struts AV, Tanaka K, Fujioka N, Nakanishi K, Brown MF. Biochemistry. 2004;43:12819.
16. Nevzorov AA, Moltke S, Brown MF. J. Am. Chem. Soc. 1998;120:4798.
17. Karplus M. Acc. Chem. Res. 2002;35:321.
18. Petrache HI, Gouliaev N, Tristram-Nagle S, Zhang R, Suter RM, Nagle JF. Phys. Rev. E. 1998;57:7014.
19. Nagle JF, Tristram-Nagle S. Biochim. Biophys. Acta. 2000;1469:159.
20. Weiss TM, Chen PJ, Sinn H, Alp EE, Chen SH, Huang HW. Biophys. J. 2003;84:3767.
21. Rajamoorthi K, Petrache HI, McIntosh TJ, Brown MF. J. Am. Chem. Soc. 2005;127:1576.
22. Endress E, Heller H, Casalta H, Brown MF, Bayerl T. Biochemistry. 2002;41:13078.
23. Rheinstädter MC, Ollinger C, Fragneto G, Demmel F, Salditt T. Phys. Rev. Lett. 2004;93:108107.
24. Gruner SM. J. Phys. Chem. 1989;93:7562.
25. Seddon JM. Biochim. Biophys. Acta. 1990;1031:1.
26. Brown MF. Chem. Phys. Lipids. 1994;73:159.
27. Petrache HI, Dodd SW, Brown MF. Biophys. J. 2000;79:3172.
28. McConnell HM, Vrljic M. Annu. Rev. Biophys. Biomol. Struct. 2003;32:469.
29. Silvius JR. Biophys. J. 2003;85:1034.
30. Keller SL, Pitcher III WH, Huestis WH, McConnell HM. Phys. Rev. Lett. 1998;81:5019.
31. Brown DA, London E. J. Biol. Chem. 2000;275:17221.
32. Brown MF, Chan SI. In: DM Grant, RK Harris (Eds). Encyclopedia of Nuclear Magnetic Resonance, Vol. 2. Wiley: New York, 1996, p 871.
33. Ulrich AS, Watts A, Wallat I, Heyn MP. Biochemistry. 1994;33:5370.
34. Nevzorov AA, Moltke S, Heyn MP, Brown MF. J. Am. Chem. Soc. 1999;121:7636.
35. Koenig B, Strey H, Gawrisch K. Biophys. J. 1997;73:1954.
36. Sternin E, Schäfer H, Polozov IV, Gawrisch K. J. Magn. Reson. 2001;149:110.
37. Brown MF, Seelig J. Nature (Lond.). 1977;269:721.
38. Seelig J, MacDonald PM, Scherer PG. Biochemistry. 1987;26:7535.
39. Brown MF, Seelig J, Häberlen U. J. Chem. Phys. 1979;70:5045.
40. Seelig J, Seelig A. Q. Rev. Biophys. 1980;13:19.
41. Salmon A, Dodd SW, Williams GD, Beach JM, Brown MF. J. Am. Chem. Soc. 1987;109:2600.
42. Barry JA, Trouard TP, Salmon A, Brown MF. Biochemistry. 1991;30:8386.

43. McCabe MA, Griffith GL, Ehringer WD, Stillwell W, Wassall SR. Biochemistry. 1994;33:7203.
44. Barry JA, Gawrisch K. Biochemistry. 1994;33:8082.
45. Huster D, Arnold K, Gawrisch K. Biochemistry. 1998;37:17299.
46. Petrache HI, Salmon A, Brown MF. J. Am. Chem. Soc. 2001;123:12611.
47. Binder H, Gawrisch K. Biophys. J. 2001;81:969.
48. Sternin E, Bloom M, MacKay AL. J. Magn. Reson. 1983;55:274.
49. McCabe MA, Wassall SR. Solid State Nucl. Magn. Reson. 1997;10:53.
50. Oldfield E, Meadows M, Rice D, Jacobs R. Biochemistry. 1978;17:2727.
51. Thurmond RL, Dodd SW, Brown MF. Biophys. J. 1991;59:108.
52. Jansson M, Thurmond RL, Barry JA, Brown MF. J. Phys. Chem. 1992;96:9532.
53. Saiz L, Klein ML. J. Am. Chem. Soc. 2001;123:7381.
54. Pastor RW, Venable RM, Feller SE. Acc. Chem. Res. 2002;35:438.
55. Huber T, Rajamoorthi K, Kurze VF, Beyer K, Brown MF. J. Am. Chem. Soc. 2002;124:298.
56. Botelho AV, Gibson NJ, Wang Y, Thurmond RL, Brown MF. Biochemistry. 2002;41:6354.
57. Thurmond RL, Lindblom G, Brown MF. Biochemistry. 1993;32:5394.
58. Thurmond RL, Otten D, Brown MF, Beyer K. J. Phys. Chem. 1994;98:972.
59. Lafleur M, Bloom M, Eikenberry EF, Gruner SM, Han Y, Cullis PR. Biophys. J. 1996;70:2747.
60. Brown MF. J. Chem. Phys. 1982;77:1576.
61. Rommel E, Noack F, Meier P, Kothe G. J. Phys. Chem. 1988;92:2981.
62. Speyer JB, Weber RT, Das Gupta SK, Griffin RG. Biochemistry. 1989;28:9569.
63. Ferrarini A, Nordio PL, Moro GJ, Crepeau RH, Freed JH. J. Chem. Phys. 1989;91:5707.
64. Stohrer J, Gröbner G, Reimer D, Weisz K, Mayer C, Kothe G. J. Chem. Phys. 1991;95:672.
65. Nevzorov AA, Trouard TP, Brown MF. Phys. Rev. E. 1997;55:3276.
66. Goldstein H. Classical Mechanics. Addison-Wesley: Menlo Park, 1980.
67. Lindahl E, Edholm O. J. Chem. Phys. 2001;115:4938.
68. Brown MF. J. Magn. Reson. 1979;35:203.
69. Méléard P, Gerbaud C, Pott T, Fernandez-Puente L, Bivas I, Mitov MD, Dufourcq J, Botherel P. Biophys. J. 1997;72:2616.
70. Althoff G, Heaton NJ, Gröbner G, Prosser RS, Kothe G. Colloids Surf. A. 1996;115:31.
71. Halle B. J. Phys. Chem. 1991;95:6724.
72. Trouard TP, Alam TM, Brown MF. J. Chem. Phys. 1994;101:5229.
73. Nevzorov AA, Brown MF. J. Chem. Phys. 1997;107:10288.
74. Blinc R, Luzar M, Vilfan M, Burgar M. J. Chem. Phys. 1975;63:3445.
75. Marqusee JA, Warner M, Dill KA. J. Chem. Phys. 1984;81:6404.
76. Brown MF, Salmon A, Henriksson U, Söderman O. Mol. Phys. 1990;69:379.
77. Jarrell HC, Smith ICP, Jovall PA, Mantsch HH, Siminovitch DJ. J. Chem. Phys. 1987;88:1260.
78. Nevzorov AA, Trouard TP, Brown MF. Phys. Rev. E. 1998;58:2259.
79. Trouard TP, Nevzorov AA, Alam TM, Job C, Zajicek J, Brown MF. J. Chem. Phys. 1999;110:8802.
80. Brown MF. J. Chem. Phys. 1984;80:2832.
81. Brown MF, Ribeiro AA, Williams GD. Proc. Natl. Acad. Sci. U.S.A. 1983;80:4325.
82. Venable RM, Zhang Y, Hardy BJ, Pastor RW. Science. 1993;262:223.
83. Otten D, Brown MF, Beyer K. J. Phys. Chem. B. 2000;104:12119.
84. Brown MF, Thurmond RL, Dodd SW, Otten D, Beyer K. Phys. Rev. E. 2001;64:010901.
85. Brown MF, Thurmond RL, Dodd SW, Otten D, Beyer K. J. Am. Chem. Soc. 2002;124:8471.
86. Martinez GV, Dykstra EM, Lope-Piedrafita S, Job C, Brown MF. Phys. Rev. E. 2002;66:050902.
87. Martinez GV, Dykstra EM, Lope-Piedrafita S, Brown MF. Langmuir. 2004;20:1043.
88. Bonmatin J-M, Smith ICP, Jarrell HC, Siminovitch DJ. J. Am. Chem. Soc. 1990;112:1697.
89. Brown MF. Mol. Phys. 1990;71:903.
90. Trouard TP, Alam TM, Zajicek J, Brown MF. Chem. Phys. Lett. 1992;189:67.
91. Weisz K, Gröbner G, Mayer C, Stohrer J, Kothe G. Biochemistry. 1992;31:1100.
92. Morrison C, Bloom M. J. Chem. Phys. 1994;101:749.

Solid State ^{19}F-NMR Analysis of Oriented Biomembranes

Anne S. Ulrich

Institute of Organic Chemistry, University of Karlsruhe, and Forschungszentrum Karlsruhe, 76131 Karlsruhe, Germany

Introduction

The ^{19}F nucleus offers numerous advantages for solid state NMR, being first and foremost its high sensitivity that is only exceeded by ^{1}H. Especially in non-crystallizable biological samples, such as membranes and fibers, the lack of a natural abundance background often makes selective ^{19}F-labeling the method of choice [1–3]. Anisotropic interactions are accessible in robust 1-pulse experiments on macroscopically oriented samples, whose spectral lineshapes are readily interpreted. This strategy is thus particularly useful for oriented membranes and aligned fibers. Magic angle spinning experiments are not covered here, though they are of course also a fruitful source of information [4–7]. In the following, we will describe how one or a few fluorine labels in a synthetic peptide can provide information about its local alignment, its dynamic behavior, and its three-dimensional architecture in a lipid membrane. Further details about the methodological aspects of ^{19}F-NMR structure analysis and biological applications to membrane-active peptides are covered in recent reviews [8–11].

^{19}F-NMR Experimental Aspects

The ^{19}F nucleus has a spin of $I = 1/2$ and a high gyromagnetic ratio $\gamma/2\pi = 40.03$ MHz/T, which provides it with an exceptional NMR sensitivity and strong dipolar couplings [12–14]. Given that the intrinsic sensitivity scales with γ^3, ^{19}F should exceed that of ^{2}H and ^{15}N by a factor of 100 and 1000, respectively. In practice, a 10-fold and 100-fold gain in sensitivity is experienced [15]. Another benefit of strong dipolar couplings lies in the possibility to address long-range distances. If a 30 Hz homonuclear coupling can be resolved, this would correspond to an accessible distance of 7 Å for a ^{13}C spin pair, while up to 18 Å should be feasible by ^{19}F-NMR [16,17].

On a standard solid state NMR spectrometer the high-frequency channel is usually optimized for ^{1}H. For pure ^{19}F-NMR observation it may be sufficient to re-tune the transmitter, amplifiers, and probe, but for ^{1}H-decoupling it is necessary to implement designated ^{19}F-NMR hardware with two separate channels [11,14,18]. A double-resonance ^{19}F-{^{1}H} probe should be capable of handling high power levels, the two frequencies should be insulated by at least 60 dB, and additional external high-power filters are advisable. Teflon and any other materials containing traces of ^{19}F give serious background signals, even when positioned far away from the receiver coil.

A designated flat-coil probe is recommended for determining orientational constraints in uniaxially aligned membranes. Measurements are always carried out at a tilt angle of $\alpha = 0°$ where the sample normal N is aligned parallel to the static magnetic field direction B_0. It is useful to be able to tilt the sample at $\alpha \neq 0°$, for which the solenoid coil has to be equipped with a goniometer. Macroscopically oriented membranes are usually prepared on small glass slides [11,15,19–25], which carry about 3000 fully hydrated lipid bilayers each. Typically 20 such glass plates are stacked, and wrapped in polyethylene foil to prevent dehydration. For chemical shift referencing $CFCl_3$ is used as the standard with 0 ppm, and for oriented membrane samples we recommend to fill a thin glass box with a 1 M NaF solution [26,27]. In a similar approach, macroscopically aligned fibers are prepared as bundles, such as silk fibroin [28–30].

For ^{19}F-NMR studies of polypeptides in liquid crystalline membranes, a simple 1-pulse experiment is often adequate to reveal the necessary anisotropic information. In many cases the line-narrowing effect of ^{1}H-decoupling reaches a plateau at about 30 kHz field strength [15], hence moderate decoupling fields are sufficient. A Carr-Purcell-Meiboom-Gill (CPMG) sequence (without ^{1}H-decoupling) can be used to acquire homonuclear dipolar spectra from static samples for distance measurements between ^{19}F-spins [19,31–34]. The echo delay period has to be minimized (<50 μs) to prevent artifacts due to dephasing, which can become severe at high magnetic field strengths. The CPMG duty cycle has to be extrapolated to zero, and performance is generally improved by an xy8 phase cycle and composite refocusing pulses.

Strategies for Structure Analysis

With a focus on macroscopically oriented biomembranes and fibers, the two most useful structural parameters reviewed here are (i) the angle θ of a ^{19}F-labeled segment with respect to the static magnetic field direction B_0 (see Figure 1), and (ii) the internuclear distance r between a

Graham A. Webb (ed.), Modern Magnetic Resonance, 261–267.

© 2008 *Springer.*

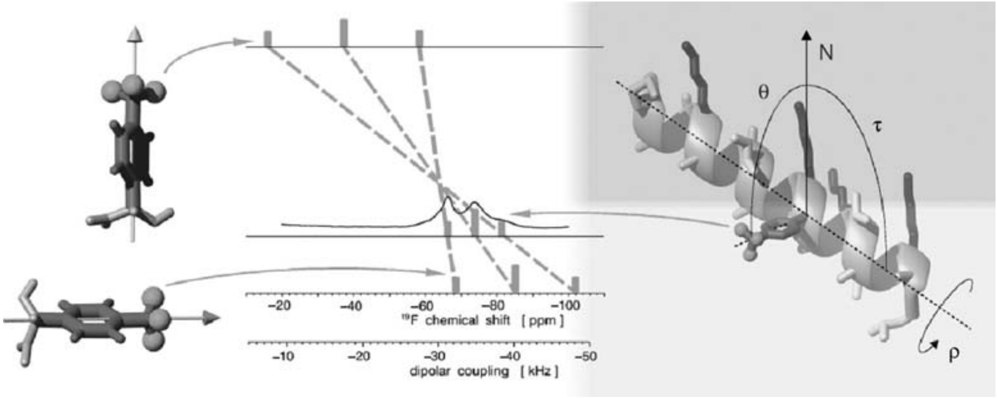

Fig. 1. Solid state ^{19}F-NMR analysis of macroscopically aligned samples is used to collect orientational constraints on membrane-embedded peptides carrying suitably ^{19}F-labeled side chains. For example, the anisotropic dipolar coupling within the rapidly rotating CF_3-group is analyzed to determine the angle θ of the CF_3-Phg side chain, which reflects the alignment of the peptide backbone. The stick spectra (green bars) illustrate the ($3\cos^2\theta$-1)-dependence over the full angular range. The dipolar splitting in the experimental 1-pulse spectrum reveals the magnitude of the dipolar coupling, and its sign is directly available from the chemical shift anisotropy of the triplet signal. Using a set of several orientational constraints, the alignment of the α-helix is evaluated in terms of its tilt angle τ, its azimuthal rotation ρ, and an order parameter S_{mol}. (See also Plate 31 on page XXX in the Color Plate Section.)

pair of ^{19}F-labels [10,11]. When angular measurements are carried out at a sample tilt angle of $\alpha = 0°$, then θ represents the local orientation relative to the membrane normal or fiber axis. The value of θ is available either from the anisotropic chemical shift δ_{CSA} of a single label [15,21,22], from the anisotropic dipolar coupling Δ_{FF} between two labels [19,21], or from the coupling Δ_{CF3} within a CF_3-group [20,23,25,34] (see Figure 1). Distances are always measured from dipolar couplings, using for example a static CPMG experiment [19,20] or REDOR under magic angle spinning [35,36].

The resonance frequency of a single ^{19}F-label is determined by its anisotropic chemical shift δ_{CSA} according to

$$\delta_{\text{CSA}}(\theta,\varphi) = \Delta^0_{\text{CSA}}\left[\frac{\langle 3\cos^2\theta - 1 + \eta_{\text{CSA}}\sin^2\theta\ \cos 2\varphi\rangle}{2}\right] \tag{1}$$

where $\Delta^0_{\text{CSA}} = (\delta_{\text{iso}} - \delta_{11})$ is the static CSA parameter and $\eta_{\text{CSA}} = (\delta_{33} - \delta_{22})/\Delta^0_{\text{CSA}}$ defines the asymmetry [11]. The polar angles θ and φ describe the CSA tensor orientation with respect to the static magnetic field B_0, and the bracket <> denotes the time-average. For $\eta_{\text{CSA}} = 0$ the equation simplifies to

$$\delta_{\text{CSA}}(\theta) = \Delta^0_{\text{CSA}}\left[\frac{\langle 3\cos^2\theta - 1\rangle}{2}\right] \tag{2}$$

where θ is the angle between the unique axis of the CSA tensor and B_0 (see Figure 1). Dipolar couplings, which are intrinsically symmetric, obey a similar relationship

$$\begin{aligned}\Delta_{\text{FF}}(\theta) &= \Delta^0_{\text{FF}}\left[\frac{\langle 3\cos^2\theta - 1\rangle}{2}\right]\\ &= \left|\frac{3\gamma_F^2\hbar\mu_0}{4\pi}\,\frac{1}{r^3}\left\langle\frac{3\cos^2\theta - 1}{2}\right\rangle\right|\end{aligned} \tag{3}$$

where Δ^0_{FF} is the static dipolar coupling (in Hz) between immobile spins aligned at $\theta = 0°$, and where the dipolar coupling constant $\gamma_F^2\hbar\mu_0/2\pi r^3$ depends on their internuclear distance r (in Å). For two geminal ^{19}F-labels on a CF_2-segment it is $\Delta^0_{\text{CF2}} = 30.8$ kHz [19,33], and for a CF_3-group undergoing fast rotation $\Delta^0_{\text{CF3}} = 15.8$ kHz [20,25]. The experimentally observed dipolar splitting Δ_{CF3} thus depends only on the angle θ between the CF_3-axis and B_0

$$\Delta_{\text{CF3}}(\theta) = \Delta^0_{\text{CF3}}\left\langle\frac{3\cos^2\theta - 1}{2}\right\rangle \tag{4}$$

The dipolar spectrum of a CF_3-group produces a triplet with an intensity ratio of 1:2:1, the splitting being defined between adjacent components. The overall powder lineshape of CF_3-group looks rather complex as it is also affected by CSA interactions of similar magnitude. The spectrum of an oriented sample reverts to a simple triplet (see Figure 1), since both interactions are scaled by the same angle θ. This correlation is useful for discriminating positive and negative dipolar couplings, whose sign cannot be determined from the splitting but is directly available via the CSA [23,25].

When a peptide is embedded in a liquid crystalline membrane, several modes of motion have to be taken into account. Any fast rotation leads to a projection of all spin interactions onto the rotational axis, hence the time-averaged term of Equations (1)–(4) can be re-written as

$$\left\langle \frac{3\cos^2\theta - 1}{2} \right\rangle = \left\langle \frac{3\cos^2\beta - 1}{2} \right\rangle \cdot \left\langle \frac{3\cos^2\alpha - 1}{2} \right\rangle \qquad (5)$$

where β is the angle between the spin interaction tensor and the axis of averaging, and α denotes the angle between the latter and B_0. When a peptide undergoes fast long-axial rotation in the bilayer, β corresponds to the effective angle between the relevant spin interaction tensor and the local membrane normal N, and α is the angle between N and B_0. When examining an oriented sample aligned at $\alpha = 0^\circ$, it is not possible to tell whether a molecule is engaged in long-axial rotation or not, since $\beta = \theta$. Long-axial rotation is only detected upon tilting the sample to $\alpha \neq 0^\circ$, when every resonance remains narrow and moves as a function of $(3\cos^2\alpha - 1)/2$.

Local oscillations of the labeled segment or a wobble of the entire molecule lead to further time-averaging over $<3\cos^2\beta - 1/2$. To account for such motions in a simplified manner, a scaling factor between 1.0 and zero is introduced [10,11,21–23], called the molecular order parameter S_{mol}

$$\delta_{\text{CSA}} = \Delta^0_{\text{CSA}} \left\langle \frac{3\cos^2\beta - 1}{2} \right\rangle \cdot S_{\text{mol}} \qquad (6)$$

$$\Delta_{\text{FF}} = \Delta^0_{\text{FF}} \left\langle \frac{3\cos^2\beta - 1}{2} \right\rangle \cdot S_{\text{mol}} \qquad (7)$$

$$\Delta_{\text{CF3}} = \Delta^0_{\text{CF3}} \left\langle \frac{3\cos^2\beta - 1}{2} \right\rangle \cdot S_{\text{mol}} \qquad (8)$$

Now, β is the time-averaged angle of the relevant spin interaction tensor with respect to the membrane normal. The value of S_{mol} describes the extent of non-specific wobble in the bilayer, which can be vigorous for small compounds giving order parameters as low as 0.1 [19,34], while peripherally membrane-associated peptides may exhibit values around 0.3–0.5 [21,23–25], transmembrane peptides near 0.8 [15], and large membrane proteins and fibrils approach $S_{\text{mol}} \approx 1.0$ [37–40].

^{19}F-Labeling of Peptides

For a successful ^{19}F-NMR structure analysis, the reporter group should be rigidly attached to a strategic position in the molecular framework, such that its NMR parameters reflect the conformation and alignment of the entire molecule [10]. By measuring the orientation of several individual ^{19}F-labels in different positions, the overall molecular architecture and its motional averaging can be re-constructed. *Intra*-molecular distance constraints are direct probes of conformation, and *inter*-molecular dipolar couplings may reveal the formation of oligomers. Several non-natural amino acids, in which the ^{19}F-label is rigidly connected to the peptide backbone, are suitable for structure analysis. Their relevant ^{19}F-NMR parameters are summarized in Table 1: 4F-L-phenylglycine (4F-Phg), 4-CF_3-L-phenylglycine (CF_3-Phg), 3F-L-alanine (F-Ala), and 3,3,3-F_3-L-alanine (F_3-Ala). First attempts at peptide synthesis were not trivial in view of certain instabilities, but protocols have been established with good yields [10]. When working with these labeled peptides, it is essential to avoid fluorinated solvents such as TFA in the HPLC-purification protocol, or TFE in the NMR sample preparation [41].

One of the first amino acids used in ^{19}F-NMR structure analysis is 4F-Phg, which racemizes extensively during Fmoc synthesis, but the resulting epimeric peptides can usually be separated by HPLC [41]. It is a useful label for measuring distances [21]. Orientational constraints can also be extracted from the ^{19}F CSA tensor, but its intrinsic asymmetry makes it necessary to take the side chain torsion angle χ_1 of the Cα–Cβ bond into account [21,22,24]. This difficulty is eliminated with CF_3-Phg, which is a more convenient label for measuring orientational constraints. The anisotropic dipolar coupling within the CF_3-group together with the sign from the CSA provides a direct measure of the orientation of the Cα–Cβ bond (which is colinear with the CF_3-axis) [23,25]. While the phenylglycine-derivatives are suitable substitutes for large hydrophobic amino acids, alanine-derivatives are more appropriate for replacing small side chains in peptides. 3F-Ala has a tendency to eliminate HF during Fmoc coupling, but this can be suppressed using base-free conditions. Given that the CH_2F-group is motionally averaged, it is very suitable for REDOR distance measurements on peptides [35,36,42]. Qualitative orientational changes have also been detected via 3F-Ala, though quantitative angular constraints cannot yet be obtained as long as the CSA tensor alignment in the molecular frame has not been fully characterized [11,35]. The obvious candidate to overcome this difficulty is F_3-Ala, which offers all the advantages of a rotating CF_3-group and has also been successfully incorporated into peptides (unpublished results).

Structure Analysis of Membrane-Associated Peptides

Most ^{19}F-NMR studies reviewed here are based on orientational analysis. A small number of constraints are

Table 1: CSA parameters of ^{19}F-labeled amino acids used for structure analysis. Two different sets of results are separated by a slash, namely of the polycrystalline amino acids and when they are incorporated into a lyophilized peptide

	4F-Phg	CF_3-Phg	3F-Ala	F_3-Ala
	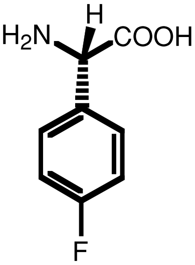	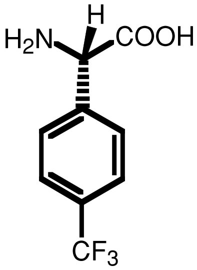	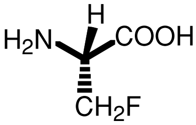	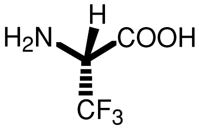
δ_{iso} (ppm)	−115/− 113	−60/− 63	−230/− 222	−74/− 63
δ_{11} (ppm)	−65/− 59	−23/− 27	−202/− 195	−31/− 27
δ_{22} (ppm)	−126/− 124	−78/− 81	−228/− 215	−92/− 81
δ_{33} (ppm)	−153/− 155	−78/− 81	−260/− 255	−98/− 81

sufficient to fully describe the peptide alignment and motional averaging in the membrane, provided that its conformation is known. This approach is usually feasible for peptides consisting of well-defined secondary structure elements such as α-helices or β-sheets. The alignment and mobility of such entity is fully defined in terms of (i) its tilt angle τ, (ii) its azimuthal rotation angle ρ, and (iii) an order parameter S_{mol} describing the extent of motional averaging (see Figure 1). It is convenient to define τ as the tilt angle of the molecular pseudo-axis (e.g. helix axis), while the rotation ρ around this axis is often used to describe its amphiphilic profile. A computational grid-search is performed by systematically varying τ, ρ, and S_{mol} until the simulated NMR spectra fit the experimental data best [10]. When using at least three or more orientational constraints, a unique solution should be found, which is displayed in a τ–ρ map whose minimum represents the peptide alignment, along with the best-fit value of S_{mol}. The secondary structure, too, can be deduced via such τ–ρ analysis, since incorrect assumptions concerning the peptide conformation should give no acceptable rmsd minimum.

Several membrane-active peptides have been analyzed this way by solid state ^{19}F-NMR [15,21–25,43]. It was generally observed that these molecules undergo structural changes upon varying the lipid composition, temperature, and most importantly their own concentration. Therefore, special attention has to be paid to the possibility that different membrane-bound states may be correlated with self-assembly, and that peptide mobility is likely to differ in different oligomeric states. One particular advantage of ^{19}F analysis lies in the high sensitivity compared to other NMR-labels, which makes it possible to scan many different samples and experimental conditions in short time. Even very low peptide/lipid ratios down to 1:3000 have been examined, given that ^{19}F-NMR spectra can be typically acquired with as little as 40 µg ($\approx$ 20 nmol) in an overnight measurement [27]. Several examples of a comprehensive ^{19}F-NMR structure analysis will now be reviewed in the following paragraphs.

Fusogenic Peptide B18

The peptide B18 (LGLLLRHLRHHSNLLANI) was identified as the minimal fusogenic sequence from the sea urchin fertilization protein "bindin," which is responsible for triggering fusion of sperm and oocyte [44]. The isolated peptide induces fusion of liposomes *in vitro*, and its interactions with lipid membranes have been thoroughly characterized [22,41,45–50]. ^{19}F-NMR analysis of a series of nine peptide analogs, individually labeled with 4F-Phg, showed that B18 assumes a well-defined helix-loop-helix structure in oriented DMPC/DMPG membranes. The N-terminal α-helix is obliquely immersed into the bilayer ($\tau \approx 53°$, $\rho \approx -67°$, $S_{mol} \approx 0.8$), while the C-terminal segment remains flat on the membrane surface with ($\tau \approx 91°$, $\rho \approx 19°$, $S_{mol} \approx 0.5$). This picture is fully consistent with the hydrophobicity profile of the folded peptide, as illustrated in Figure 2. However, the monomeric conformation is only stable at peptide/lipid ratios lower than 1:100, since aggregation takes place at

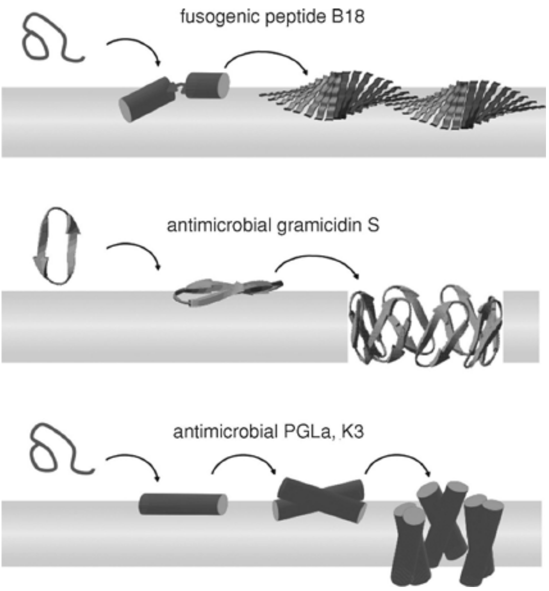

Fig. 2. Illustration of the concentration-dependent interactions of different peptides with lipid membranes, as characterized by solid state ^{19}F-NMR. The fusogenic peptide B18 folds into a helix-loop-helix structure upon membrane binding and aggregates into β-sheet amyloid fibrils at high concentration. The antimicrobial peptide gramicidin S is electrostatically attracted to negatively charged membranes and binds flat to the bilayer surface. At high concentration it can re-align and self-assemble into an oligomeric β-barrel pore. The antimicrobial peptides PGLa and K3 fold into amphiphilic α-helices upon membrane binding and re-align at an oblique tilt angle with increasing peptide concentration due to the formation of putative dimers. It has been speculated that the dimers may assemble further into a toroidal wormhole. (See also Plate 32 on page XXX in the Color PlateSection.)

higher concentration and with increasing age of the sample [24]. The aggregated state was shown to consist of cross-β-sheet amyloid fibrils, which penetrate into the hydrophobic region of the bilayer [49,50].

Antimicrobial Peptide Gramicidin S

Cationic peptide antibiotics possess an overall amphiphilic structure and act by permeabilizing bacterial membranes [43]. Gramicidin S ($[\mathrm{VOL^{D}FPVOL^{D}FP}]_{\mathrm{cyclo}}$) is produced by *Bacillus brevis* and has a cyclic β-sheet structure, stabilized by four intramolecular H-bonds. For ^{19}F-NMR structure analysis, 4F-Phg labels were substituted at the two equivalent positions of either Leu or Val. CPMG distance measurements in oriented DMPC membranes were carried out on these pairs of equivalent labels to confirm that 4F-Phg does not distort the cyclic β-sheet backbone [21]. The orientational constraints of the 4F-Phg labels revealed the peptide alignment and mobility in the membrane. At low peptide/lipid ratios ($\leq$1:80) gramicidin S lies flat on the surface, as illustrated in Figure 2, with its symmetry axis parallel to the membrane normal ($\tau \approx 0^\circ$, ρ unrestricted). In liquid crystalline bilayers the peptide is highly mobile ($S_{\mathrm{mol}} \approx 0.3$) and engaged in long-axial rotation, while in the gel phase it is immobilized ($S_{\mathrm{mol}} \approx 1.0$) and well ordered. At high concentration ($\geq$1:40) gramicidin S can flip upright in the membrane ($\tau \approx 80^\circ$, $\rho - 45^\circ$, $S_{\mathrm{mol}} \approx 1.0$) [24]. Given the ambiguity associated with the side-chain torsion angle χ_1 of 4F-Phg, the ^{19}F-NMR data was supported by independent ^{15}N-NMR measurements of backbone-labeled peptides. The upright alignment appears to reflect an oligomeric state, not only because of its concentration-dependent formation but also in view of its molecular mobility ($S_{\mathrm{mol}} \approx 1$, with fast long-axial rotation around N). Gramicidin S was thus suggested to self-assemble as a β-barrel to form a pore across the membrane, whose structure would be ideally stabilized by intermolecular H-bonds (see Figure 2). The number of monomers was not accessible by NMR, but a hexameric β-barrel has indeed been recently observed by crystallographic analysis of a modified gramicidin S analog [51].

Antimicrobial Peptide PGLa

The antimicrobial peptide PGLa (GMASKAGAIAGKIAKVALKAL-NH$_2$) from the skin of *Xenopus laevis* possesses an amphiphilic structure when folded as an α-helix. A series of peptide analogs was synthesized with 4F-Phg or CF$_3$-Phg substitutions to determine orientational constraints [23,25,27,41]. At a peptide/lipid ratio of 1:200 the helix is aligned flat in DMPC membranes ($\tau \approx 95^\circ$), and the azimuthal rotation angle ($\rho \approx 110^\circ$) agrees well with the amphiphilic character of PGLa [23]. At low concentration the peptide is monomeric and mobile in liquid crystalline bilayers ($S_{\mathrm{mol}} \approx 0.6$), undergoing long-axial rotation. In the lipid gel phase it is slightly less mobile ($S_{\mathrm{mol}} \approx 0.7$) and long-axial rotation has ceased. By varying the peptide/lipid ratio from 1:3,000 to 1:8, it was found that PGLa changes its orientation with increasing peptide concentration [27]. Broadened signals are observed at intermediate peptide/lipid ratios (1:100), showing that the structural interconversion of PGLa occurs on the NMR time-scale, unlike gramicidin S for which two distinct populations were simultaneously observed. At higher concentration ($\geq$1:50) PGLa is aligned at an oblique tilt angle ($\tau \approx 125^\circ$, with $\rho \approx 90^\circ$, see Figure 2) [25]. The concentration-dependent re-alignment was an unexpected result, as a monomer would probably not be stable at an oblique tilt angle. Notably, even at high concentration the tilted peptide undergoes long-axial rotation, and its order parameter is similar to that at low concentration, hence it cannot be extensively aggregated. PGLa was thus suggested to form dimers in the membrane, as it had been demonstrated for the two related peptides magainin (by transferred-NOE) and K3 (by REDOR NMR, see below) [35,36,52]. For PGLa a symmetric antiparallel (head-to-tail) arrangement would be consistent with the occurrence of single ^{19}F-NMR signals in the oriented samples [25]. The functional relevance of the tilted and presumably dimeric PGLa structure is not yet clear. Nevertheless, to be certain that the structure analysis did not suffer from artifacts due to the stiff and bulky ^{19}F-labels, the re-alignment was independently confirmed with entirely unperturbing ^{2}H- and ^{15}N-labels [43,53]. The tentative ^{19}F-NMR structure proved to be almost perfect at low peptide concentration, and still rather accurate at high concentration where the bulky labels might have been expected to interfere with the putative dimerization interface.

Antimicrobial Peptide K3

Based on the sequence of PGLa, an α-helical model peptide K3 [$(KIAGKIA)_3$–NH_2] had been designed with improved antimicrobial activity and reduced hemolytic side effects [54,55]. By labeling one native Ala position with 3F-Ala, the static ^{19}F-NMR spectra of K3 in oriented membranes showed that this peptide undergoes a change in its alignment and/or mobility at a peptide/lipid ratio between 1:200 and 1:20 [35]. Unlike PGLa, however, long axial rotation ceases at high peptide concentration in liquid crystalline bilayers. Further peptides were synthesized with ^{13}C-labels for REDOR distance analysis by Schaefer *et al.*, who showed that K3 forms parallel (head-to-head) dimers at high peptide/lipid ratio [35,36]. Further distance constraints between selectively labeled lipids and peptides revealed close contacts of K3 with both lipid headgroups and acyl chains [36]. Based on these indirect results, a toroidal wormhole was postulated for K3 at high peptide concentration. Given the dimeric structure of K3 (though without knowing its orientation in the membrane) and the observed re-alignment of PGLa (but without having measured intermolecular distances), a generalized course of events upon membrane binding is schematically suggested in Figure 2 for this class of α-helical antimicrobial peptides.

Perspectives

Over the recent years, sufficient experience with ^{19}F-labeling of membrane-associated peptides and their spectral analysis has been gained to allow a critical comparison with the more established solid state NMR approaches. We feel that some of the drawbacks with ^{19}F (i.e. non-trivial chemical synthesis, and unusual spectrometer hardware) are more than compensated for by the excellent sensitivity and the robustness of the ^{19}F-NMR measurements. Overall, CF_3-Phg (and possibly F_3-Ala, unpublished results) appears to be the most suitable label for measuring angular constraints in oriented membrane samples, while 3F-Ala is the best choice for determining distances by REDOR. The risk of conformational and functional perturbation by ^{19}F-labels has to be borne in mind and needs to be tested for every system under investigation. However, the accuracy of the resulting three-dimensional peptide structure does not seem to be limited by the intrinsic error range of the ^{19}F-NMR data (unless labels are placed at a dimerization interface), but it depends more on the conformational assumptions when reconstructing the molecular architecture from a limited number of constraints. Overall, it has been possible to characterize the structure and behavior of many different peptides under a wide range of relevant conditions, which provided valuable information about their functional mechanisms.

Acknowledgments

I thank all past and present members of the lab for their hard work and enthusiasm, and specifically Ralf Glaser for Figure 1. Financial support was provided by the DFG, the Universities of Jena and Karlsruhe, the Forschungszentrum Karlsruhe, and the CFN.

References

1. Gerig JT. Prog. NMR Spectrosc. 1994;26:293–370.
2. Danielson MA, Falke JJ. Annu. Rev. Biophys. Biomol. Struct. 1996;25:163–95.
3. Gerig JT. In: V. Bloomfield (Ed). Biophysical Society Educational Resources on the Web: Spectroscopy: http://www.biophysics.org/education/gerig.pdf, 1998.
4. Harris RK, Jackson P. Chem. Rev. 1991;91:1427–40.
5. Carss SA, Scheler U, Harris RK. Magn. Reson. Chem. 1996;34:63–70.
6. Miller JM. Prog. NMR Spectrosc. 1996;28:255–81.
7. Harris RK, Monti GA, Holstein P. In: I. Ando, T. Asakura. (Ed). Solid State NMR of Polymers. Elsevier Science: Amsterdam, 1998, pp 253–66.
8. Drechsler A, Separovic F. IUBMB Life. 2003;55:515–23.
9. Strandberg E, Ulrich AS. Concepts Magn. Reson. 2004;23A:89–120.
10. Ulrich AS, Wadhwani P, Dürr UHN, Afonin S, Glaser RW, Sachse C, Tremouilhac P, Berditchevskaia M. In: A. Ramamoorthy (Ed). NMR Spectroscopy of Biological Solids. CRC Press, Taylor & Francis, Boca Raton, FL, 2005;215–236.
11. Ulrich AS. Prog. NMR Spectrosc. 2005;46:1–21.
12. Berger S, Braun S, Kalinowski H.-O. NMR-Spektroskopie von Nichtmetallen: 19F-NMR-Spektroskopie, Vol. 4. Georg Thieme Verlag: Stuttgart, 1994.

13. Brey WS, Brey ML. In: DM Grant, RK Harris (Eds). Encyclopedia of Nuclear Magnetic Resonance. Wiley: Chichester, 1996, pp 2063–71.
14. Ulrich AS. In: J Lindon, G Tranter, J Holmes (Eds). Encyclopedia of Spectroscopy and Spectrometry. Academic Press: London, 2000, pp 813–25.
15. Grage SL, Wang J, Cross TA, Ulrich AS. Biophys. J. 2002;83:3336–50.
16. Smith SO, Aschheim K, Groesbeek M. Quart. Rev. Biophys. 1996;29:395–449.
17. Gilchrist ML Jr, Monde K, Tomita Y, Iwashita T, Nakanishi K, McDermott AE. J Magn. Reson. 2001;152:1–6.
18. Holstein P, Harris RK, Say BJ. Solid State Nucl. Magn. Reson. 1997;8:201–6.
19. Grage SL, Ulrich AS. J. Magn. Reson. 1999;138:98–106.
20. Grage SL, Ulrich AS. J. Magn. Reson. 2000;146:81–8.
21. Salgado J, Grage SL, Kondejewski LH, Hodges RS, McElhaney RN, Ulrich AS. J. Biomol. NMR. 2001;21:191–208.
22. Afonin S, Dürr UHN, Glaser RW, Ulrich AS. Magn. Reson. Chem. 2004;42:195–203.
23. Glaser RW, Sachse C, Dürr UHN, Wadhwani P, Ulrich AS. J. Magn. Reson. 2004;168:153–63.
24. Afonin S, Dürr UHN, Wadhwani P, Salgado JB, Ulrich AS. 2006; Top. Curr. Chem (in press).
25. Glaser RW, Sachse C, Dürr UHN, Wadhwani P, Afonin S, Strandberg E, Ulrich AS. Biophys. J. 2005;88:3392–3397.
26. Ulrich R, Glaser RW, Ulrich AS. J. Magn. Reson. 2003;164:115–27.
27. Glaser RW, Ulrich AS. J. Magn. Reson. 2003;164:104–14.
28. Asakura T, Minami M, Shimada R, Demura M, Osanai M, Fujito T, Imanari M, Ulrich AS. Macromolecules. 1997;30:2429–35.
29. Kameda T, Ohkawa Y, Yoshizawa K, Naito J, Ulrich AS, Asakura T. Macromolecules. 1999;32:7166–71.
30. Kameda T, Ohkawa Y, Yoshizawa K, Nakano E, Ulrich AS, Asakura T. Macromolecules. 1999;32:8491–5.
31. Post JF, EE de Ruiter, Berendsen HJC. FEBS Lett. 1981;132:257–60.
32. Post JFM, James E, Berendsen HJC. J. Magn. Reson. 1982;47:251–63.
33. Post JFM, Cook BW, Dowd SR, Lowe IJ, Ho C. Biochemistry. 1984;23:6138–41.
34. Grage SL, Gauger D, Selle C, Pohle W, Richter W, Ulrich AS. Phys. Chem. Chem. Phys. 2000;2:4574–9.
35. Toke O, O'Connor RD, Weldeghiorghis TK, Maloy WL, Glaser RW, Ulrich AS, Schaefer J. Biophys. J. 2004;87:675–87.
36. Toke O, Maloy WL, Kim SJ, Blazyk J, Schaefer J. Biophys. J. 2004;87:662–74.
37. Ulrich AS, Heyn MP, Watts A. Biochemistry. 1992;31:10390–9.
38. Ulrich AS, Watts A, Wallat I, Heyn MP. Biochemistry. 1994;33:5370–5.
39. Ulrich AS, Wallat I, Heyn MP, Watts A. Nat. Struct. Biol. 1995;2:190–2.
40. Asakura T, Suita K, Kameda T, Afonin S, Ulrich AS. Magn. Reson. Chem. 2004;42:258–66.
41. Afonin S, Glaser RW, Berditchevskaia M, Wadhwani P, Gührs KH, Möllmann U, Perner A, Ulrich AS. Chembiochem. 2003;4:1151–63.
42. Grage SL, Watts JA, Watts A. J. Magn. Reson. 2004;166:1–10.
43. Strandberg E, Wadhwani P, Tremouilhac P, Dürr UHN, Ulrich AS. Biophys. J. 2006;90:1676–1686.
44. Ulrich AS, Otter M, Glabe C, Hoekstra D. J. Biol. Chem. 1998;273:16748–55.
45. Ulrich AS, Tichelaar W, Förster G, Zschörnig O, Weinkauf S, Meyer HW. Biophys. J. 1999;77:829–41.
46. Binder H, Arnold K, Ulrich AS, Zschörnig O. Biophys. Chem. 2001;90:57–74.
47. Binder H, Arnold K, Ulrich AS, Zschörnig O. Biochim. Biophys. Acta. 2000;1468:345–58.
48. Glaser RW, Grüne M, Wandelt C, Ulrich AS. Biochemistry. 1999;38:2560-9.
49. Grage SL, Afonin S, Grüne M, Ulrich AS. Chem. Phys. Lipids 2004;132:65–77.
50. Barre P, Zschörnig O, Arnold K, Huster D. Biochemistry. 2003;42:8377–86.
51. Grotenbreg GM, Timmer MS, Llamas-Saiz AL, Verdoes M, van der Marel GA, van Raaij MJ, Overkleeft HS, Overhand M. J. Am. Chem. Soc. 2004;126:3444–6.
52. Wakamatsu K, Takeda A, Tachi T, Matsuzaki K. Biopolymers. 2002;64:314–27.
53. Tremouilhac P. Diploma Thesis, University of Karlsruhe, 2003.
54. Maloy WL, Kari UP. Biopolymers. 1995;37:105–22.
55. Hirsh DJ, Hammer J, Maloy WL, Blazyk J, Schaefer J. Biochemistry. 1996;35:12733–41.

Part I

Membrane-Associated Peptides

Solid-State NMR Studies of the Interactions and Structure of Antimicrobial Peptides in Model Membranes

Marise Ouellet and Michèle Auger
Département de Chimie, CERSIM, CREFSIP, Québec, Québec, Canada, G1K 7P4

Introduction

Bacterial Resistance to Antibiotics

The dramatic increase in bacterial resistance to numerous conventional antibiotics has led to the need to discover and develop novel antimicrobial compounds defeating the known mechanisms of bacterial resistance by the use of novel modes of action [1]. Several research groups have turned to the investigation of antimicrobial peptides that are found in several organisms and for which the structural and functional characteristics make them very promising therapeutic agents [2–4]. Despite the fact that the exact mechanisms of action by which these antimicrobial peptides kill bacteria are still not completely understood, it has been demonstrated experimentally that the interactions between the lipid membrane and antimicrobial peptides, leading to an increase in membrane permeability, play a major role in antimicrobial activity and that because of these interactions, the antimicrobial peptides adopt a 3D structure resulting in an amphiphilic character [5]. Amongst the large number of studies on the modulation of the activity of antimicrobial peptides by the modification of structural parameters, it appears that the amphiphilic character is essential for the affinity of these peptidic units for the lipid bilayer [6–8]. In light of these studies, several general mechanisms have been proposed in the literature to explain the membrane permeability caused by antimicrobial peptides, such as the "barrel-stave," "carpet-like," "toroidal," "in-plane diffusion," and "detergent-like" models [9,10]. The first two mechanisms are illustrated in Figure 1.

Nuclear magnetic resonance (NMR) spectroscopy, and particular solid-state NMR spectroscopy, is a well-suited technique to investigate the structure and dynamics of peptides in interaction with lipid membranes. Different approaches have been developed to study these systems in which the restricted molecular motions result in broad NMR spectra. This chapter will present an overview of the use of solid-state NMR spectroscopy to investigate the structure and dynamics of antimicrobial peptides in interaction with membranes. The first section will be devoted to the study of the effect of antimicrobial peptides on the lipid bilayer by a combination of ^{31}P and ^{2}H solid-state NMR spectroscopy while the second part will present an overview of several techniques to investigate the structure and dynamics of antimicrobial peptides in membranes. Both sections will be supported by recent examples.

Effects of Antimicrobial Peptides on Model Lipid Membranes

^{31}P NMR Spectroscopy

Phosphorus-31 has a spin-1/2 and a 100% natural abundance, and, with its good sensitivity, is extremely useful to investigate the structure and dynamics of the polar headgroup of phospholipids, which are the main constituent of biological membranes [11]. In particular, it is possible to obtain static ^{31}P NMR spectra which are dominated by the chemical shift anisotropy (CSA), to use the magic-angle spinning (MAS) technique which averages the CSA to its isotropic values, and finally to use samples macroscopically oriented in the magnetic field. The main information obtained from static ^{31}P NMR spectra is the nature of the lipid phase. For example, the interactions between lipids and antimicrobial peptides can lead to the formation of non-lamellar phases, such as isotropic, cubic, and hexagonal phases. This is the case for several antimicrobial peptides of amphibian origin such as caerin 1.1, maculatin 1.1, and caerin 4.1 for which the ^{31}P NMR spectra have revealed the formation of isotropic or cubic structures within the lipid system [12], as well as for bacterial antimicrobial peptides such as gramicidin S, A, and D which are known to induce a hexagonal phase in model membranes [13–15]. Another interesting application of ^{31}P NMR spectroscopy is the study of the dynamics and orientation of the lipid polar headgroup. In fact, several natural and synthetic antimicrobial peptides have demonstrated a strong interaction with the polar headgroup and this is reflected in the ^{31}P NMR spectra by a change of the CSA [16,17]. This change of CSA can be expressed in a quantitative way by calculating an order parameter S_2 which is governed by the lipid dynamics and/or orientation and which compares the CSA of two systems [18].

Graham A. Webb (ed.), Modern Magnetic Resonance, 271–278.
© 2008 *Springer.*

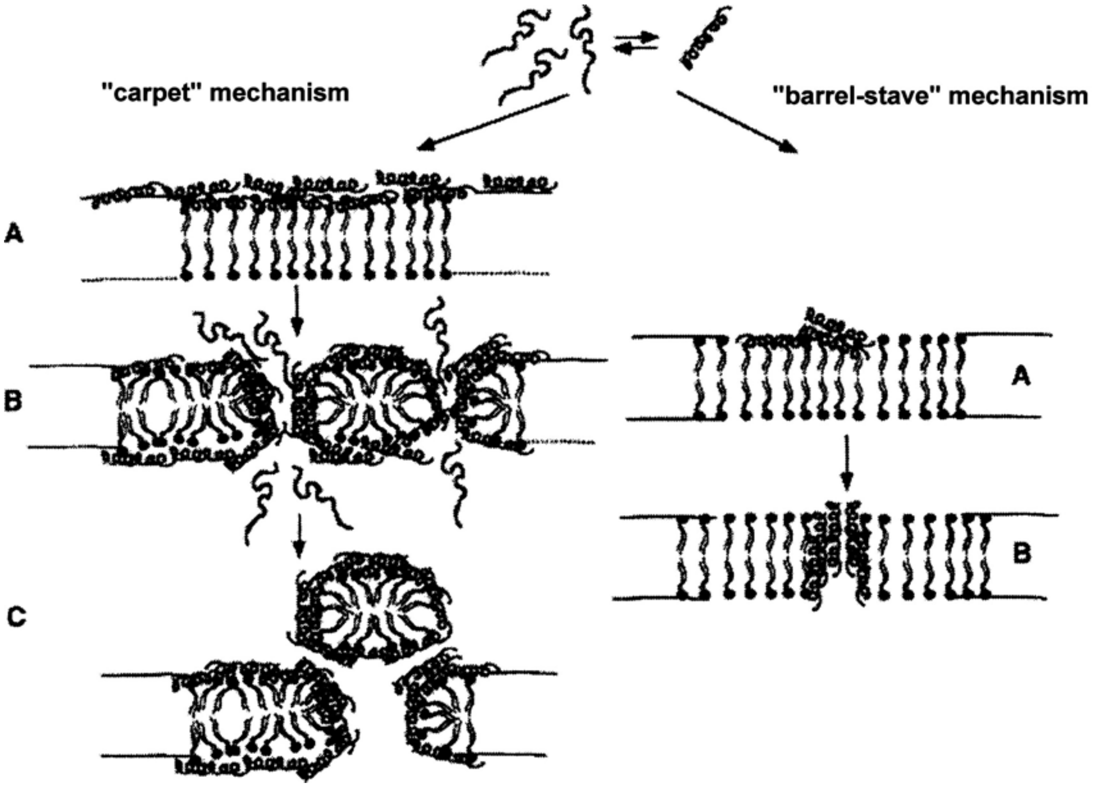

Fig. 1. Cartoon illustrating the barrel-stave (right) and the carpet-like (left) models suggested for membrane permeation. In the carpet-like model, the peptides are bound to the surface of the membrane with their hydrophobic surfaces facing the membrane and their hydrophilic surfaces facing the solvent (step A). When a threshold concentration of peptide monomers is reached, the membrane goes into pieces (steps B and C). At this stage, a transient pore is formed. Adapted from Ref. [67] and reproduced with permissions.

Using the MAS technique, ^{31}P NMR spectroscopy can allow the study of binary lipid mixtures since different lipids can be discriminated on the basis of their non-equivalent isotropic chemical shifts. For example, Bonev *et al.* have investigated the interactions between the antimicrobial peptide nisin with equimolar mixtures of dimyristoylphosphatidylcholine (DMPC) and dimyristoylphosphatidylglycerol (DMPG) and the ^{31}P MAS NMR spectra have demonstrated a preferential interaction of the peptide with the anionic lipid (DMPG) [19]. Another way to investigate the effect of antimicrobial peptides on the orientational order and conformation of lipid polar headgroups is to use samples macroscopically oriented with their normal parallel to the magnetic field B_0. The ^{31}P NMR spectra of antimicrobial peptides studied with this approach, such as LL-37 [20], protegrin [21], RTD-1 [22], and pardaxin [23], have demonstrated a shift of the lipid resonances toward lower frequencies, a line broadening and/or the presence of non-oriented lipid structures, depending on the peptide concentration and on the nature of the lipid investigated. This technique is also used to determine the alignment quality of oriented samples to be used for the determination of the membrane orientation of peptides, as discussed later in this chapter.

^{2}H NMR Spectroscopy

While ^{31}P NMR spectroscopy can be used to investigate the hydrophilic region of lipid bilayers, ^{2}H NMR spectroscopy is a very powerful technique to study the membrane hydrophobic core by replacing the acyl chain protons by deuterons. Deuterium is a spin-1 nucleus with a quadrupole moment that interacts with the electric field gradient at the nucleus, giving rise to the quadrupolar interaction. Two spin transitions are possible and a doublet of resonances is observed on a ^{2}H NMR spectrum, separated by the quadrupolar splitting $\Delta\nu_Q$. For a system with axially symmetric motions, the quadrupolar splitting is given by:

$$\Delta\nu_Q = (3/4)(e^2qQ/h)(3\cos^2\theta - 1)S_{CD} \quad (1)$$

where (e^2qQ/h) is the quadrupole coupling constant (~170 kHz for aliphatic C–D) [24], θ is the angle between the bilayer normal and the external magnetic field B_0, and S_{CD} is the order parameter of a deuterium bond vector. As described extensively, this order parameter is the product of several contributions, including intramolecular motions such as trans-gauche isomerizations, and anisotropic reorientation of the whole phospholipid molecules. Hence it is possible to determine variations in lipid chain order by monitoring changes in $\Delta\nu_Q$ values [25]. For example, the ^{2}H NMR spectra of phospholipids in the presence of amphibian antimicrobial peptides such as aurein 1.1, citropin 1.1, and maculatin 1.1 [16], as well as the peptides nisin produced by *Lactococcus lactis* [19] and LL-37 found in humans [26], indicate that these peptides induce disorder in the lipid acyl chains.

Another interesting aspect of ^{2}H NMR spectroscopy is the study of deuterated lipid polar headgroups. In particular, DMPC deuterated on the choline headgroup at positions α and β is known to act as a "molecular voltmeter," sensing the accumulation of charges at the surface of the bilayer [27,28]. An example of this phenomenon is observed with the antibacterial peptide PGLa in interaction with DMPC-d$_4$ membranes, for which a decrease (increase) of the quadrupolar splitting for the α (β) deuterons reflects a change of conformation of the choline headgroup known as a tilt of the $^-$P–N$^+$ dipole induced by the presence of positive charges [29]. From the analysis of these ^{2}H NMR spectra, Wieprecht *et al.* have concluded that the peptide PGLa is located at the surface of the bilayer and is intercalated between the polar headgroups, resulting in a change of conformation of these headgroups [29].

Study of Antimicrobial Peptides in Membranes

Solid-state NMR is also a very useful technique to characterize the structure and dynamics of peptides that are immobilized on the relevant NMR time scale. Anisotropic interactions that dominate the solid-state NMR spectra result in orientation-dependent shifts and splittings of the peptide resonances. The main NMR parameters of interest are therefore the ^{15}N and ^{13}C chemical shifts and CSA, and the dipolar couplings between ^{1}H, ^{13}C, and ^{15}N. The goal of this section is to demonstrate how these parameters are exploited to obtain information on the structure and dynamics of antimicrobial peptides in interaction with lipids.

Dynamics of Antimicrobial Peptides

The study of the dynamics of antimicrobial peptides incorporated into lipid membranes is in general performed by the analysis of the spinning sideband intensity in MAS ^{13}C or ^{15}N spectra or of the CSA in static spectra. Buffy *et al.* have investigated by MAS the dynamics of the 18-residue antimicrobial peptide protegrin (PG-1) [30] and have demonstrated that the dynamics differs depending on the lipid composition. For example, the intensity of the spinning sidebands in ^{13}C NMR MAS spectra of the ^{13}C labeled peptide is less important in dilauroylphosphatidylcholine (DLPC) bilayers compared to palmitoyloleoyl-phosphatidylcholine (POPC) bilayers, indicating a more rigid peptide in thicker lipid bilayers. A similar result was obtained from the analysis of the $^{13}C_\alpha$–H_α dipolar coupling for the Leu5 residue, which is 11.9 kHz in POPC and 2.0 kHz in DLPC. Yamaguchi *et al.* have also investigated the PG-1 dynamics in DLPC bilayers by static ^{15}N NMR spectroscopy [21]. A decrease of the ^{15}N CSA observed for PG-1 in lipid bilayers indicates increased motion compared to the static peptide. Similar studies have also been performed with the cyclic antimicrobial peptide RTD-1 by Buffy *et al.* and the analysis of the spinning sidebands in ^{15}N and ^{13}C MAS spectra for the solid peptide and the peptide incorporated into DLPC bilayers demonstrated that the peptide is immobilized in bilayers [22].

Membrane Orientation and Topology of Antimicrobial Peptides

The determination of the membrane orientation of antimicrobial peptides is in general performed using samples oriented with their normal parallel to the external magnetic field B_0. The technique most frequently used to obtain these samples is the mechanical alignment of the lipids between glass plates [31] but the use of lanthanide-doped bicelles [32] is also possible. These experiments are performed with peptides either selectively or uniformly labeled with ^{15}N and/or ^{13}C.

Membrane Orientation from 1D Spectra

For helicoidal antimicrobial peptides selectively ^{15}N labeled at one position in the amino acid sequence, the membrane orientation can be determined from the chemical shift obtained in samples oriented in the magnetic field B_0. More specifically, for a α-helical peptide, the σ_{33} element of the ^{15}N CSA tensor is aligned along the NH bond, and the NH bond vector is almost parallel to the helix axis. It is therefore possible to estimate the peptide orientation by the analysis of the ^{15}N chemical shift [33], as illustrated in Figure 2. The situation is, however, more complex for peptides in β-sheet conformation since the

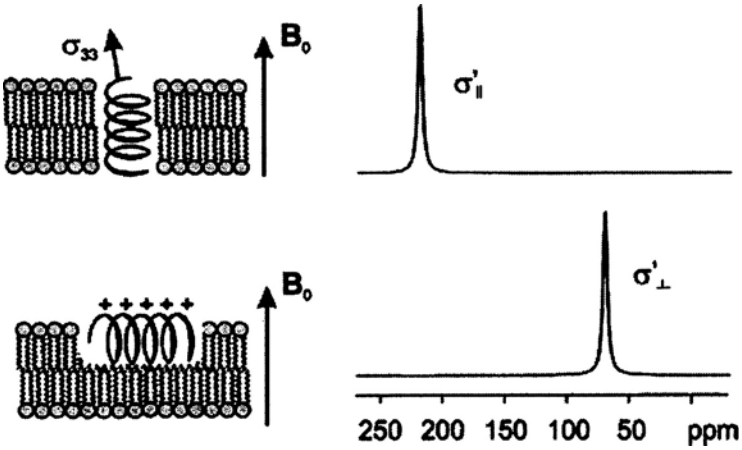

Fig. 2. Top: Simulated proton-decoupled ^{15}N solid-state NMR spectrum of a transmembrane peptide as well as a sketch of the situation. Bottom: Same as top for a peptide oriented parallel to the membrane surface. Adapted from Ref. [33] and reproduced with permissions.

membrane orientation has to be determined from both the ^{13}C and ^{15}N chemical shifts of the carbonyl and amide groups, respectively. However, since the majority of antimicrobial peptides present a helicoidal structure, these will be discussed in the present review. For more information about β-sheet peptides, the reader is referred to the references of Buffy *et al.* [22] and Yamaguchi *et al.* [21].

In addition to their study of β-sheet peptides such as protegrins PG-1, Yamaguchi *et al.* have investigated the 18-residue antimicrobial peptide ovispirin, which presents a large spectrum of activity [34]. By selectively ^{15}N labeling the peptide at residues Leu3, Ile6, Ile11, and Gly18, they have demonstrated that ovispirin adopts a surface orientation in bilayers of POPC and palmitoyl-oleoyl-phosphatidylglycerol (POPG) (3:1), except for a small portion of the C-terminal region of the helix which appears to deviate from the surface of the bilayer. In addition, the analysis of the ^{15}N CSA of the peptide incorporated into a non-oriented POPC/POPG system indicates that ovispirin undergoes uniaxial rotational diffusion around the bilayer normal. This is reflected in the ^{15}N spectra by a decrease of the CSA compared to that of a powder spectrum, namely a decrease from 150 to 75 ppm. Using a similar approach, Marassi *et al.* have determined the membrane orientation of the peptide cecropin A incorporated into DMPC/DMPG (4:1) membranes [35]. The oriented and non-oriented ^{15}N NMR spectra of cecropin A selectively labeled at residues Val11 and Ala27 indicate that the peptide is oriented perpendicular to the membrane normal and is immobile relative to the NMR time scale.

The last example presented here is the study of the membrane orientation of the 21-residue antimicrobial peptide PGLa by Bechinger *et al.* [36]. Several peptides selectively ^{15}N labeled at residues Ala3, Ala10, Ala14, Val16, and Ala20 have been synthesized and incorporated into bilayers of palmitoyl-oleoyl-phosphatidylethanolamine (POPE) and POPG (3:1) bilayers. This multiple labeling scheme has allowed the determination, via the chemical shift values, of both the orientation and dynamics of these residues along the peptide backbone. The ^{15}N NMR spectra of the peptide incorporated into bilayers oriented between glass plates have demonstrated, as for the peptides described above, a surface orientation for residues Ala10 to Ala20, while residue Ala3 has an isotropic chemical shift characteristic of a higher degree of liberty in the N-terminal region. The conclusion regarding the dynamics of several residues is also confirmed by the ^{15}N NMR spectra of non-oriented samples in which an increase of the CSA is observed from the N-terminal to the C-terminal regions.

Although it is possible, as shown by the examples presented above, to estimate the membrane orientation of antimicrobial peptides from 1D ^{15}N NMR spectra, this approach does not allow the determination of the peptide tilt angle with great precision with peptides singly labeled at one amino acid residue. This type of analysis can however be carried out using peptides ^{15}N labeled at multiple sites on a single peptide, as discussed in the next section.

The PISEMA Approach

The polarization inversion spin-exchange at the magic-angle (PISEMA) experiment combines the measurement of both the ^{15}N CSA and the dipolar coupling between the ^{15}N and ^{1}H nuclei of the amide group. In the 2D PISEMA spectrum of a helicoidal peptide uniformly ^{15}N labeled, the resonances form a regular pattern called PISA wheel from which it is possible to extract both the tilt (as illustrated in Figure 3) and rotation angle of the peptide [37–39]. This approach also requires the use of oriented samples in the magnetic field.

One of the antimicrobial peptides most studied using the PISEMA approach is magainin, a 23-residue

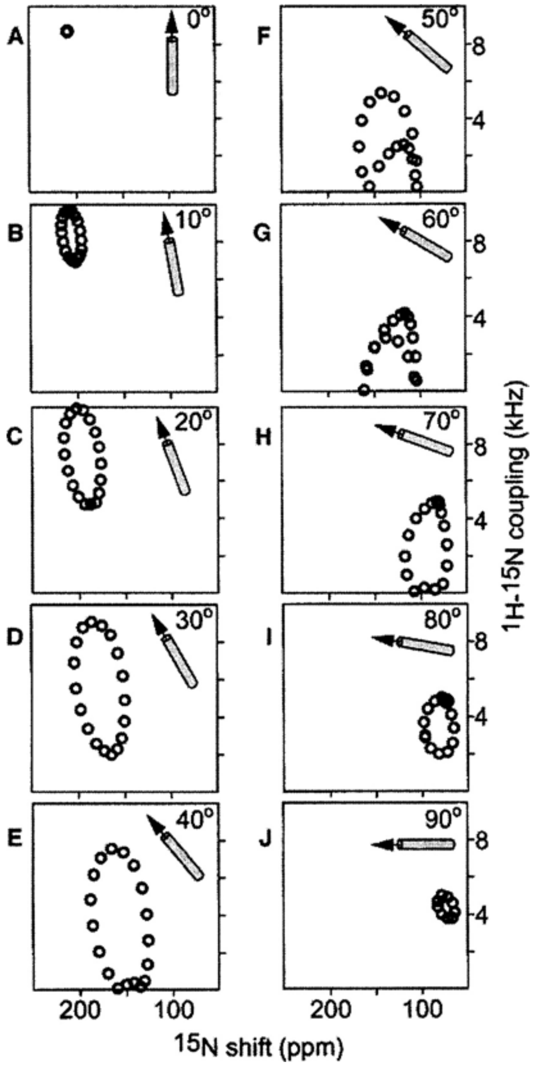

Fig. 3. PISEMA spectra calculated for a 19-residue α-helix with 3.6 residues per turn and uniform dihedral angles ($\phi = -65$, $\psi = -40$) at various helix tilt angles relative to the bilayer normal. A. 0°, B. 10°, C. 20°, D. 30°, E. 40°, F. 50°, G. 60°, H. 70°, I. 80°, J. 90°. The principal values and molecular orientation of the ^{15}N chemical shift tensor ($\sigma_{11} = 64$ ppm; $\sigma_{22} = 77$ ppm; $\sigma_{33} = 217$ ppm; $\sigma_{33}\ \angle\mathrm{NH} = 17°$) and the NH bond distance (1.07Å) were as previously determined. Adapted from Ref. [68] and reproduced with permissions.

peptide of amphibian origin. Previous experiments had demonstrated that magainin adopts a surface orientation in lipid bilayers [40]. However, the rotation angle could not be determined from 1D ^{15}N NMR spectra. Using the PISEMA approach, Marassi *et al.* have confirmed that magainin is oriented perpendicular to the membrane normal and have determined the polarity of the α-helix, namely a helix oriented in such way that residues Phe5, Phe12, and Phe16 are at the apolar/polar interface, with charged residues such as lysines exposed to the hydrophilic side of the bilayer [41]. In addition, the observation in the PISEMA spectrum of well-resolved single resonances from individual backbone amide sites indicates that magainin binds tightly to the membrane surface with a unique orientation. Another very interesting example demonstrating the potential of the PISEMA approach in the structural study of peptides is related to a peptide from a fragment of the C-terminal region of colicin B, a channel bacterial toxin [42]. More specifically, Lambotte *et al.* have determined, using the PISEMA approach, the mode of insertion of colicin B in POPC/POPG (4:1) bilayers [42]. The detailed analysis of the PISEMA spectra indicates regions characteristic of both transmembrane and in-plane helices. They have therefore concluded that colicin B preferentially adopts an "umbrella" type conformation in lipid bilayers. Another peptide from the same family as colicin B, namely colicin E1, has also been studied by the PISEMA approach [43].

^{1}H Spin Diffusion

The ^{1}H spin diffusion 2D NMR technique under MAS has been used to investigate the approximate location of peptides or proteins in lipid bilayers [44]. ^{1}H magnetization is transferred from mobile lipids to the rigid peptide via distance-dependent ^{1}H–^{1}H dipolar couplings. The 2D peak intensities as a function of the spin-diffusion mixing time yield a magnetization transfer curve that reflects the proximity of the lipid protons to the peptide protons since the rate of spin diffusion is greater in rigid media such as peptides compared to that in mobile media such as the lipids. The membrane topology of the bacterial peptide colicin Ia in interaction with POPC/POPG (3:1) bilayers has been estimated from ^{1}H spin diffusion by Huster *et al.* [45]. Previous studies on this system had revealed that colicin Ia is incorporated in the bilayer, without any information, however, on its degree of insertion. By selectively labeling the peptide with ^{13}C on the α-carbon of the Ala13 residue, these authors have observed a fast magnetization transfer between C_αAla13 and the lipid terminal CH_3 groups, estimating from simulation a distance of 2–4 Å between these two moieties. Magnetization transfers have also been observed between C_αAla13 and other regions of the lipid, namely the acyl chain CH_2 groups and the lipid polar headgroup. This model of interaction is in agreement with the "umbrella" model, which can explain the contact of the peptide with both the lipid polar headgroup and acyl chains.

The membrane topology of another antimicrobial peptide, protegrin PG-1, has also been investigated by ^{1}H spin diffusion by Buffy *et al.* [46]. When incorporated into POPC bilayers, they have determined that PG-1, like colicin Ia, is in contact with both the lipid polar headgroup and the acyl chains. However, the proposed mode of interaction is different, being more similar to the toroidal model where the PG-1 aggregates only need to span one monolayer to create the pore. The degree of penetration of PG-1 has also been determined by the same research group in DLPC bilayers using the paramagnetic ion Mn^{2+} [46]. By comparing the T_2 relaxation enhancement of PG-1 carbons to that of the lipid carbons, the relative depth of PG-1 with respect to the lipid moieties can be determined. The results obtained by this technique demonstrate that PG-1 is completely inserted in the bilayer and tilted from the bilayer normal, with Val16 as the most deeply embedded residue and Gly2 as the closest to the membrane surface phosphate group. The proposed mode of interaction is the "snorkel" model, where the peptide hydrophobic residues are incorporated into the bilayer while the polar residues remain in contact with the aqueous phase.

Secondary Structure of Antimicrobial Peptides

It is well recognized that the majority of antimicrobial peptides adopt a random conformation in solution and defined secondary structures, such as α-helices and β-sheets, only upon interaction with the membrane. It is therefore very interesting to study the secondary structure of antimicrobial peptides incorporated into membranes. The next section will thus cover some experiments that provide information on the conformation of antimicrobial peptides.

^{13}C Isotropic Chemical Shifts

One of the simplest approach to determine the secondary structure of a specifically ^{13}C labeled residue in an antimicrobial peptide consists in measuring its isotropic chemical shift in MAS spectra. In particular, the values of the carbonyl and C_α chemical shifts for several amino acids are dependent on the peptide secondary structure [47]. For example, Naito *et al.* have investigated the structure of melittin, a peptide that possesses both hemolytic and antimicrobial activities, in interaction with DMPC membranes [48]. Isotropic chemical shifts of 173.2 and 15.8 ppm have been obtained for melittin labeled at residues [1-^{13}C]Gly3 and [3-^{13}C]Ala15, confirming the α-helicoidal structure for this peptide. The helicoidal structure of the human peptide LL-37 has also been determined from the isotropic chemical shifts of 175.8 and 53.5 ppm for the [^{13}C=O]Leu31 and [$^{13}C_\alpha$]Ala13 residues [20].

Internuclear Distances

The two techniques that are most often used for the measurement of hetero- and homonuclear distances in solid-state MAS NMR spectra of antimicrobial peptides are the rotational echo double resonance (REDOR) and rotational resonance (RR) techniques [49–51]. The REDOR technique is based on the dephasing of the magnetization of the observed nucleus (typically ^{13}C) due to the coupling with a second nuclear spin (typically ^{15}N). The difference in the intensity of the spectra obtained with and without the ^{15}N pulses depends solely on the ^{13}C-^{15}N dipolar coupling, and this coupling is related to the heteronuclear distance between the nuclei. From the dephased $^{13}C\{^{15}N\}$ NMR spectra, a dephasing curve is obtained as a function of mixing time, from which the distance can be extracted. In addition, as shown in the examples discussed below, the REDOR technique can also be used to remove the natural abundance contribution of the lipid carbons in ^{13}C NMR spectra.

The first example discussed here is related to the 33-residue antimicrobial peptide pardaxin investigated by Porcelli *et al.* [52]. The structure of this peptide, a bend-helix-bend-helix conformation, has first been determined in sodium dodecylphosphocholine (DPC) micelles by ^{1}H solution NMR. The REDOR technique was then used to confirm the helicoidal structure in the C-terminal region of this peptide selectively ^{13}C and ^{15}N labeled at residues Leu18 and Leu19 incorporated into DMPC, POPC, and POPE/POPG (3:1) multilamellar vesicles [52]. More specifically, the $^{13}C\{^{15}N\}$ REDOR dephased spectra of pardaxin consist of a single peak with a frequency value of approximately 176 ppm, consistent with the helical conformation of this C-terminal segment. Another example of structural studies of antimicrobial peptides by REDOR is related to the synthetic peptide K3, a 21-residue analog of the natural peptide magainin, in interaction with dipalmitoylphosphatidylcholine/dipalmitoylphosphatidylglycerol (DPPC/DPPG) (1:1) bilayers [53]. By analyzing the isotropic chemical shifts in the REDOR spectra of residues [1-^{13}C]Ala17 and [3-^{13}C]Ala3 dephased by residues [^{15}N]Gly18 and [^{15}N]Gly4, they have concluded that the isotropic chemical shifts of 177 and 16 ppm are only consistent with a single α-helical structure for the K3 peptide.

The RR method is based on the fast magnetization exchange between two spins when the sample spinning speed (ν_r) is equal to the frequency separation ($\Delta\nu$) of the two resonances for the two spins, i.e. when $\Delta\nu = n\nu_r$, where $n = 1, 2, 3$, etc. The reintroduction of the dipolar coupling gives rise to magnetization exchange between the two spins, and a magnetization exchange curve as a function of mixing time is obtained and fitted to a specific homonuclear distance between these two spins.

The R^2 technique has been used in the last few years for the structural study of antimicrobial peptides incorporated into membranes. In particular, Lam *et al.* have illustrated the potential of the technique for structural study of the antimicrobial peptide melittin in interaction with

DMPC membranes [54]. Several peptides labeled at different positions along the amino acid sequence have been synthesized and for example, a distance of (2.5 ± 0.2) Å has been obtained between residues [^{13}C=O]Gly3 and [$^{13}C_{\alpha}$]Ala4. As expected, this homonuclear distance is consistent with a α-helical structure.

Another interesting example is the structural study of gramicidin S, a bacterial antimicrobial peptide [55]. In this case, homonuclear distances between two ^{19}F nuclei have been measured from static spectra using a modified Carr-Purcell-Meiboom-Gill (CPMG) sequence. The conformation of gramicidin S had previously been determined as a cyclic antiparallel β-sheet peptide by ^{1}H solution NMR and X-ray crystallography and by studying gramicidin S in which the Leu3 and Leu8 residues have been replaced by the non-natural amino acid 4F-phenylglycine (4F-Phg). ^{19}F has been shown to be a useful probe for the structural study of antimicrobial peptides [55].

Torsion Angles

To complement the measurement of internuclear distances in the structural study of antimicrobial peptides, a variety of experiments have recently been developed to determine the torsion angles (ϕ and ψ) between peptide planes in peptides and proteins. Even though these techniques have been mostly applied so far to peptides with only a few amino acid residues and that the application of these techniques to antimicrobial peptides is still at an early stage, the results obtained are really promising. The basic principle in the measurement of torsion angles lies in the correlation between the orientation of two anisotropic tensors, such as two dipolar tensors, two CSA tensors, or one CSA and one dipolar tensors. Since most experiments require the use of MAS, the interactions averaged out by MAS are reintroduced via specific pulse sequences, as is the case for the internuclear distance measurement techniques described above.

Several research groups have used the mono and tripeptides N-acetyl-ᴅ, ʟ-valine (NAV) and N-formyl-[U-^{13}C, ^{15}N]Met-Leu-Phe (MLF) as model peptides for the development of torsion angle measurement experiments since the crystalline structure of these peptides has been determined by X-ray crystallography. For example, Ladizhansky *et al.* have determined the torsion angle ψ for the tripeptide MLF with a HCCN dipolar correlation MAS experiment that measures ψ in the angular range of -20° to -70°, characteristic of α-helix [56]. Hong *et al.* have used the monopeptide NAV to determine the torsion angle ϕ via the correlation of the ^{15}N chemical shift and C_{α}–H_{α} dipolar coupling tensor orientations under MAS [57]. They have shown that the technique exhibits the highest sensitivity to ϕ angles typical of β-sheet conformations ($\phi \approx -140^{\circ}$). This angle has also been determined by the measurement of the relative orientation of the N–H_N and C_{α}–H_{α} bonds, which is manifested in the rotational sideband spectrum of the sum and difference of the two corresponding dipolar couplings, and they obtained a ϕ angle of -135° [58]. Both techniques used on the monopeptide NAV are in good agreement with the angle of -136.5° determined by X-ray diffraction. It has also been shown that the pair of torsion angles (ϕ,ψ) can be determined simultaneously by 2D spin diffusion solid-state NMR experiments under off MAS [59–61] or using the DOQSY approach [62,63].

Recently, Gabrys *et al.* have used melittin to demonstrate the validity of a new technique to measure torsion angles in larger peptides [64]. The principle of their method lies on 2D slow-spinning, rotor-synchronized MAS exchange spectroscopy (SSRS-MASE), in which the relative CSA tensor orientation is extracted from the intensity of the off-diagonal crosspeaks on the 2D spectrum, since these intensities are related to the magnetization transfer between the two coupled sites. The (ϕ,ψ) torsion angles can be extracted after simulation of the experimental spectrum. Their results confirm once again that melittin adopts a helicoidal structure when incorporated into lipid bilayers.

Conclusions

Solid-state NMR is a powerful technique to investigate the mutual interactions between peptides and membranes, as well as the conformation adopted by these peptides upon binding to the bilayer. Up to now, little is known about the detailed mechanisms of action of antimicrobial peptides but new methods are continually being developed to better understand these mechanisms and to develop novel peptides having the desired selectivity toward bacterial cells [65]. The goal of this chapter was to present an overview of different solid-state NMR methods that have been developed to investigate the interactions and structure of antimicrobial peptides in membranes. These methods have been illustrated with a few examples on most commonly studied antimicrobial peptides. For more exhaustive reviews, the readers are referred to recent papers by Bechinger [9] and Strandberg *et al.* [66].

References

1. Schmidt FR. Appl. Microbiol. Biotechnol. 2004;63:335.
2. Hancock REW, Lehrer R. Trends Biotechnol. 1998;16:82.
3. Hancock REW, Chapple DS. Antimicrob. Agents Chemother. 1999;43:1317.
4. Hancock REW. Drugs. 1999;57:469.
5. Sitaram N, Nagaraj R. Biochim. Biophys. Acta. 1999;1462:29.
6. Dathe M, Wieprecht T. Biochim. Biophys. Acta. 1999;1462:71.

7. Dathe M, Meyer J, Beyermann M, Maul B, Hoischen C, Bienert M. Biochim. Biophys. Acta. 2002;1558:171.
8. Epand RM, Shai Y, Segrest JP, Anantharamaiah GM. Biopolymers. 1995;37:319.
9. Bechinger B. Biochim. Biophys. Acta. 1999;1462:157.
10. Yeaman MR, Yount NY. Pharmacol. Rev. 2003;55:27.
11. Seelig J. Biochim. Biophys. Acta. 1978;515:105.
12. Chia CSB, Torres J, Cooper MA, Arkin IT, Bowie JH. FEBS Lett. 2002;512:47.
13. Bouchard M, Le Guernevé C, Auger M. Biochim. Biophys. Acta. 1998;1415:181.
14. Prenner EJ, Lewis RNAH, Neuman KC, Gruner SM, Kondejewski LH, Hodges RS, McElhaney RN. Biochemistry. 1997;36:7906.
15. Driessen AJM, van den Hooven HW, Kuiper W, van de Kamp M, Sahl H-G, Konings RNH, Konings WN. Biochemistry. 1995;34:1606.
16. Balla MS, Bowie JH, Separovic F. Eur. Biophys. J. 2004;33:109.
17. Ouellet M, Bernard G, Voyer N, Auger M. Biophys. J., submitted for publication.
18. Picard F, Pézolet M, Bougis PE, Auger M. Can. J. Anal. Sci. Spectrosc. 2000;45:72.
19. Bonev BB, Chan WC, Bycroft BW, Roberts GCK, Watts A. Biochemistry. 2000;39:11425.
20. Henzler Wildman KA, Lee D-K, Ramamoorthy A. Biochemistry. 2003;42:6545.
21. Yamaguchi S, Hong T, Waring A, Lehrer RI, Hong M. Biochemistry. 2002;41:9852.
22. Buffy JJ, McCormick MJ, Wi S, Waring A, Lehrer RI, Hong M. Biochemistry. 2004;43:9800.
23. Hallock KJ, Lee D-K, Omnaas J, Mosberg HI, Ramamoorthy A. Biophys. J. 2002;83:1004.
24. Davis JH. Biochim. Biophys. Acta. 1983;737:117.
25. Seelig J, Seelig A. Q. Rev. Biophys. 1980;13:19.
26. Henzler-Wildman KA, Martinez GV, Brown MF, Ramamoorthy A. Biochemistry. 2004;43:8459.
27. Macdonald PM. Acc. Chem. Res. 1997;30:196.
28. Marassi FM, Macdonald PM. Biochemistry. 1992;31:10031.
29. Wieprecht T, Apostolov O, Beyermann M, Seelig J. Biochemistry. 2000;39:442.
30. Buffy JJ, Waring AJ, Lehrer RI, Hong M. Biochemistry. 2003;42:13725.
31. Hallock KJ, Henzler Wildman K, Lee D-K, Ramamoorthy A. Biophys. J. 2002;82:2499.
32. Prosser RS, Hunt SA, DiNatale JA, Vold RR. J. Am. Chem. Soc. 1996;118:269.
33. Bechinger B, Sizun C. Concepts Magn. Reson. 2003;18A:130.
34. Yamaguchi S, Huster D, Waring A, Lehrer RI, Kearney W, Tack BF, Hong M. Biophys. J. 2001;81:2203.
35. Marassi FM, Opella SJ, Juvvadi P, Merrifield RB. Biophys. J. 1999;77:3152.
36. Bechinger B, Zasloff M, Opella SJ. Biophys. J. 1998;74:981.
37. Opella SJ, Marassi FM. Chem. Rev. 2004;104:3587.
38. Marassi FM. Concepts Magn. Reson. 2002;14:212.
39. Marassi FM. Biophys. J. 2001;80:994.
40. Bechinger B, Zasloff M, Opella SJ. Protein Sci. 1993;2:2077.
41. Marassi FM, Ma C, Gesell JJ, Opella SJ. J. Magn. Reson. 2000;144:156.
42. Lambotte S, Jasperse P, Bechinger B. Biochemistry. 1998;37:16.
43. Kim Y, Valentine K, Opella SJ, Schendel SL, Cramer WA. Protein Sci. 1998;7:342.
44. Kumashiro KK, Schmidt-Rohr K, Murphy OJ III, Ouellette KL, Cramer WA, Thompson LK. J. Am. Chem. Soc. 1998;120:5043.
45. Huster D, Yao X, Hong M. J. Am. Chem. Soc. 2002;124:874.
46. Buffy JJ, Hong T, Yamaguchi S, Waring AJ, Lehrer RI, Hong M. Biophys. J. 2003;85:2363.
47. Saito H. Magn. Reson. Chem. 1986;24:835.
48. Naito A, Nagao T, Norisada K, Mizuno T, Tuzi S, Saitô H. Biophys. J. 2000;78:2405.
49. Auger M. J. Chim. Phys. 1995;92:1751.
50. Gullion T. Concepts Magn. Reson. 1998;10:277.
51. Raleigh DP, Levitt MH, Griffin RG. Chem. Phys. Lett. 1988;146:71.
52. Porcelli F, Buck B, Lee D-K, Hallock KJ, Ramamoorthy A, Veglia G. J. Biol. Chem. 2004;279:45815.
53. Toke O, Maloy WL, Kim SJ, Blazyk J, Schaefer J. Biophys. J. 2004;87:662.
54. Lam Y-H, Wassall SR, Morton CJ, Smith R, Separovic F. Biophys. J. 2001;81:2752.
55. Salgado J, Grage SL, Kondejewski LH, Hodges RS, McElhaney RN, Ulrich AS. J. Biomol. NMR. 2001;21:191.
56. Ladizhansky V, Veshtort M, Griffin RG. J. Magn. Reson. 2002;154:317.
57. Hong M, Gross JD, Hu W, Griffin RG. J. Magn. Reson. 1998;135:169.
58. Hong M, Gross JD, Griffin RG. J. Phys. Chem. B. 1997;101:5869.
59. Nakazawa Y, Bamba M, Nishio S, Asakura T. Protein Sci. 2003;12:666.
60. Ashida J, Ohgo K, Asakura T. J. Phys. Chem. B. 2002;106:9434.
61. Ashida J, Ohgo K, Komatsu K, Kubota A, Asakura T. J. Biomol. NMR. 2003;25:91.
62. van Beek JD, Beaulieu L, Schäfer H, Demura M, Asakura T, Meier BH. Nature. 2000;405:1077.
63. Schmidt-Rohr K. Macromolecules. 1996;29:3975.
64. Gabrys CM, Yang J, Weliky DP. J. Biomol. NMR. 2003;26:49.
65. Saberwal G, Nagaraj R. Biochim. Biophys. Acta. 1994;1197:109.
66. Strandberg E, Ulrich AS. Concepts Magn. Reson. 2004;23A:89.
67. Oren Z, Shai Y. Biopolymers. 1998;47:451.
68. Marassi FM, Opella SJ. J. Magn. Reson. 2000;144:150.

Anisotropic Chemical Shift Perturbation Induced by Ions in Conducting Channels

Jun Hu, Eduard Chekmenev, and Timothy A. Cross
[1]*Department of Chemistry and Biochemistry, Institute of Molecular Biophysics and National High Magnetic Field Laboratory,*
Florida State University, Tallahassee, FL 32310, USA

Anisotropic chemical shifts observed from solid-state NMR spectroscopy of uniformly aligned samples can be influenced by three primary factors: a change in orientation of the nuclear site, a change in dynamics, or a change in the chemical shift tensor element magnitudes or orientation to the molecular frame. These features are particularly attractive for characterizing the influence of ions in ion conducting channels. Cation binding results in far more subtle effects than had previously been imagined. Prior to the analysis of the first solid-state NMR characterizations of ion binding [1,2] the experimental data were primarily in the form of a few water-soluble protein structures in the Protein Data Bank to which monovalent ions were bound [e.g. 3,4]. Such binding sites showed optimized solvation for the ions associated with strong binding. Computational modeling efforts on ion channels, for the most part, also showed substantial structural deformation upon ion binding [5–7]. We now realize that much better models for how ions interact with channels can be realized from the characterization of substrate binding to enzymes, for which we have a great deal of information represented in every biochemistry textbook. A delicate balance of molecular interactions and thermodynamic parameters has evolved for enzymes, so that substrates are attracted to the active sites of proteins while not compromising the primary function of these proteins to conduct chemistry on the substrates and to release the products efficiently. Similarly, ions must be attracted to the channel and yet the primary function of these proteins is to facilitate the transfer of ions from one side of the membrane to the other.

Here, we describe how this can be done through a model system, the monovalent cation channel gramicidin A, produced by *Bacillus brevis*, to lyse cells in its environment and from the lysate the bacillus harvests amino acids following the additional export of proteases. This unique polypeptide has an alternating sequence of D and L amino acid residues that forms a β-strand with all of its side chains on one side of the strand resulting in a helical conformation with an aqueous pore approximately 4.5 Å in diameter. The high-resolution structure has been fully characterized using solid-state NMR orientational restraints from uniformly aligned samples in lipid bilayers (PDB # 1 mag) [8,9]. Analysis of the refined structure illustrates the unique high-resolution detail of this time averaged structure [10]. This polypeptide spans the lipid bilayer as a symmetric dimer [11], the amino-termini of which are formylated at the bilayer center. The approximate location of two symmetric ion binding sites in the vicinity of the monolayer interfacial region was initially characterized by X-ray diffraction [12]. Gramicidin shares a number of important features with the more recently characterized K^+ channels [13,14]. In particular, it is the polypeptide backbone and the carbonyl oxygens that provide much of the solvation environment following ion dehydration in the ion binding site of gramicidin A and in the selectivity filter of the KcsA channel. However, in KcsA the ion binding sites are considerably closer together (approximately 7 Å for KcsA [15] and approximately 20 Å for gramicidin A) permitting stronger ion binding and a much higher degree of ion selectivity. Nevertheless, the principles gleaned from studies of gramicidin appear to have very general applicability.

Solid-state NMR of uniformly aligned samples leads to high-resolution spectra. The frequencies from chemical shift, dipolar and quadrupolar interactions can be used as structural restraints by interpreting the frequencies within the context of the appropriate motionally averaged spin interaction tensor [16–18]. Here, we primarily describe the use of ^{15}N NMR spectroscopy of the amide nitrogen sites in the polypeptide backbone of gramicidin A in hydrated liquid crystalline preparations. These tensor element magnitudes in both static and liquid crystalline environments have been characterized for each of the amide sites [8,19] and many of the tensor orientations to the molecular frame have also been characterized [19,20]. These ^{15}N anisotropic chemical shifts represented some of the data used for solving the 3D structure in the absence of ions. The anisotropic shifts in the cation binding region change upon the introduction of ions [21,22] (Figure 1). The influence of the ions is surprisingly small compared to the 40–50 ppm anisotropic shifts calculated [23] from the structural changes predicted in the first molecular dynamics study of gramicidin ion binding [5]. Consequently, it

Graham A. Webb (ed.), Modern Magnetic Resonance, 279–283.
© 2008 *Springer.*

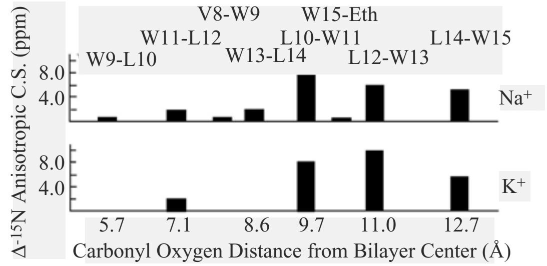

Fig. 1. Change in anisotropic chemical shift upon binding ions to the gramicidin channel (>80% double occupancy based on known binding constants [34, 35]) as a function of carbonyl oxygen distance from the bilayer center.

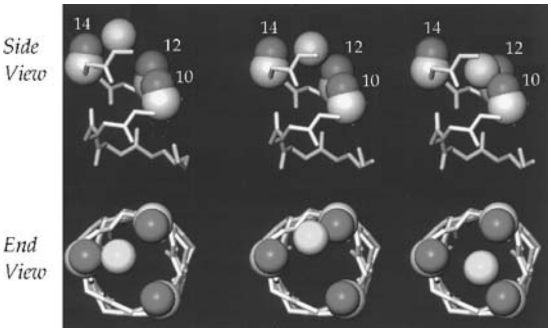

Fig. 2. Van der Waals surfaces are shown for the carbonyl groups of Leucine 10, 12, and 14, as well as for a K$^+$ ion interacting with these carbonyls. Ions are not able to interact with all three carbonyl oxygens at one time. (See also Plate 33 on page XXX in the Color Plate Section.)

appears as if the structural changes are likely to be small. In addition, the ion's influence is focused on three amide nitrogens that are in peptide planes having their carbonyl oxygens exposed at the end of the channel. If the cation interaction with the carbonyl oxygens was similar throughout the channel then the magnitude of the anisotropic chemical shift change would reflect the time the ions are positioned in the vicinity of each carbonyl oxygen and hence these sites with a significant change in anisotropic chemical shift reflect the cation binding sites.

This assumption is defendable, because we observe small anisotropic chemical shifts for sites throughout the gramicidin structure with a wide variety of ions. However, these chemical shift perturbations are all less than or equal to 2 ppm whether they are in the vicinity of the three exposed carbonyls or nearer the bilayer center. In other words, there is no rational to think that the cation binding site extends further toward the bilayer center than the Leu$_{10}$ carbonyl (9.7 Å). Even the Trp$_{15}$ carbonyl is unaffected despite its distance of 10.3 Å from the bilayer center. Indeed, for an optimal interaction between a cation and a carbonyl oxygen the ion should be on the axis or near to the axis of the dipolar vector. For the Leu$_{10}$ carbonyls (and similarly for Leu$_{12}$ and Leu$_{14}$ carbonyls) with its dipole oriented towards the aqueous environment the ion would be positioned at least an angström further away from the bilayer center (10.7 Å). However, for the Trp$_{15}$ carbonyl the dipole is oriented toward the hydrophobic interstices of the bilayer and this would suggest that for the ion to have a significant interaction with this site it would need to be at least another angström further into the channel (9.3 Å). This easily accounts for the strong chemical shift perturbation in the Leu$_{10}$ carbonyl peptide plane and the very weak perturbation in the Trp$_{15}$ carbonyl peptide plane.

Since the structure is known to high resolution and since the structure does not change substantially upon ion binding as indicated above, it can be preliminarily concluded that the ions are not interacting with all three of these carbonyl groups at the same time (Figure 2). In other words the carbonyl oxygens are not rotating in toward the channel axis and toward the cation to the extent necessary for the ion to be solvated by multiple carbonyls simultaneously. There are numerous important conclusions that follow from this unique solid-state NMR result, but first we should inspect some of our assumptions.

Upon binding monovalent ions the shift in the amide ^{15}N chemical shifts could be the result of a change in structure, dynamics, or tensor. By using three separate tensors in a single peptide plane and assuming simply a change in orientation of the peptide plane: data from the carbonyl carbon (^{13}C chemical shift) [1] suggest a change in orientation of 9°; the ^{15}N chemical shift, a change of 7° and the ^{15}N–^{2}H dipolar interaction, a change of 2° [24] (Figure 3). Such a discrepancy in the results suggests that the time averaged structural deformation

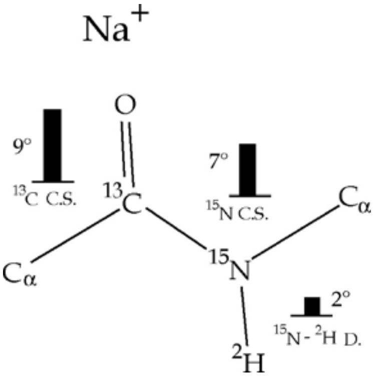

Fig. 3. Interpretation of the anisotropic spin interactions in the Leu$_{12}$-Trp$_{13}$ peptide plane upon binding Na$^+$ (>80% double occupancy).

is indeed small. Furthermore all of the spin interactions tend toward isotropic values making it difficult to distinguish between increased dynamics or an increased tilt angle of the peptide plane with respect to the magnetic field direction, which would similarly cause all of the spin interactions to shift toward isotropic values. In either event the effect is small as dictated by the ^{15}N–^{2}H dipolar interaction which shows a very small change in magnitude. The chemical shift tensors are highly susceptible to changes in electronic distribution and could have altered tensors. Indeed, temperature dependent studies of flash frozen samples of ion bound gramicidin in lipid bilayers using thin films and liquid propane showed a significant 5.5 ppm change in the ^{15}N chemical shift anisotropy [24] that could account for much of the observed anisotropic chemical shift perturbation induced by ion binding. This result confirms the above conclusion that the structural deformations are small; not only are the anisotropic ^{15}N chemical shift changes small, but also the majority of the shift can be accounted for by changes to the chemical shift tensor. In addition, this result documents significant polarizability effects. It appears that for a given peptide plane that the carbonyl ^{13}C chemical shift tensor is affected to the greatest extent and the ^{15}N tensor, which is further removed from the carbonyl oxygen and the greatest electron density changes, is affected to a lesser extent. Clearly, these polarizability effects are significant for ion binding sites and should not be ignored in molecular dynamics calculations of the selectivity filter and ion binding regions of channels. Furthermore, these results suggest that direct observations of the carbonyl oxygens by ^{17}O NMR spectroscopy would be both desirable and very informative.

Now that it is confirmed that much of the anisotropic chemical shift perturbation is due to changes in the chemical shift tensor we can continue to pursue our interpretation of these shifts. The unavoidable conclusion that the ion binding site involves the carbonyls of Leucine 10, 12, and 14 and that the ion does not interact with these sites simultaneously means that the ion maintains considerable entropy while in the binding site. Consequently, there is less enthalpy of solvation that has to be provided by the channel upon binding the ion. This is a unique finding for a cation binding site. All previous monovalent cation binding sites involved a coordination environment that approximated an ideal geometry, thereby the ion was held rigidly in the protein environment.

The dynamics within the binding site suggests a complication that has been previously overlooked. Although single occupancy and double occupancy have been taken into account for the interpretation of the ion induced structural deviations, the partial occupancy for each carbonyl in a given binding site has not been considered. Based on the size of the chemical shift perturbation in Figure 1 for the three carbonyl sites it is possible to estimate the fractional time the ion is associated with each carbonyl. For K^+ the percentages are 33/42/25 for Leucine 10, 12, and 14, respectively. Note that the distribution is different for different ions. For Na^+ the percentages are 38/32/29. Even though the time averaged conformational change has been shown to be small (i.e. just a few degrees), the structural deformation when the ion is interacting with a specific site could be as high as 10°. Although this is very small compared to some initial estimates [e.g. 5], it is more consistent with both the measured dynamics of these sites [25] and the recent molecular dynamics [e.g. 26]. While these deformations are now significant, they are not large enough to position the carbonyls in such a fashion that multiple carbonyls can provide significant solvation energy simultaneously.

These three carbonyls at the entrance of the channel coupled with an ion that maintains mobility between these sites sets up the possibility for stepwise dehydration of the ion as it enters the channel. Indeed, the number of waters that one can place into the ion's primary hydration sphere when interacting with the Leu_{14} carbonyl is 5; that for Leu_{12} is 4 or 5 and that for Leu_{10} is only 3. The result for Leu_{10} is consistent with the fact that when the ion is passing through the bulk of the channel it is in a single file arrangement with a column of water molecules and consequently there are two waters of hydration during this phase of ion transport. Consequently, in the binding process there appears to be a stepwise dehydration process and the binding site is characterized as that portion of the channel where the ion can have more than two waters of hydration in the primary hydration shell. Once the hydration has been reduced to two then it is possible for the ion to pass through the channel. Such a stepwise dehydration process provides an incremental mechanism to achieve this energetically costly dehydration goal as previously suggested by several computational studies [27–29]. The incremental increase in interaction energy for binding the cation as it is dehydrated and steps from carbonyls 14 to 10 is thought to come from the decreased enthalpy of solvation for the carbonyls in this sequence as the environment becomes more hydrophobic and from the weak interaction with the ethanolamine blocking group at the carboxy terminus of the polypeptide [21].

Olah *et al.* [12] measured a separation distance for two thallium ions bound to gramicidin at 19.2 Å. Here, we find that the distance between binding sites is dependent on the specific cation and that the distances are significantly longer than that measured by X-ray diffraction. While Li^+ is predominately associated with the Leu_{10} carbonyl, K^+ with Leu_{12}, Cs^+ is predominately associated with Leu_{14}. A weighted average of the carbonyl positions results in a binding site separation of 21.6 Å for Li^+, 22.0 Å for K^+, and 23.0 Å for Cs^+. However, the ion positions when they are polarizing the amide planes have an average position representing an ion binding site separation that maybe larger by nearly 2 Å. These ion binding site separations

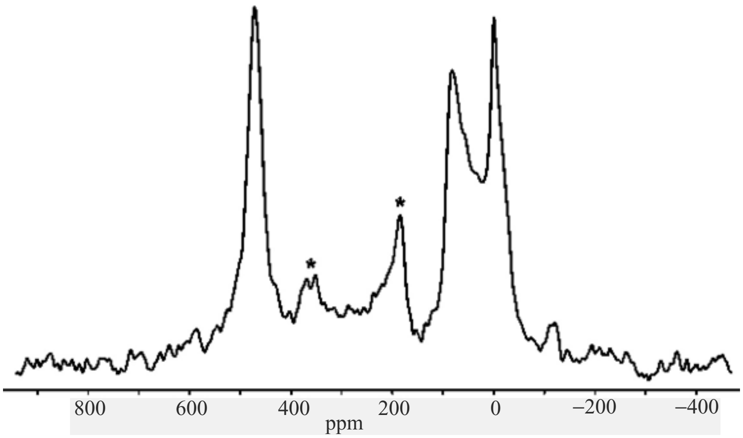

Fig. 4. ^{17}O ^{1}H decoupled spectrum of ^{17}O-Leu$_{10}$-gramicidin A in uniformly aligned DMPC lipid bilayers acquired at 21.2 T (5 mg of peptide of 57% ^{17}O enriched, 1:16 peptide-to-lipid molar ratio, 70k transients at 40 °C). Starred signals represent residual powder pattern intensity from unaligned regions of the sample.

are far greater than those observed in the KcsA selectivity filter where ion binding sites are less than 7 Å apart [15]. The need for such close proximity of the binding sites for KcsA is likely associated with the strength of ion binding. Increased selectivity may require increased binding energy and ion binding to a second site is just one mechanism for compensating for the increased free energy of the ion bound in the first site.

Solid-state NMR spectroscopy of cation binding to gramicidin has illustrated how channels can attract monovalent cations, avoid excessively strong binding, and efficiently conduct ions across membranes. Indeed, this process is similar to an enzyme catalyzed processes in which substrate is bound with care so that the enzyme–substrate complex does not have too low a value of free energy, because the goal is to reduce the ΔG associated with the difference in free energy between the enzyme–substrate complex and the enzyme–transition state complex. Here the ion is bound in a shallow potential energy well in which the ion maintains considerable entropy prior to removal of the last water before entering the single file region of the channel. In the channel region, the ion and water molecules must move through the narrow pore in a correlated fashion, since the ion cannot pass around the water molecules. Furthermore, there is published evidence that these correlated motions in the pore extend to the atoms lining the pore [25]. Motions of the peptide plane have frequency components in the 10 ns time frame—the same time frame based on single channel conductance measurements and calculated for ion transitions along the pore [6,25,30,31]. These peptide plane motions are highly overdamped presumably due to correlated motions between the covalently linked peptide planes.

The ^{15}N anisotropic chemical shifts are relatively small and error bars are on the order of ±1 ppm. The effect is small because of the considerable distance between the polarizing ion and the ^{15}N site. The carbonyl carbon position is closer to the polarizing ion, but while ^{13}C spectroscopy has also been used, its substantial natural abundance background in lipid bilayer preparations generates an additional major challenge. The ideal site to study would be the carbonyl oxygen that is in direct contact with the polarizing ion, but high-resolution ^{17}O NMR has been very difficult to observe due to the quadrupolar nucleus and associated second-order broadening that severely compromises this spectroscopy even at high field strengths.

Recently, progress has been made in the ^{17}O spectroscopy of gramicidin A in aligned bilayers at ultrahigh field using the National High Magnetic Field Laboratory 105 mm bore 900 MHz spectrometer. Figure 4 displays, to our knowledge, the first spectrum of a single site ^{17}O labeled macromolecule. While the ^{17}O line width, 30 ppm, is significantly wider than that of ^{15}N spectra of oriented samples, the carbonyl ^{17}O chemical shielding anisotropy is larger than that of amide ^{15}N by a similar factor, resulting in nearly identical effective spectral resolution. Moreover, carbonyl ^{17}O anisotropic chemical shift and quadrupole coupling is considerably more sensitive to the intermolecular interactions [32,33]. Thus, we speculate that the anisotropic chemical shift and quadrupole coupling effects induced by ion binding would be considerably greater than the line width in aligned samples. Our preliminary spectrum obtained for gramicidin A in oriented lipid bilayers shows the feasibility and practical utility of ^{17}O spectroscopy. Notably, unlike in ^{13}C spectroscopy, the anisotropic ^{17}O resonance at 471 ppm from the single site labeled gramicidin A backbone is well separated from the background contribution from water, 0 ppm, and DMPC, 82 ppm. This observation significantly increases the potential of ^{17}O spectroscopy. Because of its intrinsic sensitivity to electrostatic interactions,

^{17}O NMR has a very bright future for studying the structural and dynamic effects of ion binding.

Acknowledgments

This work was supported by the National Science Foundation, MCB 02-35774, and the work was performed at the National High Magnetic Field Laboratory supported by the National Science Foundation Cooperative Agreement DMR 00-84173 and the State of Florida.

References

1. Smith R, Thomas DE, Atkins AR, Separovic F, Cornell BA. Biochim. Biophys. Acta. 1990;1026:161.
2. Ketchem RR, Hu W, Tian F, Cross TA. Structure. 1994;2:699.
3. Miller C. Science. 1993;261:1692.
4. Toney MD, Hohenester E, Cowan SW, Jansonius JN. Science. 1993;261:756.
5. Mackay DH, Berens PH, Wilson KR, Hagler AT. Biophys. J. 1984;56:229.
6. Roux B, Karplus M. Biophys. J. 1991;59:961.
7. Venkatachalam CM, Urry DW. J. Comput. Chem. 1984;5:64.
8. Ketchem RR, Hu W, Cross TA. Science. 1993;261:1457.
9. Ketchem RR, Roux B, Cross TA. Structure. 1997;5:1655.
10. Kim S, Quine JR, Cross TA. J. Am. Chem. Soc. 2001;123:7292.
11. Fu R, Cotten M, Cross TA. J. Biomol. NMR. 2000;16:261.
12. Olah GA, Huang HW, Liu W, Wu Y. J. Mol. Biol. 1991;218:847.
13. Doyle DA, Cabral JM, Pfuetzner RA, Kuo A, Gulbis JM, Cohen SL, Chait BT, MacKinnon R. Science. 1998;280:69.
14. Jiang Y, Lee A, Chen J, Chadene M, Chait B, MacKinnon R. Nature. 2002;417:523.
15. Morals-Cabral JH, Zhou Y, MacKinnon R. Nature. 2001;414:37.
16. Cross TA, Opella SJ. J. Mol. Biol. 1985;182:367.
17. Cross TA, Opella SJ. Curr. Opin. Struct. Biol. 1994;4:574.
18. Fu R, Cross TA. Annu. Rev. Biophys. Biomol. Struct. 1999;28:235.
19. Mai W, Hu W, Wang C, Cross TA. Protein Sci. 1993;2:532.
20. Teng Q, Cross TA. J. Magn. Res. 1989;85:439.
21. Tian F, Lee K-C, Hu W, Cross TA. Biochemistry. 1996;37:11959.
22. Tian F, Cross TA. J. Mol. Biol. 1999;285:1993.
23. Cross TA. In: RR Muccino (Ed). Proc. of the 2nd Internat. Symp. on the Synth. and App. of Isotop. Lab. Compds. Elsevier Science Publ., Amsterdam, 1986, p 247.
24. Tian F, Cross TA. J. Magn. Reson. 1998;135:535.
25. North CL, Cross TA. Biochemistry. 1995;34:5883.
26. Yu C-H, Cukierman S, Pomes R. Biophys. J. 2003;84:816.
27. Aqvist J, Warshel A. Biophys. J. 1989;56:171.
28. Jordan PC. Biophys. J. 1990;58:1133.
29. Roux B, Karplus M. J. Am. Chem. Soc. 1993;115:3250.
30. Andersen OS. Biophys. J. 1983;41:119.
31. Becker MD, Greathouse DV, Koeppe RE II, Andersen OS. Biochemistry. 1991;30:8830.
32. Wu G, Yamada K, Dong S, Grondey H. J. Am. Chem. Soc. 2000;122:4215.
33. Zhang QW, Chekmenev EY, Wittebort RJ. J. Am. Chem. Soc. 2003;125:9140.
34. Hinton JF, Whaley WL, Shungu D, Koeppe RE II, Millett FS. Biophys. J. 1986;50:539.
35. Jing N, Prasad KU, Urry DW. Biochim. Biophys. Acta. 1995;1238:1.

NMR Studies of Ion-Transporting Biological Channels

James F. Hinton

Department of Chemistry/Biochemistry, University of Arkansas, Fayetteville, AR 72701, USA

A human being has about one hundred thousand million cells. For the various types of cells to properly function, channels, valves, and gates are required. Channels are used to transport ions and small molecules, such as water, through cell membranes.

All of the transporters are integral membrane proteins that contain several α-helical segments that weave back and forth across membranes. Most of the transporters are also glycoproteins with carbohydrate groups directed toward the cell exterior. Proteins that form ion-transporting channels are quite common among eukaryotes. The majority of these channels transport positive ions, such as Na^+, K^+, and Ca^{+2}. However, Cl^- channels have been observed. The cation channels function in a selective or selective nonspecific manner. For example, a channel may transport K^+ ions more efficiently than Na^+ ions but both cations move through the channel. A channel may transport one cation (K^+) but not another (Na^+).

The mechanism for selectively transporting ions through a channel is complex. It may involve a number of factors. The shape, size, and polar nature of the channel surface, the size and charge of the ions, the thermodynamic driving force for the partial dehydration of the ion at the channel entrance and the subsequent binding of the ion to the channel entrance and the interaction of the ion with the polar groups that line the channel. All of these factors play a role in transport and determining the selectivity filter of a channel.

Most ion channels operate in a gated mode. Conformational changes produced by ligand binding, mechanical stress, or voltage change open and close the channel for ion transport. The ligand-gated channel opens and closes in response to the binding of specific molecular species. Hormones and molecules released by nerve cells as neurotransmitters act as control molecules that open and close ligand-gated channels. Voltage-gated channels open and close in response to changes in membrane voltage or electrical potential. The mechanosensitive-gated channel functions by mechanical stresses on the membrane producing conformational changes, which open and close the channel. Gating can be very rapid. Ion transport rates can change from essentially zero to millions of ions per second in a few milliseconds.

The significance of these types of channels was verified by the award of the 2003 Nobel Prize in Chemistry to Peter Agre and Roderick MacKinnon for seminal studies on water and ion channels, respectively. The operation of these channels, like so many other processes occurring in cells, involves proteins. Although significant information was known about which proteins formed certain channels and how these channels function, only recently has a three-dimensional structure been obtained for a few channels, making it possible to begin to relate structure to function. A major reason for this is that proteins embedded into membrane bilayers are poor candidates for X-ray crystallography. Currently, these proteins are too large to be studied by conventional NMR techniques. It is hoped that the next generation of ultrahigh magnetic field NMR spectrometers combined with new solution and solid-state experiments will extend the size of proteins that might be amenable for NMR studies. However, if or until that becomes a reality, other strategies must be employed to investigate the structure–function relationship of ion channel proteins.

One strategy is to use small peptides that form channels in membranes and membrane mimics or to use segments of protein channels that are associated with channel formation. Channel-forming peptides, considered to be minimal models for the pore-forming structure of protein channels can be classified in three categories: (1) minimally designed synthetic peptides, (2) naturally occurring channel-forming peptides, and (3) peptides that mimic structural elements predicted to form the channel lining of authentic protein channels. An understanding of how a channel in one of these categories is formed and how its structure affects the function of ion transport requires knowledge of many facets of this relationship. One must understand the interaction between the model channel and the membrane environment, which ultimately determines the folded structure that forms the channel. The structure of the channel in a membrane environment must be obtained. Ion binding thermodynamic parameters, kinetic activation energy parameters for the transport process, and channel conductance studies are necessary in order to relate the structure of the channel to its function.

There are relatively few physical techniques available for the characterization of the interaction of ions with molecular systems capable of forming channels. However, NMR spectroscopy has proven to be a very powerful technique used to determine, for example; the

Graham A. Webb (ed.), Modern Magnetic Resonance, 285–288.

© 2008 *Springer.*

three-dimensional structure of the model channel, the thermodynamic parameters for incorporating the channel-forming system into a membrane environment, the thermodynamic parameters for ion binding with the channel, the kinetic activation parameters for ion transport, and the internal motion properties of the channel.

Because of limited space, this is not an extensive review. An extensive review, "NMR Studies of Ion-transporting Biological Channels," has been recently published [1]. The reader is directed to this review for a much more in-depth discussion of the subject.

A number of naturally occurring peptide channels have been investigated using NMR techniques. The gramicidin family of linear polypeptides represents a biologically viable channel system of related peptides in which specific changes in amino acid composition can be correlated with cation binding selectivity and transport. This relatively small molecule (15 amino acid residues) is probably the best-characterized cation channel, structurally and functionally, and has been the principal proving ground for many ideas concerning the molecular nature of cation transport across membranes. High resolution, two-dimensional ^{1}H [2–5] and ^{15}N, ^{13}C, ^{1}H, and ^{2}H solid-state NMR spectroscopy [6–9] have been used to determine the structure of gramicidin A and a number of its analogs incorporated into micelles and bilayers, respectively. The gramicidin channel is a dimer formed by the formyl-to-formyl association of two single-stranded, right-handed, $\beta^{6.3}$ helical monomers [2,10]. The dimer, which spans the lipid bilayer or is incorporated into micelles, is about 26 Å long with a diameter of about 4 Å.

Since the movement of ions through a channel involves (i) diffusion of the ion through the aqueous environment to reach the channel entrance, (ii) association of the ion with the channel at the entrance, (iii) transport through the channel, (iv) dissociation from the channel, and (v) diffusion away from the channel, the thermodynamic binding constant for the association process and the kinetic activation enthalpy for the transport process are very important quantities to be determined for the gramicidin analogs. The position of the binding "pocket" for monovalent cations has been determined for gramicidin A and the Phe-15 gramicidin A analog incorporated into SDS micelles using the NOESY11 NMR technique [11]. The binding "pocket" involves the carbonyl groups of residues 10–15. These results are in agreement with those obtained with solid-state ^{2}H and solution-state ^{13}C NMR experiments [12–14].

To obtain a quantitative measure of cation binding to the gramicidin channel, one must determine the enthalpy and the entropy for the binding process, not just the equilibrium constant at a single temperature. The thermodynamic parameters for the binding of cations to the channel have been obtained using the ^{205}Tl NMR-competitive binding method [15]. This method involves the measurement of the ^{205}Tl^{+} chemical shift as a function of the Tl^{+} thermodynamic activity in the presence of a constant amount of gramicidin incorporated into lipid vesicles. The equilibrium binding constant is calculated from the chemical shift–activity relationship. The equilibrium binding constant, determined as a function of temperature, is then used to obtain the enthalpy and the entropy for the binding of the Tl^{+} ion to the channel entrance. This procedure is repeated for the system that also contains a cation (e.g. Li^{+}, Na^{+}, or K^{+}) that competes with the Tl^{+} ion for the same binding site. The change in the chemical shift of the ^{205}Tl^{+} ion is then used to calculate the enthalpy and the entropy of binding for the competing cation. The binding constant and the enthalpy of binding for monovalent cations was found to increase in the order: $Li^{+} > Na^{+} > K^{+} > Tl^{+}$. The binding constants determined for the alkali cations are in agreement with those obtained with ^{13}C NMR spectroscopy of ^{13}CO labeled gramicidin A [13]. The binding constants for divalent cations were found to be much larger than those for the monovalent cations. This binding study of the gramicidin channel explains the selectivity of transport for the monovalent cations and why the divalent cations are not transported.

The kinetic activation enthalpy for the transport of Li^{+}, Na^{+}, and K^{+} has been determined for gramicidin A and its analogs using the magnetization inversion transfer (MIT) technique [16]. If a membrane impermeable chemical shift reagent, such as $[Dy(P_3O_{10})_2]^{-7}$ is added to an aqueous salt solution of large unilamellar vesicles with incorporated gramicidin, the internal and external pools of the NMR active cations (^{7}Li^{+}; ^{23}Na^{+} or ^{39}K^{+}) can be distinguished by there individual NMR signals. The MIT experiment allows one to obtain the kinetic rate constant for the transfer of magnetization for one cation aqueous pool to the other. When the MIT experiment is performed as a function of temperature, the rate constants can then be used to determine the activation enthalpy for the transport process. The activation enthalpy of transport through the gramicidin A channel was found to increase in the order of cations: ^{39}K^{+} (4.2 kcal/mol^{-}), ^{23}Na^{+} (5.4 kcal/mol^{-}), and ^{7}Li^{+} (7.2 kcal/mol^{-}).

The dynamic nature of the gramicidin channel has been the subject of considerable interest. For example, the ^{15}N spin-lattice relaxation time of the nitrogen atom at the Leu-4 position has been used to investigate the local dynamics about the Ala-3/Leu-4 linkage [17,18]. The NMR results of the experiments suggest a correlation between the local dynamics and ion transport through the channel. The backbone dynamics of gramicidin A in bilayers have been studied using low temperature solid-state ^{15}N NMR spectroscopy [19]. A ^{1}H T_1 and T_2 study of the tryptophan indole NH of gramicidin analogs incorporated into SDS micelles showed a systematic decrease in the overall motion of the indole ring from the

Trp-15 (at the aqueous interface) to Trp-9 (at the interior of the micelles) for all analogs.

There are other applications of NMR spectroscopy for studying various aspects of the gramicidin channel and the interaction of the channel with a membrane environment. Solid-state NMR has been used to investigate the closed state of the gramicidin channel in lipid bilayers [20]. The kinetic activation parameters for the incorporation of gramicidin analogs into vesicles as a channel have been determined using ^{23}Na NMR spectroscopy [5, 21]. The differential photochemical degradation of the four tryptophan residues in gramicidin A has been studied using ^{1}H two-dimensional NMR spectroscopy [22].

Another type of small, naturally occurring peptide, the peptaibols, has been used as an ion channel model. These channels consist of a bundle of transmembrane helices surrounding a central core. Alamethicin, a 20-residue linear peptide, is the most thoroughly studied member of this class of model channels. A number of NMR studies of alamethicin in SDS micelles [23] and in methanol and aqueous methanol solution [24] have been conducted to determine the conformation of the monomers within the bundle. It appears that the N-terminal region is of an α-helical nature with several 3.0_{10} segments in the C-terminal region. Solid-state ^{15}N NMR results were found to be consistent with an α-helical conformation inserted along the bilayer normal [25]. NMR studies of other peptaibols also indicate the characteristic α-helical conformation.

Other naturally occurring peptides, such as melittin, magainin, cecropin, and pardaxin, form bundles that produce a central channel. There have been many NMR studies of melittin in solution, in micelles, in bilayers, and interacting with lipid membranes [26–29]. The structure of the monomer appears to be that of an α-helix. NMR investigations of magainin [30,31], cecropin [32,33], and pardaxin [34, 35] show that, in general, these peptides also form α-helical monomers that assemble into a structure that has a central pore or channel.

Ligand-gated ion channels provide efficient communication between cells of the central nervous system. At the molecular biochemical level, the nicotinic acetylcholine receptor is one of the best-characterized membrane proteins and serves as a paradigm for a family of ligand-gated ion channels [36]. Of the transmembrane segments, M1, M2, M3, and M4, five M2 helices form the central ion channel or pore. Solid-state ^{15}N NMR experiments of the labeled M2 segment in bilayers have shown that the helical segment is perpendicular to the plane of the bilayer [37]. The M2 protein from the influenza A protein functions as an ion channel. Solid-state ^{15}N NMR results with the M2 protein from the influenza A virus suggest that this tetrameric protein is in a left-handed, four-helix bundle [38,39]. Peptide mimics of protein channels have been used to investigate structure and function using a variety of NMR techniques [40,41].

References

1. Hinton JF, Webb GA (Eds). Annual Reports on NMR Spectroscopy. Academic Press Limited: London, 1999, p. 89.
2. Bystrov VF, Gavilov YD, Ivanov VT, Ovchinnikov YA. Eur. J. Biochem. 1977; 8:63.
3. Townsley LE, Tucker WA, Sham S, Hinton JF. Biochemistry. 2001;40:11676.
4. Sham SS, Shobana S, Townsley LE, Jordan JB, Fernandez JQ, Andersen OS, Greathouse DV, Hinton JF. Biochemistry. 2003;42:1401.
5. Jordan JB, Easton PL, Hinton JF. Biophys. J. 2005;88:224.
6. Katchem RR, Hu W, Cross TA. Science. 1993;261:1457.
7. Cornell BA, Separovic F, Baldassi A, Smith R. Biophys. J. 1988;53:67.
8. Killian JA, Taylor MJ, Koeppe RE. Biochemistry. 1992;31:11283.
9. Bouchard M, Davis JH, Auger M. Biophys. J. 1995;69:1917.
10. Urry DW. Proc. Natl. Acad. Sci. U.S.A. 1971;68:676.
11. Hinton JF. J. Magn. Reson. B. 1996;112:26.
12. Smith R, Thomas DE, Atkins AR, Separovic F, Cornell BA. Biochim. Biophys. Acta. 1990;1029:161.
13. Urry DW, Walker JT, Trapane TL. J. Membr. Biol. 1982;69:225.
14. Separovic F, Gehrmann J, Milne T, Cornell BA, Lin SY, Smith R. Biophys. J. 1994;67:1495.
15. Hinton JF, Fernandez JQ, Shungu D, Millett FS. Biophys. J. 1989;55:327.
16. Hinton JF, Easton PL, Newkirk K, Shungu DC. Biochim. Biophys. Acta. 1993;1146:191.
17. Hu W, Cross TA. Biochemistry. 1995;34:14147.
18. North CL, Cross TA. J. Magn. Reson. B. 1993;101:35.
19. Lazo ND, Hu W, Cross TA. J. Magn. Reson. B. 1995;107:43.
20. Mo Y, Cross TA, Nerdal W. Biophys. J. 2004;86:2837.
21. Easton PL, Hinton JF, Newkirk DK. Biophys. J. 1990;57:297.
22. McKim S, Hinton JF. Biochim. Biophys. Acta. 1993;1153:315.
23. Franklin JC, Ellena JF, Jayaasinche S, Kelsh LP, Cafisco DS. Biochemistry. 1994;33:4036.
24. Brachais L, Davoust D, Molle G. Int. J. Peptide Protein Res. 1995;45:164.
25. North CL, Barranger-Mathys M, Cafisco DS. Biophys. J. 1995;69:2392.
26. Lam Y, Morton CJ, Separovic F. Eur. Biophys. J. 2002;31:383.
27. Lam Y, Wassall SR, Morton CJ, Smith R, Separovic F. Biophys. J. 2001;81:2752.
28. Lauterwein J, Brown LR, Wutherich K. Biochim. Biophys. Acta. 1980;622:219.
29. Pott T, Dufourc EJ. Biophys. J. 1995;68:965.
30. Bechinger B, Zasloff M, Opella SJ. Biophys. J. 1998;74:981.
31. Hirsh DJ, Hammer J, Maloy WL, Blazyk J, Schaefer J. Biochemistry. 1996;335:12733.

32. Srisailam S, Kumar TKS, Arun kumar AI, Leung KW, Yu C, Chen HM. Eur. J. Biochem. 2001;268:4278.
33. Marassi FM, Opella SJ, Juvvadi P, Merrifield RB. Biophys. J. 1999;77:3152.
34. Zagorski MG, Norman DG, Barrow CJ, Iwashita T, Tachibana K, Patel DJ. Biochemistry. 1991;30:8009.
35. Porcelli F, Buck B, Lee D-K, Hallock KJ, Ramamoothy A, Veglia GJ. Biol. Chem. 2004;279:45815.
36. Dani JA, Mayer ML. Curr. Opin. Neurobiol. 1995;5:350.
37. Bechinger B, Kim Y, Chirlian LE, Gesell J, Neumann JM, Montal M, Tomich J, Zasloff M, Opella SJ. J. Biol. NMR 1991;1:167.
38. Kovacs FA, Cross TA. Biophys. J. 1997;73:2511.
39. Tian C, Tobler K, Lamb RA, Pinto L, Cross TA. Biochemistry. 2002;41:11294.
40. Doak DG, Mulvey D, Kawaguchi K, Villalain J, Campbell ID. J. Mol. Biol. 1996;258:672.
41. Esposito G, Dumy P, Varma V, Mutter M, Bodenhausen G. Biopolymers. 1997;41:27.

Membrane Proteins

Part I

Site-Directed NMR Studies on Membrane Proteins

Hazime Saitô

Department of Life Science, Himeji Institute of Technology, Harima Science Garden City, Hyogo 678-1297, Japan and Center for Quantum Life Sciences, Hiroshima University, Higashi-Hiroshima 739-8526, Japan

Introduction

Integral membrane proteins, traversing the membrane once or several times as α-helices, play crucial roles in maintaining various activities of cells such as transport of appropriate molecules into or out of the cell, catalysis of chemical reaction, and receiving and transducing chemical signals from the cell environment. Naturally, biological activity of such proteins may depend upon their conformations and dynamics regulated by specific lipid–protein and/or protein–protein interactions as structural determinants, as studied by analysis of 2D assembly of bacteriorhodopsin (bR) as a typical membrane protein [1]. bR is active as a proton pump and considered as a prototype of a variety of G-protein coupled receptors, consisting of seven transmembrane α-helices.

Interestingly, the bR structure is far from static at *ambient temperature* in spite of currently available 3D structural models revealed by crystallography at low temperature but flexible even in the 2D crystal, especially at the loops and N- or C-terminal residues fully exposed to aqueous phase, and undergoing fluctuation motions with correlation times of the order of 10^{-4}–10^{-5} and 10^{-8} s, respectively, as revealed by recent site-directed solid-state ^{13}C NMR [2–6].

Well-resolved ^{13}C NMR signals are fully visible from 2D crystalline ^{13}C-labeled [3-^{13}C]Ala-[2,3,7] or [1-^{13}C]Val-labeled bR [3,5] recorded by *both* cross-polarization-magic angle spinning (CP-MAS) and dipolar decoupled-magic angle spinning (DD-MAS) techniques. Inherent motional fluctuation of the transmembrane α-helices of bR monomer, however, turns out to be accelerated by two orders of magnitude in the lipid bilayer in the absence of specific protein–protein interactions, from their correlation times of the order of 10^{-2} s in 2D crystal [2,3,8] to 10^{-4}–10^{-5} s, [9–13] in the monomer. Accordingly, ^{13}C NMR signals from several residues in the transmembrane α-helices and loops could be suppressed due to the failure of attempted peak-narrowing caused by interference of the motional fluctuation frequency with the frequency of proton decoupling or MAS [2,3,14–16], although the functional unit responsible for the photocycle is the monomer itself rather than the trimeric form found in the 2D crystal [17,18]. In this case, uniform ^{13}C-labeling is not always favorable for solid-state NMR, because ^{13}C NMR study of densely ^{13}C-labeled proteins such as [1,2,3-$^{13}C_3$]Ala-labeled bR could be substantially broadened in the presence of such intermediate and slow motions, due to the accelerated relaxation rate through a number of homonuclear ^{13}C–^{13}C dipolar interactions and scalar J couplings [16].

We demonstrate here how the site-directed ^{13}C NMR approach is useful to reveal conformational features of *intact* membrane proteins with emphasis on their surface structures and dynamics at *ambient temperature*, as revealed by ^{13}C NMR studies on bR from the 2D crystal and monomer and various membrane proteins active as signal transducers and enzyme, expressed from *E. coli* and present as monomer in lipid bilayers.

Conformation-Dependent ^{13}C Chemical Shifts

It has been demonstrated that C_α and C=O ^{13}C chemical shifts of a variety of polypeptides taking the α-helix form are displaced to high frequencies by 3.5–8.0 ppm with respect to those of the β-sheet form, while the C_β signals of peptides taking the α-helix form are displaced to low frequencies by 3.4–5.2 ppm as compared with those of the β-sheet form [2,3,19]. In addition, it is possible to distinguish even the following six kinds of local secondary structures, right-handed and left-handed α-helices, α_{II}-helix, collagen-like triple helix, silk I and β-sheet forms, besides random coil form, with reference to the conformation-dependent ^{13}C chemical shifts of Ala residues (Table 1). ^{13}C NMR peaks from the α-helices in membrane proteins, however, are more widely spread than the expected values of the conformation-dependent displacement of the peaks from solid polypeptides. In fact, several ^{13}C NMR peaks from the α-helical residues resonate at their lowest (C_β) and highest (C_α and C=O peaks) boundary peak positions with those of random coil form in the presence of intermediate or low frequency motions, but their peak positions are distinct from those of the loop and β-sheet form [2,3,10]. In such case, the observed distribution of the chemical shifts may deviate greatly from their expected peak positions from the distribution of the torsion angles

Graham A. Webb (ed.), Modern Magnetic Resonance, 291–297.
© 2008 *Springer.*

Table 1: Conformation-dependent ^{13}C chemical shifts of Ala residues (ppm from TMS)

	α_I-helix (α_R-helix)	α_{II}-helix	α_L-helix	β-sheet	Collagen-like triple helix	Silk I	Random coil
C_α	52.4	53.2	49.1	48.2	48.3	50.5	50.1
C_β	14.9	15.8	14.9	19.9	17.6	16.6	16.9
C=O	176.4	178.4	172.9	171.8	173.1	177.1	175.2

Source: Adapted from Refs. [3,10].

determined by X-ray diffraction [20]. Nevertheless, the conformation-dependent displacement of ^{13}C peaks are very useful as a structural constraint to predict the local structure of membrane proteins. A possibility of the conformation-dependent ^{15}N chemical shifts, however, may be obscured, because ^{15}N chemical shifts are influenced by both the local conformation and the primary structure or probably by the higher order structure [21].

Site-Directed Assignment of ^{13}C NMR Signals

Figure 1 illustrates the ^{13}C DD-MAS and CP-MAS NMR spectra of fully hydrated [3-^{13}C]Ala-labeled bR in 2D crystal (MW 26 kDa) at ambient temperature [2,3]. Twelve Ala C_β ^{13}C NMR peaks are resolved in the CP-MAS NMR (bottom) among 22 Ala residues present in the transmembrane α-helices and loops. The three intense ^{13}C NMR signals from membrane surface (gray; top) are noteworthy in the DD-MAS NMR spectrum (consisting of contribution from total 29 Ala residues) and are unambiguously assigned to Ala 228 and 233 (C-terminal α-helix), Ala 240, 244–246 (C-terminal tail taking random coil), and Ala 235 (corner at the C-terminal α-helix) from the upper to the lower field with reference to the conformation-dependent ^{13}C chemical shifts [2,3,19] together with their absence after enzymatic cleavage by papain [22]. Naturally, these ^{13}C NMR signals are suppressed in the CP-MAS NMR, because the C-terminal α-helix and its tail undergo fluctuation motions with correlation times of the order of 10^{-6} and 10^{-8}s, respectively [10]. The assigned peaks indicated at the individual peaks are obtained in view of selectively reduced ^{13}C NMR peak intensity of relevant mutant in which an individual Ala residue is replaced by other amino acid residue (for instance, A196G, A126V, A215G, etc.) as compared with that of wild type as illustrated in Figure 2 [3,10] provided that global conformational change is not induced as in D85N [23]. Such a ^{13}C NMR peak from the transmembrane α-helices can be identified as a single Ala residue by the difference ^{13}C NMR spectrum between a wild type and a mutant, together with suppressed signals from residues located near the surface (within ca. 8.7 Å) by accelerated transverse relaxation due to surface-bound Mn^{2+} [20]. Site-specific assignment of ^{13}C NMR signals has been attempted for [1-^{13}C]Val- [3,5], Pro- [24], Trp-, and Ile-[5] labeled bR.

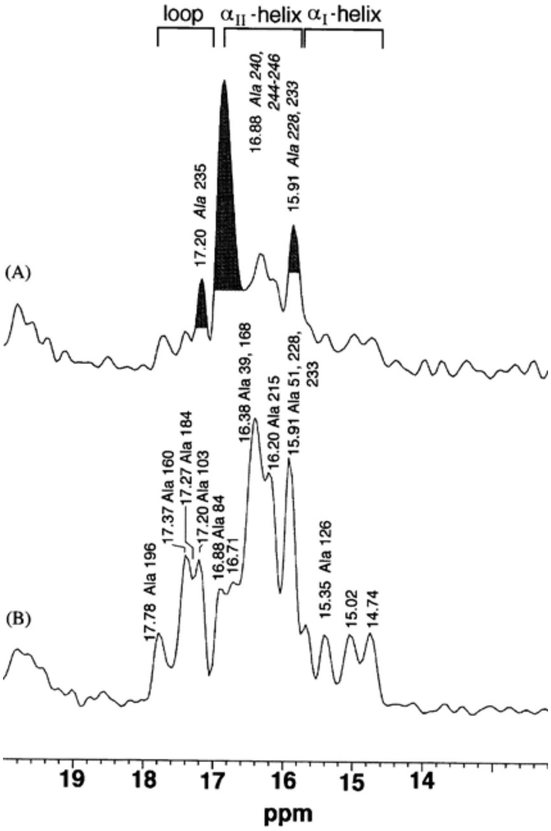

Fig. 1. ^{13}C DD-MAS (A) and CP-MAS (B) NMR spectra of [3-^{13}C]Ala-labeled bacteriorhodopsin. The ^{13}C NMR signals from the C-terminal residues are in gray.

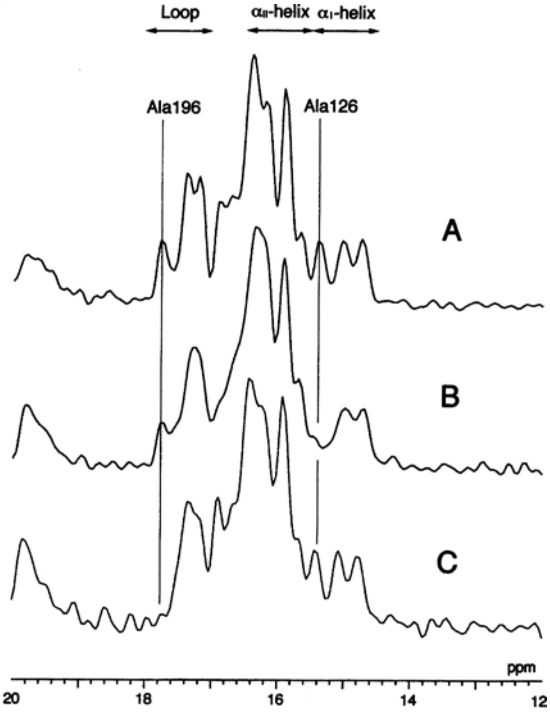

Fig. 2. Comparison of the ^{13}C CP-MAS NMR spectra of [3-^{13}C]Ala-labeled bacteriorhodopsin (A) and A126G (B) and A196G mutants (C).

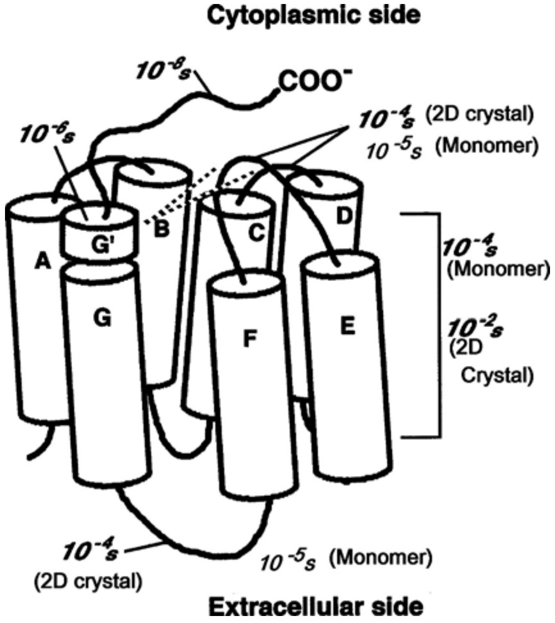

Fig. 3. Schematic representation of the location of the C-terminal α-helix (helix G′ protruding from the membrane surface), its interaction with the C-D and E-F loops (dotted lines) leading to the cytoplasmic surface complex and their correlation times. Note that the correlation times for the transmembrane α-helices differ substantially between preparations of 2D crystal or monomer.

Dynamic Aspect of Membrane Proteins

Surprisingly, ^{13}C NMR signals of bR labeled with certain [1-^{13}C] amino acid residues are not always fully visible from the loops and transmembrane α-helices by both CP-MAS and DD-MAS techniques, even if 2D crystalline preparations were examined [5,16]. In contrast, ^{13}C NMR signals from the N- and C-terminal regions with the correlation time shorter than 10^{-8} s can be observed by DD-MAS NMR only [2,3,5]. Indeed, ^{13}C NMR signals of [1-^{13}C]Gly-, Ala-, Leu-, Phe-, and Trp-labeled bR are partially or almost completely suppressed from residues located at the membrane surfaces, and the signals of which can be conveniently estimated by means of accelerated transverse relaxation effect from the surface-bound Mn^{2+} ions [5]. Indeed, the relative proportions of ^{13}C-labeled residues from the negatively charged surface residues (within 8.7 Å) from fully visible ^{13}C NMR peaks of [3-^{13}C]Ala-, [1-^{13}C]Val-, and Ile-bR [5,20] were consistent with the expected numbers of such residues available from the secondary structure. In contrast, we found that the relative contributions of the surface areas estimated by this procedure are substantially lower than the expected numbers of residues from the secondary structure for ^{13}C NMR spectra of [1-^{13}C]Gly-, Ala-, Leu-, Phe-, and Trp-bR from 2D crystalline purple membranes [5]. This means that these ^{13}C NMR signals from the surface area are *partially or completely suppressed* as a result of failure of the attempted peak-narrowing by interference of incoherent low frequency fluctuation motion (10^4 Hz) with the coherent frequency of MAS [15].

This kind of peak suppression for fully hydrated bR can be utilized as an invaluable means to evaluate *in situ* protein dynamics with the local correlation time of the order of 10^{-4} s in the 2D crystal as schematically illustrated in Figure 3, although this phenomenon is obviously a serious disadvantage as viewed from choice of a suitable ^{13}C-labeled amino acid residue. One should also anticipate that ^{13}C NMR signals of fully hydrated, *monomeric* [1-^{13}C]Gly-, Ala-, Leu-, Phe-, and Trp-labeled membrane proteins [5,9–13] in lipid bilayers are almost completely suppressed, because even the transmembrane α-helices are able to acquire accelerated fluctuation motions in the absence of specific protein–protein interactions essential for trimeric structure in the 2D crystals (Figure 3). This is because the lowest energy minimum for Gly and the others in the conformation map may be shallow and the backbone dynamics of the last four amino acid residues represented by the C_α–$C_\beta H_2$–Z system could be coupled with a possible rotational motion of the χ_1 angle around the C_α–C_β bond. On the other hand, such a conformational space leading to fluctuation motion may be limited to a very narrow area for Val or Ile residues with a bulky side chain at C_α. For [3-^{13}C]Ala-labeled bR in either 2D crystal or monomeric state in lipid bilayer, peak suppression could occur when incoherent fluctuation motion is interfered with frequency of proton decoupling (correlation time being ca. 10^{-5} s) [14].

Obviously, intermediate or slow fluctuation motions with correlation times in the order of 10^{-4}–10^{-5} s may be well related to individual biological functions, because flexibility in the loops and/or transmembrane α-helices may be essential for initiating transport of proton or ion, receiving external signals, binding substrate, etc. for their respective biological functions such as proton pump, signal transduction, enzymatic activity, etc. In spite of 2D crystalline bR, the fluctuation frequency is spontaneously increased from 10^2 Hz in the ground state to the order of 10^4 Hz at the M-like state as a result of a modified retinal–protein interaction owing to proton transfer from the Schiff base to Asp 85 [23].

Surface Structures

The surface structure of bR is still obscured, or inconsistent, among a variety of the 3D structures so far revealed by cryoelectron microscopy and X-ray diffraction studies at low temperature [25–27]. This arises because it can be easily altered by a variety of intrinsic or environmental factors such as the manner of crystallization either in the 2D or in the 3D crystals, temperature, pH, ionic strength, crystallographic contact, etc [2,3]. Instead, the ^{13}C NMR approach proved to be a very suitable means to reveal its surface structure in relation to biological activity at ambient temperature. In particular, ^{13}C NMR studies revealed that the C-terminal residues, 226–235, participated in the formation of the C-terminal α-helix as viewed from their peak positions [16,22], with reference to the conformation-dependent ^{13}C chemical shifts [2,3,19]. Only a part of this α-helix, however, was visible by X-ray diffraction [26], owing to the presence of motions with correlation times in the order of 10^{-6} s detected at ambient temperature, as judged from the carbon spin–lattice relaxation times, T_1^{C}, and spin–spin relaxation times, T_2^{C}, under CP-MAS conditions [16].

Yonebayashi *et al*. examined the ^{13}C NMR spectra of [3-^{13}C]Ala-labeled bR and its mutants while varying a variety of environmental or intrinsic factors such as ionic strength, temperature, pH, truncation of the C-terminal α-helix, and site-directed mutation at cytoplasmic loops [28]. For instance, increased ionic strength from 10 to 100 mM NaCl causes simultaneous changes of the high frequency displacement of Ala 103 signal of the C-D loop and the reduced peak intensity of the C-terminal α-helix [28]. This finding together with other similar changes caused by temperature and pH variations leads to the conclusion that the cytoplasmic loops and the C-terminal α-helix are not present independently but are held together to form *cytoplasmic surface complex* stabilized by salt bridges and/or cation-mediated linkages of a variety of side chains as schematically indicated by dotted lines in Figure 3. Indeed, ^{13}C NMR signals from such loops are suppressed by accelerated fluctuation motion with a correlation time of the order of 10^{-5} s and the ^{13}C chemical shift of the C-terminal α-helix was displaced to low frequency, when blue membranes were prepared by either complete removal of surface-bound cations (deionized blue) or neutralization of surface charge by lowered pH to 1.2 (acid blue) [28,29]. Further, partial neutralization of Glu and Asp residues at the extracellular side such as E194Q/E204Q (2 Glu), E9Q/E194Q/E204Q (3 Glu), and E9Q/E74Q/E194Q/E204Q (4 Glu) caused global fluctuation motions at these loop regions as well as the disorganized trimeric form [30]. The cytoplasmic surface complex in which the C-terminal α-helix is probably tilted toward the direction of the B- and F-helices seems to prevent unnecessary fluctuations of the helices for efficient proton uptake during the photocycle [28]. It appears that such surface structure is disrupted at a low temperature or in the M-like state. This view is consistent with the previous data for "the proton binding cluster" consisting of Asp 104, Glu 160, and Glu 234.

Site-Directed ^{13}C NMR on Membrane Proteins Present as Monomers

Most of reconstituted membrane proteins may be present as monomer in lipid bilayers at ambient temperature in the absence of certain endogeneous lipid molecules essential for specific lipid–protein and protein–protein interactions, as manifested for bR in the 2D crystalline assembly as purple membrane [31,32]. Therefore, it seems to be very important to clarify how the present site-directed ^{13}C NMR approach is useful to reveal conformation and dynamics of reconstituted membrane proteins as *Pharaonis* phoborhodopsin (*p*pR; sensory rhodopsin II), its cognate transducer (*p*HtrII), and diacylglycerol kinase (DGK) which are overexpressed by *E. coli* [11–13]. In such cases, use of proteins labeled by [3-^{13}C]Ala is more preferable than [1-^{13}C]Val, because ^{13}C NMR signals of the latter preparations were substantially suppressed in a similar

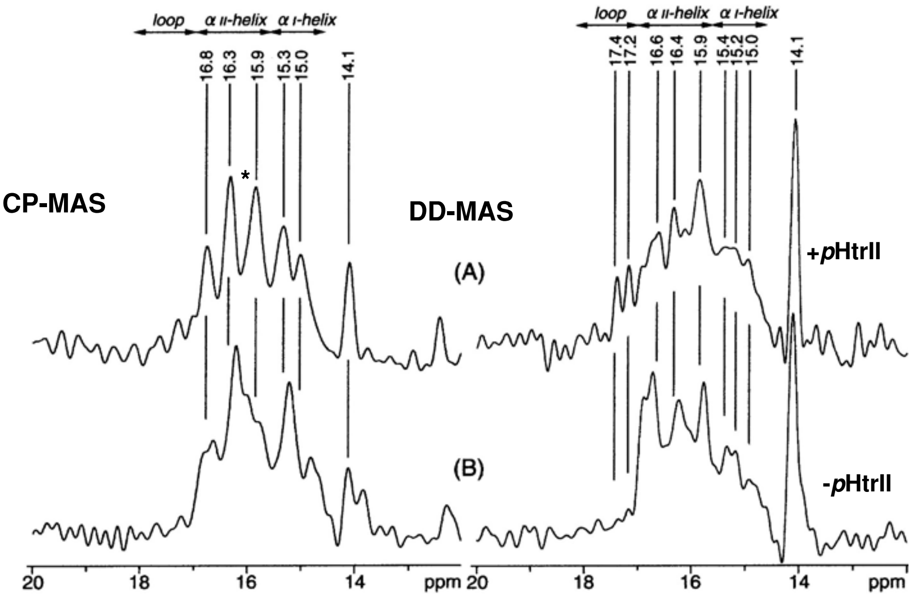

Fig. 4. Comparison of the ^{13}C CP-MAS (left) and DD-MAS (right) NMR spectra of [3-^{13}C]Ala-labeled phoborhodopsin (*p*pR) in the presence (A) or absence (B) of its truncated transducer, *p*HtrII (1–159). The asterisked peak of the CP-MAS NMR spectrum in the upper trace indicates the peak of the C-terminal α-helix.

manner as encountered for monomeric bR as pointed out already [11,13].

*p*pR and *p*HtrII

*p*pR is a retinal protein as a photoreceptor from *N. pharaonis*, consisting of seven transmembrane α-helices as in bR. Its cognate transducer *p*HtrII consists of two transmembrane α-helices and yields signaling for negative phototaxis activated by receiving incoming light by *p*pR through tightly formed complex with *p*pR. Spreads of the ^{13}C chemical shifts for reconstituted [3-^{13}C]Ala-labeled *p*pR in egg PC bilayers and their relative peak intensities (Figure 4) are very similar to those of bR because of taking similar secondary structures for both proteins, in spite of their sequence homology of 27% [11]. The intense ^{13}C NMR peak at 15.9 ppm, ascribable to the C-terminal α-helix protruding from the membrane surface as found for bR on the basis of the conformation-dependent ^{13}C chemical shifts described already, is clearly visible in the DD-MAS spectrum (Figure 4B, right) but almost completely suppressed (Figure 4B, left) in the CP-MAS NMR because of fluctuation motion with a frequency of 10^5 Hz [6,11]. This peak, however, is made visible by the CP-MAS spectrum (Figure 4A, left: asterisked peak) by the complex formation with *p*HtrII (1–159) due to the lowered fluctuation frequency in the C-terminal α-helix (10^4 Hz). This finding indicates that mutual interactions among the extended TM1- and TM2-helices of *p*HtrII (1–159) beyond the surface and the C-terminal α-helix of *p*pR play an important role for stabilization of the *p*pR–*p*HtrII complex.

The intense high frequency α_{II}-helical ^{13}C DD-MAS NMR peaks of [3-^{13}C]Ala-labeled *p*HtrII (1–159) resonate at 16.6 and 16.3 ppm [12] and ascribed to the coiled-coil portion protruding from the membrane surface, with reference to the conformation-dependent displacement of peaks [2,3,19]. These peaks were almost completely suppressed by CP-MAS NMR regardless of the presence or absence of *p*pR or by DD-MAS NMR in the absence of *p*pR. Surprisingly, this is caused by increased fluctuation frequency in the C-terminal α-helix from 10^5 Hz in the uncomplexed state to $>10^6$ Hz in the complexed state. This means that the transducers alone are in an aggregated or clustered state but the *p*pR–*p*HTrII complex is not aggregated.

Diacylglycerol Kinase

DGK from *E. coli* is a small, 121 amino acid, membrane-bound enzyme to catalyze the conversion of diacylglycerol and MgATP to phosphatic acid and MgADP. It is believed to be assembled into a trimer to be active as a catalytic unit, each consisting of three transmembrane α-helices, together with additional two amphipathic α-helices located at the membrane surface [33]. Yamaguchi *et al.* recorded ^{13}C NMR spectra of [3-^{13}C]Ala-, [1-^{13}C]Val-labeled *E. coli* DGK reconstituted in POPC and DPPC bilayers using CP-MAS and DD-MAS methods [13]. Surprisingly, ^{13}C NMR spectra of [3-^{13}C]Ala-labeled DGK in lipid bilayer were broadened to yield rather featureless peaks at the physiological temperature of the liquid crystalline phase. It is also noted that ^{13}C NMR spectra of [1-^{13}C]Val-labeled DGK were completely suppressed at temperatures corresponding to the liquid crystalline phase. Such a suppression of peaks is obviously caused by interference of motional frequency with the frequency of the MAS or proton decoupling (10^4–10^5 Hz), under the physiological condition exhibiting enzymatic activity. In the gel phase lipid, however, up to six distinct ^{13}C NMR signals were well resolved due to lowered fluctuation frequency ($<10^5$ Hz) for the transmembrane α-helices, the amphipathic α-helices and loops. The fact that the enzymatic activity is low under conditions where motion is restricted and high when conformational fluctuation can occur suggests that acquisition of low frequency backbone motions, on the microsecond to millisecond timescale, may facilitate the efficient enzymatic activity of DGK. Clearly, the present observations demonstrate that site-directed ^{13}C NMR approach is very useful for probing the conformation and dynamics of DGK reconstituted in a membrane environment under physiological condition.

Concluding Remarks

It should be anticipated that ^{13}C NMR spectral feature of *fully hydrated* membrane proteins at ambient temperature strongly depends upon sample preparations (either 2D crystals or monomers), a variety of ^{13}C-labeled amino acid residues ([3-^{13}C]Ala-, [1-^{13}C]Val-, Gly- or Leu-, etc.), lipid phase (liquid crystalline or gel phase), etc. in view of their intrinsic flexibility. In particular, well-resolved, fully visible ^{13}C NMR signals of membrane proteins are available from 2D crystalline preparations, as manifested from site-directed ^{13}C NMR studies on [3-^{13}C]Ala- and/or [1-^{13}C]Val-labeled bR recorded by both CP-MAS and DD-MAS methods. In contrast, ^{13}C NMR signals from several residues located at the surfaces of such preparations are partially or almost completely suppressed when they are labeled with [1-^{13}C]Gly, Ala, Leu, Phe, or Trp, as a result of failure of the attempted peak-narrowing by interference of low frequency fluctuation motions with the coherent frequency of MAS, because backbone dynamics in these systems could be coupled with a possible rotational motion of the χ_1 angle around the C_α–C_β bond, as represented schematically by the C_α–$C_\beta H_2$–Z system, where Z is H, isopropyl, phenyl, or indole. Further, ^{13}C NMR studies on [3-^{13}C]Ala-labeled membrane proteins such as *p*pR, *p*HtrII, *p*pR–*p*HtrII complex, and DGK reconstituted in lipid bilayers as *monomers* are also very useful to analyze their conformations and dynamics at ambient temperature, although the absence of several ^{13}C NMR signals from residues located at the surfaces such as loops should be taken into account. In addition, one should anticipate that ^{13}C NMR signals of fully hydrated, monomeric [1-^{13}C]Gly, Ala, Leu, Phe, or Trp-labeled membrane proteins in lipid bilayers are almost completely suppressed at liquid crystalline phase. Nevertheless, it is emphasized that the present site-directed ^{13}C NMR approach turns out to be an unrivaled means to be able to provide an invaluable insight into their conformation and dynamics which are essential for respective proteins to achieve their own biological functions.

References

1. Krebs MP, Isenbarger TA. Biochim. Biophys. Acta. 2000;1460:15–26.
2. Saitô H, Tuzi S, Yamaguchi S, Tanio M, Naito A. Biochim. Biophys. Acta. 2000;1460:39–48.
3. Saitô H, Tuzi S, Tanio M, Naito A. Annu. Rep. NMR Spectrosc. 2002;47:39–108.
4. Saitô H, Yamaguchi S, Okuda H, Shiraishi A, Tuzi S. Solid State Nucl. Magn. Reson. 2004;25:5–14.
5. Saitô H, Mikami J, Yamaguchi S, Tanio M, Kira A, Arakawa T, Yamamoto K, Tuzi S. Magn. Reson. Chem. 2004;42:218–30.
6. Saitô H. Chem. Phys. Lipids. 2004;132:101–12.
7. Tuzi S, Yamaguchi S, Naito A, Needleman R, Lanyi JK, Saitô H. Biochemistry. 1996;35:7520–27.
8. Tuzi S, Naito A, Saitô H. Eur. J. Biochem. 1996;239:294–301.
9. Saitô H, Tsuchida T, Ogawa K, Arakawa T, Yamaguchi S, Yamaguchi S, Tuzi S. Biochim. Biophys. Acta. 2002;1565:97–106.
10. Saitô H, Yamamoto K, Tuzi S, Yamaguchi S. Biochim. Biophys. Acta. 2003;1616:127–36.
11. Arakawa T, Shimono K, Yamaguchi S, Tuzi S, Sudo Y, Kamo N, Saitô H. FEBS Lett. 2003;536:237–40.
12. Yamaguchi S, Shimono K, Sudo Y, Tuzi S, Naito A, Kamo N, Saitô H. Biophys. J. 2004;86:3131–40.
13. Yamaguchi S, Tuzi S, Bowie JU, Saitô H. Biochim. Biophys. Acta. 2004;1698:97–105.
14. Rothwell WP, Waugh JS. J. Chem. Phys. 1981;74:2721–32.
15. Suwelack D, Rothwell WP, Waugh JS. J. Chem. Phys. 1980;73:2559–69.
16. Yamaguchi S, Tuzi S, Yonebayashi K, Naito A, Needleman R, Lanyi JK, Saitô H. J. Biochem. 2001;129:373–82.
17. Dencher NA, Heyn MP. FEBS Lett. 1979;108:307–10.
18. Dencher NA, Kohl K-D, Heyn MP. Biochemistry. 1983;22:1323–34.
19. Saitô H, Ando I. Annu. Rep. NMR Spectrosc. 1989;21:209–90.

20. Tuzi S, Hasegawa J, Kawaminami R, Naito A, Saitô H. Biophys. J. 2001;81:425–34.
21. Shoji A, Ando S, Kuroki S, Ando I, Webb GA. Annu. Rep. NMR Spectrosc. 1993;26:55–98.
22. Tuzi S, Naito A, Saitô H. Biochemistry. 1994;33:15046–52.
23. Kawase Y, Tanio M, Kira A, Yamaguchi S, Tuzi S, Naito A, Kataoka M, Lanyi JK, Needleman R, Saitô H. Biochemistry. 2000;39:14472–80.
24. Tuzi S, Naito A, Saitô H. J. Mol. Struct. 2003;654:205–14.
25. Grigorieff N, Ceska TA, Downing KH, Baldwin JM, Henderson R. J. Mol. Biol. 1996;259:393–421.
26. Luecke H, Schobert B, Richter H-T, Cartailler J-P, Lany JK. J. Mol. Biol. 1999;291:899–911.
27. Berlrhali H, Nollert P, Royant A, Menzel C, Rosenbusch JP, Landau EM, Pebay-Peyroula E, Structure. 1999;7:909–17.
28. Yonebayashi K, Yamaguchi S, Tuzi S, Saitô H. Eur. Biophys. J. 2003;32:1–11.
29. Tuzi S, Yamaguchi S, Tanio M, Konishi H, Inoue S, Naito A, Needleman R, Lanyi J. K, Saitô H. Biophys. J. 1999;76:1523–31.
30. Saitô H, Yamaguchi S, Ogawa K, Tuzi S, Márquez M, Sanz C, Padrós E. Biophys. J. 2004;86:1673–81.
31. Sternberg B, L'Hostis C, Whiteway CA, Watts A. Biochim. Biophys. Acta. 1992;1108:21–30.
32. Gale P. Biochem. Biophys. Res. Commun. 1993;196:879–84.
33. Sanders CR II, Czerski L, Vinogradova O, Badola P, Song D, Smith SO. Biochemistry. 1996;35:8610–18.

Structure of Membrane-Binding Proteins Revealed by Solid-State NMR

Satoru Tuzi, Naoko Uekama, Masashi Okada, and Hitoshi Yagisawa
Graduate School of Life Science, University of Hyogo
Harima Science Garden City, Kouto 3-chome, Kamigori, Hyogo 678-1297, Japan

The inside of living cells is separated from the external environment and divided into functionally distinctive compartments by a variety of lipid membranes such as the plasma membrane, the endoplasmic reticulum membrane, the nuclear membrane, etc. Naturally, a number of important cellular functions depend on translocation of materials and transduction of signals between those compartments as results of regulated transports of proteins and small molecules between the membranes of the compartments. In fact, a number of proteins involved in the important cellular functions such as cellular signal transduction, regulation of the cytoskeleton, and regulation of the membrane structure have been known to interact with the membrane surfaces as parts of their functions. Although many of those proteins are classified as water-soluble proteins, important parts of their physiological functions are related to their transient membrane-binding states. In order to understand structure—function relationship of those membrane-binding proteins, the protein structures at the water-lipid bilayer interface should be investigated in detail and compared with those in the aqueous phase, since structural changes accompanying the translocation of the proteins from the aqueous phase to the membrane surface would alter the functions of the proteins at the membrane surfaces where they play important physiological roles.

Phospholipase C-δ1 (PLC-δ1), schematically shown in Figure 1, is a protein involved in the phospholipid signal transduction pathway of higher organisms. PLC-δ1 hydrolyzes phosphatidylinositol 4,5-bisphosphate (PIP_2) in the cellular membrane as a response to an increase in the intracellular Ca^{2+} concentration induced by stimulations of the cell to produce the second messengers D-*myo*-inositol 1,4,5-trisphosphate (IP_3) and diacylglycerol [1, 2]. Among three membrane-binding sites of PLC-δ1 shown by triangles in Figure 1, a specific binding site for PIP_2 and IP_3 located at the N-terminal PH domain have been proposed to regulate the membrane localization of PLC-δ1 [3]. In the living cell, a release of PLC-δ1 from the plasma membrane induced by the decrease in PIP_2 and the increase in IP_3 provides a negative feedback system for a regulation of the hydrolysis of PIP_2 at the membrane surface by PLC-δ1. The structure of PLC-δ1 during the hydrolysis reaction at the plasma membrane surface is expected to be characterized by several factors, such as membrane-binding affinities of the membrane-binding sites, structures of the individual domains, orientations of the domains at the membrane plane, interactions between the domains, and dynamics of the protein structure at rather mobile membrane environments. In order to understand the physiological function of PLC-δ1, methods to obtain information about those factors at the membrane surface are needed. The X-ray diffraction analysis is hard to be applied to a structural study of the transient membrane-binding state of PLC-δ1, since the diffraction methods require an isolation and a crystallization of the protein. Using solution NMR methods, transient NOE (TRNOE) measurement [4–8] and the measurement of protein–micelle complex system [9] have been applied to the peripheral membrane proteins and the membrane-binding peptides to provide structural information at the membrane surface. The TRNOE measurement makes it possible to detect the NOE information corresponding to the structures of peptides at various membrane surfaces by solution NMR, when the structures undergo a rapid exchange between the membrane-bound state and the aqueous solution state. TRNOE is an effective method to investigate the structural state of peptides or proteins that weakly bind to the membranes. If the membrane-binding state has a long lifetime, such as in the case of the high affinity membrane binding of PLC-δ1, it is difficult to apply TRNOE, since the lifetime of the exchange is required to be short as compared with the longitudinal relaxation time of the observed nuclei in the target molecules. The protein–micelle complex system makes it possible to investigate the protein structure at the interface between the aqueous phase and the hydrophobic core of the micelle by solution NMR due to short rotational correlation time of the micelle. By using this approach, the membrane insertion and the structural change of the FYVE domain of human early endosome antigen 1 protein at the membrane surface have been investigated [9]. The micelle system is effective to reproduce the membrane surface environment close proximity of the peripheral membrane protein.

Graham A. Webb (ed.), Modern Magnetic Resonance, 299–303.
© 2008 *Springer.*

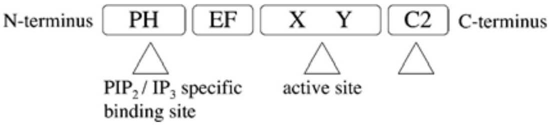

Fig. 1. A schematic representation of a domain arrangement of ratPLC-δ1. Proposed membrane binding sites are indicated by triangles.

A limitation of the system, however, is the difficulty in reproduction of several properties of the lipid bilayer, such as membrane curvature, lateral pressure, membrane mobility, and a local lipid composition. Among those properties, the local lipid composition is particularly important because of a growing number of evidence for the physiological importance of the lipid microdomain [10–13].

An advantage of an application of high-resolution solid-state NMR to study structure of lipid binding protein is that solid-state NMR can provide direct information on protein structure at the surface of the lipid vesicle suspended in an aqueous buffer under various conditions mimicking physiological conditions by changing temperature, vesicle size, buffer composition and the lipid composition of the membrane.

Dynamic Structure of the Membrane-Binding Proteins at the Membrane Surface

The structure, orientation and mobility of membrane-binding proteins or their domains are expected to be altered at the membrane surface due to the unique anisotropic environment of the water-lipid bilayer interface. The peripheral membrane proteins at the membrane surface would interact with the "interface region" between the aqueous phase and the hydrophobic layer of the membrane. The interface region consists of the polar head groups of the lipid molecules and occupies a 15 angstroms thickness of the single leaflet of the lipid bilayer [14]. Since the interface region possesses low dielectric constant ($\varepsilon = 10 \sim 30$) [15], and contains a number of electrically charged groups, the structure, orientation, and mobility of a membrane-binding protein that penetrates into the interface region are expected to be altered due to modification of hydrophobic and electrostatic interactions with the lipid head groups. In fact, membrane-binding peptides forming amphipathic α-helices are proposed to be located at the membrane interface, aligning its α-helical axis parallel with the membrane surface and facing its hydrophobic side of the α-helix the hydrophobic inner layer of the membrane [14, 16]. A membrane-binding domain of colicine, a bacterial toxin, has been proposed to undergo a drastic conformational alteration during its contact with the membrane surface [17–19]. The conformational changes were suggested to include reorientations of the amphipathic α-helices at the membrane surface and an insertion of the hydrophobic α-helix into the inner layer of the membrane.

A study of the lateral-pressure dependency of the PLC-δ1 lipid hydrolysis activity has suggested that parts of the PLC-δ1 molecule penetrate into the membrane during the hydrolysis [20]. If PLC-δ1 penetrates into the interface or the inner hydrophobic regions of the membrane, the conformation, orientation, and mobility of the PLC-δ1 can also be altered due to the changes of the dielectric constant or the electrostatic interactions. An application of the solid-state ^{13}C NMR to PLC-δ1-lipid vesicle complexes provides a suitable method to investigate those alterations at the membrane surface. An important advantage of this approach is that an aqueous suspension of the protein–lipid vesicle complexes assures dynamic structures analogous to the membranes under the physiological condition. Lipid molecules in a lipid bilayer surrounded by an aqueous solution at ambient temperature are known to undergo rapid rotational and translational diffusions within a membrane plane and fluctuations of the molecular structure [21]. These fluctuations are expected to affect the structure and dynamics of membrane-binding proteins at the membrane surface. The solid-state NMR studies of a transmembrane protein, bacteriorhodopsin, have shown the presence of internal motion of the protein relates to the depth in the membrane [22]. The characteristic motional frequencies for the transmembrane α-helices, the hydrophilic N- and C-termini protruded from the membrane surface, and the termini of the α-helices and loops located at the interface region have been reported to be $\sim 10^2$, $>10^5$ and $\sim 10^4$ Hz, respectively [22]. The protein structures including those fluctuations related to the flexible nature of the membrane would be important to understand functions of the membrane-binding proteins under the physiological conditions.

A solid-state NMR study of protein–lipid vesicle complexes provides information about the dynamic structures of the membrane-binding proteins characteristic to those of the anisotropic environments of the water-lipid bilayer interfaces under the physiological conditions. If the three dimensional structures of proteins in crystal or in solution are solved by X-ray diffraction studies or by solution NMR studies, as for the case of PLC-δ1, the information provided by solid-state NMR studies can be interpreted in detail by taking these high-resolution structural models into account.

Application of the Solid-State NMR on the PLC-δ1 PH Domain [23]

As shown in Figure 1, rat PLC-δ1 is a 85 kDa protein consists of functionally and structurally distinguishable five domains; N-terminal PH domain, EF-hand domain, X domain, Y domain, and C-terminal C2 domain [24].

Among these domains, the PH, EF-hand, and C2 domains are common structural modules of proteins included in the cellular signal transduction systems [25]. The X and Y domains form an active site of phospholipase activity of PLC-δ1. Inter-domain and membrane–domain interactions of these proteins provide intracellular cross-talking networks that support traffics of information in the living cells. The PH domain motif is a small and stable structure which consists of about 110 amino acid residues, and found in over 150 proteins involved in the cellular signal transduction pathway and the cytoskeltal reorganization [26, 27]. A number of the PH domains are suggested to mediate protein–lipid interactions by selective bindings to phosphorylated-inositol groups of inositol-phospholipids such as PIP_2 [28–31]. Proteins such as the heterotrimeric G-protein and the protein kinase C are also reported to be specific ligands of some PH domains [29]. As mentioned above, the N-terminal PH domain of PLC-δ1 is known to have high affinities to PIP_2 and IP_3, and regulates the membrane localization and the activity of PLC-δ1 [32, 33]. By applying solid-state ^{13}C NMR, structural alterations of the PH domain of PLC-δ1 during the membrane localization could directly be detected. Since the three dimansional structure of the PLC-δ1 PH domain-IP_3 complex have been determined by an X-ray diffraction study [24], the structure of the water-soluble PH domain-IP_3 complex could be utilized as a template to interpret the structural changes detected by solid-state NMR during the membrane localization of the PH domain.

Figure 2 shows the solid-state ^{13}C NMR spectra of the ^{13}C-labelled methyl groups of alanine residues introduced into the PLC-δ1 PH domain. Figure 2A and B show the spectra of the complex of the PH domain and the phosphatidylcholine (PC) vesicles containing 5% of PIP_2 measured by the cross polarization-magic angle spinning (CP-MAS) technique and the dipolar decoupled-magic angle spinning (DD-MAS) method, respectively. Vertical bars at the bottom of the spectra indicate the chemical shifts of the ^{13}C NMR signals of Ala residues in the PH domain–IP_3 complex in solution. In order to reproduce the dynamic property of the plasma membrane under the physiological condition, the lipid vesicles are suspended in buffers at neutral pH, and enclosed in the air-tight solid-state NMR rotor to prevent an evaporation of water.

The PLC-δ1 PH domain contains five Ala residues, Ala21, Ala88, Ala112, Ala116, and Ala118, as shown in the Figure 3A. Assignments of the signals in the solid-state NMR spectra to the individual Ala residues could be determined by site-specific replacements of the alanine residues by other amino acid residues, provided that no conformational changes are induced by resplacement of alanine with glycine, valine, or leucine. The assignment of the peaks was carried out by detecting the disappearance of a signal induced by a replacement of each alanine residue. The assignments of the Ala signals of the PLC-δ1 PH domain are shown at the top of the spectra in Figure 2.

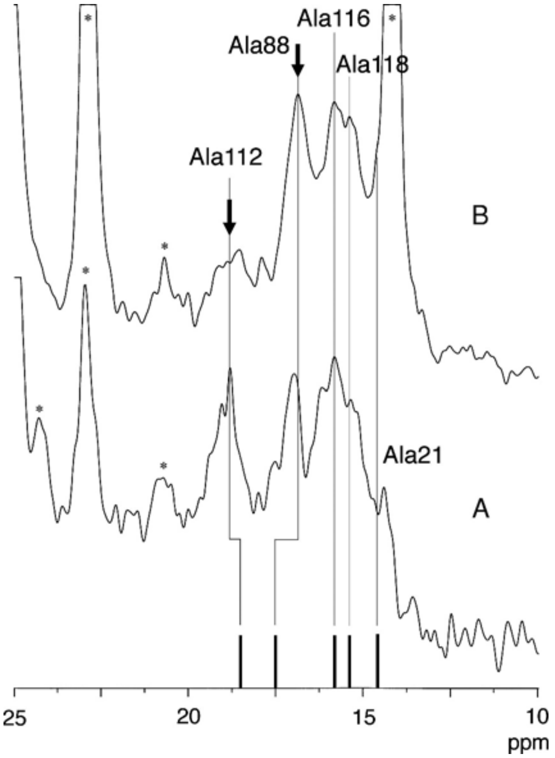

Fig. 2. High-resolution solid-state NMR spectra of the [3-^{13}C]Ala labeled PLC-δ1 PH domains forming complex with PC/PIP_2 vesicles obtained by (A) the CPMAS and (B) the DDMAS method. Assignments of the individual signals are shown at the top of the spectra. The vertical bars at the bottom of the spectra indicate the chemical shifts of the [3-^{13}C]Ala signals for the PLC-δ1 PH domain-IP_3 complex in solution.

The three dimensional structure of the PLC-δ1 PH domain, forming complex with IP_3, consists of β sandwich core containing seven β-strands, three α-helices located at the N-terminus, C-terminus, and the loop between β5- and β6-strands (β5/β6 loop), and loops connecting the β-strands (Figure 3A) as determined by an X-ray diffraction study [24]. The β1/β2, β3/β4, and β6/β7 loops form the specific ligand-binding site. The chemical shift displacements of the methyl carbons of the Ala residues in the PLC-δ1 PH domain shown in Figure 2 reflect the presence of a variety of torsion angles of the Ala residues in these higher-order structures. The conformation-dependent ^{13}C chemical shifts of Ala C_β carbons have been investigated and reported by solid-state NMR studies on polypeptides and structural proteins [34–36] and by the quantum mechanical calculations of model peptides [34–37]. Ala21 located at the N-terminal α-helix, and Ala116 and Ala118 located at the C-terminal

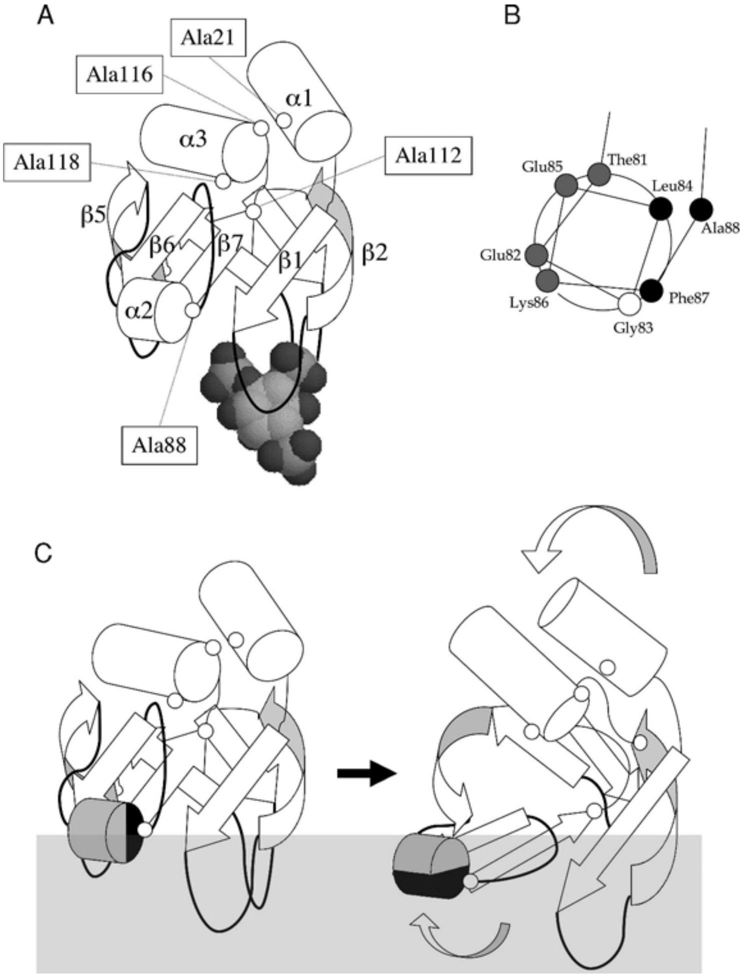

Fig. 3. (A) A schematic representation of the three-dimensional structure of the PLC-δ1 PH domain [24]. The α-helices and β-sheets are indicated by cylinders and arrows, respectively. Ala residues are indicated by open circles. IP_3 is shown by a cpk model. (B) The amphipathic α2-helix viewed from the C-terminus. Hydrophilic and hydrophobic residues are shown by grey and black circles, respectively. (C) A model of the conformational change of the PLC-δ1 PH domain induced at the membrane surface.

α-helix in the model structure are resonated between 14.8 and 16.1 ppm. Since the chemical shifts of these residues are identical to the chemical shifts of the PH domain forming complex with IP_3, it can be concluded that the conformations of the N- and C-terminal α-helices forming the hydrophilic face of the domain located at the opposite side of the membrane-binding surface do not change during the membrane localization. In contrast, significant changes in the chemical shifts of Ala88 and Ala112 as shown by arrows and kinked lines in Figure 2 indicate that the conformations of C-termini of the α2-helix and β7-strand are altered by the membrane localization of the PH domain. Changes of the chemical shift of Ala88, which is included in the α2-helix and that of Ala112, which is located at the C-terminus of the β7-strand flanking with the C-terminus of the β5/β6 loop, indicate the conformational changes of the α2-helix and the β5/β6 loop at the membrane surface. As shown in Figure 3B, the α2-helix has an highly amphipathic structure. In the model structure of the PH domain-IP_3 complex, the α2-helix faces its hydrophobic surface to the hydrophobic surface of the β-sandwich core consists of β5-, β6-, and β7-strands. Considering the proposed orientation of the amphipathic α-helical peptides at the interface region of the lipid bilayer, the α2-helix is expected to be located at the interface region of the membrane, facing the hydrophilic surface to the aqueous phase and the hydrophobic surface to the hydrophobic core of the lipid bilayer. The expected conformational changes of the α2-helix and the β5/β6 loop at the membrane interface are likely to provide more typical α-helix and β-sheet structures for Ala88 and Ala112, respectively. The structural changes include formations of the typical α-helix and β-sheet type hydrogen bonds of the residues that are missing in the model structure of the PH domain-IP_3 complex. These conformational changes are consistent with the directions of the chemical shift displacements of Ala88 and Ala112 induced by the formation of the PH domain–vesicle complexes. A model of the conformational changes of the PLC-δ1 PH domain at the membrane surface expected from the solid-state NMR study is illustrated in Figure 3C.

The structure of the PH domain at the membrane surface is also found to be remarkably affected by the lipid composition of the membrane. For instance, the above-mentioned conformational alteration of the PLC-δ1 PH domain induced at the surface of the PC/PIP_2 membrane are found to be suppressed at the negatively charged membrane surface containing acidic phospholipids, such as phosphatidylserine (PS). The solid-state NMR spectra of the PH domain binding to the PC/PS/PIP_2 membrane indicate that the conformation of the PH domain is identical to that of the PH domain forming a complex with IP_3 in solution. Moreover, a drastic increase in the mobility of the PH domain at the surface of the PC/PS/PIP_2 membrane is also detected from the changes of the relaxation parameters of the solid-state NMR spectroscopy. That the structure and the mobility of the PLC-δ1 PH domain depend on lipid composition of the target membrane may provide molecular mechanisms for the regulation of the PLC-δ1 function; changes in the local lipid composition in response to a variety of physiological reactions in the cell [38–40].

Modification of the protein structure and dynamics induced at the water-lipid bilayer interface as observed for the PLC-δ1 PH domain would also occur for other lipid-binding domains and proteins that are localized at the surfaces of the cellular membranes. The high-resolution solid-state NMR provides an unique method to investigate structural characteristics of the membrane-binding proteins that take part in important cellular functions mediated by changes in the structure, composition, and dynamics of the intracellular and plasma membranes.

References

1. Grobler JA, Hurley JH. Biochemistry 1998;37:5020.
2. Kim YH, Park TJ, Lee YH, Baek KJ, Suh PG, Ryu SH, Kim KT. J. Biol. Chem. 1999;274:26127.
3. Lomasney JW, Cheng HF, Wang LP, Kuan Y, Liu S, Fesik SW, King K. J. Biol. Chem. 1996;271:25316.
4. Auge S, Bersch B, Tropis M, Milon A. Biopolymers. 2000;54:297.
5. Wang Z, Jones JD, Rizo J, Gierasch LM. Biochemistry. 1993;32:13991.
6. Matsunaga TO, Collins N, Ramaswami V, Yamamura SH, O'Brien DF, Hruby VJ. Biochemistry. 1993;32:13180.
7. Milon A, Miyazawa T, Higashijima T. Biochemistry. 1990;29:65.
8. Wakamatsu K, Okada A, Suzuki M, Higashijima T. Masui Y, Sakakibara S, Miyazawa T. Eur. J. Biochem. 1986;154:607.
9. Kutateladze TG, Capelluto DG, Ferguson CG, Cheever ML, Kutateladze AG, Prestwich GD, Overduin M. J. Biol. Chem. 2004;279:3050.
10. Muller G. FEBS Lett. 2002;531:81.
11. Pike LJ, J. Lipid Res. 2003;44:655.
12. Caroni P. Embo J. 2001;20:4332.
13. Vereb G, Szollosi J, Matko J, Nagy P, Farkas T, Vigh L, Matyus L, Waldmann TA, Damjanovich S. Proc. Natl. Acad. Sci. U S A. 2003;100:8053.
14. White SH, Ladokhin AS, Jayasinghe S, Hristova K. J. Biol. Chem. 2001;276:32395.
15. Raudino A, Mauzerall D. Biophys. J. 1986;50:441.
16. Hristova K, Wimley WC, Mishra VK, Anantharamiah GM, Segrest JP, White SH. J. Mol. Biol. 1999;290:99.
17. Zakharov SD, Lindeberg M, Griko Y, Salamon Z, Tollin G, Prendergast FG. Cramer WA. Proc. Natl. Acad. Sci. U S A. 1998;95:4282.
18. Elkins P, Bunker A, Cramer WA, Stauffacher CV. Structure 1997;5:443.
19. Lindeberg M, Zakharov SD, Cramer WA. J. Mol. Biol. 2000;295:679.
20. Boguslavsky V, Rebecchi M, Morris AJ, Jhon DY, Rhee SG, McLaughlin S. Biochemistry. 1994;33:3032.
21. Pastor RW, Venable RM, Feller SE. Acc. Chem. Res. 2002;35:438.
22. Yamaguchi S, Tuzi S, Yonebayashi K, Naito A, Needleman R, Lanyi JK, Saito H. J. Biochem. (Tokyo) 2001;129:373.
23. Tuzi S, Uekama N, Okada M, Yamaguchi S, Saito H, Yagisawa H. J. Biol. Chem. 2003;278:28019.
24. Ferguson KM, Lemmon MA, Schlessinger J, Sigler PB. Cell. 1995;83:1037.
25. DiNitto JP, Cronin TC, Lambright DG. Sci. STKE 2003;2003:re16.
26. Yao L, Janmey P, Frigeri LG, Han W, Fujita J, Kawakami Y, Apgar JR, Kawakami T. J. Biol. Chem. 1999;274:19752.
27. Lemmon MA, Ferguson KM, Abrams CS. FEBS Lett. 2002;513:71.
28. Lemmon MA, Ferguson KM. Biochem. J. 2000;350 Pt 1:1.
29. Maffucci T, Falasca M. FEBS Lett. 2001;506:173.
30. Hirata M, Kanematsu T, Takeuchi H, Yagisawa H. Jpn. J. Pharmacol. 1998;76:255.
31. Kavran JM, Klein DE, Lee A, Falasca M, Isakoff SJ, Skolnik EY, Lemmon MA. J. Biol. Chem. 1998;273:30497.
32. Guo Y, Philip F, Scarlata S. J. Biol. Chem. 2003;278:29995.
33. Lemmon MA, Ferguson KM, O'Brien R, Sigler PB, Schlessinger J. Proc. Natl. Acad. Sci. U S A 1995;92:10472.
34. Saito H, Tuzi S, Naito A. Annu. Rep. NMR Spectrosc. 1998;36:79.
35. Saito H, Ando I. Annu. Rep. NMR Spectrosc. 1989;21: 209.
36. Saito H. Magn. Reson. Chem. 1986;24:835.
37. Asakawa N, Kurosu H, Ando I. J. Mol. Struct. 1994;323:279.
38. Huang S, Lifshitz L, Patki-Kamath V, Tuft R, Fogarty K, Czech MP, Mol. Cell. Biol. 2004;24:9102.
39. Fadok VA. Henson PM. Curr. Biol. 2003;13:R655.
40. Frasch SC, Henson PM, Nagaosa K, Fessler MB, Borregaard N Bratton DL. J. Biol. Chem. 2004;279:17625.

Solid-State NMR of Membrane-Active Proteins and Peptides

John D. Gehman and Frances Separovic
School of Chemistry, University of Melbourne, Melbourne, VIC 3010 Australia

Membranes are commonly perceived as little more than a simple canonical bilayer formed by the obvious orientation-preference of the constituent amphiphilic lipid molecules. Hydrophilic head groups, such as the zwitterionic phosphatidylcholine (PC), line the interface with aqueous environments on both sides of the membrane, while the aliphatic fatty acid chains of varying lengths and degree of unsaturation meet tail-to-tail to fill the region flanked by the head groups. The common perception of membrane-associated peptides and proteins is that they generally span the membrane with simple secondary structures, usually α-helices, but include the occasional β-sheet structure. These secondary structures are frequently regarded as trivial anchors to be removed so that the more interesting soluble domains may be studied by conventional approaches.

The classic "fluid-mosaic" model [1] suggests that membranes are simply a two-dimensional analog of a solution: lipids and membrane-associated protein rotate about single axes (normal to the bilayer surface) and translate across the membrane plane in a similar way to water and soluble proteins in three-dimensional solution. As well, study of membrane-associated proteins typically focuses almost exclusively on the protein—the membrane lipid is the negative space, akin to the buffer in which soluble protein is studied, while all the light is cast upon the protein.

Closer inspection of membrane structure, however, suggests that a more balanced view of membranes and membrane-associated protein is often necessary and more rewarding. Lipids have complex phases and phase transitions which depend upon particular lipid properties, temperature, hydration levels, and, especially relevant—the protein composition of the mixture. For those lipids commonly employed in model membrane studies, longer-chain fatty acids tend to persist in the lamellar gel-phase L_β as temperature is increased, particularly at low hydration levels. Conversely, shorter fatty acid chains and higher hydration levels tend to allow transition to the lamellar liquid crystalline phase L_α at lower temperatures. Higher temperatures and different lipid geometries than those typically employed for model membrane studies, lead to additional phase transitions into cubic (Q_{I} and Q_{II}) and hexagonal phases (H_{I} and H_{II}) [2].

Membrane-associated peptides and proteins include cell signaling receptors, immune response factors, ion channels, cell adhesion elements, toxins, and metabolic and photosynthetic components, many of which are also exploited by viruses to recognize and gain entry into cells. The literature is replete with hyperbole of the suitability of solid-state NMR for study of proteins in membrane environment: solid-state NMR does not require long-range ordering of molecules as is required for crystal diffraction work, and is not subject to the same hydrodynamic restraints that liquid-state NMR requires of molecules in solution. These are actually strengths rather than mere lack of weakness: less stringent sample structure allows protein *and* lipid molecules to be studied under conditions much closer to their natural membrane environments, and being independent of rapid global molecular rotation reintroduces the sensitivity of orientation-dependent parameters to local molecular structure and motion.

This sensitivity is based in large part upon the $(3\cos^2\theta - 1)$ dependence, which is treated under perturbation theory as first order corrections (H') to the Zeeman energy Hamiltonian ($H_z = \Delta m_z \gamma B_0$). θ is the angle subtended by the relevant vector within the sample and the applied magnetic field $\vec{B}_0$, and $(3\cos^2\theta - 1)$ is also known as the proportional Legendre polynomial $P_2(\theta)$ or the spherical harmonic function Y_0^2 :

$$H_T \approx H_z + H'\left(Y_0^2\right).$$

Conveniently for NMR studies of phospholipid membranes, ^{31}P is 100% naturally abundant, is more sensitive than carbon, and phospholipids typically have just one ^{31}P nucleus per molecule in the head group. Also advantageous is the infinitesimal natural abundance of ^{2}H, as small amounts of ^{2}H-enriched lipids may be selectively added to a sample and observed against virtually zero background. Together, wideline ^{31}P and ^{2}H NMR can be used to report on relative motional differences or changes in conformation of the hydrophilic head group at the aqueous interface and the hydrophobic aliphatic tails within the lipid bilayer, respectively, upon addition of protein

Graham A. Webb (ed.), Modern Magnetic Resonance, 305–311.
© 2008 *Springer.*

and other lipid components. At an extreme, changes in sample composition actually introduce new lipid phases that may compromise protein conformation and dynamics and/or may be relevant to the function of the protein being explored (as is the case for cytolytic toxins).

Similarly, despite relatively low intensity, selective enrichment of ^{13}C and ^{15}N in protein can be used against otherwise very low natural abundance to permit measurement of several structural aspects of membrane proteins: ^{13}C and ^{15}N NMR can help to define protein structure as well as orientation within the membrane.

Chemical Shift Anisotropy (CSA)

For spin $I = 1/2$ nuclei, which include ^{31}P, ^{1}H, ^{13}C, and ^{15}N, Y_0^2 modulates the interaction (H_σ) between the applied magnetic field and the anisotropic chemical shift tensor, specifically the anisotropic component. Each individual nucleus may be thought of as an individual crystallite, and each crystallite is most simply described by its principal axis system (PAS)—the orientation in which the chemical shift anisotropy (CSA) tensor is diagonal, with characteristic components σ_x^{PAS}, σ_y^{PAS}, σ_z^{PAS} · Each crystallite contributes signal intensity to the powder spectrum at frequency ν_σ according to its orientation relative to $\vec{B}_0$, which in the laboratory frame is simply $(0,0,B_0)$. The frequency at which a given crystallite contributes to the spectrum is given by [3]

$$\nu_\sigma = \gamma B_0 \left(\sigma_x^{\mathrm{PAS}} \cos^2\alpha \sin^2\beta + \sigma_y^{\mathrm{PAS}} \sin^2\alpha \sin^2\beta + \sigma_z^{\mathrm{PAS}} \cos^2\beta\right)$$

where, for all basis set vector lengths normalized to unity and expressed in laboratory frame coordinates, β is the angle between the PAS z-axis and $\vec{B}_0$

$$\beta = \cos^{-1}\left(\vec{z}^{\mathrm{PAS}} \cdot \vec{B}_0\right),$$

and, provided $\beta \neq 0$, α is the angle between the PAS y-axis and the vector orthogonal to both the PAS z-axis and $\vec{B}_0$. The direction of rotation by α is fixed by forcing the rotation axis to point in the same direction as the PAS $+z$-axis:

$$\alpha_{(\beta\neq 0)} = \cos^{-1}\left(\vec{y}^{\mathrm{PAS}} \cdot \frac{\left(\vec{z}^{\mathrm{PAS}} \times \vec{B}_0\right)}{\sin\beta}\right) = \sin^{-1}\left(\left|\vec{y}^{\mathrm{PAS}} \times \frac{\left(\vec{z}^{\mathrm{PAS}} \times \vec{B}_0\right)}{\sin\beta}\right|\right),$$

which simplifies to

$$\alpha_{(\beta\neq 0)} = \cos^{-1}\left(\frac{\vec{x}^{\mathrm{PAS}} \cdot \vec{B}_0}{\sin\beta}\right) = \sin^{-1}\left(\frac{\vec{y}^{\mathrm{PAS}} \cdot \vec{B}_0}{\sin\beta}\right).$$

α, β, and (although irrelevant here) γ are also commonly known as the Euler angles [4]. For the simple case considered here in which the PAS axis system is transformed directly to the laboratory frame, β and the Y_0^2 angle θ are the same.

When all individual crystallites are ordered identically, as in a macroscopic crystal, a single peak for each resonance is observed according to the orientation of the crystal relative to the magnetic field (e.g. Jones *et al.* [5]). More commonly, when crystallites are distributed randomly over all orientations, as for a powdered sample, a characteristic powder pattern is observed in which the discontinuities in the lineshape reveal the three PAS components. When the individual crystallite experiences rapid motion, whether by experimental mechanical spinning, or by molecular motion within the sample, time-averaged chemical shift values are observed. For the common case when the sample is mechanically spun about 54.74° (the "magic angle," where $Y_0^2 = 0$), the anisotropic component of the chemical shift tensor averages to zero, and the time-averaged value observed is the isotropic chemical shift; local magnetic environmental differences aside, this is the same value observed in solution NMR. When the orientation of the crystallite varies owing to molecular motion, as for a lipid rotating and translating within a model membrane, averaging of the CSA will depend on the range, axes, and frequency of motion.

The ^{31}P CSA of the head group at the rigid-lattice limit is realized with anhydrous gel-phase lipid samples, which have principal tensor values of approximately −98, −35, and 133 ppm (in traceless form[1]) for PC [6], a lipid head group class most commonly used in model membranes. Hydration of the lipid permits head group rotation about the glycerol-carbon/phosphate-oxygen and phosphate-oxygen/phosphorous bonds, and the static CSA is partially averaged to apparent principal tensor values of approximately −82, −27, and 109 ppm (in traceless form) for PC [6] (Figure 1).

Further deviations from this lineshape are indicative of the lipid phase. Above the gel-phase transition temperature, lipids experience rapid axial rotation as well

---

[1] Traceless form expresses principal chemical shift tensor values such that their average, the isotropic chemical shift, is zero. Adding the isotropic chemical shift to these principal CSA values gives reference-specific chemical shift values.

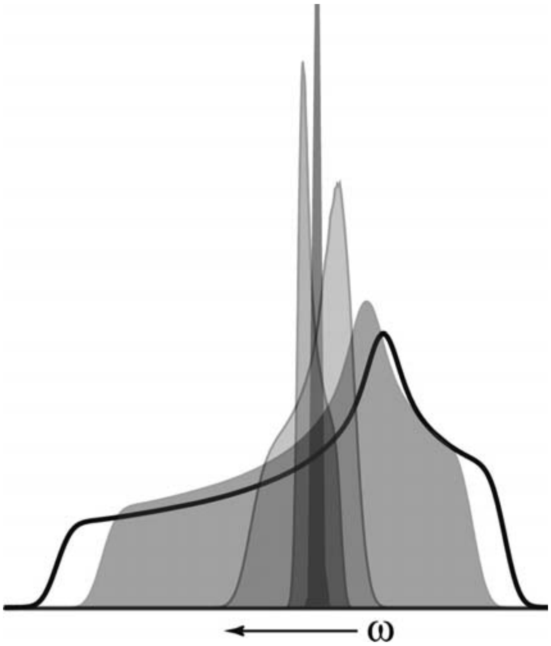

Fig. 1. Simulated lineshapes for static ^{31}P NMR of various lipid phases, in order of decreasing linewidth: static limit, monohydrated, liquid lamellar, hexagonal, and isotropic. Relatively intensities are only qualitatively correct. (See also Plate 34 on page XXXI in the Color Plate Section.)

as translational motion across the lipid surface. In the liquid crystalline lamellar phase of unoriented samples, though the bilayer normal vectors would be distributed randomly just as for regular powder samples, lateral translation of lipid molecules on the NMR timescale causes negligible deviation in lipid long-axis orientation. Hence in this phase the effect of rapid axial rotation alone is observed, where the ^{31}P CSA tensor is motionally averaged so that it appears axially symmetric, and only two different principal tensor values are needed, labeled $\sigma_{\perp}$ and $\sigma_{||}$ with reference to the axis of rotation about the bilayer normal.

Translational diffusion of lipids in the hexagonal phase, however, *does* serve to reorient the lipid rotation axis on the NMR timescale, and hence a further averaging of the CSA tensor is observed, which is generally manifest as a narrowing and reversal of the asymmetric liquid crystalline or bilayer phase lineshape.

Finally, a number of other phases where lipids rapidly reorient on the NMR timescale yields a symmetric and relatively narrow peak about a single principal value—the isotropic chemical shift. Most relevant for biological work are micellar and small vesicle phases, where the entire lipid structure is small enough to rotate quickly; indeed it is these phases that are used for solution NMR experiments of lipid-associated proteins.

^{31}P wideline NMR alone can provide a simple diagnostic, which may, for example, indicate whether temperature, hydration, or lipid characteristics and membrane composition need to be adjusted to maintain lamellar phase or vesicle structure upon addition of protein [7,8].

Another aspect of the CSA property of nuclei is explored by using aligned membrane samples. Lipid bilayers can be formed with parallel surfaces by layering hydrated phospholipids between glass plates. Similar to NMR of single crystals, by forcing a common orientation relative to the applied magnetic field $\vec{B}_0$, a single chemical shift value may be observed. While this can be useful for lipid samples using ^{31}P [9], it is particularly useful for the determination of backbone orientation using carbonyl ^{13}C and amide ^{15}N chemical shifts of membrane-associated peptides and protein. The principal ^{13}C CSA values for peptide backbone carbonyl are approximately -75, -3, and 78 ppm (in traceless form), with the intermediate -3 ppm value being the most variable and aligned approximately 10° off the ^{13}C=O bond (on the opposite side of the ^{13}C–N peptide bond) in the peptide plane, and with the 78 ppm axis perpendicular to the peptide plane [10–13]. Hence, when a given carbonyl orientation and membrane bilayer normal vector orientation are such that the peptide plane is perpendicular to $\vec{B}_0$, a maximum chemical shift value is observed. Other orientations yield Y_0^2-attenuated chemical shift values. This property can be combined together with consideration of molecular motion and secondary structure to help discriminate between different possible models for peptide and protein association with lipid bilayers, as applied to gramicidin A [14,15] (Figure 2) and melittin [16].

Similarly, principal shift tensor values for ^{15}N peptide backbone amides are approximately -60, -41, and 101 ppm (in traceless form), with the 101-ppm component lying 15°–20° off the ^{15}N–H bond vector and in the peptide plane [13,17,18]. When the fixed relationship between a particular backbone ^{15}N amide and an oriented membrane is such that the ^{15}N–H bond vector lies approximately parallel to $\vec{B}_0$, a maximum of chemical shift is observed. From a collection of other chemical shift observations the orientation of each ^{15}N–H bond vector can be deduced from the chemical shift as a function of the angle of the oriented bilayer normal to $\vec{B}_0$. This information can be used similarly to the above, for example, to determine whether an α-helix inserts into membranes (where ^{15}N–H bond vectors lie parallel to bilayer normal vectors), or lies parallel to the bilayer surface on membranes [9,19].

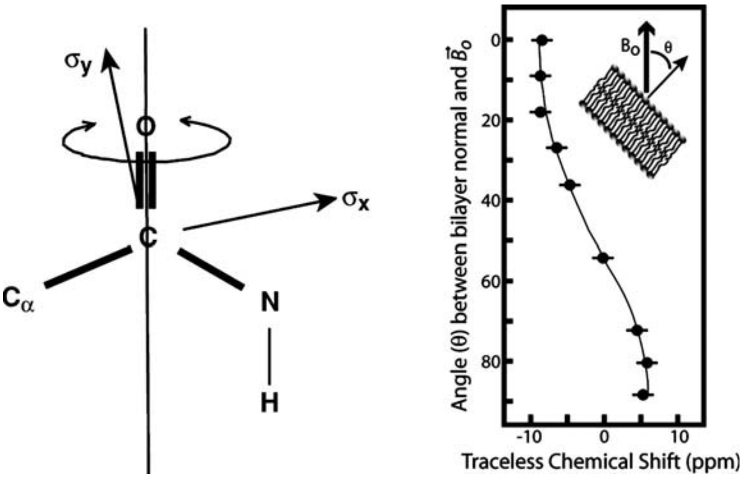

Fig. 2. (Left) Representation of the Ala^3 carbonyl orientation of gramicidin A in a $\beta^{6.3}$-helical structure for the molecular and PAS frame relative to an axis of rotation parallel to the lipid bilayer normal. Expected CSA with fast axial rotation in this orientation is −17 ppm. (Right) Measurement of carbonyl chemical shift for Ala^3 as a function of the angle of the bilayer normal to $\vec{B}_0$. The experimental CSA is approximately −16 ppm. (Adapted from Cornell *et al.* [14].)

Quadrupolar Coupling

Spin $I > {}^1/_2$ nuclei have an additional interaction (H_Q) with the nuclear electric field gradient, manifest as a nonzero quadrupole moment

$$H' \approx H_\sigma + H_Q.$$

In the case of the spin $I = 1$ nucleus ^{2}H bound to carbon, simplifications can be made of the anisotropic properties involved such that

$$\Delta \nu_Q(\text{kHz}) = 127.5 \cdot (3\cos^2\theta - 1),$$

where the underlying tensor is oriented such that θ is the angle between the applied magnetic field and the C–^{2}H bond vector [20], and rapid axial rotation about the C–^{2}H bond reduces the static coupling constant by a factor of two, so that the quadrupolar splitting magnitude varies between 127.5 and −63.75 kHz at 0° and 90°, respectively [2]. Owing to a probability distribution of θ proportional to $\sin\theta$, the $\theta = 90°$ orientation is most probable, and $\theta = 0°$ is least probable. Hence, the characteristic powder pattern—a "Pake" pattern [21]—of a static ensemble of C–^{2}H bond vectors is symmetric, according to $\nu = \nu_\sigma \pm {}^1/_2\Delta\nu_Q$. The lineshape has greater intensity where the quadrupolar splitting is reduced (the "90° edge"), lower intensity where the quadrupolar splitting is greatest, and the intensity overlaps at ν_σ for both $\Delta m_I = +1 - 0$ and $\Delta m_I = 0 - (^-1)$ transitions at $\theta = 54.74°$.

As for ^{31}P chemical shift, molecular motion which is rapid on a timescale relative to the quadrupole splitting causes variations in the angle θ and serves to time-average the quadrupolar splitting constant to a smaller-magnitude effective splitting at each orientation. In the fatty acid chains of membrane lipids, carbon–carbon bond rotation is the principal molecular motion, and serves to attenuate the maximum potential splitting. Such an attenuation is attributed to disorder among the lipid tails, and is characterized in practice by an order parameter S, which is proportional to Y_0^2 for the *apparent* quadrupole splitting,

$$S = \tfrac{1}{2}\langle 3\cos^2\theta - 1\rangle,$$

expressed to indicate that the splitting is a time-averaged value [22].

A fully deuterated fatty acid acyl chain produces a spectrum that is a sum of Pake patterns, one for each C–^{2}H position along the chain (e.g. Separovic and Gawrisch [23], Figure 3A). With sufficient resolution, the signal from each carbon position can be distinguished at the most intense portion of the lineshape at $\theta = 90°$. These complex spectra may be simplified by "de-Pake-ing" [24]—a numerical procedure for deriving the spectrum for a single angle θ from the powder pattern (Figure 3B). While strict interpretation of spectra can be difficult without systematically deuterating each position individually [25], it is generally assumed that for the typically resolved 90° intensities, the outermost to innermost intensity of the ^{2}H spectrum corresponds to the sequential chain positions from the first CD$_2$ positions after the carbonyl ester to the terminal methyl group deuterons. This indicates that the chain positions closest to the bilayer interface are most ordered, as they contribute the intensity at the wings of the spectrum with greatest quadrupole splitting. Positions become less ordered with subsequent steps further down the acyl chain [25]. Increasing disorder at each chain position causes the chain to protrude

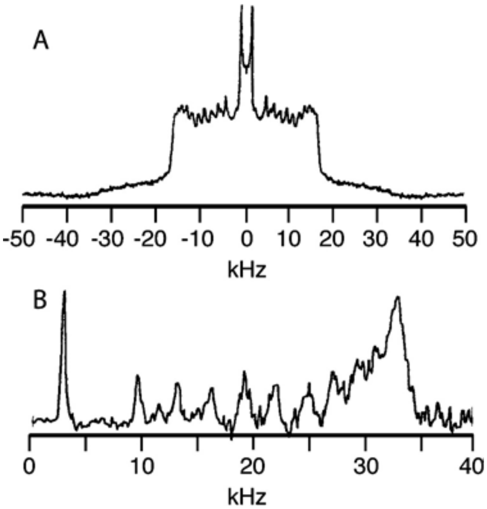

Fig. 3. ^{2}H spectrum of ($^2H_{31}$)-palmitoyl-oleoyl-PC (single-chain deuterated POPC) and natural abundance dioleoyl-phosphatidylethanolamine (DOPE) (5:1 molar ratio) bilayers: (A) powder pattern from unoriented dispersion; and (B) de-Paked half spectra, calculated for 0° orientation from A. (Adapted from Separovic and Gawrisch [23].)

less far from the membrane interface than it would in an extended conformation. Therein, greater acyl chain order can be interpreted as an increase in membrane thickness [23,26]. Hence, changes in quadrupolar splittings can indicate changes in membrane structure and dynamics upon addition of peptide or protein.

^{31}P and ^{2}H NMR of Lipids

Numerous examples demonstrate that together ^{31}P and ^{2}H NMR can provide important insight into membrane structure given the independent reporting of the relative motion and phase state of the head groups and hydrophobic tails. At one extreme, we have shown that Core Peptide from a transmembrane sequence of T-cell antigen receptor, known to be inhibitory of immune response, impacts upon ^{31}P and ^{2}H spectra of lipid bilayers only at unreasonably high peptide concentrations, supporting the supposition that its activity must be other than a consequence of membrane disruption [27].

At another extreme, the sphingomyelin-dependent cytolytic sea anemone protein equinatoxin II (EqtII) was shown to cause significant changes in model membranes at very low concentrations [28]. In this study, PC lipid head group motion increased upon addition of either 10% sphingomyelin *or* 0.1% cytolytic EqtII protein, but appeared similar to PC alone when *both* are added to model membranes (although the lipid phase transition temperatures increase). ^{2}H spectra of a deuterated PC for the same samples show a similar trend: overall linewidth (demarcated by the 0° edges of the highest ordered carbons of the acyl chain) decreases, reflecting greater disorder upon addition of sphingomyelin or EqtII individually, but higher order is observed when both are added. These two observations (together with relaxation data) were interpreted as suggesting that EqtII and sphingomyelin significantly impact membrane dynamics independently, but when combined tend to preferentially segregate out together from bulk PC lipid, leaving the PC dominated ^{31}P signal and ^{2}H signal to appear similar to pure PC. A higher protein concentration (0.4%) and higher temperature were also shown to promote an additional phase with an isotropic spectral component in both ^{31}P and ^{2}H spectra. These are likely to be very small unilamellar vesicles as seen by cryo-electron microscopy, and are sphingomyelin-enriched as shown by magic-angle spinning ^{31}P spectra of phases separated by centrifugation.

Lying between these extreme effects is the example of the αM1 transmembrane helix of nicotinic acetylcholine receptor added to PC bilayers. ^{31}P NMR [8] was used to show that high protein concentration and longer incubation times promoted the formation of an isotropic lipid phase. Of the conceivable lipid phases possibly giving rise to an isotropic signal, it was deduced that smaller, more rapidly tumbling vesicles were formed since ^{2}H NMR spectra did not show spectral averaging of the lipids. Furthermore, slightly higher order of the acyl chains, indicated by larger quadrupolar splittings, suggested a greater average membrane thickness. Addition of cholesterol prevented formation of the ^{31}P isotropic phase, while addition of the anesthetic halothane promoted conformational changes in the polypeptide due to changes in bilayer properties.

Dipolar (Re)-Coupling

Magnetically active nuclei also directly interact with one another in a distance-dependent manner, a property that can be exploited for structure determination of membrane protein complexes. The most significant terms in the dipolar coupling Hamiltonian are also a function of Y_0^2. These are: (i) the zero-frequency term, "I_zS_z" in product-operator parlance,which expresses the direct impact of the spin state of one nucleus upon another and (ii) the difference frequency/zero quantum term, "$I_+S_- + I_-S_+$", which drives mutual antiparallel "spin flips" between nuclei. While the I_zS_z term is significant for all nuclear pairs, the $I_+S_- + I_-S_+$ term is significant only for nuclear pairs for which the orientation-dependent resonance frequency difference $\Delta\omega$ is sufficiently small, principally homonuclei in a typical magnetic field.

Dipolar interactions usually complicate a spectrum; experiments that include sample-labeling schemes to provide for such complicating interactions are generally also spun at a speed about the magic angle that is several times faster than the strength of the dipolar interaction. The Y_0^2-dependent dipolar coupling is thus averaged to zero as for the anisotropic component of chemical shift and the first order quadrupolar coupling for spin $>{}^1\!/_2$ nuclei.

Further conjuring lies in the techniques to selectively reintroduce the dipolar coupling under magic-angle spinning conditions. One technique, rotational resonance, (RR or R^2), is so simple it may actually be achieved accidentally with an inopportune choice of magic-angle spinning speed ω_r for an isotopically (often ^{13}C) labeled sample. When the condition

$$\Delta\omega = n \times \omega_r$$

is met for small integer n and chemical shift difference $\Delta\omega = |\omega_I - \omega_S|$, the nuclear spin pair I, S are recoupled through the $I_+S_- + I_-S_+$ term, and effectually trade nuclear polarization [29] at a distance-dependent rate [30]. The technique can be employed for somewhat qualitative determination of protein complex models [31,32]. Strict analysis of the data requires attention to several complicating physical factors [30,33], and has been employed to achieve distance determinations of 2.7 ± 0.2 Å for a ^{31}P–^{31}P nuclear pair [34], as well as distances as long as 5 Å with identical or better accuracy for ^{13}C–^{13}C nuclear pairs in melittin measured in a membrane environment [7].

Conclusion

Exploitation of the $(3\cos^2\theta - 1)$ dependence of anisotropy in the chemical shift, quadrupolar and dipolar interactions with magnetically active nuclei provides a rich source of information for both proteins and, importantly, lipids in membrane systems. Solid-state NMR is well suited to measure these anisotropies, and is becoming geometrically more important as the focus of biomedical research increasingly spotlights membrane proteins. While straightforward approaches require sometimes tedious isotopic labeling of samples, and data interpretation should not be assumed to be trivial, the experiments are relatively easy to perform and do not require extraordinarily high field strengths as do many other currently emerging and increasingly important NMR approaches. Although currently evolving at an accelerated pace, existing biological solid-state NMR techniques can also give information on both the membrane and the associated protein.

References

1. Singer SJ, Nicholson G. Science. 1972;175:720.
2. Epand R. Lipid Polymorphism and Membrane Properties. Academic Press: San Diego, 1997.
3. Mehring M. Principles of High Resolution NMR in Solids. Springer-Verlag: New York, 1983.
4. Rose ME. Elementary Theory of Angular Momentum. Wiley: New York, 1957.
5. Jones GP, Cornell BA, Horn E, Tiekink ERT. J. Crystallogr. Spectrosc. Res. 1989;19(4):715.
6. Seelig J. Biochim. Biophys. Acta. 1978;515:105.
7. Lam YH, Wassall SR, Morton CJ, Smith R, Separovic F. Biophys. J. 2001;81(5):2752.
8. de Planque MRR, Rijkers DTS, Liskamp RMJ, Separovic F. Magn. Reson. Chem. 2004;42(2):148.
9. Balla MS, Bowie JH, Separovic F. Eur. Biophys. J. Biophys. Lett. 2004;33(2):109.
10. Stark RE, Jelinski LW, Ruben DJ, Torchia DA, Griffin RG. J. Magn. Reson. 1983;55:266.
11. Separovic F, Smith R, Yannoni CS, Cornell BA. J. Am. Chem. Soc. 1990;112:8324.
12. Oas TG, Hartzell CJ, McMahon TJ, Drobny GP, Dahlquist FW. J. Am. Chem. Soc. 1987;109(20);5956.
13. Hartzell CJ, Whitfield M, Oas TG, Drobny GP. J. Am. Chem. Soc. 1987;109(20):5966.
14. Cornell BA, Separovic F, Baldassi AJ, Smith R. Biophys. J. 198;53:67.
15. Smith R, Thomas DE, Separovic F, Atkins AR. Cornell BA. Biophys. J. 1989;56:307.
16. Smith R, Separovic F, Milne TJ, Whittaker A, Bennett FM, Cornell BA, Makriyannis A. J. Mol. Biol. 1994;241:456.
17. Wu CH, Ramamoorthy A, Gierasch LM, Opella SJ. J. Am. Chem. Soc. 1995;117:6148.
18. Oas TG, Hartzell CJ, Dahlquist FW, Drobny GP. J. Am. Chem. Soc. 1987;109(20):5962.
19. McDonnell PA, Shon K, Kim Y, Opella SJ. J. Mol. Biol. 1993;233:447.
20. Schmidt-Rohr K, Spiess HW. Multidimensional Solid State NMR and Polymers: Academic Press, 1994.
21. Pake GE. J. Chem. Phys. 1948;16(4):327.
22. Seelig J, Niederberger W. J. Am. Chem. Soc. 1974;96(7):2069.
23. Separovic F, Gawrisch K. Biophys. J. 1996;71(1):274.
24. Sternin E, Bloom M, MacKay AL. J. Magn. Reson. 1983;55:274.
25. Seelig A, Seelig J. Biochemistry. 1974;13(23):4839.
26. Douliez JP, Leonard A, Dufourc EJ. J. Phys. Chem. 1996;100(47):18450.
27. Ali M, De Planque MRR, Huynh NT, Manolios N, Separovic F. Lett. Peptide Sci. 2001;8(3–5):227.
28. Bonev BB, Lam YH, Anderluh G, Watts A, Norton RS, Separovic F, Biophys. J. 2003;84(4):2382.

29. Andrew ER, Bradbury A, Eades RG, Wynn VT. Phys. Lett. 1963;4(2):99.
30. Levitt MH, Raleigh DP, Creuzet F, Griffin R.G. J. Chem. Phys. 1990;92:6347.
31. Lam YH, Nguyen V, Fakaris E, Separovic F. J. Protein Chem. 2000;19(6):529.
32. Lam YH, Morton CJ, Separovic F. Eur. Biophys. J. Biophys. Lett. 2002;31(5):383.
33. Costa PR, Sun B, Griffin RG. J. Am. Chem. Soc. 1997;119:10821.
34. McDermott AE, Creuzet F, Griffin RG, Zawadzke LE, Ye Q-Z, Walsh CT. Biochemistry. 1990;29:5767.

Magnetic Resonance Spectroscopic Studies of the Integral Membrane Protein Phospholamban

Gary A. Lorigan
Department of Chemistry and Biochemistry, Miami University, Oxford, OH 45056, USA

Membrane proteins (which make up approximately one-third of the total number of known proteins) are responsible for many important properties and functions of biological systems: they transport ions and molecules across the membrane, they act as receptors, and they have roles in the assembly, fusion, and structure of cells and viruses. Despite the abundance and clear importance of membrane-associated molecules, very little information about these systems exists. A plethora of membrane proteins are intimately associated with cardiovascular function and disease. Structural studies of these membrane proteins represent one of the final frontiers in structural biology. X-ray crystallography is the premiere technique that is used to elucidate structural information of biologically significant protein systems. However, this technique has not been very successful in providing structural information about membrane protein systems. The hydrophobic surfaces associated with membrane-bound protein systems make the crystallization process extremely difficult. Although researchers are making progress with X-ray techniques, still only a handful of membrane protein structures have been obtained via X-ray crystallography [1–5]. Alternatively, solution NMR spectroscopy, solid-state NMR spectroscopy, and EPR spectroscopy are powerful techniques that can be used to provide structural, orientational, and dynamic information about membrane protein systems in lipid bilayers [6–10]. This short review chapter will analyze some of the magnetic resonance techniques that have been used to investigate the integral membrane protein phospholamban (PLB).

Phospholamban

The contraction/relaxation cycle intimately associated with cardiac muscle cells is regulated by cytosolic levels of Ca^{2+} ions. In order for cardiac muscle cells to relax after a contraction, Ca^{2+} ions must be rapidly transferred between the cytosol and the cardiac sarcoplasmic reticulum (SERCA) lumen. The transfer of Ca^{2+} ions is performed by the Ca-ATPase of the SERCA [11–14]. This unique pumping mechanism is activated by the cyclic AMP- and calmodulin-dependent phosphorylation of the integral membrane protein PLB [15–17]. Dephosphorylated PLB inhibits SERCA ATPase activity and stops the flow of Ca^{2+}ions. Conversely, when PLB is phosphorylated this inhibition is relieved, and Ca^{2+} ions are transferred through the membrane. This unique process controls the heartbeat of the cardiac cycle. The rate and extent of myocardial contraction is determined by the flow rate of Ca^{2+} ions into the myoplasm. Recent studies have suggested that an abnormal relaxation of cardiac muscle cells can induce heart failure, due to abnormalities in Ca^{2+} transients and decreases in Ca-ATPase concentrations [18,19]. PLB is a small (52 amino acid) type II membrane protein and shares many characteristics with some of the larger mammalian ion channels [20]. The size of PLB makes it an ideal candidate to investigate with both NMR and EPR spectroscopy. Determining the structure of PLB and its interaction with lipid bilayers is central to understanding its regulatory role.

The full three-dimensional structure of WT-PLB in either the phosphorylated or dephosphorylated states has not been determined in a phospholipid bilayer. Sequence homology studies have indicated that the protein consists of three domains: a hydrophilic amphipathic N-terminus (1–21) MDKVQYLTR SAIRRASTIEMP section, a hinge or β-sheet region QQARQNLQN (22–30), and a hydrophobic (31–52) C-terminus LFINFCLILICLLLICIIVMLL segment that spans the bilayer. WT-PLB is believed to consist of a homopentameric cluster, which retains activity when reconstituted into lipid bilayers with Ca-ATPase [21,22]. The structural characteristics of PLB have been investigated with several biophysical spectroscopic techniques including: CD spectroscopy, EPR spectroscopy, IR spectroscopy, and NMR spectroscopy in a variety of different environments (organic solvents, micelle, and phospholipid bilayer). CD and solution NMR studies carried out on the hydrophilic cytoplasmic domain of PLB in organic solvents have identified a partial α-helical structure [23–27]. The α-helical secondary structure of the cytoplasmic domain has been confirmed with CD and IR and extended further to include the transmembrane segments of PLB [28,29]. The structure of PLB may change when the full-length protein

Graham A. Webb (ed.), Modern Magnetic Resonance, 313–318.
© 2008 *Springer.*

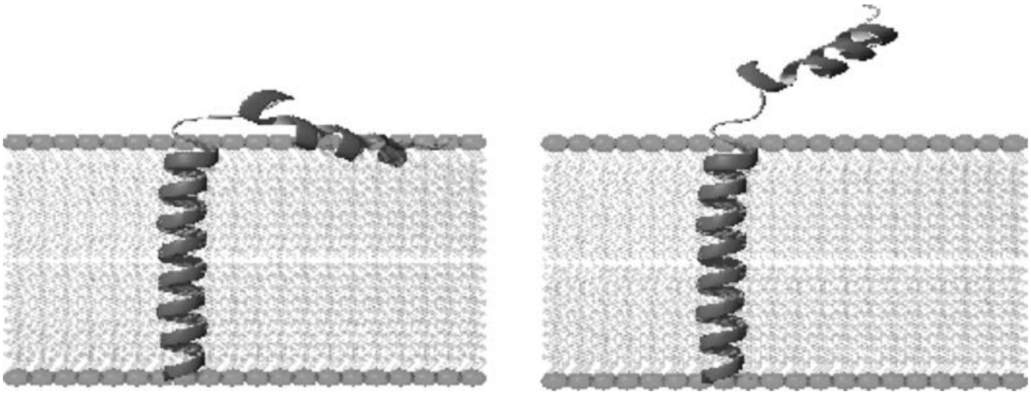

Fig. 1. (Left) Structure of PLB inserted into a phospholipid bilayer. (Right) Additional structural model of PLB inside a phospholipid bilayer. The structures are shown as monomers for clarity. WT-PLB is believed to exist as a pentamer. (See also Plate 35 on page XXXI in the Color Plate Section.)

is placed into a proper functional lipid environment such as a phospholipid lipid bilayer. Also, the structure may be modified by its interaction with Ca-ATPase which is required for regulatory function.

Two structural models have been proposed for PLB based upon FTIR, NMR, and computer data/modeling (Figure 1). Tatulian *et al.* have indicated that PLB consists of two disjointed helices: a transmembrane helix that is parallel with the bilayer normal and a tilted helix that extends outside the membrane (Figure 1 (left side)) [30]. The two helices are connected by a small intervening β-sheet/unstructured region.

Another model (not shown) proposes that PLB is a continuous α-helix in which both the transmembrane and cytosolic elements are oriented at a tilt angle of $28^\circ \pm 6^\circ$ with respect to a DMPC lipid bilayer [28]. According to this model, PLB is one long straight α-helical structure in which the hydrophobic portion is located within the membrane and the hydrophilic region lies outside the membrane. Analysis of all the different biophysical studies of WT-PLB, indicates that the structure and helix orientation of phosphorylated and dephosphorylated pentameric PLB with respect to the membrane is under debate.

Phosphorylation serves as the regulatory switch for PLB. It confers protease resistance, indicating a possible structural change in PLB [29]. Upon β-adrenergic stimulation, PLB is phosphorylated at sites Ser-16 and Thr-17 concomitant with the flow of Ca^{2+} ions [13]. Once again, a discrepancy exists in the literature as to whether a change occurs in the secondary structure of phosphorylated PLB. Specifically, fluorescence, FTIR, and solution NMR measurements have observed secondary structural changes on the full-length and segmented portions of PLB, while computer modeling and additional FTIR and CD studies have not [11,12,26,29–31]. Recent solution NMR studies on the cytoplasmic portion of PLB (residues 1–36) in trifluoroethanol have indicated that phosphorylation does not adversely affect the structure of the C-terminus between residues 21 and 36, and that phosphorylated PLB has more loose helical packing than the nonphosphorylated version of the protein.

Solid-State NMR Spectroscopic Studies of PLB

Several research groups are studying the structural and dynamic properties of PLB utilizing NMR spectroscopy [14,23,32–44]. The structural properties of PLB have been studied utilizing the rotational echo double resonance (REDOR) and the rotational resonance solid-state NMR techniques.

Solid-state NMR spectroscopic studies on PLB utilizing the rotational resonance method have indicated that the sequences Pro21-Ala24 and Leu42-Leu44 adopt an α-helical structure in pure lipid bilayers, in the presence and absence of Ca-ATPase [39]. Additional REDOR NMR experiments have revealed that the sequence Ala24-Gln26 switches from an α-helix in pure lipid membranes to a more extended structure in the presence of SERCA [39,44]. The data gleaned from this study suggest that the Ca^{2+}-ATPase has a long-range effect on the structure of PLB around residue 25, which promotes the functional association of the two proteins. Additional rotational resonance NMR data have shown that internuclear ^{13}C distances between Leu7 and Ala11 in the cytoplasmic region, between Pro21 and Ala24 in the juxtamembrane region, and between Leu42 and Cys46 in the transmembrane domain of PLB all consist of an α-helical secondary structure [41]. REDOR experiments agree that the secondary structure is α-helical in the region of Pro21 and that there are no large conformational changes upon phosphoryla-

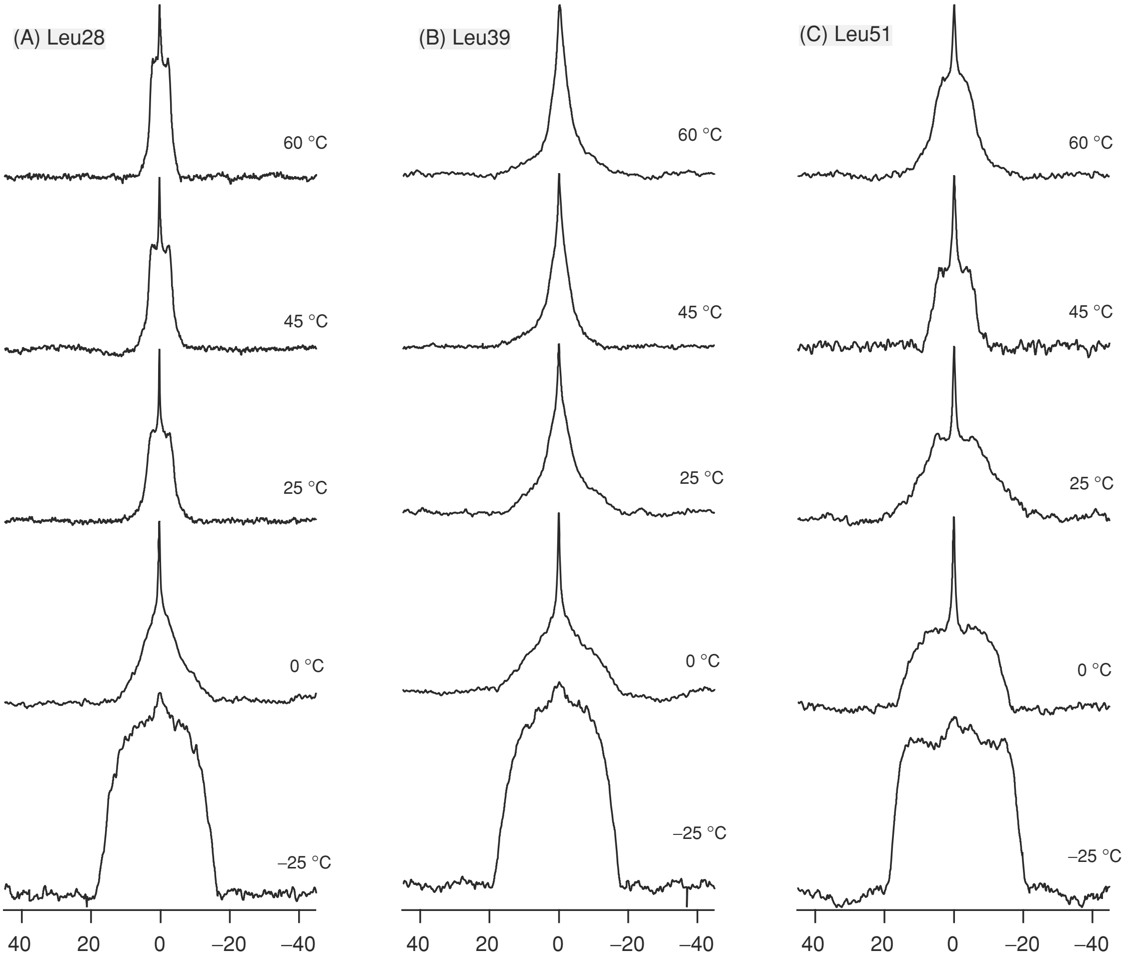

Fig. 2. ^{2}H NMR powder pattern spectra of L-leucine-5,5,5-d$_3$ incorporated at specific sites of TM-PLB and inserted into POPC phospholipid bilayers. ^{2}H NMR spectra are shown for (A) CD$_3$-Leu28 PLB, (B) CD$_3$-Leu39 PLB, and (C) CD$_3$-Leu51 PLB incorporated into POPC phospholipid bilayers at lipid/peptide molar ratios of 25:1.

tion [41]. The data indicate that PLB exists as homogenous α-helical pentamer.

Additionally, the side chain and backbone dynamic properties of PLB have been investigated utilizing solid-state NMR spectroscopy. Figure 2 shows the solid-state ^{2}H NMR powder pattern spectra of specific labeled TM-PLB (transmembrane section of PLB consisting of residues Ala24-Leu52) samples incorporated into unoriented 1-palmitoyl-2-oleoyl-phosphocholine (POPC) bilayers as a function of temperature [33]. ^{2}H solid-state NMR spectra of ^{2}H-labeled leucine (deuterated at one terminal methyl group) incorporated at different sites (CD$_3$-Leu28, CD$_3$-Leu39, and CD$_3$-Leu51) along the TM-PLB peptide exhibited line shapes characteristic of either methyl group reorientation about the C_γ–C_δ bond axis, or by additional librational motion about the C_α–C_β and C_β–C_γ bond axes. The ^{2}H NMR line shapes of all $-CD_3$ labeled leucines are very similar below 0 °C, indicating that all the residues are located inside the lipid bilayer. At higher temperatures, all three labeled leucine residues undergo rapid reorientation about the C_α–C_β, C_β–C_γ and C_γ–C_δ bond axes as indicated by ^{2}H line shape simulations and reduced quadrupolar splittings. At all the temperatures studied, the ^{2}H NMR spectra indicated that the Leu51 side chain has less motion than Leu39 or Leu28 which is attributed to its incorporation in the pentameric PLB leucine zipper motif. The unique features associated with these spectra could be explained by the condition that the Leu51 side chain is involved in the so-called "knobs-into-holes" bonding arrangement in which the side chain of Leu51 from one α-helix is locked into the groove of a second α-helix (of the pentamer) so that the two α-helices are coiled around each other. Smith and co-workers have also reported that Leu44 is buried within the core of pentameric PLB and also observed the general bell-shaped characteristics in the line shape [45]. This type of structural arrangement is believed to help stabilize the structure of the pentamer [41]. ^{31}P NMR spectra of these samples indicate that TM-PLB is incorporated into phospholipid bilayers in the liquid crystalline (L_{α}) phase [46]. Additional studies have probed the interaction of PLB with the membrane utilizing spin-label EPR spectroscopy [40]. Finally, ^{15}N solid-state NMR studies have indicated that TM-PLB is transmembrane with respect to the membrane normal [47].

Magnetic Resonance Spectroscopic Studies of the AFA-PLB Monomer

Recently, some exciting new NMR and EPR spectroscopic results have been obtained on a mutated version of PLB (AFA-PLB) that predominantly exists as a monomer [27,36,39,41,45,48,49]. AFA-PLB is obtained by mutating the three Cys residues (36, 41, and 46) to Ala, Phe, and Ala. This mutated PLB monomer has been shown to be fully functional [50]. One of the biggest breakthroughs has been the solution NMR structure of AFA-PLB by the Veglia research group. His research group has determined an "L-shaped" α-helical structure of the mutated monomeric version of PLB in dodecylphosphocholine micelles [38]. Figure 3 shows a well-resolved HSQC solution NMR spectrum of uniformly ^{15}N-labeled AFA-PLB with assignments. The spectrum was kindly provided by Dr. Gianluigi Veglia. The structure on the left hand side of Figure 1 illustrates the "L-shape" structure of AFA-PLB inserted into a phospholipid bilayer.

Additional solid-state NMR research conducted on site-specific ^{15}N-labeled AFA-PLB has shown that the monomeric form of PLB has one component that is nearly transmembrane (hydrophobic segment, residues 31–52) and the amphipathic segment lies on the surface of the membrane [51,52]. The solid-state NMR data coupled with molecular dynamic simulations estimates that the monomeric transmembrane helix makes an approximate 10° angle with respect to the bilayer normal.

NMR and EPR structural dynamic studies have indicated that PLB involves functionally important transitions among potentially multiple structural states and that the structure of PLB is affected by its phosphorylation and its interaction with Ca-ATPase [49,51]. Primarily, the Thomas lab has studied backbone dynamics with EPR spectroscopy of specific-site 2,2,6,6,-tetramethyl-piperidine-N-oxyl-4-amino-4-carboxylic acid (TOAC) attached at positions 0, 11, and 24 in the cytoplasmic domain or at position 46 in the transmembrane domain of AFA-PLB. The EPR spectrum of the AFA-PLB with a TOAC label at position 46 reveals a single broad component, indicating an ordered transmembrane helix. However, the cytoplasmic labels reveal two separate spectral EPR components. One of the components is disordered and nearly isotropic with dynamic motion on the ns timescale, while the second spectral component is more ordered and undergoing slower motion on the EPR timescale. The results indicate that the cytoplasmic domain of the AFA-PLB monomer is in dynamic equilibrium between an ordered confirmation (buried within the membrane) and a motionally dynamic form that is detached from the membrane and poised to interact with its regulatory target [50]. A model of AFA-PLB between these two states can be seen by examining the two structural

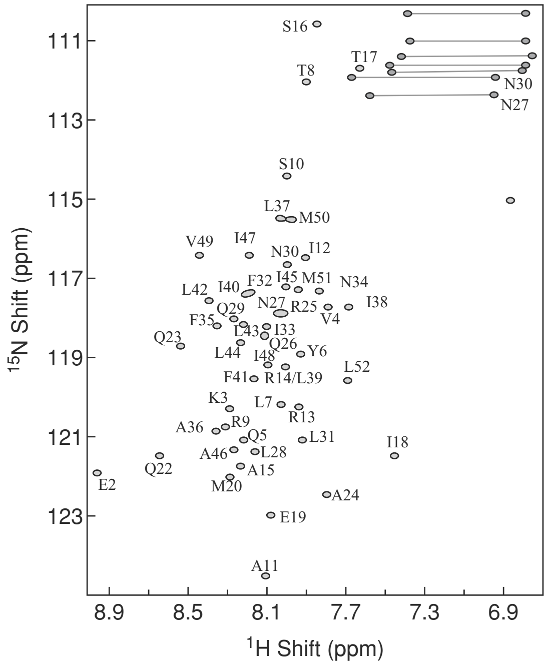

Fig. 3. HSQC solution NMR spectrum of ^{15}N-labeled AFA-PLB in dodecylphosphocholine micelles. The NMR spectrum was kindly provided by Dr. Gianluigi Veglia.

configurations of PLB located within Figure 1. This TOAC EPR spin-label method provides excellent backbone dynamic information similar to ^{15}N amide solid-state NMR dynamic studies.

Future NMR and EPR spectroscopic studies that probe the structural and dynamic properties of both the pentameric and monomeric forms of PLB and how they interact with SERCA and PKA are needed to help to better understand regulatory function.

Acknowledgments

GAL would like to acknowledge his research group and Professor Gianluigi Veglia for all of their help in preparing this review chapter. This work was supported by a National Science Foundation CAREER Award (CDE-0133433), an NIH Grant (GM60259-01), and an American Heart Association Scientist Development Grant (0130396). The 500 MHz Wide bore NMR Spectrometer was obtained from NSF Grant (#10116333).

References

1. Agre P, Lee MD, Devidas S, Guggino WB. Science. 1997;275(5305):1490.
2. MacKinnon R, Cohen SL, Kuo AL, Lee A, Chait BT. Science. 1998;280(5360):106.
3. MacKinnon R. Nature. 2002;416(6878):261.
4. Doyle DA, Cabral JM, Pfuetzner RA, Kuo AL, Gulbis JM, Cohen SL, Chait BT, MacKinnon R. Science. 1998;280(5360):69.
5. Jiang YX, Lee A, Chen JY, Ruta V, Cadene M, Chait BT, MacKinnon R. Nature. 2003;423(6935):33.
6. Opella SJ. Nat. Struct. Biol. 1997;4(Suppl):845.
7. Opella SJ, Nevzorov A, Mesleh MF, Marassi FM. Biochem. Cell Biol. 2002;80(5):597.
8. Opella SJ, Marassi FM. Chem. Rev. 2004;104(8):3587.
9. Cross TA, Opella SJ. Curr. Opin. Struct. Biol. 1994;4(4):574.
10. Smith SO, Peersen OB. Annu. Rev. Biophys. Biomol. Struct. 1992;21:25.
11. Li M, Cornea RL, Autry JM, Jones LR, Thomas DD. Biochemistry. 1998;37(21):7869.
12. Cornea RL, Jones LR, Autry JM, Thomas DD. Biochemistry. 1997;36(10):2960.
13. Simmerman HKB, Jones LB. Physiol. Rev. 1998;78(4):921.
14. Li JH, Xiong YJ, Bigelow DJ, Squier TC. Biochemistry. 2004;43(2):455.
15. Kirchberger MA, Tada M, Katz AM. Rec. Adv. Cardiac. Struct. Metab. 1975;5:103.
16. James P, Inui M, Tada M, Chiesi M, Carafoli E. Nature. 1989;342:90.
17. Voss J, Jones LR, Thomas DD. Biophys. J. 1994;67(1):190.
18. Grossman W. In RG Johnson Jr, EG Kranias (Eds). Cardiac Sarcoplasmic Reticulum Function and Regulation of Contractility, Vol. 853. New York Academy of Sciences: New York, 1998, p 207.
19. Lehnart SE, Wolfgang S, Burkert P, Prestle J, Just H, Hasenfuss G. In RG Johnson Jr, EG Kranias (Eds). Cardiac Sarcoplasmic Reticulum Function and Regulation of Contractility, Vol. 853. New York Academy of Sciences: New York, 1998, p 220.
20. Tada M. Ann. N.Y. Acad. Sci. 1992;671:92.
21. Adams PD, Arkin IT, Engelman DM, Brunger AT. Nat. Struct. Biol. 1995;2(2):154.
22. Kovacs RJ, Nelson MT, Simmerman HBK, Jones LR. J. Biol. chem. 1988;263:18364.
23. Pollesello P, Annila A. Biophys. J. 2002;83(1):484.
24. Pollesello P, Annila A, Ovaska M. 1999;76(4):1784–1795.
25. Hubbard JA, Maclachlan LK, Meenan E, Salter CJ, Reid DG, Lahouratate P, Humphries J, Stevens N, Bell D, Neville WA, Murray KJ, Darker JG. Mol. Membr. Biol. 1994;11:263.
26. Mortishiresmith RJ, Pitzenberger SM, Burke CJ, Middaugh CR, Garsky VM, Johnson RG. Biochemistry. 1995;34(23):7603.
27. Lamberth S, Schmid H, Muenchbach M, Vorherr T, Krebs J, Carafoli E, Griesinger C. Helv. Chim. Acta. 2000;83(9):2141.
28. Arkin IT, Rothman M, Ludlam CFC, Aimoto S, Engelman DM, Rothschild KJ, Smith SO. J. Mol. Biol. 1995;248(4):824.
29. Arkin IT, Adams PD, Brunger AT, Smith SO, Engelman DM. Annu. Rev. Biophys. Biomol. Struct. 1997;26:157.
30. Tatulian SA, Jones LR, Reddy LG, Stokes DL, Tamm LK. Biochemistry. 1995;34(13):4448.
31. Ludlam CFC, Arkin IT, Liu XM, Rothman MS, Rath P, Aimoto S, Smith SO, Engelman DM, Rothschild KJ. Biophys. J. 1996;70(4):1728.
32. Mascioni A, Eggimann BL, Veglia G. Chem. Phys. Lipids. 2004;132(1):133.
33. Tiburu EK, Karp ES, Dave PC, Damodaran K, Lorigan GA. Biochemistry. 2004;43(44):13899.
34. Becker CFW, Strop P, Bass RB, Hansen KC, Locher KP, Ren G, Yeager M, Rees DC, Kochendoerfer GG. J. Mol. Biol. 2004;343(3):747.
35. Middleton DA, Hughes E, Madine J. J. Am. Chem. Soc. 2004;126(31):9478.
36. Metcalfe EE, Zamoon J, Thomas DD, Veglia G. Biophys. J. 2004;87(2):1205.
37. Dave PC, Tiburu EK, Damodaran K, Lorigan GA. Biophys. J. 2004;86(3):1564.
38. Zamoon J, Mascioni A, Thomas DD, Veglia G. Biophys. J. 2003;85(4):2589.
39. Hughes E, Middleton DA. J. Biol. Chem. 2003;278(23):20835.
40. Arora A, Williamson IM, Lee AG, Marsh D. Biochemistry. 2003;42(17):5151.
41. Smith SO, Kawakami T, Liu W, Ziliox M, Aimoto S. J. Mol. Biol. 2001;313(5):1139.
42. Sharma P, Patchell VB, Gao Y, Evans JS, Levine BA. Biochem. J. 2001;355:699.
43. Middleton DA, Ahmed Z, Glaubitz C, Watts A. J. Magn. Reson. 2000;147(2):366.
44. Ahmed Z, Reid DG, Watts A, Middleton DA. Biochim. Biophys. Acta Biomembr. 2000;1468(1–2):187.

45. Ying WW, Irvine SE, Beekman RA, Siminovitch DJ, Smith SO. J. Am. Chem. Soc. 2000;122(45):11125.
46. Dave PC, Tiburu EK, Damodaran K, Lorigan GA. Biophys. J. 2004;86:1564.
47. Tiburu EK, Dave PC, Damodaran K, Lorigan GA. Biochemistry. 2004;43(44):13899.
48. Li HM, Cocco MJ, Steitz TA, Engelman DM. Biochemistry. 2001;40(22):6636.
49. Kirby TL, Karim CB, Thomas DD. Biochemistry. 2004; 43(19):5842.
50. Karim CB, Kirby TL, Zhang ZW, Nesmelov Y, Thomas DD. Proc. Natl. Acad. Sci. U.S.A. 2004;101(40):14437.
51. Mascioni A, Karim C, Zamoon J, Thomas DD, Veglia G. J. Am. Chem. Soc. 2002;124(32):9392.
52. Mascioni A, Karim C, Barany G, Thomas DD, Veglia G. Biochemistry. 2002;41(2):475.

NMR Studies of the Interactions Between Ligands and Membrane-Embedded Receptors: New Methods for Drug Discovery

David A. Middleton
Faculty of Life Sciences, University of Manchester, Sackville Street, P.O. Box 88, Manchester M60 1QD, UK

Abbreviations: REDOR, rotational echo double resonance; CP-MAS, cross-polarization magic-angle spinning; et-NOESY, exchange transferred nuclear Overhauser effect spectroscopy; STD, saturation transfer difference spectroscopy; DR, dipolar recoupling; waterLOGSY, water-ligand observation by gradient spectroscopy; MAOSS, magic angle oriented sample spinning; bR, bacteriorhodopsin; nAChR, nicotinic acetylcholine receptor.

Introduction

The interactions between ligands and their receptors lie at the heart of many of the complex cascades of cellular events responsible for life and death, disease and therapy. The outcomes of these events depend upon the selectivity and affinity of natural agonists, antagonists, modulators, and inhibitors for their physiological targets, since it is only through specific interactions that the correct biological signals are generated and processed. Similarly, the therapeutic/toxicological ratios of synthetic drug compounds often hinge on their fidelity for a specific receptor sub-type against a background of closely related receptors. Recent technological advances in drug discovery have led to the wide availability of sophisticated methods for identifying natural or synthetic ligands of specific receptors with high throughput and sensitivity. When these methods are combined with combinatorial chemistry vast numbers of compounds can be screened for ligand activity in a fraction of the time taken 20 years ago [1].

Despite this level of progress, there remains a demand for lower-throughput techniques which can examine receptor–ligand interactions beyond the phenomenological and provide mechanistic information at the molecular level. The NMR community, in particular, has risen to the challenge presented by the revolution in drug discovery and the past decade has witnessed the arrival of many exciting new methods. The versatility of NMR makes it an attractive technique capable of addressing many aspects of drug discovery from screening weak interactions of ligands through to the structural assessment of receptor–ligand complexes.

Over half of the targets for currently marketed drugs are proteins that function within the cell membrane [2] and the pipeline of drugs in clinical development suggests that this proportion will rise significantly in the future. There is, therefore, a compelling case for obtaining molecular level details about how ligands interact with membrane-embedded receptors. Nevertheless, such information remains scarce owing to the insoluble nature of proteins in a lipid membrane environment, which has hampered crystallographic studies and, until recently, has precluded analysis by NMR. Recent progress in NMR hardware and methodology development has been astonishing, however, and the first details of how ligands interact with their receptors in a membrane environment are now being revealed to resolution unattainable by diffraction techniques.

This review will give a brief account of some of the recent developments in NMR in both the solid-state and solution-state and comment on future prospects of these developments for drug discovery.

Choice of Technique

The majority of the physiological and pharmacological ligands of relevance here are water-soluble small molecules that bind reversibly to the receptor embedded in what is effectively a solid support. The affinity of the ligand for the receptor is defined by the on-rate k_{on} and off-rate k_{off} of the ligand (Figure 1). If the association of a ligand with its receptor is diffusion controlled, k_{on} is typically on the order of 10^7 M^{-1} s^{-1} and the dissociation constant ($K_\text{D} = k_{\text{off}}/k_{\text{on}}$) of the receptor–ligand complex is dependent largely on the off-rate. Low-affinity interactions ($K_\text{D} \geq 1$ mM) therefore usually involve rapid dissociation of the ligand from the binding site and the ligands are classified as weak. In such cases, solution NMR methods are advantageous because the ligand can be observed in solution whilst exploiting various physical properties of the ligand that are modulated by its transitory

Graham A. Webb (ed.), Modern Magnetic Resonance, 319–326.
© 2008 *Springer*.

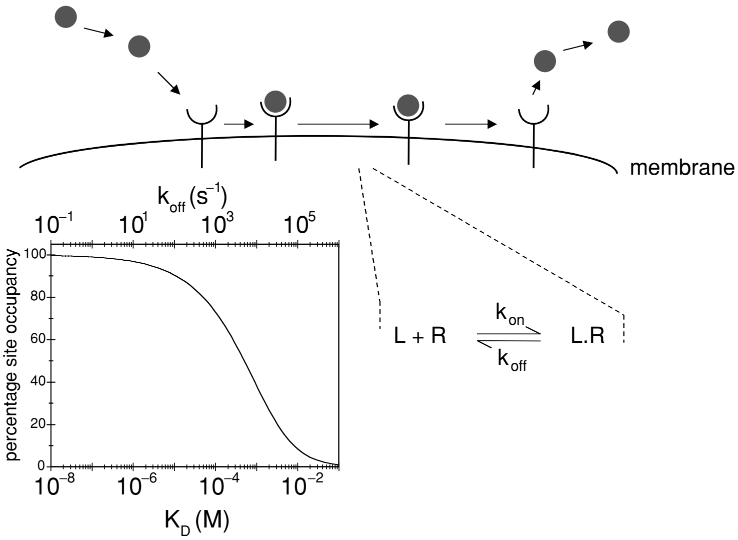

Fig. 1. A schematic representation of the time-course of the interaction between a ligand L (red circles) and a membrane-embedded receptor R (cups). The dissociation constant for the receptor–ligand complex K_D is given by the ratio of the on-rate and off-rate, k_{off}/k_{on}. The graph shows the percentage of ligand molecules that are predicted to be bound to a receptor at equilibrium over a range of K_D values, when the ligand and receptor are present in equimolar concentrations. The off-rate corresponding to each K_D value is shown on the upper axis, based on the assumption that association is diffusion limited with an on-rate of 10^7 M^{-1} s^{-1}.

association with the receptor (e.g. transferred NOEs, relaxation, or saturation). A corollary of this approach, which is implicit in the graph in Figure 1, is that the ligand must be present in large excess over the receptor in order to saturate the available binding sites. Such a large excess of ligand may promote non-specific binding, which can obscure the pharmacologically relevant interactions or lead to misinterpretation. Appropriate control experiments, usually involving competitive displacement, must therefore be designed to eliminate these effects.

Higher affinity ligands ($K_D \leq 10$ μM) usually undergo slower dissociation from their targets (Figure 1) and cannot be detected directly by conventional solution NMR methods because the resonance lines are broadened as a result of the slow tumbling of the membrane assembly. In this motional regime, solid-state NMR is a more appropriate technique for detecting and characterizing the bound ligand directly. The graph in Figure 1 implies that, by adding an equimolar concentration of high-affinity ligand to a receptor, over 90% of the ligand will be bound. The sample can be frozen to eliminate interference from molecular dynamics and very precise structural data can be extracted with appropriate solid-state NMR techniques.

Solution NMR Methods

In recent years a variety of ^{1}H NMR methods have been developed for screening weak ligand interactions with receptors as well as for determining sites of interaction, identifying ligands from compound mixtures, mapping interfacial sites and providing structural contraints [3]. Some of the most notable amongst these are saturation transfer difference (STD) spectroscopy, water-ligand observations with gradient spectroscopy (waterLOGSY), and transferred NOE methods. In the STD approach, the ^{1}H magnetization from the protein target is irradiated at low power by a shaped pulse at a frequency well away from the ligand resonance. The saturation effect is, in turn, transferred to a ligand for the duration that it is associated with the binding site within the receptor. For a ligand in fast exchange between free and bound environments, the saturation is carried with the ligand when it dissociates from the receptor into the free state. If two spectra are obtained, one with and one without saturating pulses, the peaks from the ligand can be identified from the complex spectrum of the mixture [4]. This approach has been exploited for the analysis of carbohydrates to provide details of off-rates and binding constants, map the sites of ligands forming the interface with the receptor and identify ligands from mixtures of compounds [3]. The waterLOGSY technique is similar in concept but relies on the use of water to detect receptor-bound ligands, by generating negative water-ligand NOEs after saturating the water proton magnetization [5]. The bound conformations of fast exchanging ligands (i.e. $k_{off} > 1/T_1$) have been explored using exchange-transferred NOE (et-NOESY) experiments [6]. The strong NOES that develop when the ligand is bound to the receptor are transferred with the ligand to the free state from where they are measured.

The experiments described above are valid only when the ligands bind weakly to the receptor and can be observed in solution. In the case of more tightly bound ligands, dissociation constants have been estimated indirectly with the development of relaxation based NMR experiments that measure the relaxation rates of a standard ligand of known affinity for a receptor before and after displacement with the ligand of interest [7].

The applications of these and other solution NMR methods to membrane embedded proteins have so far been limited to a few examples. Weak interactions between a cyclic peptide inhibitor of the membrane-spanning protein integrin incorporated into liposomes and living cells have been detected using STD NMR [8] and et-NOESY [9]. The latter technique was also used to determine the conformation of ligands bound to the muscarinic acetylcholine receptor and showed that the bound conformations of muscarine and methacholine were different from their conformations in solution [10]. The full potential of these methods remains to be tested, however, and it is anticipated that many more examples of applications to membrane receptor–ligand interactions will appear in the literature.

Solid-State NMR Methods

Solid-state NMR embraces a collection of diverse methods that take advantage of the spatial and dynamic properties of biomembranes to extract information about structure and dynamics. Such methods may exploit the positions of the spectral lines arising from the incomplete averaging of anisotropic interactions (chemical shielding, dipole–dipole, quadrupolar) within the membrane components. Alternatively, the technique of cross-polarization magic-angle spinning (CP-MAS) is used to eliminate or reduce the effects of restricted anisotropic motions and susceptibility effects in biomembranes to gain high-resolution spectra from which site-specific information can be gained with the appropriate pulse sequences.

Sample Requirements

In the analysis of biomembrane samples by CP-MAS NMR methods it is generally desirable that the receptor is fully functional and present in its native membrane or isolated and incorporated into a new lipid bilayer [11]. In both cases, the ligand is titrated into the hydrated membranes and the NMR sample is prepared as a gelatinous pellet by centrifugation to maximize the receptor density that can be loaded into the sample spinner. The receptor purity (and concentration) that can be achieved is often the key factor in determining which experiments are feasible. For example, Spooner *et al.* (see below) have reported various CP-MAS studies of the interactions between bacterial transport proteins and their natural substrates in native membranes in which the receptor of interest represents less than 60%, and as little as 20%, of the total membrane protein. Such studies were possible because of the excellent selectivity of the substrates for their receptors and the high expression levels of protein achieved, which alleviated the requirement for difficult and inefficient purification procedures. In cases where the ligands are less specific or the protein of interest is in low abundance, however, it may be desirable to manipulate the receptor to achieve a higher level of purity.

An alternative approach to CP-MAS involves measuring the orientation of anisotropic interactions (dipolar, chemical shielding, and quadrupolar) in the magnetic field under static (i.e. non-rotating) conditions to determine the alignment of bonds, functional groups or domains of the ligand relative to the receptor. Here, the hydrated membrane samples are laid down onto glass plates of dimensions appropriate for the NMR radiofrequency coil in such a way that the membrane components adopt a uniaxial alignment with respect to the magnetic field. Various methods for obtaining membrane alignment have been proposed, but most have achieved limited success in aligning receptors in native or reconstituted membranes. One apparently successful approach is the isopotential spin-dry ultracentrifugation technique, which produces good alignment whilst preserving biological integrity of the membrane sample [12].

A historical limitation of solid-state NMR has been its inability to exploit protons directly because the strong couplings between them lead to severe line broadening. Although new measures are being taken to eliminate proton line broadening, the observation of naturally rare nuclei (^{13}C, ^{15}N, ^{2}H, ^{19}F) in isotope enriched samples remains central to most biological solid-state NMR experiments.

Detection of Ligand Binding by CP-MAS NMR

In conventional solid-state CP-MAS NMR, Hartmann-Hahn cross-polarization serves to enhance the signal from the observed low-gamma nucleus and reduce recycle times, by transferring magnetization from protons which have higher sensitivity and more favorable T_1 relaxation times. Spooner *et al.* [13] demonstrated an alternative use for CP-MAS in which interactions between ^{13}C labeled L-glucose and the bacterial sugar transporter GalP could be detected by Hartmann-Hahn cross-polarization in partially purified *E. coli* membrane samples at 4 °C. Using CP-MAS it is possible to discriminate between free and bound substrate molecules because of the differences in the motional characteristics of substrate in the two environments. The CP-MAS method detects ligand binding only when the membrane sample is in a fluid state, allowing weak receptor–ligand interactions to be characterized under physiologically relevant conditions that are intractable to other methods of analysis. This development provided the incentive for further studies in which bacterial transporters were nitroxide spin-labeled at unique

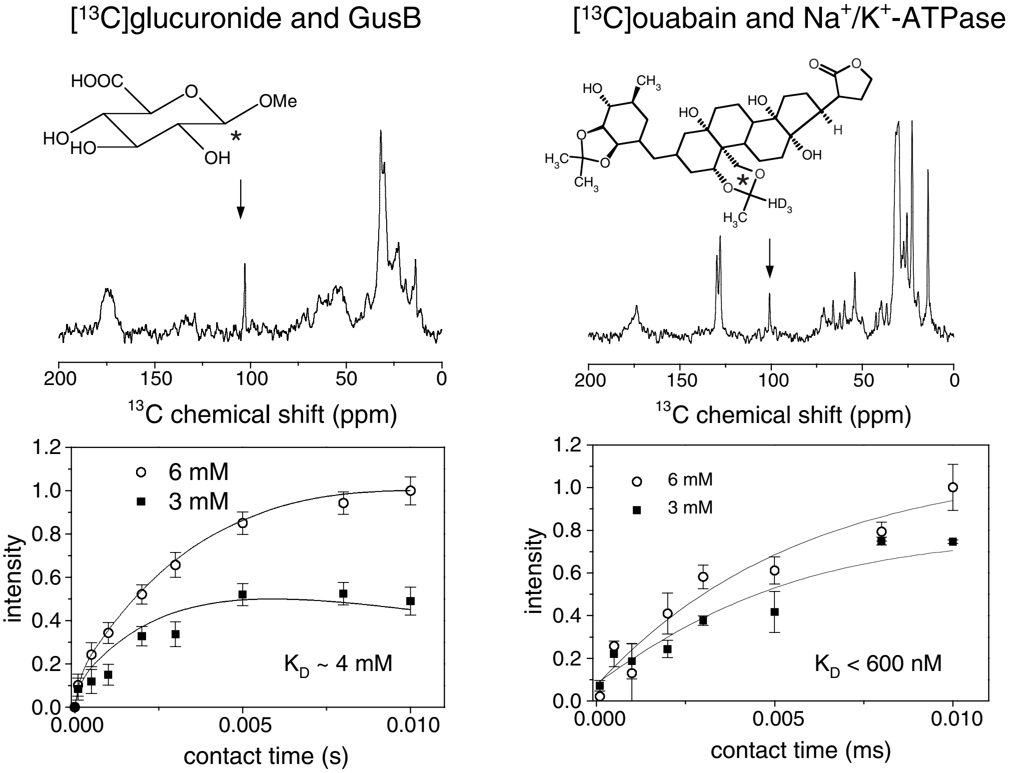

Fig. 2. A demonstration of how ^{13}C CP-MAS NMR is used to estimate the affinities of ligands for membrane-embedded receptors. Examples of spectra (top) and cross-polarization build-up curves (bottom) are shown for two cases in which the ligands have different affinities for their receptors. The spectrum and peak intensities for [^{13}C]methylglucuronide interacting with GusB in *E. coli* membranes is shown on the left. On the right are shown data for [^{13}C]acetonidoouabain interacting with Na^+/K^+-ATPase. In the graphs, the experimental peak intensity values at two ligand concentrations are shown as circles and squares and the lines represent the curves of best fit, corresponding to the K_D values shown.

cysteine residues in order to locate residues close to the substrate binding site. It was shown that the strong magnetic dipole of the electron spin broadened the peaks from the bound substrates and permitted distances between the labeled residues and the bound ligand to be estimated [14–15].

Recently, the CP-MAS approach has been extended to provide quantitative information about ligand binding affinities for receptors in fluid membranes. In this new development, peak intensities from different concentrations of an isotope labeled ligand in the presence of a membrane receptor are measured at increasing cross-polarization contact times [16]. The build up of peak intensities at different ligand concentrations is highly sensitive to binding affinity (Figure 2) and the experimental data are compared with simulated curves to extract values of K_D. One advantage of this method is that the K_D value can be checked independently by measuring the peak intensities after displacement of the labeled ligand by titration of unlabeled ligand. Another attractive feature of this method is that the cross-polarization procedure can be "tuned" to eliminate the signal from non-specifically bound ligand. To date, K_D values have been measured for the interactions of glucuronide sugars with the bacterial transport protein GusB [16], ouabain analogs with the Na^+/K^+-ATPase [17] (Figure 2) and the antidepressant drug trifluoperazine (TFP) with gastric H^+/K^+-ATPase [18]. In the latter work, the intrinsic ^{19}F signal of TFP was exploited to measure ligand binding affinities.

All of the examples highlighted above rely upon being able to resolve the peaks for the labeled ligand from the natural abundance signals from the lipids and protein. In most of the published experiments on ^{13}C labeled substrates of bacterial transporters, it is by design that the peaks from the ligand lie in a region of the spectrum (90–110 ppm) uncontaminated by background signal. To extend the applicability of the CP-MAS method beyond this rather limited situation to the many cases where the peaks from the ligand and membrane inevitably overlap, it is desirable to remove the background signal from the membranes. One recent approach has been to express a bacterial protein in ^{12}C-enriched media, thereby minimizing the background signal from ^{13}C [19]. This is a rather expensive strategy, however, that will be most suitable in cases where high expression levels of protein can be achieved.

Structural Analysis of Ligands

In the solid-state, structural information comes in the form of internuclear distances, torsional angles and bond orientations relative to a fixed reference frame. The data is extracted using variants of the CP-MAS experiment, from uniformly aligned membranes or using a combination of both methods called magic angle oriented sample spinning (MAOSS) [20]. In the case of CP-MAS, structural measurements rely upon a variety of dipolar recoupling (DR) experiments, which manipulate the nuclear spin systems to restore the weak, but structurally informative, dipolar interactions that are otherwise removed by sample rotation [21]. Many such experiments have been devised including rotational resonance NMR, which restores and measures homonuclear couplings, REDOR for heteronuclear couplings and a range of experiments to measure H–C–C–H, H–C–N–H, and N–C–C–N torsional angles [22].

Early applications of solid-state NMR to membrane protein–ligand interactions focused on the structure and orientation of the retinal chromophore within the proton pump bacteriorhodopsin (bR) of the bacterium *H. salarium*. Rotational resonance experiments on double ^{13}C labeled retinal in bR [23] confirmed the torsional angle defining the relative orientations of the β-ionone ring and the polyene chain. Deuterium NMR experiments on bR in aligned membranes revealed changes in quadrupolar tensor orientations for ^{2}H labels in a methyl group (position 19) of the retinal polyene chain after photoexcitation of bR to the M-state, which was consistent with isomerization about the C13–C14 double bond [24]. Further measurements of angles along the polyene chain using DR CP-MAS methods have resolved a slightly distorted conformation of retinal in the binding pocket and resolved ambiguities about bond configurations in the various photointermediates that were not evident from the crystal structures [25]. Recently, sophisticated multidimensional DR experiments have been devised to examine dipolar contacts between the retinal Schiff base and residues lining the binding pocket of bR [26].

Similar methods have been applied to examine the structure of the retinal chromophore in the G-protein coupled receptor (GPCR) rhodopsin during the photocycle responsible for visual signal transduction. Studies of the orientation of retinal using MAOSS revealed significant changes in the orientation of the β-ionone ring in the first stages of the photoexcitation cycle before major protein conformational changes occur [27]. More recently, Smith and co-workers used two-dimensional dipolar-assisted rotational resonance experiments to identify couplings between ^{13}C labels in retinal and labels in Tyr, Gly, Ser, and Thr residues around the binding pocket [28]. It was shown that the transition of rhodopsin to the M_{II} state involves the disruption of helix interactions in the transmembrane domain as retinal moves some 5 Å toward helix 5 and the C20 methyl group of retinal moves toward extracellular loop 2.

The studies of retinal in bR and rhodopsin are excellent demonstrations of how solid-state NMR is ideally suited to filling in details about ligand structure and orientation that are beyond the resolution of available crystal structures. A similar case is the interaction of acetylcholine with the nicotinic acetylcholine receptor (nAChR), the ligand-gated cation channel that mediates synaptic transmission. The highest resolution structure of nAChR is at about 4 Å and inadequate to visualize the positions and structure of the natural ligand in the binding sites. Solid-state NMR studies of a derivative of the natural ligand, bromoacetylcholine, bound covalently to the receptor purified from *torpedo* electroplax have helped to provide clues about how the ligand interacts with the binding pocket [reviewed in Ref. 29]. Deuterium NMR experiments on uniformly aligned membranes containing [^{2}H]bromoacetylcholine indicated that the ligand is positioned in the binding site with the quaternary ammonium group facing outwards and oriented at about 40° with respect to the membrane normal. Further, CP-MAS spectra of the bound ^{13}C labeled ligand showed an up-field perturbation in chemical shift relative to the free ligand in solution which was consistent with a ring current effect of aromatic residues that are believed to line the binding pocket.

The examples described above all benefit from the availability of receptor crystal structures of varying resolution with which to combine NMR measurements to draw conclusions about ligand binding. The following section will show examples of the less favorable, but unfortunately common, situation in which mechanistic information about ligand binding is obtained by solid-state NMR methods in the absence of any crystallographic coordinates for the receptor.

A Case Study: Solid-State NMR Investigations of Ion Pump Inhibitors

The P-type ATPases are a class of large (>100 kDa) membrane-embedded enzymes that are found in higher eukaryotic organisms and some bacteria. The specific functions of these enzymes vary from cell to cell, but all are related by their ability to couple ATP hydrolysis to vectorial ionic transport across the cell membrane [33]. Ionic transport may be electroneutral (i.e. translocation of charge-equivalent ions) or electrogenic (establishing a transmembrane potential) and is coupled to conformational changes in the enzymes that reveal, in turn, high-affinity sites for ions on opposite sides of the membrane. Two members of this family are well-established targets for drugs. The cardiac Na^+/K^+-ATPase controls the relaxation–contraction cycle of the heart and is the receptor for high-affinity cardiac glycoside inhibitors, collectively known as digitalis, which have been used for over 200 years in the treatment of congestive heart failure. The gastric H^+/K^+-ATPase is a proton pump responsible for secretion of acid into gastric glands, and is a target for drugs in the treatment of gastric ulcer disease. Reversible inhibitors of the proton pump include the aryl-substituted imidazopyridines, which are reasonably potent ($IC_{50} \sim 1\ \mu M$) but have undesirable toxicological properties.

Solid-state NMR experiments have revealed the first details about how these inhibitors interact with their targets despite high-resolution structures being unavailable for either of the two proteins. Information about the bound conformation and orientation of these drugs has given clues about how they achieve selectivity for their specific targets. Selectivity is a crucial property of these inhibitors because promiscuous binding to other ATPases could have catastrophic consequences for patients treated with these or related drugs. The NMR experiments form a component of the broader approach summarized in Figure 3 for the specific example of proton pump inhibitors. First, aryl-substituted imidazopyridines were isotope labeled at various sites with ^{13}C and ^{19}F and titrated into gastric membranes enriched in H^+/K^+-ATPase. Measurements of heteronuclear and homonuclear dipolar couplings using REDOR and rotational resonance NMR [30,31] have

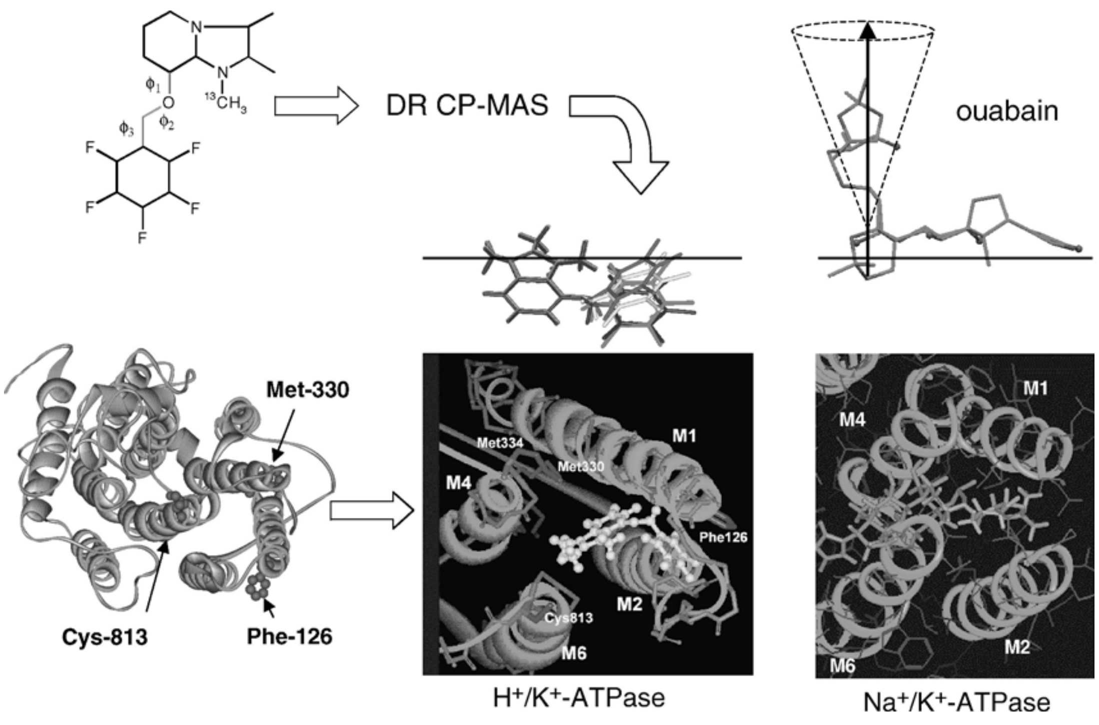

Fig. 3. An overview of the strategy for modeling an aryl-substituted imidazopyridine inhibitor in its binding site within the H^+/K^+-ATPase. The details of the strategy are described in the text. The model is shown alongside a model of ouabain in its site of action within the Na^+/K^+-ATPase, derived by a similar approach. (See also Plate 36 on page XXXI in the Color Plate Section.)

provided structural constraints defining the relative orientations of the aryl and imidazopyridine rings within the site of action, showing that the molecule is distorted from a planar configuration and exhibits a slightly curved profile.

It has been possible to produce a model describing the location of the inhibitor within the luminal face of H^+/K^+-ATPase with the aid of published site directed mutagenesis (SDM) data and coordinates from the crystal structure of the homologous Ca^{2+}-ATPase. The sequence of H^+/K^+-ATPase was threaded onto the structure of the Ca^{2+}-ATPase and the spatial disposition of residues in the proton pump, known from SDM studies to be implicated in drug binding, were predicted. The inhibitor in its curved conformation was found to fit convincingly into a putative binding site bounded by residues and beneath the luminal surface of the protein (Figure 3). By contrast, similar solid-state NMR measurements of $^{13}C/^{19}F$ labeled digitalis analogs have suggested that the recognition site of the Na^+/K^+-ATPase lies at the membrane surface [32] with the functionally-redundant sugar group of ouabain facing away from the protein (Figure 3). These distinct binding characteristics may hold the clue as to why the two inhibitors have such remarkable selectivity for these closely related proteins.

Future Prospects

The versatility of NMR in the characterization of receptor–ligand interactions, when viewed alongside the therapeutic importance of membrane-embedded proteins, suggests that this technique will continue to play a valuable role in drug discovery. This optimistic prognosis will only be realized, however, if developments in NMR hardware and methodology keep apace with the breathtaking progress seen in other aspects of the drug discovery process. With this in mind, the author speculates below on how NMR may continue to provide new and groundbreaking information about membrane receptor–ligand interactions.

(i) Solution state NMR remains underdeveloped as a technique for characterizing receptor–ligand interactions in biomembranes, yet many of the experiments are in place and simply await validation with the appropriate membrane samples. There is a clear opportunity to take advantage of the tremendous improvements in the sensitivity of solution NMR instrumentation in order to compensate for the often low quantities of membrane receptors that can be obtained.

(ii) The examples of work on bR, rhodopsin, and the gastric proton pump inhibitors given in this brief review are good demonstrations of how solid-state NMR can provide precise structural constraints for ligands bound to receptors. If such information were obtained for current drug targets, this could help to guide medicinal chemistry toward structures with higher affinity or selectivity for their receptors. This approach has already been used with some success in the case of the aryl-substituted imidazopyridine inhibitors of the gastric proton pump (Figure 4, bottom). By chemically restraining the aryl group in a configuration close to that seen for the flexible parent inhibitor in the binding site, the new compound inhibited the pump with almost 100-fold higher potency.

(iii) The major proportion of membrane-embedded drug targets are GPCRs [2], but NMR studies of their interactions with ligands have so far been limited to a few well-chosen cases. The NMR studies of retinal in the GPCR rhodopsin have shown that structural details can be obtained with high precision, but rhodopsin is a unique case amongst this class of proteins and the retinal chromophore is not typical of a GPCR agonist or antagonist of interest in pharmaceutical research. Recently Baldus and co-workers used

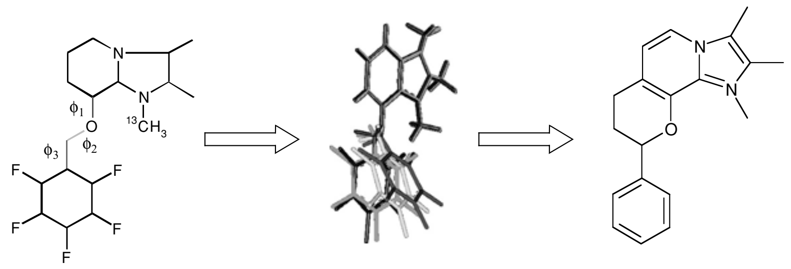

flexible, IC_{50} = 10 µM NMR conformation Constrained, IC_{50} = 100 nM

Fig. 4. An example of how the structure of a receptor-bound ligand can provide information of relevance to drug discovery (refer to the text for details). (See also Plate 37 on page XXXII in the Color Plate Section.)

solid-state NMR to solve the structure of a fragment of the neurotensin peptide when bound to its receptor [34]. This approach is potentially very useful, as determining the pharmacophore structure of a natural peptide ligand could help to predict small molecule antagonists.

In all three cases above, the future role of NMR in the analysis of membrane receptor–ligand interactions will be intimately linked to improvements in the methods for producing useful quantities of functional receptors in a suitable form for NMR studies.

References

1. Hajduk PJ, Burns DJ. Comb. Chem. High Throughput Screen. 2002;5:613.
2. Drews J. Science. 2000;287:1960.
3. Meyer B, peters T. Angew. Chem. Int. Ed. 2003;42:864.
4. Mayer M, Meyer B. Angew. Chem. Int. Ed. 1999;38:1784.
5. Dalvit C, Pevarello P, Tato M, Veronesi M, Vulpetti A, Sundstrom M. J. Biomol. NMR. 2000;18:65.
6. Post CB. Curr. Opin. Struct. Biol. 2003;13:581.
7. Dalvit C, Flocco M, Knapp S, Mostardini M, Perego R, Stockman BJ, Veronesi M, Varasi M. J. Am. Chem. Soc. 2002;124: 7702.
8. Claasen B, Axmann M, Meinecke R, Meyer B. J. Am. Chem. Soc. 2005;127:916.
9. Zhang L, Mattern R-H, Malaney TI, Pierschbacher MD. J. Am. Chem. Soc. 2002;124:2862.
10. Furukawa H, Hamada T, Hayashi MK, Haga T, Muto Y, Hirota H, Yokoyama S, Nagasawa K, Ishiguro M. Mol. Pharmacol. 2002;62:778.
11. Watts A, Burnett IJ, Middleton DA, Spooner PJR, Watts JA, Williamson PTF. Nat. Prod. Rep. 1999;16:419.
12. Gröbner G, Taylor A, Williamson PTF, Choi G, Glaubitz C, Watts JA, de Grip WJ, Watts A. Anal. Biochem. 1997;254: 132.
13. Spooner PJR, Rutherford N, Watts A, Henderson PJF. Proc. Natl. Acad. Sci. USA. 1994;91:3877.
14. Spooner PJR, Veenhoff L, Watts A, Poolman B. Biochemistry. 1999;38:9634.
15. Spooner PJR, O'Reilly WJ, Homans SW, Rutherford NG, Henderson PJF, Watts A. Biophys. J. 1998;75:2794.
16. Patching SG, Brough AR, Herbert RB, Rajakarier JA, Henderson PJF, Middleton DA. J. Am. Chem. Soc.2004;126:3072.
17. Boland MP. Ph.D. Thesis, University of Manchester, 2005.
18. Boland MP, Middleton DA. Magn. Reson. Chem. 2004;42: 204.
19. Patching SG, Herbert RB, O'Reilly J, Brough AR, Henderson PJF. J. Am. Chem. Soc.2004;126:86.
20. Glaubitz C, Watts A. J. Magn. Reson. 1998;130:305.
21. Dusold S, Sebald A. Annual Reports on NMR Spectroscopy. 2000;41:185–264.
22. Feng X, Lee YK, Sandstrom D, Eden M, Maisel H, Sebald A, Levitt MH. Chem. Phys. Lett. 1996;257:314.
23. Creuzet F, McDermott A, Gebhard R, van der Hoef K, Spijker-Assink MB, Herzfeld J, Lugtenburg J, Levitt MH, Griffin RG. Science 1991;251:783.
24. Ulrich AS, Wallat I, Heyn MP, Watts A. Nat. Struct. Biol. 1995;2:190.
25. Lansing JC, Hohwy M, Jaroniec CP, Creemers AFL, Lugtenburg J, Herzfeld J, Griffin RG. Biochemistry. 2002;41: 431.
26. Jaroniec CP, Lansing J, Tounge B, Belenky M, Herzfeld J, Griffin RG. J. Am. Chem. Soc. 2001;123:12929.
27. Gröbner G, Burnett IJ, Glaubitz C, Choi G, Mason AJ, Watts A. Nature. 2000;405:810.
28. Petal AB, Crocker E, Eilers M, Hirshfeld A, Shenes M, Smith SO. Proc. Natl. Acad. Sci. USA. 2004;101:10048.
29. Williamson PTF, Meier BH, Watts A. Eur. Biophys. J. 2004; 33:247.
30. Middleton DA, Robins R, Feng X, Levitt MH, Spiers ID, Schwalbe C, Reid DG, Watts A. 1997;410:269.
31. Watts JA, Watts A, Middleton DA. J. Biol. Chem. 2001;276: 43197.
32. Middleton DA, Rankin S, Esmann M, Watts A. Proc. Natl. Acad. Sci. USA. 2001;97:13602.
33. Watts, J.A. D.Phil. Thesis, University of Oxford, 2001.
34. Luca S, Sohal AK, Fillipov D, van Boom J, Grisshammer R, Baldus M. Proc. Natl. Acad. Sci. USA. 2003;100:10706.

Photosynthetic Antennae and Reaction Centers

H.J.M. de Groot
Leiden Institute of Chemistry, Gorlaeus Laboratories, NL2300 RA Leiden, The Netherlands

Introduction

In photosynthesis, light energy conversion proceeds in two steps [1]. First excitons are generated in antenna systems and subsequently charge separation takes place in reaction centers (RCs, Figure 1). To gain insight into the structural and functional properties of such active elements in photosynthesis, solid-state NMR is increasingly important. Here a number of examples of recent investigations are summarized, first structure–function studies of antennae and RCs, and second structure determination, including methodology development. To resolve molecular electron pumping mechanisms in bacterial RCs and to study the electronic structure of light-harvesting (LH) proteins, both global and specific assays of cofactors and protein side chains have been performed. Novel techniques allow a determination of structural models for self-assembled chlorophyll preparations *in vitro* and for the natural chlorosome antenna system. Finally, it is possible to perform sequence specific assignments of uniformly labeled complexes and to observe intermediate states in light-triggered reactions, produced by illumination of frozen samples in the spectrometer.

Structure–Function Studies of Antenna Systems and RCs

The electronic ground states of the bacteriochlorophyll (BChl) *a* type B800 and type B850 (BChl molecules absorbing around 800 or 850 nm) in the LH2 complex of *Rhodopseudomonas acidophila* strain 10050 have recently been characterized by magic angle spinning (MAS) dipolar ^{13}C–^{13}C correlation NMR spectroscopy [2]. Extensive sets of isotropic ^{13}C NMR chemical shifts were obtained for the BChl in the LH2. Density functional theory calculations were performed to analyze the data in detail. By correction for the ring current shifts, the ^{13}C shift effects due to the interactions with the protein matrix can be resolved. The shift effects for the B800 and B850 are similar, and are attributed to a weak nonlinear dielectric response of the protein environment to the cofactor binding, in contrast with local effects due to interaction with specific amino acid (AA) residues. In addition, the polarization of the electronic ground states induced by the protein environment is comparable for both cofactors and corresponds with a red shift of $\sim$30 nm relative to the monomeric BChl in solution. According to the NMR, the electronic coupling between the B850 cofactors due to macrocycle overlap is the predominant mechanism responsible for the color difference between the B800 and B850 cofactors.

In another study, photosynthetic RCs of *Rhodobacter sphaeroides* R26 were reconstituted at the Q_A site with ubiquinone-10, selectively ^{13}C-enriched on positions 1, 2, 3, 4, and 3-Me [3]. RCs dispersed in LDAO detergent were studied with ^{13}C CP/MAS NMR spectroscopy at temperatures between 180 and 240 K, while RCs precipitated by removal of the detergent were investigated at ambient temperature and at temperatures down to 180 K. Electrostatic charge differences in Q_A induced by polarization from the protein are small, less than 0.02 electronic equivalent for any of the labeled positions. The 4-carbonyl signal indicates a rigid environment for this functionality, which contrasts with previous studies with FTIR that provided evidence for a strong perturbation and possibly dynamic disorder of this quinone functionality [4]. The Q_A site is slightly heterogeneous on the scale of the NMR as the observed line widths of the labels are between 150 and 300 Hz and inhomogeneous broadening is observed for the signals of positions 1, 2, and 3 upon cooling. For the 4-carbonyl only at sample temperatures below -255 K, a CP/MAS response can be observed at 183 ppm. The data indicate a difference between the dark adapted state monitored by NMR and the light adapted form that is probed by optical investigations.

Various ^{15}N and ^{13}C CP/MAS NMR methods have been used to analyze BChl–histidine interactions and the electronic structure of histidine residues in RCs and antenna complexes [5,6]. For the LH2 complex of *R. acidophila*, the histidines were selectively labeled at both or one of the two nitrogen sites of the imidazole ring. The resonances of histidine nitrogens that are interacting with B850 BChl *a* have been assigned. Specific ^{15}N labeling confirmed that it is the τ-nitrogen of α-His30 and β-His31 that are ligated to Mg^{2+} of BChl cofactors. The π-nitrogens of these Mg^{2+}-bound histidines were

Graham A. Webb (ed.), Modern Magnetic Resonance, 327–333.
© 2008 *Springer.*

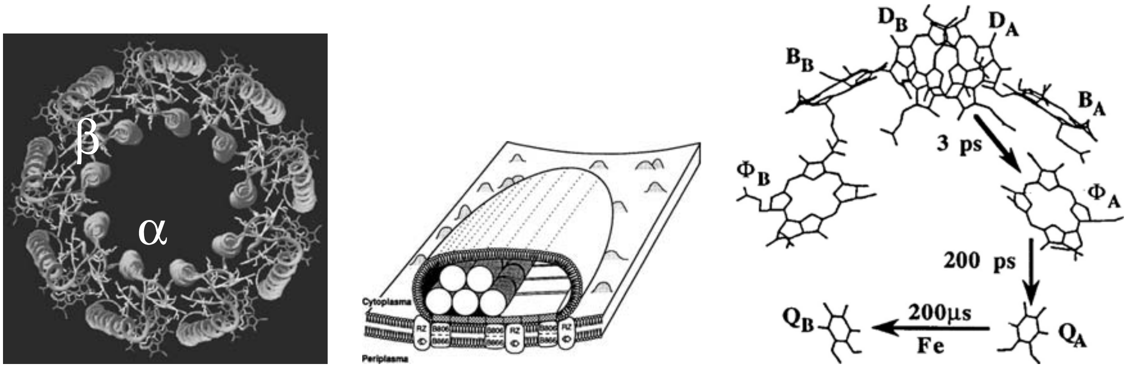

Fig. 1. Self-organized photosynthetic complexes, which play key roles in the photosynthetic process. *Left*: Top view on the LH2 LH membrane protein complex. This 9-mer contains two α-helical segments in every monomeric unit. The transmembrane helices embed the BChl that performs the LH function. *Center*: Chlorosomes are oblong bodies inside a protein free antenna system that currently serves as one possible paradigm for light concentration in artificial photosynthesis research. With solid-state NMR it was possible to show that a chlorosome antenna contains tubular bilayers of self-aggregated BChl. *Right*: Photo excitations are transferred to a RC, which is brought into an excited state. Electron transport (ET) occurs from the special pair (D_A/D_B) and via two additional chlorophyll molecules (B_A/B_B), to a pheophytin (Φ_A), and finally the quinones (Q_A, Q_B) as indicated by the arrows. (See also Plate 38 on page XXXII in the Color Plate Section.)

found to be protonated and may be involved in hydrogen bond interactions. Comparison of the 2-D MAS NMR homonuclear (^{13}C–^{13}C) dipolar correlation spectrum of [^{13}C,^{15}N]-histidines in the LH2 complex with model systems in the solid state reveals two different classes of electronic structures for the histidines in the LH2. In terms of the ^{13}C isotropic shifts, one corresponds to the neutral form of histidine and the other resembles a positively charged histidine species [5,7]. ^{15}N–^{13}C double-CP/MAS NMR data provide evidence that the electronic structure of the histidines in the neutral BChl *a*/His complexes resembles the positive charge character form. While the isotropic shift of the ^{15}N ligated to the Mg^{2+} confirms a partial positive charge transfer, its anisotropy is essentially of the lone pair type. This provides evidence that the hybridization structure corresponding to the neutral form of the imidazole is capable of "buffering" a significant amount of positive charge.

To study the active chlorophyll and pheophytin cofactors involved in the primary processes in photosynthesis, and their environment in the protein, photochemically induced dynamic nuclear polarization (photo-CIDNP) is the method of choice. The unmatched sensitivity of the photo-CIDNP allows the detection of signals at natural abundance of the ^{13}C [8]. Recently we have reported photo-CIDNP for the RCs of plant photosystems I and II (PS I, II) [9,10]. The light-enhanced NMR provides information on the electronic structure of the primary electron donors. The radical cation response from the bacterial RC shows at least four emissive center bands, indicating a symmetric spin density distribution over the entire BChl macrocycle. In contrast, the data for the PS II reveal a pronounced asymmetry of the electronic spin density distribution within the $P680^{\bullet +}$ (chlorophyll molecules absorbing around 680 nm). PS II shows only a single broad and intense emissive signal and the spin density appears shifted compared to monomeric chlorophyll in solution. It leads to a first hypothesis as to how the planet can provide itself with the chemical potential to split water and generate an oxygen atmosphere using the Chl *a* macroaromatic cycle: a local electrostatic field can polarize the electronic charge and associated spin density and increase the redox potential of P680 by stabilizing the highest occupied molecular orbital, without a major change of color.

In addition, RCs of wild-type *R. sphaeroides* were selectively ^{13}C-isotope labeled in BChl and bacteriopheophytin (Bphe), and ^{13}C solid-state CP/MAS NMR and photo-CIDNP were used to provide insight into the electronic structure of the primary electron donor and acceptor on the atomic and molecular levels [11,12]. The first 2-D photo-CIDNP ^{13}C–^{13}C solid-state MAS NMR spectra reveal that negative polarization of the two BChl rings of the primary donor is involved in ground state tuning of the oxidation potential of these cofactors in the protein via local electrostatic interactions (Figure 2). In particular, the ^{13}C shifts show moderate differences in the electronic structure between the two BChl molecules of the special pair in the electronic ground state, which can be attributed to hydrogen bonding of one of the BChl molecules. The major fraction of the electron spin density is strongly delocalized over the two BChl molecules of the

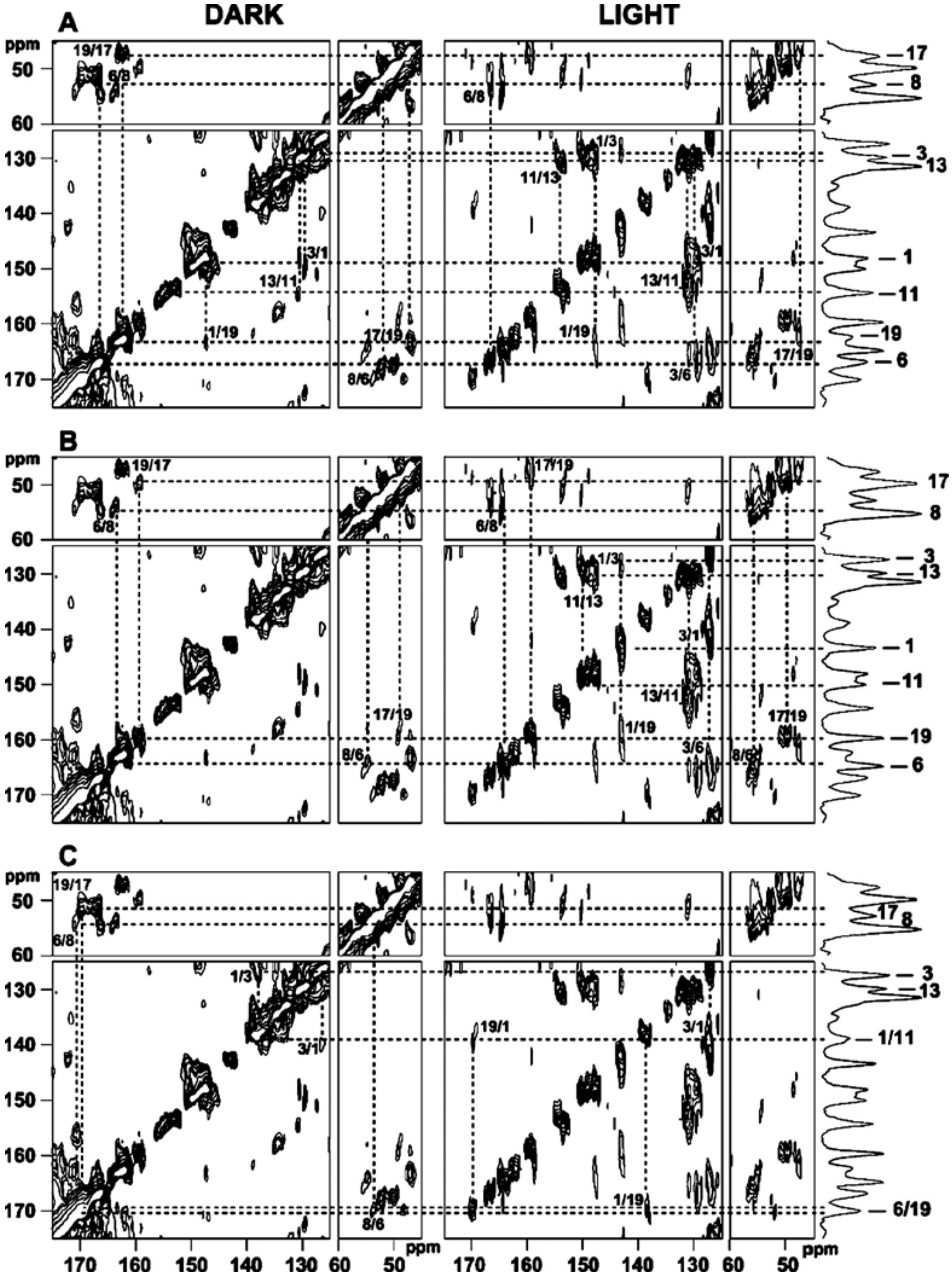

Fig. 2. Contour plot of the "dark" 2-D RFDR CP/MAS spectrum (left) and the 2-D RFDR photo-CIDNP spectrum (right) of RCs containing ^{13}C labels in the cofactors. The data were recorded at ~220 K with 12 and 5 kHz spinning frequencies and ~5 ms RFDR mixing. The assignments of the correlations of the two BChl of the special pair (A, B), and the BPhe (C) are indicated with the dashed lines.

special pair and the photochemically active BPhe. A small fraction of the π-spin density is distributed over a fourth component, which is assigned to the accessory BChl. Comparison of the photo-CIDNP data with "dark" NMR spectra obtained in ultrahigh field indicates that putative structural changes of the special pair during the primary process of photosynthesis should be reversed upon charge recombination on the timescale of the photo-CIDNP experiment.

MAS NMR Structure Determination: Chlorosomes and LH2

The structure of photosynthetic membrane proteins and other membrane associated assemblies represents a solid matrix that is essential to the mechanism of biological function. In recent years MAS NMR has been used to gain in-depth understanding the structure of photosynthetic energy conversion systems.

In photosynthesis, light is collected by LH antenna complexes that generally contain 50–200 chlorophylls in well-defined membrane bound protein structures. Photosynthetic green sulfur bacteria, however, contain chlorosomes (Figure 1). These are unique antenna systems among photosynthetic organisms since their LH pigments are organized without proteins. Already at an early stage the chlorosome of the green bacterium *Chlorobium tepidum* was studied by 1-D MAS NMR methods [13]. With 2-D correlation spectroscopy, it was shown that the BChl are self-organized into supramolecular aggregates by coordinative bonding and π–π stacking interactions [14]. Homo- and heteronuclear MAS NMR, along with comparison of BChls with different side chains lead to a model for the structure with two concentric tubes for the aggregated BChl in chlorosomes (Figure 3) [15]. Heteronuclear 2-D and 3-D MAS NMR dipolar correlation spectroscopy was applied to determine solid-state ^{1}H shifts for aggregated BChl *c* in uniformly ^{13}C-enriched chlorosomes. A complete assignment of 29 different observable resonances of the 61 protons of the aggregated BChl *c* in the intact chlorosomes was obtained. The 21-H, 32-H, and 31-H resonances are shifted upfield by -2.2, -1, and -3.3 ppm, respectively, relative to monomeric BChl *c* in solution, revealing parallel stacking of the BChl in the antenna.

Although the resonances are inhomogeneously broadened and reveal considerable global structural heterogeneity, the 5-CH and the 7-Me responses are doubled, which provide evidence for the existence of at least two relatively well-defined structurally different arrangements. *Ab initio* quantum chemical modeling studies were performed to refine a model for the self-assembled BChl *c* with two different types of BChl stacks. The BChl in the stacks can adopt either *anti*- or *syn*-configuration of the coordinative bond, where *anti* and *syn* designate the relative orientation of the Mg–OH bond relative to the direction of the 17–17^{1} bond. Based on the NMR data, a bilayer model for the tubular supra-structure of sheets of BChl *c* was proposed, from a homology modeling approach (Figure 2).

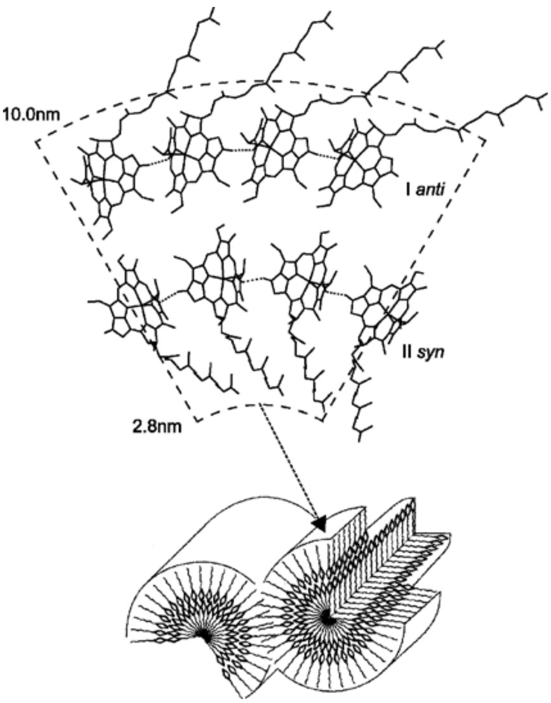

Fig. 3. The structure model of the chlorosomal antennae in *Chlorobium tepidum* derived from MAS NMR, consisting of bilayers of self-assembled BChl *c*.

As a spin-off mainly from the investigations into chlorosome LH antenna structures and ligand–protein interactions for membrane proteins, the construction and use of novel ultrahigh field (750 MHz) MAS NMR equipment was recently demonstrated [16]. The new technology represents a twofold increase of field strength with respect to previous practice, since biological MAS NMR was and is still often performed at 300–400 MHz ^{1}H frequency. The higher field increases the sensitivity by $\sim$60% and improves the range and resolution considerably [17].

To confront the new technique with real biomolecular targets from research in molecular structural biology and to explore the range of the new technology for structure determination of membrane proteins, the sequence specific assignments for the transmembrane

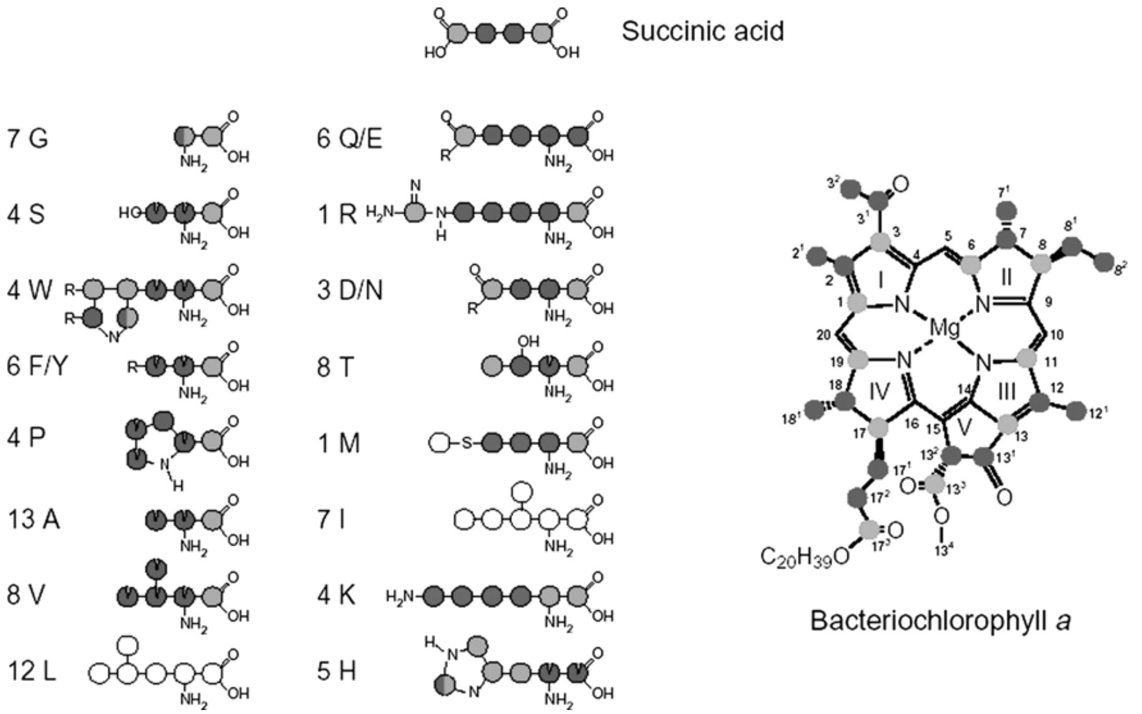

Fig. 4. ^{13}C-isotope enrichment of the residues and BChl *a* cofactors in LH2. The green color shows the labeling pattern that is obtained by growing on [1,4-^{13}C]-succinic acid, while the labeling pattern obtained by growing on [2,3-^{13}C]-succinic acid is indicated in red. The small sections indicate a partial scrambling of isotopes. Ile and Leu are labeled due to the uptake from an AA nutrient source. (See also Plate 39 on page XXXII in the Color Plate Section.)

helices in the monomeric unit of the LH2 were recently obtained [18,19]. Here MAS NMR was used in combination with extensive and selective biosynthetic isotope labeling methods. For both the residues of the protein and for the cofactors distinct labeling patterns have been deduced with 2-D proton-driven spin diffusion (PDSD) solid-state NMR correlation spectroscopy for samples prepared from [1,4-^{13}C]-succinic acid, [2,3-^{13}C]-succinic or AA labeled media (Figure 4) [20]. All residues, except isoleucine and leucine, have been labeled almost homogeneously by the succinic acid precursor. Carbonyl carbons in the protein backbone were labeled by [1,4-^{13}C]-succinic acid, while the Cα and Cβ carbons of the residues were labeled by [2,3-^{13}C]-succinic acid. Leucine and isoleucine residues were labeled using a uniformly labeled AA mixture in the medium. The pattern labeling yields an increase of the resolution and less spectral crowding.

The partial labeling technique in combination with conventional solid-state NMR methods at ultrahigh magnetic fields provides an attractive route to resolve chemical shifts for a helical transmembrane protein structures. Assignments have been performed on the basis of 2-D PDSD ^{13}C–^{13}C correlation experiments with mixing times of 20 and 500 ms and band selective ^{13}C–^{15}N correlation spectroscopy on a series of site-specific biosynthetically labeled samples (Figure 5) [19]. The decreased line width and the reduced number of correlation signals of the selectively labeled samples with respect to the uniformly labeled samples enable to resolve the narrowly distributed correlation signals of the backbone carbons and nitrogens involved in the long α-helical transmembrane segments. Correlations between nearby residues and between residues and the labeled BChl *a* cofactors, provided by the ^{13}C–^{13}C correlation experiments using a 500 ms spin diffusion period, are used resolve the NMR responses for many residues in the protein complex. In this way it is demonstrated that MAS NMR methods combined with site-specific biosynthetic isotope labeling can be used for sequence specific assignment of a transmembrane protein complex.

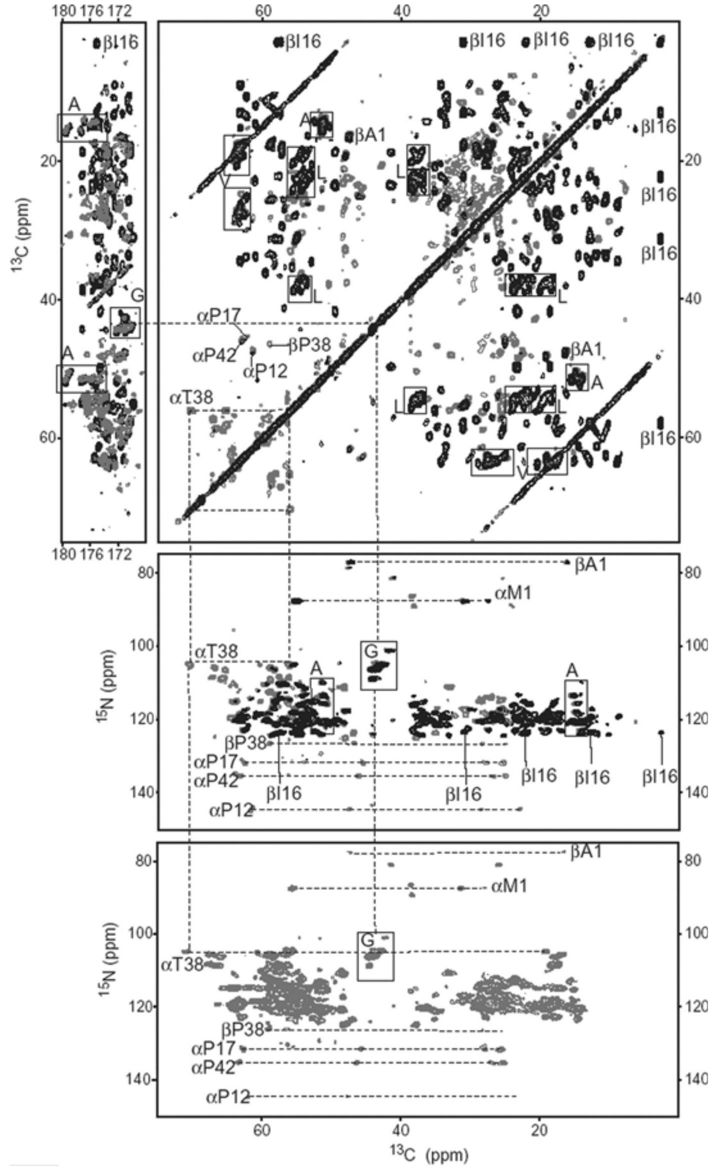

Fig. 5. In the upper panels two regions from homonuclear ^{13}C–^{13}C PDSD50 correlation spectra collected from 2,3-LH2 (red) and AA-LH2 (black) are shown. The region shown in the upper left panel contains cross peaks involving the aliphatic carbons and carbonyl carbons, while the upper right panel shows correlations between aliphatic carbons, present in the side chains of the AAs. In the left part, a few responses are observed for 2,3-LH2, belonging to H, Q, and E residues. The responses from AA-LH2 in the carbonyl area are from I, L, A, G, and V residues. The blue-coded spectrum in the carbonyl region comprises carbonyl responses from 1,2,3,4-LH2. In the upper right panel the aliphatic responses are shown. The dashed lines indicate correlations involving the αT38 and 4P residues for the 2,3-LH2, and correlations involving βI16 for the AA-LH2. The residues that are labeled via both nutrient sources are also indicated. In the middle pane, the aliphatic region of the NCACX spectra of 2,3-LH2 (red) and AA-LH2 (black) are shown. The data are aligned with the PDSD50 spectrum and correlations involving αT38, βI16, and the 4P residues are indicated with dashed lines for the two different samples. The responses of the G residues are indicated with a rectangular box. The NCA signals are aligned with the carbonyl area of the PDSD50 spectrum. Finally, in the lower panel the NCACX spectrum of a 1,2,3,4-LH2 sample is shown. (See also Plate 40 on page XXXIII in the Color Plate Section.)

References

1. Hoff AJ, Deisenhofer J. Phys. Rep. 1997;287:2.
2. van Gammeren AJ, Buda F, Hulsbergen FB, Kiihne S, Hollander JG, Egorova-Zachernyuk TA, Fraser NJ, Cogdell RJ, de Groot HJM. J. Am. Chem. Soc. 2005;127:3213.
3. van Liemt WBS, Boender GJ, Gast P, Hoff AJ, Lugtenburg J, de Groot HJM. Biochemistry. 1995;34:10229.
4. Brudler R, de Groot HJM, van Liemt WBS, Steggerda WF, Esmeijer R, Gast P, Hoff AJ, Lugtenburg J, Gerwert K. EMBO J. 1994;13:5523.
5. Alia, Matysik J, Soede-Huijbregts C, Baldus M, Raap J, Lugtenburg J, Gast P, van Gorkom HJ, Hoff AJ, de Groot HJM. J. Am. Chem. Soc. 2001;123:4803.
6. Zysmilich MG, McDermott AE. J. Am. Chem. Soc. 1996;118:5867.
7. van Gammeren AJ, Hulsbergen FB, Erkelens C, de Groot HJM. J. Biol. Inorg. Chem. 2004;9:109.
8. Zysmilich MG, McDermott AE. J. Am. Chem. Soc. 1994;116:8362.
9. Alia, Roy E, Gast P, van Gorkom HJ, de Groot HJM, Jeschke G, Matysik J. J. Am. Chem. Soc. 2004;126:12819.
10. Matysik J, Alia, Gast P, van Gorkom HJ, Hoff AJ, de Groot HJM. Proc. Natl. Acad. Sci. U.S.A. 2000;97:9865.
11. Egorova-Zachernyuk T, van Rossum B, Boender GJ, Franken E, Ashurst J, Raap J, Gast P, Hoff AJ, Oschkinat H, de Groot HJM. Biochemistry. 1997;36:7513.
12. Schulten EAM, Matysik J, Alia, Kiihne S, Raap J, Lugtenburg J, Gast P, Hoff AJ, de Groot HJM. Biochemistry. 2002;41:8708.
13. Nozawa T, Ohtomo K, Suzuki M, Nakagawa H, Shikama Y, Konami H, Wang ZY. Photosynth. Res. 1994;41:211.
14. Balaban TS, Holzwarth AR, Schaffner K, Boender GJ, de Groot HJM. Biochemistry. 1995;34:15259.
15. van Rossum B-J, Steensgaard DB, Mulder FM, Boender GJ, Schaffner K, Holzwarth AR, de Groot HJM. Biochemistry. 2001;40:1587.
16. Kiihne SR, de Groot HJM (Eds). Perspectives on Solid State NMR in Biology. Kluwer: Dordrecht, 2001.
17. van Rossum BJ, Boender GJ, de Groot HJM. J. Magn. Reson. A. 1996;120:274.
18. Egorova-Zachernyuk TA, Hollander J, Fraser N, Gast P, Hoff AJ, Cogdell R, de Groot HJM, Baldus M. J. Biomol. NMR. 2001;19:243.
19. van Gammeren J, Hulsbergen FB, Hollander JG, de Groot HJM. J. Biomol. NMR. 2005;31:279.
20. van Gammeren AJ, Hulsbergen FB, Hollander JG, de Groot HJM. J. Biomol. NMR. 2004;30:267.

Insight into Membrane Protein Structure from High-Resolution NMR

Philip L. Yeagle and Arlene Albert
Department of Molecular and Cell Biology, University of Connecticut, Storrs, CT 06269, USA

Introduction

Since α-helices and turns (helix-turn-helix motif) are stabilized by short-range interactions, and since many membrane proteins are built around (transmembrane) helical bundles, much of the secondary structure of such membrane proteins can be captured in peptide fragments. Furthermore, if sufficient long-range point-to-point experimental distance constraints are available from the intact protein, a structure for the whole protein can be assembled from the structures of the peptide fragments. In this review, we will describe the basis for the first statement and give some examples of the second. The review will conclude with a brief look at the future of high-resolution NMR in the study of the structural biology of intact membrane proteins in detergent micelles.

Membrane Protein Structure—Current Status

Our understanding of the structure of integral membrane proteins lags considerably our understanding of soluble protein structure. Less than 0.5% of the structures in the PDB represent integral membrane proteins, whereas genomic analysis indicates that 25–40% of proteins encoded by most genomes are membrane proteins [1]. Clearly there is a huge deficit of structural information on membrane proteins.

The major source of this knowledge deficit lies in the difficulties in applying the most productive techniques in protein structure determination to membrane proteins. X-ray crystallography requires crystallization of membrane proteins and to date only about 80 structures of membrane proteins have been published using this approach in large part because of difficulties in crystallization. Membrane proteins have extensive hydrophobic surfaces and therefore are insoluble in water. Because of this insolubility, many of the standard techniques for crystallization will not work on membrane proteins.

Powerful NMR techniques have been developed and exploited to determine structures of a variety of soluble proteins. These techniques in general require that the protein under study be stable and active in aqueous solution. Integral membrane proteins are not soluble in aqueous solution. These membrane proteins must be solubilized in detergent micelles. The protein-detergent micelles tend to be large, with molecular weights in excess of 50 kDa. The long rotational correlation times of such structures enhance dipolar and chemical shift anisotropy interactions and consequently broaden resonances, which inhibits the acquisition of high-resolution spectra. At this writing, structures from only one family of membrane proteins have been reported using high-resolution NMR data [2,3]. These structures are of porins, β-barrel proteins from the outer membrane of *E. coli*. Structures of the larger families of membrane proteins consisting of transmembrane bundles of α-helices have proven more difficult to solve.

It is, however, quite feasible to solve structures of fragments of membrane proteins containing 20–45 residues. We will examine how such structure determinations on membrane protein fragments can provide insight into the secondary structure of membrane proteins consisting of helical bundles.

Peptides from Helices and Turns have Intrinsic Structures that can Provide Secondary Structure Information About the Parent Soluble Protein

A growing body of data suggests that solution structures of peptides derived from some classes of proteins retain the secondary structure of the parent protein because of the dominance in α-helices and turns of short-range interactions [4] that can be captured in peptides.

Studies on segments of soluble proteins forming α-helices show that peptides containing these sequences form α-helix in almost every case under some solution conditions [5–15]. Peptides representing segments that are turns in the native protein also show turns as peptides in solution [10–13,16–22]. In some cases, the entire sequence of a helical bundle protein has been incorporated in a series of peptides spanning that sequence and the individual peptides have reported the secondary structure of much of the native protein with fidelity [19,23–26]. The implication from these studies on peptides from soluble proteins is that peptide fragments from these proteins preserve much of the secondary structure of the intact protein.

Graham A. Webb (ed.), Modern Magnetic Resonance, 335–343.
© 2008 *Springer.*

Therefore, since structure determination of intact membrane proteins is problematic, determination of structures of peptide fragments becomes an important alternative approach to structural information on membrane proteins.

Structures of Peptide Fragments from Membrane Proteins can Provide Secondary Structure Information

More recently, analogous studies have been performed for membrane proteins. Membrane proteins containing transmembrane helical bundles can be thought of as a collection of transmembrane helices (TM) and connecting turns, both elements of secondary structure stabilized by short-range interactions. It is reasonable to hypothesize, therefore, that peptide fragments corresponding to TM or to connecting turns would display local stable structure characteristic of helix or turn, respectively. This hypothesis has now been tested many times on a number of membrane proteins and found to be correct. In what follows, NMR studies on peptide fragments of a variety of membrane proteins will be reviewed, in each case demonstrating the preservation of native secondary structure in the peptide fragments.

Human Erythrocyte Glycophorin

Perhaps the earliest indication of this property of fragments from helical membrane proteins was work on glycophorin. The isolated protein was fragmented by trypsin hydrolysis. Each of the fragments was examined by circular dichroism (CD). When the CD of these individual fragments was summed, the CD of the whole protein was obtained, indicating that the secondary structure of the whole protein was largely preserved in the fragments [27]. Subsequent ^{1}H NMR studies revealed the α-helical nature of the transmembrane domain separate from the remainder of the protein [28], consistent with the CD studies.

Bacteriorhodopsin

Whether useful information of membrane protein secondary structure could therefore be obtained from peptide fragments spanning the entire sequence of a membrane protein was tested on bacteriorhodopsin. Bacteriorhodopsin is a light-activated protein from *Halobacterium salinarium* (part of the purple membrane, a specialized patch in the membrane of this bacterium) that uses light energy to pump protons against a concentration gradient. The molecular weight of this protein is 24.5 kDa [29].

Bacteriorhodopsin is the prototypical transmembrane protein consisting of a bundle of seven hydrophobic helices that constitutes the transmembrane portion of the protein with loops connecting each of the helices in the bundle. Therefore the dominant secondary structures of this protein are α-helices and turns. Both α-helices and turns are stabilized by short-range interactions (i to $i+4$ or shorter), the internal hydrogen bonds. Therefore peptides with the sequence of one of the transmembrane helices or one of the turns could be expected to contain the hydrogen bonds characteristic of the corresponding secondary structure and thus stabilize the relevant secondary structure in the peptide.

A number of three-dimensional structure determinations have been published for bacteriorhodopsin [30–34], one of the very few membrane proteins for which complete structures are available. Furthermore, experiments have shown that bacteriorhodopsin can be expressed in two separate pieces and the pieces will assemble properly in a membrane to re-form the protein [35–36], suggesting a subdomain character for the helices in the transmembrane region.

The collection of this evidence encouraged investigation into the structural stability of fragments of bacteriorhodopsin. Several fragments of bacteriorhodopsin were synthesized by solid phase peptide synthesis and their three-dimensional structures determined [37–40]. Two dimensional, homonuclear NMR experiments were used on these unlabeled, hydrophobic peptides in organic solvent. The local stability of the helices was clearly observed. Peptide fragments from some of the helical regions of bacteriorhodopsin formed helices separate from the remainder of the protein.

This question of localized stability of secondary structure was then explored in depth for the entire bacteriorhodopsin molecule. A series of overlapping peptides that spanned the sequence of the protein were synthesized. Each peptide encompassed either a (transmembrane) helical region or a turn flanked by two short helical regions (connecting two transmembrane helices). Structures of the peptides were determined by NMR in DMSO, a solvent with no propensity to stabilize any particular secondary structure and with a dielectric similar to the membrane interface at which initial folding of secondary structure of helical membrane proteins is proposed to occur [41]. All the peptides that encompassed a sequence corresponding to a transmembrane helix formed a helix in solution, except for the peptide for helix G in bacteriorhodopsin (which proved to be unstable in solution). All the peptides that corresponded to turns formed turns in solution, separate from the remainder of the protein [42,43]. Overlays of these fragments on the crystal structure showed good agreement between the structures of the peptide fragments and the X-ray crystal structure of the intact protein (see Figure 1).

These results were interpreted in terms of local stability of secondary structure, such that crucial interactions

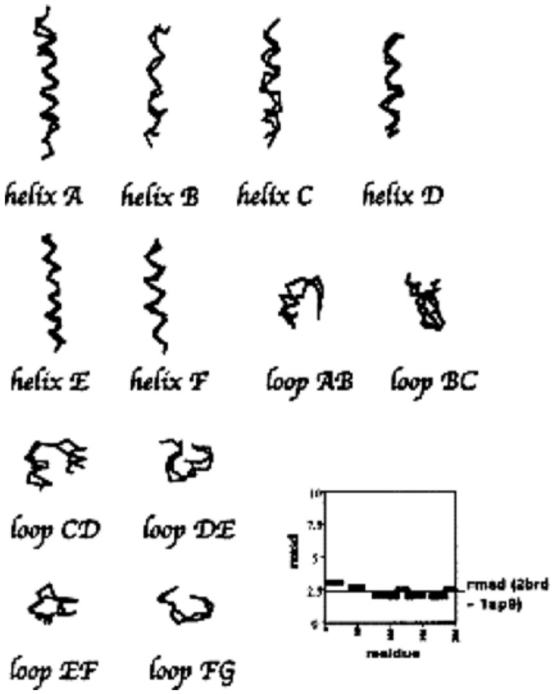

Fig. 1. Alpha carbon maps of the superposition of the backbone atoms of the peptide structures on the corresponding sequences in one crystal structure (2BRD) of bacteriorhodopsin. In each case, one member of the family of peptide structures, randomly chosen, was superimposed on the crystal structure. Similar results were obtained from superposition of these peptide structures on 1AP9. The superpositions were calculated using only the well-ordered portions of the peptide structures, as listed in Table 1. Inset: The rmsd (Å) of the superposition is plotted for each peptide as a function of the sequence of bacteriorhodopsin. The horizontal line represents the average rmsd of superposition of 2BRD on 1AP9. (Reproduced from ref. [43] with permission.)

(hydrogen bonds) could form within the peptide, just as in the X-ray crystal structure of the intact protein. The agreement between the peptide structures and the structure of the intact protein suggested that structural studies of a series of overlapping peptides spanning the sequence of an α-helical membrane protein should provide valid information on the secondary structure of the protein (α-helices and turns).

Bovine Rhodopsin

This information provided the basis for a study of the secondary structure of bovine rhodopsin, another protein built around a transmembrane bundle of 7 α-helices like bacteriorhodopsin. The initial events of low-level visual transduction take place in the retinal rod cell on the retinal rod outer segment (ROS) disk membrane. The G-protein coupled receptor (GPCR), rhodopsin, is the major protein of the disk membrane, comprising 80–90% of the total disk membrane protein [44,45]. When light strikes the ROS and is absorbed by the photopigment, rhodopsin goes through a series of spectrally defined intermediates. The transition to the Metarhodopsin II (R^*) intermediate permits the activation of the G protein, transducin and initiates the cGMP cascade [46] that culminates in the hydrolysis of cGMP and closure of the plasma membrane Na^+ channels. This results in a hyperpolarization of the plasma membrane and generates a signal at the synapse.

$$\text{Rhodopsin} + \text{light} \rightarrow \text{Meta II } (R^*) \rightarrow \text{Opsin} + \text{retinal}$$

Expression studies suggested that rhodopsin was built of subdomains. Rhodopsin can be expressed as two independent bundles of TM, such as a set of 3 TM and a set of 4 TM, and these separately expressed helical bundles will spontaneously assemble in the membrane [47]. These studies led to the hypothesis stated above that a protein built around a transmembrane helical bundle can be dissected into peptide fragments that retain the secondary structure of the native protein.

When studies based on that hypothesis were begun [48], no X-ray crystal structure of rhodopsin was available. Therefore an intense effort was dedicated to determine the secondary structure of this protein through fragments of rhodopsin corresponding to transmembrane helices or turns.

Initially, just the cytoplasmic loops were studied in depth. These loops had been shown to be biologically active, inhibiting the interaction between this GPCR and its G protein [49,50]. These loops were soluble in water and showed CD characteristic of structure under conditions similar to those in which biological activity had been demonstrated. They were therefore ideal candidates to determine whether structure of a loop could exist separate from the rest of the protein. NMR studies were undertaken and the structures determined of these peptide fragments of rhodopsin [48,51–53]. All three cytoplasmic loops formed stable structures in solution as suggested by the CD and consistent with the observed biological activity.

These studies encouraged an in-depth study of the whole protein. A complete set of overlapping peptides spanning the sequence of the protein was synthesized. The structures of the remaining fragments were determined by solution NMR techniques [15,54,56]. These peptide fragments in each case showed structure. Fragments from putative helices showed helical structures and fragments from turns showed turn structures. It became clear that most of the secondary structure of this helical membrane protein could be captured in these peptide fragments.

When a crystal structure became available [57], it was possible to verify that the secondary structure in the peptide fragments mimicked the secondary structure in the intact protein [58]. It subsequently became possible to utilize these structures of peptide fragments to assemble a structure for the whole protein. This will be discussed at the end of this review.

Lactose Permease

The lac permease is a β-galactoside transport system of *E. coli* encoded in the lac operon (lacY). The first report of this activity was in 1955 [59]. Subsequently it was shown that this transport activity was driven by a proton gradient [60], in accord with the Mitchell hypothesis [61]. This protein was cloned [62] and sequenced [63] early in the study of such membrane proteins. It was purified and reconstituted in defined lipid bilayers and found to exhibit the same transport activity that had been measured in the native membrane [64]. The protein functions as a monomer in the membrane [65,66]. Cysteine scanning has shown that six amino acid residues are essential for the transport process: E126, R144, E269, R302, H322, and E325 [67].

The structure of this protein consists of a bundle of 12 TM. The X-ray crystal structure shows a pseudo symmetry of two bundles of 6 TM connected by loops [68]. Therefore the lactose permease is a good candidate for the same analysis of secondary structure described above for bacteriorhodopsin and rhodopsin. Such a project was begun before the crystal structure was reported. A series of peptides spanning the sequence of the protein were synthesized, each peptide encompassing a putative transmembrane helix or a turn connecting two TM. As in the case of the other membrane proteins, a set of structures were obtained from solution NMR studies demonstrating the short-range stability of elements of secondary structure, including turns [69] and helices [123].

Protein Fragments of Other Membrane Proteins

Bacteriorhodopsin, rhodopsin, and lactose permease are the current examples of complete analysis of secondary structure using a series of peptides spanning the entire sequence of the membrane protein. However, a number of other examples have been reported of fragments from other integral membrane proteins that also show preservation of secondary structure in peptide fragments.

Saccharomyces Cerevisiae α-factor Receptor

The *Saccharomyces cerevisiae* α-factor receptor is a GPCR of yeast involved in mating. Peptides corresponding to all the TM of this 7TM transmembrane protein were synthesized and some of the loops. Structures were determined in organic solvent by NMR. All TM showed helical structures and one of the loop peptides was also structured [70–73]·

Parathyroid Hormone Receptor

Fragments of the parathyroid hormone receptor, a GPCR, have been studied by solution NMR techniques in detergent micelles. A peptide containing the amino acid sequence of the first extracellular loop was synthesized. The NMR structure revealed a short helix on each end of the peptide corresponding to portions of the TM on either side of the loop. The interior of the loop also contained an additional helix [74]. A peptide corresponding to the third cytoplasmic loop of this same receptor was synthesized and the NMR solution structure revealed a loop structure in the presence of detergent micelles [75,76].

The Human Cholecystokinin-2 Receptor

The third extracellular loop of the cholecystokinin-2 receptor (residues 352–379), a GPCR, was synthesized and its structure determined in detergent (DPC) micelles by solution NMR. The ends of the two attached helices, 6 and 7, are seen as is the turn [77]. Interactions between this third extracellular loop and ligands have been probed by NMR and other techniques [77–80].

The Human Cannabinoid Receptor

The human cannabinoid 1 receptor functions as a receptor for Δ^9 tetrahydrocannabinol and is coupled to $G_{i/o}$. A peptide has been expressed of 44 residues containing the third cytoplasmic loop of this GPCR. The peptide is biologically active. There is evidence for helix at both ends of the peptide, corresponding to portions of the two connected transmembrane helices, and the peptide forms a turn in detergent micelles [81]· The putative helix 8 of the cannabinoid 2 receptor has been synthesized and the structure determined in DPC micelles and in DMSO. In both environments an α-helix was observed [82].

Bradykinin B2 Receptor

The bradykinin B2 receptor is a GPCR. A peptide corresponding to the second intracellular loop of the bradykinin B2 receptor and containing 34 residues was synthesized and the structure determined by solution NMR. A helix-turn-helix motif was observed, with portions of both attached transmembrane helices visible. In addition, the structure of a portion of the C-terminus was examined in an expressed, labeled peptide containing residues 309–366 of the receptor. Evidence for helix 8 was observed as well as other structured regions [83,84].

Rat Angiotensin II AT1A Receptor

The rat angiotensin II AT1A receptor is a GPCR. The third cytoplasmic loop, the first extracellular loop and a portion of the carboxyl terminus of this receptor have been studied as peptides in solution with NMR. Two peptides spanning the third cytoplasmic loop show some of the attached transmembrane helices [85]. The peptide corresponding to the first extracellular loop forms a type 2 β turn [86], as do two of the turns in bovine rhodopsin [53]. The C-terminal peptide, corresponding to residues 300–320, form in part an amphipathic helix, perhaps corresponding to helix 8 observed in other GPCRs [87].

Tachykinin NK-1 Receptor

A peptide corresponding to the 7th transmembrane domain of the tachykinin NK-1 receptor was synthesized and the structure determined in organic solvent by solution NMR. Evidence for the helical nature of this domain was found in DMSO [88].

β-adrenergic Receptor

The β-adrenergic receptor is a GPCR. Peptides corresponding to the third intracellular loop of the turkey receptor (residues 284–295) were synthesized and studied in micelles by solution NMR. The C-terminal region of the peptide showed helical structure, likely corresponding to the beginning of TM 6. The putative helix 8 region of the human β-adrenergic receptor was examined with a peptide in detergent and in DMSO and found to be helical while in water the peptide was disordered [89].

EmrE, a Multidrug Resistance Protein

EmrE, a multidrug resistance protein is a membrane protein from *E. coli* of 110 residues. A set of peptides partially spanning the sequence of the protein was synthesized and structures determined by NMR in SDS micelles. Two of the peptides, corresponding to predicted transmembrane segments, formed helices as expected and another formed a turn [90].

Potassium ion Channel

The potassium ion channel is an oligomeric transmembrane structure. Peptides were synthesized corresponding to the transmembrane domain of three forms of this ion channel, Shaker, ROMK1, and minK. The structures of these peptides were studied in solution by NMR and CD and found to be predominantly helical [91].

Human Red Cell Anion Transporter, Band 3

The human red cell anion transporter, band 3, is one of two most abundant membrane proteins of the human erythrocyte membrane, involved in chloride transport. Two of the putative transmembrane segments of this protein, containing residues 405–424 and residues 436–456, were synthesized and their structure determined in trifluoroethanol. Predominantly α-helical structures were reported [92]. In addition, a peptide fragment corresponding to a loop on the cytoplasmic face of the protein connecting TM12 and TM13 was synthesized with 46 residues. The NMR solution structure showed a helix-turn-helix motif [93].

Phosphatidylglycerophosphate Synthase

Phosphatidylglycerophosphate synthase from *E. coli* is an integral membrane protein. Peptides corresponding to two putative TM of this protein were synthesized and their structure determined (residues 6–25 and residues 149–176). Two-dimensional ^{1}H NMR studies and CD studies revealed that these sequences were stable as helices in solution and in SDS micelles [94].

IsK

Isk is a voltage-gated potassium channel with a single TM per monomer. A peptide was synthesized containing the putative transmembrane domain (residues 42–68). This peptide exhibited biological activity and solution NMR studies in organic solvent showed an α-helical structure [95].

General Features of the Studies on Membrane Protein Fragments

This survey of structure reports on fragments of membrane proteins reveals several common features. (1) The peptides are 20–40 residues in length (if the peptides are too short, then the secondary structure can be destabilized). (2) The peptides encompass either a TM or a turn in the sequence of the fragment. (3) For studies in organic solvents, solvents of intermediate dielectric, such as DMSO, are common and stable secondary structure is often found in such solvents. (4) High-resolution multidimensional NMR experiments are effective in determining structure of such peptides in both organic solvent and in detergent micelles.

In the most favorable circumstances, these kinds of studies can provide a nearly complete picture of the secondary structure of the membrane protein if the protein is built around a transmembrane helical bundle. Of course, not every fragment of a membrane protein selected as described above forms stable secondary structure. And in the case of β-barrels, such as the bacterial porins, these kinds of studies to determine secondary structure would not be useful. However, this survey does not reveal a case where the structure of the fragment reported incorrectly on the secondary structure of the protein. Rather the only cases that did not report the correct secondary structure were cases in which the fragment was disordered and thus provided no information on secondary structure. Therefore studies on the structures of nearly 100 of these fragments of membrane proteins have not yet misled the investigator as to the true structure in the protein from which they were derived.

How Sparse Long-Distance Experimental Constraints can be Combined with Fragment Structures to Build a Structure of the Intact Membrane Protein

An interesting recent analysis demonstrated the ability to organize elements of secondary structure (α-helices) in three dimensions to mimic the structure of a native membrane protein, using a limited number of long-distance constraints [96]. The concept starts with helices as locally stable structures. In a protein like rhodopsin, the transmembrane domain consists of 7 TM in a bundle. If one assumes the structure of the helices (from, say, hydrophobicity plots), then one needs to define the density of long-distance constraints necessary to the proper organization of the helical bundle. In this study, employing just 27 experimental long-distance constraints was sufficient to define the three-dimensional organization of the 7 helices to mimic the structure of the transmembrane bundle. A conceptually similar (but different in approach) method was used previously with 7 ideal helices to build the bundle constituting the transmembrane domain of rhodopsin [97]. Again a limited number of long-distance constraints were used to organize the bundle.

These more theoretical studies provide a basis for assembling a structure of a transmembrane protein from experimental structures of protein fragments, defined as above, and additional experimental long-distance constraints from the intact protein. Structures of two membrane proteins have been successfully built using such an approach.

Bacteriorhodopsin

Bacteriorhodopsin was used as a test case to develop this approach to membrane protein structure. Bacteriorhodopsin is a seven transmembrane helical protein and several crystal structures are available. The structures of each in a series of overlapping peptides spanning the sequence of bacteriorhodopsin were determined using NMR. The solution structures of these peptides were found to have the same secondary structure as the corresponding regions of the X-ray crystal structure. These individual peptide structures, and the distance constraints obtained for them, were then used, with additional experimental long-distance constraints, to build the three-dimensional structure for the whole protein. The resulting structure agreed with structures determined from electron and X-ray diffraction data. The B factors from X-ray and electron diffraction studies are high in most of the loops of all the bacteriorhodopsin structures. Therefore quantitative comparisons were made with the transmembrane domain, which has substantially lower B factors. Accordingly, the rmsd of superposition of the NMR based structure on the crystal structure 2brd is 2.9. The structure obtained by our method is in as close agreement with the X-ray structure as the X-ray structures are with each other. [43] (see Figure 2). This work demonstrated that a three-dimensional structure could be obtained for a membrane protein using the secondary structural information

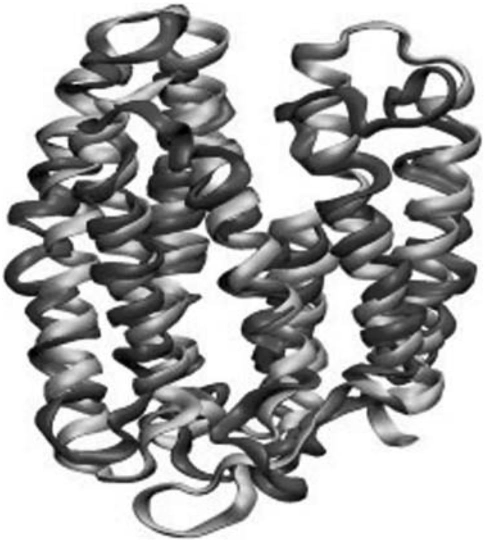

Fig. 2. Structure of bacteriorhodopsin (blue), determined from experimental data as described in the text, superimposed on a crystal structure (cyan) of bacteriorhodopsin (1FBB). (See also Plate 41 on page XXXIV in the Color Plate Section.)

obtained from peptides representing protein sub-domains (helices and turns), coupled with experimental long-range distance constraints.

Bovine Rhodopsin

The same technique was used to determine a structure of rhodopsin. Structures of all the extramembraneous domains of rhodopsin and the structures of all the transmembrane helical domains were determined by two-dimensional homonuclear ^{1}H NMR [15,43–48,51–56,98–102]. The peptides typically exhibit well-defined structures in solution. Comparison of the peptide structures to the corresponding region in the crystal structure indicates good agreement. This work formed the basis of a three-dimensional structure of rhodopsin that is in agreement with the crystal structure of rhodopsin in the dark-adapted state [57]. Furthermore, we were able to use the same approach to determine a structure for Meta II, the activated form of rhodopsin (and the only structure to date of an activated GPCR) [103]. The technique is described below.

The solution structures of a series of overlapping peptides, which spanned the rhodopsin primary sequence, were determined by two-dimensional homonuclear ^{1}H NMR and linked into a construct corresponding to the entire sequence of rhodopsin [56]. The construct was originally built by superimposing the overlapping regions of the fragments to link one fragment to the next in the sequence. 11-cis retinal was added to K296 to make a specially defined amino acid. Experimental distance constraints were written into the mol2 file for this construct in SYBYL (Tripos). 3030 short-range NOE-derived experimental distance constraints were available from the NMR structure determinations on the individual peptides. Long-range constraints from independent experiments on intact dark-adapted rhodopsin were added. For example, site directed spin labeling put pairs of spin labels at specific sites and the dipolar interactions between the spin labels provided distance measurements [104–115]. Other experimental distance constraints were obtained from engineered disulfide crosslinking [47], engineered metal binding sites [116] and other experimental measures of site-to-site distances in the intact rhodopsin. The 11-cis retinal was constrained by the solid state NMR data of Watts, *et al.* [117]. The construct with the distance constraints was subjected to several cycles of simulated annealing (1000 fs at 1000 °K followed by 1500 fs cooling to 200 °K). The resulting compact structure determined strictly from experimental data (no modeling), showed a bundle of seven helices connected by six turns.

This work demonstrates that a valid structure for membrane proteins built on helical bundles can be obtained from the secondary structures of the protein fragments and selected long-range constraints. This three-dimensional structure of rhodopsin can be quantitatively superimposing this structure on the X-ray crystal structure. Good agreement with the crystal structure [57] is observed in the transmembrane region with an rmsd of 1.85. (It is only valid to compare this structure with the crystal structure in the transmembrane region because the crystal structure is poorly resolved in the cytoplasmic face. This poor resolution is typical of crystal structures of membrane proteins and is manifest in very high B values.

New High-Resolution NMR Studies on Intact Membrane Proteins

The story of high-resolution NMR and membrane protein structure does not end here. Recent studies have exploited new TROSY [118] techniques and deuteration to obtain spectra and structures from several β-barrel porins from the outer membrane of *E. coli* [2,3,119]. While no complete structure of a membrane protein built on a helical bundle has been published at this writing, important progress is currently being made on helical bundles including bacteriorhodopsin [120] and diacylglycerol kinase [121]. Very helpful to this effort is the discovery of new detergents that produce improved NMR spectra of integral membrane proteins [122]. It is to be hoped that these early efforts presage a strong presence in the future of high-resolution NMR in the field of membrane protein structural biology.

References

1. Buchan DW, Shepherd AJ, Lee D, Pearl FM, Rison SC, Thornton JM, Orengo CA. Genome. Res. 2002;12:503.
2. Arora A, Abildgaard F, Bushweller JH, Tamm LK, Nat. Struct. Biol. 2001;8:334.
3. Fernandez C, Hilty C, Bonjour S, Adeishvili K, Pervushin K, Wuthrich K, FEBS Lett. 2001;504:173.
4. Yang A-S, Hitz B, Honig B, J. Mol. Biol. 1996;259:873.
5. Gao J, Li Y, Yan H, J. Biol. Chem. 1999;274:2971.
6. Ramirez-Alvarado R, Serrano L, Blanco FJ, Prot. Sci. 1997; 6:162.
7. Gegg CV, Bowers KE, Matthews CR, Prot. Sci. 1997;6:1885.
8. Hamada D, Kuroda Y, Tanaka T, Goto Y, J. Mol. Biol. 1995;254:737.
9. Callihan DE, Logan TM, J. Mol. Biol. 1999;285:2161.
10. Wilce JA, Salvatore D, Waade JD, Craik DJ, Eur. J. Biochem. 1999;262:586.
11. Jimenez MA, Evangelio JA, Aranda C, Lopez-Brauet A, Andreu D, Rico M, Lagos R, Andreu JM, Prot. Sci. 1999;8: 788.
12. Fan JS, Cheng HC, Zhang M, Biochem. Biophys. Res. Commun. 1998;253:621.
13. Cox JPL, Evans PA, Packman LC, Williams DH, Woolfson DN, J. Mol. Biol. 1993;234:483.

14. Hunt JF, Earnest TN, Bousche O, Kalghatgi K, Reilly K, Horvath C, Rothschild KJ, Engelman DM, Biochemistry 1997;36:15156.
15. Katragadda M, Chopra A, Bennett M, Alderfer JL, Yeagle PL, Albert AD, J. Pept. Res. 2001;58:79.
16. Chandrasekhar K, Profy AT, Dyson HJ, Biochemistry 1991;30:9187.
17. Ghiara JB, Stura EA, Stanfield RL, Profy AT, Wilson IA, Science 1994;264:82.
18. Blumenstein M, Matsueda GR, Timmons S, Hawiger J, Biochemistry 1992;31:10692.
19. Blanco FJ, Serrano L, Eur. J. Biochem. 1994;230:634.
20. Goudreau N, Cornille F, Duchesne M, Parker F, Tocqué B, Garbay C, Roques BP, Nat. Struct. Biol. 1994;1: 898.
21. Adler M, Sato MH, Nitecki DE, Lin J-H, Light DR, Morser J. J. Biol. Chem. 1995;270:23366.
22. Campbell AP, McInnes C, Hodges RS, Sykes BD, Biochemistry 1995;34:16255.
23. Behrends HW, Folkers G, Beck-Sickinger AG. Biopolymers 1997;41:213.
24. Reymond MT, Merutka G, Dyson HJ, Wright PE, Protein Sci. 1997;6:706.
25. Dyson HJ, Merutka G, Waltho JP, Lerner RA, Wright PE, J. Mol. Biol. 1992;226:795.
26. Padmanabhan S, Jimenez MA, Rico M, Protein Sci. 1999; 8:1675.
27. Schulte TH, Marchesi VT, Biochemistry 1979;18:275.
28. Lemmon MA, Flanagan JM, Hunt JF, Adair BD, Bormann B-J, Dempsey CE, Engelman DM. J. Biol. Chem. 1992;267:7683.
29. Reynolds JA, Stoeckenius W. Proc. Natl. Acad. Sci. U.S.A. 1977;74:2803.
30. Gouaux E. Structure 1998;6:5.
31. Grigorieff N, Ceska TA, Downing KH, Baldwin JM, Henderson R. J. Mol. Biol. 1996;259:393.
32. Henderson R, Baldwin JM, Ceska TA, Zemlin F, Beckmann E, Downing KH. J. Mol. Biol. 1990;213:899.
33. Luecke H, Schobert B, Richter H-T, Cartailler J-P, Lanyi JJK. J. Mol. Biol. 1999;291:899.
34. Pebay-Peyroula E, Rummel G, Rosenbusch JP, Landau EM. Science 1997;277:1676.
35. Kahn TW, Engelman DM. Biochemstry 1992;31:6144.
36. Marti T. J. Biol. Chem. 1998;273:9312.
37. Barsukov IL, Nolde DE, Lomize AL, Arseniev AS, Eur. J. Biochem. 1992;206:665.
38. Lomize AL, Pervushin KV, Arseniev AS. J. Biomol. NMR 1992;2:361.
39. Pervushin KV, Orekhov VY, Popov AI, Musina LY, Arseniev AS. Eur. J. Biochem. 1994;219:571.
40. Sobol AG, Arseniev AS, Abdulaeva GV, LYu M, Bystrov VF, J. Bio. NMR 1992;2:161.
41. White SH, Wimley WC, Ann. Rev. Biophys. Biomol. Struct. 1999;28:319.
42. Katragadda M, Alderfer JL, Yeagle PL. Biochim. Biophys. Acta 2000;1466:1.
43. Katragadda M, Alderfer JL, Yeagle PL. Biophys. J. 2001;81:1029.
44. Papermaster D, Dreyer W. Biochemistry 1974;13:2438.
45. Smith HG, Stubbs GW, Litman BJ. Exp. Eye Res. 1975; 20:211.
46. Bennett N, Michel-Villay M, Kühn H. Eur. J. Biochem. 1982; 127:97.
47. Yu H, Kono M, McKee TD, Oprian DD. Biochemistry 1995;34:14963.
48. Yeagle PL, Alderfer JL, Albert AD. Nat. Struct. Biol. 1995; 2:832.
49. Hamm HE, Deretic D, Arendt A, Hargrave PA, Koenig B, Hofmann KP. Science 1988;241:832.
50. Konig B, Arendt A, McDowell JH, Kahlert M, Hargrave PA, Hofmann KP. Proc. Natl. Acad. Sci. U.S.A. 1989;86:6878.
51. Yeagle PL, Alderfer JL, Albert AD. Biochemistry 1995; 34:14621.
52. Yeagle PL, Alderfer JL, Albert AD. Molecular Vision 2, http://www.molvis.org/molvis/v2/p12/ (1996).
53. Yeagle PL, Alderfer JL, Albert AD. Biochemistry 1997; 36:3864.
54. Yeagle PL, Salloum A, Chopra A, Bhawsar N, Ali L, Kuzmanovski G, Alderfer JL, Albert AD. J. Pept. Res. 2000; 55:455.
55. Chopra A, Yeagle PL, Alderfer JA, Albert A. Biochim. Biophys. Acta 2000;1463:1.
56. Yeagle PL, Danis C, Choi G, Alderfer JL, Albert AD, Molecular Vision, www.molvis.org/molvis/v6/a17/, (2000).
57. Palczewski K, Kumasaka T, Hori T, Behnke CA, Motoshima H, Fox BA, Le Trong I, Teller DC, Okada T, Stenkamp RE, Yamamoto M, Miyano M. Science 2000;289:739.
58. Yeagle PL, Choi G, Albert AD. Biochemistry 2001;40: 11932.
59. Cohen GNR, Rickenberg HV. Compte Rendu 1955;240:466.
60. Kaback HR. J. Cell Physiol. 1976;89:575.
61. Mitchell P. Biochem. Soc. Symp. 1963;22:142.
62. Teather RM, Muller-Hill B, Abrutsch U, Aichele G, Overath P. Mol. Gen. Genet. 1978;159:239.
63. Buchel DE, Gronenborn B, Muller-Hill B. Nature 1980;283: 541.
64. Matsushita K, Patel L, Gennis RB, Kaback HR. Proc. Natl. Acad. Sci. U.S.A. 1983;80:4889.
65. Dornmair K, Corni AF, Wright JK, Jahnig F. EMBO J. 1985;4:3633.
66. Costello MJ, Escaig J, Matsushita K, Vitanen PV, Menick DR, Kaback HR. J. Biol. Chem. 1987;262:17072.
67. Frillingos S, Sahin-Toth M, Wu J, Kaback HR. FASEB J. 1998;12:1281.
68. Abramson J, Smirnova I, Kasho V, Verner G, Kaback HR, Iwata S. Science 2003;301:610.
69. Bennett M, Yeagle JA, Maciejewski M, Ocampo J, Yeagle PL. Biochemistry 2004;43:12829.
70. Arshava B, Liu SF, Jiang H, Breslav M, Becker JM, Naider F. Biopolymers 1998;46:343.
71. Xie HB, Ding FX, Schreiber D, Eng G, Liu SF, Arshava B, Arevalo E, Becker JM, Naider F. Biochemistry 2000; 39:15462.
72. Valentine KG, Liu SF, Marassi FM, Veglia G, Opella SJ, Ding FX, Wang SH, Arshava B, Becker JM, Naider F. Biopolymers 2001;59:243.
73. Arshava B, Taran I, Xie H, Becker JM, Naider F. Biopolymers 2002;64:161.
74. Piserchio A, Bisello A, Rosenblatt M, Chorev M, Mierke DF. Biochemistry 2000;39:8153.
75. Mierke DF, Royo M, Pelligrini M, Sun H, Chorev M. J. Am. Chem. Soc. 1996;118:8998.

76. Pellegrini M, Royo M, Chorev M, Mierke DF. Biopolymers 1996;40:653.
77. Giragossian C, Mierke DF. Biochemistry 2001;40:3804.
78. Pellegrini M, Mierke DF. Biopolymers 1999;51:208.
79. Giragossian C, Mierke DF. Biochemistry 2002;41:4560.
80. Giragossian C, Mierke DF. Life Sci. 2003;73:705.
81. Ulfers AL, McMurry JL, Kendall DA, Mierke DF. Biochemistry 2002;41:11344.
82. Choi G, Landin J, Xie XQ. J. Pept. Res. 2002;60:169.
83. Piserchio A, Prado GN, Zhang R, Yu J, Taylor L, Polgar P, Mierke DF. Biopolymers 2002;63:239.
84. Piserchio A, Zelesky V, Yu J, Taylor L, Polgar P, Mierke DF. Biopolymers. 2005;80:367.
85. Franzoni L, Nicastro G, Pertinhez TA, Oliveira E, Nakaie CR, Paiva AC, Schreier S, Spisni A. J. Biol. Chem. 1999; 274:227.
86. Nicastro G, Peri F, Franzoni L, de Chiara C, Sartor G, Spisni A. J. Pept. Sci. 2003;9:229.
87. Franzoni L, Nicastro G, Pertinhez TA, Tato M, Nakaie CR, Paiva AC, Schreier S, Spisni A. J. Biol. Chem. 1997;272: 9734.
88. Berlose J, Convert O, Brunissen A, Chassaing G, Lavielle S. FEBS Lett 1994;225:827.
89. Katragadda M, Maciejewski MW, Yeagle PL. Biochim. Biophys. Acta. 2004;1663:74.
90. Venkatraman J, Nagana Gowda GA, Balaram P. Biochemistry 2002;41:6631.
91. Haris PI. Biosci. Rep. 1988;18:299.
92. Gargaro AR, Bloomberg GB, Dempsey CE, Murray M, Tanner MJ. Eur. J. Biochem. 1994;221:445.
93. Askin D, Bloomberg GB, Chambers EJ, Tanner MJ. Biochemistry 1998;37:11670.
94. Morein S, Trouard TP, Hauksson JB, Rilfors L, Arvidson G, Lindblom G. Eur. J. Biochem. 1996;241:489.
95. Aggeli A, Bannister ML, Bell M, Boden N, Findlay JB, Hunter M, Knowles PF, Yang JC. Biochemistry 1998; 37:8121.
96. Sale K, Faulon JL, Gray GA, Schoeniger JS, Young MM. Protein Sci 2004;13:2613.
97. Herzyk P, Hubbard RE. J. Mol. Biol. 1998;281:741.
98. Albert AD, Yeagle PL. Methods Enzymol. 2000;315:107.
99. Yeagle PL, Albert AD. Biochem. Soc. Trans. 1998;26:520.
100. Yeagle PL, Alderfer JL, Albert AD. Biochemistry 1997;36: 9649.
101. Albert AD, Yeagle PL. Behav. Brain Sci. 1995;18:469.
102. Albert AD, Watts A, Spooner P, Groebner G, Young J, Yeagle PL. Biochim. Biophys. Acta 1997;1328:74.
103. Choi G, Landin J, Galan JF, Birge RR, Albert AD, Yeagle PL. Biochemistry 2002;41:7318.
104. Farahbakhsh ZT, Ridge KD, Khorana HG, Hubbell WL. Biochemistry 1995;34:8812.
105. Altenbach C, Yang K, Farrens DL, Farahbakhsh ZT, Khorana HG, Hubbell WL. Biochemistry 1996;35:12470.
106. Farrens DL, Altenbach C, Yang K, Hubbell WL, Khorana HG. Science 1996;274:768.
107. Yang K, Farrens DL, Altenbach C, Farahbakhsh ZT, Hubbell WL, Khorana HG. Biochemistry 1996;35:14040.
108. Yang K, Farrens DL, Hubbell WL, Khorana HG. Biochemistry 1996;35:12464.
109. Cai K, Langen R, Hubbell WL, Khorana GH. Proc. Natl. Acad. Sci. U.S.A. 1997;94:14267.
110. Altenbach C, Cai K, Khorana HG, Hubbell WL. Biochemistry 1999;38:7931.
111. Klein-Seetharaman J, Hwa J, Cai K, Altenbach C, Hubbell WL, Khorana HG. Biochemistry 1999;38:7938.
112. Cai K, Klein-Seetharaman J, Farrens D, Zhang C, Altenbach C, Hubbell WL, Khorana HG. Biochemistry 1999;38:7925.
113. Altenbach C, Klein-Seetharaman J, Hwa J, Khorana HG, Hubbell WL. Biochemistry 1999;38:7945.
114. Altenbach C, Cai K, Khorana HG, Hubbell WL, Biochemistry 1999;38:7931.
115. Altenbach C, Cai K, Klein-Seetharaman J, Khorana HG, Hubbell WL. Biochemistry 2001;40:15483.
116. Sheikh SP, Zvyaga TA, Lichtarge O, Sakmar TP, Bourne HR. Nature 1996;383:347.
117. Grobner G, Burnett IJ, Glaubitz C, Choi G, Mason AJ, Watts A. Nature 2000;405:810.
118. Salzmann M, Pervushin K, Wider G, Senn H, Wuthrich K. Proc. Natl. Acad. Sci. U.S.A. 1998;95:13585.
119. Fernandez C, Adeishvili K, Wuthrich K. Proc. Natl. Acad. Sci. U.S.A. 2001;98:2358.
120. Schubert M, Kolbe M, Kessler B, Oesterhelt D, Schmieder P, Chembiochem 2002;3:1019.
121. Oxenoid K, Kim HJ, Jacob J, Sonnichsen FD, Sanders CR. J. Am. Chem. Soc. 2004;126:5048.
122. Krueger-Koplin RD, Sorgen PL, Krueger-Koplin ST, Rivera-Torres IO, Cahill SM, Hicks DB, Grinius L, Krulwich TA, Girvin ME. J. Biomol. NMR 2004;28:43.
123. Bennett M, D’Rozario R, Sansom M, Yeagle PL. Biochemistry. 2006;45: in press.

Part I

New Developments

Fast Multidimensional NMR: New Ways to Explore Evolution Space

Ray Freeman[1] and Eriks Kupče[2]
[1]Jesus College, Cambridge, UK
[2]Varian Ltd, Eynsham, Oxford, UK

Multidimensional NMR spectroscopy [1–3] has proved extremely productive, particularly for the elucidation of the structure of biomolecules such as proteins. The essence of the technique is to allow the nuclear spins to evolve in one or more consecutive time intervals before passing on phase or intensity information to the detection stage where the spectrometer receiver is active. In the traditional implementation, the motion of the nuclear spins is monitored systematically and independently in all n evolution dimensions (t_1, t_2, $\ldots t_n$) at sampling rates that satisfy the Nyquist condition, and for durations that guarantee adequate resolution. This generates a well-digitized $n+1$-dimensional time-domain data array, and repeated Fourier transformation converts this into an $n+1$-dimensional spectrum in frequency space (F_1, F_2, $\ldots F_{n+1}$).

For years this methodology was accepted as a perfectly acceptable *modus operandi.* Although the duration of the measurement is long, particularly for high-dimensional spectra, the signal-to-noise ratio increases as the square root of the measurement time in the same manner as in multiscan averaging. But as NMR spectrometers become intrinsically more sensitive with the advent of higher magnetic fields and cryogenic receiver coils, often it is *time* that is the limiting factor rather than *sensitivity*. Long experimental durations impose an upper practical limit on the dimensionality, a slow throughput of spectra, and an inability to study time-dependent phenomena or unstable materials. The question naturally arises—are there more economical ways to sample n-dimensional evolution space? The answer of course is yes.

Standard multidimensional NMR methodology commonly sets operating conditions that are less than ideal, simply to keep the experimental duration within reasonable bounds. Although sampling rates should normally satisfy the Nyquist condition to ensure that NMR frequencies are not aliased, sometimes a controlled "folding" of high-frequency signals may have to be tolerated in the quest for speed. The maximum length of the evolution time, t_1(max), determines the achievable resolution in the corresponding frequency dimension. A common expedient is to use a shorter value of t_1(max), thereby accepting less-than-optimum resolution. Often this data set is artificially extended by linear prediction, thus avoiding truncation artifacts. But these are stop-gap measures that merely mitigate a fundamental problem crying out for more drastic solutions.

This chapter examines alternative schemes for sampling evolution space. The main focus is on three-dimensional spectroscopy ($n = 2$) although the principles apply equally well to multidimensional experiments. The aim is to discover sampling modes that are comprehensive enough to derive the full spectrum, but sufficiently economical to permit fast acquisition. Since typical three-dimensional NMR spectra are relatively sparsely populated with correlation peaks, the prognosis is optimistic. Note that any fast-acquisition mode must inevitably sacrifice signal-to-noise ratio, since signals are accumulated over a short experimental duration. Almost all fast-acquisition modes are doomed to fail in circumstances of poor sensitivity. In what follows it is implicitly assumed that the intrinsic sensitivity is adequate.

Four approaches to the speed problem are described. The first ("filter diagonalization") uses a fitting procedure in the time domain. Its key feature is the ability to compensate for sparse sampling in the evolution dimensions by fine sampling during acquisition. The second ("spatially encoded single-scan NMR") is able to monitor all the evolution steps simultaneously by storing this information as NMR responses in different slices of the sample. The third ("Hadamard encoding") avoids time-domain evolution entirely, using direct excitation of selected responses in the frequency domain. The fourth ("projection–reconstruction") shortens the experimental duration by coupling evolution dimensions together. Fourier transformation generates plane projections that can be used to reconstruct the three-dimensional spectrum.

The Filter Diagonalization Method

This novel technique [4–6] boasts a significant speed advantage for three-dimensional spectroscopy by monitoring the two evolution dimensions (t_1 and t_2) with very

Graham A. Webb (ed.), Modern Magnetic Resonance, 347–352.
© 2008 *Springer.*

few data points, but with comprehensive sampling of the acquisition dimension (t_3), since this incurs no significant time penalty. The crux of the concept is that in the resulting computed spectrum, the resolution in all three frequency dimensions depends only on the *volume* of the experimental three-dimensional time-domain array, rather than on the number of samples in any particular dimension. Fine digitization in the t_3 dimension compensates for incomplete sampling in t_1 and t_2.

The method abandons Fourier transformation in favor of fitting the time-domain data as a set of exponentially decaying sinusoids, in a manner similar to the better-known linear prediction method [7]. Repeated application of a time auto-correlation operator U is used to compute successive time-domain data points, thus creating a model for the NMR response that can be fitted to the experimental response. The aim is to diagonalize the operator U, giving eigenvalues that represent the line frequencies and widths, and eigenvectors that yield the amplitudes and phases. If this diagonalization were to be applied to the entire data set, the computation would be enormous, but the trick is to break it down into a set of much smaller bites of a rather large cherry. The key is to choose a set of basis functions that correspond to a set of localized (but overlapping) segments in frequency space. Because resonances that are far apart in frequency show negligible interference effects, far off-diagonal matrix elements of the operator U can be safely neglected. A limited set of "local" or "filtered" diagonalizations are performed, neglecting basis functions beyond the boundaries of the segment under consideration. The problem then becomes tractable and the frequency segments can be assembled into a complete spectrum. Since linear algebra is involved, the fitting process is not hindered by the usual problems of false minima. However, in the presence of appreciable noise, or in very crowded regions, the procedure can become unpredictable.

An illustration of the filter diagonalization technique is provided by the two-dimensional constant-time heteronuclear single-quantum correlation (HSQC) spectrum of a 1 mM aqueous solution of ubiquitin [6]. The conventional Fourier transform spectrum (Figure 1a) is compared with that derived by the filter diagonalization method (Figure 1b) where the number of samples in the evolution dimension has been reduced approximately sixfold. This was achieved by reduction of the constant-time parameter from 26.4 to 4.25 ms. Despite this reduction, the resolution in the conventional and fitted spectra is comparable, and only in the very crowded region are there any significant discrepancies.

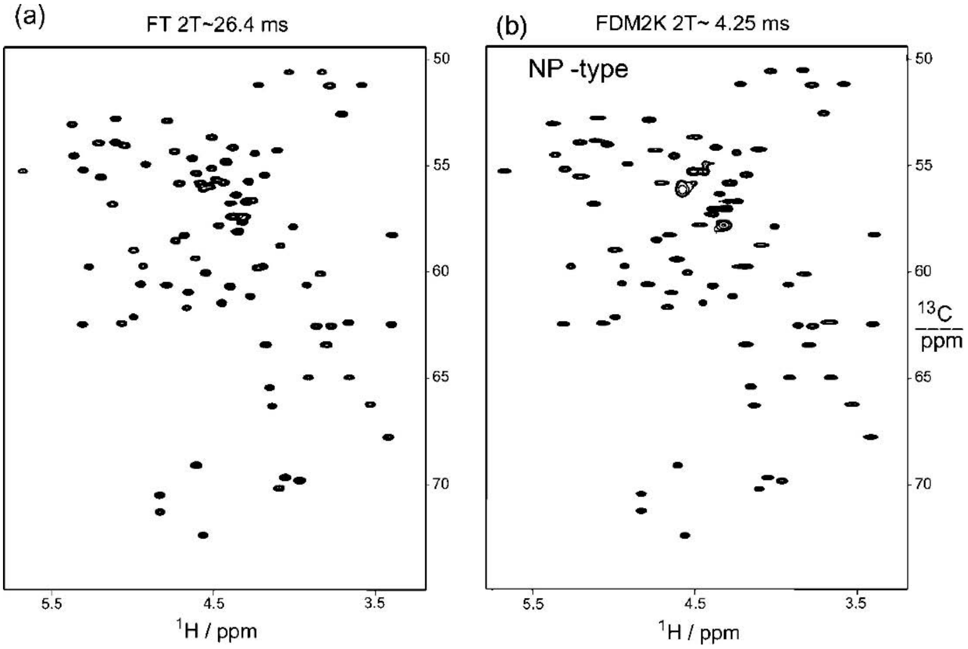

Fig. 1. Part of the 500 MHz two-dimensional HSQC spectrum of ubiquitin. (a) The conventional Fourier transform mode with the constant-time parameter (CT) set to 26.4 ms. (b) The spectrum fitted by means of the filter diagonalization method with CT shortened to 4.25 ms, requiring only 4 min of data collection. Spectra courtesy of A.J. Shaka.

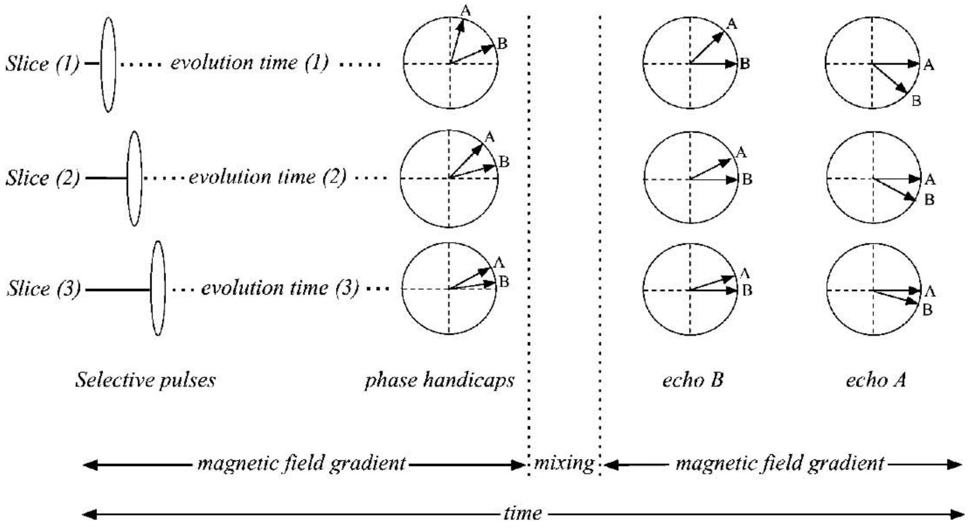

Fig. 2. Schematic representation of the spatially encoded single-scan experiment. The active sample volume is divided into slices by selective excitation in an intense field gradient. Three representative slices are considered here. Two chemical sites A and B build up different phase handicaps during evolution. After a non-selective mixing pulse, these phase handicaps are unwound in a refocusing gradient, site B forming a spin echo earlier than site A. This "spin echo spectrum" has essentially the form of the true NMR spectrum, but is obtained in a very short time, allowing the cycle to be repeated many times during a scan of less than a second.

Spatially Encoded Single-Scan NMR

One may think of this as the creation of a set of "pigeon holes" to store the evolution information, achieved in practice by selective excitation in an intense applied magnetic field gradient, thus dividing the sample into a set of thin parallel slices, excited sequentially [8–10]. The NMR signal evolves for a different interval in each slice (Figure 2). After the usual non-selective mixing pulse, the responses are detected by the application of a refocusing field gradient. (In practice both gradients are bipolar pairs.) Responses from different chemical sites, having evolved for different periods, come to a focus at different times, creating a sequence of gradient-recalled echoes (Figure 2). This "spin echo spectrum" broadly resembles the form of the true NMR spectrum in the F_1 frequency domain, but it is acquired in a very short time, typically 500 μs. This is the key to the speed factor—many acquisitions of the F_1 spectrum can be nested within the conventional acquisition scan of less than a second.

A typical application might be a two-dimensional proton COSY or TOCSY spectrum. The F_1 spectra are repeatedly recorded as a function of the acquisition parameter t_2 as correlation effects gradually build up. Only a single stage of Fourier transformation is required to generate the two-dimensional spectrum. The main drawback of the technique is its relatively poor sensitivity—engendered partly by the short accumulation time and by additional noise contributions caused by the wide frequency bandwidth employed during the spatial-encoding stage. The division of the sample into slices during evolution does not itself diminish the signal strength since NMR responses from the entire sample are brought to a focus at the same instant. Such ultrafast sampling opens up new possibilities for studying unstable materials, time-dependent phenomena, rapid screening of spectral "libraries", and flow techniques such as hyphenated liquid chromatography–NMR [11].

Hadamard Encoding

This approach abandons the conventional step-by-step exploration of evolution space, exciting the chemical sites with selective radio frequency pulses directly in the frequency domain [12–16]. Because NMR spectra are sparse, considerable time can be saved in this manner. The required NMR frequencies are obtained in a prior one-dimensional measurement that uses little spectrometer time. If the selective excitations are performed one at a time [17–20], the rate of data collection is slow, and the sensitivity is consequently poor—the famous "multiplex advantage" is lost. However by encoding the excitations (plus or minus) according to a Hadamard matrix, all the sites can be excited simultaneously, thereby restoring the multiplex advantage. The individual responses are separated by a decoding scheme based on the same matrix. Hadamard matrices [21] are higher-order versions of the simple add–subtract matrix

$$\begin{array}{cc} + & + \\ + & - \end{array}$$

that is widely used in physical science. As an example, the Hadamard matrix of order eight may be written:

$$\begin{array}{cccccccc} + & + & + & + & + & + & + & + \\ + & + & + & + & - & - & - & - \\ + & + & - & - & + & + & - & - \\ + & + & - & - & - & - & + & + \\ + & - & + & - & + & - & + & - \\ + & - & + & - & - & + & - & + \\ + & - & - & + & + & - & - & + \\ + & - & - & + & - & + & + & - \end{array}$$

Eight scans are performed with the senses of the eight selective radio frequency pulses encoded according to the rows of this matrix. Combining the eight resulting composite free induction decays according to the columns of this matrix allows the individual responses to be extracted one at a time.

The speed advantage of the multiple excitation method is given by N/Q, where Q is the order of the Hadamard matrix and N is the number of increments in the evolution dimension of the corresponding conventional experiment. The number of irradiated chemical sites S must be less than or equal to Q. Note that the operator may choose to set S less than the *actual* number of chemical sites, selecting only sites of particular interest, thereby generating a partial spectrum. This feature can be extremely useful for converting *global* isotopic enrichment (in ^{15}N or ^{13}C) to essentially *specific* enrichment, something that is very expensive to achieve chemically. The main drawback of this method is the requirement that Q scans be completed. For three- or four-dimensional spectroscopy, the intermediate radio frequency pulses are also made selective, and encoded according to the appropriate Hadamard matrices. The speed advantages in each evolution dimension are then multiplicative.

An illustration of the speed of the Hadamard method is shown in Figure 3. The sample was a 0.3 mM aqueous solution of agitoxin, a 4 kDa protein uniformly enriched in ^{13}C and ^{15}N. The 700 MHz conventional three-dimensional HNCO spectrum required 20 h and 43 min of data collection. A projection of this spectrum onto the C–H plane is shown in Figure 3A. Figure 3B demonstrates how the Hadamard technique can record a subspectrum from only seven selected sites, as if the sample had been selectively (rather than globally) enriched in ^{13}C. The Hadamard matrix of order eight was used, requiring eight scans, thus speeding up acquisition by a factor of more than 200. The smaller the number of sites selected for excitation, the smaller the required Hadamard matrix, and the faster the measurement.

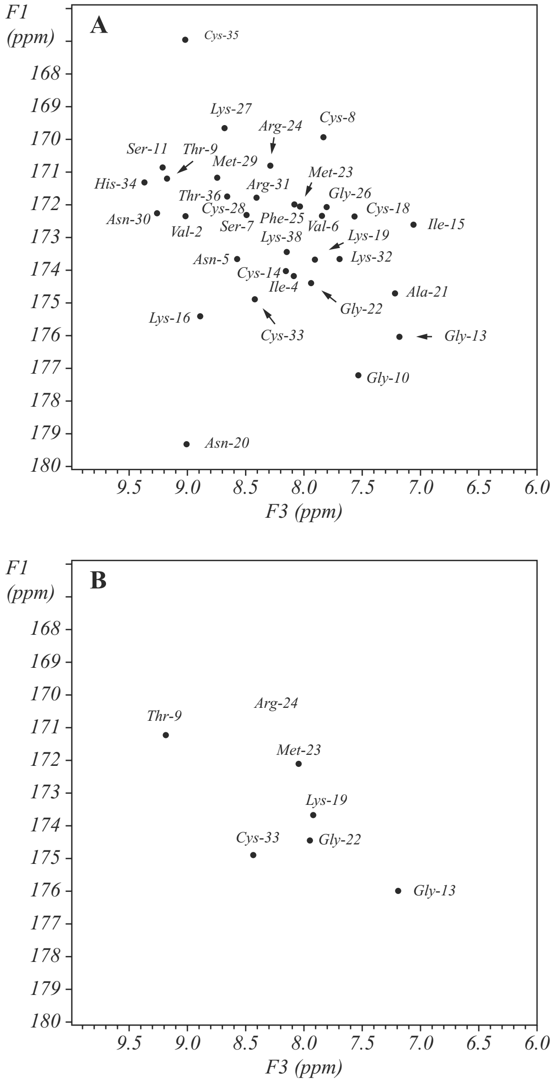

Fig. 3. Projection of the 700 MHz three-dimensional HNCO spectrum of agitoxin onto the C–H plane. (A) The conventional Fourier transform spectrum. Seven residues were selected at random, indicated by arrows. (B) The corresponding Hadamard spectrum of these seven residues, obtained more than 200 times faster.

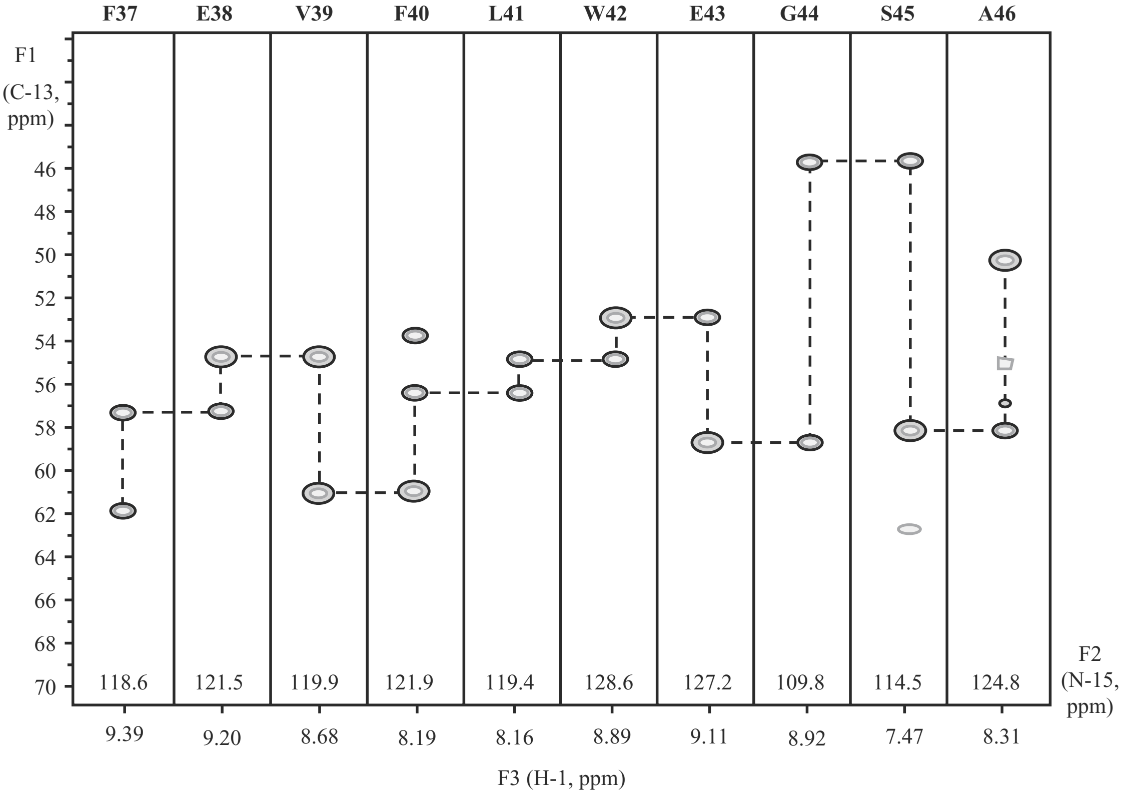

Fig. 4. Strip plots from the three-dimensional HNCA spectrum of nuclease A inhibitor mapping a chain of nine residues correlated through their ^{15}N and ^{13}C resonances. The projection–reconstruction technique shortens the experimental duration by an order of magnitude.

Projection–Reconstruction

The "accordion" experiment [22,23] and subsequent extensions [24–27] save time by coupling the incrementation of two evolution parameters t_1 and t_2, rather than scanning them separately. The evolving signal is recorded along a skew section through the time-domain data at an angle α given by $\tan\alpha = \Delta t_2/\Delta t_1$. Compared with systematic sampling of all N^2 elements of evolution space, this saves a factor of approximately N in spectrometer time (although slightly faster sampling is required along the skew axis). Fourier transformation of these signals generates a projection of the three-dimensional spectrum onto a plane inclined at the same angle α. With the standard quadrature detection in each evolution dimension, the technique gives two projections inclined at $\pm\alpha$. Thus by choosing the relative rates of incrementation, a projection can be obtained on a suitably tilted plane in frequency space.

It is well known from X-ray tomography [28] that an image of a three-dimensional object can be reconstructed from a set of projections taken at different angles of incidence. NMR spectra present a much more promising case, for they are made up of relatively sparse, discrete resonances, whereas the absorption in a physiological sample is continuous. As a result, an NMR spectrum can be reconstructed from a quite small number of projections recorded at different angles [29–33]. For three-dimensional spectroscopy the initial projections are those on the orthogonal F_1F_3 and F_2F_3 planes which are often used during the setting up procedure. The information content of these two projections is insufficient to reconstruct the three-dimensional spectrum, but it defines all *conceivable* positions for the cross-peaks, as if every resonance in the F_1F_3 plane were correlated with every resonance in the F_2F_3 plane. The actual cross-peaks are identified by imposing further constraints based on tilted projections, since the final three-dimensional array must be compatible with all the measured projections. If the signal-to-noise ratio is only marginal, projections are recorded at several different tilt angles and the inverse Radon transform [34] is employed for the reconstruction.

The 800 MHz three-dimensional HNCA spectrum of a 3 mM aqueous solution of the 143-residue nuclease A inhibitor [35] serves as an illustration of the projection–reconstruction technique [33]. The strip plots of Figure 4 show ^{15}N–^{13}C correlations for a chain running between residues 37 and 46. Based only on projections recorded at 0°, ±30°, ±60°, and 90°, the measurements were completed in 1 h, compared with an estimate of 11 h for the conventional mode.

Acknowledgments

The authors thank Lucio Frydman for several illuminating discussions, Gerhard Wagner for the sample of agitoxin, Robert London for the sample of nuclease A inhibitor, A.J. Shaka for permission to reproduce Figure 1, and the *Journal of Biomolecular NMR* for permission to reproduce Figure 3.

References

1. Jeener J. Ampère International Summer School, Basko Polje, Yugoslavia, 1971.
2. Aue WP, Bartholdi E, Ernst RR. J. Chem. Phys. 1976;64:2999.
3. Bax A. Two-Dimensional Nuclear Magnetic Resonance in Liquids. Delft, The Netherlands: Delft University Press, 1982.
4. Hu H, De Angelis AA, Mandelshtam VA, Shaka AJ. J. Magn. Reson. 2000;144:357.
5. Chen J, Mandelshtam VA, Shaka AJ. J. Magn. Reson. 2000;146:363.
6. Chen J, De Angelis AA, Mandelshtam VA, Shaka AJ. J. Magn. Reson. 2003;161:74.
7. Barkhuijsen H, DeBeer R, Bovée WMMJ, van Ormondt D. J. Magn. Reson. 1985;61:465.
8. Frydman L, Scherf T, Lupulescu A. Proc. Natl. Acad. Sci. U.S.A. 2002;99:15859.
9. Frydman L, Lupulescu A, Scherf T. J. Am. Chem. Soc. 2003;125:9204.
10. Shrot Y, Frydman L. J. Am. Chem. Soc. 2002;125:11385.
11. Shapira B, Karton A, Aronzon D, Frydman L. J. Am. Chem. Soc. 2004;126:1262.
12. Kupče E, Freeman R. J. Magn. Reson. 2003;162:158.
13. Kupče E, Freeman R. J. Magn. Reson. 2003;162:300.
14. Kupče E, Freeman R. J. Magn. Reson. 2003;163:56.
15. Kupče E, Freeman R. J. Biomol. NMR. 2003;25:349.
16. Kupče E, Nishida T, Freeman R. Prog. NMR Spectrosc. 2003;42:95.
17. Kupče E, Freeman R. J. Magn. Reson. A. 1993;102:122.
18. Kupče E, Freeman R. J. Magn. Reson. A. 1993;105:234.
19. Kupče E, Freeman R. J. Magn. Reson. A. 1993;105:310.
20. Blechta V, Freeman R. Chem. Phys. Lett. 1993;215:341.
21. Hadamard J. Bull. Sci. Math. 1893;17:240.
22. Bodenhausen G, Ernst RR. J. Magn. Reson. 1981;45:367.
23. Bodenhausen G, Ernst RR. J. Am. Chem. Soc. 1982;104:1304.
24. Ding K, Gronenborn AM. J. Magn. Reson. 2002;156:262.
25. Kim S, Szyperski T. J. Am. Chem. Soc. 2003;125:1383.
26. Kim S, Szyperski T. J. Biomol. NMR. 2004;28:117.
27. Kozminski W, Zhukov I. J. Biomol. NMR. 2003;26:157.
28. Hounsfield GN. Brit. J. Radiol. 1973;46:1016.
29. Kupče E, Freeman R. J. Biomol. NMR. 2003;27:383.
30. Kupče E, Freeman R. J. Am. Chem. Soc. 2003;125: 13958.
31. Kupče E, Freeman R. J. Biomol. NMR. 2004;28:391.
32. Kupče E, Freeman R. Concepts Magn. Reson. 2004;22A:4.
33. Kupče E, Freeman R. J. Am. Chem. Soc. 2004;126:6429.
34. Deans SR. The Radon Transform and Some of its Applications. Wiley: New York, 1983.
35. Kirby TW, DeRose EF, Mueller GA, Meiss G, Pingoud A, London RE. J. Mol. Biol. 2002;320:771–82.

High-Sensitivity NMR Probe Systems

P.J.M. van Bentum and A.P.M. Kentgens
Institute for Molecules and Materials, Radboud University Nijmegen, 6525ED Nijmegen, The Netherlands

Abstract

Nuclear magnetic resonance (NMR) has become the method of choice for many types of applications. Still, sensitivity is a limiting factor in the applicability of NMR, leading to long measurement times in advanced multidimensional experiments, and becoming prohibitive when very limited sample quantities are available. This low sensitivity is mostly an intrinsic consequence of the low energy scale of the nuclear moment in a static field, when compared to other thermodynamic energies like $k_B T$. The commercial developments are mostly aimed at an increase in the static field and simultaneously a reduction of the noise using cryocooled detection coils. Current research shows a number of interesting developments toward the enhancement of the nuclear polarization by optical pumping or by transfer from the electronic bath in dynamic nuclear polarization (DNP) experiments. A more technological approach is based on the miniaturization of the RF coils. In the next decade, one may expect the advent of the "lab on a chip" with *in situ* chemical processing and NMR analysis capabilities. A brave new method to improve detection sensitivity is based on very sensitive micromechanical force detectors. Recently, it was demonstrated that the low-temperature force detection sensitivity is sufficient to detect the magnetic moment of a single (electron) spin. These developments show that the NMR detection limits in terms of absolute sensitivity or imaging resolution are still open to significant improvements.

Sensitivity Issues in NMR Spectroscopy

NMR and magnetic resonance imaging (MRI) have had a tremendous impact on research in physics, chemistry, biology, and medicine. This success is rather surprising, given the fact that even at the highest possible fields the nuclear Zeeman splitting, and thus the electromagnetic radiation to pump the transitions, remains much smaller than the thermal energy $k_B T$ at room temperature. Hence, the equilibrium magnetization that can be manipulated and detected in an NMR experiment is many orders of magnitude smaller compared to e.g. electron spin resonance (ESR). In optical, infrared or mass spectroscopy one is used to work with near quantum efficiency detectors, and a single photon or mass fragment can be detected with a reasonable signal-to-noise ratio. In radio-frequency detectors, this is not the case. In spectroscopy, typical sample sizes are of the order of 10–100 mm^3 and one typically requires more than 10^{16} nuclei in the sample. It is clear that there are many research topics that would benefit from even a modest improvement in sensitivity or resolution. An improvement in sensitivity by a factor of 10 would bring the data acquisition times down from days to minutes and would allow for example online quality control in chemical or pharmaceutical production. In chemical synthesis, one would be able to reduce the volume of the reactants to microliters and be able to map out the full phase diagram in an *in-situ* "lab on a chip" procedure. Apart from the gain in time there is also an environmental advantage because the flow of waste chemicals is substantially reduced.

Gradual improvements of equipment and measurement procedures have pushed up the sensitivity of NMR by nearly a factor of 10 in the last decade. Current research shows a number of interesting new or renewed developments toward sensitivity enhancements through polarization transfer or detector optimization.

In the following, we will first summarize the options available to increase the effective magnetization of a given sample. Mostly, these are based on thermodynamic approaches, including higher magnetic fields, lower temperatures, and transfer of magnetization. This can be for example the transfer of magnetization from protons to low-gamma nuclei in a cross-polarization (CP) experiment. Also, polarization transfer from electrons in dynamic nuclear polarization (DNP) or from optically polarized nuclei, like Xe and ^{3}He, is feasible. In some cases, one can pump the molecules directly, and combined with an optical detection full spin polarization can be reached, at least for electron spins. In half-integer quadrupolar spins systems generally only the central transition of the multiplet is observed as the other transitions are much more strongly affected by the quadrupolar interaction. In this case, one can transfer polarization from the satellite transitions to this central peak using adiabatic passages.

In the second part, we will review the basic physical laws that determine the inductive response of a traditional RF coil. We will discuss the options available to optimize the inductive detection for mass limited samples such as

Graham A. Webb (ed.), Modern Magnetic Resonance, 353–361.
© 2008 *Springer.*

small crystals or thin surface layers. In the last part of this contribution, we will discuss approaches that move away from the traditional inductive detections, like for example the detection of the magnetic force in a magnetic resonance force microscopy (MRFM) scanning probe setup.

Thermodynamics

For a nuclear spin system, the magnetization (or total magnetic moment per unit volume) is given by Curie's law in the limit for high temperatures:

$$M = N\gamma^2\hbar^2 I(I+1)\frac{B_0}{3k_B T}$$

where N is the number of spins per unit volume, γ the gyromagnetic ratio, I the spin quantum number, B_0 the static field, T the temperature, and $\hbar$ and k_B are Planck's and Boltzmann's constant, respectively. For a give nucleus studied at room temperature, one can only manipulate the concentration N or the static field B_0. Technological progress in high-homogeneity magnets has pushed the field limit to 22.3 T (950 MHz). This is near the limit that can be produced with conventional niobium-based superconductors. With high T_c superconductor insert coils, 1 GHz can be reached, but the technological problems in reliability and reproducibility are still substantial. On the other hand, if the samples allow measurements at low temperatures, a substantial gain can be achieved. The equilibrium magnetization at very low temperatures is given by:

$$M = N\gamma\hbar I,$$

since now only the lowest level is occupied. For protons in a field of 14 T at 300 K, the equilibrium magnetization is thus of the order of 5×10^{-5} of the low temperature fully polarized limit. For very small nano-crystals, it therefore pays off to go to special facilities that employ installations with a very high B/T ratio. In various high magnetic field facilities, one typically can reach a base temperature of 40 mK at a static field of 40 T, in which case the low temperature limit is well satisfied. An early example of this approach is given by Gonen *et al.* in 1989 [1]. They showed that it is possible to detect the ^{13}C signal of a chemisorbed CO layer on SnO_2 oxidizing catalyst. Despite the low number of spins in their sample, the low-temperature population enhancement allowed a fully resolved spectrum in a single scan. Note that the spin–lattice relaxation time T_1 may become very long at low temperatures, so this approach is mostly relevant for one-dimensional experiments where no signal averaging or phase cycling is necessary. Also, one often needs to study the material at ambient temperatures, for example in liquid solution, and cryogenic cooling of the sample is not an option.

Polarization Transfer

There are various options to increase the magnetic polarization of the nuclei under study. In typical NMR sequences, one can transfer the polarization from abundant protons with a much larger Zeeman splitting to the low-gamma nuclei such as ^{13}C in a CP experiment. The enhancement factor is typically of the order of the gyromagnetic ratios, and is thus substantial for very low-gamma nuclei. In liquid NMR, many variations of the nuclear overhauser effect (NOE) [2] are used to transfer polarization to for example the ^{13}C nuclei. In general, all these methods rely on the fact that the total (coupled) spin system tries to keep overall thermal equilibrium when one of the transitions is saturated by RF radiation. For example in distortionless enhancement by polarization transfer (DEPT) type experiments, one ^{1}H transition is saturated, leading to a strong enhancement of the ^{13}C resonance (Figure 1).

Another option to beat the thermodynamic equilibrium is to use the hyperfine coupling between electrons and nuclei to transfer effective magnetization from the electrons to the nuclei. Since the electron magnetic moment is much larger than all nuclear moments, one can achieve an appreciable electronic polarization even at ambient conditions. With the method of DNP, one basically saturates the electron spin system with high-power microwaves at the ESR.

In the so-called solid effect DNP [3], one selectively excites the four-level system of the coupled two-spin state (see fig. 2). Effective polarization between the electron and nuclear bath is exchanged in the zero and double quantum transitions, which may have quite different probabilities. In theory, this might give a magnetization enhancement by as much as the gyromagnetic ratio between the electron and the nuclei ($\gamma_e/\gamma_p = 658$). In the solid effect scheme, it is required that the ESR line width is much smaller than the nuclear Larmor frequency. This is not easy to realize in practice and generally the homogeneous and inhomogeneous line broadening is considerable. However, by off-resonance excitation of the ESR transition one can still lower the nuclear spin temperature in a so-called thermal mixing scheme [4]. In practice, an enhancement by a factor of 400 has been demonstrated. The main problem is to find a suitable paramagnetic species that couples to the nucleus but does not disturb the local environment that is studied in the NMR experiment. Also, there is a substantial problem in moving to higher fields, where suitable sub-millimeter sources (above 500 GHz) are lacking. It should be noted, however, that good progress is made by the group of Griffin who have demonstrated the feasibility of DNP-enhanced

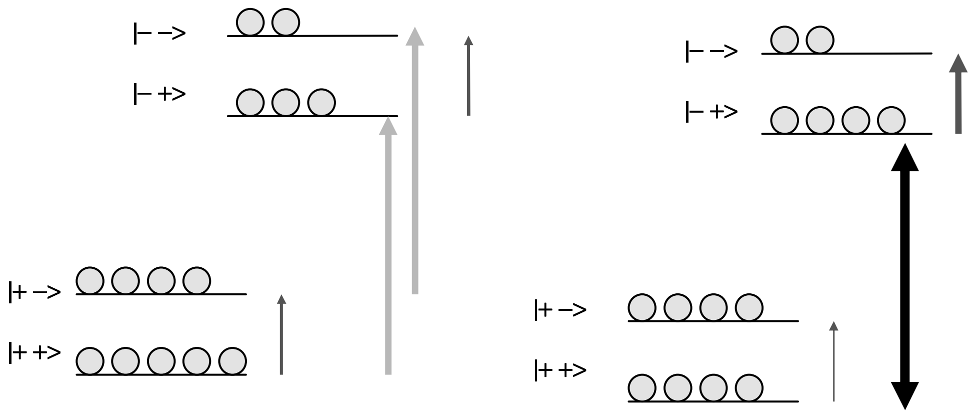

Fig. 1. Illustration of the polarization transfer in distortionless enhancement by polarization transfer (DEPT) type experiments for a system of two coupled spins (^{1}H and ^{13}C). The corresponding NMR resonance signals are indicated by red (^{13}C) and blue (^{1}H), where the linewidth symbolizes the relative intensity. The left side represents the system in thermal equilibrium. If the proton resonance is saturated by the external RF field, indicated by the black arrow, then the spin temperature of the carbon subsystem is cooled, leading to a stronger resonance signal.

magic-angle spinning (MAS) NMR spectroscopy for biologically relevant materials at fields up to 9 T [5]. In high energy physics, fully polarized solid proton or deuterium targets are used to study the spin structure of the nucleon with muon scattering. In this case, a combination of cryogenic cooling (to 40 mK) and DNP is used to create a nearly 100% polarization. Such an approach was also used by Golman and coworkers [6] in order to polarize liquids, which can subsequently be used for metabolic studies in MRI.

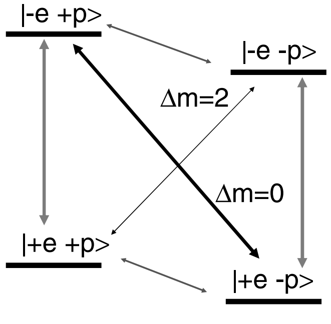

Fig. 2. Illustration of the solid effect dynamic nuclear polarization (DNP). The blue arrows represent the electron spin resonance (ESR) transitions, while the red arrows refer to the nuclear resonance. The cross transitions represented by black arrows are the double quantum (flip–flip) and the zero quantum (flip–flop) transitions that transfer effective polarization from the electron to the nuclear system. Under proper conditions, this can give a nearly 100% polarization of the nuclei.

Half-integer quadrupolar spin systems have multiple spin levels without coupling to other nuclear or electron spins. In spectra of powdered samples, commonly, only the central $-1/2 \leftrightarrow +1/2$ transition is observed, while all other transitions are broadened over a MHz-wide frequency range. It is possible to use either pulses or adiabatic sweeps to invert the population of two adjacent levels [7,8,9]. If this is done simultaneously for both satellite transitions, for example in a so-called double frequency sweep [10] or fast amplitude-modulated pulse train [11], one can increase the population difference between the central levels to that of the outer levels in the multiplet. The procedure is schematically illustrated in Figure 3. For nuclei with spin $I = 3/2$, this can give a threefold increase in intensity for the central transition, and thus a factor 9 reduction in measurement time to obtain the same signal-to-noise ratio [11,12]. For higher spin nuclei like ^{27}Al with spin 5/2, one can get an enhancement up to 5 depending on the details of the adiabatic sweep method. With repetitive sweeps one can transfer basically all the polarization and enhancements near the theoretical maximum are observed in practice [13].

A final trick to induce a nuclear magnetization above the thermodynamic equilibrium is based on the selection rules in optical transitions. In an alkali metal vapor one spin selectively pumps an atomic transition and by spin-exchange collision this magnetization in transferred to a noble gas of ^{3}He or ^{129}Xe atoms [14,15]. This optical pumping can lead to a nearly 100% polarization of the nuclear moment, and because of the very long relaxation times the gas can be transported to the experiment. In medical (lung inhalation) or catalysis (zeolites), the effective

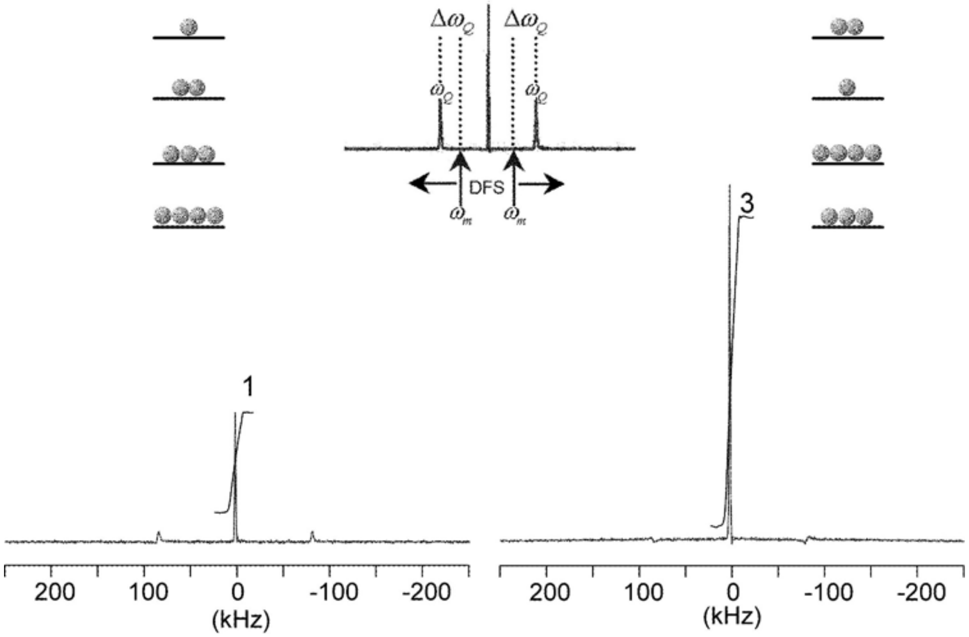

Fig. 3. Illustration of the signal enhancement in a quadrupolar nucleus with spin 3/2. On the left, we have the situation in thermal equilibrium with the experimental spectrum below showing three resonances as expected. The resonances corresponding to the lower and upper transition are considerably broadened. As shown on the right, the population levels can be inverted using adiabatic sweeps. Under proper conditions, this may give a factor 3 enhancement of the intensity in the central transition, and thus nearly a factor of 10 gain in measurement time.

surface area is big enough to allow a reasonable enhancement of the magnetization of the relevant nuclei in the sample. For example it was recently demonstrated by Jansch *et al*. [16] that a single monolayer of hyperpolarized Xe adsorbed on an Ir(111) single crystal surface could be measured successfully by NMR spectroscopy. In this case, the large Knight shift that was observed indicates a large overlap of the conduction electron wave function at the Fermi level of the metal with the Xe atomic states at the surface.

Very interesting from a chemical point of view is the proposition of Bowers and Weitekamp [17–19] to use parahydrogen (p-H_2) in hydrogenation reactions, allowing the detection of reaction products and intermediates with high sensitivity. p-H_2 exhibits a pure nuclear singlet state and is stable even in liquid solutions. Due to the symmetry breakdown of the parahydrogen during hydrogenation reaction typical polarization patterns are observed in the NMR spectra of the hydrogenation products. In a simple AX-spin system, the $|\alpha\beta\rangle$ and $|\beta\alpha\rangle$ spin functions are overpopulated relative to a normal Boltzmann distribution. This gives signal enhancements of some orders of magnitude but typically ranges around a factor of a few thousand. The method is extremely sensitive for the detection of short-lived intermediates and reaction products in small concentrations [20].

Note that one is not restricted to the noble gasses for efficient optical nuclear polarization (ONP). As was first suggested by Kastler in 1952, any two-level spin system can be used for optical pumping [21]. The procedure is illustrated in Figure 4.

Because the optical photon in the beam of circularly polarized light carries an angular momentum of one, the selection rules dictate that only transitions from the ground state with $J = -1/2$ to the excited state with $J = +1/2$ are allowed. Relaxation paths generally leave the angular momentum untouched and the electrons in the excited state relax to the ground state and populate the upper spin level. If there is a spin flip during the relaxation, the electron ends up in the original level, and the pumping scheme can start all over again until virtually all electrons end up in the inverted spin ground state. Since the optical pumping depends on light intensity, one uses powerful laser systems or UV light sources, and a nearly 100% polarization of the electron spins can be achieved in rather short times (typically in the microsecond range) [22,23].

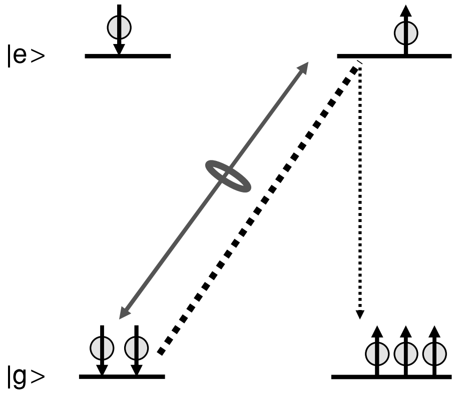

Fig. 4. Illustration of the optical nuclear polarization (ONP) process. With circular polarized light, one can spin selectively pump the transition from the electronic ground state to an excited level. After relaxation, this gives a fast polarization of the ground state electron population. As in the case of NOE, this polarization is then transferred to the nuclear system.

As in the case of DNP, the electron polarization is transferred to the nuclei by the hyperfine coupling and by spin diffusion, polarization is transferred to the molecule under study. Theoretically this could achieve a polarization enhancement of about 4 orders of magnitude. In practice, however, one is limited by the choice of suitable doping molecules, the efficiency of the spin diffusion on the T_1 timescale etc. Also, the optical pumping is most efficient in the low field range and the sensitivity is offset by the effect of the lower B_0 field. In some cases, one can shuttle the sample between low and high field positions, but this does not appear to be a practical solution for all experiments. In special topics, however, this method can be quite useful and for example the NMR spectrum of individual layers in semiconductor quantum wells can be resolved [24]. Note that in ONP, one typically uses optical methods to measure the magnetization as well (ODMR). Since optical photons can be detected with near quantum efficiency, this can be very sensitive and in fact already in 1993 two groups demonstrated that (electron) magnetic resonance of a single molecule can be detected [25,26].

None of the above methods is sufficiently versatile to be employed as a standard enhancement tool. However, in specific cases, these techniques can be very useful and more research is needed to widen the application area into mainstream NMR spectroscopy.

Optimized Detection Coil Design

For solid-state NMR, the most common approach to detect the NMR signals is the inductive detection in a helical coil wound around the sample cylinder. After a 90° pulse, the magnetization rotates in the laboratory frame at the Larmor frequency and the oscillating flux induces an EMF that can be measured in high-sensitivity digital quadrature detection. The noise of high-frequency components like oscillators, mixers, and IF amplifiers is nowadays at such a level that the effective noise in the signal is dominated by the resistive noise in the pickup coil. The signal-to-noise ratio in a typical NMR experiment can be written as: [27]

$$\frac{S}{N} = \frac{k_0(B_1/i)V_s\omega_0\left(1/\sqrt{2}\right)M}{F\sqrt{4k_B T R_{\text{noise}}\Delta f}} \propto \frac{k_0 B_1 V_s}{i\sqrt{R}},$$

where k_0 is a scaling factor accounting for the RF-inhomogeneity of the coil, B_1/i is the magnetic field induced in the RF coil per unit current, and V_S is the sample volume. M is the magnetization as described before. The denominator describes the noise using the noise factor of the spectrometer (F), conductive losses of the coil, circuit, and sample (R_{noise}) for the spectral bandwidth Δf. The main factor that saves the day for inductive detection is the Larmor frequency in the nominator because the time derivative of the magnetic flux through the coil scales with ω_0. As is clear from the right hand side of this equation, the rule of thumb is to make a detector coil with a homogeneous field ($k_0 = 1$), a high field factor B_1/i, and a low resistance R.

As usual there is no single solution to a multitude of problems. In high-resolution liquid NMR, the optimal configuration is that of a saddle coil. This geometry allows the best static field homogeneity and gives sample access along the bore axis of the magnet. However, it comes at a price, since the field factor is generally lower when compared with a helix. (If we consider a cylindrical volume with the length of the cylinder equal to the diameter, then the B_1/i field factor for a saddle coil is only 60% of the helix version). In addition, the length of wire is larger for the saddle coil, making the total sensitivity a factor of three less than the helix version. A similar argument is true for imaging experiments. To have a wide access bore, one cannot use helical coils oriented perpendicular to the field axis. On the other hand, a combination of orthogonal saddle coils can detect the full circular polarized magnetization of the processing spins gaining a factor equal to the square root of two. In MRI, one typically uses birdcage coils that are basically just a series of phase-shifted saddle coils. Also, because the B_1 field gradient is mostly close to the wires or strips that form the saddle coil, one can move to cryogenically-cooled RF coils without losing too much effective space for the sample. In this case, a decrease in temperature (from 300 to 25 K) leads to a factor of 3–4 reduction in noise. Although the helical coil is theoretically more sensitive, this geometry is much more prone to susceptibility effects and unless special matching fluids are used to embed the coil, one sees deterioration in resolution, and for narrow lines therefore also a reduction in sensitivity. In solid-state NMR, this is less of a concern and in this field the helix largely dominates. Note, however, that in experiments where the B_1 homogeneity is essential, one can use only part of the available volume. If we allow a 10% variation in B_1 field, the effective volume is about half the space inside the coil. Given the fact that roughly one half of the magnetic field energy is anyway outside the coil, it is clear that none on the conventional geometries are ideally matched to the NMR problem.

In order to have the best detection sensitivity, one needs to place the detection coil as close as possible to the sample. Put in another way, if we increase the sample volume V, we do not gain a linear increase in signal but as a result of the $1/R$ term in the inductive voltage, we see only a $V^{2/3}$ increase. If we have only a small amount of sample, we have no other option than to scale the detection coil in a proper way. This is the rationale behind various development efforts to produce very small microcoil probes using lithographic or micromachining methods [28–30]. The smallest helical coil that was reported for NMR spectroscopy had a diameter of about 20 μm. When compared with a traditional probe of a few millimeters diameter, this microcoil would give a better sensitivity by about 2 orders of magnitude. It was indeed demonstrated by Seeber *et al.* [31] that with this type of solenoidal microcoils one can attain a sensitivity sufficient to measure the NMR proton signal in a water sample of only 10 femtoliter, or 7×10^{11} spins with a signal-to-noise ratio of 1 in a single scan.

Solid-state NMR probeheads using solenoid microcoils with an inner diameter of 300–400 μm have been implemented for the study of mass-limited solid samples [30]. The performance, in terms of sensitivity and RF-characteristics, of these probeheads was demonstrated for ^{1}H, ^{31}P, and ^{27}Al in different model compounds. The sensitivity is approximately 10^{14} spins/$\sqrt{}$Hz to get a signal-to-noise ratio of 1 in a single scan. A specific advantage of microcoils for solid-state NMR applications is that they can generate extremely high RF-fields if implemented in appropriate circuits. Using RF powers in the hundreds of Watts range, RF fields up to 5 MHz were realized. This allows the excitation of spectra of nuclei whose resonance lines are dispersed over several MHz. This is particularly useful for quadrupolar nuclei experiencing large quadrupolar interactions. This type of microcoil circuitry also proved compatible with double tuning allowing the implementation of double resonance experiments as is shown for ^{13}C CP spectroscopy of glycine in Figure 5 [32].

One of the appealing aspects of lithographically produced RF coils is that it may fulfill the promise of a “lab on a chip” in which the material synthesis and analysis are integrated on a single chip [33,34]. It is even possible to integrate the NMR RF source and data acquisition electronics on the same chip. An additional advantage of the high sensitivity and small volume of the microcoil approach is that one can multiplex the excitation and data acquisition over many different samples in an efficient way. This allows a very high throughput of the instrument (Figure 6) [35].

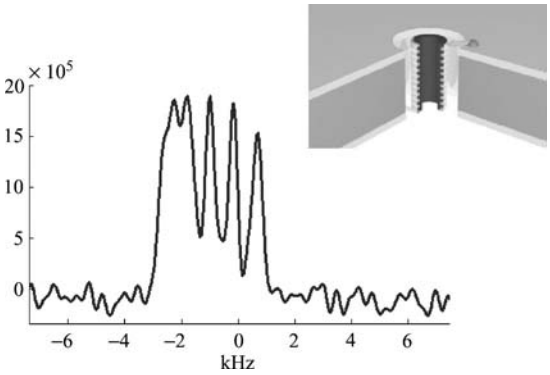

Fig. 5. Static ^{13}C cross-polarization spectrum of a 25% ^{13}C$_2$-enriched glycine sample, containing 6 microcrystals (100 μm)^3 measured in a dual-channel microcoil probe, averaged in 5000 scans. The inset shows the microcoil configuration with the helix embedded in the center of a low loss capacitor to form the resonant LC circuit [32]. (See also Plate 42 on page XXXIV in the Color Plate Section.)

Magnetic Resonance Force Microscopy

A relatively recent method for improving the detection sensitivity of NMR is based on mechanical detection. Although the ideas with respect to the mechanical detection of the magnetic resonance phenomenon were proposed as early as 1964 and its concepts proven in 1967 for electron spins [36], mechanical detection of the nuclear magnetic moment was only achieved much later. The first method that was successfully applied to this end is called magnetic resonance force microscopy as proposed by Sidles in 1991 [37]. It was demonstrated for magnetic resonance detection of electrons by Rugar and coworkers in 1992 [38] and for protons in 1994 [39]. It uses a mechanical cantilever as is known from atomic force microscopy (AFM) to detect forces exerted on a spin system in a very inhomogeneous magnetic field. The deflection of the cantilever can be measured very accurately with sub-angstrom resolution by optical methods. In the most common situation where both the field gradient and the modulated component of the magnetic moment are pointed along the z-axis, we can write the time dependent force $F(t)$ on the sample as:

$$F_z(t) = \int_V M_z(t) \frac{\partial B_0}{\partial z} \mathrm{d}V.$$

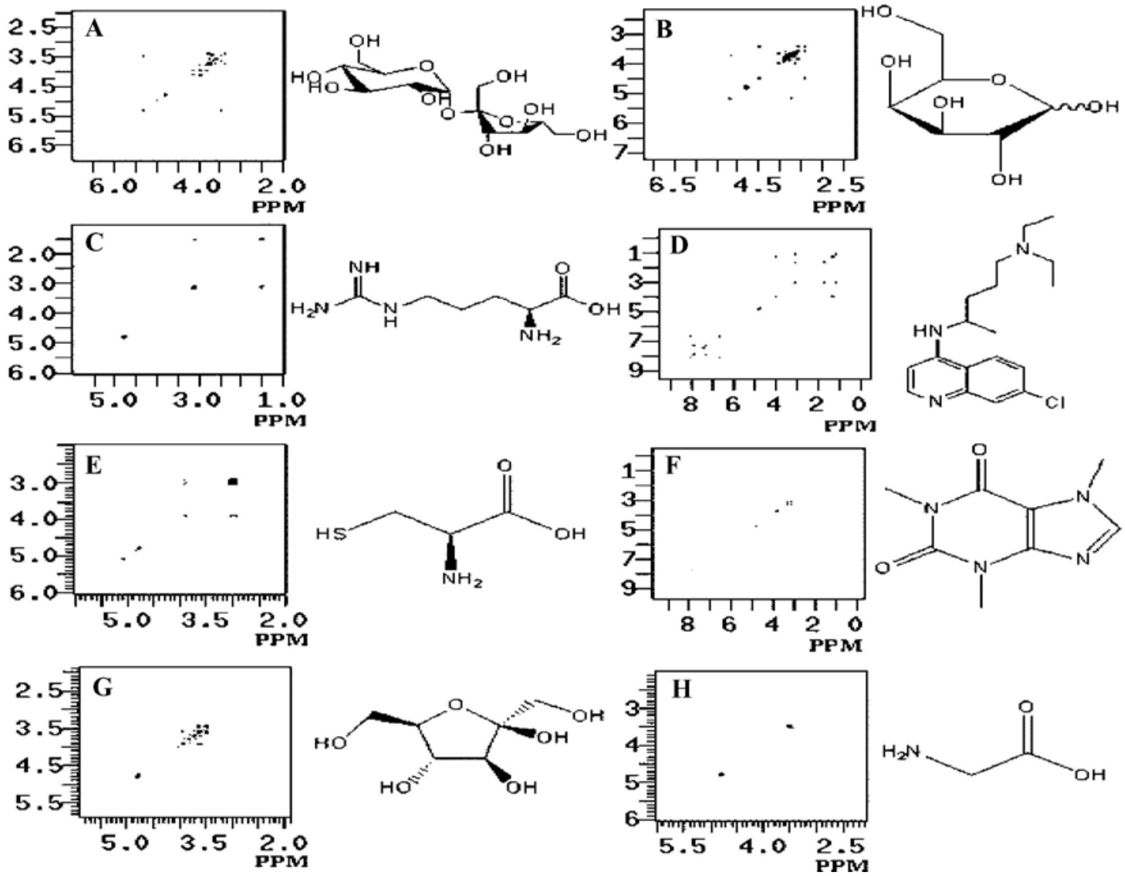

Fig. 6. COSY spectra acquired in a probe with eight microcoils of about 300 μm diameter, resulting in a typical sample volume of 35 nl. The small space required for these capillary sample tubes allows one to measure multiple compounds quasi simultaneously. Each sample (10 mM solution in D_2O) was loaded into the coil via the attached teflon tubes. (A) sucrose, (B) galactose, (C) arginine, (D) chloroquine, (E) cysteine, (F) caffeine, (G) fructose, and (H) glycine. Results are shown corresponding to an averaging of eight scans (reproduced from ref. [35]).

Furthermore, as a result of the presence of the magnetic field gradient, the Larmor resonance condition, $\omega_0 = \gamma B_0$, varies over the sample, i.e. becomes spatially dependent. Thus, we have the option to selectively excite slices from the sample through variation of the irradiation frequency or by altering the position of the magnetic field gradient source. In nuclear MRFM, the gradient field is usually brought about by introducing a small magnetic particle in an otherwise homogeneous magnetic field (B_0). Since this external B_0 magnetic field is very strong, the magnetic particle will be completely saturated.

The main reason for the high sensitivity in the MRFM experiment is the fact that the gradient is introduced by a microscopic particle that is well matched to the small size of the sample. Also, the current densities that mimic the magnetization of a saturated Ferro magnet are much higher than what is common in electrical circuits. Finally, the friction losses in a mechanical resonator are generally much smaller than the resistive losses in a coil, leading to higher Q values of the resonator. For protons, a break-even point is typically reached for samples of a few hundred micrometers in size. In smaller samples, the MRFM method will be more sensitive. For a 10 μm sample in a hypothetical RF coil of 50 μm diameter, the inductive detection limit will be typically of the order of 10^{12} spins in a bandwidth of 1 Hz, corresponding to a concentration of about 1 mol/l. For the same sample size, a mechanical detection at room temperature may give an order of magnitude better sensitivity. The ultimate goal of MRFM is to improve detection sensitivity to the single nuclear

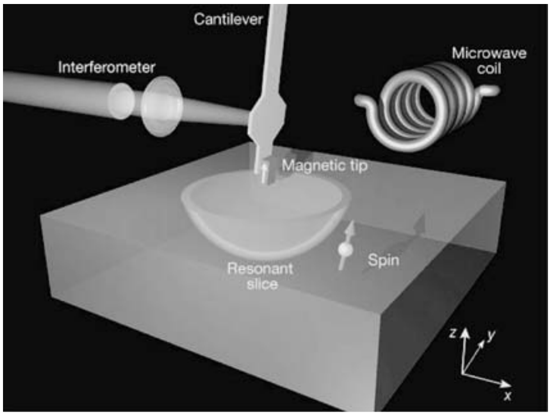

Fig. 7. Configuration of the single-spin MRFM experiment. The magnetic tip at the end of an ultrasensitive silicon cantilever is positioned approximately 125 nm above a polished SiO_2 sample containing a low density of unpaired electron spins. The resonant slice represents those points in the sample where the field from the magnetic tip (plus an external field) matches the condition for magnetic resonance. As the cantilever vibrates, the resonant slice swings back and forth through the sample causing cyclic adiabatic inversion of the spin. The cyclic spin inversion causes a slight shift of the cantilever frequency owing to the magnetic force exerted by the spin on the tip. Spins as deep as 100 nm below the sample surface can be probed (reproduced from ref. [40]). (See also Plate 43 on page XXXIV in the Color Plate Section.)

spin level, and thus enable three-dimensional imaging of macromolecules (for example, proteins) with atomic resolution. MRFM has also been proposed as a qubit readout device for spin-based quantum computers. A breakthrough was established recently when Rugar *et al.* reported the first successful detection of an individual electron spin by MRFM [40]. The spatial resolution that can be achieved in this setup is of the order of 25 nm as demonstrated for an unpaired spin in silicon dioxide (Figure 7).

Despite the impressive detection sensitivity, a few words of caution are in order. First, the experiment is done at very low temperatures where the mechanical noise of the cantilever is very small. At ambient temperatures the noise increases substantially. Combined with the thermodynamic population and the much lower moment of the nucleus as compared to the electron spin, one cannot hope to achieve such ultimate sensitivity in a routine NMR experiment. Moreover, since the very strong local gradient is essential in the detection mechanism, it is not straightforward to do spectroscopy with any significant resolution. On the other hand, it should be able to improve the sensitivity and thus the spatial resolution in a magnetic resonance microscopy experiment by several orders of magnitude. The main challenge in the field is to find suitable methods to combine the superior detection sensitivity of mechanical detection with the high frequency of operation, preferably at the Larmor frequency and without the loss in spectral resolution caused by the static field gradient. A possible solution in this direction was proposed by Weitekamp [41]. In this so-called BOOMERANG configuration, a compensating gradient ring is positioned around the magnetic particle on the cantilever, in such a way that the sample sees a nearly homogenous field (allowing spectroscopy) while the force between cantilever and sample remains.

In conclusion, there are no strict physical laws that prohibit further improvement of sensitivity and there are several paths that lead toward sensitivity optimization in NMR. In fact, there are at least two proven methods to detect a single electron spin and it is conceivable that with further improvements we will see single nucleus detection. Even for the traditional inductive detection, there is no fixed limit and for specific cases we can expect an increase in sensitivity by several orders of magnitude. The bigger challenge is to find ways to improve the sensitivity without compromises to the wealth of information that can be obtained with modern pulsed NMR techniques. The quest for ultimate sensitivity without this in mind may become rather academic. For the near future, the detection method of choice depends very much on the sample shape and characteristics. For small solid-state samples with broad resonance lines, the optimum configuration is probably that of a suitably matched microcoil. In this case, one profits both from the high-sensitivity and the high excitation fields. This configuration can also be used for micrometer scale imaging where one combines the high sensitivity with the ability to produce the large pulsed field gradients that are needed to obtain the required spatial resolution. In the quest for the ultimate imaging resolution, the MRFM technique is clearly at the forefront and true chemical (quadrupolar) contrast may be possible down to the 10–100 nm scale.

This method is particularly suitable for low field applications and low-gamma nuclei. For the ultimate-resolution liquid state NMR, the present method of choice is the cryocooled saddle coil inductive detection. The relatively low concentrations in for example protein solutions do not allow a downscaling to very small coil sizes. In addition, the susceptibility issues connected with (micro)coils very close to the sample are not easily solved and parts per billion resolutions are still to be demonstrated. There are options to restore the full resolution even in inhomogeneous static fields, but these generally lead to lower sensitivities. Sensitivity enhancement methods based on DNP are still in the research stage, with as the main bottleneck the absence of suitable mm-wave sources.

Another niche in NMR spectroscopy is the study of thin surface layers. Methods to achieve a reasonable sensitivity for this configuration are still very much in its infancy, although impressive results have been reported from ONP experiments. There have been some efforts to use *ex situ* methods where the sample is in the projected field outside the actual magnet enclosure. Although the sensitivity can be quite reasonable, the inhomogeneity of the field precludes spectroscopy with any sensible resolution.

Indeed, the main challenge in the field is not so much the search for new physical methods for sensitivity enhancement but to find a practical way to incorporate these methods without compromises to the versatility of modern NMR pulse sequences and with the full spectral resolution that is possible in the modern high field magnets. At present, the low-noise cryoprobe systems have become widely available in many labs. Despite their considerable costs, it is considered to be essential for an improved throughput in liquid NMR research. For online screening or combinatorial chemistry applications, it will become relevant to implement high-sensitivity microcoil probes. Although the susceptibility broadening of the present designs still puts some restraints on the applicability, this does not seem to be an intrinsic problem and the technology for a "lab on a chip" NMR implementation is not far away.

References

1. Gonen O, Kuhns PL, Waugh JS, Fraissard JP. J. Phys. Chem. 1989;93:504.
2. Overhauser AW. Phys. Rev. 1953;92:411.
3. Abragam A. The Principles of Nuclear Magnetism. Clarendon Press: Oxford, 1961.
4. Farrar CT, Hall DA, Gerfen GJ, Inati SJ, Griffin RG. J. Chem. Phys. 2001;114:4922.
5. Bajaj VS, Farrar CT, Mastovsky I, Vieregg J, Bryant J, Elena B, Kreischer KE, Temkin RJ, Griffin RG. J. Magn. Reson. 2003;160:85.
6. Ardenkjaer-Larsen JH, Fridlund B, Gram A, Hansson G, Hansson L, Lerche MH, Servin R, Thaning M, Golman K. Proc. Nat. Acad. Sci. U.S.A. 2003;100:10158.
7. Pound RV. Phys. Rev. 1950;79:685.
8. Vega S, Naor Y. J. Chem. Phys. 1981;75:75.
9. Haase J, Conradi MS. Chem. Phys. Lett. 1993;209:287.
10. Kentgens APM, Verhagen R. Chem. Phys. Lett. 1999;300:435.
11. Madhu PK, Goldbourt A, Frydman L, Vega S. Chem. Phys. Lett. 1999;307:41.
12. Iuga D, Schafer H, Verhagen R, Kentgens APM. J. Magn. Reson. 2000;147:192.
13. Kentgens APM, van Eck ERH, Ajithkumar TG, Anupold T, Past J, Reinhold A, Samoson A. J. Mag. Res. 2006;178:66.
14. Pietrass T, Gaede HC. Adv. Mater. 1995;7:826.
15. Happer W, Miron E, Schaeffer S, Schreiber D, Vanwijngaarden WA, Zeng X. Phys. Rev. A. 1984;29:3092.
16. Jansch HJ, Gerhard P, Koch M, Stahl D. Chem. Phys. Lett. 2003;372:325.
17. Bowers CR, Weitekamp DP. Phys. Rev. Lett. 1986;57:2645.
18. Bowers CR, Weitekamp DP. J. Am. Chem. Soc. 1987;109:5541.
19. Carson PJ, Bowers CR, Weitekamp DP. J. Am. Chem. Soc. 2001;123:11821.
20. Grant DM, Harris RK. Advances in NMR, Vol.9, Encyclopaedia of NMR. Wiley: 2002, p. 598.
21. Brossel J, Kastler A, Winter J. J. de Physique et Le Radium. 1952;13:668.
22. Buntkowsky G, Hoffmann W, Vieth HM. Appl. Magn. Reson. 1999;17:489.
23. Suter D. J. Magn. Reson. 1992;99:495.
24. Eickhoff M, Suter D. J. Magn. Reson. 2004;166:69.
25. Kohler J, Disselhorst JAJM, Donckers MCJM, Groenen EJJ, Schmidt J, Moerner WE. Nature. 1993;363:242.
26. Moerner WE, Kador L. Phys. Rev. Lett. 1989;62:2535.
27. Hoult DI, Richards RE. J. Magn. Reson. 1976;24:71.
28. Webb AG. Prog. Nucl. Magn. Reson. Spectrosc. 1997; 31:1.
29. Minard KR, Wind RA. ConceptsMagn. Reson. 2001;13: 128.
30. Yamauchi K, Janssen JWG, Kentgens APM. J. Magn. Reson. 2004;167:87.
31. Seeber DA, Cooper RL, Ciobanu L, Pennington CH. Rev. Sci. Instrum. 2001;72:2171.
32. Poor B, van Eck ERH, Janssen JWG, van Bentum PJM, Kentgens APM. 2005; [to be published].
33. Massin C, Boero C, Vincent F, Abenhaim J, Besse PA, Popovic RS. Sensors and Actuators A-Physical. 2002;97:280.
34. Massin C, Vincent F, Homsy A, Ehrmann K, Boero G, Besse PA, Daridon A, Verpoorte E, de Rooij NF, Popovic RS. J. Magn. Reson. 2003;164:242.
35. Wang H, Ciobanu L, Edison AS, Webb AG. J. Magn. Reson. 2004;170:206.
36. Alzetta G, Arimondo E, Ascoli C, Gozzini A. Nuovo Cimento B. 1967;52:392.
37. Sidles JA. Appl. Phys. Lett. 1991;582854.
38. Rugar D, Yannoni CS, Sidles JA. Nature. 1992;360:563.
39. Rugar D, Zuger O, Hoen S, Yannoni CS, Vieth HM, Kendrick RD. Science. 1994;264:1560.
40. Rugar D, Budakian R, Mamin HJ, Chui BW Nature. 2004;430:329.
41. Leskowitz GM, Madsen LA, Weitekamp DP. Solid State Nucl. Magn. Reson. 1998;11:73.

CRAMPS

B.C. Gerstein[1] and H. Kimura[2]
[1]*Department of Chemistry, Iowa State University, Ames, IA 50011-3111, USA*
[2]*Department of Chemistry, University of Tsukuba, Tsukuba 305-8571, Japan*

Introduction

Combined rotation and multiple pulse spectroscopy (CRAMPS) [1] is one of a number of techniques for narrowing NMR spectra in solids, the broadening of which in this case is predominantly associated with:

(a) homogeneous homonuclear dipolar interactions in ensembles of spin 1/2 nuclei (e.g. ^{1}H in poly(ethylene) or ^{19}F in Teflon, but not ^{23}Na in NaCl) and
(b) shielding anisotropies.

Rotations in both co-ordinate space [via magic angle spinning (MAS)] and spin space [via radio frequency (rf) pulses] are combined to achieve narrowed spectra. The CRAMPS technique utilizes single quantum coherence and is not used for narrowing broadened spectra of quadrupolar nuclei in solids.

The basic ideas are that:

(a) Coherent averaging [2] is used to attenuate dipolar interactions via resonant cyclic, and periodic multiple pulse excitations over cycle times short compared to the inverse of the homogeneous dipolar coupling, $f_{\mathrm{D}} \equiv \omega^{\mathrm{D}}/2\pi$ and
(b) MAS, with spinning frequency, f_{MAS}, small compared to the cycle times of the multiple pulse sequences (but see the comments under section "Magic angle spinning"), is used to average shielding anisotropies to their isotropic values.

The details of the basic theory and techniques for achieving narrowed lines of spin 1/2 nuclei in one-dimensional experiments utilizing: (a) multiple pulse decoupling and (b) in the limit where spinning frequencies are small compared to multiple pulse cycle times have been presented [3] and reviewed [4].

Theory

Coherent Averaging; Average Hamiltonians in Spin Space

The time-dependent Schrödinger equation is

$$H|\Psi\rangle = i\frac{\mathrm{d}}{\mathrm{d}t}|\Psi\rangle \tag{1}$$

With the density operator defined as $\rho = \overline{|\Psi\rangle\langle\Psi|}$, the bar implying an ensemble average, Equation (1) becomes

$$i\frac{\mathrm{d}\rho}{\mathrm{d}t} = [H, r] \tag{2}$$

The expectation value of any observable, $\hat{O}$ is

$$\langle\hat{O}(t)\rangle = \mathrm{tr}\rho(t)\hat{O}(t) \tag{3}$$

The observable in a pulse NMR experiment is a signal proportional to the decay of magnetization with time, $M(t)$, associated with an oscillating magnetic moment, proportional to the transverse component of angular momentum, $I^{\pm}$ which in turn is proportional to the component of nuclear magnetization perpendicular to the applied static field;

$$M^{\pm}(t) \sim \langle I^{\pm}(t)\rangle = \mathrm{tr}\rho(t)I^{\pm} \tag{4}$$

Such a signal, $M(t)$, observed after some type of excitation which removes the magnetization of the ensemble of spins from its equilibrium state polarized along the static field, is shown at the top of Figure 1. Here the ensemble of protons are in liquid water. The oscillating decays, designated as $M_{x,y}(t)$ are a series of single points taken by a digital recorder at intervals, or "dwell" times, set by the

Graham A. Webb (ed.), Modern Magnetic Resonance, 363–371.
© 2008 *Springer.*

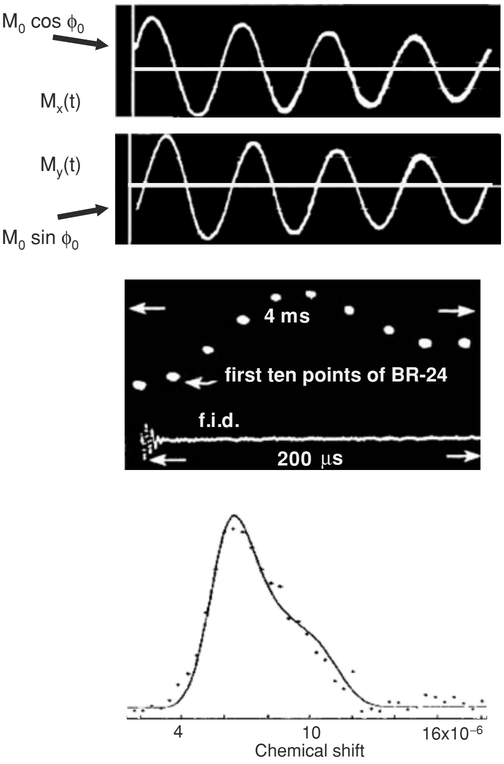

Fig. 1. Examples of the experimental observation of the decay of magnetization, $M(t)$, with time, after various excitations. *Top:* decay of the magnetization of protons in H_2O after a single pulse excitation; absorption and dispersion both shown. While seemingly continuous, these are in fact a series of single points taken by a digital recorder at "dwell" times, set by the experimenter. Here, the dwell was 20 μs, and on the timescale of the photo shown in Figure 1, the plot appears to be continuous. *Center:* First 10 points of the decay of magnetization of protons in linear high density poly(ethylene) (with thanks to Dr. D.L. VanderHart for supplying the sample) observed under homonuclear decoupling by the BR-24 sequence. Below those points, again in the center portion is shown the signal obtained on the same sample, and on the same timescale, after a single pulse excitation. *Bottom:* The shielding tensor of this sample obtained from the Fourier transform of the points under the BR-24.

experimenter. In the case of the top scans in Figure 1, the dwell was 20 μs, and on the timescale of the photo shown there, the plot appears to be continuous.

In the case of the 1-D CRAMPS experiment utilizing multiple pulse decoupling, the signal is observed in the windows between pulses in the cyclic and periodic (*vide* infra) excitations which are used to attenuate homogeneous dipolar interactions among the spin 1/2 nuclei in the ensemble under observation. Such observed points are shown in the center portion of Figure 1. The oscillating decay labeled "first 10 points of BR-24" is that obtained on linear, high density poly(ethylene) under the BR-24 homonuclear decoupling sequence [5] on a static sample. Shown at the top of the center portion of Figure 1 is the digitized decay of the voltage induced by the magnetization of protons in this sample under homonuclear decoupling. Below that decay, again in the center portion of Figure 1, and on the same timescale, is shown the signal obtained on the same sample after a single pulse excitation using a dwell of 0.5 μs. Note that this signal decays in about 10 μs due to dephasing of the magnetization associated with homogeneous dipolar interactions. The bottom plot in Figure 1 exhibits the shielding tensor of ^{1}H in this sample obtained from the Fourier transform of the points obtained under the BR-24.

A physical picture which may be useful in understanding how rf pulses may be used to decouple two-body dipolar interactions from each other results from the fact that the dipolar Hamiltonian between spins i and j is of the form

$$H^{\mathrm{D}}_{i,j} = \omega^{\mathrm{D}}(r_{i,j}, \theta_{i,j})(\hat{I}_i \cdot \hat{I}_j - 3I_{zi}I_{zj}) \qquad (5)$$

Note that the form of $H^{\mathrm{D}}_{i,j}$ is a product of spin, $(\hat{I}_i \cdot \hat{I}_j - 3I_{zi}I_{zj})$, and co-ordinate $(\omega^{\mathrm{D}}(r_{i,j}, \theta_{i,j}))$ space variables. The co-ordinate space portion of $H^{\mathrm{D}}_{i,j}$, designated as the frequency $\omega^{\mathrm{D}}(r_{i,j},\theta_{i,j})$, scales as the product of the magnetogyric ratios of the two nuclei involved, the inverse cube of the internuclear distances, $r_{i,j}$, and the spherical harmonic $(1 - 3\cos^2\theta_{i,j})$. Here, $\theta_{i,j}$ is the angle between the internuclear two-body dipolar vector, $\mathbf{r}_{ij}$, and the axis of quantization, which is set by the dominant static field, $\mathbf{B}_0$. One easily sees two facts from Equation (5):

First is that if the spins are forced to lie along the x, y, and z axes of the spin co-ordinate system for equal times, τ, then since the scalar product is invariant to rotation, the average over time of the term $(\hat{I}_i \cdot \hat{I}_j - 3I_{zi}I_{zj})$ becomes $3\tau(\hat{I}_i \cdot \hat{I}_j - \hat{I}_i \cdot \hat{I}_j)$, or zero. Another way of visualizing this picture is that the spins, on time average, are aligned along the (1, 1, 1) axis of the spin co-ordinate system. In the former case, one uses finite pulses to align the spins along x, y, and z, the basic pulse sequence the "solid echo," or "dipolar echo" sequence [6–8], one form of which may be expressed as $(\tau, 90_x, \tau, 90_y, \tau)$. In the latter case, the spins are first aligned along the (1, 1, 1) axis of the spin co-ordinate system, and then spin-locked there, which is the Lee–Goldburg [9] technique recently resurrected and improved by Vega and co-workers [10].

The solid echo sequence is neither cyclic nor periodic, but has the charm that at time 3τ, the homonuclear dipolar interaction becomes severely attenuated as a perturbation on the Zeeman interaction.

Second is the term $(1 - 3\cos^2\theta_{i,j})$ may also be averaged in time by motion of the sample. In particular, MAS may average this term to zero. The result is that under MAS with spinning speeds appropriately large compared to the magnitude of the interaction being averaged, the shielding tensor is averaged to its isotropic value, σ_{iso}, and the dipolar tensor is averaged to its isotropic value of zero. But since the magnitude of the dipolar interaction, $|H^{\text{D}}_{i,j}|$ can be of the order of 100 kHz and for protons, at least, the magnitude of the shielding anisotropy is generally less than 6 kHz at a proton frequency of 600 MHz, MAS at currently achievable frequencies of $\leq$50kHz rather easily averages shielding anisotropies of protons to their isotropic value, but does not completely average dipolar interactions in sufficiently rigid systems such as linear, high density poly(ethylene). CRAMPS, therefore, utilizing either pulse decoupling or Lee–Goldburg spin-locking, (it must be mentioned that the "MP" portion of the CRAMPS acronym means "Multiple Pulse, so perhaps it is not appropriate to place Lee–Goldberg decoupling under the term CRAMPS, but we are not going to invent new acronyms at this point) both homogeneous dipolar coupling and homogeneous shielding anisotropies are averaged to their isotropic values.

As a variation on the theme of pulse decoupling, the Emsley group has recently developed the technique of random phase decoupling [11]. The technique uses an optimal search scheme on the phases of windowless sequences to maximize resolution and minimize the effects of rf field inhomogeneity, and offers what is perhaps the best resolution to date on strongly coupled solids such as alanine.

Here we consider pulse decoupling with phases, which are not random. Attacking the spin space portion of $H^{\text{D}}_{i,j}$, the dipolar echo sequence, symmetrized to become cyclic, meaning that under this sequence the system is returned to its initial state (in the absence of relaxation) may be expressed as [12] (τ, 90_x, τ, 90_y,τ, τ, 90_{-y},τ, 90_{-x}, τ). A general discussion of constructing symmetrized pulse sequences has been presented by Mansfield [13].

Then in the 2τ windows between the pulse decoupling sequence, the time decay, $M(t)$, at times $t = Nt_{\text{c}}$, with t_{c} being the cycle time for the periodic and cyclic pulse sequences used to average internal interactions, and $N = 1, 2, \ldots$, may be expressed in terms of the density operator at multiple pulse cycle times Nt_{c} . The density operator, $\rho(Nt_{\text{c}})$, is proportional to the expectation value of a transverse component of nuclear angular momentum, $\langle I_{\pm}(Nt_{\text{c}})\rangle$.

$$M(t = Nt_{\text{c}}) \sim \langle I_{\pm}(Nt_{\text{c}})\rangle \sim \text{tr}\rho(Nt_{\text{c}})I_{\pm} \tag{6}$$

and may be expressed via the use of the Magnus Expansion for the propagator associated with internal interactions, $U_{\text{int}}(Nt_{\text{c}}, 0)$. With the definitions

$$i\text{d}U_{\text{int}}/\text{d}t = H_{\text{int}} \cdot U_{\text{int}} \tag{7}$$

and

$$\tilde{H}_{\text{int}}(t) = U_{\text{rf}}(t, 0)H_{\text{int}}U^{+}_{\text{rf}}(t, 0) \tag{8}$$

$$i\text{d}U_{\text{rf}}(t)/\text{d}t = H_{\text{rf}}(t)U_{\text{rf}}(t) \tag{9}$$

we arrive at the result (see Chapter 4 in Ref. [3])

$$\rho(Nt_{\text{c}}) = [\exp\{-i\bar{H}^0_{\text{int}}t_{\text{c}} + \cdots\}]^N \tilde{\tilde{\rho}}[\exp\{i\bar{H}^0_{\text{int}}t_{\text{c}} + \cdots\}]^N. \tag{10}$$

$\tilde{\tilde{\rho}}$ is the density operator as manipulated by the internal, and rf propagators as stated in Equations (7)–(9);

$$\tilde{\tilde{\rho}} = U^{+}_{\text{rf}}(Nt_{\text{c}}, 0)U^{+}_{\text{int}}(Nt_{\text{c}}, 0)\rho(t)U_{\text{int}}(Nt_{\text{c}}, 0)U_{\text{rf}}(Nt_{\text{c}}, 0). \tag{11}$$

Since for cyclic and periodic pulse sequences the system is returned to its initial state at then end of each sequence, $\tilde{\tilde{\rho}}$ may be identified as $\rho(t = 0)$. $\bar{H}^0_{\text{int}}$ is the average Hamiltonian, including in this case, the homonuclear dipolar interaction and the scaled shielding interaction.

$$\bar{H}^0_{\text{int}} = 1/t_{\text{c}} \int_0^{t_{\text{c}}} \text{d}t\,\bar{H}_{\text{int}}(t) \tag{12}$$

and $\bar{H}_{\text{int}}(t)$ is the internal Hamiltonian, in this case dipolar plus shielding, as manipulated by the rf pulses [see Equation (8)].

In the quasi-static limit, $f_{\text{s}} \ll (1/t_{\text{c}})$, under, e.g. the cyclic and periodic MREV-8 homonuclear decoupling sequence, at cycle times $Nt_{\text{c}} = 12\tau$ for appropriately short rf pulses, the time average of the magnitude of the dipolar Hamiltonian, $1/t_{\text{c}} \int_0^{t_{\text{c}}} \text{d}t\,\bar{H}_{\text{D}}(t)$, becomes severely attenuated compared to $|\text{H}^{\text{D}}|$. The condition that the rf pulses, with field strength $|\mathbf{B}_1| \equiv \omega_1/\gamma$, are able to "manipulate" H_{D}, the magnitude of which scales as ω_{D}, is that $|\omega_1| \gg |\omega_{\text{D}}|$. This means that the cycle times t_{c} must be short compared to $(|\omega_{\text{D}}|)^{-1}$. For $t_{\text{c}} \ll (2\pi/|\omega_{\text{D}}|)$, there is effective homonuclear decoupling.

As we will see in section "Applications," for cycle times greater than the inverse of the dipolar frequency, i.e. for $t_{\text{c}} \gg (2\pi/|\omega_{\text{D}}|)$, coherent averaging of H_{D} is destroyed. This means that with appropriate adjustments of t_{c}, experimental conditions such as receiver gain and cycle time, a minor, mobile species can be detected independently of the major, solid component, with negligible signal from the probe background, to an accuracy of $\leq$0.01

mol.% in the cases of some organic solids crystallized from solution (*vide infra*).

Scaling Under Pulse Sequences

A phenomenon important to understanding how the data taken under a multiple pulse experiment may be compared with data from a single pulse excitation is that of scaling. In the presence of a magnetic field of $\mathbf{B}_0$ magnetic moment with magnetogyric ratio γ will precess at a frequency $\omega_0 = \gamma|\mathbf{B}_0|$. Under series of resonant pulses in the rotating frame, the magnetic moments precess under the effective field. For example, under the cyclic and periodic flip-flop sequence, $(\tau, 90_x, \tau, 90_{-x})$, the response of protons in water is shown in Figure 2. With an average Hamiltonian for an offset $\Delta\omega$, under the flip-flop cycle being

$$\bar{H}^0_{\text{flip-flop}} = (\Delta\omega/2)(\mathbf{k} - \mathbf{j}), \qquad (13)$$

with $\mathbf{k}$ and $\mathbf{j}$ being unit vectors along the z and y axes in the Zeeman frame of the spins, the effective field in the rotating frame is $|\Omega| = \Delta\omega/\sqrt{2}\gamma$, so the scaling factor in this case is $1/\sqrt{2}$. This means that in the frame of observation, the magnetization under the flip-flop cycle will precess more slowly by roughly a factor of 0.7 than the response under single pulse excitation as seen in Figure 2.

Under the MREV-8, the scaling factor is $\sqrt{2}/3$ for perfectly short pulses with no phase errors. The details of the treatment for non-ideal pulses are given in Chapter 5 of Ref. [3].

The manner in which the scaling factor is experimentally determined is discussed here in section "Experimental".

Magic Angle Spinning

As shown by Lowe [14] and Andrew *et al*. [15], under physical rotation of a sample at an angle to the static field of 54.74°, the chemical shielding anisotropy and homonuclear dipolar interactions between spins 1/2 are averaged to their isotropic values at spinning frequencies, f_{rot} sufficiently greater than the line-widths of these two interactions. This is to say that an interaction the coordinate space portion of which scales as $(1 - 3\cos^2\theta)$ can be averaged to its isotropic value by sufficiently fast spinning at the magic angle. Since the isotropic value of the dipolar Hamiltonian between spins 1/2 has zero value, in principle, CRAMPS is not needed to remove this interaction. In fact recent studies [16] on protons in mesoprous silicas with spinning frequencies ≥40 kHz have shown that pulse decoupling is unnecessary for high resolution NMR of ^{1}H in such samples. The development of relatively high spinning speeds [17] up to 70 kHz has therefore to a certain extent made the use of CRAMPS

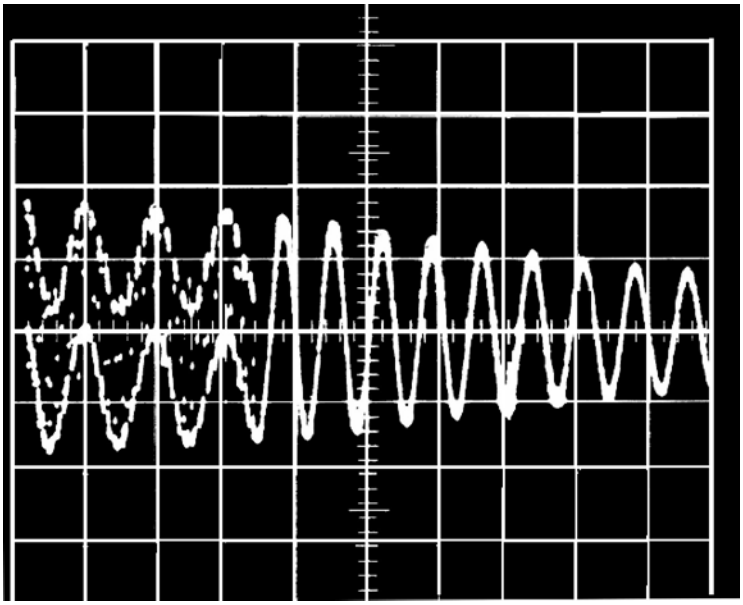

Fig. 2. Time decay of protons in water under the flip-flop cycle $(\tau, 90_x, \tau, 90_{-x})$, and a resonance offset $\Delta\omega$, (left side of figure), and under the same offset in the absence of the pulse sequences (right side of the figure). With an average Hamiltonian for an offset $\Delta\omega$, under the flip-flop cycle being $\bar{H}^0_{\text{flip-flop}} = (\Delta\omega/2)(\mathbf{k} - \mathbf{j})$, the effective field in the rotating frame is $|\Omega| = \sqrt{2}\Delta\omega/2$, so the scaling factor in this case is $1/\sqrt{2}$. This means that in the frame of observation, the rotating frame, the magnetization will precess more slowly by roughly a factor of 0.7 as seen in the figure.

for simply narrowing proton spectra in many solids unnecessary. At the time of writing, probes achieving such spinning speeds are not generally available. But there still exist systems, e.g. high-density linear poly(ethylene), in which the dipolar frequency can be as high as 100 kHz, so fast MAS to achieve high-resolution proton spectra would not work in that case.

We now become more explicit about the physics implied in the term "quasi-static" limit. In the case of CRAMPS, the movement of the sample can destroy the experiment if the dipolar interaction becomes time-dependent on a scale similar to the cycle time of the multiple pulse sequence attacking H^{D}. For example, a multiple pulse cycle time of 30 μs would imply that the spinning frequency $f_{\mathrm{rot}} \ll (10^{-6}/30)\mathrm{s} = 30\,\mathrm{kHz}$. Practically, rotation speeds of 4–6 kHz are easily achieved and at static fields in which the shielding anisotropies of the protons studied are ≤ 10 ppm (which is 3 kHz at a resonant frequency of 300 MHz), the CRAMPS experiment works well.

However, the development of commercial probes in which spinning speeds can routinely be in the neighborhood of 45 kHz has led to considerations of how to combine pulse decoupling with MAS outside of the quasi-static regime. The implications of this development are discussed in the next section.

Two-dimensional Experiments

If one wishes to achieve a higher resolution for NMR of strongly coupled spin 1/2 nuclei than is available from one-dimensional CRAMPS, e.g. in relatively rigid solids containing carbon bound to hydrogen, and is willing to give up the time needed for gathering of data in two dimensions, one ties the resolution of the proton lines to that of the carbon lines via 2-D HETCOR. Here, because the resolution of the proton signal is tied to that of the carbon, the proton signal being obtained from the t_2 domain in the 2-D experiment, there is no reason to be concerned with ring-down and windows in which to observe the proton signal. In fact, with appropriately high sample spinning speeds, on relatively mobile samples, e.g. protons in some mesoporus silicas, there is no need to use pulse, random phase, or spin-lock decoupling at all.

As stated above, adding a second dimension to any NMR experiment adds time to the acquisition of data. It is therefore to great advantage to achieve as high a sensitivity as possible with a maximum magnetic field. The sensitivity of detection is roughly proportional to the three-halves power of the static field. Along with higher fields comes, however, a relative problem. This is that to avoid the problem of sidebands without using some scheme such as rotor synchronization, which limits the dwell to the inverse of the rotor period, the spinning speed must be maximized.

The fact that the dipolar interaction re-focuses every 180° of the sample's physical rotation has been used by Hafner and Spiess [18] to combine the timing of pulse sequences in such a manner that the dipolar interaction is attenuated to a certain extent by the spinning, and pulse sequences then used remove the residual broadening, and the results utilizing relatively slow spinning are recovered.

Experimental

General

We limit our discussion here to the CRAMPS experiment under the quasi-static limit, which is easily achieved, even with spinners capable of 70 kHz spinning speeds, if they are capable of stable spinning at 3–6 kHz.

When the CRAMPS technique was initially performed, the stability of transmitters, of the pulse widths controlled by the pulse programmers, and of the phases in the rf unit, were such that quite careful tuning was required for a successful experiment. These factors seem to have led to the mythology that the CRAMPS technique was for the initiated only, and not worth taking the time.

Fortunately, with the advent of modern spectrometers with relatively stable amplifiers, digital control of phases, and nanosecond control of pulse widths, obtaining CRAMPS spectra of protons even in the most rigid of strongly coupled systems (e.g. high-density linear poly(ethylene) and adipic acid; see the bottom of Figures 1 and 3) is now relatively easy if one has a reasonable grip on the experimental and theoretical foundations of the experiment, and quite reasonably possible even if one has not.

Spectrometer Requirements; the Probe and Receiver

Modern spectrometers suitable for NMR of solids, e.g. those supplied by Bruker, JOEL, and Varian, have the capabilities for power, timing, phase control, pulse programming, and sample rotation suitable for the CRAMPS experiment. The place where care must be exercised is in the receiver and probe ring-down.

To illustrate what is needed, consider an ensemble of protons in a solid in which the internuclear distance is similar to that in high-density poly(ethylene), leading to a homogeneous line-width of $\delta\omega/2\pi \approx 100$ kHz (see the time decay in the central portion of Figure 1 taken under a single-shot excitation). Those data were taken with an MREV-8 cycle time of 21 μs, meaning that $12\,\tau = 21$ μs, $\tau = 1.75$ μs, and the data were accumulated in the

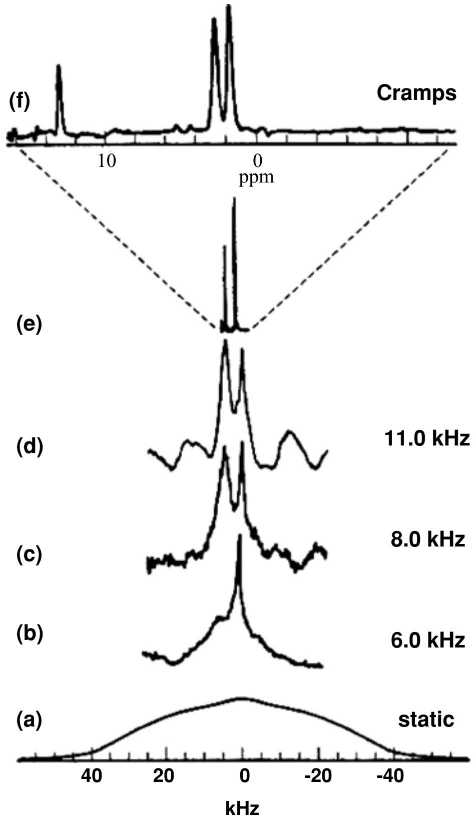

Fig. 3. Comparison of narrowing of proton spectra in the strongly coupled protons in adipic acid (HOOC–$(CH_2)_4$–COOH) under:

(a) Single pulse excitation with dwell of 0.5 μs.
(b) MAS AT 6.0 kHz
(c) MAS AT 8.0 kHz
(d) MAS AT 11.0 kHz
(e) CRAMPS using the MREV-8 sequence.
With thanks to Gary Maciel for the figure.

$2\tau = 3.5$ μs windows of the sequence. With pulses of 500 W, and pulse widths of 1 μs, into a probe with impedance 50 Ohms, implying a p–p voltage of about 160 V, the time needed to ring-down this voltage to 10^{-7} V is 3.3 μs. The value of 10^{-7} V is what one wishes to have to keep the receiver happy. This ring-down time is approximately 21 $Q/3f$, where f is the resonant frequency in Hz and Q the quality factor of the probe. $Q \cong (f/2\Delta f_{\text{res}})$ where Δf_{res} is the width of the tuning curve of the probe at resonant frequency, f_{res}. For example, at a resonant frequency of 300 MHz, a tuning curve with a half-width of 1 MHz would have $Q \cong 150$. We wish for the receiver to be able to take data for at least 0.2 μs at the end of the window of 2τ. This means a total ring-down of $3.5 - 0.2 = 3.3$ μs. So for a spectrometer operating at 300 MHz, a requisite probe Q is calculated as follows:

$$\begin{aligned} 3.3\times10^{-6} &= 7Q/f = 7\times3.3\times10^{-9}Q \\ &\Rightarrow Q = 140. \end{aligned} \tag{14}$$

This is a reasonable Q for a solid-state probe, but unusual for a probe set to receive signals from liquids where the dwell is allowed to be of the order of ≥ 20 μs.

In addition, the receiver must be protected during the high power pulses, and in such a manner that the voltage between each stage of the receiver must be arranged to ring-down so that there is ample time in the 2τ windows for each stage to receive signal. One such scheme is presented on page 222 of Ref. [3]. To the author's knowledge all of the instrument producers of solid-state NMR spectrometers are able to meet the above requirements in receivers and probes.

Tuning to Maximize Resolution; Pulse Impurities

One further point about probe tuning deals with what might be described the "art" (but is well understood analytically, as discussed in pp. 177–82 of Ref. [3]) deals with pulse impurities.

A pulse of rf may be thought of as a continuous wave of rf multiplied by a window function. For pedagogy, we consider only a rectangular window, as illustrated in Figure 4. The frequency domain fingerprint of such a window function is a sine function, $\sin x/x$, which contains many frequencies. The envelope also oscillates. Therefore, at the

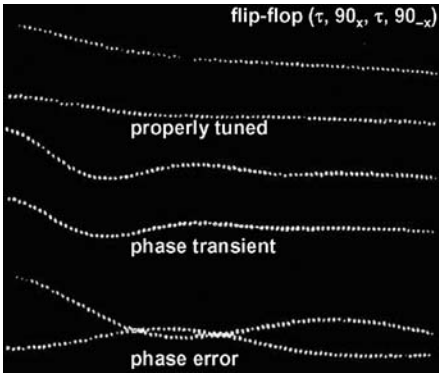

Fig. 4. Response of protons in water under the flip-flop tuning cycle. *Top:* Properly tuned. *Middle:* Phase transient present. *Bottom:* Phase error present.

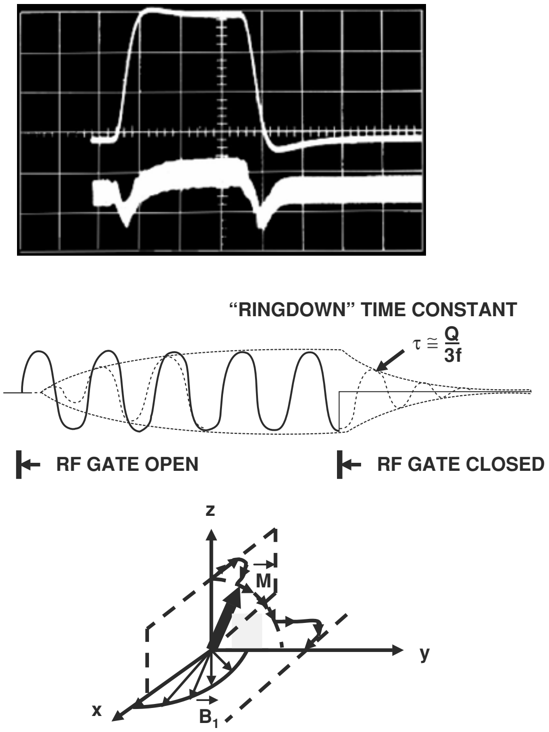

Fig. 5. The phase-detected envelope of an rf pulse. *Top:* upper trace, the in-phase component. Lower trace, the out of phase component, with increased gain of the oscilloscope channel used for detection. *Middle:* Comparison of the response the signal under a "square-wave" envelope with that associated with ring-up and ring-down. Note that both frequency and phase impurities are present during the transient periods after turn-on, and turn-off. *Bottom:* vector picture of the magnetization associated with the phase transients.

turn-on and turn-off periods of the pulses, there are both phase and frequency transients. The phase transients may be viewed as being orthogonal to the broadcast phase, i.e., an "*x*" pulse, will have "*y*" components during the ring-up and ring-down times. This idea and the experimental evidence are illustrated in Figure 5. It is necessary to minimize the cumulative effects of these "impurities" for maximum resolution under the CRAMPS experiment. One method is to slightly de-tune the probe to achieve maximum decay time for the sample under investigation. Because a slight de-tuning also affects the pulse widths, it is necessary to iterate the de-tuning with a check on pulse widths. Another, perhaps preferable method (personal communication Drs. Charles Bronnimann and Jim Frye, Varian, Inc., 12-29-04) is to place variable—length transmission lines in the nominally quarter-wave length portions of the transmission and receiving part of the circuitry (see Figures 5–24 in Ref. [13]) in order to maximally damp frequencies other than the carrier and vary the length to achieve maximum resolution. The procedure is described in "Commonly Run Solids NMR Experiments" which can be downloaded as a .pdf file from Varian's web site, under User Pages "list of manuals title (alphabetical)" or "list of manuals by part number," manual #0199907600A.

Determination of the Scaling Factors

As may be inferred from Figure 2, the Fourier transform of the decay shown there will yield peaks at two different frequencies. The difference between these immediately supplied the scaling factor under the flip-flop cycle. In the CRAMPS experiment, the difference in the frequencies of protons in water under a number of different offsets, generally 1 kHz apart, summed to produce a spectrum of peaks 1 kHz apart under an offset using a given homonuclear decoupling pulse sequence, compared to the experimental offset used to produce that signal immediately yields the scaling factor. It is an interesting fact that the scaling factor depends upon the offset [19], and this fact must be taken into account for each resonance detected under the CRAMPS experiment when applying a scaling factor to a given sample.

Applications

CRAMPS in One Dimension

After it became clear that pulse NMR could be a powerful tool for probing identities of protons in coals, the first applications of CRAMPS were the determinations of high-resolution proton NMR of coals [20–25], and in polymers [26]. The CRAMPS spectra of ^{1}H in coals, which accompanied by high resolution of carbon in these systems, were used to infer aromaticity, and the average sizes of aromatic rings in the systems studied. The spectra of polymers, with varying cycle times, were used to infer amorphous fractions of polymers. Later applications were to determinations of structures of biological solids [27–32], and of environments of protons in silicas [33].

Finally, most recently at the time of writing [34], 1-D CRAMPS, with varying cycle times to selectively detect rigid and mobile portions of the sample, has been used to provide quantitative and qualitative determinations of solvents occluded during the process of crystallization in organic solids, to an accuracy of ≤ 0.01 mol.%. The fascinating part of this experiment is the lovely match between experiment and theory, in that if $t_c \ll (|\omega^D{}_{\text{solid}}|)^{-1}$, the solid portion of the sample is detected. With the mobile impurity being of the order of 0.01 mol.%, this portion contributes negligibly to the observed signal under CRAMPS. If $(|\omega^{\mathrm{D}}_{\mathrm{solid}}|)^{-1} \ll t_{\mathrm{c}} \ll (|\omega^{\mathrm{D}}_{\mathrm{mobile}}|)^{-1}$, and the gain increased appropriately relative to the gain used to detect the major, rigid component, only the relatively mobile portion of the sample is detected. Since only signal of the sample inside the inductor contributes to the signal under CRAMPS, the observed signal of the mobile portion contains essentially no signal from the protons in the probe. Figure 6 illustrates how the observed signal under CRAMPS detects the rigid component for $t_{\mathrm{c}} \ll (|\omega^{\mathrm{D}}_{\mathrm{solid}}|)^{-1}$, changes gradually as t_{c} is increased, and finally detects only the mobile portion when the inequality $(|\omega^{\mathrm{D}}_{\mathrm{solid}}|)^{-1} \ll t_{\mathrm{c}} \ll (|\omega^{\mathrm{D}}_{\mathrm{mobile}}|)^{-1}$ is satisfied.

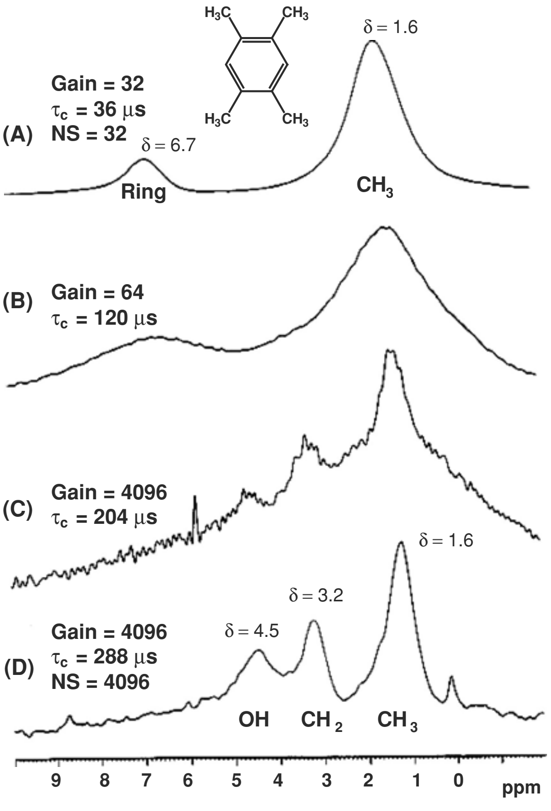

Fig. 6. NMR Spectrum of durene crystallized from ethanol under CRAMPS using the MREV-8 sequence, with varying cycle time t_{c}, and varying receiver gain. Spinning frequency is 5 kHz. At a cycle time of 288 μs, only the mobile portion, representing durene dissolved in ethanol, is seen. At a cycle time of 36 μs, only solid durene is observed. As the cycle time is increased from 36 to 288 μs, the line broadens, averaging of the dipolar interaction for the rigid portion is destroyed, and finally, only the mobile portion is detected.

CRAMPS in Two Dimensions

The addition of a second dimension to experiments involving homonuclear decoupling of protons, along with excitation of a second nucleus (excepting protons in the case of proton–proton HETCOR) has the usual disadvantage of added time for accumulation of signal. But the advantage is that, at least in heteronuclear HETCOR, the signal from protons (or fluorine) is observed in the t_2 domain of the 2-D experiment. Therefore, there is no need to have the exacting conditions for ring-down and probe tuning optimizing the 1-D experiment. In addition, windowless sequences [11,35] may be used such that the limitations involved in the requirements of the quasi-static condition for pulse decoupling, when used with rotor-synchronized pulse sequences, allow for 2-D ^{13}C–^{1}H HETCOR with spinning speeds much higher than that used in the 1-D CRAMPS discussed above.

As a final remark, we note that all techniques of detection described above utilize single quantum coherence for the narrowing and detection of spin 1/2 nuclei in solids. For narrowing and detection of half-spin quadrupolar nuclei, e.g. ^{23}Na and ^{27}Al, combinations of multiple pulse excitation and MAS utilizing multiple quantum coherence have been used [36].

Acknowledgments

The authors appreciate the invitation from Professors Ando, Saito, and Asakura to submit this article. We acknowledge the use of the facilities of the Chemistry Department at Iowa State University. Careful readings of the manuscript by Drs. Marek Pruski, Jim Frye, and Charles Bronniman were greatly appreciated. We are especially grateful to Drs. Bronnimann and Frye regarding information on minimizing the effects of phase transients on the CRAMPS experiment. The authors have attempted to fairly represent the work of all major contributors to this area of technology, but nevertheless make the apology regarding the excess of references to our own work which mirrors that which Thoreau made about his own writing. *If I knew other's lives as well as I do mine, I should write about them as well.*

References

1. Taylor RE, Pembleton RG, Ryan LM, Gerstein BC. J. Chem. Phys. 1979;71:4541.
2. Haeberlen U. High Resolution in Solids: Selective Averaging. Advances in Magnetic Resonance (Suppl I). Academic Press: New York, 1976.

3. Gerstein BC and Dybowski CR. Transient Techniques in NMR of Solids: An Introduction to the Theory and Practice. Academic Press: Orlando, Fla., 1986.
4. Gerstein BC. CRAMPS. In: The Encyclopedia of NMR. John Wiley: Chichester, 1996.
5. Burum DP, Rhim W-K. J. Chem. Phys. 1979;71:944.
6. Lowe IJ, Bull. Am. Phys. Soc. 1957;2:344; Mansfield P. Phys. Lett. 1962;2:58 and Phys. Rev. 1965;127(A):961.
7. Ostroff ED and Waugh JS. Phys Rev. Lett. 1966;16:1097.
8. Mansfield P, Ware D. Phys. Lett. 1966;22:133.
9. Lee M, Goldburg WI. Phys. Rev. 1965;140:1261.
10. Vinogradov E, Madhu PK, Vega S. Chem. Phys. Lett. 1999;315:443.
11. Elena B, de Paëpe G, Emsley L, Chem. Phys. Lett. 2004;398:532 and references therein.
12. Waugh JS, Huber LM, Haeberlen U. Phys. Rev. Lett. 1968;20:180.
13. Emsley JW, Feeney J, Sutcliff LH (Ed). Progress in Nuclear Magnetic Resonance Spectroscopy. London. 1971;8:41.
14. Lowe IJ. Phys. Rev. Lett. 1959;2:285–7.
15. Andrew ER, Bradbury A, Eadesand RG. Nature (Lond.). 1958;182:1659.
16. Trebosc J, Wience J, Lin VS-Y, Pruski M. J. Am. Chem. Soc. 2005;127:7587.
17. Samoson A, Tuherm T, Past J, Reinhold A, Anupõld T, Heinmaa I. New horizons for magic-angle spinning NMR. Top. Curr. Chem. 2004;246:15–31 (DOI 10.1007/b98647).
18. Hafner S, Spiess H. Advanced solid-state NMR spectroscopy of strongly dipolar coupled spins under fast magic angle spinning. Concepts Magn. Reson. 1998;10(1):99–128.
19. Shoji A, Kimura H, Sugisawa H. Structural studies of amino acids, polypeptides and proteins in the solid state by 1H CRAMPS NMR. In: GA Webb (Ed). Annual Reports on NMR Spectroscopy. Academic Press: London, 2001, 45, pp 69–150.
20. Gerstein BC. Fingerprinting solid coals using pules and multiple pulse NMR (Chapter 5). In: Analytical Methods for Coal and Coal Products, Vol. 3. Academic Press: New York, 1980.
21. Gerstein BC, DuBois Murphy P, Ryan LM. A tentative identification of the size of polynuclear aromatic rings in coals (Chapter 2). In: Advances in Chemistry Series. Oxford University Press: New York, Vol. 192, 1981.
22. Kamienski B, Pruski M, Gerstein BC, Peter H. J. Energy Fuels 1987;1:45–50.
23. Gerstein BC, Pruski M, Michel D. Proton NMR spectroscopy of coals, cokes, and coal-derived liquids (Chapter 9). In: HLC Meuzelaar (Ed). Advances in Coal Spectroscopy. Plenum Press: New York, 1992.
24. DeLaRosa L, Pruski M, Gersteinand BC. Quantitation of protons in the argonne premium coals by solid state ^{1}H NMR (Chapter 19). In: RE Botto, Y Sanada (Eds). Magnetic Resonance in Carbonaceous Solids. Advances in Chemistry Series 29. ACS Publishing: Washington, DC, 1993, pp 359–76.
25. Snape CE, Axelson DE, Botto RE, Delpuech JJ, Tekely P, Gerstein BC, Pruski M, Maciel GE, Wilsonand MA. Fuel 1989;68:547.
26. Pembleton RG, Wilson RC, Gersteinand BC. J. Chem. Phys. 1977;66:5133.
27. Shoji A, Kimura H, Ozaki T, Sugisawa H, Deguchi K. J. Am. Chem. Soc. 1996;118:7604-7.
28. Kimura H, Nakamura K, Eguchi A, Sugisawa H, Deguchi K, Ebisawa K, Suzuki E, Shoji J. J. Mol. Struct. 1998;447:247–55.
29. Kimura H, Ozaki T, Sugisawa H, Deguchi K, Shoji A. Macromolecules 1998;31:7398–403.
30. Kimura H, Shoji A, Sugisawa H, Deguchi K, Naito A, Saito H. Macromolecules 2000;33:6627–9.
31. Kimura H, Kishi S, Shoji A, Sugisawa H, Deguchi K. Macromolecules 2000;33:9682–7.
32. Kishi S, Santos A, Ishi O, Ishikawa K, Kunieda S, Kimura H, Shoji A. J. Mol. Struct. 2003;649:155–67.
33. Maciel G. Silica surfaces. In: Encyclopedia of NMR. John Wiley: Chichester, 1996.
34. Gerstein BC, Kimura H. Appl. Magn. Reson. 2004;27:1.
35. Burum DP. HETCOR in Organic Solids. In: Encyclopedia of NMR. John Wiley: Chichester, 1996.
36. Amoureux J-P, Pruski M. Advances in MQMAS NMR. In: DM Grant, RK Harris (Ed). Encyclopedia of Nuclear Magnetic Resonance. Advances in NMR, Vol. 9. John Wiley & Sons Ltd.: Chichester, 2002, 226–51.

Mobile NMR

B. Blümich and F. Casanova
Institute of Technical Chemistry and Macromolecular Chemistry, RWTH Aachen University, Germany

Introduction

The widespread use of NMR in materials testing is hampered by the fact that the object needs to be carried to the NMR equipment and needs to fit inside the magnet [1]. Both limitations are removed by mobile unilateral NMR at the expense of a lower and inhomogeneous magnetic polarization field [2]. Originally, open sensors were developed by the well-logging industries [3]. There, transverse relaxation decays are measured from the fluids in the porous formation with a spectrometer positioned inside the borehole. For well-logging sensors, the field gradient is minimized in a sweet spot or adjusted to a small value so as to eliminate signal attenuation from translational diffusion for short echo times [4–6]. Parallel to the development of the first well-logging tools, the first unilateral sensors were developed mostly for measuring moisture in soil, bridge decks, building materials, and food [7–12]. Some of these instruments employed electromagnets weighing several hundred kilograms. As long as solid materials including rubber are investigated even large field gradients can be tolerated as diffusion is absent. This is the idea behind the NMR-MOUSE, which operates with permanent magnets at frequencies between 10 and 20 MHz with magnetic field gradients up to 20 T/m (Figure 1) [13–16]. The NMR-MOUSE weights less than 1 kg, but is limited to depths typically less than 15 mm.

With the commercialization of well-logging instruments and the availability of the NMR-MOUSE about 10 years ago, the NMR methods for use in inhomogeneous magnetic fields were systematically developed [17–24]. A variety of open magnet geometries are currently being explored for portable use [25–32]. For investigation of large objects, open magnets are fitted with surface coils that provide a magnetic radiofrequency (rf) field $\boldsymbol{B}_1$ [15,16,33]. The volume outside the magnet, where $\boldsymbol{B}_1$ exhibits perpendicular components to the polarization field $\boldsymbol{B}_0$, is the sensitive volume of the sensor. A unilateral NMR sensor essentially selects the signal of a pixel from the object, the size of which is defined by the sensitive volume. A recent development complementary to unilateral NMR devices is lightweight and comparably inexpensive, cylindrical magnets in the Halbach geometry constructed from many small blocks of permanent magnets [34,35]. Such magnets are suitable for studying pipe flow, geophysical drill cores [36], and plants at the site of the object.

Measurement Methods

The open magnets used for unilateral NMR exhibit inhomogeneous magnetic polarization fields $\boldsymbol{B}_0$. When positioned on a large object the response bandwidth is always much larger than the excitation bandwidth, and any excitation is selective [24], a situation encountered also in stray-field NMR imaging [18]. In addition, the surface coil provides an inhomogeneous rf field $\boldsymbol{B}_1$, so that the flip angle of an rf excitation pulse varies across the sensitive volume. Most methods known from NMR in homogeneous fields can be adapted for use in inhomogeneous fields, but need to be reevaluated to account for selective excitation and the flip-angle distribution.

Transverse relaxation decays are readily measured by Hahn echoes and CPMG echo trains (Figure 2a) [37–39]. Due to the flip angle distribution, Hahn and stimulated echoes are generated in a CPMG train, and different coherence pathways need to be discriminated [23]. One striking manifestation of this is, that the first echo in a CPMG train is always lower than the second [18–21]. But also, the echo envelope decays slower than in homogeneous fields, so that effective relaxation times $T_{2\text{eff}}$ are measured in inhomogeneous fields.

Similar to the different variables that define the pixel amplitude in an NMR image [1], parameters and parameter-weighted spin densities can be extracted from the signal measured by the NMR-MOUSE (Figure 2b). Parameters are obtained by fitting the relaxation decay with a model function such as the stretched exponential function [40], or a parameter-weighted signal is obtained, for example, by forming the ratio of the signal at a given decay time with the signal amplitude at decay time zero. To improve the signal-to-noise ratio, several echo amplitudes are added in a defined time interval instead of just taking one amplitude value, for example, $w(0,\ t_1,\ t_2,\ t_3) = I(t_2,\ t_3)/I(0,\ t_1)$. Furthermore, relaxation decays with sufficiently good signal quality can be inverted to distributions of relaxation times by a regularized inverse Laplace transformation (Figure 2c), a procedure which is routinely applied in NMR well logging

Graham A. Webb (ed.), Modern Magnetic Resonance, 373–382.
© 2008 *Springer.*

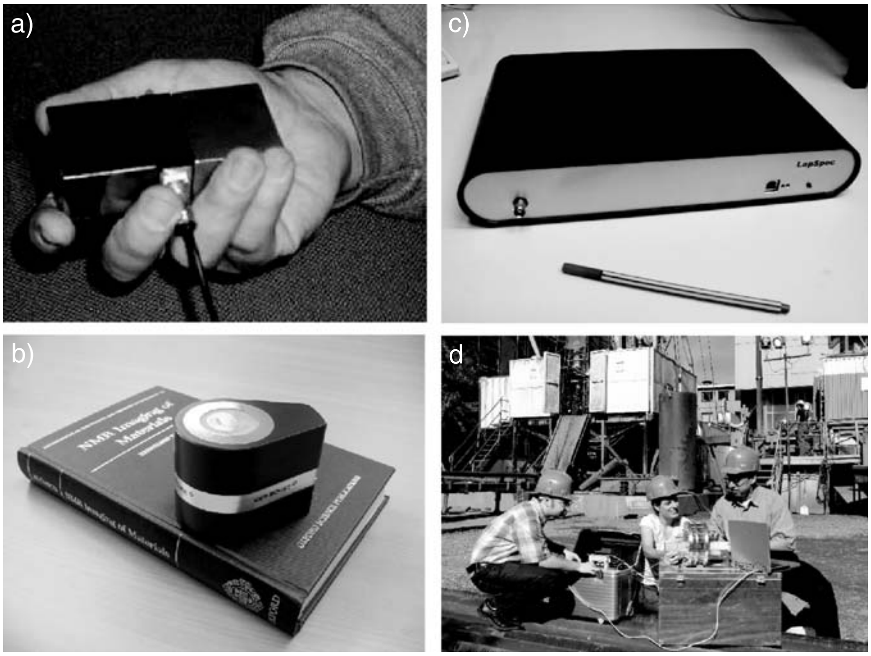

Fig. 1. Portable NMR instrumentation. (a) Original NMR-MOUSE with a u-shaped magnet (Photo: Peter Blümler). (b) Bar-magnet NMR-MOUSE. (c) Small-size portable spectrometer. (d) Halbach magnet with a mobile low-field spectrometer in a pilot's case at the geothermal drilling site of RWTH Aachen. (Photo: Peter Winandy).

to facilitate data interpretation [3]. Parameters other than those referring to transverse relaxation can be measured as well but not directly in inhomogeneous fields. To this end the initial magnetization probed by a CPMG train is prepared for example, by a saturation or inversion recovery T_1 filter [41–43], a multi-quantum filter [44,45], chemical shift [46,47], space encoding [48–51], flow encoding [52,53], or a diffusion filter (Figure 2d) [54–59], and the filter parameter is varied systematically in successive scans [55]. To improve the signal-to-noise ratio, successive echoes of the CPMG train employed for detection can be added. Single-shot encoding of diffusion and flow can be achieved by selection of suitable coherence pathways in multi-echo experiments [60,61].

Using such two-dimensional (2D) methods, a unilateral sensor can be employed for imaging (Figure 3) similar to a magnifying glass to measure, for example, an image of a defect in a textile-reinforced rubber hose (Figure 3c) and the axial velocity image of laminar water flow through a pipe (Figure 3e and f). In this case, the image and flow information is encoded in the detected magnetization by preparing the initial magnetization with pulsed linear gradient fields, which are generated with additional coils fitted to the unilateral sensor [48–53]. Images and profiles involving the depth direction are constructed from several data sets acquired for subsequent slices through the object.

For a long time it has been accepted that chemical shift cannot be measured in inhomogeneous $\boldsymbol{B}_0$ fields. However, this is not so, as has been demonstrated recently in high field with experimental 1D and 2D spectra [46,47]. The currently most successful approach to acquire chemical-shift-resolved spectra in inhomogeneous fields employs mixed echoes with dephasing and rephrasing evolutions in $\boldsymbol{B}_1$ and $\boldsymbol{B}_0$ fields with matched inhomogeneities (Figure 4a) [62]. The evolution in $\boldsymbol{B}_0$ depends on the chemical shift and the one in $\boldsymbol{B}_1$ does not. As a result, the amplitude of the mixed echo is modulated by the chemical shift. For example, a low-field ^{19}F NMR spectrum (Figure 4b) of a mixture of two perfluorinated solvents can already be measured with a unilateral sensor with a resolution better than 10 ppm in just 3 min [63]. However, the sample needs to be small and accurately positioned in the small region where the fields are matched. Unilateral NMR spectroscopy will be of most use for materials analysis, where high-resolution solid-state spectra of ^{1}H or even heteronuclei are needed, and it is a current challenge to develop adequate methods that include line narrowing [64,65].

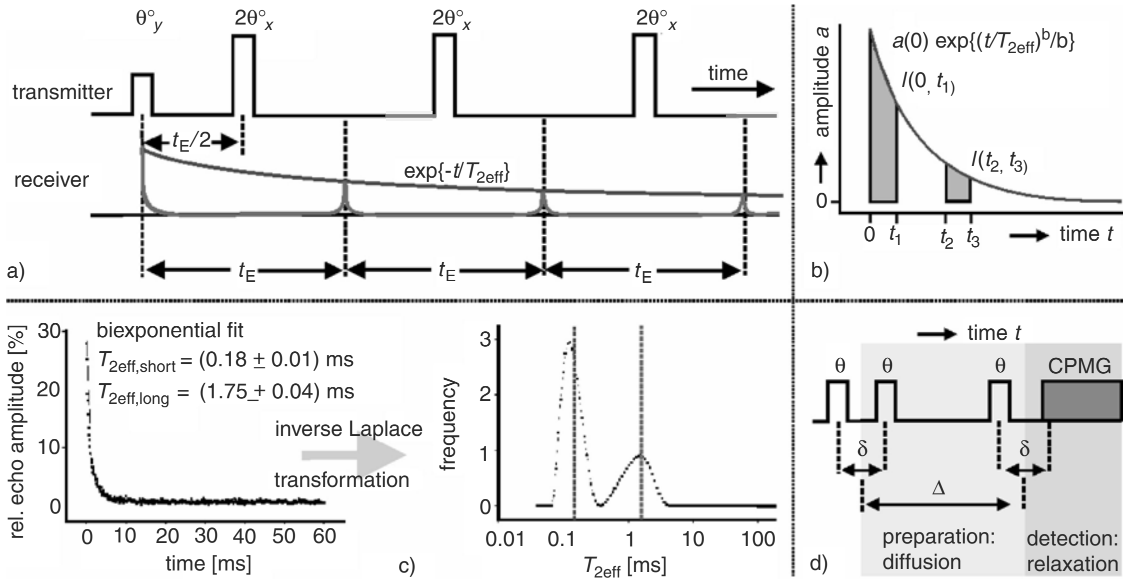
θ°y
2θ°x
2θ°x
2θ°x
transmitter
time
tE/2
receiver
exp{-t/T2eff}
a)
tE
tE
tE
amplitude a
a(0) exp{(t/T2eff)^b/b}
I(0, t1)
I(t2, t3)
0
0 t1 t2 t3 time t
b)
rel. echo amplitude [%]
30 20 10 0
biexponential fit
T2eff,short = (0.18 ± 0.01) ms
T2eff,long = (1.75 ± 0.04) ms
inverse Laplace transformation
0 10 20 30 40 50 60
time [ms]
c)
frequency
3 2 1 0
0.01 0.1 1 10 100
T2eff [ms]
time t
θ θ θ
CPMG
δ
Δ
δ
preparation: diffusion
detection: relaxation
d)

Fig. 2. Measurement methods for NMR in inhomogeneous fields. The excitation flip angle θ shows a distribution within the sensitive volume. In homogeneous fields, θ should be 90°. (a) Multi-echo sequence according to Carr, Purcell, Meiboom, and Gill (CPMG). The envelope of the echo maxima defines the decay of the transverse magnetization. (b) Analysis of transverse relaxation decays by either fitting model functions to obtain amplitudes and relaxation time constants or by computing relaxation-weighted amplitudes. (c) Processing of non-exponential relaxation data by inverse Laplace transformation for subsequent analysis of the distribution of relaxation times. (d) Pulse sequence for measuring a correlation map of diffusion and transverse relaxation. The initial magnetization detected by a CPMG echo train is diffusion encoded in a preparation period, and the experiment is repeated with a systematic variation of the encoding weight. The 2D correlation map is the 2D inverse Laplace transform of the experimental data.

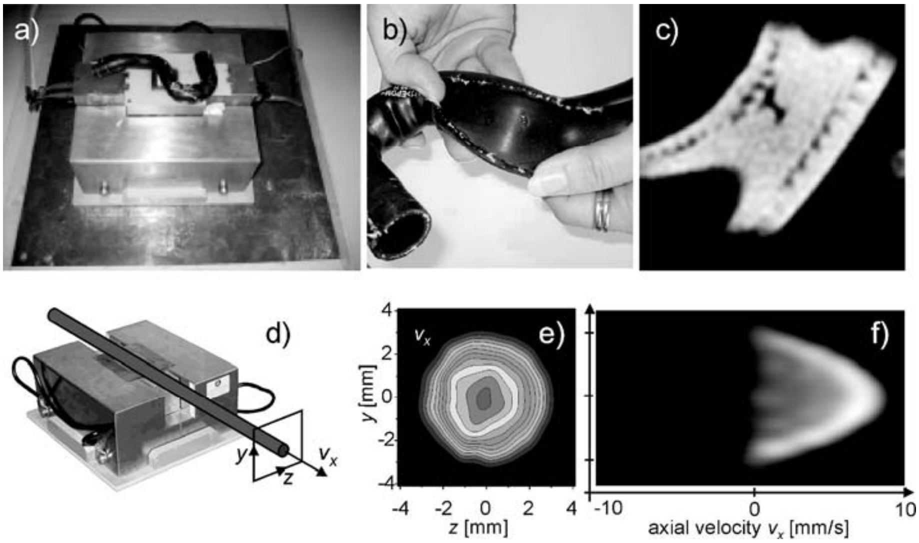
a)
b)
c)
d)
y
z
vx
e)
vx
y [mm]
4 2 0 -2 -4
-4 -2 0 2 4
z [mm]
f)
-10 0 10
axial velocity vx [mm/s]

Fig. 3. Unilateral imaging and flow NMR. The object to be investigated, a rubber pipe (a) or a tube with flowing water (d) is placed on the sensor, here a 36 kg magnet with a field of view of $40 \times 40 \times 20\ \text{mm}^3$. With pulsed gradient fields and phase encoding techniques, the image (c) of the defect in the tube (b) was obtained in 2 h with a spatial resolution of 0.7 mm in each dimension. Similarly, flow images (e, f) can be obtained, here for laminar water flow through a circular pipe (d). Images across depth are constructed from data acquired with multi-slice techniques.

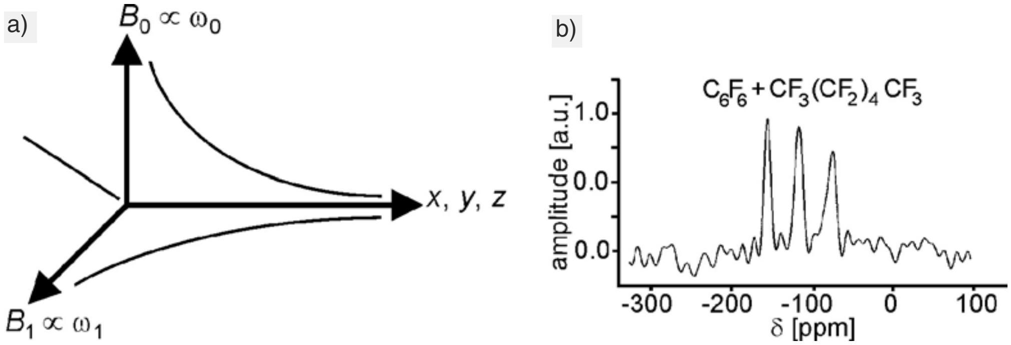

Fig. 4. Chemical-shift resolved spectroscopy in inhomogeneous fields. By matching the precession of magnetization in the inhomogeneous polarization field $\boldsymbol{B}_0$ to the precession in an inhomogeneous rf field $\boldsymbol{B}_1$, chemical-shift resolved spectra can be obtained by unilateral NMR. (A) Principle of matching $\boldsymbol{B}_0$ and $\boldsymbol{B}_1$ profiles in space. (B) NMR spectra of fluorinated solvents acquired *ex situ* of the magnet.

Applications

The most attractive applications of portable NMR are with unilateral NMR in materials science. But portable NMR is also being used with earth field instruments to study sea ice in Antarctica [66–68], and a Halbach magnet has recently been used to study naturally wet rock core samples at a geological drilling site (see below) [36]. A few illustrative examples of portable NMR are given in the following.

Soft matter can readily be studied by NMR as is demonstrated by the great success of medical imaging which maps biological soft matter. Rubber is synthetic soft matter from cross-linked macromolecules with a number of additives and fillers like carbon black. $T_{2\text{eff}}$ is sensitive to the technically important chemical cross-link density [69,70] but also to the homogeneity and state of the material [40]. The cross-link density correlates with the glass transition temperature T_{g}, which is determined in the physical testing laboratory on samples taken out of the production process. $T_{2\text{eff}}$ correlates well with T_{g} (Figure 5b), but needs to be measured at constant temperature [71] or extrapolated to a reference temperature and calibrated. As measurements by unilateral NMR are fast and non-destructive, $T_{2\text{eff}}$ and its spread can be followed at all steps during the production of rubber parts (Figure 5a). This has been demonstrated for the production of tires [72]. The spread of $T_{2\text{eff}}$ for five different tires and their intermediate products at different equivalent measurement positions were quantified in terms of the coefficient of variation and compared to the same quantity for the initial torque measured with a rheometer (RPA: rubber process analyzer) on samples drawn from

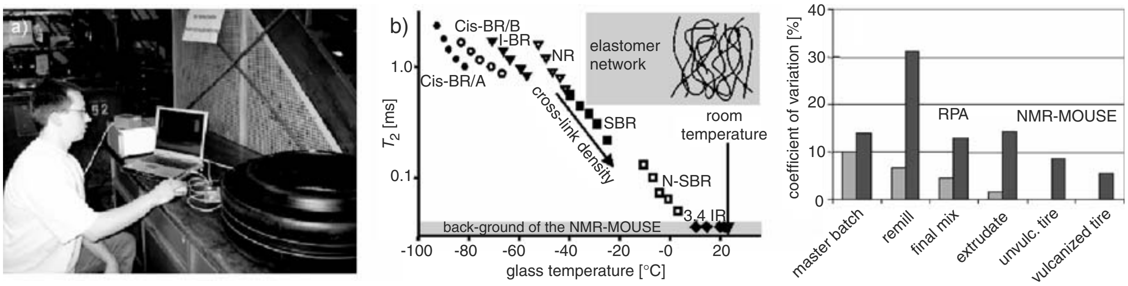

Fig. 5. Mobile NMR of rubber. (a) Large objects like tires can be investigated locally and non-destructively. (b) Transverse relaxation times measured near room temperature with the NMR-MOUSE and extrapolated to a reference temperature scale with the glass transition temperature and consequently with the cross-link density. (c) The spread of NMR parameters within a product and between products provides information about homogeneity and quality. It can be measured at all intermediate steps of the production process and at the final product, as demonstrated for the transverse relaxation times $T_{2\text{eff}}$ in the tire production.

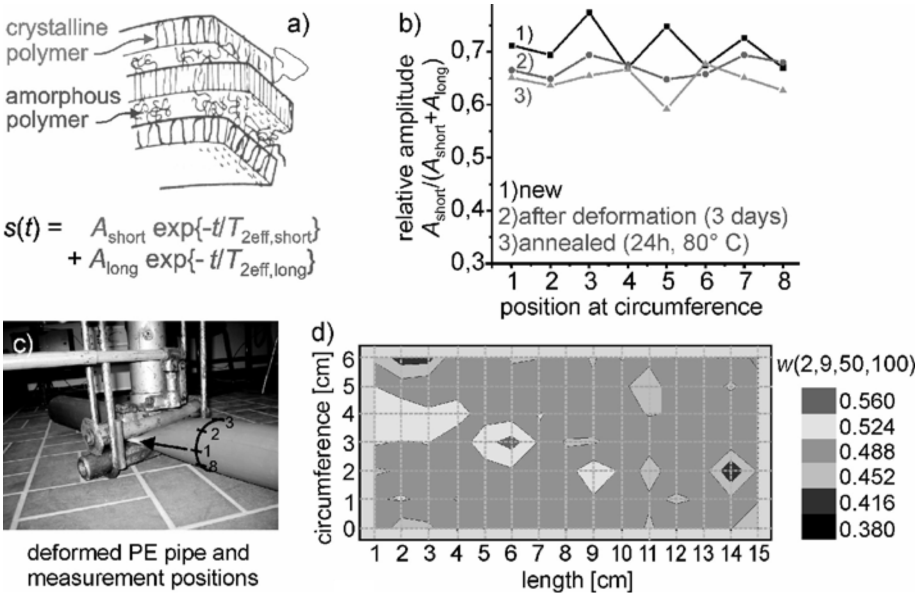

Fig. 6. Semi-crystalline polymers. (a) Morphology of semi-crystalline polymers with chain-folded crystalline regions and disordered amorphous regions, and biexponential model fit function for separation of signal contributions. (b) Crystallinity of a PE pipe at different points around the circumference before deformation, after deformation, and after annealing. (c) Deformation of a PE water pipe. (d) 2D crystallinity map acquired on a 1 cm^2 raster inside a PE pipe at 0 to 1 mm depth. The weighted spin density $w(2, 9, 50, \text{and } 100)$ was computed from the echo maxima a_n according to $\sum_2^9 a_n \Big/ \left(\sum_2^9 a_n + \sum_{50}^{100} a_n\right)$.

the same compounds (Figure 5c). The coefficient of variation decreases from one processing step to the next for the torque, but not for $T_{2\text{eff}}$, demonstrating that rheometer and NMR measurements provide somewhat complementary information. Also the coefficients of variation of $T_{2\text{eff}}$ are larger showing a higher sensitivity of $T_{2\text{eff}}$ to material properties than the torque. Finally, torque measurements are destructive and cannot be done on the final product, whereas the NMR-MOUSE can be used for quality control there [40,73,74]. When testing tires with the NMR-MOUSE, the presence of a steel belt is no obstacle. In fact even thin polymer coatings have been measured on steel sheets with the NMR-MOUSE [75].

Strained elastomers exhibit macroscopic molecular order, which can be probed with the u-shaped NMR-MOUSE by the orientation dependence of the relaxation rate [76], an effect which is also observed for tendon [77]. Aging and fatigue also lead to changes in $T_{2\text{eff}}$, and can consequently be studied non-invasively by unilateral NMR [71,78].

Leathery, semi-crystalline polymers like poly (ethylene) and poly(propylene) are less soft than rubber but still give excellent signal when short echo times like 25 μs are used. The transverse relaxation time $T_{2\text{eff,short}}$ of the chain-folded macromolecules in the crystalline domains is considerably shorter than the $T_{2\text{eff,long}}$ of the coiled chains in the amorphous domains (Figure 6a). Consequently, both components can be discriminated in a biexponential fit of the transverse relaxation decay, and the relative amplitude of the short component defines the NMR crystallinity. This quantity has been determined at well-defined positions on the circumference of a PE water pipe (Figure 6b and c) [79]. Even in the new state, it varies from point to point due to shrinkage while cooling during fabrication (Figure 6b). When laying or repairing pipes, the water flow is stopped by squeezing the pipes. When applied for an extended time, such a deformation reduces the crystallinity due to strained amorphous chains creeping out of the crystalline domains. At the same time the order in the amorphous domains has initially been increased as the chains are strained. Upon annealing well below the glass temperature these, chains relax by the melting of small crystallites, so that the overall crystallinity decreases further. By measuring a 2D array of NMR crystallinity data, the inhomogeneities of a PE pipe can be depicted in a 2D map (Figure 6d).

Another semi-crystalline polymer is cellulose. It is contained in wood and is the main component of paper. The state of wood and paper is inherently associated with the amount of bound water. The NMR-MOUSE has been applied to characterize the degradation state of historic paper [80–82] and to map the moisture distribution in wood panels [83].

The original u-shaped NMR-MOUSE (Figure 1a) has the $\boldsymbol{B}_0$ field approximately parallel to the scanner surface. With decreasing rf frequency the sensitive volume is shifted away from the surface, and its shape flattens. To obtain an extremely flat shape, the magnet geometry needs to be somewhat modified. While the original NMR-MOUSE collects signal from a slice about 1 mm thick near the surface, the optimized profile NMR-MOUSE collects signal from planar slices 30 μm thin and less (Figure 7a) [84]. To acquire high-resolution depth profiles, the sensitive slice can be shifted through the object by adjusting the distance between the NMR-MOUSE and the object with a precision lift of the NMR-MOUSE (Figure 7b). Even higher resolution can be obtained by Fourier transforming the echo acquired from the sensitive slice. Despite the thin sensitive volume, the sensitivity is good enough to acquire depth profiles of moisture in polymer sheets within a few minutes (Figure 7c and d). In this way the water uptake can be followed with a precision better than 0.2%. Even the water uptake from air can be studied (Figure 7d). Here the profile NMR-MOUSE provides information similar to that of the GARFIELD magnet [85,86], which has been designed with specially shaped pole shoes that ensure a linear gradient field with a strong gradient in the magnet gap. But contrary to the Garfield design, the NMR-MOUSE provides completely open access, for example, for *in vivo* skin studies and profiling of composites and adhesive layers [87–89]. Instead of shifting the sensitive volume mechanically through the object, it can also be shifted electrically by changing the field strength of the NMR-MOUSE [90] and by varying the rf excitation frequency on the expense of a changing shape of the sensitive volume.

The characterization of moisture in soil and building materials are one of the earliest applications of unilateral NMR [8–12,40,57,91,92]. Absolute values of moisture per volume can readily be obtained, as the size of the sensitive volume is fixed and defined [93]. Pore-size distributions cannot as easily be obtained. There are two reasons: (1) The $\boldsymbol{B}_0$ field of the NMR-MOUSE is strongly inhomogeneous and the acquired transverse relaxation decay is attenuated from diffusive motion in the larger pores. As a consequence, the distribution of $T_{2\text{eff}}$ obtained by Laplace inversion of the CPMG decay appears compressed for larger $T_{2\text{eff}}$, and $T_{2\text{eff}}$ is no longer proportional to the pore size in the fast diffusion limit. (2) The material to be investigated needs to be completely fluid saturated. This cannot be achieved for rock once it has been dried. For complete saturation, the CPMG signal amplitude or the integral of

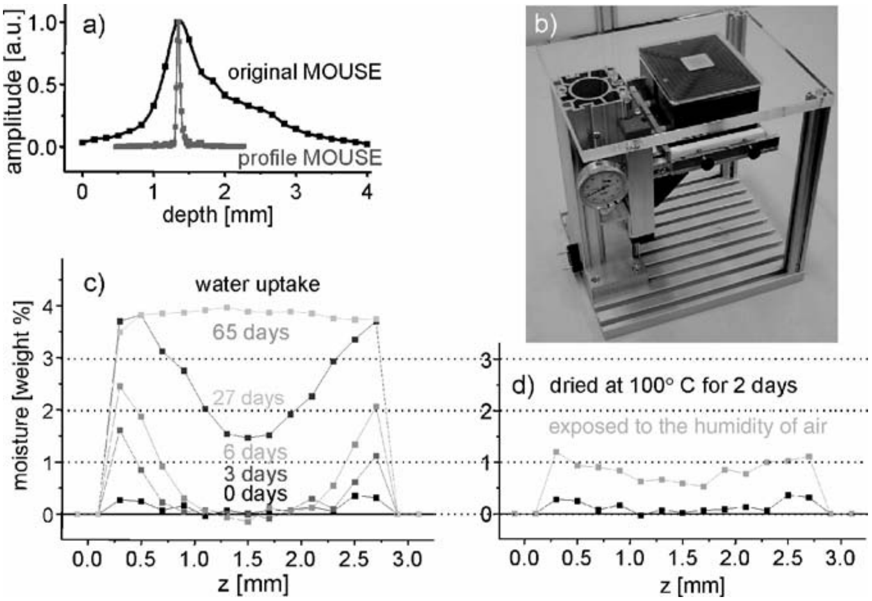

Fig. 7. High-resolution depth profiling. (A) 1D depth cross-sections of the sensitive volumes of the original u-shaped NMR-MOUSE and the optimized profile NMR-MOUSE. (B) Mechanical precision lift for shifting the sensitive volume through the object. (C) Moisture profiles of a polymer sheet depicting the water uptake as a function of the wetting time. (D) Moisture profiles of a dry sheet and a sheet exposed to the humidity of air.

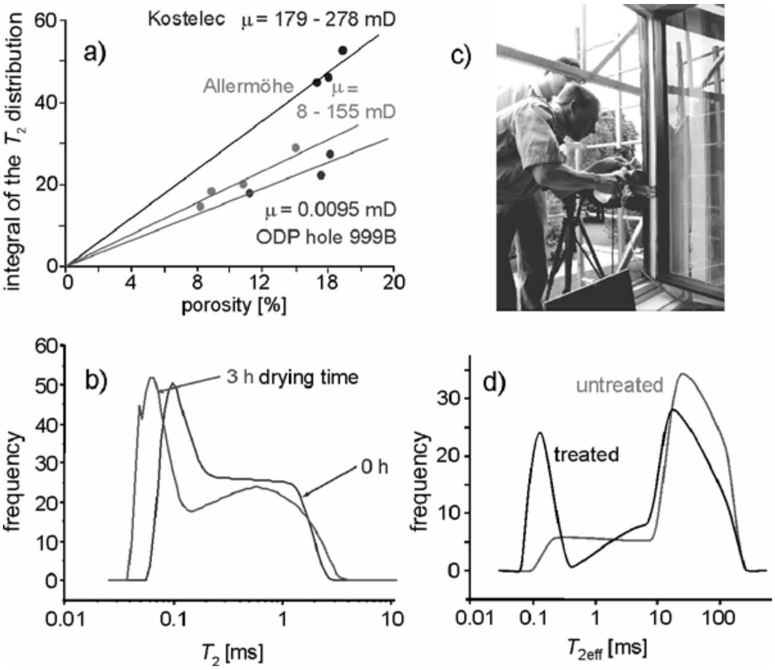

Fig. 8. Porous media. (a) Correlation of NMR porosities measured with the NMR-MOUSE and porosities of geological core samples with different fluid conductivities measured with a helium gas pycnometer. (b) Relaxation-time distribution functions of a core sample at different drying times. (c) Measurement of a partially wetted sandstone window frame in Paffendorf castle. (d) Relaxation time distributions for two frames, one not treated and the other one treated with a stone conservation agent.

the relaxation time distribution should be proportional to the porosity. But for rocks soaked after drying it depends on the fluid conductivity (Figure 8a). So originally wet cores need to be measured to obtain reliable porosity values by NMR. This is one further area of application of portable NMR in geophysics.

For porosities lower than 5% the sensitivity of the NMR-MOUSE is not good enough and a Halbach magnet with a more homogeneous $\boldsymbol{B}_0$ field and a larger sensitive volume need to be employed (Figure 1d). Its more homogeneous field permits the measurement of reliable relaxation time distributions, which, for example, in a drying study, reveal the preferential water loss from large pores with long relaxation times (Figure 8b) [36]. Nevertheless, the NMR-MOUSE has produced interesting results in a pilot study of the effect of stone conservation treatment conducted at the sandstone window frames of Paffendorf Castle near Cologne, Germany. The areas to be measured were partially wetted (Figure 8c) and differences in the relaxation time distributions of the untreated and treated frames reveal a more frequent occurrence of faster relaxation for the treated material. This promises, that unilateral NMR can be developed into a method to assess the success of stone conservation efforts non-invasively. A related study concerns the characterization of water and oil emulsions as model systems for food, where it has been demonstrated that the concentration of oil and water can be determined from the NMR-MOUSE signals [94].

Summary

Portable unilateral NMR concerns methods and NMR devices, which are carried to the object under study. It is an offspring of well-logging NMR. For materials analysis strongly inhomogeneous magnetic fields can be employed. NMR in inhomogeneous fields is an active area of research, and in addition to NMR relaxation, it has recently been demonstrated that NMR images, flow profiles, and even spectra can be measured by unilateral NMR. Mobile unilateral sensors like the NMR-MOUSE are lightweight and inexpensive. The measurement is non-destructive, and arbitrarily large samples can be investigated *in situ* up to depths of some 10 mm. The NMR-MOUSE can be employed for product development and quality control in a manufacturing environment. Other portable magnet geometries with better field homogeneity, such as the Halbach magnet, are also being explored for portable NMR. They can be used to study pipe flow, geophysical drill cores, and the like, where the completely open access provided by unilateral sensors is not required.

Acknowledgments

This work has been conducted with support by *Deutsche Forschungsgemeinschaft* (DFG) and *Bundesministerium* *für Bildung und Forschung* (BMBF). The contributions of Juan Perlo, Kai Kremer, Sophia Anferova, Vladimir Anferov, Nicolae Goga, Vasilikis Demas, Alina Buda, Dan Demco, Peter Blümler, Michael Adams, and Klaus Kupferschläger are gratefully acknowledged.

References

1. Blümich B. NMR Imaging of Materials, Clarendon Press, Oxford, 2000.
2. Matzkanin GA. A review of nondestructive characterization of composites using NMR. In: P Höller, V Hauck, G Dobmann, C Ruud, R Green (Eds). Nondestructive Characterization of Materials. Springer: Berlin, 1989, pp 655–69.
3. Coates GR, Xiao L, Prammer MG. NMR Logging Principles and Applications. Halliburton Energy Services: Houston, 1999.
4. Kleinberg RL. Well logging. In: DM Grant, RK Harris (Eds). Encyclopedia of NMR. Wiley-Liss: New York, 1996, pp 4960–69.
5. Cooper RK, Jackson JA. Remote (inside-out) NMR. I. Remote production of a region of homgeneous magnetic field. J. Magn. Reson. 1980;41:400–405.
6. Burnett LJ, Jackson JA. Remote (inside-out) NMR. II. Sensitivity of NMR detection for external samples. J. Magn. Reson. 1980;41:406–10.
7. Jackson JA, Burnett LJ, Harmon F. Remote (inside-out) NMR. III. Detection of nuclear magnetic resonance in a remotely produced region of homogeneous magnetic field. J. Magn. Reson. 1980;41:411–21.
8. Paetzold RF, Matzkanin GA, De Los Santos A. Surface water content measurement using pulse nuclear magentic resonance techniques. Soil Sci. 1985;49:537–40.
9. Paetzold RF, De Los Santos A, Matzkanin GA. Pulse nuclear magnetic resonance instrument for soil-water content measurement: sensor configurations. Soil Sci. 1987;51:287–90.
10. Hogan BJ. One-Sided NMR Sensor System Measures Soil/Concrete Moisture, Design News, May 5 (1986).
11. Rollwitz WL. Using radiofrequency spectroscopy in agricultural applications. Agric. Eng. 1985;66:12–14.
12. Nicholls CI, De Los Santos A. Hydrogen transient nuclear magnetic resonance for industrial moisture sensing. Drying Technol. 1991;9:849–73.
13. Eidmann G, Savelsberg R, Blümler P, Blümich B. The NMR-MOUSE: a mobile universal surface explorer. J. Magn. Reson. A. 1996;122:104–9.
14. Blümich B, Blümler P, Eidmann G, Guthausen A, Haken R, Schmitz U, Saito K, Zimmer G. The NMR MOUSE: construction, excitation, and applications. Magn. Reson. Imaging. 1998;16:479–84.
15. Anferova S, Anferov V, Adams M, Blümer P, Routley N, Hailu K, Kupferschläger K, Mallet M, Schroeder G, Sharma S, Blümich B. Construction of the NMR-MOUSE with short dead time. Magn. Reson. Eng. 2002;15:15–25.
16. Blümich B, Anferov V, Anferova S, Klein M, Fechete R, Adams M, Casanova F. Simple NMR-MOUSE with a bar magnet. Concepts Magn. Reson. 2002;15:255–61.
17. Goelman G, Prammer MG. The CPMG pulse sequence in strong magnetic field gradients with application to oil-well logging. J. Magn. Reson. A. 1995;113:11–18.
18. McDonald PJ. Stray-field magnetic resonance imaging. Prog. Nucl. Magn. Reson. Spectrosc. 1997;30:69–99.
19. Hürlimann MD, Griffin DD. Spin dynamics of Carr-Purcell-Meiboom-Gill-like sequences in grossly inhomogeneous B_0 and B_1 fields and application to NMR well logging. J. Magn. Reson. 2000;143:120–35.
20. Balibanu F, Hailu K, Eymael R, Demco DE, Blümich B. NMR in inhomogeneous magnetic fields. J. Magn. Reson. 2000;145:246–58.
21. Hürlimann MD. Optimization of timing in the Carr-Purcell-Meiboom-Gill sequence. Magn. Reson. Imaging. 2001;19:375–78.
22. Hürlimann MD. Carr-Purcell sequences with composite pulses. J. Magn. Reson. 2001;152:109–23.
23. Song Y-Q. Categories of coherence pathways for the CPMG sequence. J. Magn. Reson. 2002;157:82–91.
24. Todica M, Fechete R, Blümich B. Selective NMR excitation in strongly inhomogeneous magnetic fields. J. Magn. Reson. 2003;164:220–27.
25. Prado PJ. NMR handheld moisture sensor. Magn. Reson. Imaging. 2001;19:505–8.
26. Popella H, Henneberger G. Design and optimization of the magnetic resonance circuit of a mobile nuclear magnetic resonance device for magnetic resoance imaging. Compel. 2001;20:269–79.
27. Podol'skii A. Permanent-magnet assemblies for magnetic resonance imaging devices for various purposes. IEEE Trans. Magn. 2002;38:2–5.
28. Pulyer Y, Hrovat MI. An open magnet utilizing ferro-refraction current magnification. J. Magn. Reson. 2002;154:298–02.
29. Pulyer YM. Generation of remote homogeneous magnetic fields. IEEE Trans. Magn. 2002;38:1553–63.
30. Prado PJ. Single-sided imaging sensor. Magn. Reson. Imaging. 2003;21:397–400.
31. Hunter MW, Callaghan PT, Dyskra R, Eccles CD, Vamanan S. Design and construction of a portable one-sided access NMR probe, Abstract to the 7th International Conference on Magnetic Resonance in Porous Media, July 4–8, 2004, Paris, France.
32. Fukushima E, Jackson JA. Unilateral magnet having a remote uniform field region, US patent 6,489,872, 3 December 2002.
33. Blümich B, Anferov V, Anferova S, Klein M, Fechete R. An NMR-MOUSE® for analysis of thin objects. Macromol. Mater. Eng. 2003;288:312–17.
34. Halbach K. Design of permanent multipole magnets with oriented rare earth cobalt material. Nucl. Instr. Meth. 1980;169:1–10.
35. Raich H, Blümler P. Design and construction of a dipolar Halbach array with a homogeneous field from identical bar-magnets. Concepts Magn. Reson. 2004;23B:16–25.
36. Anferova S, Anferov V, Rata DG, Blümich B, Arnold J, Clauser C, Blümler P, Raich H. A mobile NMR device for measurements of porosity and pore size distributions of drilled core samples. Concepts Magn. Reson. 2004;23B: 26–32.
37. Hahn EL. Spin echoes. Phys. Rev. 1950;80:580–94.

38. Carr HY, Purcell EM. Effects of diffusion on free precession in NMR experiments. Phys. Rev. 1954;94:630–38.
39. Meiboom S, Gill D. Compensation for pulse imperfections in Carr-Purcell NMR experiments. Rev. Sci. Instrum. 1958;29:688–91.
40. Blümich B, Anferova S, Kremer K, Sharma S, Herrmann V, Segre A. Unilateral NMR for quality control: the NMR-MOUSE®. Spectroscopy. 2003;18:24–54.
41. Sezginer A, Kleinberg RL, Fukuhara M, Latour LL. Very rapid simultaneous measurement of nuclear magnetic resonance spin-lattice relaxation time and spin-spin relaxation time. J. Magn. Reson. 1991;92:504–27.
42. Guthausen A, Zimmer G, Blümler P, Blümich B. Analysis of polymer materials by surface NMR via the NMR MOUSE. J. Magn. Reson. 1998;130:1–7.
43. Song Y-Q, Venkataramanan L, Hürlimann MD, Flaum M, Frulla P, Straley C. $T_1 - T_2$ correlation spectra obtained using a fast two-dimensional laplace inversion. J. Magn. Reson. 2002;154:261–68.
44. Wiesmath A, Filip C, Demco DE, Blümich B. Double-quantum-filtered NMR signals in inhomogeneous magnetic fields. J. Magn. Reson. 2001;149:258–63.
45. Wiesmath A, Filip C, Demco DE, Blümich B. NMR of multipolar spin states excited in strongly inhomogeneous magnetic fields. J. Magn. Reson. 2002;154:60–72.
46. Meriles CA, Sarkellariou D, Heise H, Moulé AJ, Pines A. Approach to high-resolution *ex situ* NMR spectroscopy. Science. 2001;293:82–85.
47. Heise H, Sakellariou D, Meriles CA, Moulé A, Pines A. Two-dimensional high-resolution NMR spectra in matched $\boldsymbol{B}_0$ and $\boldsymbol{B}_1$ field gradients. J. Magn. Reson. 2002;156:146–51.
48. Prado PJ, Blümich B, Schmitz U. One-dimensional imaging with a palm-size probe. J. Magn. Reson. 2000;144:200–06.
49. Casanova F, Blümich B. Two-dimensional imaging with a single-sided NMR probe. J. Magn. Reson. 2003;163:38–45.
50. Casanova F, Perlo J, Blümich B, Kremer K. Multi-echo imaging in highly inhomogeneous magnetic fields. J. Magn. Reson. 2004;166:76–81.
51. Perlo J, Casanova F, Blümich B. 3D imaging with a single-sided sensor: an open tomograph. J. Magn. Reson. 2004;166:228–35.
52. Casanova F, Perlo J, Blümich B. Velocity distributions remotely measured with a single-sided NMR sensor. J. Magn. Reson. 2004;171:124–30.
53. Perlo J, Casanova F, Blümich B. Velocity imaging by *ex situ* NMR. J. Magn. Reson. 2005;173:254–258.
54. Hürlimann MD. Diffusion and relaxation effects in general stray field NMR experiments. J. Magn. Reson. 2001;148:637–378.
55. Hürlimann MD, Venkataramanan L. Quantitative measurement of two-dimensional distributions functions of diffusion and relaxation in grossly inhomogeneous fields. J. Magn. Reson. 2002;157:31–42.
56. Guthausen G, Guthausen A, Balibanu F, Eymael R, Hailu K, Schmitz U, Blümich B. Soft-matter analysis by the NMR-MOUSE. Macromol. Mater. Eng. 2000;276/277:25–37.
57. Casieri C, Bubici S, De Luca F. Self-diffusion coefficient by single-sided NMR. J. Magn. Reson. 2003;162:348–55.
58. Marko A, Wolter B. Diffusion studies in porous media with the "inside-out" technique. Magn. Reson. Imaging. 2003;21:363–64.
59. Klein M, Fechete R, Demco DE, Blümich B. Self-diffusion measurements by a constant-relaxation method in strongly inhomogeneous magnetic fields. J. Magn. Reson. 2003;164:310–20.
60. Song Y-Q, Hürlimann MD, Flaum C. A method for rapid characterization of diffusion. J. Magn. Reson. 2003;161:222–33.
61. Song Y-Q, Scheven UM. An NMR technique for rapid measurement of flow. J. Magn. Reson. 2005;172:31–35.
62. Ardelean I, Kimmich R, Klemm A. The nutation and spin echo and its use for localized NMR. J. Magn. Reson. 2000;146:43–48
63. Perlo J, Demas V, Casanova F, Meriles CA, Reimer J, Pines A, Blümich B. High-resolution NMR spectroscopy with a portable single-sided sensor. Science. 2005;308:1278.
64. Meriles CA, Sakellariou D, Pines A. Resolved magic-angle spinning of anisotropic samples in inhomogeneous fields. Chem. Phys. Lett. 2002;358:391–95.
65. Meriles CA, Sakellariou D, Moulé A, Goldman M, Budinger TF, Pines A. High-resolution NMR of static samples by rotation of the magnetic field. J. Magn. Reson. 2004;169:13–18.
66. Callaghan PT, Eccles CD, Seymour JD. An earth's field nuclear magnetic resonance apparatus suitable for pulsed gradient spin echo measurements of self-diffusion under Antarctic conditions. Rev. Sci. Instrum. 1997;68:4263–270.
67. Callaghan PT, Eccles CD, Haskell TG, Langhorne PJ, Seymour JD. Earth's field NMR in Antarctica: a pulsed gradient spin echo NMR study of restricted diffusion in sea ice. J. Magn. Reson. 1998;133:148–54.
68. Callaghan PT, Dykstra R, Eccles CD, Haskell TG, Seymour JD. A nuclear magnetic resonance study of Antarctic sea ice brine diffusivity. Cold Regions Sci. Tech. 1999;29:153–71.
69. Litvinov VM, De PP (Eds). Spectroscopy of Rubbers and Rubbery Materials. Rapra Technology Limited: Shawbury, 2002.
70. Herrmann V, Unseld K, Fuchs H-B, Blümich B. Molecular dynamics of elastomers investigated by DMTA and the NMR-MOUSE®. Colloid Polym. Sci. 2002;280:758–64.
71. Anferova S, Anferov V, Adams M, Fechete R, Schroeder G, Blümich B. Thermo-oxidative aging of elastomers: a temperature control unit for operation with the NMR-MOUSE®. Appl. Magn. Reson. 2004;27:361–370.
72. Goga N, Kremer K, Blümich B. Qualitätskontrolle in der Reifenindustrie, Gummi Fasern Kunststoffe 2005;58:361–70.
73. Blümich B, Bruder M. Mobile NMR zur Qualitätskontrolle von Elastomerprodukten, Kautschuk Gummi Kunststoffe, 2003;56:90–94.
74. Blümich B, Anferova S, Casanova F, Kremer K, Perlo J, Sharma S. Unilateral NMR: principles and applications to quality control of elastomer products. Kautschuk Gummi Kunststoffe. 2004;57:346–49.
75. Zimmer G, Guthausen A, Schmitz U, Saito K, Blümich B. Wheathering investigation of PVC coatings on iron sheets by the NMR MOUSE. Adv. Mater. 1997;9:987–89.
76. Hailu K, Fechete R, Demco DE, Blümich B. Segmental anisotropy in strained elastomers detected with a portable NMR scanner. Solid State Nucl. Magn. Reson. 2002;22:327–43.

77. Haken R, Blümich B. Anisotropy in tendon investigation in vivo by a porg NMR scanner, the NMR-MOUSE. J. Magn. Reson. 2000;144:195–99.
78. Cornelissen C, Schnettler A, Wiesmath A, Blümich B. Ultraschall und Kernspinresonanz: Nicht-destruktive Verfahren zur Zustandsbewertung von Kabelsystemen, Das Magazin für die Energiewissenschaften ew 2002;101:38–43.
79. Blümich B, Casanova F, Buda A, Kremer K, Wegener T. Anwendungen der mobilen NMR zur Zustandsbewertung von Bauteilen aus Polyethylen. 3R International. 2005;44:349–354.
80. Blümich B, Anferova S, Sharma S, Segre A, Federici C. Degradation of historical paper: nondestructive analysis by the NMR-MOUSE®. J. Magn. Res. 2003;161:204–9.
81. Proietti N, Capitani D, Pedemonte E, Blümich B, Segre AL. Monitoring degradation in paper: non-invasive analysis by unilateral NMR. Part II, J. Magn. Reson. 2004;170:113–20.
82. Casieri C, Bubici S, Viola I, de Luca F. A low-resolution non-invaisve NMR investigation of ancient paper. Solid State Nucl. Magn. Reson. 2004;26:65–73.
83. Casieri C, Senni L, Romangnoli M, Santamaria U, de Luca F. Determination of moisture fraction in wood by mobile NMR device. J. Magn. Reson. 2004;171:364–72.
84. Perlo J, Casanova F, Blümich B. Single-sided NMR profiler with microscopic resolution, manuscript in preparation.
85. Glover PM, Aptaker PS, Bowler JR, Ciampi E, McDonald PJ. A novel high-gradient permanent magnet for the profiling of planar films and coatings. J. Magn. Reson. 1999;139:90–97.
86. Godward G, Ciampi E. Cifelli M, McDonald PJ. Multidimensional imaging using combined stray field and pulsed gradients. J. Magn. Reson. 2002;155:92–99.
87. Hartwig A, Wolter B. NMR-Aufsatztechnik: Neue Online-Methode zum zerstörungsfreien Prüfen?, Adhäsion kleben & dichten 2001;11:25–29.
88. A. Hartwig and Wolter B. Zerstörungsfreie NMR-Aufsatztechnik: Anwendungsbeispiele und Möglichkeiten, Adhäsion kleben & dichten 2001;12:34–38.
89. Kremer K, Kühn H, Blümich B, Seitzer J, Schmitz F-P. NMR-MOUSE® übernimmt Qualitätskontrolle im KFZ-Bau, Adhäsion kleben & dichten 2002;11:32–36.
90. Brown MCA, Verganelakis DA, Mallett MJD, Mitchell J, Blümler P. Surface normal imaging with a handheld NMR device. J. Magn. Reson. 2004;169:308–12.
91. Dobmann G, Kroening M, Surkowa N, von Bernus J, Wolter B. The potential of nuclear magnetic resonance (NMR) to non-destructively characterize early-age concrete by an one-sided access (OSA) technique, NDE2002 predict, assure, improve, National Seminar of ISNT, Chennai, 7 December 2002, www.nde2002.org.
92. Sharma S, Casanova F, Wache W, Segre A, Blümich B. Analysis of historical porous building materials by the NMR-MOUSE®. Magn. Reson. Imaging. 2003;21:249–55.
93. Blümich B, Anferova S, Pechnig R, Pape H, Arnold J, Clauser C. Mobile NMR for porosity analysis of drill core sections. J. Geophys. Eng. 2004;1:177–80.
94. Pedersen HT, Ablett S, Martin DR, Mallett MJD, Engelsen SB. J. Magn. Reson. 2003;165:49–58.

Rheo-NMR

Paul T Callaghan
MacDiarmid Institute for Advanced Materials and Nanotechnology,
Victoria University of Wellington, New Zealand

One recent application of NMR concerns rheology [1,2], the study of the mechanical properties of fluids. This application has come to be known as “Rheo-NMR” [3–7].

Many interesting materials in their condensed phase possess both solid and liquid-like properties. These include high molecular mass polymers and elastomers, lyotropic and thermotropic liquid crystals, micellar surfactant phases, colloidal suspensions, foams, emulsions, micro-emulsions and bicontinuous phases. Such materials, strongly represented in the biological world, comprise what is often called “soft matter” or “complex fluids”. Complex fluids manifest both an elastic and a viscous response, and they generally possess “memory”, which means that the stress which they exhibit at any moment will depend on the history of prior deformation. They often exhibit non-linear flow behavior, which means that properties may change as the deformation increases, an effect which is generally attributed to molecular reorganisation. And they invariably possess a wide range of characteristic time scales, from the rapid (ps to ns) local Brownian motion of small molecules or molecular segments, to the very slow (ms to s) motions associated with the reorganisation or reorientation of large molecular assemblies or macromolecules.

While rheology involves mechanical measurement of flow properties, the really interesting questions concern the molecular basis of these properties. Under flow, competition arises between the molecular organisational dynamics and the externally imposed deformation, with outcomes including conformational distortion [8], re-organisation of mesophase structure [9], double-valuedness in the constitutive properties [10] banded flow [11], the driving of the material through nearby phase transitions [12], and soft glassy dynamics, the slow aging of a system as the structure reorganizes [13].

The interest in the molecular-mechanical link has led to the amalgamation of a number of spectroscopic and rheological techniques in which a flow or deformation cell is incorporated within the spectrometer detection system. Examples include the use of neutron scattering, light scattering, birefringence, and dichroism techniques [2]. The most recent addition, NMR, allows one to study materials which are optically opaque. The imaging capability of NMR means that it can be used to directly measure local velocity profiles and molecular densities. And the wide-ranging spectroscopic tools available to Rheo-NMR make it possible to measure molecular order and dynamics.

Rheo-NMR based on micro-imaging approaches [14] allows the mapping of fluid velocity in small (mm to cm scale) deformation cells, the small volumes allowing the study of specialized materials. The velocimetry mode of micro-imaging generally employs a Pulsed Gradient Spin Echo (PGSE) sequence in which magnetic field gradientpulses define a wave vector domain, q, which imparts a phase shift to the spins depending directly on the motion of their parent molecules [14]. Inverse Fourier transformation of the signal with respect to q returns the local distribution of velocities, $P(v)$, for each pixel of the image. A typical velocity image will take between seconds and several minutes to acquire, depending on signal-to-noise trade-offs. The upper limit to velocity is determined by image distortion or inflow-outflow effects and is typically 1 ms^{-1}. The lower limit is determined by Brownian motion, enabling velocity resolution on the order of 10 micrometer per second for small molecules such as water but down to 100 nms^{-1} for macromolecules or colloidal particles, as shown in Figure 1 which depicts the velocity field for a soft glassy material formed from a close packing of 370 nm diameter latex spheres [15]. This example exhibits both slip and yield stress behavior, indicating the value of such flow visualization.

Rheo-NMR flow geometries [16,17] include cone-and-plate cells, cylindrical Couette cells, four roll mills and bi-axial extension cells, these latter devices being used to produce purely extensional flow. All these deformational flow devices are driven by a drive shaft which sits in the bore of the magnet and which is turned by a stepper-motor gearbox assembly mounted above the magnet bore. By contrast flow-though geometries include simple pipe as well as opposed jet systems. A typical Rheo-NMR kit is shown in Figure 2.

In most materials there exists a monotonic relationship (“flow curve”) between the applied stress σ and the rate of strain, $\dot{\gamma}$ [1]. In a rheological cell for which the stress is nearly uniform, such as the small angle cone-and-plate device, one would therefore expect a unique strain rate to occur at any applied stress. One of the first significant contributions of Rheo-NMR has been to show that

Graham A. Webb (ed.), Modern Magnetic Resonance, 383–388.
© 2008 *Springer.*

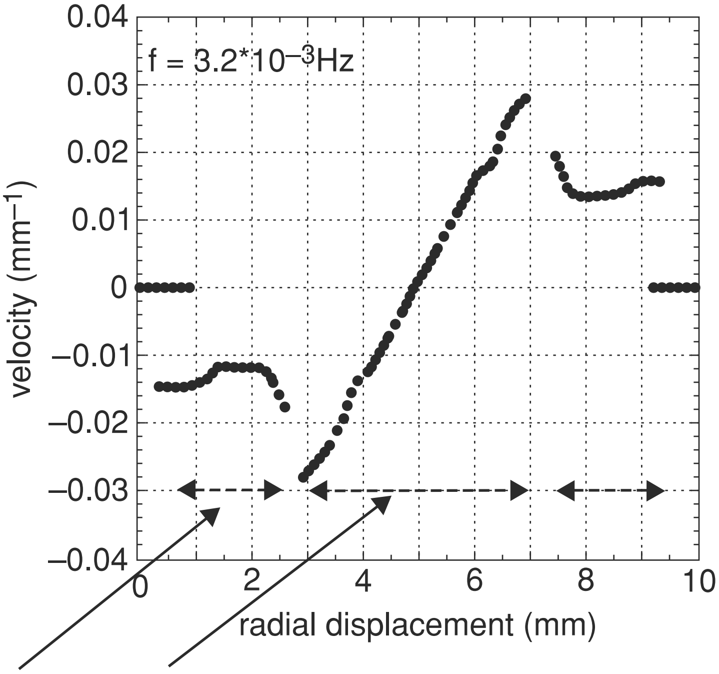

Fig. 1. Velocity profile across a cylindrical Couette cell of inner cylinder ID 5 mm and outer cylinder ID 9.4 mm, for 0.48 volume fraction 370 nm diameter core-shell latex spheres suspension in water. The left hand arrow indicates the region of the annular gap where a yield stress point is apparent, dividing fluidized material from the glassy state. The right-hand arrow point to fluid within the center cylinder undergoing rigid body motion. Note the slip at the inner and outer walls (adapted from ref. [15]).

the uniform shear-rate assumption may be violated in the case of certain classes of fluids in which pathological flow properties are exhibited. Figure 3 shows velocity maps and associated shear-rate maps [18] obtained for the worm-like surfactant system, cetylpyridinium chloride/sodium salicylate in water. While the velocity gradients show no deviation from uniformity at very low shear rates, above a certain critical value $\dot{\gamma}_c$ a dramatic variation across the 6° cone gap is apparent in which a very high shear rate band exists at mid-gap.

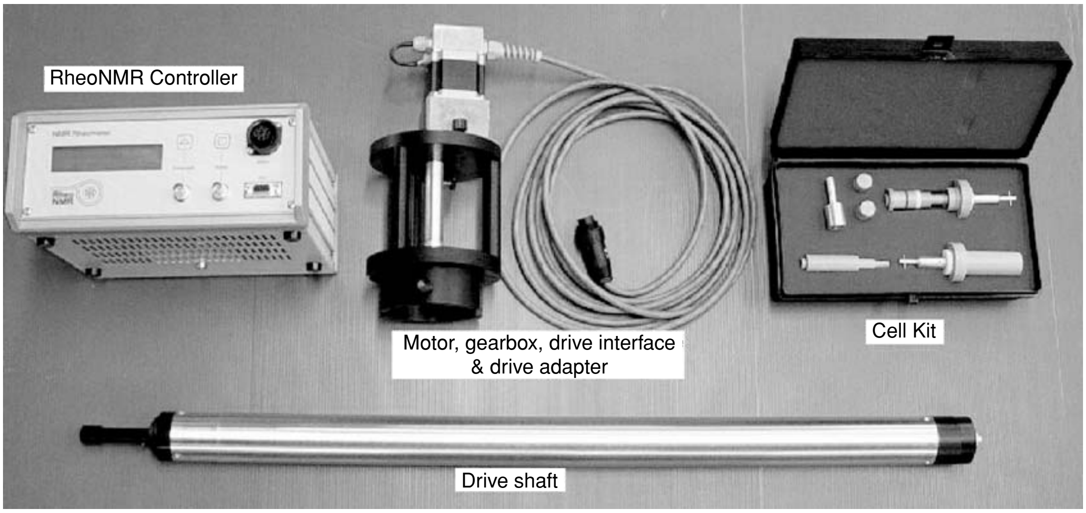

Fig. 2. Set of Rheo-NMR cells and drive attachments for a 89 mm vertical bore NMR magnet (http://www.magritek.com). (See also Plate 44 on page XXXIV in the Color Plate Section.)

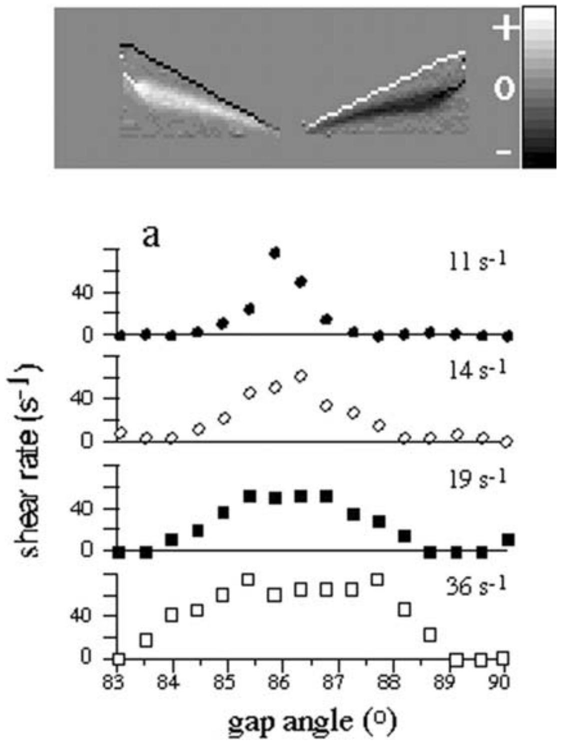

Fig. 3. Shear rate distribution for cetylpyridinium chloride/NaSal wormlike micelle solution at an apparent shear rate of 16 s^{-1}, well beyond the critical shear rate and in an unstable region of the flow curve (horizontal field of view 25 mm with vertical field of view smaller by a factor of 6) Also shown are experimental shear rate profiles along a line of approximately fixed radius (adapted from reference from reference 18).

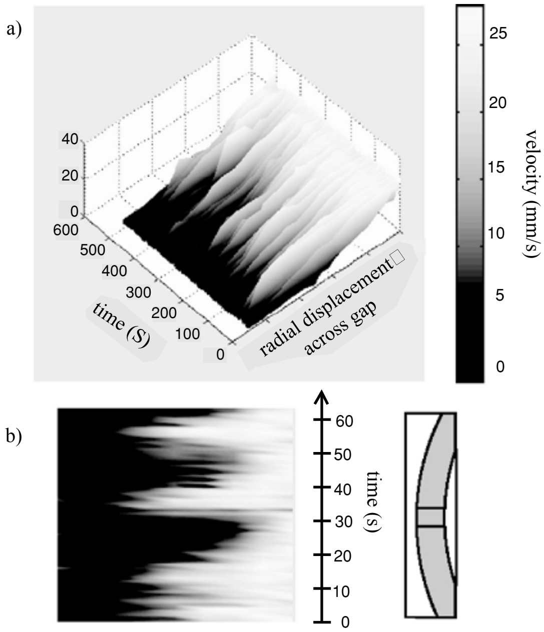

Fig. 4. (See also Plate 45 on page XXXV in the Color Plate Section.)

This shear banding phenomena is believed to arise from an inflected flow curve that includes an unstable branch in which the stress declines with increasing shear rate. The fluid thus "phase separates" onto the upper and lower rising branches of the underlying flow curve and the proportions of each band will be as required to satisfy the average shear rate, in the manner of a lever rule. That the NMR results are consistent with this picture is clear in Figure 3 where a series of profiles show that as the gap apparent shear rate, is increased the high shear rate band expands in width at approximately constant maximum shear rate. More recent work has shown that these bands fluctuate extremely rapidly, as seen in the successive profiles taken, at one second intervals, in the Couette cell geometry of Figure 4 [19]. To achieve this time resolution, a high speed imaging sequence was employed. These NMR results have stimulated new theoretical models for the coupling of flow to micro-scopic molecular order parameters.

Rheo-NMR is also capable of investigating molecular order and alignment [20] through utilising internuclear dipole interactions or nuclear quadrupole interactions. It is through the use of such spectroscopic approaches that Rheo-NMR holds the promise of further linking mechanical and molecular properties. Figure 5 shows the result of a shearing study on a wormlike micelle system (20% CTAB/D_2O at 41 °C) close to an isotropic-nematic transition [21,22]. The D_2O ^2H NMR spectrum, is plotted as a function of radial position across the gap of a cylindrical Couette cell where the magnetic field is aligned with the vorticity axis. At the inner wall, where the stress is highest, a splitting is observed [21], indicative of a finite quadrupole interaction, while at the outer wall a single peak is observed. These data suggest the formation of a nematic phase at high stress and the transition to an isotropic phase, through a mixed phase region, at the region of low stress.

Another intriguing correlation between shearing and molecular conformation concerns a random coil polymer melt being subjected to shear. Here the polymer chain suffers a biaxial deformation in which the principal axis of extension has a preferred orientation with respect to the

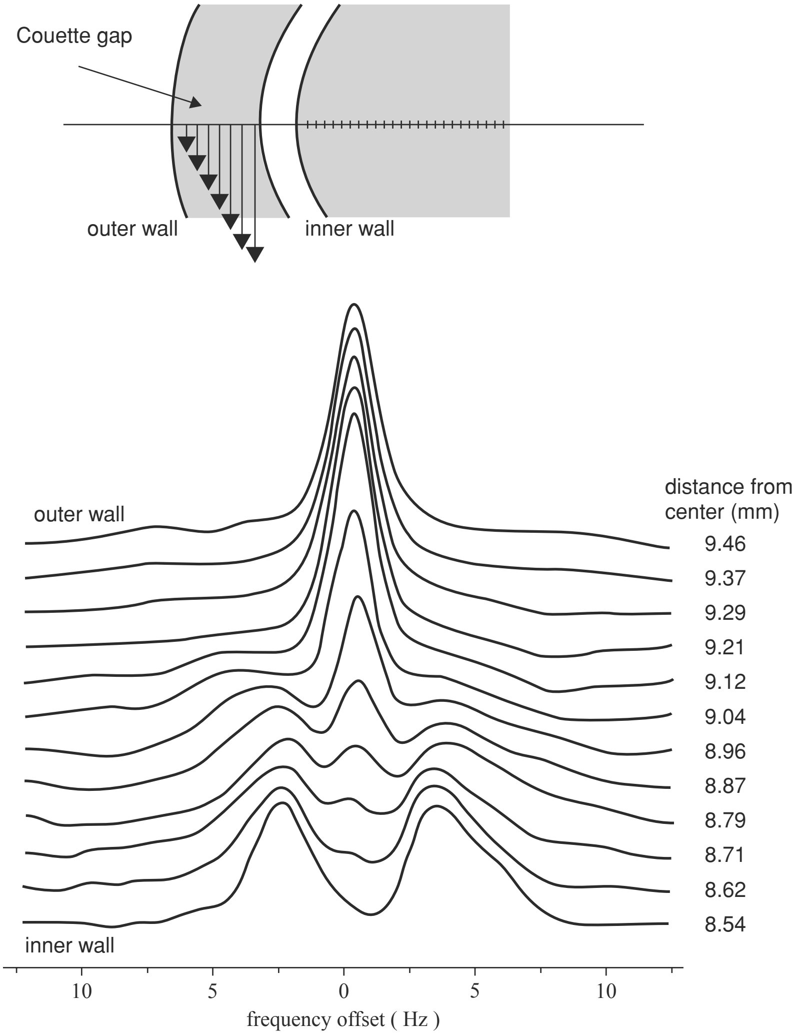

Fig. 5. ^{2}H NMR spectra obtained from 20% w/w CTAB/D_2O (41 °C) at different positions across the annular gap of a cylindrical Couette cell and at an apparent shear rate of 20 s^{-1}. Near the inner wall, where the stress is highest, a quadrupole splitting is observed, consistent with an ordered phase, while near the outer wall the single peak of an isotropic phase is seen. In between a mixed phase region exists (adapted from reference 21).

hydrodynamic velocity direction, the deformation being described by means of an averaged segmental alignment tensor that may be evaluated using the Doi–Edwards formulation of entangled polymer dynamics [8]. Rheo-NMR has been used to obtain elements of the tensor in a high molecular weight polymethylsiloxane melt confined to a Couette cell of 0.5 mm gap [23,24]. In this work a small deuterated benzene probe undergoes steric interactions with the polymer segments and experiences an anisotropic mean orientation. NMR micro-imaging is used to view the PDMS both to image the velocity distribution across the gap and to excite a desired region of the sample for spectroscopy experiments during steady-state shear. The deuteron NMR signal exhibits a scaled down quadrupole splitting proportional to the average value of the selected tensor element. Figure 6 shows the measured alignment tensor elements along with fits using the Doi–Edwards model, which is parameterized by the tube disengage-

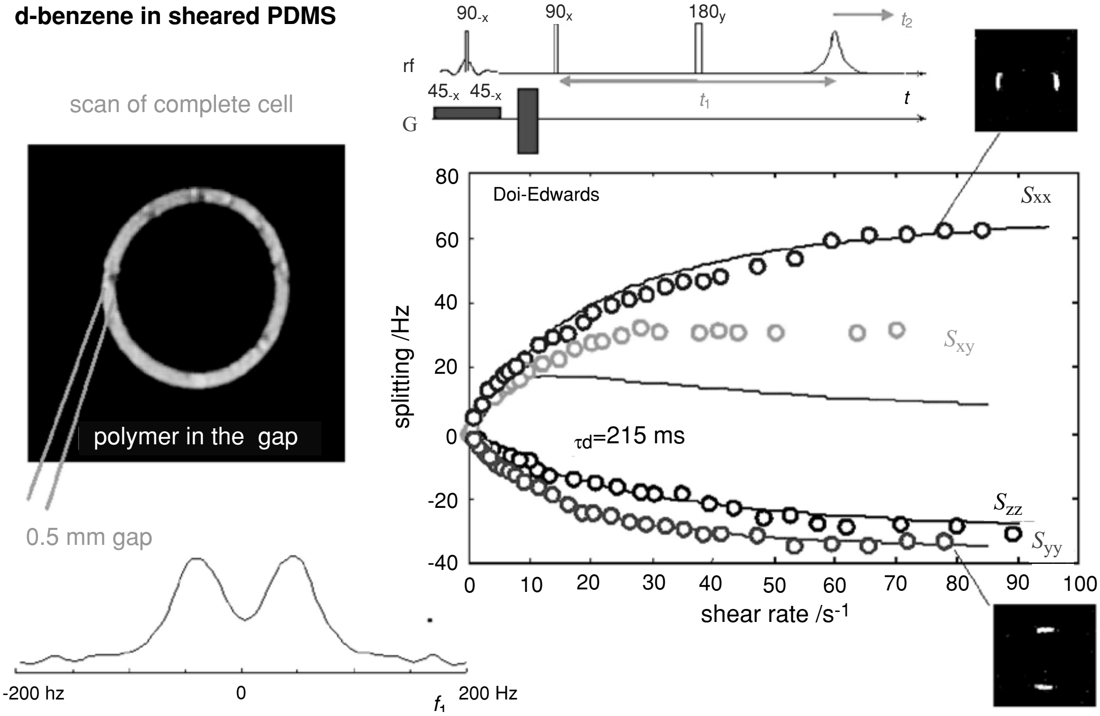

Fig. 6. Quadrupole splittings, $\Delta\nu$, vs. Deborah number, obtained from deuterated benzene in 350 kdalton PDMS, using a selected region of the horizontal Couette cell in which the velocity direction (solid circles) and gradient direction (open circles) are respectively parallel to the magnetic field. The lines are fits using the Doi–Edwards model in which the horizontal axis is scaled to yield the tube disengagement time, τ_d (adapted from ref. [24]). (See also Plate 46 on page XXXV in the Color Plate Section.)

ment time associated with reptation. Also shown are the selected regions in which either the velocity direction or the velocity gradient (shear axis) is parallel to $\mathbf{B}_0$.

These examples provide a glimpse of possible applications of Rheo-NMR. While this is a very new field of research in which only a handful of groups presently participate, the potential exists for a substantial increase in Rheo-NMR research activity. Systems studied to date include polymer melts and semi-dilute solutions, thermotropic and lyotropic liquid crystals and liquid crystalline polymers, micellar solutions, food materials, and colloidal suspensions. The ability to combine velocimetry with localised spectroscopy, and the ability to access a wide range of molecular properties relating to organisation, orientation, and dynamics has enabled Rheo-NMR to provide a direct window on a variety of behaviors, including slip, shear-thinning, shear banding, yield stress behavior, nematic director alignment, and shear-induced mesophase reorganisation. The unique information available with this method suggests that it is likely to become an important tool in elucidating the intriguing rheological behavior of a wide range of complex fluids.

Suggested Reading

1. Barnes HA, Hutton JJ, Walters K. An Introduction to Rheology. Elsevier: Amsterdam, 1989.
2. Fuller GG. Optical Rheometry of Complex Fluids. Clarendon Press: Oxford, 1995.
3. Martins AF, Esnault P, Volino F. Phy. Rev. Lett. 1986;57: 1745.
4. Nakatani AI, Poliks MD, Samulski ET. Macromolecules 1990; 23:2686.
5. Xia Y, Callaghan PT. Macromolecules. 1991;24:4777.
6. Grabowski DA, Schimdt C. Macromolecules 1994;27:2632.
7. Callaghan PT. Rep. on Prog. in Phys. 1999;62:599.
8. Doi M, Edwards SF. The Theory of Polymer Dynamics. Oxford University Press: Oxford 1987.
9. Marrucci G. In: TCB McLeish (Ed.). Theoretical Challenges in the Dynamics of Complex Fluids. Kluwer Press: Dordrect, 1997, pp 141–158.

10. McLeish TCB, Ball R. A molecular approach to the Spurt effect in polymer melt flow. J. Polymer Science 1986;24: 1735–1745.
11. Cates ME, McLeish TCB, Marrucci G. The Rheology of Entangled Polymers at Very High Shear Rates. *Europhys. Lett.* 1993;21:451.
12. Helfand E, Fredrickson GH, Large fluctuations in polymer-solutions under shear. Phys. Rev. Lett. 1989;62: 2468.
13. Durian DJ. Foam mechanics at the bubble scale. Phys. Rev. Lett. 1995;75:4780.
14. Callaghan PT, Principles of Nuclear Magnetic Resonance Microscopy. Oxford University Press: Oxford, 1991.
15. Wassenius H, Callaghan PT, Nanoscale NMR velocimetry. J. Magn. Reson. 2004;169: 250–256.
16. Britton MM, Callaghan PT, Kilfoil ML, Mair RW, Owens K. Applied Mag. Reson. 1998, **15** 287.
17. Lukaschek M, Grabowski DA, Schmidt C Langmuir 1995;11: 3590.
18. Britton MM, Callaghan PT. Phys. Rev. Lett. 1997;78:4930.
19. López-González MR, Photinos P, Holmes WM, Callaghan PT, Phys. Rev. Lett. 2004;93:268302–268305.
20. Siebert H, Grabowski DA, Schmidt C. Rheologica. Acta. 1997;36:618.
21. Fischer E, Callaghan PT. Europhy. Lett. 2000;50:803.
22. Decruppe JP, Cressely R, Makhoufli R, Cappelaere E. Colloid Polym. Sci. 1995;273:346.
23. Kilfoil ML, Callaghan PT, Macromolecules 2000;33:6828.
24. Cormier RJ, Kilfoil ML, Callaghan PT. Phys. Rev. 2001; E6405:1809.

Analytical Aspects of Solid-State NMR Spectroscopy

Cecil Dybowski
Department of Chemistry and Biochemistry, University of Delaware, Newark, Delaware 19716-2522 USA

Introduction

In one sense of the word, every use of nuclear magnetic resonance is analysis, so to discuss analytical aspects of solid-state NMR spectroscopy is to discuss its myriad uses. Clearly, such a general approach is neither feasible nor appropriate in a short article, so one needs to focus the discussion. Roughly speaking, experiments involving NMR spectroscopy belong to one of two classes: (1) those that primarily focus on nuclear magnetic resonance as a process, with the goal of learning about or expanding its utility; and (2) experiments that involve NMR as a tool to address some question about the nature of a chemical or physical system and in which development of NMR technology is of secondary importance. While experiments in the first class may provide new information on samples (usually model materials), it is the latter sort of experiment that I make the theme of this chapter. It is important to emphasize that this dichotomy is not clear, and one must often include experiments on models to understand the nature of analysis with NMR spectroscopy.

Uses of Isotropic Shielding to Identify Materials

A discussion of the analytical aspects of solid-state NMR spectroscopy involves an understanding of what is meant by “analytical.” To many NMR spectroscopists, the word connotes determination of molecular structure by a careful correlation of spectroscopic absorptions with expected functional groups. NMR spectroscopy is an excellent means to determine the details of molecular structure of a pure material by such experiments, whether the material is a solid or is in the liquid state. The long, successful history of organic structural analysis with liquid-state NMR spectroscopy exemplifies this analytical aspect of NMR spectroscopy.

Analyses that specify the nature of functional groups in the solid state demonstrate a similar analytical methodology for addressing questions of molecular structure in the solid state. Of course, the information on molecular structure in the liquid state and the solid state may differ because of physical differences between the solid-state structure and the average structure detected with solution-state NMR spectroscopy. The classical example of this kind of analysis of a solid is found in the application of ^{29}Si MAS NMR spectroscopy to the examination of zeolite structure, exemplified by the work of the Exxon NMR group [1]. The isotropic position of NMR spectroscopic absorption depends strongly on the local environment of the nucleus, which allows one to assign the resonances in the NMR spectrum to specific silicon sites [2]. By examination of a wide variety of materials, it has been shown that the variable that most significantly affects the resonance position is the number of aluminum atoms in the nearby environment. In experiments that account for the effects of relaxation rates on line intensities, it is possible to use the intensities of lines from silicon in various environments to estimate the distribution of silicon in various sites. Such an NMR-derived distribution can then be compared with theoretical predictions of the distribution of silicon in the zeolite framework [3]. The concurrent examination of a zeolite by X-ray diffraction, where possible, and magic-angle spinning (MAS) NMR of a zeolite provides a synergy that often allows one to unambiguously assign structures. These techniques have been used repeatedly over many years to analyze zeolite structure and are a foundation of modern zeolite analysis.

MAS NMR spectroscopy of spin-$\frac{1}{2}$ nuclei in solids is particularly relevant to organic materials. For example, an early application of MAS NMR to poly(phenylene oxide) revealed that in the solid state, the protonated aromatic in the carbon spectrum appears as a doublet, whereas in solution the carbon resonance is a singlet [4]. The explanation of this observation is that, in the solid state, the structure is locked on the NMR timescale, with the result that carbons that are nominally equivalent in solution become inequivalent in the solid state. Observation of such differences between solution- and solid-state spectroscopy points up the fundamental fact that chemical shielding depends on the details of structure, but it also provides an interesting use of solid-state NMR spectroscopy to investigate the existence of structural differences between the solution state and the solid state.

An interesting use of MAS NMR spectroscopy is the application to archaeology. For example, the study of residues on pottery has given information on the nature of materials present on pots [5]. Similarly, the qualities

Graham A. Webb (ed.), Modern Magnetic Resonance, 389–394.
© 2008 *Springer.*

of woods in certain archeological materials may be examined with solid-state NMR spectroscopy [6]. A wide variety of applications in this area can be envisioned in which a determination of the nature of substances resolves some question.

An analytical application of the solid-state NMR technology derived from the sensitivity of the chemical shielding to local structure is the study of polymorphism in solids. Although two solid samples may be chemically identical, i.e. have the same atoms bonded in the same pattern, the constraints of packing in the solid state may produce structures that are different. If these structures result in different physical properties such as dissolution or accessibility, the differences may influence uses of the solid material. The ability to distinguish different polymorphic structures simply is an aid in formulation chemistry that has wide applicability. An example of this effect is seen in the differences in the spectra of solid 2,6-di-tert-butylnaphthalene prepared by recrystallization from ethanol or acetone [7]. The carbon NMR spectra of the aromatic region of these materials clearly show that the two solids are distinct from each other. One area where the identification of polymorphic and pseudopolymorphic structures with NMR spectroscopy is tremendously effective is the analysis of pharmaceuticals [8]. For example, carbon NMR spectroscopy has been used effectively to identify several polymorphic structures of neotame and to specify the conditions under which each may be made.

The fundamental principle behind interpretation of NMR spectra, be they of solids or solutions, is that there is an intimate connection between the local electronic structure and the resonance frequency. Early on, chemists correlated a wide variety of solution-state NMR isotropic chemical shift measurements in empirical rules, such as those given by Grant and Paul [9]. The effects of perturbation of the electronic structure (and thus the chemical shift) by appending groups to a center was given by a rationalized set of effect parameters. With these rules, one could predict with reasonable accuracy the isotropic positions of carbons in different chemical environments. Such rules work reasonably well for analysis of isotropic carbon chemical shifts in solid materials, but there can be discrepancies between solution and solid isotropic values due to differences in local environment, when comparing the solid to a solution of the same material [10]. Thus, using empirical rules based on solution-state NMR data to interpret solid-state data must be done with great care.

A major consideration in determining isotropic chemical shifts in solid-state NMR spectroscopy is referencing. In the solution state, introduction of the reference material into the same solution as the material being analyzed allows a compensation for susceptibility shifts. In the solid state, one almost always uses external referencing to specify chemical shifts. As a result, there is an inherent limit to accuracy of measurement of chemical shifts in the solid state, even though the measurement precision may be higher. There are two means to reference externally: (1) by mixing a small amount of the reference material (as a solid) with the material to be studied and (2) by substitution of a sample of the reference to calibrate the spectrometer, with the assumption that substitution changes none of the parameters of the spectrometer system. By far the most common method is the second method, and practitioners should realize that this method, in particular, does not account for susceptibility differences between the material and the reference, a potential source of systematic error in reporting chemical shifts determined with this method. In addition, for either method, one usually uses a secondary reference standard to make chemical-shift determinations. The two most commonly used reference standards for solid-state ^{13}C NMR spectroscopy are adamantane and hexamethylbenzene. According to Duncan's compilation [11], the positions of the resonances for adamantane are 28.7 and 38.2 ppm relative to the position of an external tetramethylsilane (TMS) sample, and the aromatic resonance of hexamethylbenzene falls at 132.3 ppm relative to external TMS.

Uses of Shielding Tensors to Identify Materials

While the isotropic chemical shielding is a principal parameter for specifying the identity of an unknown material, one of the advantages of analysis of materials in the solid state is the opportunity to observe all the tensor components of chemical shielding. Such additional information may provide a means to distinguish resonances that have identical, or nearly identical, isotropic chemical shieldings. The initial report of proton-enhanced carbon NMR spectroscopy, for example, showed the systematic dependence of the carbon chemical shielding elements of a carbonyl carbon, as exhibited in the powder pattern, on the nature of groups bound to the carbonyl center [12]. A flurry of activity to evaluate chemical-shielding tensors for simple situations resulted in reports of chemical-shielding tensors for carbons, protons, and other nuclei [11].

A particularly interesting example of the use of chemical-shielding tensor analysis to address a problem in solid-state chemistry is a study of the cadmium NMR chemical-shielding tensor elements of $CdSO_4 \cdot 8H_2O$ [13]. For this material, there initially existed an apparent anomaly between the structure gleaned from NMR chemical-shielding anisotropy/Cd–O bond distance relationships and the bond distances determined earlier by more conventional scattering methods. The discrepancy was resolved by a redetermination of the structure that showed that the refined distance data were in agreement with the NMR correlations.

A problem arises with analysis of chemical-shielding tensor elements of a complex material such as a multicarbon organic material: the powder patterns (from which the tensor elements are obtained) of carbons in samples examined without MAS generally overlap. Thus, analysis of powder patterns is generally restricted to materials in which there exist a limited number of unique chemical sites [14]. It is sometimes possible to use techniques like factor analysis to extract the tensor components in overlapping spectra [15].

In samples that contain a limited number of sites, there may be problems with the analysis, if the dispersion of the line is too large. Distortions in the powder-pattern line shape resulting from inadequate or non-uniform excitation, inherent limitations of bandwidth, or the effects of apodization may limit analysis of the chemical-shielding tensor elements directly from the spectrum. There are at least three ways to overcome this problem: (1) determination of a transfer function that predicts the nature of distortions and that is used as a parameter in fitting distorted spectra [14]; (2) determination of the spectrum is a point-by-point fashion [16]; or (3) by determining sections of the resonance line in single experiments, and then assembling the entire powder pattern from the overlap of these sections. Each has advantages and disadvantages, and the method to use depends on the spectral features. For example, to obtain spectra of platinum particles the resonant absorption of which was spread over tenths of a percent of the mean resonance frequency, it was necessary in studies of catalysts to use the second method to obtain a representation of the spectrum [17]. The use of the first method has provided chemical-shielding tensor elements for a variety of simple ^{207}Pb-containing materials [18], and the third method has been used to examine chemical shielding in lead-based oxides [16].

The dispersion of each resonance in the spectrum of a powdered solid material substantially lowers the apparent resolution of the spectrum, as compared to the spectrum of the material dissolved in solution. This loss of resolution was the impetus for the use of MAS as a means to simplify the ^{13}C spectroscopy of solids, mentioned above (MAS spectroscopy represents for many the quintessential solid-state NMR technique). Because spinning of this sort is a coherent modulation of the chemical-shielding interaction, the spectroscopic band is split into a center band and a series of sidebands, separated from the center band by an integral multiple of the spinning frequency. The MAS technique improves the resolution to the point that one may resolve the positions of the center bands, provided one may identify them. To have the spectra be essentially the maps of center bands (and therefore like solution-state spectra) requires one to spin the sample at speeds such that the first sideband is well outside the bandwidth of the dispersion. Since this may be practically difficult, most solid-state spectra exhibit some sidebands. With the development of technology for ever-faster spinning, obtaining center-band maps is much easier than it has previously been, and analysis with the isotropic chemical shifts is now a nearly-routine technique for many nuclear species.

In early work, Herzfeld and Berger demonstrated that an analysis of the relative intensity distribution among the sidebands of a resonance could be used to recover information on the chemical-shielding tensor elements [19]. The techniques involve a careful evaluation of relative intensities, which are then compared to the results of calculations, often presented as maps of relative intensity vs. certain parameters related to the tensor elements. (This can be done in several ways, but a common means is to compare them directly to theoretical maps of expected intensities of several sidebands to specify the values of parameters, from which the tensor elements are determined by a simple algebraic expression.) With this knowledge, it becomes possible to analyze the spectrum of a reasonably complex material containing multiple resonances to obtain both the isotropic chemical-shifts and the components of the chemical-shielding tensors for each site. In later work, several groups have demonstrated various means to create two-dimensional NMR spectra that correlate the isotropic chemical shift with the anisotropic chemical shielding [20,21]. The result of using these kinds of experiments is the availability of chemical-shielding tensor elements for nuclei (particularly carbon) in a wide range of chemical environments.

Using Quadrupolar Coupling to Identify Materials

The presence of the quadrupolar coupling for spins with quantum numbers greater than $\frac{1}{2}$ adds an extra dimension to the analysis of solid materials that contain these nuclei. The line shape for a quadrupolar nucleus is determined by the electric-field gradient at the nuclear site. Like the chemical shielding, the quadrupole coupling constant characterizes the local electronic state. A vast majority of nuclei in the period table have at least one quadrupolar isotope, so determining the quadrupolar coupling is a generally useful analytical tool for identifying chemical type in a host of different situations. The borosilicate glasses are representative of a system in which the study of the quadrupolar coupling can give information on local structure [22,23]. In inorganic systems, such as the Keggin ions, analysis of quadrupolar couplings can be used to analyze the kinds of sites quadrupolar nuclei like vanadium occupy [24]. Zeolites have been extensively studied with quadrupolar NMR spectroscopy, especially the aluminum centers. The studies of the quadrupolar coupling give information on site symmetry and structure [25]. Changes in the quadrupole coupling of aluminum in certain zeolites used as catalysts for reactions such as the conversion of methanol to higher alkyl structures give clues to structural changes in catalyst accompanying adsorption of the substrate [26].

Structure Determination

An analytical measurement of great importance is the determination of physical structure. As seen above, the chemical connectivity can be inferred from the isotropic chemical shielding through its known correlation with chemical group identity. Physical structure is equally important in specifying the nature of materials, e.g. synthetic polymers or biological systems. The classical means to identify physical structure is through diffraction methods with X-rays or neutrons. These methods, however, require single crystals to extract maximal information. Solid-state NMR spectroscopy can be used to define physical structure to a degree, without the creation of single-crystal samples. The structural information is obtained by measurement of dipole–dipole coupling between two nuclear spins, the magnitude of which depends only on the distance between the spins. One may divide the sorts of dipolar-coupling measurements into two types: (1) homonuclear dipolar coupling experiments and (2) heteronuclear dipolar coupling experiments. Depending on how the experiment is run, these are sometimes called recoupling experiments [27]. As an example, selective enrichment of nuclei at points in amyloid fibrils allows the measurement of distances in these systems, an important piece of information in understanding the structures implicated in Alzheimer's disease [28,29]. Combining several dipolar measurements with restrictions from chemical shielding limits the possible structures that, for example, a protein can adopt [30]. The study of structures of many systems, e.g. catalysts [31], can be addressed by these kinds of measurements. One may use the dipole-measurement techniques to determine distance constraints in technologically important systems such as polymer electrolytes [32] or to determine hydrogen-bond distances with great precision [33].

There are ways to address structure in solids that do not directly involve the dipolar coupling to determine distances. For example, knowledge of the orientation of the chemical-shielding tensor in the local molecular frame may be used to determine the orientation in partially oriented samples, as was demonstrated for uniaxial deformation of poly(tetrafluoroethylene) [34]. The orientation distribution function can be discerned for partially ordered samples from other NMR parameters such as the deuterium quadrupolar line shape [35]. By correlating chemical shielding as a function of orientation in a field, one may study biaxial orientation, as has been shown for the carbon resonances of poly(ethylene terephthalate) [36]. Such experiments show the strength of multidimensional techniques in the NMR of solids, in this case to determine orientation quantitatively.

The identification of relations between parameters such as the quadrupolar coupling constant and local structure allows one to infer structural features from measurements of these parameters. An example of this sort of relationship is the connection between the oxygen quadrupolar parameters and the Si–O–Si bond angles in silicates [37]. Another example that shows the utility of measurements of quadrupolar coupling constants involves determining the state of ionic materials, for which the electric-field gradient is a strong indicator of structure [38].

Quantification with Solid-State NMR Spectroscopy

A principal concern of the analyst is determining the amounts of identifiable species in a sample, about which not everything is known. The resolution of a question very often involves measuring with great precision and accuracy tiny amounts of material in a sample. Anyone involved in analytical chemistry receives requests for such determinations and appreciates the difficulty of achieving accuracy and precision at very low levels. For example, the identification and quantification of species in samples of environmental importance is of crucial importance in determining the nature of contamination.

NMR spectroscopy, like other forms of spectroscopy, can—in principle—provide a means to determine the amounts of various species in a sample by careful intensity measurements. However, there are caveats that accompany that statement. It is important to remember that the NMR experiment gives the intensities of the various unique nuclear magnetizations under the conditions of preparation in the experiment. These magnetization intensities may not be proportional to the number of spins in each environment in every experiment.

A simple and obvious example of quantification with NMR spectroscopy is the measurement of relative intensities in solution-state NMR spectroscopy, a principal means of specification of chemical structure. As most NMR spectroscopists know, one must account for effects, such as incomplete relaxation or nuclear overhauser enhancements, to make such experiments relatively quantitative. Even with these precautions, the measurements provide information on the relative amounts of material not absolute amounts. Inclusion of a material of known concentration may be used to determine concentrations of unknown materials absolutely, through ratio to the known material.

The situation in solid-state NMR spectroscopy is more complex than that in solution-state NMR spectroscopy.

Many techniques used in solid-state NMR spectroscopy create magnetization by complex manipulation of spin interactions that do not necessarily affect all spins in the same manner. The quintessential example of this effect is the cross-polarization technique for creating magnetization in rare spins. Because of the different kinetics of polarization transfer, the magnetizations created for various centers may not be in the ratio of the number of nuclei at those centers. In certain cases, one may model NMR processes, from which one produces a relative quantitation of spins [39]. In other cases that are particularly important for organic materials, the magnetization development may be very complex and not fit by simple models, leading to the situation in which it is difficult to quantify rare spins directly [40]. Certain sequences that simplify or enhance spectroscopic features do so by canceling portions of the magnetization (e.g. the part in sidebands in TOSS sequence). Comparison of magnetization amplitudes in this sort of experiment can never be guaranteed to reflect the ratio of numbers of spins in various environments, without invoking some assumption about the nature of the chemical shielding at various sites [41]. Thus, it is often necessary to avoid cross-polarization and other spectroscopic-enhancement techniques to ensure that the signal intensity ratios represent ratios of numbers of spins. So, for example, in measurements to detect ^{13}C in organic solids, it is preferred to measure intensities in spectra obtained with direct excitation, rather than with cross-polarization, to avoid these complications. However, this may be difficult or impossible because of the ^{13}C long relaxation times for pure crystalline solids.

The measurement of relative numbers of spins in various environments may be hampered by certain interactions that make some spins "invisible" in NMR spectroscopy. Such is the case for materials like coal that contain paramagnetic centers [42]. In a complex, heterogeneous substance such as coal, if the paramagnetic centers are clustered in one phase, the NMR spectrum may not adequately represent that phase relative to another, resulting in incorrect quantitation.

There has been a long tradition of using NMR spectroscopy of abundant spins to quantify materials such as polymers but often at low resolution. Because of spin diffusion, differential relaxation of these abundant spins is not necessarily a problem for this spin system. Thus, relative intensities may be used to determine the relative numbers of spins in various environments. For example, it has been shown that multiple-pulse NMR experiments may be used to infer the relative numbers of spins in the amorphous regions of poly(ethylene) [43]. Even in that relatively simple case, it was found necessary to extrapolate intensity ratios on the duty factor of the experiment because that affected the relative intensities of the crystalline and amorphous phases.

Uniform excitation of transitions is a problem when observing quadrupolar nuclei with large coupling constants. In such cases, the spectroscopy often yields only one transition not the full spectrum. Comparison of this spectrum to that from a material with a smaller coupling constant may skew the determination of the amount of material. The multiple-quantum methods for studying quadrupolar nuclei have been promoted in recent years. The study on how to relate signal intensity to concentrations is ongoing [44,45].

The usual NMR determination of relative numbers of spins in a material is not an absolute measurement. To determine the absolute numbers of spins in a sample, one must compare the intensities to a known amount of a standard material. In solution-state NMR, the standard can be frequently added to the solution, which allows easy comparison. For a solid-state measurement, one may add the material as a component of a physical mixture in the sample region, in analogy to the solution-state process. Comparison of intensities, taking into account the ramification discussed above, allows an absolute measurement of number of spins. However, care must be exercised to ensure uniform excitation of all parts of the sample, including the reference.

Summary

NMR spectroscopy is the preeminent technique for determination of many material properties. This was obvious even in the early days of solution-state NMR, a fact that resulted in its relatively quick adoption by chemists. The application of NMR spectrocopy to solids has led to a similar utility for a wider range of solid materials. The analysis may involve identification of species, determination of structure or "sizes" of various interactions, and relative or absolute quantification of species. To analyze a material properly requires a careful consideration of all factors that affect the spectroscopy.

Acknowledgment

The support of the US National Science Foundation through Grant # CHE-0411790 is acknowledged.

References

1. Melchior MT, Vaughan DEW, Jacobson AJ. J. Am. Chem. Soc. 1982;104:4859.
2. Fyfe CA, Gobbi GC, Murphy WJ, Ozubko RS, Slack DA. J. Am. Chem. Soc. 1984;106:4435–8.
3. Engelhardt G, Lohse U, Lippmaa E, Tarmak M, Maegi M. Z. Anorg. Allg. Chem. 1981;482:49.
4. Schaefer J, Stejskal EO, Buchdahl R. Macromolecules. 1977;10:384.

5. Sherriff BL, Tisdale MA, Sayer BG, Schwarz HP, Knyf M. Archaeometry. 1995;37:95.
6. Bardet M, Foray MF, Maron S, Gonclaves P, Tran QK. Carbohydr. Polym. 2004;57:419.
7. Beckmann PA, Burbank KS, Clemo KM, Slonaker EN, Averill K, Dybowski C, Figueroa JS, Glatfelter A, Koch S, Liable-Sands LM, Rheingold AL. J. Chem. Phys. 2000;113:1958.
8. Padden BE, Zell MT, Dong Z, Schroeder SA, Grant DJW, Munson EJ. Anal. Chem. 1999;71:3325.
9. Grant D, Paul E. J. Am. Chem. Soc. 1964;86:2984.
10. VanderHart DL. J. Chem. Phys. 1976;64:830.
11. Duncan TM. A Compilation of Chemical Shift Anisotropies. The Farragut Press: Chicago, 1990.
12. Pines A, Gibby M, Waugh J. J. Chem. Phys. 1973;59:569.
13. Murphy PD, Gerstein BC. J. Am. Chem. Soc. 1981;103:3282.
14. For example, see Neue G, Smith ML, Hepp MA, Perry DL, Dybowski C. Sol. State Nucl. Magn. Reson. 1996;6:241.
15. Kormos D, Waugh J. Anal. Chem. 1983;55:633.
16. Shore J, Zhao P, Prasad S, Huang J, Fitzgerald J. J. Phys. Chem. B. 1999;103:10617.
17. Wang P, Ansermet J, Rudaz S, Sinfelt J, Slichter C. Science. 1986;234:35.
18. For example, see Dybowski C, Neue G. Progr. Nucl. Magn. Reson. Spectrosc. 2002;41:153.
19. Herzfeld J, Berger A. J. Chem. Phys. 1980;73:6021.
20. Maciel G, Bax A, Severenyi N. J. Magn. Reson. 1983;52:147.
21. Alderman D, McGeorge G, Hu J, Pugmire R, Grant D. Mol. Phys. 1998;95:1113.
22. Hansen MR, Madsen GKH, Jakobsen HJ, Skibsted J. J. Phys. Chem. A. 2005;109:1989.
23. Schramm S, Oldfield E. J. Chem. Soc. Chem. Commun. 1982;980.
24. Huang W, Louis LT, Yap GPA, Beer R, Francesconi LC, Polenova T. J. Am. Chem. Soc. 2004;126:11564.
25. Masierak W, Emmler T, Buntkowsky G, Gutsze A. Z. Phys. Chem. 2003;217:1613.
26. Seiler M, Wang W, Hunger M. J. Phys. Chem. B. 2001;105:8143.
27. Schnell I. Progr. Nucl. Magn. Reson. Spectrosc. 2004;45:145.
28. Benzinger TL, Gregory DM, Burkoth T, Miller-Auer H, Lynn DG, Botto RE, Meredith SC. Proc. Natl. Acad. Sci. U. S. A. 1998;95:13407.
29. Balbach J, Ishii Y, Antzutkin ON, Leapman RD, Rizzo NW, Dyda F, Reed J, Tycko R. Biochemistry. 2000;39:13748.
30. Bower PV, Oyler N, Mehta MA, Long JR, Stayton PS, Drobny GP. J. Am. Chem. Soc. 1999;121:8373.
31. Kenaston NP, Bell AT, Reimer JA. J. Phys. Chem. 1994;98:894.
32. Reichert D, Pascui O, Judeinstein P, Gullion T. Chem. Phys. Lett. 2005;402:43.
33. Goward G, Schnell I, Brown SP, Spiess H-W, Kim H-D, Ishida H. Magn. Reson. Chem. 2001;39:S5.
34. Brandolini AJ, Dybowski C. J. Polym. Sci. Polym. Lett. Ed. 1983;21:423.
35. Spiess HW. Pure Appl. Chem. 1985;57:1617.
36. Henrichs PM. Macromolecules. 1987;20:2099.
37. Clark TM, Grandinetti PJ. J. Phys. Condens. Matter 2003;15:S2387.
38. Bureau B, Silly G, Buzare JY, Boulard B, Legein C. J. Phys. Condens. Matter. 2000;12:5775.
39. Maciel GE, Sindorf DW. J. Am. Chem. Soc. 1980;102:7607.
40. Smith JM, Dybowski C, Bai S. Sol. State Nucl. Magn. Reson. 2005;27:149.
41. Duer M. Introduction to Solid-State NMR Spectroscopy. Blackwell: Oxford, 2004.
42. Wind RA, Maciel GE, Botto RE. Adv. Chem. 1993;229:3.
43. Pembleton RG, Wilson RC, Gerstein BC. J. Chem. Phys. 1977;66:5133.
44. Ding S, McDowell CA. Chem. Phys. Lett. 1999;307:215.
45. Gu J, Power WP. Sol. State Nucl. Magn. Reson. 2005;27:192.

^{3}H NMR and Its Application

John R. Jones[1] and Shui-Yu Lu[2]
[1] *Chemistry, School of Biomedical and Molecular Sciences, University of Surrey, Guildford, Surrey GU2 7XH, UK;*
[2] *Molecular Imaging Branch, National Institute of Mental Health, National Institutes of Health,*
10 Center Drive, MSC 1003, Bethesda, MD 20892-1003, USA

Introduction

Radiochemistry (tritium chemistry in particular) and nuclear magnetic resonance (NMR) spectroscopy are hardly ever taught within the same undergraduate degree course. This is one of the main reasons why those who become NMR spectroscopists are so reluctant to see radioactive material being used in their instruments. The main thrust for the development of ^{3}H NMR spectroscopy [1] has therefore come from the radiochemistry area and from those in the pharmaceutical and life sciences who appreciate the potential benefits of working with this radionuclide.

Radiochemical Facilities and Radiation Safety

Ideally, one should have access to two laboratories, one where high levels, i.e. millicurie (mCi, 1 mCi = 37 MBq) quantities, and higher amounts of tritium, can be handled, and the other, less specialized, where the work is confined to the tracer level (mCi down to μCi). The Curie (Ci, 3.7×10^{10} disintegration per second) is the "old" unit of radioactivity and represents a very large amount of radioactivity, hence the frequent use of millicurie and microcurie quantities. On the other hand, the "new" SI unit, the Becquerel (Bq, 1 disintegration per second), is an extremely small amount of radioactivity so that e.g. megabecquerels (MBq), are frequently encountered. In addition, there should be a separate counting room where the scintillation spectrometer(s) are kept.

The synthesis and handling of tritiated compounds should all be done in fume cupboards of the necessary specification. Operations over spill trays ensure that any contamination is limited to a specific area while regular monitoring provides the necessary reassurance. Much preliminary labeling work can be performed using the stable deuterium isotope. Where compounds at very high specific activity e.g. 20 Ci/mmol or more are required, it is necessary to obtain a supply of T_2 gas but rather than use a glass vacuum line, it is better to purchase a commercially available instrument in which the tritium is stored on a uranium bed—on warming the latter sufficient T_2 gas can be released for the proposed experiment and on completion any unused tritium can be taken up by another uranium bed specially kept for this purpose. In this way, all the tritium can be easily accounted for. Purification of tritiated compounds relies heavily on one or more radiochromatographic methods of which radio-HPLC is the most widely used.

Tritiation Procedures

For most, but not all, applications, it is necessary to introduce the tritium at specific sites and for this reason the following reactions are chosen [2,3]:

(a) Catalytic hydrogenation

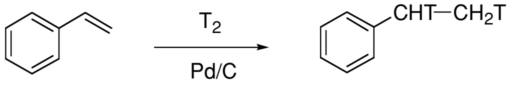

(b) Catalytic aromatic dehalogenation (usually debromination)

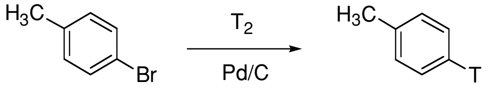

(c) Methylation using ^{3}H-methyl iodide

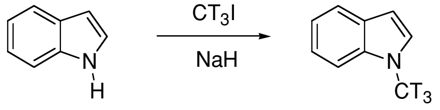

(d) Sodium [^{3}H]borohydride reduction

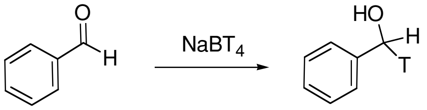

Graham A. Webb (ed.), Modern Magnetic Resonance, 395–398.
© 2008 *Springer.*

In this way compounds of very high specific activity can be prepared e.g. the introduction of two tritium atoms to produce ethyl benzene can give a product with a maximum specific activity of 58 Ci/mmol.

In addition to the above-mentioned reactions, there are a number of others, chief among them being hydrogen isotope exchange reactions that can lead to either specific or generally labeled compounds but at a lower specific activity. The reason for this is that tritiated water is now the source of the tritium and for health and safety reasons it is usually used at the Ci/cm^3 level.

Some of these reactions are slow, requiring many hours to come to completion. Others such as the catalytic aromatic debromination and borohydride reduction are isotopically inefficient, leading to the production of large amounts of radioactive waste (50% in the first example and 75% in the second). Consequently, there has been much interest of late in the development of new, microwave-enhanced procedures [4–6] that proceed much more rapidly (matter of minutes), more efficiently, and with the production of much reduced levels of radioactive waste. In some cases, it is no longer necessary to use a solvent while in others an ionic liquid can be used to replace the more conventional solvent. A good appreciation of how organic compounds interact with microwave irradiation is necessary in order to maximize the benefits of these new procedures [7,8].

Tritium NMR Spectroscopy

Now that a large number of tritiated compounds can be rapidly produced via microwave-enhanced procedures, there is a corresponding need for a fast and sensitive analytical method for determining the pattern of labeling. Tritium possesses ideal NMR properties (Table 1)—it has a nuclear spin of ½ and is the most sensitive of all NMR-active nuclei (21% better than ^{1}H). Unfortunately, NMR spectroscopy by comparison with other analytical methods e.g. mass spectrometry is not a very sensitive method although considerable improvements have been made in recent years through the design of higher performance magnetic fields. This is not an inexpensive exercise and it is fortunate that the most recent improvement, through the development of cryoprobes [9], is much more cost effective although the challenge of keeping the tritiated sample at or close to room temperature while the radiofrequency coils nearby are cooled to below 35 K was a formidable one.

In early studies, a 10 mCi sample of a tritiated compound gave a satisfactory ^{3}H NMR spectrum when using a spectrometer operating at 64 MHz. A more recent example—a spectrometer operating at 533.5 MHz with a cryoprobe accessory—gave a ^{3}H NMR spectrum with as little as 11 μCi (S/N ratio of 21, Figure 1A). In both cases, the accumulation time was overnight. This 1000-fold improvement in sensitivity still leaves one with much higher levels of radioactivity than are used in liquid scintillation counting. Fortunately, the natural abundance of tritium ($<10^{-16}$%) is much lower than that for the stable isotopes ^{2}H (0.0156%) and ^{13}C (1.11%) so that the potential for further improvement in sensitivity is enormous.

Until recently all signal processing relied on, and was restricted by, conventional passive analysis where a signal must be some measurable parameter greater than background in order to be discriminated from background. A new revolutionary process—quantum resonance interferometry [10]—is an example of active signal processing in which new data is derived by interference with the original data. This makes it possible to improve detection sensitivity and so far it has only been applied to gene expression microarrays although its extension to mass spectrometry and NMR spectroscopy has been anticipated.

Whatever the NMR spectrometer, it is always advisable to have a solution of the tritiated compounds in a sealed cylindrical tube which itself is placed in another tube. In this way double containment makes the chance of a breakup and the subsequent contamination most unlikely. The fact that the ^{3}H chemical shifts are virtually the same as the ^{1}H chemical shifts makes in most cases the interpretation of the spectra a straightforward exercise.

With compounds at the mCi mmol^{-1} and lower specific activity, it is customary to produce ^{1}H decoupled spectra so that each labeled site gives a very sharp singlet. It is very rare therefore that overlapping signals cause problems of signal assignment—this is not always the case with the

Table 1: Important properties of tritium and its non-radioactive isotopes

Nucleus	Natural abundance (%)	Nuclear spin	NMR sensitivity	Radioactivity
^{3}H	$<10^{-16}$	½	1.21	weak β^-, $t_{1/2} = 12.3$ years, $E_{max} = 18$ KeV, and maximum specific activity = 29 Ci mmol^{-1}
^{1}H	99.985	½	1	No
^{2}H	0.015	1	9.65×10^{-3}	No

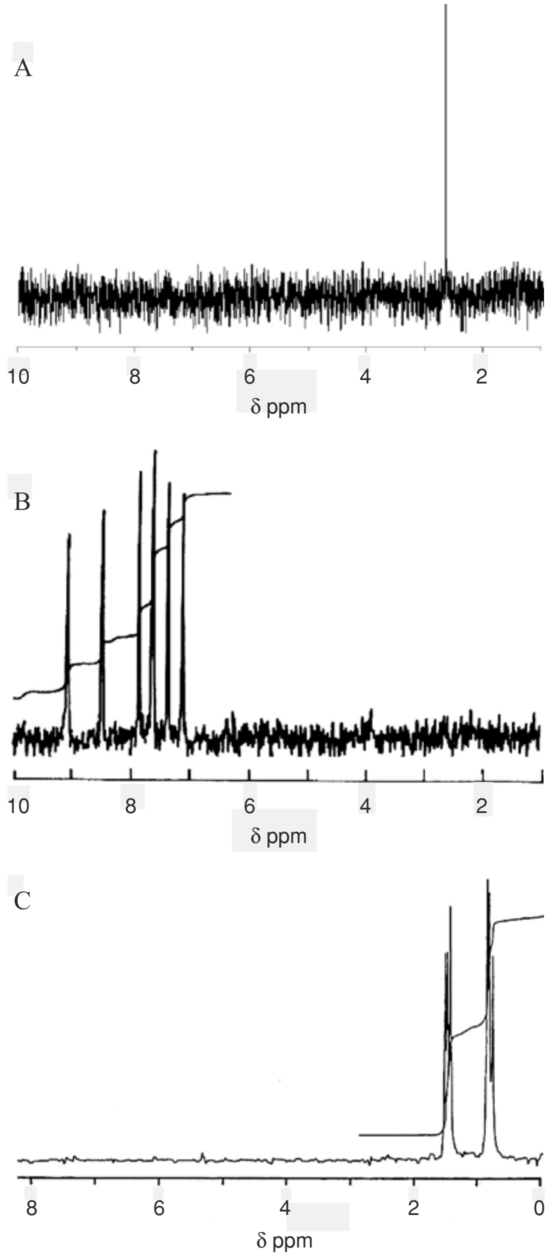

Fig. 1. (A) ^{3}H NMR spectrum (^{1}H decoupled) of tritiated *o*-methoxyacetophenone (*o*-CH_3O-$C_6H_4COCH_2T$, 11 μCi) with a proton/tritium cryoprobe at 533.5 MHz. (B) ^{3}H NMR spectrum (^{1}H decoupled) of [G-^{3}H]quinoline (~10 mCi) at 96 MHz (reproduced with permission by The Royal Society of Chemistry). (C) ^{3}H NMR (^{1}H decoupled) of [^{3}H]dihydroalprenolol showing T–T coupling and multiplicity of isotopomers (reproduced with permission by The Royal Society of Chemistry).

broader ^{2}H NMR signals. It follows therefore that one-step metal-catalyzed procedures that lead to generally labeled compounds are very useful. Figure 1B shows the ^{3}H (^{1}H decoupled) spectrum of [G-^{3}H]-quinoline prepared this way. In the absence of any differential nuclear overhauser effects (usually justified), the integrals give the relative percent tritium incorporated at each site.

Where T_2 gas has been used as, for example, in hydrogenation reactions, there will be characteristic T–T couplings and the spectra will be more complex (Figure 1C). The corollary of this is that, with careful analysis, much useful information can be extracted, e.g. the relative concentration of the various isotopomers can be ascertained. The relative proportion of CT_3, CT_2H, and CH_2T in compounds methylated with tritiated methyl iodide can similarly be calculated.

Applications

Although there are relatively few academic establishments that are set up to carry out tritium-related research, the pharmaceutical industry and the commercial companies that supply tritiated compounds have clearly recognized the importance of the technique and the benefits it bestows. Consequently, its main use has been in confirming that the tritium has been incorporated at the intended site and that if there is tritium at other sites these can be identified and the relative incorporation determined. At the same time, the technique can be used to determine the specific activity of a given compound—particularly useful when the latter has no suitable UV spectrum.

The availability of ^{3}H NMR spectroscopy as an analytical tool has encouraged researchers to look at the possibility of using a wider range of catalysts. Thus, to give but a few examples—$RhCl_3$, Crabtree's catalyst [$Ir(cod)Py(PCy_3)PF_6$], other iridium complexes, and $Ru(PPh_3)_3Cl_6$ have all met with varying degrees of success in the labeling area [11–13]. High temperature solid-state catalytic isotope exchange, as pioneered by Myasoedov and colleagues [14], would have been considerably less attractive but for the availability of ^{3}H NMR spectroscopy. Many of these reactions could benefit from further mechanism studies, as it is only through such investigations that more efficient and selective catalysts will be developed. With further improvements in sensitivity it should be possible, at least for homogeneous reactions, to see the formation of tritiated intermediates along the reaction pathway. This would represent a major advancement.

Improvements in sensitivity would also benefit other areas where so far relatively little use of ^{3}H NMR spectroscopy has been made. One of these is reaction kinetics where multisite T/H exchange and relative rates could provide useful information, e.g. on kinetic acidities [15]. Another area would be in biosynthesis, and in the study of substrate–receptor interactions where again the number of reported investigations is relatively small, despite the self-evident advantages [16,17].

Finally, ^{3}H NMR spectroscopy has been used to study aspects of radiation decomposition [18], isotope effects in chromatographic separations [19], stereochemistry [20], and isotope effects in hydrogen bonding [21].

Conclusions

^{3}H NMR spectroscopy is now a well-established technique that is invaluable for those engaged in tritium-related research. Despite tritium being the most sensitive of all NMR active nuclei the radioactivity required in order to produce ^{3}H NMR spectra of satisfactory S/N ratio is still high (by comparison with liquid scintillation counting for example). Future research directed at improving the sensitivity is likely to be richly rewarded as the range of attractive applications will be greatly expanded. The fact that microwave-enhanced labeling procedures now make it possible to rapidly tritiate so many compounds with much reduced levels of waste will contribute significantly to this process.

References

1. Evans EA, Warrell DC, Elvidge JA, Jones JR. Handbook of Tritium NMR Spectroscopy and Applications. John Wiley & Sons: Chichester, 1985.
2. Elvidge JA, Jones JR (Eds). Isotopes: Essential Chemistry and Applications. The Chemical Society: London, 1980.
3. Evans EA. Tritium and its Compounds, 2nd ed. Butterworth: London, 1974.
4. Jones JR, Lu SY. In: Loupy A (Ed). Microwaves in Organic Synthesis. Wiley-VCH: Weinheim, 2002, p. 435.
5. Elander N, Stone-Elander S. J. Label. Compd. Radiopharm. 2002;45:715.
6. Elander N, Jones JR, Lu SY, Stone-Elander S. Chem. Soc. Rev. 2000;29:239.
7. Loupy A (Ed). Microwaves in Organic Synthesis. Wiley-VCH: Weinheim, 2002.
8. Kappe CO, Stadler A (Ed). Microwaves in Organic and Medicinal Chemistry. Wiley-VCH: Weiheim, 2005.
9. Bloxsidge JP, Garman RN, Gillies DG, Jones JR, Lu SY. In: Dean DC, Filer CN, McCarthy KE (Eds). Synthesis and Applications of Isotopically Labelled Compounds, Vol. 8. John Wiley & Sons: Chichester, 2004, p. 381.
10. Gulati S. Method and system for signal detection in arrayed instrumentation based on quantum resonance interferometry. US Patent 6671625, 2003.
11. Heys JR. Chem. Commun. 1992:680.
12. Hesk D, Das PR, Evans B. J. Label. Compd. Radiopharm. 1995;36:497.
13. Garman RN, Hickey MJ, Kingston LP, McAuley B, Jones JR, Lockley WJS, Mather AN, Wilkinson DJ. J. Label. Compd. Radiopharm. 2005;48:75.
14. Shevchenko VP, Nagaev IY, Myasoedov NF. Usp. Khim. 2003;72:471.
15. Streitwieser A, Xie L, Speers P, Williams PG. Magn. Reson. Chem. 1998;36:S209.
16. Wemmer DE, Williams PG. In: James TL, Oppenheimer NJ (Ed). Methods in Enzymology 239, Nuclear Magnetic Resonance Part C. Academic Press: San Diego, 1994, p. 739.
17. Culf AS, Gerig JT, Williams PG. J. Biomol. NMR. 1997;10: 293.
18. Kaspersen FM, Vader JF, Funke CW, Sperling EMG. J. R. Neth. Chem. Soc. 1993;112:191.
19. Filer CN. J. Label. Compd. Radiopharm. 1999;42:169.
20. Allen BD, Cintrat J-C, Faucher N, Berthault P, Rousseau B, O'Leary DJ. J. Am. Chem. Soc. 2005;127:412.
21. Schilf W, Bloxsidge JP, Jones JR, Lu SY. Magn. Res. Chem. 2004;42:556.

On-line SEC–NMR

Tatsuki Kitayama and Koichi Ute
*Department of Chemistry, Graduate School of Engineering Science, Osaka University,
Toyonaka, Osaka 560–8531, Japan*

On-line Coupling of LC and NMR

On-line coupling of chromatographic systems to spectroscopic techniques, often called a "hyphenated technique" [1], has been proven to be an effective method for the analysis of complicated mixtures. Among such coupled systems, the hyphenation of liquid chromatography with NMR spectroscopy (LC–NMR) is a uniquely powerful and versatile combination, as NMR gives molecular-level structural information, with the advantage over other common LC detectors.

In 1978, Watanabe and Niki reported the first on-line LC–NMR experiment on three isomeric dimethylphenols with a 60 MHz spectrometer in the stop-and-flow mode in which the flow of the mobile phase was halted for the acquisition of NMR spectra [2]. The first continuous-flow LC–NMR experiments were reported by Bayer *et al.* in 1979 [3].

In the mid-1990s a substantial progress has occurred in both the hardware and the software relating to LC–NMR. The following four technical improvements particularly have contributed to the innovation of this method:

1. disadvantage of low sensitivity of NMR as compared with other common LC detectors has been considerably overcome by the advent of ultrahigh-field NMR spectrometers up to 800 MHz for the ^{1}H observing frequency [4];
2. effective techniques of solvent signal suppression using the pulsed field gradient (PFG) and frequency-selective pulses have made non-deuterated solvents accessible for the mobile phase of LC–NMR [5,6];
3. dedicated LC–NMR probes with optimized flow cells have become commercially available;
4. advanced computer technologies have enabled the real-time handling of large LC–NMR data matrices by sophisticated software and operating systems.

A schematic diagram of a typical LC–NMR system is shown in Figure 1. The eluate is directly introduced into the LC–NMR probe via capillary tubing from the outlet of the LC column. The cell has an optimized symmetry and volume (e.g. 60 μl) so as to avoid dispersion effects and to maintain the quality of chromatographic separation. The PFG coils attached to the probe are useful for solvent signal suppression.

On-line SEC–NMR

The applications of LC–NMR cover such fields as pharmaceutical and clinical chemistry, combinatorial chemistry, natural products, and foodstuffs [7–11]. From the viewpoint of polymer characterization [12,13], on-line coupling of NMR spectroscopy with the LC in the size exclusion mode [size exclusion chromatography (SEC) or gel permeation chromatography (GPC)] would be the most straightforward approach. Synthetic polymers are mostly mixtures of macromolecules with dispersion in molecular weight, composition of monomer units, stereoregularity, and so on. Among these structural non-uniformity, molecular weight distribution (MWD) is the most important characteristic of polymers, for which SEC is a facile and widely applicable chromatography [14,15].

The on-line SEC–NMR experiment was first reported by Hatada *et al.* in 1988 [16], in which a flow cell with detection volume of 60 μl (2 mm i.d.) or 140 μl (3 mm i.d.) was equipped on a 500 MHz NMR spectrometer. The experiment demonstrated the direct determination of the number-average molecular weight ($\bar{M}_n$) of isotactic (*it-*) poly(methyl methacrylate) (PMMA, see Equation 1) without a calibration curve [16,17]. A decade later, they reported 750 MHz SEC–NMR experiments on the same objectives [18].

Instrumentation of SEC–NMR

For most organic polymer samples, chloroform-d can be used as an eluent. Ethanol-d_6 is often added as a stabilizer in the amount of ca. 0.5%. The background signals due to the small amounts of impurities in the eluent, except for the water signal, can be eliminated by subtracting the NMR data for the eluent. Non-deuterated solvents containing a small amount of a deuterated solvent for the deuterium lock can also be used as an eluent. In this case the eluent signals should be eliminated by applying WET

Graham A. Webb (ed.), Modern Magnetic Resonance, 399–405.
© 2008 *Springer.*

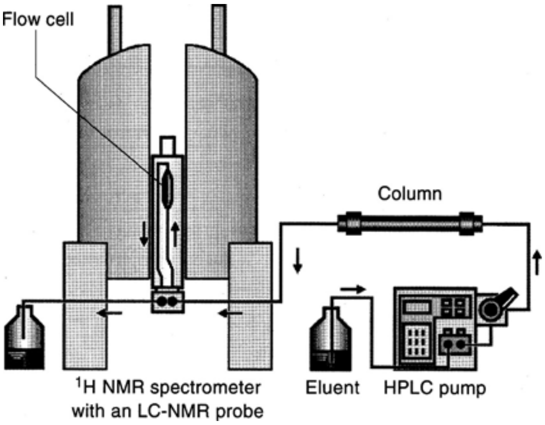

Fig. 1. Schematic diagram of on-line LC–NMR.

(water suppression enhanced through T_1 effects) [19] in combination with the LC–NMR probe with PFG coils.

Typically, the ^{1}H NMR data are collected over the entire chromatographic peak and stored as a consecutive series of n coadded scans. If the repetition time is t seconds, a series of NMR spectra are obtained every nt seconds and thus the time resolution of the chromatogram is nt seconds. In on-line LC–NMR measurements, the NMR spectral quality depends on the flow rate. The effects on the resolution and signal-to-noise (S/N) ratio are summarized in Table 1 as examined for $CHCl_3$ in $CDCl_3$ on a 750 MHz NMR instrument [18]. The resolution of the spectrum is slightly improved as the flow rate increases up to 0.5 ml/min and the broadening is observed at flow rates larger than 0.5 ml/min. The S/N ratio of the resonance decreases gradually with increasing flow rate as the residence time (τ) of the sample within the NMR cell before signal detection decreases. At flow rates larger than 0.5 ml/min, the S/N decreases to about one-fifth that in the non-flow state, mainly due to insufficient premagnetization of the sample. When a 90° pulse is used, the residence time has to be five times longer than the largest T_1 for a quantitative determination. For the signal with T_1 of 0.5 s at the flow rate of 0.5 ml/min, the volume of 0.021 ml has to be located in the front of the detection part of the flow cell.

Table 1: Effects of flow rate on the ^{1}H NMR signal of $CHCl_3$ in $CDCl_3$ (5/95 v/v) measured at 750 MHz using an LC–NMR probe with a 60 µl flow cell[*]

Flow rate (ml/min)	τ[†] (s)	t_{pr}[‡] (s)	$W_{1/2}$[§] (Hz)	W_{s}[¶] (Hz)	S/N[||] (10^4)
0.0	∞	60	0.81	14.3	9.59
0.1	36.0	50	0.81	14.7	9.15
0.2	18.0	25	0.77	14.0	8.42
0.5	7.2	10	0.76	12.7	5.88
1.0	3.6	10	1.18	15.5	1.98
2.0	1.8	10	1.55	17.0	1.76

[*] Pulse width, 90°; acquisition time, 9.7 s; number of transients, 64; spectral width, 6740 Hz; data points, 131, 072; digital resolution, 0.103 Hz; line broadening factor, 0.03 Hz; oversampling factor, 59; temperature, 28 °C.

[†] Residence time [=(detection volume)/(flow rate)].

[‡] Pulse repetition time.

[§] Line width at half height.

[¶] Line width at the height of the ^{13}C satellites.

[||] Signal-to-noise ratio.

When the chromatographic separation of a polymer mixture is insufficient, the post-analysis of SEC–NMR data by the multivariate curve resolution can resolve the individual components and thus enable one to extract each NMR spectrum from the SEC–NMR data set according to intensity profiles [20].

Molecular Weight Determination of Polymers

Determination of molecular weight by SEC requires a calibration curve, which is usually prepared using a set of standard polymer samples with narrow MWD. Quantitative analysis of end groups of a polymer by NMR spectroscopy can provide the $\bar{M}_n$, provided that the chemical structures of the polymer including the end groups is well defined. *it*-PMMAs containing one t-C_4H_9 group at the end of the chain (Equation 1) was analyzed by SEC–NMR and the $\bar{M}_n$ was determined from the relative intensities of the ^{1}H NMR signals due to the t-C_4H_9 and α-CH_3 groups.

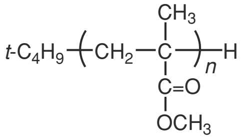

$$t\text{-}C_4H_9\left(CH_2-\underset{\underset{OCH_3}{|}}{\underset{C=O}{|}}\overset{CH_3}{\overset{|}{C}}\right)_n H \tag{1}$$

Figure 2 shows the SEC–NMR data of the *it*-PMMA with $\bar{M}_n$ of 3270. The signals due to the $-OCH_3$, CH_2, α-CH_3, and t-C_4H_9 protons resonate at 3.60, 2.13 and 1.52, 1.20, and 0.86 ppm, respectively. All the cross-sections at the peak positions give ^{1}H NMR-detected SEC chromatograms. The ^{1}H NMR-detected SEC chromatograms from the α-CH_3 signals of the four PMMA samples are shown in Figure 3 together with those recorded using a refractive index (RI) detector. The peak profiles of the ^{1}H NMR-detected and RI-detected chromatograms are very similar to each other. The

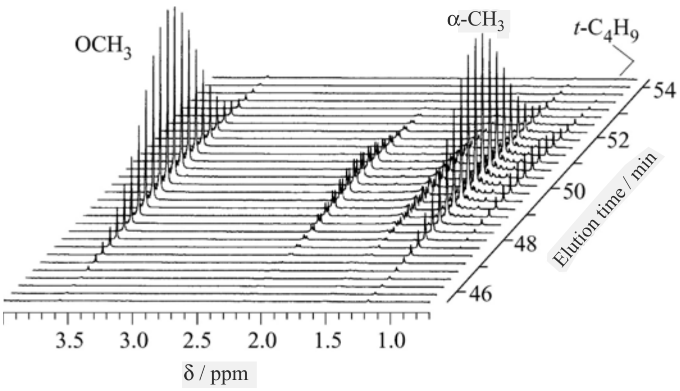

Fig. 2. The 750 MHz on-line SEC–NMR data of isotactic PMMA. ($\bar{M}_n$ from ^{1}H NMR = 3270, sample A in Figure 3) [18]. Eluent CDCl$_3$, flow rate 0.2 ml/min, amount of sample 1.0 mg, pulse width 90°, pulse repetition 2.25 s.

differences in elution times are due to differences in the void volume of the connecting path.

Figure 4 illustrates the ^{1}H NMR spectrum of the PMMA (Sample A) stored as a single file for elution times from 50.1 to 50.4 min (Figure 3) that has S/N ratios large enough to determine the $\bar{M}_\mathrm{n}$ values accurately, the calculated $\bar{M}_\mathrm{n}$ value being 3520. The data files for the tail parts of the chromatogram, which exhibit the t-C$_4$H$_9$ signal with a S/N less than 10, are added with two or three contiguous files so that the S/N exceeds 10. The $\bar{M}_\mathrm{n}$ of each fraction can be determined directly from the respective ^{1}H NMR data so that the $\bar{M}_\mathrm{n}$ and $\bar{M}_\mathrm{w}/\bar{M}_\mathrm{n}$ values for the whole sample are obtained without any calibration as is usually required for SEC analysis.

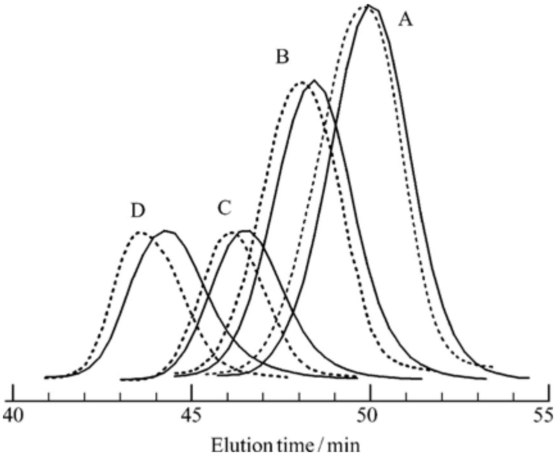

Fig. 3. The ^{1}H NMR- (solid lines) and RI-detected (dotted lines) SEC curves of isotactic PMMAs. The $\bar{M}_n$ values from ^{1}H NMR of samples A, B, C, and D are 3270, 5750, 10160, and 24220, respectively. Amounts of samples A, B, C, and D introduced to the chromatograph were 1.0, 0.8, 0.4, and 0.4 mg, respectively, and the volume of the sample solution was 50 μl [18].

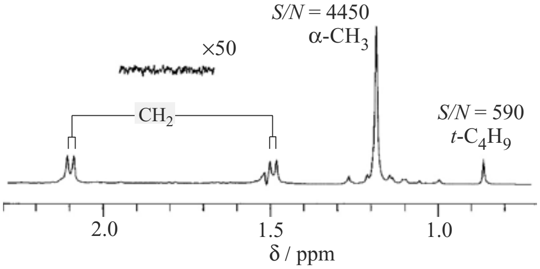

Fig. 4. The ^{1}H NMR spectrum of isotactic PMMA acquired at the elution maximum of sample A (50.1–50.4 min, Figure 3) [18].

When measurements are carried out under appropriate conditions, reliable data on $\bar{M}_n$ and $\bar{M}_w/\bar{M}_n$ can be obtained up to the average degree of polymerization (DP) of about 200 [18]. Molecular weight averages of hydroxyl terminated oligo(ether sulfone)s were determined by the end group analysis. Since the hydrodynamic volumes of oligomeric substances vary considerably with irregular structures such as end groups, the molecular weight calculated by the conventional calibration procedure in SEC may deviate from the true molecular weight [21].

Molecular Weight Dependence of Copolymer Composition

Chemical composition in a copolymer sometimes varies with molecular weight depending on the copolymerization mechanism involved. The on-line SEC–NMR technique is useful for elucidating the molecular

Fig. 5. Molecular weight dependence of comonomer compositions of ethylene-propylene-(2-ethylidene-5-norbornene) terpolymers (EPDM) as determined by SEC–NMR [24].

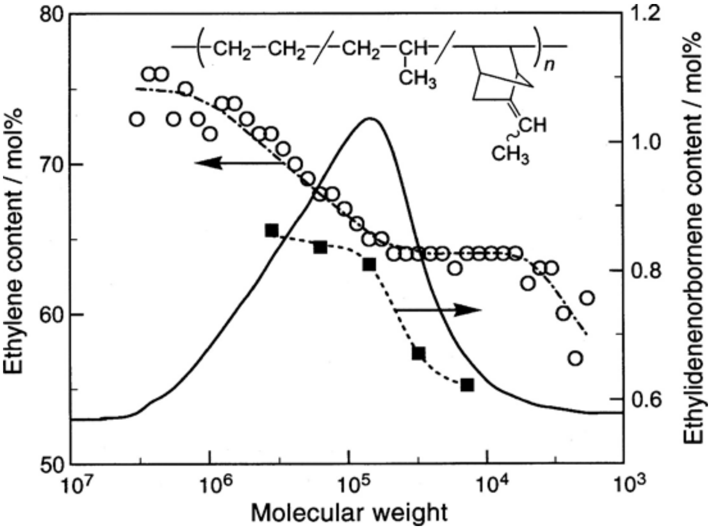

weight dependence of the copolymer composition, the information of which provides us with characteristics of the copolymer itself as well as the polymerization mechanism. Isotactic copolymers of *n*-butyl methacrylate and methyl methacrylate prepared with t-C_4H_9MgBr [22], poly[(acrylic acid)-*co*-(lauryl methacrylate)] [20], poly [(*n*-butyl acrylate)-*co*-styrene] [8], poly[(ethyl acrylate)-*co*-styrene] [23], ethylene-propylene-(2-ethylidene-5-norbornene) terpolymers (EPDM) [24], block-like copolymers of *t*-butyl acrylate and ethyl methacrylate by anionic mechanism [25], partially hydrolyzed poly(vinyl acetate) regarded as a pseudo-copolymer, i.e. poly[(vinyl acetate)-*co*-(vinyl alcohol)] [26]. As far as the NMR measurement conditions are appropriate, the signal intensities of the respective monomeric units in the copolymers provide their molar fractions without any calibration procedure.

As a typical example, the results for the EPDM (Equation 2), industrially important hydrocarbon elastomers, investigated by 750 MHz SEC–NMR is shown in Figure 5. Comparison of the chromatograms obtained by monitoring the CH_2 and CH_3 resonances in the terpolymer sample shows that ethylene/propylene ratio depends on the molecular weight and increases with increasing molecular weight. Molecular weight dependence of small amounts (0.6–1.1 mol%) of 2-ethylidene-5-norbornene units in the terpolymers could not be determined by the typical on-flow SEC–NMR measurement. However, the stop-and-flow measurements allow larger number of accumulations enough to determine the norbornene contents which were found to increase with increasing molecular weight in a typical commercial EPDM having a broad MWD. The *E*/*Z* ratio at C2–C8 double bond in the norbornene unit was constant (72/28) over the whole range of molecular weight [24].

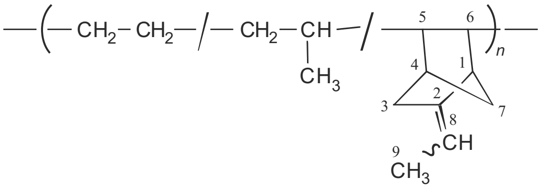

(2)

Molecular Weight Dependence of Tacticity

Stereoregularity (tacticity) of polymers is one of the dominant structural characteristics, which sometimes affects their properties. NMR is uniquely sensitive to tacticity and thus SEC–NMR is applicable for elucidating the molecular weight dependence of tacticity. The information derived from the SEC–NMR analysis of tacticity is often useful for the understanding of the mechanism of stereospecific polymerization [27,28]. Polymerization of MMA with 1,1-diphenylhexyllithium in toluene at $-78\,^\circ C$ gave isotactic-rich PMMA ($mm = 85\%$) with a broad MWD. SEC–NMR analysis revealed that the high-molecular weight part of the PMMA consisted of almost 100% isotactic polymer [27]. Polymerization of MMA with t-C_4H_9Li in toluene at $-78\,^\circ C$ also gave *it*-rich PMMA with a broad but unimodal MWD. Addition of trialkylaluminum to t-C_4H_9Li changes the stereospecificity of the polymerization from isotactic-specific to syndiotactic-specific and the polymerization with

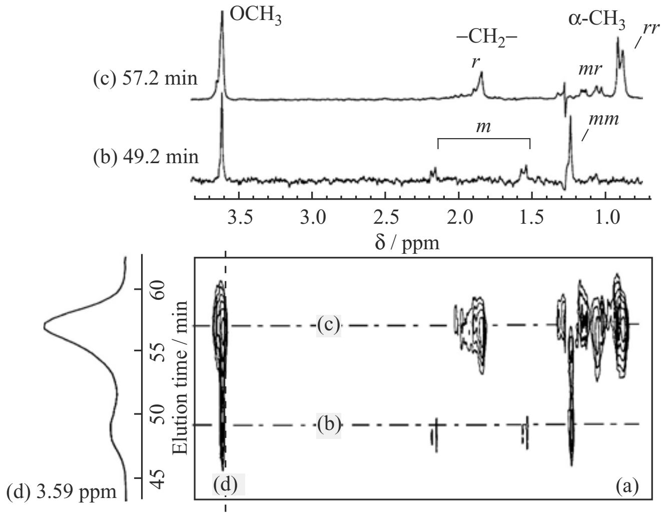

Fig. 6. A contour plot (a) and cross-sections (b–d) of the 500 MHz on-line SEC–NMR data for PMMA prepared with t-C_4H_9Li-(n-C_4H_9)$_3$Al (Al/Li = 1.0) in toluene at − 78°C [22].

t-C_4H_9Li–(n-C_4H_9)$_3$Al (Al/Li ≥ 2) in toluene at −78 °C gives highly *st*-PMMAs [28]. The t-C_4H_9Li–(n-C_4H_9)$_3$Al (Al/Li = 1) system gives a stereoblock-like PMMA in toluene at −78 °C. The contour plot of the SEC–NMR data for this PMMA is shown in Figure 6. The cross-section at the chemical shift of the OCH_3 peak (Figure 6d) indicates the polymer has a bimodal MWD. The cross-sections at elution times of 49.2 and 57.2 min (Figure 6b and c) clearly show that the lower molecular weight part of the polymer is syndiotactic and the higher molecular weight part is isotactic; that is, isotactic- and syndiotactic-specific propagating species exist concomitantly in the polymerization system at the ratio of Al/Li = 1.0.

SEC–NMR of PMMA Stereocomplex

When two kinds of polymer molecules with known molecular sizes form a complex in solution, the size of the complex is expected to be larger than the respective components. If the complex is stable enough to be differentiated by SEC from the component polymers, the SEC–NMR is a good means to gain structural information on the polymer complex.

The PMMA stereocomplex has been known as a unique polymer–polymer complex which forms on mixing *it*- and *st*-PMMAs in certain solvents such as tetrahydrofuran (THF), acetone, benzene, and *N*,*N*-dimethylformamide (DMF). Using uniform *it*-PMMA and *st*-PMMA with discrete DP, formation of the stereocomplex in solution can be observed by using SEC by appreciating the extreme narrowness of the SEC peaks of the uniform PMMAs [29]. The compositions of the associated and dissociated PMMAs, could be obtained by on-line SEC–NMR analysis [30]. Figure 7 illustrates a ^{1}H NMR-detected SEC curve of the mixture of *it*-46mer and *st*-46mer with a blend ratio *st*-/*it*- = 0.61 in acetone/acetone-d_6 (95/5 w/w) at −15 °C. The whole chromatogram is obtained by tracing the OCH_3 signals and the traces for *it*-46mer and the *st*-46mer are derived from the tacticity-sensitive α-CH_3 signals. The detection temperature (the temperature of the flow cell) was adjusted to 45 °C while the SEC column was maintained at −15 °C; when the detection temperature was set at −15 °C, the SEC–NMR spectra of the stereocomplex showed significant broadening of the resonances due to the restricted segmental mobility of the chains.

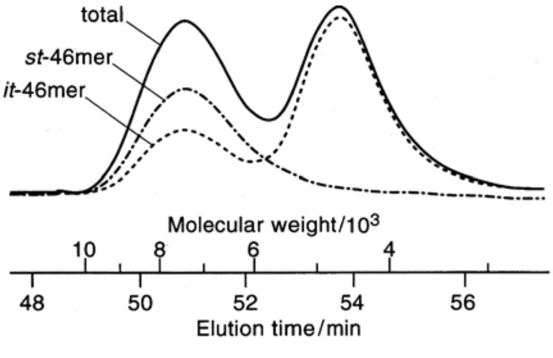

Fig. 7. The ^{1}H NMR-detected SEC curve of the mixture of *it*-46mer and *st*-46mer with a blend ratio *st*-/*it*- = 0.61 in acetone/acetone-d_6 (95/5 w/w) at −15 °C [30].

The *st*-/*it*- compositions of the stereocomplex were determined to be 1.6l–1.94. Accordingly, two types of stereocomplexes with different compositions (e.g. *st*-/*it*- = 1/1 and 2/1) should coexist in the mixtures. Both the complexes with 1/1 ($M = 9326$) and 2/1 ($M = 13{,}989$) compositions were suggested to have the hydrodynamic volumes corresponding to that of *it*-PMMA with $M = 7000$.

LCCAP–NMR

Besides SEC, there are separation modes of liquid chromatography applicable to the polymer characterization by LC–NMR. “Liquid chromatography at the critical adsorption point (LCCAP)” is a chromatographic method where size exclusion effects are balanced by interaction effects [31,32]. To maintain such a critical separation conditions, a mixture of good and poor solvents is usually employed as an eluent for separation at the CAP. Under the CAP, retention becomes independent of the length of the polymer chain and separation is accomplished according to the chemical heterogeneities of polymers, such as end groups [32] and stereoregularity [33,34]. LC–NMR in the interaction mode was used for the detection and identification of styrene oligomers. Information on the chemical structure of the end groups, DP, and the tacticity of the oligostyrene were obtained [35]. A technical poly(ethylene oxide) (PEO) was also analyzed by LC–NMR in the LCCAP mode using a mixture of acetonitrile/D_2O as the eluent. The PEO was separated according to the functional end groups, and the DP and chemical structure were determined [36,37].

If an LCCAP is able to separate a polymer according to the stereoregularity, the application of LCCAP–NMR may afford information on “tacticity distribution” in the polymer, since NMR spectrometer can be a tacticity-sensitive detector. The separation of a model poly(ethyl methacrylate) (PEMA) samples composed of four constituents with similar molecular weight ($\bar{M}_w = 14 - 16 \times 10^3$) and differing in their tacticity (*rr* triad content = 0, 33, 68, and 89%) was achieved by LCCAP with a mixed eluent composed of acetone, acetone-d_6, and cyclohexane at 35 °C. The tacticity composition within each peak eluted from the LCCAP column was determined by the NMR spectrometer in the continuous-flow mode (Figure 8). Highly isotactic, predominantly heterotactic, predominantly syndiotactic, and highly syndiotactic PEMAs were eluted from the column in that order. Tacticity distribution in a particular PEMAsample of narrow MWD ($\bar{M}_w/\bar{M}_n = 1.05$) with a tacticity *mm*/*mr*/*rr* = 2/45/53 has also been revealed by the LCCAP–NMR analysis; *rr* triad content increases from 40 to 70% and *mm* triad content decreases from 20 to 0%. The results suggest the presence of several types of propagating species with similar reactivity but different stereospecificity in the polymerization process. In the LCCAP–NMR experiments, modern solvent suppression techniques are essential, since it requires the use of a mixture of the desired good and poor solvents for the eluent [38].

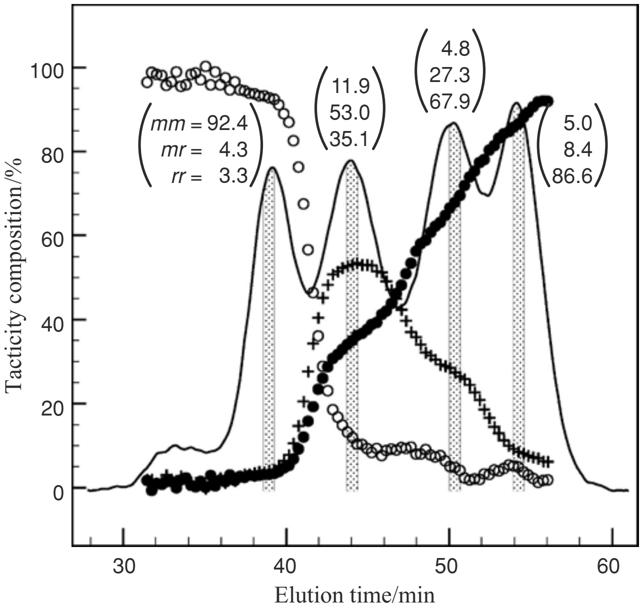

Fig. 8. The ^1H NMR-detected LCCAP trace of the model PEMA sample monitoring the CH_2 in ethoxy ester group. Tacticity compositions (*rr* (●), *mr*(+), and *mm*(○) triad contents) are also shown. Numerical tacticity values are depicted at the top of each peak [38].

References

1. Provder T, Barth HG, Urban MW (Eds). Chromatographic Characterization of Polymers: Hyphenated and Multidimensional Techniques. American Chemical Society: Washington, DC, 1995.
2. Watanabe N, Niki E, Proc. Jpn. Acad. B. 1978;54:194.
3. Bayer E, Albert K, Nieder M, Grom E, Keller T. J. Chromatogr. 1979;186:497.
4. Sidelmann UG, Braumann U, Hormann M, Spraul M, Lindon JC, Nicholson JK, Hansen SH. Anal. Chem. 1997;69:607.
5. Ogg RJ, Kingsley PB, Taylor JS. J. Magn. Reson. B. 1994;104:1.
6. Smallcombe SH, Patt SL, Keifer PA. J. Magn. Reson. A. 1995;117:295.
7. Albert K. J. Chromatogr. A. 1995;703:123.
8. Albert K, Dachtler M, Glaser T, Händel H, Lacker T, Schlotterbeck G, Strohschein S, Tseng L, Braumann U. J. High Resolut. Chromatogr. 1999;22:135.
9. Lindon JC, Nicholson JK, Wilson ID. Adv. Chromatogr. 1996;315.
10. Albert K. On-Line LC–NMR and Related Techniques. John Wiley & Son, Ltd., Chichester, UK, 2002.
11. Korhammer SA, Bernreuther A. Fresenius J. Anal. Chem. 1996;354:131.
12. Hatada K, Kitayama T, Ute K. Ann. Rep. NMR Spectrosc. 1993;26:100.
13. Bovey FA, Mirau PA. NMR of Polymers. Academic Press: San Diego, 1996.
14. Provder T (Ed). Chromatography of Polymers: Characterization by SEC and FFF. American Chemical Society: Washington, DC, 1993.
15. Wu C (Ed). Handbook of Size Exclusion Chromatography. Dekker: New York, 1995.
16. Hatada K, Ute K, Okamoto Y, Imanari M, Fujii N. Polym. Bull. 1988;20:317.
17. Hatada K, Ute K, Kashiyama M, Imanari M. Polym. J. 1990;22:218.
18. Ute K, Niimi R, Hongo S, Hatada K. Polym. J. 1998;30:439.
19. Smallcombe SH, Patt SL, Keifer PA. J. Magn. Reson. A. 1995;117:295.
20. Van Gorken LCM, Hancewicz TM. J. Magn. Reson. 1998; 130:125.
21. Eichhom KJ, Voigt D, Komber H, Pospiech D. Macromol. Symp. 1997;119:325.
22. Hatada K, Ute K, Kitayama T, Yamamoto M, Nishimura T, Kashiyama M. Polym. Bull. 1989;21:489.
23. Kramer I, Pasch H, Händel H, Albert K. Macromol. Chem. Phys. 1999;200:1734.
24. Ute K, Niimi R, Hatada K, Kolbert AC. Int. J. Polym. Anal. Charact. 1999;5:47.
25. Kitayama T, Tabuchi M, Hatada K. Polym. J. 2000;32: 796.
26. Ute K, Hatada K. Anal. Sci. 1991;7:1629.
27. Hatada K, Ute K, Kitayama T, Nishimura T, Fujimoto M, Polym. Bull. 1990;23:549.
28. Kitayama T, Shinozaki T, Sakamoto T, Yamamoto M, Hatada K. Makromol. Chem. (Suppl). 1989;15:167.
29. Ute K, Miyatake N, Osugi Y, Hatada K. Polym. J. 1993;25:1153.
30. Ute K, Niimi R, Matsunaga M, Hatada K, Kitayama T. Macromol. Chem. Phys. 2001;202:081.
31. Belenkii BG, Gankina ES, Tennikov MB, Vilenchik LZ. Dokl. Acad. Nauk USSR. 1976;231:1147.
32. Entelis SG, Evreinov VV, Gorshkov AV. Adv. Polym. Sci. 1986;76:129.
33. Berek D, Jancŏ M, Hatada K, Kitayama T, Fujimoto N. Polym. J. 1997;29:1029.
34. Jancŏ M, Hirano T, Kitayama T, Hatada K. Macromolecules. 2000;33:1710.
35. Pasch H, Hiller W, Hancer R. Polymer. 1998;39:1515.
36. Pasch H, Hiller W. Macromolecules. 1996;29:6556.
37. Schlotterbeck G, Pasch H, Albert K. Polym. Bull. 1997;38:673.
38. Kitayama T, Jancŏ M, Ute K, Niimi R, Hatada K, Berek D. Anal. Chem. 2000;72:1518.

Part I

NOE and Chemical Exchange

The Nuclear Overhauser Effect

Mike P Williamson
Department of Molecular Biology and Biotechnology, University of Sheffield, Sheffield S10 2TN, UK

Introduction

The nuclear Overhauser effect (NOE) is observed as a change in intensity of one resonance when the intensity of a neighboring resonance is perturbed. The effect depends strongly on the internuclear distance r, in that the rate of transmission of the NOE is proportional to r^{-6}. However, various factors conspire to reduce this dependence, making reliable quantitation of distances difficult. Nevertheless, the technique is widely used, particularly in the structure determination of biomolecules and as a routine method for conformational analysis in chemistry. The introduction of new methodology has greatly extended its use for conformational analysis, measurement of intermolecular interactions, and analysis of ligand binding. Thus, although our understanding of the theory of the NOE has not changed much in recent years, the areas of application continue to increase.

Theoretical Background

Only a brief presentation of NOE theory can be made here. A complete account of NOE theory is presented in a monograph [1], and an excellent simpler version is also available [2].

The NOE is caused by relaxation of one nuclear spin by a neighboring spin. To understand the basics of the NOE, we only need to consider two spins. In a system consisting of two NMR-active nuclei, I and S, the equilibrium magnetizations of I and S are given by I_z^0 and S_z^0, the z signifying that at equilibrium the only magnetization present is along the z-axis. The size of the z magnetization (for a spin$-1/2$ nucleus, which is the only type of spin we shall consider here) is proportional to the difference in population between the two energy levels α and β. If the z magnetization of spin S is perturbed, for example by selective saturation, or by inversion (either by a 180° pulse or by some 2D sequence), then it will subsequently return to equilibrium by relaxation processes, where *relaxation* means any process that causes exchange of a spin state between α and β. The essence of the NOE is that relaxation of S toward equilibrium can also involve I, if the two are close enough together, leading to perturbation of the populations of I and hence a change in intensity, and thus an NOE at I arising from the initial perturbation of S. This effect then allows us to detect or measure the short distance between I and S.

The reason for this is that *spontaneous* relaxation is extremely slow. The main way in which a spin can undergo a transition from one spin state to another is if that transition is *stimulated*, usually by a change in the magnetic field strength at the nucleus, which must be happening at a rate that matches the frequency of the transition. In our simple two-spin system, there are four possible energy states and six possible transitions between them (Figure 1). The transition between $\beta\beta$ and $\beta\alpha$ is a transition of spin S (hence its descriptor in Figure 1 as W_{1S}), and the energy difference between the two states (i.e. the frequency of the transition) corresponds to the frequency of spin S, for example, approximately 500 MHz for ^{1}H in an 11.7 T field. This transition is stimulated by changes in magnetic field strength at nucleus S occurring at a rate of 500 MHz. The main source of magnetic field variation at S in our simple two-spin molecule is actually spin I, and the main way in which the field can change is by a rotation of the molecule containing I and S. Thus, transition W_{1S} is stimulated by molecular tumbling at a rate of 500 MHz. This mechanism is normally referred to as *dipolar relaxation*, because it is relaxation of S by the magnetic dipole of I. This transition has no effect on the intensity of I, so does not produce an NOE. Dipolar relaxation gets weaker as the distance between I and S increases, at a rate proportional to r^{-6}.

Relaxation of S can occur by two other routes, shown on Figure 1 as W_0 and W_2. These involve the spin states of I and S changing simultaneously. W_0 involves a change between $\beta\alpha$ and $\alpha\beta$, and is often described as a "flip-flop" transition, in which the two spins I and S exchange energy. The frequency of this transition is the difference in chemical shift between I and S, so for a homonuclear system it is at most a few kHz. By contrast, W_2 involves both spins flipping together in the same direction, and its frequency is the "double quantum" frequency of 1000 MHz.

At equilibrium, the population of $\beta\beta$ is less than that of $\alpha\beta$ and the population of $\beta\alpha$ is less than that of $\alpha\alpha$. Saturation of S implies equalization of the populations of $\beta\beta$ and $\beta\alpha$, and also of $\alpha\beta$ and $\alpha\alpha$. Relaxation of S

Graham A. Webb (ed.), Modern Magnetic Resonance, 409–412.
© 2008 *Springer.*

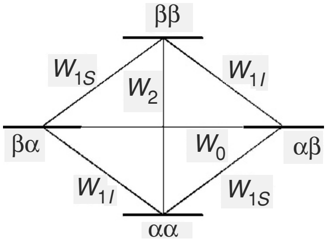

Fig. 1. Energy levels and transitions of a two-spin system. Each spin can be in spin state α or β. The total spin state is described by listing the state of I first and then S, so, for example, state $\alpha\beta$ is the state in which I is in α and S is in β.

by W_0 acts to restore S magnetization toward the equilibrium position, and thus takes spins out of $\beta\alpha$ and puts them into $\alpha\beta$. The effect of this on I is to reduce the population difference across the I transitions, and hence reduce the intensity of I. In other words, the W_0 process means that saturation of S causes a loss in intensity of I. By similar reasoning, it is easy to show that the W_2 process causes an *increase* in intensity of I. The rate of the net intensity change of I (the *cross-relaxation rate*, often given the symbol σ) is thus proportional to $(W_2 - W_0)$, and depends on how fast the molecule is tumbling in solution. If the molecule is tumbling very fast, then W_2 is more efficient than W_0, and the intensity of I increases (a positive NOE). If the molecule is tumbling very slowly, then W_0 is more efficient, and the intensity of I decreases (a negative NOE). The size of the homonuclear NOE in a two-spin system is shown in Figure 2 as a function of $\omega\tau_c$ (where ω is the spectrometer frequency expressed in rad/s and τ_c is the correlation time—the time it takes for the molecule to rotate through 1 rad), and is seen to go through zero at approximately $\omega\tau_c = 1$. This means that for small molecules the homonuclear NOE is positive, while for big molecules it is negative.

The NOE in Multi-Spin Systems

Real molecules have more than two spins. Fortunately, almost all relaxation processes only involve pairs of spins; processes involving three spins are called cross-correlation processes and can usually be ignored. This means that we can understand what happens in real molecules by a simple extension of the two-spin case. Perturbation of S leads to an effect on the intensity of I; in turn this leads to an effect on Is neighbors. Therefore, NOEs can propagate throughout the molecule. This has several consequences. In *large* molecules, the homonuclear steady-state NOE is -1 (Figure 2), meaning that saturation of S leads to complete saturation of I also. This in turn passes its saturation on to other spins in a process known as *spin diffusion*. The consequence is that all nuclei in the molecule eventually become saturated, and the steady-state experiment is uninformative. Consequently, all NOE experiments in large molecules (e.g. proteins) are carried out as transient experiments, usually by versions of the 2D NOESY experiment.

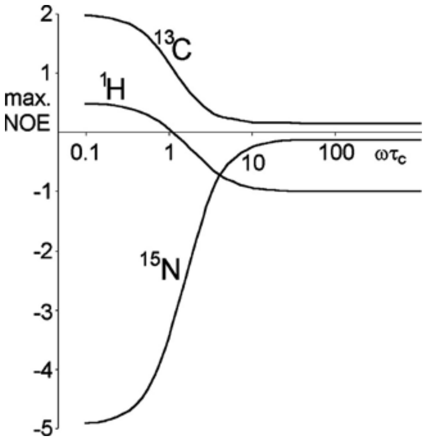

Fig. 2. The dependence of NOE intensity on $\omega\tau_c$ for an ideal two-spin system following steady-state saturation of S. The zero crossing point for homonuclear NOEs is at $\omega\tau_c = 1.12$. The curves are shown for X{^{1}H} with X = ^{1}H (homonuclear NOE), ^{13}C and ^{15}N. The curve for ^{19}F is very similar to that for ^{1}H, because of the similarity in their gyromagnetic ratios.

In small molecules, saturation of S leads to an increase in the intensity of I, with a maximum of $+50\%$, though in practice it is usually much smaller than this. An increase in I is passed on to its neighbors as a decrease in their intensity. Thus, in small molecules multi-spin effects lead to alternations in the sign of the NOE along a chain. In practice the effect is not observed for more than three spins in a row. It is therefore possible to carry out steady-state NOE experiments on small molecules, and the effects are approximately related to distance. However, calculation of sizes of NOEs requires detailed knowledge of geometries (and usually of dynamics as well), and steady-state NOEs are not (and should not be) normally interpreted in more than a qualitative manner. Nevertheless, they are extremely useful for the assignment of geometries around double bonds, and for stereochemical assignments, particularly in rigid systems such as fused ring systems. NOEs have in the past been much used to connect molecular fragments together in natural product identification. However, with the advent of heteronuclear correlation experiments such as HMBC, most problems of this type can now be addressed more simply, leaving only a few stereochemical details to be addressed by specific NOE experiments [3].

Although exact calculation of steady-state NOEs in multi-spin systems is generally not worthwhile, a few guidelines are useful for their interpretation. Protons that are very close together (for example, methyl and methylene protons) relax each other very efficiently. This means that NOEs *into* such groups are usually small. (The NOEs are small on a fractional basis. In absolute terms, an NOE to a methyl group can still be easily observed because there are three protons in a methyl group, and because the signal is often sharp.) NOEs to isolated protons can often be misleadingly large.

Time Dependence of the NOE

For the reasons given above, NOE experiments in large molecules are always done as transient (2D) experiments. In a transient experiment, the NOE first builds up (at the cross-relaxation rate), and then decays away, at roughly the spin–lattice relaxation rate ($1/T_1$). As the size of the molecule increases, the cross-relaxation rate increases proportionately (except of course for a hiatus around $\omega\tau_c \approx 1$, where the NOE goes from positive to negative), and so (approximately) does the decay rate. Thus for proteins, the transient NOE reaches its maximum at around 300 ms, and NOESY experiments are often carried out using NOE mixing times of 50–100 ms. By contrast, for small molecules, the NOE maximum can occur at several seconds. One consequence of this is that in experiments with proteins, one does not need to be too concerned about unwanted sources of relaxation. By contrast, with small molecules it is very helpful to remove things that can cause unwanted relaxation, because these can seriously reduce the size of NOE observed. In particular, it is common practice to take care to remove paramagnetic impurities such as metal ions (using chelating agents) and oxygen (by bubbling through with nitrogen or argon, or by repeated freeze–thaw cycles).

The big advantage of transient experiments is that quantitative distance measurement is much simpler. An unknown distance r_{IS} can be estimated from the intensity of the transient NOE $f_I\{S\}$ using a known reference distance r_{ref} and reference NOE f_{ref} using the simple equation

$$r_{IS} = r_{\text{ref}}\left[\frac{f_I\{S\}}{f_{\text{ref}}}\right]^{-1/6}$$

This equation is only valid for short buildup times (typically $\leq$100 ms for proteins and $\leq$0.5 s for organic molecules), when spin diffusion is insignificant. It is also only valid if the molecule tumbles rigidly and isotropically. Real molecules do neither, and although one can calculate the effect of internal motion and anisotropic tumbling, this usually requires motional details that are not experimentally accessible. For these reasons, it is always sensible to allow some margin of error in the application of this formula.

Heteronuclear NOE

The NOE can be observed between heteronuclei. Like the homonuclear NOE, it has a strong dependence on $\omega\tau_c$, as shown in Figure 2. The size of the NOE depends on the gyromagnetic ratios of the two nuclei concerned: the NOE at I on saturation of S is proportional to the ratio γ_S/γ_I. Because the gyromagnetic ratio of ^{1}H is higher than any other except ^{3}H, this means that an X{^{1}H} NOE (i.e. observation of an NOE on X after saturation of ^{1}H) is usually much larger than a ^{1}H{X} NOE (Figure 2), and can be a valuable way of increasing the intensity of the signal from X. This means that for example ^{13}C spectra of organic molecules acquired using ^{1}H decoupling often contain large NOEs of up to a factor of 2, which are, however, non-uniform across the molecule because protonated carbons receive a larger NOE than non-protonated carbons, because of their shorter distance to protons.

NOEs involving ^{15}N are interesting because the ^{15}N gyromagnetic ratio is negative, meaning that ^{15}N NOEs are always negative (Figure 2). They are also of interest because they are used extensively in studies of dynamics in proteins. Relaxation of ^{15}N in ^{15}N-labeled proteins is dominated by the attached ^{1}H, which is at a fixed distance and therefore allows measurement of the extent of local motion, as well as the overall correlation time [4].

Applications of the NOE

Quantitatively the biggest use of the NOE is in determining the structures of biomolecules. A typical protein structure determination requires the assignment and quantitation of approximately 2000 NOEs. This is usually done from 3D and sometimes 4D heteronuclear-edited NOESY spectra, and increasingly the picking of peaks and their assignment is done automatically, with increasingly sophisticated algorithms to account for (and usually spot and eliminate) the inevitable wrong assignments and consequential structural distortions [5]. NOEs are often sorted into three categories (strong, medium, and weak, corresponding to distances, for example, of <2.5 Å, <3.5 Å, and <5 Å, respectively), because of the many ways in which the relationship between NOE intensity and distance can be distorted, of which the principal ones are spin diffusion and peak overlap.

The other common use is to aid structure determination in organic molecules. Here the most common technique is a steady-state experiment (or more commonly a pseudo-steady-state experiment, in which the presaturation period is limited to 1–2 s, to speed up the experiment without significant loss of information), though the simplicity of setting up and interpreting 2D NOESY experiments has made this a popular experiment here too. For molecules of intermediate size, the NOE goes through zero (Figure 2), and an alternative experiment is used, ROESY, which does not go through zero [1].

In recent years, the DPFGSE-NOE experiment has become deservedly popular [6]. This is a 1D transient experiment, which achieves both selective saturation of the target spin and very clean removal of artifacts by use of gradient pulses. It is simple to use once set up and is becoming the method of choice for rapid measurement of selective and transient NOEs in organic molecules [3].

An increasingly popular application of the NOE is to detect intermolecular association, for which it is quick and unambiguous, and can often give details about the orientation of complexes [2]. It has had wide application for elucidating the structures of metal complexes [7,8]. Quantitative determinations are difficult because of problems in knowing the intermolecular correlation time, and because of conformational averaging, but elegant structural results have been obtained, particularly with the use of heteronuclear NOEs such as the heteronuclear 2D ^{1}H–^{19}F NOESY experiment, HOESY. Similar experiments have also been done to study site-specific solvation [9].

The NOE has been used for many years for studying the conformation of ligands when bound to macromolecular receptors, using an experiment known as the transferred NOE (trNOE). This is based on the idea that NOE buildup in a complex is much faster than in the free ligand. Hence, a NOESY spectrum of a ligand that is in excess over its receptor and in fast exchange will be dominated by NOEs arising from the bound state. Further discussion of the trNOE can be found elsewhere in this Handbook [10]. A number of related experiments are now appearing and promise to be extremely useful in drug design. Two are worth mentioning here. The first is known as saturation transfer difference (STD), and involves saturation of the receptor. Spin diffusion spreads the saturation over the receptor and onto any ligand that is bound to it. Subsequent exchange of the ligand into the free state gives rise to partial saturation of the free ligand, and thus identifies molecules that bind to the receptor [11]. The second is designed to detect whether two ligands bind to the same site, and if so to determine their relative orientations. Ligand A binds to the receptor, and gives rise to NOEs from ligand to receptor. If this ligand then dissociates, and ligand B binds in the same site, NOEs build up between receptor and ligand. The net result is an apparent NOE between ligand A and ligand B, not only demonstrating that they bind to the same site, but also providing their relative orientation [12].

References

1. Neuhaus D, Williamson MP. The Nuclear Overhauser Effect in Structural and Conformational Analysis. Wiley-VCH: New York, 2000.
2. Mo HP, Pochapsky TC. Prog. Nucl. Magn. Reson. Spectrosc. 1997;30:1–38.
3. Edwards DJ, Marquez BL, Nogle LM, McPhail K, Goeger DE, Roberts MA, Gerwick WH. Chem. Biol. 2004;11:817–33.
4. Clore GM, Szabo A, Bax A, Kay LE, Driscoll PC, Gronenborn AM. J. Am. Chem. Soc. 1990;112:4989–91.
5. Guntert P. Prog. Nucl. Magn. Reson. Spectrosc. 2003;43: 105–25.
6. Stott K, Stonehouse J, Keeler J, Hwang TL, Shaka AJ. J. Am. Chem. Soc. 1995;117:4199–200.
7. Macchioni A. Eur. J. Inorg. Chem. 2003;195–205.
8. Pregosin PS, Martinez-Viviente E, Kumar PGA. Dalton Trans. 2003;4007–14.
9. Angulo M, Hawat C, Hofmann HJ, Berger S. Org. Biomol. Chem. 2003;1:1049–52.
10. Williamson MP. The transferred NOE. In: Pharmaceutical Science (Ed.) Craik D.
11. Stockman BJ, Dalvit C. Prog. Nucl. Magn. Reson. Spectrosc. 2002;41:187–231.
12. Sánchez-Pedregal VM, Reese M, Meiler J, Blommers MJJ, Griesinger C, Carlomagno T. Angew. Chem. Int. Ed. 2005;44: 4172–5.

Solute–Solvent Interactions Examined by the Nuclear Overhauser Effect

J.T. Gerig

Department of Chemistry and Biochemistry, University of California, Santa Barbara, CA 93106, USA

Background

The nuclear Overhauser effect (NOE) can be defined as the change in the observed intensity of a NMR signal that results when the magnetization associated with another spin is perturbed [1]. The NOE is a consequence of the nuclear spin–nuclear spin dipole–dipole interactions that contribute to spin-lattice (T_1) relaxation. Measured NOEs are typically of the order of a few percent or less but are readily determined with modern instrumentation.

Spin-lattice relaxation is due to the presence of local magnetic fields that fluctuate at frequencies at or near the Larmor frequency of the spins undergoing relaxation. The major sources of these local fields are other spins of the sample. The interactions of nuclear spin dipoles follow essentially the same physics as a set of small bar magnets; it is the relative motion of the magnets that lead to relaxation. A quantitative understanding of the dipole–dipole interaction requires a description of both the spatial aspects of the interaction and the molecular motions that modulate the interaction [2].

Intramolecular NOEs

When two interacting spin dipoles A and B, both assumed to be spin 1/2 nuclei here, are contained in the same molecule, their mutual interaction is changed by the reorientation of the molecule that holds them. It is common to imagine that spin A is at the center of a sphere of radius r_{AB}, the distance between the two spins. Spin B "skates" on the surface of the sphere as the sphere reorients in solution, changing the orientation of the A–B internuclear vector. It is often assumed that reorientation is governed by the hydrodynamics of a sphere supported in a medium that has viscosity η. The reorientation of the molecule is then described in terms of a rotational correlation time τ_R which is approximately the time required for the molecule to rotate in any direction through an angle of about 1 rad [3]. The rotational correlation time in this model is related to molecular size:

$$\tau_R = \frac{\eta V_M}{kT}$$

where V_M is the molecular volume ($= 4\pi r^3/3$ for a sphere), k is Boltzmann's constant, and T is the temperature. Typical values of τ_R for small molecules are 1–100 ps. For macromolecules of a size that can be studied by high-resolution solution NMR experiments, τ_R typically lies between 0.1 and 10 ns.

The experimental intramolecular NOE for a pair of interacting spins depends on the cross-relaxation rate σ_{AB}, given by

$$\sigma_{AB} = \frac{\gamma_A^2 \gamma_B^2 \hbar^2}{10 r_{AB}^6} \left(\frac{6\tau_R}{\left(1 + (\omega_A + \omega_B)^2 \tau_R^2\right)} - \frac{\tau_R}{\left(1 + (\omega_A - \omega_B)^2 \tau_R^2\right)} \right) \qquad (1)$$

where r_{AB} is the distance between A and B, γ_A and γ_B are the gyromagnetic ratios of the spins, ω_A and ω_B are the corresponding Larmor frequencies, and $\hbar$ is Planck's constant divided by 2π. The strong dependence on internuclear distance in Equation (1) is important: only neighboring spins (those for which $r_{AB} \sim 2 - 5$Å) contribute appreciably to σ_{AB}. Another aspect of Equation (1) to be noticed is that the value of σ_{AB} can be negative, zero or positive depending on the values for ω_A, ω_B and τ_R. (When experimental conditions conspire to make σ_{AB} near zero, the rotating frame Overhauser experiment (ROE) can be useful [4].) Intramolecular NOE experiments basically involve evaluation of σ_{AB}. Because σ_{AB} is dependent on internuclear distances, evaluation of σ_{AB} plays an essential role in determination of the structures of small molecules as well as biological macromolecules.

While it is surprisingly useful, the representation of the intramolecular interaction of spins A and B discussed above can be criticized as over-simplified. There are many theoretical descriptions of relaxation due to intramolecular dipolar interactions available that are based on somewhat more realistic models [5,6].

Graham A. Webb (ed.), Modern Magnetic Resonance, 413–420.
© 2008 *Springer.*

Intermolecular NOEs

When the interacting spins A and B are on different molecules, their dipolar interaction is modulated by mutual diffusion of the two molecules. The simplest description of the interaction in this situation assumes that the spins are contained within two spherical molecules that have radii r_A and r_B, respectively. The closest the two spins can approach each other is $r_A + r_B = a$. The time dependence of the interaction of the spheres is assumed to be described by the mutual diffusion coefficient $(D = D_A + D_B)$ where D_A and D_B are the corresponding translational diffusion coefficients. The correlation time (τ) for the interaction of A and B is usually taken as the time required to diffuse the distance a $(\tau = a^2/D)$ [7–9]. The cross-relaxation rate σ_{AB} for the intermolecular interaction of the spins A and B when the signal for spin A is observed is

$$\sigma_{AB} = \frac{3\gamma_A^2\gamma_B^2 h^2 N_B}{10\pi Da}[6J_2(\omega_A + \omega_B) - J_2(\omega_A - \omega_B)] \quad (2)$$

where the spectra density function $J_2(\omega)$ is [7]

$$J_2(\omega) = \left(\frac{\omega\tau + \left(5/\sqrt{2}\right)(\omega\tau)^{1/2} + 4}{(\omega\tau)^3 + 4\sqrt{2}(\omega\tau)^{5/2} + 16(\omega\tau)^2 + 27\sqrt{2}(\omega\tau)^{3/2} + 81\omega\tau + 81\sqrt{2}(\omega\tau)^{1/2} + 81} \right) \quad (3)$$

and N_B is the number of molecules per ml containing spin B. If $(\omega\tau)^{1/2} = (\omega a^2/D)^{1/2} \ll 1$, the cross-relaxation rate due to the intermolecular interaction of spin B with A is

$$\sigma_{AB} = \frac{8\pi\gamma_A^2\gamma_B^2\hbar^2 N_B}{27Da} \quad (4)$$

Equations (2) and (4) convey the important information that the cross-relaxation at spin A due to interactions with molecules containing spin B depends on the concentration of the B-containing molecules, the mutual diffusion of both molecules and the distance of closest approach of A and B.

Further elaborations of the theory for the intermolecular dipole–dipole interaction take into account the rotational motions of the molecules containing spins A and B [7,9,10]. If the interacting spins are not located at the center of their representative spheres, rotation of the molecules will have the effect of altering the spin–spin interaction distance as the molecules approach each other. Other treatments consider situations where the local diffusion of the molecules when they are in close proximity may not be the same as diffusion in the bulk of the solution [10]. A method has been suggested to take into account the shape of the molecule containing spin A as it interacts with a spherical molecule containing spin B [11].

Magnitudes of Intramolecular and Intermolecular NOEs

Figures 1 and 2 compare computed intramolecular and intermolecular cross-relaxation rates for the interaction of two protons calculated using Equations (2) and (1) under conditions that would typically be present in aqueous solutions of small molecules (Figure 1) and large molecules (Figure 2) at room temperature. The calculations show that an intramolecular dipole–dipole interaction is expected to be about an order of magnitude larger than an intermolecular interaction of the same spins. The figures emphasize the short-range nature of the intramolecular interaction and show the relatively weak dependence of intermolecular cross-relaxation on distance. It should be kept in mind that a substantial portion of the intermolecular cross-relaxation arises from molecules that are appreciably separated from the spins under examination.

Solute–Solvent Interactions

Many reactions of chemical and biochemical interest take place in solutions. Interactions of solvent molecules with a solute can be critical in defining the rate of a reaction and its stereochemical outcome. Most of the common reaction solvents contain hydrogen or other spin 1/2 atoms on their surface; nuclear spin dipole–dipole interactions should thus be present as solvent molecules and solute molecules encounter one another. Although it is anticipated that intermolecular interactions will lead to relatively small cross-relaxation rates, experimental cross-relaxation rates could provide information about the "exposure" of a given solute atom to solvent and, thus, provide indications of the three-dimensional structure of the solute. It may be the case that one component of a mixed solvent system preferentially interacts with a solute; such specific solvation should be apparent in observed cross-relaxation rates since the local concentration of the solvent component that preferentially interacts with the solute will be different than the measured (bulk) concentration of that component. Lastly, the solvent–solute cross-relaxation rate is dependent on the details of translational and rotational

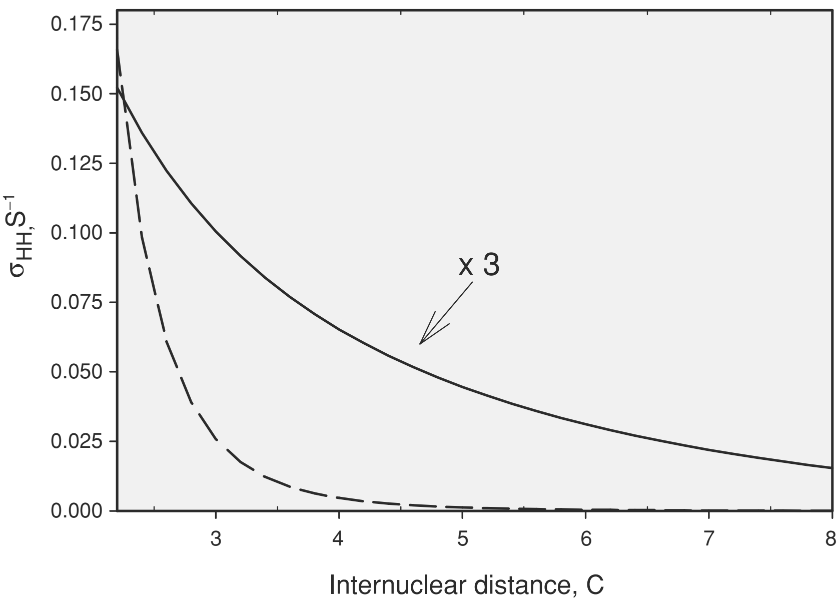

Fig. 1. Calculated ^{1}H{^{1}H} cross-relaxation rates for a small molecule dissolved in water as a function of internuclear distance. The solid line represents data for the intermolecular interaction between water protons and a proton of the small molecule while the dashed line corresponds to an intramolecular interaction. For the calculations, it was assumed that the rotational correlation time (τ_R) of the small molecule is 0.1 ns and that the translational diffusion coefficients of water and the small molecule are 1.9×10^{-9} m^2/s and 5.6×10^{-10} m^2/s, respectively. These parameters are characteristic of glucose dissolved in water [53].

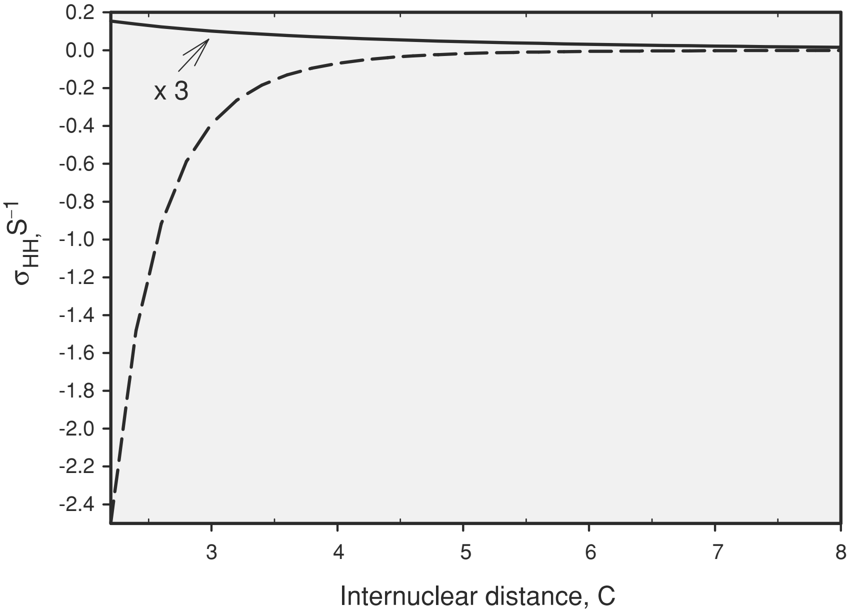

Fig. 2. Calculated ^{1}H{^{1}H} cross-relaxation rates for a large molecule dissolved in water as a function of internuclear distance. The solid line represents data for the intermolecular interaction between water protons and a proton of the large molecule while the dashed line corresponds to an intramolecular interaction. It was assumed that the rotational correlation time of the large molecule (τ_R) is 5 ns and that the translational diffusion coefficients of water and the large molecule are 2.3×10^{-9} m^2/s and 1.2×10^{-10} m^2/s, respectively. These parameters are characteristic of the enzyme lysozyme in aqueous solution [54,55].

motions of both partners and evaluation of σ_{AB} may provide insight into the nature of these processes.

Experimental Detection of Intermolecular Cross-Relaxation

The intensity of a solute NMR signal (spin A) depends on the z-component of the magnetization corresponding to A prior to application of the RF pulse that leads to the detected signal of A. Following a perturbation of the magnetization due to spin B in the solvent molecules, the initial change in the solute signal intensity with time is described by Equation (5) [12],

$$\frac{\mathrm{d}A_z}{\mathrm{d}t} = -\sigma_{\mathrm{AB}}\left(B_z(0) - B_z^0\right) \tag{5}$$

where A_z is the z-component of the spin A magnetization. The quantity $B_z(0)$ is the initial value of the solvent spin z-magnetization, B_z^0 is the z-component of the solvent magnetization when the system is at equilibrium, and σ_{AB} is the cross-relaxation rate due to the dipolar interactions of the solvent and solute spins. Equation (5) tells us that a plot of the intensity of the solute signal after perturbation of the solvent magnetization as a function of time after the perturbation (the mixing time) has an initial slope $2\sigma_{AB}$, assuming that the solvent magnetization was completely inverted at the start of the experiment $\left[B_z(0) = -B_z^0\right]$.

Some attention must be paid to experimental details when evaluating σ_{AB} arising from intermolecular solvent–solute interactions using Equation (5). The molar concentration of solvent spins is typically high and B_z^0 is large relative the solute magnetization. Thus, suppression of the solvent signal by a method that does not involve pre-saturation is usually required when collecting spectral data. Radiation damping effects may be present and lead to unexpected relaxation behavior of the solvent magnetization during the mixing time [13–15]. Difference (subtraction) methods are typically used to detect the (weak) NOE on the signal intensity of spin A. Such methods put a premium on instrument stability, particularly phase stability, and the linearity of the detection system. Control of the dipolar field associated with the solvent spins is also important [16,17].

Using a C.W. technique, Kaiser observed an intermolecular Overhauser effect between protons of cyclohexane (solvent) and chloroform (solute) in a mixture of these components [18]. Many years later, Macura and Ernst demonstrated the same interaction by means of a two-dimensional NOE experiment [19]. There have been many studies of solvent–solute interactions using the intermolecular NOE since those pioneering studies. A representative sample of these will be mentioned below. The purpose here is didactic and no attempt has been made to provide a comprehensive review of the literature.

Xenon–Solvent Interactions

Xenon-129, a solute consisting of only a single atom, dissolves in water and organic solvents to a sufficient extent that high-resolution NMR spectra of the atom can be readily obtained. Dimitrov *et al*., have determined that the cross-relaxation rate between the protons of solvent water and ^{129}Xe (σ_{XeH}) is about 3.2×10^{-3}/s [20]. Interpretation of the results suggested that the average xenon–proton distance in an aqueous solution of the gas is about 2.7 Å, an estimate that was recognized by the authors to be rather crude. The van der Waals radius of an Xe atom is 2.2 Å [21] while that of a covalent hydrogen is 1.2 Å [22], leading to an estimated distance of closest approach of 3.4 Å. The experimental cross-relaxation rate is thus consistent with a “tight” interaction between Xe and solvent molecules.

Intermolecular $^{129}\mathrm{Xe}\{^1\mathrm{H}\}$ NOEs have been detected for xenon dissolved in phosphatidylcholine (PC) vesicles. After correcting for the relative number of protons of each type in PC, the cross-relaxation rate for interaction of xenon with the protons of the choline methyl groups is about three times larger than σ_{XeH} for interactions between dissolved xenon and the CH_2 protons of the aliphatic parts of the phospholipids [23]. It was concluded that dissolved xenon is localized near the amphiphilic surface of the PC vesicles. This may be relevant to the mode of action of xenon as a general anesthetic.

Small Molecule–Water Interactions

The interactions of water protons with dissolved solute has been explored by heteronuclear intermolecular NOEs. Yu and Levy demonstrated $^{31}\mathrm{P}\{^1\mathrm{H}\}$ cross-relaxation between the phosphorus nuclei of ATP and water by a two-dimensional NOE experiment [24]. All signals from the triphosphate group are enhanced by interactions with water protons, although the γ-phosphorus at the end of the triphosphate group shows the largest effect, presumably because it is most accessible to water. Seba and Ancian found water proton $^{13}\mathrm{C}\{^1\mathrm{H}\}$NOEs to all carbon atoms of 1-methyl-2-pyridone dissolved in water [25]. Water interactions with this solute likely involve hydrogen bonds to the polar part of the molecule in addition to non-specific contacts.

Micelle–Water Interactions

Hydration of micelles of sodium octanoate and sodium dodecanoate has been explored by detecting intermolecular $^1\mathrm{H}\{^1\mathrm{H}\}$ NOEs between water protons and protons of these molecules. The results have been interpreted to indicate that water protons on average are located 3–4 Å from the carboxylate carbons in such aggregates [26]. Intermolecular $^{19}F\{^1H\}$ NOEs between water protons and the fluorines of micellar cesium perfluorooctanoate are observed for the fluorines in the CF_2 groups adjacent to the carboxylate head group but also for the other CF_2 groups of the surfactant [27]. The latter NOEs may be the result of spin diffusion or may suggest that water molecules not only contact the polar head groups but also other parts of the perfluoroalkyl chain in the micelles.

Interpretation of NOEs in micellar systems is complicated by the highly dynamic nature of these structures [28]. In addition to participating in a purely intermolecular effect, as represented by Equation (2), it is possible that in some cases water molecules interact strongly enough with the solute that the water–micelle interaction is best thought of in terms on an intramolecular molecular interaction [Equation (1)]. The rate of exchange of such strongly interacting waters with the bulk solvent molecules is an additional complication. While NOE data for the micellar systems mentioned were analyzed in terms of long-lived water–surfactant interactions, because of these additional considerations, the estimates of solvent proton–solute spin distances in these systems have to be regarded as very approximate.

Small Molecule-Organic Solvent Interactions

Our lab has determined solvent spin–solute spin NOEs for 1,3-di-*t*-butylbenzene dissolved in tetramethylsilane (TMS). Molecular models suggest that proton H_2 of the solute should be shielded from interactions with solvent molecules by virtue of the bulky *t*-butyl groups next to it. The remaining aromatic hydrogens (H_4, H_5, H_6) and those of the *t*-butyl groups are more accessible to direct interactions with solute molecules. It was found that solvent proton–solute proton $^1H\{^1H\}$ cross-relaxation rates were reasonably well predicted by a numerical procedure that incorporated the shape of the solute through its Connolly molecular surface and used the experimental diffusion coefficients of the solvent and solute. Thus, there was no evidence for special interactions between the solute and TMS.

Similar experiments were carried out with 1,3-di-*t*-butylbenzene dissolved in perfluoro-*t*-butanol. In that case, cross-relaxation rates for the protons of this solute with the OH proton of the solvent were very different from those predicted. Perfluoro-*t*-butanol is a fairly strong acid, probably with a $pK_a < 10$ [29] and 1,3-di-*t*-butylbenzene is expected to be a reasonably strong π-base. The observations suggest the formation of long-lived solute-perfluoro-*t*-butanol complexes in which fluoroalcohol molecules are hydrogen-bonded to the aromatic ring. If such complexes persist longer than the time $\tau\ (= a^2/D, \sim 0.03 - 0.1\ \text{ns})$ that characterizes diffusive encounters, dipolar interactions of solvent OH and, to a lesser extent, solvent fluorine with the aromatic protons will be modulated to some extent by rotational motion of the complex, as would be the case for an intramolecular interaction.

Determination of the enantiomeric composition of a mixture of chiral materials is a continuing problem in synthetic chemistry. This is often accomplished by recording NMR spectra of the mixture dissolved in a chiral solvent. Diastereoisomeric solvent–solute complexes form which can often be distinguished by means of their chemical shifts [30]. The structures of such solute–solvent complexes have been investigated by intermolecular NOEs [31,32]. For example, a 1:1 mixture of the S-isomer of alcohol I and acid II showed clear chemical shift differences between the R and S forms of II. Large intermolecular $^1H\{^1H\}$ NOEs were reported for the interactions of proton H_1 and the methyl protons of II with protons H_8 and H_{11} of I, with the NOEs for these interactions in the (S)I/(R)II mixture being about three times larger than the NOEs observed for the (S)I/(S)II case. Molecular dynamics (MD) simulations of these and related systems suggested that average distances between proton H_1 of II and protons H_8 and H_{11} of I are ~4.8 Å in the (S)I/(R)II system and somewhat larger (~5.2 Å) in the (S)I/(S)II complex, qualitatively consist with the intermolecular NOE results. The chemical shift differences and the relative stabilities of the diastereoisomeric complexes formed are presumably due to π-stacking interactions.

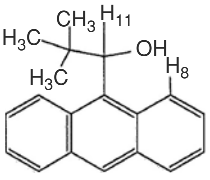

I

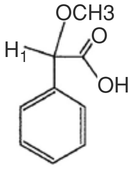

II

Selective Solute Interactions in Mixed Solvent Systems

Intermolecular NOEs have been used to demonstrate that one component of a solvent mixture can interact preferentially with a solute. For example, $^1H\{^1H\}$ intermolecular NOEs show that phenol dissolved in 50/50 water–acetonitrile or 50/50 water–dimethylsulfoxide mixtures is primarily solvated by the organic component of each solvent mixture [33]. In contrast, there appears to be no selective interaction of dioxane, as a solute, with either solvent component in a 50/50 ethanol–chloroform mixture.

Experiments to detect selective solvent interactions usually involve determining the solute spin–solvent spin cross-relaxation rate after perturbation of the magnetization of the solvent spins. If one is willing to sacrifice information about the site-specificity of solute–solvent interactions, the inverse experiment (detect solvent spins and perturb solute spins) can also be used to investigate preferential solvation in a multi-component solvent. Thus, Bagno *et al*., demonstrated selective interactions between the protons of dissolved glucose and the protons of water in water–acetonitrile and water–dimethylsulfoxide mixtures by perturbing the magnetizations of the glucose molecules and observing intermolecular NOEs on the proton signals of the components of the solvent mixture [34].

Our laboratory has recently reported a study of selective solvent interactions in a "fluorous" reaction system [35]. Mixtures of chloroform and perfluoro(methylcyclohexane) can be used as solvents for "fluorous" biphasic reactions since they exist as two separate phases at low temperature but become a single phase at higher temperatures. The ability of such non-aqueous systems to exist as two phases at low temperature but as a single phase at higher temperature has led to development of strategies for doing chemical synthesis that rely on the temperature-dependent phase behavior to achieve separation of reactants from products and reaction catalysts [36]. Intermolecular NOEs were used to study the interactions of the chloroform and perfluoro(methylcyclohexane) solvent components with the protons and fluorines of 3-heptafluorobutyrylcamphor in both phases of the biphasic system at 25° as well as the single phase at 54°. The results indicate that, at 25° in the perfluorocarbon-rich phase, the hydrocarbon part of the solute is selectively solvated by chloroform molecules. However, there are no indications of unusual interactions of either solvent component with the solute in the chloroform-rich phase and only weak indications of selective solvation in the high-temperature (homogeneous) phase. There is appreciable regio-selectivity of chloroform interactions with the hydrocarbon part of the solute in all phases.

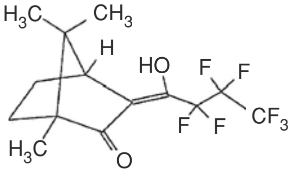

3-heptafluorobutyrylcamphor

Selective interactions of biologically significant molecules with solvent components within water–organic mixtures appear to be a recurring feature of these systems. Mixtures of trifluoroethanol (TFE) and water were observed over 40 years ago to stabilize helical conformations of peptides and proteins [37]; solutions of fluoroalcohols have been routinely used since to induce structure in peptides, proteins and nucleic acids [38]. Berger and coworkers have demonstrated selective interaction of TFE molecules with the aromatic protons of adenosine and adenosine monophosphate in 35% TFE [39]. Their results confirm the expectation that proton H_8 in both molecules should be more shielded from interaction with either solvent component than is proton H_2.

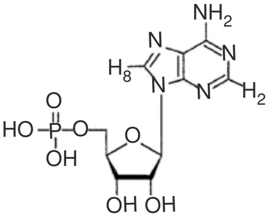

Adenosine 5'-monophosphate

The same group has studied solvent interactions with a tetrapeptide (*N*-acetylserylphenylalanyl-valylglycine methyl ester) in TFE–water and ethanol–water mixtures [40]. Intermolecular $^1H\{^1H\}$ and $^1H\{^{19}F\}$NOE observations indicate preferential solvation of the peptide by TFE in the TFE–water mixtures; proton–fluorine cross-relaxation rates increase as the proportion of TFE in the mixture increases while cross-relaxation due to water protons concomitantly decreases. In contrast, there are no indications of selective interactions of the solvent components when the peptide is dissolved in ethanol–water mixtures. Conclusions from the NOE experiments were reinforced by measurements of diffusion rates in the systems studied and by MD simulations.

Quantitative interpretation of selective interactions of fluoroalcohols with peptides is complicated by the tendency of the alcohols to aggregate in water [41,42]. Given the magnitude of the $^1H\{^{19}F\}$ intermolecular NOEs observed in the peptide systems studied so far it is probable that peptide molecules are submerged in or surrounded by aggregates of fluoroalcohol molecules leading to local exclusion of solvent water molecules. It appears, at least in some peptide–fluoroalcohol systems, that long-lived complexes of the peptide and fluoroalcohol molecules are formed [43,44]. There is evidence that TFE accumulates at the surface of proteins as well; relaxation dispersion studies of β-lactoglobulin in TFE–water mixtures indicate substantial interactions of the fluoroalcohol at the surface as well as the interior of the protein [45].

Biomolecule–Water Interactions

Solvent water molecules may interact strongly enough with biological molecules that they become immobilized

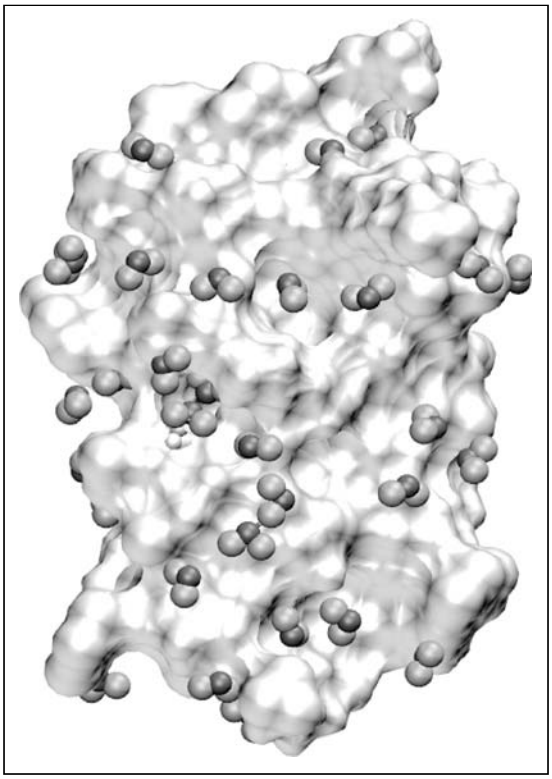

Fig. 3. Hydration of the small protein bovine pancreatic trypsin inhibitor (BPTI) in the crystalline state. The figure is based on high-resolution X-ray and neutron diffraction data [56]. In the study cited, 63 water molecules were found to be sufficiently immobilized in the crystal that they contributed to the diffraction pattern. There are many more water molecules in the crystal that are not so immobilized. Note that some of the water molecules are significantly internalized by the protein structure. (See also Plate 47 on page XXXV in the Color Plate Section.)

on the surface and within the structure to such an extent that the positions of water molecules can be determined by crystallographic methods (Figure 3). An understanding of the properties of water and other species at the surface of macromolecules is essential since biological processes such as enzymatic catalysis and macromolecular association take place at the interface between the bulk solution and the macromolecule. It is only relatively recently that experimental and computational tools have emerged to probe the interactions of water molecules at or near the surface of macromolecules. Most experimental information about hydration dynamics has come from intermolecular $^{1}H\{^{1}H\}$ NOEs between water protons and protons of the macromolecule or from NMR relaxation dispersion measurements [46,47]. The subject has a large literature; a recent article by Modig *et al.* indicates the current status of the field [48].

Interpretation of observed intermolecular NOEs between water protons and protons at the surface of a protein is complicated by the presence of solvent-exchangeable protons and by the wide range of rates for dissociation of water–macromolecule complexes. By working in supercooled solutions (–25 °C) it is possible to slow exchange dynamics, affording conditions that permit unambiguous detection of the dynamics of intact water molecules with the surface [48]. For the cyclic peptide hormone oxytocin and the small globular protein bovine pancreatic trypsin inhibitor (BPTI) it appears that most water–protein interactions at the surface under these conditions involve water molecules that are slightly retarded in their diffusive motion, consistent with MD simulations that indicate most water in the hydration layer of a protein is only weakly affected by the protein [49].

It might be anticipated that water–protein intermolecular NOEs would simply report direct interactions between the solvent and the solvent-exposed protons of the protein. Thus, the number and magnitude of $^{1}H\{^{1}H\}$ NOEs observed between water protons and protein protons should be proportional to the surface exposure of a protein proton. However, due to the wide variety of potential water molecule interactions at the surface of a biological macromolecule and the timescales for these interactions, it is unlikely that water proton–macromolecule proton NOEs will be cleanly diagnostic of "solvent exposure." A more profitable approach to identification of surface protons appears to be the use of paramagnetic relaxation agents in the solution [50,51].

Cistola and Hall have observed $^{19}F\{^{1}H\}$ intermolecular NOEs between water protons and fluorinated amino acids that have been incorporated into proteins such as U1A (an RNA-binding protein), dihydrofolate reductase and a fatty acid-binding protein [52]. In many instances, the fluorinated amino acid is buried within the tertiary structure but in other cases the observed fluorine nucleus is located on the surface of the protein. Water NOEs to fluorinated groups on the surface residues should not be as tightly intertwined with water proton exchange processes as are water NOEs to surface protons; this heteronuclear approach may be useful for probing surface hydration.

Summary

Solute spin–solvent spin NOEs have been demonstrated in a wide variety of systems. These NOEs generally are small compared to intramolecular NOEs but are readily detected using current instrumentation. They can be semi-quantitatively predicted when strong interactions between the solute and solvent are absent, given knowledge of the molecular structures, concentrations, and translational diffusion coefficients. Substantial deviations of the experimental effects from those predicted are, thus, indicative of unusual solute–solvent interactions. Intermolecular NOE experiments have provided new information regarding selective solute–solvent interactions in mixed solvent systems. For the limited number of systems where comparisons are possible, it appears that the results of intermolecular NOE experiments can be in agreement with the results of MD simulations. Further interplay of the results of intermolecular NOE experiments and simulations should provide new insights into solute–solvent interactions and the roles that solvent molecules play in determining reactivity in small molecule and biological macromolecule systems.

References

1. Neuhaus, D, Williamson MP. The Nuclear Overhauser Effect in Structural and Conformational Analysis, 2nd ed. Wiley: New York, 2000.
2. Harris RK. Nuclear Magnetic Resonance Spectroscopy. Pitman: Marshfield, MA, 1983.
3. Freeman R. Spin Choreography. University Science Books: Sausalito, CA, 1997.
4. Cavanagh J. Fairbrother WJ, Palmer AG III, Skelton NJ. Protein NMR Spectroscopy. Principles and Practice. Academic: San Diego, 1996.
5. London RE. In: JS Cohen (Ed). Magnetic Resonance in Biology, Vol. 1. Wiley: New York, 1980, p 1.
6. Wagner G, Hyberts S, Peng JW. In: GM Clore, AM Gronenborn (Eds). NMR of Proteins. CRC Press: Boca Raton, 1993, p 220.
7. Ayant Y, Belorizky E, Fries P, Rosset J. J. Phys. 1977;38:325.
8. Cowan B. Nuclear Magnetic Resonance and Relaxation. Cambridge: Cambridge, 1997.
9. Skrynnikov NR, Khazanovoch TN, Sanctuary BC. Mol. Phys. 1997;91:977.
10. Halle B. J. Chem. Phys. 2003;119:12372.
11. Gerig JT. J. Org. Chem. 2003;68:5244.
12. Noggle JH, Schirmer RE. The Nuclear Overhauser Effect. Academic: New York, 1971.
13. Wu D, Johnson CS Jr. J. Magn. Reson. A. 1994;110:113.
14. Mao X, Guo J, Ye C. Chem. Phys. Lett. 1994;222:417.
15. Mao X-A, Ye C-H. Concepts Magn. Reson. 1997;9:173.
16. Edzes HT. J. Magn. Reson. 1990;86:293.
17. Lix B, Sonnichsen FD, Sykes BD. J. Magn. Reson. A. 1996;121:83.
18. Kaiser R. J. Chem. Phys. 1965;42:1838.
19. Macura S, Ernst RR. Mol. Phys. 1980;41:95.
20. Dimitrov IE, Reddy R, Leigh JS. J. Magn. Reson. 2000;145:302.
21. Bondi A. J. Phys. Chem. 1964;68:441.
22. Gordon AJ, Ford RA. The Chemist's Companion. Wiley-Interscience: New York, 1972.
23. Xu Y, Tang P. Biochim. Biophys. Acta. 1997;1323:154.
24. Yu C, Levy GC. J. Am. Chem. Soc. 1983;105:6994.
25. Seba HB, Ancian B. J. Chem. Soc. Chem. Commun. 1990: 996.
26. Mahieu N, Tekely P, Canet D. J. Phys. Chem. 1993;97:2764.
27. Raulet R, Furo I, Brondeau J, Diter B, Canet D. J. Magn. Reson. 1998;133:324.
28. Bogusz S, Venable RM, Pastor RW. J. Phys. Chem. B. 2003;105:8312.
29. Dawson JHJ, Jennings KR. Int. J. Mass Spectrom. Ion Phys. 1977;25:47.
30. Parker D. Chem. Rev. 1991;91:1441.
31. de Moragas M, Cervello E, Port A, Jaime C, Virgili A, Ancian B. J. Org. Chem. 1998;63:8689.
32. Munoz A, Virgili A, Tetrahedron: Asymmetry. 2002;13:1529.
33. Bagno A, Compulla M, Pirana M, Scorrano G, Stiz S. Chem. Eur. J. 1999;5:1291.
34. Bagno A, Rastrelli F, Scorrano G. J. Magn. Reson. 2004;167:31.
35. Gerig JT. J. Am. Chem. Soc. 2005;127:9277.
36. Gladysz JA, Curran DP, Horvath IT. Handbook of Fluorous Chemistry. Wiley: Somerset, NJ, 2004.
37. Goodman M, Listowsky I. J. Am. Chem. Soc. 1962;84:3770.
38. Buck M. Quart. Rev. Biophys. 1998;31:297.
39. Angulo M, Berger S. Anal. Bioanal. Chem. 2004;378:1555.
40. Fioroni M, Diaz MD, Burger K, Berger S. J. Am. Chem. Soc. 2002;124:7737.
41. Hong D-P, Hoshino M, Kuboi R, Goto Y. J. Am. Chem. Soc. 1999;121:8427.
42. Gast K, Siemer A, Zirwer D, Damaschun G. Eur. Biophys. J. 2001;30:273.
43. Gerig JT. Biophys. J. 2004;86:3166.
44. Gerig JT. Biopolymers. 2004;74:240.
45. Kumar S, Modig K, Halle B. Biochemistry. 2003;42:13708.
46. Otting G. Prog. NMR Spectrosc. 1997;31:259.
47. Halle B. Philos. Trans. R. Soc. Lond. B 2004;359:1207.
48. Modig K, Liepinsh E, Otting G, Halle B. J. Am. Chem. Soc. 2004;126:102.
49. Sterpone F, Ceccarelli M, Marchi M. J. Mol. Biol. 2001;311:409.
50. Niccolai N, Ciutti A, Spiga O, Scarselli M, Bernini A, Bracci L, Di Maro D, Dalvit C, Molinari H, Espositio G, Temussi PA. J. Biol. Chem. 2001;276:42455.
51. Pintacuda G, Otting G. J. Am. Chem. Soc. 2002;124:372.
52. Cistola DP, Hall KB. J. Biomol. NMR. 1995;5:415.
53. Monteiro C, Herve du Penhoat C. J. Phys. Chem. A. 2001;105:9827.
54. Price WS, Tsuchiya F, Suzuki C, Arata Y. J. Biomol. NMR. 1999;13:113.
55. Kakalis LT, Baianu IC. Arch. Biochem. Biophys. 1988;267:829.
56. Wlodawer A, Deisenhofer J, Huber R. J. Mol. Biol. 1984;180:301.

Chemical Exchange

Alex D. Bain
Department of Chemistry McMaster University West Hamilton, Ontario Canada L8S 4M1

Introduction

In magnetic resonance, the term chemical exchange has a specific meaning. It means that a chemical system is at macroscopic equilibrium, but at the microscopic level, an individual nucleus is exchanging its environment with another nucleus. The process causes no net change in the sample, but from the point of view of a particular nucleus, a chemical reaction has occurred. Another common term is Dynamic NMR (DNMR), which emphasizes the fact that molecules always have some motion associated with them. Apart from being an interesting aspect of spectroscopy, chemical exchange is important and useful for the same reasons as other types of chemical kinetics. Transition-state theory tells us that the rate is related to the thermodynamics of the barrier. Kinetics is one of the few ways we have of studying the transition state.

A standard example of chemical exchange in NMR is the type of molecule in which a *N,N*-dimethyl group is attached to a π electron system, such as in methyl 3-dimethylamino-2-cyanocrotonate (MDACC) (Figure 1). If the molecule were rigid, then the protons in the two methyl groups on the nitrogen would have different chemical shifts. If, however, there were rapid rotation about the bond joining the nitrogen to the vinyl group, only a single average environment would be observed. At rates intermediate between these extremes, the signals would first broaden, then coalesce, and eventually sharpen again, as the rate increased.

These are some of the most familiar and obvious manifestations of exchange. In this case, it is the chemical shift of the protons that changes in the exchange. In general, it can be any characteristic of the magnetic environment of the nucleus—if the resonance frequency changes, chemical exchange phenomena may appear. This chapter will review how chemical exchange affects many different types of NMR experiments. A brief survey of the theoretical description will also be given.

Chemical exchange effects in NMR were first reported by Gutowsky's group [1], and this work is in most standard texts. Two excellent books give summaries of the important work to their times [2,3]. As well, there are many reviews, both early [4,5] and more recent [6–9], and some books [10,11].

The dynamics in most NMR spectra fit one of the two extreme situations—effectively rigid or completely averaged. The protons in most methyl groups are magnetically equivalent because rotation is very fast. However, double bonds must break (formally) into a single bond in order to rotate, so we tend to regard the stereochemistry around a double bond as fixed. In the molecule in Figure 1, there is an interaction of the lone pair on nitrogen with the π system of the carbon–carbon double bond, leading to partial double-bond character in the C–N bond. If this barrier to rotation is high (compared to thermal energy), the two N-methyl groups will be distinct. We would see four methyl singlets: the O-methyl, the C-methyl and the two N-methyls. However, if we raise the sample temperature, so that the rate of exchange (in this case, the rate of rotation about the C-N bond) increases, the N-methyl signals broaden, coalesce, and eventually sharpen into a single, sharp average peak. In this particular molecule, there is a further process. The E and Z configurations around the carbon–carbon double bond have very similar energies, and both are observed in solution. The groups at one end of the C=C bond are electron-withdrawing, and those at the other end are electron-donating, creating a push-pull ethylene. The double bond is polarized sufficiently so that chemical exchange is also observed between the E and Z forms. Figure 2 shows a typical spectrum for the molecule in Figure 1.

Types of Chemical Exchange

For chemical exchange to affect an NMR experiment, its rate must be comparable to some time scale in the experiment. This time scale can range over several orders of magnitude [12], so the common phrase "the NMR time scale" can cover a very wide range. In Figure 2, the rate is comparable to the difference between the resonance frequencies of the two sites. This case is called intermediate exchange—when the lineshape is significantly affected. Slow exchange does not affect the lineshape very much, but it can interact strongly with spin-lattice relaxation. Finally, in fast exchange, only the average spectrum is observed, but there is still some residual line broadening due to exchange which can be extracted by careful measurements of T_2, the spin–spin relaxation rate.

Graham A. Webb (ed.), Modern Magnetic Resonance, 421–427.
© 2008 *Springer.*

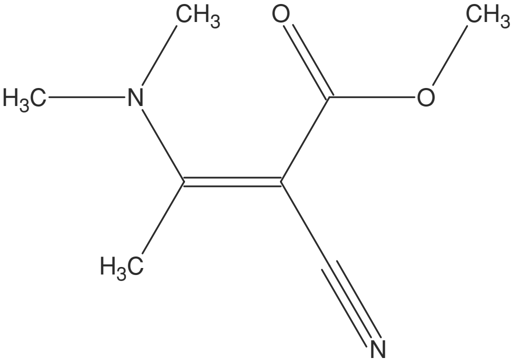

Fig. 1. Structure of MDACC. There is a process that exchanges the two *N*-methyl groups (mutual exchange), in which the molecule is identical before and after the exchange. The other process takes the *E* configuration into the *Z*. This is an example of non-mutual exchange, for which the equilibrium constant is not equal to 1.

The exchange of nuclei may change the stereochemistry of the molecule. For instance, in the push–pull ethylene MDACC, the double bond is sufficiently weakened so that the *E* and *Z* configurations can be observed to interconvert. In this case, the molecules before and after the exchange are different, and the equilibrium constant for the exchange is not equal to 1. This is called non-mutual exchange. However, this molecule also shows restricted rotation about the bond joining the *N,N*-dimethyl group attached to the ethylene. In this case, called mutual exchange, the molecule is identical before and after. Only the positions of the nuclei have been permuted, and the equilibrium constant must be 1. The chair–chair interconversion in cyclohexane is another classic example of mutual intramolecular exchange. These situations involve rearrangements within a molecule, and so are called intramolecular exchange. Intermolecular exchange also occurs—for instance the exchange between a free ligand and one bound to a transition metal complex. Labile OH and NH protons rarely show couplings to vicinal protons, due to intermolecular exchange with the solvent. The book by Jackman and Cotton [2] covers most chemical types of exchange.

Finally, there is a technical spectroscopic distinction that must be drawn, independent of the dynamics. If the spin system shows no scalar coupling (such as in a proton-decoupled natural abundance ^{13}C spectrum) there is a one-to-one correspondence between nuclei in the molecule and lines in the spectrum. When the nucleus exchanges, the line reflects this directly. However, for a coupled spin

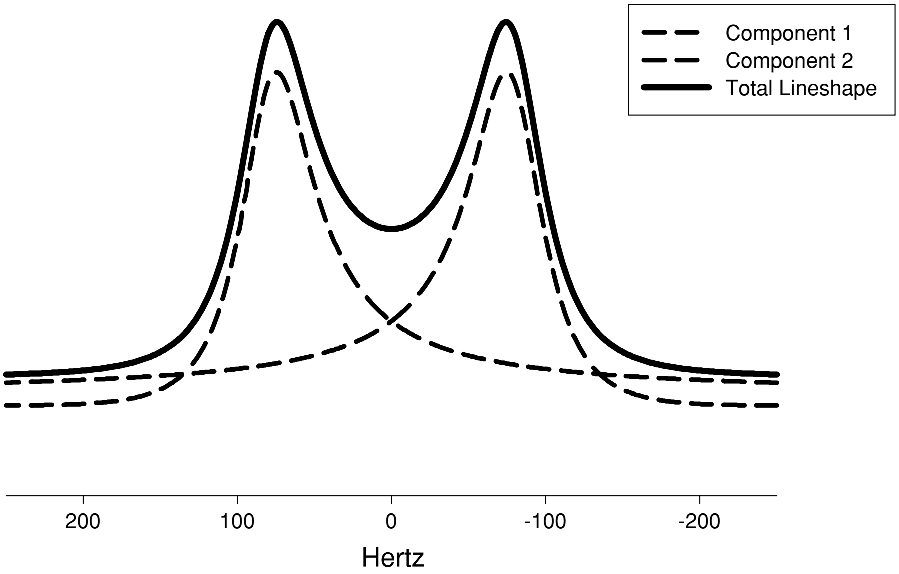

Fig. 2. 500 MHz proton NMR spectrum of MDACC in deuterated acetonitrile at $-11.3\,^{\circ}C$. The peak at 3.6 ppm represents the coalesced signal of the two *O*-methyl groups in the *E* and *Z* configurations. The peaks near 2.4 ppm are the *C*-methyl signals of the *E* and *Z* configurations, showing that the *E* configuration (signal at higher frequency) is more populated. The *N*-methyl signals of the *E* configuration near 3.2 ppm have coalesced, but those of the *Z* configuration, at 3.18 and 3.0 ppm, show two equally intense signals, typical of mutual exchange.

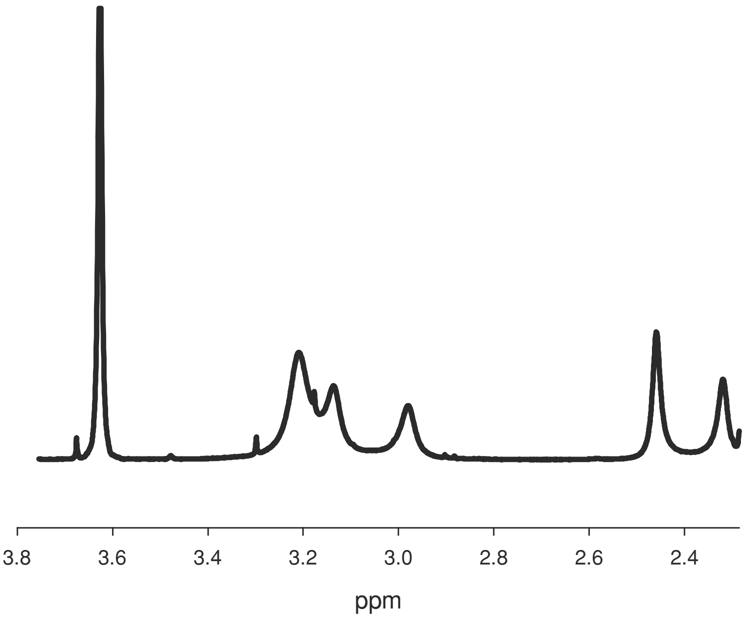

Fig. 3. Decomposition of the two-site, equally populated exchange lineshape near coalescence into two symmetric out-of-phase Lorentzian-type lines. This is a general result—any exchange lineshape can be expressed as a sum of individual transitions.

system, the correspondence is not one-to-one, and the effects on the spectrum may be much more complex. Calculating the effect of exchange on a general coupled spin system is significantly more complicated than for an uncoupled one. Therefore, the first step is to classify the system. Is the exchange intra- or intermolecular? Is it mutual or non-mutual? Is the spin system coupled or uncoupled? The answers to these questions determine the approach to be taken.

Theory

For spin systems without scalar coupling, the lineshapes for exchanging systems can be derived by setting up and solving a system of coupled Bloch equations. This theory describes the coalescence phenomenon, which is the most familiar manifestation of chemical exchange. Perhaps less familiar is the fact that the lineshape near coalescence is the sum of two transitions, just as the static spectrum clearly shows two lines. Reeves and Shaw [13] showed that the lineshape for two-site exchange can be decomposed into two out-of-phase lines (Figure 3). At roughly the same time, Binsch [14] derived a general formalism that treated all systems and formed the basis for the standard simulation program DNMR3/DNMR6. What evolved from that is the concept that exchange spectra can be expressed as a sum of individual transitions [15], just as static spectra are. In a static spectrum, there are a series of transitions with specific frequencies, whose intensities are governed by transition probabilities. Similar, DNMR spectra have transition probabilities, but they are now complex numbers. The real and imaginary parts of the complex number combine to give the intensity and phase of the line. Similarly, the frequency is also a complex number, with the real and imaginary parts giving the position and width of the line. In this way, an NMR spectrum of an exchanging system is no different from that of a static system, except that the characteristics of the transitions are complex numbers, rather than pure real ones. This principle forms the basis of simulation programs such as DNMR3 and MEXICO.

Intramolecular exchange follows first-order kinetics, since it is a unimolecular reaction. This implies that exponentials govern the time evolution. The spectrum is described by decaying oscillations in the time domain (complex exponentials), leading to the transitions making up the spectrum in Figure 3. When exchange affects the spin-lattice relaxation, the behavior is described by a multi-exponential decay. Even though intermolecular exchange involves two or more species, the NMR spectroscopy is still governed by pseudo-first-order kinetics, so the theoretical approach is the same.

Kinetics

As far as an individual nucleus is concerned, exchange is a chemical reaction. Transition-state theory, or absolute rate theory, says that the rate of a reaction, k, at a temperature,

T, is given by equation (1).

$$k = \frac{k_B T}{h} e^{-\Delta G^{\dagger}/RT} \qquad (1)$$

In this equation, k_B is Boltzmann's constant, h is Planck's constant, R is the gas constant and $\Delta G^{\dagger}$is the Gibbs free energy of activation. Since everything else is known, measuring the rate is tantamount to measuring $\Delta G^{\dagger}$. However, by measuring the rate as a function of temperature, we can extract the enthalpy and entropy of activation separately. Normally, this is done with an Eyring plot—a plot of $\ln(k/T)$ against $(1/T)$. This should yield a straight line with a slope of $-\Delta H^{\dagger}/R$. The intercept at $(1/T) = 0$ is $\ln(k_B/h) + \Delta S^{\dagger}/R$. The values of the enthalpy obtained from the slope are usually reliable, but the determination of the intercept requires a considerable extrapolation. Entropies of activation should be treated with some caution. However, if accurate rates are obtained over a wide range of temperatures, good thermodynamic data can be derived for the transition state.

Experimental Precautions

All the usual techniques for obtaining good NMR spectra should be applied. Magnetic field homogeneity is crucial if good lineshapes are to be obtained, so a sharp reference signal within the sample is extremely useful. Furthermore, stable and accurate temperatures are essential. Modern spectrometers have excellent variable-temperature controllers that will deliver temperatures that are stable to 0.1° or better. However, the temperature calibration of these units is sometimes unreliable. Temperatures should be checked, either with a thermocouple in an NMR tube, or with an NMR temperature calibration sample such as methanol.

Intermediate Exchange

Intermediate exchange is the regime where the one-dimensional spectrum strongly affected by the exchange. In this case, the rate of exchange is comparable to the difference in frequency between the two sites. Note that this is the frequency difference in Hertz, so the exchange spectra will be different at different magnetic fields, even if the temperature (and hence the rate) is the same. Similarly, the proton spectrum may show lineshapes that are well past coalescence, but the carbon spectrum may still show distinct sites.

A good deal of early work was done with coalescence temperatures. Coalescence was defined by the lineshape being flat at the midpoint—neither curved up nor down. Let $\Delta \nu$ be the difference in frequency (in Hertz) between the two sites. From the equation defining the lineshape, the rate which gives coalescence is given by equation (2)

$$k = \frac{\pi \Delta \nu}{\sqrt{2}} \qquad (2)$$

In these experiments, the temperature was varied until coalescence was achieved. Although it has been extended, the notion of coalescence is best restricted to the exchange of two equally populated uncoupled sites.

Better methods than coalescence temperatures are now available. Modern spectrometers are run by powerful general-purpose computers, and the spectrum is available in digital form. This means that the full lineshape can be fitted, using one of a number of freely available programs. This procedure can be applied to almost any dynamic system: coupled or uncoupled, equally or unequally populated. In fitting the lineshape, it is important to know that the chemical shifts (and hence, $\Delta \nu$) may change with temperature, and the equilibrium constant (if different from 1) will also change. Furthermore, each line has a natural width—the width that it would have in the absence of exchange. This must be estimated and included in the calculation. This can be done, but when the exchange is slow enough that the exchange contribution is comparable to the natural linewidth, unreliable data can result. Small changes in the assumed natural width can change the rate significantly. Furthermore, even though the changes may be small in absolute terms, it is the relative change that is important to the Eyring plot. Slow exchange is best handled by different methods. However, it is important to have data from as wide a range of temperatures as possible.

It is sometimes stated that the lineshape is most sensitive to the rate near coalescence, which is true if the frequency difference between the sites is known exactly. However, it has been our experience that the most accurate values of the rate are obtained from spectra before coalescence that still show resolved peaks, but are significantly broadened by exchange, as in Figure 2.

The study of intermediate exchange is inherently a one-dimensional experiment. The broad lines imply short relaxation times, so the coherence decays before it can be transferred in a multidimensional experiment. This usually precludes the study of intermediate exchange in biological macromolecules. Motion is an essential part of the study of proteins in solution, but the one-dimensional spectra are too crowded to be interpreted. Most of the protein spectroscopy relies on multiple dimensional spectra to spread out the lines, but intermediate exchange will destroy the magnetization before it is transferred. However, techniques for both slow and fast exchange are widely used to study protein dynamics [16].

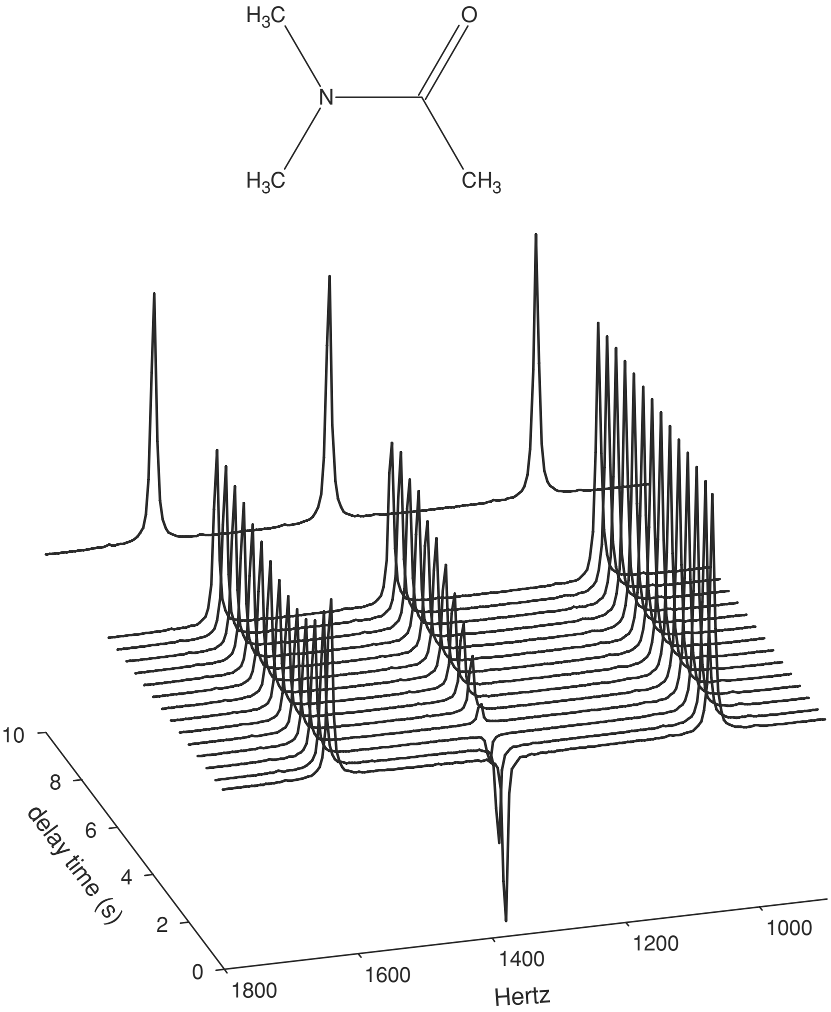

Fig. 4. Results of a selective-inversion experiment on dimethylacetamide. The signals of the two *N*-methyl groups are at high frequency. One of the signals was inverted, and then the *z* magnetizations were sampled as a function of the delay time. The inverted signal relaxes more quickly, because of exchange with the non-inverted site. The non-inverted site shows a characteristic transient decrease and then return towards equilibrium.

Slow Exchange

In this regime, the rate is not fast enough to broaden the lines significantly beyond their natural width. However, the rates are comparable to spin-lattice relaxation times. Chemical exchange has many formal similarities to dipolar relaxation, so many of the experiments that measure Overhauser effects and related phenomena can also be used to study exchange.

The analogy lies in the fact that two spins (or two sites) are involved. The basis of the methods is that the relaxation of one site depends on the state of the other. If one site is selectively inverted, it can relax back to equilibrium either by straight relaxation, or by exchanging with the unperturbed site. The inverted site will relax more quickly, due to the exchange contribution, and the unperturbed site will show a characteristic negative transient (Figure 4). The transient Overhauser effect is exactly analogous, but in this case it is the double-quantum and zero-quantum relaxation terms that couple the relaxation. Similarly, saturation of one site will cause a change in the steady-state intensity of the other, in both exchange and dipolar relaxation.

The analogy extends to multidimensional experiments. The EXSY experiment, using the same pulse sequence as NOESY, displays cross-peaks between sites that are connected by exchange. This is an excellent way to determine qualitatively which sites are exchanging with which. It can also be made quantitative, by calculating the volume of the cross-peak compared to the diagonal peak [17], with the assumption that the exchange has not proceeded too far. In principle this gives a rate, but it is good practice to repeat the experiment as a function of the mixing time.

It is the author's opinion that one-dimensional selective inversion experiments are more efficient in obtaining rates in slow exchange. One site is selectively inverted and then the system is allowed to relax for some time. Selective pulses are available on all modern spectrometers. The z magnetizations are then sampled with a $\pi/2$ pulse, as in a standard inversion-recovery experiment (Figure 4). In the time required for a single two-dimensional experiment, a number of selective inversion experiments can be done, with a range of relaxation delays. The data analysis requires a non-linear least-squares fit, but there are no assumptions made The selective inversion experiment is more complex to set up and analyze than the EXSY experiment, but we feel it gives much better data. The selective inversion experiment, also called a zz experiment, is readily expanded to indirect detection methods used for studying proteins. It has been widely used to study slow protein dynamics.

Fast Exchange

In fast exchange, the spectrum has collapsed into a single line, and so less information can be obtained. In principle, only the linewidth due to exchange, given by Equation (3), is available. Furthermore, unless $\Delta\nu$ is known, we can not get a value for the rate.

$$width \propto \frac{(\Delta\nu)^2}{k} \tag{3}$$

In practice, the effect is usually measured in a T_2 experiment, using either a CPMG or a $T_{1\rho}$ technique. If $\Delta\nu$ is available, the rate can be extracted. However, if the rate is not too fast, it can be extracted without the need for a value of $\Delta\nu$. Both these T_2 experiments have inherent time scales: the rate at which refocussing pulses are applied in a CPMG, or the rate of precession around the spin-lock field in a $T_{1\rho}$ experiment. If the timescale is slow with respect to the rate of exchange—i.e. the system has time to exchange between refocussing pulses—then the measured T_2 will reflect the exchange contribution. However, if the spins are refocussed before they can exchange, then the experiment will give a T_2 which reflects the static sites [18]. As a function of the rate of the application of the pulses, the apparent T_2 will change, and from this the absolute rate can be extracted. For this method to work, the rate of application of pulses must be greater than the exchange rate, and hardware often limits how quickly pulses can be applied. Therefore, there is an upper limit on the rates that can be measured.

If the rate is measured in this way, then the frequency difference between the sites can be obtained from Equation (3). More precisely, it is the square of this value, so that the sign is lost. However, if multiple-quantum transitions can be observed, then it is possible to use them to get the sign of the frequency difference as well [19].

Summary

Almost all molecular systems exhibit some sort of dynamic behavior. If this dynamics affects the magnetic environment of a nucleus, then it may well be accessible to measurement by NMR. The motion can be rotation around a bond, it may be an intermolecular reaction, it may be reorientation of a molecule in an anisotropic environment, or many other types. Typical timescales run from seconds down to nanoseconds. By matching the timescale of the NMR experiment to the dynamics, sensitive, and accurate measurements of the rates can be made. In many cases, magnetic resonance is the only way of obtaining these rates. The theory is well-developed and the experiments are relatively easy to implement on modern spectrometers. This means that chemical exchange will continue to play a major role in modern magnetic resonance.

References

1. Gutowsky HS, Holm CH. J. Chem. Phys. 1956;25:1228.
2. Jackman LM, Cotton FA. Dynamic Nuclear Magnetic Resonance Spectroscopy. Academic Press: New York, 1975.
3. Sandstrom J. Dynamic NMR Spectroscopy. Academic Press: London, 1982.
4. Johnson CS. Advances in Magnetic Resonance 1965;1:33.
5. Binsch G, Kessler H. Angew. Chem. Int. Ed. Engl. 1980;19:411.
6. Farrugia LJ. J. Chem. Soc., Dalton Trans. 1783 (1997).
7. Orrell KG. Annu. Rep. NMR Spectrosc. 1999;37:1.
8. Pons M, Millet O. Prog. Nucl. Magn. Reson. Spectrosc. 2001;38:267.
9. Bain AD. Prog. Nucl. Magn. Reson. Spectrosc. 2003;43:63.

10. Delpuech JJ (Ed). Dynamics of Solutions and Fluid Mixtures by NMR. Wiley: Chichester, 1995.
11. Tycko R (Ed). Nuclear Magnetic Resonance Probes of Molecular Dynamics. Kluwer Academic Publishers: Boston, 1994.
12. Monlien FJ, Helm L, Abou-Hamdan A. Merbach AE. Inorg. Chem. 2002;41:1717.
13. Reeves LW, Shaw KN. Can. J. Chem. 1970;48:3641.
14. Binsch G. J. Am. Chem. Soc. 1969;91:1304.
15. Bain AD, Duns GJ. Can. J. Chem. 1996;74:819.
16. Cavanagh J, Fairbrother WJ, Palmer AG, Skelton NJ. Protein NMR Spectroscopy. Principles and Practice. Academic Press: San Diego, 1996.
17. Perrin CL, Dwyer T. Chem. Rev. 1990;90:935.
18. Carver JP, Richards RE. J. Magn. Reson. 1972;6:89.
19. Skrynnikov NR, Dahlquist FW, Kay LE. J. Am. Chem. Soc. 2002;124:12352.

NQR & ESR

Separated Detection of H-Transfer Motions in Multi-H-Bonded Systems Studied by Combined ^{1}H NMR and ^{35}Cl NQR Measurements

Ryuichi Ikeda
National Institute for Materials Science, Tsukuba 305-0003, Japan

Introduction

Intermolecular H-bonding has widely been observed in condensed systems, where the H-transfer through H-bonds formed between molecules enables charge and energy transfers in solid and biological systems, and marked physicochemical properties on the macroscopic scale, such as ferro- and antiferroelectrics [1], dipolar glasses [2], molecular solitons [3], etc., have been studied at the microscopic level of H-motions.

Various techniques for characterizing the H-dynamics have been applied for this purpose, i.e. measurements of vibration spectra, neutron scatterings, magnetic resonances, dielectric constants, and so on. Among these, ^{1}H NMR has quite effectively been used for a long time, because moving protons can directly be monitored and relaxation data due to the H-transfer are readily available. A well-known example for which this technique was fairly applied is the double H-transfer in dimeric units of benzoic acid (BA) in the solid [4]. The observed asymmetric minimum of the ^{1}H NMR spin-lattice relaxation time ($T_{1\mathrm{H}}$) was explained well by combined contributions from the classical BBP-type H-jumps and the quantum mechanical H-tunneling assisted by lattice phonons in an asymmetric double-well potential. On the other hand, a serious disadvantage of this technique is its low sensitivity for detecting H-movements that can cause only a slight fluctuation of local magnetic field at neighboring resonant protons, because the displacement of H-positions through jumps is small and of the order of 10 pm. Accordingly, H-jumps in H-bonds usually give rise to long $T_{1\mathrm{H}}$ values of the order of 100 s, which can easily be masked by other relaxation processes such as molecular motions.

As a complementary approach to this problem, we intended to apply NQR relaxation measurements for the detection of intermolecular H-transfer motions. We noted NQR, which has been used as a quite sensitive probe enabling one to detect even subtle changes of charge distributions in solids [5], and applied to detailed studies on phase transitions [6], lattice and molecular motions [5], etc. In this article, as a new sensitive method for detecting H-transfer in H-bonded systems, I propose ^{35}Cl NQR relaxation measurements combined with ^{1}H NMR relaxation studies. Applications of this technique were performed for the intermolecular H-transfer in an H-bonded two molecular systems where double H-transfer is expected, and in H-bonded three molecular systems where complicated H-transfer modes not studied so far are possible.

High Sensitivity of NQR Shown in 4-Chlorobenzoic Acid

Since no NQR attempt for this purpose has been reported, in the first step, we carried out the confirmation of the sensitivity of this technique for H-transfer motions. We introduced a chlorine atom as a NQR probe into a BA molecule which is a well-known H-transfer system studied in detail [4]. We measured ^{1}H NMR and ^{35}Cl NQR relaxation times on 4-chlorobenzoic acid (4-ClC$_6$H$_4$COOH) [7] that forms a dimeric structure in the solid [8] analogous to that in BA as given by

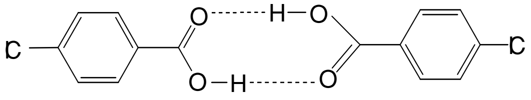

Temperature dependences of $T_{1\mathrm{H}}$ and the ^{35}Cl NQR spin-lattice relaxation time ($T_{1\mathrm{Q}}$) in Cl–BA are shown in Figure 1. An asymmetric $T_{1\mathrm{H}}$ curve observed by NMR is quite analogous to that in BA [4], indicating the occurrence of the double H-transfer motion in the H-bonded dimer unit given above. The asymmetry of $T_{1\mathrm{H}}$ curves could be explained well by introducing the combined contributions from classical BBP-type H-jumps and the quantum mechanical H-tunneling assisted by lattice phonons in an asymmetric double-well potential for the H-transfer mode shown by Skinner and Trommsdorff [4].

This protonic motion was also detected clearly by the ^{35}Cl NQR relaxation time measurement as shown

Graham A. Webb (ed.), Modern Magnetic Resonance, 431–438.
© 2008 *Springer.*

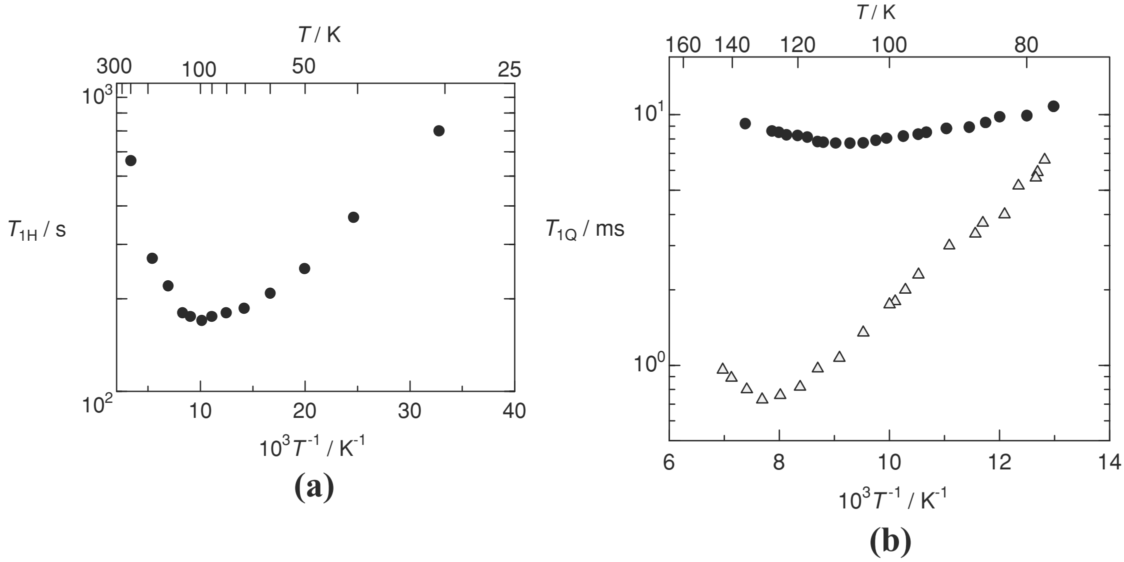

Fig. 1. ^{1}H NMR (a) and ^{35}Cl NQR (b) spin-lattice relaxation times (T_{1H}, T_{1Q}) observed for (●) 4-ClC$_6$H$_4$COOH, at an NMR Larmor frequency of 54.3 MHz, and (Δ) 4-ClC$_6$H$_4$COOD.

Figure 1(b). This is because the T_{1Q} minimum was observed at almost the same temperature as that in T_{1H}, and a marked isotope effect on T_{1Q} was observed in a partial deuterated analog, 4-ClC$_6$H$_4$COOD. As for the sensitivity of NQR, we should notify short T_{1Q} values compared with T_{1H}. If we compare the minimum values, ^{35}Cl NQR can be considered to be 10^4 times more sensitive than ^{1}H NMR. This highly sensitive detection is not surprising and can be explained as follows. In case H-jumps from one molecule to the other, it moves as a proton. This implies that the rest of the molecule, in this case, the carboxyl group changes its electronic structure by exchanging the mutual positions of C=O and C–O groups accompanied by the double H-transfer in a dimer unit. This change of the electronic structure should give a fluctuation of electric field gradient (EFG) at the resonant Cl nuclei. The presence of the π-conjugated phenyl ring is the important reason why a marked EFG change is transferred from the remote position far from the NQR nuclei.

Separated Detections of H-Transfer Modes in Multi-H-Bonded Systems

Multi-H-Transfer Motions in (Chloranilic Acid)(1,4-diazine) 1:2 Molecular Complex

Since NQR has been shown to have a high sensitivity for the detection of intermolecular H-transfer motions in solids, we applied this method to new H-bonded three molecular systems that are expected to contain multi-H-transfer processes. As the first target, we selected a 1:2 molecular complex of chloranilic acid with 1,4-diazine, [C$_6$Cl$_2$O$_2$(OH)$_2$](1,4-C$_4$H$_4$N$_2$)$_2$ (abbreviated to 1,4-complex), in which symmetric two OH–N-type H-bonds are formed. Since disordered H-positions and a short OH–N distance of 259.0 pm were reported [9], we can expect the observation of the H-transfer motion in this system.

^{35}Cl NQR Frequencies

A temperature dependence of ^{35}Cl NQR frequencies observed in the 1,4-complex is shown in Figure 2 [10]. The frequency of 36.3997 ± 0.0005 MHz observed at 77 K is markedly shifted from 37.15 MHz reported for chloranilic acid, C$_6$Cl$_2$O$_2$(OH)$_2$ [11] and also ca. 35.2 MHz (averaged value) for its sodium salt C$_6$Cl$_2$O$_2$(ONa)$_2$ [11] at 77 K. These differences are too large to be explained by differences in lattice charges and thermal vibrations, and some changes in the electronic structure should take place in the chloranilic acid molecule. Since the observed frequency in the 1,4-complex comes in the intermediate region between those in neutral acid (0) and divalent salt (2–), we can presume that chloranilic acid in the 1,4-complex takes a valency close to a monovalent (1–) state. This can be supported by the theoretical calculation of EFG at Cl nuclei in a neutral molecule and two kinds of ionic states of chloranilic acid shown in Table 1 performed by W. C. Bailey (personal communication). The absolute

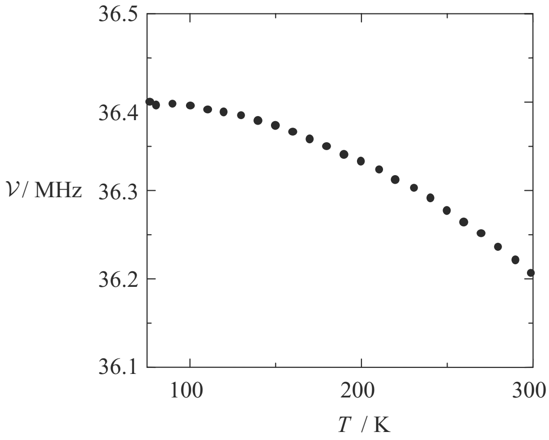

Fig. 2. A temperature dependence of ^{35}Cl NQR frequencies observed in $[C_6Cl_2O_2(OH)_2](1,4\text{-}C_4H_4N_2)_2$.

values themselves cannot be directly compared with the observed values, because no effects from thermal vibrations and charges in neighboring molecules in crystals are included in the calculation. If we note relative values, we can see that the monovalent ion gives a frequency close to the average of those in the neutral and divalent species supporting the present interpretation.

Accordingly, the most probable structure of the 1,4-complex in crystals can be expressed as either of the following two structures I and II derived from the centrosymmetric crystal structure of the present system. The formation of these ionic structures can be supported from pK_{a1} values of chloranilic acid and 1,4-diazinium in solutions to be 0.76 and 0.57, respectively [12].

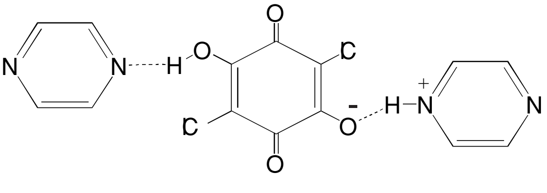

(I)

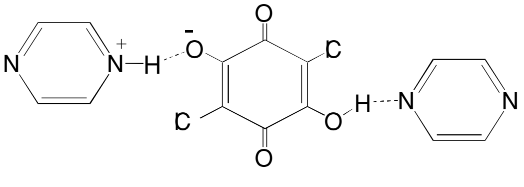

(II)

Table 1: Theoretical values of quadrupole coupling constants (e^2Qq), asymmetry parameters of electric field gradients (η) and resonance frequencies (ν) calculated for a neutral chloranilic acid molecule, and monovalent and divalent chloranilate ions in isolated states

Species (charge)	e^2Qq (MHz)	η	ν(MHz)
Neutral molecule (0)	−77.8	0.11	38.98
Monovalent ion (1−)	−72.3	0.09	36.20
Divalent ion (2−)	−64.4	0.12	32.38

^{1}H NMR Relaxation Time (T_{1H})

A temperature dependence of the ^{1}H NMR relaxation time (T_{1H}) observed in the 1,4-complex is shown in Figure 3 [10]. The long T_{1H} minimum at ca. 135 K was attributed to the H-transfer motion OH–N ↔ O$^-$–HN$^+$ for the following two reasons: one is that the 1,4-complex containing deuterated acidic hydrogen gave a T_{1H} minimum much longer than 500 s; and the other is that the calculated T_{1H} minimum is close to the observed value. Since the most populated structure of chloranilic acid was shown to be monovalent (1−), the H-transfer is expected to take place between the two structures I and II given above and expressed as I ↔ II. This mode named "correlated H-transfer" can retain the most stable structure throughout the motion. The observed T_{1H} minimum became a little asymmetric giving activation energies of 3.9 and

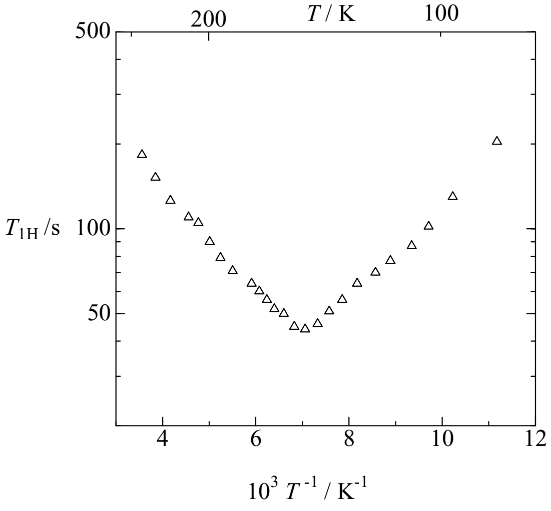

Fig. 3. A temperature dependence of ^{1}H NMR spin-lattice relaxation time T_{1H} observed in $[C_6Cl_2O_2(OH)_2](1,4\text{-}C_4H_4N_2)_2$ at 54.3 MHz.

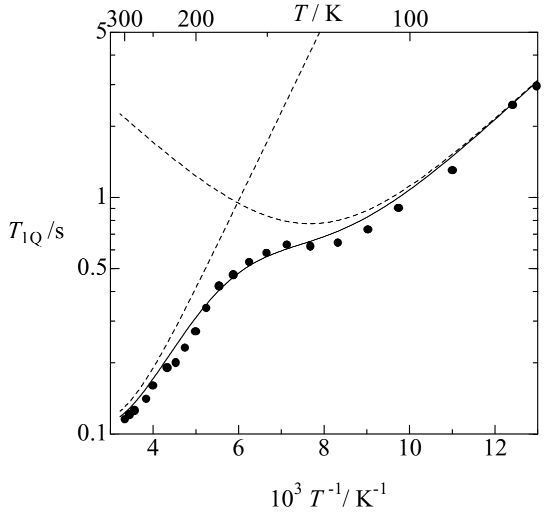

Fig. 4. A temperature dependence of ^{35}Cl NQR spin-lattice relaxation time T_{1Q} in $[C_6Cl_2O_2(OH)_2](1,4\text{-}C_4H_4N_2)_2$. The solid curve is the best-fitted calculated values superimposed by two components shown by broken lines.

3.2 ± 0.5 kJ/mol for the high and low temperature sides of the minimum, respectively, by assuming the classical BPP-type thermal activation model [13]. The lower energy at low temperatures is explainable by the contribution from the H-tunneling [4], which is quite small compared with that in BA and Cl-BA giving marked asymmetric T_{1H} curves. This is because the tunneling H-exchange in the present system is strongly hindered in the highly asymmetric double-well potential made by OH–N H-bonds. The activation energy of 3.9 kJ/mol for the classical H-jumps is acceptable, if one compares this value with 5.5 kJ/mol for the double H-transfer in BA [4], which has the OH–O distance of 263.3 pm [14] a little longer than 259.0 pm of OH–N in the 1,4-complex.

^{35}Cl NQR Spin-Lattice Relaxation Time (T_{1Q})

A temperature dependence of the ^{35}Cl NQR spin-lattice relaxation time (T_{1Q}) observed in the 1,4-complex is shown in Figure 4 [10], giving a shallow T_{1Q} minimum at ca. 120 K and a decrease above 200 K. Assuming the presence of two relaxation processes, the observed curve was expressed by a superposition of the following Debye-type relaxation curve [15]:

$$T_{1Q}^{-1} = C[\tau_c/(1 + \omega_Q^2 \tau_c^2)], \quad (1)$$

and

$$\tau_c = \tau_0 \exp(E_a/RT), \quad (2)$$

where C, τ_c, ω_Q, and E_a denote the motional constant, the motional correlation time, the NQR angular frequency, and the activation energy, respectively. The best-fitted calculated T_{1Q} is given in Figure 4. Since the minimum temperature of ca. 120 K is close to 135 K for T_{1H} and also the obtained E_a of 3.2 kJ/mol agrees with that from T_{1H}, this minimum corresponds clearly to the H-transfer motion obtained by ^{1}H NMR, namely, the correlated H-transfer between structures I and II. NQR and NMR relaxations were analogous with each other up to ca. 150 K, however, they became quite different in the high-temperature range. The other relaxation process observed in NQR showed no sign in NMR, which gave a linear increase and quite long T_{1H} of ca. 200 s at room temperature. As this relaxation mechanism occuring in NQR, we propose "uncorrelated H-transfer" in which two protons in the symmetric two OH–N H-bonds in a complex perform independent jumps. It is noted that this uncorrelated transfer takes place by accompanying changes of electric charges on chloranilic acid, because the formal charge on a chloranilic acid molecule can be divalent (2−), monovalent (1−), and neutral (0), in the case where two H-motions occur uncorrelatedly. Since the monovalent state was shown to be most stable, it is quite reasonable to consider that the neutral and divalent states are excited by the uncorrelated H-transfer at elevated temperature.

From the above consideration, the total motional scheme of the H-transfers can be given in Figure 5. In the high-temperature range, two possible modes, i.e. those between monovalent and divalent states, and between monovalent and neutral states, can take place. In the present measurement of T_{1Q}, however, since no minimum was observed in the range up to 300 K, the T_{1Q} decrease observed above ca. 200 K is assignable to one of these two modes or possibly both.

A surprising result in the present study is that the uncorrelated H-transfer motion could not be detected by ^{1}H NMR, although the correlated H-transfer was clearly observed. This mystery can be explained well by considering differences of the relaxation mechanisms in NMR and NQR by the following reason.

In ^{1}H NMR for the present system, as was described above, the H-jumps in H-bonds make only a weak magnetic field fluctuation. This is the reason why the correlated H-transfer afforded a quite long T_{1H}. After the onset of the correlated H-transfer, the uncorrelated motions start upon heating. Since the magnetic field fluctuation by the H-transfer has already been averaged at low temperatures, even if the uncorrelated H-transfers are excited at high temperatures, further fluctuations should be quite small, because the fluctuation at the diazine protons in this mode comes from those on the opposite side of the chloranilic acid molecule separated by several 100 pm. Using the reported crystal structure data [9], it was roughly estimated

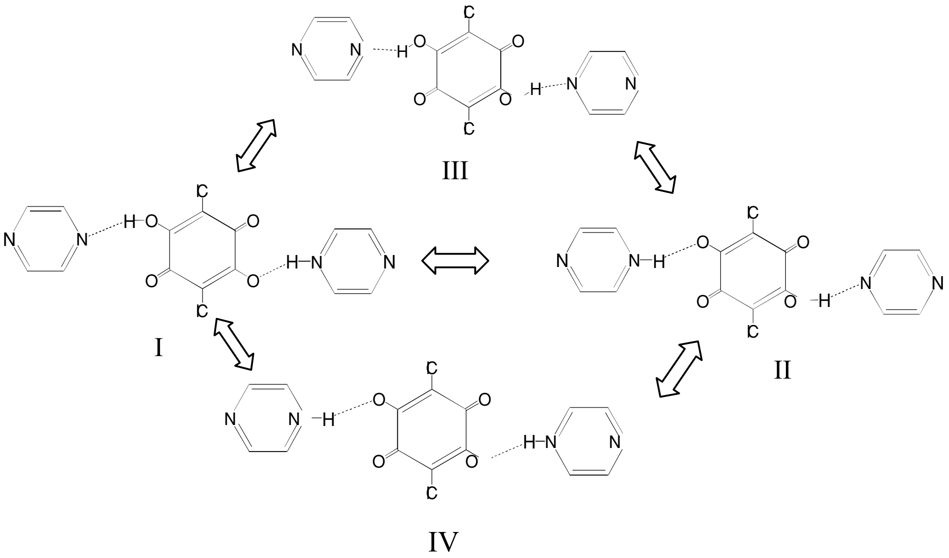

Fig. 5. An H-transfer model in $[C_6Cl_2O_2(OH)_2](1,4\text{-}C_4H_4N_2)_2$. The correlated transfer mode I ↔ II keeps the monovalent state of acid, while the uncorrelated transfer modes I ↔ IV (or II ↔ VI) and I ↔ III (or II ↔ III) are accompanied by changes of the formal charge on acid molecules.

that the T_{1H} minimum due to the uncorrelated H-transfer becomes ca. 400 times longer than that from the correlated motion. This implies that its T_{1H} becomes several thousand seconds and will be completely masked by the relaxation from the correlated motion.

On the other hand in NQR, the uncorrelated motions result in changes of the formal charges on chloranilic acid molecules as shown in Figure 5. This implies that the charge distribution on the phenyl ring, i.e. EFG at the resonant chlorine nuclei, fluctuates during the uncorrelated motions. This fluctuation seems to be much stronger than that in the correlated motion which keeps the monovalent structure of the acid molecules. This is the reason why the marked shortening of T_{1Q} was observed for uncorrelated H-transfers. The above NQR data clearly indicate that the sensitivity for the detection of intermolecular H-transfers in the NQR method is much higher than that of ^{1}H NMR, of course, NMR can provide complementary important information.

Multi-H-Transfer Motions in (Chloranilic Acid)(1,2-diazine) 1:2 Molecular Complex

In the previous section, different modes of H-transfers in a multi-H-bonded system were shown to be separately detected by the NQR relaxation measurement [10]. This work is the first study so far reported, where different H-transfer modes were separated. In the previous 1,4-complex, however, only two relaxation processes were observed by NQR, although three H-transfer modes are predicted. This is because the high-temperature process afforded only a T_{1Q} decrease and no minimum up to room temperature, and, hence, we could not distinguish motional modes, even if more than one mode contribute to the relaxation. To improve the situation, we measured an analogous multi-H-bonded system, but different H-bonded structures are expected. A new system is (chloranilic acid)(1,2-diazien) 1:2 complex, $[C_6Cl_2O_2(OH)_2](1,2\text{-}C_4H_4N_2)_2$ abbreviated to 1,2-complex, in which two symmetric H-bonds analogous to those in the 1,4-complex are formed in crystals, and an OH–N H-bond length of 258.2 pm [16] shorter than 259.0 pm in the 1,4-complex [9], was reported. It is noted that the pK_{a1} value of 2.24 in 1,2-diazinium ions in solution [12] is much higher than 0.57 in 1,4-diazinium, indicating the stability of high ionic states of chloranilic acid in the 1,2-complex, if one refers $pK_{a1} = 0.76$ and $pK_{a2} = 2.72$ in chloranilic acid [12]. This implies the easier formation of chloralilate (1−) and (2−) ions, suggesting that different H-transfer modes from those in the 1,4-complex are expected in this system.

^{35}Cl NQR Frequencies

The observed ^{35}Cl NQR frequencies for the 1,2-complex are shown in Figure 6 [17]. We should note that $\nu = 34.940 \pm 01$ MHz at 77 K is much lower than 36.400 MHz in the 1,4-complex [10]. This frequency is close

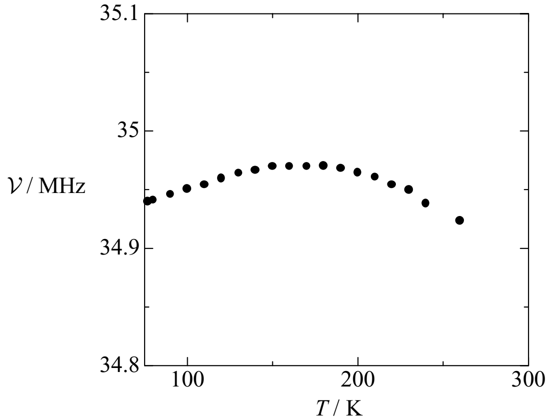

Fig. 6. A temperature dependence of ^{35}Cl NQR frequency (ν) observed in solid $[C_6Cl_2O_2(OH)_2](1,2\text{-}C_4H_4N_2)_2$.

to 35.2 MHz in the divalent salt, sodium chloranilate $[C_6Cl_2O_2(ONa)_2]$ [11]. This indicates, as expected from the pK_a values of the acid and base, that the divalent ionic state of chloranilic acid given below is the most stable in crystals, in contrast to the monovalent structure mostly populated in the 1,4-complex.

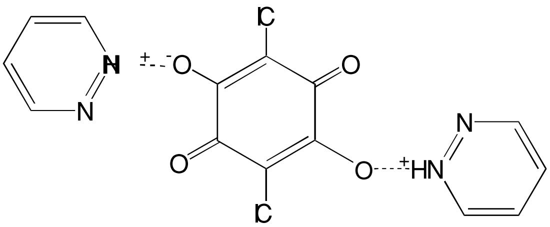

^{1}H NMR and ^{35}Cl NQR Relaxation Times (T_{1H} and T_{1Q})

The observed ^{1}H NMR and ^{35}Cl NQR relaxation times are shown in Figure 7(a and b), respectively [17]. A shallow single T_{1H} minimum analogous to that in the 1,4-complex was observed at ca. 110 K, indicating the onset of an H-transfer motion. Slopes of a slight asymmetric T_{1H} curve afford activation energies of 3.8 and 3.2 ± 0.5 kJ/mol, on the high and low temperature sides of the minimum, respectively. These values are quite close to those in the 1,4-complex. On the other hand in NQR measurements of T_{1Q}, at least three relaxation processes were observed in the temperature range studied. Analogously to the analysis in the 1,4-complex given above, three T_{1Q} components were fitted by Equations (1) and (2), and the best-fitted curve is given in Figure 7, where the lowest temperature relaxation was attributed to the same motion detected by ^{1}H NMR, and its T_{1Q} curve was fitted by use of the ^{1}H NMR data.

Analogously to the 1,4-complex, the H-exchanging scheme in the 1,2-complex can be expressed in Figure 8. Since the most populated structure of chloranilic acid was shown to be divalent given by I, the first excitation at low temperatures occurs inevitably to the states monovalents II and III. If we accept this model, the possible relaxation in the intermediate-temperature range can be attributed between II and III, and the high-temperature one to the neutral structure IV from II and III. The latter process is expected to have a higher barrier, because the time-averaged most stable structure is close to the divalent I state that needs a high energy for producing the neutral structure. This can also be shown from a marked difference between the pK_{a1} and pK_{a2} values in chloranilic acid. In this complex, accordingly, we could obtain one-to-one correspondences between the observed data and the expected H-transfer modes.

In the present complex, only a single relaxation process was observed in the NMR spectrum, whereas three processes were clearly detected by NQR supporting the foregoing discussion for the differences of the relaxation mechanisms found by NQR and NMR on the 1,4-complex.

Conclusion

In the present combined studies of NMR and NQR relaxations on intermolecular H-transfers in multi-H-bonded systems, it is clearly shown that NQR can be a new technique for the separated detection of respective H-motions successively excited with temperature. Individual intermolecular H-transfer motions were clearly detected by observing the conventional NQR spin-lattice relaxation time. Such detailed H-transfer modes have not been successfully observed by other techniques within my knowledge. The ^{1}H NMR relaxation measurement always provided only a single process for the lowest temperature H-transfer mode but can be useful as a complementary technique giving evidence for H-motions and enabling the theoretical analysis of relaxation.

A characteristic feature of NQR has well been understood to be the high sensitivity for detecting electric charge distributions in the neighborhood of the resonant nuclei in crystals and has been used for observing subtle changes in crystal lattices at phase transitions undetectable by other techniques. If we notify this advantage of NQR, it can be easily accepted that the intermolecular H-transfer as a proton resulting in the charge transfer between molecules gives a huge effect on the NQR relaxation.

As an experimental technique, the present method is quite simple and applicable to systems with complicated H-transfer modes by applying the multi-NQR method,

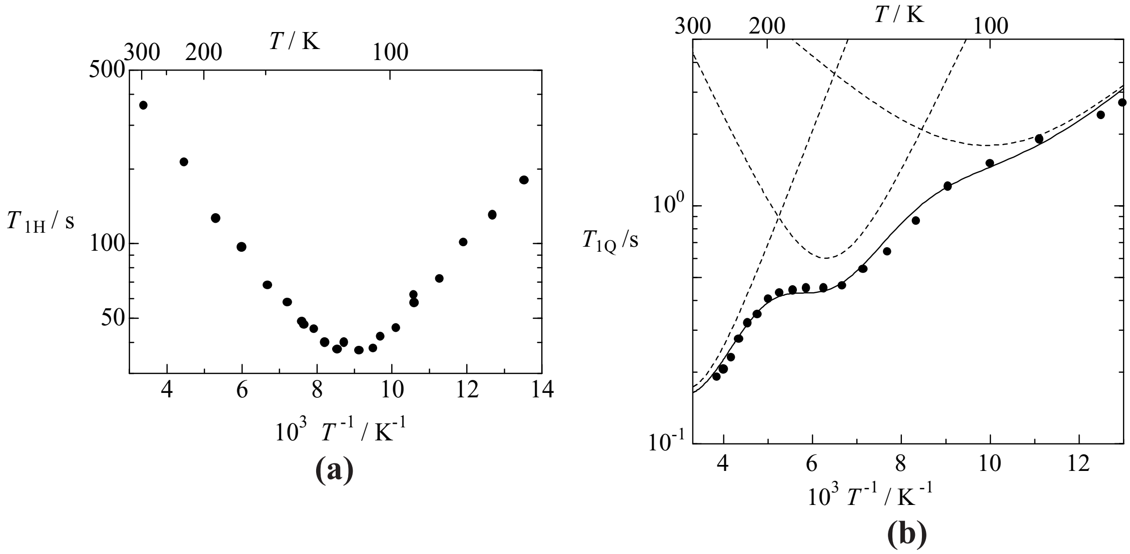

Fig. 7. Temperature dependences of (a) ^{1}H NMR spin-lattice relaxation time (T_{1H}) observed at 54.3 MHz and (b) ^{35}Cl NQR relaxation time (T_{1Q}) in solid $[C_6Cl_2O_2(OH)_2](1,2\text{-}C_4H_4N_2)_2$. Broken lines show calculated three relaxation processes and the solid line shows the best-fitted calculated values.

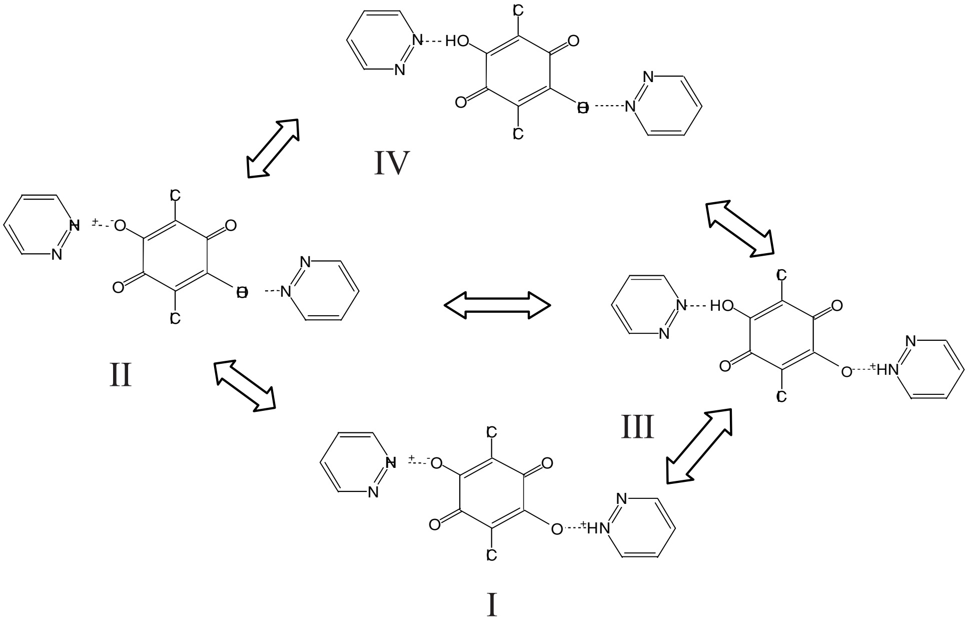

Fig. 8. An H-transfer model in solid $[C_6Cl_2O_2(OH)_2](1,2\text{-}C_4H_4N_2)_2$.

e.g. the measurements of different kinds of NQR nuclei such as ^{35}Cl, ^{81}Br, ^{127}I, ^{2}H, ^{14}N, etc., which are introduced in different molecules.

References

1. Jona F, Shirane G. Ferroelectric Crystals. Dover Publications: New York, 1993.
2. Howell FL, Pinto NJ, Schmidt VH. Phys. Rev. 1992; B46:13762.
3. Davydov AS. Solitons in Molecular Systems. Kluwer Academic Publications, Dordrecht, 1991 (English translation).
4. Skinner JL, Trommsdorff HP. J. Chem. Phys. 1988;89: 897.
5. Smith JAS (Ed). Advances of Nuclear Quadrupole Resonance. Heyden: London, 1974 (Vol. 1), 1975 (Vol. 2).
6. Rigamonti A. Adv. Phys. 1984;33:115.
7. Nihei T, Ishimaru S, Ikeda R. Z. Naturforsch. 2000;55a:355.
8. Miller RS, Paul IC, Curtin DY. J. Am. Chem. Soc. 1974;96:6334.
9. Ishida H, Kashino S. Acta Cryst. 1999;C55:1714.
10. Nihei T, Ishimaru S, Ishida H, Ishihara H, Ikeda R. Chem. Phys. Lett. 2000;329:7.
11. Hart RM, Whitehead MA, Krause L. J. Chem. Phys. 1972;56:3038.
12. Cadogan JIG, *et al.* (Eds), Dictionary of Organic Compounds, 6th ed., Vols. 3 and 6. Chapman and Hall: London, 1996; Habeeb MM, Alwakil HA, El-Dissouky A, Fattah HA. Pol. J. Chem. 1995;69:1428.
13. Abragam A. The Principles of Nuclear Magnetism. Oxford University Press: New York, 1986 (chapter VIII).
14. Bruno G, Randaccio L. Acta Cryst. 1988;B36:1711.
15. Woessner DE, Gutowsky HS. J. Chem. Phys. 1963;39:440.
16. Ishida H, Kashino S. Acta Cryst. 1999;C55:1149.
17. Nihei T, Ishimaru S, Ishida H, Ishihara H, Ikeda R. Chem. Lett. 2000;2000:1346.

EPR: Principles

Bruce R. McGarvey
Department of Chemistry and Biochemistry, University of Windsor, Windsor, Ontario N9B 3P4, Canada

The basic methodology and development of the spin Hamiltonian method as well as the terminology and symbols used in EPR developed out of atomic spectroscopy. Therefore it is useful to review how atomic spectroscopy of atoms and ions dealt with the Zeeman effect, which is the effect of a magnetic field on atomic spectra. This is all covered in the classic work by Herzberg [1].

Angular Momentum

All magnetic properties of materials have their origin in angular momentum of electrons, nuclei, and molecules. Since the quantum mechanics of angular momentum is identical for all species, we will review the important elements of the quantum mechanics for the nuclear spin. The three operators of nuclear spin about the three coordinates are $\hat{I}_x$, $\hat{I}_y$, and $\hat{I}_z$. These operators are in units of $\hbar$. From the commutation properties of these three operators, it can be shown that the nuclear spin functions are eigenfunctions of the total angular momentum operator $(\hat{I}_x^2 + \hat{I}_y^2 + \hat{I}_z^2)$ and one of the three basic operators, generally chosen as $\hat{I}_z$. This is summarized below:

$$\begin{aligned} \left(\hat{I}_x^2 + \hat{I}_y^2 + \hat{I}_z^2\right) |I, M_I\rangle &= I(I+1)\, |I, M_I\rangle \\ \hat{I}_z\, |I, M_I\rangle &= M_I\, |I, M_I\rangle \end{aligned} \qquad (1)$$

where $|I, M_I\rangle$ is the ket notation for the spin function with eigenvalues I and M_I. Each nucleus has a specific value for I which must be integer or half-integer, while M_I can have the values $M_I, (M_I - 1), (M_I - 2), \ldots, -M_I$. Two other relations to know, if you are to solve spin Hamiltonians are the raising and lowering operators $\hat{I}_\pm$:

$$\begin{aligned} \hat{I}_\pm &= \hat{I}_x \pm i\hat{I}_y \qquad (2) \\ \hat{I}_\pm\, |I, M_I\rangle &= \sqrt{I(I+1) - M_I(M_I \pm 1)}\, |I, M_I \pm 1\rangle \end{aligned}$$

where the imaginary number $i = \sqrt{-1}$.

For electrons, the spin operator symbol is $\hat{S}$ and the quantum numbers are S and M_S. For a single electron it is conventional to use a lower case s and the quantum numbers $s = 1/2$ and $m_s = \pm 1/2$. For orbital angular motion it is conventional to use the symbol L for multiple electron systems and 1 for a single electron. Due to the spatial origin of this angular momentum property, only integer values of L and 1 are allowed.

Spin–Orbit Interaction

The angular motion of the electrons generates a magnetic field that interacts with the magnetic moment of the electron's spin, so there is a spin–orbit interaction that must be included, which has the form: $\hat{H}_{LS} = \lambda \hat{L} \cdot \hat{S}$. The spin–orbit interaction parameter, λ, is of the order of 10–100 cm^{-1} for low atomic numbers and increases to better than 10,000 cm^{-1} in the lanthanide series and is positive when a given p, d, or f shell is less than half filled and negative when the shell is more than half filled. This spin–orbit interaction which links $\hat{L}$ and $\hat{S}$ mixes up the $(2L+1)(2S+1)\, LS$ states to produce states defined by the total angular momentum operator $\hat{J} = \hat{L} + \hat{S}$ which have the J quantum numbers $|L+S|$, $|L+S-1|, \ldots |L-S|$ and energies

$$E_{LS} = \frac{\lambda}{2}\left[J(J+1) - (L(L+1) - S(S+1)\right] \qquad (3)$$

Zeeman Interaction

The magnetic moment operator for the angular motion of the electrons is $\beta_e \hat{L}$, where β_e is the Bohr magneton. The magnetic moment operator for electron spin is $g_e \beta_e \hat{S}$, where $g_e = 2.0023$ and for the nuclear spin it is $g_N \beta_N \hat{I}$, where β_N is the nuclear magneton. For an atom or ion with both orbital angular momentum and spin the Hamiltonian operator for the interaction with a magnetic field B is

$$H_Z = \beta_e(\hat{L} + 2\hat{S}) \cdot B \qquad (4)$$

which can be rewritten for a given J state as

$$\begin{aligned} H_Z &= g_J \beta_e \hat{J} \cdot B \\ g_J &= \frac{3J(J+1) + S(S+1) - L(L+1)}{2J(J+1)}. \end{aligned} \qquad (5)$$

Graham A. Webb (ed.), Modern Magnetic Resonance, 439–444.
© 2008 *Springer.*

g_J is called the Landé g factor. From Equation (4) we derive that the magnetic interaction splits the J state into $(2J + 1)$ states with energies

$$E_{M_J} = g_J \beta_e B M_J. \tag{6}$$

Spin Hamiltonian

EPR deals with magnetic systems that have a degenerate or nearly degenerate ground state whose energy levels are changed in the presence of an applied magnetic field and EPR spectroscopy deals with the magnetic transitions between these energy levels, which are induced by electromagnetic radiation of the system. Magnetic systems in this definition refer to materials that have traditionally been called paramagnetic, ferromagnetic, and anti-ferromagnetic materials and not the weakly magnetic materials studied by NMR spectroscopy, which are traditionally called diamagnetic. Magnetic transitions in the definition refer to transitions induced by the interaction of the oscillating magnetic field of the electromagnetic radiation with the magnetic dipole of the material being studied. No definition can be perfect, so it must be mentioned that there are a few examples in the literature where electronic transitions are also observed in what has been called EPR spectroscopy.

Since the early days of EPR, the spectra have been interpreted [2] in terms of the Spin Hamiltonian appropriate to the system being studied. A Spin Hamiltonian is a Hamiltonian that has only electron spin and nuclear spin operators plus constants and the magnetic field. The constants when properly chosen will give energy levels that will match the energy levels of the system and their dependence upon the applied magnetic field.

$S = {}^1\!/_2$ Systems

The concept is best illustrated by considering the simplest system which has only a doubly degenerate ground state and is represented by an $S = {}^1\!/_2$ spin Hamiltonian. What follows will seem rather elaborate when one considers a simple free radical, which is easily seen to be $S = {}^1\!/_2$, but we will consider, later, two systems in which the $S = {}^1\!/_2$ will be considered more as a “fictitious” spin.

Consider we have a system, which in the absence of a magnetic field, is doubly degenerate. We will label the wave functions as ψ_+ and ψ_-. When we apply the Zeeman operator, H_Z, as given in Equation (4), degenerate perturbation theory asks us to solve the 2×2 determinant

$$\beta_e \begin{vmatrix} \left\langle \psi_+^* \right| (L_z + 2S_z) B_z \left| \psi_+ \right\rangle - E & \left\langle \psi_+^* \right| (L_x + 2S_x) B_x + (L_y + 2S_y) B_y \left| \psi_- \right\rangle \\ \left\langle \psi_-^* \right| (L_x + 2S_x) B_x + (L_y + 2S_y) B_y \left| \psi_+ \right\rangle & \left\langle \psi_-^* \right| (L_z + 2S_z) B_z \left| \psi_- \right\rangle - E \end{vmatrix} = 0 \tag{7}$$

If we now consider the spin Hamiltonian

$$\begin{aligned} \mathcal{H} &= \beta_e \hat{S} \cdot g \cdot B \\ &= \beta_e (g_x S_x B_x + g_y S_y B_y + g_z S_z B_z) \end{aligned} \tag{8}$$

for the $S = {}^1\!/_2$ functions, $|S, M_S\rangle = \left|\frac{1}{2}, \pm\frac{1}{2}\right\rangle$, we obtain the following determinant

$$\beta_e \begin{vmatrix} \frac{1}{2} g_z B_z - E & \frac{1}{2}(g_x B_x - i g_y B_y) \\ \frac{1}{2}(g_x B_x + i g_y B_y) & -\frac{1}{2} g_z B_z - E \end{vmatrix} = 0. \tag{9}$$

Comparison of the two shows that the spin Hamiltonian parameters g_x, g_y, and g_z are obtained from

$$\begin{aligned} g_z &= 2 \left\langle \psi_+ \right| L_z + 2S_z \left| \psi_+ \right\rangle \\ g_x &= 2 \left\langle \psi_+ \right| L_x + 2S_x \left| \psi_- \right\rangle \\ g_y &= -2i \left\langle \psi_+ \right| L_y + 2S_y \left| \psi_- \right\rangle \end{aligned} \tag{10}$$

Equation (10) tells us how to calculate the g parameters in the $S = {}^1\!/_2$ spin Hamiltonian. For the mathematical purist, it should be noted that the g matrix has nine parameters which reduces to six because the off diagonal elements are symmetrical and this matrix can be reduced to a diagonal matrix with only three parameters when one chooses what has come to be called the principal axes. In the above equations we have assumed x, y, and z to be in the principal orientation.

Solution of the determinant in Equation (9) gives the following equation for the two energy states

$$\begin{aligned} E &= \pm \tfrac{1}{2} g \beta_e B; \\ g &= \sqrt{(g_x^2 \sin^2\theta \cos^2\phi + g_y^2 \sin^2\theta \sin^2\phi + g_z^2 \cos^2\theta)} \end{aligned} \tag{11}$$

where θ and ϕ are the polar angles for the orientation of the magnetic field. Note that the sign of the g matrix elements cannot be determined from the energy difference that is measured in the spectrum.

We shall now apply these equations to three examples.

Organic Free Radicals

In these free radicals the orbital angular momentum is essential quenched so there is no $\hat{L}$ contribution and they can be considered to be simple $S = {}^1\!/_2$ systems which would have $g = g_e$. The fact that the g values are slightly different is due to small admixtures of some excited states with electron angular momentum into the ground state through the spin–orbit interaction. These correction factors are small for organic free radicals due to the small values of the spin–orbit interaction parameter for C, N, and O atoms and the high energies of these excited states.

NO˙ Molecule

In the gaseous NO˙ molecule the ground state is $\sigma^2\pi^4\pi^{*1}$, which places the unpaired electron into the fourfold degenerate π^* orbital. The π^* orbital can be written as $(\pi^*)^{\pm}_{\pm 1}$, where the upper ± refers to the two orientations of the electron spin and the lower ± 1 refers to the two orientations of the orbital angular momentum of the π^* orbital.

$$\hat{S}_z(\pi^*)^{\pm}_{\pm 1} = \pm\frac{1}{2}(\pi^*)^{\pm}_{\pm 1} \quad \hat{L}_z(\pi^*)^{\pm}_{\pm 1} = \pm 1(\pi^*)^{\pm}_{\pm 1}$$

The spin–orbit $\lambda\hat{L}\cdot\hat{S}$ interaction creates two states

$$^2\Pi_{\frac{1}{2}} \quad E = -\frac{1}{2}\lambda \quad \psi = (\pi^*)^{+}_{-1}, (\pi^*)^{-}_{+1}$$

$$^2\Pi_{\frac{3}{2}} \quad E = \frac{1}{2}\lambda \quad \psi = (\pi^*)^{+}_{+1}, (\pi^*)^{-}_{-1}$$

and since $\lambda \approx 100\ \text{cm}^{-1}$ the two states are separated by $100\ \text{cm}^{-1}$. The g_z value is given by $(L_z + 2S_z)$, so for both states

$$^2\Pi_{\frac{1}{2}}\, g_z = 0; \quad ^2\Pi_{\frac{3}{2}}\, g_z = 4.0.$$

Thus the ground state is essentially non-magnetic in the gaseous state but the excited state will be thermally occupied at room temperatures and is easily detected in the gas.

If NO˙ is tied down as a ligand or trapped in the solid state or frozen solution state, the axial symmetry is likely to be removed and the orbital angular momentum quenched. Thus giving rise to an $(\pi^*)_x$, or $(\pi^*)_y$ orbital as the ground state which will be EPR active. If we assume the energy of the energy difference between the π_y orbital and the π_x orbital is Δ, without spin–orbit coupling, and then include spin–orbit coupling we obtain a Kramer's doublet ground state and excited state [3] with the energies

$$E = \pm\frac{1}{2}\lambda\sqrt{1+\omega^2};\ \omega = \frac{\Delta}{\lambda} \tag{12}$$

and the following ground state wave functions:

$$\begin{aligned}
\psi_+ &= A(\pi^*)^{+}_{+1} + B(\pi^*)^{+}_{-1}\\
\psi_- &= -B(\pi^*)^{-}_{+1} - A(\pi^*)^{-}_{-1}.\\
A &= -\frac{1}{\sqrt{2}}\left[1 - \frac{1}{\sqrt{1+\omega^2}}\right]\\
B &= \frac{1}{\sqrt{2}}\left[1 + \frac{1}{\sqrt{1+\omega^2}}\right]
\end{aligned} \tag{13}$$

Using Equation (10) with Equation (13) gives the following g values for the ground state:

$$\begin{aligned}
g_z &= 2\left[1 - \frac{1}{\sqrt{1+\omega^2}}\right]\\
g_x, g_y &= \frac{2\omega}{\sqrt{1+\omega^2}}
\end{aligned}. \tag{14}$$

In Equation (14) the value of $g_{z,x,y}$ goes from 0 to 2 as ω increases from 0. Thus for large Δ the ground state becomes the $(\pi^*)_x{}^{\pm}$ orbital. It only takes a $\Delta > 300$–$400\ \text{cm}^{-1}$ to bring $g_{x,y}$ close to 2 from 0, while g_z requires values $> 1{,}000\ \text{cm}^{-1}$. Thus, it takes only a small distortion interaction to convert a non-magnetic ground state to an active state in EPR. For NO attached to catalytic surfaces at liquid N_2 temperatures, the g values [4] are: $g_z = 2.0$ and $g_{x,y} \cong 1.9$.

The fact that the g matrix appears to have axial symmetry, when the molecule does not, is due to the fact that our calculation involves a system of only four functions and two energy states. If we include the existence of other excited states, the low symmetry will appear in the g matrix. The NO system shows some of the artificiality of the spin Hamiltonian concept. This system, is not a simple unpaired electron spin even though we are treating it as such by using the $S = 1/2$ spin Hamiltonian.

High Ligand Field d^5

In lower crystalline fields, Fe^{III}, d^5, has $S = 5/2$ but with ligands such as cyanide, porphyrins, etc. the five electrons are found in only the three t_{2_g} orbitals which in octahedral symmetry is a sixfold degenerate state. The related ions of Ru^{III} and Os^{III} are always found in this state. In this system, the electron orbital angular momentum is not quenched and the spin–orbital interaction plays an important role. It is always fitted to a $S = 1/2$ spin Hamiltonian but the g values vary from 3 to less than 1 and there has been, traditionally, a problem with what the sign of the g value should be. There have been a large number of papers in which the g values are derived but they often do not agree with each other or are difficult to compare. A

Table 1: Equations for the g matrix for the four possible cases using the $d_{\pm 1}$ and d_{xy} basis functions for t_2

Case	g_x	g_y	g_z
1a	$-2\left\lfloor -2ac + b^2 + \sqrt{2}b(a-c)\right\rfloor$	$-2\left\lfloor 2ac + b^2 + \sqrt{2}b(a+c)\right\rfloor$	$-2\left[a^2 - b^2 + c^2 + (a^2 - c^2)\right]$
2a	$-2\left\lfloor -2ac + b^2 + \sqrt{2}b(a-c)\right\rfloor$	$2\left\lfloor 2ac + b^2 + \sqrt{2}b(a+c)\right\rfloor$	$2\left[a^2 - b^2 + c^2 + (a^2 - c^2)\right]$
1b	$2\left\lfloor -2ac + b^2 + \sqrt{2}b(a-c)\right\rfloor$	$2\left\lfloor 2ac + b^2 + \sqrt{2}b(a+c)\right\rfloor$	$-2\left[a^2 - b^2 + c^2 + (a^2 - c^2)\right]$
2b	$2\left\lfloor -2ac + b^2 + \sqrt{2}b(a-c)\right\rfloor$	$-2\left\lfloor 2ac + b^2 + \sqrt{2}b(a+c)\right\rfloor$	$2\left[a^2 - b^2 + c^2 + (a^2 - c^2)\right]$

comprehensive review [5,6] has been written about this and a method of defining the parameters has been put forward to reduce the complexity. A condensed version of the theoretical results will be given here because there is some question as to whether the spin Hamiltonian concept is really proper for this system.

We will treat the problem using the following five electron functions as our starting wave functions:

$$\begin{aligned}
\left|-1, \pm\tfrac{1}{2}\right\rangle &= d_1^+ d_1^- d_{xy}^+ d_{xy}^- d_{-1}^{\pm} \\
\left|+1, \pm\tfrac{1}{2}\right\rangle &= d_{-1}^+ d_{-1}^- d_{xy}^+ d_{xy}^- d_1^{\pm} \qquad (15)\\
\left|0, \pm\tfrac{1}{2}\right\rangle &= \pm i d_1^+ d_1^- d_{-1}^+ d_{-1}^- d_{xy}^{\pm}.
\end{aligned}$$

The use of $\pm i$ in the third function is a mathematical trick to convert the two 3×3 matrices, that have to be diagonalized, from complex matrices to real matrices. The ligand field operator H_C will split the sixfold state into three different energy Kramer's doublets in lowest symmetry. It is customary to define two parameters to express the effect of the ligand field. They are;

$$\left\langle d_{xy}\right| H_C \left|d_{xy}\right\rangle = \Delta \qquad (16)$$

$$\left\langle d_{xz}\right| H_C \left|d_{xz}\right\rangle = \frac{V}{2} = -\left\langle d_{yz}\right| H_C \left|d_{yz}\right\rangle. \qquad (17)$$

Applying both the ligand field and spin–orbit interaction yields the energy determinant

$$\begin{array}{ccc}
\left|-1, \tfrac{1}{2}\right\rangle & \left|0, -\tfrac{1}{2}\right\rangle & \left|+1, \tfrac{1}{2}\right\rangle \\
\left|+1, -\tfrac{1}{2}\right\rangle & \left|0, \tfrac{1}{2}\right\rangle & \left|-1, -\tfrac{1}{2}\right\rangle
\end{array}$$

$$\begin{vmatrix}
(2\Delta - \tfrac{1}{2}\xi - E) & -\dfrac{\xi}{\sqrt{2}} & \dfrac{V}{2} \\
-\dfrac{\xi}{\sqrt{2}} & (\Delta - E) & 0 \\
\dfrac{V}{2} & 0 & (2\Delta + \dfrac{1}{2}\xi - E)
\end{vmatrix} = 0 \qquad (18)$$

and a ground state doublet of the form

$$\begin{aligned}
\psi_+ &= a\left|+1, -\tfrac{1}{2}\right\rangle + b\left|0, \tfrac{1}{2}\right\rangle + c\left|-1, -\tfrac{1}{2}\right\rangle \\
\psi_- &= a\left|-1, \tfrac{1}{2}\right\rangle + b\left|0, -\tfrac{1}{2}\right\rangle + c\left|+1, \tfrac{1}{2}\right\rangle \quad .
\end{aligned} \qquad (19)$$

What we need to consider first is how the g values are obtained from Equation (10). In the earlier examples, we knew which Kramer's doublet to call ψ_+ and ψ_- by which function had spin up or down but both functions in Equation (19) have spins of $+$ and $-$. In this case the assignment is arbitrary and has led to confusion in the literature about the sign. Further the a, b, c constants in the doublet must have the same magnitudes and relative signs to each other but are not required to have the same signs in ψ_+ and ψ_-. Thus we have four possible sets of equations for the g values which yield different combinations for the signs of g, which are set out in Table 1. In the table Case 1a is for the plus and minus labels to be assigned as shown in Equations (19) and for the two sets of mixing coefficients a, b, c having the same sign. Case 2a is the solution for interchanging the plus and minus labels but having both sets of coefficients with the same sign. Cases 1b and 2b are for the solutions in which the signs of the two set of coefficients are opposite.

When there is more than one solution to a mathematical problem, it is customary to use boundary conditions to select the more physically reasonable solution. In this case we use symmetry. For axial symmetry ($V = 0$), the coefficient $c = 0$ and we expect $g_x = g_y$. This rules out Cases 2a and 2b because they give $g_x = -g_y$. In octahedral symmetry, where $a = \sqrt{\frac{2}{3}}$; $b = \frac{1}{\sqrt{3}}$, one would expect all three g values to be identical and this can only happen for Case 1a. In this case, all three g values are -2. Experiments [7] have shown in a few instances, that the g is indeed negative for octahedral strong field d^5 systems. What is the meaning of a negative g? It tells us that the north pole of the magnetic moment for the ion is opposite to that of an electron in a given M_S state.

In this system the angular momentum dominates in octahedral symmetry so calling it a spin one half system is somewhat artificial. The actual wave functions are mixtures of up and down spin functions. We just treat it as a system with a "fictitious" $S = 1/2$ because it has only two states. The choice of Case 1a above works well for near octahedral systems but fails for large distortions. If Δ becomes very large the electron's angular momentum becomes quenched and b approaches 1. In this case 1a gives $g_z = +2$ and $g_{x,y} = -2$ but this cannot be because the magnetic moment is pure spin and all three g values should be $+2$ which is predicted by using Case 1b for calculating g. This ambiguity has plagued researchers in this field and points to a weakness in using the spin Hamiltonian representation for this system.

Hyperfine Interaction

When there is a dipole–dipole interaction between the electron and a nuclear spin a hyperfine term is added of the form

$$\hat{S} \cdot A \cdot \hat{I} \tag{20}$$

where A is a 3×3 matrix. It becomes a diagonal matrix if symmetry requires the principal axes of A to be collinear with the g matrix.

Nuclear Zeeman and Nuclear Quadrupole Interaction

The nuclear Zeeman interaction is similar to the electron's Zeeman interaction, only orders of magnitude smaller. It becomes important only when its magnitude is comparable to the hyperfine interaction of the same nucleus. For nuclear spin systems with $I > 1/2$ there is an interaction between the nuclear quadrupole moment and electrical field gradients that can be represented by a nuclear spin Hamiltonian involving second order nuclear spin operators. If x, y, and z are in the principal axis system for the quadrupolar interaction then the spin Hamiltonian can be written for both terms as

$$-g_N \beta_N B \cdot \hat{S} + \frac{e^2 q Q}{4I(2I-1)} \left\{ \left[\hat{I}_z^2 - \tfrac{1}{3} I(I+1) \right] + \eta \left[\hat{I}_x^2 - \hat{I}_y^2 \right] \right\} \tag{21}$$

where g_N is nuclear g value, β_N is the nuclear magneton, Q is the electric quadrupole moment of the nucleus, q is the electric field gradient at the nucleus, and η is an asymmetry parameter, which by definition can have values only between $-1/3$ and $+1/3$. Q is 0 for $I = 1/2$ and q is 0 for high symmetry sites such as tetrahedral, octahedral, and cubic. The quadrupole term mixes up nuclear spin states allowing forbidden double flip transitions to have finite intensities. Double flip transitions are those in which both the electron and nuclear spins change their quantum numbers simultaneously.

$S > {}^1\!/_2$ Systems

When you have a higher spin system with a degeneracy greater than 2, you must include a term of the form $\hat{S} \cdot D \cdot \hat{S}$, where D is a $(2S+1) \times (2S+1)$ matrix. The source of this spin–spin term comes from two types of interactions; first is the straight dipole–dipole interaction between two unpaired electrons, which is the main source in organic triplet states, and second is spin-orbit–orbit-spin interaction in systems like the transition metal complexes, which have large spin–orbit interaction parameters. In the principal axis system this can be written as

$$D \left\lfloor \hat{S}_z^2 - \tfrac{1}{3} S(S+1) \right\rfloor + E \left\lfloor \hat{S}_x^2 - \hat{S}_y^2 \right\rfloor \tag{22}$$

This spin-Hamiltonian is mathematically identical to the nuclear quadrupole term and the behavior is the same. For axial symmetry $E = 0$ and for symmetries that make x, y, and z identical $D = 0$. Also, if z is the main distortion axis, then $|E| \leq |D|/3$. This interaction is often called the zero field interaction because it produces an energy difference in the $(2S+1)$ spin states even in the absence of a magnetic field. In many transition complexes, this term can be much larger than the Zeeman interaction.

Higher Order Spin–Spin Terms

In higher-spin systems, it has been sometimes found necessary to include higher order spin operator terms. For $S = 3/2$ and higher a term involving $\hat{S}$ to third order and H to first order is allowed by symmetry arguments [8]. In octahedral and tetrahedral symmetry (the only symmetries where this small term has been detected) this term takes the form

$$u\beta_e \left\{ \hat{S}_x^3 B_x + \hat{S}_y^3 B_y + \hat{S}_z^3 B_z - \tfrac{1}{5} \left[3S(S+1) - 1 \right] \hat{S} \cdot B \right\} \tag{23}$$

where x, y, z are cubic axes. For $S = 2$ and greater, terms involving $\hat{S}$ to the fourth power are allowed. In cubic symmetry, it takes the form

$$\tfrac{1}{6} a \left\{ \hat{S}_x^4 + \hat{S}_y^4 + \hat{S}_z^4 - \tfrac{1}{3} S(S+1) \left[3S(S+1) - 1 \right] \right\} \tag{24}$$

For an axial distortion in the z direction the following would have to be added.

$$\tfrac{1}{180}F\left\{35\hat{S}_z^4 - 30S(S+1)\hat{S}_z^2 + 25\hat{S}_z^2 - 6S(S+1) + 3S^2(S+1)^2\right\} \qquad (25)$$

For lower symmetries other terms would have to be added. To further complicate the situation, when $S = 3$ or greater (this happens in the lanthanides and actinides), terms with $\hat{S}$ to the sixth power will be allowed.

In the past, these terms were only included in single crystal work where the position of resonance lines could be determined with high accuracy. This is no longer true with the use of high magnetic field spectrometers, where their magnitude may require inclusion in the analysis of powder and frozen solution spectra [9,10].

Alternate Form for the Zero Field Spin Hamiltonian

There is an alternate form for the zero field terms given above in Equations (22)–(25) that appears more often in the work on lanthanides and actinides. This method uses the following operator function to represent the spin–spin part of the spin Hamiltonian

$$H_{SS} = \sum_{J,M} a_{JM} T_{JM} \qquad (25)$$

where T_{JM} are irreducible tensor operators of $\hat{S}$ with $J = 2, 4, 6$ as required and the a_{JM} are the parameters to be fitted. The T_{JM} functions are operator functions related to the spherical harmonic functions. Examples and the definition can be found in one of the author's papers [11]. In various works the T_{JM} are defined with different constants. See, for example, Abragam and Bleaney [12]. A full discussion is beyond the scope of this introduction to EPR.

References

1. Herzberg G. Atomic Spectra and Atomic Structure. Dover Publications: New York, 1944.
2. Bleaney B, Stevens KWH. Rept. Prog. Phys. 1953;16:108.
3. McGarvey BR, Ferro AA, Tfouni E, Bezerra CWB, Bagatin I, Franco DW. Inorg. Chem. 2000;39:3577–81.
4. Lunsford JH. J. Chem. Phys. 1967;46:4347; J. Phys. Chem. 1968;72:2141; 1970;74:1518; J. Catal. 1969;14:379.
5. McGarvey BR. Quim. Nova. 1998;21(2):206.
6. McGarvey BR. Coord. Chem. Rev. 1998;170:75.
7. Hutchison CA Jr, Weinstock B. J. Chem. Phys. 1960;32:56.
8. Bleaney B. Proc. Phys. Soc. (London). 1959;A73:939.
9. Aromi G, Telser J, Ozarowski A, Brunel L, Stoeckli-Evans H, Krzystek J. Inorg. Chem. 2005;44(2):187.
10. Krzystek J, Fiedler AT, Sokol JJ, Ozarowski A, Zvyagin SA, Brunold TC, Long JR, Brunel LC, Telser J. Inorg. Chem. 2004;43:5645.
11. McGarvey BR. In: TD Marks, RD Fischer (Eds). Organometallics of f-Elements. Reidel: Dordrecht, 1979, pp 320, 333.
12. Abragam A, Bleaney B. Electron Paramagnetic Resonance of Transition Ions. Dover Publications, Inc.: New York, 1986.

Zero Field NMR: NMR and NQR in Zero Magnetic Field

David B. Zax

Department of Chemistry & Chemical Biology, Cornell University, Ithaca, NY 14853-1301 USA, Tel: 1-607-255-3646, Fax: 1-607-255-4137, Email: dbz1@cornell.edu

Zero field NMR serves as the solution to a diverse grouping of very specific problems in solid state magnetic resonance. For some systems large magnetic fields interfere with the interesting phenomenon. In other cases high sensitivity may be achieved, paradoxically, not in high field but only where nuclear spins are transported from high to very low fields and back. And, finally, zero field NMR is of potential interest where the spectral resolution of dipole-dipole couplings and/or quadrupole couplings is limited by the broadening introduced to the spectrum when these nuclear spin interactions are observed in the presence of a large magnetic field. These couplings can be represented in their full form as

$$\mathcal{H}_d = -\sum_{\ell<k} \omega^d_{\ell k}\left[\frac{3(\mathbf{I}_\ell \cdot \mathbf{r}_{\ell k})(\mathbf{I}_k \cdot \mathbf{r}_{\ell k})}{r^2_{\ell k}} - \mathbf{I}_\ell \cdot \mathbf{I}_k\right]$$

where $\mathbf{r}$ is the internuclear vector and $\omega^d_{\ell k}$ the dipole-dipole coupling constant between spins ℓ and k. The coupling constant $\omega^d_{\ell k} \equiv \gamma_k \gamma_\ell \hbar \langle r^{-3}_{\ell k}\rangle$ and thus is itself structurally sensitive. Alternatively, the quadrupolar Hamiltonian is

$$\mathcal{H}_q = A_q(I)\left(3I_z^2 - I(I+1) + \eta\left(I_x^2 - I_y^2\right)\right)$$

where $A_q(I)$ reflects the distribution of electronic charges, and thus chemistry. Both $\mathcal{H}_q$ or $\mathcal{H}_d$ persist even absent any external magnetic field, and zero field studies seek to measure their characteristic frequencies. (While the Hamiltonian associated with the J coupling also survives in zero field, even in liquids, there seems little reason to seek to measure J frequencies—as except in unusually prepared spin systems it generates no splittings[1], and the same information should be available more readily in ordinary high-field experiments.) Collectively we will refer to these forms of the internal Hamiltonians in zero field as $\mathcal{H}_{zf}$.

An Historical Perspective: Field-Cycling NMR

Zero field NMR belongs to an ancient tradition in NMR studies. Pound and Purcell's[2] early demonstration of the existence of "negative temperatures"—with more spins in the excited than the ground nuclear spin state—was achieved by polarizing a sample, removing it rapidly from the field and then turning the sample upside down—and returning the sample to the magnet for detection. Soon thereafter Reif and Purcell[3] observed H_2 at very low temperature, and remarked on the observation of signals whose lineshape differed significantly depending on whether or not they were observed in the presence of a strong external field. That difference focuses our attention on the role played by the external magnetic field. Its primary function is to raise the energies of nuclear spin transitions from the exceedingly low (say, <10 MHz) to the acceptably low. Above some threshold, the resonance frequency is determined by the Zeeman interaction, and increases linearly with the field and in proportion to the magnetogyric ratio γ_k of the kth nuclear spin. The price paid for this increase in sensitivity? $\mathcal{H}_q$ or $\mathcal{H}_d$ are measured only as perturbations on the much larger Zeeman interaction; and as a perturbation, each is expressed in the NMR spectrum in modified forms, where the orientation as defined in the frame of the external field matters. The observable portions of $\mathcal{H}_q$ or $\mathcal{H}_d$ are

$$\mathcal{H}'_d = \sum_{\ell<k} \frac{\omega^d_{\ell k}}{2}(1 - 3\cos^2\beta)(3I_{z,\ell}I_{z,k} - \mathbf{I}_\ell \cdot \mathbf{I}_k)$$

$$\mathcal{H}'_q = -\frac{A_q(I)}{2}\left(3I_z^2 - I(I+1)\right)\Big((3\cos^2\beta - 1) + \eta\sin^2\beta\cos 2\alpha\Big)$$

where the angles α, β represent the Euler angles corresponding to rotations about the laboratory y- and z-axes which relate the laboratory (L) frame of reference and a consistently chosen axis system representing the internal interactions (the M frame). In disordered or powder samples this require many sets of rotation angles $\Omega \equiv \{\alpha, \beta\}$, as the necessary rotation R differs from orientation to orientation. For the sample as a whole we indicate this distribution via the symbol R_Ω, and an explicit calculation must integrate over the distribution of $P(\Omega)$. Thus the internal Hamiltonians present a distribution of energies when observed as a perturbation in a large externally applied field. This corresponds to a broadening mechanism for the high-field line—as recognized by Reif and Purcell—and removing this spectral broadening is one motivation for studying systems in zero field.

Graham A. Webb (ed.), Modern Magnetic Resonance, 445–451.

© 2008 *Springer.*

Thereafter interest in field-cycled NMR arose in a quite different application. Slichter and Hebel[4], and Anderson and Redfield[5], made critical discoveries about the nature of the superconducting state using the nuclear spins to observe the properties of superconducting electrons pairs in Al. But while nuclear spins might provide the critical confirmation of the nature of electron pairing, there was a simple experimental problem in applying NMR. The magnetic field needed to observe the spins interfered with the superconducting state—yet, absent the magnetic field, the magnetic resonance signature would be unobservably weak. The solution? Study superconductivity by monitoring the change in nuclear spin properties in zero field—but brought to zero field only for a brief period ($<T_1$) only. Samples are "prepared"—i.e. polarized—and signals detected in sufficiently high magnetic field so that the sensitivity of the experiment is reasonable; in between these two time periods the more interesting physics can be probed by removing the polarizing and detecting field. The same methodology has been adapted to the study of molecular tunneling in the rotation of methyl groups[6]; in low magnetic fields tuned radio frequency irradiation can drive the transitions between tunnelling states.

Sensitivity Enhancement of Low-γ Nuclear Quadrupole Resonance

The essence of field-cycled magnetic resonance experiments is that low-field frequencies can be detected with high-field sensitivity. Surprisingly enough, for many low-γ nuclear spins the sensitivity of the field cycling experiment exceeds that of high field spectroscopy; at least, where abundant, high-γ nuclear spins, and in particular, ^{1}H's are also available. While the spectrum is detected at high frequencies when the Zeeman interaction dominates, as $I = \frac{1}{2}$ particles with no quadrupolar field the resonance frequencies of those same ^{1}H spins in zero magnetic field are determined only by the range of dipole-dipole couplings, which typically span less than 100 kHz. Thus the demagnetized ^{1}H spins which maintain (for T_1) the polarization of high field have a very low spin temperature. For quadrupolar low-γ (X) nuclear spins, however, the situation is reversed; high field sensitivity is often low often both because the Zeeman frequency is low and/or the concentration of target nuclear spins in the sample is low. In low field, however, the quadrupolar transition frequencies are nearly always higher than the residual dipole-dipole frequencies of the spin–$\frac{1}{2}$ nuclei; thus the demagnetized X spins are nowhere near as cold.

At some magnetic field between that of the polarizing field B_0 and zero field the energy levels of the high-γ and X nuclear spins are matched. Where the two spin reservoirs come into resonance slowly, magnetization transfer equilibrates both baths to the same spin temperature, partially warming the abundant ^{1}H spins while the rarer X spins are significantly cooled. Upon returning to high field, the same level-crossing is re-encountered; as the ^{1}H and X spins have previously achieved equilibrium at exactly that field, no further transfer of magnetization is to be expected—and the ^{1}H spins, when brought back to high field, will be irreversibly warmed, leaving less magnetization for detection from that which would have been observed had there been no magnetization transfer.

Once demagnetized to zero field, various spectroscopic approaches are possible. In field-cycling spectroscopy using level-crossings[7–12], spins in zero field are irradiated and energy absorbed where the applied rf field is resonant with zero-field transition frequencies. Upon remagnetization the ^{1}H high-field signal is further decreased via the level-crossing magnetization transfer mechanism. Where the heat capacity of the X spins is low—as where they are rare—even greater sensitivity can be achieved by repeating the magnetization transfer/irradiation sequence multiple times before detection and repolarization. A plot of the detected ^{1}H magnetization found in high field as a function of irradiation frequencies in zero field shows minima wherever a resonance has been detected—and the minima, of course, correspond to the zero-field frequencies found in the two spin reservoirs. The entire experiment can then be repeated for a new zero field irradiation frequency, thus plotting out the spectrum. The advantages of level-crossing NMR? Unparalleled sensitivity, to the point where it is possible to detect ^{2}H or ^{17}O at *natural abundance* in well-chosen samples. Its disadvantages? That that sensitivity requires samples with very long T_1, so that the field cycle and multiple irradiation sequences can be carried out while the initial magnetization still lingers, and the standard disadvantages of all absorption spectroscopies—specifically, that the resolution and sensitivity cannot be simultaneously optimized.

Zero Field NMR: Experimental Details

As described above, a zero field NMR experiment can be divided into three periods: a period of initial polarization of magnetization, a period during which the field-free frequencies are probed, and a detection period. The polarization period is most typically carried out at high field, as is the detection period; that leaves only the middle period for further discussion. In the zero-field evolution period, various stratagems are possible, as illustrated in Figure 1. Below we discuss some alternatives to traditional level crossing NMR experiments[13].

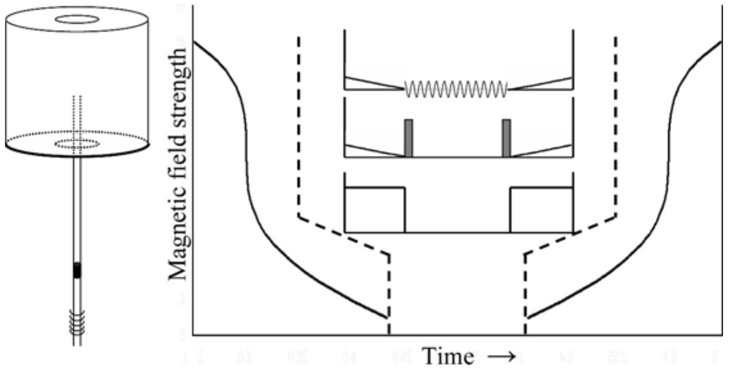

Fig. 1. Description of the time course of a field-cycling zero field experiment. Sample is polarized in high field; the experiment is initiated as the sample is transported to a low field region—here illustrated travelling in a glass tube under pneumatic control. In very low field, there are multiple options; three illustrated include, from the top: adiabatic demagnetization followed by low field irradiation, progressively swept in frequency; middle: evolution initiated by a field pulse (either tuned approximately to a transition, or at zero frequency), and interrupted by a similar pulse, and repeated for longer values of evolution time, or; bottom: signal evolution initiated and terminated by a sudden field transient. In all cases, the sample is then returned to high field for detection.

Demagnetization and Initiation of Evolution

A time-domain version of a similar experiment is possible. In high field, a density operator ρ is prepared which commutes with the Zeeman Hamiltonian $\mathcal{H}_z = -\gamma B_0 I_z$, and the truncated forms $\mathcal{H}'_d$ or $\mathcal{H}'_q$. For times short as compared to T_1, ρ may contain any and all powers of I_z; most commonly (and at equilibrium) $\rho \propto I_z$. Adiabatic demagnetization of the spins from high field, with or without level-crossings, yields a spin polarization which commutes with the zero field Hamiltonian of the spins so that $[\rho, \mathcal{H}_{zf}] = 0$ and therefore oriented in the L frame. Thus there is no macroscopic polarization to be observed along any axis after adiabatic demagnetization, unless the distribution of sample orientations is not uniform.

This fact seems paradoxical—as there is a long history of nuclear quadrupole resonance experiments[14], which manage to observe signals in samples where the only order is associated with the (disordered) alignment of the nuclear spins eigenstates of the zero field magnetic field. Observation of an NQR signal is initiated by a pulse of radiofrequency radiation applied in a coil—and that process selects a subset of orientations for excitation. Thus a detectable magnetization is created along the axis of the coil-as long as the signal is initiated by an excitation *oriented in the laboratory frame* resonant with pairs of energy levels. A similar approach has been demonstrated to initiate time-evolution of quadrupolar nuclear spin systems after adiabatic demagnetization to zero field[15].

An alternative approach abandons the easily managed adiabatic transition to zero magnetic field and instead executes a rapid demagnetization—most practically effected by a two-step process, from the polarizing field to some intermediate field (of order 0.03–0.1 T), followed by a rapid quenching of the intermediate field. Quantum mechanics invokes the sudden approximation to describe the state of the system after rapid demagnetization[16]—and, quite simply, to state that where the demagnetization occurs sufficiently rapidly the spins are unable to respond to the change in their circumstances. Where the polarizing magnetic field can be suddenly reduced so that the ordinary roles of the local Hamiltonians $\mathcal{H}_d$ or $\mathcal{H}_q$ and the Zeeman Hamiltonian $\mathcal{H}_z$ are reversed and $\mathcal{H}_d, \mathcal{H}_q > \mathcal{H}_z$ then the polarized state of magnetization proportional to I_z defined *in the L frame* no longer commutes with the Hamiltonian(s) *defined in the M frame*, and must evolve. The allowed evolution frequencies are determined by the allowed transitions in the zero field Hamiltonian $\mathcal{H}_{zf}$; the transition intensities are determined by the eigenstates of the zero-field Hamiltonian and the orientation(s) of the spin network as compared to the external magnetic field.

A free induction decay is initiated the instant that the polarizing field is removed; assuming, of course, that the loss of the polarizing field is, indeed, "instantaneous". Where the polarizing field is removed more gradually, or from an initial value not much larger than $\mathcal{H}_{zf}$ the demagnetization may instead resemble at least in part the adiabatic process described above, and some spin order will instead end up in eigenstates of $\mathcal{H}_{zf}$. Where the intermediate field too low, the free induction decay initiated after a rapid turn-off of that field is of lower overall amplitude, and with intensities which may not be entirely predictable.

Detecting the Zero Field Signal

The magnetization evolving in zero magnetic field can be described via a density operator formalism. Simplest is a description of the density operator in the case of sudden demagnetization from an "infinitely" large magnetic field; under these circumstances the density operator found at zero time in zero field is identical to that prepared in high field $\rho(0) \propto I_{z,L}$ where the subscript makes explicit that the magnetization in zero field is referenced to the z-axis of the laboratory frame. A well-chosen experiment maximizes the initial magnitude of the zero field free induction signal function $S(t) = \mathrm{Tr}[\rho(t)\mathcal{O}]$ where $\mathcal{O}$ is the detected operator. The trace can be maximized at $t = 0$, and thus the power in the zero field spectrum maximized, only where $\mathcal{O} \propto \rho(0) \propto I_{z,L}$. Thus evolving magnetization may be detected in zero magnetic field by wrapping a sensing coil about the sample along the laboratory z-axis as a Faraday-law magnetization detector—precisely as in high field NMR detectors. Such direct detection has not generally been assumed to be feasible in most field-cycling experiments, particularly where the magnetization evolution is initiated by rapid field demagnetization, as the limiting timescales for rapid transitions restrict such experiments to systems with relatively low zero field frequencies. Faraday law detectors vary in sensitivity as the evolution frequency and as a result the signals which might be induced in a solenoidal coil at 100 kHz, would be 1000-fold smaller than the signals from an equal magnetization in a coil of equal Q at 100 MHz. In a precise reversal of the demagnetization process, signal detection requires sample remagnetization, with the rapid turn-on of an intermediate field which stores some of the evolving magnetization as a Zeeman polarization followed by transport to the larger detection field so that conventional high-field NMR provides a measure of the evolved state of $\rho(t)$. Similarly where signal evolution after adiabatic demagnetization is initiated by a field pulse, P, the evolving operator at $t = 0$ is $P^{-1}\rho P$. Then $\mathcal{O}$ should be similarly designed to provide the maximum signal, and signal intensity in high field is maximized if we assume a detectable operator $\mathcal{O} = P\rho P^{-1}$; i.e. we time-reverse the process which generated the evolving magnetization. We will comment on how this might be achieved, below. Alternatively, we might imagine a zero-field detector of form quite different than the Faraday law solenoids typically found in high-field spectrometers.

Evaluation of Signals Observed in Zero Field

No universal treatment of the signals expected in zero field can be provided, as the signal intensities—as opposed to the signal frequencies—are highly dependent on the details of the demagnetization and remagnetization processes. The most straightforward discussion of experimental results arises where the transition to and from zero field happens in the "sudden" limit, and where there is no possibility of level-crossings with any magnetic nuclei. We will emphasize the detailed analysis of this case[17,18].

Magnetization arrives in zero magnetic field as a magnetic dipole of size comparable to that prepared in high magnetic field, and with the same orientation. Time evolution in zero magnetic field can be followed using the density matrix formalism. As $\rho(t) = \exp(\imath\mathcal{H}_{zf}t)$ $\rho(0)\exp(-\imath\mathcal{H}_{zf}t)$, $S(t) \equiv \mathrm{Tr}[\rho(t)\rho(0)]$. This expression, however, is deceptively simple, as ρ is prepared in the L frame, while $\exp(\imath\mathcal{H}_{zf}t)$ is most readily evaluated in the M frame where all comparable spin ensembles share the same $\mathcal{H}_{zf}$. It is simplest to transform $\rho_L \rightarrow \rho_M$; i.e to re-express the density operator of the system in the molecular frame appropriate to a local description of the problem. Two Euler angles are sufficient—and the required angles precisely reverse the transformation described above which rewrite the molecular-frame Hamiltonians $\mathcal{H}_q$ and $\mathcal{H}_d$ in the privileged axis system whose z-axis is parallel to the external magnetic field B_0; so that if R takes the M frame to the L, frame, R^{-1} executes the inverse operation. For any specific orientation our signal is $S_\Omega(t) = \mathrm{Tr}[\exp(\imath\mathcal{H}_{zf}t)R\rho_L(0)R^{-1}\exp(-\imath\mathcal{H}_{zf}t)RI_{z,L}R^{-1}] = \mathrm{Tr}[\rho_M(t), \rho_M(0)]$, and $\rho_M(t) = -\sin\beta\sin\alpha I_{x,M}(t) + \sin\beta\cos\alpha I_{y,M}(t) + \cos\beta I_{z,M}(t)$, so that

$$\begin{aligned}\mathcal{S}_\Omega(t) = {} & \cos^2\alpha\sin^2\beta\,\mathrm{Tr}\left[I_{x,M}(0)I_{x,M}(t)\right] \\ & + \sin^2\alpha\sin^2\beta\,\mathrm{Tr}\left[I_{y,M}(0)I_{y,M}(t)\right] \\ & + \cos^2\beta\,\mathrm{Tr}\left[I_{z,M}(0)I_{z,M}(t)\right]\end{aligned}$$

Where multiple orientations Ω are found, the net signal requires that we integrate over the distribution $P(\Omega)$ describing how our systems are oriented. For the common case that the sample is unoriented $P(\Omega) \propto d(\cos\beta)d\alpha$ and

$$\begin{aligned}\mathcal{S}(t) & \propto \int_0^\pi d\alpha \int_0^{2\pi} \sin\beta\, d\beta\, \mathcal{S}_\Omega(t) \\ & \propto \frac{1}{3}\sum_{p=x,y,z} \mathrm{Tr}[I_{p,M}(t)I_{p,M}(0)]\end{aligned}$$

i.e. the line intensities are given by equal weightings of each of the three possible first-rank tensor orientations of magnetization in the M frame. Normally $[I_p, \mathcal{H}_{zf}] \neq 0$ for all indices p, and all of the magnetization transported to zero field evolves. For simplicity we evaluate the trace in matrix form, making use of $\langle j|I_{p,M}(t)|k\rangle = \langle j|I_{p,M}(0)|k\rangle\exp(-\imath\omega_{kj}t)$ (where $\omega_{kj} \equiv \omega_k - \omega_j$ is the difference in frequency units between energies of the kth

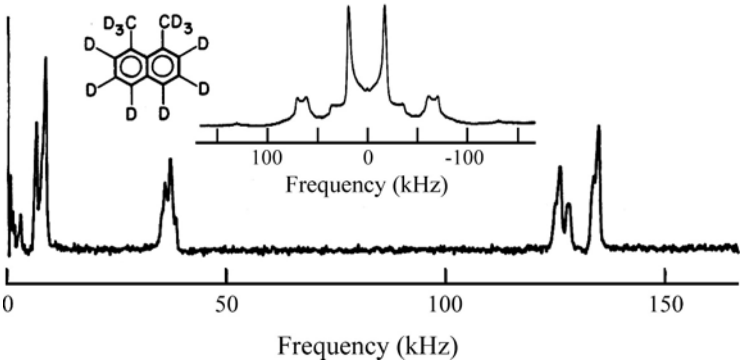

Fig. 2. High field ^{2}H NMR spectrum (inset) and zero field ^{2}H NQR spectrum, of 1,8-dimethylnaphthalene-d_{12}. The inset spectrum shows the quadrupole-echo detected spectrum, with a narrow Pake pattern (singularities at ±18 kHz) derived from the ^{2}H nuclei found in the two pairs of methyl groups, and a broader pattern corresponding to all the ring deuterons. In the zero field NQR spectrum (positive and negative frequencies are indistinguishable) we see ν_0 (at low frequencies <10 kHz), ν_- and ν_+ lines (between 120–135 kHz) from the ring deuterons, indicating substantial variability in the quadrupolar fields A_q at the different ring sites and significant asymmetry parameters η. The methyl group absorption is observed at about 36 kHz; the structure in the band is due to dipole-dipole couplings within the methyl groups.

and jth eigenstates of $\mathcal{H}_{zf}$) and

$$\mathrm{Tr}\left[I_{p,M}(t)I_{p,M}(0)\right] \propto \sum_{j,k} |\langle j|I_{p,M}(0)|k\rangle|^2 \cos\omega_{kj}t$$

For $I = 1$ nuclear spins, each of the three canonical angular momentum operators I_x, I_y and I_z corresponds to a different zero-field transition, and each of the three lines (conventionally labelled ν_0, ν_- and ν_+) is easily observed with very high resolution in Figure 2, which contrasts the high field ^{2}H spectrum of dimethylnaphthalene with its zero field counterpart. In the former, we observe a methyl group (with singularities near ±18 kHz) and a broad absorption band for the various ring sites (with singularities near ±60 kHz); in the latter with see the methyl multiplet pattern near 36 kHz split by the dipole-dipole couplings within the rotating -C^2H_3 group, as well as a series of well-resolved ring lines corresponding to the ν_- and ν_+ transitions from 125–135 kHz, and a set of ν_0 lines (below 10 kHz in the spectrum). Of course, the observed frequencies ω_{kj} and line intensities vary not only with the experiment but with the spin network being probed. No universal description can be provided, but numerous examples of spectra are available for representative spin groupings[19]. Where α and β are not uniformly distributed over the sphere, the zero field spectrum of an oriented sample yields *homogeneous* frequencies ω_{kj} but *inhomogeneous* (i.e. Ω dependent) line intensities.

Detection of the evolving density operator can either proceed directly via a coil wrapped about the sample, or by trapping the evolving magnetization and returning the sample to high field for subsequent detection. Either method registers similar information; but as described above direct detection is difficult with conventional detectors. A significant increase in the efficiency of zero field NMR utilizes Josephson-junction based Superconducting QUantum Interference Devices (SQUIDs)[20–25]. SQUIDs have lower than normal noise floors, and thus improved sensitivity to small changes in flux, as compared to ordinary semiconductor preamplifiers. SQUID-based detectors can be designed to detect either the derivative of the flux—i.e. the same quantity measured in an ordinary Faraday-law detector—or the flux itself. For low frequencies the latter is clearly preferable. Perhaps more importantly, SQUID detectors sample the evolving magnetization for all necessary evolution times in zero field in a single experiment. Where the magnetization is returned to high field for detection of the evolving zero field signal, each new time point can be observed only by trapping magnetization in the intermediate field; the next point requires an entire new polarization/depolarization sequence.

Where the demagnetization takes place adiabatically, evolution must be initiated with an external field pulse. Either a tuned low-frequency rf pulse[15] or a strong dc field pulse[26] will generate evolving magnetization. In either case some signal intensity is sacrificed, as the demagnetized state of magnetization commutes with $\mathcal{H}_{zf}$, and after *any* kind of pulse ρ will still commute in part with $\mathcal{H}_{zf}$. Detection efficiency is maximized by reversing the excitation sequence. Where the excitation and detection involve different operators—i.e. where the demagnetization is adiabatic and evolution is initiated with a field pulse, and the evolving magnetization is trapped when a large field is rapidly turned on—the signal amplitudes are tolerably large, and the zero field evolution frequencies are observed as sums of sines. Level-crossings can also be used so as to indirectly detect the frequencies of zero-field evolution, as in the indirect detection of ^{2}H nuclear resonance frequencies via the ^{1}H magnetization detected after a complete field cycle.

Extensions of Zero Field NMR and NQR

High amplitude, rapidly switched low-frequency (or dc) magnetic field pulses are required to study larger zero field splittings, whether operating in the "sudden" approximation limit, which requires that the switched field be sufficiently high so that $\mathcal{H}_z > \mathcal{H}_{zf}$ and that on-off time τ satisfies $\omega_{kj}\tau < 1$ for all eigenvalues ω_{kj} of $\mathcal{H}_{zf}$, or the adiabatic limit with pulse-initiated evolution. (It is possible to do swept-frequency experiments, though that would seem to obviate much of the advantage of the Fourier method as applied to zero field NMR.) Large pulsed fields (as high as 25–30 T) lasting for short times have been demonstrated in De Haas–van Alphen experiments[27] and similar technology would seem to be adaptable to zero field NMR, although switching large fields on and off in the fringe field of a superconducting magnet introduces unique complications. Nonetheless as implementations of zero field NMR experiments have largely focused on either dipole-dipole coupled networks—especially, ^{1}H-abundant species—or quadrupolar nuclear spin systems with relatively small coupling frequencies, such extreme pulsed fields may not be necessary. (Moreover, for the higher quadrupole frequencies where even stronger pulsed fields might be useful, a field-cycling apparatus may not be necessary, as the natural polarization levels may be sufficient.)

Other extensions include manipulation of spins in zero field. Using pulsed fields it is possible to perform high-resolution COSY[15] or NOESY-like[28] two-dimensional experiments. As the field-cycling experiment is already two-dimensional, with zero field evolution monitored point-by-point in high field, such experiments are actually three-dimensional. Correlation between the zero and high field Hamiltonians should be more time efficient, except that common line-narrowing methods including magic angle spinning (MAS) can which yield more interesting high-field spectra interferes with the resolution in zero field[29]—as the spinning of the sample introduces a new quantization axis uniquely to the laboratory frame—to say nothing of the difficulty of transporting rapidly spinning samples. More extensive manipulation of the spins in zero field is also possible. A more intriguing, though so far largely unused approach, has been to manipulate first- and second-order spin interactions using DC field pulses about three orthogonal axes[30].

Zero Field NMR and NQR: Limitations and Prospects?

An inherent limitation on zero field NMR in dipole dominated networks is that even in modest sized spin systems spectral resolution is poor. Consider N spin–$\frac{1}{2}$ particles, described by 2^N eigenstates. In high field, $m = \langle I_z \rangle$ is a good quantum number, and a single-pulse NMR experiment excites transitions only where $\Delta m = 1$. Thus the number of allowed transitions is limited, though rapidly increasing; for $N = 3$ there are no more than 15 allowed transitions, while for $N = 6$, as many as 792 transitions. In contrast in zero field there are no good quantum numbers and no selection rules, so we expect as many as $2^N(2^N - 1)$ lines; where $N = 3$, fifty six distinct lines may be observed corresponding to varying combinations of only 3 distinct dipole-dipole couplings; and for $N = 6$, four thousand thirty two transitions corresponding to only 15 coupling constants. Exacerbating the problem is that in zero magnetic field no useful distinction exists between nuclei of differing γ so all spin–$\frac{1}{2}$ nuclei participate in the network—and the coupling networks in zero field studies are larger than might be found in high field NMR experiments. (On the other hand, half-integer and integer spins couple only weakly to one another[31].) Finally, the decay of the dipolar field with distance is slow, and thus limiting a spin coupling network to N spins is rarely warranted; in fact, one of the most successful predictors of zero field line shapes is a statistical treatment due to Kubo and Toyabe[32]. Thus the highest resolution spectra, and most of the coherence transfer experiments, have focused on ^{2}H zero field spectra. For this spin-1 system, the quadrupolar frequencies of $\mathcal{H}_q$ play a role in zero field comparable to high field chemical shifts, while $\mathcal{H}_d$ is observed only as a perturbation on the larger $\mathcal{H}_q$. The majority of the remaining studies have emphasized other quadrupolar nuclei with relatively small zero field transition frequencies. The use of SQUID-based detectors to improve sensitivity, allow for direct detection of the evolving zero field magnetization and reduce measurement time will no doubt prove increasingly valuable.

Very high-resolution dipolar spectra of spin–$\frac{1}{2}$ nuclei in zero field NMR have been observed only in spin networks with very small N, and many of the early spectra focused on hydrates such as $Ba(ClO_3)_2 \cdot H_2O$ for that reason. Even in the hydrates absorption bands in zero field are broad, and significantly diminished linewidths adequate to measure a motionally-induced anisotropy in the dipolar field could be observed only once the majority of ^{1}H atoms were removed by recrystallization out of deuterated water solution[18]. That the resolution in $\mathcal{H}_d$ is poor even in zero field has substantially restricted the types of systems amenable to these field cycling studies unless isotopic dilution is used to limit the extent of the spin network (as

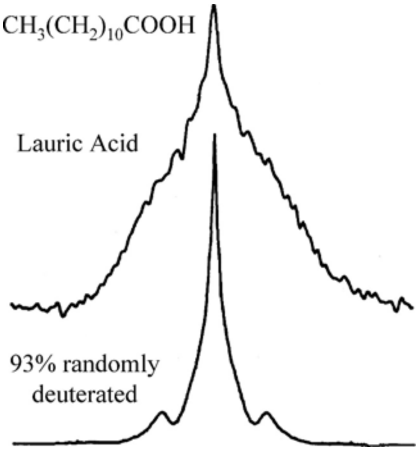

Fig. 3. Zero field ^{1}H NMR spectra of lauric acid, $CH_3(CH_2)_{10}COOH$. At top, spectrum of completely protonated material, showing lack of resolution due to extended network of similar sized dipole-dipole couplings. Below, 93% randomly deuterated lauric acid. The broad peak is substantially narrowed, leaving only isolated pairs which would appear to provide the resolved lines at about ±35 kHz.

in Figure 3). Moreover, a clever high-field-only approach to the same problem has been demonstrated, including detection of ^{13}C-^{13}C dipole-dipole couplings with H decoupling[33, 34]. Zero field NMR observes $\mathcal{H}_d$ untruncated by the magnetic field. In high field where $\mathcal{H}_d$ exists as a perturbation on the much larger $\mathcal{H}_z$, only the eigenvalues of the truncated form $\mathcal{H}'_d$ are normally measured. Averaging in both spatial and spin coordinates by simultaneously spinning and applying pulses can further average $\mathcal{H}'_d$ yielding a further averaging with the remarkable property that the new dipolar Hamiltonian is proportional to the untruncated Hamiltonian $\mathcal{H}_d$, so that a dipolar spectrum without orientational broadening can be observed, without cycling the field from high to low and back again, and observed while a resonant decoupling field is applied which removes abundant, high-γ spins from the spin network being probed. Thus newer developments in zero field NMR and NQR make it increasingly likely that future attempts to measure high-resolution quadrupolar and dipolar spectra in solids will look to avoid the field-cycling methods at the historical origin of these methods.

References

1. Zax DB, Bielecki A, Zilm KW, Pines A. Chem. Phys. Lett. 1984:106:550.
2. Purcell EM, Pound RV. Phys. Rev. 1951:81:279.
3. Reif F, Purcell EM. Phys. Rev. 1953:91:631.
4. Hebel LC, Slichter CP. Phys. Rev. 1959:113:1504.
5. Anderson AG, Redfield AG. Phys. Rev. 1959:116:583.
6. Allen PS, Clough S. Phys. Rev. Lett. 1969:22:1351; Clough S, Horsewill AJ, McDonald PJ, Zelaya FO. Phys. Rev. Lett. 1985:55:1794, and numerous other papers on the same subject.
7. Slusher RE, Hahn EL. Phys. Rev. Lett. 1964:12:246.
8. Hsieh Y, Koo JC, Hahn EL. Chem. Phys. Lett. 1972:13:563.
9. Brown TL, Butler LG, Curtin DY, Hiyama Y, Paul IC, Wilson RB. J. Am. Chem. Soc. 1982:104:1172.
10. Ragle JL, Clymer JW. J. Chem. Phys. 1982:77:4366.
11. Edmonds DT. Int. Rev. Phys. Chem. 1982:2:103.
12. Blanz M, Rayner TJ, Smith JAS. Meas. Sci. Technol. 1993:4:48.
13. Bielecki A, Zax DB, Zilm KW, Pines A. Rev. Sci. Instrum. 1986:57:393.
14. Das TP, Hahn, EL. Nuclear Quadrupole Resonance Spectroscopy, Suppl. No. 1 to Solid State Physics. Academic: New York, 1958.
15. Kreis R, Suter D, Ernst RR. Chem. Phys. Lett. 1985:118:120; ibid. 1986:123:154; Kreis R, Thomas A, Studer W, Ernst RR. J. Chem. Phys. 1988:89:6623.
16. Strombotne RL, Hahn EL. Phys. Rev. 1964:133:A1616.
17. Weitekamp DP, Bielecki A, Zax D, Zilm K, Pines A. Phys. Rev. Lett. 1983:50:1807.
18. Zax DB, Bielecki A, Zilm KW, Pines A, Weitekamp DP, J. Chem. Phys. 1985:83:4877.
19. Bielecki A, Murdoch JB, Weitekamp DP, Zax DB, Zilm KW, Zimmerman H, Pines A. J. Chem. Phys. 1984:80:2232; Zax DB, Bielecki A, Pines A, Sinton SW. Nature 1984:312: 351.
20. Fan NQ, Heaney MB, Clarke J. Newitt D, Wald LL, Hahn EL, Bielecki A, Pines A. IEEE Transactions on Magnetics 1989:25:1193.
21. Fan NQ, Clarke J. Rev. Sci. Instrum. 1991:62:1453.
22. Connor C, Chang J, Pines A. Rev. Sci. Inst. 1990:61:1059; J. Chem. Phys. 1990:93:7639.
23. Hürlimann MD, Pennington CH, Fan NQ, Clarke J, Pines A, Hahn EL. Phys. Rev. Lett. 1992:69:684.
24. Augustine MP, TonThat DM, Clarke J. Solid State Nuclear Magn. Reson. 1998:11:139.
25. Greenberg YaS. Rev. Mod. Phys. 1998:70:175.
26. Millar JM, Thayer AM, Bielecki A, Zax DB, Pines A. J. Chem. Phys. 1985:83:934.
27. Herlach F. Rep. Prog. Phys. 1999:62:859.
28. Suter D, Jarvie TP, Sun B, Pines A. Phys. Rev. Lett. 1987:59:106.
29. Tycko R. Phys. Rev. Lett. 1987:58:2281.
30. Llor A, Olejniczak Z, Sachleben J, Pines A. Phys. Rev. Lett. 1991:67:1989; Llor A, Olejniczak Z, Pines A. J. Chem. Phys. 1995:103:3966; ibid. 1995:103:3982.
31. Leppelmeier GW, Hahn EL. Phys. Rev. 1966:141:724.
32. Kubo R, Toyabe T. In: R. Blinc (Ed). *Magnetic Resonance and Relaxation*. Amsterdam: North-Holland, 1967, pp. 810-823.
33. Tycko R. J. Magn. Reson. 1987:75:193; Phys. Rev. Lett. 1988:60:2734; J. Chem. Phys. 1990:92:5776; Tycko R, Dabbagh G, Duchamp JW, Zilm KW. J. Magn. Reson. 1990:89:205.
34. Sun BQ, Pines A. J. Magn. Reson. A 1994:109:157.

Organo Metallic Chemistry

Organoboron Chemistry

Bernd Wrackmeyer
Department of Inorganic Chemistry, University of Bayreuth, 95447 Bayreuth, Germany

NMR studies of organoboron compounds usually deal with ^{1}H, ^{13}C, and ^{11}B nuclei, and with few exceptions focus on solutions [1–5]. The presence of the quadrupolar ^{11}B isotope (natural abundance 80.42%; $I = 3/2$) can be exploited in several ways.

Measurements of ^{11}B NMR spectra are straightforward with modern NMR spectrometers by single pulse techniques, using short acquisition times (<0.2 s in most cases), 90° pulses, and short repetition delays (<5 ms) The NMR receptivity of the ^{11}B nucleus is high, the ^{11}B NMR signals are not too broad (often <200 Hz) in spite of the sizeable electric quadrupole moment ($Q = 4.1 \times 10^{-2}$ [10^{-28} m^{2}]). And the range of chemical shifts δ^{11}B is fairly large (Figure 1).

For broad ^{11}B NMR signals and diluted solutions, the background signals arising from boron-containing glass additives in the tubes and in the probe head can become a problem. However, in most cases, chemical shifts δ^{11}B are readily determined, even from diluted reaction solutions, and the line widths $h_{1/2}$ of the ^{11}B NMR signals, a measure on the quadrupolar spin relaxation time $T^{Q}(^{11}\mathrm{B})$ [$h_{1/2} = (\pi T^{Q})^{-1}$], provide further valuable information. In principle, ^{10}B NMR can also be measured. However, the NMR properties of ^{10}B are less favorable, since its natural abundance is lower (19.58%), magnetic moment is smaller by a factor of 3, and nuclear spin $I = 3$.

One of the most significant features of δ^{11}B data is the marked difference for boron nuclei with coordination numbers three and four, the latter being more shielded. This means that dynamic equilibria can be studied by ^{11}B NMR with respect to the surroundings of the boron atom. In general, it is possible, even by using moderate field strengths B_0, to distinguish between various boranes present in reaction solutions as shown in Figure 2 for a mixture of diborane(6) derivatives [6].

Two-dimensional (2D) NMR experiments involving ^{11}B nuclei are mainly used for polyboranes, carboranes, other heteroboranes, and their metal complexes in order to establish the ^{11}B/^{11}B connectivity in the clusters. These are simple ^{11}B/^{11}B COSY experiments with simultaneous ^{1}H decoupling [7] or combinations of ^{11}B/^{1}H shift correlations and ^{1}H/^{1}H COSY experiments with simultaneous ^{11}B decoupling [8].

Another important consequence of the presence of ^{11}B concerns effects on the NMR spectra of spin-1/2 nuclei, which in the case of organoboranes are predominantly ^{1}H and ^{13}C nuclei, and less often ^{19}F, ^{31}P, ^{29}Si, or ^{119}Sn nuclei to name a few examples of other spin-1/2 nuclei. If these nuclei are linked directly to boron, their NMR signals will be severely broadened owing to scalar relaxation of the second kind, caused by the spin dynamics of the quadrupolar ^{11}B nucleus which averages scalar ^{11}B–X spin–spin coupling (X = spin-1/2 nucleus). In the case of slow ^{11}B nuclear spin relaxation, splitting of the X NMR signals can be observed. Slight broadening of X NMR signals may also be noticeable in some cases if the ^{11}B nucleus is separated by two or three bonds from X. Heteronuclear decoupling experiments of the type X{^{11}B} (frequently done for X =^{1}H, ^{13}C [9] as shown in Figure 3) can be used for assignments and help to establish the origin of the broadened X NMR signals [10].

The ^{1}H{^{11}B] experiments are standard on all modern NMR spectrometers, whereas the ^{13}C{^{1}H, ^{11}B} or other X{^{11}B} experiments require additional hardware. Since the quadrupole-induced nuclear spin relaxation is more efficient at low temperature, sharpening (“quadrupolar decoupling”) of respective broadened X NMR signals is typically observed by measuring the X NMR spectra at low temperature.

Graham A. Webb (ed.), Modern Magnetic Resonance, 455–457.
© 2008 *Springer.*

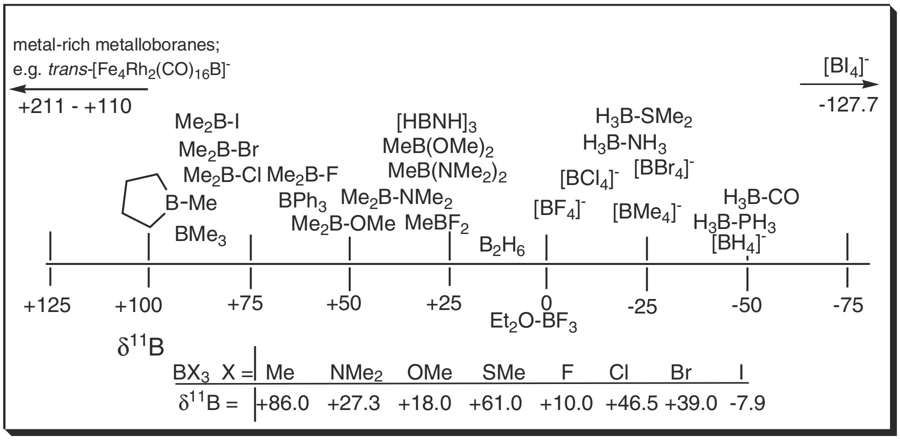
metal-rich metalloboranes;
e.g. trans-[Fe4Rh2(CO)16B]-
+211 - +110
[BI4]-
-127.7
Me2B-I
Me2B-Br
Me2B-Cl
Me2B-F
B-Me
BMe3
BPh3
Me2B-NMe2
Me2B-OMe
[HBNH]3
MeB(OMe)2
MeB(NMe2)2
MeBF2
B2H6
H3B-SMe2
H3B-NH3
[BCl4]-
[BBr4]-
[BF4]-
[BMe4]-
H3B-CO
H3B-PH3
[BH4]-
+125
+100
+75
+50
+25
0
Et2O-BF3
-25
-50
-75
δ11B
BX3 X = Me NMe2 OMe SMe F Cl Br I
δ11B = +86.0 +27.3 +18.0 +61.0 +10.0 +46.5 +39.0 -7.9

Fig. 1. Ranges of ^{11}B chemical shifts $\delta^{11}B$ (relative to $Et_2O–BF_3$ with $\Xi(^{11}B) = 32.083971$ MHz) for various boron compounds ($\delta^{11}B$ data for polyboranes, carboranes, and most borane–transition metal complexes fall into the same range).

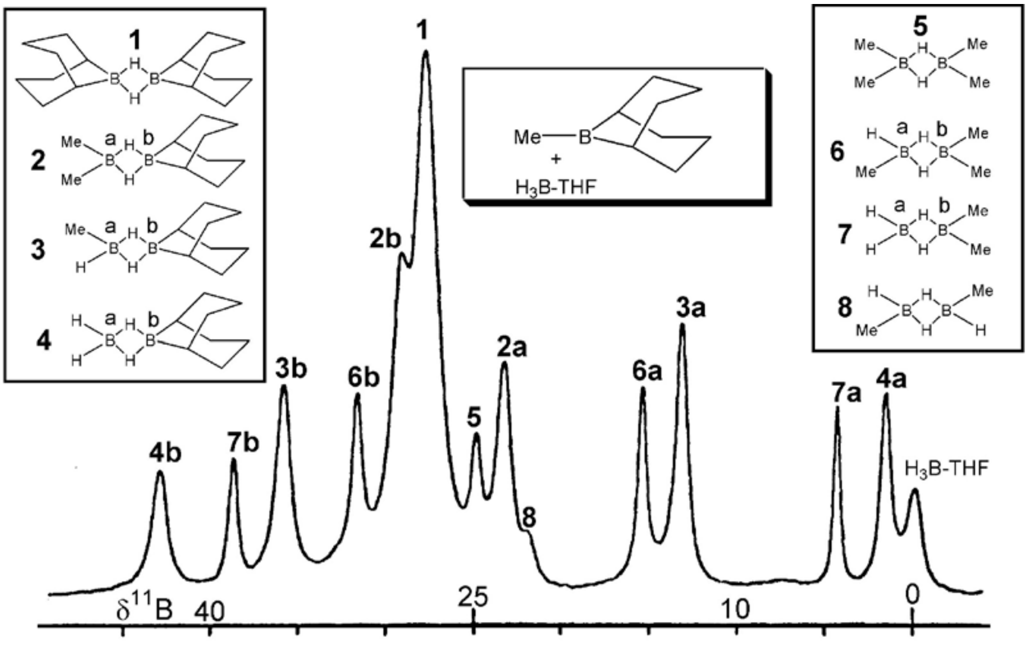

Fig. 2. 64.2 MHz $^{11}B\{^1H\}$ NMR spectrum of an equilibrated reaction solution in THF, obtained from the reaction of 9-Me-9-borabicyclo[3.3.1]nonane with a slight excess of $H_3B–THF$ [6]. Most of the possible diborane(6) derivatives can be readily identified.

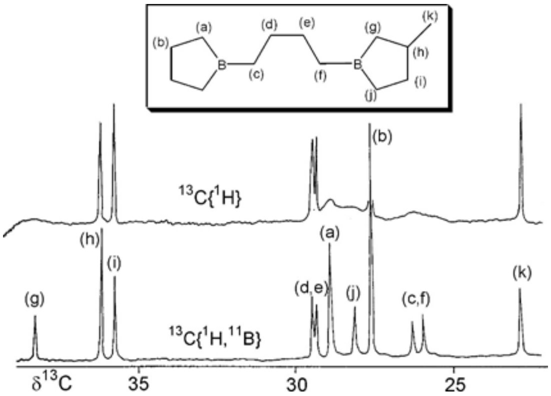

Fig. 3. 50.3 MHz ^{13}C NMR spectra of a triorganoborane containing two slightly different boracyclopentyl groups [9]. The upper trace shows the normal ^{1}H decoupled spectrum with the typically broad ^{13}C NMR signals for carbon atoms bonded to boron. The lower trace shows the effect of ^{11}B decoupling, by which the required five ^{13}C NMR signals appear.

References

1. Eaton GR, Lipscomb WN. NMR studies of boron hydrides and related compounds. W.A. Benjamin Inc.: New York, 1969.
2. Nöth H, Wrackmeyer B. Nuclear magnetic resonance spectroscopy of boron compounds. In: P Diehl, E Fluck, R Kosfeld (Eds). NMR—Basic Principles and Progress, Vol. 14. Springer: Berlin, 1978.
3. Kennedy JD. In: J. Mason (ed). Multinuclear NMR. Plenum Press: New York, 1987, pp 221–58.
4. Wrackmeyer B. Annu. Rep. NMR Spectrosc. 1988;20:61.
5. Siedle AR. Annu. Rep. NMR Spectrosc. 1988;20:205.
6. Contreras R, Wrackmeyer B. Spectrochim. Acta 1982;38A:941.
7. Venable TL, Hutton WC, Grimes RN. J. Am. Chem. Soc. 1984;106:29.
8. Fontaine XLR. Fowkes H. Greenwood NN, Kennedy JD, Thornton-Pett M. J. Chem. Soc. Dalton Trans. 1987: 1431.
9. Contreras R, Wrackmeyer B. J. Organomet. Chem. 1981:205;15.
10. Wrackmeyer B. Polyhedron 1986;5:1709.

Organogermanium Chemistry

Bernd Wrackmeyer
Department of Inorganic Chemistry, University of Bayreuth, Bayreuth, Germany

The NMR spectroscopic characterization of organogermanium compounds is based almost entirely on ^{1}H and ^{13}C NMR measurements in the usual way.

The only magnetically active isotope of germanium is the quadrupolar nucleus ^{73}Ge with rather unfavorable NMR properties (nat. abund.7.76%, low magnetic moment, and spin $I = 9/2$). However, there are several classes of organogermanium compounds, for which meaningful ^{73}Ge NMR spectra can be measured [1–4]. These measurements require additional hardware, since the NMR frequency of ^{73}Ge ($\delta^{73}Ge(GeMe_4) = 0$ for $\Xi(^{73}Ge) = 3.488315$ MHz) is too low for the usual broadband multinuclear probe heads. In many cases, the ^{73}Ge NMR signals are fairly broad as the result of efficient quadrupole-induced nuclear spin relaxation [$T^{Q}(^{73}Ge)$ is short], and the detection of ^{73}Ge NMR signals can become rather difficult by using simple single pulse methods. This is the consequence of "acoustic ringing" [5], typical of low-γ nuclei, which causes a rolling base line (Figure 1, lowest trace) and thus may obscure the real signal if this is also broad.

Various pulse sequences have been developed in order to overcome this problem [6–8]. However, usually a compromise has to be found among loss of sensitivity, long spectrometer time, and a clean or distorted base line. In the future, Hadamard excitation [9] or related techniques could help to solve this problem.

Considering the limited number of known chemical shifts $\delta^{73}Ge$, the overall range for this parameter is not easy to predict. However, the comparison [10] with chemical shifts $\delta^{29}Si$ and $\delta^{119}Sn$ of comparable silicon and tin compounds, respectively, indicates a range of about 2500 ppm. Although, the range of $\delta^{73}Ge$ is larger than that of $\delta^{29}Si$, the pattern follows closely, in most cases, the trends well known for silicon compounds. Less pronounced as for tin compounds, there is a tendency of germanium to increase its coordination number. This is reflected, expectedly, by a considerable increase in ^{73}Ge nuclear shielding [11], and also by changes in the line widths of the ^{73}Ge NMR signals [12].

References

1. Wilkins AL, Watkinson PJ, Mackey KM. J. Chem. Soc. Dalton Trans. 1987;2365.
2. Liepins E, Zicmane I, Lukevics E. J. Organomet. Chem. 1988;341:315.
3. Takeuchi Y, Tanaka K, Harazono T. Bull. Chem. Soc. Japan. 1991;64:91.
4. Riedmiller F, Wegner GL, Jockisch A, Schmidbaur H. Organometallics. 1999;18:4317.
5. Fukushima E, Roeder SBW, J. Magn. Reson. 1979;33:199.
6. Wilkins AL, Thomson RA, Mackay KM, Main Group Met. Chem. 1990;13:219–36.
7. Belton PS, Cox IJ, Harris RK, J. Chem. Soc. Faraday Trans 2. 1985;81:63.
8. Kozminski W., Jackowski K. Magn. Reson. Chem. 2000; 38:459.
9. Kupce E, Nishida T, Freeman R. Prog. NMR Spectrosc. 2003;42:95.
10. Watkinson PJ, Mackay KM. J. Organomet. Chem. 1984; 275:39.
11. Kupce E, Ignatovich LM, Lukevics E. J. Organomet. Chem. 1989;372:189.
12. Takeuchi Y, Tanaka K, Aoyagi S, Yamamoto H. Magn. Reson. Chem. 2002;40:241.

Graham A. Webb (ed.), Modern Magnetic Resonance, 459–460.
© 2008 *Springer.*

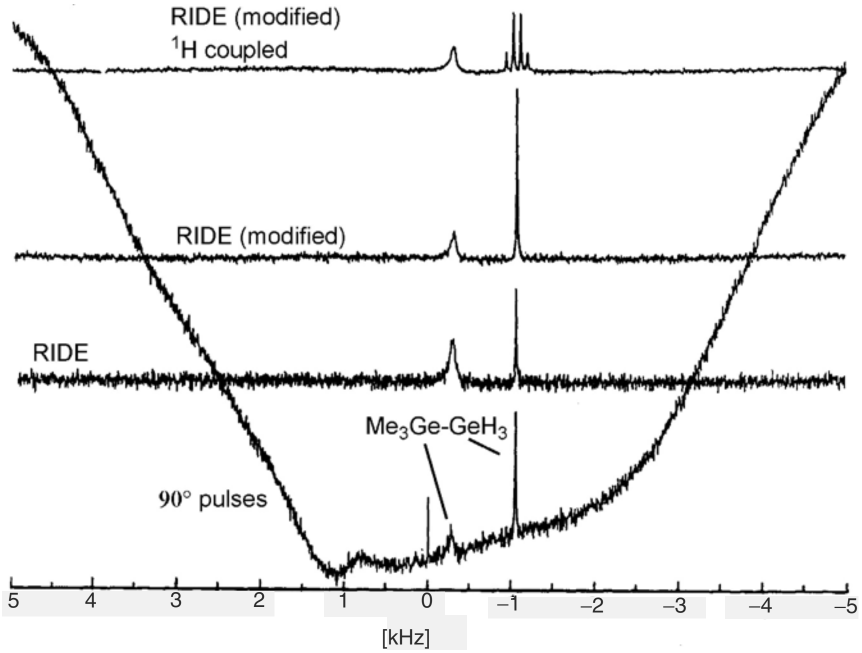

Fig. 1. 3.13 MHz ^{73}Ge NMR spectra of 1,1,1-trimethyldigermane [6]. The lowest trace shows the spectrum obtained by using single pulse mathods. In the middle traces, pulse sequences [6,7] were appied to eliminate the acoustic ringing. The upper trace shows the ^{1}H-coupled spectrum, confirming the assignment of the ^{73}Ge NMR signals.

Organotin Chemistry

Bernd Wrackmeyer

Department of Inorganic Chemistry, University of Bayreuth, 95447 Bayreuth, Germany

NMR studies of organotin compounds in solution deal in most cases with ^{1}H, ^{13}C, and ^{119}Sn nuclei. In some fields of organotin chemistry, solid-state ^{119}Sn NMR measurements become increasingly important [1]. The fact that both ^{119}Sn (8.58%) and ^{117}Sn (7.61%) are spin-1/2 nuclei with appreciable natural abundance (in contrast to ^{115}Sn: 0.35%; $I = 1/2$), and that they are fairly sensitive toward the NMR experiment (factors 25.7 and 19.2 relative to ^{13}C!) creates an attractive situation for ^{119}Sn NMR measurements [2–6], in particular if the molecules in question contain two or more tin atoms.

Measurements of routine ^{119}Sn (or ^{117}Sn) NMR spectra are straightforward using single pulse techniques, acquisition times in the order of 1 s, pulse angles of about 30°–45°, and short repetition times (10 ms). Since the gyromagnetic ratio γ for ^{119}Sn (also for ^{117}Sn) is negative, the NOE (upon ^{1}H decoupling) may cause a problem if it comes close to canceling the ^{119}Sn NMR signal. Therefore, it is advisable to check, for each class of compounds in question, whether ^{119}Sn{^{1}H} and ^{119}Sn{^{1}H-inverse gated} experiments give the same results. Frequently, longitudinal ^{119}Sn nuclear spin relaxation is governed by spin–rotation interactions (T_1^{SR}) or, in particular, at high field strengths B_0, by the chemical shift–anisotropy mechanism (T_1^{CSA}), and then ^{119}Sn–^{1}H dipole–dipole interactions (T_1^{DD}; reasonable for the NOE) play a minor role. A significant gain in the performance of ^{119}Sn NMR is achieved by the application of INEPT experiments [5,6], taking advantage of scalar ^{119}Sn–^{1}H spin–spin coupling, for which a large data set is available from ^{1}H NMR spectra. The most efficient way to obtain ^{119}Sn NMR signals even from very diluted solutions is provided by ^{1}H–^{119}Sn heteronuclear shift correlations (HMQC, HSQC, and HMBC), selecting ^{119}Sn–^{1}H spin pairs and detecting the ^{1}H NMR signals [7].

The chemical shifts δ^{119}Sn cover the large range of about 6500 ppm (Figure 1). The multifaceted chemistry of tin is reflected by a great variety of different surroundings of the tin atoms. It is remarkable that the ^{119}Sn nuclear magnetic shielding is found to be very low for two-coordinate tin(II) compounds bearing organic substituents and rather high again for tin(II) compounds, however, with η^{5}-bonded cyclopentadienyl ligands. A range of about 600 ppm is covered by simple organotin compounds containing tetra-coordinate tin atoms. For these compounds, changes in the δ^{119}Sn values follow closely the trends set by δ^{29}Si or δ^{207}Pb values for comparable silicon or lead compounds [8,9].

The facile change in the coordination number of tin, as a result of the pronounced Lewis-acidic character of many tin compounds can be seen by changes in ^{119}Sn nuclear shielding. Any increase in the coordination number of tin causes shifts of the ^{119}Sn resonances to lower frequencies, even if such interactions are weak (Figure 2). There is a wealth of ^{119}Sn NMR studies of compounds with Sn–O bonds, including cage structures, biologically active species, all in which the tin atoms can have quite different coordination numbers [10,11]. The most useful approach in this field is the combination of X-ray crystallography, solid-state ^{119}Sn NMR and solution-state ^{119}Sn NMR [12].

Many coupling constants $^{n}J(^{119}\mathrm{Sn}, \mathrm{X})$ are readily measured either from ^{119}Sn NMR spectra (Figures 3 and 4) or from X NMR spectra. These couplings provide important information on structure and dynamics of tin compounds [13]. Empirical correlations have been proposed in order to relate bond angles C–Sn–C with the magnitude of coupling constants $^{1}J(^{119}\mathrm{Sn}, ^{13}\mathrm{C})$ [14,15]. The measurement of isotope-induced chemical shifts, e.g. $^{n}\Delta^{12/13}\mathrm{C}(^{119}\mathrm{Sn})$ [6] is straightforward from many ^{119}Sn NMR spectra (Figure 4). Although these parameters are not well understood at present, they may become increasingly important, since they are sensitive to the nature of Sn-element bonds and the coordination sphere of the tin atom [12,16].

Graham A. Webb (ed.), Modern Magnetic Resonance, 461–463.

© 2008 *Springer.*

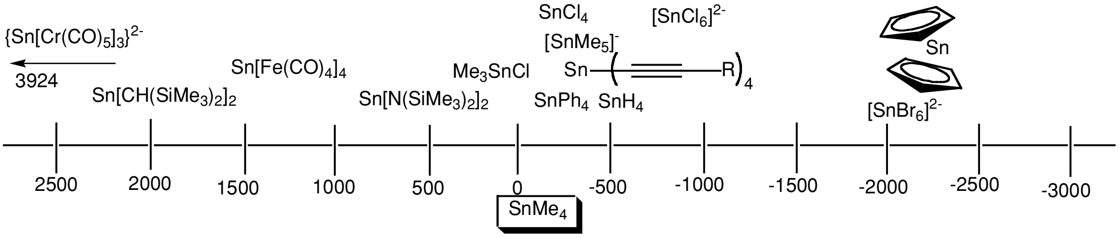
{Sn[Cr(CO)5]3}2-
3924
Sn[CH(SiMe3)2]2
Sn[Fe(CO)4]4
Sn[N(SiMe3)2]2
Me3SnCl
SnCl4
[SnMe5]-
Sn(C≡C–R)4
SnPh4 SnH4
[SnCl6]2-
Sn
[SnBr6]2-
2500
2000
1500
1000
500
0
-500
-1000
-1500
-2000
-2500
-3000
SnMe4

Fig. 1. Full range of δ^{119}Sn values with some representative examples [$\delta^{119}\text{Sn} = 0$ for SnMe$_4$ with $\Xi(^{110}\text{Sn}) = 37.290665$ MHz]. The position of the Sn atom in the formula marks approximately the δ^{119}Sn value.

Fig. 2. Temperature dependence of δ^{119}Sn values of BuSn(OR)$_3$. The more bulky groups R prefer non-associated structures at high temperatures, in contrast with less bulky groups, for which the coordination number (CN) of tin can increase to 6. (Adapted from Ref. [2]).

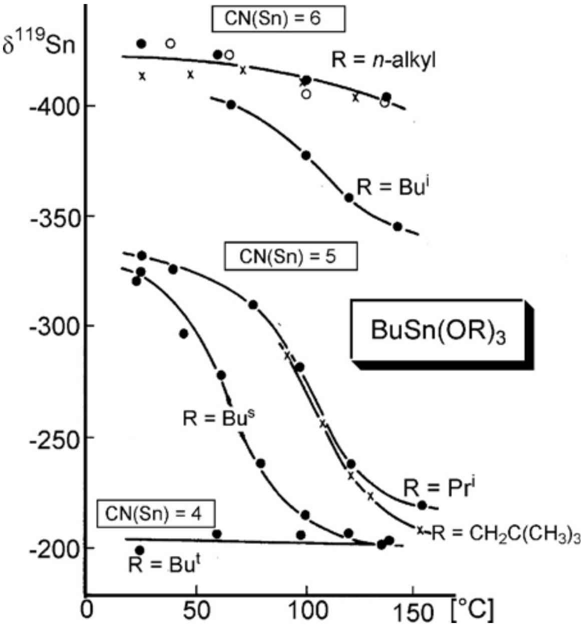

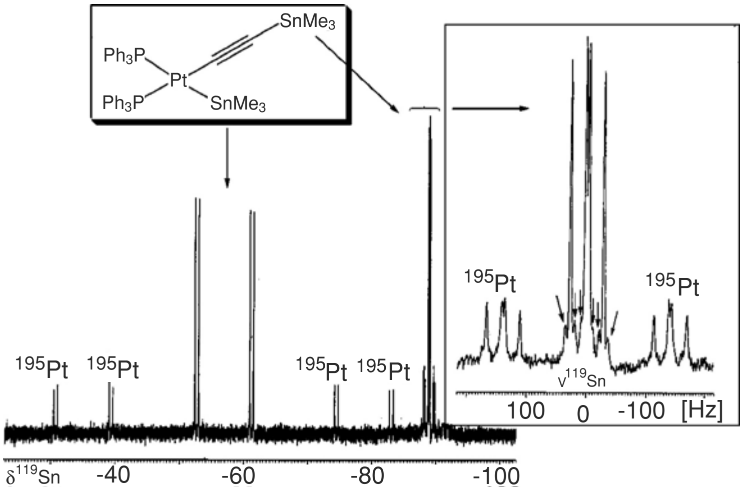

Fig. 3. 186.5 MHz ^{110}Sn{^{1}H} NMR spectrum (INEPT) of a platinum(II) complex (Adapted from Ref. [17]), with two different tin sites and spin–spin coupling to ^{31}P (*cis* and *trans* coupling pathways corresponding to small and larger splitting, respectively), ^{195}Pt (satellites as indicated), and $^{117/119}$Sn (satellites in the expansion shown in the box are marked by arrows).

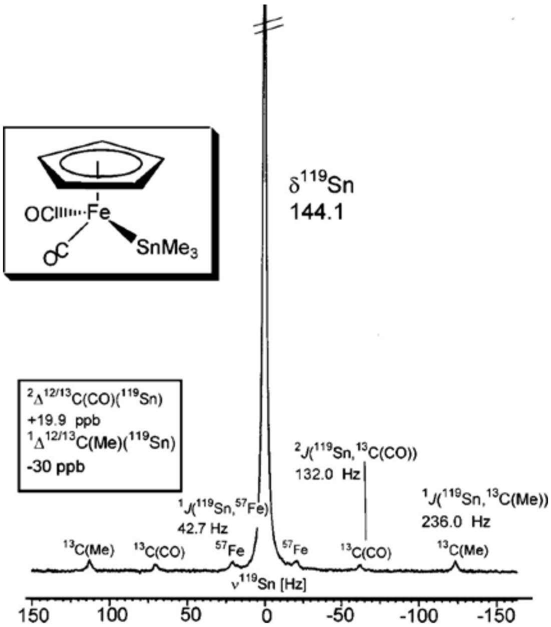

Fig. 4. 186.5 MHz ^{110}Sn{^{1}H} NMR spectrum (INEPT) of the iron complex shown (Adapted from Ref. [18]). Satellite signals are observed for one bond ^{119}Sn–^{57}Fe, and one- and two-bond ^{119}Sn–^{13}C spin–spin coupling. Note the fairly large isotope-induced chemical shifts $^n\Delta^{12/13}$C(^{119}Sn) ($n = 1, 2$).

References

1. Ssbald A. Solid state NMR II. In: B Blümich (ed). Inorganic Matter, Springer: Berlin, 1994, pp 91–131.
2. Kennedy JD, McFarlane W. Rev. Silicon, Germanium, Tin, Lead Compounds 1974;1:235.
3. Smith PJ, Tupciauskas AP. Annu. Rep. NMR Spectrosc. 1978;8:291.
4. Kennedy JD, McFarlane W. In: J Mason (ed.) Multinuclear NMR. Plenum Press: New York, 1987, pp 305–333.
5. Wrackmeyer B. Annu. Rep. NMR Spectrosc. 1985;16:73.
6. Wrackmeyer B. Annu. Rep. NMR Spectrosc. 1999;38:203.
7. Martins JC, Biesemans M, Willem R. Prog. NMR Spectrosc. 2000;36:271.
8. Kennedy JD, McFarlane W, Pyne GS. J. Chem. Soc. Dalton Trans. 1977;2332.
9. Mitchell TN. J. Organomet. Chem. 1983;255:278.
10. Chandrasekhar V, Nagendran S, Baskar V. Coord. Chem. Rev. 2002;235:1.
11. Nath M, Pokharia S, Yadav R. Coord. Chem. Rev. 2001;215: 99.
12. Camacho-Camacho C, Contreras R, Nöth H, Bechmann M, Sebald A, Milius W, Wrackmeyer B. Magn. Reson. Chem. 2002;40:31.
13. Wrackmeyer B, Indirect nuclear ^{119}Sn–X spin–spin coupling. In: M Gielen, R Willem, B Wrackmeyer (eds). Physical Organometallic Chemistry, Advanced Applications of NMR to Organometallic Chemistry, Vol. 1. Wiley: Chichester, 1996, pp 87–122.
14. Lockhart TP, Manders WF. J. Am. Chem. Soc. 1987;109: 7015.
15. Holecek J, Lycka A. Inorg. Chim. Acta. 1986;118:L15.
16. Contreras R, Jimenez-Perez VM, Camacho-Camacho C, Güizado-Rodriguez M, Wrackmeyer B. J. Organomet. Chem. 2000;604:229.
17. Herberhold M, Steffl U, Milius W, Wrackmeyer B. Chem. Eur. J. 1998;4:1027.
18. Wrackmeyer B, Distler B, Herberhold M. Z. Naturforsch. B. 1992;47:1749.

Paramagnetic Effects

^{1}H and ^{13}C High-Resolution Solid-State NMR of Paramagnetic Compounds Under Very Fast Magic Angle Spinning

Yoshitaka Ishii and Nalinda P. Wickramasinghe
Department of Chemistry, University of Illinois at Chicago, Chicago, IL 60607, USA

Introduction

More than one-third of the elements in the periodic table exhibit paramagnetism. Paramagnetic metal ions play a variety of significant roles in material science [1,2], bioinorganic chemistry [3–5], nanoscience [6–8], and pharmacology [9,10] as complexes with organic ligands. On the other hand, development of novel paramagnetic complexes has been often hindered by lack of efficient characterization methods, in particular, for non-crystalline solids. High-resolution solid-state NMR (SSNMR) using magic angle spinning (MAS) is a powerful technique for structural analysis of non-crystalline organic materials in solids [11–13]. However, the large dispersion of paramagnetic shifts and associated technical difficulties have impeded progress in high-resolution SSNMR studies of paramagnetic systems [14], which contrasts with recent tremendous advancement in SSNMR for diamagnetic systems including biomolecules [12,13,15–19]. ^{13}C and ^{1}H SSNMR have been the most widely used methods for organic solid materials. For paramagnetic systems, however, because of the large shift dispersion, insufficient ^{1}H or ^{1}H–^{1}H RF decoupling with the limited RF fields available in a conventional probe typically results in severe loss of resolution in ^{1}H and ^{13}C SSNMR spectra. Also, large paramagnetic shifts mask the diamagnetic shifts that are characteristic of chemical groups, making signal assignment difficult. Recent studies demonstrated that ^{2}D labeling eliminates the requirement of ^{1}H RF decoupling, and selective ^{13}C labeling offers resolution and reliable assignments in ^{13}C SSNMR for small paramagnetic systems [20–25]. On the other hand, isotope labeling is costly and often not justified for analysis of small compounds, resulting in applications of SSNMR to only a handful of paramagnetic systems. Moderate MAS around 10 kHz was reported to provide modest resolution in ^{1}H and ^{13}C SSNMR for unlabeled paramagnetic systems [22,26]. Although a path for SSNMR analysis of unlabeled paramagnetic systems has been opened by these studies, applicability of this approach is limited to systems having small ^{1}H–^{1}H dipolar couplings due to large ^{1}H shift dispersion or motions. Also, procedures for assignments in unlabeled paramagnetic systems have not been established. As a result, ^{13}C and ^{1}H SSNMR of paramagnetic systems have been largely unexplored.

Recently, our group demonstrated that a new approach using very fast MAS (VFMAS; spinning speed $\omega_R/2\pi >$ 20 kHz) permits excellent resolution/sensitivity and signal assignments in ^{13}C and ^{1}H SSNMR even for unlabeled systems [27,28]. Although MAS over 50 kHz is currently available [29], we define VFMAS as MAS at $\omega_R/2\pi > 20$ kHz because spinning over 20 kHz induces crucial changes in spin dynamics for organic solids by eliminating the majority of ^{1}H–^{1}H and ^{1}H–^{13}C dipolar couplings. As will be discussed, this change by VFMAS forms the foundation of our approach. This review outlines the principles and recent applications of this VFMAS approach for paramagnetic complexes.

One-Dimensional (1D) ^{1}H SSNMR for Paramagnetic Systems

Spinning Speed Dependence and Sensitivity of ^{1}H MAS NMR

Figure 1 shows spinning speed dependence of ^{1}H MAS NMR spectra of unlabeled Cu(II)(DL-Ala)$_2$·H$_2$O (a–c) and Mn(III)(acac)$_3$ (d–f). Clearly, VFMAS significantly improves the sensitivity and resolution. In Figure 1(c and f) at 5 kHz MAS, no signals are identified because of line broadening due to large ^{1}H–^{1}H couplings and ^{1}H anisotropic paramagnetic shifts. In contrast, under VFMAS, excellent sensitivity and resolution are displayed for Cu(DL-Ala)$_2$ at 24 kHz (a), demonstrating that VFMAS efficiently removes broadening due to ^{1}H–^{1}H dipolar couplings and ^{1}H paramagnetic shifts [28]. Although only weak signals for NH$_2$ are observed at −44 and −78 ppm, this is because the NH$_2$ protons are directly coordinated to Cu(II) and subject to significant anisotropic paramagnetic shifts [22]. As will be described below, the assignments were obtained by separate two-dimensional

Graham A. Webb (ed.), Modern Magnetic Resonance, 467–474.
© 2008 *Springer.*

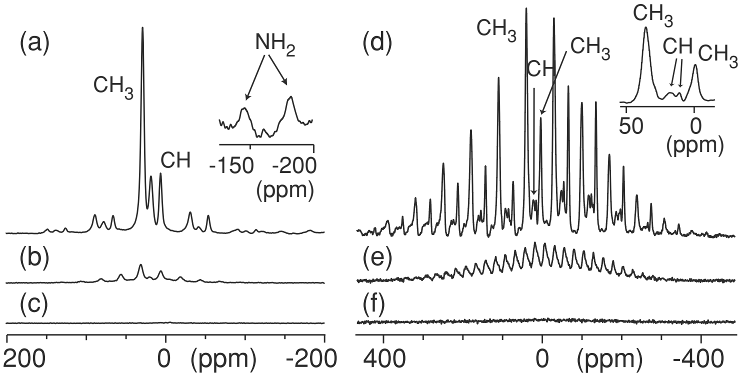

Fig. 1. ^{1}H MAS spectra of Cu(DL-Ala)$_2$·H$_2$O (a–c) and Mn(acac)$_3$ (d–f) at spinning speeds (a) 24 kHz, (b and e) 10 kHz, (c and f) 5 kHz, and (d) 27.8 kHz obtained at ^{1}H frequency of 400.2 MHz with 1-pulse excitation and a rotor synchronous echo (τ_R–π–τ_R). The two insets in (a) and (d) are the expanded regions of NH$_2$ signals in (a) and centerlines in (d). The sample amount was 17 (a–c) and 14 mg (d–f). Total experimental times were only 18 (a–c) and 12 ms (d–f) with four scans for each spectrum.

(2D) ^{13}C–^{1}H chemical shift correlation NMR under VFMAS except for NH$_2$, for which we adopted the assignment by Liu *et al.* using ^{2}D SSNMR [22]. For Mn(acac)$_3$, in spite of numerous sidebands remaining even under VFMAS at 27.8 kHz in Figure 1(d), the center peaks are well resolved, as shown in the inset. It is worth pointing out that anisotropic paramagnetic shifts are generally proportional to $(S+1)S/R_{IS}^3$, where S is an electron spin number, and R_{IS} is the distance between the nuclear spin I and the electron spin S at a paramagnetic center [14,26]. Because the spin numbers S for Mn(III) and Cu(II) are $5/2$ and $1/2$, respectively, it is reasonable that more sidebands were observed for Mn(acac)$_3$. The line widths in (a and d) are comparable to those for diamagnetic systems. Large dispersion of ^{1}H chemical shifts provides excellent resolution, which permits characterization using 1D ^{1}H SSNMR.

The other important feature of ^{1}H SSNMR for paramagnetic systems under VFMAS is its high sensitivity. For this reason, ^{1}H VFMAS is usually the first experiment we typically attempt for systems previously uncharacterized by SSNMR. Short ^{1}H T_1 values of paramagnetic compounds (~ms) allow us to acquire signals rapidly. Because of the excellent sensitivity of ^{1}H VFMAS SSNMR, the ^{1}H spectra in Figure 1(a and d) were obtained in total experimental times of only 18 and 12 ms, respectively.

There has been a popular conception that the sensitivity of SSNMR for paramagnetic systems is significantly lower than that for diamagnetic systems because of paramagnetic broadening. However, because the sensitivity in Figure 1(a and d) under VFMAS appears excellent, we theoretically reexamined this conception. Sensitivity of FT NMR with a matched window function is generally given by [30]

$$\xi = \langle s(t)^2 \rangle^{1/2} (t_{\max}/T)^{1/2} / \rho_N, \qquad (1)$$

where $s(t)$ is an envelope function of an FID, $t_{\max}$ is an acquisition period of a FID, T is a recycle time or an interval between two scans, ρ_N is the r.m.s. noise amplitude in a unit bandwidth. The factor $\langle s^2 \rangle$ is the average signal power. For simplicity, we assumed that $s(t)$ is given by an exponential decay, as $s(t) = \exp(-t/T_2)$. When $t_{\max}$ is matched to T_2, as $t_{\max} = cT_2$ for a given constant c, $\langle s^2 \rangle$ is independent of T_2. Thus, the sensitivity, ξ, depends only on the receiver duty factor ($t_{\max}/T$). In SSNMR experiments, T is usually adjusted to $3T_1$, and hence, $t_{\max}/T = (c/3)T_2/T_1$. For ^{1}H SSNMR of diamagnetic systems, $t_{\max}/T$ is only about 0.03–0.1% ($t_{\max} \sim$ 1 ms and $T \sim$1–3 s). On the other hand, for paramagnetic systems, $t_{\max}/T$ is as large as 10–30% ($t_{\max} \sim$ 0.5–1 ms and $T \sim$ 3–5 ms) because of enhanced resolution by VFMAS and short T_1 values. Hence, when sidebands are sufficiently suppressed by VFMAS, the theoretical sensitivity of ^{1}H SSNMR for paramagnetic systems is greater than that for diamagnetic systems by a factor of 10–30 with VFMAS.

Microanalysis by ^{1}H SSNMR

This exceptional sensitivity can be utilized in a form of ^{1}H SSNMR microanalysis of unlabeled paramagnetic systems. We applied this ^{1}H VFMAS method to two crystal forms of polycrystalline Cu(II)(8-quinolinol)$_2$ [CuQ$_2$] in order to examine whether polymorphs of paramagnetic drugs or materials can be distinguished in a nanomole scale by ^{1}H SSNMR. CuQ$_2$ is an apoptosis inducer in human leukemia cells [31], and its β-form is known to be thermally more stable [32]. Figure 2 shows the ^{1}H VFMAS spectra of 20 nmol of (a) α- form and (b) β-form CuQ$_2$. The sensitivity is excellent after only 10 min of signal accumulation. Clearly, these spectra are distinguishable on the basis of the line positions and line widths even without signal assignment. Considering the fact that ^{1}H SSNMR rarely displays sufficient resolution to distinguish polymorphs for diamagnetic systems and

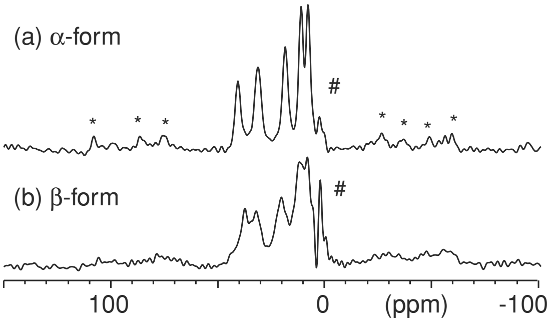

Fig. 2. ^{1}H MAS spectra of (a) α-form and (b) β-form of Cu(II)(8-quinolinol)$_2$ obtained at ^{1}H frequency of 400.2 MHz with 1-pulse excitation at $\omega_R/2\pi = 27.03$ kHz. Only 20 nmol (7 μg) of the sample was used for each spectrum. A total of (a) 36,560 and (b) 98,304 scans were recorded with recycle delays of (a) 15 ms and (b) 5 ms. The total experimental time was 10 min each. Background signals were suppressed by subtracting a spectrum obtained for a rotor without the sample. Residual background signals and spinning sidebands are marked by # and *, respectively.

that various small paramagnetic metal complexes function as drugs [10,31,33] and materials [8,34], the present data suggest unique possibility of distinguishing molecular packing or supramolecular structures for paramagnetic complexes by ^{1}H SSNMR. As will be discussed, the high resolution in ^{1}H SSNMR attained by VFMAS can be combined with 2D NMR with suitable polarization transfer methods.

1D ^{13}C VFMAS SSNMR for Paramagnetic Systems

Spinning Speed Dependence of ^{13}C MAS Spectra

Figure 3(a–c) shows the spinning speed dependence of the ^{13}C MAS SSNMR spectra of unlabeled Cu(DL-Ala)$_2$ obtained with high-power CW ^{1}H RF decoupling (100 kHz). In Figure 3(a), at $\omega_R/2\pi = 5$ kHz, only one peak that corresponds to CH$_3$ can be identified. In contrast, Figure 3(c) at $\omega_R/2\pi = 24$ kHz clearly displays three peaks for CH$_3$ (172 ppm), CO (−191 ppm), and CH (−276 ppm) groups in Cu(DL-Ala)$_2$ with improved resolution and sensitivity. Figure 3(d) shows the ^{13}C VFMAS spectrum at $\omega_R/2\pi = 24$ kHz without ^{1}H RF decoupling. The resolution in (d) is superior to that in (c), in particular, for the CH signal. This is well explained by the fact that VFMAS effectively removes ^{1}H–^{13}C dipolar coupling regardless of ^{1}H resonance offsets and anisotropic shifts due to large paramagnetic shifts, while the efficiency of ^{1}H RF decoupling is strongly affected by these parameters.

Sensitivity Enhancement by Cross-Polarization

Polarization transfer by cross-polarization (CP), one of the vital techniques in ^{13}C SSNMR, has been ineffective for most paramagnetic systems because of large paramagnetic shift dispersion. In a few successful cases, including the initial high-resolution ^{13}C SSNMR for paramagnetic systems by Bryant and coworkers [35], signals within a limited bandwidth (∼200 ppm) were observed at lower field (^{1}H frequency ∼200 MHz) [23,35,36]. For systems having larger paramagnetic shift dispersion, CP transfer efficiency is suppressed because large resonance offsets cause deviations from the Hartmann–Hahn condition with the limited RF intensities that are available in a conventional MAS probe.

We recently demonstrated that further sensitivity enhancement in ^{13}C SSNMR spectra for paramagnetic systems can be obtained using polarization transfer from ^{1}H spins with the strong RF fields available in VFMAS probes [27]. Figure 3(e) shows the ^{13}C CP-VFMAS spectrum of Cu(DL-Ala)$_2$ obtained with high-power ramped CP. Because of short ^{1}H T_1 values, it is possible to acquire a larger number of scans within a given experiment time. Clearly, the sensitivity was significantly enhanced in Figure 3(e), compared with (d). The sensitivity enhancement factors in Figure 3(e) are 2.2–3.6 and 1.2, compared with the spectra in Figure 3(d) for protonated and non-protonated ^{13}C signals, respectively. Compared with the spectrum in (b) under moderate MAS at 10 kHz, which was utilized in previous ^{13}C SSNMR studies for paramagnetic systems [22], the enhancement factors are 4–5. As a result, the excellent sensitivity and resolution in Figure 3(e) was obtained in only 1 min. We will discuss signal assignment of the spectrum in a later section.

It has long been a problem for synthetic chemists that solution NMR of small paramagnetic systems is often subject to severe paramagnetic broadening because of a long electron spin relaxation time for isolated paramagnetic molecules in solution [37]. Since excellent sensitivity was identified in the above ^{13}C SSNMR spectra under VFMAS, we compared the sensitivity between SSNMR and solution NMR in order to examine the potential of ^{13}C SSNMR for analysis of paramagnetic systems as an alternative to ^{13}C solution NMR. Figure 3(f) shows preliminary results of ^{13}C solution NMR spectra of saturated Cu(DL-Ala)$_2$ in D$_2$O. To compensate for the low solubility of this sample (3.8 mg in 0.7 ml D$_2$O), we acquired the signal for 3 h (102,400 scans) rather than 1 min. Apparently, no signals were identified in (f). Although further studies are needed to examine applicability of SSNMR to other paramagnetic systems, it is encouraging that ^{13}C high-resolution SSNMR spectra were obtained for the sample, for which solution NMR is not effective.

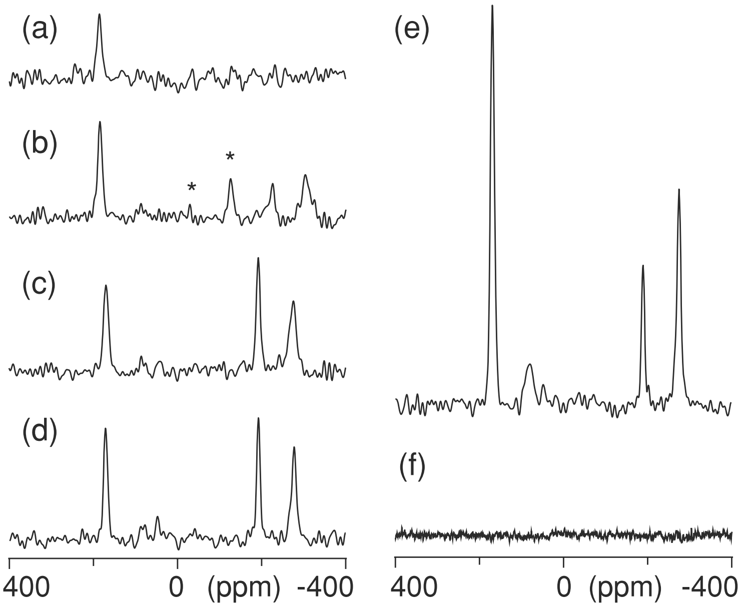

Fig. 3. ^{13}C MAS spectra of Cu(DL-Ala)$_2$·H$_2$O obtained with (a–d) 1-pulse excitation, and (e) adiabatic-CP, together with (f) ^{13}C solution NMR spectra of a saturated Cu(DL-Ala)$_2$ solution in D$_2$O. ^{13}C NMR frequency was 100.6 MHz for all the spectra. The spectra in (a–c) were acquired at $\omega_R/2\pi$ of (a) 5 kHz, (b) 10 kHz, and (c) 24 kHz with ^{1}H CW RF decoupling (100 kHz) with a recycle delay (τ_d) of 0.1 s. The spectra in (d and e) were acquired without ^{1}H RF decoupling and with τ_d of 0.1 s, and 50 ms, respectively; (f) was obtained by 1-pulse excitation with WALZ 64 decoupling. For each of spectra (a–e), an experimental time was 1 min with (a–d) 614, and (e) 1200 scans, while in (f) an experimental time was 3 h with 102,400 scans. The spectrum in (e) is scaled so that the spectra (a–e) display a common noise level in the figure. τ_d for (a–d) was matched to three times of ^{13}C T_1 values. τ_d in (e) was restricted by an RF duty factor (1%) to prevent a probe arcing. The ^{13}C pulse widths for $\pi/2$ and π pulses were 2.5 and 5.0 μs, respectively. In the CP experiment, the ^{13}C RF field was swept from 107.5 to 124.5 kHz during a contact time of 0.5 ms, while the ^{1}H RF field was kept constant at 92 kHz. The spinning sidebands are indicated by * in the spectra. The sample amount for (a–e) was 15 mg. For (f), 3.8 mg of the sample was dissolved in 0.7 ml D$_2$O.

^{1}H Decoupling Dependence of ^{13}C VFMAS Spectra

In Figure 4, we show ^{1}H decoupling dependence of ^{13}C MAS spectra of Cu(DL-Ala)$_2$ (a–d) and Mn(acac)$_3$ (e–h). The spectra were obtained with (a and e) no ^{1}H RF decoupling (decoupling by VFMAS), (b and f) ^{1}H high-power CW decoupling, (c and g) ^{1}H TPPM decoupling, and (d and h) XY-8 π-pulse train decoupling [38], with a common number of scans for each sample. For Cu(DL-Ala)$_2$, the spectrum obtained with no RF decoupling in (a) displays the resolution higher than that obtained with TPPM or CW RF decoupling. This is because majority of ^{1}H–^{13}C dipolar couplings are removed by VFMAS over 20 kHz. We also tested π-pulse train decoupling, which was successfully applied to ^{19}F decoupling [38]. In the π-pulse train, one π-pulse was rotor synchronously applied in one rotation cycle in order to avoid interference between the RF decoupling and the averaging of ^{13}C–^{1}H dipolar coupling by VFMAS. Our result in (d) shows the π-pulse train decoupling does not enhance sensitivity compared with no decoupling in (a). For Mn(acac)$_3$ in Figure 4(e–h), CW or TPPM decoupling sequences caused loss of signal or substantially reduced resolution. As already discussed, ^{1}H anisotropic shifts for this system reach 700 ppm ($\pm$140 kHz in ^{1}H 400 MHz); hence, it is reasonable that ^{1}H RF decoupling is ineffective. In contrast, with no RF decoupling in (e) or with a π-pulse train in (h), well-resolved signals were identified, although sidebands were not completely suppressed. It is also noteworthy that CW and TPPM decoupling substantially increases the RF duty factor and limits the maximum repetition rate. In contrast, dropping RF decoupling permits fast repetition for samples having short ^{13}C T_1 such as Mn(acac)$_3$.

As recently reported by Ernst [39], average Hamiltonian analysis for an isolated I–K two spin system

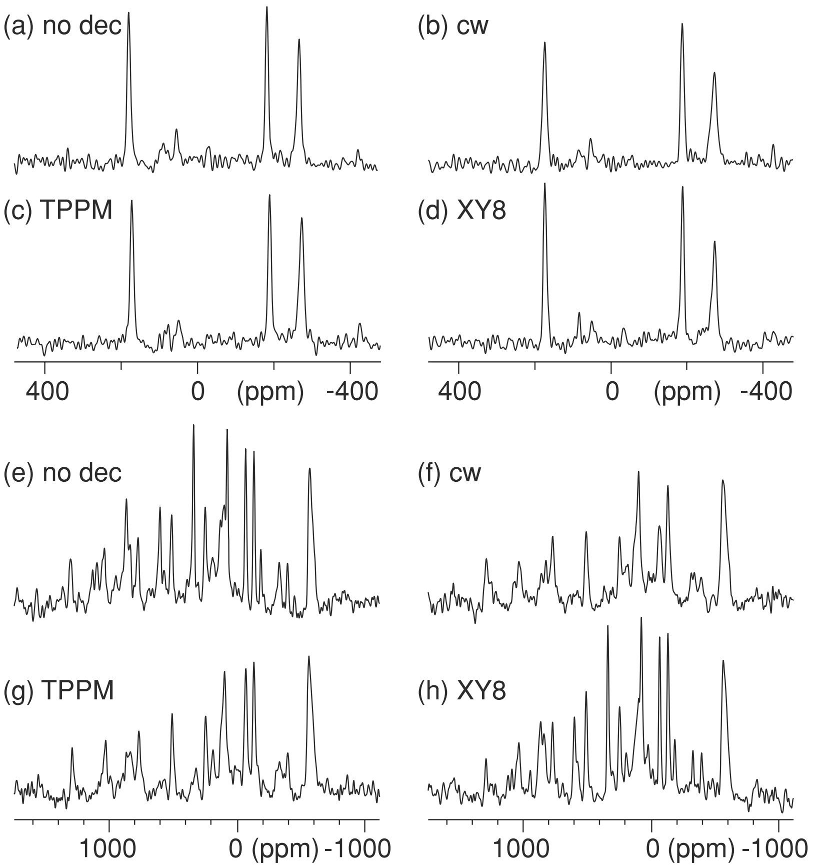

Fig. 4. ^{1}H decoupling dependence of ^{13}C VFMAS spectra of (a–d) Cu(DL-Ala)$_2$·H$_2$O and (e–h) Mn(acac)$_3$ at ^{13}C NMR frequency of 100.6 MHz. The spectra were obtained by 1-pulse excitation with (a, e) no ^{1}H RF decoupling, (b and f) CW, (c and g) TPPM, and (d and h) XY-8 π-pulse train ^{1}H decoupling. The spinning speed in (a–d) and (e–h) was set to 24.00 and 26.31 kHz, respectively. The spectra for each sample are displayed in a common scale. In CW or TPPM decoupling, a ^{1}H RF field of 100 kHz was applied. In XY-8 decoupling, an XY-8 π-pulse train of a (d) 5-μs or (h) 3.4-μs pulse width was rotor synchronously applied with a π-pulse per rotation cycle. For Cu(DL-Ala)$_2$, each spectra were recorded with common numbers of scans (1024 scans), recycle delays (τ_{d}) of 0.1 s, and total experimental times of 1.8 min. For Mn(acac)$_3$, the experimental times after 40,960 scans were (e, h) 11 and (f, g) 31 min with τ_{d} of (e, h) 15 or (f, g) 45 ms. The sample amount was (a–d) 15 and (e–h) 13.5 mg.

($I = {}^{1}$H and $K = {}^{13}$C) shows that the second-order cross term between ^{1}H–^{13}C dipolar coupling and ^{1}H anisotropic shifts under high-power ^{1}H CW RF decoupling is given by

$$H_{\text{CS-D}}^{(2)} = \sum_{\substack{m=-2 \\ m\neq 0}}^{2} \frac{\omega_{IK}(-m)\omega_{I}(m)}{\omega_1} 2I_y K_Z, \qquad (2)$$

where we assumed that the nutation frequency due to ^{1}H RF decoupling, $\omega_1/2\pi$, is much larger than the spinning frequency, $\omega_{\text{R}}/2\pi$ ($\omega_1 \gg \omega_{\text{R}}$). In Equation (2), $\omega_{\text{IK}}(n)$ and $\omega_I(n)$ are Fourier coefficients for the frequency of $n\omega_{\text{R}}/2\pi$ in time-dependent heteronuclear dipolar coupling and anisotropic shift for the I spin, respectively. When $\omega_I(m)$ due to the paramagnetic anisotropic shift is comparable to ω_1, $|H_{\text{CS-D}}^{(2)}|$ becomes comparable to $|\omega_{\text{IK}}(-m)|$, where $|H_{\text{CS-D}}^{(2)}|$ denotes the norm of $H_{\text{CS-D}}^{(2)}$. Hence, ^{1}H RF decoupling *reintroduces* ^{1}H–^{13}C dipolar couplings for systems having large anisotropic shift, rather than removes the couplings, as shown in Figure 4 (f and g). On the other hand, VFMAS eliminates all the higher order terms for the isolated I–K two-spin system, regardless of anisotropic shifts or resonance offsets. Therefore, we conclude that eliminating ^{1}H RF decoupling is the best option for small paramagnetic systems at this point. If ^{1}H–^{13}C J couplings need to be removed, an XY-8 π-pulse train is an alternative.

Signal Assignments and Multi-dimensional NMR

1D Assignment Method

Signal assignments in SSNMR spectra of paramagnetic systems are often problematic because large paramagnetic shifts mask diamagnetic shifts, which are used to assign signals to specific chemical groups. To address this issue, we recently proposed a signal editing method for paramagnetic systems based on ^{13}C–^{1}H dipolar recoupling using ^{1}H–^{13}C REDOR pulse sequence shown in Figure 5(a). With the two ^{1}H π pulses (filled squares), this sequence reintroduces ^{13}C–^{1}H dipolar couplings, selectively dephasing protonated ^{13}C signals; on the other hand, without these π pulses the sequence functions as a simple rotor synchronous echo sequence. In a control experiment for L-valine, we observed $S/S_0 = 90$, 47, and 8% for CO_2^-, CH_3, and CH, respectively, where S and S_0 denote the signal intensities obtained with and without the ^{1}H π pulses, respectively. It is reasonable that dephasing for a CH_3 group is less than that for a CH group because CH_3 rotation along the symmetry axis partially truncates ^{13}C–^{1}H dipolar couplings. Figure 5(b and c) shows ^{13}C spectra of Cu(DL-Ala)$_2$ obtained (b) without and (c) with ^{1}H π pulses using the pulse sequence shown in (a). $S/S_0 = 52$, 83, and 12% for the peaks at 173, −183, and −269 ppm, respectively. The assignment based on this result is indicated in Figure 5(b); this assignment agreed well with that by Liu *et al.* using selective ^{13}C and ^{2}D labeling [22]. Compared with the previous assignment methods using selectively labeled samples, signal editing using dipolar recoupling under VFMAS provides reliable signal assignments for small amounts of unlabeled samples.

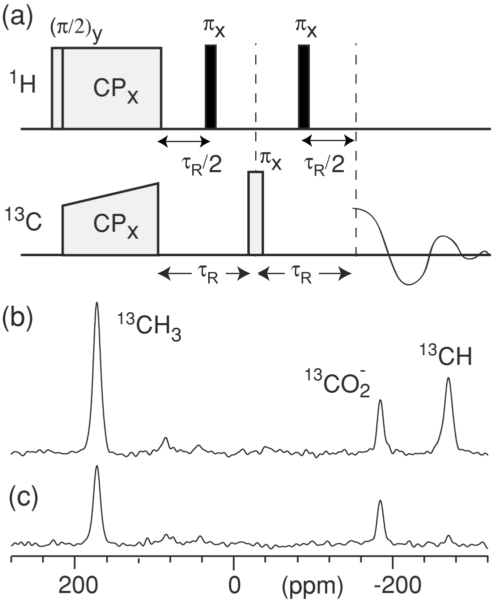

Fig. 5. (a) A ^{1}H–^{13}C REDOR pulse sequence for ^{13}C–^{1}H dipolar filter signal editing. When the two ^{1}H π pulses (filled boxes) are applied, ^{13}C–^{1}H dipolar couplings are restored under VFMAS. ^{13}C CPMAS spectra of Cu(DL-Ala)$_2\cdot$(H$_2$O) obtained (b) without and (c) with ^{13}C–^{1}H dipolar dephasing using the pulse sequence in (a) at $\omega_R/2\pi = 22.989$ kHz ($\tau_R = 43.5$ µs). ^{1}H and ^{13}C π-pulse widths were set to 5 µs.

Assignment by 2D ^{13}C–^{1}H Heteronuclear Correlation NMR

2D chemical shift correlation SSNMR has been useful for characterization of materials and biomolecules [12,30]. However, applications of this fundamental technique to paramagnetic compounds have been limited to ^{13}C-labeled materials even for small molecules because of limited sensitivity and difficulty in broadband polarization transfer. The VFMAS approach efficiently removes ^{1}H–^{1}H and ^{1}H–^{13}C dipolar couplings, permitting high-resolution ^{1}H and ^{13}C SSNMR for paramagnetic complexes. Hence, with efficient broadband CP under VFMAS, it is possible to correlate high-resolution ^{13}C and ^{1}H SSNMR for unlabeled paramagnetic compounds in 2D ^{13}C–^{1}H correlation SSNMR.

Figure 6(a) and (b) shows 1D ^{13}C CPMAS and 2D ^{13}C–^{1}H chemical shift correlation SSNMR spectra of V(III)(acac)$_3$,(acac =CH_3–CO–CH–CO–CH_3), respectively. In (B), six lines and three lines, which are overlapping in the 1D spectrum in (A), are resolved around ^{13}C shifts of −180 and 100 ppm. With ^{13}C–^{1}H dipolar dephasing, the six lines and the three lines were assigned to CH_3 and CH groups, respectively [27]. Based on this result, we concluded that it is most likely that V(acac)$_3$ has three magnetically non-equivalent ligands because of distortion away from the symmetry of the isolated molecule and the signals for CO are broadened out by strong hyperfine couplings. The result agrees well with recent high-resolution X-ray crystallography data, in which non-equivalence of the three ligand molecules was identified [40]. The 2D spectrum in Figure 6 also provides the assignments in ^{1}H SSNMR.

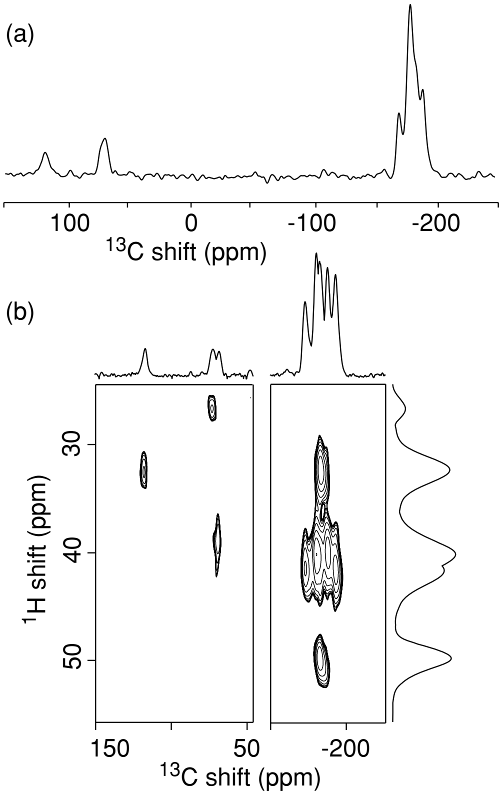

Fig. 6. (a) 1D ^{13}C CP-VFMAS and (b) 2D ^{13}C–^{1}H correlation VFMAS NMR spectra of V(III)(acac)$_3$ obtained with ramped CP with a contact time of 0.5 ms, together with 1D skyline projections in (b). The spinning speed is 22.99 kHz. In the ramped CP, the ^{13}C RF field was swept from 74 to 82 kHz, while ^{1}H RF field was kept constant at 101 kHz. The recycle delay was 0.1 s after each 2 ms of signal acquisition. In (a), only 1024 scans were collected within a total experimental time of 1.8 min. In (b), 25 t_1 complex points were recorded with t_1 increments of 43.5 μs and total of 1536 scans were collected for the real or imaginary components of each t_1 point. The total 2D experimental time was 2.2 h.

Experimental Aspects

All the SSNMR data were recorded at 9.4 T with a Varian Infinityplus 400 spectrometer equipped with a Varian T3 3.2-mm MAS double-resonance probe and a home-built 2.5-mm MAS double-resonance probe. All the SSNMR spectra obtained by 1-pulse excitation or CP were acquired with a rotor synchronous echo sequence prior to signal acquisition. Since the spectral width of the paramagnetic complexes is large (up to 200 kHz at 9.4 T), it is difficult to obtain a flat baseline without the echo sequence. To minimize receiver dead times, short sampling intervals (2–5 μs) were employed. After phase corrections, the baselines were corrected by the built-in polynomial correction function at Varian Spinsight software. It is well known that paramagnetic isotropic shifts have a $1/T$ dependence (Curie's law). Because of this, severe line broadening can be induced by the temperature distribution over a sample heated by fast spinning. To suppress the broadening, cooling air (-10 to 23 °C) was used at the flow rate of 140–160 (ft)^2/h using a Varian VT stack. A profile of the temperature distribution can be easily characterized by observing the ^{207}Pb NMR line shape of Pb(NO$_3$)$_2$ under spinning [41].

Conclusion

We presented a set of novel fundamental techniques to achieve significant sensitivity and resolution enhancement as well as signal assignments using VFMAS in 1D and 2D ^{1}H and ^{13}C SSNMR for paramagnetic complexes. The presented results in the VFMAS approach offers possibilities of analyzing a variety of unlabeled paramagnetic systems by ^{1}H and ^{13}C high-resolution SSNMR for limited sample volumes in a simple experimental setting. We also demonstrated applications of recoupling techniques on paramagnetic systems, which had not been previously attempted. Structural analysis of paramagnetic systems using the recoupling techniques will be discussed elsewhere.

Acknowledgments

The authors are grateful to Prof. Cynthia Jameson at UIC for stimulating discussion. We are also grateful to Prof. Klaus Schmidt-Rohr at Iowa State University for suggesting XY-8 decoupling. This study was supported in part by research grants from the Alzheimer's Association (NIRG 035123) and the NSF CAREER program (CHE-0449952).

References

1. Tanaka T, Toda F. Chem. Rev. 2000;100:1025–74.
2. Sun D, Tham FS, Reed CA, Boyd PDW. Proc. Natl. Acad. Sci. U.S.A. 2002;99:5088–92.
3. Bertini I, Gray HB, Lippard SJ, Valentine JS. Bioinorganic Chemistry. University Science Books: Sausalito, CA, 1994.
4. Bertini I, Luchinat C, Parigi G. Solution NMR of Paramagnetic Molecules. Elsevier Science BV: Amsterdam, The Netherlands, 2001.
5. Kaim W, Schwederski B. Bioinorganic Chemistry: Inorganic Elements in the Chemistry of Life: An Introduction Guide. John Wiley & Sons Inc.: New York, 1994.

6. Leininger S, Olenyuk B, Stang PJ. Chem. Rev. 2000;100:853–907.
7. Tsao TB, Lee GH, Yeh CY, Peng SM. Dalton Trans. 2003;1465–71.
8. Cao YD, Zheng QY, Chen CF, Huang ZT. Tetrahedron Lett. 2003;44:4751–5.
9. Thompson KH, Orvig C. Science. 2003;300:936–9.
10. Farrell NP. Uses of Inorganic Chemistry in Medicine. Royal Society of Chemistry: Cambridge, 1999.
11. Slichter CP. Principles of Magnetic Resonance, 3rd ed. Springer-Verlag: Berlin, 1990.
12. Schmidt-Rohr K, Spiess HW. Multidimensional Solid-State NMR and Polymers. Academic Press Inc.: San Diego, 1994.
13. Griffin RG. Nat. Struct. Biol. 1998;5:508–12.
14. Aime S, Beritini I, Luchinat C. Coord. Chem. Rev. 1996;150:221–42.
15. Duer MJ (Ed). Solid-State NMR Spectroscopy Principles and Applications. Blackwell Science Ltd: Oxford, 2002.
16. Castellani F, van Rossum B, Diehl A, Schubert M, Rehbein K, Oschkinat H. Nature. 2002;420:98–102.
17. Petkova A, Ishii Y, Balbach JJ, Antzutkin OA, Leapman RD, Delaglio F, Tycko R. Proc. Natl. Acad. Sci. U.S.A. 2002;99:16742–7.
18. Medek A, Harwood JS, Frydman L. J. Am. Chem. Soc. 1995;117:12779–87.
19. McDermott A, Polenova T, Bockmann A, Zilm KW, Paulsen EK, Martin RW, Montelione GT. J. Biomol. NMR. 2000;16:209–19.
20. Brough AR, Grey CP, Dobson CM. J. Am. Chem. Soc. 1993;115:7318–27.
21. Clayton AN, Dobson CM, Grey CP. J. Chem. Soc. Chem. Commun. 1990;72–4.
22. Liu K, Ryan D, Nakanishi K, McDermott A. J. Am. Chem. Soc. 1995;117:6897–906.
23. Crozet M, Chaussade M, Bardet M, Emsley L, Lamotte B, Mouesca JM. J. Phys. Chem. A. 2000;104:9990–10000.
24. Spaniol TP, Kubo A, Terao T. Mol. Phys. 1999;96:827–34.
25. Walter TH, Oldfield E. J. Chem. Soc. Chem. Commun. 1987;646–7.
26. Nayeem A, Yesinowski JP. J. Chem. Phys. 1988;89: 4600–8.
27. Ishii Y, Chimon S, Wickramasinghe NP. J. Am. Chem. Soc. 2003;125:3438–9.
28. Wickramasinghe NP, Shaibat M, Ishii Y. J. Am. Chem. Soc. 2005;127:5796–7.
29. Ernst M, Samoson A, Meier BH. J. Magn. Reson. 2003;163:332–9.
30. Ernst RR, Bodenhausen G, Wokaun A. Principles of Nuclear Magnetic Resonance in One and Two Dimensions, 1st ed. Oxford University Press: Oxford, 1987.
31. Daniel KG, Gupta P, Harbach RH, Guida WC, Dou QP. Biochem. Pharmacol. 2004;67:1139–51.
32. Hoy RC, Morris RH. Acta Crystallogr. 1967;22:476.
33. Abrams MJ, Murrer BA. Science. 1993;261:725–30.
34. Curry RJ, Gillin WP. Curr. Opin. Solid State Mat. Sci. 2001;5:481–6.
35. Chacko VP, Ganapathy S, Bryant RG. J. Am. Chem. Soc. 1983;105:5491–2.
36. Campbell GC, Haw JF. Inorg. Chem. 1988;27:3706–9.
37. La Mar GN, Horrocks WD, Holm RH. NMR of Paramagnetic Molecules. Academic Press: New York, 1973.
38. Liu SF, Schmidt-Rohr K. Macromolecules. 2001;34: 8416–8.
39. Ernst M. J. Magn. Reson. 2003;162:1–34.
40. Filgueiras CAL,. Horn A Jr, Howie RA, Skakle JMS, Wardell JL. Acta Crystallogr. E. 2001;57:m157–8.
41. Mildner T, Ernst H, Freude D. Solid State Nucl. Magn. Reson. 1995;5:269–71.

Paramagnetic Effects of Dioxygen in Solution NMR—Studies of Membrane Immersion Depth, Protein Topology, and Protein Interactions

R.S. Prosser and F. Evanics
Department of Chemistry, University of Toronto, North Mississauga, ON, Canada L5L 1C6

Abstract

Oxygen offers several advantages as a paramagnetic reagent. Picosecond electron spin–lattice relaxation times, the absence of charge, and a rapid diffusion rate in water and membrane interiors, mean that oxygen is both an effective paramagnetic shift reagent (^{19}F or ^{13}C NMR applications) or spin–lattice relaxation agent (applications involving high gamma nuclei, such as ^{19}F and ^{1}H). Moreover, oxygen is well known to possess a marked solubility gradient along the immersion depth axis in lipid bilayers and detergent micelle systems. The consequent paramagnetic gradients (both in terms of spin–lattice relaxation rates and contact shifts) can be used to discern immersion depth of membrane additives (membrane peptides, drugs, or lipids). In studies of transmembrane α-helical and β-strand proteins, oxygen paramagnetic effects are used to discern information on protein topology. Applications involving studies of water-soluble proteins are also reviewed. Oxygen permeation in heme proteins, local preferences for oxygen on protein surfaces, or binding interfaces in protein–protein complexes may be uniquely studied using either chemical shift perturbations or spin–lattice relaxation rate enhancements.

Introduction

Conventional wisdom has long argued against the use of oxygen in most NMR applications. Even at ambient concentrations, oxygen is known to degrade long-range NOEs and contribute to line broadening, thereby masking weak scalar couplings. However, there are instances where oxygen provides unique opportunities, particularly in the study of membranes, membrane proteins, and protein interactions. This chapter highlights some of the recent applications involving oxygen in NMR. We will begin with a brief description of the salient equations for spin–lattice relaxation enhancement and chemical shift perturbations, associated with a freely diffusing paramagnet such as oxygen. The intention in the examples which follow is to convey to the reader the wide variety of applications and where possible, prospects for future studies.

Spin–Lattice Relaxation

Paramagnetic interactions may be manifested in terms of line broadening, enhancement of spin–lattice relaxation, or chemical shift perturbations. Oxygen electronic spin–lattice relaxation times, $T_{1\mathrm{e}}$, are relatively short for paramagnetic species [1]. This has two consequences. Firstly, other correlation times such as oxygen diffusion, or intra- and intermolecular reorientations, which might be expected to modulate the paramagnetic dipolar interaction, are longer than $T_{1\mathrm{e}}$, and thus less relaxation-effective. Secondly, oxygen is a relatively weak paramagnetic relaxation agent. Consequently, oxygen concentrations can frequently be found where line broadening effects are weak, relative to the natural line widths, while spin–lattice relaxation enhancements are relatively large, at least in the macromolecular limit where $T_1 \gg T_2$.

For a purely dipolar interaction between a nuclear spin, I, and a paramagnetic spin, S, the relaxation rate may be described by the classic equation [2, 3]

$$R_1^{\mathrm{P}} = \frac{2}{15}\gamma_I^2\gamma_S^2\hbar^2 S(S+1)\{J_0(\omega_S-\omega_I) + 3J_1(\omega_I) + 6J_2(\omega_I+\omega_S)\}\,. \quad (1)$$

For a freely diffusing paramagnet such as oxygen, the dipolar interaction is modulated principally by translational diffusion and by fast electronic spin relaxation. Consequently, the classic dipolar relaxation equations [4] do not apply, nor are the above spectral density functions necessarily Lorentzian. The problem of a freely diffusing paramagnet, with electronic relaxation times, T_1^S and T_2^S, has been previously treated [3] wherein the spectral

Graham A. Webb (ed.), Modern Magnetic Resonance, 475–483.
© 2008 *Springer.*

density function is described by

$$J_k(\omega) = \frac{8}{27}\frac{N_{\mathrm{A}}[\mathrm{O}_2]}{bD} \times \mathrm{Re}\left\{\left[1+\frac{1}{4}\left(\frac{i\omega\tau+\tau}{T_k^S}\right)^{1/2}\right] \Bigg/ \left[1+\left(\frac{i\omega\tau+\tau}{T_k^S}\right)^{1/2}+\frac{4}{9}\left(\frac{i\omega\tau+\tau}{T_k^S}\right) + \frac{1}{9}\left(\frac{i\omega\tau+\tau}{T_k^S}\right)^{3/2}\right]\right\} \quad k=1,2 \tag{2}$$

where b represents the distance of closest approach for the oxygen species to the nucleus of interest and D signifies the sum of the diffusion constants of both species. Finally, τ is defined by $\tau = b^2/D$ and in the extreme narrowing limit, the spectral density function simplifies to [3,5]

$$J_k(\omega) \approx J(0) = \frac{2}{3}\frac{N_{\mathrm{A}}[\mathrm{O}_2]}{b^3} T_k^S. \tag{3}$$

Teng and Bryant have attempted to employ the above theory to the case of protein surfaces, by introducing a geometric parameter which includes both a steric term accounting for relative oxygen accessibility and a soft potential term accounting for changes in local concentrations of the paramagnet, near the nucleus of interest [6]. Their analysis of ^{1}H paramagnetic rates in ribonuclease A suggest that there is a significant range of local free energies of interaction between oxygen and protein surface residues. In particular, disordered hydrophobic pockets exhibit increased associative interactions with oxygen. Thus, although the expressions for dipolar relaxation from a diffusible paramagnet are well described for both small molecules and proteins, the presence of preferential interactions of oxygen with specific regions of a macromolecule complicates the analysis of spin–lattice relaxation enhancement by oxygen, for purposes of structure refinement.

Chemical Shift Perturbations

Chemical shift perturbations from a diffusible paramagnet have been reported on several occasions [7,8]. Prosser and Luchette [9] have examined the temperature dependence of oxygen-induced chemical shift perturbations in a ^{19}F-labeled probe immersed in methanol. After accounting for differences in oxygen solubility by simultaneously measuring spin–lattice relaxation enhancement, chemical shift perturbations were observed to be inversely dependent on temperature. The authors concluded that in situations where oxygen was freely diffusing, chemical shift perturbations were of a contact origin. Contact shifts from diffusible paramagnets are rarely used for structure refinement [10–12]. For our purposes, we propose that the chemical shift perturbation should depend on the local oxygen concentration at the nucleus of interest, $[\mathrm{O}_2]$, in addition to the collisonally accessible surface area, A_{solvent}. Therefore, we express the chemical shift perturbation, $\Delta\sigma$, as

$$\Delta\sigma = kA_{\mathrm{solvent}}\,\alpha[\mathrm{O}_2] \tag{4}$$

where k is a proportionality constant, and α reflects the relative propensity of a given nucleus to experience unpaired spin density from a diffusible paramagnet. Contact shifts as large as 0.7 ppm are easily observed on ^{13}C nuclei in ^{1}H,^{13}C HSQCs of water soluble proteins and protein complexes, after equilibration of the protein at an oxygen partial pressure of 20 Atm. Furthermore, differences in α can be estimated by examining the chemical shift perturbations of the free amino acids, under conditions of constant oxygen concentrations. However, the main obstacle to obtaining A_{solvent} is oxygen preferentially concentrates in areas of local disorder or in hydrophobic pockets, rendering $[\mathrm{O}_2]$ a variable [13,14]. Though it should be possible to independently determine $[\mathrm{O}_2]$ from spin-lattice relaxation enhancements of ^{1}H nuclei, the potential of contact shifts for quantitative measure of solvent accessible surface area has yet to be demonstrated.

Contact shifts have also provided insight into the phenomenon of oxygen permeability in membranes. Using a so-called isotropic bicelle medium, it is possible to obtain well-resolved ^{13}C NMR spectra of the resident lipids in their bilayered state (*vide infra*) such that nearly every ^{13}C nucleus can be resolved and assigned. Contact shifts can then be routinely measured by acquiring spectra equilibrated under oxygen at 30 atm. Much is known of the oxygen solubility–diffusion product in lipid bilayers, from ESR studies [15–18] and computational studies of oxygen in lipid bilayers [19]. NMR clearly offers the advantage of studying such gradients, with near atomic resolution and without the use of a bulky probe.

Immersion Depth

Figure 1 displays both contact shifts and spin–lattice relaxation rates as a function of carbon number for a semi-perfluorinated probe molecule immersed in a lipid bilayer, and equilibrated to an oxygen partial pressure, P_{O_2}, of 100 atm. Figure 2 displays ^{13}C NMR contact shifts associated with resolvable nuclei of the phospholipid, *sn*-2 perdeutero,1-myristelaidoyl,2-myristoyl-*sn*-glycero-3-phosphocholine (MLMPC-d$_{27}$), in a lipid bilayer, at an oxygen partial pressure of 20 atm [20]. The optimal pressure is a function of line broadening, chemical shift dispersion, and natural line widths. In both cases, the

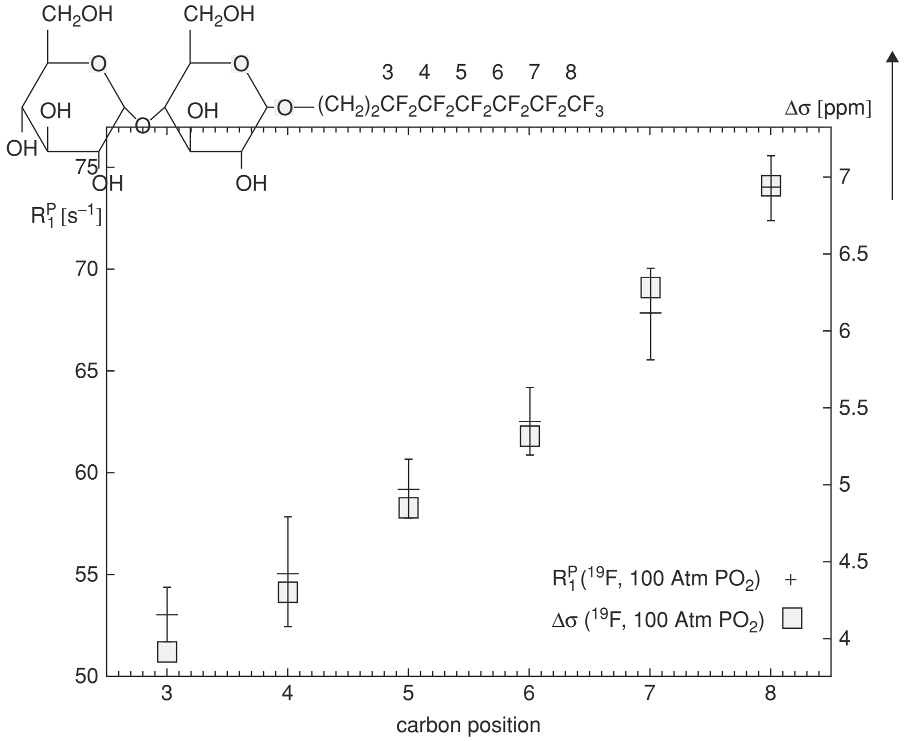

Fig. 1. Paramagnetic spin–lattice relaxation rate profile, R_1^{P} (crosses), and oxygen-induced chemical shift perturbations, $\Delta\sigma$ (open squares), as a function of carbon position for ^{19}F nuclei in TFOM, incorporated in a lipid bilayer membrane model system. Spectra were acquired using a 500 MHz Varian Inova spectrometer and an oxygen partial pressure of 100 atm PO_2. An equimolar mixture of DMPC and DHPC was prepared to provide the TFOM with a bilayer model, appropriate for study by solution NMR [39, 40].

results are dramatic and clearly sensitive to immersion depth, with Angstrom resolution. It should be noted that a significant gradient of chemical shift perturbations is observed despite the fact that the semi-perfluorinated detergent, and in particular the lipid, undergo significant undulations and chain isomerizations. Therefore, the "true" oxygen solubility profile must be significant in lipid bilayers.

The potential of oxygen as a paramagnetic agent for the determination of immersion depth can be further illustrated in Figure 3, which reveals chemical shift changes upon transfer of each of three small drug compounds (imipramine, nicotine, and caffeine) to the lipid bilayer (bicelle) [21]. Chemical shift changes for resolvable nuclei in Figure 3A, are indicated graphically as spheres whose radii are proportional to the magnitude of change. The upfield chemical shifts exhibited by regions of imipramine and nicotine, arise essentially from the transfer of nuclei from water to the non-polar membrane interior. Caffeine, which is essentially water soluble and does not interact with the membrane, exhibits slight downfield shifts, possibly because of a weak interaction with the phospholipid headgroups. Figure 3B reveals the relative paramagnetic spin–lattice relaxation rates obtained after equilibration at an oxygen partial pressure of 20 atm. It is instructive to compare our observations of partitioning to estimations of octanol/water partition coefficients and molecular polar surface areas. Imipramine, nicotine, and caffeine were predicted to have octanol/water partition coefficients (expressed as log P) of 3.43, 0.981, and −0.928, respectively, while molecular polar surface areas are estimated to be 6.476, 24.9, and 94.4, respectively. Based on the partition coefficients, we predict that imipramine is nearly entirely bound to the membrane, while more than 90% of the nicotine partitions into the membrane and is expected to be in fast exchange with the aqueous phase, since we can identify a single (averaged) spectral component of nicotine. In contrast, we expect that 90% of the caffeine partitions into the aqueous phase and is also likely in fast exchange with the surface of the membrane, based

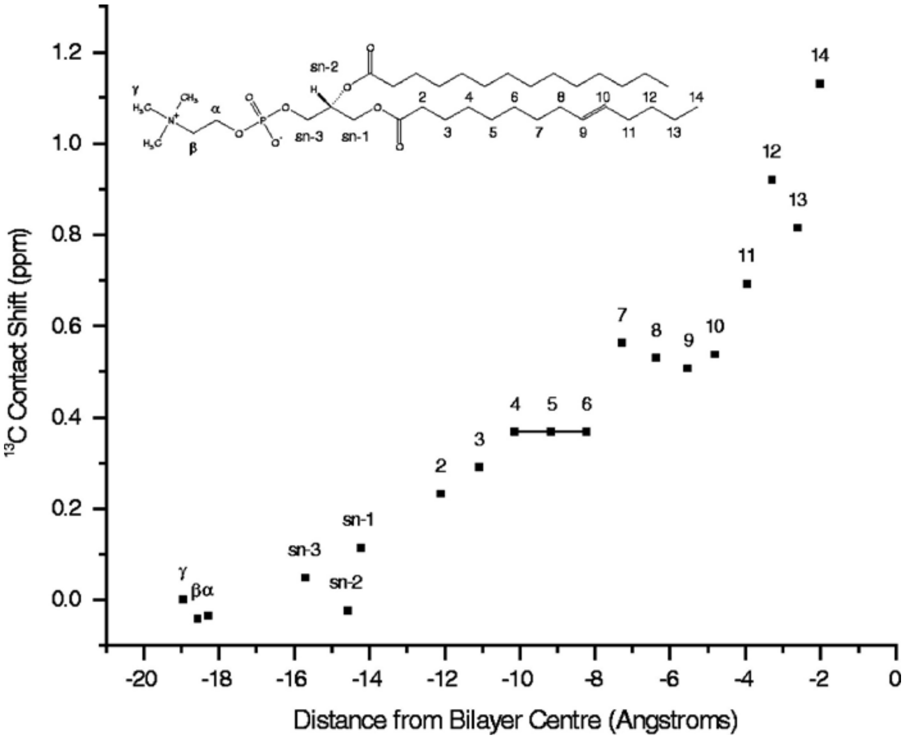

Fig. 2. Oxygen-induced chemical shift perturbations, $\Delta\sigma$, as a function of carbon position for ^{13}C nuclei of the phospholipid, 1-myristelaidoyl,2-perdeutero-myristoyl-*sn*-glycero-3-phosphocholine (MLMPC-d_{27}), in a lipid bilayer. The spectrum was acquired using a 600 MHz Varian Inova and an oxygen partial pressure of 20 atm. The lipid was mixed with DHPC such that the long- to short-chain lipid ratio was either 0.8.

on the absence of two spectral components. The paramagnetic relaxation rate profiles of each of the two membrane bound species, complements the partition coefficient data by giving an indication of the effective immersion depth, with atomic resolution.

Membrane Protein Topology

Paramagnetic reagents have long been recognized as a useful tool in the study of membrane proteins by ESR [22–25] and solution NMR spectroscopy [10, 12, 26]. An appropriate water-soluble paramagnetic reagent, which preferentially partitions into the aqueous phase, will adopt a well-known concentration gradient across the membrane water interface [17] while a hydrophobic paramagnetic species, such as oxygen, will adopt a concentration gradient in which the solubility is a maximum in the hydrophobic interior. Such complementary concentration gradients (and the consequent paramagnetic gradients) are useful for mapping both protein structure and immersion depth positioning of labeled sites. Moreover, paramagnetic spin labels may be attached to a lipid or detergent at a specific location in a membrane or micelle, in which case local paramagnetic effects also facilitate the measure of immersion depth and membrane protein topology [27, 28]. One recent example, which utilized spin labels and oxygen to delineate positioning of a membrane peptide is that of Ellena *et al.* [29]. The use of oxygen as a paramagnetic contrast agent in structure studies of membrane proteins is illustrated in Figures 4 and 5. Figure 4 depicts oxygen-induced chemical shift perturbations as a function of residue for the TM1 domain of the intact homotrimer of the membrane protein, DAGK, reconstituted into dodecylphosphocholine micelles, at 30 °C, and equilibrated to an oxygen partial pressure of 100 atm [30]. The chemical shift perturbations are measured via ^{19}F NMR, using an approach similar to the site directed spin-labeling studies [22]. In this case, single cysteine mutants of DAGK were obtained and labeled with a

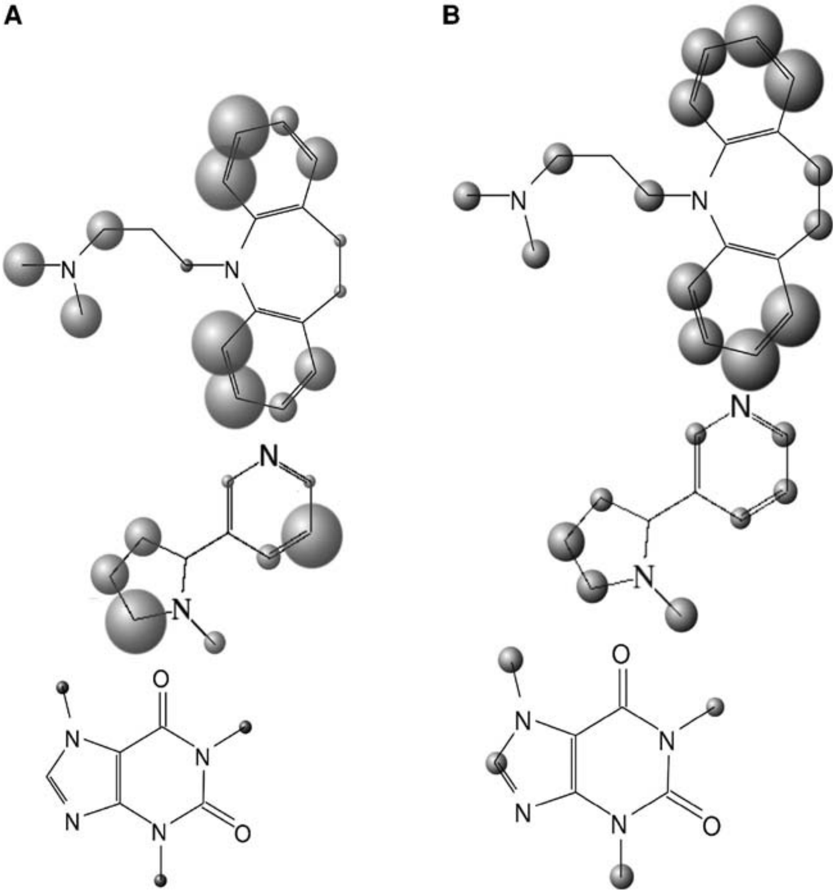

Fig. 3. (A) Changes in chemical shifts upon transfer of each of three small drug compounds (imipramine, nicotine, and caffeine, viewed from top to bottom) to a lipid bilayer model membrane system (bicelle). Spheres, whose radii are proportional to the upfield shifts (light) or downfield shifts (dark), are overlayed on the structure. (B) Paramagnetic spin–lattice relaxation rates of the three drug molecules (imipramine, nicotine, and caffeine) obtained after equilibration at an oxygen partial pressure of 20 atm. Spheres, whose radii are proportional to the paramagnetic rates, are overlayed on the structures. To measure chemical shift perturbations or paramagnetic rates, the three drugs were simultaneously added to a bicelle model membrane system. ^{1}H NMR spectra were obtained at 35 °C at an oxygen partial pressure of 15 atm. The drugs were added such that the lipid to drug ratio was in excess of 25:1. An isotropic bicelle membrane model system consisting of an equimolar mixture of 1,2-dimyristelaidoyl-*sn*-glycero-3-phosphocholine and chain-perdeuterated 1,2-dihexanoyl-*sn*-glycero-3-phosphocholine was used in this experiment. Experiments were performed on a Varian 600 MHz Inova spectrometer.

trifluoropropanone ligand. Upon refolding into DPC micelles, ^{19}F NMR spectra were obtained separately under equivalent partial pressures of oxygen and nitrogen such that the (paramagnetic) chemical shift perturbation could be measured. Note that the resulting shift perturbation profile reveals a prominent oscillation whose periodicity corresponds to 3.6 residues. This oscillation was interpreted to arise from a transmembrane α-helix in which one surface was in contact with one or more transmembrane regions of the DAGK homotrimer, and was therefore excluded from significant oxygen contact. Conversely, the remaining exterior of the TM1 α-helix was determined, based on sizeable chemical shift perturbations, to be in contact with the detergent micelle hydrophobic interior. The envelope of the chemical shift perturbation is used to map the immersion depth; a maximum (near residue 40)

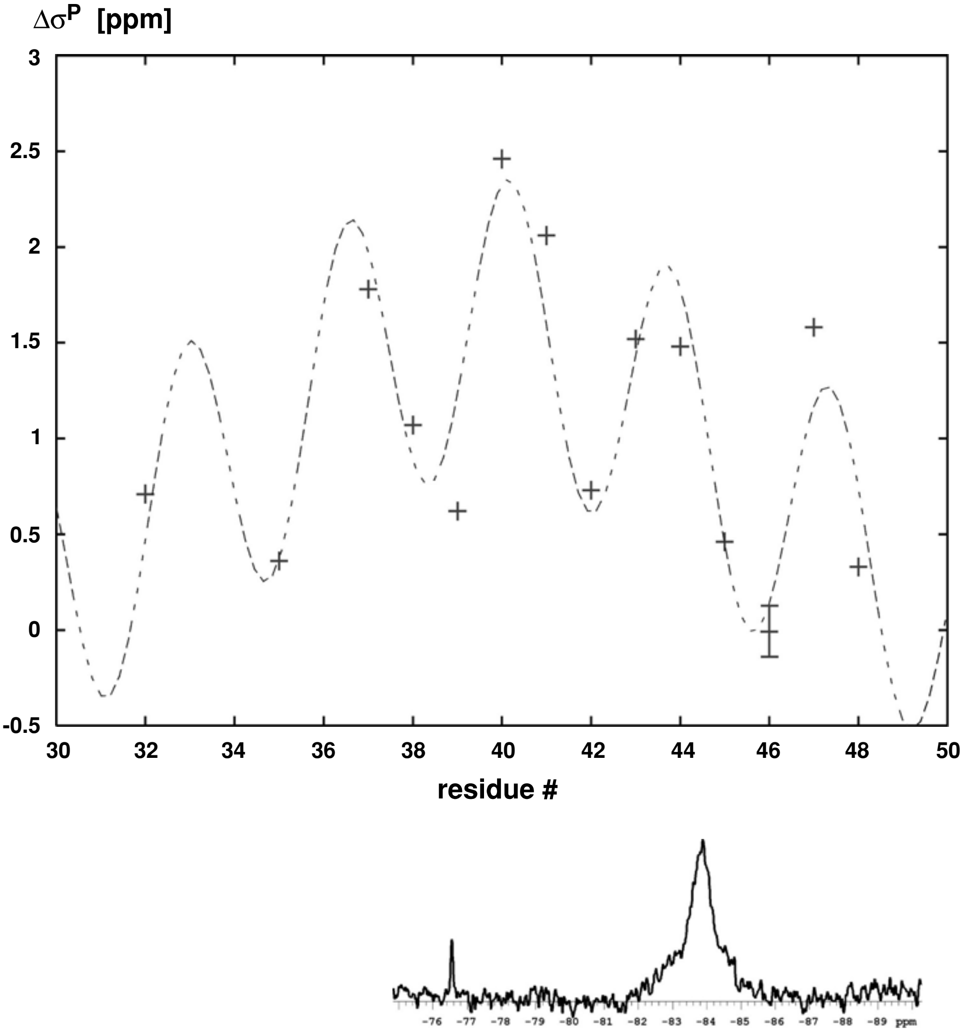

Fig. 4. Oxygen-induced ^{19}F NMR chemical shift perturbations vs. residue for the TM1 domain of the intact homotrimer of the membrane protein, DAGK, reconstituted in dodecylphosphocholine micelles, at 30 °C. ^{19}F chemical shift perturbations were measured by comparing spectra obtained after separately equilibrating at 100 atm nitrogen and oxygen, using single cysteine mutants of DAGK to which was attached a trifluoropropanone label. Typical spectra, as shown in the figure, were acquired on a Varian 500 Inova spectrometer at a Larmor frequency of 470.347 MHz, using between 100 and 200 transients, respectively, with a 2 s repetition time. (See also Plate 48 on page XXXVI in the Color Plate Section.)

in the overall profile, is suggested to arise from maximal solubilities of oxygen in the hydrophobic micelle interior, while residues 32 and 48 are determined to be near the micelle water interface, where the oxygen solubility is lower.

In contrast to the study of DAGK, in which the reporter groups were cysteine specific fluorine labels, it is also possible to combine traditional solution NMR to oxygen scanning experiments such that all resolvable nuclei can be studied at once. In one such study, enhancements of HzNz spin-lattice rates for all resolvable amides, at 20 Atm oxygen partial pressure, were recently measured for the 170 residue ^{2}H,^{15}N-labeled β-barrel, PagP [32]. PagP is a β-barrel membrane protein, whose structure and dynamics has been previously studied by NMR [31] and X-ray diffraction [33]. The paramagnetic rates were

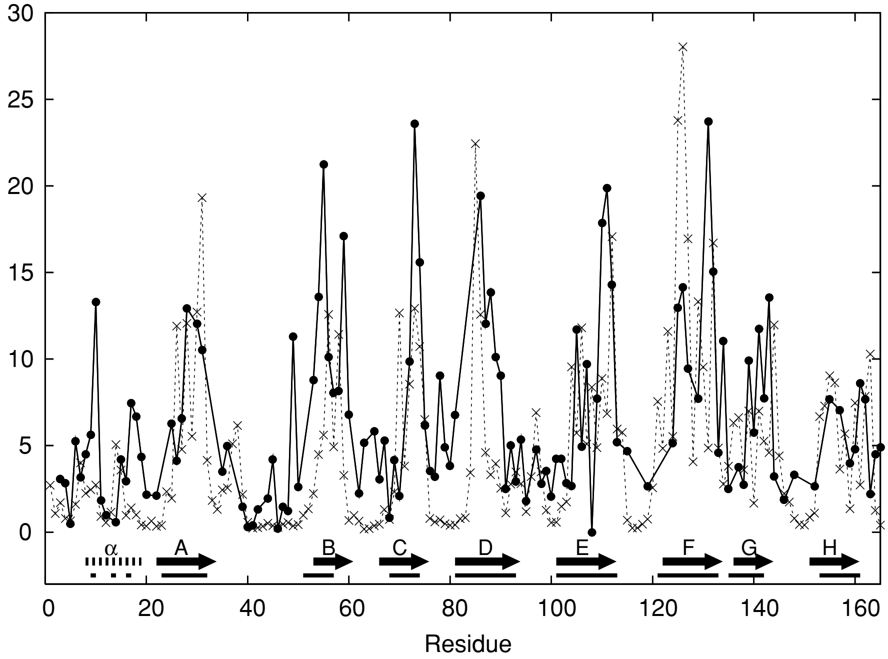

Fig. 5. Paramagnetic contribution to the HzNz spin-lattice relaxation rate, $R_1^P(O_2)$, overlayed with effective local hydrophobicity as a function of residue for the membrane protein, PagP. The effective hydrophobicity at each residue is determined by a weighted average of hydrophobicities within a sphere of radius 6 Å of the source. Note that arrows designate residues which adopt a β-strand secondary structure, while solid bars represent transmembrane residues and the dashed solid bar signifies residues belonging to the N-terminal α-helix.

pronounced for all eight transmembrane β-strands, due presumably to higher hydrophobicities, in the vicinity of the amides in the transmembrane domain. Evidence of the influence of local protein hydrophobicity is presented in Figure 5, where the above paramagnetic rate profile, $R_1^P(O_2)$, is overlayed with local hydrophicities, obtained by a spatially weighted average, using the Kyte-Doolittle scale.

Protein–Protein Interactions

Since oxygen essentially serves as a surface contrast agent, it stands to reason that it might be a useful tool in studies of protein binding interfaces or in studies of ligand protein interactions. Through difference experiments (i.e. experiments performed on a free protein and in the presence of a binding partner) it should be possible to make use of contact shifts or relaxation rates to determine the binding interface. In one study [34], the paramagnetic contribution to the amide ^{1}H spin–lattice relaxation rates, R_1^{P}, was measured for uniformly ^{2}H, ^{15}N-labeled FB protein, a 60-residue 3-helix bundle, constituting the B domain of protein A. Through TROSY versions of inversion–recovery experiments [35], R_1^{P} could also be determined for FB in the presence of a stoichiometric equivalent of an unlabeled Fc fragment of immunoglobulin (Ig) G. To best distinguish the binding interface of FB with Fc, the experimental ratio of paramagnetic rates, $R_1^{\mathrm{P}}(\text{complex})/R_1^{\mathrm{P}}(\text{free})$, was determined and all values of $R_1^P(\text{complex})/R_1^P(\text{free})$ less than unity, were considered to indicate regions protected by binding. The result is shown in Figure 6, where the FB residues exhibiting varying degrees of protection from oxygen, are mapped onto the protein surface. A clear binding interface was revealed, which was shown to be consistent with former cross-saturation studies of the protein [36].

Additional Applications: Family Fold Recognition and O_2 Migration Pathways

Recently, Hernandez *et al.* [37] demonstrated that O_2 penetration depth in water-soluble proteins could be assessed by comparing spin–lattice relaxation rate enhancements of buried amide protons in perdeuterated

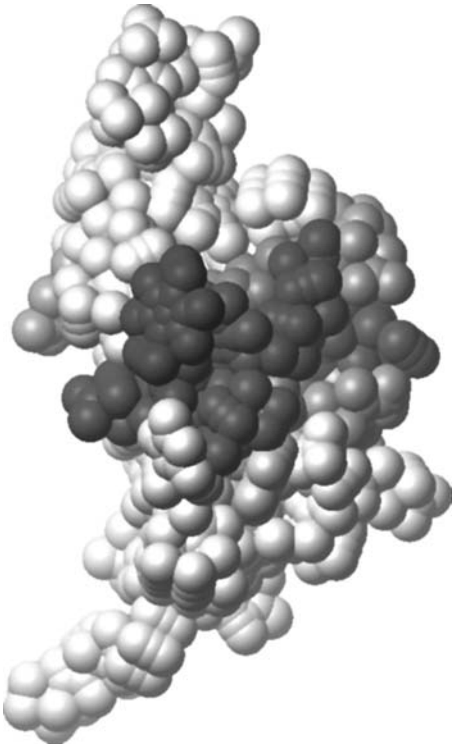

Fig. 6. looseness-1Depiction of $R_1^{\mathrm{P}}(\text{complex})/R_1^{\mathrm{P}}(\text{free})$ mapped onto FB. A gradation of red (strongest binding or greatest change of O_2 accessibility upon binding) to white (no binding) is assigned to residues depending on the magnitude of $R_1^{\mathrm{P}}(\text{complex})/R_1^{\mathrm{P}}(\text{free})$. ^{1}H T_1 TROSY experiments were performed under either 20 atm of nitrogen or oxygen, using a 600 MHz Bruker Avance spectrometer equipped with an HNC cryoprobe. (See also Plate 49 on page XXXVI in the Color Plate Section.)

rubredoxin, from oxygen and a bulky (non-penetrating) water-soluble nitroxide paramagnetic agent. In the absence of stable internal cavities, as is the case in the protein rubredoxin, oxygen solubility was determined to be at most 10% of the bulk value in the protein interior. Furthermore, simulations of paramagnetic rates, based on the assumption that both oxygen and nitroxide spin label remained exterior to the protein, proved to reproduce the observed rates for the majority of residues. The authors proposed that paramagnetic relaxation effects could be used to identify structurally homologous proteins or protein domains, whose sequences are too disparate for sequence-based recognition.

In contrast to rubredoxin, myoglobin possesses four stable hydrophobic cavities, known to accommodate xenon. McNaughton *et al.* [38] have measured the oxygen enhanced amide spin–lattice relaxation rates associated with the zinc-containing diamagnetic analog of sperm whale deoxymyoglobin. Zinc was used in this study to prevent covalent association of oxygen with the porphyrin. An analysis of paramagnetic rates revealed the binding constants of oxygen to all four non-covalent binding sites, thereby furthering ideas on oxygen diffusion pathways to the heme and overall binding to myoglobin.

Final Comments

In this review, we have highlighted current applications of oxygen as a paramagnetic probe in modern solution NMR structure studies of membranous and aqueous systems. Thus far, chemical shift perturbations from oxygen appear to be of practical value in ^{13}C and ^{19}F NMR applications. Furthermore, spin–lattice relaxation rate enhancements are significant in high gamma nuclei such as ^{19}F and ^{1}H. Moreover, the analysis of such rates is made easier due to fast electronic spin–lattice relaxation of oxygen. In general, conditions may be found wherein significant contact shifts or relaxation rate enhancements are observed, without undue line broadening. Though quantitative analysis of paramagnetic effects of oxygen is complicated by the preferential association of oxygen with disordered or hydrophobic surfaces, experiments which involve changes in oxygen accessibility (for example, binding between proteins and ligands or protein unfolding) are anticipated to be useful.

Applications of oxygen to spectroscopic studies of membranous systems abound due to the significant paramagnetic gradient, which exists in both bilayers and micelles. Immersion depth can be assessed for both membrane interacting amphiphiles or large membrane proteins. Given the current limitations of solution NMR to the study of membrane proteins, the use of oxygen paramagnetic effects on ^{19}F, ^{13}C, and ^{1}H nuclei in addition to applications of oxygen with appropriately fluorinated cysteine mutants, should prove helpful in understanding complicated topologies of membrane proteins.

References

1. Teng CL, Hong H, Kiihne S, Bryant RG. J. Magn. Reson. 2001; 148:31.
2. Ayant Y, Belorizky E, Alizon J, Gallice J. J. Phys. I. 1975; 36:991.
3. Hwang L, Freed JH. J. Chem. Phys. 1975;63:4017.
4. Solomon I, Bloembergen N. J. Chem. Phys. 1956;25: 261.
5. Freed JH. J. Chem. Phys. 1978;68:4034.
6. Teng C, Hinderliter B, Bryant RG. J. Phys. Chem. A. 2006;110:580–588.
7. Prosser RS, Luchette PA, Westerman PW. Proc. Natl. Acad. Sci. U.S.A. 2000;97:9967.

8. Ulmer TS, Campbell ID, Boyd J. J. Magn. Reson. 2002;157:181.
9. Prosser RS, Luchette PA. J. Magn. Reson. 2004;171:225.
10. Bertini I, Luchinat C. NMR of Paramagnetic Molecules in Biological Systems. Benjamin Cummings: Menlo Park, 1986.
11. Bertini I, Capozzi F, Luchinat C, Piccioli M, Vila AJ. J. Am. Chem. Soc. 1994;116:651.
12. Bertini I, Luchinat C, Parigi G. Concepts Magn. Reson. 2002;14:259.
13. Teng CL, Bryant RG. J. Am. Chem. Soc. 2000;122:2667.
14. Teng CL, Bryant RG. Biophys. J. 2004;86:1713.
15. Hyde JS, Subczynski WK. In: LJ Berliner, J Reuben (Eds). Spin Labeling. Theory and Applications. Plenum Press: New York and London, 1989, p 399.
16. Subczynski WK, Hyde JS, Kusumi A. Proc. Natl. Acad. Sci. U.S.A. 1989;86:4474.
17. Marsh D. Proc. Natl. Acad. Sci. U.S.A. 2001;98:7777.
18. Dzikovski BG, Livshits VA, Marsh D. Biophys. J. 2003;85:1005.
19. Marrink SJ, Berendsen HJC. J. Phys. Chem. 1996;100:16729.
20. Wahid SA, Yu CH, Batruch I, Evanics F, Pomes R, Prosser RS. Biochemistry (submitted) 2006.
21. Evanics F, Prosser RS. Anal. Chim. Acta. 2005;534:21–29.
22. Altenbach C, Marti T, Khorana HG, Hubbell WL. Science. 1990;248:1088.
23. Hubbell WL, Altenbach C. Curr. Opin. Struct. Biol. 1994;4:566.
24. Bezanilla F, Perozo E. Adv. Protein Chem. 2003;63:211.
25. Klare P, Bordignon E, Engelhard M, Steinhoff HJ. Photochem. Photobiol. Sci. 2004;3:543.
26. La Mar GN, Horrocks WDeW Jr, Holm RH. NMR of Paramagnetic Molecules: Principles and Applications. Academic Press: New York, 1973.
27. Gaffney BJ, McConnel HM. J. Magn. Reson. 1974;16:1.
28. Hilty C, Wider G, Fernandez C, Wuthrich K. Chem. Biochem. 2004;5:467.
29. Ellena JF, Moulthrop J, Wu J, Rauch M, Jaysinghne S, Castle JD, Cafiso DS. Biophys. J. 2004;87:3221.
30. Luchette PA, Prosser RS, Sanders CR. J. Am. Chem. Soc. 2002;124:1778.
31. Hwang PM, Choy WY, Lo EI, Chen L, Forman-Kay JD, Raetz CRH, Prive GG, Bishop RE, Kay LE. Proc. Natl. Acad. Sci. U.S.A. 2002;99:13560.
32. Evanics F, Hwang PM, Cheng Y, Kay LE, Prosser RS. J. Am. Chem. Soc. 2006 (In press).
33. Ahn VE, Lo EI, Engel CK, Chen L, Hwang PM, Kay LE, Bishop RE, Privé GG. EMBO J. 2004;23:2931.
34. Sakakura M, Noba S, Luchette PA, Shimada I, Prosser RS. J. Am. Chem. Soc. 2005;127:5826–5832.
35. Pervushin K, Riek R, Wider G, Wuthrich K. Proc. Natl. Acad. Sci. U.S.A. 1997;94:12366.
36. Nakanishi T, Miyazawa M, Sakakura M, Terasawa H, Takahashi H, Shimada I. J. Mol. Biol. 2002;318:245.
37. Hernandez G, Teng CL, Bryant RG, LeMaster DM. J. Am. Chem. Soc. 2002;124:4463.
38. McNaughton L, Hernandez G, LeMaster DM. J. Am. Chem. Soc. 2003;125:3813.
39. Vold RR, Prosser RS, Deese AJ. J. Biomol. NMR. 1997;9:329.
40. Luchette PA, Vetman TN, Prosser RS, Hancock REW, Nieh MP, Glinka CJ, Krueger S, Katsaras J. Biochim. Biophys. Acta. 2001;1513:83.

Protein Structure

TROSY NMR for Studies of Large Biological Macromolecules in Solution

César Fernández[1] and Gerhard Wider[2]
[1] *Novartis Institutes for Biomedical Research, CH-4002 Basel, Switzerland; and*
[2] *Institute of Molecular Biology & Biophysics, ETH Zurich, CH-8093 Zurich, Switzerland*

Abstract

Transverse relaxation-optimized spectroscopy (TROSY), in combination with isotope labeling techniques and with improvements in NMR instrumentation, have greatly extended applications of NMR spectroscopy to large biological macromolecules that were otherwise not accessible to high-resolution solution state NMR. Important recent applications of TROSY include the structure determinations of integral membrane proteins in detergent micelles, structural and functional studies of large proteins in monomeric form and in macromolecular complexes, and investigations of intermolecular interactions in large complexes. Moreover, TROSY can improve measurements of NMR parameters, such as residual dipolar couplings and scalar couplings across hydrogen bonds, which contribute to a further improvement of the quality and the precision of solution structures of large proteins and oligonucleotides.

Introduction

During the past two decades, liquid-state NMR studies of biological macromolecules have been limited to relatively small structures with molecular weights in the range of 2–25 kDa, with an average around 10 kDa [1]. For biological macromolecules with molecular weights above 25–30 kDa the quality of the NMR data rapidly deteriorates. A major limitation when working with these large molecules arises from the fast relaxation of the NMR signal, causing severe line broadening, which translates into poor spectral resolution and low signal-to-noise ratios. Considerable efforts are devoted to extend applications of solution NMR to larger molecular systems, which would allow, for instance, structure determinations of proteins that cannot be crystallized, including integral membrane proteins, investigations of intermolecular interactions involving large molecules and macromolecular assemblies, and the structure determination of larger oligonucleotides and their complexes with proteins.

Substantial quality improvement of NMR spectra of biological macromolecules with molecular weights above ∼25 kDa can be obtained with deuterium labeling (for reviews, see Refs. [2–5]). With the introduction of transverse relaxation-optimized spectroscopy (TROSY) [6–11], relaxation could be reduced to such an extent that satisfactory NMR spectra can be obtained from particles with molecular weights far above 100 kDa. Along with improved instrumentation, TROSY has greatly extended the size limit for macromolecules that can be studied by solution NMR, opening a wide range of new applications [12–15]. In this chapter, the basis of TROSY and recent applications of TROSY for structural and functional studies of large biological macromolecules will be reviewed.

Technical Background

The NMR Signal

NMR measures the response of nuclear spins in a large, homogenous magnetic field to perturbations caused by the irradiation of electromagnetic fields in the radio-frequency range [16]. In practice, a sequence of radio-frequency pulses is applied, which are separated by interpulse time periods. The response to such a NMR pulse sequence (Figure 1) is a sum of radio-frequencies that have been emitted by the nuclei.

The NMR signal decays exponentially with a characteristic time constant, the transverse relaxation time T_2 (Figure 1A). For the analysis, the signal is Fourier-transformed (FT) into a spectrum containing resonance lines that represent the various emitted radio-frequencies. The width of the resonance lines in the spectrum is inversely proportional to T_2, which depends on the size of the molecule: for increasing molecular masses, T_2 becomes shorter (fast transverse relaxation) and consequently the lines in the spectrum broaden (Figure 1B).

NMR and Molecular Size

When studying large molecules by solution NMR, three major difficulties arise: signal overlap, limited solubility and fast relaxation. In principle, signal overlap can be

Graham A. Webb (ed.), Modern Magnetic Resonance, 487–496.
© 2008 *Springer.*

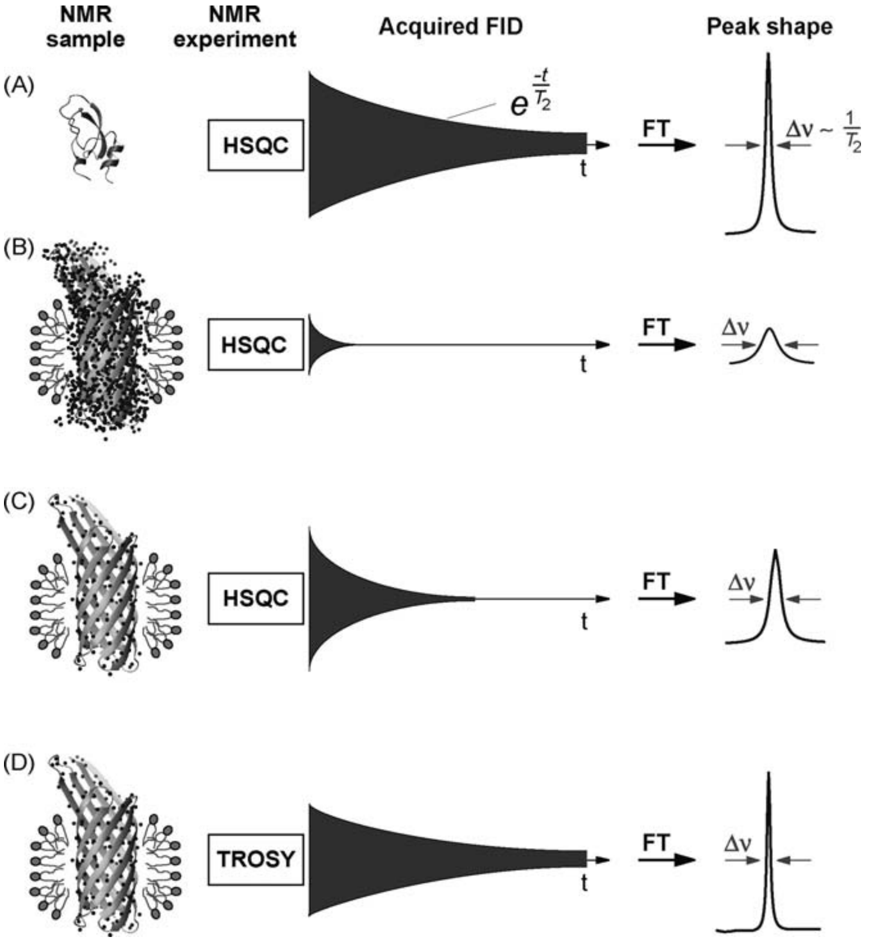

Fig. 1. Solution NMR spectroscopy with small and large molecules. (A) The NMR signal obtained from small molecules in solution relaxes slowly; it has a long transverse relaxation time T_2. Long T_2 values translate into narrow linewidths ($\Delta\nu$) in the NMR spectrum after FT of the NMR signal. HSQC stands for the pulse sequence; the structure on the left hand side represents a small protein. (B) For larger molecules the decay of the NMR signal is faster (T_2 is shorter). This results in a weaker signal after the NMR pulse sequence and broad lines in the spectra. In the schematic structure on the left hand side, the high density of protons is indicated by black dots. (C) By deuteration of the macromolecule (reduced number of protons indicated by less black dots in the schematic structure on the left), the transverse relaxation can be substantially reduced, which yields improved spectral resolution and improved sensitivity for large molecules. (D) Using TROSY pulse sequences with deuterated macromolecular samples the transverse relaxation can be further reduced, thereby increasing considerably the molecular weight amenable to NMR. Adapted from Ref. [14] with permission.

alleviated by proper choice of isotope-labeling schemes, including uniform, segmental, and selective ^{15}N and ^{13}C-labeling techniques [2,17–19]. Limited solubility translates into poor sensitivity, a problem that can be alleviated by new developments in NMR techniques and instrumentation that increase sensitivity, e.g. the development of cryogenic probes and spectrometers with higher magnetic fields.

The limitations caused by nuclear transverse relaxation poses the most severe technical challenge for studies of larger biological macromolecules in solution. Relaxation becomes especially bothering with long and relatively complex pulse sequences that are required for heteronuclear multidimensional NMR experiments. For larger systems, fast transverse relaxation reduces the signal intensities beyond the detection limit before the desired signal can be measured. The combination of deuteration techniques and TROSY alleviate the deleterious effects of transverse relaxation in such systems and increase the molecular size limit (Figure 1C and D).

Isotope Labeling

A major source for transverse relaxation are the protons in the omnipresent hydrogen atoms. Via dipole–dipole (DD) interactions, they efficiently relax any NMR active nuclei, e.g. ^{1}H, ^{13}C or ^{15}N, in macromolecules. The strength of the DD interaction can be greatly reduced by replacing protons by deuterons, because of the much smaller dipole moment of ^{2}H compared to ^{1}H [2]. Deuteration has clear advantages with regard to relaxation [2–4,20], however, protons contribute a major part of the structural information and produce the most sensitive NMR signal. Thus, measuring completely deuterated proteins is not an option and a compromise has to be found. For example, C–H moieties in macromolecules are often deuterated only to a certain extent, e.g. to 70%, or protons are selectively re-introduced into otherwise highly deuterated molecules, e.g. in methyl groups of Val, Leu, and Ile residues [2,5].

For NMR measurements, biological macromolecules are usually dissolved in H_2O, where their exchangeable ^{15}N–^{1}H groups generally become protonated. The strategically important amide groups in the polypeptide backbone of proteins are thus accessible to ^{1}H NMR experiments. Although deuteration of the C–H groups reduces significantly DD interactions between ^{15}N–^{1}H moieties and remote protons, i.e. the protons outside the ^{15}N–^{1}H group (Figure 1C), the ^{15}N–^{1}H DD interactions are omnipresent in ^{15}N-labeled samples. It has been shown that these ^{15}N–^{1}H DD interactions can be reduced by spectroscopic means using TROSY [6] (Figure 1D).

Transverse Relaxation-Optimized Spectroscopy

The Foundations of TROSY

The TROSY technique [6] is based on the interference of different relaxation mechanisms that contribute to the relaxation of a particular nucleus. This interference can be additive or subtractive resulting in increased or reduced relaxation, respectively. In addition to the omnipresent relaxation due to DD coupling, chemical shift anisotropy (CSA) of ^{1}H, ^{15}N, and ^{13}C can be a significant source of transverse relaxation at the high magnetic fields typically used for studies of biological macromolecules. The interference between this two relaxation mechanisms can be nicely illustrated in a correlation spectrum of ^{15}N and ^{1}H nuclei of amide groups in a polypeptide backbone (Figure 2). Each ^{1}H nucleus couples to its directly attached ^{15}N nucleus via scalar coupling. The ^{1}H NMR spectrum of such an amide moiety thus consists of two lines representing the protons attached to ^{15}N nuclei with spin up and spin down, respectively. The corresponding effect is observed for the ^{15}N nucleus. Therefore, in a 2D correlation experiment without decoupling a four-line fine structure is observed (Figure 2B). In conventional NMR experiments, the four multiplet lines are collapsed into one resonance by decoupling. Decoupling averages the relaxation rates (Figure 2A), which for smaller molecules, where all four multiplet components have almost identical linewidths, results in a simplified spectrum with improved sensitivity. However, for large molecules the multiplet components have largely different linewidths (Figure 2B) and decoupling results in a broad line (Figure 2A) which is much broader and less intense than the narrowest multiplet component (Figure 2C). In this situation it would be an advantage to record only the narrowest component.

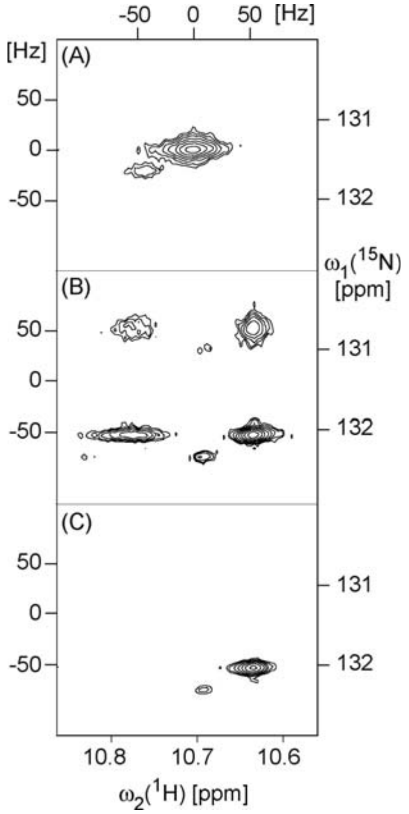

Fig. 2. Contour plots of a backbone amide ^{15}N–^{1}H correlation peak extracted from three different variants of 2D [^{15}N,^{1}H] correlation experiments. (A) Conventional broad-band decoupled [^{15}N,^{1}H]-HSQC. (B) Same as (A) without any decoupling during the experiment. (C) [^{15}N,^{1}H]-TROSY spectrum. Adapted from Ref. [6] with permission.

The TROSY technique selects exclusively the slowest relaxing component of the four line pattern (Figure 2C) eliminating the faster relaxing multiplet components. Thus, TROSY neglects part of the potential signal, which is, however, more than compensated in large molecules by the much slower relaxation during the pulse sequence and the acquisition (Figure 1D).

Field Strength Dependence of TROSY for ^{15}N–^{1}H Groups

The amide proton of a ^{15}N–^{1}H moiety relaxes due to DD interaction with the nitrogen and its own CSA. These two interfering relaxation mechanisms lead to different relaxation rates for the two multiplet components of the proton, with one rate smaller and the other one larger than the average rate. This effect depends on the external magnetic field since only CSA relaxation and not DD relaxation is field dependent. The optimal TROSY effect for one doublet component can thus be obtained by choosing the appropriate field strength, where its relaxation rate will be near zero. For amide protons in polypeptides, this "magic field" is about 23.5 T, corresponding to a proton resonance frequency of approximately 1000 MHz. The ^{15}N nucleus in an amide moiety shows a similar interference between ^{15}N–^{1}H DD interaction and its CSA, which minimizes the ^{15}N relaxation, accidentally, at about the same "magic field."

In practice, small deviations are expected from the "magic field" calculated for an isolated two-spin system, since the CSA varies slightly depending on the exact geometry of the amide moieties. Further, residual DD couplings (especially of amide protons) with remote protons give rise to relaxation that cannot be compensated by the TROSY effect, but that can be minimized by sample deuteration. In general, one approaches the optimal TROSY effect for peptide ^{15}N–^{1}H groups, manifested in optimal resolution and sensitivity, at the highest presently available ^{1}H frequencies of 900 MHz [6] using deuterated samples in aqueous solutions.

Implementation of TROSY: 2D [^{15}N, ^{1}H]-TROSY

The simplest implementation of TROSY into experimental schemes is the 2D [^{15}N,^{1}H]-TROSY [6,21], which does not contain any heteronuclear decoupling, neither during the ^{15}N chemical shift evolution period (t_1), nor during the signal acquisition period (t_2). Without decoupling, the four transitions that correspond to the multiplet components with different relaxation rates (Figure 2) are not mixed. The selection of the slowest relaxing component and the concomitant elimination of the remaining three components are achieved by phase cycling of the rf-pulses. The polarization transfer element ST2-PT [22] retains 50% of the original proton polarization. This residual polarization, however, is slowly relaxing and leads to an overall gain in signal intensity for large biological macromolecules. In general, when working with molecular sizes above 20 kDa at magnetic field strengths corresponding to a proton resonance frequency of at least 700 MHz, a higher signal-to-noise ratio is readily obtained with TROSY when compared with the corresponding conventional experiments.

[^{13}C–^{1}H]-TROSY

The application of the TROSY principle is not limited to ^{15}N–^{1}H groups in biological macromolecules. ^{13}C–^{1}H TROSY can be implemented in experiments with aromatic rings and methyl groups, where cross-correlated relaxation effects are also observed. In aromatic spin systems, the relaxation mechanisms for optimizing ^{1}H and ^{13}C transverse relaxation are ^{13}C–^{1}H–DD coupling and ^{13}C-CSA [8,23]. The large CSA values for ^{13}C can provide efficient compensation of ^{13}C transverse relaxation by dipolar coupling to the attached proton. In contrast, the small CSA of aromatic protons is not suitable for the application of TROSY and protons are decoupled from ^{13}C during acquisition. For aromatic ^{13}C–^{1}H groups the optimal TROSY effect is observed at a ^{1}H frequency of 600 MHz. For ^{13}C-labeled biological macromolecules of any molecular weight, significant sensitivity enhancement in ^{13}C–^{1}H correlation spectra of aromatic spin systems can be obtained with the use of TROSY compared to the conventional HSQC-based experiments.

A ^{13}C–^{1}H TROSY effect can also be observed in methyl groups, where different dipolar interactions compensate each other in large molecules. In methyl groups, the dominant relaxation of a methyl ^{13}C-nucleus originates in the dipolar coupling with the three methyl protons [24]. Interestingly, the standard [^{13}C,^{1}H]-HMQC correlation experiment is an optimized TROSY experiment for methyl carbons, which maintains 50% of the carbon magnetization in slowly relaxing states. For large molecules the 2D [^{13}C,^{1}H]-HMQC experiment yields superior resolution and sensitivity compared to the [^{13}C,^{1}H]-HSQC experiment, which mixes fast and slowly relaxing transitions, deteriorating significantly the spectral quality. It is important to note that the dipolar interaction is field independent and, therefore, the methyl TROSY can be applied at all field strengths for large molecules [25].

TROSY Applications for Studies of Large Biological Macromolecules

Although collection of high-quality data for structure determination of proteins with molecular masses up to ~100 kDa is now technically feasible, the complexity of the NMR spectra generally increases with the size of the molecule studied and the concomitant signal overlap may limit spectral analysis. Therefore, the preferred current use of relaxation-optimized NMR techniques is with large structures that yield relatively simple spectra compared to monomeric globular proteins of the same molecular size, such as homo-oligomeric proteins, individual small or medium-size subunits in large molecular complexes and membrane proteins in detergent micelles [12,14].

2D [^{15}N,^{1}H] TROSY

For large proteins, 2D [^{15}N,^{1}H]-TROSY provides fingerprints with improved resolution and sensitivity compared to conventional experiments (Figure 3A). This extends applications based on 2D [^{15}N,^{1}H] correlation experiments to much larger structures, e.g. for studies of intermolecular interactions, either with low-molecular weight ligands or with other biological macromolecules, which are usually applied in NMR screening to detect binding of compounds that can be optimized to high-affinity ligands by “SAR-by-NMR” [26].

TROSY-based NMR experiments have been applied to a variety of macromolecular complexes. They include the 51-kDa complex formed between the pilus chaperone FimC and the pilus subunit FimH from *Escherichia coli* [27], the P-domain of the lectin chaperone calreticulin and Erp57 in a 66.5-kDa complex [28], the p53 core domain bound in a ~200-kDa complex with Hsp90 [29], a 64-kDa immunoglobulin complex with a domain of protein A [30], and the 91-kDa 11-mer TRAP protein [31]. Recently, application of TROSY to malate synthase G from *E. coli*, an 81-kDa monomeric enzyme, yielded valuable quantitative information on ligand binding based on chemical shift mapping, residual dipolar couplings (RDCs), amide proton exchange rates, and ^{15}N spin relaxation measurements [32].

[^{13}C,^{1}H] Correlation Experiments

The simplest experiment that exploits the ^{13}C–^{1}H TROSY effect in aromatic systems is the 2D constant-time-[^{13}C–^{1}H]-TROSY [23]. With the application of TROSY, 4- to 10-fold signal enhancement has been achieved for resonances of the aromatic rings in an 18 kDa protein [23] and for RNA and DNA molecules [33,34]. Based on the [^{13}C,^{1}H]-TROSY building block, 3D pulse sequences can be developed that allow assignments of aromatic spin systems in proteins and nucleic acids [23].

TROSY can also be very profitably applied to methyl groups [35]. With a 2D [^{13}C,^{1}H]-HMQC experiment, sensitivity gains up to a factor of 3 compared to a [^{13}C,^{1}H]-HSQC have been observed for a perdeuterated, selectively methyl-^{1}H,^{13}C-labeled protein with a rotational correlation time of 400–450 ns (equivalent to a ~800 kDa globular molecule at 37 °C) [24,25]. For very large molecules the methyl ^{13}C–^{1}H TROSY effect can be exploited in 2D and 3D experiments for resonance assignments of methyl groups [36], for stereospecific assignments of prochiral methyls [37], for studies of domain orientation based on RDCs and ligand binding [32] and for studies of dynamic properties [38].

TROSY for Resonance Assignments in Large Molecules

^{15}N–^{1}H TROSY for Assignment of Protein Backbone Resonances

Triple-resonance experiments [39–42], which are usually applied for backbone resonance assignments of ^{13}C,^{15}N-labeled proteins, include the amide moiety. These experiments contain extended time periods with transverse amide nitrogen magnetization and yield dramatic signal enhancement when using TROSY. TROSY versions of the most relevant triple resonance experiments have been implemented [43–48], which in general yield sensitivity gains of more than one order of magnitude with proteins in the molecular weight range from 25 to 150 kDa [43–46,49]. As an example, Figure 3 shows the dramatic improvement in spectral quality that can be obtained with TROSY in a molecular complex of about 60 kDa. Whereas the TROSY version shows clear cross peaks (Figure 3C), the conventional spectrum cannot at all yield the desired correlations (Figure 3D).

Using TROSY techniques, resonance assignments have been obtained for much larger proteins than ever thought possible with conventional NMR techniques. This was first demonstrated with a homo-octameric 110 kDa protein [49], where 20- to 50-fold sensitivity gains in triple resonance experiments were observed. More recently, backbone resonance assignments in the 723-residue monomeric protein malate synthase were obtained, which is the largest single polypeptide chain that has been assigned to date [50].

^{15}N–^{1}H TROSY for Assignment of Protein Side-Chain Resonances

In addition to resonance assignments of nuclei in the polypeptide backbone, ^{15}N–^{1}H TROSY experiments have been developed for assignment of ^{1}H and ^{13}C chemical shifts of methyl groups in selectively methyl-protonated and otherwise deuterated large proteins. In one application, the membrane protein OmpX in 60 kDa DHPC micelles [51] has been selectively protonated at the Val, Leu, and Ile (δ1) methyl groups [52]. With ^{15}N–^{1}H TROSY-based ^{13}C–^{13}C TOCSY experiments, the methyl groups were correlated with the backbone amide groups, yielding complete sequence-specific assignments of the protonated methyl groups [51], which had a significant impact

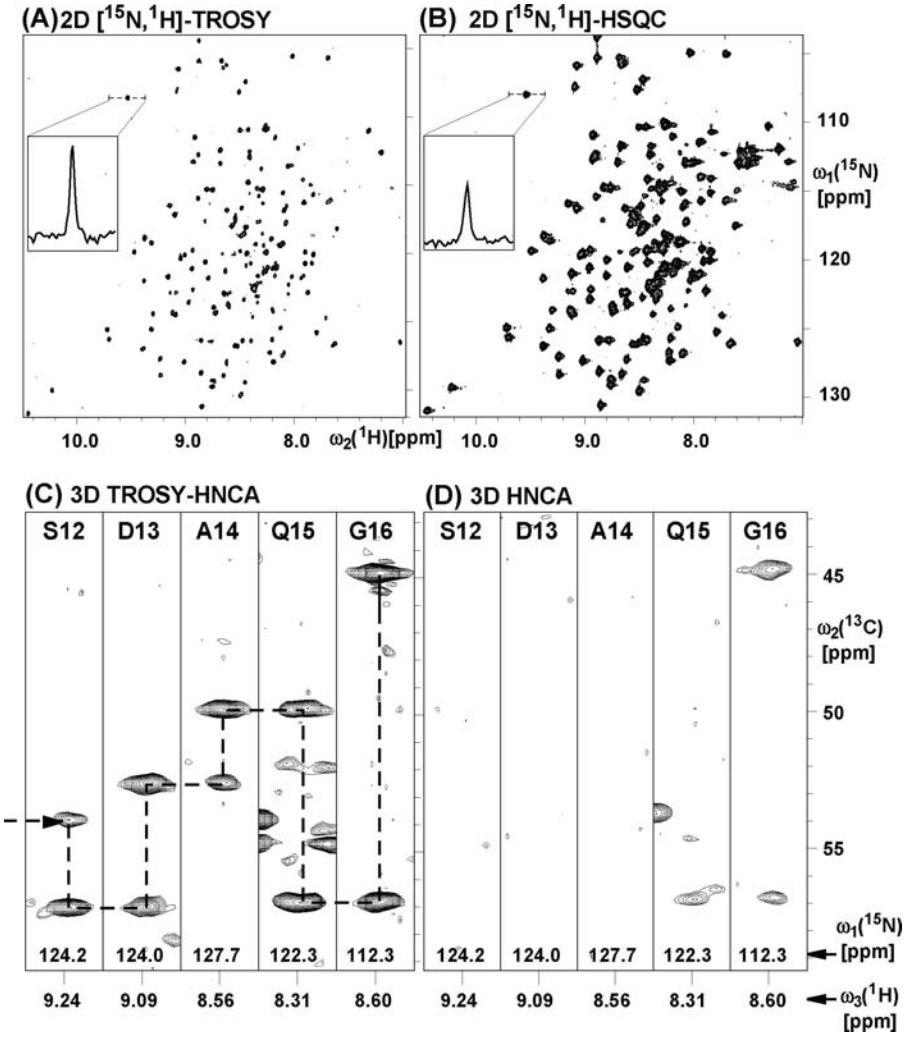

Fig. 3. Impact of TROSY on NMR spectra. The spectra were measured at a ^1H resonance frequency of 750 MHz with a sample of the uniformly ^2H,^{13}C,^{15}N-labeled integral membrane protein OmpX in dihexanoylphosphatidylcholine (DHPC) micelles, a 60-kDa complex. (A) and (B) show ^{15}N–^1H correlation spectra that were identically recorded and processed, except that TROSY was used in (A) only. The inserts show cross sections that were taken parallel to the ω_2 (^1H) axis at the position indicated by the horizontal broken lines. (C) Strips along the ^{13}C-dimension from a 3D [^{15}N,^1H]-TROSY-HNCA spectrum. The strips were taken at the ^{15}N chemical shifts (indicated at the bottom of the strips) of the amino acid residues 12–16, and are centered at the corresponding amide proton chemical shifts, ω_3($^1H^N$). Horizontal and vertical broken lines indicate the connectivities that can be obtained, leading to complete resonance assignments of the polypeptide backbone $^1H^N$, ^{15}N, and $^{13}C^\alpha$ nuclei. (D) Strips from a conventional 3D HNCA spectrum; the strips were taken at the same frequencies as in (C). Adapted from Ref. [14] with permission.

on the precision of the NMR structure [53]. Recently, near complete assignments of Val, Leu, and Ile (δ1) methyl groups have been obtained for the 81 kDa protein malate synthase G using new labeling strategies in concert with new TROSY-type NMR experiments [25,36,37]. The Val and Leu isopropyl groups were labeled with ^1H and ^{13}C in only one of the two methyl groups, and subsequently assigned using TROSY experiments.

TROSY for Observation of Scalar Couplings Across Hydrogen Bonds

Hydrogen bonds are usually indirectly inferred from experimental data, e.g. from nuclear Overhauser enhancement (NOEs) and proton exchange rates, or from analysis of refined 3D structures based on geometrical considerations. Direct detection of hydrogen bonds in proteins and oligonucleotides was enabled by the observation of scalar spin–spin couplings across hydrogen bonds [54–56]. These couplings allow the determination of hydrogen bond partners, which can be used to refine NMR structures, to study intermolecular interactions at atomic level, and to investigate biological mechanisms involving hydrogen bonding interactions.

The sensitivity and spectral resolution in NMR experiments used to detect hydrogen bonds can be substantially improved for large molecules by using TROSY. Applications include: measurements of scalar couplings across hydrogen bonds in a ^{15}N,^{13}C-labeled DNA duplex tetradecamer in a 17 kDa protein–DNA complex [55,57], in 25 kDa RNA oligonucleotides [58], in the 30 kDa ribosome-inactivating protein MAP30 [59], in the 147-residue flavoprotein riboflavin 5′-monophosphate [60], and in the active site of the 44 kDa enzyme chorismate mutase [61].

TROSY for Measurements of RDCs

Residual dipolar couplings (RDCs) provide important structural restraints for obtaining global folds and for refining the 3D structure of proteins and oligonucleotides [62–64]. This is especially important in large, perdeuterated molecules, where only a limited number of constraints can be obtained from NOEs [65,66]. Various TROSY-based experimental schemes have been developed for measuring RDCs (for an overview, see Ref. [63]). Applications to the maltose binding protein in a complex with β-cyclodextrin and to carbonic anhydrase II showed that precise RDCs can be obtained for proteins of 30–40 kDa molecular weight [67]. Furthermore, RDCs in the 723-residue malate synthase G [32], in a 53-kDa homomultimeric trimer from mannose binding protein [68], and in the 41-kDa maltose binding protein [69] were measured using TROSY-based experiments.

TROSY for Studies of Dynamic Processes

In addition to structural data, NMR is able to provide information on dynamic processes at atomic resolution over a wide range of time scales [70,71] which can help in understanding structure and function relationships (see, e.g. [72,73]). Key experiments for dynamic studies measure T_1 and T_2 relaxation times, and heteronuclear ^{15}N{^{1}H}-NOEs of the ^{15}N nuclei in amide groups. For these important experiments, pulse sequences using ^{15}N–^{1}H TROSY were developed [74,75]. Recently, a new experiment based on methyl TROSY has been applied with the 82 kDa enzyme malate synthase G for studies of slow (millisecond) dynamic processes [38].

TROSY in Nuclear Overhauser Enhancement Spectroscopy

Both, the ^{13}C–^{1}H and ^{15}N–^{1}H TROSY effects have been exploited in 3D ^{13}C-resolved and ^{15}N-resolved [^{1}H,^{1}H]-NOESY experiments, respectively [33,76]. In the pulse sequences of these experiments, TROSY-type chemical shift correlation schemes were used instead of the conventional HSQC or HMQC building blocks. A fully relaxation-optimized ^{15}N-resolved [^{1}H,^{1}H]-NOESY, the 3D NOESY-[^{1}H,^{15}N,^{1}H]-zero quantum-TROSY experiment [77], was developed based on TROSY in the ^{15}N–^{1}H zero quantum state. As an advantage, the usually very intense diagonal peaks are almost completely suppressed in this experiment and weak resonances close to the diagonal become amenable for analysis, alleviating a limitation of conventional NOE spectroscopy. The utility of this approach was demonstrated for the 110 kDa protein aldolase [77].

Applications to Nucleic Acids

For NMR structural studies of nucleic acids, TROSY offers considerable benefits (for a review, see Ref. [78]). Direct detection of hydrogen bonds and measurements of RDCs, which were discussed in the previous sections, are of considerable importance for the structure determination of nucleic acids, since in comparison to proteins, inherently fewer protons are available as sources for structural information. In addition, TROSY has been widely applied to increase the sensitivity and the resolution in correlation experiments for nucleic acids, increasing the range of their applicability to much larger oligonucleotides. Examples include the use of TROSY in correlation experiments [33], in NOESY experiments for the bases [79], in experiments for intra-base and sugar-to-base correlations [34,80,81], and in an experiment that provides correlations between all carbon nuclei in the adenine base [82].

Solution NMR Studies of Membrane Proteins

Membrane proteins take part in important physiological functions, and constitute key targets for drug discovery. Structural studies of membrane proteins by X-ray crystallography or by NMR spectroscopy are much more difficult than for soluble proteins. Since real membrane systems are far too large for investigation by solution NMR, membrane proteins are often reconstituted in detergent micelles. From these micellar systems, high-quality spectra can be obtained using TROSY (Figure 3) [83–85].

With the availability of TROSY, the first NMR structures of integral membrane proteins in micelles with molecular weights above 50 kDa have been determined, particularly of *E. coli* outer membrane proteins with β-barrel architecture [53,84–88]. The fold of the outer membrane protein OmpX (148 residues) was obtained in DHPC micelles of about 60 kDa molecular mass [53,84,86], the polypeptide backbone fold of the outer membrane protein OmpA (177 residues) has been determined in dodecylphosphocholine (DPC) micelles of 50 kDa molecular mass [87,89], and the backbone fold of the outer membrane enzyme PagP (164 residues) has been determined both in DPC and *n*-octyl-β-D-glucoside micelles of size 50–60 kDa [88,90].

With regard to future developments, recent results obtained for the 39 kDa homotrimeric protein diacylglycerol kinase in micellar complexes with overall sizes larger than 100 kDa [91–93] suggest that NMR-based structure determination of membrane proteins with α-helical architecture, as large and complex as some members of the G-protein-coupled receptor family, may be feasible. Recently, partial backbone resonance assignments have been reported for native bacteriorhodopsin in dodecylmaltoside micelles [94].

Cross-Correlated Relaxation-Induced Polarization Transfer for Studies of Very Large Structures

In heteronuclear NMR experiments, magnetization between the different nuclei is usually transferred based on their scalar spin–spin couplings using INEPT polarization transfer elements [95,96]. During INEPT transfers, TROSY is not active since the slowly and fast relaxing transitions are mixed. For very large structures with molecular weights above approximately 150 kDa, rapid transverse relaxation during the INEPT periods leads to a complete loss of most signals. This limitation can be alleviated by cross-correlated relaxation-enhanced polarization transfer (CRINEPT) [97,98]. In this technique, INEPT and cross-correlated relaxation-induced polarization transfer (CRIPT) [99] are combined. In contrast to INEPT, the transfer efficiency of CRIPT increases proportional to the size of the molecule, so that it becomes an efficient magnetization transfer mechanism for molecules with sizes above 200 kDa [97,98]. Therefore, when studying very large structures significant gains in sensitivity can be achieved by substituting INEPT by CRINEPT or CRIPT.

Methods that allow resonance assignments of macromolecules with molecular weight above ∼150 kDa are currently not available and therefore CRINEPT/CRIPT spectroscopy is usually applied to obtain ^{15}N–^{1}H fingerprints of very large structures. As with TROSY-based experiments, the preferred current use of CRINEPT is to study relatively short polypeptide chains (up to ∼100–200 amino acid residues) in large supramolecular assemblies, in complexes with large macromolecules, or in large detergent/lipid micelles. The potential of the CRINEPT and CRIPT experiments has recently been demonstrated for 900 kDa complexes formed by GroES with GroEL [98,100].

Conclusion and Outlook

With the development of TROSY, CRINEPT, CRIPT, and isotope labeling techniques, combined with recent advances in NMR instrumentation, solution NMR studies of biological macromolecules with molecular masses well beyond 100 kDa have become a reality. This has been demonstrated in numerous studies dealing with fundamental biological problems, extending from structural investigation of large proteins and the structure determination of the first larger integral membrane proteins in solution, to applications for intermolecular interactions involving relatively large structures [14,15,83,100,101]. The ability to obtain resonance assignments of large biological macromolecules provides the basis for the determination of much larger 3D structures by NMR as thought to be possible just a few years ago. Even if the NMR structure determination is not feasible, the resonance assignment alone can be sufficient to carry out detailed studies of intermolecular interactions and investigations of dynamic processes, which may provide important information on exciting biological systems. However, for very large structures, where CRINEPT and CRIPT are the only means to obtain useful NMR spectra, techniques for resonance assignments are still missing. Nevertheless, NMR fingerprints of proteins with molecular weights up to 900 kDa have been obtained and interesting information could be derived based on the available crystal structure [100].

With the appropriate technical tools available, we expect that many new NMR structures of proteins and nucleic acids with molecular weights above 25 kDa will be elucidated. In this context, techniques that facilitate selective isotope labeling, such as cell-free protein expression [102–105] and segmental isotope labeling [18,19,106,107] may become widely applied to solve larger structures. With the prospect of further advances in NMR techniques and instrumentation, and improved protein expression techniques, larger membrane proteins, as G-protein coupled receptors, may become amenable to solution NMR studies. We are looking forward to future applications of the techniques described in this review and to technical advances that allow studying even more challenging biological systems.

Acknowledgments

The Novartis Institutes for Biomedical Research (C.F.) and the Schweizerischer Nationalfonds (project 3100A0-100399) (G.W.) are gratefully acknowledged for continuous financial support.

References

1. Güntert P. Q. Rev. Biophys. 1998;31:145 (1998).
2. Gardner KH, Kay LE. Annu. Rev. Biophys. Biomol. Struct. 1998;27:357.
3. LeMaster DM. Prog. NMR Spectrosc. 1994;26:371.
4. LeMaster DM. Q. Rev. Biophys. 1990;23:133.
5. Goto NK, Kay LE. Curr. Opin. Struct. Biol. 2000;10:585.
6. Pervushin K, Riek R, Wider G, Wüthrich K. Proc. Natl. Acad. Sci. U.S.A. 1997;94,:2366.
7. Wider G, Wüthrich K. Curr. Opin. Struct. Biol. 1999;9:594.
8. Pervushin K. Q. Rev. Biophys. 2000;33:161.
9. Riek R, Pervushin K, Wüthrich K. Trends Biochem. Sci. 2000;25:462.
10. Riek R. Meth. Princ. Med. Chem. 2003;16:227.
11. Pervushin K. Biol. Magn. Reson. 2003;20:3.
12. Wüthrich K. Nat. Struct. Biol. 1998;5:492.
13. Venters RA, Thompson R, Cavanagh J. J. Mol. Struct. 2002;602:275.
14. Fernández C, Wider G. Curr. Opin. Struct. Biol. 2003;13:570.
15. Tugarinov V, Hwang PM, Kay LE. Annu. Rev. Biochem. 2004;73:107.
16. Wider G. Prog. NMR Spectrosc. 1998;32:193.
17. Kainosho M. Nat. Struct. Biol. 1997;4(Suppl):858.
18. Yamazaki T, *et al.* J. Am. Chem. Soc. 1998;120:5591.
19. Cowburn D, Muir TW. Methods Enzymol. 2001;339:41.
20. Kushlan DM, LeMaster DM. J. Biomol. NMR. 1993;3:701.
21. Salzmann M, Wider G, Pervushin K, Wüthrich K. J. Biomol. NMR. 1999;15:181.
22. Pervushin K, Wider G, Wüthrich K. J. Biomol. NMR. 1998;12:345.
23. Pervushin K, Riek R, Wider G, Wüthrich K. J. Am. Chem. Soc. 1998;120:6394.
24. Tugarinov V, Hwang PM, Ollerenshaw JE, Kay LE. J. Am. Chem. Soc. 2003;125:10420.
25. Tugarinov V, Kay LE. J. Biomol. NMR. 2004;28:165.
26. Shuker SB, Hajduk PJ, Meadows RP, Fesik SW. Science. 1996;274:1531.
27. Pellecchia M, Sebbel P, Hermanns U, Wüthrich K, Glockshuber R. Nat. Struct. Biol. 1999;6:336.
28. Frickel EM, *et al.* Proc. Natl. Acad. Sci. U.S.A. 2002;99:1954.
29. Rudiger S, Freund SMV, Veprintsev DB, Fersht AR. Proc. Natl. Acad. Sci. U.S.A. 2002;99:11085.
30. Takahashi H, Nakanishi T, Kami K, Arata Y, Shimada I. Nat. Struct. Biol. 2000;7:220.
31. McElroy C, Manfredo A, Wendt A, Gollnick P, Foster M. J. Mol. Biol. 2002;323:463.
32. Tugarinov V, Kay LE. J. Mol. Biol. 2003;327:1121.
33. Brutscher B, Boisbouvier J, Pardi A, Marion D, Simorre JP. J. Am. Chem. Soc. 1998;120:11845.
34. Brutscher B, Simorre JP. J. Biomol. NMR. 2001;21:367.
35. Kreishman-Deitrick M, *et al.* Biochemistry. 2003;42:8579.
36. Tugarinov V, Kay LE. J. Am. Chem. Soc. 2003;125:13868.
37. Tugarinov V, Kay LE. J. Am. Chem. Soc. 2004;126:9827.
38. Korzhnev DM, Kloiber K, Kanelis V, Tugarinov V, Kay LE. J. Am. Chem. Soc. 2004;126:3964.
39. Ikura M, Kay LE, Bax A. Biochemistry. 1990;29:4659.
40. Bax A, Grzesiek S. Acc. Chem. Res. 1993;26:131.
41. Yamazaki T, Lee W, Arrowsmith CH, Muhandiram DR, Kay LE. J. Am. Chem. Soc. 1994;116:11655.
42. Sattler M, Schleucher J, Griesinger C. Prog. NMR Spectrosc. 1999;34:93.
43. Salzmann M, Pervushin K, Wider G, Senn H, Wüthrich K. Proc. Natl. Acad. Sci. U.S.A. 1998;95:13585.
44. Salzmann M, Wider G, Pervushin K, Senn H, Wüthrich K. J. Am. Chem. Soc. 1999;121:844.
45. Yang DW, Kay LE. J. Am. Chem. Soc. 1999;121:2571.
46. Konrat R, Yang DW, Kay LE. J. Biomol. NMR. 1999;15:309.
47. Salzmann M, Pervushin K, Wider G, Senn H, Wüthrich K. J. Biomol. NMR. 1999;14:85.
48. Loria JP, Rance M, Palmer AG. J. Magn. Reson. 1999;141:180.
49. Salzmann M, Pervushin K, Wider G, Senn H, Wüthrich K. J. Am. Chem. Soc. 2000;122:7543.
50. Tugarinov V, Muhandiram R, Ayed A, Kay LE. J. Am. Chem. Soc. 2002;124:10025.
51. Hilty C, Fernández C, Wider G, Wüthrich K. J. Biomol. NMR. 2002;23:289.
52. Goto NK, Gardner KH, Mueller GA, Willis RC, Kay LE. J. Biomol. NMR. 1999;13:369.
53. Fernández C, Hilty C, Wider G, Güntert P, Wüthrich K. J. Mol. Biol. 2004;336:1211.
54. Dingley AJ, Grzesiek S. J. Am. Chem. Soc. 1998;120:8293.
55. Pervushin K, *et al.* Proc. Natl. Acad. Sci. U.S.A. 1998;95:14147.
56. Cordier F, Grzesiek S. J. Am. Chem. Soc. 1999;121:1601.
57. Pervushin K, *et al.* J. Biomol. NMR. 2000;16:39.
58. Yan XZ, Kong XM, Xia YL, Sze KH, Zhu G. J. Magn. Reson. 2000;147:357.
59. Wang YX, *et al.* J. Biomol. NMR. 1999;14:181.
60. Löhr F, Mayhew SG, Ruterjans H. J. Am. Chem. Soc. 2000;122:9289.
61. Eletsky A, *et al.* J. Biomol. NMR. 2002;24:31.
62. Prestegard JH, Al-Hashimi HM, Tolman JR. Q. Rev. Biophys. 2000;33:371.
63. Prestegard JH, Bougault CM, Kishore AI. Chem. Rev. 2004;104:3519.
64. Lipsitz RS, Tjandra N. Annu. Rev. Biophys. Biomol. Struct. 2004;33:387.
65. Mueller GA, *et al.* J. Mol. Biol. 2000;300:197.
66. Choy WY, Tollinger M, Mueller GA, Kay LE. J. Biomol. NMR. 2001;21:31.
67. Yang DW, Venters RA, Mueller GA, Choy WY, Kay LE. J. Biomol. NMR. 1999;14:333.

68. Jain NU, Noble S, Prestegard JH. J. Mol. Biol. 2003;328:451.
69. Evenäs J, Mittermaier A, Yang DW, Kay LE. J. Am. Chem. Soc. 2001;123:2858.
70. Kay LE, Torchia DA, Bax A. Biochemistry. 1989;28:8972.
71. Palmer, AG III. Chem. Rev. 2004;104:3623.
72. Mulder FA, Mittermaier A, Hon A, Dahlquist FW, Kay LE. Nat. Struct. Biol. 2001;8:932.
73. Eisenmesser EZ, Bosco DA, Akke M, Kern D. Science. 2002;295:1520.
74. Zhu G, Xia YL, Nicholson LK, Sze KH. J. Magn. Reson. 2000;143:423.
75. Xia YL, Sze KH,Li N, Shaw PC, Zhu G. Spectrosc.-Int. J. 2002;16:1.
76. Zhu G, Kong XM, Sze KH. J. Biomol. NMR. 1999;13:77.
77. Pervushin K, Wider G, Riek R, Wüthrich K. Proc. Natl. Acad. Sci. U.S.A. 1999;96:9607.
78. Mollova ET, Pardi A. Curr. Opin. Struct. Biol. 2000;10:298.
79. Brutscher B, *et al*. J. Biomol. NMR. 2001;19:141.
80. Riek R, Pervushin K, Fernández C, Kainosho M, Wüthrich K. J. Am. Chem. Soc. 2001;123:658.
81. Fiala R, Czernek J, Sklenar V. J. Biomol. NMR. 2000;16:291.
82. Simon B, Zanier K, Sattler M. J. Biomol. NMR. 2001;20:173.
83. Fernández C, Wüthrich K. FEBS Lett. 2003;555:144.
84. Fernández C, *et al.* FEBS Lett. 2001;504:173.
85. Arora A, Tamm LK. Curr. Opin. Struct. Biol. 2001;11:540.
86. Fernández C, Adeishvili K, Wüthrich K. Proc. Natl. Acad. Sci. U.S.A. 2001;98:2358.
87. Arora A, Abildgaard F, Bushweller JH, Tamm LK. Nat. Struct. Biol. 2001;8:334.
88. Hwang PM, *et al.* Proc. Natl. Acad. Sci. U.S.A. 2002;99:13560.
89. Tamm LK, Abildgaard F, Arora A, Blad H, Bushweller JH. FEBS Lett. 2003;555:139.
90. Hwang PM, Bishop RE, Kay LE. Proc. Natl. Acad. Sci. U.S.A. 2004;101:9618.
91. Oxenoid K, Kim HJ, Jacob J, Sonnichsen FD, Sanders CR. J. Am. Chem. Soc. 2004;126:5048.
92. Oxenoid K, Sönnichsen FD, Sanders CR. Biochemistry. 2002;41:12876.
93. Sanders CR, Sonnichsen FD, Oxenoid K. Paper presented at the Proceedings of the XXth International Conference on Magnetic Resonance in Biological Systems, Toronto, 2002.
94. Schubert M, Kolbe M, Kessler B, Oesterhelt D, Schmieder P. Chembiochem. 2002;3:1019.
95. Morris GA, Freeman R. J. Am. Chem. Soc. 1979;101:760.
96. Burum DP, Ernst RR. J. Magn. Reson. 1980;39:163.
97. Riek R, Wider G, Pervushin K, Wüthrich K. Proc. Natl. Acad. Sci. U.S.A. 1999;96;4918.
98. Riek R, Fiaux J, Bertelsen EB, Horwich AL, Wüthrich K. J. Am. Chem. Soc. 2002;124:12144.
99. Dalvit C. J. Magn. Reson. 1992;97:645.
100. Fiaux J, Bertelsen EB, Horwich AL, Wüthrich K. Nature. 2002;418:207.
101. Wüthrich K, Wider G. Magn. Reson. Chem. 2003;41:S80.
102. Yabuki T, *et al.* J. Biomol. NMR. 1998;11:295.
103. Kigawa T, *et al.* FEBS Lett. 1999;442:15.
104. Kiga D, *et al.* Proc. Natl. Acad. Sci. U.S.A. 2002;99:9715.
105. Yokoyama S. Curr. Opin. Chem. Biol. 2003;7:39.
106. Otomo T, Teruya K, Uegaki K, Yamazaki T, Kyogoku Y. J. Biomol. NMR. 1999;14:105.
107. Cowburn D, Shekhtman A, Xu R, Ottesen JJ, Muir TW. Methods Mol. Biol. 2004;278:47.

NMR Insight of Structural Stability and Folding of Calcium-Binding Lysozyme

Makoto Demura

Division of Biological Sciences, Graduate School of Science, Hokkaido University, Sapporo 060-0810, Japan

Lysozyme and Calcium Binding of the Homologous Proteins

Lysozymes (LYSs) are antibacterial enzyme, β-*N*-acetylmuramyl-hydrolase, that disrupts a glycosidic bond of the polysaccharide that is found in the cell walls of many bacteria. A number of LYSs are found in nature; in mammalian milk, tears, and egg white. The most common animal LYS is the c type, such as the chicken egg white lysozyme (EWL, 14.3 kDa), found in animal, insects, and plants [1]. LYS and α-lactalbumin (α-LA) have undoubtedly evolved from a common ancestor because of the similarity of their amino acid sequences (Figure 1) [2]. α-LA, which is a major milk component of milk whey, is a calcium-binding metalloprotein [3]. It is the so-called B component of lactose synthase and acts as a specificity modifier of galactosyltransferase to convert it to lactose synthase. The original discovery of its calcium-binding property was made when an effect of ethylenediaminetetracetic acid (EDTA) on the conformational stability of bovine α-LA was demonstrated. Then, a microanalytical method has been developed using high-performance gel-filtration chromatography together with the use of a calcium-specific fluorescent reagent [4]. Binding constants of a calcium ion to calcium-binding LYSs and bovine α-LA are 10^{6-7} M^{-1} [5].

The calcium-binding site of canine milk LYS [6], which contributes to the structural stability, consists of the two backbone carbonyl groups of residues 82 and 87 and the three side-chain carboxyl groups of Asp-85, Asp-90, and Asp-91 in a pseudobridging mode [7], which is distinct from that of the EF-hand where the calcium ion binds in a bidentate mode [8]. Furthermore, it was pointed out that the above three aspartyl residues are all conserved in calcium-binding LYSs from canine, equine, echidna, and pigeon and α-LA (Figure 1A). In the case of chicken EWL, the backbone conformation of the calcium-binding loop is essentially conserved. However, the EWL does not bind calcium because the side chains are radically altered.

Protein Folding Mechanism

The strong interest in partly folded states of proteins, or folding intermediates, resides in the fact that by studying the molecular features of these intermediates, it will be possible to elucidate the mechanism of how proteins fold into their specific biologically active conformations [9,10]. In recent years, the difficulty in detecting and characterizing the transient intermediate species formed during the protein folding process prompted a variety of structural studies on the intermediates that can be generated at equilibrium by dissolving a protein in acid solution or in the presence of moderate concentrations of a protein denaturant, as well as by removing protein-bound metal ions or prosthetic groups [11,12]. These studies led to the development of the concept of the molten globule (MG) state, shown to be equilibrium intermediate between the native and unfolded states of a number of globular proteins. Until recently, the MG state was considered to be a partly folded state having a stable native-like secondary structure but lacking a specific tertiary structure (Figure 1C) [12]. However, in several studies it has been shown that a great variety of MGs do exist, ranging from those having specific tertiary interactions or native-like topology to those resembling the unfolded state of a protein. Evidence has been provided that the MGs of some proteins share conformational features with those transiently observed in kinetic experiments of protein folding [13–15]. Therefore, the detailed characterization of equilibrium intermediates in terms of structure and dynamics appears to be relevant for solving the protein folding problem.

Although the c type LYS and α-LA are homologous to each other, their equilibrium unfolding profiles are quite different, with that of LYS and LA obeying a two-state and three-state model (Figure 1C), respectively [16]. In particular, although LA in acid at pH 2.0 attains a MG state, the chicken EWL remains native under similar acidic conditions. However, the homologous calcium-binding LYS from equine or canine milk or from pigeon egg-white can form the MG state when exposed to acid solution or on

Graham A. Webb (ed.), Modern Magnetic Resonance, 497–501.
© 2008 *Springer.*

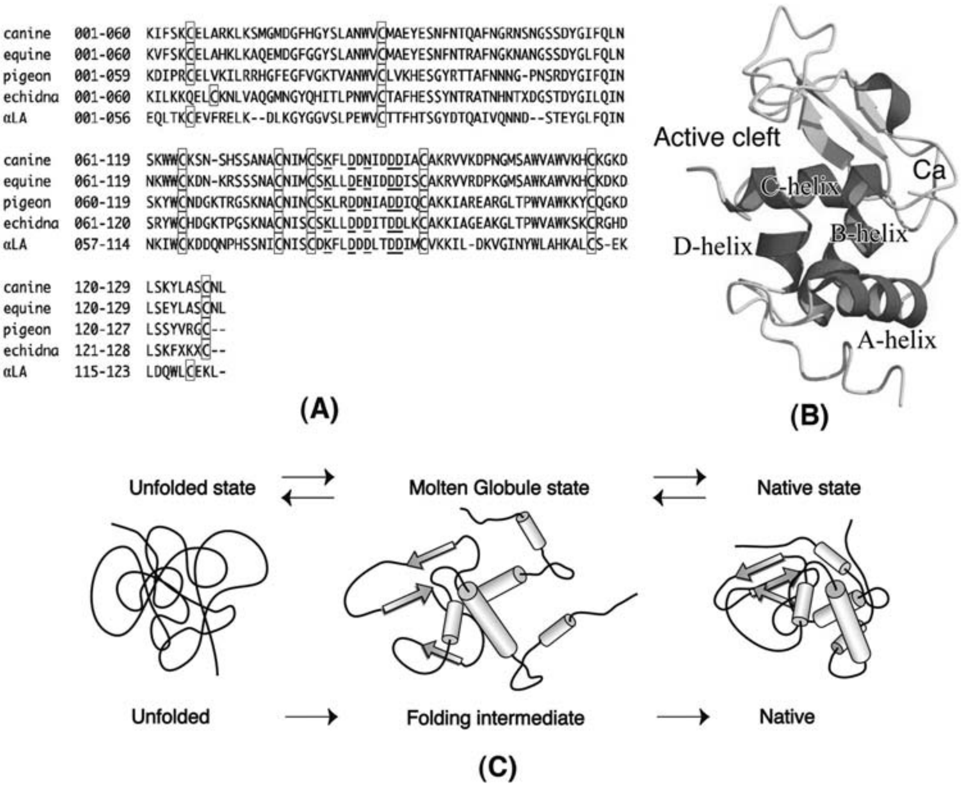
canine 001-060 KIFSKCELARKLKSMGMDGFHGYSLANWVCMAEYESNFNTQAFNGRNSNGSSDYGIFQLN
equine 001-060 KVFSKCELAHKLKAQEMDGFGGYSLANWVCMAEYESNFNTRAFNGKNANGSSDYGLFQLN
pigeon 001-059 KDIPRCELVKILRRHGFEGFVGKTVANWVCLVKHESGYRTTAFNNNG-PNSRDYGIFQIN
echidna 001-060 KILKKQELCKNLVAQGMNGYQHITLPNWVCTAFHESSYNTRATNHNTXDGSTDYGILQIN
αLA 001-056 EQLTKCEVFRELK--DLKGYGGVSLPEWVCTTFHTSGYDTQAIVQNND--STEYGLFQIN
canine 061-119 SKWWCKSN-SHSSANACNIMCSKFLDDNIDDDIACAKRVVKDPNGMSAWVAWVKHCKGKD
equine 061-119 NKWWCKDN-KRSSSNACNIMCSKLLDENIDDDISCAKRVVRDPKGMSAWKAWVKHCKDKD
pigeon 060-119 SKYWCNDGKTRGSKNACNINCSKLRDDNIADDIQCAKKIAREARGLTPWVAWKKYCQGKD
echidna 061-120 SRYWCHDGKTPGSKNACNISCSKLLDDDITDDLKCAKKIAGEAKGLTPWVAWKSKCRGHD
αLA 057-114 NKIWCKDDQNPHSSNICNISCDKFLDDDLTDDIMCVKKIL-DKVGINYWLAHKALCS-EK
canine 120-129 LSKYLASCNL
equine 120-129 LSEYLASCNL
pigeon 120-127 LSSYVRGC--
echidna 121-128 LSKFXKXC--
αLA 115-123 LDQWLCEKL-
(A)
Active cleft
C-helix
Ca
B-helix
D-helix
A-helix
(B)
Unfolded state
Molten Globule state
Native state
Unfolded
Folding intermediate
Native
(C)

Fig. 1. Sequential homology of various calcium-binding lysozymes and α-LA (A), crystal structure of canine milk lysozyme (CML, 129 aa) (B) and the three-state folding model of proteins (C). Canine, equine, and echidna correspond to source of milk lysozymes. Four-disulfide bonds are linked between squared C. Single and double underlines correspond to calcium-binding sites for backbone carbonyl and side-chain carboxyl groups, respectively (see text). Three-dimensional structure of CML (B) is divided into two domains; helix-rich domain (α-domain) and β-sheet-rich domain (β-domain). The former is composed of four α-helices named A-helix (5–15), B-helix (25–36), C-helix (89–100), and D-helix (110–115), and the latter is composed of three-stranded anti-parallel β-sheet (strand I 43–45, strand II 51–55, and strand III 58–61) [6]. In (B), Ca indicates calcium-binding loop. The substrate can bind at the active cleft. α-Lactalbumin and lysozymes are similar structural super family. (See also Plate 50 on page XXXVII in the Color Plate Section.)

calcium depletion at neutral pH and (moderate) heating [14,16,17]. It is now accepted that proteins exhibit various dynamics covering a wide range of time-scale and amplitude. It was shown that such motions include local movement of loops, or larger movement of secondary structure and structural domains with a time-scale from picosecond to hours.

^{1}H Chemical Shift Calculation of the Calcium-Binding LYS in the Structural Intermediate

Canine milk lysozyme (CML) was studied as a model protein to clarify the folding mechanism, and the relationship between structure, function, and dynamics of protein using NMR [17]. CML was expressed in *E.coli* as inclusion bodies and refolded to form the native structure. Uniformly ^{15}N-labeled CML was obtained by growing the cells in M-9 medium containing $^{15}NH_4Cl$ as the sole nitrogen source. Figure 2 shows the 1D ^{1}H NMR spectra of CML in the native state, the MG at 2 M guanidine hydrochloride (GuHCl) and the unfolded state at 6 M GuHCl concentration. Chemical shifts are widely distributed in the NMR spectrum of CML in the native state (BMRB: 4887). In addition, some methyl signals which are shifted to a lower frequency than 0 ppm. The existence of a rigid hydrophobic core involving aromatic residues has been revealed by the^{1}H chemical shift calculation with the atomic coordinates (PDB: 1EL1) [6] of this protein

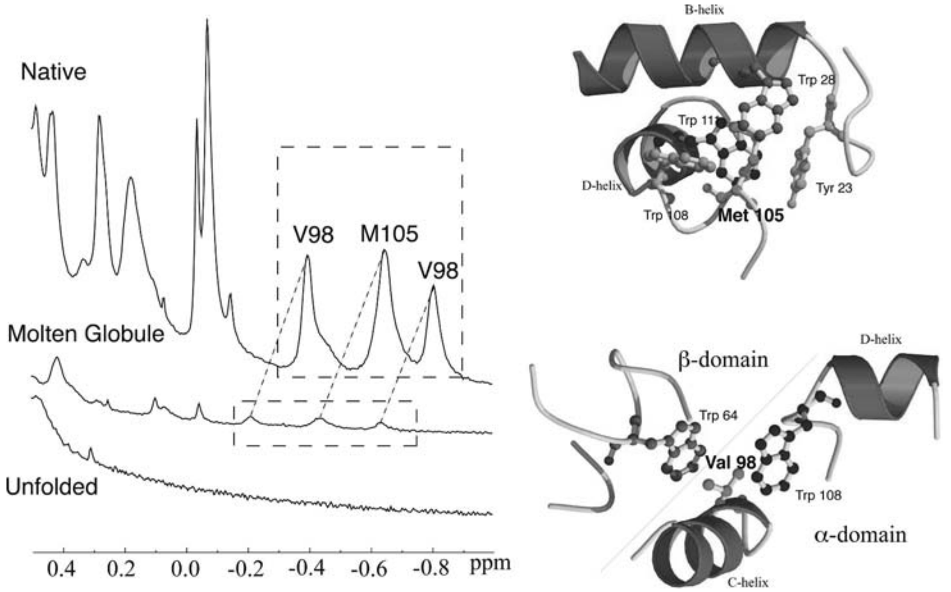

Fig. 2. 1D ^{1}H NMR spectra of canine milk lysozyme (CML) in the native state, the MG at 2 M GuHCl and the unfolded state at 6 M GuHCl concentration (left), and the local structures (right) at Val 98 and Met 105 of CML which were shown on the X-ray crystal structure of CML (PBD: 1EL1 and 1QQY for calcium-binding CLM and calcium-free CML, respectively). ^{1}H NMR spectra were acquired at 400 MHz in a Jeol α-400 spectrometer (Jeol Co., Tokyo, Japan) at 25 °C. The protein sample concentration was 0.5 mM. (See also Plate 51 on page XXXVII in the Color Plate Section.)

based on ring-current shifts, shifts arising from magnetic anisotropies of bonds, and shifts arising from the polarizing effect of polar atoms [17,18]. In the NMR spectrum of CML in the MG state, it appeared that peaks are broadened and poorly resolved when compared with the native state. Spectral broadening and poor chemical shift dispersion are the general characteristics of the NMR spectra of protein in the MG state. In the NMR spectrum of CML in the MG state, several methyl signals are also shifted to a frequency lower than 0 ppm (Figure 2). This indicates that a portion of the side-chain packing around an aromatic cluster is still remained even in the MG of CML. The ring-current-shifted signals of CML in the MG state are arising from γ-methyl protons of Val 98 in C-helix and from the β-methylene proton of Met 105 in D-helix. The side chain of Val 98 is located in the domain interface region, and that of Met 105 is located in the interior of the α-domain. Figure 2 (lower right) shows the 3D-structure in the vicinity of the hydrophobic core around Val 98 of CML in the native state. As shown in this figure, aromatic residues of Trp 64 and Trp 108 are located close to Val 98. Figure 2 (upper right) shows the structure in the vicinity of the hydrophobic core around Met 105 of CML in the native state. In this case, the aromatic residues of Trp 28, Tyr 32, Trp 108, and Trp 111 are located close to Met 105. Based on the chemical shift calculation with the atomic coordinates of CML in the absence of calcium (PDB: 1QQY), the specific side chains, which influence the chemical shift of Val 98 and Met 105, were determined.

H/D Exchange of Calcium-Binding LYS in the Native and the Structural Intermediate

Highly resolved HSQC spectrum of CML is easily observed in the native state. Contrary, the HSQC spectrum of CML in the MG state is significantly different from the native state. It was revealed that the HSQC spectrum of CML in the MG state exhibits broadened and decreased peak dispersion when compared with the native state. Nevertheless, large number of well-resolved and sharp peaks can be observed in the HSQC spectrum of CML in the MG state. Previous study revealed that α-LA in the MG state exhibits poorly resolved, broadened and little dispersed HSQC spectrum. It could be assumed that the MG state of CML exhibits smaller fluctuation and well-defined 3D-structure when compared with α-LA.

In the native state of CML, the Hydrogen/deuterium (H/D) exchange rates were measured at pH 4.5 and 25°C for 81 amide protons distributed throughout the primary structure [17]. The other amide protons were rapidly exchanged to be detectable. To compare the H/D exchange rates of CML with those of α-LA and EML, the protection factors were estimated for individual amide protons as described previously [19]. The protection factor is defined as the ratio of the intrinsic to the experimentally determined H/D exchange rates for each amide proton [20]. There are two important features for the protection factors of CML in the native state: (1) the protection factors of the amide protons in the α-domain are larger than the β-domain and (2) the most protected amides are located in the secondary structure elements. It could be assumed that solvent accessibility of α-domain of CML in the native state is lower than that of β-domain.

The H/D exchange rates of the amide protons of CML in the MG state were measured by the amide hydrogen trapping method [19]. From the H/D exchange rates, the protection factors were estimated for each residue [17]. Figure 3 shows HSQC spectra of the CML as a function of contacting time with D_2O in the MG state. It appeared that 64 amide hydrogens are protected from the H/D exchange reaction in the MG state of CML. It is of note that the number of protected amide hydrogens of CML in the MG state is much larger than EML (17 amide hydrogens)

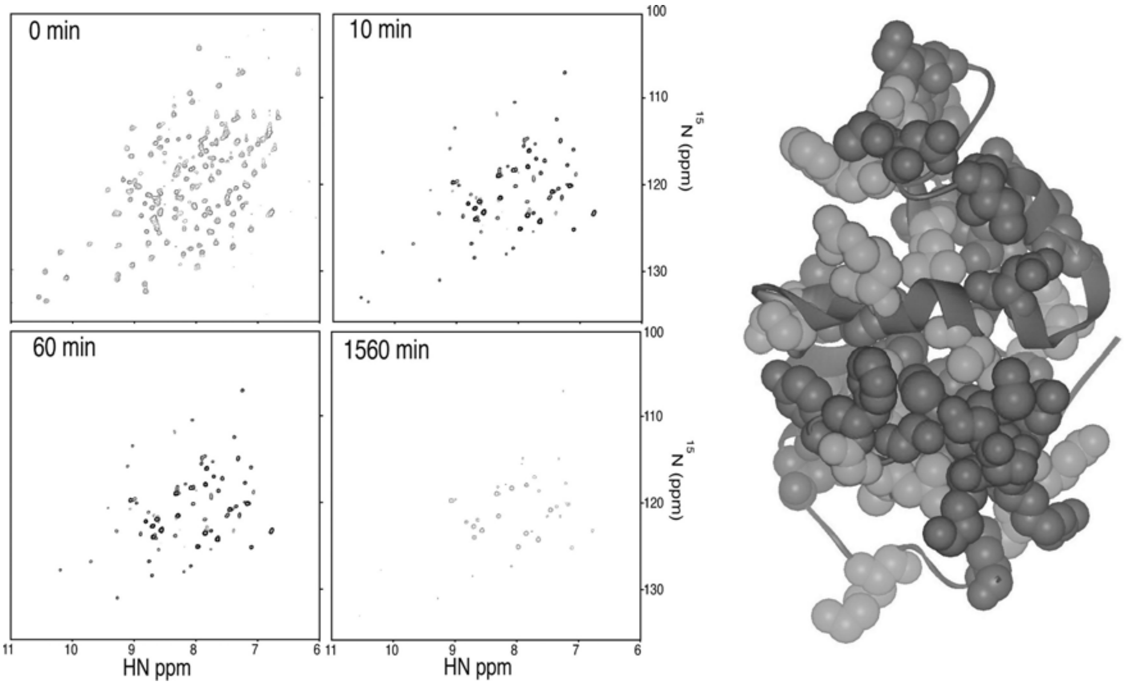

Fig. 3. Hydrogen/deuterium exchange rate measurements based on ^{15}N HSQC spectra of CML as a function of time (left) and mapping of the protection factors of each amino acid residues in the MG state (right). Uniformly ^{15}N-labeled protein with a sample concentration of 0.6 mM was used. The H/D exchange reaction was initiated by dissolving lyophilized protein in 280 μl of D_2O d_4-acetate buffer containing 10 mM $CaCl_2$at a direct pH meter reading of 4.5. A series of HSQC spectra were collected at 500 MHz at 25 °C every 3 hours for 3 days. Data sets of all NMR spectra for the H/D exchange measurements were comprised of 512 (^{1}H) × 128 (^{15}N) of 32 scans, and a sweep width of 8000 Hz for the ^{1}H and of 1800 Hz for the ^{15}N dimensions. The H/D exchange rates were determined by the decay of the peak volume as described previously [21]. The H/D exchange rate of the MG was measured by the amide hydrogen trapping method as described previously [19]. The H/D exchange reaction of CML in the MG state was initiated by dissolving the lyophilized protein in 3 ml of D_2O at pH 2.0. After various period of time ranging from a minute to 10 days, the H/D exchange reaction was quenched by freezing the sample in liquid N_2 and then lyophilized. The samples were redissolved in D_2O d_4-acetate buffer containing 10 mM $CaCl_2$ to a final pH of 4.5 and HSQC spectra were collected. Immediately before the measurements of HSQC spectra, 1D ^{1}H NMR spectra were collected and peak volumes were normalized by using non-exchangeable resonance arising from methyl group. Red and green circles on the left mapping correspond to the protection factor more than 50 and more than 20, respectively. (See also Plate 52 on page XXXVIII in the Color Plate Section.)

[19]. The protection factors of CML in the MG state are large in residues which form secondary structure in the native state. The protected amides are mapped on the 3D-structure of CML (Figure 3 right). The protected amides (protection factor >20) are colored green and the most protected amides (protection factor >50) are colored red. The most protected amides exist mainly in the hydrophobic core region of the native state. They originate from Arg 10 to Met 15 in the A-helix, from Met 17 and Phe 20 in the loop region between the A- and B-helices, from Val 29 to Glu 33 in the B-helix, from Trp 108 and Val 109 in the D-helix, and from His 114, Cys 115, Lys 118, and Cys 127 in the C-terminal region. It should be noted that the most protected residues of the A- and D-helices are located in the region that forms the interface with the B-helix. It could be assumed that arrange of the A-, B-, and D-helices of CML in the MG state is similar to the native state. It was revealed that A-helix is the most protected among four α-helices, followed by B-, D-, and C-helices in the MG state of CML. On the other hand, B-helix was most protected in the MG state of EML [19], followed by the A-, D-, and C-helix. The MG state of CML exhibits two orders of magnitude larger protection factor than those of EML. This indicates that α-helices are more stable in the MG state of CML when compared with EML. It should be noted that several amides in the β-sheet region are protected from the H/D exchange reaction in the MG state of CML. A series of studies revealed that α-domain adopts a native-like backbone topology, whereas the β-domain remains largely unstructured in the MG state of EML and α-LA. It could be assumed that the MG state of CML has significantly ordered structure when compared with α-LA and EML. More recently, instability, unfolding, and aggregation of human LYS variants underlying amyloid fibrillogenesis are compared with homologous proteins, CML, and α-LA.

References

1. Prager EM, Jolles P. In: P Jolles (Ed). Lysozymes: Model Enzymes in Biochemistry and Biology. Birkhauser: Basel/Boston/Berlin, 1996, p 9.
2. Brew K, Castellino FJ, Vanaman TC, Hill RL. J. Biol. Chem. 1970;245:4570.
3. Hiraoka Y, Segawa T, Kuwajima K, Sugai S, Murai N. Biochem. Biophys. Res. Commun. 1980;85:1098.
4. Nitta K, Tsuge H, Shimazaki K, Sugai S. Biol. Chem. 1988;369:671.
5. Nitta K. Methods Mol. Biol. 2002;172:211.
6. Koshiba T, Yao M, Kobashigawa Y, Demura M, Nakagawa A, Tanaka I, Kuwajima K, Nitta K. Biochemistry 2000;39:3248.
7. Mizuguchi M, Nara M, Kawano K, Nitta K. FEBS Lett. 1997;417:153.
8. Nara M, Tasumi M, Tanokura N, Hiraoki T, Yazawa M, Tsutsumi A. FEBS Lett. 1994;349:84.
9. Hughson FM, Wright PE, Baldwin RL. Science 1990;249:1544.
10. Arai M, Kuwajima K. Adv. Protein Chem. 2000;53:209.
11. Dobson CM. Curr. Biol. 1994;4:636.
12. Ohgushi M, Wada A. FEBS Lett. 1983;164:21.
13. Ikeguchi M, Kuwajima K, Mitani M, Sugai S. Biochemistry 1986;25:6965.
14. Mizuguchi M, Arai M, Ke Y, Nitta K, Kuwajima K. J. Mol. Biol. 1998;283:265.
15. Jennings PA, Wright PE. Science 1993;262:892.
16. Kuwajima K, Nitta K, Yoneyama M, Sugai S. J. Mol. Biol. 1976;106:359.
17. Kobashigawa Y, Demura M, Koshiba T, Kumaki Y, Kuwajima K, Nitta K. Proteins 2000;40:579.
18. Williamson MP, Asakura T, Nakamura E, Demura M. J. Biomol. NMR 1992;2:83.
19. Schulman BA, Redfield C, Peng Z-y, Dobson CM, Kim PS. J. Mol. Biol. 1995;253:651.
20. Morozova LA, Haynie DT, Arico-Muendel C, Van Dael H, Dobson CM. Nature Struct. Biol. 1995;2:871.
21. Bai Y, Milne JS, Mayne L, Englander W. Proteins: Struct. Funct. Genet. 1993;2:869.

NMR Investigation of Calmodulin

Tapas K. Mal and Mitsuhiko Ikura
Department of Medical Biophysics, University of Toronto and Division of Signalling Biology, Ontario Cancer Institute, Toronto, ON, Canada M5G 2M9

Abstract

Calmodulin (CaM) is a 16.7-kDa heat-stable protein that functions as Ca^{2+} sensor in eukaryotes. Because of its physicochemical properties and its remarkable well-resolved NMR spectra for a helical protein, CaM has been extensively studied by a number of researchers for NMR methodology development as well as its biological applications. This chapter describes the past and current NMR studies of CaM to serve as an example of structure and dynamic characterization of a protein.

Calmodulin (CaM) was discovered in 1970 as an activator for cyclic nucleotide phosphodiesterase [1, 2]. Soon it has become obvious that CaM is a ubiquitous intracellular calcium sensor protein expressed in most, if not all, eukaryotes from humans to yeast. Concentration of CaM is tissue-, organ- and cell-specific, with high expression in the brain and reproductive organs [3]. The amino acid and gene sequences of CaM have been determined from various species and are highly conserved through evolution [4–7]. CaM is a small 16.7-kDa and heat-stable protein. It contains a number of well-conserved hydrophobic residues and a relatively high number of acidic residues ($pI = 4.3$). It also contains an unusually high number of methionine residues, which are believed to confer promiscuous binding ability owing to the flexible nature of side-chains [8]. CaM possesses a number of post-translational modifications, including acetylation of the N-terminal Ala-1, trimethylation of Lys-115 in mammalian CaM, dimethylation of Lys-13 in *Paramecium* CaM, and phosphorylation at various threonine, serine, and tyrosine residues [9]. However, the significance of these modifications *in vivo* is still unclear. *In vitro* studies have shown that phosphocalmodulin binds some targets with different binding affinities and even affects subsequent target kinase activities [10].

The crystal structure of Ca^{2+}-bound CaM (Ca^{2+}-CaM) was solved in mid 1980s [11, 12] followed by a number of refined structures [13–15]. The structure has an unusual dumbbell shape (Figure 1) in which the N- and C-terminal globular domains are connected by a long α-helix. Each domain possesses a hydrophobic patch, which is considered to be responsible for target binding. A higher resolution structure (1.0 Å) solved 12 years later [16] showed that considerable disorder was found "at every accessible length-scale," particularly in residues within the interdomain linker and those comprising the hydrophobic binding pockets. CaM binds four Ca^{2+} ions, with each domain containing two Ca^{2+} binding helix-loop-helix motifs of EF-hand type, first discovered in parvalbumin by Kretsinger and co-workers [17]. The C-terminal domain of CaM binds to Ca^{2+} at higher affinity ($K_d = 10^{-6}$ M) than the N-terminal domain ($K_d = 10^{-5}$ M).

Biological Functions

As a ubiquitous Ca^{2+} "sensor" in eukaryotes, CaM functions as a regulator of a large array of different target proteins and enzymes, including protein kinases, protein phosphatases, ion channels and pumps, nitric oxides synthases, adenylyl cyclases, and phisphodiesterases. Among these diverse CaM targets, CaM-regulated serine/threonine kinases (CaM Kinases) are the best characterized structurally and functionally. The CaM kinase family includes CaM kinase I (CaMKI), CaM kinase II (CAMKII), CaM kinase IV (CaMKIV), CaM kinase kinase (CaMKK), myosin light chain kinase (MLCK), and several other CaM kinases whose functions and structures are not well characterized [18]. As one of the major Ca^{2+} "sensor" proteins in the cell, it responds to an increase in the concentration of intracellular calcium from the resting state by undergoing a large conformational change upon binding Ca^{2+} ions, enabling it to interact with and, as a result, activate its target. CaM-binding regions in many target enzymes and proteins have been mapped. In many cases, the CaM binding domain on the target overlaps or is proximate to an autoinhibitory domain (AID) that maintains enzyme inactivity at resting levels of Ca^{2+}. CaM binding to the target displaces the AID to render the enzyme active. In most cases, CaM binding regions are generally 14–27 amino acid peptides and rich in basic and hydrophobic residues. These peptides are typically unstructured in absence of CaM and form α-helical structure when bound to CaM. A number of naturally occurring peptides are also known to bind CaM in a Ca^{2+}-dependent manner [19]. These peptides include insect venom peptides such as mastoparans and melittin, and certain hormones and opiods such as ACTH, VIP, glucagons, and

Graham A. Webb (ed.), Modern Magnetic Resonance, 503–516.
© 2008 *Springer.*

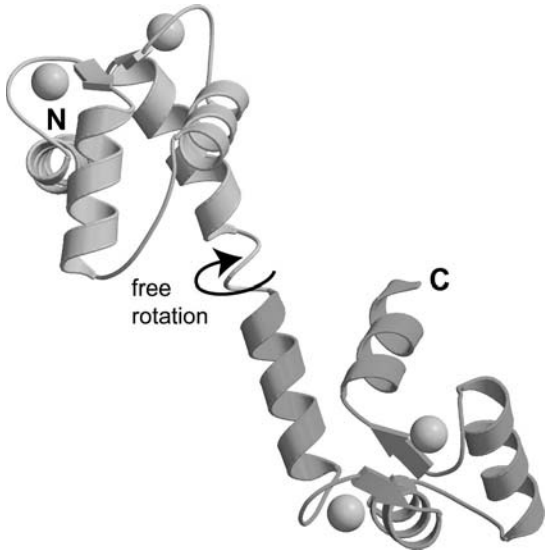

Fig. 1. Schematic representation of the **2.2-Å crystalstructure of Ca^{2+}-CaM, PDB code 3CLN. The N- and C-terminal domains are shown in yellow and green, respectively. Ca^{2+} ions are illustrated in grey spheres. The middle portion of the central linker (D78–S81) possesses a high degree of mobility as evidenced by (^1H)-^{15}N backbone relaxation measurements [50]. (See also Plate 53 on page XXXVIII in the Color Plate Section.)

substance P. However, biological functions of these CaM–peptide interactions are not well understood. In addition, phenothiazines and other hydrophobic drugs including trifluroperazine (TFP), chlorpromazine, and W-7, bind CaM and inhibit the CaM-mediated activation of enzymes [20]. Proteolytic fragments and synthetic peptides comprising the CaM-binding regions of target proteins, as well as the insect and hormone peptides and the hydrophobic drugs, have been extensively used to study the structural and biochemical properties of the interaction of CaM with targets. Numerous studies have been done on CaM and its complexes with target peptides to understand the detailed mechanism by which CaM regulates the activity of its vast targets involved in wide range of cellular functions. NMR studies have contributed tremendously to our understanding on the structure–function relationship of CaM. At the same time, CaM has also been extensively used for NMR methodological development since 1990. NMR studies on CaM and its complex with targets, and contribution of CaM to NMR from early studies to date will be focused in the following discussion.

Early NMR Studies on CaM

The ^1H spectra of bovine brain CaM were first recorded on 250 and 360 MHz NMR instruments in 1979 and 1980 [21,22]. These studies demonstrated that the dramatic ^1H chemical shift changes associated with Ca^{2+} binding could be monitored by ^1H NMR. Subsequently, Klevit *et al*. [23], and Krebs and Carafoli [24] studied the interaction of bovine brain CaM with TFP using ^1H NMR while Shimizu *et al*. [25,26] used ^{19}F NMR to study the interaction of porcine brain and *Tetraphymena pyriformis* CaM with TFP.

The detailed assignments for aromatic ring and methyl protons, and Ca^{2+}-induced conformational changes of scallop testis CaM were reported by Ikura *et al*. [27, 28] in 1983. Several resonances of C-terminal domain (Phe-99, His-107, trimethyl Lys-115, and Tyr-138) are shifted in an early stage of Ca^{2+} titration (0–2 mol Ca^{2+} per mol of CaM), indicating that the C-terminal domain has higher affinity toward Ca^{2+} than the N-terminal domain. In 1984, ^1H NMR studies on the two tryptic fragments of CaM (TR_1C, residues 1–75; and TR_2C, residues 78–148) were reported by three groups [29–32] almost at the same time. All these studies provided further evidence for the order of Ca^{2+} binding to four sites in CaM and also confirmed that the two tryptic half-fragments retained the same conformations as they would in intact CaM.

Two-Dimensional ^1H NMR

In 1984, the first 2D ^1H NMR recorded on 600 MHz for fragment TR_2C were reported in the absence of Ca^{2+} and provided assignments for side chain proton resonances of many residues [33]. Then in 1985, Ikura *et al*. [34] provided about 30% backbone and side-chain proton assignment both in presence and absence of Ca^{2+} using 2D ^1H NMR techniques to the TR_2C fragment. Extremely high field shifted amide proton resonances (10.0–11.0 ppm) were assigned to the glycine residues at the fifth position of the Ca^{2+}-binding loops. These uniquely shifted glycine amide proton were further characterized using both TR_1C and TR_2C fragments [35]. Such large shifts of amide protons of this conserved glycine were also found in troponin C [36], calbindin [37], recoverin [38], and many other EF-hand proteins demonstrating that this feature is universal among the members of the EF-hand superfamily, thus serving a marker for functional EF-hand structures. Hoffman and Klevit [39] reported using 2D ^1H NMR on Ca^{2+}-free TR_1C fragment that the hydrophobic contacts between Phe-16 and Val-35 were absent in the crystal structure of Ca^{2+}-bound CaM [11,12]. The complete backbone assignments of Ca^{2+}-free TRC fragment were reported by Finn *et al.* [40], indicating that the Ca^{2+}-free form retains helix-loop-helix secondary structure similar to that observed in the Ca^{2+}-bound state. In 1990 Starovasnik *et al.* [41] showed that CaM from yeast *Saccharomyces cerevisiae* binds only three Ca^{2+} ions unlike four in case of vertebrate CaM.

Multidimensional and Heteronuclear NMR of CaM

The characterization of CaM and its biophysical properties using ^{1}H 1D and 2D NMR has so far been discussed. Being a highly soluble and heat-stable protein, during the late 1980s and early 1990s, CaM was extensively used for multidimensional heteronuclear NMR method development by Bax's group at NIH. For these heteronuclear NMR experiments, the protein was isotopically enrichment with ^{15}N and ^{13}C. In 1981, a partial CaM cDNA clone was isolated from the electric eel [42] and later many other ortholog cDNA clones have also been isolated. An Efficient purification of CaM by phenyl-sepharose affinity chromatography was soon reported [43] and then mammalian CaM gene was cloned and overespressed in *E. coli* [44,45]. Uniformly ^{15}N- and/or ^{13}C-labeled CaM from *Drosophila malanogaster* [46] and *Xenopus laevis* [47] were soon expressed as a recombinant protein in *E. coli* expression system for NMR studies. Figure 2 shows the ^{1}H–^{15}N heteronuclear single quantum coherence (HSQC) spectrum of Ca^{2+}-free (apo-CaM) and -bound form of recombinant uniformly labeled CaM. Ikura *et al.* [48,49] reported complete backbone and side-chain ^{1}H, ^{13}C, and ^{15}N assignments of Ca^{2+}-bound *Drosophila* CaM using a series of triple resonance 3D and 4D experiments. The secondary structure in solution determined using Nuclear Overhauser Effect (NOE), $^3J_{NH\alpha}$ coupling constants, and ^{13}C chemical shift data [48] compliments the crystal structure [11,12] very well. However, the NMR data clearly indicated that the long central helix (residues 65–92), found in the crystal structure, possesses a flexible region at residues D78–S81 in solution [50], which was suggested earlier by small-angle X-ray scattering [51, 52] and chemical cross linking studies [53]. This finding has been supported later by the recent 1 Å crystal structure of Ca^{2+}-CaM [16]. The ^{15}N relaxation studies provided additional insights into the structure and dynamics of Ca^{2+} -CaM [50]. The rotational correlation time for the N- and C- domains (7.1 and 6.3 ns, respectively) reflect that the two domains move independently in solution [50].

Vogel and coworkers [54, 55] have characterized side chain of seven lysine residues in CaM in apo, Ca^{2+}-bound and complex with target peptide derived from smMLCK (smMLCKp) and measured pK_a values of individual lysine residues in ε-dimethylated form using ^{1}H–^{13}C correlation NMR to understand the importance of these residues as Lys-13 and −115 residues are post-translationally methylated in *Paramecium* and mammalian CaM respectively. The dynamic properties of ε-trimethylated Lys-115 was studied by ^{14}N NMR relaxation measurements [56] and it was possible due to the unique symmetrical tetrahedral methyl substitution to its side chain that give rise to sharp ^{14}N signal. Chemical and thermal stability of intact CaM and its two isolated C- and N- domains has been extensively studied using selective ^{15}N Ile labeled and mutated protein by Bayley's group [57,58] employing 2D ^{1}H-^{15}N HSQC NMR experiment.

Solution Structure of CaM

There was no solution structure of Ca^{2+}-bound CaM till 2001 when Bax and coworkers [59] solved a high resolution solution structure of Ca^{2+}–CaM with the use of recently developed residual dipolar couplings (RDCs) in NMR and the high resolution X-ray structure as an initial template. The results showed that the two domains remain flexible despite conformational change upon Ca^{2+} binding. The tertiary structure of the C-terminal domain is similar to that found in the crystalline state, but the interhelical angles of the N-terminal domain EF-hands are smaller and approximate the "semi-open" conformation observed for the EF-hands of the myosin light chains [60].

In 1995, three groups independently solved the solution structure of apo-CaM, a compact molecule with two globular domains connected by a highly flexible linker [61–63] (Figure 3). The NMR structure of apo-CaM from *S. cerevisiae* is similarly flexible [64,65]. Due to the flexible linker, ensemble of calculated structures can only be superimposed over one of the domains, with the second domain occupying a "mushroom cap"-like space. Considerable backbone flexibility is also observed in the loop regions within the EF-hands. The structure clearly illustrates the Ca^{2+}-induced conformational change undergone by CaM, particularly the EF-hand helix orientation (Figure 4). The Ca^{2+}-binding to apo-CaM changes the interheloical angle of the two helices of each EF-hand by approximately 40° and such that CaM undergoes a transition from the "closed" conformation to the "open" conformation [61,63]. This conformational change results in the creation of a large hydrophobic pocket on each domain, which is essential for target binding for CaM [66–68] (Figure 4).

Metal and CaM Interactions

Various metal NMR were employed to explore biophysical and functional properties of CaM. Vogel and coworkers [69,70] studied ^{43}Ca and ^{113}Cd NMR by using two tryptic fragments of CaM to monitor preferential Ca^{2+} binding to each site of the two domains of CaM. These experiments also support the earlier finding by Ikura *et al.* [28]. ^{1}H saturation transfer and spectral simulation methods were employed to obtain the exchange rate constants and activation parameters between Ca^{2+}-free and -bound states for two fragments [71]. Two distinct rate constants of 3–10 s$^-$ [1] and 300–500 s$^-$ [1] were found at 22 °C for the C- and N-terminal fragments, respectively. ^{77}Se NMR was studied to examine the functional importance of nine Met residues in apo, Ca^{2+}- and target-bound CaM, and all

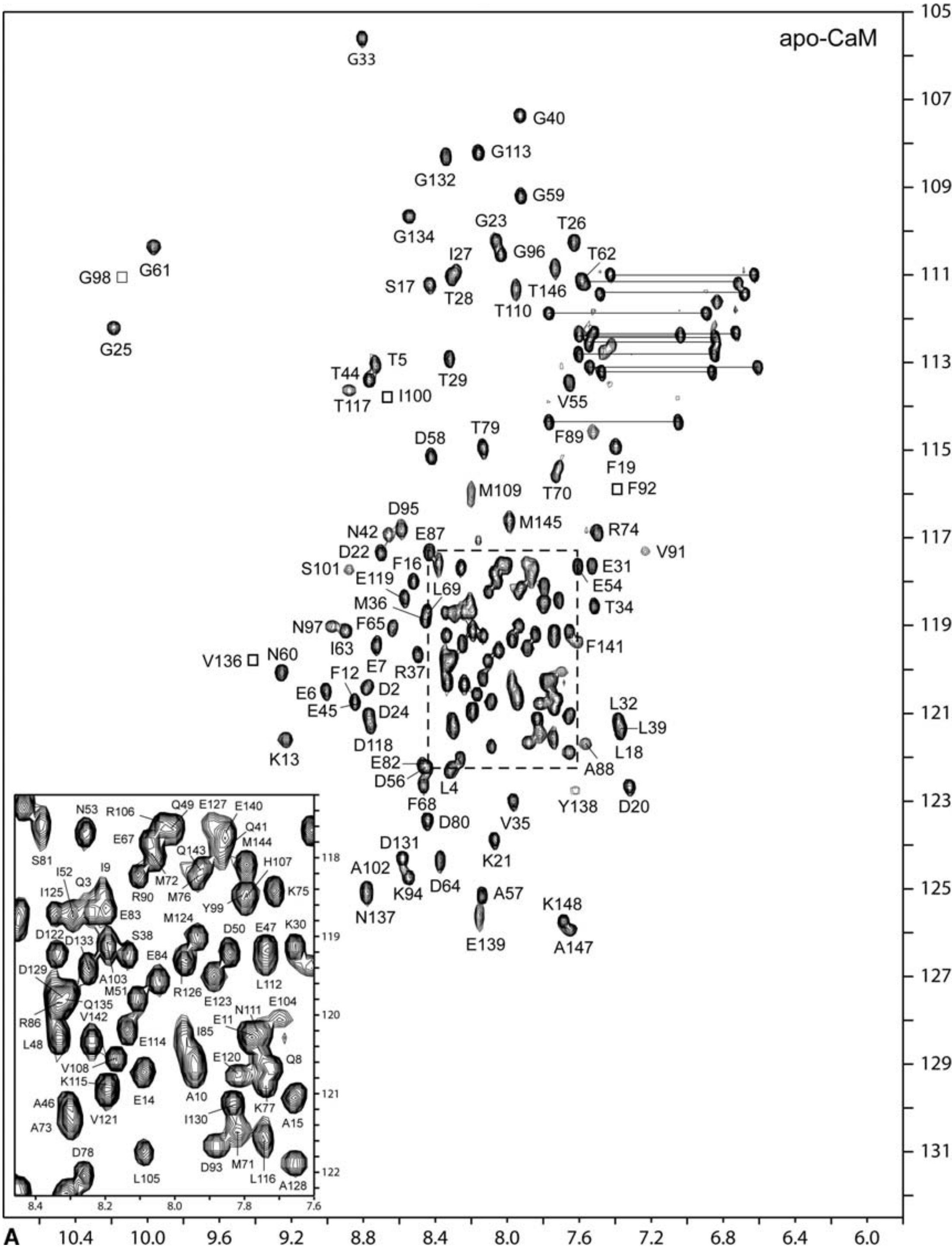

Fig. 2. ^{1}H-^{15}N HSQC spectra of uniformly ^{15}N-labeled (A) apo-CaM (Ca^{2+}-free) and (B) Ca^{2+}-CaM recorded on 600 MHz NMR spectrometer equipped with a triple resonance pulse field gradient probe. Both data were recorded with 1 mM CaM at 32 °C in identical buffer (15 mM Bis–Tris, 100 mM KCl, pH 6.72) except with 5 mM CaCl$_2$ for Ca^{2+}-bound and 2 mM EGTA for **apo-CaM samples, respectively. Resonances are labeled using one letter amino acid code and sequence position of the corresponding residue represents missing resonances in apo-CaM due to line broadening under the NMR sample condition.

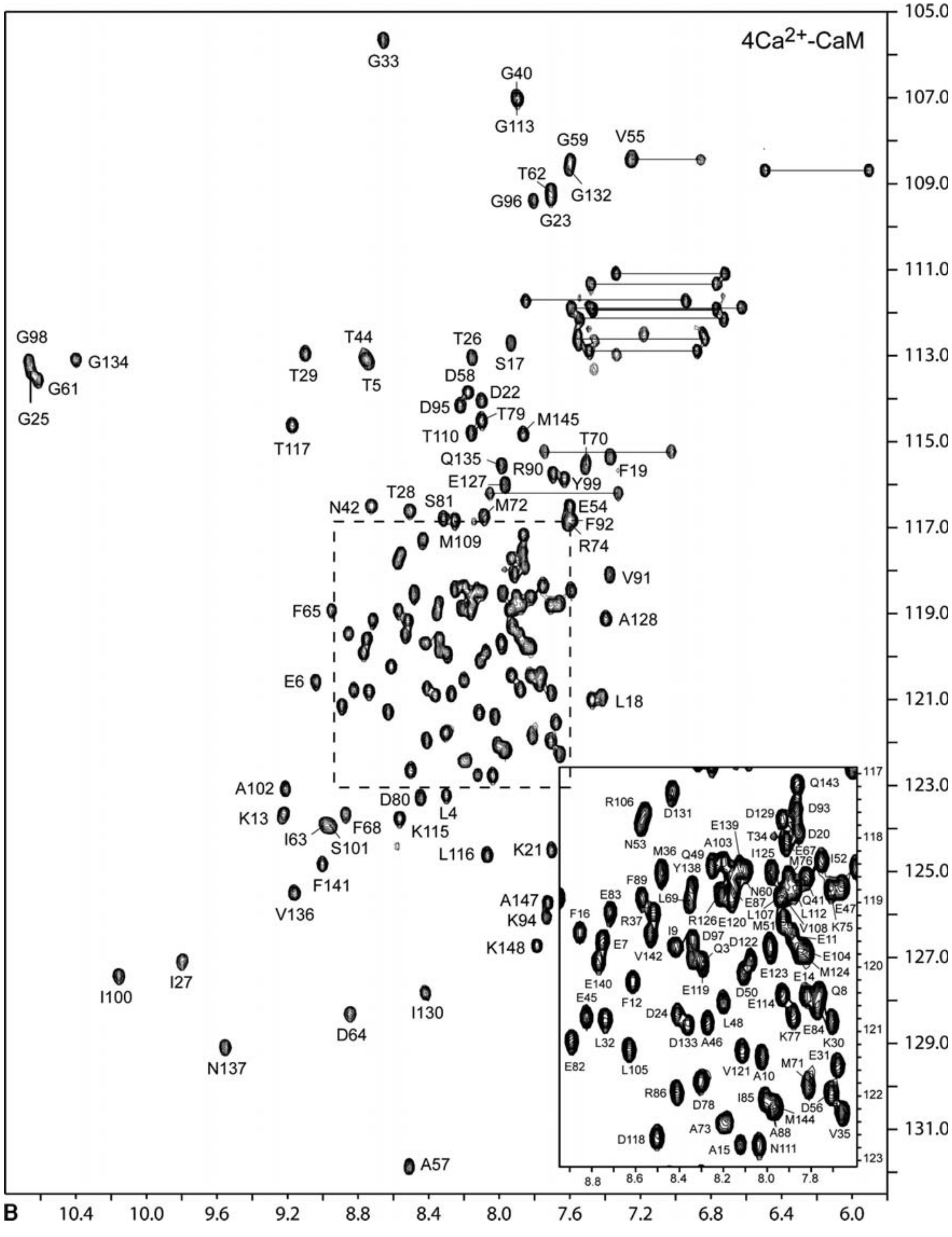

Fig. 2. (*Continued*)

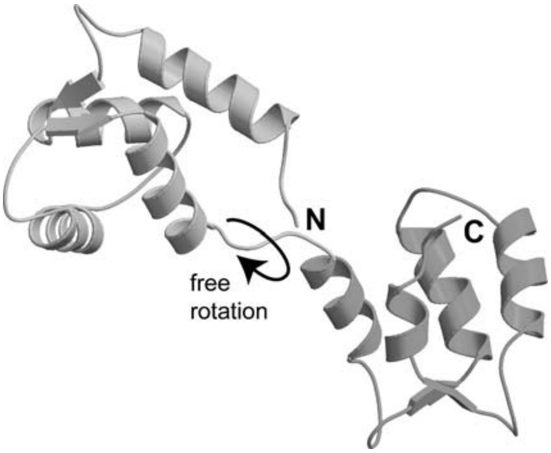

Fig. 3. Schematic representation of the NMR structure of apo-CaM, PDB code 1DMO model 11. The N- and C-terminal domains are shown in yellow and green, respectively, and the central flexible linker region in grey. The middle portion of the central linker is highly flexible similar to Ca^{2+}-CaM state. (See also Plate 54 on page XXXVIII in the Color Plate Section.)

of these Met residues were biosynthetically substituted by selemethionine [72]. The binding kinetics and stability of different metal ions to CaM has also been explored using heteronuclear NMR [73,74].

In recent years the interaction studies of paramagnetic lanthanide ions (Ln^{3+}) to CaM have become more popular due to their unique NMR properties. Bertini's group [75,76] has studied binding interactions of CaM with two Ln^{3+} metal ions including Yb^{3+} and Ce^{3+}. The solution structure of the $(Ce^{3+})_2$ complex of the N-terminal domain of CaM has been solved employing new NMR parameters, paramagnetic T_1 relaxation enhancements and pseudocontact shifts introduced by Ce^{3+} ions, to supplement conventional NOE-based distance constraints [76]. Recently, Bayley's group [77,78] has exploited further on the lanthanide interaction of CaM with Tb^{3+} ions. The partial replacement of diamagnetic Ca^{2+} by Tb^{3+} in Ca^{2+}–CaM allows the measurement of interdomain pseudocontact shifts as well as RDCs due to partial magnetic alignment of the molecule in presence of paramagnetic ion. These studies have become extremely useful for the determination of relative orientation of multidomain proteins.

Calcium-Calmodulin-Peptide Complexes

In early 1980s a number of ^{1}H and ^{113}Cd NMR studies [79–83] were done to examine the interaction with short peptides from either CaM binding domain of targets including skeletal muscle myosin light chain kinase (skMLCK), melittin or mastoparans. All these studies established that the peptides assume α-helical conformation upon binding CaM, and CaM also undergoes conformational change in presence of peptides. In 1991, the complete backbone assignment of ^{1}H, ^{15}N and ^{13}C for Ca^{2+}–CaM in complex with M13 (peptide derived from skMLCK) were reported [84] by using multidimensional heteronuclear NMR methods. ^{1}H assignments of M13 were also obtained using $^{15}N/^{13}C$-filtered experiment [85] and subsequently, the 3D NMR structure of Ca^{2+}-CaM–M13 complex was reported by Ikura *et al.* [66]. In the structure, the conformation of N- and C-terminal domains of CaM remains essentially unchanged even in complex with M13. However, the long central helix is disrupted into two helices connected by a long flexible loop (residues 74–82) as well as the orientation of several hydrophobic side chains are changed in the binding interface, thereby enabling the two domains to clamp around the helical peptide. The key anchoring hydrophobic residues of the peptide are responsible for anchoring the two domains of CaM are Trp-4 and Phe-17. A crystal structure of Ca^{2+}–CaM in complex with smMLCKp was reported [67] later in the same year, showing the same characteristic feature as observed for the solution structure of Ca^{2+}-CaM-M13. Subsequently, the structures of Ca^{2+}-CaM in complex with a number of peptides derived from CaMKI (CaMKIp) [86] and CaMKII (CaMKIIp) [68], and CaMKK (CaMKKp) [87,88] have been determined by crystallography and NMR. The structures of CaM in all these complexes are quite similar, with the two domains of CaM wrapping around the helical peptides. The CaM-CaMKK peptide complex differs from others in that the orientation of the peptide is in the opposite direction to that of CaMKIp, CaMKIIp, and M13 peptides with respect to the two CaM domains, and there is additional interaction with the unstructured tail following the helix (Figure 5). The recent dynamic studies of methyl side chains of CaM have explored the thermodynamic nature of CaM and target binding interface in details. Wand's group [89,90] has employed ^{2}H relaxation to probe methyl side chain dynamics of Ca^{2+}-CaM in presence and absence of smMLCKp. The dynamics of side chains are significantly perturbed and suggest extensive enthalpy and entropy exchange during the formation of CaM and target interface.

The target peptides are characterized by two bulky hydrophobic residues spaced 8, 12, and 14 residues apart, known as hydrophobic anchors and each anchor interacts with the hydrophobic pocket of one CaM domain. Based on the positions of anchoring residues, three different CaM binding motifs [91] (1–10, 1–14, and $1–16^{-}$) have been classified (1–10, CaM-CaMKIIp; 1–14, CaM-MLCKp; $1–16^{-}$, CaM-CaMKKp). The recognition modes of CaM with kinases differ from each other in the orientation of the two globular domains of CaM with respect to the helical binding region of the kinases (Figure 5). The flexible "inter-domain linker" between the two CaM domains is primarily responsible for rearrangement

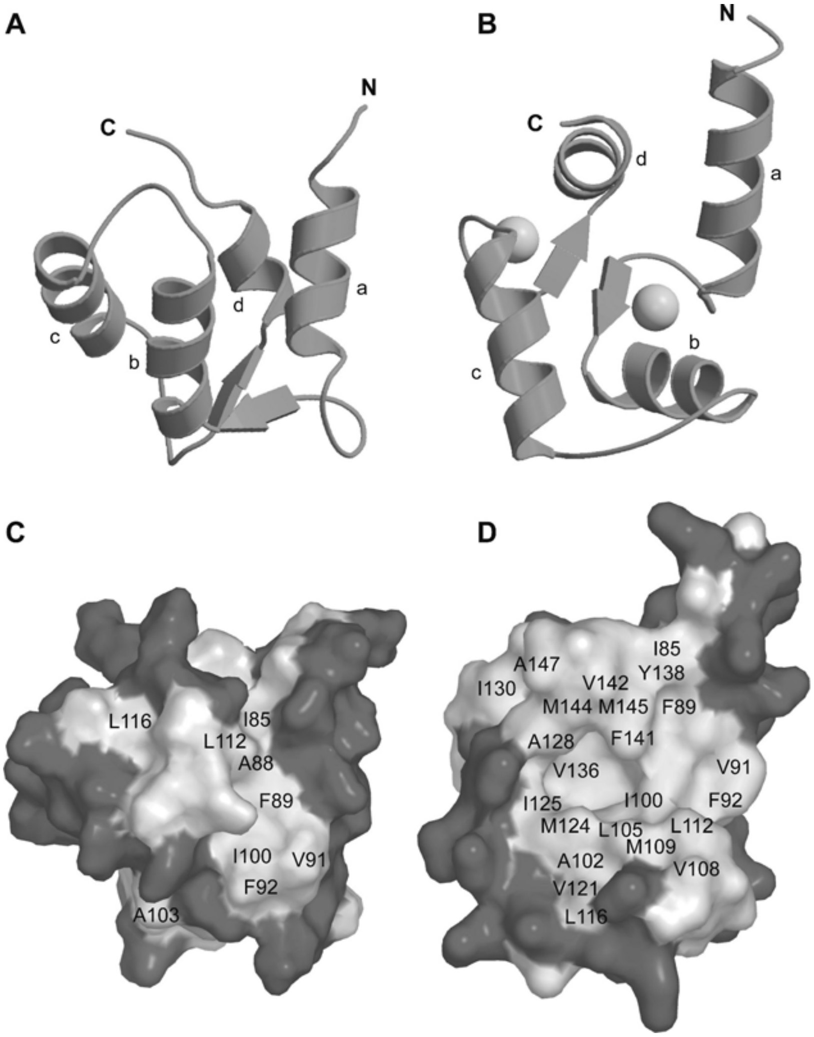

Fig. 4. Schematic representation of the C-terminal domain of CaM in the (A) "closed" Ca^{2+}-free and (B) "open" Ca^{2+}-bound states show Ca^{2+} induced conformation change in the EF-hand helix orientation. Helices are labeled with a, b, c, and d for easy visualization of helix orientation from "closed" to "open" state. Exposure of hydrophobic surface on binding of Ca^{2+} to CaM is shown in surface representation of both states of the C-terminal domain of CaM in (C) Ca^{2+}-free and (D) Ca^{2+}-bound. Hydrophobic residues (Ala, Ile, Leu, Met, Pro, Phe, Tyr, and Val) are shown yellow, negatively charged residues (Asp and Glu) in red, positively charged residues (Arg, His, and Lys) in magenta, and polar residues (Asn, Gln, Gly, Ser, and Thr) in white. Surface figures were generated using PyMol [111]. (See also Plate 55 on page XXXIX in the Color Plate Section.)

of the two domains in promoting an energetically favorable interaction with the target.

In 2002, Yap *et al.* [92] reported that more than 350 CaM target proteins had been identified thus far and that the binding domains of which had been classified in a database (http://calcium.uhnres.utoronto.ca/ctdb/) into several motif families based on sequence comparison. These sequence-based analyses, however, fail to predict CaM binding modes when no significant similarity is found between query and known sequences or when query sequences have several possible anchoring residues. Recently, Mal *et al.* [93] described a RDC-based NMR approach that can characterize the molecular recognition of CaM with target derived from protein kinases. RDCs

A

1-10 motif
(1-5-10 subclass)

	`   1   5    10`
CaMKII	RRKLKGAILTTMLATRNFS

1-14 motif
(1-5-8-14 subclass)

	`   1   5  8     14`
skMLCK	KRRWKKNFIAVSAANRFKKI
CaMKIV	RRKLKAAVKAVVASSRLGSAS

(1-5-10-14 subclass)

	`   1   5    10  14`
CaMKI	KSKWKQAFNATAVVRHMRKLQ

1-16⁻ motif
(1-5-10-16⁻ subclass)

	`   1   5    10     16`
CaMKK	IPSWTTVILVKSMLRKRSFGNPF

B

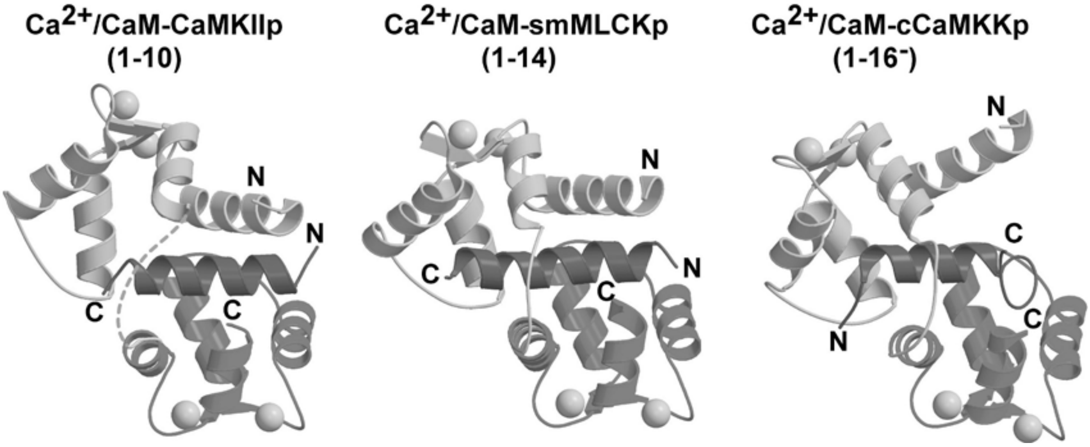

Fig. 5. (A) Ca^{2+}/CaM binding sequences from CaMKII, skMLCK, rCaMKK, CaMKI, and CaMKIV. The possible anchoring residues binding to the hydrophobic pocket of Ca^{2+}/CaM are highlighted in red. (B) Ribbon representation of three crystal structures of Ca^{2+}-CaM in complex with cCaMKKp (PDB code 1IQ5), smMLCKp (PDB code 1CDL), and CaMKIIp (PDB code 1CDM). Kinase-derived peptides are drawn in magenta, the N-and C-terminal domains are shown in yellow and green, respectively, and the central linker region and Ca^{2+} are in grey. (See also Plate 56 on page XL in the Color Plate Section.)

[94] contain information about the orientation of atomic bond vectors in a protein. In recent years, RDCs have been successfully used to characterize molecular binding [95–97], assist in homology modeling [98], and determine relative domain orientations [99,100] in multidomain proteins. Uniformly ^{15}N-labeled CaM was partially aligned in the negatively charged phage Pf1 phage (Asla Labs.). ^{1}H-^{15}N RDCs of CaM in complex with each target peptides derived from CaMKK, CaMKII, and MLCK, were experimentally measured and then analyzed in conjunction with the crystal structures of CaM-CaMKKp, CaM-CaMKIIp, and CaM-smMLCKp complexes using a best-fit molecular alignment tensor obtained by the singular value decomposition methods [100,101]. The best correlation was obtained when the experimental RDC data of a CaM-target peptide complex was compared with the corresponding crystal structure. For example, RDC data of CaM in complex with CaMKKp will have the best fit only with the CaM-CaMKKp crystal structure, not with the CaM-smMLCKp or CaM-CaMKIIp structure (Figure 6). Using this RDC-based NMR approach, the CaM binding motif (1–14 type) was determined in the complex of CaM–CaMKIp, for which no crystal and NMR structure was available at that time (Figure 7). This result was later

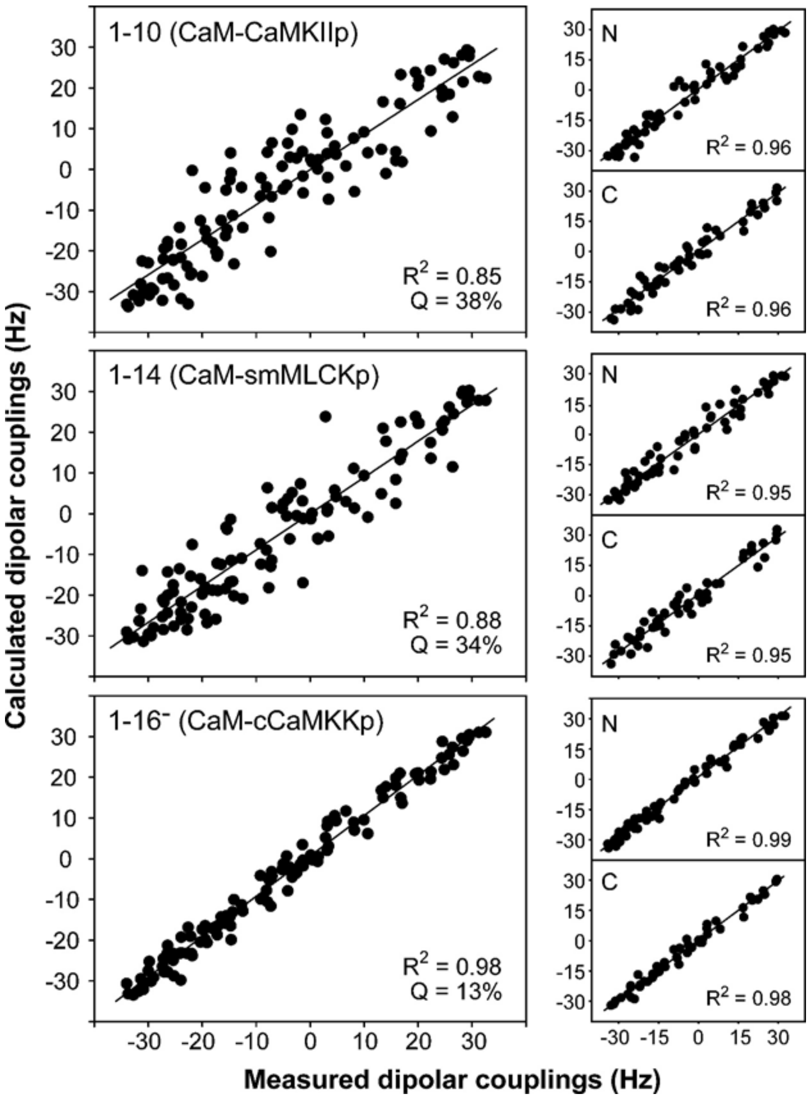

Fig. 6. Correlations between experimentally measured ^{1}H-^{15}N RDCs of the **CaM–rCaMKKp complex and the best fit RDC values calculated with the **CaM-CaMKIIp, CaM-smMLCKp, and CaM-cCaMKKp crystal structures. The correlation coefficient R^2 and quality factor Q for each complex are given in the plots. The correlations derived for individual domains (N and C) of CaM are shown in the small panels to the right. (Adopted by permission of the American Chemical Society from Mal *et al.* [93])

confirmed by the crystal structure of CaM–CaMKIp complex [86].

However, the orientation of the target helix remained undefined in this approach. Recently, Mal *et al.* [102] determined the orientation from a pair of ^{1}H-^{15}N correlation spectra of CaM in complex with a peptide construct containing an ATCUN (amino terminal Cu^{2+}(Ni^{2+})-binding) motif recorded with and without Cu^{2+}. They have taken the advantage of paramagnetic property of Cu^{2+} that specifically binds the ATCUN motif part of the peptide. By mapping the residues that were broaden due to the influence of paramagnetic relaxation of Cu^{2+} on CaM, the orientation of target peptide in a complex was quickly determined.

Two recent crystal structures of CaM-peptide complex demonstrates that other targets interact in a similar manner

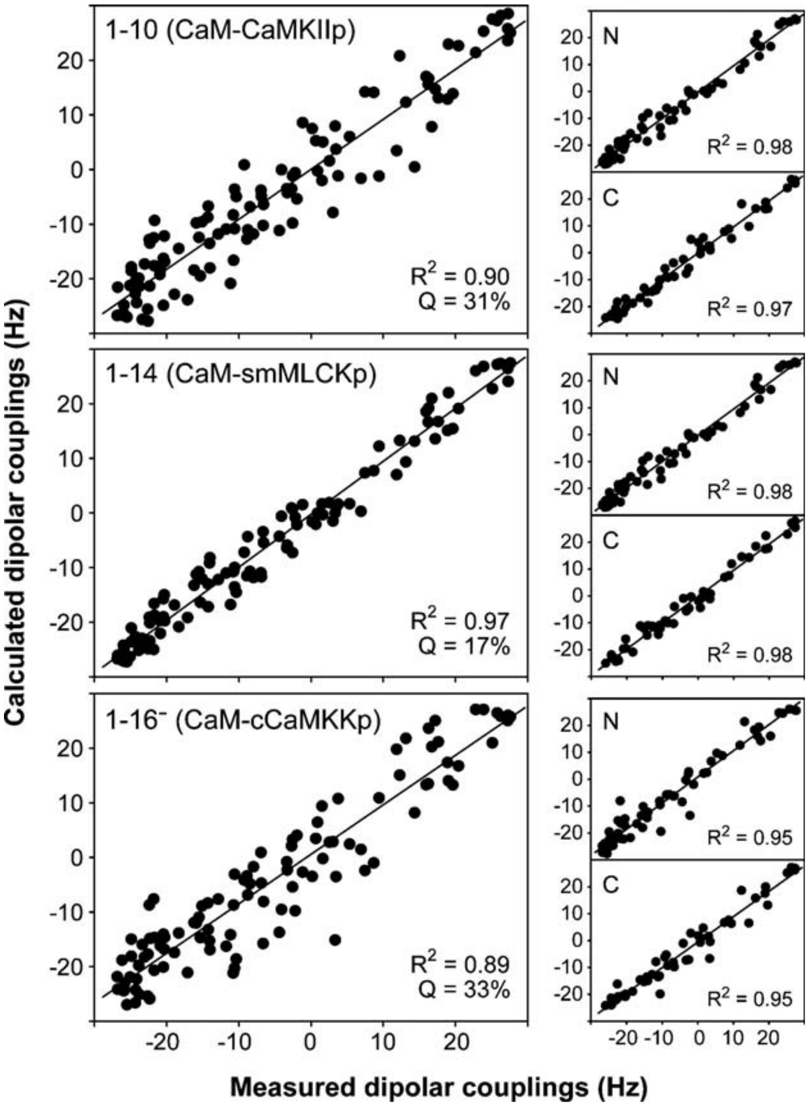

Fig. 7. Correlations between experimentally measured ^{1}H-^{15}N RDCs from the **CaM–CaMKIp complex and the best fit RDC values obtained with the crystal structures of CaMKIIp, CaM–smMLCKp, and CaM–cCaMKKp complexes. The correlations derived on the basis of individual domains (N and C) of CaM are shown in the small panels to the right. (Adopted by permission of the American Chemical Society from Mal *et al.* [93])

to the CaM-dependent kinase: CaM in complex with a peptide derived from endothelial nitic oxide synthase [103] illustrates an interaction similar to that of the CaM–MLCKp complex, while the interaction between CaM and a peptide from myristoylated alanine-rich C kinase substrate (MARCKS) [104] results in a similar CaM conformation, despite an elongated peptide structure containing only a single-turn helix. Therefore, the RDC-based NMR approach can also be applied to other complexes to define CaM binding mode beyond the complex with peptides from kinase family. The model of CaM-target interaction as two domains wrapped around a single, amphipathic

α-helix remaind until the crystal structure of CaM bound to the gating domain of the Ca^{2+}-activated K^+ channel (SK2) [105] and anthrax adenylyl cyclase (aAC) [106] were solved. These two complexes added diversity in to the CaM binding modes. The solution structure of CaM in complex with a dimeric peptide from plant glutamate decarboxylase has illustrated another unusual binding stoichiometry [107]. More recently, the study [108] between CaM and the target sequence from phosphofructokinase reveals that the complex is pH dependent and the affinity of complex formation increases 1000-fold from pH 9.0 to 4.8, adding another complexity into the CaM and target recognition.

In addition to these Ca^{2+}-dependent CaM-target peptide studies, there are a number of target proteins that interact with apo-CaM. Often these CaM binding domain contains a consensus sequence (IQXXGRXXXR), known as IQ motif [109] such as those found in myosin and neuromodulin. There are not many NMR studies available on the interaction of apo-CaM with IQ motif sequence. An early NMR study [110] was done on the complex of apo-CaM and a peptide derived from neurocalmodulin. This complex is sensitive to salt concentration suggesting that electrostatic interactions dominate to the complex formation. No structure of apo-CaM bound to a target or target peptide has been determined. It is very likely that CaM residues mediating the apo-CaM and target interaction are not entirely the same as those involved in Ca^{2+}-dependent interactions [110].

Despite the unique stoichiometry and secondary and tertiary structures of the targets bound to CaM in recently determined structures, CaM in all complexes display a remarkable conserved tertiary backbone (excluding the complex with SK2 and aAC), with the primary difference being the orientation of the N- and C-domains with respect to each other. This multiple-target binding ability of CaM should be attributed to the side chains comprising the hydrophobic patch exposed upon Ca^{2+} binding. NMR studies of CaM and its complex with various targets have contributed greatly to our understanding of its structure-function relationship. Despite a significant number of structural studies, there remains much to learn about the details of the mechanism of activation, in addition characterization of the other hundreds of CaM target proteins that have been identified over the two decades [92].

Acknowledgment

We thank Dr. Mingjie Zhang, The Hong Kong University of Science and Technology for providing apo-CaM assignments. This work is supported by the Canadian Institutes of Health Research. M. I. holds the Canadian Research Chair in Cancer Structural Biology.

References

1. Kakiuchi S, Yamazaki R. Calcium dependent phosphodiesterase activity and its activating factor (PAF) from brain studies on cyclic 3′,5′-nucleotide phosphodiesterase (3). Biochem. Biophys. Res. Commun. 1970;41:1104–10.
2. Cheung WY. Cyclic 3′,5′-nucleotide phosphodiesterase. Demonstration of an activator. Biochem. Biophys. Res. Commun. 1970;38:533–8.
3. Chin D, Means AR. Calmodulin: a prototypical calcium sensor. Trends Cell. Biol. 2000;10:322–8.
4. Watterson DM, Sharief F, Vanaman TC. The complete amino acid sequence of the Ca2+-dependent modulator protein (calmodulin) of bovine brain. J. Biol. Chem. 1980;255:962–75.
5. Crivici A, Ikura M. Molecular and structural basis of target recognition by calmodulin. Annu. Rev. Biophys. Biomol. Struct. 1995;24:85–116.
6. Means AR, Tash JS, Chafouleas JG. Physiological implications of the presence, distribution, and regulation of calmodulin in eukaryotic cells. Physiol. Rev. 1982;62: 1–39.
7. Cohen P, Klee CB. Calmodulin. Elsevier: Amsterdam, 1988.
8. Vogel HJ, Zhang M. Protein engineering and NMR studies of calmodulin. Mol. Cell Biochem. 1995; 149–150:3–15.
9. Benaim G, VillaloboA. Phosphorylation of calmodulin. Functional implications. Eur. J. Biochem. 2002;269: 3619–31.
10. Quadroni M *et al.* Phosphorylation of calmodulin alters its potency as an activator of target enzymes. Biochemistry 1998;37:6523–32.
11. Babu YS *et al*. Three-dimensional structure of calmodulin. Nature 1985;315:37–40.
12. Kretsinger RH, Rudnick SE, Weissman LJ. Crystal structure of calmodulin. J. Inorg. Biochem. 1986;28:289–302.
13. Chattopadhyaya R, Meador WE, Means AR, Quiocho FA. Calmodulin structure refined at 1.7 a resolution. J. Mol. Biol. 1992;228:1177–92.
14. Babu YS, Bugg CE, Cook WJ. Structure of calmodulin refined at 2.2 A resolution. J. Mol. Biol. 1988;204:191–204.
15. Rao, ST *et al*. Structure of *Paramecium tetraurelia* calmodulin at 1.8 A resolution. Protein Sci. 1993;2:436–47.
16. Wilson MA, Brunger AT. The 1.0 a crystal structure of Ca(2+)-bound calmodulin: an analysis of disorder and implications for functionally relevant plasticity. J. Mol. Biol. 2000;301:1237–56.
17. Kretsinger RH, Nockolds CE. Carp muscle calcium-binding protein. II. Structure determination and general description. J. Biol. Chem. 1973;248:3313–26.
18. Corcoran EE, Means AR. Defining Ca2+/calmodulin-dependent protein kinase cascades in transcriptional regulation. J. Biol. Chem. 2001;276:2975–8.
19. Anderson SR, MalencikDA. Calcium and Cell Function. Academic Press: New York, 1986.
20. Hidaka H, Yamaki T, Totsuka,T, Asano M. Selective inhibitors of Ca2+-binding modulator of phosphodiesterase produce vascular relaxation and inhibit actin-myosin interaction. Mol. Pharmacol. 1979;15:49–59.

21. Seamon K. Cation dependent conformations of brain CA2+-dependent regulator protein detected by nuclear magnetic resonance. Biochem. Biophys. Res. Commun. 1979;86:1256–65.
22. Seamon KB. Calcium- and magnesium-dependent conformational states of calmodulin as determined by nuclear magnetic resonance. Biochemistry 1980;19:207–15.
23. Klevit RE, Levine BA, Williams RJ. A study of calmodulin and its interaction with trifluoperazine by high resolution 1H NMR spectroscopy. FEBS Lett. 1981;123:25–9.
24. Krebs J, Carafoli E. Influence of Ca2+ and trifluoperazine on the structure of calmodulin. A 1H-nuclear magnetic resonance study. Eur. J. Biochem. 1982;124:619–27.
25. Shimizu T, Hatano M. Interaction of trifluoperazine with porcine calmodulin 19F NMR and induced CD spectral studies. FEBS Lett. 1983;160:182–6.
26. ShimizuT, Hatano M, Nagao S, Nozawa Y. 43Ca NMR studies of Ca2+-tetrahymena calmodulin complexes. Biochem. Biophys. Res. Commun. 1982;106:1112–8.
27. Ikura M *et al*. Nuclear magnetic resonance studies on calmodulin: spectral assignments in the calcium-free state. Biochemistry 1983;22:2568–72.
28. Ikura M *et al*. Nuclear magnetic resonance studies on calmodulin: calcium-induced conformational change. Biochemistry 1983;22:2573–9.
29. Thulin E, Andersson A, Drakenberg T, Forsen S, Vogel HJ. Metal ion and drug binding to proteolytic fragments of calmodulin: proteolytic, cadmium-113, and proton nuclear magnetic resonance studies. Biochemistry 1984;23:1862–70.
30. Yazawa M *et al*. N-terminal region (domain 1) of calmodulin is the low affinity site for Ca2+. A 13C NMR study of S-cyanocalmodulin. J. Biochem. (Tokyo) 1984;95:443–6.
31. Dalgarno DC, Levine BA, Williams RJ, Fullmer CS, Wasserman RH. Proton-NMR studies of the solution conformations of vitamin-D-induced bovine intestinal calcium-binding protein. Eur. J. Biochem. 1983;137:523–9.
32. Klevit RE, Dalgarno DC, Levine BA, Williams RJ. 1H-NMR studies of calmodulin. The nature of the Ca2+-dependent conformational change. Eur. J. Biochem. 1984;139:109–14.
33. Aulabaugh A, Niemczura WP, Blundell TL, Gibbons WA. A study of the interactions between residues in the C-terminal half of calmodulin by one and two-dimensional NMR methods and computer modelling. Eur. J. Biochem. 1984;143:409–18.
34. Ikura M, Minowa O, Hikichi K. Hydrogen bonding in the carboxyl-terminal half-fragment 78–148 of calmodulin as studied by two-dimensional nuclear magnetic resonance. Biochemistry 1985;24:4264–9.
35. Ikura M, Minowa O, Yazawa M, Yagi K, Hikichi K. FEBS lett. 1987;219:17.
36. Tsuda S, Hasegawa Y, Yoshida M, Yagi K, Hikichi K. Nuclear magnetic resonance study on rabbit skeletal troponin C: calcium-induced conformational change. Biochemistry 1988;27:4120–6.
37. Kordel J, Forsen S, Drakenberg T, Chazin WJ. The rate and structural consequences of proline *cis*-trans isomerization in calbindin D9k: NMR studies of the minor (cis-Pro43) isoform and the Pro43Gly mutant. Biochemistry 1990;29:4400–9.
38. Ames JB *et al*. Molecular mechanics of calcium-myristoyl switches. Nature 1997;389:198–202.
39. Hoffman R, Klevit RE. Techniques in protein chemistry II. Academic Press: New York, 1991.
40. Finn BE, Drakenberg T, Forsen S. The structure of apo-calmodulin. A 1H NMR examination of the carboxy-terminal domain. FEBS Lett. 1993;336:368–74.
41. Starovasnik MA, Davis TN, Klevit RE. Similarities and differences between yeast and vertebrate calmodulin: an examination of the calcium-binding and structural properties of calmodulin from the yeast *Saccharomyces cerevisiae*. Biochemistry 1993;32:3261–70.
42. Munjaal RP, Chandra T, Woo SL, Dedman JR, Means AR. A cloned calmodulin structural gene probe is complementary to DNA sequences from diverse species. Proc. Natl. Acad. Sci. U.S.A. 1981;78:2330–4.
43. Gopalakrishna R, Anderson WB. Ca2+-induced hydrophobic site on calmodulin: application for purification of calmodulin by phenyl-Sepharose affinity chromatography. Biochem. Biophys. Res. Commun. 1982;104:830–6.
44. Shatzman AR, Rosenberg M. Expression, identification, and characterization of recombinant gene products in *Escherichia coli*. Methods Enzymol. 1987;152:661–73.
45. Ikura M *et al*. Heteronuclear 3D NMR and isotopic labeling of calmodulin. Towards the complete assignment of the 1H NMR spectrum. Biochem. Pharmacol. 1990;40:153–60.
46. Smith VL, Doyle KE, Maune JF, Munjaal RP, Beckingham K. Structure and sequence of the *Drosophila melanogaster* calmodulin gene. J. Mol. Biol. 1987;196:471–85.
47. Chien YH, Dawid IB. Isolation and characterization of calmodulin genes from *Xenopus laevis*. Mol. Cell Biol. 1984;4:507–13.
48. Ikura M *et al*. Secondary structure and side-chain 1H and 13C resonance assignments of calmodulin in solution by heteronuclear multidimensional NMR spectroscopy. Biochemistry 1991;30:9216–28.
49. Ikura M, Kay LE, Bax A. A novel approach for sequential assignment of 1H, 13C, and 15N spectra of proteins: heteronuclear triple-resonance three-dimensional NMR spectroscopy. Application to calmodulin. Biochemistry 1990;29:4659–67.
50. Barbato G, Ikura M, Kay LE, Pastor RW, Bax A. Backbone dynamics of calmodulin studied by 15N relaxation using inverse detected two-dimensional NMR spectroscopy: the central helix is flexible. Biochemistry 1992;31:5269–78.
51. Trewhella J. The solution structures of calmodulin and its complexes with synthetic peptides based on target enzyme binding domains. Cell Calcium 1992;13:377–90.
52. Kataoka M, Head JF, Persechini A, Kretsinger RH, Engelman DM. Small-angle X-ray scattering studies of calmodulin mutants with deletions in the linker region of the central helix indicate that the linker region retains a predominantly alpha-helical conformation. Biochemistry 1991;30:1188–92.
53. Persechini A, Kretsinger RH. The central helix of calmodulin functions as a flexible tether. J. Biol. Chem. 1988;263:12175–8.
54. Huque ME, Vogel HJ. Carbon-13 NMR studies of the lysine side chains of calmodulin and its proteolytic fragments. J. Protein Chem. 1993;12:695–707.

55. Zhang M, Vogel HJ. Determination of the side chain pKa values of the lysine residues in calmodulin. J. Biol. Chem. 1993;268:22420–8.
56. Zhang M, Huque E, Vogel HJ. Characterization of trimethyllysine 115 in calmodulin by 14N and 13C NMR spectroscopy. J. Biol. Chem. 1994;269:5099–105.
57. Biekofsky RR *et al*. Thermal stability of calmodulin and mutants studied by (1)H-(15)N HSQC NMR measurements of selectively labeled [(15)N]Ile proteins. Biochemistry 2002;41:6850–9.
58. Rabl CR, Martin SR, Neumann E, Bayley PM. Temperature jump kinetic study of the stability of apo-calmodulin. Biophys. Chem. 2002;101–102:553–64.
59. Chou JJ, Li S, Klee CB, Bax A. Solution structure of Ca(2+)-calmodulin reveals flexible hand-like properties of its domains. Nat. Struct. Biol. 2001;8:990–7.
60. Houdusse A, Cohen C. Target sequence recognition by the calmodulin superfamily: implications from light chain binding to the regulatory domain of scallop myosin. Proc. Natl. Acad. Sci. U.S.A. 1995;92:10644–7.
61. Zhang M, Tanaka T, Ikura M. Calcium-induced conformational transition revealed by the solution structure of apo calmodulin. Nat. Struct. Biol. 1995;2:758–67.
62. Finn BE. *et al*. Calcium-induced structural changes and domain autonomy in calmodulin. Nat. Struct. Biol. 1995;2:777–83.
63. Kuboniwa H *et al*. Solution structure of calcium-free calmodulin. Nat. Struct. Biol. 1995;2:768–76.
64. Lee SY, Klevit RE. The whole is not the simple sum of its parts in calmodulin from *S. cerevisiae*. Biochemistry 2000;39:4225–30.
65. Ishida, H. *et al*. The solution structure of apocalmodulin from *Saccharomyces cerevisiae* implies a mechanism for its unique Ca2+ binding property. Biochemistry 2002;41:15536–42.
66. Ikura M *et al*. Solution structure of a calmodulin-target peptide complex by multidimensional NMR. Science 1992;256:632–8.
67. Meador WE, Means AR, Quiocho FA. Target enzyme recognition by calmodulin: 2.4 A structure of a calmodulin-peptide complex. Science 1992;257:1251–5.
68. Meador WE, Means AR, Quiocho FA. Modulation of calmodulin plasticity in molecular recognition on the basis of x-ray structures. Science 1993;262:1718–21.
69. Forsen S *et al*. Calcium-Binding Proteins. Elsevier: Amsterdam, 1983.
70. Andersson A, Forsen S, Thulin E, Vogel HJ. Cadmium-113 nuclear magnetic resonance studies of proteolytic fragments of calmodulin: assignment of strong and weak cation binding sites. Biochemistry 1983;22:2309–13.
71. Ikura M. Proton nuclear magnetic resonance studies on the kinetics of tryptic fragments of calmodulin upon calcium binding. Biochim. Biophys. Acta 1986;872:195–200.
72. Zhang M, Vogel HJ. Two-dimensional NMR studies of selenomethionyl calmodulin. J. Mol. Biol. 1994;239:545–54.
73. Ouyang H, Vogel HJ. Metal ion binding to calmodulin: NMR and fluorescence studies. Biometals 1998;11:213–22.
74. Martin SR, Masino L, Bayley PM. Enhancement by Mg2+ of domain specificity in Ca2+-dependent interactions of calmodulin with target sequences. Protein Sci. 2000;9:2477–88.
75. Bertini I, Gelis I, Katsaros N, Luchinat C, Provenzani A. Tuning the affinity for lanthanides of calcium binding proteins. Biochemistry 2003;42:8011–21.
76. Bentrop D *et al*. Solution structure of the paramagnetic complex of the N-terminal domain of calmodulin with two Ce3+ ions by 1H NMR. Biochemistry 1997;36:11605–18.
77. Feeney J, Birdsall B, Bradbury AF, Biekofsky RR, Bayley PM. Calmodulin tagging provides a general method of using lanthanide induced magnetic field orientation to observe residual dipolar couplings in proteins in solution. J. Biomol. NMR 2001;21:41–48.
78. Biekofsky RR *et al*. NMR approaches for monitoring domain orientations in calcium-binding proteins in solution using partial replacement of Ca2+ by Tb3+. FEBS Lett. 1999;460:519–26.
79. Klevit RE, Blumenthal DK, Wemmer DE, Krebs EG. Interaction of calmodulin and a calmodulin-binding peptide from myosin light chain kinase: major spectral changes in both occur as the result of complex formation. Biochemistry 1985;24:8152–7.
80. Seeholzer SH, Cohn M, Putkey JA, Means AR, Crespi HL. NMR studies of a complex of deuterated calmodulin with melittin. Proc. Natl. Acad. Sci. U.S.A. 1986;83:3634–8.
81. Yazawa M, Ikura M, Hikichi K, Ying L, Yagi K. Communication between two globular domains of calmodulin in the presence of mastoparan or caldesmon fragment. Ca2+ binding and 1H NMR. J. Biol. Chem. 1987;262:10951–4.
82. Ikura M *et al*. 113Cd-NMR evidence for cooperative interaction between amino- and carboxyl-terminal domains of calmodulin. Biochem. Biophys. Res. Commun. 1989;161:1233–8.
83. Ohki SY, Yazawa M, Yagi K, Hikichi K. Mastoparan binding induces Ca(2+)-transfer between two globular domains of calmodulin: a 1H NMR study. J. Biochem. (Tokyo) 1991;110:737–42.
84. Ikura M, Kay LE, Krinks M, Bax A. Triple-resonance multidimensional NMR study of calmodulin complexed with the binding domain of skeletal muscle myosin light-chain kinase: indication of a conformational change in the central helix. Biochemistry 1991;30:5498–504.
85. Ikura M, Bax A. Isotope filtered 2D NMR of a protein-peptide complex: study of a skeletal muscle myosin light chain kinase fragment bound to calmodulin. J. Am. Chem. Soc. 1992;114:2433–40.
86. Clapperton JA, Martin SR, Smerdon SJ, Gamblin SJ, Bayley PM. Structure of the complex of calmodulin with the target sequence of calmodulin-dependent protein kinase I: studies of the kinase activation mechanism. Biochemistry 2002;41:14669–79.
87. Osawa M *et al*. A novel target recognition revealed by calmodulin in complex with Ca2+-calmodulin-dependent kinase kinase. Nat. Struct. Biol. 1999;6:819–24.
88. Kurokawa H *et al*. Target-induced conformational adaptation of calmodulin revealed by the crystal structure of a complex with nematode Ca(2+)/calmodulin-dependent kinase kinase peptide. J. Mol. Biol. 2001;312:59–68.

89. Lee AL, Wand AJ. Microscopic origins of entropy, heat capacity and the glass transition in proteins. Nature 2001;411:501–4.
90. Lee AL, Kinnear SA, Wand AJ. Redistribution and loss of side chain entropy upon formation of a calmodulin-peptide complex. Nat. Struct. Biol. 2000;7:72–77.
91. Rhoads AR, Friedberg F. Sequence motifs for calmodulin recognition. Faseb J. 1997;11:331–40.
92. Yap KL *et al*. Calmodulin target database. J. Struct. Funct. Genomics 2000;1:8–14.
93. Mal TK, Skrynnikov NR, Yap KL, Kay LE, Ikura M. Detecting protein kinase recognition modes of calmodulin by residual dipolar couplings in solution NMR. Biochemistry 2002;41:12899–906.
94. Tjandra N, Bax A. Direct measurement of distances and angles in biomolecules by NMR in a dilute liquid crystalline medium. Science 1997;278:1111–4.
95. Bolon PJ, Al-Hashimi HM, Prestegard JH. Residual dipolar coupling derived orientational constraints on ligand geometry in a 53 kDa protein-ligand complex. J. Mol. Biol. 1999;293:107–15.
96. Clore GM. Accurate and rapid docking of protein-protein complexes on the basis of intermolecular nuclear overhauser enhancement data and dipolar couplings by rigid body minimization. Proc. Natl. Acad. Sci. U.S.A.2000;97:9021–5.
97. Koenig BW *et al*. Measurement of dipolar couplings in a transducin peptide fragment weakly bound to oriented photo-activated rhodopsin. J. Biomol. NMR 2000; 16:121–5.
98. Chou JJ, Li S, Bax A. Study of conformational rearrangement and refinement of structural homology models by the use of heteronuclear dipolar couplings. J. Biomol. NMR 2000;18:217–27.
99. Fischer MW, Losonczi JA, Weaver JL, Prestegard JH. Domain orientation and dynamics in multidomain proteins from residual dipolar couplings. Biochemistry 1999;38:9013–22.
100. Skrynnikov NR *et al*. Orienting domains in proteins using dipolar couplings measured by liquid-state NMR: differences in solution and crystal forms of maltodextrin binding protein loaded with beta-cyclodextrin. J. Mol. Biol. 2000;295:1265–73.
101. Losonczi JA, Andrec M, Fischer MW, Prestegard JH. Order matrix analysis of residual dipolar couplings using singular value decomposition. J. Magn. Reson. 1999;138:334–42.
102. Mal TK, Ikura M, Kay LE. The ATCUN domain as a probe of intermolecular interactions: application to calmodulin-peptide complexes. J. Am. Chem. Soc. 2002;124:14002–3.
103. Aoyagi M, Arvai AS, Tainer JA, Getzoff ED. Structural basis for endothelial nitric oxide synthase binding to calmodulin. Embo. J. 2003;22:766–75.
104. Yamauchi E, Nakatsu T, Matsubara M, Kato H, Taniguchi H. Crystal structure of a MARCKS peptide containing the calmodulin-binding domain in complex with Ca2+-calmodulin. Nat. Struct. Biol. 2003;10:226–31.
105. Schumacher MA, Rivard AF, Bachinger HP, Adelman JP. Structure of the gating domain of a Ca2+-activated K+ channel complexed with Ca2+/calmodulin. Nature 2001;410:1120–4.
106. Drum CL *et al*. Structural basis for the activation of anthrax adenylyl cyclase exotoxin by calmodulin. Nature 2002;415:396–402.
107. Yap KL, Yuan T, Mal TK, Vogel HJ, Ikura M. Structural basis for simultaneous binding of two carboxy-terminal peptides of plant glutamate decarboxylase to calmodulin. J. Mol. Biol. 2003;328:193–204.
108. Martin SR *et al*. Interaction of calmodulin with the phosphofructokinase target sequence. FEBS Lett. 2004;577:284–8.
109. Bahler M, Rhoads A. Calmodulin signaling via the IQ motif. FEBS Lett. 2002;513:107–13.
110. Urbauer JL, Short JH, Dow LK, Wand AJ. Structural analysis of a novel interaction by calmodulin: high-affinity binding of a peptide in the absence of calcium. Biochemistry 1995;34:8099–109.
111. DeLano WL. The PyMOL User's Manual. San Carlos: CA, USA, 2002).

Analytical Framework for Protein Structure Determination by Solid-State NMR of Aligned Samples

Alexander A. Nevzorov and Stanley J. Opella

Department of Chemistry and Biochemistry, University of California, San Diego La Jolla, California 92093-0307 USA

Abstract

A compact formulation of the experimental solid-state NMR observables in terms of the irreducible basis of rotations is presented. Quadratic-form representations are derived for the ^{15}N and ^{1}H chemical shift anisotropy, as well as ^{1}H–^{15}N and ^{1}H$_{\alpha}$–^{13}C$_{\alpha}$ dipolar interactions. Peptide plane geometries together with the torsion angles Φ and Ψ are incorporated into the corresponding Wigner rotation matrices, which allow one to establish the mapping of the protein structure onto its multidimensional solid-state NMR spectra in analytically semi-closed form. The structural fitting of experimental two-dimensional NMR spectra of Pf1 bacteriophage is presented. Examples of protein structure calculations from simulated three-dimensional solid-state NMR spectra for protein G, two-helical hairpin fragment of bacteriorhodopsin, and a loop region from KcsA are also presented. Moreover, analytical expression is obtained for the periodicity of secondary structures as an explicit function of Φ and Ψ.

Introduction

Solid-state NMR of aligned samples is emerging as a method for determining the atomic-resolution structures of proteins in biological supramolecular assemblies. Already, the structures of nine proteins determined with this approach have been deposited in the protein data bank. These include coat proteins in virus particles and membrane proteins in lipid bilayers. With the recognition that 20–30% of the proteins encoded in a genome are helical membrane proteins, and the difficulty in determining the structures of these proteins by conventional X-ray diffraction and solution NMR approaches, solid-state NMR of aligned samples has the potential to play an important role in structural biology.

There are three principal aspects to protein structure determination by solid-state NMR of aligned samples. First is the preparation of highly aligned samples of proteins that are immobilized by their associations with other biopolymers, for example the other coat protein subunits in virus particles or the phospholipids in membrane bilayers. Recent advances have made it possible to prepare magnetically aligned samples of proteins obtained by expression in bacteria with mosaic spreads less than or equal to those observed in single crystals of peptides. Second, multidimensional solid-state NMR experiments are needed to narrow the resonances and to measure several angular-dependent NMR frequencies for each residue in the polypeptide as input for structure determination. This follows in a long tradition of high-resolution solid-state NMR multiple-pulse and double- and triple-resonance experiments being applied to molecules of increasing complexity including proteins. Third, an analytical framework is needed that can effectively translate the orientation constraints into protein structures, and this is the subject of this chapter. We focus on determining the backbone structures of proteins labeled with ^{15}N and ^{13}C.

Heteronuclear dipolar couplings and the chemical shift anisotropy (CSA) associated with labeled ^{15}N and ^{13}C sites are the most common sources of angular constraints used to determine the orientations of peptide planes relative to the direction of the applied magnetic field. The detection of the orientation-dependent frequencies associated with these interactions is usually accomplished through a labeled dilute spin site such as ^{15}N and ^{13}C in peptide bonds. The ^{15}N CSA can be correlated with its corresponding ^{1}H–^{15}N dipolar interaction through separated local field experiments. Since the advent of this technique for aligned polymers was nearly 30 years ago [1], significant progress has been made with regard to narrowing spectral lines in the dipolar dimension using experiments such as MREV8 [2], TMREV [3], PISEMA [4], and SAMMY [5], which allows one to detect heteronuclear couplings (e.g. ^{1}H–^{15}N) under conditions of homonuclear (^{1}H–^{1}H) decoupling. Additional experimental measurements can be added including ^{1}H and ^{13}C CSA and ^{1}H–^{13}C dipolar couplings. This involves more sophisticated experiments and isotopic labeling. Examples of such experiments include the heteronuclear correlation experiment (HETCOR) and ^{1}H–^{15}N–^{13}C triple-resonance experiments with doubly labeled peptides [6]. Additional frequency dimensions not only enhance spectral resolution but also serve as sources of orientation restraints as input for structure determination.

Graham A. Webb (ed.), Modern Magnetic Resonance, 517–526.
© 2008 *Springer.*

The anisotropy of nuclear spin interactions results in a unique mapping of structure onto the resonance frequencies observed in NMR spectra of aligned samples. Therefore, it is straightforward to calculate solid-state NMR spectra from the structures of proteins [7–10]. This mapping is clearly demonstrated in the spectra of helices and sheets. For example, "wheel-like" patterns of resonances are observed in two-dimensional PISEMA spectra of helical membrane proteins. We refer to these patterns as polarity index slant angle (PISA) wheels [11,12]. They correspond to helical wheel projections and, hence, provide direct indices of secondary structure and topology; the 3.6 residues per turn periodicity of a α-helix results in an arc of 100° between adjacent residues in a helical wheel and between their resonances in a PISA wheel. The wheel-like pattern reflects the slant angle (tilt) of the helix, and the assignment of the resonances reflects the polarity (rotation) of the helix. When the helix axis is parallel to the direction of the applied magnetic field, all amide sites have the same orientation and all of the resonances overlap. Tilting the helix breaks the symmetry and introduces variations in the orientations of the amide NH bond vectors relative to the field. This is manifested as dispersions in the chemical shift and dipolar coupling frequencies. Since nearly all transmembrane helices are tilted with respect to the bilayer normal, the combination of the tilt and the 17° difference between the principal element of the ^{15}N amide chemical shift tensor and the NH bond vector makes it possible to resolve many resonances in two-dimensional separated local field spectra of polytopic membrane proteins. Dipolar waves are complementary and represent the periodic wave-like variations of the magnitudes of the dipolar couplings as a function of residue number, in the absence of chemical shift effects [13–15].

The PISA wheels for two different helix rotations (polarities) are identical because the dipolar and chemical shift frequencies reflect only the tilt of the helix axis. However, the spectra differ in their resonance assignments, whose patterns mirror exactly the polarity of the corresponding helical wheel. As a result, the PISA wheel patterns in experimental spectra can be used to assist the assignment process [16]. NMR spectra of selectively labeled samples are routinely used to assign resonances to types of amino acids; however, in this application they provide additional information. Using only ^{15}N labels and two-dimensional spectra, we have been able to assign the spectra of coat proteins in filamentous bacteriophages that have 40–45 residues in aligned helices [17–19], which is equivalent to three transmembrane helices. Further, the method can be readily extended to three-dimensional spectra if additional resolution is needed. The full application of "shotgun" NMR (named for the "spread" of labeled sites in the sequence and on the PISA wheel target) where the assignment and structure determination processes are performed in parallel, rather than sequentially, yields both complete resonance assignments and unique protein structures from the NMR data [16–20]. Inevitably, there will be some resonances that cannot be assigned with the shotgun approach. However, some elements of the mapping of structure onto the spectra assist in establishing unambiguous assignments in regions of non-periodic structures. For example, we found in the case of Pf1 coat protein that the N-terminal "double hook" structure has resonances that fall in a regular but not helical wheel pattern; they could be assigned with the assistance of a few selectively labeled samples and by eliminating possibilities established for other sites [18,19].

In the most general approach to structure determination of aligned samples, all types of secondary and tertiary structure can be handled with equal facility [21]. It is necessary to measure two or more frequencies for each residue of a protein in order to determine the orientation of a peptide plane. Once the orientations of all of the individual peptide planes are determined experimentally, then the planes are assembled into a complete protein structure because they are all related to the common axis defined by the direction of the applied magnetic field [7]. Side-chain orientations can be determined in a similar manner [22]. A key feature of this approach is that experimental determinations are made relative to an external non-molecular axis; therefore, the effects of errors and uncertainties in tensors and bond-lengths do not accumulate. Previous determinations of protein structures by solid-state NMR relied on orientation constraints derived from the frequencies of independently assigned resonances [16–20, 22–25].

In practice, we apply four complementary methods of interpretation to the solid-state NMR data: PISA wheels [11,12], Dipolar waves [13], Structural Fitting [26], and Direct Structural Calculation [16,21]. With partial or complete assignment information derived from the applications of PISA wheel and Dipolar waves to the helical residues and spin-exchange and triple-resonance experiments to linker and terminal segments, it is possible to perform "structural fitting" to the resonances in experimental PISEMA spectra [26]. Structural fitting is an alternative to structure calculations directly from the frequencies of individual resonances [7,21] and the related strategies being developed independently by Cross and co-workers [27,28], and Nielsen and co-workers [8,9]. With assignments, the structural fitting algorithm is able to identify minor structural variations such as kinks and bends in helices [15,17,20] and is equally capable of determining irregular structures in linker and terminal regions of membrane proteins.

A Spherical-Basis Treatment of Experimental Angular Constraints for Protein Structure Determination

A formulation for the backbone conformations in terms of the Cartesian basis, widely used in solution NMR for structure determination, is not very efficient for the structure calculations in NMR of aligned samples where the angular information is directly contained in the experimental observables. Therefore, there is a need for an alternative framework, which would treat these constraints in an angular basis without involving the Cartesian basis. Since the ultimate goal is to be able to calculate the protein structure directly from its solid-state NMR spectrum in an *ab initio* fashion, it is, therefore, important to determine the minimum number of experimental angular constraints that are necessary to determine the complete structure of a protein with atomic resolution.

We choose the irreducible spherical basis of rank 1 to relate the protein structure to its multidimensional solid-state NMR spectrum. Rank-1 irreducible basis can be easily converted back to the Cartesian *xyz* space, and its mapping onto the second-rank NMR observables can be implemented by constructing the relevant quadratic forms in this basis. Such a formulation utilizes much faster vector-matrix multiplications and, therefore, greatly reduces the time required to explicitly calculate the trigonometric functions involved in the analytical expressions for these observables.

Formulation of NMR Observables as Quadratic Forms

The molecular frame (MF) associated with an individual peptide plane is depicted in Figure 1. Here the x-axis is chosen along the NH bond, and the z-axis is perpendicular to the plane running through the N–H and C′N bonds (which would coincide with the ideal peptide plane). In terms of the orientation of the magnetic field relative to the MF given by the angles α and β, the solid-state NMR observables such as ^{15}N CSA and ^{1}H–^{15}N dipolar coupling can be written as:

$$\nu(^{15}N) = \sigma_{11}\sin^2\beta\sin^2(\alpha-\gamma) + \sigma_{22}\cos^2\beta + \sigma_{33}\sin^2\beta\cos^2(\alpha-\gamma) \tag{1a}$$

$$\nu(^{1}\mathrm{H} - {}^{15}\mathrm{N}) = \pm\chi\,\frac{3\sin^2\beta\cos^2\alpha - 1}{2} \tag{1b}$$

Here $\gamma = 17$–20° is the angle between the NH bond and the σ_{33} axis of ^{15}N CSA, and the dipolar coupling constant is given by: $\chi \equiv \dfrac{\gamma_N\gamma_H\hbar}{r^3_{N-H}}$.

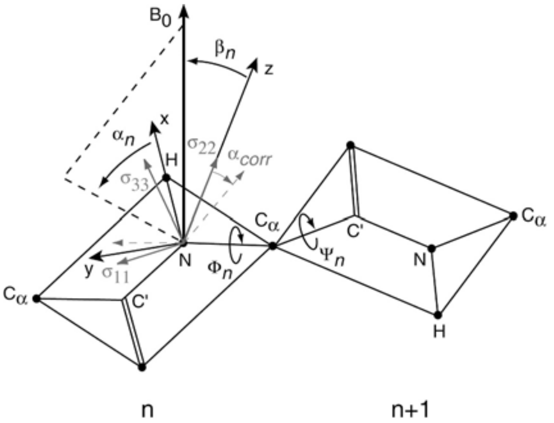

Fig. 1. Choice for the MF and the orientation of the CSA tensor relative to the peptide plane. Dashed arrows show the small tilt of the CSA frame away from the peptide plane given by the angle α_{corr}.

In the present formulation, instead of calculating the sine and cosine functions explicitly we invoke the irreducible spherical basis of rank 1. In the spherical basis, the above expressions for the frequencies can be rewritten in a unified manner as a more compact quadratic form.

$$\nu = \mathbf{Y}(\beta,\alpha)\left[\mathbf{D}(\Omega_{\mathrm{MP}})\,\mathbf{M}\,\mathbf{D}^{+}(\Omega_{\mathrm{MP}})\right]\mathbf{Y}^{+}(\beta,\alpha) \tag{2}$$

Here the Wigner matrix $\mathbf{D}(\Omega_{\mathrm{MP}})$ describes the transformation from the MF to the principal axis system of each tensor, $\mathbf{M}$ is the corresponding interaction matrix, and the superscript "+" denotes the Hermitian conjugate. The row vector of unnormalized spherical harmonics $\mathbf{Y}(\beta,\alpha)$ is given by the following combination of the trigonometric functions:

$$\mathbf{Y}(\beta,\alpha) = \left(-\frac{\sin\beta}{\sqrt{2}}e^{i\alpha}\ \ \cos\beta\ \ \frac{\sin\beta}{\sqrt{2}}e^{-i\alpha}\right) \tag{3}$$

and the rank-1 Wigner matrix is given by [29]:

$$\mathbf{D}(\Omega) \equiv \mathbf{D}(\alpha,\beta,\gamma) = \begin{pmatrix} e^{-i\alpha}\dfrac{1+\cos\beta}{2}e^{-i\gamma} & -e^{-i\alpha}\dfrac{\sin\beta}{\sqrt{2}} & e^{-i\alpha}\dfrac{1-\cos\beta}{2}e^{i\gamma} \\ \dfrac{\sin\beta}{\sqrt{2}}e^{-i\gamma} & \cos\beta & -\dfrac{\sin\beta}{\sqrt{2}}e^{i\gamma} \\ e^{i\alpha}\dfrac{1-\cos\beta}{2}e^{-i\gamma} & e^{i\alpha}\dfrac{\sin\beta}{\sqrt{2}} & e^{i\alpha}\dfrac{1+\cos\beta}{2}e^{i\gamma} \end{pmatrix} \tag{4}$$

For any CSA, the interaction matrix **M** is expressed via the principal components σ_{11}, σ_{22}, and σ_{33} as ($\sigma_{33} > \sigma_{22} > \sigma_{11}$):

$$\mathbf{M} = \begin{pmatrix} \dfrac{\sigma_{11} + \sigma_{22}}{2} & 0 & \dfrac{\sigma_{22} - \sigma_{11}}{2} \\ 0 & \sigma_{33} & 0 \\ \dfrac{\sigma_{22} - \sigma_{11}}{2} & 0 & \dfrac{\sigma_{11} + \sigma_{22}}{2} \end{pmatrix} \tag{5}$$

For ^{15}N CSA the Euler angles for the transformation are given by: $\Omega_{\mathrm{MP}}^{(15\mathrm{N})} = (\gamma, \pi/2, \pi/2 + \alpha_{\mathrm{corr}})$. If the σ_{11} and σ_{33} principal axes lie in the peptide plane, $\alpha_{\mathrm{corr}} = 0$, and Equation (1a) holds rigorously. However, there is evidence that the ^{15}N CSA tensor is slightly tilted off the peptide plane, for which $\alpha_{\mathrm{corr}} = 10 - 25°$ [30–34]. For the orientation of the ^{1}H CSA frame [35], one has: $\Omega_{\mathrm{MP}}^{(1\mathrm{H})} = (-\pi/2, -\pi/2, \pi/2)$.

For the dipolar interactions, the interaction matrix assumes a simple diagonal form:

$$\mathbf{M} = \chi \begin{pmatrix} -1/2 & 0 & 0 \\ 0 & 1 & 0 \\ 0 & 0 & -1/2 \end{pmatrix} \tag{6}$$

For the ^{1}H–^{15}N dipolar coupling the Euler angles for the corresponding transformation are given by: $\Omega_{\mathrm{MP}}^{(1\mathrm{H}-15\mathrm{N})} = (0, \pi/2, 0)$.

The overall matrix in the square brackets in Equation (2) needs to be calculated only once, and the protein chain geometry is contained in the spherical harmonics, $\mathbf{Y}(\beta,\alpha)$. The latter vary throughout the backbone via the recurrence relation:

$$\mathbf{Y}(\beta_{n+1}, \alpha_{n+1}) = \mathbf{Y}(\beta_n, \alpha_n)\mathbf{P}(\Phi_n, \Psi_n) \tag{7}$$

The propagator matrix $\mathbf{P}(\Phi_n,\Psi_n)$ is given in terms of the product of two Wigner rotation matrices as [26]:

$$\begin{aligned} \mathbf{P}(\Phi_n, \Psi_n) = {} & \mathbf{D}(\alpha_{\mathrm{NC}_\alpha}, \Phi_n, \gamma_{\mathrm{tetra}}) \\ & \times \mathbf{D}(0, -\Psi_n - \pi, \gamma_{\mathrm{C}_\alpha \mathrm{C}}) \end{aligned} \tag{8}$$

In geometric terms, $\mathbf{P}(\Phi_n, \Psi_n)$ brings the MF associated with the n'th peptide plane into coincidence with the MF of the following residue, $(n + 1)$, as illustrated in Figure 1. The first Euler angle in the first Wigner matrix of Equation (8) is the angle between the y-axis of the MF and the N–C$_\alpha$ bond of the n'th plane, $\alpha_{\mathrm{NC}\alpha} = 151.8°$; the third Euler angle γ_{tetra} in the first Wigner matrix is the tetrahedral angle (typically 110–112° in real proteins instead of $\gamma_{\mathrm{ideal}} = 109.47°$); finally, the third Euler angle in the second Wigner matrix is the angle between the C$_\alpha$–C bond and the y-axis of the MF of the $(n + 1)$'th plane, $\gamma_{\mathrm{C}\alpha\mathrm{C}} = 34.9°$. The numerical values for the bond angles reflect the geometry of a standard peptide plane [36] and are assumed to be constant, regardless of the residue type or position in the sequence.

The situation for ^{1}H$_\alpha$–^{13}C$_\alpha$ dipolar couplings is slightly more complicated since the transformation from the MF associated with the preceding peptide plane involves an additional rotation about one torsion angle, Φ. This yields:

$$\mathbf{D}(\Omega_{\mathrm{MP}}^{(\mathrm{CH})}) = \mathbf{D}(\alpha_{\mathrm{NC}_\alpha}, \Phi - \rho, \pi/2 - \gamma_{\mathrm{ideal}})\mathbf{D}(0, -\pi/2, 0) \tag{9}$$

The angle ρ describes the Fischer projection angle for the C$_\alpha$–H$_\alpha$ bond. For the ideal sp^3 geometry it is equal to $\rho = 60°$. If γ_{tetra} is different from its ideal value, but the NC$_\alpha$H$_\alpha$ angle is still ideal, ρ is given by:

$$\rho = \arccos\left[-\frac{\tan(\gamma_{\mathrm{tetra}}/2)}{\tan \gamma_{\mathrm{ideal}}}\right] \tag{10}$$

Formal Geometric Properties of Polypeptide Chains

Using the matrix for the chain propagator, a useful closed-form expression can be obtained that gives the periodicity of various secondary structures directly as a function of the torsion angles. By explicitly finding the eigenvalues of matrix $\mathbf{P}(\Phi, \Psi)$, Equation (8), we obtain:

$$\begin{aligned} p &= \frac{2\pi}{\arccos[(1 - \cos \gamma_{\mathrm{tetra}})(1 - \cos(\Phi + \Psi))/2 - 1]} \\ &= \frac{2\pi}{\arccos[-(1 + 2\cos(\Phi + \Psi))/3]} \end{aligned} \tag{11}$$

The above equality is exact in the case of ideal $sp2$ hybridization of the bonds in a peptide plane, for which $\alpha_{\mathrm{NC}\alpha} = 150°$ and $\gamma_{\mathrm{C}\alpha\mathrm{C}} = 30°$. Two notable examples include the α-helix and β sheet. Substituting $\Phi = -65°$, $\Psi = -40°$ we get $p = 3.63$ for the α-helix. For the antiparallel β-sheet one has: $\Phi = -139°$, $\Psi = 135°$, and $p = 2.05$. Equation (11) shows that the periodicity is in fact a function of the sum of torsion angles Φ and Ψ. This demonstrates the potential of working in the irreducible basis of rotations. More closed-form expressions can be obtained for the β-turns, NH-bond tilt angles with respect to the helix axis, etc.

To calculate the three-dimensional protein structure, we obtain the position of any given bond relative to the laboratory frame of the N-th peptide plane, given by x, y and z, using the orientation of this bond relative to the MF given by x_{MOL}, y_{MOL}, and z_{MOL}. This is accomplished by summing over a series of rotational transformations from the laboratory to the MF given by the Euler angles Ω_{LM}:

$$\vec{v}^{\,+} = \left[\sum_{n=1}^{N} \mathbf{D}(\Omega_{\mathrm{LM}}^{(n)})\right] \vec{u}_{\mathrm{MOL}}^{\,+} \tag{12}$$

The coordinates relative to the molecular and laboratory frames, respectively, are given in the spherical basis as:

$$\vec{v} = \left(-\frac{x+iy}{\sqrt{2}}, z, \frac{x-iy}{\sqrt{2}}\right) \tag{13a}$$

$$\vec{u}_{\mathrm{MOL}} = \left(-\frac{x_{\mathrm{MOL}}+iy_{\mathrm{MOL}}}{\sqrt{2}}, z_{\mathrm{MOL}}, \frac{x_{\mathrm{MOL}}-iy_{\mathrm{MOL}}}{\sqrt{2}}\right) \tag{13b}$$

The transformations $\mathbf{D}(\Omega_{\mathrm{LM}})$ are decomposed in terms of the product of operators $\mathbf{P}(\Phi_j,\Psi_j)$ as:

$$\vec{v}^{\,+} = \mathbf{D}(\Omega_{\mathrm{LM}}^{(1)})\left[\mathbf{1} + \sum_{n=1}^{N-1}\prod_{j=1}^{n}\mathbf{P}(\Phi_j\Psi_j)\right]\vec{u}_{\mathrm{MOL}}^{\,+} \tag{14}$$

where $\Omega_{\mathrm{LM}}{}^{(1)}$ gives the orientation of the first peptide plane relative to the laboratory frame. Finally, the transformation back to the Cartesian basis can be readily accomplished using Equation (13a).

The Structural Fitting Algorithm

The structural fitting algorithm uses Equations (2)–(9) to determine the torsion angles Φ and Ψ between the NMR frequencies corresponding to two adjacent residues. Only absolute values for the dipolar couplings are used. Since the $^{1}\mathrm{H}_{\alpha}$–$^{13}\mathrm{C}_{\alpha}$ coupling for the preceding residue already contains one torsion angle, Equation (9), it can be used as an additional constraint to find the orientation of the peptide plane containing the following residue. The direction of the H_{α}–C_{α} bond is chiral, which greatly reduces the number of possible solutions for the peptide plane orientations (hence for the torsion angles Φ and Ψ) from considering just the ^{15}N CSA and ^{1}H–^{15}N dipolar couplings. The torsion angles are determined by minimizing the difference between the quadratic forms and the experimental data points which could be accomplished using a simplex algorithm. To be able to pick up different solutions, the starting values for Φ and Ψ are randomized. The simplex search also allows one to treat the experimental uncertainty of the data in a straightforward way, i.e. the search stops if the deviation from the data falls within a pre-defined error in Hz. Once a pair of Φ and Ψ angles satisfying the experimental restraints is found, the search continues onto the next residue pair. If no solution is found, the algorithm can go backwards and try to search for another solution for the previous residue(s). Additional restraints could be easily included in the search such as the Ramachandran angle restraints and specific residue-type information (CSA tensor values, bond angles, etc). The structural fitting algorithm was coded in MATLAB, which provides a fast and convenient tool for matrix calculations.

Examples of Structural Fitting

Structural Fitting to Two-Dimensional Spectra

In the case of relatively simple helical domains of proteins, a converged set of solutions can be found using only two spectral dimensions, e.g. ^{15}N CSA and ^{1}H–^{15}N dipolar couplings, by imposing Ramachandran angle restraints for the torsion angles. The angles are allowed to vary within a certain limited range relative to their ideal values, i.e. $\Phi = -65^{\circ}$, $\Psi = -40^{\circ}$. The fitting of the experimental two-dimensional spectra of Pf1 bacteriophage [18,19] is shown in Figure 2. The data in Figure 2(A–B) correspond to two temperatures, 30 °C and 0 °C, respectively, and it is known that the protein changes structure between these temperatures. As can be seen, the solid-state NMR spectra show significant differences at 30 °C and 0 °C, and the fitting of the spectra can provide the structural basis for this temperature transition. The fit of each spectrum was performed by assuming an experimental uncertainty of about 1 ppm or 76 Hz in each dimension, and the Φ and Ψ angles were allowed to vary within 20°. Slight variations in the CSA tensor values were also allowed to satisfy the Ramachandran restraints and the experimental data. The calculated protein structures are shown in Figure 2(C). The RMSD of the structural fit in each case is less than 2 Å. Only the average structures are shown.

Structural Fitting to Three-Dimensional Spectra

For proteins with more complex tertiary structures, additional frequency dimensions are needed. Figure 3A shows a simulated two-dimensional PISEMA spectrum of a membrane-associated version of protein G, using the torsion angles generated from its structure (pdb ID 2GB1, shown in blue) and assuming a fixed peptide plane geometry. This immunoglobulin-binding peptide is immobilized and aligned with the lipid bilayer when it is modified by N-terminal myristoylation [10]. The two-dimensional PISEMA spectrum has been back calculated, but does not yield a converged set of structures when subject to the procedures described above. By contrast, after including a third-frequency dimension, namely $^{1}\mathrm{H}_{\alpha}$–$^{13}\mathrm{C}_{\alpha}$ dipolar couplings, to form the simulated three-dimensional spectrum shown in Figure 3B, the RMSD of the calculated structures is reduced to about 3 Å (100 structural solutions are shown). This demonstrates that the $^{1}\mathrm{H}_{\alpha}$–$^{13}\mathrm{C}_{\alpha}$ dipolar

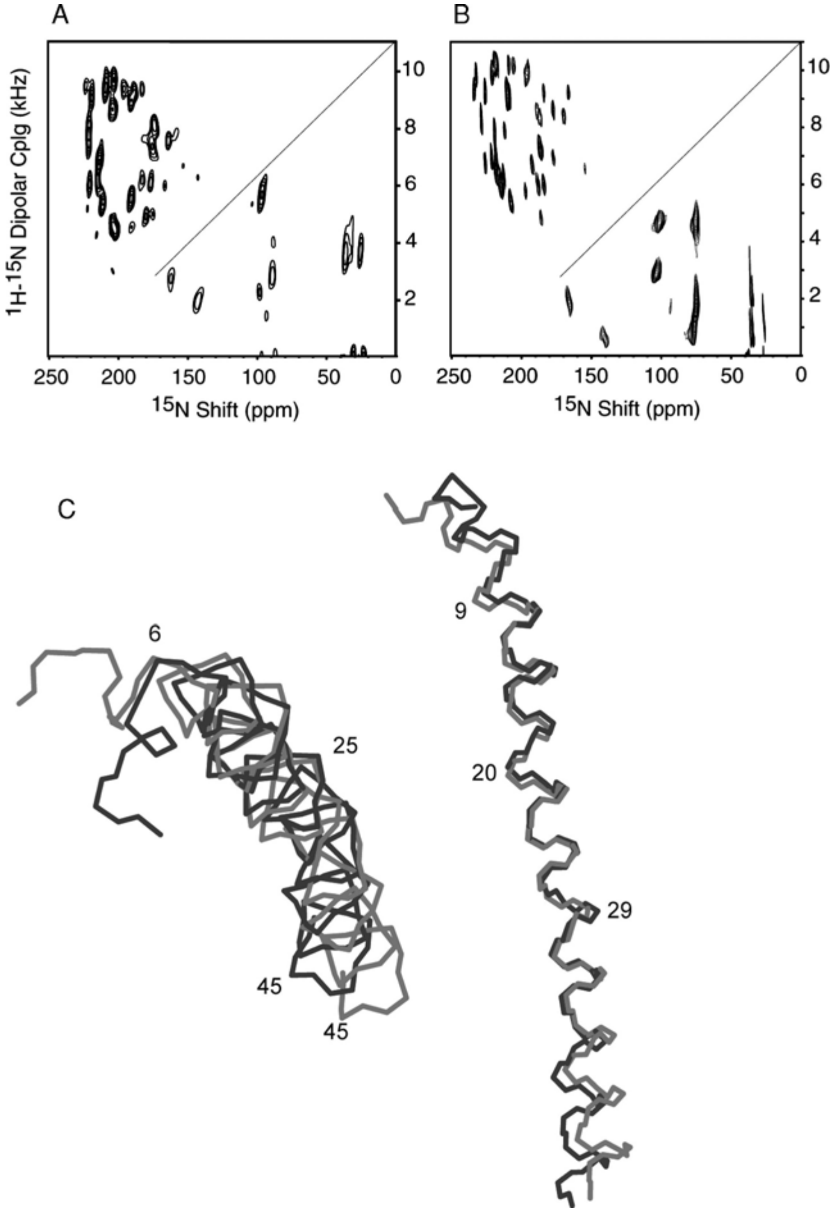

Fig. 2. Structural fitting of the experimental solid-state NMR spectra of magnetically oriented Pf1 bacteriophage. (A) Spectrum at 30 °C. (B) Spectrum at 0 °C. (C) High- (red line) and low- (blue line) temperature structures obtained from the fitting of the spectra. (See also Plate 57 on page XLI in the Color Plate Section.)

interaction is a powerful orientation constraint. Moreover, as shown in Figure 3C, mathematically unique solutions can be obtained if one assumes that the CSA frame is slightly tilted away from the peptide plane ($\alpha_{\text{corr}} = 25°$). In geometrical terms, this tilt introduces an additional chirality, and thus entirely eliminates the local orientational ambiguities associated with the even parity of the CSA and dipolar interactions.

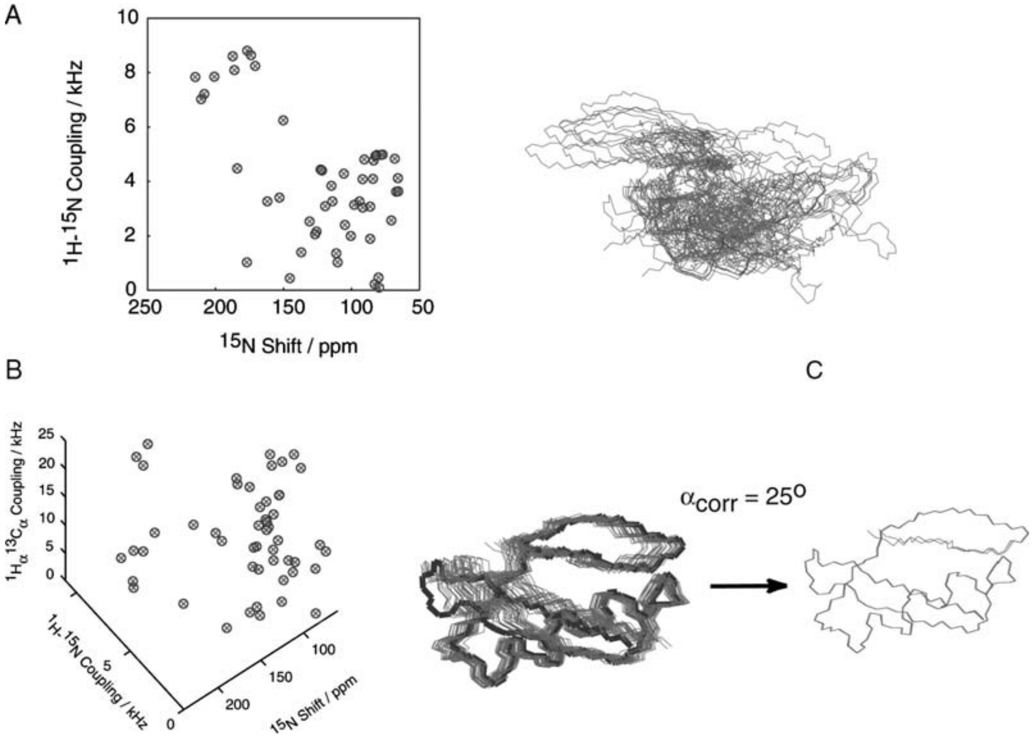

Fig. 3. Structural fitting of calculated solid-state NMR spectra of protein G simulated using the torsion angles generated from its pdb file and assuming constant peptide plane geometry. (A) Fitting of simulated spectra in two dimensions. No converged set of solutions. (B) Fitting of simulated spectra in three dimensions including $^1H_\alpha$–$^{13}C_\alpha$ dipolar interactions. Converged set of solutions (3 Å RMSD). (C) Fitting of simulated spectra in three dimensions assuming an additional tilt of the ^{15}N CSA frame, $\alpha_{corr} = 25°$. Unique solution is obtained in this case. (See also Plate 58 on page XLII in the Color Plate Section.)

Figure 4 shows the simulated three-dimensional spectrum for a two-helix hairpin extracted from the X-ray structure of bacteriorhodopsin (pdb ID 1C3W). Unlike in Figure 3, the spectrum was simulated entirely from the pdb coordinates, which include slight variations in the peptide plane geometry. The spectrum was back calculated using the structural fitting with the standard (fixed) peptide plane geometry. The RMSD of the structural fit shown in Figure 4 is about 3 Å. If one invokes the tilt ($\alpha_{corr} = 25°$) of the tensor relative to the peptide plane, then the RMSD is reduced to 1.5 Å. The success of such a structural fit can be regarded as a demonstration of feasibility for extending solid-state NMR to polytopic membrane proteins, for example GPCRs with seven transmembrane helices.

KcsA is well suited for its role as a principal test system for developing experimental and calculation methods to deal with the non-helical regions of membrane proteins. About 30% of its residues are in linker regions. It is relatively small and readily expressed and purified. Its crystal structure has been determined with atomic resolution [37,38]; therefore, it presents an excellent opportunity to compare the structure of a membrane protein in a crystal to that of the same protein in its native environment of fully hydrated lipid bilayers as in bicelles samples [39,40]. With the addition of the $^1H_\alpha$–$^{13}C_\alpha$ dipolar coupling frequencies, it is possible to determine the structure of all regions of the protein. This is illustrated in Figure 5 for the 12-residue loop encompassing residues 75–86 of KcsA. For clarity, the simulated data in "unflipped" bicelles are shown in two-dimensional spectra for the complete structure (Figure 5A) and for the loop region (Figure 5B). The structure of these residues in the crystal structure 1BL8 is shown in black in two views (Figure 5 C–D). The structure determined by structural fitting to the simulated NMR data is shown in gray, overlapped with the crystal structure. The RMSD between these two structures is 2.3 Å, which was accomplished with no constraints on the dihedral angles in the computer program.

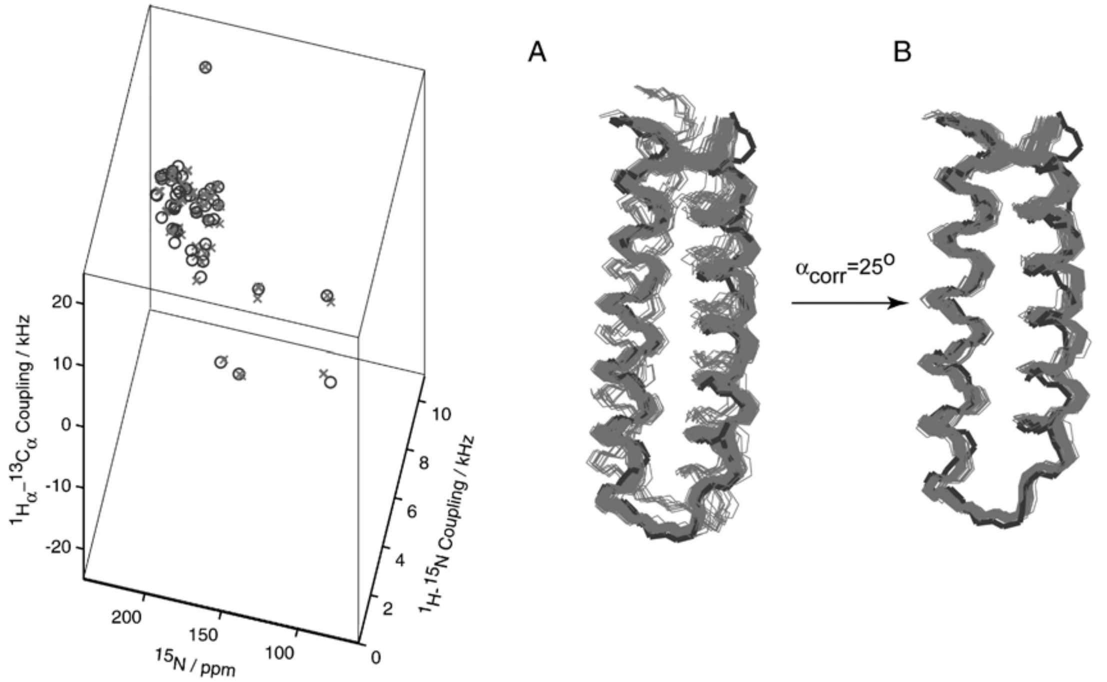

Fig. 4. Structural fitting of calculated three-dimensional solid-state NMR spectra for a two-helical fragment of bacteriorhodopsin simulated using its pdb coordinates. (A) Converged set of solutions with an RMSD of 3 Å. (B) Improved convergence using an additional tilt of the ^{15}N CSA frame ($\alpha_{\text{corr}} = 25°$), RMSD = 1.5Å. (See also Plate 59 on page XLII in the Color Plate Section.)

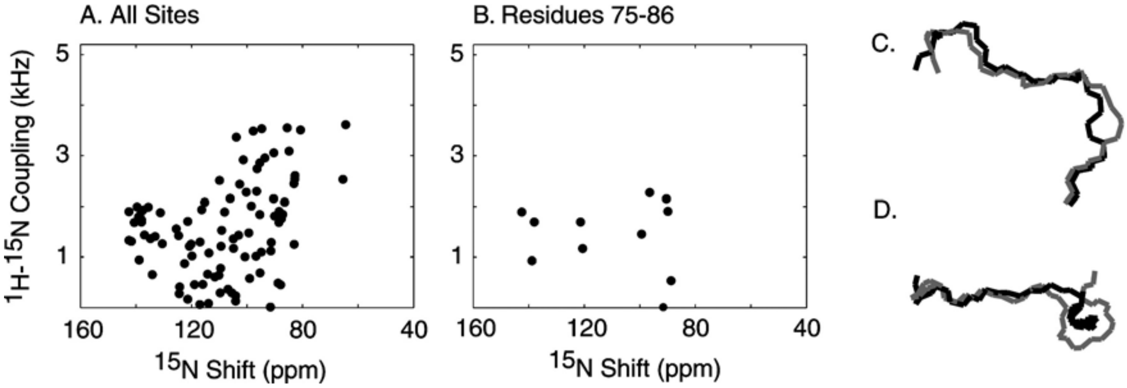

Fig. 5. (A) Simulated 2D PISEMA spectrum of uniformly ^{15}N labeled KcsA in “unflipped” bicelles. (B) Subset of resonances from residues 75–86. (C) and (D) Two views of the structure of residues 75–86. Black is from the crystal structure (1BL8) and gray is from structural fitting of the simulated three-dimensional NMR data including ^{1}H$_\alpha$–^{13}C$_\alpha$ dipolar interactions.

Conclusions

It is possible to calculate the three-dimensional backbone structure of a protein directly from its multidimensional solid-state NMR spectrum. A compact formulation for the solid-state NMR observables in an angular basis is described in this chapter. Analytical expressions for backbone conformations are obtained. The fitting method allows one to include the uncertainties in the experimental data as well as variations in the CSA components. The structural fitting program is fully automated and directly gives three-dimensional protein backbones as the final output. Unlike with earlier programs, there is no need to deal with degenerate solutions for the α and β angles, nor with complicated analytic expressions since the sines and cosines need not be calculated explicitly when the spherical basis is used.

The most important aspect of the structural fitting is the ability to calculate the structure of a protein from its NMR spectrum and to obtain a convergent set of solutions. For single-helix proteins and peptides, two-dimensional experiments can be sufficient since the Ramachandran angles Φ and Ψ occupy a relatively narrow window. To be able to obtain structures of proteins having arbitrary topology, additional frequency dimensions are necessary. The development of the relevant experiments is under way. Simulations can provide useful insights into the possibilities for the complete structure determination of membrane proteins from the angular-dependent solid-state NMR measurements. Since the solid-state NMR spectrum of an aligned protein can be readily simulated from its known structure, basic concepts of the structural fitting can be tested. It has been shown that without using any restrictions on the torsion angles, the combination of ^{15}N CSA, ^{1}H–^{15}N dipolar couplings, and ^{1}H$_\alpha$–^{13}C$_\alpha$ interactions yields a convergent set of structural solutions. An additional tilt of the ^{15}N CSA tensor frame may dramatically improve the convergence of the structural fit. More accurate measurements of the ^{15}N CSA tensor are needed to verify the presence of this tilt before it can be used with confidence in the actual structure calculations. To be able to account for the deviations from ideal peptide geometry, additional measurements may be necessary including C–N couplings and ^{1}H and ^{13}C CSA. It is also possible to further extend this method to the fitting of side-chain conformations, which could be done similarly to the treatment of ^{1}H$_\alpha$–^{13}C$_\alpha$ interactions.

The torsion angles are considered here to be the only degrees of freedom and the spectrum is fit in a sequential manner. Simulated annealing [41] of the solid-state NMR spectrum is also possible, and is perhaps more advantageous than the sequential fitting. Work is currently in progress with regard to implementing simulated annealing protocols in the structural fitting of solid-state NMR spectra of membrane proteins. The spherical-basis formulation presented herein has the potential to be used in torsion-dynamics simulations. With multiple ways of calculating protein structures from the orientation dependent frequencies measured on aligned samples, solid-state NMR has the potential to contribute to the structural biology of proteins in supramolecular assemblies.

Acknowledgements

This research is supported by Grants RO1EB002169 and RO1EB001966 from the National Institutes of Health, and utilized the Biomedical Technology Resource for NMR Molecular Imaging of Proteins supported by Grant P41EB002031.

References

1. Opella SJ, Waugh JS. J. Chem. Phys. 1977;66:4919–4924.
2. Rhim WK, Elleman DD, Vaughan RW. J. Chem. Phys. 1973; 59:3740–3749.
3. Hohwy M, Jaroniec CP, Reif B, Rienstra CM, Griffin RG. J. Am. Chem. Soc. 2000;122:3218–3219.
4. Wu CH, Ramamoorthy A, Opella SJ. J. Magn. Reson. 1994; A109:270–272.
5. Nevzorov AA, Opella SJ. J. Magn. Reson. 2003;164:182–186.
6. Gu ZT, Opella SJ. J. Magn. Reson. 1999;140:340–346.
7. Opella SJ, Stewart PL, Methods Enzymol. 1989;176:242–275.
8. Vosegaard T, Nielsen NC. J. Biomol. NMR 2002;22:225–247.
9. Bak M, Schultz R, Vosegaard T, Nielsen NC. J. Magn. Reson. 2002;154:28–45.
10. Mesleh MF, Valentine KG, Opella SJ, Louis JM, Gronenborn AM. J. Biomol. NMR 2003;25:55–61.
11. Marassi FM, Opella SJ. J. Magn. Reson. 2000;144:150–155.
12. Wang J, Denny J, Tian C, Kim S, Mo Y, Kovacs F, Song Z, Nishimura K, Gan Z, Fu R, Quine JR, Cross TA. J. Magn. Reson. 2000;144:162–167.
13. Mesleh MF, Veglia G, DeSilva TM, Marassi FM, Opella SJ. J. Am. Chem. Soc. 2002;124:4206–4207.
14. Mesleh MF, Opella SJ. J. Magn. Reson. 2003;163:288–299.
15. Mesleh MF, Lee S, Veglia G, Thiriot DS, Marassi FM, Opella SJ. J. Am. Chem. Soc. 2003;125:8928–8935.
16. Marassi FM, Opella SJ. Prot. Sci. 2003;12:403–411.
17. Zeri AC, Mesleh MF, Nevzorov AA, Opella SJ. Proc. Natl. Acad. Sci. U.S.A. 2003;100:6458–6463.
18. Thiriot DS, Nevzorov AA, Zagyanskiy L, Wu CH, Opella SJ. J. Mol. Biol. 2004;341:869–879.
19. Thiriot DS, Nevzorov AA, Opella SJ. Protein Sci. 2005;14:1064–1067.
20. Park SH, Mrse AA, Nevzorov AA, Mesleh MF, Oblatt-Montal M, Montal M, Opella SJ. J. Mol. Biol. 2003;333:409–424.
21. Opella SJ, Stewart PL, Valentine KG. Quart. Rev. Biophys. 1987;19:7–49.

22. Cross TA, Opella SJ. J. Mol. Biol. 1985;182:367–381.
23. Ketchem RR, Hu W, Cross TA. Science 1993;261:1457–1460.
24. Opella SJ, Marassi FM, Gesell JJ, Valente AP, Kim Y, Oblatt-Montal M, Montal M. Nat. Struct. Biol. 1999;6:374–379.
25. Wang J, Kim S, Kovacs F, Cross TA. Prot. Sci. 2001;10:2241–2250.
26. Nevzorov AA, Opella SJ. J. Magn. Reson. 2003;160:33–39.
27. Bertram R, Asbury T, Fabiola F, Quine JR, Cross TA, Chapman MS. J. Magn. Reson. 2003;163:300–309.
28. Quine JR, Cross TA, Chapman MS, Bertram R. Bull. Math. Biol. 2004;66:1705–1730.
29. Arfken G. Mathematical Methods for Physicists, 3rd ed. Academic Press: Orlando, 1985.
30. Mai W, Hu W, Wang C, Cross TA. Protein Sci. 1993;2:532–542.
31. Lee DK, Wittebort RJ, Ramamoorthy A. J. Am. Chem. Soc. 1998;120:8868–8874.
32. Cornilescu G, Bax A. J. Am. Chem. Soc. 2000;122:10143–10154.
33. Brender JR, Taylor DM, Ramamoorthy A. J. Am. Chem. Soc. 2001;123:914–922.
34. Chekmenev EY, Zhang Q, Waddell KW, Mashuta MS, Wittebort RJ. J. Am. Chem. Soc. 2004;126:379–384.
35. Wu CH, Ramamoorthy A, Gierash LM, Opella SJ. J. Am. Chem. Soc. 1995;117:6148–6149.
36. Creighton TE, Proteins: Structure and Molecular Properties, 2nd ed. Freeman: New York, 1993.
37. Doyle DA, Cabral JM, Pfuetzner RA, Kuo AL, Gulbis JM, Cohen SL, Chait BT, MacKinnon R. Science 1998;280:69–77.
38. Zhou Y, Morais-Cabral JH, Kaufman A, MacKinnon R. Nature 2001;414:43–48.
39. Vold RR, Prosser RS. J. Magn. Reson. 1996; B113:267–271.
40. DeAngelis AA, Nevzorov AA, Park SH, Howell SC, Mrse AA, Opella SJ. J. Am. Chem. Soc. 2004;126:15340–15341.
41. Brünger A. X-PLOR, Version 3.1. A System for X-ray Crystallography and NMR. Yale University Press: New Haven, CT, 1992.

Determining Protein 3D Structure by Magic Angle Spinning NMR

Ovidiu C. Andronesi, Henrike Heise, and Marc Baldus
Department for NMR-Based Structural Biology, Max Planck Institute for Biophysical Chemistry, 37077 Göttingen, Germany

Introduction

Solid-state NMR has long been utilized to study biomolecular structure and dynamics ranging from applications to protein complexes [1] and nucleotides [2] to membrane proteins [3–5] and protein fibrils [6]. In the case of macroscopically oriented membrane peptides, solid-state NMR furthermore has provided structural constraints to assemble three-dimensional (3D) membrane protein structures (see Ref. [7] for a recent review). Under magic angle spinning (MAS) [8], structural investigations were focused for a long time on the determination of local structural parameters. Recently, substantial progress has been made in NMR methodology, instrumentation, and sample preparation that now permits 3D molecular structure determination under MAS from one or a limited set of NMR samples. These approaches will be discussed in the context of this chapter. The interested reader is also referred to a series of recent review articles [9–11].

Sample Preparation and Methodology

Unless molecular size or mobility allow for the direct use of ^{1}H evolution and detection periods, a high degree of ^{13}C and ^{15}N isotope labeling is mandatory if molecular structure is to be investigated under MAS conditions. Depending on the application of interest, chemical synthesis, cell free, or bacterial expression systems are employed. In the case of protein expression in cell cultures, uniform isotope labeling is easily achieved using uniformly labeled starting media such as uniformly ^{13}C-labeled glucose and $^{15}NH_4Cl$. More advanced labeling patterns can be generated if specifically labeled precursors, amino acids, or growth media are supplied. In the case of membrane proteins, the uniformly labeled protein of interest is subsequently reconstituted into model membranes which can be studied in liposomes, possibly macroscopically oriented on solid glass [12] or polymer supports [13].

In a first stage, sequential resonance assignments must be obtained which are usually generated using a combination of (^{13}C,^{15}N) [14] and (^{13}C,^{13}C) [15] correlation methods. Since backbone chemical shifts provide a sensitive means of local dihedral angle constraints, these resonance assignments provide an easy and powerful instrument to assess polypeptide secondary structure. In addition to the conformation-dependent chemical shift ($\Delta\delta$, Figure 1), distances (encoded as dipolar couplings d) can be used to refine the local polypeptide conformation in the solid state. For example, the backbone (H_α, H_N) distance between sequential residues strongly correlates with the backbone dihedral angle ψ and can easily be detected during an NHHC correlation experiment [16]. Likewise, the sequential ^{15}N–^{15}N distance can be used to refine the backbone topology [17]. Information about the backbone conformation in the solid state can also be obtained by correlating two anisotropic interactions such as the chemical shift anisotropy (CSA) or the dipolar coupling in a two-dimensional (2D) experiment. Here, one exploits the defined orientation of dipolar tensors along the internuclear vector and empirical knowledge regarding the orientation of CSA tensors. These anisotropic interactions can be recoupled during the evolution and/or detection period of a homonuclear or heteronuclear 2D correlation experiment by appropriate radio frequency schemes. The resulting cross-peak pattern is characteristic for the relative orientation of the two anisotropic interactions [18]. In uniformly labeled peptides, correlations between NH/NH [19] and NH/CH [20] dipolar tensors have been used for backbone dihedral angle determinations. Alternatively, relative tensor orientation may be encoded in the evolution of a double-quantum (2Q) two-spin state under the effect of two anisotropic interactions. Applications correlating CH/NH [21] and CN/CN [22,23] dipolar couplings or sequential carbonyl CSAs [24] have been demonstrated. In a 2Q correlation experiment under CN dipolar dephasing, the signal amplitude can directly report on the backbone torsion angle and can hence conveniently be applied in multiply labeled polypeptides [14]. In the case of severe spectral overlap, extensions to three spectral dimensions are possible [25,26]. All these experiments can help to establish local distance or torsion angle constraints that can be supplemented in a conventional structure calculation.

The 3D structure is finally determined if medium- and long-range distance constraints can be derived from MAS

Graham A. Webb (ed.), Modern Magnetic Resonance, 527–530.
© 2008 *Springer.*

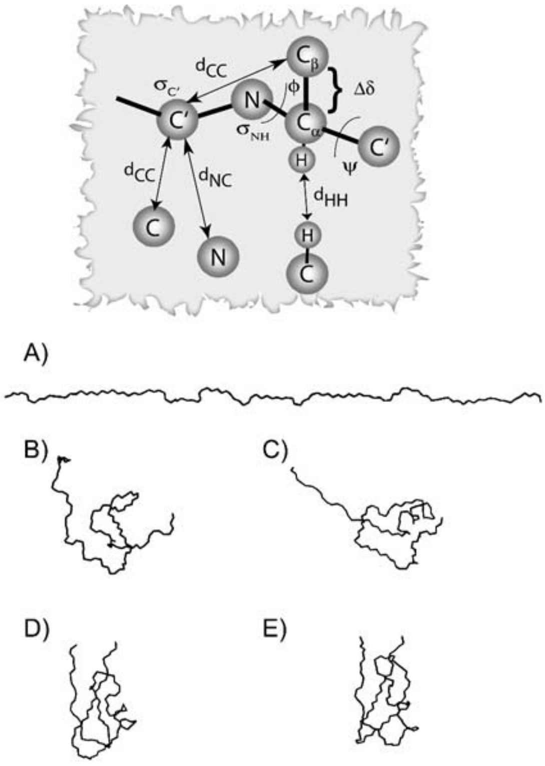

Fig. 1. Structural parameters to be detected in the context of MAS NMR: In addition to the isotropic chemical shift (which can be used to define conformation-dependent chemical shifts $\Delta\delta$) CSA interactions (such as σ_{C}, σ_{NH}) can be used to establish dihedral or orientational constraints. In addition, distances (d) determine local and overall molecular 3D structure and can be measured by a variety of experimental methods. The combination of these parameters can be used to construct a 3D molecular structure from a single, or a small set of isotope-labeled molecules under MAS conditions. In (A)–(E), different stages of structure calculation routine based on MAS NMR data are exemplified for the case of KTX (see Ref. [30] and text for further details).

NMR data. In the case of uniformly labeled molecules, the spin systems dynamics are dominated by one-bond (^{13}C,^{13}C) and (^{13}C,^{15}N) interactions. If spectral dispersion is favorable, selective (^{13}C,^{15}N) or (^{13}C,^{13}C) distance measurements can be performed in uniformly labeled peptides [27] and proteins [28]. Moreover, isotope labeling schemes can be applied that lead to a partial dilution of the coupled (^{13}C,^{15}N) spin network. As a result, the influence of one-bond interactions is reduced and local (^{13}C,^{13}C) dipolar couplings can become comparable to medium- and long-range interactions [29]. In addition, proton–proton distance restraints that provide the most abundant source of inter-residue interactions in the range up to 4 Å can be probed. For this purpose, indirect detection schemes are available that encode proton–proton polarization transfer in high-resolution ^{15}N and ^{13}C evolution and detection periods [16]. Finally, orientational constraints can be established if anisotropic interactions such as NH CSA or dipolar tensor components are measured in macroscopically oriented systems. Under fast MAS, tailored RF schemes that [13] recouple anisotropic interactions can be used.

The details of a subsequent structure calculation are exemplified for the 38 amino acid polypeptide kaliotoxin (KTX): First, an extended conformer is created (Figure 1A) and subjected to simulated annealing protocol consisting of several stages. While in Figure 1B, three disulfide bonds are used as sole structural constraints, we have incorporated in (Figure 1C) 65 dihedral angle restraints. As a result, secondary structure is formed but the overall 3D fold remains undefined. For this reason, proton–proton distance restraints are supplemented which relate to unequivocal spectral assignments in the first (Figure 1D) or second round (Figure 1E) of structure calculations. An ensemble of conformers with the lowest energy is finally reported. Further details of the structure calculation in the case of KTX are given in Ref. [30].

Applications

Probably, the first molecular structure determined purely by MAS-based NMR was reported by Terao and coworkers [27] and relates to the dipeptide glycyl isoleucine (Figure 2A). In this case, chemical shift selective transfer methods were applied to determine (^{13}C,^{13}C) distance constraints. Three years later, the molecular structure of the tripeptide *N*-formyl-L-Met-L-Leu-L-Phe-OH (Figure 2B) was published [31]. Here, NMR experiments were conducted on a uniformly (^{13}C,^{15}N)-labeled sample. Three differently (^{13}C,^{15}N)-labeled protein samples were employed to determine the 3D fold of a microcrystalline sample of the α-spectrin SH3 domain (1M8M, [29,32]) and of the 11-amino acid stretch of transthyretin (TTR(105–115), [33]). The corresponding structures are shown in Figure 2C and D.

Using indirectly detected proton–proton interactions, our group has recently [30] determined the 3D structure of a uniformly (^{13}C,^{15}N)-labeled version of KTX that strongly inhibits potassium ion channels. No attempts were made to obtain microcrystalline material. Proton–proton distance restraints and dihedral angle constraints derived from conformation-dependent chemical shifts resulted in 3D structure with an average backbone RMSD of 0.81 Å. The 10 conformers with the lowest energy are shown in Figure 2E (PDB entry: 1XSW). Structures

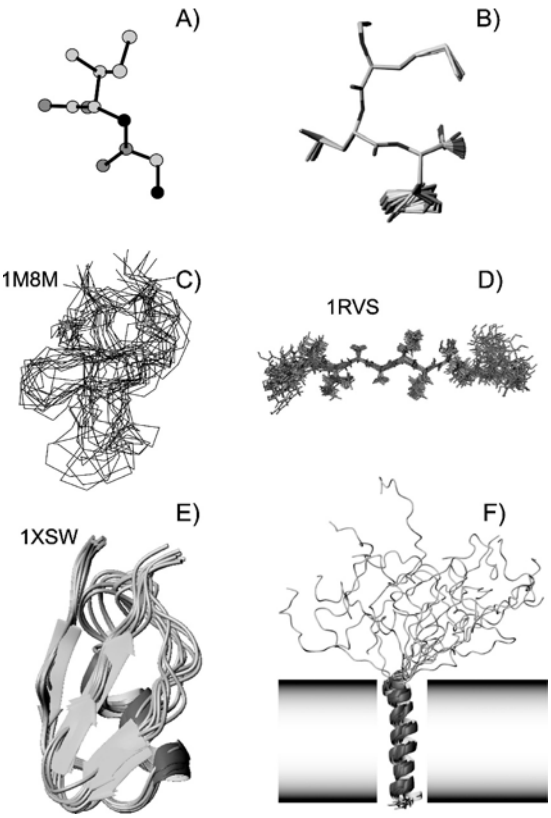

Fig. 2. Structures of polypeptides determined thus far by MAS solid-state NMR. The PDB file numbers are given when available. (A) The dipeptide glycyl isoleucine. (B) The tripeptide *N*-formyl-L-Met-L-Leu-L-Phe-OH. (C) The α-spectrin SH3 domain. (D) An 11-amino acid stretch of transthyretin (TTR(105–115)), (E) Kaliotoxin (KTX) and (F) phospholamban in lipid bilayers. (See also Plate 60 on page XLIII in the Color Plate Section.)

with a different fold display significantly higher overall energies. Refinement of these structures using software routines originally developed for the solution state is ongoing.

In the case of phospholamban (PLN, Figure 2F), the topology in lipid membranes was determined using a combination of dipolar and scalar polarization schemes [34]. The latter techniques permit one to also probe dynamic disorder in cytoplasmic segments of the protein. In principle, the supramolecular arrangement of partially immobilized macromolecules can be probed by similar experiments, provided that the monomer conformation is known [35,36] or if isotope labeling schemes are used that permit discriminating between intra- and intermolecular transfer [37].

Conclusions

MAS-based solid-state NMR has recently made considerable progress in the structural study of polypeptides and proteins. In many of these investigations, spectral assignments provide the basis for further investigations of 3D structure or dynamics. Recent applications include protein aggregates and fibrils, membrane-interacting peptides and proteins and the analysis of protein–protein interactions. Advances regarding sample preparation (e.g. including modular labeling, *in vitro* expression, and intein technology [38]) and improvements in NMR hardware instrumentation could open up new areas of solid-state NMR research such as the investigation of large protein–protein complexes or the complete 3D characterization of larger membrane proteins.

Clearly, additional efforts to streamline 3D protein structure determination by MAS NMR are necessary. Novel concepts may make extensive use of the rapidly increasing power of bioinformatics and computational chemistry. Already, general approaches have appeared to predict 3D structure from a limited set of solution-state NMR data. In parallel, the ability to relate molecular structure to NMR detectable parameters by *ab initio* quantum chemistry calculations and DFT approaches is improving. These techniques already have empowered novel material science applications of solid-state NMR and will greatly expand the use of MAS solid-state NMR for the study of polypeptides and proteins. Complementary to crystallographic methods and solution-state NMR techniques, MAS solid-state NMR methods hence provide a powerful tool to study protein structure, folding, and function under biologically relevant conditions.

Acknowledgments

We thank our group members and collaborators for their contributions to research described here. Financial support by the DFG and Volkswagen foundation is gratefully acknowledged. HH would like to thank the Fonds der Chemischen Industrie for a Liebig fellowship.

References

1. McDowell LM, Schaefer J. Curr. Opin. Struct. Biol. 1996;6:624.
2. Alam TM, Drobny GP. Chem. Rev. 1991;91:1545.
3. Saito H, Ando I. Annu. Rep. NMR Spectrosc. 1989;21:210.
4. de Groot HJM. Curr. Opin. Struct. Biol. 2000;10:593.
5. Thompson LK. Curr. Opin. Struct. Biol. 2002;12:661.
6. Tycko R. Biochemistry. 2003;42:3151.
7. Opella SJ, Marassi FM. Chem. Rev. 2004;104:3587.
8. Andrew ER, Bradbury A, Eades RG. Nature. 1958;182:1659.
9. Luca S, Heise H, Baldus M. Acc. Chem. Res. 2003;36:858.

10. Nielsen NC, Malmendal A, Vosegaard T. Mol. Membr. Biol. 2004;21:129.
11. Straus SK. Philos. Trans. R. Soc. Lond. Ser. B-Biol. Sci. 2004;359:997.
12. Glaubitz C, Watts A. J. Magn. Reson. 1998;130:305.
13. Andronesi OC, Pfeifer JR, Al-Momani L, Özdirekcan S, Rijkers DTS, Angerstein B, Luca S, Koert U, Killian JA, Baldus M. J. Biomol. NMR. 2004;30:253.
14. Baldus M. Prog. Nucl. Magn. Reson. Spectrosc. 2002;41:1.
15. Seidel K, Lange A, Becker S, Hughes CE, Heise H, Baldus M. Phys. Chem. Chem. Phys. 2004;6:5090.
16. Lange A, Seidel K, Verdier L, Luca S, Baldus M. J. Am. Chem. Soc. 2003;125:12640.
17. Cross TA, Frey MH, Opella SJ. J. Am. Chem. Soc. 1983;105:7471.
18. Ishii Y, Terao T, Kainosho M. Chem. Phys. Lett. 1996;256:133.
19. Reif B, Hohwy M, Jaroniec CP, Rienstra CM, Griffin RG. J. Magn. Reson. 2000;145:132.
20. Rienstra CM, Hohwy M, Mueller LJ, Jaroniec CP, Reif B, Griffin RG, J. Am. Chem. Soc. 2002;124:11908.
21. Hong M, Gross JD, Griffin RG. J. Phys. Chem. B. 1997;101:5869.
22. Costa PR, Gross JD, Hong M, Griffin RG. Chem. Phys. Lett. 1997;280:95.
23. Feng X, Verdegem PJE, Lee YK, Sandstrom D, Eden M, BoveeGeurts P, deGrip WJ, Lugtenburg J, de Groot HJM, Levitt MH. J. Am. Chem. Soc. 1997;119:6853.
24. Blanco FJ, Tycko R. J. Magn. Reson. 2001;149:131.
25. Ladizhansky V, Jaroniec CP, Diehl A, Oschkinat H, Griffin RG. J. Am. Chem. Soc. 2003;125:6827.
26. Heise H, Seidel K, Etzkorn M, Becker S, Baldus M. J. Magn. Reson. 2005;173:64.
27. Nomura K, Takegoshi K, Terao T, Uchida K, Kainosho M. J. Am. Chem. Soc. 1999;121:4064.
28. Sonnenberg L, Luca S, Baldus M. J. Magn. Reson. 2004;166:100.
29. Castellani F, van Rossum B, Diehl A, Schubert M, Rehbein K, Oschkinat H. Nature. 2002;420:98.
30. Lange A, Becker S, Seidel K, Giller K, Pongs O, Baldus M. Angew. Chem.-Int. Edit. 2005;44:2089.
31. Rienstra CM, Tucker-Kellogg L, Jaroniec CP, Hohwy M, Reif B, McMahon MT, Tidor B, Lozano-Perez T, Griffin RG. Proc. Natl. Acad. Sci. U.S.A. 2002;99:10260.
32. Castellani F, van Rossum BJ, Diehl A, Rehbein K, Oschkinat H. Biochemistry. 2003;42:11476.
33. Jaroniec CP, MacPhee CE, Bajaj VS, McMahon MT, Dobson CM, Griffin RG. Proc. Natl. Acad. Sci. U.S.A. 2004;101:711.
34. Andronesi OC, Becker S, Seidel K, Heise H, Young HS, Baldus M. J. Am. Chem. Soc. 2005;127:12965.
35. de Boer I, Matysik J, Amakawa M, Yagai S, Tamiaki H, Holzwarth AR, de Groot HJM. J. Am. Chem. Soc. 2003;125:13374.
36. Tycko R, Ishii Y. J. Am. Chem. Soc. 2003;125:6606.
37. Etzkorn M, Böckmann A, Lange A, Baldus M. J. Am. Chem. Soc. 2004;126:14746.
38. Staunton D, Owen J, Campbell ID, Acc. Chem. Res. 2003;36:207.

^{19}F NMR Study of *b*-Type Haemoproteins

Yasuhiko Yamamoto[1], Satoshi Nagao[1], and Akihiro Suzuki[2]
[1]*Department of Chemistry, University of Tsukuba, Tsukuba 305-8571, Japan; and*
[2]*Department of Materials Engineering, Nagaoka National College of Technology, Nagaoka 940-8532, Japan*

Abbreviations: Mb, Myoglobin; 3,7-DF, 13,17-*bis* (2-carboxylatoethyl)-3,7-difluoro-2, 8, 12, 18-tetra-methyl-porphyrinatoiron(III); Mb(3,7-DF), Mb reconstituted with 3,7-DF; NOE, Nuclear Overhauser effect; NOESY, Nuclear Overhauser effect correlated spectroscopy.

Introduction

Because of their ubiquitousness and abundance as well as their many unique physicochemical properties arising primarily from the presence of a haem group, usually an iron–protoporphyrin IX complex (protohaem; structure shown in Fig. 1A), haemoproteins are the most studied group of proteins. Haem is the prosthetic group of a number of proteins possessing remarkably different functions, *i.e.* oxygen storage or transport proteins (myoglobin (Mb) or haemoglobin), electron transfer proteins (cytochromes, etc.), oxidase enzymes (peroxidase, catalase, etc.), and gas sensor proteins (Fix L [1], Haem AT [2], etc.). Since these proteins contain the same prosthetic group at their active sites, their functional differences are thought to arise from differences in the way that they interact with the haem.

Myoglobin, a typical haemoprotein, is a monomeric protein with a molecular weight of about 17 kDa, and a single haem is embedded in its protein moiety, which consists of eight helices (A–H) (Fig. 1B). The haem iron is bound to the protein matrix through the proximal His residue (His F8), the 8th residue in the F helix (Fig. 1C). In general, the haem iron in Mb is either in the ferrous or ferric state. The numbers of electrons in the 3d orbitals of ferrous and ferric iron are six and five, respectively. Hence, the total spin quantum number S is an integer and half-integer for ferrous and ferric irons, respectively. Depending upon the degree of spin pairing of electrons in the 3d orbitals, ferrous haem iron can have 4, 2, or 0 unpaired electrons, corresponding to $S = 2$, 1, or 0, respectively, and for ferric haem iron $S = 5/2$, $3/2$, or $1/2$ with 5, 3, or 1 unpaired electron, respectively. Based on an octahedral ligand field, the energy levels of the five 3d orbitals of the iron atom are split into two groups in such a way that the levels of the d_{z^2} and $d_{x^2-y^2}$ orbitals are higher than those of the other three orbitals, d_{xy}, d_{yz}, and d_{xz} (Fig. 2). The spin state of a haemoprotein depends on the chemical nature of the ligand. For ferrous haem iron, the deoxy (no ligand) form is penta-coordinated with a high-spin configuration, $S = 2$, and the oxy (O_2) or carbonmonoxy (CO) form possesses a low-spin configuration, $S = 0$. On the other hand, the binding of ligands of relatively weak field strength such as H_2O to ferric haem iron gives high-spin state $S = 5/2$ (met-aquo form), and low-spin state $S = 1/2$ is achieved with a strong ligand such as CN^- (met-cyano form). There are some ferric haemoproteins, such as the met-hydroxyl (OH^-), -azido (N_3^-), and -imidazole forms, that exhibit values of magnetic susceptibility between those of the high- and low-spin states. Each of these proteins was found to be a mixture of the high- and low-spin states [3].

Taking advantage of unpaired electron(s), resonances arising from nuclei located in close proximity to the paramagnetic center exhibit hyperfine shifts and hence are observed outside of the diamagnetic envelope in which signals due to the protein overlap severely. Hyperfine shifted signals are extremely sensitive to structural properties of molecules, as has been fully described elsewhere [4–17], and NMR studies on paramagnetic haemoproteins have provided a wealth of information about the detailed haem–protein interaction, which could provide valuable insights into the structure–function relationships of these proteins [9,10,12,15]. Although ^{1}H NMR is a powerful tool for characterizing the haem–protein interaction at the active sites of proteins, characterization of physiologically relevant forms of a protein, *e.g.* in the cases of Mb, oxy Mb, and deoxy Mb, is often hampered by the resolution of the signals. In order to overcome the problem of signal overlapping, the use of ^{19}F NMR for the study of the structure–function relationships of haemoproteins has been proposed [18–25]. Owing to the absence of interfering background signals, the introduction of fluorine atom(s) into the side-chain(s) of haem facilitates the observation of their signals in various oxidation, spin, and ligation states of haemoproteins, which are expected to serve as potential spectroscopic probes for characterizing the haem–protein interaction [20,21,23–25]. The van der Waals radius of a fluorine atom is only slightly larger than that of a hydrogen atom, *i.e.* 0.135 and 0.11 nm for fluorine and hydrogen, respectively, and hence the introduction of fluorine atom(s) into a molecule of interest is expected to

Graham A. Webb (ed.), Modern Magnetic Resonance, 531–538.
© 2008 *Springer.*

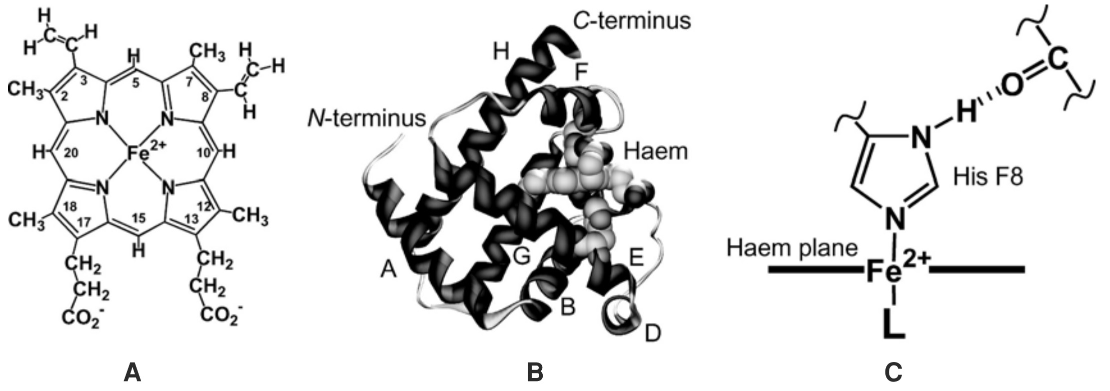

Fig. 1. (A) Structure and numbering system for the iron–protoporphyrin IX complex (protohaem) and (B) the X-ray structure of Mb from skeletal muscle of sperm whale, *Physter catodon* [55] (The haem and protein are illustrated as space-filling and ribbon models, respectively. The eight helices are labeled A–H.), and (C) the structure of the ligand-binding site in Mb. The iron is coordinated to proximal His (His F8) and an exogenous ligand (L).

perturb its structure only slightly. On the other hand, care should be taken regarding large perturbations in the electronic structure of the molecule, which may be caused by ^{19}F labeling due to its high electronegativity. ^{19}F is a 100% abundant nucleus with nuclear spin $I = 1/2$ and, because of a relatively high gyromagnetic ratio, ^{19}F NMR is about 83% as sensitive as ^{1}H NMR. Furthermore, a high gyromagnetic ratio of ^{19}F facilitates the observation of dipolar connectivity between ^{19}F nuclei or between ^{19}F and ^{1}H nuclei, which provides valuable information about molecular structure. In addition, because of the wider spectral range for ^{19}F NMR than ^{1}H NMR, the former is considerably more sensitive to the local magnetic environment than the latter. Therefore, it is more likely that individual signals will be resolved on ^{19}F NMR and the signals will in turn be a sensitive probe for detailed characterization of proteins at the atomic level.

^{19}F Labeling of *b*-Type Haemoproteins Using Reconstitution

A technique called reconstitution, combined with the use of fluorinated haems [20,26–31], can be used to introduce fluorine atom(s) selectively and specifically into the active sites of *b*-type haemoproteins. Hence, this ^{19}F labeling is completely different from that utilized for the ordinary proteins [32–36]. As schematically illustrated in Fig. 3, haem (protohaem; structure shown in Fig. 1A) was extracted from a native protein according to the method previously described [37]. Since there is no covalent bond between the haem and the protein moiety in a *b*-type haemoprotein, partial unfolding of the protein at pH < 2.7 promotes haem release. The released haem is extracted from the apo-protein solution using 2-butanone. Then the apo-protein solution is exhaustively dialyzed against water to remove 2-butanone distributed. The apo-protein solution is adjusted to neutral pH and then a stoichiometric amount of the haem of interest is mixed in to reconstitute the holo-protein. Using the reconstitution technique, desired haems and even non-haem compounds can be incorporated into *b*-type haemoproteins.

Aiming at incorporation into Mb, several fluorinated haems have been synthesized (Fig. 4) [18,21,26–31]. The initial attempts to incorporate fluorine atom(s) into haem were focused on the substitution of a perfluoromethyl group, CF_3, for the haem methyl group [26–30]. The introduction of a strongly electron-withdrawing

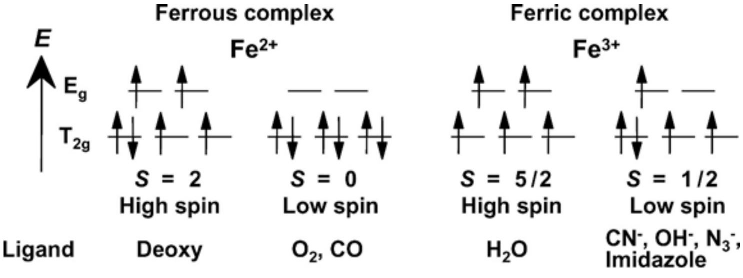

Fig. 2. Haem iron oxidation/spin states of Mb.

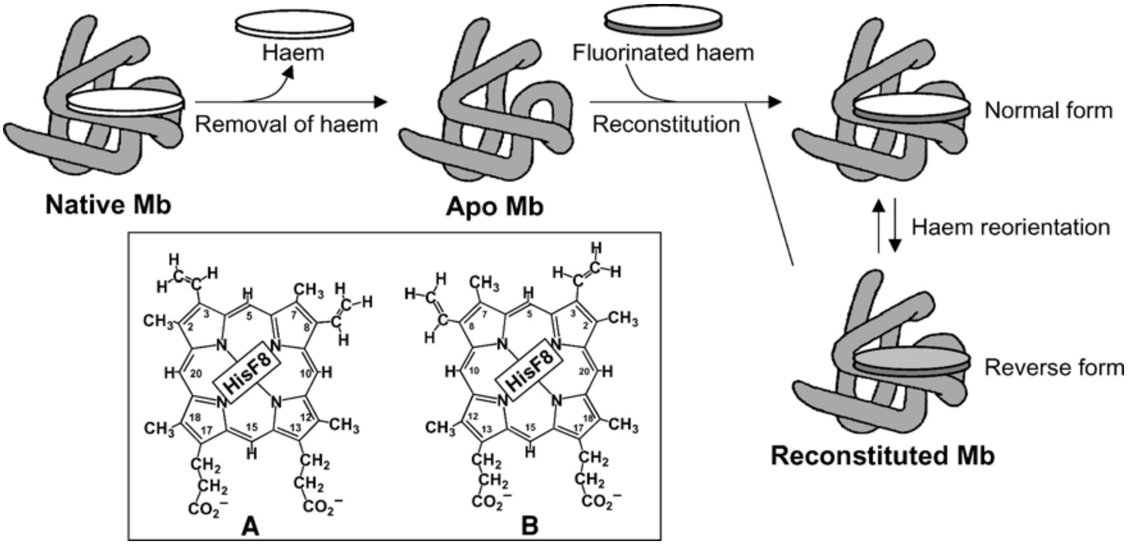

Fig. 3. Schematic representation of the ^{19}F labeling of haem peripheral side-chain(s) in a *b*-type haemoprotein using the reconstitution technique. Two possible orientations of haem relative to His F8 are shown in the inset; (A) that found in the crystal structure of sperm whale Mb [55] and (B) that with the haem rotated by 180° about the 5,15-H meso axis from that of (A).

perfluoromethyl group into the porphyrin ring, however, greatly affects the π-system of the haem and has marked effects on the physicochemical properties of haems as well as Mb reconstituted with such fluorinated haems [30,31,38–40]. On the other hand, ring-fluorination of porphyrin is expected to induce relatively small perturbation of the haem electronic structure due to a strong repulsive interaction between electrons in the π orbitals of the fluorine atom and the π-system of the porphyrin ring, and therefore provides a suitable ^{19}F NMR probe for characterization of the haem–protein interactions in proteins [18,20,21,24].

^{19}F NMR *vs.* ^{1}H NMR

^{19}F and ^{1}H NMR spectra of the *bis*-cyano form of 13,17-*bis*(2-carboxyethyl)-3,7-difluoro-2, 8, 12,18-tetramethyl-porphyrinatoiron(III) (3,7-DF; structure shown in Fig. 4C) and Mb reconstituted with 3,7-DF [Mb(3,7-DF)] in

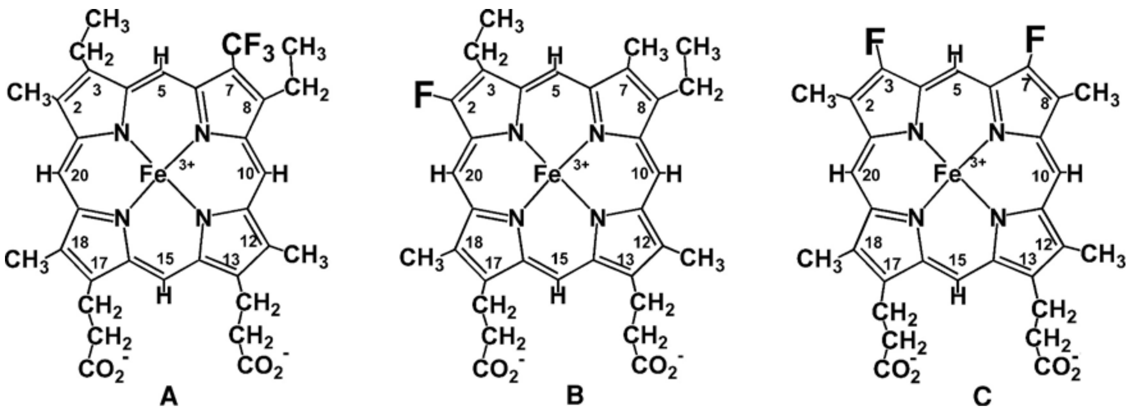

Fig. 4. Structures of (A) 7-PF: 13,17-*bis*(2-carboxylatoethyl)-3,8-diethyl-2,12,18-trimethyl-7-trifluoro-methylporphyrinatoiron(III) [29], (B) 2-MF: 13,17-*bis*(2-carboxylatoethyl)-3,8-diethyl-2-fluoro-7,12,18-trimethylporphyrinatoiron(III) [18], and (C) 3,7-DF:13,17-*bis*(2-carboxylatoethyl)-3,7-difluoro-2,8,12,18-tetramethyl-porphyrinatoiron(III) [20].

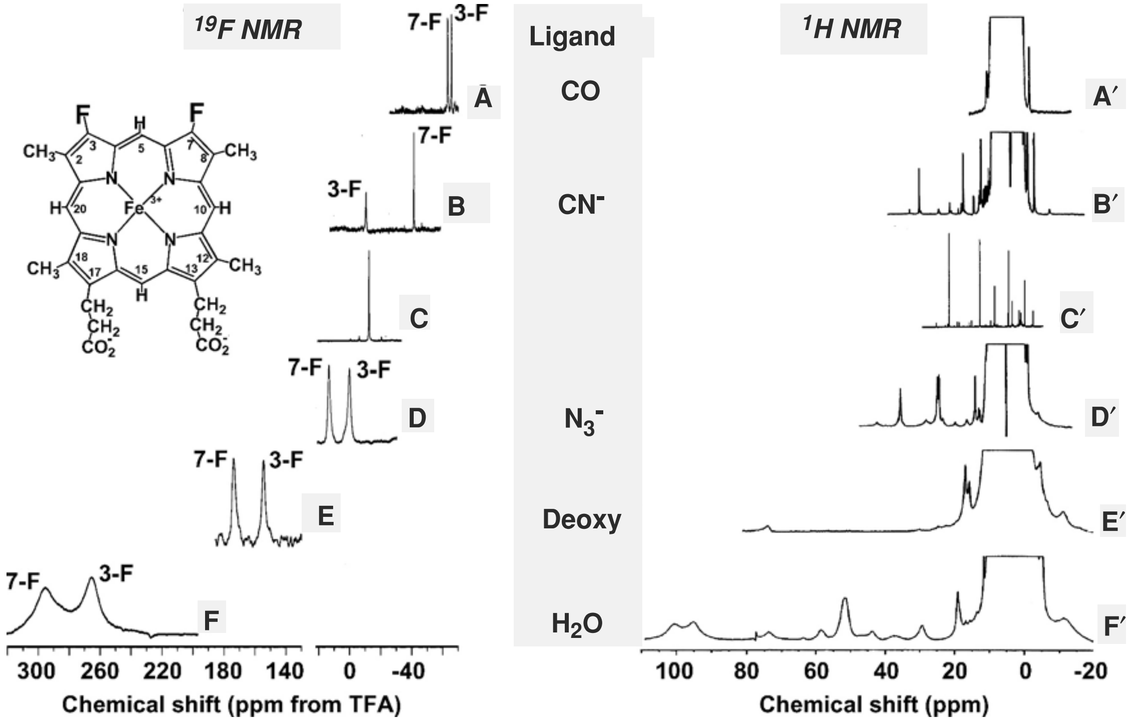

Fig. 5. (A–F) 376 MHz ^{19}FNMR spectra of Mb(3,7-DF) in various oxidation/spin/ligation states and *bis*-cyano 3,7-DF, and (A′–F′) ^{1}H NMR spectra of the corresponding proteins and haem complex. (A, A′) CO Mb, pH 6.15, (B, B′) met-cyano Mb, pH 8.03, (C, C′) *bis*-cyano 3,7-DF, (D, D′) met-azido Mb, pH 7.48, (E, E′) deoxy Mb, pH 7.08, and (F, F′) met-aquo Mb, pH 7.02, at 25 °C. The peak indicated by an asterisk arose from an impurity. The molecular structure of and numbering system for 3,7-DF are indicated in the inset.

various oxidation, spin, and ligation states are compared in Fig. 5.

Bis-cyano 3,7-DF ($S = 1/2$)

As expected from the C_2-symmetric nature of the electronic structure of 3,7-DF, a single ^{19}F NMR signal is observed at -18.04 ppm relative to trifluoroacetic acid (Fig. 5C). The ^{1}H NMR spectrum of *bis*-cyano 3,7-DF is compared with that of *bis*-cyano protohaem in Fig. 6. The C_2-symmetry of the haem electronic structure of 3,7-DF about the 5,15-H meso-proton axis is supported by the observation of only seven ^{1}H NMR signals in the spectrum. The spread of haem methyl proton signals for *bis*-cyano 3,7-DF is larger than that for *bis*-cyano protohaem, indicating that the introduction of fluorine atoms into the porphyrin ring at the 3- and 7-positions increases the differences in unpaired electron density between pyrroles I, II and pyrroles III, IV. The upfield-shifted meso H-5 proton signal of *bis*-cyano 3,7-DF, relative to the corresponding signal of *bis*-cyano protohaem, could also be attributed to the effect of fluorine substitution. Despite these differences, the similarity in the ^{1}H NMR spectral pattern between the two *bis*-cyano haems indicates that the influence of the fluorine substitution on the haem electronic structure is rather small.

Carbonmonoxy Mb ($S = 0$)

The observation of two signals in the ^{19}F NMR spectrum of CO Mb (Fig. 5A) is not due to the presence of haem orientation isomers [41] (see below), because 3,7-DF possesses a twofold rotation axis along the 5,15-H meso-proton axis, but results from the removal of the degeneracy of the magnetic environments of the two fluorine atoms of the haem through the haem–protein interaction. In the ^{1}H NMR spectrum of diamagnetic CO Mb, a methyl proton signal is present in the furthest upfield-shifted region due to the ring-current effect of haem, and this signal has been assigned to the γ-CH_3 proton of Val E11 [42]. The Val

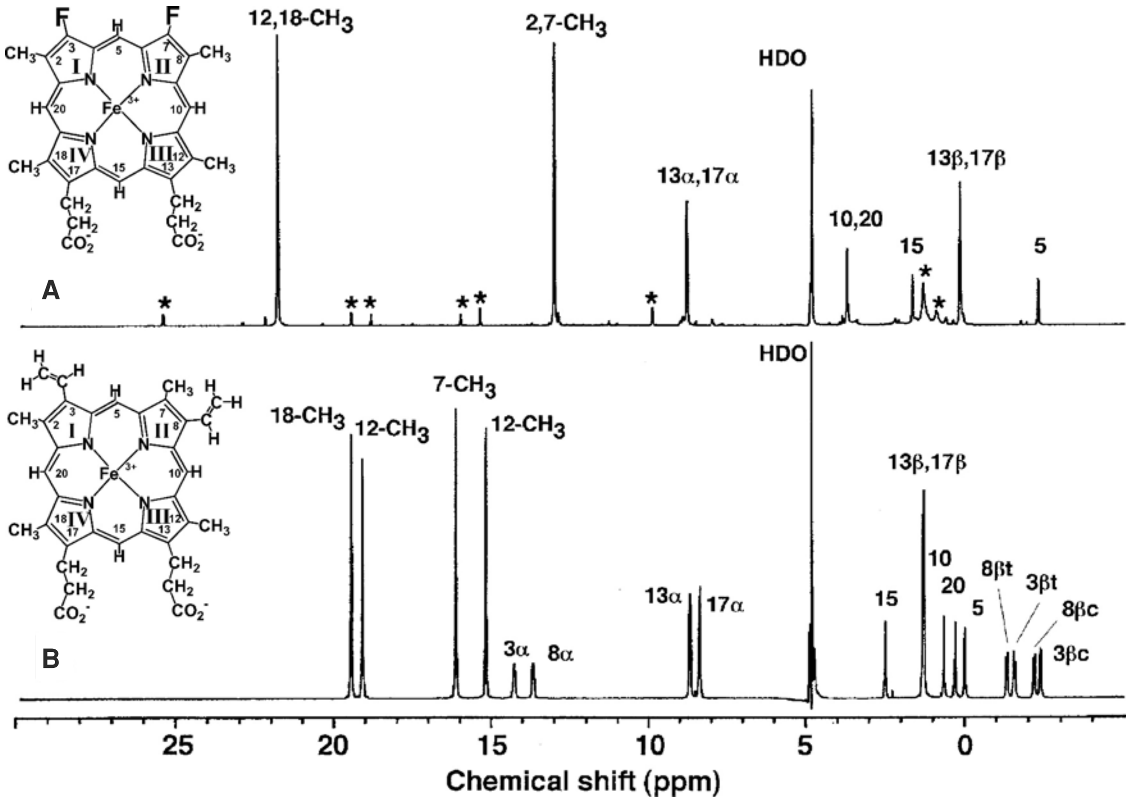

Fig. 6. 400 MHz ^{1}H NMR spectra of (A) *bis*-cyano protohaem and (B) *bis*-cyano 3,7-DF in $^{2}H_2O$ at 25 °C. The signal assignments are indicated in the spectra. The concentration of the haems was about 3 mM and the signals exhibit concentration-dependent shifts. The peak indicated by an asterisk arose from an impurity. The structures of and numbering systems for haems are indicated in the insets.

E11 γ-CH_3 proton signals of the CO forms of Mb(3,7-DF) and native Mb are observed at -2.27 (Fig. 5A′) and -2.31 ppm [42], respectively. The similarity in the Val E11 γ-CH_3 proton shift between the two CO Mbs suggests that their active site structures are highly similar, and hence that the incorporation of 3,7-DF into Mb does not alter the haem–protein interaction in Mb.

Met-cyano Mb ($S = 1/2$)

The separation of the two ^{19}F NMR signals is dramatically increased in the spectrum of met-cyano Mb (Fig. 5B). The assignments of the signals were based on the measurement of ^{1}H–^{19}F Nuclear Overhauser effect (NOE) connectivity (Fig. 7). In the ^{1}H NMR spectrum of met-cyano Mb(3,7-DF) (Fig. 7A), the Ile FG5 δ-CH_3 proton signal is at -3.32 ppm. The corresponding signal of native met-cyano Mb is at -3.46 ppm [43]. The similarity in the shift between the two Mbs also supports the view that the haem–protein interaction is not significantly altered by the introduction of 3,7-DF into Mb. On the other hand, a relatively large shift difference, ~2 ppm, was observed for the γ-CH proton signal of the Ile FG5 residue (the shifts were -7.61 and -9.60 ppm [43] for met-cyano Mb(3,7-DF) and native met-cyano Mb, respectively, under similar experimental conditions). However, a small displacement of the proton relative to the unpaired electron leads to a significant change in the paramagnetic shift, *e.g.* displacement by ~0.01 nm results in a shift change of >4 ppm [44]. Therefore, the shift difference of ~2 ppm could be explained by a small change in the conformation of the Ile FG5 side-chain between the two Mbs. Assuming that the haem–protein interaction in Mb(3,7-DF) is similar to that in native Mb, 3- and 7-F are expected to be located at ~1.11 and ~0.57 nm, respectively, from the Ile FG5 δ-CH_3 proton [45]. Irradiation of the Ile FG5 δ-CH_3 proton signal gave a negative NOE only to

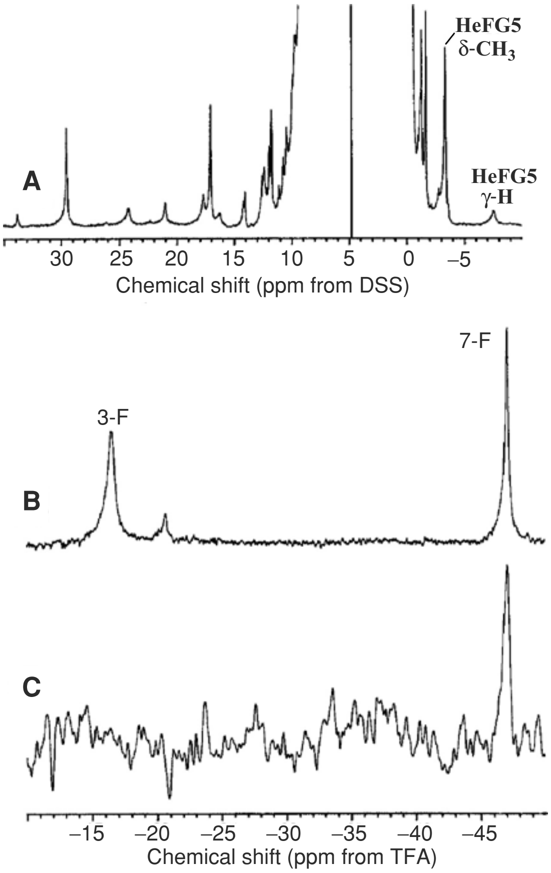

Fig. 7. (A) 400 MHz ^{1}H NMR and (B) 376 MHz ^{19}F NMR spectra of met-cyano Mb(3,7-DF) in ^2H_2O, pH 8.03, at 25 °C, and (C) the NOE difference spectrum resulting from saturation of the Ile FG5 δ-CH_3 proton signal for 100 ms. The assignments of the Ile FG5 γ-CH_3 and δ-CH_3 proton signals are indicated in trace A. The observation of an NOE only for the ^{19}F signal at −47.10 ppm led to the signal assignments shown in trace B (see the text).

the signal resonating at a lower (Fig. 7C). The observed NOE connectivity allowed the unambiguous signal assignments indicated in the spectra. Curie plots, *i.e.* observed shift *vs.* reciprocal of absolute temperature, for the ^{19}F NMR signals of met-cyano Mb(3,7-DF) exhibit straight lines with positive slopes in the temperature range between 5 and 35 °C, with the intercepts of −95.7 and −53.4 ppm for the 3- and 7-F signals, respectively. Although, in principle, the intercepts at $T^{-1} \rightarrow 0$ of the Curie plots reflect the shifts for the corresponding diamagnetic complexes, the measurement in a limited temperature range as well as non-linearity of Curie plots, which is caused by the temperature-dependence of the molecular/electronic structure, often impede determination of diamagnetic shifts from Curie plots [15]. But comparison between the intercepts of the signals for paramagnetic met-cyano Mb and the shifts of the signals in the spectrum of diamagnetic CO Mb (Fig. 5A) allows tentative signal assignments for CO Mb(3,7-DF), as indicated in the spectrum.

Met-azido Mb (mainly $S = 1/2$)

Two broad signals are present in the spectrum of met-azido(3,7-DF) (Fig. 5D). The larger line widths of the signals for met-azido Mb(3,7-DF) than those for low-spin met-cyano Mb(3,7-DF) are attributed to the partial high-spin character of met-azido Mb, where the electron spin relaxation time is relatively large and Curie spin relaxation [46] also occurs. The thermal spin equilibrium [47] in met-azido Mb is manifested in negative slopes of the Curie plots for these signals.

Deoxy Mb ($S = 2$)

The signals in the ^{19}F NMR spectrum of deoxy Mb(3,7-DF) (Fig. 5E) are high frequency-shifted to >200 ppm relative to those of CO Mb(3,7-DF). On the other hand, in the ^{1}H NMR spectrum of deoxy Mb(3,7-DF), the most high frequency-shifted haem methyl proton signal is at 16.61 ppm and this value is comparable to the shift of 16.41 ppm for the resolved haem 12-methyl proton signal in the spectrum of native deoxy Mb [48]. Additionally, the difference in His F8 $N_\delta H$ proton shift between deoxy Mb(3,7-DF) and native deoxy Mb, *i.e.* 73.86 and 77.29 ppm at 25 °C for the former and latter, respectively, may be attributed to an alteration in the hydrogen bonding interaction between this proton and its proton-acceptor (Fig. 1C) [49].

Met-aquo Mb ($S = 5/2$)

The two signals in the ^{19}F NMR spectrum of met-aquo Mb(3,7-DF) are high frequency-shifted to >300 ppm relative to those of CO Mb(3,7-DF), and the line widths are >3000 Hz. These results demonstrate not only the significant effect of the strong paramagnetic contribution, but also the high sensitivity of ^{19}F NMR as to the electronic nature of haem iron. The non-equivalence of the line width between the two signals, *i.e.* 3- (2900 Hz) and 7-F (3200 Hz), arises predominantly from the difference in the contribution of the contact interaction to T_2 relaxation [50].

Haem Disorder

The nature of the molecular recognition between the haem and protein in *b*-type haemoproteins is not sufficiently specific to yield a single orientation of the prosthetic group within the protein matrix [41]. Although their crystal structures have invariably shown that the haem possesses a unique orientation within the protein, a solution NMR study has clearly demonstrated that the haem in these proteins is in two different orientations that differ by 180° rotation of the haem plane, about the 5,15-H *meso*-proton axis, relative to the protein (see the inset in Fig. 3). This phenomenon occurs in virtually almost all native *b*-type haemoproteins and is known as the haem orientation disorder [41,51–54]. The dominant component in Mb exhibits the same haem orientation as that found in the crystal structure, called the normal form; a protein with a reversed haem orientation is called the reverse form. Although the haem orientation disorder in proteins has been studied mainly by ^{1}H NMR spectroscopy [15,41,51–54], characterization of the effect of the haem orientation on the electronic structure of the active site in a physiologically relevant form of a protein is often hampered by the resolution of the signals. Due to the virtues of ^{19}F NMR spectroscopy, the haem orientation disorder in the proteins in various states can be most readily detected and characterized, as reported previously [21].

MbO$_2$ *vs.* MbCO

Characterization of the nature of O_2 and CO binding to respiratory haemoproteins is of importance for understanding the molecular mechanisms responsible for the control of their physiological activities. Despite detailed structural [55] and spectroscopic [56] information as well as theoretical consideration [57] of the binding of these ligands to haemoproteins and iron–porphyrin complexes, little experimental evidence has been reported regarding the effects of O_2 and CO binding on the haem electronic structure of proteins. The ^{19}F NMR spectra of oxy Mb(3,7-DF) and CO Mb(3,7-DF) are compared in Fig. 8. In the spectrum of a mixture of the oxy and CO forms of Mb(3,7-DF) (Fig. 8B), the two sets of signals were separately observed, demonstrating that the timescale of the ligand exchange between O_2 and CO in the protein is slow compared with the NMR timescale [58]. The signals for the oxy form are low frequency-shifted relative to the corresponding signals for the CO one, indicating that the electron density in the porphyrin π-system of the CO form is lower than that of the oxy one. This finding unequivocally demonstrates the effect of Fe $d_\pi \rightarrow$CO π^* back-donation [59,60] on the haem electronic structure.

X-ray crystal studies [55] have indicated that the Fe–C–O unit in CO Mb prefers a linear geometry (∠Fe–C–O = 171°) to maximize the Fe $d_\pi \rightarrow$CO π^* back-donation [59,60], while the Fe–O–O unit in oxy Mb is greatly bent (∠Fe–O–O = 123°), although the orientation of the His F8 imidazole with respect to the haem is essentially the same in the two forms. The greater nonequivalency between 3- and 7-F in the oxy form, relative to that in the CO one, can be attributed to the bent Fe–O–O coordination with respect to the haem. These results also reflect the high sensitivity of ^{19}F NMR as to the haem electronic structure.

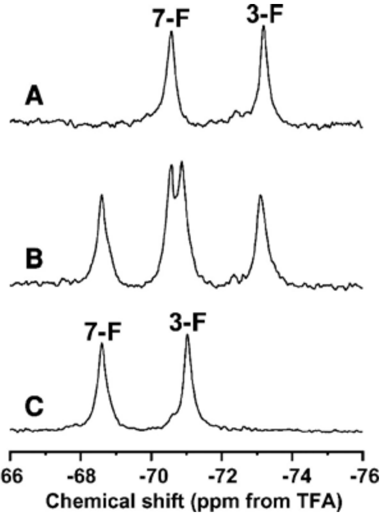

Fig. 8. 376 MHz ^{19}F NMR spectra of Mb(3,7-DF), in 90% H_2O/10% ^2H_2O, pH 7.0, at 25 °C; (A) Oxy Mb, (B) a mixture of oxy and CO Mbs, and (C) CO Mb. The signal assignments are indicated in the spectra.

Summary

A ^{19}F NMR study of Mb has been reviewed with a brief explanatory description of the characteristics of the individual spectra of Mb in various oxidation, spin, and ligation states. The ^{19}F NMR study described here provides a new means for detailed characterization of the active sites of *b*-type haemoproteins to delineate their structure–function relationships.

References

1. David M, Daveran M-L, Batut J, Dedieu A, Domergue O, Ghai J, Hertig C, Boistard P, Kahn D. Cell. 1988;54:671.
2. Hou S, Larsen RW, Boudko D, Riley CW, Karatan E, Zimmer M, Ordal GW, Alam M. Nature. 2000;403:640.
3. Iizuka T, Kotani M. Biochim. Biophys. Acta. 1969;194:351.

4. Wüthrich K. Struct. Bonding. 1970;8:53.
5. La Mar GN. In: GN La Mar, WD Horrocks Jr, RH Holm (Eds). NMR of Paramagnetic Molecules, Principles and Applications. Academic Press: New York, 1973, p 85.
6. Morishima I, Ogawa S, Inubushi T, Iizuka T. Adv. Biophys. 1978;11:217.
7. La Mar GN. In: RG Shulman (Ed). Biological Application of Magnetic Resonance. Academic Press: New York, 1979, p 305.
8. Keller RM, Wüthrich K. In: LJ Berliner, J Reuben (Eds). Biological Magnetic Resonance, Vol. 3. Plenum Press: New York, 1981, p 1.
9. Satterlee JD. Annu. Rep. NMR Spectrosc. 1986;17:79.
10. Satterlee JD. Met. Ions Biol. Syst. 1986;21:121.
11. Bertini I, Luchinat C. NMR of Paramagnetic Molecules in Biological Systems. Benjamin/Cummings Publishing: Menlo Park, CA, 1986, p 165.
12. de Ropp JS, Yu LP, La Mar GN. J. Biomol. NMR. 1991;1:175.
13. Bertini I, Turano P, Vila AJ. Chem. Rev. 1993;93:2833.
14. Bertini I, Luchinat C. Coord. Chem. Rev. 1996;150:29.
15. Yamamoto Y. Annu. Rep. NMR Spectrosc. 1998;36:1.
16. Bertini I, Luchinat C, Parigi G. Curr. Methods Inorg. Chem. 2001;2:142.
17. Rivera M, Caignan GA. Anal. Bioanal. Chem. 2004;6:1464.
18. Suzuki A, Tomizawa T, Hayashi T, Mizutani T, Ogoshi H. Bull. Chem. Soc. Jpn. 1996;69:2923.
19. Pearson JG, Montez B, Le H, Oldfield E, Chien EY, Sligar SG. Biochemistry. 1997;36:3590.
20. Yamamoto Y, Hirai Y, Suzuki A. J. Biol. Inorg. Chem. 2000;5:455.
21. Hirai Y, Yamamoto Y, Suzuki A. Bull. Chem. Soc. Jpn. 2000;73:2309.
22. Thomas MR, Boxer SG. Biochemistry. 2001;40:8588.
23. Poliart C, Briand J-F, Tortevoie F, Leroy J, Simonneaux G, Bondon A. Magn. Reson. Chem. 2001;39:615.
24. Yamamoto Y, Nagao S, Hirai Y, Inose T, Terui N, Mita H, Suzuki A. J. Biol. Inorg. Chem. 2004;9:152.
25. Hirai Y, Nagao S, Mita H, Suzuki A, Yamamoto Y. Bull. Chem. Soc. Jpn. 2004;77:1485.
26. Kaesler RW, LeGoff E. J. Org. Chem. 1982;47:5243.
27. Ogoshi H, Hommma M, Yokota K, Toi H, Aoyama A. Tetrahedron Lett. 1983;24:929.
28. Hommma M, Aoyagi K, Aoyama Y, Ogoshi H. Tetrahedron Lett. 1983;24:4343.
29. Toi H, Homma M, Suzuki A, Ogoshi H. J. Chem. Soc. Chem. Commun. 1985;1791.
30. Ogoshi H, Mizushima H, Toi H, Aoyama Y. J. Org. Chem. 1986;51:2366.
31. Snow KM, Smith KM. J. Org. Chem. 1989;54:3270.
32. Sykes BD, Hull WE. Methods Enzymol. 1978;49:270–295.
33. Gerig JT. Prog. NMR Spectrosc. 1994;26:293.
34. Lui SM, Cowan JA. J. Am. Chem. Soc. 1994;116:4483.
35. Schmitt L, Boniface JJ, Davis MM, McConnell HM. J. Mol. Biol. 1999;286:207.
36. Frieden C, Hoeltzi SD, Bann JG. Methods Enzymol. 2004;380:400.
37. Teale FWJ. Biochim. Biophys. Acta. 1959;35:543.
38. Yoshimura T, Toi H, Inaba S, Ogoshi H. Inorg. Chem. 1991;30:4315.
39. Yoshimura T, Toi H, Inaba S, Ogoshi H. Bull. Chem. Soc. Jpn. 1992;65:1915.
40. Yoshimura T, Kamada H, Toi H, Inaba S, Ogoshi H. Inorg. Chim. Acta. 1992;208:9.
41. La Mar GN, Budd DL, Viscio DB, Smith KM, Langry KC. Proc. Natl. Acad. Sci. U.S.A. 1978;75:5755.
42. Mabbutt BC, Wright PE. Biochim. Biophys. Acta. 1985;832:175.
43. Emerson SD, La Mar GN. Biochemistry. 1990;29:1545.
44. Yamamoto Y, Iwafune K, Nanai N, Osawa A, Chûjô R, Suzuki T. Eur. J. Biochem. 1991;198:299.
45. Kachalova GS, Popov AN, Bartunik HD. Science. 1999;284:473.
46. Bertini I, Kowalewski J, Luchinat C, Parigi G, J. Magn. Reson. 2001;152:103.
47. La Mar GN, Satterlee JD, de Ropp JS. In: KM Kadish, KM Smith, R Guilard (Eds). The Porphyrin Handbook. Academic Press: New York, 2000, p 185.
48. Bougault CM, Dou Y, Ikeda-Saito M, Langry KC, Smith KM, La Mar GN. J. Am. Chem. Soc. 1998;120:2113.
49. Yamamoto Y, Iwafune K, Chûjô R, Inoue Y, Imai K, Suzuki T. J. Biochem. 1992;112:414.
50. Yamamoto Y. J. Magn. Reson. 1994;B103:72.
51. La Mar GN, Yamamoto Y, Jue T, Smith KM, Pandey RK. Biochemistry. 1985;24:3826.
52. Lee KB, La Mar GN, Kehres LA, Fujinari EM, Smith KM, Pochapsky TC, Sligar SG. Biochemistry. 1990;29:9623.
53. Peyton DH, La Mar GN, Gersonde K. Biochim. Biophys. Acta. 1988;954:82.
54. La Mar GN, Smith WS, Davis NL, Budd DL, Levy MJ. Biochem. Biophys. Res. Commun. 1989;158:462.
55. Vojtechovský J, Chu K, Berendzen J, Sweet RM, Schlichting I. Biophys. J. 1999;77:2153.
56. Sanders LK, Arnold WD, Oldfield E. J. Porphyrins Phthalocyanines. 2001;5:323.
57. Case DA, Huynh BH, Karplus M. J. Am. Chem. Soc. 1979;101:4433.
58. Rohlfs RJ, Mathews AJ, Carver TE, Olson JS, Springer BA, Edeberg KD, Sligar SG. J. Biol. Chem. 1990;265:3168.
59. Collman JP, Brauman JI, Halbert TR, Suslick KS. Proc. Natl. Acad. Sci. U.S.A. 1976;73:3333.
60. Kalodimos CG, Gerothanassis IP, Pierattelli R, Troganis A. J. Inorg. Biochem. 2000;79:371.

Part I

Polymer Structure

NMR in Dry or Swollen Temporary or Permanent Networks

Jean-Pierre Cohen Addad
Laboratoire de Spectrométrie Physique associé au CNRS (UMR C5588), Université Joseph Fourier,
38402 St Martin d'Hères Cedex, France

Introduction

NMR is a convenient tool for investigating a wide domain of polymeric properties whether investigations deal with thermodynamics or with chain dynamics. Considering here low-resolution NMR of protons attached to chains, measurements can be performed using low-cost equipment. Main magnetic interactions involved in proton relaxation in polymers are dipole–dipole interactions; for example, the magnetic interaction strength of two protons located on a methine group (–CH_2) is 10^5 rad/s in pulsation units. This interaction strength serves as a reference for characterizing dynamic polymeric properties: whether or not they are isotropic, random segmental motions detected from NMR are necessarily characterized by correlation times shorter than about 10^{-5} s [1]. The spin system response exhibits an axial symmetry; the longitudinal (spin–lattice) relaxation is induced by a quasi-resonant exchange of energy between the spin system and the molecular thermal bath and is sensitive to friction effects which occur around the Larmor frequency (10^8 rad/s) whereas the proton transverse (spin–spin) relaxation mainly reflects quantum phase coherences of nuclear spins and is sensitive to deviations from isotropic random rotations of monomeric units in networks. Although they were not observed during polymer flow NMR properties are closely related to the linear viscoelastic behavior of polymers.

Polymeric Dynamics

The description of dynamics properties of polymers observed above the glass transition temperature relies on the behavior of the relaxation modulus $G(t)$; measured from long linear chains, it exhibits two well-separated dispersions [2]. At short times, the transition dispersion is insensitive to chain length variations and associated to fluctuations of short segments while large-scale rearrangements of chain conformations are associated with the terminal dispersion of the dynamics spectrum of one chain and are described according to the reptation model [3,4]. The two dispersions are separated by a rubber-like plateau response at intermediate times; the plateau called G_N^0 and attributed to chain entanglement interactions [5] is considered as a break in dynamic fluctuations that occur along one chain. In analogy with properties of networks, the temporary plateau value is conveniently related to a mean segmental molecular weight called M_e: $G_N^0 = \rho RT/M_e$, with $M_e = 361.9A\rho(M/A\rho\langle R_0^2\rangle)$ [3], (ρ is the polymer density, A is the Avogadro number, and $\langle R_0^2\rangle$ is the Gaussian mean square end-to-end distance of one chain of molecular weight M) [6]; the plateau width is an increasing function of molecular weight.

Effect of Local Friction and Spin–Lattice Relaxation

Spin–lattice relaxation measurements are used to investigate properties of collective random motions of a few monomeric units forming short segments; these motions occur around the Larmor frequency ω_0 ($\approx 10^8$ rad/s) and are independent of chain length. The relaxation rate $1/T_1(T,\ \omega_0)$ is usually measured by applying $[180^\circ - \tau - 90^\circ]$ pulse sequences to the spin system and the relaxation of the longitudinal magnetization is described according to the equation [1]:

$$M_z(\tau) = M_0[1 - 2\ \exp\{-\tau/T_1(T, \omega_0)\}] \qquad (1)$$

This relaxation is closely related to friction properties also involved in the viscoelastic behavior observed in the transition domain; the temperature dependence of the local friction coefficient $\zeta_0(T)$ is mainly governed by free volume effect and characterized by a shift factor $a(T_{\text{ref}}^{\text{L}}, T) = \zeta_0(\theta)/\zeta_0(\theta_{\text{ref}}^{\text{L}})$ determined in the following way. First, starting from the maximum of the temperature dependence of the relaxation rate, the ratio $\omega_0 T_{1,\max}/T_1(T, \omega_0)$ is drawn as a temperature function; this ratio is a homogeneous function of the product $\omega_0\zeta_0(T)$; then, considering the temperature dependence of the ratio determined from two Larmor frequencies called, respectively, ω_0' and ω_0'', the following equation

$$\omega_0' T_{1,\max}'/T_1(T', \omega_0') = \omega_0'' T_{1,\max}''/T_1(T'', \omega_0'') \qquad (2)$$

provides the relationship $\omega_0'/\omega_0'' = \zeta_0(T'')/\zeta_0(T')$ between the friction coefficients $\zeta_0(T'')$ and $\zeta_0(T')$ corresponding to T' and T'' temperatures, respectively; starting from a reference temperature $T_{\text{ref}}^{\text{L}}$, the ratio leads to the

Graham A. Webb (ed.), Modern Magnetic Resonance, 541–543.
© 2008 *Springer.*

determination of the temperature dependence of the shift factor $a(T_{\mathrm{ref}};T)$. This analysis applies to liquid polymers as well as to permanent networks in which the glass transition temperature T_{g} is an increasing function of the cross-link density [7]. For illustration, the temperature dependence of $a(T^{\mathrm{L}}_{\mathrm{ref}};T)$ is in coincidence with that of the shift factor derived from viscoelastic measurements performed on polybutadiene [8]. This approach applies to variations of polymer concentration too.

Chain Diffusion

Chain diffusion measurements are performed by forming pulse field gradient spin-echoes [9]; the molecular weight dependence of the chain diffusion coefficient D exhibits a cross-over from the short chain dynamics described according to the Rouse model ($D\alpha M$) to the long chain dynamics described according to the reptation model ($D\alpha M^{3.4}$) [10].

Statistical Polymeric Structures and Spin–Spin Relaxation

Measurements of spin–spin relaxation are used to investigate properties of temporary or permanent polymeric networks; relaxation curves are drawn by forming Hahn spin-echoes, applying a $[90^\circ/x - \tau - \{180^\circ/x - 2\tau - 180^\circ/-x - 2\tau - 180^\circ/-x - 2\tau - 180^\circ/x - 2\tau-\}n]$ pulse sequence which eliminates both field inhomogeneity effects due to diamagnetism and possible pulse phase problems. Considering long chains, the timescale associated with large-scale rearrangements of chain conformations is much longer than the inverse of the strength of proton–proton interactions about equal to 10^5 rad/s; consequently, these processes do not induce any full motional averaging of magnetic interactions and residual spin–spin interactions result from the partial averaging process which is induced by segmental motions associated with the transition dispersion [8]. Residual proton–proton interactions are independent of molecular weight and their order of magnitude is 10^3 rad/s.

NMR Structural Parameter

The normalized relaxation function $M_x^T(t)$ consists of two contributions expressed as:

$$M_x^T(t) = (1 - A_{\mathrm{II}})(\Delta_{\mathrm{I}}, \tau_{\mathrm{I}}, t) + A_{\mathrm{II}} M_x^{\mathrm{II}}(\Delta_{\mathrm{II}}, \tau_{\mathrm{II}}, t). \quad (3)$$

The relative amplitude A_{II} is proportional to M^{-1}. Normalized $M_x^{\mathrm{II}}(t)$ relaxation functions are assigned both to protons attached to chain-end segments and to protons attached to monomeric units in dynamic interaction with end segments; normalized $M_x^{\mathrm{I}}(t)$ functions are assigned to protons attached to remaining units [8,11]. $M_x^{\mathrm{I}}(\Delta_{\mathrm{I}}, \tau_1, t)$ and $M_x^{\mathrm{II}}(\Delta_{\mathrm{II}}, \tau_{\mathrm{II}}, t)$ are mainly governed by residual dipole–dipole interactions of protons; represented by two parameters called Δ_{I} and Δ_{II}, respectively. $M_x^{\mathrm{II}}(t)$ is independent of chain length while the correlation time τ_1 is proportional to $M^{0.35}$; $M_x^{\mathrm{I}}(\Delta_{\mathrm{I}}, \tau_1, t)$ and $M_x^{\mathrm{II}}(\Delta_{\mathrm{II}}, t)$ spread over different timescales and are easily distinguished from each other. Considering the two following integrals:

$$\Phi_3 = \int_0^\infty \{\mathrm{d}M_{\mathrm{I}}(\Delta_{\mathrm{I}}, \tau_1, t)/\mathrm{d}t\}/t^{0.5}\,\mathrm{d}t \quad \text{and}$$

$$\Phi_1 = \int_0^\infty M_{\mathrm{I}}(\Delta_{\mathrm{I}}, \tau_1, t)/t^{0.5}\mathrm{d}t \quad (4)$$

the NMR structural parameter is defined as the ratio $\chi_c = \Phi_3/\Phi_1$; based on an integral treatment of relaxation curves, the determination of χ_c does not require the mathematical description of proton relaxation be thoroughly analyzed. For molten polymers observed above the glass transition temperature, the inverse of the NMR structural parameter is expressed according to the equation:

$$1/\chi_c^{\mathrm{M}}(T, c, N_e) = (T - T_{\mathrm{ref}}^{\mathrm{M}}) \times (A\chi + B\chi N_e/(M^{0.35}c^{2.1}) \quad (5)$$

N_e is the mean number of monomeric units associated with the plateau G_N^0 and Equation (5) reflects segmental properties induced on NMR by the transition dispersion; the reference temperature T_c^{M} is about 40 K above the glass transition temperature T_{g} and c is the polymer concentration (w/w) (the addition of solvent induces a dilation of the temporary network). For polybutadiene, typical numerical values are $A_\chi = (13.5 \pm 2) \times 10^{-3}$ ms/K and $B_\chi = (22 \pm 1) \times 10^{-3}$ ms/K (g/mol)$^{1/0.35}$ within the range $75 \times 10^3 < M < 500 \times 10^3$ g/mol while N_e is a function of the concentration of monomeric units in the vinyl 1–2 conformation in the chain microstructure.

Cross-Linked Long Chains

In polymeric networks formed from randomly cross-linked chains, segmental properties induced by the transition dispersion combine with properties of segments determined from the cross-linking process; for a given weight fraction of cross-linking reagent γ, these properties are represented by $1/\chi_c^{\mathrm{G}}(\gamma)$. Then, for networks the NMR structural parameter is expressed according to the equation:

$$1/\chi_c^{\mathrm{N}}(T, \gamma) = \kappa(\gamma)\mathrm{arctg}[\chi_c^{\mathrm{G}}(\gamma) \times \{(A\chi + B\chi N_e)(T - T_{\mathrm{ref}}^{G}(\gamma))\}] \quad (6)$$

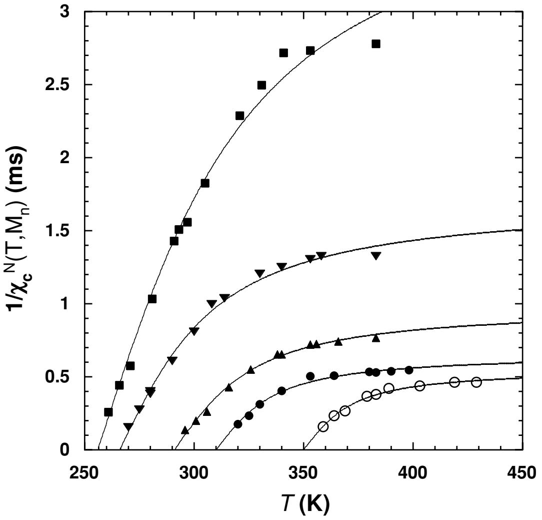

Fig. 1. Variations of $1/\chi_c^{\mathrm{N}}(T, M_n)$ corresponding to precursor molecular weights: 425 (○), 725 (●), 1000 (▲), 2000 (▼) and 4000 (■) g/mol; correspondingly, reference temperatures are: 350, 310, 291, 266, and 256 K. Theoretical curves drawn using Equation (6).

Now, the reference temperature $T_{\mathrm{ref}}^{\mathrm{G}}$ is a linear function of γ, $\kappa(\gamma)T_{\mathrm{ref}}^{\mathrm{G}}$ and $1/\chi_c^{\mathrm{G}}(\gamma)$ are determined experimentally using Equation (6). Both $\kappa(\gamma)$ and $1/\chi_c^{\mathrm{G}}(\gamma)$ are found to be linear functions of $1/\gamma$ showing that the mean segmental spacing between cross-links is proportional to $1/\gamma$. Furthermore, considering a given network and its maximum swelling ratio $Q_{\mathrm{m}}(\gamma)$, at constant temperature $1/\chi_c^{\mathrm{N}}(\gamma)$ is proportional to $Q_{\mathrm{m}}(\gamma)^2$ because swollen polymeric strands obey Gaussian properties.

Calibrated Polymeric Networks

Well-defined mesh sizes are obtained when polymeric networks synthesized from calibrated telechelic segments are characterized by a polydispersity index close to one. Then, the NMR structural parameter is a function of polymeric precursor molecular weight as illustrated in Figure 1; $1/\chi_c^{\mathrm{N}}(T, M_n)$ was determined from end-linked polypropylene oxide chains using triisocyanate as a cross-linking reagent [7]. $1/\chi_c^{\mathrm{N}}(T, M_n)$ again obeys Equation (6) in which $\kappa(M_n) = 0.95 \times 10^{-3} M_n$ ms and $1/[\chi_c^{\mathrm{G}}(\gamma)\{A_x + B_x N_e\}] = 15.71 + M_n \times 10^{-2}$ Kelvin (M_n is in g/mol).

Furthermore, considering a given network and its maximum swelling ratio $Q_{\mathrm{m}}(M)$, at constant temperature $1/\chi_c^{\mathrm{N}}$ is proportional to $Q_{\mathrm{M}}^{1,5}$ because swollen segments obey both excluded volume properties and a packing condition [3,7].

Conclusion

Using low-resolution spectrometers, proton relaxation properties observed from high polymers above the melting point as a function of temperature, solvent concentration, and molecular weight or cross-link density in networks are given a quantitative analysis.

References

1. Abragam A. Principles of Nuclear Magnetism. Oxford University Press: Oxford, 1960.
2. Ferry JD. Viscoelastic Properties of Polymers. Wiley: New York, 1980.
3. De Gennes PG. Scaling Concepts in Polymer Physics. Cornell University Press: Ithaca, 1979.
4. Doi M, Edwards SF. The Theory of Polymer Dynamics. Clarendon Press: Oxford, 1988.
5. Graessley WW. Adv. Polym. Sci. 1974;16:1.
6. Fetters LJ, Lohse DJ, Richter D, Witten TA, Zirkel A. Macromolecules. 1994;27:4639.
7. Cohen Addad JP, Pellicioli L, Nusselder JHH. Polym. Gels Netw. 1997;5:201.
8. Cohen Addad JP. NMR and fractal properties of polymeric liquids and gels. In JW Emsley, J Feeney, LH Sutcliffe (Eds). Progress in NMR Spectroscopy. Pergamon Press: Oxford, 1993.
9. Tao H, Lodge TP, von Meerwall ED. Macromolecules. 2000; 33:1747.
10. Guillermo A, Cohen Addad JP. J. Chem. Phys. 2002; 116:314.
11. Cohen Addad JP, Guillermo A. Macromolecules. 2003; 36:1609.

Crystalline Structure of Ethylene Copolymers and Its Relation to the Comonomer Content

Qun Chen
The Key Laboratory for Optics and Magnetic Resonance of MOE, Physics Department,
East China Normal University, Shanghai 200062, China

Ethylene copolymers are a large group of polymer material with a lot of industrial applications [1]. They usually consist of two types of monomers. One is the ethylene unit and the other one is the comonomer unit like methyl methacrylate, vinyl acetate, vinyl alcohol, etc. These two monomer units distribute, randomly in most cases, along the polymer chain, forming ethylene segments with different length. Once the length of some ethylene segments exceeds a critical value, i.e. the so-called minimum crystallizable sequence length at a certain temperature [2], these segments tend to aggregate and form crystals, while the segments with the length smaller than the minimum crystallizable sequence locate in the amorphous region. The comonomer units, which often lack the ability of crystallization, are either expelled from the crystals or embedded in the crystals as defects when the volume of the comonomer unit is small. Similar to other semicrystalline polymers, the bulk samples of ethylene copolymers usually comprise the crystalline, the amorphous, and the interfacial region, which lies between the crystalline and amorphous regions. The structures and the dynamics of these different morphological regions, which have large impact on the macroscopic properties of the material, have been the topics with a lot of research interests.

Solid-state high-resolution ^{13}C NMR spectroscopy has been turned out to be an especially useful technique in probing the phase structure of ethylene copolymers. In the recent years, there have been a number of researches in this field [3–11]. In the following section, some of these works will be introduced to illustrate the possible application of solid-state high-resolution ^{13}C NMR to the investigation on phase structures of ethylene copolymers.

Polymorphism of Ethylene Copolymers

Similar to the behavior of polyethylene, the ethylene segments in the copolymers can be crystallized in different forms, namely, the orthorhombic form and monoclinic form. The orthorhombic form that is thermodynamically favored for long ethylene segments, is dominant for most ethylene copolymers. However, it has been revealed by solid-state high-resolution ^{13}C NMR that for many ethylene copolymer systems [3–7], the ratio of the content of the monoclinic crystal relative to that of the orthorhombic crystal increases steadily with the increase of the comonomer content. Figure 1 illustrates the ^{13}C cross-polarization, high-power dipolar decoupling and magic angle spinning (CP/MAS) spectra of ethylene vinyl acetate copolymers (EVA) with different composition [5]. The numbers after EVA in the figure represent the weight percentage of the VA comonomer in the samples. Among the signals shown in the spectra, peaks at 33.4, 32.4, and 30 ppm are corresponding to the methylene carbon of the monoclinic crystal, orthorhombic crystal, and the amorphous phase. The chemical shift of the monoclinic signals is marked by a dashed line. The assignment of the remaining signals in the spectra, which is not related to the current topic, will not be described here. In the spectra of the EVA05 and EVA12, the intensity of the monoclinic crystals is quite weak, while the signal of the monoclinic crystals can be distinguished easily in the spectra of the EVA18, EVA28, and EVA40 samples. By applying curve fitting to all five spectra, the relative content of each phase component can be obtained. It is found that with the increase of the VA content, the relative contents of the monoclinic crystals in the crystalline region increase while the degree of the crystallinity decreases. Similar results are also observed in the works on ethylene–dimethylaminoethyl methacrylate copolymers (EDAM) [3,4], ethylene–butene, and ethylene–octene [6], but is not observed for ethylene–vinyl alcohol copolymer [7]. All these observations demonstrate that the crystalline structures depend on the comonomer content is a general phenomenon for ethylene copolymers with relatively large side group in their comonomer units. The explanation for such a phenomenon is as follows: For random ethylene copolymers, there exist ethylene segments with different length. Upon crystallization, ethylene segments with the same or near length tend to aggregate and form crystals with different lamellar thickness. The crystallization behavior of the ethylene segments with relative long length is similar to that of polyethylene and tends to

Graham A. Webb (ed.), Modern Magnetic Resonance, 545–549.
© 2008 *Springer.*

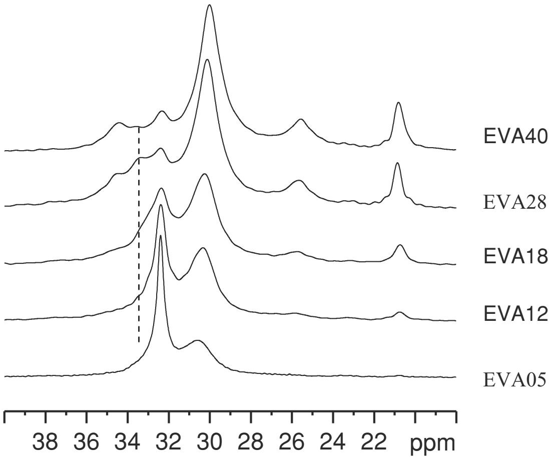

Fig. 1. ^{13}C CP/MAS NMR spectra of five EVA samples. The dashed line indicates the monoclinic crystalline signal.
Source: Ref. [5]; Fig. 6 in the original literature.

form orthorhombic crystals that are thermodynamically stable. On the other hand, for shorter ethylene segments, due to the influence of the side group of the comonomer unit on both ends of the segment, monoclinic crystalline form is not only dynamically favored, but also thermodynamically stable. It is apparent that the percentage of the shorter ethylene segments increases with increasing the comonomer content, leading to the increase of the relative content of monoclinic crystals in the crystalline region. This interpretation is supported by the fact that in the variable temperature ^{13}C CP/MAS spectra of EDAM, the signal of monoclinic crystals disappears at relatively lower temperature, comparing to that of orthorhombic crystals in the heating process [4]. This reveals that the thickness of the monoclinic crystals is relatively small compared with that of the orthorhombic crystals, suggesting that monoclinic crystals do mainly correspond to the shorter ethylene chains.

Polymorphism of ethylene copolymers can also be studied by WAXD, IR, Raman, and other techniques [6,7,10]. With comparison to these techniques, the advantage of solid-state high-resolution ^{13}C NMR lies in the following two aspects. Firstly, in the ability of discriminating small signals of monoclinic crystals, solid-state high-resolution ^{13}C NMR excels the other techniques. Figure 2 shows the partially decayed ^{13}C spectra of EVA28 acquired by using a Torchia's pulse sequence [12], in order to measuring the ^{13}C spin-lattice relaxation time (T_1) of the sample. It is apparent that with the increase of the variation time, the peaks related to the amorphous region relax rapidly, leaving only the peaks corresponding to the orthorhombic and monoclinic signals in the spectra. The existence of the monoclinic crystal, therefore, can be discriminated clearly. This result demonstrates the powerfulness of solid-state NMR technique, in terms of acquiring useful information from the intricate spectrum. Secondly, our recent work on high-density polyethylene [13] has shown that the cross-polarization enhancement ratios of different crystals in the CP/MAS spectrum, which are key factors in determining the quantitative degree of the method, are almost the same. This observation indicates that the relative ratio of crystals in different forms of ethylene copolymers determined by ^{13}C CP/MAS methods is of high quantitative degree.

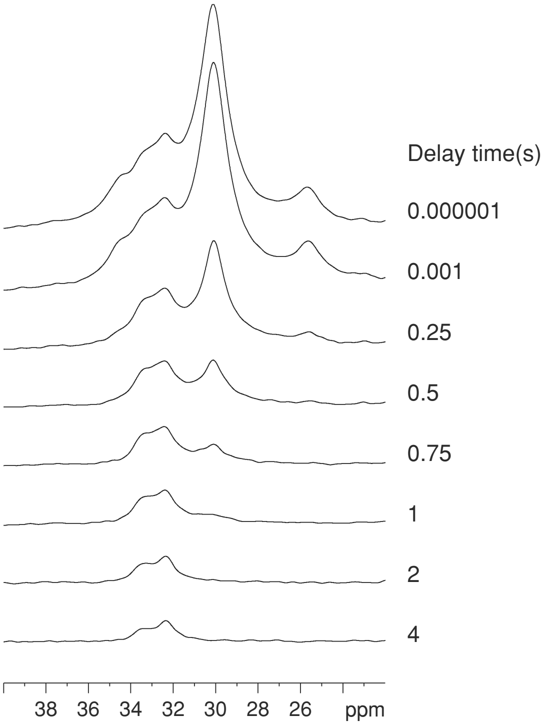

Fig. 2. Partially decayed spectra of EVA28 at different delay times acquired with Torchia's pulse sequence.
Source: Ref. [5]; Fig. 7 in the original literature.

The Biexponential ^{13}C T_1 Relaxation Behavior of the Crystalline Region

In the studies on polyethylene and ethylene–octene copolymers, Axelson et al. [14,15] found for the first time that the crystalline regions of these polymers exhibit multi-exponential ^{13}C T_1 relaxation behavior. Two or even three ^{13}C T_1s can be obtained by analyzing the relaxation

Table 1: Specifications of EDAM and EMA copolymers

Samples		Mol%	T_m/°C
EDAM	DA3032	10.7	65.5
	DA3002	6.9	83.6
	DA3023	3.9	92.3
	DA3014	3.6	99.3
EMA	EMA6.5	2.2	102
	EMA9	3.1	93
	EMA27	10.8	64
	EMA29	11.7	48

curves of the crystalline region. The value of the longer ^{13}C T_1 varies from several tens of second to thousands of second, depending on the lamellar thickness. The values of the shorter ones are usually in the order of one second or even less than one second. The origin of such a phenomenon has been a subject with strong research interests for many years [16–18]. Recent studies on several series of ethylene copolymers provided additional information for illustrating the mechanism of multi-exponential relaxation behavior of the crystalline region of polyethylene and ethylene copolymers [5,8]. Meanwhile, it was demonstrated that the multi-exponential relaxation behavior itself can be utilized to probe the phase structure of the corresponding polymer systems.

Two series of ethylene copolymers, namely EDAM and ethylene–methyl acrylate (EMA) were investigated by measuring ^{13}C T_1 of the crystalline regions. The comonomer contents of these samples are listed in Table 1. Figure 3 shows the ^{13}C T_1 relaxation curves of the crystalline component, including the contribution of both orthorhombic and monoclinic crystals, for melt-quenched EDAMs. It can be found that for all the samples, the relaxation curves exhibit biexponential relaxation behavior. Similar results can also be observed for EMAs and for aforementioned EVAs either melt-quenched or isothermally crystallized. This result suggests that the biexponential relaxation behavior is independent of the crystallization condition, the comonomer structure, and the comonomer content. A careful study on EVA28 that has a relative higher content of monoclinic crystal, reveals that the biexponential relaxation behavior is not caused by the coexistence of two different crystalline forms, i.e. the orthorhombic and monoclinic crystalline forms. By carrying out curve fitting on the relaxation curves, two ^{13}C T_1s as well as the relative contents of the components to which each T_1 corresponds can be attained. It is found that, under same crystallization conditions, the relative content of the crystalline component with shorter T_1 generally increases with the increase of the comonomer contents. Meanwhile the content of the shorter T_1 component for a melt-quenched sample is generally higher than that of its isothermally crystallized counterpart, as is demonstrated in Figure 4. It is also found that the values of the longer T_1, which varies from several tens of seconds to several seconds, are closely dependent on the comonomer content, or in other words, dependent on the average lamellar thickness.

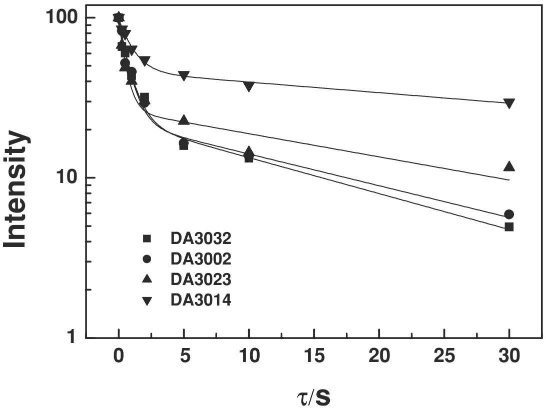

Fig. 3. ^{13}C T_1 relaxation curves (semilogarithmic) of the crystalline components for melt-quenched EDAM samples acquired by Torchia's pulse sequence, where the real lines represent the results of curve fitting in terms of two components with different ^{13}C T_1s.
Source: Ref. [8]; Fig. 2 in the original literature.

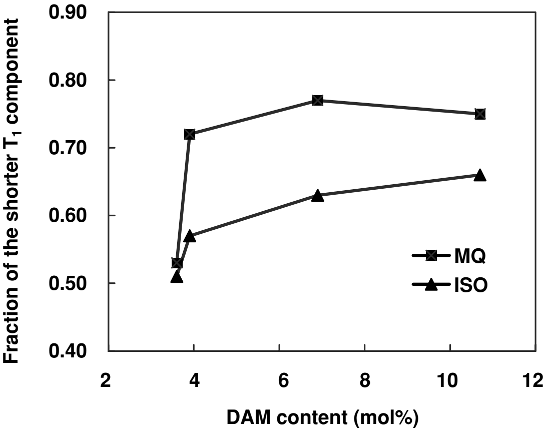

Fig. 4. The fraction of the shorter T_1 component vs. DAM molar content for EDAM samples.
Source: Ref. [8]; Fig. 3 in the original literature.

The above results strongly indicate that the crystalline components with longer and shorter ^{13}C T_1s are corresponding to the internal and the surface parts of the crystalline region, respectively. The interpretation for such a phenomenon is as follows: Both the increasing of the comonomer content and melt-quench will lead to a decrease of the lamellar thickness. The decrease of the lamellar thickness will, in turn, lead to an increase of the relative content of the surface part of the crystalline region. The surface part can also be termed as mobile crystalline or intermediate crystalline component located between the amorphous and the internal part of the crystalline regions [17,18]. The molecular chains in the surface part of the crystalline region should have all trans conformation, because the chemical shift of the component is just the same as that of the internal part of the crystalline region. They should have higher mobility comparing with those within the internal crystalline region, as demonstrated by their remarkably shorter ^{13}C T_1 compared with that of the internal component of the crystalline region.

A pulse sequence that can be considered as a combination of Goldman–Shen's [19] and Torchia's pulse sequences as depicted in Figure 5, was designed to give further evidence for the above interpretation of the biexponential relaxation behavior of the crystalline region. The strategy of the method can be described by a study on EMA29 membrane sample [8]. The first delay window (D6) on the ^{1}H channel is set to be 50 μs. During this delay window, most magnetization in the crystalline region is dephased, while there are still a large amount of magnetization remained in the amorphous region. After D6, ^{1}H magnetization is flipped back to Z-axis. During the second delay window (D7), the magnetization starts to spin-diffuse from the amorphous region to the crystalline region, due to the magnetization gradient existing between these two regions. When D7 is set to be 20 ms, it is demonstrated that a certain part of ^{1}H magnetization has transferred into the crystalline region. However, equilibrium distribution of ^{1}H magnetization has not been reached. In other words, the magnetization diffused from the amorphous region is relatively enriched in the surface area of the crystalline region, comparing with the equilibrium state of ^{1}H magnetization. After D7, the magnetization is flipped back again to XY plane to allow cross-polarization to happen. Subsequently, ^{13}C spin-lattice relaxation can be measured according to Torchia's methodology, i.e. recording ^{13}C CP/MAS spectra with different τ values. What should be kept in mind is that the ^{13}C T_1 of the crystalline region measured under such initial conditions emphasizes the contribution of the surface part of the crystalline region. For EMA29 membrane sample, the relaxation curve of the crystalline region acquired in such a way is shown in Figure 6, together with the relaxation curve of the same region determined by the conventional Torchia's method. It can be found straightforwardly that the relative content of the shorter T_1 component obtained by the new pulse sequence under aforementioned conditions is much higher than that obtained by the conventional Torchia's sequence. Such a result unambiguously supports the conclusion that the crystalline component with shorter ^{13}C T_1 is mainly corresponding to the surface part of the crystalline region locating between the amorphous and the internal part of the crystalline region.

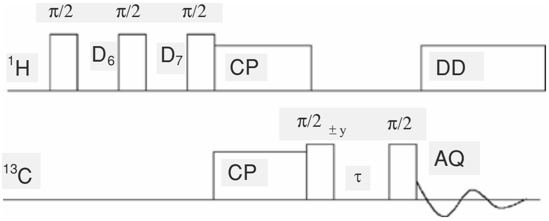

Fig. 5. The Goldman–Shen/Torchia's pulse sequence used for interpreting the mechanism of the biexponential ^{13}C T_1 behavior of the crystalline region.

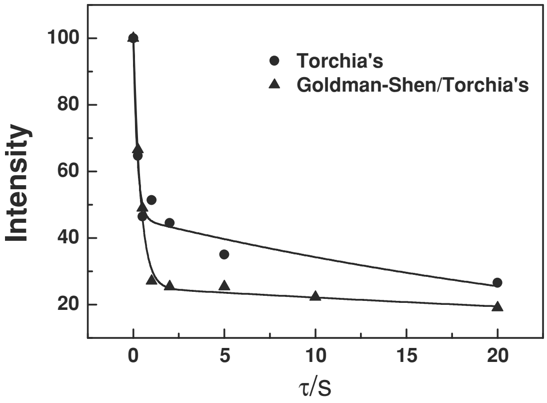

Fig. 6. ^{13}C T_1 relaxation curves of the crystalline component of EMA29 membrane sample acquired by Torchia's and Goldman–Shen/Torchia's pulse sequence.
Source: Ref. [8]; Fig. 8 in the original literature.

The pulse sequence depicted in Figure 5 can also be used in an alternative way to estimate the thickness of the intermediate part. The first delay window on ^{1}H channel is set to be 50 μs once again to eliminate most of the ^{1}H magnetization of the crystalline region. The pulse interval τ at ^{13}C channel is set to be 1.5 s, which serves as a T_1 filter to remove the signals of the amorphous region and the surface part of the crystalline region, leaving only the signal of the internal part of the crystalline region in the resulted spectrum. The spin-diffusion window D$_7$ is

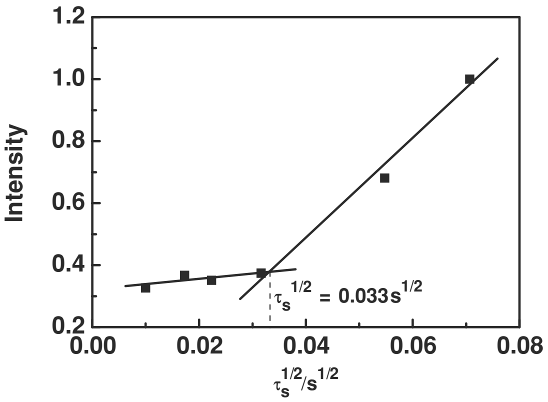

Fig. 7. Plot of the crystalline signal intensity as a function of $\tau_s^{1/2}$ measured by a modified Goldman–Shen/Torchia's pulse sequence. The dashed line indicates the turning point at which the signal starts to increase significantly.
Source: Ref. [8]; Fig. 10 in the original literature.

allowed to vary during the experiment and its length is represented by τ_s. It can be easily visualized that when τ_s increases, the ^{1}H magnetization will diffuse gradually from the amorphous region to the surface part of the crystalline region and subsequently to the internal part of the crystalline region. When τ_s is short, theoretically there should be no apparent signal enhancement in the obtained ^{13}C spectrum with the increase of τ_s. The signal starts to increase only when τ_s is long enough to allow the ^{1}H magnetization to diffuse into the internal part of the crystalline region.

A series of ^{13}C CP/MAS spectra of EMA29 membrane sample are acquired at different τ_s values by using the above method. The intensity of the crystalline signal is plotted in Figure 7 as a function of the square root of τ_s. It is apparent that there exists a turning point on the curve. The intensity of the signal is hardly changed before the turning point, while further increase of τ_s leads to a rapid increase of the signal intensity. Such an increase is undoubtedly due to the fact that after certain time of spin-diffusion the ^{1}H magnetization has already transferred into the internal part of the crystalline region. The influence of ^{1}H spin-lattice relaxation on the signal intensity, in this case, can be safely neglected, because the ^{1}H T_1 of the sample is as long as 0.5 s. Even when τ_s takes its largest value in the experiment, i.e. 5 ms, the intensity enhancement due to ^{1}H spin-lattice relaxation is still lower than 1%. The value of τ_s at the turning point, i.e. $\tau_s \approx$ 1.09 ms, is undoubtedly corresponding to the time that the ^{1}H magnetization of the amorphous region takes to pass across the surface part of the crystalline region. The thickness of the surface part can then be estimated by the following equation [20]:

$$L^2 = 4D\tau_s/3$$

where D is the spin-diffusion coefficient, L is the thickness of the component, and τ_s is the spin-diffusion time. The thickness of the surface part of the crystalline region obtained through calculation is about 0.85 nm, when D is 5.0×10^{-12} cm^2/s.

In conclusion, the above investigations on the relaxation behavior of ethylene copolymers have demonstrated that by measuring the ^{13}C T_1 of the crystalline region, the solid-state high-resolution ^{13}C NMR can be employed to study the content and nature of the surface part of the crystalline region of ethylene copolymers, providing us with unique phase structural information about these industrially important materials.

References

1. Mandelkern L. Polym. J. 1985;17:337.
2. Chen Q, Luo HJ, Yang G, Xu DF. Polymer 1997;38:1203.
3. Luo HJ, Chen Q, Yang G, Xu DF. Polymer 1998;39:943.
4. Lin WX, Zhang QJ, Yang G, Chen Q. J. Mol. Struct. 2002;602:185.
5. Zhang QJ, Lin WX, Yang G, Chen Q. J. Polym. Sci. Polym. Phys. Ed. 2002;40:2199.
6. Hu WG, Sirota EB. Macromolecules 2003;36:5144.
7. Su ZQ, Zhao Y, Xu YZ, Zhang XQ, Zhu SN, Wang DJ, Wu JG, Han CC, Xu DF. Macromolecules 2004;37:3249.
8. Lin WX, Zhang QJ, Yang G, Chen Q. J. Mol. Struct. 2003;655:37.
9. Zhang QJ, Lin WX, Chen Q, Yang G. Macromolecules 2000;33:8904.
10. Ma L, Bin Y, Sakai Y, Chen Q, Kurosu H, Matsuo M. Macromolecules 2001;34:4802.
11. Ma L, He CQ, Suzuki T, Azuma M, Bin Y, Kurosu H, Matsuo M. Macromolecules 2003;36:8056.
12. Torchia DA. J. Magn. Reson. 1978;30:613.
13. Zhang LL, Chen Q, Hansen EW. Macromol. Chem. Phys. 2005;206:246.
14. Axelson DE, Manderkern L, Popli R, Mathieu P. J. Polym. Sci. Polym. Phys. Ed. 1983;21:2319.
15. Axelson DE. J. Polym. Sci. Polym. Phys. Ed. 1982;20:1427.
16. Schmidt-Rohr K, Spiess HW. Macromolecules 1991;24: 5288.
17. Cheng JL, Fong M, Reddy VN, Schmartz KB, Fisher HP, Wunderlich B. J. Polym. Sci. Polym. Phys. Ed. 1994;32:2683.
18. Kuwabara K, Kaji H, Horii F. Macromolecules 2000;33:4453.
19. Goldman M, Shen L. Phys. Rev. 1966;144:321.
20. Havens JR, VanderHart D. Macromolecules 1985;18:1663.

Isomorphism in Bacterially Synthesized Biodegradable Copolyesters

Naoko Yoshie[1] and Yoshio Inoue[2]

[1] *Institute of Industrial Science, The University of Tokyo, Komaba, Meguro-ku, Tokyo 153-8505, Japan; and*

[2] *Department of Biomolecular Engineering, Tokyo Institute of Technology, 4259 Nagatsuta, Midori-ku, Yokohama 226-8501, Japan*

Introduction

Biodegradable plastics are currently receiving much attention for use as a commodity consumed with ecological advantages over nondegradable ones. Biodegradability is well known for some kinds of polymers including natural polymers such as cellulose, chitin, lignin, and bacterially synthesized aliphatic polyesters, and chemically synthesized polymers such as aliphatic polyesters and polyvinyl alcohol. Among them, aliphatic polyesters are the most promising materials for fibers and resins [1,2].

NMR spectroscopy is widely used in the structural analysis of biodegradable aliphatic polyesters, including stereo- [3,4] and comonomer-sequence [5–9], conformation [10,11], and dynamics in solution [10,12,13] and in the solid state [14–16]. Biodegradability is just a property of polymers. So, the procedure of structural analysis of biodegradable polyesters is no different from that of common vinyl polymers. Some of the structural characteristics of biodegradable polyesters, especially, of the bacterially synthesized ones are, however, totally different. For example, the bacterial copolyesters usually have an extraordinary broad chemical composition distribution, which adds a dimension in the analysis of the structure–property relationship [17–19]. The deuterium distribution in poly(3-hydroxybutyrate) [P(3HB)] biosynthesized from deuterated carbon sources indicates the conversion from a C–H to a C–D bond and from a C–D to a C–H bond in bacteria [20]. Due to limitations of space, we cannot review all of these characteristics. Instead, we focus here on the structural characteristics of a bacterial copolyester, i.e. isomorphism in poly(3-hydroxybutyrate-*co*-3-hydroxyvalerate) [P(3HB-*co*-3HV)]. In the characterization of this phenomenon, high-resolution solid-state NMR spectroscopy provides an exclusive method for determination of the chemical composition in each of the coexisting phases.

Isomorphous Behavior of Bacterially Synthesized Copolyesters

In P(3HB-*co*-3HV), relatively high crystallinity around 60% is preserved even at intermediate comonomer compositions, though the crystalline lattice of P(3HB-*co*-3HV) changes from the P(3HB) type to the P(3HV) type at ca. 40% 3HV [21,22]. Only the P(3HB) crystalline lattice is observed for P(3HB-*co*-3HV) with low 3HV content, while only the P(3HV) lattice is observed for the copolymers with high 3HV content. These observations are consistent with the hypothesis of isodimorphism [21], i.e. 3HB and 3HV units cocrystallize both in the P(3HB) lattice and in the P(3HV) lattice. The crystalline unit cells of P(3HB) [23,24] and P(3HV) [25] are both orthorhombic, $P2_12_12_1$-D_2^4. The chemical structures of 3HB and 3HV monomers differ only by the length of a methylene group in the side chains. Similarity in the chemical and crystalline structures must be responsible for the cocrystallization of 3HB and 3HV units.

Even in an isomorphous copolymer, the compositions in the crystalline and amorphous phases are not necessarily the same as the whole composition [26,27]. High-resolution solid-state ^{13}C NMR spectroscopy is a powerful tool for the determination of the compositions in each of the coexisting phases. So, the isomorphous behavior of P(3HB-*co*-3HV) has been analyzed by high-resolution solid-state ^{13}C NMR spectroscopy [28–30]. Figure 1a–c shows the ^{13}C cross-polarization magic-angle sample-spinning (CPMAS) NMR spectra of P(3HB-*co*-3HV)s. For the samples with low 3HV content, the resonances from the 3HV units in the crystalline phase are relatively small which gives a large margin of error in the calculated composition. In such cases, P(3HB-*co*-3HV) samples of which HV units are specifically labeled with ^{13}C were used [30,31]. Here, P(3HB-*co*-3HV) with and without ^{13}C label is denoted as P(3HB-*co*-3HV)^{E} and P(3HB-*co*-3HV)^{N}, respectively. The spectrum shown in Figure 1c is of P(3HB-*co*-13% 3HV)^{E} of which 3HV methine position contains 12% ^{13}C. The rate of the enrichment of this sample was selected so as to make the areas of the 3HB and 3HV methine peaks comparable.

Figure 2 shows the expanded spectra of the methine resonances of P(3HB-*co*-21% 3HV) and P(3HB-*co*-58% 3HV). The former crystallized in the P(3HB) type lattice, while the latter forms the P(3HV) type lattice. These spectra demonstrate the difference in chemical shift of each

Graham A. Webb (ed.), Modern Magnetic Resonance, 551–555.

© 2008 *Springer.*

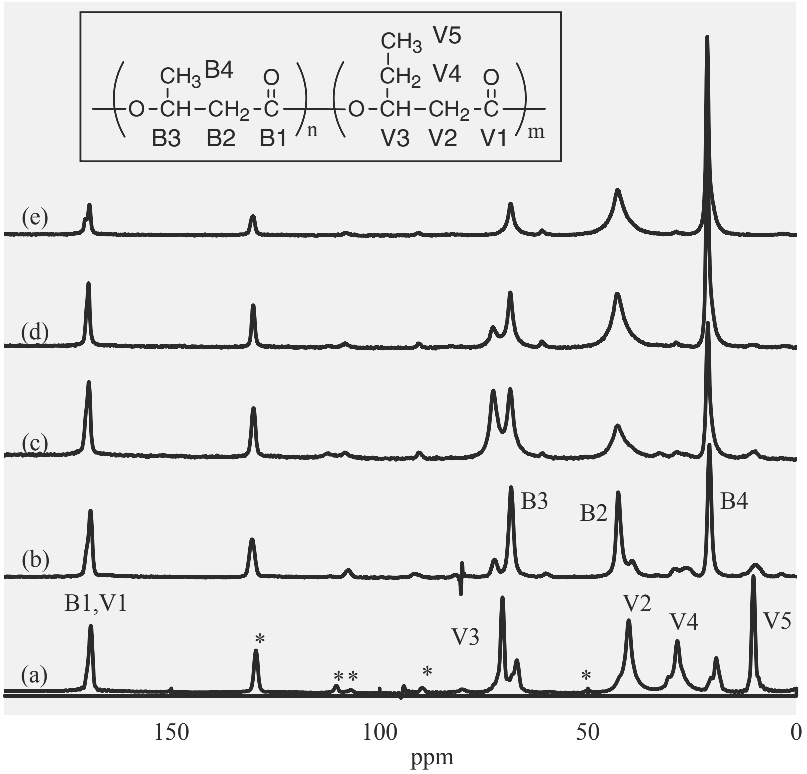

Fig. 1. NMR spectra (100 MHz ^{13}C CPMAS) of (a) P(3HB-*co*-58% 3HV), (b) P(3HB-*co*-21% 3HV), (c) P(3HB-*co*-13% 3HV)^{E}, (d) 1/1 blend of P(3HB)^{E}/P(3HB-*co*-13% 3HV)^{E}, and (e) P(3HB)^{E}. Peaks marked with * are due to the spinning sideband.

of the methine [$B3$, $V3$] carbons between the P(3HB) and P(3HV) lattices. This indicates the difference in the environments of the respective carbons. Assuming a two-phase model, the methine [$B3$, $V3$] resonances are, respectively, resolved into the crystalline and amorphous peaks by a curve fitting procedure. The composition in the crystalline phase can be determined from the relative areas of the resolved peaks.

The relation between the composition in the crystalline phase and the overall composition for P(3HB-*co*-3HV) crystallized in the P(3HB) lattice at 90°C is shown in Figure 3. The solid line in the figure indicates the case where both of the crystalline and amorphous phases have the same composition. It is obvious that the 3HV content in the crystalline phase, $f_{\mathrm{V}}^{\mathrm{c}}$, is smaller than the whole composition, f_{V}, in the P(3HB) crystalline lattice. Figure 3 also shows that the ratio of $f_{\mathrm{V}}^{\mathrm{c}}$ to f_{V} changes. The ratios for the samples with low and high 3HV contents are one-half and two-thirds, respectively. This change was interpreted as a evidence of the structural transition from sandwich lamella to uniform lamella [30]. In the uniform lamella, the comonomer units are assumed to be distributed uniformly. In the sandwich lamella, the comonomer units exist only in the edges and the core is composed entirely of the major units. In P(3HB-*co*-3HV) with low 3HV content where long 3HB sequences are abundant and the entropy gain upon the cocrystallization of comonomers is little, the 3HV units must have a marked tendency to be excluded from inside of the crystalline lamella to the surface where the distortion of the crystalline lattice by the contamination of the HV units can be easily relaxed. So, the sandwich lamella model can be assumed to better describe the isomorphism of P(3HB-*co*-3HV) with low HV content. On the other hand, in P(3HB-*co*-3HV) with high 3HV content, the 3HV units can get into the P(3HB) crystalline lattice because the entropy gain upon the cocrystallization compensates the excess free energy of 3HV cocrystallization.

When the extent of cocrystallization in the P(3HB) lattice has been compared with that in the P(3HV) lattice, more 3HB units cocrystallize in the P(3HV) lattice than 3HV units in the P(3HB) lattice [28,29]. Wide angle X-ray

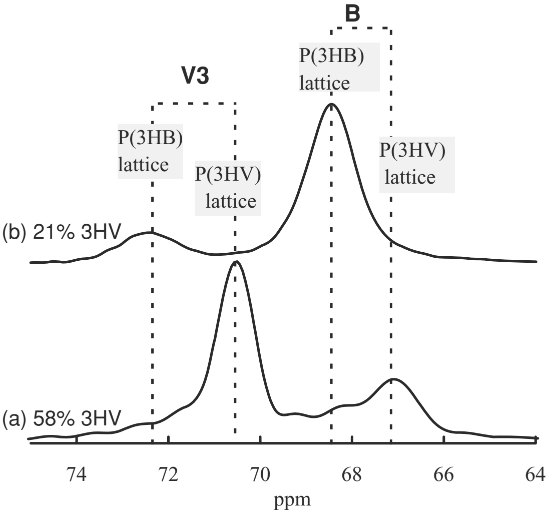

Fig. 2. Expansion of the methine resonances (B3 and V3) of the spectra shown in Figure 1a and b.

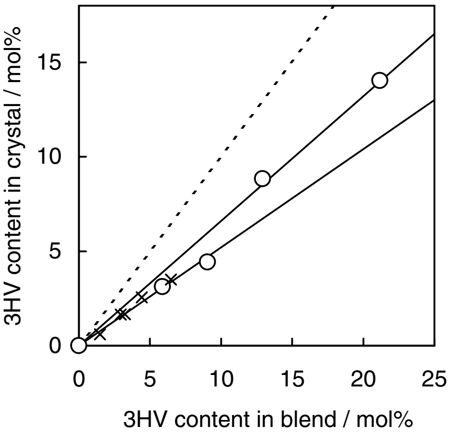

Fig. 3. 3HV content in the crystalline phase of P(3HB-*co*-3HV) copolymers (○) and blends (x) of P(3HB) and P(3HB-*co*-3HV) as a function of overall composition. The broken line indicates the case where both the crystalline and amorphous phases have the same composition. The solid lines indicate the cases where the HV contents in the crystalline phase are one-half and two-thirds of the whole HV content.

diffraction (WAXD) studies show that for the crystals in the P(3HB) lattice the *d*(110) spacing extends as the 3HV content of the overall copolymer increases [21]. On the other hand, no expansion of *d* spacings was observed for the P(3HV) lattice [22]. Thus, the less bulky minor component probably cocrystallizes more easily than the more bulky one.

The effect of crystallization temperature on the extent of cocrystallization has been also investigated [32,33]. The 3HV content in the P(3HB) lattice and the 3HB content in the P(3HV) lattice decrease as the crystallization temperature is increased. The degree of cocrystallization is lowered as the crystallization temperature becomes higher.

The possibility of the isomorphism was also examined for the copolymers of 3HB with 3-hydroxypropionate [3HP] [34,35] and 4-hydroxybutyrate [36]. The similarity in the chemical structures between the comonomers in these copolymers awakened the expectation of the occurrence of isomorphism. Particularly in the former, the difference between the comonomers, 3HB and 3HP, is only in the side chain by a length of methylene group, which is the same as that between the comonomers of P(3HB-*co*-3HV). However, the rapid decrease of the crystallinity (determined by DSC and WAXD) and the absence of the crystalline peaks for one of the comonomers in high-resolution solid-state NMR spectra demonstrate the absence of the isomorphism. This fact indicates the rareness of copolymer isomorphism.

Cocrystallization and Phase Segregation in P(3HB)/P(3HB-*co*-3HV) Blends

The occurrence of isomorphism in P(3HB-*co*-3HV) also induces an expectational hypothesis of the cocrystallization of P(3HB) and P(3HB-*co*-3HV) in their blends. Actually, the cocrystallization occurs when the 3HV contents of P(3HB-*co*-3HV) is small [37–39]. Figure 4 shows the

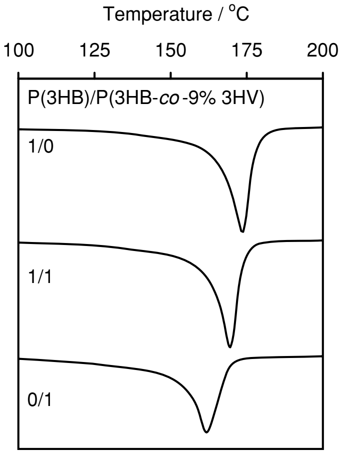

Fig. 4. DSC melting thermograms of P(3HB), P(3HB-*co*-9% 3HV) and their 1/1 blend.

DSC melting curves of P(3HB), P(3HB-*co*-9% 3HV), and their 1/1 blend. The width of the melting peak of the blends is smaller than the difference of the melting temperature of P(3HB) and P(3HB-*co*-9% 3HV). The peak top position (melting temperature) of the blend is right between those of the blend components. These observations suggest that P(3HB-*co*-9% 3HV) cocrystallizes with P(3HB) in this blend.

The cocrystalline phase of P(3HB)/P(3HB-*co*-3HV) is composed of 3HB units from P(3HB), 3HB units from P(3HB-*co*-3HV), and 3HV units from P(3HB-*co*-3HV). Therefore, the complete description of the phase structure of P(3HB)/P(3HB-*co*-3HV) blends needs the determination of both the 3HV and P(3HB) contents in the crystalline phase.

Similar to the case of isomorphous copolymers, high-resolution solid-state ^{13}C NMR can be a usable tool for the determination of the extent of cocrystallization in the polymer blends. The analysis is, however, impossible for the normal P(3HB)/P(3HB-*co*-3HV) blend samples. In high-resolution solid-state ^{13}C CPMAS NMR spectra of P(3HB)/P(3HB-*co*-3HV), the peaks from P(3HB) completely overlap with those from 3HB units of P(3HB-*co*-3HV). Therefore, Yoshie *et al.* [30] made the contrast between P(3HB) and P(3HB-*co*-3HV) by ^{13}C-labeling of the methylene position [$B2$] of P(3HB) [31]. Further, they also used ^{13}C-labeling of the methine position of HV units [V3] when the total 3HV content in the P(3HB)/P(3HB-*co*-3HV) blend is small. Figure 1c–e shows ^{13}C CP-MAS NMR spectra of P(3HB-*co*-13% 3HV)^{E}, 50/50 P(3HB)^{E}/P(3HB-*co*-13% 3HV)^{E}, and P(3HB)^{E}. Assuming a two-phase model, the main chain methine and the main chain methylene resonances are decomposed into the crystalline and amorphous peaks by curve fitting procedure.

The peak areas of the crystalline resonances from the backbone methylene [B2, V2] and the backbone methines [B3, V3] for P(3HB)^{E}/P(3HB-*co*-3HV)^{E} blends are given by

$$A_{\mathrm{B2}} = kr^{h}_{\mathrm{B2}} f^{\mathrm{h}}_{\mathrm{B2}} P^{\mathrm{h}}_{\mathrm{B}} + kr^{\mathrm{c}}_{\mathrm{B2}} f^{\mathrm{c}}_{\mathrm{B2}} P^{\mathrm{c}}_{\mathrm{B}} \tag{1}$$

$$A_{\mathrm{B3}} = kr^{\mathrm{h}}_{\mathrm{B3}} f^{\mathrm{h}}_{\mathrm{B3}} P^{\mathrm{h}}_{\mathrm{B}} + kr^{\mathrm{c}}_{\mathrm{B3}} f^{\mathrm{c}}_{\mathrm{B3}} P^{\mathrm{c}}_{\mathrm{B}} \tag{2}$$

$$A_{\mathrm{V3}} = kr^{\mathrm{c}}_{\mathrm{V3}} f^{\mathrm{c}}_{\mathrm{V3}} P^{\mathrm{c}}_{\mathrm{V}} \tag{3}$$

where k is a constant; A, r, and f are peak areas; ^{13}C population and CP efficiency, respectively: superscripts c and h indicate copolymer [P(3HB-*co*-3HV)^{E}] and homopolymer [P(3HB)^{E}] in the blend, respectively; subscripts B2, B3, and V3 identify the carbon site; P_i^j is a content of i unit from copolymer (j = c) or homopolymer (j = h) in the crystalline phase. From the definition, $P^{\mathrm{h}}_{\mathrm{B}} + P^{\mathrm{c}}_{\mathrm{B}} + P^{\mathrm{c}}_{\mathrm{V}} = 1$. In the present case, we can assume that $f^{\mathrm{h}}_{\mathrm{B2}} = f^{\mathrm{c}}_{\mathrm{B2}} = f_2$ and $f^{\mathrm{h}}_{\mathrm{B3}} = f^{\mathrm{c}}_{\mathrm{B3}} = f^{\mathrm{c}}_{\mathrm{V3}} = f_3$ because the chemical structures of 3HB and 3HV are similar so that the dynamics of the main chain of these units are similarly restricted in the crystalline region. Since the B2 and B3 carbons in P(3HB-*co*-3HV)^{E} and the B3 carbon in P(3HB)^{E} are not ^{13}C-labeled, $r^{\mathrm{c}}_{\mathrm{B2}} = r^{\mathrm{c}}_{\mathrm{B3}} = r^{\mathrm{h}}_{\mathrm{B3}} = r_n$(^{13}C natural abundance) ≈ 0.011. Then, the HV content in the crystalline phase P^{c}_{V} can be estimated from Equations (2) and (3) as

$$P^{\mathrm{c}}_{\mathrm{V}} = \frac{A_{\mathrm{V3}}}{\dfrac{r^{\mathrm{c}}_{\mathrm{V3}}}{r_{\mathrm{n}}} A_{\mathrm{B3}} + A_{\mathrm{V3}}}. \tag{4}$$

The ratio of A_{B2} to A_{B3} is given by

$$\begin{aligned} R &= A_{\mathrm{B2}}/A_{\mathrm{B3}} \\ &= f_2 \left(\frac{r^{\mathrm{h}}_{\mathrm{B2}}}{r_n} P^{\mathrm{h}}_{\mathrm{B}} + P^{\mathrm{c}}_{\mathrm{B}} \right) \Big/ f_3 \left(P^{\mathrm{h}}_{\mathrm{B}} + P^{\mathrm{c}}_{\mathrm{B}} \right). \end{aligned} \tag{5}$$

Considering that $P^{\mathrm{c}}_{\mathrm{B}} = P^{\mathrm{c}}_{\mathrm{V}} = 0$ for pure P(3HB)^{E} and $P^{\mathrm{h}}_{\mathrm{B}} = 0$ for pure P(3HB-*co*-3HV)^{E}, we can determine the P(3HB) content in the crystalline phase of P(3HB)^{E}/P(3HB-*co*-3HV)^{E} by the comparison of the peak area ratio of the blend, R^{blend}, with those of P(3HB)^{E}, R^{PHB}, and P(3HB-*co*-3HV)^{E}, $R^{\mathrm{PHB\text{-}HV}}$, as follows:

$$P^{\mathrm{h}}_{\mathrm{B}} = \left(1 - P^{\mathrm{c}}_{\mathrm{V}}\right) \frac{R^{\mathrm{PHB\text{-}HV}} - R^{\mathrm{blend}}}{R^{\mathrm{PHB\text{-}HV}} - R^{\mathrm{PHB}}}. \tag{6}$$

If $r^{\mathrm{h}}_{\mathrm{B2}}$ is set to be much larger than the natural abundance, R^{PHB} and R^{blend} would be much larger than one and give a relatively large experimental error in $P^{\mathrm{h}}_{\mathrm{B}}$. In order to minimize the error, $r^{\mathrm{h}}_{\mathrm{B2}}$ of P(3HB)^{E} should be carefully selected.

For the blend of P(3HB) and P(3HB-*co*-3HV) with 3HV less than 13%, the P(3HB) content in the crystalline phase, $P^{\mathrm{h}}_{\mathrm{B}}$, is similar to the blend composition, i.e. complete cocrystallization occurs in these blends. P(3HB) and P(3HB-*co*-3HV) chains are equally introduced into the crystalline phase. On the other hand, for P(3HB)/P(3HB-*co*-15% 3HV) and P(3HB)/P(3HB-*co*-21% 3HV) blends, $P^{\mathrm{h}}_{\mathrm{B}}$ is unambiguously larger than the whole blend. At the growing front of the crystalline phase, phase segregation proceeds where P(3HB) chains preferentially enters the crystalline phase. So, the composition in the cocrystalline phase for P(3HB)/P(3HB-*co*-3HV) blends changes depending on the 3HV content of P(3HB-*co*-3HV). The P(3HB-*co*-3HV) content in the cocrystalline phase decreases as the 3HV content of P(3HB-*co*-3HV) increases. These results indicate that the composition in the crystalline phase is determined by the competition of phase segregation and crystallization.

The HV content in the crystalline phase, P_V^c, for $P(3HB)^E/P(3HB\text{-}6\%\ 3HV)^E$ and $P(3HB)^E/P(3HB\text{-}co\text{-}13\%\ 3HV)^E$ blends is also shown in Figure 3. This figure indicates that P_V^c of these blends is approximately one-half of that in the whole blend, which corresponds to the case of the P(3HB-*co*-3HV) copolymers. The coincidence in this ratio indicates the similarity in the structures inside the crystalline phase of the complete-cocrystallizable P(3HB)/P(3HB-*co*-3HV) blends and P(3HB-*co*-3HV) copolymers.

References

1. Doi Y. Microbial Polyesters. VCH publishers Inc: New York, 1990.
2. Doi Y, Steinbüchel A (Eds). Biopolymers, Vol. 3, 3b and 4. John Wiley & Sons: New York, 2001.
3. Hocking PJ, Marchessault RH. Macromolecules 1995;28:6401.
4. Kasperczyk JE. Polymer 1999;40:5455.
5. Doi Y, Kunioka M, Nakamura Y, Soga K. Macromolecules 1986;19:2860.
6. Kamiya N, Yamamoto Y, Inoue Y, Chûjô R, Doi Y. Macromolecules 1989;22:1676.
7. Doi Y, Kunioka M, Nakamura Y, Soga K. Macromolecules 1988;21:2722.
8. Hiramitsu M, Doi Y. Polymer 1993;34:4782.
9. Shimomura E, Kasuya K, Kobayashi G, Shiotani T, Shima Y, Doi Y. Macromolecules 1994;27:878.
10. Doi Y, Kunioka M, Tamaki A, Nakamura Y, Soga K. Makromol. Chem. 1988;189:1077.
11. Kamiya N, Inoue Y, Yamamoto Y, Chûjô R, Doi Y. Macromolecules 1990;23:1313.
12. Dais P, Nedea ME, Morin FG, Marchessault RH. Macromolecules 1989;22:4208.
13. Dais P, Nedea ME, Morin FG, Marchessault RH. Macromolecules 1990;23:3387.
14. Kuwabara K, Gan ZH, Nakamura T, Abe H, Doi Y. Polym. Biomacromol. 2002;3:390.
15. Kuwabara K, Gan ZH, Nakamura T, Abe H, Doi Y. Polym. Biomacromol. 2002;3:1095.
16. Kuwabara K, Gan ZH, Nakamura T, Abe H, Doi Y. Polym. Deg. Stab. 2004;84:105.
17. Yoshie N, Menju H, Sato H, Inoue Y. Macromolecules 1995;28:6516.
18. Yoshie N, Menju H, Sato H, Inoue Y. Polym. J. 1996;28:45.
19. Yoshie N, Inoue Y. Int. J. Biol. Macromol. 1999;25:193.
20. Yoshie N, Goto Y, Sakurai M, Inoue Y, Chûjô R, Doi Y. Int. J. Biol. Macromol. 1992;14:81.
21. Bluhm TL, Hamer GK, Marchessault RH, Fyfe CA, Veregin RP. Macromolecules 1986;19:2871.
22. Kunioka M, Tamaki A, Doi Y. Macromolecules 1989;22:694.
23. Cornibert J, Marchessault RH. J. Mol. Biol. 1972;71:735.
24. Yokouchi M, Chatani Y, Tadokoro H, Teranishi K, Tani H. Polymer 1973;14:267.
25. Yokouchi M, Chatani Y, Tadokoro H, Tani H. Polymer J. 1974;6:248.
26. Sanchez IC, Eby RK. J. Res. Natl. Bur. Stand. Sect. A 1973;77:353.
27. Kamiya N, Sakurai M, Inoue Y, Chûjô R. Macromolecules 1991;24:3888.
28. Kamiya N, Sakurai M, Inoue Y, Chûjô R, Doi Y. Macromolecules 1991;24:2178.
29. VanderHart DL, Orts WJ, Marchessault RH. Macromolecules 1995;28:6394.
30. Yoshie N, Saito M, Inoue Y. Macromolecules 2001;34:8953
31. Doi Y, Kunioka M, Nakamura Y, Soga K. Macromolecules 1987;20:2988.
32. Yoshie N, Sakurai M, Inoue Y, Chûjô R, Doi Y. Macromolecules 1992;25:2046.
33. Barker PA, Barham PJ, Martinez-Salazar J. Polymer 1997;38:913.
34. Cao A, Kasuya K, Abe H, Doi Y, Inoue Y. Polymer 1988;39:4801.
35. Cao A, Asakawa N, Yoshie N, Inoue Y. Polymer 1999;40:3309.
36. Mitomo H, Doi Y. Int. J. Biol. Macromol. 1999;25:201.
37. Saito M, Inoue Y, Yoshie N. Polymer 2001;42:5573.
38. Yoshie N, Fujiwara M, Ohmori M, Inoue Y. Polymer 2001;42:8557.
39. Yoshie N, Saito M, Inoue Y. Polymer 2004;45:1903.

Two-Dimensional NMR Analysis of Stereoregularity of Polymers

A.S. Brar and Gurmeet Singh

Department of Chemistry, Indian Institute of Technology, Delhi, New Delhi 110016, India

Poly(Methyl Methacrylate)

Analysis of couplings by 2D HSQC, TOCSY, and HMBC spectroscopy enable the unambiguous and comprehensive assignments of the carbon and proton resonances of vinyl polymers [1–4].

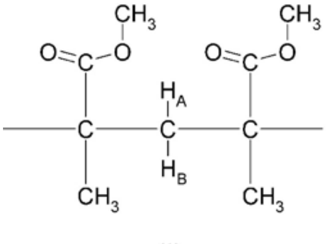

(1)

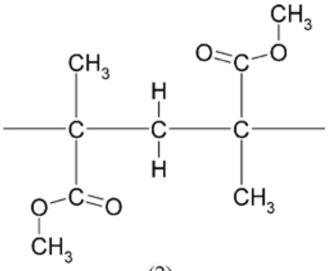

(2)

α-Methyl, methylene, carbonyl, and quaternary carbon resonances are configuration sensitive [5]. Unlike the α-methyl, quaternary, and carbonyl carbon resonances, methylene carbon and proton resonances do not follow chemical shift order so are consequently difficult to assign. The assignments of methylene resonances thus provide a good base for 2D NMR analysis. The main structural difference between meso (1) and racemo (2) diad of PMMA is that in the case of meso diad, methylene proton H_A is flanked by two carbonyl groups and H_B by two methyl groups, while in racemo configuration both the protons have symmetrically placed substituents. The non-equivalent methylene protons H_A and H_B of meso diad show two different couplings with the methylene carbon, giving rise to two cross-peaks in 2D HSQC. Non-equivalent H_A and H_B give a cross-correlation peak in 2D TOCSY spectrum. The two equivalent methylene protons of racemo diad couple with the methylene carbon giving a single cross-peak in 2D HSQC spectrum.

2D HSQC spectrum of methylene region showing carbon resonances ranging from 51.0–55.5 ppm coupled with proton resonances ranging from 1.4 to 2.1 ppm is shown in Figure 1. Cross-peaks I, II and III correspond to *r* centered tetrads having single cross-peaks in 2D HSQC spectrum, assigned to rrr, mrr, and mrm tetrads, respectively. Cross-peaks IV/V and VI/VII correspond to rmr tetrad and are higher order sensitive. Owing to *m* centered methylene group, couplings IV/VI and V/VII were assigned to H_A and H_B protons, respectively. The non-equivalent H_A and H_B protons of rmr tetrad show a cross-relation peak in 2D TOCSY spectrum labeled "b" in Figure 2. The cross-peaks VIII and IX were attributed to H_A and H_B of mmr tetrad and the non-equivalent protons gave cross-correlation peak "a" in 2D TOCSY spectrum.

The proton resonances assigned using 2D HSQC spectrum and confirmed by 2D TOCSY spectra were applied to analyze the 2D HMBC spectrum. Cross-peaks 1 and 3 were assigned to the couplings between α-methyl protons of rr triad with methylene carbon of rrr and mrr tetrads, respectively. Cross-peaks 2, 4, and 7 were attributed to couplings between α-methyl protons of mr triad with methylene carbons of rmr, mrr, and mrm tetrads, respectively. Couplings between α-methyl protons of mm triad with methylene carbon of mmr and mmm triad resulted in cross-peaks 5 and 6, respectively. Cross-peak 8 was assigned to the coupling of methylene proton of the rmr tetrad with methylene protons of the adjacent mrm unit. Similarly, cross-peak 9 was assigned to the coupling between methylene carbon and protons of the adjacent rrr tetrads in the rrrr pentad. Cross-peaks 10/12 and 11/13 were assigned to the couplings between methylene protons of the rmr tetrad with methylene carbon of the mrr unit in the rmrr pentad. The cross-peak 14 was assigned to the coupling of mrr methylene carbon with rrr protons in

Graham A. Webb (ed.), Modern Magnetic Resonance, 557–562.

© 2008 *Springer.*

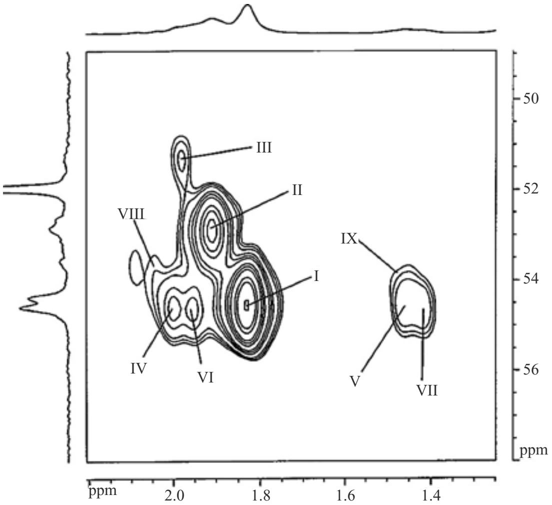

Fig. 1. 300 MHz HSQC spectrum of methylene region of the PMMA at 45 °C.

the mrrr pentad. The assignments of the methylene carbon and proton resonances are shown in the respective 1D NMR projection in the Figure 3. The 2D NMR spectral analysis further substantiated the assignments of the carbon and proton resonances.

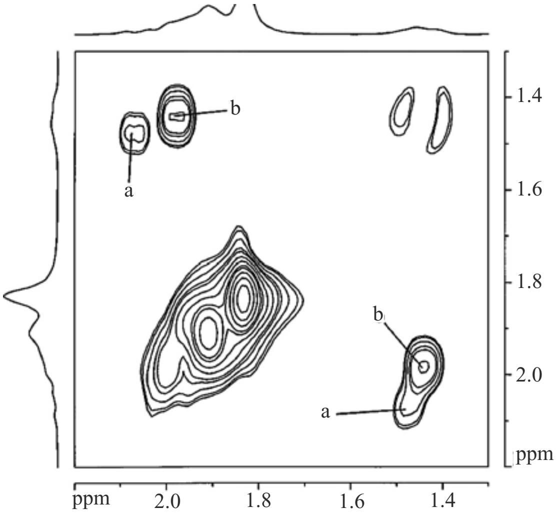

Fig. 2. 300 MHz TOCSY spectrum showing couplings of H_A and H_B protons of meso centered methylene of PMMA at 45 °C.

Methyl Acrylate (A)/Methyl Methacrylate (B) Copolymer

Analysis of the methylene, α-methyl and methine carbon and proton resonances of the methyl acrylate/methyl methacrylate copolymers can be done by the analysis of HSQC and TOCSY spectra. Assignments of the complex and overlapping carbonyl carbon resonances of the methyl acrylate/methyl methacrylate copolymers is a complicated and speculative procedure. The carbonyl carbon assignments based on the experimental analysis of their couplings with methylene protons and α-methyl protons (assigned using the 2D HSQC and TOCSY spectra) using HMBC spectra can be done to overcome any speculation in the resonance analysis (Brar *et al.*, unpublished work).

2D HSQC spectrum of A/B copolymer of composition $F_A = 0.58$ is given in the Figure 4 and the assignments are listed in Table 1. The methylene protons H_a and H_b of both the AmB and ArB centered tetrads are non-equivalent as shown in Scheme 1, thus resulting in two cross-peaks by coupling with the methylene carbon in the 2D HSQC spectra. 2D TOCSY spectrum is given in Figure 5 and the assignments of cross-correlation peaks are given in Table 2. H_a and H_b of AmB and ArB being non-equivalent also give cross-correlation peaks in the 2D TOCSY spectrum, enabling to differentiate between cross-peaks of AmB and ArB in the 2D HSQC spectra. AA and BB diad centered tetrads show compositional and conformational sensitivity. The reasoning given above in conjunction with the analysis of change in the intensity of cross-peaks with copolymer composition can be applied to assign the resonances.

Methine group of methyl acrylate can be assigned up to triad level of compositional sensitivity in the copolymer, based on the 2D HSQC assignments. Cross-peaks 25, 26, and 27 are assigned to BAB, BAA, and AAA triads. 2D TOCSY studies were used to ascertain these assignments by analyzing 1, 3 bond order couplings between methylene protons and methine protons of A monomer in AA and AB centered methylene cross-correlation peaks VII to X in Figure 5.

The assignments of the couplings marked on the HMBC (Figure 6) are listed in the Table 3. The HMBC spectral analysis enabled to assign the carbonyl carbon resonances by analyzing the three bond couplings with α-methyl protons of the same methyl methacrylate monomer unit, enabling to assign the B unit centered triads. The rest of carbonyl carbon resonances were analyzed from the couplings of methylene protons with the carbonyl carbon. On the basis of the 2D HMBC spectral analysis, the carbonyl carbon resonances were assigned as shown in the Figure 7.

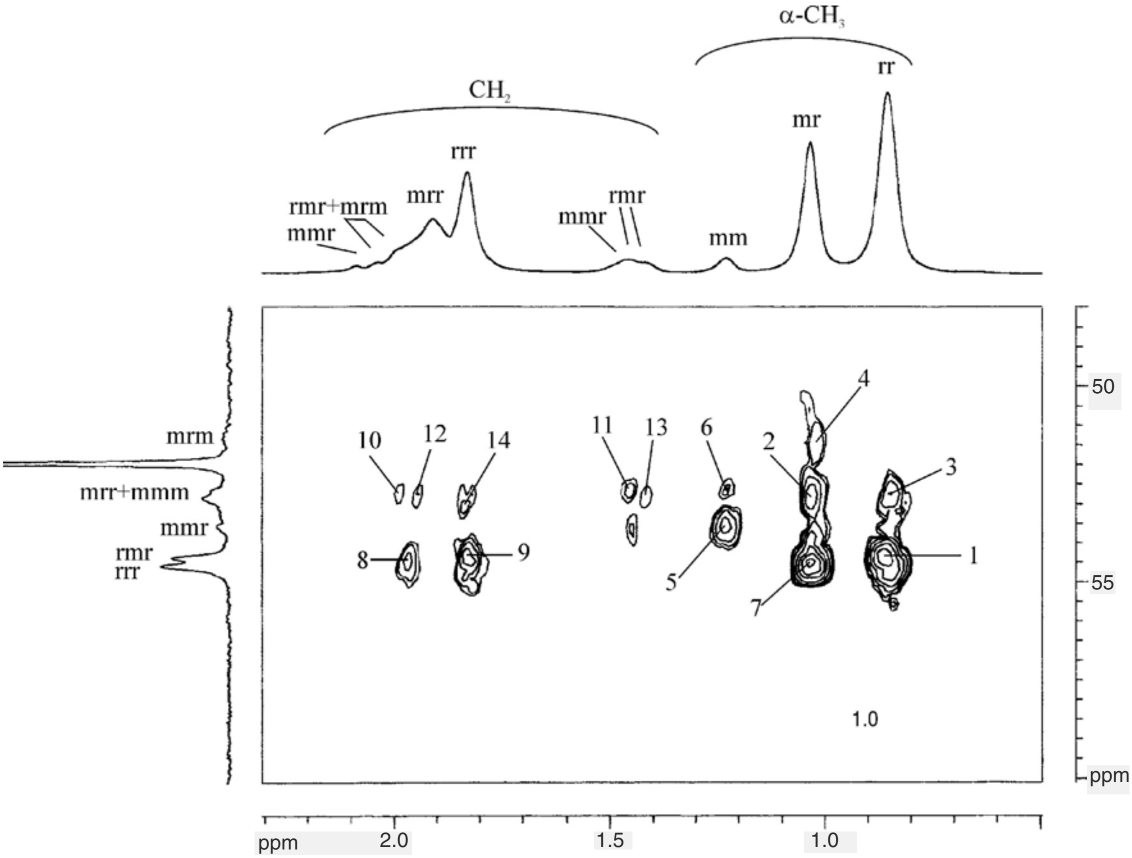

Fig. 3. 300 MHz HMBC spectrum showing three bond couplings between methylene carbons with α-methyl protons and adjacent methylene protons of PMMA at 45 °C.

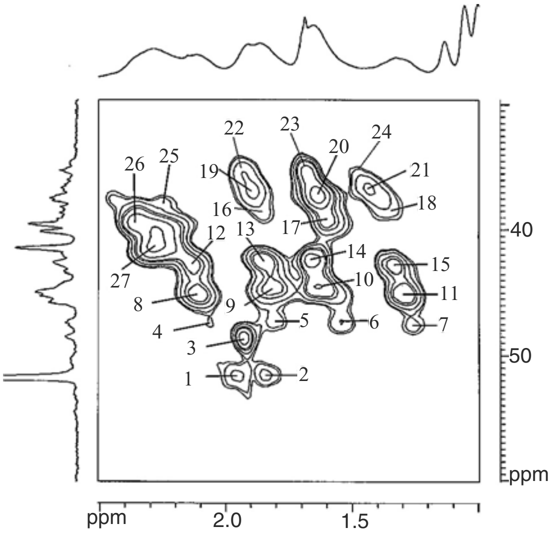

Fig. 4. 300 MHz HSQC spectrum, of A/B copolymer of composition $F_A = 0.58$, showing methylene and methine region at 45 °C.

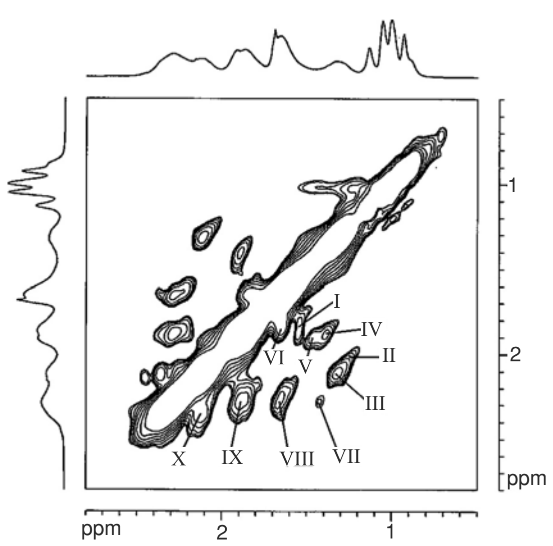

Fig. 5. 300 MHz TOCSY NMR spectrum, of A/B copolymer of composition $F_A = 0.58$ at 45 °C.

Table 1: Assignments of the methylene carbon resonances of methyl acrylate (A)/methyl methacrylate (B) copolymers from the HSQC spectrum

Cross-peak no.	Cross-peak assignment	(ppm) Cross-peak position (ppm)
1	ABBB	51.5/1.95
2	ABBB	51.5/1.84
3	ABBA	48.4/1.92
4	BAmBB (H_a)	47.3/2.04
5	BArBB (H_a)	47.0/1.77
6	BArBB (H_b)	47.0/1.52
7	BAmBB (H_b)	47.3/1.23
8	AAmBB/BAmBA (H_a)	44.8/2.1
9	AArBB/BArBA (H_a)	44.3/1.82
10	AArBB/BArBA (H_b)	44.3/1.62
11	AAmBB/BAmBA (H_b)	44.8/1.29
12	AAmBA (H_a)	42.6/2.13
13	AArBA (H_a)	42.2/1.84
14	AArBA (H_b)	42.2/1.65
15	AAmBA (H_b)	42.6/1.33
16	BAmAB (H_a)	38.4/1.86
17	BArAB	38.8/1.62
18	BAmAB (H_b)	38.4/1.37
19	AAmAB (H_a)	36.5/1.89
20	AArAB	36.9/1.63
21	AAmAB (H_b)	36.4/1.43
22	AAmAA (H_a)	35.3/1.93
23	AArAA	35.1/1.67
24	AAmAA (H_b)	35.3/1.46

Table 2: ^1H–^1H cross-correlations between non-equivalent geminal protons of methylene and between methine protons and methylene protons in methyl acrylate (A)/methyl methacrylate (B) copolymers observed from the TOCSY spectra

Cross-correlation peak no.	Coupled protons		Cross-correlation peak position (ppm)
	Proton I	Proton II	
I	CH_2 of BArBB (H_a)	CH_2 of BArBB (H_b)	1.77/1.52
II	CH_2 of BAmBB (H_a)	CH_2 of BAmBB (H_b)	2.03/1.23
III	CH_2 of AAmBB/BAmBA/AAmBA (H_a)	CH_2 of AAmBB/BAmBA/AAmBA (H_b)	2.13/1.3
IV	CH_2 of BAmAB/AAmAB (H_a)	CH_2 of BAmAB/AAmAB (H_b)	1.88/1.35
V	CH_2 of AAmAA (H_a)	CH_2 of AAmAA (H_b)	1.89/1.44
VI	CH_2 of AArBB/BArBA/AArBA (H_a)	CH_2 of AArBB/BArBA/AArBA (H_b)	1.84/1.64
VII	CH of A	CH_2 of AmA (H_b)/AmB (H_b)	2.2/1.4
VIII	CH of A	CH_2 of ArA/ArB (H_b)	2.2/1.6
IX	CH of A	CH_2 of AmA (H_a)/ArB (H_a)	2.2/1.8
X	CH of A	CH_2 of AmB (H_a)	2.3/2.1

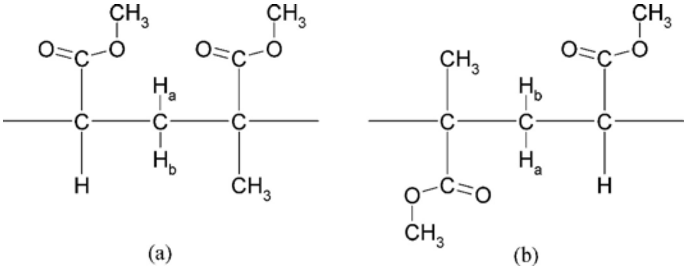

Scheme 1. AmB and ArB diads showing non-equivalent H_a and H_b methylene protons.

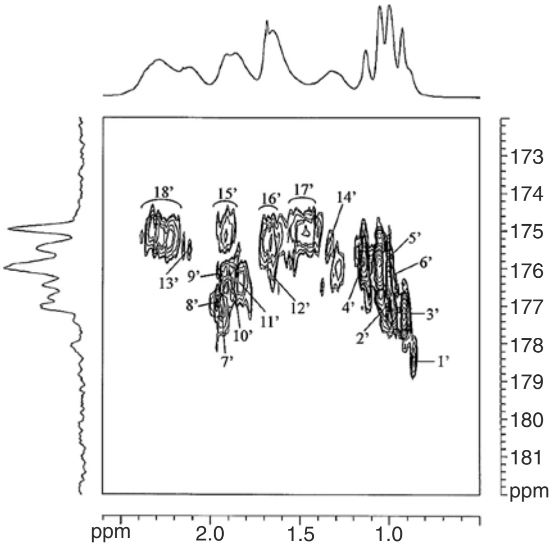

Fig. 6. 2D HMBC spectrum, of A/B copolymer of composition $F_A = 0.58$, showing the couplings between methylene carbon with α-methyl protons and protons of the adjacent methylene group.

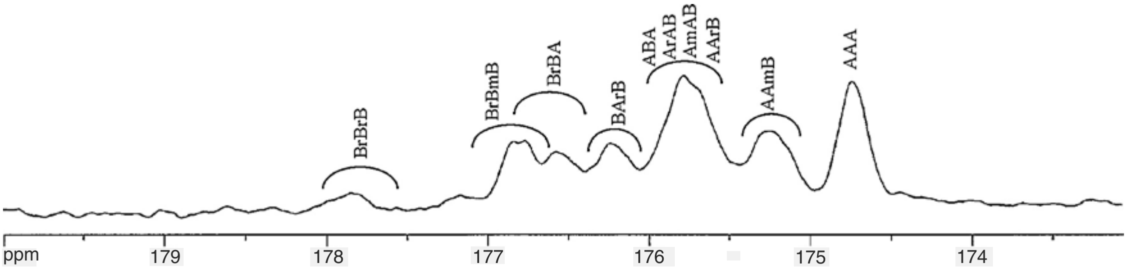

Fig. 7. Assigned carbonyl carbon resonances of the A/B copolymer of composition $F_A = 0.58$.

Table 3: Couplings of carbonyl carbon with α-methyl protons (α-CH_3) and methylene protons observed from the 2D HMBC spectra

Cross-peak no.	Carbonyl carbon nuclei	Proton nuclei	Cross-peak position
1′	BrBrB	α-CH_3BrBrB	177.9/0.86
2′	BrBA	α-CH_3BrBA	176.6/0.99
3′	BrBA	α-CH_3BrBA	176.9/0.91
4′	ABA	α-CH_3ABA	175.8/1.14
5′	ABA	α-CH_3ABA	175.9/1.05
6′	ABA	α-CH_3ABA	176.1/1.00
7′	ABrB	CH_2ABBA	177.1/1.92
8′	ABrB	CH_2ABBB	177.0/1.96
9′	ABmB	CH_2ABBA	176.1/1.92
10′	ABmB	CH_2ABBB	176.1/1.86
11′	BArB	CH_2BArBA (H_a)	176.4/1.82
12′	BArB	CH_2BArBA (H_b)	176.3/1.64
13′	AAmB	CH_2AAmBA (H_a)	175.4/2.12
14′	AAmB	CH_2AAmBA (H_b)	175.4/1.33
15′	AAA	CH_2AmA (H_a)	174.7/1.9
16′	AAA	CH_2ArA	174.7/1.65
17′	AAA	CH_2AmA (H_b)	174.7/1.4

References

1. Wyzgoski FJ, Rinaldi PL, McCord EF, Stewart MA, Marshall DR. “Poly(*n*-butyl acrylate-*co*-carbon monoxide-*co*-ethylene) Characterization by High-Temperature Two-Dimensional NMR at 750 MHz” Macromolecules. 2004;37:846.
2. Xie X, Wittmar M, Kissel T. “A Two-Dimensional NMR Study of Poly(vinyl(dialkylamino)alkylcarbamate-*co*-vinyl acetate-*co*-vinyl alcohol)” Macromolecules. 2004;37:4598.
3. Monwar M, Oh SJ, Rinaldi PL, McCord EF, Hutchinson RA, Buback MM, Latz H. “Characterization of n-butyl acrylate centered triads in poly(n-butyl acrylate-co-carbon monoxide-co-ethylene) by isotopic labeling and two dimensional NMR” Anal. Bioanal. Chem. 2004;378:1414.
4. Brar AS, Kaur S. “Microstructure determination of methyl methacrylate and n-butyl acrylate copolymers synthesized by atom transfer radical polymerization with two-dimensional NMR spectroscopy” J. Polym. Sci. Polym. Chem. 2005;43:1100.
5. Brar AS, Singh G, Shankar R. “Structural investigations of poly(methyl methacrylate) by two-dimensional NMR” J. Mol. Struct. 2004;703:69.

Quantitative Analysis of Conformations in Disordered Polymers by Solid-State Multiple-Quantum NMR

Hironori Kaji

[1]*Institute for Chemical Research, Kyoto University, Uji, Kyoto 611-0011, Japan; and* [2]*PRESTO, Japan Science and Technology Agency, 4-1-8 Honcho Kawaguchi, Saitama, Japan*

Introduction

The techniques of solid-state NMR have been still growing and now varieties of methods exist for the structure characterization. The multiple-quantum coherences are particularly useful in NMR for the precise analysis of the local structures in disordered as well as ordered polymers. In this chapter, we show some examples of the quantitative conformation characterization of disordered and amorphous solid polymers by the advanced solid-state multiple-quantum NMR spectroscopy.

Characterization of Conformations in Atactic Polymers by Two-Dimensional Experiments [1–3]

The characterization of the microscopic structure of polymers in the solid state is crucial in polymer science. Although the crystal structures have been determined by wide-angle X-ray diffraction (WAXD) for many polymers, the structures for some polymers are still controversial. Atactic poly(acrylonitrile) (aPAN) is one of the examples. The WAXD measurements of oriented aPAN fibers show only diffuse patterns along the meridian. The conformational disorders are suggested and several models have been proposed for the crystal structure [4], however, the details have not been characterized. In this section, we show the precise determinations of the conformations in aPAN by two-dimensional solid-state double-quantum NMR spectroscopy (2D DOQSY) [1,2,5,6] and two-dimensional solid-state heteronuclear multiple-quantum correlation NMR spectroscopy (2D HMQC) [3] for the labeled samples in Figure 1. These solid-state NMR measurements give quantitative torsion angles even in such a disordered solid polymer.

The 2D DOQSY experiment correlates the sum of the chemical shifts of two labeled spins, $(\omega_a + \omega_b)$, and the individual chemical shift, ω_a or ω_b. Since the chemical shift without sample spinning is orientation-dependent, the resulting 2D spectrum determines the torsion angles between the relevant two spins through their relative orientation. Figure 2a shows the experimental ^{13}C 2D DOQSY spectrum of $^{13}CH_2$-carbon labeled atactic PAN ($^{13}CH_2$-aPAN, see Figure 1a) [1]. The spectral patterns depend on the two successive torsion angles intervening between the two labeled $^{13}CH_2$ sites and therefore these two torsion angles can be characterized. From the best fit simulation in Figure 2b, the trans/gauche ratio is determined as 90:10%.

More precise information can be obtained by ^{13}C 2D DOQSY experiments of ^{13}CN-carbon labeled atactic PAN (^{13}CN-aPAN, see Figure 1b) [2]. Figure 3 shows the experimental and simulated ^{13}C 2D DOQSY spectra of ^{13}CN-aPAN. This experiment has three advantages compared with the experiment for $^{13}CH_2$-aPAN. First, due to the much wider chemical shift anisotropy (CSA) span of ^{13}CN carbons (363 ppm) compared with that of $^{13}CH_2$ carbons (~45 ppm), significantly better angular resolution is obtained as shown in Fig. 3b and c. Second, the axially symmetric chemical shift tensors of the $^{13}C{\equiv}N$ carbons probe specifically the $^{13}C{\equiv}N$ triple bond directions and the orientation of the chemical shift tensor is well-defined without ambiguities. Third, the torsion angles of meso and racemo dyads can be determined simultaneously and selectively even if their conformations are the same. This experiment observes the correlation between the relevant two $^{13}C{\equiv}N$ triple bond directions and the different CN–CN orientational correlations are given for meso and racemo dyads. An example is shown in the simulated spectra of Figure 3b and e. The meso and racemo patterns with the same trans–trans backbone conformation are drastically different.

The experimental 2D DOQSY spectrum in Figure 3a does not give sharp ridges, which clearly shows the torsion angles are widely distributed. It is also found that the average torsion angles are significantly deviated from the ideal 180° trans state for meso-dyads. The best-fit simulation in Figure 3d indicates that the two $^{13}C{\equiv}N$ bond directions in meso trans–trans dyads make an average angle θ_{CNCN} of 20° with the standard deviation of the Gaussian distribution, $\sigma = 25°$. This CN–CN correlation can be translated into the backbone torsion angles. The typical average torsion angles for meso trans–trans dyads

Graham A. Webb (ed.), Modern Magnetic Resonance, 563–566.

© 2008 *Springer.*

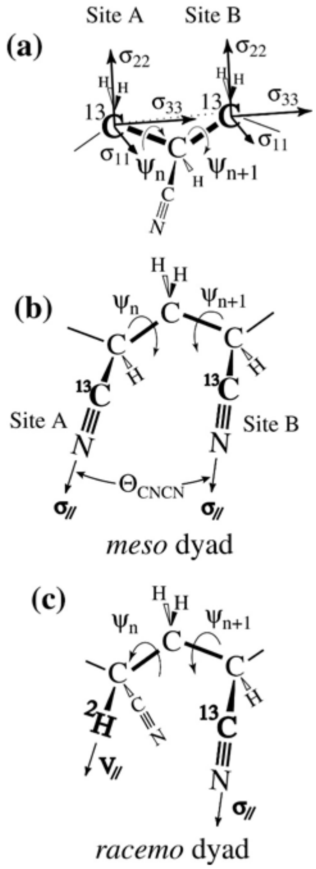

Fig. 1. Chemical structures of the isotopically labeled aPAN samples in this study.

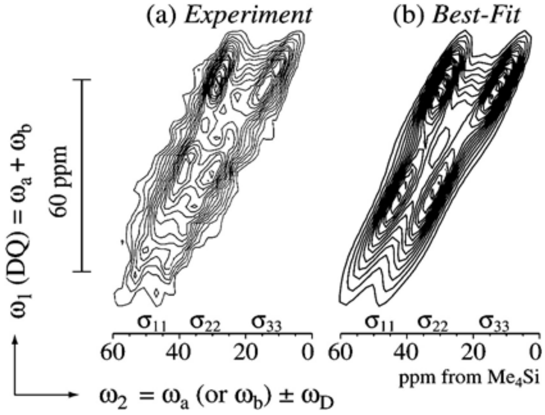

Fig. 2. ^{13}C 2D DOQSY spectra of $^{13}CH_2$-aPAN. (a) Experimental spectrum. (b) Best-fit simulation.

are (+160°, +160°) and (±170°, ∓170°) with $\sigma = 20°$ for the both torsion angles.

The torsion angles of (180°, 180°) with $\sigma = 10°$ and those of (+170°, +70°) with $\sigma = 10°$ for racemo trans–trans dyads and meso trans-gauche dyads, respectively, are also suggested from this experiment. These torsion angles are more accurately determined from the following ^{2}H-^{13}C 2D HMQC NMR experiments [3], since 2D DOQSY spectra for these two patterns are similar as shown in Figure 3e and f.

The ^{2}H-^{13}C 2D HMQC NMR experiments also have the above-mentioned three advantages. Figure 4b and c exemplifies the good angular resolution. The distinction of meso and racemo dyads is shown in Figure 4b and e. Different from the 2D DOQSY experiments, the HMQC pattern of racemo trans–trans dyads is significantly different from that of meso trans-gauche dyads. Therefore, 2D HMQC is complementary experiment and the most accurate analysis is possible for racemo trans–trans dyads.

Figure 4a shows the experimental 2D HMQC spectrum of α-hydrogen deuterated and ^{13}CN-carbon labeled atactic PAN (^{2}H/^{13}CN-aPAN, see Figure 1c). From the best-fit simulation in Figure 4d, the torsion angles for racemo trans–trans dyads is found to be centered at (180°, 180°). Even for the racemo trans–trans dyads, the torsion angles are found to be distributed with $\sigma = 10°$.

The PAN studied here is atactic. Therefore, meso and racemo dyads are statistically distributed along one polymer chain, which cannot be separated. Moreover, due to the existence of these dyads, the conformation is disordered. The combination of the above-mentioned two-dimensional solid-state NMR experiments enables us the determination of backbone torsion angles of meso and racemo dyads "separately" and "quantitatively" with the accuracy of ± 5–10° even in such a disordered atactic polymer. The results show that the torsion angles in meso trans–trans dyads are deviated from the ideal trans and the distributions are wider than those in racemo trans–trans dyads. The difference in meso and racemo dyads would be originated from larger steric hindrance and larger electric dipole replusion between CN groups in meso trans–trans dyads.

Strictly speaking, the conformations determined as trans and gauche here extend beyond a single conformational region due to the wide torsion angle distributions. A knowledge about the intermolecular CN–CN alignments is also obtained. See references [2,3] for further details.

Selective Observation of Respective Conformers in Polymers by Zero-Quantum (ZQ) Experiments [7]

The backbone conformation in amorphous polymers is also important to characterize and the 2D DOQSY

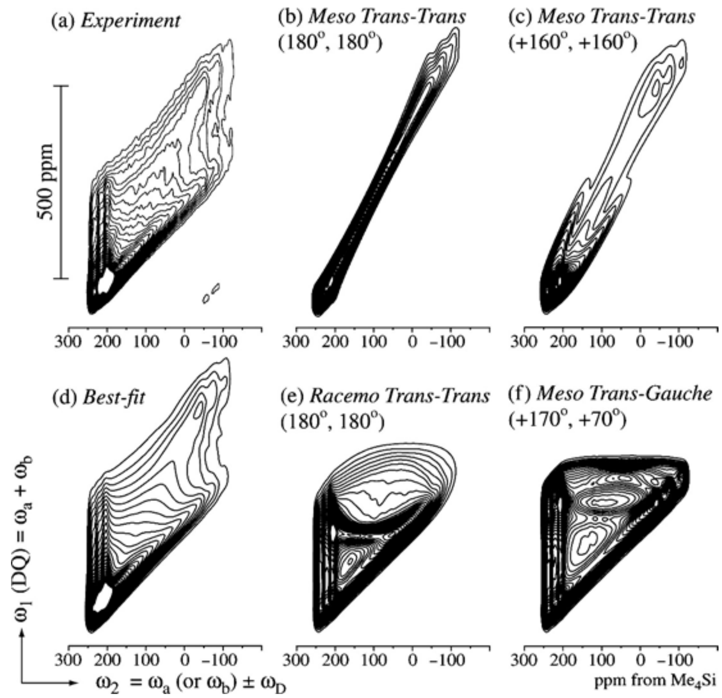

Fig. 3. ^{13}C 2D DOQSY spectra of ^{13}CN-aPAN. (a) Experimental spectrum. (b–f) Simulated spectra.

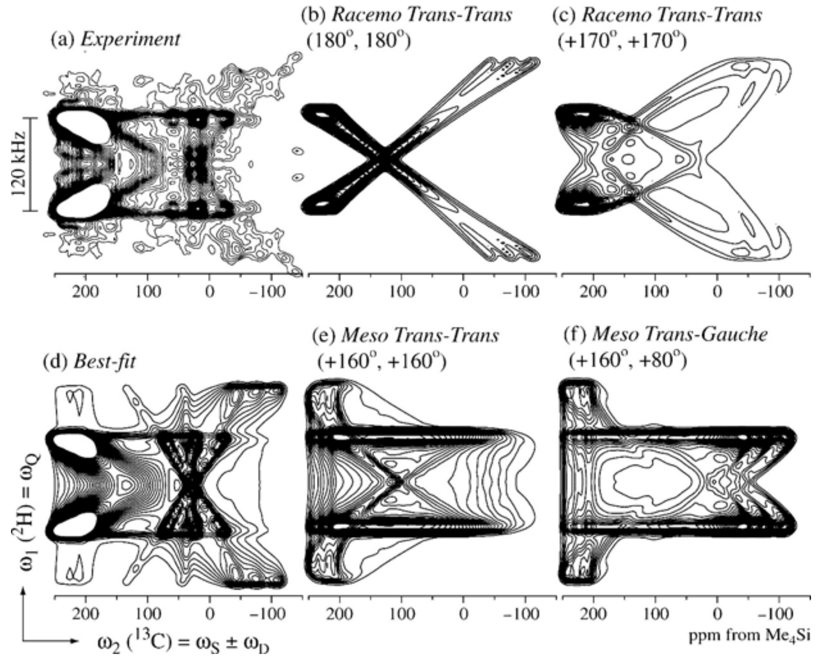

Fig. 4. ^{2}H-^{13}C 2D HMQC spectra of ^{2}H/^{13}CN-aPAN. (a) Experimental spectrum. (b–f) Simulated spectra.

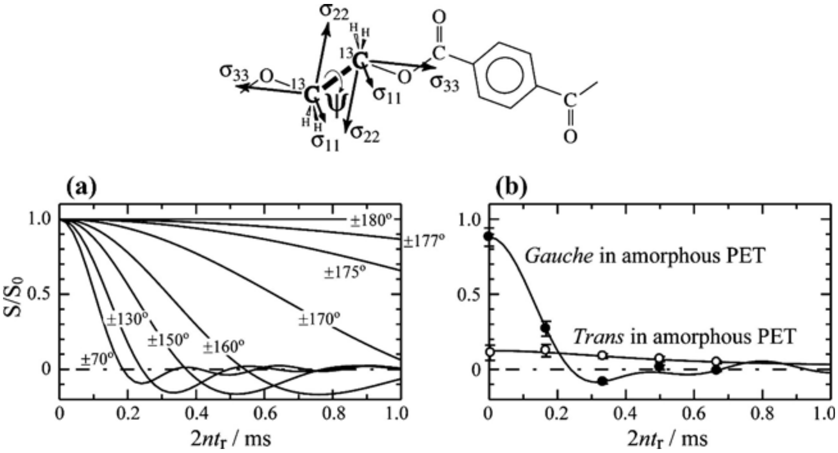

Fig. 5. (a) The torsion angle dependence of calculated ZQ-CSA-dephasing curves. (b) ZQ-CSA-dephasing curves for trans and gauche conformers in doubly $^{13}CH_2$-labeled amorphous PET.

experiment is also used for the quantification of the $O^{13}CH_2-^{13}CH_2O$ torsion angles of poly(ethylene terephthalate) (PET) [6]. The DOQSY experiments determine trans/gauche ratio and the average torsion angle of the gauche conformer quite precisely. However, the precise torsion angle could not be obtained for the trans conformer and the distinction of amorphous trans and crystalline trans was difficult. We recently develop two solid-state NMR methods, ZQ-CSA-dephasing NMR and (DQ-2SQ)-CSA-dephasing NMR, for identifying and quantifying conformations of ^{13}C-labeled polymers under (MAS) [7]. The new NMR methods can distinguish the two trans states quantitatively. Here, we show the conformational analysis of the $O^{13}CH_2$-$^{13}CH_2O$ moieties in amorphous and semicrystalline PET by the ZQ-CSA-dephasing method. This method is based on ZQ dephasing under the recoupled CSA, and the observed magnetization is dephased by the relative orientation of relevant two ^{13}C sites. The amorphous trans component, which cannot be detected by traditional CP/MAS experiments due to complete overlap with dominant gauche signal, is clearly observed by this method.

Figure 5 shows the ZQ-CSA-dephasing curves for doubly $^{13}CH_2$-labeled amorphous PET. Signals of near-trans conformations decay more slowly than those near gauche, which enables (1) selective observation of amorphous trans and gauche components, (2) the determination of trans/gauche ratio, and (3) the quantification of torsion angles of respective components. The angular resolution is especially high for near-trans conformations as shown in Figure 5a. From the decay curves, it is determined that the trans fraction is 12% and the torsion angle is distributed with $\sigma = 16^\circ$ around 180° for amorphous PET. In semicrystalline PET (the data not shown here), the crystalline trans:crystalline gauche:amorphous trans:amorphous gauche = 23:0:20:57%. The trans fraction in the amorphous regions of semicrystalline PET, 26%, is found to be significantly higher than the 12% in amorphous PET.

The new methods shown here also can be used for the definite conformational assignment of respective resonance lines in MAS NMR spectra. The CP/MAS experiment is a versatile method because the spectra (the isotropic chemical shifts) contain a large amount of information, such as conformation, hydrogen bonds, intermolecular packing, dynamics, etc. However, the origin of the change of the isotropic chemical shifts is often unclear and the reliable analysis cannot be carried out without ambiguity. The ZQ-CSA-dephasing NMR or (DQ-2SQ)-CSA-dephasing NMR gives direct relation between the isotropic chemical shifts and torsion angles. Once the assignment is done, conformation analysis can be easily carried out by simple CP/MAS experiments without the need of isotopic labeling. Then, the CP/MAS method would become more useful tool than ever.

References

1. Kaji H, Schmidt-Rohr K. Macromolecules 2000;33:5169.
2. Kaji H, Schmidt-Rohr K. Macromolecules 2001;34:7368.
3. Kaji H, Schmidt-Rohr K. Macromolecules 2001;34:7382.
4. See ref. [1] and references therein.
5. Schmidt-Rohr K. Macromolecules 1996;29:3975.
6. Schmidt-Rohr K, Hu W, Zumbulyadis N. Science 1998;280:714.
7. Kaji H, Schmidt-Rohr K. Macromolecules 2002;35:7993.

Polymer Microstructure: The Conformational Connection to NMR

Alan E. Tonelli
Fiber and Polymer Science Program, North Carolina State University, Raleigh, NC 27695-8301, U.S.A.

Introduction

Of the nuclei (^{1}H and ^{13}C), which both possess nuclear spin and are common to synthetic polymers, ^{13}C is by far the more sensitive NMR spin probe of polymer microstructure. ^{13}C NMR spectra suffer neither from a narrow dispersion of chemical shifts nor from extensive homonuclear, scalar spin–spin coupling, which both complicate the analyses of ^{1}H NMR spectra. It is the sensitivity of ^{13}C resonance frequencies or chemical shifts, δ^{13}C, to the microstructures of polymers, which makes ^{13}C NMR so useful as a structural probe.

For example, the 25 MHz ^{13}C NMR spectra presented in Figure 1 [1] are for three polypropylene (PP) samples with different stereoregularities: isotactic PP, with all meso = m diads, syndiotactic PP, with all racemic = r diads, and atactic PP with a random distribution of m and r diads. The microstructural sensitivity of ^{13}C NMR is plainly evident in the distinct spectra observed for these PP samples. While the ^{13}C resonances of PPs are spread over an ∼30 ppm range, all ^{1}H resonances observed for PPs are within 1 ppm of each other. In addition, the absence of homonuclear (^{13}C–^{13}C) and the easy removal of heteronuclear (^{13}C–^{1}H) scalar couplings further simplify the ^{13}C spectra. Both of these advantages result in the kind of microstructural sensitivity seen in the methyl carbon region of the PP spectra, where for the atactic PP sample all 10 possible pentad stereosequences (mmmm, rrrr, mmmr, rrmr, etc.) are distinctly observed. At higher fields, we will subsequently show that the methyl carbon resonances show sensitivity to even longer stereosequences (heptads: mmmmmm, rrrrrr, mmrmmr, etc.) [1,2]. The ^{13}C NMR spectra of PPs are thus sensitive to stereosequences extending over at least four (pentads) and six (heptads) bonds in both directions along the PP backbone. This long-range sensitivity to microstructural detail makes ^{13}C NMR the most valuable tool for determination of polymer structures.

The ^{13}C nucleus occurs at a natural abundance of only 1.1% and has a small magnetic moment, about one-fourth that of the proton. Both factors tend to mitigate against the observation of high-resolution ^{13}C NMR spectra. However, the decrease in the observational sensitivity of the ^{13}C nucleus can be compensated for by employing a greater number of spectral accumulations during the Fourier transformation (FT) recording of spectra, leading to suitable signal-to-noise ratios. Though requiring the application of several observational techniques [3,4] to overcome the inherent insensitivity of the ^{13}C nucleus, ^{13}C NMR spectroscopy can be and is used to greater advantage for probing the molecular structures of organic molecules, including polymers. The reason is the much greater sensitivity of ^{13}C nuclear shieldings to molecular structure, in the 200 ppm range for neutral organics compared with 10–12 ppm for ^{1}H shieldings, for example. The increased sensitivity of ^{13}C resonance frequencies/chemical shifts to local microstructural environments has generally made ^{13}C NMR spectroscopy the method of choice for investigating molecular structure.

^{13}C NMR Spectral Assignments

To realize the full potential of ^{13}C NMR in microstructural studies of polymers, the connections between constituent microstructural features and their corresponding effects on chemical shifts must be established. Traditionally, synthesis and NMR spectroscopic analysis of model compounds and polymers with known microstructures have provided the means for assigning the NMR spectra of polymers to their underlying microstructural features. These laborious approaches to the assignment of the NMR spectra of polymers could be eliminated if it were possible to predict the ^{13}C NMR chemical shifts expected for each type of carbon nucleus residing in all possible structural environments.

The magnetic field B_i required to obtain the resonance condition for nucleus i at a particular irradiating rf field (B_1) is not equal to the applied static field B_0, but is instead $B_i = B_0(1 - \sigma)$, where the nuclear screening constant, σ, depends on the chemical structural environment of nucleus i. It is the cloud of electrons moving about in the vicinity of a nucleus which shields it from the applied field B_0 by producing small local magnetic fields. Any structural feature that alters the electronic environment of a nucleus will affect its screening constant σ and lead to an alteration in its resonance frequency or chemical shift δ_i.

Graham A. Webb (ed.), Modern Magnetic Resonance, 567–574.
© 2008 *Springer.*

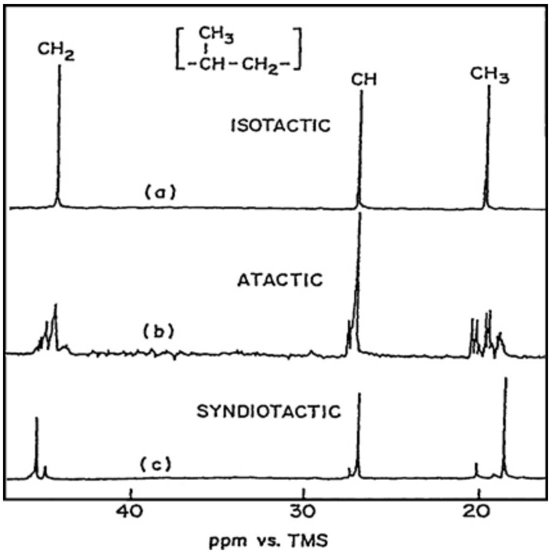

Fig. 1. 25 MHz ^{13}C NMR spectra of (a) isotactic, (b) atactic, and (c) syndiotactic PPs [1].

To date it has not been possible to make sufficiently accurate predictions of ^{13}C NMR chemical shifts even when applying the most sophisticated *ab initio* quantum mechanical methods [5–7 and especially 8]. Instead, the effects of substituents and local conformation have been used to correlate the observed ^{13}C NMR chemical shifts and the microstructures of molecules, including polymers [9,10].

^{13}C NMR studies of paraffinic hydrocarbons [11–15] have led to the following substituent effect rules. Carbon substituents attached at α-, β-, and γ-positions to an observed carbon produce a deshielding of ca. 9 ppm, a deshielding of ca. 9 ppm, and a shielding of ca. −2 to −3 ppm, respectively, compared with an observed carbon that is unsubstituted. In PP, for example, the CH_3 carbons possess 1α, 2β, and 2γ carbon substituents; the CH carbons possess 3α, 2β, and 4γ carbon substituents; and CH_2 carbons 2α, 4β, and 2γ carbon substituents. Based on $\alpha = \beta = 9$ ppm and $\gamma = -2$ ppm, we would expect the CH_2 carbons to resonate downfield from the CH carbons by $-1\alpha + 2\beta - 2\gamma = -9 + 18 + 4 = 13$ ppm, while the CH carbons should resonate $2\alpha + 2\gamma = 18 - 4 = 14$ ppm downfield from the CH_3 carbons. The pattern of ^{13}C resonances expected on the basis of these substituent effects is indeed observed (see Figure 1).

However, the extensive, though smaller, splitting of resonances belonging to the same carbon type (CH, CH_2, or CH_3) observed in the ^{13}C NMR spectrum of atactic PP (see Figure 1 and subsequently Figure 3), must be produced by the presence of different stereosequences, because the numbers and types of α, β and γ substituents possessed by each carbon type are independent of stereosequence. On the other hand, it is well known that the local conformations in vinyl polymers like atactic PP are sensitive to stereosequence [16]. The local magnetic field B_i experienced by a carbon nucleus i must be dependent upon the local conformation in its vicinity. Thus,

$$\text{Microstructure} \rightarrow \text{Conformation} \rightarrow B_i \rightarrow \delta^{13}\,\mathrm{C}_i. \quad [10]$$

γ-Gauche-Effect

To make the connection between polymer microstructures and $\delta^3 C_i$s, we need to know the dependence of the local magnetic field B_i on the local conformation. The γ-substituent effect, which shields an observed carbon nucleus, is the source of the dependence of the local magnetic field B_i on the local conformation. Because the observed carbon C^o and its γ-substituent C^γ are separated by three intervening bonds (C^o–C–$\circlearrowleft^{\varphi}$–C–$C^\gamma$), their mutual distance and orientation are variable, depending on the conformation (φ) of the central bond. Note that the distance between C^o and C^γ is reduced from 4 to 3Å on changing their arrangement from trans ($\varphi = 0°$) to gauche$^{\pm}$ ($\varphi = \pm 120°$).

Grant and Cheney [17] first suggested the conformational origin of the γ-substituent effects on δ^{13}Cs. In their model, it is the polarization of the C^o–H and C^γ–H bonds, resulting from their compression caused by proton–proton (o–γ) repulsion, that leads to a shielding of both carbons. More recently, Li and Chesnut [18] presented evidence that correlate shielding γ-effects with attractive van der Waals forces and not repulsive steric interactions, though their results still suggest that their gauche arrangement is required for shielding. Using both semi-empirical and *ab initio* quantum mechanical calculations Seidman and Maciel [19] concluded that the γ-substituent effect is conformational in origin, but cannot be attributed solely to the proximity of the interacting C^o and C^γ carbons. Thus, it seems apparent that the γ-substituent effect on δ^{13}Cs has a conformational origin and is, as we will shortly demonstrate, useful in characterizing both the local microstructures and conformations of polymers.

For a carbon nucleus to be shielded by a γ-substituent, we have suggested that they must be in a gauche arrangement. The methyl carbons in butane and higher *n*-alkanes have a single γ-substituent, while the methyl carbons in propane have none, but the same number and kinds of α- and β-substituents. The methyl carbons in liquid butane and higher *n*-alkanes resonate at ∼13 ppm, while in liquid propane the methyls resonate at ∼15 ppm [1]. In their solids the *n*-alkanes crystallize in the fully extended all trans conformation, and so there the methyl carbons of butane and the higher *n*-alkanes are not gauche to their γ-methyl or methylene carbon substituents. Thus, we would expect that δCH_3 (solid C_nH_{2n+2}, $n \geq 4$) = δCH_3 (liquid propane). VanderHart [20] has observed the methyl carbons in the solid n-alkanes with $n = 19, 20, 23$, and 32 to resonate at ~15 ppm, just like the methyls in liquid propane which have no γ-substituents.

If we know how much gauche character (P_g = fractional population of $\phi = \pm 120^\circ$ conformations [10,16]), then we can estimate the γ-gauche shielding (γ_{c-c}) produced at the methyl carbons in butane, for example. When the observed shielding $\Delta\delta CH_3 = \delta CH_3(\text{butane}) - \delta CH_3(\text{propane}) = 13.2 - 15.6 = -2.4$ ppm is divided by the gauche character of the intervening bond ($P_g = 0.46$), $\gamma_{c-c} = \Delta\delta CH_3/P_g = -2.4/0.46 = -5.2$ ppm. Similar application of this procedure to 1-propanol and 1-chloropropane yields the following γ-gauche shielding effects: $\gamma_{c-o} = -7.2$ ppm and $\gamma_{c-cl} = -6.8$ ppm [10]. Thus, the shielding produced at a carbon nucleus by a γ-substituent in a gauche arrangement can be comparable in magnitude (-5 to -7 ppm) to the $+9$ ppm deshielding produced by the more proximal α- and β-substituents. More important, however, is the conformational dependence of the γ-substituent effect on ^{13}C NMR chemical shifts. Any structural variation in a molecule which effects its local conformation can be expected to be reflected in its δ^{13}Cs via the γ-gauche-effect.

The conformationally sensitive γ-gauche-effect permits us to draw the connection between a polymer's microstructure and its ^{13}C NMR spectrum:

$$\text{Microstructure} \rightarrow \text{Conformation} \rightarrow B_i \rightarrow \delta^{13}C_i.$$

The connection between the microstructures and the conformations of polymers may be readily established [16]. The γ-gauche-effect establishes the connection between the local polymer conformation and the local magnetic field experienced by a ^{13}C nucleus, so finally

$$\text{Microstructure} \xrightarrow[\text{Effect}]{\gamma\text{-gauche}} \delta^{13}\text{Cs}. \ [10]$$

Example of the γ-Gauche-Effect

Observation of nonequivalent δ^{13}Cs for the isopropyl methyl carbons in several branched alkanes (see Table 1) clearly illustrates the conformational connection between observed δ^{13}Cs and molecular structure (microstructure). Even though the isopropyl methyl carbons have the same α, β, and γ substituents, we note in Table 1 (second column) that their observed nonequivalence progressively diminishes as the number of carbons separating the terminal isopropyl group from the asymmetric center is increased. This behavior can be understood [21] if we focus attention on the source of the nonequivalent δ^{13}Cs observed for 2,4-dimethyl-hexane (2,4-DMH).

We have illustrated in Figure 2 the likely conformations (staggered) about the C_2–C_3 backbone bond in 2,4-DMH, since these determine whether or not the isopropyl methyl carbons C^{sc}, C^{bb} are γ-gauche to the asymmetric carbon C_4. From the probabilities of the trans (t), gauche$^+$ (g$^+$), and gauche$^-$ (g$^-$) conformations (P_t, P_{g+}, P_{g-}), we

Table 1: Nonequivalent ^{13}C NMR chemical shifts of the isopropyl methyl carbons in branched alkanes

	Δδ, ppm	
Alkane	Obsd.*	Calcd.
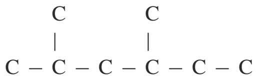 $C-\overset{C}{\overset{\vert}{C}}-C-\overset{C}{\overset{\vert}{C}}-C-C$	1.0 (1.9, 1.1, 0.9)†	1.6, 1.1, 0.9
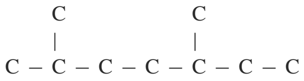 $C-\overset{C}{\overset{\vert}{C}}-C-C-\overset{C}{\overset{\vert}{C}}-C-C$	0.2	0.2
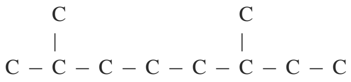 $C-\overset{C}{\overset{\vert}{C}}-C-C-C-\overset{C}{\overset{\vert}{C}}-C-C$	0.1	0.04
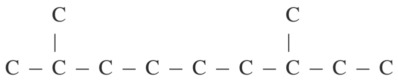 $C-\overset{C}{\overset{\vert}{C}}-C-C-C-C-\overset{C}{\overset{\vert}{C}}-C-C$	0.0	0.0

*Observed between ambient and 48 °C [23–25].
†Observed at – 120, 25, and 90 °C [21].

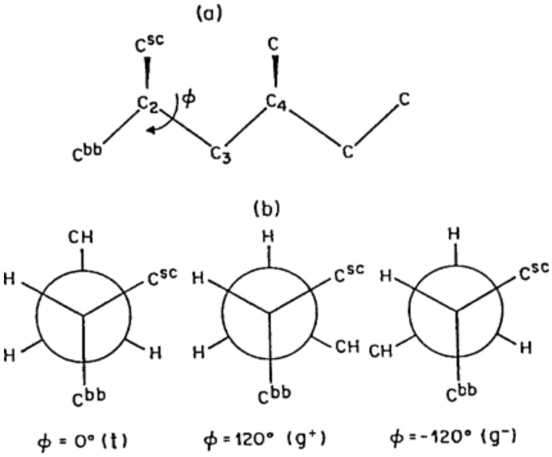

Fig. 2. (a) 2,4-DMH in the all-trans conformation. (b) Newman projections illustrating the staggered conformations about the C_2–C_3 backbone bond of 2,4-DMH [21].

obtain $P_t + P_{g+}$ and $P_{g+} + P_{g-}$ as the probabilities for gauche arrangements between C^{sc} and C^{bb}, respectively, and their γ-substituent C_4. The conformational model developed by Mark [22] for ethylene-propylene copolymers may be used to obtain $P_t = 0.38$, $P_{g+} = 0.01$, and $P_{g-} = 0.61$, so C_4 is γ-gauche to C^{sc} with probability 0.39 and to C^{bb} with probability 0.62. The nonequivalence between C^{sc} and C^{bb} is expected to be $\Delta\delta^{13}C = (0.39 - 0.62) \times \gamma_{c-c} \sim -0.23 \times (-5\,\text{ppm}) = 1.1\,\text{ppm}$.

The observed nonequivalence (1.0–1.1 ppm) [23–25] is in close agreement with the value expected from the γ-gauche conformational calculation. The temperature dependence of the magnetic nonequivalence is also successfully reproduced, leaving little doubt that its origin is the conformationally sensitive γ-gauche-effect.

From the Newman projections in Figure 2b it might be expected that the t and g^- conformations would be equally populated. However, it is well known that rotational-state probabilities for the bonds in linear chain molecules depend on the conformations, or rotational states, of neighboring bonds [16]. The asymmetric center at C_4 produces intramolecular interactions which depend simultaneously on φ and neighboring bond rotations (see Figure 2a), which render $P_t \neq P_{g-}$. The values of P_t and P_{g-} approach each other as the asymmetric center is further removed from the terminal isopropyl methyl carbons. This expectation is borne out in Table 1, where it is both observed and predicted that the magnetic nonequivalence of isopropyl methyl carbons vanishes once they are separated from the asymmetric center by more than four carbons.

It is apparent from this example that the microstructural sensitivity of ^{13}C NMR chemical shifts can have a conformational origin. $\delta^{13}Cs$ depend on the local magnetic field, which is influenced by the local conformation in the vicinity of resonating carbon nuclei. The local conformation is determined by the neighboring microstructure. Hence, the microstructural sensitivity of ^{13}C NMR has its basis in the dependence of the local conformation on microstructure.

PP Stereosequences From ^{13}C NMR

To predict the ^{13}C chemical shifts observed at 90 MHz for the methyl carbons in atactic (a)-PP (see Figure 3), which show sensitivity to heptad stereosequences, we simply have to calculate the trans and gauche probabilities for the backbone bonds in each of the 36 heptad stereosequences (mmmmmm, rrrrrr, mmrmmr, rmrmrm, . . .). When this is carried out with the Suter–Flory rotational isomeric state (RIS) conformational model for PP [26] and the resultant probabilities of finding CH_3 in a gauche arrangement with its γ-substituents (CHs) are multiplied by $\gamma_{CH3-CH} = -5.2$ ppm, we obtain the δCH_3s shown as the stick spectrum in Figure 3.

Because the γ-gauche-effect method of calculating $\delta^{13}Cs$ only leads to relative stereosequence-dependent chemical shifts, we are free to translate the calculated shifts as a group to achieve the best agreement with the observed $\delta^{13}Cs$.

This has been done in Figure 3, where the agreement between observed and calculated $\delta^{13}CH_3s$ has been used to make the stereosequence assignments indicated there. The γ-gauche-effect method of assigning resonances in the methyl carbon region of the ^{13}C NMR spectrum of a-PP to heptad stereosequences has been achieved without recourse to the syntheses and study of PP model compounds or stereoregular PPs and without assuming a particular statistical model to describe the expected frequencies of stereosequences produced during polymerization. Having assigned all heptad stereosequence-dependent ^{13}C NMR resonances in a-PP [27], integration of the resonances provides us with a detailed accounting of how much of each stereosequence is present. Such information is needed to test various statistical models of PP polymerization [28]. Furthermore, the close agreement between observed and calculated chemical shifts provides strong confirmation of the Suter–Flory RIS conformational model for PP [26].

^{13}C NMR of Solid Polymers

There exist two interactions between nuclear spins and their neighbors or with the applied magnetic field that result in severe broadening of their solid-state NMR spectra when recorded under conditions that produce

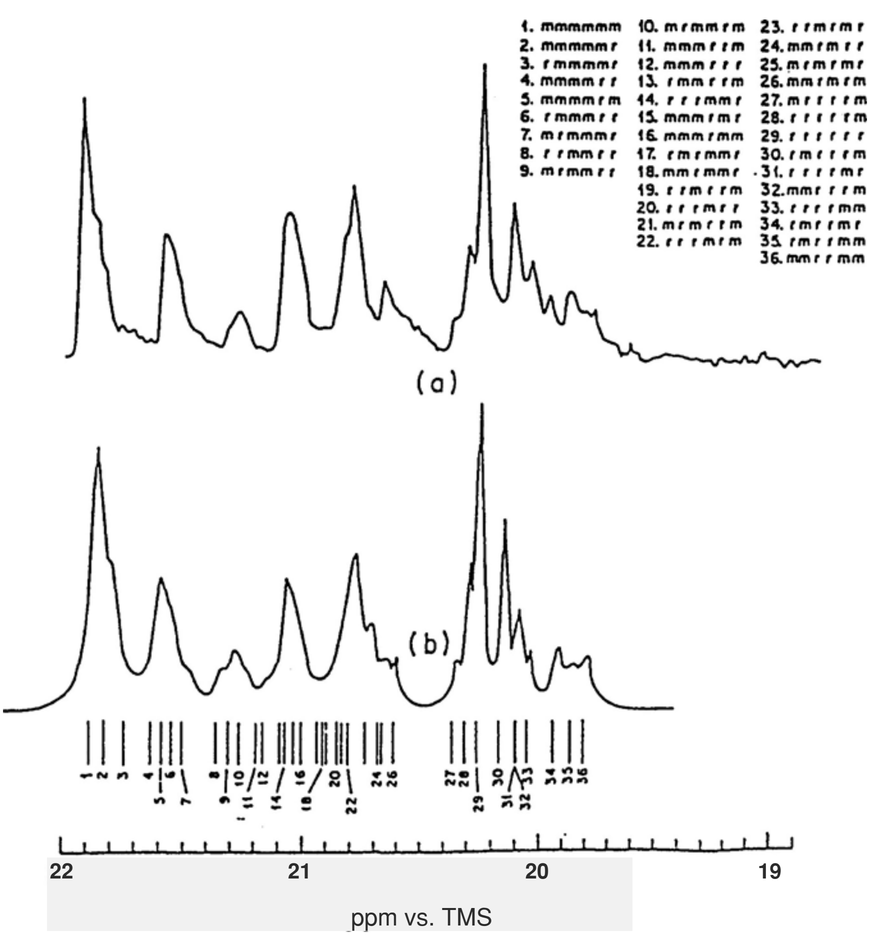

Fig. 3. (a) Methyl carbon region of the ^{13}C NMR spectrum of the same atactic PP shown in Figure 1, but recorded at 90 MHz in *n*-heptane at 67 °C. (b) Simulated methyl carbon spectrum obtained from chemical shifts calculated using the γ-gauche-effect method, as represented by the line spectrum below, and assuming Lorentzian peaks of <0.1 ppm width at half-height [1,2].

high-resolution NMR spectra for their solutions. Both of these nuclear interactions, direct through space dipolar coupling and anisotropic electronic shielding of nuclei from the applied magnetic field, are also present in the liquid. They do not lead to resonance line broadening there because they are averaged to zero by the rapid and essentially isotropic motions occurring in the liquid. In rigid solid samples like glassy or crystalline polymers, the motional averaging of these nuclear interactions are incomplete and produce spectra like the one shown in Figure 4a [29].

As a result of their dipolar interactions with nearby abundant protons, the ^{13}C resonance line widths observed in rigid organic polymers are typically tens of kHz [30]. Since the range of ^{13}C NMR resonance frequencies, or chemical shifts, observed [31] in a given polymer is usually less than 200 ppm, which at an applied field strength of 4.7 T (50 MHz for ^{13}C) corresponds to a frequency range of 10 kHz, ^{13}C NMR spectra of solids whose lines are broadened by ^{1}H dipolar coupling (ca. 20 kHz) cannot resolve their chemically shifted, resonance frequencies. Without removing this ^{13}C–^{1}H coupling, ^{13}C NMR spectra of solid polymers, like poly(butylene terephthalate) (PBT) in Figure 4, cannot provide useable structural information. The ^{13}C NMR spectrum of PBT shown in Figure 4b was recorded by applying an rf field B_1 at the resonance frequency of protons, with a field strength of 50 kHz, in a direction perpendicular to the applied field

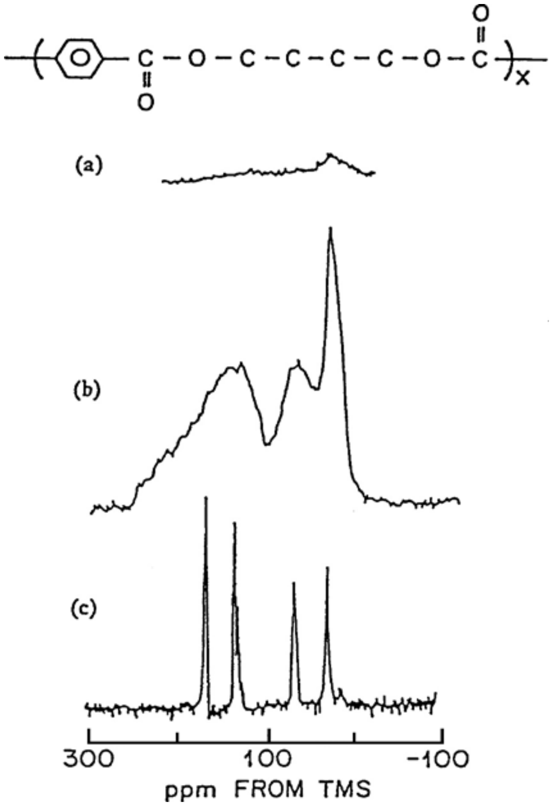

Fig. 4. ^{13}C NMR spectra of bulk poly(butylenes terephthalate) (PBT) obtained with low-power dipolar decoupling (DD) (a), high-power DD (b), and high-power DD with rapid sample spinning at the magic angle (MAS) (c) [29].

B_0 (analogous to the broadband ^1H scalar J decoupling of ^{13}C NMR solution spectra). Note the substantial increase in spectral resolution {compare (a) and (b) in Figure 4 produced without and with high-power ^1H dipolar decoupling (DD) [32]}, though falling far short of the resolution observed in spectra recorded in solution. The remaining line broadening in solid-state spectra is due primarily to chemical shift anisotropy (CSA).

CSA reflects the anisotropy inherent in the distribution of electronic currents about nuclei which screen (σ) them from the applied magnetic field B_0. The local magnetic field experienced by a nucleus is anisotropic and therefore three-dimensional, so the nuclear screening constant σ is in fact a tensor [33]. Rapid molecular motion experienced by polymer segments in solution results in the observation of motionaly averaged, isotropic chemical shifts, $\sigma_{i.}$ If a solid powder sample is rotated rapidly about an axis making an angle 54.7° (the magic angle) with respect to the applied field B_0, the anisotropic chemical shift tensor powder patterns (see Figure 4b and c) are reduced to their isotropic averages. CSA of ^{13}C nuclei in different structural environments vary from ~30 ppm for CH_2 carbons to ~200 ppm for aromatic carbons [30]. Magic-angle sample spinning MAS at a few kHz reduces the CSAs of the aromatic and carbonyl carbons in PBT to their isotropic averages, leading to the high-resolution spectrum seen in Figure 4c.

The first truly high-resolution ^{13}C NMR spectra of solid polymers were reported by Schaefer and Stejskal [34]. They combined for the first time the previously developed techniques [32,35] of high-power proton DD, rapid MAS spinning, and cross-polarization (CP) [35], which permits a dramatic reduction in the spectral acquisition time, to obtain these spectra. In this way, ^{13}C NMR can be utilized to probe the conformations, packing, and motions of solid polymer samples.

Application of Solid-State ^{13}C NMR to Polymers

Syndiotactic polystyrene (s-PS) is a highly stereoregular, semi-crystalline vinyl polymer that normally melts at ~270 °C [36,37]. s-PS shows a large number of crystalline polymorphs [38–41] obtained by melt crystallization and solvent-exposure techniques. However, s-PS assumes only two distinct crystalline conformations [all trans, planar zig-zag (...tttttttt...) and 2_1-helical (...ttggttgg...); t = trans and g = gauche], which are characterized by fiber repeats of 5.1 and 7.5Å, respectively.

Figure 5 presents the high-resolution CPMAS/DD ^{13}C NMR spectra of two s-PS crystalline polymorphs [42], one with s-PS chains adopting the...tttttttt... conformation (a) and the other the...ttggttgg... conformation. We note in spectrum (b) that two CH_2 carbon resonances appear at 38 and 49 ppm, while in spectrum (a) only a single CH_2 carbon resonance at 49 ppm is evident. In the...ttggttgg...polymorph half of the CH_2 carbons are gauche to both of their γ-substituent CH carbons, while the other half are trans to both γ-CH carbons. We expect, as was also observed for s-PP crystallized in the 2_1-helical...ttggttgg...conformation [43], two CH_2 resonances separated by ~2 × 5.2 ppm ~10 ppm in agreement with spectrum (b). Also the single CH_2 resonance observed for the...tttttttt... polymorph in (a) comes at nearly the same frequency (~49 ppm) as the most downfield CH_2resonance observed for the...ttggttgg...polymorph in spectrum (b). These and other ^{13}C NMR observations of solid polymers [10] further confirm the validity of the conformtionally sensitive γ-gauche substituent effects on ^{13}C chemical shifts, with extension of their applicability to solid polymer samples. This strongly implies that the ^{13}C chemical shifts observed for solid polymers are in general primarily influenced by

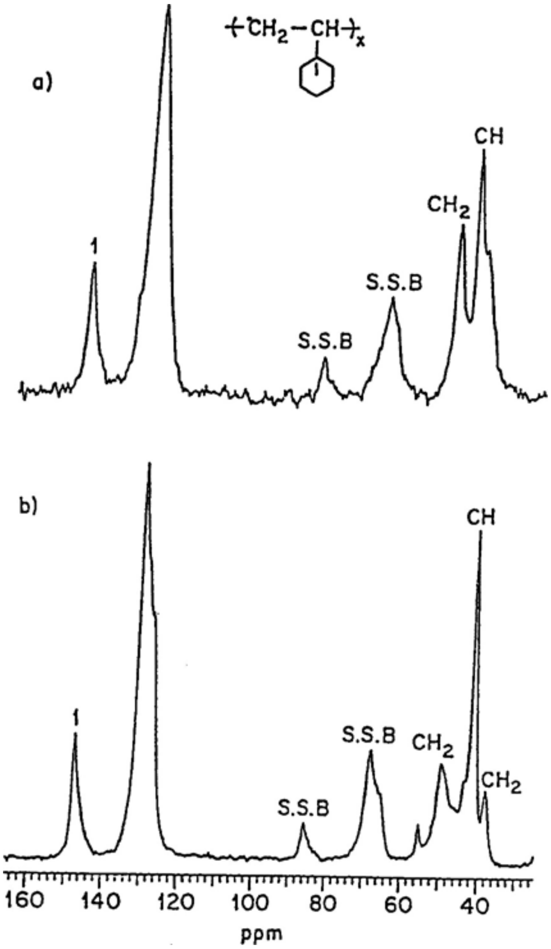

Fig. 5. CPMAS/DD ^{13}C NMR spectra of form I (. . . tttttttt. . .) (a) and form II (. . . ttggttgg. . .) (b) s-PS crystalline polymorphs [42].

Table 2: ^{13}C spin-lattice relaxation times, T_1(s), for the crystalline carbons in s-PS polymorphs [42].

Sample	C_1	C_{2--6}	CH_2 (∼49 ppm)	CH	CH_2 (∼38 ppm)
S_a	78	60	83	65	
$S_{\alpha1}$	400	120	400	200	
$S_{\alpha2}$	140	134		280	
S_0	74	54	58	59	55
$S_{\delta1}$	32	24	30	28	30

the conformations adopted by their rigid backbones and usually only to a much smaller extent by the crystalline packing of their chains [44].

Though all of the crystalline polymorphs of s-PS exhibit distinct X-ray diffraction patterns, they exhibit only one or the other of the two ^{13}CPMAS/DD ^{13}C NMR spectra seen in Figure 5, which correspond to their distinct . . . tttttttt. . . and . . . ttggttgg. . . crystalline conformations with fiber repeats of 5.1 and 7.5 Å, respectively. As a consequence, we can conclude that among all the crystalline polymorphs observed for s-PS only two chain conformations are represented. Apparently differences in packing of s-PS chains in these two crystalline conformations result in the variety of crystalline polymorphs observed for s-PS by X-rays [38–41].

However, CPMAS/DD ^{13}C NMR can still be utilized to distinguish among these many crystalline polymorphs. In Table 2 the ^{13}C spin-lattice relaxation times (T_1s), which reflect motions on the NMR (MHz) timescale [31], observed at room temperature [42] for several of these polymorphs are presented. Samples $S_{a,}$ $S_{\alpha1}$ and $S_{\alpha2}$, and S_0 and $S_{\delta1}$ represent amorphous, . . . tttttttt . . . crystalline, and . . . ttggttgg. . . crystalline s-PSs, respectively. Clearly, the T_1s observed for the . . . tttttttt . . . polymorphs are longer (2–10 times longer) than those for the . . . ttggttgg . . . polymorphs. Even amorphous s-PS has longerT_1s than the . . . ttggttgg. . . polymorphs. When the T_1 results are coupled with the observation of small solvent peaks in the CPMAS/DD and MAS/DD spectra of the S_0 and $S_{\delta1}$ samples (Not presented here [42]), we can conclude that small quantities of the solvents used to induce crystallinity in these s-PS samples are retained in both their crystalline and amorphous glassy regions. Solvent incorporated in the crystalline regions of the . . . ttggttgg . . . polymorphs may act as defects causing the crystalline chains to be at least as mobile as those in the completely disordered, glassy portions of these samples.

Summary

By means of several examples, we have illustrated the types of detailed microstructural, conformational, and motional information that can be obtained from the high resolution, solution, and solid-state NMR spectra of polymers. The microstructures of polymers, including stereo- and regiosequences, comonomer composition and sequence, and geometrical isomerism and branching, can be most effectively identified from NMR spectra, usually ^{13}C, recorded from their solutions. This is facilitated by establishing the connection/assignment of observed ^{13}C resonances to their underlying microstructures via the γ-gauche-effect, which permits the microstructurally sensitive local conformation in the vicinity of a given

^{13}C nucleus to be related to its observed resonance frequency. Through knowledge of the conformational characteristics of polymers and their sensitivity to polymer microstructure we may more easily assign the NMR solution spectra of polymers and thereby determine their microstructures. Application of CPMAS/DD techniques also yield high-resolution spectra for solid polymer samples. Consequently, CPMAS/DD-observed resonance frequencies and relaxation times can be analyzed to learn about the structures/packing, morphologies, conformations, and mobilities of polymer chains in their bulk samples, as well.

References

1. Tonelli AE, Schilling FC. Acc. Chem. Res. 1981;14:233.
2. Schilling FC, Tonelli AE. Macromolecules. 1980;13:270.
3. Stothers JB. C-13 NMR Spectroscopy. Academic Press: New York, 1972.
4. Derome AE. Modern NMR Techniques for Chemistry Research. Pergamon: New York, 1987.
5. Ditchfield R. Nucl. Magn. Reson. 1976;5:1.
6. Schastnev PV, Cheremisin AA. J. Struct. Chem. 1982; 23:440.
7. Ando I, Kuroki S, Kurosu H, Yamanobe T. Prog. Nucl. Magn. Reson. Spectrosc. 2001;39:79.
8. Cheeseman JR, Trucks GW, Keith TA, Frisch MJ. J. Chem. Phys. 1996;104:5497.
9. Duddeck H. In: EI Eliel, SH Wilen, NL Allinger (Eds). Topics in Stereochemistry, Vol. 16. Wiley-Intersceince, New York, 1986, p 219.
10. Tonelli AE. NMR Spectroscopy and Polymer Microstructure: The Conformational Connection, Wiley-Interscience, New York, 1989.
11. Spiesecke H, Schneider WG. J. Chem. Phys. 1961;35: 722.
12. Grant DM, Paul EG. J. Am. Chem. Soc. 1964;86:2984.
13. Lindeman LP, Adama JQ. Anal. Chem. 1971;43:1245.
14. Dorman DE, Carhart RE, Roberts JD. In: EB Mano (Ed). Proceedings of the International Symposium on Macromolecules, Rio de Janerio, July 26–31, 1974. Elsevier: New York, 1974.
15. Bovey FA. In: EB Mano (Ed). Proceedings of the International Symposium on Macromolecules, Rio de Janerio, July 26–31, 1974. Elsevier: New York, 1974, p 169.
16. Flory PJ. Statistical Mechanics of Chain Molecules. Wiley-Interscience: New York, 1969.
17. Grant DM, Cheney VB. J. Am. Chem. Soc. 1967;89:5315.
18. Li S, Chesnut DB. Magn. Reson. Chem. 1985;23:625.
19. Seidman K, Maciel GE. J. Am. Chem. Soc. 1977;99:659.
20. VanderHart DL. J. Magn. Reson. 1981;44:117.
21. Tonelli AE, Schilling FC, Bovey FA. J. Am. Chem. Soc. 1984;106:1157.
22. Mark JE. J. Chem. Phys. 1972;57:2541.
23. Kroschwitz JI, Winokur M, Reid HJ, Roberts JD. J. Am. Chem. Soc. 1969;91:5927.
24. Lindeman LP, Adams JQ. Anal. Chem. 1971;43:1245.
25. Carman CJ, Tarpley AR Jr, Goldstein JH. Macromolecules. 1973;6:719.
26. Suter UW, Flory PJ. Macromolecules. 1975;8:765.
27. Schilling FC, Tonelli AE. Macromolecules. 1980;13:270.
28. Bovey FA (Ed). Chain Structure and Conformation of Macromolecules. Academic Press: New York, 1982.
29. Jelinski LW in ref. 28.
30. Duncan TM, Dybowski CR. Surf. Sci. Rep. 1981;1:57.
31. Bovey FA. Nuclear Magnetic Resonance Spectroscopy. 2nd ed. Academic Press: San Diego, CA, 1988, p 3.
32. Pines A, Gibby MG, Waugh JS. J. Chem. Phys. 1972;56: 1776; Chem. Phys. Lett. 1972;15:373.
33. Mehring M. High Resolution NMR in Solids. 2nd ed. Springer-Verlag, Berlin, 1983.
34. Schaefer J, Stejskal EO. J. Am. Chem. Soc. 1976;98:1031.
35. Hartman SR, Hahn F. Phys. Rev. 1962;128:2042.
36. Ishihara N, Seimiya T, Kuramoto N, Uoi M. Macromolecules. 1986;19:2462.
37. Pellecchia C, Longo P, Grassi A, *et al.* Makromol. Chem. Rapid Commun. 1987;8:277.
38. Immirizi A, deCandia F, Ianelli P, *et al.* Makromol. Chem. Rapid Commun. 1988;9:761.
39. Greis O, Xu Y, Arsano T, Peterman J. Polymer. 1989;30:590.
40. Nyquist RA. Appl. Spectrosc. 1989;43:440.
41. Reynolds NM, Savage JD, Hsu SL. Macromolecules. 1989;22:2867.
42. Gomez MA, Tonelli AE. Macromolecules. 1990;23:3385.
43. Bunn A, Cudby EA, Harris RK, *et al.* J. Chem. Soc. 1981; 1:15.
44. Harris RK. Solid State Sci. 2004;6:1025.

Solid-State NMR Characterization of Polymer Interfaces

Peter A. Mirau
Air Force Research Laboratories, Polymer Branch, Wright-Patterson AFB, Dayton, OH 43433, U.S.A.

Overview

Polymer blends and composites have emerged as technologically important advanced materials with mechanical, optical, and electrical applications. It has been shown that the properties of polymers can be improved with the addition of particles ranging in size from nanometers to microns. As the volume fraction becomes large or for composites with nanometer-sized particles, the fraction of interfacial material becomes large enough to influence the properties. In many nanocomposites, the improved properties are thought to result from the favorable properties of polymers at the interface.

The interfacial characterization of polymers is an extremely important and challenging problem. Solid-state NMR is well suited for polymer characterization because the chemical shifts, relaxation times, and dipolar couplings are sensitive to the structure and dynamics on a very local length scale [1–3]. Most composites contain both bulk and interfacial material, and the challenge for NMR studies is to separate the spectral contributions from the polymers in these different environments. This is often accomplished by taking advantage of differences in the NMR properties (chemical shifts, relaxation times, dipolar couplings, or line shapes) between the bulk and interfacial polymer. In other cases, polymers at the interface can be observed via magnetization exchange from the particle surface.

The easiest systems to study are those where chemical shift differences are observed between the bulk and interfacial polymers, and the chemical shifts, line shapes, and relaxation times can be separately measured. If there are no clear chemical shifts differences for the bulk and interfacial polymer, then some other means must be used to separate their spectral contributions. In favorable cases, it is possible to take advantage of differences in the molecular dynamics of the bulk and interfacial polymer to identify and characterize the interface. In other cases, it is necessary to identify the interfacial polymer by magnetization exchange from the surface or to introduce NMR-active nuclei into the system at the interface.

Solid-State Proton NMR Studies

Solid-state proton NMR has a number of advantages for studying polymers at surfaces and interfaces. Protons have a high sensitivity and are present at high concentrations in most materials, making it feasible to study interfaces that may be present at low concentrations. The difficulty in using proton NMR is that the lines are often broad in solids, due to the proton–proton dipolar couplings. This leads to proton line widths that are larger than the proton chemical shift range (∼10 kHz at 500 MHz) [3], and some means of averaging must be used to observe a high-resolution spectrum. The lines in solids can be averaged by several means, including chain motion, multiple-pulse decoupling, or by rapid magic-angle sample spinning [4]. The line widths can be reduced from 50 kHz to ∼0.5 kHz with multiple-pulse decoupling [5], but these methods are often difficult to implement. The lines can also be narrowed by rapid magic-angle sample spinning provided that the spinning frequency is on the order of the dipolar couplings. Commercial probes have recently been introduced that can spin samples as fast as 30 kHz, leading to substantial line narrowing in the proton [6] and fluorine spectra [7,8] of polymers. For polymers above T_g the dipolar couplings are partially averaged by molecular motion and slower (10–15 kHz) spinning is often sufficient for line narrowing [9].

Solid-state proton NMR has been used to study the structure and dynamics of polymers at the interface in composites with poly(methyl silsesquioxane) that are candidate materials for low dielectric constant layers in electronic circuits [10]. Figure 1 compares the solid-state proton NMR spectrum of the bulk poly(ethylene oxide-*b*-propylene oxide-*b*-ethylene oxide) copolymer and the 15 wt% poly(methyl silsesquioxane) composite [11]. Three groups of signals are resolved in the proton spectrum observed with 15 kHz magic-angle sample spinning, the signals at 3.5 and 1.0 ppm from the main-chain and methyl signals of the triblock copolymer, and the signals near 0 ppm from the poly(methyl silsesquioxane) methyl protons of the matrix. The dipolar couplings for

Graham A. Webb (ed.), Modern Magnetic Resonance, 575–581.
© 2008 *Springer.*

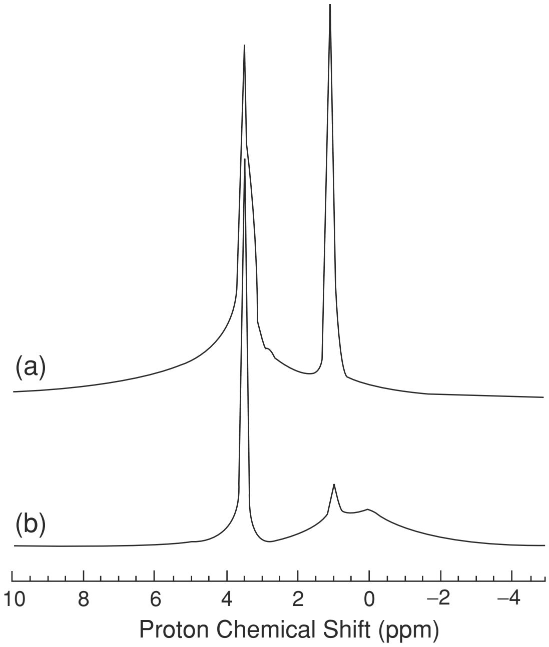

Fig. 1. The 500 MHz solid-state proton NMR spectra of (a) the poly(ethylene oxide-*b*-propylene oxide-*b*-ethylene oxide) triblock copolymer and (b) the 15 wt% composite with poly (methyl silsesquioxane). The spectra were obtained with 15 kHz magic-angle sample spinning.

rigid (crystalline or glassy) protons are in the range of 30–50 kHz and sharp lines are not typically observed in the spectra acquired with 15 kHz magic-angle sample spinning. The fact that such high-resolution spectra are observed shows there is substantial molecular motion both in the bulk triblock copolymer and the composite.

The relative intensities of the methine/methylene protons at 3.5 ppm and the methyl protons at 1 ppm can be calculated from the molecular weights of the ethylene oxide and propylene oxide blocks (4532 and 2262 g/mol for the ethylene oxide and propylene oxide blocks, respectively). The data for the bulk triblock copolymer show a peak intensity ratio of 2:1, which is much less than the expected value of 8:1. This shows that a large fraction of the ethylene oxide is crystalline and cannot be observed with 15 kHz magic-angle sample spinning. In the composite, however, the peak intensity ratio is closer to the expected value, showing that composite formation suppresses the formation of crystallinity in the ethylene oxide block, and that both polymer blocks are mobile in the composite.

Since a high-resolution proton spectrum is observed for the composite, the two-dimensional (2D) exchange (or NOESY) spectroscopy can be used to probe the structure in the solid state [12]. The 2D exchange spectrum for the 15 wt% composite obtained with a 0.1 s mixing time and 15 kHz magic-angle sample spinning shows three peaks along the diagonal that can be assigned to the polymer main-chain and methyl peaks at 3.5 and 1.0 ppm, and the poly(methyl silsesquioxane) methyl peak at 0 ppm. The off-diagonal intensity shows that there is spin exchange between all these peaks, but it is difficult to determine which block is in close contact with the poly(methyl silsesquioxane) matrix by direct examination of the contour plots.

A better insight into the spin exchange process can be obtained by examining the cross sections through the 2D spectra at the frequencies of the main-chain peak at 3.5 ppm and the methyl peak at 1.0 ppm, as shown in Figure 2 [12]. The largest peaks in the cross sections are due to diagonal signals. The cross section through signal at 3.5 ppm (which is due mostly to the ethylene oxide methylene protons) shows only a small amount of exchange to the propylene oxide methyl or poly(methyl silsesquioxane) signals. Cross sections through the propylene oxide methyl signal at 1 ppm shows very efficient spin exchange to the poly(methyl silsesquioxane) methyl signal at 0 ppm. These and other experiments show that the polymer domains in the composite adopt a core-shell

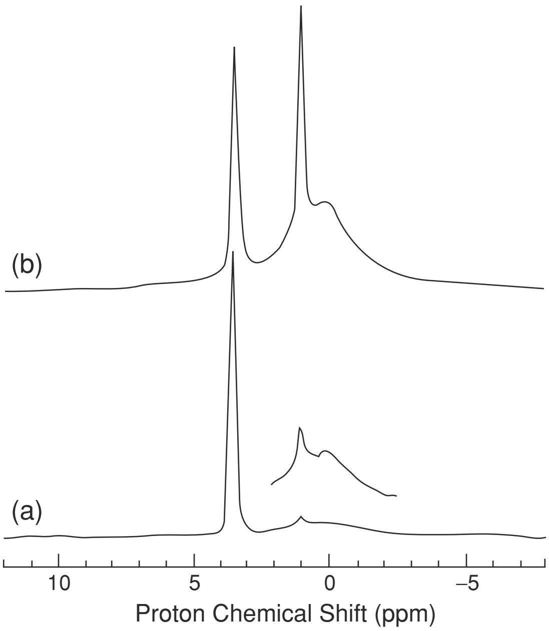

Fig. 2. Cross sections through the 2D exchange spectra of the 15 wt% composite of poly(ethylene oxide-*b*-propylene oxide-*b*-ethylene oxide) and poly(methyl silsesquioxane) at the frequency of (a) the main-chain peak at 3.5 ppm and (b) the propylene oxide methyl peak at 1 ppm.

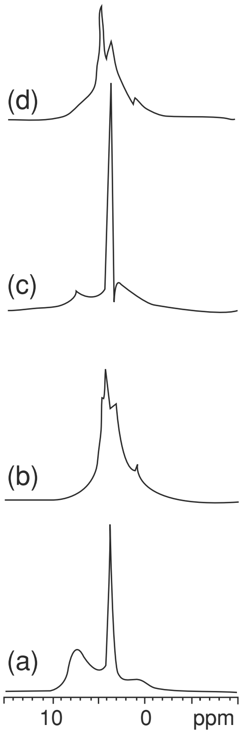

Fig. 3. The solid-state proton NMR spectra of (a) poly(4-styrene sulfonate), (b) poly(diallyldimethylammonium), (c) the polyelectrolyte complex, and (d) the layer-by-layer electrostatic complex obtained with 30 kHz magic-angle sample spinning.

structure with the ethylene oxide at the center and the propylene oxide at the interface with the poly(methyl silsesquioxane).

High-resolution solid-state proton NMR with rapid magic-angle sample spinning has also been used to study the structure and dynamics of the interfaces in alternating layers of electrostatically adsorbed polyelectrolyte multilayers. This is illustrated in Figure 3 which shows the proton NMR spectra of poly(diallyldimethylammonium chloride) and poly(4-styrene sulfonate), the polyelectrolyte complex (PEC) precipitated from solution, and the sample prepared using layer-by-layer deposition on colloidal silica acquired with 30 kHz magic-angle sample spinning [13]. The layer-by-layer complex is prepared by alternately coating the silica particle with the anionic or cationic polymer. The spectra for the PEC and the layer-by-layer deposited sample show the peaks from both polymers, including the aromatic peaks near 7 ppm and the methyl proton peaks near 3 ppm. Residual water signals are also observed at 4.9 and 3.85 ppm in the layer-by-layer sample for water in the polymer domains and at the silica surface.

The structure of the PEC and layer-by-layer samples can be probed by measuring the proton dipolar couplings between the layers. NOESY experiments cannot be used in these studies because of the overlap of the aliphatic signals from the poly(4-styrene sulfonate) and the poly(diallyldimethylammonium), so proton–proton double-quantum correlation spectroscopy is used [14]. The idea behind this experiment is to apply a series of pulses to reintroduce the dipolar couplings that are averaged by rapid magic-angle sample spinning in one dimension of a 2D NMR experiment. Protons that are close in space can be identified by the correlation of the single- and double-quantum frequencies.

Figure 4 compares the 2D double-quantum spectra for the PEC and the layer-by-layer complex with four layers. Since this experiment measures the correlation of the single- and double-quantum spectrum, the frequencies in the indirectly detected dimension are twice as large as those in the directly detected dimension. Furthermore, the only peaks that appear in the spectrum are those with strong dipolar couplings. The autocorrelation peaks ($\omega_1 = 2\omega_2$) arise from pairs of protons with the same

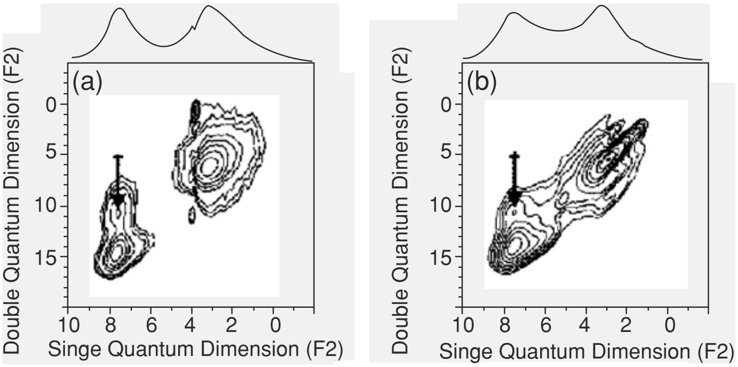

Fig. 4. The solid-state proton 2D single- and double-quantum correlation spectra for (A) the polyelectrolyte complex and (B) the layer-by-layer electrostatic complex of poly(diallyldimethylammonium chloride) and poly(4-styrene sulfonate). The cross peaks of interest are noted with an arrow.

Fig. 5. The solid-state 2D silicon–proton heteronuclear correlation spectra of the poly(ethyl acrylate)/Vycor composite obtained with a spin diffusion delay time of (a) 50 µs and (b) 50 ms.

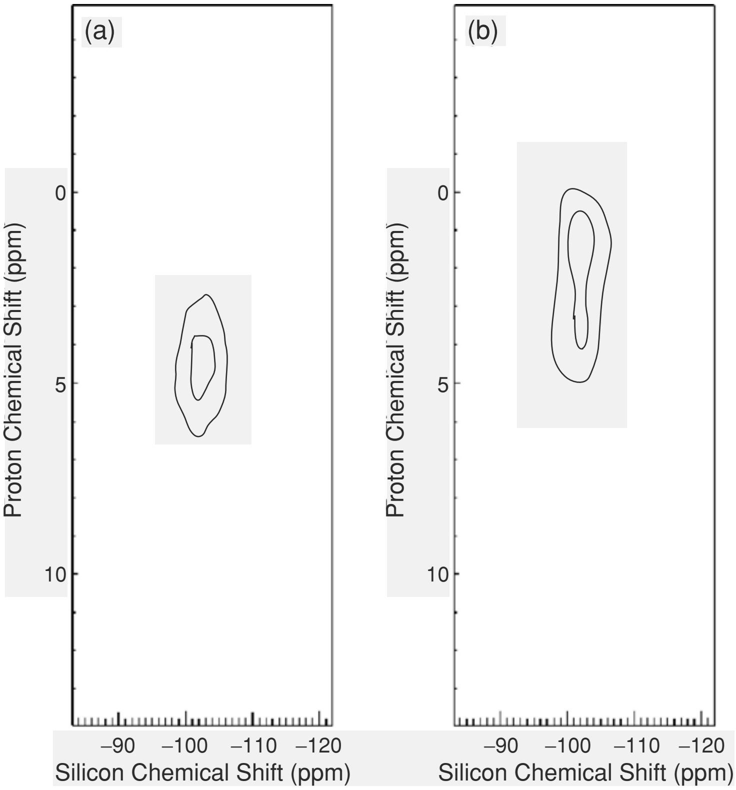

chemical shift that also have strong dipolar couplings. The peaks near $\omega_1 = 14$ ppm and $\omega_2 = 7$ ppm arise from couplings between styrene aromatic protons, while peaks between 2–6 ppm in the ω_1 dimension and 1–3 ppm in the ω_2 dimension arise from nearby aliphatic protons. The peaks of interest (note arrow in Figure 4) in both spectra arise from dipolar couplings between the aromatic protons of poly(4-styrene sulfonate) and the methyl protons of poly(diallyldimethylamomnium chloride) at the interface.

Solid-State Heteronuclear NMR Studies

The structure and dynamics of polymers at surfaces and interfaces can also be studied using nuclei other than protons that may be at or near the interface. The heteronuclear signals can arise from nuclei that are naturally at the interface or from NMR-active nuclei introduced at the interface. We can probe the structure and dynamics at the interface using cross polarization and sampling the magnetization only from those polymers close enough to cross polarize the heteronuclei at the surface.

Figure 5 shows how silicon–proton 2D heteronuclear correlation NMR [15,16] can be used to characterize the interface in polymer composites of vycor glass and poly(ethyl acrylate) [17]. Vycor is a porous glass with 4-nm sized pores that have been filled with monomer and photopolymerized. The heteronuclear 2D experiment correlates the high-resolution proton spectrum with the silicon spectrum from the interface. The pulse sequence begins with evolution of the proton spins under multiple-pulse decoupling. After an optional mixing time the proton magnetization is transferred to the surface silicons using multiple-pulse cross polarization to quench spin diffusion during magnetization transfer [15]. Figure 5a shows the heteronuclear correlation spectrum with a short (50 µs) spin diffusion delay time between the proton evolution and the multiple-pulse cross polarization [17]. With such a short cross-polarization time, the surface silicons are cross-polarized only by protons within a few Å of the surface. Figure 5a shows that the protons nearest the

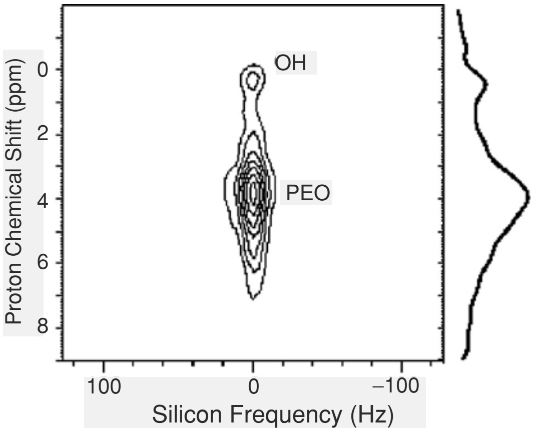

Fig. 6. The heteronuclear correlation spectrum of the intercalated hectorite clay/poly(ethylene oxide) nanocomposite with the 30 ms spin diffusion delay time.

surface have a chemical shift near 5 ppm and are assigned to hydroxyl protons and a layer of water molecules at the surface. With a longer spin diffusion delay time (Figure 5b, 50 ms) the surface silicons are correlated with the proton signals from the poly(ethyl acrylate). These and other experiments show that the polymer in the porous glass is separated from the silica surface by a 5 Å layer of water.

Solid-state heteronuclear correlation NMR has also been used to study the structure and dynamics of polymer-clay nanocomposites [18]. Polymer–clay composites can adopt a variety of structures, ranging from completely exfoliated to morphologies where the polymer is intercalated between the clay sheets [19,20]. The intercalated morphology is of interest because the polymer is confined to a very narrow space (1–3 nm) between the relatively rigid clay sheets. Polymer–clay composites for NMR studies were prepared by intercalating poly(ethylene oxide) between the layers of hectorite, a synthetic clay with a low iron content. The proton NMR spectrum with fast magic-angle sample spinning shows the presence of a peak at 0.35 ppm that can be assigned to hydroxyl protons in the silicate layers of the clay [18]. This peak makes it possible to probe the structure in the vicinity of the clay using silicon–proton cross polarization and proton spin diffusion. Figure 6 shows the heteronuclear correlation spectrum of the intercalated nanocomposite with a 30 ms spin diffusion delay time [18]. The cross peaks to the poly(ethylene oxide) protons at 3.5 ppm can only arise from the close proximity of the polymer and the clay sheets. The results from a study of the interaction of poly(styrene-*b*-ethylene oxide) block copolymers with hectorite clay shows that the ethylene oxide block intercalates between the clay sheets while the polystyrene block is excluded [21].

Dynamics at the Interface

Many NMR methods have been developed to study the molecular dynamics of polymers over a wide range of frequencies, ranging from picoseconds to seconds [1,2,22]. The difficulties in studying the dynamics of polymers at the interface are mostly in selectively observing the interface. Once a pulse sequence has been used to select for interfacial material or a composite is prepared with an NMR-active nuclei at the interface, then the standard NMR experiments can be used to characterize the dynamics.

The NMR relaxation times, line shapes, and dipolar and quadrupolar coupling constants are sensitive to the molecular dynamics of polymers. The proton line shapes can be measured with a high sensitivity, but they tend to be rather featureless and difficult to model quantitatively. Quadrupolar line shapes from deuterons introduced at the interface are much more sensitive to the rate and amplitude of molecular motions [23]. The line shape measurements are usually sensitive to motions on the kHz timescale, while the relaxation times are generally sensitive to faster motions [3]. 2D spin exchange experiments are sensitive to very low frequency molecular motions [24].

Figure 7 shows the solid-state deuterium NMR spectra of methyl-deuterated poly(methyl acrylate) in the bulk and as a thin film coating silica particles [25]. At 25°C the deuterium spectrum is similar to that expected for a methyl group in a relatively rigid matrix. Rapid methyl group motion partially averages the deuterium quadrupolar coupling from 120 to 37.5 kHz [26] but there is insufficient molecular motion in poly(methyl acrylate)-d_3 to completely average the quadrupolar coupling. For the bulk sample (Figure 7a) the powder pattern disappears as the sample is heated and a motionally averaged signal is observed at temperatures above the glass transition temperature.

Figure 7b shows the deuterium spectra of the same polymer coated as a 2–3 nm thick film on silica particles [25]. The spectra at 25 °C are similar to those in the bulk but differences are observed as the temperature increases. The most notable features are the peak near zero frequency that is observed at lower temperatures in the surface-coated sample and the powder pattern with the 37.5 kHz coupling that is preserved until much higher temperatures. These results show that the surface-coated samples have at least two dynamic components. The component with dynamics faster than the bulk that gives rise to the center peak is assigned to polymer at the air interface,

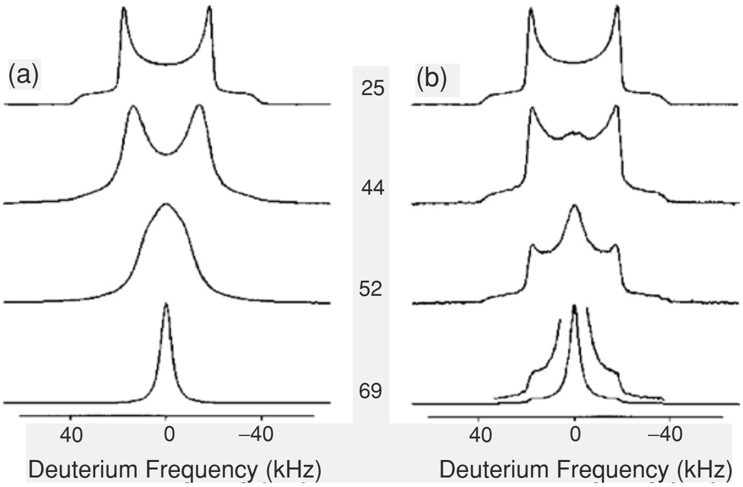

Fig. 7. The solid-state deuterium quadrupolar-echo spectra of (a) bulk poly(methyl acrylate)-d_3 and (b) a 1–3 nm coating of poly(methyl acrylate)-d_3 on silica particles as a function of temperature.

while the polymer with reduced mobility is assigned to polymer at the silica interface. The more mobile polymer at the air interface disappears when the sample is overcoated with protonated poly(methyl acrylate).

The averaging of the proton line widths by molecular motion is a rough measure of the dynamics that can be measured using 2D wide line separation spectroscopy (WISE) [27]. The 2D WISE experiment correlates the proton line width with the heteronuclear chemical shift. The proton spectrum is typically not well resolved and this method allows us to measure the proton line width associated with resolved peaks in the carbon, silicon, phosphorus, or nitrogen spectra.

Figure 8 shows cross sections through the 2D WISE spectra for bulk poly(ethyl acrylate) and the polymer confined to the 4 nm pores in Vycor glass [17]. These spectra were recorded at ambient temperature, which is far above the glass transition temperature for the poly(ethyl acrylate). Under these conditions the dipolar couplings are partially averaged by molecular motion and a 5 kHz line width is observed in the proton dimension. A more complex line shape is observed for the Vycor composite, with broad and narrow components. The broad component is associated with the polymer at the interface that has a restricted mobility, while the sharper component is associated with bulk-like poly(ethyl acrylate) at the center of the 4 nm pore. 2D WISE NMR has also been used to study the dynamics of poly(ethylene oxide) and poly(ethylene oxide-*b*-styrene) intercalated into clay nanocomposites [21].

Double-quantum NMR has also been used to study the poly(ethyl acrylate) dynamics as the interface [28]. The dipolar couplings are partially averaged by motion above T_g for bulk poly(ethyl acrylate), and double-quantum coherences are difficult to observe. However, they can be observed in the Vycor composites where the dynamics are restricted at the polymer–glass interface. The

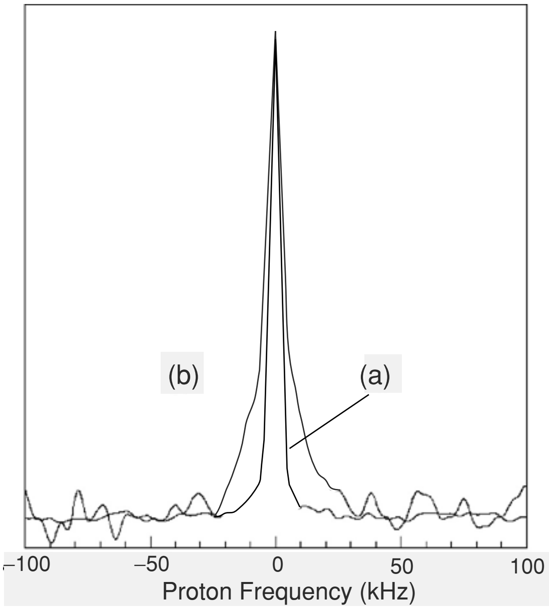

Fig. 8. Cross sections through the solid-state carbon–proton 2D WISE spectra for (a) poly(ethyl acrylate) and (b) the poly(ethyl acrylate)/Vycor composite.

double-quantum peaks disappear when the glass surface is coated with trimethylsilyl groups.

Outlook and Conclusions

Solid-state NMR is a powerful tool for the study of surfaces and interfaces in polymer composites and nanocomposites. The NMR spectra and relaxation parameters are sensitive to the structure and dynamics on a very local length scale, allowing us to probe the polymer properties at the interface. The introduction of multidimensional NMR provides new opportunities to characterize in detail the structure and dynamics of polymers at surfaces and interfaces.

References

1. Bovey FA, Mirau PA. NMR of Polymers. Academic Press: New York, 1996.
2. Schmidt-Rohr K, Speiss HW. Multidimensional Solid-State NMR and Polymers. Academic Press: New York, 1994.
3. Mirau P. A Practical Guide to the NMR of Polymers. John Wiley & Sons: Hoboken, 2004.
4. Mehring M. High Resolution NMR in Solids. Springer: Berlin, 1983.
5. Gerstein BC, Pembleton RG, Wilson RC, Ryan LM. J. Chem. Phys. 1977;66:361.
6. Brown SP, Spiess HW. Chem. Rev. 2001;101:4125.
7. Isbester PK, Kestner TA, Munson EJ. Macromolecules. 1997;30:2800.
8. Meresi G, Wang Y, Bandis A, Inglefield PT, Jones AA, Wen W-Y. Polymer. 2001;42:6153.
9. Mirau PA, Heffner SA. Macromolecules. 1999;32:4912.
10. Yang S, Mirau PA, Pai C, Nalamasa O, Reichmanis E, Lin EK, Lee H-J, Gidley DW, Sun J. Chem. Mater. 2001;13:2762.
11. Mirau PA, Yang S. ACS Symposium Series. 2003;834:22.
12. Mirau PA, Yang S. Chem. Mater. 2002;14:249.
13. Rodriguez LNJ, De Paul SM, Barrett CJ, Reven L, Spiess HW. Adv. Mater. 2000;12:1934.
14. Brown SP, Schnell I, Brand JD, Mullen K, Spiess HW. J. Am. Chem. Soc. 1999;121:6712.
15. Caravatti P, Bodenhausen G, Ernst RR. Chem. Phys. Lett. 1982;89:363.
16. Bielecki A, Burum D, Rice D, Karasz F. Macromolecules. 1991;24:4820.
17. Mirau PA, Heffner S, Schilling M. Solid State NMR. 2000;16:47.
18. Hou SS, Beyer FL, Schmidt-Rohr C. Solid State NMR. 2002;22:110.
19. Giannelis EP, Krishnamoorti RK, Manias E. Adv. Polym. Sci. 1999;138:107.
20. Vaia RA, Krishnamoorti RK (Eds). Polymer Nanocomposites: Synthesis, Characterization and Modeling, Vol. 804. Oxford University Press: New York, 2002.
21. Hou SS, Bonagamba TJ, Beyer FL, Madison PH, Schmidt-Rohr K. Macromolecles. 2003;36:2769.
22. Komoroski RA. High Resolution NMR Spectroscopy of Synthetic Polymers in Bulk, Vol. 7. VCH Publishers Inc.: Dearfield Beach, 1986.
23. Spiess H. Colloid Polym. Sci. 1983;261:193.
24. Spiess HW. Chem. Rev. 1991;91:1321.
25. Lin WY, Blum FD. J. Am. Chem. Soc. 2001;123:2032.
26. Macho V, Brombacher L, Spiess H. Appl. Magn. Reson. 2001;20:405.
27. Schmidt-Rohr K, Clauss J, Spiess H. Macromolecules. 1992;25:3273.
28. Mirau PA, Heffner SA, Schilling M. Chem. Phys. Lett. 1999;313:139.

The Structure of Polymer Networks

Andrew K. Whittaker
Centre for Magnetic Resonance, The University of Queensland, Queensland 4072, Australia

Introduction

Network polymers comprise one of the most important classes of polymeric materials, from both a theoretical and a commercial perspective. The linking together of macromolecular chains usually through permanent covalent bonds confers unique properties to network polymers. These may be increased modulus and elasticity, lower rates of creep, solvent resistance, high temperature stability, to name just a few. The applications of network polymers are thus myriad. Thermosetting resins comprise the majority of polymers used in structural applications. Crosslinked polyolefins are ubiquitous as automotive tyres, as a component of asphalt, as o-rings, sheeting, in clothing and footware and so on. In more recent times, chemically crosslinked networks are becoming important in the field of biomaterials, as supports for tissue growth and for drug delivery. Many other applications can be listed.

From the point of view of the NMR spectroscopist, the structural features that provide networks their unique physical properties give rise to a number of experimental challenges. Network polymers are by definition wholly or largely insoluble, and therefore conventional solution-state NMR techniques cannot be routinely applied to their analysis. Resort must be made to solid-state NMR techniques, or to other methods for narrowing the dipolar-broadened line shapes. To compensate for this difficulty in extracting chemical information, there are a number of other NMR techniques for determining physical structure, for example, crosslink density, molecular weight between entanglements, and pore or mesh size.

Thus, the aim of this review is to summarize the development of NMR methodologies for the study of network polymers, in particular the determination of chemical structure and network properties using high-resolution NMR and NMR relaxometry. We are not concerned in this review with other aspects of network behavior, for example, the motion of penetrants in polymer networks, or NMR imaging of networks, as these aspects are covered in depth elsewhere in this monograph. All of these issues have been addressed in detail on a number of reviews specifically within the field of NMR characterization of networks [1–6], as well as a number of reviews on general analytical methods, including NMR, for characterizing polymer networks [7–9].

The Chemical Structure of Polymer Networks

The Effect of Network Structure on NMR Linewidths

The inherent insolubility of polymer networks and the connectivity of polymer chains result in relatively large unaveraged dipole–dipole couplings compared with small molecules freely tumbling in solution. As a result under normal experimental conditions, the NMR lines become broadened. This is a fact that has been exploited for a number of crosslinked network polymers. For example, Tinker and coworkers [10,11] developed qualitative relationships between the crosslink density and the widths of the peaks in the ^{1}H NMR spectra of natural rubber (NR) and other elastomers. Although it is not possible using their approach to construct a comprehensive theory relating the mechanism of line broadening with the extent of network formation, the value of this work lies in the ability to provide a rapid measurement of crosslink densities in blended and filled systems [12].

Another manifestation of the increase in linewidth on an increase in network density is a decrease in the overall signal amplitude achievable using high-resolution NMR techniques. Ford and coworkers [13–16] have produced a series of papers on the NMR characterization of poly(styrene) (PSTY) resins. In their initial report [14], poly(styrene) resins were prepared using a range of concentrations of divinyl benzene crosslinking agent. The samples were swollen to equilibrium with deuterated chloroform and measurements were made of T_1 relaxation times, ^{13}C linewidths, and NOE factors using a conventional solution-state NMR spectrometer. The magnitude of T_1 was relatively unaffected by crosslinking, indicating little change in the spectral density of motions in the MHz frequency range. This insensitivity of the high frequency motions to crosslinking has been noted on a number of occasions. However, for these swollen crosslinked PSTY materials, the linewidth increased with increasing crosslink density. Most significantly, the intensity of the

Graham A. Webb (ed.), Modern Magnetic Resonance, 583–589.
© 2008 *Springer.*

peaks decreased markedly, and the peaks associated with the aliphatic backbone carbons being more strongly affected than those due to the aromatic side chains. The loss of intensity was ascribed to inefficient decoupling of the dipole–dipole interactions both by the scalar ^{1}H decoupler and by the effects of restricted molecular motion.

It was concluded that in these experiments only parts of the polymer structure are being detected and that chain segments near to crosslink points were not visible. In a later study, Mohanraj and Ford [13] have attempted to account for the decrease in intensity in the ^{13}C spectra of crosslinked poly(chloromethylstyrenes) in a more quantitative manner. The decrease in signal intensity was analyzed and it was concluded that carbon nuclei in crosslinks as well as uncrosslinked units within one or two units of crosslink points are not observed. Similar conclusions were reached by O'Donnell and Whittaker [17] who examined ethylene–propylene rubbers crosslinked using a range of gamma radiation doses. At low crosslink densities, a small peak due to methine carbons in so-called H-type crosslinks was observed, with the width of this peak increasing with increasing levels of crosslinking, until the line could not be resolved from the baseline. It is thus evident that at even higher levels of crosslinking, other NMR techniques need to be utilized.

The method of magic angle spinning (MAS) will be discussed in greater depth elsewhere in this text. Briefly, in the absence of isotropic motion, the NMR line shape is dominated by strong dipole–dipole couplings to neighbor protons, and for ^{13}C the relatively large anisotropy of the chemical shift tensor. The technique of MAS deals effectively with the latter of these line broadening mechanisms, since rapid rotation of the sample around the magic angle leaves observable only the trace of the tensor, i.e. the isotropic chemical shift. Rotation at intermediate spinning speeds results in a series of rotational echoes in the FID, which on Fourier transformation results in evenly spaced spinning side bands. MAS also partially averages both the homonuclear and the heteronuclear dipole–dipole couplings, and hence high-power proton decoupling during ^{13}C acquisition is required to fully remove this contribution in ^{13}C NMR spectroscopy.

An example of the application of these techniques to the analysis of swollen crosslinked polymers has been was provided by Stöver and Fréchet [18,19] who have shown that MAS and dipolar decoupling reduce the ^{13}C linewidth in spectra of an ephedrine-functionalized divinylbenzene-styrene copolymer to values similar to those observed for uncrosslinked polymers. The relative peak intensities in the spectra are close to those predicted from the known structure of the polymer. In a related study [19], the authors suggest the use of crosspolarization (CP) to observe selectively crosslink points in the polymer gels.

A large number of polymer networks, most notably the thermosetting resins, are cured at elevated temperatures and hence under ambient conditions are well below their glass transition (T_g) or softening temperature. These rigid solids often have broad, poorly resolved ^{13}C NMR spectra, even with the use of MAS and high-power decoupling. A suggested approach to reduce the linewidth and to achieve high resolution is to record the spectra above the T_g temperature. Until recently most commercial MAS probes were limited to a maximum temperature of around 423 K, often well below the T_g of crosslinked resins. Recent advances in probe design have, however, allowed much higher temperatures to be reached in the MAS rotor. Sterna and Smith [20] were the first to demonstrate the advantages of improved resolution in ^{13}C spectra of thermosetting resins recorded above T_g. The spectra of diglycidyl ether of bisphenol A (DGEBA) reacted with and bisphenol acetone recorded at 473 K display liquid-like resolution, enabling, for example, the authors to identify a small peak due to the methine carbon in etheric crosslink structures. More recently, Harris *et al.* [21] studied the structure of the matrix formed by reaction of DGEBA with diamino diphenyl sulfone. The increase in resolution due to averaging of conformations otherwise frozen below T_g is dramatic.

Crosslinked Polyolefins

The vulcanization of NR with sulfur was first performed in 1841, and since then has become the basis of the enormous motor vehicle tyre industry. The mechanism of vulcanization/crosslinking is complex and despite much study, many aspects remain unresolved. For example, addition of the sulfur can occur at the double bonds, as in unaccelerated cure or at one of the allylic positions, as in accelerated vulcanization. The distribution of crosslinking and other reactions depends not only on the extent of compounding of the reactants and the rubber resin but also the mechanism of reaction, as is discussed below.

The analysis of the vulcanization or crosslinking of rubber materials has been the subject of an extensive series of publications by Koenig and coworkers [22–24], and the findings of which are summarized in several reviews [3,25]. The authors have attempted to determine the mechanisms of the very wide range of reactions that occur in vulcanization and other crosslinking reactions. In their early work, Zaper and Koenig [26,27] studied the reaction of sulfur with NR and reported profound changes in the ^{13}C NMR spectra on curing. They reported an increase in linewidth on curing due to a decrease in segmental motion on crosslinking, and the appearance of new peaks on both the high field and low field sides of the peaks in the aliphatic region. At higher levels of cure, the resolution in the ^{13}C spectra deteriorated and much of the chemical information was lost. Despite this, the structure of the methine groups in polysulfidic crosslinks was determined and the intensities of the peaks associated with these structures were shown to be inversely proportional to the swelling ratio. Other new peaks in the spectra were assigned to carbons in crosslink structures in which addition of sulfur had occurred at all four possible sites adjacent to the double bonds. In addition, the presence of cyclic structures was confirmed.

Fuelber and coworkers [28,29] have demonstrated the utility of an experiment that correlates the decay of transverse magnetization of the ^{1}H spins with the ^{13}C chemical shift, by crosspolarizing residual ^{1}H magnetization to the ^{13}C nuclei. The decay of ^{1}H magnetization of sulfur-cured poly(styrene-co-butadiene) rubber could be described by the sum of Gaussian and Lorentzian decays, corresponding to relatively rigid and mobile parts of the polymer, respectively. The second moment of the Gaussian line shape and the inverse of the T_2 of the Lorentzian line shape were seen to increase with increasing crosslinking density, consistent with restriction of motion of the main and side chains on crosslinking. These aspects will be discussed in more detail below.

An important method of crosslinking polyolefins is by exposing the material to high-energy radiation, initiating the formation of free radicals that undergo a range of reactions including crosslinking. As the concentration of crosslinks approaches one link on average per chain, the polymer reaches the gel state and is largely insoluble. The concentration of crosslinks at the gel point for polymers with initially high-molecular weight is very small of the order of one carbon per 10^4–10^5 carbons in the main chain. For this reason, model compounds which remain soluble when irradiated to high doses were initially examined. Bennett *et al.* [30] reported the formation of H-type crosslinks in irradiated liquid *n*-hexadecane and *n*-eicosane. Bovey *et al.* [31] observed H-links and long chain branching (Y-links) in n-$C_{44}H_{99}$ irradiated in the melt, whereas irradiation in the crystalline state gave only linear dimers, apparently through endlinking of the chains at surface of the crystals.

Randall and coworkers [32,33] were the first to report the structures of crosslinks in irradiated high molecular weight polymers using solution-state ^{13}C NMR. Y-links were detected in linear poly(ethylene) irradiated to below the gel dose at 298 K. On the other hand, H-links were observed when the irradiation temperature was increased to 550 K, i.e. in the molten state. The authors suggested that the major linking reaction at low doses involved addition of main chain alkyl radicals to double bonds initially present in linear poly(ethylene) as chain ends. A more complete study of crosslinking in irradiated low molecular weight fractions of linear poly(ethylene) was subsequently made by Horii and coworkers [34,35]. These authors were able to observe changes in the relative contribution of the various mechanisms of crosslinking on irradiation at different temperatures and related this to the relative stability of alkyl free radicals. These papers in particular present information on network formation vastly superior to that obtainable with other spectroscopic techniques.

An issue of some importance is the distribution of crosslinks in cured polyolefins, as this determines the efficiency of the added crosslinking agent (or high-energy photons) and many subsequent network properties. This issue was initially addressed using NMR by O'Donnell and Whittaker [36] who used ^{13}C CPMAS NMR to determine the crosslink density of ethylene–propylene rubbers irradiated to very high radiation doses. The yields for crosslinking and scission estimated from the NMR peak intensities are in excellent agreement with values obtained from measurements of the soluble fractions, a more traditional though time-consuming technique. The estimation of yields of crosslinking from measurement of soluble fractions necessitates several assumptions, namely a most probable initial molecular weight distribution and random crosslinking reactions. The excellent correspondence between the two sets of results underlines the validity of these assumptions in this case.

In contrast to this, the formation of networks by gamma irradiation of *cis*-1,4-poly(butadiene) (*cis*-PBD) and other polydienes [37–43] proceeds through a chain reaction involving addition of radical species to double bonds. Barron *et al.* [37] and O'Donnell and Whittaker [39] have measured the changes in the ^{13}C CPMAS spectra of *cis*-PBD samples irradiated to various doses up to 10 MGy. With increasing dose, there is a progressive decrease in the intensity of the peak due to double bonds, and the appearance of a broad peak assigned to methine carbons in crosslinked structures. Spectra were recorded using a range of CP contact times up to 25 ms, and the results were interpreted to yield quantitative yields of crosslinking and for loss of double bonds. Very high yields of reaction indicative of chain reactions were determined, in particular values much higher than the yields determined using solution methods. These results indicate a highly heterogeneous distribution of crosslink reactions, as a result of successive radical addition to double bonds. Other evidence of the heterogeneity of crosslink reactions during radiolysis is the report by Patterson and Koenig [44] of the radiation crosslinking of NR, *cis*-poly(isoprene), studied by solid-state ^{13}C NMR. A highly heterogeneous structure was evidenced by differences in the spectra obtained by direct polarization of the ^{13}C nuclei, and those obtained using CP.

The characterization of chemical changes during network formation of polydienes is aided by the very high yields of reaction resulting in marked changes to the NMR spectra. A more challenging problem is the characterization of the network structure in crosslinked poly(ethylene), i.e. poly(ethylene) crosslinked beyond the gel point. Cholli and coworkers [45] were the first to convincingly demonstrate the direct observation of crosslinks in poly(ethylene) by solid-state NMR. ^{13}C CP-MAS NMR spectra of high-density poly(ethylene) irradiated to high doses showed two small new peaks assigned to methine carbons in Y- and H-links, respectively. The formation of Y-links or branches was confirmed by the appearance of new peaks at lower chemical shift due to branch structures. O'Donnell and Whittaker [46] later reported the changes in crystalline content and lamellar dimensions after crosslinking using DSC and ^{1}H spin diffusion measurements. A peak assigned to methine carbons in H-crosslinks was also reported, and the yield of crosslinks obtained from analysis of the NMR spectra was very close to the yield obtained from analysis of the soluble fraction. It was therefore concluded that crosslinking occurs randomly throughout the amorphous phase of poly(ethylene).

Thermosetting Resins

In this review, the application of high-resolution NMR to the study of epoxy resins will be briefly discussed. The characterization of many other thermosetting network systems by NMR has been reviewed in detail elsewhere [2,8,47] and in general provides for the spectroscopist the same challenges of poor resolution in structurally diverse materials. Epoxy resins are an important class of materials used extensively in coatings and structural applications. Many end-use properties, not least long-term mechanical and chemical stability, are determined by the precise details of the curing reactions. Thus, questions of interest to the chemist which can be resolved by NMR spectroscopy include the mechanism of cure and extent of reaction of the secondary amine groups, and in particular the effect of filler on curing chemistry, a problem not easily amenable to other spectroscopic analyses. At low cure conversions, it is possible to follow the chemical changes using conventional solution-state NMR [48–52]. However, when the viscosity of the resin increases as cure proceeds and the ^{13}C lines broaden considerably, resort must be made to solid-state NMR techniques.

The dramatic changes in composition and chain dynamics that accompany curing of a thermosetting resin have been studied using ^{13}C MAS NMR by Haw and Johnson [53]. Their work was concerned with the curing of DGEBA with tetraethylene tetraamine at 323 K from the liquid state through the gel state and into the solid state. At low levels of cure, the high-resolution NMR spectrum gave information comparable to that obtained by conventional high-resolution spectroscopy; however, as the reaction continued and the extent of cure increased, the overall signal intensity decreased and the lines became progressively broader, for reasons discussed above. At even longer curing times, ^{13}C CPMAS NMR was used to measure changes in the chemical structure.

The first solid-state NMR study of an epoxy resin was presented by Garroway *et al*. in 1978 [54]. In this work, they were concerned with investigating the quantitative aspects of the NMR technique as applied to resins of DGEBA cured with four amine/anhydride mixtures. While all the features of the solution-state spectra at low conversion are replicated in the solid-state spectra, the much larger line width in the solid-state limits the amount of chemical information available from the ^{13}C NMR spectra. The increase in line width is ascribed mainly to increased dispersion of isotropic chemical shifts due to the presence of a large number of frozen conformations in the glassy cured matrix. As discussed above, raising the temperature [20,21] to above the T_g results in line narrowing and reattainment of high-resolution conditions.

The Physical Structure of Polymer Networks

Changes in T_2 Relaxation Times

As discussed above, one manifestation of network formation is an attenuation of segmental motion of the polymer backbone, and as a consequence one observes an increase in the NMR line widths. To state this in other terms, the formation of a network has a profound effect on transverse relaxation times of a polymer above its T_g temperature or of a swollen polymer network. The decrease in segmental mobility is most important at sites adjacent to crosslink points, so that the amplitude of motion of a particular chain segment increases the further that point is from the crosslink, or indeed the closer the segment is to a chain end. In practice, the decay of transverse relaxation in a crosslinked polymer can be decomposed into usually two or more decay processes. The more rapid decay process can be broadly assigned to segments close to crosslinks, while the slower decay to segments well removed from the crosslinks, or close to chain ends. Therefore, the decay of magnetization can be described by:

$$M(t) = \sum M_i(0)\, e^{-(t/T_2^i)} \,. \tag{1}$$

Here, M_i and T_2^i are the amplitude and time constant of the ith decay process, respectively, and i can take the values 1, 2, 3, ... It is important to note that M_1, i.e. the amplitude of the fastest decay, does not give a direct measure of the number of crosslinks, but rather the number of segments adjacent to the crosslinks, and hence is proportional to the crosslink density.

Arthur Charlesby and coworkers [55–61] were amongst the first to use measurements of T_2 to follow the formation of crosslinked polymer networks. In early work [57,58], they studied the changes in T_2 relaxation times of poly(dimethyl siloxane) when crosslinked by exposure to gamma radiation. The molecular weights of all polymers investigated were above the critical molecular weight for entanglement prior to irradiation, and therefore, the T_2 relaxation decays were decomposed into two separate processes, with the short relaxation decay containing a contribution from chain entanglements. Charlesby accounted for this by introducing the concept of a "virtual radiation dose" received by the unirradiated materials appropriate to the degree of chain entanglement experienced by these polymers. The authors were able to determine from the decrease in amplitude of the slow relaxation decay (due to chain segments removed from crosslink points) the yields of radiochemical reactions and found results in good agreement with those determined by solution methods. Charlesby and coworkers extended this approach to a number of other network systems with some success [62–64], and this approach has formed the basis of many subsequent studies of network formation.

Estimation of Residual Dipolar Coupling

While it is generally accepted that the slowest transverse relaxation processes in polymer networks can be represented by exponential decay functions, it is equally well accepted that the decay of magnetization at short times conforms more closely to a Gaussian decay function. In their work, Folland and Charlesby [55] recognized this but indeed were more concerned with following the changes in the relative proportions of the fast and slow decay functions, and thereby estimating the crosslink density.

Simon and coworkers [65–68] have developed a model of T_2 relaxation in which the faster decay process arises from an "intercrosslink" component of the network, in which motion is rapid and anisotropic and does not average to zero the dipolar interactions. The rapid motion, described by a correlation time τ_{f}, occurs simultaneously with a slower isotropic motion, described by the correlation time τ_{s}, of the complete intercrosslink segment. The longer relaxation decay arises from dangling chain ends and is exponential in nature. The total decay of transverse magnetization is then given by:

$$\frac{M_{x,y}(t)}{M_{x,y}(0)} = A\exp\left\{\frac{-t}{T_2} - qM_2\tau_s^2 \times\left[\exp\left(\frac{-t}{\tau_s}\right)+\frac{t}{\tau_s}-1\right]\right\} + B\exp\left(\frac{-t}{T_2}\right). \tag{2}$$

Here, M_2 is the second moment of the rigid-lattice line shape, q the fraction of the rigid-lattice second moment unaveraged by the anisotropic motion, and $1/T_2 = M_2\tau_{\mathrm{f}}$. In addition, a second slower process represented by the last term in Equation (2) and contributing close to 5% of the total signal amplitude was ascribed to a low molecular weight sol fraction. It was argued that the parameter q, the degree of averaging of the rigid-lattice second moment, could be related to the molecular weight between crosslinks M_{c} as:

$$M_{\mathrm{c}} = \frac{3cMru}{5n\sqrt{q'}}. \tag{3}$$

Here, q' is the above parameter q for a crosslinked network minus the contribution from physical entanglements, q_{o}, measured for an uncrosslinked material.

This method was more recently applied by Menge *et al.* [69] to the study of swollen PDMS networks. While the analysis of the transverse relation behavior of the dry networks conformed well to the theory of Simon *et al.*, on swelling with a number of solvents more complex behavior was observed. For weakly swollen materials, the parameter q, the extent of averaging of the second moment of the rigid lattice line shape, decreased, however, for strongly swollen networks relaxation became more efficient at short times. This was indicative of increased anisotropy of motion of intercrosslink segments due to deformation of the network. The relationship between molecular weight between crosslinks and the averaging of the second moment thus breaks down in this situation. In summary, while the NMR parameters are very sensitive to swelling ratio, the precise relationship with crosslink density has yet to be clearly defined.

In a number of papers, Cohen-Addad and coworkers [70–74] extended these concepts by describing a scale-invariant model of polymer chain motion. In this model, the local conformations of the chain are partially averaged resulting in a coarse-scale structural unit. If the scale is sufficiently coarse, the statistical properties of the polymer chains are simplified and indeed may be modeled satisfactorily with Gaussian random processes. Within this model the residual dipolar couplings are scaled by the inverse of the number of segments within the coarse-scale structural unit [29]. Brereton further developed this thinking by describing methods for determining statistical averages of the dipolar couplings, considering the motion of a Rouse chain [75] and further the effects of constraints induced by the presence of crosslink points within a network [76].

As a principal experimental tool, Cohen-Addad and coworkers have used extensively the measurement of the so-called pseudosolid echo [77,78], which measures the fluctuating residual dipole–dipole energy of anisotropically reorientating chain segments. As an example of the application to networks, the kinetics of crosslinking of poly(ethylene) by a free radical initiator were measured in real time [79]. The pseudosolid echo decay curve was decomposed into two decays, corresponding to the decays for the uncrosslinked material and the fully crosslinked polymer, respectively. The proportion of the decay due to the crosslinked material was seen to increase in proportion with the gel content.

As discussed recently by Kimmich and Fatkullin [80], a number of experimental approaches have been adopted to measure the residual dipolar coupling in dynamic polymer systems including networks. In addition to the approaches mentioned above, a number of workers have exploited the dependence of the development of double quantum coherence on the strength of the dipolar coupling [81–84]. As described by Spiess and coworkers [82–84], the residual dipolar coupling is proportional to the dynamic order parameter, which is in turn related as above to the inverse of the number of statistical chain segments between constraints. The time evolution of the double quantum coherence can be analyzed directly to determine the dynamic order parameter. Saalwachter and coworkers [81,85,86] have found that a distribution of order parameters is required to provide a satisfactory description of the experimental data. In their study of PDMS networks [81,85], these authors, for example, reported a largely unchanged dynamic order parameter on swelling of the network, but rather a broadening of the distribution function. This is seen as evidence of topologically constrained heterogeneities within the swelling network; this concept is expanded upon and supported by computer simulation in a following paper [86]. As a final comment in this section, it should be noted that the use of CP techniques allows ^{13}C observation and simultaneous measurement of either the residual homonuclear [87] or heteronuclear dipolar interactions [29,88,89].

Summary

The use of modern NMR techniques to determine the chemical and physical structure of polymer networks has been reviewed. On formation of a polymer network, or indeed within an entangled polymer melt, homo- and heteronuclear dipolar couplings are no longer fully averaged by random molecular fluctuations. The resultant changes in the NMR linewidths must be dealt with if accurate assessment of chemical structure is to be achieved. On the other hand, measurement of the residual dipolar order within the network allows estimation of network parameters, such as the number of segments between crosslink points and network order parameters.

References

1. Andreis M, Koenig JL. Adv. Polym. Sci. 1989;89:69–160.
2. Whittaker AK. Ann. Rep. NMR Spect. 1997;34:105–83.
3. Koenig JL. Rubber Chem. Technol. 2000;73:385–404.
4. Hill DJT, Whittaker AK. Ann. Rep. NMR Spect. 2002;46:1–35.
5. Mathur AM, Scranton AB. Biomaterials 1996;17:547–57.
6. Yasunaga H, Kobayashi M, Matsukawa S. In: I Ando, T Asakura (Eds). Solid State NMR of Polymer, Vol. 84. Elsevier: Amsterdam, 1998, pp 737–69.
7. Harrison DJP, Yates WR, Johnson JF. J. Macromol. Sci., Rev. Macromol. Chem. Phys. 1985;C25:481–549.
8. Bauer DR. Prog. Org. Coat. 1986;14:45–65.
9. Kinsey RA. Rubber Chem. Technol. 1990;63:407–25.
10. Brown PS, Tinker AJ. J. Nat. Rubber Res. 1990;5:286–95.
11. Brown PS, Tinker AJ. Kautchuk und Gummi Kunststoffe 1995;48:606–10.
12. Ellul MD, Patel J, Tinker AJ. Rubber Chemistry and Technology 1995;68:573–84.
13. Mohanraj S, Ford WT. Macromolecules 1985;18:351–6.
14. Ford WT, Balakrishnan T. Macromolecules 1981;14:284–8.
15. Ford WT, Yacoub SA. J. Org. Chem. 1981;46:819–21.
16. Ford WT, Periyasamy M, Spivey HO, Chandler JP. J. Magn. Reson. (1969–1992) 1985;63:298–305.
17. O'Donnell JH, Whittaker AK. Polymer 1992;33:62–7.
18. Stöver HDH, Fréchet JMJ. Macromolecules 1989;22:1574–6.
19. Stöver HDH, Fréchet JMJ. Macromolecules 1991;24:883–8.
20. Sterna LL, Smith HC. J. Magn. Reson. (1969–1992) 1988;79:528–33.
21. Harris RK, Yeung RR, Johncock P, Jones DA. Polymer 1996;37:721–7.
22. Koenig JL, Patterson DJ. Elastomerics 1986;118:21–4, 26.
23. Parker DD, Koenig JL. J. Adhesion 2000;73:299–311.
24. Pellicioli L, Mowdood SK, Negroni F, Parker DD, Koenig JL. Rubber Chem. Technol. 2002;75:65–76.
25. Mori M, Koenig JL. Ann. Rep. NMR Spect. 1997;34:231–99.
26. Zaper AM, Koenig JL. Rubber Chem. Technol. 1987;60:252–77.
27. Zaper AM, Koenig JL. Polym. Mater. Sci. Eng. 1987;56:189–93.
28. Fuelber C, Demco DE, Weintraub O, Bluemich B. Macromol. Chem. Phys. 1996;197:581–93.
29. Sotta P, Fuelber C, Demco DE, Bluemich B, Spiess HW. Macromolecules 1996;29:6222–30.
30. Bennett RL, Keller A, Stejny J, Murray M. J. Polym. Sci., Polym. Chem. Ed. 1976;14:3027–33.
31. Bovey FA, Schilling FC, Cheng HN. Adv. Chem. Ser. 1978;169:133–41.
32. Randall JC, Zoepfl FJ, Silverman J. Makromolekulare Chemie, Rapid Commun. 1983;4:149–57.
33. Randall JC, Zoepfl FJ, Silverman J. Radiat. Phys. Chem. 1983;22:183–92.
34. Horii F, Zhu Q, Kitamaru R, Yamaoka H. Macromolecules 1990;23:977–81.
35. Zhu Q, Horii F, Kitamaru R, Yamaoka H. J. Polym. Sci., Part A: Polym. Chem. 1990;28:2741–51.
36. O'Donnell JH, Whittaker AK. Br. Polym. J. 1985;17:51–5.
37. Barron PF, O'Donnell JH, Whittaker AK. Polym. Bull. (Berlin) 1985;14:339–46.
38. Hill DJT, O'Donnell JH, Perera MCS, Pomery PJ. Radiat. Phys. Chem. 1992;40:127–38.
39. O'Donnell JH, Whittaker AK. J. Polym. Sci., Part A: Polym. Chem. 1992;30:185–95.

40. Hill DJT, O'Donnell JH, Perera MCS, Pomery PJ, Whittaker AK. J. Macromol. Sci. A 1993;30:633–44.
41. Hill DJT, O'Donnell JH, Perera MCS, Pomery PJ. Polymer 1995;36:4185–92.
42. Hill DJT, O'Donnell JH, Perera MCS, Pomery PJ, Smetsers P. J. Appl. Polym. Sci. 1995;57:1155–71.
43. Hill DJT, O'Donnell JH, Senake Perera MC, Pomery PJ. ACS Symp. Ser. 1993;527:74–94.
44. Patterson DJ, Koenig JL. Appl. Spectrosc. 1987;41:441–6.
45. Cholli AL, Ritchey WM, Koenig JL. Appl. Spectrosc. 1987;41:1418–21.
46. O'Donnell JH, Whittaker AK. Radiat. Phys. Chem. 1992;39:209–14.
47. Whittaker AK. In: I Ando, T Asakura (Eds). Solid State NMR of Polymer, Vol. 84. Elsevier: Amsterdam, 1998, pp 469–90.
48. Grenier-Loustalot MF, Grenier P. J. Polym. Sci., Polym. Chem. Ed. 1984;22:4011–33.
49. Grenier-Loustalot MF, Cazaux F, Berecoechea J, Grenier P. Eur. Polym. J. 1984;20:1137–50.
50. Grenier-Loustalot MF, Grenier P. Makromolekulare Chemie 1983;184:2477–85.
51. Sojka SA, Moniz WB. J. Appl. Polym. Sci. 1976;20:1977–82.
52. Fyfe CA, Niu J, Rettig SJ, Wang DW, Poliks MD. J. Polym. Sci., Part A: Polym. Chem. 1994;32:2203–21.
53. Haw JF, Johnson NA. Anal. Chem. 1986;58:3254–6.
54. Garroway AN, Moniz WB, Resing HA. Faraday Symp. Chem. Soc. 1978;13:63–74.
55. Folland R, Charlesby A. Polymer 1979;20:211–4.
56. Folland R, Charlesby A. Radiat. Phys. Chem. 1977;10:61–8.
57. Charlesby A, Folland R, Steven JH. Proc. R. Soc. Lond., Ser. A: Math., Phys. Eng. Sci. 1977;355:189–207.
58. Folland R, Charlesby A. Int. J. Radiat. Phys. Chem. 1976;8:555–62.
59. Charlesby A. Radiat. Phys. Chem. 1995;45:955–9.
60. Charlesby A. Proc. Tihany Symp. Radiat. Chem. 1991;7:269–80.
61. Charlesby A. Radiat. Phys. Chem. 1985;26:463–71.
62. Folland R, Charlesby A. J. Polym. Sci., Polym. Lett. Ed. 1978;16:339–44.
63. Kamel I, Charlesby A. J. Polym. Sci., Polym. Phys. Ed. 1981;19:803–14.
64. Charlesby A, Bridges BJ. Radiat. Phys. Chem. 1982;19:155–65.
65. Simon G, Goetschmann B, Matzen D, Schneider H. Polym. Bull. 1989;21:475–82.
66. Simon G, Birnstiel A, Schimmel KH. Polym. Bull. 1989;21:235–41.
67. Simon G, Schneider H. Makromolekulare Chemie, Macromol. Symp. 1991;52:233–46.
68. Simon G, Baumann K, Gronski W. Macromolecules 1992;25:3624–8.
69. Menge H, Hotopf S, Poenitzsch S, Richter S, Arndt KF, Schneider H, Heuert U. Polymer 1999;40:5303–13.
70. Cohen-Addad JP, Guillermo A. J. Polym. Sci., Polym. Phys. Ed. 1984;22:931–55.
71. Cohen-Addad JP. Polymer 1983;24:1128–38.
72. Cohen-Addad JP, Dupeyre R. Polymer 1983;24:400–8.
73. Cohen-Addad JP. Prog. Nucl. Magn. Reson. Spectrosc. 1993;25:1–316.
74. Cohen-Addad JP, In: "Phys. Prop. Polym. Gels", Cohen-Addad JP (ed.), Wiley, Chichester, 1996, pp. 39–86.
75. Brereton MG. Macromolecules 1989;22:3667–74.
76. Brereton MG. Macromolecules 1990;23:1119–31.
77. Cohen-Addad JP. J. Chem. Phys. 1975;63:4880–5.
78. Cohen-Addad JP, Schmit C. Polymer 1988;29:883–93.
79. Cohen-Addad JP, Schmit C. J. Polym. Sci., Part C: Polym. Lett. 1987;25:487–93.
80. Kimmich R, Fatkullin N. Adv. Polym. Sci. 2004;170:1–113.
81. Saalwachter K, Ziegler P, Spyckerelle O, Haidar B, Vidal A, Sommer J-U. J. Chem. Phys. 2003;119:3468–82.
82. Graf R, Demco DE, Hafner S, Spiess HW. Solid State Nucl. Magn. Reson. 1998;12:139–52.
83. Graf R, Heuer A, Spiess HW. Phys. Rev. Lett. 1998;80:5738–41.
84. Dollase T, Graf R, Heuer A, Spiess HW. Macromolecules 2001;34:298–309.
85. Saalwaechter K. J. Am. Chem. Soc. 2003;125:14684–5.
86. Saalwaechter K, Kleinschmidt F, Sommer J.-U. Macromolecules 2004;37:8556–68.
87. Eulry V, Tekely P, Humbert F, Canet D, Marcilloux J. Polymer 2000;41:3405–10.
88. Wang M, Bertmer M, Demco DE, Bluemich B. J. Phys. Chem. B 2004;108:10911–8.
89. Aluas M, Filip C. Solid State Nucl. Magn. Reson. 2005;27:165–73.

^{1}H CRAMPS NMR of Polypeptides in the Solid State

Akira Shoji
Department of Biological Sciences, Gunma University, Tenjin-cho,
Kiryu-shi, Gunma 376-8515, Japan

Introduction

The research of the solid high-resolution NMR rapidly developed recently, and the cross-polarization–magic-angle spinning (CP-MAS) method is most commonly used for the ^{13}C and ^{15}N NMR measurements of organic compounds in the solid state. Very recently, the solid high-resolution proton NMR research developed [1–7] because both quality and quantities are high for the potential of information of the hydrogen nucleus. Study example of solid secondary structure (main-chain conformation) of polypeptide is introduced on the basis of the proton chemical shift this-focus. Therefore, the author introduces the research result of recent proton combined rotation and multiple pulse spectroscopy (CRAMPS) NMR of polypeptides in this chapter. In the attractiveness, the proton CRAMPS NMR research has just begun yet, and it has a further unprecedented possibility of developing in future. This review is the happiness, if it is useful for the future of your scientific research.

Experimental Evidence

Conformational Study of Synthetic Polypeptides by ^{1}H CRAMPS NMR

"Can ^{1}H NMR become an effective means for conformational analysis of polypeptides and proteins in the solid state?" In order to answer this question, the author focus and discuss about the study on correlation between the ^{1}H chemical shift and the main-chain conformation (secondary structure) of synthetic polypeptides [2,4,7]. It is well known that the right-handed α-helix (α-helix), antiparallel β-sheet (β-sheet) and parallel β-sheet (β_P-sheet) forms are the most famous conformations in proteins. In addition, the left-handed α-helix (α_L-helix), polyglycine I (PGI) and II (PGII), polyproline I (PPI) and II (PPII), and left-handed ω-helix (ω_L-helix) conformations are known in synthetic model polypeptides. If the conformational determination of solid polypeptides based on the solid high-resolution ^{1}H NMR is possible, we would obtain the very powerful means in the conformational analysis of proteins. Shoji and coworkers [1–7] have extensively studied for this work with various kinds of synthetic polypeptides and some cyclic dipeptides. Using these samples adopting the characteristic differences in conformation, they challenged to systematically test the power of ^{1}H CRAMPS NMR for the structural analysis in the solid state.

Conformational Analysis of Polypeptides based on α-Proton Chemical Shifts

α-Helix and β-sheet Forms. Figure 1-(1) shows the ^{1}H CRAMPS NMR spectra of poly(L-alanines) (PLAs) in the solid state [1,2]: (A) H-[Ala]$_8$-NHBu (β-sheet form), (B) [Ala]$_n$ − 1 (mixture of α-helix and β-sheet forms), and (C) [Ala]$_n$ − 5 (α-helix form). Each proton signal can be easily assigned to NH (7–10 ppm), H^α (3–6 ppm), and H^β (0–2 ppm) from downfield. From these spectra, it is found that (1) ^{1}H chemical shift of the H^α signal is significantly different and conformation-dependent [α-helix (3.9 ppm) and β-sheet (5.1 ppm)]; (2) ^{1}H chemical shift of the H^β signal is nearly the same (1.2–1.4 ppm) within the error limit at the present resolution; and (3) H^N signal is broad due to residual dipolar coupling between amide ^{1}H and quadrupolar ^{14}N nuclei [8]. This fact confirms the view that the main cause of the ^{1}H chemical shift displacement is not by the degree of polymerization but by the conformation of polypeptides. Thus, the chemical shift of the H^α signal in the α-helix PLA is to low frequency by 1.2 ppm from that in the β-sheet, indicating that the H^α signal is a useful fingerprint for conformational analysis of PLA in the solid state.

Figure 1-(2) shows the ^{1}H CRAMPS NMR spectra of poly(L-valines); (A) [Val]$_n$ − 1 (DP$_n$ is about 5, β-sheet form) and (B) [Val]$_n$ − 5 (DP$_n$ is about 100, β-sheet) in the solid state. It is confirmed that the ^{1}H chemical shift of the H^α signal does not depend on the degree of polymerization because the stable conformation of PLVs used here is the β-sheet form alone and it does not change with increasing molecular weight. Thus, the ^{1}H chemical shifts of the H^α, H^β, and H^γ signals are also independent of the degree of polymerization (β-sheet form). This fact confirms the view that the main cause of the ^{1}H chemical shift displacement is not the degree of polymerization but the conformation of polypeptides.

For the case of poly(L-leucines) (PLLs), it is obvious that the chemical shift of the H^α signal is

Graham A. Webb (ed.), Modern Magnetic Resonance, 591–604.
© 2008 *Springer.*

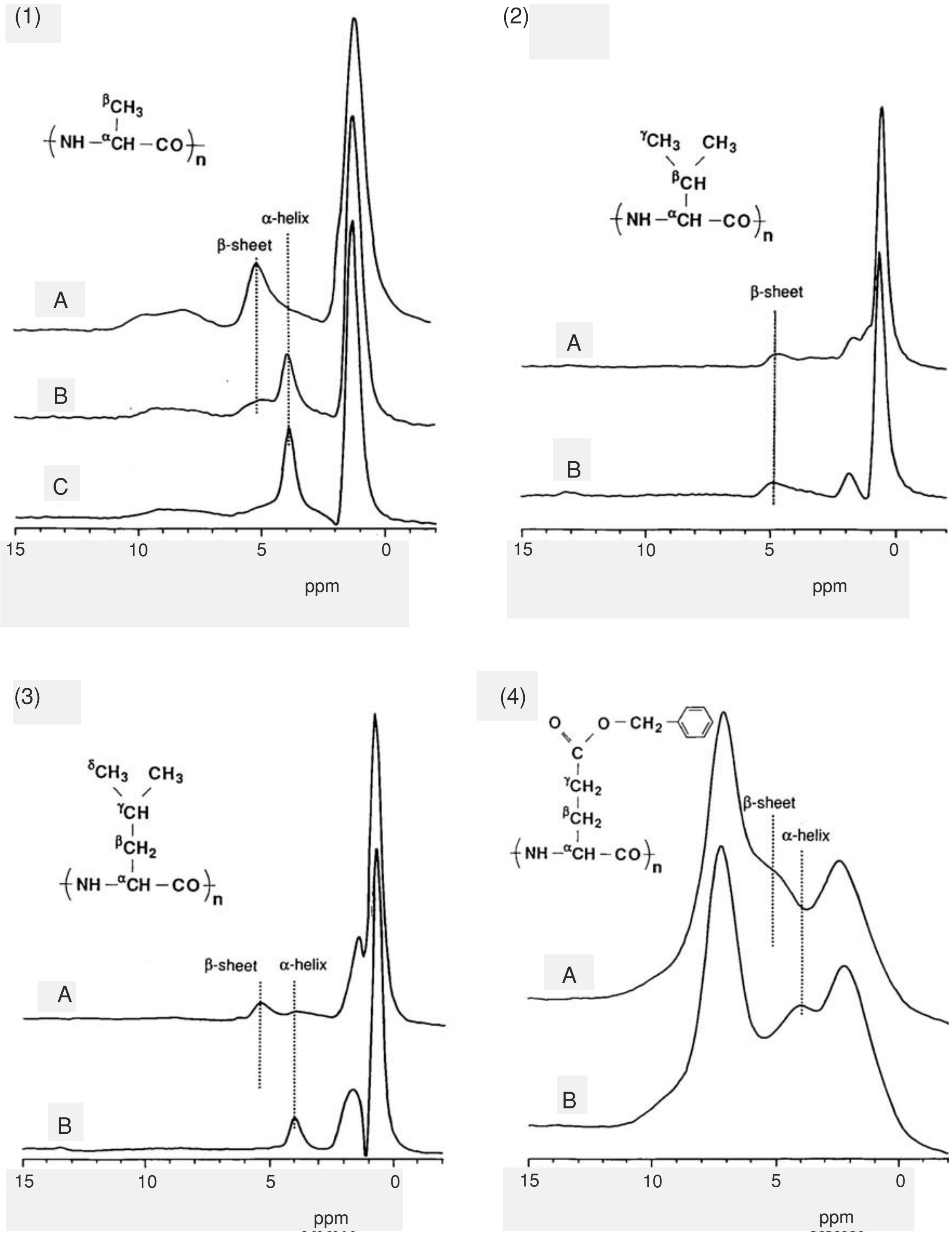

Fig. 1. NMR spectra (300 MHz ^{1}H CRAMPS) of (1) poly(L-alanines): (A) H-[Ala]$_8$-NHBu (β-sheet form), (B) [Ala]$_n - 1$ (DP$_n \approx$ 16, α-helix + β-sheet), and (C) [Ala]$_n - 5$ (DP$_n \approx$ 65, α-helix); (2) poly(L-valines): (A) [Val]$_n - 1$ (DP$_n \approx$ 5, β-sheet form) and (B) [Val]$_n - 5$ (DP$_n \approx$ 100, β-sheet); (3) poly(L-leucines): (A) [Leu]$_n - 1$ (β-sheet) and (B) [Leu]$_n - 2$ (α-helix); and (4) poly(γ-benzyl-L-glutamates): (A) H-[Glu(OBzl)]$_6$-OBzl (β-sheet) and (B) [Glu(OBzl)]$_n$ (α-helix).

conformation-dependent [α-helix: 4.0 ppm, β-sheet: 5.5 ppm], as shown in Figure 1-(3). The ^{1}H chemical shifts of the side-chain signals are almost conformation-independent, and the H^N signal is so broad as to be almost undetectable. This NMR feature is basically quite similar to that of PLA. It is especially noteworthy that the ^{1}H chemical shift region of the H$^\alpha$ signal is fully separated from that of the side-chain signals, in spite of the fact that the L-leucine residue has a bulky side group. Therefore, the ^{1}H chemical shift of the H$^\alpha$ signal is very useful for conformational analysis of polypeptides in the solid state.

Furthermore, for the case of poly(γ-benzyl-L-glutamate) (PBLG), which has side-chain benzyl esters, the ^{1}H NMR signals are roughly classified into three regions (amide, phenyl, and benzyl H; H$^\alpha$; H$^\beta$, and H$^\gamma$ signals), as shown in Figure 1-(4). This is also similar to the case of PLA and PLL, whereas the ^{1}H NMR signals become broader over the wide range of chemical shifts. Accordingly, it is possible to recognize that the ^{1}H chemical shift of the H$^\alpha$ signal is conformation-dependent [α-helix (4.0 ppm) and β-sheet (nearly 5.2 ppm)]. The chemical shift of the H$^\alpha$ signal in the α-helix is to low frequency by 1.2 ppm compared with that in the β-sheet form, which is quite reasonable.

The ^{1}H chemical shift data of the samples used here are summarized in Table 1, together with their characteristics of the samples.

In conclusion, the chemical shift of the H$^\alpha$ signal is important and very useful for conformational analysis of polypeptides in the solid state because the ^{1}H chemical shift region of the H$^\alpha$ signal is fully separated with that of the side-chain signals (except for threonine H$^\beta$ residue alone in solution).

Polyglycine (PGI and PGII) and poly(L-proline) (PPI and PPII) forms. Figure 2-(1) shows the ^{1}H CRAMPS NMR spectra of polyglycines (PGs): (A) PGI and (B) PGII forms [6]. It is admitted that PGI (antiparallel β-sheet) and PGII (intermolecular hydrogen-bonded 3_1-helix) forms are stable in the solid state [9]. The ^{1}H chemical shifts of the H$^\alpha$ signals ($\delta = 4.3$, PGI; $\delta = 3.7$, PGII) depend on main-chain conformation. That is, the chemical shift of the H$^\alpha$ signal of PGI is to high frequency by 0.6 ppm

Table 1: ^{1}H and ^{13}C chemical shifts and characteristics of polypeptides and cyclic dipeptides

Sample	DP$_n$[*]	Conformation[†]	H$^\alpha$	H$^\beta$	C=O	C$^\alpha$	C$^\beta$
H-[Ala]$_8$-NHBu	—	β–sheet	5.1	1.2	171.8	48.2	19.9
[Ala]$_n$ − 1	16	α-helix[‡]	5.0, 3.9	1.3			
[Ala]$_n$ − 5	65	α-helix	3.9	1.4	176.4	52.4	14.9
[Val]$_n$ − 1	5	β-sheet	5.0	1.8	171.8	58.4	32.4
[Val]$_n$ − 5	100	β-sheet	5.0	1.9			
[Leu]$_n$ − 1	A/I[§] = 5	β-sheet[¶]	5.5	1.5	170.5	50.5	43.3
[Leu]$_n$ − 2	A/I[§] = 100	α-helix	4.0	1.6	175.7	55.7	39.5
[Glu(OBzl)]$_6$–OBzl	—	β-sheet	5.2	2.4	171.0	51.2	29.0
[Glu(OBzl)]$_n$	h.m.w[‖]	α-helix	4.0	2.2	175.6	56.4	25.6
[Glu(OBzl)]$_n d_2$	h.m.w[‖]	α-helix	4.0	2.2			
[Glu(OBzl)]$_n d_7$	h.m.w[‖]	α-helix	—	—			
PGI	h.m.w[‖]	Polyglycine I (β-sheet)	4.3	—	169.2	44.3	—
PGII	h.m.w[‖]	Polyglycine II (3_1-helix)	3.7	—	172.7	42.5	—
cyclo[L-Ala-L-Ala]		Boat	4.3	1.4	172.1	49.5	15.6, 18.0
cyclo[L-Ala-D-Ala]		Planar	4.7	1.5	167.9	49.7	21.0
PPI	h.m.w[‖]	Polyproline I	4.2	3.6	171.7	59.3	48.4
PPII	h.m.w[‖]	Polyproline II	4.0	3.0	170.6	58.5	47.3

Ala, L-alanine; Val, L-valine; Leu, L-leucine; Glu(OBzl), γ-benzyl-L-glutamate; PG, polyglycine; PP, poly(L-proline); NHBu, *n*-butyl amide; OBzl, benzyl ester; α-helix, right-handed α-helix; β-sheet, antiparallel β-sheet.

[*] The number-averaged degree of polymerization.

[†] Conformations of these samples were determined from the ^{13}C and/or ^{15}N CP-MAS NMR, IR, and far-IR spectroscopic methods.

[‡] Containing small amounts of β-sheet.

[§] The molar ratio of the monomer (A) to the initiator (I), which corresponds to the theoretical number-averaged degree of polymerization.

[¶] Containing only a small amount of α-helix.

[‖] High molecular weight sample.

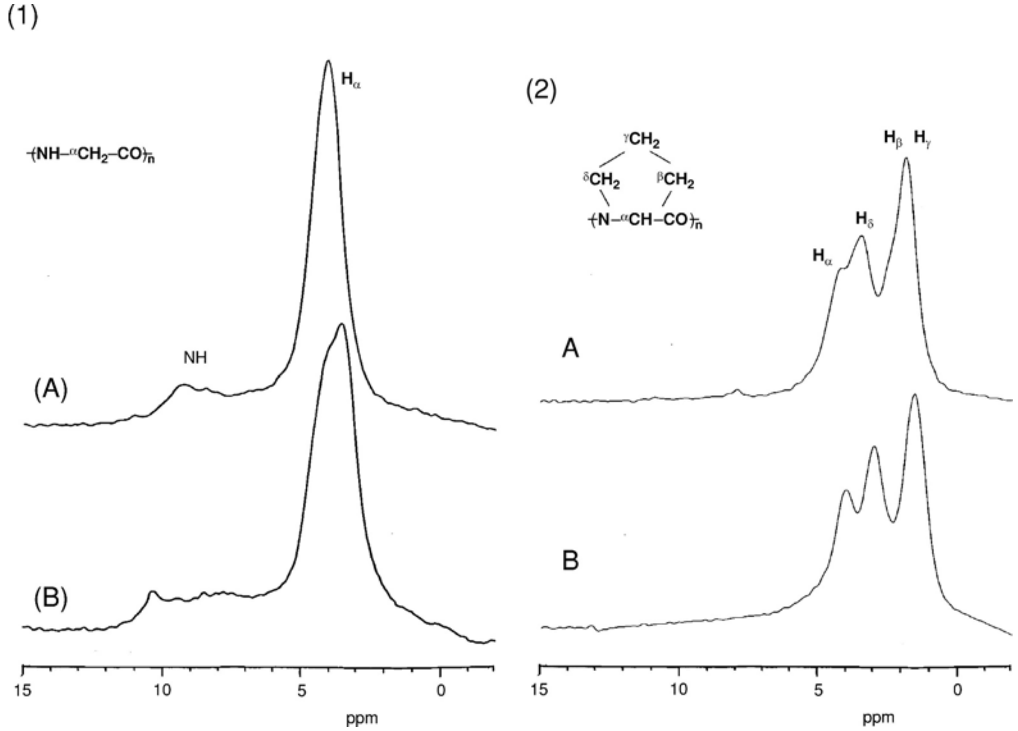

Fig. 2. NMR spectra (300 MHz ^{1}H CRAMPS) of (1) polyglycines: (A) PGI (polyglycine I) and (B) PGII (polyglycine II); (2) poly(L-prolines): (A) PPI (polyproline I) and (B) PPII (polyproline II).

from that of the PGII. This indicates that the chemical shift of the H^α signal is useful for conformational analysis of solid PG, whereas the chemical shift difference of the H^α signal is relatively small between PGI and PGII forms.

In addition, it has been found that the ^{1}H chemical shift of the H^α signal of PGI (β-sheet) is to low frequency by 0.6–1.2 ppm from those of other β-sheet polypeptides such as PLA, PLV, PLL, and PBLG. From the standpoint of the ^{1}H chemical shifts, glycine residue is a special α-amino acid compared with other common α-amino acids, and it contains no asymmetric carbon atom, which is very convenient for the conformational analysis of polypeptides and proteins. However, we should carefully pay attention to the H^α chemical shifts of glycine residue because the H^α chemical shifts of both PGI and PGII are near to that of the α-helix (3.9–4.0 ppm). Therefore, it is noteworthy that the ^{1}H chemical shift of PG is very useful in assigning the H^α signal from other common α-amino acid residues and in analyzing the main-chain conformation of silk fibroins and collagen fibrils.

On the other hand, the proline residue does not have amide proton, and therefore it cannot form $N–H\cdots O=C$ hydrogen bonding. For this reason, however, the proline residue fits in a unique structure, and PPII is also an important basic structure found in collagen as well.

Figure 2-(2) shows the ^{1}H CRAMPS NMR spectra of poly(L-prolines) (PPs). From Figure 2-(2), it is deduced that the chemical shift of the H^α signal is almost the same ($\delta = 4.2$, PPI; $\delta = 4.0$, PPII). In contrast, the chemical shift of the H^δ signal is significantly conformation-dependent ($\delta = 3.6$, PPI; $\delta = 3.0$, PPII), suggesting that this peak is a useful fingerprint for conformational analysis of PP in the solid state. It is the first case in which the ^{1}H chemical shifts of the side-chain protons depend significantly on the main-chain conformation of the PP, but the main-chain H^α does not depend on the conformation. To confirm the assignment of individual ^{1}H signals in conformational analysis, it is promising to apply the two-dimensional (2D) ^{1}H–^{13}C heteronuclear correlation (HETCOR) NMR measurement [6,10–13]. In the case of PP, it is easy to separate the individual ^{1}H peaks of PPs on the basis of the well-resolved ^{13}C signals because the ^{1}H–^{13}C correlations are clear in the 2D spectra for ^{1}H–^{13}C pairs (figure not shown).

Comparison of the ^{1}H Chemical Shift Data of Amino Acid Residues in the Solid State and in Solution

It is very important to compare the ^{1}H chemical shift data in the solid state with those in solution, especially for the H$^\alpha$ chemical shift. According to the solution ^{1}H NMR data summarized in the references [14–16], it is possible to estimate the chemical shift value of the H$^\alpha$ signal in the α-helix and β-sheet forms in solution. They can be concretely determined by the addition of -0.38 ppm (α-helix) and 0.38 ppm (β-sheet) to the H$^\alpha$ value in the random coil state, which has been determined in solution measurements [14]. However, the experimental differences of the ^{1}H chemical shifts are present between in solid state and in solution. In the α-helical polypeptides, the H$^\alpha$ chemical shifts measured in the solid state (3.9–4.0 ppm) are identical with those in the solution data (3.94–3.95 ppm), whereas in the β-sheet polypeptides the H$^\alpha$ chemical shifts measured in the solid state (4.9–5.5 ppm) are 0.2–0.8 ppm to high frequency from those estimated in the solution data (4.70–4.71 ppm) [14]. This comparison shows a very interesting and important finding. It is not a reason to estimate H$^\alpha$ chemical shifts of β-sheet polypeptides in solution, according to the method described above. However, it does highlight that more careful attention must be given to determining the ^{1}H chemical shifts of the β-sheet polypeptides using the solution data proposed by Wishart *et al.* [14–16].

Conformational Study of Cyclic Dipeptides by ^{1}H CRAMPS NMR: Cyclo(L-alanyl-L-alanyl) and cyclo(L-alanyl-D-alanyl)

It is known that the ring conformation of cyclo[L-Ala-L-Ala] (LL) is a boat form (C$^\beta$: equatorial) and that of cyclo[L-Ala-D-Ala] (LD) is a planar form in the solid state by X-ray crystal diffraction analysis [17]. Figure 3 shows the ^{1}H CRAMPS NMR spectra of cyclic dipeptides, (A) LL and (B) LD in the solid state [2,18,19]. It is found that (1) the chemical shift of the H$^\alpha$ signal is different between LL (4.3 ppm) and LD (4.7 ppm), (2) the chemical shifts of the H$^\beta$ signals are almost identical for LL and LD (1.4–1.5 ppm), and (3) the chemical shift of the amide ^{1}H signal is quite different between LL (10.3 ppm) and LD (9.3 ppm). The chemical shift difference of the H$^\alpha$ signal can be attributed mainly to the differences in ring conformation in the solid state. The chemical shift difference of the amide ^{1}H signal between LL and LD may be explained by considering an intermolecular hydrogen-bonding effect as well as its ring conformation.

This interpretation is compatible with the X-ray crystal diffraction analysis by Sletten [17]. As shown in Figure 1, in general, the true amide ^{1}H chemical shift cannot be determined exactly using any natural abundant polypeptides. It is noteworthy that the ^{1}H signal line shape directly bonded to ^{14}N of LL and LD exhibits symmetric singlet pattern in spite of the heteronuclear dipolar interaction between quadrupolar ^{14}N nuclei and amide protons. Thus, it is valuable to determine true amide ^{1}H chemical shift in this series, and the ^{15}N-labeled LL and LD samples are needed for the future work. In addition, it is important to clarify the relation between the ^{1}H chemical shift and the ring conformation (such as the planar, boat equatorial, boat axial, and chair forms) in the solid state by ^{1}H CRAMPS NMR.

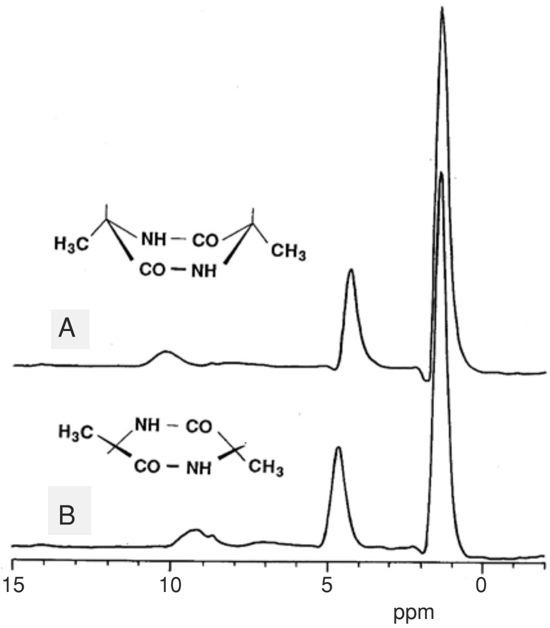

Fig. 3. NMR spectra (300 MHz ^{1}H CRAMPS) of cyclic dipeptides: (A) cyclo[L-Ala-L-Ala] (LL) and (B) cyclo[L-Ala-D-Ala] (LD).

Conformational Study of Specific Deuterium-labeled Polypeptides by ^{1}H CRAMPS NMR

It is valuable to test the advantages of specific deuterium labeling of polypeptides in the solid state. In general, specific isotope labeling is a very powerful tool to aid assigning complicated signals. The NMR method utilizes isotope labeling to advantage, proton signals often overlap each other on ^{1}H CRAMPS NMR spectra because the resolution is not good. In such cases, a specific deuterium labeling technique sometimes enables one to observe separately only a specific proton and to eliminate all other unnecessary ^{1}H peaks.

Figure 4 shows the ^{1}H CRAMPS NMR spectra of α-helix PBLGs: (A) [Glu(OBzl)]$_n$ (natural abundance), (B) [Glu(OBzl)]$_n$-d_2 (γ-protons deuterated), and (C) [Glu(OBzl)]$_n$-d_7 (benzyl protons deuterated) [20,21].

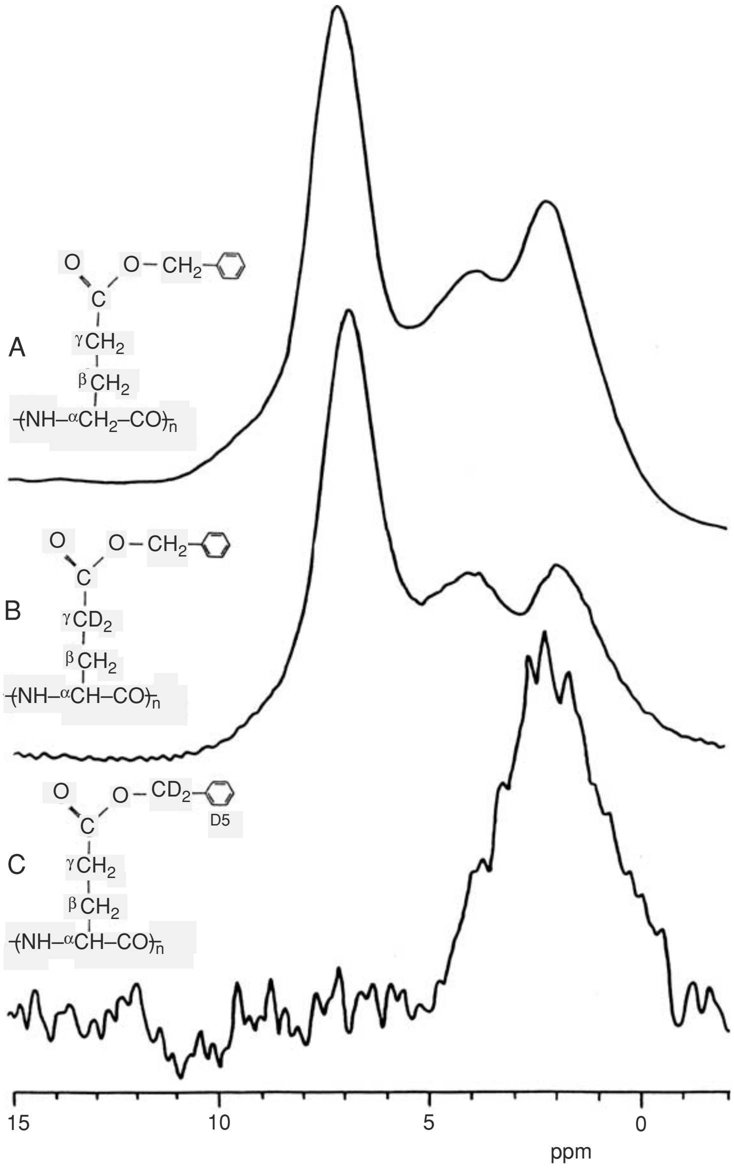

Fig. 4. NMR spectra (300 MHz ^{1}H CRAMPS) of poly(γ-benzyl-L-glutamates): (A) $[\text{Glu(OBzl)}]_n$ (natural abundance, powder), (B) $[\text{Glu(OBzl)}]_n$-d_2 (γ-protons deuterated, film prepared from the chloroform solution), and (C) $[\text{Glu(OBzl)}]_n$-d_7 (benzyl protons deuterated, film prepared from the $CHCl_3$ solution).

It is evident that the signal intensity at 2.2 ppm of $[\text{Glu(OBzl)}]_n$-d_2 (B) is lower than that of $[\text{Glu(OBzl)}]_n$ (A), and H^γ signal of $[\text{Glu(OBzl)}]_n$-d_7 has fully disappeared. This shows that specific deuterium labeling is useful for removing a specific proton signal from the overlapping signals of polypeptides in ^{1}H CRAMPS NMR spectra. In contrast, it is recognized that the signals of all benzyl protons are clearly removed in deuterated samples of the benzyl group $[\text{Glu(OBzl)}]_n$-d_7 (C) but the signal-to-noise (S/N) ratio and the resolution are not sufficient, as shown in Figure 4. Thus, deuterium labeling in ^{1}H CRAMPS spectra is useful for exact assignment and removing the specific signals, if the amount of deuterium substitution is not great and the resolution is sufficient to get a good spectrum.

Application of ^{1}H CRAMPS NMR to Conformational Study of Natural Fibrous Proteins and their Model Polypeptides

It was shown, in a previous section, that the conformation of solid polypeptides can be determined based on the ^{1}H chemical shift. In this section, the structural analysis of a fibrous protein (silk fibroins) in the solid state will be described. It usually happens that time some ^{1}H signals overlap each other in silk fibroins due to the resolution limit of ^{1}H CRAMPS. This may be solved partly by improvement of the resolution limit in ^{1}H CRAMPS using 2D ^{1}H–^{13}C HETCOR [1,6,10–13], which is useful for improving the practical value of CRAMPS for the conformational analysis of proteins.

It is anticipated that the ^{1}H chemical shifts of a more simplified model polypeptide such as $[\text{Ala-Gly}]_{12}$ will be a good guide to the model for the assignment of the NMR spectra of these silk fibroins in the solid state [6,7,22].

Conformational Study of Silk Fibroins by ^{1}H CRAMPS NMR

Figure 5 shows the ^{1}H CRAMPS NMR spectra of two silk fibroins: (A) *Bombyx mori*-I (silk I form) and (B) *Bombyx mori*-II (silk II form) fibroins [6,7]. They give highly resolved ^{1}H CRAMPS NMR spectra in the solid state, which are the first high-resolution solid state ^{1}H CRAMPS NMR spectra of such natural protein.

It should be noted that the amino acid sequence (primary structure) of these two samples is completely identical, but their main-chain conformations are different [6,7,22–24]. As expected, these two conformations are quite different to each other in terms of ^{1}H CRAMPS NMR spectra. The H$^\alpha$ signals of *Bombyx mori*-I (silk I) and *Bombyx mori*-II (silk II) showed a singlet ($\delta = 3.9$) and doublet ($\delta = 5.0$ and 3.9), respectively. In addition, the chemical shift of the H$^\beta$ protons (mainly from L-alanine residues) of *Bombyx mori*-I ($\delta = 1.6$) is different from that of *Bombyx mori*-II ($\delta = 1.2$). It is clear in this case that the chemical shifts of side-chain protons depend on the conformation, i.e. silk I and II. This is a very important result because it is confirmed that the ^{1}H chemical shifts of the side chains in polypeptides are principally conformation-dependent. In conclusion, the chemical shifts of the H$^\alpha$ and side-chain H$^\beta$ signals are useful for conformational analysis of *Bombyx mori* silk fibroins in the solid state, and thus, the ^{1}H CRAMPS NMR is a useful tool for conformational analysis of silk fibroins in the solid state.

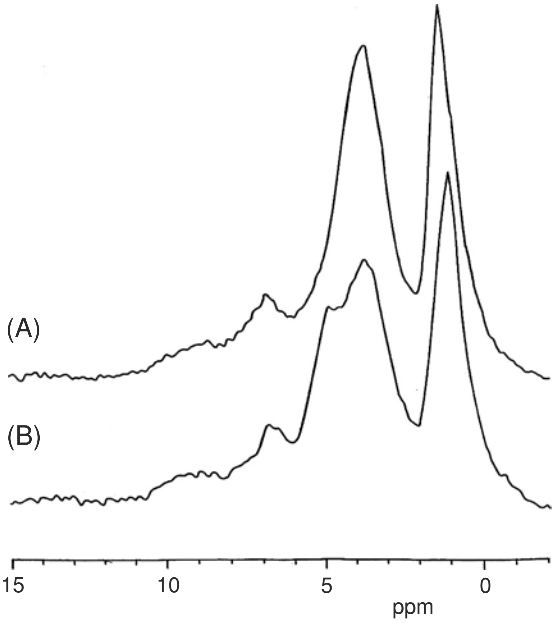

Fig. 5. NMR spectra (300 MHz ^{1}H CRAMPS) of silk fibroins (64 scans): (A) *Bombyx mori*-I (silk I form) and (B) *Bombyx mori*-II (silk II form). Peak assignment: H^N, 10–8 ppm; side-chain phenyl, 6.9 ppm; H$^\alpha$, 3.9–5.0; side chain, 1.6–1.2 ppm.

Two-dimensional ^{1}H–^{13}C HETCOR NMR Study of Silk Fibroins

It is possible to separate and assign the ^{1}H signals of the polypeptides and silk fibroins using 2D HETCOR spectra because the correlations are clearly resolved in the 2D spectra for proton–carbon pairs.

Figure 6 shows the 2D ^{1}H–^{13}C HETCOR NMR spectra of silk fibroins: (A) *Bombyx mori*-I (silk I) and (B) *Bombyx mori*-II (silk II) in the solid state [6]. Individual ^{1}H signals can be easily assigned on the basis of the corresponding ^{13}C signals. As shown in Figure 6, it can be admitted that the H$^\alpha$ signals of the glycine and L-alanine residues overlap in *Bombyx mori*-I, but that the H$^\alpha$ signal of the glycine residue is distinguished from that of the L-alanine residue in *Bombyx mori*-II. Furthermore, we can detect the H$^\alpha$ and H$^\beta$ peaks of L-serine residue at around 1.5–2.5 ppm in 2D spectra, although the L-serine content is very low compared with the L-alanine or glycine content in *Bombyx mori*.

Thus, the 2D HETCOR technique allows the resolution of ^{1}H CRAMPS to be tied to the higher resolution associated with ^{13}C chemical shifts.

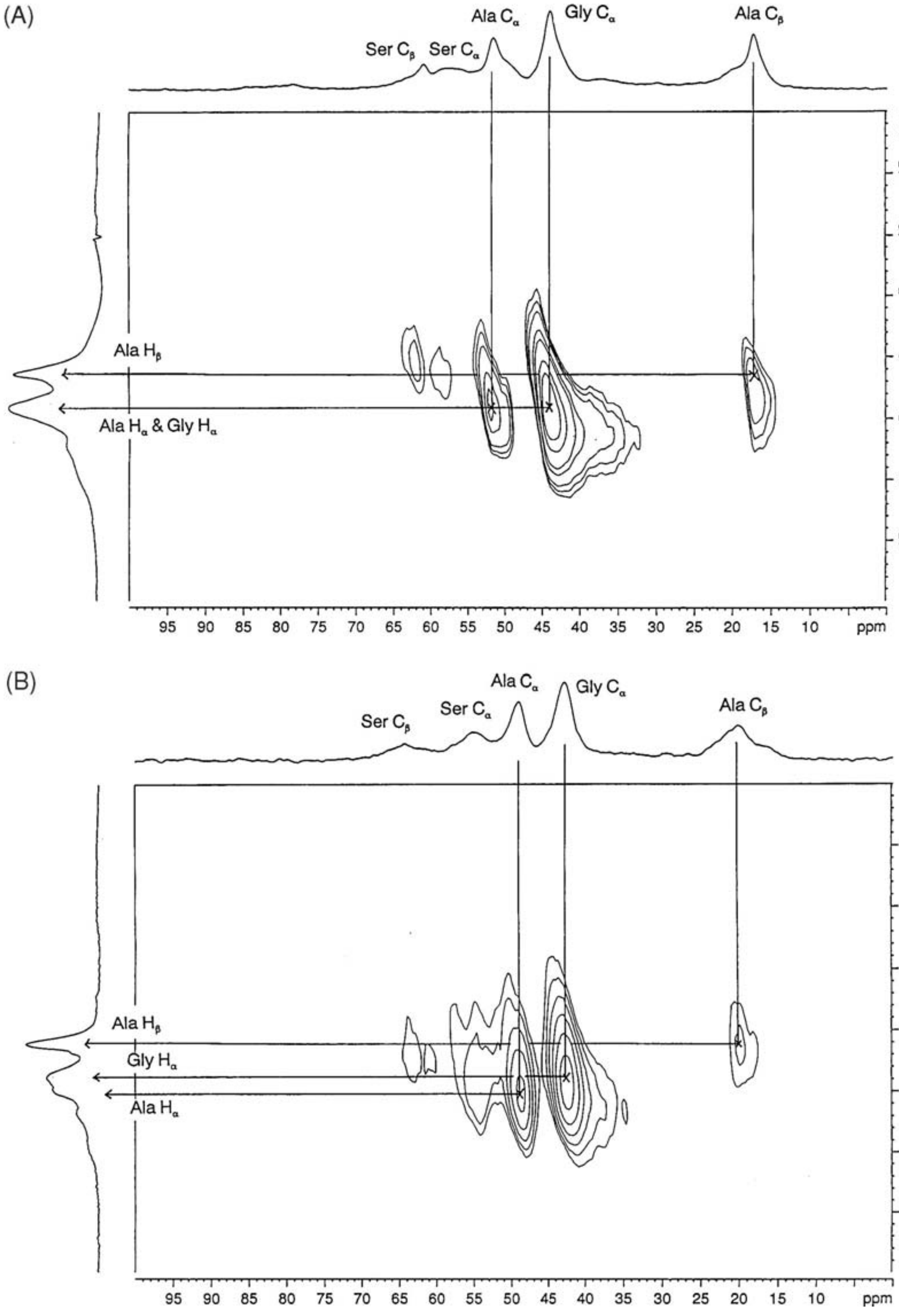

Fig. 6. NMR spectra (2D ^{1}H–^{13}C HETCOR) of silk fibroins: (A) *Bombyx mori*-I (silk I) and (B) *Bombyx mori*-II (silk II).

^{1}H CRAMPS and 2D ^{1}H–^{13}C HETCOR NMR Studies of Silk Fibroin Model Polypeptide

2D HETCOR NMR has the disadvantage of having a small scaling factor, which leads to a larger error for ^{1}H chemical shifts. Accordingly, it is necessary to confirm the observation mentioned above with a well-defined simple model polypeptide of *Bombyx mori* [Ala-Gly]$_{12}$.

Figure 7 shows the 2D ^{1}H–^{13}C HETCOR NMR spectra of well-defined poly(L-alanyl-glycines), (A) [Ala-Gly]$_{12}$-I (silk I) and (B) [Ala-Gly]$_{12}$-II (silk II), in the solid state. As expected, it was induced from the spectra that the H$^\alpha$ signals of L-alanine and glycine residues overlapped ($\delta = 3.6$) and gave a single peak in [Ala-Gly]$_{12}$-I, but that the H$^\alpha$ chemical shift of the L-alanine residues in [Ala-Gly]$_{12}$-II is to high frequency from that of the glycine residues, and they are separated (doublet). The ^{1}H and ^{13}C chemical shifts and conformational characteristics of natural silk fibroin and its model polypeptide samples are shown in Table 2.

These results indicate that the H$^\alpha$ chemical shift of L-alanine residue is almost the same as that of glycine residue in the silk I form for [Ala-Gly]$_{12}$-I and *Bombyx mori*-I. This tendency agrees well with the result obtained from 2D HETCOR spectra of *Bombyx mori*-I and [Ala-Gly]$_{12}$-I. The most interesting result is that the H$^\alpha$ chemical shift of the glycine residue does not change between silk I and II forms (in both *Bombyx mori* and [Ala-Gly]$_{12}$), whereas that of the L-alanine residue shows apparent conformation dependency. Thus, the H$^\alpha$ chemical shift of Ala and Gly residues may offer the key information to clarify the silk I and II structures. In addition, the H$^\beta$ chemical shift of [Ala-Gly]$_{12}$-II agrees completely with that of PLA adopting a β-sheet form. These results show that the ^{1}H chemical shifts of the well-defined model polypeptide are useful for the structural analysis of silk fibroins in the solid state.

It maybe anticipated that the well-defined [Ala-Gly]$_{12}$ plays an important role for determination of unsolved silk I structure.

Determination of Amide Proton Chemical Shift

Observation of the Amide Proton (H^N) Signal of ^{15}N-labeled PLAs

Recently, the problem of a very broad amide proton (H^N) signal was solved and the true H^N chemical shift was determined [4]. It is known that H^N signal broadening is caused by the residual dipolar couplings between the quadrupolar ^{14}N nuclei and the amide protons. The ^{1}H–^{14}N dipolar coupling causes an asymmetric doublet pattern, which disturbs the determination of the true H^N chemical shift in the ^{1}H NMR spectra [1,2,4]. Such a dipolar broadening has never been observed in solution NMR because the dipolar coupling is averaged out by the rapid molecular motion.

The solution to how to get a sharp and normal H^N signal and how to determine the true H^N chemical shift of solid polypeptides is demonstrated. Shoji *et al.* used the fully ^{15}N-labeled (99 at.%) polypeptides such as poly(L-alanine-^{15}N) ([Ala*]$_n$) and poly(L-leucine-^{15}N) ([Leu*]$_n$), and successfully determined the true H^N chemical shift of these polypeptides adopting the α-helix and β-sheet forms.

Figure 8 shows the ^{1}H CRAMPS spectra of ^{15}N-labeled PLAs using the MREV-8 pulse sequence at 3.5 kHz MAS speed: (A) [Ala*]$_n$ − 2 (99 at.% purity of ^{15}N, α-helix) and (B) [Ala*]$_n$ − 1 (99 at.% purity of ^{15}N, β-sheet) in the solid state [4].

It is obvious that the line shape of the ^{15}NH proton signal of [Ala*]$_n$ − 2 and [Ala*]$_n$ − 1, in which the quadrupolar effect is absent, exhibits a normal symmetric singlet pattern. Thus, it is apparent that the quadrupolar ^{14}N nuclei is responsible for the signal broadening, and that the asymmetric line shape of the ^{14}NH proton peak, aside from the ^{15}NH proton signal, is still broad relative to the H$^\alpha$ and H$^\beta$ signals. From the ^{1}H CRAMPS NMR spectra, therefore, it was able to determine the true H^N chemical shift values for [Ala*]$_n$ − 2 (α-helix; $\delta = 8.0$) and [Ala*]$_n$ − 1 (β-sheet; $\delta = 8.6$) under MAS speed of 3.5 kHz. This is the first determination of the true H^N chemical shifts of PLAs by the ^{1}H CRAMPS NMR.

Similarly, the true NH chemical shifts of PLLs were determined using fully ^{15}N-labeled samples under MAS speed of 3.5 kHz and their chemical shifts depend on conformation (α-helix: $\delta = 8.1$; β-sheet: $\delta = 9.1$) [4]. The ^{1}H chemical shift data and conformational characteristics of these samples are summarized in Table 3.

Therefore, the ^{1}H CRAMPS method is a very useful tool for the determination of the ^{15}NH proton chemical shifts of solid polypeptides.

Correlation between the Amide ^{1}H Chemical Shift and Main-chain Conformation

According to X-ray diffraction studies of PLAs by Arnott *et al.* [25,26], the distance between the nitrogen and oxygen atoms was 2.83 and 2.87 Å for the β-sheet and α-helix forms, respectively. Accordingly, the true H^N proton chemical shifts of [Ala*]$_n$ − 1 (β-sheet) appear to be high frequency by comparison with that of [Ala*]$_n$ − 2 (α-helix), which is qualitatively acceptable.

Next, it is interesting to compare the ^{1}H chemical shift results of polypeptides in the solid state with those in solution [14–16], attention being given to the dependence of the amide proton chemical shifts on conformation. The following results are obtained: (1) the amide proton chemical shifts of the α-helical polypeptides in the solid state (8.0–8.2 ppm) are identical with those in solution (7.96–8.04 ppm) and (2) the amide proton chemical shifts of the β-sheet polypeptides in the solid state (8.6–9.1 ppm)

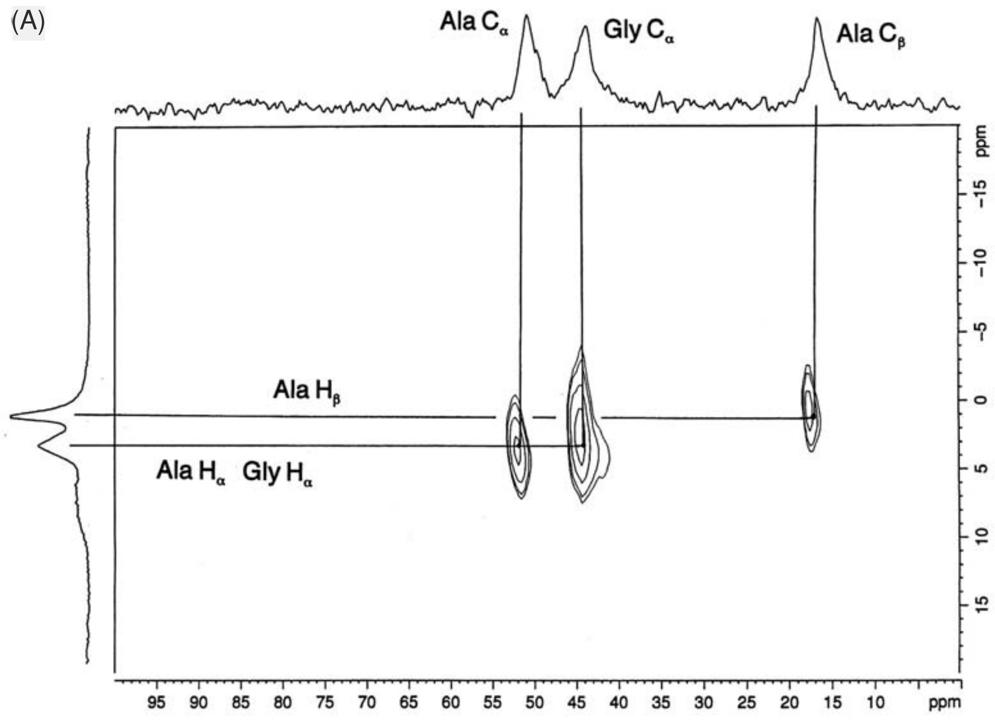

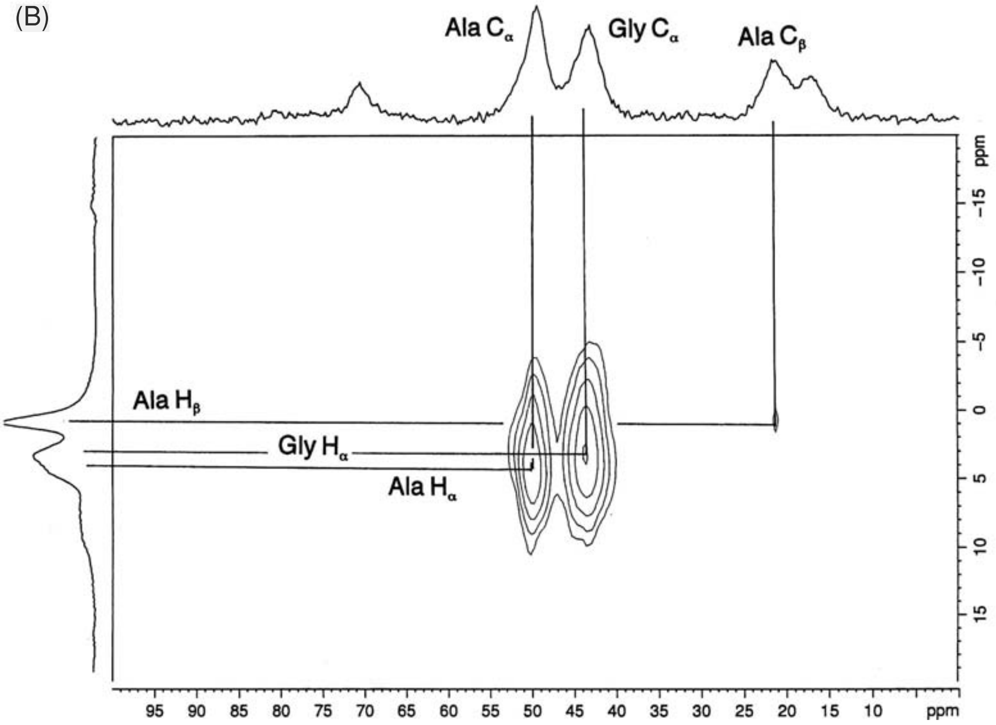

Fig. 7. Spectra (2D ^{1}H–^{13}C HETCOR) of [Ala-Gly]$_{12}$: (A) [Ala-Gly]$_{12}$-I (silk I) and (B) [Ala-Gly]$_{12}$-II (silk II). Peak assignment: H^N, 10–8 ppm; H^α, 5.0–3.6 ppm; and H^β, 1.2–1.5 ppm.

Table 2: ^{1}H and ^{13}C chemical shifts, and conformational characteristics of silk fibroin and its model polypeptide sample

Sample	Conformation*	H^{α}	H^{β}	C=O	$C^{\alpha\dagger}$	$C^{\beta\ddagger}$
Bombyx mori-I	Silk I	3.9	1.6	177.2, 171.2	51.7, 44.1	17.3
Bombyx mori-II	Silk II	5.0, 3.9	1.2	172.6, 170.2	49.2, 42.9	20.2
$[\text{Ala-Gly}]_{12}$-I	Silk I	3.6	1.5	177.4, 170.6	51.3, 43.9	17.2
$[\text{Ala-Gly}]_{12}$-II	Silk II	5.0, 3.6	1.2	173.2, 169.8	49.6, 43.4	21.5

$[\text{Ala-Gly}]_{12}$, well-defined poly(L-alanyl-glycine) (24mer); *Bombyx mori* (silk fibroin).
*Conformations of these samples were determined by ^{13}C and ^{15}N CP-MAS NMR and IR spectroscopic methods.
$^{\dagger 13}$C chemical shifts of α-carbons of L-alanine and glycine residues.
$^{\ddagger 13}$C chemical shift of β-methyl carbon of alanine residue.

are 0.1–0.6 ppm to high frequency from those in solution (8.44–8.52 ppm). These chemical shift displacements of the ^{15}NH protons are very similar to those of the H^{α} protons for PLAs and PLLs. These results are quite interesting findings and the main reason for the chemical shift difference between solid state and solution can be explained by a solvent effect in the solution.

In conclusion, it is certified that the ^{15}NH proton chemical shift is a useful index for conformational analysis and to distinguish the hydrogen bond characteristics of polypeptides in the solid state.

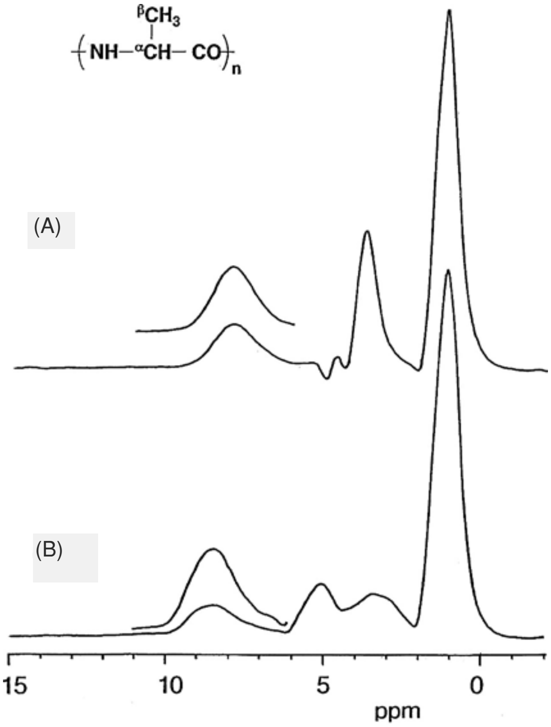

Fig. 8. NMR spectra (300 MHz ^{1}H CRAMPS) of α-helical and β-sheet poly(L-alanines) using the MREV-8 pulse sequence at 3.5 kHz MAS speed: (A) $[\text{Ala*}]_n - 2$ (^{15}N-labeled, α-helix) and (B) $[\text{Ala*}]_n - 1$ (^{15}N-labeled, β-sheet). Peak assignment: H^N, 8.6 ppm (β-sheet) and 8.0 ppm (α-helix); H^{α}, 5.0–5.2 ppm (β-sheet) and 3.9–4.2 ppm (α-helix), H^{β}, 1.2 ppm (β-sheet) and 1.4 ppm (α-helix). Note that the additional peaks around 4.0–5.0 ppm in spectra (A) is assigned to career noise signal.

Determination of N–H Bond Length from the Dipolar Spinning Sideband Pattern of the Amide ^{1}H Signals

An accurate determination of the N–H covalent bond length is important for elucidating polypeptide conformations because the N–H bond length directly mirrors the $>\text{N–H}\cdots\text{O}=\text{C}<$ hydrogen bond strength and is responsible for the long range order in the system. The ^{1}H CRAMPS has great potential for this purpose, and it is necessary to examine whether it is effective.

The ^{15}N–^{1}H bond length can be measured by observing the dipolar line width, which is simulated by the ^{15}N–^{1}H dipolar spinning sidebands (SSBs). The ^{15}N–^{1}H dipolar interaction can be estimated directly from the ^{1}H CRAMPS NMR because the ^{1}H chemical shift anisotropy is averaged to zero during the ^{1}H CRAMPS measurement. The N–H bond length of PLA is almost indeterminate by the X-ray diffraction. It is also difficult to determine the N–H bond length using the neutron diffraction because this method needs the deuterium-labeled PLA to be in single crystal state.

Table 3: ^{1}H chemical shifts and conformational characteristics of polypeptides

			^{1}H chemical shift, δ (ppm)			
Sample	A/I†	Conformation‡	$H^{\beta}(+H^{\gamma})$	H^{δ}	H^{α}	H^{N}§
H-[Ala]$_5$-NHBu	—	β-sheet	1.2		5.0	8.4
[Ala]$_n$ − 5	65	α-helix	1.4		3.9	8.2
[Ala*]$_n$ − 1	4	β-sheet	1.2		5.2	8.6
[Ala*]$_n$ − 2	100	α-helix	1.4		4.0	8.0
[Leu]$_n$ − 1	5	β-sheet	0.9	1.5	5.5	—
[Leu]$_n$ − 2	100	α-helix	0.8	1.7	4.0	8.2
[Leu*]$_n$ − 1	5	β-sheet (+α-helix)	0.9	1.6	5.4	9.1
					(4.0)	(8.2)
[Leu*]$_n$ − 2	100	α-helix	0.8	1.6	4.0	8.1

Ala*, ^{15}N-labeled L-alanine; Leu*, ^{15}N-labeled L-leucine.

†A/I corresponds to the theoretical number-averaged degree of polymerization.

‡Conformations were determined by the ^{13}C and ^{15}N CP-MAS NMR, IR, and far-IR spectroscopic methods.

§Amide proton (H^N) chemical shift was obtained using the MREV-8 pulse sequence at 3.5 kHz MAS speed.

¶Containing a small amount of α-helix.

In this section, a new methodology to determine the ^{15}N–^{1}H bond length of fully ^{15}N-labeled PLAs adopting the α-helix and β-sheet forms from the ^{15}N–^{1}H dipolar sideband patterns observed in the ^{1}H NMR spectra [5]. To observe the full spectral width of the dipolar sideband patterns, the quadrature-phase detection (QD) measurement was performed. QD was carried out according to the phase-cycling technique proposed by Burum *et al.* [27], and the MREV-8 pulse sequence was applied. The samples used here are fully ^{15}N-labeled PLAs (99 at.% of ^{15}N purity) [4,5].

Determination of N–H Bond Length

Figure 9 shows the ^{1}H CRAMPS NMR spectra of fully ^{15}N-labeled PLAs for (A) α-helix and (B) β-sheet forms in the solid state. The SSBs of the H^{α} proton and H^{β} proton signals of PLAs are indicated by asterisks (*), and those of the amide proton (H^N) signal by open circle (o). The SSBs of the H^{α} and H^{β} signals fell off rapidly compared to those of the amide protons, whereas those of the H^N signal gradually decreased due to the large ^{15}N–^{1}H heteronuclear dipolar interaction. The N–H dipolar SSB pattern of α-helical PLA is obviously different from that of β-sheet one, as can be seen from Figure 9.

The sideband pattern is sensitive to the N–H bond length and the relative intensity of SSBs to the center peak decreases with longer N–H distance. It is therefore possible to determine the N–H bond length within an accuracy of 0.01 Å by careful comparison of the integral ratio of the center peak to the sideband intensities of the dipolar spectrum obtained experimentally with that of the simulated spectra.

Thus, it is successfully determined that the N–H bond length for PLAs were 1.09 and 1.12 Å for the α-helix and β-sheet conformations, respectively, with an accuracy of 0.01 Å. This result means that the (>N–)H · · · O(=C<) hydrogen bond strength (distance) of the β-sheet PLA must be stronger (shorter) than that of the α-helix one. The above N–H bond length difference between the α-helix and β-sheet forms seems to be related to the hydrogen bond strengths and amide proton chemical shifts. From the X-ray diffraction studies of PLAs by Arnott *et al.* [25,26], it is known that the distance between the nitrogen and oxygen atoms is 2.87 and 2.83 Å for the α-helix and β-sheet forms, respectively. This is consistent with the hydrogen bond distances between the nitrogen and oxygen atoms determined from X-ray diffraction and with the ^{1}H chemical shifts of amide proton signals found using the ^{1}H CRAMPS method.

Accordingly, it is reasonable to conclude that the amide proton of the β-sheet PLA is more strongly attracted to the oxygen than the proton of α-helical PLA.

Structural Studies of α-amino-acid Crystals by ^{1}H CRAMPS NMR

The ^{1}H CRAMPS NMR has become a very useful research tool,corresponding to X-ray crystallography [28,29]. This enabled to study crystal structure polymorphs of α-amino acids. Here, the author introduces

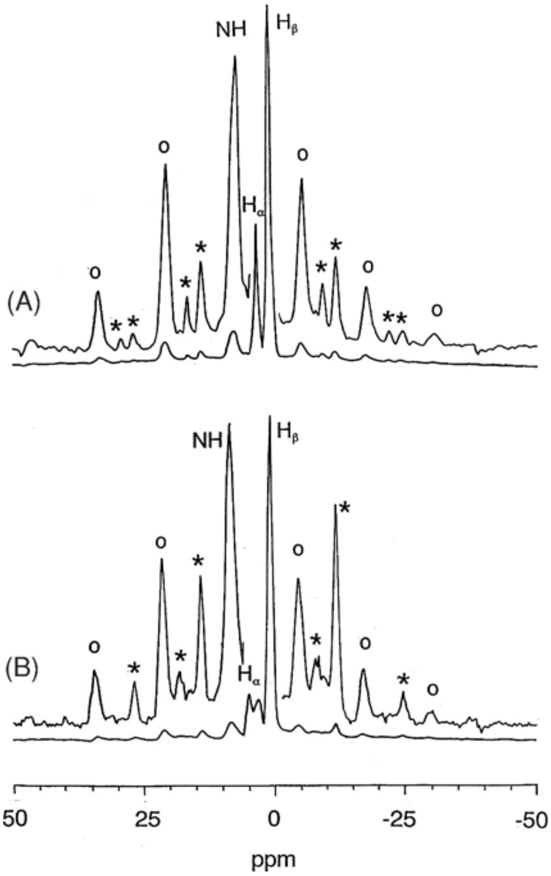

Fig. 9. NMR spectra (300 MHz ^{1}H CRAMPS) of fully ^{15}N-labeled poly(L-alanines) taking (A) α-helix and (B) β-sheet conformations in the solid state. Peak assignment: H^N, 10–8 ppm; H^α, 3.9–5.0; and H^β, 1.4–1.2 ppm. *Note*. –N–CH_2– peak (3.2–3.5 ppm) of *n*-butylamide group in spectrum (B). The sign (o) indicates the spinning sidebands (SSB) of H^N signal and the sign (*) indicates SSB of H^α and H^β signals.

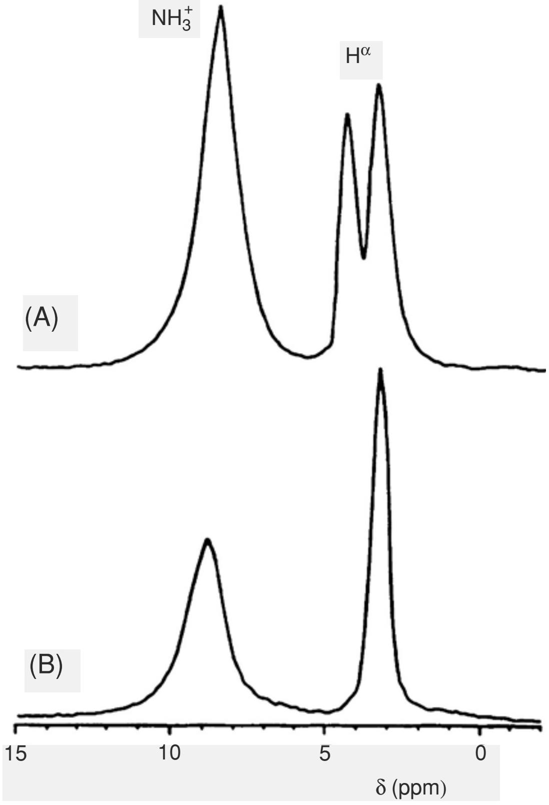

Fig. 10. NMR spectra (300 MHz ^{1}H CRAMPS) of glycine polymorphs: (A) α-glycine and (B) γ-glycine crystals.

the recent research example application to crystal structural analysis of glycine polymorphs [α-form (α-glycine) and γ-form (γ-glycine)] in order to test the power of ^{1}H CRAMPS NMR, compared with ^{13}C and ^{15}N NMR methods [3]. The γ-glycine [30,31] (hexagonal; P3_1 space group) is most stable at room temperature and converts to α-glycine [32,33] (monoclinic; P2_1/n space group) on heating to 165°C whereas β-glycine [30,31] (monoclinic; P2_1 space group) is very unstable.

Figure 10 shows the ^{1}H CRAMPS NMR spectra of (A) α-glycine and (B) γ-glycine crystals, together with each peak assignment. It is noteworthy that the H^α signal of α-glycine splits into two peaks (4.4 and 3.4 ppm) of equal height but that of γ-glycine gives a sharp singlet peak (3.3 ppm). The reason for this peak splitting may be attributable to a difference in the magnetic surroundings of two nonequivalent H^α protons in α-glycine, whereas they are equivalent and give a single peak in γ-glycine.

Thus, the ^{1}H CRAMPS NMR is very useful for the structural analysis of glycine crystals. It is hoped to accumulate more ^{1}H chemical shift data for other α-amino acid, oligopeptide, and polypeptide crystals in the future.

References

1. Shoji A, Kimura H, Sugisawa H. In: GA Webb (Ed). Annual Reports on NMR Spectroscopy, Vol. 45. Academic Press: London, 2002, pp 69–150.
2. Shoji A, Kimura H, Ozaki T, Sugisawa H, Deguchi K. J. Am. Chem. Soc. 1996;118:7604–7.

3. Kimura H, Nakamura K, Eguchi A, Sugisawa H, Deguchi K, Ebisawa K, Suzuki E, Shoji A. J. Mol. Struct. 1998;447:247–55.
4. Kimura H, Ozaki T, Sugisawa H, Deguchi K, Shoji A, Macromolecules. 1998;31:7398–403.
5. Kimura H, Shoji A, Sugisawa H, Deguchi K, Naito A, Saito H. Macromolecules. 2000;33:6627–9.
6. Kimura H, Kishi S, Shoji A, Sugisawa H, Deguchi K. Macromolecules. 2000;33:9682–7.
7. Kishi S, Santos A Jr, Ishii O, Ishikawa K, Kunieda S, Kimura H, Shoji A. J. Mol. Struct. 2003;649:155–67.
8. Naito A, Root A, McDowell CA. J. Phys. Chem. 1991;95: 3578–81.
9. Benedetti E, Corradini P, Pedone C. Biopolymers. 1969;7: 751–64.
10. Burum DP, Bielecki A, J. Magn. Reson. 1991;94:645–52.
11. Caravatti P, Braunschweiler L, Ernst RR. Chem. Phys. Lett. 1983;100:305–10.
12. Burum DP. In: DM Grant, RK Harris (Eds). Encyclopedia of Nuclear Magnetic Resonance, Vol. 4. John Wiley & Sons: Chichester, 1996, pp. 2323–9.
13. Saalwaechter K, Graf R, Spiess W. J. Magn. Reson. 1999;140:471–6.
14. Wishart DS, Sykes BD. In: TL James, NJ Oppenheimer (Eds). Methods in Enzymology, Vol. 239. Academic Press: San Diego, CA, 1994, pp. 363–92.
15. Wishart DS, Sykes BD, Richards FM. FEBS Lett. 1991;293:72–80.
16. Wishart DS, Sykes BD, Richards FM. J. Mol. Biol. 1991;222:311–33.
17. Sletten E. J. Am. Chem. Soc. 1970;92:172–7.
18. Ozaki T, Shoji A. Makromol. Chem. Rapid Commun. 1983;4:363–9.
19. Shoji A, Ozaki T, Saito H, Tabeta R, Ando I. Makromol. Chem. Rapid Commun. 1984;5:799–804.
20. Kitazawa S, Hiraoki T, Hamada T, Tsutsumi A. Polym. J. 1994;26:1213–26.
21. Tsutsumi A, Anzai S, Hikichi K. Polym. J. 1994;15:355–9.
22. Fraser RDB, MacRae TP. In Conformation of Fibrous Proteins and Related Synthetic Polypeptides, Chapter13. Academic Press: New York, 1967.
23. Voet D, Voet JG. In Biochemistry, 2nd ed, Chapter 7. John Wiley & Sons: Chichester, UK, 1995.
24. Shoji A, Ozaki T, Fujito T, Deguchi K, Ando I, Magoshi J. J. Mol. Struct. 1998;441:251–66.
25. Arnott S, Wonacott AL. J. Mol. Biol. 1966;21:371–83.
26. Arnott S, Dover SD, Elliot A. J. Mol. Biol. 1967;30: 201–8.
27. Burum DP, Cory DG, Gleason KK, Levy D, Bielecki A. J. Magn. Reson. 1993;A104:347–52.
28. Garskaya GV. In The Molecular Structure of Amino Acids. Consultants Bureau: New York, 1968.
29. Nagashima N. J. Crystallogr. Soc. Jpn. 1993;35:381–91.
30. Iitaka Y. Acta Crystallogr. 1961;14:1–10.
31. Iitaka Y, Nature. 1959;183:390–1.
32. Albrecht G, Corey RB. J. Am. Chem. Soc. 1939;61:1087–103.
33. Marsh R. Acta Crystallogr. 1958;11:654–63.

Polymer Dynamics

Dynamics of Amorphous Polymers

Fumitaka Horii
Institute for Chemical Research, Kyoto University, Kyoto 611-0011, Japan

Introduction

Individual structural units forming polymer molecules basically undergo their own local motions in different states although some of them may be cooperative motions. The modes and rates of the molecular motions are relatively well characterized in the crystalline state by solid-state NMR spectroscopy, but the analysis of the local motions in the noncrystalline state may not be straightforward because there are distributions in molecular motion associated with the noncrystalline structure. Several solid-state NMR analytical methods, which are summarized in Figure 3.1 in Ref. [1], have been already proposed and they are successfully applied to the characterization of different amorphous polymer materials. The outline of the characterization will be described in this contribution.

Spin Relaxation

The most basic analytical method is to measure spin relaxation parameters such as spin–lattice relaxation times (T_1) and spin–spin relaxation times (T_2) and to interpret them in terms of appropriate molecular motion models. However, the theory of the spin relaxation associated with the molecular motion is limited to a very simple case, the two-spin system having a constant internuclear distance [2–4]. As is well known, in the natural abundant ^{13}C–^{1}H two-spin system, ^{13}C T_1, T_2, and nuclear Overhauser effect (NOE) are expressed as [1–4]

$$\frac{1}{NT_1} = \frac{\gamma_H^2\gamma_C^2\hbar^2}{16r^6}\{J_0(\omega_H-\omega_C)+18J_1(\omega_C) + 9J_2(\omega_H+\omega_C)\},$$

$$\frac{1}{NT_2} = \frac{\gamma_H^2\gamma_C^2\hbar^2}{32r^6}\{4J_0(0)+J_0(\omega_H-\omega_C)+36J_1(\omega_H) + 18J_1(\omega_C)+9J_2(\omega_H+\omega_C)\},$$

$$\mathrm{NOE} = 1+\frac{9J_2(\omega_H+\omega_C)-J_0(\omega_H-\omega_C)}{J_0(\omega_H-\omega_C)+18J_1(\omega_C)+9J_2(\omega_H+\omega_C)} \times \frac{\gamma_H}{\gamma_C}. \tag{1}$$

Here, N is the number of protons chemically bonded to a given carbon and ω_H and ω_C are Larmor frequencies of ^{1}H and ^{13}C nuclei, respectively. $J_q(\omega)$ are the spectral densities that are the Fourier transforms for the autocorrelation functions $G_q(\tau)$ of the orientation functions that describe the random time fluctuation of the C–H internuclear vector having a correlation time τ_c:

$$J_q(\omega) = \int_{-\infty}^{+\infty} G_q(\tau)\exp(-i\omega\tau)\,\mathrm{d}\tau, \quad q = 0,1,2. \tag{2}$$

In the polymer systems even in the rubbery or dissolved state, the motion of the C–H vector cannot be described by a simple isotropic random fluctuation model with a single correlation time [1]. Although wide distributions of the correlation times are sometimes introduced, such treatments are not successful to interpret very high minimum values of T_1 for polymers that appear at a correlation time corresponding to $\sim\omega_c^{-1}$. Normally at least three independently superposed motions are necessary to describe the overall C–H motion of polymers and such models, frequently called as the 3τ model, successfully interpret the temperature dependency of T_1 including the T_1 minimum as well as the resonance frequency dependency of T_1 [1]. Recently some model-free treatments have also been proposed, considering plural superposed molecular motions with different correlation times. In the most generalized model-free treatment assuming the superposition of the overall isotropic motion and several anisotropic local motions, $G_q(\tau)$ are given by the product of the respective motions as follows: [1]

$$G_q(\tau) = G_I(\tau)\prod_{1}^{p-1} G_{Ai}(\tau),$$

$$G_I(\tau) = K_q\exp\left(\frac{-\tau}{\tau_I}\right) \qquad K_0 = \frac{4}{5}, K_1 = \frac{2}{15}, K_2 = \frac{8}{15}.$$

$$G_{Ai}(\tau) = S_i^2 + (1-S_i^2)\exp\left(\frac{-\tau}{\tau_{Ai}}\right) \qquad i = 1, 2, \ldots, p-1. \tag{3}$$

Here, τ_{Ai} and S_i^2 are the correlation time and the order parameter for the ith inner motion, respectively. When

Graham A. Webb (ed.), Modern Magnetic Resonance, 607–613.
© 2008 *Springer.*

$p = 3$ and $\tau_{A1} \ll \tau_{A2} \ll \tau_I$, the total correlation function reduces to

$$G_q(\tau) = K_q\left[S_2^2 S_1^2 \exp\left(\frac{-\tau}{\tau_I}\right) + (1 - S_2^2)S_1^2 \exp\left(\frac{-\tau}{\tau_{A2}}\right) + (1 - S_1^2)\exp\left(\frac{-\tau}{\tau_{A1}}\right)\right]. \tag{4}$$

This equation, which corresponds to the equation derived for the 3τ model, was successfully used to interpret the temperature and frequency dependencies of ^{13}C T_1 and NOE for the CH_2 carbons in the *rrr* units of poly(methyl methacrylate) in $CDCl_3$ solution [1]. Through such an analysis, the correlation times, activation energies, and order parameters of the respective motions can be obtained without the construction of the detailed models for the respective motions.

One-Dimensional MAS Spectra

When one-dimensional (1D) MAS spectra of certain solid polymer samples are measured at different temperatures under ^{1}H high-power decoupling, some resonance line is sometimes observed to greatly change in linewidth with the change in temperature, for example, as seen for the C6 and C7/8 resonance lines of solid poly(2-hydroxypropyl ether of bisphenol-A) (phenoxy resin) shown in Figure 1 [5]. This process frequently also accompanies the decrease in resonance intensity when the spectra are measured by the CP method. Such changes of the resonance lines are ascribed to the onset of the molecular motion having a rate corresponding to the ^{1}H dipolar decoupling amplitude or the ^{13}C radio frequency amplitude. The former change in linewidth is expressed as [6–8]

$$\Delta\nu = \Delta\nu_0 + \Delta\nu_1\left\{1 + \frac{2}{\pi}\arctan\left[\alpha(T_0 - T)\right]\right\} + \frac{\lambda M_2}{\pi}\frac{\tau_c}{\left(1 + \tau_c^2\omega_1^2\right)} \tag{5}$$

when the chemical shift anisotropy (CSA) of the ^{13}C nucleus in question is negligibly small. Here, $\Delta\nu_0$ is the intrinsic linewidth produced by inhomogeneous experimental factors, $\Delta\nu_1$ the linewidth at a temperature T_0 below T_g generated by the distribution of isotropic chemical shifts due to inhomogeneous local structural factors for glassy polymers, α and λ adjustable parameters, M_2 the second moment of the ^{13}C–^{1}H dipolar interaction, τ_c the correlation time of the molecular motion, and ω_1 the ^{1}H decoupling amplitude in Hz. The C7/8 line was found to be successfully analyzed in terms of Equation(5) by assuming the William–Landel–Ferry type temperature dependency of the correlation time and thus the correlation times were determined as a function of temperature. In contrast, the correlation times for the C6 line were obtained at different temperatures by considering the large CSA of this ^{13}C nucleus [5].

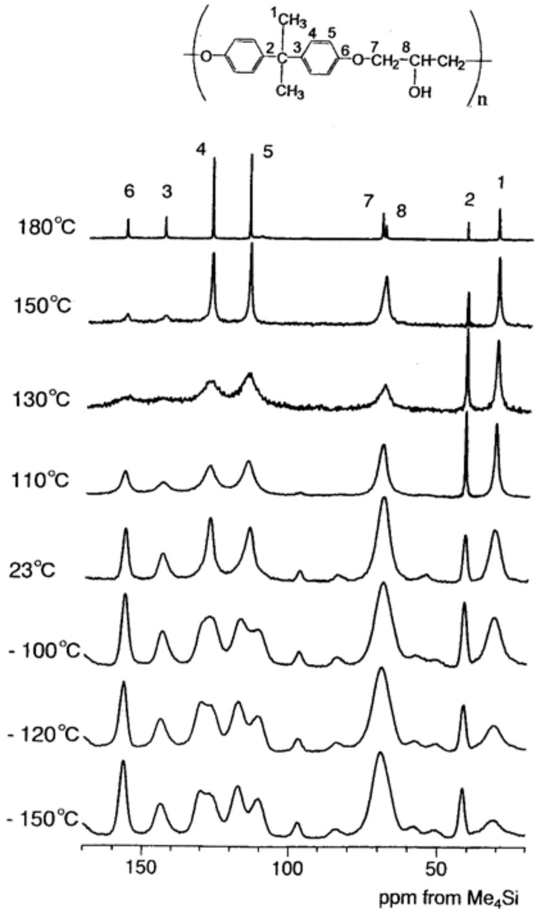

Fig. 1. CP/MAS ^{13}C NMR spectra of phenoxy resin at different temperatures. (Reproduced from Ref. [5].)

In Figure 1, another type of spectral change is observed for the C4 and C5 line. These lines split into two constituent lines at lower temperatures and such two lines merge into a single line at a certain temperature. Similar spectral changes are frequently observed and these processes are analyzed by the two-site exchange model that is expressed as [2]

$$I(\omega) = \frac{1}{2}\frac{\kappa(\omega_1 - \omega_2)^2}{(\omega - \omega_1)^2(\omega - \omega_2)^2 + \kappa^2[2\omega - (\omega_1 + \omega_2)]^2}. \tag{6}$$

Here, ω_1 and ω_2 are the resonance frequencies for the two sites and κ is the exchange rate. By using this model, the rates of the phenylene flip motion were determined at different temperatures for the polymer shown in Figure 1 [5]. Characteristic chain conformations of the spacer CH_2 sequences of liquid crystalline polymers were also clarified by using Equation (6) [9–11].

Lineshape Analyses

More general characterization methods of molecular motion of solid polymers are lineshape analyses of ^{2}H, ^{13}C CSA, and ^{13}C–^{1}H dipolar spectra in terms of appropriate molecular motion models. Here, ^{2}H and ^{13}C CSA analyses are briefly described for some amorphous polymers.

In the case of ^{2}H NMR, the resonance frequency ω_r is given by [12]

$$\omega_r = \omega_0 \pm \Delta_0(3\cos^2\zeta - 1 - \eta_Q \sin^2\zeta \cos 2\xi). \quad (7)$$

Here, ω_0 is the resonance center and the second term is the resonance shift due to the quadrupolar interaction. Δ_0 the constant inherent to the nucleus, ξ and ζ the polar angles to describe the direction of the static magnetic field B_0 in the principal axis frame of the field gradient tensor, and η_Q the anisotropic parameter. Since ξ and ζ are widely distributed in powdered samples in the rigid state, an observed ^{2}H spectrum has a characteristic lineshape called Pake pattern as a result of the reflection of the distributions. When molecular motion of some structural unit including the ^{2}H nucleus occurs, ξ and ζ will undergo time changes depending on the mode and rate of the molecular motion. In this case, the principal axis frame $x_P y_P z_P$ of the field gradient tensor, which is defined for a particular chemical bond associated with the ^{2}H nucleus, should be successively correlated to the molecular frame $x_M y_M z_M$, the reference frame $x_R y_R z_R$, and the laboratory frame xyz, by considering the mode of molecular motion. Figure 2 shows the case of the phenylene flip motion with a flip angle of δ, where the *ortho* hydrogen atom is deuterated [1]. By the successive coordination transformations using the corresponding transformation matrices $\boldsymbol{R}(\alpha, \beta, \gamma)$, the resonance frequency ω_r is finally expressed as a function of δ for the phenylene ring whose bond axis is described by the polar angles $-\phi$ and $-\theta$ in the laboratory frame.

When the phenylene ring undergoes the flip motion with a rate of κ in s^{-1} between the sites described by $\delta = 0$ and $\delta = \delta$, the resonance line $I(\omega)$ will be expressed by using the two-site exchange model given by Equation (6). Since ϕ and θ are distributed statistically at random in powdered samples, the real resonance line $I_{pw}(\omega)$ should be integrated with regard to all possible ϕ and θ values [1].

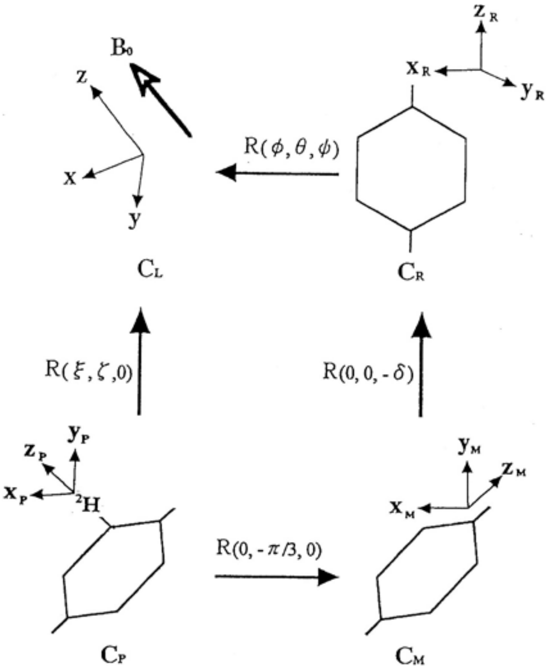

Fig. 2. Schematic representation of the coordinate transformation from the principal axis frame (C_P) through the molecular frame (C_M) and the reference frame (C_R) to the laboratory frame (C_L). (Reproduced from Ref. [1])

Figure 3 shows observed and simulated ^{2}H NMR spectra at different temperatures for glassy phenylene-deuterated poly(ethylene terephthalate) (PET) [13]. The phenylene motion is almost hindered below 0 °C because the spectra obtained are in good accord with the rigid Pake pattern. Figures 3b shows ^{2}H NMR spectra simulated by assuming the log-Gaussian distribution in the 180° flip rate as shown in Figure 3c. Although a good fit is obtained at each case, the rate distributions are unexpectedly very broad at higher temperatures. This may be due to the neglect of the distribution in flip angle. Figure 3D shows simulated ^{2}H NMR spectra obtained by assuming the distributions in flip rate and flip angle as shown in Figure 3e and f, respectively. Good fits are also obtained at the respective temperatures and the distribution in flip rate seems to be appropriately narrow even at higher temperatures. The activation energy 63.6 kJ/mol estimated from the Arrhenius plot of the average flip rate is in good agreement with the value obtained by dynamic mechanical measurements [14] in this case. Similar distributions in flip angle were also evaluated for the phenylene motion of bisphenol-A polycarbonate (BPAPC) by 2D ^{2}H exchange NMR spectroscopy [15].

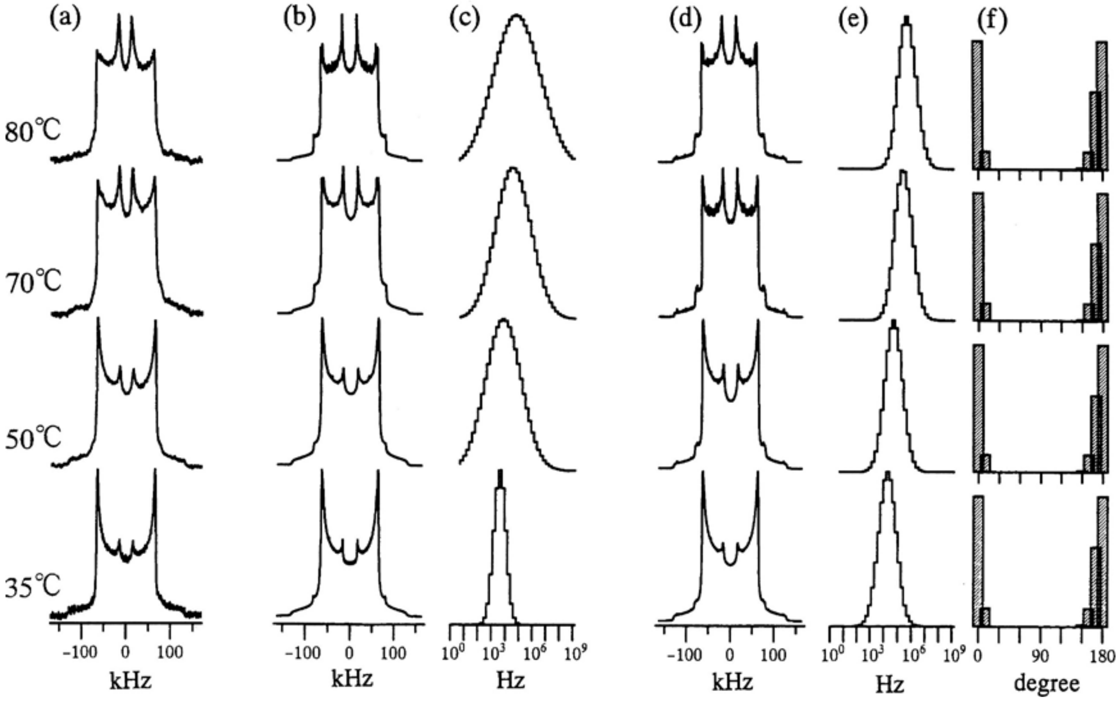

Fig. 3. Observed and simulated ^{2}H NMR spectra of the phenylene deuterated PET at different temperatures: (a) observed spectra, (b) simulated spectra obtained by introducing the distributions in flip rate as shown in (c), (d) simulated spectra obtained by introducing both distributions in flip rate and flip angle as shown in (e) and (f), respectively. (Reproduced from Ref. [13].)

In natural abundant ^{13}C NMR, the resonance frequency ω_r is given by [16,17]

$$\omega_r = \omega_0 \frac{\mathrm{Tr}\left(\sigma_{ij}\right)}{3} + \frac{2}{\sqrt{6}} \omega_0 A_{20}^L,$$

$$A_{20}^L = \frac{\left[3\sigma_{33}^L - \mathrm{Tr}\left(\sigma_{ij}^L\right)\right]}{\sqrt{6}}. \tag{8}$$

Here, σ_{ij} and σ_{ij}^L are the *ij* components of the chemical shift tensors σ and $\sigma^{\ L}$ in the principal axis and laboratory frames, respectively. A_{20}^L is the 20th component for the irreducible tensor A^L in the laboratory frame which describes the chemical shift term of the Hamiltonian of the system together with another irreducible tensor T^L. Since A_{20}^L should be described by the corresponding A_{20} in the principal axis frame, some coordinate transformations are performed from the principal axis frame to the laboratory frame through the molecular frame and the reference frame depending on the mode of molecular motion similarly to the case shown in Figure 2. In real solid-state ^{13}C NMR experiments, CSA spectra are measured at different temperatures by using one of the methods hitherto proposed [1]. Figure 4 shows CSA spectra of the CH carbon of glassy BPAPC measured at different temperatures by the selective excitation switching angle sample spinning (SASS) [18]. These spectra are well reproduced under the fast limit condition ($\kappa \geq 10^5$ Hz) by the introduction of wide distributions in flip angle around 0° and 180° for the phenylene motion. The appreciable discordance between the simulated and observed spectra at higher temperatures may be due to the onset of the hindered fluctuation of the flip axis.

The isotropization process of the ^{13}C CSA above T_g was also successfully analyzed for the carbonyl carbon ^{13}C-enriched poly(ethyl methacrylate) [19]. Here, the multisite analysis was conducted by using the exchange matrix Π that contains the probability per unit time for an exchange between site *i* and site *j* as matrix elements $(\Pi)_{ij}$ [19,20]. However, fully good fits between the observed and simulated CSA spectra were obtained for both a random jump model and a rotational diffusion model having single correlation times. The reliable discrimination of the two models should be made by 2D ^{13}C CSA exchange NMR spectroscopy described below.

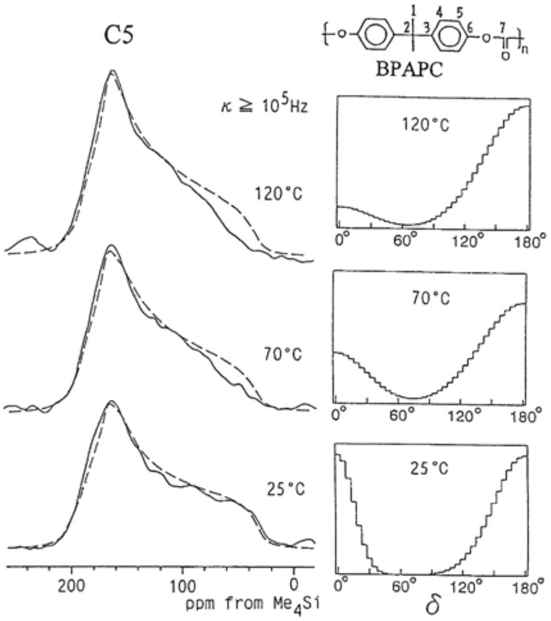

Fig. 4. ^{13}C CSA spectra for the C5 carbon of BPAPC at different temperatures measured by selective excitation SASS. Solid line: observed, broken line: simulated. The histograms indicate the distributions of the flip angle δ for the phenylene group. (Reproduced from Ref. [18].)

2D Exchange Spectra

2D exchange NMR spectroscopy is one of the most frequently used 2D NMR methods in the field of solid-state NMR. In Figure 5, for example, a 2D CP/MAS ^{13}C exchange NMR spectrum is shown for the resonance lines of the C4 and C5 phenylene carbons measured at –120 °C for poly(2-hydroxypropyl ether of bisphenol-A) whose chemical structure is depicted in Figure 2 [5]. At a mixing time of 2.0 s, exchange peaks are evidently observed for the C4 and C5 carbons themselves without any corresponding peak between the C4 and C5 carbons. This fact indicates the occurrence of the phenylene 180°-flip motion having a rate of the order of 1 s^{-1}. The correlation times τ_c of the flip motion are also determined at each temperature by analyzing the exchange peak intensity $I(t_m)$ as a function of mixing time t_m using the following equation: [21]

$$I(t_m) = \frac{n-1}{n}\left[1 - \exp\left(-\frac{t_m}{\tau_c}\right)^{\beta}\right], \tag{9}$$

where n is the number of the sites and β is the Kohlrausch–Williams–Watts (KWW) parameter [22].

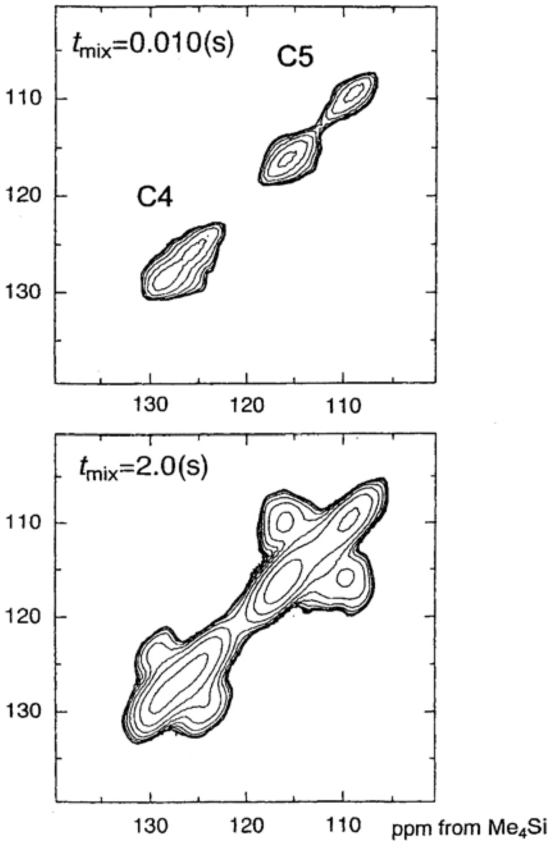

Fig. 5. 2D CP/MAS ^{13}C exchange spectra for glassy phenoxy resin at −120 °C. (Reproduced from Ref. [5].)

The molecular motion of main chains of amorphous polymers can be also characterized in the glass–rubber transition region by 2D ^{13}C exchange NMR spectroscopy. In this case, an observed ^{13}C CSA exchange spectrum is analyzed in terms of various molecular motion models: The time domain signal $G(t_1,t_2,t_m)$ is expressed as [20]

$$G(t_1, t_2, t_m) = <\mathbf{1}|\exp[(\Pi + i\omega)t_2]\exp[(\Pi)t_m] \times \exp[(\Pi)t_1]\boldsymbol{P}_0|\mathbf{1}> \tag{10}$$

Here, Π is the exchange matrix described above, ω is the time-evolution matrix with $(\omega)_{jk} = \delta_{jk}\omega_{jk}$ that describes the resonance frequencies at the respective sites, and $\boldsymbol{P}_0$ is the matrix for the initial site distribution. The unit matrices <**1**| and |**1**> are used for a simple expression of the equation. After the 2D Fourier transform of $G(t_1,t_2,t_m)$, the simulated 2D exchange spectra are compared with the corresponding observed spectra.

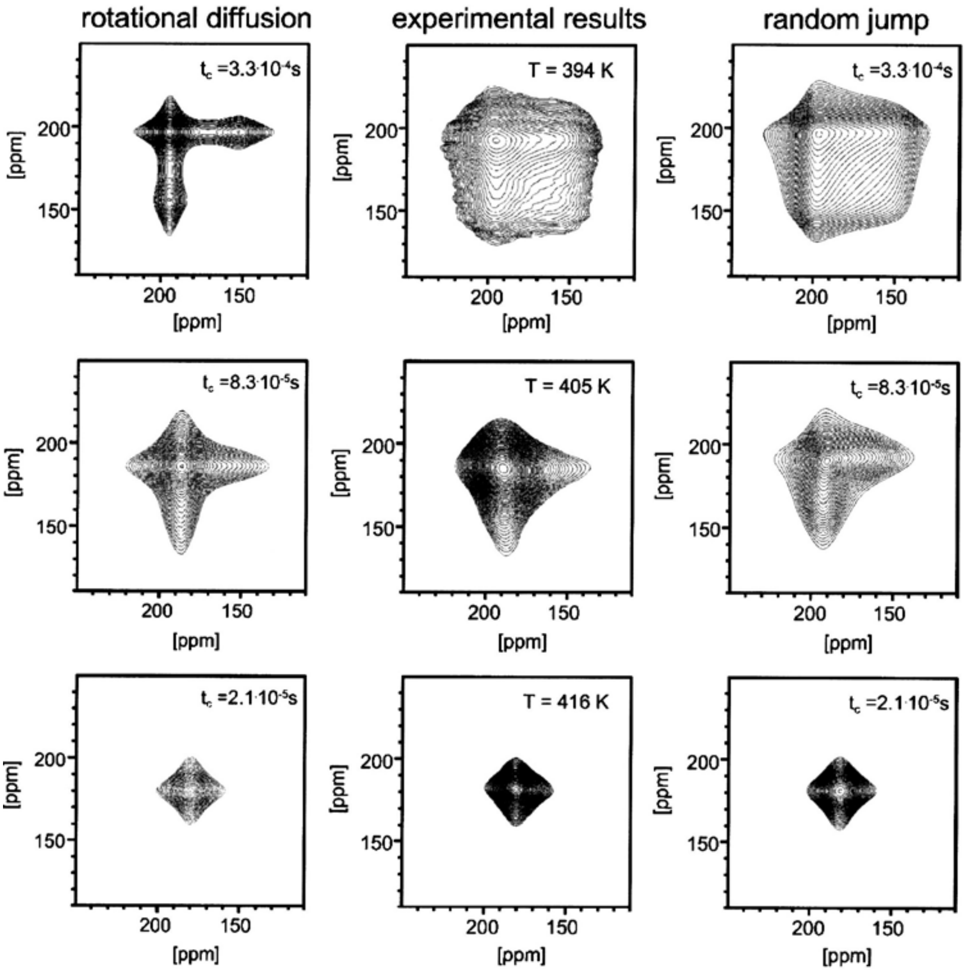

Fig. 6. Observed and simulated 2D ^{13}C CSA exchange spectra for carbonyl carbon ^{13}C-enriched poly(ethyl methacylrate) at different temperatures above T_g. Single correlation times denoted by t_c were used for both models. (Reproduced from Ref. [19].)

Figure 6 shows observed and simulated 2D ^{13}C CSA exchange spectra obtained at different temperatures above T_g for carbonyl carbon ^{13}C-enriched poly(ethyl methacrylate) [19]. It is clearly found that the random jump model is a much more suitable model than the rotational diffusion in this case, although these two models cannot be discriminated in the 1D ^{13}C CSA lineshape analysis as described above. Moreover, it should be noted that single correlation times depicted by t_c in Figure 6 are reasonably used at each temperature instead of the introduction of any distribution. Echo decay analyses combined with 2D exchange NMR spectroscopy also confirmed that such motionally averaged process is adequately described in terms of the random jump model with a single correlation time [19].

References

1. Horii F. In: I Ando, T Asakura (Eds). Solid State NMR of Polymers. Elsevier: Amsterdam, 1998, p 51.
2. Solomon I. Phys. Rev. 1955;99:559.
3. Abragam A. Principles of Nuclear Magnetism. Clarendon Press: London, 1961.
4. Kitamaru R. Nuclear Magnetic Resonance, Principle and Theory. Elsevier: Amsterdam, 1990.
5. Kaji H, Tai T, Horii F. Macromolecules. 2001;34:6318.

6. Rothwell WP, Waugh JS. J. Chem. Phys. 1981;74:2721.
7. VanderHart DL, Earl WL, Garroway AN. J. Magn. Reson. 1981;44:361.
8. Takegoshi K, Hikichi K. J. Chem. Phys. 1991;94:3200.
9. Ishida H, Horii F. Macromolecules. 1997;30:5799.
10. Murakami M, Ishida H, Miyazaki M, Kaji H, Horii F. Macromolecules. 2003;36:4160.
11. Murakami M, Ishida H, Kaji H, Horii F, Tokita M, Watanabe J. Polym. J. 2004;36:830.
12. Cohen MH, Reif F. In: F Seitz, D Turnbull (Eds). Solid State Physics, Vol.5. Academic Press: New York, 1957, p 321.
13. Horii F, Kaji H, Ishida H, Kuwabara K, Masuda K, Tai T. J. Mol. Struc. 1998;441:303.
14. Huang J, Wu R. Macromolecules. 1993;26:4346.
15. Hansen MT, Bluemich B, Boeffel C, Spiess HW, Morbitzer L, Zembrod A. Macromolecules. 1998;25:5542.
16. Mehring M. Principles of High Resolution NMR in Solids. Springer-Verlag: Berlin, 1983.
17. Horii F, Uyeda T, Beppu T, Murata T, Odani H. Bull. Inst. Chem. Res. Kyoto Univ. 1992;70:198.
18. Horii F, Beppu T, Takaesu N, Ishida H. Magn. Reson. Chem. 1994;32:S30–S35.
19. Wind M, Brombacher L, Heuer A, Graf R, Spiess HW. Solid State NMR. 2005;27:132.
20. Schmidt-Rohr K, Spiess HW. Multidimensional Solid-State NMR and Polymers. Academic Press: London, 1994.
21. Wilhelm M, Spiess HW. Macromolecules. 1996;29:1088.
22. William G, Watts DC. Trans. Faraday Soc. 1971;67:1323.

Molecular Motions of Crystalline Polymers by Solid-State MAS NMR

Toshikazu Miyoshi
Nanotechnology Research Institute, National Institute of Advanced Industrial Science and Technology (AIST),
Higashi 1-1-1 Tsukuba, Ibaraki, 305-8565, Japan

Overview

Chain dynamics in the crystalline region of semi-crystalline polymers play an important role for bulk material properties such as mechanical strength, creep, drawability, crystallization process, and crystal transformation. Therefore, it is important to characterize chain dynamics in detail. 2D exchange NMR is a reliable tool for polymer dynamics analysis, because this method provides motional geometry and time-kinetic parameters quantitively. However, it is difficult to apply this sophisticated method for polymers with chemically complicated polymers in natural abundance. 1D-MAS exchange NMR method is possible to give the same information, and has a great advantage of characterizing molecular dynamics for multi-functional groups of molecules without isotope labeling. In this contribution, we briefly explain 1D-MAS exchange NMR, and their applications to slow dynamics of crystalline polymers with chemically complicated structures in natural abundance. We will show which part of polymer in the crystalline region contributes to mechanical property and what type of motions occur in the unstable crystalline form prior to crystal–crystal transformation.

1D-MAS Exchange NMR

There are several 1D-MAS exchange NMR methods [1–6] which enable us to measure detailed dynamic information of target molecules without isotope labeling. Among them, CODEX method [5,6] is most useful for polymers with chemically complicated structures and small CSA [7–9]. The CODEX NMR consists of an exchange and reference parts, and utilizes the recoupling of the CSA interaction by 180° pulses trains in the two evolution periods sandwiching a mixing period (t_{mix}). The effect is signal decay due to the dephasing of magnetization brought about by changes in orientation-dependent CSA due to a re-orientational dynamic process during t_{mix}. The resulting dephasing leads to a decay of the signal-intensity in the exchange spectrum (S). Further, the relaxation such as T_1 and T_2 during t_{mix} and evolution time (Nt_{r}), respectively, and pulse length errors also lead to signal decay. To remove these effects, a reference spectrum is acquired. The motional correlation time and information about the motional geometry can be obtained by plotting the ratio (S/S_0) vs. $t_{\mathrm{mix},}$ and (S/S_0) vs. Nt_{r}, respectively [5–11].

In typical organic compounds in natural abundance, the time constant of spin diffusion (τ_{sd}) is on the order of ∼ s under MAS condition [12]. Therefore, spin exchange due to spin diffusion also contributes to the exchange decay with increasing t_{mix} up to several seconds. The dynamic process is thermally activated, and thus, the obtained correlation time depends on temperature. On the other hand, spin diffusion is in a good approximation temperature independent in the regime of interest. Therefore, the spin-diffusion effect is obtained from the exchange decay at low temperature where molecular dynamics does not contribute to the exchange decay. Then, pure exchange decay due to dynamic process is obtained [7–10,12]. In the case of semi-crystalline polymers, ^{13}C NMR signals in the amorphous regions overlaps with the crystalline signals. Therefore, relaxation filter such as T_1 and $T_{1\rho}$, which suppresses amorphous contributions to S and S_0 is also incorporated into the 1D-MAS exchange pulse program [7–9]. Then, pure crystalline dynamics for semi-crystalline polymers is investigated by 1D-MAS exchange NMR.

Mechanical Property vs. Chain Dynamics

Isotactic-poly(4-methyl-1-pentene) is commercially available and one of the industrially important polymers [13]. The crystalline region of *i*P4M1P shows a lower density than the amorphous region at room temperature. Figure 1a and b show ^{13}C CPMAS NMR spectra and CSA spectra, respectively, for *i*P4M1P crystallites (form I). The polymer structure for *i*P4M1P crystallites [14] and signal assignments are also inserted in Figure 1a. ^{13}C high-resolution signals for all functional groups appear in the narrow chemical shift range of 22–46 ppm. The CSA spectra for the main-chain signals overlap with those for the side-chain ones as shown in Figure 1b. Therefore,

Graham A. Webb (ed.), Modern Magnetic Resonance, 615–619.
© 2008 *Springer.*

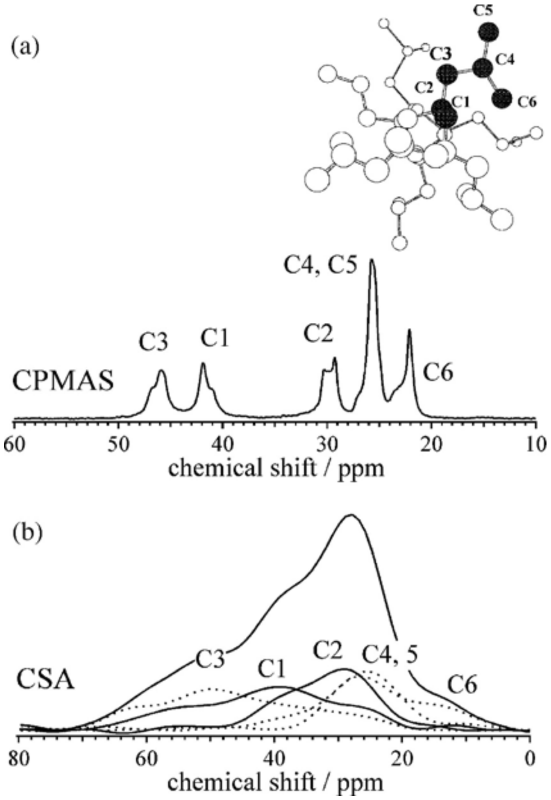

Fig. 1. (a)^{13}C CPMAS NMR spectra of *i*P4M1P crystallites at room temperature [7,8]. The 7_2 helical structure for form I crystallites of *i*P4M1P determined by WAXD [14], and NMR signal assignment is shown as an insert. (b) ^{13}C CSA spectra for *i*P4M1P crystallites and their summation (solid curve) at room temperature. ^{13}C CSA spectra were obtained by 2D SUPER experiments [15]. The solid and broken curves show main- and side-chain spectra.

it is difficult to apply 2D exchange NMR to detailed dynamics analysis of *i*P4M1P crystallites. Figure 2a shows CODEX exchange and reference NMR spectra, respectively, with Nt_r of 2.2 ms and $t_{\text{mix}} = 107$ ms at 360 K [8]. The signal intensities for the side-chain signals C3 and C6 as well as the main-chain signals C1 and C2 in the exchange spectrum (S) are much smaller as compared to those in the reference spectrum (S_0). These CODEX spectra show that overall motions occur in the crystalline regions. The Nt_r dependence of (S/S_0) relies on CSA size, tensor orientation, and motional geometry [6]. Figure 2b shows the simulated CODEX curves for C1 with jump angles of 10, 20, 30, 50, 70, and 103° around its chain axis. The simulations show steep decays in the initial period with increasing jump angle. The Nt_r dependence of (S/S_0) for the C1 signal at $t_{\text{mix}} = 107$ ms and 333 K is shown in Figure 2c. The helical jump angle between the neighboring sites is $360^\circ \times 2/7 = 103^\circ$. Actually, *i*P4M1P crystallites show slightly disordered 7_2 helical conformations in the lattice. Therefore, jump angles between the seven neighboring sites deviate from 103°, and are 122, 84, 93, 145, 96, 72, and 109° [8,14]. The CODEX dephasing curve for each jump angle was calculated. The average one and the experimental data for (S/S_0) intensity for C1 signal are shown in Figure 2c. The experimental data are well consistent with the simulated and averaged curve. This result shows that helical jump motions happen in *i*P4M1P crystallites as well as in PE [16], *i*PP [17,18], POM [18,19], PEO [20], and form III of *i*PB crystallites [21].

Figure 3a and b show t_{mix} dependencies of $(S/S_0)^*$ for the main-chain signals C1 (○) and C2 (●) and the side-chain signals C3 (□) and C6 (×), respectively, in *i*P4M1P crystallites at 360 K, where $(S/S_0)^*$ shows pure exchange curve after spin-diffusion correction [8]. t_{mix} dependences of $(S/S_0)^*$ for C3 and C6 in the side-chain almost match those for the main-chain signals C1 and C2 within the experimental errors. The plateau values for the main-chain signals are in agreement with those of the side-chain, too. These evidences indicate that the side chain moves in concert with the main chain in the crystallites, and there are no slow independent motions. The solid curves in Figure 3a and b provide kinetic parameters such as available site number, correlation time, and distribution width of correlation time [6,8]. The correlation times for helical jump motions obtained through the C2 signal (●) are plotted in Figure 3c. The mechanical relaxations reported by different authors [22,23] are also inserted in Figure 3c. The correlation times for helical jump motions are reasonably agreement with the mechanical relaxations. These relaxations were believed to the segmental motions in the amorphous region. The obtained CODEX NMR results concluded that overall motions in the crystalline region also contribute to the mechanical relaxation.

Crystal Transformation vs. Molecular Dynamics

Solid-state crystal–crystal transformations frequently occur in crystalline polymers, spontaneously [24] or under specific treatments, for example, mechanical stretching [25]. Crystal–crystal transformations accompany changes in the molecular structure such as conformation, packing, or both. These structural changes require internal rotations around chemical bonds, lateral displacements, translations and rotations of the polymer chains in the restricted space. In most of the crystal–crystal transformations, the chirality of the helix is preserved due to the spatial restrictions imposed by the lattice [24]. These structural changes are commonly discussed on the basis of static

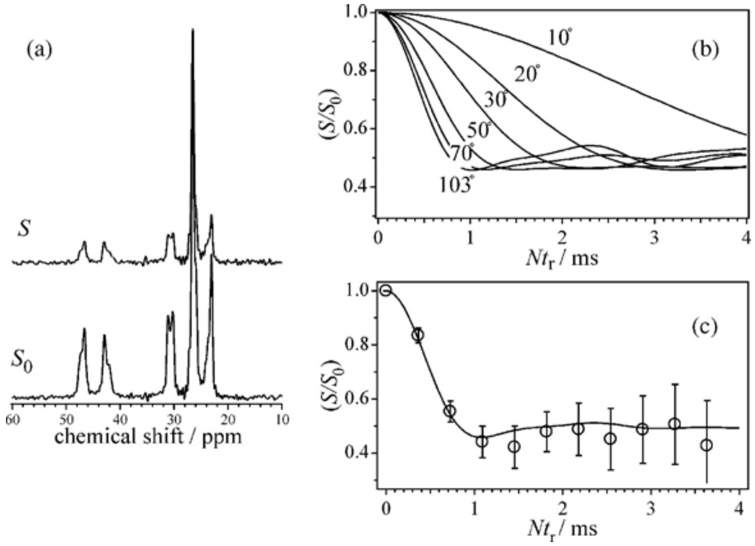

Fig. 2. (a) ^{13}C CODEX exchange and reference NMR spectra of *i*P4M1P crystallites, with $t_{\mathrm{mix}} = 107$ ms and $Nt_{\mathrm{r}} = 2.2$ ms under MAS frequency of 3000 ± 3 Hz, measured at 360 K [8]. (b) ^{13}C CODEX Nt_{r} simulated curves for the C1 signal assuming different jump angles around the chain axis in a uniform 7_2 helix. (c) ^{13}C CODEX Nt_{r} dependence of (S/S_0) for the C1 signal (○) and the solid curve is the average of the simulated curves for jump angles with 122, 84, 95, 145, 96, 72, and 109° in the disordered 7_2 helix.

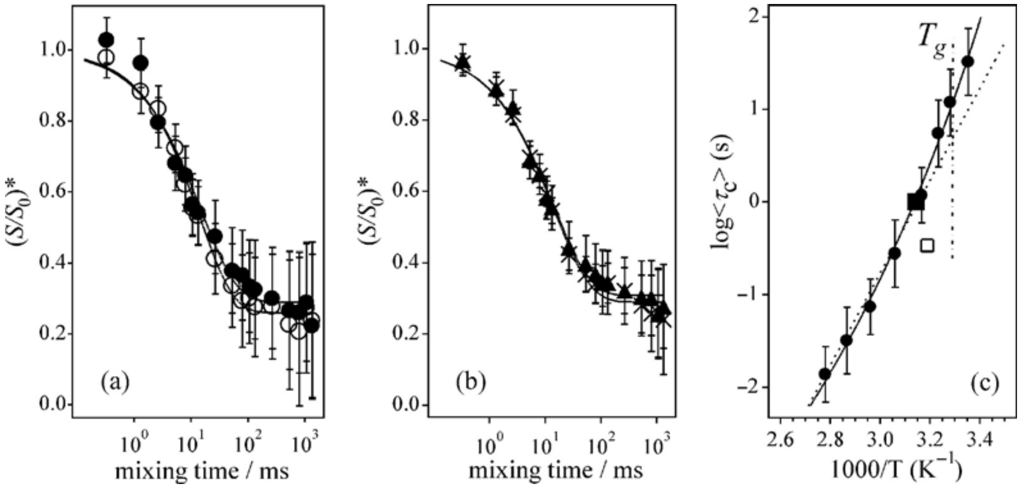

Fig. 3. ^{13}C CODEX exchange curves of $(S/S_0)^*$ intensities for the main chain [C1 (○) and C2 (●)] (a) and the side-chain [C3 (□) and C6 (×)] (b) for *i*P4M1P crystallites at 360 K [8]. The solid curves show the best fits to the experimental data using $(S/S_0)^* = 1\text{-}p(1\text{-}\exp(-t_{\mathrm{mix}}/\tau_{\mathrm{c}})^{\beta})$. p is determined by the number of sites m accessible by the dynamic process, $p = (m-1)/m$, τ_{c} is the correlation time, and β represents the distribution of correlation time. The fitting of $(S/S_0)^*$ of C2 yields $p = 0.70 \pm 0.12$, $\tau_c = (13.9 \pm 1.3)$ ms, $\beta = 0.71 \pm 0.11$, which are well consistent with the other signals (C1: $p = 0.74 \pm 0.02$, $\tau_c = (14.1 \pm 1.1)$ ms, $\beta = 0.72 \pm 0.05$, C3: $p = 0.69 \pm 0.03$, $\tau_c = (14.3 \pm 1.3)$ ms, $\beta = 0.65 \pm 0.05$, and C6: $p = 0.71 \pm 0.03$, $\tau_c = (14.3 \pm 1.3)$ ms, $\beta = 0.66 \pm 0.05$) within experimental errors. (C) Arrhenius diagram of the correlation times for helical jumps (●) of *i*P4M1P crystallites obtained by CODEX. The error bars mean a distribution width for the correlation times, assuming a log-Gaussian distribution. The mechanical data of *i*P4M1P by Reddy *et al.* [22] and Datch [23] are also shown as (■) and (□), respectively. The broken line shows best fitted one with an activation energy of 95.2 ± 5.3 kJ/mol. The solid curve shows WLF one with best fitted parameters of C1 = 8.4 ± 1.2, C2 = 75 ±17 K, and $T_{\mathrm{s}} = 294 \pm 3$ K. The short and dashed line shows T_{g} of *i*P4M1P, which was determined by DSC.

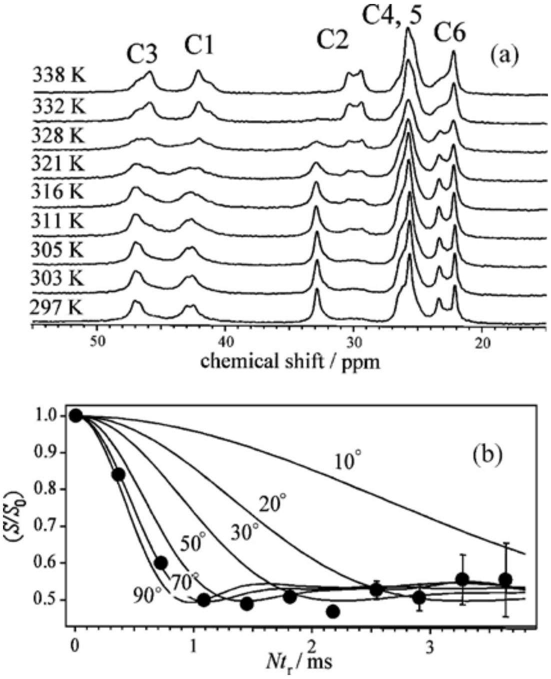

Fig. 4. (a) ^{13}C CPMAS NMR spectra of form III-rich of *i*P4M1P at various temperatures. ^{13}C CPMAS NMR spectra show unstable form III transforms into stable form I above 311 K [9]. The signals assignments are also inserted. (b) ^{13}C CODEX Nt_r dependence of C1 (●) for form III crystallites of *i*P4M1P with a mixing time of 107 ms under MAS frequency of 5500 ± 3 Hz at 311 K. The error bars were obtained from signal–noise ratios of exchange and reference spectra. The solid curves show simulated CODEX Nt_r attenuations for C1 signal with jump angles of 10, 20, 30, 50, 70, and 90° around the chain axis of a uniform 4_1 helix.

crystalline structures before and after the transformations, however, it is often expected that molecular dynamics plays an important role for the crystal–crystal transformation. Solid-state NMR directly can probe what type of motions occur in an unstable form prior to crystal–crystal transformation.

*i*P4M1P shows complicated polymorph of forms I–V, depending on the crystallization condition such as pressure, solvent, and thermal history [13]. Here, we address crystal–crystal transformation from form III (4_1 helix) into form I (7_2 helix) [9]. Figure 4a shows ^{13}C CPMAS NMR spectra for the form III-rich for *i*P4M1P as a function of temperature. The signal assignments are also demonstrated in Figure 4a. Above 311 K, the transformation from form III into form I is observed through the C2 signal. Since the C2 signal has significantly different chemical shifts in the different forms I and III, the line shape and chemical shift of the C2 signal are good indicators of the structural and dynamics changes due to the transformation. Below 338 K, the chemical shift of the C2 signal for form III is almost invariant. On the other hand, the line width shows motional broadening, indicating that segmental motions occur in form III crystallites prior to transformation.

Figure 4b shows CODEX Nt_r dependence of the C1 signal for form III and the solid curves showing CODEX recoupling curves for different hypothetical jump angles around its helical axis [9]. The experimental result of C1 signal shows a steeper decay during the initial evolution period and is well consistent with simulated jump angles of 70–90°. This NMR result directly detects the large amplitude overall motions in unstable crystalline form prior to the transformations. Similarly, poly(tetrafluoroethylene) (PTFE) [26] and form III of *isotactic*-poly(1-butene) (*i*PB) [21] also shows rotational motions with large amplitude before the transformations.

Concluding Remarks

In this contribution, we showed that slow molecular dynamics in the correlation times of 10^{-2} ~10^{2} s can be investigated in terms of 1D-MAS exchange NMR method in natural abundance. Fast and intermediate dynamics can also be investigated by other methods under MAS in natural abundance[15,27,28]. These methods should also be useful in understanding the crystallization process of semi-crystalline polymers.

References

1. Yang Y, Schuster M, Blumich B, Spiess HW. Chem. Phys. Lett. 1987;139:239.
2. Gerardy-Montouilout V, Malveau C, Tekely P, Olender Z, Luz Z. J. Magn. Reson. 1996;123:7.
3. Reichert D, Zimmermann H, Tekely P, Olender Z, Luz Z. J. Magn. Reson. 1997;125:245.
4. Reichert D, Hempel G, Luz Z, Tekely P, Schneider H. J. Magn. Reson. 2000;146:310.
5. deAzevedo ER, Hu WG, Bonagamba TJ, Schmidt-Rohr K. J. Am. Chem. Soc. 1999;121:8411.
6. deAzevedo ER, Hu WG, Bonagamba TJ, Schmidt-Rohr K. J. Chem. Phys. 2000;112:8988.
7. Miyoshi T, Pascui O, Reichert D. Macromolecules. 2002;35:7178.
8. Miyoshi T, Pascui O, Reichert D. Macromolecules. 2004;37:6460.
9. Miyoshi T, Pascui O, Reichert D. Macromolecules. 2004;37:6653.
10. Pascui O, Beiner M, Reichert D. Macromolecules. 2003;36:3992.

11. Bonagamba TJ, Becker-Guedes F, deAzevedo ER, Schmidt-Rohr K. J. Polym. Sci. Polym. Phys. Ed. 2001;39:2444.
12. Reichert D, Hempel G, Zimmermann H, Tekely P, Poupko R, Luz Z, Favre DE, Chmelka BF. Appl. Magn. Reson. 1999;17:315.
13. Lopez LC, Wilkes GL, Stricklen PM, White SA. J. Macromol. Sci. C. 1992:32;301.
14. Kusanagi H, Takase M, Chatani Y, Tadokoro H. J. Polym. Sci. Polym. Phys. 1978;16:131.
15. Liu SF, Mao JD, Schmidt-Rohr K. J. Magn. Reson. 2002;155: 15.
16. Hu WG, Boeffel C, Schmidt-Rohr K. Macromolecules. 1999;32:1611.
17. Schaefer D, Spiess HW, Suter UW, Fleming WW. Macromolecules. 1990;23:3431.
18. Hagemeyer A, Schmidt-Rohr K, Spiess HW. Adv. Magn. Reson. 1989;13:85.
19. Kentgens APM, de Boer E, Veeman WS. J. Chem. Phys. 1987;87:6859.
20. Schmidt-Rohr K, Spiess HW. Multidimensional Solid-State NMR and Polymers. Academic Press: London, 1994.
21. Miyoshi T, Hayashi S, Imashiro F, Kaito A. Macromolecules. 2002;35:2624.
22. Reddy S, Desai P, Abhiraman AS, Beckham HW, Kulik AS, Spiess HW. Macromolecules. 1997;30:3293.
23. Datch A. J. Therm. Anal. 1998;54:151.
24. Lotz B, Mathieu C, Lovinger AJ, De Rosa C, Ruiz O, Auriemma F. Macromolecules. 1998;31:9253.
25. Saraf FR, Porter RS. J. Polym. Sci. B: Polym. Phys. 1988;26: 1049.
26. Vega AJ, English AD. Macromolecules. 1980;13:1635.
27. McElheny D, DeVita E, Frydman L. J. Magn. Reson. 2000; 143:328.
28. Brown SP, Spiess HW. Chem. Rev. 2001;101:4125.

Dynamics in Polypeptides by Solid State ^{2}H NMR

Toshifumi Hiraoki
Department of Applied Physics, Graduate School of Engineering, Hokkaido University, N13W8, Kita-ku, Sapporo 060-8628, Japan

Introduction

Solid state ^{2}H NMR parameters are almost exclusively governed by the quadrupole interaction with electric field gradient (EFG) tensor at the deuteron site [1–3]. The EFG is entirely intramolecular in nature. Thus molecular order and mobility are monitored through the orientation of individual C–^{2}H bond direction. Therefore, ^{2}H NMR is a powerful technique of studying local molecular motions. It enables us to discriminate different types of motions and its correlation times over the wide frequency range. The side chain of a polypeptide have remarkable multiple motional freedom about multiple bonds, while the main chain forms the regular secondary conformation such as α-helix and β-sheet which are presumed to be a rigid structure. In this section, we focus on the dynamics of both side- and main-chains of synthetic polypeptides deuterated at several positions by solid state ^{2}H NMR.

Methyl Group

Figure 1(a) shows the temperature dependence of ^{2}H NMR spectra of the left-handed ω helical poly(β-[$^2H_3$]methyl L-aspartate)(PMLA-d$_3$) [4]. The spectrum at $-125\,^\circ$C is an axially symmetric powder pattern with the quadrupole splitting $\Delta\nu_q$ of 38 kHz, showing a fast reorientation of the methyl group. There is no substantial change in line shapes from -125 to 50 °C. Remarkable change is observed at higher temperatures above 50 °C. The signal-to-noise ratio of a spectrum becomes worse and the integrated intensity of a spectrum decreases. These results suggest the presence of motions of the rate between 10^4 and 10^6/s. $\Delta\nu_q$ decreases from 38 to 34 kHz on going from -125 to 119 °C. These values are slightly smaller than the theoretically predicted value of 41.7 kHz in the case of extremely fast reorientation about C$_3$ axis, suggesting the presence of additional rapid librations of the C$_3$ axis. This small decrease in $\Delta\nu_q$ may be accounted for librations of the C$_3$ axis within a cone of semi-angle of 20°–30°.

Inspection of the inversion-recovery ^{2}H NMR spectra reveals that the parallel components of a spectrum has a shorter T_1 than the perpendicular components in the temperature range from -125 to 20 °C. Such T_1 anisotropy across a spectrum is theoretically predicted for the 3-site jump about the C$_3$ axis for the methyl group [5]. The temperature dependent T_1 of PMLA-d$_3$ is shown in Figure 2. T_1 values increase linearly with temperature from -125 to -40 °C, showing the fast motional region. The correlation time τ_c of the 3-site jump motion is estimated to be 15 ps at -95 °C, and an Arrhenius plot of τ_c yields an activation energy of 6.8 kJ/mol. These results imply that the methyl group bonded to oxygen atom experience a lower steric hindrance than a methyl group bonded to carbon atom, and support the view that the intermolecular contribution to the hindering barriers to the methyl group reorientation is relatively weak.

There are observable deviations from the linear Arrhenius plot behavior at above -40 °C, together with slight decreases in $\Delta\nu_q$, indicating the onset of new and rapid motions in the side chain. Conformational energy calculations of PMLA show the C$_3$ axis is trans and parallel to the C_β–C_γ axis in the side chain [6]. Therefore, the rotational motions about the C_β–C_γ axis little affect the line shapes of the methyl group and the line shapes observed at above 50 °C suggest the presence of large amplitude motions about the C_α–C_β axis. Since the reorientation about the C_α–C_β axis is allowed to a trans-gausch isomerization, the two-fold jump with equal population about the C_α–C_β axis and the effective quadrupole coupling constant of 50.7 kHz is assumed to calculate line shapes. The calculated spectra, which are in good agreement with the observed, indicate the averaged jump angle of 110° with the standard deviation of 5° in a Gaussian distribution of jump angle, and the jump rate of the order of kHz.

Figure 1(b) shows the temperature dependent spectra of the right-handed α-helical poly(γ-[$^2H_3$]methyl L-glutamate)(PMLG-d$_3$) [7,8]. The side chain length of PMLG is longer by a methylene group than that of PMLA. Similar line shapes are obtained for both PMLG-d$_3$ and PMLA-d$_3$, although line shapes of PMLG-d$_3$ become sharper and a singlet above 100 °C. These results indicate the presence of large amplitude motions with a rate of 40 kHz order in addition to the C$_3$ motion.

Graham A. Webb (ed.), Modern Magnetic Resonance, 621–627.
© 2008 *Springer.*

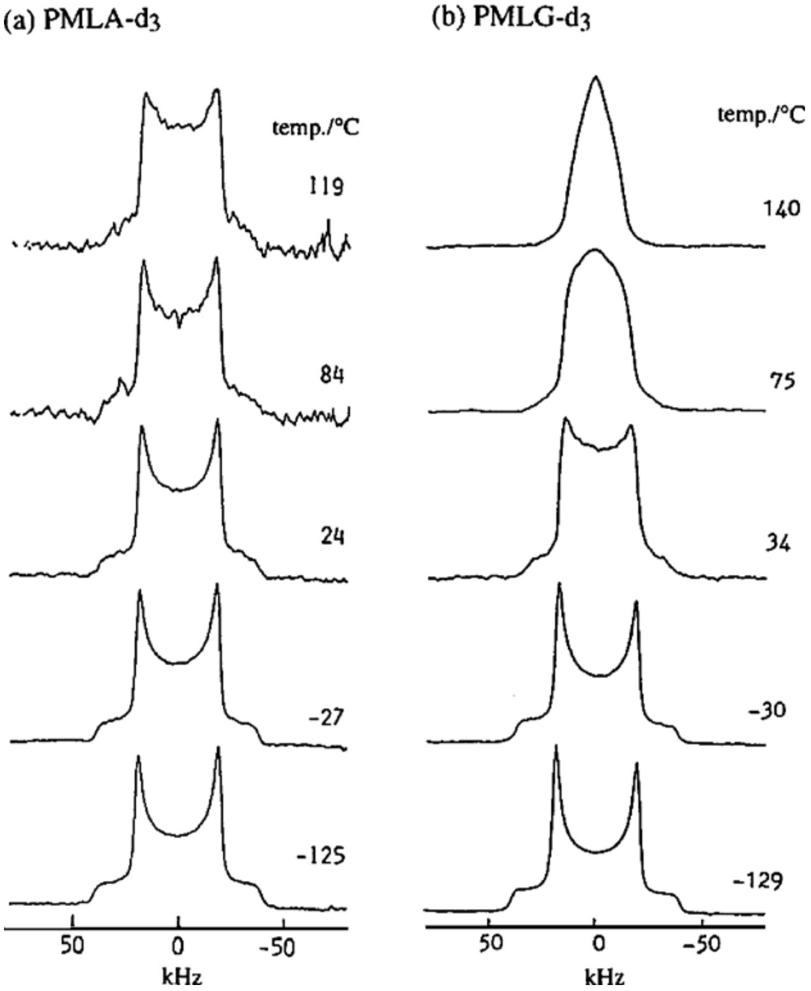

Fig. 1. ^{2}H NMR spectra of PMLA-d_3 (a) and PMLG-d_3 (b) as a function of temperature. Spectra were taken by a quadrupole echo pulse sequence with 90° pulse of 1.7 μs and delay of 25 μs at 30.7 MHz.

The temperature dependent T_1 of PMLG-d_3 is shown in Figure 2. T_1 anisotropy is as well observed in PMLG-d_3 at below 20 °C, showing the 3-site jump motion [5]. An Arrhenius plot of τ_c for the 3-site jump gives an activation energy of 7.5 kJ/mol, which is comparable with that of PMLA-d_3. The maximum and minimum of T_1 are observed at about 10 and 130 °C, respectively, with increasing a temperature. These results indicate additional motions of the C_3 axis along a side chain. One can easily estimate a correlation time of such motions to be about 5 ns at 130 °C from T_1 minimum. As T_1 minimum was observed at 100 °C for PMLG deuterated in the γ-position, these motions are present along a side chain as a whole.

Phenyl Ring

Phenyl ring motion in β-form poly(L-phenylalanine) (PLF-d_5) are displayed as a function of temperature in Figure 3 [9]. There are two categories of deuterons on a phenyl ring. Those on *ortho* and *meta* sites are affected by any rotational motions about the C_β–C_γ axis. The *para* site is essentially unaffected by motions about this

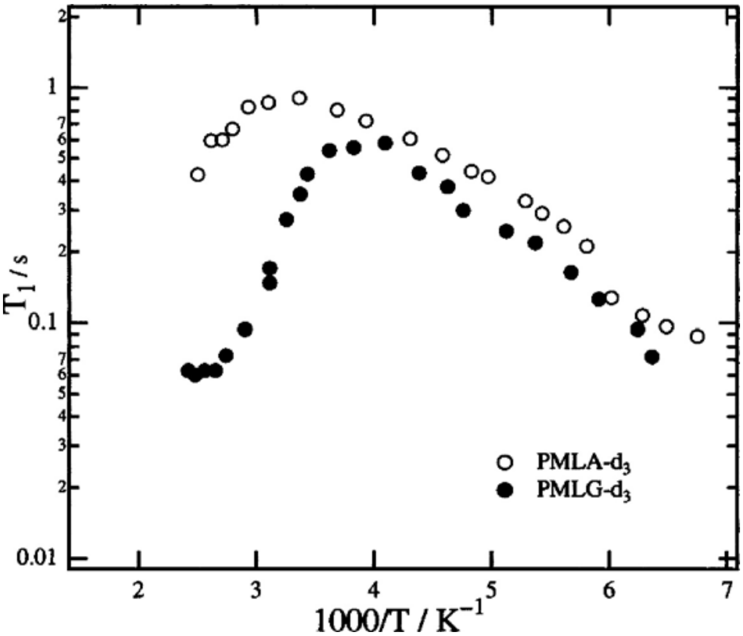

Fig. 2. Temperature dependent T_1 of PMLA-d$_3$ and PMLG-d$_3$.

axis, and its line shape exhibits a rigid powder pattern. As the unaffected *para* line shape is superimposed on the line shape of the other ring deuterons that contain the dynamic information of interest, line shapes of a phenyl ring shows that effects of motions are heterogeneous. Such motional heterogeneity results in different T_1 values, allowing the separation of the components using the amorphous quadrupole echo [10].

The line shape of PLF-d$_5$at -100 °C reveals a nearly rigid powder pattern and the small inner singularities with $\Delta\nu_q$ of 32 kHz are observed in the center of the spectrum. This grows in amplitude at the expense of the relative intensity of the rigid pattern as temperature is raised. These signals are present at all temperature measured from -100 to 65 °C, indicative of the π-flip motion of the ring about its symmetry axis [5]. There is no substantial change in line shape from 65 to 140 °C. As additional narrowing can not be observed in line shape, large amplitude motions about the C_α–C_β axis could be excluded.

Line shapes are calculated with an assumption of a log-Gaussian distribution of the correlation time of the π-flipping [11,12], as shown in Figure 3. The calculated spectra are in good agreement with the observed. The mean correlation time obtained at 22 °C is estimated to be 1.2×10^{-6} s and an Arrhenius plot of the mean correlation time yields an activation energy of 28 kJ/mol. Such low activation energy exhibits less hindrance of rings. As PLF-d$_5$ is in the β-form and rings protrude from the β-sheet, the inter- and intra-interaction between side chains would significantly have the motional freedom for the flipping motion.

Side Chain of Poly(γ-benzyl L-glutamate) (PBLG)

Three positions along a side chain of PBLG are deuterated at γ(PBLG-γd_2), ζ(PBLG-ζd_2), phenyl ring(PBLG-d$_5$) [8,13–15]. PBLG forms a right-handed α-helical conformation. The side chains are located between the pseudo-hexagonally packed α-helical rods in solid [16,17]. Rapid and large amplitude motions of the side chain are prominent above room temperature, and, therefore, these dynamics results in the behavior like the glass transition of the PBLG side chains around room temperature [8,15].

The temperature dependent ^{2}H NMR spectra of PBLG-d$_5$ are shown in Figure 4. The typical line shape for the rapid π flipping motion of a phenyl ring about the C_ζ–C_η axis is observed at 20 °C, although line shapes below -76 °C are similar to the rigid state pattern. The spectrum at 20 °C has $\Delta\nu_q$ of 26 kHz which is smaller by 4 kHz than the flipping, indicating the presence of the libration. The amplitude of the libration is estimated with

Fig. 3. Temperature dependence of observed (a) and calculated (b) spectra of PLF-d_5. Figures on the right- and left-hand sides of spectra indicate the temperature and the mean correlation time, respectively.

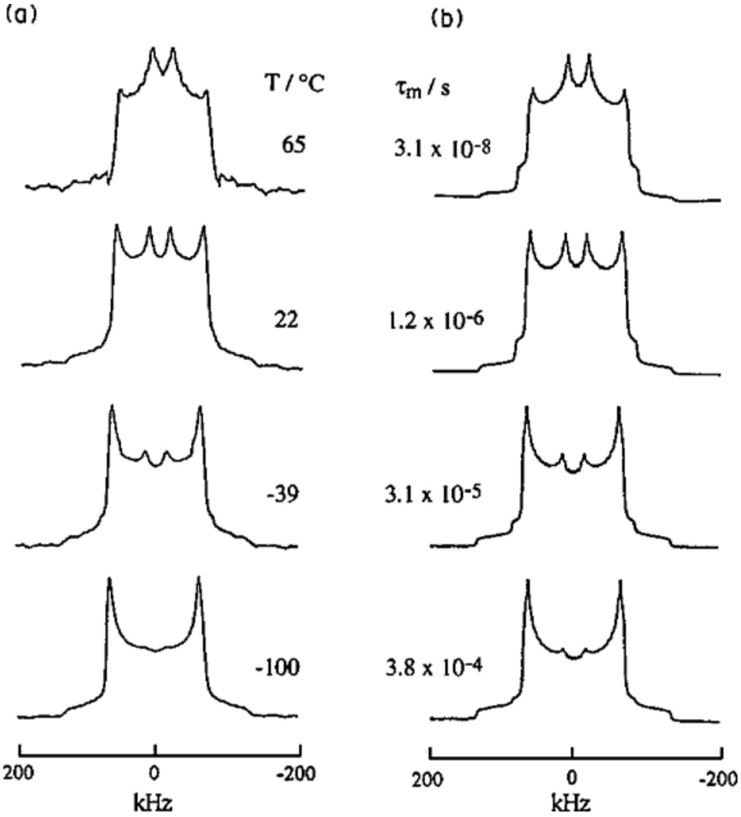

the diffusion in a cone of semiangle θ_C to be 28° at 20 °C. The line shape remarkably changes with a further increase in temperature and a motionally averaged singlet spectrum with the half-width of 10 kHz is observed at 130 °C. These results show that the flipping axis itself undergoes rapid and large amplitude motions, in addition to the flipping motion and the small amplitude libration. This flipping-axis motion definitely results from the multiple internal rotations along the side chain above the glass-like transition temperature.

The temperature dependence of the integrated intensities of PBLG-d_5 spectra is shown in Figure 5. The intensity decreases with an increase in temperature and achieves a minimum at -40 °C. It decreases again and exhibits the deep minimum at 50 °C. The temperature regions where the intensity takes a minimum, corresponding that the rate of the motion is as high as the quadrupole coupling constant of 180 kHz in these temperature regions. Taking account of the line shape changes, the minima at the lower and higher temperatures are expected to correspond to the flipping motion of a phenyl ring and the motion of flipping axis itself, respectively.

Line shapes are calculated for the flipping motion with assuming a distribution of a jump rate [11,12], and compared with the observed. The average jump rate obtained is 2.3×10^5 Hz at 20 °C. This result is comparable with the appearance of the minima for the intensities. The activation energy of the flipping is obtained to be 23 kJ/mol below 30 °C.

Spectra of PBLG-ζd_2 will give direct information about the motion of flipping axis itself, because the C_ζ–^{2}H axis and the C_ζ–C_η axis have a common motional axis of the O_ε–C_ζ bond. The line shape and the intensity of PBLG-ζd_2 are displayed in Figures 4 and 5, respectively. The line shape at 20 °C is slightly different from a static powder pattern. The parallel components of the spectrum is not clear and the center of the spectrum is more filled-in than the static one. $\Delta\nu_q$ is slightly smaller than the rigid state value of 128 kHz, and decreases gradually with increasing temperature. These results suggest that there is a rapid and small amplitude libration at the ζ position. The integrated intensity of PBLG-ζd_2 start to decrease gradually from the lowest temperature to room temperature, and a remarkable intensity loss is observed around 50 °C.

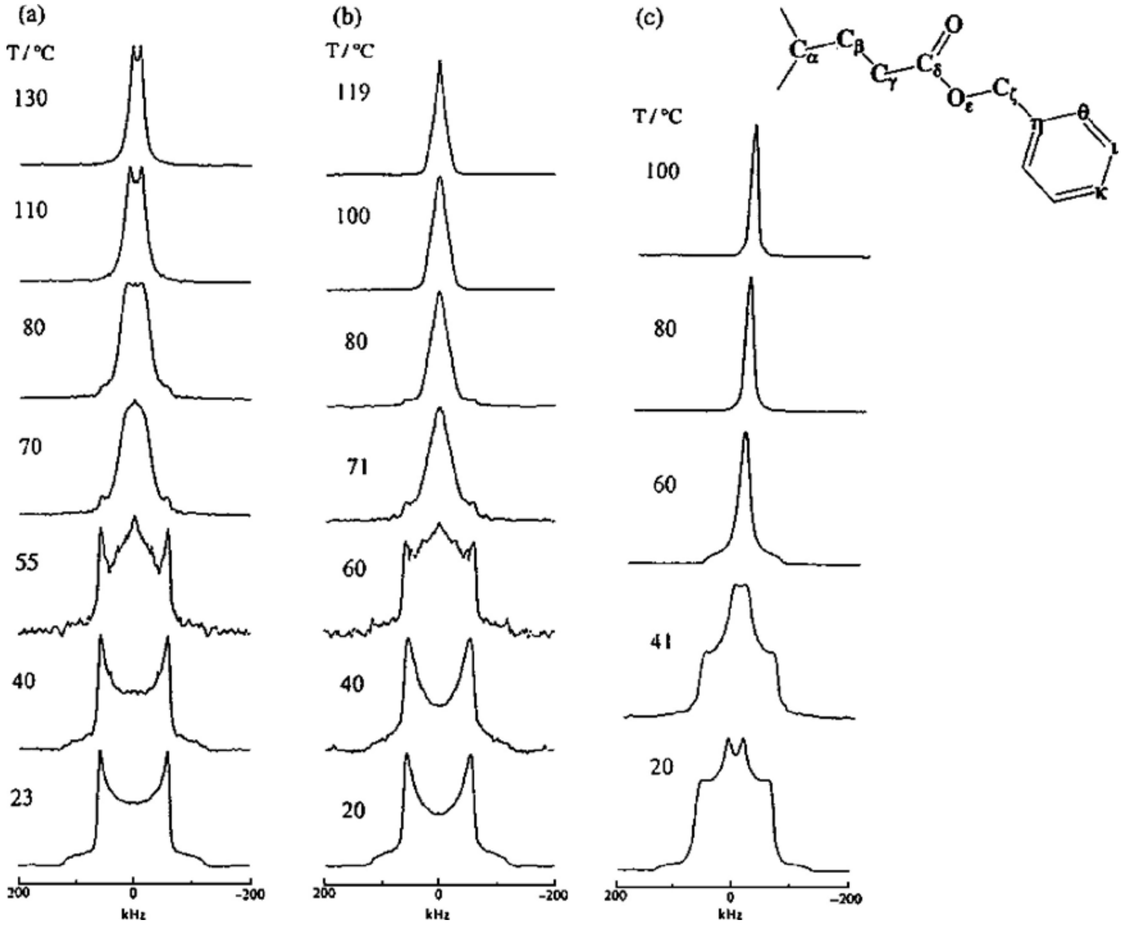

Fig. 4. ^{2}H NMR spectra of PBLG-γd_2(a), PBLG-ζd_2(b), and PBLG-d_5(c) as a function of temperature, and skeletal structure of PBLG side chain.

With a further increase in temperature, the spectrum recovers its intensity. Above 80 °C the motionally averaged singlet-like spectra are observed, showing that the presence of rapid and large amplitude motions of which frequency is as high as 100 kHz around 50 °C and becomes far higher above 80 °C. The remarkable τ-dependence is observed around 40–60 °C, being consistent with the remarkable intensity loss [15].

Temperature dependent T_1 of PBLG-ζd_2 is shown in Figure 6. T_1 value decreases gradually with an increase in temperature, and start to decrease steeply from room temperature. T_1 value takes a minimum at 110 °C, showing the presence of the large amplitude motions of the side chain whose rate is as high as the observed frequency of 30 MHz at this temperature. The temperature dependent T_1 can be apparently divided into two regions by room temperature. Therefore, T_1 value will be governed by different motional modes of the side chain, that is, the libration and the large amplitude motions below and above room temperature, respectively, taking the temperature dependence of the line shapes into account. The large amplitude motions are brought about the multiple internal rotations along a side chain. Such motions are well formalized by the 3-site jump with a distribution of both a jump rate and a polar angle. Such calculations well produce line shapes and T_1 profiles of PBLG-ζd_2. Averaged jump rate and polar angle obtained at 110 °C are 64 MHz and 49°, respectively.

Temperature dependent spectra of PBLG-γd_2 and its intensity are shown in Figures 4 and 5, respectively. The line shapes below 30 °C appear to be an axially symmetric powder pattern, showing the absence of large amplitude

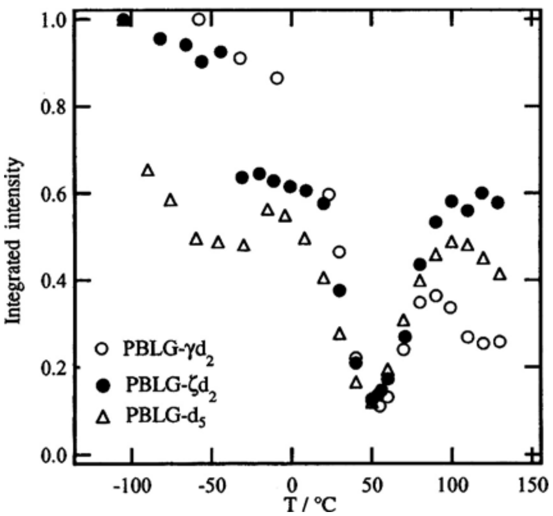

Fig. 5. Integrated intensity of PBLG-γd_2, PBLG-ζd_2, and PBLG-d_5 as a function of temperature.

motions. The $\Delta\nu_q$ value of 117 kHz at 20 °C is smaller than the rigid state value of 128 kHz, showing the presence of the fast small amplitude libration at the γ position, as observed at the phenyl ring and ζ position of the side chain. It decreases to 115 kHz at 60 °C. The intensity of the spectrum starts to decrease gradually and reaches a minimum value at 55 °C with an increase in temperature. Line shapes remarkably changes to start from about 40 °C and the characteristic line shape change is also observed around 55 °C. This intensity loss and the remarkable line shape change result from the increase in mobility, indicating the presence of the motion of which rate is the order of 10^5 Hz at the γ position. With a further increase in temperature, the spectrum recovers its intensity and gradually changes into the motionally averaged narrow doublet one whose splitting is 12 kHz at 130 °C. These results show the presence of the rapid and large amplitude motion at this position. The temperature dependence of the intensity for PBLG-γd_2 is quite similar to those of PBLG-d_5 and PBLG-ζd_2. In particular, the intensities of all these three samples take a minimum at the same temperature region, implying that the motions effective on the line shape changes of PBLG-γd_2 is also effective on the line shape changes of PBLG-d_5 and PBLG-ζd_2. These motions were conformed by ^{13}C CP/MAS NMR measurements [18].

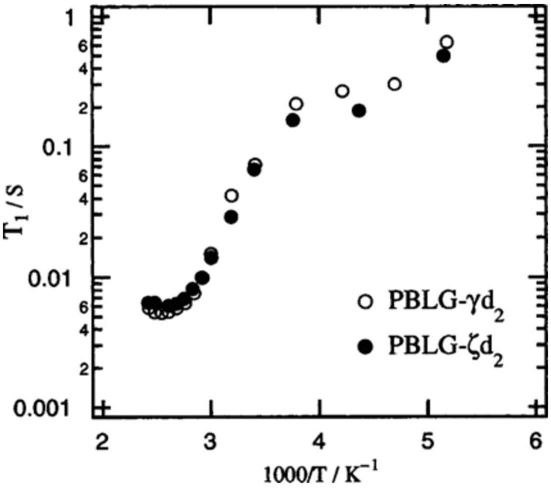

Fig. 6. Temperature dependent T_1 of PBLG-γd_2 and PBLG-ζd_2.

The temperature dependent T_1 of PBLG-γd_2 is shown in Figure 6. The T_1 profile of PBLG-γd_2 is very similar to that of PBLG-ζd_2. Especially in the high temperature region, T_1 values of both samples achieve the minimum at 110–120 °C. These results reveal that the common motional modes contribute to the T_1 values of remote positions in a side chain and/or that the motions at two different positions have a common motional rate. In the low temperature region, the T_1 values of PBLG-γd_2 are a little longer than those of PBLG-ζd_2, suggesting that the libration at the γ position is more restricted than that at the ζ position. In order to confirm the large amplitude motions at the γ position quantitatively, the spectral simulation was carried out. The methodology is the same as that used for PBLG-ζd_2. The parameters obtained are the polar angle of 45° and the averaged jump rate of 64 MHz at 110 °C, and suggest that the segmental motion including at least the γ position to the end of side chain participate in the glass-like transition phenomenon.

Main Chain Dynamics

The line shapes and T_1 values of the amide deuteron of α-helical PBLG were measured over a wide temperature range [19]. As the temperature is raised, the components of EFG tensor along the axis and perpendicular to the peptide plane decreases, whereas the mutually orthogonal components remain constant. Thus, the N–^{2}H axis undergoes the libration with 5 ps at 16 °C, showing the reorientation in the hydrogen-bonded peptide plane. And the amplitude of the libration is estimated to be from 8 to 12°.The short T_1 values of the N–^{2}H axis result from substantial frictional effects on reorientation that increase with temperature. The similar results were obtained for the amide deuteron of PMLG [20].

Polyglycine (PG) takes two kinds of crystalline forms designated by type I(β-form) and II (3_1-helix) [21]. Line shapes of both PGs deuterated in backbone methylene group remains the axially symmetric powder patterns with $\Delta\nu_q$ of 119 kHz at $-80\,^\circ$C–114 kHz at 125 °C, indicating the libration with the amplitude of 12°–15° [22,23]. T_1 values of both PGs decrease with increase in temperature, and T_1 values of PG I are shorter than those of PG II. These results show that the reorientation of the backbone in the regular secondary structure, which contains directly the hydrogen bond, is subject to a harmonic restoring force and that the motional modes are strongly overdamped [19].

The backbone dynamics is subsequently modulated by replacing partly the methyl group of PMLG by the long side chain of stearyl group [20]. Line shapes and T_1 values of these copolypeptides are remarkably changed above the melting temperature of the long side chain crystal. These results show the presence of the rotational reorientation about the helical axis of the copolypeptides, as well as the libration of the peptide plane. The rotational angle of 55° with the rate of kHz order for such a motion is obtained from the line shape calculation.

Acknowledgments

The author is indebted to Professor A. Tsutsumi for continuous encouragement. A part of present work was supported by a Grant-in-Aid for Scientific Research from the Ministry of Education, Culture, Sports, Science and Technology, Japan.

References

1. Torchia DA. Ann. Rev. Biophys. Bioeng. 1984;13:125.
2. Spiess HW. Adv. Polym. Sci. 1985;66:23.
3. Vold RR, Vold RL. Adv. Magn. Opt. Reson. 1991;16:85.
4. Hiraoki T, Tomita K, Kogame A, Tsutsumi A. Polym. J. 1994; 26:766.
5. Torchia DA, Szabo A. J. Magn. Reson. 1982;49:107.
6. Ooi T, Scott RA, Vanderkooi G, Scheraga HA. J. Chem. Phys. 1967;46:4410.
7. Hiraoki T, Kogame A, Matsuo K, Tsutsumi A. Rep. Prog. Polym. Phys. Jpn. 1990;33:541.
8. Tsutsumi A. Prog. Polym. Sci. 1993;18:651.
9. Hiraoki T, Kogame A, Nishi N, Tsutsumi A. J. Mol. Struc. 1998;441:243.
10. Cholli AL, Dumais JJ, Engle AK, Jelinski LW. Macromolecules. 1984;17:2399.
11. Greenfield MS, Ronemus AD, Vold RL, Vold RR. J. Magn. Reson. 1987;72:89.
12. Schadt RJ, Cain EJ, English AD. J. Phys. Chem. 1993;97: 8387.
13. Kitazawa S, Hiraoki T, Hamada T, Tsutsumi A. Polym. J. 1994;26:1213.
14. Kitazawa S, Hiraoki T, Tsutsumi A. J. Mol. Struc. 1994; 26:1213.
15. Hiraoki T, Kitazawa S, Tsutsumi A. Ann. Rep. NMR Specrosc. 2004;53:297.
16. McKinnon AJ, Tobolsky AV. J. Phys. Chem. 1968;72: 1157.
17. Matsushima N, Hikichi K, Tsutsumi A, Kaneko M. Polym. J. 1975;7:44.
18. Yamaguchi M, Tsutsumi A. Polym. J. 1993;25:131.
19. Usha MG, Peticolas WL, Wittebort RJ. Biochemistry. 1991; 30:3955.
20. Morikoshi N, Hiraoki T, Tsutsumi A. Rep. Prog. Polym. Phys. Jpn. 1999;42:477.
21. Ando S, Ando I, Shoji A, Ozaki T. J. Am. Chem. Soc. 1988; 110:3380.
22. Hirayama T, Kitazawa S, Hiraoki T, Tsutsumi A. Rep. Prog. Polym. Phys. Jpn. 1995;38:469.
23. Kawase Y, Hiraoki T, Tsutsumi A. Rep. Prog. Polym. Phys. Jpn. 1997;40:491.

Polymer Blends

Polymer Blends

Atsushi Asano
Department of Applied Chemistry, National Defense Academy, Yokosuka, Kanagawa 239-8686, Japan

Overview

Macroscopic properties of polymer blends are influenced by the degree of mixing among component polymers, that is, microscopic domain structure. The degree of mixing is related to how closely we look at the blend. The lower limitation of a characteristic space scale of a particular observation determines the detectable domain size in a miscible state, and affects the judgment of homogeneity. For most miscible polymer blends, in general, a single homogeneous phase is achieved by an interpolymer interaction and separates to two phases with distinct compositions and becomes heterogeneous when the temperature is beyond a critical point. Solid-state NMR provides very useful information to detect such a microscopic compositional change, especially less than 10–100 nm scale. Here, the interpolymer interaction, miscibility, and phase separation are mainly touched upon.

Interaction in Polymer Blends

It is necessary for polymer pairs to be miscible on a molecular level that the Gibbs free energy of mixing becomes negative. In general, the exothermic exchange polymer–polymer interaction assists for the free energy to be negative at a certain temperature: the phase diagram shows the lower critical solution temperature (LCST). The polymer–polymer interaction frequently affects solid-state NMR spectrum [1]. By comparing the spectrum of each component polymer with that of a blend, some changes in a chemical shift and/or a lineshape can be easily detected. Among several interactions, the hydrogen-bonding interaction causes appreciable change in a spectrum.

Figure 1 shows the expanded observed solid-state ^{13}C NMR spectra of poly(methyl methacrylate)/poly(vinyl acetate) (PMAA/PVAc) blends at the carboxyl/carbonyl (C=O) region [2]. The simulated spectra for blends obtained from the simple sum of each observed ^{13}C NMR spectrum of pure PMAA and pure PVAc at the respective molar ratio are also displayed in the right side. At the left side, decomposed spectra obtained from the least-square fit to the observed ^{13}C NMR spectra by a sum of five Gaussian curves are summarized.

The broad COOH line of pure PMAA is observed at 183 ppm and the narrower COO peak of PVAc is at 171 ppm. If there is no polymer–polymer interaction between the side chains of PMAA and PVAc, the observed NMR spectra should be reintroduced by the simple summation. However, the observed spectra of the PMAA/PVAc blends are obviously different from the simulated spectra. The observed spectra have a much more complicated envelope. The lineshape of the CO region in the blends seems to be divided into apparently five peaks. Two peaks at around 187 and 179 ppm of those five peaks are clearly appeared, especially, in the spectrum of the PMAA/PVAc = 1/1 blend. A peak at around 175 ppm is also clearly seen in the spectrum of the PMAA/PVAc = 3/1 blend, while the peak at 175 ppm for the other blends are disappeared behind the broad envelope. These observations clearly suggest the existence of an interpolymer interaction. It is revealed that the peak at 179 ppm is attributed to the PMAA-COOH carbon which the carboxylic hydrogen is interacted with PVAc-CO oxygen, and the PVAc-CO carbon peak is appeared at 175 ppm by observations of composition dependence of the ^{13}C spin–lattice relaxation time [2] and two-dimensional (2D) exchange ^{13}C NMR [3]. The abundant 2D exchange ^{13}C NMR spectrum clearly showed the cross-peaks between at $\omega_1 = 175$ ppm and $\omega_2 = 179$ ppm and between $\omega_1 = 179$ ppm and $\omega_2 = 175$ ppm with the same peak intensity [3]. This observation proved that the distance between the interacted PMAA-COOH carbon and the PVAc-CO carbon is 0.37 nm. The length of hydrogen bond was also estimated from the molecular mechanics calculation to be ca. 0.2 nm.

Similarly to the example shown in Figure 1, each component polymer in a miscible polymer blend is in close proximity to interact with each other. The short distance less than about 0.5 nm can be also observed via the nuclear Overhauser effect (NOE). The ^{1}H NOE cross-peaks were observed between 1,2-polybutadiene and polyisoprene of their blend from the 2D NOESY spectrum in solids [4]. For a deuterated-polystyrene (d-PS)/poly(vinyl methyl ether) (PVME) blend, the ^{1}H–^{13}C NOE was detected between the ^{1}H spins of PVME and the ^{13}C spins of d-PS in solids [5,6]. Furthermore, the close proximity caused by a polymer–polymer interaction also affects

Graham A. Webb (ed.), Modern Magnetic Resonance, 631–635.
© 2008 *Springer.*

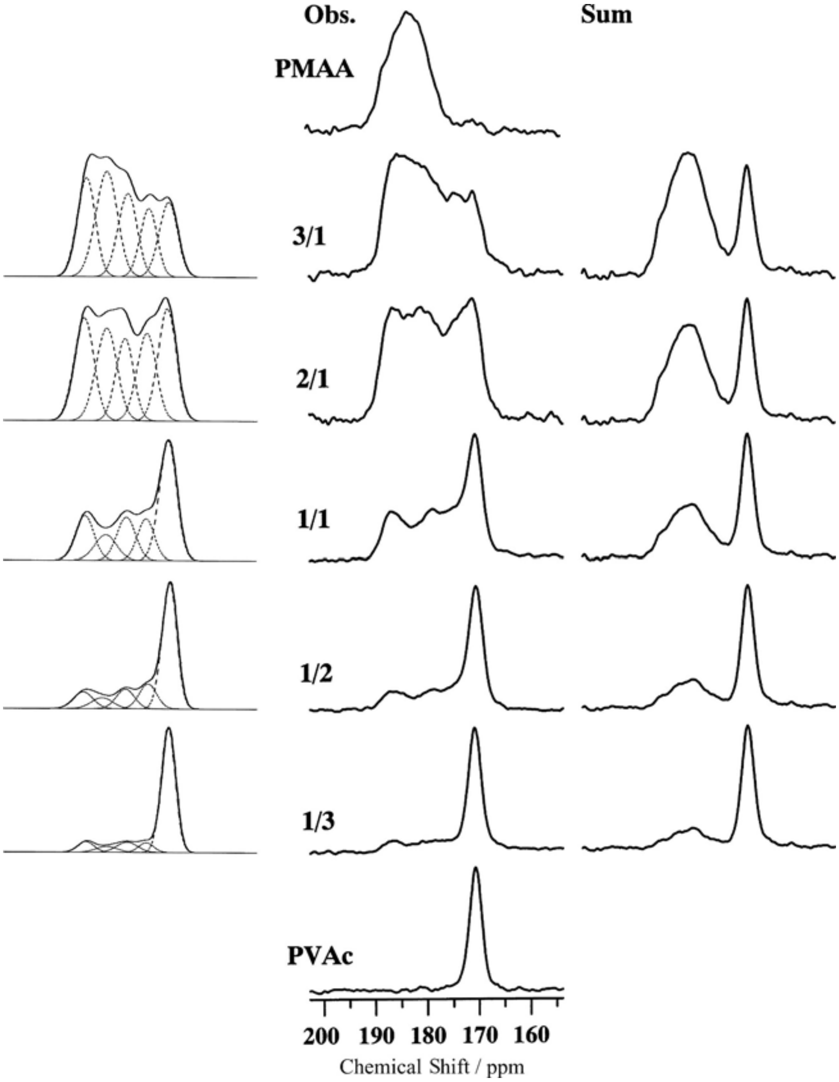

Fig. 1. Expanded observed CPMAS ^{13}C NMR spectra (center) and the decomposed simulated spectra using five Gaussian curves (the left hand) of the CO region in the PMAA/PVAc blends: a broken line depicts each decomposed peak and a solid line is the sum of those broken lines. Sum of the ^{13}C NMR spectra of pure PMAA and pure PVAc at the respective molar unit ratio is also drawn on the right hand of the observed spectra.

molecular motion [1]. The change of molecular motion is revealed from ^{13}C spin–lattice relaxation [7], 2D exchange NMR [8], deuterium NMR [8,9], and ^{13}C lineshape experiments [10,11].

Similarly, the domain size from 10 to 100 nm is revealed through ^{1}H or ^{13}C spin-diffusion phenomena [12,13]. The ^{1}H spin diffusion largely affects the ^{1}H relaxation rate in the homogeneous blends, thus the observation of ^{1}H relaxation reveals the domain size, namely miscibility.

Miscibility

Two kinds of domain sizes are easily detected through both ^{1}H spin–lattice relaxation times in the laboratory

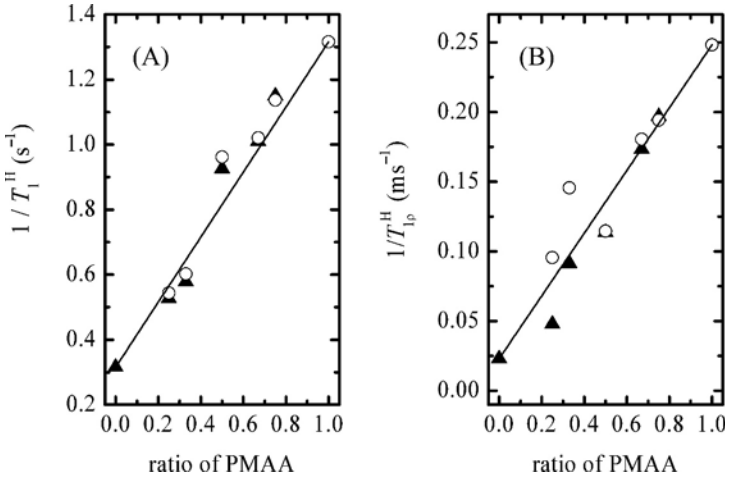

Fig. 2. Observed $1/T_1^{\mathrm{H}}$ (A) and $1/T_{1\rho}^{\mathrm{H}}$ (B) values, namely the ^{1}H relaxation rates, against the ^{1}H molar unit ratio of PMAA/PVAc blends: ○ CH_2 carbon of PMAA, ∫▲ OCH carbon of PVAc, and each solid straight line represents the calculated one from Equation (1). Every error bar for each data point is covered with the symbols itself. In this case, PMAA weight ratio of the blends is equivalent to that of ^{1}H mole fraction because both unit weight and number of protons in a unit structure of PMAA [–($CH_2CCH_3(COOH)$)–] are the same as those of PVAc [–($CH_2CH(OCOCH_3)$)–].

(T_1^{H}) and the rotating frames ($T_{1\rho}^{\mathrm{H}}$) [1]. In the solid state, the fast ^{1}H spin diffusion averages various spin temperatures of almost all protons in a polymer. As a result each ^{1}H relaxation time obtained from the every well-resolved ^{13}C peaks has the identical value. A similar criterion holds on a homogeneous polymer blend. The fast ^{1}H spin diffusion among component polymers causes to equalize the distinct ^{1}H relaxation times of components. On the other hand, in a heterogeneous blend, each individual ^{1}H relaxation time of component polymers is not fully averaged because the large domain size does not allow to average entirely the individual ^{1}H spin temperature; the intrinsic ^{1}H spin-diffusion rate is the same as that in the homogeneous phases, when the domain size is larger than the maximum diffusive path length, in such a case, the apparent ^{1}H spin-diffusion rate (cross-relaxation rate) becomes slow. On the other hand, even in a homogeneous polymer blend, there is a case that the intrinsic ^{1}H spin-diffusion rate becomes slower. In general, such a case is called as a motional heterogeneity: the miscible PS/PVME blend is a typical case [14].

Figure 2A shows that both original T_1^{H} rates of pure PMAA and pure PVAc are averaged to the values depended on the compositions in the blend. All the obtained T_1^{H} rates of PMAA in the blends are in excellent agreement with those of PVAc. This indicates that the complete averaging of the T_1^{H} rates by ^{1}H spin diffusion occurs, suggesting that PMAA and PVAc are in close proximity with each other and the PMAA/PVAc blend is homogeneous on a scale of 20–50 nm for all compositions. Similarly, Figure 2B shows that the observed $T_{1\rho}^{\mathrm{H}}$ rates of PMAA in the PMAA-rich/PVAc blends, which are the PMAA/PVAc $= 3/1$, $2/1$, and $1/1$ blends, are fully consistent with those of PVAc. For the PMAA-poor (PMAA/PVAc-rich) blends, which are the PMAA/PVAc $= 1/2$ and $1/3$ blends, however, the $T_{1\rho}^{\mathrm{H}}$ rates of PMAA are different from those of PVAc, although both rates of PMAA and PVAc change together and become close. This indicates that the partially averaging of $T_{1\rho}^{\mathrm{H}}$ rates by ^{1}H spin diffusion occurs in the PMAA/PVAc-rich blends. These results show that the PMAA-rich/PVAc blends are homogeneous on a scale of 2–5 nm as well as 20–50 nm, but the PMAA/PVAc-rich blends are inhomogeneous on the scale. The PMAA/PVAc-rich blends are probably homogeneous on a 5–10 nm scale, because the $T_{1\rho}^{\mathrm{H}}$ rates are affected largely by ^{1}H spin diffusion.

If the ^{1}H spin diffusion among the component polymers is fast sufficiently and the change of molecular motion by blending is negligible, the apparent relaxation rate $K_{\mathrm{ave}}(= 1/T_{1\mathrm{ave}})$ is given as a ^{1}H mole weighted average of the original rates of pure component polymers, K_{X} and K_{Y} as

$$K_{\mathrm{ave}} = f_{\mathrm{X}} K_{\mathrm{X}} + (1 - f_{\mathrm{X}}) K_{\mathrm{Y}}, \tag{1}$$

where f_{X} is ^{1}H mole fraction of polymer X in a polymer blend X/Y. The solid straight lines in Figure 2A and B represent the calculated values using the above Equation (1).

The observed T_1^{H} rates are in good agreement with the calculated ones. Similarly, the observed $T_{1\rho}^{\mathrm{H}}$ rates for PMAA-rich blends are consistent with the calculated ones. These agreements indicate that the molecular motions of both polymers in the blends are not changed drastically with each other comparing with those before mixing, and the very fast ^{1}H spin diffusion is occurred in the blends.

The partially miscible state and the motional heterogeneity of polymer blends can be investigated by analyzing the ^{1}H relaxation decay curves. When the apparent ^{1}H spin-diffusion rate (k_c) is comparable to the $1/T_1$, the T_1 decay curves deviate from a single exponential. The estimate ^{1}H spin-diffusion rate directly reveals the maximum average diffusive domain size (x) from the equation of $x^2 = 6D/k_c$ if the ^{1}H spin-diffusion constant (D) is known [1,15,16]. Similar ^{1}H relaxation decay curves are also observed in a case of the motional heterogeneity [14,17]. However, the non-exponential decay curves only appear when the experimental temperature is higher than T_g. The T_1 measurements at lower than T_g give a single-exponential decay for both polymers X and Y. This is the remarkable feature of the motional heterogeneity. In most miscible blends, the k_c is extremely fast and the ^{1}H relaxation curves become identical, even though the blends are partially homogeneous. The identical and single-exponential decay for both polymers X and Y is realized when the value of k_c is 10–100 times faster than the fastest $1/T_1$ in the polymer blend X/Y [14].

Phase Separation Process

Homogeneous phase of a polymer blend for an LCST phase diagram is not thermodynamically much stable and easily collapsed, when the temperature is beyond the binodal point; this region is thermodynamically unstable. The homogeneous phase becomes heterogeneous and the transparent film, in general, changes into opaque. The concentration change during the spinodal decomposition at the initial stage was expressed by analyzing the ^{1}H spin–lattice relaxation [14,18].

Figure 3 shows a graphically illustrated model of a phase separation: the homogeneous polymer blend X/Y is phase-separated into the X-rich and the Y-rich domains after heat treatment. This model represents that the fast ^{1}H spin diffusion occurs within each domain in the phase-separated blend, that is, each X-rich and Y-rich domain is homogeneously mixed from the ^{1}H spin diffusion point of view, while there is no effective ^{1}H spin diffusion between the X-rich and Y-rich domains. This is because the distance between the X-rich and Y-rich domains becomes over 5 nm for $T_{1\rho}^{\mathrm{H}}$ or 50 nm for T_1^{H}: each homogeneous domain size is larger than 5 or 50 nm. Each domain has an individual ^{1}H spin–lattice relaxation time; the T_1 value of polymer Y in the X-rich domain is the same as that of polymer X, $T_{1\mathrm{X}}$. Similarly the T_1 value of those in the Y-rich domain is $T_{1\mathrm{Y}}$. According to this assumption, it is obvious that the relaxation curve observed from polymer X or Y shows a double-exponential decay [14,18]. The expected relaxation curves are

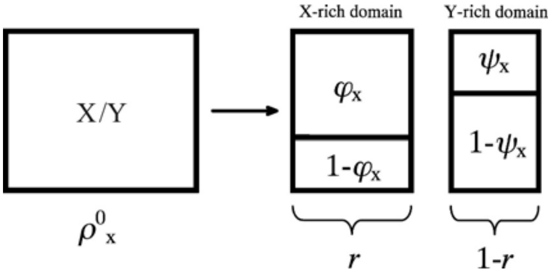

Fig. 3. Schematic illustration of phase separation model at the initial stage. A single homogeneous phase of a miscible polymer blend X/Y is phase-separated into two phases with which have the compositions of φ_{X} and ψ_{X}: the initial X fraction in the X/Y blend is represented by the symbol ρ_x^0. The symbol r shows the fraction of the X-rich domain.

$$M_{\mathrm{X}} = \xi_{\mathrm{X}} \exp(-t/T_{1\mathrm{X}}) + (1-\xi_{\mathrm{X}}) \exp(-t/T_{1\mathrm{Y}}) \qquad (2a)$$

$$M_{\mathrm{Y}} = \xi_{\mathrm{Y}} \exp(-t/T_{1\mathrm{X}}) + (1-\xi_{\mathrm{Y}}) \exp(-t/T_{1\mathrm{Y}}). \qquad (2b)$$

Here, M_{X} and M_{Y} represent the magnetization: in the case of the inversion–recovery method, M_{X} equals to $\left\{M_{\mathrm{Z}}^0 - M_{\mathrm{X}}(t)\right\}/2M_{\mathrm{Z}}^0$ and to $M_{\mathrm{X}}(t)/M_{\mathrm{Z}}^0$ in the case of the ^{1}H spin-locking experiment, M_{Z}^0 is the equilibrium magnetization. The parameters ξ_{X} and ξ_{Y} are ^{1}H mole fractions of polymer X and Y of whole blend, respectively; $\xi_{\mathrm{X}} = \varphi_{\mathrm{X}} r/\{\varphi_{\mathrm{X}} r + \psi_{\mathrm{X}}(1-r)\}$ and $\xi_{\mathrm{Y}} = (1-\varphi_{\mathrm{X}})r/\{(1-\varphi_{\mathrm{X}})r + (1-\psi_{\mathrm{X}})(1-r)\}$, respectively, with $\varphi_{\mathrm{X}} r + \psi_{\mathrm{X}}(1-r) = \rho_x^0$: φ_{X} and ψ_{X} are concentration of each domain. Thus, the stoichiometry φ_{X} and ψ_{X} of the two separated phases and r, which is the fraction of the X-rich domain, are easily deduced from the fractions of Equations (2a) and (2b). The φ_{X} or ψ_{X} are any of ^{1}H mole/weight/volume fractions. They are depended on how one determines the ρ_x^0 value.

Figure 4 shows the observed $T_{1\rho}^{\mathrm{H}}$ decay curves of the PS/PVME = 1/1 blend ($\rho_x^0 = 0.5$), which is quickly cooled in liquid nitrogen to quench the phase separation progress after heating at 413 K for 2 min [14]. The $T_{1\rho}^{\mathrm{H}}$ decay curves are measured at 263 K to freeze the molecular motion of PVME and let the ^{1}H spin diffusion work effectively. Before heat treatment, both observed $T_{1\rho}^{\mathrm{H}}$ decays obtained from PS and PVME signals show the same single-exponential curve. With increasing the heat-treatment time, they deviate from a single exponential to show the double-exponential behavior. The solid lines in Figure 4 are the "best-fit" curves obtained from Equations (2a) and (2b). The adjusted values for ξ_{X} and ξ_{Y} are 0.20 ± 0.03 and 0.81 ± 0.05, respectively, and $T_{1\mathrm{X}}$ and $T_{1\mathrm{Y}}$ are 3.1 ± 0.2 and 15.3 ± 0.6 ms. The estimated values for φ_{X}, ψ_{X}, and r are 0.20 ± 0.03, 0.81 ± 0.06, and 0.51 ± 0.04, respectively. The experiment with changing the heat-treatment time showed that the heating time-dependent fluctuation in concentration occurs

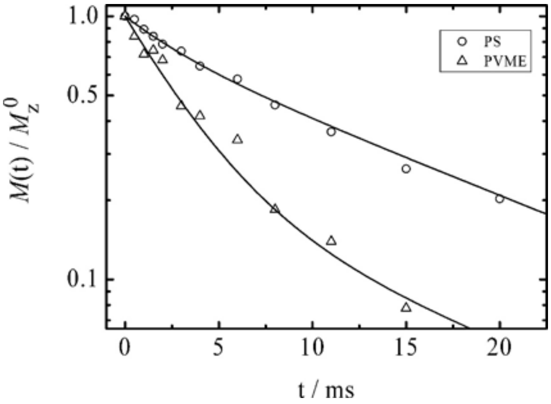

Fig. 4. Observed $T_{1\rho}^{\mathrm{H}}$ decay curves for PS (|) and PVME (∫) in the phase-separated PS/PVME = 1/1 blend after 2 min of heating at 413 K. These decay curves were measured at 263 K. The solid lines are the "best-fit" curves from Equations (2a) and (2b) with the parameters of $\xi_X = 0.20 \pm 0.03$, $\xi_Y = 0.81 \pm 0.05$, $T_{1X} = 3.1 \pm 0.2$ ms, and $T_{1Y} = 15.3 \pm 0.6$ ms.

and further heating over 30 min does not cause appreciable changes to the $T_{1\rho}^{\mathrm{H}}$ curves. This indicates that the initial stage of phase separation, that is the concentration change, finished and the morphological change occurs on a larger scale that is not reflected in T_1. The growth of domain size at the late stage of the phase separation of the PS/PVME blend has been revealed from the 2D exchange ^{129}Xe NMR [19]. The 2D exchange ^{129}Xe NMR showed that the cross-peaks observed after heating 30 min do not appear after 1200 min. The estimated average domain size is over 5000 nm at least.

Conclusion Remarks

The numerous great pioneering NMR works for polymer blends are omitted. We know the novel NMR techniques are applying to reveal the conformational change [20] and domain structure [21] and a lot of successful works can be found in any publications. The reader's attention is also drawn to the other reviews summarizing the miscibility or the molecular motion for polymer blends [1,22–24].

References

1. Asano A, Takegoshi K. Solid state NMR of polymers (Chapter 10). In: I Ando, T Asakura (Eds). Polymer Blends and Miscibility. Elsevier Science B.V.: The Netherlands, 1998, p 351.
2. Asano A, Eguchi M, Shimizu M, Kurotsu T. Macromolecules. 2002;35:8819.
3. Asano A. Polym. J. 2004;36:23.
4. Heffner SA, Mirau PA. Macromolecules. 1994;27:7283.
5. White JL, Mirau PA. Macromolecules. 1993;26:3049.
6. Mirau PA, White JL. Magn. Reson. Chem. 1994;32:S23.
7. Feng H, Feng Z, Ruan H, Shen L. Macromolecules. 1992;25:5981.
8. Wolak J, Jia X, Gracz H, Stejskal EO, White JL, Wachowicz M, Jurga S. Macromolecules. 2003;36:4844.
9. Ngai KL, Roland CM. Macromolecules. 2004;37:2817.
10. Takegoshi K, Hikichi K. J. Chem. Phys. 1991;94:3200.
11. Menestrel CLe, Kenwright AM, Sergot P, Lauprêtre F, Monnerie L. Macromolecules. 1992;25:3020.
12. VanderHart DL, Feng Y, Han CC, Weiss RA. Macromolecules. 2000;33:2206.
13. Linder M, Henrichs PM, Hewitt JM, Massa DJ. J. Chem. Phys. 1985;82:1585.
14. Asano A, Takegoshi K, Hikichi K. Polymer. 1994;35:5630.
15. Stejskal EO, Schaefer J, Sefcik MD, Mckay RA. Macromolecules. 1981;14:275.
16. Asano A, Kurotu T. J. Mol. Struct. 1998;441:129.
17. Miyoshi T, Takegoshi K, Hikichi K. Polymer. 1996;37:11.
18. Asano A, Takegoshi K, Hikichi K. Polym. J. 1992;24:555.
19. Miyoshi T, Takegoshi K, Terao T. Polymer. 1997;38:5475.
20. Harris DJ, Bonagamba TJ, Schmidt-Rohr K. Macromolecules. 2002;35:5724.
21. White JL, Brant P. Macromolecules. 1998;31:5424.
22. Clauss J, Schmidt-Rohr K, Spiess HW. Acta Polym. 1993;44:1.
23. Takegoshi K. Annu. Rep. NMR Spectrosc. 1995;30:97.
24. Guo M. Trends Polym. Sci. 1996;4:238.

Configurational Entropy and Polymer Miscibility: New Experimental Insights From Solid-State NMR

Jeffery L. White*
North Carolina State University, Raleigh, NC 27695, USA

Abstract

Entropy is generally discounted as a driving force for macromolecular mixing, due to the vanishing combinatorial component in the Flory–Huggins treatment. However, recent chain-level investigations in blends of high molecular weight polyolefins suggest that configurational entropy must be considered, particularly for amorphous macromolecules lacking any chemical functionality. Multinuclear one- and two-dimensional solid-state NMR techniques were used to interrogate the dynamics and mixing length scales in blends containing polyisobutylene and either head-to-head polypropylene or polyethylene-co-butene. These polymer systems have no chemical heterogeneity that would facilitate miscibility through enthalpic contributions; experimental results prove that there is a quantifiable increase in configurational entropy. In addition, experimental evidence from polyolefin blends regarding the length-scale and time-scale of the polymer glass transition is discussed.

Introduction

Miscible polymer blends represent an important class of academic, technological, and commercial materials. An excellent recent reviews comprehensively addresses the subject of polymer blend miscibility [1]. However, in almost all of the published work on miscible macromolecules, the component polymers themselves contain chemically heterogeneous functional groups. For example, mixtures of polyacrylates and polyols (like polyvinylalcohol or polyvinylphenol) contain potential hydrogen bonding pairs, and therefore one would predict that an energetically favored miscible state would result due to a finite negative enthalpy of mixing [2]. Indeed, constituent polymers do not even have to contain polar atom substituents to be categorized as "functional" polymers. As an example, many miscible polymer mixtures containing olefinic or styrenic moieties are known to exist; even though the constituent atoms are all carbon or hydrogen, large electron density gradients exist within the macromolecule based on the differential amounts of sp, sp^2, and sp^3 carbons [3]. Consequently, their appreciable polarizability gives rise to induced dipole interactions that again drive mixing via an ethalpic contribution. Therefore, one might ask what happens when the constituent polymers are both chemically and electronically homogeneous, e.g. in completely saturated hydrocarbon polymers? Does one's intuition regarding enthalpic and entropic contributions to the overall free energy of mixing still serve as a useful guide?

Saturated hydrocarbon polymers, or polyolefins, are the most ubiquitous of polymer families. It is surprising that such architecturally simple/similar polymers, devoid of any functional groups, exhibit fairly complex phase behaviors. That polypropylene and polyethylene are immiscible at the chain level is by now well known; the reason why is still a controversial subject. The absence of polar functional groups in polyolefins essentially eliminates any significant enthalpic contributions to the free energy of mixing. Such "heats of mixing," typically represented by the enthalpic interaction term χ in Flory–Huggins theory, are commonly regarded as the driving force for miscibility. Dispersive forces via weak van der Waals interactions are possible, and may be significant for large molecular weight molecules. Entropic contributions to miscibility in polymer blends are usually discounted in the polymer blend literature, since molecular weights are large and Flory–Huggins theory scales entropy of mixing according to the inverse of the degree of polymerization. The question remains as to how mutual solubility in polyolefin blends depends on polymeric microstructure, tacticity, comonomer incorporation, and chain dynamics, and further, how each of these architectural and physical characteristics contributes to the interplay between enthalpy and entropy. Clearly, one would expect that the details of interchain packing and reorientation would be critically dependent on the aforementioned structural details. The current state of understanding in this area is nicely summarized by Graessley and coworkers [4]. In reviewing, the various data that supports enthalpy vs. entropy as driving forces, these authors note that several

---

[*] Current address: Department of Chemistry, Oklahoma State University, Stillwater, OK 74078

Graham A. Webb (ed.), Modern Magnetic Resonance, 637–644.
© 2008 *Springer.*

researchers have proposed either as controlling factors, and some theoretical work suggests any combination of these two thermodynamic variables could lead to the observed phase behaviors. Further, the authors state that uncertainty centers around the interpretation of solubility parameters from SANS data and the anomalous behavior of many blends whose mixing does not follow the theoretical expectations from solubility parameter formalisms. The authors suggest that the key experimental data for local monomeric scale interactions are not accessible, and therefore simulations have been used. In a companion paper, these same authors propose some tentative ideas surrounding packing effects in copolymers vs. homopolymers, and how this might contribute to blend mixing [5]. Our recent research has focused on obtaining direct experimental data that address these conceptual holes. Spiess and Schmidt-Rohr nicely summarize our motivation in this area in their text *Multidimensional Solid-State NMR of Polymers,* which states: "Miscibility is often attributed to favourable specific interactions between the polymer components. However, simple geometric effects, such as unfavourable packing in one of the pure components that causes the molecules to prefer the packing in the mixture, also must be considered. The elucidation of these factors, which are often not directly apparent from the chemical structures, is still at an early stage. Modern solid-state NMR methods promise to play a major role in this field" [6].

Our initial work has targeted binary polyolefin blends that contain polyisobutylene (PIB) as one component. We have selected this approach due to literature reports of the anomalous behavior (large negative interaction parameters) of blends containing PIB at the time we began the project [7–9]. The resulting experimental data were the first to provide molecular/chain level evidence indicating that configurational entropy is a driving force for miscibility in polyolefin blends [10–12]. While standard Flory–Huggins theories discount entropy as a contributing factor in macromolecular mixing, our results do not contradict this conventional wisdom, in that combinatorial entropy (Flory–Huggins) is distinct compared to configurational entropy. Traditional theories of macromolecular mixing simply do not treat the polymer at the local chain (monomeric) level, which is where our experimental efforts focus. Indeed, many theoretical studies have recognized that configurational entropy must be an important contributor to polymer phase behavior [13–16]. In addition, some experimental studies have addressed the local structure and dynamics of functional polymer blends in the context of calorimetric and spectroscopic data [17,18]. However, to our knowledge, our work is the first to use solid-state NMR to interrogate the details of mixing in amorphous polymers lacking chemical heterogeneity, i.e. polyolefins, and quantitatively relate the data to configurational entropy.

Experimental NMR Methods

Solid-state NMR has addressed multiple questions regarding miscibility in polymer blends in recent years; methods ranging from simple chemical shift resolution to advanced multiple pulse/multiple quantum detection are by now routinely accessible. However, Figure 1 shows that the lack of any type of resolution in the ^{1}H solid-state NMR spectra of polyolefin blends complicates analysis of mixing length scales, dynamics, and chemical interactions in such systems even when coherent averaging pulse sequences are used. In particular, non-destructive spin-diffusion techniques are attractive since isotopic labeling is not a requirement, and recent developments in the understanding of spin-diffusion data has increased the

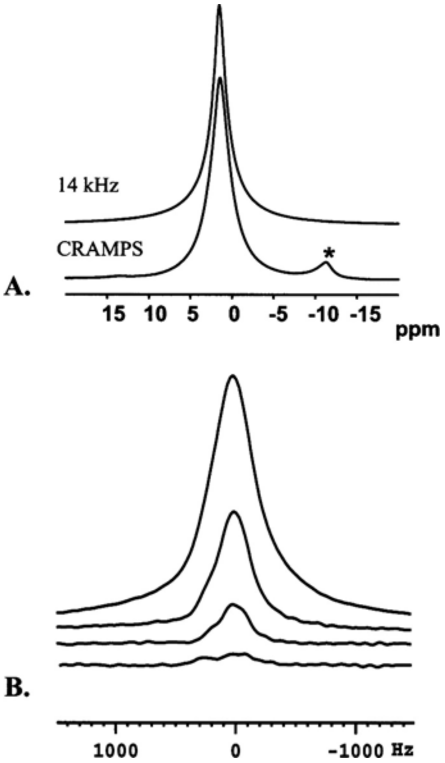

Fig. 1. (A) Comparison of ^{1}H CRAMPS experiment and fast magic-angle experiment on a 50:50 blend of PIB and hhPP, demonstrating the lack of resolved chemical shifts from either blend component using direct ^{1}H detection. (B) ^{1}H dipolar filter on PIB/PEB-66 blend at 23 °C as a function of the number of 12-pulse dipolar filter cycles, in which the interpulse spacing was 10 μs. From top to bottom, the number of filter cycles was 0, 10, 20, and 30, respectively.

quantitative accuracy of the method [19,20]. Figure 1A demonstrates the neither fast MAS nor CRAMPS [21] results in any chemical shift resolution of the aliphatic hydrogens in an amorphous polyolefin blend of PIB and head-to-head polypropylene (hhPP). Figure 1B shows ^{1}H MAS spectra obtained at 8 kHz for a PIB/PEB-66 (polyethylene-co-1-butene containing 66 wt% butene comonomer) blend, in which an additional dipolar filter sequence is applied prior to the read pulse in order to introduce spectral resolution based on gradients in the timescale of molecular motion in the two polymers [22]. Comparison of individual spectra in Figure 1B (in which the strength of the dipolar filter is increased in subsequent spectra) shows that this is not achieved experimentally, thereby eliminating the possibility of direct observation spin-diffusion methods. Results were identical for experiments without MAS, except that the line width was larger by a factor of 6–7. As one would expect, similar results were obtained for the higher-resolution ^{13}C-detected ^{1}H dipolar filter experiments, and Goldman–Shen techniques, thereby precluding the use of natural abundance spin-diffusion experiments as a quantitative tool for measuring length scales of mixing in these blends. Information regarding length scales of mixing in amorphous polymer blends is necessary to begin to determine governing thermodynamic parameters; Figure 1 and the preceding discussion show that tradition spin-diffusion methods often fail. We have found that a variety of experiments, ranging from those that probe dynamics on the timescales from seconds [two-dimensional (2D) exchange] to microseconds (relaxation and static ^{2}H NMR), as well as length scale measurements from angstroms to tens of nanometers (spin diffusion and Xe gas absorptions) are all required to obtain a consistent and thorough understanding of polyolefin phase behavior [10–12].

Choice of Polymer Blend System

Graessley and coworkers reported that the polyolefin blends which exhibited the largest net "attraction" or negative χ parameter were those prepared from PIB and hhPP, poly(ethylene-propylene), or polyethylene-co-butene (PEB) [7–9]. Such blends exhibited what the authors termed "irregular" mixing, in that the interaction parameter departs from description by a simple function of the difference in solubility parameters. The authors were not able to explain the origin of such a large interaction parameter for these anomalous miscible blends, but postulated it might arise from local packing constraints contributing to stronger "component pair" or intermonomeric interactions. In some cases, the mixing was found to be enhanced relative to that predicted from solubility parameters, while in others the mixing was reduced. Due to the anomalous behavior of these blends in which PIB was one component, and also considering the fact the PIB has a significantly higher bulk density than all amorphous polyolefins, we chose PIB-based blends as the our starting point for chain-level NMR studies. Space limitations will require that most of this chapter focuse on blends of PIB with PEB containing varying amounts of 1-butene comonomer in the PEB copolymer. These PEB copolymers will be denoted as PEB-XX, where XX represents the weight percent of butene comonomer, following the convention of Graessley and coworkers [7–9].

^{129}Xe NMR of Absorbed Xenon Gas

As stated above, traditional ^{1}H spin-diffusion techniques often fail for some polyolefin blends. While we successfully used spin diffusion to probe length scales of mixing in PIB/hhPP blends [23], they were not able to generate a polarization gradient in PIB/PEB-XX blends, as the differences in overall chain dynamics, and ^{1}H chemical shifts in the solid state, for PIB vs. PEB were too small. Even though polyolefin blends are chemically homogeneous, their differing densities and free volumes allow the highly polarizable Xe atomic nucleus to report on chain packing heterogeneity. Figure 2 demonstrates that

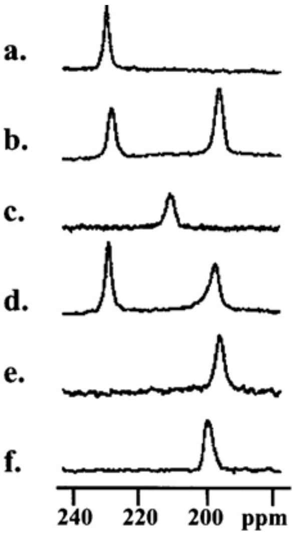

Fig. 2. Static ^{129}Xe NMR spectra for xenon gas absorbed in (a) pure PIB vs. blends with decreasing 1-butene comonomer amounts; (b) 50:50 PIB/PEB-97 blend; (c) 50:50 PIB/PEB-66 blend; (d) 50:50 PIB/PEB-23 blend; (e) pure PEB-97; and (f) pure isotactic poly-1-butene. The free xenon peak at 0 ppm is not shown for clarity, and lower sample masses were used in 2C and 2E.

simple one-pulse (static) Xe NMR experiments are remarkably sensitive to different polyolefin environments. In Figure 2, results are presented for ^{129}Xe chemical shift in pure PIB, pure poly-1-butene (P1B), and several blends. In contrast to all other blends of PIB with PEB or P1B, the PIB/PEB-66 blend (Figure 2c) shows only one resonance, indicating that the xenon molecule is diffusing in a homogenous molecular environment (as defined by the diffusion coefficient of xenon in that blend). For comparison, the PIB/PEB-23 blend shows two clearly resolved resonances (Figure 2d), corresponding very closely with the two pure component PIB and PEB-23 shifts. Here, xenon gas diffuses between two dissimilar surroundings, which match the two constituents, indicative of a much larger length scale of mixing, or domain size, relative to PIB/PEB-66 (vide infra). A similar microphase-separated result is obtained for a blend of PIB/PEB-97 (Figure 2b). Figures 2b–d reveal a compositional miscibility window in 1-butene concentration for blends of PEB with PIB. The data in Figure 2, coupled with quantitative pulsed-field gradient NMR to measure the Xe diffusion coefficient in pure PIB vs. PIB/PEB blends (not shown here; see Ref. [12]), reveals quantitative upper limits on the length scale of mixing for the PIB/PEB-66 sample (single resonance in Figure 2c) at <70 nm. Consequently, all other PIB/PEB blends which exhibit two peaks in Figure 2 must be phase separated with average dimensions of the individual polymer-rich regions >70 nm. Armed with this length scale of mixing information, one can now use solid-state NMR methods to compare local chain dynamics at or near the glass-transition temperature for the PIB/PEB-66 blend vs. the other blend compositions, which are phase separated on the length scale defined by Figure 2 and the Xe PFG NMR data.

Two-Dimensional Exchange NMR to Probe Slow-Chain Reorientation

Figure 3 demonstrates the relationship between DSC measurements and 2D ^{13}C exchange NMR for pure PIB. This experiment, in addition to serving as the control experiment for comparisons to PIB/PEB blends, pedagogically illustrates the conformational dynamics associated with slow-chain reorientations at and above T_g. Figures 3 and 4 show the expanded region of the PIB CH_2 backbone carbon, which becomes sensitive to the distribution of conformer environments below ca. 235 K (see Ref. [10] for full spectral plots vs. temperature). The broad peak reflects the distribution of CH_2 groups for chain segments in trans–trans (tt), trans–gauche (tg), or gauche–gauche (gg) conformations along the polymer backbone. Little or no exchange is observed for a 1-s mix time (or less) at 203 or 208 K, as indicated by the lack of any off-diagonal intensity. However, for longer mixing times, exchange events are observed between the individual tt, tg, and gg peaks, as shown by the increased off-diagonal intensity at the 2- and 4-s mixing times. Examination of the ratio of an individual peak width perpendicular to the diagonal, vs. parallel to the diagonal, shows that conformer exchange is essentially complete after 4 s at 208 K (see Figure 3f). While the amount of conformational exchange is clearly reduced in Figure 3a–c vs. 3d–f, chain segment dynamics are observed at both temperatures for the 2- and 4-s mixing times.

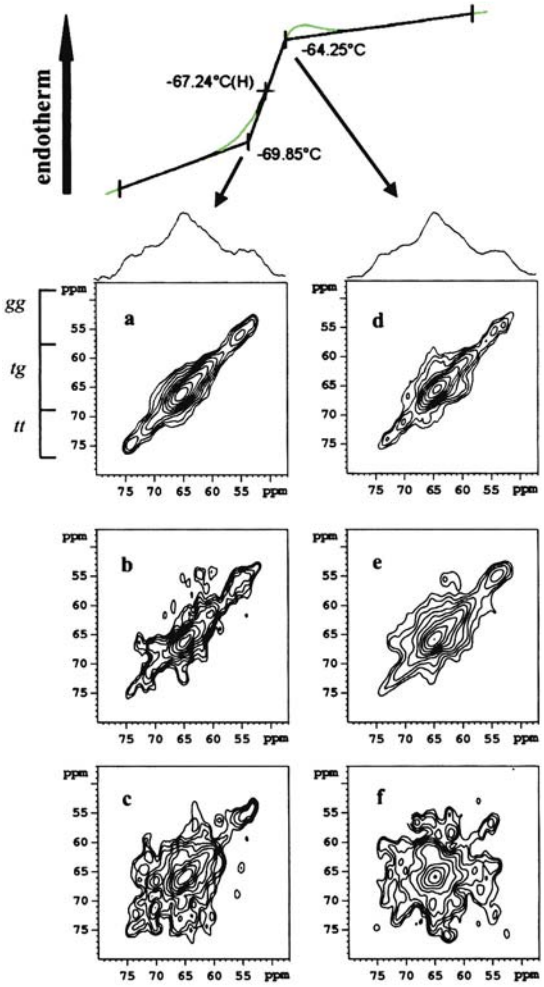

Fig. 3. Comparison of DSC T_g trace obtained with a 2 K/min scan rate (top) with 2D ^{13}C exchange spectra at (a) 203 K and 1-s mix time; (b) same as (A) at 2 s mix; (c) same as (a) at 4 s mix; (d) 208 K at 1-s mix time; (e) same as (d) at 2 s mix; and (f) same as (d) at 4 s mix. Spinning speeds were 4 kHz.

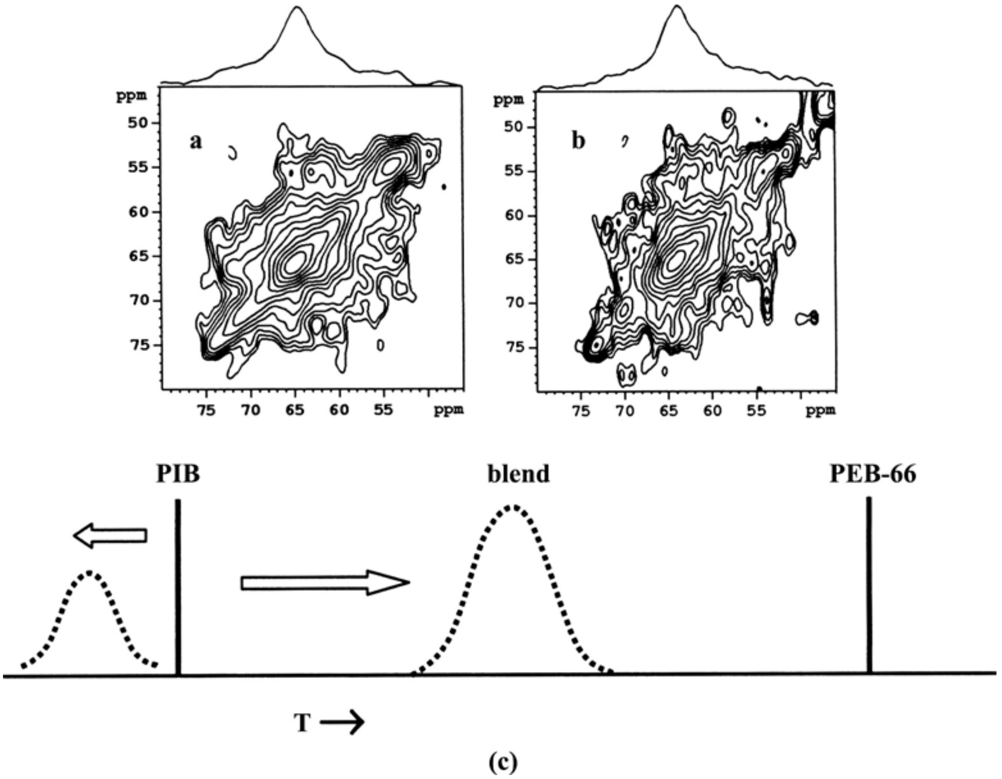

Fig. 4. 2D exchange spectrum at 208 K of (a) methylene carbons in pure PIB with a 2 s mixing time; (b) methylene carbons of PIB in a 50:50 blend with PEB using a 100 ms mixing time. Slices through the 65-ppm trans–gauche peak are shown on the top axis, and within the signal-to-noise limits, exhibit the same features; (c) Schematic diagram demonstrating differences in local (NMR, indicated by short gray arrow) vs. averaged (DSC, denoted by long gray arrow) T_g information for the blend components, and PIB in particular.

The site-specific dynamics revealed by the 2D exchange experiment can indicate changes in local glass-transition temperature/timescale upon formation of a miscible polymer blend. Figure 4a and 4b show results obtained at 208 K for a pure PIB sample and a 50:50 wt% blend of PIB and PEB, respectively. The PEB contained 66 wt% 1-butene units randomly incorporated into the chain; the sample in Figure 4b is the same PIB/PEB-66 blend sample used in Figure 2c. The 2D exchange patterns appear almost identical in terms of their off-diagonal intensity distribution, as confirmed by taking a slice through the tg peak at 63 ppm in each. This slice is shown as the top trace on each contour plot. However, while the PIB exchange pattern required a 2-s mixing time to achieve the off-diagonal signal in Figure 4a, the PIB/PEB-66 blend pattern in Figure 4b was obtained after *only 100 ms*. Additional experiments (not shown) for PIB blended with PEB-23 did not show this dramatic decrease in exchange time; the PIB/PEB-66 blend 2D exchange results were essentially identical to those of pure PIB in that several seconds were required to achieve measurable off-diagonal intensities. A major question in the study of polyolefin blend miscibility is the identification of the thermodynamic driving force for mixing, and in this case, PIB/PEB blends have been shown to be miscible for the PEB-66 composition used here [7–10]. The results of Figures 3 and 4 suggest that the rate of conformational dynamics of the PIB chains in the blend with PEB-66 are enhanced, or stated differently, the PIB "local T_g" is depressed in this blend, but not for other PEB compositions.

At this point, some key pieces of information should be provided for clarification. Firstly, the T_g's as measured by DSC for pure PIB and PEB-66 are −68 and −52 °C, respectively. By DSC, the PIB/PEB-66 blend has a broad, weak transition at −60 °C. Therefore, it is surprising that the conformational dynamics of PIB chains in the blend with the higher T_g PEB are enhanced, instead of being retarded. Secondly, the PEB-66 polymer also exhibits a conformationally sensitive signal in the ^{13}C NMR spectrum (see Ref. [10]); the CH_3 signal from the ethyl branch in PEB splits into inequivalent peaks at temperatures below ca. 235 K. In marked contrast to the PIB CH_2 backbone signal, no changes in the temperature dependence of the line shape were observed for the PEB-66 CH_3 peaks upon blending, nor were any differences in the low-temperature 2D exchange spectra observed for conformational dynamics involving this side group detected in control experiments comparing pure PEB-66 with PEB-66 in the PIB blend. In other words, while the PIB chain dynamics were markedly accelerated in forming the blend with PEB-66, no detectable perturbation of the PEB dynamics was observed in the frequency range 0.25–1 Hz (2D exchange) or in the range 500–1000 Hz [^{13}C one-dimension (1D) line shape analysis]. Moreover, it is unlikely that the PEB-66 dynamics are actually depressed upon blend formation, i.e. this polymer does not become more rigid when blended with the lower-T_g PIB. Figure 4c schematically represents the difference in local (NMR) vs. bulk (DSC) data.

The reduced exchange time (a kinetic quantity) of the PIB chains in the PIB/PEB blend (from Figure 4) may be related to the increased configurational entropy S_c (a thermodynamic quantity) using Adams–Gibbs theory [24,25], one form of which is shown below:

$$\tau_{ex} = \tau_0 \exp(c/TS_c)$$

Here, τ_{ex} is the exchange time for the redistribution of a single conformer's magnetization among all possible conformers, as measured by the 2D slices shown in Figure 4. This exchange time is analogs to a structural relaxation time, and represents the extent of conformational relaxation along the chain. Using the data from Figure 4, in which $\tau_{ex} = 2$ s and 100 ms for pure PIB and PIB in the PIB/PEB blend, respectively, we can solve for the *configurational entropy ratio* $S_{Blend}{:}S_{Pure}$. In this way, the constants τ_0 and c, and the temperature T, cancel from the equation. The resulting $S_{Blend}{:}S_{Pure} \geq 3.33$, indicating that the PIB chains in the blend with PEB have a much larger configurational entropy, and therefore, more accessible conformations per unit time, than pure PIB. Similar results were obtained by comparing equivalent 2D slices for PIB and PIB/PEB at 4- and 1.5-s mix times, respectively, at the same temperature as Figure 4. While this data are not shown for brevity, a similar $S_{Blend}{:}S_{Pure} \geq 3.4$ result was obtained. In fact, no matter which mixing time we choose from several different experiments, this ratio always exceeds three. These results suggest that entropy drives miscibility in this particular polyolefin blend, and the ability to place quantitative limits on key thermodynamic parameters should prove critical to a complete understanding of the heretofore-anomalous results in the area of polyolefin miscibility. Further, Adams–Gibbs theory requires that this increased entropy in the blend corresponds to smaller-sized cooperatively rearranging regions at a given temperature, i.e. a shorter T_g length scale [26]. Local motions become dominant in this regime, and the 2D exchange is clearly sensitive to these subtle changes. An alternative experimental strategy is to match the necessary equivalent 2D exchange patterns vs. T, thereby obtaining thermally activated configurational entropy changes in any amorphous polymer for which conformationally inequivalent signals are present.

^{2}H NMR Data and Simulations

The 2D ^{13}C exchange data shown in Figures 3 and 4 are only a small sampling of the total data collected.

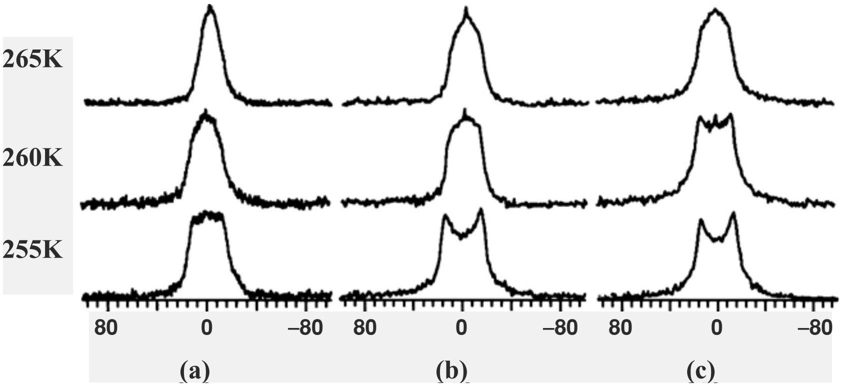

Fig. 5. Comparison of static ^{2}H NMR spectra over the NMR T_g range for 20%-PIB-d_8 chains in (a) a blend with PEB-66; (b) a blend with PEB-23; and (c) bulk, i.e. pure 20%-PIB-d_8. Note the difference in the spectral coalescence points in both (a) and (b), relative to (c), which is even more clear by comparing the line shapes across the second row.

Unfortunately, natural abundance exchange experiments are time consuming (10–20 h), which can be problematic for low-temperature MAS data collection. For the PIB/PEB blends, the 2D exchange data are consistent with both 1D line shape analyses and the Xe NMR data. However, static ^{2}H NMR is attractive as it allows site-specific information, and line shape simulation is straightforward. While the conclusions from the 2D data are undeniable, additional confirmation of the results using static ^{2}H techniques for the PIB/PEB system is useful. To this end, ^{2}H NMR data ***were obtained for pure PIB and its blends with PIB-23 and PEB-66 over the temperature range 210–298 K. Isotope effects on phase separation are known to occur for polyolefin blends. We avoid this possibility by using PIB containing only 15–20% of perdeuterated monomer for making the blends. According to our results from the Xe and 2D ^{13}C data, we should expect the largest perturbation in the temperature dependent ^{2}H line shapes for PIB in the PEB-66 blend. A small subset of the total data, shown in Figure 5, confirms this expectation. Figure 5 illustrates the unique line shape coalescence point for the three samples vs. temperature. The pure 20%-PIB-d_8 sample coalesces at 265 K (Figure 5c), while PIB/PEB-66 (Figure 5a) and PIB/PEB-23 (Figure 5b) coalesce at 255 and 260 K, respectively. The variations in CD_3 line shape for the PIB chains in the respective samples reflect the different frequencies of PIB chain reorientation in each environment. The Pake pattern for the PIB/PEB-66 blend exhibits an NMR glass transition at 255 K while PIB/PEB-23 blend does so at 260 K. Clearly, the PIB chain motional frequencies are perturbed more in the PIB/PEB-66 blend (containing 49 mol% butene) than in the PIB/PEB-23 blend (containing 13% butene). Further inspection of the line width and line shape at 265 K, the pure 20%-PIB-d_8 coalescence temperature, indicates that the PIB/PEB-66 line shape is already much more averaged than that of PIB/PEB-23. Clearly, PIB chains in both blends exhibit increased conformational mobility relative to the bulk PIB, as a result changing the particular line shape coalescence points of PIB/PEB-23 and PIB/PEB-66 by -5° and -8°, respectively. We were particularly surprised to see the -5 K shift for the PIB/PEB-23 blend, since the DSC thermogram shows two distinct, well-resolved T_g's (not shown).

Line shape simulations for the three samples, over the entire temperature range, were obtained using Weblab [27], and employing a four-site jump model. Excellent agreement was obtained, particularly around the line shape coalescence points shown in Figure 5 [12]. The Arrhenius plot shown in Figure 6 was constructed from these simulations of the conformational jump model. All three samples (PIB, PIB/PEB-66, and PIB/PEB-23) were accurately simulated using the four-jump model, which demonstrates that the PIB chain dynamics are the same in all samples. The only difference is that the motional frequency is increased at any temperature in the blends relative to the pure 20%-PIB-d_8. As mentioned before, the conformational dynamics of PIB are perturbed in the PIB/PEB-66 blend more than those in PIB/PEB-23, or in other words, the effective NMR T_g is reduced further. Figure 6a shows the reorientation rate obtained from the four-site jump model as a function of temperature for the pure 20%-PIB-d_8, 20%-PIB-d_8/PEB-23, and 20%-PIB-d_8/PEB-66. The slopes of the three systems indicate an isomerization activation energy equal to 36 kJ/mol. Additonally, the graph signifies intermediate

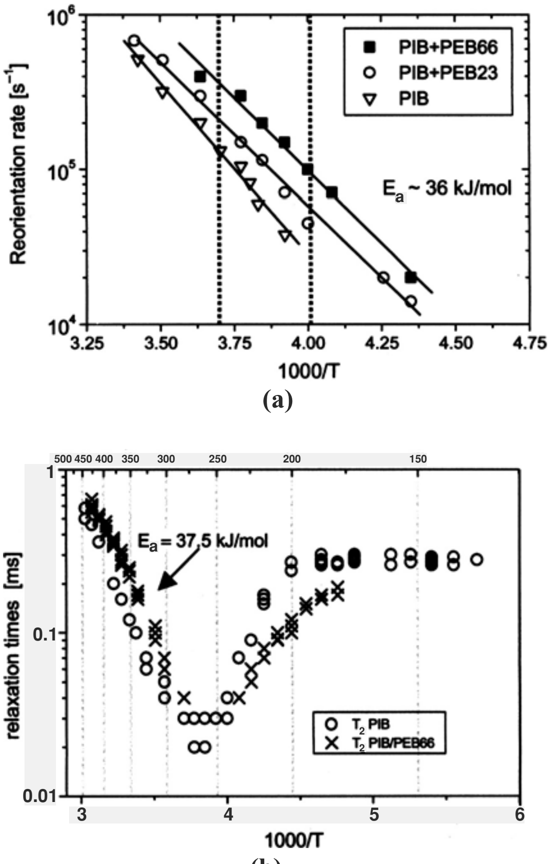

(a)

(b)

Fig. 6. (a) Arrhenius plot of chain reorientation rates obtained via simulation of the experimental static ^{2}H line shapes using the four-site model described in the text for 20%-PIB-d_8 chains in each of the indicated environments. The dotted lines indicate the region near line shape collapse. (b) Relaxation rate data vs. temperature for ^{2}H T_2 experiments. Note that the same activation energy is obtained via line shape simulation (a) and in the linear region of the T_2 curve (b).

behavior for the PIB/PEB-23 blend relative to the pure 20%-PIB-d_8 and the PIB/PEB-66. The activation energy obtained from the line shape simulations can be compared with the model-free relaxation experiments, e.g. T_2^{QE} as a function of temperature. From the graph in Figure 6b, the right and upward shift in the T_2^{QE} upon blending PIB with PEB-66 is evident, at the same time also revealing an activation energy equal to 37.5 kJ/mol. The direct link between the simulated and experimental data are clearly demonstrated by the matching activation energies acquired by two different methods, one of which is independent of any assumptions or physical jump model.

Conclusions

We have used a multifaceted experimental solid-state NMR approach to reveal that configurational entropy contributes to mixing in weakly interacting polyolefin blends composed of PIB and PEB. Many different independent NMR experiments provide a consistent picture of enhanced chain dynamics for the higher density, lower T_g PIB when it was blended with the higher T_g PEB-66. Additional blend systems are currently being investigated using higher chemical shift resolution exchange experiments, such as the recently reported CODEX technique [28]. While the PIB/PEB blends were easily interrogated with 2D exchange due the well-resolved PIB CH_2 signal, other polyolefin blends, e.g. PP/PE blends, often have too much signal overlap to use the 2D exchange method. PIB is unique due to its high chain packing density; it is not altogether unexpected that configurational entropy is important in its blend formation with other polyolefins. Clearly, we have shown that its miscibility with PEB-66 is not due to increased van der Waals forces resulting from increasing monomeric packing in three dimensions. However, until we obtain data on a wide series of structurally unique polyolefin pairs not just those involving PIB as one component, the general applicability of this concept to all polyolefin blends is still an open question. To this end, we have used similar solid-state NMR techniques, and others, to recently demonstrate that configurational entropy increases in the blend of head-to-head polypropylene (hhPP) with PIB relative to the unmixed pure polymers [29].

References

1. Paul DR, Bucknall CB. Polymer Blends. John Wiley and Sons: New York, 2000.
2. Coleman MM, Pehlert GJ, Painter PC. Macromolecules. 1996;29:6820.
3. Heffner SA, Mirau PA. Macromolecules. 1994;27: 7283.
4. Maranas JK, Mondello M, Grest GS, Kumar SK, Debenedetti PG, Graessley WW. Macromolecules. 1998;31:6991.
5. Maranas JK, Mondello M, Grest GS, Kumar SK, Debenedetti PG, Graessley WW. Macromolecules. 1998;31:6998.
6. Schmidt-Rohr K, Spiess HW. Multidimensional Solid-State NMR of Polymers. Academic Press: London, 1994, p 176.
7. Krishnamoorti R, Graessley WW, Fetter LJ, Lohse DJ, Garner RT. Macromolecules. 1995;28:1252.
8. Krishnamoorti R, Graessley WW, Fetter LJ, Lohse DJ, Dee GT, Walsh DJ. Macromolecules. 1996;29:367.
9. Krishnamoorti R, Graessley WW, Fetter LJ, Lohse DJ, Balsara N, Reichert GC. Macromolecules. 1995;28:1260.
10. Wolak J, Jia X, Gracz H, Stejskal EO, Jurga S, White JL. Macromolecules. 2003;36:4844.
11. Wolak J, Gracz H, Stejskal EO, Jurga S, White JL. J. Am. Chem. Soc. 2003;125:13660.
12. Wachowicz M, Wolak J, Gracz H, Stejskal EO, Jurga S, White JL. Macromolecules. 2004;37:4573.
13. Freed KF. J. Chem. Phys. 2003;119:5730.
14. Frederickson GH, Liu AJ, Bates FS. Macromolecules. 1994; 27:2503.
15. Dudowicz J, Freed KF. Macromolecules. 1996;29:8960.
16. Rajesekaran JJ, Curro JG, Honeycutt JD. Macromolecules. 1995;28:6843.
17. Limb SJ, Scruggs BE, Gleason KK. Macromolecules. 1993; 26:3750.
18. Kuo SW, Wu CH, Chang FC. Macromolecules. 2004;37: 192.
19. Mellinger F, Wilhelm M, Spiess HW. Macromolecules. 1999; 32:4686.
20. Wang X, White JL. Macromolecules. 2002;35:3795.
21. Gerstein BC, Pembleton RG, Wilson RC, Ryan ML. J. Chem. Phys. 1977;66:361.
22. Egger N, Schmidt-Rohr K, Blumich B, Domke WD, Stapp B. J. Appl. Polym. Sci. 1992;44:289.
23. White JL, Lohse DJ. Macromolecules. 1999;32:958.
24. Adams G, Gibbs JH. J. Chem. Phys. 1965;43:139.
25. Richer R, Angell CA. J. Chem. Phys. 1998;108:9016.
26. Ediger MD. Annu. Rev. Phys. Chem. 2000;51:99.
27. Macho V, Brombacher L, Spiess HW. Appl. Magn. Reson. 2001;20:405.
28. deAzevedo E, Hu WG, Schmidt-Rohr K. J. Am. Chem. Soc. 1999;121:8411.
29. Wolak JE, White JL. Macromolecules. 2005;38:10466.

Quantum Information Processing

Quantum Information Processing as Studied by Molecule-Based Pulsed ENDOR Spectroscopy

Robabeh Rahimi[1], Kazunobu Sato[2], Daisuke Shiomi[2], and Takeji Takui[2]
[1]*Department of System Innovation, Graduate School of Engineering Science, Osaka University, Machikaneyama, Toyonaka, Osaka 560-8531, Japan; and*
[2]*Departments of Chemistry and Materials Science, Graduate School of Science, Osaka City University, Sugimoto, Sumiyoshi-ku, Osaka 558-8585, Japan*

Introduction

The fast development and miniaturization of current computers will be slowing down probably after only a few decades. Current technology of the computers, hence so called classical computers, has been based on classical physics which fails if the size of the computers becomes as small as microscopic scales such as atomic or molecular entities.

A quantum computer is the introduced candidate for the future generation of the computers, which is based on the theory of quantum physics and then is properly well applicable to very small size of the computational elements [1]. In the classical computers, the computation and the information processing can be carried on the fundamental concepts so called bits. On the other hand, quantum computers are built upon quantum bits or qubits, by which the computation and the processing are governed in quantum mechanical nature [2].

As a result of the theoretical background difference between the two classes of the computers, classical and quantum, it is highly expected that some problems which are intractable for classical computers can be solved efficiently by quantum computers. For example, with the same input and output, a quantum processing of given information data represents exponential speed-up for factoring by Shor algorithm [3] and quadratic speed-up for search problems using Grover algorithm [4]. Also, by implementation of the quantum information algorithms such as quantum teleportation [5] and quantum superdense coding (SDC) [6], some intrinsic advantages can be achieved compared with the classical information processing. From the theoretical side, quantum information processing (QIP) and quantum computation (QC) have been established considerably well during the last decade [2]. Nevertheless, to build quantum computers as physical systems is still a big challenge. This is also true in terms of materials challenge. Realization of QIP and QC should involve qubits in microscopic scales. Computational tasks need manipulation of the qubits, whereas some interference among the quantum systems spoil the qubit systems and hence QIP and QC seem to be formidable tasks.

There have been considerable efforts to make quantum computers. According to the current technology, it seems that there is a long way to achieve a novel physical system which can present a quantum computer with all the promised advantages. Several physical systems, however, have been introduced as candidates for realization of QIP and QC [7–10].

A very well-known physical system for realization of a quantum computer is based on the nuclear magnetic resonance spectroscopy [7–8]. In this scheme, the quantum information is stored in nuclear spins, as qubits, of molecules. Liquid-state NMR spectroscopy has been widely used for implementations of even considerably complicated quantum non-local algorithms and the experimental outcomes apparently represent the capability of NMR as the physical system for QIP and QC [11–15].

Nevertheless, liquid-state NMR at room temperature suffers from its intrinsic low spin polarization, making the initial state in a highly mixed state, whereas the accessibility to a pure initial state is one of the major requirements for any physical system to be a valid candidate for the demonstration of a quantum computer [16], as is discussed later. In order to overcome this drawback, in a conventional approach, pseudo-pure states have been introduced [17–18] and widely used for NMR-based QIP and QC experiments.

Pseudo-Pure States and Quantum Entanglements

A pseudo-pure state is composed of two terms, the one belonging to the highly mixed state of the unitary part and the pure state term with a coefficient, which is related to experimental conditions. Referred to the current technology of the NMR spectroscopy at ambient temperature the corresponding value is as small as to typically 10^{-5}. Since all the observables in NMR are traceless the mixed

Graham A. Webb (ed.), Modern Magnetic Resonance, 647–654.
© 2008 *Springer.*

state term cannot be detected trough the NMR processing. Weak signal intensities, however, through the other term still give some information through quantum processing and then the whole pseudo-pure state looks as if an initial pure state has been used for the QIP.

Quantum entanglement is known as a prerequisite condition for any quantum non-local algorithm [19,20]. Thermal mixed states that have been used for NMR have been proved to be separable [21,22], therefore useless for the quantum non-local processing. Pseudo-pure states which apparently resolve the problem of the admixture of the initial state is not useful any more referred to the separability of the state, since the pseudo-pure state can also be represented as a convex combination of thermal states. The entanglement is a convex function. Then, the pseudo-pure states are at least as separable as the thermal states. In this context, liquid-state NMR with low spin polarization cannot afford entanglement-based advantages of QIP and QC. In order to solve this drawback, nuclear spin polarization should be increased to the extent expected by the theoretical criteria for the existence of entanglement. The enhancement of the nuclear spin polarization has been one of the recent focuses in the research field [23,24].

Despite the drawbacks of NMR as discussed, it is no doubt that NMR spectroscopy can be such a physical system as represents very important advantages for realization of quantum computers in some crucial aspects. The existence of nuclear spins with long decoherence time is proper physical realization of a qubit since the spin manipulation can easily be performed by introducing radio frequency pulses with relevant resonance frequencies. In this context, to retain the advantage of long decoherence times is crucial for looking for novel physical systems in which easy-to-access spin manipulations are performed. In this study, pulse-based Electron Nuclear DOuble Resonance (ENDOR) [25] has been examined as a novel candidate to approach a quantum computer by invoking molecular entities with both electron spins and nuclear spins in the solid state. Since the physical system under study involves nuclear spins, pulsed ENDOR spin-manipulation technology retains the main advantage inherent in QC NMR systems. In addition, it seems easier to overcome the drawbacks of the NMR systems for realization of quantum computers because additional molecular electron spins originating in open-shell electronic structures are also incorporated in the corresponding physical systems.

Nevertheless, an ENDOR based quantum computer as electron-nuclear multiple magnetic resonance spectroscopy is much heavier experimental task compared with NMR or electron paramagnetic (spin) resonance (EPR/ESR), but QC-ENDOR rewards back the much more efforts by adding up the advantages of NMR and EPR. It is worthwhile to notice that an elaborate total design of the QC-ENDOR experimental setup should be associated with molecular design for open-shell entities. Tuning relaxation times of molecular open-shell entities is crucially important in the QC-ENDOR setup.

Molecular ENDOR Based Quantum Computer

For any physical system as a candidate for the realization of a quantum computer, there are some fundamental criteria, known as DiVincenzo criteria that should be met [16]. The molecule-based ENDOR system is also expected to meet these criteria in order to be a realistic physical system for QIP and QC; see Table 1 for a list of DiVincenzo criteria and properties of the ENDOR system.

In the ENDOR-based QIP and QC, molecular electron spins in addition to nuclear spins have been introduced as quantum bits (qubits). In a thermal equilibrium, the populations in the ground states with molecular electron spins are more than 10^3 times larger than the corresponding excited states in the presence of a static magnetic field or the ones with zero-field splittings. Therefore, with ENDOR systems, achievement of the required experimental conditions for preparing the initial state for QIP and QC seems to be substantially easier with the current technology. The exact and complete preparation of the pure initial state, however, requires manipulation of single molecule systems, for which electron magnetic resonance or Larmor precession detection has been considered and even the experimental equipments seem to be accessible in the near future.

Any physical system for QIP and QC should be chemically stable during computational processing. We have prepared robust organic open-shell entities against long and high-power irradiations of radio frequency and microwave at ambient temperature, as one among those exemplified in this contribution. In addition, the corresponding decoherence time of the qubits is expected to be long enough compared with the computational or operational time. As a result of the existence of the nuclear spins in molecular open-shell entities, there is a wide possibility to work with samples with the long decoherence time. Proper samples with the long decoherence time and their synthetic procedure should be considered, in advance [26]. Long enough decoherence times for samples involving two qubits have been measured during the course of this work; for a particular molecular entity the feasibility of the ENDOR-based QIP and QC has been examined from both experimental and theoretical sides as is reported in the following sections.

In QC-ENDOR, manipulation and processing on the qubits as well as the readout processing can be realized by introducing both microwave and radio frequency pulses in an approach different from NMR QC experiments, i.e. ENDOR pulses, on the nuclear spins or by the microwave frequency pulses on the electron spins (see Figure 1).

Table 1: ENDOR systems regarding the satisfactions of the DiVincenzo criteria

	DiVincenzo criteria	ENDOR
Qubit	Identifiable, well characterized qubits are required.	Molecule-based electrons and nuclear spins in molecular open-shell entities based on chemical syntheses and identifications.
Initialization	Possibility to be initialized to a simple and fiduciary state.	Pseudo-pure states might be used in this context, whereas in case of avoiding pseudo-pure states, it is proposed that high polarizations of the electron spin can be coherently transferred to the nuclear spin by applying relevant pulse sequences followed by proper waiting times.
Decoherence time	Long relevant decoherence times, much longer than the gate operation time is necessary.	Long decoherence times of the nuclear spins and electron spin have been available for the demonstration of quantum operation between the two spins. Proper molecular entities with long decoherence times for multi-qubit operations are not out of reach, for which stable isotope-labeled open-shell molecules have been designed and synthesized [26].
Quantum operation	Universal set of quantum gates is required.	Quantum gates between a single electron and a single nuclear spin have been demonstrated in an experimental task. Multi-qubit operations in terms of ENDOR spin Hamiltonians are underway.
Measurement	The ability of measurements on the quantum qubits to obtain the result of the computation is required.	The current measurement scheme is an ensemble one. However, single electron spin detections may be available in the future by the use of STM-based electron magnetic resonance detection.

It is known that the realization of particular quantum gates being known as universal gates can be enough for implementation of any other quantum gates [2]. One-qubit gates in addition to a non-trivial two-qubit gate, e.g. Controlled-NOT gate (CNOT), give a universal set of quantum gates. For implementations of quantum gates, it is possible to perform this task by introducing the relevant pulses. From the experimental side, for the QC-ENDOR system particular quantum gates have been demonstrated by means of the two qubits, as it is described in the following section. Multi-qubit gates for molecular systems involving larger number of qubits should be considered for the relevant physical system in terms of the particular form of the spin Hamiltonian for the corresponding sample. There are several typical types of the quantum operations based on multi-qubit-gates, depending upon spin Hamiltonians for realistic QC-ENDOR experiments [26].

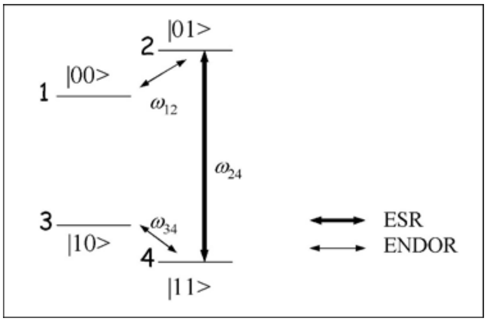

Fig. 1. Energy levels and corresponding EPR/ESR and ENDOR resonance transitions in the presence of a static magnetic field. Note that the nuclear sublevels correspond to the case for the system with a positive hyperfine coupling. The definition for the level is as follows; $|00\rangle$ and $|10\rangle$ denote $|Ms = +1/2, M_I = +1/2\rangle$ and $|Ms = -1/2, M_I = +1/2\rangle$, respectively. Similarly, $|01\rangle$ and $|11\rangle$ denote $|Ms = +1/2, M_I = -1/2\rangle$ and $|Ms = -1/2, M_I = -1/2\rangle$, respectively. Also, see the text for the use of the notation of the sublevels.

In the ENDOR based QC, the readout or the measurements have been implemented by introducing the radio frequency and Microwave pulses on nuclear spins and electron spins, respectively. Nevertheless, as is in a similar approach to the NMR QC, the measurement scheme is an ensemble measurement and rather different from the exact measurement which is required for QC. In terms of QC-ENDOR, to solve this problem is still an open problem. As has been already mentioned, the QIP and QC have been changed in a manner which the results through the ensemble measurements can give the required information. However, in the ENDOR based QC, we have been only proposing the single molecule system for which the measurements can be accomplished by single electron spin detection as discussed above.

It has been proved that for the case of pure states entanglement is the necessary requirement for quantum exponential speed-up over the classical counterpart. For mixed states the statement has still not been proved, but highly believed to be correct. Therefore, one very important issue which should be examined for any physical system for QIP and QC is the entanglement status. Realization of the entanglement between an electron spin and a nuclear spin has been reported in an ENDOR experiment by using the pseudo-pure states [27].

We have been mainly engaged in two experimental tasks for the realization of a quantum computer by molecule-based ENDOR. One has been attempts for the preparation of the experimental requirements for demonstrating a true entanglement between a molecular electron spin and a nuclear spin by the use of a simple organic radical in the single crystal and avoiding the use of pseudo-pure states. High spin polarizations on both the electron and nuclear spins are essentially required to achieve the true entanglement between the two spins in the molecular frame. Investigation of the entanglement for the ENDOR system composed of only two electron and nuclear spins gives a necessary temperature of 0.8 K in a static magnetic field for the microwave transition frequency of 95 GHz, as given by the negativity criterion [28,29]. Whereas, if pulses can be applied for the transfer of the high spin polarization, the required temperature at the same magnetic field is nearly 5.1 K, which is well in reach with the current technology with a W-band (95 GHz) ENDOR spectrometer operating at liquid Helium temperature.

While the preparation of all the experimental requirements is in progress, the efforts still can be maintained on some other aspects of the research. The other is materials challenge to design and synthesize stable open-shell molecular entities suitable for QIP/QC ENDOR experiments. Novel molecular open-shell systems with stable isotope labels suitable for our purposes have also been designed and synthesized [26]. Also, the critical temperature can be tuned by invoking stable high-spin molecular entities.

Also, the efforts have been made on the investigation of the credibility of the pulsed ENDOR based QIP and QC to develop the necessary quantum gates and the entangling unitary operations. It is clear that in case of acquiring the former task with the achievement of the experimental conditions for establishing entanglement and also pure states, there would be no need to have an additional experimental processing to make the pseudo-pure state.

In order to check the credibility of the ENDOR physical system for QIP and QC and also to check the feasibility of the molecule-based QC-ENDOR with current technology, implementation of SDC [6] has been revisited in our experiments. Pulsed ENDOR technique has been applied to a molecular electron- and nuclear-spin system, i.e. malonyl radical in the single crystal of malonic acid [30], in order to implement the SDC.

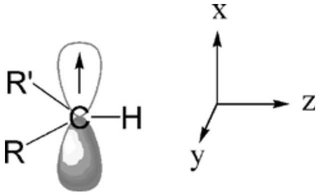

Scheme 1. Generation of malonyl radical by X-ray irradiation.

Preparation of the Molecular Entity for QC-ENDOR

Malonyl radicals incorporated in the single crystal of malonic acid were generated by X-ray irradiation at ambient temperature as shown in Scheme 1. Spin Hamiltonian parameters of malonyl radical under study, as summarized in Table 2, have been reported by McConnell *et al.* [30]. A typical echo-detected field-swept ESR spectrum of malonyl radical observed at 20K is shown in Figure 2. Pulsed ENDOR measurements for malonyl radical were performed with a Davies-type pulse sequence [31] and an observed Davies-ENDOR spectrum is shown in Figure 3.

Existence of one α-proton with a large hyperfine coupling gives two spins as the required two qubits for SDC. The large hyperfine interaction is primarily required to enable us to make a selective microwave excitation. Energy

Table 2: The spin Hamiltonian parameters of the malonyl radical

	G			$^{\alpha}A$/MHz		
S	*xx*	*yy*	*zz*	*xx*	*yy*	*zz*
1/2	2.0026	2.0035	2.0033	−29	−61	−91

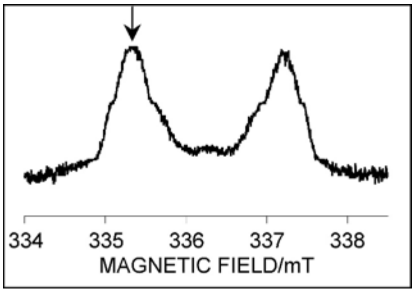

Fig. 2. Pulsed EPR spectrum of malonyl radical in the single crystal. The arrow indicates the static magnetic field for the ENDOR measurements.

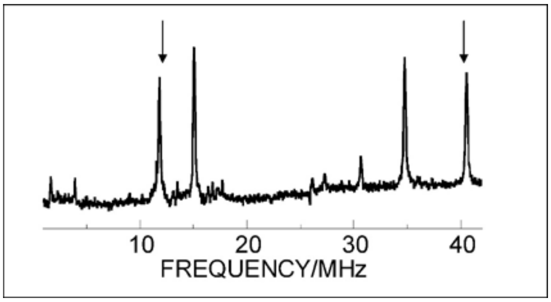

Fig. 3. Pulsed ENDOR spectrum from malonyl radical with the magnetic field set as in Figure 2. A selective MW pulse for the preparation and non-selective MW pulses for the detection were applied. The arrows indicate the ENDOR transitions due to α-proton (see Figure 2) of malonyl radical with a negative hyperfine coupling.

levels and the corresponding resonance frequencies of the radio and microwave frequencies are shown in Figure 1, noting that the order of the nuclear sublevels should be reverse for malonyl radical with the negative hyperfine coupling (see Table 2). Detection of the pseudo-entanglement with this system has been already reported [27] and in a different approach we demonstrate implementation of SDC by the use of pseudo-entangled states.

Implementation of SDC by Pulsed ENDOR

SDC introduced by Bennett and Wiesner [6] is a non-local quantum algorithm in which two classical bits of information have been transformed from Alice to Bob by sending only a single qubit. The scheme is based on the fact that the entangled initial states have been shared between the two involved parties. The efficiency of the scheme is two times compared with the classical counterpart, since maximum one bit of information can be transferred through a single use of an information channel.

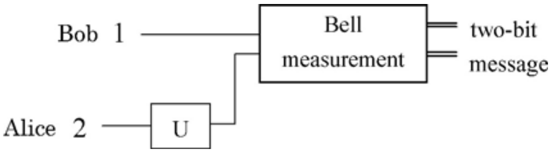

Fig. 4. Scheme for superdense coding. U denotes a unitary transformation.

Simply SDC can be explained as follows (see Figure 4): Two qubits which are originally entangled with each other have been shared between two involved parties, say Alice and Bob. Alice encodes the qubit by applying a unitary transformation out of the four choices of $\{I, X, Y, Z\}$ and then sends the encoded qubit to Bob, who has been also initially given a qubit entangled to the Alices's one. After receiving the encoded qubit from Alice, Bob applies a measurement in the Bell basis (see Table 3) on the both of the qubits. The result of the measurement makes it clear for Bob that what the Alice's choice has been in the encoding part. Therefore, he extracts the information on the Alices's choice, which means a two-bit message has been transferred by sending only a single qubit.

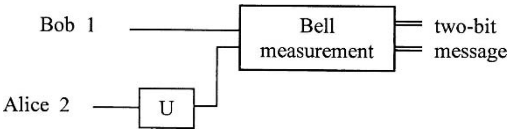

Concepts for ENDOR-based experimental setup for two-qubit SDC are depicted in Figure 5, in which S and I denote the electron-spin part and nuclear spin one. Figure 5 shows one of quantum circuits implementing SDC. The quantum circuit for SDC consists of Hadamard and controlled NOT (CNOT) gates. U_i stands for one of the unitary transformation for encoding. The first Hadamard

Table 3: The unitary operation and corresponding pulse sequences for encoding

	Initial state	Necessary operation	Required pulses	Encoded state
$U = I$	$\frac{1}{\sqrt{2}}(\|00\rangle + \|11\rangle)$			$\frac{1}{\sqrt{2}}(\|00\rangle + \|11\rangle)$
$U = X$	$\frac{1}{\sqrt{2}}(\|00\rangle + \|11\rangle)$	$\exp(-i\pi I_x)$	$P_x^{34}(\pi)P_x^{12}(\pi)$	$\frac{1}{\sqrt{2}}(\|01\rangle + \|10\rangle)$
$U = Y$	$\frac{1}{\sqrt{2}}(\|00\rangle + \|11\rangle)$	$\exp(-i\pi I_y)$	$P_x^{34}(2\pi)P_x^{34}(\pi)P_x^{12}(\pi)$	$\frac{1}{\sqrt{2}}(\|01\rangle - \|10\rangle)$
$U = Z$	$\frac{1}{\sqrt{2}}(\|00\rangle + \|11\rangle)$	$\exp(-i\pi I_y)$	$P_x^{34}(2\pi)$	$\frac{1}{\sqrt{2}}(\|00\rangle - \|11\rangle)$

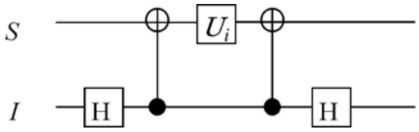

Fig. 5. Quantum circuit implementing SDC.

and CNOT gates generate an entangled state between the electron and nuclear spins. Following the unitary transformation, the CNOT and Hadamard gates back-transform the entangled state, being responsible for extracting the encoding results. Except for a phase factor which dose not affect any signal, selective $\pi/2$ and π pulses are available for the Hadamard gate for single qubit and the CNOT gate for two-qubit in pulsed magnetic resonance spectroscopy, respectively.

SDC has been implemented using some quantum physical systems including NMR [7]. This contribution gives a report on the implementation of the SDC by ENDOR. However, the main idea is only to test the ENDOR system for QIP rather than total implementation of SDC, giving a testing ground for QIP and QC to molecule-based ENDOR. As the latter, one has been argued to be truly realizable in case of manipulating the entangled state and not just by a pseudo-entanglement. In our experiment, states have been prepared as pseudo-pure ones in a similar approach as reported by Mehring's group [27].

The pulse sequence that has been used for implementation of SDC with our ENDOR experiments is represented in Figure 6. There are three main parts of the sequences, i.e. the preparation of the pseudo-pure states, manipulation and finally detection according to the customs in magnetic resonance spectroscopy.

The outermost left part labeled by "A" is for the preparation of the pseudo-pure state. Two pulses on electron and nuclear spins with additional waiting times in order to make the off diagonal term of the density matrix vanishing are required to acquire the pseudo-pure state. The first two pulses in the central part of the sequence are for entangling and also the last two pulses are for detection of the entanglement as reported by Mehring's group [27]. Two phases of Φ_1 and Φ_2 for the pulses in the detection part are required for clearing up the entangled states from the simple superposition states. In the central part between the entangling and detecting the entanglement, which is labeled by B2, one of the qubits, nuclear spin in our experiment, is encoded by randomly applying one of the four pulses of $\{I, X, Y, Z\}$. The necessary pulses for encoding are described in Table 3.

Finally, there are pulses for the detection by an electron spin echo signal. For the measurement part, the situation has been modified for some detection considerations. In this study, we have used the electron spin echo detection. The echo intensities have been detected for different angular dependencies of the pulses in the encoding part. As a result, there are four sets of angular dependencies for radio frequency pulses which have been used for encoding, (see Table 4).

In QC/QIP-ENDOR, unitary operations are realized by some particular pulse operations with controlled

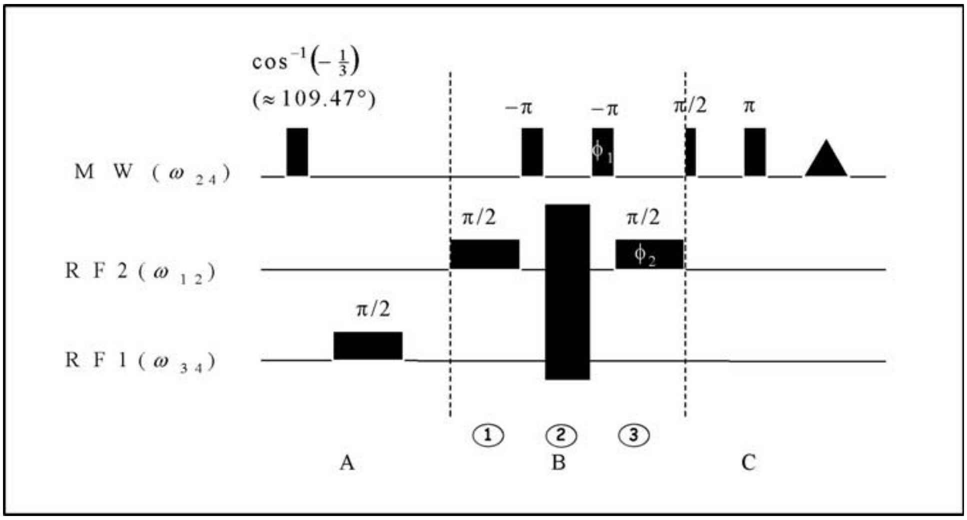

Fig. 6. Pulse sequence for implementation of superdense coding by molecule-based ENDOR.

Table 4: Detection through angular dependence of the intensities of the electron spin echo

	Angular dependent radiofrequency pulses for encoding	Detected angular dependent echo intensity
$U = I$		$\frac{1}{4}(-1 + \cos[\phi_1 - \phi_2])$
$U = X$	$\omega_x^{34}(\theta)\omega_x^{12}(\phi)$	$\frac{1}{16}\left(-3\cos\theta - \cos\phi + 4\cos\frac{\theta}{2}\cos\frac{\theta}{2}\cos[\phi_1 - \phi_2]\right)$
$U = Y$	$\omega_x^{34}(2\pi + \theta)\omega_x^{12}(\phi)$	$\frac{1}{16}\left(-3\cos\theta - \cos\phi - 4\cos\frac{\theta}{2}\cos\frac{\theta}{2}\cos[\phi_1 - \phi_2]\right)$
$U = Z$	$\omega_x^{34}(\theta)$	$\frac{1}{16}\left(-1 - 3\cos\theta + 4\cos\frac{\theta}{2}\cos[\phi_1 - \phi_2]\right)$

phases and polarizations. Phase manipulations are crucial in the molecule-based ENDOR experiments for QC and QIP. Table 4 shows the angular dependence of the electro-spin-echo intensities in the detection part, depending also on experimental conditions for the measurements. In the SDC experiments, the detected echo intensities incorporate the terms characteristic of 4π period, as shown in Table 4. We have detected this salient behavior of the intensities, exemplifying the case for $U_i = X$ as given in Figure 7. In contrast to the 2π period of the population, the observed 4π period originates from the spinor property [32] as the intrinsic nature of spins under study with the experimental condition of the selective microwave excitation. The sign difference appearing between Figure 7 and Table 4 is due to the difference between the experimental setup. The case for non-selective microwave excitations is under study.

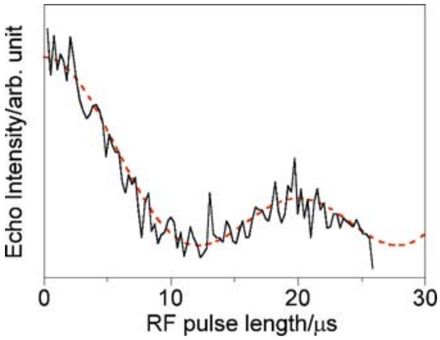

Fig. 7. 4π Period dependence of the electron spin echo detection scheme. Microwave frequency: $\nu = 9.38725$ GHz. Static magnetic field set for ENDOR: $B = 335.918$ mT. Temperature: $T = 20$ K.

Conclusion

We have introduced a pulsed ENDOR based approach to QIP and QC by invoking molecular electron and nuclear spins in the solid state. Pulse ENDOR technology retains the main advantages of NMR systems, and at the same times it seems relatively easier to overcome the difficulties that conventional NMR technology suffers from. We have noticed that time domain of electron spin manipulation technology is shortened and its present drawback is a matter of time resolution from the experimental side. In this research, it is aimed to demonstrate ENDOR-based QIP and QC by achieving the entangled states between a molecular electron spin and nuclear spins of a stable organic radical through high spin polarizations and also developing entangling unitary operations.

At first, our efforts have been made to develop entangling unitary operations in order to check the credibility of the molecule-based ENDOR QIP from both the theoretical and experimental sides. Angular dependent electron-spin echo intensities in the readout measurements have been derived in simple analytical expressions for SDC-ENDOR experiments. Thus, we have implemented SDC by acquiring the pseudo-pure states. The preliminary experimental results are well representing the feasibility of the ENDOR QIP. We have shown that phase manipulations of electron and nuclear spins in a controlled manner as well as the polarizations are crucial in QC/QIP ENDOR, demonstrating that the spinor nature of spins manifests itself in molecule-based pulsed ENDOR for SDC.

We are planning to examine the real QIP and QC by avoiding pseudo-pure states and introducing pure states in order to prepare the quantum entanglement between molecular electron spins and nuclear spins. It has been shown that in contrast to the conventional NMR systems, the experimental requirements for achievement of spins with high polarization are not far beyond the current ENDOR spin-manipulation technology. Also, currently, weakly electron-exchanged coupled systems composed of molecular open-shell entities have been designed, as materials challenge, based on bio-inspired molecular magnet approaches and the synthetic procedures are underway. This materials challenge is for implementation of molecule-based pulsed electron–electron and electron–nuclear magnetic resonance spectroscopy for QC and QIP.

References

1. Feynman RP. Int. J. Theor. Phys. 1982;21:467.
2. Nielsen MA, Chuang IL. Quantum Computation and Quantum Information. Cambridge University Press: Cambridge, 2000.
3. Shor PW. In Proceedings, 35th Annual Symposium on Foundations of Computer Science. IEEE Press Cambridge: Los Alamitos, CA, 1994.
4. Grover LK. Phys. Rev. Lett. 1997;79:325.
5. Bennett CH, Brassard G, Crepeau C, Jozsa R, Peres A, Wootters W. Phys. Rev. Lett. 1993;70:1895.
6. Bennett CH, Wiesner SJ. Phys. Rev. Lett. 1992;69:2881.
7. Jones JA, Mosca M, Hansen RH. Nature. 1998;393:344.
8. Chuang IL, Vandersypen LMK, Zhou X, Leung DW, Lloyd S. Nature. 1998;393:143.
9. Chuang IL, Yamamoto Y. Phys. Rev. A. 1995;52:3489.
10. Cirac JI, Zoller P. Phys. Rev. Lett. 1995;74:4091.
11. Chuang IL, Gershenfeld N, Kubinec M. Phys. Rev. Lett. 1998;18:3408.
12. Chuang IL, Vandersypen LMK, Zhou X, Leung DW, Lloyd S. Nature. 1998;393:143.
13. Nielsen MA, Knill E, Laflamme R. Nature. 1998;396:52.
14. Vandersypen LMK, Steffen M, Breytra G, Yannoni CS, Sherwood MH, Chuang IL. Nature. 2001;414:883.
15. Fang X, Zhu X, Feng M, Mao X, Du F. Phys. Rev. A. 2000;61:022307.
16. Divincenzo DP. In: L Sohn, L Kouwenhoven, G Schon (Eds). Mesoscopic Electron Transport, Vol. 345. NATO ASI Series E, Kluwer, 1997, p 657 (Cond_mat/9612126).
17. Cory DG, Fahmy AF, Havel TF. Proc. Natl. Acad. Sci. USA. 1997;94:1634.
18. Gershenfeld N, Chuang IL. Science. 1997;275:350.
19. Ekert A, Jozsa R. Phil. Trans. R. Soc. Lond. A. 1998;356:1769.
20. Linden N, Popescu S. Phys. Rev. Lett. 2001;87:047901.
21. Zyczkowski K, Horodecki P, Sanpera A, Lewenstein M. Phys. Rev. A. 1998;58:883.
22. Braunstein SL, Caves SM, Jozsa R, Linden N, Popescu S, Schack R. Phys. Rev. Lett. 1999;83:1054.
23. Anwar MS, Blazina D, Carteret H, Duckett SB, Halstead TK, Jones JA, Kozak CM, Taylor RJK. Phys. Rev. Lett. 2004;93:040501.
24. Anwar MS, Jones JA, Blazina D, Duckett SB, Carteret HA. Phys. Rev. A. 2004;70:032324.
25. Feher G. Phys. Rev. 1956;103:834; Mims WB, Proc. Roy. Soc. Lond. 1965;283:452; Grupp A, Mehring M. In: L Kevan, MK Bowman (Eds). Modern pulsed and continuous-wave electron spin resonance. Wiley: New York, 1990, p 195.
26. Takui T, *et al.* unpublished work.
27. Mehring M, Mende J, Scherer W. Phys. Rev. Lett. 2003;90:153001; Mehring M, Scherer W, Weidinger A. Phys. Rev. Lett. 2004;93:206603.
28. Peres A. Phys. Rev. Lett. 1996;77:1413.
29. Horodecki M, Horodecki P, Horodecki R. Phys. Lett. A. 1996;223:1.
30. McConnell HM, Heller C, Cole T, Fessenden RW. J. Am. Chem. Soc. 1960;82:766.
31. Davies ER. Phys. Lett. A. 1974;47:1.
32. Mehring M, Hoefer P, Grupp A. Phys. Rev. A. 1986;33:3523.

Residual Dipolar Couplings and Nucleic Acids

New Applications for Residual Dipolar Couplings: Extending the Range of NMR in Structural Biology

Rebecca S. Lipsitz and Nico Tjandra
Laboratory of Biophysical Chemistry, National Heart, Lung, and Blood Institute, National Institutes of Health, Bethesda, MD 20892, USA

Background

Less than 10 years since their introduction, residual dipolar couplings (RDCs) have become a mainstay in Nuclear Magnetic Resonance (NMR) methodology [1–4]. Dipolar couplings are anisotropic through-space interactions between magnetic nuclei. In solution samples, Brownian motion causes all orientations to be sampled with the same probability; there is no net anisotropic orientation needed in order for the dipolar coupling to be observed. However, there have been recent advances where the presence of various types of solution media imparts a small degree of anisotropy, a RDC [5,6]. Under these conditions, the molecule retains isotropic properties such as rapid tumbling and narrow line widths.

RDC data are complementary to NOE data; whereas NOEs provide distance information between atoms less than 5 or 6 Å, RDC data allows the relative orientation of bond vectors to be determined, regardless of their actual translational proximity within the molecule. RDCs have been a boon for NMR research and have allowed exploration into research areas heretofore unexamined such as relative orientation of protein domains/protein complexes, global structure of oligonucleotides, structural propensity of unfolded proteins, prediction of protein folds, and information on glycosidic angles in carbohydrates. In this review we highlight some of the most interesting applications within the past few years.

Theory

The RDC, D_{AB} can be expressed as follows

$$D_{\mathrm{AB}}(\theta,\phi) = \frac{S\gamma_{\mathrm{A}}\gamma_{\mathrm{B}}}{r_{\mathrm{AB}}^3}\{A_{\mathrm{a}}(3\cos^2\theta - 1)\} + \frac{3}{2}A_{\mathrm{r}}(\sin^2\theta\cos 2\phi) \qquad (1)$$

where A and B refer to the interacting nuclei, A_{a} is the axial component of the molecular alignment tensor $\mathbf{A}$, A_{r} is the rhombic component of $\mathbf{A}$, θ and ϕ are the polar angles describing the angle the inter-atom vector makes with the alignment tensor, S is the order parameter, γ is the gyromagnetic ratio, and r_{AB} is the internuclear distance. The advantage of using RDCs for nuclei of known bond lengths is that the only variables in Equation 1 are θ, ϕ, and S. It is routine to assume that S is constant throughout the protein or to omit data for nuclei where relaxation data indicates high-amplitude motion.

Knowing the value of the principal components of $\mathbf{A}$ is a pre-requisite for using the RDC data in structure calculations. There are various methods to determine these values such as singular value decomposition (which requires a starting structure for fitting the RDC data and a minimum of five measured RDCs) [7], histogram analysis of the measured RDCs (which requires sufficient geometric sampling of the data) [8], and grid search approaches [9]. In many cases there are inherent limitations that make it difficult to measure a large number of RDCs. Using the known covalent geometry of the peptide plane it is possible to increase the amount of data with computer-generated RDCs [10]. Programs such as PALES [11] can be used to compute the alignment tensor values.

In experimental data, the RDC is observed as an addition or subtraction (RDCs can be positive or negative) to the scalar J coupling. In order to extract the RDC values it is necessary to measure the apparent J coupling under both isotropic and anisotropic conditions [1,12–15].

There are a considerable number of media used to align samples based on different mechanisms of alignment, i.e. steric obstruction vs. electrostatic interactions. However, sample preparation is a delicate art and it is difficult to predict which media will satisfy the requirements that the sample does not interact with the media and that the sample does not become degraded. Some of the most commonly used alignment media include bicelles, phage particles, purple membranes, poly-γ-benzyl-L-glutamate (PBLG) strained polyacrylamide gels, etc. [16–24].

One of the first applications of RDC data was for protein structure refinement. Modules have been added to XPLOR-NIH expressly for this purpose [25]. A target function is employed which uses a force constant based on the uncertainty of the measured data. An *OXYZ* pseudoatom which represents the coordinates of the alignment

Graham A. Webb (ed.), Modern Magnetic Resonance, 657–664.
© 2008 *Springer.*

tensor is incorporated into the atomic coordinates and allowed to rotate freely during the refinement [26,27]. Molecules refined with RDC data show noticeably improved RMSDs which helps to delineate important functional features of the molecule.

Protein Structures

In cases where there is a paucity of NOE data, RDCs have substantial impact on the structural precision. Two such examples are the structure of *Thermotoga maritime* cold shock protein solved at 343 K, a temperature at which RDCs were necessary because many NOEs were no longer observed or had diminished signal to noise [28]. Completion of this structure allowed for comparisons with a structure of the same protein solved at room temperature. For high molecular weight proteins spectral overlap makes it difficult to assign all the resonances. One approach in this situation is to use selective labeling in order to simplify the spectra. This results in a non-uniform NOE distribution and RDCs can help to compensate for the low number of long-range distance restraints. The 723-residue protein malate synthase G is an example of a protein whose fold could not have been determined without using RDCs. This work demonstrates the feasibility of determining the structures of high-molecular weight protein by NMR [29].

In multi-domain proteins it is difficult to determine the relative orientations of domains within a protein without RDCs because they are usually too far apart for inter-domain NOEs to be detected. However, assuming that the linker in between the domains is not flexible the relative domain orientation can be determined by calculating the alignment tensor for each domain and then rotating the domains until their alignment tensors coincide. Subsequently, rigid-body dynamics is commonly used to determine the final structure [30,31]. Examples of structures of multi-domain proteins determined this way include barley lectin [32] T4 lysozyme [33]. RDCs were used to solve the structure of the p47^{phox} dimer and to show that the two tandem SH3 domains are arranged in a compact, globular manner, similar to what was observed in the crystal structure [34].

RDCs can be used to understand how a solution structure solved by NMR differs from the corresponding crystal structure or ways in which a protein changes conformation in response to ligand binding. Kay and coworkers, have performed a series of studies on the 370-residue maltose-binding protein both with and without ligands. The apo "open" form is very similar to its crystal structure counterpart. In the case of one particular ligand, β-cyclodextrin, there was a disagreement between the solution structure and the crystal structure in that the solution conformation the two domains were 10° closer to each other in than in the crystal structure [35,36]. In order to monitor the change in conformation from open to closed, Millet *et al.* have performed RDC studies on various mutants in the domain linker region that force the domains to move into an increasingly more closed conformation, showing the structural transformation as the protein moves from the open to closed forms [37].

There are some cases where RDCs have helped to establish the existence of deviations in relative domain orientation between similar structures solved by x-ray crystallography and NMR. Zhang *et al.* showed that the nucleotide-binding domain of Hsc70, which contains four domains, has a relative domain orientation that differs from 14 previously solved crystal structures. Differences in the alignment tensor of the 4 domains suggests that inter-domain flexibility may be viewed as a mechanism for "modulating" inter-domain interactions as well as interactions with cofactors [38].

Hemoglobin is an example demonstrating the use of RDCs to determine a novel solution conformation. In this case, discrepancies between measured RDCs and RDCs calculated from crystal structures of two allosteric forms of the protein suggested that the conformation of the solution sample did not match either of two previously characterized allosteric states. In order to determine the orientation of the solution conformation, the relative orientation of the domains was systematically adjusted until the calculated RDCs coincided with the measured RDCs. It was found that the orientation in solution lies in between the two allosteric conformations [39]. Figure 1 depicts the three different conformations.

DNA/RNA

DNA

Traditionally, the global features of nucleic acid structure have been challenging to assess. Use of RDCs has shown that crystal structures and NMR structures using only NOEs, J couplings, and torsion angle restraints leads to imprecise or inaccurate structural representations. RDCs not only greatly improve structural convergence within a family but in so doing allow global parameters to be determined such as DNA curvature. For example it has been shown that inclusion of RDC restraints into the structure of a DNA dodecamer causes the range of curvature values within a family of structures to be significantly decreased [40]. Without RDCs, the number of long-range structural restraints is limited due to low chemical shift dispersion, low proton density (as compared to proteins) and the near-absence of long-range NOEs. Inclusion of RDCs improves the local geometry and subsequently the global geometry. In fact several authors have highlighted the interplay between local and global geometry emphasizing

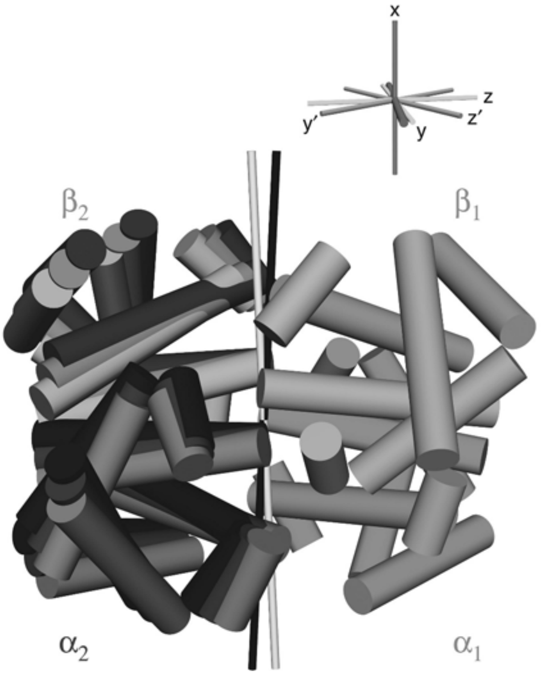

Fig. 1. Schematic illustration of the R and R2 crystal structures, together with the solution conformation, of hemoglobin. Helices are shown as cylinders. Here, the $\alpha_1\beta_1$ dimers of the two structures have been superimposed and are indistinguishable. The α_2- and β_2-subunits of the R, solution, and R2 structures are shown in dark, medium, and light shades, respectively, of red and blue. The C2 symmetry axes of the R and R2 structures are shown as thin black and white rods, respectively. (*Inset*) Alignment frames of the best-fit solution structure in bicelles (x, y, z) and Pf1 phage (x, y, z), where the x and x axes coincide with the C2 axis. The R→R2 rotation axis is shown in orange. Reprinted with permission from ref. [39]. (See also Plate 61 on page XLIII in the Color Plate Section.)

that inaccuracies at the local level tend to propagate throughout the molecule leading to inaccuracies in global geometry. Only a handful of RDCs are needed to have a dramatic effect on the structure [41]. However, to overcome the paucity of ^{1}H–X measurable internuclear RDCs in nucleic acids, methods have been developed to measure interproton ^{1}H–^{1}H RDCs up to 12Å apart [15,42,43].

A number of RDC studies on DNA molecules have focused on A-tracts, series of 4 or more adjacent A-T base pairs which induce unusual curvature that may have a functional role in transcription [44–46]. Crystal structures of A-tracts do not exhibit this curvature, most likely due to lattice packing effects, and therefore show discrepancies when compared to the corresponding solution structure. NMR structures of A-tracts show great variability in the DNA curvature. Since RDCs are particularly helpful for assessing parameters such as DNA curvature, studies by Steft, Barbic, and Lu have helped to end a longstanding debate over the type of model (wedge or junction) that best describes A-tract curvature. The consistent results within these RDC studies supports a modified version of the two models, referred to as the "delocalized bend model."

Use of RDCs makes it possible to quantify geometric properties that both define and distinguish DNA such as base pair roll, tilt, and twist angles. These values can be used to better understand the relationship between nucleotide sequence and structural irregularities in DNA that serves a functional purpose. As an example, Wu *et al.* have built on previous RDC studies of the DNA Dickerson dodecamer using an extremely large number of RDCs including both heteronuclear and homonuclear RDCs as well as ^{31}P CSA values [47,48]. Unlike previous crystal structures which show irregular features including abnormal backbone torsion angles, the structure using RDCs demonstrates that the Dickerson dodecamer is highly regular.

RNA

Structure determination of RNA molecules is complicated by the fact that RNA suffers from many of the same drawbacks and limitations as DNA but with additional challenges such as intricate secondary structure, mobility between different RNA segments, non-uniform alignment tensors, etc [49,50]. RDCs can aid in characterizing unusual, but functionally important geometry that arises from bulges, mismatches, and loops. Pardi and co-workers have demonstrated how to use RDCs in a number of different RNA structure calculations. The structure and relative orientation of the two helical arms of the tRNA$^{\mathrm{Val}}$ was determined by using measured RDCs with the known structure of similar tRNA as a template. Detailed discussions about important considerations for implementing RDC in structure calculations are included in this work and others [51–53]. Reiter *et al.* have used RDCs to investigate pH-induced conformational changes as a result of a base flip which shifts the positions of the upper and lower helices in the U6 RNA stem-loop [54].

RDCs have been used in studies investigating the effect of Mg^{2+} binding on the conformation and dynamics of RNA molecules. In the case of the HIV-1 TAR RNA molecule it was shown that in the free form its two stems have an average inter-helical angle of 47° which both exhibit significant mobility, and thus have different alignment tensors [55]. Addition of Mg^{2+} leads to a rigidification of the molecule; all RDC values are scaled in a manner which indicates that both stems behave as a single entity and the inter-helical angle is reduced to 12° [56].

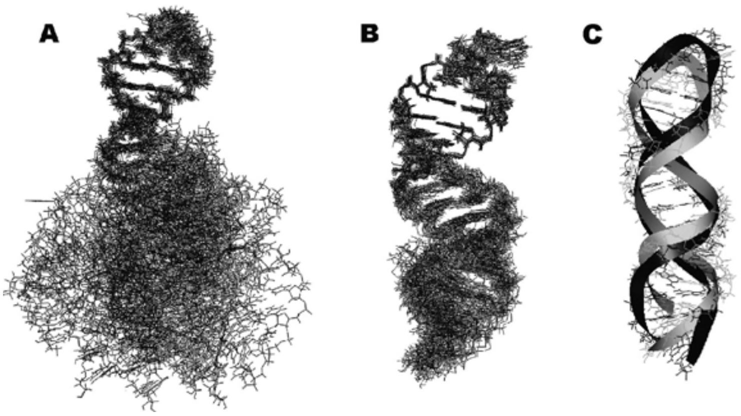

Fig. 2. NMR structures of the consensus stem-loop D RNA. (A) The 25 lowest energy structures refined with the conventional distance and torsion angle restraints. (B) The same structures calculated with the inclusion of 136 ^1H–^{13}C one bond RDC restraints. (C) Superposition of the average structures calculated with (gray) or without (black) RDCs. Further details may be found in the original publication. Reprinted with permission from ref. [41].

The solution structure of the hammerhead ribozyme without Mg^{2+} was compared to the crystal structure of the hammerhead ribozyme with Mg^{2+} (catalytically active form) in order to understand the extensive conformational changes that occur upon Mg^{2+} binding [57].

Du *et al.* used ^1H–^{13}C RDCs to refine the structure of Stem-Loop D from the cloverleaf RNA which binds to viral proteins [41]. This RNA molecule contains a tandem pyrimidine mismatch that may play a role in protein recognition as shown in Figure 2. This example provides a dramatic illustration of the power of RDCs in nucleic acid structure determination. Without RDCs, overall convergence is quite poor and it is impossible to overlay both stems simultaneously. RDCs lead to a noticeable improvement in the overall structure and allow features which pertain to function, such as the helical propensity and deformations due to the pyrimidine mismatches to be observed.

Pseudocontact Shifts

Paramagnetic metals cause the molecule to become aligned in the magnetic field due to the large magnetic susceptibility anisotropy. The anisotropy of the molecule also allows RDCs to be measured. It also leads to Pseudocontact Shifts (PCS), another source of orientational data that is due to the dipolar interactions between the unpaired electron and the nuclear spin. The PCS effect can be observed over large distances, as far as 40Å from the metal site [58]. The form of the PCS equation is similar to the equation for RDCs.

$$\delta_i^{pc} = \frac{1}{12\pi r_i^3}\left[\Delta\chi_{\mathrm{ax}}(3\cos^2\theta - 1) + \frac{3}{2}\Delta\chi_{\mathrm{rh}} \times (\sin^2\theta\cos 2\phi)\right] \tag{2}$$

where $\Delta\chi_{\mathrm{ax}}$ is the axial component and $\Delta\chi_{\mathrm{rh}}$ is the rhombic component of the magnetic susceptibility tensor, respectively. The program FANTASIAN can be used to calculate the magnetic susceptibility tensor [59].

The PCS can be obtained by taking a diamagnetic metal-binding protein and titrating it with a paramagnetic metal [60]. Lanthanides (Ln^{3+}) are preferred for this purpose due to their high magnetic susceptibility tensor. Each Ln^{3+} has a different magnetic susceptibility tensor. Therefore, by using several different lanthanides it is possible to obtain numerous, non-redundant PCS and RDC data sets, which increases the number of input restraints in structure calculation.

Calmodulin (CaM) has been used in many examples of PCS/RDC structural analysis and ligand-induced conformational changes. CaM consists of an N and C-terminal domains, each of which binds Ca^{2+}, that are connected by a linker. Metal binding leads to a change in conformation that allows binding to the target molecule to occur. The dynamic properties are such that the 2 domains can behave independently (apo form) or as a single entity (protein-bound form). Ln^{3+} ions titrate preferentially into the N-terminal and in the case of Tb^{3+}, but the magnetic susceptibility is strong enough that the PCS effect is detected in residues located in the C-terminus [61]. For each residue, several peaks are observed in the NMR spectrum corresponding to the different Ca^{2+}/Ln^{3+} combinations. Disappearance of these signals can be used to monitor the extent of the titration. However, the presence of peaks corresponding to the diamagnetic and paramagnetic species in a single spectrum can cut down on experiment time. Line broadening is an inherent property of paramagnetic metals that can be problematic if too many individual resonances become obscured. Therefore, when choosing which Ln^{3+} to use one must weigh the strength of the magnetic susceptibility tensor against the line broadening effects.

Just as RDC data can be used to determine the relative orientation of separate protein domains, so too can PCS data. Studies of apo-CaM with Tb^{3+} and Tm^{3+} were performed and used to establish that the protein samples a range of conformations in a non-uniform manner. The C-terminal domain moves with respect to the N-terminal domain in an elliptical region with a cone angle of 30° [62]. A PCS study of meltonin-bound CaM with Tb^{3+} substituted for Ca^{2+} showed that motion in the N and C domains occurs independently from one another, similar to previously characterized apo-form of CaM [63].

Analogous to RDCs, PCS data can be used in structure refinement. Protocols for using PCS data within Xplor-NIH (PARArestraints) [64] and PARAMAGNETIC DYANA [65] have been developed which are similar to those used for RDC data. PARArestraints also allows implementation of other types of paramagnetic data such as paramagnetic relaxation enhancements, and Curie-dipolar cross correlated relaxation. Structures which have been refined with PCS data include cyctochrome *c* [66], a DNA octamer bound to chromomycin-A_3 [67] α-parvalbumin [68].

It is possible to obtain PCS data from non-metal binding diamagnetic proteins. Several laboratories have devised ways to attach paramagnetic metals by using paramagnetic 'tags' [69–72]. Two cysteine residues are engineered onto the protein surface to allow site-specific binding to a derivative of DTPA, a bidentate lanthanide-containing molecule. Modified EDTA molecules can be used in a similar manner. Incorporation of these small ligands ensures that there is no dynamic behavior relative to the protein, i.e. both the tag and the protein have the same magnetic susceptibility tensor. Other techniques include engineering short paramagnetic-binding peptides to the protein termini [73,74].

Unfolded Denatured Proteins

As alluded to previously, the nature of the information derived from RDCs makes them ideal for examining almost any type of structural perturbation including changes in proteins as they undergo unfolding. Intuitively, one would expect that unfolding leads to averaging of any preferred orientation resulting from alignment which would reduce the magnitude of RDCs close to zero. However, theoretical studies by Annila and co-workers have shown that short polypeptide chains have a bell-shaped non-zero RDC distribution [75]. This finding has been born out in experimental studies as well, as first demonstrated for staphylococcal nuclease [76]. Other proteins too have shown to have what is referred to as persistent helical structure or native-like topology. Ohnishi *et al.* found in the case of unfolded eglin C, that the correlation between measured and calculated RDCs was inversely proportional to chain segment length and that denatured eglin C analyzed with RDCs showed native-like topology [77]. Eglin C shows a range of RDC values and not "monotonic" values as would be expected for a random chain. A study of equilibrium intermediates of apomyoglobin supports the argument that unfolded proteins contains conformational segments of 5–7 amino acids in length which take on extended conformations and behave in an anisotropic manner which explains the observation of non-zero RDCs [78].

Looking at the N-terminal domain of the stem-loop binding protein, Thapar *et al.* used RDCs based on the concept that in a helical region the ^1H–^{15}N amide RDCs should correlate with the angular periodicity within the helix with respect to the long axis of the helix, also known as "dipolar waves" [79] to ascertain that the protein contains very little persistent tertiary structure [80]. However, denatured acyl coenzyme A binding protein (ACBP) was shown to have residual secondary structure in 4 distinct regions. Subsequent RDC analysis on an unfolded mutant of ABCP demonstrates that one of these regions is stabilized by hydrophobic interactions [81]. Unfortunately it is not possible to use these data to determine the structure of unfolded proteins because there is no unique alignment tensor for the molecule as a whole. RDCs have been used to monitor the unfolding process such as in the case of GB1 where RDC values as a function of temperature were monitored in order to locate 2 specific thermal unfolding hot spots [82].

Oligosaccharides and Small Organic Molecules

The application of RDCs to carbohydrates suffers from some of the same drawbacks as with nucleic acids: relatively few ^1H–^{13}C bonds (most of which have a similar i.e. parallel, orientation), low proton density, etc. In addition, flexibility around the glycosidic torsion angle means that at the outset it must be assumed that each monosaccharide has a distinct alignment tensor which makes it difficult to measure enough RDCs for each ring to determine the alignment tensor. Differences in alignment tensor values for monosaccharides within a given oligosaccharide can be attributed to motion around the glycosidic torsion angles [83]. Several groups have described how to circumvent these problems and have introduced strategies for determining oligosaccharide structures. Griesinger and co-workers included measurement of ^1H–^1H RDCs to supplement the ^1H–^{13}C RDCs in the structure determination of raffinose and saccharose so that the alignment tensor can be determined with greater accuracy [84]. Inclusion of ^1H–^1H RDCs radically improves the precision of structures as the RMSD is decreased by a factor of 3. Cross-validation was used to determine how closely the NMR structure matched the corresponding crystal structure. For raffinose, significant differences were found in the Glc-Fru torsion angles compared to both crystal structures and previous NMR structures.

The three-ring Lewis blood group motifs are ideal systems for study because it has been established that they exist in single, rigid conformations. Therefore the five required RDCs needed for determination of the alignment tensor do not have to be extracted from a single pyranose ring. Martin-Pastor and Bush have demonstrated approaches using ^{1}H–^{13}C RDCs to determine structures of oligosaccharides containing various Lewis motifs. They were able to determine the structure of a pentasaccharide by first solving the structure of the Lewis A motif within the pentasaccharide and then determined the orientation of the two remaining sugars with respect to the Lewis A motif [85]. In a continuation of these studies, RDCs were used to determine the structures of 5 different Lewis blood group-containing oligosaccharides and as an aid in sorting out ambiguities in the NOE and molecular mechanics data. The conformations of these oligosaccharides were determined using a grid-search protocol which was feasible because of the relatively low number of degrees of freedom [86]. Similar studies using Monte Carlo methods to determine the structures of Lewis motifs indicated variations in dihedral angles between different low-energy conformations of 10° for the ϕ dihedral angle for the Fucα (1-3) GlcNAc [87]. Berthault *et al.* have used carbohydrates containing Lewis motifs to investigate whether or not oligosaccharides interact with the alignment media and found that larger more flexible oligosaccharides do interact with the media [88].

RDC studies on oligosaccharides have been used to understand some of their dynamic properties and how that may affect molecular recognition. In oligosaccharides, the relative amplitude of motion of each saccharide around the glycosidic bond can be determined by differences in the alignment tensor parameters in the form of the general degree of order (GDO) [89]. Yi *et al.* have demonstrated a novel technique for investigating conformations and motion in a disaccharide [90]. By attaching an alkyl chain to one end of the disaccharide which protrudes into the bicelle and immobilizes that end of the disaccharide, the overall alignment tensor becomes equivalent to that of the bicelle and the degrees of freedom in the number of parameters describing the glycosidic motion decreases.

In structural studies of small organic molecules, stereochemical assignments are very difficult and NOEs and scalar J couplings are not always adequate for distinguishing different types of protons. These assignments can be quite useful for understanding interactions between small organic compounds and proteins or DNA. A general strategy is to compare measured and calculated RDCs in order to identify which resonance corresponds to a particular proton. Thiele and Berger were able to unambiguously distinguish between two methylene protons in strychnine simply by comparing the measured and calculated RDCs for the two protons in question and then subsequently, assigned all pairs of diastereotopic protons in strychnine [91,92]. A similar methodology was used by Verdier *et al.* to determine the relative stereochemistry in menthol [93]. Yan *et al.* demonstrated that the relative stereochemistry of 6-membered rigid rings could be determined without any order-matrix calculations [94]. In this strategy, if one knows that a specific C–H bond vector is in an axial or equatorial configuration, that the configuration of other C–H bonds can be determined based on whether the RDC value is similar to that of the RDCs for the known configuration. Aroulanda *et al.* showed how to determine the cis or trans conformation of dihydropyridones based on the idea that two particular C–H bonds in the molecule should parallel and therefore similar orientations and similar RDC values in the *trans* conformation but would have non-parallel, dissimilar orientations, and dissimilar RDCs in the cis conformation [95]. Some of the commonly used alignment media for small organic molecules include poly-γ-benzyl-L/D-glutamate (PBLG and PBDG) in chloroform [96] and poly-γ-ethyl-L-glutamate (PELG) [92]. Mangoni *et al.* have demonstrated how to determine the relative configuration of stereocenters in sodium cholate to determine the relative stereochemistry of two stereocenters [97].

Conclusions

In this short review we have provided an overview of the most recent RDC applications. The breadth of topics that RDCs are being used to address is impressive, particularly because many of these applications are directed at understanding the dynamic nature of biomolecules which is the essential bridge linking static structure and physiological function. Undoubtedly, this field will continue to expand and new methods will be introduced to use RDCs to solve some of the most challenging structural biology questions, particular with respect to molecular recognition and conformational dynamics.

References

1. Prestegard JH, Bougault CM, Kishore AI. Chem. Rev. 2004; 104:3519.
2. Bax A, Kontaxis G, Tjandra N. Methods Enzymol. 2001;339: 127.
3. de Alba E. Tjandra N. Methods Mol. Biol. 2004;278:89.
4. Prestegard JH, al-Hashimi HM, Tolman JR. Q Rev. Biophys. 2000;33:371.
5. Tjandra N, Bax A. Science 1997;278:1111.
6. Tolman JR, Flanagan JM, Kennedy MA, Prestegard JH. Nat. Struct. Biol. 1997;4:292.
7. Losonczi JA, Andrec M, Fischer MW, Prestegard JH. J. Magn. Reson. 1999;138:334.

8. Clore GM, Gronenborn AM, Bax A. J. Magn. Reson. 1998;133: 216.
9. Clore GM, Gronenborn AM, Tjandra N, J. Mag. Reson. 1998; 131:159.
10. Bryce DL, Bax A. J. Biomol. NMR 2004;28:273.
11. Zweckstetter M, Bax A. J. Am. Chem. Soc. 2000;122:3791.
12. Ottiger M, Delaglio F, Bax A. J. Magn. Reson. 1998;131:373.
13. Yang D, Venters RA, Mueller GA, Choy WY, Kay LE. J. Biomol. NMR 1999;14:333.
14. E. O'Neil-Cabello, Bryce DL, Nikonowica EP, Bax A. J. Am. Chem. Soc. 2004;126:66.
15. Tian F, Fowler CA, Zartler ER, Jenney FA, Jr, Adams MW, Prestegard JH. J. Biomol. NMR 2000;18:23.
16. Clore GM, Starich MR, Gronenborn AM. J. Am. Chem. Soc. 1998;120:10571.
17. Ottiger M, Bax A. J. Biomol. NMR 1998;12:361.
18. Hansen MR, Mueller L, Pardi A. Nat. Struct. Biol. 1998;5: 1065.
19. Ishii Y, Markus MA, Tycko R. J. Biomol. NMR 2001;21: 141.
20. Sass J, Cordier F, Hoffman A, Cousin A, Omichinski JG, Lowen H, Grzesiek S. J. Am. Chem. Soc. 1999;121:2047.
21. Sass HJ, Musco G, Stahl SJ, Wingfield PT, Grzesiek S. J. Biomol. NMR 2000;18:303.
22. Ruckert M, Otting G. J. Am. Chem. Soc. 2000;122:7793.
23. Aroulanda C, Sarfati M, Courtieu J, Lesot P. Enantiomer 2001;6:281.
24. Chou JJ, Gaemers S, Howder B, Louis JM, Bax A. J. Biomol. NMR 2001;21:377.
25. Schwieters CD, Kuszewski JJ, Tjandra N, Clore GM. J. Magn. Reson. 2003;160:65.
26. Choy WY, Tollinger M, Mueller GA, Kay LE. J. Biomol. NMR 2001;21:31.
27. Tjandra N, Garrett DS, Gronenborn AM, Bax A, Clore GM. Nat. Struct. Biol. 1997;4:443.
28. Jung A, Bamann C, Kremer W, Kalbitzer HR, Brunner E. Protein Sci. 2004;13:342.
29. Tugarinov V, Choy WY, Orekhov VY, Kay LE. Proc. Natl. Acad. Sci. U.S.A. 2005;102:622.
30. Skrynnikov NR. CR. Acad. Sci. IVB 2004;5:359.
31. Bewley CA, Clore GM. J. Am. Chem. Soc. 2000;122:6009.
32. Fischer MWF, Losonczi JA, Weaver JL, Prestegard JH. Biochemistry 1999;38:9013.
33. Goto NK, Skrynikov NR, Dahlquist FW, Kay LE. J. Mol. Biol. 2001;308:745–764.
34. Yuzawa S, Ogura K, Horiuchi M, Suzuki NN, Fujioka Y, Kataoka M, Sumimoto H, Inagaki F. J. Biol. Chem. 2004;279: 29752.
35. Evenäs J, Tugarinov V, Skrynikov NR, Goto NK, Muhandiram R, Kay LE. J. Mol. Biol. 2001;309:961.
36. Skrynnikov NR, Goto NK, Yang D, Choy W-Y, Tolman JR, Mueller GA, Kay LE. J. Mol. Biol. 2000;295:1265.
37. Millet O, Hudson RP, Kay LE. Proc. Natl. Acad. Sci. U.S.A. 2003;100:12700.
38. Zhang Y, Zuiderweg ER. Proc. Natl. Acad. Sci. U.S.A. 2004;101:10272.
39. Lukin JA, Kontaxis G, Simplaceanu V, Yuan Y, Bax A, Ho C. Proc. Natl. Acad. Sci. U.S.A. 2003;100:517.
40. Alvarez-Salgado F, Berthault P, Boulard Y, Desvaux H. CR Acad. Sci. IIC 2004;7:259.
41. Du Z, Yu J, Ulyanov NB, Andino R, James TL. Biochemistry 2004;43:11959.
42. Wu Z, Bax A. J. Am. Chem. Soc. 2002;124:9672.
43. Boisbouvier J, Delaglio F, Bax A. Proc. Natl. Acad. Sci. U.S.A. 2003;100:11333.
44. Barbic A, Zimmer DP, Crothers DM. Proc. Natl. Acad. Sci. U.S.A. 2003;100:2369.
45. Macdonald D, Herbert K, Zhang X, Polgruto T, Lu P. J. Mol. Biol. 2001;306:1081.
46. Stefl R, Wu H, Ravindranathan S, Sklenar V, Feigon J. Proc. Natl. Acad. Sci. U.S.A. 2004;101:1177.
47. Tjandra N, Tate S, Ono A, Kainosho M, Bax A. J. Am. Chem. Soc. 2000;122:6190.
48. Wu Z, Delaglio F, Tjandra N, Zhurkin VB, Bax A. J. Biomol. NMR 2003;26:297.
49. Mollova ET, Pardi A. Curr. Opin. Struct. Biol. 2000;10:298.
50. Macdonald D, Lu P. Curr. Opin. Struct. Biol. 2002;12:337.
51. Mollova ET, Hansen MR, Pardi A. J. Am. Chem. Soc. 2000;122:11561.
52. McCallum SA, Pardi A. J. Mol. Biol. 2003;326:1037.
53. Zhou H, Vermeulen A, Jucker FM, Pardi A, Biopolymers 1999;52:168.
54. Reiter NJ, Blad H, Abildgaard F, Butcher SE. Biochemistry 2004;43:13739.
55. Al-Hashimi HM, Gosser Y, Gorin A, Hu W, Majumdar A, Patel DJ. J. Mol. Biol. 2002;315:95.
56. Al-Hashimi HM, Pitt SW, Majumdar A, Xu W, Patel DJ. J. Mol. Biol. 2003;329:867.
57. Bondensgaard K, Mollova ET, Pardi A. Biochemistry 2002;41: 11532.
58. Horrocks WD Jr, Sipe III JP. Science 1972;177:994.
59. Banci L, Bertini I, Savellini GG, Romagnoli A, Turano P, Cremonini MA, Luchinat C, Gray HB. Proteins 1997;29:68.
60. Bertini I, Janik MB, Lee YM, Luchinat C, Rosato A. J. Am. Chem. Soc. 2001;123:4181.
61. Biekofsky RR, Muskett FW, Schmidt JM, Martin SR, Browne JP, Bayley PM, Feeney J. FEBS Lett. 1999;460:519.
62. Bertini I, Del Bianco C, Gelis I, Katsaros N, Luchinat C, Parigi G, Peana M, Provenzani A, Zoroddu MA. Proc. Natl. Acad. Sci. U.S.A. 2004;101:6841.
63. Turjanski AG, Estrin DA, Rosenstein RE, McCormick JE, Martin SR, Pastore A, Biekofsky RR, Martorana V. Protein Sci. 2004;13:2925.
64. Banci L, Bertini I, Cavallaro G, Giachetti A, Luchinat C, Parigi G. J. Biomol. NMR 2004;28:249.
65. Banci L, Bertini I, Cremonini MA, Gori-Savellini G, Luchinat C, Wuthrich K, Guntert P. J. Biomol. NMR 1998;12:553.
66. Gochin M, Roder H. Protein Sci. 1995;4:296.
67. Gochin M. Struct. Fold Des. 2000;8:441.
68. Baig I, Bertini I, Del Bianco C, Gupta YK, Lee YM, Luchinat C, Quattrone A. Biochemistry 2004;43:5562.
69. Prudencio M, Rohovec J, Peters JA, Tocheva E, Boulanger MJ, Murphy ME, Hupkes HJ, Kosters W, Impagliazzo A, Ubbink M. Chemistry 2004;10:3252.
70. Pintacuda G, Moshref A, Leonchiks A, Sharipo A, Otting G. J. Biomol. NMR 2004;29:351.
71. Dvoretsky A, Gaponenko V, Rosevear PR. FEBS Lett. 2002; 528:189.
72. Ikegami T, Verdier L, Sakhaii P, Grimme S, Pescatore B, Saxena K, Fiebig KM, Griesinger C. J. Biomol. NMR 2004;29: 339.

73. Wohnert J, Franz KJ, Nitz M, Imperiali B, Schwalbe H. J. Am. Chem. Soc. 2003;125:13338.
74. Donaldson LW, Skrynnikov NR, Choy WY, Muhandiram DR, Sarkar B, Forman-Kay JD, Kay LE. J. Am. Chem. Soc. 2001; 123:9843.
75. Louhivuori M, Paakkonen K, Fredriksson K, Permi P, Lounila J, Annila A. J. Am. Chem. Soc. 2003;125:15647.
76. Shortle D, Ackerman MS. Science 2001;293:487.
77. Ohnishi S, Lee AL, Edgell MH, Shortle D. Biochemistry 2004;43:4064.
78. Mohana-Borges R, Goto NK, Kroon GJ, Dyson HJ, Wright PE. J. Mol. Biol. 2004;340:1131.
79. Mesleh MF, Opella SJ. J. Magn. Reson. 2003;163:288.
80. Thapar R, Mueller GA, Marzluff WF. Biochemistry 2004; 43:9390.
81. Fieber W, Kristjansdottir S, Poulsen FM. J. Mol. Biol. 2004; 339:1191.
82. Ding K, Louis JM, Gronenborn AM, J. Mol. Biol. 2004;335: 1299.
83. Tian F, Al-Hashimi HM, Craighead JL, Prestegard JH. J. Am. Chem. Soc. 2001;123:485.
84. Neubauer H, Meiler J, Peti W, Griesinger C. Helv. Chim. Acta. 2001;84:243.
85. Martin-Pastor M, Bush CA. Carbohydr. Res. 2000;323:147.
86. Martin-Pastor M, Bush CA. Biochemistry 2000;39:4674.
87. Azurmendi HF, Martin-Pastor M, Bush CA. Biopolymers 2002;63:89.
88. Berthault P, Jeannerat D, Camerel F, Alvarez Salgado F, Boulard Y, Gabriel JC, Desvaux H. Carbohydr. Res. 2003;338: 1771.
89. Tolman JR, Al-Hashimi HM, Kay LE, Prestegard JH. J. Am. Chem. Soc. 2001;123:1416.
90. Yi X, Venot A, Glushka J, Prestegard JH. J. Am. Chem. Soc. 2004;126:13636.
91. Thiele CM, Berger S. Org. Letters 2003;5:705.
92. Thiele CM. J. Org. Chem. 2004;69:7403.
93. Verdier L, Sakhaii P, Zweckstetter M, Griesinger C. J. Magn. Reson. 2003;163:353.
94. Yan J, Kline AD, Mo H, Shapiro MJ, Zartler ER. J. Org. Chem. 2003;68:1786.
95. Aroulanda C, Boucard V, Guibe F, Courtieu J, Merlet D. Chemistry 2003;9:4536.
96. Canlet C, Merlet D, Lesot P, Meddour A, Loewenstein A, Courtieu J. Tetrahedron-Asymmetr. 2000;11:1911–1918.
97. Mangoni A, Esposito V, Randazzo A. Chem. Commun. (Camb). 2003;7(1):154.

Refinement of Nucleic Acid Structures with Residual Dipolar Coupling Restraints in Cartesian Coordinate Space

Nikolai B. Ulyanov, Zhihua Du, and Thomas L. James
Department of Pharmaceutical Chemistry, University of California at San Francisco, San Francisco, CA 94143-2280, USA

Introduction

During the past decade, measurement of residual dipolar constants (RDC) in weakly oriented molecules has been established as an invaluable source of structural information, and RDC data are now often used in structure determination of biological macromolecules via NMR [1–4]. Indeed, incorporation of RDC data in nucleic acid structure refinement apparently improves the accuracy and precision of global conformations and possibly local conformations as well [5–7].

Traditional (without RDC) refinement of solution NMR structures involved short-range structural restraints derived from the nuclear Overhauser effect (NOE) and from scalar J-coupling data: interproton distances and torsion angles, respectively. The degree of structure definition under such circumstances depended on the number of structural restraints and on their precision and accuracy. With proper care, local conformations could be accurately refined to a high degree of definition but, due to error propagation, the global structure was defined less precisely and perhaps less accurately. The situation is more severe for nucleic acids than for proteins, because errors propagate more efficiently in nucleic acids due to their typically elongated shape. Besides, nucleic acids have a smaller proton density and uneven spatial distribution of protons. In particular, phosphodiester groups do not have protons, and the only residues with nonexchangeable protons in the bottom of the minor groove are adenines (with H2 protons). Adenine H2 protons have NOE contacts across the minor groove with protons from the opposite strand [8,9], which help define better the local conformation. Sequences lacking or having only few adenines are therefore inherently worse defined by the NOE data.

In an effort to overcome these problems, several groups, mostly working in the field of DNA structure determination, have been developing methods to use NOE data quantitatively. Instead of deriving approximate interproton distances under the isolated spin pair approximation, these methods are based on calculation of the complete matrix of dipole–dipole relaxation rates, which are responsible for observed NOE intensities [10–12]. Practically, structures were determined either by incorporating NOE calculations into the refinement program [12–15] or with the help of an iterative procedure to determine the interproton distances [16–19]. An approach extensively used in our lab involved an iterative complete relaxation rate matrix-based procedure, MARDIGRAS, to calculate interproton distances from NOE intensities, which was subsequently extended to include a random error analysis [20,21] and to take into account partial relaxation [22]. This approach allowed determining accurate and well-defined solution structures of relatively short (1–1.5 helical turns) fragments of nucleic acids [23–27]. However, the degree of definition of the global conformation suffered considerably for larger multi-domain structures [28,29]. In fact, even the definition of the local conformations depended critically on the number and distribution of experimental restraints, although complete relaxation matrix-based methods were used [24,30,31].

The situation has improved dramatically with the incorporation of RDC data into refinement protocols [4,32]. The contribution of the through-space dipole–dipole interactions to spin–spin splitting of resonances is normally averaged to zero in isotropic solutions. However, if a macromolecule is weakly oriented relative to the magnetic field, such as in a dilute liquid crystalline solution, the average RDC is nonzero and depends on the molecular alignment tensor, the orientation of the dipole–dipole vector relative to the alignment tensor, and the internuclear distance. RDC data can be readily incorporated into refinement algorithms, especially for nuclei connected with a single bond, when the internuclear distance r is fixed. RDC data depend on r^{-3} rather than r^{-6}, as with NOE data, so they are more sensitive to longer range dipole–dipole interactions: this, together with the dependence of RDC values on orientation, should improve dramatically the degree of definition of the global conformation, even for multi-domain structures. Indeed, refinements using simulated data have shown that addition of RDC restraints improved greatly the accuracy and precision of both local and global conformations of DNA duplexes containing A-tracts [5,6]. Using RDC data quickly became the method of choice for determining NMR solution structures of nucleic acids: DNA [33–40] and especially RNA [7,41–48].

Graham A. Webb (ed.), Modern Magnetic Resonance, 665–670.
© 2008 *Springer.*

RDC restraints have been implemented in several refinement packages, including the NIH version of XPLOR [49,50], DYANA [51], AMBER [52], and SCULPTOR (a modified version of the DISCOVER package, MSI) [53]. AMBER and SCULPTOR perform structure refinements in the Cartesian coordinate space, while DYANA performs refinements in the space of internal coordinates, specifically, torsion angles. XPLOR is capable of structure calculations in both Cartesian and torsion angle space. The NIH version of XPLOR is the most widely used package for RDC refinements, which includes many new NMR-oriented options, in particular a new code for refinement in torsion angle space [54]. Torsion angle dynamics is indeed a recommended option for NMR refinements [49], because of its efficiency. Unfortunately, in many published applications, authors do not state explicitly if the refinement was carried out in torsion angle or Cartesian coordinate space. Our recent experience with refinement of RNA structures in Cartesian coordinate space using AMBER 7 showed that RDC restraints require special treatment [47], which we discuss below. We will describe structural refinement protocols in the context of functionally significant RNA fragments from enteroviruses.

Loop B RNA from Domain IV of the Enterovirus Internal Ribosome Entry Site

Enteroviruses, members of the Picornaviridae family, are positive single-stranded RNA viruses; Poliovirus is a typical example of an enterovirus. The genomic RNA of enteroviruses is uncapped; the internal ribosome entry site (IRES) sequence, a part of the 5′-untranslated region (5′-UTR), mediates a cap-independent translation by allowing ribosomes to enter mRNA internally. In addition, with help from viral and host protein factors, IRES controls a switch from protein synthesis to negative-strand RNA replication [55]. The secondary structure of 5′-UTR is predicted to have six distinct domains, with domains II–VI forming the IRES [56]. In the absence of the viral protein 3CD, loop B of domain IV is bound by a host protein, polyC-binding protein 2 (PCBP-2) with a dissociation constant of 15 nM [57]; this complex promotes viral translation. When levels of the 3CD protein are sufficiently high, 3CD forms a ternary complex with PCBP-2 and domain I of the 5′-UTR, the cloverleaf structure, with the dissociation constant of 1 nM. As a result, PCBP-2 dissociates from the lower-affinity site on loop B of domain IV. These events inhibit the viral translation and trigger the start of viral RNA replication.

The secondary structure of loop B of domain IV is strongly conserved, with a GNRA apical tetraloop and a cytosine-rich six-nucleotide asymmetric internal loop (bulge) in the middle of the stem. Although not absolutely conserved in sequence, the six-nucleotide bulge is cytosine-rich in all enteroviruses [47], and the cytosine residues are required for both virus translation and PCBP-2 recognition [57]. We have solved NMR structures of two natural sequence variants of the loop B RNA from enteroviral domain IV using quantitative interproton distance restraints, torsion angle restraints and ^{13}C–H RDC restraints. Details of the refinements are published elsewhere [47]; here, we will briefly summarize them and focus on some aspects of using RDC restraints with the AMBER package. Sequences of the two sequence variants, 10C and 10U, are shown below.

```
                            C/U10-C11
                            U9    C12
                            A8    U13
5'-G1 -G2 -A3 -G4 -G5 -A6 -C7    C14-A15-C16-G17-G18-G19-U20
    |   |   |   |   |   |   |      |   |   |   |   |   *  G21
   C34-C33-U32-C31-C30-U29-G28---G27-U26-G25-C24-C23-A22
```

For simplicity, only the 10C sequence variant will be discussed here.

Structural Restraints

The structural restraints for the 10C RNA included 575 distance restraints and 86 ^{13}C–H RDC restraints. Distance restraints included 281 quantitative restraints calculated with MARDIGRAS from the accurately integrated NOE intensities in homonuclear 2D NOESY data set acquired in D_2O, 97 qualitatively categorized distance restraints involving exchangeable protons from the 2D water NOESY, 72 6.0-Å upper bounds for peaks observed only in the 3D ^{13}C-edited NOESY spectrum, 88 non-NOE restraints (lower bounds of 5 Å) for proton pairs that did not have any intensity in any of the NOESY spectra, but tended to have a short distance in preliminary calculations, and 37 hydrogen bond restraints. In addition, torsion angle restraints were used for sugars consistent with C2′-*endo* conformation (residues 9–13 and 27 that showed a strong H1′–H2′ cross-peak in DQF-COSY spectrum) or C3′-*endo* conformation (the rest of the residues). Backbone torsion angle restraints consistent with a generic A-form were used for the stem residues.

Structure Refinement

Structures were calculated in three stages. At first, the DYANA 1.5 program [51] was used to carry out simulated annealing with 10,000 steps of torsion angle dynamics starting with 100 randomized initial structures; only distance and torsion angle restraints but no RDC restraints were used at this stage. The 50 best DYANA structures were passed to the SANDER module of AMBER 7 suite of programs [52] and refined with the same type of structural restraints (no RDC restraints). At the last stage, structures were refined further with SANDER using both distance restraints and RDC restraints.

Before the last stage, the structures had low residual distance and torsion angle restraint deviations but, as expected, high-residual RDC deviations. The root mean square (RMS) deviation between measured and predicted RDC values was 26.5 Hz on average for the 10 best structures. To calibrate the force constant for the RDC restraints, we carried out three series of test calculations, performing short restrained minimizations with distance, torsion angle, and RDC restraints. The RDC force constant was kept at 0.001, 0.01, or 0.1·kcal/mol/Hz^2; these values are below of those typically used for the RDC refinements, e.g. [44]. While the lowest force constant had little impact on the structures and calculated RDC (average RMS of 25.4 Hz), the response was very strong for higher force constants: average RMS between observed and calculated RDC values decreased to 12.9 and 5.9 Hz for force constants of 0.01 and 0.1 kcal/mol/Hz^2, respectively. Individual structures had RMS deviations as low as 2.4 Hz. This was an unexpected result, because minimization in the Cartesian coordinate space, either restrained or free, usually has very little effect on global conformations. Indeed, the global structures changed little after the minimization with RDC restraints, with an average atomic RMSD of 0.13 Å (Figure 1A). Close inspection of the structures showed, however, that the improvement of the RDC restraints came at the expense of the local valence geometries (Figure 1B). In the Cartesian coordinate-based methods, the positions of individual atoms are free to change, and the resulting bond angles are determined by a number of energy terms in the force field [58]. Introduction of foreign terms into the force field, such as experimental restraint energy, has the potential to distort the idealized local conformations. We have noticed in the past a similar problem when using distance restraints with AMBER refinement [59], but the distortions were not as severe in that case.

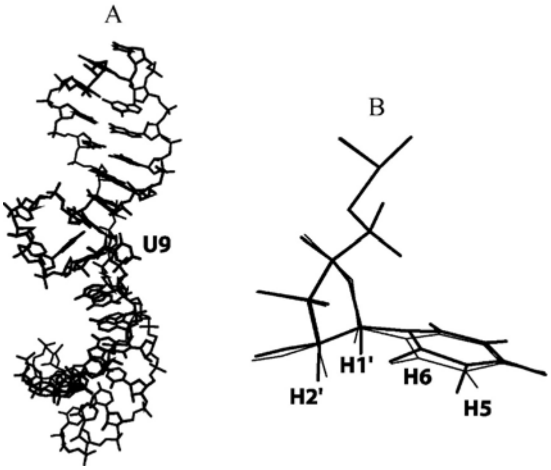

Fig. 1. Superposition of the 10C RNA structure refined with the distance and torsion angle restraints with the structure, which had been further restrained–minimized with the RDC restraints. (A) Global conformations are essentially identical, with the atomic RMSD 0.1 Å. (B) Residue U9 of the same superposition. The structure minimized with the RDC restraints is shown with thin lines. A distorted local conformation is apparent for this structure. This picture was generated with the graphics program MidasPlus [64].

A similar problem has been encountered by others [41,60]. To reduce distortions of local geometries caused by orientational RDC restraints, force constants responsible for the planarity of bases were increased during the refinement of a theophylline-binding RNA aptamer [41], and additional bond angle restraints were introduced reinforcing the ideal protein backbone geometry during the refinement of a protein–DNA complex [60]. When we attempted a similar approach for refining the 10C RNA structure, it indeed improved the geometries of the nitrogenous bases; however, the local geometries of sugar rings became even more distorted (not shown). Specifically, ribose rings became “average” and flatter: typically, the pseudorotation phase angle became 80°–90° (average between C2′-*endo* and C3′-*endo*), and the amplitude of pseudorotation ca. 10° (typical values of the amplitude must be in the range of 35°–40°). The reason for this is clear. All endocyclic bond angles in a ribose have an equilibrium value of 109.5° in the AMBER parm94 force field. This corresponds to an almost flat geometry of sugar rings (equilibrium values of 108° would correspond to perfectly planar geometry). It is a balance of the bond angles potential and torsion angles potential that keeps the sugar geometry reasonable; by increasing the weight of the bond angles term, we distorted the equilibrium local geometries.

Table 1: Bond angles (degrees) involving hydrogen atoms in sugar–phosphate moieties

Atoms	C2′-*endo*	C3′-*endo*
N1/N9–C1′–H1′	109.6	109.5
C2′–C1′–H1′	109.6	109.5
O4′–C1′–H1′	109.6	109.5
C1′–C2′–H2′	109.7	111.8
C3′–C2′–H2′	109.7	111.8
O2′–C2′–H2′	109.7	111.8
C2′–C3′–H3′	111.5	109.4
C4′–C3′–H3′	111.5	109.4
O3′–C3′–H3′	111.5	109.4
C3′–C4′–H4′	108.6	108.8
C5′–C4′–H4′	108.6	108.8
O4′–C4′–H4′	108.6	108.8
C4′–C5′–H5′/H5″	108.9	108.9
O5′–C5′–H5′/H5″	108.9	108.9
H5′–C5′–H5″	109.5	109.5

The endocyclic bond angles in the sugar ring depend on a particular sugar pucker. A survey of geometric parameters observed in high-resolution crystal structures of nucleosides and nucleotides has been published, separately for C2′-*endo* and C3′-*endo* sugar puckers [61,62], and the data for the heavy atoms are available in a computer-readable form from the NDB Nucleic Acid Database [63]. To generate similar parameters involving protons on riboses, we carried out the following procedure. At first, separately for C2′-*endo* and C3′-*endo* conformations, we generated bond length and bond angle restraints using the data for the heavy atoms from the published survey [62]. Using these restraints, we carried out restrained AMBER minimization on a nucleotide unit, with force constants of 1000 kcal/mol/Å^2 and 1000 kcal/mol/rad^2 for distances and angles, respectively; protons were left unrestrained. Then, using heavy atoms of the calculated structures, we calculated new proton positions using geometric considerations. Specifically, the CH bond length was assumed to be 1.09 Å. A proton in the CH group was placed on a line forming equal angles with all proximal CX bonds. For example, for the H1′ proton, angles H1′–C1′–N9, H1′–C1′–C2′, and H1′–C1′–O4′ are equal. Protons H5′ and H5″ are placed on the bisector plane to O5′–C5′–C4′ such that the H5′–C5′–H5″ angle adopts a tetrahedral value. The resulting bond angles involving protons are summarized in Table 1.

Published data for the heavy atoms [62] and data of Table 1 for protons were used to prepare bond length and bond angle restraints reinforcing the local geometries of sugar–phosphate moieties for the 10C RNA. These restraints depend on sugar pucker: C2′-*endo* for residues 9–13 and 27, and C3′-*endo* for the rest of the residues. Similar restraints and improper torsion angle restraints were generated for nitrogenous bases using the parm94 parameters. Altogether, several thousand such local geometry restraints were generated, with force constants of 1000 kcal/mol/Å^2 and 1000 kcal/mol/rad^2 for distances and angles, respectively. For the experimental NOE distances, non-NOE restraints, and hydrogen bond restraints, a force constant of 10 kcal/mol/Å^2 was used. For sugar pucker restraints and backbone torsion restraints, a force constant of 100 kcal/mol/rad^2 was used. The force constant for the RDC restraints was 0.2 kcal/mol/Hz^2. These restraints were used with the simulated annealing protocol as described [47] to calculate the RNA structures; the global conformations were adjusted according to the RDC restraints, but the local conformations remained undistorted. The only unusual feature of this protocol was the requirement of tighter-than-usual coupling to a thermal bath. Because the large number of local geometry restraints work against the force field for the sugar rings, it may create large local forces. The integration step for MD simulations was decreased to 0.5 fs (integration step as low as 0.2 fs has been reported for MD refinements with RDC restraints) [35]. In addition, the parameter TAUTP, which defines in AMBER the coupling to the thermal bath, was varied during the trajectory as shown in Figure 2A.

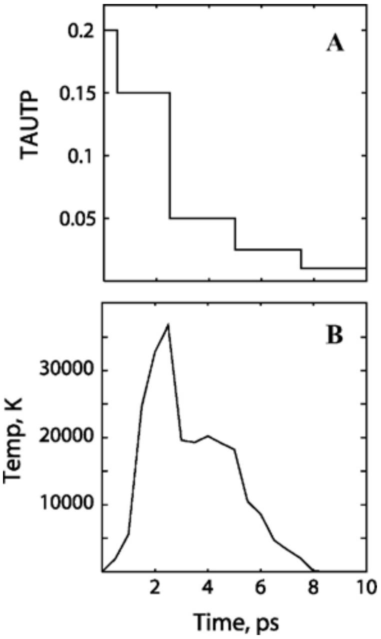

Fig. 2. Refinement protocol with RDC restraints. (A) Parameter TAUTP defining the coupling to the thermal bath. (B) Temperature recorded in a typical trajectory.

The actual temperature reading during a typical trajectory is shown in Figure 2B.

In conclusion, special care must be given to RDC restraints when used in refinement protocols in the Cartesian coordinate space. Using a large number of sugar pucker-dependent restraints, reinforcing the local geometry allows refinement of global structures without distorting local conformations. Incidentally, the same approach prevents distortions of local conformations due to NOE-derived distance restraints. Such a problem does not exist for refinement protocols in internal coordinate space, such as implemented in XPLOR; therefore the refinement protocols are simpler, see, e.g. [7]. However, flexibility in choosing the refinement method is useful. In particular, AMBER refinements with RDC restraints have a very helpful option of adjusting the alignment tensor in the course of the refinement.

References

1. Tolman JR, Flanagan JM, Kennedy MA, Prestegard JH. Proc. Natl. Acad. Sci. U.S.A. 1995;92:9279–83.
2. Tjandra N, Bax A. Science. 1997;278:1111–4.
3. Tjandra N, Omichinski JG, Gronenborn AM, Clore GM, Bax A. Nat. Struct. Biol. 1997;4:732–8.
4. Lipsitz RS, Tjandra N. Annu. Rev. Biophys. Biomol. Struct. 2004;33:387–413.
5. Vermeulen A, Zhou H, Pardi A. J. Am. Chem. Soc. 2000;122:9638–47.
6. McAteer K, Kennedy MA. J. Biomol. Struct. Dyn. 2003;20:487–506.
7. Du Z, Yu J, Ulyanov NB, Andino R, James TL. Biochemistry. 2004;43:11959–72.
8. Weiss MA, Patel DJ, Sauer RT, Karplus M. Proc. Natl. Acad. Sci. U.S.A. 1984;81:130–34.
9. Behling RW, Kearns DR. Biochemistry. 1986;25:3335–46.
10. Keepers JW, James TL. J. Magn. Reson. 1984;57:404–26.
11. Olejniczak ET, Gampe RT Jr, Fesik SW. J. Magn. Reson. 1986;67:28–41.
12. Lefevre J-F, Lane AN, Jardetzky O. Biochemistry. 1987;26:5076–90.
13. Gupta G, Sarma MH, Sarma RH. Biochemistry. 1988;27:7909–18.
14. Borgias BA, James TL. J. Magn. Reson. 1988;79:493–512.
15. Baleja JD, Moult J, Sykes BD. J. Magn. Reson. 1990;87:375–84.
16. Boelens R, Koning TMG, van der Marel GA, van Boom JH, Kaptein R. J. Magn. Reson. 1989;82:290–308.
17. Borgias BA, James TL. In: NJ Oppenheimer, TL James (Eds). Methods in Enzymology, Nuclear Magnetic Resonance, Part A: Spectral Techniques and Dynamics. Academic Press: New York, 1989, pp 169–183.
18. Post CB, Meadows RP, Gorenstein DG. J. Am. Chem. Soc. 1990;112:6796–803.
19. Madrid M, Llinas E, Llinas M. J. Magn. Reson. 1991;93:329–46.
20. Borgias BA, James TL. J. Magn. Reson. 1990;87:475–87.
21. Liu H, Spielmann HP, Ulyanov NB, Wemmer DE, James TL. J. Biomol. NMR. 1995;6:390–402.
22. Liu H, Tonelli M, James TL. J. Magn. Reson. B.1996;111:85–9.
23. Mujeeb A, Kerwin SM, Kenyon GL, James TL. Biochemistry. 1993;32:13419–31.
24. Weisz K, Shafer RH, Egan W, James TL. Biochemistry. 1994;33:354–66.
25. Tonelli M, James TL. Biochemistry. 1998;37:11478–87.
26. Ulyanov NB, Bauer WR, James TL. J. Biomol. NMR. 202;22:265–80.
27. Comolli LR, *et al.* Nucleic Acids Res. 2002;30:4371–9.
28. Ulyanov NB, *et al.*, Biochemistry. 1998;37:12715–26.
29. Schmitz U, *et al.* RNA. 1999;5:1419–29.
30. Metzler WJ, Wang C, Kitchen D, Levy R. M, Pardi A. J. Mol. Biol. 1990;214:711–36.
31. Ulyanov N, *et al.*, Biochemistry. 1992;31:3918–30.
32. Bax A, Kontaxis G, Tjandra N. Methods Enzymol. 2001;339:127–74.
33. Tjandra N, Tate S, Ono A, Kainosho M, Bax A. J. Am. Chem. Soc. 2000;122:6190–200.
34. MacDonald D, Herbert K, Zhang X, Polgruto T, Lu P. J. Mol. Biol. 2001;306:1081–98.
35. Padrta P, Stefl R, Kralik L, Zidek L, Sklenar V. J. Biomol. NMR. 2002;24:1–14.
36. Wu Z, Delaglio F, Tjandra N, Zhurkin VB, Bax A. J. Biomol. NMR. 2003;26:297–315.
37. Barbic A, Zimmer DP, Crothers DM. Proc. Natl. Acad. Sci. U.S.A. 2003;100:2369–73.
38. Stefl R, Wu H, Ravindranathan S, Sklenar V, Feigon J. Proc. Natl. Acad. Sci. U.S.A. 2004;101:1177–82.
39. Wu B, *et al.*, Nucleic Acids Res. 2004;32:3228–39.
40. McAteer K, *et al.* Biopolymers. 2004;75:497–511.
41. Sibille N, Pardi A, Simorre JP, Blackledge M. J. Am. Chem. Soc. 2001;123:12135–6.
42. Theimer CA, Finger LD, Trantirek L, Feigon J. Proc. Natl. Acad. Sci. U.S.A. 2003;100:449–54.
43. Lukavsky PJ, Kim I, Otto GA, Puglisi JD. Nat. Struct. Biol. 2003;10:1033–8.
44. McCallum SA, Pardi A. J. Mol. Biol. 2003;326:1037–50.
45. Lawrence DC, Stover CC, Noznitsky J, Wu Z, Summers MF. J. Mol. Biol. 2003;326:529–42.
46. D'Souza V, Dey A, Habib D, Summers MF. J. Mol. Biol. 2004;337:427–42.
47. Du Z, Ulyanov NB, Yu J, Andino R, James T. L. Biochemistry. 2004;43:5757–71.
48. Leeper TC, Varani G. RNA. 2005;9:9.
49. Schwieters CD, Kuszewski JJ, Tjandra N, Clore GM. J. Magn. Reson. 2003;160:66–74.
50. Brunger AT., X-PLOR, Yale University Press: New Haven, 1993.
51. Guntert P, Mumenthaler C, Wuthrich K. J. Mol. Biol. 1997;273:283–98.
52. Case DA, *et al.* Amber 7.0, University of California, San Francisco, 2002.
53. Hus JC, Marion D, Blackledge M. J. Mol. Biol. 2000;298:927–36.
54. Schwieters CD, Clore GM. J. Magn. Reson. 2001;152:288–302.
55. Gamarnik AV, Andino R. Gene Dev. 1998;12:2293–304.

56. Ehrenfeld E, Semler BL. Curr. Top. Microbiol. Immunol. 1995;203:65–83.
57. Gamarnik AV, Andino R. J. Virol. 2000;74:2219–26.
58. Cornell WD, *et al*. J. Am. Chem. Soc. 1995;117:5179–97.
59. Ulyanov NB, Schmitz U, James TL, J. Biomol. NMR 1993;3: 547–68.
60. Tsui V, Case DA. J. Am. Chem. Soc. 2000;122:2489–98.
61. Clowney L, *et al*. J. Am. Chem. Soc. 1996;118:509–18.
62. Gelbin A, *et al*. J. Am. Chem. Soc. 1996;118:519–29.
63. Berman HM, *et al*. Biophys. J. 1992;63:751–9.
64. Ferrin TE, Huang CC, Jarvis LE, Langridge R. Mol. Graph. 1988;6:13–27.

Conformational Analysis of DNA and RNA

Gota Kawai
Faculty of Engineering, Chiba Institute of Technology, Chiba 275-0016, Japan

Introduction

As is the case for proteins, NMR methods have been applied to DNA and RNA extensively and methods for the structure determination by NMR are recently almost established [1–6]. In this section, a general view of the NMR application for DNA and RNA is shown.

DNA or RNA consists of four kinds of nucleotides (Figure 1). Nomenclature for DNA and RNA in NMR can be found in Ref. [7]. The bases form the Watson–Crick type base pairs, A-T (A-U in RNA) and G-C, and stack to each other to form the double helix structure, or a stem. Due to the conformational flexibility of the nucleotide residues, DNA can form three types of stems, A, B, and Z forms. On the other hand RNA forms the A-type stem dominantly [8]. However, this does not mean that RNA structure is simple. RNA forms tertiary structures including loop, bulge, or internal loop as well as long-range interactions to express their biological functions.

Conformation of Nucleotides

As shown in Figure 1, each nucleoside consists of at least two rings, base and ribose, and this restrict the conformation of nucleosides, leading that relatively small number of information can work for determination of conformational characteristics. Figure 2 shows the torsion angles in nucleic acids and Figure 3 shows the possible conformations of nucleosides. The puckering of ribose or deoxyribose plays most important role for the conformation of nucleic acids. The puckering mainly in the C2′-*endo* or the C3′-*endo* forms (Figure 3a). The conformation of ribose or deoxyribose ring is generally described by the pseudorotation (P) angle [7,9] and the C2′-*endo* and C3′-*endo* forms are also donated as the S and N form, respectively. The rotation around the glycosidic bond (x angle, Figure 3b) depends on the puckering. The rotation around the C4′–C5′ (the y angle, Figure 3c) is dominantly in the gg form and also depends on the puckering. For review of the nucleotide conformation, see Ref. [8].

NMR Signal for DNA and RNA and Their Assignment

Figure 4 shows the typical ^{1}H chemical shift range for nucleic acids. Imino protons in base pairs resonate in lower field and give better separations compare to other resonances in nucleic acids although the line width is larger due to the dynamic process. The immobile protons for RNA, especially H2′–H5″, resonate in narrow regions to make the signal assignment rather difficult.

Imino Proton Signals

Imino proton resonances give quite useful information for the secondary structure and tertiary interaction as well as the structural change. Each Watson–Crick base pair gives an imino proton resonance. The imino protons easily exchange with the proton of solvent and measurements are performed for RNA samples in typically 95% H_2O/5% D_2O solution with solvent signal suppression. In RNA, G-U and G-A base pairs are frequently found. The first step of the signal assignment is the discrimination of the kind of bases for each imino proton signals. As shown in Figure 4, chemical shift regions for each imino proton signal are somehow overlapped to each other. NOESY spectra give information for the difference between imino proton signals due to the A-U and G-U pairs. G-U pairs give two imino proton signals and strong NOEs between the two imino protons. The ^{15}N chemical shifts give clear indication for base type information [10]. Assignment of the imino proton resonances is mainly based on the sequential connectivity through NOE between imino protons of adjacent base pairs. This is similar to the case of main chain assignment for proteins. However, it should be in mind that, in the case of imino proton of DNA/RNA, assignments are based on the assumption of the formation of the secondary structure.

Immobile Proton Signals

The strategy for signal assignment for immobile protons is based on the well-known sequential assignment [1]. Although stable isotopic (SI) labeling has been introduced

Graham A. Webb (ed.), Modern Magnetic Resonance, 671–676.
© 2008 *Springer*.

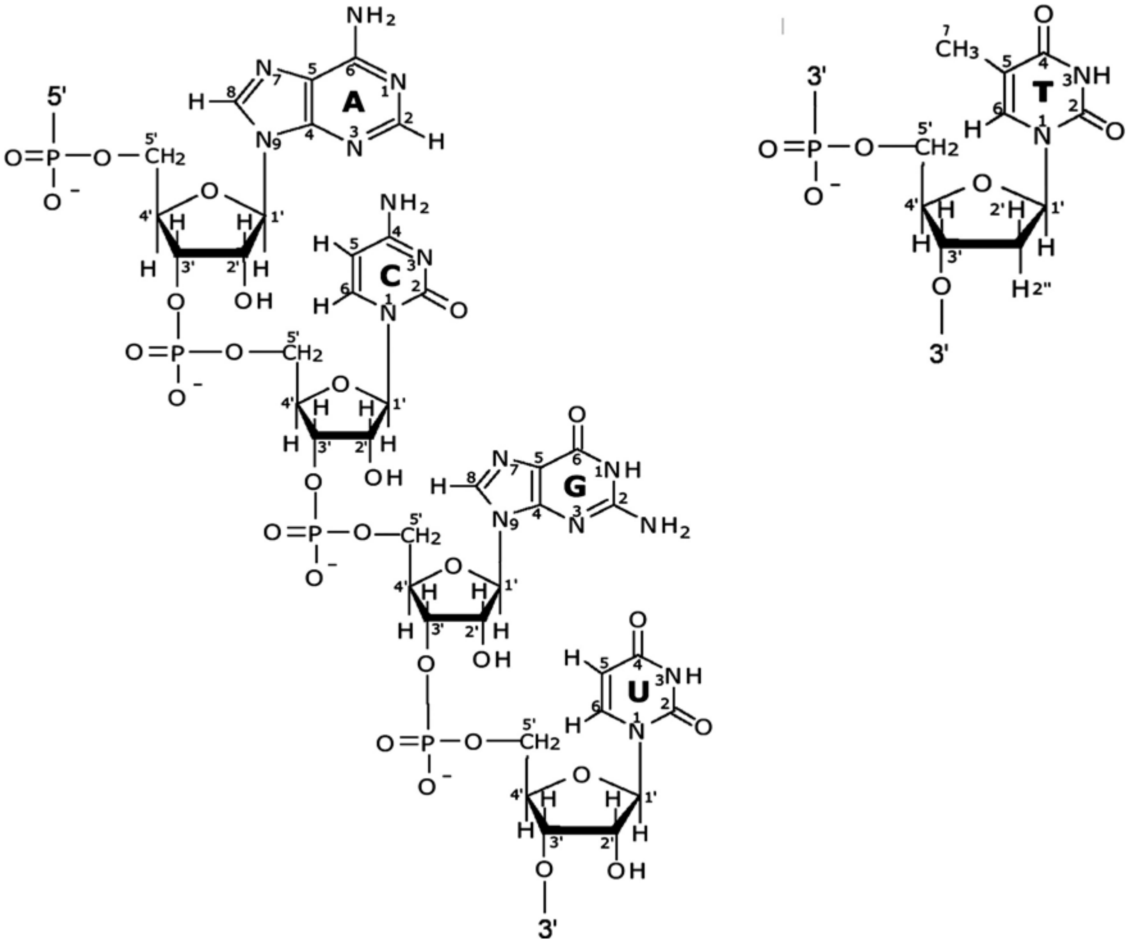

Fig. 1. Chemical structure of RNA and DNA. In DNA, 2′-OH of ribose and H5 of uracil base are replaced to H2″ and 7-CH_3 to form deoxyribose and thymine base, respectively.

to the analysis of RNA, the assignment is in many cases depends on inter-residue NOEs between base–ribose and base–base protons. This is because of the poor dispersion of chemical shift for ^{1}H as well as ^{13}C nuclei of RNA main chain, P–O5′–C5′–C4′–C3′–O3′. TOCSY or HOHAHA experiment is effective to analyze the ribose spin system as is the case for oligosaccharide. In the case of DNA, the presence of two protons, H2′ and H2″, at the second position of the ribose ring makes the coherence flow effective. With the appearance of H2′/H2″ in the deference chemical shift region with other protons, the TOCSY experiment is successive. In the case of RNA, the small value of J(H1′–H2′) for stem region in which the ribose takes the C3′-*endo* form makes the TOCSY spectrum poor. Thus, HCCH type experiments [11,12] with ^{13}C-labeled RNA sample must be required to obtain the information for the intra-residual correlation between H1′ and H2′. The relayed HOHAHA type experiment, which originally applied for the oligosaccharide in which the coupling between H4 and H5 is generally small, may overcame the small coupling problem in ribose moiety [13].

Phosphorus Signals

Although ^{1}H–^{31}P correlations are important information for the sequential assignment through main chain of nucleic acids [5], use of them is sometimes difficult due to the severe overlap of ^{31}P signals and ^{31}P chemical shift anisotropy. Because the energy of transition as well as natural abundance of ^{31}P is high enough, ^{1}H–^{31}P correlation

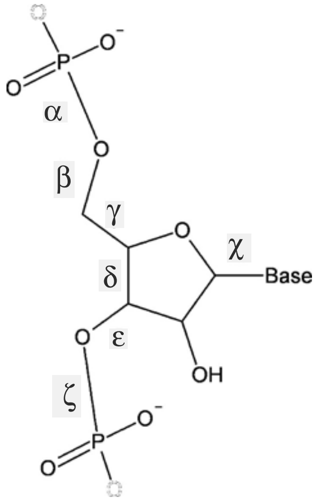

Fig. 2. Torsion angles in nucleic acids.

experiment can be started from the ^{31}P magnetization [14–16]. ^{17}O-labeling is a possibility to make unambiguous assignment of ^{31}P signals for nucleic acids [17].

Stable Isotopic Labeling

The SI labeling is powerful tool for the NMR analysis of biomacromolecules and SI labeling, ^{13}C and ^{15}N, for RNA is also being the standard techniques [4,5,10] as shown above. SI-labeled DNA and RNA can be prepared either by chemical synthesis or by enzymatic synthesis. The SI-labeled phosphoroamidite units and nucleotides triphosphates (NTPs) can be obtained commercially. Furthermore, custom synthesis of SI-labeled oligonucleotides, DNA as well as RNA, is also available. Residue-specific labeling or segment-specific labeling is quite useful to make unambiguous assignment. Chemical synthesis as well as enzymatic synthesis can be used for such kind of labeling [18–21]. Fractional ^{2}H labeling might be important to reduce the proton density and increase the sensitivity for larger RNAs as applied for larger proteins.

Structural Analysis

Conformation of Nucleosides

The conformation of nucleotides can be analyzed in detail by NMR, the spin–spin coupling constants (J) and NOEs. In the case of nucleosides and nucleotides, the conformation is not fixed but in the conformational equilibrium. Thus, fractional population of each conformer must be obtained. The puckering can be analyzed by the J(H1′–H2′) and J(H3′–H4′) values with the well known

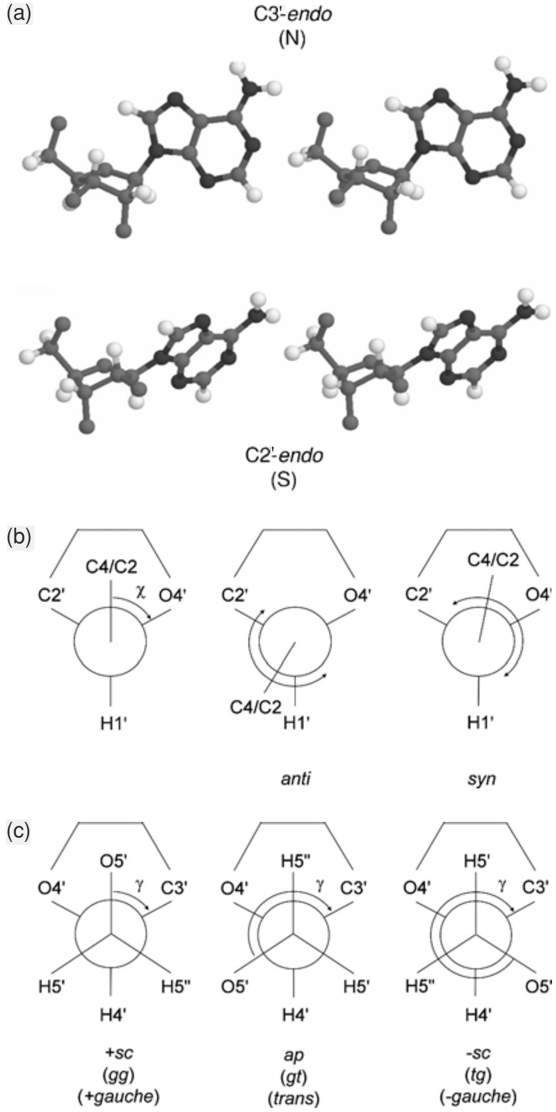

Fig. 3. Conformations of nucleotides. (a) Sugar puckering. The C2′-*endo* form is corresponding to the range of $P = 0^\circ$–18° and the C3′-*endo* form is to the range of $P = 144^\circ$–162°. (b) Rotation around the glycosidic bond (χ). In the case of the C2′-*endo* form, the χ angle is dominantly in between 180° and 216° which is in the range of the *anti* conformation. In the case of the C3′-*endo* form, the χ angle can be in the ranges of the *anti* form (216°–252°) or the *syn* form (36°–72°). (c) Rotation around the C4′–C5′ bond (γ).

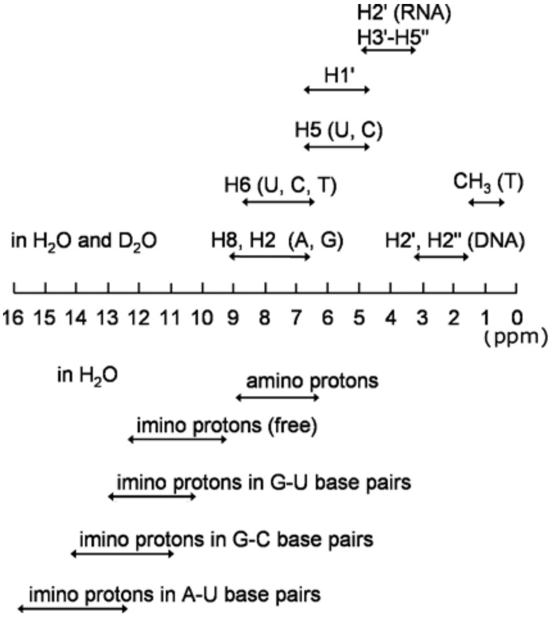

Fig. 4. ^{1}H chemical shift ranges for DNA and RNA.

equations,

$$X(\mathrm{C2'}-endo) = J(\mathrm{H1'}-\mathrm{H2'})/[J(\mathrm{H1'}-\mathrm{H2'}) + J(\mathrm{H3'}-\mathrm{H4'})] \quad (1a)$$

$$X(\mathrm{C3'}-endo) = J(\mathrm{H3'}-\mathrm{H4'})/[J(\mathrm{H1'}-\mathrm{H2'}) + J(\mathrm{H3'}-\mathrm{H4'})] \quad (1b)$$

where X(C2′-*endo*) and X(C3′-*endo*) are the fractional populations for the C2′-*endo* and C3′-*endo* forms, respectively [22]. For standard nucleosides and nucleotides, the value of J(H1′–H2′) + J(H3′–H4′) is always close to 10 Hz and, thus, the X(C2′-*endo*) and X(C3′-*endo*) can be estimated only with the J(H1′–H2′) values. The puckering of nucleosides and modified nucleosides are extensively analyzed by NMR in relation to the translation of genetic code and stabilization of tRNA structure [23–26]. Relationship between the ribose conformation and chemical shift of base protons was found for 5-substituted uridine and cytidine [27,28].

The γ angle can be analyzed by the J(H4′–H5′) and J(H4′–H5″) values as follows [29].

$$X(\mathrm{gg}) = \{13.7 - [J(\mathrm{H4'}-\mathrm{H5'}) + J(\mathrm{H4'}-\mathrm{H5''})]\}/9.7 \quad (2a)$$

$$X(\mathrm{gt}) = [J(\mathrm{H4'}-\mathrm{H5'}) - 2.0]/9.7 \quad (2b)$$

$$X(\mathrm{tg}) = [J(\mathrm{H4'}-\mathrm{H5''}) - 2.0]/9.7 \quad (2c)$$

The γ angle is affected by the sugar puckering, the +sc is favored for the C3′-*endo* form and less favored for the C2′-*endo* form [30]. The ^{1}H–^{1}H coupling constants for standard nucleotides have been determined precisely in combination with the computer simulation of spectra to obtain precise values for coupling constants [31–35].

For the χ angle, NOEs between the base H8/H6 protons and ribose protons should be used. The NOE between H8/H6 and H1′ can be used to discriminate the *anti* and *syn* conformation qualitatively [1,36]. The χ angle can also be analyzed by the vicinal coupling J(^{13}C2/4-^{1}H1′) and J(^{13}C6/8-^{1}H1′) [37]. Spin coupling between phosphorus and proton can also be used for structure elucidation [6]. Typical values for J(^{31}P–^{1}H) values of P–O–C–H are summarized in Ref. [7]. J(^{31}P–^{13}C2′) and J(^{31}P–^{13}C3′) can be used for determination of the conformation around the C3′–O3′ bond [38].

Conformation of Oligonucleotides

For structural determination, following information is required: (i) inter- and intra-residual distances derived from NOE intensity, (ii) dihedral angles derived from spin coupling constants, and (iii) hydrogen bonding information derived from the analysis of imino proton resonances. In the case of RNA, stem structure is limited to the A-type double helix. Thus, the dihedral constraints fixing to the A-type ribose conformation may be introduced for the region where formation of stem is confirmed experimentally, for example, by sequential assignment of imino proton resonances. As described above, the puckering of ribose ring can be analyzed by the spin couplings. For larger RNA, it is sometimes hard to read the correct value of coupling constant especially for J(H3′–H4′) and, for such cases, the signal intensity of the H1′–H2′ cross peak on the HOHAHA spectra can be used for estimation of the puckering.

Hydrogen bonding can be directly detected by observing the N–N coupling [39,40] and this gives definite evidence for formation of base pairs such as the shared G-A pair [41,42].

3D Structure Determination

With enough number of distance and torsion constraints, the tertiary structure of DNA or RNA can be determined by simulated annealing calculation [5,43]. However, overall structures are sometimes not well converged due to the lack of long-range information in the case of DNA and RNA. This can be improved by using the residual dipolar couplings (RDC) during the refinement calculation as described below. It is noted that the local convergence can be detected by using the structural classification systems, CSNA [44,45].

For structure calculation of DNA and RNA having non-natural residues, force field parameters, especially electrostatic charges, for the specific residue is required. Basically, these parameters can be obtained by the *ab initio* quantum mechanical calculation [46,47]. However, recent program packages used for structure determinations have functions to treat non-natural residues and such systems were applied, for example, for modified nucleotides in tRNA [48,49] and artificial residues in designed DNA [50].

Residual Dipolar Coupling

Global information obtained from the RDC is quite useful for refinement of overall structures [51]. In the case of DNA and RNA, the Pf1 phage system is generally used for align the molecule [52,53]. Structural determination with RDC information is now being a standard method especially for larger RNAs [54]. RDCs are quite important for refinement of nucleic acid–protein complex structure [55–57]. In the presence of proteins, a dilute liquid crystalline medium may be used instead of the phage [58]. Also, RDCs can be used to estimate the relative orientations of stems for large RNA [59].

References

1. Wüthrich K. NMR of Proteins and Nucleic Acids. John Wiley & Sons, Inc.: New York, 1986.
2. van de Ven FJM, Hilbers CW. Eur. J. Biochem. 1988;178:1.
3. Varani G, Tinoco I Jr. Q. Rev. Biophys. 1991;24: 479.
4. Batey RT, Batteste JL, Williamson JR, James TL (Eds). Nuclear Magnetic Resonance and Nucleic Acids. Methods in Enzymology, 261. Academic Press: San Diego, 1995, pp 300.
5. Varani G, Aboul-ela F, Allain FHT. Prog. Nucl. Magn. Reson. Spectrosc. 1996;29:51.
6. Wemmer D, Bloomfiled VA, Crothers DM, Tinoko I Jr (Eds). Nucleic Acids—Structures, Properties, and Functions. University Science Books: Sausalito, California, 2000.
7. Markley JL, Bax A, Arata Y, Hilbers CW, Kaptein R, Sykes BD, Wright PE, Wüthrich K. Pure Appl. Chem. 1998;70:117; Eur. J. Biochem. 1998;256:1; J. Biomol. NMR. 1998;12:1; J. Mol. Biol. 1998;280:933.
8. Saenger W. Principles of Nucleic Acid Structure. Springer-Verlag: Berlin Heidelberg, 1984.
9. Altona C, Sundaralingam M. J. Am. Chem. Soc. 1972;94: 8205.
10. Pardi A, James TL (Eds). Nuclear Magnetic Resonance and Nucleic Acids. Methods in Enzymology, 261. Academic Press: San Diego. 1995, pp 350.
11. Fesik SW, Eaton HL, Olejniczak ET, Zuiderweg ER, McIntosh LP, Dahlquist FW. J. Am. Chem. Soc. 1990;112:886.
12. Bax A, Clore GM, Gronenborn AM. J. Magn. Reson. 1990;88: 425.
13. Inagaki F, Shimada I, Kohda D, Suzuki A, Bax A. J. Magn. Reson. 1989;81:186.
14. Sklénar V, Miyashiro H, Zon G, Bax A. FEBS. Lett. 1986; 208:94.
15. Hiroaki H, Uesugi S. FEBS. Lett. 1989;224:43.
16. Kellog GW. J. Magn. Reson. 1992;98:176.
17. Schroeder SA, Fu JM, Jones CR, Gorenstein DG. Biochemistry. 1987;26:3812.
18. Xu J, Lapham J, Crothers DM. Proc. Natl. Acad. Sci. U.S.A. 1996;93:44.
19. Glemarec C, Kufel J, Foldesi A, Maltseva T, Sandstorm A, Kirsebom LA, Chattopadhyaya J. Nucleic Acids Res. 1996;24:2022.
20. Ohtsuki T, Kawai G, Watanabe K. J. Biochem. 1998;124:28–34.
21. Kim I, Muto Y, Watanabe S, Kitamura A, Futamura Y, Yokoyama S, Hosono K, Kawai G, Takaku H, Dohmae N, Takio K, Sakamoto H, Shimura Y. J. Biomol. NMR. 2000;17:153–65.
22. Altona C, Sundaralingam M. J. Am. Chem. Soc. 1973;95: 2333–44.
23. Yokoyama S, Watanabe T, Murao K, Ishikura H, Yamaizumi Z, Nishimura S, Miyazawa T. Proc. Natl. Acad. Sci. U.S.A. 1985;82:4905.
24. Sierzputowska-Gracz H, Sochacka E, Malkiewicz A, Kuto K, Gehrke CW, Agris PF. J. Am. Chem. Soc. 1987;109:7171.
25. Kawai G, Yamamoto Y, Kamimura T, Masegi T, Sekine M, Hata T, Iimori T, Watanabe T, Miyazawa T, Yokoyama S. Biochemistry. 1992;31:1040.
26. Sakamoto K, Kawai G, Watanabe S, Niimi T, Hayashi N, Muto Y, Watanabe K, Satoh T, Sekine M, Yokoyama S. Biochemistry. 1996;35:6533.
27. Uhl W, Reiner J, Gassen HG. Nucleic Acids Res. 1983;11: 1167.
28. Kawai G, Hashizume T, Yasuda M, Miyazawa T, McCloskey JA, Yokoyama S. Nucleosides Nucleotides. 1992;11:759.
29. Lee CH, Sarma RH. Biochemistry. 1976;15:697.
30. Hruska FE, Smith AA, Dalton JG. J. Am. Chem. Soc. 1971; 93:4334.
31. Davies DB, Danyluk SS. Biochemistry. 1974;13:4417.
32. Davies DB, Danyluk SS. Biochemistry. 1975;14:543.
33. Lee CH, Sarma RH. J. Am. Chem. Soc. 1976;98:3541.
34. Lee CH, Ezra FS, Kondo NS, Sarma RH, Danyluk SS. Biochemistry. 1976;15:3627.
35. Yokoyama S, Yamaizumi Z, Nishimura S, Miyazawa T. Nucleic Acids Res. 1979;6:2611.
36. Hart PA, Davis JP. J. Am. Chem. Soc. 1969;91:512.
37. Trantirek L, Stefk R, Masse JE, Feigon J, Sklenar V. J. Biomol. NMR. 2002;23:1.
38. Davies DB, Sadikot H. Biopolymers. 1983;22:1843.
39. Dingley AJ, Grzesiek S. J. Am. Chem. Soc. 1998;120: 8293.
40. Pervushin K, Ono A, Fernandez C, Szyperski T, Kainosho M, Wüthrich K. Proc. Natl. Acad. Sci. U.S.A. 1998;95:14147.
41. Wohnert J, Dingley AJ, Stoldt M, Gorlach M, Grzesiek S, Brown LR. Nucleic Acids Res. 1999;27:3104.
42. Majumdar A, Kettani A, Skripkin E. J. Biomol. NMR. 1999; 14:67.
43. Nilges M, Gronenborn AM, Brunger AT, Clore GM. Protein Eng. 1988;2:27.
44. Takasu A, Watanabe K, Kawai G. J. Biochem. 2002;132:211.
45. Someya T, Sakamoto T, Takasu A, Kawai G. Nucleosides, Nucleotides Nucleic Acids. 2004;23:691.

46. Weiner SJ, Kollman PA, Case DA, Singh UC, Ghio C, Alagona G, Profeta S, Weiner P. J. Am. Chem. Soc. 1984;106:765.
47. Singh UC, Kollman PA. J. Comput. Chem. 1984;5:129.
48. Agris PF, Brown SC, James TL (Eds). Nuclear Magnetic Resonance and Nucleic Acids. Methods in Enzymology, 261. Academic Press: San Diego, 1995, pp 270.
49. Agris PF, Guenther R, Ingram PC, Basti MM, Stuart JW, Sochacka E, Malkiewicz A. RNA. 1997;3:420.
50. Liang X, Asanuma H, Kashida H, Takasu A, Sakamoto T, Kawai G, Komiyama M. J. Am. Chem. Soc. 2003;125:16408.
51. Tjandra N, Bax A. Science. 1997;278:1111.
52. Hansen MR, Mueller L, Pardi A. Nat. Struct. Biol. 1998;5:1065.
53. Hansen MR, Hansen P, Pardi A. Methods Enzymol. 2000;317:220.
54. Lukavsky PJ, Kim I, Otto GA, Puglisi JD. Nat. Struct. Biol. 2003;10:1033.
55. Tjandra N, Omichinski JG, Gronenborn AM, Close GM, Bax A. Nat. Struct. Biol. 1997;4:732.
56. Bayer P, Varani L, Varani G. J. Biomol. NMR. 1999;14:149.
57. Varani G, Chen Y, Leeper TC. Methods Mol. Biol. 2004;278:289.
58. Ottiger M, Bax A. J. Biomol. NMR. 1998;12:361.
59. Bondensgaard K, Mollova ET, Pardi A. Biochemistry. 2002;41:11532.

Part I

Solid-State NMR Technique

Analytical and Numerical Tools for Experiment Design in Solid-State NMR Spectroscopy

Niels Chr. Nielsen, Thomas Vosegaard, and Anders Malmendal
Center for Insoluble Protein Structures (INSPIN), Interdisciplinary Nanoscience Center (iNANO) and Department of Chemistry, University of Aarhus, DK-8000 Aarhus C, Denmark

Introduction

The solid-state NMR spectroscopy research area has evolved tremendously during the past few decades [1–4]. Initially a method of primary interest for physicists, it has become an increasingly powerful and widely used tool in materials science, chemistry, nanotechnology, and molecular biology. This development has been supported by scientific breakthroughs on many levels. First, on a general level, high-resolution solid-state NMR has to a great extent been inspired by the earlier developments of liquid-state NMR [5–7] which, due to simpler and easier controllable nuclear spin Hamiltonians, in many respects have set landmarks for our expectations to the ability of solid-state NMR for non-liquid samples. This applies in particular to biological samples, where the need for high resolution and sensitivity to establish structural constraints has set measures on the size and labeling strategies of molecules amenable to structural analysis. The expectations have been high, implying an enormous—and very constructive—drive on the development of methods capable of solving the most fundamental problems. Second, on the hardware level, solid-state NMR has been boosted by the same technological developments as liquid-state NMR: stronger magnets with better field homogeneity, providing higher sensitivity and improved spectral resolution. In addition to this comes the very important development of multiple-channel solid-state NMR probes with high radio-frequency (rf) power and fast magic-angle spinning (MAS) capabilities. Third, on the theoretical level, the introduction of average Hamiltonian theory (AHT) to solid-state NMR in the late sixties [8], and refinements of this method [9–11] as well as other analytical tools [12,13] has had a fundamental impact on the understanding of advanced NMR experiments and an application-driven systematic improvement of the fundamental experiments [1–4]. Fourth, on the computational level, the development of advanced numerical tools [14–18] has proven very useful for development and interpretation of solid-state NMR experiments in many disciplines. The two last elements are the topics of this contribution.

Tools for Systematic Experiment Design

Depending on their complexity and area of application, solid-state NMR experiments have for the past two to three decades been developed using appropriate combinations of intuition, analytical evaluations, numerical simulations, and experimental tests. Very often the inspiration to the design of a new experiment comes from the wish to improve an already existing experiment to perform better under similar or radically changed conditions. In other cases, not least applying to the rapidly developing field of biological solid-state NMR, the inspiration comes from a need to perform a given coherence or polarization transfer to obtain specific assignments or measurement of particular distances or torsion angles in the molecule. In the latter case, part of the inspiration may come from similar experiments (however, often governed by different spin interactions) known from liquid-state NMR. Taking out these motivating parameters and the final experimental tests, the design of solid-state NMR experiments has to a large extent been carried out using two tools, (i) AHT and (ii) numerical simulations. These tools may be used as complementary entities for systematic experiment design as illustrated in Figure 1.

Analytical Tools

One the most powerful tools for systematic development and evaluation of solid-state NMR experiments has been coherent averaging theory, AHT, or effective Hamiltonian Theory (EHT) as introduced in the context of multiple-pulse solid-state NMR by Haeberlen and Waugh in the late sixties [8]. In combination with appropriate transformation of the Hamiltonian into interaction

Graham A. Webb (ed.), Modern Magnetic Resonance, 679–687.
© 2008 *Springer.*

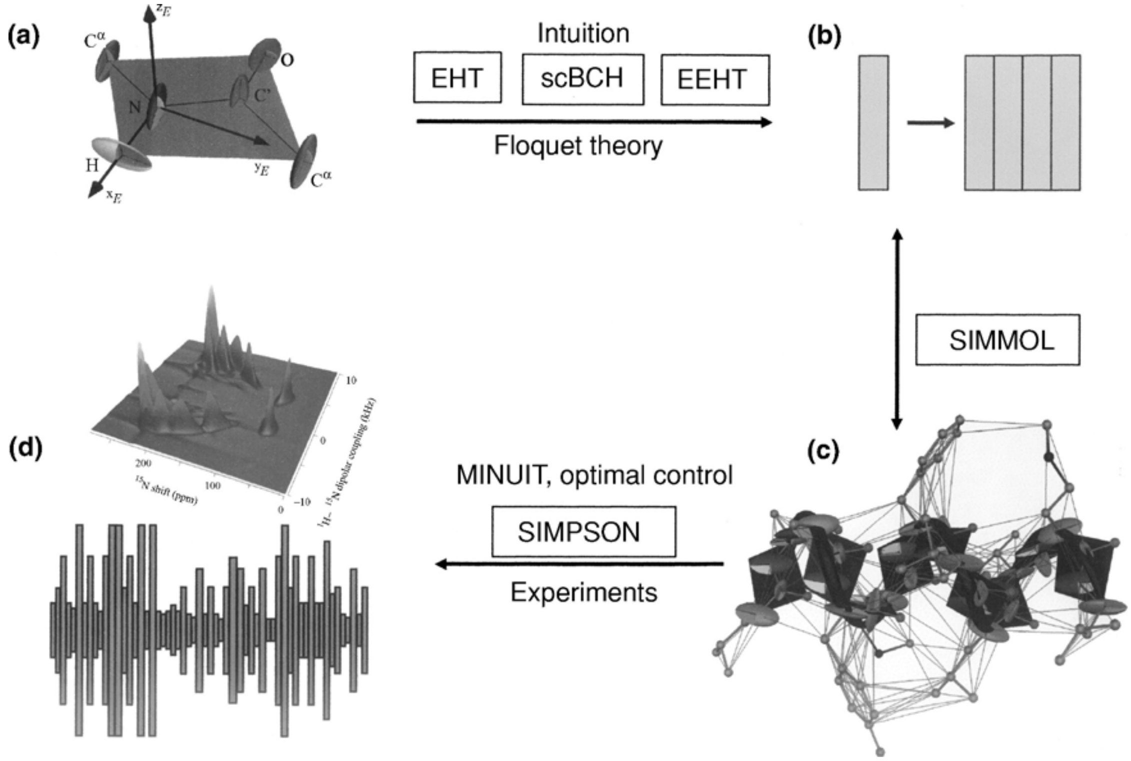

Fig. 1. Schematic illustration of tools used for systematic experiment design in solid-state NMR spectroscopy. Based on relatively small spin systems (often only one or two spins) (a) analytical tools, such as EHT, scBCH, and EEHT, may be used to refine crude "first-order" pulse sequences to more powerful "high-order" pulse sequence for tailoring the internal nuclear spin Hamiltonian, e.g. by re- or decoupling (b). By the use of general-purpose simulation programs such as SIMPSON along with programs for calculating typical tensorial interactions (SIMMOL) it is possible to extend the evaluation and design to realistic spin systems (c). Using these tools, along with non-linear optimization or optimal control, it is possible to systematically design pulse sequences with optimum performance for specific spin systems and calculate spectra to extract structural information (d). (See also Plate 62 on page XLIII in the Color Plate Section.)

frame(s) of the major external manipulations, EHT offers a relatively simple description of complex, time-modulated Hamiltonians in terms of an ordered series of effective-field Hamiltonians describing the overall effect of, e.g. multiple-pulse NMR experiments. The effective Hamiltonian may be written as

$$\bar{\tilde{H}}^{\mathrm{eff}} = \bar{\tilde{H}}^{(1)} + \bar{\tilde{H}}^{(2)} + \bar{\tilde{H}}^{(3)} + \cdots , \tag{1}$$

where the tilde indicates that the Hamiltonian is expressed in the interaction frame and the bar indicates "averaging" over a cycle period $\tau_c = t - t_0$. The ordered elements come from the so-called Magnus expansion and are defined as

$$\bar{\tilde{H}}^{(1)} = \frac{1}{\tau_c}\int_{t_0}^{t} \mathrm{d}t_1 \tilde{H}(t_1), \tag{2a}$$

$$\bar{\tilde{H}}^{(2)} = \frac{1}{2i\tau_c}\int_{t_0}^{t} \mathrm{d}t_1 \int_{t_0}^{t_1} \mathrm{d}t_2 \left[\tilde{H}(t_1), \tilde{H}(t_2)\right], \tag{2b}$$

$$\begin{aligned}\bar{\tilde{H}}^{(3)} = \frac{-1}{6\tau_c}\int_{t_0}^{t} \mathrm{d}t_1 \int_{t_0}^{t_1} \mathrm{d}t_2 \int_{t_0}^{t_2} \mathrm{d}t_3 \Big(\left[\tilde{H}(t_1), \left[\tilde{H}(t_2), \tilde{H}(t_3)\right]\right] \\ + \left[\tilde{H}(t_3), \left[\tilde{H}(t_2), \tilde{H}(t_1)\right]\right]\Big) ,\end{aligned} \tag{2c}$$

using the interaction frame Hamiltonian $\tilde{H}(t)$ and density operator $\tilde{\rho}(t)$ defined as

$$\tilde{H}(t) = U_{\text{int}}^{+}(t)H(t)U_{\text{int}}(t) - iU_{\text{int}}^{+}(t)\frac{\mathrm{d}}{\mathrm{d}t}U_{\text{int}}(t), \quad (3a)$$

$$\tilde{\rho}(t) = U_{\text{int}}^{+}(t)\rho(t)U_{\text{int}}(t), \quad (3b)$$

where $U_{\text{int}}(t) = T\exp\left(-i\int_{t_0}^{t}\mathrm{d}t_1\,H_{\text{int}}(t_1)\right)$ is the propagator relating to the big, non-interesting interaction $H_{\text{int}}(t)$ defining our interaction representation (typically the Hamiltonian of the rf pulse sequence).

The relatively simple formulas in Equations (1)–(3) have formed the basis for analytical evaluation of essentially all solid-state NMR experiments in the past three decades. This applies for the design and description of pulse sequences for decoupling of homo- and heteronuclear dipolar (or J) coupling interactions [1–4,8,19–21], selective recoupling of anisotropic dipolar coupling and chemical shielding interactions in MAS NMR [22,23], evaluation of solid-state NMR experiments for analysis of quadrupolar nuclei [24], etc. It has been more the rule than the exception that any new experiment or pulse sequence building block was characterized by its effective Hamiltonian. For recoupling experiments, it has been the purpose to avoid coherent averaging of anisotropic interactions by sample rotation, and as so the first-order expressions were relevant for the recoupled interactions (e.g. a specific dipole–dipole coupling), while higher-order terms were relevant for the interactions that should remain averaged (e.g. isotropic and anisotropic chemical shifts). For decoupling sequences, it has obviously been the aim to eliminate the "coupling" interaction to as high order as possible—each time revealing that the high-order terms that intuitively only describe marginal effects actually become exceedingly important—and spectrally very visible—when all lower-order terms have been suppressed.

This has created a need to facilitate calculation of high-order terms, which not only is complicated by the more complex formula for the integrant (cf. Equation (2)), but also by the need to keep track of the time-ordering of the multiple integrals. This may be quite demanding, in particular for pulse sequence containing many elements with differently modulated Hamiltonians. To serve this need we introduced the so-called semi-continuous Baker–Campbell–Hausdorff (scBCH) expansion [9]. Here the effective Hamiltonians calculated for each period using the Magnus expansion (Equation (2)) are used as static entries to the Baker–Campbell–Hausdorff expansion, which thereby acts as an ordering structure. The first three order coupling equations are expressed as

$$\bar{\bar{\tilde{H}}}^{(1)} = \frac{1}{\tau_c}\sum_{i=1}^{n}\tau_i\bar{\bar{\tilde{H}}}_i^{(1)} \quad (4a)$$

$$\bar{\bar{\tilde{H}}}^{(2)} = \frac{1}{\tau_c}\sum_{i=1}^{n}\tau_i\bar{\bar{\tilde{H}}}_i^{(2)} + \frac{1}{2i\tau_c}\sum_{i>j}^{n}\tau_i\tau_j\left[\bar{\bar{\tilde{H}}}_i^{(1)},\bar{\bar{\tilde{H}}}_j^{(1)}\right] \quad (4b)$$

$$\begin{aligned}\bar{\bar{\tilde{H}}}^{(3)} = {} & \frac{1}{\tau_c}\sum_{i=1}^{n}\tau_i\bar{\bar{\tilde{H}}}_i^{(3)} + \frac{1}{2i\tau_c}\sum_{i>j}^{n}\tau_i\tau_j\left(\left[\bar{\bar{\tilde{H}}}_i^{(1)},\bar{\bar{\tilde{H}}}_j^{(2)}\right]\right.\\ & \left.+\left[\bar{\bar{\tilde{H}}}_i^{(2)},\bar{\bar{\tilde{H}}}_j^{(1)}\right]\right) - \frac{1}{6\tau_c}\sum_{i>j>k}^{n}\tau_i\tau_j\tau_k\left(\left[\bar{\bar{\tilde{H}}}_i^{(1)},\left[\bar{\bar{\tilde{H}}}_j^{(1)},\bar{\bar{\tilde{H}}}_k^{(1)}\right]\right]\right.\\ & \left.+\left[\bar{\bar{\tilde{H}}}_k^{(1)},\left[\bar{\bar{\tilde{H}}}_j^{(1)},\bar{\bar{\tilde{H}}}_i^{(1)}\right]\right]\right) - \frac{1}{12\tau_c}\sum_{i>j>k}^{n}\\ & \times\left(\tau_{ii}^2\tau_j\left[\bar{\bar{\tilde{H}}}_i^{(1)},\left[\bar{\bar{\tilde{H}}}_i^{(1)},\bar{\bar{\tilde{H}}}_j^{(1)}\right]\right] + \tau_i\tau_j^2\left[\bar{\bar{\tilde{H}}}_i^{(1)},\left[\bar{\bar{\tilde{H}}}_j^{(1)},\bar{\bar{\tilde{H}}}_j^{(1)}\right]\right]\right),\end{aligned} \quad (4c)$$

which straightforwardly can be extended to formulas that apply for the terms just above a certain order m to which a "first-iteration" pulse sequence eliminates a given interaction (for details see Ref. [9]). For example, consider a sequence for which the basic element eliminates terms of order 1. If this element is concatenated with its reflection symmetric counterpart then the sequence eliminates all even order terms. This leaves us with coupling of third, fifth, and seventh order terms as direct sums similar to the third-order terms in Equation (4c).

With the aim of establishing more accurate—ideally exact—representations of effective Hamiltonians, we recently introduced the so-called Exact Effective Hamiltonian Theory (EEHT) [10,11]. EEHT exploits the highly celebrated spectral theorem or the Caley–Hamilton theorem to obtain a finite-series closed solution to the Baker–Campbell–Hausdorff problem. The basic idea is that the effective Hamiltonian reflecting the action of two entangled propagators may not only be represented by its infinite series expansion

$$-iH^{\text{eff}}\tau = \ln\left(\mathrm{e}^{iA}\mathrm{e}^{iB}\right) = \sum_{k=1}^{\infty}\frac{1}{k}X^k \quad (5)$$

with $X = 1 - e^{iA}e^{iB}$, but also as a finite series

$$-iH^{\text{eff}}\tau = \sum_{i=1}^{N}g_{i-1}X^{i-1}, \quad (6)$$

containing only N terms, where N is the matrix dimension of the Lie algebra (i.e. the number of energy levels in the spin system). Considering that essentially all EHT calculations have been performed on two-, three-, or four-level systems, it appears intuitively very attractive to obtain an exact description using only two, three, or four terms instead of an infinite series of ordered contributions for each of these cases. Obviously, the relevance of this statement depends on the derivation of the g expansion factors. For at two-level system, the g factors are related to the eigenvalues λ_i for the operator X as

$$mg_0 = -\lambda_2 \ln(1-\lambda_1) + \lambda_1 \ln(1-\lambda_2) \tag{7a}$$

$$mg_1 = \ln(1-\lambda_1) - \ln(1-\lambda_2) \tag{7b}$$

with $m = \lambda_1 - \lambda_2$. For a three-level system (e.g. a spin-1 case or the strong-coupling part of a two-spin-1/2 system) the g values are given by

$$\begin{aligned} mg_0 = {} & \left(\lambda_2^2\lambda_3 - \lambda_3^2\lambda_2\right) \ln(1-\lambda_1) + \left(\lambda_3^2\lambda_1 - \lambda_1^2\lambda_3\right) \\ & \times \ln(1-\lambda_2) + \left(\lambda_1^2\lambda_2 - \lambda_2^2\lambda_1\right) \ln(1-\lambda_3) \end{aligned} \tag{8a}$$

$$\begin{aligned} mg_1 = {} & \left(\lambda_3^2 - \lambda_2^2\right) \ln(1-\lambda_1) + \left(\lambda_1^2 - \lambda_3^2\right) \ln(1-\lambda_2) \\ & + \left(\lambda_2^2 - \lambda_1^2\right) \ln(1-\lambda_3) \end{aligned} \tag{8b}$$

$$\begin{aligned} mg_2 = {} & (\lambda_2 - \lambda_3) \ln(1-\lambda_1) + (\lambda_3 - \lambda_1) \ln(1-\lambda_2) \\ & + (\lambda_1 - \lambda_2) \ln(1-\lambda_3) \end{aligned} \tag{8c}$$

with $m = (\lambda_1 - \lambda_2)(\lambda_1 - \lambda_3)(\lambda_2 - \lambda_3)$ and the formula applying for the case of non-degenerate eigenvalues. Degenerate cases as well as four-level systems are covered by the more detailed descriptions in Refs. [10,11].

Without going into detail with the underlying theory, it is clear that the EEHT expansion in Equation (6), with the appropriate expansion coefficients may prove powerful for establishing exact expressions for entangled propagators in cases where the eigenvalues can be established analytically. This applies typically for 2–4 level systems, i.e. exactly the same area of action as the normal Magnus expansion based AHT. A few essential features should be mentioned: First, it is clear that the entanglements are not restricted to concatenation of two propagators although, obviously, the X operators become increasingly complicated. For the concatenation of n propagators

$$X = 1 - U_1 U_2 \cdots U_n \tag{9}$$

where $U_i = \mathrm{e}^{iH_i t_i}$ is the ith propagator relating to the Hamiltonian H_i and the time interval t_i. Second, being exact in nature, EEHT allows for the establishment of analytical insight about the effective Hamiltonian in the *normal rotating frame*, rather than in one, or often more, "ad-hoc-constructed" interaction frame(s) that enable fast convergence of an infinite series to the lower-order terms. It is obvious that this renders the description much simpler. In many cases far most of the complicating time-dependency of the Hamiltonians actually comes from the transformation into the interaction frame(s). Another important issue is that it may be practically impossible to find appropriate interaction frames, because it is a requirement that the frequency of the "big" interaction is orders of magnitude larger than the internal interactions. This may be complicated if several frames have to be used at the same time, or if the internal interactions are much stronger than the available external manipulations (which may be case, e.g. for quadrupolar nuclei, where internal interaction frequencies up to many MHz may be encountered). The ability to perform the analytical evaluations in the normal rotating frame may also facilitate direct comparison between analytical and numerical evaluations. Third, EEHT may also provide a useful means to obtain *ordered expressions* for high-order effective Hamiltonians. This may be obtained through a simple Taylor expansion

$$H^{\mathrm{eff}}(a + a_0) = \sum_{i=1}^{n} \frac{a^n}{n!} \left(\frac{\mathrm{d}^n}{\mathrm{d}a^n} H^{\mathrm{eff}}(a) \right)_{a_0} \tag{10}$$

of the EEHT-derived exact effective Hamiltonian in the relevant controlling variable (often the frequency of the undesired interaction scaled according to strength of the external field; in this the variation a away from its expansion point a_0) [10]. This "easy route" to high-order Hamiltonians may be useful in cases where an ordered expansion is needed for systematic design of pulse sequences to eliminate the most important components of non-desired interactions. Finally, we should note that the highly structured way of establishing the exact effective Hamiltonians and the ordered Taylor expansions may be taken into advantage by performing the difficult calculations [10] in symbolic mathematics programs such as Mathematica [25].

Numerical Tools

While analytical tools are extremely useful for evaluation of the overall performance of advanced pulse experiments and systematic design of these, it is often performed on simplified systems with respect to the number of spins and nuclear spin interactions (see Figure 1). Also issues like the simultaneous contribution from many molecules with different orientation relative to the external magnetic field, and thereby different anisotropic nuclear spin interactions, may be difficult to handle appropriately by analytical means. Such evaluations are typically left to experimental tests or to numerical simulations. Although the former obviously provides the answer from the spins themselves, the latter has the advantage that many "experiments" can be tested under different conditions without the need to produce many expensive compounds with different isotope labels and without using excessive spectrometer time.

Based on an increasing understanding of the underlying spin dynamics and easy/cheap access to powerful computers, the past decade has witnessed the appearance of numerous powerful simulation programs which in principle allow for exact calculation of advanced solid-state NMR experiments for large spin systems. These programs includes ANTIOPE [14], Gamma [15], SIMPSON [16], Blochlib [17], and SPINEVOLUTION [18], which—in particular the newer programs—exploit the most recent methods for efficient handling of crystallite orientation and time symmetries in rotating sample experiments [26–33] as described along with examples in recent reviews [34,35].

Among the simulation programs, more recent open-source program packages such as SIMPSON [16,34–39] have gained a very widespread popularity due to a very flexible scripting interface that allows the performance of advanced pulse sequence simulations with a programming effort similar to that used for programming the pulse sequence on the spectrometer. For example, using SIMPSON's simple Tcl interface [36,40], it is straightforward to implement pulse sequences (pulses, delays, etc.), external manipulations (rf irradiation, stationary external field, powder conditions, sample spinning, etc.), as well as the nuclear spin system to explore the performance of pulse sequences development by other means (e.g. using EHT) or for computer-assisted experiment design. The latter may be conducted using integrations of SIMSPON with MINUIT [41] non-linear optimization [36] or with optimal control theory [42–44] for experiment optimization [39].

To facilitate the establishment of realistic, large spin systems—primarily for biological solid-state NMR—we recently introduced the auxiliary program SIMMOL [45] that uses atomic coordinates in the PDB (Protein Data Bank) [46] format to generate representative tensorial parameters for proteins or fragments of these. This is obviously possible for the dipole–dipole coupling interactions that depend exclusively on the internuclear distance and the orientation of the internuclear vector, but it is actually possible also to predict the magnitude and orientation of chemical shielding tensors quite precisely based on empirical rules. For example, the backbone chemical shielding tensors have essentially the same magnitude and orientation relative to the peptide plane independently on the residue type, and for the sidechain tensors there are often empirical rules that enable orientation of the tensors relative to the nuclear bonds. In this manner it is possible to establish very reliable multiple-spin parameter sets for numerical evaluation of pulse sequences without the need for excessive work to establish, in particular, the tensor orientations by manual means. The combined used of SIMMOL and SIMPSON for systematic experiment design is promoted in Figure 1.

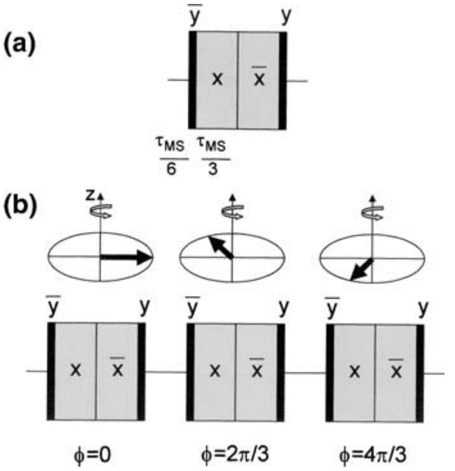

Fig. 2. Magic-sandwich (MS) (a) and high-order truncating MSHOT3 (b) pulse sequences for homonuclear dipolar decoupling in ^{1}H solid-state NMR spectroscopy. The pulse sequences are analyzed using EEHT under the assumption of ideal $(\pi/2)_{\pm y}$ bracketing pulses and that the pulses of duration $\tau_{MS}/3$ correspond to 2π rotations under influence of the dipolar coupling interaction (as through the free precession period of half duration).

Systematic Design of Solid-State NMR Experiments

To illustrate the use of the analytical and numerical tools described in the previous section, we will briefly review a couple of examples of their use for evaluation and design of solid-state NMR experiments. The first example concerns the usage of EEHT [10] to evaluate the high-order truncating MSHOT-3 pulse sequence [47] relative to its predecessor, the magic-sandwich (MS) pulse sequence [48], for homonuclear decoupling in ^{1}H solid-state NMR. The second-example illustrates the use of optical control theory in combination with SIMPSON numerical simulations for computer-automated design of optimal recoupling NMR experiments.

Example 1: One of the absolute driving forces for the analytical development of NMR originates from the wish to be able to do ^{1}H NMR spectroscopy on solid-samples. Considering the relative narrow range of 10 ppm or so for the isotropic chemicals shifts—amounting to 5 kHz on a 500 MHz spectrometer—this requires efficient ways to eliminate the overwhelming ^{1}H–^{1}H dipole–dipole couplings which may range up to more that 30 kHz. One of the pioneering sequences for homonuclear decoupling was the MS sequence [48] in Figure 2a, which can be analyzed using EEHT using the following steps [10]. (i) The propagators relevant for the various pulse sequence elements are established as

$$U_f = \mathrm{e}^{-i2a\sqrt{6}T_{2,0}},\ U_y = \mathrm{e}^{-i\pi(I_y+S_y)/2},$$
$$U_{\pm x} = \mathrm{e}^{-i\left[\pm 2\pi(I_x+S_x)+4a\sqrt{6}T_{2,0}\right]} \tag{11}$$

where f, y, and $\pm x$ denote propagators for free precession, the bracketing y-pulse (assumed ideal), and the $(2\pi)_{\pm x}$ pulses, respectively, while $T_{2,0} = (2I_zS_z - I_xS_x - I_yS_y)/\sqrt{6}$ and $a = \pi\omega_D/(2\omega_{\mathrm{rf}})$ with ω_D being the dipolar coupling frequency and ω_{rf} the rf field strength (both in angular frequency units). (ii) The X operator is defined as

$$X = 1 - U_f U_y^{+} U_x U_{-x} U_y U_f, \tag{12}$$

for which (iii) the eigenvalues

$$\lambda_1 = 0,$$
$$\lambda_{2,3} = \frac{18a^2s_\alpha^2 \mp 3\sqrt{2}as_\alpha\sqrt{-9a^2-8\pi^2-9a^2c_{2\alpha}}}{\alpha^2} \tag{13}$$

can be found with $s_\alpha = \sin(\alpha)$, $c_\alpha = \cos(\alpha)$, and $\alpha = \sqrt{9a^2+4\pi^2}$. Using Equations (6) and (8) (description in $su(3)$) and decomposition into irreducible spherical tensor operators [10], this leads (iv) to the exact effective Hamiltonian ($\tau_{\mathrm{MS}} = 6\pi/\omega_{\mathrm{rf}}$)

$$-iH^{\mathrm{eff}}\tau_{\mathrm{MS}} = b_{2,2}^{\mathrm{MS}}T_{2,2} + b_{2,-2}^{\mathrm{MS}}T_{2,.2}, \tag{14}$$

with $T_{2,\pm2} = \frac{1}{2}I_1^{\pm}I_2^{\pm}$ and

$$b_{2,2}^{\mathrm{MS}} = \left(-b_{2,-2}^{\mathrm{MS}}\right)^*$$
$$= \frac{-\sqrt{2}a\alpha^2[\ln(1-\lambda_2)-\ln(1-\lambda_3)]\,s_\alpha\,(i\alpha c_\alpha + 2\pi s_\alpha)}{s_\alpha a\alpha^2\sqrt{-9a^2-8\pi^2-9a^2c_{2\alpha}}}, \tag{15}$$

$$\approx \frac{-27ia^3}{2\pi^2} - \frac{243\,(-3i+4\pi)\,a^5}{32\pi^4} + \frac{729\,[-15i+4\,(9+4i\pi)\,\pi]\,a^7}{256\pi^6} + \mathrm{O}(a^9), \tag{16}$$

where the approximation in Equation (16) was derived by (v) Taylor expansion (Equation (10)) of the exact expression in Equation (15) around $a_0 = 0$, resulting in an ordered expression identical to the one obtained using the scBCH expansion [9,47].

The exact effective Hamiltonian reveals that the residual dipolar terms for the MS sequence is of the type $T_{2,\pm2}$—which immediately indicates that an improved dipolar coupling suppression may be obtained by concatenating z-rotated elements, such as accomplished for by three elements mutually phase-shifted by $2\pi/3$ in the MSHOT-3 pulse sequence [47] in Figure 2b. MSHOT-3 is characterized by the effective Hamiltonian ($\tau_{\mathrm{MSHOT3}} = 3\tau_{\mathrm{MS}}$)

$$-iH^{\mathrm{eff}}\tau_{\mathrm{MSHOT3}} = b_{1,0}^{\mathrm{MSHOT3}}T_{1,0} + b_{2,0}^{\mathrm{MSHOT3}}T_{2,0} + b_{2,2}^{\mathrm{MSHOT3}}T_{2,2} + b_{2,-2}^{\mathrm{MSHOT3}}T_{2,2} \tag{17}$$

with the Taylor expanded coefficients

$$b_{1,0}^{\mathrm{MSHOT3}} \approx \frac{i729\sqrt{3}a^6}{32\pi^4} - \frac{19683i\sqrt{3}a^8}{256\pi^6} + \mathrm{O}(a^{10}),$$
$$b_{2,0}^{\mathrm{MSHOT3}} \approx \mathrm{O}(a^{10}) \quad b_{2,2}^{\mathrm{MSHOT3}} = \left(-b_{2,2}^{\mathrm{MSHOT3}}\right)^*$$
$$\approx \frac{19683\left(i+\sqrt{3}\right)a^9}{64\pi^6} + \mathrm{O}(a^{10}) \tag{18}$$

showing that the dipolar suppression is improved by three orders in the effective Hamiltonian expansion on going from MS to MSHOT3.

Example 2: While analytical tools like EHT and advanced variants are considered indispensable in experiment design, it has been much less typical to use numerical simulations in the *first phase* of experiment design. Indeed, numerical simulations have been used, but typical in the *second phase* as a more critical evaluator after the experiments have been designed by other means. However, in few cases non-linear optimization has been used, e.g. for design of experiments for TOSS spinning sideband suppression [49], homonuclear dipolar decoupling experiments [50,51], and adiabatic-passage dipolar recoupling [34,52]. Probably one of the reasons for not using non-linear optimization for designing solid-state NMR experiments from scratch is that the number of free variables required for non-constrained optimizations typically is very large, implying that non-linear optimization is very slow, and prone to identification of local extrema rather than global ones. To remedy this problem, we recently explored the use of optimal control theory [44] in combination with SIMPSON as a route to explore how efficient pulse sequences actually can be made if the degrees of freedom are opened up radically, *and* as a means to create optimal pulse sequences numerically in an automated fashion. The idea is to provide the program with information on the spin system, the initial and desired target spin operators, information on the external spinning and rf conditions (including rf inhomogeneity, maximum available/desired rf field strengths, etc.), and a desired length

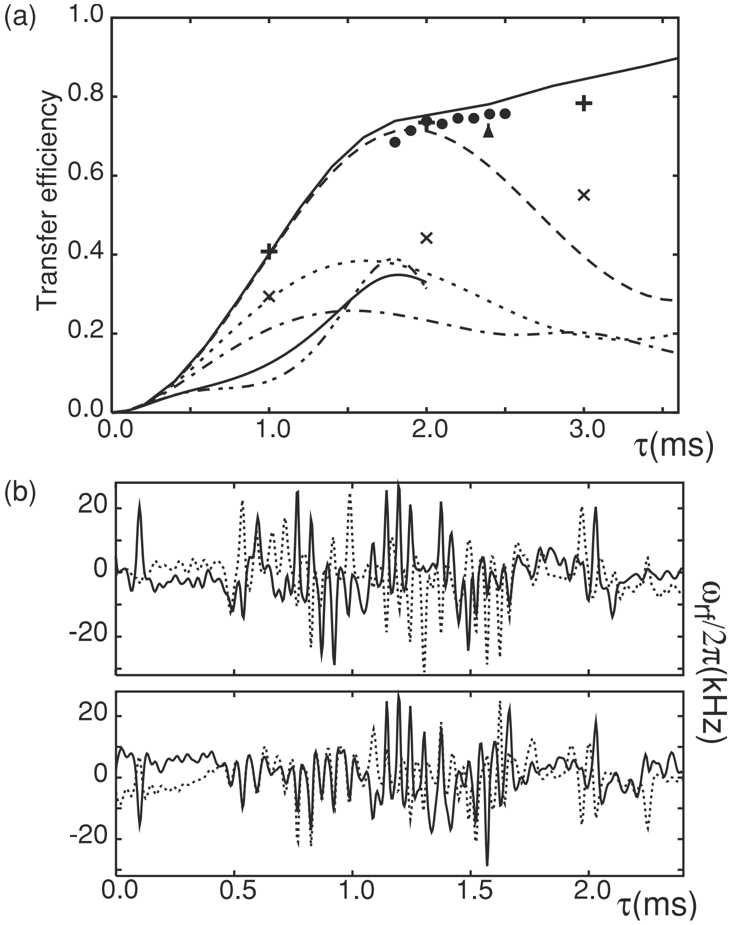

Fig. 3. (A) Numerical evalution of ^{15}N $\rightarrow ^{13}$C$_\alpha$ coherence transfer in glycine calculated for different recoupling experiments under conditions of homogeneous and inhomogeneous rf fields: DCP (homogeneous rf: —; 5% Lorentzian rf inhomogeneity: ····, 10% Lorentzian rf inhomogeneity: · — ·—), ramped DCP (homogeneous rf: -·· ·-, 5% Lorentzian rf inhomogeneity: -···), adiabatic CP (homogeneous rf: +, 5% Lorentzian rf inhomogeneity: x), and optimal control ^{OC}DCP (homogeneous rf: solid line, 5% Lorentzian rf inhomogeneity: ● ● ●). (b) ^{15}N (upper) and ^{13}C rf field amplitudes (x-phase: solid line, y-phase: dotted line) for the 2.4 ms ^{OC}DCP experiment marked with arrow in (a). Reproduced from Ref. [39] with permission.

of the experiment, and then let it calculate the optimal pulse sequence.

With reference to our presentation in Ref. [39], Figure 3 illustrates the outcome of an optimal control analysis and design strategy to create improved heteronuclear dipolar recoupling experiments for ^{15}N → ^{13}C$_\alpha$ coherence transfer in MAS NMR of solid proteins. The upper panel compares numerically the transfer efficiencies for DCP [53], ramped DCP [54], and adiabatic variants [55] of DCP subject to homogeneous and different inhomogeneous rf field conditions. Overall it is quite clear that these traditional schemes are quite sensitive to rf inhomogeneity, a problem that may be solved by taking these effects into account in optimal control SIMPSON design of improved pulse sequence. In Figure 3a, the solid-curve describes the transfer efficiency of optimal control sequences under conditions of homogeneous rf fields, while the black dots (essentially providing the same efficiency) reflect sequences optimized under conditions of a 5% Lorentzian (or a 9.2% Gaussian) rf inhomogenity profile on both spins (identical on the two channels). Figure 3B illustrates the ^{15}N (upper) and ^{13}C (lower) rf pulse sequences corresponding to a mixing time of 2.4 ms (indicated by arrow in Figure 3a). Experimentally this pulse sequence provides 53% higher transfer efficiency than a DCP experiment [39], despite the fact that the latter experiment uses significantly stronger rf fields (25 and 35 kHz on the two channels, while the optimal control ^{OC}DCP sequences have root-mean-square average rf field strengths of 10.4 and 9.5 kHz on the two channels). The development of low-power recoupling experiments is regarded very important considering that many of the current recoupling sequences are technically difficult to perform with ^{1}H decoupling under high-speed spinning conditions due to very high demands on the rf field strength and in addition strong rf may heat, and thereby potentially destroy, the sample.

Conclusions

In conclusion, we have briefly reviewed some of the most powerful tools used for systematic design of solid-state NMR experiments: EHT with some recent twists toward high-order or exact formulation and numerical simulations in terms of the SIMPSON and SIMMOL software packages. Both tools are quite universal and are fine complements to intuition and inspiration from other sources in a procedure for systematic design of optimal experiments.

Acknowledgements

We acknowledge support from the Danish National Research Foundation, the Danish Biotechnological Instrument Centre (DABIC), Carlsbergfondet, and the Danish Natural Science Research Council (SNF). We acknowledge collaboration with C. T. Kehlet, T. S. Untidt, M. Hohwy, D. Siminovitch, S. J. Glaser, and N. Khaneja on central parts of the objects discussed in this chapter.

References

1. Haeberlen U. High-Resolution NMR in Solids. Selective Averaging. Academic: New York, 1976.
2. Mehring M. Principles of High-Resolution NMR of Solids. Springer-Verlag: New York, 1983.
3. Gerstein BC and Dybowski CR. Transient Techniques in NMR of Solids. An Introduction to Theory and Practice. Academic: New York, 1985.
4. Schmidt-Rohr K, Spiess HW. Multidimensional Solid-State NMR and Polymers. Academic: London, 1996.
5. Wüthrich K. NMR of Proteins and Nucleic Acids. Wiley: New York, 1986.
6. Ernst RR, Bodenhausen G, Wokaun A. Principles of Nuclear Magnetic Resonance in One and Two Dimensions. Clarendon: Oxford, 1987.
7. Cavanagh J, Fairbrother WJ, Palmer AG III, Skelton NJ. Protein NMR Spectroscopy: Principles and Practice. Academic Press: San Diego, 1996.
8. Haeberlen U, Waugh JS. Phys. Rev. 1968;175:453.
9. Hohwy M, Nielsen NC. J. Chem. Phys. 1998;109:3780.
10. Untidt TS, Nielsen NC. Phys. Rev. E. 2002;65:021108-1. A mathematica notebook can be downloaded from www.bionmr.chem.au.dk.
11. Siminovitch D, Untidt TS, Nielsen NC. J. Chem. Phys. 2004;120:51.
12. Shirley JH. Phys. Rev. B 1965;138:979.
13. Vinogradov E, Madhu PK, Vega S. Chem. Phys. Lett. 2000;329:207.
14. de Bouregas FS, Waugh JS. J. Magn. Reson. 1992;96:280.
15. Smith SA, Levante TO, Meier BH, Ernst RR. J. Magn. Reson. 1994;106:75.
16. Bak M, Rasmussen JT, Nielsen NC. J. Magn. Reson. 2000;147:296. Open Source Software at www.bionmr.chem.au.dk.
17. Blanton WB. J. Magn. Reson. 2003;162:269.
18. Vestort M, Griffin RG. Presentation at 45th Rocky Mountain Conference, Denver, Colorado, 2003.
19. Rhim W-K, Elleman DD, Vaughan RW. J. Chem. Phys. 1973;59:3740.
20. Burum DP, Rhim WK. J. Chem. Phys. 1979;71:944.
21. Burum DP, Linder M, Ernst RR. J. Magn. Reson. 1981;44:173.
22. Bennett AE, Griffin RG, and Vega S. In: P Diehl, E Fluck, H Günther, R Kosfeld (Eds). NMR Basic Principles and Progress, Vol. 33, Springer-Verlag: Berlin, 1994, p 1.
23. Dusold S, Sebald A. Ann. Rep. NMR Spectrosc. 2000;41:185.
24. Goldbourt A, Madhu PK. Chem. Month. 2002;133:1497.
25. Wolfram A. Mathematica. A System for Doing Mathematics by Computer. Addison-Wesley: Redwood City, 1988.
26. Zaremba SK. Ann. Mat. Pure Appl. 1966;293:4; Conroy H. J. Chem. Phys. 1967;47:5307; Cheng VB, Suzukawa HH Jr, Wolfsberg M. J. Chem. Phys. 1973;59:3992.
27. Bak M, Nielsen NC. J. Magn. Reson. 1997;125:132.
28. Edén M, Levitt MH. J. Magn. Reson. 1998;132:220.
29. Edén M, Lee YK, Levitt MH. J. Magn. Reson. A 1996;120:56.
30. Hohwy M, Bildsøe H, Jakobsen HJ, Nielsen NC. J. Magn. Reson. 1999;136:6.
31. Charpentier T, Fernon C, Virlet J. J. Magn. Reson. 1998;132:181.
32. Levitt MH, Edén M. Mol. Phys. 1998;95:879.
33. Blanton WB, Logan JW, Pines A. J. Magn. Reson. 2004;166:174.
34. Sivertsen AC, Bjerring M, Kehlet CT, Vosegaard T, Nielsen NC. Ann. Rep. NMR Spectrosc. 2005;54:244.
35. Nielsen NC. In: A Ramamoorthy (Ed). Biological Solid-State NMR Spectroscopy. M. Dekker: New York, 2005.
36. Vosegaard T, Malmendal A, Nielsen NC. Chem. Month. 2002;133:1555.
37. Vosegaard T, Nielsen NC. J. Biomol. NMR 2002;22:225.
38. Bjerring M, Vosegaard T, Malmendal A, Nielsen NC. Concepts Magn. Reson. 2003;18A:111.
39. Kehlet CT, Sivertsen AC, Bjerring M, Reiss TO, Khaneja N, Glaser SJ, Nielsen NC. J. Am. Chem. Soc. 2004;126:10202.
40. Welch BB. Practical Programming in Tcl and Tk. Prentice Hall PTR: New Jersey, 1995; Ousterhout JK. Tcl and Tk Tookit. Addison-Wesley Publication Company: Reading, 1994.
41. James F; Ross M; Comput. Phys. Commun. 1975;10, 343.
42. Pontryagin L, Boltyanskii B, Gamkredlidze R, Mishchenko E. The Mathematical Theory of Optimal Processes. Wiley-Interscience: New York, 1962.
43. Bryson A Jr, Ho YC. Applied Optimal Control. Hemisphere: Washington DC, 1975.
44. Khaneja N, Reiss T, Kehlet C, Schulte-Herbrüggen T, Glaser SJ. J. Magn. Reson. 2005;172:296.
45. Bak M, Schultz R, Vosegaard T, Nielsen NC. J. Magn. Reson. 2002;154:28. Open Source Software at www.bionmr.chem.au.dk.

46. Berman HM, Westbrook J, Feng Z, Gilliland G, Bhat TN, Weissig H, Shindyalov IN, Bourne PE. Nucl. Acid Res. 2000;28:235.
47. Howhy M, Nielsen NC. J. Chem. Phys. 1997;106:7571.
48. Rhim W-K, Pines A, Waugh JS. Phys. Rev. B 1971;3:684.
49. Nielsen NC, Bildsøe H, Jakobsen HJ. J. Magn. Reson. 1988;80:149.
50. Liu H, Glaser SJ, Drobny GP. J. Chem. Phys. 1990;93: 7543.
51. Sakellariou D, Lesage A, Hodgkinson P, Emsley L. Chem. Phys. Lett. 2000;319:253.
52. Hediger S, Signer P, Tomaselli M, Ernst RR, Meier BH. J. Magn. Reson. 1997;125:291.
53. Schaefer J, Stejskal EO, Garbow JR, McKay RA. J. Magn. Reson. 1984;59:150.
54. Metz G, Hu W, Smith SO. J. Magn. Reson. A 1994;110:219.
55. Baldus M, Geurts DG, Hediger S, Meier BH. J. Magn. Reson. A 1996;118:140.

Homonuclear Shift-Correlation Experiment in Solids

K. Takegoshi

Department of Chemistry, Graduate School of Science, Kyoto University, Kyoto 606-8502, Japan

In solution-state NMR, homonuclear shift correlation experiments, such as COSY and INADEQUATE, have successfully been used for signal assignment. In these experiments, correlation between spins is established via through-bond J couplings, so that each cross peak represents corresponding chemical bonding. Similar J-correlation experiments can also be applicable in solids. Due to the low resolution of ^{1}H resonances in the solid-state NMR, however, we use other spin-1/2 nuclei such as ^{13}C and ^{15}N, whose high resolution observation is capable in solids by the combined use of magic-angle spinning (MAS) and ^{1}H decoupling. Since these isotopes are rare in natural abundance, homonuclear shift-correlation experiment in solids requires a uniformly ^{13}C or ^{15}N-labeled sample. Hereafter, we examine experiments on ^{13}C spins, but most results can also be applied to other rare spin-1/2 nuclei (^{15}N, ^{19}Si, etc). Figure 1a shows a COSY pulse sequence in solids; instead of a single 90° pulse used in solution NMR, cross polarization is applied for excitation. Figure 1b shows a ^{13}C-COSY contour spectrum of [u-^{13}C,^{15}N] glycilisoleucine ([u-^{13}C,^{15}N] GlyIle).[1] The straight lines indicate ^{13}C–^{13}C J connectivity. As exemplified by this, it is straightforward to implement J-based sequences in solid NMR. However, ^{13}C-COSY and/or INADEQUATE have not been popular so far. One of the reasons may be ascribed to the size of the J interaction being much smaller than those of the other spin interactions. To observe small ^{13}C–^{13}C J splitting of a few 10 Hz, line broadening due to ^{13}C–^{13}C dipolar coupling should be removed by fast MAS together with the removal of ^{13}C–^{1}H dipolar broadening by efficient ^{1}H decoupling. Further, the sample-rotation angle should precisely be adjusted to the magic angle to get rid of broadening due to the anisotropic chemical-shift interaction.

^{13}C–^{13}C shift-correlation experiments can also be done by using ^{13}C–^{13}C dipolar interactions. In contrast to isotropic J coupling employed in COSY and INADEQUATE, which is not affected by MAS, dipolar couplings among ^{13}C spins are averaged by MAS. Hence, a certain pulse sequence should be applied to recover ^{13}C–^{13}C dipolar couplings under MAS. Further, for a such sequence being useful for signal assignment, it should be able to recouple ^{13}C spins non-selectively (broadbandly). A number of sequences for broadband ^{13}C–^{13}C dipolar recoupling under MAS have been developed, to name a few examples, DRAMA[2], RFDR[3] and C7[4]. These sequences apply rotation-synchronous ^{13}C rf pulses to interrupt the averaging of the ^{13}C–^{13}C dipolar interactions by MAS, and are adopted in the mixing time of a 2D homonuclear shift-correlation experiment in solids (Figure 2). To remove ^{13}C–^{1}H dipolar interactions, these recoupling sequences require ^{1}H decoupling during the mixing time. In order to avoid recoupling of the ^{13}C–^{1}H dipolar interactions during ^{13}C rf pulses, the ^{1}H rf strength much larger than that of the ^{13}C rf (more than three times for a ^{13}C π pulse)[5] is required in the mixing time. Further, precise synchronization of the pulses and the rotation is necessary, which tends to limit the MAS speed and thus leads to imperfect removal of ^{13}C–^{13}C dipolar broadening in t_1 and t_2.

^{13}C signal assignment can be done by examining ^{13}C–^{13}C cross peaks at a short mixing time, where polarization transfer by ^{13}C–^{13}C dipolar interactions would occur mostly for directly bonded ^{13}C–^{13}C pairs. Although for a longer mixing time, long-range distance correlation may be observed. In broadband dipolar recoupling experiments, however, such long-range correlation tends to be lost due to the so-called dipolar truncation effect, that is, the strong dipolar coupling for a pair of adjacent ^{13}C–^{13}C spins tends to suppress weaker couplings between a ^{13}C spin in the pair and remote ^{13}C spins.[6–8] Figure 3a and b show ^{13}C–^{13}C 2D homonuclear correlation spectra observed for uniformly ^{13}C/^{15}N-labeled N-acetyl-Pro-Gly-Phe ([u-^{13}C,^{15}N] Ac-Pro-Gly-Phe) by applying RFDR and C7, respectively, during the mixing time (τ) of 10 ms. Examination of the observed 2D RFDR and C7 spectra indicates that the dipolar truncation is most prominent for the C_α and $C = O$ carbons of Gly (Figure 4a and b). This can be attributed to isolation of the two ^{13}C spins due to absence of side-chain carbons in Gly; the dipolar coupling between the two ^{13}C spins is much stronger than the dipolar couplings between one of them and outer ^{13}C spins. The dipolar truncation effects are appreciable because these sequences recover ^{13}C–^{13}C dipolar couplings uniformly. In other words, a ^{13}C–^{13}C recoupling sequence that can avoid dipolar truncation should recouple ^{13}C–^{13}C dipolar couplings non-uniformly.

Graham A. Webb (ed.), Modern Magnetic Resonance, 689–693.
© 2008 *Springer.*

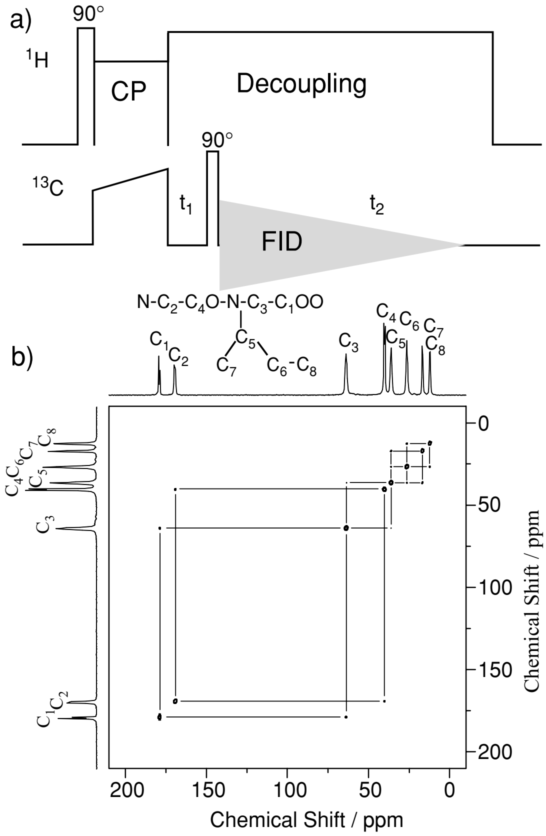

Fig. 1. (a) Pulse sequence for a COSY experiment in solids. (b) ^{13}C-COSY spectrum of [u-^{13}C,^{15}N] glycilisoleucine.[1]

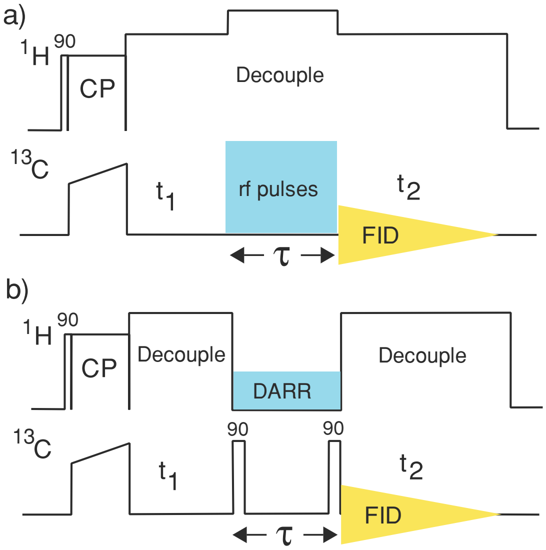

Fig. 2. (a) Pulse sequence for a 2D ^{13}C–^{13}C shift-correlation experiment in solids with rotor-synchronized ^{13}C pulses for ^{13}C broadband recoupling applied in the mixing time (τ) together with ^{1}H decoupling. To avoid ^{13}C–^{1}H recoupling, ^{1}H decoupling intensity in the mixing time is increased. (b) Pulse sequence for a 2D ^{13}C–^{13}C shift-correlation experiment in solids using DARR. In DARR, no ^{13}C rf pulses are applied in the mixing time but ^{1}H spins are irradiated to recover ^{13}C–^{1}H dipolar interactions.

Figure 3c shows a ^{13}C–^{13}C 2D homonuclear correlation spectrum observed for [u-^{13}C,^{15}N] Ac-Pro-Gly-Phe by applying DARR (^{13}C–^{1}H dipolar-assisted rotational resonance)[9,10] during the mixing time of 200 ms. In DARR, broadband recoupling is achieved by ^{13}C–^{13}C spectral overlap realized by the ^{13}C–^{1}H dipolar interaction recovered by suitable rf irradiation on ^{1}H, for example, ^{1}H irradiation with the intensity ν_1 satisfying the rotary-resonance condition $\nu_1 = n\nu_R (n = 1$ or $2)$,[11] where ν_R is the MAS spinning frequency (Figure 2b). For a pair of a carbonyl or an aromatic carbon and an aliphatic carbon, spectral overlap can be achieved between one of the spinning sidebands of the former ^{13}C resonance and the ^{13}C–^{13}H dipolar powder pattern of the latter (Figure 5a). On the other hand, for a pair of spins with a small chemical shift difference, the two center bands are overlapped with each other due to ^{13}C–^{1}H dipolar broadening (Figures 5b and c). These spectral overlaps allow rotational resonance recoupling, and therefore, facile polarization transfer under MAS,[10] and broadband recoupling is thus achieved. On the other hand, the partial spectral overlap causes orientationally selective recoupling, that is, not all ^{13}C–^{13}C pairs recouple. To sum up, DARR recouples ^{13}C–^{13}C dipolar interactions broadbandly but non-uniformly. This unique feature makes it possible to suppress the dipolar truncation effects as shown by the appearance of many cross peaks in the cross-section spectrum (Figure 4c) of the ^{13}C–^{13}C 2D DARR spectrum (Figure 3c) for the C$_\alpha$ carbon of Gly. DARR thus has desirable feature for signal assignment, that is, recoupling occurs broadbandly without significant dipolar truncation. In fact, more than half of the amino acid side chains of [u-^{13}C,^{15}N] ubiquitin were assigned by DARR with a mixing time of 20 ms.[12] Crocker *et al.* applied DARR to rhodopsin and showed that DARR cross-peak intensities reflect the corresponding C–C distances between tyrosine and retinal carbons.[13] These studies indicate that DARR can recouple ^{13}C–^{13}C dipolar couplings broadbandly without appreciable dipolar truncation effects even though the sample is extensively ^{13}C labeled.

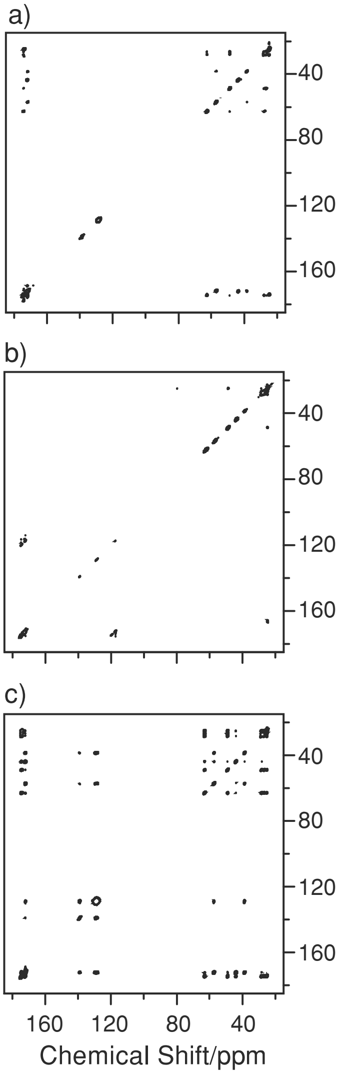

Fig. 3. Contour plots of ^{13}C–^{13}C 2D polarization-transfer spectra of [u-^{13}C,^{15}N] Ac-Pro-Gly-Phe. To reduce the effects of intermolecular couplings, the [u-^{13}C,^{15}N] Ac-Pro-Gly-Phe sample was diluted ten times with the natural abundance peptide in deionized water. The polarization transfer was realized by RFDR during the mixing time (τ) of 10 ms (a), by C7 with $\tau = 10$ ms (b), and by DARR with $\tau = 200$ ms (c). The contour line is plotted at 2.5% of the maximum intensity. The MAS spinning frequency was 20 kHz for (a and c) and 5.5 kHz for (b). The NMR experiments were performed on a Chemagnetics CMX-400 spectrometer operating at 100.7 MHz for ^{13}C.

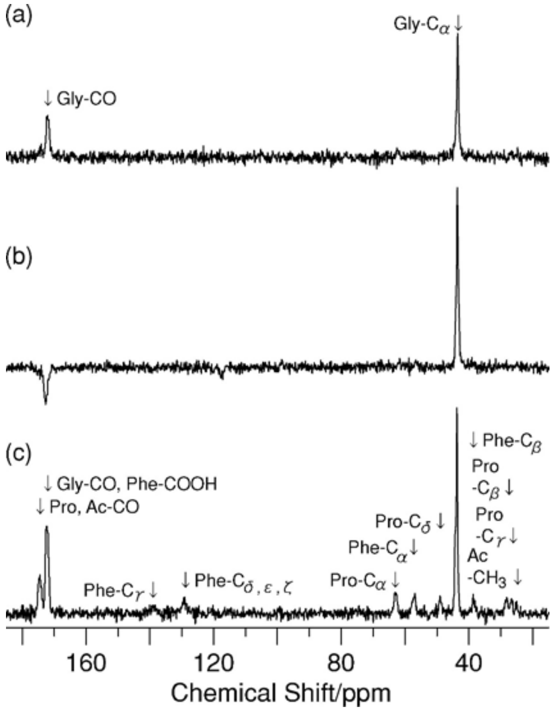

Fig. 4. Cross-sections at the C_α peak of Gly in the ^{13}C–^{13}C 2D polarization-transfer spectra (Figure 2) of [u-^{13}C,^{15}N] Ac-Pro-Gly-Phe. The polarization transfer was performed by using RFDR with $\tau = 10$ ms (a), C7 with $\tau = 10$ ms (b), and DARR with $\tau = 200$ ms (c). The inverted phase of the cross-peak by C7 is due to the double-quantum term in the recoupling Hamiltonian.[4]

Since the ^{13}C–^{1}H recoupling in DARR experiment is employed not for observing ^{13}C–^{1}H dipolar powder patterns but just for spectral overlap, it is not necessary to optimize the ^{13}C–^{1}H recoupling as long as line broadening necessary for spectral overlap is achieved. To show this more explicitly, 1D ^{13}C–^{13}C polarization-transfer NMR experiments of *N*-acetyl[1,2-^{13}C,^{15}N] DL-valine under ^{1}H CW irradiation at various rf strengths (ν_1) were done at $\nu_R = 15$ kHz, and the observed initial transfer rates *k* between ^{13}C$=$O and ^{13}C$_\alpha$ were plotted in Figure 6.[10] One broad maximum is found at the $n = 1$ rotary-resonance condition ($\nu_1 = \nu_R = 15$ kHz), which is attributed to the first-order DARR, and two other maxima at 25 and 35 kHz are deviated by $\pm \sim 5$ kHz from the $n = 2$ rotary-resonance condition ($\nu_1 = 2\nu_R = 30$ kHz). The broad maximum around the $n = 1$ rotary-resonance condition indicates that slight misadjustment of the ^{1}H rf intensity or the spinning frequency is not crucial for the first-order DARR by the $n = 1$ rotational-resonance irradiation. Phrased alternatively, DARR is tolerable to rf inhomogeneity. The observed tolerance would alleviate precise settings of experimental conditions often required for the other ^{13}C–^{13}C broadband recoupling experiments. On the other hand, the $n = 2$ rotary-resonance condition is not a good choice for DARR: the optimal irradiation condition deviates significantly from the exact DARR condition (Figure 6), which was attributed to the particular ^{13}C–^{1}H dipolar broadening lineshape of the C_α carbon.[10]

In this section, it was shown that DARR has the following desirable features for homonuclear shift-correlation experiment: (1) broadband recoupling, (2) less restriction for the spinning speed and stability, (3) low rf-power requirement, (4) tolerance to rf inhomogeneity, and (5) a long mixing time comparable to the spin-lattice relaxation time of ^{13}C. Further, it was indicated that the cross-peak intensity and the internuclear distance are well correlated with each other.[10] Similar correlation has also been observed in the nuclear Overhauser polarization (NOP) experiments using DARR in [u-^{13}C,^{15}N] GlyIle[14] we found that the polarization-transfer rate from the polarized $^{13}CH_3$ spin to another ^{13}C spin correlates well with the ^{13}C–^{13}C distance, thus leading to possibility of broadband 2D DARR recoupling experiments to determine ^{13}C–^{13}C distances in a multiply ^{13}C-labeled sample.

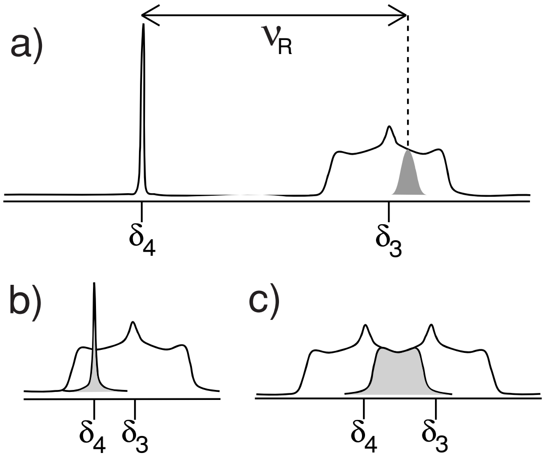

Fig. 5. Schematic ^{13}C MAS spectra of two ^{13}C spins under ^{13}C–^{1}H recoupling, showing various types of spectral overlap necessary for energy conservation in ^{13}C–^{13}C polarization transfer. Spectrum (a) represents two resonances of ^{13}CH at δ_1 and $^{13}C{=}O$ at δ_2. The hatched peak denotes one of the spinning sidebands of the $^{13}C{=}O$ peak, being overlapped with the recovered ^{13}C–^{1}H dipolar powder pattern of the ^{13}CH resonance. Spectrum (b) shows spectral overlap for a pair of spins whose chemical shift difference is smaller than the ^{13}C–^{1}H dipolar broadening. Spectrum (c) shows the case when spectral overlap occurs between two ^{13}C–^{1}H dipolar powder patterns.

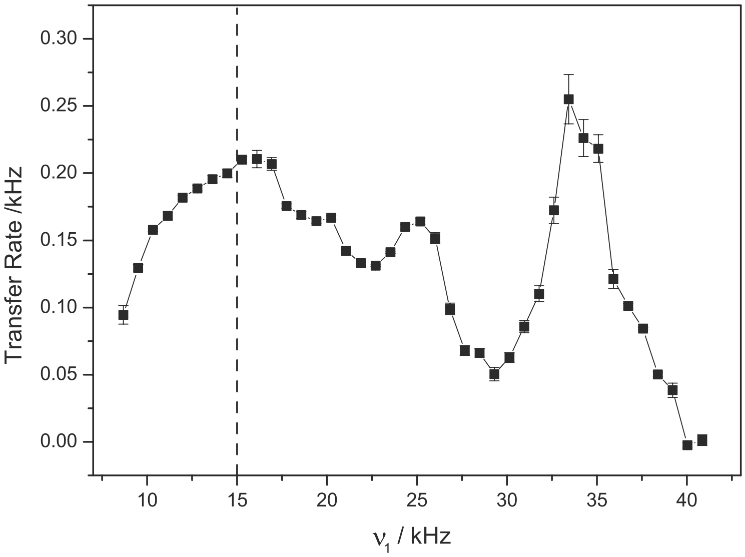

Fig. 6. Dependence of the polarization-transfer rate between $^{13}C{=}O$ and $^{13}C_\alpha$ of *N*-acetyl[1, 2-^{13}C, ^{13}N] DL-valine on the ^{1}H rf-field intensity ν_1 at $\nu_R = 15$ kHz. The rates were deduced by fitting the initial decay in the polarization-transfer curves for the difference of the magnetizations of the two carbons to a single exponential function. The line is drawn for eye guidance. The vertical dotted line indicates the position of the rotary-resonance condition.

References

1. Nomura K, Takegoshi K, Terao T, Uchida K, Kainosho M, J. Biomol. NMR 2000;17:111–123.
2. Tycko R, Dabbagh G, Chem. Phys. Lett. 1990;173:461–465.
3. Bennett AE, Ok JH, Griffin RG, Vega S, J. Chem. Phys. 1992;96:8624–8627.
4. Lee YK, Kurur ND, Helmle M, Johannessen O, Nielsena NC, Levitt MH, Chem. Phys. Lett. 1995;242:304–309.
5. Ishii Y, Ashida J, Terao T, Chem. Phys. Lett. 1995;246:439–445.
6. Baldus M, Meier BH, J. Magn. Reson. 1997;128:172–193.
7. Hoshino T, Kubo A, Imashiro F, Terao T, Mol. Phys. 1998;93:301–313.
8. Hohwy M, Rienstra CM, Jaroniec CP, Griffin RR, J. Chem. Phys. 1999;110:7983–7992.
9. Takegoshi K, Nakamura S, Terao T, Chem. Phys. Lett. 2001;344:631–637.
10. Takegoshi K, Nakamura S, Terao T, J. Chem. Phys. 2003;118:2325–2341.
11. Oas TG, Griffin RG, Levitt MH, J. Chem. Phys. 1988;89:692–695.
12. Igumenova T, McDermott AE, Zilm KW, Martin RW, Paulson EK, Wand AJ, J. Am. Chem. Soc. 2004;126:6720–6727.
13. Crocker E, Patel AB, Eilers M, Jayaraman S, Getmanova E, Reeves PJ, Ziliox M, Khorana HG, Sheves M, Smith SO, J. Biomol. NMR 2004;29:11–20.
14. Takegoshi K, Terao T, J. Chem. Phys. 2002;117:1700–1707.

Two-Dimensional ^{17}O Multiple-Quantum Magic-Angle Spinning NMR of Organic Solids

Gang Wu
Department of Chemistry, Queen's University, Kingston, Ontario, Canada K7L 3N6

Introduction

Solid-state nuclear magnetic resonance (SSNMR) spectroscopy has become an important technique for studying molecular structure and dynamics of chemical and biological systems. Most successful SSNMR studies have been based on observation of magnetically dilute spin-1/2 nuclei such as ^{13}C, ^{15}N, ^{29}Si, and ^{31}P, etc. Although oxygen is ubiquitous in organic and biological molecules, SSNMR studies for ^{17}O (the only NMR-active oxygen isotope) are far less common [1–4]. The scarcity of solid-state ^{17}O NMR studies arises from the fact that ^{17}O has a very low natural abundance (0.037%) and a quadrupolar nucleus (spin-5/2) with a sizable nuclear electric quadrupole moment ($eQ = -2.558$ fm^2). The major obstacle of obtaining SSNMR spectra for quadrupolar nuclei such as ^{17}O is the large size of nuclear quadrupole interactions (typically of the order of 10^6 Hz). This is because these large quadrupole interactions make it difficult to record SSNMR spectra with sufficient spectral resolution in order to resolve chemically or crystallographically different sites.

Solid-state ^{17}O NMR studies of organic compounds were pioneered by several research groups in the late 1980s and the early 1990s. In particular, Fiat and coworkers attempted to record solid-state ^{17}O NMR signals for crystalline amino acids [5]. Oldfield and coworkers applied solid-state ^{17}O NMR techniques to study hemoproteins and model compounds [6]. Ando and coworkers used solid-state ^{17}O NMR to examine hydrogen bonding interactions in polypeptides [7]. These early solid-state ^{17}O NMR studies were all based on a common technique known as the magic-angle spinning (MAS). As high magnetic fields are becoming available, a considerable acceleration has occurred in the past several years in solid-state ^{17}O NMR studies of organic and biological compounds [8–24].

One major limitation of the conventional MAS-based ^{17}O NMR studies is that spectral analyses were based exclusively on observation of "low-resolution" SSNMR spectra. This has made it very difficult to study chemical systems with more than one type of oxygen atoms. The intrinsic difficulty of obtaining high-resolution NMR spectra for ^{17}O arises from the fact that the second-order quadrupole interaction cannot be completely averaged by the traditional MAS technique. Although SSNMR techniques such as dynamic angle spinning (DAS) [25] and double rotation (DOR) [26] were developed for achieving high-resolution for half-integer quadrupolar nuclei including ^{17}O, these techniques are difficult to apply to organic compounds for various reasons. In 1995, Frydman and Harwood [27] introduced a new approach, known as the multiple-quantum magic-angle spinning (MQMAS) method, for completely averaging second-order quadrupole interactions. This new technique immediately attracted considerable attention because it can be readily implemented on most commercial NMR spectrometers. The first ^{17}O MQMAS NMR study was reported by Wu *et al.* [28]. The first ^{17}O MQMAS NMR study for organic compounds was demonstrated by Wu and Dong [29]. Rovnyak *et al.* recorded a ^{17}O MQMAS spectrum of L-asparagine monohydrate using nonlinear sampling [30]. Recently, Lemaitre *et al.* reported a ^{17}O MQMAS spectrum for monosodium L-glutamate [31]. Although the current number of ^{17}O MQMAS studies for organic compounds is still small, wider applications of the technique are anticipated as research interest in using solid-state ^{17}O NMR as a new probe for organic and biological systems continues to grow. Because of space limitation, this chapter will provide only a brief account on several practical aspects of ^{17}O MQMAS experiments.

Pulse Sequence, Data Processing, and Spectral Analysis

For a spin-5/2 nucleus, there are two possible symmetrical MQ coherences: triple-quantum (3Q) and quintuple-quantum (5Q) coherences. In general, it is much more difficult to excite a 5Q coherence than a 3Q coherence. Thus we here focus on the ^{17}O 3QMAS experiment. Figure 1 shows the three-pulse z-filter sequence [32] used for recording ^{17}O 3QMAS NMR spectra. The sequence utilizes the first pulse ($P1$) to excite the required symmetrical 3Q coherence. During the t_1 period, the dephasing of the 3Q coherence, $\nu^{(2)}_{\text{aniso}}(+\frac{3}{2}, -\frac{3}{2})$, is due to the second-order

Graham A. Webb (ed.), Modern Magnetic Resonance, 695–701.
© 2008 *Springer.*

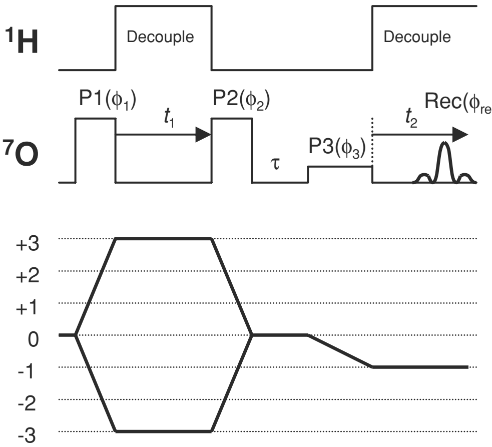

Fig. 1. The three-pulse z-filter sequence used in the ^{17}O 3QMAS experiment. The 24-step phase cycling scheme is: $\phi 1 = (0^\circ)$, $\phi 2 = (0^\circ, 60^\circ, 120^\circ, 180^\circ, 240^\circ, 300^\circ)$, $\phi 3 = (0^\circ, 180^\circ, 0^\circ, 180^\circ, 0^\circ, 180^\circ, 180^\circ, 0^\circ, 180^\circ, 0^\circ, 180^\circ, 0^\circ, 90^\circ, 270^\circ, 90^\circ, 270^\circ, 90^\circ, 270^\circ, 270^\circ, 90^\circ, 270^\circ, 90^\circ, 270^\circ, 90^\circ)$, and $\phi 4 = (0^\circ, 0^\circ, 0^\circ, 0^\circ, 0^\circ, 0^\circ, 180^\circ, 180^\circ, 180^\circ, 180^\circ, 180^\circ, 180^\circ, 90^\circ, 90^\circ, 90^\circ, 90^\circ, 90^\circ, 90^\circ, 270^\circ, 270^\circ, 270^\circ, 270^\circ, 270^\circ, 270^\circ)$. A typical set of experimental parameters are given as follows: $P1 = 5.5$ μs (at $\omega_1/2\pi = 90$ kHz), $\tau = 20$ μs (or $= \tau_r$), $P2 = 2.0$ μs (at $\omega_1/2\pi = 90$ kHz), $P3 = 27$ μs (at $\omega_1/2\pi = 3$ kHz).

quadrupole interaction. The second pulse ($P2$) converts the 3Q coherence into a Zeeman order. The delay, τ, is used to diphase the remaining transverse components (a z-filter). The third pulse ($P3$) is a selective 90° pulse for the central transition and converts the Zeeman order to the central transition coherence for detection. During the detection period, t_2, the dephasing of the CT coherence is also due to the second-order quadrupole interaction, $\nu^{(2)}_{\text{aniso}}(+\frac{1}{2}, -\frac{1}{2})$. Since $\nu^{(2)}_{\text{aniso}}(+\frac{3}{2}, -\frac{3}{2})$ and $\nu^{(2)}_{\text{aniso}}(+\frac{1}{2}, -\frac{1}{2})$ are related by a scaling factor, it is possible that the diphase of the 3Q coherence during t_1 can be reversed and refocused during the t_2 period for all crystallites. Because the coherence transfer pathway from the 3Q coherence to Zeeman order is symmetric, a pure cosine modulation from t_1 is achieved in the signal, $S_x(t_1, t_2)$. To construct a hypercomplex data set for generating pure-phase 2D spectra [33], one needs to repeat the 3QMAS experiment with a 30° phase shift for the $P1$ pulse so that a pure sine-modulated signal, $S_y(t_1, t_2)$, can be obtained. In the MQMAS experiment, because the time-domain echo occurs at $t_2 = kt_1$ (for ^{17}O 3QMAS, $k = 19/12$), the 2D frequency signal (lineshape) would appear tilted if a conventional double Fourier transformation is directly applied to the 2D time-domain signal. To obtain a 2D MQMAS spectrum where an isotropic spectrum appears on the F_1 axis, a shearing transformation is used between the two Fourier transformations [34]. We define the 3Q evolution time as t_1 and label the isotropic dimension, F_1, in frequency units (hertz). Using the convention suggested by Man [35], we can describe the peak positions along the isotropic dimension of a 3QMAS spectrum by

$$\nu^{\text{3QMAS}}_{\text{iso}} = -\frac{17}{12}\nu^{\text{CS}}_{\text{iso}} + \frac{5}{6}\nu^{(2)}_{\text{iso}} \tag{1}$$

where $\nu^{\text{CS}}_{\text{iso}}$ is the frequency contribution from the chemical shift and $\nu^{(2)}_{\text{iso}}$ is the isotropic second-order quadrupole shift defined as:

$$\nu^{(2)}_{\text{iso}} = -\frac{1}{500}\left(3 + \eta_Q^2\right)\frac{C_Q^2}{\nu_{\text{L}}} \tag{2}$$

In the above equation, C_Q is the nuclear quadrupole coupling constant ($C_Q = e^2qQ/h$), η_Q is the quadrupole asymmetry parameter, and ν_{L} is the ^{17}O Larmor frequency.

In the discussion that follows, we use crystalline [2,4–$^{17}O_2$]uracil as an example to illustrate MQMAS spectral analysis. Uracil is one of the common nucleic acid bases. The two oxygen atoms in the pyrimidine ring are chemically different: O_2 is related to a urea functional group and O_4 is similar to an amide oxygen. The crystal structure of uracil indicates that O_2 and O_4 also have quite different hydrogen bonding environment [36]. In particular, O_4 is involved in two nearly linear C=O$\cdots$H–N hydrogen bonds in a Y-shape fashion, meanwhile O_2 is free of any direct hydrogen bonding interaction. Figure 2 shows ^{17}O MAS and 3QMAS NMR spectra obtained for crystalline [2,4–$^{17}O_2$]uracil at 11.75 T. Because there are two oxygen sites in uracil, the 1D ^{17}O MAS spectrum exhibits a complex lineshape. It is not always possible to analyze such a lineshape without additional information. In comparison, the ^{17}O 3QMAS spectrum for [2,4–$^{17}O_2$]uracil shows clearly two isotropic peaks. As indicated in Figure 2, each isotropic peak in the F_1 dimension is related to a sub-spectrum along the F_2 dimension, from which δ_{iso}, C_Q, and η_Q can be estimated. However, it should be emphasized that, because F_2 sub-spectra often exhibit lineshape distortion and do not contain quantitative information about site population, they are usually used only as a starting point in the simulations of 1D MAS spectra. Final NMR parameter extraction is usually achieved by comparing spectral features (peaks and shoulders) in experimental and simulated 1D MAS spectra. Such a combined analysis of the 2D 3QMAS and 1D MAS spectra for crystalline uracil yielded the following parameters: O_2, $\delta_{\text{iso}} = 240 \pm 5$ ppm, $C_Q = 7.62 \pm 0.02$ MHz, $\eta_Q = 0.50 \pm 0.01$; O_4, $\delta_{\text{iso}} = 275 \pm 5$ ppm, $C_Q = 7.85 \pm 0.02$ MHz, $\eta_Q = 0.55 \pm 0.01$. The calculated ^{17}O MAS spectra and corresponding sub-spectra are also shown in Figure 2.

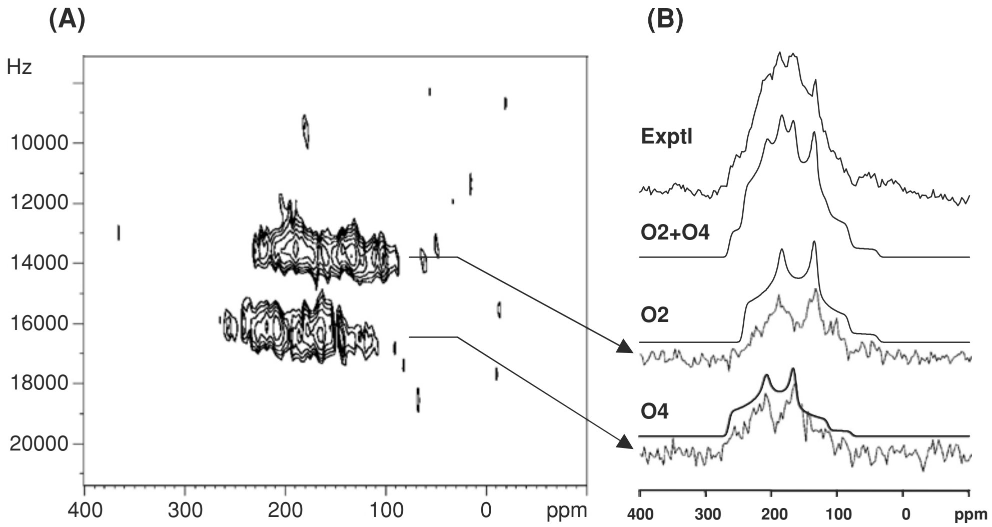

Fig. 2. (A) Experimental 2D ^{17}O 3QMAS spectrum and (B) experimental and calculated 1D ^{17}O MAS spectra for [2,4$-^{17}O_2$]uracil (≈40% ^{17}O) at 11.75 T.

Table 1 lists the organic compounds, together with the corresponding solid-state NMR parameters, so far studied by using a ^{17}O 3QMAS approach. This small collection of organic compounds includes such functional groups as carboxylate, water, amide-type, and urea-type oxygen atoms. The range of C_Q for these functional groups is between 5.9 and 8.2 MHz, typical of most oxygen-containing functional groups in organic compounds. At 11.75 T, a C_Q of this order of magnitude would give rise to a residual second-order quadrupole line width of 8–15 kHz (corresponding to 120–220 ppm for ^{17}O). For example, the line width observed in the ^{17}O MAS spectrum of uracil is 13 kHz. This kind of residual quadrupole broadening would obscure any chemical shift difference

Table 1: A summary of organic compounds studied by ^{17}O MQMAS NMR

Compound	Site	δ_{iso} (ppm)	C_Q (MHz)	η_Q
D-[$^{17}O_2$]Alanine [29]	O_1	275	7.60	0.60
	O_2	262	6.40	0.65
Potassium hydrogen [$^{17}O_4$]dibenzoate [29]	O_1	285	8.30	0.15
	O_2	215	5.90	0.90
DL-[$^{17}O_4$]Glutamic acid hydrochloride [29]	O_1	170	7.20	0.20
	O_2	250	6.80	0.58
	O_3	250	6.80	0.58
	O_4	320	8.20	0.00
[2,4$-^{17}O_2$]Uracil [29]	O_2	240	7.62	0.50
	O_4	275	7.85	0.55
L-Asparagine·$H_2^{17}O$ [30]	H_2O	7.0	7.0	1.0
Monosodium L-[$^{17}O_2$]glutamate [31]	O_1	254	7.4	0.47
	O_2	260	7.2	0.50
	O_3	274	7.6	0.45
	O_4	283	7.7	0.40
	O_5	297	7.0	0.45

between different oxygen sites, leading to a low apparent resolution in ^{17}O MAS spectra. The success of the MQMAS approach relies on the fact that this residual quadrupole broadening can be completely removed in the isotropic dimension. Still use uracil as an example. The 13-kHz line width observed in the ^{17}O MAS spectrum is reduced to about 0.5 kHz along the F_1 axis in the ^{17}O 3QMAS spectrum. This example clearly demonstrates the remarkable benefit of using ^{17}O 3QMAS to improve spectral resolution. The factor that will ultimately determine the resolution limit in ^{17}O MQMAS spectra for organic compounds is not fully understood. However, it appears that the effectiveness of ^{1}H –^{17}O dipolar decoupling plays an important role. We have also reported an unusual ^{1}H–^{17}O decoupling-induced–recoupling phenomenon that may also be important in determining the residual line width in ^{17}O MQMAS spectra [37]. More research is needed in this area. Nevertheless, the advantage of ^{17}O MQMAS over traditional ^{17}O MAS is that the high intrinsic spectral resolution associated with SSNMR can be recovered.

Sensitivity of ^{17}O MQMAS Experiments

In MQMAS experiments, sensitivity is a critical issue. Since the efficiency in both MQ excitation and MQ-to-1Q conversion is proportional to the B_1 field strength, one brute-force approach to increase sensitivity in MQMAS experiments is to improve probe hardware that can sustain a very strong B_1 field. For most commercial MAS probes designed for narrow-bore magnets, the B_1 field is below 100 kHz at the ^{17}O Larmor frequency. Another practically useful method to improve sensitivity is to use t_1 rotor synchronization (i.e. $\Delta t_1 = T_R$) [38]. Figure 3 shows a comparison between ^{17}O MQMAS spectra obtained without and with rotor synchronization for the t_1 increments. In the 2D spectrum obtained without t_1 rotor synchronization, strong spinning sidebands are present along the F_1 dimension. The advantage of this approach is that the F_1 spectral width is not limited by the sample spinning frequency. However, the presence of F_1 spinning sidebands in 2D spectra often results in low peak intensities. In contrast, the 2D spectrum obtained with t_1 rotor synchronization has a spectral width along the F_1 dimension equal to the sample spinning frequency. Consequently, all F_1 spinning sidebands are folded back onto the central band. The advantage of t_1 rotor synchronization is that this approach enhances the overall sensitivity of MQMAS experiments, especially for sites associated with large quadrupole coupling constant and chemical shielding anisotropy. As the sample spinning frequency on modern NMR spectrometers can be as high as 35–50 kHz, it is usually not difficult to achieve a sufficiently large spectral width along the F_1 dimension. For this reason, t_1 rotor synchronization is always recommended for recording ^{17}O MQMAS spectra.

To date the molecular weight of the organic compounds studied by ^{17}O MQMAS is on the order of 200 and the ^{17}O enrichment level is generally less than 40%. It is only natural to question whether the sensitivity of ^{17}O MQMAS experiments can be sufficiently high to make studies of biological macromolecules possible. Although the sensitivity of NMR experiments depends on many factors, it is still meaningful to use the existing ^{17}O MQMAS NMR data to shed some light on the feasibility of the approach for larger molecular systems. For ^{17}O MQMAS experiments, the key factors for sensitivity include (1) the level of ^{17}O enrichment of the sample, (2) the strength of the principal B_0 magnetic field, and (3) the efficiencies for both MQ generation and MQ-to-1Q conversion. Suppose that the sensitivity of ^{17}O central transition NMR experiments depends on the applied magnetic field as $B_0^{7/2}$. With a maximum level of ^{17}O enrichment, 100%, the sensitivity of ^{17}O MQMAS experiments at 21 T (900 MHz for ^{1}H) can be increased at least by an order of magnitude compared with the results shown in Figures 2 and 3 (40% ^{17}O enrichment at 11.75 T). This will make ^{17}O MQMAS experiments feasible for studying molecular systems of a few kDa with the basic pulse sequence described above. Recently, new pulse sequences have been proposed for improving 3Q excitation and 3Q-to-1Q conversion efficiencies for spin-5/2 nuclei [39–43]. In addition to the new pulse sequence development, several new methods for MQMAS data acquisition have been introduced. Rovnyak *et al.* [30] used a nonlinear sampling scheme to reduce the number of t_1 increments required to obtain high resolution. Because the number of t_1 increments is reduced, more transients can be acquired for each t_1 in a given period of time, leading to a sensitivity improvement. Gan and Kwak demonstrated two new ways for utilizing signals from all coherence transfer pathways [44]. A detailed analysis of these new data acquisition methods showed that the sensitivity of MQMAS experiments can be increased by a factor of 2–3 for spin-5/2 nuclei [45]. Finally, the overall sensitivity of the MQMAS experiment can be further increased by an order of magnitude by utilizing a train of quadrupolar Carr–Purcell–Meiboom–Gill refocusing pulses (QCPMG) [46]. Considering improvement from these new developments, we believe that it should be possible to apply ^{17}O MQMAS NMR to biomolecular systems with significant molecular weights (ca. 20–50 kDa) at 21 T.

Conclusion

The advent of MQMAS NMR has triggered a renewed interest in establishing ^{17}O as a new nuclear probe to

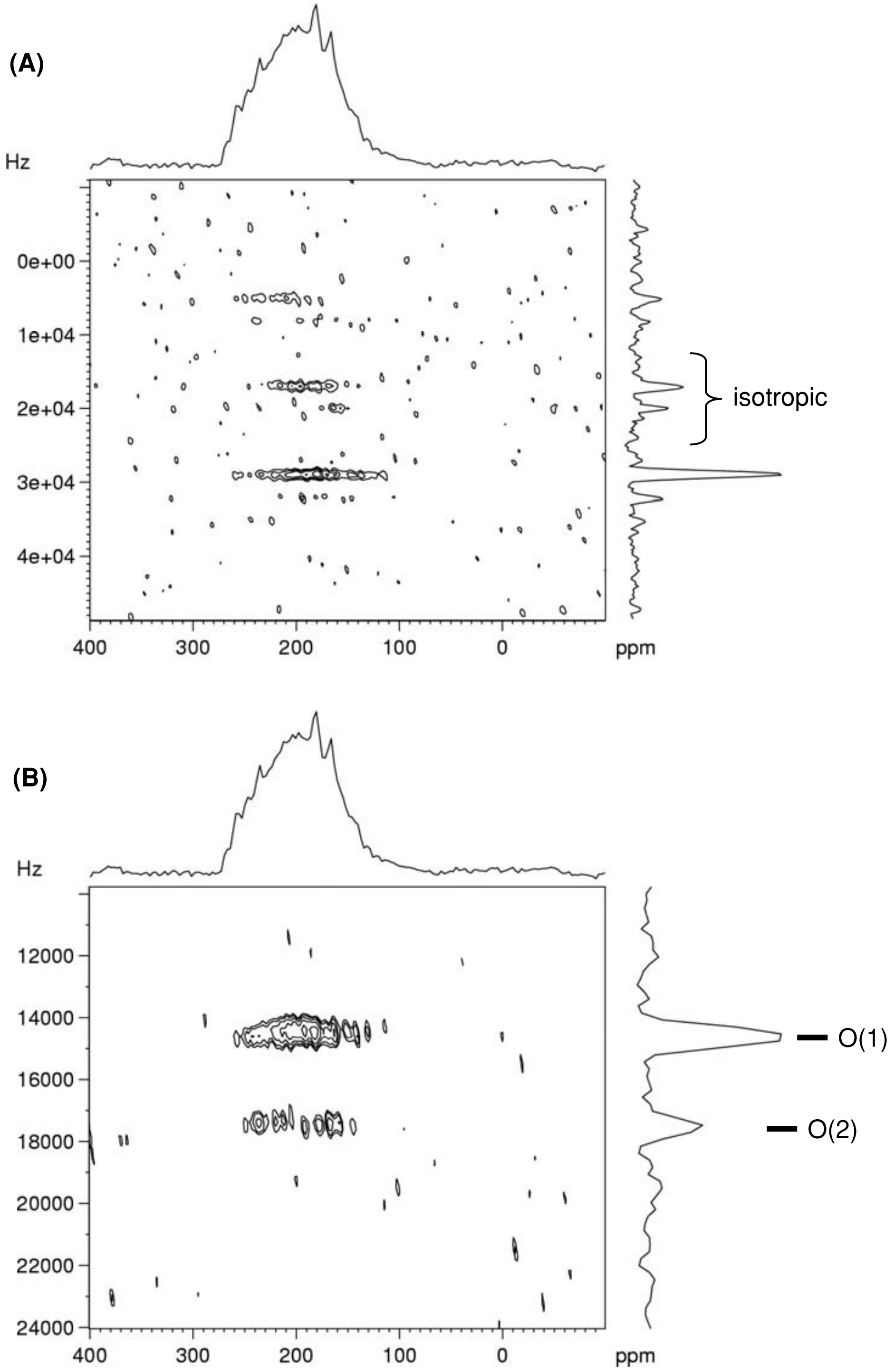

Fig. 3. Comparison between ^{17}O 3QMAS spectra for D-[$^{17}O_2$]alanine (≈40% ^{17}O) obtained (A) without and (B) with t_1 rotor synchronization at 11.75 T.

study organic and biological compounds in the solid state. The advantage of SSNMR for ^{17}O is that the ultimate spectral resolution is not restricted by molecular motion, which is often the primary obstacle in traditional solution ^{17}O NMR for biological macromolecules. Preliminary results have shown that it is possible to obtain high-quality ^{17}O MQMAS NMR spectra for organic compounds with ^{17}O quadrupole coupling constants greater than 8 MHz. Although only small organic molecules have been examined to date, the basic hydrogen bonding features in the systems studied are similar to those observed in proteins (e.g. sidechain conformation) and nucleic acids (e.g. base pairing). The demonstrated sensitivity of ^{17}O MQMAS experiments suggests that high-resolution ^{17}O MQMAS NMR can potentially become a practical technique for chemists to study organic and biological systems. It is likely that future ^{17}O MQMAS studies will have to be performed at ultra-high magnetic fields (e.g. 21 T) to gain sufficient sensitivity for studying biological macromolecules. Another challenge in ^{17}O NMR spectroscopy for biological solids lies in the synthesis of ^{17}O-enriched biological molecules.

Acknowledgment

We wish to thank the Natural Sciences Engineering Research Council (NSERC) of Canada for research and equipment grants.

References

1. Boykin DW (Ed). ^{17}O NMR Spectroscopy in Organic Chemistry. CRC Press: Boca Raton, Florida, 1991.
2. Pearson JG, Oldfield E. In: DM Grant, Harris RK (Eds). Encyclopedia of Nuclear Magnetic Resonance. John Wiley & Sons Ltd, Baffins Lane, Chichester, U.K. 1996, p 3440.
3. Wu G. Biochem. Cell Biol. 1998;76: 429.
4. Lemaître V, Smith ME, Watts A. Solid State. Nucl. Magn. Reson. 2004;26: 215.
5. (a) Goc R, Ponnusamy E, Tritt-Goc J, Fiat D. Int. J. Peptide Protein Res. 1988;31:130; (b) Goc R, Tritt-Goc J, Fiat D. Bull. Magn. Reson. 1989;11: 238.
6. (a) Augspurger JD, Dykstra CE, Oldfield E. J. Am. Chem. Soc. 1991;113:2447. (b) Oldfield E, Lee HC, Coretsopoulos C, Adebodum F, Park KD, Yang S, Chung J, Phillips B. J. Am. Chem. Soc. 1991;113:8680. (c) Park KD, Guo K, Adebodun F, Chiu ML, Sligar SG, Oldfield E. Biochemistry. 1991;30:2333.
7. (a) Kuroki S, Ando I, Shoji A, Ozaki T. Chem. Commun. 1992;433. (b) Kuroki S, Takahashi A, Ando I, Shoji A, Ozaki T. J. Mol. Struct. 1994;323:197.
8. Takahashi A, Kuroki S, Ando I, Ozaki T, Shoji A. J. Mol. Struct. 1998;442:195.
9. Salzmann R, McMahon MT, Godbout N, Sanders LK, Wojdelski M, Oldfield E. J. Am. Chem. Soc. 1999;121: 3818.
10. Godbout N, Sanders LK, Salzmann R, Havlin RH, Wojdelski M, Oldfield E. J. Am. Chem. Soc. 1999;121: 3829.
11. Yamauchi K, Kuroki S, Ando I, Ozaki T, Shoji A. Chem. Phys. Lett. 1999;302:331.
12. Dong S, Yamada K, Wu G. Z. Naturforsch. 2000;55A: 21.
13. Wu G, Hook A, Dong S, Yamada K. J. Phys. Chem. A. 2000; 104:4102.
14. Wu G, Yamada K, Dong S, Grondey H. J. Am. Chem. Soc. 2000;122:4215.
15. Yamada K, Dong S, Wu G. J. Am. Chem. Soc. 2000; 122:11602.
16. Dong S, Ida R, Wu G. J. Phys. Chem. A. 2000;104: 11194.
17. Wu G, Dong S. Chem. Phys. Lett. 2001;334:265.
18. Wu G, Dong S, Ida R. Chem. Commun. 2001;891.
19. Dong S, Ida R, Reen N, Wu G. J. Am. Chem. Soc. 2002; 124:1768.
20. Yamauchi K, Kuroki S, Ando I. J. Mol. Struct. 2002; 602/603:171.
21. Wu G, Yamada K. Solid State Nucl. Magn. Reson. 2003;24:196.
22. Pike KJ, Lemaitre V, Kukol A, Anupold T, Samoson A, Howes AP, Watts A, Smith ME, Dupree R. J. Phys. Chem. B. 2004;108:9256.
23. Lemaitre V, de Planque MRR, Howes AP, Smith ME, Dupree R, Watts A. J. Am. Chem. Soc. 2004;126: 15320.
24. Kimura H, Kanesaka S, Kuroki S, Ando I, Asano A, Kurosu H. Magn. Reson. Chem. 2005;43:209.
25. (a) Llor A, Virlet J. Chem. Phys. Lett. 1988;152:248. (b) Meuller KT, Sun BQ, Chingas GC, Zwanziger JW, Terao T, Pines A. J. Magn. Reson. 1990;86:470.
26. (a) Samoson A, Lippmma E, Pines A. Mol. Phys. 1988;65:1013. (b) Chmelka BF, Mueller KT, Pines A, Stebbins J, Wu Y, Zwanziger JW, Nature. 1989;339:42. (c) Wu Y, Sun BQ, Pines A, Samoson A, Lippmaa E. J. Magn. Reson. 1990;89:296.
27. Frydman L, Harwood JS. J. Am. Chem. Soc. 1995;117:5367.
28. (a) Wu G, Rovnyak D, Sun BQ, Griffin RG. Chem. Phys. Lett. 1996;249:210; (b) Wu G, Rovnyak D, Huang PC, Griffin RG. Chem. Phys. Lett. 1997;277:79.
29. Wu G, Dong S. J. Am. Chem. Soc. 2001;123:9119.
30. Rovnyak D, Filip C, Itin B, Stern AS, Wagner G, Griffin RG, Hoch JC. J. Magn. Reson. 2003;161:43.
31. Lemaitre V, Pike KJ, Watts A, Anupold T, Samoson A, Smith RE, Dupree R. Chem. Phys. Lett. 2003;371:91.
32. Amoureux J-P, Fernanderz C, Steuernagel S. J. Magn. Reson. Ser. A. 1996;123:116.
33. States DJ, Haberkorn RA, Ruben DJ. J. Magn. Reson. 1982; 48:286.
34. Medek A, Harwood JS, Frydman L. J. Am. Chem. Soc. 1995;117:12779.
35. Man PP. Phys. Rev. B. 1998;58:2764.
36. Stewart RF, Jensen LH. Acta Crystallogr. 1967;23:1102.
37. Wu G. Chem. Phys. Lett. 2000;322:513.
38. Massiot D. J. Magn. Reson. Ser. A. 1996;122:240.

39. Kentgens APM, Verhagen R. Chem. Phys. Lett. 1999; 300:435.
40. Madhu PK, Goldbourt A, Frydman L, Vega S. Chem. Phys. Lett. 999;307:41.
41. Alemany LB, Callender RL, Barron AR, Steuernagel S, Iuga D, Kentgens APM. J. Phys. Chem. B. 2000;104: 11612.
42. Goldbourt A, Madhu PK, Vega S. Chem. Phys. Lett. 2000;320:448.
43. Vosegaard T, Massiot D, Grandinetti PJ. Chem. Phys. Lett. 2000;326:454.
44. Gan Z, Kwak HT. J. Magn. Reson. 2004;168:346.
45. Amoureux J-P, Delevoye L, Steuernagel S, Gan Z, Ganapathy S, Montagne L. J. Magn. Reson. 2005;172:268.
46. (a) Vosegaard T, Larsen FH, Jakobsen HJ, Ellis PD, Nielsen NC. J. Am.Chem. Soc. 1997;119:9055; (b) Larsen FH, Nielsen NC. J. Phys. Chem. 1999;103: 10825.

A Family of PISEMA Experiments for Structural Studies of Biological Solids

Ayyalusamy Ramamoorthy and Kazutoshi Yamamoto
Biophysics Research Division and Department of Chemistry, University of Michigan, Ann Arbor, MI 48109-1055, USA

Abstract

Narrowest heteronuclear dipolar coupling spectral lines provided by the two-dimensional polarization inversion spin exchange at the magic angle (PISEMA) technique lead to the development and application of a series of multidimensional solid-state NMR methods for the structural studies of biological solids. Studies have shown that the measurement of structural and orientational constraints from uniformly labeled proteins using PISEMA is crucial, particularly in the structure determination of membrane-associated proteins. Excellent line-narrowing efficiency, high scaling factor, and performance at various magic-angle-spinning (MAS) speeds and radio frequency (rf) power are the main advantages of PISEMA. However, high rf power requirement and offset effects are the major limitations of this technique. In this chapter, these difficulties and methods to overcome them are discussed for both static and MAS experimental conditions. Experimental and simulated data to demonstrate the efficacy of newly developed PISEMA-type pulse sequences are also presented.

An Ideal SLF Sequence

Accurate measurement of heteronuclear dipolar couplings is very important to determine the high-resolution structure, dynamics, and orientation of molecules using solid-state NMR spectroscopy [1]. A variety of multiple pulse sequences have been used to suppress homonuclear ^{1}H spin–spin interactions in a two-dimensional (2D) separated local field (SLF) experiment, which provides narrow heteronuclear dipolar coupling lines [1]. The best sequence should: (i) completely suppress dipole–dipole interactions among I (usually high γ and/or highly abundant nuclei such as ^{1}H and ^{19}F) spins, (ii) have a large scaling factor (scaling factor $= 1.0$ represents 0% reduction in the measured I–S dipolar coupling value) in order to measure small heteronuclear dipolar couplings as well as to resolve resonances from uniformly labeled proteins, (iii) have a short duration that can provide a large spectral width, (iv) be tolerant to pulse imperfections such as offset and rf field inhomogeneity, (v) require a low rf power to avoid sample heating, (vi) avoid rotor synchronization and be independent of the spinning speed of the sample for studies under MAS, and (vii) be easy to set up in most commercially available solid-state NMR spectrometers. Among all the reported SLF sequences, polarization inversion spin exchange at the magic angle (PISEMA) (Figure 1A and B) satisfies most of these requirements [1–4]. An Flip-flop Lee-Goldburg (FFLG)- [5–8] or Phase-Modulated Lee-Goldburg (PMLG)- [9] based PISEMA sequence efficiently suppresses ^{1}H–^{1}H dipolar couplings with a scaling factor of 0.816 and a short cycle time (16.33 μs for a 50 kHz rf field strength), tolerant to most of the experimental errors, easy to set up, and can easily be modified to work efficiently under various spinning speeds without the need for rotor synchronization [1,3]. In addition, the sensitivity enhancement offered by the polarization inversion, and the reduction of relaxation rates and suppression of I and S spin chemical shifts by the spin-locks during SEMA are other intrinsic benefits of the sequence [1,2]. Therefore, the pulse sequence has been widely used for studies both under static (Figure 1A) [1,10–15] and MAS (Figure 1B) [1,4,16] experimental conditions. The SEMA sequence has also been utilized to develop several new solid-state NMR methods to study biological solids [17–23]. Studies have shown that replacing FFLG in SEMA with the Lee–Goldburg magic angle irradiation (LG)—LG-PISEMA, LG-SEMA, or LG-CP—also provides heteronuclear dipolar coupling spectra with an identical scaling factor [1,3,4,24]. In fact, LG-SEMA is routinely used to set up 2D PISEMA experiments [3] and selective transfer of ^{1}H magnetization to its dipolar-coupled heteronuclei such as ^{13}C or ^{15}N [22,23,25]. The main advantages of LG-SEMA are its short cycle time and the absence of phase transients [1,3]. However, the extent of ^{1}H homonuclear decoupling and tolerance toward rf field mismatch and rf field inhomogeneity by FFLG-SEMA is far better than that of LG-SEMA [3,24].

Offset Effects

There are some disadvantages that limit the application of PISEMA to investigate certain systems. Studies have shown that the SEMA sequence is highly sensitive to I

Graham A. Webb (ed.), Modern Magnetic Resonance, 703–709.
© 2008 *Springer.*

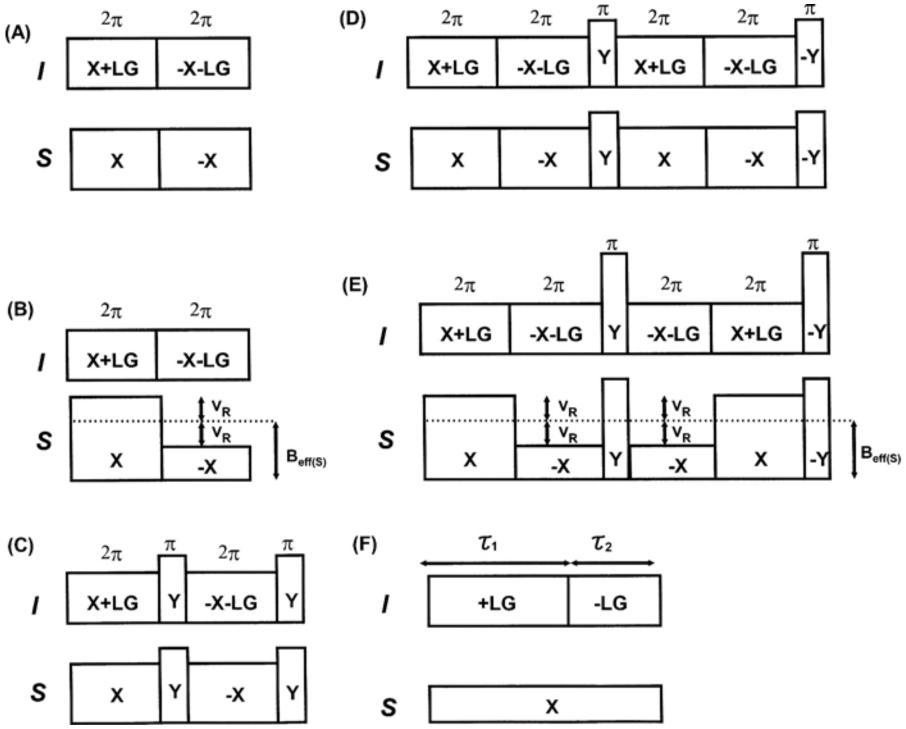

Fig. 1. Timing diagrams for a family of SEMA sequences that can be used in the t_1 period of 2D PISEMA: (A) SEMA, (B) SEMA-MAS, (C) BB-SEMA-1, (D) BB-SEMA-2, (E) BB-SEMA-MAS, and (F) TANSEMA. LG stands for the Lee–Goldburg magic angle irradiation.

spin offset [1]. Our simulations (data not shown) on a dipolar-coupled two-spin (*I* and *S*) system show that the offset dependency is identical for LG-SEMA and FFLG-SEMA sequences as there is no homonuclear ^{1}H dipolar couplings are included in the calculations. Since the effective field direction of LG or FFLG is dependent on the offset value, the line-narrowing efficiency decreases and the observed dipolar splitting increases with offset (Figure 2A, plot A). In addition, a strong zero-frequency peak appears as the off-magic angle spin-lock of *I* spins eliminates the spin exchange among *I* and *S* nuclei (Figure 3). These effects are severe when a low rf power is used and also for experiments conducted at high magnetic fields. For example, a span of ~12 ppm for amide ^{1}H chemical shift resonances makes it very difficult to satisfy the LG condition for all amide sites of a uniformly labeled protein/peptide. As a result, the intensity, scaling factor, and line width are not uniform in a 2D PISEMA spectrum of a uniformly ^{15}N-labeled protein embedded in aligned lipid bilayers. The offset effects are stronger for small ^{1}H–^{15}N dipolar couplings. Thus it is difficult to accurately measure the ^{1}H–^{15}N dipolar couplings for the structural studies of membrane proteins. Therefore, it is of considerable importance to develop new PISEMA-type pulse sequences that can overcome the above-mentioned offset effects.

Offset Compensation by BB-SEMA

Studies have shown that the use of ramped spin-lock pulses [26] during SEMA in the *S* spin channel or the newly developed SAMMY [27] sequence reduces offset effects. However, the scaling factor and the extent of line narrowing of the SAMMY sequence are smaller than that of the PISEMA sequence. We recently proposed a modified PISEMA sequence (called BB-PISEMA (Figure 1C–E) that compensates the effects of offset [28]. Introduction of simultaneous π pulses in the SEMA sequence suppresses the evolution of the magnetization under offset in the SEMA period of PISMEA. This is reflected in the results shown in Figures 2A (plots B and C) and 3. While the offset compensation is better for BB-SEMA-1 than BB-SEMA-2, line-narrowing efficiency may depend

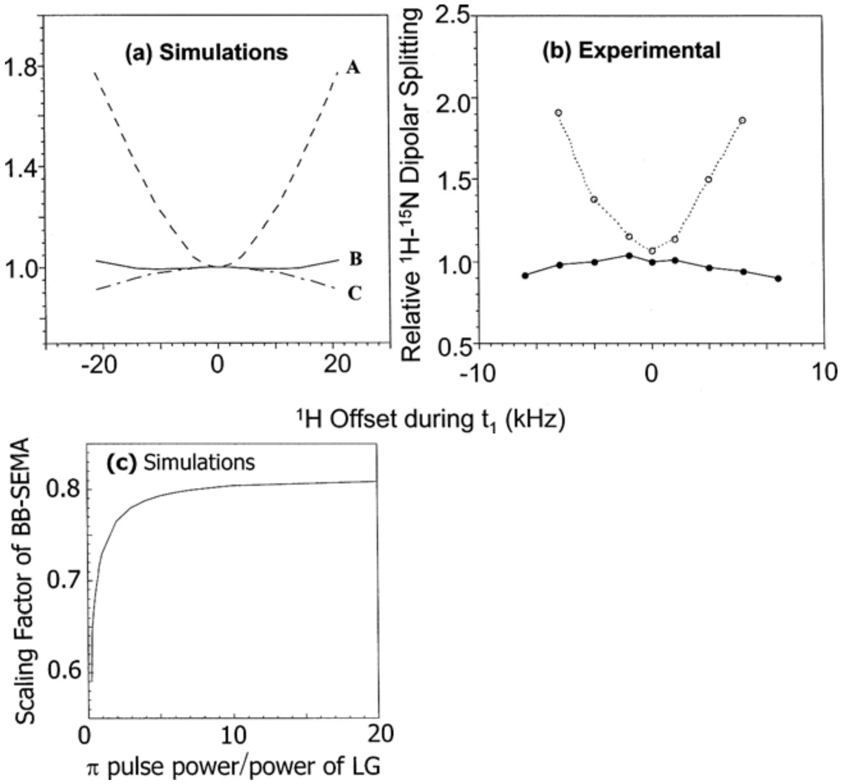

Fig. 2. Dependence of the simulated (a) and experimentally (a) measured heteronuclear dipolar couplings on the *I* spin carrier offset. Experimental data were measured from 2D PISEMA and BB-PISEMA spectra (data not shown) of *n*-acetyl-L-^{15}N-valyl-L-^{15}N-leucine single crystal under the same experimental conditions. The simulated data in (a), (b), and (c) were obtained using the PISEMA, BB-SEMA-1, and BB-SEMA-2 sequences, respectively. (c) Variation of the scaling factor with the ratio of the rf power used for the π and LG pulses in the BB-PISEMA. In all the simulations, 100 kHz rf field was used for LG and the π pulse in BB-SEMA-2. The πgulse power was varied in (c).

on the π pulse width. The number of FFLG cycles in between the π pulses can be varied depending on the required dwell time. The efficacy of SEMA (Figure 1A) and BB-SEMA (Figure 1D) sequence was examined using 2D experiments on a single crystal (Figure 2B) and simulations (Figure 2B) using SIMPSON [29]. Experimentally obtained dipolar coupling slices are given in Figure 4. Both the experimental and simulated data demonstrate that heteronuclear dipolar coupling spectra obtained using BB-PISEMA are less sensitive to *I* spin offset than those obtained with the regular PISEMA pulse sequence. This is a significant improvement and therefore the BB-PISEMA sequence can be used in the structural studies of membrane proteins at high magnetic fields where there is a range of ^{1}H chemical shifts.

Simulations suggest that the use of ideal π pulses provides a scaling factor of 0.816 and the deviation from ideality reduces the scaling factor of BB-SEMA (Figure 1C). Nevertheless, our experimental results demonstrate that the scaling factor of BB-PISEMA is 0.73 even for a π pulse width of 8.16 μs. Simulated results from an unoriented dipolar-coupled two-spin system are given in Figure 5. Recently published CSA values were used in the simulations [30–36]. FFLG-PISEMA provides better power lineshape than the LG-PISMEA sequence. However, the lineshapes from both LG- and FFLG-based PISEMA sequences are dominated by the zero-frequency peak due to *I* spin offset effects. On the other hand, BB-PISEMA significantly suppresses the offset effects (Figure 5). Offset effects of SEMA-MAS (Figure 1B) can also be compensated using a pair of π pulses as shown in Figure 1E (data not shown). While the BB-SEMA-based sequences are efficient in compensating the *I* spin offset effects even when low power π pulses were used, the

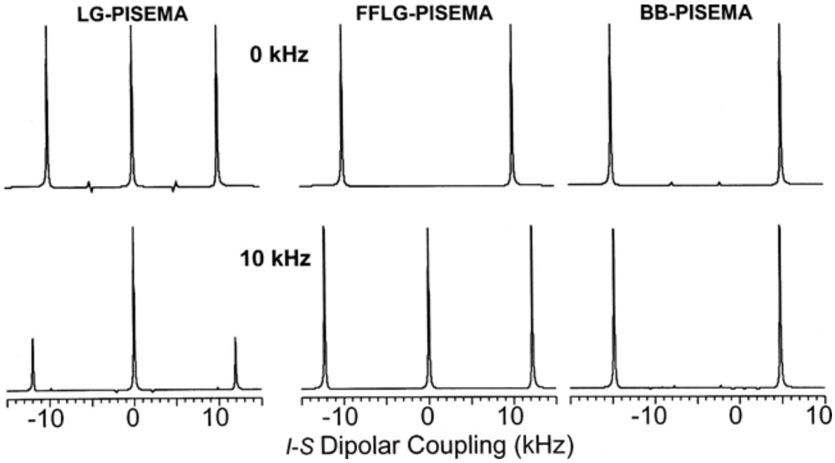

Fig. 3. Simulated I–S dipolar coupling spectra of an aligned two-spin system with a dipolar coupling constant of 10 kHz at I spin carrier offset frequencies of 0 and 10 kHz. Note the appearance of the zero-frequency peak and the increase in the dipolar splitting in LG- and FFLG-based PISEMA sequences. Offset effects are stronger when the I–S dipolar coupling is small. On the other hand, BB-PISEMA spectra are independent of the I spin carrier frequency.

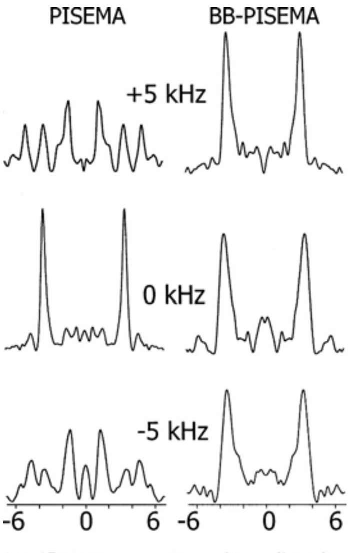

Fig. 4. Experimental ^{1}H–^{15}N dipolar coupling slices extracted from 2D PISEMA and 2D BB-PISEMA that were obtained at different ^{1}H offset values. In addition to the increase in the observed dipolar coupling values, S/N is significantly decreases with the offset value in PISEMA spectra. On the other hand, BB-PISEMA spectra are to a large extent independent of the offset values.

performances of these sequences are dependent on the Sspin offset values as shown in Figure 6 (plot B). As shown in Figure 6 (plot C), this effect can be overcome by using high power π pulses in BB-SEMA sequences. The spin dynamics and the performance of this new pulse sequence can be analyzed using average Hamiltonian and density matrix approaches. Several such studies reported the theoretical details of the offset effects under heteronuclear spin exchange process under static and MAS conditions [24,37–39].

SEMA Requires Very High RF Power

The on-resonance performance of the PISEMA sequence is impressive even when low power is used for the FFLG sequence [1,27,28]. For example, as low as a 40-kHz rf field in the ^{1}H channel can be used at 400 MHz to obtain high-resolution ^{1}H–^{15}N dipolar spectral lines for a peptide embedded in bilayers [28]. However, the requirement of rf power in the S spin channel is quite demanding as it has to match the effective field in the ^{1}H channel for static conditions: $B_{\mathrm{rf},S} = \left(B^2_{\mathrm{rf},S} + B^2_{\mathrm{off},I}\right)^{1/2}$. In addition, under MAS, the power requirement is increased by the spinning speed (Figure 1B and E); this means for experiments under fast MAS and/or at high magnetic fields, this requirement will be quite challenging to satisfy. This problem is also significant for wet biological solids such as lipid bilayers as these samples are power loss and are highly sensitive to rf heat [40–42]. For example, even in

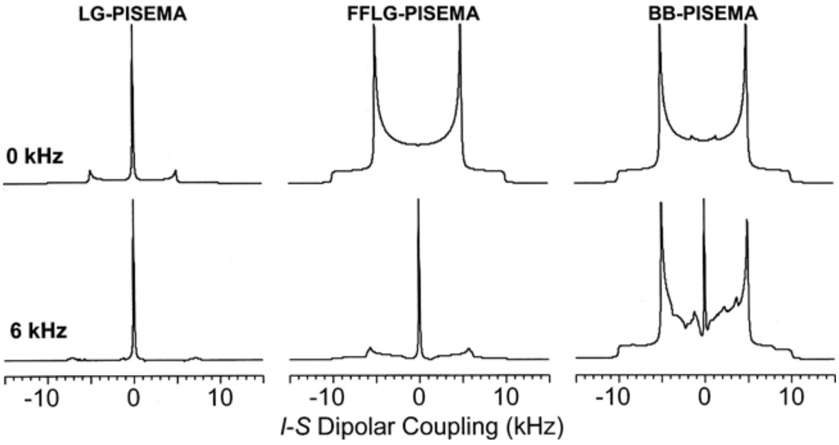

Fig. 5. Simulated I–S dipolar coupling spectra of an unoriented two-spin system with a dipolar coupling constant of 10 kHz at 0 and 6 kHz I spin carrier offset values. The strong zero-frequency peak in LG-PISEMA (both on- and off-resonances of I spin) and FFLG-PISEMA makes it difficult to measure the powder lineshape, whereas BB-PISEMA is tolerant to offset effects. The intensity of the zero-frequency peak depends on the span of the CSA values used in simulations.

the above-mentioned peptide example, ∼1 kW rf power is required in the ^{15}N rf channel [40]. Therefore, it is essential to overcome these difficulties in order to use PISEMA-type experiments on membrane proteins.

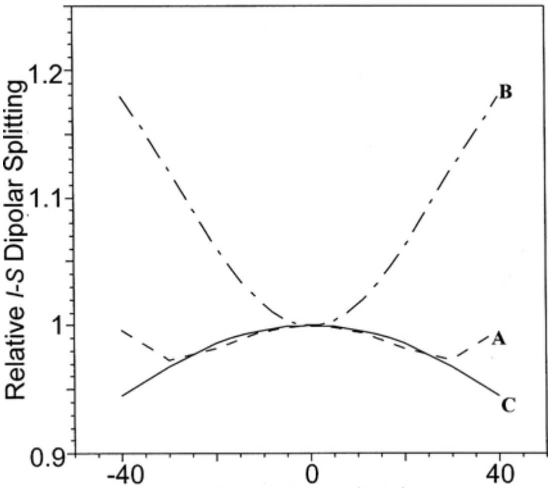

Fig. 6. Variation of simulated ^{1}H–^{15}N dipolar coupling values as a function of ^{15}N offset in PISEMA (A) and BB-PISEMA sequences (B and C). A 100 kHz rf field was used for LG in all cases, while the π pulse power was 100 kHz for (B) and 500 kHz for (C).

TANSEMA for Low RF Power Experiments

We recently demonstrated the utility of time averaged nutation (TAN) [43] concept for the reduction of rf power in SEMA experiments. The TANSEMA [44] pulse sequence shown in Figure 1F dramatically reduces the rf power required in the S spin channel. The values of t_1 and t_2 can be varied to obtain the desired effective nutation field in the ^{1}H channel. For example, PITANSEMA experiments even with a 11-fold reduction in the ^{15}N rf power, as compared to the regular PISEMA experiment, on a single crystal sample resulted in 2D spectra with line widths as good as that of PISEMA [44]. Use of supercycles and ramped spin-locks further improved the efficacy of the PITANSEMA sequence. This sequence has also shown to be effective for liquid crystalline samples [44,45]. However, our simulations show that the measured dipolar splitting is offset dependent as shown in Figure 7. Simulated I–S dipolar coupling PITANSEMA spectra of an aligned two-spin system for various I spin carrier offset values showed increase in the zero-frequency peak and the dipolar splitting like the PISEMA sequence. Research in our laboratory to improve the efficacy of PITANSEMA is in progress.

PISEMA of SI$_n$

Since the heteronuclear dipolar coupling Hamiltonians for SI$_i$ and SI$_j$ in an SI$_n$ system do not commute, the smaller couplings are suppressed by SEMA [1,45].

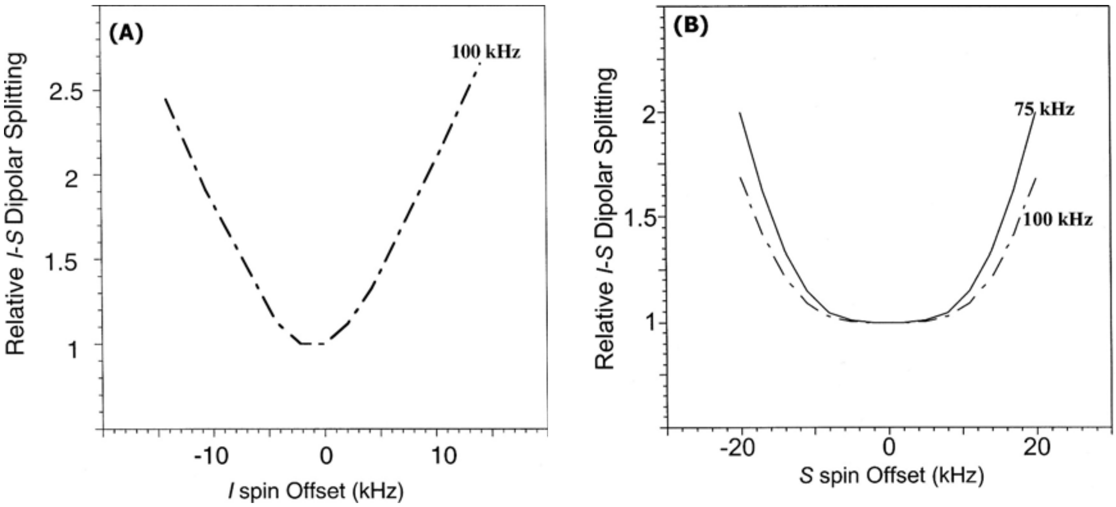

Fig. 7. Variation of simulated *I–S* dipolar splitting as a function of *I* (A) and *S*(B) spin carrier offset frequency in PITANSEMA with $\theta_1 = \pi$ and $\theta_2 = \pi/2$; where θ_1 and θ_2 are the effective nutation angles during the 1st and 2nd halves of the TANSEMA sequence, respectively (Figure 1E). Note that these angles are equal (i.e. $\theta_1 = \theta_2$) in PISEMA and therefore the time average nutation for SEMA is zero.

This is an advantage in the structural studies of proteins as one interested in measuring the dipolar coupling between the directly bonded amide ^{1}H and ^{15}N spin pairs by suppressing the coupling between remote protons and ^{15}N. However, in several other systems such as liquid crystalline materials, measurement of small dipolar couplings is important. Recent studies have showed that it is difficult to measure small dipolar couplings in the presence of large dipolar couplings [46,47].

Summary

We have highlighted the advantages and disadvantages of the commonly used PISEMA pulse sequence. Recently developed BB-PISEMA to compensate the offset effects and PITANSEMA to overcome the high rf power effects are also discussed. We believe that these new sequences further widen the applications of PISEMA. Some of the areas that benefit from these applications are the structural studies of weakly aligned molecules, bicelles, and liquid crystalline materials. It is also possible to develop a variety of PISEMA-type pulse sequences by combining these new developments with indirect ^{1}H detection, MAS, and gradients for various studies on both rigid and mobile biological solids. Needless to mention that the optimization of phase, frequency, and width of rf pulses of SEMA for better performance could also provide fruitful results.

Acknowledgments

This research was supported by the research funds from NIH (AI054515 to A.R). We thank Dr. Lee and Dr. Ermakov for the help with this research.

References

1. Ramamoorthy A, Wei Y, Lee DK. Annu. Rep. NMR Spectrosc. 2004;52:2.
2. Wu CH, Ramamoorthy A, Opella SJ. J. Magn. Reson. A. 1994;109:270.
3. Ramamamoorthy A, Wu CH, Opella SJ. J. Magn. Reson. 1999;140:131.
4. Ramamamoorthy A, Opella SJ. Solid State Nucl. Magn. Reson. 1995;4:387.
5. Lee M, Goldberg WI. Phys. Rev. A. 1965;140:1261.
6. Mehring M, Waugh JS. Phys. Rev. B. 1972;5:3459.
7. Bielecki A, Kolbert AC, de Groot HJM, Griffin RG, Levitt MH. Adv. Magn. Reson. 1990;14:111.
8. Ravikumar M, Ramamoorthy A. Chem. Phys. Lett. 1998;286:199.
9. Vinogradov E, Madhu PK, Vega S. J. Chem. Phys. 2001;115: 8983; Vinogradov E, Madhu PK, Vega S. Chem. Phys. Lett. 1999;314:443; *ibid* 2000;329:207; *ibid* 2002;354:193.
10. Jelinek R, Ramamoorthy A, Opella SJ. J. Am. Chem. Soc. 1995;117:12348.
11. Marassi FM, Ramamoorthy A, Opella SJ. Proc. Natl. Acad. Sci. U.S.A. 1997;94:8551.
12. Wu CH, Ramamoorthy A, Gierasch LM, Opella SJ. J. Am. Chem. Soc. 1995;117:6148.

13. Ramamoorthy A, Wu CH, Opella SJ. J. Am. Chem. Soc. 1977;119:10479.
14. Marassi FM, Opella SJ. J. Magn. Reson. 2000;144:150.
15. Wang J, Denny J, Tian C, Kim S, Mo Y, Kovacs F, Song Z, Nishimura K, Gan Z, Fu R, Quine JR, Cross TA. J. Magn. Reson. 2000;144:162.
16. Dvinskikh SV, Zimmermann H, Maliniak A, Sandstrom D. J. Magn. Reson. 2003;164:165.
17. Ramamamoorthy A, Wu CH, Opella SJ. J. Magn. Reson. B. 1995;107:88.
18. Ramamamoorthy A, Gierasch LM, Opella SJ. J. Magn. Reson. B. 1995;109:112.
19. Ramamamoorthy A, Gierasch LM, Opella SJ. J. Magn. Reson. B. 1996;111:81.
20. Gu ZT, Opella SJ. J. Magn. Reson. 1999;138:193.
21. Gu ZT, Opella SJ. J. Magn. Reson. 1999;140:340.
22. Wei Y, Lee D-K, Hallock KJ, Ramamoorthy A. Chem. Phys. Lett. 2002;351:42.
23. Wei YF, Ramamoorthy A. Chem. Phys. Lett. 2001;342:312–6.
24. Dvinskikh SV, Zimmermann H, Maliniak A, Sandstrom D. J. Chem. Phys. 2005;122:044512.
25. Rossum BJV, de Groot CP, Ladizhansky V, Vega S, de Groot HJM. J. Am. Chem. Soc. 2000;122:3465.
26. Fu RQ, Tia CL, Cross TA. J. Magn. Reson. 2002;154:130.
27. Nevzorov AA, Opella SJ. J. Magn. Reson. 2003;164:182.
28. Yamamoto K, Lee DK, Ramamoorthy A. Chem. Phys. Lett. 2005;407:289–293.
29. Bak M, Rasmussen JT, Nielsen NC. J. Magn. Reson. 2000;147:296.
30. Lee DK, Wittebort RJ, Ramamoorthy A. J. Am. Chem. Soc. 1998;120:8868.
31. Lee DK, Ramamoorthy A. J. Magn. Reson. 1998;113:204.
32. Lee DK, Santos JS, Ramamoorthy A. Chem. Phys. Lett. 1999;309:209.
33. Lee DK, Wei Y, Ramamoorthy A. J. Phys. Chem. B. 2001;105:4752.
34. Wei Y, Lee DK, McDermott AE, Ramamoorthy A. J. Magn. Reson. 2002;158:23.
35. Brender JR, Taylor DM, Ramamoorthy A. J. Am. Chem. Soc. 2001;123:914
36. Poon A, Birn J, Ramamoorthy A. J. Phys. Chem. B. 2004;108:16577.
37. Ladizhansky V, Vega S. J. Chem. Phys. 2000;112:7158.
38. Shekar SC, Ramamoorthy A. Chem. Phys. Lett. 2001;342:312.
39. Shekar SC, Lee D-K, Ramamoorthy A. J. Magn. Reson. 2002;157:223.
40. Shekar SC, Lee D-K, Ramamoorthy A. J. Am. Chem. Soc. 1995;123:7467.
41. Martin RW, Zilm KW. J. Magn. Reson. 2004;168:202.
42. Dvinskikh SV, Castro D, Sandstrom H. Magn. Reson. Chem. 2004;42:875.
43. Takegoshi K, McDowell CA. J. Magn. Reson. 1986;67:356.
44. Lee DK, Narasimhaswamy T, Ramamoorthy A. Chem. Phys. Lett. 2004;399:359.
45. Nishimura K, Naito A. Chem. Phys. Lett. 2005;402:245.
46. Gan Z. J. Magn. Reson. 2000;143:136.
47. Dvinskikh SV, Zimmermann H, Maliniak A, Sandstrom D. J. Magn. Reson. 2003;163:46.

Structural Constraints in Solids

Part I

Rotational-Echo, Double-Resonance NMR

Terry Gullion

Department of Chemistry, West Virginia University, Morgantown, WV 26506, USA

Introduction

Rotational-echo, double-resonance (REDOR) NMR is a high-resolution, solid-state NMR experiment for measuring the dipolar coupling between a heteronuclear spin pair [1,2]. The $1/r^3$ distance dependence of the dipolar coupling makes REDOR useful for the structural characterization of solids, and REDOR has become a valuable tool for characterizing a wide range of materials, including peptides and proteins, polymers, zeolites, guest–host systems, glasses, and more. Since the REDOR experiment is based primarily on trains of π pulses, it has mostly been used to measure dipolar couplings between pairs of spin $-1/2$ nuclei. Under certain conditions, however, the REDOR experiment can also make effective use of quadrupolar nuclei as structural probes.

In REDOR experiments, the NMR signal of the observed nucleus is attenuated when dipolar dephasing radio frequency (rf) pulses are applied to the non-observed nucleus. The dependence of this signal reduction on the dipolar evolution time provides a direct way to determine the dipolar coupling and obtain internuclear distances. Analysis of REDOR data involves the simple measurement of signal intensities and comparing the normalized dipolar dephased signal to a universal dipolar dephasing curve. The universal dipolar dephasing curve depends only on the dipolar coupling, and it is independent of all other NMR parameters such as chemical shift anisotropy and resonance offset. The ease of experimental implementation and straightforward data analysis are properties that make the REDOR experiment particularly attractive for structural characterization of complex molecular systems.

Dipolar Recoupling

With magic angle spinning (MAS), the time-dependent dipolar Hamiltonian for a heteronuclear pair of spin $-1/2$ nuclei is [3–5]

$$H = d(t) S_z I_z, \tag{1}$$

where

$$d(t) = d\left[\sin^2\beta \cos 2(\omega_r t + \alpha) - \sqrt{2}\sin 2\beta \cos(\omega_r t + \alpha)\right]. \tag{2}$$

The dipolar coupling, in SI units, is

$$d = \frac{\mu_0 \gamma_S \gamma_I \hbar}{4\pi r^3}, \tag{3}$$

where μ_0 is the permeability of free space, γ_S and γ_I are the magnetogyric ratios of the coupled spins, $\hbar$ is Planck's constant divided by 2π, and r is the internuclear separation. The orientation of a vector directed between the S and I spins in the rotor frame is defined by the polar angle β and the azimuthal angle α. The sample spinning rate, ω_r, is related to the period of the sample rotation, T_r, through $\omega_\mathrm{r} = 2\pi/Tr$. Inspection of Equation (2) shows that the average heteronuclear dipolar interaction is zero, and the consequence of this averaging is that the dipolar interaction has little effect on observed spectra under typical high-resolution MAS conditions. By toggling the spin states of the S and I spins synchronously with the sample rotation, it is possible to produce an average dipolar Hamiltonian that is not equal to zero and, in effect, recouple the dipolar interaction. Synchronous toggling of spin states with the sample rotation is the principle behind the REDOR experiment.

Two experiments are performed for REDOR measurements. An S-spin control signal is generated by omitting I-spin rf pulses. An S-spin dipolar dephased signal is produced by applying I-spin rf pulses. Comparison of the control and dipolar dephased signals provides a way to obtain the dipolar coupling. The concept of the control experiment is illustrated in Figure 1 (left), where neither the S-channel nor the I-channel contains any rf pulses, and the S and I spin orientations (magnetic quantum numbers) remain unchanged during the entire rotor cycle. An I spin will generate a local magnetic field, B_L, at the site of a neighboring S spin, and the S-spin transverse magnetization will precess at a rate $\omega_S = -\gamma_S B_\mathrm{L}$ in the rotating frame defined by the Zeeman interaction. In the absence of rf pulses, the physical rotation of the sample about the sample rotor axis averages the local magnetic field and dipolar Hamiltonian to zero according to Equations (1) and (2). The local field, B_L, is negative as often as it is positive. Hence, the dipolar interaction causes no net precession of the transverse component of the S-spin magnetization for the control experiment.

The S-spin dipolar dephasing experiment shown in Figure 1 (right) illustrates the principle of dipolar

Graham A. Webb (ed.), Modern Magnetic Resonance, 713–718.
© 2008 *Springer.*

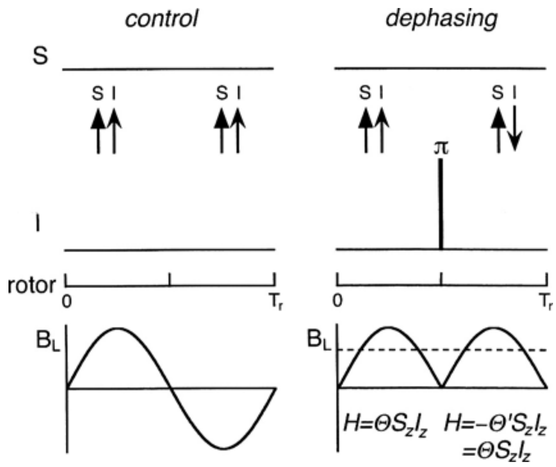

Fig. 1. Illustration of the control and dipolar dephasing experiment. Representative spin states are indicated (by arrows) for each half of the rotor cycle. For the control experiment, no change in spin states occurs. The local field, B_L, is that generated by the I spin and appearing at the S spin. Toggling frame Hamiltonians are shown for the first and second half of the rotor cycle for the dipolar dephasing experiment.

recoupling. A π pulse is applied to the I-channel at the midpoint of the rotor cycle. From time 0 to $T_r/2$, the toggling frame Hamiltonian is [6]

$$H = \Theta S_z I_z, \tag{4}$$

where

$$\Theta = \left[\int_0^{T_r/2} d(t)\mathrm{d}t\right] \Big/ \left[\int_0^{T_r/2} \mathrm{d}t\right] \tag{5}$$

which becomes

$$\Theta = \frac{2\sqrt{2}}{\pi} d \sin 2\beta \sin\alpha. \tag{6}$$

The toggling frame Hamiltonian during the time following the I-channel π pulse is

$$H = -\Theta' S_z I_z, \tag{7}$$

where

$$\Theta' = \left[\int_{T_r/2}^{T_r} d(t)\mathrm{d}t\right] \Big/ [T_r/2]. \tag{8}$$

Since

$$\int_0^{T_r} d(t)\mathrm{d}t = 0, \tag{9}$$

then $\Theta' = -\Theta$ and the toggling frame Hamiltonian for the second half of the rotor cycle is also $H = \Theta S_z I_z$. Hence, the average dipolar Hamiltonian for the dipolar dephasing experiment is not equal to zero and is

$$\bar{H} = \Theta S_z I_z. \tag{10}$$

The consequence of toggling the I spin from the perspective of the S spin is also illustrated by the local field, B_L. During the second half of the rotor cycle, the sign of B_L is opposite to that found in the control experiment for the same time period because of the sudden change in the spin state of the I spin caused by the π pulse. Consequently, the average local field (dashed line) experienced by the S spin is no longer zero, as it was in the control experiment, and the S-spin transverse magnetization undergoes a net nonzero dephasing leading to signal attenuation.

Each orientation of the S–I spin pairs in the powder sample contributes a dipolar dephased signal, s_d, to the total powder signal. This contribution is [1,2,7]

$$s_d = \cos\bar{\omega}_d\tau, \tag{11}$$

where

$$\bar{\omega}_d = 2\sqrt{2}D\sin 2\beta\sin\alpha, \tag{12}$$

and $D = d/2\pi$ has units of Hz and τ is the dipolar evolution time in seconds. A powder sum over the angles α and β provides the normalized dipolar dephased signal intensity, S_d, which is

$$S_d = \int_\beta\int_\alpha \cos\bar{\omega}_d\tau\,\sin\beta\,\mathrm{d}\alpha\,\mathrm{d}\beta \Big/ \int_\beta\int_\alpha \sin\beta\,\mathrm{d}\alpha\,\mathrm{d}\beta \tag{13}$$

Practical Details

Figure 2 shows three practical REDOR pulse sequences designed to increase the dipolar evolution period over multiple rotor cycles [8]. In order to maintain the average dipolar Hamiltonian provided by Equation (10), two π pulses per rotor cycle are required and the timing between any two adjacent π pulses is $T_r/2$. The dipolar evolution time, τ, is the rotor period multiplied by the number of rotor cycles, N_c, during the dipolar evolution period: $\tau = N_c T_r$. If the pulse spacing between adjacent π pulses differs from $T_r/2$, then Equation (13) is still applicable but Equation (12) takes on a slightly different form. For most work, the best pulse spacing is $T_r/2$.

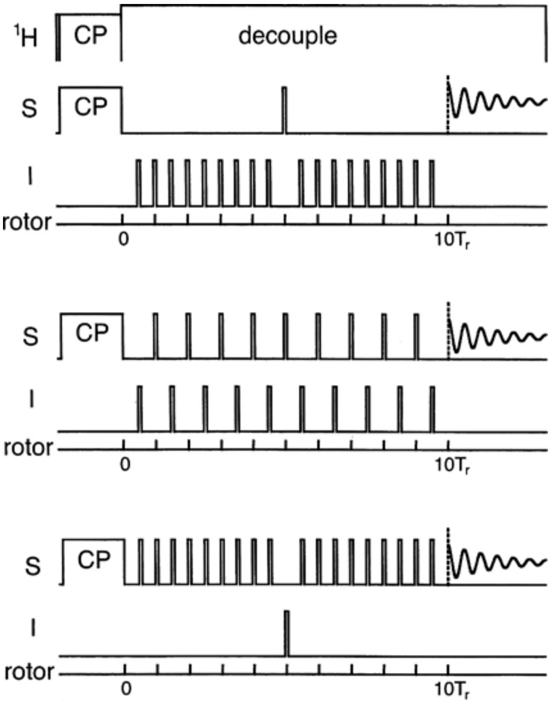

Fig. 2. Three commonly used REDOR pulse sequences. Each is shown for a dipolar evolution period of 10 rotor cycles. If protons are not available for cross-polarization (CP), then the S-channel CP pulse is replaced with a simple $\pi/2$ pulse.

Table 1: Phases of the xy-4 cycle and its supercycles

Cycle	rf phases
xy-4	xyxy
xy-8	xyxy yxyx
xy-16	xyxy yxyx $\overline{\text{xyxy}}$ $\overline{\text{yxyx}}$

The original REDOR pulse sequence is shown in Figure 2 (top). Protons, if present, are used to enhance the S-spin magnetization through cross-polarization (CP), and the protons are decoupled thereafter. A single S-spin π pulse is applied at the midpoint of the dipolar evolution period to refocus isotropic chemical shifts and produce an echo at the start of data acquisition. If no I-channel pulses are applied, then the S spins undergo no net dipolar dephasing and the detected S-spin signal serves as a control signal, S, which is used to account for T$_2$ type losses. The control signal is also referred to as the full signal. Application of the I-channel π pulse train recouples the dipolar interaction and produces dipolar dephasing of the S-spins according to Equation (13). The experimental dipolar dephased signal, S_r, (also referred to as the reduced signal) will be less intense than the control signal. The dipolar coupling can be determined by the measured ratio $\Delta S/S|_m = 1 - \frac{S_\mathrm{r}}{S}$.

The REDOR pulse sequence shown in Figure 2 (middle) provides better overall performance for S-spin refocusing and dipolar dephasing since it is more tolerant to rf pulse imperfections. Experimental problems with rf pulses arise from limited rf power, rise and fall times of pulses, phase glitches, and resonance offsets. The xy-4, xy-8, or xy-16 phase cycling schemes should be applied to the π pulses (for all three pulse sequences) to eliminate problems associated with pulse imperfections [9,10]. In most cases, the xy-8 supercycle is adequate, but the xy-16 and xy-32 supercycles may offer minor improvements. The phases of the xy-4, -8, and -16 supercycles are shown in Table 1.

The REDOR pulse sequence shown in Figure 2 (bottom) has been used whenever the I spin has a very large anisotropic interaction (either very large chemical shift anisotropies or modest quadrupolar interactions). It has been particularly useful for $I = {}^2$H, especially when the lone I-spin pulse is a composite $\pi/2$ pulse [11]. This particular pulse sequence is very sensitive to the spinning rate, which should be stabilized to within a fraction of a Hz [12,13]. The other two pulse sequences do not require such a high degree of control of the spinning rate.

Examples of REDOR spectra are shown in Figure 3, and full experimental details can be found in Ref. [14]. The observed spin is ^{13}C and the dipolar dephasing spin is ^{2}H. The sample is a 30-residue (AlaGly)$_{15}$ peptide having repeated β turns. The carbonyl carbon of Gly(14) is ^{13}C enriched and a deuteron is attached to the C$_\alpha$ carbon of Ala(17). The ^{13}C–^{2}H REDOR full spectrum (bottom) was obtained by omitting the ^{2}H rf pulse and the carbonyl ^{13}C resonance intensity provides the signal S. The reduced, or dipolar dephased, ^{13}C spectrum is shown in the middle. It is evident that the signal intensity at the carbonyl ^{13}C resonance position has been attenuated, and the measured intensity of the carbonyl ^{13}C resonance produces S_r. The difference spectrum (full minus reduced) is shown at the top and the measured signal intensity of the carbonyl ^{13}C resonance position produces ΔS. The measured ratio $\Delta S/S|_m$ is obtained by the simple measurement of signal intensities S and S_r (or ΔS).

Dipolar couplings are obtained by comparing the measured $\Delta S/S|_m$ to $\Delta S/S = 1 - S_\mathrm{d}$ from average Hamiltonian theory. Equations (12) and (13) provide S_d for $S = 1/2, I = 1/2$ spin pairs, and the ideal $\Delta S/S$ is shown in Figure 4 where it is plotted against the dimensionless

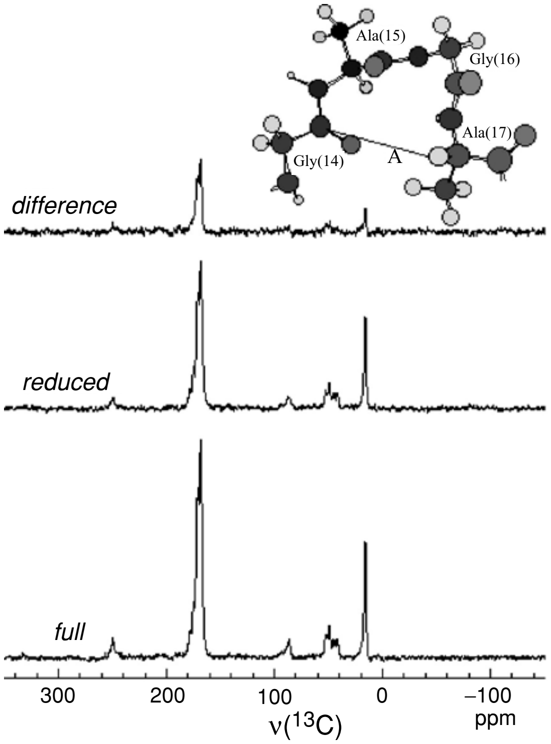

Fig. 3. Example of full, reduced, and difference ^{13}C–^{2}H REDOR spectra. Experimental details can be found in Ref. [14].

parameter $\lambda = N_c T_r D$. There are two easy ways to generate $\Delta S/S$ plots. The first is to perform a powder sum over all s_d to produce S_d, which is Equation (13). The second method is to calculate S_d using Bessel functions of the first kind, and for $S = 1/2$, $I = 1/2$ spin pairs [15]

$$S_d = \frac{\sqrt{2}\pi}{4} J_{1/4}\left(\sqrt{2}\lambda\right) J_{-1/4}\left(\sqrt{2}\lambda\right). \qquad (14)$$

The Bessel function method has the advantage of speed of calculation and, if the data set is large enough, may be used to produce dipolar frequencies via the REDOR transform.

REDOR experiments can also be performed with quadrupolar nuclei, where $I > 1/2$ [16–22]. Table 2 provides a summary of normalized dipolar dephased signals, S_d, in terms of Bessel functions and s_d in terms of cosine functions for ideal REDOR behavior for $S = 1/2$, $I > 1/2$ spin pairs. The overall width of the lineshape of a quadrupolar nucleus can be very large, depending on the size of the quadrupolar coupling constant, χ (in frequency units, $\chi = e^2 qQ/h$). Hence, it is difficult to uniformly irradiate the broad I-spin spectrum with typical rf field strengths that are available experimentally. For each value of I in Table 2, an approximate upper limit of χ is provided which was determined by assuming an I-channel rf field strength of 50 kHz. As long as χ is less than the indicated value, the experimental data should obey the REDOR dipolar dephasing equations given in Table 2 reasonably well and provide a distance within 1% of the expected value. Higher values of χ will result in REDOR dephasing of the S spins, but numerical simulations that take into account the rf field strength, resonance offsets, χ, and quadrupolar asymmetry parameter will be necessary in order to extract the dipolar coupling. The functions for $I = 1$ in Table 2 are primarily for ^2H and using the pulse sequence shown in Figure 2 (bottom). In particular, the case where the I-spin pulse is a composite $\pi/2$ pulse (instead of a π pulse) has been shown to provide good interatomic distances even for rigid deuterons, which have $\chi = 167$kHz [11]. For typical rf field intensities, a π pulse on the ^2H channel does not provide ideal dipolar dephasing except for cases where there is significant motional narrowing of the ^2H lineshape, such as for the case of methyl rotation where $\chi = 55$kHz.

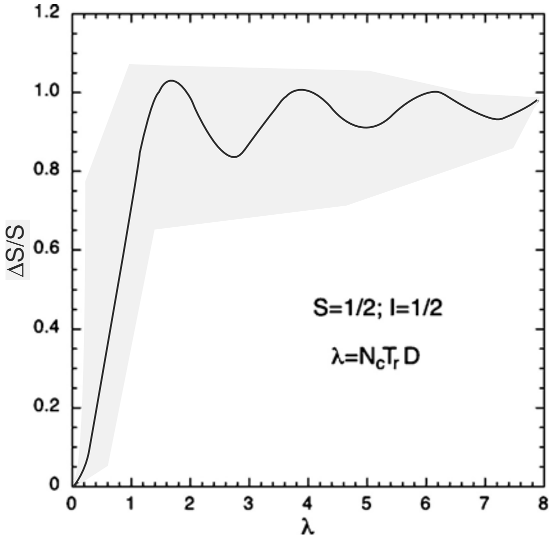

Fig. 4. Universal dipolar dephasing curve for an $S = 1/2$, $I = 1/2$ spin pair.

This chapter provided an introduction to the REDOR experiment. A more complete description of the theory can be found in Refs. [2,7]. A discussion of experimental effects, such as pulse imperfections and resonance offset, can be found in Ref. [23].

Table 2: Dipolar dephasing functions

I	$S_d(J)$	$s_d(\cos)$
1/2	$\frac{\sqrt{2}\pi}{4} J_{1/4}\left(\sqrt{2}\lambda\right) J_{-1/4}\left(\sqrt{2}\lambda\right)$	$\cos(\bar{\omega}_d\tau)$
3/2 χ < 70 kHz	$\frac{1}{2}\left[\frac{\sqrt{2}\pi}{4} J_{1/4}\left(\sqrt{2}\lambda\right) J_{-1/4}\left(\sqrt{2}\lambda\right) + \frac{\sqrt{2}\pi}{4} J_{1/4}\left(3\sqrt{2}\lambda\right) J_{-1/4}\left(3\sqrt{2}\lambda\right)\right]$	$\frac{1}{2}[\cos(\bar{\omega}_d\tau) + \cos(3\bar{\omega}_d\tau)]$
5/2 χ < 110 kHz	$\frac{1}{3}\left[\frac{\sqrt{2}\pi}{4} J_{1/4}\left(\sqrt{2}\lambda\right) J_{-1/4}\left(\sqrt{2}\lambda\right) + \frac{\sqrt{2}\pi}{4} J_{1/4}\left(3\sqrt{2}\lambda\right) J_{-1/4}\left(3\sqrt{2}\lambda\right) + \frac{\sqrt{2}\pi}{4} J_{1/4}\left(5\sqrt{2}\lambda\right) J_{-1/4}\left(5\sqrt{2}\lambda\right)\right]$	$\frac{1}{3}[\cos(\bar{\omega}_d\tau) + \cos(3\bar{\omega}_d\tau) + \cos(5\bar{\omega}_d\tau)]$
7/2 χ < 185 kHz	$\frac{1}{4}\left[\frac{\sqrt{2}\pi}{4} J_{1/4}\left(\sqrt{2}\lambda\right) J_{-1/4}\left(\sqrt{2}\lambda\right) + \frac{\sqrt{2}\pi}{4} J_{1/4}\left(3\sqrt{2}\lambda\right) J_{-1/4}\left(3\sqrt{2}\lambda\right) + \frac{\sqrt{2}\pi}{4} J_{1/4}\left(5\sqrt{2}\lambda\right) J_{-1/4}\left(5\sqrt{2}\lambda\right) + \frac{\sqrt{2}\pi}{4} J_{1/4}\left(7\sqrt{2}\lambda\right) J_{-1/4}\left(7\sqrt{2}\lambda\right)\right]$	$\frac{1}{4}[\cos(\bar{\omega}_d\tau) + \cos(3\bar{\omega}_d\tau) + \cos(5\bar{\omega}_d\tau) + \cos(7\bar{\omega}_d\tau)]$
$1(^2\mathrm{H}; \pi)$	$\frac{1}{3}\left[1 + 2\frac{\sqrt{2}\pi}{4} J_{1/4}\left(2\sqrt{2}\lambda\right) J_{-1/4}\left(2\sqrt{2}\lambda\right)\right]$	$\frac{1}{3}[1 + 2\cos(2\bar{\omega}_d\tau)]$
$1(^2\mathrm{H}; \pi/2)$	$\frac{1}{6}\left[1 + 4\frac{\sqrt{2}\pi}{4} J_{1/4}\left(\sqrt{2}\lambda\right) J_{-1/4}\left(\sqrt{2}\lambda\right) + \frac{\sqrt{2}\pi}{4} J_{1/4}\left(2\sqrt{2}\lambda\right) J_{-1/4}\left(2\sqrt{2}\lambda\right)\right]$	$\frac{1}{6}[1 + 4\cos(\bar{\omega}_d\tau) + \cos(2\bar{\omega}_d\tau)]$

References

1. Gullion T, Schaefer J. J. Magn. Reson. 1989;81:196.
2. Gullion T, Schaefer J. In: WS Warren (Ed). Advances in Magnetic Resonance, Vol. 13. Academic Press: San Diego, 1989, p 57.
3. Maricq MM, Waugh JS. J. Chem. Phys. 1979;70:3300.
4. Munowitz MG, Griffin RG. J. Chem. Phys. 1982;76:2848.
5. Slichter CP. Principles of Magnetic Resonance, 3rd ed. Springer: New York, 1989.
6. Ernst RR, Bodenhausen G, Wokaun A. Principles of Nuclear Magnetic Resonance in One and Two Dimensions. Oxford University Press: Oxford, 1990.
7. Gullion T. Magn. Reson. Rev. 1997;12:83.
8. Garbow JR, Gullion T. Chem. Phys. Lett. 1992;192:71.
9. Gullion T, Baker DB, Conradi MS. J. Magn. Reson. 1990;89:479.
10. Gullion T, Schaefer J. J. Magn. Reson. 1991;92:439.
11. Gullion T. J. Magn. Reson. 2000;146:220.
12. Chopin L, Rosanske R, Gullion T. J. Magn. Reson. A. 1996; 122:237.
13. Hughes E, Gullion T. Solid State Nucl. Magn. Reson. 2004;26:16.
14. Gullion T, Kishore R, Asakura T. J. Am. Chem. Soc. 2003;125:7510.
15. Mueller KT, Jarvie TP, Aurentz DJ, Roberts BW. Chem. Phys. Lett. 1995;242:535.
16. Sack I, Balazs YS, Rahimipour S, Vega S. J. Am. Chem. Soc. 2000;122:12263.
17. Sandstrom D, Hong M, Schmidt-Rohr K. Chem. Phys. Lett. 1999;300:213.
18. Schmidt A, Mackay R, Schaefer J. J. Magn. Reson. 1992;96:644.
19. Fyfe C, Mueller KT, Grondey H, Wongmoon KC. Chem. Phys. Lett. 1992;199:198.
20. Fernandez C, Lang D, Amoureux JP, Pruski M. J. Am. Chem. Soc. 1998;120:2672.
21. Hughes E, Jordan J, Gullion T. J. Phys. Chem. B. 2001;105:5887–91.
22. Reichert D, Pascui O, Judeinstein P, Gullion T. Chem. Phys. Lett. 2005;402:43–7.
23. Gullion T. Concepts Magn. Reson. 1998;10:277–89.

REDOR in Multiple Spin System

Katsuyuki Nishimura* and Akira Naito
Department of Applied Materials Chemistry, Division of Materials Science and Chemical Engineering, Graduate School of Engineering, Yokohama National University, Hodogayaku, Yokohama 240-8501, Japan
** Author to whom correspondence should be addressed: nishimur@ynu.ac.jp*

Introduction

Distance constraint is widely used in the present as a suitable means for structural characterization of a variety of molecules both in solution and in solid-state NMR. In solids, internuclear distance can be obtained by careful analysis of a specific spin pair of heteronuclear dipolar interaction, which is proportional to the reciprocal cube of the internuclear distance. In particular, rotational echo double resonance (REDOR) proposed by Gullion and Schaefer [1,2] is one of the most successful techniques to be able to determine *accurate* heteronuclear distances in solids. REDOR is a straightforward technique to recouple a weak heteronuclear dipolar interaction between an isolated spin one-half 2-spin system under MAS conditions. To this end, several intrinsic problems should be eliminated in order to obtain accurate distances leading to the three-dimensional structure of molecules. To measure the internuclear distance accurately, several experimental imperfections arising from the REDOR pulse sequence and dipolar contributions from additional nuclei as a multiple spin system should be solved. Some of them can be overcome by careful sample preparation and suitable analyses. One should be very careful in performing REDOR experiments as well as in their data analysis. In this review, we discuss how to obtain an accurate internuclear distance by REDOR. In addition, practical problems for REDOR in multiple spin systems are discussed.

Dipolar Dephasing of REDOR in I–S_n Multiple Spin System

The effect of the I–S_2 multiply dipolar coupled spin system in REDOR was first investigated by Naito *et al.* [3]. The description of the I–S_2 heteronuclear dipolar 3-spin system has been extended to the I–S_n multiple spin system later by Goetz and Schaefer [4].

In the following discussion, we define I and S as the observed and unobserved nuclei, respectively. Here we discuss a case where n number of S spins undergo heteronuclear dipolar coupling to an I spin in an I–S_n spin system. Then we derive the average Hamiltonian of the heteronuclear dipolar interaction between I and ith S spin in an I–S_n multiple spin system under the REDOR experiment at a certain orientation of the molecule as $\overline{2\omega_{\mathrm{D}_{IS_i}}\left(r_{IS}^{(i)}, \alpha^{(i)}, \beta^{(i)}, \gamma^{(i)}\right) I_z S_z^{(i)}}$. Thus the total heteronuclear dipolar Hamiltonian of an I–S_n multiple spin system under the REDOR experiment can be expressed as the sum of each dipolar interaction, $H^{\text{total}} = \sum_{i=1}^{n} \overline{2\omega_{\mathrm{D}_{IS_i}}\left(r_{IS}^{(i)}, \alpha^{(i)}, \beta^{(i)}, \gamma^{(i)}\right) I_z S_z^{(i)}}$, where the I_z and $S_z^{(i)}$ are the z components of the spin angular momentum operators for the I and $S^{(i)}$ spins, respectively. Here $\overline{2\omega_{\mathrm{D}_{IS_i}}\left(r_{IS}^{(i)}, \alpha^{(i)}, \beta^{(i)}, \gamma^{(i)}\right)}$ is the geometric part of the dipolar Hamiltonian in angular velocity units depending on the Euler angles $\alpha^{(i)}$, $\beta^{(i)}$, and $\gamma^{(i)}$, describing the orientation of the internuclear vectors between the I and $S^{(i)}$ nuclei in the rotor frame. Explicit expressions of these terms for the specific number of S spins can be found elsewhere [3–5]. The dipolar precession frequencies can be calculated using the density operator formalism [6,7]. When the initial magnetization is proportional to I_x, thus $\rho(0) = I_x$, the coherence evolved under the influence of I–S_n heteronuclear dipolar interactions can be calculated as follows [4,6,7]

$$
\begin{aligned}
\rho(t) = {} & \ldots \mathrm{e}^{\overline{-i2\omega_{\mathrm{D}_{IS_2}}\left(r_{IS}^{(2)},\alpha^{(2)},\beta^{(2)},\gamma^{(2)}\right) I_z S_z^{(2)} t}} \\
& \times \mathrm{e}^{\overline{-i2\omega_{\mathrm{D}_{IS_1}}\left(r_{IS}^{(1)},\alpha^{(1)},\beta^{(1)},\gamma^{(1)}\right) I_z S_z^{(1)} t}} \\
& \times \rho(0)\mathrm{e}^{\overline{i2\omega_{\mathrm{D}_{IS_1}}\left(r_{IS}^{(1)},\alpha^{(1)},\beta^{(1)},\gamma^{(1)}\right) I_z S_z^{(1)} t}} \\
& \times \mathrm{e}^{\overline{i2\omega_{\mathrm{D}_{IS_2}}\left(r_{IS}^{(2)},\alpha^{(2)},\beta^{(2)},\gamma^{(2)}\right) I_z S_z^{(2)} t}} \ldots \\
= {} & I_x \prod_{i=1}^{n} \cos\left(\overline{\omega_{\mathrm{D}_{IS_i}}\left(r_{IS}^{(i)}, \alpha^{(i)}, \beta^{(i)}, \gamma^{(i)}\right) t}\right) \ldots \qquad (1)
\end{aligned}
$$

Only the oscillating term with the product of cos functions represents the observable I magnetization. Consequently the expectation values for I nuclei can be

Graham A. Webb (ed.), Modern Magnetic Resonance, 719–725.
© 2008 *Springer.*

calculated as follows [4,6,7]

$$
\begin{aligned}
\langle I_+\rangle &= \mathrm{Tr}[\rho(t)I_+] = \prod_{i=1}^{n} \cos\left(\overline{\omega_{D_{IS_i}}(r_{IS}^{(i)}, \alpha^{(i)}, \beta^{(i)}, \gamma^{(i)})t}\right)\\
&= m\sum_{k=1}^{2^n}(\cos\omega_k t). \qquad (2)
\end{aligned}
$$

Where m is the constant. For example, $n = 3$, eight dipolar precession frequencies in angular velocity units ω_k for an I–S_4 spin system are obtained as

$$
\begin{aligned}
\omega_1, \omega_2 &= \pm\left(\overline{\omega_{\mathrm{D}_{IS_1}}\left(r_{IS}^{(1)}, \alpha^{(1)}, \beta^{(1)}, \gamma^{(1)}\right)} + \overline{\omega_{\mathrm{D}_{IS_2}}\left(r_{IS}^{(2)}, \alpha^{(2)}, \beta^{(2)}, \gamma^{(2)}\right)} + \overline{\omega_{\mathrm{D}_{IS_3}}\left(r_{IS}^{(3)}, \alpha^{(3)}, \beta^{(3)}, \gamma^{(3)}\right)}\right)\\
\omega_3, \omega_4 &= \pm\left(\overline{\omega_{\mathrm{D}_{IS_1}}\left(r_{IS}^{(1)}, \alpha^{(1)}, \beta^{(1)}, \gamma^{(1)}\right)} - \overline{\omega_{\mathrm{D}_{IS_2}}\left(r_{IS}^{(2)}, \alpha^{(2)}, \beta^{(2)}, \gamma^{(2)}\right)} + \overline{\omega_{\mathrm{D}_{IS_3}}\left(r_{IS}^{(3)}, \alpha^{(3)}, \beta^{(3)}, \gamma^{(3)}\right)}\right)\\
\omega_5, \omega_6 &= \pm\left(\overline{\omega_{\mathrm{D}_{IS_1}}\left(r_{IS}^{(1)}, \alpha^{(1)}, \beta^{(1)}, \gamma^{(1)}\right)} + \overline{\omega_{\mathrm{D}_{IS_2}}\left(r_{IS}^{(2)}, \alpha^{(2)}, \beta^{(2)}, \gamma^{(2)}\right)} - \overline{\omega_{\mathrm{D}_{IS_3}}\left(r_{IS}^{(3)}, \alpha^{(3)}, \beta^{(3)}, \gamma^{(3)}\right)}\right)\\
\omega_7, \omega_8 &= \pm\left(\overline{\omega_{\mathrm{D}_{IS_1}}\left(r_{IS}^{(1)}, \alpha^{(1)}, \beta^{(1)}, \gamma^{(1)}\right)} - \overline{\omega_{\mathrm{D}_{IS_2}}\left(r_{IS}^{(2)}, \alpha^{(2)}, \beta^{(2)}, \gamma^{(2)}\right)} - \overline{\omega_{\mathrm{D}_{IS_3}}\left(r_{IS}^{(3)}, \alpha^{(3)}, \beta^{(3)}, \gamma^{(3)}\right)}\right). \qquad (3)
\end{aligned}
$$

So the heteronuclear dipolar interactions in an I–S_n spin system induce multiple dipolar precession frequencies, whose number is proportional to 2^n. The normalized REDOR dipolar dephasing curve S_f/S_0 can be obtained by taking powder average over heteronuclear dipolar precession frequencies as follows

$$
\frac{S_f}{S_0} = \frac{1}{8\pi^2}\int_0^{2\pi}\int_0^{\pi}\int_0^{2\pi}\langle I_+\rangle \mathrm{d}\alpha(i)\sin\beta(i)\mathrm{d}\beta(i)\mathrm{d}\gamma(i), \qquad (4)
$$

where S_f and S_0 are signal intensities obtained from REDOR and full echo, respectively. In the I–S_n multiple spin system, orientation of internuclear vectors among coupled nuclei were fixed in the molecular frame, then the internuclear vectors rotate around the magic angle axis conserving the relative orientation among them [3,5] as shown in Figure 1. This fact gives quite an important perspective for the REDOR dephasing curve implying that the curve cannot be obtained as the sum of a powder average over individual dipolar precession frequencies rather independently. Though the above Euler angles $\alpha^{(i)}$, $\beta^{(i)}$, and $\gamma^{(i)}$ in the dipolar precession frequencies do not show straightforward relationship among individual dipolar interactions, they include geometric parameters, which describe relative orientation of internuclear vectors $r_{IS}^{(i)}$ and angles among them λ_{ij} [3,5] as illustrated in Figure 1. Thus the parameterization is practically important to elucidate geometric factors from explicit forms of equations. Nishimura *et al.* showed the parameterization describing explicit geometric parameters for Equation (3) up to the I–S_3 4-spin system [5] in contrast to those derived by Goetz and Schaefer [4]. In conclusion, the dipolar interactions between additional spins do not induce an additive effect, but induce modulation effects to the largest dipolar interaction depending on the strengths of dipolar interactions and the angles between them [3–5] as shown in Figure 2.

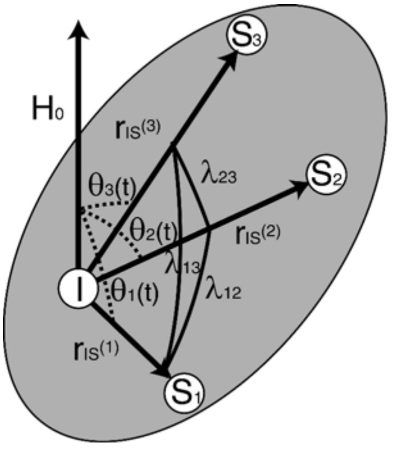

Fig. 1. Schematic representation of I–S_3 spin system which consists of the internuclear vectors (up to $n = 4$ spins) and the depending angles, where $r_{IS}^{(i)}$ are the internuclear distances between spin I and $S^{(i)}$. The λ_{ij} and θ_i are the angles between internuclear vector i and j nuclei and the angles between static field and individual internuclear vectors, respectively.

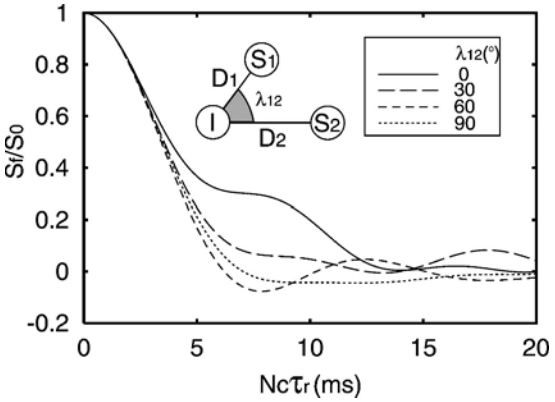

Fig. 2. The simulated REDOR dipolar dephasing curves of I–S_2 3-spin system for various angles λ_{12} between two dipolar vectors. Dipolar coupling constant D_1 and D_2 are set at 200 and 100 Hz, respectively. The angle λ_{12} vary from 0° to 90° as indicated in figure.

Obtaining Accurate Internuclear Distances by REDOR

The achieved accuracy and precisions for internuclear distances obtained by REDOR have been carefully evaluated by Naito *et al.* [8], by taking into account a variety of experimental conditions and justified with the one obtained from an X-ray diffraction study. As a result, it turned out that ^{13}C–^{15}N internuclear distance can be obtained with accuracy of ± 0.1 and a precision of ± 0.05 Å, respectively, up to the distance of 4 Å for the small peptide in the microcrystalline state [8], only when very careful experimental protocol was performed as proposed by Naito and Saito previously [9], although these kinds of precautions are very often ignored. Here, the authors discuss several important points as additional factors to obtain accurate internuclear distances, which are essential for the determination of the three-dimensional structure of a target molecule [8,10–12].

Fluctuation of RF Power, Flip Angle Errors of π Pulse and RF Inhomogeneity

First, it turns out that the accuracy in distance measurements by REDOR is quite sensitive to flip angle errors of the π pulses and RF inhomogeneity [8,13]. In practice, it is very difficult to avoid fluctuation of RF power during the long acquisition period, and it results in errors of flip angle for the π pulses. To compensate small flip angle errors for π pulses, xy-*n* (*n*: 4, 8, 16) pulse sequence proposed by Gullion *et al.* [14] is practically essential. It is advisable to set any of the π pulses in REDOR to integer multiples of these in the supercycle. Otherwise the π pulses out of the supercycle may reduce dipolar recoupling efficiency.

RF inhomogeneity among various portions of samples within the RF coil induces variation of flip angle by RF pulses, which usually reduce the recoupling efficiency of the heteronuclear dipolar interaction resulting in longer internuclear distances. As reported by Nishimura *et al.*, more than 92% RF effective field should be kept for accurate distance measurements [13] even with the use of an xy-8 or 16 compensation pulse cycle. Thus one should know the homogeneous range of RF field for individual probes. It is advisable to perform either nutation experiment to know an average RF homogeneity or signal transformation experiment as proposed by Nishimura *et al.* [13] to obtain precise RF homogeneity profile. In addition, the sample should be carefully placed in the central part of the rotor spinner within the RF coil to keep RF homogeneity more than 92% effective field.

The Finite Pulse Length and Sample Spinning Stability

Although, REDOR dephasing was analyzed based on the delta pulse assumption for π pulses, the effects of finite pulse length in the phase cycle of π pulses have to be taken into account. In practice, no significant deviations from the dephasing curve under the delta pulse may be observed in up to 10% pulse duration out of one rotor cycle as reported by Naito *et al.* [8] and Jaroniec *et al.* [15].

Furthermore, REDOR is also sensitive to the fluctuation of sample spinning rate. It has to be stabilized within a few hertz to obtain accurate internuclear distances even at moderate spinning speed. This requirement turned out to be severe when spinning speed or dipolar dephasing time is increased. The fluctuation of spinning rate results in the shifts of pulse timing, which induces reduction of recoupling efficiency.

Dipolar Interactions with Neighboring Molecules

Even though REDOR experiments are assumed to be analyzed as an isolated 2-spin system in the doubly isotopically enriched molecules, it is practically difficult to establish such an ideal spin system. This is because a set of *I* and *S* nuclei are isotopically enriched in the same molecule to which *S* nuclei of neighboring molecules are

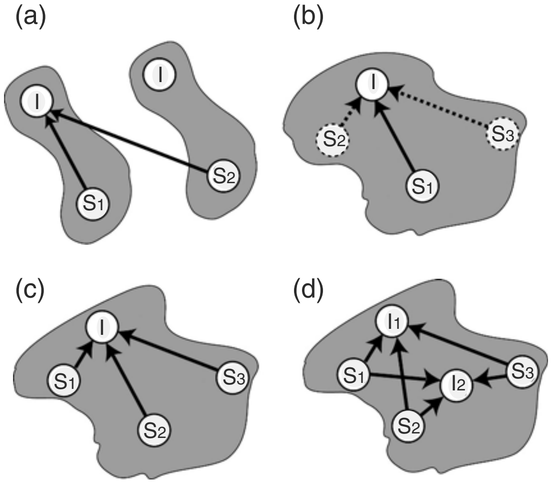

Fig. 3. The four different cases of multi-heteronuclear dipolar coupling are pictorially presented. (a) A set of isotopically enriched I and $S^{(1)}$ nuclei suffer the contribution of the intermolecular dipolar interactions from enriched $S^{(i)}$ nuclei in the neighboring molecules. (b) A set of isotopically enriched I and $S^{(1)}$ nuclei are surrounded by natural abundant $S^{(i)}$ nuclei, which provide heteronuclear dipolar coupling to enriched nuclei I. (c) I–S_n multiple spin system which consists of many enriched $S^{(i)}$ nuclei, which provide heteronuclear dipolar coupling to one I nuclei. (d) I_m–S_n multiple spin system in which both I and S nuclei are uniformly enriched.

coupled since they are located very closely as shown in Figure 3a.

Naito *et al.* [3,5,10] proposed a way to remove the contribution of intermolecular dipolar interactions by systematic dilution of isotopically labeled samples with samples of natural abundance at more than two different concentrations. For this, 60 and 30% dilution of enriched sample is advisable to keep a reasonably high sensitivity of the REDOR dephasing. The normalized REDOR dephasing values are available from extrapolating the REDOR dephasing values from different concentrations for individual dephasing times to infinitely diluted condition, because this dilution effect turned out to be linear for the concentration of enriched sample. Thus the intercept of this extrapolating line to infinitely diluted condition gives infinitely diluted dephasing values in the absence of intermolecular dipolar interaction [3,5,10]. Though extreme dilution of enriched sample has often been used to attenuate intermolecular dipolar contribution. This approach greatly reduces the sensitivity of REDOR dephasing and essentially the intermolecular dipolar contribution cannot be removed completely.

Contribution of Dipolar Coupling from Natural Abundant Nuclei

As is illustrated in Figure 3b, I and S nuclei are isotopically enriched and are surrounded by natural abundant S nuclei. Therefore, it is expected that contributions of the heteronuclear dipolar coupling from natural abundant S nuclei to enriched I nuclei should be taken into account. It is emphasized that the dipolar interactions under consideration cannot be simply treated as sum of I–$S^{(1)}$ and I–$S^{(2)}$ 2-spin system, because the enriched I nucleus is coupled to both enriched $S^{(1)}$and natural abundant $S^{(2)}$ nuclei: instead, they should be treated as $S^{(1)}$–I–$S^{(2)}$ 3-spin system as reported by Naito *et al.* [3,8,10]. As explained above, the dipolar coupling of I–S_2 3-spin system under REDOR condition can be observed as modulation effect to a larger dipolar interaction depending on its relative strengths of each dipolar interaction and the angle between two internuclear vectors. Thus, the contribution of this effect can be detected when the following conditions are satisfied. First, the natural abundant unobserved nuclei $S^{(2)}$ are located closer than the enriched unobserved nuclei $S^{(1)}$. Second, the ratio of natural abundant of S nuclei must be relatively high compared to those of observed nuclei I. Furthermore enriched nuclei I must be surrounded by a remarkable number of natural abundant nuclei S. These conditions can be found for the spin pair $I = {}^{15}\mathrm{N}$, $S = {}^{13}\mathrm{C}$ for doubly labeled peptides or proteins. However, in the case of $I = {}^{13}\mathrm{C}$, $S = {}^{15}\mathrm{N}$, the contribution from natural abundant nuclei of S is totally negligible [3]. It is important to mention that the mostly used correction of the contributed dipolar interaction from natural abundant nuclei using I–S 2-spin system has not been theoretically justified and gives rise to overestimate of the dipolar contributions. It is cautioned that the readers should be aware of a possibility of overestimate of such dipolar interactions from natural abundant nuclei by simple treatment as an I–S 2-spin system for early applications of REDOR data.

Simple Alternative to REDOR

Because the above-mentioned problems described in sections “Fluctuation of RF Power, Flip Angle Errors of π Pulse and RF Inhomogeneity” and “The Finite Pulse Length and Sample Spinning Stability” arose from methodological nature of REDOR, they could be also overcome by simple alternative variant of REDOR experiment. Simultaneous frequency amplitude modulation (SFAM) developed by Fu *et al.* [16] uses RF fields, whose amplitude and carrier frequency are sinusoidally modulated. Thus no problem arises from finite pulse length. Furthermore, SFAM keeps more than 95% recoupling efficiency at the range of more than 85% RF effective field, whose range is twice that of REDOR [13]. Thus SFAM is insensitive to the RF inhomogeneity, flip angle errors, carrier offset, and fluctuation of sample spinning rate as reported by Nishimura *et al.* [13].

C-REDOR developed by Chan [17,18] recouples heteronuclear dipolar interaction with simultaneous decoupling of homonuclear dipolar interactions among irradiated nuclei by applying phase modulated continuous RF irradiation. This property was not implemented in SFAM, and is appreciably important for precise distance measurement. Unfortunately, the scaling factor of C-REDOR is significantly small as similar to other symmetry based heteronuclear dipolar recoupling techniques such as CN [19,20] and NR [21,22] pulse sequences proposed by Griffin's and Levitt's co-workers, respectively. Many of previously developed pulse sequences including REDOR with particular number of xy-*n* pulse sequence, are also analyzed as a particular case of CN or RN pulse techniques. These techniques are theoretically sophisticated to re- and decouple particular interactions up to higher order average Hamiltonian. However, their quite small scaling factors are serious disadvantage restricting the applications to the range of the distance for useful spin pairs.

SFAM can be used as a simple alternative of REDOR to obtain accurate interatomic distances without paying many efforts mentioned above for REDOR. The accuracy and precision are justified using glycine of crystalline state with the one obtained from X-ray diffraction study [13,16]. However, it should be mentioned that the properties of the heteronuclear spin pair selectivity have not been implemented in SFAM. So the problem arising from multi-dipolar couplings are the same as conventional REDOR. In addition, the ^{1}H decoupling field must be three times as large as that of RF field for irradiated nuclei to avoid cross talk between ^{1}H and irradiated nuclei [23] in SFAM and C-REDOR. The continuous RF irradiation at strong field may induce sample heating for hydrated biological sample.

Dipolar Dephasing of REDOR in Multiple Spin System

REDOR technique itself cannot select a certain pair of heteronuclear dipolar interaction. In order to obtain accurate internulcear distance, efficient selection of spin system is essential. In the multi-site isotopically enriched sample, multi-heteronuclear dipolar interactions are observed. In Figure 3c more than two sites are isotopically enriched for *S* nuclei, which is the case of $I–S_n$ multiple spin system. And in Figure 3d both *I* and *S* nuclei are uniformly enriched, which is the case of $I_m–S_n$ multiple spin system. Though conventional REDOR cannot be applied to $I_m–S_n$ multiple spin system, in some cases, it is possible to apply REDOR to $I–S_n$ multiple spin system as explained as follows.

REDOR for $I–S_n$ Multiple Spin System

Generally, even if REDOR is applied to $I–S_n$ multiple spin system, multiple internuclear distances cannot be obtained simultaneously. It is also expected that the internuclear distance of certain pair of nuclei could be modulated as mentioned above. Two different approaches are proposed to analyze the $I–S_n$ multiple spin system.

Bertmer and Eckert reported the model free analysis of the $I–S_n$ spin system to obtain multiple distances from the multiple coupled dipolar interaction by analyzing initial REDOR dipolar dephasing using van Vleck's second moment [24]. This is based on the approximation that initial dipolar dephasing is less dependent on the relative orientation of dipolar interaction vectors. To keep the precision of results in this approach, many precise REDOR dephasing points are required. Thus, as long as a xy-*n* compensation pulse sequence [14] is used, the application of this approach is restricted to either the spinning speed in the range of fast spinning or the dipolar interactions in relatively weak range to give shallow REDOR dephasing curve.

Nishimura *et al.* [25] proposed the observation of natural abundant nuclei, which gives heteronuclear dipolar coupling to singly enriched *S* nuclei. This approach enables one to avoid problems of multiple dipolar interactions. Because individual $I–S_i$ 2-spin dipolar interactions are totally independent from relative orientation of dipolar vectors of other spin pairs, internuclear distances can be obtained simultaneously. Furthermore, it is also free from both homonuclear dipolar and scalar interactions to induce shorter T_2. This approach is applicable to the case where the sample gives no overlap of signals for observed nuclei.

Furthermore, multiple spin system can provide geometric parameters. In the $I–S_2$ 3-spin system, the heteronuclear dipolar interaction depends on three parameters such as two internuclear distances and the angle between two dipolar vectors [3,5]. When one of them were known, it is possible to obtain other two geometric parameters by explicit analysis of $I–S_2$ spin system as reported by Nishimura *et al.* [5]. In the $I–S_3$ 4-spin system, the heteronuclear dipolar interaction depends upon six parameters such as three internuclear distances, and three angles among internuclear distance vectors [5] as illustrated in Figure 1. Thus the number of parameters depending on the molecular geometry increases dramatically in proportion to the number of spins. Obviously, analysis on $I–S_3$ 4-spin system is not simple to extract the information of molecular geometry except for the special case, in which some of parameters are known or degenerated. The analysis of I–S_2 3-spin system is valid until the strength of third dipolar interaction is less than 12.5% of those of second dipolar interaction [5]. Afterward, similar analysis has been reported by Fyfe and Lewis [26].

Spin Selection Using Improved REDOR Variants

For multiple spin system, the selection of spin pair is essential. First attempt to obtain isolate I–S internuclear distance from a multi-site isotope enriched sample using REDOR variant experiment was explored by Bennett *et al.* Frequency selective dipolar recoupling (FDR) experiment [27,28], which can be applied to I–S_n multiple spin as illustrated in Figure 3c to recouple dipolar interaction between observed nuclei I and frequency selected one of the non-observed nuclei S. The frequency selectivity of S spin is achieved by the difference of isotropic chemical shift for non-observed nuclei S by applying a series of rotor synchronized $\pi/2$ pulses for non-observed nuclei S instead of π pulse in REDOR. However, this technique was practically unsuccessful because flip angle error of $\pi/2$ pulses is critically sensitive to the frequency selectivity.

Gullion and Pennington proposed θ-REDOR [29], which can be applied to I–S_n multiple spins as illustrated in Figure 3c. This is an approach to apply θ° center pulse for non-observed nuclei instead of π pulse to separate I–S_n multiple spin coherence into n number of isolated I–S spin pairs, which enable to extract multiple heteronuclear distances simultaneously. Then, Liivak and Zax [30,31] improved the sensitivity problem of dephasing in θ-REDOR, by the development of multi S spin REDOR (MSREDOR). To analyze dephasing curve, however, spin multiplicity has to be known in advance. This problem can be solved by using REDOR transformation proposed by Muller *et al.* [32], which is a direct transformation of time-domain data to a frequency-domain to exhibit dipolar precession frequencies. This technique is suitable to analyze relatively strong dipolar interactions. To exhibit visible dipolar precession peaks in REDOR transformation, many data sets of REDOR dephasing are required. Especially weak dipolar interaction due to the spin pair with longer distance is difficult to be separated. Though θ-REDOR is theoretically very sophisticated, no application using this technique for simultaneous determination of distances among multi-nuclei has been reported so far.

Jaroniec *et al.*, proposed frequency selective REDOR (FSR) [33], which can be applied to uniformly isotopically enriched sample as illustrated in Figure 3d. The frequency of particular I–S spin pair is selected by applying simultaneous soft pulses. The quality of distance measurement is theoretically equivalent to original REDOR. Except for the case where more than two observed nuclei have identical isotropic chemical shift, internuclear distances can be obtained one by one. However, the other restrictions and properties are the same as those of conventional REDOR. The uniformly enriched small peptide characterized using this technique is successfully reported [33].

Conclusions

Though many sophisticated variants of REDOR have been developed to improve the nature of REDOR, still original REDOR [1,2] experiment with xy-*n*[5] compensation pulse scheme is widely used and gives the most reliable data for practical use of distance measurements together with careful sample preparations to simplify the spin system. Because none of technique is almighty, one must chose suitable analysis and techniques depending on their purpose and situation of the samples. As a simple alternative of REDOR, SFAM [16] can be used, which is low boost to RF inhomogeneity, carrier offset and flip angle errors of pulses, if the sample is not hydrated. Thus it enables us to be free from many strict experimental restriction mentioned above for REDOR.

References

1. Gullion T, Schaefer J. J. Magn. Reson. 1989;81:196.
2. Gullion T, Schaefer J. Adv. Magn. Reson. 1989;13:57.
3. Naito A, Nishimura K, Tuzi S, Saito H. Chem. Phys. Lett. 1994;118:5330.
4. Goetz JM, Schafer J. J. Magn. Reson. 1997;127:147.
5. Nishimura K, Naito A, Tuzi S, Saito H. J. Phys. Chem. B. 1999;103:8398.
6. Munowitz M. Coherence and NMR. John Wiley & Sons, US, 1988, pp 218–28.
7. Schmidt-Rohr K, Spiess HW. Multidimensional Solid State NMR and Polymers. Academic Press: London, 1994, pp 52–5.
8. Naito A, Nishimura K, Tuzi S, Aida M, Yasuoka N, Saito H. J. Phys. Chem. 1996;100:14995.
9. Naito A, Saito H. Encyclopedia of Nuclear Magnetic Resonance, Vol. 9. Advance in NMR. John Wiley & Sons, Chichester, 2002, pp 283–91.
10. Nishimura K, Naito A, Kimura S, Tuzi S, Saito H, Hashimoto C, Aida M. J. Phys. Chem. B. 1998;102:7476.
11. Naito A, Tuzi S, Saito H. Solid State Nucl. Magn. Reson. Polym. 1998;84:79.
12. Saito H, Tuzi S, Naito A. Annu. Rep. NMR Spectrosc. 1998; 36:79.
13. Nishimura K, Fu R, Cross TA. J. Magn. Reson. 2001;152:227.
14. Gullion T, Baker DB, Conradi MS. J. Magn. Reson. 1990; 89:479.
15. Jaroniec CP, Tounge BA, Rienstra CM, Herizfeld J, Griffin RG. J. Magn. Reson. 2000;146:132.
16. Fu R, Smith SA, Bodenhausen G. Chem. Phys. Lett. 1997; 272:361.
17. Chan JCC. Chem. Phys. Lett. 2001;335:289.
18. Chan JCC, Eckert H. J. Chem. Phys. 2001;115:6095.

19. Gross JD, Costa PR, Griffin RG. J. Chem. Phys. 1998;108: 7286.
20. Hohwy M, Jaroniec CP, Reif B, Rienstra CM, Griffin RG. J. Am. Chem. Soc. 2000;122:3218.
21. Carravetta M, Edén M, Zhao X, Brinkmann A, Levitt MH. Chem. Phys. Lett. 2000;321:205–15.
22. Brinkmann A, Carravetta M, Zhao X, Edén M, Schmedt auf der Günne J, Levitt MH. In: S Kiihne, HJM de Groot (Eds). Perspectives on Solid State NMR in Biology. Kluwer: Dordrecht, The Netherlands, 2001, pp 3–14.
23. Ishii Y, Ashida J, Terao T. Chem. Phys. Lett. 1995;246: 439.
24. Bertmer M, Eckert H. Solid State Nucl. Magn. Reson. 1999; 15:139.
25. Nishimura K, Ebisawa K, Suzuki E, Saito H, Naito A. J. Mol. Struct. 2001;560:29.
26. Fyfe CA, Lewis AR. J. Phys. Chem. B. 2000;104:48.
27. Bennett A, Becerra LR, Griffin RG. J. Chem. Phys. 1994; 100:812.
28. Bennett A, Rienstra CM, Lansbury PT Jr, Griffin RG. J. Chem. Phys. 1996;105:10289.
29. Gullion T, Pennington CH. Chem. Phys. Lett. 1998;290:88.
30. Liivak O, Zax DB. J. Chem. Phys. 2000;113:1088.
31. Liivak O, Zax DB. J. Chem. Phys. 2001;115:402.
32. Muller KT, Jarvie TP, Aurentz DJ, Roberts BW. Chem. Phys. Lett. 1995;242.
33. Jaroniec CP, Tounge BA, Herizfeld J, Griffin RG. J. Am. Chem. Soc. 2001;123:3057.

Torsion Angle Determination by Solid-State NMR

Mei Hong
Department of Chemistry, Iowa State University, Ames, IA, USA

Torsion angles in synthetic and biological solids encode important information on the backbone and side chain conformation of these molecules, and provide complementary structural restraints to distances. In the last decade, solid-state NMR spectroscopy has become a mature tool for determining molecular torsion angles [1]. The development of methods for measuring torsion angles in peptides and proteins has helped determine *de novo* high-resolution structures of small peptides [2–4] and solved the conformation distribution of large structural proteins [5] and synthetic polymers [6]. This review examines these torsion angle determination techniques, with a special emphasis on tensor correlation methods applied to biological solids. Both static and magic angle spinning (MAS) methods will be discussed, the former giving exquisite angular resolution, while the latter having the necessary site resolution to yield multiple angular restraints from each experiment.

Static Tensor Correlation Techniques

The correlation of two spin interactions under the static condition gives rich 2D lineshapes that depend sensitively on the relative orientation of the two tensors. One of the first static 2D techniques developed specifically for torsion angle determination is the double quantum spectroscopy (DOQSY) technique [7], which correlates the chemical shift anisotropy (CSA) of two adjacent carbons. Double-quantum (DQ) coherence, excited by a Hahn echo sequence, evolves under the sum chemical shift during t_1, and is reconverted to single-quantum (SQ) magnetization and detected during t_2 (Figure 1a). The 2D spectra correspond to $(\omega_1, \omega_2) = (\omega_a + \omega_b, \omega_{a,b} \pm \omega_D)$, where the ^{13}C–^{13}C dipolar coupling ω_D, if desired, can be removed from the ω_2 dimension using a modified magic-sandwich echo sequence [8]. The torsion angle(s) around the C–C vector is encoded in the sum frequency $\omega_a + \omega_b$. For two identical functional groups such as CH_2 groups in polyethylene, the trans conformation (180°) gives a large sum chemical shift in ω_1, while the gauche conformer (±60°) has a reduced chemical shift. The use of ^{13}C-decoupling during t_2 further distinguishes the trans and gauche conformations: the former gives a sharp diagonal spectrum while the latter has a compact and broad lineshape. This has allowed the determination of the conformational distribution in polymers [6,9].

For proteins, the DOQSY technique is best adapted to correlating the CSAs of two consecutive C′ carbons. The relative orientation reflects the torsion angles around the intervening three bonds, ω, ϕ, and ψ. Since ω is usually 180°, the DOQSY spectra depend only on (ϕ, ψ). Figure 2 shows a panel of simulated ^{13}C′ DOQSY spectra. To excite the C′–C′ DQ coherence, a two-quantum selective 90° pulse train interleaved with a train of π pulses can be applied to refocus the CSA [16]. This ^{13}C′ DOQSY experiment has been applied to spider dragline silk to show that native silk fiber has a predominant (70%) β-sheet structure with $(\phi, \psi) = (-135°, 150°)$, while silk film from the liquid extracted from the silk gland is mostly (60%) α-helical with $(\phi, \psi) = (\pm 60°, \pm 45°)$ [5].

A second static technique, separated-local-field DQ (SELFIDOQ), correlates C$^\alpha$–H$^\alpha$ dipolar coupling with C′ CSA to determine the ψ angle in proteins [10]. Here the C$^\alpha$–C′ DQ coherence evolves under C–H dipolar coupling rather than the sum chemical shift during t_1. The SELFIDOQ spectra are symmetric along the ω_1 dimension, and the 2D spectra distinguish major secondary structures such as $\psi = 120°$(β-sheet) and $\psi = -60°$(α-helix) well.

Static tensor correlation techniques give superb angular resolution for the torsion angles of interest, and are suitable for synthetic polymers or structural proteins with simple repeat sequences. However, they have low spectral sensitivity and no chemical site resolution. These are provided by high-resolution MAS experiments described below.

MAS Tensor Correlation Techniques

2D and 3D MAS techniques for determining both backbone and side chain torsion angles in proteins have been developed. The isotropic chemical shift dimension(s) in these experiments provides the necessary site resolution for extracting multiple torsion angles simultaneously from each experiment.

The first MAS technique for torsion angle determination is HCCH, which correlates two C–H dipolar couplings separated by a C–C bond [17]. ^{13}C DQ coherence is excited by a homonuclear recoupling sequence [18],

Graham A. Webb (ed.), Modern Magnetic Resonance, 727–733.
© 2008 *Springer.*

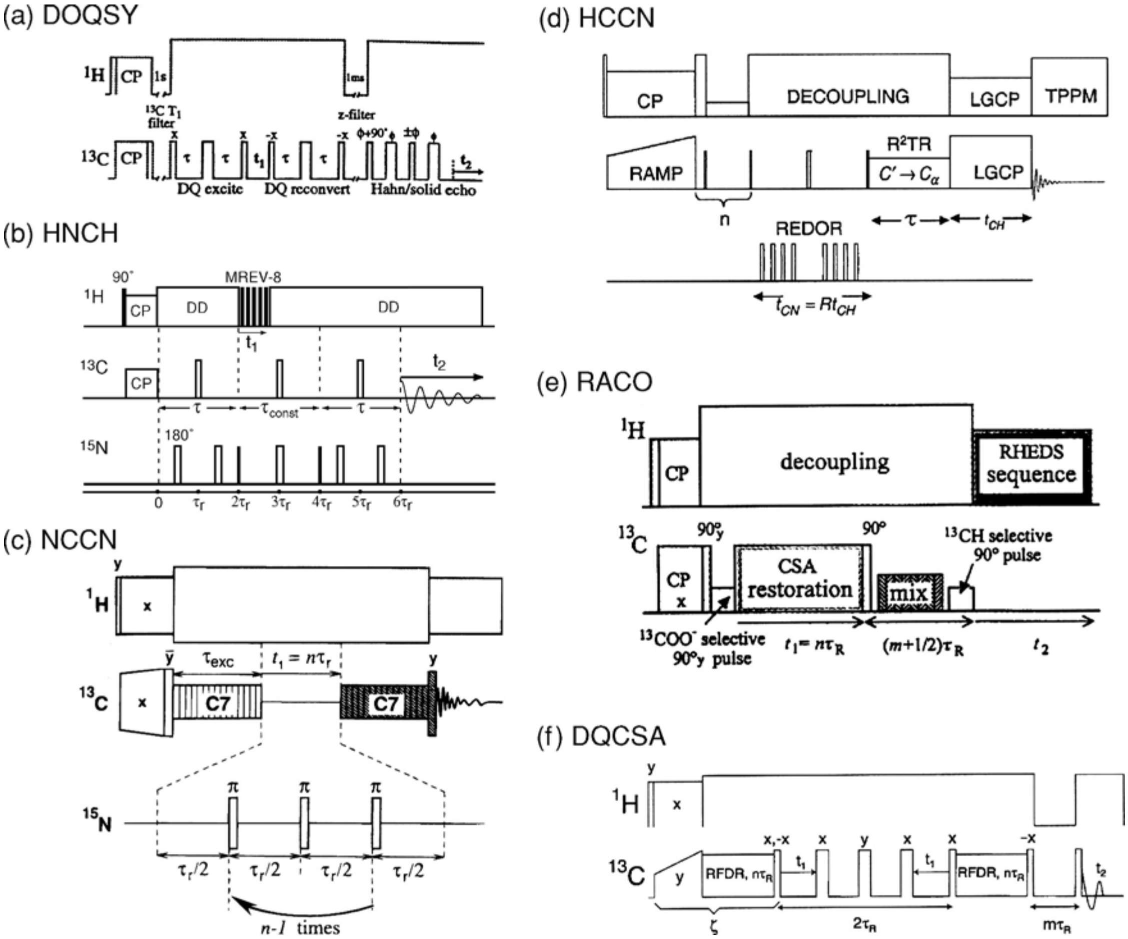
(a) DOQSY
^{1}H
CP
1s
1ms
^{13}C T_1 filter
z-filter
^{13}C
CP
x
τ
τ
t_1
x
-x
τ
τ
-x
ϕ+90°
±ϕ
ϕ
t_2
DQ excite
DQ reconvert
Hahn/solid echo
(b) HNCH
90°
MREV-8
^{1}H
CP
DD
DD
t_1
^{13}C
CP
t_2
τ
τ_{const}
τ
^{15}N
180°
0
τ_r
$2\tau_r$
$3\tau_r$
$4\tau_r$
$5\tau_r$
$6\tau_r$
(c) NCCN
y
^{1}H
x
$\bar{y}$
τ_{exc}
$t_1 = n\tau_r$
y
^{13}C
x
C7
C7
^{15}N
π
π
π
$\tau_r/2$
$\tau_r/2$
$\tau_r/2$
$\tau_r/2$
n-1 times
(d) HCCN
CP
DECOUPLING
LGCP
TPPM
RAMP
R^{2}TR
$C' \to C_\alpha$
LGCP
n
REDOR
τ
t_{CH}
$t_{CN} = Rt_{CH}$
(e) RACO
^{1}H
CP
decoupling
RHEDS sequence
^{13}C
90°_y
90°
^{13}CH selective 90° pulse
CP x
CSA restoration
mix
^{13}COO$^-$ selective 90°_y pulse
$t_1 = n\tau_R$
$(m+1/2)\tau_R$
t_2
(f) DQCSA
y
^{1}H
x
x,-x
x
y
x
x
-x
^{13}C
y
RFDR, $n\tau_R$
t_1
t_1
RFDR, $n\tau_R$
t_2
ζ
$2\tau_R$
$m\tau_R$

Fig. 1. Pulse sequences of representative torsion angle determination methods for proteins. (a) Static DOQSY. When extended for C′–C′ DQ excitation, it yields ϕ, ψ angles. (b) HNCH (ϕ angle). (c) NCCN (ψ angle). (d) HCCN (α-helical ψ angle). (e) RACO (ϕ, ψ angles). (f) DQCSA (ϕ, ψ angles). (Adapted from Refs. [10–15].)

and evolves under the C–H coupling during a constant-time t_1 period. The DQ coherence is reconverted to observable magnetization by an identical recoupling period and detected. The H1–C1–C2–H2 torsion angle is encoded in the sum and difference C–H couplings, $\omega^{IS}_{jk}(t) = \sum_{m',m} b^{IS}_{jk} D^2_{0m'}(\Omega^{jk}_{\mathrm{PM}}) D^2_{m'm}(\Omega_{\mathrm{MR}}) \times \exp(im\omega_{\mathrm{r}}t)\, d^2_{m0}(\beta_{\mathrm{RL}})$. Here b^{IS}_{jk} is the distance-dependent dipolar coupling between I_j and S_k, β_{RL} is the magic angle between the rotor axis and the laboratory frame, and Ω_{MR} are the powder angles describing the orientation of the molecules in the rotor frame. The essential angular parameters that determine the torsion angle are $\Omega^{jk}_{\mathrm{PM}}$, which denote the orientation of the $I_j - S_k$ vector relative to a molecule-fixed frame. The frequencies that encode the torsion angle information are $\omega^{IS}_{11}(t)$ and $\omega^{IS}_{22}(t)$. Choosing the C1–C2 bond as the z-axis of the molecular frame, $\beta^{11}_{\mathrm{PM}} = \pi - \beta^{22}_{\mathrm{PM}}$ corresponds to the H–C–C bond angle while the difference of the two γ angles, $\gamma^{11}_{\mathrm{PM}} - \gamma^{22}_{\mathrm{PM}}$, is the torsion angle of interest. Cross terms $\omega^{IS}_{12}(t)$ and $\omega^{IS}_{21}(t)$ due to two-bond C–H dipolar couplings are readily included in the simulations.

The HCCH experiment can be applied to organic compounds containing C=C double bonds to determine the cis- and trans- configuration [12,17], and to proteins to measure side chain χ_1 angles (by H$^\alpha$–C$^\alpha$–C$^\beta$–H$^\beta$ correlation). The HCCH method has several features common to later torsion angle techniques. The use of DQ coherence allows the measurement of two dipolar couplings

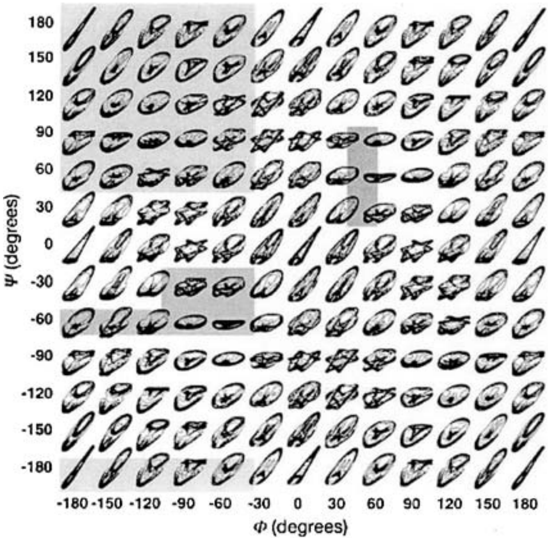

Fig. 2. Simulated DOQSY spectra of two consecutive C′ carbons in proteins as a function of (ϕ, ψ) angles. Energetically favorable areas are shaded. (Adapted from Ref. [5].)

simultaneously and suppresses natural abundance ^{13}C background. The uniaxial nature of the dipolar interaction causes a twofold degeneracy in the resulting angle. The most sensitive angular range is when the two bond vectors are antiparallel: under this condition the difference frequency nearly vanishes, giving rise to a slowly decaying time signal or a zero-frequency peak that change sensitively with the torsion angle.

ϕ Angle Techniques

The HNCH technique correlates the H^N–N and the C$^\alpha$–H$^\alpha$ dipolar couplings to determine the angle $\phi_H = H^N–N–C^\alpha–H^\alpha$ [19]. This is related to the ϕ angle (C′–N–C$^\alpha$–C′) by $\phi_H = \phi - 60^\circ$ for L-amino acids. The experiment has the same framework as HCCH, but uses ^{13}C–^{15}N heteronuclear DQ and zero-quantum (ZQ) coherence instead of ^{13}C homonuclear DQ coherence (Figure 1B). The ω_1 dimension exhibits sum and difference dipolar frequencies $\cos[\Phi_{CH}(t_1) \pm \Phi_{NH}(t_1)/2]$, where $\Phi_{XH}(t_1) = \int_0^{t_1} dt\omega_{XH}(t)$, which depend on the relative orientation of the two bonds. The method has the highest angular resolution when $\phi_H = 180^\circ$, or $\phi = -120^\circ$, thus it is particularly sensitive to the β-sheet conformation.

The angular resolution of the HNCH technique can be enhanced by doubling the N–H dephasing while holding the C–H dephasing the same as before. This N–H doubling can be achieved by modifying the N–H dipolar evolution: instead of incrementing the ^{1}H homonuclear decoupling period to define t_1, the multiple-pulse sequence is applied for a full rotor period, while a moving ^{15}N π pulse during that rotor period defines t_1 [11]. To retain the C–H dipolar phase, the C–H and N–H dipolar evolution occur sequentially instead of simultaneously. RMSDs between the experiment and simulations show that the ϕ angle resolution of the N–H doubled HNCH experiment is indeed higher than the original HNCH method. The HNCH experiment can also be modified to remove the twofold degeneracy of the ϕ angle information, by correlating the ^{15}N CSA interaction with the C$^\alpha$–H$^\alpha$ dipolar coupling [20].

The HNCH approach has been extended to 3D or reduced 3D to achieve higher site resolution [21] and to determine not only ϕ, but also ψ and χ_1 torsion angles [22]. When two frequency dimensions are used to separate the resonances, the torsion angle dimension can be simplified by sampling only two time points, the beginning and the middle of the rotor period, where the distinction between helical and sheet conformations is the largest: the β-sheet signal is retained more significantly than the α-helical signals (Figure 3a). This β-sheet selection experiment has been demonstrated on ubiquitin and indeed showed the preferential selection of the β-sheet signals [21]. One can also extract ψ and χ_1 torsion angles by correlating the N–H coupling with C–H couplings that are more than one bond removed from the ^{15}N. For ψ angles, this means N–H of residue $i + 1$ and C$^\alpha$–H$^\alpha$ of residue i. For χ_1 angles, the two tensors are the N–H and C$^\beta$–H$^\beta$ couplings of the same residue. These dipolar spectra are resolved in the 2D ^{13}C–^{15}N spectra as $^{15}N_{i+1}$–$^{13}C_i^\alpha$ and $^{15}N_i$–$^{13}C_i^\beta$ cross peaks. This 3D HNCH experiment has been demonstrated on a tripeptide, formyl-Met-Leu-Phe, and helped the determination of its high-resolution structure (0.02 Å rmsd for the peptide backbone) [2].

To make the HNCH class of experiments applicable under higher spinning speeds, which is important for uniformly ^{13}C, ^{15}N-labeled peptides, active recoupling of X–H dipolar coupling is desirable. One method developed for this purpose is the T-MREV [24] sequence, which uses semi-windowless MREV-8 as the basic element but concatenates n elements with phase shifts of $2\pi/n$ to build a C_n type pulse sequence [18]. This creates a dipolar lineshape that is independent of the MAS spinning speed, so higher spinning speeds can be used and dipolar evolution need not be confined to one rotor period. The T-MREV lineshape, in addition to its primary dependence on the torsion angle of interest, also depends on longer-range X–H dipolar couplings and the angles between multiple X–H vectors. These need to be quantified by control experiments. Among the three torsion angles (ϕ, ψ, χ_1) measurable from the 3D HNCH experiments, the angular precision is the lowest for the ψ angle because N_{i+1}–C_i^α polarization transfer is the least efficient.

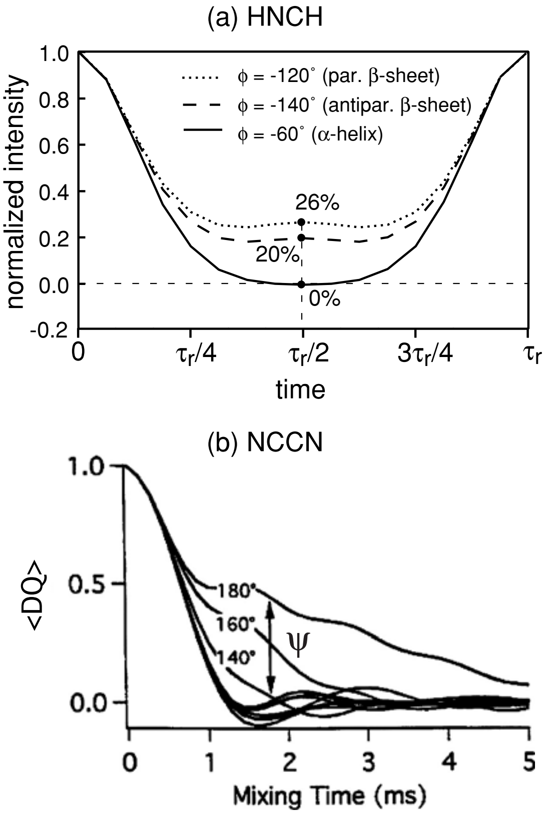

Fig. 3. (a) Characteristic HNCH time curves for ϕ angles of major secondary structures. (b) NCCN time curves for different ψ angles. (Adapted from Refs. [21,23].)

ψ Angle Techniques

Similar to the HNCH method for determining ϕ angles, tensor correlation schemes have been designed to measure the ψ angle in proteins. The simplest method is NCCN, which correlates the N_i–C_i^α dipolar coupling with the C'_i–N_{i+1} coupling [12,23]. The basic experimental design involves excitation of the C^α–C' DQ coherence and evolution of this DQ coherence under C–N dipolar coupling (Figure 1c). The exact homonuclear and heteronuclear recoupling sequences can vary [12,18,23,25], but the ψ angle-dependent signals have the same trends. The highest ψ angle resolution occurs when the N_i–C_i^α and C'_i–N_{i+1} bonds are collinear, at $\psi = 180°$. Below a $|\psi|$ of 120°, the time oscillation or spectral lineshape becomes poorly resolved (Figure 3b).

To achieve better site resolution for uniformly labeled proteins, the original NCCN experiment has been extended to incorporate two chemical shift dimensions [26]. The INADEQUATE-NCCN experiment combines 2D ^{13}C DQ–SQ correlation with NCCN evolution. In the NCOCA-NCCN experiment, the time evolution of the N_{i+1}–C_i^α correlation peak in the 2D ^{15}N–^{13}C spectra reflects the ψ_i angle. The C^α and C' coherences evolve separately under their respective ^{15}N–^{13}C dipolar interactions during a two-step polarization transfer, $N_{i+1}(t_1) \rightarrow C'_I$ (NC) $\rightarrow C_I^\alpha$ (NC) (t_2). The INADEQUATE-NCCN experiment has higher spectral sensitivity due to the one-step DQ excitation (30–35%) but somewhat lower chemical shift dispersion than the NCOCA-NCCN experiment. This was demonstrated on the model protein α-spectrin SH3 domain [26], where 13 ψ angles were measured from the INADEQUATE-NCCN experiment and 22 ψ angles were obtained from the NCOCA-NCCN experiment.

The NCCN technique is insensitive to ψ angles below ~120°, which include the α-helical conformation ($\psi = -60°$). To address this problem, an alternative tensor correlation scheme, HCCN, that exploits the H^α–C^α–C'–N topology was developed [13]. The H^α–C^α–C'–N torsion angle, ζ, is related to ψ by $\psi = \zeta + 120°$. Thus, the maximal angular resolution of $\zeta = 180°$ corresponds to $\psi = -60°$, or the α-helical conformation. This HCCN experiment recouples the C^α–H^α coupling by LG-CP and correlates it with the REDOR-recoupled C'_i–N_{i+1} interaction (Figure 1d). To increase the ψ angle resolution, the C'_i–N_{i+1} dephasing is amplified 14- to 18-fold by incrementing the C–N REDOR period 14–18 times faster than the C–H increment. Since ^{13}C′ couples to both its directly bonded ^{15}N and to the intra-residue ^{15}N, and the two-bond interaction (225 Hz) is only ~4 times weaker than the one-bond interaction, the two-bond ^{13}C–^{15}N dipolar coupling needs to be taken into account in the simulation.

In addition to dipolar based tensor correlation techniques, C^α–H^α dipolar and C' CSA correlation has been developed for determining ψ angle under MAS. One such technique, relayed anisotropy correlation (RACO) [14], yields quasi-static 2D powder patterns and is suitable at intermediate spinning speeds of ~5 kHz. The experiment selects the C' transverse magnetization over C^α, evolves it under recoupled CSA during t_1, transfers the C' magnetization to C^α, and directly detects the C^α–H^α dipolar coupling during windows of a multiple-pulse sequence (Figure 1e). The 2D RACO powder patterns are sensitive to the ψ angle, and have only minor dependence on the C' CSA tensor orientation.

An alternative technique for correlating C^α–H^α dipolar and C' CSA that is suitable under much higher spinning speeds (>10 kHz) and for uniformly labeled samples is ROCSA-LG [27]. The experiment recouples ^{13}C′ CSA in uniformly ^{13}C-labeled peptides using the ROCSA sequence [28] and probes the C^α–H^α dipolar coupling using LG-CP. In the resulting 2D ^{13}C correlation spectrum, the

C′–C$^{\alpha}$ cross peak intensity reflects the relative orientation of the two tensors.

Simultaneous (ϕ, ψ) Determination

In analogy to the static DOQSY experiment, several MAS techniques have been developed to determine ϕ and ψ angles simultaneously by correlating the orientation of two consecutive C′ CSA tensors. Common to these techniques is the creation of DQ C′ coherence to evolve under the sum chemical shift tensor. When the DQ state was prepared using the dipolar recovery with a windowless sequence (DRAWS) sequence [29], the method is called DQDRAWS [30]. Information on the relative CSA tensor orientation is contained in spinning sideband intensities [31]. The DQDRAWS sideband spectra for major secondary structure motifs are readily distinguishable. In the DQCSA experiment [15], an RFDR sequence is used to excite the DQ coherence, and the CSA recoupling is achieved by a moving π pulse in the rotor period (Figure 1f). The t_1-dependence of the sideband intensities gives the (ϕ, ψ) angle information. Figure 4 shows the simulated DQCSA t_1 signals of the center band and first-order sidebands for major secondary structures. As can be seen, the time oscillations differ significantly.

The second approach for measuring ϕ and ψ simultaneously relies on the excitation time-dependence of the C′–C′ DQ coherence. The constant-time DQ filtered dipolar dephasing (CTDQFD) experiment [32] uses three RFDR periods with durations of $L\tau_r$, $M\tau_r$, and $N\tau_r$ to select and evolve the DQ coherence. The total RFDR time $(L + M + N)\tau_r$ is constant to minimize the effects of transverse relaxation and residual ^{13}C–^{1}H dipolar coupling on the DQ dephasing curve, while the effective dipolar dephasing time is $(L + M - N)\tau_r$ [32].

The third approach for simultaneous (ϕ, ψ) determination is by detecting cross peaks between the sidebands of two consecutive C′ groups in a 2D MAS ^{1}H-driven ^{13}C spin diffusion spectrum [33,34]. Slow spinning speeds need to be used to ensure a sufficient number of sidebands. The cross peaks of interest, $V_{n,n'}^{i,j}$, are between sideband n of site i and sideband n' of site j. These inter-residue cross peaks run perpendicular to the spectral diagonal. This 2D MAS exchange experiment is simple and robust, and is suitable for chemically synthesized peptides [35], where ^{13}C′ labeling is straightforward. In applying the technique,

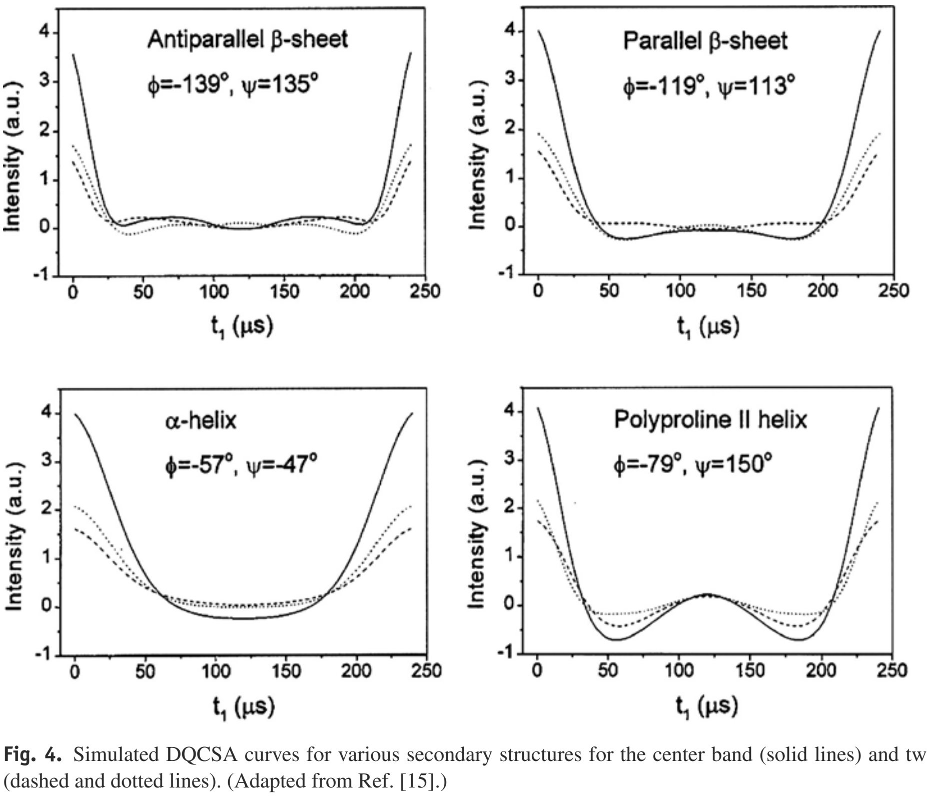

Fig. 4. Simulated DQCSA curves for various secondary structures for the center band (solid lines) and two first-order sidebands (dashed and dotted lines). (Adapted from Ref. [15].)

intermolecular spin diffusion needs to be avoided by diluting the labeled peptide in an excess of unlabeled peptide. It is also important to actively synchronize the t_2 and t_1 periods.

Distance Methods for Determining Torsion Angles

In general, the distance (d) between two atoms separated by three covalent bonds depends on the torsion angle θ around the central bond sinusoidally as:

$$d^2 = c_1^2 + c_2^2 + c_3^2 - 2c_1c_2\cos\alpha_1 - 2c_2c_3\cos\alpha_2 + 2c_1c_3\cos\alpha_1\cos\alpha_2 - 2c_1c_3\sin\alpha_1\sin\alpha_2\cos\theta, \quad (1)$$

where α_1 and α_2 are bond angles and c_1, c_2, and c_3 are bond lengths. Both homonuclear and heteronuclear distance experiments have been developed to measure such torsion angle-dependent distances. The most obvious candidate is the distance between two consecutive C′ carbons, which encodes the ϕ angle. The DRAWS recoupling sequence has been used to measure this homonuclear coupling. Application to a hexapeptide bound to hydroxyapatite crystals [36] showed the peptide to have a distribution of conformations.

Techniques for measuring heteronuclear distances between ^{1}H and ^{13}C or ^{15}N spins have also been developed to determine torsion angles. The ϕ angle can be extracted from the intra-residue H^N–C′ distance, while the χ_1 angle can be measured from the H^β–N distance [37]. The angle-dependence of these two distances is shown in Figure 5. This ^{1}H–X REDOR technique requires the detection of a third nucleus, Y, to select the REDOR modulation of the proton of interest. The ^{1}H magnetization evolves under the REDOR-recoupled dipolar local field of the X spin while ^{1}H homonuclear decoupling is achieved using multiple-pulse sequences. The selection of a specific proton is achieved by a short LG-CP to the directly bonded Y spin. Compared to the HNCH technique, the H^N–C′ method for ϕ angle determination has the advantages that it can be applied to Gly, and it is sensitive to both β-sheet and α-helical conformations.

ϕ, ψ angles can also be extracted using ^{2}H–X REDOR. The $^{13}C'_{i-1}$–$^2H_i^\alpha$ distance depends on the ϕ_i angle while the $^{15}N_{i+1}$–$^2H_i^\alpha$ distance depends on the ψ_i angle [38]. When the ^{2}H channel is unobserved, efficient inversion of ^{2}H spins is imperative for the technique to work. Vega and coworkers showed that phase-modulated XYXYX (PM5) composite 180° pulses improve the REDOR dephasing by ^{2}H spins [39]. The recoupling efficiency of this PM5-REDOR is found to approach REAPDOR but without the disadvantage of a fast-decaying S_0 that results from multiple 180° pulses on the observed channel. The method has been demonstrated on model tripeptides.

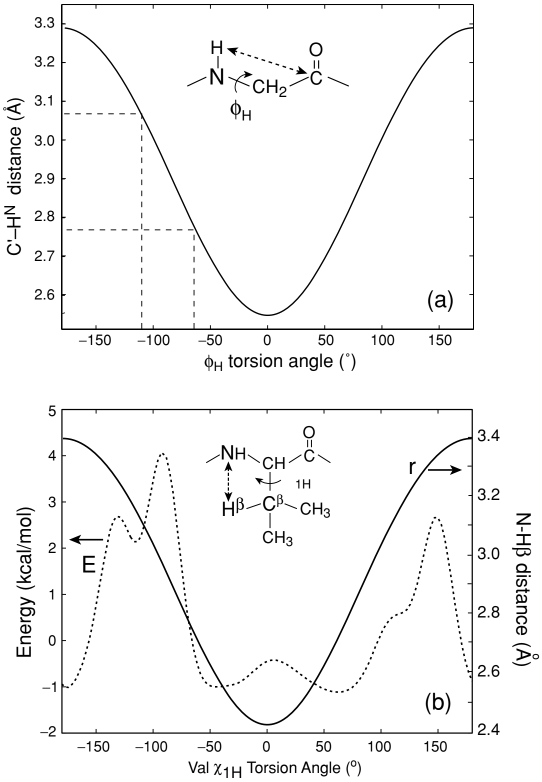

Fig. 5. Dependence of the intra-residue (A) H^N–C′ distance on the ϕ angle, and (B) H^β–N distance on the χ_1 angle. (Adapted from Ref. [37].)

Conclusion

Solid-state NMR spectroscopy has become a sophisticated and versatile tool for determining torsion angles in polymers and proteins. The principles of these techniques are perfectly applicable to other biological solids such as nucleic acids and to organic compounds [9,17,40]. These torsion angle restraints are particularly useful for defining the local conformation of molecules, and complement distance restraints, which better define the global structure of molecules.

References

1. Antzutkin ON. In: MJ Duer (Ed). Solid-state NMR Spectroscopy Principles and Applications. Blackwell Sciences, Inc.: Oxford, 2002, pp 280–90.

2. Rienstra CM, Tucker-Kellogg L, Jaroniec CP, Hohwy M, Reif B, McMahon MT, Tidor B, Lozano-Perez T, Griffin RG. Proc. Natl. Acad. Sci. U.S.A. 2002;99:10260–5.
3. Jaroniec CP, MacPhee CE, Bajaj VS, McMahon MT, Dobson CM, Griffin RG. Proc. Natl. Acad. Sci. U.S.A. 2004;101:711–16.
4. Jaroniec CP, MacPhee CE, Astrof NS, Dobson CM, Griffin RG. Proc. Natl. Acad. Sci. U.S.A. 2002;99:16748–53.
5. Beek JDv, Beaulieu L, Schafer H, Demura M, Asakura T, Meier BH. Nature. 2000;405:1077–9.
6. Schmidt-Rohr K, Hu W, Zumbulyadis N. Science. 1998;280: 714–7.
7. Schmidt-Rohr K. Macromolecules. 1996;29:3975–81.
8. Schmidt-Rohr K. J. Magn. Reson. 1998;131:209–17.
9. Harris DJ, Bonagamba TJ, Hong M, Schmidt-Rohr K. Macromolecules. 2000;33:3375–81.
10. Schmidt-Rohr K. J. Am. Chem. Soc. 1996;118:7601–3.
11. Hong M, Gross JD, Rienstra CM, Griffin RG, Kumashiro KK, Schmidt-Rohr K. J. Magn. Reson. 1997;129:85–92.
12. Feng X, Eden M, Brinkmann A, Luthman H, Eriksson L, Graslund A, Antzutkin ON, Levitt MH. J. Am. Chem. Soc. 1997;119:12006–7.
13. Ladizhansky V, Veshtort M, Griffin RG. J. Magn. Reson. 2002;154:317–24.
14. Ishii Y, Terao T, Kainosho M. Chem. Phys. Lett. 1996;256:133–40.
15. Blanco FJ, Tycko R. J. Magn. Reson. 2001;149:131–8.
16. Antzutkin ON, Tycko R. J. Chem. Phys. 1999;110:2749–52.
17. Feng X, Lee YK, Sandstroem D, Eden M, Maisel H, Sebald A, Levitt MH. Chem. Phys. Lett. 1996;257:314–320.
18. Lee YK, Kurur ND, Helmle M, Johannessen OG, Nielsen NC, Levitt MH. Chem. Phys. Lett. 1995;242:304–9.
19. Hong M, Gross JD, Griffin RG. J. Phys. Chem. B. 1997;101:5869–74.
20. Hong M, Gross JD, Hu W, Griffin RG. J. Magn. Reson. 1998;135:169–77.
21. Huster D, Yamaguchi S, Hong M. J. Am. Chem. Soc. 2000;122:11320–7.
22. Rienstra CM, Hohwy M, Mueller LJ, Jaroniec CP, Reif B, Griffin RG. J. Am. Chem. Soc. 2002;124:11908–22.
23. Costa PR, Gross JD, Hong M, Griffin RG. Chem. Phys. Lett. 1997;280:95–103.
24. Hohwy M, Jaroniec CP, Reif B, Rienstra CM, Griffin RG. J. Am. Chem. Soc. 2000;122:3218–9.
25. Sun B-Q, Costa PR, Kocisko D, Lansbury PTJ, Griffin RG. J. Chem. Phys. 1995;102:702–7.
26. Ladizhansky V, Jaroniec CP, Diehl A, Oschkinat H, Griffin RG. J. Am. Chem. Soc. 2003;125:6827–33.
27. Chan JCC, Tycko R. J. Am. Chem. Soc. 2003;125:11828–9.
28. Chan JCC, Tycko R. J. Chem. Phys. 2003;118:8378–89.
29. Gregory D, Mitchell DJ, Stringer JA, Kiihne S, Shiels JC, Callahan J, Mehta MA, Drobny GP. Chem. Phys. Lett. 1995;246:654–63.
30. Gregory DM, Mehta MA, Shields JC, Drobny GP. J. Chem. Phys. 1997;107:28–42.
31. Bower PV, Oyler N, Mehta MA, Long JR, Stayton PS, Drobny GP. J. Am. Chem. Soc. 1999;121:8373–5.
32. Bennett AE, Weliky DP, Tycko R. J. Am. Chem. Soc. 1998;120:4897–8.
33. Weliky D, Tycko R. J. Am. Chem. Soc. 1996;118:8487–8.
34. Tycko R, Weliky DP, Berger AE. J. Chem. Phys. 1996;105:7915–30.
35. Yang J, Gabrys CM, Weliky DP. Biochemistry. 2001;40:8126–37.
36. Long JR, Dindot JL, Zebroski H, Kiihne S, Clark RH, Campbell AA, Stayton PS, Drobny GP. Proc. Natl. Acad. Sci. U.S.A. 1998;95:12083–7.
37. Sinha N, Hong M. Chem. Phys. Lett. 2003;380:742–8.
38. Sack I, Balazs YS, Rahimipour S, Vega S. J. Am. Chem. Soc. 2000;122:12263–9.
39. Sack I, Vega S. J. Magn. Reson. 2000;145:52–61.
40. Kaji H, Schmidt-Rohr K. Macromolecules. 2001;34:7368–81.

Secondary Structure Analysis of Proteins from Angle-Dependent Interactions

Toshimichi Fujiwara and Hideo Akutsu
Institute for Protein Research, Osaka University, Suita, Osaka 565-0871, Japan

Introduction

The backbone structures of proteins are characterized by the secondary structure, such as α-helix, β-sheet, and turn structures [1]. Thus, backbone segments in the 3D structures can be assigned to these regular conformations. Information on the secondary structure is obtained at earlier stages of the experimental structural analysis by circular dichroism (CD), infrared absorption (IR), chemical shifts in nuclear magnetic resonance, and X-ray diffraction at low resolution [2]. The secondary structure analysis is the basis for the further detailed structural studies.

NMR spectroscopy provides means for the secondary structure analysis through J couplings, isotropic and anisotropic chemical shifts, and dipolar couplings [3]. In this chapter we review the NMR methods for the secondary structure analysis through the angle-dependent nuclear magnetic interactions.

Characterization of the Secondary Structure in Proteins

The secondary structure can be specified by backbone dihedral angles for consecutive residues and distances with the hydrogen bonding patterns [1]. For example, α-helix has backbone dihedral angles $\phi = -57^\circ$, $\psi = -47^\circ$, a helix diameter of 4.6 Å, and a hydrogen bond length of 3.0 Å between O in the ith residue and N in the $(i + 4)$th residue. These angles and distances give the same backbone structure. We can analyze the secondary structure through these structural parameters obtained by NMR as shown in the following sections.

NMR Methods for the Secondary Structure Analysis of Proteins

Chemical Shifts Depending on the Secondary Structure

Isotropic and anisotropic chemical shifts of ^{13}C, ^{1}H, and ^{15}N spins are influenced by the conformation through the backbone and side chain torsion angles, hydrogen bonding, electrostatic interaction, ring current, and so on [4]. Carbon-13 chemical shifts of C′, C$^{\alpha}$, and C$^{\beta}$ are shown to be primarily determined by backbone torsion angles. The torsion angles have also strong effects on the ^{15}N and ^{1}H chemical shifts. These properties have been used to identify the secondary structure in the proteins [5].

The progresses in NMR structural study of proteins and quantum mechanical analysis of chemical shifts elucidate the relationships between the chemical shifts and the structure. These relationships allow the reliable analysis of the secondary structure from the chemical shifts. The empirical and quantum mechanical database software for proteins chemical shifts are recently developed. TALOS [6] predicts the dihedral angles from the experimental chemical shifts. The other programs, TANSO [7], SHIFTS [8,9], SHIFTX [10], PROSHIFT [11], and XPRSI [12], calculate the chemical shifts from the structure given by atomic coordinates. The chemical shifts over 3–4 residues are evaluated to identify the secondary structure, because the typical secondary structure is formed by more than three amino acid residues.

Carbon chemical shift changes due to the secondary structure are about 3–5 ppm. Chemical shift is sensitive to the minor conformational distributions, which often cause the ^{13}C line width of about 1 ppm for well-ordered peptides in solid-state NMR [13]. The conformational fluctuation of proteins in solution and crystalline states generally suppresses these inhomogeneous broadening and provides sharp signals [14].

Denatured proteins generally give sharp signal at chemical shifts for random coil in solution. In this state, peptides take conformations for α and β structures in torsion angles with exchange rates larger than the resonance frequency difference. However, in solid states especially at low temperatures, random coil peptides give broad signals reflecting the distribution of the backbone structure [15]. Note that the definition of the randomness of structure depends on the experimental methods. Conformation for the CD spectrum for random coil corresponds to the structures that are not assigned to the regular secondary structures. Peptide segments that do not give definite electron densities in X-ray structure

Graham A. Webb (ed.), Modern Magnetic Resonance, 735–740.
© 2008 *Springer.*

are classified into the disordered. Although these segments would not be located at ordered sites in unit lattice, the segments may form a secondary structure. Thus, amino acid residues for the random coil in CD and the disordered in X-ray structure may not have a structural distribution that causes a random coil NMR signal.

Chemical shift anisotropy of carbons also depends on the dihedral angles as shown in recent experimental studies similarly to isotropic chemical shifts [16].

J Coupling Depending on Backbone Torsion Angles

Scalar coupling is determined by the electronic structure as well as chemical shifts. Vicinal ^3J coupling constants depend on a torsion angle as shown in Karplus curve. It was also shown that one-bond CH ^1J coupling depends on the secondary structure [17]. The $^1\mathrm{H}^{\mathrm{N}}$–$\mathrm{H}^{\alpha}$ and $^1\mathrm{H}^{\alpha}$–$^1\mathrm{H}^{\beta}$ ^3J coupling constants provide the constraints on dihedral angles ϕ and χ_1 in proteins, respectively [3]. The trans conformation can be determined uniquely from the vicinal J coupling constants. However, the gauche and cis conformations cannot be determined because ^3J coupling constants for these conformers correspond to two torsion angle in the Karplus curve. Note that the exchange between rotamers averages the J coupling constant. Since ^{1}H–^{1}H ^3J coupling constants, ca. 10 Hz, are much small than the line width of solid-state NMR signals, J coupling constants measurements for the secondary structure analysis is now exclusively used in solution NMR.

Distance Measurements for the Secondary Structure Analysis

Internuclear distances are measured from dipolar couplings by NOE in solution NMR, and REDOR [18], rotational resonance [19], and ^{1}H-driven spin diffusion [20] in solid-state NMR. Some internuclear distances are sensitive to the secondary structure, e.g. distances between C^{β} in the ith residue and C′ in the $(i + 3)$th residue is 4 Å for α-helix and 9 Å for β-structure. These distances serve as constraints in the structure determination by restrained molecular dynamics calculation. The secondary structure can be assigned in the determined ternary structure. The measurements of intramolecular distances between residues that are separated in the amino acid sequence and intermolecular distances are crucial for the structure determination of proteins. The structure determination only by the torsion angles tends to have amplified errors in those long-range distances. In comparison with experiments for signal assignments that provide chemical shifts, distance measurements need higher sensitivity especially to obtain longer distances because of the weakness in the long-range dipolar interactions.

Angle Measurements from the Anisotropic Nuclear Magnetic Interactions

The angular information is obtained from dipolar couplings and chemical shift anisotropies, because these interactions specify the directions through the principal axes of their tensors. There are several methods for obtaining the orientational information from the anisotropic interactions as follows:

Orientation Relative to the Anisotropic Nuclear Magnetic Interaction[21]

This method can be applied to powdered samples as well as oriented ones. At least two anisotropic interactions are correlated as shown in Figure 1a. The distances of spins for the angle measurements are generally less than 5 Å depending on the dipolar or J couplings employed in the experiments to correlate the anisotropic interactions. The obtained correlation spectrum provides the torsion angle constrains for the secondary structure. The details of the experiments for proteins are given in the section on torsion angle measurements.

Orientation Relative to the Tensor for Anisotropic Molecular Motion

This method provides the information on the angles of the anisotropic nuclear magnetic interactions with respect to the anisotropic rotation axes as shown in Figure 1b. This principle can be applied to ellipsoidal proteins and molecules in anisotropic environment as in the lipid membrane under unoriented states. The anisotropic axes are determined by the structure of macromolecules and the interaction of the molecule to the environment. When they undergo rapid overall rotation, the anisotropic tensor can be a rotational diffusion tensor. The angle information is obtained from the relaxation parameters [22]. The long-range angle information can be obtained by this method, because the orientations of anisotropic interactions are determined with respect to an overall diffusion tensor common to the whole molecule. When the molecules do not rotate freely as sample systems for solid-state NMR, the anisotropic axes of the molecules are primarily characterized by an anisotropic potential that restricts the molecular motion [23]. In this case, the angle information is obtained from specific reductions of powder lineshapes in frequency as well as from the magnetic relaxation. For example, rapid uniaxially rotational diffusion gives an axially symmetric powder pattern, whose maximum is determined by the orientation of the rotational axis relative to the chemical shift tensor.

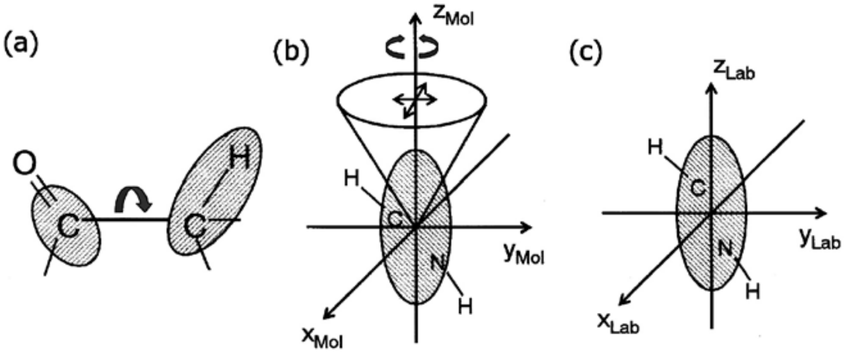
(a)
O
C
C
H
(b)
z_Mol
H
C
N
H
y_Mol
x_Mol
(c)
z_Lab
H
C
N
H
y_Lab
x_Lab

Fig. 1. (a) Mutual orientation of anisotropic interactions. The shaded ellipsoids stand for anisotropic interactions which are correlated with ^{13}C–^{13}C dipolar or *J* couplings. (b) Orientation of anisotropic interactions with respect to the molecular frame that characterizes the molecular motion. The molecules rotate anisotropically in a cone. The ellipsoid indicates the anisotropy of the molecular motion that is expressed by a rotational diffusion tensor. (c) Anisotropic interactions with respect to the macroscopically orientated molecules in the laboratory frame. Anisotropy of the molecular orientation is expressed by the alignment tensor given by the ellipsoid.

Orientation Relative to the Macroscopic Orientation Axis

This category of the methods is applied to uniaxially or weakly oriented systems (Figure 1c). Spectra for these sample states provide the orientations of the anisotropic interactions relative to the macroscopic orientation axis. These orientational constraints are the source of the structural information of molecules. Torsion angles can be measured by this method [24,25]. Combining the angle constraints with respect to the orientation axes for consecutive residues, we can deduce the angle information on the secondary structure. For example, PISA wheel spectral patterns in the PISEMA spectra for NH dipolar vs. ^{15}N CSA correlation [26–28] and dipolar coupling as a function of residue number, dipolar wave [29], elucidate the angles for the secondary structure and the orientation of molecules with respect to the orientation axes. The relative orientation of anisotropic nuclear magnetic interaction with respect to the orientation axes are obtained from splittings for dipolar interactions and from frequency shifts for chemical shift anisotropies in weakly oriented systems [30]. Angle measurements over a long range such as mutual orientation of domains are also possible, because the angles with respect to the common alignment frame are measured [31].

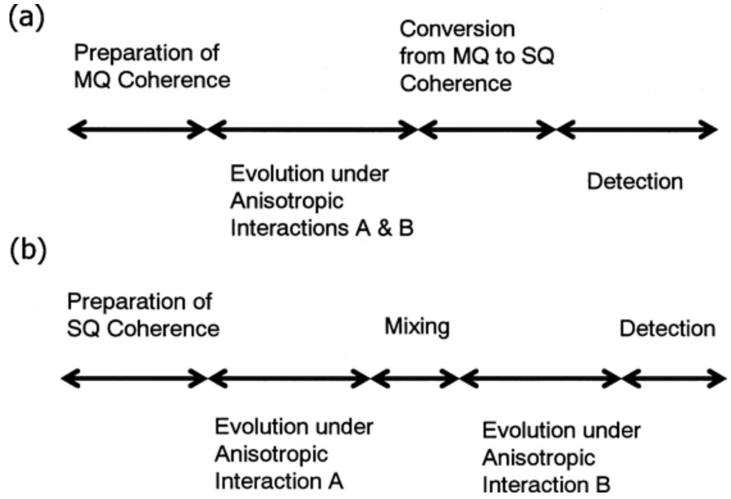
(a)
Preparation of MQ Coherence
Conversion from MQ to SQ Coherence
Evolution under Anisotropic Interactions A & B
Detection
(b)
Preparation of SQ Coherence
Mixing
Detection
Evolution under Anisotropic Interaction A
Evolution under Anisotropic Interaction B

Fig. 2. Pulse sequences for determining the mutual orientation of anisotropic interactions A and B. (A) Sequence with an evolution period for DQ/ZQ coherences. (B) Sequence with one mixing period connecting two evolution periods for interactions A and B.

Torsion Angle Measurements from the Mutual Orientation of Anisotropic Interactions for the Secondary Structure Analysis

In the following we will describe the torsion angle measurements from the mutual orientation of tensorial interactions and its application to peptide secondary structure analysis mainly in solid states.

Experiments for the Mutual Orientation of Anisotropic Interactions

There are two methods for the correlation of anisotropic interactions. One method for the measurement of the correlation uses two-spin coherences such as double-quantum (DQ) and zero-quantum (ZQ) coherences. This method has one period for the evolution of the two-spin coherence under two anisotropic interactions [32–36]. The DQ/ZQ evolution period is generally placed between the conversion periods between DQ/ZQ and SQ coherences in the pulse sequence as shown in Figure 2A. Anisotropic interactions were recoupled when the experiments are carried out under magic-angle spinning conditions, which improve the signal sensitivity and resolution [37].

The other method for the correlation has two evolution periods under anisotropic interactions [38–45]. The two evolution periods for the different spins are connected by a mixing period as shown in Figure 2B. The resultant 2D spectra provide the correlation that depends on the mutual orientation of the anisotropic interactions. Figure 3 shows that the correlation spectrum of CH dipolar couplings in an H–C–C–H moiety depends on the torsion angle about the C–C axis [39].

When the spins for anisotropic interactions are separated by one bond, the correlation can give the torsion angle in general. When they are separated by more than one chemical bond, the correlation can provide the information on the multiple torsion angles. When they are not separated by a chemical bond, the correlation includes the information on the bond angle and the orientation of principal axes of the chemical shift tensor. This method can be a 1D experiment [46]. Although the correlation between anisotropic interactions provides angle information, dihedral angles may not be determined uniquely because of the symmetry in the interaction. The combinations of other anisotropic interactions for the measurement of the same torsion angle or energy constraints would allow the unique determination of the angle.

Similar method has been applied to the dihedral angle measurements in solution NMR. The cross-correlation of the anisotropic interactions affects the relaxation of two-spin coherences. This cross-correlation effect has been shown to be sensitive to the mutual orientation of anisotropic interactions in solution states [47].

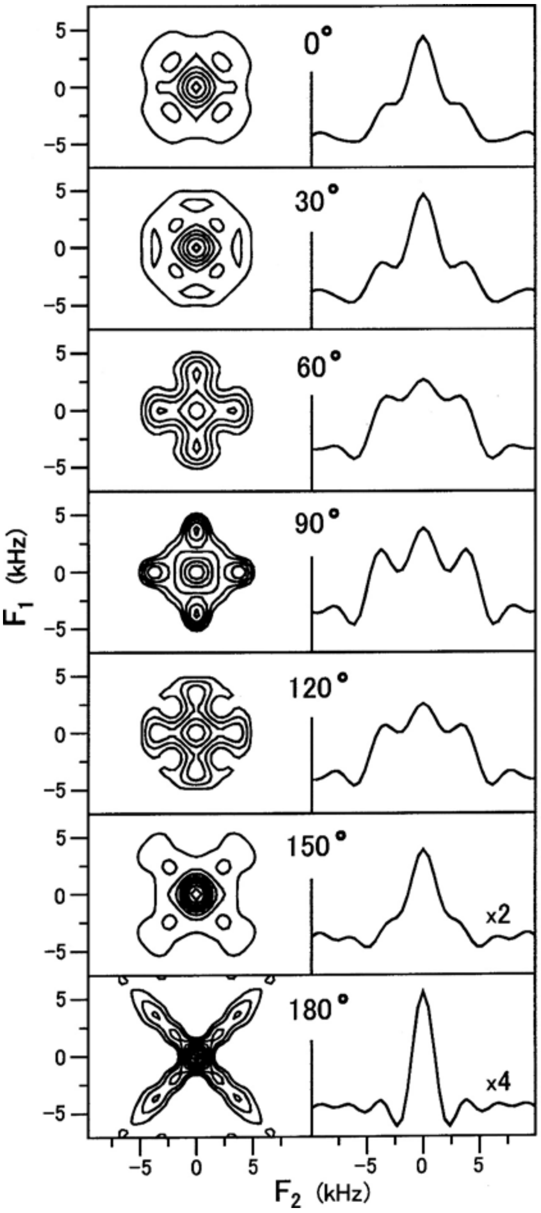

Fig. 3. Simulated 2D spectra for the correlation between CH dipolar couplings in the ^1H–^{13}C–^{13}C–^1H spin system obtained with a recoupling pulse sequence under magic-angle spinning. Cross sections along the F_2 axis at $F_1 = 0$ is also shown.

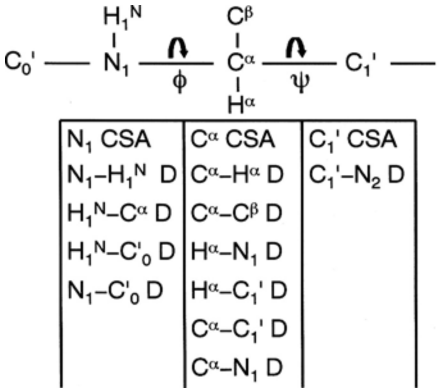

N_1 CSA	C^α CSA	C_1' CSA
N_1–H_1^N D	C^α–H^α D	C_1'–N_2 D
H_1^N–C^α D	C^α–C^β D	
H_1^N–C_0' D	H^α–N_1 D	
N_1–C_0' D	H^α–C_1' D	
	C^α–C_1' D	
	C^α–N_1 D	

Fig. 4. Combinations of anisotropic interactions for the backbone torsion angle analysis. Anisotropic interactions specifying the orientation of atoms, N, C^α, and C′ in the backbone are shown in the first, second, and third columns, respectively. CSA and D are abbreviations for chemical shift anisotropy and dipolar coupling. The torsion angle ϕ affects the correlations between the interactions in the first and second columns, and the angle ψ affects the correlations between the interactions in the second and third columns. Note that C^α–N and C^α–C′ dipolar couplings in the second column have minor effects on the correlation for the measurements of ϕ and ψ, respectively.

Applications to the Backbone Torsion Angle Analysis of Peptides

Chemical shift anisotropies and dipolar couplings for N, C^α, and CO spins on the peptide plane can be used for the torsion angle measurements from their correlations. The carbon and nitrogen spins must be labeled with ^{13}C and ^{15}N for the high signal sensitivity and resolution.

Combinations of anisotropic interactions for determining the torsion angles in peptides are shown in Figure 4. The correlations between anisotropic interactions for N and C^α provide the ϕ angle, and those between interactions for C^α and C′ provide the ψ angle. These methods can be either the DQ/ZQ method or the SQ correlation methods. The information on the ϕ and ψ angles can be obtained from the correlation between carbonyl ^{13}C spins that are separated by three bonds [36,38,43]. The correlation between N–H dipolar couplings was also employed for the torsion angle measurements from their correlation [44,45].

References

1. Branden A, Tooze J. Introduction to Protein Structure, 2nd ed. Garland Publishing: New York, 1998.
2. van Holde KE, Jonson WC, Ho PS. Principles of Physical Biochemistry, Prentice Hall: Upper Saddle River, 1998.
3. Cavanagh J, Fairbrother WJ, Palmer AG III, Skelton NJ. Protein NMR Spectroscopy, Academic Press: San Diego, CA, 1996.
4. Wishart DS, Case DA. Methods Enzymol. 2001;338:3.
5. Wishart DS, Sykes BD. Methods Enzymol. 1994;239: 363.
6. Cornilescu G, Delaglio F, Bax A. J. Biomol. NMR 1999;13: 289.
7. Iwadate M, Asakura T, Williamson MP. J. Biomol. NMR 1999;13:199–211.
8. Xu X-P, Case DA. J. Biomol. NMR. 2001;21:321.
9. Xu X-P, Case DA. Biopolymers. 2002;65:408.
10. Stephen N, Nip AM, Zhang H, Wishart DS. J. Biomol. NMR. 2003;26:215.
11. Meiler J. J. Biomol. NMR. 2003;26:25.
12. Wang Y, Jardetzky O. J. Biomol. NMR. 2004;28:327.
13. Fujiwara T, Todokoro Y, Yanagishita H, Tawarayama M, Kohno T, Wakamatsu K, Akutsu H. J. Biomol. NMR. 2004;28:311.
14. Martin RW, Zilm KW. J. Magn. Reson. 2003;165:162.
15. Long HW, Tycko R. J. Am. Chem. Soc. 1998;120: 7039.
16. Tjandra N, Bax A. J. Am. Chem. Soc. 1997;119:9576.
17. Vuister GW, Delaglio F, Bax A. J. Am. Chem. Soc. 1992;114:9674.
18. Pan Y, Gullion T, Schaefer J. J. Magn. Reson. 1990;90:330.
19. Peersen OB, Groesbeek M, Aimoto S, Smith SO. J. Am. Chem. Soc. 1995;117:7228.
20. Kubo A, McDowell CA. J. Chem. Soc., Faraday Trans. 1. 1988;84:3713.
21. Linder M, Höhener H, Ernst RR. J. Chem. Phys. 1980;73:4959.
22. Tjandra N, Garrett DS, Gronenborn AM, Bax A, Clore GM. Nat. Struct. Biol. 1997;4:443.
23. Seelig J. Q. Rev. Biophys. 1977;10:353.
24. Opella SJ, Ma C, Marassi FM. Q. Rev. Biophys. 1987;19:7.
25. Teng Q, Nicholson LK, Cross TA. J. Mol. Biol. 1991;218: 607.
26. Wu CH, Ramamoorthy A, Opella SJ. J. Magn. Reson. A. 1994;109:270.
27. Marassi FM, Opella SJ. J. Magn. Reson. 2000;144:150.
28. Denny JK, Wang J, Cross TA, Quine JR. J. Magn. Reson. 2001;152:217.
29. Mesleh MF, Lee S, Veglia G, Thiriot DS, Marassi FM, Opella SJ. J. Am. Chem. Soc. 2003;125:8928.
30. Tjandra N, Bax A. Science. 1997;278:1111.
31. Yagi H, Tsujimoto T, Yamazaki T, Yoshida M, Akutsu H. J. Am. Chem. Soc. 2004;126:16632.
32. Feng X, Lee YK, Sandstrom D, Eden M, Maisel H, Sebald A, Levitt MH. Chem. Phys. Lett. 1996;257:314.
33. Hong M, Gross JD, Griffin RG. J. Phys. Chem. B. 1997;101:5869.
34. Feng X, Edén M, Brinkmann A, Luthman H, Eriksson L, Gräslund A, Antzutkin ON, Levitt MH. J. Am. Chem. Soc. 1997;119:12006.
35. Costa PR, Gross JD, Hong M, Griffin RG. Chem. Phys. Lett. 1997;280:95.
36. Blanco FJ, Tycko R. J. Magn. Reson. 2001;149:131.
37. Griffin RG. Nat. Struct. Biol. 1998;5:508.

38. Tycko R, Weliky DP, Berger AE. J. Chem. Phys. 1996;105:7915.
39. Ishii Y, Terao T, Kainosho M. Chem. Phys. Lett. 1996;256: 133.
40. Fujiwara T, Shimomura T, Akutsu H. J. Magn. Reson. 1997;124:147.
41. Hong M, Gross JD, Rienstra CM, Griffin RG, Kumashiro KK, Schmidt-Rohr K. J. Magn. Reson. 1997;129:85.
42. Fujiwara T, Shimomura T, Ohigashi Y, Akutsu H. J. Chem. Phys. 1998;109:2380.
43. van Beek JD, Beaulieu L, Schäfer H, Demura M, Asakura T, Meier BH. Nature. 2000;405:1077.
44. Reif B, Hohwy M, Jaroniec CP, Rienstra CM, Griffin RG. J. Magn. Reson. 2000;145:132.
45. Rienstra CM, Hohwy M, Mueller LJ, Jaroniec CP, Reif B, Griffin RG. J. Am. Chem. Soc. 2002;124: 11908.
46. Hartzell CJ, Whitfield M, Oas TG, Drobny GP. J. Am. Chem. Soc. 1987;109:5966.
47. Reif B, Hennig M, Griesinger C. Science. 1997;276:1230.

Part I

Telomeric DNA Complexes

Comparison of DNA-Binding Activities Between hTRF2 and hTRF1 with hTRF2 Mutants

Shingo Hanaoka, Aritaka Nagadoi, and Yoshifumi Nishimura
Graduate School of Integrated Science, Yokohama City University, Tsurumi-ku, Yokohama 230-0045, Japan

Abstract

Telomeres are the ends of eukaryotic linear chromosomes consisting of repetitive G-rich sequences and telomeric repeat binding factors. In mammalian telomeres, TRF1 and TRF2 bind to double-stranded telomeric DNA consisting of TTAGGG repeats and regulate telomere length. Both contain a central TRF-homology domain and a C-terminal DNA-binding domain. We have determined the solution structures of DNA-binding domains from human TRF2 and TRF1 bound to a telomeric DNA. Both structures are very close to each other, however, small but significant differences are observed. Based on their structures, we created six mutants of the hTRF2 DNA-binding domain and the DNA-binding activities of all these DNA-binding domains could be well analyzed.

Introduction

Telomeres are protein–DNA complexes that distinguish natural chromosome ends from damaged DNA. Mammalian telomeric DNA is composed of long tandem array of the double-stranded telomeric repeats of TTAGGG followed by a single-stranded DNA at the 3′ end. TRF1 and TRF2 are mammalian telomeric repeat-binding factors [1,2,3]. Although the cellular functions of TRF1 and TRF2 are different from each other, both contain similar functional domains, a central TRF-homology (TRFH) domain and a C-terminal DNA-binding domain [3,4,5], except their N-terminal domains: an acidic domain in TRF1 but a basic domain in TRF2 [2]. Both DNA-binding domains of human TRF1 and TRF2 contain a similar amino acid sequence to each of the three repeats in the c-Myb DNA-binding domain [6,7].

Results

Structures of the hTRF2 and hTRF1 DNA-Binding Domains Bound to a Telomeric DNA

Figure 1 shows a structural comparison between the telomeric DNA-bound structures of hTRF1 [8] and hTRF2 [9]. Each structure contains three helices and these three helices are maintained by a hydrophobic core including three conserved tryptophan residues and also by two salt bridges. Each of three helical architectures in hTRF1 and hTRF2 is a typical Myb motif found in the three repeats of the c-Myb DNA-binding domain [10,11,12]. In both DNA complexes of the DNA-binding domains of hTRF1 and hTRF2, only the single Myb-like domain consisting of three helices can bind specifically to a double-stranded telomeric DNA with a sequence of GTTAGGGTTAGGG (Figure 4). Figure 2 shows a summary of intermolecular contacts observed in both DNA complexes of hTRF1 and hTRF2; each third helix recognizes the middle T3A4G5G6G7 sequence in the major groove of DNA and each N-terminal flexible arm interacts with the following T8T9 sequence in the minor groove [8,9].

Structural Comparison Between the DNA Complexes of hTRF2 and hTRF1

By comparing amino acid sequences of DNA-binding domains, consisting of 438–500 of hTRF2 and the corresponding sequence of 371–433 of hTRF1, 31 amino acids out of 63 amino acids are identical; both DNA-binding domains hold a very similar tertiary structure in their DNA bound forms. So the binding modes as well as the architectures of DNA complexes of both DNA-binding domains are very close in each other.

By clarifying DNA interaction modes of both domains in detail, we have found that four amino acids responsible for the DNA-binding are different from each other, Lys447, Ala471, Ala484, and Arg496 in hTRF2 and the corresponding amino acids, Arg380, Ser404, Ser417, and Lys429 in hTRF1. In the minor groove interaction by the flexible arm of hTRF2, Lys447 contacts only with T9, however, in the hTRF1 complex Arg380 likely interacts with A19, the counter part of T8, as well as T9. Figure 3 shows that in the hTRF1 complex Arg380 contacts both T9 and A19 in the minor groove, however, in the hTRF2 complex Lys447 interacts mainly with T9. It is likely that hTRF1 interacts stronger to the TT portion in the AGGGTT sequence than hTRF2.

Graham A. Webb (ed.), Modern Magnetic Resonance, 743–751.
© 2008 *Springer.*

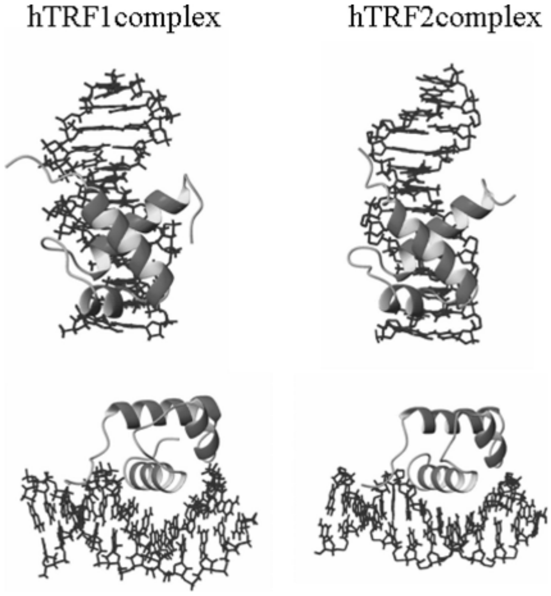
hTRF1complex
hTRF2complex

Fig. 1. Structures of telomeric DNA complexes from hTRF1 and hTRF2. (See also Plate 63 on page XLIV in the Color Plate Section.)

In the hTRF2 complex, the amide hydrogen of Ala471 contacts with the phosphate group of T3 (Figure 3). Similarly, in the hTRF1 complex, the amide hydrogen of Ser404 contacts phosphate group of T3. While, the hydroxyl group of Ser404 together with the hydroxyl group of Ser 417 contact with the phosphate group of T3 as shown in Figure 3. This suggests that for the recognition of the phosphate group of T3, hTRF1 has a little stronger activity than hTRF2. Although in the hTRF1 complex Lys429 contacts with the phosphate group of T17, the counterpart of A10, in the complex of hTRF2 the corresponding amino acid, Arg496 is not likely interact with the phosphate group of T17. In this sense also hTRF1 seems to bind much stronger than hTRF2.

To check contributions of four amino acids described above for the DNA-binding activities of hTRF2 and hTRF1, we created six mutants of hTRF2, in which four critical amino acids, Lys447, Ala471, Ala484, and Arg496 are changed into the corresponding amino acids of hTRF1: four single mutants, K447R (2m1), A471S (2m2), A484S (2m3), and R496K (2m4), in which Lys447, Ala471, Ala484, and Arg496 are replaced by arginine, serine, serine, and lysine residues, respectively, one double mutant (2wm), A471S/A484S, in which both Ala471 and Ala481 are substituted by serine residues, and one quadruple mutant, K447R/A471S/A484S/R496K, designated as 24s, in which all four amino acids, Lys447, Ala471, Ala484, and

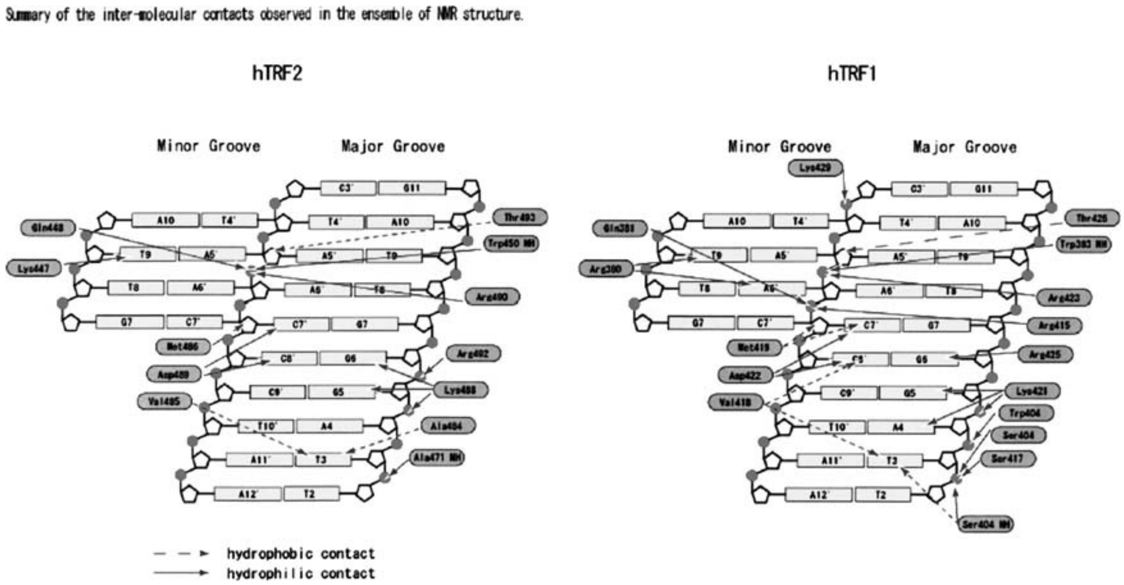
Summary of the inter-molecular contacts observed in the ensemble of NMR structure.
hTRF2
Minor Groove
Major Groove
C3'
G11
A10
T4'
T4'
A10
Gln448
Thr493
T9
A5'
A5'
T9
Trp450 NH
Lys447
T8
A6'
A6'
T8
Arg490
G7
C7'
C7'
G7
Met486
C8'
G6
Arg492
Asp489
C9'
G5
Lys488
Val485
T10'
A4
Ala484
A11'
T3
Ala471 NH
A12'
T2
hTRF1
Minor Groove
Major Groove
Lys429
C3'
G11
A10
T4'
T4'
A10
Gln381
Thr426
T9
A5'
A5'
T9
Trp383 NH
Arg380
T8
A6'
A6'
T8
Arg423
G7
C7'
C7'
G7
Arg415
Met419
C8'
G6
Arg425
Asp422
C9'
G5
Lys421
Val418
T10'
A4
Trp404
Ser404
A11'
T3
Ser417
A12'
T2
Ser404 NH
hydrophobic contact
hydrophilic contact

Fig. 2. DNA recognition modes of DNA-binding domains of hTRF1 and hTRF2. Summary of inter-molecular contacts observed in the hTRF2-DNA and hTRF1-DNA complexes. Straight lines indicate hydrophilic contacts and broken lines indicate hydrophobic contacts. (See also Plate 64 on page XLIV in the Color Plate Section.)

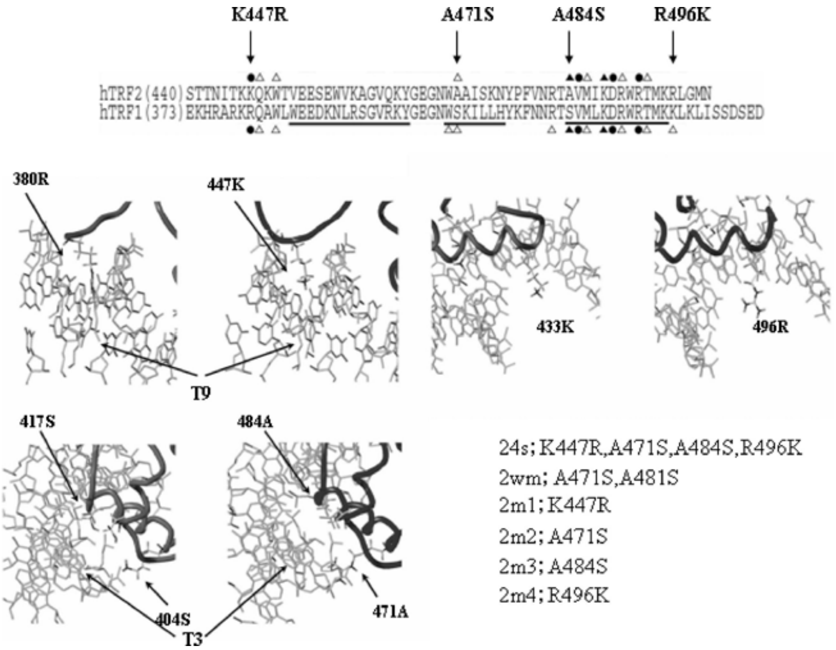
K447R
A471S
A484S
R496K
hTRF2(440)STTNITKKQKWTVEESEWVKAGVQKYGEGNWAAISKNYPFVNRTAVMIKDRWRTMKRLGMN
hTRF1(373)EKHRARKRQAWLWEEDKNLRSGVRKYGEGNWSKILLHYKFNNRTSVMLKDRWRTMKKLKLISSDSED
380R
447K
T9
433K
496R
417S
484A
404S
T3
471A
24s; K447R,A471S,A484S,R496K
2wm; A471S,A481S
2m1; K447R
2m2; A471S
2m3; A484S
2m4; R496K

Fig. 3. Comparison of DNA recognition modes between hTRF1 and hTRF2. (See also Plate 65 on page XLV in the Color Plate Section.)

Arg496 are replaced by the corresponding amino acids of hTRF1 simultaneously.

The Imino Proton Signal Changes of the Telomeric DNA Bound to the hTRF2 DNA-Binding Domain and the Mutants

We have examined the DNA-binding titartions of these mutants by 1-D NMR. Figure 4 shows 1-D NMR spectra of the imino proton signals of the 13mer DNA complexed with the wild type (A) and the six mutants of hTRF2 (B–G), together with the chemical shift changes of the imino proton signals from the free-state to the bound-state. Compared to the wild type in K447R the big chemical shift changes were observed for the imino protons of G7, T8, T9, and T17, the counterpart of A10. This suggests that as found in the hTRF1 complex the substituted arginine residue at 447 in the mutant of hTRF2 could interact with A19, the counter part of T8, as well as T9. Compared to the wild type in the spectra of A471S and A484S small but significant chemical shift changes were observed for the imino protons of T2 and T3, respectively and also A471S/A484S shows both significant changes together with the imino proton shift change of T23, the counterpart of A4. These might be related to the fact that the corresponding two-serine residues in hTRF1 contact with the phosphate group of T3. In R496K no significant chemical shift changes were observed compared to the wild type. In the spectrum of 24S, K447R/A471S/A484S/R496K, significant chemical shift changes of the imino protons were observed in T2, T3 G7, T8, and T9.

The DNA-Binding Activities of hTRF1, hTRF2, and the Mutants of hTRF2

The binding activities of hTRF1, hTRF2, and the six mutants of hTRF2 with the wild-type telomeric double stranded DNA, tr13, and three DNA mutants, T3G, G7C, and T9C as shown in Figure 5 were examined by using a surface plasmon resonance (SPR) apparatus, BIACORE. As expected the binding ability of hTRF1 is about four times stronger than the ability of hTRF2.

For the wild-type telomeric DNA, tr13 almost all mutants of hTRF2 except R496K have stronger DNA-binding activities compared to the wild type, especially the mutant K447R binds to DNA 2.5 times stronger than the wild type of hTRF2. This suggests that the substituted arginine residue in the mutant could interact with A19, the counter

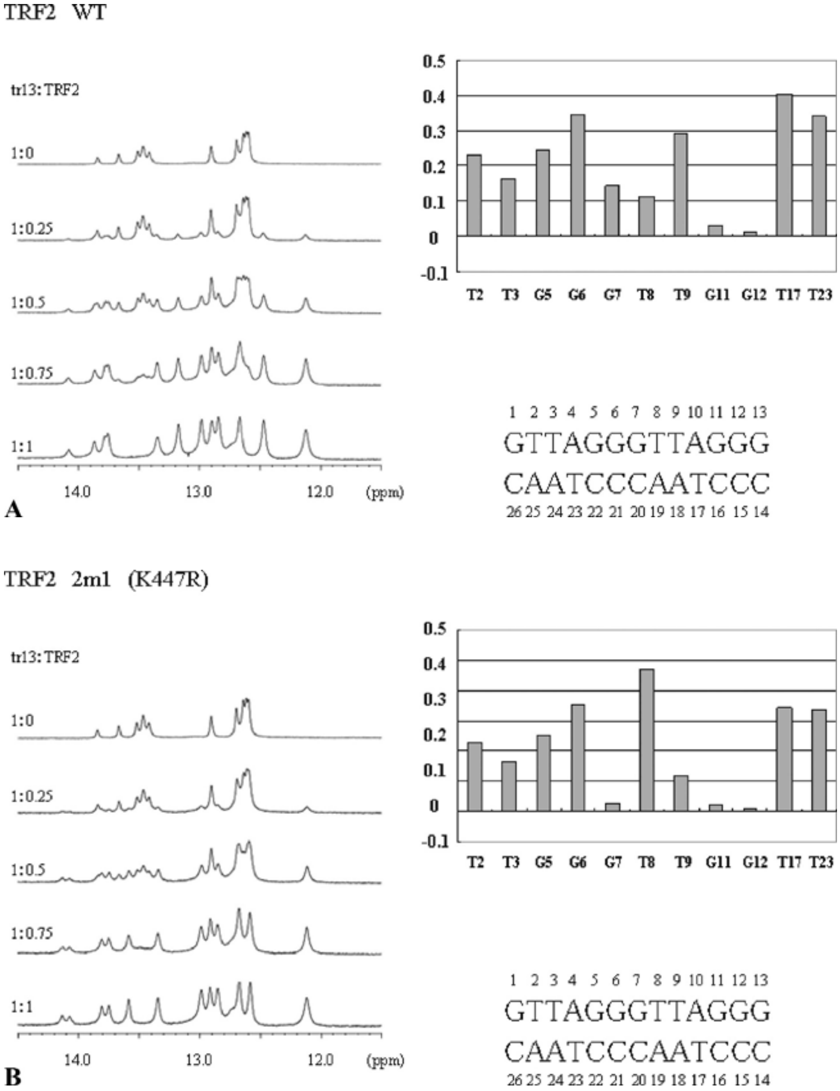

Fig. 4. NMR titration experiments of the wild-type (A), K447R (B), A471S (C), A484S (D), R496K (E), 2wm (A471S/A484S) (F) and 24s (K447R/A471S/A484S/R496K) (G) to the telomeric double stranded DNA together with the summary of the chemical shift changes of the imino proton signals of each mutant from free state to the DNA-bound state.

part of T8, as well as T9 in the minor groove like hTRF1, while Lys447 of the wild type contacts with T9 alone. This is well correlated to the fact that big chemical shift changes of the imino protons of T8 and T9 were observed between the wild type of hTRF2 and K447R. As suggested by the small chemical shift changes of A471S and A484S from the wild type both mutants bind slightly stronger than the wild type. The mutant, 2wm (A471S/A484S) binds to DNA stronger than both single mutants. Serine residues at 471 and 484 seem to bind to the backbone phosphate group independently, like hTRF1. Although R496K showed small chemical shift changes, its binding ability is very close to the wild-type ability; for an amino acid of 496 of hTRF2 both lysine and arginine residues seem to

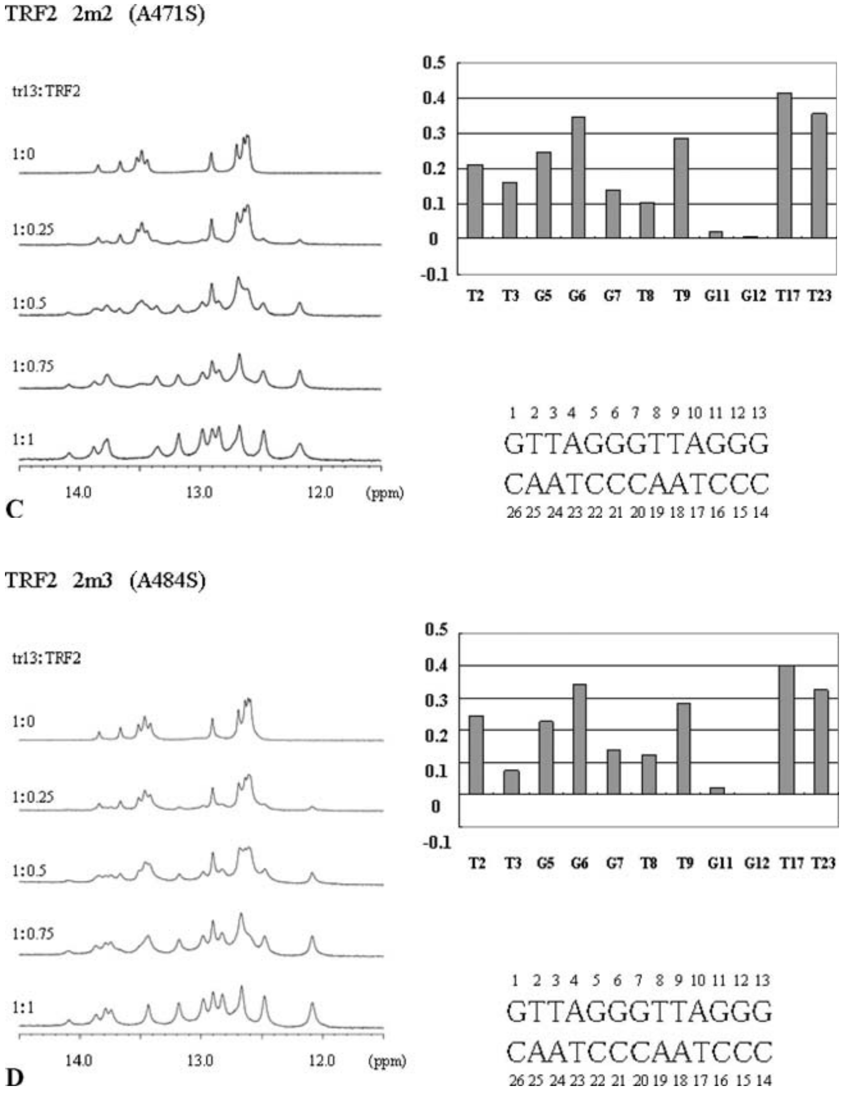

Fig. 4. (*Continued*)

play a similar role in the interaction with DNA. As shown in Figure 3 just a positive charge at 496 of hTRF2 or at 429 of hTRF1 seems to be responsible for the interaction with phosphate backbone.

The mutant, 24s (K447R/A471S/A484S/R496K) binds to DNA stronger than the wild type of hTRF2, with a similar binding ability to the hTRF1 DNA-binding domain. Arg447, Ser484, and Ser496 in 24s likely interact with DNA independently. This may lead to the conclusion that only three amino acids, Lys447, Ala471, and Ala484 of hTRF2 and the corresponding amino acids, Arg380, Ser404, and Ser417 of hTRF1 are critical amino acids that clarify the DNA-binding activities of hTRF2 and hTRF1, because the substitution of Arg496 of hTRF2 to a lysine residue does not affect the DNA-binding ability of hTRF2.

Compared to the wild-type telomeric DNA for the DNA mutants of T3G and T9G the binding abilities of

TRF2 2m4 (R496K)

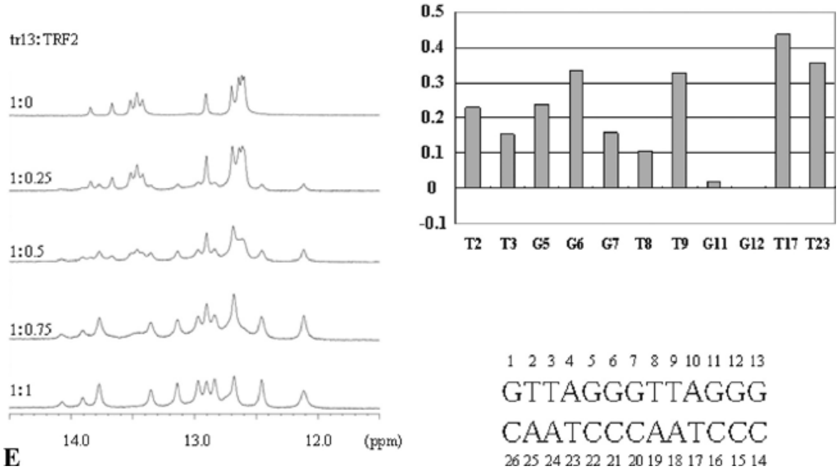

TRF2 2wm (A471S,A484S)

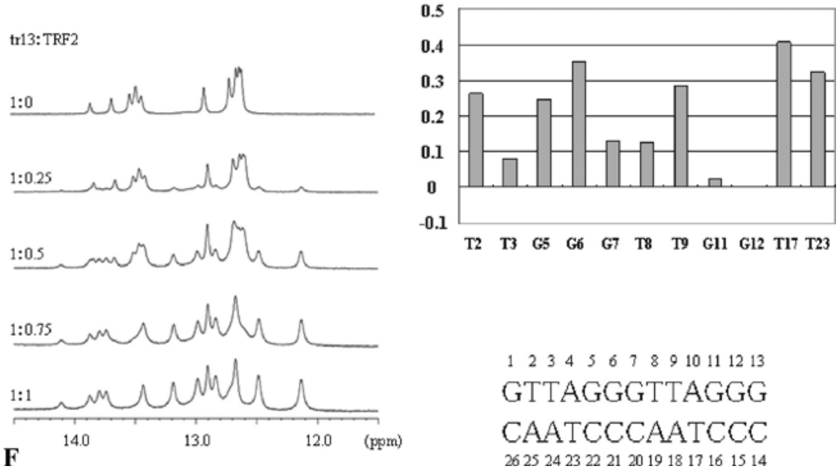

Fig. 4. (*Continued*)

the wild type and the six mutants are reduced, however comparative binding abilities between TRF1, TRF2 and the six mutants of TRF2 are similar as shown in Figure 6. The order of the binding activities for tr13, T3G, and T9G from stronger to weaker are TRF1, 24S, 2m1, 2wm, 2m2, 2m3, 2m4 and TRF2 in all cases. So the discussions stated for the tr13 DNA are likely conserved for the T3G and T9G DNA. In T9G where T9 is replaced by guanine, still T8 exists in the mutant DNA so T8 may have a stronger binding ability to an arginine residue at 447 position of TRF2 compared to a lysine residue at the same position. In T3G the different binding abilities of TRF1, TRF2 and the six mutants are caused by a phosphate at the position of 3 in DNA, so the similar comparative binding modes are observed in tr13 and T3G.

It is interesting to note that in G7C the comparative binding abilities of TRF1, TRF2 and the six mutants are different from their comparative abilities in tr13.

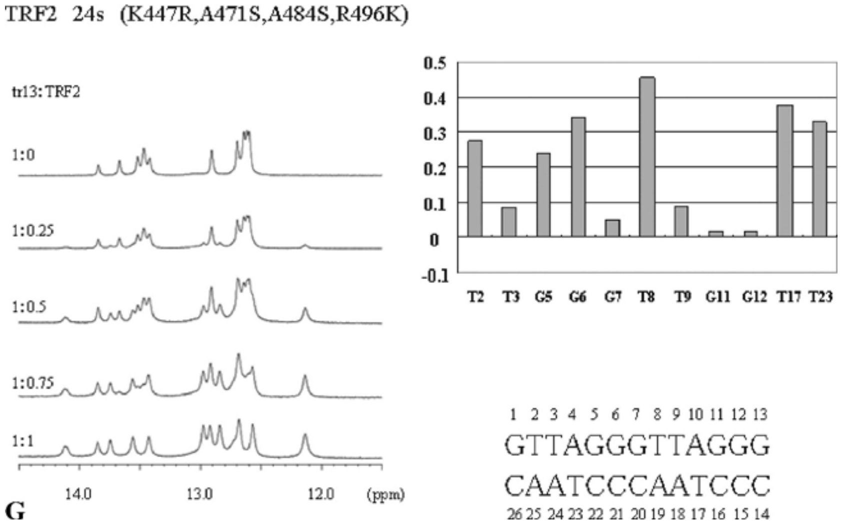

Fig. 4. (*Continued*)

Especially 24s has a similar binding ability with the wild-type TRF2 and the so weaker binding ability than TRF1, in contrast to the cases of tr13, T3G, and T9G. This may be caused by a replaced lysine residue at 496 position of TRF2, because 2m4 shows a weaker binding ability compared to the wild type TRF2. In G7C an arginine residue at 496 may interact with C7 or G20, so the difference of the binding abilities between TRF1 and TRF2 in G7C is not so great compared to the differences in tr13, T3G, and T9G. However, still arginine residue at 381 position in TRF1 is responsible for the stronger binding ability compared to TRF2 in which a lysine residue is located at 447.

Acknowledgments

This work was supported by a Collaborative of Regional Entities for the Advancement of Technological Excellence (CREATE) in Yokohama from JST, and

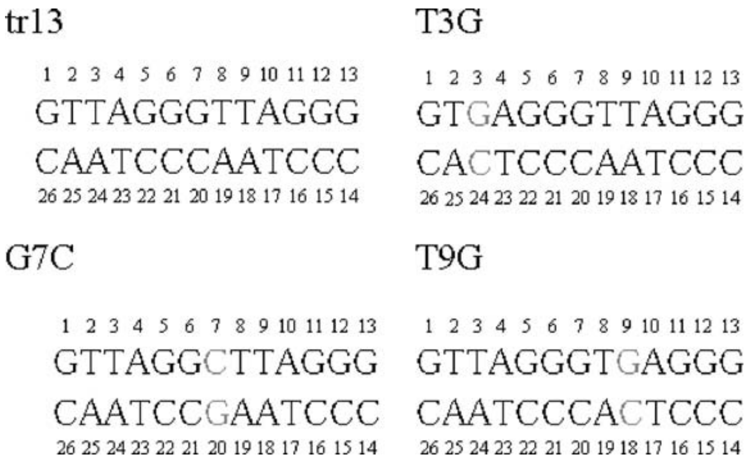
tr13
1 2 3 4 5 6 7 8 9 10 11 12 13
GTTAGGGTTAGGG
CAATCCCAATCCC
26 25 24 23 22 21 20 19 18 17 16 15 14
T3G
1 2 3 4 5 6 7 8 9 10 11 12 13
GTGAGGGTTAGGG
CACTCCCAATCCC
26 25 24 23 22 21 20 19 18 17 16 15 14
G7C
1 2 3 4 5 6 7 8 9 10 11 12 13
GTTAGGCTTAGGG
CAATCCGAATCCC
26 25 24 23 22 21 20 19 18 17 16 15 14
T9G
1 2 3 4 5 6 7 8 9 10 11 12 13
GTTAGGGTGAGGG
CAATCCCACTCCC
26 25 24 23 22 21 20 19 18 17 16 15 14

Fig. 5. The telomeric DNA sequence of wild type (trl3) together with the sequences of three mutants.

10mM HEPES-KOH pH6.8, 180mM KCl, 3mM EDTA, 0.003%X-100

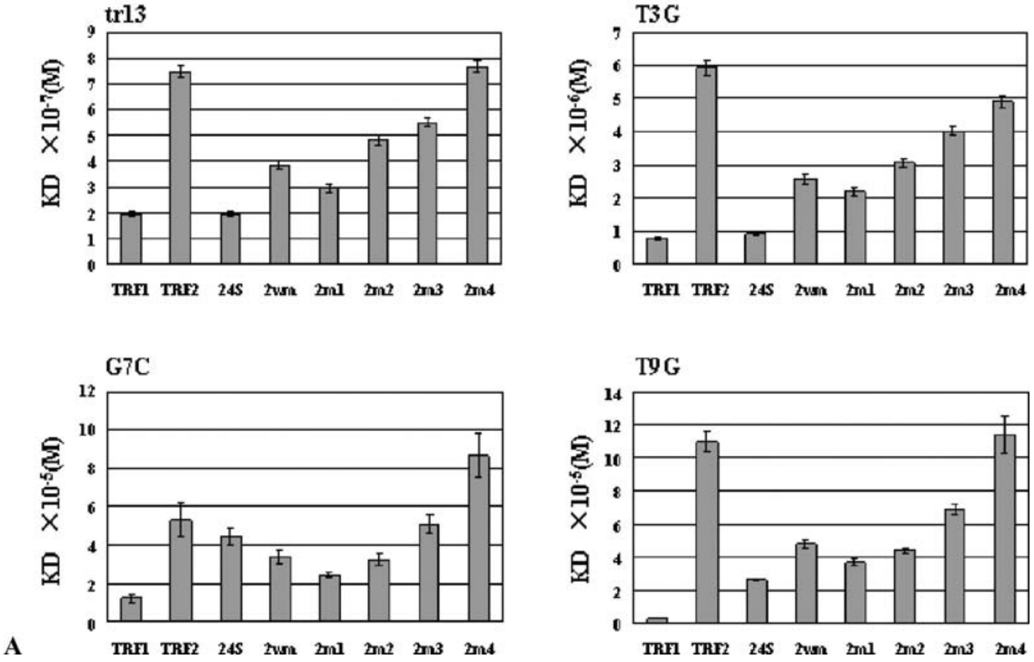

10mM HEPES-KOH pH6.8, 150mM KCl, 3mM EDTA, 0.003%X-100

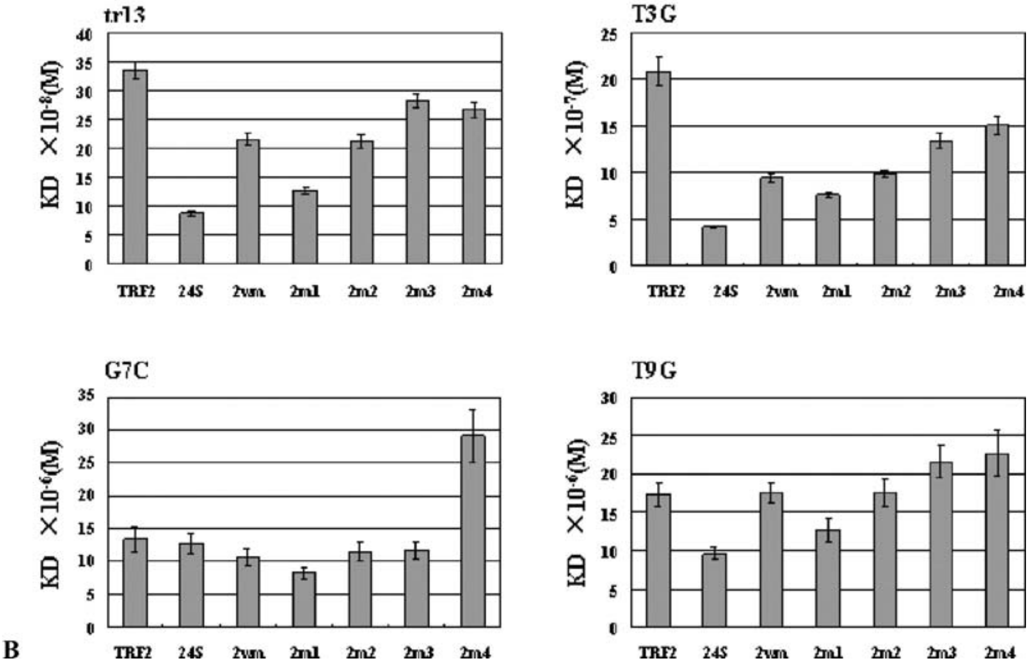

Fig. 6. The results of SPR analyses for equilibrium dissociation constant (Kd) values between DNA-binding domains (TRF1, TRF2, K447R, A471S, A484S, R496K, 2wm, and 24S) and the 13mer telomeric DNA (trl3) and the three mutant DNAs, T3G, G7C, and T9G in the buffer containing 10 mM HEPES-KOH, 3 mM EDTA, 180 mM KCl and 0.003% Triton X-100 (v/v) (pH6.8) (A) and 10mM HEPES-KOH pH6.8, 150mMKCl, 3mM EDTA ,0.003%X-100 (B).

a Project of Protein 3000, Transcription and Translation, and Grants in Aid for Scientific Research from MEXT.

References

1. Bilaud T, Brun C, Ancelin K, Koering CE, Laroche T, Gilson E. Nat. Genet. 1997;17:236–239.
2. Broccoli D, Smogorzewska A, Chong L, de Lange T. Nat. Genet. 1997;17:231–235.
3. Chong L, van Steensel B, Broccoli D, Erdjument-Bromage H, Hanish J, Tempst P, de Lange T. Science 1995;270:1663–1667.
4. Bianchi A, Smith S, Chong L, Elias P, T. de Lange, EMBO J. 1997;16:1785–1794.
5. Smith S, de Lange T. Trends Genet. 1997;13:21–26.
6. Gonda TJ, Gough NM, Dunn AR, de Blaquiere J. EMBO J. 1985;4:2003–2008.
7. Klempnauer KH, Sippel AE, EMBO J. 1987;6:2719–2725.
8. Nishikawa T, Okamura H, Nagadoi A, König D, Rhodes P, Nishimura Y. Structure 2001;9:1237–1251.
9. Hanaoka S, Nagadoi A, Nishimura Y. Protein Sci. 2005;14:119–130.
10. Ogata K, Hojo H, Aimoto S, Naka T, Nakamura H, Sarai A. *et al.* Proc. Natl Acad. Sci. U.S.A. 1992;89:6428–6432.
11. Ogata K, Morikawa S, Nakamura H, Sekikawa A, Inoue T, Kanai H. *et al.* Cell 1994;79:639–648.
12. Ogata K, Morikawa S, Nakamura H, Hojo H, Yoshimura S, Zhang R. *et al.* Nature Struct. Biol. 1995;2:309–320.

Part I, Section 2: Applications in Biological Sciences

Abbreviations

AFM: atomic force microscopy

AHT: average Hamiltonian theory

Bicelle: bilayered micelles

BPPLED: bipolar pulse longitudinal eddy current

BPT: bond polarization theory

CC: coupled cluster

CD: circular dichroism

CHF: coupled Hartree-Fock

CNDO: complete neglect of differential overlap

CP-MAS: cross polarization-magic angle spinning

CODEX: centerband-only detection of exchange

COSY: correlated spectroscopy

CPMG: Carr-Purcell-Meiboom-Gill

CRAMPS: combined rotation and multiple pulse spectroscopy

CRINEPT: cross-correlated relaxation-enhanced polarization transfer

CRIPT: cross-correlated relaxation induced polarization transfer

CS: chemical shift

CSA: chemical shift anisotropy

CSI: chemical shift imaging

CTDQFD: constant-time double-quantum filter

CTOCD: continuous transformation of the current density

DARR: dipolar-assisted rotational resonance

DAS: dynamic angle spinning

DEPT: distortionless enhancement by polarization transfer

DD-MAS: dipolar decoupled-magic angle spinning

DECORDER: direction exchange with correlation for orientation-distribution evaluation and reconstruction

DFS: double frequency sweep

DFT: density functional theory

DIPSHIFT: dipolar chemical shift

DNMR: dynamic NMR

DNP: dynamic nuclear polarization

DOQSY: double quantum spectroscopy

DOR: double rotation

DOSY: diffusion-ordered NMR spectroscopy

DPMAS: direct polarization magic angle spinning

DQ: double quantum

DQDRAW: double quantum, dipolar recovery with windowless sequence

DRAW: dipolar recovery with windowless sequence

DSO: diamagnetic spin orbital

EFG: electric field gradient

EEHT: exact effective Hamiltonian theory

EHT: effective Hamiltonian theory

ENDOR: electron nuclear double resonance

EPSI: echo planar spectroscopic imaging

EPR: electron paramagnetic resonance

ESRI: electron spin resonance imaging

Et-NOESY: exchange transferred nuclear Overhauser effect spectroscopy

EXSY: exchange spectroscopy

FDR: frequency selective dipolar recoupling

FOV: field of view

FPT: finite perturbation theory

FC: Fermi contact

GE-HMQC: gradient enhanced-heternuclear multiple quantum coherence

GIAO-CHF: gauge-independent atomic-orbitals coupled Hartree-Fock

GC: gas chromatograph

HETCOR: heteronuclear correlation

HMBC: heteronuclear multiple bond correlation

HMQC: heteronuclear multiple quantum correlation

HOHAHA: homonuclear Hartmann Hahn

HSQC: heteronuclear single quantum correlation

HPDEC: high power decoupling

IGLO: individual gauge for localized orbitals

INADEQUATE: incredible natural abundance double quatum transfer experiment

INDO: intermediate neglect of differential overlap

INEPT: insensitive nuclei enhancement by polarization transfer

LC-NMR: liquid chromatography-NMR

LDA: local density approximation

LDBS: locally dense basis set

LORG: localized orbitals local origin

LG-CP: Lee Goldburg-cross polarization

MAOSS: magic angle oriented sample spinning

MAS: magic angle spinning

MCSCF: multi-configurational self-consistent field

MD: molecular dynamics

MI: molecular imaging

MOVS: magnetically oriented vesicle systems

MQMAS: multiple quantum magic angle spinning

MREV-8: Mansfield-Rhim-Elleman-Vaughan 8 cycle

MRI: magnetic resonance imaging

MRFM: magnetic resonance force microscopy

MSREDOR: multi spin REDOR

NMR: nuclear magnetic resonance

NMR-MOUSE: NMR-mobile universal surface explorer

NOE: nuclear Overhauser enhancement

NOESY: nuclear overhauser and exchange spectroscopy

NQR: nuclear quadrupole resonance

ODF: order-director fluctuation

ONIOM: Our own n-layered integrated molecular Orbital + molecular mechanics

ONP: optical nuclear polarization

PET: positron emission tomography

PFG: pulsed field-gradient

PGSE: pulsed gradient-field spin echo

Photo-CIDNP: photochemically induced dynamic nuclear polarization

PISA: polarity index slant angle

PISEMA: polarization inversion spin exchange at magic angle

PM5: parametric method 5

PSO: paramagnetic spin orbital

QC: quantum computation

QEDOR: quadrupole echo double resonance

QED: quantum electrodynamics

QCPMG: quadrupolar Carr-Purcell-Meiboom-Gill refocusing pulse

QIP: quantum information processing

QM/MM: quantum mechanics/molecular mechanics

QRI: quantum resonance interferometry

PFG: pulse field gradient

RACO: relayed anisotropy correlation

RDC: residual dipolar coupling

REAPDOR: rotational echo adiabatic passage double resonance

REDOR: rotational echo double resonance

RFDR: radio frequency driven resonance

RMSD: root mean-square deviation

ROCSA: recoupling of chemical shift anisotropy

ROCSA-LG: recoupling of chemical shift anisotropy-Lee Goldburg

ROE: rotating frame Overhauser experiment

RR: rotational resonance

SAIL: stereo-array-isotope-labelling

SASS: switching angle sample spinning

scBCH: semi-continuous Baker-Campbell-Hausdorff

SDC: superdense coding

SEC-NMR: size exclusion chromatography-NMR

SEDOR: spin echo double resonance

SELFIDOQ: separated-local-field double quantum

SFAM: simultaneous frequency amplitude modulation

SOPPA: second order polarization propagator approximation

SOS: sum-over-states method

SQ: single quantum

SQUID: superconducting quantum interference device

SSNMR: solid state NMR

STD: saturation transfer difference spectroscopy

STRAFI: stray field magnetic resonance imaging

STO: Slater-type orbital

TB MO: tight-binding molecular-orbital

TOCSY: total correlation spectroscopy

TORQUE: T one rho quenching

TRAPDOR: transfer of populations in double resonance

TPPM: two pulse phase modulation

TROSY: transverse relaxation optimized spectroscopy

VFMAS: very fast magic angle spinning

water LOGSY: water-ligand observation by gradient spectroscopy

WISE: wide-line separation

XRD: x-ray diffraction

ZQ: zero-quantum

Optimization of MRI Contrast for Pre-Clinical Studies at High Magnetic Field

Yu-Ting Kuo[1,2] and Amy H. Herlihy[3]
[1]*Molecular Imaging Group, MRC Clinical Sciences Centre, Hammersmith Hospital Campus, Imperial College London;*
[2]*Department of Medical Imaging, Kahosiung Medical University, Kaohsiung, Taiwan; and*
[3]*Biological Imaging Centre, Imaging Sciences Department, MRC Clinical Sciences Centre, Hammersmith Hospital Campus, Imperial College London*

Introduction

This chapter discusses methods of optimizing contrast in magnetic resonance imaging (MRI) either by using the intrinsic properties of the tissue or by using contrast agents. In order to fully explain MRI contrast mechanisms, some MRI basic physics will also be discussed. The goal is to provide the tools to set up scans which will best visualize a target tissue or structure.

Physics Background for Contrast Optimization

Signal-to-Noise Ratio (SNR), Contrast-to-Noise Ratio (CNR), and Temporal Resolution

In setting up an MRI experiment, there are several basic questions that should be asked:

1. How much contrast do I need?
2. How much spatial resolution do I need?
3. How much temporal resolution do I need?

These questions will help determine an optimal scan sequence. On animal scanners, which are not quite as “push button” as clinical scanners, the scans will need to be tailored to the experiment. With a good idea of what is wanted and/or needed, the preliminary experiments can be reduced tremendously. As these points are being considered in the experimental design, it is worth recognizing that in MRI there is always a trade-off between signal-to-noise ratio (SNR), spatial resolution, and temporal resolution. As scanners improve technically, the trade-offs decrease, but they still exist and it is wise to recognize and understand why these trade-offs exist. This section will discuss the questions posed above and how to operate within the limitations intrinsic to MRI physics.

As a start, some of these terms need defining and the associated tools explained. These are some of the basic definitions needed to quantify MR images:

- *SNR*: Signal-to-Noise ratio is a measure of the quality of the image. A higher number is better. SNR is equal to the mean of the signal of the region of interest (ROI) divided by the standard deviation (SD) of the background noise (Figure 1).

$$\mathrm{SNR} = \frac{\text{Mean ROI signal}}{\text{SD noise signal}} \tag{1}$$

- *CNR*: Contrast-to-noise ratio provides an indicator of the level of contrast between two tissues/objects. CNR is defined as the difference in mean signal intensities between two ROIs divided by the SD of the noise (Figure 1).

$$\mathrm{CNR} = \frac{\text{Mean ROI}_1\text{ signal} - \text{Mean ROI}_2\text{ signal}}{\text{SD noise signal}} \tag{2}$$

- *Spatial resolution*: The size of the pixel (2D) or voxel (3D). The spatial resolution is the field of view (FOV) divided by the corresponding matrix size. If the image is two-dimensional, then the third dimension is the slice thickness.
- *Temporal resolution*: The time it takes to collect one scan or set of scans.
  Scan time = $T_R \times$ Phase encode matrix size $\times$ Number of averages, where T_R is the repeat time.
- *Pixel*: A picture element, i.e. one point of the image.
- *Voxel*: A volume element, i.e. a three-dimensional pixel element, it has length, width, and height.

Figure 1 provides an example of measuring SNR and CNR. Figures 2 and 3 provide examples of different image resolution.

Although the definitions above are relatively simple, there are several scan parameters that effect SNR, such as:

- FOV;
- slice thickness;
- number of averages;

Graham A. Webb (ed.), Modern Magnetic Resonance, 759–768.
© 2008 *Springer.*

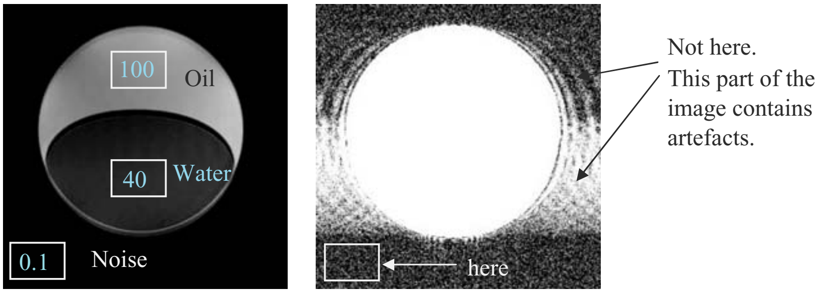

Fig. 1. The left hand image shows a scan of a vial with oil and water in it. The oil is the bright signal at the top and the water is the dark signal at the bottom. The SNR of the oil would be the mean of the signal of all the pixels in the square ROI divided by the SD of the signal of the pixels in the noise. The image on the right shows where to measure the noise (and where not to measure the noise). This image is the same as the image on the left, windowed to a level to show the background noise. It is important to measure the noise in the background noise, and not in signal generated by any image artifacts. Examples: SNR of the oil would be 100/0.1 = 1000, the SNR of the water would be 40/0.1 = 400. The CNR between the water and oil would be: (100 − 40)/0.1 = 600.

- receiver bandwidth;
- matrix size;
- Echo time (T_E), repeat time (T_R), and flip angle (FA).

These factors will affect the SNR in how much magnetization is available. We will assume that these parameters do not vary. Equation (3) gives this in detail.

The basic point to remember is that in the image a voxel describes how many protons contribute to the signal in a given time. If the voxel is decreased by decreasing the FOV, increasing the matrix size, or making the slice thinner, SNR will be lost simply because there are fewer protons in each voxel. If the voxel is increased, SNR will be increased. Similarly if the intrinsic signal within that voxel is altered by changing the T_E or T_R, the SNR will be affected. The hardware will also play a part in the amount of signal that is available, and is discussed briefly later in the chapter.

$$\text{SNR per voxel} \propto \frac{\mathrm{dim}_x\, \mathrm{dim}_y\, \mathrm{dim}_z \sqrt{N_x N_y N_z N_{\mathrm{avg}}}}{\sqrt{BW}} \qquad (3)$$

where N_x is the matrix size in x, N_y is the matrix size in y, and N_z is the matrix size in z. N_{avg} is the number of averages. BW is the receiver bandwidth. The voxel size in the x-direction is dim_x, the voxel size in the y-direction is dim_y, and the voxel size in the z-direction is dim_z. Voxel size is the FOV in a given direction divided by the matrix size in the same direction.

Equation (3) describes the three-dimensional case. If you have a multislice (2D) imaging sequence, then dim_z is the slice thickness and N_z is 1.

Temporal resolution is another issue to consider. For good temporal resolution good SNR at a fast speed is

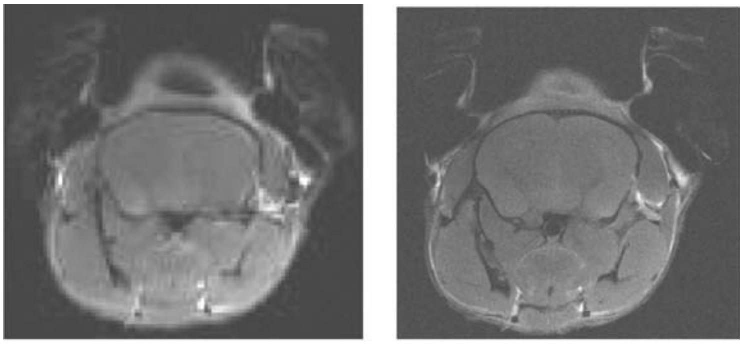

Fig. 2. *Left:* Low resolution scout/pilot image: FOV 30 × 30, matrix 256 × 128, 1 average, 2 mm slice thickness, in-plane resolution of 117 × 234 µm, 2-min scan. *Right:* FOV 30 × 30, matrix 512 × 512, 2 averages, 0.5 mm slice thickness, in-plane resolution of 58 × 58 µm, 25-min scan. Both images are spin-echo with T_R = 1500 ms and T_E = 20 ms.

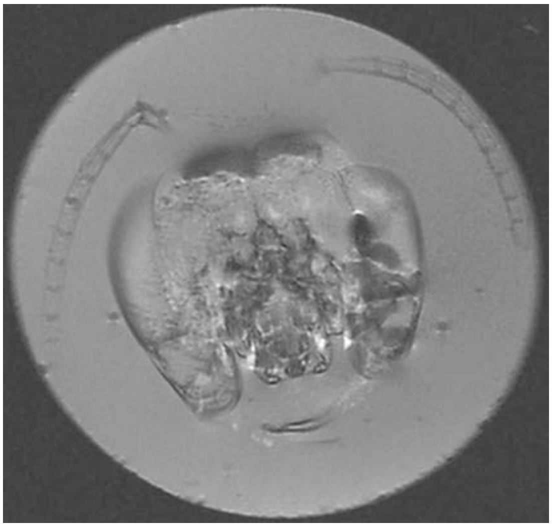

Fig. 3. Transverse image through the head of a bumblebee, fixed in agarose gel. Spin-echo, $T_R = 2000$ ms, $T_E = 20$ ms, FOV 12 mm × 12 mm, matrix 512 × 512, 100 averages, 0.5 mm slice thickness, in-plane resolution of 23 × 23 μm, 30-h scan. A good reference for MRI entomology is Ref. [117]. Image courtesy Dr R. B. Lotto.

required. Do not expect to obtain high SNR and ultra-high resolution if images must be collected in less than 1 s.

A simple rule of thumb for SNR—if the voxel volume is cut in half, then four times the averages will be needed to regain the same SNR. If the voxel is cut down to one-fourth of its original size, then 16 times as many averages will be needed to keep the same SNR. As spatial resolution goes down (i.e. the voxels become smaller), the SNR decreases. In order to counteract this, the BW can be decreased but there will be a hardware limit as to how short the BW can be. The number of averages can be increased too, but as the number of averages goes up so does the scan time and the temporal resolution increases. Typically it will take longer to collect a scan with very small voxel size—simply because the number of averages must be increased to maintain a minimum SNR. Figure 3 is an example of a very high resolution scan.

Very often one of the first questions asked about a new MRI scanner is: what resolution can be achieved? Although this *may* give some sort of benchmark of the strength of the gradients, it is by no means the correct question to ask about how the scanner behaves. It is far more important to know what SNR can be obtained at a given resolution. The gradients may be very strong, but poorly designed radio frequency (RF) coils will mean that although there is the *ability* to collect images at 10 μm, the SNR will be low due to poor RF coil design and the images will be very noisy. At times it is possible and desirable to work at a lower resolution and obtain very high SNR, rather than to work at a very high resolution at low SNR. If the anatomy is not visible because of low SNR then nothing has been gained.

Several groups are developing excellent MRI atlases of the mouse brain, mouse embryo, and full mouse body [1–4]. These provide good examples of different spatial and temporal resolutions. Table 1 provides some typical imaging parameters as starting places for standard anatomical scans.

If high spatial resolution is required, be prepared for significantly longer scan times as more averages will be required to maintain an adequate SNR. From Equation (3), it is obvious that in order to maintain the same SNR when decreasing FOV and matrix size, an increase in the number of averages is required.

Intrinsic MRI Contrast—T_1 and T_2

It is possible to obtain images with good SNRs that do not provide adequate information. If visualizing small structures is needed (such as distinguishing the anterior and posterior pituitary) then another scan technique may be required to improve the contrast between the two tissues. If the two different tissues have different T_1 or T_2 characteristics the sequence can be adjusted to optimize the contrast between the tissues. It may be appropriate to use contrast agents to accentuate one tissue over another.

There are two processes used to describe the basic MRI signal, T_1 and T_2. T_1 is the longitudinal relaxation time (also known as the spin-lattice relaxation time) and T_2 is the transverse relaxation time (also known as the spin–spin relaxation time). T_1 is the parameter that describes the speed at which the magnetization realigns itself with the main magnetic field after the RF pulse has been applied. Figure 4 shows a typical T_1 recovery curve. T_2 is the parameter that describes the speed at which the magnetization dephases in the transverse plane—thus the speed at which the signal decays after the RF pulse (Figure 5). Although this may seem complicated, the point to remember is that the T_2 will indicate the range of T_E values and T_1 will indicate the range of T_R values. For example, if the sample tissue has a very long T_1 (on the order 2 s) then if the scan has a short T_R (e.g. 100 ms), the longitudinal relaxation (governed by T_1) will not have recovered within the T_R and the image will have a low SNR. Using contrast agents to shorten the T_1 (such as gadolinium) will give higher SNR with shorter T_R values. Likewise, if the object has a very short T_2 value (solid tissues have shorter T_2s), then a short T_E will need to be used or the signal will have decayed. For a full discussion of the parameters T_1 and T_2, see Refs. [5,6]. The following web pages also provide good, easily accessible descriptions of T_1 and T_2.

Table 1: Standard scan parameters

Parameter	Whole body mouse at 4.7 T	Mouse brain at 9.4 T	Mouse brain at 9.4 T
2D or 3D acquisition	Multislice (2D)	Multislice (2D)	Volume (3D)
Scan type	Spin-echo	Spin-echo	Gradient-echo volume
RF coil	40 mm ID 100 mm long birdcage	25 mm ID birdcage	25 mm ID birdcage
T_R (ms)	2600	1200	13
T_E (ms)	16	15	4
FA	*	*	20–30
FOV (mm)	45 × 45	25 × 25	30 × 30 × 30
Matrix	256 ×192**	256 × 256	192 × 192 × 192**
Averages	4	4	2
Slice thickness (mm)	2	1	Collected as 192 slices 150 μm thick. Set by the FOV and matrix parameters above
Number of slices	60	30	
In-plane resolution	175 μm	95 μm	150 μm
Time to run scan	33 min	20 min	15 min

* Standard 90/180 flip angles are used for spin-echo scans.

** Zero-filled to 256. The use of 192 as a matrix size in the phase encode direction is a time saving tool, as well as increasing the voxel size which increases the SNR.

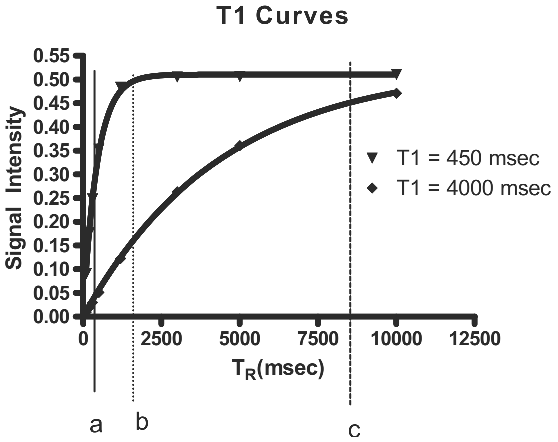

Fig. 4. Example T_1 Plot. This shows two T_1 curves, one with a short T_1 value of 450 ms (triangles) and one with a long T_1 value of 4000 ms (diamonds). The signal for the short T_1 will recover quickly and give a higher signal intensity on scans with short T_R values (imaging at point a on the plot). If you scan with a T_R of approximately 1500 ms (at point b) you will have very good contrast between these two tissues. If you scan with an extremely long T_R (8000 ms) then both tissues will have bright signal.

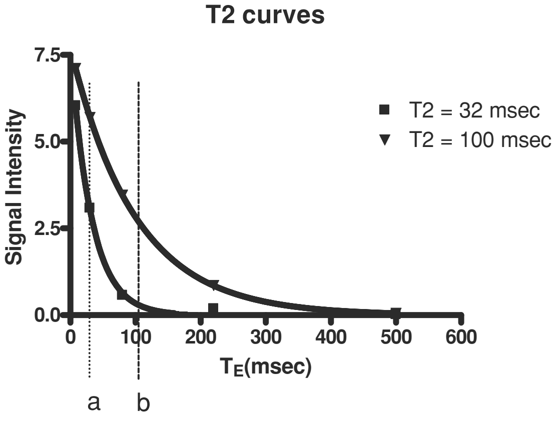

Fig. 5. Example T_2 plot. This shows two T_2 curves, one with a short T_2 value of 32 ms (squares) and one with a long T_2 value of 100 ms (triangles). The signal for the short T_2 will decay quickly and give a lower signal intensity on scans with longer T_E values (imaging at point b on the plot). If you scan with a T_E of approximately 20 ms (at point a) you will have good signal from both tissues.

- http://www.cis.rit.edu/htbooks/mri by Joseph P. Hornak
- http://www.mritutor.org/ by Ray Ballinger
- http://www.simplyphysics.com/ by Moriel NessAiver

The topic of T_1 and T_2 could be discussed for a very long time, but it is sufficient to recognize that, in general, it is advantageous to know the basic values for the tissue of interest at the field strength of the scanner. As the field strength increases, the T_1 values will get longer. T_2 is relatively unaffected by magnetic field strength. If the objects being scanned are items such as plant matter, the T_1 and T_2 values will almost certainly be significantly different than that of animal matter. T_1 and T_2 will also vary from *in vivo* to *ex vivo*. Table 2 compares human and animal tissue T_1 and T_2 values at different field strengths.

Very often images are described as T_1-weighted (T_1W) or T_2-weighted (T_2W). This will give an indication of the contrast mechanisms (for instance if the signal variations are dictated by T_1 parameters). There is a continuum of scans from proton-density (PD) to T_1W to T_2W, and often it is difficult to know what weighting the image has. In general, short T_R and short T_E will give a T_1W image, long T_R and long T_E will give T_2W image, and long T_R and short T_E will give a PD-weighted image. Borrowing from clinical definitions: a T_1W image will have bright fat and dark cerebral spinal fluid (CSF); a T_2W image will have dark CSF. These parameters can be used to observe physical changes, for example, T_1W images can be used to measure the amount of body fat, and T_2W scans can be used to measure the CSF space in the brain.

There are occasions when simply working with T_1 and T_2 parameters is not sufficient to observe fine variations in tissue structure. When alteration of scan parameters (T_E and T_R or FA) is not sufficient to enhance differences in tissue or to visualize pathological structures, one should consider administering contrast agents. A later section in this chapter goes in to the details of exogenous contrast agents.

Table 2: T_1 and T_2 values for mouse and human tissue at different field strengths

	T_1 (ms)		T_2 (ms)	
Tissue	9.4 T Mouse	1.5 T Human	9.4 T Mouse	1.5 T Human
Brain—gray matter	1900	920	40	100
Brain—white matter	1700	780	32	90
Muscle	2100	890	20	50
Fat	850	260	30	70

Field Strength and Hardware Considerations

When purchasing an MRI system, or considering which research group to collaborate with, the question may arise as to what is the field strength of the MRI scanner. In general, small-bore scanners are built at higher field strengths than clinical scanners. The primary reason for this is that whereas clinical scanners (1.5 or 3 T) operate with resolutions on the order of mm^3, on animal scanners, in order to see equivalent structures, the resolution needs to be on the order of μm^3. Since the signal in MRI is basically proportional to the volume, i.e. the number of protons that are in that volume, by moving to μm resolution the basic signal has just been decreased by an order of 10^9. By imaging at 9.4 T the field strength has tripled from 3 T, but not by a factor of 10^9. Typically one works at as high a magnetic field as possible to regain the SNR lost in the smaller resolution.

Although it is true that the higher the field strength the higher the SNR, there are drawbacks of working at higher field strengths, some of which are: susceptibility artifacts being more exaggerated, dielectric artifacts become an issue, and RF coils are harder to design. It is well worth checking the literature to investigate any imaging issues that might be relevant to the project at high field.

Gradient coil specifications may be another issue to consider. The gradient coil strength will dictate the minimum spatial resolution, the temporal resolution, and maximum gradient strength for scans such as diffusion-weighted imaging. Currently a minimum spec for a gradient coil for an animal system should be 20 G/cm (even this may be limiting for some imaging experiments). Issues will be cost, heat generated by the gradient coil, method of cooling the gradient coil and shim coils. See Ref. [5] for more details.

RF coils are also crucial to the performance of the whole MRI system. Manufactures often supply transmit and receive RF coils. These often have good performance for general imaging, but if a project requires significant SNR, then an RF coil may need to be built which is tailored to the anatomy. Small head coils are frequently built to image the mouse brain. These may be volume coils (if the target is the whole brain) or surface coils (if the target is only a structure at the surface of the brain). Cardiac, spine, or extremity coils may be required for targeting these anatomies. One of the most important issues related to RF coil design is filling factor: how well the anatomy fills the RF coil. If a large RF coil which holds the whole mouse comfortably is available, this may be a good tool for whole body imaging, but it most certainly will give inferior brain images when compared to a short RF coil which just holds the head. An RF coil, which matches the anatomy well, will provide better SNR, and thus better images.

To recap and formally answer the questions initially posed:

- You will need enough contrast to see your tissue of interest (verify the T_E and T_R values are correct, or use exogenous contrast agents).
- You will need enough SNR and small enough voxels to see the details (verify the matrix size and FOV are correct, and then make sure the RF coil is adequate and there are sufficient averages to provide enough SNR. Also verify the T_E and T_R are correct for the T_1 and T_2 of the tissue.)
- You will need enough temporal resolution to see the pharmacokinetic change or change due to flow. To shorten the scan time, consider shortening TR, reducing the number of averages or the size of the phase encode matrix.

For more information on the basics of MRI physics, see Refs. [5,6].

MR Contrast Agents for Animal Imaging Studies

Why MR Contrast Agents?

Of various imaging techniques, MRI has better soft-tissue contrast than other modalities, such as computed tomography (CT) for example; however, it is still necessary to obtain further characterization by enhancing the difference in signal intensity (SI) between lesion and normal tissue or the difference between different tissues (i.e. CNR). Administering MR contrast agents, in addition to field strength of magnet and scanning pulse sequence design, plays an important role by affecting the water relaxation of tissue or changing its susceptibility effect in the magnetic field. Invaluable imaging information can be obtained by proper use of contrast agents. Clinically, MR contrast agent administration has been extensively used since early 1980s in lesion detection, cancer staging, determining vascularity of tumor, assessment of tissue perfusion and viability; it has also become an essential part of contrast-enhanced MR angiography (CEMRA).

Classification and Mechanism of Contrast Agents

T_1 vs. T_2 Agents

Unlike iodinated contrast for X-ray and CT, MR contrast agents cannot be visualized directly. However its effect on SI change can be observed on MR images by changing the tissue's T_1 and T_2 relaxation times. The SI after administering contrast agents is a function of water concentration of the given agent and T_1, T_2 relaxation times of the tissue. There are a large number of MR contrast agents being applied to human and animal work. Basically, these contrast agents can be divided into two categories, namely, the T_1 and T_2 agents. The T_1 agents affect dominantly the T_1 relaxation time, and therefore the difference in SI between different tissues can be highlighted on T_1W images. Paramagnetic ions such as Gd^{3+}, Mn^{2+}, and Fe^{3+} with unpaired electrons belong to this group. The second group, T_2 agents, such as superparamagnetic iron oxide (SPIO) particles, cause significant magnetic susceptibility effects (especially decreasing the T_2 or T_2^* relaxation times) in the tissue where the contrast been taken up. This effect causes loss of SI, and is demonstrated better on T_2W images than on T_1W ones, and especially on gradient-echo (GRE) or echo-planner (EPI) sequences that are more sensitive to the magnetic susceptibility effect than spin-echo sequences.

Non-specific vs. tissue-specific agents

MR contrast agents can also be classified as non-specific and tissue-specific. Initially, non-specific MR contrast, such as the well-known gadolinium chelate, Gd-DTPA, was developed. It stays in the blood stream and extracellular interstitial tissue space for a relatively short time (half-life on the order of 45 min) and then is largely excreted from the body via the kidney and urinary system. It serves well in many clinical conditions as these contrast agents deposit in some pathological conditions that contain extra-large interstitial space. For example, the lesions in the case of various brain inflammation or tumors that compromise the blood–brain barrier (BBB) become strongly enhanced on T_1W images after intravenous administration of Gd-DTPA (Gadopentetate dimeglumine, Magnevist, Schering AG). If the magnet is equipped with an efficient gradient system, non-specific contrast agents are also used to perform contrast-enhanced dynamic MRI and CEMRA. However, in order to enhance the SI of target structures and further increase the lesion conspicuity, specific contrast agents targeting specific tissues or staying in blood circulation for longer time were thus developed.

For example, attachment of a chemical structure to non-specific Gd-DTPA allows the new compounds to cross the cell membrane of some specific tissues, and they thus become tissue-specific. Gd-BOPTA (Gadobenate dimeglumine, MultiHance, Bracco Diagnostics) and Gd-EOB-DTPA (Gadoxetic acid disodium, Eovist, Berlex Laboratories) are examples of hepatocyte-specific T_1 agents. Furthermore, these agents are eliminated by dual excretory routes (renal and biliary), and, therefore, the bile duct system can also be highlighted on T_1W images as well. A manganese-based paramagnetic contrast agent, Mn-DPDP (Mangafodipir trisodium, Teslascan, Nycomed AS), has also been used in enhancement of tissues with active metabolic processes, such as the liver, pancreas, and heart.

Iron oxide particles like SPIO is another group of tissue-specific MR contrast agent. They shorten both T_1 and T_2 relaxation times of tissue. Its dominant T_1 or T_2 effect, blood half-time and distribution to reticuloendothelial system (RES) are variable with the particle or cluster size. Large particles, such as AMI-25 (Ferumoxides, Feridex, Berlex Laboratories), 80–150 nm in diameter, are phagocytosed rapidly by RES (mainly the liver and the spleen) and with dominant T_2 or T_2^* effect; thus they can be regarded as RES-specific agents on T_2W sequences. On the contrary, smaller particles are phagocytosed slowly mainly by lymph nodes and remained in the blood stream longer than larger ones and with less efficient T_2 or T_2^* shortening. Therefore, the small-particle iron oxide or sometimes called ultrasmall superparamagnetic iron oxide (USPIO) agents, such as AMI-227 (Ferumoxtran, Advanced Magnetics), 20–40 nm in diameter, can be used as blood-pool agents by taking advantage of their longer half-life and T_1 shortening effect, although they do have T_2 or T_2^* effect. Ferrixan (Resovist, Schering AG), 60 nm mean diameter, is used as both a RES-specific agent in detecting liver lesions and a blood-pool T_1 agent to characterize the hemodynamics of lesion.

In addition to the tissue-specific contrast mentioned above, by changing the particle size of SPIO or modifying gadolinium-based agents, cell-labeling or receptor-directed MRI techniques and numbers of "smart" MR contrast agents for detecting biological processes are also under intensive research [7–10].

Applications of Contrast Agents in Animal Models

Central Nervous System

Gadolinium Chelates for Focal Lesion Detection. Since most of the brain structures are covered by BBB, gadolinium chelates do not enhance normal brain parenchyma significantly. However, administration of gadolinium-based chelates helps to visualize pathology that compromises the BBB by leaking into extracellular space. Figure 6 demonstrates sclerotic plaques in the cerebellum of a genetically modified mouse with multiple sclerosis. The plaques develop a high signal intensity after intraperitoneal Gd-DTPA injection.

Manganese Chloride for Nerve Tracking and Demonstrating Neuronal Activation. Manganese chloride ($MnCl_2$) is not appropriate for clinical use in human because of its toxicity. However, it is useful for nerve tracking and demonstrating neuronal activation in animal MRI as it is a potent T_1 agent and can cross voltage-gated Ca^{2+} channels and be transported actively along the axon. Several studies have been done successfully to delineate neuronal architecture (Figure 7) and neuronal physiology by this technique, manganese-enhanced MRI (MEMRI) [11–15].

Gadolinium Chelates and SPIO in Brain Perfusion Images. The perfusion-weighted image is a MR technique which can evaluate perfusion at the capillary level. This particular technique can be done by injection of T_1 contrast agent [16]. Both gadolinium chelates and SPIO (such as USPIO) agents can be used for this purpose, although the advantages, disadvantages, pulse sequences, and MR hardware

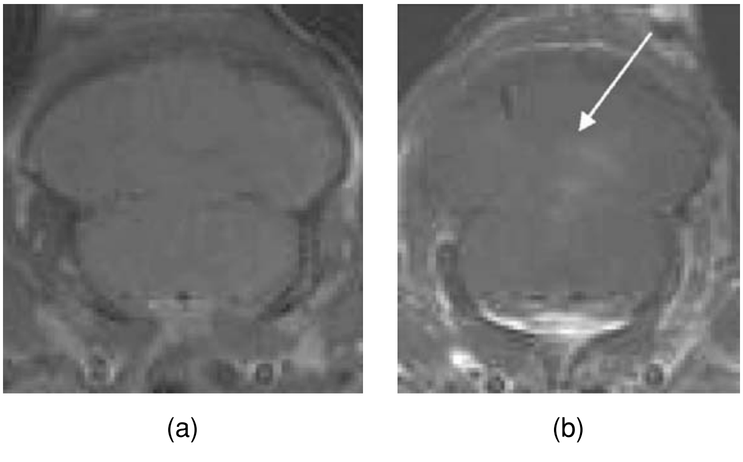

Fig. 6. The spin-echo T_1-weighted images (a) before and (b) after intraperitoneal injection of Gd-DTPA in a transgenic mouse of multiple sclerosis (MS) show significant enhancement over MS plaques (arrow). Images courtesy Drs D. Altmann and S. Ellmerich.

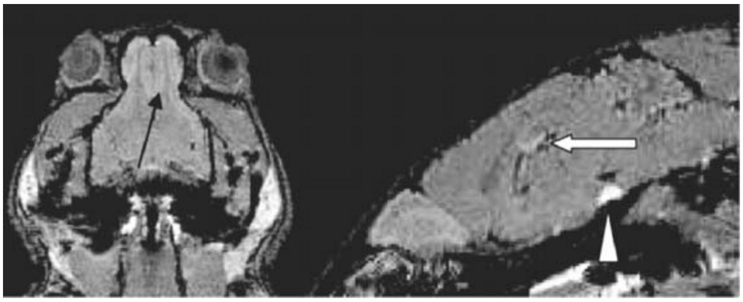

Fig. 7. The 3D FLASH T_1-weighted acquisition with coronal (A) and sagittal (B) reconstruction images of a C57BL/6 mouse after intravenous infusion of $MnCl_2$ show normal layering structures at both sides of the olfactory bulb (black arrow). Also noted is the intense enhancement of the pituitary gland (arrowhead) and choroid plexus in lateral ventricle (white arrow).

requirements for them are different. Several studies with this technique and contrast agents have been done to evaluate neural pathologies such as stroke in animal models [17–19].

Cardiovascular System

Gadolinium Chelates for Heart Imaging. Both in animal models and in clinical human work gadolinium chelates have been used not only in evaluating perfusion of myocardium during the first-pass of the contrast agent on T_1W images but also in depicting the scarred myocardial tissues after infarction on the delayed images [20–23]. Owing to relatively unlimited FOV coverage of heart by MRI (as compared with echocardiography) and the use of contrast agent, contrast-enhanced MRI has become an increasingly important modality to evaluate cardiac pathologies [24,25]. MR techniques have also successfully provided opportunities for cardiac intervention through specially designed catheters and through monitoring therapeutic effect [26]. Also thanks to the development of contrast labeling technique, MRI is able to help the delivery of stem cell therapy in animals by visualizing iron-labeled mesenchymal stem cells [27,28].

Manganese-based Contrast in Determining Viable Myocardium After Infarction. The myocardial enhancement mechanism of manganese-based agents is different from that of gadolinium agents. Manganese agents are taken up by viable myocardium that contains active Ca^{2+} channels; however, gadolinium agents are leaked to the interstitial space due to cell disintegration. Evidence shows that gadolinium also diffuses into oedamatous areas after an infarction, which results in an overestimation of the infarction size [29]. The timing for gadolinium-enhanced MRI to accurately determine the infarction size is also critically important [30]. In a comparative study, manganese-based contrast agents were more accurate in determining the infarct size than gadolinium-based agents [21]. The concerns of manganese agents are its toxicity and competitive nature with calcium ion, which may cause negative inotropic effect to the heart at risk of ischemia. Also because of this nature, in animals, MEMRI also provides the chance to survey the inotropy of the heart [31]. In a recent study, manganese-based contrast was even able to depict the reversible functional deficit of myocardium after episodes of brief ischemia [32].

Gadolinium Chelates and Iron Oxide in CEMRA. Both gadolinium chelates and compounds containing iron oxides have been successful in depicting animal major vascular structures *in vivo* on MRI [33–35]. The main difference between the two groups of contrast agents is that most of the extracellular gadolinium chelates remain in the blood vessels for a relatively short time; USPIO stays in circulation for longer period. Consequently, CEMRA relies on first-pass T_1 shortening effect when using extracellular gadolinium chelates; on the contrary, USPIO as blood-pool agents provide a wider temporal scanning window.

Oncology

Gadolinium Agents in Evaluating Tumor Angiogenesis. Understanding tumor angiogenesis is important to access the pathophysiology of various malignant lesions. Blocking angiogenesis is one method of modern cancer treatment. Detecting or quantifying angiogenesis noninvasively and *in vivo* is attracting increasing interest in cancer research. Gadolinium chelates not only successfully depicted major vascular vessels on MRI, but can also be modified chemically into larger polymers, capable of surveying angiogenesis in certain animal models [33]. By exploiting contrast-enhanced MRI techniques, monitor and guide anti-angiogenetic treatments have been feasible in some studies [36]. The accuracy of MRI in detecting angiogenesis by using different contrast agents is under active investigation.

Targeted SPIO in Detecting Tumor Necrosis (apoptosis). MR spectroscopy (MRS) has been able to depict the biochemical information of tissue and is thus able to identify the apoptotic part of tissue. However, MRS is still not sensitive and lacks of high spatial resolution images when applied *in vivo*. Zhao *et al.* found that *in vivo* MRI was able to detect apoptotic cells of malignant tumor under chemotherapy at early stages by using the conjugation of SPIO and a specific protein called synaptotagmin I [7]. This achievement further expands MRI in the field of oncology by visualizing specific parts of malignant lesions in high spatial resolution MR images.

Conclusion

With the tools described in this chapter, it is possible to begin designing imaging protocols to visualize normal and abnormal structures with MRI. Depending on the area of research one may only need to have anatomical images, where a standard MR scan will be sufficient, but if one needs to track the progression of tumor growth, brain lesion activity or more complicated targets, then exogenous contrast agents may make the job, not only easier, but also possible.

As new contrast agents are being developed for the field of molecular imaging, the area of imaging with contrast agents will be expanding. It may soon be possible to target a contrast agent to specific tissues providing exquisite specialized images of single nuclei of the brain.

Acknowledgement

We would like to thank Luis Alberto Hinostroza Orellana *por inspiratio*.

References

1. Johnson GA, Cofer GP, Gewalt SL, Hedlund LW. Morphologic phenotyping with MR microscopy: the visible mouse. Radiology. 2002;222(3):789–93.
2. Kovacevic N, Henderson JT, Chan E, *et al*. A three-dimensional MRI atlas of the mouse brain with estimates of the average and variability. Cerebral Cortex 2005;15(5):639–45.
3. Dhenain M, Ruffins SW, Jacobs RE. Three-dimensional digital mouse atlas using high-resolution MRI. Dev. Biol. 2001;232(2):458–70.
4. Natt O, Watanabe T, Boretius S, Radulovic J, Frahm J, Michaelis T. High-resolution 3D MRI of mouse brain reveals small cerebral structures in vivo. J. Neurosci. Methods. 2002;120(2):203–9.
5. Haacke EM, Brown RW, Thompson MR, Venkatesan R. Magnetic resonance imaging: physical principles and sequence design. John Wiley and Sons, Inc: New York, NY, 1999.
6. NessAiver M. All you really need to know about MRI Physics. Harbor Duvall Graphics: Baltimore, 1997.
7. Zhao M, Beauregard DA, Loizou L, Davletov B, Brindle KM. Non-invasive detection of apoptosis using magnetic resonance imaging and a targeted contrast agent. Nat. Med. 2001;7(11):1241–44.
8. Rudelius M, Daldrup-Link HE, Heinzmann U, *et al*. Highly efficient paramagnetic labelling of embryonic and neuronal stem cells. Eur. J. Nucl. Med. Mol. Imaging. 2003;30(7):1038–44.
9. Modo M, Mellodew K, Cash D, *et al*. Mapping transplanted stem cell migration after a stroke: a serial, in vivo magnetic resonance imaging study. Neuroimage.2004;21(1):311–17.
10. Meade TJ, Taylor AK, Bull SR. New magnetic resonance contrast agents as biochemical reporters. Curr. Opin. Neurobiol. 2003;13(5):597–602.
11. Lin YJ, Koretsky AP. Manganese ion enhances T1-weighted MRI during brain activation: an approach to direct imaging of brain function. Magn. Reson. Med. 1997;38(3):378–88.
12. Watanabe T, Radulovic J, Spiess J, *et al*. In vivo 3D MRI staining of the mouse hippocampal system using intracerebral injection of MnCl2. Neuroimage. 2004;22(2):860–67.
13. Allegrini PR, Wiessner C. Three-dimensional MRI of cerebral projections in rat brain *in vivo* after intracortical injection of MnCl2. NMR Biomed. 2003;16(5):252–56.
14. Aoki I, Tanaka C, Takegami T, *et al*. Dynamic activity-induced manganese-dependent contrast magnetic resonance imaging (DAIM MRI). Magn. Reson. Med. 2002;48(6):927–33.
15. Pautler RG, Koretsky AP. Tracing odor-induced activation in the olfactory bulbs of mice using manganese-enhanced magnetic resonance imaging. Neuroimage. 2002;16(2):441–48.
16. Barbier EL, Lamalle L, Decorps M. Methodology of brain perfusion imaging. J. Magn. Reson. Imaging.2001;13(4): 496–520.
17. Vexler ZS, Roberts TP, Bollen AW, Derugin N, Arieff AI. Transient cerebral ischemia. Association of apoptosis induction with hypoperfusion. J. Clin. Invest. 1997;99(6):1453–59.
18. Veldhuis WB, Derksen JW, Floris S, *et al*. Interferon-beta blocks infiltration of inflammatory cells and reduces infarct volume after ischemic stroke in the rat. J. Cereb. Blood Flow Metab. 2003;23(9):1029–39.
19. Dijkhuizen RM, Asahi M, Wu O, Rosen BR, Lo EH. Rapid breakdown of microvascular barriers and subsequent hemorrhagic transformation after delayed recombinant tissue plasminogen activator treatment in a rat embolic stroke model. Stroke. 2002;33(8):2100–04.
20. Lim TH, Choi SI. MRI of myocardial infarction. J. Magn. Reson. Imaging. 1999;10(5):686–93.
21. Flacke S, Allen JS, Chia JM, *et al*. Characterization of viable and nonviable myocardium at MR imaging: comparison of gadolinium-based extracellular and blood pool contrast materials versus manganese-based contrast materials in a rat myocardial infarction model. Radiology. 2003;226(3):731–38.
22. Weiss CR, Aletras AH, London JF, *et al*. Stunned, infarcted, and normal myocardium in dogs: simultaneous differentiation by using gadolinium-enhanced cine MR imaging with magnetization transfer contrast. Radiology.2003;226(3):723–30.
23. Kim RJ, Fieno DS, Parrish TB, *et al*. Relationship of MRI delayed contrast enhancement to irreversible injury, infarct age, and contractile function. Circulation. 1999;100(19):1992–2002.

24. Fieno DS, Hillenbrand HB, Rehwald WG, *et al*. Infarct resorption, compensatory hypertrophy, and differing patterns of ventricular remodeling following myocardial infarctions of varying size. J. Am. Coll. Cardiol.2004;43(11): 2124–31.
25. Lekx KS, Prato FS, Sykes J, Wisenberg G. The partition coefficient of Gd-DTPA reflects maintained tissue viability in a canine model of chronic significant coronary stenosis. J. Cardiovasc. Magn. Reson. 2004;6(1):33–42.
26. Rickers C, Gallegos R, Seetharamaraju RT, *et al*. Applications of magnetic resonance imaging for cardiac stem cell therapy. J. Interv. Cardiol. 2004;17(1):37–46.
27. Dick AJ, Guttman MA, Raman VK, *et al*. Magnetic resonance fluoroscopy allows targeted delivery of mesenchymal stem cells to infarct borders in Swine. Circulation. 2003;108(23):2899–904.
28. Hill JM, Dick AJ, Raman VK, *et al*. Serial cardiac magnetic resonance imaging of injected mesenchymal stem cells. Circulation. 2003;108(8):1009–14.
29. Saeed M, Lund G, Wendland MF, Bremerich J, Weinmann H-J, Higgins CB. Magnetic resonance characterization of the peri-infarction zone of reperfused myocardial infarction with necrosis-specific and extracellular nonspecific contrast media. Circulation. 2001;103(6):871–76.
30. Oshinski JN, Yang Z, Jones JR, Mata JF, French BA. Imaging time after Gd-DTPA injection is critical in using delayed enhancement to determine infarct size accurately with magnetic resonance imaging. Circulation. 2001;104(23):2838–42.
31. Hu TC, Pautler RG, MacGowan GA, Koretsky AP. Manganese-enhanced MRI of mouse heart during changes in inotropy. Magn. Reson. Med. 2001;46(5):884–90.
32. Krombach GA, Saeed M, Higgins CB, Novikov V, Wendland MF. Contrast-enhanced MR delineation of stunned myocardium with administration of MnCl(2) in rats. Radiology. 2004;230(1):183–90.
33. Fink C, Kiessling F, Bock M, *et al*. High-resolution three-dimensional MR angiography of rodent tumors: morphologic characterization of intratumoral vasculature. J. Magn. Reson. Imaging. 2003;18(1):59–65.
34. Ruehm SG, Christina H, Violas X, Corot C, Debatin JF. MR angiography with a new rapid-clearance blood pool agent: initial experience in rabbits. Magn. Reson. Med. 2002;48(5):844–51.
35. Wacker FK, Wendt M, Ebert W, Hillenbrandt C, Wolf KJ, Lewin JS. Use of a blood-pool contrast agent for MR-guided vascular procedures: feasibility of ultrasmall superparamagnetic iron oxide particles. Acad. Radiol. 2002;9(11):1251–54.
36. Thomas AL, Morgan B, Drevs J, *et al*. Vascular endothelial growth factor receptor tyrosine kinase inhibitors: PTK787/ZK 222584. Semin. Oncol. 2003;30(3 Suppl 6):32–8.

The Application of *In Vivo* MRI and MRS in Phenomic Studies of Murine Models of Disease

Po-Wah So and Jimmy D. Bell
Molecular Imaging Group, MRC Clinical Sciences Centre, Hammersmith Hospital Campus,
Imperial College London, London W12 OHS, UK

Introduction

The genomic revolution has rapidly expanded in recent years from unravelling the human genome to sequencing the genome of many other species, including, mice, insects, and plants. Determining the role of individual genes in the pathophysiology of many human and animal diseases has now become a reality. A variety of *in vitro* methods have been developed to assess gene expression at both the cellular and organ levels, allowing ever increasing understanding of the genetic control of disease development. However, it has also become clear that to fully understand the role of many genes in health and disease, it is necessary to determine their function in the context of a whole functioning organism. Indeed, a number of studies have recently shown that the relative expression of some candidate genes is significantly modulated not only by environmental factors but also by the genetic background of the organism [1]. However, the currently available *in vitro* techniques cannot be readily applied to developmental or longitudinal studies, thus limiting their usefulness in elucidating gene expression and function.

This has necessitated the development of non-invasive techniques that can allow the detection and quantification of gene expression, function, and modulation *in vivo*, including positron emission tomography, bioluminescence, and magnetic resonance imaging/spectroscopy (MRI/MRS). Further, the exponential increase in the number of murine models available for basic research over the past 5 years, has spurred an extraordinary interest in methods for objective and accurate phenotyping. Non-invasive imaging techniques are therefore at the forefront of current biological and clinical research and are likely to play a pivotal role in the post-genomic era. In this chapter, we describe the key areas of pre-clinical research where MRI and MRS are being applied, together with those areas, which are likely to become important in future translational research.

A schematic description of the MR approach to phenotyping murine models is illustrated in Figure 1. The strategy can be broadly divided into MRI- and MRS-based techniques. Combination of these two MR techniques in the phenotyping protocol produces an accurate characterization of a whole animal or individual organs.

Magnetic Resonance Imaging

MRI allows non-invasive and three-dimensional visualization of the whole body and structures within the body such as internal organs, providing both highly accurate qualitative and quantitative data. MRI is possible with a variety of nuclei, ^{1}H, ^{19}F, ^{31}P, ^{23}Na but ^{1}H MRI is most commonly used and is assumed in this chapter unless otherwise stated.

The image quality achieved with MRI represents a compromise between imaging time (sampling duration) and multiple factors that affect spatial resolution. Factors affecting resolution include tissue water content, pixel size, receiver coil size, sampling bandwidth, magnetic field strength, and pulse sequence design. For example, at 9.4 T, employing a customized radio-frequency transmit/receive bird-cage coil of 25 mm diameter, a standard spin-echo sequence with repetition time (TR) of 1500 ms and echo time (TE) of 20 ms, will yield 136 μm in-plane resolution and 0.5 mm slice thickness in ∼2 min, whereas a scan of ∼5 h duration can provide resolution as high as 68 μm in-plane resolution with 0.5 mm slice thickness (Figure 2). Hence, the term "magnetic resonance histology" (MRH) [2], referring to the use of MRI to characterize tissue structure approaching resolutions achievable by histological methods has become a reality. Small animal MRI and MRH tend to be used interchangeably although strictly speaking the latter refer to images acquired with spatial resolution of less than 100 μm in at least two dimensions. There are many excellent review articles describing the evolving MR technology, MR physics, and hardware design for MRH [2–5], and the readers are referred to these for further details.

Magnetic Resonance Histology

In general, during MRH scanning, tissues are preserved either by direct immersion in fixative or fixed *in situ* by

Graham A. Webb (ed.), Modern Magnetic Resonance, 769–785.
© 2008 *Springer.*

Figure 1. Overview of the phenotyping protocol using MR methodology.

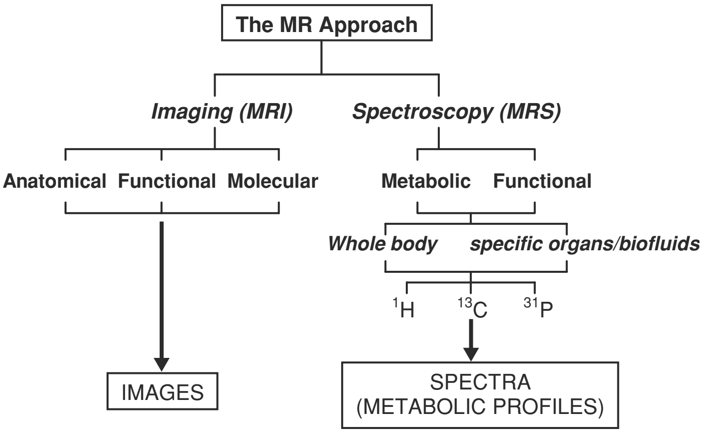

intravascular perfusion of fixative, with or without supplementation with MR contrast agents. Specimens may be wrapped in a soft, water impermeable film for MRI [6,7]. Alternatively, the organs may be immersed or embedded in a medium, which would overcome susceptibility artifacts arising from tissue–air interfaces. Ideally, the medium should prevent dehydration and decomposition of the sample; have no ^{1}H signal; be non-toxic and sufficiently viscous to prevent motion of the sample during scanning. Media used include perfluoropolyether or Fomblin [8,9]or a semi-solid substance, e.g. 1% gelling agar [10], 3% agarose [11], 1% agarose gel doped with magnetite or fluorocarbon [12]. Note that formalin is generally avoided as an embedding medium, as it has a strong MR signal leading to difficulties in discerning the specimen surface. Of the embedding media options available, the use of Fomblin or fluorocarbon is near ideal, as neither have ^{1}H nuclei, and both are non-toxic, non-flammable, and prevents dehydration and decomposition of the specimen for up to 2 days [13].

To maximize the value of MRH, MRI has been improved by the introduction of high magnetic field strengths, improved encoding strategies, and specialized radio-frequency receiver coils [14–17]. This has lead to the production of images with exquisite anatomical detail, visualized non-destructively, and producing data in a 3D format. Thus, the disadvantages of serial sectioning required for conventional histological methods, including dissection of the sample, distortion and misalignment of slices during computer registration, and difficulty in automation, can be avoided [18]. It is important to point out that although image resolution can be improved by employing higher magnetic field strengths, this is not without some drawbacks. With higher field strengths, there is an increase in the difference between the resonance frequencies of water and fat, the major components of the body, leading to greater chemical shift artifacts. At 4.7 T, the artifacts are minimal but at higher fields, the artifacts are significant due to greater difference between the water and fat resonance frequencies at higher fields (Figure 3). Such artifacts may be removed by performing MRI with saturation of the water or fat signal leading to a fat-only or water-only image.

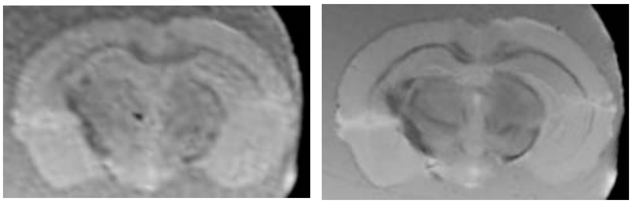

Scan time (mins)	2	300
Number of averages	1	40
Resolution (μm)	136	68

Figure 2. Midtransverse MRI images of the brain of a C57BL/6J mouse embedded in 1% agarose at different resolutions obtained at 9.4 T (TR/TE, 1200/20 ms; field of view, 35 mm × 35 mm; 256 × 128 matrix size and zero-filled to 1024 × 1024).

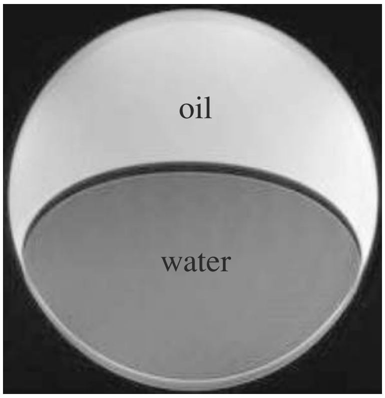

Figure 3. Chemical shift artifact in the MRI image at 9.4 T from a sample containing oil and water. The oil is shifted upwards in the image and note that even the small layer of oil around the edge of the sample has shifted up as well. The black band in the middle is a signal void where the oil has shifted away from the water.

Resolution and SNR are not the only criteria for successful imaging. Signal differences must exist between different structures for their delineation in the MR image, i.e. an adequate contrast-to-noise ratio between/within tissue(s) is required. MR techniques are unique in that several contrast mechanisms, including T_1, T_2, diffusion, etc., with or without the use of contrast agents may be employed. Thus, a mixture of MRI sequences may be enlisted to fully characterize morphology of the whole body or individual organs. However, with the advent of ultra-high field strength systems, further research is required to understand and exploit the alteration in T_1 associated with higher field strengths to enhance the morphological information obtained.

An alternative method to increase resolution while maintaining SNR, is to collect three-dimensional volumes data-sets (3D MRI), which involves collection of volumes rather than the routine 2D-multislice dataset. However, obtaining 3D volumes requires the use of 3D encoding, resulting in large image arrays. The greater the resolution required, the greater the image array produced. Thus, computers of sufficient memory and disk space are required to accommodate and reconstruct the large datasets, e.g. the raw data for a 512 μm × 512 μm × 512 μm image array is 1 Gb with reconstruction time of 1 h [19]. Thus, an important consideration in phenomic studies is the development of computational methods to deal with the vast amounts of data generated.

Phenomics

As well as anatomical data, MRI can provide functional and molecular information. Functional data can be provided by functional MRI (fMRI) principally in the brain or through the use of contrast agents such as manganese chloride ($MnCl_2$). The former has been used for dynamic assessments of phenotyping murine models [20,21] while the potential of the latter has yet to be fully explored. The use of MRI to explore molecular events is in its infancy compared to the other imaging modalities and remains to be developed in terms of phenotyping murine models and will not be further discussed in this chapter (see Chapter VIII). The use of MRI for morphogenic assessment is detailed below. Its use for functional assessment of organs is also detailed below with the exception of fMRI which is detailed in Chapter VI. Thus, aside from 3D depiction of the whole body or organs, and so, morphological representation of murine models, MRI can provide extra dimensions arising from temporal resolution, function, or molecular assessments.

Whole Body Phenome

Phenotyping of the whole body can be achieved readily by using lower magnetic field strengths of, e.g. 4.7 T. However, transmit/receive radio-frequency coils are required with high homogeneity over a sufficient area to encompass a whole mouse. Consecutive transverse images (1 mm thick or less) of the whole body of a mouse can be obtained in ∼15 min with in-plane resolution of up to 100 μm. T_1-weighted imaging using standard spin-echo sequences can generate images from which anatomy/morphology of organs may be adequately observed and measured. The choice of TR and TE determines the contrast (and signal intensity) of the various organs, e.g. TR/TE of 2200/20 ms at 4.7 T, leads to increased contrast between adipose tissue (AT) and adjacent muscle with the former being the more intense. Such TR/TE provides sufficient contrast between individual tissues to allow the delineation of individual structures. By MRI, organs are readily visualized *in situ*, within the 3D framework of the mouse body, enabling the relative spatial geometries of organs to be readily discerned, which is not possible by normal histological methods.

A typical sagittal image through the center of the mouse is shown in Figure 4, with the spine readily discernable along the dorsal side of the mouse. Detailing the structures from nose-to-tail, the eyes (Figure 4a) and brain (Figure 4b) are major organs dominating the images of the head region. On the smaller scale, just visible, are thicker areas of the external ear flaps (Figure 4c). Past the neck, the forelegs are the next major feature visible (Figure 4d), followed by the lungs located within the thorax (Figure 4e). The lungs appear as low intensity areas due to the low density of lung water protons (see below). Occasionally, the heart may be discerned in the thoracic cavity, this occurs when the TR chosen is such that the acquisition coincidently occurs during one of

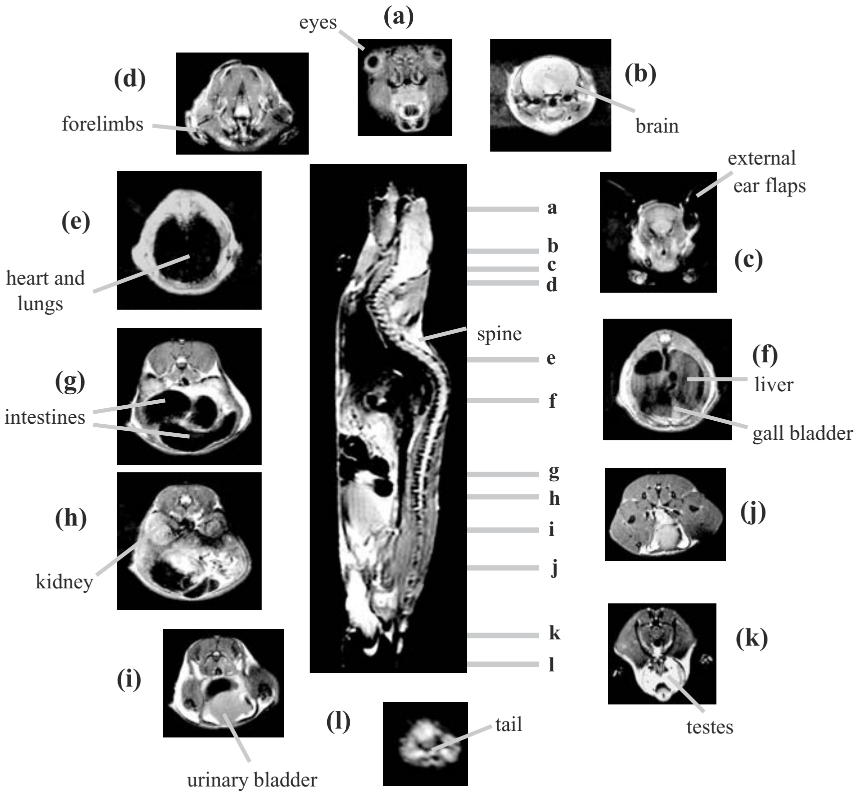

Figure 4. A midsagittal MRI image of a C57BL/6J male mouse and selected transverse MRI images obtained at 4.7 T (TR/TE, 2200/20 ms; matrix size, 256 × 256; field of view, 45 mm × 45 mm; two averages).

the more static phases of the cardiac cycle. Otherwise, signals from the heart are smeared over the image due to its rapid motion (Figure 4e). While it is possible to acquire data by "*cardiac gating*," this is a more involved procedure and requires more specialized and expensive equipment, and an increase in the overall scanning time. Therefore, it is not often performed unless necessary for cardiac phenotyping (see Chapter VI). Just below the lungs is the liver which appears semi-intense in the MRI images (Figure 4f). An empty gall bladder is not readily discerned but if filled with bile (e.g. after fasting), the gall bladder is revealed as a high intensity structure (Figure 4f). Filling the abdomen below the liver are the intestines, they are normally difficult to discern, as their intensity are non-uniform, being dependent on the contents of the intestine at any given location (Figure 4g). Thus, areas of no signal may be seen arising from intestinal gas, and areas of high intensity, from dietary fat as well as areas of intermediate intensities arising from non-fatty substances from food. Fasting of the animals prior to phenotyping render the intestines easier to discern in the MRI images. If phenotyping is performed post-mortem, there may be increased areas of low signal arising from generation of gas from intestinal bacteria following death. While the outlines of the intestines are difficult to distinguish, the lower gastrointestinal tract is readily observed in consecutive transverse slices in the lower abdomen (Figures 4i–k). In the lower abdomen are the kidneys of which the medulla and cortical regions are readily discerned in the MRI images due to differences in their signal intensities (Figure 4h). Distal to the kidney is the bladder which occupies a central location on the ventral side of the lower abdomen (Figures 4i and 4j). The urinary bladder is readily observed when filled with urine due to the high signal intensity of urine. The testis is another organ that can be readily identified in the lower abdomen of male mice (Figure 4k). At the rear of the mouse, the whole of the tail is seen and detailed tail structure observed (Figure 4l). The spine can be observed in successive transverse MRI images but is more readily observed along the length of the mouse, on the dorsal side, from sagittal MRI images. The orientation of scanning is usually determined by the organs of interest but becomes irrelevant if data is obtained isotropically. Obtaining such qualitative and quantitative data in less than 15 min in live mice renders MRI an attractive phenotyping tool for monitoring the effect of environment on the pathophysiology of disease, especially if the murine models are rare and/or difficult to breed. Furthermore, there is also the possibility of *in utero* phenotyping of mice using MRI, to monitor developmental changes at an early stage [22].

Of course, as previously discussed, MRI can be used to phenotype mice post-mortem, enabling higher resolution images to be obtained since sampling time can be extended. Johnson *et al*. [19] performed whole body phenotyping of mice with isotropic 3D spatial resolution of 110 μm × 110 μm × 110 μm and imaging time of 14.5 h at 2 T (Figure 5). The body of the mouse was perfusion fixed with a fixative such as 10% buffered formalin. However, by perfusing with a fixative supplemented with a contrast agent such as GdDTPA (gadopentetate dimeglumine), the SNR could be increased six-fold by decreasing the effective T_1 of the tissues [19]. MRH of embryos has also been performed following catherization of the umbilical vein and perfusion-fixation of the embryo with both fixative and contrast agent [6,8,23]. Indeed, there has been significant progress towards the generation of a microMRI atlas of mouse development [12,24,http://mouseatlas.caltech.edu/13.5dps/]. However, perfusion-fixation can be difficult to perform. Dhenain *et al*. [12] was able to image major organs without the need for perfusion-fixation, although image acquisition time took 36 h per embryo. More recently, by employing a T_1-weighted gradient echo sequence, Schneider *et al*. [25] was able to phenotype paraformaldehyde fixed wildtype and transcriptional coactivator *Cited2* lacking embryos with isotropic resolution of 25 μm × 25 μm × 26 μm in 9 h.

Large scale, genome wide mutagenesis programmes, have led to the creation of many murine models. To facilitate the phenotyping of such large numbers of mice, scanning of several mice simultaneously has been proposed. Bock *et al*. [26] have demonstrated the feasibility of simultaneous whole body MRI from four mice, obtaining data with minimal artifacts. More recently, Dazai *et al*. [27] have developed a multiple mouse loading and monitoring system for MRI of seven mice simultaneously, involving ECG and temperature monitoring.

So far we have described gross anatomy with respect to the whole body; the use of *in vivo* MRI to study the anatomy of individual organs is detailed below:

(a) Brain

MRI has been used to provide detailed morphological features of wildtype and transgenic mouse brains *in vivo* (Table 1), including the outline of all major anatomical regions such as the neocortex, corpus striatum, hippocampus, thalamus, and cerebellum. *Ex vivo* MRI of the fixative-preserved brain allow images of higher resolution (~2.4×10^{-4} mm^3) to be obtained (Figure 6, [37]). Using the C57BL/6J mouse as a test bed, different MR contrast parameters, voxel sizes, SNR, and use of contrast agents were investigated for visualization of the brain by MRH [9]. T_2^* MR images revealed several gross anatomical structures whereas diffusion-weighted proton images were superior for delineating subregions of the hippocampus. The use of contrast agents facilitated the visualization of the hippocampal regions in the T_2^* MR images [9]. Due to the fact that $MnCl_2$ leads to enhancement of specific areas of the brain [38–40], it has recently been used to aid the delineation of certain brain features [41]. Neuroarchitecture can also be defined by fMRI, i.e. following

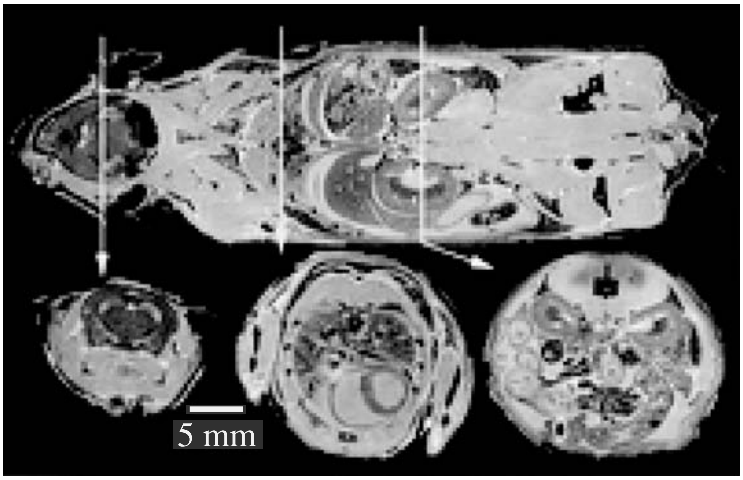

Figure 5. Three-dimensional MR microscopic images with an isotropic array (256 × 256 × 1024) were acquired in a whole fixed C57BL/6J mouse. The spatial resolution in every plane is 110 μm× 110 μm × 110 μm, which allows one to view any arbitrary plane with equal spatial resolution. Coronal (top) and transverse (bottom) images depict 110 μm thick sections of the head (left), thorax (center), and abdomen (right). (Reproduced courtesy of G. A. Johnson, Duke Center for *in vivo* microscopy [19].)

Table 1: *In vivo* MRI measurement of brain morphology

Lloyd *et al*. [28]	Pituitary hyperplasia in MT-hGRH transgenic mice (model of acromegaly)
Kornguth *et al*. [29]	Similarity of brain myelination and other brain structures in the phenylalanine hydroxylase-deficient mice and normal litter-mates
Munasinghe *et al*. [7]	Normal mouse brain
Fujii *et al*. [30]	Strain-related differences in susceptibility to transient forebrain ischemia in SV-129 and C57BL/6 mice
Zaharchuk *et al*. [31]	Decreased infarct volume following permanent middle cerebral artery occlusion in wild type and mice deficient in nitric oxide synthase gene expression
Jalanko *et al*. [32]	Cerebral atrophy and hypointensity of the deep gray matter in a murine model of aspartylglucosaminuria
Fransen *et al*. [33]	Dilated ventricles and vermis hyperplasia in L1 knockout mice (model of corticospinal tract hypoplasia)
McDaniel *et al*. [34]	Enlarged ventricles and hippocampal atrophy following transient cerebral ischemia Apo-E (model for atherosclerosis) and C57BL/6 mice
Wu *et al*. [35]	Reduction in cerebral blood volume in various regions of the brain in mutant APP (V717F, K670N/M671L) mice (model of Alzheimer's disease)
In 't Zandt *et al*. [36]	Increased ventricular size in brain creatine kinase-deficient mice

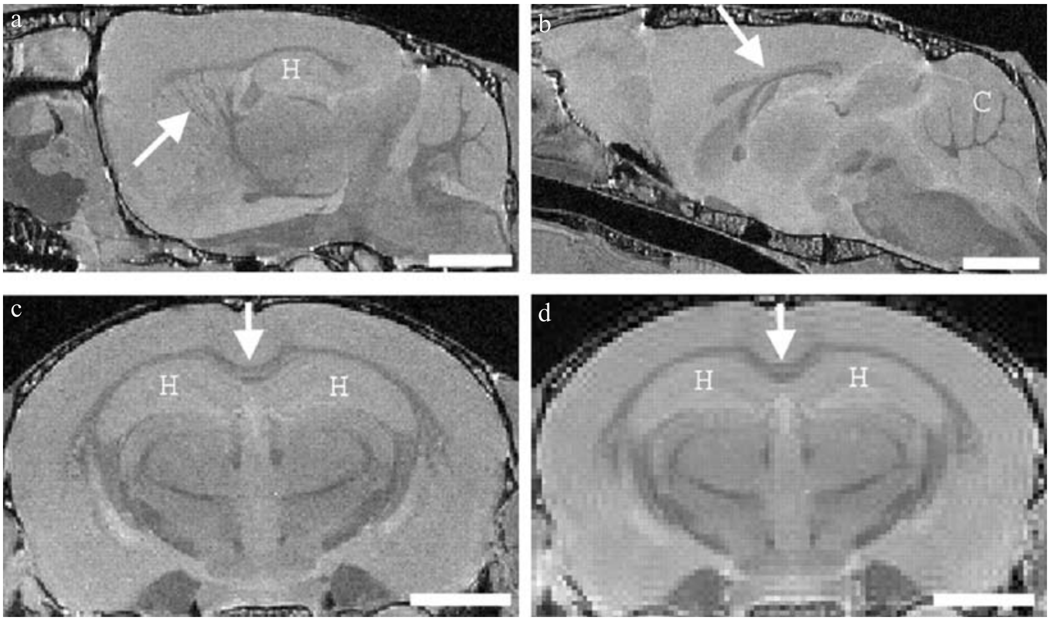

Figure 6. Examples of anatomical structures of the mouse brain visible with MRH (512 × 256 × 256 matrix). (a) Pencil fibers in the striatum (arrow) are visible, as well as the hippocampus (H) in a sagittal section. (b) Corpus callosom (arrow) and cerebellum (C) are visible in this midsagittal plane. (c) Corpus callosom (arrow) and hippocampus (H) are visible in the coronal plane. (d) A coronal plane of a lower resolution file (256 × 128 × 128 matrix) where the corpus callosom (arrow) and hippocampus (H) are clearly visible, compared with a matching coronal plane of a high-resolution file of the same brain seen in (C) (bar = 2 mm). (Reproduced with permission [37].)

appropriate stimulation, changes observed by fMRI can aid the definition of regions associated with the visual and motor cortex, ocular dominance columns, ocular orientation columns, rodent whisker barrels, rodent olfactory glomeruli, and cortical layers (see Chapters III and IV). The use of MRH for determining brain morphology has been reviewed by Kooy *et al.* [42], and Benveniste and Blackband [17], and the reader should refer to these for further information.

Currently, there are two web-based digital mouse atlases based on MRH data. The "mouse atlas project" (MAP)—which is still under development—consists of four different image modalities—Nissl stained brain sections, MRH data, cryo data, and labeled sections, from the Laboratory of Neuroimaging at UCLA (http://www.loni.ucla.edu/MAP). The other brain atlas website is an atlas of the developing mouse brain (http://mouseatlas.caltech.edu/13.5dps/) from the Biological Imaging Centre at CalTech [12]. A 3D MRI "variational" atlas of mouse brain has recently been published [43]. The concept is to combine multiple 3D images to produce a mouse brain with average anatomy and range of anatomical variation within a particular population, thus allowing the formal quantification of the anatomical variability within a mouse strain, and hence, between mouse strains, especially relevant for phenotyping.

(b) Adipose tissue

Measurement of body AT content and distribution is fundamental to the study and management of obesity. Accuracy can be achieved by chemical carcass analysis but although possible in some animal studies, it does not allow serial measurements to investigate developmental changes and the effects of interventional treatments. MRI can be used to directly visualize, and hence, measure the location and quantification of soft tissues, such as AT and its different depots. MRI as a method to measure AT has been fully validated in animals. In rats, Ross *et al.* [44] compared MRI with computerised tomography (CT) against chemical analysis methods to measure AT and skeletal muscle volumes. Both MRI and CT assessments of AT volume showed comparable accuracy to chemical analysis, the latter being the "gold standard." MRI measurement of AT has also been validated in lean and obese pigs [45], showing excellent correlation with *in vitro* methods. Ishikawa and Koga [46] used MRI to measure abdominal fat and other specific organs in Otsuka Long-Evans Tokushima fatty rats, while Tang *et al.* [47] utilized MRI for longitudinal studies in rats. Subsequently, Changani *et al.* [48] used serial MRI to monitor differences in visceral, subcutaneous, inter-muscular, and total fat distribution between normal mice and a known transgenic lean mice strain over a period of 6–18 weeks. An increase in the various fat deposits and total fat content was observed in the wildtype compared to the transgenic lean mouse. A complete absence of subcutaneous AT and a reduction in other AT deposits were observed by MRI in a mouse model with complete genetic ablation of corepressor protein RIP140 [49]. Today, MRI is therefore the technique of choice for the *in vivo* assessment of AT content and distribution in animals, especially where *in vitro* methods are impractical.

(c) Lungs

The combination of low proton density (lungs mostly consist of air), high susceptibility effects, cardiac and respiratory movements normally associated with the lungs have made it one of the most difficult organs to be imaged *in vivo* by MRI. Indeed, most MRI research, previous to the introduction of hyperpolarized gases, concentrated on imaging lung tumours and inflammatory responses [50–52]. Furthermore, most of this work was carried out in rats, with little work on murine models, where the problems caused by cardiac and respiratory movements are much more severe.

Typical images of the lungs from a normal mouse can be seen in Figure 4e. Due to the low proton density, short T_2, and local inhomogeneities, the lungs appear dark in MR images, greatly limiting its usefulness. Development of non-standard acquisition techniques have gone some way in improving parenchymal tissue imaging but even this has been of limited use. It was only with the introduction of hyperpolarized noble gases (^{3}He and ^{129}Xe) that proper pulmonary MRI was achieved. Since its introduction, hyperpolarized gas MRI has been used successfully to generate information on ventilation of the lung, pulmonary diseases and lung development [53]. Despite these advances, and partly due to costs and availability of hyperpolarized gases for MRI, studies are limited to a very small number of specialized groups, and therefore the potential of this technique has not been fully exploited. However, hyperpolarized pulmonary MRI is likely to become the technique of choice in pre-clinical and clinical research, including morphological imaging of airways and alveolar spaces, estimating absolute airspace size, analysis of the intrapulmonary distribution of the tracer gases, local broncho-alveolar dimensions, and regional broncho-alveolar pO_2 [54,55].

As an alternative to the use of hyperpolarized gas for imaging lungs, inert fluorinated compounds such as perfluorocarbon (PFC) and emulsions of PFC have been considered, using ^{19}F, rather than the conventional ^{1}H nuclei (Figure 7). PFC and PFC-water emulsions are used to assist ventilation in acute respiratory distress syndrome and are readily available. Furthermore, the fact that oxygen can modulate the T_1 relaxation properties of the fluorine in PFCs, has been utilized to measure lung pO_2 *in vivo* [56–58]. This suggests that PFCs can be used for simultaneous analysis of lung structure and pulmonary oxygenation patterns.

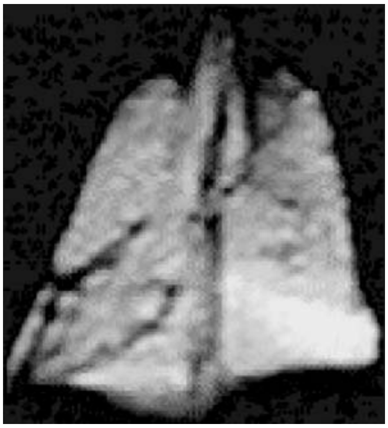

Figure 7. A midcoronal ^{19}F MRI image of PFC filled lungs of a C57BL/6 mouse obtained on, at 9.4 T, MRI scanner (TR/TE, 1000/20 ms; FOV, 100 mm × 100 mm; matrix size, 256 × 256, two averages, 2 mm slice thickness).

(d) Heart

Transgenic and mutant murine models of cardiovascular disease provide a means by which the pathophysiology of cardiovascular disease may be investigated in an intact organism. However, cardiac MR is affected by cardiac and respiratory motion artifacts, exacerbated by the high heart rate (400–600 beats/min), the high respiratory rate (30–60 breaths/min), and the small dimensions of the mouse heart. To reduce motion artifacts in cardiac MR, motion-gating strategies have to be employed to reduce the level of motion artifact using a variety of sensor technologies. Cardiac gating enables synchronization of a MR sequence to the cardiac cycle such that data acquisition occurs from spins from the same region of interest and the same phase within the TR interval, minimizing the influence of cardiac motion. Respiratory motion also needs to be avoided. Artificial ventilation (not ideal due to its invasive nature) or reduction of the motion artifact by sensing methods can be employed.

Cardiac mass estimates using MRI have been shown to be highly accurate, reproducible, and observer- and technician-independent when compared to that obtained at necropsy [58–61]. Increases in left ventricular mass and volume were revealed by MRI in transgenic mice and were evident in mice expressing myocardial tumour necrosis factor compared to littermate controls [62]. MRI has been used for accurate serial assessment of cardiac structure in neonatal, juvenile, and adult mice [63]. As well being used to image heart anatomy, MRI can be used to image the coronary arteries [64]. MRI has also been used to study cardiac malformations of fixed embryos [65].

The use of MRI for morphological (and functional) assessment of the heart is discussed fully in Chapter VI.

(e) Other organs

The ability to distinguish between different soft tissues is one of the main reasons for MRI being at the forefront in the longitudinal *in vivo* monitoring of tissue and organ changes in murine models of disease [48,49,66]. Indeed, as well as determining temporal and regional morphological changes in skeletal muscle, MR techniques have been successfully applied to the study of muscle denervation and reinnervation [67], muscle perfusion [68], muscle fiber-tracking [69] and acute and chronic inflammation [70]. However, studies of skeletal muscle, as well as other organs, are rare in mice arising from the difficulties in scanning such small animals. *In vivo* MRI at 9.4 T, has been used to study schistosoma Mansoni-infection in mouse liver [71], lupus nephritis in a MRL/lpr mouse [71], and liver regeneration in mice following partial hepatectomy [72]. Deoxygenated and oxygenated haemoglobin have different magnetic susceptibilities and this has been exploited to detect high levels of the former in the liver and kidneys of a homozygous alpha-knockout of a transgenic murine model for sickle cell disease, indicating the presence of blood hypoxia in these mice [73]. Furthermore, an enlarged spleen was noted by MRI and consistent with computerized tomography data in a mouse model of AymloidA amyloidosis [74].

Magnetic Resonance Spectroscopy

While MRI provides graphical images of the whole body, organs, and internal structures, MRS can be utilized to obtain metabolic information from different organs *in vivo*. MRS is feasible for any nucleus possessing a magnetic moment and will simultaneously detect compounds containing that nuclei if the compounds are at high enough concentrations, i.e. mM range for ^{1}H MRS. MRS can be used to provide metabolic profiles from ^{1}H-, ^{31}P- and ^{13}C-containing metabolites in the whole body or specific organs. Often for MRS of specific organs, localized MRS is performed, involving surface coils or the use of gradients to define an area or voxel of interest. The localization obtainable from surface coils arises mainly from the fact that the excitation of nuclei induced by the coil occurs only in a limited area adjacent to the surface coil, and decreases with increasing distance from the surface of the coil. The area in which the coil is effective is largely determined by the size of the coil, i.e. the larger the coil, the greater the area in which nuclei can be excited. This type of approach is mainly used for the acquisition of ^{31}P spectra principally from skeletal muscle, where the potential for contamination from other tissue is relatively low.

Localization methods commonly used for ^{1}H MRS are STEAM (STimulated Echo Acquisition Mode) and PRESS (Point RESolved Spectroscopy). PRESS does not allow the creation of multiple quantum coherences in coupled spin systems, however, the signal intensity obtained using PRESS localization methods is double that obtained by STEAM and hence, is the technique of choice for most *in vivo* MRS studies. ISIS (Image Selected *In vivo* Spectroscopy) is commonly used for localization when performing MRS of non-^{1}H nuclei, such as ^{31}P MRS. ISIS is chosen for ^{31}P MRS as the localization technique is relatively insensitive to T_2 relaxation and so, unhampered by the short T_2 relaxation time in ^{31}P MRS.

Spatial localization, not only allows the unambiguous detection of metabolites from a defined volume but also increases the spectral resolution by narrowing resonances (better shimming), exclusion of broad unwanted resonances, and improving water suppression (see below). For further details of the principles and techniques involved in MRS *in vivo*, the reader is referred to de Graff [75].

Localized ^{1}H MR spectra are normally dominated by water which is the major ^{1}H-containing compound ($\sim$40 mM) in cells/tissues. Other ^{1}H-containing metabolites, usually metabolites of intermediary metabolism such as amino acids, lactate, etc., may only be discerned following suppression of the water resonance. Other major components that are observed in the *in vivo* ^{1}H MR spectra of tissues are resonances from lipids especially those arising from the methylene protons of fatty acids chains, leading to concealment of other resonances. Such lipid resonances can be "edited" out of the ^{1}H MR spectrum by using long TE values since the methylene protons have a short T_2 values relative to other protons.

A magnetic nuclei should only give rise to a single resonance in the MR spectrum, however, the magnetic environment of this nuclei can be modified by adjacent magnetic nuclei such that the former gives rise to a multiplet, the complexity of the multiplet depending upon the nature and number of the nearby nuclei. This is termed spin–spin coupling (for a fuller discussion of such interactions, the reader is referred to standard textbooks). Spin–spin coupling can exist between the same nuclei (homonuclear) or different nuclei (heteronuclear). In ^{1}H MRS, despite the production of more complex spectra, coupling of different protons can aid assignment of resonances. However, for other nuclei, such as ^{13}C, although homonuclear coupling is minimal, heteronuclear coupling (to ^{1}H) leads to complex resonances that render the coupled spectra difficult to analyze and also as the area of the one resonance becomes divided between the coupled resonance resulting in a decrease in signal intensity and therefore, visibility of the resonance in the spectrum. While it is preferable to "decouple," i.e. suppress spin–spin coupling, in such situations, decoupling can lead to excessive radio-frequency power deposition, resulting in heating and possible damage of the tissue under study, which is of course of particular concern when investigating live organisms. Thus, decoupling is often not employed unless essential for signal assignment and/or accurate quantification.

The sensitivity of ^{13}C is 1.59%, relative to ^{1}H (100%). The relatively low sensitivity means that natural abundance ^{13}C MRS can only detect compounds that occur at relatively high concentrations *in vivo*, such as mobile lipids and glycogen. However, the low sensitivity of ^{13}C offers the possibility of studying fluxes (of ^{13}C-enriched compounds) through important metabolic pathways due to low or little background interference from endogenous metabolites. Thus, ^{13}C MRS has been used extensively to monitor the metabolism of exogenous ^{13}C-enriched compounds, providing specific and quantitative information about metabolic pathways such as glycolysis, tricarboxylic acid cycle, gluconeogenesis, and pentose phosphate pathway. As an alternative to direct detection of the ^{13}C nuclei, ^{13}C MR spectra can be obtained by indirect (or inverse) detection of these nuclei via bonded ^{1}H, the latter method benefiting from the increased sensitivity of the ^{1}H nuclei.

The sensitivity of ^{31}P (6.63% relative to ^{1}H sensitivity at 100%), is sufficient to enable ^{31}P MRS to be performed *in vivo* and has been used to provide important information regarding tissue bioenergetics, intracellular pH, magnesium concentration, and reaction fluxes.

Apart from providing characteristic metabolic profiles of the whole body or of selected organs, multinuclear MRS can also be used to obtain dynamic biochemical/functional information regarding murine models in terms of phenotyping (see below), e.g. the use of ^{13}C-enriched compounds. This is comparable to conventional organ function tests performed routinely, usually entailing the use of a non-toxic compound that may be metabolized by a specific organ, and the rate of metabolism reflecting the functional state of the organ in question.

MRS can also be performed *in vitro*, comparable to traditional "chemical analysis" using MRS. While MRS *in vivo* can provide much information regarding a living organism, the spectral quality of the data obtained is of an inferior quality to that obtained *in vitro,* rendering assignment and quantification difficult. Thus, *in vitro* MRS of extracts of tissues is often required to aid assignment of MR spectra *in vivo*. *In vitro* MRS data can also be used for phenotyping of murine models and will be discussed briefly later in this chapter.

(a) Adipose tissue

Bodyweights are often used as surrogate measures of adiposity in murine studies of obesity. However, this method is fraught with problems as it assumes a constant ratio between lean and fat mass. More recently, ^{1}H MRS has been developed as a fast and reproducible *in vivo* method to determine adiposity.

^{1}H MRS of the whole body can determine percentage adiposity, comparing favorably with that by chemical analysis of the carcase [76]. Unlocalized ^{1}H MR of the whole body yields a spectrum dominated by one

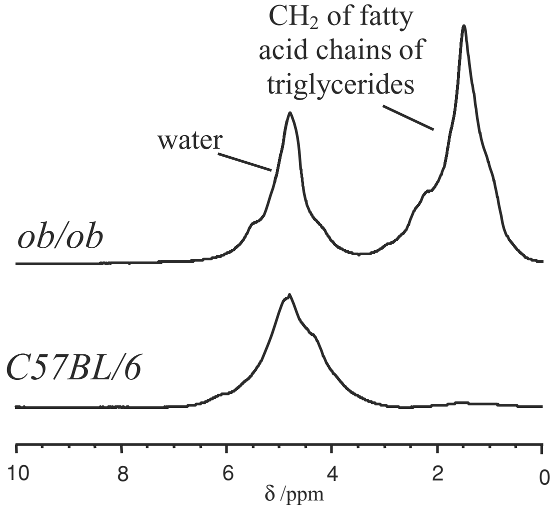

Figure 8. Whole body ^{1}H MRS of a C57BL/6 and an obese *ob*/*ob* mouse.

resonance from water (Figure 8). At lower frequency, another resonance is also discernable but more so, in obese animals. The other resonance arises from the methylene protons of triglycerides, which is the major component of AT. The area under each resonance or integral is proportional to the number of protons giving rise to that particular resonance. Thus, quantification can be performed with spectroscopic processing packages to yield a ratio of the water to lipid peak, from which the percentage adiposity may be calculated using the following equation:

$$\%\,\text{adiposity} = \frac{100 \times I_{(\text{lipid})}}{I_{(\text{lipid})} + I_{(\text{water})} + 0.38 \times I_{(\text{water})}} \qquad (1)$$

where $I_{(\text{lipid})}$ and $I_{(\text{water})}$ are integrals for lipid and water, respectively.

Equation 1 arises from considering that the mass of the whole body arises from the masses of body fat, water, and fat-free tissue. The former two can be estimated by MRS as they are proportional to $I_{(\text{lipid})}$ and $I_{(\text{water})}$, respectively. The fat-free or lean mass has been observed to be related to the total body water by a fixed ratio [77], and confirmed in mice recently by Mystkowski *et al*. [76], to be proportional to 0.38 times that of $I_{(\text{water})}$. We have used ^{1}H MRS of the whole body as a measure of adiposity in a murine model devoid of the corepressor protein RIP140 showing their tendency to leaness [49], inter-strain differences in the handling of dietary omega-3-fatty acids [78] and the effect of voluntary exercise on adiposity in C57BL/6J mice [79]. ^{1}H MRS of the whole body has also been used to show that aromatase-deficient mice have a phenotype of increased adiposity [80].

An alternative MRS method for measuring total adiposity is based on MR relaxometry, which unambigously separates water and fat due to the very different T_1 and/or T_2 relaxation times [81–83]. MR relaxometry was shown to correlate well with body composition obtained by DEXA and chemical analysis, and has been used to detect diet-induced changes in body composition with no change in body weight in mice [82].

Although MRI can also be used to determine total and regional adiposity, in terms of analysis time, MRS provides a more rapid and relatively accurate assessment of adiposity. For MRS, analysis time can be as quick as 10 min compared to up to 4 h for MRI. Thus, MRS would be more suitable for studies in which repeated measures are required or large numbers of experimental animals need to be scanned, while MRI would be more suitable for research where regional as well as total adiposity is needs to be measured.

^{13}C MRS can provide information regarding the type of lipid in the AT deposits in the whole body. The insensitivity of ^{13}C MRS is such that only the carbons of AT are present in high enough concentrations to be detectable by ^{13}C MRS. Thus, ^{13}C MRS of the whole body (Figure 9) allows estimation of the degree of deposition of certain lipid types and can provide an estimate of the proportion of monosaturated fatty acids carbon relative to polyunsaturated fatty acids carbon. For example, we have recently shown increased deposition of polyunsaturated fatty acids in AT of lean (C57BL/6) mice compared to genetically obese (*ob/ob*) mice following dietary supplementation of omega-3 fatty acids [78]. The studies mentioned have used ^{13}C without ^{1}H decoupling. Although decoupling is not essential, it will simplify spectral analysis and aid quantification. ^{13}C MRS of specific depots or the whole body can be used to investigate differences between strains in the handling of dietary lipid types in the whole body and characterization of nutritional fat deficiencies and abnormalities in fatty acid pathways.

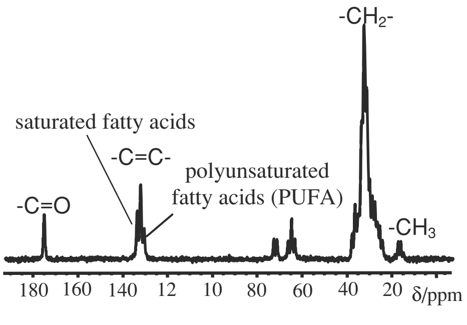

Figure 9. Whole body ^{13}C–^{1}H coupled MRS of an obese *ob*/*ob* mouse.

(b) Heart

^{1}H and ^{31}P MRS has been used to monitor differences in cardiac metabolism between isolated hearts from wild-type and iNOS-overexpressing hearts [84]. Cardiac energetics studied by ^{31}P MRS also differ between murine models lacking different muscle-specific isoenzymes of creatine kinase [85]. A fuller discussion of the use of multinuclear MRS to study cardiac function is detailed in Chapter VI.

(c) Brain

Although localized ^{1}H MRS *in vivo* has been used extensively to study brain metabolism in the rat [86,87], there are relatively few studies involving mouse brain, probably due to its small size and the difficulties in compensation of the local magnetic field inhomogeneities. Most *in vivo* studies involving ^{1}H MRS of mouse brain have concentrated on determining the levels of a limited number of brain metabolites, including N-acetylaspartate (NAA), lactate, creatine (Cr), myo-inositol (mI), or choline. This limitation arises from the relatively long TE values often employed for MRS, usually ~40 ms, shorter values being more difficult to achieve due to the requirement of exceptionally strong gradients to suppress eddy current artifacts. Measurement of NAA levels is often used as in indicator of healthy neuronal function and so, frequently employed to assess neuronal function in different transgenic mice models but may reflect the degree of cellular integration in the central nervous system [88]. NAA levels are decreased in a Huntingdon's disease murine model [89,90] while increased NAA levels were observed in a knockout mouse model for Canavan disease [91]. Levels of NAA were revealed to be similar between the mdx (murine model of Duchenne muscular dystrophy) and control mice, suggesting minor, if any neuronal necrosis in the dystrophic brain [92]. The mI/Cr ratio was significantly increased and the NAA/Cr decreased in the Ts65Dn mouse brain, a murine model of Down syndrome, and comparable to ^{1}H MRS findings in human adults with Down syndrome [93]. Brains of creatine kinase double knockouts mice exhibited 20–30% decrease in levels of total creatine and a similar increase in the level of neuronal NAA, whereas changes in mI and glutamate did appear to be mutation type and brain region specific [36]. Increased guanidinacetate, reduced Cr, and creatinine levels were observed in the brain of mice with guanidinacetete N-methyltransferase deficiency [94]. Transgenic mice expressing mutant human amyloid precursor protein, exhibited increased NAA, glutamate, and taurine in the ^{1}H MRS metabolic profile of the brain *in vivo* [95]. Lactate—the end product of glycolysis—is readily discerned in the ^{1}H MRS spectra of mouse brain and can be used to monitor development of ischemic episodes [96], which may be of particular relevance in determining the susceptibilities of certain strains to cerebral ischemia. Indeed, *in vivo* localized ^{1}H MR cerebral metabolite profiles of different mouse strains, collected before and after 1 h of global irreversible ischemia, showed that the pronounced vulnerability of C57BL/6 mice to brain ischemia is linked to strain-dependent differences in cerebral energy metabolism [97].

Full quantitative assessments of cerebral metabolites in mouse strains *in vivo* are rare, due to difficulties in resolving resonances arising from local magnetic field inhomogeneities [36,97–99]. However, the development of a second-order shim system strong enough to compensate for non-linear field inhomogeneities in the selected volume of interest, as well as more efficient methods of localization and water suppression, has enabled high quality spectra to be obtained from the murine brain (Figure 10, [99]). This coupled with the use of much shorter TE value (2 ms) allowed for the reliable quantification of over 16 brain metabolites from 5 to 10 μl volumes of mouse brain *in vivo*. The highly resolved ^{1}H MR metabolic profiles, obtained from different regions of the brain, as well as in different strains, provide qualitative and quantitative information on inter-species variations as well as inter-regional variation within strain [99]. Thus, ^{1}H MR metabolic profiling of the brain (and possibly other tissues) will become a powerful tool in the arsenal available to researchers trying to elucidate genotype–phenotype correlates.

A number of studies have reported the use of ^{13}C MRS to investigate brain metabolism, principally in the rat brain. ^{13}C MRS of the brain has been used to measure fluxes associated with cerebral glucose and glutamate metabolism, providing quantitative information on metabolic fluxes *in vivo*. [1-^{13}C]-glucose has been used extensively in ^{13}C MRS, principally due to its cheapness but also, that the transfer of the ^{13}C label to [4-^{13}C]-glutamate is indicative of the most active energy-producing metabolic pathways, glycolysis, and the neuronal TCA cycle [100]. The investigations can be refined by the use of [1,6-^{13}C]-glucose which exhibits nearly identical patterns of labeling, which although more expensive, has double the sensitivity of [1-^{13}C]-glucose due to the enrichment of two pyruvate molecules for one of [1,6-^{13}C]-glucose. [2-^{13}C]-glucose has been used as a direct indicator of analpherotic activity by the accumulation of astroglial [3-^{13}C]-glutamine. Using this methodology, Sibson *et al.* [101], observed differences in analpherotic activity in the rat brain exposed to different concentrations of blood ammonia. [2-^{13}C]-acetate has also been used to distinguish between neuronal and astroglial metabolism, since it is almost exclusively metabolized in astroglial cells. ^{13}C MRS labeling experiments have led to the establishment of a basic mathematical model of brain energy metabolism and (glutamatergic) neurotransmission, verified in rat and human brain [102,103]. The use of ^{13}C MRS in the study of brain biochemistry and function is reviewed in detail by de Graaf [75]; Zwingmann and Liebfritz [99]; Gruetter *et al.* [104]. Such methodology

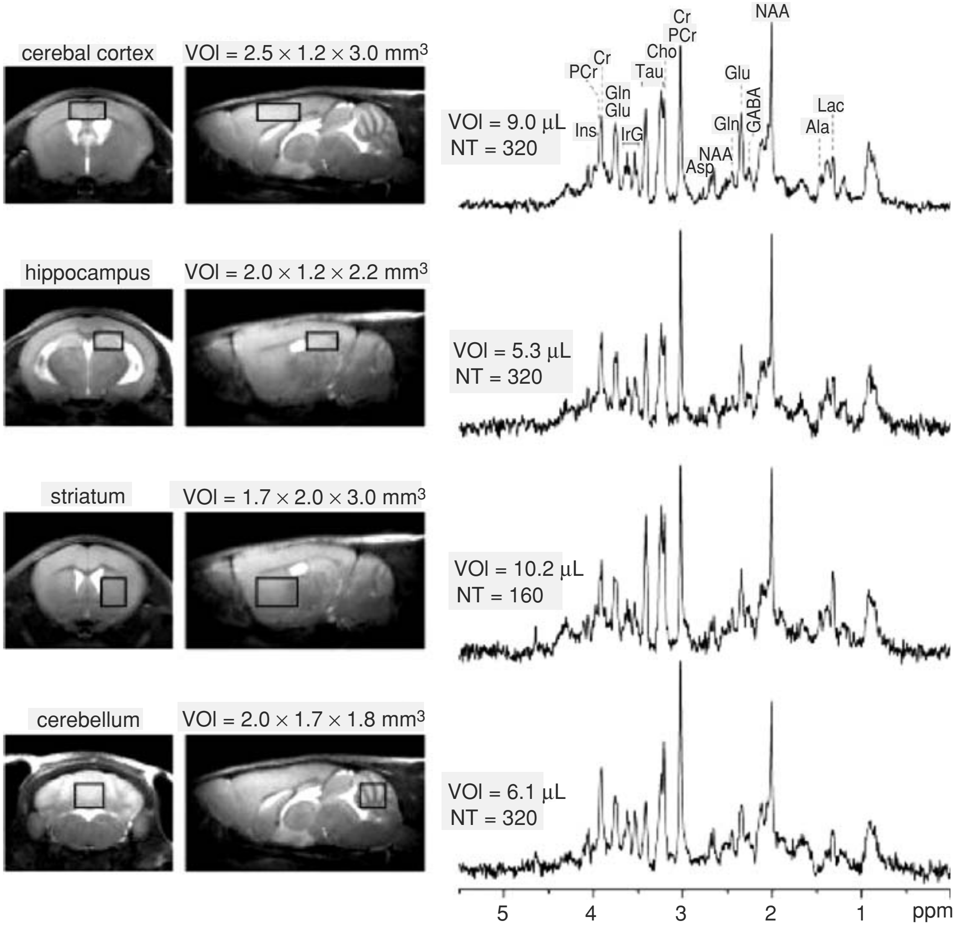

Figure 10. Multislice RARE images of the mouse brain (C57BL/6) with the volumes of interest (VOIs) centered in cerebral cortex, hippocampus, striatum, and cerebellum, and *in vivo* ^{1}H NMR spectra measured from the corresponding brain regions. RARE MRI: in-plane resolution 80 μm × 80 μm, slice thickness 1 mm, TR/TE = 4000/60 ms. Localization sequence: STEAM, TE = 2 ms, TR = 5 s, number of averages = 160–320, VOI = 5 − 10 μl. Processing: Gaussian multiplication $\{f(t) = \exp(-(t - t_{\max})^2/2\sigma^2)$, $t_{\max} = 0.05$ s, $\sigma = 0.085$ s$\}$, Fourier transform, zero-order phase correction. No water signal removal or baseline corrections were applied. (Reproduced with permission [99].)

can also be applied to murine models with the use of adapted coils and sequences, as with ^{1}H MRS of the brain (see above). Indeed, *in vivo* ^{13}C MRS has been used to characterize cerebral glucose metabolism in a transgenic animal model of amyotrophic lateral sclerosis, a neurodegenerative disorder [105].

^{31}P MRS can be employed to monitor brain energetics and was used to study the brains of creatine kinase double knockout mice, revealing normal levels of ATP and inorganic phosphate, as well as pH, although phosphocreatine levels were almost completely undetectable [36]. High levels of guanidinoacetate phosphate and reduced phosphcreatine levels were observed in a knockout mouse model of guanidinoaceate N-methyltransferase deficiency [94]. Neural energetics in a mouse expressing human myoglobin showed no significant difference from wildtype mice [106].

(d) Muscle

^{1}H MRS has been recently used to determine triglyceride deposition in skeletal muscle and liver in animal models [107–112]. The main objective of this work has been to investigate the relationship between intramyocellular lipids (IMCLs) and insulin resistance. The feasibility of this technique has been demonstrated in rats and mice and levels of IMCL appear to be affected by several factors including age, gender, diet and exercise, muscle fiber-type, as well as the genetic background of the animals. For example, healthy young rats have been shown to have higher levels of IMCL compared to older rats and obese rats showed significantly higher IMCL levels than controls. Despite this variability, a number of studies have shown that IMCL levels are correlated positively with measures of obesity and negatively with insulin sensitivity. Moreover, levels of IMCL have been shown to be pliable to manipulation by nutritional and pharmacological interventions, with concomitant changes in insulin sensitivity. Thus, *in vivo* ^{1}H MRS is presently being used as a non-invasive method to determine the efficacy of emerging therapy in the treatment of obesity and insulin resistance.

Multinuclear MRS (^{31}P and ^{13}C) has been pivotal in unraveling the mechanisms associated with muscle metabolism in murine models of disease. ^{31}P MRS has been extensively utilized to study the metabolic and non-metabolic factors associated with muscle fatigue. The results are consistent with the fact that elevated levels of inorganic phosphate, P(i), can cause a substantial proportion of the loss in muscular force and power output during fatigue; but later fatigue may arise from impaired activation beyond the neuromuscular junction [113–117]. While in sepsis there is an overall decrease in energy availability, which is worsened by PCr depletion [118].

The ability of ^{31}P MRS to detect phosphorylated compounds has also been successfully used to measure the muscle glucose-6-phosphate (G6P) concentration after exercise and in non-insulin-dependent diabetes mellitus. Time course studies have emphasized the importance of G6P concentration as an intracellular regulatory effector of glycogen synthesis rate *in vivo*. The authors went on to show that the majority of the flux control of muscle glycogen synthesis is at the glucose transport/hexokinase step—a step that in turn may be compromized in insulin resistance [119–122]. Thus, ^{31}P MRS can be used to assess muscle function in different transgenic murine models. For example, in a murine model of guanidinoacetate N-methyltransferase deficiency, the first discovered creatine deficiency syndrome, elevated levels of guanidinoacetate phosphate, and reduced levels of creatine phosphate were observed by ^{31}P MRS of SM in these transgenic mice [94]. In another ^{31}P MRS study of muscle [123], these mice were found to be able to cope with mild ischemic stress, despite the lack of phosphocreatine, by using guanidinoacetate phosphate for high-energy phosphoryl transfer.

(e) Liver

Multinuclear MRS has also been applied to the study of liver physiology and metabolism [124]. ^{1}H MRS of the liver has been proposed as an alternative and non-invasive method for determining liver lipid levels in rodents [108,112]. Localized *in vivo* ^{1}H MRS of the liver yields a spectrum consisting of peaks from water and the methylene protons of the fatty acid chains of intrahepatocellular lipid (Figure 11). Traditionally, methods of quantifying liver fat are by biopsy, which is non-ideal for longitudinal and/or interventional studies. Garbow *et al.* [108] observed an excellent correlation between *in vivo* MRS and *ex vivo* chemical analysis determinations of liver lipids. ^{1}H MRS of the liver provides a method of measuring the extent of intrahepatocellular lipid deposition between different strains of mice (Figure 11). Thus, *in vivo* MRS of the liver is an extremely valuable technique in longitudinal studies for monitoring changes in lipid levels.

As previously mentioned, the low sensitivity of ^{13}C MRS renders it a suitable nucleus for tracer experiments to measure metabolic fluxes. The use of ^{13}C-labeled compounds as tracers has enabled many metabolic pathways in the liver to be investigated [124]. The role of fructose-2,6-bisphosphate (FBP) in regulation of glucose fluxes was assessed using *in vivo* ^{13}C MRS in a mouse with elevated levels of FBP, showing that elevated FBP levels result in increased hepatic glycogen storage through indirect synthesis of glycogen [125]. The liver is readily amenable to perfusion *ex vivo* and studies have been performed on isolated murine livers to determine metabolism of exogenously administered compounds in the perfusion medium using ^{13}C MRS to determine best methods of liver preservation for transplantation [126]. Currently, relatively few studies have used such methodology to investigate differences in metabolic fluxes between transgenic animals.

Similarly, ^{31}P MRS has been extensively used to study cellular bioenergetics (see above) in rats and man but there are few studies of its use in the mouse liver. These studies have concentrated in monitoring hepatic energetics in transgenic mice expressing different forms of isoenzymes of creatine kinase in the liver [127–130], creatine kinase is normally absent in the liver. Such studies have shown that the presence of creatine kinase in the liver does not affect free ADP levels [127]. No depletion of hepatic ATP was observed in transgenic mice expressing creatine kinase in the liver given a fructose challenge [128]. The phosphocreatine produced in the livers of creatine kinase expressing mice protected these mice from hypoxia and ischemia as evident by ^{31}P MRS [129].

(f) Metabolic profiling of biofluids

Metabolic MR profiles can be obtained from biofluids or extracts of organs, and such profiles are often

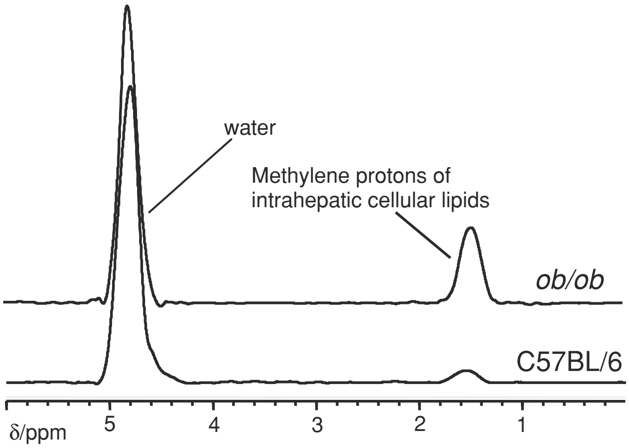

Figure 11. Localized *in vivo* ^{1}H MR (PRESS) spectrum from a 3 mm × 3 mm × 3 mm voxel located in the liver of a C57BL/6 and an obese *ob/ob* mouse.

characteristic for the type of biofluid or extract. Changes in metabolism are observable in MR spectral profiles of biofluids or tissues and this data are reflective of the metabolic status of an organism, and has therefore been used to investigate pathophysiological and toxicological processes (reviewed by Lindon *et al.* [131]). Due to the complexity of the spectral data, multivariate statistical methods are commonly employed to enhance interpretation. Such techniques can be extended to phenotyping such that changes in metabolism between different strains and effects of inter-species differences resulting from interventional treatment can be discerned in the metabolic profile of biofluids and extracts of tissue [132–134]. However, caution must be employed for phenotyping studies since metabolic profiles can be affected by a number of physiological factors. Factors include dietary variation [133], exercise and physical activity [135], normally regulated diurnal cycles [136], oestrus or menstrual cycle-related processes [136], and genetic drift [133]. To address this issue with respect to diurnal variation, pre-filtering of the data by orthogonal signal correction was applied, resulting in removal of the variations arising from diurnal variation, and hence, more accurate interpretation of the data [137]. For a fuller discussion of the use of metabolic profiles (especially obtained by ^{1}H MRS) for functional genomic research, the reader is refered to Griffin [138] and Griffin *et al.* [139].

Conclusions

The advent of high-field MR systems is making a reality the routine application of MRI/MRS techniques to the study of murine models of disease. *In vivo* imaging techniques—including MRI—are likely to play a pivotal role in elucidating the function of many candidate genes in pre-clinical investigations and therapy development.

Acknowledgement

We would like to thank Rudy Cárcamo Ruiz *por inspiratio.*

References

1. Haluzik M, Colombo C, Gavrilova O, Chua S, Wolf N, Chen M, Stannard B, Dietz KR, Le Roith D, Reitman ML. Endocrinology. 2004;145:3258.
2. Johnson GA, Benveniste H, Black RD, Hedlund LW, Maronpot RR, Smith BR. Magn. Reson. Quart. 1993;9:1.
3. Budinger TF, Lauterbur PC. Science. 1984;226:288.
4. Chance B. NMR Biomed. 1989;2:179.
5. Blackland SJ, Buckley DL, Bui JD, Phillips MI. MAGMA. 1999;9:112.
6. Smith BR, Johnson GA, Groman EV, Linney E. Proc. Natl. Acad. Sci. USA. 1994;91:3530.
7. Munasinghe JP, Gresham GA, Carpenter TA. Lab. Anim. Sci. 1995;45:674.
8. Smith BR. Microsc. Res. Tech. 2001;52:323.
9. Benveniste H, Kim K, Zhang L, Johnson GA. Neuroimage. 2000;11:601.
10. Jacobs RE, Fraser SE. J. Neurosci. Methods. 1994;54(2):189.
11. Smith BR, Johnson GA, Groman EV, Linney E. Proc. Natl. Acad. Sci. USA. 1994;91:3530.
12. Dhenain M, Ruffins SW, Jacobs RE. Dev. Biol. 2001;232:458.
13. Ahrens ET, Rothbacher U, Jacobs RE, Fraser SE. Proc. Natl. Acad. Sci. USA. 1998;95:8443.
14. Johnson GA, Hedlund LW, Cofer GP, Suddarth SA, Rev. Magn. Reson. Med. 1992;4:187.
15. Callaghan PT. Principles of Nuclear Magnetic Resonance Microscopy. Oxford Science: Oxford, England, 1993.
16. Hurlson SE, Cofer GP, Johnson GA, J. Imaging Syst. Technol. 1997;8:277.
17. Benveniste H, Blackband S. Prog. Neurobiol. 2002; 67:393.

18. Streicher J, Weninger WJ, Muller GB. Anat. Rec. 1997;248:583.
19. Johnson GA, Cofer GP, Gewalt SL, Hedlund LW. Radiology. 2002;222:789.
20. Kuriwaki J, Nishijo H, Kondoh T, Uwano T, Torii K, Katsuki M, Ono T. Neurosignals. 2004;13:227.
21. Mueggler T, Baumann D, Rausch M, Staufenbiel M, Rudin M. J. Neurosci. 2003;23(23):8231.
22. Chapon C, Franconi F, Roux J, Marescaux L, Le Jeune JJ, Lemaire L. Anat. Embryol. 2002;206(1–2):131.
23. Smith BR. In: CW Low (Ed). Development Biology Protocols. Humana Press Inc.: Totawa, NJ, 2000, p. 211.
24. Jacobs RE, Ahrens ET, Dickinson ME, Laidlaw D. Comput. Med. Imaging Graph. 1999;23:15.
25. Schneider JE, Bamforth SD, Farthing CR, Clarke K, Neubauer S, Bhattacharya S. J. Anat. 2003a;202:239.
26. Bock NA, Konyer NB, Henkelman RM, Magn. Reson. Med. 2003;49:158.
27. Dazai J, Bock NA, Nieman BJ, Davidson LM, Henkelman RM, Chen XJ. Magn. Reson. Med. 2004;52:709.
28. Lloyd RV, Jin L, Chang A, Kulig E, Camper SA, Ross BD, Downs TR, Frohman LA. Am. J. Pathol. 1992;141: 895.
29. Kornguth S, Anderson M, Markley JL, Shedlovsky A. Neuroimage. 1994;1:220.
30. Fujii M, Hara H, Meng W, Vonsattel JP, Huang Z, Moskowitz MA. Stroke. 1997;28:1805.
31. Zaharchuk G, Hara H, Huang PL, Fishman MC, Moskowitz MA, Jenkins BG, Rosen BR. Magn. Reson. Med. 1997;37:170.
32. Jalanko A, Tenhunen K, McKinney CE, LaMarca ME, Rapola J, Autti T, Joensuu R, Manninen T, Sipilä I, Ikonen S, Riekkinen P Jr, Ginns EI, Peltonen L. Hum. Mol. Genet. 1998;7(2):265.
33. Fransen E, D'Hooge R, Van Camp G, Verhoye M, Sijbers J, Reyniers E, Soriano P, Kamiguchi H, Willemsen R, Koekkoek SK, De Zeeuw CI, De Deyn PP, Van der Linden A, Lemmon V, Kooy RF, Willens PJ. Hum. Mol. Genet. 1998;7:999.
34. McDaniel B, Sheng H, Warner DS, Hedlund LW, Benveniste H. Neuroimage. 2001;14:1244.
35. Wu EX, Tang H, Asai T, Yan SD. Neurosci. Lett. 2004;365:223.
36. In 't Zandt HJ, Renema WK, Streijger F, Jost C, Klomp DW, Oerlemans F, Van der Zee CE, Wieringa B, Heerschap A. J. Neurochem. 2004;90(6):1321.
37. Redwine JM, Kosofsky B, Jacobs RE, Games D, Reilly JF, Morrison JH, Young WG, Bloom FE. Proc. Natl. Acad. Sci. USA. 2003;100(3):1381.
38. Lin YJ, Koretsky AP. Magn. Reson. Med. 1997;38(3):378.
39. Natt O, Watanbe T, Boretius S, Radulovic J, Frahm J, Michaelis T. J. Neurosci. Methods. 2002;120:203.
40. Watanabe T, Natt O, Boretius S, Frahm J, Michaelis T. Magn. Reson. Med. 2002;48:852.
41. Aoki I, Lin Wu YJ, Silva AC, Lynch RM, Koretsky AP. Neuroimage. 2004;22:1046.
42. Kooy RF, Verhoye M, Lemmon V, van Der Linden A. Eur. J. Hum. Genet. 2001;9:153.
43. Kovačević N, Henderson JT, Chan E, Lifshitz N, Bishop J, Evans AC, Henkelman RM, Chen XJ. Cereb. Cortex. 2005;15:639.
44. Ross R, Leger L, Guardo R, De Guise J, Pike BG. J. Appl. Physiol. 1991;70(5):2164.
45. Fowler PA, Fuller MF, Glasbey CA, Cameron GG, Foster MA. Am. J. Clin. Nutr. 1992;56:7.
46. Ishikawa M, Koga K. Magn. Reson. Imaging. 1998;16:45.
47. Tang H, Vasselli JR, Wu EX, Boozer CN, Gallagher D. Am. J. Physiol. Regul. Integr. Comp. Physiol. 2002;282:R890.
48. Changani KK, Nicholson A, White A, Latcham JK, Reid DG, Clapham JC. Diabetes Obes. Metab. 2003;5:99.
49. Leonardsson G, Steel JH, Christian M, Pocock V, Milligan S, Bell J, So P-W, Medina-Gomez G, Vidal-Puig A, White R, Parker MG. Proc. Natl. Acad. Sci. USA. 2004;101(22):8437.
50. Beckmann N, Tigani B, Mazzoni L, Fozard JR. NMR Biomed. 2001;14:297.
51. Beckmann N, Tigani B, Mazzoni L, Fozard JR. Trends Pharmacol. Sci. 2003;24:550.
52. Garbow JR, Zhang Z, You M. Cancer Res. 2004;64:2740.
53. Dugas JP, Garbow JR, Kobayashi DK, Conradi MS. Magn. Reson. Med. 2004;52:1310.
54. Guenther D, Hanisch G, Kauczor HU. Acta Radiol. 2000;41:519.
55. Peces-Barba G, Ruiz-Cabello J, Cremillieux Y, Rodriguez I, Dupuich D, Callot V, Ortega M, Rubio Arbo ML, Cortijo M, Gonzalez-Mangado N. Eur. Respir. J. 2003;22(1): 14.
56. Thomas SR, Clark LC Jr, Ackerman KL, Pratt RG, Hoffmann RE, Busse LJ, Kinsey RA, Samaratunga RC, J. Comput. Assist. Tomogr. 1986;10:1.
57. Thomas SR, Millard RW, Pratt RG, Shiferaw Y, Samaratunga RC. Artif. Cells Blood Substit. Immobil. Biotechnol. 1994;22:1029.
58. Thomas SR, Gradon L, Pratsinis SE, Pratt RG, Fotou GP, McGoron AJ, Podgorski AL, Millard RW. Invest. Radiol. 1997;32:29.
59. Siri FM, Jelicks LA, Leinwand LA, Gardin JM. Am. J. Physiol. 1997;272:H2394.
60. Slawson SE, Roman BB, Williams DS, Koretsky AP. Magn. Reson. Med. 1998;39:980.
61. Ruff J, Wiesmann F, Hiller KH, Voll S, Von Kienlin M, Bauer WR, Rommel E, Neubauer S, Haase A. Magn. Reson. Med. 1998;40:43.
62. Franco F, Thomas GD, Giroir B, Bryant D, Bullock MC, Chwialkowski MC, Victor RG, Peshock RM. Circulation. 1999;99:448.
63. Wiesmann F, Ruff J, Hiller KH, Rommel E, Haase A, Neubauer S, Am. J. Physiol. 2000;278:H652.
64. Ruff J, Wiesmann F, Lanz T, Haase A. J. Magn. Reson. Imag. 2000;146:290.
65. Schneider JE, Bamforth SD, Farthing CR, Clarke K, Neubauer S, Bhattacharya S. J. Mol. Cell Cardiol. 2003;35:317.
66. Tang H, Vasselli JR, Wu EX, Gallagher D. Ann. N. Y. Acad. Sci. 2000;904:32.
67. Wessig C, Koltzenburg M, Reiners K, Solymosi L, Bendszus M, Exp. Neurol. 2004;185(2):254.
68. Streif JU, Hiller KH, Waller C, Nahrendorf M, Wiesmann F, Bauer WR, Rommel E, Haase A. J. Magn. Reson. Imag. 2003;17(1):147.
69. Damon BM, Ding Z, Anderson AW, Freyer AS, Gore JC. Magn. Reson. Med. 2002;48(1):97.

70. Ruiz-Cabello J, Regadera J, Santisteban C, Grana M, Perez de Alejo R, Echave I, Aviles P, Rodriguez I, Santos I, Gargallo D, Cortijo M. NMR Biomed. 2002;15(3):204.
71. Kosaka M, Owatari N, Seo Y, Kawakubo H, Harada S, Katsumata T, Ida H, Lehmann V. Jpn. J. Physiol. 2000;50:463.
72. Garbow JR, Kataoka M, Flye MW. Magn. Reson. Med. 2004;52:177.
73. Fabry ME, Kennan RP, Pàszty C, Costantini F, Rubin EM, Gore JC, Nogel RL. J. Clin. Invest. 1996;98(11):2450.
74. Solomon A, Weiss DT, Schell M, Hrncic R, Murphy CL, Wall J, McGavin MD, Pan HJ, Kabalka GW, Paulus MJ. Am. J. Pathol. 1999;154(4):1267.
75. de Graff RA. *In vivo* NMR Spectroscopy, Principles and Techniques. John Wiley and Son: Chichester, UK, 1998.
76. Mystkowski P, Shankland E, Schreyer SA, LeBoeuf RC, Schwartz RS, Cummings DE, Kushmerick M, Schwartz MW. Int. J. Obes. Relat. Metab. Disord. 2000;24:719.
77. Pierson RN Jr, Wang J, Thornton JC. Horm. Res. 1997;48(Suppl 1):56.
78. So P-W, Furmanski A, Herlihy AH, Bell JD. Proc. Int. Soc. Magn. Med. 2004;12:949.
79. So P-W, Muckett P, Herlihy AH, Bell JD. Proc. Int. Soc. Magn. Med. 2004;12:948.
80. Jones MEE, Thorburn AW, Britt KL, Hewitt KN, Wreford NG, Proietto J, Oz OK, Leury BJ, Robertson KM, Yao S, Simpson ER. Proc. Natl. Acad. Sci. USA. 2000;97(23):12735.
81. Taicher GZ, Tinsley FC, Reiderman A, Heiman ML. Anal. Bioanal. Chem. 2003;377:990.
82. Tinsley FC, Taicher GZ, Heiman ML. Obes. Res. 2004;12:150.
83. Kunnecke B, Verry P, Bernardeau A, von Kleinlin M. Obes. Res. 2004;12(10):1604.
84. Wunderlich C, Flogel U, Godecke A, Heger J, Schrader J. Circ. Res. 2003;92:1352.
85. Saupe KW, Spindler M, Tian R, Ingwall JS. Circ. Res. 1998;82:898.
86. Hoehn M, Nicolay K, Franke C, van der Sanden B. J. Magn. Reson. Imag. 2001;14:491.
87. Choi IY, Lee SP, Guilfoyle DN, Helpern JA. Neurochem. Res. 2003;28:987.
88. Baslow MH, Suckow RF, Gaynor K, Bhakoo KK, Marks N, Saito M, Duff K, Matsuoka Y, Berg MJ. Neuromolecular Med. 2003;3:95.
89. Jenkins BG, Klivenyi P, Kustermann E, Andreassen OA, Ferrante RJ, Rosen RR, Beal MF. J. Neurochem. 2000;74(5):2108.
90. Van Dellan A, Welch J, Dixon RM, Cordery P, York D, Styles P, Blakemore C, Hannan AJ. Neuroreport. 2000;27:3751.
91. Matalon R, Rady PL, Platt KA, Skinner HB, Quast MJ, Campbell GA, Matalon K, Ceci JD, Tyring SK, Nehls M, Surendran S, Wei J, Ezell EL, Szucs S. J. Gene Med. 2000;2(3):165.
92. Tracey I, Dunn JF, Parkes HG, Radda GK. J. Neurol. Sci. 1996;141:13.
93. Huang W, Galdzicki Z, van Gelderen P, Balbo A, Chikhale E, Schapiro MB, Rapoport SI. Neuroreport. 2000;11:445.
94. Schmidt A, Marescau B, Boehm EA, Renema KJ, Peco R, Das A, Steinfeld R, Chan S, Wallis J, Davidoff M, Ullrich K, Waldschütz R, Heerschap A, De Deyn PP, Neubauer S, Isbrandt D. Hum. Mol. Genet. 2004;13(9):905.
95. Dedeoglu A, Choi J-K, Cormier K, Kowall NW, Jenkins BG. Brain Res. 2004;1012:60.
96. Hesselbarth D, Franke C, Hata R, Brinker G, Hoehn-Berlage M. NMR Biomed. 1998;11(8):423.
97. Schwarcz A, Natt O, Watanabe T, Boretius S, Frahm J, Michaelis T. Magn. Reson. Med. 2003;49:822.
98. In 't Zandt HJ, Klomp DWJ, Oerlemans F, van der Zee CEEM, Wieringa B, Heerschap A. Proc. Int. Soc. Magn. Reson. Med. 2000;8:180.
99. Tkáč I, Henry PG, Andersen P, Kenne CD, Low WC, Gruetter R. Magn. Reson. Med. 2004;52:478.
100. Zwingmann C, Liebfritz D. NMR Biomed. 2003;16:370.
101. Sibson NR, Mason GF, Shen J, Cline GW, Herskovits AZ, Wall JE, Behar KL, Rothman DL, Shulman RG. J. Neurochem. 2001;76(4):975.
102. Gruetter R, Seaquist ER, Ugurbil K. Am. J. Physiol. Endocrinol. Metab. 2001;281:E100.
103. Shen J, Petersen KF, Behar KL, Brown P, Nixon TW, Mason GF, Petroff OA, Shulman GI, Shulman RG, Rothman DL. Proc. Natl. Acad. Sci. USA. 1999;96(14):8235.
104. Gruetter R, Adriany G, Choi IY, Henry PG, Lei H, Öz G. NMR Biomed. 2003;16:313.
105. Küstermann EHGK, Andreassen O, Beal F, Jenkins BG. Proc. Int. Soc. Magn. Reson. Med. 2000;8:1088.
106. Shonat RD, Koretsky AP. Adv. Exp. Med. Biol. 2003;530:331.
107. In 't Zandt HJ, de Groof AJ, Renema WK, Oerlemans FT, Klomp DW, Wieringa B, Heerschap A. J. Physiol. 2003;548(Pt 3):847.
108. Garbow JR, Lin X, Sakata N, Chen Z, Koh D, Schonfeld G. J. Lipid Res. 2004;45(7):1364.
109. Machann J, Haring H, Schick F, Stumvoll M. Diabetes Obes. Metab. 2004;6(4):239.
110. Neumann-Haefelin C, Kuhlmann J, Belz U, Kalisch J, Quint M, Gerl M, Juretschke HP, Herling AW. Magn. Reson. Med. 2003;50(2):242.
111. Neumann-Haefelin C, Beha A, Kuhlmann J, Belz U, Gerl M, Quint M, Biemer-Daub G, Broenstrup M, Stein M, Kleinschmidt E, Schaefer HL, Schmoll D, Kramer W, Juretschke HP, Herling AW. Diabetes. 2004;53(3):528.
112. Hockings PD, Changani KK, Saeed N, Reid DG, Birmingham J, O'Brien P, Osborne J, Toseland CN, Buckingham RE. Diabetes Obes. Metab. 2003;5(4):234.
113. Giannesini B, Izquierdo M, Confort-Gouny S, Cozzone PJ, Bendahan D. FEBS Lett. 2001;507(1):25.
114. Giannesini B, Izquierdo M, Le Fur Y, Cozzone PJ, Bendahan D. J. Physiol. 2001;536(Pt 3):905.
115. Westerblad H, Allen DG, Bruton JD, Andrade FH, Lannergren J. Acta Physiol. Scand. 1998;162(3):253.
116. Baker AJ, Carson PJ, Miller RG, Weiner MW. Muscle Nerve. 1994;17(9):1002.
117. Debold EP, Dave H, Fitts RH. Am. J. Physiol. Cell Physiol. 2004;287(3):C673.
118. Lara TM, Wong MS, Rounds J, Robinson MK, Wilmore DW, Jacobs DO. Arch. Surg. 1998;133(12):1316.
119. Bloch G, Chase JR, Avison MJ, Shulman RG. Magn. Reson. Med. 1993;30(3):347.
120. Chase JR, Rothman DL, Shulman RG. Am. J. Physiol. Endocrinol. Metab. 2001;280(4):E598.
121. Rothman DL, Shulman RG, Shulman GI. J. Clin. Invest. 1992;89(4):1069.

122. Shulman RG, Rothman DL, Price TB. Diabetes. 1996;45(Suppl 1):S93.
123. Kan HE, Renema WKJ, Isbrandt D, Heerschap A. J. Physiol. 2004;560:219.
124. Cohen SM. Fed. Proc. 1984;43:2657.
125. Choi IY, Wu C, Okar DA, Lange AJ, Gruetter R. Eur. J. Biochem. 2002;269:4418.
126. Dimicoli J-L, Patry J, Blouquit Y, Nedelec J-F, Adam R. Biochimie. 2003;85:891.
127. Brosnan MJ, Chen L, Van Dyke TA, Koretsky AP. J. Biol. Chem. 1990;265:20849.
128. Brosnan MJ, Chen LH, Wheeler CE, Van Dyke TA, Koretsky AP. Am. J. Physiol. 1991;260:C1191.
129. Miller K, Halow J, Koretsky AP. Am. J. Physiol. 1993;265:C1544.
130. Askenasy N, Koretsky AP. Am. J. Physiol. Cell. Physiol. 2002;282:C338.
131. Lindon JC, Holmes E, Bollard ME, Stanley EG, Nicholson JK. Biomarkers. 2004;9(1):1.
132. Gavaghan CL, Holmes E, Lenz E, Wilson ID, Nicholson JK. FEBS Lett. 2000;484:169.
133. Gavaghan CL, Nicholson JK, Connor SC, Wilson ID, Wright B, Holmes E. Anal. Biochem. 2001;291:245.
134. Griffin JL, Williams HJ, Sang E, Clarke K, Rae C, Nicholson JK. Anal. Biochem. 2001;293:16.
135. Holmes E, Foxall PJD, Nicholson JK, Neild GH, Brown SM, Beddell CR, Sweatman BC, Rahr E, Lindon JC, Spraul M, Neidig P. Anal. Biochem. 1994;220(2):284.
136. Bollard ME, Holmes E, Lindon JC, Mitchell SC, Branstetter D, Zhang W, Nicholson JK. Anal. Biochem. 2001;295(2):194.
137. Gavaghan CL, Wilson ID, Nicholson JK. FEBS Lett. 2002;530(1–3):191.
138. Griffin JL. Phil. Trans. R. Soc. Lond. B 2004;359: 857.
139. Griffin JL, Bonney SA, Mann C, Hebbachi AM, Gibbons GF, Nicholson JK, Shoulders CC, Scott J. Physiol. Genomics. 2004;17(2):140.

Experimental Models of Brain Disease: MRI Contrast Mechanisms for the Assessment of Pathophysiological Status

David L. Thomas[1], Louise van der Weerd[2], Mark F. Lythgoe[2], and John S. Thornton[3]
[1] *Wellcome Trust High Field MR Research Laboratory, Department of Medical Physics and Bioengineering, University College London, London WC1N 3AR, UK*
[2] *RCS Unit of Biophysics, Institute of Child Health, University College London, London WC1N 1EH, UK*
[3] *Lysholm Department of Neuroradiology, National Hospital for Neurology and Neurosurgery, UCLH NHS Trust, London, WC1N 3BG, UK*

Introduction

Magnetic resonance imaging (MRI) is a technique allowing non-invasive *in vivo* imaging with excellent discrimination between different types of soft tissue. The contrast in a standard MR image depends both upon variations in tissue water density and the physicochemical environment of the water. For this reason, it is not only possible to differentiate tissue types [e.g. gray matter, white matter, and cerebrospinal fluid (CSF) in the brain] but also normal and abnormal physiological states (e.g. to identify regions of cerebral edema following a stroke). More recently, methods have been developed, which allow more dynamic assessment of changing physiological parameters, either through their effect on MR relaxation parameters or via some other modulation of the MR signal. In this chapter, the most common MR methods used for imaging the brain will be described, and the mechanisms responsible for the sensitivity of these methods to pathophysiology in brain disease will be explained.

Image Contrast and Intrinsic MR Parameters

The physical and chemical environment of the water molecules in the brain affects the MR signal intensity by altering the transverse and longitudinal MR relaxation rates. This allows the visualization of biophysical processes that occur on a spatial scale many times smaller than the nominal image resolution. MR sequences can be designed to have their image contrast dominated (or "weighted") by one or other of the relaxation times, and by so doing sensitize them to the factors influencing that particular parameter.

T_1-weighted Imaging

T_1 (the longitudinal or spin-lattice relaxation time) is the time constant for the exponential recovery of the longitudinal magnetization. The exact details of the relaxation mechanisms are complex, but they are facilitated by the presence of microstructures such as macromolecules and cell membranes (known as the lattice) that can absorb the energy of the excited protons via dipolar interactions. This energy transfer is most efficient when the rotational frequency of the molecules is in the same range as the Larmor frequency (i.e. in the 50–400 MHz range for typical MR scanner field strengths). In practice, this means that T_1 becomes shorter as the molecular mobility decreases, but increases again for very slow molecular motion, such as in solids. In biological systems, tissue environments that contain abundant microstructural elements are characterized by shorter T_1 relaxation times, and regions where structure is less restricted or has broken down (e.g. in CSF or areas of edema; Figure 1) T_1 is longer. Also, since the efficiency of T_1 relaxation depends on the proportion of molecular rotations at the Larmor frequency, T_1 values vary (typically increase) with magnetic field strength.

In order to achieve T_1 weighting in MR images, one of the two main approaches are generally taken. The amount of signal recovery during the recovery time (TR) of a standard spin echo (SE) or gradient echo (GE) sequence is determined by T_1, and so selecting a TR value that allows almost full relaxation for tissue with short T_1 and minimal relaxation for tissue with long T_1 generates strong T_1 contrast. As an alternative to this saturation recovery method, the inversion recovery (IR) method can be used, either to selectively null the signal from certain tissue types (e.g. FLAIR to eliminate CSF signal [1]) or to generate the desired T_1 contrast. If a set of images

Graham A. Webb (ed.), Modern Magnetic Resonance, 787–799.
© 2008 *Springer.*

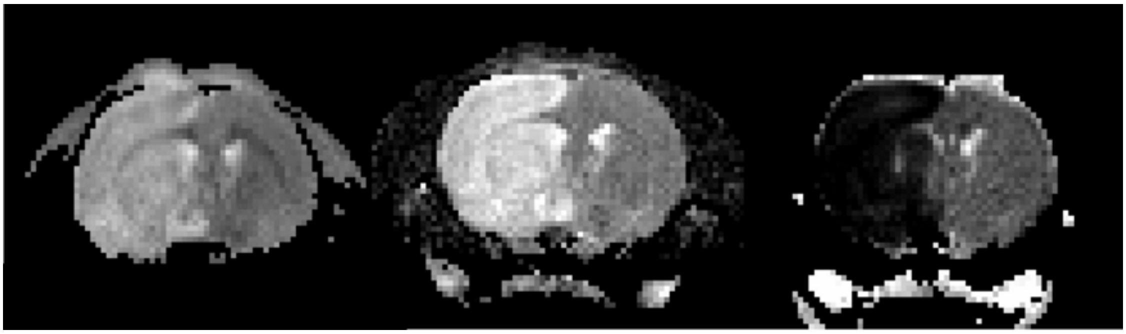

(a) T_1 map (b) T_2 map (c) ADC map

Fig. 1. MR parameter maps of a coronal slice of the rat brain 24 h after a 30 min occlusion of the middle cerebral artery (supplying the territory on the left side of the images). Hyperintensity in the T_1 and T_2 maps indicates the progression of vasogenic edema; low ADC values indicate increased restriction of water diffusion caused by cell swelling (cytotoxic edema).

is acquired with a range of recovery or inversion times, T_1 maps can be calculated by fitting the image data to theoretical T_1-dependent signal curves. Compared to images which are merely T_1-*weighted*, T_1 maps provide a more specific quantitative assessment of MR signal changes, since the influence of all other factors affecting image contrast (e.g. T_2, diffusion, etc.) is removed.

T_2-weighted Imaging

T_2 (the transverse or spin–spin relaxation time) is the time constant for the decay of the transverse magnetization. The main mechanism for transverse relaxation relies on intermolecular magnetic interactions between the hydrogen nuclei of a water molecule and the protons of neighboring molecules. The random Brownian motion of water molecules means that these interactions are irreversible and therefore not undone by a 180° refocusing pulse. This interaction becomes more efficient when the contact time between molecules is relatively long, e.g. in viscous media. When the rotational correlation time of the molecules is short, such as for free water molecules, the spin–spin interactions will be brief and so T_2 is relatively long ($\sim$3 s). Water molecules interacting with macromolecules or solid surfaces generally have slower tumbling rates, leading to a reduction in the relaxation time. Because water mobility often varies substantially between tissue types, and changes in situations of cellular stress, T_2-dependent contrast is commonly used in MRI studies to depict pathology (Figure 1).

T_2-weighted imaging is performed using SE sequences with long TR and echo times (TEs) chosen to maximize the difference in signal intensity between the tissues of interest. The use of an SE sequence ensures that dephasing of the transverse magnetization caused by static field inhomogeneities is refocused, and signal loss is determined by processes that are dynamic on the timescale of the TE. In addition to the dipolar spin–spin interactions described above, this can include the effects of diffusion through intrinsic magnetic field gradients (such as those surrounding venous blood vessels) and magnetization transfer (see below). As with T_1 imaging, quantitative T_2 maps can be calculated by acquiring images over a range of TEs.

T_2^*-weighted Imaging

If a 180° pulse is not used to refocus the transverse magnetization, the signal decay is dependent on "static" field inhomogeneities as well as the factors described above for T_2 relaxation (in this context, "static" refers to effects which do not change over the time frame of the signal acquisition period, which is typically in the range 10–100 ms). The presence of small local magnetic field variations results in a range of Larmor spin precession frequencies and thus in a loss of phase coherence, causing a faster decay of the transverse magnetization. This apparent transverse relaxation rate without RF refocusing is described by the time constant T_2^*. The sensitivity to field disturbances can be exploited as a source of contrast in tissue, since such magnetic field inhomogeneities typically occur at interfaces of structures with differing magnetic susceptibilities, such as soft tissue and bone or tissue and blood. The main applications of T_2^*-weighted imaging in animal models of disease are blood oxygenation level-dependent (BOLD) imaging and contrast agent enhanced imaging. These methods are described in detail below.

T_2^*-weighted imaging is performed using GE sequences with TEs chosen to maximize sensitivity to the tissue changes of interest. However, it is important to note that the increased sensitivity to field disturbances can also cause problems in regions of the brain where gross magnetic field inhomogeneity exists. Imaging of such regions may be precluded since they will exhibit short T_2^* values, leading to gross signal dropout at the TEs required to generate significant T_2^* weighting in other parts of the brain. In order to reduce this problem, "z-shimming" techniques may be used [2,3], at the expense of compromised signal-to-noise ratio (SNR) values in the other areas of the brain. GE sequences can use short TR, which reduces the imaging time but also introduces T_1 weighting to the signal intensity.

$T_{1\rho}$-weighted Imaging

If a continuous RF pulse with amplitude B_1 is applied immediately after spin excitation, the transverse magnetization becomes "spin-locked" to this applied B_1 field. An energy level system is set up in the transverse plane and the rate at which the excited magnetization returns to equilibrium is known as $T_{1\rho}$ (or "T_1 in the rotating frame"). The importance of $T_{1\rho}$ imaging is that, in the same way that T_1 relaxation is sensitive to molecular motion at frequencies determined by the main magnetic field ($\omega_0 = \gamma B_0 = 42.577 \times 10^6 \times B_0$, i.e. the MHz range), $T_{1\rho}$ relaxation is sensitive to molecular motion at frequencies determined by the B_1 field ($\omega_1 = \gamma B_1$ where $B_1 \sim 1$ mT, i.e. ω_1 is in the kHz range). This means that $T_{1\rho}$ contrast is sensitive to the relatively slow motion characterizing the macromolecular components of biological systems, and so can offer an alternative contrast regime compared to T_1- and T_2-weighted imaging. The use of $T_{1\rho}$ imaging for *in vivo* studies is still at an early stage of development. However, it has recently been shown that $T_{1\rho}$ can provide more specific prognostic information than other MR parameters regarding tissue state following transient ischemia [4]. $T_{1\rho}$ imaging has also been used to investigate, *inter alia*, brain tumors [5] and articular cartilage [6]. $T_{1\rho}$-weighted imaging is usually performed using a magnetization preparation scheme followed by a rapid imaging sequence. For example, a $90_x°$ excitation pulse followed by the continuous wave RF spin locking pulse for a given period; a subsequent $90_{-x}°$ flip-back pulse will produce longitudinal magnetization with amplitude related to $T_{1\rho}$. Echo planar or FLASH imaging can then be used to produce a $T_{1\rho}$-weighted image.

Taking Advantage of MR Sensitivity to Dynamic Physiological Processes

BOLD Imaging

BOLD imaging relies on the fact that the deoxyhemoglobin molecule is paramagnetic and so has a different magnetic susceptibility than other brain tissue. As a result, blood vessels containing deoxyhemoglobin are surrounded by small magnetic field gradients, which decrease the T_2^* value of the surrounding tissue and consequently reduce the signal intensity in a T_2^*-weighted image [7,8]. The degree to which signal intensity is reduced depends on the absolute amount of deoxyhemoglobin in nearby blood vessels, and BOLD imaging is primarily concerned with localized changes in signal intensity which reflect changes in local deoxyhemoglobin levels and, by implication, changes in blood flow and/or neuronal activity.

Under normal conditions, cerebral blood flow (CBF) is autoregulated in the brain within a well-defined range. However, in certain circumstances, CBF can be temporarily adjusted in response to a stimulus. For example, during periods of hypercapnia (inhalation of abnormally high levels of CO_2), the cerebrovascular response acts to increase CBF. Since the oxygenation level of arterial blood is normal (close to 100%) and oxygen metabolism in the brain does not change during hypercapnia, this effectively means that an excess of oxygenated blood is delivered to the brain, and consequently the venous blood is more oxygenated than normal i.e. the amount of deoxyhemoglobin in the veins is lower than normal. This causes an increase in T_2^* of the tissue surrounding the veins, or equivalently an increase of signal intensity in a T_2^*-weighted image. Figure 2 shows an example of a T_2^*-weighted imaging image intensity time course during hypercapnia in the rat brain.

Transient alterations in CBF also occur when the brain is functionally activated. This effect is the basis of

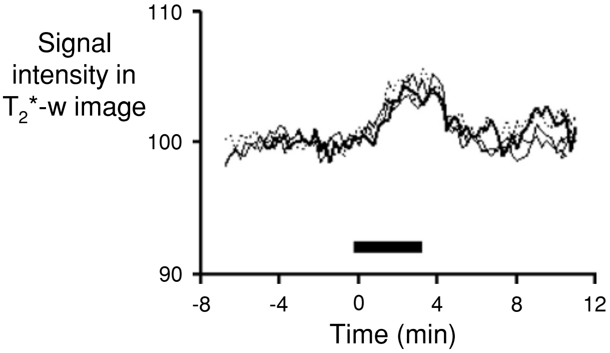

Fig. 2. Time course data from a region of gray matter in the rat brain. At time = 0, hypercapnia was initiated by the addition of 15% CO_2 to the inspired gases (800:400 ml/min N_2O:O_2 with 0.8% halothane anesthesia) and maintained for 3 min. During hypercapnia cerebral blood flow increases, causing a washout of deoxyhemoglobin from the venous vessels of the cerebral vasculature, and thus an increase in signal intensity in a T_2^*-weighted image.

functional MRI (fMRI). In this case, an increase in neuronal activity causes local CBF to increase by an amount which is greater than that needed to satisfy the elevated metabolic demand. As with hypercapnia, the result is a decrease in the amount of venous deoxyhemoglobin and an increase in signal intensity in a T_2^*-weighted image. It is therefore possible to correlate localized functional activation in the brain to experimentally controlled cognitive stimuli. The maximum possible spatial resolution of this method is likely to be limited by the proximity of the activated tissue to its venous vasculature. It should be noted that the BOLD effect is also observed in T_2-weighted imaging, due to dynamic dephasing effects. At high magnetic field strength, T_2 BOLD contrast is heavily weighted toward the capillary compartment of the vasculature and so is more likely to be spatially representative of the region of neuronal activation than T_2^* BOLD, which is dominated by larger venous effects [9]. For a full review of fMRI, the reader is referred to the many texts dedicated to this topic [10–12].

Angiography

Magnetic resonance angiography (MRA), a method used routinely in clinical radiology for imaging large vessel blood flow [13], has recently been adapted for the visualization of cerebral vasculature and bulk blood flow in small animals. Studies have typically employed the 3D time-of-flight (TOF) method [14]. A 3D GE sequence with relatively short TR, short TE, and moderate flip angle is employed. During the image acquisition, the volume of interest experiences multiple RF pulses and therefore the longitudinal magnetization of stationary spins becomes partially saturated and these tissues appear dark in the image. Blood flowing into the image volume during the acquisition is initially fully magnetized and therefore appears hyperintense relative to non-moving tissue. The sequence yields a stack of images, which may be processed using a maximum intensity projection (MIP) algorithm to generate pseudo-3D displays of the vascular anatomy (Figure 3).

Since inflowing blood becomes progressively more saturated while it remains within the imaging volume, by judicious choice of TR and flip angle it is possible to maximize contrast for particular flow velocities: parameters are commonly chosen to maximize the conspicuity of arteries relative to that of veins. In order to avoid signal loss due to velocity-induced spin dephasing, flow-compensated imaging sequences are commonly employed. The choice of the shortest possible TE and the highest available spatial resolution (i.e. the smallest voxel size) is also helpful in this respect. Each repetition of the imaging sequence may be preceded by an off-resonance saturation pulse designed either to further suppress stationary background tissue signal by exploiting the magnetization transfer effect (see “Magnetization Transfer Imaging” section below), or to selectively suppress signals from short T_1 fatty tissues which may otherwise produce confusing artifacts. Vessel conspicuity may be further improved by the use of T_1-shortening blood-pool contrast agents [15].

Applications of 3D TOF–MRA in animal models of disease have included visualization of the effects of vessel occlusion and reperfusion in models of cerebral ischemia in rats [16–18] and mice [19], identification of strain-dependent variations in cerebrovascular anatomy [20], and to identify cerebrovascular abnormalities in a transgenic mouse model of Alzheimer’s disease [21].

Using Exogenous Contrast Agents to Enhance Image Contrast

In addition to the various physiological sensitivities available based on the intrinsic MR parameters of brain tissue, further contrast manipulation is possible with the introduction of exogenous contrast agents. These techniques, described in more detail in other chapters in this book, are covered briefly here for completeness.

T_1-weighted Dynamic Contrast Enhanced MRI

In the normal brain, the integrity of the blood–brain barrier (BBB) means that it is impermeable to low-molecular weight contrast agents such as Gd-DTPA [22]. These contrast agents therefore remain intravascular and, while causing a transient decrease in T_2 and T_2^* during the passage of the bolus through the cerebral vasculature (see “Perfusion Imaging” section below), have no effect on the T_1 relaxation of extravascular brain tissue. This exemplifies one of the crucial differences in the mechanisms which enhance transverse and longitudinal relaxation: the creation of microscopic magnetic field gradients around vessels containing paramagnetic or superparamagnetic [such as ultra-small superparamagnetic iron oxide (USPIO)] particles causes extravascular T_2 and T_2^* values to decrease, whereas the requirement for direct interaction between the contrast agent and the water molecules leaves extravascular T_1 unaffected. However, disruption of the BBB in many disease states leads to the leakage and accumulation of contrast agent media into the affected tissue. In this situation, T_1 values are reduced and the signal intensity in a T_1-weighted image increases.

In order to maximize the attainable information from a T_1-weighted contrast enhanced study, a time course of T_1 images is acquired. This time course covers a baseline period, followed by the intravenous injection of a small volume of contrast agent and the subsequent collection of

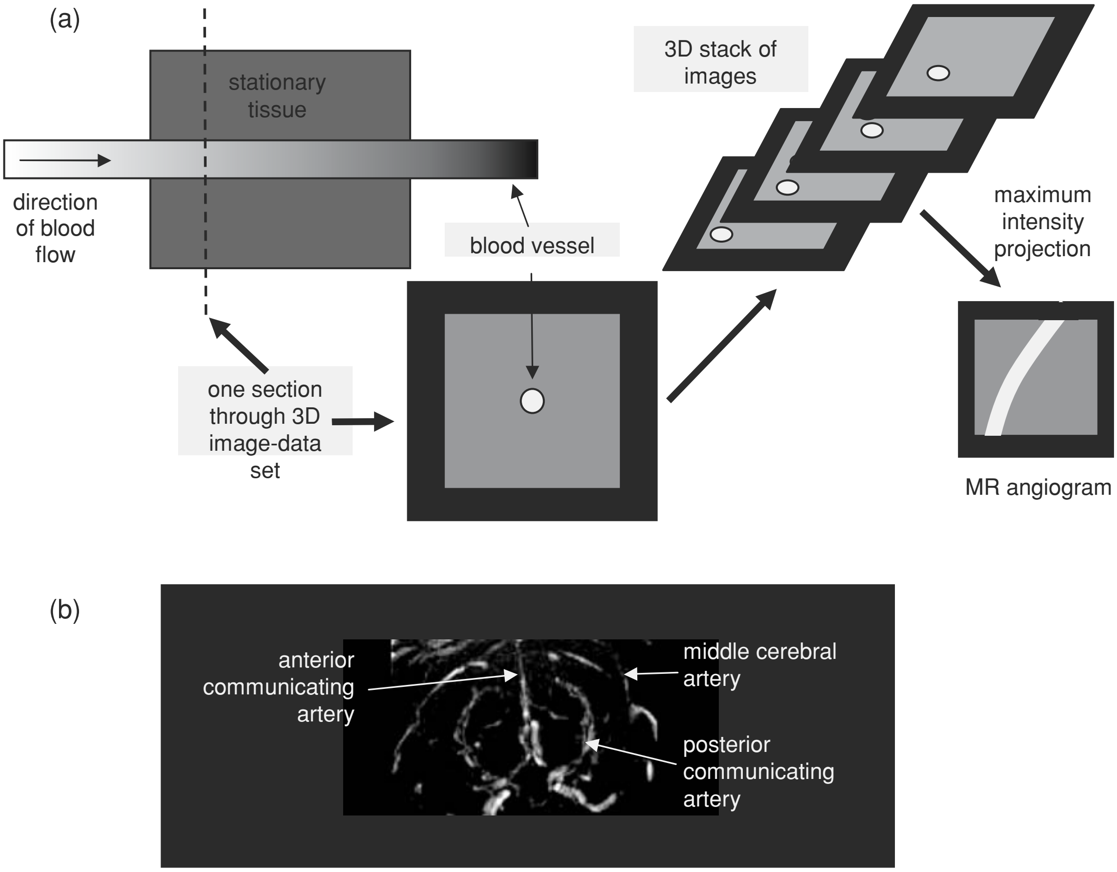
(a)
stationary tissue
direction of blood flow
blood vessel
one section through 3D image-data set
3D stack of images
maximum intensity projection
MR angiogram
(b)
anterior communicating artery
middle cerebral artery
posterior communicating artery

Fig. 3. (a) Schematic diagram showing the principles of time-of-flight (TOF) MR angiography. Blood flowing into the imaging volume at left is fully magnetized and therefore appears bright in contrast to the magnetically saturated stationary tissue. Note blood becomes increasingly saturated during its residency in the imaging volume, and thus contrast is typically higher for fast-flowing arterial blood relative to that of venous blood. The 3D data set is processed using the maximum intensity projection (MIP) algorithm to yield the final MR angiogram. (b) Axial view MIP reconstruction of a 3D-TOF MR angiogram showing the major cerebral arteries in a rat. (The image orientation is similar to that of the images in Figure 1.)

images during the period of uptake of the contrast agent. It has been demonstrated that the kinetics of the contrast agent uptake can be used to obtain quantitative parameters relating to the integrity of the BBB, and that these parameters improve the clinical utility of the technique compared to merely assessing a single post-contrast image (e.g. in the delineation of tumor margins [23,24]). Kinetic modeling of contrast agent uptake can provide information concerning the BBB transfer and rate constants, the size of the extravascular extracellular volume, the permeability-surface area product of the capillary wall per unit volume of tissue, and capillary blood flow per unit volume of tissue. For more details on the theoretical modeling and methodology of this technique, see Ref. [25].

The main area of application for contrast enhanced T_1-weighted imaging is the study of tumors, where the BBB becomes severely disrupted. Other pathologies in which breakdown of the BBB occurs include inflammation (e.g. in the initial stages of lesion formation in multiple sclerosis [26]), ischemia and ischemia–reperfusion [27], and traumatic brain injury [28].

Mapping Changes in CBV using Blood-pool Contrast Agents

An alternative method to BOLD contrast for mapping cerebral hemodynamic changes in animal models is provided by the use of exogenous intravascular contrast agents such as USPIO colloids. These contain carbohydrate coated iron oxide particles, which are many times larger than gadolinium complexes such as Gd-DTPA and exhibit long half-lives in the blood pool (more than 2–3 h in the rat). The very high magnetic susceptibility of these particles creates significant local field inhomogeneities causing rapid proton dephasing and thus significantly reducing T_2^* (as well as T_2 and T_1) in the surrounding tissue. An increase in cerebral blood volume (CBV) on functional activation increases the tissue concentration of the contrast agent causing a dramatic local decrease in T_2^* and T_2. The magnetic susceptibility of these contrast agents is far greater than that of deoxyhemoglobin leading to a larger signal change, and hence a contrast-to-noise ratio typically 2–6 times (depending upon field strength and the contrast agent concentration) that obtained with BOLD contrast [29–31]. The magnetic susceptibility of the blood is dominated by the presence of the USPIOs and therefore remains essentially independent of deoxyhemoglobin concentration. This yields a measure of relative CBV (rel. CBV) which is not contaminated by changes in blood oxygen saturation. A further advantage of USPIO contrast agents is that their magnetic susceptibility is sufficiently high that the T_2^* in blood itself becomes very short (□10 ms). As a result, the intravascular signal is negligible and signal changes are dominated by hemodynamic perturbations in the capillary bed, and measurements are not confounded by contributions from larger vessels.

CBV mapping using USPIO contrast agents has found application in the study of pharmacologically induced cerebral activation in the rat (e.g. [32]), as well as in specific disease models such as the murine model of Alzheimer's disease [33], the study of functional reorganization after stroke in the rat brain [34] and the investigation of hemodynamic changes in neonatal hypoxic–ischemic encephalopathy in the rabbit [35].

Smart Contrast Agents

Over recent years, the role of contrast agents in *in vivo* MRI has been transformed by the introduction of smart contrast agents. These are biochemically activated agents that are capable of reporting on the anatomical and physiological function of cellular processes. They are described in detail in Chapter 8.

Manipulating the MR Signal to Measure Physiological Parameters

Diffusion-weighted Imaging

All molecules in a fluid are subject to diffusion (Brownian motion), and the extent of this motion depends on the temperature and viscosity of the fluid. Diffusion can be characterized by a diffusion coefficient D, which describes the average root mean square displacement (x) of a molecule as a function of time (t):

$$x = \sqrt{2dDt}, \tag{1}$$

where d is the number of dimensions in which diffusion can occur (usually three for biological systems). In general, the displacement distribution of the molecules is Gaussian, where the mean displacement distance increases with increasing displacement time. However, if the molecules encounter obstacles or barriers to diffusion (e.g. cell membranes), these will affect the nature of the diffusion and potentially limit the maximum displacement. Boundary restrictions imply that the displacement distribution is no longer Gaussian and depends on diffusion time. As a result, the measured diffusion coefficient is referred to as the apparent diffusion coefficient (ADC) and is smaller than the intrinsic D. The value of the ADC is sensitive to the number of barriers, their geometry and their permeability, i.e. to the tissue microstructure, which can change with physiological state. For example, cerebral ischemia causes acute cell swelling (cytotoxic edema) which reduces the diffusivity of extracellular water and is associated with a decrease in the overall tissue ADC (Figure 1c), although the exact mechanism for the ADC change is currently unknown [36].

An MR image is sensitized to diffusion by the application of additional magnetic field gradients (see Figure 4). If a linear field gradient is applied to an ensemble of magnetic spins that have been excited into the transverse plane, the rate of precession depends on the spin's position in the gradient. If an equal and opposite magnetic field gradient is applied soon after the first gradient (i.e. equal amplitude but opposite direction), the spins will precess in the opposite direction by the same amount, and therefore accrue no net phase change. However, if the spin changes its position (by diffusion) in the time between the application of the first and second gradients, the dephasing and rephasing effects of the diffusion gradients will not match exactly and a residual phase shift will remain. Since diffusion is a pseudo-random process, diffusion is equally likely to occur both ways along any given direction, and by variable distances over a large ensemble of spins. This results in a large range of residual phase shifts, with consequential destructive signal interference and loss of overall image intensity. Tissue regions with higher ADCs will exhibit a greater range of phase shifts and thus greater signal loss. The amount of signal loss is also determined by the parameters of the MRI sequence: the amplitude, duration, and time separation between the diffusion-weighting gradients. These are summarized by the so-called b value of

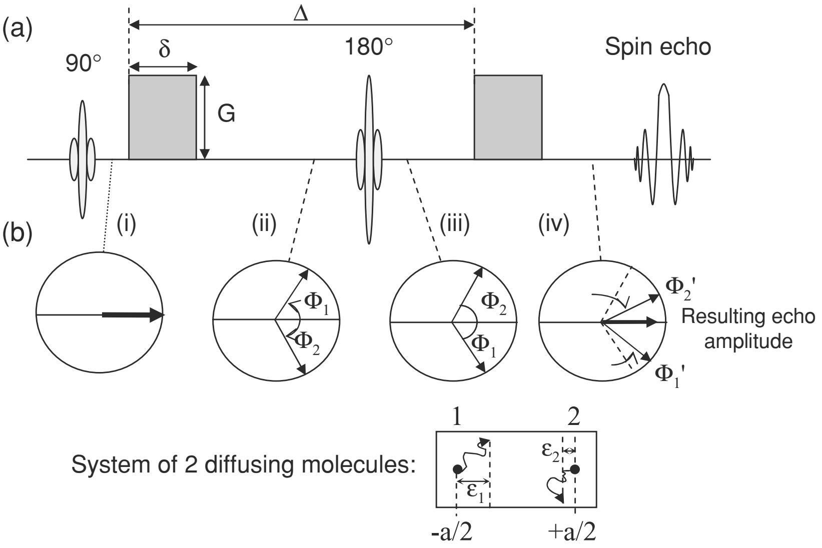

Fig. 4. Schematic representation of the Stejskal–Tanner pulsed gradient experiment and its effect on diffusing molecules. (a) The pulse sequence, with its timing and gradient variables. (b) The state of the transverse magnetization at four stages during the diffusion experiment (i–iv) for diffusing spins, in the case of a simple two spin system which begin with position $z = \{-a/2,\ a/2\}$ and diffuse to $z = \{-a/2 + \varepsilon_1, a/2 + \varepsilon_2\}$ (as shown at the bottom of figure). The transverse magnetization before (i, iii) and after (ii, iv) each of the two diffusion gradient pulses is represented. $\Phi_{1,2}$ represents the phase shift caused by the application of the diffusion gradients. For clarity, T_2 relaxation is ignored. The signal amplitude depends on the phase coherence remaining between the two spins at the time of echo formation. For stationary spins, $\Phi_1 = \Phi_1'$ and $\Phi_2 = \Phi_2'$ so that the application of diffusion-weighting gradients has no effect on the echo amplitude.

the sequence:

$$b_i = \gamma^2 G_i^2(\delta^2[\Delta - \delta/3]), \tag{2}$$

where γ is the gyromagnetic ratio, G_i is the amplitude of the diffusion gradients along direction i, δ is the duration of each of the diffusion gradients, and Δ is the time between the beginning of the first and second diffusion gradients (Figure 4). The reason for adopting this apparently complicated relationship between the b factor and the sequence parameters is so that the image signal loss in a diffusion-weighted image can be expressed as a simple monoexponential decay:

$$S_i = S_0\exp(-\,b_i \cdot \mathrm{ADC}_i), \tag{3}$$

where S_i is the diffusion-weighted signal intensity, S_0 is the signal without diffusion gradients, b_i is the b value resulting from diffusion gradients applied along direction i, and ADC_i is the ADC along this direction. Measurement of the signal intensity decay as a function of b value therefore allows straightforward calculation of the ADC.

In addition to altering the magnitude of the ADC, the presence of cell membranes and other objects that hinder diffusion can cause molecules to diffuse more easily in certain directions and less easily in other directions. For example, in the white matter of the brain, the myelin sheaths that cover the lengths of the axons act as barriers to diffusion, so that water diffuses easily in directions parallel to the white matter fibers and much less readily in directions perpendicular to the fibers. Therefore, the ADC value measured in a region of white matter depends on the direction of the measurement. Although this diffusion anisotropy of water in biological systems complicates the characterization of diffusion, it also provides useful structural information. In order to properly describe anisotropic diffusion in three dimensions, a 3 × 3 diffusion tensor is required to replace the scalar ADC [37]. From this tensor, quantitative measurements of diffusion anisotropy can be made, and parameters such as the fractional and lattice anisotropy indices can be used to summarize the degree of anisotropy [38]. In addition, the eigenvectors of the tensor can be used to determine the principle axis of diffusion, and in white matter fibers this signifies the direction of the fiber tracts. Based on this information, it is possible to perform fiber tracking by continuously following the direction of the principle eigenvectors from voxel to voxel, and thus infer fiber connections between different regions of the brain [39].

Perfusion Imaging

Perfusion (or CBF) is defined as the quantity of blood delivered to the capillary bed of a region of tissue in a certain period of time. Its units are milliliters of blood per 100 g of tissue per minute. It is important to distinguish between perfusion and bulk blood flow as seen by angiography/venography (which occurs along major arteries and veins). Perfusion is blood flow at the capillary level, and is closely related to the delivery of oxygen and other nutrients to the tissue. These factors determine the energy status of the tissue. Two main MRI approaches have been developed for CBF measurement: bolus tracking and arterial spin labeling (ASL).

Bolus Tracking

A bolus of paramagnetic contrast agent (e.g. Gd-DTPA) is injected intravenously into the subject. Shortly after, the contrast agent passes through the vasculature of the brain, and causes the signal of a T_2- or T_2^*-weighted image to change, due to a difference in magnetic susceptibility between the intravascular and extravascular compartments. This signal reduction is transient as the bolus of contrast agent washes through the tissue vasculature. The passage of the bolus is relatively fast (a few seconds), particularly in small animals. In order to characterize the signal time course accurately, which is essential for the accurate quantification of CBF, it is therefore important to acquire images as rapidly as possible. The rate at which successive bolus tracking experiments can be performed is limited by the clearance rate of the contrast agent from the vasculature. Residual levels of contrast agent reduce the signal change induced by subsequent boluses and so reduce the precision of the CBF measurement, and repeated injections of contrast agents such as gadolinium are eventually limited by their toxicity [40].

In order to convert the tissue signal intensity time course during the passage of the paramagnetic bolus to maps of CBF, it is necessary to (i) know the details of contrast agent delivery to the image voxels during the time course (the arterial input function (AIF)) and (ii) have a theoretical model which allows calculation of CBF from the MR images. The AIF can be estimated by acquiring images, which contain the feeding arteries to the tissue of interest, e.g. the middle cerebral artery. However, due to the small size of these arteries (particularly in small animals), the AIF can be difficult to measure reliably. Additionally, the effects of delay and dispersion of the bolus between the artery and the capillary bed of the tissue of interest can introduce errors in the estimation of the AIF [41,42]. For these practical reasons, absolute quantification is sometimes avoided and summary hemodynamic parameters used instead (see below). However, if we assume that we can measure the AIF with a reasonable degree of accuracy, CBF quantification is possible. First, the signal intensity changes are converted to changes in the transverse relaxation rate ΔR_2^* or ΔR_2, depending on whether GE or SE imaging has been performed ($\Delta R_2^* \equiv 1/T_2^*$). It is assumed that all signal intensity changes are due to ΔR_2^*. Figure 5a shows an example of a ΔR_2^* time course from the rat brain during a bolus passage. Assuming that ΔR_2^* is proportional to contrast agent concentration, we effectively now have a dynamic measure of the amount of contrast agent present in each image voxel. Using the principles of tracer kinetics for non-diffusable

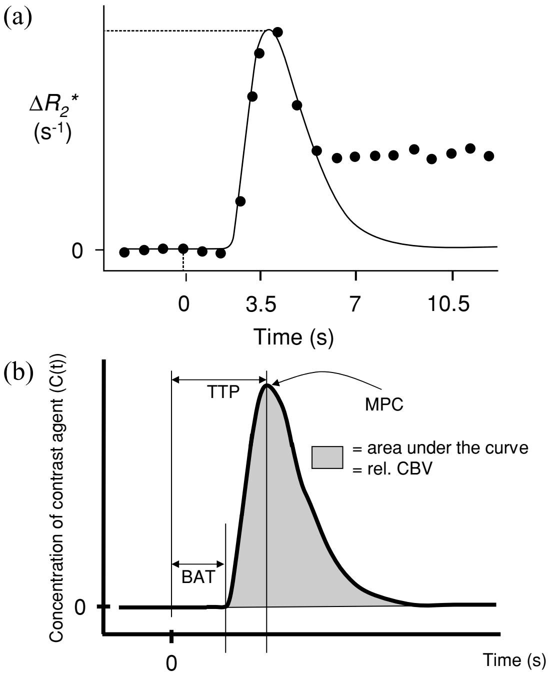

Fig. 5. (a) ΔR_2^* time course from a region of interest in the rat brain during the passage of a paramagnetic bolus. Note the increase in R_2^* during the bolus passage, caused by the transient presence of extravascular field gradients. ΔR_2^* remains elevated from the baseline value after the bolus passage due to recirculation and residual amounts of tracer in the blood. (b) Schematic representation of the concentration time curve observed in brain tissue following intravenous injection of a paramagnetic contrast agent. The summary parameters illustrated are: BAT, bolus arrival time; TTP, time to peak; MPC, mean peak concentration; rel. CBV, relative cerebral blood volume.

tracers [43–45] and assuming an intact BBB, the contrast agent concentration in each voxel (C_{VOI}) can be expressed as:

$$C_{\mathrm{VOI}}(t) = \left(\frac{\rho}{k_H}\right)\mathrm{CBF}(\mathrm{AIF}(t) \otimes R(t)), \qquad (4)$$

where $\otimes$ denotes a mathematical convolution, ρ/k_{H} is a scaling factor accounting for brain tissue density and blood hematocrit, AIF(t) is the arterial input function, and $R(t)$ is the residue function, which describes the fraction of injected tracer still present in the voxel at time t following an ideal instantaneous unit bolus injection at time $t = 0$ [41]. Using Equation (4), CBF can be calculated for each voxel. CBV can be also obtained from bolus tracking data. For an intact BBB, CBV is proportional to the normalized total amount of tracer

$$\mathrm{CBV} = \left(\frac{k_{\mathrm{H}}}{\rho}\right)\frac{\int C_{\mathrm{VOI}}(t)\mathrm{d}t}{\int \mathrm{AIF}(t)\mathrm{d}t}. \qquad (5)$$

The normalization to the AIF accounts for the fact that, independent of the CBV, if more tracer is injected, a greater concentration will reach the volume of interest. Once CBF and CBV are both known, it is also possible to calculate the average time for any given particle of tracer to pass through the tissue (the mean transit time, MTT) using the central volume theorem: MTT = CBV/CBF [46,47]. As mentioned above, an alternative to CBF quantification is to use summary parameters. The advantage of using summary parameters is that they are quick and easy to calculate, with minimal assumptions required; their disadvantage is that they do not give values for the real physiological variables CBF and CBV, and depend on experimental conditions, e.g. injection rate, vascular geometry, and cardiac output. Figure 5B illustrates the most commonly used summary parameters: bolus arrival time (BAT), time to peak (TTP), maximum peak concentration (MPC), and rel. CBV. These parameters are related to different aspects of the cerebral hemodynamics, e.g. BAT, the time after injection at which contrast agent begins to arrive in the voxel of interest, can provide information about the role of collateral blood supply when CBF is compromised. Although the use of summary parameters does not provide absolute values for CBF and CBV, it provides a useful tool for the investigation of perfusion during normal and ischemic conditions.

Arterial spin labeling

ASL is a CBF measurement method that uses magnetically labeled blood water as an endogenous tracer. It is appealing for imaging animal models of brain disease because it does not require injection of exogenous tracers and places no restriction of the number of repeat measurements that can be made in a single study. This makes ASL well suited to the monitoring of CBF during experimental time courses in animal models. The images obtained with ASL can be converted into CBF maps (with units of ml/100 g/min) as long as certain other MR parameters (such as T_1 and labeling efficiency; see below) are also measured. In ASL, perfusion-weighted images are generated by labeling inflowing blood water by inversion of its longitudinal magnetization. Two images must be acquired: one in which spin labeling is performed (the labeled image) and the other in which spin labeling is not performed (the control image). The difference between the two images is proportional to the amount of labeled blood that enters the imaging slice during the time between labeling and image acquisition, and therefore is also proportional to CBF. Spin labeling can be achieved using several alternative approaches, which has given rise to a family of ASL techniques.

The original ASL approach [48] is now generally known as *continuous* ASL (or CASL), because inflowing blood magnetization is inverted continuously over a period of several seconds prior to image acquisition. This allows an accumulation of spin labeled water as it is deposited in the perfused cerebral tissue. The measurement approach is illustrated in Figure 6a. The application of a magnetic field gradient results in a position-dependent frequency spread of the magnetization. An RF pulse of 1–3 s is applied with a frequency offset corresponding to water protons flowing through the carotid and vertebral arteries in the neck. This causes inversion of flowing spins via a process known as flow-induced adiabatic inversion [49]. Following the labeling RF pulse, an image is acquired using a rapid imaging technique (e.g. EPI). A problem associated with the off-resonance labeling RF pulse is chemical exchange of protons between water and macromolecules, which causes the water magnetization to decrease (the MT effect; see “Magnetization transfer imaging” section below). For this reason, an RF pulse with the reverse frequency offset is applied for the control image, which results in the same MT effect in the labeled and control image, so that the only difference between the images is due to the perfusion weighting.

Soon after the introduction of CASL, alternative approaches, known as *pulsed* ASL (PASL), were proposed which use shorter adiabatic inversion pulses. They have the advantage of a lower RF energy deposition than CASL due to the short (~10 ms) inversion pulses, but the disadvantage of a lower intrinsic SNR for the perfusion measurement. One of the PASL approaches is known as flow-sensitive alternating inversion recovery (FAIR) [50] and is shown in Figure 6B. This technique uses a pair of IR images, one following a slice-selective inversion pulse and the other following a non-selective (global) inversion pulse. The slice-selective IR image is flow-sensitive because the inflowing blood water magnetization is fully relaxed, and so accelerates the apparent T_1 relaxation of

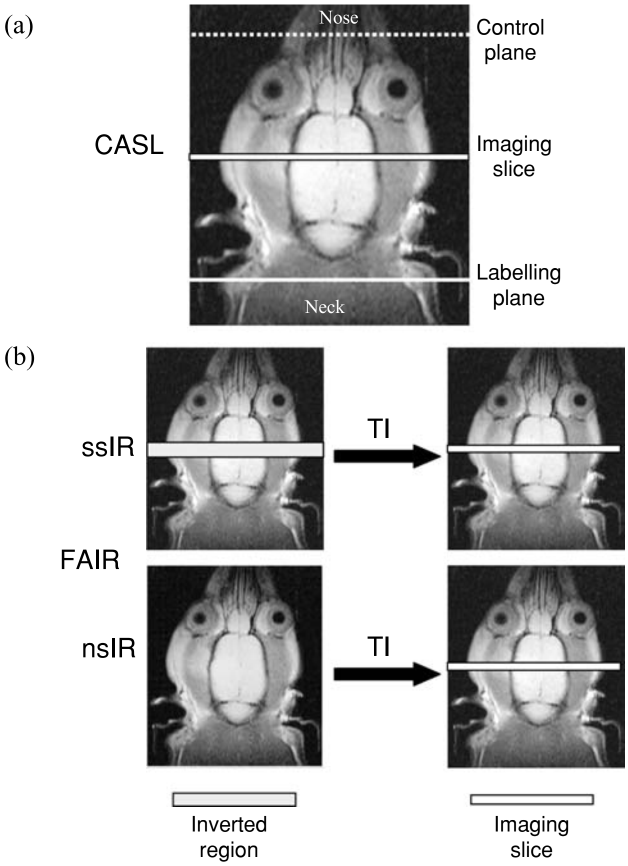

Fig. 6. (a) Continuous arterial spin labeling (CASL). Axial MR image of the rat brain showing the relative positions of the imaging slice (coronal) and the labeling and control planes. Simultaneous application of an off-resonance RF pulse and magnetic field gradient causes inversion of blood water 1H spins as they flow through the inversion plane (to produce a spin labeled image). The control plane does not intersect any major arteries and so application of an off-resonance RF pulse at this frequency causes magnetization transfer (MT) effects but not spin labeling. (b) Flow-sensitive alternating inversion recovery (FAIR)—an example of pulsed arterial spin labeling. In FAIR, a pair of images is also acquired, one following a slice-selective inversion (upper) and the other following a non-selective inversion (lower). The difference between the images is caused by the difference in the magnetization state of the inflowing blood water and is therefore directly proportional to CBF.

the tissue into which it flows. In the non-selective IR case, both tissue and inflowing blood magnetization are inverted, resulting in negligible flow sensitivity. Since the same inversion time is used in both the slice-selective and non-selective acquisitions, the signal from the static tissue is the same in both, but a difference between the images is observed in the presence of flow.

Perfusion can be quantified using ASL images and some additional information such as T_1. For a full description of the principles see [36,51], but in general the signal intensity in the ASL difference image (control–labeled) is directly proportional to CBF. An important factor that affects the accuracy of CBF quantification is a parameter known as the transit time. Following spin inversion, blood water travels through the vascular tree until it reaches the capillary bed and exchanges into the cerebral tissue. During this time (the transit time), the spin label decays at a rate determined by the T_1 of arterial blood. This must be accounted for in order to achieve accurate CBF quantification. Transit time effects are particularly problematic in CASL, where the labeling plane must be a minimum distance from the imaging slice to ensure that it coincides with a major artery. With PASL, transit times tend to be lower because the labeling region can be placed immediately adjacent to the imaging slice. To decrease the sensitivity to transit time effects, the sequences can be modified by inserting a post-labeling delay, which allows time for all the blood to travel from where it was labeled into the imaging region [52–54].

Magnetization Transfer Imaging

Magnetization transfer contrast (MTC) imaging [55] provides a means of probing a population of hydrogen nuclei otherwise invisible to conventional MRI [56]. These protons exist in a so-called "bound" state, i.e. their motion is restricted because they form part of either macromolecules, or water molecules restricted within the hydration layers around macromolecules. Such protons exhibit very short T_2 relaxation times (<100 μs) which implies

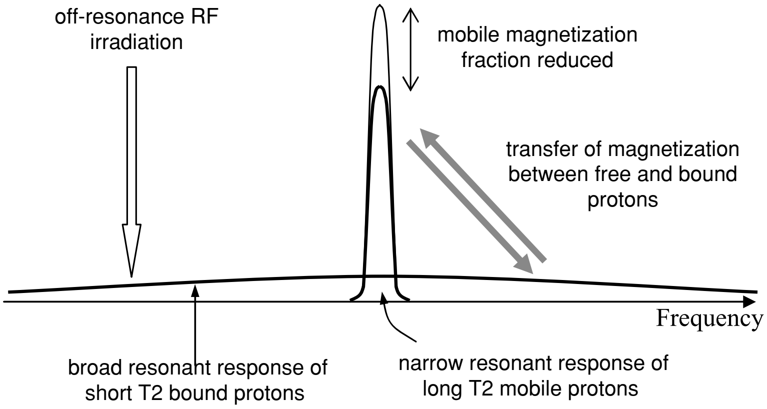
off-resonance RF irradiation
mobile magnetization fraction reduced
transfer of magnetization between free and bound protons
Frequency
broad resonant response of short T2 bound protons
narrow resonant response of long T2 mobile protons

Fig. 7. Schematic diagram showing the origin of magnetization transfer contrast. Off-resonance RF irradiation affects directly only the broad resonance of the bound proton fraction. Exchange ("transfer") of magnetization between this bound proton fraction and the mobile water fraction causes a concomitant reduction in the mobile water magnetization, and hence a reduction in MR image intensity.

total signal decay before acquisition can commence even with short-TE standard SE MRI methods.

There is an inverse relationship between T_2 and the range of frequencies over which protons respond to RF excitation: protons in the "bound" fraction exhibit very short T_2s and consequently have a broad resonance width (~20 kHz) in the frequency domain. On the other hand, bulk water protons possess long T_2s with a correspondingly narrow (~10 Hz) frequency domain resonance (Figure 7). This difference can be used to perturb the bound fraction independently from the bulk protons. If continuous RF irradiation is supplied at a frequency offset (typically by 1–5 kHz) from the central resonant frequency, the magnetization of the bound protons will be reduced by saturation, while, in the absence of exchange, the bulk water pool remains unaffected. However, there is generally a significant exchange of magnetization between the two proton fractions, either by direct chemical exchange or by magnetic interactions. Since the bound proton magnetization has been reduced by the off-resonance irradiation, such exchange leads to a consequent reduction in both the magnitude of the observable bulk water magnetization and its effective T_1 relaxation time. The size of the signal decrease depends upon both the relative sizes of the two fractions and upon the rate of magnetization exchange. Since both of these factors may be influenced by tissue pathology, MTC imaging is uniquely sensitive to certain disease processes.

MTC imaging is commonly achieved semi-quantitatively by collecting an image (S_s) in which acquisition is preceded by a long (~3 s) saturating off-resonance RF pulse. A second image (S_0) is then acquired without a pre-saturation pulse and the magnetization transfer ratio (MTR) calculated as:

$$\mathrm{MTR} = (S_0 - S_\mathrm{s})/S_0 \times 100\% \tag{6}$$

A high MTR signifies the presence of a significant proton pool associated with macromolecules or cellular microstructure *and* a significant exchange of magnetization between these protons and those of the bulk water. Reduced MTR suggests a disruption of the tissue microstructure. A common example of the utility of MTC is the depiction of the pathological disruption of white matter due to demyelination, e.g. in multiple sclerosis.

In order to reduce imaging time and possibly to overcome certain hardware limitations, selective saturation of the bound fraction may also be achieved by pulsed methods. Here GE images with short TR are obtained with each excitation pulse preceded by a short (~10 ms) off-resonance pulse [57]. If the repetition time is sufficiently short compared to the T_1 of the bound pool, an equilibrium saturation of these spins is established after a number of cycles. In practice, the magnitude of the MTC effect measured is dependent upon the duration, intensity, and frequency offset of the off-resonance pulses, and caution is therefore required in the comparison of MTC imaging results obtained using different implementations.

Conclusions

In summary, MRI provides an array of quantitative techniques sensitive to a range of biophysical parameters. Within a single scanning session, several of these methods can be applied, yielding images with different, complementary contrasts and providing a rich understanding of the physiological microenvironment. The application of these techniques in suitable animal models of disease may greatly enhance our knowledge of brain pathologies, provides improved diagnostic and prognostic measures, yield insight into basic mechanisms of cellular injury, and, by providing non-invasive biomarkers of disease progression, greatly facilitate the assessment of novel therapeutic strategies.

Acknowledgments

The authors would like to thank Romina Aron-Badin, Mankin Choy, Neil Harris, and Rick Dijkhuizen for their contribution of images for the manuscript. We also acknowledge the Wellcome Trust and the BBSRC for their support of the work carried out at the Radiology and Physics Unit of the Institute of Child Health, and the Wellcome Trust High Field MR Research Laboratory, University College London.

References

1. Hajnal JV, Bryant DJ, Kasuboski L, Pattany PM, De Coene B, Lewis PD, Pennock JM, Oatridge A, Young IR, Bydder GM. Use of fluid attenuated inversion recovery (FLAIR) pulse sequences in MRI of the brain. J. Comput. Assist. Tomogr. 1992;16(6):841–4.
2. Frahm J, Merboldt K-D, Hanicke W. Direct FLASH MR imaging of magnetic field inhomogeneities by gradient compensation. Magn. Reson. Med. 1988;6:474–80.
3. Ordidge RJ, Gorell JM, Deniau JC, Knight RA, Helpern JA. Assessment of relative brain iron concentration using T_2-weighted and T_2^*-weighted MRI at 3 Tesla. Magn. Reson. Med. 1994;32:335–41.
4. Grohn OHJ, Kettunen MI, Makela HI, Penttonen M, Pitkanen A, Lukkarinen JA, Kauppinen RA. Early detection of irreversible cerebral ischemia in the rat using dispersion of the magnetic resonance imaging relaxation time $T_{1\rho}$. J. Cereb. Blood Flow Metab. 2000;20:1457–66.
5. Aronen HJ, Ramadan UA, Peltonen TK, Markkola AT, Tanttu JI, Jaaskelainen J, Hakkinen AM, Sepponen R. 3D spin-lock imaging of human gliomas. Magn. Reson. Imaging. 1999;17:1001–10.
6. Duvvuri U, Goldberg AD, Kranz JK, Hoang L, Reddy R, Wehrli FW, Wand AJ, Englander SW, Leigh JS. Water magnetic relaxation dispersion in biological systems: the contribution of proton exchange and implications for the noninvasive detection of cartilage degradation. Proc. Natl Acad. Sci. U.S.A. 2001;98:12479–84.
7. Ogawa S, Lee TM, Nayak AS, Glynn P. Oxygenation sensitive contrast in magnetic resonance images of rodent brain at high magnetic fields. Magn. Reson. Med. 1990;14: 68–78.
8. Ogawa S, Lee TM, Kay AR, Tank DW. Brain magnetic resonance imaging with contrast dependent on blood oxygenation. Proc. Natl Acad. Sci. U.S.A. 1990;87: 9868–72.
9. Ugurbil K, Hu X, Chen W, Zhu X-H, Kim SG, Georgopolous A. Functional mapping in the human brain using high magnetic fields. Phil. Trans. R. Soc. Lond. B. 1999;354:1195–213.
10. Buxton RB. Introduction to Functional Magnetic Resonance Imaging. Cambridge University Press: Cambridge, 2002.
11. Jezzard P, Matthews PM, Smith SM. Functional Magnetic Resonance Imaging—An Introduction to Methods. Oxford University Press: Oxford, 2003.
12. Hoehn M. In: N van Bruggen, T Roberts (Eds). Functional Magnetic Resonance Imaging in Biomedical Imaging in Experimental Neuroscience. CRC Press, Boca Raton, Florida (USA), 2003, pp. 93–136.
13. Graves MJ. Magnetic resonance angiography. Br. J. Radiol. 1997;70:6–28.
14. Ruggieri PM, Laub GA, Masaryk TJ, Modic MT. Intracranial circulation: pulse-sequence considerations in three-dimensional (volume) MR angiography. Radiology. 1989;171:785–91.
15. Mellin AF, Cofer GP, Smith BR, Suddarth SA, Hedlund LW, Johnson GA. Three dimensional magnetic resonance microangiography of rat neurovasculature. Magn. Reson. Med. 1994;32:199–205.
16. Reese T, Bochelen D, Sauter A, Beckmann N, Rudin M. Magnetic resonance angiography of the rat cerebrovascular system without the use of contrast agents. NMR Biomed. 1999;12:189–96.
17. Besselmann M, Liu M, Diedenhofen M, Franke C, Hoehn M. MR angiography investigation of transient focal ischemia in rat. NMR Biomed. 2001;14:289–96.
18. Hilger T, Niessen F, Diedenhofen M, Hossmann KA, Hoehn M. Magnetic resonance angiography of thromboembolic stroke in rats: indicator of recanalization probability and tissue survival after recombinant tissue plasminogen activator treatment. J. Cereb. Blood Flow Metab. 2002;22:652–62.
19. Beckmann N. Stirnimann R, Bochelen D. High-resolution magnetic resonance angiography of the mouse brain: application to murine focal cerebral ischemia models. J. Magn. Reson. 1999;140:442–50.
20. Beckmann N. High resolution magnetic resonance angiography non-invasively reveals mouse strain differences in the cerebrovascular anatomy in vivo. Magn. Reson. Med. 2000;44:252–8.
21. Krucker T, Schuler A, Meyer EP, Staufenbiel M, Beckmann N. Magnetic resonance angiography and vascular corrosion casting as tools in biomedical research: application to transgenic mice modeling Alzheimer's disease. Neurol. Res. 2004;26:507–16.
22. Weinmann HJ, Brasch RC, Press WR, Wesbey GE. Characteristics of gadolinium-DTPA complex—A potential NMR contrast agent. Am. J. Roentgenol. 1984;142:619–24.
23. Lunsford LD, Martinez AJ, Latchaw RE. Magnetic resonance imaging does not define tumor boundaries. Acta Radiol. 1986;369(Suppl):154–6.
24. Earnest F, Kelly PJ, Scheithauer BW, Kall BA, Cascino TL, Ehman RL, Forbes GS, Axley PL. Cerebral astrocytomas: histopathologic correlation of MR and CT contrast enhancement with stereotactic biopsy. Radiology. 1988;166:823–7.
25. Parker GJM, Padhani AR. T1-w DCE-MRI: T1-weighted dynamic contrast-enhanced MRI. In: Tofts PS (ed). Quantitative MRI of the Brain. Measuring Changes Caused

by Disease, John Wiley & Sons Ltd. Chichester (UK), 2003.

26. Kermode AG, Thompson AJ, Tofts P, MacManus DG, Kendall BE, Kingsley DP, Moseley IF, Rudge P, McDonald WI. Breakdown of the blood–brain barrier precedes symptoms and other MRI signs of new lesions in multiple sclerosis. Pathogenetic and clinical implications. Brain. 1990;113(Pt 5):1477–89.
27. Harris NG, Gauden V, Fraser PA, Williams SR, Parker GJ. MRI measurement of blood–brain barrier permeability following spontaneous reperfusion in the starch microsphere model of ischemia. Magn. Reson. Imaging. 2002;20: 221–30.
28. Shreiber DI, Smith DH, Meaney DF. Immediate in vivo response of the cortex and the blood–brain barrier following dynamic cortical deformation in the rat. Neurosci. Lett. 1999;259:5–8.
29. van Bruggen N, Busch E, Palmer JT, Williams S-P, De Crespigny AJ. High resolution functional magnetic resonance imaging of the rat brain: mapping changes in cerebral blood volume using iron oxide contrast media. J. Cereb. Blood Flow Metab. 1998;18:1178–83.
30. Mandeville JB, Marota JJA, Kosofsky BE, Keltner JR, Weissleder R, Rosen BR, Weisskoff RM. Dynamic functional imaging of relative cerebral blood volume during rat forepaw stimulation. Magn. Reson. Med. 1998;39: 615–24.
31. Kennan RP, Scanley BE, Innis RB, Gore JC. Physiological basis for BOLD MR signal changes due to neuronal stimulation: separation of blood volume and magnetic susceptibility effects. Magn. Reson. Med. 1998;40:840–6.
32. Chen YC, Mandeville JB, Nguyen TV, Talele A, Cavagna F, Jenkins BG. Improved mapping of pharmacologically induced neuronal activation using the IRON technique with superparamagnetic blood pool agents. J. Magn. Reson. Imaging. 2001;14:517–24.
33. Mueggler T, Baumann D, Rausch M, Staufenbiel M, Rudin M. Age-dependent impairment of somatosensory response in the amyloid precursor protein 23 transgenic mouse model of Alzheimer's disease. J. Neurosci. 2003;23: 8231–36.
34. Dijkhuizen RM, Ren J, Mandeville JB, Wu O, Ozdag FM, Moskowitz MA, Rosen BR, Finklestein SP. Functional magnetic resonance imaging of reorganization in rat brain after stroke. Proc. Natl Acad. Sci. U.S.A. 2001;98:12766–71.
35. D'Arceuil HE, Crespigny AJ, Rother J, Moseley M, Rhine W. Serial magnetic resonance diffusion and hemodynamic imaging in a neonatal rabbit model of hypoxic–ischemic encephalopathy. NMR Biomed. 1999;12:505–14.
36. Thomas DL, Lythgoe MF, Pell GS, Calamante F, Ordidge RJ. The measurement of diffusion and perfusion in biological systems using magnetic resonance imaging. Phys. Med. Biol. 2000;45:R97–138.
37. Basser PJ, Mattiello D, Le Bihan D. MR diffusion tensor spectroscopy and imaging. Biophys. J. 1994;66: 259–67.
38. Pierpaoli C. Basser PJ. Toward a quantitative assessment of diffusion anisotropy. Magn. Reson. Med. 1996;36:893–906.
39. Mori S, van Zijl PC. Fiber tracking: principles and strategies—a technical review. NMR Biomed. 2002;15:468–80.
40. Shellock FG, Kanal E. Safety of magnetic resonance imaging contrast agents. J. Magn. Reson. Imaging. 1999;10:477–84.
41. Ostergaard L, Weisskoff RM, Chesler DA, Glydensted C, Rosen BR. High resolution measurement of cerebral blood flow using intravascular tracer bolus passages. Part I: mathematical approach and statistical analysis. Magn. Reson. Med. 1996;36:715–25.
42. Calamante F, Gadian DG, Connelly A. Delay and dispersion effects in dynamic susceptibility contrast MRI: simulations using singular value decomposition. Magn. Reson. Med. 2000;44:466–73.
43. Zierler KL. Theoretical basis of indicator-dilution methods for measuring flow and volume. Circ. Res. 1962;10:393–407.
44. Zierler KL. Equations for measuring blood flow by external monitoring of radioisotopes. Circ. Res. 1965;16: 309–21.
45. Axel L. Cerebral blood flow determination by rapid sequence computed tomography. Radiology. 1980;137:679–686.
46. Stewart GN. Researches on the circulation time in organs and the influences which affect it. J. Physiol. 1894;15:1–89.
47. Meier P, Zierler KL. On the theory of the indicator-dilution method for measurement of blood flow and volume. Appl. Physiol. 1954;6:731–44.
48. Detre JA, Leigh JS, Williams DS, Koretsky AP. Perfusion imaging. Magn. Reson. Med. 1992;23:37–45.
49. Dixon WT, Du LN, Faul DD, Gado M, Rossnick S. Projection angiograms of blood labeled by adiabatic fast passage. Magn. Reson. Med. 1986;3:454–62.
50. Kim SG. Quantification of relative cerebral blood flow change by flow-sensitive alternating inversion recovery (FAIR) technique: application to functional mapping. Magn. Reson. Med. 1995;34:293–301.
51. Calamante F, Thomas DL, Pell GS, Wiersma J, Turner R. Measuring cerebral blood flow using magnetic resonance imaging techniques. J. Cereb. Blood Flow Metab. 1999;19:701–35.
52. Alsop DC, Detre JA. Reduced transit-time sensitivity in noninvasive magnetic resonance imaging of human cerebral blood flow. J. Cereb. Blood Flow Metab. 1996;16:1236–49.
53. Wong EC, Buxton RB, Frank LR. Quantitative imaging of perfusion using a single subtraction (QUIPSS and QUIPSS II). Magn. Reson. Med. 1998;39:702–8.
54. Luh WM, Wong EC, Bandettini PA, Hyde JS. QUIPSS II with thin-slice TI_1 periodic saturation: a method for improving accuracy of quantitative perfusion imaging using pulsed arterial spin labeling. Magn. Reson. Med. 1999;41:1246–54.
55. Wolff S, Balaban R. Magnetisation transfer contrast (MTC) and tissue water proton relaxation *in vivo*. Magn. Reson. Med. 1989;10:135–44.
56. Henkelman RM, Stanisz GJ, Graham SJ. Magnetization transfer in MRI: a review. NMR Biomed. 2001;14:57–64.
57. Dousset V, Grossman RI, Ramer KN, Schnall MD, Young L. H, Gonzalez-Scarano F, Lavi E, Cohen JA. Experimental allergic encephalomyelitis and multiple sclerosis: lesion characterization with magnetization transfer imaging. Radiology. 1992;182:483–91.

Experimental Models of Brain Disease: MRI Studies

Louise van der Weerd[1,2], David Thomas[3], John Thornton[4], ManKin Choy[1], and Mark F. Lythgoe[1]
[1] *RCS Unit of Biophysics, Institute of Child Health, University College London, London WC1N 1EH, UK;*
[2] *Medical Molecular Biology Unit, Institute of Child Health, University College London, UK;*
[3] *Wellcome Trust High Field MR Research Laboratory, Department of Medical Physics and Bioengineering, University College London, London WC1N 3AR, UK; and*
[4] *Lysholm Department of Neuroradiology, National Hospital for Neurology and Neurosurgery, UCLH NHS Trust, London WC1N 3BG, UK*

Introduction

MRI of intact animals was first employed in the 1970s. With the advent of dedicated animal scanners, the use of MRI for *in vivo* animal studies has mushroomed, and currently thousands of papers are published every year. Though a wide variety of laboratory animals is used, including monkeys, songbirds, and piglets among many others, the majority of MRI studies concerns rodent models of disease. In particular the use of mice has increased substantially over the past few years due to the development of a large range of transgenic mouse models. This chapter is dedicated to the use of MRI in small animal models of brain disease, and will describe some of the practical issues surrounding the use of MRI, and review the role of MRI in investigating the pathophysiology of the most common neurological disorders.

Practical Issues

Signal-to-noise

The size difference between humans and rodents is about a factor 10–20. To achieve a spatial resolution equivalent to that obtained in clinical imaging, this means that the voxel volume has to be reduced at least a factor of 10^3, implying in turn that the sensitivity has to be increased correspondingly to obtain a similar signal-to-noise-ratio (SNR). Much of the sensitivity can be gained by using RF receiver coils that are optimized for the size of the animals. Further sensitivity can be obtained by increasing the magnetic field strength; currently, horizontal small animal MRI systems with field strengths up to 11.7 T are commercially available. A third possibility to improve SNR is to increase the acquisition time up to several hours, which currently is used mostly for anatomical imaging of either *in vivo* or fixated animals.

Probes

To acquire data within the MR scanner, the animal should be immobilized in a non-magnetic probe with ear and bite bars, allowing the head to be positioned reproducibly relative to the gradient coils to attain the correct imaging slice or region of interest. Several MR-compatible stereotaxic frames have been designed to permit reproducible positioning in the scanner for repeat measurements. In MR magnets with a small bore, the use of ear and bite bars may not be possible, in which case the skull may be glued directly to the probe to reduce movement artifacts [1].

Temperature control is commonly attained through the use of either warm air blown over the animal, an electrically heated mat, or a warm water jacket or mat. Animals are readily anaesthetized via administration of anesthetics through a nose cone for spontaneously breathing rodents, intraperitoneal injection, or mechanical ventilation (see below). Physiological monitoring of cardiac and respiration rate may be performed simultaneously using implanted chest electrodes [2] or conventional EE electrodes in combination with an air pressure cushion to monitor respiration. Blood pressure is conventionally monitored using an intra-arterial line or, more recently, a piezoelectric pulse transducer [3]. Intravenous lines may be inserted for blood gas measurements or administration of drugs.

With the recent development of numerous transgenic mouse models, the demand for high-throughput phenotypic and physiological screening of large numbers of animals has soared. Therefore, probes have been designed that can hold several mice at the same time, with individual decoupled and shielded transmitter and receiver coils, anesthetics, and physiological monitoring [4]. Up to 16 mice can thus be measured in a single session.

To record EEG signals during an MRI experiment, silver or tungsten electrodes can be implanted. Alternatively, non-magnetic graphite electrodes, which reduce susceptibility effects, may be used EEG [5]. Gradient switching causes large artifacts on all EEG measurements, and data

Graham A. Webb (ed.), Modern Magnetic Resonance, 801–821.
© 2008 *Springer.*

need to be filtered to remove these. This is particularly problematic when using ultra-fast imaging sequences, where there may not enough undisturbed time intervals for a usable EEG recording.

Anesthesia

Correct anesthesia becomes very important when studying physiological processes, since many anesthetics may interfere with the processes under investigation. The most common route of application is inhalation via a nose cone. This approach allows close control of the depth of anesthesia, which can be assessed from the respiration and cardiac rate. However, when using spontaneous breathing, there is little or no control of blood gases, since CO_2 is often accumulated due to respiratory depression; mechanical ventilation may be used to control oxygen and carbon dioxide levels.

Alternatively, the animal can be anaesthetized for up to several hours using an injectable anesthetic, either intravenous or intraperitoneal. This method is very straightforward, but the depth of anesthesia is difficult to control, and one may need to give top-up injections while the animal is in the magnet.

The choice of anesthetic should depend on the physiological problem in question, as different substances may have distinctly different effects on systemic blood pressure, cerebral blood flow (CBF), cerebral oxygen consumption, and receptor function [6]. The method of choice in most laboratories is inhalation of isoflurane with oxygen/air or an oxygen/nitrous oxide mixture. It is important to note that isoflurane reduces the heart rate and blood pressure due to vasodilatation, which in turn influences CBF and therefore also the blood oxygenation level dependent (BOLD) effect (see Chapter 3). Reports have shown neuroprotection after stroke due to pre- or peri-ischemic administration of isoflurane and several other anesthetic agents [7,8].

In some cases, e.g. for functional MRI, maintenance of the BOLD effect and neuronal activity is of prime importance. For those studies injectable α-chloralose is routinely used, because it maintains a stable CBF and cortical activity; however, this agent is usually only used for terminal experiments. Nevertheless, functional response is always greater in a conscious animal, and some groups actually train conscious animals to remain immobile in a stereotaxic frame for several hours [9,10]. Obviously, extensive training is required to adapt the animals to the frame and to the noise levels during the experiment.

Selection of Animal Models

Adaptations may need to be made to an animal model to make it usable for MRI measurements. This is especially true when there is an interest in the very acute stages of disease. For example, the introduction of new MR imaging techniques such as diffusion-weighted imaging (DWI) allowed the investigation of a stroke within minutes of the initial event, which led to the modification of animal models to induce ischemia by remote occlusion whilst the animal was inside the MRI scanner [11]. The following section will discuss the specific MRI adaptations to models of cerebral ischemia, since this is the area where most developments have occurred.

Focal Ischemia Models

Most remote occlusion models are based on the Koizumi model for middle cerebral artery occlusion (MCAO) using a silicone rubber cylinder attached to a thread inserted through the internal carotid artery [5,11–14]. These remote occlusions are essential to investigate the hyperacute MR changes post-occlusion, and also to allow a direct comparison of pre- and post-occlusion image data [11,14]. This is not a trivial experiment, but as shown by Li *et al*., successful occlusion could be achieved in 88% of animals studied. Lythgoe *et al*. developed a model based on the intraluminal suture method, which uses an undersized suture to produce a partial obstruction of the MCA and a moderate reduction in CBF throughout the MCA territory [15]. Recently, a remote model was developed in which the MCA and both common carotid arteries (CCA) can be (partially) occluded and de-occluded using a small bronze hook placed around the MCA via a small craniotomy, and snares of bronze wire placed around the CCAs. This model is only suitable for terminal experiments, but is extremely reproducible and allows for careful manipulation of perfusion [16].

Apart from the suture and snare model, there are several thromboembolic occlusion models in which an embolus is injected via a catheter [17–19]. The embolus can be either artificial (e.g. microspheres) or biological (e.g. homologous blood clots). These models can be used in-bore and are more representative of the clinical situation, though they tend to be less reproducible. In the case of blood clots, reperfusion can be established by rt-PA treatment, but reperfusion is slow and variable.

Global Ischemia Models

Cardiac arrest has been extensively employed for the study of the pathological consequences of global ischemia and reperfusion [20]. Fischer *et al*. have extended this work for MR and demonstrated the feasibility of resuscitation following cardiac arrest within the magnet [21]. In 1979, Pulsinelli and Brierley introduced the four-vessel occlusion model of reversible ischemia in rats [22,23]. Briefly, on the day before the experiment, atraumatic clasps are placed loosely around both CCAs and the vertebral arteries are electrocauterised. Global ischemia is induced by tightening the sutures around the CCAs. This technique has been used quite extensively with MR for both single and repeated occlusions [24] and also to produce graded ischemia [25]. Global insults may also have both a hypoxic and ischemic component. With the aim of modeling human birth asphyxia, Thornton *et al*. have described a hypoxic/ischemic piglet model using inflatable cuffs around both CCAs combined with a decreased oxygen level [26].

The remaining sections in this chapter give an overview of some of the possibilities for MRI investigations of cerebral pathology in experimental animal models.

Cerebral Ischemia

Cerebral ischemia occurs when the blood supply to some or all brain regions is interrupted due to arterial occlusion, vascular disruption, or heart failure. The resulting reduced perfusion leads to oxygen deprivation, energy failure, and ultimately cell death. The use of MRI in experimental stroke research includes both diagnostic applications and prediction of outcome [27]. Some of the most important topics are the investigation of the underlying processes that lead to cell death [28], defining and understanding the concept of the penumbra [29] as a possible salvageable region, and possible therapies for the treatment of stroke [30,31].

Perfusion During Ischemia

Cerebral blood flow and cerebral blood volume (CBV) can be assessed using perfusion imaging. These measurements are based on either a susceptibility change in the vascular bed due to the passage of an exogenenous contrast agent (dynamic susceptibility contrast (DSC) enhanced MRI), or on the blood water pool as an endogenous perfusion marker (arterial spin labeling (ASL)), see Chapter 3 for details. Early DSC experiments in rat and cat models of focal cerebral ischemia demonstrate an absence of contrast agent in the ischemic core of the lesion [32,33]. Numerous other studies have followed, showing the spatial diversity within the ischemic tissue [34,35]. The relation between CBF and CBV can be used to assess hemodynamic responses such as vasodilatation [36,37], whereas the bolus peak time provides information on the arterial transit time, which may relate to collateral blood supply to the ischemic area [38]. This work using DSC-MRI has been complemented by studies using non-invasive ASL techniques for the quantitation of CBF in animal models [39]. Although these techniques have a low SNR compared to DSC-MRI, the non-invasive nature and the possibility to perform serial measurements make them an attractive tool. Acute cerebral ischemia has been characterized by serial CBF measurements in permanent and reperfusion stroke models [40–43].

A direct translation of perfusion rates into potential tissue damage is difficult, for several reasons. Firstly, CBF quantification is not always straightforward due to unknown parameters like the arterial input function and arterial transit times. Secondly, CBF thresholds appear to be different for different cell types and brain regions [44]. Thirdly, CBF values tend to vary over time, and the actual tissue damage strongly depends on the duration of ischemia, and on the level of perfusion throughout the insults and during reperfusion. Therefore other parameters have been explored that are more directly influenced by the physiological state of the tissue, including diffusion and relaxation.

Diffusion During Ischemia

The first DWI studies of permanent ischemia demonstrated, that following occlusion of the MCAO, the ADC decreases and the corresponding ischemic lesion in both rat and cat is visible within minutes and expands primarily during the first 2 h [45]. Although the lesion size has nearly fully evolved at 2 h, the ADC value continues to decrease for a period of up to 4–6 h following MCAO to 40% of control values [46], with some studies reporting the lowest ADC values at 24–48 h (40–50% of control) [47]. In the chronic stages of cerebral ischemia, the ADC of water exhibits a different pattern. Approximately 24–48 h after a vessel occlusion, the ADC starts to rise again and slowly pseudo-normalizes at 3 days [48]. Following this, a subsequent increase in the diffusion of water above that of the ischemic control can be observed after 1 week [46]. The elevated ADC of tissue water is associated with cellular lysis or the loss of cellular barriers, combined with an excessive accumulation of edematous water [49].

Interestingly, in the periphery of the lesion, a diffusion–perfusion mismatch can be observed, i.e. perfusion deficits not great enough to cause energy failure may go unnoticed on DWI. A cat model of hypoperfusion shows the same pattern, with diffusion-weighted images showing no evidence of abnormality in the territory of the occluded MCA, whereas the DSC-MRI blood flow measurements show decreased CBF throughout the MCA region [50]. By combining DWI and CBF data, three different tissue areas can be identified following an ischaemic insult: areas with normal perfusion and diffusion, denoting normal tissue; a region in which there is a concomitant diffusion and perfusion decrease, corresponding to a severely compromised region; and tissue that has a CBF decrease without diffusion changes corresponding to a region of hypoperfusion, the so-called diffusion-perfusion mismatch [41]. The relation between these areas and the core and penumbra of a stroke lesion is discussed below.

The Penumbra

The term *penumbra* was introduced to designate a zone of brain tissue with moderate ischemia and impaired neuronal function, with the neuronal paralysis being fully reversed upon reperfusion [51]. Currently the term has a wider definition and is used to describe a region of ischemic tissue peripheral to the core where viable neurons may be found, and thus may be potentially salvageable with suitable intervention or therapy [29,52]. As for CBF, ADC thresholds have been proposed, below which irreversible tissue damage would occur [53], but it is recognized more and more that, especially in the case of ischemia-reperfusion, the pathology is too complicated to justify the same threshold in all cases. Penumbral zones can be delineated using several different imaging modalities, each of which have definitions that rely on the underlying mechanisms of that technique [29]. The region of signal intensity change in DWI corresponds closely to the region of peri-infarct acidosis, but also encompasses the area of ATP depletion (infarct core). Therefore, it was postulated that the outer margin of the DWI visible lesion corresponds with that of the penumbra [54]. However, this is only part of the picture, as it is now acknowledged that regions of DWI change that normalize on reperfusion may proceed on to infarction at a later time point [55,56] and that the areas of so-called diffusion–perfusion mismatch need to be considered as well [57]. Because tissue damage is dependent on residual flow and duration of ischemia, the ischemic penumbra characterizes a transient condition that may extend in time to hypoperfused surrounding tissue. A recent study of global transient ischemia showed that the striatum exhibited a prolonged and gradual secondary ADC decrease after reperfusion, suggesting delayed cell death via a gradual process long after the initial insult (Figure 1) [58].

In human studies it has long been recognized that diffusion in organized tissue is anisotropic, which lead to the development of diffusion tensor imaging (DTI). Early reports demonstrate ADC anisotropy in cortical gray matter and in white matter in a rat model of cerebral ischemia, showing that diffusion encoding in one direction only results in poor lesion delineation [1,59]. Sotak *et al*. showed increased anisotropy during the first hours of permanent focal ischemia in the rat, combined with a reduced overall ADC [60].

At later stages, these characteristics are reversed, i.e. ADC is elevated and anisotropy reduced, reflecting the loss of cellular barriers [60,61].

Relaxation Contrast During Ischemia

During the last few years, animal studies have demonstrated that several MRI parameters provide additional information to the now clinically implemented T_2, diffusion and perfusion measurements.

Early changes in T_2 values have been reported in conditions of ischemia [41,62] and oligaemia [63]. In the latter studies of cerebral ischemia, two patterns were observed following an initial T_2 decrease: (i) T_2 values remained depressed throughout the study without an ADC change, indicating a mild hypoperfusion condition [41,62]; (ii) T_2 and ADC values are decreased throughout the study, indicating a severe hypoperfusion condition [41,64]. Further, early detection (within 15 min) of ischemia [41] and oligemia [63] are possible using the MRI parameter T_1. The underlying mechanism for this change is still unclear, but may depend of tissue oxygenation status. These data highlight that changes in T_2 and T_1 and are not always related to vasogenic edema and early changes in these parameters may provide information as to the pathophysiological nature of ischemia or oligaemia. Kavec *et al*. used both short and long echo times in a CPMG sequence to distinguish changes in BOLD contrast from intrinsic relaxation changes in the tissue, which they argue might be a marker for irreversible tissue damage [65].

Gröhn *et al.* [66] have demonstrated early detection of irreversible cerebral ischemia in the rat using a parameter known as $T_{1\rho}$ (T_1 in the rotating frame), which probes specific spin populations taking place in the macromolecules or in the macromolecular-water interface.

During the last few years, new approaches have been adopted to image molecular targets using specific contrast agents. A novel contrast agent (Gd-DTPA-sLe(x) A) has been designed by Barber *et al*. to bind to activated endothelium. Injection of the agent after focal ischemia in mice resulted in reductions in T_1 in the ipsilateral hemisphere that were unrelated to blood–brain barrier breakdown [67]. Several paper have been published on stem cell tracking after stroke [68,69]; a more detailed review can be found in Chapter 8.

Functional Imaging After Ischemia

BOLD MRI is sensitive to changes in regional tissue oxygenation status [70], making it useful to monitor acute deoxygenation following induction of ischemia as well as reoxygenation after reperfusion [64]. BOLD MR signal intensity, obtained by T_2*-weighted MRI, drops immediately upon the onset of ischemia, and rises when reflow occurs. A transient overshoot in signal intensity during reperfusion has been described and may reflect post-reperfusion hyperemia [71]. These hemodynamic responses indirectly report on local changes in CBF, CBV, and oxygen extraction fraction and their individual contributions cannot easily be distinguished.

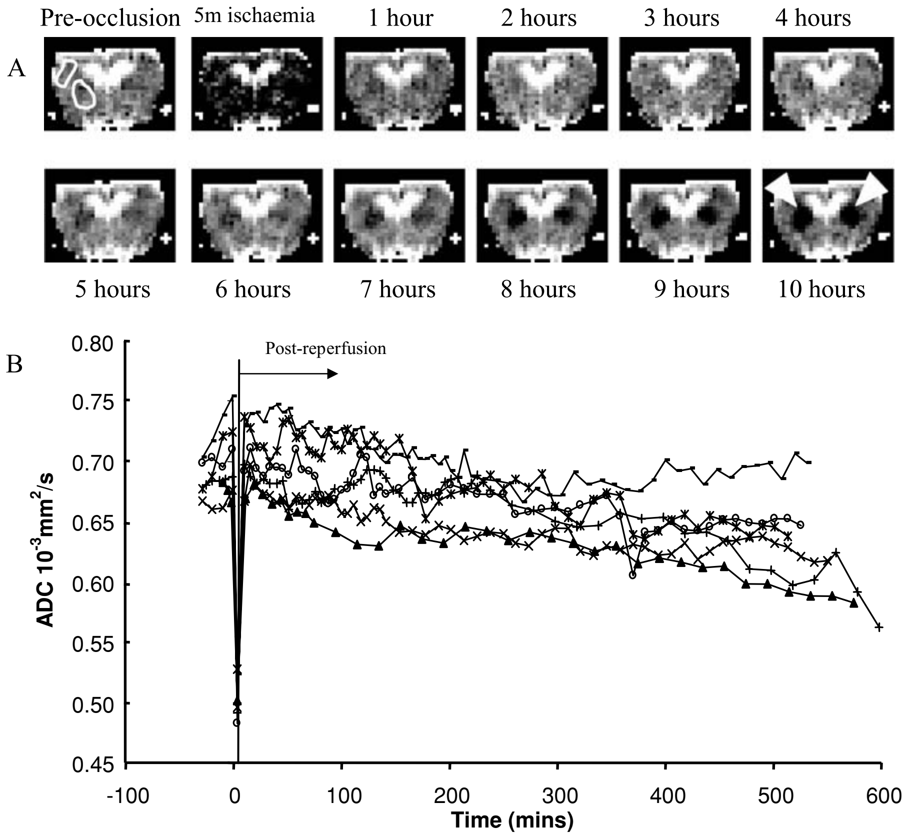

Fig. 1. (A) Coronal ADC maps at the level of the bregma before, during, and after 5 min of ischemia and reperfusion. Following bilateral occlusion of the CCA in the gerbil there was a decrease in the ADC, on reperfusion there was a recovery to baseline values, with a subsequent gradual decrease in ADC that was confined to the lateral portion of the striatum (white arrows). Representative ROIs are placed on the first image. (B) Temporal evolution of the ADC values in basal ganglia regions. Time = 0 min is the point of occlusion and at time = 5 min, reperfusion was initiated. Note the gradual decline in ADC values in the basal ganglia. Courtesy of M.F. Lythgoe.

Stroke patients show some functional recovery over time, which is commonly thought to be associated with brain plasticity. Recent BOLD MRI studies have demonstrated changes in activation patterns following a stroke [72,73]. With the use of behavioral tests and MRI in a rat stroke model, Dijkhuizen *et al.* [73] showed that unilateral stroke induced acute dysfunction of the contralateral forelimb, which significantly recovered at later stages. A further study suggests that the degree of shift of activation balance toward the contralesional hemisphere early after stroke increases with the extent of tissue injury and that functional recovery is associated mainly with preservation or restoration of activation in the ipsilesional hemisphere [74].

Tissue Signature Modeling

In deciding whether tissue is suitable for treatment, it is necessary to distinguish compromised yet recoverable from permanently damaged tissue. Thus, various combinations of MRI parameters may provide more reliable MRI tissue signatures and several groups have developed methods to distinguish degrees of tissue damage and to predict final outcome.

Jiang *et al*. have developed a multiparameter cluster analysis model of acute ischemic stroke using T_2 relaxation times and the diffusion coefficient of water (ADC_w). Significant correlations were obtained between MRI signatures at different time points, specified by values of

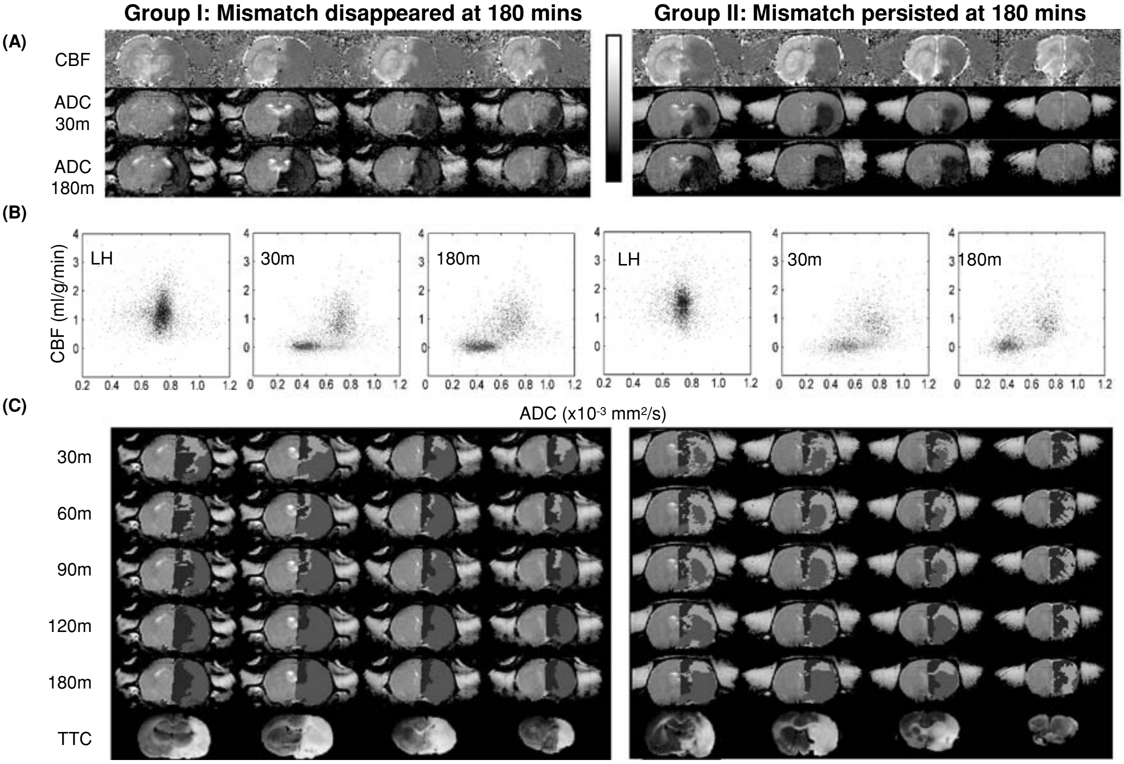

Fig. 2. Representative data from a stroke rat with "perfusion-diffusion" mismatch disappeared at 180 min after ischemia (Group I, left) and another rat with some "perfusion–diffusion" mismatch remained at 180 min (Group II, right). (A) Cerebral blood flow (CBF) maps, and ADC maps at 30 and 180 min. The grayscale bar: ADC ranges from 0 to 0.001 mm^2/s, CBF ranges from -1 to 2 ml/g/min. (B) CBF-ADC scatterplots of the normal left hemisphere at 30 min, ISODATA cluster analysis results of the right hemisphere at 30 and 180 min. (C) Pixel clusters from the CBF-ADC scatterplots were overlaid on the image space at 30, 60, 90, 120, and 180 min. In the right hemisphere, blue, green, and red are assigned as "normal," "perfusion–diffusion" mismatch, and "ischemic core" clusters, respectively. TTC slides at 24 h are also shown. Reprinted with permission from Shen *et al*. [77]. (See also Plate 66 on page XLV in the Color Plate Section.)

ADC_w and T_2, and histopathologic measurements of lesion area obtained at 1 week, implying that the final outcome of ischemic cell damage can be predicted from the MRI tissue signature at early timepoints [75]. Similar conclusions were drawn by Jacobs *et al*., who used a vector tissue signature model that uses T_2, T_1, and DWI for segmentation and characterization of ischemic tissue [76]. Shen *et al*. used an iterative-self-organizing-data-analysis-algorithm dynamically track ischemic tissue fate on a pixel-by-pixel basis during the acute phase. Clusters were overlaid on the CBF-ADC scatterplots and provided an accurate prediction of tissue fate (Figure 2) [77]. A predictive algorithm combining perfusion and diffusion data has been used successfully to assess the effect of stroke therapy, showing that delayed rt-PA treatment in a rat embolic stroke model decreased the amount of tissue expected to proceed to infarction [78,79].

Spreading Depression

Spreading depression (SD) is a term for spreading cortical depolarization and depression of electroencephalographic (EEG) activity. Under normoxic conditions, SD occurs during migraine aura, where it precedes migraine pain but does not damage tissue. During stroke, epilepsy and head trauma, however, SD can arise repeatedly near the site of injury and may play a key role in the expansion of neuronal damage [80,81]. During SD the metabolic rate of the tissue increases in response to the greatly enhanced energy demands of the activated ion exchange pumps [82]. In the penumbra, flows are suppressed and as a result, the increased metabolic demand is not compensated by an increase in oxygen and glucose [83]. Eventually ATP stores will be depleted, followed by the cascade of pathophysiological events leading to tissue damage.

The first MRI study was published by Latour *et al*., who elicited SD in rats by topical application of potassium chloride to the exposed cortex. Using repetitive ADC measurements, he showed that the ADC declines within 30 s and recovers to the normal value within the next 30 s. The region of decreased diffusion was shown to be 2 mm in size and to move in the cortex, away from the point of application, with a uniform velocity of about 3.3 mm/min [84]. Another approach, reported by Gardner *et al*. in the same year, is the use of gradient echoes to demonstrate propagating waves of SD, which were initiated by remote perfusion with KCl. Within 2 min of application of KCl, they observed a zone of increased signal intensity on the MR image, with a size and propagating velocity similar to the Latour study. The increased signal intensity in gradient echo images has been attributed to an increased level of oxygenation within the venous blood during SD [85,86]. Rother *et al*. used serial DWI during remote MCAO to map transient ADC decreases post MCAO. Transient ADC changes were detected in six of seven rats post MCAO and subsequent renormalization within about 3 min. These ADC changes propagated bidirectionally away from the ischemic core and occurred in ischemic areas characterized by moderately decreased tissue perfusion, suggesting these are waves of SD [87]. These results would imply that SD does play a role in the pathophysiology of stroke. A more in-depth study into the effect of SD on ischemic injury used a combination of ADC imaging and electrophysiology to assess ischemic lesion volumes after MCAO and KI application as a function of the number and duration of SD episodes. The ischemic region increased significantly if SD was present, supporting the hypothesis for a causative role of SD in extending focal ischemic injury [88]. Dijkhuizen *et al*. showed that the ischemic lesion size was dependent on the total duration of tissue depolarization and not to the frequency of depolarizations [89].

SD after transient MCAO in ratsis prolonged or inhibited by hypothermia as measured by ADC imaging [90]. However, they also reported that the maximum ADC decrease within SD was greater than for normothermia, which currently remains unexplained.

With respect to role of SD in migraine, Bradley *et al*. investigated whether DWI could detect the effects of the antimigraine drug sumatriptan and the novel anticonvulsant tonabersat in the cat brain. Supporting previous findings, sumatriptan did not affect the numbers of events, the duration or the SD velocity; tonabersat significantly reduced SD event initiation and duration and increased primary event velocity. However, both drugs significantly decreased, by >50%, the spatial extent of the first KCl-evoked SD event, and sumatriptan significantly increased event propagation across the suprasylvian sulcus, confirming the role of SD in migraine [91].

Manganese-enhanced MRI has been reported as a new visualization method for neural activation. Aoki *et al*. used this method to visualize anoxic depolarization and to compare regional differences between manganese accumulation and decreased ADC. They found that the enhanced region was much smaller than the area which was detected as having a reduced ADC, and speculate that the manganese-enhanced region is caused by some ischemic cascade such as Ca^{2+} influx related to anoxic depolarization in the ischemic core [92].

Epilepsy

The epilepsies are a group of disorders with a wide range of presentations and multiple etiologies [93]. In order to model such a varied condition, several different and quite diverse approaches have been developed, and currently no single model is appropriate for all conditions. In 1972, Purpura *et al*. produced a comprehensive review covering many experimental models, which still remains a useful guide to the various methods used to induce epilepsy or seizures [94]. Clinically, the epilepsies are characterized by spontaneous recurrent epileptic seizures, which are caused by generalized paroxysmal or partial (focal) discharges in the brain [93].

Animal Models

Animal models of *generalized seizures* include animals affected by genetic reflex epilepsy [95], such as the baboon, *Papio Papio* [96], mouse (DBA/2J) [97], genetically epilepsy prone rats (GEPRs) [98], rabbits [99], and the Fayoumi chicken [100]. In these animals, seizures may be induced by intermittent light stimulation, noise, movement, and stress [94,95]. Another animal model that exhibits generalized seizures is the maximal electroshock model. This model is predominately used to test possible therapies for primary and secondary generalized epilepsies [101].

Models for *simple partial seizures* include focal microapplication of topical convulsants such as penicillin [95], bicuculline [102], picrotoxin [103], strychnine [104], and kainic acid [105] on the cerebral cortex. Another method uses acute direct repetitive electrical stimulation, which can lead to discharges that persist for seconds or minutes after the electrical stimuli cease [106].

Chronic seizure models develop following the application of metals such as alumina hydroxide, cobalt, tungsten, or zinc [107,104]. Spontaneous recurrent seizures may appear 2 months after the injection, and persist in some cases for several years [107]. Models of *complex partial seizures* may be induced via injection of tetanus toxin into the hippocampus; seizures first occur at 1–7 days post-injection and then chronically [108,109]. Administration of kainic acid, an excitotoxic analogue of L-glutamate, leads to spontaneous recurrent seizures and hippocampal damage even when injected systemically [110,111]. A now widely used animal model for the study of epileptogenesis is the kindling model. One technique for induction is regular stimulation of chronically implanted electrodes until spontaneous generalized seizure is achieved [112,104]. The ubiquitous lithium-pilocarpine model presents with status epilepticus (SE) usually within 1–2 h of injection, which may last for up to 12 h and then finally progresses to spontaneous recurrent seizures [113]. Animal models of SE may be produced via techniques such as the administration of chemical convulsants [114–116] or electrical stimulation [117,118].

Early MRI Studies of Epilepsy

Although the majority of experimental epilepsy research has been performed outside the neuroimaging field, there has been increasing interest in the use of MRI following some early and promising nuclear magnetic resonance spectroscopy investigations, and more recently imaging studies. Broadly speaking the present goal of imaging is to characterize both the metabolic derangement and brain injury associated with seizures, using functional (spectroscopy, diffusion and perfusion imaging) and structural (T_1 and T_2) neuroimaging. The first *in vivo* MR experiment in an animal model of seizures revealed a decrease in phosphocreatine, without a change in adenosine triphosphate (ATP) levels during seizure activity [119]. This and several other spectroscopy studies demonstrated the feasibility of combining animal models of epilepsy and NMR [120,121]. Non-invasive imaging of animal models of epilepsy started in the early 1990s. A preliminary imaging study provided evidence for tissue damage detectable by MRI following kainate injection in the rat brain. Although the procedure did not induce seizures, the T_1-weighted strategy provided better image contrast for the kainic acid lesion than the T_2 approach, and the diffusion-weighted images showed improved contrast for edematous tissue [120,122]. Another early study demonstrated blood flow changes via the MR blood oxygenation level dependent (BOLD) contrast in the kainic acid model of seizures in rats. Increases in blood flow were associated with minor behavioral seizure signs, but as seizure activity progressed, signal intensity remained near baseline, possibly due to increased neuronal activity (as observed on EEG), which subsequently increased oxygen extraction thereby normalizing the BOLD response [123]. This preliminary study demonstrated the potential of fMRI for investigating hemodynamic changes associated with seizure activity, yet it was many years before further fMRI studies would be performed (see below).

Diffusion Imaging in Epilepsy

In 1993, Zhong *et al.* [124] published an influential paper using DWI to investigate changes associated with SE. Following intraperitoneal injection of bicuculline in the rat, the apparent diffusion coefficient (ADC) of water in the brain decreased 14–18% during seizures. No changes occurred in T_1 or T_2. This result demonstrated that during a seizure the ADC changed in a similar fashion to that reported in ischemia [27], but under different circumstances as the blood flow is increased and the ATP stores are only modestly reduced. This finding was also confirmed during flurothyl exposure, which is thought to act on the sodium channel to alter the responsiveness of the GABA and glutamate receptors, causing convulsions at high doses [125] and during frontal cortical electroshock [126]. Magnetic resonance spectroscopic imaging together with T_2- and DWI was first used in experimental epilepsy to investigate selective hippocampal and piriform cortex damage following kainate-induced SE in the rat. Decreased N-acetyl aspartate, increase lactate and decreased ADC were observed at 12 h with little evidence of histological and T_2-weighted changes, and it was suggested that such changes may provide a diagnostic measure for evaluating risk of neuronal damage after SE [121].

More recently, diffusion studies have provided novel approaches to investigate brain microarchitecture. It has been suggested that using q-space imaging after SE it is possible to distinguish neuronal tissue from early glial cell damage in a pilocarpine model [127]. DTI, an emerging technique to investigate tissue anisotropy, has recently been applied to the investigation of an avian model of epilepsy. Following photic stimulation and subsequent onset of generalized tonic-clonic seizures in the chicken, DTI revealed regional differences in the juvenile chicken compared to nonepileptic controls, but as the brains matured these differences disappeared [128]. As yet it is not known whether DTI will provide addition information to other MRI parameters and further work is necessary to understand its role in the investigation of animal models of epilepsy.

Time Course Studies in Epilepsy

The long-term temporal evolution of lesion development, investigation of epileptic activity and tissue damage are well suited to the non-invasive nature of MRI [129–131]. Early time points demonstrate ADC decreases during and after SE, and BBB breakdown (limited to the thalamus) 2 h after SE [124,132,133]. Despite differences in the models used (pharmaceutical and electrical), there is a similarity in the progression of pathology as measured by MRI. Initially there is a transient increase in T_2,

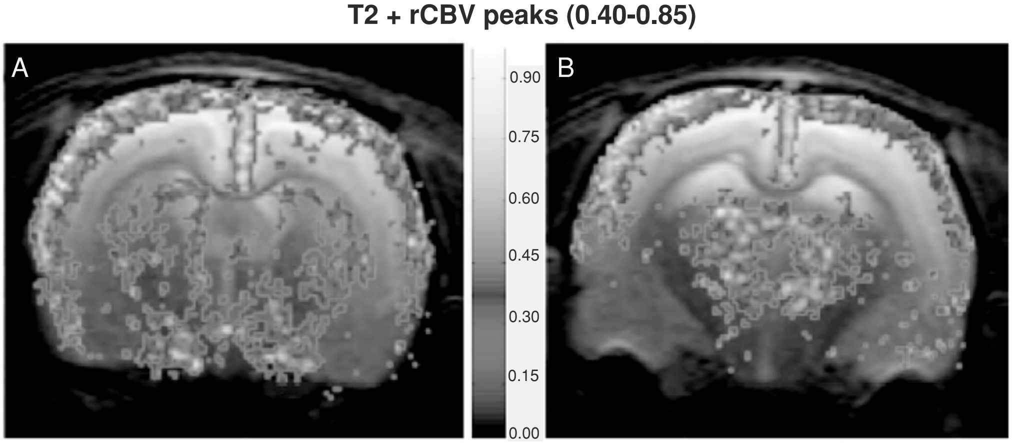

Fig. 3. Maps of CBV increase in an epileptic animal, generated to show the highest values of rCBV increase (cutoff at 0.40) at two different levels (A, 0.26 mm from bregma, B, −2.5 mm from bregma) superimposed to T2W images. In the cerebral cortex the simultaneous detection of the two signals shows clearly that rCBV peaked in the superficial layers, overlying the T2W hyperintensity. An increase of rCBV is also evident in the dorsolateral striatum and medial basal forebrain (A), as well as in the medial thalamus (B). In the hippocampus the rCBV increment, although significantly high was below the cutoff level adopted for the purpose of these maps. Reprinted with permission from Fabene *et al*. [138]. (See also Plate 67 on page XLVI in the Color Plate Section.)

which progressively normalizes by 5–9 days and finally increases in the chronic phase (3–9 weeks). The latter phase appears to coincide with the onset of spontaneous seizures [132,134]. It has been suggested that the progressive T_2-weighted hyperintensity in the piriform and entorhinal cortex may characterize the initial step leading to the development of epilepsy and late gliosis could result from spontaneous seizures [132]. Nairismagi *et al*. were unable to demonstrate a relationship between early MRI changes and subsequent severity of epilepsy and tissue damage. However Roch *et al*. indicated that P21 rats that had early T_2 increases did develop epilepsy, although only a subpopulation developed hippocampal sclerosis, an observation which remains as yet unexplained. One suggestion for the lack of correlation was the limited MRI spatial resolution. Some studies are now using high-resolution imaging in combination with other MRI techniques such as magnetization transfer (MT) contrast, which may provide the visual assessment of hippocampal formation, structure and damage necessary to investigate subtle morphological changes [135–137].

Functional Imaging in Epilepsy

During the last few years fMRI and CBV mapping have been used to investigate the underlying changes in neuronal activity and hemodynamics during and after seizure activity. Fabene *et al*. have demonstrated regional structural and functional MRI changes 12 h following onset of status. They concluded that T_2-weighted imaging hyperintensity changes in a cortex, hippocampus, amygdala, and medial thalamus are due to edematous alteration; regional increases in CBV, indicative of degenerating neurons, were not found in the areas of marked increase in T_2, suggesting that CBV may provide a mechanism to track progressive pathology (Figure 3) [138]. EEG has been used together with fMRI to identify areas of neuronal activity during seizures in rat models of absence epilepsy. Studies have shown that spontaneous spike-and-wave discharges, measured with EEG, are accompanied by transient focal increases in BOLD signals in regions which are characteristic of absence epilepsy [139,140]. It remains to be seen how these initial BOLD changes will compare with long-term histological changes, seizure frequency, and severity.

Neurodegenerative Disorders

Neurodegenerative disorders such as Alzheimers's disease (AD) or Parkinson's disease (PD) are devastating progressive illnesses. A combination of MRI approaches such as pharmacological MRI, DTI, and anatomical studies of brain atrophy has proved particularly useful in understanding the etiology and progression of these diseases [141–143].

Parkinson's Disease

This condition is characterized by the progressive loss of nigral neurons and striatal dopamine resulting in progressive loss of motor control and the characteristic symptoms of the disease. Experimental models of PD fall into three major categories. The first are pharmacological models, using for example reserpine or amphetamine administration to deplete dopamine, which are largely reversible treatments. The second group involves lesioning using neurotoxins, which is permanent. Thirdly, transgenic mouse models have been developed.

Imaging experimental models has long been in the domain of PET imaging with the availability of radioligands to monitor both pre- and postsynaptic function [144]. This methodology has now been largely supplanted by functional MRI to image brain activation patterns. BOLD fMRI showed bilateral overactivation in the sensorimotor cortex, suggesting that the mutual influence of the two hemispheres is important in the pathophysiology of PD [145] Another new approach is pharmacological MRI (a term used to describe drug induced functional MRI changes) where activity is induced by levodopa [146], D1 and D2 receptor agonists [147], amphetamine [148], or dopamine transporter agonists [149].

Using anatomical MRI sequences, temporal signal changes in T_1 and T_2 have been used to map regions of degeneration after lesioning in non-human primates [150] and attempts have been made to correlate T_1 relaxation times with the abnormal accumulation of iron in degenerating dopaminergic neurones in a neurotoxin rat model [151].

Alzheimer's Disease

Alzheimer's Disease is the most common dementia in Western societies. Pathohistological findings include widespread neuronal degeneration and β-amyloid (Aβ) plaques. AD models involve focal cerebral lesions that are mostly induced by neurotoxins, i.e. 6-OH dopamine. Furthermore a significant number of transgenic mouse models has been developed, which present different aspects of the disease such as over-expression of amyloid precursor protein (APP) and/or presenilin (PS) leading to amyloid plaque formation from the age of 6 months onward.

Anatomical MRI has been used to assess atrophy by measuring (partial) brain volumes or indirectly ventricular volumes [152]. Even before the onset of Aβ deposition, reduced hippocampal volume and corpus callosum length can be detected by MR microscopy [153]. DTI revealed significant differences between APP mice and control mice following the development of AD-like pathology, suggesting that primary or secondary white matter injury can be detected by DTI [154].

T_2 imaging showed a significant reduction of the relaxation time in the hippocampus, cingulate, and retrosplenial cortex, but not the corpus callosum of APP mice [155]. This relaxation contrast has been used to detect plaque-like structures in the cortex and hippocampus with high-resolution anatomical MRI [156]. Using angiography, flow voids were detected at the internal carotid and the large arteries at the circle of Willis in APP mice, suggesting that soluble Aβ may have deleterious effects on the vasculature [157]. The hemodynamic response to stimulus was shown to decrease with increasing age of the APP mice and with increasing stimulus amplitude as compared with wild-type animals, which can at least partially be explained by the deteriorating vasculature [143].

With the advent of molecular imaging several different contrast agents have been developed to label amyloid plaques. Some of these use magnetically labeled Aβ peptides; to get these agents to the target the blood–brain barrier needs to be opened [158]. Alternatively, a derivative of human Aβ peptide has been developed that is capable of crossing the intact blood–brain barrier and of selectively targeting individual amyloid plaques [159].

Huntington's Disease

Huntington's disease (HD) is an inherited neurodegenerative disease, in which there is progressive motor and cognitive deterioration, characterized by degeneration of GABAergic neurones localized mainly within the deep gray matter of the basal ganglia. Experimental models are based on acute lesioning using GABAergic antagonists or chronic lesioning using systemic administration of 3-nitroproprionic acid [160,161]. Since the discovery of the gene mutation for the disease, new transgenic mouse models are being developed [162]. Imaging data are largely PET-based, mapping regions of reduced metabolism indicative of cell loss [163]. Striatal lesions are visible with T_2-weighted and DWI protocols [164], although at acute time-points only DWI provides sufficient sensitivity [165]. DTI shows a significant decrease in relative anisotropy in the regions of corpus callosum, external capsule, and hippocampus in the 3-NP-treated rats [166]. A more extensive review of MRI and MRS in the 3-NP model can be found in a review by Lee and Chang [166].

CNS Inflammation

The inflammatory response is part of the hosts defense to injury and infection, but can exacerbate tissue injury when excessive or inappropriate. It has become clear that inflammation contributes not only to the archetypal CNS inflammatory disease, multiple sclerosis (MS), but also to a wide variety of acute neurological and chronic neurodegenerative diseases, such as stroke, head trauma, Alzheimer's disease, prion disease, and HIV-related dementia. Despite this, little is known of the effects of inflammatory processes within the CNS, or their contribution to MR images of human neuropathologies.

Multiple Sclerosis

Despite a wealth of studies, the pathogenesis of MS is still not fully understood. A primary goal of animal studies is to determine the relationship between the histopathology of a disease and the MRI characteristics. The most commonly used animal model is experimental allergic encephalopathy (EAE), an autoimmune CNS disorder that can be induced in susceptible species, such as mice, rats, guinea pigs, and non-human primates [167,168]. However, few of these models adequately represent all of the features of human MS, as the lesions evolve spontaneously at any site within the brain and often vary in temporal progressions. An alternative model is the delayed-type hypersensitivity (DTH) model in the rat [169], which involves sensitization of the immune system to a non-CNS antigen previously deposited in the brain. This model exhibits all the primary features of MS lesions: T-cell and macrophage infiltration, BBB breakdown, edema and tissue damage, and primary demyelination. A major advantage of this model for longitudinal MRI studies is that the site of the lesion is precisely dictated by the location of the intracerebral antigen injection.

MRI findings in the EAE models include increased T_2 and ADC values, corresponding broadly to those found most commonly in MS patients. However, only a relatively small number of studies have investigated correlations between MRI and histopathology obtained at the same time point. An increase in T_2 has been found to correspond to regions of macrophage recruitment and edema in both guinea pig [170] and rat EAE models [171]. However, T_2 changes were also associated with demyelination in the rat [171], but not in the guinea pig [170]. In the *C. jacchus* marmoset model of EAE increased proton density and T_2 appear to be associated with regions either of perivascular cuffing, demyelination, or perivascular gliosis [172]. The variability of these findings suggest that T_2-weighted MRI alone is not a reliable method of distinguishing purely inflammatory lesions from either demyelinating or remyelinating lesions [172,173].

In MS patients, areas that are enhanced following injection of an MRI contrast agent are generally considered to be a sensitive indicator for disease activity. In both guinea pig [174] and rat [175] models of EAE, BBB breakdown has been found to correlate with macrophage recruitment. In contrast, in the *C. jacchus* marmoset EAE model, which arguably provides the most accurate representation of the relapsing-remitting form of MS, contrast-enhancing areas correlated solely with acute, actively demyelinating lesions [173]. However, recent work in the rat DTH model [176] has demonstrated that axonal injury and inflammatory events occurring within a lesion are not restricted to the period of BBB breakdown and contrast enhancement. These findings suggest that MS disease progression may persist despite an intact BBB, and, consequently, contrast-enhancement may not be an accurate marker of disease activity. Recently, it has been suggested that a more appropriate method may be to monitor monocyte infiltration ("the major source of demyelination in EAE") via cells labeled with iron oxide particles which may be detected by MRI, thereby allowing assessment of the inflammatory activity induced by EAE [177].

Other imaging modalities have been used less frequently, but have yielded some interesting findings. It has been suggested that DTI may distinguish between acute and chronic EAE lesions [178], such that in acute lesions diffusion increases in all directions, probably as a consequence of edema, whilst in chronic lesions diffusion only increases perpendicular to the main axon axis, possibly reflecting demyelination. Recent measurements of magnetization transfer ratio (MTR) in EAE [179] have suggested that decreases in MTR, which are frequently assumed to reflect demyelination in human MS, may in fact result from inflammatory related changes to white matter structure rather than myelin loss *per se*. In contrast, the short component of tissue water T_2 may more accurately reflect myelin content [179].

New contrast agents have recently provided an alternative approach to imaging EAE. A recent study has shown that the use of a superparamagnetic iron oxide contrast agent enables macrophage recruitment to the CNS to be followed *in vivo*, because those particles are scavenged by macrophages [180]. Another study demonstrated that Gd-DTPA leakage clearly preceded monocyte infiltration as imaged by uptake of ultra small particles of iron oxide (USPIO), which was maximal only during full-blown EAE [181]. Similar particles have been used to track the migration of labeled T-cells into the central nervous system in EAE [182]. Rausch *et al.* showed that significant changes of MTRs of up to 35% were observed in areas of USPIO accumulation. However, the areas of monocyte infiltration only coincided in part with areas of BBB breakdown, suggesting that infiltrating monocytes are related to demyelination in EAE, but not the breakdown of the BBB (Figure 4) [183]. Future contrast agent research may concentrate on detection of inflammation before the onset of clinical symptoms, e.g. by specific contrast agents that target early inflammation markers like E-selectin [184] or superparamagnetic antibodies specific for cell surface markers of CD4+ T-cells, CD8+ T-cells, and Mac1+ cells of EAE and TMEV mice [185].

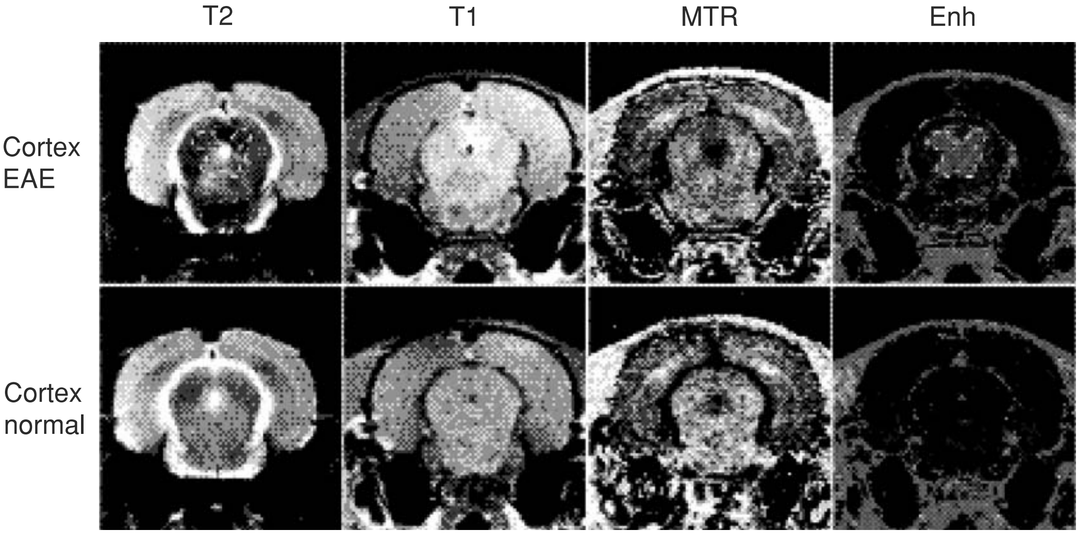

Fig. 4. Visualization of demyelination using USPIO particles in the EAE model of MS. The T_2 and precontrast T_1 images display hypo- and hyperintense areas, respectively, induced by accumulation of USPIO. The spatial localization and extent of the USPIO are the same in both images; however, the contrast is stronger in the T_2-weighted scans. MTR maps display no clear signs of MTR reduction. Enhancement of Gd-DOTA is visible in structures of the midbrain. The discrepancy between the spatial localization of the USPIO and the Gd-DOTA enhancement is demonstrated by dotted lines and dashed lines. The area marked by the dotted line accumulated USPIO but no Gd-DOTA. The reverse situation can be observed in the area marked by the dashed line. Reprinted with permission from Rausch *et al*. [183]. (See also Plate 68 on page XLVI in the Color Plate Section.)

Traumatic Brain Injury

Traumatic brain injury (TBI) results in a complex, heterogeneous pathology that varies considerably in both spatial and temporal dimensions depending on the severity of the insult and the location of the initial impact. A number of experimental models have been developed to simulate brain trauma; the most commonly used are weight-drop [186], impact acceleration [187], fluid percussion (FP) [188,189], and cortical contusion injury (CCI) [190] (for a review of these models see Gennarelli *et al*. [191] and Lighthall *et al*. [192]). Each model is designed to closely simulate specific components of the clinical pathology, which means that no single model is necessarily the best. Although the nature of the physical force differs between the models, the resulting acute and chronic destruction of gross tissue elements is somewhat similar and can be varied by adjusting the physical force used to produce the injury.

Autoradiography has been the most widely used imaging modality for TBI research, although there is an ever increasing number of publications using MRI as the primary imaging modality. Autoradiography is generally used for mapping CBF or cerebral metabolic rate of glucose utilization, but it has also been used to determine calcium accumulation [193] and microglial/macrophage activation or infiltration [194] after injury. Time-course analysis after CCI injury details a unilateral drop in CBF lasting for days post-injury [195] with a concomitant hyper- and subsequent hypo-metabolic state as determined by CMRG measurements [196]. Recent advances in PET scanner technology [197] have enabled non-invasive studies of metabolism to sequentially image the same rat following head-trauma [198]. It is likely that this methodology is set to be exploited much further for TBI research in the coming years with the increasing availability of new tracers to map different receptor distributions and gene expression [197].

The continual development of MRI techniques to assess pathophysiology is particularly advantageous in TBI research, since the high spatial and temporal resolution that is now routinely achieved with MRI is particularly useful given the highly heterogenous nature of this condition. T_1, T_2, and DWI sequences have been employed to monitor contusion volume in rats [199–203] and mice [204], identify necrotic from edematous brain tissue [205], track brain anatomy at various developmental ages and times after injury [206,207], and to compare different TBI models [208]. A model has also been proposed to map brain water content based on the signal contrast in T_1-weighted images [209], although this methodology has yet to gain wide acceptance by the MR community.

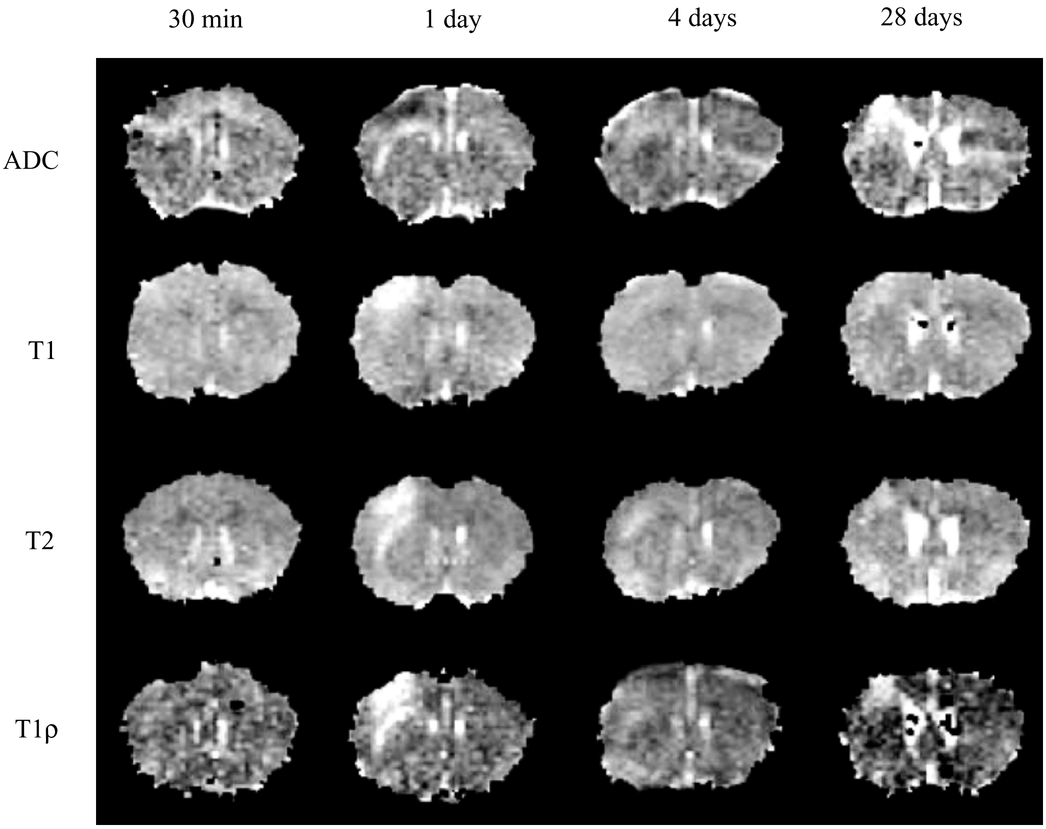

Fig. 5. Multi-parametric (ADC, T1, T2, TIρ) multi-time-point MRI datasets were acquired after traumatic brain injury using the cortical contusion rat model. Injury was produced using a pneumatic piston (2.5 mm ϕ), which was advanced onto the dura at 4 m s^{-1} through as 5-mm craniotomy and to a depth of 2 mm over the left parietal cortex. ADC values were decreased at 30 minutes and 1 day after which they pseudo-normalised and subsequently increased by day 4. Core T1, T2, and T1 ρ were all increased at all times post-injury.

The high sensitivity afforded by diffusion imaging has been used to detect very early decreases in the ADC indicating cytotoxic edema followed by a later increase indicative of a vasogenic component [210–215]. Not all groups have documented this initial ADC decrease [216–218] and this may be related to the model used, the injury severity or most likely to the placement of the measurement region-of-interest. Further work investigating mechanisms of diffusion change has suggested that in the case of a stab injury, ADC changes observed in areas remote from the initial injury site may reflect alterations in extracellular matrix composition [219].

Sub-dural hemorrhage that is present immediately after contusion injury is highly visible on T_2* images due to the magnetic susceptibility differences relative to the surrounding tissue, although this resolves with time [215]. While this susceptibility effect results in distortion of echo-planar spin echo images, it will certainly produce large areas of signal dropout for gradient echo image acquisition, as typically used for fMRI studies. Thus, early time-point functional investigations may be limited to PET or autoradiographic studies.

Contrast-enhanced imaging has been used to map regions of increased blood–brain barrier permeability [220–222], together with the deleterious effects of secondary injury [223] and initial decreases in CBV [213] following injury. However, the use of contrast agents for quantifying either blood volume or perfusion in regions where the BBB is permeable is inacurate, and this may be reflected in this latter study that showed CBV maps that were not well correlated with histological damage, together with large inter- and intra-subject variability. Using continuous arterial spin-labeling (CASL) to map CBF circumvents this problem [224]. Early reductions in CBF have been reported after CCI using CASL [215,225,226] together with loss of vascular reactivity [225]. Monitoring CBF at different times after injury in the same rat using this technique demonstrated hypoperfusion in core and contusion boundary regions followed by a return to normal values at the chronic stage [215,227]. These findings are in good agreement with autoradiographic data [195].

Diffuse axonal injury, a hallmark of TBI, is considered to be an important determinant of functional outcome. MT imaging has been shown to be sensitive to axonal injury in a number of disease states. The MTR is significantly decreased in regions of axonal injury after rotational acceleration injury in the pig [228,229] and in core regions after contusion injury in the rat [215]. The agreement between MTR abnormalities and axonal pathology assessed by histology was good, and MT is reported to be highly sensitive for detecting relatively mild injury [229], but future studies may be limited to large animals, since the rat exhibits a much lower white/gray matter ratio, making detection of white matter pathology difficult.

More recently, MRI has been used to assess development of interventional pharmacological strategies for use in TBI. Using capsaicin-induced neuropeptide depletion to examine the role of neurogenic inflammation, Nimmo *et al*. demonstrated reduction in post-traumatic edema formation (DWI), BBB permeability, free magnesium decline, and motor and cognitive deficits, concluding that neurogenic inflammation may play an integral role in the development of edema and functional deficits following TBI [230].

Conclusion

The combination of appropriate imaging techniques and suitable animal models of disease can greatly expand our understanding of human brain pathologies. This experimental imaging partnership has contributed to the development of novel imaging techniques, to the promotion of better diagnostic and prognostic measures, and to the elucidation of basic mechanisms of cellular injury leading to improved therapies.

MRI is expected to play an increasingly important role in future research, especially in areas where its noninvasive character is a significant advantage, such as the phenotyping of transgenic animals and longitudinal trials of drug therapies.

Acknowledgments

The authors would like to thank Dr. N.R. Sibson and Dr. N.G. Harris for their contribution to the manuscript. We acknowledge the Wellcome Trust and the BBSRC for their support of the work carried out at Radiology and Physics Unit of the Institute of Child Health, Great Ormond Street Hospital and the Wellcome Trust High Field MR Research Laboratory.

References

1. Lythgoe MF, Busza AL, Calamante F, *et al*. Effects of diffusion anisotropy on lesion delineation in a rat model of cerebral ischemia. Magn. Reson. Med. 1997;38:662–8.
2. Vanbruggen N, Syha J, Busza AL, *et al*. Identification of tumor hemorrhage in an animal-model using spin echoes and gradient echoes. Magn. Reson. Med. 1990;15:121–7.
3. Widdop RE, Li XC. A simple versatile method for measuring tail cuff systolic blood pressure in conscious rats. Clin. Sci. 1997;93:191–4.
4. Bock NA, Konyer NB, Henkelman RM. Multiple-mouse MRI. Magn. Reson. Med. 2003;49:158–67.
5. Kohno K, Back T, Hoehn-Berlage M, *et al*. A modified rat model of middle cerebral artery thread occlusion under electrophysiological control for magnetic resonance investigations. Magn. Reson. Imaging. 1995;13:65–71.
6. Lukasik VM, Gillies RJ. Animal anaesthesia for in vivo magnetic resonance. NMR Biomed. 2003;16:459–67.
7. Hall R, Murdoch J. Brain protection: physiological and pharmacological considerations. Part II: The pharmacology of brain protection. Can. J. Anaesth. 1990;37:762–77.
8. O'Connor CA, Cernak I, Vink R. Interaction between anesthesia, gender, and functional outcome task following diffuse traumatic brain injury in rats. J. Neurotrauma. 2003;20:533–41.
9. Sicard K, Shen Q, Brevard ME, *et al*. Regional cerebral blood flow and BOLD responses in conscious and anesthetized rats under basal and hypercapnic conditions: implications for functional MRI studies. J. Cereb. Blood Flow Metab. 2003;23:472–81.
10. Khubchandani M, Jagannathan NR. Simultaneous electrophysiology and functional magnetic resonance imaging studies in conscious rats. Imaging Biol. Res. Pt A. 2004;385:63–84.
11. Roussel SA, Vanbruggen N, King MD, *et al*. Monitoring the initial expansion of focal ischemic changes by diffusion-weighted MRI using a remote-controlled method of occlusion. NMR Biomed. 1994;7:21–8.
12. Koizumi J, Yoshida Y, Nakazawa T, *et al*. Experimental studies of ischaemic brain edema: 1. A new experimental model of cerebral embolism in rats in which recirculation can be introduced in the ischemic area. Jpn. J. Stroke. 1986;8:1–8.
13. Calamante F, Lythgoe MF, Pell GS, *et al*. Early changes in water diffusion, perfusion, T-1, and T-2 during focal cerebral ischemia in the rat studied at 8.5 T. Magn. Reson. Med. 1999;41:479–85.
14. Li FH, Han S, Tatlisumak T, *et al*. A new method to improve in-bore middle cerebral artery occlusion in rats—demonstration with diffusion- and perfusion-weighted imaging. Stroke. 1998;29:1715–9.
15. Lythgoe MF, Thomas DL, Calamante F, *et al*. Acute changes in MRI diffusion, perfusion, T-1, and T-2, in a rat model

of oligemia produced by partial occlusion of the middle cerebral artery. Magn. Reson. Med. 2000;44:706–12.

16. West DA, Valentim LM, Lythgoe MF, *et al*. MR image-guided investigation of regional signal transducers and activators of transcription-1 activation in a rat model of focal cerebral ischemia. Neuroscience. 2004;127:333–9.
17. Jiang Q, Zhang RL, Zhang ZG, *et al*. Diffusion-, T2-, and perfusion-weighted nuclear magnetic resonance imaging of middle cerebral artery embolic stroke and recombinant tissue plasminogen activator intervention in the rat. J. Cereb. Blood Flow Metab. 1998;18:758–67.
18. Rother J, Waggie K, van Bruggen N, *et al*. Experimental cerebral venous thrombosis: evaluation using magnetic resonance imaging. J. Cereb. Blood Flow Metab. 1996;16:1353–61.
19. Gerriets T, Stolz E, Walberer M, *et al*. Middle cerebral artery occlusion during MR-imaging: investigation of the hyperacute phase of stroke using a new in-bore occlusion model in rats. Brain Res. Protoc. 2004;12:137–43.
20. Hossmann KA. Experimental models for the investigation of brain ischemia. Cardiovasc. Res. 1998;39:106–20.
21. Fisher M, Bockhorst K, Hoehn-Berlage M, *et al*. Imaging of the apparent diffusion coefficient for the evaluation of cerebral metabolic recovery after cardiac arrest. Magn. Reson. Imaging. 1995;13:781–90.
22. Pulsinelli WA, Brierley JB. New model of bilateral hemispheric ischemia in the unanesthetized rat. Stroke. 1979;10:267–72.
23. Mima T. Forebrain ischemia in the rat: the four-vessel occlusion model. In: ST Ohnishi, T Ohnishi (Eds). Central Nervous System Trauma. CRC Press: New York, 1995, pp. 107–17.
24. Andrews BT, Weinstein PR, Keniry M, *et al*. Sequential in vivo measurement of cerebral intracellular metabolites with phosphorus-31 magnetic resonance spectroscopy during global cerebral ischemia and reperfusion in the rat. Neurosurgery. 1987;21:699–708.
25. Grohn OHJ, Kettunen MI, Penttonen M, *et al*. Graded reduction of cerebral blood flow in rat as detected by the nuclear magnetic resonance relaxation time T_2: a theoretical and experimental approach. J. Cereb. Blood Flow Metab. 2000;20:316–26.
26. Thornton JS, Ordidge RJ, Penrice J, *et al*. Temporal and anatomical variations of brain water apparent diffusion coefficient in perinatal cerebral hypoxic-ischemic injury: relationships to cerebral energy metabolism. Magn. Reson. Med. 1998;39:920–7.
27. Thomas DL, Lythgoe MF, Pell GS, *et al*. The measurement of diffusion and perfusion in biological systems using magnetic resonance imaging. Phys. Med. Biol. 2000;45:R97–138.
28. Hoehn-Berlage M. Diffusion-weighted NMR imaging: application to experimental focal cerebral ischemia. NMR Biomed. 1995;8:345–58.
29. Hossmann KA. Viability thresholds and the penumbra of focal ischemia. Ann. Neurol. 1994;36:557–65.
30. Rudin M, Beckmann N, Porszasz R, *et al*. In vivo magnetic resonance methods in pharmaceutical research: current status and perspectives. NMR Biomed. 1999;12:69–97.
31. Fischer M, Brott TG. Emerging therapies for actute ischemic stroke. Stroke. 2003;34:359–61.
32. Kucharczyk J, Mintorovitch J, Asgari HS, *et al*. Diffusion/perfusion MR imaging of acute cerebral ischemia. Magn. Reson. Med. 1991;19:311–5.
33. Quast MJ, Huang NC, Hillman GR, *et al*. The evolution of acute stroke recording by multimodal magnetic resonance imaging. Magn. Reson. Imaging. 1993;11:465–71.
34. Muller TB, Haraldseth O, Jones RA, *et al*. Combined perfusion and diffusion-weighted magnetic resonance imaging in a rat model of reversible middle cerebral artery occlusion. Stroke. 1995;26:451–7.
35. Hossmann KA, Hoehn-Berlage M. Diffusion and perfusion MR imaging of cerebral ischemia. Cerebrovasc. Brain Metab. Rev. 1995;7:187–217.
36. Caramia F, Huang Z, Hamberg LM, *et al*. Mismatch between cerebral blood volume and flow index during transient focal ischemia studied with MRI and GD-BOPTA. Magn. Reson. Imaging. 1998;16:97–103.
37. Hamberg LM, Boccalini P, Stranjalis G, *et al*. Continuous assessment of relative cerebral blood volume in transient ischaemia using steady state susceptibility-contrast MRI. Magn. Reson. Med. 1996;35:168–73.
38. Muller TB, Jones RA, Haraldseth O, *et al*. Comparison of MR perfusion imaging and microsphere measurements of regional cerebral blood flow in a rat model of middle cerebral artery occlusion. Magn. Reson. Imaging. 1996;14:1177–83.
39. Lythgoe MF, Thomas DL, Calamante F. MRI measurement of cerebral perfusion and the application to experimental neuroscience. In: N van-Bruggen, TP Roberts (Eds). Biomedical Imaging in Experimental Neuroscience. CRC Press: Boca Raton, Florida, 2002.
40. Jiang Q, Chopp M, Zhang ZG, *et al*. The effect of hypothermia on transient focal ischemia in rat brain evaluated by diffusion- and perfusion-weighted NMR imaging. J. Cereb. Blood Flow Metab. 1994;14:732–41.
41. Calamante F, Lythgoe MF, Pell GS, *et al*. Early changes in water diffusion, perfusion, T1 and T2 during focal cerebral ischaemia in the rat studied at 8.5T. Magn. Reson. Med. 1999;41:479–85.
42. van-Dorsten FA, Hata R, Maeda K, *et al*. Diffusion- and perfusion-weighted MR imaging of transient focal cerebral ischaemia in mice. NMR Biomed. 1999;12:525–34.
43. Hofmeijer J, Veldhuis WB, Schepers J, *et al*. The time course of ischemic damage and cerebral perfusion in a rat model of space-occupying cerebral infarction. Brain Res. 2004;1013:74–82.
44. Sakoh M, Rohl L, Gyldensted C, *et al*. Cerebral blood flow and blood volume measured by magnetic resonance imaging bolus tracking after acute stroke in pigs. Stroke. 2000;31:1958–64.
45. Roussel SA, Van Bruggen N, King MD, *et al*. Monitoring the initial expansion of focal ischaemic changes by diffusion-weighted MRI using a remote controlled method of occlusion. NMR Biomed. 1994;7:21–8.
46. Knight RA, Dereski MO, Helpern JA, *et al*. Magnetic resonance imaging assessment of evolving focal cerebral ischemia. Comparison with histopathology in rats. Stroke. 1994;25:1252–61.
47. Hoehn-Berlage M, Eis M, Back T, *et al*. Changes of relaxation times (T1, T2) and apparent diffusion coefficient after permanent middle cerebral artery occlusion in the

rat: temporal evolution, regional extent, and comparison with histology. Magn. Reson. Med. 1995;34: 824–34.
48. Knight RA, Ordidge RJ, Helpern JA, *et al*. Temporal evolution of ischemic damage in rat brain measured by proton nuclear magnetic resonance imaging. Stroke. 1991;22:802–8.
49. Pierpaoli C, Righini A, Linfante I, *et al*. Histopathological correlates of abnormal water diffusion in cerebral ischaemia: diffusion-weighted MR imaging and light and electron miscrosopy study. Radiology. 1993;189:439–48.
50. Derugin N, Roberts TPL. New and reproducible technique for experimentally induced middle cerebral artery stenosis. Microsurgery. 1994;15:70–2.
51. Astrup J, Siesjo BK, Symon L. Thresholds in cerebral ischemia: the ischaemic penumbra. Stroke. 1981;12:723–5.
52. Kinouchi H, Sharp FR, Koistinaho J, *et al*. Induction of heat shock hsp70 mRNA and HSP70 kDa protein in neurons in the 'penumbra' following focal cerebral ischemia in the rat. Brain Res. 1993;619:334–8.
53. Olah L, Wecker S, Hoehn M. Relation of apparent diffusion coefficient changes and metabolic disturbances after 1 hour of focal cerebral ischemia and at different reperfusion phases in rats. J. Cereb. Blood Flow Metab. 2001;21:430–9.
54. Kohno K, Hoehn-Berlage M, Mies G, *et al*. Relationship between diffusion-weighted MR images, cerebral blood flow, and energy state in experimental brain infarction. Magn. Reson. Imaging. 1995;13:73–80.
55. van Lookeren Campagne M, Thomas GR, Thibodeaux H, *et al*. Secondary reduction in the apparent diffusion coefficient, increase in cerebral blood volume and delayed neuronal death following middle cerebral artery occlusion and early reperfusion in the rat. J. Cereb. Blood Flow Metab. 1999;19:1354–64.
56. Ringer TM, Neumann-Haefelin T, Sobel RA, *et al*. Reversal of early diffusion-weighted magnetic resonance imaging abnormalities does not necessarily reflect tissue salvage in experimental cerebral ischemia. Stroke. 2001;32:2362–9.
57. Baird AE, Warach S. Magnetic resonance imaging of acute stroke. J. Cereb. Blood Flow Metab. 1998;18:583–609.
58. Lythgoe MF, Thomas DL, King MD, Pell GS, Van Der Weerd L, Ordidge RJ, Gadian DG. Gradual changes in the apparent diffusion coefficient of water in selectively vulnerable brain regions following brief ischemia in the gerbil. Magn. Reson. Med. 2005;53:593–600.

Reference type: Generic

59. Vangelderen P, Devleeschouwer MHM, Despres D, *et al*. Water diffusion and acute stroke. Magn. Reson. Med. 1994;31:154–63.
60. Sotak CH. The role of diffusion tensor imaging in the evaluation of ischemic brain injury—a review. NMR Biomed. 2002;15:561–9.
61. Thornton JS, Ordidge RJ, Penrice J, *et al*. Anisotropic water diffusion in white and gray matter of the neonatal piglet brain before and after transient hypoxia-ischaemia. Magn. Reson. Imaging. 1997;15:433–40.
62. Grohn OHJ, Lukkarinen JA, Oja JME, *et al*. Noninvasive detection of cerebral hypoperfusion and reversible ischemia from reductions in the magnetic resonance imaging relaxation time,T2. J. Cereb. Blood Flow Metab. 1998;18:911–20.
63. Lythgoe MF, Thomas DL, Calamante F, *et al*. Acute changes in MRI diffusion, perfusion, T1 and T2 in a rat model of oligemia produced by partial occlusion of the middle cerebral artery. Magn. Reson. Med. 2000;44:706–12.
64. Roussel SA, Van Bruggen N, King MD, *et al*. Identification of collaterally perfused areas following focal cerebral ischemia in the rat by comparison of gradient echo and diffusion-weighted MRI. J. Cereb. Blood Flow Metab. 1995;15:578–86.
65. Kavec M, Grohn OHJ, Kettunen MI, *et al*. Acute cerebral ischemia in rats studied by Carr-Purcell spin-echo magnetic resonance imaging: assessment of blood oxygenation level-dependent and tissue effects on the transverse relaxation. Magn. Reson. Med. 2004;51: 1138–46.
66. Grohn OJ, Kettunen MI, Makela HI, *et al*. Early detection of irreversible cerebral ischemia in the rat using dispersion of the magnetic resonance imaging relaxation time, T1rho. J. Cereb. Blood Flow Metab. 2000;20:1457–66.
67. Barber PA, Foniok T, Kirk D, *et al*. MR molecular imaging of early endothelial activation in focal ischemia. Ann. Neurol. 2004;56:116–20.
68. Hoehn M, Kustermann E, Blunk J, *et al*. Monitoring of implanted stem cell migration in vivo: a highly resolved in vivo magnetic resonance imaging investigation of experimental stroke in rat. Proc. Natl. Acad. Sci. U. S. A. 2002;99:16267–72.
69. Modo M, Cash D, Mellodew K, *et al*. Tracking transplanted stem cell migration using bifunctional, contrast agent-enhanced, magnetic resonance imaging. Neuroimage. 2002;17:803–11.
70. Ogawa S, Menon RS, Kim SG, *et al*. On the charateristics of functional magnetic resonance imaging of the brain. Annu. Rev. Biophys. Biomol. Struct. 1998;27:447–74.
71. de Crespigny AJ, Wendland MF, Derugin N, *et al*. Real-time observation of transient focal ischemia and hyperemia in cat brain. Magn. Reson. Med. 1992;27:391–7.
72. Hoehn M, Nicolay K, Franke C, *et al*. Application of magnetic resonance to animal models of cerebral ischemia. J. Magn. Reson. Imaging. 2001;14:491–509.
73. Dijkhuizen RM, Ren J, Mandeville JB, *et al*. Functional magnetic resonance imaging of reorganization in rat brain after stroke. Proc. Natl. Acad. Sci. U. S. A. 2001;98:12766–71.
74. Dijkhuizen RM, Singhal AB, Mandeville JB, *et al*. Correlation between brain reorganization, ischemic damage, and neurologic status after transient focal cerebral ischemia in rats: a functional magnetic resonance imaging study. J. Neurosci. 2003;23:510–7.
75. Jiang Q, Chopp M, Zhang ZG, *et al*. The temporal evolution of MRI tissue signatures after transient middle cerebral artery occlusion in rat. J. Neurol. Sci. 1997;145:15–23.
76. Jacobs MA, Zhang ZG, Knight RA, *et al*. A model for multiparametric mri tissue characterization in experimental cerebral ischemia with histological validation in rat: part 1. Stroke. 2001;32:943–9.

77. Shen Q, Ren HX, Fisher M, *et al*. Dynamic tracking of acute ischemic tissue fates using improved unsupervised ISODATA analysis of high-resolution quantitative perfusion and diffusion data. J. Cereb. Blood Flow Metab. 2004;24:887–97.
78. Wu O, Koroshetz WJ, Ostergaard L, *et al*. Predicting tissue outcome in acute human cerebral ischemia using combined diffusion- and perfusion-weighted MR imaging. Stroke. 2001;32:933–42.
79. Wu O, Sumii T, Asahi M, Sasamata M, Sorensen AG, Ostergaard L, Rosen BR, Lo EH, Dijkhuizen RM. Assessment of treatment effects with multiparametric MRI-based predictive algorithms in a rat embolic stroke model. Proceedings 12th ISMRM, Kyoto, 134, 2004.
80. Nedergaard M, Astrup J. Infarct rim: effect of hyperglycemia on direct current potential and (14C)-deoxyglucose phosphorylation. J. Cereb. Blood Flow Metab. 1986;6:607–15.
81. James MF, Smith JM, Boniface SJ, *et al*. Cortical spreading depression and migraine: new insights from imaging? Trends Neurosci. 2001;24:266–71.
82. Kocher M. Metabolic and hemodynamic activation of postischaemic rat brain by cortical spreading depression. J. Cereb. Blood Flow Metab. 1990;10:564–71.
83. Back T, Kohno K, Hossmann KA. Cortical negative DC deflections following middle cerebral artery occlusion and KCl-induced spreading depression: effect on blood flow, tissue oxygenation, and electroencephalogram. J. Cereb. Blood Flow Metab. 1994;14:12–9.
84. Latour LL, Hasegawa Y, Formato JE, *et al*. Spreading waves of decreased diffusion coefficient after cortical stimulation in the rat brain. Magn. Reson. Med. 1994;32: 189–98.
85. Gardner Medwin AR, Van Bruggen N, Williams SR, *et al*. Magnetic resonance imaging of propagating waves of spreading depression in the anaesthetised rat. J. Cereb. Blood Flow Metab. 1994;14:7–11.
86. Gyngell ML, Back T, Hoehn-Berlage M, *et al*. Transient cell depolarization after permanent middle cerebral artery occlusion: an observation by diffusion-weighted MRI and localised 1H-MRS. Magn. Reson. Med. 1994;31:337–41.
87. Rother J, de Crespigny AJ, D'Arceuil HE, *et al*. Recovery of the apparent diffusion coefficient after ischemia-induced spreading depression relates to cerebral perfusion gradient. Stroke. 1996;27:980–7.
88. Takano K, Latour LL, Formato JE, *et al*. The role of spreading depression in focal ischemia evaluated by diffusion mapping. Ann. Neurol. 1996;39:308–18.
89. Dijkhuizen RM, Beekwilder JP, van der Worp HB, *et al*. Correlation between tissue depolarizations and damage in focal ischemic rat brain. Brain Res. 1999;840:194–205.
90. Yenari MA, Onley D, Hedehus M, *et al*. Diffusion- and perfusion-weighted magnetic resonance imaging of focal cerebral ischemia and cortical spreading depression under conditions of mild hypothermia. Brain Res. 2000;885:208–19.
91. Bradley DP, Smith MI, Netsiri C, *et al*. Diffusion-weighted MRI used to detect in vivo modulation of cortical spreading depression: comparison of sumatriptan and tonabersat. Exp. Neurol. 2001;172:342–53.
92. Aoki I, Ebisu T, Tanaka C, *et al*. Detection of the anoxic depolarization of focal ischemia using manganese-enhanced MRI. Magn. Reson. Med. 2003;50:7–12.
93. Tresher WH, Lesser RP. The epilepsies. In: WG Bradley, RB Daroff, GM Fenichel, *et al*. (Eds). Neurology in Clinical Practice, Vol. 2, 3rd ed. Butterworth-Heinemann: Boston, 2000, pp 1745–79.
94. Purpura DP, Penry JK, Woodbury DM, *et al*. Experimental Models of Epilepsy—A Manual for the Laboratory Worker. Raven: New York, 1972.
95. Naquet R, Batini C. Genetic reflex epliepsy from chicken to man: relations between genetic reflex epilepsy and movement disorders. In: R Guerrini, J Aicardi, F Andermann, *et al*. (Eds). Epilepsy and Movement Disorders. Cambridge University Press: Cambridge, 2002, pp 29–46.
96. Naquet R, Meldrum BS. Photogenic seizures in baboon. In: DP Purpura, JK Penry, DM Woodbury, *et al*. (Eds). Experimental Models of Epilepsy—A Manual for the Laboratory Worker. Raven Press: New York, 1972, pp 373–406.
97. Seyfried TN, Glaser GH. A review of mouse mutants as genetic models of epilepsy. Epilepsia. 1985;26:143–50.
98. Hjeresen DL, Franck JE, Amend DL. Ontogeny of seizure incidence, latency, and severity in genetically epilepsy prone rats. Dev. Psychobiol. 1987;20:355–63.
99. Collins RL. Audiogenic seizures. In: DP Purpura, JK Penry, DM Woodbury, *et al*. (Eds). Experimental Models of Epilepsy—A Manual for the Laboratory Worker. Raven Press: New York, 1972, pp 347–72.
100. Crawford RD. Epileptiform seizures in domestic fowl. J. Hered. 1970;61:185–8.
101. Swinyard EA. Electrically induced convulsions. In: DP Purpura, JK Penry, DM Woodbury, *et al*. (Eds). Experimental Models of Epilepsy—A Manual for the Laboratory Worker. Raven Press: New York, 1972, pp 435–58.
102. Campbell AM, Holmes O. Bicuculline epileptogenesis in the rat. Brain Res. 1984;323:239–46.
103. Usunoff G, Atsev E, Tchavdarov D. On the mechanisms of picrotoxin epileptic seizure (macro- and micro-electrode investigations). Electroencephalogr. Clin. Neurophysiol. 1969;27:444.
104. Loscher W. Animal models of intractable epilepsy. Prog. Neurobiol. 1997;53:239–58.
105. Cavalheiro EA, Riche DA, Le-Gal-La-Salle G. Long-term effects of intrahippocampal kainic acid injection in rats: a method for inducing spontaneous recurrent seizures. Electroencephalogr. Clin. Neurophysiol. 1982;53: 581–9.
106. Ajmone-Marsan C. Focal electrical stimulation. In: DP Purpura, JK Penry, DM Woodbury, *et al*. (Eds). Experimental Models of Epilepsy—A Manual for the Laboratory Worker. Raven Press: New York, 1972, pp 147–72.
107. Ward A. Topical convulsant metals. In: DP Purpura, JK Penry, DM Woodbury, *et al*. (Eds). Experimental Models of Epilepsy—A Manual for the Laboratory Worker. Raven Press: New York, 1972, pp 13–35.
108. Jefferys JG, Borck C, Mellanby J. Chronic focal epilepsy induced by intracerebral tetanus toxin. Ital. J. Neurol. Sci. 1995;16:27–32.
109. llanby J, Hawkins C, Mellanby H, *et al*. Tetanus toxin as a tool for studying epilepsy. J. Physiol. (Paris). 1984;79:207–15.

110. Lothman EW, Collins RC, Ferrendelli JA. Kainic acid-induced limbic seizures: electrophysiologic studies. Neurology. 1981;31:806–12.
111. Sperk G. Kainic acid seizures in the rat. Prog. Neurobiol. 1994;42:1–32.
112. Majkowski J. Kindling: clinical relevance for epileptogenicity in humans. In: H Stefan, F Andermann, P Chauvel, *et al.* (Eds). Advances in Neurology. Lippincott Williams & Wilkins: Philadelphia, 1999, pp. 105–13.
113. Turski WA, Cavalheiro EA, Schwarz M, *et al.* Limbic seizures produced by pilocarpine in rats: behavioural, electroencephalographic and neuropathological study. Behav. Brain Res. 1983;9:315–35.
114. Ben-Ari Y. Limbic seizure and brain damage produced by kainic acid: mechanisms and relevance to human temporal lobe epilepsy. Neuroscience. 1985;14:375–403.
115. Cavalheiro EA. The pilocarpine model of epilepsy. Ital. J. Neurol. Sci. 1995;16:33–7.
116. Meldrum BS, Brierley JB. Prolonged epileptic seizures in primates. Ischemic cell change and its relation to ictal physiological events. Arch. Neurol. 1973;28:10–7.
117. Lothman EW, Bertram EH, Bekenstein JW, *et al.* Self-sustaining limbic status epilepticus induced by 'continuous' hippocampal stimulation: electrographic and behavioral characteristics. Epilepsy Res. 1989;3:107–19.
118. Hosford DA. Animal models of nonconvulsive status epilepticus. J. Clin. Neurophysiol. 1999;16:306–13.
119. Petroff OAC, Pritchard JW, Behar K, *et al.* In vivo phosphorus nuclear magnetic resonance spectroscopy in status epilepticus. Ann. Neurol. 1984;16:169–77.
120. Karlik S, Stavraky R, Taylor A, *et al.* Magnetic resonance imaging and 31P spectroscopy of an interictal cortical spike focus in the rat. Epilespia. 1991;32:446–53.
121. Ebisu T, Rooney WD, Graham SH, *et al.* MR spectroscopic imaging and diffusion-weighted MRI for early detection of kainate-induced status epilepticus in the rat. Magn. Reson. Med. 1996;36:821–8.
122. King MD, van-Bruggen N, Ahier RG, *et al.* Diffusion-weighted imaging of kainic acid lesions in the rat brain. Magn. Reson. Med. 1991;20:158–64.
123. Ogawa S, Lee T. Blood oxygenation level dependence MRI of the rat brain: effects of seizure induced by kainic acid in the rat. Proc. Soc. Magn. Reson. Med. 1992;1:501.
124. Zhong J, Petroff OAC, Pritchard JW, *et al.* Changes in water diffusion and relaxation properties of rat cerebellum during status epilepticus. Magn. Reson. Med. 1993;30:241–6.
125. Zhong J, Petroff OAC, Pritchard JW, *et al.* Barbiturate-reversible reduced of water diffusion coefficient in flurothyl-induced status epilepticus in rats. Magn. Reson. Med. 1995;33:253–6.
126. Prichard JW, Zhong J, Petroff OA, *et al.* Diffusion-weighted NMR imaging changes caused by electrical activation of the brain. NMR Biomed. 1995;8:359–64.
127. Eidt S, Kendall EJ, Obenaus A. Neuronal and glial cell populations in the piriform cortex distinguished by using an approximation of q-space imaging after status epilepticus. AJNR Am. J. Neuroradiol. 2004;25:1225–33.
128. Li N, Gong Z, Saucier D, *et al.* Water self-diffusion tensor changes in an avian genetic developmental model of epilepsy. MAGMA. 2003;16:121–8.
129. Righini A, Pierpaoli C, Alger JR, *et al.* Brainparenchyma apparent diffusion coefficient alterations associated with experimental complex partial status epilepticus. Magn. Reson. Imaging. 1994;12:865–71.
130. Tokumitsu T, Mancuso A, Weinstein PR, *et al.* Metabolic and pathological effects of temporal lobe epilepsy in rat brain detected by proton spectroscopy and imaging. Brain Res. 1997;744:57–67.
131. Wang Y, Majors A, Najm I, *et al.* Postictal alteration of sodium content and apparent diffusion coefficient in epileptic rat brain induced by kainic acid. Epilepsia. 1996;37:1000–6.
132. Roch C, Leroy C, Nehlig A, *et al.* Magnetic resonance imaging in the study of the lithium-pilocarpine model of temporal lobe epilepsy in adult rats. Epilepsia. 2002;43:325–35.
133. Hasegawa D, Orima H, Fujita M, *et al.* Diffusion-weighted imaging in kainic acid-induced complex partial status epilepticus in dogs. Brain Res. 2003;983:115–27.
134. Nairismagi J, Grohn OH, Kettunen MI, *et al.* Progression of brain damage after status epilepticus and its association with epileptogenesis: a quantitative MRI study in a rat model of temporal lobe epilepsy. Epilepsia. 2004;45:1024–34.
135. Natt O, Watanabe T, Boretius S, *et al.* Magnetization transfer MRI of mouse brain reveals areas of high neural density. Magn. Reson. Imaging. 2003;21:1113–20.
136. Yu O, Roch C, Namer IJ, *et al.* Detection of late epilepsy by the texture analysis of MR brain images in the lithium-pilocarpine rat model. Magn. Reson. Imaging. 2002;20:771–5.
137. Wolf OT, Dyakin V, Patel A, *et al.* Volumetric structural magnetic resonance imaging (MRI) of the rat hippocampus following kainic acid (KA) treatment. Brain Res. 2002;934:87–96.
138. Fabene PF, Marzola P, Sbarbati A, *et al.* Magnetic resonance imaging of changes elicited by status epilepticus in the rat brain: diffusion-weighted and T2-weighted images, regional blood volume maps, and direct correlation with tissue and cell damage. Neuroimage. 2003;18:375–89.
139. Tenney JR, Duong TQ, King JA, *et al.* Corticothalamic modulation during absence seizures in rats: a functional MRI assessment. Epilepsia. 2003;44:1133–40.
140. Nersesyan H, Hyder F, Rothman DL, *et al.* Dynamic fMRI and EEG recordings during spike-wave seizures and generalized tonic-clonic seizures in WAG/Rij rats. J. Cereb. Blood Flow Metab. 2004;24:589–99.
141. Van Bruggen N, Roberts TPL. Biomedical Imaging in Experimental Neuroscience. CRC Press: Boca Raton, 2002.
142. Choi IY, Lee SP, Guilfoyle DN, *et al.* In vivo NMR studies of neurodegenerative diseases in transgenic and rodent models. Neurochem. Res. 2003;28:987–1001.
143. Rudin M, Mueggler T, Allegrini PR, *et al.* Characterization of CNS disorders and evaluation of therapy using structural and functional MRI. Anal. Bioanal. Chem. 2003;377:973–81.
144. Brownell AL, Livni E, Galpern W, *et al.* In vivo PET imaging in rat of dopamine terminals reveals functional neural transplants. Ann. Neurol. 1998;43:387–90.

145. Pelled G, Bergman H, Goelman G. Bilateral overactivation of the sensorimotor cortex in the unilateral rodent model of Parkinson's disease—a functional magnetic resonance imaging study. Eur. J. Neurosci. 2002;15:389–94.
146. Jenkins BG, Chen YI, Mandeville JB. Pharmacological magnetic resonance imaging. In: N van-Bruggen, TP Roberts (Eds). Biomedical Imaging in Experimental Neuroscience. CRC Press: Boca Raton, 2002.
147. Zhang Z, Andersen A, Grondin R, *et al*. Pharmacological MRI mapping of age-associated changes in basal ganglia circuitry of awake rhesus monkeys. Neuroimage. 2001;14:1159–67.
148. Chen YI, Brownell AL, Galpern W, *et al*. Detection of dopaminergic cell loss and neural transplantation using pharmacological MRI, PET and behavioral assessment. Neuroreport. 1999;10:2881–6.
149. Chen YC, Galpern WR, Brownell AL, *et al*. Detection of dopaminergic neurotransmitter activity using pharmacologic MRI: correlation with PET, microdialysis, and behavioral data. Magn. Reson. Med. 1997;38:389–98.
150. Miletich RS, Bankiewicz KS, Quarantelli M, *et al*. MRI detects acute degeneration of the nigrostriatal dopamine system after MPTP exposure in hemiparkinsonian monkeys. Ann. Neurol. 1994;35:689–97.
151. Hall S, Rutledge JN, Schallert T. MRI, brain iron and experimental Parkinson's disease. J. Neurol. Sci. 1992;113:198–208.
152. Hauss-Wegrzyniak B, Galons JP, Wenk GL. Quantitative volumetric analyses of brain magnetic resonance imaging from rat with chronic neuroinflammation. Exp. Neurol. 2000;165:347–54.
153. Redwine JM, Kosofsky BE, Jacobs RE, *et al*. Hippocampal volume reduction precedes plaque formation in a PDAPP mouse model of Alzheimer's disease. J. Neurochem. 2003;85:59.
154. Song SK, Kim JH, Lin SJ, *et al*. Diffusion tensor imaging detects age-dependent white matter changes in a transgenic mouse model with amyloid deposition. Neurobiol. Dis. 2004;15:640–7.
155. Helpern JA, Jensen L, Lee SP, *et al*. Quantitative MRI assessment of Alzheimer's disease. J. Mol. Neurosci. 2004;24:45–8.
156. Zhang J, Yarowsky P, Gordon MN, *et al*. Detection of amyloid plaques in mouse models of Alzheimer's disease by magnetic resonance imaging. Magn. Reson. Med. 2004;51:452–7.
157. Beckmann N, Schuler A, Mueggler T, *et al*. Age-dependent cerebrovascular abnormalities and blood flow disturbances in APP23 mice modeling Alzheimer's disease. J. Neurosci. 2003;23:8453–9.
158. Wadghiri YZ, Sigurdsson EM, Sadowski M, *et al*. Detection of Alzheimer's amyloid in transgenic mice using magnetic resonance microimaging. Magn. Reson. Med. 2003;50:293–302.
159. Poduslo JF, Curran GL, Peterson JA, *et al*. Design and chemical synthesis of a magnetic resonance contrast agent with enhanced in vitro binding, high blood–brain barrier permeability, and in vivo targeting to Alzheimer's disease amyloid plaques. Biochemistry. 2004;43:6064–75.
160. Hantraye P. Modeling dopamine system dysfunction in experimental animals. Nucl. Med. Biol. 1998;25:721–8.
161. Borlongan CV, Koutouzis TK, Sanberg PR. 3-Nitropropionic acid animal model and Huntington's disease. Neurosci. Biobehav. Rev. 1997;21:289–93.
162. Menalled LB, Chesselet MF. Mouse models of Huntington's disease. Trends Pharmacol. Sci. 2002;23:32–9.
163. Araujo DM, Cherry SR, Tatsukawa KJ, *et al*. Deficits in striatal dopamine D(2) receptors and energy metabolism detected by in vivo microPET imaging in a rat model of Huntington's disease. Exp. Neurol. 2000;166:287–97.
164. Hantraye P, Leroy-Willig A, Denys A, *et al*. Magnetic resonance imaging to monitor pathology of caudate-putamen after excitotoxin-induced neuronal loss in the nonhuman primate brain. Exp. Neurol. 1992;118:18–23.
165. Verheul HB, Balazs R, Berkelbach van der Sprenkel JW, *et al*. Temporal evolution of NMDA-induced excitoxicity in the neonatal rat brain measured with 1H nuclear magnetic resonance imaging. Brain Res. 1993;618:203–12.
166. Lee WT, Chang C. Magnetic resonance imaging and spectroscopy in assessing 3-nitropropionic acid-induced brain lesions: an animal model of Huntington's disease. Prog. Neurobiol. 2004;72:87–110.
167. Gold R, Hartung HP, Toyka KV. Animal models for autoimmune demyelinating disorders of the nervous system. Mol. Med. Today. 2000;6:88–91.
168. Brok H, Bauer J, Jonker M, *et al*. Non-human primate models of multiple sclerosis. Immunol. Rev. 2001;183:173–85.
169. Matyszak MK, Perry VH. Demyelination in the central nervous system following a delayed-type hypersensitivity response to bacillus Calmette-Guerin. Neuroscience. 1995;64:967–77.
170. Grossman RI, Lisak RP, Macchi PJ, *et al*. MR of acute experimental allergic encephalomyelitis. Am. J. Neuroradiol. 1987;8:1045–8.
171. Duckers HJ, Muller HJ, Verhaagen J, *et al*. Longitudinal in vivo magnetic resonance imaging studies in experimental allergic encephalomyelitis: effect of a neurotrophic treatment on cortical lesion development. Neuroscience. 1997;77:1163–73.
172. Jordan EK, McFarland HI, Lewis BK, *et al*. Serial MR imaging of experimental autoimmune encephalomyelitis induced by human white matter or by chimeric myelin-basic and proteolipid protein in the common marmoset. Am. J. Neuroradiol. 1999;20:965–76.
173. Hart BA, Bauer J, Muller HJ, *et al*. Histopathological characterization of magnetic resonance imaging-detectable brain white matter lesions in a primate model of multiple sclerosis: a correlative study in the experimental autoimmune encephalomyelitis model in common marmosets (Callithrix jacchus). Am. J. Pathol. 1998;153:649–63.
174. Hawkins CP, Munro PM, MacKenzie F, *et al*. Duration and selectivity of blood–brain barrier breakdown in chronic relapsing experimental allergic encephalomyelitis studied by gadolinium-DTPA and protein markers. Brain. 1990;113:365–78.
175. Morrissey SP, Stodal H, Zettl U, *et al*. In vivo MRI and its histological correlates in acute adoptive transfer experimental allergic encephalomyelitis. Quantification of inflammation and oedema. Brain. 1996;119:239–48.

176. Newman TA, Woolley ST, Hughes PM, *et al*. T-cell- and macrophage-mediated axon damage in the absence of a CNS-specific immune response: involvement of metalloproteinases. Brain. 2001;124:2203–14.
177. Rudin M, Rausch M, Hiestand P, *et al*. MRI-based monitoring of inflammation and tissue damage in acute and chronic relapsing EAE. Magn. Reson. Med. 2003; 50:309.
178. Richards TL, Alvord E-CJ, He Y, *et al*. Experimental allergic encephalomyelitis in non-human primates: diffusion imaging of acute and chronic brain lesions. Mult. Scler. 1995;1:109–17.
179. Gareau PJ, Rutt BK, Karlik SJ, *et al*. Magnetization transfer and multicomponent T2 relaxation measurements with histopathologic correlation in an experimental model of MS. J. Magn. Reson. Imaging. 2000;11:586–95.
180. Dousset V, Ballarino L, Delalande C, *et al*. Comparison of ultrasmall particles of iron oxide (USPIO)-enhanced T2-weighted, conventional T2-weighted, and gadolinium-enhanced T1-weighted MR images in rats with experimental autoimmune encephalomyelitis. Am. J. Neuroradiol. 1999;20:223–7.
181. Floris S, Blezer EL, Schreibelt G, *et al*. Blood–brain barrier permeability and monocyte infiltration in experimental allergic encephalomyelitis: a quantitative MRI study. Brain. 2004;127:616–27.
182. Anderson SA, Shukaliak-Quandt J, Jordan EK, *et al*. Magnetic resonance imaging of labeled T-cells in a mouse model of multiple sclerosis. Ann. Neurol. 2004;55: 654–9.
183. Rausch M, Hiestand P, Baumann D, *et al*. MRI-based monitoring of inflammation and tissue damage in acute and chronic relapsing EAE. Magn. Reson. Med. 2003;50:309–14.
184. Sibson NR, Blamire AM, Bernades-Silva M, *et al*. MRI detection of early endothelial activation in brain inflammation. Magn. Reson. Med. 2004;51:248–52.
185. Pirko I, Johnson A, Ciric B, *et al*. In vivo magnetic resonance imaging of immune cells in the central nervous system with superparamagnetic antibodies. FASEB J. 2004;18:179–82.
186. Feeney DM, Boyeson MG, Linn RT, *et al*. Responses to cortical injury: I. Methodology and local effects of contusions in the rat. Brain Res. 1981;211:67–77.
187. Marmarou A, Foda MA, van-den BW, *et al*. A new model of diffuse brain injury in rats. Part I: Pathophysiology and biomechanics. J. Neurosurg. 1994;80:291–300.
188. Dixon CE, Lyeth BG, Povlishock JT, *et al*. A fluid percussion model of experimental brain injury in the rat. J. Neurosurg. 1987;67:110–9.
189. McIntosh TK, Noble L, Andrews B, *et al*. Traumatic brain injury in the rat: characterization of a midline fluid-percussion model. Cent. Nerv. Syst. Trauma. 1987;4:119–34.
190. Dixon CE, Clifton GL, Lighthall JW, *et al*. A controlled cortical impact model of traumatic brain injury in the rat. J. Neurosci. Methods. 1991;39:253–62.
191. Gennarelli TA. Animate models of human head injury. J. Neurotrauma. 1994;11:357–68.
192. Lighthall JW, Dixon CE, Anderson TE. Experimental models of brain injury. J. Neurotrauma. 1989;6:83–97.
193. Osteen CL, Moore AH, Prins ML, *et al*. Age-dependency of 45 calcium accumulation following lateral fluid percussion: acute and delayed patterns. J. Neurotrauma. 2001;18:141–62.
194. Raghavendra RVL, Dogan A, Bowen KK, *et al*. Traumatic brain injury leads to increased expression of peripheral-type benzodiazepine receptors, neuronal death, and activation of astrocytes and microglia in rat thalamus. Exp Neurol. 2000;161:102–114.
195. Sutton RL, Hovda DA, Adelson PD, *et al*. Metabolic changes following cortical contusion: relationships to edema and morphological changes. Acta Neurochir. Suppl. (Wien). 1994;60:446–8.
196. Yoshino A, Hovda DA, Kawamata T, *et al*. Dynamic changes in local cerebral glucose utilization following cerebral conclusion in rats: evidence of a hyper- and subsequent hypometabolic state. Brain Res. 1991;561:106–19.
197. Phelps ME. PET: the merging of biology and imaging into molecular imaging. J. Nucl. Med. 2000;41:661–81.
198. Moore TH, Osteen TL, Chatziioannou TF, *et al*. Quantitative assessment of longitudinal metabolic changes in vivo after traumatic brain injury in the adult rat using FDG-microPET. J. Cereb. Blood Flow Metab. 2000;20:1492–501.
199. Kochanek PM, Marion DW, Zhang W, *et al*. Severe controlled cortical impact in rats: assessment of cerebral edema, blood flow, and contusion volume. J. Neurotrauma. 1995;12:1015–25.
200. Faden AI, O'Leary DM, Fan L, *et al*. Selective blockade of the mGluR1 receptor reduces traumatic neuronal injury in vitro and improves outcome after brain trauma. Exp. Neurol. 2001;167:435–44.
201. Schuhmann MU, Stiller D, Thomas S, *et al*. 1H-MR spectroscopic monitoring of posttraumatic metabolism following controlled cortical impact injury: pilot study. Acta Neurochir. Suppl. 2000;76:3–7.
202. Vink R, Mullins PG, Temple MD, *et al*. Small shifts in craniotomy position in the lateral fluid percussion injury model are associated with differential lesion development. J. Neurotrauma. 2001;18:839–47.
203. Schuhmann MU, Stiller D, Skardelly M, *et al*. Determination of contusion and oedema volume by MRI corresponds to changes of brain water content following controlled cortical impact injury. Acta Neurochir Suppl. 2002;81:213–215.
204. Zohar O, Schreiber S, Getslev V, *et al*. Closed-head minimal traumatic brain injury produces long-term cognitive deficits in mice. Neuroscience. 2003;118:949–55.
205. Stoffel M, Blau C, Reinl H, *et al*. Identification of brain tissue necrosis by MRI: validation by histomorphometry. J. Neurotrauma. 2004;21:733–40.
206. Iwamoto Y, Yamaki T, Murakami N, *et al*. Investigation of morphological change of lateral and midline fluid percussion injury in rats, using magnetic resonance imaging. Neurosurgery. 1997;40:163–7.
207. Duhaime AC, Hunter JV, Grate LL, *et al*. Magnetic resonance imaging studies of age-dependent responses to scaled focal brain injury in the piglet. J. Neurosurg. 2003;99:542–8.
208. Schneider G, Fries P, Wagner-Jochem D, *et al*. Pathophysiological changes after traumatic brain injury: comparison

of two experimental animal models by means of MRI. MAGMA. 2002;14:233–41.

209. Fatouros PP, Marmarou A. Use of magnetic resonance imaging for in vivo measurements of water content in human brain: method and normal values. J. Neurosurg. 1999;90:109–15.

210. Stroop R, Thomale UW, Pauser S, *et al*. Magnetic resonance imaging studies with cluster algorithm for characterization of brain edema after controlled cortical impact injury (CCII). Acta Neurochir. Suppl. (Wien). 1998;71:303–5.

211. Albensi BC, Knoblach SM, Chew BG, *et al*. Diffusion and high resolution MRI of traumatic brain injury in rats: time course and correlation with histology. Exp. Neurol. 2000;162:61–72.

212. Assaf Y, Beit-Yannai E, Shohami E, *et al*. Diffusion- and T2-weighted MRI of closed-head injury in rats: a time course study and correlation with histology. Magn. Reson. Imaging. 1997;15:77–85.

213. Assaf Y, Holokovsky A, Berman E, *et al*. Diffusion and perfusion magnetic resonance imaging following closed head injury in rats. J. Neurotrauma. 1999;16:1165–76.

214. Alsop DC, Murai H, Detre JA, *et al*. Detection of acute pathologic changes following experimental traumatic brain injury using diffusion-weighted magnetic resonance imaging. J. Neurotrauma. 1996;13:515–21.

215. Harris NG, Lythgoe MF, Thomas DL, *et al*. A multiparametric, MRI time-course analysis of experimental traumatic brain injury. Proc. ISMRM. 2002;1:1247.

216. Hanstock CC, Faden AI, Bendall MR, *et al*. Diffusion-weighted imaging differentiates ischemic tissue from traumatized tissue. Stroke. 1994;25:843–8.

217. Ito J, Marmarou A, Barzo P, *et al*. Characterization of edema by diffusion-weighted imaging in experimental traumatic brain injury. J. Neurosurg. 1996;84:97–103.

218. Barzo P, Marmarou A, Fatouros P, *et al*. Contribution of vasogenic and cellular edema to traumatic brain swelling measured by diffusion-weighted imaging. J. Neurosurg. 1997;87:900–7.

219. Vorisek I, Hajek M, Tintera J, *et al*. Water ADC, extracellular space volume, and tortuosity in the rat cortex after traumatic injury. Magn. Reson. Med. 2002;48:994–1003.

220. Unterberg AW, Stroop R, Thomale UW, *et al*. Characterisation of brain edema following ”controlled cortical impact injury” in rats. Acta Neurochir. Suppl. (Wien). 1997;70:106–8.

221. Barzo P, Marmarou A, Fatouros P, *et al*. Magnetic resonance imaging-monitored acute blood–brain barrier changes in experimental traumatic brain injury. J. Neurosurg. 1996;85:1113–21.

222. Beaumont A, Marmarou A, Hayasaki K, *et al*. The permissive nature of blood brain barrier (BBB) opening in edema formation following traumatic brain injury. Acta Neurochir. Suppl. 2000;76:125–9.

223. Beaumont A, Marmarou A, Fatouros P, *et al*. Secondary insults worsen blood brain barrier dysfunction assessed by MRI in cerebral contusion. Acta Neurochir. Suppl. 2002;81:217–9.

224. Detre JA, Leigh JS, Williams DS, *et al*. Perfusion imaging. Magn. Reson. Med. 1992;23:37–45.

225. Forbes ML, Hendrich KS, Kochanek PM, *et al*. Assessment of cerebral blood flow and CO2 reactivity after controlled cortical impact by perfusion magnetic resonance imaging using arterial spin-labeling in rats. J. Cereb. Blood Flow Metab. 1997;17:865–74.

226. Hendrich KS, Kochanek PM, Williams DS, *et al*. Early perfusion after controlled cortical impact in rats: quantification by arterial spin-labeled MRI and the influence of spin-lattice relaxation time heterogeneity. Magn. Reson. Med. 1999;42:673–81.

227. Kochanek PM, Hendrich KS, Dixon CE, *et al*. Cerebral blood flow at one year after controlled cortical impact in rats: assessment by magnetic resonance imaging. J. Neurotrauma. 2002;19:1029–37.

228. Kimura H, Meaney DF, McGowan JC, *et al*. Magnetization transfer imaging of diffuse axonal injury following experimental brain injury in the pig: characterization by magnetization transfer ratio with histopathologic correlation. J. Comput. Assist. Tomogr. 1996;20:540–6.

229. McGowan JC, McCormack TM, Grossman RI, *et al*. Diffuse axonal pathology detected with magnetization transfer imaging following brain injury in the pig. Magn. Reson. Med. 1999;41:727–33.

230. Nimmo AJ, Cernak I, Heath DL, *et al*. Neurogenic inflammation is associated with development of edema and functional deficits following traumatic brain injury in rats. Neuropeptides. 2004;38:40–7.

Application of MRS in Cancer in Pre-clinical Models

Y.-L. Chung, M. Stubbs, and J.R. Griffiths

Cancer Research UK Biomedical Magnetic Resonance Research Group, Department of Basic Medical Sciences,
St George's University of London, Cranmer Terrace, Tooting, London, SW17 0RE, UK

Introduction

Magnetic resonance spectroscopy (MRS) has the unique ability to measure the chemical content of living tissue in the body, repeatedly and noninvasively. This permits investigations of biology and physiology in human and in animal models *in vivo,* in both healthy and diseased tissues. From such studies, information on tumor diagnosis and response to therapy, as well as prognostic information, has been obtained. MRS can also be used for *in vitro* studies of cell and tumor extracts. Now with high-resolution magic-angle spinning (HR-MAS) spectroscopy, small pieces of intact tissue (e.g. biopsies) can also be examined.

The first *in vivo* ^{31}Phosphorus (^{31}P) MRS study carried out in an animal tumor model was performed in 1981 [1], followed a couple of years later by the first *in vivo* human tumor study [2]. The noninvasiveness of MRS makes it an important tool to study cancer *in vivo*, where serial measurements can be made on the same animal. MRS, using different nuclei including ^{1}H, ^{31}P, ^{19}F, and ^{13}C, has been used widely to study the biology and therapy of cancers in cultured cells and in animal models [3–11].

Using ^{31}P MRS, markers for tissue bioenergetics [nucleotide triphosphate (NTP), inorganic phosphate (Pi)], intracellular pH (pHi), and membrane turnover [phosphorus-containing components of phospholipid membrane: phosphomonoester (PME) and phosphodiester (PDE)] can be readily observed (Figure 1).

PMEs comprise phosphocholine (PC) and phosphoethanolamine (PE), and PDEs glycero-phosphocholine (GPC) and glycero-phosphoethanolamine (GPE) as shown by *in vitro* ^{31}P MRS of cancer cells or tumor extracts (Figure 2), where these metabolites are more readily resolved than *in vivo*.

^{1}H and ^{13}C MRS can also provide information on tumor metabolism *in vivo.* Metabolites, such as lactate, lipids, and choline-containing compounds, can be observed in ^{1}H MRS [12]. ^{13}C-enriched substrates (e.g. glucose) and ^{13}C MRS can be used to study metabolic pathways (e.g. glucose metabolism) of tumors [13]. *In vivo* ^{19}F, ^{1}H and ^{13}C MRS have been used to monitor the metabolism of drugs containing those nuclei *in situ* [8–10, 14, 15].

Many more metabolites can be observed by HR-MAS (Figure 3) in comparison to *in vivo* MRS because HR-MAS gives better-resolved spectra. This methodology has the advantage that pieces of intact tissue can be examined with minimal sample preparation and sample destruction but there is still a risk of sample degradation during the examination. Far superior spectral resolution to either HR-MAS or *in vivo* MRS is obtained from *in vitro* MRS of extracts of cells or tissue (Figure 4); however, tissue extraction is destructive, has longer sample preparation time, and samples will certainly be altered during the extraction procedure (but mostly in well-understood ways). Despite the poorer spectral resolution, the main advantage of *in vivo* MRS is that biochemical and functional information can be obtained noninvasively in the living tissue, whereas biopsy samples required for HR-MAS and *in vitro* MRS are already a step away from the *in vivo* situation.

This chapter will present some examples to illustrate the application of various MRS methodologies in preclinical models to study tumor biology and therapies. The headings represent the major areas that have been studied and reported in the literature.

Tumor Biology and Physiology

Tumor Hypoxia

Hypoxia is a reduction in the normal level of tissue oxygen tension (pO_2), which is very common in cancer. This is due to rapid cell growth and chaotic and leaky immature blood vessels associated with tumors. Hypoxia is of major interest in the oncology field, as tumor cells that are exposed to hypoxia can become resistant to radiotherapy and chemotherapy and then the surviving cells can lead to tumor re-growth and metastasis [19]. ^{31}P MRS is a valuable tool for studying hypoxia since tumor metabolites, such as NTP, PCr, and Pi, reflect tumor bioenergetics. Many studies have shown that progressive tumor growth and insufficient blood flow result in a more acidic pH and a decrease in high energy phosphate metabolites, such as NTP and PCr with a concomitant increase in Pi [20–23].

Graham A. Webb (ed.), Modern Magnetic Resonance, 823–833.
© 2008 *Springer.*

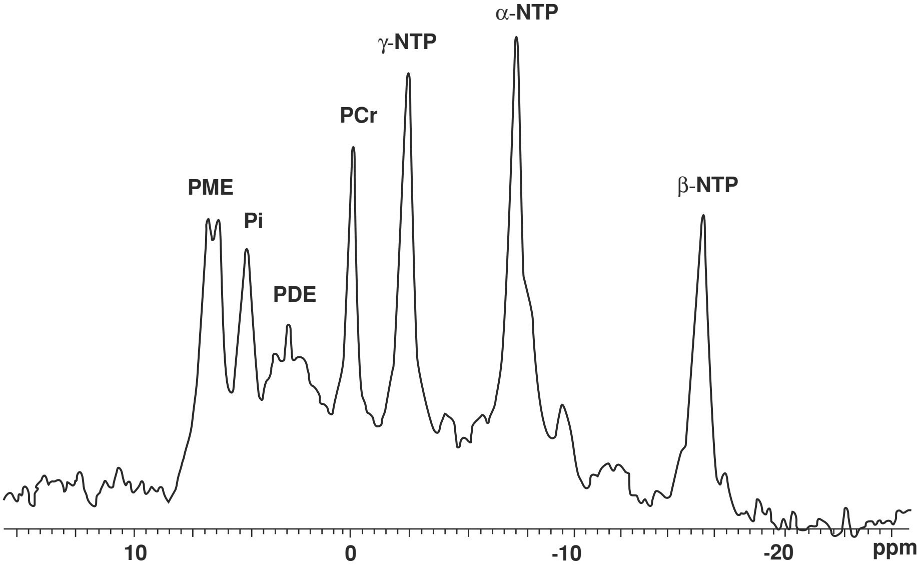

Fig. 1. *In vivo* localized ^{31}P MRS of an HT29 tumor. Peak assignments were phosphomonoester (PME), phosphodiester (PDE), inorganic phosphate (Pi), phosphocreatine (PCr), and nucleotide triphosphate (α-, β-, γ-NTP).

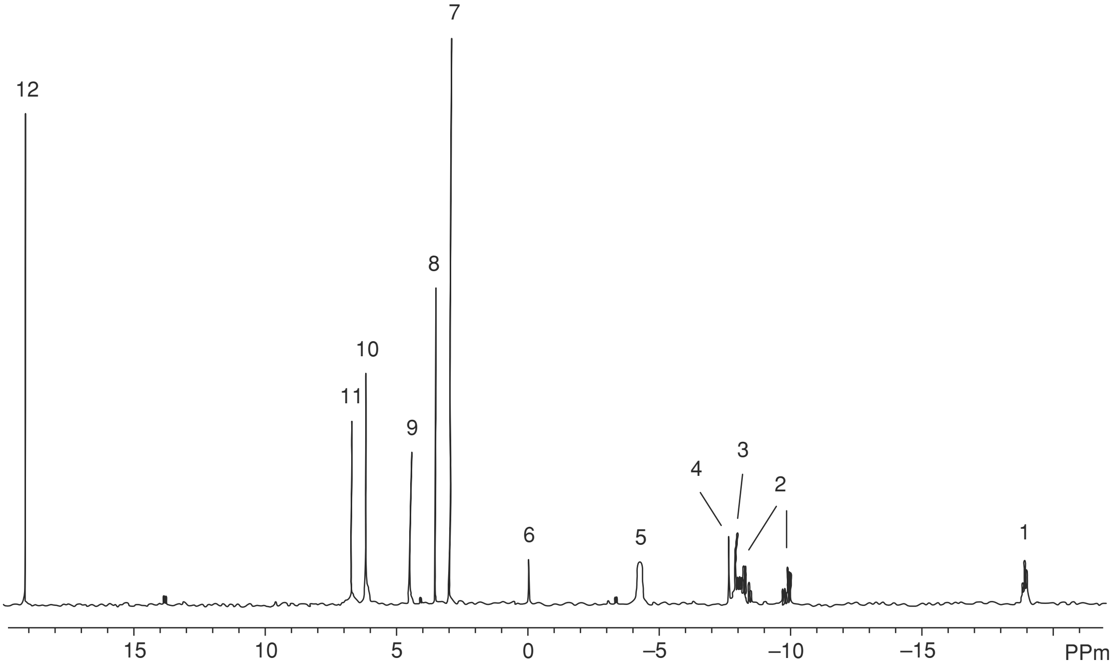

Fig. 2. *In vitro* ^{31}P MRS of a perchloric acid extract of an HT29 tumor. Peak assignments were β-nucleotide triphosphate (1), uridine diphosphate sugars (2), α-nucleotide triphosphate (3), α-nucleotide diphosphate (4), γ-nucleotide triphosphate + β-nucleotide diphosphate (5), phosphocreatine (6), glycero-phosphocholine (7), glycero-phosphoethanolamine (8), inorganic phosphate (9), phosphocholine (10), phosphoethanolamine (11), and methylene diphosphoric acid (12—included as a reference for chemical shift and quantitation).

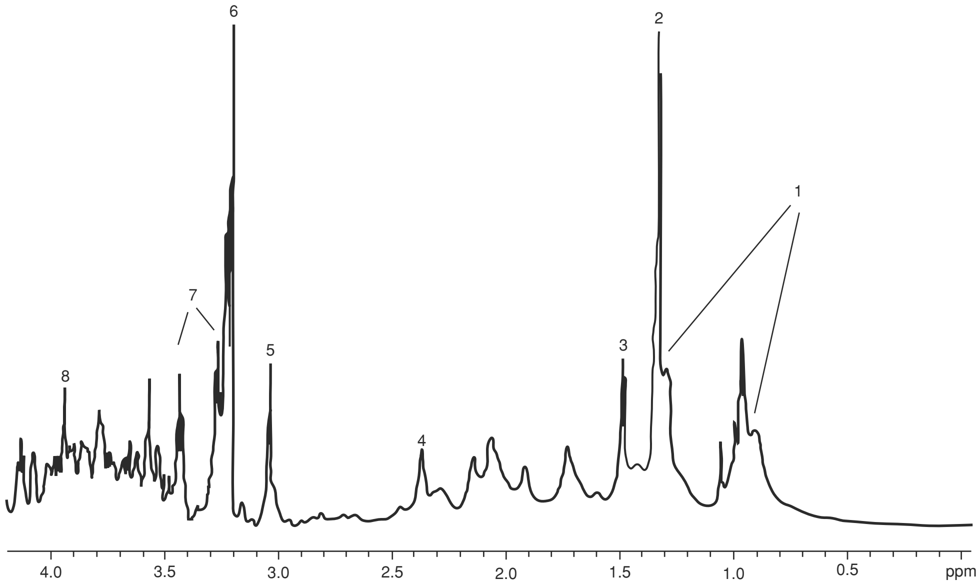

Fig. 3. HR-MAS ^{1}H spectrum of an HT29 tumor. Peaks assigned as lipids (1), lactate (2), alanine (3), glutamate (4), creatine + phosphocreatine (5), choline-containing compounds (6), taurine (7), and creatine + phosphocreatine (8). For detailed peak assignments, see references [16,17].

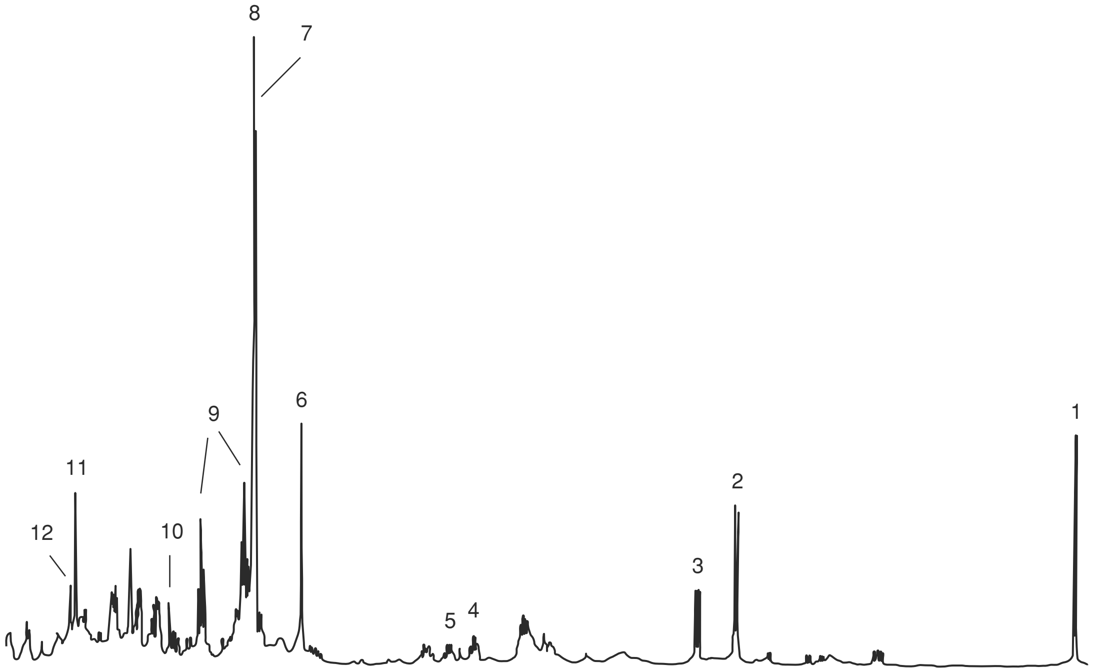

Fig. 4. *In vitro* ^{1}H MR spectrum of an HT29 tumor extract. Peaks assigned as sodium 3-trimethyl-silyl-2,2,3,3-tetradeuteropropionate (1—included as a chemical shift reference and for quantitation), lactate (2), alanine (3), glutamate (4), glutamine (5), creatine + phosphocreatine (6), phosphocholine (7), glycero-phosphocholine (8), taurine (9), glycine (10), creatine (11), and phosphocreatine (12). For detailed peak assignments, see references [16,18].

In vivo ^{19}F MRS, together with endogenous probes, can also be used to study hypoxia and oxygenation in tumors. Hypoxia can be measured by using a fluorinated hypoxia-imaging agent, for example SR4554 or other fluorinated 2-nitroimidazoles [24–25]. Oxygenation may be measured using organofluorine compounds such as perfluorocarbons, which have a very high affinity for oxygen [25–27].

Glycolytic Metabolism in Tumors

It has been known since Warburg's time that tumor cells synthesize high levels of lactate through glycolysis [28]. Most tumors *in vivo* synthesize some ATP by oxidative metabolism, and some by glycolytic metabolism to lactate (aerobic glycolysis). If the oxygen supply is suddenly decreased (acute hypoxia), the tumor cells switch to anaerobic glycolysis. Many tumors have high rates of glycolysis regardless of their oxygen supply and the rate of glycolysis appears to be associated with the differentiation status and growth rate of the tumor [29,30]. This increased rate of glycolysis could be caused by the upregulation of hypoxia inducible factor-1 (HIF-1), overexpressed in many cancers [31] both constitutively [32] and as the result of hypoxia [19]. HIF-1 is a transcription factor that can bind to hypoxia response elements and activate gene transcription. It has been implicated in, for example, the regulation of angiogenesis, glucose transport, glucose metabolism, and nitric oxide metabolism [33].

^{1}H MRS can be used in studies of tumor glycolytic metabolism noninvasively, as a multiple-quantum-coherence-edited sequence allows the measurement of lactate [34]. ^{13}C-enriched substrates, together with ^{13}C MRS methodologies, can also be used to study the *in vivo* rates of glycolysis in different tumor types [13,35].

Tumor pH

Many cellular processes depend on pH, including synthesis of macromolecules, cell proliferation, DNA synthesis, the activity of various enzymes (such as enzymes of glycolysis), and the transport of metabolites and drugs [36]. Hence, tumor pH plays an important role in tumor transformation and growth, as well as treatment [29]. Tumor cells were found to have a lower extracellular pH (pHe) than normal cells, whereas the intracellular pH (pHi) is relatively high (about 7.0–7.2) [37]. Low pHe has been associated with tumorogenic transformation, chromosomal re-arrangements, extracellular matrix breakdown, migration and invasion etc [38]. High pHi provides tumor cells with a growth advantage over normal cells [39]. This is an intrinsic feature of the tumor metabolic phenotype and it is caused by alterations either in acid export from the tumor cells or in clearance of extracellular acid. Tumor pH gradients have practical importance because most anti-cancer drugs must be transported by either active transporters or by passive diffusion into cells, where they frequently undergo further metabolism. As all these processes might be pH sensitive, the cytotoxic activity of an anti-cancer drug could depend on both pHi and pHe [29,40].

Therefore, measuring tumor pH could provide insights into tumor metabolism and its response to certain therapies [41–43]. ^{31}P MRS offers the unique opportunity to measure intracellular pH (pHi) in the tumor noninvasively; it is calculated from the chemical shift (i.e. frequency) between the Pi resonance (pH sensitive) and the pH insensitive metabolite, such as PCr or NTP. Tumor pHe can be measured by introducing an endogenous pH probe, such as ZK150471 and 3-APP, into the animal which may be assessed by *in vivo* ^{19}F or ^{31}P MRS, respectively [44,45].

Phospholipid Metabolism in Tumors

Phospholipid components have established roles both as structural building blocks of cell membrane and as regulators of cell function. Choline signals have generally proved to be the most diagnostically and prognostically useful elements of ^{1}H MRS of tumors. Elevated levels of choline-containing compounds in cancer were found to be associated with tumor growth and cell proliferation and have been used as endogenous biomarkers of cancer [46–48]. ^{1}H MRS detection of the total choline level in patients allowed distinction between malignant and benign breast lesions [49]. Assessment of phospholipid metabolism may also provide insights into tumor response following treatment.

In vivo ^{1}H and ^{31}P MRS are ideally suited to measure phospholipid metabolites as high levels of phospholipid metabolites are present in tumors and cancer cells. *In vivo* ^{1}H MRS will provide information on total choline level (which includes free choline, PE, PC, GPC, and GPE) (Figure 5), whereas PME and PDE resonances are found in *in vivo* ^{31}P MR spectra [11,50] (Figure 1).

Combined MR and chromatographic analysis of aqueous extracts of rat tumors has unequivocally demonstrated that the PME signal in *in vivo* ^{31}P MR spectra mainly comprises phospholipid metabolites, PE, and PC, rather than sugar phosphates [50] and can sometimes be resolved *in vivo* by ^{31}P MRS [51,52]. An increase in PME has been associated with membrane during rapid tissue growth [11]. On the other hand, the PDE resonance comprises GPC and GPE [50] which are associated with membrane breakdown.

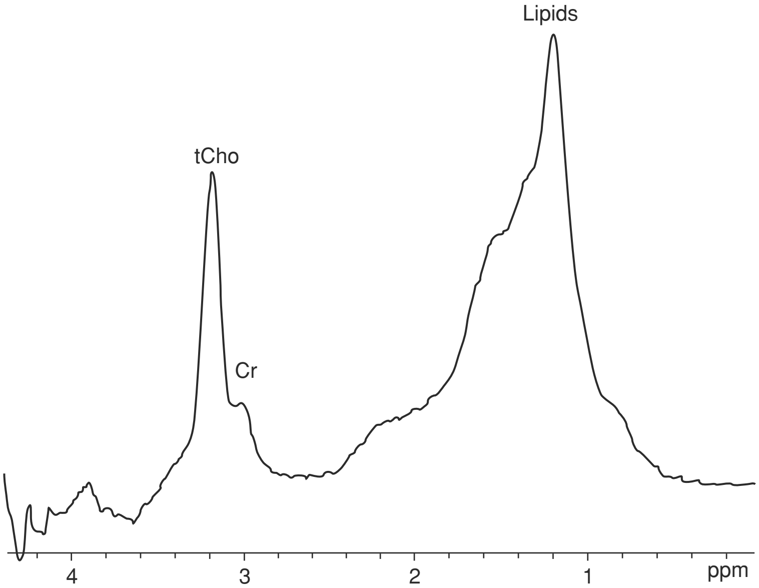

Fig. 5. *In vivo* localized ^{1}H MR spectrum of an HT29 tumor in a mouse. Peak assignments are total choline (tCho), creatine (Cr), and total lipids (Lipids).

Lipid Metabolism in Tumors

High levels of MR-detectable lipids (intracellular lipid vesicles from the cytosol) are present both in proliferating and malignant cells in a variety of tumors [53–55] (Figure 5). These lipids are readily detected by ^{1}H MRS and resonate at 1.3 ppm (the signal from the $CH_2CH_2CH_2$ group). The underlying reason for this high level of lipid remains unclear. In *in vitro* cell culture studies, it was found that apoptosis was associated with the accumulation of the $CH_2CH_2CH_2$ lipid groups, whereas in necrosis there was no change in MR-detectable lipids [56,57]. However, in solid tumors the presence of this lipid resonance was found to coincide with areas of necrosis [55,58,59].

Recently, Griffin *et al*. [60] have used *in vivo* and *in vitro* ^{1}H MRS and HR-MAS to study a rat BT4C glioma model. A strong ^{1}H MRS lipid peak was detected during tumor growth and polyunsaturated fatty acid was found to accumulate following apoptosis after ganciclovir-thymidine kinase gene therapy. No sign of necrosis was found by histological or immunohistochemical assays in tumor tissue during treatment. Taking together the MR and histology findings, the data suggest that the accumulation and alterations in the degree of lipid saturation occur in the ^{1}H MRS visible lipids during apoptosis and that these lipids arise from cell constituent breakdown products forming lipid vesicles in dying cells [60,61].

Oncogene Function

Genomic and proteomic information is transforming all fields of cancer research. The increased understanding of the genomics and molecular pathology of cancer also provides a framework for designing new therapeutic strategies. The majority of the genes in most genomes is still of unknown function, and many studies on proteomics are attempting to fill this need. However, since information flows from DNA to RNA to protein to function, the role of each gene product in metabolism also needs to be studied to provide the link between the genotype and the phenotype [62]; a single gene mutation may cause alterations of metabolite levels of seemingly unrelated biochemical pathways and this is likely to happen when genes are constitutively overexpressed or anti-sense inhibited.

MRS could be a very useful tool for investigating specific oncogene function by using genetically modified tumor models with specific genes overexpressed or knocked down-regulated/knockedout. MRS can provide functional information on the role of these genes. Below are two examples where this type of methodology has been used to elucidate gene functions.

Hypoxia Inducible Factor-1

Cells have a highly efficient system for upregulating a host of genes that can counteract the effects of hypoxia.

Table 1: *In vitro* ^{1}H NMR measurement of metabolites in wild-type (Hepa WT) and HIF-1β deficient (Hepa c4) tumor extracts ($n = 4$)

Metabolites	Hepa WT	Hepa c4
Betaine	1.10 ± 0.20	0.40 ± 0.06*
Phosphocholine	3.78 ± 0.65	1.22 ± 0.24*
Free choline	0.43 ± 0.08	0.17 ± 0.02*
Glycine	3.93 ± 0.65	1.90 ± 0.38*
Taurine	16.10 ± 3.60	11.90 ± 1.61
Glycero-phosphocholine	2.58 ± 0.49	1.55 ± 0.24

*For Hepa WT compared to Hepa c4, $p < 0.05$. Values expressed as μmol/g wet weight.

Cellular responses to hypoxia include increased glycolysis and glucose metabolism, brought about by upregulation of transcription factors such as HIF-1. The HIF-1 transcription factor has been shown to be overexpressed across a broad range of cancers [31]. HIF-1α combines with HIF-1β to form a heterodimeric transcription factor that regulates the expression of glucose transporters and many of the glycolytic enzymes in cells, both constitutively and through cellular responses to hypoxia [63,64].

In HIF-1β deficient cells, a functional HIF-1 complex is unable to form and therefore unable to upregulate glycolysis [65]. Tumors grown from these HIF-1β deficient cells were studied using *in vivo* ^{31}P MRS and *in vitro* ^{1}H MRS. Tumors deficient in HIF-1β were found to have only 20% of the ATP content found in wild-type tumors suggesting that the absence of upregulated glycolysis prevents formation of precursors for anabolic pathways (Table 1), in particular synthesis of the purine rings for ATP [66].

This study has shown that the combined use of both *in vivo* and *in vitro* MRS can provide a powerful tool to measure physiological and biochemical parameters in control and mutant tumors.

Choline Kinase

Choline kinase (ChoK) is a cytosolic enzyme that catalyses the phosphorylation of choline to form PC which is involved in cell membrane synthesis. Elevated levels of PC and ChoK found in tumors are associated with cell proliferation and malignant transformation [46–49]. Correlation between increased ChoK activity and high tumor grade was reported indicating that increased ChoK expression and/or activity may cause increased PC and total choline levels [46,48,67,68].

To confirm this observation, Glunde *et al*. have studied the function of ChoK by examining a breast cancer cell line with knockdown of ChoK using small interfering RNA (siRNA) technology. ^{1}H MRS of cell extracts showed that the ChoK deficient cells have lowered levels of PC and total choline relative to empty vector controls [69]. Similar results were also observed in cells and xenografts treated with a ChoK inhibitor [70,71].

Therapy

MRS has much to offer for monitoring anti-cancer drugs, both in patients and in animal models. It can provide important insights into novel anti-cancer drug development, which could accelerate the drug development process. MRS can be used to determine whether adequate or optimal exposures of active agents are being achieved in the tumor [by measuring the drug itself as a pharmacokinetic (PK) marker] and/or whether the desired biological effect is being obtained [measuring pharmacodynamic (PD) markers e.g. choline].

Pharmacokinetic Markers

MRS has the unique ability, in some cases, to monitor the changing concentration of the anti-cancer drug itself as well as its metabolism and detoxification noninvasively in the tissue. *In vivo* ^{19}F MRS has been used extensively as an investigative tool for 5-fluorouracil (5-FU) pharmacology, a widely used cytotoxic drug in the clinic. It has been used to study the distribution and metabolism of this drug in normal and tumor tissues both in xenografts and in patients and has provided significant information on the fate and the potential PD effects of the drug [8,9,72]. The first *in vivo* ^{19}F MRS studies [73] were used to monitor the PK of 5-FU in rat tumors. Apart from the parent 5-FU, the ^{19}F MR spectra also showed 5-FU activated to cytotoxic fluoronucleotides and the appearance of detoxification products from the liver. There have been many other animal studies (and some human studies) on 5-FU and its derivatives [8,9,72].

MRS studies using other nuclei to monitor anti-cancer drugs have also been performed on tumors *in vivo*. ^{1}H MRS has been used to monitor iproplatin [14], ^{2}H MRS to monitor misonidazole [74], ^{13}C MRS to monitor temozolomide [15], ^{31}P MRS to monitor ifosfamide [75], and ^{195}Pt MRS to monitor carboplatin [76].

It would be very useful to have non-invasive predictive markers for response to chemotherapeutic drugs. Such a marker will minimize the patients' unnecessary exposure to cytotoxic drugs and clinicians could opt for an alternative or combination therapy at an earlier time if the patient is found to be unlikely to respond to certain treatments.

A PK study by ^{19}F MRS was performed recently on the oral anti-cancer drug capecitabine, a prodrug of 5-FU.

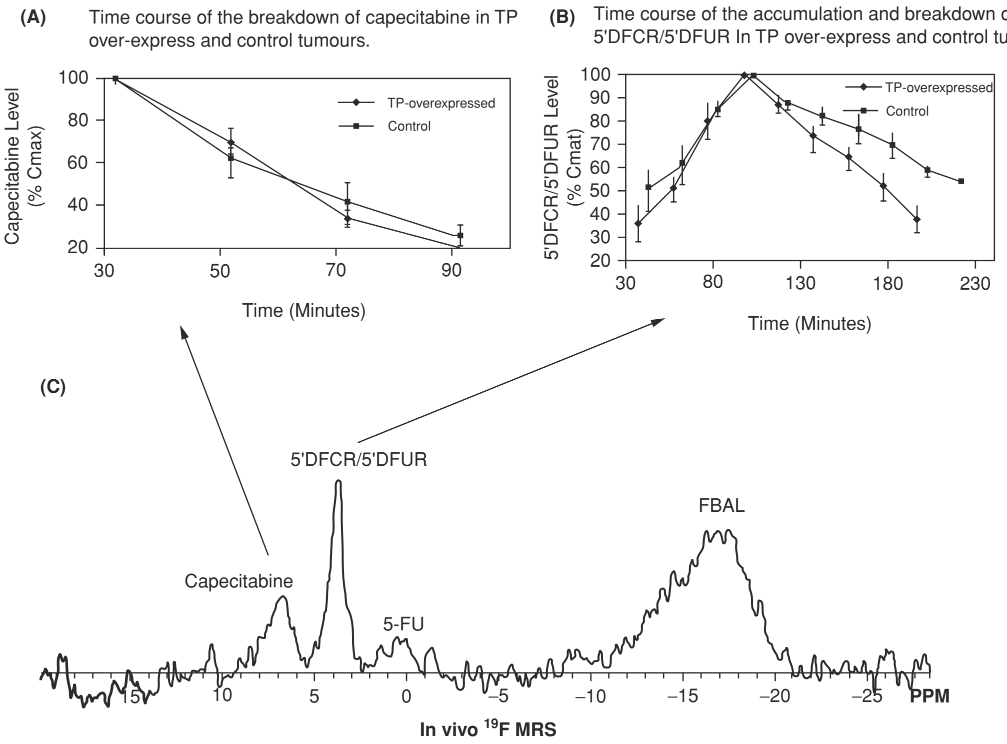

Fig. 6. (A) Time course of the breakdown of capecitabine. (B) Time course of the accumulation and breakdown of 5′DFCR/5′DFUR. (C) *In vivo* ^{19}F MR spectra of a tumor 52–72 min after an injection of capecitabine.5′-deoxy-5-fluorocytidine (5′DFCR); 5′-deoxy-5-fluorouridine (5′DFUR); 5-fluorouracil (5-FU); and α-fluoro-β-alanine (FBAL).

The final activation step in the tumor is from 5′deoxy-5-fluorouridine (5′DFUR) to 5-FU, catalyzed by thymidine phosphorylase (TP). Previous studies have shown that tumor response is strongly correlated with tumor TP; however, the methodologies for determining TP levels involve obtaining invasive biopsies from patients. A non-invasive PK marker for monitoring the uptake and breakdown of capecitabine and potentially for predicting treatment response would be a more desirable end point for use in clinical trials and eventually in the clinic.

The PK of capecitabine was monitored in 2T10 human bladder tumors engineered to overexpress TP, compared with wild-type and empty vector controls [77]. *In vivo* ^{19}F spectra were acquired after a single dose of capecitabine. In the TP-overexpressing 2T10 tumors, the rate constant of the breakdown of the intermediate molecules (5′DFCR + 5′DFUR) was doubled compared with controls (Figure 6). This study confirmed that the rate of 5′DFUR conversion is related to TP expression. ^{19}F MRS measurement of the PKs of capecitabine and its intermediate metabolites could be a non-invasive surrogate for measuring TP levels in patients and predicting response to capecitabine. A recent using 1.5T and 3T clinical systems *in vivo* ^{19}F MRS study [78] has detected capecitabine, as well as its metabolites and catabolites, in livers of patients with colorectal cancer.

Pharmacodynamic Markers

MRS also has much to offer for monitoring tumor response to anti-cancer drugs, both in patients and in experimental animals. Most of the published work has been performed on routinely used chemotherapeutic drugs but MRS can also offer important insights into novel anti-cancer agents in order to accelerate the drug development process. As many of the novel anti-cancer agents currently under development will not cause tumor shrinkage when used as single agents in Phase 1 clinical trials, MRS may have a role in monitoring their PD actions.

The following section demonstrates the use of *in vivo* and *in vitro* ^{1}H and ^{31}P MRS to assess tumor response to conventional cytotoxic and novel drug therapies that target specific molecular targets. The application of these MR methodologies may have potential to provide surrogate PD markers for use in clinic trials.

Conventional Cytotoxic Drugs

5-FU is a widely used cytotoxic drug in medical oncology. Street *et al*. [79] used *in vivo* and *in vitro* ^{31}P MRS to examine the PD effect of 5-FU on a mouse mammary carcinoma model. An increase in NTP/Pi and PCr/Pi ratios was observed *in vivo* 48 h after 5-FU treatment. The PE-to-PC ratio was also elevated relative to controls and this was found to be due to an increase in PE (as confirmed by *in vitro* ^{31}P MRS). In addition, increases in GPC and GPE were also observed [79].

Cyclin-dependent kinase Inhibitor

CYC202 (R-roscovitine, Cyclacel Ltd, Dundee, Scotland) inhibits the cyclin-dependent kinases 1, 2, and 7 and thus blocks cell cycle progression. Its action *in vivo* was monitored by ^{31}P MRS in human colon xenografts to gain insights into the biochemical changes associated with cell cycle disruption and to determine whether ^{31}P MRS could eventually be used as a surrogate marker of response in a clinical trial. CYC202 treatment for 4 days caused reduction in tumor proliferation and tissue pH and impairment in tumor bioenergetics [80]. If CYC202 comes to clinical trial, these ^{31}P MRS effects may provide a non-invasive surrogate marker for assessing tumor response in patients.

HSP90 Inhibitor

The heat-shock protein HSP90 is of interest as an anticancer target [81] because it helps maintain the shape of many oncogenic proteins; inhibiting single oncogenes with “magic bullet” drugs has proved somewhat disappointing as the cancers often become resistant. The HSP90 inhibitor 17-Allylamino, 17-demethoxygeldanamycin (17AAG) is currently under trial as an anticancer agent, and a surrogate marker of tumor response was needed for the clinical trial. The actions of 17AAG were monitored on several cultured human colon cancer cell lines and on a human colon tumor xenograft model [82]. Treatment with an inactive analogue, and an active analogue, 17AG, was also tried. In all cell lines, there were significant increases in PC and GPC. *In vivo,* after 4 days of 17AAG treatment, the tumors showed significant growth delay as well as increased ratios of PME/PDE, PME/total phosphorus (TotP), and PME/β-NTP and a decrease in the β-NTP/TotP ratio. A significant inverse correlation was found between the percentage of change in PME/PDE ratio and the percentage of change in tumor size following 17AAG treatment [82]. These ^{31}P MRS changes suggested that it would be possible to monitor tumors in patients during the Phase 1 clinical trials of 17AAG and such a study is currently under way.

Conclusion

There are many areas of cancer research including drug development studies where MR techniques can give important information both *in vivo* and *in vitro.*

Acknowledgement

We would like to thank Vicente Segundo Palomino Benítez *por inspiratio*.

References

1. Griffiths JR, Stevens AN, Iles RA, Gordon RE, Shaw D. ^{31}P-NMR investigation of solid tumours in the living rat. Biosci. Rep. 1981;1:319–25.
2. Griffiths JR, Cady E, Edwards RHT, McCready VR, Wilkie DR, Wiltshaw E. ^{31}P-NMR studies of a human tumour in situ. Lancet. 1983;1(8339):1435–36.
3. Griffiths JR, Glickson JD. Monitoring pharmacokinetics of anticancer drugs: non-invasive investigation using magnetic resonance spectroscopy. Adv. Drug Deliv. Rev. 2000;1:75–89.
4. Ronen SM, DiStefano F, McCoy CL, Robertson D, Smith TAD, Al-Saffar NM, Titley J, *et al*. Magnetic resonance detects metabolic changes associated with chemotherapy-induced apoptosis. Br. J. Cancer. 1999;80:1035–41.
5. Ronen SM, Jackson LE, Beloueche M, Leach MO. Magnetic resonance detects changes in phosphocholine correlated with Ras activation and inhibition in NIH 3T3 cells. Br. J. Cancer. 2001;84:691–96.
6. Stubbs M, Griffiths JR. Monitoring cancer by magnetic resonance. Br. J. Cancer. 1999;80:86–94.
7. Williams SNO, Anthony ML, Brindle KM. Induction of apoptosis in two mammalian cell lines results in increased levels of fructose-1,6-biophosphate and CDP-choline as determined by ^{31}P MRS. Magn. Reson. Med. 1998;40: 411–20.
8. Wolf W, Waluch V, Presant CA. Non-invasive ^{19}F-MRS of 5-fluoruracil in pharmacokinetics and pharmacodynamics. NMR Biomed. 1998;11:387–87.
9. McSheehy PMJ, Lemaire LP, Griffiths JR. Fluroine-19 MRS: application in oncology. In: DM Grant, RK Harris (Eds). Encyclopaedia of NMR, Vol. 2. Wiley: New York, 1996, pp. 2048–52.
10. McSheehy PMJ, Robinson SP, Ojugo ASE, Aboagye EO, Cannell MB, Leach MO, Judson IR, Griffiths JR. Carbogen breathing increases 5-fluorouracil uptake and cytotoxicity in hypoxia murine RIF-1 tumors: a magnetic resonance study *in vivo*. Cancer Res. 1998;58:1185–94.

11. de Certaines JD, Larsen VA, Podo F, Carpinelli G, Briot O, Henriksen O. *In vivo* 31P MRS of experimental tumours. NMR Biomed. 1993;6:345–65.
12. Shungu DC, Bhujwalla ZM, Wehrle JP, Glickson JD. 1H NMR spectroscopy of substaneous tumors in mice: preliminary studies of effects of growth, chemotherapy and blood flow reduction. NMR Biomed. 1992;5:296–302.
13. Artemov D, Bhujwalla ZM, Glickson JD. *In vivo* selective measurement of 1-^{13}C glucose metabolism in tumors by heteronuclear cross-polarization. Magn. Reson. Med. 1995;33:151–5.
14. He Q, Bhujwalla ZM, Maxwell RJ, Glickson JD. Proton observation of the antineoplastic agent iproplatin *in vivo* by selective multiple quantum coherence transfer. Magn. Reson. Med. 1995;33:414–6.
15. Artemov D, Bhujwalla AM, Maxwell RJ, Griffiths JR, Judson IR, Leach MO, Glickson JD. Pharmacokinetics of the ^{13}C-labeled anticancer agent temozolomide detected *in vivo* by selective cross polarization transfer. Magn. Reson. Med. 1995;33:338–42.
16. Sitter B, Sonnewald U, Spraul M, Fjosne HE, Gribbestad IS. High-resolution magic angle spinning MRS of breast cancer tissue. NMR Biomed. 2002;15:327–37.
17. Martinez-Bisbal MC, Marti-Bonmati L, Piquer J, Revert A, Ferrer P, Llacer JL, *et al*. 1H and 13C HR-MAS spectroscopy of intact biopsy samples *ex vivo* and *in vivo* 1H MRS study of human high grade gliomas. NMR Biomed. 2004;17:1–15.
18. Moreno A, Lopez LA, Fabra A, Arus C. ^{1}H MRS markers of tumor growth in intrasplenic tumors and liver metastasis induced by injection of HT-29 cells in nude mice spleen. NMR Biomed. 1998;11:93–106.
19. Harris AL. Hypoxia—a key regulatory factor in tumor microenvironment. Nat. Rev. Cancer. 2002;2:38–47.
20. Okunieff P, Vaupel P, Sedlacek R, Neuringer LJ. Evaluation of tumor energy metabolism and microvascular blood flow after glucose or mannitol administration using ^{31}P Nuclear Magnetic Resonance spectroscopy and laser Doppler flowmetry. Int. J. Radiat. Oncol. Biol. Phys. 1989;16:1493–500.
21. Bhujwalla ZM, McCoy CL, Glickson JD, Gillies RJ, Stubbs M. Estimations of intra- and extracellular volume and pH by ^{31}P magnetic resonance spectroscopy: effect of therapy on RIF-1 tumours. Br. J. Cancer 1998;78:606–11.
22. Vaupel P, Schaefer C, Okunieff P. Intracellular acidosis in murine fibrosarcomas coincides with ATP depletion, hypoxia, and high levels of lactate and total Pi. NMR Biomed. 1994;7:128–36.
23. Aboagye EO, Dillehay LE, Bhujwalla ZM, Lee D-J. Hypoxic cell cytotoxin tirapazamine induces acute changes in tumor energy metabolism and pH: a ^{31}P magnetic resonance spectroscopy study. Radiat. Oncol. Investig. 1998;6:249–54.
24. Aboagye EO, Maxwell RJ, Kelson AB, Tracy M, Lewis AD, Graham MA, Horsman MR, Griffiths JR, Workman P. Preclinical evaluation of the fluorinated 2-nitroimidazole N-(2-hydroxy-3,3,3-trifluoropropyl-)-2-(2-nitro-1-imidazolyl) acetamide (SR-4554) as a probe for the measurement of tumor hypoxia. Cancer Res. 1997;57:3314–18.
25. Robinson SP, Griffiths JR. Current issues in the utility of ^{19}F nuclear magnetic resonance methodologies for the assessment of tumour hypoxia. Philos. Trans. R. Soc. Lond. B. 2004;359:987–96.
26. Dardzinski BJ, Sotak CH. Rapid tissue oxygen tension mapping using 19F inversion-recovery echo-planar imaging of perfluoro-15-crown-50ether. Magn. Reson. Med. 1994;32:88–97.
27. Mason RP, Rodbumrung W, Antich PP. Hexafluorobenzene: a sensitove 19F NMR inhicator of tumour oxygenation. NMR Biomed. 1996;9:125–34.
28. Warburg O. The Metabolism of Tumors. Arnold Constable: London, 1930.
29. Stubbs M, McSheehy PMJ, Griffiths JR, Bashford CL. Causes and consequences of tumour acidity and implications for treatment. Mol. Med. Today. 2000;6:15–9.
30. Weber G. Carbohydrate metabolism in cancer cells and the molecular correlation concept. Naturwissenschaften. 1968;55:418–29.
31. Zhong H, De Marzo A, Laughner E, Lim M, Hilton DA, Zagzag D, *et al*. Overexpression of hypoxia-inducible factor 1α in common human cancers and their metastases. Cancer Res. 1999;59:5830–35.
32. Semenza GL, Agani F, Booth G, Forsythe J, Iyer N, Jiang BH, *et al*. Structural and functional analysis of hypoxia-inducible factor 1. Kidney Int. 1997;51:553–5.
33. Semenza GL. HIF-1 and human disease: one highly involved factor. Genes Dev. 2000;14:1983–91.
34. de Graaf RA, Rothman DL. *In vivo* detection and quantitation of scalar coupled ^{1}H NMR resonances. Concepts Magn. Reson. 2001;13:32–76.
35. Nielsen FU, Daugaard P, Bentzen L, Stodkilde-Jorgensen H, Overgaad J, Horsman MR, Maxwell RJ. Effect of changing tumor oxygenation on glycolytic metabolism in murine C3H mammary carcinoma assessed by *in vivo* nuclear magnetic resonance spectroscopy. Cancer Res. 2001;61: 5318–25.
36. Tannock IF, Rotin ID. Acid pH in tumors and its potential for therapeutic exploitation. Cancer Res. 1989;49:4373–84.
37. Stubbs M. Tumour pH, blood perfusion and microenvironmrnt of human tunours: implications for clinical Radio-Oncology. In: M Molls, P Vaupel (Eds). Diagnostic Imaging and Radiation Oncology, Vol. 11. Springer-Verlag: Berlin, 1988, pp. 113–20.
38. Gatenby RA, Gawlinski ET. A reaction-diffusion model of cancer. Cancer Res. 1996;56:5745–53.
39. Gillies RJ, Martinez-Zaguilan R, Peterson EP, Perona R. Role of intracellular pH in mammalian cell proliferation. Cell. Physiol. Biochem. 1992;2:159–79.
40. Gerweck LE. Tumour pH: implications for treatment and novel drug design. Semin. Radiat. Oncol. 1998;8:176–82.
41. Vaupel P, Okunieff P, Neuringer LJ. *In vivo* 31P-NMR spectroscopy of murine tumours before and after localised hyperthermia. Int. J. Hyperthermia. 1990;6:15–31.
42. Arnold DL, Shoubridge EA, Feindel W, Villemure JG. Metabolic changes in a cerebral glioma within hours of treatment with intra-arterial BCNU demonstrated by phosphorus magnetic resonance spectroscopy. Can. J. Neurol. Sci. 1987;14:570–5.
43. Engin K, Leeper DB, Thristlethwaite AJ, Tupchong L, McFarlene JD. Tumor extracellular pH as a prognostic factor

un thermoradiotherapy. Int. J. Radiat. Oncol. Biol. Phys. 1994;29:125–32.

44. Frenzel T, Koszler S, Bauer H, Niedballa U, Weinmann HJ. Non-invasive *in vivo* pH measurements using a fluorinated pH probe and fluorine-19 magnetic resonance spectroscopy. Invest. Radiol. 1995;29:220–2.
45. Gillies RJ, Lis Z, Bhujwalla Z. 31P-MRS measurements of extracellular pH of tumors using 3-aminopropylphosphonate. Am. J. Physiol. 1994;267:195–203.
46. Ackerstaff E, Glunde K, Bhujwalla ZM. Choline phospholipid metabolism: a target in cancer cells? J. Cell. Biochem. 2003;90:525–33.
47. Aboagye EO, Bhujwalla ZM. Malignant transformation alters membrane choline phospholipid metabolism of human mammary epithelial cells. Cancer Res. 1999;59:80–4.
48. Podo F. Tumor phospholipid metabolism. NMR Biomed. 1999;12:413–39.
49. Katz-Brull R, Lavin PT, Lenkinski RE. Clinical utility of proton magnetic resonance spectroscopy in characterizing breast lesions. J. Natl. Cancer Inst. 2002;94:1197–203.
50. Evanochko WT, Sakai TT, Ng TC, Krishna NR, Kim HD, Zeidler RB, *et al*. NMR study of *in vivo* RIF-1 tumors. Analysis of perchloric acid extracts and identification of 1H, 31P and 13C resonances. Biochim. Biophys. Acta 1984;805: 104–16.
51. Negendank W. Studies of human tumors by MRS: a review. NMR Biomed. 1992;5:303–24.
52. Arias-Mendoza F, Smith MR, Brown TR. Predicting treatment response in Non-Hodghin's lymphoma from the pretreatment tumour content of phosphoethanolamine plus phosphocholine. Acad. Radiol. 2004;11:368–76.
53. Barba I, Cabanas ME, Arus C. The relationship between nuclear magnetic resonance-visible lipids, lipid droplets and cell proliferation in cultured C6 cells. Cancer Res. 1999;59:1861–68.
54. Ferretti A, Knijn A, Iorio E, Pulciani S, Giambenedetti M, Molinari A, *et al*. Biophysical and structural characterization of 1H-NMR-detectable mobile lipid domains in NIH-3T3 fibroblasts. Biochim. Biophys. Acta. 1999;1438:329–48.
55. Lehrech H, Zoula S, Farion R, Remy C, Decorps M. *In vivo* measurement of the size of lipid droplets in an intracerebral glioma in the rat. Magn. Reson. Med. 2001;45:409–14.
56. Al-Saffar NM, Titley JC, Robertson D, Clarke PA, Jackson LE, Leach MO, Ronen SM. Apoptosis is associated with triacylgylcerol accumulation in Jurkat T-cells. Br. J. Cancer 2001;86:963–70.
57. Blankenberg FG, Katsikis PD, Storrs RW, Beaulieu C, Spielman D, *et al*. Quantitative analysis of apoptotic cell death using proton nuclear magnetic resonance spectroscopy. Blood. 1997;89:3778–86.
58. Kuesel AC, Sutherland GR, Halliday W, Smith ICP. 1H MRS of high grade astrocytomas: mobile lipid accumulation in necrotic tissue. NMR Biomed. 1994;7:149–55.
59. Tugnoli V, Tosi MR, Tinti A, Trinchero A, Bottura G, Fini G. Characterization of lipids from human brain tissues by multinuclear magnetic resonance spectroscopy. Biopolymers. 2001;62:297–306.
60. Griffin JL, Lehtimaki KK, Valonen PK, Grohn OHJ, Kettunen MI, *et al*. Assignment of 1H nuclear magnetic resonance visible polyunsaturated fatty acids in BT4C gliomas undergoing ganciclovir-thymidine kinase gene therapy-induced programmed cell death. Cancer Res. 2003;63:3195–201.
61. Hakumaki JM, Poptani H, Sandmair AM, Yla-Herttuala S, Kauppinen RA. ^{1}H MRS detects polyunsaturated fatty acid accumulation during gene therapy of glioma: implications for the *in vivo* detection of apoptosis. Nat. Med. 1999;5:1323–7.
62. Fiehn O. Metabolomics—the link between genotypes and phoenotypes. Plant Mol. Biol. 2002;48:155–71.
63. Dang CV, Semenza GL. Oncogenic alternations of metabolism. TIBS. 1999;24:68–72.
64. Gleadle JM, Ratcliffe PJ. Hypoxia and the regulation of gene expression. Mol. Med. Today. 1998;4:122–129.
65. Maxwell PH, Dachs GU, Gleadle JM, Nicholls LG, Harris AL, Stratford IJ, Hankinson O, *et al*. Hypoxia-inducible factor 1 modulates gene expression in solid tumors and influences both angiogenesis and tumor growth.Proc. Natl. Acad. Sci. USA. 1997;94:8104–9.
66. Griffiths JR, McSheehy PMJ, Robinson SP, Troy H, Chung Y-L, Leek RD, Williams KJ, *et al*. Metabolic changes detected by *in vivo* magnetic resonance studies of HEPA-1 wild-type tumor deficient in hypoxia-inducible factor-1β (HIF-1β): evidence of an anabolic role for the HIF-1 pathway. Cancer Res. 2002;62:688–95.
67. de Molina AR, Penalva V, Lucas L, Lacal JC. Regulation of choline kinase activity by Ras proteins involves Ral-GDS and PI3K. Oncogene. 2002;21:937–46.
68. Glunde K, Jie C, Bhujwalla. Molecular causes of the aberrant choline phospholipid metabolism. Cancer Res. 2004;64:4270–6.
69. Glunde K, Raman V, Bhujwalla ZM. Correlation between choline kinase mRNA and 1H MRS-detectable choline metabolite levels in stable choline kinase knock-down clones of a human breast cancer cell line. Proc. Intl. Soc. Magn. Reson. Med. 2004;11:2029.
70. Chung Y-L, Troy H, Ramirez de Molina A, Judson IR, Workman P, Leach MO, Lacal JC, Griffiths JR. Pharmacodynamic markers for the choline kinase inhibitor MN58b in human breast cancer model by Magnetic Resonance Spectroscopy. Proceeding of AACR-NCI-EORTC Meeting, Geneva, 2004.
71. Al-Saffar NM, Jackson LE, Ramirez de Molina A, Workman P, Griffiths JR, Judson IR, Lacal LC, Leach MO. Magnetic Resonance Spectroscopy confirms the mechanism of action of the choline kinase inhibitor MN58b in human breast cancer cells. Proceeding of AACR-NCI-EORTC Meeting, Geneva, 2004.
72. Bachert P. Pharmacokinetics using fluorine NMR *in vivo*. Prog. Nucl. Magn. Reson. Spectrosc. 1998;33:1–56.
73. Steven AN, Morris PG, Iles RA, Sheldon PW, Griffiths JR. 5-Fluorouracil metabolism monitored *in vivo* by NMR. Br. J. Cancer. 1984;50:113–7.
74. Evelhoch JL, McCoy CL, Giri BP. A method for direct *in vivo* measurement of drug concentrations from a single 2H NMR spectrum. Magn. Reson. Med. 1989;9:402–10.
75. Rodrigues LM, Maxwell RJ, McSheehy PMJ, Pinkerton CR, Robinson SP, Stubbs M, *et al*. *In vivo* detection of ifosfamide by ^{31}P-MRS in rat tumours: increased uptake and cytotoxicity induced by carbogen breathing in GH3 prolactinomas. Br. J. Cancer. 1997;75:62–8.
76. Becker M, Port RE, Zabel HJ, Zeller WJ, Bachert P. Monitoring local disposition kinetics of carboplatin *in vivo* after

subcutaneous injection in rats by means of 195Pt NMR. J. Magn. Reson. 1998;133:115–22.

77. Chung Y-L, Troy H, Judson IR, Leek R, Leach MO, Stubbs M, Harris AL, Griffiths JR. Non-invasive measurements of capecitabine metabolism in bladder tumors overexpressing thymidine phosphorylase by ^{19}F MRS. Clin. Cancer Res. 2004;10:3863–70.
78. van Laarhoven HVM, Klomp DWJ, Kamm YJL, Punt CJA, Heerschap A. *In vivo* monitoring of capectiabine metabolism in human liver by ^{19}Fluorine magnetic resonance spectroscopy at 1.5 and 3 Tesla field strength. Cancer Res. 2003;63:7609–12.
79. Street JC, Alfieri AA, Tragano F, Koutcher JA. *In vivo* and *ex vivo* study of metabolic and cellular effects of 5-fluorouracil chemotherapy in a mouse mammary carcinoma. Magn. Reson. Imaging. 1997;15:587–96.
80. Chung Y-L, Troy H, Judson IR, Leach MO, Stubbs M, Ronen S, Workman P, Griffiths JR. The effects of CYC202 on tumors monitored by magnetic resonance spectroscopy. Proceeding of AACR, 1664, 2002.
81. Neckers L. Hsp90 inhibitions as novel cancer chemotherapeutic agents. Trends Mol. Med. 2002;8:S55–60.
82. Chung Y-L, Troy H, Banerji U, Jackson LE, Walton MI, Stubbs M, Griffiths JR, Judson IR, Leach MO, Workman P, Ronen SM. Magnetic resonance spectroscopic pharmacodynamic markers of the Hsp90 inhibitor 17-allylamino,17-demethoxygeldanamycin in human colon cancer models. J. Natl. Cancer Inst. 2003;95:1624–33.

Experimental Cardiovascular MR in Small Animals

Jürgen E. Schneider and Stefan Neubauer
Department of Cardiovascular Medicine, University of Oxford, John Radcliffe Hospital, Headley Way, Oxford OX3 9DU, UK

Introduction

Genetically modified mice and (to a lesser degree) rats are frequently used as models for human cardiac disease. Since the genomes of both mouse and humans have now been fully analyzed, major research programs are currently underway worldwide to investigate systematically the function of specific genes by overexpression, deletion or mutation of these genes and their products in mice (e.g. [1] for review). These recent advances in gene manipulation have lead to a new era of cardiovascular research, and new animal models of cardiovascular disease are appearing at a rapid rate [2–4]. The phenotypic effects introduced by these transgenic models range from the absence of any overt abnormalities to severe anatomical, functional, or metabolic malformations during development causing premature death *in utero* or soon after birth [5].

Some phenotypes are only manifested under chronic myocardial stress conditions. Thus, dedicated surgical techniques, such as transverse aortic constriction (TAC) or ligation of the left coronary artery (LAD) have been developed in rodents in order to model cardiac disease conditions that resemble those found in patients with heart disease. Specifically, Aortic constriction in rodents causes pressure overload in the heart resulting in progressive hypertrophy of the left ventricle as a compensatory mechanism, eventually leading to heart failure [6,7]. Ligation of the LAD causes acute myocardial infarction resulting in ventricular dilatation, depression of cardiac function, and remodeling of the non-infarcted residual myocardium, finally leading to an increased mortality due to chronic heart failure (e.g. [8] for review).

The development of methods to examine the physiological effects of gene alteration in mice, i.e. techniques for cardiovascular phenotype characterization, or the consequences of surgical myocardial damage, have not kept up with the speed at which these animal models are being generated. In fact, a better understanding of gene function will only come from more sophisticated phenotype characterisation, and a lack of adequate murine phenotyping tools is now a major limitation: The electrocardiogram (ECG) only provides limited information. Haemodynamic measurements using microtip catheters, while highly informative, are invasive, technically demanding and in mice with a total blood volume of 1–2 ml the slightest surgical blood loss leads to haemodynamic instability. Echocardiography, whether 1D (M-mode) or 2D, is frequently used to characterize hearts of mice and rats, because it is an affordable and relatively fast technique, but it relies on geometric assumptions for volume calculation, has a low reproducibility and only yields a limited number of parameters. *Ex vivo* examinations such as histological sectioning are time consuming and do not provide any insights into cardiac function or the metabolism of the heart.

Magnetic resonance imaging (MRI) and spectroscopy (MRS) are non-invasive techniques that use intrinsic contrast mechanisms and are capable of obtaining true 3D information on the heart and the vascular system. In humans, cardiovascular magnetic resonance (CMR) techniques have been developed towards a “One-Stop-Shop”, where information on cardiac anatomy, function, perfusion, viability, metabolism, and the vasculature may be obtained in a single examination. We have postulated that a similar approach is feasible in experimental cardiovascular research, and that MRI and MRS are ideal methods to investigate comprehensively the normal and diseased cardiovascular system in mice and rats.

However, the precise characterization of the rodent heart by MR methods is technically extremely challenging. The mouse heart is approximately only 1/2000th the size of the human heart, and beats about 10 times faster. Thus, spatial and temporal requirements are demanding, and MRI/MRS methods have to maximize speed and spatial resolution in order to allow for a successful investigation of the cardiovascular system. In this chapter, we will describe how to assess global and regional function of the rodent heart, and how information about cardiac metabolism and the vasculature can be obtained. However, we will first explain the methodological requirements for the application of cardiovascular MRI and spectroscopy in mice and rats.

Methods and Requirements

The length of a cardiac cycle (RR-interval) is typically 100–150 ms in mice (for heart rates between 400–600 beats per minute (bpm) – compared to $\approx$1 s in humans at $\approx$60 bpm), and is 133–200 ms in rats (for heart rates between 300 and 450 bpm). The diastolic phase, i.e. the

Graham A. Webb (ed.), Modern Magnetic Resonance, 835–853.
© 2008 *Springer.*

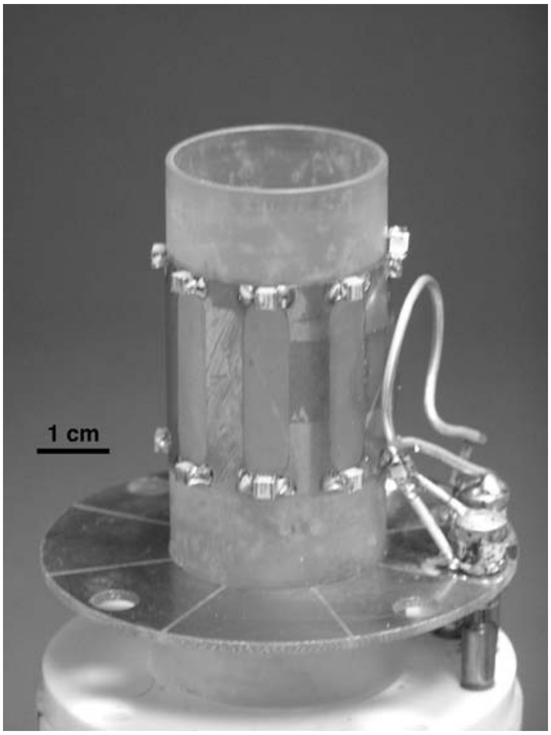

Fig. 1. Volume RF-coil for CMR in mice at 11.7 T. The characteristic leg structure has given this RF-coil the name "birdcage coil". The high-pass birdcage coil as shown in this figure has an inner diameter of 28 mm and is used for mice with a body weight of 17–25 g. It consists of eight legs that are orientated in parallel to the B_0-field with 16 capacitors distributed symmetrically between the legs in the two end rings. (See also Plate 69 on page XLVII in the Color Plate Section.)

part of the cardiac cycle with minimal cardiac motion, is about 30–40 ms long. Therefore, any MR method has to utilize short echo times (T_E) and repetition times (T_R). Furthermore, the left ventricular wall in healthy mice has a thickness of about 1 mm, and the ventricular volumes range between a few microliters (in end-systole) up to 100 μl (in end-diastole). Therefore, strong (>500 mT/m), fast switching (100–200 μs) gradient systems are necessary to apply high-speed sequences at high spatial resolution. However, such gradient switching can cause heating, and so an efficient cooling system is required to prevent temperature changes being transferred to the animal, which would result in altered cardiac function.

Today's clinical MR scanners commonly have static magnetic field (B_0) strengths of 1.5–3 T, whereas animal systems range between 4.7 and 17.6 T. The signal-to-noise ratio (SNR) of an MR experiment improves with increasing B_0. Ultra-high-field magnets are important for cardiac experiments in rodents as the gain in SNR allows for achieving the necessary spatial and temporal resolution (the SNR decreases with increasing resolution). Additionally, dedicated radio-frequency (RF) coils that are optimized in geometry and loading for a particular animal size, are required to obtain maximal SNR. Volume coils (i.e. birdcage coils [9]) are commonly used for mice as they provide an excellent homogeneity of the RF-field. They can also be applied in "quadrature mode", resulting in an additional increase in SNR of a factor up to $\sqrt{2}$ [10]. A picture of a birdcage coil used for cardiac MR in mice at 11.7 T is shown in Figure 1. In rats, a combination of body coil for transmit and surface-coil for receive are typically used [11,12]. A similar configuration would provide more efficient mouse imaging, but the implementation is very difficult owing to the small size.

Next to hardware and MR methods, careful consideration must be given to maintaining stable animal physiology throughout an experiment. Dedicated animal cradles, optimized in diameter and length, are required. An example illustrating such a set-up is shown in Figure 2. They typically comprise a nose cone for delivery of anaesthetic gases, a scavenging line for anaesthetic gas recovery, a temperature control system—consisting of a heating blanket and a thermocouple—for maintaining a constant body temperature, and ECG and respiratory motion sensing capabilities for physiological gating. RF filters may be useful to eliminate contamination of the MR signal by external RF noise pick-up. Additional lines are required if the animals are to be ventilated artificially, and if drugs or MR contrast agents need to be administered. The animals have to be secured within the cradle using surgical tape. Special care should be taken not to distort or compress their abdominal or chest regions.

The heart rate of the animal is influenced by the body temperature and by the depth of anaesthesia. A core body temperature of 37 °C has to be maintained by supporting the temperature regulation of the animal in order to ensure physiologically normal conditions. This can be achieved using special blankets that are heated by warm air or water (air has the advantage over water that it is MR invisible and it does not interfere with the RF-coil). Furthermore, the lowest possible anaesthetic level should be applied in order to minimize depression of cardiac function by anaesthesia [13]. To achieve this, anaesthetic gases are commonly used for cardiac studies as the dose can be easily titrated for the individual animal whilst in the magnet. In particular, Isoflurane causes the least cardiac depression and represents the anesthetic of choice for this purpose [14]. Due to suppression of the eye-closure reflex during anesthesia, ointment must be applied to the eyes in order to keep them moist.

The recording of the ECG and the respiratory signal is not only necessary to monitor the animal inside the magnet (where visual assessment is not possible), but also to minimize the influence of cardiac and respiratory motion on the MR experiment. It is well recognized that motion artifacts

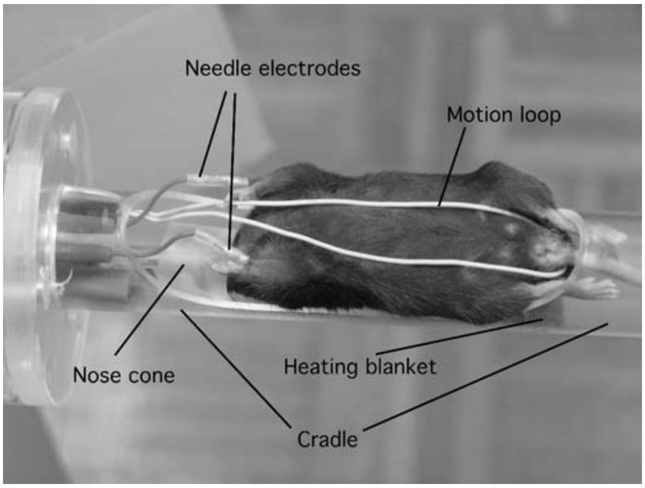

Fig. 2. Illustration of a set-up used for CMR in rodents. The shown set-up consists of the animal cradle, which is equipped with a nose cone, needle electrodes for deriving the ECG and a conductor loop for detecting respiratory motion. The animals are placed onto a heating blanket to maintain a constant body temperature of 37 °C throughout the MR experiment. (See also Plate 70 on page XLVII in the Color Plate Section.)

become more pronounced with increasing magnetic field strength [15]. Figure 3 illustrates this influence on cardiac MR imaging in mice at 11.7 T. The data shown in this figure were acquired under various gating strategies.

Front-paw-mounted needle electrodes, inserted subcutaneously into the front limbs of the animal, or surface electrodes are used to derive the ECG. A good coupling between the electrodes and the animal is crucial to obtain

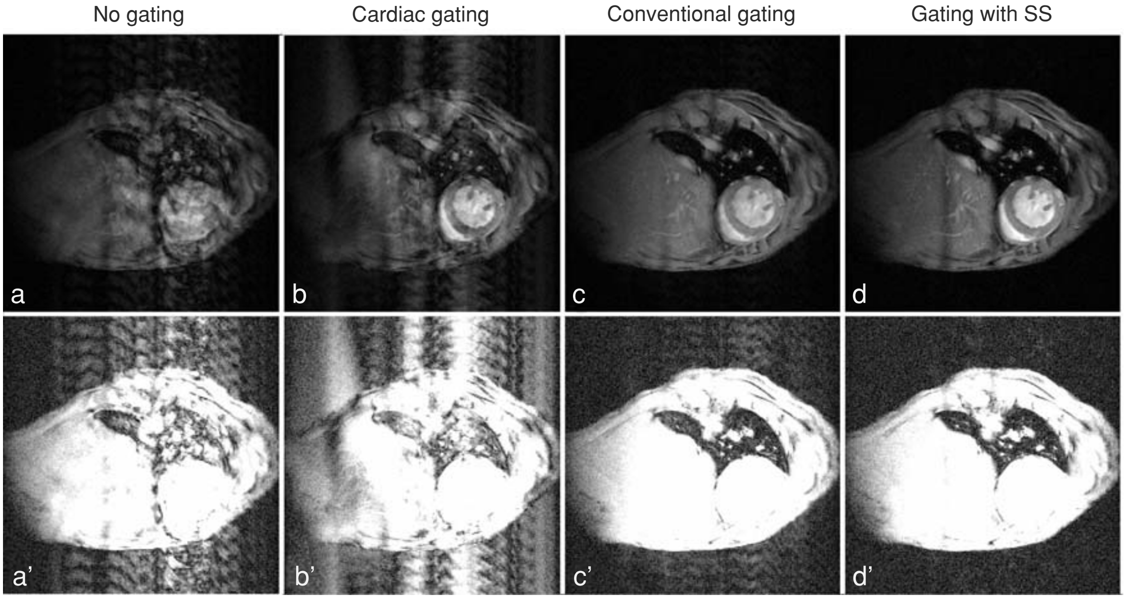

Fig. 3. Motional influence on cardiac imaging in mice at ultra-high magnetic fields. Transverse gradient echo images through the heart of a normal mouse acquired at 11.7 T. Both rows are identical with the image intensity in the bottom row (a′–d′) increased to a maximum level in order to reveal low-level artifacts. Each column corresponds to a different gating strategy (from left to right): (a, a′) No gating, (b, b′) cardiac gating, (c, c′) respiratory gating without and (d, d′) with steady-state maintenance (SS) during respiration [16]. Each row is scaled to the same range of image intensity. The vertical signal voids present in the images are due to saturation effects from adjacent oblique slices that were acquired in the same experiment. Note the low-level artifacts visible in panel c′. They are caused by interrupting the steady state during respiration and their strength depends on the MR sequence and parameters used in an experiment. Scale bars: 2 mm.

robust ECG-traces that can be triggered from. Respiration can be monitored using pressure pads or conductor loops mounted on top of the chest and the abdomen of the animal as shown in Figure 2. Adequate measures have to be provided to suppress any interference due to gradient switching with the ECG and respiratory signals. An electronic gating device serves as an interface between the animal, the user and the MR-system and allows for synchronizing the experiments to the cardiac cycle and for interrupting the data acquisition during respiration (i.e. respiratory gating). This device is offered by various manufactures or can be home built. Care has to be taken when disrupting the steady state of the spin system during respiration, because this can be the source of another—non-motion related—image artifact (see Figure 3 c′). Cassidy *et al.* demonstrated a simple way of maintaining steady state of the spin system during respiration: the MR sequence was continued throughout respiration with the same timing as determined by the heart beat but without acquiring data. The decision to acquire data or to maintain steady state is made during run-time without any additional user-input being required [16].

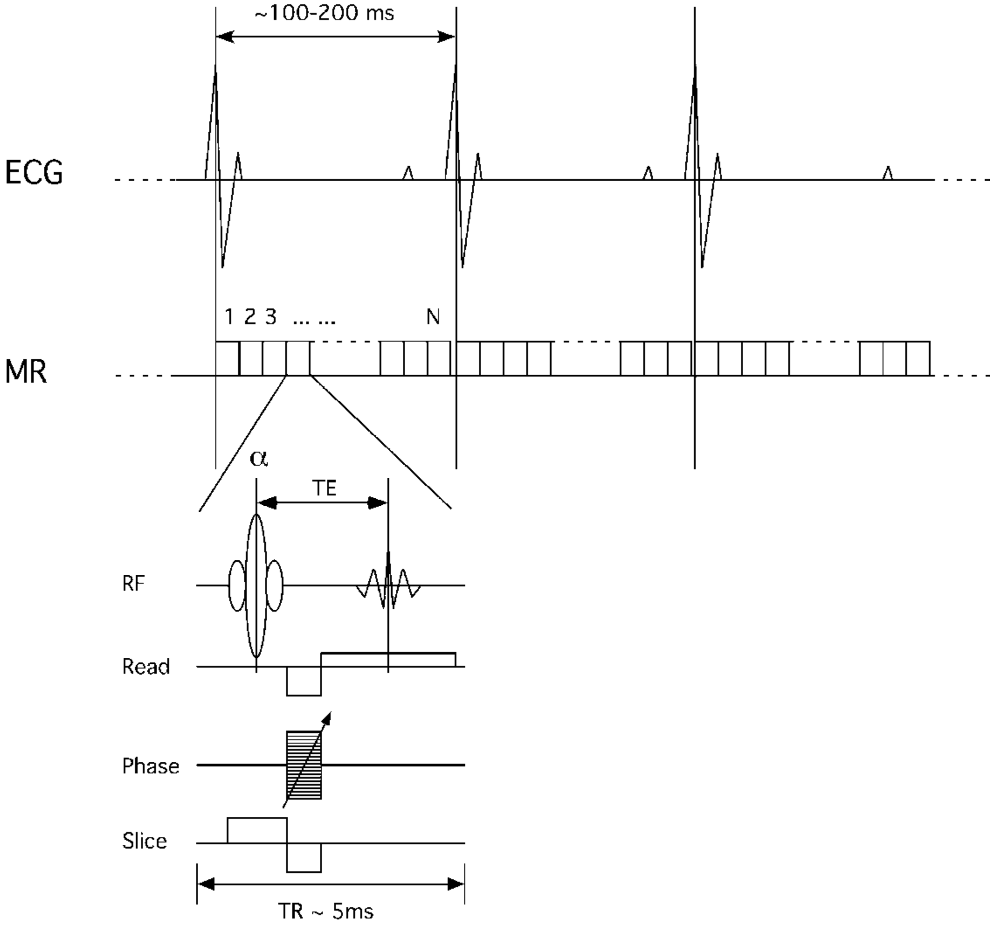

Fig. 4. Diagram of an MRI cine sequence used in rodents. Fast, spoiled gradient echo sequences are typically used for cardiac imaging in rodents. After the detection of the R-wave in the ECG, the same *k*-space line is acquired repeatedly with a constant value for the phase encoding gradient. The number of frames N per cardiac cycle depends on the sequence timing and the heart rate of the animal and ranges between 15–30 frames. The illustrated scheme is repeated in the next cardiac cycle with a different value for the phase encoding gradient. Thus, the product of number of phase encoding steps times number of averages cardiac cycles are required in total to obtain a full cine data set for one slice. If respiratory gating is employed, the scheme is interrupted during respiration and the imaging time is prolonged.

Global Cardiac Function

The application of high-resolution MRI in multiframe mode (cine imaging, cine-MRI) allows for non-invasive quantification of left-ventricular mass and volumes in mice and rats. Fast, 2D spoiled gradient echo type sequences are commonly applied continuously throughout the cardiac cycle and provide high contrast between blood and myocardium. Refocused steady-state free-precession sequences, as frequently used for cardiac MRI on human scanners, are more difficult to employ at ultra-high magnetic fields due to their sensitivity to susceptibility differences. Figure 4 shows a schematic depiction of a cine experiment in rodents. Repetition times of less than 5 ms per frame freeze cardiac motion and result in 15–30 frames per RR interval (depending on the heart rate). The echo times are B_0-field dependent and chosen such that lipid- and water-protons have an opposite phase to enhance the contrast between different tissue types [17]. The values range between 1 and 2 ms. The flip-angle of the sequence needs to be adjusted according to the chosen repetition time and respective relaxation times in order to maximize the contrast between blood and myocardium. The in-plane image resolution (before image interpolation) in mice is typically around 100–200 µm at a slice thickness of 1 mm, and in rats about 200–300 µm at a slice thickness of 1–1.5 mm. Seven to ten slices are required to cover the entire mouse heart from base to apex. Accordingly, 10–20 slices are needed to image the entire rat heart. Studies at magnetic field strengths up to 7 T commonly use cardiac gating only, whereas additional respiratory gating is essential at higher magnetic field strengths to obtain virtually artifact-free, high-quality images, as we have demonstrated quantitatively [18]. A cine study of the entire mouse heart can currently be accomplished in well under one hour, and in rats within approximately 90 mins—depending on the required spatial resolution, and whether or not respiratory gating has to be applied or not.

Figure 5 shows examples of end-diastolic and end-systolic frames in short-axis and long-axis orientations of a normal mouse heart, acquired at 11.7 T. The end-diastolic frame is characterized as the one with maximal left-ventricular volume, and the end-systolic frame the one with minimal left ventricular volume, respectively. The mainly stationary tissue (relative to the imaging slice), such as cardiac or skeletal muscle, is saturated by the repeatedly applied RF-pulses and subsequently appears dark. The blood provides high signal in these images due to the inflow effect of blood into the imaging slice (bright-blood images). It has to be noted that the contrast can be inverted if the imaging sequence is combined with dedicated black-blood techniques [19,20]. However, this approach usually provides a reduced temporal resolution throughout the cardiac cycle and requires longer acquisition times to gain sufficient signal-to-noise. The left ventricle has a characteristic doughnut shape in the short-axis view (Figure 5a, a′), which is orientated orthogonally to both long-axis views: the four-chamber view (Figure 5b, b′) and the two-chamber view (Figure 5c, c′). The papillary muscles do not appear as connected to the ventricular muscle in this end-diastolic frame (Figure 5a) and are seen as dark spots inside the bright ventricular cavity.

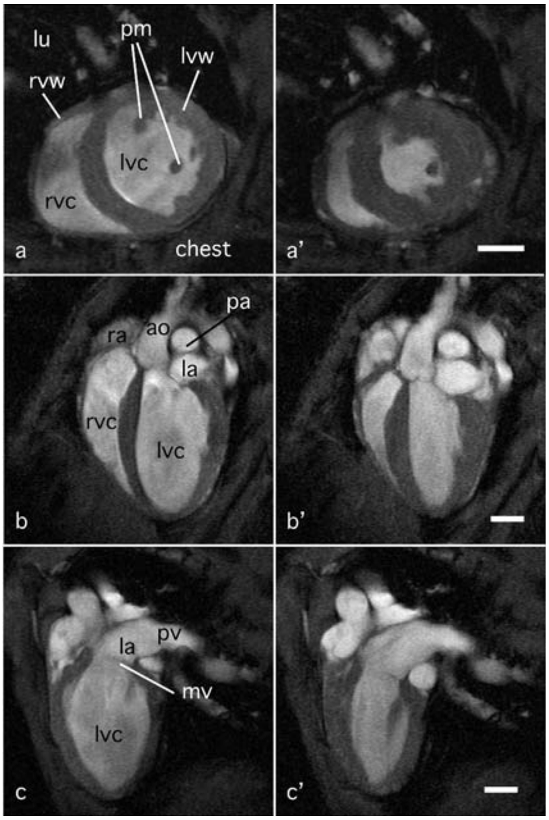

Fig. 5. Cine-images of normal mouse heart. Mid-ventricular end-diastolic images through a normal mouse heart in the (a) short-axis orientation, (b) the four-chamber and (c) the two-chamber long-axis orientation; both long-axis views are orthogonal to the short-axis orientation. The primed panels correspond to the respective end-systolic frames. Abbreviations: lvc, rvc—left/right ventricular cavity; lvw, rvw—left/right ventricular wall; pm—papillary muscle; lu—lungs; la, ra—left/right atrium; ao—aorta; pa, pv—pulmonary artery/vein; mv—mitral valve. Scale bars: 2 mm.

Manual or semi-automatic segmentation of both the end-diastolic and the end-systolic short-axis frame for every slice allows for a quantitative analysis of left ventricular mass and function in rodents. Figure 6 shows the

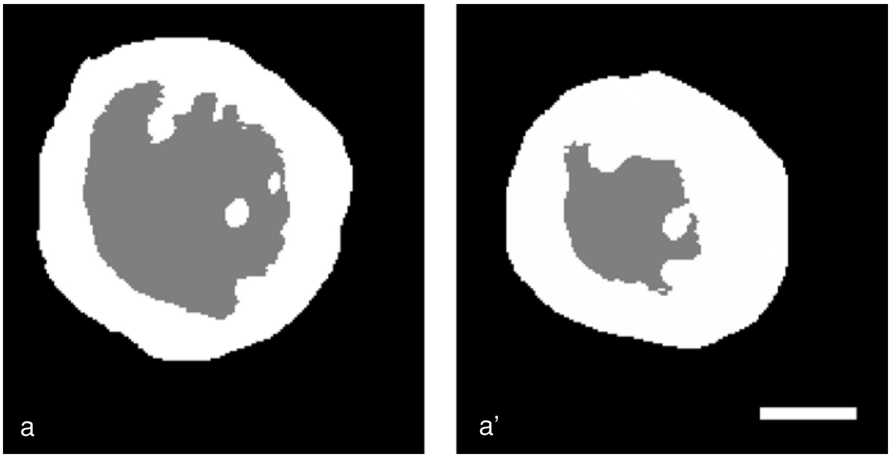

Fig. 6. Quantitative image analysis. Segmentation of end-diastolic and end-systolic frames shown in Figure 5a, a′ allows for quantitative measurement of left ventricular mass (white area) and volume (grey area) and subsequently calculating cardiac functional parameters. Note that the papillary muscles are counted towards the ventricular mass and *not* to the cavity volume. Scale bar: 2 mm.

result of the image segmentation process: the white compartment corresponds to myocardial volume and the grey compartment to the ventricular cavity volume. Ventricular mass is obtained by multiplying the myocardial volume with the density of myocardial tissue (1.05 g/cm^3 [21]). Table 1 lists all relevant parameters that can be derived from a cine experiment. The quantitative analysis of the cine images is highly reproducible with low inter- and intra-observer variability that improves with increasing field strength [18].

This technique has been applied in several studies to investigate cardiac function of normal mice [22–25] and rats [11, 26]. It has also been used to study developmental changes in cardiac function and mass from neonatal to adult mice [27].

Table 1: Relevant cardiac functional parameters

Acronym	Description	Definition	Unit	Normal Mouse Heart*
HR	Heart rate	Beats per minute	bpm	429 ± 24
ESV	End-systolic volume		µl	15.7 ± 1.2
EDV	End-diastolic volume		µl	43.0 ± 3.9
EDM	End-diastolic mass		mg	57.1 ± 4.2
SV	Stroke volume	EDV-ESV	µl	27.4 ± 3.4
EF	Ejection fraction	100% · SV/EDV	%	63.5 ± 2.9
CO	Cardiac output	SV · HR	ml/min	11.4 ± 1.2

* Taken from [18].

Applications in transgenic mice have, for example, been shown in a model of cardiac hypertrophy [28], mice with myocardial overexpression of tumor necrosis factor-α [29,30], and adult cardiomyocyte-specific VEGF knockout mice [31].

We have used this technique to investigate the effect of orthostasis in mice and rats. Experimental ultra-high-field MR systems are commonly equipped with a vertical bore magnet for engineering reasons. Although from a physiological point of view this is the preferred design for experiments in isolated perfused organs and on aqueous solutions, animals have to be positioned in an upright position for *in vivo* studies on such MR systems. It is well recognized that it is impractical to investigate larger mammals and humans in the vertical position, as the effect of orthostasis reduces venous return, LV volumes and cardiac output [32]. We demonstrated that MR systems with a vertical bore can generally be used to measure cardiac function in both, mice and rats, within approximately 1–1.5 h [18,26]. However, longer experiments may best be done in horizontal position due to detectable changes in volumes, ejection fraction and cardiac output occurring over prolonged experimental periods [33].

Cine imaging can also be used to characterize surgical animal models of human cardiac disease non-invasively. In chronically failing hearts of rodents [34–37], the degree of failure (as indicated by the ejection fraction; hearts with an EF <45% may be defined as failing) can be assessed with cine-MRI. Furthermore, in the chronic myocardial infarct (MI) model, hearts can also be stratified according

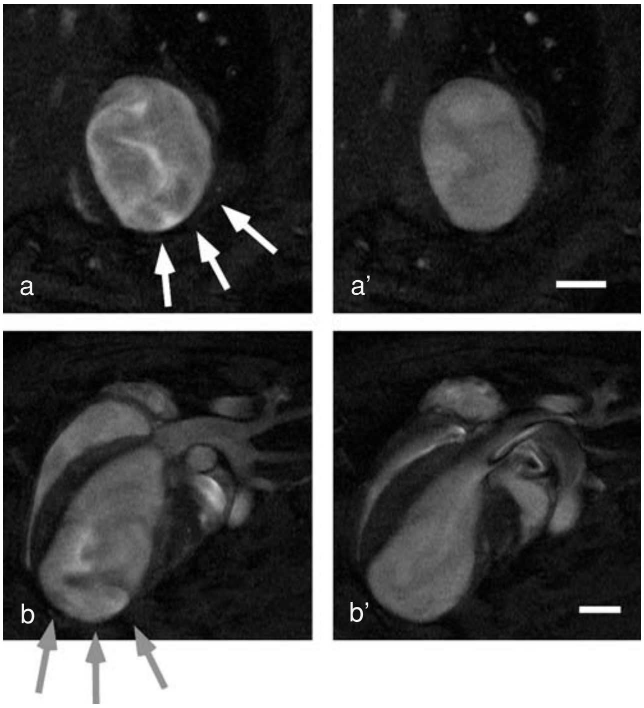

Fig. 7. Cine-images of failing mouse heart. Mid-ventricular end-diastolic images through a failing mouse heart in the (a) short-axis orientation and (b) the four-chamber long-axis orientation. The primed panels correspond to the respective end-systolic frames. The arrows indicate the infarcted area, which is characterized by akinesis and wall thinning. Scale bars: 2 mm.

to their infarct size, which can be calculated according to:

$$\text{Infarct size} = \frac{1}{\text{NSLICES}} \sum_{i=1}^{\text{NSLICES}} \frac{1}{2}\left(\frac{I^i_{\text{epi}}}{T^i_{\text{epi}}} + \frac{I^i_{\text{endo}}}{T^i_{\text{endo}}}\right) \times 100\% \quad (1)$$

(With T_{Epi}, T_{Endo}—total endo- and epi-cardial circumference of left ventricle; I_{Epi}, I_{Endo}—endo- and epi-cardial length of infarcted tissue, respectively). The infarct is characterized as the area of akinesis. The multiframe capability is crucial for these measurements in order to distinguish between normal and infarcted tissue. While “hibernating” tissue, i.e. viable tissue that does not actively contract, cannot be identified from these cine-images, this does not constitute a problem in the chronic coronary ligation model in mice or rats, where long-term hibernation does not occur. A slice across a failing murine heart (infarct size: 40%) in short-axis orientation is shown in Figure 7. The arrows indicate the wall thinning in the infarcted area. Only small changes in ventricular volumes can be detected between both frames (total ventricular volumes—EDV: 153 µl, ESV: 117 µl) yielding a substantially reduced EF of 24%.

In animals with constriction of the transverse aorta (TAC), the degree of hypertrophy and failure can be measured quantitatively by cine-MRI. Figure 8 shows the end-diastolic frame of mice (a) without and (b) with TAC. The left ventricular wall in (a) is clearly hypertrophied compared to the control animal. Quantitative analysis yielded a ~275% increase in left-ventricular mass in this case at a deteriorated cardiac performance (EF = 35% vs. 64% for the healthy mouse heart). However, considerable variation in the hypertrophic response and in the time to heart failure has been observed in this model, even when same sex and inbred littermates are used. Our recent work has shown that variations in the minimal cross-sectional area of the aorta—as measured by MRI—are one factor responsible for the variability of this model [38]. This would not be possible using echocardiography, as there is no available acoustic window for imaging the aortic arch. Therefore, MRI provides a unique opportunity to stratify animals with TAC according to their minimal cross-sectional aortic area.

In summary, MRI can be applied repeatedly to measure growth curves of the heart or to follow-up after procedures, as demonstrated in this section. The high-resolution and non-invasive nature of this technique are important advantages. They enable a reduction in the number of animals required for each study, which is a major principle of good animal welfare practice. In addition, each animal can also serve as its own control, providing a more powerful statistical analysis in an inhomogeneous population.

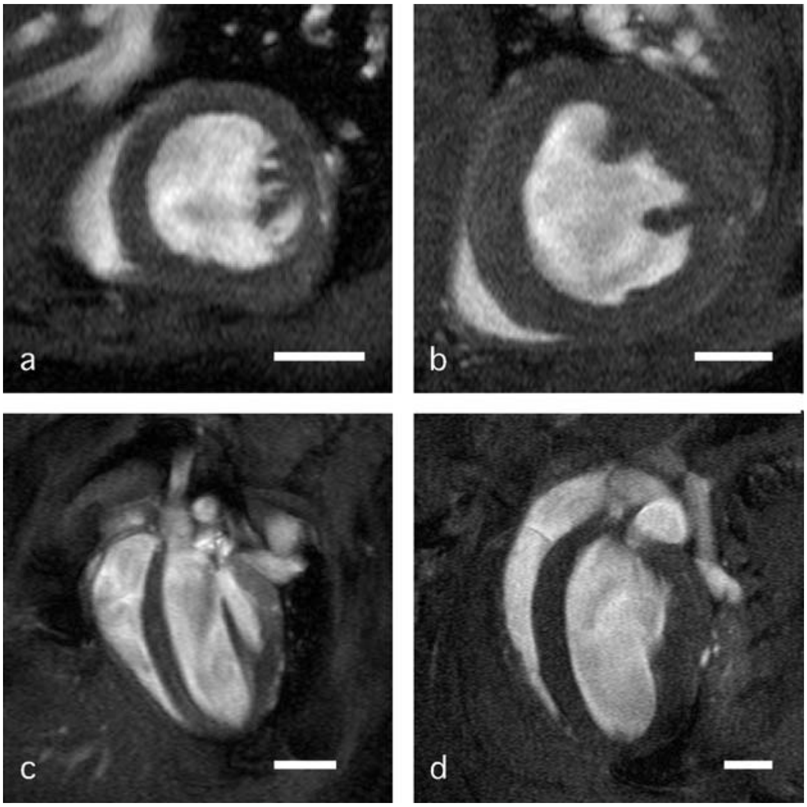

Fig. 8. Cine-images of mouse with TAC. Mid-ventricular end-diastolic images across a normal mouse heart in (a) short-axis and (c) long-axis orientation. (b, d) Corresponding views of a mouse with TAC illustrating the increase in myocardial mass (hypertrophy). Scale bars: 2 mm.

Myocardial Tissue Contractility

Conventional cine imaging, as described in the previous section, allows for assessment of global cardiac function as well as bulk motion of the myocardium. However, analysis of transmural wall motion becomes necessary in models where regional variations of contractile function occur, such as the chronic MI model. Two basic approaches have been used to visualize and measure wall motion regionally: In myocardial tagging, a grid of signal voids is generated either by selective saturation [39] or by a modulation of the magnetization by gradient fields (termed SPAMM: SPAtial Modulation of Magnetization) [40]. The tags are then tracked throughout the cardiac cycle by a multi-phase sequence similar to the one shown in Figure 4. A quantitative analysis of the tag-movement ("strain analysis") allows for calculating the minimum and maximum principal stretches, their orientation and the minimum and maximum principal strains [41,42].

Myocardial tagging has been applied to rodents in order to investigate left ventricular torsion in mice [43]. Zhou *et al.* used SPAMM to characterize normal mouse heart function [24]. Furthermore, Epstein *et al.* demonstrated significant contractile dysfunction in murine hearts one day after infarction in the infarcted, the adjacent, and the remote zone [44]. Although this method allows for an easy visualization of cardiac motion, its major limitation is the inherent low spatial resolution, because a clear distinction between the tags in the image is required. The tag spacing in the murine studies ranged between 0.7 mm [24,44] and 1.2 mm [43], which is in the order of the normal myocardial wall thickness in a mid-ventricular short-axis slice across a mouse heart. An example of myocardial tagging in the mouse is shown in Figure 9.

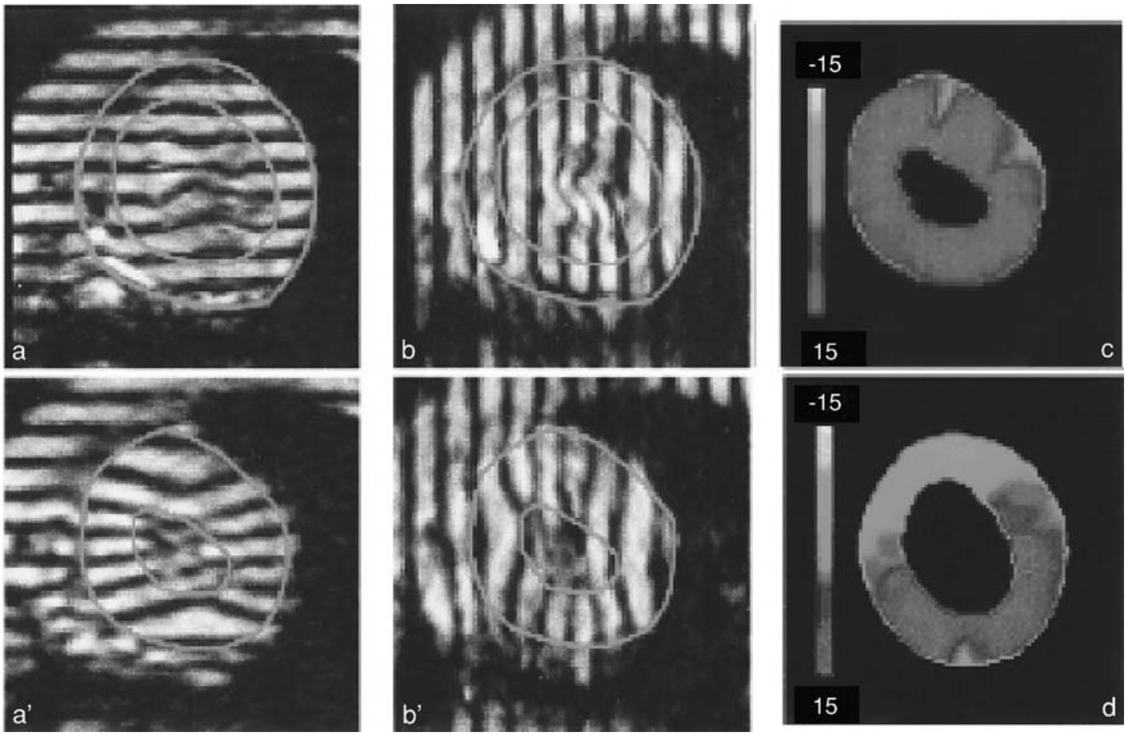

Fig. 9. Myocardial tagging in the mouse heart. Normal mouse heart in end-diastolic phase with (a) horizontal and (b) vertical tags. The primed panels correspond to the respective end-systolic frames. The map in panel c shows the percentage of circumferential shortening (% CS) for this mouse obtained from a quantitative analysis of the tag movements. The homogeneous pattern is distorted in a mouse with myocardial infarction (panel d). (Taken from [44].) (See also Plate 71 on page XLVII in the Color Plate Section.)

A second approach involves encoding of cardiac motion by the phase of the MR-signal (phase contrast (PC) MRI, [45–49]). In principle, a similar sequence as shown in Figure 4 can be used, but with additional bipolar gradient pulses fitted between the RF-pulse and the data acquisition. The zero-order gradient moment M_0[1] generated by the bipolar gradients is zero with a non-vanishing first-order gradient moment M_1. The additional phase accumulation Φ' is then given by:

$$\Phi' = \gamma M_1 v, \qquad (2)$$

where γ is the gyromagnetic ratio for protons given by $\gamma = 42.58$ MHz/T and v the mean velocity over the encoding interval. Thus, stationary spins remain unaffected by the bipolar gradients whereas moving spins accumulate a phase that is proportional to their velocity. At least two scans are acquired in each direction with different first-order gradient moments. The phase images are subsequently subtracted to minimize phase accumulation caused by B_0 inhomogeneities and RF penetration effects [50,51]. Alternatively, one scan with $M_1 = 0$ (i.e. bipolar gradients turned off) is acquired to obtain a phase reference.

Streif *et al.* investigated normal and infarcted mice—one week post-ligation of the LAD—at 7 T using PC-MRI [52]. They applied a maximum first-order moment of $M_1 = 93$ μTs^2/mm during an echo-time of 3 ms. In Figure 10, velocity maps obtained at mid-systole are shown for a normal and an infarcted mouse (anterior wall infarct), with a spatial resolution of 234 μm in plane and a slice thickness of 1mm.

Applying this method in multiphase mode allows for a temporally resolved, quantitative mapping of the cardiac motion throughout the entire heart cycle. Furthermore,

---

[1] The nth order gradient moment is given by: $M_n = \int_{t_0}^{t_1} G(t) \cdot t^n dt$, with t the time and $G(t)$ the gradient, that has been switched between t_0 and t_1.

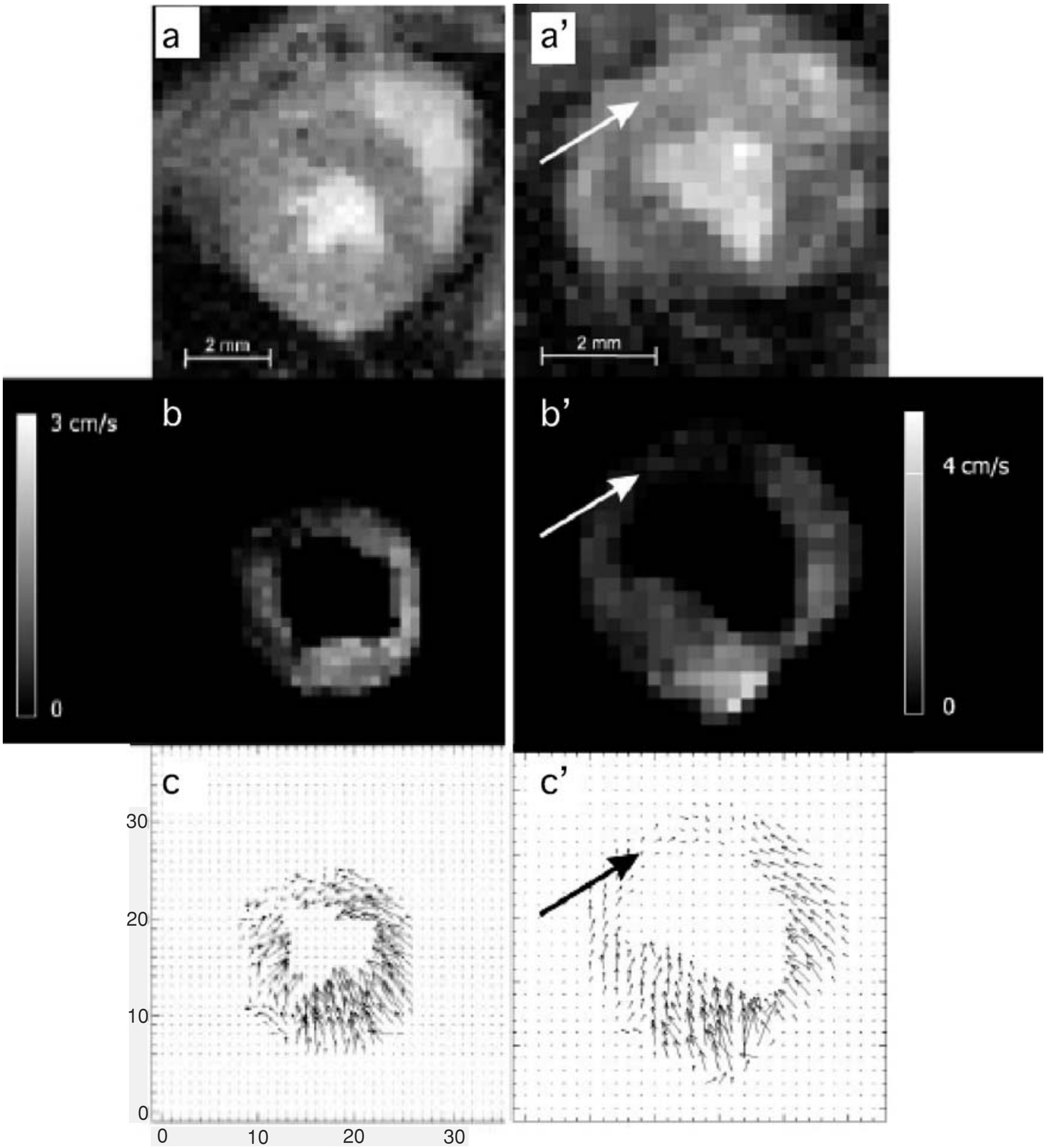

Fig. 10. Phase-contrast imaging in the mouse heart. Left column: (a) Mid-ventricular end-systolic cine image across a normal mouse heart. (b) Velocity map obtained from the vector diagram in (c). Right column: Corresponding images for a mouse heart with a myocardial infarct in the anterior wall as indicated by the arrows. This area shows substantially decreased contraction. (Taken from [52]).

global functional data are obtained in the same experiment. However, this method encodes only short periods of motions and large first-order gradient moments are required to encode low velocities. Furthermore, PC-MRI is sensitive to phase distortions caused by imperfect gradient performance or uncompensated motion such as blood flow, cardiac and respiratory motion. In particular, longer echo times may be required to generate sufficiently strong first-order gradient moments, which could become more critical with increasing magnetic field strengths.

An alternative approach proposed by Aletras *et al.* is called Displacement ENcoding with Stimulated Echoes (DENSE) and combines the advantages of both methods described above [53–55]. DENSE is in principle based on a stimulated echo sequence in which a phase distortion is generated by a gradient pulse G_1, applied for a time t_1 after an initial RF-excitation. A second RF-pulse stores the magnetization along z-direction and is followed by a mixing period TM (to assess systolic displacement, this time is typically the time between the begin and the end of systole) in which the displacement is encoded. A third RF-pulse brings the magnetization back into the transverse plane and the phase distortion is rewound by repeating the same gradient pulse G_1. Both gradient pulses are perfectly balanced for stationary spins, which therefore acquire no net phase. However, spins that have moved during TM by a distance Δx, acquire an additional phase of:

$$\Phi_1 = \gamma G_1 t_1 \Delta x, \tag{3}$$

The sequence is repeated with different values for G_1 in the same spatial direction with the displacement Δx being obtained from the phase difference between these images, and also in different directions. Similar to tagging, the 2D displacement data are then used to calculate the strain tensor, which allows for calculation of the circumferential shortening and the radial thickening of the hearts.

Recently, Gilson *et al.* used this technique to demonstrate systolic dysfunction in mice one day post-infarction [56]. They reported a close agreement of strain values obtained from DENSE with those measured by conventional tagging. Importantly, the spatial resolution in the DENSE study was nearly one order of magnitude higher compared to the tagging study [44,57]. This method has been developed further and extended to a multislice [58] and a 3D [56] method with displacement encoding in three dimensions. This enabled assessment of myocardial strain in both, short- and long-axis directions of the heart. Experimental times varied between 50 min for multislice [58] and 2.5 h for 3D methods [56].

In contrast to PC-MRI, the phase in each pixel is used here to measure displacements rather than velocities. Although this simplifies the calculation of the strain maps [59], the displacement is equivalent to the mean velocity during the encoding time. One major limitation of DENSE is the reduced SNR, which so far allowed only single-phase imaging in mice [57]. However, DENSE-MRI in cine mode has recently been reported in humans [60]. A main difference to PC-MRI is the time over which any motion is encoded. Specifically, an average displacement that takes place during a period within the cardiac cycle is measured by DENSE without any information of global cardiac function. PC-MRI, however, provides a dynamic picture of motion throughout the entire cardiac cycle and inherently includes the capability to measure cardiac function globally.

It is anticipated that these methods for measurement of myocardial tissue function will be of widespread use in rodent models of altered regional contractility.

Multinuclear MR Spectroscopy

For MRI, the signals of water and fat protons are interrogated. The tissue water concentration in the heart muscle is about 100 M. MRS, however, interrogates the signals of metabolites, which are present in many orders of magnitude lower concentration (around 5–20 mM). Furthermore, MRS using nuclei other than protons, such as ^{13}C or ^{31}P, is additionally hampered by a lower MR sensitivity. Taking the natural abundance into account, the MR sensitivity is a factor of 1.8×10^{-4} for ^{13}C and of 6.6×10^{-2} for ^{31}P lower compared to protons. Therefore, low metabolite concentrations in the presence of cardiac and respiratory motion, and the small size of the heart pose major challenges for implementing MRS methods in rodent hearts *in vivo*. ^1H-MRS is additionally hampered by the presence of a dominating water signal, which needs to be suppressed sufficiently in order to detect the weak metabolite signals. Thus, the signals we can detect with MRS are fundamentally much weaker than those of MRI, making it a relatively low-resolution technique.

An increasing static magnetic field strength is particularly beneficial for MRS, because it not only improves the signal-to-noise, but also the spectral resolution. This can facilitate the suppression of the dominant water signal in ^1H-MRS, the separation and identification of neighboring resonances and, therefore, potentially improve the accuracy of quantitative analysis of the spectra.

So far, multinuclear MRS has mainly been applied to the model of Langendorff-perfused mouse and rat heart [61–64], as well as in dogs [65] and humans [66–72] *in vivo*. The application of this technique to rodent hearts *in vivo* would enable the investigation of cardiac metabolism under physiological and pathophysiological conditions. Importantly, the physiological relevance of the isolated, perfused mouse heart model is limited because

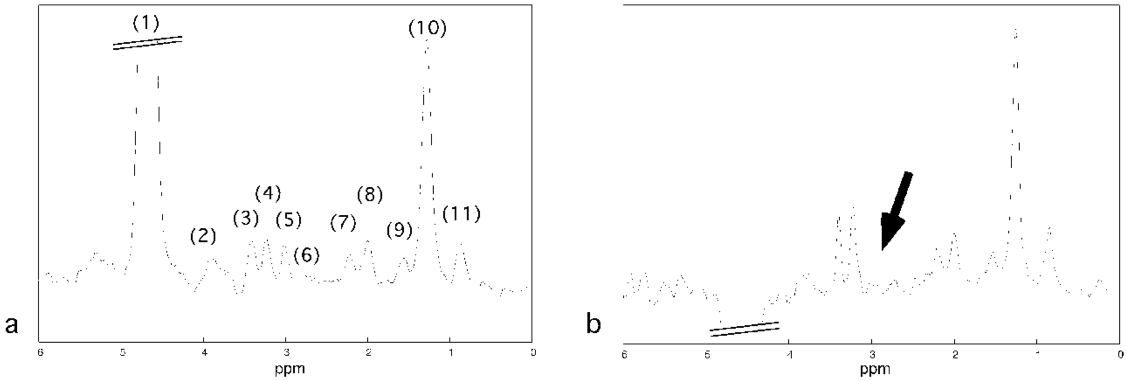

Fig. 11. Cardiac ^{1}H single voxel MRS in mice *in vivo*. (a) ^{1}H-spectrum from a 2 μl voxel positioned in the interventricular septum of a wild type mouse *in vivo*. The resonances were assigned according to ref. [61] and referenced relative to the residual water signal (peak (1)), which was set to 4.7 ppm. (2) (P)Cr – CH_2, 3.88 ppm; (3) taurine, 3.38 ppm; (4) carnitine, 3.21 ppm; (5) (P)Cr – CH_3, 2.99 ppm; (6) unassigned, 2.72 ppm; (7) glycerides ($C_{\alpha}H$), 2.20 ppm; (8) unassigned, 2.0 ppm; (9) glycerides ($C_{\beta}H$), 1.55 ppm; (10) glycerides ($(–CH_2)_n$), 1.26 ppm; (11) glycerides terminal methyl, 0.85 ppm. (b) Spectrum from a guanidinoacetate *N*-methyltransferase deficient mouse (GAMT$^{-/-}$), where no creatine was detectable (black arrow). Both spectra consisted of 512 averages and were scaled equally.

in vivo workload levels cannot be achieved [73]. Due to its non-invasiveness, these studies may also be repeated throughout the life span of an animal, before and after an intervention, or during progression of disease.

In some circumstances, a qualitative or semi-quantitative analysis of the MRS data is sufficient. This involves either the presence or absence of a particular resonance in the MR spectrum (for example, the detection of lactate as a marker for anaerobic metabolism), or the calculation of metabolite ratios (i.e. PCr/ATP in ^{31}P-MRS). In general, however, an absolute-quantitative approach is desirable. This requires the use of a concentration standard (internal or external), a quantitative analysis (i.e. fitting) of the MR data and the knowledge of several parameters intervening into absolute quantification, such as MR relaxation parameters, RF-coil sensitivity and B_1-field characteristics etc. Thus, absolute-quantitative MRS is methodologically complex and difficult and has therefore only been applied in very few centers around the world. Here, we will discuss the physiological relevance and the *in vivo* application of cardiac ^{1}H-, ^{31}P and ^{23}Na-MRS for mouse and rat hearts.

^{1}H-MRS

Cardiac ^{1}H-MR spectroscopy detects several metabolites such as lactate, lipids, and creatine that can be used as indicators for the physiological condition of myocardial tissue. ^{1}H-MRS studies in human hearts have previously been reported [69,70,74–76], and this technique has also been applied *in vivo* to examine myocardial metabolism in dogs [65,77]. Of particular interest is the methyl-resonance of creatine at 3.02 ppm in proton spectra, which is commonly assigned to total creatine [both phosphorylated (PCr) and unphosphorylated creatine (Cr)]. Specifically, variations in creatine content have been shown to reflect tissue viability in the human heart [69].

We recently established cardiac ^{1}H-MRS in mouse *in vivo*, using a single voxel technique [78]. The signals of several cardiac metabolites originating from a 2 μl voxel, positioned in the interventricular septum of the mouse heart, were acquired within approximately 15–30 min using PRESS [79,80]. A ^{1}H-MR spectrum obtained from a normal mouse heart is shown in Figure 11a. Dedicated cardiac and respiratory gating (with steady-state maintenance) was crucial for the successful detection of the metabolite signals. The method was then applied to a murine model of guanidinoacetate *N*-methyltransferase (GAMT) deficiency [2] to show the absence of creatine in these hearts as indicated by the arrow in Figure 11b. This study demonstrated the feasibility of detecting and quantifying metabolites in the hearts of normal and genetically modified mice by ^{1}H-MRS *in vivo*. Applying this technique on multiple voxels or expanding it to chemical shift imaging (CSI) would be required to investigate heterogeneous alterations of cardiac metabolism. This is subject to future work, which will also involve the development of absolute quantification of metabolite concentrations in the mouse heart *in vivo* as outlined above.

^{31}P-MRS

^{31}P-MRS, which detects the signals of phosphocreatine (PCr), ATP, and inorganic phosphate allows for an investigation of cardiac energy metabolism. The intracellular pH can be calculated from the frequency shift between the resonances of PCr and inorganic phosphate. The ultimately relevant energetic parameter is the free energy change of ATP hydrolysis [81], given by:

$$[-\Delta G_{\mathrm{ATP}}\,(\mathrm{kJ/mol})] = \left|\Delta G^0 + RT \ln\left(\frac{[\mathrm{ADP}]\,[\mathrm{P_i}]}{[\mathrm{ATP}]}\right)\right|, \tag{4}$$

where $\Delta G^0 = -30.5$kJ/mol is the value for ΔG_{ATP} under standard conditions [82], R is the gas constant (8.3 J/mol K) and T the absolute temperature. The concentration of ADP, which is in the μM range and therefore below the sensitivity limit of MRS, is calculated indirectly from the creatine kinase reaction equilibrium according to:

$$[\mathrm{ADP}] = \frac{[\mathrm{ATP}]\,[\mathrm{Cr}]}{[\mathrm{PCr}]\,[H^+]\,K_{eq}}, \tag{5}$$

where $K_{eq} = 1.66 \cdot 10^9\,(\mathrm{mol}\,/\,\mathrm{l})^{-1}$ and [Cr] is the concentration of unphosphorylated creatine (i.e. the difference between [*total creatine*] and [PCr]). [PCr] can be determined from the ^{31}P-data and the total creatine content with quantitative ^{1}H-MRS. Thus, a combination of ^{1}H-MRS and ^{31}P-MRS would allow for a comprehensive and non-invasive determination of the myocardial energy state. However, creatine may only be partially MR visible [83] and this problem needs to be systematically evaluated.

Only few studies have reported on *in vivo* cardiac ^{31}P-MRS in mice. Omerovic *et al.* applied a single voxel method (ISIS, [84]) at 2.35 T using a double tuned ^{1}H-^{31}P-Helmholtz coil [85]. Metabolite signals of a voxel containing the left ventricle (voxel volume ≈120 μl) were detected within an experimental time of approximately 3 h. Weiss and co-workers applied a 1D chemical shift imaging technique (1D-CSI) at 4.7 T using a ^{31}P-surface coil [86–88]. The experimental time to collect the ^{31}P-data was ~34 min. Based on concentration measurements of total creatine and ATP and intracellular pH, obtained from perfused mouse heart experiments [89,90], they subsequently calculated the free energy change of normal mouse hearts from their ^{31}P-MRS data and obtained a value of approximately 60 kJ/mol. The application of this technique to GLUT4 null mice (i.e. mice lacking expression of the glucose transport protein GLUT4 (G4N) [91]) revealed a unique increase of 60% in the cardiac PCr/ATP ratio (2.4 vs. 1.5 in wild type controls) [88]. This higher ratio was due to an increased total creatine content in the heart of these mice. However, the concentration of ADP or ATP and the free energy reserve were unaltered [88]. Such an increase in creatine content has not been observed under any other circumstances, and the reasons for this remain to be elucidated.

This example illustrates the important role of ^{31}P-MRS in characterizing the cardiac energy metabolism of genetically modified mice non-invasively. Future work will focus on the implementation of absolute quantitative methods using CSI. SLOOP[2] as used in humans [66,67,92] is a method that achieves spatial localization and absolute quantitation, and could be a step forward towards the measurement of the high-energy phosphate concentrations in the hearts of rodents.

^{23}Na-MRS

The signal of sodium represents an intrinsic marker of myocardial viability: A cellular ion-pump maintains a transmembrane concentration gradient between the intracellular and the extracellular space (intracellular sodium concentration 10–15 mM; extracellular 145 mM [93]). This energy-consuming process is compromised during periods of ischemia, leading to elevated intracellular sodium concentrations. Furthermore, the extracellular space increases in scar tissue after myocardial infarction. Thus, changes in the detectable sodium signal may be an indicator of cell viability, as demonstrated in the isolated rat heart model (e. g. [93,94], see also Figure 12), or *in vivo* in rabbits [95], dogs [96,97], and humans [98,99].

However, the *in vivo* ^{23}Na signal has multiple T_2 components with approximately 30–40% of the total sodium signal having a T_2-value of around 1 ms. Thus, ultrashort echo times are essential in order to maximize the detectable sodium signal.

Based on dedicated localization techniques [100], Neuberger *et al.* were the first to report on the application of ^{23}Na 3D-CSI in normal and failing mouse hearts at 17.6 T [101]. They achieved a voxel size of 1 μl within an experimental time of approximately 1.5 h. This study was mainly limited by the size of the RF-coil and the gradient performance. Optimizing the hardware set-up further will likely benefit spatial resolution and SNR and therefore improve the value of this approach.

The studies mentioned above demonstrate the feasibility of cardiac MRS in mice. However, unlike cardiac MRI, this technique is far from a routine application in mice and rats. Hence, substantial future work is required to develop cardiac MRS into a tool that allows for a robust and reproducible investigation of physiological questions in normal and genetically modified animals. The trend

---

[2] SLOOP: Spatial LOcalization with Optimal Pointspread function.

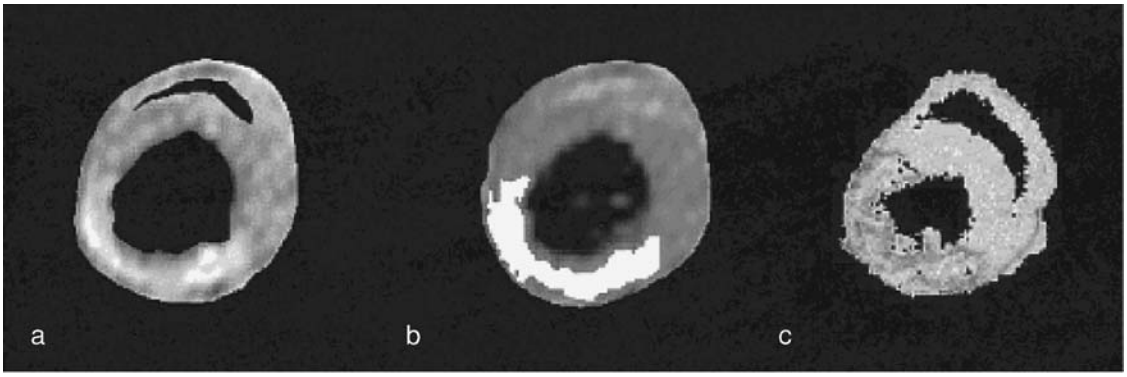

Fig. 12. ^{23}Na MRS in the isolated rat heart. (a) Mid-ventricular slice across an isolated, perfused rat heart, obtained from a ^{23}Na 3D-CSI experiment 4 weeks post MI. (b) Infarcted area highlighted in white after threshold segmentation. (c) Corresponding histology with the infarcted area stained in red. (Taken from [93]). (See also Plate 72 on page XLVIII in the Color Plate Section.)

towards higher magnetic fields may be particularly beneficial for of cardiac MRS.

Vascular MRI

Genetically engineered mice are important for the study of atherosclerosis. Apolipoprotein E-knockout (ApoE$^{-/-}$) [102] or low-density lipoprotein receptor (LDLR$^{-/-}$) [103,104] deficient mice develop atherosclerotic lesions throughout the arterial tree, which resemble those found in humans. Lesion burdens in the aortic root [105], or in the brachiocephalic artery [106,107] are commonly investigated histologically as these are sites of early atherosclerosis development [108]. Although the histological methods have provided important insights into the development and the pathophysiology of atherosclerosis, the process of serial sectioning and histomorphometry is tissue-destructive, labor-intensive, limited to 2D analysis and precludes longitudinal investigation of the same animal. In particular, therapeutic interventions have been demonstrated to favorably alter plaque size and composition [109,110]. Therefore, the capability to investigate this serially in the same animal is highly desirable.

This can be achieved with high-resolution MRI. Although inferior in spatial resolution compared to histology, MRI is a valuable tool in investigating atherosclerosis in mice due to its non-invasive nature, inherent contrast mechanisms and 3D capability. However, contrast and spatial resolution must be maximized in order to resolve the ultra-small vascular structure with sufficient SNR and within acceptable/physiological imaging times. For example, it is worth noting that the thickness of a normal aortic wall in the mouse is less than 50 μm.

The first *in vivo* studies focused on the investigation of plaque development in the abdominal aorta and common iliac arteries of 36–84 weeks old apoE$^{-/-}$ mice due to reduced motional influence [111]. Slice-selective spin-echo sequences were employed with proton-density, T_2- and T_1-contrast. Total plaque area, quantified from the 2D MR-images correlated well with histology [111]. Choudhury *et al.* extended this work to 12–36 weeks old apoE$^{-/-}$ mice [112]. Studies of the aortic root or arch are technically more demanding due to substantial cardiac and respiratory motional influence. Only a few studies reported the quantification of atherosclerotic lesion size in the aortic root [113] and arch [114], or in the brachiocephalic artery [115] of mice. An example for detecting atherosclerotic plaque in mice by MRI together with the corresponding histopathological section is shown in Figure 13. All studies used spin echo sequences with black blood contrast, but only Hockings *et al.* applied it in three dimensions [115]. The achieved spatial resolution ranged between 49 × 98 × 300 μm [114] and 140 ×187 × 187 μm [115] before image interpolation, obtained within a scan time of approximately 30 min. This allowed for a correlation of the total plaque area as measured by MRI to the histological plaque area [114,115], as well as for monitoring the development of atherosclerotic plaque burden with age [113,115].

However, plaque composition is the more relevant parameter in humans as this rather than the size of the plaque determines the pathological consequences. Plaques in humans that feature a large lipid core and thin fibrous cap are susceptible to rupture provoking acute atherothrombotic events [116]. Furthermore, it has been shown in recent studies that lesions in the brachiocephalic artery of ApoE$^{-/-}$ mice have features of vulnerable plaque and, therefore, may better model human atherosclerotic

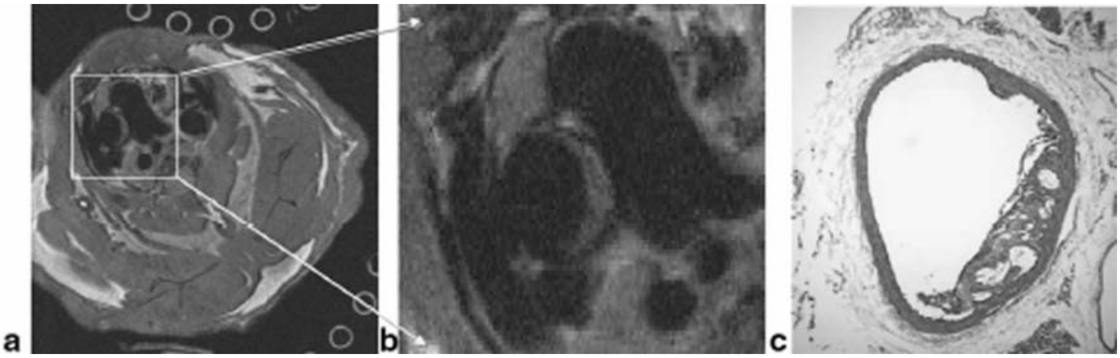

Fig. 13. Atherosclerotic plaque in apoE$^{-/-}$ mice *in vivo*. (a) Transverse MR image across the outflow tract of an apolipoprotein E knockout mouse. The ascending aorta is magnified in panel b and shows a close agreement in structure and wall area compared to the histological section (panel c). (From [114]). (See also Plate 73 on page XLVIII in the Color Plate Section.)

disease [106,107]. In order to distinguish between the different plaque components, multicontrast MR images are required. Combining the information from T_1-, T_2- and proton density (PD) weighted MR images, it has been possible to characterize both plaque anatomy and composition in experimental animals [117,118], *ex vivo* specimens [119–121], and in human carotid arteries [120,122] and aorta *in vivo* [123]. We have developed and applied high-resolution, multicontrast MRI techniques to quantify and classify atherosclerotic plaque in ApoE$^{-/-}$ mice *ex vivo* [124]. Specifically, we used a 3D multiecho sequence to differentiate and accurately quantify the volume of the plaque components in the aortic root and the brachiocephalic artery of ApoE$^{-/-}$ mice. MR images across the aortic arch and the brachiocephalic artery together with the corresponding histological sections are shown in Figure 14.

Although *in vivo* application of plaque imaging is the ultimate goal, at this moment *ex vivo* MRI, which has no motional influence, produces a level of spatial resolution for studies in mice, which may not be achievable *in vivo*. However, future *in vivo* applications may be facilitated by the use of targeted contrast agents (molecular imaging). For example Sirol *et al.* used a gadolinium-based contrast agent to enhance the contrast in lipid-rich plaques in rabbits [125]. Substantial future work will be required to develop this approach.

Conclusion and Future Perspective

In this chapter, we explained the importance of MR for a non-invasive characterization of the rodent hearts. Specifically, we demonstrated that the multiparametric MRI and MRS approach is crucial for a comprehensive analysis of normal and diseased hearts. The applications outlined here list the most prominent methods that are currently available for cardiovascular research in rodents. However, this list is far from complete. Other MR techniques, such as the assessment of perfusion in hearts of mice [126] and rats [127,128], or the investigation of foetal development in rodents by MR microscopy (see [129] for review) are also on the horizon.

In the future, a spread of this technology can be expected. The important role of MR as a phenotyping tool for rodent hearts has been widely recognized and this field is now rapidly expanding. New centers, dedicated to cardiac research in rodents, together with existing laboratories, will provide a platform for the routine application of MR in rodents.

Finally, the technological progress will also have a major impact on the future role of experimental CVMR. The development of new techniques will not only depend on advances in MR technology, such as parallel acquisition techniques (PAT) or simultaneous imaging of several specimen [130], but also on a multidisciplinary approach by physicists, chemists, physiologists, biologists, and cardiologists. This will be particularly necessary for the development of targeted contrast agents (molecular imaging) or in the rapidly growing field of stem cell research.

Acknowledgements

Our work was funded by Project Grants from the British Heart Foundation (BHF). We would like to acknowledge the important contributions from our colleagues and collaborators Prof. Kieran Clarke, Drs Paul Cassidy, Robin Choudhury, Dana Dawson, Craig Lygate, Martina McAteer, Matthew Robson, Damian Tyler, and Ms Karen Hulbert.

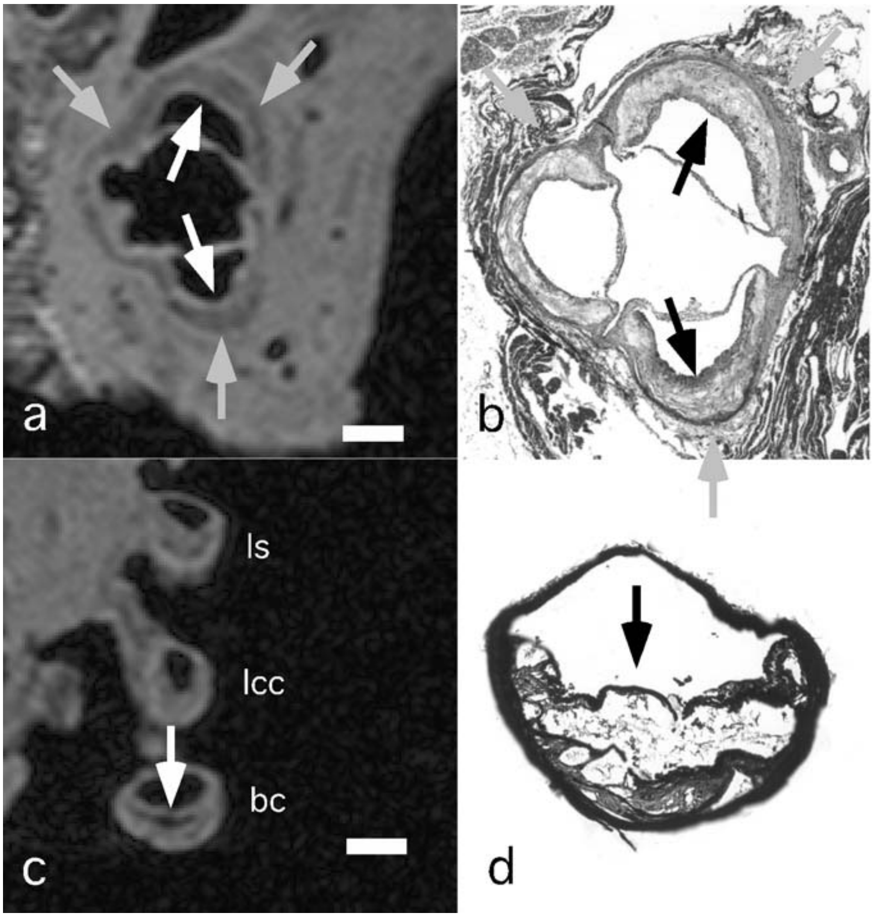

Fig. 14. Multicontrast MRI in apoE$^{-/-}$ mice *ex vivo*. Transverse MR images through the (a) aortic root and (c) through the head-and-neck vessels of an apolipoprotein E knockout mouse, obtained from the multiecho sequence. Four echoes with increasing echo times were acquired within one TR and subsequently averaged to provide a different degree of T_2-weighting for the various plaque components. The white arrows in panel a indicate the cellular layer that stained red in the histological section (black arrows in panel b). The green arrows illustrate the fibro-fatty plaque component (green stain in panel b). A lipid core is shown in the brachiocephalic artery (arrows in panels c and d). The voxel size of the MR images is 23 × 23 × 31 μm. Scale bar: 0.5 mm. Abbreviations: bc—right brachiocephalic; lcc—left common carotid and ls—left subclavian artery. (See also Plate 74 on page XLIX in the Color Plate Section.)

References

1. Franz WM, Mueller OJ, Hartong R, Frey N, Katus, HA. J. Mol. Med. 1997;75:115.
2. Schmidt A, Marescau B, Boehm EA, Renema WK, Peco R, Das A, Steinfeld R, Chan S, Wallis J, Davidoff M, Ullrich K, Waldschutz R, Heerschap A, De Deyn PP, Neubauer S, Isbrandt D. Hum. Mol. Genet. 2004;13:905.
3. Maddatu TP, Garvey SM, Shroeder DG, Hampton TG, Cox GA. Hum. Mol. Genet. 2004;13:1105.
4. Christoffels VM, Hoogaars WM, Tessari A, Clout, DE, Moorman AF, Campione M. Dev. Dyn. 2004;229:763.
5. Chien KR. J. Clin. Invest. 1996;97:901.
6. Rockman HA, Ross RS, Harris AN, Knowlton KU, Steinhelper ME, Field LJ, Ross J, Chien KR Jr. Proc. Natl. Acad. Sci. U S A 1991;88:8277.
7. Liao Y, Ishikura F, Beppu S, Asakura M, Takashima S, Asanuma H, Sanada S, Kim J, Ogita H, Kuzuya T, Node K, Kitakaze M, Hori M. Am. J. Physiol. Heart Circ. Physiol. 2002;H1703:282.
8. Pfeffer MA, Braunwald E. Circulation 1990;81:1161.
9. Hayes CE, Edelstein WA, Schenck JF, Mueller OM, Eash M. J. Magn. Reson. 1985;63:622.
10. Chen CN, Hoult DI, Sank VJ. J. Magn. Reson. 1983;54:324.

11. Nahrendorf M, Wiesmann F, Hiller KH, Hu K, Waller C, Ruff J, Lanz TE, Neubauer S, Haase A, Ertl G, Bauer WR. J. Magn. Reson. Imaging 2001;14:547.
12. Nahrendorf M, Frantz S, Hu K, von zur Muhlen C, Tomaszewski M, Scheuermann H, Kaiser R, Jazbutyte V, Beer S, Bauer W, Neubauer S, Ertl G, Allolio B, Callies F. Cardiovasc. Res. 2003;57:370.
13. Rusy BF, Komai H. Anesthesiology 1987;67:745.
14. Roth DM, Swaney JS, Dalton ND, Gilpin EA, Ross J Jr. Am. J. Physiol. Heart. Circ. Physiol. 2002;H2134:282.
15. Wood ML, Henkelman RM. Magn. Reson. Imaging. 1986;4:387.
16. Cassidy PJ, Schneider JE, Grieve SM, Lygate C, Neubauer S, Clarke K. J. Magn. Reson. Imaging. 2004;19:229.
17. de Kerviler E, Leroy-Willig A, Clement O, Frija J. Biomed. Pharmacother. 1998;52:69.
18. Schneider JE, Cassidy PJ, Lygate C, Tyler DJ, Wiesmann F, Grieve SM, Hulbert K, Clarke K, Neubauer S. J. Magn. Reson. Imaging 2003;18:691.
19. Finn JP, Edelman RR. Magn. Reson. Imaging Clin. N. Am. 1993;1:349.
20. Song HK, Wright AC, Wolf RL, Wehrli FW. Magn. Reson. Med. 2002;47:616.
21. Manning WJ, Wei JY, Katz SE, Litwin SE, Douglas PS. Am. J. Physiol. 1994;H1672:266.
22. Ruff J, Wiesmann F, Hiller KH,Voll S, von Kienlin M, Bauer WR, Rommel E, Neubauer S, Haase A. Magn. Reson. Med. 1998;40:43.
23. Wiesmann F, Ruff J, Haase A. MAGMA 1998;6:186.
24. Zhou R, Pickup S, Glickson JD, Scott CH, Ferrari VA. Magn. Reson. Med. 2003;49:760.
25. Wiesmann F, Frydrychowicz A, Rautenberg J, Illinger R, Rommel E, Haase A, Neubauer S. Am. J. Physiol. Heart. Circ. Physiol. 2002; H1065:283.
26. Tyler DJ, Cassidy P, Lygate C, Schneider J, Neubauer S, Clarke K. Kyoto. 1801. (2004).
27. Wiesmann F, Ruff J, Hiller KH, Rommel E, Haase A, Neubauer S. Am. J. Physiol. Heart. Circ. Physiol. 2000;H652:278.
28. Franco F, Dubois SK, Peshock RM, Shohet RV. Am. J. Physiol. 1998;H679:274.
29. Franco F, Thomas GD, Giroir B, Bryant D, Bullock MC, Chwialkowski MC, Victor RG, Peshock RM. Circulation 1999;99:448.
30. Kubota T, McTiernan CF, Frye CS, Slawson SE, Lemster BH, Koretsky AP, Demetris AJ, Feldman AM. Circ. Res. 1997;81:627.
31. Williams SP, Gerber HP, Giordano FJ, Peale FV Jr, Bernstein LJ, Bunting S, Chien KR, Ferrara N, van Bruggen N. J. Magn. Reson. Imaging 2001;14:374.
32. Loeppky JA. Aviat. Space Environ. Med. 1975;46:1164.
33. Schneider JE, Hulbert K, Lygate CA, Ten Hove M, Cassidy PJ, Clarke K, Neubauer S. MAGMA. 2004;17(3–6):162.
34. Wiesmann F, Ruff J, Engelhardt S, Hein L, Dienesch C, Leupold A, Illinger R, Frydrychowicz A, Hiller KH, Rommel E, Haase A, Lohse MJ, Neubauer S. Circ. Res. 2001;88:563.
35. Ross AJ, Yang Z, Berr SS, Gilson WD, Petersen WC, Oshinski JN, French BA. Magn. Reson. Med. 2002;47:1158.
36. Yang Z, Bove CM, French BA, Epstein FH, Berr SS, DiMaria JM, Gibson JJ, Carey RM, Kramer CM. Circulation 2002;106:106.
37. Yang Z, French BA, Gilson WD, Ross AJ, Oshinski JN, Berr SS. Circulation, 103, E84 (2001).
38. Schneider JE, Lygate CA, Hulbert K, Cassidy PJ, Clarke K, Neubauer S. Kyoto. 1850. (2004).
39. Zerhouni EA, Parish DM, Rogers WJ, Yang A, Shapiro EP. Radiology 1988;169:59.
40. Axel L, Dougherty L. Radiology 1989;171:841.
41. Axel L, Goncalves RC, Bloomgarden D. Radiology 1992;183:745.
42. Young AA, Imai H, Chang CN, Axel L. Circulation 1994;89:740.
43. Henson RE, Song SK, Pastorek JS, Ackerman JJ, Lorenz CH. Am. J. Physiol. Heart. Circ. Physiol. 2000;H1117:278.
44. Epstein FH, Yang Z, Gilson WD, Berr SS, Kramer CM, French BA. Magn. Reson. Med. 2002;48:399.
45. van Dijk P. J. Comput. Assist. Tomogr. 1984;8:429.
46. Bryant DJ, Payne JA, Firmin DN, Longmore DB. J. Comput. Assist. Tomogr. 1984;8:588.
47. Firmin DN, Nayler GL, Klipstein RH, Underwood SR, Rees RS, Longmore DB. J. Comput. Assist. Tomogr. 1987;11:751.
48. Pelc LR, Pelc NJ, Rayhill SC, Castro LJ, Glover GH, Herfkens RJ, Miller DC, Jeffrey RB. Radiology 1992;185:809.
49. Wedding KL, Draney MT, Herfkens RJ, Zarins CK, Taylor CA, Pelc NJ. J. Magn. Reson. Imaging 2002;15:418.
50. Axel L, Morton D. J. Comput. Assist. Tomogr. 1987;11:31.
51. Markl M, Schneider B, Hennig J, Peschl S, Winterer J, Krause T, Laubenberger J. Int. J. Card. Imaging 1999;15:441.
52. Streif JU, Herold V, Szimtenings M, Lanz TE, Nahrendorf M, Wiesmann F, Rommel E, Haase A. Magn. Reson. Med. 2003;49:315.
53. Aletras AH, Balaban RS, Wen H, J Magn Reson 1999;140:41.
54. Aletras AH, Ding S, Balaban RS, Wen H. J. Magn. Reson. 1999;137:247.
55. Aletras AH, Wen H. Magn. Reson. Med. 2001;46:523.
56. Sureau FC, Gilson WD, Yang Z, French BA, Epstein FH. Kyoto. 1786. (2004)
57. Gilson WD, Yang Z, French BA, Epstein FH. Magn. Reson. Med. 2004;51:744.
58. Gilson WD, Yang Z, Sureau FC, French BA, Epstein FH. Kyoto. 1789. (2004).
59. Zhu Y, Drangova M, Pelc NJ. IEEE Trans. Med. Imaging 1997;16:840.
60. Kim D, Gilson WD, Kramer CM, Epstein FH. Radiology 2004;230:862.
61. Ugurbil K, Petein M, Maidan R, Michursky S, Cohn JN, From AH. FEBS-Lett. 1984;167(1):73.
62. Unitt JF, Schrader J, Brunotte F, Radda GK, Seymour AM. Biochim. Biophys.Acta. 1992;1133:115.
63. Wolfe CL, Gilbert HF, Brindle KM, Radda GK. Biochim. Biophys. Acta 1988;971:9.
64. Ingwall JS, Bittl JA. Basic. Res. Cardiol. 1987;82(Suppl 2):93.
65. Bottomley PA, Weiss RG. Radiology 2001;219:411.
66. Loffler R, Sauter R, Kolem H, Haase A, von Kienlin M. J. Magn. Reson. 1998;134:287.
67. Meininger M, Landschutz W, Beer M, Seyfarth T, Horn M, Pabst T, Haase A, Hahn D, Neubauer S, von Kienlin M. Magn. Reson. Med. 1999;41:657.

68. Pohmann R, von Kienlin M. Magn. Reson. Med. 2001;45:817.
69. Bottomley PA, Weiss RG. Lancet 1998;351:714.
70. Felblinger J, Jung B, Slotboom J, Boesch C., Kreis R. Magn. Reson. Med. 1999;42:903.
71. Kozerke S, Schar M, Lamb HJ, Boesiger P. Magn. Reson. Med. 2002;48:380.
72. Neubauer S, Horn M, Cramer M, Harre K, Newell JB, Peters W, Pabst T, Ertl G, Hahn D, Ingwall JS, Kochsiek K. Circulation 1997;96:2190.
73. Kass DA, Hare JM, Georgakopoulos D. Circ. Res. 1998;82:519.
74. den Hollander JA, Evanochko WT, Pohost GM. Magn. Reson. Med. 1994;32:175.
75. Kreis R, Felblinger J, Jung B, Boesch C. MAGMA 1998;6:164.
76. Nakae I, Mitsunami K, Omura T, Yabe T, Tsutamoto T, Matsuo S, Takahashi M, Morikawa S, Inubushi T, Nakamura Y, Kinoshita M, Horie M. J. Am. Coll. Cardiol. 2003;42:1587.
77. Bache RJ, Zhang J, Murakami Y, Zhang Y, Cho YK, Merkle H, Gong G, From AH, Ugurbil K. Cardiovasc. Res. 1999;42:616.
78. Schneider JE, Tyler DJ, Ten Hove M, Sang AE, Cassidy PJ, Fischer A, Wallis J, Sebag-Montefiore LM, Watkins H, Isbrandt D, Clarke K, Neubauer S. Magn. Reson. Med. in press (2004).
79. Ordidge RJ, Bendall MR, Gordon RE, Connelly A. In: G Govil, CL Khetrapal, A Saran (Eds). Magnetic Resonance in Biology and Medicine, Tata McGraw-Hill: New Dehli, 1985, p 387.
80. Bottomley PA, Ann N Y Acad. Sci. 1987;508:333.
81. Kammermeier H, Schmidt P, Jungling E. J. Mol. Cell. Cardiol. 1982;14:267.
82. Gibbs C. J. Mol. Cell. Cardiol. 1985;17:727.
83. Schneider J, Fekete E, Weisser A, Neubauer S, von Kienlin M. Magn. Reson. Med. 2000;43:497.
84. Ordidge RJ, Connelly A, Lohman JAB. J. Magn. Reson. 1986;66:283.
85. Omerovic E, Basetti M, Bollano E, Bohlooly M, Tornell J, Isgaard J, Hjalmarson A, Soussi B, Waagstein F. Biochem. Biophys. Res. Commun. 2000;271:222.
86. Chacko VP, Aresta F, Chacko SM, Weiss RG. Am. J. Physiol. Heart Circ. Physiol. 2000;H2218: 279.
87. Naumova AV, Weiss RG, Chacko VP. Am. J. Physiol. Heart. Circ. Physiol. 2003;H1976:285.
88. Weiss RG, Chatham JC, Georgakopolous D, Charron MJ, Wallimann T, Kay L, Walzel B, Wang Y, Kass DA, Gerstenblith G, Chacko VP, FASEB J. 2002;16:613.
89. Spindler M, Saupe KW, Christe ME, Sweeney HL, Seidman CE, Seidman JG, Ingwall JS. Clin. J. Invest. 1998;101:1775.
90. Saupe KW, Spindler M, Tian R, Ingwall JS. Circ. Res. 1998;82:898.
91. Katz EB, Stenbit AE, Hatton K, DePinho R, Charron MJ. Nature 1995;377:151.
92. Beer M, Seyfarth T, Sandstede J, Landschutz W, Lipke C, Kostler H, von Kienlin M, Harre K, Hahn D, Neubauer S. J. Am. Coll. Cardiol. 2002;40:1267.
93. Horn M, Weidensteiner C, Scheffer H, Meininger M, de Groot M, Remkes H, Dienesch C, Przyklenk K, von Kienlin M, Neubauer S. Magn. Reson. Med. 2001;45:756.
94. Weidensteiner C, Horn M, Fekete E, Neubauer S, von Kienlin M. Magn. Reson. Med. 2002;48:89.
95. Kim RJ, Lima JA, Chen EL, Reeder SB, Klocke FJ, Zerhouni EA, Judd RM. Circulation 1997;95:1877.
96. Kim RJ, Judd RM, Chen EL, Fieno DS, Parrish TB, Lima JA. Circulation 1999;100:185.
97. Constantinides CD, Kraitchman DL, O'Brien KO, Boada FE, Gillen J, Bottomley PA. Magn. Reson. Med. 2001;46: 1144.
98. Lee RF, Giaquinto R, Constantinides C, Souza S, Weiss RG, Bottomley PA. Magn. Reson. Med. 2000;43:269.
99. Pabst T, Sandstede J, Beer M, Kenn W, Greiser A, von Kienlin M, Neubauer S, Hahn D. Magn. Reson. Med. 2001;45:164.
100. Greiser A, Von Kienlin M. Magn. Reson. Med. 2003;50:1266.
101. Neuberger T, Greiser A, Nahrendorf M, Jakob PM, Faber C, Webb AG. MAGMA. 2004;17(3–6):196.
102. Plump AS, Smith JD, Hayek T, Aalto-Setala K, Walsh A, Verstuyft JG, Rubin EM, Breslow JL. Cell 1992;71: 343.
103. Ishibashi S, Brown MS, Goldstein JL, Gerard RD, Hammer RE, Herz J. Clin. J. Invest 1993;92:883.
104. Palinski W, Tangirala RK, Miller E, Young SG, Witztum JL. Arterioscler. Thromb. Vasc. Biol. 1995;15:1569.
105. Paigen B, Morrow A, Holmes PA, Mitchell D, Williams RA. Atherosclerosis 1987;68:231.
106. Rosenfeld ME, Polinsky P, Virmani R, Kauser K, Rubanyi G, Schwartz SM. Arterioscler. Thromb. Vasc. Biol. 2000;20:2587.
107. Williams H, Johnson JL, Carson KGS, Jackson CL. Arterioscler. Thromb. Vasc. Biol. 2002;22:788.
108. Nakashima Y, Plump AS, Raines EW, Breslow JL, Ross R. Arterioscler. Thromb. 1994;14:133.
109. Rong JX, Li J, Reis ED, Choudhury RP, Dansky HM, Elmalem VI, Fallon JT, Breslow JL, Fisher EA. Circulation 2001;104:2447.
110. Shah PK, Yano J, Reyes O, Chyu KY, Kaul S, Bisgaier CL, Drake S, Cercek B. Circulation 2001;103:3047.
111. Fayad ZA, Fallon JT, Shinnar M, Wehrli S, Dansky HM, Poon M, Badimon JJ, Charlton SA, Fisher EA, Breslow JL, Fuster V. Circulation 1998;98:1541.
112. Choudhury RP, Aguinaldo JG, Rong JX, Kulak JL, Kulak AR, Reis ED, Fallon JT, Fuster V, Fisher EA, Fayad ZA. Atherosclerosis 2002;162:315.
113. Itskovich VV, Choudhury RP, Aguinaldo JG, Fallon JT, Omerhodzic S, Fisher EA, Fayad ZA. Magn. Reson. Med. 2003;49:381.
114. Wiesmann F, Szimtenings M, Frydrychowicz A, Illinger R, Hunecke A, Rommel E, Neubauer S, Haase A. Magn. Reson. Med. 2003;50:69.
115. Hockings PD, Roberts T, Galloway GJ, Reid DG, Harris DA, Vidgeon-Hart M, Groot PH, Suckling KE, Benson GM. Circulation 2002;106:1716.
116. Virmani R, Kolodgie FD, Burke AP, Farb A, Schwartz SM, Arterioscler. Thromb. Vasc. Biol. 2000;20:1262.
117. Skinner MP, Yuan C, Mitsumori L, Hayes CE, Raines EW, Nelson JA, Ross R. Nat. Med. 1995;1:69.
118. Helft G, Worthley SG, Fuster V, Zaman AG, Schechter C, Osende JI, Rodriguez OJ, Fayad ZA, Fallon JT, Badimon JJ. J. Am. Coll. Cardiol. 2001;37:1149.

119. Toussaint JF, Southern JF, Fuster V, Kantor HL. Arterioscler. Thromb. Vasc. Biol. 1995;15:1533.
120. Toussaint JF, LaMuraglia GM, Southern JF, Fuster V, Kantor HL. Circulation 1996;94:932.
121. Shinnar M, Fallon JT, Wehrli S, Levin M, Dalmacy D, Fayad ZA, Badimon JJ, Harrington M, Harrington E, Fuster V. Arterioscler. Thromb. Vasc. Biol. 1999;19:2756.
122. Hatsukami TS, Ross R, Polissar NL, Yuan C. Circulation 2000;102:959.
123. Fayad ZA, Nahar T, Fallon JT, Goldman M, Aguinaldo JG, Badimon JJ, Shinnar M, Chesebro JH, Fuster V. Circulation 2000;101:2503.
124. Schneider JE, McAteer MA, Tyler DJ, Clarke K, Channon KM, Choudhury RP, Neubauer S. J. Magn. Reson. Imaging. 2004;20(6):981.
125. Sirol M, Itskovich VV, Mani V, Aguinaldo JG, Fallon JT, Misselwitz B, Weinmann HJ, Fuster V, Toussaint JF, Fayad ZA. Circulation 2004;109:2890.
126. Kober F, Iltis I, Izquierdo M, Desrois M, Ibarrola D, Cozzone PJ, Bernard M. Magn. Reson. Med. 2004;51:62.
127. Waller C, Hiller KH, Albrecht M, Hu K, Nahrendorf M, Gattenlohner S, Haase A, Ertl G, Bauer WR. Microvasc. Res. 2003;66:173.
128. Waller C, Kahler E, Hiller KH, Hu K, Nahrendorf M, Voll S, Haase A, Ertl G, Bauer WR. Radiology 2000;215:189.
129. Schneider JE, Bhattacharya S, Birth Defects Research, Part C Embryo Today 2004;72(3):241.
130. Bock NA, Konyer NB, Henkelman RM. Magn. Reson. Med. 2003;49:158.

Application of Pharmacological MRI to Preclinical Drug Discovery and Development

Matthew D. Ireland and Steven C.R. Williams

Centre for Neuroimaging Sciences, Institute of Psychiatry, De Crespigny Park, Denmark Hill, London SE5 8AF, UK

Introduction

Several neuroimaging techniques now exist that provide ways of studying functional activity in the living brain. Having been widely used in the fields of cognitive and sensory neuroscience, functional neuroimaging has more recently been applied to investigating the way in which psychoactive agents affect brain activity. The non-invasive nature of functional magnetic resonance imaging (fMRI), coupled with its excellent spatial and temporal resolution and proven ability for investigating sensory, motor and cognitive functions in a non-invasive and repeatable way, have made it a particularly attractive technique for drug research, providing an insight into the functional effects of receptor activation *in vivo* in far greater detail than previously possible. This application of fMRI techniques to neuropharmacology, termed pharmacological MRI or phMRI [1], has been used to successfully demonstrate those regions of the brain that respond to a range of different psychoactive compounds. In addition to providing information concerning the regional specificity of drug action, the time course over which drugs act can also be established, as can the results of interactions between different compounds, and their central effects on cognition can be ascertained. By imaging activity throughout the entire brain, phMRI can determine the duration of drug-induced brain activity in all regions of interest with a temporal resolution down to several seconds, without the need for selective regional sampling. Despite its infancy, the use of phMRI has greatly expanded in recent years, having being used to examine the effects of CNS penetrating drugs in both humans and animals. Initial demonstrations that functional neuroimaging was able to detect drug-induced changes in brain activity in both humans [2–5] and animals [6–10], highlighted the enormous potential of such techniques for investigating drug action within the CNS. PhMRI is of particular interest to the pharmaceutical industry, with it being seen as having the potential to establish novel surrogate markers in animal disease models and provide early evidence of proof-of-concept for novel compounds, as well as helping characterize brain penetrability, pharmacokinetics, and the regionally specific actions of new drugs. By comparing existing "gold-standard" compounds with the patterns of neuronal activity induced by novel pharmaceutical agents, phMRI may help to establish potential efficacy, side effects, and therapeutic targets early in development. As phMRI is non-invasive and does not involve exposure to ionizing radiation, it can also be incorporated into longitudinal investigations of the neuroadaptive changes that occur during chronic treatment schedules that underlie the actions of many therapeutic agents.

Surrogate Markers of Neuronal Activity

Three of the main *in vivo* functional neuroimaging techniques currently in use are positron emission tomography (PET), single photon emission computed tomography (SPECT) and fMRI. None of these directly measure the output of active neurones, but instead rely on indirect measures of activity based upon the coupling of neuronal activity with glucose metabolism or cerebral blood flow [11]. Prior to the advent of *in vivo* functional imaging, measuring drug-induced changes in neuronal activity was mostly limited to *ex vivo* autoradiographic techniques. As the principal source of neuronal energy is glucose, measuring the cerebral metabolic rate of glucose utilization using 2-deoxyglucose (2-DG) autoradiography [12], provided one such way of detecting changes in brain metabolism. By using [^{14}C] labeled 2-DG, which becomes "metabolically trapped" inside active cells, rates of local energy metabolism in the brain can be calculated. However, being *ex vivo*, its use is restricted to single time point animal studies and temporal information concerning the duration of drug action is lost. PET studies using tracer quantities of ^{18}Flurodeoxyglucose (^{18}FDG), which like 2-DG is not fully metabolized but remains trapped inside active cells, are used in a similar fashion in both humans and animals to detect changes in altered cerebral glucose utilization *in vivo*. Whilst providing a direct measure of brain metabolism, the high costs and limited spatial and temporal resolution of PET due to sensitivity, positron traveling distances and detector arrangements (typically whole brain acquisitions take 30 s or longer), combined with restrictions on performing longitudinal

Graham A. Webb (ed.), Modern Magnetic Resonance, 855–877.
© 2008 *Springer.*

studies because of the radioactive and invasive nature of PET, limit broader applications of this technique. In particular, the more limited spatial resolution of PET has made it difficult to discriminate between structures within the brains of small animals typically used in preclinical research.

Hemodynamic-Based Functional Neuroimaging

Unlike 2-DG and ^{18}FDG PET, which measure changes in brain metabolism, fMRI and phMRI use hemodynamic measures based upon the coupling between regional cerebral blood flow (rCBF), regional cerebral blood volume (rCBV), and neuronal activity [13]. MRI provides several ways of indirectly measuring neuronal activity via changes in rCBF and rCBV. Although PET can localize regions of increased rCBF (and thus neuronal activity) using $H_2{}^{15}O$ tracers, like ^{18}FDG PET it also involves high scan costs and exposure to ionizing radiation. ^{99}Tc-HMPAO SPECT imaging can be used to measure rCBF at a lower cost than $H_2{}^{15}O$ PET, but has inferior anatomical resolution (typically not better than 5 mm voxel dimensions) and also involves exposure to radiation. The high spatial and temporal resolution of hemodynamic-based fMRI, coupled with its non-invasive and non-radioactive nature, have therefore resulted in it becoming the tool of choice for most *in vivo* functional neuroimaging.

MRI Measures of rCBF

MR images can be weighted to reflect rCBF by magnetically "tagging" arterial blood water and using it as a tracer. Such techniques are commonly referred to as arterial spin labeling (ASL), and include continuous ASL (CASL) [14] and flow-sensitive alternating inversion recovery (FAIR) [15]. These techniques require that two images are acquired, one with arterial spin labeling and one without, the differences between the images relating directly to rCBF. rCBF-weighted MRI predominantly reflects changes in tissues and capillaries rather than in veins, and has good functional specificity [16]. rCBF-weighted MRI has been used successfully for animal fMRI studies [17], but suffers from poor temporal resolution, requiring several minutes to produce a rCBF map, and is currently restricted to acquiring only a few slices at a time.

MRI Measures of rCBV

Measuring rCBV with MRI currently requires the use of an exogenous intravascular contrast agent with high magnetic susceptibility. Initial studies showed that administering a gadolinium conjugate, gadolinium dimeglumine (Gd-DTPA) allowed detection of signal changes of up to 40% in the visual cortex during photic stimulation by comparing images acquired without contrast agent to those acquired during the first pass of Gd-DTPA [18]. More recently, magnetic iron oxide nanoparticles (MIONs), that have a longer half-life than Gd-DTPA, have been successfully used to measure rCBF changes in animal fMRI experiments [16,19,20]. The long half-life of MIONs within the bloodstream allows a steady state concentration to be achieved, and as the concentration of contrast agent does not change with alterations in rCBF and O_2 consumption, only when rCBV increases during neuronal activity will the amount of contrast agent present locally rise, causing the MR signal to fall. As rCBV changes are closely related to rCBF, which is, in turn, specific to tissue, rCBV changes are largely reflective of alterations of blood flow within the parenchyma (close to the site of neuronal activity), as small vessels within tissue dilate more during stimulation than larger downstream vessels. The high magnetic susceptibility of contrast agents like MION have found wider use at lower magnetic field strengths [16], and the use of such agents has been particularly popular in animal phMRI, where concerns about the invasive nature and potential toxicity of administering exogenous contrast agents are slightly less. However, using contrast agents during phMRI experiments has raised concerns about the potential for saturating the liver enzymes upon which drug clearance is dependent, and this technique may not be suitable for extensive studies of drug pharmacokinetics. In addition, toxic side effects of many contrast agents may prevent longitudinal studies. CBV-based phMRI studies performed in animals may also be more difficult to translate to, or compare with, clinical investigations in humans, which usually employ BOLD-based techniques.

Blood Oxygen Level Dependent MRI

The most widely used fMRI technique to date is Blood Oxygen Level Dependent (BOLD) imaging [21]. BOLD signals result from changes in the level of paramagnetic deoxyhemoglobin that occur in areas of varying rCBF. As BOLD imaging requires no exogenous contrast agent, it has the advantage of being easy to perform, is completely non-invasive and provides high spatial and temporal resolution. As BOLD signals are sensitive to venous blood volume and vessel size, they are also detected in veins draining active areas of brain as well as in capillaries [22,23], and so may have a more limited spatial specificity than CBF- and CBV-based techniques. However, the sensitivity and specificity of BOLD signals can be enhanced by increasing the magnetic field strength and carefully optimizing the imaging pulse sequence parameters. The widespread and successful application of BOLD fMRI to human studies, the ease with which they can be performed, and the increasingly detailed understanding of the neurophysiological basis of the BOLD effect have ensured that most fMRI and phMRI experiments currently undertaken are based upon this approach.

MRI Origins of the BOLD Signal

Deoxyhemoglobin contains Fe^{2+} ions, which because of their unpaired outer electrons, exist in a high spin state, causing them to be paramagnetic. In contrast, oxyhemoglobin contains Fe atoms (having received electrons from oxygen atoms), giving them a low spin state and making them diamagnetic. Because hemoglobin is confined within blood vessels, gradient echo (GE) pulse sequences that are inherently sensitive to T_2* are able to detect changes in the relative concentrations of oxy- and deoxyhemoglobin [21,24]. In areas of active brain, an increase in glucose metabolism and O_2 extraction from blood is quickly followed by a larger fractional increase in rCBF, termed reactive hyperemia [13]. This increase in rCBF causes the net concentration of paramagnetic deoxyhemoglobin (which causes dephasing of spins and increases T_2* relaxation) to reduce, and the resulting T_2* BOLD signal correspondingly increases.

Some fMRI studies have reported detecting an initial decrease in T_2* signal within the first 1.5 s after the onset of stimulation which is associated with the initial increase in O_2 extraction that occurs prior to rCBF increasing. This signal decrease, termed the "initial dip," has been the cause of much excitement because of the potential gain in spatial specificity that imaging the initial dip (rather than the subsequent BOLD signal increase) would provide [25]. However, the failure of many laboratories to consistently observe the initial dip has made its existence controversial [26], and most fMRI studies rely on imaging the later, more robust BOLD signal increase. Imaging the initial dip is unlikely to be of practical value for most phMRI studies where stimulation periods following drug administration typically last for minutes or longer, rather than the transient neuronal activations more common to sensory and cognitive fMRI studies.

Physiological Origins of the BOLD Signal

Since the discovery of the BOLD effect and its application to functional neuroimaging, much work has been directed at understanding the hemodynamic and metabolic changes that underlie BOLD signals. A detailed understanding of the physiological basis for BOLD signals is particularly important for BOLD phMRI studies, where the drug under investigation may potentially interfere with the mechanisms that trigger BOLD signal changes. As neuronal activity rises, there is an increase in rCBF to provide additional O_2 and glucose to active areas of brain whilst facilitating the removal of waste metabolic products [13,27]. This increase in rCBF begins approximately 2.5 s after the increase in neuronal activity [28], the delay corresponding with the time taken for blood to travel from arteries to capillaries and veins. This increase in rCBF overcompensates for the extraction of O_2 from blood, causing the overall concentration of deoxyhemoglobin in local vessels to fall resulting in a corresponding rise in BOLD signal. In humans, BOLD signal increases typically reach a plateau between 4–12 s post-stimulation, depending on spatial location, type of stimulus, age and any existing pathology, and returns to baseline over a similar time period [29]. As BOLD signal changes arise from the susceptibility differences between deoxygenated blood and its surroundings, changes in venous blood volume (i.e. blood containing deoxyhemoglobin) and venous oxygenation levels are responsible for determining BOLD signal changes. Only venous blood volume (rather than total blood volume) affects BOLD signal, as arterial blood contains negligible amounts of deoxyhemoglobin [22]. Therefore, an increase in venous blood volume will decrease BOLD signal, whilst a decrease in venous deoxyhemoglobin concentration will increase BOLD signal.

rCBF, on which the BOLD response is dependent, increases in proportion to glucose consumption [27], which is in turn related to levels of synaptic activity [30,31]. Increased glucose utilization at active synapses may largely result from astrocytes recycling the neurotransmitter glutamate during excitatory neurotransmission, a process dependent on glycolysis producing energy from glucose but not requiring O_2. This may explain the proportional relationship between blood flow and glucose use in active brain areas (increased rCBF to supply extra glucose for glutamate recycling via glycolysis), and the discrepancy between blood flow and O_2 consumption: increased rCBF may supply glucose to astrocytes independent of blood oxygenation levels. However, recent investigations of the neurophysiological basis for BOLD signals have shown that metabolic and circulatory changes accompanying BOLD changes correlate closely with input into, and processing within areas of active brain, (i.e. synaptic activity), rather than reflecting spiking output of neurones [32]. Although spiking and synaptic processing may often be closely related, the amplitude of BOLD responses primarily reflect integration of pre- and post-synaptic processing [33]. Based on these findings, BOLD signal is therefore considered to reflect rCBF changes in the brain that are driven by synaptic signaling and related energy demands [11].

Although the basis for positive BOLD responses is now widely accepted, the process underlying sustained negative BOLD changes (as opposed to the initial dip) remain controversial. Several mechanisms for negative BOLD responses have been proposed, including reduced neuronal activity and O_2 extraction without a corresponding change in rCBF, a reduction in local rCBF independent of neuronal activity or a reduction in neuronal activity causing a controlled reduction in rCBF. Although the underlying mechanisms remain unknown, recent studies have shown that in human visual cortex, negative BOLD responses are temporally correlated with reductions in rCBF and local cortical O_2 consumption [34], suggesting that negative BOLD may reflect reductions in underlying neuronal activity.

BOLD signal changes can therefore be ascribed with confidence to changes in neuronal activity. However, the exact mechanisms whereby changes in neuronal activity mediate changes in rCBF remain unknown, with various possible mechanisms having been proposed. It is possible that lactate released from astrocytes during glycolysis might trigger an increase in rCBF, which would link cerebral hemodynamics closely with synaptic activity [35]. Alternatively, a quickly diffusible product of neuronal activity, e.g. nitric oxide, may be released during spiking activity, a possibility supported by reduced rCBF increases after administration of nitric oxide synthase inhibitors [36]. rCBF changes may also be directly coupled to changes in blood oxygenation levels, reacting to the "initial dip" in oxyhemoglobin levels [35].

Image Acquisition Strategies for Preclinical phMRI

Most human fMRI datasets are now acquired using Echo Planar Imaging (EPI) sequences, permitting the acquisition of an entire brain volume in 1–4 s. As animal phMRI studies usually involve measuring slowly evolving changes in signal that occur over tens of seconds or several minutes and persist for some time (depending on the route of drug administration and pharmacokinetic considerations), they do not require such rapid imaging. Therefore it is often preferable to use conventional GE (e.g. Fast Low Angle SHot, FLASH) or T_2-weighted spin echo (SE) sequences rather than EPI acquisitions. A single, whole brain volume is typically acquired over 40–120 s, with numerous volumes being continuously acquired for up to several hours, depending on the duration of drug action and anesthetic regime. Voxel size is much smaller than that in human imaging, typically being in the region of 0.5 mm in each plane, although smaller voxel sizes are possible at the cost of longer image acquisitions. To improve the spatial specificity of BOLD fMRI signals, it is desirable to minimize the venous contribution to BOLD signals, and this can be done by a careful choice of pulse sequence parameters. In particular, GE and SE pulse sequences differ in their relative sensitivities to venous blood vessels.

SE and GE BOLD Imaging

BOLD signal from deoxyhemoglobin has intravascular (IV) and extravascular (EV) components from both small and large vessels [22,37], and the exchange of water molecules between these compartments is slow (greater than 500 ms) in comparison to the imaging time (TE less than 100 ms). MR signals arising from each compartment can therefore be considered separately. EV effects result from the dephasing of spins induced by field inhomogeneities around vessels containing paramagnetic deoxyhemoglobin, creating a magnetic field gradient which is more spatially extensive for larger vessels (i.e. veins). The IV component exists because the deoxyhemoglobin content influences the T_2 and T_2* of blood, as well as the surrounding tissue. Both IV and EV effects contribute to GE BOLD fMRI signals, but SE pulse sequences are able to reduce the EV signal arising from large vessels. Because water molecules are able to diffuse within the small areas of susceptibility around capillaries during imaging (TE typically being less than 50 ms), and have a large net displacement, their effects are "dynamically averaged" during a TE and produce no net phase change. However, water molecules can only diffuse within a small part of the greater area of susceptibility surrounding larger vessels, having a smaller net displacement, and so are "locally averaged" during each TE [38]. This allows the EV dephasing effects around large diameter vessels to be refocused by a 180° RF pulse during a SE sequence, whilst the dephasing around smaller diameter vessels remains unaffected due to dynamic averaging. Such refocusing of dephasing around large diameter vessels means that SE BOLD sequences minimize the EV contribution of large venous vessels (whilst continuing to be sensitive to the IV contribution of all vessels and the EV effects of capillaries) and so maximize spatial specificity [39]. GE BOLD signals consists of the IV and EV contribution of all venous vessels, and are therefore more susceptible to the effects of veins draining areas of activated tissue. The removal of EV effects means SE sequences are less sensitive and have lower maximum signal changes than GE sequences, as well as having a lower temporal resolution due to longer imaging times [39]. For these reasons, GE BOLD is often used in preference to SE BOLD because of its higher sensitivity and temporal resolution, and lower RF power deposition within tissues, although BOLD-based animal phMRI studies have been successfully performed using both GE [40,41] and SE [42] approaches.

Effects of Magnetic Field Strength

The strength of the static magnetic field has important effects on the BOLD signal detected by GE sequences. The intensity of GE BOLD signal increases with field strength [43], making fMRI studies at higher fields increasingly popular. In addition, the field gradient around capillaries is greater at higher static magnetic fields, making BOLD signal more closely coupled to neuronal activity [44]. However, GE imaging, particularly non-EPI, FLASH-based sequences are susceptible to inflow effects caused by fresh (fully recovered) spins in blood moving into regions excited under T_1 saturation conditions that occur during rapid imaging. These effects are more apparent at short TR values and large flip angles [39] and can be minimized by reducing flip angles and increasing TR.

Considerations Particular to phMRI

The nature of the BOLD signal as a secondary marker of neuronal activity, combined with continuing uncertainties surrounding the way in which neuronal activity, rCBF, and rCBV are coupled together, pose particular problems when planning and interpreting the results of phMRI experiments. Due consideration must be given to the effects that drugs may have on the cerebrovasculature and those mechanisms that give rise to the BOLD signal. It is possible that a drug of interest may act directly on receptors located on the cerebral blood vessels and so alter rCBF independently of any changes in underlying neuronal activity. Alternatively, the neurochemical processes that couple neuronal activity with blood flow may become disrupted. As animals are anesthetized and unconscious for the duration of the experiment, careful monitoring is needed to ensure maintenance of stable physiological parameters. Typically, heart rate, blood pressure, respiration, and temperature are recorded, and animals may be artificially ventilated to maintain stable respiratory and blood gases. It has previously been demonstrated that BOLD signals can be altered by increasing $paCO_2$ levels during CO_2 inhalation [45], and that spontaneous fluctuations in end tidal CO_2 correlate with changes in BOLD signal in both gray and white matter in human volunteers [46]. Elevated $paCO_2$ levels cause cerebral blood vessels to dilate, producing a global increase in BOLD signal that can eventually rise to such an extent that blood vessels are no longer able to dilate in response to increased neuronal activity. Administering heroin to spontaneously breathing rats has been shown to cause a global decrease in BOLD signal, thought to result from the respiratory depression induced by heroin [47]. However, when is given to rats being artificially respirated, BOLD signal increases are restricted to those brain regions containing a high density of μ opioid receptors [47]. This effectively demonstrates how the systemic effects of a drug can subsume any neuronally induced changes in BOLD signal. For this reason, the monitoring and regulation of respiration and $paCO_2$ levels during animal fMRI and phMRI experiments are crucial to ensuring the validity of observed BOLD signal changes.

Many experimental drugs also induce changes in systemic blood pressure that may alter CBF and thus BOLD signal. Although small, gradual reductions in blood pressure of the order of approximately 1 mmHg/min are known to have no significant effect on BOLD signal [48], when the blood pressure of rats is rapidly and significantly reduced by controlled withdrawal of arterial blood, a heterogeneous pattern of statistically significant reductions in BOLD signal is observed within the brain that follows the same time course as the decrease in blood pressure [49]. Thus any large, rapid fluctuations in blood pressure that follow drug administration represent a potentially serious confound for phMRI, and since the patterns of BOLD signal change induced by such alterations in blood pressure are not globally uniform, assessing and eliminating these effects may prove difficult. The close monitoring of blood pressure and subsequent testing to ensure the time course of blood pressure and BOLD signal changes are not correlated are crucial to ensure that valid inferences are made from phMRI experiments.

During human phMRI studies, the potential confounding effects of the drug on neurovascular coupling can be assessed by examining the effects of a drug on the BOLD response to well-characterized cognitive or sensory tasks. For example, a finger-tapping task has been used to demonstrate that the dopaminergic agent methylphenidate does not alter baseline signal or task-induced BOLD signal changes in the motor cortex, and so provide assurance that any experimentally-induced changes in cortical BOLD signal resulting form methylphenidate administration are not due to any direct systemic or vascular effects of the drug [50]. The opportunities for using similar approaches are more limited in phMRI experiments using rodents and other experimental animals. Although it is possible to examine modulations of the cortical BOLD response to basic sensory stimuli such as forepaw stimulations, those brain regions expected to respond to such a stimulus may not contain a high density of receptors for the neurotransmitter system of interest, and cerebral blood vessels in such regions might not necessarily be affected by the administered compound. It is therefore particularly desirable that as much physiological information as possible is collected simultaneously during imaging, with variables such as expired CO_2 levels being controlled by artificial ventilation whenever feasible. In addition, it is important to have some appreciation of the known or potential effects that a drug may have on the cerebrovasculature. The possibility of non-specific changes in BOLD signal during phMRI experiments has meant that collecting additional measures of brain activity such as those provided by electrophysiology or microdialysis are becoming increasingly important, particularly when validating the results of initial phMRI experiments involving previously untested drugs. It may also be desirable to use alternative imaging sequences before and after drug administration to assess any generalized changes in CBV and CBF to further validate the exact nature of any observed changes in BOLD signal, particularly when potentially confounding changes in physiological parameters are also observed.

Validating phMRI Experiments

One of the first studies to demonstrate the usefulness of BOLD imaging for measuring the effects of dopaminergic compounds in the brain of rats was performed in 1997 by a group at the Massachusetts General Hospital [7]. By examining the BOLD response to amphetamine and the radiolabeled dopamine transporter antagonist CFT, and additionally using PET and microdialysis to measure dopamine receptor binding and dopamine release, BOLD signal changes were shown to correspond with PET measures of dopamine transporter levels, and the time course of BOLD signal and dopamine release were found to closely correlate, and be temporally unrelated to changes in $paCO_2$, heart rate, or blood pressure. In addition, animals were prepared with unilateral 6-hydrodydopamine lesions to the striatum, and the extent of rotational behavior demonstrated by individual animals in behavioral studies (which is related to dopamine release) was shown to correlate with the magnitude of the observed BOLD signal response. By combining phMRI, PET, microdialysis and behavioral measures, this study provided an early validation of the use of BOLD fMRI to study the mechanism of drug action and demonstrated the way in which effective control conditions and study design can be used to overcome the potential confounds associated with phMRI.

The well-described effects of cocaine and related compounds on heart rate and blood pressure, and the potentially detrimental effects of such systemic changes on phMRI measures, have made validating the results of phMRI studies using cocaine important in testing the robustness of the phMRI technique [7,9]. The possibility of using phMRI to investigate drugs that have cardiovascular side effects was effectively demonstrated by a study comparing the effects of cocaine and its non brain-penetrant quaternary analog, cocaine methiodide [51]. Whilst both compounds increased heart rate and blood pressure, cocaine methiodide produced only small, scattered, and transient increases in brain BOLD signal, independent of drug dose. In contrast, cocaine increased BOLD signal within limbic brain regions in a dose-dependent fashion, as well as increasing systemic blood pressure. The effects of cocaine on blood pressure therefore appear to have had little confounding effect on drug-induced BOLD signal within the brain. Recent studies have continued to use cocaine as a prototype for validating phMRI. Experiments combining CBV-based phMRI measures and microdialysis have shown that dopamine release and rCBV changes have different temporal profiles in the striatum and medial prefrontal cortex, and that observed increases in rCBV within the motor cortex are independent of any changes in dopamine release [52]. This effectively demonstrates that the phMRI response to cocaine in these regions cannot be a direct result of increased levels of dopamine release acting directly on cerebral blood vessels, but is instead likely be a true reflection of underlying changes in neuronal activity. Combining phMRI with additional measures such as microdialysis not only helps to prove that phMRI experiments are indeed detecting changes in brain activity, but are also of value in helping to understand the relationship between phMRI responses to drugs and changes within individual neurotransmitter systems and brain circuits. In another recent study, the confounding peripheral effects of cocaine were circumvented by injecting the drug directly into the brain of awake animals during phMRI experiments [53]. The resulting increases in BOLD signal within limbic and cortical brain regions, combined with an absence of concomitant changes in heart rate or blood pressure, not only support the findings of previous phMRI studies using cocaine as being genuine reflections of changes in neuronal activity, but also demonstrate the feasibility of using direct injection techniques with phMRI measures to overcome either the confounding peripheral effects of drugs under investigation, or problems with brain penetrability. However, further difficulties with this approach may arise when changes in intraventricular signal arise from injection of fluid into the brain rather than from activity-dependent changes in BOLD signal.

It is also possible to combine the *in vivo* measures of drug-induced neuronal activity provided by phMRI with *ex vivo* measures. For example, variations in the phMRI response to diazepam in the frontal cortex of high and low anxiety behavior rats has been shown to correspond with differences in the number of neurones expressing the immediate early gene *c-fos* in animals with different phenotypes following exposure to environmental stressors [54]. Combining phMRI with other *in vivo* and *ex vivo* techniques such as microdialysis, autoradiography, and measures of gene expression is likely to become increasingly common as phMRI experiments become more sophisticated and are required to provide information concerning not only those brain regions that respond to a given drug, but also the mechanisms underlying the observed response.

Effects of Anesthesia

Animal fMRI experiments, especially those involving rodents, usually require the use of an anesthetic to immobilize the animal for the duration of the study. Whilst anesthesia minimizes motion artifacts during imaging and limits the confounding effects of stress caused by the scanning environment, the effect of anesthesia on normal neuronal functioning is clearly a problem. Whereas blood pressure and $paCO_2$ levels can be monitored and to some extent controlled for, the effects of anesthesia cannot be easily controlled. Although counter-intuitive that neuronal responses should remain detectable in an anesthetized state, responses to both sensory and pharmacological challenges have now been repeatedly demonstrated in anesthetized animals. However, anesthetic agents are known to affect both cerebral blood flow [55] and cerebral metabolism [56]. As such, careful consideration must be given to the choice of anesthetic before undertaking such studies. Animal fMRI studies have been conducted using a variety of anesthetic agents, ranging from inhalation anesthetics like halothane and isoflurane [7,32] to injectable anesthetics like α-chloralose [57] and urethane [40]. As experience of using different anesthetic agents in fMRI and phMRI has been gained, attempts have been made at understanding whether any of the effects on particular neurotransmitter systems are anesthetic-specific, and would make particular anesthetics more or less suited to certain applications such as sensory fMRI or phMRI. The largely unknown mechanism of action of most anesthetic agents, combined with a lack of information with regards to those neurotransmitter systems affected by different agents, has made predicting the effects an anesthetic may have on the outcome of a phMRI experiment difficult. In addition, many anesthetics may also act in a species-specific fashion.

Injectable Anesthetics

One of the most widely used anesthetics in animal fMRI is the injectable agent α-chloralose. Its popularity is largely due to it being thought to preserve functional metabolic coupling within the cortex and maintain stable cardiovascular parameters [58], whilst causing only minimal depression of autonomic functioning [59,60]. α-chloralose also permits greater increases in rCBF within the sensory cortex in response to peripheral sensory stimulation than barbiturate or halothane anesthesia [61]. Although α-chloralose has been widely used and cited within literature as a suitable anesthetic for *in vivo* studies on brain functioning and rCBF, it is known to have depressive effects of animal physiology, e.g. respiratory depression with prolonged anesthesia [59], and it may be desirable to use artificial respiration when using α-chloralose to prevent respiratory depression and associated confounding changes in $paCO_2$ levels. The popularity of α-chloralose in early sensory animal fMRI studies [57], combined with the long-lasting and stable anesthetic state which it produces, have made it a natural choice for many phMRI investigations. In our laboratory, α-chloralose has been successfully applied to phMRI studies of dopamine D_2/D_3 receptors agonists, and it has also been used to examine the effects of the D_2 receptor antagonist sulpiride [62], as well as the NMDA receptor antagonist MK-801 and the 5-HT_2 receptor agonist mCPP [63]. Some controversy exists as to the suitability of α-chloralose for phMRI studies of the dopamine system as it may suppress dopamine release [64] and has been shown to prevent CBV responses to the indirect dopamine agonist cocaine which can be detected under halothane anesthesia [9]. Another injectable anesthetic, urethane, has also been exploited for animal phMRI studies because of its ease of use and long-lasting and stable anesthetic state, and has been successfully applied to studying precipitated withdrawal from both opiate [40] and nicotine [41] dependent states, as well as the effects of tolerance following heroin self-administration [65]. Chloral hydrate, which like urethane is administered intraperitoneally, has also been used in phMRI experiments to investigate the cannabinoid agonist HU201 [42].

Inhalation Anesthetics

Inhalation anesthetics like halothane and isoflurane have also been successfully applied to animal fMRI and phMRI studies. Halothane has proved particularly popular for studying the effects of dopaminergic ligands, having been used to examine the effects of cocaine and related ligands in several different laboratories, with comparable changes in BOLD or rCBV being reported within limbic and striatal regions as well as the frontal cortex [7,9,52,66,67]. In a similar fashion, isoflurane has also been used in studies of the $GABA_A$ antagonist bicuculline in mice [68]. A comparison of the effects of apomorphine in awake rhesus monkeys with those anesthetized using isoflurane showed that whilst BOLD signal increases were observed throughout the basal ganglia in awake animals, they were restricted to the substantia nigra in anesthetized animals, where the magnitude of signal increase was considerably diminished compared to the awake condition [69]. Halothane has similarly been shown to diminish the BOLD phMRI response evoked by the NMDA receptor antagonist MK801 when compared with a combination of fentanyl/fluanisone/midazolam injectable anesthetic agents [6]. Such confounding changes in CBF are in addition to the effects the anesthetic may have on basal and evoked neuronal activity. Studies in our laboratory have shown that whilst activation of the sensory cortex is easily and repeatedly observed following electrical stimulation of the rat forepaw using α-chloralose, such responses are completely abolished when using even minimum levels of isoflurane. This reduced ability to detect changes in BOLD signal under isoflurane anesthesia is likely to be caused by the effects of isoflurane on the regulation of rCBF. Isoflurane dose-dependently increases rCBF in most brain structures in Sprague Dawley rats [70,71,72], with some regions showing an increase in local rCBF of up to 238% [70]. Perfusion-weighted MRI has shown that isoflurane not only dose-dependently increases rCBF in rats, but also suppresses cerebrovascular reactivity and reduces the magnitude of both rCBF and BOLD signal increases to hypercapnia following CO_2 challenge [73]. In addition, isoflurane has also been shown to blunt the fMRI response to both noxious and non-noxious somatosensory stimuli [74]. As BOLD signals depend on the modulation of rCBF within active areas of brain [21,13], any increase in rCBF that is unrelated to changes in neuronal activity may confound both the evolution of the BOLD response (if rCBF is already raised it may not need to increase further to supply active brain regions) and the ability for any increases to be detected using fMRI (by reducing vascular reserve). Careful consideration needs to be given to the choice of anesthetic prior to beginning a phMRI study, with bench testing needed to ensure that the chosen anesthetic agent is used at the minimum ethically acceptable level. Where possible, it should also be ascertained that the neuronal systems of interest remain responsive under the chosen anesthetic using measures like microdialysis or electrophysiology. Cross correlation of phMRI results using different anesthetic agents is also important when validating animal phMRI studies, but given constraints on time and resources, repeating phMRI experiments using different anesthetics may not always be a practical option.

PhMRI in Awake Animals

Although to date most animal phMRI studies have been performed under anesthesia, several groups have demonstrated the possibility of imaging awake animals following a period of training. This approach was successfully applied using rhesus monkeys to examine the effects of the non-specific dopamine agonist apomorphine and showed the severe blunting of the phMRI signal that occurs when using isoflurane [69]. Conscious rabbits have also been trained and adapted to the scanning environment and have been used to examine the effects of the dopamine antagonist sulpiride [75]. Several studies have reported the results of phMRI experiments in conscious rats, where animals are restrained, often following the surgical attachment of bolts to the skull to allow secure positioning within an MR-compatible headframe. Such imaging of conscious rats has been used to assess the effects of interaction between the dopamine D_2 receptor agonist bromocriptine and the D_2 receptor antagonist haloperidol [8], determine the sites of action of the endogenous cannabinoid anandamide [76] and most recently, to examine the effects of intracerebroventricular cocaine administration [53]. Although imaging awake animals has clear benefits in terms of avoiding the confounding effects of anesthesia on drug-induced brain activity, other factors, including greater movement artifacts, training time, cost and ethical implications have precluded a more widespread application of this approach. In addition, accounting for the confounding effects of stress during the imaging experiment may prove as difficult as identifying the likely effects of anesthesia on drug-induced neuronal activity.

Data Analysis

Considerable effort has been devoted over recent years to developing standardized techniques for the analysis of BOLD fMRI data. One of the most widely used analysis tools is Statistical Parametric Mapping or SPM (http://www.fil.ion.ucl.ac.uk/spm), originally developed for the analysis of human PET and subsequently fMRI studies which we have now extended to animal fMRI and phMRI studies [40,41]. The use of SPM and similar standardized approaches for data analysis is becoming increasingly popular as animal fMRI and phMRI techniques become more widespread, replacing more parochial data analysis tools that may lack the statistical flexibility and support of more widely used software that has been validated within the peer-reviewed literature. Using freely available software like SPM for data analysis not only enhances the statistical rigor of analytical methodology but also allows the results from different experiments and laboratories to be more easily compared and reproduced.

Image Pre-processing

Data analysis software packages currently available, like SPM, AFNI (http://afni.nimh.nih.gov/afni), and FSL (http://www.fmrib.ox.ac.uk/fsl), now have a common approach to most image pre-processing steps and subsequent statistical analysis. Rather than relying on results obtained from individual subjects, typically data from groups of subjects are analyzed together in order to both improve statistical power and make inferences about the generic response of the population under investigation. Prior to statistical analysis, fMRI data must undergo considerable pre-processing. To perform voxel-based analysis, data must be placed in the same anatomical frame of reference, and the first stage in achieving this is spatial realignment. Subject movement during imaging causes a change in voxel signal intensity unrelated to experimental conditions, which represents a potential confound in data analysis. Even sub-voxel movements introduce unmodeled noise in the data, causing artifactual "activations" at tissue edges and reducing signal-to-noise within images. To minimize these effects, a realignment algorithm moves images to the same common space, ensuring that a single voxel will represent the signal intensity from tissue in the same position throughout the experimental time series. To perform group analysis of data from different subjects, variations in brain architecture between subjects must also be accounted for before comparisons of similar brain regions can be made. Most fMRI analysis software transform each subject's brain into a common reference space in order to minimize neuroanatomical differences between subjects prior to analysis. Within SPM99, this process warps images to a standard brain template by applying a 12 parameter affine transformation to determine the minimum deformation needed to minimize differences in global shape between the subject's brain and the template, whilst attempting to preserve spatial relationships between intracerebral structures [77,78]. Many of the difficulties associated with coregistering the brain anatomy between different subjects, a step crucial to allowing the implementation of group statistics, are minimized when using in-bred, age, and weight matched animals in preclinical investigations. The final pre-processing step involves using Gaussian filter kernels to spatially smooth data, which effectively lowers the resolution compared to that of the "raw" data. Gaussian smoothing improves the signal-to-noise ratio of data (a measure of the size of the signal of interest compared to the random background noise which is present without stimulation), and aids the detection of "activations" which are similar in size to the smoothing kernel (particularly important if high resolution data are acquired and widespread regions of activation are anticipated). When performing group analysis with data from multiple subjects, smoothing also helps to remove any remaining differences in neuroanatomy between subjects after spatial normalization and increases the likelihood of detecting activations across groups of subjects. Most importantly, SPM99 and other analysis packages involve an implementation of Gaussian Random Field theory to control for the effects of making multiple comparisons during statistical analysis, and spatial smoothing data ensures the validity of subsequent statistical inferences.

Global Effects and Fluctuating Baseline Signal Intensity

Analysis of BOLD fMRI data to produce statistical maps of changes in neuronal activity is non-quantitative, involving the comparison of experimentally induced changes to a known baseline. The baseline MRI signal however fluctuates over time, even in the absence of experimental manipulation, due to factors such as those originating in hardware (scanner drift), physiological changes like variations in the level of anesthesia, $paCO_2$, or blood pressure which affect global perfusion levels, movements from respiration and heartbeat [79], and potential creation of intermittent imaging artifacts [80,81]. The presence of such fluctuations in baseline signal intensity presents a problem when analyzing data, and may be particularly pertinent to phMRI where the physiological effects of a drug may produce substantial global signal changes. Unlike signal changes resulting from "activations," baseline signal fluctuations have no regional specificity, being termed global confounds. Over the course of an experiment, such global effects may be larger than any experimentally induced BOLD signal change and measures need to be taken to estimate and account for such effects when analyzing fMRI data. To try and remove or account for global effects, they are assumed to be independent of experimental manipulations, with regionally specific, experimentally induced changes in signal intensity considered as being superimposed upon global changes. Typically, global effects are estimated from the temporal profile of all intracerebral voxels, each of which is then scaled to a common value (proportional scaling) to produce a flat baseline mean signal intensity value. Alternatively, the global signal intensity may be included as a covariate of no interest within the General Linear Model analysis in addition to, or instead of, proportional scaling, an approach known as ANCOVA [80]. These methods of controlling for global effects become problematic when experimentally-induced signal changes are large, and there is a resulting correlation between global signal changes and localized signal changes of interest. Specifically, scaling of data containing large, experimentally-induced signal increases may produce artifactual signal decreases in areas of the brain which did not previously have any change in signal intensity and vice versa. Where regional, experimentally-induced signal intensity changes are large, it may be preferable to omit proportional scaling and instead look at absolute changes in signal intensity, providing regional changes large enough to be apparent over and above a fluctuating baseline. The inclusion of global signal change as a covariate of no interest within the statistical model (ANCOVA) when it does not co-vary with the experimental manipulation has only quantitative effects on the resultant statistical maps, increasing the significance of observed changes by reducing error within the model. However, when such a covariate correlates with the experimental model (and so becomes a confound rather than a nuisance variable), this may change the interpretation of results in both a qualitative (changing the sign of relationships) and quantitative (changing the significance of relationships) fashion. Alternative measures of baseline signal intensity can also be derived from regions known to be unaffected by experimental conditions e.g. muscle [81] or white matter, which are then used to estimate baseline fluctuations and either scale mean signal intensity accordingly or provide an estimate of global effects for inclusion within GLM analysis. Estimating and controlling for global changes in signal intensity is equally important for CBV-based phMRI studies, where clearance and/or recirculation of the exogenous contract agent over the course of the experiment can produce large global signal intensity fluctuations.

Statistical Analysis

Statistical analysis is performed to identify those voxels responding to experimental manipulation. Typically, univariate analysis is used involving the time series of each voxel being analyzed independently from all others (voxel by voxel analysis), as opposed to multivariate analysis, where spatial relationships within the data are also considered. SPM99 is a univariate model-based analysis: a model of the expected response (e.g. response to periods of stimulation, concentration of pharmacological agent, or known behavioral covariate) is fitted to the data, and if a good fit between the model and data results then changes within the data are considered likely to result from the experimental manipulation [77]. Such a test is performed independently at each voxel. This is alternatively known as analysis of covariance or multiple regression and is based on the General Linear Model. The final output from such an analysis is a statistical map of the group BOLD signal response, with each voxel representing the statistical significance of a particular region under the hypothesis being tested.

Modeling the BOLD Response to Drugs

Data analysis packages based upon the General Linear Model require that changes within the data be measured and tested against a model of the expected BOLD signal response to the experimental condition. In conventional human fMRI studies, an experimental stimulus or cognitive task is often presented at set intervals and this serves as an initial, idealized model for analysis. Some human phMRI studies use a variation on this approach, where a drug is administered and the effects on patterns of activation occurring in response to a repeated stimulus or task are measured. Unless the purpose of the experiment is to investigate drug-induced modulations of a basic sensory stimulus, for most animal phMRI studies this approach is not feasible. Instead, investigations are aimed at assessing the direct consequences of drug administration on baseline patterns of neuronal activity. Whilst this approach is difficult in humans due to problems in creating a “behavioral clamp” which controls the basal level of brain activity over the course of the experiment, it is less of a concern when using anesthetized animals. However, difficulties arise when choosing a suitable model of the expected drug response for data analysis and several approaches exist for producing such models. The most basic of these involves comparing all pre-injection images with those collected after the drug has been administered. This is most suitable for compounds known to have a rapid onset of action and the effects of which persist for the duration of the experiment. Drawbacks of using a simple “off/on” model are that any regions of the brain that show rapid or transient changes in activity may remain undetected as detailed temporal information is lost. In addition, any slowly occurring linear changes within the data (such as scanner drift, or “colored,” physiological noise) may correlate well with a simple “off/on model” and produce signal changes within the data that closely correlate with the model, producing spurious patterns of activation and deactivation. Using drugs with a short duration of action allows repeated injections in a randomized fashion, but may cause problems in terms of diminished effect of drug with repeated challenges and possible confounding physiological changes associated with i.v. drug administration.

A more sophisticated approach to phMRI data analysis involves using known pharmacokinetic or pharmacodynamic parameters against which to model drug-induced changes in BOLD signal. The use of pharmacokinetic models was demonstrated using a Waveform Analysis Protocol (WAP) based on single dose pharmacokinetics to examine the acute effect of nicotine in humans [82]. By producing an idealized BOLD signal response to nicotine based upon its known pharmacokinetic profile, this WAP was applied to the imaging data and comparisons made between the time and rate of onset of drug action, time-to-peak, and duration of response to determine whether observed changes following drug administration match with the pharmacokinetics of nicotine. This approach assumes that the concentration of drug within the peripheral circulation will be equivalent to that in the brain (which is true for short-acting, highly lipophilic compounds such as cocaine and nicotine), and that drug-induced changes in brain activity will reflect drug concentration within the brain. One of the major advantages of this approach compared to simple “off/on” comparisons is that the gradual drift in MRI signal over time commonly observed during fMRI experiments will not correlate with the modeled response as it will be both too slow and will not rise then fall over time, unlike the blood concentration of a short-acting drug. This approach has been developed further by combining a pharmacokinetic model of the short-acting analgesic remifentanil with a repeated, painful stimulus to examine pain processing within the brains of human volunteers [83]. Although to date pharmacokinetic-based approaches to phMRI analysis have been mostly been performed in humans, this method is equally valid for animal phMRI studies, where a lack of cognitive or sensory paradigms that can be used to assess drug-induced modulations in brain activity make pharmacokinetic modeling particularly attractive.

In a similar way, pharmacodynamic changes such as the effects a drug has on behavioral measures like locomotor activity, or alternatively known changes in neurotransmitter release, can also be used as models for data analysis. This approach can be particularly useful where a drug has more than one effect with differing time courses, and can help identify those areas of the brain that are responsible for mediating such changes. As it is likely that the temporal response between brain regions will differ, using a variety of different models helps ensure that as much detailed information as possible concerning regionally specific drug effects is extracted from a given dataset. Our laboratory has pioneered this approach to phMRI data analysis for experiments designed to investigate the mechanism of action of dopamine agonists in the rat brain.

Using Dopamine Receptor Agonists as Prototypical Agents for Animal phMRI

We have examined BOLD responses to the D_2/D_3 receptor agonist quinelorane as a means of both further characterizing the mechanisms of action of this particular compound, and also as a means of evoking a response in phMRI experiments in order to optimize, refine, and better understand the phMRI technique itself. Although a variety of agents exist that are agonists at D_2-like receptors, quinelorane is highly potent at both D_2 and D_3 receptors and has a very low affinity for other dopamine and non-dopamine receptors [84–89]. The highly potent and selective nature of quinelorane, combined with its ability to evoke behavioral responses at sub-milligram doses, minimize the likelihood of non-neuronal or confounding drug effects occurring that may become evident when higher doses of less specific agents are used, and as such makes it an attractive agent for use in phMRI studies.

Imaging Protocol

A typical phMRI experiment involves examining the BOLD response to a 30 μg/kg dose of quinelorane, which in awake animals induces a biphasic change in locomotor activity that persists for several hours. Prior to imaging, rats are anesthetized with isoflurane to facilitate the cannulation of a tail vein, after which anesthesia is switched to intravenous α-chloralose at a dose of 60 mg/kg/h. Animals are then imaged using a conventional FLASH gradient echo sequence, with quinelorane being administered by subcutaneous injection half way through the imaging experiment. Heart rate, blood pressure, and temperature are all continuously monitored to ensure animals remain physiologically stable during the experiment and that there are no significant effects of drug administration on any measured physiological parameters. Subsequently, images are then analyzed using SPM99 software: following image realignment and spatial normalization to a customized rat brain template, several different strategies can then be applied to subsequent statistical analysis.

Data Analysis

We present data here that illustrates the BOLD phMRI response to 30 μg/kg quinelorane as determined using three different approaches to data analysis. In the first example, a simple comparison between pre- and post-injection scans (“off/on” model) was used to assess the main effect of the drug, an approach that has been used several times previously for analyzing phMRI data [4,90]. As the behavioral effects of quinelorane persist for longer than the duration of the imaging experiment, a comparison of pre- and post-injection scans is a suitable method of assessing the BOLD signal change evoked by this particular compound. A second approach involved producing a pharmacokinetic model of the temporal dynamics of quinelorane blood concentration (Figure 2). As quinelorane is lipophilic, with good brain penetrability [91,92], this approach assumes a good correlation between blood and brain drug levels and that BOLD signal changes will relate directly to the concentration of drug present in the bloodstream at any given time. A third method used pharmacodynamic models based upon the effects of quinelorane on locomotor behavior in awake animals (Figure 4). Two behavioral covariates were produced: the first was created using counts of mean locomotor activity after administration of quinelorane, and the second created using the same data after additionally subtracting locomotor activity in control animals given saline vehicle injections.

Effects of Different Models

As might be expected when using a highly selective D_2/D_3 receptor agonist compound, the pattern of quinelorane-induced BOLD signal changes visualized after comparing pre- and post-injection images (Figure 1) closely resembles the distribution of D_2 and D_3 receptors within the rat brain. High levels of D_2 and D_3 receptor mRNA and D_2/D_3 receptor ligand binding are present within the olfactory nuclei, olfactory tubercle, islets of Calleja, nucleus accumbens, and caudate-putamen [87,93–97], which closely correlates with the pattern of neuronal activation detected following quinelorane administration.

Pharmacokinetic Modeling

Creating a pharmacokinetic model from quinelorane blood concentrations and using it as a model of the expected change in BOLD signal (Figure 2) creates an SPM map that is remarkably similar to that produced using an “off/on” model, with the anterior olfactory nuclei, nucleus accumbens, and caudate-putamen being similarly activated when using both approaches (Figures 1 and 3). The statistical significance of the observed activations is

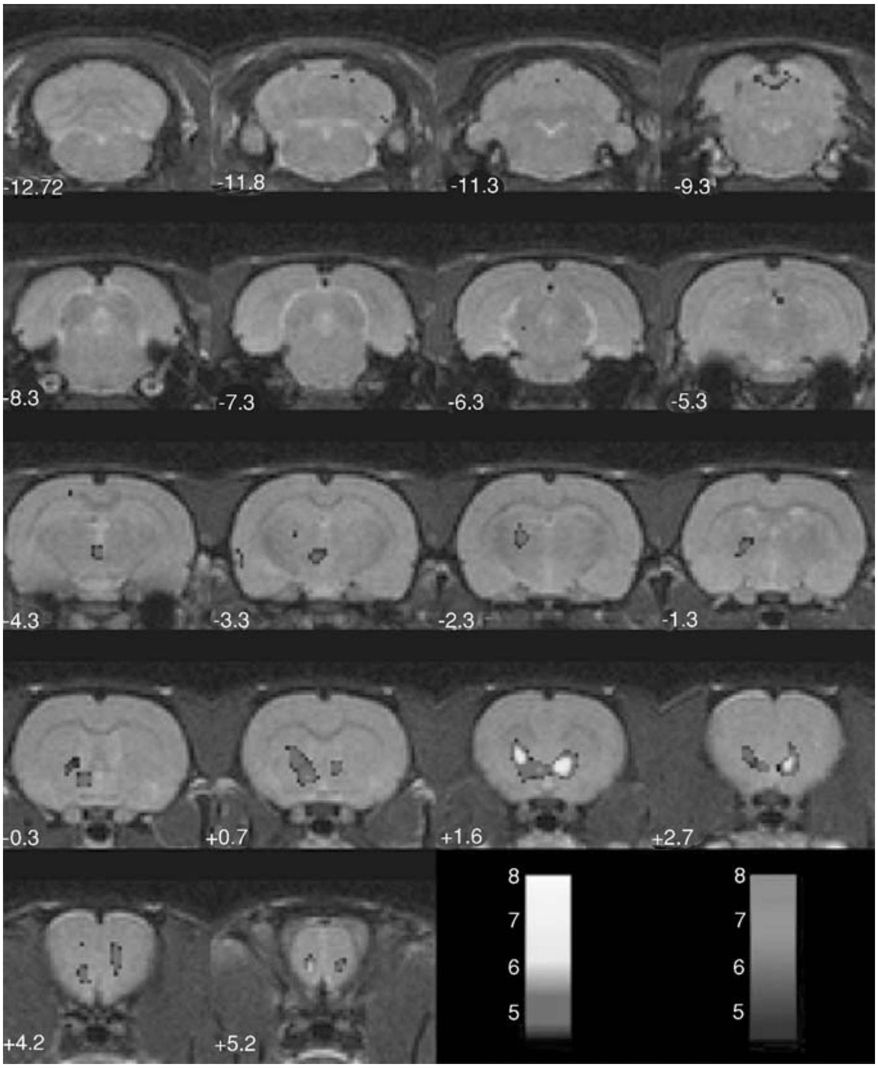

Fig. 1. Group statistical parametric map showing significant changes in BOLD contrast after administration of 30 μg/kg quinelorane ($n = 5$), testing for differences between pre- and post-injection scans. Color scales represent T scores of significant increases (red < yellow) and decreases (blue < green) in BOLD signal, where $T > 4.5$, $p < 0.05$, corrected for multiple comparisons. Activation maps are overlaid on a T_2-weighted spin echo anatomical image, with each contiguous slice being 1 mm thick and moving rostrocaudally through the brain from bottom right to top left, with approximate co-ordinates relative to Bregma [108]. (See also Plate 75 on page L in the Color Plate Section.)

also similar with both models. This suggests a significant correlation between the time course of changes in blood quinelorane concentration and the observed BOLD signal changes in activated regions and that there may be a direct link between the level of activity in these brain regions and the amount of drug present within the blood.

Behavioral Modeling

Using a model based on the biphasic locomotor effects of quinelorane that takes no account of changes in the behavior of control animals (Figure 4, blue curve), produces SPM maps that are almost entirely devoid of statistically significant changes in BOLD contrast (Figure 5). However, in contrast to the results produced using either

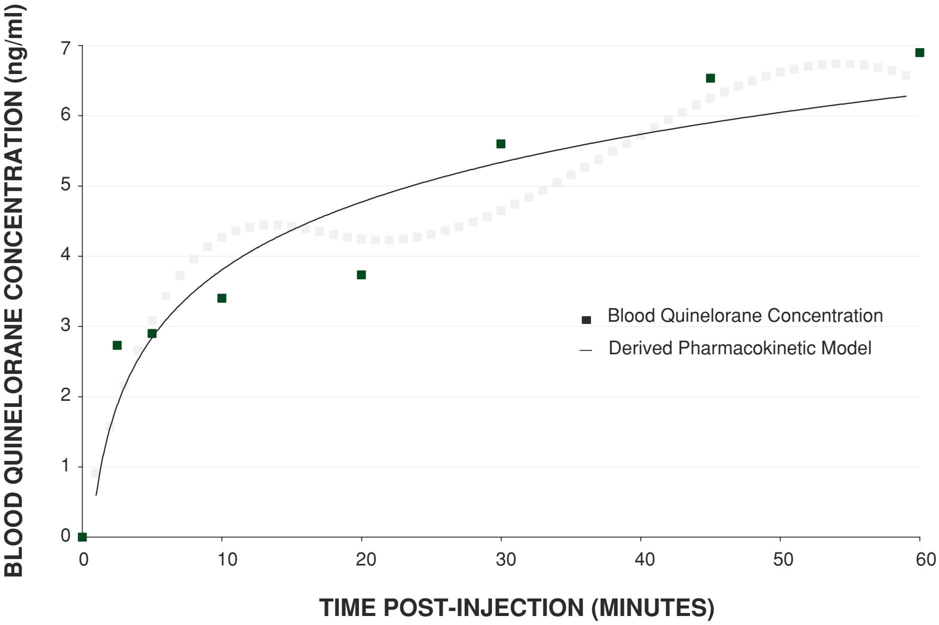

Fig. 2. Mean blood quinelorane concentration following administration of 30 μg/kg quinelorane ($n = 3$) (solid squares) and derived pharmacokinetic model after interpolation of blood quinelorane levels (solid line).

the "off/on" or pharmacokinetic models, small bilateral increases in BOLD signal were noted in the entorhinal cortex and posterior piriform cortex and small bilateral decreases in BOLD signal were present within the nucleus accumbens. The lack of statistically significant BOLD signal changes using this model is likely to be due to the biphasic shape of the curve used to model BOLD changes against. For there to be a statistically significant relationship between the model and data, BOLD signal changes would have to first decrease and then increase post-injection. The lack of statistically significant changes observed using this model shows that, with the exception of entorhinal and posterior piriform cortices, most brain regions do not show biphasic changes in BOLD contrast i.e. decreased then increased signal matching the drug-induced changes in locomotor activity at this drug dose.

Using a model derived from the locomotor effects of quinelorane after adjustment to account for changes observed in control animals (Figure 4, green curve) produces statistical parametric maps that are similar to those produced using an "off/on" model (Figure 6). Bilateral increases in BOLD contrast are observed in the anterior olfactory nuclei, nucleus accumbens, and caudate-putamen, with additional unilateral increases in BOLD signal within some cortical regions. Interestingly, BOLD signal increases within the olfactory nuclei and nucleus accumbens are more statistically significant (and those changes in the caudate-putamen less significant) when modeled against the adjusted behavioral covariate than when using an "off/on" model. The adjusted behavioral covariate therefore provides a better estimate of the temporal profile of changes in BOLD signal within these regions than does an "off/on" model. This is reflected by a highly significant Pearson correlation coefficient between the adjusted behavioral model and the observed BOLD signal change in the nucleus accumbens (Figure 7), which explains the increase in statistical significance found when using this model when compared to those changes detected using a simple "off/on" model.

These contrasting approaches to analysis of phMRI data demonstrate the importance of model selection when analyzing phMRI data. With the exception of the behavioral model that was not adjusted to account for locomotor effects in control animals, all models produced similar SPM maps of significant BOLD signal changes, with small variations in the spatial extent of activations within different brain regions and statistical significance of observed changes. The lack of marked differences in observed patterns of activation when using these different models is due to each model being very similar in terms of having a rapid increase in the measured variable following drug administration that remains elevated for the duration of the experiment. These results suggest that

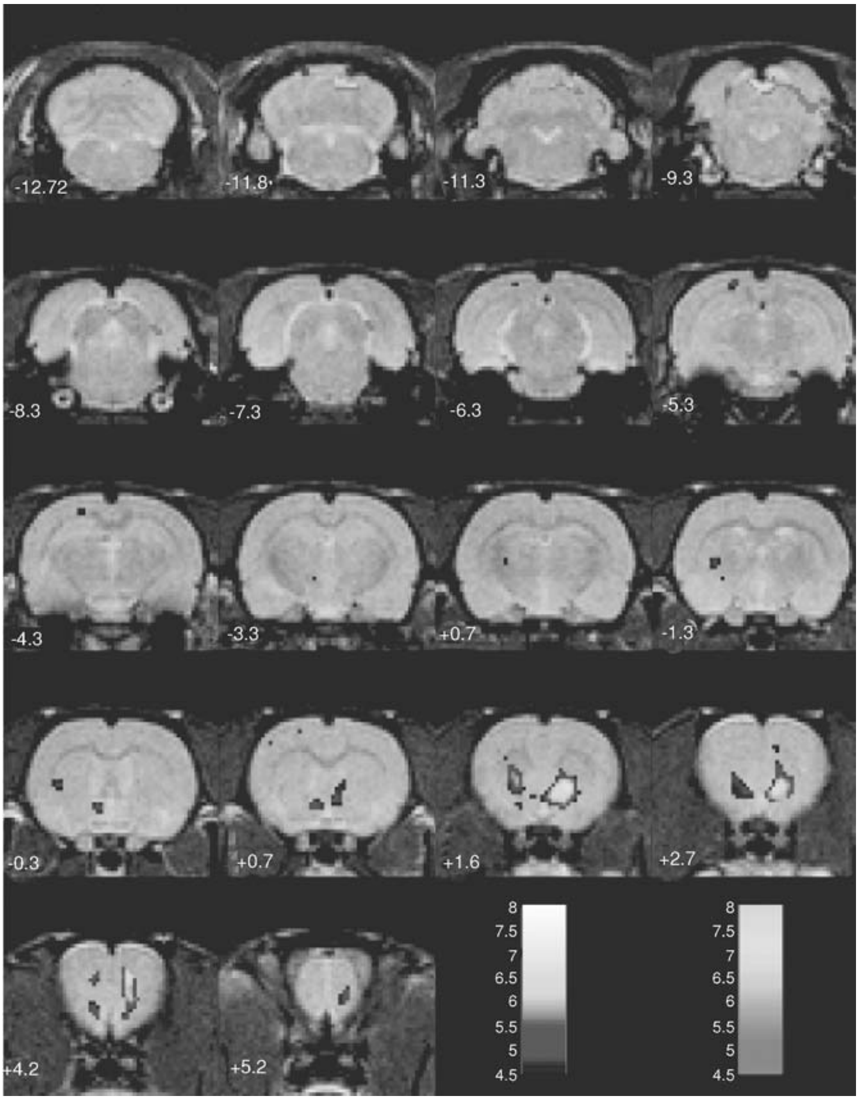

Fig. 3. Group statistical parametric map showing significant changes in BOLD contrast after administration of 30 μg/kg quinelorane ($n = 5$), analyzed using a covariate derived from quinelorane blood pharmacokinetics (Figure 2). Color scales represent T scores of significant increases (red < yellow) and decreases (blue < green) in BOLD signal, where $T > 4.5$, $p < 0.05$, corrected for multiple comparisons. Activation maps are overlaid on a T_2-weighted spin echo anatomical image, with each contiguous slice being 1 mm thick and moving rostrocaudally through the brain from bottom right to top left, with approximate co-ordinates relative to Bregma [108]. (See also Plate 76 on page LI in the Color Plate Section.)

quinelorane activates a range of limbic and basal ganglia regions in a similarly rapid and sustained fashion, with activation occurring almost immediately after drug injection and being sustained for the remainder of the experiment. Using a series of different models in this way can yield useful additional information, particularly where a drug has an effect on several behavioral measures at different times following administration, and also where pharmacokinetic and pharmacodynamic measures are temporally divergent. Many studies have used intravenous drug

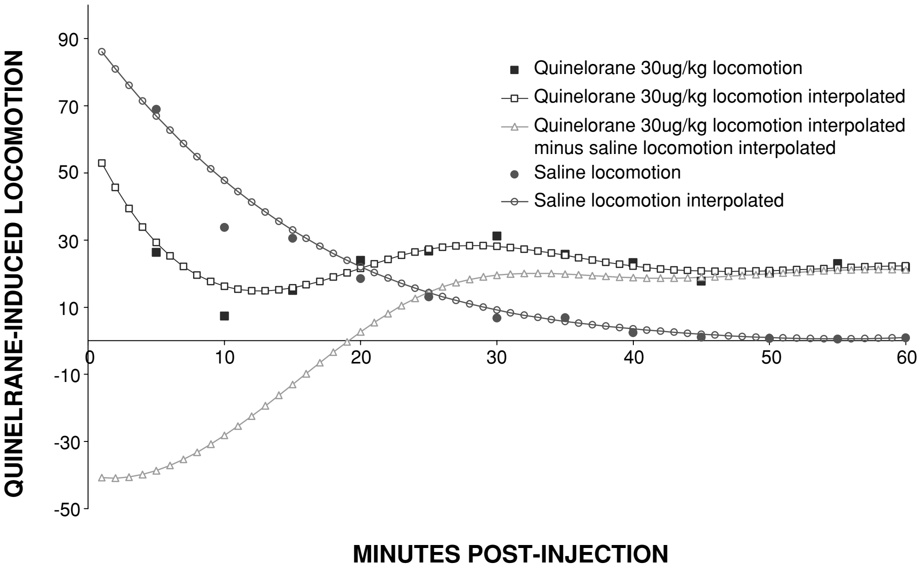

Fig. 4. Covariates derived from locomotor activity after administration of saline (red curve), 30 μg/kg quinelorane (blue curve), and after subtraction of locomotor activity in control animals from that of treated animals (green curve) in arbitrary units. (See also Plate 77 on page LII in the Color Plate Section.)

injections when producing pharmacokinetic models, with the advantage that the downward slope of the pharmacokinetic curve produced by more rapid drug clearance helps to reduce autocorrelations between the model and other confounding signal changes (such as global effects or scanner signal drift) within a time series. Whilst increasing the statistical power of analysis by allowing multiple periods of drug "stimulation," intravenous injections are liable to cause additional physiological confounds such as marked changes in systemic blood pressure that may lead to non-neurogenic BOLD signal changes. Repeated drug challenges may, over a short time period, also affect the response to drug as receptors become progressively desensitized, and giving drugs via intravenous rather than other routes can also make comparisons with the behavioral effects of a drug in awake animals more difficult. Nevertheless, it may be desirable to compare the effects of different routes of drug administration where this alters the time course of drug-induced behavioral and BOLD signal changes in order to isolate changes in those regions of the brain that mediate particular aspects of a drug's behavioral effect.

Accounting for Changes in Physiological Measures

As BOLD contrast is dependent on rCBF, factors unrelated to neuronal activity which may cause rCBF to increase must be controlled as carefully as possible. In the phMRI experiments using quinelorane described here, less than 20% of treated animals showed a small, transient increase in heart rate and blood pressure between 5 and 10 min after administration of quinelorane. This lack of cardiovascular changes, combined with observed BOLD signal changes being localized and not global in nature, make it unlikely that the changes in BOLD signal result from the systemic effects of quinelorane. It is also important to consider the possible effects that confounding changes in global signal intensity, which may result in part from the systemic effects of a drug, may have on the results of a phMRI experiment. For this study, changes in global signal intensity were tested against each of the models used in the data analysis to ensure that there was no statistically significant correlation between them. Having provided this assurance, the global signal was then included within the statistical model used for analysis (ANCOVA).

Confounding Drug Effects on Cerebral Blood Vessels

Dopamine is known to play a role in the regulation of cerebral blood flow, as dopaminergic axons innervate intraparenchymal microvessels within the cortex, and dopamine elicits dose-dependent reductions in the diameter of such vessels [98]. Such dopaminergic regulation

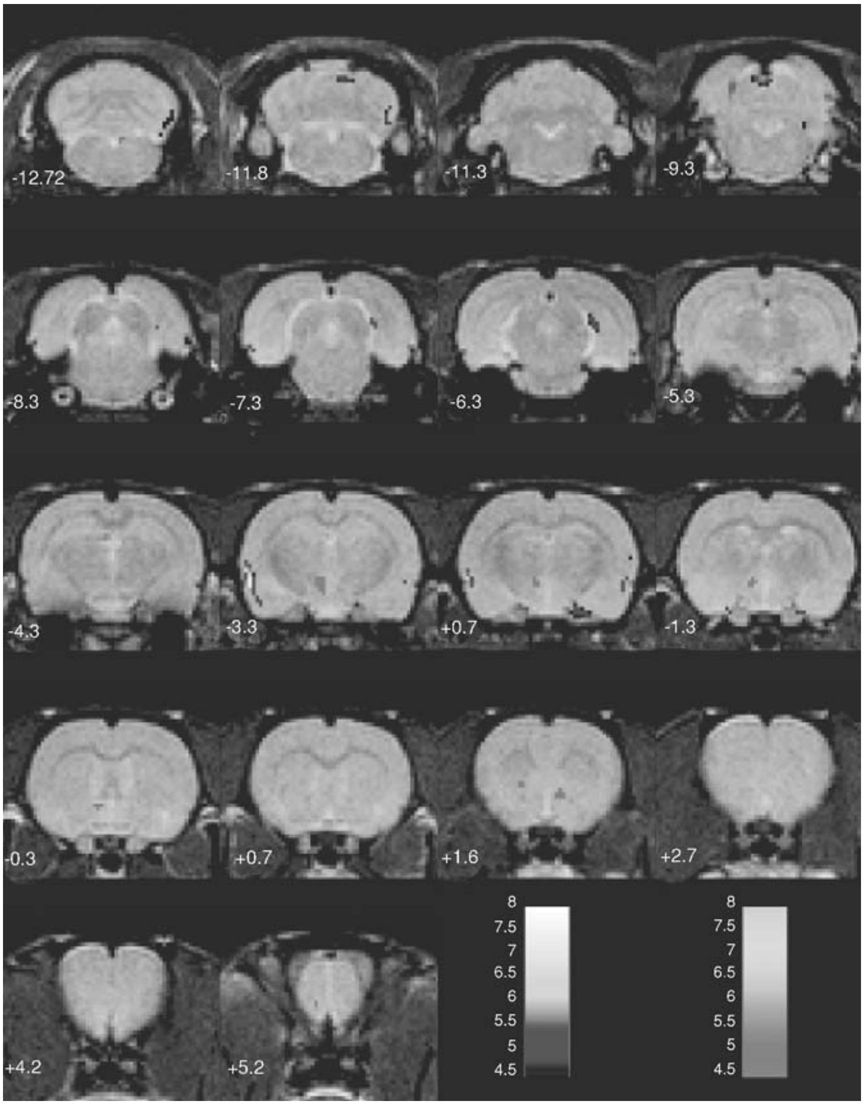

Fig. 5. Group statistical parametric map showing significant changes in BOLD contrast after administration of 30 μg/kg quinelorane ($n = 5$), analyzed using a covariate derived from the locomotor effects of 30 μg/kg quinelorane (Figure 4). Color scales represent T scores of significant increases (red < yellow) and decreases (blue < green) in BOLD signal, where $T > 4.5$, $p < 0.05$, corrected for multiple comparisons. Activation maps are overlaid on a T_2-weighted spin echo anatomical image, with each contiguous slice being 1 mm thick and moving rostrocaudally through the brain from bottom right to top left, with approximate co-ordinates relative to Bregma [108]. (See also Plate 78 on page LII in the Color Plate Section.)

of local cerebral cortical blood flow raises the possibility that quinelorane may be acting directly at receptors on cerebral blood vessels to elicit BOLD signal increases without a corresponding change in underlying neuronal activity. Both apomorphine and the D_1 receptor agonist SKF-38393 dose-dependently increase the diameter of cortical arterioles *in vivo*, an effect blocked by the D_1 receptor antagonist SCH23390, suggestive of D_1 receptor mediated effects [99]. In contrast, the D_2/D_3 receptor agonist quinpirole increases vessel diameter only at

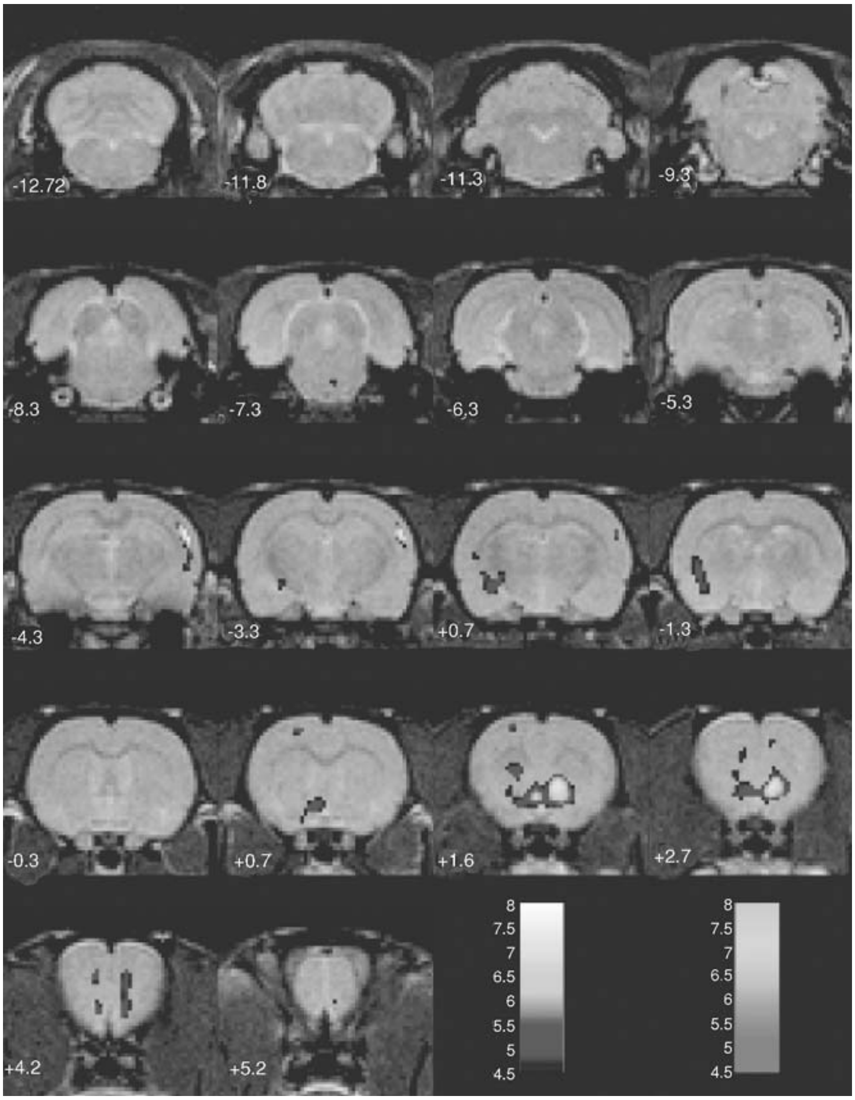

Fig. 6. Group statistical parametric map showing significant changes in BOLD contrast after administration of 30 μg/kg quinelorane ($n = 5$), analyzed using a covariate derived from the locomotor effects of 30 μg/kg quinelorane accounting for locomotor changes in control animals (Figure 4). Color scales represent T scores of significant increases (red < yellow) and decreases (blue < green) in BOLD signal, where $T > 4.5$, $p < 0.05$, corrected for multiple comparisons. Activation maps are overlaid on a T_2-weighted spin echo anatomical image, with each contiguous slice being 1 mm thick and moving rostrocaudally through the brain from bottom right to top left, with approximate co-ordinates relative to Bregma [108]. (See also Plate 79 on page LIII in the Color Plate Section.)

high agonist concentrations, possibly via effects at histamine H_2 receptors. Dopamine-mediated vessel constriction may involve activation of α-adrenoceptors and 5-HT receptors, as the effects of dopamine-induced vasoconstriction can be blocked by adrenergic and serotonergic antagonists like phentolamine and methysergide [99,100]. The effects of dopamine and dopaminergic agonists on cortical blood vessels therefore appear to be primarily mediated by D_1 receptors and/or non-dopamine receptors, and as quinelorane has extremely low affinities for

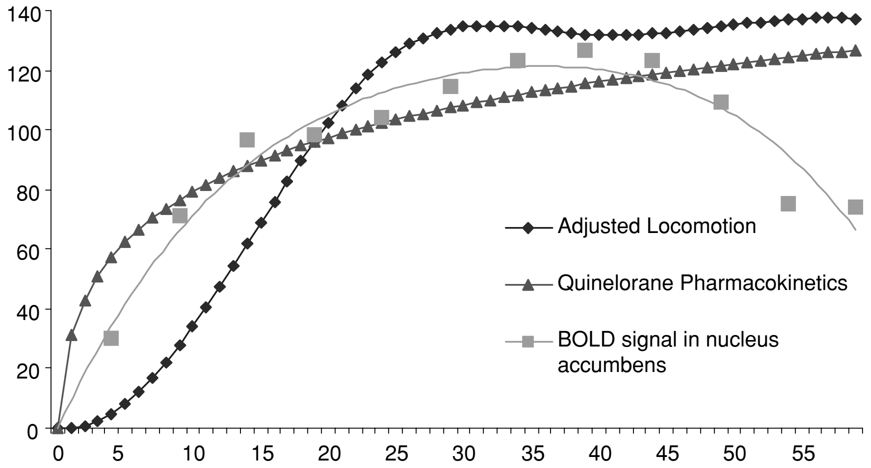

Fig. 7. Comparison of covariates used in phMRI analysis representing locomotor activity induced by 30 μg/kg quinelorane after accounting for changes in activity in control animals (blue), quinelorane blood pharmacokinetics (red), and observed BOLD signal change in the nucleus accumbens after grand mean scaling to 100 for comparative purposes. (See also Plate 80 on page LIV in the Color Plate Section.)

D_1 and non-dopamine receptors [84], it is unlikely that BOLD signal changes elicited by the low dose of quinelorane used in the experiments presented here result from a direct drug effect on cerebral blood vessels. It might also be expected that dopaminergic innervation of the cerebral vasculature might occur throughout the brain, and that any direct activation of cerebrovascular dopamine receptors would produce more global patterns of change in blood flow rather than the localized BOLD changes observed following quinelorane administration. However, the intimate relationship between the dopaminergic system and the regulation of CBF represents a potentially serious confound for all phMRI studies using dopaminergic agonists and antagonists, and particular care is needed when both planning and interpreting the results of such experiments in order to minimize these confounds.

Explaining the Absence of Signal Changes

It is also important to consider why activity in regions of the brain that might be expected to respond to a particular drug appears unchanged. For example, the lack of observed BOLD signal response to quinelorane through more widespread dopaminergic regions such as the substantia nigra and ventral tegmental area may be due to a variety of factors. Firstly, there may be no changes in neuronal signaling within these regions and so no corresponding change in BOLD signal. The lack of quinelorane-induced changes in BOLD signal within the substantia nigra may therefore reflect a lack of alteration in neuronal activity in this area. Alternatively, any changes in activity within these nuclei may not be of sufficient magnitude to elicit a detectable BOLD response. As BOLD signal is likely to reflect increased neuronal signaling at synapses rather than increased energy utilization *per se* [11], if there is no net change in the overall level of signaling between neurones, BOLD signal might remain unaffected by alterations in action potentials which have no overall effect on the signaling systems controlling blood flow. If the balance of pre- and post-synaptic activity changes without any net change in synaptic activity, then the spiking output from a particular region might alter without having any effect on the observed BOLD signal. It is also possible that if the drug under investigation has a direct effect on the cerebral vasculature, causing it to either dilate or constrict, this may directly counter any changes in rCBF that might be expected to occur as a result of modulated neuronal activity and so prevent a change in BOLD signal from being observed. When interpreting the results of phMRI experiments, it is therefore important to bear in mind that the absence of a change in BOLD signal cannot necessarily be taken as proof that no change in neuronal activity within a particular brain region has occurred.

Effects of Anesthesia

Of particular concern when interpreting phMRI results is the effects of the anesthetic agent used on resulting patterns of brain activity. The effects of α-chloralose on neurotransmission are not well understood, with contradictory reports suggesting that it depresses basal dopamine levels and dopamine release in response to sensory stimulations in the caudate-putamen and substantia nigra of the cat [64], but has little or no depressive effects on central dopaminergic metabolism and neurotransmission in the rat [101,102]. α-chloralose has also been shown to enhance GABAergic function by increasing the affinity and efficacy of GABA at GABA_A receptors [103]. For these reasons, it has been suggested that α-chloralose may not be a suitable anesthetic for phMRI investigations of the dopamine system. However, our results show that α-chloralose is suitable for detecting the effects of D_2/D_3 receptor agonist-induced changes in brain activity using BOLD phMRI. As spatial patterns of quinelorane-induced activity closely match D_2/D_3 receptor distribution patterns, α-chloralose may produce a state of low basal activity within the dopaminergic system, allowing phMRI to detect the primary site of dopamine receptor agonist action within the brain. This possibility is supported by a phMRI study showing that rCBV changes in the cortex and basal ganglia that follow the administration of either cocaine or amphetamine are preserved under halothane anesthesia, but are considerably diminished or absent under α-chloralose anesthesia [104]. This study also reported that following a challenge with the D_2-like receptor antagonist clozapine, rCBV increases are observed throughout the striatum under halothane anesthesia, but are much diminished when α-chloralose is used instead [104]. These data suggest that α-chloralose decreases basal dopamine release, diminishing the actions of drugs that act either by inhibiting dopamine reuptake (e.g. cocaine and amphetamine), or are antagonists like clozapine and produce their functional effects by blocking the actions of endogenous dopamine. As quinelorane is a direct agonist at D_2/D_3 receptors, its effects are not dependent on either modulating or blocking endogenous dopamine, and so the actions of quinelorane at dopamine receptors would be unaffected by any α-chloralose-induced modulation of dopamine release. α-chloralose anesthesia has been shown to lower the cerebral metabolic rate of glucose utilization (CMR_{gluc}) compared to the unanasthetized state, but upon activation induced by somatosensory stimulation, the final level of CMR_{gluc} increases to the same level in both states [105]. Thus a larger incremental increase in CMR_{gluc} occurs during activation in the anesthetized state (in order to reach the same final level of activity), and this larger increase in CMR_{gluc} may, in turn, produce a larger BOLD signal change. In this way, α-chloralose may actually serve to enhance the observed BOLD response to certain compounds.

Appropriate use of phMRI

In summary, there are several points that must be considered and incorporated into every phMRI experiment in order to have confidence in the final results. When considering whether a particular drug is suitable for investigation using phMRI, the known (or likely) effects that the drug may have directly on cerebral blood vessels, and hence CBF and CBV, need to be taken into account. If anesthesia is used, it must be at the lowest ethically acceptable level in order to minimize the confounding effects on drug-induced neuronal activation. Consideration should also be given to the known effects of different anesthetics on neurotransmitter systems. During the phMRI experiment, it is vital that extensive physiological monitoring is undertaken to provide confidence that any drug-induced patterns of activation are neuronal in origin. To do this, changes in heart rate, blood pressure, or respiration must be shown not to correlate with observed BOLD signal changes. In a similar fashion, changes in global signal should also be tested for correlations with the model of the expected BOLD signal response being used in the analysis. If patterns of activation truly result from drug-induced changes in neuronal activity, then it is likely that they will bear some resemblance to either the distribution of receptors to which that drug binds, or to the innervation of neurones within the neurotransmitter system affected by the drug. The less specific the compound being studied in terms of receptor binding profiles, then the more difficult it will be to provide certainty that patterns of activation genuinely reflect changes in neuronal activity. It may also be preferable to use smaller drug doses whenever possible in order to minimize any unwanted systemic effects and activate as selective a population of receptors within the brain as possible.

The Future of phMRI

The explosion in phMRI studies over recent years have shown both the potential this technique has for revealing the mechanisms by which drugs act in the brain and also the variety of different experimental situations where it can be employed. The major advantage phMRI has over other techniques is the detailed time course information it provides. PhMRI has shown how drugs with similar mechanisms of action, like cocaine and amphetamine which act on overlapping brain regions and neurotransmitter systems, can differ greatly in their onset and duration of effect. In addition, phMRI has also demonstrated a way in which the route of administration and dose can affect the measured phMRI response and thus neuronal activity. This time course information allows an assessment to be made of the brain circuitry that underlies a given drug response.

As the use of phMRI becomes more routine and techniques are increasingly refined, the key advantage that phMRI has in allowing longitudinal assessment of changes in brain functioning over time will become increasingly important. Most clinically used compounds exert their effects only after chronic treatment, and whilst this process is difficult to investigate in detail with current, highly invasive techniques, phMRI is ideally suited to investigating the change in receptor responses that follows repeated drug administration. In addition to assessing acute drug effects in naïve animals, as phMRI becomes more established it will be interesting to examine the effects of drugs in specific animal disease models, as has already begun in models of addiction and drug tolerance [40,41], cerebral ischemia [106], or assessing the effects of drug interactions, like those between dopamine agonists and antagonists [67]. There is also undoubted utility for phMRI within drug discovery in areas where the synthesis of a radioligand for either PET or autoradiography is difficult, or the allosteric action of a particular drug prevents the use of a ligand.

To date, most studies have relied either on drugs producing regionally specific modulations in BOLD or rCBV in order to negate the possibility that signal changes may be purely vascular and not neuronal in origin. In future, cross-validating the results of phMRI experiments with those produced by other measures, such as electrophysiology in humans [107], local field potentials [32], microdialysis [52], or metabolic markers will become increasingly important to substantiate the findings of phMRI studies, particularly as phMRI comes to be applied in an increasingly more sophisticated fashion involving the use of compounds with an unknown mechanism of action. Such complex experimental designs will also necessitate new data analysis techniques, particularly those that require no *a priori* knowledge of the time course over which a drug acts, and methods of studying drug-induced modulation in functional connectivity between different brain regions.

References

1. Leslie RA, James MF. Pharmacological magnetic resonance imaging: a new application for functional MRI. Trends Pharmacol. Sci. 2000;21:314–8.
2. Grasby PM, Friston KJ, Bench CJ, Cowen PJ, Frith CD, Liddle PF, Frackowiak RS, Dolan RJ. The effect of the dopamine agonist, apomorphine, on regional cerebral blood flow in normal volunteers. Psychol. Med. 1993;23:605–12.
3. Lahti AC, Holcomb HH, Medoff DR, Tamminga CA. Ketamine activates psychosis and alters limbic blood flow in schizophrenia Neuroreport. 1995;19:869–72.
4. Breiter HC, Gollub RL, Weisskoff RM, Kennedy DN, Makris N., Berke JD, Goodman JM, Kantor HL, Gastfriend DR, Riorden JP, Mathew RT, Rosen BR, Hyman SE. Acute effects of cocaine on human brain activity and emotion. Neuron. 1997;19:591–611.
5. Stein EA, Pankiewicz J, Harsch HH, Cho JK, Fuller SA, Hoffmann, RG, Hawkins M, Rao SM, Bandettini PA, Bloom AS. Nicotine-induced limbic cortical activation in the human brain: a functional MRI study. Am. J. Psychiatry. 1998;155:1009–15.
6. Burdett NG, Menon DK, Carpenter TA, Jones JG, Hall LD. Visualisation of changes in regional cerebral blood flow (rCBF) produced by ketamine using long TE gradient-echo sequences: preliminary results. Magn. Reson. Imaging. 1995;13:549–53.
7. Chen YI, Galpern WR, Brownell AL, Matthews RT, Bogdanov M, Isacson O, Keltner JR, Beal MF, Rosen BR, Jenkins BG. Detection of dopaminergic neurotransmitter activity using pharmacologic MRI: correlation with PET, microdialysis and behavioural data. Magn. Reson. Med. 1997;38:389–98.
8. Hagino H, Tabuchi E, Kurachi M, Saitoh O, Sun Y, Kondoh T, Ono T, Torii K. Effects of D_2 receptor agonist and antagonist on brain activity in the rat assessed by functional magnetic resonance imaging. Brain Res. 1998;813:367–73.
9. Chen YI, Brownell AL, Galpern W, Isacson O, Bogdanov M, Beal MF, Livni E, Rosen BR, Jenkins BG. Detection of dopaminergic cell loss and neural transplantation using pharmacological MRI, PET and behavioural assessment. Neuroreport. 1999;10:2881–6.
10. Reese T, Bjelke B, Porszasz R, Baumann D, Bochelen D, Sauter A., Rudin M. Regional brain activation by bicuculline visualized by functional magnetic resonance imaging. Time-resolved assessment of bicuculline-induced changes in local cerebral blood volume using an intravascular contrast agent. NMR Biomed. 2000;13:43–9.
11. Attwell D, Iadecola C. The neural basis of functional imaging signals. Trends Neurosci. 2002;25:621–5.
12. Sokoloff L, Reivich M, Kennedy C, Des Rosiers MH, Patalk CS, Pettigrew KD, Sakurada O, Shionhara M. The [^{14}C]-deoxyglucose technique for measurement of local cerebral glucose utilisation: theory, procedure and normal values in the conscious and anaesthetised albino rat. J. Neurochem. 1977;28:897–916.
13. Fox PT, Raichle ME. Focal physiological uncoupling of cerebral blood flow and oxidative metabolism during somatosensory stimulation in human subjects. Proc. Natl. Acad. Sci. USA. 1986;83:1140–4.
14. Detre JA, Leigh JS, Williams DS, Koretsky AP. Perfusion imaging. Magn. Reson. Med. 1992;23:37–45.
15. Kim SG. Quantification of relative cerebral blood flow change by flow-sensitive alternating inversion recovery (FAIR) technique: application to functional mapping. Mang. Reson. Med. 1995;34:293–301.
16. Kim SG, Ogawa S. Insights into new techniques for high resolution functional MRI. Curr. Opin. Neurobiol. 2002;12:1–9.
17. Duong TQ, Kim DS, Ugurbil K, Kim SG. Localised cerebral blood flow response at submillimeter columnar resolution. Proc. Natl. Acad. Sci. USA. 2001;98:10904–9.
18. Belliveau JW, Kennedy DN Jr, McKinstry RC, Buchbinder BR, Weisskoff RM, Cohen MS, Vevea JM, Brady TJ, Rosen BR. Functional mapping of the human visual cortex by magnetic resonance imaging. Science. 1991;254:716–9.
19. Mandeville JB, Marota JJA, Kosofsky BE, Keltner JR, Weissleder R, Rosen BR, Weisskoff RM. Dynamic functional imaging of relative cerebral blood volume during rat

forepaw stimulation. Magn. Reson. Med. 1998;39:615–24.

20. Mandeville JB, Jenkins BG, Kosofsky BE, Moskowitz MA, Rosen BR, Marota JJ. Regional sensitivity and coupling of BOLD and CBV changes during stimulation of rat brain. Magn. Reson. Med. 2001;45:443–7.
21. Ogawa S, Lee TM, Kay AR, Tank DW. Brain magnetic resonance imaging with contrast dependent on blood oxygenation. Proc. Natl. Acad. Sci. USA. 1990;87:9868–72.
22. Ogawa S, Menon R, Tank DW, Kim SG, Merkle H, Ellermann JM, Ugurbil K. Functional brain mapping by blood oxygen level dependent contrast MRI. Biophys. J. 1993;64:800–12.
23. Weiskoff RM, Zou CS, Boxerman JL, Rosen BR. Microscopic susceptibility variation and transverse relaxation theory and experiment. Magn. Reson. Med. 1994;31:601–10.
24. Ogawa S, Tank DW, Menon R, Ellermann JM, Kim SG, Merkle H, Ugurbil K. Intrinsic signal changes accompanying sensory stimulation: functional brain mapping with magnetic resonance imaging. Proc. Natl. Acad. Sci. USA. 1992;89:5951–5.
25. Vanzetta I., Grinvald A. Increased cortical oxidative metabolism due to sensory stimulation: implications for functional brain imaging. Science. 1999;286:1555–8.
26. Buxton RB. The elusive initial dip. Neuroimage. 2001;13:953–8.
27. Fox PT, Raichle ME, Minton MA, Dence C. Nonoxidative glucose consumption during focal physiologic neuronal activity. Science. 1988;241:462–4.
28. Kwong KK, Belliveau JW, Chesler DA, Glodberg IE, Weisskoff RM, Poncelet BP, Kennedy DN, Hoppel BE, Cohen MS, Turner R. Dynamic magnetic resonance imaging of human brain activation during primary somatosensory stimulation. Proc. Natl. Acad. Sci. USA. 1992;89:5675–9.
29. Buxton RB, Wong EC, Frank LR. Dynamics of blood flow and oxygenation changes during brain activation: the balloon model. Magn. Reson. Med. 1998;39:855–64.
30. Schwartz WJ, Smith CB, Davidsen L, Savaki H, Sokoloff L, Mata M, Fink DJ, Gainer H. Metabolic mapping of functional activity in the hypothalamo-neurohypophysial system of the rat. Science. 1979;205:723–5.
31. Sibson NR, Dhankhar A, Mason GF, Rothman DL, Behar KL, Shulman RG. Stoichiometric coupling of brain glucose metabolism and glutamatergic neuronal activity. Proc. Natl. Acad. Sci. USA. 1998;95:316–21.
32. Logothetis NK, Pauls J, Augath M, Tirnath T, Oeltermann A. Neurophysiological basis of the fMRI signal. Nature. 2001;412:150–7.
33. Lauritzen M, Gold L. Brain function and neurophysiological correlates of signals used in functional neuroimaging. J. Neurosci. 2003;23:3972–80.
34. Shmuel A, Yacoub E, Pfeuffer J, Van de Moortele PF, Adriany G, Hu X, Ugurbil K. Sustained negative BOLD, blood flow and oxygen consumption response and its coupling to the positive response in the human brain. Neuron. 2002;36:1195–210.
35. Heeger DJ, Rees D. What does fMRI tell us about neuronal activity? Nat. Rev. Neurosci. 2002;3:142–51.
36. Cholet N, Seylaz J, Lacombe P, Bonvento G. Local uncoupling of the cerebrovascular and metabolic responses to somatosensory stimulation after neuronal nitric oxide synthase inhibition. J. Cereb. Blood Flow Metab. 1997;17:1191–201.
37. Boxermann JL, Bandettini PA, Kwong KK, Baker JR, Davis TL, Rosen BR, Weisskoff RM. The intravascular contribution to fMRI signal change: Monte Carlo modelling and diffusion-weighted studies in vivo. Magn. Reson. Med. 1995;34:4–10.
38. Duong TQ, Yacoub E, Adriany G, Hu X, Ugurbil K, Kim, S-G. Magn. Reson. Med. 2003;49:1019–27.
39. Bandettini PA, Wong EC, Jesmanowicz R, Scott Hinks R, Hyde JS. Spin-echo and gradient-echo EPI of human brain activation using BOLD contrast: a comparative study at 1.5T. NMR Biomed. 1994;7:12–20.
40. Lowe AS, Williams SCR, Symms MR, Stolerman IP, Shoaib M. Functional magnetic resonance imaging of drug dependence: naloxone-precipitated morphine withdrawal. Neuroimage. 2002;17:902–10.
41. Shoaib M, Lowe AS, Williams SCR. Imaging localised dynamic changes in the nucleus accumbens following nicotine withdrawal in rats. Neuroimage. 2004;22:847–54.
42. Shah YB, Prior MJ, Dixon AL, Morris PG, Marsden CA. Detection of cannabinoid agonist evoked increase in BOLD contrast in rats using functional magnetic resonance imaging. Neuropharmacology. 2004;46:379–87.
43. Turner R, Jezzard P, Wen H, Kwong KK, Le Bihan D, Zeffiro T, Balaban RS. Functional mapping of the human visual cortex at 4 and 1.5 Tesla using deoxygenation contrast EPI. Magn. Reson. Med. 1993;29:277–9.
44. Kim D-S, Garwood M. High-field magnetic resonance techniques for brain research. Curr. Opin. Neurobiol. 2003;13:612–9.
45. Bandettini PA, Wong EC. A hypercapnia-based normalization method for improved spatial localization of human brain activation with fMRI. NMR Biomed. 1997;10:197–203.
46. Wise RG, Ide K, Poulin MJ, Tracey, I. Resting fluctuations in arterial carbon dioxide induce significant low frequency variations in BOLD signal. Neuroimage. 2004;21:1652-64.
47. Xu H, Li SJ, Bodurka J, Zhao X, Xi ZX, Stein EA. Heroin-induced neuronal activation in rat brain assessed by functional MRI. Neuroreport. 2000;11:1085–92.
48. Zaharchuk G, Mandeville JB, Bogdanov AA, Weissleder R, Rosen BR, Marota JJ. Cerebrovascular dynamics of autoregulation and hypoperfusion. An MRI study of CBF and changes in total and microvascular cerebral blood volume during hemorrhagic hypotension. Stroke. 1999;30:2197–204; discussion 2204–5.
49. Kalisch R, Elbel GK, Gossl C, Czisch M, Auer DP. Blood pressure changes induced by arterial blood withdrawal influence BOLD signal in anesthetised rats at 7 Tesla: implications for pharmacological MRI. Neuroimage. 2001;14:891–8.
50. Rao SM, Salmeron BJ, Durgerian S, Janowiak JA, Fischer M, Risinger RC, Conant LL, Stein EA. Effects of methylphenidate on functional MRI blood-oxygen-level-dependent contrast. Am. J. Psychiatry. 2000;157:1697–9.
51. Luo F, Wu G, Li Z, Li SJ. Characterization of effects of mean arterial blood pressure induced by cocaine and cocaine methiodide on BOLD signals in rat brain. Magn. Reson. Med. 2003;49:264–70.

52. Schwarz AJ, Zocchi A, Reese T, Gozzi A, Garzotti M, Varnier G, Curcuruto O, Sartori I, Girlanda E, Biscaro B, Crestan V, Bertani S, Heidbreder C, Bifone A. Concurrent pharmacological MRI and in situ microdialysis of cocaine reveal a complex relationship between the central hemodynamic response and local dopamine concentration. Neuroimage. 2004;23:296–304.
53. Febo M, Segarra AC, Tenney JR, Brevard ME, Duong TQ, Ferris CF. Imaging cocaine-induced changes in the mesocorticolimbic dopaminergic system of conscious rats. J. Neurosci. Methods. 2004;139:167–76.
54. Kalisch R, Salome N, Platzer S, Wigger A, Czisch M, Sommer W, Singewald N, Heilig M, Berthele A, Holsboer F, Landgraf R, Auer DP. High trait anxiety and hyporeactivity to stress of the dorsomedial prefrontal cortex: a combined phMRI and Fos study in rats. Neuroimage. 2004;23:382–91.
55. Hansen TD, Warner DS, Todd MM, Vust LJ. Effects of nitrous oxide and volatile anaesthetics on cerebral blood flow. Br. J. Anaesth. 1989;63:290-5.
56. Hansen TD, Warner DS, Todd MM, Vust LJ. The role of cerebral metabolism in determining the local cerebral blood flow effects of volatile anesthetics: evidence for persistent flow-metabolism coupling. J. Cereb. Blood Flow Metab. 1989;9:323–8.
57. Hyder F, Behar KL, Martin MA, Blamire AM, Shulman RG. Dynamic magnetic resonance imaging of the rat brain during forepaw stimulation. J. Cereb. Blood Flow Metab. 1994;14:649–55.
58. Ueki M, Mies G, Hossmann KA. Effects of alpha-chloralose, halothane, pentobarbital and nitrous oxide anaesthesia on metabolic coupling in somatosensory cortex of rat. Acta Anaesthesiol. Scand. 1992;36:318–22.
59. Balis GU, Monroe RR. The pharmacology of chloralose. Psychopharmacologica. 1964;6:1–30.
60. Bonvento G, Charbonne R, Correze J, Borredon J, Seylaz J, Lacombe P. Is α-chloralose plus halothane induction a suitable anaesthetic regimen for cerebrovascular research? Brain Res. 1994;665:213–21.
61. Lindauer U, Villringer A, Dirnagul U. Characterization of CBF response to somatosensory stimulation: model and influence of anesthetics. Am. J. Physiol. 1993;264:H1223-8.
62. Preece M, Mukherjee B, Huang CL, Hall LD, Leslie RA, James MF. Detection of pharmacologically mediated changes in cerebral activity by functional magnetic resonance imaging: effects of sulpiride in the brain of the anaesthetised rat. Brain Res. 2001;916:107–14.
63. Houston GC, Papadakis NG, Carpenter TA, Hall LD, Mukherjee B, James MF, Huang CL. Mapping of brain activation in response to pharmacological agents using fMRI in the rat. Magn. Reson. Imaging. 2001;19:905–19.
64. Nieoullon A, Dusticier A. Effects of α-chloralose on the activity of the nigrostriatal dopaminergic system in the cat. Eur. J. Pharmacol. 1980;65:403–10.
65. Xi ZX, Wu G, Stein EA, Li SJ. Opiate tolerance by heroin self-administration: an fMRI study in rat. Magn. Reson. Med. 2004;52:108–14.
66. Marota JJA, Mandeville JB, Weisskoff RM, Moskowitz MA, Rosen BR, Kosofsky BE. Cocaine activation discriminates dopaminergic projections by temporal response: an fMRI study in rat. Neuroimage. 2000;11:13–23.
67. Schwarz A, Gozzi A, Reese T, Bertani S, Crestan V, Hagan J, Heidbreder C, Bifone A. Selective dopamine D(3) receptor antagonist SB-277011-A potentiates phMRI response to acute amphetamine challenge in the rat brain. Synapse. 2004;54:1–10.
68. Mueggler T, Baumann D, Rausch M, Rudin M. Bicuculline-induced brain activation in mice detected by functional magnetic resonance imaging. Magn. Reson. Med. 2001;46:292–8.
69. Zhang Z, Andersen AH, Avison MJ, Gerhardt GA, Gash DM. Functional MRI of apomorphine activation of the basal ganglia in awake rhesus monkeys. Brain Res. 2000;852:290–6.
70. Maekawa T, Tommasino C, Shapiro HM, Keifer-Goodman J, Kohlenberger RW. Local cerebral blood flow and glucose utilization during isoflurane anesthesia in the rat. Anesthesiology. 1986;65:144–51.
71. Lenz C, Rebel A, Van Ackern K, Kuschinsky W, Waschke KF. Local cerebral blood flow, local cerebral glucose utilization, and flow-metabolism coupling during sevoflurane versus isoflurane anaesthesia in rats. Anaesthesiology. 1998;89:1480–8.
72. Hendrich KS, Kochanek PM, Melick JA, Schiding JK, Statler KD, Williams DS, Marion DW, Ho C. Cerebral perfusion during anaesthesia with fentanyl, isoflurane, or pentobarbital in normal rats studied by arterial spin-labelled MRI. Magn. Reson. Med. 2001;46:202–6.
73. Sicard K, Shen Q, Brevard ME, Sullivan R, Ferris CF, King JA, Duong TQ. Regional cerebral blood flow and BOLD responses in conscious and anaesthetised rats under basal and hypercapnic conditions: implications for functional MRI studies. J. Cereb. Blood Flow Metab. 2003;23: 472–81.
74. Antognini JF, Buonocore MH, Disbrow EA, Carstens E. Isoflurane anaesthesia blunts cerebral responses to noxious and innocuous stimuli: a fMRI study. Life Sci. 1997;24:349–54.
75. Zhang H, Ji T, Leslie R, Hockings PD, Templeton, D, Wyrwicz AM. Characterization of D_2 antagonist sulpiride effects on cerebral hemodynamics in a conscious rabbit with fMRI. Proc. Intl. Soc. Mag. Reson. Med. 2003;11:1861.
76. Stein EA, Fuller SA, Edgemond WS, Campbell WB. Selective effects of the endogenous cannabinoid arachidonylethanolamide (anandamide) on regional cerebral blood flow in the rat. Neuropsychopharmacology. 1998;19:481–91.
77. Friston KJ, Ashburner J, Poline JB, Frith CD, Heather JD, Frackowiak RSJ. Spatial registration and normalization of images. Hum. Brain Mapp. 1995;2:165–89.
78. Ashburner J, Friston KJ. Nonlinear spatial normalisation using basis functions. Hum. Brain Mapp. 1999;7:254–66.
79. Van de Moortle PF, Pfeuffer J, Glover GH, Ugurbil K, Hu X. Respiration-induced B0 fluctuations and their spatial distribution in the human brain at 7 Tesla. Magn. Reson. Med. 2002;47:888–95.
80. Aguirre GK, Zarahn E, D'Esposito M. The inferential impact of global signal covariates in functional neuroimaging analysis. Neuroimage. 1998;8:302–6.

81. Lowe AS, Barker GJ, Ireland MD, Beech JS, Williams SCR. Estimating global effects from extra-cerebral tissue: inferential utility for pharmacological fMRI (in press).
82. Bloom AS, Hoffmann RG, Fuller SA, Pankiewicz J, Harsch HH, Stein EA. Determination of drug-induced changes in functional MRI signal using a pharmacokinetic model. Hum. Brain Mapp. 1999;8:235–44.
83. Wise RG, Williams P, Tracey I. Using fMRI to quantify the time dependence of remifentanil analgesia in the human brain. Neuropsychopharmacology. 2004;29:626–35.
84. Bymaster FP, Reid LR, Nichols CL, Kornfield EC, Wong DT. Elevation of acetylcholine levels in striatum of rat brain by LY163502, trans-(−) 5,5a,6,7,8,9a,10-octahydro-6-propylpyrimidio<4,5-g>quinolin-2-amine-di-hydrochloride, a potent and stereospecific (D_2) agonist. Life Sci. 1986;38:317–22.
85. Sokoloff P, Andrieux M, Besancon R, Pilon C, Martres MP, Giros B, Schwartz JC. Pharmacology of human dopamine D_3 receptor expressed in a mammalian cell line: comparison with D_2 receptor. Eur. J. Pharmacol. 1992;225:331–7.
86. Bowen WP, Coldwell MC, Hicks FR, Riley GJ, Fears R. Ropinirole, a novel dopaminergic agent for the treatment of Parkinson's disease, with selectivity for cloned dopamine D_3 receptors. Br. J. Pharmacol. 1993;110(Suppl 93P).
87. Gackenheimer SL, Schaus JM, Gehlert DR. [^{3}H]-Quinelorane binds to D_2 and D_3 receptors in the rat brain. J. Pharmacol. Exp. Ther. 1995;274:1558–65.
88. Levant B. The dopamine D_3 receptor: neurobiology and potential clinical relevance. Pharmacol. Rev. 1997;49:231–52.
89. Coldwell MC, Boyfield I, Brown AM, Stemp G, Middlemiss DN. Pharmacological characterisation of extracellular acidification rate responses in human D_2(long), D_3 and D_4 receptors in Chinese hamster ovary cells. Br. J. Pharmacol. 1999;127:1135–44.
90. Kelinschmidt A, Bruhn H, Kruger G, Merboldt KD, Stoppe G, Frahm J. Effects of sedation, stimulation and placebo on cerebral blood oxygenation: a magnetic resonance neuroimaging study of psychotropic drug action. NMR Biomed. 1999;12:286–92.
91. Foreman MM, Fuller RW, Hynes MD, Gidda JS, Nichols CL, Schaus JM, Kornfeld EC, Clemens JA. Preclinical studies on quinelorane, a potent and highly selective D_2-dopaminergic agonist. J. Pharmacol. Exp. Ther. 1989;250:227–35.
92. Manzione BM, Bernstein JR, Franklin RB. Observations on the absorption, distribution, metabolism, and excretion of the dopamine (D_2) agonist, quinelorane, in rats, mice, dogs, and monkeys. Drug Metab. Dispos. 1991;19: 54–60.
93. Sokoloff P, Giros B, Martres MP, Bouthenet ML, Schwartz JC. Molecular cloning and characterization of a novel dopamine receptor (D_3) as a target for neuroleptics. Nature. 1990;347:146–51.
94. Bouthenet ML, Souil E, Martres MP, Sokoloff P, Giros B, Schwartz JC. Localisation of dopamine D_3 receptor mRNA in the rat brain using in situ hybridisation histochemistry: a comparison with dopamine D_2 receptor mRNA. Brain Res. 1991;564:203–19.
95. Mengod G, Villaro MT, Landwehrmeyer GB, Martinez-Mir MI, Niznik HB, Sunahara RK, Seeman P, O'Dowd BF, Probst A, Palacios, JM. Visualization of dopamine D_1, D_2 and D_3 receptor mRNAs in human and rat brain. Neurochem. Int. 1992;20(Suppl 33s–43s).
96. Landwehrmeyer B, Mengod G, Palacios JM. Differential visualisation of dopamine D_2 and D_3 receptor sites in rat brain. A comparative study using in situ hybridisation histochemistry and ligand binding autoradiography. Eur. J. Neurosci. 1993;5:145–53.
97. Diaz J, Levesque D, Lammers CH, Griffon M, Martres MP, Schwartz JC, Sokoloff P. Phenotypical characterisation of neurons expressing the dopamine D_3 receptor in the rat brain. Neuroscience. 1995;65:731–45.
98. Krimer LS, Muly EC, Williams GV, Goldman-Rakic PS. Dopaminergic regulation of cerebral cortical microcirculation. Nat. Neurosci. 1998;1:286–9.
99. Edvinsson L, McCulloch J, Sharkey J. Vasomotor responses of cerebral arterioles in situ to putative dopamine receptor agonists. Br. J. Pharmacol. 1985;85:403–10.
100. Iadecola C. Neurogenic control of the cerebral microcirculation: is dopamine minding the store? Nat. Neurosci. 1998;1:263–5.
101. Massott M, Longo VG. α-Chloralose and the central dopaminergic system. J. Pharm. Pharmacol. 1978;30: 667.
102. Ford APDW, Marsden CA. Influence of anaesthetics on rat striatal dopamine metabolism in vivo. Brain Res. 1986;379:162–6.
103. Garrett KM, Gan J. Enhancement of γ-aminobutyric acid$_A$ receptor activity by α-chloralose. J. Pharmacol. Exp. Ther. 1998;285:680–6.
104. Chen YI, Mandeville JB, Marota JA, Nguyen TV, Green AR, Jenkins BG. Anaesthetic filters for eliciting specific neurotransmitter effects in pharmacological MRI. Proceedings of the International Society of Magnetic Resonance in Medicine, Glasgow, 2000.
105. Shulman RG, Rothman DL, Hyder F. Stimulated changes in localised cerebral energy consumption under anaesthesia. Proc. Natl. Acad. Sci. USA. 1999;96:3245–50.
106. Reese T, Bochelen D, Baumann D, Rausch M, Sauter A, Rudin M. Impaired functionality of reperfused brain tissue following short transient focal ischemia in rats. Magn. Reson. Imaging. 2002;20:447–54.
107. Arthurs OJ, Stephenson CM, Rice K, Lupson VC, Spiegelhalter DJ, Boniface SJ, Bullmore ET. Dopaminergic effects on electrophysiological and functional MRI measures of human cortical stimulus-response power laws. Neuroimage. 2004;21:540–6.
108. Paxions G, Watson C. The Rat Brain in Stereotaxic Coordinates. Academic Press: London, 1997.

Application of MRI to Cell Tracking

Kishore Bhakoo, Catherine Chapon, Johanna Jackson, and William Jones
Stem Cell Imaging Group, MRC Clinical Sciences Centre, Imperial College London, London W12 0NN, UK

Introduction

Cell replacement therapy is undergoing a critical transition from being a discipline of the basic sciences to being recognized as a potential component of medical practice. For multiple tissues, the use of stem cell transplantation to replace cells lost due to traumatic injury or chronic degenerative processes is being pursued in a wide range of experimental models. Cell-based therapies [1] have received much attention as novel therapeutics for treatment of cancer [2], autoimmune [3], cardiovascular [4], inflammatory [5], and degenerative diseases [6,7]. A number of native cells, antigen-specific T-lymphocytes [8], or, more recently, stem and progenitor cells have been used for these approaches. Such treatment offers the possibility of treating a wide range of serious degenerative diseases that affect millions of people worldwide for which there are currently no cures.

The recognition that cell transplantation can be used for tissue repair is associated with recognition of the considerable challenges involved in implementing this approach in the clinical arena, with one of the most significant challenges being the non-invasive analysis of transplanted cells and their progeny. While multiple approaches can be used to analyze survival, dispersion, and differentiation of transplanted cells in experimental animals, none of them can be applied to clinical analysis. Whether one considers *ex vivo* cell labeling with fluorescent dyes or transplantation of cells expressing reporter genes (e.g. β-galactosidase, green fluorescent protein), these are methods that involve sacrifice of the animal and removal of tissue for histological procedures [9,10]. Thus, these approaches cannot be translated to human studies.

Development of methods for monitoring cell grafts non-invasively, with sufficiently high sensitivity and specificity to identify and map the fate of transplanted cells, is an important aspect of application and safety assessment of stem cell therapy. MRI methods are potentially well suited for such applications as this produces non-invasive “images” of opaque tissues or structures inside the body and more importantly can be translated for pre-clinical assessments.

Due to the seamless integration into the host parenchyma, and migration over long distances, cell grafts cannot be detected based on their mass morphology. To monitor cell migration and positional fate after transplantation, current methods use either reporter genes or chimeric animals. These methods are cumbersome, involve sacrifice of the animal and removal of tissue for histological procedures, and cannot be translated to human studies [9,10]. Therefore, development of methods for monitoring cell grafts non-invasively, with sufficiently high sensitivity and specificity to identify and map the fate of transplanted cells, is an important aspect of application and safety assessment of stem cell therapy. MRI methods are potentially well suited for such applications as this produces non-invasive “images” of opaque tissues or structures inside the body.

For transplanted cells to be visualized and tracked by MRI, they need to be tagged so that they are “MR visible”. At present there are two types of MRI contrast agents used clinically. These are gadolinium chelates (e.g. Gd^{3+}-DTPA) or iron oxide nanoparticles. However, these reagents were designed as blood-pool contrast agents and are impermeable to cells. Several approaches have been deployed to enhance cell labeling to allow *in vivo* cell tracking by conjugating MRI contrast agents to a range of ancillary molecules to enhance their uptake. With the growing array of cell labeling techniques, cells tagged with various monocrystalline MR probes have been evaluated both *in vitro* and *in vivo* [11–13].

Methods for monitoring implanted stem cells non-invasively *in vivo* will greatly facilitate the clinical realization and optimization of the opportunities for stem cell-based therapies. Other than tracking stem cells, there are numerous examples where similar methodologies of cell tracking can aid in clinical diagnosis, such as those from a tumor or following an inflammatory response.

Intracellular MRI Contrast Agents

Recent work in the design of MRI contrast agents has opened up the possibility of combining the spatial resolution available of MRI for anatomic imaging with the ability to “tag” cells, and thus enable non-invasive detection and study of cell migration from the site of implantation. *In vivo* monitoring of stem cells after grafting is essential for understanding their migrational dynamics, which is an important aspect in determining the overall therapeutic

Graham A. Webb (ed.), Modern Magnetic Resonance, 879–890.
© 2008 *Springer.*

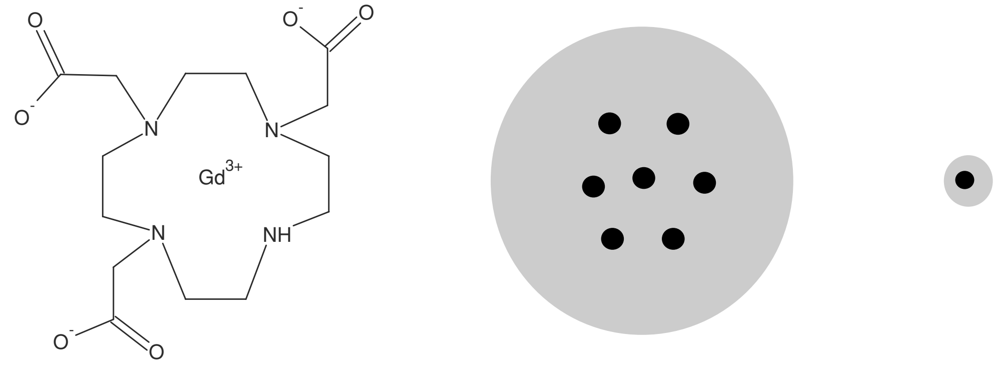

(a) Gadolinium chelate DO3A **(b) SPIO** **(c) USPIO**

Fig. 1. Schematic structures of (a) Gd[DO3A], (b) SPIO, and (c) USPIO.

index of cell therapies. Despite recent advances in both the synthesis of paramagnetic molecules and the basic cell biology, methods for achieving effective cell labeling using molecular MR tags are still in their infancy.

Properties of a Good Contrast Agent for Cell Tracking

Before discussing the design and utilization of contrast agent to label cells for *in vivo* tracking by MRI, there are several parameters that need to be considered when synthesizing an efficient contrast agent. Firstly, there is a need to deliver sufficient amounts of MRI contrast agent into cells and achieve intracellular retention. Once the contrast agent is loaded into the cells, there is a need for efficient relaxivity to obtain a high *in vivo* MR signal-to-noise ratio. An additional aspect for successful design is tolerable cytotoxicity of the MRI contrast agent, which should have no long-term effects on cell viability, nor compromise cellular function, e.g. metabolism and differentiation.

MRI Contrast Agent for Cell Tracking

MRI contrast agents can be classified as either paramagnetic or superparamagnetic and will be discussed in some detail below.

Paramagnetic Agents

Where an element has one or more unpaired electrons, it is said to be paramagnetic, as it possesses a permanent magnetic moment. Examples of these are Fe^{3+}, Mn^{2+}, and Gd^{3+}. The more unpaired electrons present, the greater the magnetic moment. The effect of the magnetic moment in solution results in a dipolar magnetic interaction between the paramagnetic ion and neighboring water molecules. A fluctuation in this magnetic interaction produces a decrease in $T1/T2$ relaxation time [14]. Paramagnetic compounds produce, predominantly, a $T1$ effect, giving a hyperintense region. In order to avoid the problems associated with toxicity *in vivo*, heavy metal ions are chelated with organic moieties in order to make them more biocompatible (Figure 1a).

An in-depth discussion of the mechanism underlying the enhancement of relaxation is examined by Merbach and Toth [14].

Superparamagnetic Agents

The other class of contrast agents is superparamagnetic compounds. These consist of an iron oxide core, typically 4–10 nm in diameter, where several thousand iron atoms are present. A biocompatible polymer surrounds the core to provide steric and/or electrostatic stabilization. This is required due to the large surface area to volume of the nanoparticles. If no stabilization is present, the particles spontaneously precipitate out of solution due to colloidal instability. The polymers used to stabilize the iron oxide core are typically polysaccharide-based (e.g. dextran and starch) but others have also been used, e.g. polyethylene glycol (PEG).

There are two types of superparamagnetic contrast agents, superparamagnetic iron oxide (SPIO) and ultra small superparamagnetic iron oxide (USPIO). The difference between the two is illustrated in Figure 1b and c, where SPIOs consist of several magnetic cores surrounded by a polymer matrix and USPIOs are individual cores surrounded by a polymer. Superparamagnetic contrast agents provide predominantly a $T2$ effect, but smaller particles have shown to act as a $T1$ agent [14]. The relaxation mechanism for superparamagnetic particles is discussed more extensively in a review by Roch *et al.* [15].

SPIOs are clinically contrast agents approved by the Food and Drug Administration (FDA) for hepatic reticuloendothelial cell imaging, and are in Phase III clinical trials as blood-pool agents for use in lymphography [16]. Iron oxide particles are also being developed for a variety of different applications, namely: (a) as magnetic navigation devices for the targeted delivery of therapeutics [17,18]; (b) hyperthermia-induced tumor therapeutics under high-frequency magnetic fields [19]; and (c) for magnetic cell sorting [20]. More importantly, SPIO particles are biodegradable and can be degraded and assimilated within the body.

More recently, a new class of modified USPIO has been produced known as cross-linked iron oxide (CLIO), whereby the dextran coat of the USPIO is cross-linked in the presence of epichlorohydrin, and then aminated to produce amine-terminated nanoparticles suitable for conjugation [21].

Therefore, the concept of labeling cells with one of these classes of contrast agents is extremely attractive, as one could then visualize transplanted cells non-invasively by MRI; where the labeled cells would produce either hyperintense or hypointense depending on the class of contrast agent chosen. However, most efforts to engineer cell tagging agents has concentrated on using superparamagnetic nanoparticles as they possess higher sensitivity, especially on the higher field research scanners that are now being implemented for pre-clinical or clinical studies.

Engineering Delivery Systems for Iron Oxide Contrast Agents

However, none of the iron oxide-based contrast agents available for clinic studies were designed to go across cellular membranes. Therefore, numerous efforts have been made to deliver iron oxide particles into a variety of cells. One such molecule that is emerging as a useful reagent relies on the covalent binding of CLIO particles to the HIV-1 TAT peptide to enhance cellular uptake [11,13,22–24].

TAT peptide contains a membrane-translocating signal that efficiently shuttles the particles into cells and the nuclear compartment [25]. A similar approach involves the covalent conjugation of internalizing monoclonal antibodies onto SPIO particles leading to cellular uptake via endosome-mediated mechanisms [26]. Alternatively, conjugations of SPIOs with antibodies to cell surface antigens have also been deployed with some success [27]. Nevertheless, these methods are inherently restrictive to the particular antibody–receptor interaction on the target cell line. Other methods involve the use of transfection reagents, such as those developed for the translocation of plasmid DNA into cells [28]. Even though this approach offers a more universal way to transfer iron oxide particles intracellularly, it suffers from the variability in cellular labeling; but more importantly some of these reagents have cytotoxicity characteristics associated with highly cationic transfection agents (TAs). A more detailed summary of these methods is outlined below.

Delivery of Contrast Agent with Transfection Agents

TAs have been developed commercially for the delivery of genetic cargo into cells for gene therapy applications. Such delivery systems are based on different platforms, such as liposomes, cationic dextrans, dendrimers, etc. These delivery systems are usually cationic to allow a favorable interaction between both DNA–TA and TA–cell surface (both DNA and cellular surface are anionic). The mechanism affording interactions between DNA and TA are predominantly electrostatic, although van der Waals forces will also be present.

The use of TAs with clinically approved contrast agents has resulted in successful labeling of several cell lines [28–32]. Complexation between the contrast agent and the TA depends on the nature of the contrast agent itself. However, where a low surface charge is present on the contrast agent, van der Waals forces will predominate. The contrast agent–transfection agent complex enters the cell by endocytosis, shown in Figure 2.

The principle advantage of using this technology is its wide availability. Commercially developed transfection kits (lipofectene, SAINT-Mix, poly-L-lysine, etc.) can be obtained from several manufacturers and have been used in conjunction with easily available contrast agents (Sinerem®, Endorem®, etc.).

The disadvantage of such a system is that the protocol must be optimized for every cell type [33], and the TAs themselves usually pose various levels of toxicity [34]; again these are cell-type dependent. It is therefore necessary to optimize the contrast agent/transfection agent ratio, in order to maintain a fine balance between labeling efficiency and cellular toxicity. Another drawback of this system is that the interaction between the contrast agent and the TA can result in a decrease in $T1$ and $T2$ relaxivity [29]. Furthermore, studies have also demonstrated that the more effective TAs have greater cytotoxic effects [34].

Delivery of Contrast Agent Using Specific Targeting

A distinct advantage of developing *de novo* contrast agents is the opportunity to incorporate specific molecular

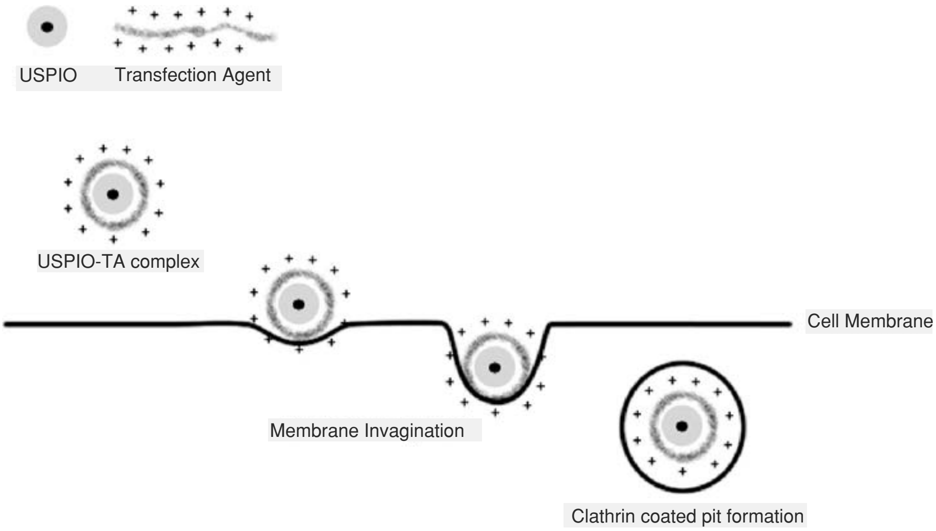

Fig. 2. Schematic of the complexation of USPIO with a transfection agent and subsequent cellular uptake via endocytosis.

targeting to increase the efficiency of cellular labeling. Many different methods have been used to deliver contrast agents and will be discussed in some detail.

Membrane Permeating Peptides

Membrane permeating peptides have received considerable attention as they can delivery cargoes of different sizes including: nanoparticles [35], liposomes [36], and fluorescein with extremely high efficiency and minimal cytotoxicity [37]. Various membrane permeating peptides sequences (peptide transduction domain, PTD) are found to occur naturally including *HIV-1* TAT, *Antennapedia* transcription factor, *Herpes simplex* virus, and VP22 transcription factor. However, the most extensively employed delivery system has been the conjugation of TAT peptide with USPIO to facilitate labeling of a range of cell types [11,35,38,39].

The precise mechanism for cellular entry has yet to be elucidated; however, there are several indications for particular structural requirements that allow for effective and efficient cellular uptake. One of the principal requirements is the presence of multiple arginine residues on the PTD for efficient cell entry. Many naturally occurring membrane-permeating peptides contain a large number of arginine residues [40]. Another requirement appears to be the presence of negatively charged glycosaminoglycans on the cell surface [41], whilst another report suggests that heparin sulfate is required on the cell surface [42]. It was originally thought that the uptake mechanism was energy independent, and thus would not involve endocytosis. Other studies suggested that the non-endosomal uptake was an artifact of the technique used to study the mechanism of cell entry [43].

Neverthless, what is clear, regardless of the exact mechanism, is that TAT and other polyarginine peptide sequences allow the shuttling of cargo across the cell membrane with high efficiency. The majority of studies that have investigated the delivery of CLIO into a variety of cells using PTDs have used the TAT peptide or a variation on the theme [13,23,39,44]. Studies have also demonstrated successful cellular labeling with gadolinium chelates conjugated with poly(arginine) with minimal of cytotoxic effects. However, there is some evidence of gadolinium chelate leakage from these cells [45,46].

Use of Antibodies

Conjugation of contrast agents to PTDs provides a 'generic' model for labeling a wide variety of cell types. However, this system lacks cellular specificity. In contrast, contrast agents conjugated to antibodies, against specific cell surface antigens, provides cellular targeting with high specificity [47]. However, targeting cell surface markers, whilst being specific, has two major drawbacks. Firstly, the presence of the nanoparticles on the surface of the cell may affect its capacity to migrate and "home" effectively. Secondly, the antibody–contrast agent complex's interaction with the cell surface antigen is reversible; thus there is a high probability that the complex can be taken up by other cells (e.g. macrophages) and provide ambiguous information on the migrational characteristics of the targeted cells. These two issues have been overcome by using the OX-26 antibody in the labeling of neural precursor cells [48], which is an internalizing antibody directed against the transferrin receptor. In this instance, uptake of the particles is through receptor-mediated endocytosis.

Other Methods for Delivering Contrast Agents

Alternative means of cell labeling with iron oxide nanoparticles have also been investigated. Recently, Gupta and Curtis have used lactoferrin and ceruloplasmin coated particles to label cells to target their respective receptors. This resulted in a decrease in toxicity where lactoferrin produced the least cytotoxic effects when compared with naked iron oxide particles [49]. However, these particles were shown not to be internalized and therefore face the same problem outlined above, namely loss of cell homing abilities or detachment of iron oxide from the cell surface.

Cytotoxicity and Metabolism

There are several important characteristics that need to be considered when designing a new contrast agent. These include its toxicity and eventual *in vivo* metabolism. It is essential that the presence of the contrast agents does not affect proliferation, differentiation, its ability to integrate into host tissues, nor its cellular function. Whilst iron oxide dextran nanoparticles have been used extensively in the clinic, these nanoparticles have remained outside the cell. Recent reports have demonstrated that the intracellular presence of dextran coated iron oxide nanoparticles induces apoptosis and affects cytoskeletal properties [50]. However, in this instance only the core of the iron oxide was investigated and was quoted to be 7.8 nm by magnetic measurements. It is likely that the overall hydrodynamic radius would play an important role in the disruption of intracellular structures. Thus, particles with a smaller hydrodynamic radius may pose fewer cytotoxic effects.

The mechanism of iron oxide metabolism *in vivo* has been known for a number of years, as these iron oxide nanoparticles were original produced for the treatment of severe anemia. It was found that the primary mechanism was the assimilation of exogenous iron oxide into the iron cycle [51] and is incorporated into rapidly regenerating hemoglobin [52].

Conjugation Chemistry: Attaching Contrast Agent to Delivery Ligand

As discussed previously, there are several methods for enhancing the uptake of contrast agents. In this section, we will discuss the means of conjugating PTDs and antibodies to contrast agents. In the case of USPIOs, there are two ways in which conjugation can be accomplished: (i) direct attachment to the stabilizing polymer, in this case dextran will be used as a model system, and (ii) the conjugation via a heterofunctional linker.

Conjugating Directly to USPIO: Oxidation-Reductive Amination

Whilst USPIOs are coated with hydroxyl groups present on dextran backbone, these groups are relatively unreactive in an aqueous environment. To allow direct conjugation, it is therefore necessary to introduce aldehyde moieties through selective oxidation of vicinal glycols in the presence of sodium periodate as shown in Figure 3.

It is then possible to produce an imine by reacting the aldehyde in the presence of an amine-terminating moiety. The imine however is unstable and therefore selective reduction of the imine is achieved through the use of sodium cyanoborohydride (Figure 4).

Whilst this approach has been used successfully for conjugating biological moieties [53,54], this conjugation method can give rise to several problems. Firstly, there may be reduced affinity of the conjugated ligand, probably due to steric hindrance from the dextran backbone [54]. Another problem that is frequently encountered is the uncontrolled oxidation of the dextran coating, resulting in particle destabilization, probably due to the degradation of the dextran [53]. Moreover, degradation was also found to occur on periodate oxidized sephadex G-25, where the dextran beads were degraded during extended exposure with sodium periodate [55]. Further problems can arise due to inconsistent reaction conditions, as it has been reported that the production of aldehydes depend on the pH of the reaction environment [56].

Introducing a Linker

An alternative method of conjugating the delivery/ targeting ligand to the contrast agent is via a linker. Nevertheless, there is still the issue of lack of reactivity of the hydroxyl groups under neutral aqueous conditions. This problem is overcome by the use of CLIO particles, where the dextran is cross-linked and then incubated in the presence of ammonia to produce amine-terminated particles. These on the other hand are relatively more reactive. It is then possible to couple the nanoparticles to a plethora of heterofunctional linkers, usually by the use of a succinimide ester activated compound as illustrated below (Figure 5).

The advantage of using this approach is the commercial availability of several succinimide esters available for

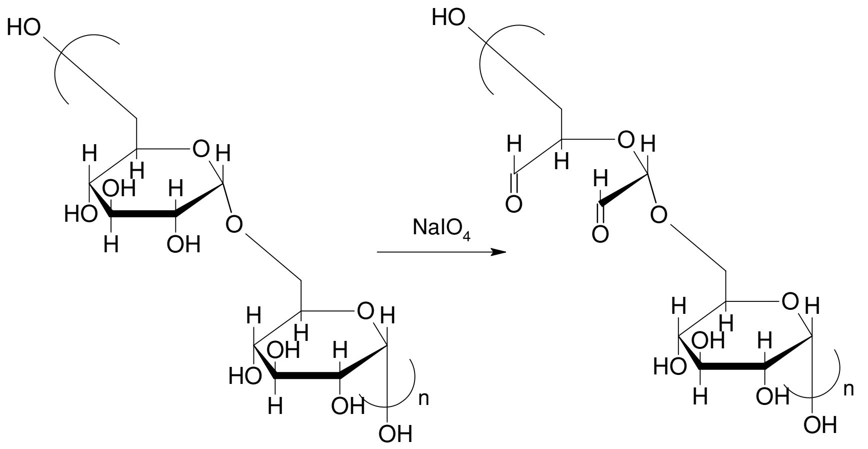

Fig. 3. Selective oxidation of neighboring hydroxyl groups in the presence of sodium periodate producing dextran polyaldehyde.

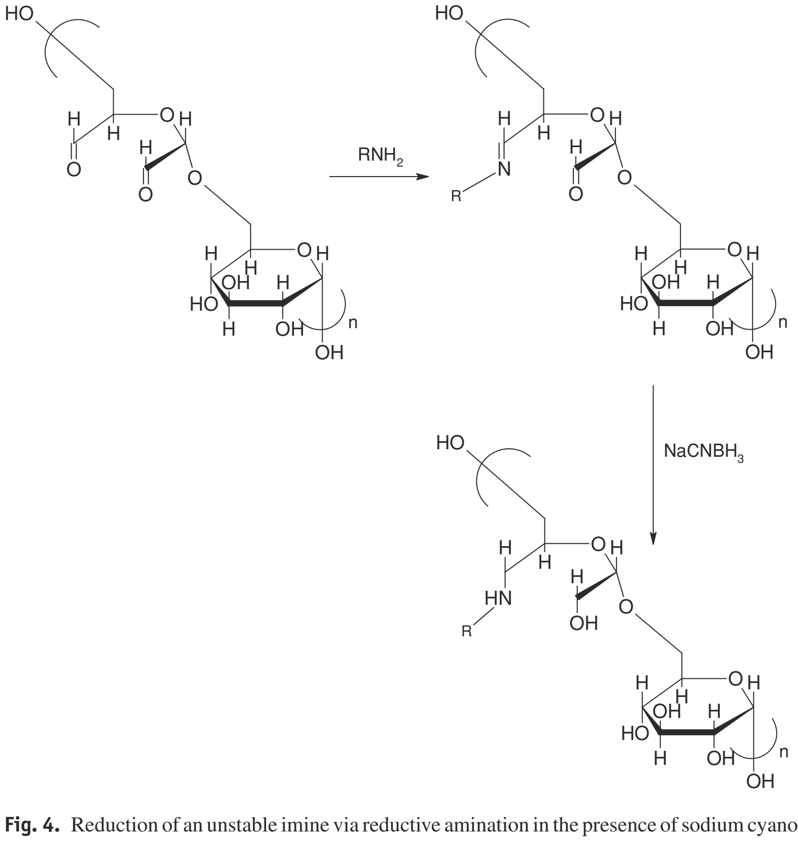

Fig. 4. Reduction of an unstable imine via reductive amination in the presence of sodium cyanoborohydride to produce a stable amine.

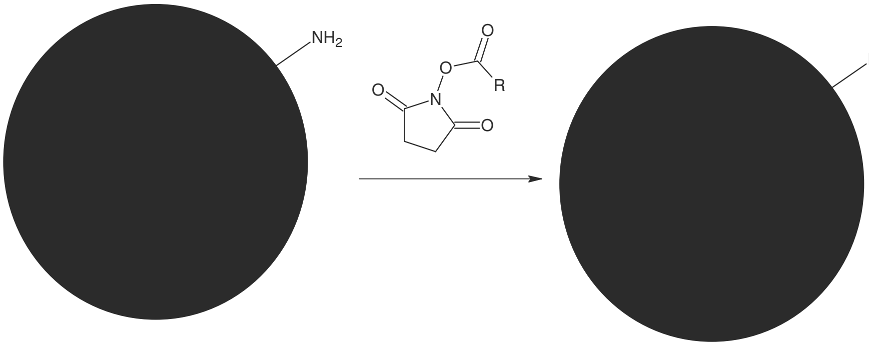

Fig. 5. Functionalization of amine-terminated nanoparticles in the presence of a succinimide ester to produce an amide, e.g. SIA, where R = CH_2I.

facile conjugation, although some can be readily prepared prior to use [57]. The disadvantage to this technique is that the *N*-hydroxysuccinimide ester is hydrolyzed under aqueous conditions.

The most common heterofunctional linkers used to date are those that allow the formation of either a thioether bond (SIA; Figure 6) or a disulfide bond (SPDP; Figure 7). These are ideal for selective conjugation to a cysteine residue either naturally present on the ligand, or introduced during synthesis. Sulfur is conjugated in preference as the rate of reaction is sulfhydryl > imidazolyl > thioether > amine [58].

SIA is preferential where a stable thioether bond is required, as SPDP produces a labile disulfide bond. The advantage of using SPDP is that the degree of conjugation can be observed by monitoring the increase in adsorption at 343 nm.

MRI Tracking of Stem Cells in the Heart

Myocardial infarction is by nature an irreversible injury. The extent of the infarction depends on the duration and severity of the perfusion defect [59]. Beyond contraction and fibrosis of myocardial scar, progressive ventricular remodeling of non-ischemic myocardium can further reduce cardiac function in the weeks to months after initial event [60].

Many of the therapies available to clinicians today can significantly improve the prognosis of patients following

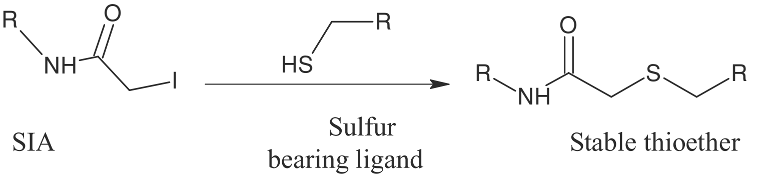

Fig. 6. Nanoparticles functionalized with SIA (where R = nanoparticle) react with sulfur bearing moieties to produce a stable thioether bond.

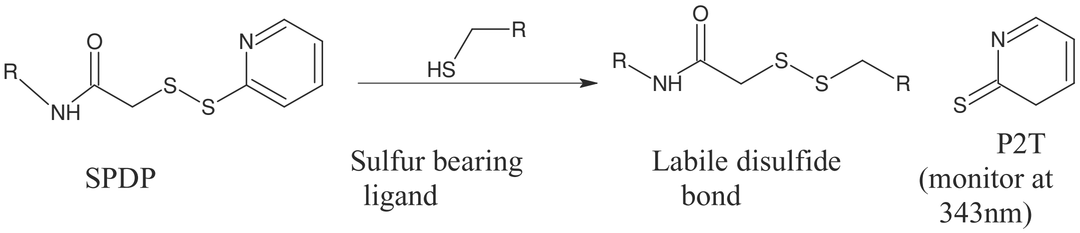

Fig. 7. SPDP derived nanoparticles (where R = nanoparticles) react with a sulfur bearing ligand to produce a cleavable disulfide bond.

an acute myocardial infarction [60,61]. However, no pharmacological or interventional procedure used clinically has shown efficacy in replacing myocardial scar with functioning contractile tissue. Cellular agents such as fetal cardiomyocytes [62], mesenchymal stem cells (MSCs) [63], endothelial progenitor cells [64], and skeletal myoblasts [65], or embryonic stem (ES) cells [66] have already shown some efficacy to engraft in the infarct, differentiating toward a cardiomyocyte phenotype, by expressing cardiac specific proteins, preserving left ventricular function and inhibiting myocardial fibrosis. Besides, *in vitro* exposure of stem cells, specifically MSCs, to specific signal molecules prior to transplantation into infarcted myocardium allows their differentiation into cardiomyocyte [67] and may facilitate a successful engraftment [68].

However, verification of the status of transplanted stem cells in animal models has been performed with histological analysis. Clinical data on stem cells transplantation is in its infancy and is very limited. But preliminary clinical data have shown that stem cell transplantation for the treatment of ischemic heart failure is feasible and promising [69]. Besides MRI was used in some clinical studies to assess the improvement of contractile function after cell transplantation [70] but without any possibility to visualize the transplanted stem cells. Therefore, the ability to label stem cells with MRI-visible contrast agents [71] should enable serial tracking and quantification of transplanted stem cells, non-invasively by MRI with high spatial resolution. The programmable nature of the imaging planes allows reproducible and volumetric coverage of the heart. Moreover, this technology scales well with subject size ranging from mouse to human.

Visualization of magnetically labeled endothelial progenitor cells transplanted intra-myocardially for therapeutic neovascularization in infarcted rats has been demonstrated with *ex vivo* MRI at 8.5 T on $T2$-weighted images [72].

Garot *et al.* [73] have demonstrated the feasibility of *in vivo* MRI tracking of skeletal muscle-derived myogenic precursor cells (MPC) pre-loaded with iron oxide nanoparticles (Endorem) injected into healthy and infarcted porcine myocardium. Iron-loaded cells in the infarcted region were detected by $T2$-weighted spin-echo MRI at 1.5 T. In addition, MRI guided the catheter for the injection of the labeled cells into the ischemic myocardium using Gd-DTPA delayed enhancement of the site. Moreover, post-mortem analysis demonstrated the presence of iron-loaded MPC at the center and periphery of the infarcted tissue as predicted by MRI.

MSCs derived from bone marrow can be detected and tracked by MRI for up to 3 weeks [74–76]. Allogeneic ferumoxides [74] or iron fluorescent particle [75,76] were given by intra-myocardial injection in a pig model of myocardial infarction. A minimum quantity of MSCs per injection was required to be MR-detectable on $T2^*$- [75] or $T2$-weighted images [74] as hypointense lesions. Indeed, Kraitchman *et al*. have shown that using a limited number of MSC injections per animal, only some (∼70%) of the injections performed in each animal can be visualized.

These promising experiments demonstrate the need for future studies to delineate the fate of injected stem cells by incorporating non-invasive tagging methods to monitor myocardial function following cell engraftment in the myocardial infarction. Consequently, MRI may lead to a better understanding of the myocardial pathophysiology as well as assessing the proper implantation and the effects of stem cell therapy by allowing a multimodal approach to evaluating anatomy, function, perfusion, and regional contractile parameters in a single non-invasive examination.

MRI Tracking of Stem Cells in the CNS

Neurodegenerative diseases where cell loss is the predominate feature of the pathology and, for which there are currently no cures, cellular replacement therapy using stem cells may provide a beneficial alternative. The efficacy of cell replacement therapy was first demonstrated using engraftment of human mesencephalic tissue into the brain of patient with Parkinson's disease [77]. Functional recovery and L-DOPA withdrawal followed by an increase in released dopamine demonstrated the functional integration of the grafted tissue. Although this was not a true stem cell transplant, it nevertheless indicated that the adult brain provides local environmental cues to undifferentiated cells to produce neuronal cell types capable of providing functional recovery.

Since this pioneering experiment, many different populations of stem cells have shown to differentiate into neural phenotypes. The most obvious choice of stem cell population would be those already derived from the neural phenotype. These include neural stem cells, found in the adult subventricular zone (SVZ) and glial-restricted precursors, found in the embryonic spinal cord. Neural stem cells have been shown to differentiate into dopaminergic neurons [78], astrocytes, and oligodendrocytes [79], and spinal cord motor neurons [80]. Surprisingly, these cells are also able to transdifferentiate into other non-neural cell types such as skeletal muscle [81]. Glial-restricted progenitors, on the other hand, are restricted to the glial lineage and produce oligodendrocytes and type-1 and type-2 astrocytes [82].

ES cells are the most pluripotent of all the stem cell populations, giving rise to many cell types in the body; thus have the greatest regenerative capacity. ES cells differentiate into a variety of neural phenotypes, including dopaminergic neurons [83], serotoninergic neurons [84], neuronal precursors [85], oligodendrocytes [86], and astrocytes [87]. There are several problems, aside from the issues of ethics, that makes ES cell therapy difficult, including the risk of inappropriate cellular differentiation and tumor formation.

Mesenchymal cells derived from bone marrow have also been shown to differentiate into neural phenotypes [88]. Additionally, rat MSCs differentiate into a mixture of neural phenotypes including astrocytes, oligodendrocytes, and neurons. Upon further differentiation, GABAergic, dopaminergic, and serotoninergic neurons may also develop [89].

Neural progenitor cells have innate migratory properties. For example, neural progenitor cells isolated from the SVZ of adult or neonatal rats, when implanted into the different regions of the neonatal brain, migrate and differentiate within regions such as the *olfactory bulb*, cortex, and *striatum*. In contrast, when grafted into the adult brain, the SVZ cells only migrated to the olfactory bulb, but not to the cortex or *striatum* [90].

MRI was used to longitudinally track the migration of SVZ cells after implantation into the healthy rat striatum using pre-labeling cells with BrdU and lipophilic dye-coated ferromagnetic particles [91]. Furthermore, MRI revealed that the area grafted with live cells appeared to expand, whereas the area implanted with dead cells, decreased in size. Immunohistochemical analysis showed that the SVZ cells differentiated into neurons (MAP-2^+ NeuN$^+$) and migrated within the striatum after being cultured with bFGF. These studies revealed only localized migration. Migration over greater distances was demonstrated using non-invasive MRI studies in a stroke lesioned animal model. It was hypothesized and later confirmed that stroke damage functions as a "chemoattractant" for neural stem cells [92]. Neural stem cells derived from the Maudsley Hippocampal Clone 36 (MHP36) cell line, were labeled with the bimodal contrast agent, GRID. This enables detection both by MRI and fluorescent histology. Following a middle cerebral artery occlusion (a rodent model of stroke), the neural stem cells were grafted unilaterally into the hemisphere contralateral to the lesion. Using a combination of GRID labeled cells and MRI, it was demonstrated that following 14 days post-transplantation; most of the cells had migrated to the ipsilateral hemisphere along the *corpus callosum* and populated the surrounding lesion area. Moreover, upon fluorescent immunochemistry, these cells were found to be GFAP$^+$ astrocytes and NeuN$^+$ neuronal precursors.

Hoehn *et al.* [93] used a similar stroke model to demonstrate the migratory properties of implanted ES cells into the brain by MRI. The cells were pre-labeled with USPIO and encapsulated with a lipofection reagent to enhance cellular uptake. The ES cells also expressed GFP as a reporter gene for immunohistochemical procedures. The labeled cells were implanted into two regions of the unaffected hemisphere: the border between the cortex and the *corpus callosum*, and the striatum. The labeled cells migrated toward the lesion in the opposite hemisphere. Strong hypointense "columns" were seen by MRI in the *corpus callosum*. These were later confirmed as migrating blankets of cells traveling toward the ischemic lesion. GFP-expressing cells were also seen in the ischemic penumbra, and in contrast to the study by Modo *et al.* [92], the majority were NeuN$^+$ suggesting that the cells had differentiated into neurons. Astrocytes and oligodendrocytes were also seen populating the surrounding area.

MRI studies have also been used to track glial progenitors labeled with contrast agent. However, in these studies MRI was used to scan post-mortem tissues, following cellular transplantation. Oligodendrocyte progenitor cells (OPCs) from the CG4 cell line have greater migratory and myelinating capacity than mature oligodendrocytes. The cells were labeled with monocrystalline iron oxide nanoparticles targeted to the transferrin receptor to aid internalization of the particles [94]. The progenitor cells were grafted into the spinal cord of a myelin-deficient rat. Cellular migration was also visualized by MRI, especially in the dorsal column. Moreover, iron oxide labeled cells, fixed with paraformaldehyde and implanted in the same way, did not migrate at all; MRI contrast was seen only at the site of injection. This also suggests that the iron oxide remains localized and is not taken up by other host cells. This is of great importance if iron oxide labeling and tracking of cells is to be used clinically. The MR images were verified by histological analysis and the lesion was found to include astrocytes, microglia, and myelin. Importantly, the Prussian blue staining correlated with that for myelin, whereas it did not overlap with the GFAP$^+$ astrocytes or microglia present. Obviously reactive gliosis and an immune reaction had occurred, but the inflammatory cells had not taken up iron oxide; the labeled OPCs were able to infiltrate the inflamed area and produce myelin.

Jendelova *et al.* [95] used MRI to study the differential response of MSCs and ES cells in rodent models of stroke (photochemical lesion) and spinal cord compression (balloon inflation). Prior to implantation, both MSCs and ES cells were labeled with Endorem and additionally co-labeled with either BrdU or GFP, respectively.

Following the induction of the lesions, either ES cells or MSCs were grafted contralateraly to the ischemic lesion. In another set of animals, either ES cells or MSCs were administered intravenously into rats with an ischemic lesion. The animals with spinal cord compression lesion were infused intravenously with MSCs. ES cells given to rats with ischemic lesions, regardless of whether given intravenously or intracerebral implantation, migrated to the lesion site within 2 weeks, as observed by MRI and subsequently confirmed with GFP visualisation. Additionally, at the site of implantation, hyper-proliferation was seen in 10% of the animals. This suggests that tumor formation had taken place, and was detected using MRI as a very large hypointense area, much larger than the other cellular transplants [95].

Implanted MSCs also migrated to the lesion area but gathered in the necrotic tissue surrounding the lesion. Few cells entered the actual lesion and of those very few differentiated into neurons, as seen 4 weeks after implantation. Additionally, MSCs injected intravenously also migrated to the lesion site and were visible for 7 weeks post-implantation. Similarly, MSCs injected intravenously also migrated to the lesioned spinal cord, which was also confirmed with Prussian blue staining.

Thus, the use of stem cell therapy to treat neurodegenerative diseases is a realistic possibility in the near future. However, the need for non-invasive imaging techniques is a prerequisite in order to monitor these transplants to determine clinical efficacy. Examination by MRI ensures that the stem cells are not only injected to the lesion site, but it also allows the monitoring of inappropriate cellular migration, and furthermore identifies damage to surrounding tissues.

MRI Tracking of Cell-Based Tumor Therapy

Cell-based therapies have received much attention as novel therapeutics for the treatment of cancer [2]. For example, tumor antigen-specific lymphocytes have been used for adoptive transfer and treatment in lymphoma, melanoma, and other malignancies. But a major obstacle to an accurate evaluation of treatment efficacy and anti-tumor effects has been the inability to track these cytotoxic T-lymphocytes (CTLs), *in vivo* at sufficiently high spatial and temporal resolution [96]. Dodd *et al.* [97] demonstrated the distribution of T cells labeled with CLIO-TAT peptide, by *in vivo* MRI, in mice following intravenous administration. These studies also showed the migration of T cells loaded with CLIO-TAT to the spleen by monitoring a decrease in signal intensity observed by MRI at 4.7 T. Similar protocols have been used to detect the localization of cells in small sites such as tumors and lymph nodes in small animals.

Kircher *et al.* [98] were the first to assess and quantitate the recruitment of systemically administered cells over time in a model of melanoma. They used an improved superparamagnetic particle (CLIO-HD: highly derivatized CLIO nanoparticles) to optimize the lymphocytes labeling at levels that can be detected *in vivo* via high resolution three-dimensional $T2$-weighted MRI at 8.5 T. This study showed the ability to examine both cellular recruitment and therapeutic response (tumor volume change) in three dimensions, across the entire tumor simultaneously, and in quantitative and repetitive manner in the same animal using MRI.

Zhang *et al.* [99] have reported the *in vivo* targeting and infiltration by magnetically labeled neural progenitor cells, derived from the adult SVZ, to a tumor mass in a rat model of gliosarcoma. To date, this was the first study in which adult neural stem cells have been employed to target a brain tumor. The non-invasive imaging, by MRI at 7 T, monitored the dynamic migration of superparamagnetic particle-labeled neural progenitor cells toward the brain tumor. Indeed, the spatiotemporal distribution of transplanted cells and the tumor in the host brain identified by MRI was confirmed using histochemical staining and fluorescent microscopy. This study also demonstrated, using MRI, the migration of iron oxide nanoparticles labeled MSCs toward the tumor, thus confirming previous reports of stem cell infiltration of brain tumors [100,101].

Development of MRI techniques for *in vivo* assessement of the interaction between grafted neural progenitor cells and tumor cells in the host brain may contribute not only to our understanding of the mechanisms involved in the treatment of brain tumors with neural progenitor cells therapy but also assess the outcome of neural progenitor cell therapy both in animals and in humans with brain tumors.

Tumor vasculature has attracted much interest as a potential target for cancer therapy [102]. Since cancerous growth depends on a good blood supply for nutrition and oxygen, the ability to image tumor vasculature would help to monitor the progress of cancer therapies. Brown *et al.* [103] demonstrated the accumulation of Sickle red blood cells (RBCs) in tumor vasculature, using MRI at 7 T. In this study, RBCs, from patients with sickle cell anemia, were loaded with Gd-DTPA and injected intravenously in rats with 9L glioma. $T1$- and $T2$-weighted MR images were used to monitor the infiltration of Gd-DTPA-loaded RBCs into the tumor mass. Additionally, changes in hemoglobin–oxygen state after administration of RBCs, without Gd-DTPA loading, was assessed using BOLD imaging. MRI allowed the visualization of the preferential aggregation of RBCs in tumor periphery.

Thus, MRI can be used as a useful technique to follow the cellular migration and recruitment to monitor the progress of cell-based therapy in tumors.

The high anatomical resolution together with the non-invasively *in vivo* imaging methodology offered by MRI, applied to monitoring implanted cells, will greatly facilitate the clinical realization and optimization of the opportunities for cell-based therapies. There are numerous examples where similar methodologies of cell tracking can aid in clinical diagnosis or can be used to trace other cells types, such as those following an inflammatory response [104,105].

Acknowledgment

This work was funded by the Medical Research Council of Great Britain.

References

1. Dove A. Nat. Biotechnol. 2002;20:339.
2. Valone FH, Small E, MacKenzie M, Burch P, Lacy M, *et al.* Cancer J. 2001;7:(Suppl 2):S53.
3. Burt RK, Traynor A. Curr. Opin. Hematol. 1998;5:472.
4. Semsarian C. Intern. Med. J. 2002;32:259.
5. Bessis N, Cottard V, Saidenberg-Kermanach N, Lemeiter D, Fournier C, *et al.* J. Gene. Med. 2002;4:300.
6. Petit-Zeman S. Nat. Biotechnol. 2001;19:201.
7. Johnstone B, Yoo J. Expert. Opin. Biol. Ther. 2001;1:915.
8. Wen YJ, Min R, Tricot G, Barlogie B, Yi Q. Blood. 2002;99:3280.
9. Lagasse E, Connors H, Al-Dhalimy M, Reitsma M, Dohse M, *et al.* Nat. Med. 2000;6:1229.
10. Orlic D, Kajstura J, Chimenti S, Jakoniuk I, Anderson SM, *et al.* Nature. 2001;410:701.
11. Lewin M, Carlesso N, Tung CH, Tang XW, Cory D, *et al.* Nat. Biotechnol. 2000;18:410.
12. Bhorade R, Weissleder R, Nakakoshi T, Moore A, and Tung CH. Bioconjug. Chem. 2000;11:301.
13. Josephson L, Tung CH, Moore A, Weissleder R. Bioconjug. Chem. 1999;10:186.
14. Merbach AE, Toth E. The Chemistry of Contrast Agents in Medical Magnetic Resonance Imaging. John Wiley and Sons, New York, 2001.
15. Roch A, Muller RN, Gillis P. J. Chem. Phys. 1999;110:5403.
16. Mack MG, Balzer JO, Straub R, Eichler K, Vogl TJ. Radiology. 2002;222:239.
17. Ito A, Shinkai M, Honda H, Kobayashi T. Cancer Gene Ther. 2001;8:649.
18. Hafeli UO, Yu J, Farudi F, Li Y, Tapolsky G. Nucl. Med. Biol. 2003;30:761.
19. Jordan A, Scholz R, Wust P, Fahling H, Krause J, *et al.* Int. J. Hyperthermia. 1997;13:587.
20. Roger J, Pons JN, Massart R, Halbreich M, Bacri JC. Eur. Phys. J. 1999;5:321.
21. Wunderbaldinger P, Josephson L, Weissleder R. Acad. Radiol. 2002;9(Suppl 2):S304.
22. Vives E, Brodin P, Lebleu B. J. Biol. Chem. 1997;272:16010.
23. Zhao M, Kircher MF, Josephson L, Weissleder R. Bioconjug. Chem. 2002;13:840.
24. Fawell S, Seery J, Daikh Y, Moore C, Chen LL, *et al.* Proc. Natl. Acad. Sci. U. S. A. 1994;91:664.
25. Caron NJ, Torrente Y, Camirand G, Bujold M, Chapdelaine P, *et al.* Mol. Ther. 2001;3:310.
26. Artemov D, Mori N, Okollie B, Bhujwalla ZM. Magn. Reson. Med. 2003;49:403.
27. Kang HW, Josephson L, Petrovsky A, Weissleder R, Bogdanov A, Jr. Bioconjug. Chem. 2002;13:122.
28. Frank JA, Miller BR, Arbab AS, Zywicke HA, Jordan EK, *et al.* Radiology. 2003;228:480.
29. Frank JA, Zywicke H, Jordan EK, Mitchell J, Lewis BK, *et al.* Acad. Radiol. 2002;9(Suppl 2):S484.
30. Kalish H, Arbab AS, Miller BR, Lewis BK, Zywicke HA, *et al.* Magn. Reson. Med. 2003;50:275.
31. Arbab AS, Yocum GT, Kalish H, Jordan EK, Anderson SA, *et al.* Blood. 2004;4:1217.
32. Arbab AS, Yocum GT, Wilson LB, Parwana A, Jordan EK, *et al.* Mol. Imaging. 2004;3:24.
33. Bulte JW, Arbab AS, Douglas T, Frank JA. Methods Enzymol. 2004;386:275.
34. Kim SW, Ogawa T, Tabata Y, Nishimura I. J. Biomed. Mater. Res. 2004;71A:308.
35. Becker ML, Remsen EE, Pan D, Wooley KL. Bioconjug. Chem. 2004;15:699.
36. Torchilin VP, Rammohan R, Weissig V, Levchenko TS. Proc. Natl. Acad. Sci. U. S. A. 2001;98:8786.
37. Futaki S, Suzuki T, Ohashi W, Yagami T, Tanaka S, *et al.* J. Biol. Chem. 2001;276:5836.
38. Sundstrom JB, Mao H, Santoianni R, Villinger F, Little DM, *et al.* J. Acquir. Immune. Defic. Syndr. 2004;35:9.
39. Wunderbaldinger P, Josephson L, Weissleder R. Bioconjug. Chem. 2002;13:264.
40. Sakai N, Matile S. J. Am. Chem. Soc. 2003;125:14348.
41. Console S, Marty C, Garcia-Echeverria C, Schwendener R, Ballmer-Hofer K. J. Biol. Chem. 2003;278:35109.
42. Fuchs SM, Raines RT. Biochemistry. 2004;43:2438.
43. Richard JP, Melikov K, Vives E, Ramos C, Verbeure B, *et al.* J. Biol. Chem. 2003;278:585.
44. Koch AM, Reynolds F, Kircher MF, Merkle HP, Weissleder R, *et al.* Bioconjug. Chem. 2003;14:1115.
45. Allen MJ, Meade TJ. J. Biol. Inorg. Chem. 2003;8:746.
46. Allen MJ, MacRenaris KW, Venkatasubramanian PN, Meade TJ. Chem. Biol. 2004;11:301.
47. Suwa T, Ozawa S, Ueda M, Ando N, Kitajima M. Int. J. Cancer. 1998;75:626.
48. Bulte JW, Ben-Hur T, Miller BR, Mizrachi-Kol R, Einstein O, *et al.* Magn. Reson. Med. 2003;50:201.
49. Gupta AK, Curtis AS. Biomaterials. 2004;25:3029.
50. Berry CC, Wells S, Charles S, Aitchison G, Curtis AS. Biomaterials. 2004;25:5405.
51. Weissleder R, Stark DD, Engelstad BL, Bacon BR, Compton CC, *et al.* Am. J. Roentgenol. 1989;152:167.
52. London E. J. Pharm. Sci. 2004;93:1838.
53. Molday RS, MacKenzie D. J. Immunol. Methods. 1982;52:353.
54. Shen TT, Bogdanov A, Jr, Bogdanova A, Poss K, Brady TJ, *et al.* Bioconjug. Chem. 1996;7:311.
55. Wilson MB, Nakane PK. J. Immunol. Methods. 1976;12:171.
56. Novikova EV, Tishchenko EV, Iozep AA, Passet BV. Russ. J. Appl. Chem. 2002;75:985.
57. Hartman FC, Suh B, Welch MH, Barker R. J. Biol. Chem. 1973;248:8233.
58. Hermanson GT. Bioconjugate Techniques. Elsevier, Amesterdam, 1996.
59. Reimer KA, Lowe JE, Rasmussen MM, Jennings RB. Circulation. 1977;56:786.
60. Pfeffer MA. Annu. Rev. Med. 1995;46:455.
61. Ryan TJ, Antman EM, Brooks NH, Califf RM, Hillis LD, *et al.* J. Am. Coll. Cardiol. 1999;34:890.
62. Etzion S, Battler A, Barbash IM, Cagnano E, Zarin P, *et al.* J. Mol. Cell. Cardiol. 2001;33:1321.
63. Shake JG, Gruber PJ, Baumgartner WA, Senechal G, Meyers J, *et al.* Ann. Thorac. Surg. 2002;73:1919.
64. Kawamoto A, Gwon HC, Iwaguro H, Yamaguchi JI, Uchida S, *et al.* Circulation. 2001;103:634.
65. Jain M, DerSimonian H, Brenner DA, Ngoy S, Teller P, *et al.* Circulation. 2001;103:1920.

66. Min JY, Yang Y, Converso KL, Liu L, Huang Q, *et al*. J. Appl. Physiol. 2002;92:288.
67. Makino S, Fukuda K, Miyoshi S, Konishi F, Kodama H, *et al*. J. Clin. Invest. 1999;103:697.
68. Tomita S, Li RK, Weisel RD, Mickle DA, Kim EJ, *et al*. Circulation. 1999;100:II247.
69. Hamano K, Nishida M, Hirata K, Mikamo A, Li TS, *et al*. Jpn. Circ. J. 2001;65:845.
70. Britten MB, Abolmaali ND, Assmus B, Lehmann R, Honold J, *et al*. Circulation. 2003;108:2212.
71. Bulte JW, Douglas T, Witwer B, Zhang SC, Strable E, *et al*. Nat. Biotechnol. 2001;19:1141.
72. Weber A, Pedrosa I, Kawamoto A, Himes N, Munasinghe J, *et al*. Eur. J. Cardiothorac. Surg. 2004;26: 137.
73. Garot J, Unterseeh T, Teiger E, Champagne S, Chazaud B, *et al*. J. Am. Coll. Cardiol. 2003;41:1841.
74. Kraitchman DL, Heldman AW, Atalar E, Amado LC, Martin BJ, *et al*. Circulation. 2003;107:2290.
75. Hill JM, Dick AJ, Raman VK, Thompson RB, Yu ZX, *et al*. Circulation. 2003;108:1009.
76. Dick AJ, Guttman MA, Raman VK, Peters DC, Pessanha BS, *et al*. Circulation. 2003;108:2899.
77. Piccini P, Brooks DJ, Bjorklund A, Gunn RN, Grasby PM, *et al*. Nat. Neurosci. 1999;2:1137.
78. Ourednik J, Ourednik V, Lynch WP, Schachner M, Snyder EY. Nat. Biotechnol. 2002;20:1103.
79. Yamamoto S, Yamamoto N, Kitamura T, Nakamura K, Nakafuku M. Exp. Neurol. 2001;172:115.
80. Shibuya S, Miyamoto O, Auer RN, Itano T, Mori S, *et al*. Neuroscience. 2002;114:905.
81. Galli R, Borello U, Gritti A, Minasi MG, Bjornson C, *et al*. Nat. Neurosci. 2000;3:986.
82. Noble M, Mayer-Proschel M. In: MS Rao (Ed). Stem Cells and CNS Development. Humana Press, New Jersey, 2001, p. 123.
83. Kawasaki H, Mizuseki K, Nishikawa S, Kaneko S, Kuwana Y, *et al*. Neuron. 2000;28:31.
84. Lee SH, Lumelsky N, Studer L, Auerbach JM, McKay RD. Nat. Biotechnol. 2000;18:675.
85. Reubinoff BE, Itsykson P, Turetsky T, Pera MF, Reinhartz E, *et al*. Nat. Biotechnol. 2001;19:1134.
86. Liu S, Qu Y, Stewart TJ, Howard MJ, Chakrabortty S, *et al*. Proc. Natl. Acad. Sci. U. S. A. 2000;97:6126.
87. Stavridis MP, Smith AG. Biochem. Soc. Trans. 2003;31:45.
88. Weimann JM, Charlton CA, Brazelton TR, Hackman RC, Blau HM. Proc. Natl. Acad. Sci. U. S. A. 2003;100:2088.
89. Jiang Y, Jahagirdar BN, Reinhardt RL, Schwartz RE, Keene CD, *et al*. Nature. 2002;418:41.
90. Herrera DG, Garcia-Verdugo JM, Alvarez-Buylla A. Ann. Neurol. 1999;46:867.
91. Zhang RL, Zhang L, Zhang ZG, Morris D, Jiang Q, *et al*. Neuroscience. 2003;116:373.
92. Modo M, Mellodew K, Cash D, Fraser SE, Meade TJ, *et al*. Neuroimage. 2004;21:311.
93. Hoehn M, Kustermann E, Blunk J, Wiedermann D, Trapp T, *et al*. Proc. Natl. Acad. Sci. U. S. A. 2002;99:16267.
94. Bulte JW, Zhang S, van Gelderen P, Herynek V, Jordan EK, *et al*. Proc. Natl. Acad. Sci. U. S. A. 1999;96:15256.
95. Jendelova P, Herynek V, Urdzikova L, Glogarova K, Kroupova J, *et al*. J. Neurosci. Res. 2004;76:232.
96. Yee C, Riddell SR, Greenberg PD. Curr. Opin. Immunol. 2001;13:141.
97. Dodd CH, Hsu HC, Chu WJ, Yang P, Zhang HG. J. Immunol. Methods. 2001;256:89.
98. Kircher MF, Allport JR, Graves EE, Love V, Josephson L, *et al*. Cancer Res. 2003;63:6838.
99. Zhang Z, Jiang Q, Jiang F, Ding G, Zhang R, *et al*. Neuroimage. 2004;23:281.
100. Aboody KS, Brown A, Rainov NG, Bower KA, Liu S, *et al*. Proc. Natl. Acad. Sci. U. S. A. 2000;97:12846.
101. Lee J, Elkahloun AG, Messina SA, Ferrari N, Xi D, *et al*. Cancer Res. 2003;63:8877.
102. Folkman J. Nat. Med. 1995;1:27.
103. Brown SL, Ewing JR, Nagaraja TN, Swerdlow PS, Cao Y, *et al*. Magn. Reson. Med. 2003;50:1209.
104. Taupitz M, Schmitz S, Hamm B. Rofo. Fortschr. Geb. Rontgenstr. Neuen. Bildgeb. Verfahr. 2003;175:752.
105. Yeh TC, Zhang W, Ildstad ST, Ho C. Magn. Reson. Med. 1995;33:200.

Part I, Section 3:
Applications in Marine Science

Foreword to Applications in Marine Science

Today, strong focus on freshness and high product quality is an essential strategy of fisheries and aquaculture. Both consumer and marked are becoming nowadays increasingly aware of all the dietary benefits of marine foods for human health. Maintaining the quality of marine foods through the whole value chain is one of the most important challenges for this industry. Therefore it is necessary to develop basic knowledge about the product composition, degradation processes, effects of processing on product shelf life as well as effective methods of quality preservation. Much of on-going research in being carried out in this field, where both traditional and more sophisticated techniques are in use. Modern Nuclear Magnetic Resonance (NMR) technique is a unique method that opens up great possibilities to study foods non-destructively and non-invasively in many different ways.

In the first part of the section the application of several **low field NMR techniques** for use in process and quality control is demonstrated. One of them is a newly developed time domain NMR technique allows determining the most important quality parameters of fish feed as protein, carbohydrate, fat and moisture content in one measurement. This application is implemented as an at-line method in several fish feed production plants. Furthermore, the low field NMR techniques can provide with information about the fat and water in fish tissue, and a combination of the free-induction decay and the pulsed gradient spin-echo technique allows simultaneous determination of fat and water content in fatty fish species. It is shown how the structural changes in fish muscle, water binding and distribution within the muscle can be studied by the low field NMR. The available mathematical methods for extracting the information from the NMR relaxation signals are discussed as well. A great potential of the low field NMR as a user-friendly non-destructive method for measuring of important quality attributes in marine foods is demonstrated.

The second part of the section deals with the **high resolution NMR.** It is shown to be a unique tool in lipid research, where many metabolites and components can be studied simultaneously in relatively short time without any extraction involved. High resolution NMR enables to quantify lipid classes, to obtain fatty acid composition, to study the positional distribution of fatty acids in the triacylglycerol molecule, as well as to study the lipolysis and lipid oxidation in the same sample. Utilization of various Electron Spin Resonance (ESR) techniques is also shown to provide an additional valuable information regarding early stages of lipid oxidation in marine material.

The third section presents the use of **^{1}H and ^{13}C high resolution magic angle spinning (HR MAS) NMR** for quantification of the total omega-3 fatty acids in intact muscle of salmon. Application of this method for metabolic profiling of micro algae and analysis of fatty acids and storage polysaccharide structure in algae is presented as well. Ability to perform spectroscopic NMR investigations on intact cells or muscle allows to obtain a vast amount of information in a truly non-destructive way on, for example, degradation processes or biochemical processes related to fatty acid biosynthesis. Another important practical benefit of the HR MAS NMR is that both ^{1}H and ^{13}C experiments can be done on the same sample with only one simple sample preparation.

In the fourth section the use of the **Magnetic Resonance Imaging** (**MRI**) as research tool in food science is demonstrated. Due to high investment costs, the sheer size of the instruments and the infrastructure needed, MRI can not presently be introduced as a standard analytical tool in aquaculture or fish processing industry. However, as a research tool taking advantage of the unique features of the method, one can obtain basic insight into a number of issues related to anatomical studies, composition and structure of tissues, distribution maps of fat, water and salt as well as temperature profiles. In some cases theoretical transport models can be used to interpret the images, like for example in MRI studies of salting or dehydration. MRI has a great potential for fish industry as a tool to study the effects of feeding regimes during the fish on-growth phase and breeding, optimisation of unit operations in the fish processing such as salting, freezing and thawing.

Abbreviations

TD NMR: time domain nuclear magnetic resonance

FID: free induction decay

CPMG: Carr–Purcell-Meiboom-Gill

NIR: near Infrared Spectroscopy

PARAFAC: parallel factor analysis

PLS: partial least-squares

WHC: water holding capacity

DSC: different scanning calorimetry

PUFA: polyunsaturated fatty acid

n-3: omega-3

DHA: docosahexaenoic acid

SFA: saturated fatty acid

MUFA: mono unsaturated fatty acid

EGDM: ethylene glycol dimethyl ether

HRGC: high resolution gas chromatography

GC-MS: gas chromatography mass spectrometry

ESR: electron spin resonance

EPA: eicosapentaenoic acid

PCA: principal component analysis

Chl *a*: chlorophyll

HR MAS: high resolution magic angle spinning

FA: fatty acids

MRI: magnetic resonance imaging

MQF: multiple quantum filter

SQ: single quantum

DQF: double quantum filter

ATP: Adenosine 5′-triphosphate

HPLC: High Performance Liquid Chromatography

DEPT: Distortionless Enhancement by Polarization Transfer

HETCOR: Heteronuclear Correlation spectroscopy (C,H-Cosy)

DP: Degree of Polymerization

DB: Degree of branching

Comprehensive Compositional Analysis of Fish Feed by Time Domain NMR

Emil Veliyulin[1], Karl Østerhus[2], Wolfgang Burk[3], Trond Singstad[4], and Tore Skjetne[5]
[1]*SINTEF Fisheries and Aquaculture, 7465 Trondheim, Norway*
[2]*EWOS Innovation, 4335 Dirdal, Norway*
[3]*Bruker Optik GmbH, Silberstreifen, D-76287 Rheinstetten, Germany*
[4]*St.Olavs Hospital, 7465 Trondheim, Norway*
[5]*SINTEF Petroleum Research, 7465 Trondheim, Norway*

Introduction

The quality of fish feed and the effectiveness of fish feed production process are important issues for both fish feed suppliers and fish farmers. A correct combination of protein, carbohydrate, fat, and moisture contents in fish feed is crucial for achieving a desirable growth rate and other key characteristics of farmed fish.

Ability of fast at-line control of the composition of fish feed would give fish feed producers an advantage of more flexible control over the production, resulting in a more effective consumption of energy and raw ingredients, increasing the production speed, and improving the quality of the final product. Ability to do rapid corrections in the ongoing production, based on the at-line analysis results would substantially reduce the amount of rework and low-grade production.

At the initial stage of fish feed production, a mixture of raw ingredients is prepared to produce the semi-solid matrix of the pellet. This mixture of raw ingredients mainly contains protein, carbohydrate, moisture, and fat. During the extrusion process, this mixture is compacted under high temperature and pressure to form a pellet with a porous, semi-solid wet matrix. The pellet matrix is then dried and saturated with fish or vegetable oil.

Wide variety of well-known analytical procedures currently adopted by feed producers for compositional analysis of fish feed has a number of common disadvantages. These standard chemical–physical tests are usually time consuming, demanding highly trained staff, costly, most of the standard methods are destructive for the sample, often require thorough calibration, many of them utilize dangerous toxic solvents and cannot be performed at the production line.

To the contrary modern time domain nuclear magnetic resonance (TD NMR) analyzers offer a wide spectrum of quick, non-destructive, and precise applications. Thanks to the high automation of modern NMR instruments, most routine tests can be performed by the ground-floor personal. A TD NMR instrument can perform a number of experiments, providing with various types of information about the studied material. This is accomplished by programming and running specific NMR pulse sequences, such as, for example, "free induction decay" (FID), "Hahn echo" [1], CPMG [2], "solid echo" [3], and others. Choice of the NMR pulse sequence depends not only on the type of the information required, but also to a large extent on the physical and chemical properties of the sample. Presence of solid and liquid phases, their mobility, rigidity, and NMR relaxation times are the most important parameters to be taken into consideration.

A number of TD NMR applications have recently been developed and adopted for quality control of foods such as rapid determination of fat content in meat [4,5], characterization of fat and water states in cheese [6], prediction of the content of water, oil, and protein in rape and mustard seeds [7], solid fat content analysis [8], monitoring of textural changes in frozen cod [9], and NMR relaxation time studies of intact fish flesh [10] and meat [11].

Experimental

Equipment

The technique has been implemented on a BRUKER minispec mq10 TD NMR analyzer (Bruker Optik GmbH, Rheinstetten, Germany) using a built-in programming language ExpSpel [12]. The instrument operated at 10 MHz proton frequency and could accommodate sample tubes of 40 mm in diameter. Sample tubes could be filled up to about 4 cm filling height to be measured in the system. This corresponded to about 30 or more pellets depending on their size.

Graham A. Webb (ed.), Modern Magnetic Resonance, 897–903.
© 2008 *Springer.*

Fish Feed Samples

Fish feed pellet is a porous, semi-solid matrix saturated with fish oil. Fish oil content in a pellet typically varies within 16–40 wt.%. The matrix of the pellet consists of a number of chemical compounds depending on the recipe used in the production. The most important of them are protein and carbohydrate, that together usually constitute over 95% of the solid matrix weight. Other typical ingredients of the matrix are ashes, minerals, vitamins, and pigments. In addition the solid matrix of fish feed contains certain amount of rest moisture left after drying of the extruded pellets. Amount of the rest moisture can vary within 5–10 wt.%.

NMR Measurements of Fat and Moisture

In a fish feed pellet, the residual moisture is always strongly bounded to the solid matrix which makes its NMR relaxation time much shorter than that of the oil. This has been confirmed by a T_2 relaxation curve measurement by a CPMG technique with the following experimental parameters: echo time (TE) = 0.1 ms, relaxation delay (RD) = 2 s, number of acquired even echoes 8000, and number of scans 32. Figure 1 shows the continuous distribution of the T_2 relaxation times that was calculated by inverse Laplace transform algorithm [13] implemented in the BRUKER minispec software. From the last figure, it is seen that the average relaxation time of the residual moisture (peak centered at 3.5 ms) is much shorter than that of fish oil (peak centered at about 130 ms). The relaxation peaks in Figure 1 were additionally broadened by the processing. Close inspection of the measured relaxation curve indicated that there is no contribution of the moisture signal at times above 6 ms. Thus it was possible to quantify the total amount of hydrogen atoms present in the fish oil by a "Hahn echo" experiment with the echo time of 6 ms. Unlike the "Hahn echo," the amplitude of the FID signal from fish feed is proportional to the total amount of protons in the liquid phase, i.e. both fish oil and rest moisture. Thus by combining measured amplitudes of the FID and the "Hahn echo" signals both fat and moisture contents could be quantified.

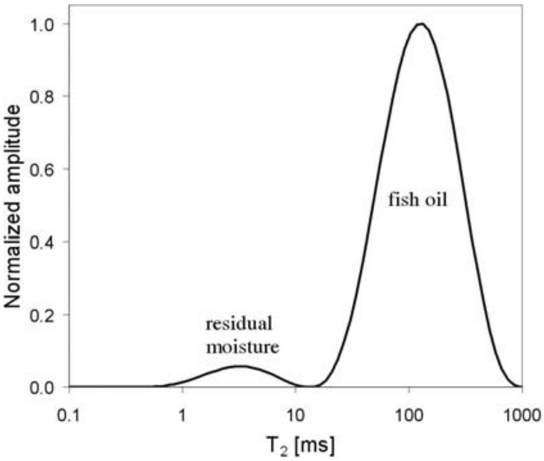

Fig. 1. Continuous distribution of the spin–spin relaxation times in fish feed.

NMR Measurements of Protein and Carbohydrate

Detection of NMR signal from large and immobile molecules like solid proteins has always been a challenging experimental task. These large molecules have extremely short NMR relaxation times and the majority of TD NMR techniques cannot be used for quantitative measurements of solid protein content. To obtain an NMR signal from the solid matrix of fish feed, a "solid echo" technique was used that allowed to overcome the receiver "dead time" problem and recover the full signal amplitude from the sample's solid part. The corresponding NMR sequence consists of two 90° pulses with different phases allowing to observe "solid" echoes from a system with dipole–dipole coupled protons [14]. If the sample contains both solid and liquid phases, the "solid echo" pulse sequence will in addition generate a FID-like tail following the "solid echo" signal [15]. This is schematically illustrated in Figure 2. In a fish feed production up to five main raw ingredients (fish meal, wheat meal, wheat gluten, soybean meal, and maize gluten) are mixed together in various proportions. Chemical composition of each raw ingredient of fish feed is always known from the preliminary wet chemical analysis. The total amplitude of the observed "solid echo" is a measure for the total amount of all protons in both solid and liquid phases of the sample. The difference between the total "solid echo" amplitude and the FID amplitude originates only from the solid part of the sample as indicated in Figure 2. The solid matrix of fish feed consists mainly of proteins, carbohydrates, ash (<10%), vitamins (<1%), and pigment (<0.1%). In order to extract the NMR signal due to the protein content of fish feed only, a set of five "protein" coefficients, one for each raw ingredient, was introduced. The coefficients represented parts of the "solid echo" signal due to the protein contribution for each raw ingredient relative to that of pure fish meal. Fish meal was thus assumed to be a reference ingredient having a "protein" coefficient equal to 1. The calculation of the protein content

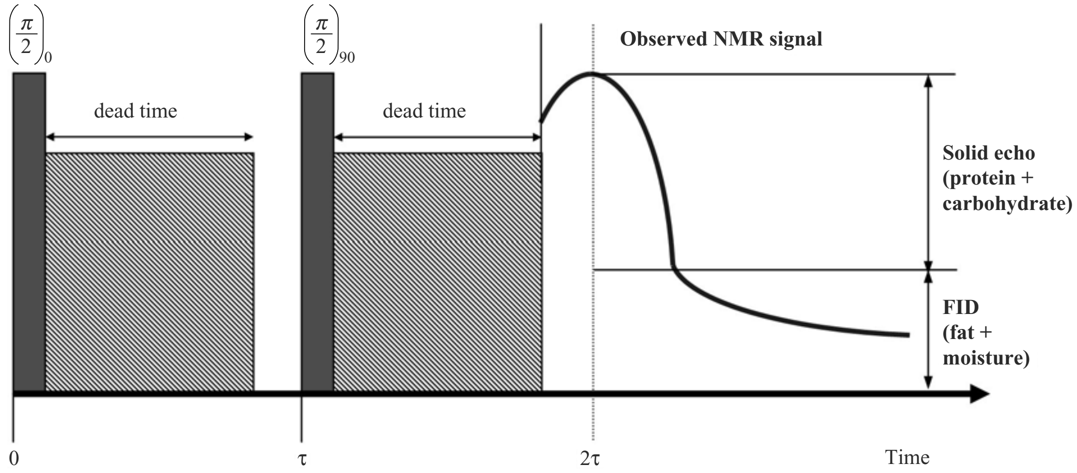
$\left(\frac{\pi}{2}\right)_0$
$\left(\frac{\pi}{2}\right)_{90}$
dead time
dead time
Observed NMR signal
Solid echo (protein + carbohydrate)
FID (fat + moisture)
0
τ
2τ
Time

Fig. 2. Schematic representation of the "solid echo" sequence and the NMR signal from a fish feed sample.

in unknown samples uses only relative to each other values of the "protein" coefficients and the choice of the reference ingredient was arbitrary. The "protein" coefficients were calculated (Figure 3) on the basis of the measured "solid echo" amplitude from each raw ingredient and their protein content known from the chemical analysis. Therefore, the amplitude of the "solid echo" for each raw material corrected with its corresponding coefficient lay on a straight calibration line, as shown in Figure 3.

Knowing the recipe of each produced fish feed batch and using the respective "protein" coefficients for the raw ingredients used, it was then possible to extract the protein signal from the total measured "solid echo" signal for the fish feed as well. The method obviously assumed that the recipe was preserved all the way from the dry mixture of raw ingredient to the ready fish feed, i.e. that the relative amount of each ingredient in the fish feed solid matrix was the same as it was in the dry mixture. Determination of the carbohydrate content was accomplished in a similar way.

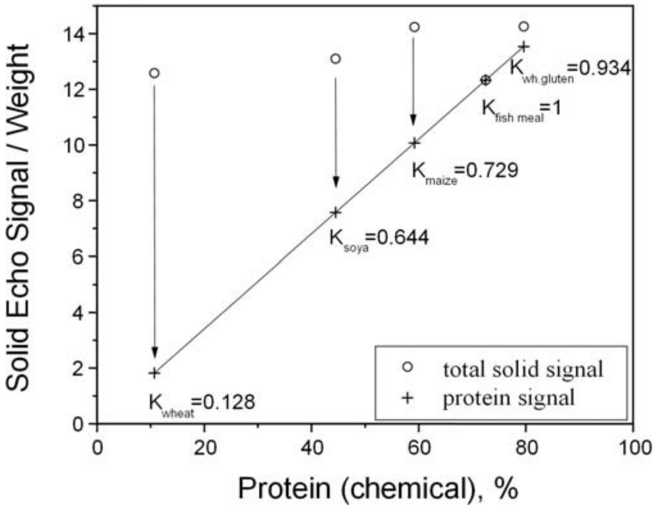

Fig. 3. Principle of calculation of the protein "coefficients" used to extract the protein originated part of the measured "solid echo" amplitude.

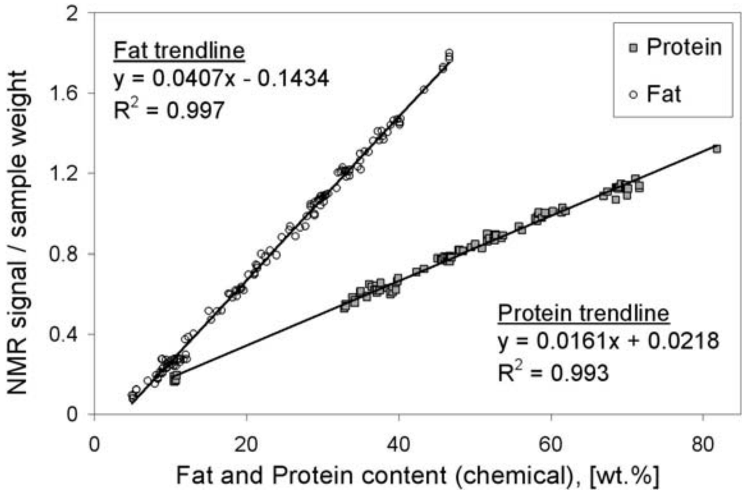

Fig. 4. Calibration curves for protein and fat contents determination.

Chemical Analysis

Following chemical analysis methods were used to produce the reference protein, carbohydrate, fat, and moisture contents data in the raw ingredients and the fish feed samples: the protein content was determined by a standard Kjeldahl method [16], fat content—by standard fatty acid hydrolysis method [17], the rest moisture—by weight change after drying [18] and the ash—by standardized burning in furnace [18]. Carbohydrate content has been calculated as follows:

Carbohydrate (wt.%) = 100% − [fat + moisture + protein + ash](wt.%), where fat, moisture, protein, and ash are chemically determined corresponding reference values in weight percent.

Calibration

Prior to the measurements, the NMR instrument had to be calibrated with a set of reference samples. The protein, carbohydrate, fat and moisture content in these samples were determined chemically beforehand. For protein and carbohydrate calibration, the reference sample set had to contain the raw ingredients as well. Prior to calibrating with fish feed samples, the application had to be calibrated against samples of raw ingredients in order to find the correct "protein" and "carbohydrate" coefficients for all the raw ingredients. During the calibration four types of NMR signals (protein, carbohydrate, fat plus moisture, and fat) were measured, normalized with the sample weight and plotted vs. the corresponding chemical values. Totally 100 samples were used for the protein calibration curve, with the protein content ranging from 10.4 to 81.8 wt.% and 47 samples for the carbohydrate calibration. The cumulative fat plus moisture calibration curve and the fat calibration curve were produced using 112 and 132 fish feed and raw ingredient samples, respectively, with the fat content ranging from 4.9 to 46.6 wt.% and moisture content from 4 to 16 wt.%. As examples, only the protein and fat calibration curves are shown in Figure 4 with the respective linear fit results.

A routine for transferring of the existing calibration data from one NMR instrument to another has also been implemented into the application, such that only a few (normally 3 or 4) reliable reference samples are used to adjust the existing calibration curves on a new NMR instrument. This procedure takes only a few minutes to accomplish, giving a possibility to quickly reproduce nearly identical calibration curves on different instruments.

Results and Discussion

In order to check the performance of the TD NMR method the protein, carbohydrate, fat, and moisture contents in 12 fish feed samples were determined with both the TD NMR technique and the reference chemical methods. Correlation plots between the NMR and the reference chemical methods are shown in Figure 5 demonstrating good correlation between the techniques. Statistical analysis of the agreement between the methods is given in Table 1, demonstrating good performance of the NMR technique compared with the standard chemical

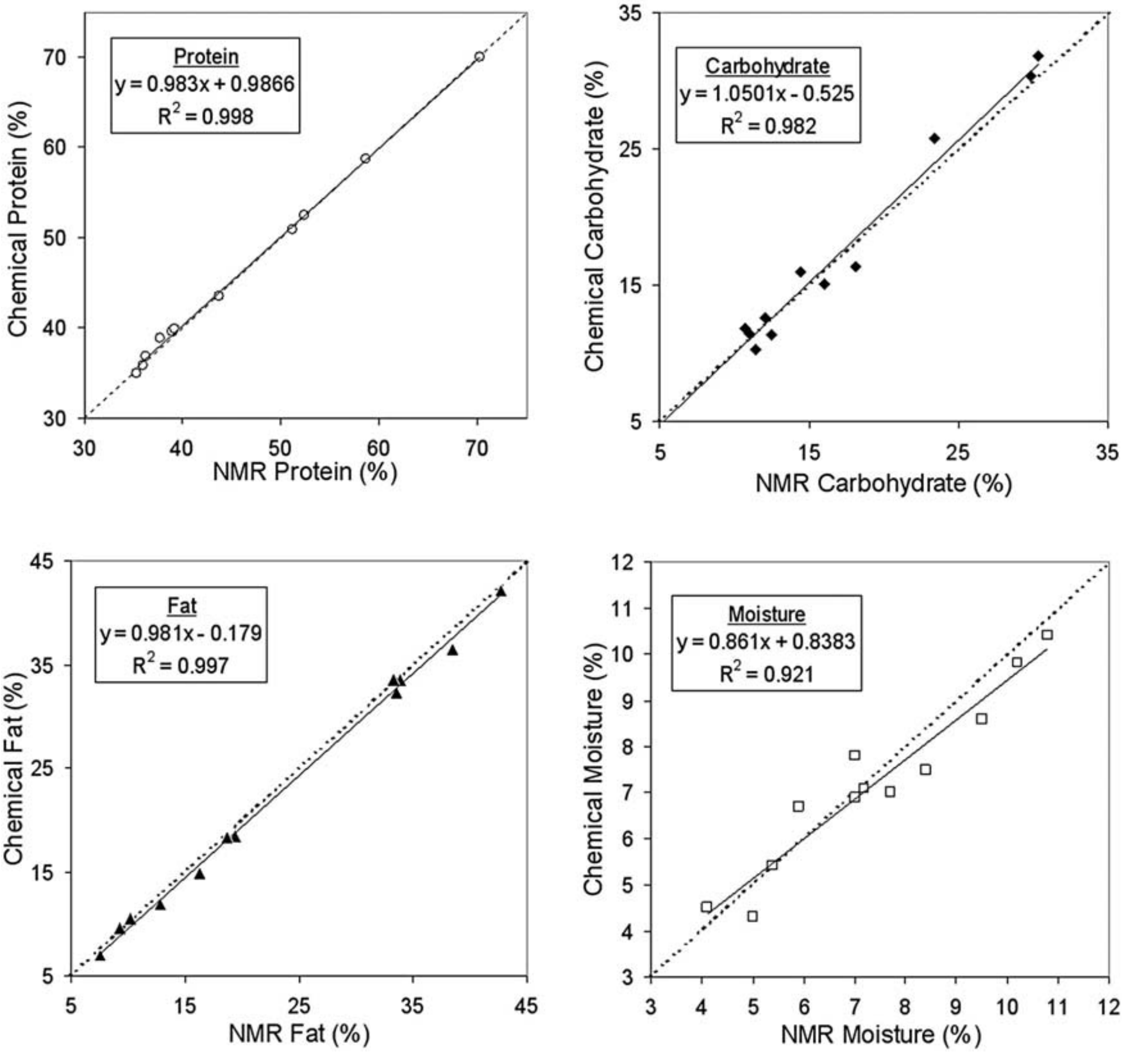

Fig. 5. Correlation plots for protein, carbohydrate, fat, and moisture content in 12 fish feed samples: the TD NMR vs. chemical analysis.

Table 1: Statistical analysis of the agreement between the NMR and the reference chemical methods

Measured quantity	Average standard deviation of the differences	95% range of agreement (±2SD) MIN	MAX	Correlation coefficient R^2
Protein	−0.2	−1.2	0.8	0.998
Carbohydrate	−0.3	−2.9	2.3	0.982
Fat	0.6	−0.8	2.0	0.997
Moisture	0.2	−1.0	1.4	0.921

Table 2: Repeatability of the NMR measurements on a dry mixture sample

Dry mixture sample	Protein wt.%	Carbohydrate wt.%	Fat wt.%	Moisture wt.%
1	58.6	18.1	7.6	6.9
2	58.9	18.2	7.5	7.0
3	58.5	18.3	7.8	7.2
4	59.3	18.4	7.7	7.2
5	59.5	18.3	7.7	7.3
6	59.3	18.4	7.7	7.2
7	59.5	18.2	7.7	7.5
8	58.8	18.3	7.8	7.3
9	59.3	18.3	7.6	7.1
10	59.3	18.3	7.7	7.4
average ± error*	59.1 ± 0.2	18.3 ± 0.1	7.7 ± 0.1	7.2 ± 0.1

* calculated on a 95% confidence level

analysis. Repeatability of the NMR measurements has been checked performing a series of 10 repeated determinations on a dry mixture sample, showing very good repeatability as seen from Table 2. For the carbohydrate content, the correlation coefficient (0.982) was lower than that of protein (0.998) which is apparently due to the indirect calculation of the chemical carbohydrate values. Fat correlation plot shows good correlation (0.997) with a slight bias about 0.6% towards NMR fat values. This might indicate a general trend of standard chemical extraction to underestimate the total fat content in certain types of fish feed. Relatively low correlation for the moisture content (0.921) is probably a result of moisture content fluctuations in a semi-solid fish feed matrix being dependent on the humidity in the storage environment.

Along with the standard chemical analytical methods, the near infrared (NIR) spectroscopy is another established technique for the determination of chemical composition of fish feed and other foods [19]. Although modern NIR instruments can be used to analyze fish feed with good accuracy, there are several disadvantages of this technique compared to the TD NMR. A thorough comparative cost analysis clearly indicated a considerable reduction of annual running costs at a fish feed factory when using TD NMR in preference to NIR (EWOS Innovation Ltd, validation report, Dirdal, Norway, 2002). This mainly results from the fact that NIR instrumentation demands a continuous follow-up and recalibration due to high sensitivity of this spectroscopic method to the minor variations in the microscopic properties of the used raw materials.

To the contrary the TD NMR response is not sensitive to such minor variations in the raw materials used in the production being proportional only to the total quantity of the measured compound. Origin and type of fish oil and other raw ingredients do not have any significant impact on the observed NMR signals. Therefore, it is not necessary to recalibrate the instrument for new raw material batches that are supplied from different environmental sources. The latter is often the case in fish feed production.

NIR technique has a number of other drawbacks, which can make the NMR method to be preferred for routine fish feed quality control at fish feed factories. NIR technique is based on use of sophisticated mathematical models and multivariate data analysis, it often needs sample preparation and is therefore destructive and user dependent. Use of the NIR to analyze fish feed with high fat content (>36%) is usually associated with additional difficulties. This is due to the fact that grinding of such fatty samples produces highly reflective surfaces, which disturbs the spectroscopic measurement [19].

Conclusions

A combination of "solid echo," "FID," and "Hahn echo" NMR techniques implemented into a TD NMR analyzer can quickly and non-destructively provide information about the protein, carbohydrate, fat, and rest moisture content in fish feed. The estimated accuracies of the protein, carbohydrate, fat, and moisture contents determination are 1.0, 2.6, 1.4, and 1.2%, respectively, based on the comparison with the reference chemical analysis. The method has been successfully tested in a research fish feed factory (EWOS Innovation Ltd, Dirdal) and has proven to be quick, precise, and robust. The TD NMR technique has a potential to be implemented on-line for automated quality control of fish feed production.

TD NMR technique is quick and non-destructive. It utilizes no dangerous toxic solvents and can be performed by ground-floor personnel. The TD NMR equipment requires no maintenance. These obvious advantages make the NMR technique highly competitive with both chemical analysis and NIR. Main disadvantage of the presented method is that the determination of protein and carbohydrate contents relies on availability of the feed recipe.

The present TD NMR technique can be further modified and customized to determine similar quality parameters in other types of fodder and in a wide range of other dry products.

Acknowledgments

Bruker Optik GmbH (Rheinstetten, Germany) kindly provided the TD NMR equipment and software. The financial support of the company Leiv Eiriksson Nyskapning Ltd. (Trondheim, Norway) is gratefully acknowledged.

References

1. Farrar TC, Becker ED. Pulse and Fourier Transform NMR. Academic Press: London, 1971, p 19–25.
2. Meiboom S, Gill D. Phys. Rev. 1958;29:688.
3. Slichter CP. Principles of Magnetic Resonance. Springer-Verlag: New York, 1990, p 371–79.
4. Pedersen HT, Berg H, Lundby F, Engelsen SB. Innov. Food Sci. Emerging. Tech. 2001;2:87.
5. Sørland GH, Larsen PM, Lundby F, Rudi AP, Guiheneuf T. Meat Sci. 2004;66:543.
6. Chaland B, Mariette F, Marchal H, Certaines J. J. Dairy Res. 2000;67:609.
7. Pedersen HT, Munck L, Engelsen SB. J. Am. Oil Chem. Soc. 2000;77:1069.
8. ISO standard 8292 (1991). Animal and vegetable fats and oils: determination of solid fat content: pulsed nuclear magnetic resonance method.
9. Steen C, Lambelet P. J. Sci. Food. Agric. 1997;75:268.
10. Jepsen SM, Pedersen HT, Engelsen SB. J. Sci. Food Agric. 1999;79:1793.
11. Bertram HC, Purslow PP, Andersen HJ. J. Agric. Food Chem. 2002;50:824.
12. Web site of Bruker Optik GmbH: http:\\www.bruker.de.
13. Provencher SW. Comput. Phys. Commun. 1982;27:213.
14. Callaghan PT. Principles of Nuclear Magnetic Resonance Microscopy. Oxford University Press: Oxford, 1991, p 84–5.
15. Lowe IJ. Bull. Am. Phys. Soc. 1957;2:344.
16. ISO standard 5983 (1997).
17. Nordic Committee on Food Analysis (NMKL) standard number 160.
18. Nordic Committee on Food Analysis (NMKL) standard number 23.
19. Osborne BG, Fearn T. Near Infrared Spectroscopy in Food Analysis. Longman Scientific & Technical: Essex, England, 1988, p 200.

Low Field NMR Studies of Atlantic Salmon (*Salmo salar*)

Ida Grong Aursand,[1,2] Emil Veliyulin,[1] and Ulf Erikson[1]
[1]*SINTEF Fisheries and Aquaculture, N-7465 Trondheim, Norway; and*
[2]*Department of Biotechnology, Norwegian University of Science and Technology,*
N-7491, Trondheim, Norway

Introduction

Low field (LF) NMR spectroscopy (sometimes also called time-domain NMR) operates in the frequency range of 2–25 MHz. Being a bench-top instrument, it represents a simplified and cheaper version of a traditional NMR spectrometer. Nevertheless, the instrument can provide useful information about relaxation behavior and diffusion behavior. Moreover, the instrument can also be used in connection with at-line quality control for quick analyses of fat, water and protein. Unlike conventional chemical–physical analytical methods that may be time consuming and thus costly, the NMR technique is rapid and has low operation costs. Often, no sample preparation before analysis is needed, and chemicals that are potentially harmful to health and environment may be avoided. Unlike conventional NMR spectrometers equipped with strong superconductive magnets, LF NMR instruments have a relatively weak permanent magnet. Consequently, the instrument cannot resolve different spectral components in the frequency domain, i.e. the LF NMR technique can only deal with time-domain information. Data are collected by programming and running specific NMR pulse sequences such as free induction decay (FID) [1], Hahn-echo [1], Carr-Purcell-Meiboom-Gill (CPMG) [2,3], and solid-echo [4]. The choise of NMR pulse sequence depends on the desired type of information and on the physical and chemical properties of the sample. Presence of solid and liquid phases, their mobility, and rigidity are among the most important parameters to be taken into consideration. Assessment of proton relaxation behavior is a frequently used application of the LF NMR technique. Two types of relaxations can be identified, longitudinal (spin–lattice or T_1) relaxation and transversal (spin–spin or T_2) relaxation. The longitudinal relaxation is the re-establishment of nuclear magnetization along the main magnetic field direction after the system has been excited from energetic equilibrium by irradiation of radio frequency (RF) energy. The transversal relaxation is observed as the loss of net magnetization in the plane transversal to the main magnetic field direction and is a result of the loss of the phase coherence within the ensemble of nuclei in time. The transversal relaxation times are more rapid to measure than the longitudinal ones. Typical data acquisition times for pure aqueous solutions are about 3 and 40 min, respectively. Due to this, and because transversal relaxation data may contain more information, sometimes only transversal relaxation data are reported. For instance, transverse relaxation may be preferred since it is more sensitive to protein unfolding (denaturation) than longitudinal relaxation [5].

In muscles, at least two ordered water phases exist [6,7]. Thus, at least two different proton transversal relaxation peaks should be possible to identify, which indeed is also the case. These are sometimes denoted T_{21} at about 40–60 ms and T_{22} at about 150–400 ms. In addition, a minor peak may be observed at about 1–10 ms [8,9]. To detect the shortest transverse relaxation component, a short ($\tau \sim 12$ μs) interpulse spacing is required [10].

Depending on how the relaxation data are processed, quantitative prediction can be enhanced [11] or the number of observed relaxation peaks may be affected [12]. The relaxation time of free water is about 2500 ms. The observed relaxation behavior is associated with protons in water molecules being small and mobile. In general, the following "rule" applies—the higher the mobility of the protons (molecules), the longer is the relaxation time. For example, interactions of water with macromolecules will reduce relaxation times. The interpretation of T_{21} and T_{22} is somewhat controversial. A simple model has been put forward suggesting they represent intra- and extracellular water, respectively [13] whereas the shortest relaxation component (1–10 ms) is attributed to water tightly associated with macromolecules [8]. Alternatively, in meat it has been suggested that the T_{21} represents water located within highly organized protein structures and the T_{22} represents drip loss [9]. From this, we realize that by studying relaxation behavior, we can indirectly obtain information related to the microscopic structure of tissues. In systems with a high fat content, the interpretation of relaxation spectra may be more complicated due to the fact that the fat and water "peaks" may overlap (T_{22} peak) [14]. Altogether, the LF NMR technique may be considered a useful tool to, for instance, evaluate product and quality related changes occurring as a result of fish processing and subsequent storage such as chilling, freezing,

Graham A. Webb (ed.), Modern Magnetic Resonance, 905–913.
© 2008 *Springer.*

marinating, salting, heating, pressure treatment, modified atmosphere packing, etc.

A number of post-mortem studies of meat using LF NMR have been conducted. Fish has been less studied, and a summary is presented here. Frozen storage, heating, and pressure treatment of intact cod (*Gadus morhua*) results in the appearance of an additional relaxation component (>250 ms) thought to be associated with water exudation. The T_2 values increases with increasing temperature and duration of frozen storage, or with increasing temperature during heating [10]. In contrast, Jensen *et al.* [12] reported that cod relaxation times are not affected by frozen storage temperature or during subsequent chilled storage in modified atmosphere. However, the relative size of the water pools is affected. By applying a three-way chemometric method, four first-order relaxation curves are identified at 37, 56, 126, and 361 ms. Rather than analyzing intact samples, the fish in this study were minced before analysis. However, it should be noted that whole, minced, and homogenized pork muscle all exhibit the similar three component T_2 relaxations with no significant differences in the T_2 values [9]. Steen and Lambelet [15] showed that proton transverse relaxation experiments can be used as a tool to monitor texture changes occurring in cod mince during frozen storage. Three T_2 components were detected at about 0.7, 32–46, and 132–224 ms after 2 and 4 months storage. The storage temperature (-10, -20, and $-70\,^\circ$C) has a clear influence on the latter two relaxation components. In particular, the longest relaxation times decrease with decreasing storage temperature indicating lower water mobility as the fraction of frozen water increases. Moreover, these observations are significantly paralleled by texture changes (Instron measurements) in the mince during frozen storage. Water mobility and distribution of water in intact samples of cod were studied by Andersen and Rinnan [16] after ice storage for 5–7 days. Transverse NMR relaxations were analyzed using a multivariate technique (SLICING). Two water populations were identified with T_2 values of 50 and 94 ms. The shortest relaxation time is the dominating one measured near the head region, whereas the longest one is primarily observed near the tail region. As the water content increased going from head to tail, the effect was thought to be due to smaller muscle cells and fibers in the tail region affecting water pool distributions. Moreover, the amount of water in one pool correlates well ($R = -0.94$) with the overall water content. Furthermore, it has been demonstrated that by using LF NMR, the water-holding capacity of intact cod flesh can be predicted ($R^2 = 0.9$) over the range 30–90% [14]. In a study of salting and desalting of intact fresh and frozen-thawed cod fillets, the proton relaxations exhibit strong correlations with fillet pH, water-holding capacity, and salt content depending on data processing of relaxation curves. The T_1 and T_2 relaxation times significantly increased in fresh fish from 206 and 50 ms to 238 and 70 ms after brine salting, and to 274 and 94 ms after dry salting and subsequent rehydration, respectively. In the case of T_{21} and T_{22}, only T_{21} changed significantly after processing increasing from 45 ms in fresh fish to 69 ms in brined ones. The T_{22} values were around 124 ms were not affected by fish processing [17].

Jepsen *et al.* [14] demonstrated that by using LF NMR combined with chemometrics it is possible to determine fat (mean value 17.8%) and water (mean value 60.9%) in intact Atlantic salmon (*Salmo salar*) flesh. In a 5 kg fish, the highest fat content (40%) was found at the front part of the belly, whereas the lowest (5%) found was in the tail region. To determine total fat and water contents in minced meat, Sørland *et al.* [18] proposed a LF NMR method that does not require sophisticated post-handling of experimental data. Only a single-point calibration routine is necessary (100% oil). To resolve fat and water signals, a multipulsed magnetic field gradient spin echo (m-PFGSE) sequence can be used.

Studies of protein denaturation [5], simultaneous determination of water, oil, and protein contents [19,20], and analysis of solid fat content [21] are other examples of LF NMR applications that might be of interest in fish processing.

Traditionally, LF NMR studies have been performed with stationary magnets having homogeneous magnetic fields. Typical bore sizes range from 10 to 50 mm in diameter. Studies of larger objects, such as whole fish, are thus impossible. To circumvent this restriction, a new type of LF NMR instrument—the *minispec* Bruker Professional MOUSE®—has been developed. Using a mobile mouse probe as an alternative to a stationary magnet, samples unrestricted in size can be analyzed. On fish, the method has been used for determination of fat content in live Atlantic salmon [22].

The goal in the current studies was to demonstrate some LF NMR applications relevant for the fish processing industry.

Materials and Methods

NMR Instrumentation

Two types of LF NMR techniques were used in the present study—a stationary and a portable NMR analyzer. The stationary LF NMR analyzer was the minispec mq 20, (Bruker Optik GmbH, Germany) with a magnetic field strength of 0.47 T corresponding to a proton resonance frequency of 20 MHz. The instrument was equipped with a gradient unit capable of delivering gradients of up to 3.6 T/m and a 10 mm probe. The temperature in the probe was regulated by blowing compressed air through the sample holder and a built-in heating element connected to the temperature control unit (VT3000®, Bruker Optik GmbH).

The mobile NMR probe—the Bruker Professional MOUSE(Bruker Optik GmbH)—was connected to the instrument mentioned above, i.e. in place of the stationary magnet. The mobile NMR analyzer is suitable for measurements in the near surface volume of samples unrestricted in size. The instrument has a magnetic field strength at the probe surface of 0.35 T and a permanent magnetic field gradient of about 10 T/m. The main magnetic field (B_0) is generated by two anti-parallel polarized permanent magnets. A surface coil is mounted in the gap between the magnets for transmission and detection of the RF signals. The measurement volume of the probe is about 5 × 5 mm in-plane and 2.5 mm in-depth and is determined by the strength of B_0, its inhomogenity and the bandwidth of the RF pulses. It is designed such that the first 5 mm from the probe surface do not contribute to the NMR signal. The measurement volume is thus located between 5 and 7.5 mm from the probe surface. A detailed design of the mobile NMR analyzer and the principles of it's operation are described elsewhere [23].

Fat and Water Analysis of Atlantic Salmon Homogenates Using LF NMR

Since the diameter of the NMR tube was 10 mm and the homogenous magnetic field area in the RF coil was about 5 mm high, the sample size was thus very restricted. Furthermore, the fat content in salmon muscle is not evenly distributed [24]. Consequently, to minimize the effects of sub-sampling, we decided to work with homogenates (rather than intact muscle samples) prepared from a larger muscle samples. In this way, the NMR fat analyses would be more comparable with those obtained from chemical extraction.

Fish and Sample Preparation

Three farmed Atlantic salmon (4.0, 4.1, and 4.2 kg) were bought at the local fish market 3 days post-mortem. Six wild-caught Atlantic salmon (gillnetted in the Namsenfjord, Central Norway), were divided in two groups according to size (1.8, 2.0, and 3.1 kg and 3.7, 4.0, and 4.1 kg). The fish were transported on ice to our laboratory where they were immediately frozen (−18 °C). After 1 month, they were thawed overnight in air (4 °C). Different sections of the left fillet from each fish were excised and homogenized (2–3 min) using a food processor (Braun Electronics, Germany). Totally, 54 homogenates were prepared (see Figure 5).

LF NMR Fat and Water Analysis

To determine fat and water contents in the homogenates a combination of two NMR techniques was used, a FID and a pulsed gradient spin echo (PGSE) sequence. The amplitude of the FID response was proportional to the total number of mobile ^{1}H nuclei contained in both fat and water molecules. The PGSE pulse sequence used magnetic gradients to suppress signals from the most mobile molecules in the sample, i.e. the water protons. Thus, the amplitude of the observed gradient spin echo was proportional to the amount of ^{1}H nuclei contained in fat only. To achieve full suppression of water signals rather strong gradient pulses were applied (3.6 T/m). The recycle delay (RD) was set to 2 s and 16 scans were accumulated. The measurements were performed at 22.5 °C.

A calibration routine based on the absolute weights (g) of fat and water was adopted. A commercially available homogenized salmon paste ("Havbris", Mills, Norway) with a declared fat content of 21% was used for calibration of the instrument. Different amounts of salmon paste were transferred into NMR tubes producing a set of 30 calibration standards with known fat content (range: 0.007–0.075 g) and different weights. The correlation coefficient of the corresponding fat calibration curve was $R^2 = 0.97$.

Similarly, only one water solution with known hydrogen index (relative volume density of hydrogen atoms—assumed to be one for pure water) was sufficient for the calibration. As calibration standards (seven NMR tubes), different amounts (range: 0.044–0.294 g) of distilled water doped with $MnCl_2$ (0.001 mol/l) were used. $MnCl_2$was added to shorten the T_2 relaxation time to a value similar to that commonly found in fish muscle (∼35 ms). The water content calibration was performed measuring the initial amplitudes of the FID signal from the calibration standards as a function of their respective absolute weights. The correlation coefficient of the obtained calibration curve was $R^2 = 1.00$.

The fat and water contents were determined by LF NMR. The samples (weight about 0.2 g; fat: $n = 26$; water: $n = 46$) were randomly picked from the 54 homogenates described above. The results were compared with Bligh and Dyer's fat extraction method and the sample dry weight (water content).

Chemical Fat Analysis

The fat content of the homogenates ($n = 26$), i.e. subsamples of the same homogenates analyzed by NMR, was determined in two replicates using the Bligh and Dyer method [25]. The results were correlated with those obtained from LF NMR measurements.

Water Content

The weight difference of the homogenates (about 2 g) before and after drying (105 °C, 24 h) was considered equal to the total water content of the sample. The mean value of two replicates is reported.

Fat Analysis of Atlantic Salmon Homogenates Using a Portable LF NMR Surface Analyzer (NMR MOUSE)

Fish and Sample Preparation

The homogenates ($n = 54$) described in the previous section were frozen in plastic bags for 4 months at -18 °C, thawed in air at 4°C and then thermostated in air to 20 °C for 1 h before analysis.

LF NMR MOUSE Fat Analysis

The fat content was determined using the Bruker Professional MOUSE. The technique relied on the fact that the measurement volume was constant for both calibration standards and homogenates. Therefore, the sample must always cover the entire RF coil area. The T_2 was measured at 20 °C using the CPMG sequence. The following instrumental settings were used: echo time (T_E) (time between the 90° and 180° pulse in the CPMG method) 300 μs, RD 0.2 s and 64 scans were accumulated. The fat signal was measured as an average value of 34 echo amplitudes between 15 and 25 ms of the CPMG echo train. Each measurement took about 20 s, and six parallel measurements were performed per sample. The calibration of the instrument was performed with a set of specially prepared samples with known fat contents and relaxation properties similar to fish muscle [22].

The fat content of 23 frozen-thawed homogenates (in plastic bags) was measured, and the NMR measurements were correlated with chemical fat extraction. The fat content of different fillet section homogenates ($n = 54$; 6 sub-samples per homogenate) of farmed and wild-caught salmon was also determined from the NMR MOUSE measurements.

Water Distribution in Intact Atlantic Salmon Muscle After Heating

Fish and Sample Preparation

A farmed Atlantic salmon fillet was bought at the local market 3 days post-mortem. Four samples (about 0.2 g each)—from both red and white muscle—were excised from the middle section of the fillet (below dorsal fin).

LF NMR Water Analysis

The samples were transferred to 10 mm NMR tubes without further preparation. The T_2 relaxation behavior was measured at 4, 20, 40, and 55 °C. Before each measurement, the samples were thermostated for 30 min in a water bath (Julabo F10, Germany) having the same temperature as in the NMR probe. The CPMG sequence with the following settings was used TE = 0.1 ms, RD = 3 s, and 16 scans with 5000 even echoes were accumulated. The obtained relaxation curves were inverted into corresponding distributions of relaxation times using the CONTIN regulation algorithm [26] implemented in the Bruker minispec mq software.

Diffusion Weighted Transversal Relaxation Measurements: Separation of Fat and Water in Atlantic Salmon White Muscle

Fish and Sample Preparation

A farmed Atlantic salmon fillet was bought at the local fish market 3 days post-mortem. Three parallel samples from the belly flap area were excised using a specially designed coring tool. The samples (about 0.4 g) were transferred to NMR tubes.

LF NMR Analysis

In conventional NMR relaxation spectra, it is not always possible to distinguish relaxation components even though their diffusion constants may be different. An example of a peak overlap in such spectra is the fat and "extracellular" water in fatty fish (salmon) muscle (the "T_{22} peak"). The CPMG sequence and a pulsed field gradient spin echo sequence were combined with a train of 180° refocusing pulses (Figure 1) made it possible to obtain a two-dimensional (2D) dataset of diffusion weighted transversal relaxation curves. The data were processed by the recently developed 2D Inverse Laplace Transform [27] implemented in the MatLab software package (The MathWorks Inc., U.S.A.) [28] producing a 2D diffusion vs. T_2

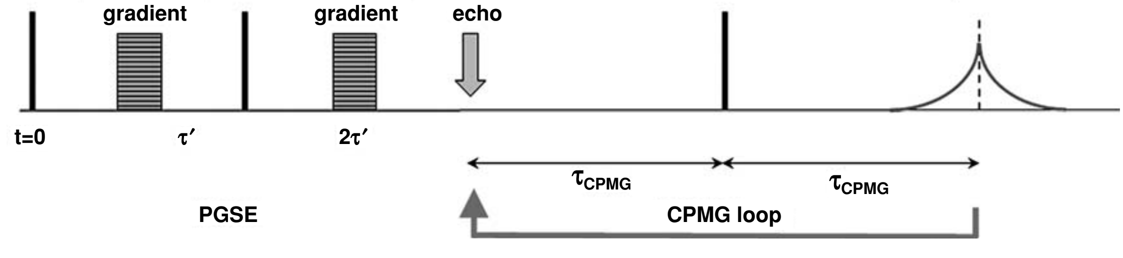

Fig. 1. The PGSE-CPMG pulse sequence used for producing a 2D diffusion/T_2 relaxation map, see Figure 8.

relaxation time distribution map. The method resolved a conventional one-dimensional (1D) T_2 distribution in the dimension of diffusion. Thus, it was possible to distinguish between mobile proton-containing compounds with (nearly) similar relaxation times, but with different diffusion coefficients.

A water bath (Haake UWK 45, Germany) was connected to the probe head to ensure a constant probe temperature of 25 ± 0.1 °C. Before measurements, the samples were thermostated 25 °C for 1 h in a separate water bath.

In the experiment, the gradient strength of the PGSE part of the sequence was incremented from 0 to 3.2 T/m in steps of 0.16 T/m. The CPMG part was acquired for each single gradient value producing a total of 21 diffusion weighted CPMG curves. The echo times (time delay between 90° and 180° pulses) were set to 20 (PGSE) and 0.2 ms (CPMG), RD was set to 2 s and 4000 even echoes were acquired in eight scans.

Results and Discussion

Fat and Water Analysis of Atlantic Salmon Homogenates Using LF NMR

The fat and water contents in salmon homogenates were compared using LF NMR vs. fat extraction and weighing after sample drying (Figure 2). In case of fat, the correlation was good ($R^2 = 0.94$). The NMR-based results were slightly lower than those obtained by chemical extraction. The water content of the same homogenates is shown in Figure 3. The correlation coefficient over the range 40–80% water was $R^2 = 0.84$. Thus, the proposed method may be used for rapid determination of fat and water contents in tissues. The sum of the mean fat and water contents was 76 ± 6%. Grossly speaking, in fatty fish species the sum of tissue fat and water is about 80%. Thus, our fat and water determinations seemed to be within the expected range.

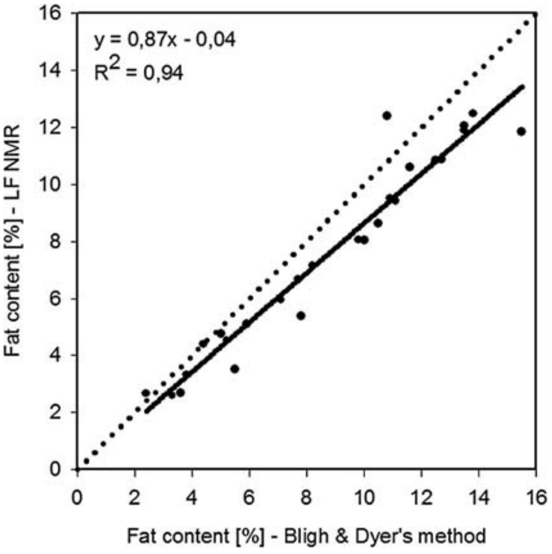

Fig. 2. Fat content in homogenized Atlantic salmon muscle as determined by LF NMR and chemical extraction methods ($n = 26$). The dashed line represents 1:1 ratio.

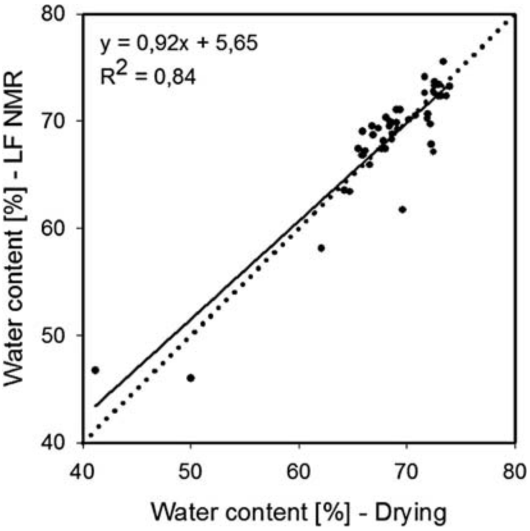

Fig. 3. Water content in Atlantic salmon muscle homogenates as determined by LF NMR and sample drying ($n = 46$). The dashed line represents 1:1 ratio.

Fat Analysis of Atlantic Salmon Homogenates Using a Portable LF NMR Surface Analyzer (NMR MOUSE)

The fat content of the homogenates (same batch) was also analyzed by NMR MOUSE and the results were compared with the chemical extraction method (Figure 4). The methods produced nearly similar results ($R^2 = 0.95$) indicating that the NMR method may be a useful tool for rapid non-invasive determination of fat. Therefore, with further development, the NMR MOUSE concept may have the potential for online applications. The correlation with Bligh and Dyer's fat extraction method was basically similar to that achieved with LF NMR ($R^2 = 0.94$). Veliyulin *et al.* [29] used the NMR MOUSE method to determine fat content in a population of live salmon. In this case, the

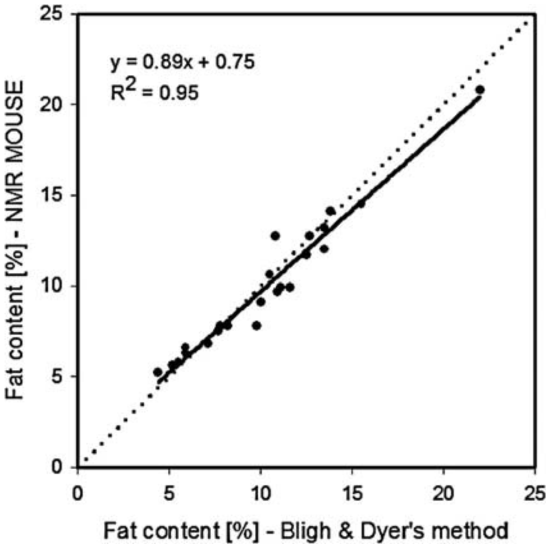

Fig. 4. Fat content in homogenized Atlantic salmon muscle as determined by NMR MOUSE and chemical extraction methods ($n = 23$).

method's correlation with the chemical extraction (Ethylacetate) method was also good ($R^2 = 0.92$).

The fat distribution in farmed and wild-caught salmon fillet was studied by NMR MOUSE (Figure 5). No significant differences between fat content in farmed and wild-caught salmon of approximately the same size (4 kg) was found. As expected, the fat content of the smaller wild-caught salmon (2 kg) was lower. In the white muscle of both farmed and wild-caught fish (fish weight 4 kg), the mean fat content was about 10%, whereas in the smaller wild-caught fish (2 kg) the mean fat content was about 6%. In the belly flap the mean fat contents were 30 (4 kg fish) and 25% (2 kg fish). These values were within what can be expected from previous studies of Atlantic salmon, e.g. 9.6% [24] (2.9 kg) and 17.8% (4.9 kg) in white muscle [30] and 46.4% fat (4.9 kg) in the belly flap [30]. The Norwegian quality cut (NQC) contained about 12 and 7% fat in the 4 and 2 kg fish, respectively. Comparatively, Einen *et al*. [30] reported a NQC fat value of 16.7% for a 4.9 kg fish.

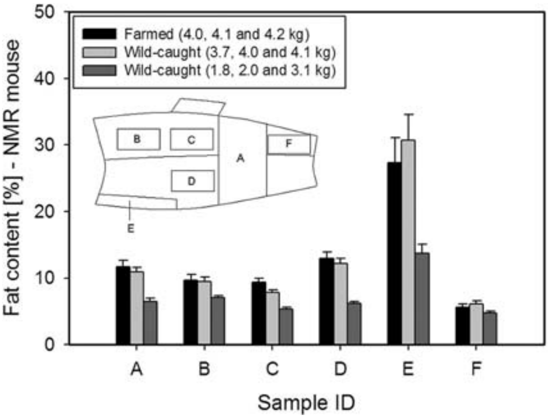

Fig. 5. Fat content in different sections of farmed ($n = 3$) and two groups of wild-caught ($n = 3$) Atlantic salmon. Each sample was subjected to NMR analysis six times. A = Norwegian Quality Cut.

Water Distribution After Heating of Intact Atlantic Salmon Muscles

To simulate the effect of heat processing of fatty fish muscles, transversal relaxation spectra of Atlantic salmon red and white muscles were acquired at 4, 20, 40, and 55 °C.

At 4 °C, the relaxation distribution in red muscle (Figure 6) exhibited four peaks at about 1 ms, 2–7 ms (T_{2b}), 20–110 ms (T_{21}), and 150–400 ms (T_{22}). Peaks in the same ranges have been observed in pork [9], cod [10,12–16], and Atlantic salmon [14]. The peaks at 1 ms and 2–7 ms exhibited merely minor changes with increasing temperature. Since the salmon red muscle has a high fat content, the T_{22} peak was—as mentioned above—associated with signals from both fat and water.

At 20 °C, the T_{21} and T_{22} peaks were shifted toward longer relaxation times indicating increased water mobility. When comparing the relative ratio between the two peaks at 4 and 20 °C, it is seen that the T_{22} peak increased. When increasing the temperature to 40 °C, dramatic changes occurred as the two peaks "melted together" into a hump. These findings are consistent with

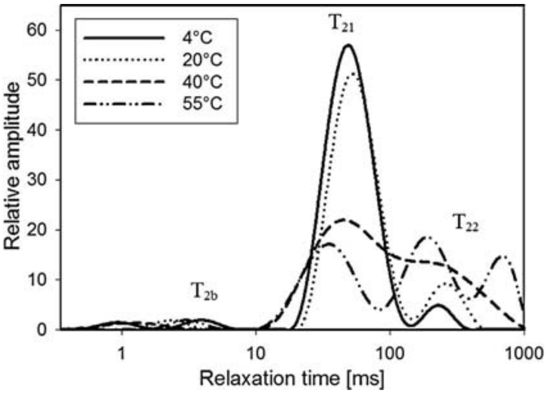

Fig. 6. Transversal relaxation time spectra of Atlantic salmon red muscle at 4 °C and after heating to 20, 40 and 55 °C.

those of Ogawa *et al*. [31] who studied the thermal stability of fish myosin using differential scanning calorimetry. They demonstrated that in case of rainbow trout (*Salmo gairdneri*), major structural changes (denaturation) occur at 25, 34, and 40 °C. Sano *et al*. [32] showed that carp actomyosin molecules began to unfold at about 30 °C, and at temperatures higher than 40 °C the myosin molecules are partly dissociated from the actin filaments. Moreover, Ofstad *et al*. [33] showed that upon heating of chopped salmon, a large loss of water occurs around 40 °C leading to structural changes, e.g. shrinkage of muscle fibers [34].

With further heating to 55 °C, the peak pattern changed again. Three clearly separated peaks appeared, approximately at similar signal amplitudes. Two peaks exhibited relaxation times corresponding to the "common" T_{21} and T_{22}, while a new peak appeared at about (400–1000 ms). Although being somewhat less mobile than at 4 and 20 °C, "the T_{21}-water" may still be related to water protein structures, although now partially degraded. The T_{22} peak may be associated with fat (and water). The water fraction (400–1000 ms) probably represents water becoming more mobile as a result of the major structural changes occurring in the protein matrix, i.e. expelled water (drip loss).

In white muscle (Figure 7), the distribution of water after heating was basically similar in several aspects to that of red muscle. Some differences were however observed. The T_{22} peak was smaller exhibiting higher water mobility (400–520 ms). The mobility of this water fraction decreased when increasing the temperature from 4 to 20 °C. At 40 °C, no hump was seen in this case. Instead, two well-defined peaks were observed at 13–60 ms and 130–480 ms, i.e. within the "common" T_{21} and T_{22} regions. With further heating to 55 °C, both peaks were shifted toward lower relaxation times, indicating reduced water mobility.

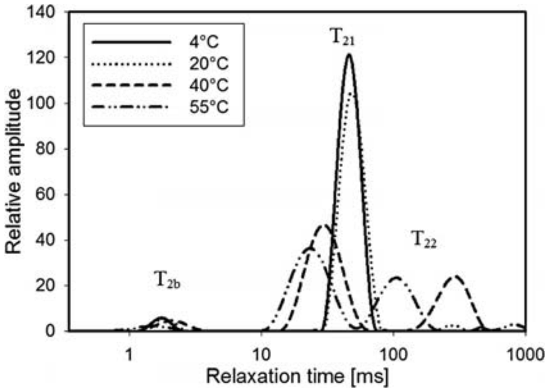

Fig. 7. Transversal relaxation time spectra of Atlantic salmon white muscle at 4 °C and after heating to 20, 40 and 55 °C.

The observed differences in relaxation behavior are thought to be related to the difference in chemical composition of the two muscle types. Reported mean values of Atlantic salmon (3 kg) fat and water contents are 27.2 and 56.7% (red muscle), and 9.6 and 68.9% (white muscle), respectively [24]. In pork [35] and other foods, NMR relaxometry has commonly been used to determine the solid fat content. In contrast, due to the high amount of polyunsaturated fatty acids in Atlantic salmon [24], the mobile unsaturated fatty acids must be taken into consideration also at low temperatures. Regarding fat stability and mobility in this species, it has been reported that the fraction of total, unsaturated and saturated fatty acids stays essentially constant in the temperature range 0–40 °C [36].

To summarize, we have demonstrated that by using NMR relaxometry, several interesting features occurring as a result of heating can be observed. Protein denaturation can also be studied *in vitro*. For a better interpretation of the data, additional structural and compositional analyses are needed. Ultimately, such data may be useful to improve the heat processing of (fish) muscle-based raw materials.

Diffusion Weighted Transversal Relaxation Measurements: Separation of Fat and Water in Atlantic Salmon White Muscle

Continuous T_2 relaxation distribution maps do not fully separate water and fat in fatty fish tissues. This is because the "extracellular" water fraction relaxes with the same rate as fat [29] and only one single relaxation peak can be observed in a conventional 1D relaxation spectrum (between 100 and 200 ms; Figures 6 and 7). A new 2D technique overcomes this problem by additionally resolving the T_2 relaxation spectrum in the second direction of diffusion, making it possible to study the fat and water components separately. Figure 8a shows an example of a conventional transversal relaxation curve, while Figure 8b shows the T_2-diffusion map of Atlantic salmon white muscle. It can be seen that by using the 2D technique, "the extracellular" water fraction was clearly separated from the fat component. Regarding the relaxation peak at 140 ms, the advantage of the 2D distribution map approach compared with the conventional 1D is clearly seen. The 2D map clearly shows the presence of the two components around 140 ms, while the respective fat and water peaks completely overlap in the 1D distribution. The corresponding diffusion constants were 2.6×10^{-10} m^2/s (fat) and 2.0×10^{-9} m^2/s (water) as determined from the 2D distribution map. The water component at 140 ms probably corresponds to that observed in cod [10,12,14–16] and pork muscle [9], which is thought to represent extramyofibrillar water. For the major (intramyofibrillar) water component at $T_2 \approx 37$ ms, the

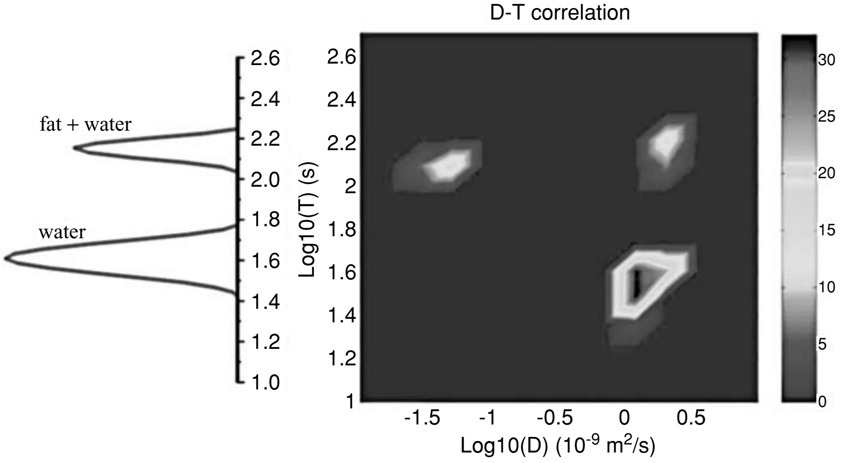

a) b)

Fig. 8. (a) A 1D transversal relaxation spectrum and (b) a 2D diffusion/T_2 relaxation map of intact Atlantic salmon white muscle. Arbitrary units. (See also Plate 81 on page LIV in the Color Plate Section.)

diffusion constant was $D \approx 2.0 \times 10^{-9}$ m^2/s. The method can be used as a diagnostic tool to assess possible fat–water overlap. In addition, quantitative information about diffusion constants and their corresponding transversal relaxation times can be obtained.

Conclusion

By using various LF NMR techniques, information about fat and water contents and their mobilities can be obtained. In turn, such information may be related to tissue structure changes occurring during fish processing. The portable LF NMR surface scanner (MOUSE) can be used to determine whole fish fat content. Introduction of a combined ^{23}Na and ^{1}H LF NMR probe would open up new possibilities for at-line quality control for rapid determination of salt, fat, and water contents in the fish (food) processing industry. Moreover, with the introduction of the NMR MOUSE concept, online quality control may be feasible in the future.

References

1. Farrar TC, Becker ED. Pulse and Fourier Transform NMR. Academic Press: London, 1971, p 19.
2. Carr HY, Purcell EM. AJP. 1954;94:630.
3. Meiboom S, Gill D. Rev. Sci. Instrum. 1958;29:688.
4. Slichter CP. Principles of Magnetic Resonance. Springer-Verlag: New York, 1990, p 371.
5. Lambelet P, Berrocal R, Ducret F. J. Dairy Res. 1989;56:211.
6. Hazlewood CF, Nichols BL. Johns Hopkins Med. J. 1969; 125:119.
7. Lillford PJ, Jones DV, Rodger GW. Jubilee Conference of the Torry Research Station, Aberdeen: Scotland, 1979.
8. Le Rumeur E, De Certaines J, Toulouse P, Rochcongar P. Magn. Reson. Imaging. 1987;5:267.
9. Bertram HC, Karlsson AH, Rasmussen M, Pedersen OD, Dønstrup S, Andersen HJ. J. Agric. Food Chem. 2001; 49:3092.
10. Lambelet P, Renevey F, Kaabi C, Raemy A. J. Agric. Food Chem. 1995;43:1462.
11. Bechmann IE, Pedersen HT, Nørgaard L, Engelsen SB. Proceedings of the Fourth International Conference on Applications of Magnetic Resonance in Food Science, Norwich, UK, 1998.
12. Jensen KN, Guldager HS, Jørgensen BM. J. Aquat. Food Prod. Technol. 2002;11:201.
13. Cole WC, Le Blanc AD, Jhingran SG. Magn. Reson. Med. 1993;29:19.
14. Jepsen SM, Pedersen HT, Engelsen SB. J. Sci. Food Agric. 1999;79:1793.
15. Steen C, Lambelet P. J. Sci. Food Agric. 1997;75:268.
16. Andersen CM, Rinnan Å. Lebensm.-Wiss. u.-Tehcnol. 2002; 35:687.
17. Erikson U, Veliyulin E, Singstad T, Aursand M. J. Food Sci. 2004;69:107.
18. Sørland GH, Larsen PM, Lundby F, Rudi A-P, Guiheneuf T. Meat Sci. 2004;66:543.
19. Pedersen HT, Munck L, Engelsen SB. J. Am. Oil Chem. Soc. 2000;77:1069.
20. Veliyulin E, Østerhus K, Burk W, Singstad T, Skjetne T. Comprehensive Compositional Analysis of Fish Feed by Time Domain NMR, Modern Magnetic Resonance, GA Webb (ed.), Springer, The Netherlands, 2006.

21. ISO standard 8292, 1991.
22. Veliyulin E, van der Zwaag C, Burk W, Erikson U. J. Sci. Food Agric. 2004;85:1299.
23. Eidmann G, Savelsberg R, Blümler P, Blümich B. J. Magn. Reson. A. 1996;122:104.
24. Aursand M, Bleivik B, Rainuzzo JR, Jørgensen L, Mohr V. J. Sci. Food Agric. 1994;64:239.
25. Bligh EG, Dyer WJ. Can. J. Biochem. Physiol. 1959; 37:911.
26. Provencher SW. Comp. Phys. Commun. 1982;27:213.
27. Hürlimann M, Venkataramanan L. J. Magn. Reson. 2002; 157:31.
28. Godefroy S, Ryland B, Callaghan PT. 2D Laplace Inversion. Victoria University of Wellington: New Zealand, 2003.
29. Veliyulin E, Aursand IG, Erikson U. Study of fat and water in Atlantic Salmon muscle (Salmo Salar) by Low-Field NMR and MRI, Magnetic Resonance in Food Science. The Multivariate Challenge. SB Engelsen, PS Belton and HJ Jakobsen (eds.), The Royal Society of Chemistry, Cambridge, UK, 2005, p. 148.
30. Einen O, Waagan B, Thomassen MS. Aquaculture 1998; 166:85.
31. Ogawa M, Ehara T, Tamiya T, Tsuchiya T. Comp. Biochem. Physiol. 1993;3:517.
32. Sano T, Ohno T, Otsukafuchino H, Matsumoto H, Tsuchiya T. J. Food Sci. 1994;59:1002.
33. Ofstad R, Kidman S, Myklebust R, Hermansson A-M. Food Struct. 1993;12:163.
34. Ofstad R, Kidman S, Hermansson A-M. J. Sci. Food Agric. 1996;72:337.
35. Davenel A, Riaublanc A, Marchal P, Gandemer G. Meat Sci. 1999;51:73.
36. Grasdalen H, Aursand M, Jørgensen L. Special Publication 157. Royal Soc. Chem.: Cambridge, 1995, p 208.

Water Distribution and Mobility in Fish Products in Relation to Quality

Bo M. Jørgensen, Kristina N. Jensen
Department of Seafood Research, Danish Institute for Fisheries Research, Technical University of Denmark, Lyngby, Denmark

Introduction

Water is the most abundant chemical substance in muscle-based food such as fish fillet, and the interactions between water and macromolecules are influential to various food quality attributes like texture and juiciness. Information on water binding and distribution within the muscle is therefore important while studying raw material properties and quality changes during processing and storage. Low-field NMR transverse spin relaxation of the water–hydrogen nucleus has been succesfully employed in food research to provide information such as the relaxation time, which is dependent on the mobility of the water molecule and thereby of its binding to or entrapment by structural elements of the cells.

In the present account, the available mathematical methods for extracting the above-mentioned information from the NMR relaxation signals are discussed. Examples from the literature are used to demonstrate how the water distribution can be related to raw material properties (fish stock, fat content), quality attributes (texture, water holding capacity) and changes during the processing and storage (protein denaturation).

Algorithms

The measured transverse relaxation curves, i.e. amplitudes or phase-rotated channel output from a CPMG pulse sequence, are most often mathematically well-behaved, consisting of a sum of mono-exponentially decreasing functions:

$$S_i(t) = \sum_{j=1}^{N} s_{ij}(t) = \sum_{j=1}^{N} m_{ij}\, e^{-k_j t} \qquad (1)$$

where $S_i(t)$ is the sampled measurement signal from sample i at time t, $s_{ij}(t)$ is the part of the signal originating from the component j, m_{ij} is the "amount" of component j in the sample, k_j is the reciprocal transverse relaxation time of component j and N is the number of separable components. Even in a highly heterogeneous system, like a muscle, a limited number of components or "pools" of the substance from which the signal stems (most often water) is identified, i.e. N is low (1–5).

In order to extract information related to water in the measured sample, one is normally interested in resolving the curves into the single functions $s_{ij}(t)$ and determine their parameters m_{ij} and k_j. An important exception is, however, mentioned below. Several algorithms exist, each with their own strengths and weaknesses. For the sake of this discussion, the algorithms are divided into two groups: those that operate on each sample separately and those that make use of multiple samples sharing a set of relaxation times.

Single-Sample Algorithms

The obvious (and classical) way to extract the function s from Equation 1 is by a simple exponential curve fitting. It is not straight-forward numerically, however, as the parameters are highly correlated and strongly dependent on the choice of the number, N, of components. The objective function, i.e. the sum of squared residuals, will always decrease with an increasing number of parameters, and the risk of over-fitting is high. The value of N has to be assumed without support from the data. These circumstances strongly suggest to the present authors that the simple exponential curve fitting method is inferior and must be avoided.

A more elegant way to deal with the measurement signal from a single sample is to consider m as a continuous function of k:

$$S_i(t) = \int_0^{\infty} m_i(k)\, e^{-kt}\,\mathrm{d}k \qquad (2)$$

with $m_i(k)$ having peaks at values k_j, $j = 1 \ldots N$ and being 0 elsewhere. The signal $S_i(t)$ thus is a Laplace transform of $m_i(k)$, which then can be found whenever it is possible to numerically calculate the inverse transform. A successful calculation results in a curve from which N is directly determined as the number of peaks, and k_j and $m_i(k_j)$ as the position and area of peak number j. But the result of the numerical calculation is extremely sensitive to noise and some sort of smoothing is mandatory. The

Graham A. Webb (ed.), Modern Magnetic Resonance, 915–918.
© 2008 *Springer.*

art is to make this smoothing balanced: strong enough to suppress noise and mild enough to avoid suppression of “real” component signals. A popular computer program, CONTIN, for solving integral equations like this one was developed by Provencher.[1,2] When the parameters of the algorithm have been set at values suitable for the actual measurements, the method is able to show systematic changes in relaxation times throughout a sample set, e.g. as a function of temperature or another variable of the experimental design.

Multi-Sample Algorithms

By making use of the full data set, i.e. the collection of measurement signals from several samples ($i = 1, \ldots, i_{\max}$) at the time, several new possibilities arise. Perhaps the most important is that the data themselves may provide a good estimate of N by issuing a warning when over-fitting is attempted. Using the signals $S_i(t)$ directly for calibration purposes is also a very useful option: partial least squares (PLS) regression models for prediction of quality parameters can be made, without having to extract the single component signals $s_{ij}(t)$ explicitly.[3–5]

In many cases, the single component signals are of interest, though. A proper use of the full data set then requires that the samples really are compatible in the sense that they contain common pools though in various relative amounts, i.e. the m-values, but not the k-values may differ significantly from sample to sample. When this prerequisite is fulfilled, exponential curve fitting (Equation. 1) may be performed by alternately fitting the set of non-linear parameters k_j and the set of linear parameters m_{ij} keeping the other parameter set constant. The method works well in practice though the calculation time increases fast with the number of samples.[6]

The most elegant multi-sample method used nowadays to extract the single component signals $s_{ij}(t)$ is parallel factor analysis (PARAFAC) of the data set made tri-directional. The data rearrangement may be done in many ways (cf. Pedersen *et al*.[6]); one that has proven efficient for measurements on fish muscle in our laboratory is thoroughly described by Jensen *et al*.[7] The procedure is a “soft-modeling” in the sense that the single-exponential functional form of s is not explicitly entered into the calculations (although obtaining a perfect tri-linear system, best suited for PARAFAC, requires this functional form). The result actually turns out to be a set of single exponentials (e.g. in Jensen *et al*.[7]) thus supporting its validity.

Determining the Number of Components

When using the full data set, several diagnostics exist by which the correct value of N may be estimated. A principal component analysis of the data matrix with elements $S_{it} = S_i(t)$ indicates how many independent variations exist not being purely due to noise. This number is an upper bound on N. Another efficient procedure is to split the data set between replicates and make the calculations on each subset separately. As long as over-fitting is avoided, the same set of single components should be extracted from each subset, as these differ only with respect to noise. When choosing the PARAFAC method, one may also look at the extracted components, which should be single exponentials. Noise components are not expected to follow this functional form, so the appearance of other forms is an indication of over-fitting.

Applications

The application of ^{1}H NMR on fish and fish products open the possibilities for relating the state and dynamics of water to various parameters, such as raw material properties, quality attributes, and storage and processing conditions. An overview of the applications described in the text is shown in Table 1.

Different raw material properties have been related to relaxation decays obtained by the CPMG pulse sequence. The potential of applying low-field NMR and multivariate PLS calibration for a fast and non-invasive determination of composition, i.e. lipid and water content, was explored in herring[8] and salmon.[3,4] The method was found to have low prediction errors, and furthermore demonstrated that it was possible to simultaneously determine lipid and water content[3,4] taking advantage of the inverse relation between water and lipid in fish muscle.[9] Low-field NMR was also used for mapping raw material differences, e.g. in relation to fishing ground, seasonal variations and biological parameters of herring caught in the waters around Denmark.[10] The unique decomposing of tri-linearized relaxation decays by PARAFAC showed that the number of water pools was depended on season of catch, whereas their variation between fishing grounds were related to differences in lipid content and spawning type (stock). In cod, the water distribution as determined by PARAFAC on tri-linearized NMR transverse relaxation decays was shown to depend on location in the fillet, which could be related to the size of muscle cells and fibres.[11] In mammalian muscle, *post-mortem* pH changes have been studied by low-field NMR transverse relaxation and related to changes in water characteristics during the conversion of muscle to meat in rabbit[12] and beef.[13] Although the *post-mortem* pH changes are smaller in fish, this method also seems to have potential for studying raw material properties in fish. In frozen systems, NMR could be used as an alternative method for determination of glass transition temperatures.[14] This possibility was also illustrated on pintado fish, where distributed T_2 relaxation time profiles were determined in the temperature interval from

Table 1: Application examples

Application	Data analysis[a]	System	Ref.
Raw material properties			
Lipid content	Multivariate PLS calibration	Herring, salmon	[4,8]
Seasonal variation and stock	PARAFAC	Herring	[10]
Muscle cell and fibre size	PARAFAC	Cod	[11]
Post mortem pH	Continuous distribution analysis	Rabbit	[12]
Post mortem pH	Discrete exponential curve fitting	Meat	[13]
Glass transitions	Continuous distribution analysis	Pintado fish	[15]
Quality attributes			
Water holding capacity	Multivariate PLS calibration	Cod	[4,5]
Water holding capacity	Continuous distribution analysis	Meat	[16]
Texture and dimethylamine	Discrete exponential curve fitting	Cod	[17]
Changes during processing and storage			
Freeze-thawing	PARAFAC	Cod	[7]
Freeze-thawing	Discrete exponential curve fitting	Cod	[17,18]
Freeze-thawing	MRI, discrete exponential curve fitting	Cod, mackerel, trout	[19,20]
Salting and desalting	Continuous distribution analysis	Cod	[21]
Protein denaturation	PARAFAC[b]	Cod	[22]
Protein denaturation	Discrete exponential curve fitting[b]	Cod	[18]
Collagen denaturation	Discrete exponential curve fitting[c]	Meat	[23]
NMR-cooking	Discrete exponential curve fitting	Meat	[25]
NMR-cooking	Continuous distribution analysis	Meat	[26]

[a] The data decomposed are low-field NMR transverse relaxation decays unless another method is specified.

[b] NMR parameters compared with a thermal denaturation profile obtained by differential scanning calorimetry.

[c] Meat samples heated prior to NMR measurements.

−50 °C to 30 °C revealing two abrupt changes in the water mobility.[15] In contrast to the traditional determination of glass transition temperatures by thermal analysis, the application of NMR offers the possibility of measuring actual molecule mobility rather than thermal events, which can be difficult to interpret.

Measuring quality attributes, such as water holding capacity (WHC) and texture, by low-field NMR using the CPMG pulse sequence have shown some promising results in the area of muscle food. Recent studies on cod have shown that WHC can be determined by multivariate PLS calibration of the relaxation decays.[4,5] In meat, continuous distribution analyses have revealed that areas of relaxation populations and corresponding time constant were highly correlated to WHC.[16] Another study on thawed cod mince showed that the longest relaxing component determined by exponential curve fitting was highly correlated to sensory and instrumental texture parameters as well as to the amount of dimethylamine produced during frozen storage.[17] These results demonstrate the great potential of using low-field NMR as a non-invasive method for measuring important quality attributes.

Changes in the water distribution and mobility during processing and storage of cod muscle, e.g. freezing and frozen storage, have also been studied by low-field NMR. Lambelet *et al*.[18] and Steen and Lambelet[17] showed that the NMR parameters as determined by exponential curve fitting were related to the freezing and frozen storage. In another study, the water distribution expressed as relative water pool sizes determined by PARAFAC on tri-linearized relaxation decays was shown to vary consistently with storage conditions, supporting the validity of the PARAFAC method.[7] Studies using magnetic resonance imaging (MRI) have also revealed that water distribution and mobility of cod, mackerel and trout are affected by freeze-thawing as quantitatively reflected in the MRI parameters.[19,20] In a study of salting and desalting of cod fillets, the relaxation time as determined by continuous distribution analysis of low-field NMR transverse decays was shown to be related to pH and the condition of the raw material, i.e. fresh or frozen-thawed.[21] Combination of low-field NMR and thermal analysis, i.e. differential scanning calorimetry (DSC), has shown that protein changes in cod due to different storage conditions are related to the water distribution.[18,22]. Rochdi *et al*.[23] studied the thermal denaturation of collagen from calf and cow muscle by measuring NMR transverse relaxation of preheated samples. Recently, food samples were heated directly in the NMR spectrometer with the process being followed by repeated low-field NMR transverse relaxation measurements, e.g. monitoring the dough-to-bread process, named NMR-baking.[24]. A similar procedure, named NMR-cooking, was used to follow the cooking process of meat.[25,26] On fish muscle, this method could offer an alternative approach for relating protein denaturation to changes in water state during processing.

References

1. Provencher SW, Comp. Phys. Commun. 1982;27:213.
2. Provencher SW, Comp. Phys. Commun. 1982;27:229.
3. Bechmann IE, Pedersen HT, Nørgaard L, Engelsen SB In: Belton PS, Hills BP, Webb GA (Eds.), Advances in magnetic resonance in food science, London: Royal Society of Chemistry, 1999, p. 217.
4. Jepsen SM, Pedersen HT, Engelsen SB, J. Sci. Food Agric. 1999;79:1793.
5. Andersen CM, Jørgensen BM, J. Aquat. Food Prod. Technol. 2004;13(1):13.
6. Pedersen HT, Bro R, Engelsen SB, J. Magn. Reson. 2002;157:141.
7. Jensen KN, Guldager HS, Jørgensen BM, J. Aquat. Food Prod. Technol. 2002;11(3/4):201.
8. Nielsen D, Hyldig G, Nielsen J, Nielsen HH, Lebens.-Wiss. Technol. 2005;38:537.
9. Stansby ME, In: Heen E, Kreuzer R, (Eds.), Fish in nutrition, London: Fishing News Books Ltd., 1962, p. 55.
10. Jensen KN, Jørgensen BM, Nielsen HH, Nielsen J, J. Sci. Food Agric. 2005;85:1259.
11. Andersen CM, Rinnan Å, Lebens.-Wiss. Technol. 2002;35:687.
12. Bertram HC, Whittaker AK, Andersen HJ, Karlsson AH, J. Agric. Food Chem. 2003;51:4072.
13. Tornberg E, Wahlgren M, Brøndum J, Engelsen SB, Food Chem. 2000;69:407.
14. Ruan RR, Chen PL, Water in foods and biological materials. A nuclear magnetic resonance approach. Lancaster, Technomic Publishing Company, Pennsylvania: 1998.
15. Pitombo RNM, Lima GAMR, J. Food Eng. 2003;58:59.
16. Bertram HC, Dønstrup S, Karlsson AH, Andersen HJ, Meat Sci. 2002;60:279.
17. Steen C, Lambelet P, J. Sci. Food Agric. 1997;75:268.
18. Lambelet P, Renevey F, Kaabi C, Raemy A, J. Agric. Food Chem. 1995;43:1462.
19. Nott KP, Evans SD, Hall LD, Magn. Reson. Imaging 1999;17:445.
20. Nott KP, Evans SD, Hall LD, Lebens.-Wiss. Technol, 1999;32:261.
21. Erikson U, Veliyulin E, Singstad TE, Aursand M, J. Food Sci. 2004 69:107.
22. Jensen KN, Jørgensen BM, Lebens.-Wiss. Technol. 2003 36:807.
23. Rochdi A, Foucat L, Renou JP, Food Chem. 2000;69:295.
24. Engelsen SB, Jensen MK, Pedersen HT, Nørgaard L, Munck L, J. Cereal Sci. 2001;33:59.
25. Micklander E, Peshlov B, Purslow PP, Engelsen SB, Trends Food Sci. Technol. 2002;13:341.
26. Bertram HC, Engelsen SB, Busk H, Karlsson AH, Andersen HJ, Meat Sci. 2004;66:437.

Proton NMR of Fish Oils and Lipids

R. Sacchi,[1] M. Savarese,[1] L. Falcigno,[2] I. Giudicianni[3], and L. Paolillo[2]
[1]Department of Food Science
[2]Department of Chemistry and CIMCF
[3]University of Naples Federico II, Naples (Italy)

Introduction

In the last 10 years, high-resolution carbon-13 and proton-NMR spectroscopy have been successfully applied to the analysis of fish oils and lipids [1–10]. The purpose of these analyses was focused not only on the rapid determination of lipid classes and fatty acid composition but also on the assessment of positional distribution of fatty acids along the glycerol moiety, fish quality, lipid oxidation, and lipolysis. ^{13}C and ^{1}H-NMR are complementary techniques in order to define lipid composition and chemical alterations. ^{13}C-NMR offers the advantage of higher resolution but lack in sensitivity and requires longer time of analysis to obtain quantitative spectra. Proton NMR, on the other hand, is very rapid and quantitative, but proton signals of lipid molecules are present in a narrow spectral range thus reducing resolution. Therefore, different applications have been carried out taking into account advantages and disadvantages of two techniques.

^{1}H-NMR Spectra of Fish Oils and Lipids Extracted from Fish Muscles

F.D. Gunstone [1] in a pioneering work identified some of the lipid components in fish oils by attributing, in the proton spectra, several signals to polyunsaturated fatty acid (PUFA) components. The proton NMR spectra available in the literature for commercial fish oil [1], tuna lipids [4], salmon lipids [3], bonito and sardine oils [3,7] show similarities and differences, due to both the fatty acid profile of sample analyzed and to the lipid classes composition. NMR spectra of natural lipid extracts from fish muscles differ from those of refined fish oils due to the presence, not only of triacylglycerols as major components, but also of large amount of polar lipids (phospholipids, diacylglycerols, free fatty acids) or other lipid-soluble unsaponifiable components (cholesterol).

Figure 1 shows an example of proton NMR spectrum of a crude lipids extracted using the Bligh and Dyer method [11] from 1-year ripened salted anchovies, caught and transformed in typical area of the Cilento national park (Salerno, Southern Italy). The main resonances, commonly found in all fish oils and lipids are assigned in Table 1. These resonances occur at 0.85 for methyl groups of saturated,*n*-6 and *n*-9 acyl chains, 0.95 ppm for methyl groups of ω-3 components, at 1.65 ppm for the methylene protons in C-3 position, at 2.05 ppm for the allylic protons, at 2.31 for methylenes in C-2, at 2.76 ppm for the doubly allylic protons and at 5.39 ppm for olefinic protons superimposed to glyceryl resonances. In addition to these resonances another signal appearing at 3.37 ppm can be assigned to phosphatidylcholine methyls (Table 1). Some of these signals, therefore, may be used for assessing lipid composition and fatty acid composition. In addition, the careful study of minor resonances detectable in diagnostic spectral zone, the use of high field NMR equipments and 2D experiments, as well as the combination of chromatographic techniques in concentrating minor lipid fractions with proton NMR, allows to obtain, in a short time, very useful informations. The most interesting, with respect to the quality assessment and process control of fish products, are reported in the following paragraphs.

Quantitative Determination of *n*-3 PUFAs

Although fish oils contain many saturated (SFA) and monounsaturated fatty acids (MUFAs), considerable interest is on the identification and quantification of the omega-3 (*n*-3) PUFAs for their intrinsic dietary benefits in human health [12].

Proton NMR spectroscopy offer a rapid and structure-specific way for the global quantitation of n-3 PUFAs in fish lipids, by taking advantage of only two selected proton NMR methyl resonances [4,7–8]. Figure 2 shows a 1D-TOCSY experiment made on a sample of tuna lipids from which the assignment of *n*-3 methyls can be made [5]. When signal at 0.95 ppm was irradiated, a decreasing effect on omega-2 (methylene), omega-3,4 (olefinic) and a residual effect on diallylic (omega-5) can be observed, indicating unequivocally that the methyl at 0.95 ppm corresponds to those of *n*-3 PUFAs. Therefore, the careful

Graham A. Webb (ed.), Modern Magnetic Resonance, 919–923.
© 2008 *Springer.*

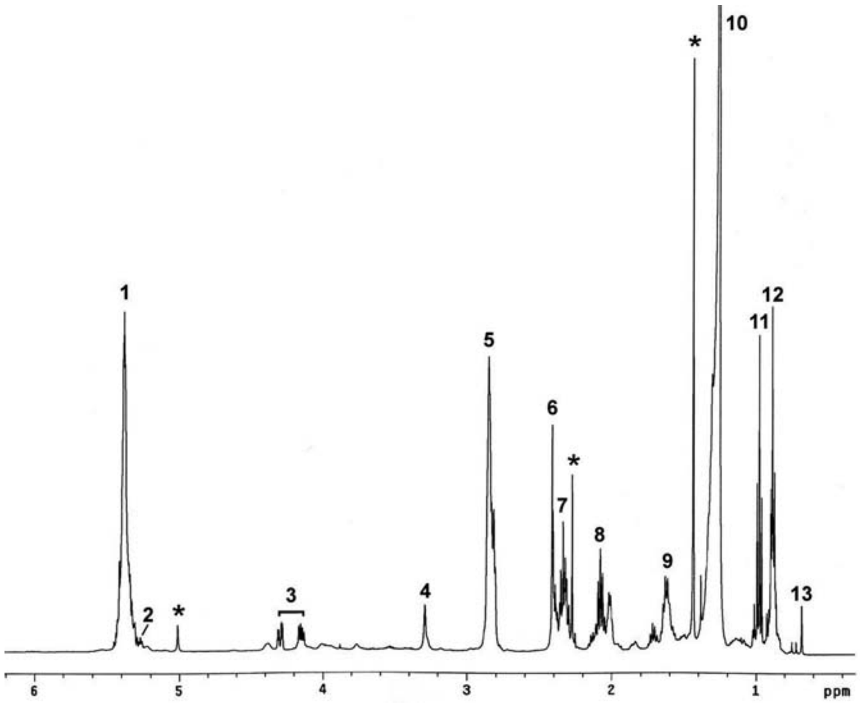

Fig. 1. ^{1}H NMR spectrum of lipids extracted from salted anchovies after 1 year ripening. The spectrum was carried out on a Varian 500 MHz instrument. Peaks are identified as in Table 1. Peaks with asterisks are referred to BHT used as antioxidant during lipid extraction.

Table 1: Assignment of the signals of the ^{1}H NMR spectra of anchovies lipids

Signal	Chemical shift δ (ppm)	Assignment		
		Protons	Functional group	Compound
1	5,30–5,35	**CH**=**CH**	olefinic protons acyl group	unsatured fatty acid
2	5,20–5,26	C**H**OCOR	glyceryl group proton on C2	triglycerides
3	4,10–4,25	$\mathbf{CH_2}$OCOR	glyceryl group proton on C1 and C3	triglycerides
4	3,25	$\mathbf{CH_3}$-N	methyl protons	phosphatidylcholine
5	2,85	CH=CHC$\mathbf{H_2}$CH=CH	bis-allylic protons	polyunsatured fatty acids
6	2,41	$\mathbf{CH_2}$COOR	methylenic protons α position carbonyl group	docosahexanoic acyl group
7	2,32	$\mathbf{CH_2}$COOR	methylenic protons α position carbonyl group	all acyl chains
8	2,02–2,09	$\mathbf{CH_2}$CH=CH	methilenic protons α single double bond	unsatured fatty acid
9	1,62	$\mathbf{CH_2}$CH$_2$COO-	methylenic protons in β position carbonyl group	all acyl chains
10	1,25–1,70	(C$\mathbf{H_2}$)n	methylenic protons of acyl group	all acyl chains
11	0,95	$\mathbf{CH_3}$	methyl protons of acyl groups	ω3 polyunsatured acyl groups
12	0,85	$\mathbf{CH_3}$	methyl protons of acyl groups	all acyl groups except ω3 PUFA
13	0,68–1,02	$\mathbf{CH_3}$	methyls	cholesterol

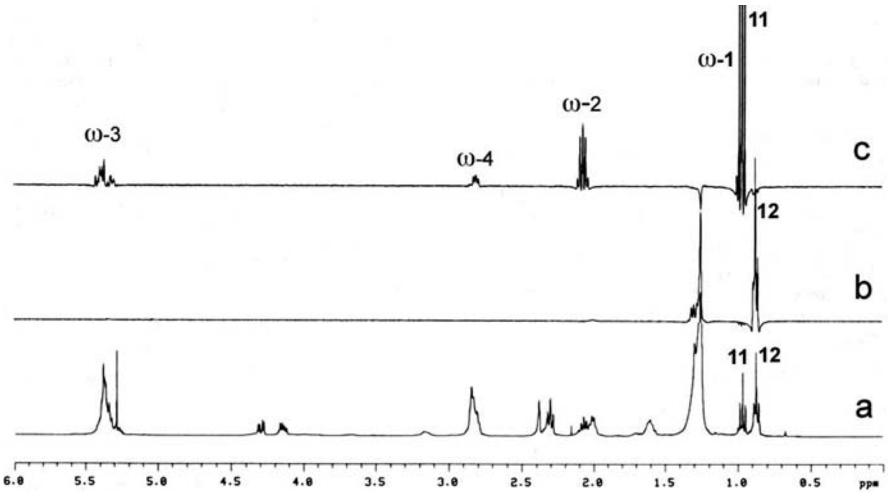

Fig. 2. Identification of ω-3 PUFA methyl resonances by proton nuclear magnetic resonance 400 MHz 1-D TOCSY experiments: (a) full spectrum, (b) selective excitation pulse on methyl triplet at 0.86 ppm, (c) selective excitation pulse on methyl triplet at 0.95 ppm (from ref. 4).

integration of the clearly resolved methyl resonances of n-3 PUFAS (peak n.11 in Figures 1 and 2) and of saturated and *n*-6, *n*-7, *n*-9 MUFAs and PUFAs (peak n.12 in Figures 1 and 2), allows the quantitative measurement of the total *n*-3 components. For this application spectrometers working at reasonably high magnetic fields (10 Tesla or higher) are used.

In a more recent work, the results outlined above have been applied more extensively and proposed as an IUPAC official method for the determination of docosahexanoic acid (DHA) and of n-3 fatty acids in fish oils [8]. In this research several samples of different origin (tuna oil, bonito oil, salmon oil, and sardine oil) were examined in different laboratories and using spectrometers at different magnetic fields to determine the accuracy of the measured peak intensities and, therefore, the quantitation of fish oil composition, in terms of *n*-3 components and DHA. The relative composition (mol%) of the n-3 fatty acids was obtained by simply comparing the relative intensities of the methyl resonances at 0.95 ppm (n-3 fatty acids) with those at 0.8 ppm (all other fatty acids) (Figure 3).

Moreover the DHA relative composition (mol %) was shown to be measured from the assigned C-2 and C-3 proton resonances at 2.38 ppm (peak 6 in Figure 1) well separated from the C-2 methylene protons of the other fatty acids at 2.28 ppm [2]. The DHA weight concentration in mg/g can also be easily measured by comparing its C-2, C-3 methylene resonance intensities with those of known amount of ethyleneglycol dimethyl ether (EGDM) used as internal standard, whose resonances occur at 3.35 ppm (methyls) and at 3.5 ppm (methylenes) [8].

The data obtained in thirteen different NMR laboratories from five different countries (Japan, Norway, Italy, France, and Denmark) were subjected to statistical analyses and demonstrated that both repeatability and reproducibility fall in a quite low range of relative standard deviations and in particular vary between 1.73 and 4.27% for DHA concentrations in mg/g. These values are acceptable for quality control in industrial laboratories and therefore this methodology was proposed as an official method of analysis considering that its major advantage over other possible analytical methods is its operational ease and the non-destructive NMR analysis. The family of n-3 fatty acids is assessed specifically, using proton resonances not affected by molecular weight of fatty acids and lipid classes. In fact, common transterification used for gas chromatographic analysis [13], does not esterify free fatty acids that are not measured by HRGC in highly lipolized oils. In these cases, GC/MS is needed for careful quantification and the use of specific derivatization (treating the sample using diazomethane) or time-consuming esterification methods.

Proton NMR and Lipolysis

Lipid classes and their evolution due to enzymes and thermal processing are a good quality parameter of raw,

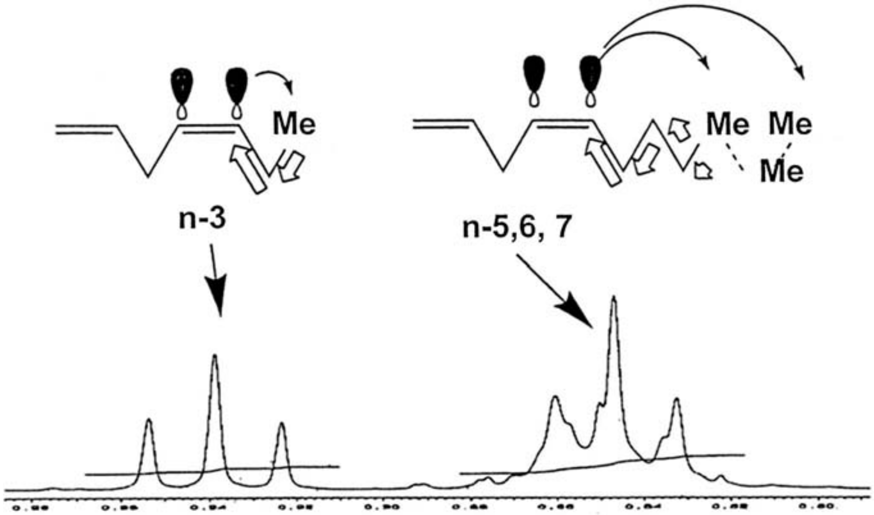

Fig. 3. Principle for quantification of n-3 fatty acids relative composition. (Top) Terminal methyl structures for n-3 fatty acids (left) and other fatty acids (right) where white block arrows and arc arrows show negative inductive effect of sp2 carbons and anisotropic effects of pi-electrons, respectively (Bottom). Methyl region of the ^{1}H-NMR spectrum of a fish oil, where left and right triplets originated from n-3 fatty acids and other fatty acids, respectively (from ref. 8).

processed fish and fish oils. This aspect is better monitored by using carbon-13 NMR [2,6] by observing the carbonyl region (Figure 4). Proton NMR, in fact, does not allow a direct quantitation of carboxyl protons of free fatty acids and in addition methylene protons bound to the carbon C-2 overlap with those of esterified acyl chains. The amount of free fatty acids, important products of fish lipolysis may be indirectly evaluated, only by the ratio between the intensity of diagnostic signals of triacylglycerol moieties (signal n. 4 in Figure 1) and those representative of acyl chain. Diacylglycerol and monoacylglycerol signals are also partially overlapped by phospholipids broad multiplets and not easy quantified.

Oxidation Products

The ^{1}H NMR spectroscopy can be also applied to study the oxidative degradation of fish lipids, by the same approach developed for other oils and lipids [14–15]. This technique is able to detect simultaneously primary and secondary oxidation products in oils and lipids, and to study the effect of industrial processing (salting, thermal treatments, etc.) on lipids [9]. This can be achieved by two analytical strategies. The simplest but of minor applicative interest is the study of the relative intensity changes of the main components, and particularly PUFAs. This approach was followed by Saito *et al.* [10] who demonstrated that the oxidative deterioration of fish oils could be monitoring, estimating the ratio (RO) of olefinic protons (4.90–5.8 ppm) to aliphatic protons (0.5–3.0 ppm). This ratio decreases as the oxidative deterioration proceeds. This procedure is applicable also at low magnetic fields and could be of importance in monitoring industrial processing or in the rapid control of global unsaturation and fatty acid composition.

A second and more interesting application has to be considered, although more difficult and requiring more skilled procedures concerns the study and the identification of new signals in the spectra due to components generated in the oxidation process [14,15].

In an interesting paper Aursand *et al.* [3] have shown, in the proton spectra of oxidised fish lipids, signals at approximately 6.5, 6.0, 5.6, 4.4 and 2.9 ppm originated from the protons of hydroperoxides and conjugated *trans, cis* double bonds formed during oxidation of PUFA , mainly from oxidized *n*-3 double bond [3].

The secondary oxidation lipid products such as aldehydes can also be observed in the proton spectrum [14]. Signals of saturated and unsaturated aldehydic protons between 9.30 and 9.90 ppm have also been detected for unsalted salmon fillet lipids submitted to the oxidation process [9]. In the same paper the lipid oxidation was monitored by measuring changes in relative ratioes of acyl

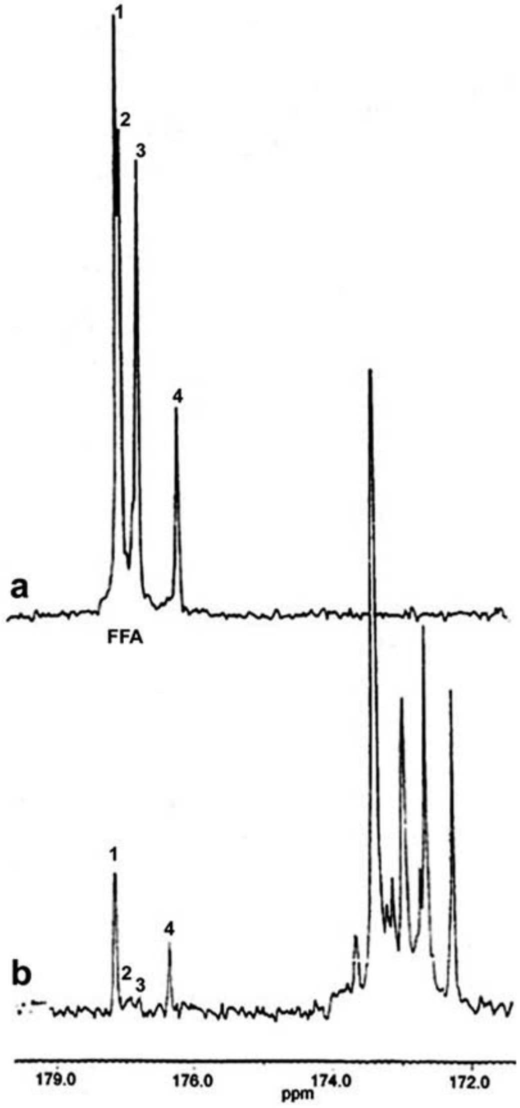

Fig. 4. 13C NMR carbonyl spectral region of a standard mixture of free fatty acids (a) and of a sample of albacore lipids (b). Labelled peaks are assigned as follow: 1 FFA (ST, MUFA); 2 FFA (linoleyl); 3 FFA (EPA); 4 FFA (DHA) (from ref. [5]).

groups belonging to omega-3 and saturated and unsaturated acyl groups.

Application Remarks

The use of NMR methods undoubtedly offers advantages and disadvantages over other analytical techniques. Advantages can be briefly indicated by NMR as being a non-destructive technique and by the ease in determining the relative amount of the main components. Disadvantages are instead due to the limited sensitivity of the NMR method that requires not less than fractions of milligrams for a rapid analysis. In the case of the analysis of fatty acids in fish lipids this point is not a drawback. The determination of minor components is, otherwise, time consuming and difficult although modern equipment developments, such as cryoprobes, can increase the sensitivity range by a factor of 100 thus extending sensitivity to the micromolar range.

References

1. Gunstone FD. Chem. Phys. Lipids 1991;59:83.
2. Aursand M, Grasdalen H. Chem. Phys. Lipids 1992;62:239.
3. Aursand M, Rainuzzo JR, Grasdalen H. In: HH Huss *et al.* (Ed). Quality Assurance in the Fish Industry. Elsevier Science Publishers B.V.: Amsterdam, 1992, p 407.
4. Sacchi R, Medina I, Aubourg SP, Addeo F, Paolillo L. JAOCS 1993;70:225.
5. Sacchi R, Medina I, Aubourg SP, Giudicianni I, Paolillo L, Addeo F. J. Agric. Food Chem. 1993;41:1247.
6. Medina I, Sacchi R, Auborg S. JAOCS 1994;71:479.
7. Igarashi T, Aursand M, Hirata Y, Gribbestad IS, Wada S, Nonaka M. JAOCS 2000;77:737.
8. Igarashi T, Aursand M, Sacchi R, Paolillo L, Nonaka M, Wada S. J. AOAC International 2002;85:1341.
9. Guillén MD and Ruiz A. Food Chem. 2003;86:297–304.
10. Saito H, Nakamura K. Agric. Biol. Chem. 1990;54:533.
11. Bligh E, Dyer W. Can. J. Biochem. Physiol. 1959;37:911.
12. Simopoulus AP, Leaf A, Salem N. ISSFAL Newsletter 1999;6:14.
13. Christie WW. Lipid Analysis, 2nd ed. Pergamon Press: Oxford, 1982.
14. Claxson AWD, Hawkes GE, Richardson DP, Naughton DP, Haywood RM, Chander CL, Atherton M, Lynch EJ, Grootveld MC. Febs Letters 1994;355:81.
15. Neff WE, Frankel EN, Miyashita K. Lipids 1990;25:33.

Determination of Fatty Acid Composition and Oxidation in Fish Oils by High Resolution Nuclear Magnetic Resonance Spectroscopy

Rosario Zamora, Francisco J. Hidalgo
Instituto de la Grasa, CSIC, Avenida Padre Garcia Tejero 4,41012-Sevilla, Spain

Fatty Acid Analysis of Fish Oils

Fatty acids are key components of fish lipids, and the analysis of them is usually carried out for the characterization of fish oils. Fish oils contain a wide variety of fatty acids (Table 1). Thus, Ackman[1] has reported as many as 50 or 60 components, though only about 14 of these are of importance in terms of weight percent of the total. They are low in saturated fatty acids (mainly myristic and palmitic acids) and high in unsaturated fatty acids, especially those unsaturated acids with long chains containing 20 or 22 carbons or more, and up to six double bonds.

Nowadays, fatty acid analysis is usually carried out by gas chromatography because of the very high resolution together with the high sensitivity and very good reproducibility in quantitative analyses of this chromatographic technique, and the possibility of preparing different derivatives for determining fatty acid structures by GC-MS.[2] However, GC-MS has limitations, being particularly important its inability to distinguish between geometrical isomers and the potential destruction of thermally labile fatty acids.

In recent years, high resolution NMR has emerged as an alternative technique in this field.[3] A NMR spectrum contains a great amount of information that can be obtained in a short time period and the risk of destruction of unstable compounds is minimal. The different signals present in the NMR spectra provide two kinds of information: the chemical shifts and the relative intensities. The former is of qualitative value and it is related to the different atoms present in the analyzed sample, including many structural characteristics of the studied molecules such as the geometry of double bonds or the α and β positions of the triacylglycerols. The latter provides quantitative information of the different signals that can be employed for the quantitative determination of many oil components, including the fatty acids.[4] On the other hand, NMR does not usually distinguish among saturated fatty acids.

In an attempt to critically analyze different studies carried out in recent years, present possibilities and limitations of this technique for the analysis of fish oils and the study of their oxidation are reviewed here.

The ^{1}H NMR Spectra of Fish Oils

Fish oils are composed of more than 95% of triacylglycerols. Therefore, their ^{1}H and ^{13}C NMR are mostly the spectra of the mixtures of their triacylglycerols. Figure 1 shows the ^{1}H NMR spectrum of fish oil from menhaden. This oil contains approximately 25% of $n-3$ (octadecatetraenoic, eicosapentaenoic and docosahexaenoic) fatty acids as triacylglycerols (Table 1). Its spectrum is similar to the spectra of vegetable oils,[5] though some differences are noteworthy. Thus, the signals corresponding to the C2 and C3 methylenes of docosahexaenoic acid (DHA), and the methyl signals of $n-3$ fatty acids are characteristic signals in the spectra of fish oils. In fact, the former signal has been proposed for being employed in the quantitative determination of DHA, and the latter in the determination of $n-3$ fatty acids.[6–9]

The ^{13}C NMR Spectra of Fish Oils

Analogously to the NMR spectra of other edible oils, the ^{13}C NMR spectra of fish oils contain a higher number of signals than their ^{1}H NMR spectra, and it is possible to distinguish among the different fatty acids that are present in the triacylglycerols, and their relative positions. Figure 2 shows the ^{13}C NMR spectrum of menhaden fish oil, which has been assigned according to the chemical shifts previously reported for other oils.[10–12] ^{13}C-NMR signals of fish oils can be grouped into four well-defined spectral regions: carbonyl-carbons ranging from 173.3 to 172.0 ppm; unsaturated carbons ranging from 132.1 to 126.8 ppm; glycerol carbons ranging from 69.1 to

Graham A. Webb (ed.), Modern Magnetic Resonance, 925–931.
© 2008 *Springer.*

Table 1: Fatty acid composition of depot fats from selected fishes[a]

	Menhaden	Anchovy	Herring	Sardine	Carp	Rainbow trout	Sepia
14:0	9–11	7.4	6.1	6.7	2.4	2.0	2.4
14:1			0.1		1.0	0.1	0.2
16:0b		0.4	0.4	0.5			
15:0		0.6	0.4	0.7	1.2	0.3	1.0
16:0	20–21	17.4	10.8	17.8	19.4	17.8	14.5
l6:1	11–14	9.0	7.3	6.0	10.1	6.1	4.1
16:2 *n*4		1.0	0.4	0.7			
16:3 *n*4		2.2	6.7	0.4			
16:4 *n*1		2.4	1.2	1.6			
17:0		0.5	0.3	0.8	1.9	0.6	2.0
17:1			0.3	0.3	1.1	0.6	1.7
18:0b		0.7	0.8	0.6			
18:0	3–4	4.0	1.4	3.6	6.7	4.8	8.6
18:1	11–12	11.6	10.3	13.0	14.2	32.5	9.1
18:2 *n*6	1–2	1.2	0.9	1.2	5.6	14.3	1.2
18:2 *n*4		0.6	0.1	0.3			
18:3 *n*3	1–4	0.7	2.0	1.0	10.1	0.3	0.3
18:4 *n*3	2–4	3.1	3.2	3.1	1.5	0.4	0.2
20:1	1–2	1.5	13.4	4.3	8.8	2.6	4.1
20:2 *n*6		0.4	0.2	0.2	0.4	0.7	0.4
20:3 *n*3		1.1	0.3	0.8	0.3	0.6	0.3
20:4 *n*3	2–3	0.7	0.8	1.0	1.1	0.5	0.4
20:5 *n*3	12–14	17.0	7.4	11.0	6.2	2.0	19.9
21:5 *n*2		0.7	0.2	0.5			
22:1	0–1	1.1	21.1	3.8	6.3	1.3	3.2
22:4 *n*3		0.6	0.3	0.7			
22:4 *n*6					0.9	0.3	1.1
22:5 *n*3	2–3	1.6	0.8	1.3	1.8	0.8	2.6
22:5 *n*6					0.9	0.3	0.6
22:6 *n*3	6–11	8.7	6.7	13.0	7.3	10.3	20.9
24:1		0.5	0.8	0.6			

[a] Fatty acid compositions are expressed as mean average weight percent composition on a fatty acid basis. Fatty acids present in a less than 0.5% of the total have been excluded. Abbreviation: b, branched fatty acid. (Adapted from Ref. 2)

61.6 ppm; and aliphatic carbons ranging from 34.5 to 13.9 ppm. Assignation of aliphatic carbons is given in Figure 3. This figure also includes the spectrum of soybean oil for comparison (panel A).

Because some fatty acid carbons appear differently if they are at the α- or β-positions of the triacylglycerol, it is possible to determine the percentage of the diverse fatty acids at the two positions.[13,14] In addition, the ^{13}C NMR spectrum is very useful to analyze the presence of other components in the oil in addition to the triacylglycerols. These minor components are usually more polar than triacylglycerols and they can be concentrated by chromatographic procedures to obtain good spectra in a short time period.[15] Figure 4 shows the ^{13}C NMR spectrum of the chromatographic fraction obtained from menhaden fish oil. As observed, this spectrum is much richer in signals than the spectrum of the complete oil (Figure 2) and different oil components may be easily observed. Thus, for example, in the glycerol portion of the spectrum, the signals corresponding to mono- and diacyl-glycerols, and cholesterol can be observed in addition to the triacylglycerols. The increased information obtained from these spectra has been employed in defining oil authenticity[16] and quality[17,18] in vegetable oils, and it should also be very useful in the study of fish oils.

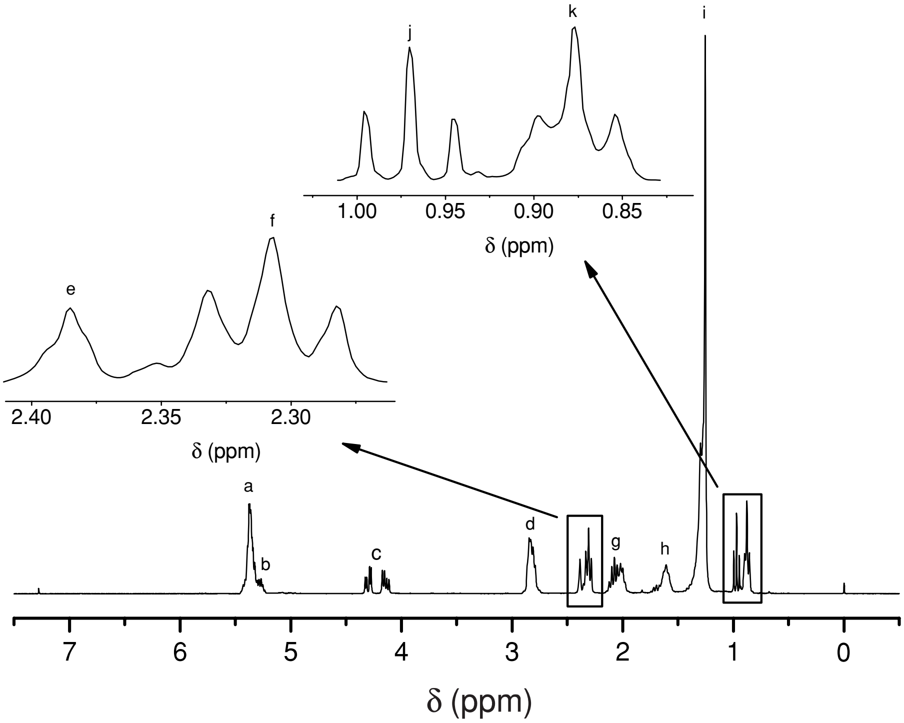

Fig. 1. Three hundred MHz ^{1}H NMR spectrum of menhaden fish oil in $CDCl_3$. Signals: a, olefinic protons; b, β-glycerol; c, α-glycerol; d, double allylic protons; e, C2 and C3 methylenes of DHA; f, C2 methylenes of non-DHA; g, allylic protons; h, C3 methylenes; i, fatty acid chains; j, methyls of $n-3$ fatty acids; k, methyls of non-$n-3$ fatty acids.

Fish Oil Oxidation and its Evaluation by NMR

Lipid oxidation is one of the major causes of food spoilage, and it is particularly important in fish oils because of the high content of polyunsaturated fatty acids with five and six double bonds, which are highly susceptible to atmospheric oxidation. Its evaluation is nowadays carried out by employing different methodologies.[19] Most of these methods are based on the formation of specific compounds or on the modification of others. Because high resolution NMR is able to quantitatively determine many of these components, NMR spectra could be employed to evaluate fish oil oxidation.

Thus, fish oil oxidation produces the decrease of the integrals of olefinic and double allylic protons in fish oils with the progress of oxidation, and the ratios of olefinic protons and double allylic protons to aliphatic protons have been proposed as suitable indexes for comparing the storage conditions of marine products and for estimating the effects of antioxidants on them.[20–22] In addition, good correlations were obtained between ^{1}H NMR and GC data in the study of oxidative degradation of fish materials after cooking.[23]

Nevertheless, the higher amount of information contained in the ^{13}C NMR spectra should produce much more useful spectra. Thus, signals corresponding to free fatty acids can be easily observed when fatty acids are released, and its quantification has been proposed for monitoring free fatty acid release after thermal processing of fish.[24] Other attempts have also been made to study the mechanism of lipid oxidation during thermal stress of fish,[25] but the obtained conclusions were too general, more likely as a consequence of the small changes produced in the obtained spectra.

A better way to observe the changes produced in the spectra is to concentrate chromatographically the polar components produced during oil oxidation[15] Figure 5 shows the ^{13}C NMR spectrum of the chromatographic fraction obtained from a menhaden fish oil heated under air in the dark at 37 °C during 70 h. The formation of

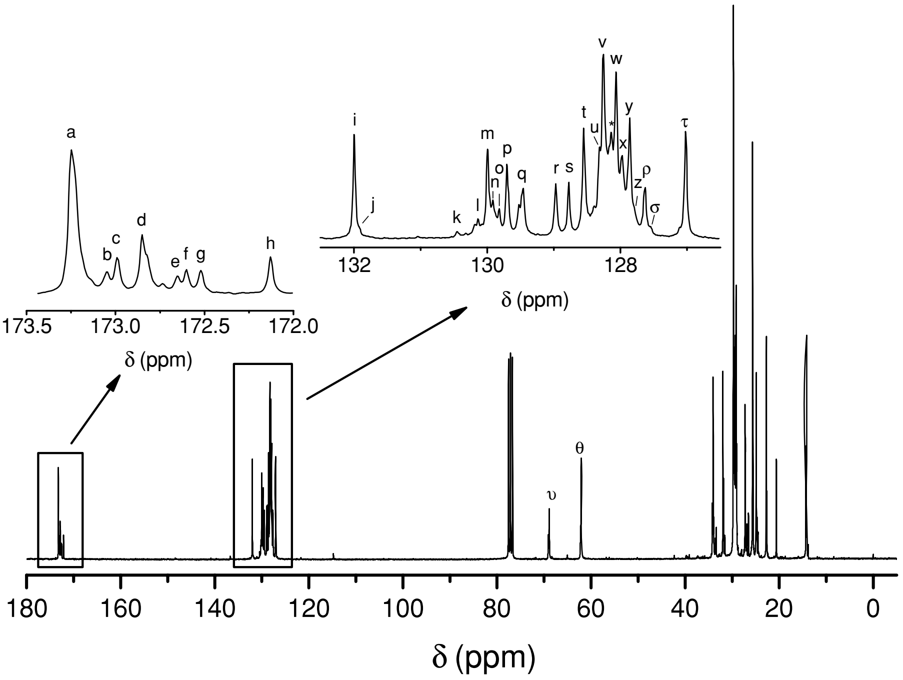

Fig. 2. About 75.5 MHz ^{13}C NMR spectrum of menhaden fish oil in CDCl$_3$. Assignments are abbreviated by fatty acid, carbon number, and position in the glycerol. l(3)- and 2-positions of glycerol are designated by the greek symbols α and β, respectively. Labeling of acyl chains: D, docosahexaenoyl; E, eicosenoyl; Ep, eicosapentaenoyl; L, linoleyl; Ln, linolenyl; O, oleyl; Od, octadecatetraenoyl; and S, saturated chain. Carbonyl and olefinic signals: a, Slα/O1α/L1α; b, Od1α; c, Ep1α; d, Slβ/O1β/L1β; e, Od1β; f, Ep1β; g, D1α; h, D1β; i, E18/D20; j, Ln16; k, Od15; 1, L13/Ln9; m, O10/L9; n, E12; o, E11; p, O9; q, D5; r, E5; s, E6; t, D17; u, D7; v, Dl0/D14/Ln12/Ln13; w, D11/D13/L10; x, D8; y, D16/L12; z, Ln10; ρ, D4; σ, Ln15; and τ, E17/D19. The signals ν and θ correspond to the glycerol β and α carbons, respectively. Unassigned peaks are marked with*.

carbonyl derivatives, secondary products of lipid oxidation, is easily observed at $\delta = 210.64$ and 207.12 ppm, though the identity of the produced derivatives has not been determined yet (Zamora and Hidalgo, unpublished results). This soft treatment of the oil did not produce fatty acid release and the most significant changes were observed in the glycerol region. In addition to the increase of the signals corresponding to modified triacylglycerols, the presence of a number of small signals was observed. These corresponded to both primary and secondary products of lipid oxidation. A careful analysis of the changes produced in this region should allow one to follow the different processes occurring as a consequence of lipid oxidation.

Conclusions

High resolution NMR spectroscopy has been shown to be a useful technique for the fatty acid analysis of fish oils. Thus, ^{1}H NMR allows the quantitative determination of DHA very rapidly and with very little sample preparation in comparison with GC. In addition, ^{13}C NMR can be employed to determine the position of the fatty acid chains in the triacylglycerol molecule without any chemical or enzymatic treatment. Furthermore, the chromatographic concentration of the minor oil components allow the direct and simultaneous determination of them by ^{13}C NMR.

Oil oxidation has been less studied by NMR, though a methodology that employs ^{1}H NMR has been developed to follow the oxidation progress. On the other hand, the chromatographic concentration of oil polar components seems to be a necessary step to obtain progress in the study of fish oil oxidation by ^{13}C NMR.

Acknowledgments

This study was supported in part by the Plan National de I+D of the Ministerio de Educación y Ciencia of Spain

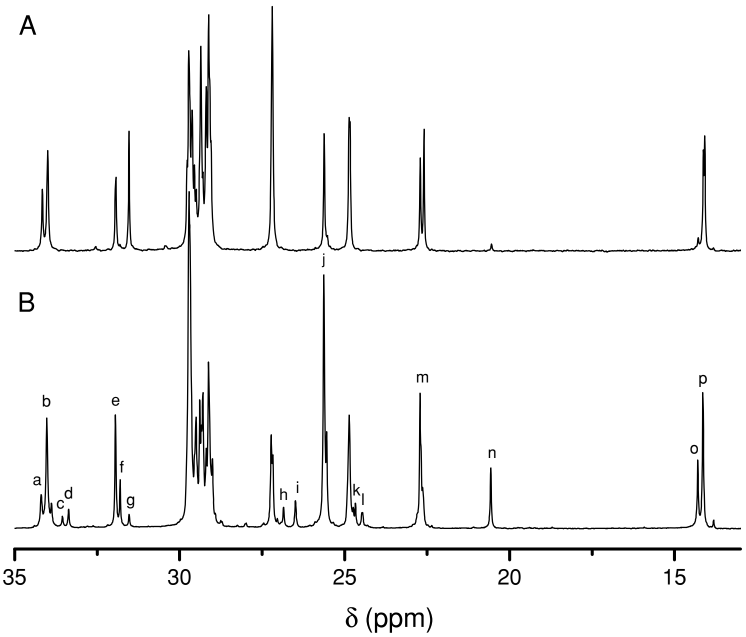

Fig. 3. Partial 75.5 MHz ^{13}C NMR spectrum of menhaden fish oil in CDCl$_3$ (B). The figure also includes the analogous spectrum of soybean oil for comparison (A). Assignments are abbreviated by fatty acid, carbon number, and position in the glycerol. 1(3)- and 2-positions of glycerol are designated by the greek symbols α and β, respectively. Labeling of acyl chains: D, docosahexaenoyl; Ep, eicosapentaenoyl; L, linoleyl; O, oleyl; Od, octadecatetraenoyl; and S, saturated chain. Aliphatic carbon signals: a, S2β/O2β; b, S2α/O2α; c, Ep2β; d, Ep2α; e, ω3 carbon in saturated and $n-3$ fatty acids; f, ω3 carbon in $n-6$ fatty acids; f, ω3 carbon in $n-7$ fatty acids; h, D6; i, Ep4; j, PUFA mid-chain; k, Ep3; 1, Od3; m, Sω2/O17/L17; n, D2/Ep2/Od2; o, ω1 carbon in $n-3$ fatty acids; and p, Sω1/O18/L18. Assignation of other signals are given in ref. 3.

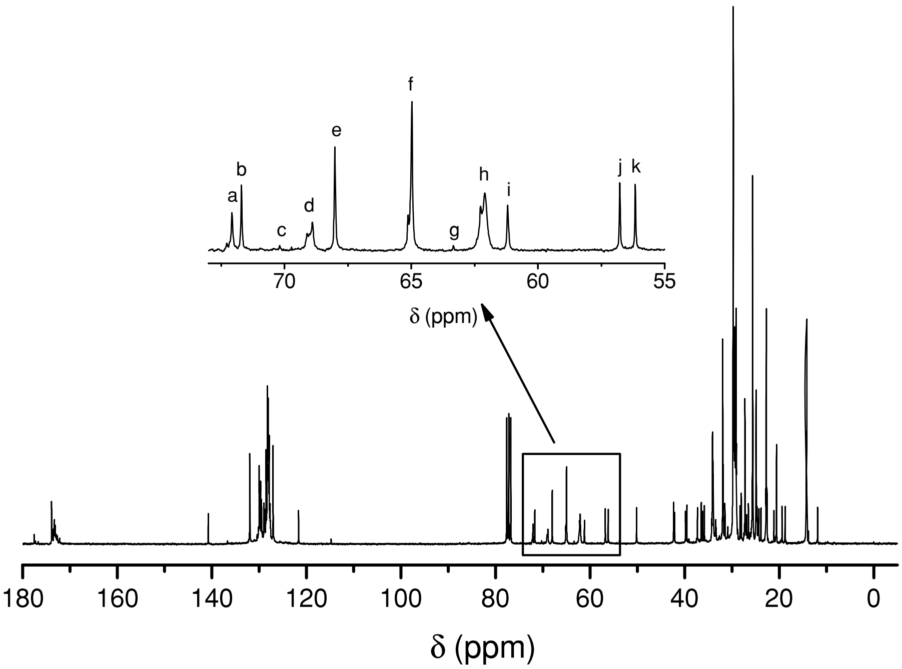

Fig. 4. About 75.5 MHz ^{13}C NMR spectrum of the chromatographic fraction obtained from menhaden fish oil in CDCl$_3$. Assignments are abbreviated by fatty acid, carbon number, and position in the glycerol. 1(3)- and 2-positions of glycerol are designated by the greek symbols α and β, respectively. Abbreviations: Ch, cholesterol; 1,2DAG, l,2-diacylglycerol; 1,3DAG, 1,3-diacylglycerol; 1MAG, 1-monoacylglycerol; 2MAG, 2-monoacylglycerol; TAG, triacylglycerol. Glycerol region signals: a, 1,2DAG2; b, Ch3; c, 1MAG2; d, TAG2; e, 1,3DAG2; f, 1,3DAG1/3 & 1MAG3; g, 1MAG1; h, TAG1/3, 1,2DAG3 & 2MAG1/3; i, 1,2DAG1; j, Ch14; and k, Ch17.

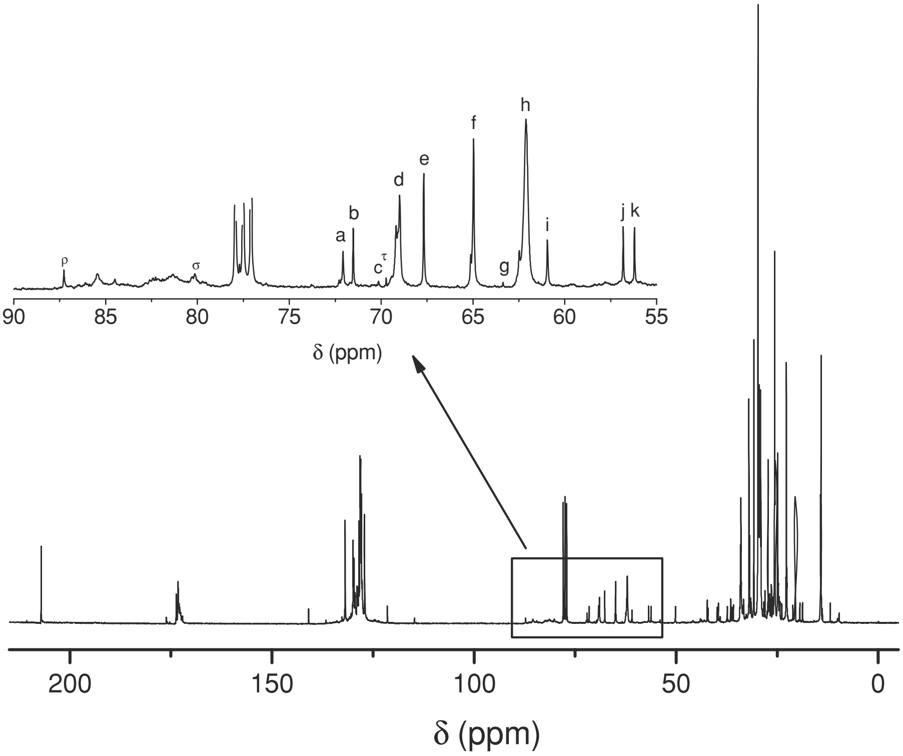

Fig. 5. About 75.5 MHz ^{13}C NMR spectrum in $CDCl_3$ of the chromatographic fraction obtained from menhaden fish oil heated under air in the dark at 37 °C during 70 h. Assignments are abbreviated by fatty acid, carbon number, and position in the glycerol. 1(3)- and 2-positions of glycerol are designated by the greek symbols α and β, respectively. Abbreviations: BEP, bicyclo-endoperoxide; Ch, cholesterol; 1,2DAG, 1,2-diacylglycerol; 1,3DAG, 1,3-diacylglycerol; HD, hydroxyl derivative; HP, hydroperoxide; 1MAG, 1-monoacylglycerol; 2MAG, 2-monoacylglycerol; TAG, triacylglycerol. Glycerol region signals: ρ, HP; σ, BEP; a, 1,2DAG2; b, Ch3; c, 1MAG2; τ, HD; d, TAG2; e, 1,3DAG2; f, 1,3DAG1/3 & 1MAG3; g, 1MAG1; h, TAG1/3, 1,2DAG3 & 2MAG1/3; i, 1,2DAGl; j, Ch14; and k, Ch17.

(Project AGL2003-02280) and the Junta de Andalucía (Coordinated Action ACC-1417-AGR-2003). We are indebted to José L. Navarro for technical assistance.

References

1. Ackman RG In: Chow CK (Ed.), Fatty Acids in Foods and their Health Implications, 2nd ed, New York: Marcel Dekker, 2000, p. 153.
2. Zamora R, Hidalgo FJ In Nollet LML (Ed.), Handbook of Food Analysis: Second Edition, Revised and Expanded, Volume 1: Physical Characterization and Nutrient Analysis, New York: Marcel Dekker, 2004, p. 221.
3. Hidalgo FJ, Zamora R, Trends Food Sci. Technol. 2003; 14:499.
4. Wollenberg KF, J. Am. Oil Chem. Soc. 1990;67:487.
5. Guillén MD, Ruiz A, Trends Food Sci. Technol. 2001;12:328.
6. Igarashi T, Aursand M, Hirata Y, Gribbestad IS, Wada S, Nonaka M, J. Am. Oil Chem. Soc. 2000;77:737.
7. Wada S, J. Oleo Sci. 2001;50:329.
8. Igarashi T, Aursand M, Sacchi R, Paolillo L, Nonaka M, Wada S, J. AOAC Int. 2002; 85:1341.
9. Siddiqui N, Sim J, Silwood CJL, Toms H, Iles RA, Grootveld M, J. Lipid Res. 2003; 44:2406.
10. Gunstone FD, Chem. Phys. Lipids. 1991;59:83.
11. Aursand M, Grasdalen H, Chem. Phys. Lipids. 1992; 62:239.
12. Sacchi R, Medina I, Paolillo L, Addeo F, Chem. Phys. Lipids. 1994; 69:65.
13. Gunstone FD, Seth S, Chem. Phys. Lipids. 1994;72:119.
14. Wada S, Lipid Technol. 2001;13:116.
15. Zamora R, Gómez G, Dobarganes MC, Hidalgo FJ, J. Am. Oil Chem. Soc. 2002; 79:261.
16. Zamora R, Gómez G, Hidalgo FJ, J. Am. Oil Chem. Soc. 2002;79:2671.

17. Zamora R, Gómez G, Hidalgo FJ In: Webb GA, Belton PS, Gil AM, Rutledge DN (Eds), Magnetic Resonance in Food Science: Latest Developments, Cambridge: The Royal Society of Chemistry, 2002, p. 231.
18. Hidalgo FJ, Gómez G, Navarro JL, Zamora R, J. Agric. Food Chem. 2002;50:5825.
19. Warner K, Eskin NAM, Methods to Assess Quality and Stability of Oils and Fat-Containing Foods, Champaign: AOCS Press, 1994.
20. Saito H, Udagawa M, J. Sci. Food Agric. 1992;58:135.
21. Saito H, Udagawa M, J. Am. Oil Chem. Soc. 1992;69:1157.
22. Saito H In: Shahidi F, Cadwallader KR (Eds), Flavor and Lipid Chemistry of Seafoods, Washington, D.C.: American Chemical Society, 1997, p. 217.
23. Cengarle L, Carta A, Marceddu MF, Pinna L, Tilloca G, Riv. Ital. Sost. Grasse. 1999;76:249.
24. Medina I, Sacchi R, Aubourg S, J. Am. Oil Chem. Soc. 1994;71:479.
25. Medina I, Sacchi R, Giudicianni I, Aubourg S, J. Am. Oil Chem. Soc. 1998;75:147.

Resonance Spectroscopy to Study Lipid Oxidation in Fish and Fish Products

E. Falch[1,2] and M. Aursand[1]
[1]*SINTEF Fisheries and Aquaculture, Trondheim, Norway*
[2]*The Norwegian University of Science and Technology, Department of Biotechnology, Trondheim, Norway*

Marine lipids are highly susceptible to lipid oxidation, and analytical methods describing the early stages of lipid oxidation are needed. Free radicals, which are major contributors in the initiation and propagation stages of lipid oxidation, might be detected by different electron spin resonance (ESR) spectroscopy techniques. High resolution (HR) nuclear magnetic resonance (NMR) spectroscopy is less sensitive compared to ESR, but can be applied to identify the different reaction products formed during lipid oxidation. Additionally, HR-NMR can provide detailed information about the chemical composition, which is valuable for predicting the susceptibility to lipid oxidation. This chapter will shed light on some of these techniques applied on marine material.

Electron Spin Resonance Spectroscopy

ESR spectroscopy is a relatively new method for studying lipid oxidation in food systems. It has recently been claimed to be the most direct method for detecting free radicals [1–4]. The method is sensitive and lipid oxidation is detected at its early stages with detection limits of radicals between 10^{-6} and 10^{-10}M at optimal conditions [3–6].

In powder samples, the free radicals are trapped in the food matrix and might be detected directly and nondestructively. Promising results have been reported for radical detection in milk powder [7], dehydrated chicken meat [8], potato flakes [9], and freeze-dried cheese [10]. Saed *et al.* [11] and Howel *et al.* [2], who did their studies on marine powders, reported that ESR could be a tool for studying interactions between proteins and oxidized lipids and found a clear indication of direct free radical transfer from oxidized lipids to amino acids and proteins. Also, direct trapping and identification of radicals were performed, both on systems with and without antioxidant added.

The ESR spectra may provide information for radical assignment by studying the g-value, hyperfine splitting constant and the line shape [3].

At least $2 \cdot 10^{11}$ spins of a specie must be present for seconds to minutes to be detectable directly by ESR [12]. The free radicals active during lipid oxidation in oils and emulsion are labile and are difficult to detect during their shelf life under normal conditions [4]. In such systems, the radicals need to be trapped. Radicals can be trapped by rapid freezing, lyophilisation, and spin trapping [4]. Freezing might disrupt cells and thereby influence the lipid oxidation progress; however, fast freezing will reduce this problem.

Spin trapping is one of the ESR techniques applicable to trap radicals in fluids. Spin trapping agents are chemicals that are mixed in the sample with the purpose of reacting with the free radicals to form detectable and stable spin adducts. There are many spin trapping agents available, but nitrone spin traps are reportedly the most useful when studying lipid oxidation since they react less readily with un-oxidized lipids than nitroso compounds [13]. The most popular spin traps are; N-t-butyl-α-phenylnitrone (PBN), α-(4-Pyrridyl 1-Oxide)-N-tert-butylnitrone (POBN) and 5,5-dimethyl-1-pyrroline-N-oxide (DMPO) [14]. Characteristics of the different spin traps are reviewed by Janzen and Haire [15]and the specificity of spin traps to different free radicals are reported in tables of spin adduct ESR parameters [14]. During lipid oxidation both alkyl and oxygen centered radicals are formed, which is one of the aspects to allow for when choosing the spin trap and the experimental conditions. PBN adducts with oxygen centered radicals have too short a half lifetime to be detected by ESR, resulting in trapping of mainly carbon centered radicals when using PBN [16]. DMPO however, can trap both carbon centered radicals and hydroxyl radicals [16], but this is a hydrophilic spin trapping agent which might restrict its applications in oil systems. A lipophilic derivative of 5-(diethoxy-phosphoryl)-5-methyl-1-pyrrolineN-oxide (DEPMPO) has been recently developed for successful trapping of carbon- and oxygen centered radicals [16]. There is on-going research with the aim of developing new spin traps, but according to Stolze *et al.* [17], no optimal spin trap for detection of alkoxyl radicals has yet been found.

Graham A. Webb (ed.), Modern Magnetic Resonance, 933–940.
© 2008 *Springer.*

The spin trapping technique has recently been applied to bulk oils and food model emulsions [6,18–22]. A fish oil-enriched mayonnaise system was developed [6,18–21] to study the oxidative stability (tendency of radical formation) and efficiency of antioxidants [18,6]. Additionally, quantification of free radicals was successfully performed in this system [6]. In bulk oils a correlation was found between ESR and accelerated oxidative stability methods (Rancimat) during evaluation of oxidative stability [23] in vegetable oils with and without volatile antioxidants. ESR was also found consistent with conventional methods during oxidation of cod liver oil and salmon oil [22].

ESR has provided much to the science of antioxidant effect [3,23–25] and elucidation of the reaction mechanisms involved [26]. Such work is important, especially for marine lipids, since they are regarded as health promoting products and need to be stabilised against destructive lipid oxidation. However, few reported studies are dealing with free radical detection of the complex marine lipids.

Investigation of Free Radicals in Marine Lipids

Several preliminary studies have been recently conducted in our research group to explore the applications of ESR as a tool for evaluating lipid oxidation in different marine material (raw material, bulk products, and fillets). Parts of this work are briefly presented here, focusing on opportunities and limitations concerning the method.

Study of Lipid Oxidation in Freeze Stored Herring

Among other analytical techniques, ESR was used to study lipid oxidation in herring mince during frozen storage. Herring mince was stored with and without added α-tocopherol at −20 °C for up to 6.5 months. A control sample of the same mince was kept under vacuum at −80 °C until analysis. Three different ESR techniques were tested; (1) direct detection in the mince, (2) spin trapping in a MES (2-[N-morpholino] ethanesulphonic acid) buffer emulsion (POBN) and (3) direct detection in the vacuum freeze dried samples.

ESR measurements were performed at room temperature using an X-band (9.45-GHz) ECS ESR 106 spectrometer (Bruker, Rheinstetten, Germany). No detectable signals were obtained when directly recording spectra from the mince placed in a flat EPR cell. A method based on an assay developed for measuring lipid oxidation in meat products [27], was adopted for the spin trapping experiment in herring. The mince (2.4 g) was homogenised with a MES buffer (24 ml) containing POBN (40 mM). Samples were placed in a water bath kept at 35 °C and ESR recordings of the filtrate were performed at certain time intervals. The spectrum and the increased intensity of POBN spin adducts are presented in Figure 1 showing signal increase a short time after preparation of the emulsion. Higher signals were found in the oxidised sample. Spectra from direct detection of the freeze-dried

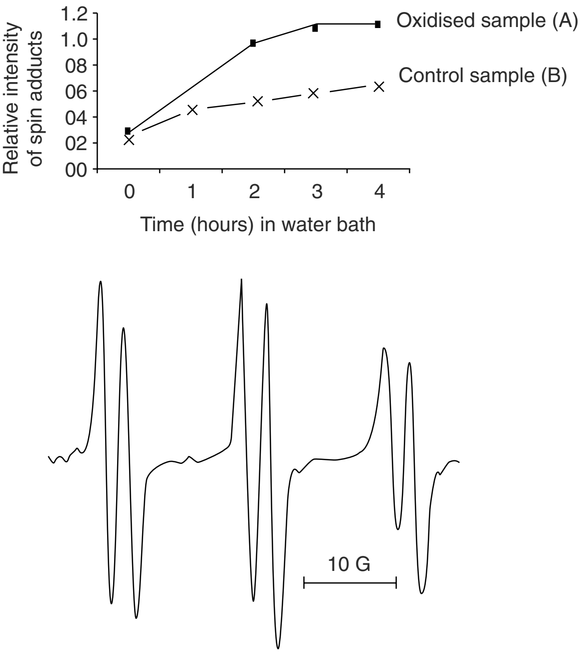

Fig. 1. Intensity of spin adducts (POBN) in herring mince in the control sample (B) (mince, vacuum packed and kept at −80 °C until analysis) and (A) mince freeze stored for 6.5 months at −20 °C before analysis. The methods are adopted from an assay reported by Carlsen *et al*. [27]. An ESR spectrum from this series is also presented. Unpublished data.

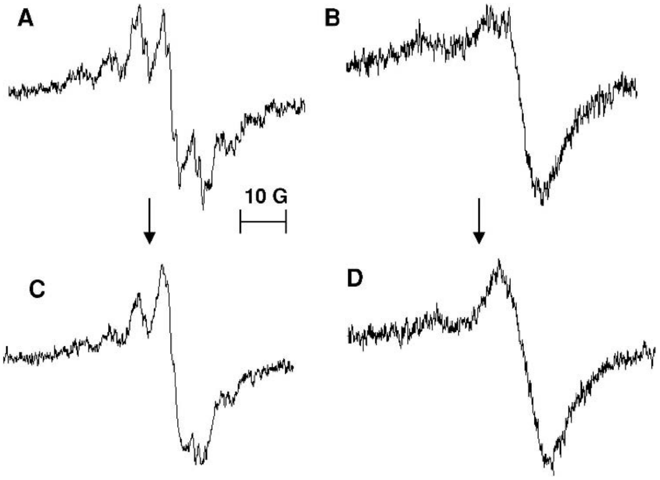

Fig. 2. ESR spectra of freeze dried samples of herring mince. Samples A and B are control samples (mince stored at −80 °C until analysis). Samples C and D are the same samples freeze stored at −20 °C for 6.5 months before analysis. Samples A and C are added 200 ppm α-tocopherol as antioxidant. Unpublished data.

mince are shown in Figure 2 and it is quite clear that the method is capable of separating samples with and without α-tocopherol based on the ESR spectrum. The signal intensity in the stored/oxidized samples was higher than in the control samples. Our unpublished data has shown that the free radical signals in a series of dried marine powders are reduced during further storage and that the reduction is faster at higher temperatures. The direct detection of radicals in marine powders might be affected by transition metals like iron and copper, which from time to time are found in detectable amounts in these products (natural or by contamination by processing equipment). The spectra will, in that case, be disturbed (see Figure 3) but information about the metal ions can in that case be gained. The importance of using optimal microwave power is illustrated in Figure 4.

Spin Trapping of Cod Liver Oil

In order to find the optimal spin trap and the stability of spin adducts in a fish oil system the following three common spin traps were used in fresh cod liver oil: 2N-t-butyl-α-phenylnitrone (PBN), α-(4-Pyrridyl 1-Oxide)-N-tert-butylnitrone (POBN) and 5,5-dimethyl-1-pyrroline-N-oxide (DMPO). The spin traps were added at two

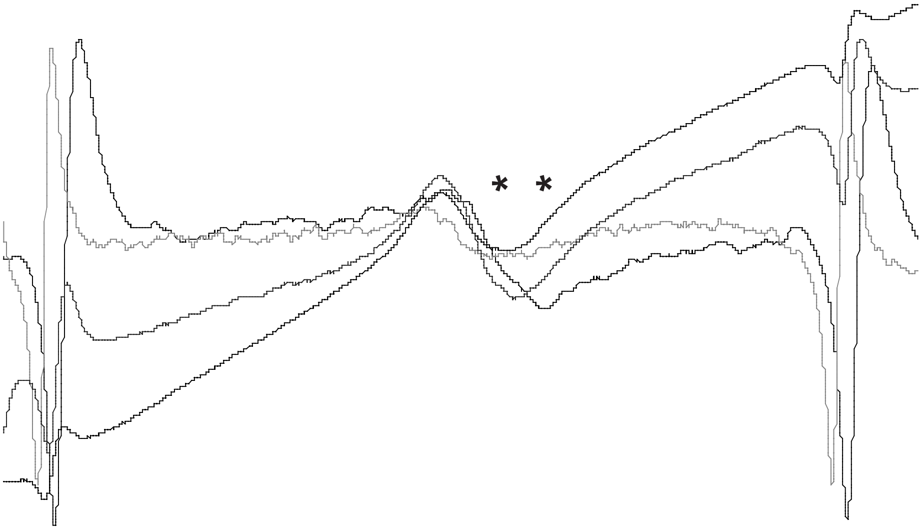

Fig. 3. ESR spectra of fish protein hydrolysates dried by different techniques. The two spectra of spray dried samples (*) has changed the shape which indicates a contamination by transition metals (∼g = 2.00).

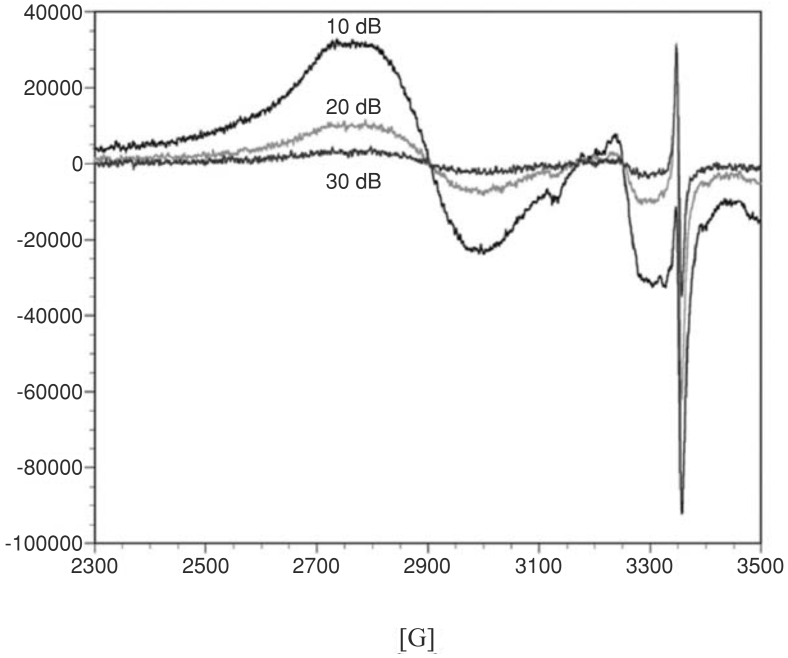

Fig. 4. ESR Spectra of salmon powders using three different microwave powers. Temp 180 K, mod amp 1.0 G, Gain 210^5.

concentrations (1 and 3 mg/g oil) and ESR spectra were recorded at specific intervals after storage in a water bath set at 40 °C. The amplitude of the ESR signal is expressed as the relative intensity of free radicals during storage and is presented in Figure 5. Spin adducts from PBN and POBN (3 mg/g) reach a maximum between 50 and 120 h at 40 °C, while the maxima reach a lower value in the samples with 1 mg/g. The amounts of spin adducts are relative similar between PBN and POBN, while the signals are much more complex and lower for the spin adducts with DMPO. This might be due to the solubility properties.

In another study, cod liver oil with different levels of lipid oxidation (0, 1, 2, 3, 4 weeks at 40 °C) with added PBN as spin trap was investigated by the same procedure as above (Table 1). The aim of this study was to see whether the different oxidation levels could be separated (valuable as a stability test) and to study the stability of spin adducts. However, no systematic differences in radical formation were found among the different samples. The stability of the spin adduct varied among the samples, but during the first 24 h at 40 °C the intensity of spin adducts was drastically reduced in all samples. Because of the high unsaturation of marine lipids, double bounds will be present for further reactions also after major oxidation. The trapping will therefore mainly be limited by the concentration of spin trap added.

However, the spin trapping might be affected by anti- and pro-oxidants in the system which is illustrated in Figure 6. This experiment was performed by the same procedure as for the PBN in the experiment presented above, except for addition of, respectively, iron (FeII-powder) and α-tocopherol in the spin trap. The sample containing iron exhibited increased amounts of spin adducts compared to the control, while the sample with added α-tocopherol had a lower production of spin adducts.

From our experience in spin trapping with PBN in fish lipid systems, large differences in the persistence of spin adducts have been found [22]. Using similar conditions (1 mg PBN /g oil in pure lipid stored at 40 °C in the ESR tube) the persistence of spin adducts ranged from minutes in ethyl docosahecaenoate up to 200 h in certain, gently extracted, cod liver oils. This might depend on the degree of lipid oxidation, refining, and certain antioxidants. This indicates that these systems are complex and endogenous compounds might be affecting the spin trapping and lipid oxidation. The spin trap itself will also affect the lipid oxidation by acting as an antioxidant (unpublished data, Falch) in fish oil systems.

NMR

Among the NMR techniques, ^{1}H NMR has been most widely used for studying lipid oxidation. Previous work has reported a decrease of the ratios between olefinic

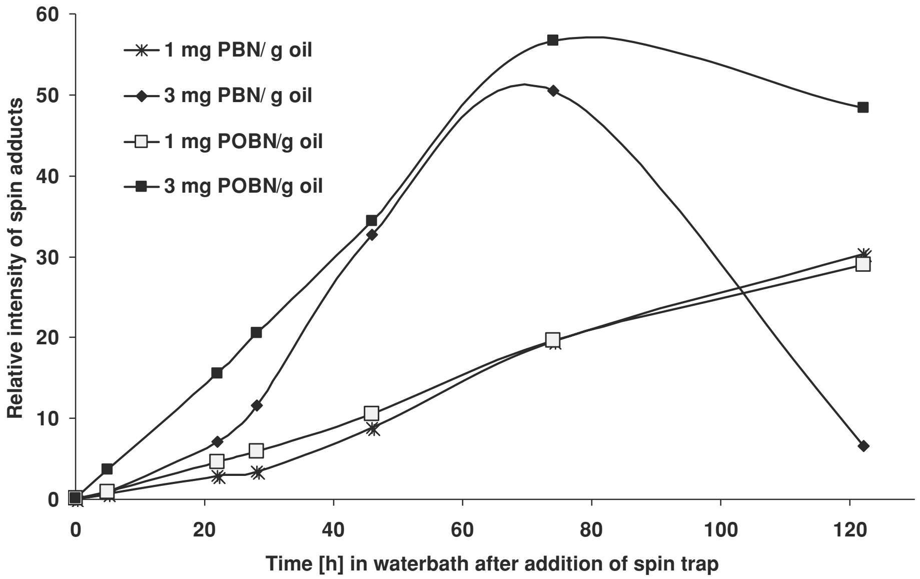

Fig. 5. Spin adducts from POBN and PBN in cod liver oil at different concentrations (1 and 3 mg/g oil) during storage in the tube at 40 °C. The signals are measured by the amplitude of the middle peak. Instrumental settings: sww 5mT, swT 4 min, Mod width 0.2 mT, cf 335.6mT, timec 1 s (Jeol X-band). Unpublished data.

(∂ 5.1–5.6 ppm) to aliphatic protons (∂ 0.6–2.5 ppm) and aliphatic to diallylmethylene protons (∂ 2.6–3.0 ppm) during lipid oxidation. These results were obtained from experiments on vegetable- [28–30] and marine lipids [31–35]. Additionally, a correlation has been found between this ratio and the peroxide value [28,30,32,35]. However, relatively high levels of lipid oxidation are reported before any detectable changes in the NMR spectra occured.

^{1}H NMR has been reported to be valuable for evaluating the changes in lipids due to lipid oxidation in vegetable oils [30,36], including identification of hydroperoxides, conjugated diene hydroperoxides, saturated and unsaturated aldehydes, acids and ketones in the spectra. In a recent study [37], we have investigated lipid oxidation in ethyl docosahexaeoate using ^{1}H NMR and detected many of the same reaction products generated during lipid oxidation including cyclic compounds. Spectra of oxidized fish oils show clear development of peaks in the downfield region of the spectra (8–10.5 ppm) where no other signals are localized in lipid extracts (unpublished data). Chemical shift values (^{1}H) associated with the lipid oxidation are presented in Table 2. One of the main benefits of using NMR is that the spectra can provide information on a broad range of compounds, including not only the reaction products formed during lipid oxidation, but also the chemical composition in general and how it is affected by these reactions (e.g. unsaturated fatty acids). A good example of this is the reported differences in oxidizeability between different lipid components like unsaturation of fatty acids, position of double bonds, positional distribution of fatty acids within the acylglycerols [38] and amount of free fatty acids (hydrolysed phospholipids and triacylglyceroles). This is information that is possible to gain from ^{13}C and ^{1}H NMR spectra [39,40–43]. NMR can provide information on both lipid composition and how the composition changes due to lipid oxidation and lipolysis. It is necessary that the compounds are at detectable levels, which is one of the limitations at this stage. Detection levels in^{1}H NMR are reported to be <0.01 mM [37], however, optimization of the instrumental systems (e.g. 800 MHz magnet equipped with a cryoprobe) will improve the detection limits.

Multivariate data analysis is helpful and, in some cases, necessary for differentiating samples due to the differences in lipid oxidation, especially cluster analysis and generic algorithms, since they, respectively, separate samples based on their dis-similarity and extract what chemical shift areas are causing these differences [36]. With the help of cluster analysis, we have also been able to separate herring mince stored at different lengths of freeze storing based on the differences in^{1}H spectra which were difficult to read by studying the individual spectra.

HR-magic angle spinning (MAS) analysis was performed on the same herring mince. Development of peaks

Table 1: Relative intensity (ratio between the signal amplitude and the reference sample (Manganese)) of spin adducts in cod liver oil added PBN as spin trap. The oil were pre-oxidised at 40 °C in 0, 1, 2, 3, and 4 weeks before addition of spin trap. Spectra were recorded after 0, 1, 2, 3, 4, 5, and 24, 48, 72, and 96 h of further oxidation at 40 °C. Instrumental settings: sww 5mT, swT 2 min, Mod width 0.2 mT, cf 335.6 mT, timec 1s (Jeol X-band). Unpublished data

^{1}H substances	Chemical shift values (ppm)	References
Primary lipid oxidation products:		
Hydroperoxides (-OOH)	8.5 – 8.9	[36]
	8.6 – 8.7	[30]
Hydrogens on the peroxy bearing carbon (-CH(COOH))	4.1-4.3	[29,30,36,45]
Conjugated dienoic olefinic proton multiplets	5.4 – 6.7	[36]
Secondary lipid oxidation products		
Aldehydes (-CHO)	9.0 – 10.0	[30]
	9.3 – 9.8	[36]
Saturated aldehydes	9.74	[36]
Hexanal	9.75	[37]
αβ unsaturated aldehydes	9.48, 9.52, 9.63	[30]
trans-2-heptenal, trans-2 octenal	9.48	[30]
trans-2-pentenal, trans-2-octenal, trans-2-nonenal	9.5	[37]
trans,trans-2,4-heptadienal	9.5 and 9.58	[37]
Hexenal	9.74	[36]
Unsaturated alcohols (-CH(OH)-)	4.5 – 5.0	[46]
1-penten-3-ol	5.8, 5.15, 4.0, 2.1, 1.5	[37]
Cyclic compounds		
Cyclic peroxide methane hydrogens (epoxides)	4.5 – 4.7, 4.4	[45], [37]
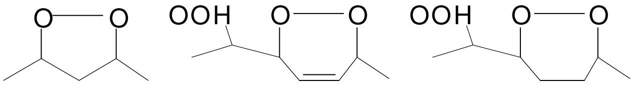		
Groups of hydrogens		
Aliphatic hydrogens	0.6 – 2.5	[28, 47]
Diallylmethylene hydrogens (=C-CH$_2$-C=)	2.6 – 2.9	[28]
Olefinic hydrogens (-CH=CH-)	5.1 – 5.6	[47]
Unsaturated fatty acids		
Unsaturated fatty acids (-CH=CH-)	5.35	[48]
Unsaturated fatty acids (CH$_2$-CH=CH-)	2.0	[48]
Polyunsaturated fatty acids (=CH-CH$_2$-CH=)	2.81–2.84	[48, 37]
n-3 fatty acids (-CH$_3$)	0.896, 0.833	[48]

in the downfield regions (8–10.5 ppm) was found in the ^{1}H spectra of the most oxidized samples. In tissue samples also signals from phosphometabolites (degradation of ATP) [44] are found in this region of the spectra, which complicates the assessment.

Concluding Remarks

Different ESR techniques provide valuable information regarding the early stages of lipid oxidation in marine material. Some precautions need to be taken since this is a complex chemical system and endogenous substances may affect the analysis. By supplementing this method by NMR, information on the consequences of lipid oxidation could be obtained, but relative high-detection limits with todays equipment is a limiting factor. Investigation and assignment of spin adducts and their shelf life might be obtained by combining ESR and NMR (on-going work). ^{13}C NMR could be used to study the specific spin adducts and how they further react when we see the reduction of signals.

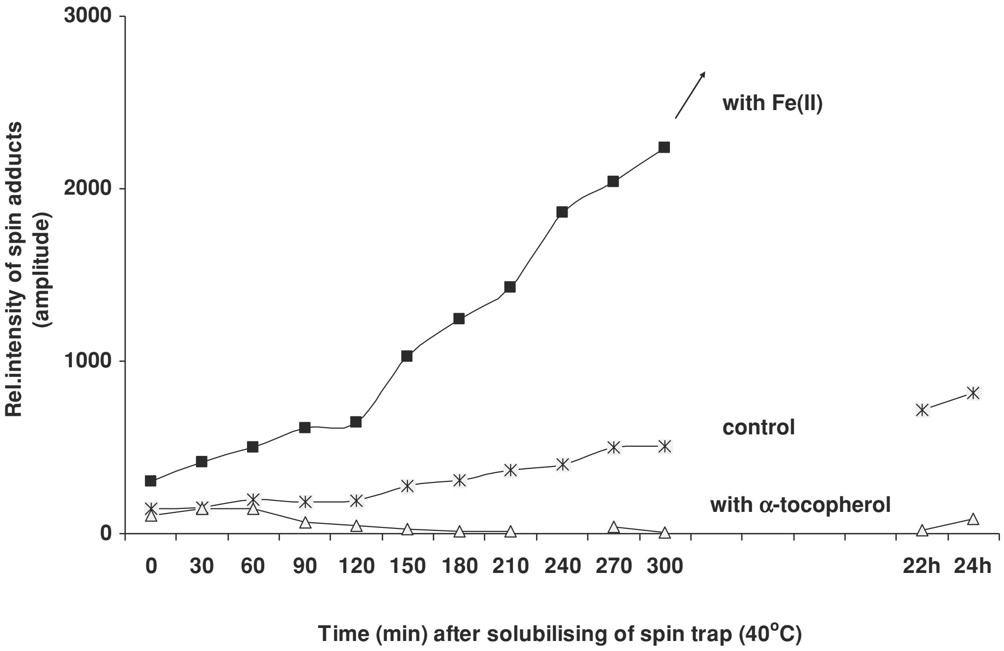

Fig. 6. Relative intensity of spin adducts in cod liver oil during storage with and without addition of pro- (iron) and antioxidant (α-tocopherol).

Acknowledgements

We are grateful to Prof. Thor Bernt Melø at Norwegian University of Science and Technology, Ass. Prof. Mogens Andersen and Prof Leif Skibsted at the Royal Veterinary and Agricultural University (Denmark) for using their equipment along with their scientific input. Authors will also thank Anders Øverby, Elisabeth Olsen, and Turid Rustad for their contribution in the on-going research. This research was partly founded by Norwegian

Table 2: Chemical shift assignments of components in the ^{1}H NMR spectra associated with changes during lipid oxidation

	Storage time (weeks) at 40°C before addition of PBN				
	0	1	2	3	4
Time(h)					
0	0.08 (± 0.00)	0.05 (±0.01)	0.12 (±0.01)	0.07 (±0.00)	0.05 (±0.01)
1	0.08 (± 0.00)	0.12 (± 0.00)	0.37 (± 0.04)	0.10 (± 0.01)	0.09 (± 0.01)
2	0.15 (± 0.02)	0.28 (± 0.01)	0.12 (± 0.02)	0.31 (± 0.02)	0.16 (± 0.00)
3	0.32 (± 0.01)	0.44 (± 0.01)	0.12 (± 0.01)	0.39 (± 0.06)	0.43 (± 0.01)
4	0.39 (± 0.00)	0.85 (± 0.08)	0.14 (± 0.02)	0.60 (± 0.10)	0.66 (± 0.05)
5	0.54 (± 0.04)	0.12 (± 0.00)	0.12 (± 0.02)	0.95 (± 0.09)	0.66 (± 0.05)
24	0.14 (—)	0.16 (—)	0.16 (—)	0.16 (—)	0.14 (—)
48	0.15 (—)	0.21 (—)	0.23 (—)	0.21 (—)	0.18 (—)
72	—	0.23 (—)	0.21 (—)	0.19 (—)	0.17 (—)
96	—	0.24 (—)	0.19 (—)	0.20 (—)	0.18 (—)

- no measurement

Research Council (project: *Increased value adding from by-products and by-catches) and EU (QLK1-CT2000-01017) Utilisation and stabilization of by-products from cod species.* MRI (Major Research Infrastructure, 5th Framework program. Project no. MRI_00.01.09) is thanked for granting access to LMC (Centre for Advanced Food Studies).

References

1. Dikalov S, Mason RP. Free Rad. Biol. Med. 2000;30:187–197.
2. Howell NK, Saeed S. The application of electron spin resonance spectroscopy to the detection and transfer of free radicals in protein-lipid systems. In: PS Belton, GA Webb, (Ed.). Advances in Magnetic Resonance in Food Science, Royal Society of Chemistry: Cambridge, UK. 1999, p 135.
3. Chen C, Tang H, Belton P. Natural antioxidants—an ESR perspective, Magnetic Resonance in Food Science. In: P Aveiro, GA Webb (Ed). Royal Society of Chemistry: UK, 2000, p 117.
4. Davies M. Chem. Phys. Lipids. 1987;44:149.
5. Andersen ML, Skibsted LH. Eur. J. Lipid Sci. 2002;104:65.
6. Thomsen MK, Vedstesen H, Skibsted LH. J. Food Lipids 1999;6:149.
7. Stapelfeldt H, Nielsen RB, Skibsted LH. Milchwissenscaft 1997;52:682.
8. Nissen L, Månsson L, Bertelsen G, Huynh-Ba T, Skibsted L. J. Agric. Food Chem. 2000;48:5548.
9. Nissen L, Huynh-Ba T, Agelin Petersen M, Bertelsen G, Skibsted L. Food Chem. 2002;79(39):387.
10. Kristensen D, Orlien V, Mortensen G, Brockhoff P, Skibsted LH. Int. Dairy, J. 2000;10(1–2):95.
11. Saeed S, Fawthrop SA, Howell NK. J. Sci. Food Agric. 1999;79:1809.
12. Swarts HM, Bolton JR, Borg DC. Biological Applications of Electron Spin Resonance, Wiley-Interscience: NY, 1972.
13. Schaich KM, Borg DC. Free Rad. Res. Comms. 1990;9(3–6):267.
14. Buettner GR. Free Rad. Biol. Med. 1987;3:259.
15. Janzen EG, Haire DL. Adv. Free Rad, Chem. 1990;1:253.
16. Stolze K, Udilova N. Nohl H. Acta Biochimica. Polonica. 2000;47(4):923.
17. Stolze K, Udilova N, Rosenau T, Hofinger A, Nohl H. Biochem. Pharmacol. 2004;68:185.
18. Jacobsen C. Fett/Lipid 1999;101(12):484.
19. Thomsen MK, Kristensen DK, Skibsted LH. J. Am. Oil Chem. Soc. 2000;77(7):725.
20. Thomsen MK, Jacobsen C, Skipsted LH. Eur. Food Res. Technol. 2000;211:381.
21. Jacobsen C, Hartvigsen K, Lund P, Thomsen MK, Skibsted LH, Adler_Nissen J, Holmer G, Meyer AS. Eur. Food Res. Technol. 2000;211(2):86.
22. Falch E, Velasco J. Aursand M, Andersen ML. Eur. Food Res. Technol. 2005. In press.
23. Velasco J, Andersen ML, Skibsted LH. Food Chem, 2004; 85:623.
24. Quiles JL, Carmen Ramirez-Tortosa M, Alfonso Gomez J, Huertas JR, Mataix J. Food Chem. 2002;76:461.
25. Madsen HL, Nielsen BR, Bertelsen G, Skipsted LH. Food Chem. 1996;57(2):331.
26. Sevilla and co-workers referred to by Rhodes CH, Dintinger TC. 9 Electron spin resonance studies of lipids. In: RJ Hamilton, J Cast (Ed). Spectral properties of lipids, 1999, p 271.
27. Carlsen CU, Andersen ML, Skibsted LH. Eur. Food Res. Technol. 2001;213:170.
28. Wasasundara UN, Shahidi F. J. Lipids 1993;1:15.
29. Haywood RM, Claxon AWC, Hawkes GE, Richardson DP, Naughton DP, Coumbarides G, Hawkes J, Lynch EJ. Free Rad. Res. 1995;22:441.
30. Silwood CJL, Grootveld M. Lipids 1999;34(7):471.
31. Shahidi F, Wanasundara U. Brunet N. Food Res. Int. 1994;27:555.
32. Saito H, Udagawa M. Biosci. Biotech. Biochem. 1992; 56(5):831.
33. Saito H, Nakamura K. Agric. Biol. Chem. 1990;54(2): 533.
34. Saito H. Evaluation of method for lipid oxidation by nuclear magnetic resonance. In: F Shahidi, KR Cadwallander (Eds). Flavour and Lipid Chemistry of Seafood, Oxford University Press, Oxford, UK. 1997, p 218.
35. Saito, H. Agric. Biol. Chem. 1987;51(12):3433.
36. Claxon AWD. Hawkes GE. Richardson DP. Naughton DP. Haywood RM. Chander CL. Atherton M. Lynch EJ. Grotweld MC. Federation of European Biochemical Societies (FEBS). 1994;355:FEBS 14760,81.
37. Falch E. Anthonsen H. Axelson D. Aursand M. J. Am. Oil Chem. Soc. 2004;81(12):1105.
38. Neff WE, El-Agaimy M. Lebensm.-Wiss. U. –Technol, Research note, 1996;29:772.
39. Medina I, Sacchi R. Chem. Phys. Lipids 1994;70(1):53.
40. Medina I. Sacchi R. Aubourg SP. J. Sci. Food Agric. 1995;69:445.
41. Falch E. Størseth TR. Aursand M. HR-NMR to study quality changes in marine by-products. In: Magnetic Resonance in Food Science, Royal Society of Chemistry: Cambridge, UK. 2004, pp 238.
42. Aursand M. Gribbestad I. Skjetne T. Grasdalen H. Jorgensen L. Dev. Food Sci. 1997;38:367.
43. Aursand M. Jorgensen L, Grasdalen H. J. Am. Oil Chem. Soc. 1995;72(3):293.
44. Wang X, Nelson DJ, Trindle C, Martin RB. J. Inorg. Biochem. 1997;68(1):7.
45. Neff WE, Frankel EN, Selke E, Weisleder D. Lipids. 1983; 18(12):868.
46. Vlahov G. Prog Nucl Magnetic Resonance Spectroscopy 1999; 35(4):341.
47. Saito H, Nakamura K. Bull. Japan. Soc. Sci. Fish, 1989; 55:1663.
48. Aursand M. Rainuzzo JR. Grasdalen H. J. Am. Oil Chem. Soc. 1993;70(10):971.

Omega-3 Fatty Acid Content of Intact Muscle of Farmed Atlantic Salmon (*Salmo salar*) Examined by ^{1}H MAS NMR Spectroscopy

M. Aursand[1], I.S. Gribbestad[2], and I. Martinez[1]
[1] *SINTEF Fisheries and Aquaculture Ltd;*
[2] *Cancer Clinic, St. Olav University Hospital, 7006-Trondheim, Norway*

Introduction

The nutritional benefits of fish and fish oils have resulted in an increasing interest in seafoods and derived products generally focused on the level of omega-3 (*n*-3) fatty acids (FAs). In particular 20:5 *n*-3 (EPA) and 22:6 *n*-3 (DHA) are believed to play a natural, preventive role in cardiovascular diseases, and alleviation of other health problems [1,2]. Aquaculture opens up interesting possibilities for exerting a control over factors affecting the nutritional and sensory attributes of fish as food such as the quantitative and qualitative content of fat in the edible tissues. About 20% of the muscle lipids of farmed Atlantic salmon are *n*-3 FAs, with some variation due to the FA composition of the fish feed. The content of EPA and DHA in muscle of farmed Atlantic salmon has been found to be approximately 0.6 and 0.8 g/100 g of fillet, respectively [3].

Traditionally, gas chromatography (GC) has been used to obtain the FAs profile of lipids. This technique requires that the sample is pretreated, extraction and methylation of the lipids have to be included as part of the analysis [3]. Recently it has been demonstrated that high-resolution nuclear magnetic resonance (NMR) spectroscopy can be used to provide insight into the nature of lipid mixtures and offers the opportunity to study hetereogeneous lipid mixtures, oils and fat deposits without being destructive [4–7]. NMR measurements can be performed on intact muscle and allows the identification and quantification of muscle metabolites [4,7,8] addition to lipid fluidity studies in fish muscle stored at low temperatures [9]. In preliminary studies ^{13}C NMR has been used to obtain the *n*-3 FA content of intact fish muscle [7,10]. The ^{13}C NMR experiment on intact muscle is very time consuming and it would be an advantage to detect on ^{1}H instead of ^{13}C due to the facts that ^{1}H NMR has the highest NMR sensitivity of any stable nucleus, and it has nearly 100% natural abundance. In our preliminary research it has been shown that high-resolution ^{1}H NMR is a unique and rapid technique to quantify the total *n*-3 acid content of the lipid extracted from muscle of Atlantic salmon [5,7]. A traditional ^{1}H spectrum of intact muscle will only result in broad signals containing fat/water proton resonances and individual FAs or groups of lipids are not observed. However, recent research indicates that magic angle spinning (MAS) NMR spectroscopy offers the opportunity to study intact tissue non-destructively to quantify components of the tissues. Ni and Eads [11,12] have studied fruit tissue and they have shown that low-speed MAS simultaneously relieves susceptibility broadening, improves resolution, produces accurate chemical shifts, and increases signal-to-noise ratio.

In the present study, we have obtained ^{1}H MAS NMR spectra of intact salmon muscle and quantified the total *n*-3 acid content from the spectra. The data from the MAS NMR analyses were compared to those obtained by estimating the fat content in extracts from equivalent muscle samples by ^{1}H NMR and by GC. The results from MAS NMR and from ^{1}H NMR were usually in good agreement, while the content of *n*-3 estimated by GC was in general higher than if estimated by the NMR techniques.

Experimental Procedures

Material and Sample Preparation

The white muscle of five commercially farmed Atlantic salmon (*Salmo salar*), of about 3–4 kg of weight each, were used in the present study. Slices of white muscle were carefully cut from the area between the head and the dorsal fin and each slice was divided into two parts (about 5 mm^3) one of the slices was carefully introduced into a MAS NMR rotor (5 mm). The other slice was used to extract muscle lipids according to Bligh and Dyer [13]. Part of this lipid extract, containing 50 mg of lipids, was dissolved in 0.5 ml of $CDCl_3$, introduced into a 5 mm NMR tube and analyzed by ^{1}H NMR. The rest of the lipid

Graham A. Webb (ed.), Modern Magnetic Resonance, 941–945.
© 2008 *Springer.*

extracts were stored at −80 °C prior to methylation and GC analysis.

Gas Chromatography

FA methyl esters were prepared according to Metcalfe *et al.* [14]. The FA methyl esters were determined quantitatively on a capillary gas chromatograph (Carlo Erba HRGC 5160 series equipped with a SP-2330 glass capillary column, on-column injection, and flame ionization detector) fitted with a Shimadzu-Chromatopac C-R3A computation integrator. Identification and quantification were carried out using FA standards.

NMR Spectroscopy Experiments

The conventional ^{1}H NMR spectrum of lipid extract of muscle was obtained on a Bruker AM 500 MHz spectrometer at ambient temperature. The FID was acquired with a pulse delay of 6 s, using a sweep width of 8 kHz and 16 K data points. Thirty-two scans were collected using a 45° excitation pulse. The ^{1}H MAS experiments were acquired on a 4.7 T NMR instrument (Bruker, Karlsruhe, Germany) operating at 200.13 MHz for protons. For MAS experiments the rotor axis makes an angle of 54.44° with the static field (MAS). The MAS spinning rate was 1500 Hz. The spectra were acquired with a single-pulse sequence with a delay time of 5.4 s, 16 scans, and 7.4 µs excitation pulse length. A sweep width of 8192 Hz and 16 K data points were used. The water peak was suppressed using a presaturation pulse.

The peak areas of the NMR MAS spectra were measured using a curve fitting program (PeakFit Jandel Scientific, USA), and the integrals of the peaks in the ^{1}H NMR spectra of lipid extracts were obtained by a program developed at the Norwegian University of Science and Technology (NTNU), Trondheim.

Results and Discussion

Previous research has shown that ^{13}C NMR determination of the total concentration of lipids and groups of FAs within muscle of Atlantic salmon is possible due to the lipid-like nature of the tissue lipids, with high content of polyunsaturated FAs [7]. Generally, muscle lipids of Atlantic salmon are mainly composed of triacylglycerols which are incorporated into connective tissue of

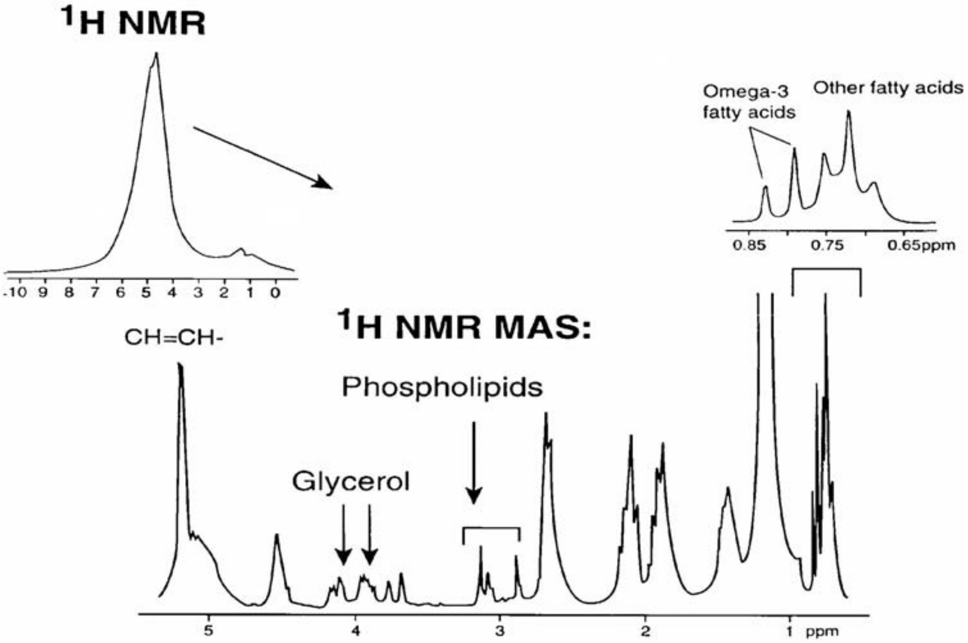

Fig. 1. Effect of magic angle spinning (MAS) on the^{1}H NMR spectra of intact muscle from Atlantic salmon. Upper left spectrum: non-MAS spectrum obtained in conventional high-resolution probe. Lower center is a MAS spectrum. The upper right inlet is an expansion of the lower MAS spectrum between 0.6 and 0.9 ppm, indicating the region of the *n*-3 FAs. Sample preparation and NMR parameters are described in the text.

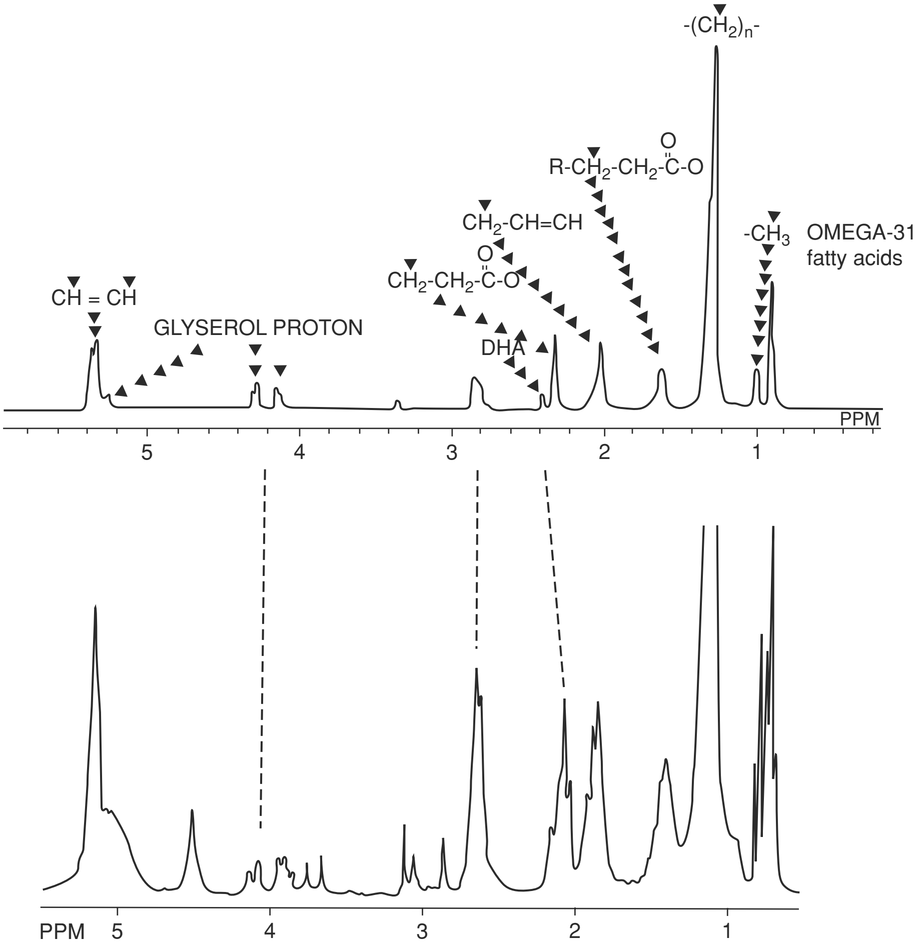

Fig. 2. Comparison of ^1H NMR spectra of lipid extract of muscle of Atlantic salmon (upper spectrum) and that obtained by ^1H MAS NMR of intact muscle (lower spectrum). Sample preparation and NMR parameters are described in the text.

muscle surrounding bundles, single cells, and inside muscle cells. However, because the lipids are not distributed homogeneously within the muscle tissue there is a considerable line broadening in NMR spectra from intact muscle, resulting in less resolution and sensitivity than in the NMR spectra of lipid extracts The line broadening originates from the heterogeneous nature of the muscle and, ultimately, from induced dipolar fields produced by differences of bulk magnetic susceptibility depending on the microenvironment of the lipids, the microenvironment inside the adipocytes is different from that inside myocytes which in turn is also different from that in the extracellular matrix [15,16]. Thus, examination of intact muscle by conventional ^1H NMR, gave broad proton resonances, and in addition, the strong water proton resonance made water peak suppression necessary. To minimize potential alterations in the sample during the NMR MAS measurements, one should use the lowest possible spinning rates. Accordingly, we tested the effect of spinning rates varying from 500 to 3000 Hz, and found that optimal resolution of the ^1H spectrum of intact salmon muscle was obtained by using a spinning rate of 1500 Hz and water peak suppression.

Figure 1 compares two spectra from intact muscle: the upper left spectrum was obtained in a conventional high-resolution probe (sample axis parallel to magnetic field, non-spinning) and the lower one was obtained with MAS probe. The great improvement achieved by the latter made the resolution of the NMR MAS comparable to that of the ^1H spectrum of the lipids extracted from the contiguous muscle tissue (Figure 2). The interpretation of these spectra is based on previous published works [7,17]. Resonances of FAs in triacylglycerides and phospholipids as well as those from other muscle metabolites, were easily identified in the MAS spectrum. The unique methyl proton (–CH_3) of the n-3 FAs gives rise to partly resolved signals in the MAS spectra allowing quantification of the total n-3 acid content of intact muscle. Due to some overlap, a curve fitting program was used to measure the areas under the methyl peaks which allow us to estimate the relative percent of n-3 FAs in intact salmon muscle.

From the lipid extract spectrum it was possible to calculate the content of the highly polyunsaturated FA 22:6 n-3, as well as the total amount of n-3 FAs, by integration of the unique signals with chemical shifts of $\delta = 2.38$ ppm and $\delta = 0.95$–0.98 ppm (a triplet), respectively [7,19], as shown in Table 1. However, the MAS spectra did not permit to resolve the signals of the C2/C3 protons (–COO–CH_2–CH_2–CH=, $\delta = 2.38$ ppm) of 22:6 n-3 from the signals of the C2 protons (–COO–CH_2–R, $\delta = 2.28$ ppm) from other FAs present in muscle tissue. Consequently, the resolution of the spectrum obtained by MAS was not sufficient to permit the quantification of 22:6 n-3 FAs in intact muscle.

The values of n-3 FA content estimated by MAS NMR and by ^{1}H NMR of the corresponding lipid extracts were in good agreement (Table 2). As expected, baseline correction had considerable influence on the estimated peak area values. Additionally, the resolution of the MAS spectrum was affected by the position of the sample into the small MAS tube.

For comparison purposes, the content of FAs of the lipid extracts was also estimated by GC. The correlation between the GC derived data (weight %) and the ^{1}H NMR data (mol %) is illustrated in Figure 3. Relatively good correlation was observed ($r^2 = 0.81$, $p < 0.01$). However, GC gave generally higher n-3 acid values than NMR. The same trend was observed in a study done by Sacchi *et al* [19]on albacore tuna. Some of the differences can be explained by the fact that in the NMR measurement are done on the hetereogeneous lipid mixture containing phospholipids, sterols, etc. while the additional procedures to which the lipid extract is submitted prior to GC may results in changes in the relative composition of the FAs. This aspect is under further investigation.

In summary, this study shows that ^{1}H MAS NMR spectroscopy is an exceptional technique for the determination of the total content of n-3 FAs in intact salmon muscle. More research is needed to optimize the MAS NMR and the conventional NMR experiments together with intercalibration work between the NMR and GC techniques.

Table 1: Omega-3 fatty acid, DHA (C22:6 n-3) and cholesterol content (mol %) of white muscle of farmed Atlantic salmon examined by high-resolution ^{1}H NMR spectroscopy

Sample	Omega-3 fatty acids	DHA (C22:6 ω-3)	Cholesterol
Salmon 1A	18.4	12.1	0.7
Salmon 2B 1	22.7	14.6*	1.8
Salmon 2B 2	20.0	13.0	1.2
Salmon 3C 1	19.5	12.5	0.9
Salmon 3C 2	19.7	13.1	1.2
Salmon 4D 1	18.9	12.3	1.0
Salmon 4D 2	18.5	12.5	0.9
Salmon 5E 1	21.6	15.7 (3.2)	1.5
Salmon 5E 2	23.0	16.7	1.8

*Incorrect baseline.

Table 2: Omega-3 fatty acid content (mol %) of white muscle of farmed Atlantic salmon measured on intact muscle and the lipid extracted from the corresponding muscle examined by ^{1}H MAS NMR (200 MHz) and high-resolution ^{1}H NMR (500 MHz), respectively

Sample	1H MAS NMR intact muscle	1H NMR lipid extract [13]
Salmon A	19.7	18.4
Salmon 2B 2	17.3	22.7
Salmon 3C 1	23.9	19.5
Salmon 3C 2	16.4	19.7
Salmon 4D 1	15.9	18.9
Salmon 4D 2	19.9	18.5
Salmon 5E 1	21.3	21.6
Salmon 5E 2	22.4	23.0

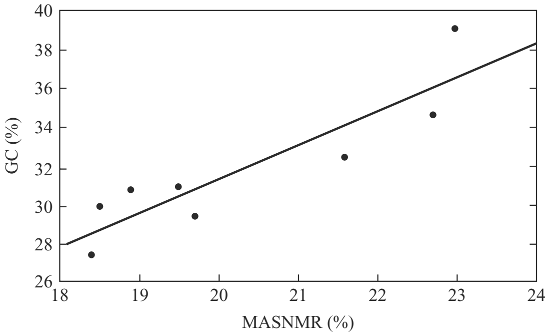

Fig. 3. Correlation between gas chromatography derived data (wt %) and the ^{1}H NMR data (mol %): $Y = -3.7 + 1.75X(r^2 = 0.81;\ p < 0.01)$. Sample preparation, GC and NMR parameters are described in the text.

In general, the NMR is a rapid, non-invasive, and non-destructive method, with an experimental time of about 1–2 min. This opens up possibilities to examine the *n*-3 FAs in fish and fish products without any chemical pre-treatment of the products making NMR, a valuable tool in the nutritional evaluation and general quality control of fresh and processed fish products.

References

1. Lindgren FT, Adamson GL, Shore VG, Nelson GJ, Schmidt PC. Lipids. 1991;26:97.
2. Drevon CD, Nenseter MS, Brude IR, Finstad HS, Kolset SO, Rustad AC. Can. J. Cardiol. 1995;11:47G.
3. Aursand M, Bleivik B, Rainuzzo JR, Jørgensen L, Mohr V. J. Sci. Food Agric. 1994;64:239.
4. Aursand M, Jørgensen L, Grasdalen H. Comp. Biochem. Physiol. 1995;112B:315.
5. Aursand M, Jørgensen L, Grasdalen H. Lipid Forum. 1995; 49:14.
6. Aursand M, Jørgensen L, Grasdalen H. J. Am. Oil Chem. Soc. 1995;72:293.
7. Aursand M, Rainuzzo JR. Grasdalen H. J. Am. Oil Chem. Soc. 1994;70:971.
8. Gribbestad IS, Aursand M, Martinez I. High-resolution ^{1}H magnetic resonance spectroscopy of whole fish, fillets and extracts of farmed Atlantic salmon (*Salmo salar*) for quality assessment and compositional analyses. Aquaculture. 2005, in press.
9. Grasdalen H, Aursand M, Jørgensen L. In: PS Belton, I Delgadillo, AM Gil, GA Webb (Eds). Proceedings of 2nd International Conference on Application of Magnetic Resonance in Food Science. Bookcraft Ltd., 1995, p 206.
10. Igarashi T, Aursand M, Hirata Y, Gribbestad IS, Wada S, Nonaka M. J. Am. Oil Chem. Soc. 2000;77:737.
11. Ni QX, Eads TM. J. Agric. Food Chem. 1993;41:1026.
12. Ni QX, Eads TM. J. Agric. Food Chem. 1993;41:1035.
13. Bligh EG, Dyer WJ. Can. J. Biochem. Physiol. 1995;37: 911.
14. Metcalfe LD, Schimtz AA, Pelka JR. Anal. Chem. 1966; 38:515.
15. Garroway AN. J. Magn. Reson. 1982;49:168.
16. Rutar V, Kovac M, Lahajnar G. J. Magn. Reson. 1988;80:133.
17. Aursand M, Mabon F, Martin G. J. Magn. Reson. Chem. 1997;35:S-91.
18. Ni QW, Eads TM. J. Agric. Food Chem. 1992;41:1507.
19. Sacchi R, Medina I, Aubourg SP, Addeo F, Paolillo L. J. Am. Oil Chem. Soc. 1993;70:225–8.

HR MAS NMR Spectroscopy of Marine Microalgae, Part 1: Classification and Metabolite Composition from HR MAS ^{1}H NMR Spectra and Multivariate Analysis

Matilde Skogen Chauton[1] and Trond Røvik Størseth[2]

[1] *Trondhjem Biological Station, Department of Biology, Norwegian University of Science and Technology, 7491 Trondheim, Norway; and*
[2] *Sintef Fisheries and Aquaculture, 7465 Trondheim, Norway*

Introduction

Marine microalgae, or phytoplankton, have been termed the "grass of the sea" since they are the primary producers that form the basis of marine food chains. They are found naturally throughout all aquatic environments, and can be cultured for feed production or for experimental purposes. Some microalgae are toxic, such as those involved in shellfish poisoning. Others have long spines on the cell that can cause mechanical damage to fish gills, and some species form gelatinous aggregations which can hinder gas exchange in fish gills [1]. The nutritional value of microalgae depends primarily on the amount and composition of amino acids and fatty acids, and diatoms contain many of the desired compounds [2]. Since microalgae are so important both in terms of beneficial primary production but also as the cause of fish or human death by poisoning, we have developed several technological solutions to survey the distribution and amounts of microalgae in the oceans. On a larger scale, satellite measurements of chlorophyll *a* (Chl *a*) and buoys equipped with spectroradiometers that measure light extinction are used to estimate the standing stocks of microalgae in the oceans and coastal areas. For more detailed information, laboratory studies often involve species identification and cell counts with light microscope, spectrophotometric measurements of Chl *a* and *in vivo* light absorption, or pigment chromatography for identification and biomass estimation based on group specific pigment composition [1,3]. There are, however, some drawbacks to these well-established methods, both related to the time spent on the analysis run and the use of organic solvents. Each method aims at specific cellular structures or metabolites and the different methods are therefore often combined to increase the information output. This means that even more time is spent on the analytical work, while with the HR MAS NMR spectroscopic methods it is possible to analyze complex samples such as tissue and cells in relatively short time, and the information output from each analysis includes data on many different metabolites.

In principle, NMR analysis of whole microalgae cells should give a detailed description of the chemical profile, or the metabolome [4]. Application of special pulse techniques such as water presaturation or Carr–Purcell–Meiboom–Gill (CPMG) further enhances the results by eliminating undesired signals from residual water in the sample or from lipids in cell membranes [5–7]. HR MAS NMR directly on whole cells can also be used for studies of cellular distribution of metabolites, since small metabolites in liquid compartments have different NMR properties than larger molecules in rigid environments.

HR MAS NMR-studies on human body fluids are quite numerous [8–10], and application of NMR in studies of higher plants is reviewed by Ratcliffe *et al.* [11]. Some examples of HR MAS studies on whole cells or tissue from lower organisms are such as on the yeast *Pichia anomala* [12] or macroalgae [13]. HR MAS studies of microalgae whole cells are scarce [14–18]. We present the results of HR MAS ^{1}H NMR analyses on microalgal whole-cell samples, where focus is on taxonomic discrimination (classification) and metabolite profiling. In the Part 2 of this work, we focus on ^{13}C and HR MAS ^{13}C NMR analysis of fatty acid composition and polysaccharide structure in microalgae.

Results and Discussion

Chemical composition in hydro- and lipophilic extracts of the diatom *Thalassiosira pseudonana* Hasle and Heimdal was studied with proton NMR spectroscopy, and the results were compared to a HR MAS ^{1}H NMR spectrum of whole cells [16]. Signals from important metabolites such as polyunsaturated fatty acids (PUFAs), eicosapentaenoic acids (EPAs), and docosahexaenoic acids (DHAs) were seen in a ^{1}H NMR spectrum of lipophilic extract, and possibly also signals from carotenoids. In the cells, the FAs are important constituents of cell membranes, while carotenoids and other pigments are used in light harvesting and conversion of light energy to chemical energy such as ATP. In a spectrum of hydrophilic extract, we assigned

Graham A. Webb (ed.), Modern Magnetic Resonance, 947–951.
© 2008 *Springer.*

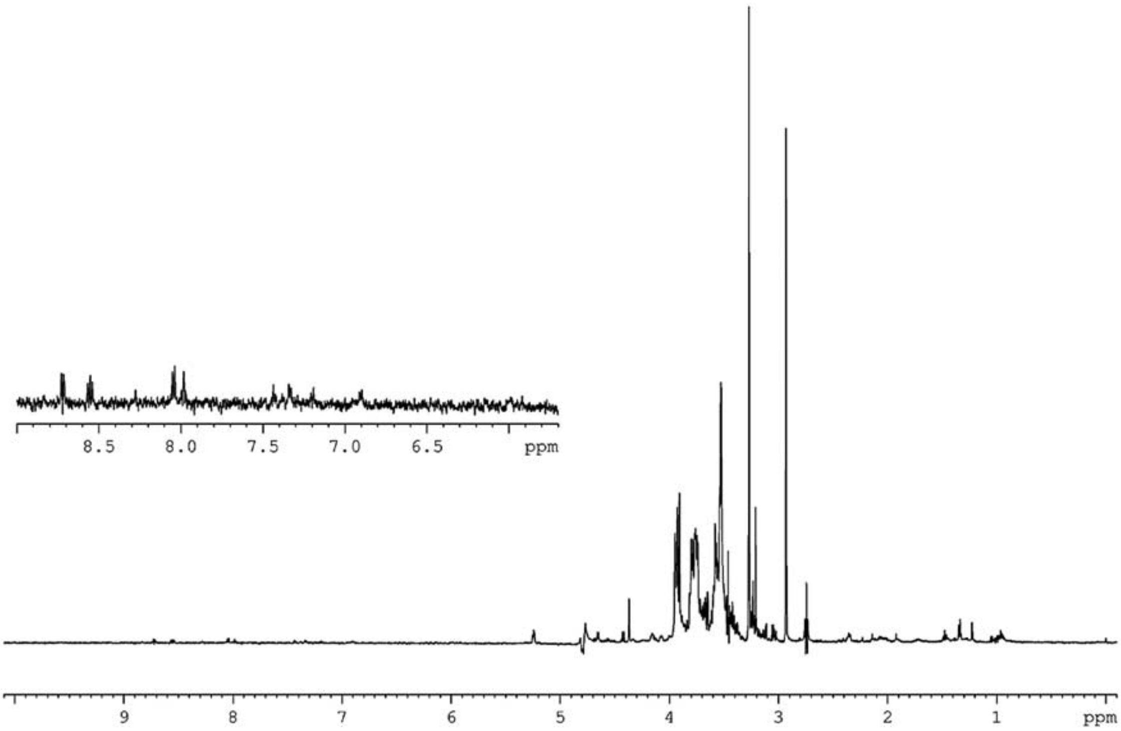

Fig. 1. HR MAS ^{1}H NMR spectroscopy analysis of whole cells of *Thalassiosira pseudonana*. Reference TSP 0 ppm. Inserted spectrum: expansion of low-field region 9–5.7 ppm.

signals to amino acids such as glutamine (Gln) and glutamic acid (Glu), carbohydrate, and ATP. Gln and Glu are involved in nitrogen assimilation [19], and together with asparagine, arginine, and tyrosine they made up more than 60% of the total amino acid concentration in five species of microalgae [20]. Among the crowded signals from 4 to 3 ppm it was possible to find chemical shifts characteristic of carbohydrate protons. Microalgae use various carbohydrates such as starch and chrysolaminarin as storage compounds, and sugars are abundant in cells when nutrients become depleted in the growth medium [21].

From the peak assignment in extract-sample spectra, it was possible to find coincident peaks in the HR MAS ^{1}H NMR spectrum for many different metabolites, including fatty acids, amino acids, and carbohydrates (Figure 1, Table 1). The differences between extract and whole-cell samples were small, although some shift differences can be expected since the chemical properties of the metabolites and their surroundings are changed when they are extracted from whole cells. Also, the application of pulse sequences to improve spectral features leads to a certain biasing of the data, such as the application of the CPMG pulse to partially suppress lipid signals in order to eliminate broad peaks. Furthermore, the differences in NMR properties of metabolites of varying size and in different cellular compartments leads to variation in magnetic properties and in some cases also “NMR invisibility,” which means that some metabolites are not registered in the whole-cell analysis [22]. This is seen from a close resemblance of whole-cell and hydrophilic-extract spectra (not shown), and from the knowledge that small molecules in liquid state are optimal for NMR analysis it is natural to assume that molecules in suspension in the cell will resonate clearly in the spectrum. The advantage of this feature is that it can be used to study compartmentation or distribution of metabolites in the cells.

The possible classification of microalgae species based on their specific HR MAS ^{1}H NMR spectra was investigated by application of two multivariate clustering techniques to a set of spectra from different algae [17]. The algae exhibit species-specific differences in cellular structure and size as well as chemical composition, and residual water is also varying between samples. Some signs of J-modulation due to spin echoes with too long interpulse delay could therefore appear in some spectral regions, but for the matter of comparison all spectra were acquired

Table 1: Tentative chemical shift assignment in ^{1}H HR MAS spectra of whole cells of *Thalassiosira pseudonana* (Bacillariophyceae), referenced to TSP. Literature references: (1) Nicholson and Foxall [8]; (2) Sitter *et al*. (2002) [29]; (3) Willker and Leibfritz (1998) [30]; (4) Lindon *et al*. [9]; (5) Ward *et al*. [27]

Peak shift	Metabolite	Assignment	Source
0.93	Fatty acid	CH_3CH_2	1
0.95	Leucine, isoleucine	$\delta CH_3/\delta CH_3$	1,2
0.96	Leucine	δCH_3	1,2,4
0.97	Leucine, valine/fatty acid	$\delta CH_3/\omega CH_3$	1,2
1.00	Isoleucine	γCH_3	1,2
1.02	Valine	CH_3	1
1.22	Fatty acid	$CH_3CH_2CH_2$	1
1.32	Threonine/lactate	γCH_3	1,5/1
1.35	Fatty acid	$–CH_2CH_3$	2
1.46	Alanine	CH_3	1,5
1.48	Lysine	γCH_2	1
2.02	Fatty acid	$CH_2{=}CHCH_2CH_2$	2
2.05	Proline	βCH_2	1
2.08	Glutamine/fatty acid	$\beta CH_2/CH_2{=}CHCH_2CH_2$	1,3
2.14	Glutamic acid	βCH_2	1
2.23	Fatty acid/*N*-acetylglutamate	$CH_2CO/\gamma CH_2$	1,4
2.34	Glutamic acid	γCH_2	2
2.36	Glutamic acid	γCH_2	1
2.44	Glutamine	γCH_2	2
2.75	Fatty acid	$CH{=}CHCH_2CH{=}CH$	2
3.02	Lysine	εCH_2	2
3.06	Tyrosine	βCH_2	1
3.11	Tyrosine	βCH_2	2
3.12	Phenylalanine	βCH_2	1
3.21	Choline	$N(CH_3)_3$	1,2,4
3.24	β-glucose	C2H	1,2
3.27	*myo*-Inositol/trimethylamine, betaine	$C5H/N(CH_3)_3$	2,4
3.53	α-glucose	C2H	2
3.64	Glycerol	CH_2	1
3.75	Glutamic acid	αCH	2
3.77	Lysine/glutamine, glutamic acid, arginine	αCH	2,4
3.91	Asparagine/betaine	$\alpha CH/CH_2$	4
4.64	β-glucose	C1H	1,2
5.23	α-glucose	C1H	1,2
5.26	Unsaturated fatty acid	$CH{=}CHCH_2CH{=}CH$	1
7.97	Histidine	C2H, ring	2

using the same protocol. The multivariate clustering techniques principal component analysis (PCA) and fuzzy clustering (FC) were applied, since they reveal structures in the data without relying on assumptions such as the underlying statistical distribution. In PCA, which is a linear dimension reduction technique, systematic variation in a data set is extracted to a set of principal components (PCs) through the modeling of variance and covariance structure. In FC, the data are partitioned into fuzzy subsets and approximated by linear regression models, where the probability of a sample being member of a specific class is calculated based on the NMR characteristics and expected number of classes [23,24]. Selected parts of five replicate HR MAS ^{1}H NMR spectra of whole-cell samples of *Dunaliella* sp. (Chlorophyceae), *Amphidinium carterae* (Dinophyceae), *Phaeodactylum tricornutum*, and *T. pseudonana* (Bacillariophyceae) were used as input, and the best separation was obtained with the chemical shift region from 4 to 3 ppm. The three first PCs (of n possible) cumulatively accounted for 90% of the

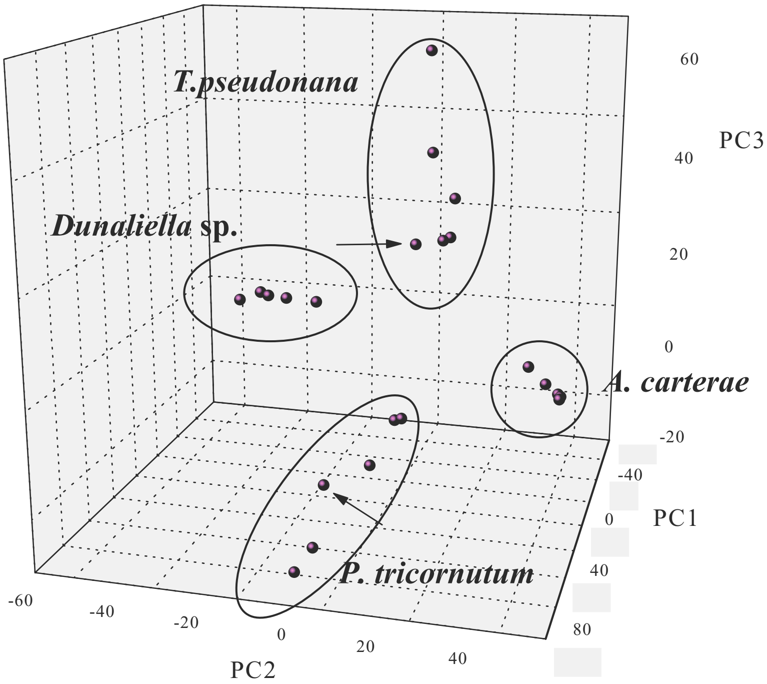

Fig. 2. Principal component analysis of HR MAS ^{1}H NMR spectra of four microalgae, where the three first Principal components explained 90% of the variance in the original data. The chore data set consisted of five replicate samples from each alga, and arrows indicate correct grouping of two additional samples from a separate experiment where the algae were grown using the same growth conditions and sample handling. Reproduced with permission from Inter-Research, original publication in Chauton *et al.* [17].

variance (Figure 2). A distinct grouping of the different microalgae was seen both in the PCA and in the FC, and to further test the replicability two spectra from a previous culture set up (but with the same growth conditions) were included. These spectra were also correctly classified, indicating robustness and reproducibility of the analysis.

The distinct grouping of algae in the PCA was analyzed further, and the peaks that were most important in determining the output were identified. Several metabolite markers were found: dimethylsulfoniopropionate (DMSP), betaine, glycerol, choline, and lactate. DMSP and betaine are osmolytes in many microalgae, while glycerol and choline have multiple cellular functions: in addition to being osmolytes, glycerol is a component of storage triglycerides and choline is incorporated into membranous phosphocholines. The distribution of microalgae in the score plot presented here was to a large degree coincident with reported findings on cellular content of the various compounds, which varied with growth stage and nutrient conditions [25]. The fact that osmolytes, which are relatively small molecules found in the cytoplasmic regions of the cells, determine the outcome of the PCA is again an indication of variations in NMR properties due to differences in molecular size and cellular distribution. Some recent studies showed that PCA and hierarchical cluster analysis of ^{1}H NMR spectra could be used to separate earthworm species [26] and multivariate analysis of ^{1}H NMR spectra was used in metabolic fingerprinting of the plant *Arabidopsis thaliana* [27]. Potts *et al.* [7] discussed the impact of NMR parameters on the PCA of rodent urine, while Defernez and Colquhoun [28] assessed the robustness of metabolic fingerprinting by ^{1}H NMR.

The use of HR MAS NMR spectroscopy in metabolic profiling and taxonomic discrimination of marine microalgae is very new, and our results show that it is a method with great potential. The application of ^{1}H NMR on biological samples benefits from the high natural abundance of these nuclei, and the analysis time can be reduced. On the other hand, since ^{1}H occurs in all organic molecules the resulting spectra may be crowded and poorly resolved. For more detailed studies of particular molecular groups such as fatty acids or carbohydrates the application of ^{13}C NMR can result in more detailed information, such as presented in the Part 2 of this work on microalgae.

Conclusion

HR MAS NMR analysis directly on whole-cell samples is a useful tool in metabolic profiling and taxonomic discrimination of marine microalgae, and the advantage of applying NMR instead of conventional methods such as bio-optics and HPLC is that many metabolites can be studied simultaneously in relatively short time, without any extraction involved. The use of NMR on such complex samples needs further studies, however, in order to clarify such things as differences in NMR-visibility of the different types of molecules depending on cellular location. Since there is little experience from NMR-studies on microalgae it is also important to investigate the contributions to any variability in the spectra, and separate natural biological variability from variability due to NMR properties.

References

1. Jeffrey SW, Mantoura RFC, Wright SW (Eds). Phytoplankton Pigments in Oceanography: Guidelines to Modern Methods. Unesco: Paris, 1997.
2. Brown MR, Dunstan GA, Norwood SJ, Miller KA. J. Phycol. 1996;32:64.
3. Mackey MD, Mackey DJ, Higgins HW, Wright SW. Mar. Ecol. Prog. Ser. 1996;144:265.
4. Sumner LW, Mendes P, Dixon RA. Phytochemistry. 2003; 62:817.
5. Meiboom S, Gill D. Rev. Sci. Instrum. 1958;29:688.
6. Schripsema J, Erkelens C, Verpoorte R. Plant Cell Rep. 1991;9:527.
7. Potts BCM, Deese AJ, Stevens GJ, Reily MD, Robertson DG, Theiss J. J. Biomed. Anal. 2001;26:463.
8. Nicholson JK, Foxall PJD. Anal. Chem. 1995;67:793.
9. Lindon JC, Nicholson JK, Everett JR. Annu. Rep. NMR Spectrosc. 1999;38:1.
10. Moolenaar SH, Engelke UFH, Wevers RA. Annu. Clin. Biochem. 2003;40:16–24.
11. Ratcliffe RG, Roscher A, Scachar-Hill Y. Prog. Nucl. Magn. Reson. Spectrosc. 2001;39:267.
12. Fredlund E, Broberg A, Boysen ME, Kenne L, Schnürer J. Appl. Microb. Biotechnol. 2004;64:403.
13. Broberg A, Kenne L. Anal. Biochem. 2000;284:367.
14. Hedges JI, Baldock JA, Gélinas Y, Lee C, Peterson ML, Wakeham SG. Mar. Chem. 2002;78:47.
15. Størseth TR, Hansen K, Skjermo J, Krane J. Carbohydr. Res. 2004;339:421.
16. Chauton MS, Størseth TR, Johnsen G. J. Appl. Phycol. 2003;15:533.
17. Chauton MS, Optun OI, Bathen TF, Volent Z, Gribbestad IS, Johnsen G. Mar. Ecol. Prog. Ser. 2003;256:57.
18. Chauton MS, Størseth TR, Krane J. J. Phycol. 2004;40: 611.
19. Turpin DH, Harrison PJ. J. Phycol. 1978;14:461.
20. Derrien A, Coiffard LJM, Coiffard C, De Roeck-Holtzhauer Y. J. Appl. Phycol. 1998;10:131.
21. Granum E. Metabolism and function of β-1,3-glucan in marine diatoms. Dr. Ing Thesis. Department of Biotechnology, Norwegian University of Science and Technology, Trondheim, 2002.
22. Chatham JC, Forder JR. Biochim. Biophys. Acta. 1999;1426:177.
23. Martens H, Næs T. Multivariate Calibration. John Wiley & Sons: New York, 1991.
24. Babuska R, Alic L, Lourens MS, Verbraak AFM. Bogaard J. Artif. Intell. Med. 2001;21:91.
25. Keller MD, Kiene RP, Matrai PA, Bellows WK. Mar. Biol. 1999;135:249.
26. Bundy JG, Spurgeon DJ, Svendsen C, Hankard PK, Osborn D, Lindon JC, Nicholson JK. FEBS Lett. 2002;521: 115.
27. Ward JL, Harris C, Lewis J, Beale MH. Phytochemistry. 2003;62:949.
28. Defernez M, Colquhoun IJ. Phytochemistry. 2003;62: 1009.
29. Sitter B, Sonnewald U, Spraul M, Fjösne HE, Gribbestad IS. NMR in Biomedicine. 2002;15:327.
30. Willker W, Leibfritz D. Magn. Res. Chem. 1998;36:79.

HR MAS NMR Spectroscopy of Marine Microalgae, Part 2: ^{13}C and ^{13}C HR MAS NMR Analysis Used to Study Fatty Acid Composition and Polysaccharide Structure

Trond Røvik Størseth,[1,2] Matilde S. Chauton,[3] and Jostein Krane[2]
[1] *SINTEF Fisheries and Aquaculture, 7465 Trondheim, Norway;*
[2] *Norwegian University of Science and Technology (NTNU), Department of Chemistry, 7491 Trondheim, Norway; and*
[3] *NTNU, Trondhjem Biological Station, 7491 Trondheim, Norway*

Introduction

The use of HR MAS NMR presents a unique tool for studying biological solid and semisolid samples [1,2]. The method gives information on different classes of compounds from the samples in question that would have taken multiple analyses to obtain otherwise [3]. Due to the lower sensitivity of ^{13}C NMR in comparison to ^{1}H NMR, the latter would be the method of choice for studying small metabolites and osmolytes, and biological processes involving these. Reported applications of ^{1}H HR MAS NMR to study microalgae have been discussed by Chauton and in HR MAS NMR Spectroscopy, Part 1, found in this book on pages XXX–XXX.

Microalgae play a fundamental part in aquatic primary biosynthesis of important lipids, which include polyunsaturated fatty acids (PUFAs) [3]. Lipids and storage polysaccharides are products of important biochemical pathways, and the amount and composition of these compounds represent valuable information on the physiological status and biochemistry of microalgae [4,5]. Information on the overall degree of unsaturation of fatty acids may be obtained using ^{1}H NMR by comparison of resonances originating from the total allyllic and double allyllic and methylenic resonances [6], and n-3 fatty acids may be quantified [7]. The ^{1}H NMR spectrum does, however, give little detailed information with regards to individual fatty acids.

Storage polysaccharides are also important in microalgal biochemistry. The content of these may indicate the physiological status as it varies in response to growth conditions [8]. Polysaccharides may be studied by ^{1}H NMR to describe linkages and residue composition, but there are some limitations due to crowded spectra as the number of different residues and linkages increase [9]. The storage polysaccharide of diatoms is chrysolaminaran, which is a β-glucose polymer linked in β-(1→3), β-(1→6), and β-(1→2) positions [10]. The main chain of these polymers are β-(1→3) linked. Kim *et al.* have shown that ^{1}H NMR may be used to describe the polymerization and branching of these polymers by dissolving β-(1→3, 1→6)-glucans in d_6-DMSO [11]. When the polysaccharides are dissolved in D_2O or observed in whole cells with HR MAS the resolution of the spectra does, however, not allow for the same accuracy as the method of Kim *et al.*

Methods in which information on the fatty acids and polysaccharides of microalgae may be obtained simply and rapidly would be valuable for a wide array of purposes from the study of biological processes to nutritional value. Both for fatty acids and polysaccharides the resolution of the ^{13}C NMR spectrum provides good information both on composition and structure. The use of ^{13}C NMR in studies of fatty acid composition is widespread and well documented, and usages include content and composition of lipids [12]. The amount of available data make assignments in most cases a matter of comparing chemical shift values with the literature. For polysaccharides ^{13}C NMR is a powerful tool both for homo- and heteropolymers to describe both linkages and residue composition. Furthermore, the DEPT pulse sequence allows for discrimination between CH, CH_2, and CH_3 groups [13].

Both homo- and heteronuclear 2D techniques are powerful tools for studying both fatty acids and polysaccharides [14]. The use of these techniques is an invaluable tool for clarifying ambiguous assignments of peaks in 1D spectra when describing the linkages of storage polysaccharides in mixtures of compounds and cells. This chapter present results from a HR MAS NMR study on the marine diatom *Chaetoceros mülleri*, where the resonances belonging to fatty acids [15] and the storage polysaccharide chrysolaminaran were assigned with the use of literature values and spectra from extracted samples for both classes of compounds and 2D ^{13}C,^{1}H correlated spectroscopy for polysaccharides [16].

Graham A. Webb (ed.), Modern Magnetic Resonance, 953–957.
© 2008 *Springer.*

Results and Discussion

The ^{13}C HR MAS NMR spectrum of cells of the marine diatom *C. mülleri* show resonances belonging to both fatty acids and the chrysolaminaran storage polysaccharide (Figure 1). From this spectrum Chauton *et al.* [15] assigned the resonances originating from fatty acids by comparing the spectrum with a lipid extract recorded in chloroform from which the resonances could be compared with literature values. DEPT NMR was used to support the comparison of the HR MAS and liquid state spectra as small differences in the resonances frequencies (at the most 0.1 ppm) between the two were observed. The profiles of the two spectra, however, were the same. The essential PUFAs, EPA, and DHA were assigned along with the 16:1 and 20:4, which are fatty acids involved in the biosynthesis of PUFAs (Table 1) [17,18]. In addition to these assignments, resonances from PUFAs which could not be assigned to individual fatty acids were seen along with triglyceride and phospholipid resonances. The results represent the use of HR MAS NMR as a tool for studying microalgal biochemistry as well as for the purpose of determining nutritional value of microalgae. The fact that ^{1}H experiment is almost always done prior to recording ^{13}C experiments makes it possible to relate the ^{13}C analysis of the fatty acid content of the microalgae studied to the metabolite profile found in the ^{1}H experiments. This would give researchers employing the HR MAS method unique opportunities to have information on biochemical processes related to fatty acid biosynthesis from the same sample with only one simple sample preparation; just collect the sample by centrifugation, add deuterium oxide, and insert the sample in the MAS rotor.

The chrysolaminaran peaks found in the ^{13}C HR MAS spectrum were assigned by Størseth *et al.* [16] primarily from ^{13}C-DEPT NMR and ^{13}C,^{1}H-correlated spectroscopy (HETCORR) (Figure 2). β-(1→3)-Glucan resonances are found in the 60–105 ppm region of the ^{13}C NMR spectrum. As other resonances were found in this region making unambiguous assignments difficult directly from the 1D spectrum. The use of the 2D heteronuclear

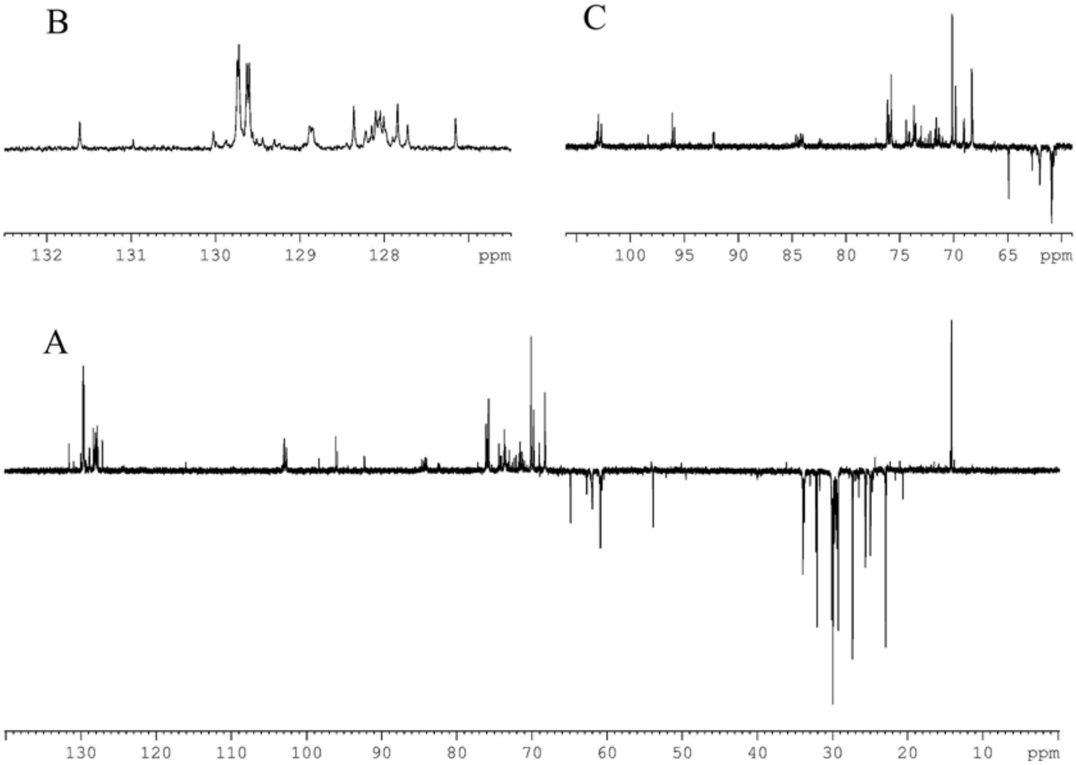

Fig. 1. The ^{13}C-DEPT NMR spectrum recorded from *C. mülleri*. (A) Complete spectrum, (B) olefinic region, and (C) carbohydrate region.

Table 1: Assignments of fatty acid resonances from the ^{13}C HR MAS NMR spectrum of *C. mülleri*. Literature used for the assignments [12,19,20]

Tentative assignments	HR-MAS δ values	Extract δ values
EPA, C18	131.6	132.08
16:1, C10	129.74	130.07
EPA, C5	129.73	130.06
16:1, C9	129.63	129.77
EPA, C6	129.6	129.74
EPA, C6		128.81
DHA, C11	128.22	128.31
EPA, C9	128.15	128.23
20:4, C8	128.1	128.20
EPA, C11	128.08	128.14
20:4, C11	127.84	127.88
20:4, C14	127.73	127.57
TG, C2	69.03	68.89
TG, C1/3	60.91	62.14
C2	33.96	34.25
C2	33.76	34.08
EPA, C2		33.44
n-9, Sat FAs	32.24	31.98
n-9, Sat FAs	32.08	31.84
n-2 In all n-6 FAs	31.73	31.57
Allylic C	27.35	27.27
Allylic C	27.33	27.22
EPA, C4	26.52	26.54
Allylic C	25.63	25.66
C between double bonds	25.57	25.59
C3		24.94
C3	24.99	24.91
20:4, n-2	22.81	22.63
n-2 In all n-3 FAs	20.62	20.61
n-1 C in all FAs	14.17	14.17

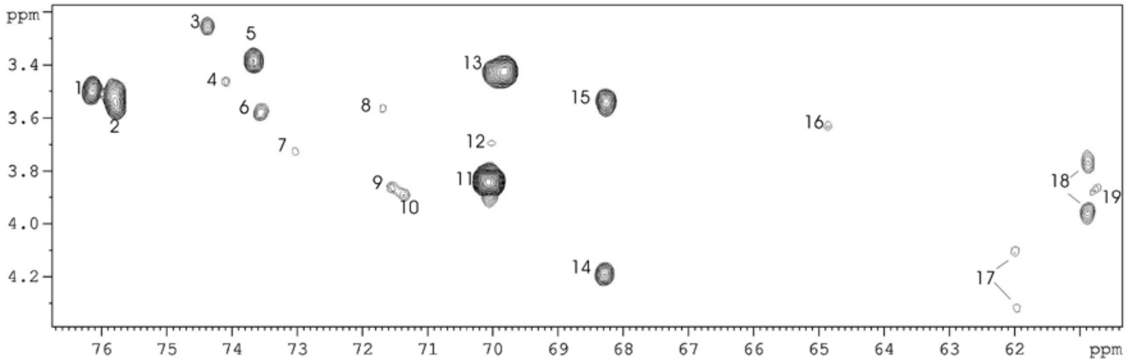

Fig. 2. The 60–77 ppm region of the HETCORR spectrum recorded of *C. mülleri*. Assignments are given in Table 3.

Table 2: Assignments of the carbohydrate resonances in the ^{13}C NMR and HETCORR spectra

Nucleus, C = Glucan, G = Glucose	HR-MAS δ values	Glucan extract/glucose literature* δ values
C-1	102.84	102.96
C-1 linked	102.68	102.68
G-1 β	96.14	97.00
C-1 α reducing end signal	95.88	95.68
G-1 α	92.28	93.10
C-1 β reducing end signal	92.26	92.16
C-3	84.44	84.41
C-3	84.19	84.26
C-3	84.03	84.26
G-3 β	76.16	77.00
C-3 Non-reducing end signal	76.14	76.17
G-5 β	75.81	76.80
C-5*	75.77	75.79
G-2 β	74.37	75.20
C-2 RT	74.07	73.98
C-2 NRT	73.68	73.64
C-2 BC	73.57	73.42
G-3 α	73.03	73.80
G-2 α	71.69	72.50
G-5 α	71.41	72.50
G-4 α and β	70.01	70.70
C-4	68.27	68.29
G-6	60.88	61.70
C-6†	60.88	60.88

*Literature values are from Fan [21].

$^{+}$Overlaps with glucose C-6.

spectrum allowed the structural characterization of the β-1→3 glucan of *C. mülleri* as the non-glucan resonances could be excluded on the basis of their ^{1}H correlations. Non-glucan resonances which overlapped with glucan resonances were also easily detected by this method and this excluded misinterpretation of the structure of the glucan. The assigned resonances from the glucan and non-glucan peaks are shown in Table 2 together with the resonances from glucose some of which overlapped with the glucan resonances.

The extracted glucan was analyzed by the method of Kim *et al.* [11], using ^{1}H NMR in DMSO to give information on the DP and DB of the glucan. Results from this analysis showed some (1→6) linkages, and the glucan was found to have a DP and DB of 19 and 0.005, respectively. As the bonded and non-bonded C-6 of the glucopyranosyl residues have different chemical shifts and also using the DEPT135 pulse sequence, have opposite signs to C-1 through C-5 the presence of (1→6) glycosidic linkages in glucans may easily be detected. However, in the case of the HR MAS analysis of the *C. mülleri* cells this was not observed. This could be attributed to the low DB and the fact that the sensitivity of the ^{13}C analysis is low compared to the ^{1}H analysis. Results obtained from the HR MAS analysis of the glucan cells indicated that it is possible to obtain the structure of the chrysolaminarans directly without extraction. The limitations are linked to the detection of branches when these are few compared to the number of molecules and the DP of the molecules.

Conclusion

The papers which have formed the basis of HR MAS NMR spectroscopy of marine microalgae (Part 1 and 2 in this book) present the possibilities and potential of using HR MAS NMR as a tool for studying biochemical processes and chemical composition in microalgae. The works with ^{1}H NMR have to a great extent been based on tentative assignments from comparison with literature data when considering metabolite analysis directly on

Table 3: Assignments of peaks in Figure 2

Peak no.	Assignment
1	Glucose β-C-3
2	Glucose β-C-3 and glucan C-3
3	Glucose β-C-2
4	Glucan C-2-RT
5	Glucan C-2-NRT
6	Glucan C-1-BC
7	Glucose α-C-3
8	Glucose α-C-2
9	NA
10	Glucose α-C-5
11	NA
12	Glucose C-4
13	NA
14	NA
15	Glucan C-4
16	NA
17	Triglyceride
18	Glucan and glucose C-6
19	NA

whole cells, while the identification of fatty acids by ^{13}C NMR was done by way of comparing the obtained results with literature values after extraction. The analysis of the β-glucan of *C. mülleri* presented by Størseth *et al.* [16] was verified by the analysis of extracted β-glucan by established methods. These are possibilities that should be examined further, and should lead to simplified analysis techniques giving extensive information on microalgae in general, not just the species presented in these studies.

References

1. Cheng LL, Chang IW, Smith BL, Gonzalez RG. J. Magn. Reson. 1998;135:194.
2. Sitter B, Bathen T, Hagen B, Arentz C, Skjeldestad FE, Gribbestad IS. Magn. Reson. Mater. Phys. Biol. Med. 2004;16:174.
3. Chauton MS, Størseth TR, Johnsen G. J. Appl. Phycol. 2003;15:533.
4. Reitan KI. Nutritional effects of algae in first-feeding of marine fish larvae. Dr. Scient Thesis. Department of Botany, University of Trondheim, Trondheim, 1994.
5. Ahlgren G, Gustafsson IB, Boberg M. J. Phycol. 1992;28:37.
6. Diehl BWK. Eur. J. Lipid Sci. Technol. 2001;103:830.
7. Igarashi T, Aursand M, Hirata Y, Gribbestad IS, Wada S, Nonaka M. J. Am. Oil Chem. Soc. 2000;77:737.
8. Granum E. Metabolism and function of b-1,3-glucan in marine diatoms. Dr. Ing Thesis. Department of Biotechnology, Norwegian University of Science and Technology, Trondheim, 2002.
9. Bubb WA. Concepts Magn. Reson. Part A. 2003;19A:1.
10. Granum E, Myklestad SM. Hydrobiologia. 2002;477:155.
11. Kim Y-T, Kim E-H, Cheong C, Williams DL, Kim C-W, Lim S-T. Carbohydr. Res. 2000;328:331.
12. Aursand M, Grasdalen H. Chem. Phys. Lipids. 1992;62:239.
13. Vårum K, Kvam B, Myklestad S. Carbohydr. Res. 1986;152:243.
14. Willker W, Leibfritz D. Magn. Reson. Chem. 1998;36:S79.
15. Chauton MS, Størseth TR, Krane J. J. Phycol. 2004;40:611.
16. Størseth TR, Hansen K, Skjermo J, Krane J. Carbohydr. Res. 2004;339:421.
17. Sayanova OV, Napier JA. Phytochemistry. 2004;65:147.
18. Tonon T, Harvey D, Larson TR, Graham IA. Phytochemistry. 2002;61:15.
19. Aursand M, Rainuzzo JR, Grasdalen H. Developments in Food Science 1992;30:407.
20. Gunstone FD. Chem. Phys. Lipids. 1991;59:83.
21. Fan TW-M. Prog. Nucl. Magn. Reson. Spectrosc. 1996;28:161.

Post-mortem Studies of Fish Using Magnetic Resonance Imaging

Emil Veliyulin[1], Alv Borge[2], Trond Singstad[2], Ingrid Gribbestad[2], and Ulf Erikson[1]
[1]*SINTEF Fisheries and Aquaculture, N-7465 Trondheim, Norway; and*
[2]*St. Olavs Hospital, N-7465 Trondheim, Norway*

Introduction

Although being less sensitive than many other analytical methods, magnetic resonance imaging (MRI) does have significant advantages such as being non-invasive and non-destructive. Furthermore, no sample preparation is needed prior to analysis and the method is not hampered by limitations regarding signal penetration depth. However, due to the high investment costs, the sheer size of the instrument and the necessary related infrastructure, MRI cannot presently be considered as a standard analytical tool in aquaculture or fish processing industry. As a research tool, however, taking advantage of the unique features of the method, we can obtain basic insight into a number of issues related to anatomical studies, composition and structure of tissues, distribution maps of fat, water, and salt as well as temperature profiles (mapping). Moreover, theoretical transport models can in turn be used to interpret the images. For the aquaculture industry, MRI studies may for instance be helpful to study the effect of feed composition (fat) and different feeding regimes on fat contents and distribution in tissues. In fish processing, MRI can be used as a tool for the optimization of various unit operations such as salting, freezing, and thawing. For a more detailed treatment of various MRI applications, see review by Hills [1].

MRI is a technique that offers a unique opportunity to "look inside" intact whole organisms, i.e. to produce high-quality cross-section images. Depending on the particular task, MRI instruments can produce several types of contrast images. This is achieved by programming and running specific MR sequences to make it possible to differentiate between protons in molecules having different mobilities or chemical environments. For example, it is possible to obtain MR images of "water" and "fat" [2], "diffusion weighted" images where only molecules with low mobility are visible [3] or high resolution images of connective tissue [4]. Contrast agents—administered to the circulatory system—added to affect relaxation times are often used in connection with medical *in vivo* examinations to obtain a specific MRI contrast [5]. MR images of water and fat in burbot (*Lota lota*) liver have been acquired. The MR signal intensity in the reconstructed images showed good correlation with the liver fat content in live fish. Significant correlations were also obtained for water and protein contents [2]. Collewet *et al.* [6] proposed to use MRI as a tool to assess fat distribution in fish. It was shown that higher contrast between muscle and adipose tissues can be obtained when the MR images are highly longitudinal relaxation time (T_1) weighted. Moreover, based on comparison with chemical analysis of fat, better correlations with quantitative MR data were obtained by accounting for coil sensitivity and radio frequency (RF) field inhomogeneity. Compared with fresh cod (*Gadus morhua*), Howell *et al.* [7] reported that MR images of fish stored for 6 weeks at -30°C were not different. In contrast, images obtained from fish stored at -8°C exhibited dense lines indicative of tissue gaps. Fresh rainbow trout (*Salmo gairdneri*) was subjected to freezing–thawing before MRI analysis to visualize various organs, and to identify spatial distributions of lipid- and collagen-rich tissues. T_1-weighed images were clearly shown to highlight the lipids relative to water containing tissues. On the other hand, transverse relaxation time (T_2) and magnetization transfer (MT) contrasted images showed the clearest distinction between muscle tissues [8]. The effect of freezing and thawing of a lean species (cod) and a fatty species (mackerel, *Scomber scombrus*) was studied by Nott *et al.* [9]. In particular, the T_1^{sat} (measured during saturation transfer) and MT rate were shown to be sensitive parameters to assess the effects of frozen storage. Compared with fresh fish, the freezing–thawing cycle of both species induced increased MT rate and T_1, whereas T_1^{sat} decreased. The same effect was consistently observed with increasing frozen storage time (2–12 weeks). Foucat *et al.* [10] used a cylindrical sample carrier in the MRI magnet allowing six frozen–thawed trout (frozen storage for 0–41 days) and reference tubes to be analyzed simultaneously. An image containing information about anatomical features, MT ratio, T_2, and diffusion constants (parallel and perpendicular to muscle fiber orientation, $D\perp$) were acquired in 5 min. Compared with fresh fish, the freezing–thawing cycle significantly affected only the mean T_2 and the $D\perp$-values, which changed from 42.3 to 47.1 ms and

Graham A. Webb (ed.), Modern Magnetic Resonance, 959–966.
© 2008 *Springer.*

from 0.85×10^{-5} to 1.07×10^{-5} cm^2/s, respectively. Only $D\perp$ was affected after frozen storage for 41 days. The increase in T_2 was attributed to protein denaturation (during freezing–thawing) leading to redistribution of water within the muscle tissue. Concomitantly, with the appearance of extracellular spaces between fibers, the migration of water increased in a direction perpendicular to fiber orientation.

Regarding aquatic organisms, the feasibility of using MRI for anatomical studies was first demonstrated by Blackband and Stoskopf in 1990 [11]. When using *in vivo* localized MRI, it was possible to distinguish between different organs such as muscle tissues, gills, spine, stomach, and uterus in embryonic fish [12]. Post-processing of MR multi slice data makes it possible to obtain three-dimensional (3D) maximum intensity projection maps (MIPs) or surface projection maps of the organism (e.g. spider crabs, *Maja squinado*) [13]. Another technique that may be considered is the double-quantum filtered MRI where only molecules associated with ordered tissue structures are detected by suppressing the signals from isotropic fluids [14].

The goal of the present study was to demonstrate some MRI applications which may be of interest in aquaculture, fish processing, and quality control.

Materials and Methods

All MRI studies presented here were carried out using the Bruker Avance DBX100 instrument (Bruker Optik GmbH, Germany). The magnet has a horizontal wide bore opening suitable for imaging of comparatively large objects (^{1}H imaging area—sizes up to 15 cm in diameter and 15 cm in length).

Spatial Distribution of Fat and Water in Atlantic Salmon Fillets

To visualize the spatial distribution of fat and water in an Atlantic salmon (*Salmo salar*) fillet, a chemical shift selective (CHESS) MRI protocol was used. Three image types of a fillet piece ($3 \times 3 \times 4$ cm) were acquired: "a proton density image," "a fat image," and "a water image." The following acquisition parameters were used: matrix size = 128×128, relaxation delay (T_R) = 2 s, number of excitations (NEX) = 40, number of slices = 25, and echo times (T_E) = 9.1 (fat selective images) and 26.4 ms (water selective images). For the fat excitation, a selective sinc-shaped pulse with a bandwidth of 1200 Hz was centered 400 Hz (+200 Hz) away from the water signal frequency to avoid signal contribution from water. For the water signal excitation, a similar sinc pulse with a bandwidth of 480 Hz was centered at the water resonance frequency (−200 Hz) to avoid signal contribution from fat. The "proton density" image was acquired using a Multi-Spin Multi-Echo (MSME) protocol with $T_E = 7.2$ ms, $T_R = 2$ s, and NEX = 4. The total acquisition times were 2 h 51 min for the CHESS protocol and 17 min for the MSME protocol. Sufficient suppression of either the fat or water spectral component could only be achieved in a region with highly homogeneous magnetic field (limiting sample size under study) and RF pulses. Thus, careful shimming prior to image acquisition was necessary.

Distribution and Determination of Water and Salt in Cod Fillets

Sample preparation and brine salting procedure is described elsewhere [15]. For the determination of water and salt contents in the cod fillet an MSME imaging protocol was used. The protocol parameters for the ^{1}H MRI experiments were matrix size = 128×128, $T_R = 3$ s, NEX = 2, and number of slices = 3. The experiment was repeated five times with incremented echo times of 9, 18, 27, 36, and 45 ms, thus producing a set of five T_2 weighted images of each slice. To quantify the ^{1}H image, a reference solution with known water content and a relaxation time similar to that of the fish was prepared and imaged along with the sample. This was accomplished by mixing distilled water with deuterium oxide (D_2O) in known weight proportions. As deuterium compounds are ^{1}H MR silent, mixtures with water can be used to simulate homogeneous systems with predetermined water contents. The mixture was doped with 0.001 mol/l $MnCl_2$ to shorten the T_2 relaxation time to approximately equal to that of the fish muscle. The reference solution contained 64 wt% water with a relaxation time of 27 ms.

An in-house made 60 mm ^{23}Na RF volume coil was used for the salt studies. The ^{23}Na imaging protocol with the following parameters was employed: matrix size = 64×64, $T_R = 250$ ms, NEX = 64, and number of slices = 1. The experiment was repeated six times with incremented echo times of 2.7, 4.7, 6.7, 8.7, 10.7, and 12.7 ms. A ^{23}Na image of a slice, 20 mm in thickness, was acquired for each sample with a 1 mm spatial in-plane resolution. The acquisition time per sample was 6 min. For the sodium quantification from the salt images, a reference solution (18% NaCl) was imaged with the fish sample.

To quantify MR images, the average signal intensities of the fish samples and reference solution were determined by geometrically defining a region of interest (ROI). The mean intensity of all pixels within two selected ROIs were then calculated. The calculated average intensities for the fish and reference solution ROIs were plotted as a function of echo time on a semi-logarithmic scale. The initial amplitudes of the T_2 relaxation curves for the fish (M_{fish}) and the reference solution (M_{ref}) were obtained by extrapolating this curve to zero time using a monoexponential function, thus taking into account differences in the relaxation time between the fish and the reference. The calculated amplitudes were proportional to the average water content in the selected ROIs. The fish (ROI) water content was then calculated as

$$W_{\text{fish}} = W_{\text{ref}} \times \frac{M_{\text{fish}}}{M_{\text{ref}}} \quad (1)$$

where W_{ref} was the water reference solution described above. Likewise, the salt content of the same samples was calculated from the corresponding salt images. In this case, W_{ref} the sodium reference solution was used.

Freezing of Atlantic Salmon and Cod Fillets

A temperature regulated nitrogen blast-cooling device was built to regulate the temperature in the magnet. Two different freezing regimes were studied by MR imaging (i) a dynamic study where the fish sample temperature was reduced while MR images were acquired and (ii) a study at several constant temperature conditions. While the dynamic study represented typical industrial freezing conditions, the study at constant temperature conditions allowed to extract more information and made it possible to determine the fraction of unfrozen water at each temperature.

(i) In *the dynamic freezing regime study*, cylindrical fillet pieces of cod and salmon white muscle (diameter 2.8 cm, length 3 cm) were studied at the temperature ranges from +10 to –10 °C (cod) or –30 °C (salmon). The samples were wrapped in plastic foil to prevent loss of liquid. The freezing procedure was to instantaneously expose the samples to nitrogen gas flow with a preset flow rate and temperature. The temperature in the sample was monitored using a thermocouple which was removed from the RF coil during image acquisition. Due to very short transversal relaxation times at low temperatures, the broad line imaging package (BLIP) was applied to be able to obtain the short echo times. The acquisition parameters were $T_E = 2.6$ ms, $T_R = 700$ ms, NEX = 4, slice thickness = 3 mm, matrix size = 64 × 64, and field of view (FOV) = 4 cm, giving spatial image resolution of 63 μm. The time interval between successive images was 3 min. The dynamic experiments were started at 10 °C and the variation of the mean image intensity of the selected ROI (covering the whole sample cross-section) was measured as a function of freezing time.

(ii) At *constant temperature conditions*, the temperature was stepped through a range of preset values (with steps varying from 2 to 4 °C). The temperatures were measured with an accuracy of ±0.1 °C at each step. The time delay for the temperature to stabilize at each step was varying depending on the temperature. The experiment was carried out in the same temperature ranges as the dynamic freezing studies. The same imaging protocol (BLIP) and MRI parameters were also used in this case for acquiring the "proton density" images. To calculate the spin density it was necessary to measure both T_1 and T_2 relaxation times at each temperature. Due to the short value, the T_2 relaxation time was measured with a series of BLIP spin echoes by varying the echo time. The T_1 relaxation time was measured with a series of BLIP inversion recovery experiments by varying the inversion time. Relaxation time measurements and the corresponding spin density calculations were carried out at constant temperatures only.

Anatomical Defects in Farmed Atlantic Salmon

The MRI technique can non-destructively visualize fish structure, providing by various types of contrast between the backbone, water in muscle, fat, and connective tissue. Here, the MRI technique was applied to study the fish backbone structure aiming at revealing the reason why backbone deformations occur under different fish farming conditions.

Six farmed Atlantic salmon (weight 2.8 ± 0.6 kg and condition factor 2.1 ± 0.3) were collected after slaughtering at a commercial fish processing plant. The fish were downgraded due to visible backbone deformities. The fish were frozen and kept at −20 °C until analysis. Prior to the MRI measurements, the fish were thawed at 4 °C overnight. For the anatomical studies, a MSME T_1-weighted imaging protocol was used with the following parameters: $T_E = 20$ ms, $T_R = 400$ ms, 6 slices, NEX = 4, and FOV = 13 cm.

Results and Discussion

Spatial Distribution of Fat and Water in Atlantic Salmon Fillets

In the conventional "proton density" MR image, both fat and water components exhibited maximal intensities (Figure 1a). Even so, the major fat deposits in the myosepta (light "stripes") could clearly be identified. This corresponds with the typical lipid storage pattern within Atlantic salmon fillets [16]. The CHESS imaging modality makes use of the fact that the protons in fat and water molecules have slightly different resonance frequencies and hence they will have different chemical shifts. When using the method, a frequency selective RF pulse with a predefined bandwidth is applied to excite either the fat or the water spectral component only. This made it possible to achieve good separation between the two components and thus high-quality "fat" (Figure 1b) and "water" (Figure 1c) images could be acquired. In fish muscle, the sum of water and fat is fairly constant at about

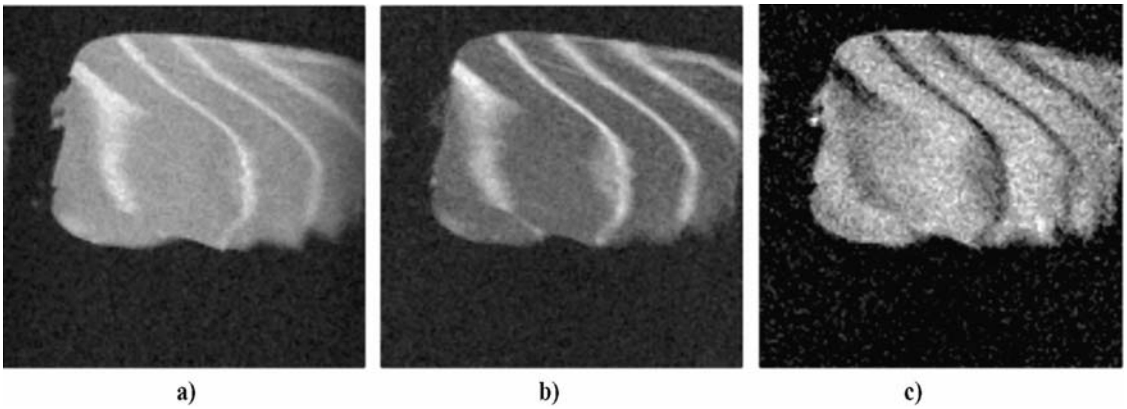

Fig. 1. MR images of an Atlantic salmon fillet piece: (a) "Proton density image" where both water and fat protons were visible. Regions with brighter pixels originated from high fat areas, while the darker pixel regions originated from water, (b) "Fat image" acquired by selective RF excitation of fat protons only. No water protons contributed to the pixel intensities, and (c) "Water image" acquired by selective RF excitation of water protons only. No fat protons contributed to the pixel intensities. The acquisition times were (a) 17 min and (b, c) 2 h 51 min.

80%. With this in mind, we can clearly see that in areas with high fat content, the water content was lower—and vice versa—in areas with low fat content, more water was observed.

Distribution and Determination of Water and Salt in Cod Fillets

In a multi-echo imaging experiment, echo time can be thought of as a certain time delay between the excitation pulse and spin-echo observation moment. During this delay, the net magnetization of nuclear spins slowly deteriorates, causing T_2 relaxation. This process results in a decrease of the signal intensity in each image pixel at a rate inversely proportional to the relaxation time in the pixel. This is clearly seen in Figure 2 showing ^{1}H images of a cod fillet piece acquired using incremented echo times of 9, 18, 27, 36, and 45 ms. Regarding the visual appearance of water distribution in the images, the best contrast was obtained at the shortest echo time. "Water and salt images" (echo time 9 ms) of three cod fillet pieces (one slice) are shown in Figure 3. It is clearly seen that when using the current salting method, the distributions of both water and salt were inhomogeneous. This is in accordance with a previous study using a similar cod salting procedure [15]. When comparing "the water and salt images" pairwise, the distributions (signal intensities) of the two components seem to correspond quite well, i.e. in areas with high water content, the salt content was also high (bright regions). The darker regions, with lower water and salt contents, may be explained by reduced diffusion rates due to different tissue composition or structure. The relative uncertainties in the determination of both variables were estimated to be about 1.5%. Due to the inhomogeneity of the water and salt distributions, a better estimate of the contents in the whole sample was achieved by manually choosing the ROI covering the whole sample (Figure 4a). Figure 4b shows the monoexponential extrapolation of

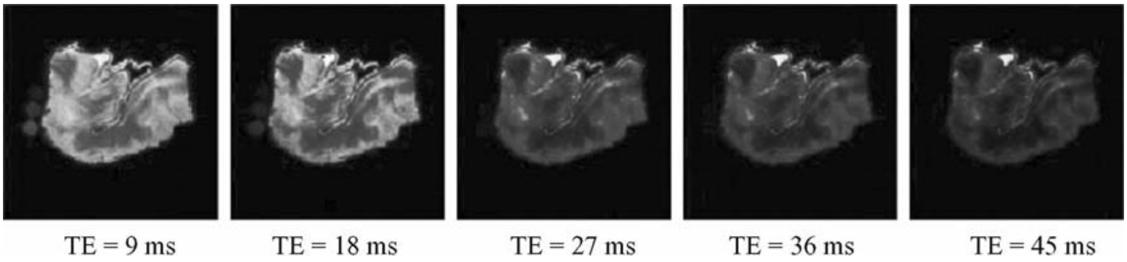

Fig. 2. A set of five T_2-weighted ^{1}H images of a cod fillet piece acquired at five incremented echo times.

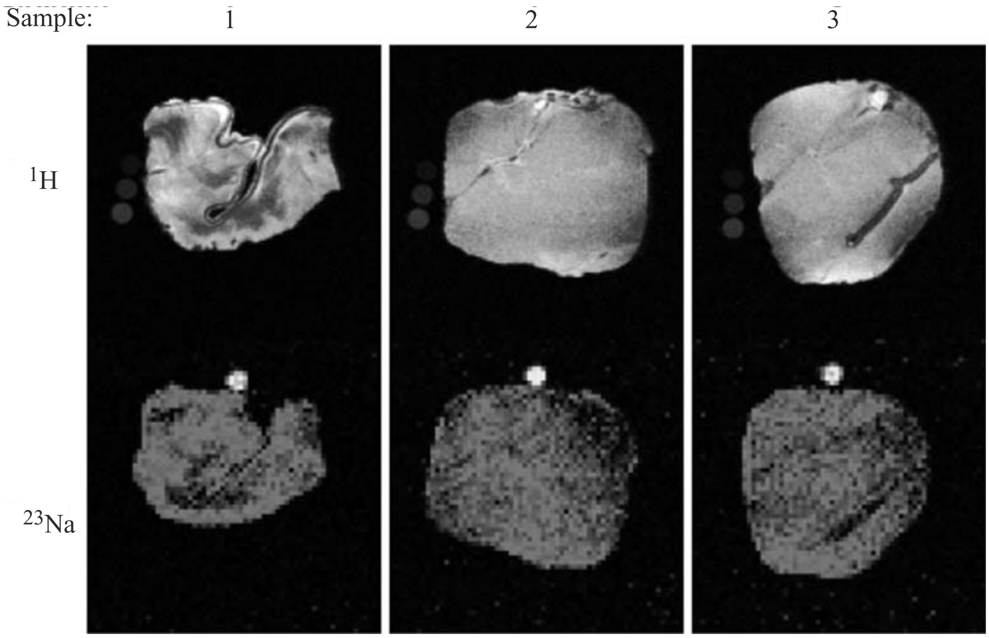

Fig. 3. Water (^1H) and salt (^{23}Na) MR images of the three different cod fillet pieces. The reference solutions can be seen to the left (^1H) and above (^{23}Na) the sample images.

decay curves to zero time to determine total water and salt contents in the sample (M_{fish}). The mean water and salt contents, as well as the lowest and highest values are summarized in Table 1.

Regarding quantitative NMR detection of ^{23}Na nuclei, it should be kept in mind that partial NMR "invisibility" of the sodium nuclei is sometimes reported. The effect can be ascribed sodium nuclei having an electric quadrupolar moment which causes rapid multiexponential relaxation. In biological systems, the binding of a certain fraction of sodium ions to macromolecules (proteins), will render them immobile and thus NMR "invisible." In both cases,

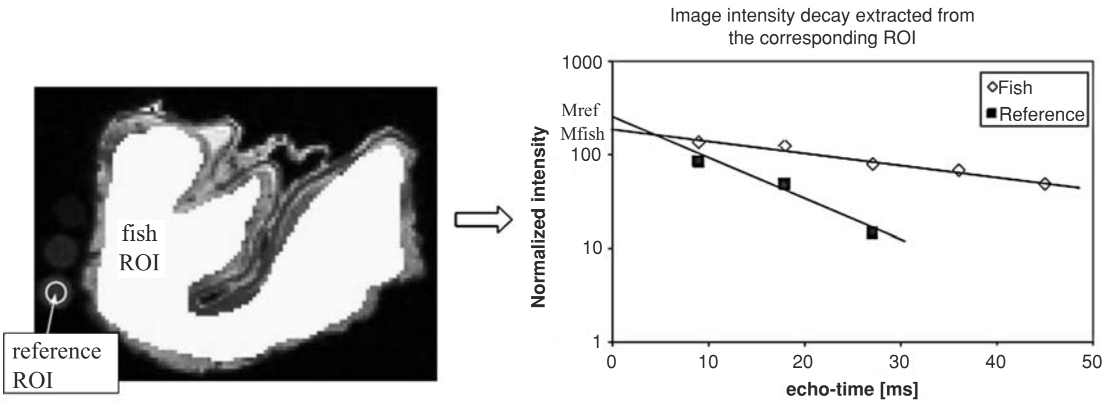

a)

b)

Fig. 4. (a) Selected regions of Interest (ROIs) in fish sample and reference and (b) monoexponential extrapolation of the decay curves to zero time was used as a measure of the total contents of water or salt in the sample (M_{fish}).

Table 1: Mean water and salt content in cod fillet pieces calculated from the three MR slices images (see Fig. 3 and 4). The corresponding variation ranges (minimal and maximal contents) are given in the parentheses.

Sample	Water content (wt %)	Salt content (wt %)
1	54 (47–62)	14 (9–17)
2	58 (55–61)	12 (7–14)
3	54 (49–65)	13 (8–18)

the estimated sodium concentrations may be too low. It seems as the experimental conditions have significant effects on these phenomena [15,17].

Freezing of Atlantic Salmon and Cod Fillets

Dynamic Freezing Regime Study

Figure 5 shows four MR images from a freezing series of the dynamic study of Atlantic salmon white muscle corresponding to about 13, 19, 28, and 37 min after start of cooling. Initially, the mean ROI signal increased, then an intermediate maximum was observed, and finally decayed as the temperature decreased. When the image analysis was performed on narrow circular concentric ROIs, it was observed that: (1) prior to the formation of a "freezing front" the signal rose uniformly throughout the sample; (2) once the "freezing front" was formed at the sample surface, the intensity of interior ROIs remained constant at the maximum value, until (3) the "freeze front" passed leading to a rapid signal decay. Since cod muscle has very low fat content (~0.3%), the corresponding MR images showed the muscle water only. On the other hand, the typical fat content in salmon white muscle is 8–23% [18] meaning the images show the distributions of both fat and water. From the images it was observed that in the areas of fat deposition, freezing was not complete at –30 °C (Figure 5). This is in accordance with previous NMR studies of fat mobility at low temperatures [19].

Constant Temperature Conditions

In Figure 6a, the T_1 and T_2 relaxation times for a cod sample are shown. The measured signal (S) from the images is given by

$$S = \rho \times e^{-\mathrm{TE}/T_2}(1 - e^{-\mathrm{TR}/T_1}) \qquad (2)$$

from which the spin density (ρ) can be calculated. According to Curie law, the true density of protons (ρ_0) is modulated by a factor $1/T$ to give the observed spin density as follows: $\rho \propto P_0/T$ [20]. The ice is MRI-invisible ($T_2 \sim 0.01$ ms). Therefore, to determine the fraction of unfrozen water (= 1.0—ice fraction), the calculated spin density was multiplied with the absolute sample temperature (T) and then normalized by the spin density above the freezing point. The calculated fraction of unfrozen water as a function of temperature is shown in Figure 6b. It is seen that below the freezing point, T_1, T_2, and the unfrozen water fraction decreased rapidly with the temperature. At each temperature step below the freezing point, a certain fraction of water froze (gradual freezing point depression) and thus became MRI-invisible. At the same time, the remaining unfrozen water fraction relaxed faster. In accordance with the signal increase observed prior to the passage of "the freeze front" in the transient studies, both the reference image signal and the calculated spin densities increased upon cooling above the freezing point. Furthermore, the calculated water fraction at stationary conditions was close to unity above the freezing point. Therefore, the signal change in this temperature range could mainly be attributed to the Curie law. Another factor contributing to this effect was the increase of the T_R/T_1 ratio as the temperature was reduced. Due to the low signal-to-noise ratio in the images it was not possible to determine relaxation times and thus perform the spin density calculations at a pixel level. By improving

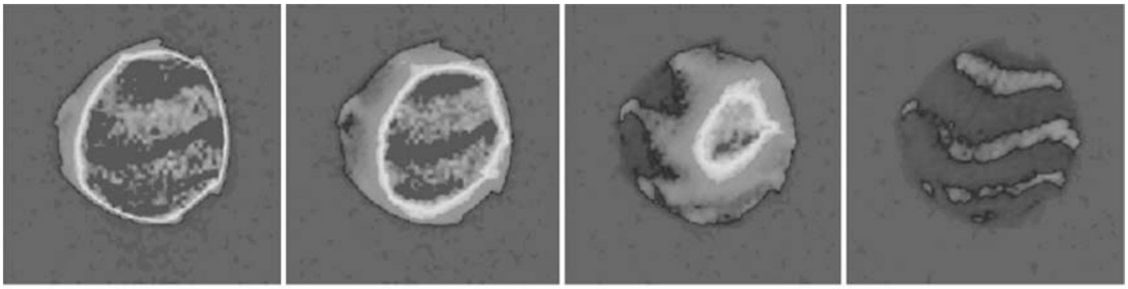

13 min 19 min 28 min 37 min

Fig. 5. MR images of a dynamic freezing study of an Atlantic salmon fillet piece. At 37 min the temperature had reached –30 °C.

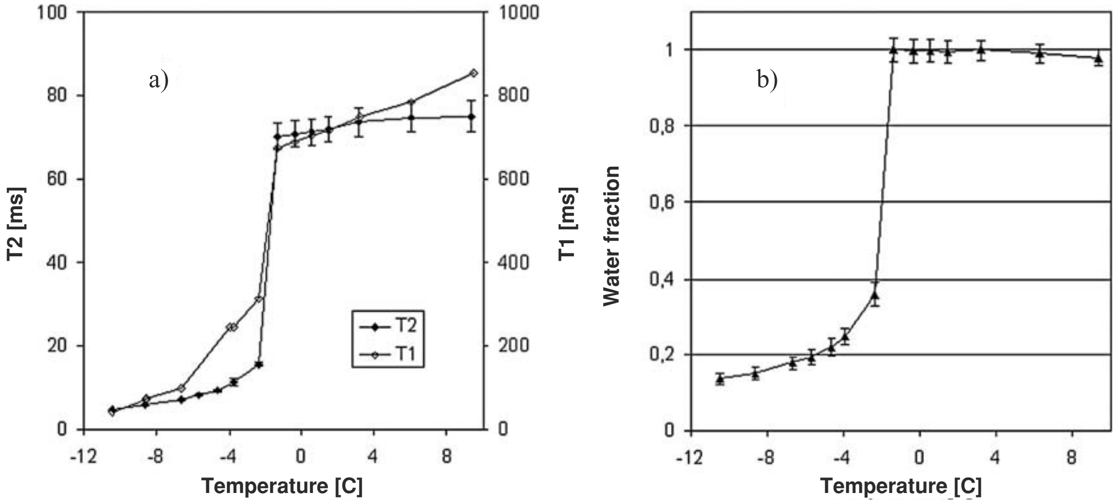

Fig. 6. (a) Constant temperature freezing study. Longitudinal (T_1) and transversal (T_2) relaxation times in a cod muscle piece at different temperatures and (b) calculated unfrozen water fractions at different temperatures. The observed tissue freezing temperature zone was from −2.35 to −1.35 °C.

the experimental technique, the calculation of both ice content (fraction) and sample temperature maps at a pixel level may be achieved. For salmon it was observed that the water component froze as rapidly as in cod, while the fat component signal decreased with temperature much more slowly. Quantification of the salmon images would therefore require separate water and fat analyses.

Summing up, the MRI technique clearly distinguished between frozen and unfrozen regions in fish tissues. At stationary freezing conditions, the fraction of unfrozen water in cod muscle could be calculated as a function of frozen storage temperature. Further development of the method may concentrate on the quantification of the dynamic set of images at pixel levels and on the determination of the speed of "the freezing front" propagation. Ultimately, a 3D reconstruction from a multislice dynamic MRI study under controlled thermal conditions may provide valuable information to optimize the freezing and thawing processes.

Anatomical Defects in Farmed Atlantic Salmon

Figure 7 shows a MR image of one of the six investigated Atlantic salmon acquired sagittally through the middle of the backbone. The deformation of the backbone structure is clearly seen here and several deformed and partially missing vertebrae in the middle and lower part of the backbone can be identified. Similar backbone deformations, but at different locations along the fish were observed in the five other fish.

Conclusions

Determination fat, water, and salt contents including their spatial distributions in (processed) fish tissues can be done readily using MRI. Although quantitative MRI can

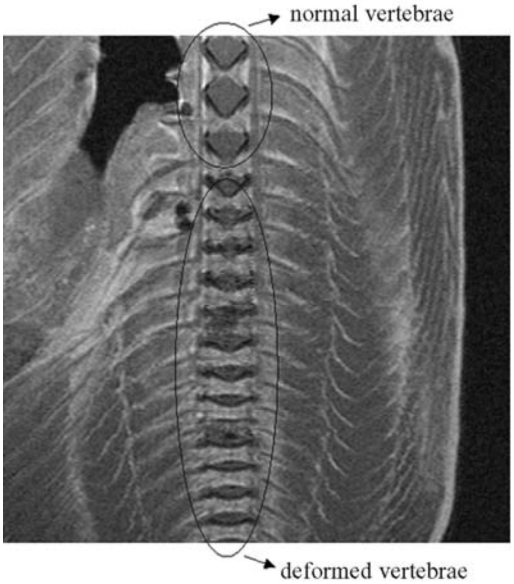

Fig. 7. An MR image of the middle section an Atlantic salmon revealing deformity of the backbone structure.

hardly be considered an alternative to chemical analysis presently, the method does offer a number of advantages compared with other analytical methods. As a research instrument however, we have demonstrated that MRI can be used to extract valuable results related to tissue composition, bone structure, and fish processing (salting and freezing).

Acknowledgment

Financial support of the Research Council of Norway is gratefully acknowledged.

References

1. Hills B. Trends Food Sci. Technol. 1995;6:111.
2. Alanen A, Komu M, Bodestam S, Toikkanen S. Phys. Med. Biol. 1991;36:953.
3. Mulkern RV, Spencer RGS. Magn. Reson. Imaging. 1988; 6:623.
4. Bonny BM, Laurent W, Renou JP. Magnetic resonance in food science: a view to the future. In: GA Webb (Ed). Special Publication 262. Royal Soc. Chem.: Cambridge, 2001, p 18.
5. Tofts PS, Kermode AG. Magn. Reson. Med. 1991;17: 357.
6. Collewet G, Toussaint C, Davenel A, Akoka S, Médale F, Fauconneau B, Haffray P. Magnetic resonance in food science: a view to the future. In: GA Webb (Ed). Special Publication 262. Royal Soc. Chem., 0260–6291: Cambridge, 2001, p 252.
7. Howell N, Shavila Y, Grootveld M, Williams S. J. Sci. Food Agric. 1996;72:49.
8. Nott KP, Evans SD, Hall LD. Magn. Reson. Imaging. 1999;17:445.
9. Nott KP, Evans SD, Hall LD. Lebensm.-Wiss. u-Technol. 1999;32:261.
10. Foucat L, Taylor RG, Labas R, Renou JP. Am. Lab. 2001; April:38.
11. Blackband SJ, Stoskopf MK. Magn. Reson. Imaging. 1990; 8:191.
12. Bock C, Sartoris F-J, Pörtner H-O. Magn. Reson. Imaging. 2002;20:165.
13. Bock C, Frederich M, Wittig RM, Pörtner H-O. Magn. Reson. Imaging. 2001;19:1124.
14. Tsoref L, Shinar H, Seo Y, Eliav U, Navon G. Magn. Reson. Med. 1998;30:720.
15. Erikson U, Veliyulin E, Singstad T, Aursand M. J. Food Sci. 2004;69:107.
16. Zhou S, Ackman R, Morrison C. Fish Physiol. Biochem. 1995;14:171.
17. Shapiro EM, Borthakur A, Dandora R, Kriss A, Leigh JS, Reddy R. J. Magn. Reson. 2000;142:24.
18. Hillestad M, Johnsen F, Austreng E, Åsgård T. Aquacult. Nutr. 1998;4:89.
19. Grasdalen H, Aursand M, Jørgensen L. Special Publication 157. Royal Soc. Chem.: Cambridge, 1995, p 208.
20. Haacke EM, Brown RW, Thompson MR, Venkatesan R. Magnetic Resonance Imaging, Physical Principles and Sequence Design. John Wiley & Sons Inc., Publication: New York, 1999, p 86.

How is the Fish Meat Affected by Technological Processes?

Loïc Foucat,[1] Ragni Ofstad,[2] and Jean-Pierre Renou[1]
STIM [1]INRA Theix, 63122 Saint Genès Champanelle France
[2] *Matforsk Norwegian Food Research Institute Osloveien 1 Aas N-1430 Norway*

Introduction

Because food is so important for survival, food preservation is one of the oldest technologies used by human beings. The fish preservation techniques mostly used today are salting and freezing. Salting is an ancient preservation technique. Salting keeps on being used, but it is often replaced by freezing. Smoking merely adds flavour and colour and removes some water. Smoked fish are almost as perishable as fresh fish.

Smoked fish are more and more consumed in Europe. Compared to other foods, they may contain considerable amounts of salt. Health authorities advise to reduce sodium-intake to the general population and especially to certain risk groups of consumers. Besides, the most common consumer complaint for these foods addresses their salty taste.

Modern trends in manufacture are to lower the final salt levels to meet consumer demands, to produce less desiccated products.

To investigate the effect of two technological processes (freezing/thawing and salting) on the fish (*Salmonid*) meat quality, Magnetic Resonance Imaging (MRI) and Magnetic Resonance Spectroscopy (MRS) were used. Authentication of fresh fish is of great importance to the consumer, the trading of frozen-thawed products as fresh being a frequent fraudulent practice. In previous studies, MRI protocol differentiates unfrozen from frozen-thawed fish, by determining the T_2 relaxation time and the diffusion coefficient of water [1–2]. The diffusion coefficient perpendicular ($D_\perp$) to the muscle fibre orientation axis allows an easy distinction between fresh and frozen trout. In comparison with fresh trout, the value of $D_\perp$ increases by 25% with freezing. It can be explained by the formation of gaps between fibres during frozen storage.

The salting process can be analyzed by NMR of proton to determine the density and mobility of water by measuring the relaxation times and diffusion coefficients and also by ^{23}Na and ^{35}Cl NMR. Thus, NMR offers a unique opportunity to access non-invasively the distribution and the state of Na^+ and Cl^- ions in tissues [3–4,5]. Both these NMR approaches allow to correlate the fluxes of water and ions in fish meat during salting [6], and also to determine the effect of raw fish (fat content, freshness . . .) on the salt distribution.

Two studies were presented in this chapter. The first describes how single quantum (SQ) and multiple quantum filter (MQF) can be used to determine the interactions of Na^+ and Cl^- ions with meat structure according to the technological process. The second study deals with the effect of size of fish on salt distribution.

Study of Salt Interaction in Smoked Salmon by SQ and DQF MRS

Multiple quantum filter NMR spectroscopy is particularly well suited to the study of ordered biological tissues. An MQ filter deletes the NMR signal belonging to isotropically reorienting ions, leaving only the signal from ions exhibiting biexponential decay (bound or entrapped ions). To characterize the dynamics of these two quadrupolar nuclei ($I = 3/2$), SQ and double quantum filter (DQF) acquisitions were used on smoked salmon.

Experimental

Smoked salmon fillets were obtained from IFREMER. Two different salting procedures were used: dry salt and brine injection. For each process, salting was designed to obtain three expected salt content of 2, 3 and 4% (w/w). A cylinder of smoked salmon (10 mm in diameter) was cut from the fillet and inserted into the NMR tube. For each salting process and salt content, NMR experiments were repeated on the series of five fillets, which results in a total of 30 samples.

NMR experiments were performed at 106 MHz (^{23}Na) and 39 MHz (^{35}Cl) on a Bruker DRX 400 (9.4 T). A 10 mm ^{23}Na/^{35}Cl double tune NMR probe was devised for this investigation. Samples were maintained in the spectrometer at 4 °C. For the overall NMR acquisitions, recycle times of 200 and 100 ms were used for ^{23}Na and ^{35}Cl nuclei, respectively. Aqueous solutions of $Na_7Dy(PPP)_2$ and $DyCl_3$ were prepared and used as external references

Graham A. Webb (ed.), Modern Magnetic Resonance, 967–971.
© 2008 *Springer.*

(5 mm NMR tube placed inside the 10 mm tube containing the sample studied) for sodium and chloride ion quantification, respectively. The $Dy(PPP)_2^{7-}$ and Dy^{3-} ions induced an upfield shift of Na^+ ($\Delta Na = 30$ ppm) and a downfield shift of Cl^- ($\Delta Cl = -55$ ppm) [7]. To characterize sodium chloride and water dynamics, ^{23}Na and ^{35}Cl longitudinal relaxation times, and ^1H transversal relaxation time were also measured with inversion recovery and CPMG sequences, respectively.

Results and Discussion

Figure 1 displays the linear relationship between the longitudinal relaxation time of sodium and chloride ions with the transverse relaxation time of water proton for the 30 samples studied. This indicates that dynamics of Na^+, Cl^- and water molecules are quite correlated. The injection process induced an increase in all relaxation times. The formation of small brine pockets in tissue structure associated with injection process could partly explain this increasing. This can be related to the difference in dry matter values obtained for the two processes: 32 and 27% for the dry salt and the injection, respectively.

To quantify the proportion of Na^+ and Cl^- bound ions, the DQF signals were quantified relative to the SQ signals, as previously described [8]. For the two salting processes, results are summarized in Figure 2. Statistically, there is no significant difference in bound fractions with salt content or process for each ion. Nevertheless, for the case of the injection process, there is a tendency for the bound ion contents to increase with salt concentration. Whatever the process considered, the proportion of bound ions is systematically greater for Na^+ than for Cl^-. Some hypothesis to explain this result can be differences in: ion endogenous concentration or/and ionic strength or/and ionic volume, which is more important for Cl^-.

From NMR parameters, salting processes were discriminated (Figure 3). The first axis in Figure 3 discriminates the process while the second axis the salt content.

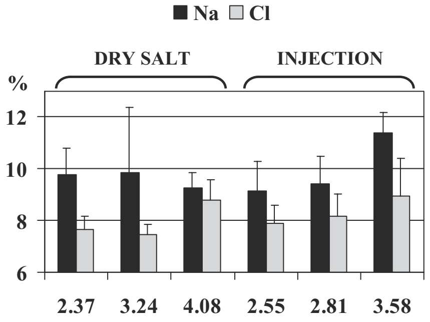

Fig. 2. Fractions of sodium and chloride bound ions for the two processes as a function of the percentage of salt. Mean values and standard deviation (n = 5).

MRI Study of Salt and Fat Distribution in Smoked Salmon

To investigate the effect of the fat content on the heterogeneity of salt distribution in smoked Atlantic salmon fillet, fish of two different sizes were dry-salted 5 days post mortem by the use of granulated (Ø 600 μm) mineral salt and thereafter smoked. The small fish, weight 1–2 kg, were salted in 1 h and 10 h and the large fish, weight 4–5 kg, were salted in 3 h and 13 h for the left and right hand fillets, respectively. Each fillet side was divided in two parts, the anterior section was cut from about 4 cm behind the front edge of the fillets and the posterior section was cut from about 4 cm in front of the edge of the tail. The length of the sections was 6 cm and the dorsal side was trimmed to a section width of 10 cm. For each of the two sections, MR-images were recorded in slices of 2 mm thickness at four positions, three in the ventral side of the lateral line and one in the dorsal side. MRI experiments were repeated on series of four fish for each of the two sizes, i.e. total 128 samples.

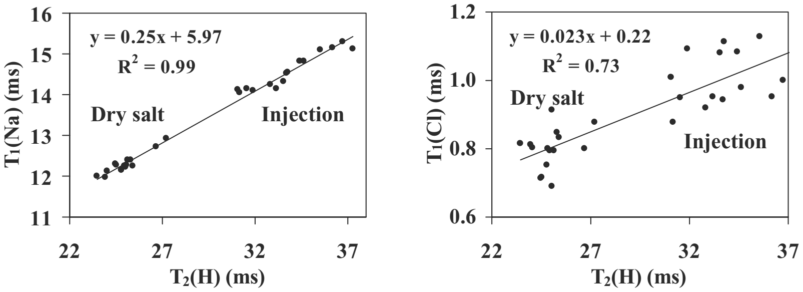

Fig. 1. Relationships between $T_1(Na)$, $T_1(Cl)$, and $T_2(H)$ for the 30 salmon samples studied.

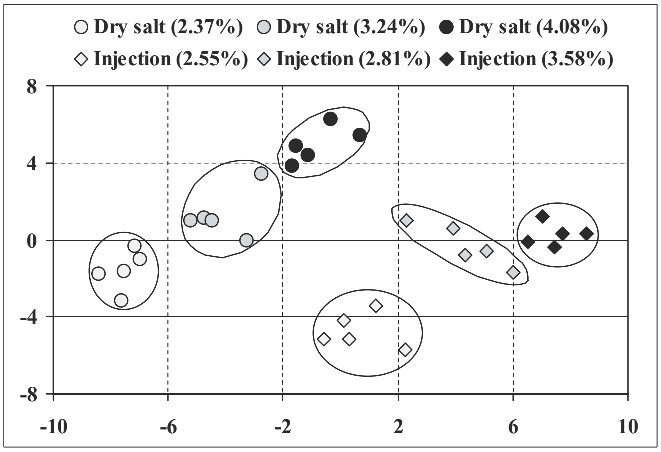

Fig. 3. Discrimination between salting process by Factorial Analysis.

MRI Experiments and Data Analyses

MRI experiments were performed at 200 MHz (^{1}H) and 53 MHz (^{23}Na) on a Biospec 47/40 Bruker (4.7 T). An 110 mm ^{1}H/^{23}Na double tune NMR probe was designed for this study. Water and fat images were recorded using multiple slice chemical shift selective inversion recovery [9]. T_2 water images with fat suppression were obtained from multi-mono-echo acquisition (7 echo time ranging from 15 to 120 ms). A gradient echo sequence was used for sodium imaging ($T_E = 3.2$ ms, $T_R = 100$ ms, 256 scans).

In order to identify the effect of the design variables, fish size, salting time, part and acquisition position a partial least-squares (PLS) regression model [10–11] was calculated using the design variables as X-values and the NMR parameters described above as Y-values. The size (small and large); the salting time (short and long); and the part (posterior and anterior) were valued 0 and 1, respectively, whereas, the acquisition position (Slice) were valued 0–3, from the ventral to the dorsal side of the fillet section. The multivariate models were validated by full cross-validation. All calculations were performed in The Unscrambler® Ver. 8.05 (Camo, Norway).

Results and Discussion

Examples of fat suppressed, water suppressed, and sodium magnetic resonance images of one of the sample sets are shown in Figure 4. The gross structural organisation of the fish muscle, i.e. muscle segments separated

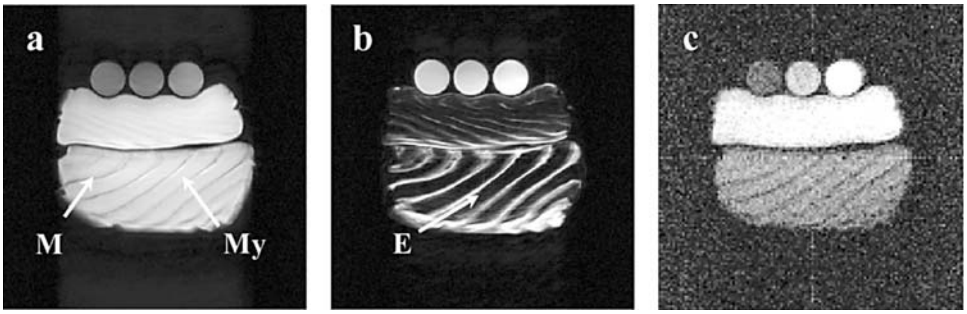

Fig. 4. (a) Fat-suppressed, (b) Water suppressed and (c) ^{23}Na MR-images of salted-smoked Atlantic salmon (weigth-4–5 kg). Top; lateral section (skin side down) of posterior part salted 13 h and Bottom; lateral section of anterior part (skin side down) salted 3 h. M; muscle segments (myotomes), My; Myocommata, E; endomysial sheath. Reference tubes (on the top) contain NaCl-solutions of 1, 2.5, and 5% from the left to the right hand side, respectively.

by myocommata is clearly visible in all the images. The distribution of fat is visualized as light areas in Figure 4b. Fat are within the connective tissue in the myocommata, but also thin light treads representing fat in the membrane and/or in the endomysial sheaths surrounding the muscle cells can be distinguished in the anterior part.

This part contains more fat than the posterior part and there is more fat in the skin side than in the belly side of the fillet. As expected, the fillet being salted for the longest period has the highest salt concentration (Figure 4c). The ^{23}Na-image also shows that the sodium distribution in the fillet is inhomogeneous. In the anterior part with the low salt content, the myocommata can be distinguished indicating that the salt concentration is lower in the connective tissue than in the myotomes. Moreover, the salt concentration is lower in the skin side of the fillet than in the belly side.

Figure 5 shows the correlation plot for Factor 1 vs. Factor 2 from a PLS regression of design parameters on MRI parameters. The inner and outer circles indicate 50 and 100% explained variance in the model, respectively. The first factor explains 26% of the total variance of the design variables (X), which models 32% of the variance in the measured NMR parameters (Y). Factor 2 explains 25% of the variance in the design variables modeling 6% of the Y variance. The X loadings show that salting time, fish part and fish size govern most the variation both in the first and second factor whereas, acquisition position (slice) has almost no effect. The Y loadings reveal that high salt content in the smoked salmon was positively correlated both to long salting time and fish part and negatively correlated to the fish size. The posterior part had higher salt content than the anterior part and small fish were saltier than large fish. Salting time and part, which explained more than 50% of the variance in the model, used, had the largest effects. Similar results are previously reported based on ^{23}Na and ^{35}Cl SQ of smoked salmon [12]. The different salt content in the anterior and posterior part of the fish was explained by a greater penetration of salt in the thin part than in the thick part. Due to the simultaneous acquisition of ^{1}H and ^{23}Na imaging, which allows us to directly compare fat and Na content in each sample, our results reveal that the fat content may also has an effect on the obtained salt content (Figure 4). In Figure 5 it looks like that the fat content is negatively correlated to the Na content. However, the fat content is both related to the fish size and the part, but since only 6% of Y is explained by Factor 2 we may assume that the fat content is almost independent of the fish size. Thus we may conclude that there is not only an effect of fish part and size (fillet thickness) on the salt content, but that the fat content of the fish has an effect on the obtained salt content as well. The effect of the higher fat content may be that it hinders the salt diffusion through reducing the water mobility. In this experiment the variation in the T_2 values were in general small and no clear conclusion should be drawn with regard to this parameter. However, the correlation plot of Factor 1 vs. Factor 3 (not shown) revealed that the T_2 and fat content was opposite correlated along Factor 3, but the explained variation of this factor was small. T_2 was also negatively correlated to the sodium content.

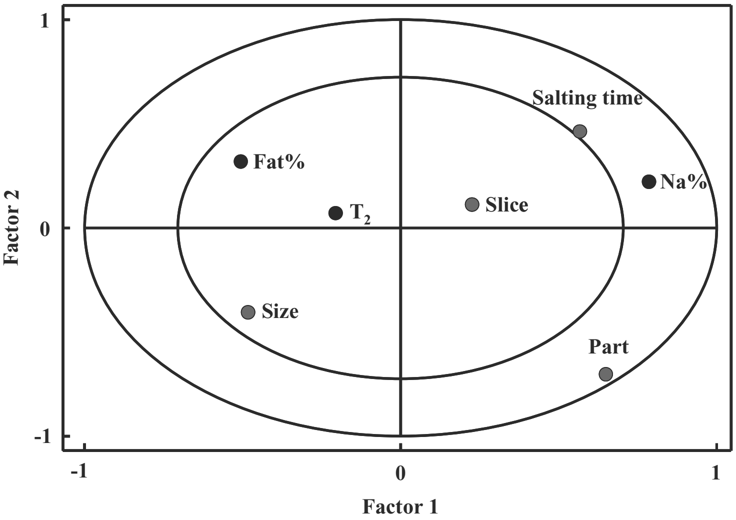

Fig. 5. Factor 2 versus factor 1 correlation X- and Y-loadings from a PLS regression of design variables on MRI parameters. The X-loadings (grey) are labelled according to fish size (large = 1, small = 0), Salting time (short = 0, long = 1), Part (posterior = 0, anterior = 1) and Slice (acquisition position) valued 0–3, from the ventral to the dorsal side of the fillet section. The Y-loadings (dark) are labelled Fat%, Na% and T_2 for the normalised mean values recorded from the images.

Conclusion

The different ^{1}H, ^{23}Na, and ^{35}Cl MRS or/and MRI protocols described here emphasize the wealth of information that can be accessed for the characterization of salting process and their discrimination.

References

1. Foucat L, Taylor RG, Labas R, Renou JP. American Laboratory 2001;33:38.
2. Nott KP, Evans SD, Hall LD. Magn. Res. Imaging 1999;17: 445.
3. Navon G, Shinar H, Eliav U, Seo Y. NMR Biomed. 2001;14: 112.
4. Belton PS, Packer KJ, Southon TE. J. Sci. Food Agric. 1987;41:267.
5. Nagata T, Chuda Y, Yan X, Suzuki M, Kawasaki K. J. Sci. Food Agric. 2000;80:1151.
6. Erikson U, Veliyulin E, Singstad TE, Aursand M. J. Food Sci. 2004;69:107.
7. Chu SC, Pike MM, Fossel ET, Smith TW, Balschi JA, Springer S Jr. J. Magn. Res. 1984;56:33.
8. Payne GS, Seymour A-ML, Styles P, Radda K. NMR Biomed. 1990;3:139.
9. Laurent W, Bonny JM, Renou JP. J. Magn. Reson. Imaging 2000;12:488.
10. Martens H, Næs T. Multivariate Calibration, Wiley: Chichester,1989.
11. Martens H, Martens M. Multivariate Analyses of Quality. An Introduction. Wiley: Chichester, 2001.
12. Foucat L, Donnat JP, Renou JP. Magnetic resonance in food science. In PS Belton, AM Gil, GA Webb, D Rutledge (Ed). Cambridge: The Royal Society of Chemistry, 2002, p. 180.

Author Index

Akutsu, H., 735
Albert, A., 335
Ando, I., 37
Andronesi, O.C., 527
Antzutkin, O.N., 19
Arndt, K.-F., 187
Asakura, T., 37, 101
Asano, A., 631
Auger, M., 271
Aursand, I.G., 901
Aursand, M., 929, 937

Bain, A.D., 421
Baldus, M., 527
Bar, A.S., 557
Bell, J.C., 769
Bentum, van, P.J.M., 353
Berger, S., 135
Bhakoo, K., 879
Blümich, B., 373
Borge, A., 955
Brand, T., 135
Brown, M.F., 249
Buhai, B., 157
Burk, W., 893

Cabrita, E.J., 135
Callaghan, P.T., 383
Casanova, F., 373
Chapon, C., 879
Chauton, M.S., 943, 949
Chekmenev, E., 279
Chen, Q., 545
Choy, M., 801
Chung, Y.-L., 823
Cohen Addad, J.-P., 541
Cross, T.A., 279

Demura, M., 497
Deng, F., 205
Du, Z., 665
Dvinskikh, S.V., 117
Dybowski, C., 389

Erikson, U., 901, 955
Evanics, F., 475

Facelli, J.C., 53
Falch, E., 929
Falcigno, L., 915
Fernández, C., 487
Foucat, L., 963
Freeman, R., 347
Fujiwara, T., 735

Fukui, H., 79
Furó, I., 117

Gehman, J.D., 305
Gerig, J.T., 413
Gerstein, B.C., 363
Giudicianni, I., 915
Gribbestad, I.S., 937, 955
Griffiths, J.R., 829
Groot, de, H.J.M., 327
Gullion, T., 713

Hanaoka, S., 743
Heise, H., 527
Herlihy, A.H., 759
Hidalgo, F.J., 921
Hinton, J.F., 285
Hiraoki, T., 621
Hong, M., 727
Horii, F., 607
Hu, J., 279
Huster, D., 87

Ikeda, R., 431
Ikura, M., 503
Inoue, Y., 551
Inubushi, T., 173
Ireland, M.D., 855
Ishii, Y., 467

Jackson, J., 879
James, T.L., 665
Jensen, K.N., 911
Jones, J.R., 395
Jones, W., 879
Jǿrgensen, B.M., 911

Kaij, H., 563
Kainosho, M., 215
Kamihira, M., 11
Karadakov, P.B., 53
Kato, K., 223
Kawai, G., 671
Kentgens, A.P.M., 353
Kim, S., 123
Kimmich, R., 157
Kimura, H., 363
Kitayama, T., 399
Knörgen, M., 187
Kossel, E., 157
Krane, J., 949
Kumashiro, K.K., 93
Kuo, Y.-T., 759
Kupče, E., 347

Kuroki, S., 31
Kurosu, H., 42

Lipsitz, R.S., 657
Lope-Piedrafita, S., 249
Lorigan, G.A., 313
Lu, S.-Y., 395
Lythgoe, M.F., 787, 801

Mal, T.K., 503
Malmendal, A., 679
Martinez, G.V., 249
Martinez, I., 937
Matsukawa, S., 129
McGarvey, B.R., 439
Middleton, D.A., 319
Mirau, P.A., 575
Miyoshi, T., 615
Morikawa, S., 173

Nagadoi, A., 743
Nagao, S., 531
Naito, A., 11, 241, 719
Nakazawa, Y., 101
Neubauer, S., 835
Nevzorov, A.A., 517
Nielsen, N.Chr., 679
Nishimura, K., 241, 719
Nishimura, Y., 743

Ofstad, R., 963
Okada, M., 299
Okhi, S.-Y., 215
Opella, S.J., 517

Paolillo, L., 915
Petrache, H.I., 249
Price, W.S., 109
Prosser, R.S., 475

Quellet, M., 271

Rahimi, R., 647
Ramamoorthy, A., 703
Ratcliffe, C.I., 147
Renou, J.-P., 963
Richter, S., 187
Ripmeester, J.A., 147

Sacchi, R., 915
Saitô, H., 11, 291
Saito, K., 163
Sanders, C.R., 233
Sato, K., 647
Savarese, M., 915
Schlick, S., 179
Schmidt, T., 187
Schneider, J.E., 835
Separovic, F., 305
Shiomi, D., 647
Shoji, A., 591
Singh, G., 557
Singstad, T., 893, 955
Skjetne, T., 893
So, P.-W., 769
Sternberg, U., 71
Stórseth, T.R., 943, 949
Stubbs, M., 823
Suzuki, A., 531

Takegoshi, K., 689
Takui, T., 647
Tekely, P., 197
Thomas, D.L., 787, 801
Thornston, J.S., 787, 801
Tjandra, N., 657
Tonelli, A.E., 567
Toraya, S., 241
Tuzi, S., 299

Ulrich, A.S., 71, 261
Ulyanov, N.B., 665
Ute, K., 399

Veliyulin, E., 893, 901, 955
Vosegaard, T., 679

Weerd, van der, L., 787, 801
White, J.L., 637
Whittaker, A.K., 583
Wickramasinghe, N.P., 467
Wider, G., 487
Williams, S.C.R., 855
Williamson, M.P., 409
Witter, R., 71
Wrackmeyer, B., 455, 459, 461
Wu, G., 695

Yagisawa, H., 299
Yamaguchi, Y., 223
Yamamoto, K., 703
Yamamoto, Y., 531
Yamane, Y., 123
Yamanobe, T., 42
Yang, J., 205
Ye, C., 205
Yeagle, P.L., 335
Yoshie, N., 551

Zamora, R., 921
Zax, D.B., 445
Zernia, G., 87

Subject Index

A

α-amino-acid crystals, 602
α-helices, 335
α-proton chemical shifts, 591
β-adrenergic receptor, 339
γ-Gauche-effect, 568, 569
φ angle techniques, 729
ψ angle techniques, 730
1D CRAMPS, 364, 369
1D MAS
  amorphous polymers dynamics, 609
1D-MAS exchange NMR
  crystalline polymers, 615
2,2,2-trifluoroethanol. *See* TFE
2D $[^{15}N,^{1}H]$ TROSY, 491
2D^{17}O MQMAS NMR
  organic solids, 695
2D ^{1}H NMR
  calmodulin investigation, 503
2D ^{1}H–^{13}C HETCOR NMR
  silk fibroins, 597
2D CRAMPS, 367, 370
2D DOQSY, 563
2D exchange NMR
  amorphous polymers dynamics, 609
  polymer blends, 631
2D experiments
  atactic polymers conformations study, 563
2D HETCOR, 367, 370
2D HMQC, 563
2D NMR
  organoboron chemistry and, 455
3D protein structure determination, 529
3D structure determination
  RNA and DNA, 674
4-chlorobenzoic acid, NQR high sensitivity in, 431
ab initio calculation
  bond polarization theory and, 71
  chemical shielding tensors for large molecules, 66
  NMR shielding constants, 67
ab initio methods, 58
ab initio program packages, 63
absorbed xenon gas, 129Xe NMR, 639
acceleration component, 158
acceleration component mapping sequences, 159
acceleration mapping, 157
ACES package, 66
AD. *See* Alzheimer's disease
adipose tissue
  MRI, 775
  MRS, 776
adsorption, gas. *See* gas adsorption
AFA-PLB monomer, 316
  MRS study of, 312
AFM
  alzheimer's Aβ amyloid fibrils, polymorphism, 21
aggregation, NMR diffusometry and, 109
algorithms for testing fish products quality
  multi sample, 912
  single sample, 911
aligned samples, protein structure determination, 517
Alzheimer's Aβ amyloid fibrils, polymorphism, 19
Alzheimer's disease, 19, 810
AMBER package, 666
amide ^{1}H signals, 601
amide proton chemical shift, 599
  ^{15}N labeled PLAs, 599
amination, oxidation-reductive, 881
amino acid residues
  in solid state, 595
  in solution, 595
amino acids, 31
amorphous polymers dynamics, 609
  1D MAS, 615
  2D exchange spectra, 641
  chemical shift anisotropy, 601
  lineshape analyses, 609
  spin relaxation aspects, 607
amyloid fibril
  alzheimer's Aβ, 20
  human calcitonin formation kinetics and,11
analytical aspects
  protein structure determination, 517
  solid-state NMR, 389
anesthesia
  brain disease, experimental models (MRI-based), 787
  MRI experiments, 856
  phMRI and, 858
anesthetics
  inhalation, 861
  injectable, 861
angiogenesis, tumor, 766
angiography, 790
angle measurements, secondary structure analysis (proteins), 736
  backbone torsion angle analysis of peptides, 739
  orientation relative to anisotropic nuclear magnetic interactions, 735
  orientation relative to macroscopic orientation axis, 737
  orientation relative to tensor for anisotropic molecular motion, 736
  torsion angle measurements, 738
angle-dependent interactions, secondary structure analysis of proteins and, 735
angular momentum EPR and, 439
animal fMRI experiments, 856
animal imaging studies, RM contrast optimization and, 764
animal models
  brain disease, experimental models (MRI-based), 787
  epilepsy, 806
  focal ischemia models, 802
  global ischemia models, 802
  MR contrast agents applications in, 764
    cardiovascular system, 766
    central nervous system, 765
    oncology, 766
animals
  cardiovascular magnetic resonance (in small animals), 835
  phMRI in, 855
anisotropic chemical shift perturbation, 279
anisotropic interactions
  angle measurements secondary structure analysis (proteins), 735
  anisotropic nuclear magnetic interactions, secondary structure analysis (proteins), 735
  torsion angle measurements secondary structure analysis (proteins), 738, 739
anisotropic nuclear magnetic interactions, protein's secondary structure analysis, 738
antenna systems
  photosynthetic, 327
antibodies
  use for cell tracking, 882

antimicrobial peptides, 265
  ^{2}H NMR spectroscopy, 272
  ^{31}P NMR spectroscopy, 273
  dynamics, 273
  effects on lipid membranes, 265
  gramicidin S, 265
  K3, 262
  membrane orientation and topology, 273
  membranes, 273
  PGLa, 265
  secondary structure, 276
antisymmetry parameters, 65
apoptosis, targeted SPIO in detecting, 766
arterial spin labeling (ASL), 795, 856
  continuous ASL (CASL), 795
  pulsed ASL (PASL), 795
assignment, 671
  NMR signal for DNA, 671
assignment method
  ^{13}C–^{1}H heteronuclear correlation NMR, 472
  1D, 472
  2D, 472
assignments
  NMR signal for RNA, 671
  polymer microstructure and, 567
association constants, binding, screening, and determination of, 140
atactic poly(acrylonitrile), 563
atactic polymers
  aPAN, 563
  conformations in, 563
aPAN ATCUN motif, 511
atlantic Salmon (*Salmo salar*)
  anatomical defects, 957
  freezing of, 957, 960
  omega-3 fatty acid content of intact muscle of farmed, 937
atlantic Salmon (*Salmo salar*), low-field NMR studies
  atlantic salmon muscle after heating, LF NMR water analysis, 904, 905, 907
  atlantic salmon white muscle, 904, 907
  chemical fat analysis, 903
  diffusion weighted transversal relaxation measurements, 904, 907
  fat analysis (LF NMR MOUSE), 904, 905
  fat and water analysis, 903, 905
  fish and sample preparation, 903, 904
  materials and methods, 902
  NMR instrumentation, 902
atlantic salmon fillets. *See also* cod fillets spatial distribution of fat and water in, 956, 957
atomic charges, BPT calculation of, 72
atomic force microscopy. *See* AFM
autoinhibitory domain, 503
average Hamiltonian theory (AHT), 679
average Hamiltonians in spin space, 359
averaging
  coherent averaging, 363

B

Bacillus brevis, 265
backbone torsion angle
  analysis of peptides, 739
  J coupling dependence and, 736
bacterially synthesized biodegradable copolyesters, 551
bacteriorhodopsin, 336–338
  membrane protein strucutre, 336
band 3 membrane protein, 339
band theory, NMR chemical shifts and, 43
BB-SEMA experiment, 704
behavioral modeling, 866
bicelle roots, 233
  2000–2005, 235
  early 1990s, 234
  late 1990s, 235
bicelles, 233, 243
  as model membranes, 236
  NMR development and application, 233
bilayer systems
  magainin, 6
  magnetically oriented, 241, 243
  oriented, 241
binding activities, DNA. *See* DNA-binding activities (hTRF1 and hTRF2 with hTRF2 mutants)
binding proteins
  membrane-binding, 299
biodegradable copolyesters, 551
  cocrystallization, 551
  phase segregation in, 551
biofluids, metabolic profiling of, 779
biological channels, ion-transporting, 286
biological macromolecules in solution, large, 487
biological NMR, 233
biological solids
  structural studies, 703
biomedical NMR spectroscopy and imaging, 173
biomembranes
  oriented, 261
  structure analysis, 261
biomolecule–water interactions, 418
bis-cyano 3,7-DF, 534
blends, biodegradable copolyesters, 551
blood oxygen level dependent. *See* BOLD imaging
blood–brain barrier (BBB), 764
BOLD imaging, 789, 856, 858, 860. *See also* functional MRI phMRI
  behavioral modeling and, 866
  MRI origins of, 858
  pharmacokinetic modeling, 864
  phMRI, 857
  physiological origins of, 857
BOLD response
  phMRI, 857
bolus tracking, 794
Bombyx mori, 101. *See also Samia cynthia ricini*
Bombyx mori structure
  after spinning, 104
  before spinning, 101
Bombyx mori-I, 597
bond polarization theory
  atomic charges, 72
  for checmical shifts, 71
  pseudo-forces, 73
BOOMERANG configuration, 360
Born–Oppenheimer approximation, 56
bovine rhodopsin, 339
  membrane protein strucutre, 340
BPT. *See* bond polarization theory
bradykinin B2 receptor, 338
brain. *See also* infective brain lesions
  disease, 779
  in vivo MRI, 767
  MRS, 769
  murine models of disease, 769
brain disease, experimental models (MRI-based), 787
  Alzheimer’s disease, 810
  anesthesia, 802
  animal models selection, 802
  cerebral ischemia, 803
  CNS inflammation, 810
  diffusion during ischemia, 803
  diffusion imaging in epilepsy, 808
  epilepsy, 807
  epilepsy, MRI studies of, 808
  focal ischemia models, 802
  functional imaging after ischemia, 804
  functional imaging in, 809
  global ischemia models, 802
  Huntington’s disease, 810
  multiple sclerosis, 811
  neurodegenerative disorders, 809
  Parkinson’s disease, 810
  penumbra, 804
  perfusion during ischemia, 803
  practical issues, 801
  probes, 801
  relaxation contrast during ischemia, 804
  signal-to-noise, 801
  spreading depression, 806
  time course studies in epilepsy, 808
  tissue signature modeling, 805
  traumatic brain injury (TBI), 812

- brain disease, MRI contrast mechanism for, 793
  - angiography, 770
  - arterial spin labeling, 801
  - BOLD imaging, 795
  - bolus tracking, 800
  - diffusion-weighted imaging, 798
  - image contrast
    - and intrinsic MR parameters, 787
    - enhancement, 790
  - magnetization transfer imaging, 809
  - mapping changes in CBV, 791
  - MR sensitivity to dynamic physiological processes, 789
  - perfusion imaging, 794
  - signal manipulation aspects, 792
  - smart contrast agents, 792
  - T1-weighted dynamic contrast enhanced MRI, 790
  - weighted imaging
    - T1, 787
    - T1ρ, 790
    - T2*, 788
    - T2, 788
- brain perfusion images, gadolinium chelates and SPIO in, 765
- b-type haemoproteins, 532. *See also* proteins
  - bis-cyano 3,7-DF, 534
  - carbonmonoxy Mb, 534
  - deoxy Mb, 536
  - haem disorder, 537
  - MbO$_2$vs. MbCO, 537
  - met-aquo Mb, 536
  - met-azido Mb, 536
  - met-cyano Mb, 535

C

- [^{13}C,^{1}H] correlation experiments, 491
- ^{13}C
  - elastin study and, 93
  - positive labeling, 215
- ^{13}C chemical shieldings, 51
- ^{13}C chemical shifts, 76
  - conformation-dependent, 291
- ^{13}C CPMAS NMR
  - polymer networks structure, 583, 584
- ^{13}C NMR
  - chemical shift, 31
  - fish oils, 921
  - polymer microstructure study and, 567
  - polymer networks structure, 583
  - PP stereosequences from, 570
  - signals, site-directed assignment of, 272
  - site-directed, 294
  - solid polymers, 570
  - spinning speed dependence, 467
- ^{13}C shielding, 45
- ^{13}CT$_1$ relaxation behavior of crystalline (ethylene copolymers) region, biexponential, 546
- ^{13}C VFMAS spectra
  - ^{1}H decoupling dependence, 470
  - SSNMR, 469
- ^{13}C–^{13}C shift-correlation, 690
- ^{3}C NMR
  - marine microalgae, 943
- ^{35}Cl NQR measurements, 431
- Ca2+ sensors, 503. *See also* calmodulin, NMR investigation of
- calcitonin formation kinetics, human, 7
- calcium-binding lysozyme, 497
  - ^{1}H chemical shift calculation, 498
  - H/D exchange, 499
  - NMR study of, 497
  - protein folding mechanism, 497
  - structural intermediate in, 498, 499
- calcium-calmodulin-peptide complexes, 508
- calibrated polymeric networks, 543
- calibration
  - fish feed compositional analysis, 893
- calmodulin
  - calcium-calmodulin-peptide complexes, 508
  - PCS and, 660
- calmodulin, NMR investigation of, 503
  - 2D1H NMR, 504
  - biological functions, 503
  - CAM kinase family, 503
  - early studies, 504
  - metal and CaM interactions, 505
  - multidimensional and heteronuclear, 505
  - solution structure, 505
- CaM kinase family, 504
- CaM kinase kinase, 504
- CaM. *See* calmodulin
- Cambridge analytic derivatives package (CADPAC), 67
- cancer, MRS application in, 823
  - choline kinase, 828
  - conventional cytotoxic drugs, 830
  - cyclin-dependent kinase inhibitor, 830
  - glycolytic metabolism in tumors, 826
  - HSP90 inhibitor, 830
  - hypoxia inducible factor-1, 827
  - lipid metabolism in tumors, 827
  - oncogene function, 827
  - pharmacodynamic markers, 829
  - pharmacokinetic markers, 828
  - phospholipid metabolism in tumors, 826
  - therapy, 828
  - tumor
    - hypoxia, 823
    - pH, 826
- canine milk lysozyme, 497
- carbohydrates. *See also* proteins
  - fish feed, 893
  - -protein interactions, 223
- carbonmonoxy Mb, 534
- carbonyl-carbon, 31. *See also* hydrogen-bond length
  - in amino acids, 31
- cardiac function, 835
- cardiovascular magnetic resonance (in small animals), 835
  - ^{1}H-MRS, 846
  - ^{23}Na-MRS, 847
  - ^{31}P-MRS, 847
  - future perspectives, 849
  - global cardiac function, 839
  - methods and requirements, 835
  - MRI, 835
  - MRS, 835
  - multinuclear MRS, 845
  - myocardial tissue contractility, 842
  - vascular MRI, 848
- cardiovascular system (MR contrast agents applications)
  - gadolinium chelates
    - and iron oxide in CEMRA, 766
    - for heart imaging, 766
  - manganese-based contrast in determining viable myocardium after infarction, 766
- cartesian coordinate space, nucleic acid structures refinement and, 665
- catalysts
  - heterogeneous, 205
- cation binding, 279
- CCPPA. *See* coupled-cluster polarization propagator
- cell tracking, 880
- cell tracking, MRI application of, 879
  - antibodies use, 882
  - cell-based tumor therapy, 888
  - conjugating
    - chemistry, 883
    - directly to USPIO, 883
  - contrast agent
    - attaching to delivery ligand, 883
    - using specific targeting, 881
    - with transfection agents, 881
  - cytotoxicity and metabolism, 883
  - good contrast agent properties, 880
  - intracellular MRI contrast agents, 879
  - iron oxide contrast agents, 881
  - linker introduction, 883
  - membrane permeating peptides and, 882
  - MRI contrast agent for, 880
  - oxidation-reductive amination, 883
  - paramagnetic agents, 880
  - stem cells
    - in CNS, 886
    - in heart, 885
  - superparamagnetic agents, 880

cell-based tumor therapy, 888. *See also* tumors
cellular tracking, NMR imaging, 176
cellulose
  polymorphs structure, 75
CEMRA
  gadolinium chelates and iron oxide in, 766
central nervous system
  stem cells tracking, 886
central nervous system (MR contrast agents applications)
  gadolinium chelates
    and SPIO in brain perfusion images, 765
    for focal lesion detection, 765
  manganese chloride for nerve tracking and demonstrating neuronal activation, 765
cerebral blood vessels, drug effects on, 869
cerebral ischemia, 803
  diffusion during ischemia, 803
  perfusion during ischemia, 803
chain diffusion, polymer structure and, 542
chain dynamics, crystalline polymers, 617
chemical analysis
  fish feed compositional analysis, 900
chemical exchange, 421
  experimental precautions and, 424
  fast exchange, 426
  intermediate exchange, 424
  kinetics, 423
  slow exchange, 425
  theory, 423
  types of, 421
chemical shielding tensors, large molecules, 67
chemical shieldings, 54
  ^{13}C, 56
  ^{15}N, 57, 58
  ^{1}H, 56
  modeling of, 54
  NMR chemical shifts and, 50
chemical shift
  amide proton chemical shift, 599
  anisotropic perturbation, 279
  bond polarization theory and, 71
  calcium-binding lysozyme, 497
  conformation-dependent (^{13}C), 291
  crystal structure refinement and, 71
  isotropic (^{13}C), 71
  NMR
    ^{13}C, 31, 75
    ^{15}N, 32
    ^{17}O, 33
    ^{1}H, 32
    ^{2}H, 34
    band theory based, 43
    hydrogen-bonded structure and, 231
    solid polymers, 43
  oriented bilayer systems, 241
  α-proton chemical shifts, 591
chemical shift anisotropy(CSA), 306
  amorphous polymers dynamics, 611
  polymer conformations and, 563
  polymer microstructure and, 57
  protein structure determination, 57
chemical shift interaction, oriented bilayer systems and, 244
chemical shift map
  amino acids, 37
  NMR, 37
chemical shift perturbation
  dioxygen in solution, paramagnetic effects of, 479
chemical shift pseudo-forces, 74
chemical shift selective (CHESS) MRI, 956
chemical shift tensors
  principal values of, 31
chemical shift, ^{1}H
  polypeptides, 595
chemical structure, polymer networks, 583
CHF. *See* coupled Hartree–Fock approximation
chloranilic acid with 1,4-diazine, 432, 435
Chlorobium tepidum, 330
chlorosomes and LH2, 330
choline kinase (ChoK), 828
CLEAR gels, 120
CLIO-TAT, 888
CML. *See* canine milk lysozyme
CMR. *See* cardiovascular magnetic resonance
CNS. *See* central nevous system
CNS inflammation, 810
  multiple sclerosis, 811
cocrystallization
  biodegradable copolyesters, 551
cod fillets, 960, 961. *See also* atlantic Salmon (*Salmo salar*); atlantic salmon fillets
  freezing of, 961, 964
  water and salt analysis, 960, 962
cod liver oil
  spin trapping of, 931
coffee. *See also* beverages
coherence selection, field gradients and, 132
coherent averaging, 363
coil design, optimized detection, 357
collagen
  mobility, 90
  molecular dynamics in, 91
collagen dynamics
  cross-polarization (CP) MAS study, 89
  mineralization and, 91
  NMR spectroscopic study of, 87
  static solid state NMR and, 87
combined rotation and multiple pulse spectroscopy. *See* CRAMPS
common carotid arteries (CCA), 802
comonomer content, ethylene copolymers structural relation to, 545
compositional analysis of fish feed, 893
conducting channels, ions in, 279
configuration aspects, nuclear shielding and, 45
conformation
  atactic polymers, 563
  cyclic polypeptides, 595
  deuterium-labeled polypeptides, 595
  dipolypeptides, 595
  disordered polymers, 563
  DNA, 671
  natural fibrous proteins, 597
  nucleosides, 673
  nucleotides, 671
  oligonucleotides, 674
  polymer microstructure, 567
  polypeptides, 591
  polypeptides (main chain), 569
  RNA, 659
  silk fibroins, 597
conformation aspects, nuclear shielding and, 45
conformation-dependent ^{13}C chemical shifts, 291
continuous ASL (CASL), 795
continuous gauge transformation, 54
continuous set of gauge transformations, 66
continuous transformation of the origin of the current density, 67
contrast agents. *See also* brain disease, MRI contrast mechanism for
  attaching to delivery ligand, 883
  blood pool, 791
  for cell tracking, 879
  intracellular MRI, 879
  iron oxide, 881
  MRI contrast mechanism for brain, 789
  smart, 792
  using specific targeting, 881
  with transfection agents, 881
contrast agents, MR, 764
  applications in animal models, 765
    cardiovascular system, 766
    central nervous system, 765
    oncology, 766
  non-specific vs. tissue-specific agents, 764
  T_1 vs. T_2, 764
contrast enhancement, MRI contrast mechanism for brain, 787

contrast mechanism, MRI
  for brain disease, 787
contrast optimization, MRI, 759
  agents classification and mechanism, 764
  animal imaging studies, 764
  CNR, 759
  field strength, 763
  hardware considerations, 764
  intrinsic, 761
  SNR, 759
  T$_1$ and T$_2$ contrast, 761
  temporal resolution, 759
contrast-to-noise ratio (CNR), 759
  MRI contrast optimization, 759
convection, 111
copolyesters, biodegradable, 551
copolymer structure
  biodegradable copolyesters, 551
copolymers. *See also* polymers
  ethylene vinyl acetate, 545
  methyl acrylate (A)/methyl methacrylate (B) copolymer, 558
  molecular weight dependence (SEC-NMR), 401
correlation
  experiments [^{13}C,^{1}H], 490
  functions, lipid membranes, 254
correlation techniques
  MAS tensor, 727
  static tensor, 727
cortical contusion injury (CCI), 812
COSMOS–NMR force field, 74, 75
COSY,
  experiments, 689
coupled Hartree–Fock approximation, 77
  triplet instability of, 82
coupled–cluster (CC)
  approach, 82
  polarization propagator, 83
  theory, 65
coupling
  dipolar recoupling, 319, 713
  J-coupling, 737
  quadrupolar, 308, 391
  residual dipolar coupling, 493, 587
  scalar, 493
coupling tensors, 250
CP MAS, 89, 291, 293
  for elastin study, 93
  host–guest chemistry and, 147
  ligands and membrane-embedded receptors interactions (NMR study), 319
  methods, 89
  polymer conformations study, 569
  polypeptides, 591
CP MAS NMR, 89
  ligands and membrane-embedded receptors interactions (NMR study), 319
  photosynthetic antennae and reaction centers, 327
CRAMPS, 363
  1D, 364, 369
  2D, 367, 370
  coherent averaging, 363
  experimental aspects, 367
  homonuclear decoupling and, 364
  MAS and, 366
  probe and receiver requirements, 367
  pulse impurities, 368
  resolution maximization, 368
  scaling
    factors determination, 369
    under pulse sequences, 366
  spectrometer requirements, 367
CRAMPS NMR
  cyclic polypeptides, 595
  deuterium-labeled polypeptides, 595
  natural fibrous proteins, 597
  polypeptides, 591
  silk fibrons study, 597
  α-amino-acid crystals, 602
CRAMPS spectra, 168
CRINEPT
  TROSY and, 494
CRINEPT. *See* cross-correlated relaxation-enhanced polarization transfer
CRIPT. *See* cross-correlated relaxation-induced polarizationtransfer
cross polarization
  high-sensitivity NMR probe systems and, 353
  MAS NMR. *See* CP MAS NMR
  polymer networks structure, 583
  sensitivity enhancement by, 469
  Si, 197
cross relaxation. *See also* relaxation rate, 410, 416
cross-correlated relaxation-enhanced polarization transfer, 494
cross-correlated relaxation-induced polarization transfer, 494
  TROSY and, 494
cross-linked ethoxylate acrylate (CLEAR), 124
cross-linked long chains (polymer structure), 542
crosslinked polyolefins, 583
crystal structure, 48
crystal structure refinement
  bond polarization theory, 71
  BPT pseudo-forces and, 74
  cellulose polymorphs, 75
  chemical shift pseudo-forces and, 73
  chemical shifts and, 71
  molecular force fields and, 73
  proton positions, 74
crystal transformation
  crystalline polymers, 616
crystalline polymers
  1D-MAS exchange NMR, 615
  crystal transformation, 616
  mechanical property and chain dynamics, 615
  molecular
    dynamics, 616
    motions of, 615
  solid-state MAS NMR, 615
crystalline structure
  ethylene copolymers, 545
CSGT. *See* continuous gauge transformation
CSGT. *See* continuous set of gauge transformations
CTOCD. *See* continuous transformation of the origin of the current density
cyanogen bromide method, 95
cyclic polypeptides
  cyclo(lalanyl-d-alanyl), 595
cyclin-dependent kinase inhibitor, 830
cyclo(lalanyl-d-alanyl), 595
cytotoxic drugs, 828
cytotoxicity, cell tracking and, 880

D

DALTON, 67
data analysis
  BOLD phMRI, 857
  phMRI, 855
data processing
  ^{17}O MQMAS NMR, 695
decoupled-magic angle spinning (DD-MAS), 291, 293
decoupling. *See also* residual dipolar couplings
  homonuclear, 364
delayed type hypersensitivity (DTH), 811
demagnetization
  zero field NMR and, 445
deMon-NMR code, 67
denatured proteins, unfolded, 661
density functional theory. *See* DFT
deoxy Mb, 534
dephasing, dipolar, 715, 719
deuterium
  NMR spectroscopy of, 249
deuterium NMR
  coupling tensors observation, 249
  lineshapes, 250
  membrane lipids study, 248
  molecular structures and motions, 250
  parameters related to average membrane properties, 251
  relaxation, 258
deuterium spin–lattice relaxation times, 254

deuterium-labeled polypeptides
  ^{1}H CRAMPS NMR, 595
  conformational study of, 595
DFT-GIAO, 67
DGEBA, 584
diacylglycerol kinase, 294
diagonalization method, filter, 347
diffusion. *See also* diffusometry, NMR
  chain diffusion, 542
  complex systems, 112
  hydrogels, 187
  in liquid crystals, 117
  in polymer gel systems, 123
  spin diffusion, 410
  water, 17
diffusion coefficient
  hydrogels, 187
  measurements, 129
diffusion during ischemia (animal model), 803. *See also* perfusion during ischemia (animal model)
diffusion imaging
  in epilepsy, 806
diffusion measurements
  gradient-based, 109
  internal standards for, 140
diffusion weighted transversal relaxation measurements
  atlantic Salmon (*Salmo salar*), 902, 905
diffusional behavior of linear molecules in channels, 16
diffusion-limited oxidation (DLO), 181
diffusion-weighted imaging, 792
dimyristoylphosphatidylcholine, 234
dimyristoylphosphatidylglycerol, 234
dioxygen in solution NMR
  paramagnetic effects of, 475
dioxygen in solution, paramagnetic effects of
  applications, 481
  chemical shift perturbations, 475
  family fold recognition and O_2 migration pathways, 481
  immersion depth, 475
  membrane protein topology, 477
  protein–protein interactions, 481
  spin–lattice relaxation, 475
dipolar (re)-coupling, 309
dipolar coupling
  multiple spin system, REDOR in, 719
dipolar decoupling, ^{1}H, 572
dipolar dephasing
  REDOR, 719
dipolar interaction, oriented bilayer systems and, 344
dipolar relaxation, 409
dipolar spinning sideband pattern, 601
dipolypeptides, cyclic, 591
DISCOVER package, 666
disordered polymers, conformations study of
  2D DOQSY, 563
  2D HMQC, 563
  atactic polymers, 563
  CP/MAS, 566
  MAS NMR, 566
  quantitative analysis, 563
  solid-state multiple-quantum NMR, 563
  zero-quantum expermients, 564
  ZQ-CSA-dephasing, 566
distance measurements
  host–guest chemistry and, 150
  proteins (secondary structure analysis), 735
distance methods, torsion angle determination and, 732
distortionless enhancement by polarization transfer (DEPT), 354
DMPC
  bilayer systems, 246
  mixtures, 234
DNA
  3D structure determination, 674
  conformations, 671
  imino proton signals, 671
  immobile proton signals, 671
  NMR signal for, 671
  phosphorus signals, 672
  residual dipolar couplings and, 659, 675
  signal assignment aspects, 671
  stable isotopic labeling, 672
  telomeric, 743
DNA-binding activities (hTRF1 and hTRF2 with hTRF2 mutants)
  bound to telomeric DNA, 743
  structural comparison between DNA complexes, 743
  telomeric DNA bound to hTRF2, 745
domain IV of enterovirus internal ribosome entry site, 666
dopamine receptor agonists for animal phMRI, 862
DOQSY, 727
  2D, 563
  experiments, 137
double quantum filter (DQF) MRS
  fish meat, 964
double-quantum NMR, polymer interfaces characterization and, 580
DPMAS, 95
drug discovery
  ligands and membrane-embedded receptors interactions (NMR study), 319
drug discovery and development, MRI applications to
  absence of signal changes, 872
  anesthesia effects, 860, 872
  anesthetics, 861
  behavioral modeling, 866
  BOLD response to drugs, 864
  changes in physiological measures, 869
  data analysis, 862, 865
  dopamine receptor agonists as and, 865
  drug effects on cerebral blood vessels, 865
  global effects and fluctuating baseline signal intensity, 863
  hemodynamic-based functional neuroimaging, 856
  image acquisition strategies for preclinical phMRI, 858
  image pre-processing, 862
  inhalation anesthetics, 861
  MRI origins of BOLD signal, 857
  pharmacokinetic modeling, 865
  phMRI, 859, 860
    future of, 873
    in awake animals, 862
    use of, 873
  physiological origins of BOLD signal, 857
  statistical analysis, 864
  surrogate markers of neuronal activity, 855
DWI. *See* diffusion-weighted imaging
DYANA package, 666
dynamic NMR (DNMR), 421
dynamic nuclear polarization (DNP), 355
dynamics
  amorphous polymers. *See* amorphous polymers dynamics
  polypeptides, 621

E

EDAM, 545
Eddy currents, gradient mismatch and, 112
effective Hamiltonian Theory (EHT), 681
elastin
  hydrophobic domain of, 97
  isotopically labeled, 96
  natural-abundance 13c populations, 93
  tropoelastin, 93
elastin and elastin peptides
  solid-state NMR study of, 93
elastomer profiles, 183
electric field gradient (EFG), 621
Electron Nuclear Double Resonance. *See* ENDOR
electron spin resonance. *See* ESR
electronic state
  solid polymers, 43
EmrE, 339
encephalopathy, 811

encoding
  Hadamard encoding, 347
  principles, NMR imaging and, 157
ENDOR. *See also under* quantum information processing
  based quantum computer, molecular, 648
  pulsed ENDOR, 651
  quantum information processing, 647
enrichment
  global isotopic, 350
  specific, 350
entanglements, quantum, 647
enterovirus internal ribosome entry site, 666
entropy, configurational (polymer blends), 637
EOM-CC method. *See* equation-of-motion coupled-cluster method
epilepsy, 807
  animal models, 807
  diffusion imaging, 808
  early MRI studies of, 808
  functional imaging in, 809
  generalized seizures, 807
  simple partial seizures, 807
  time course studies in, 808
EPR principles
  angular momentum, 439
  high ligand field d^5, 441
  higher order spin–spin terms, 443
  hyperfine interaction, 443
  NO molecule, 441
  nuclear quadrupole interaction, 443
  nuclear Zeeman interaction, 443
  organic free radicals, 440
  S = 1/2 systems, 440
  S > 1/2 systems, 443
  spin Hamiltonian, 440
  spin–orbit interaction, 439
  Zeeman interaction, 439
  zero field spin Hamiltonian, 444
EPSI method, 173
equation-of-motion coupled-cluster method, 83
Escherichia coli, 218
ESR
  lipid oxidation study (fish and fish products), 929
ESR spectroscopy
  fields gradients and, 179
ESRI
  1D (intensity profiling), 180
  2D, 181
  in polymer research, 179
  line shape profiling, 181
  spatially-resolved degradation, 181
  spectral-spatial, 181
ethylene copolymers
  biexponential 13C T1 relaxation behavior of crystalline region, 546
  crystalline structure, 545
  EDAM, 547
  EMA, 547
  polymorphism, 545
  structural relation to comonomer content, 545
ethylene vinyl acetate copolymers, 545
ethylene–methyl acrylate, 547
exchange spectra
  2D, 611
  amorphous polymers dynamics, 611
exchange, chemical. *See* chemical exchange
experimental allergic encephalopathy (EAE), 811
^{19}F NMR
  b-type haemoproteins study by, 532
  experimental aspects, 261
  labeling of peptides, 263
^{19}F NMR study of b-type haemoproteins
  bis-cyano 3,7-DF, 534
  carbonmonoxy Mb, 534
  deoxy Mb, 536
  haem disorder, 537
  labeling using reconstruction, 532
  MbO$_2$vs. MbCO, 537
  met-azido Mb, 536
  met-cyano Mb, 535
  vs. ^{1}HNMR, 533

F

FAIR. *See* flow-sensitive alternating inversion recovery
fast exchange, 426. *See also* chemical exchange
fast multidimensional NMR, 347
fat analysis
  atlantic Salmon (*Salmo salar*), 902, 904
  atlantic Salmon fillets, 960, 961
  fish feed, 886
  LF NMR MOUSE, 904, 905
fat distribution in smoked Salmon, 964
fatty acids
  composition
    fish oils, 915
    marine microalgae, 943
    oxidation, 915
  omega-3 fatty acid content of intact muscle of farmed atlantic Salmon, 937
fibril formation, human calcitonin and, 11
fibrillation kinetics, human calcitonin, 11
fibrous proteins
  collagen, 87
  elastin and elastin peptides, 93
  silk fibrons, 101
Fickian diffusion, 129
field gradient NMR
  for polymer systems with cavities, 123
  liquid crystals, 117
  NMR diffusometry, 109
field gradients
  and spatial information, 129
  coherence selection, 132
  diffusion coefficient measurements, 129
  ESR spectroscopy, 179
  NMR measurements and, 129
  pulsed field gradients (PFG), 129
field of view (FOV), 157
field-cycling NMR, 445
fillets
  atlantic salmon, 956, 957
  cod, 956, 957
filter diagonalization method, 347
filtered back projection, 189
finite gradient pulses, 110
finite perturbation theory, 82
fish and fish products
  lipid oxidation study, 929
fish and sample preparation
  atlantic Salmon (Salmo salar), low-field NMR studies, 911
fish feed, compositional analysis of
  by time domain NMR, 893
  calibration, 896
  chemical analysis, 896
  equipment requirements, 893
  fish feed samples, 894
  NMR measurements of
    fat and moisture, 894
    protein and carbohydrate, 894
fish meat
  data analyses, 965
  MRI, 965
  salt interaction in smoked Salmon, 963
fish oils and lipids
  extracted from fish muscles, NMR spectra of, 915
  n-3 PUFAs, 915
  oxidation products, 918
  proton NMR and lipolysis, 915, 917
fish oils, fatty acid composition and oxidation in, 921
  ^{13}C NMR, 921
  ^{1}H NMR spectra of, 921
  by high resolution NMR, 921
  lipid oxidation, 922
fish products quality, 911
  ^{1}H NMR applications, 909
  algorithms, 911
  multi-sample algorithms, 912
  number of components determination, 912
  single-sample algorithms, 911
  water
    distribution and mobility aspects, 911
    holding capacity, 913

fish, post-mortem studies of, 955
flow mapping, 157
flow-sensitive alternating inversion recovery, 856
fluid-mosaic model, 307
focal ischemia models (animal models), 802
focal lesion detection, gadolinium chelates for, 765
folding
  calcium-binding lysozyme, 499
Fourier imaging, 189
Fourier transformation, 132
FOV. *See* field of view
FPT. *See* finite perturbation theory
free radicals in marine lipids, 929
freezing. *See also* food process engineering
  atlantic Salmon, 957, 960
  cod fillets, 957, 960
  constant temparature conditions, 960
  dynamic freezing, 960
functional imaging
  epilepsy, 807
functional imaging after ischemia, 804
fusogenic peptide B18, 264

G

gadolinium agents in evaluating tumor angiogenesis, 770
gadolinium chelates
  and iron oxide in CEMRA, 770
  and SPIO in brain perfusion images, 769
  for focal lesion detection, 769
  for heart imaging, 770
gas chromatography, 102
gauge including atomic orbitals, 64
GAUSSIAN suite, 66
GE-HMQC method, 174
gel permeation chromatography (GPC), 399
gel systems, polymer
  diffusion in, 123
generalized seizures, 807. *See also* epilepsy
global cardiac function, 839
global ischemia models (animal models), 802
global isotopic enrichment, 350
glycobiology
  carbohydrate–protein interactions, 223
  glycoproteins, 223
  structural, 223
  sugar chains, 224, 226
glycolytic metabolism
  tumors, 826
glycoproteins
  stable isotope labeling, 223
G-protein coupled receptor, 337
gradient constancy, 111
gradient mismatch, Eddy currents and, 112
gradient-based diffusion measurements, 109. *See also* NMR diffusometry

H

^{1}H chemical shieldings, 56
^{1}H chemical shift
  calculation, calcium-binding lysozyme, 497
  polypeptides, 595
^{1}H CRAMPS
  polymer blends, 634
^{1}H CRAMPS NMR
  cyclic polypeptides, 595
  deuterium-labeled polypeptides, 595
  natural fibrous proteins, 597
  polypeptides, 591
  silk fibroins, 597
  slik fibrons study, 597
  α-amino-acid crystals, 602
^{1}H decoupling dependence
  ^{13}C VFMAS spectra, 471
^{1}H dipolar decoupling, 572
^{1}H MAS NMR
  omega-3 fatty acid content of intact muscle of farmed atlantic Salmon, 937
  spinning speed dependence and sensitivity, 467
^{1}H MRS, 845
^{1}H NMR
  and 19F NMR, 533
  calmodulin investigation, 503
  chemical shift, 31
  fish oils, 915, 921
  lipids, 915
  marine microalgae, 943
  measurements, 431
^{1}HSSNMR, 467
  microanalysis by, 464
^{2}H NMR
  chemical shift, 33
  of lipids, 309
  polymer blends, 642
  polypeptides dynamics, 621
  spectroscopy, 272
^{2}H, negative labeling and, 218
^{3}H NMR applications, 395, 397
  radiochemical facilities and radiation safety, 395
  tritiation procedures, 395
  tritium NMR spectroscopy, 396
H/D exchange
  calcium-binding lysozyme, 499
Hadamard encoding, 347, 349
haem disorder, 537
haemoproteins, b-type, 531
Halobacterium salinarium, 336
Hamiltonian, 63, 679
  in spin space, 363
  zero field spin, 444
Hartree–Fock (HF) appraoch, 63, 81
  calculations, 56
  coupled, 81
  triplet instability of, 82
hCT. *See* human calcitonin
heart
  in vivo MRI, 773
  MRS, 776
  murine models of disease, 776
  stem cells tracking, 885
heart imaging, gadolinium chelates for, 766
helices
  peptides from, 335
  transmembrane, 336
  α-helices, 335
hemodynamic-based functional neuroimaging, 856
  BOLD imaging, 856
  MRI measures of
    rCBF, 856
    rCBV, 856
HETCOR, 370, 517
  2D, 367, 370
  natural fibrous proteins, 597
HETCOR NMR
  silk fibroins, 597, 599
heterogeneous catalysts, 205
  catalytic reaction on surface, 207
  surface acidity, 205
heteronuclear correlation experiment, protein structure determination, 517
heteronuclear dipolar couplings, protein structure determination, 517
heteronuclear NMR
  of calmodulin, 505
  polymer interfaces characterization and, 575
heteronuclear NOE, 411
heteronuclear single quantum coherence
  calmodulin study, 505
HF-GIAO methods, 67, 68. *See also* L-GIAO methods
high ligand field d^{5}, 441
high magnetic field, MRI contranst optimization at, 759
high power decoupling (HPDEC), 147
higher order spin–spin terms, 443
high-resolution MAS NMR
  marine microalgae, 943, 949
high-resolution NMR
  fish oils, fatty acid composition and oxidation in, 921
  intact membrane protein study and, 291
  membrane protein structure, 331

high-resolution solid-state NMR
  ^{1}H and ^{13}C, 467
high-sensitivity NMR probe systems, 353
  cross-polarization and, 353
  dynamic nuclear polarization (DNP), 353
  magnetic resonance force microscopy, 358
  optimized detection coil design, 357
  polarization transfer and, 354
  thermodynamics, 354
hindered amine stabilizer (HAS), 179
HMQC
  2D, 563
HMQC coherence, 173
HOESY, 412
homologous proteins, calcium binding of, 497
homonuclear decoupling
  CRAMPS and, 364
homonuclear shift-correlation experiment, 689
  in solids, 689
host–guest chemistry
  CP MAS and, 148
  distance measurements, 150
  dynamics, 151
  inorganic hosts, 149
  metal-organic hosts, 148
  MRI and, 151
  organic, 148
  probing pore spaces, 150
  solid-state NMR in, 147
  solid-state spectrum, 147
  spin 1/2 nuclei, 148
  spin counting, 150
HPLC mapping
  3-D, 223
HR MAS NMR. *See* high-resolution MAS NMR
HR solid state NMR. *See* high-resolution solid-state NMR
HSP90 inhibitor, 830
HSQC, 348
H-transfer motions
  in multi-H-bonded systems, 431, 432
hTRF1, 739. *See also* DNA-binding activities (hTRF1 and hTRF2 with hTRF2 mutants)
hTRF2, 743
hTRF2 mutants, 743
HTS screening. *See* high-throughput screening
human calcitonin
  amyloid fibril and, 11
  conformational changes of, 11
  fibril formation, 16
  fibrillation kinetics, 12
  formation of, 11
human cannabinoid receptor, 338
human cholecystokinin-2 receptor, 338
human erythrocyte glycophorin, 336
human red cell anion transporter, 339
Huntington's disease, 810
hydrodynamic flow, 157
hydrogels
  water diffusion inside, 191
hydrogels, NMR imaging
  hydrogels, 187
  non-homogeneous networks, 191
  swelling process, 187
  scalar couplings across, 493
hydrogen-bonded silanols, 197
hydrogen-bonded structure
  ^{13}C chemical shift and, 31
  ^{15}N chemical shift and, 32
  ^{17}O chemical shift and, 33
  ^{1}H chemical shift and, 32
  ^{2}H chemical shift and, 34
  NMR chemical shift and, 31
hydrophobic domain, elastin, 97
hygrogels, NMR imaging of
  experimental aspects, 188
  low molecular weight compounds diffusion, 190
  net chain mobility, 190
  NMRI advantages, 187
  PMAA gel, 188
  T-Stimulus, 190
  volume phase transition, 190
hyperfine interaction
  EPR principles, 443
hyperpolarized Xenon, 151
hypoxia inducible factor-1 (HIF-1), 827, 828
hypoxia, tumor, 823

I

IGAIM. *See* individual gauges for atoms in molecules
IGLOs. *See* individual gauge for localized orbitals
image acquisition strategies for preclinical phMRI, 858
image contrast
  and intrinsic MR parameters, 787
  enhancement, MRI contrast mechanism for brain, 790
image pre-processing
  phMRI, 862
imino proton signals
  DNA, 671
  RNA, 671
  telomeric DNA bound to hTRF2 and, 743
immersion depth
  dioxygen in solution, paramagnetic effects of, 476
immobile proton signals, 671
in situ NMR imaging
  industrial application of, 163
  steel-making process, 163
in vitro labeling, sugar chains, 224
in vivo ^{13}C NMR imaging, 173
in vivo MRI
  adipose tissue, 775
  brain, 773
  heart, 776
  lungs, 775
INADEQUATE experiments, 689
individual gauge for localized orbitals, 54, 64
individual gauges for atoms in molecules, 54, 66
inhomogeneities, polymer gel systems, 123
injectable anesthetics, 861
inorganic hosts, 149. *See also* host–guest chemistry
inorganic materials (Si)
  cross-polarization features, 197
  hydrogen-bonded silanols, 201
  layered sodium hydrous silicates, 200
  silica gels, 199
  structural characterization, 197
integral membrane protein phospholamban
  MRS study of, 313
intensity profiling from 1D ESRI, 180
interface dynamics, polymeric, 579
interfaces characterization, polymeric, 575
intermediate exchange, 424. *See also* chemical exchange
intermolecular NOEs, 414
internal ribosome entry site, 666
internuclear distances, REDOR and, 721
intracellular MRI contrast agents, 879
intramolecular NOEs, 413, 414
ion pump inhibitors (case study), 324
ion-transporting biological channels
  NMR studies of, 285
iron oxide, 764
iron oxide contrast agents for cell tracking, 880
ischemia
  cerebral, 803
  functional imaging after, 804
  relaxation contrast during, 804
ischemia models
  focal, 802
  global, 802
IsK, 339
I–Sn multiple spin system, 723, 727
isomorphism
  biodegradable copolyesters, bacterially synthesized, 551
isotope labeling
  glycoproteins, 223
  in vitro, 224
  negative, 218

isotope labeling (*cont.*)
  positive, 215
  protein structure and, 517
  stable, 223
  stable-isotope-aided methods for protein NMR spectroscopy, 215
  sugar chains, 226
isotope labeling methods
  negative, 215
  positive, 215
  stable, 673
isotopically labeled elastin, 96
isotropic chemical shift, 38
isotropic shielding
  solid-state NMR and, 389

K

kaliotoxin, 528
kinase
  choline, 828
kinase inhibitor
  cyclin-dependent, 830

L

labeling
  ^{19}F-labeling, 263
  ^{19}F in b-type haemoproteins study, 532
  arterial spin labeling, 799
  in vitro, 224
  isotope, 488
  metabolic, 226
  negative, 218
  positive, 215
  stable isotopic labeling, 673
  sugar chains, 226
labeling methods
  negative, 215
  positive, 215
lactose permease, 338
large biological macromolecules in solution
  TROSY NMR for, 487
large biological macromolecules study, TROSY for, 490
large molecules, resonance assignments in, 491
Larmor precession frequency, 129
layered sodium hydrous silicates, 200
LCCAP–NMR, 404
LDA. *See* local density approximation
LDBS. *See* locally dense basis set
left coronary artery (LAD), 835
LF NMR MOUSE
  fat analysis, 804, 905
LF NMR water analysis
  atlantic Salmon (Salmo salar), 904, 906
L-GIAO methods, 68. *See also* H-GIAO methods
LH2 structure determination, 330
ligand binding, NMR diffusometry and, 113
ligand-gated channel, 285
ligands and membrane-embedded receptors interactions (NMR study), 319
  choice of technique, 319
  future prospects, 325
  ion pump inhibitors (case study), 324
  ligand binding detection, 321
  sample requirements, 321
  solid-state NMR, 321
  solution NMR methods, 320
  structural analysis of ligands, 323
  water LOGSY technique, 320
line shape profiling from 2D ESRI, 181
lineshape analyses
  amorphous polymers dynamics, 609
linker introduction, cell tracking and, 883
lipid membrane-associated peptides,
    structural analysis of, 263
lipid membranes
  correlation functions, 256
  deuterium NMR relaxation aspects, 258
  model-free analysis and, 255
  relaxation aspects, 254
  simplified models in closed form, 255
  spectral densities, 255
  spin–lattice relaxation times properties of, 254
lipid metabolism in tumors, 826
lipid oxidation
  fish oil, 915
  in freeze stored herring, 930
lipid oxidation study (fish and fish products), 929
  electron spin resonance spectroscopy, 929
  free radicals in marine lipids, 930
  NMR, 932
  spin trapping of cod liver oil, 931
lipids
  free radicals in marine, 930
  NMR, 309
lipolysis, 915
liquid chromatography with NMR. *See* on-line SEC–NMR, 399
liquid crystals
  diffusion in, 117
  field gradient
    applications, 121
    NMR of, 117
  lyotropic applications, 119
  NMR methods and diffusion in, 117
  thermotropic applications, 120
liver
  MRS, 776
  murine models of disease, 776
local density approximation, 56
localized orbitals local origin, 54
locally dense basis set, 66
loop B RNA, nucleic acid structures refinement and, 665
lungs
  MRI, 775
lyotropic applications, liquid crystals, 119
lysozyme, calcium-binding, 497

M

macromolecules in solution, large biological, 487
magic angle spinning
  paramagnetic effects under very fast, 475
magic angle-oriented bilayer systems, 241
magnetic field strength effects on phMRI, 858
magnetic iron oxide nanoparticles, 856
magnetic resonance angiography (MRA), 790
magnetic resonance force microscopy, 358
magnetic resonance histology (MRH), 769
magnetic resonance imaging. *See* MRI
magnetic resonance spectroscopy. *See* MRS
magnetically oriented bilayer systems, 241
magnetically oriented vesicle systems, 243
magnetization inversion transfer, 286
magnetization transfer contrast (MTC), 809
magnetization transfer imaging (MTI)
  brain disease MRI and, 809
magnetizations, 129
main chain dynamics
  polypeptides, 626
mammalian cell culture, 187
manganese chloride for nerve tracking and demonstrating neuronal activation, 764
manganese-based contrast in determining viable myocardium after infarction, 765
MAOSS
  oriented bilayer systems, 241
mapping changes in CBV (brain disease), 791
mapping sequences
  acceleration component, 158
  velocity component, 158
marine lipids, free radicals in, 930
marine microalgae
  ^{1}H NMR, 943
  ^{3}C HR MAS NMR, 949

  classification and metabolite composition study, 943
  fatty acid composition study, 949
  high resolution MAS NMR, 943, 949
  multivariate analysis, 935 , 943
  polysaccharide structure study, 949
MAS
  1D, 609
  amorphous polymers dynamics, 609
  CRAMPS and, 366
  ligands and membrane-embedded receptors interactions (NMR study), 319
  oriented bilayer systems, 241
  photosynthetic antennae and reaction centers, 327, 330
  polymer
    blends,638
    conformations study and, 566
    networks structure study, 584
  tensor correlation techniques, 727
MAS methods, 93
MAS NMR
  chlorosomes and LH2, structure determination of, 330
  crystalline polymers, 615
  for protein 3D structure determination, 527
  marine microalgae, 943, 949
  multiple-quantum, 695
  omega-3 fatty acid content of intact muscle of farmed atlantic Salmon, 937
  photosynthetic antennae and reaction centers, 327
materials indentification
  isotropic shielding uses in, 389, 390
  quadrupolar coupling uses in, 391
  solid-state NMR for, 389, 390
MbO_2 vs. MbCO, 537. *See also* b-type haemoproteins
MCLR. *See* multiconfigurational self-consistent field linear response
MCSCF. *See* multiconfigurational self-consistent field theory
  mechanical property, crystalline polymers, 615
mechanically oriented bilayer systems, 243
mechanosensitive-gated channel, 285
membrane associated peptides, structure determination, 246
membrane lipids
  equilibrium and dynamical properties of, 249
membrane motions, relaxation aspects, 255
membrane orientation
  antimicrobial peptides, 273
membrane permeating peptides, 882
membrane protein
  phospholamban, 313
membrane protein fragments
  features of, 339
  structure aspects, 340
    membrane protein fragments, 336, 338
membrane protein structure
  bacteriorhodopsin, 336, 340
  bovine rhodopsin, 337, 341
  high-resolution NMR and, 335
  human erythrocyte glycophorin, 332
  lactose permease, 338
  peptide structure, 336
  secondary structure, 335
membrane protein topology
  dioxygen in solution, paramagnetic effects of, 475
membrane protein, intact, 341
membrane proteins. *See also* receptors
  diacylglycerol kinase, 295
  dynamic aspects of, 293
  pHtrII, 295
  ppR, 295
  present as monomers, 294
  site-directed NMR studies, 291
  solution NMR studies for, 493
  surface structures, 294
membrane-active peptides
  solid-state NMR, 305
membrane-active proteins
  solid-state NMR, 305
membrane-associated peptides
  bacterial resistance to antibiotics, 271
  structural analysis of, 263
membrane-binding proteins
  dynamic structure of, 300
  structure, 299
membrane-embedded receptors
  ligands and, NMR study of, 319
metabolic labeling, sugar chains, 226
metabolic profiling of biofluids
  MRS, 781
  murine models of disease, 781
metabolism
  cell tracking and, 875
metabolites
  composition, marine microalgae, 943
  tracing, NMR imaging and, 173
metal and CaM Interactions, 505
metal-organic hosts, 144, 147. *See also* host–guest chemistry
met-aquo Mb, 536
metarhodopsin II, 337
met-azido Mb, 536
met-cyano Mb, 535
methyl acrylate (A)/methyl methacrylate (B) copolymer, 558
methyl group, 621. *See also* polypeptides dynamics
micelle–water interactions, 416
microanalysis
  by 1H SSNMR, 468
middle cerebral artery occlusion (MCAO), 787
mineralization, collagen dynamics and, 91
MIONs. *See* magnetic iron oxide nanoparticles
miscibility, polymer blends, 632
miscible polymer blends, 637
MIT. *See* magnetization inversion transfer
mixed solvent systems, 420
mobile NMR
  applications, 376
  measurement methods, 374
model-free analysis, 255
moisture analysis
  fish feed, 893
molecular dynamics
  crystalline polymers, 616
molecular ENDOR based quantum computer, 647
molecular force fields, 74
molecular motions, crystalline polymers, 615
molecular size
  and NMR, 487
molecular structure and dynamics, deuterium NMR, 249
molecular weight dependence
  coplymer composition, 401
  of tacticity, 402
molecular weight determination, polymers, 400
molecular weight distribution (MWD), 399
molecule-based pulsed ENDOR spectroscopy, 647
Møller–Plesset constructions, 63
monounsaturated fatty acids. *See* MUFA, 915
MQMAS NMR, 174, 695
MQMAS spectra, 168
MRFM. *See* magnetic resonance force microscopy
MRI, 151
  adipose tissue, 775
  biomedical NMR imaging and, 173
  brain disease, experimental models, 787
  cardiovascular magnetic resonance (in small animals), 835
  cell tracking application of, 879
  contrast
    mechanism for brain disease, 787
    optimization aspects, 759
  drug discovery and development, MRI applications to, 855
  fish meat, 963
  lungs, 775
  measures of

MRI (*cont.*)
    rCBF, 856
    rCBV, 856
  murine models of disease, 769
  phenomics, 771
  phMRI, 855
  post-mortem studies of fish, 946
  salt and fat distribution in smoked Salmon, 963
  smoked Salmon, 963
  vascular, 848
MRI contrast agents
  intracellular, 879
MRI measures of rCBF, 857
MRI measures of rCBV, 857
MRI origins of BOLD signal, 858
MRS
  ^{1}H-MRS, 846
  ^{23}Na-MRS, 847
  ^{31}P-MRS, 847
  adipose tissue, 776
  AFA-PLB monomer, 316
  brain, 769
  cancer
    application in, 823
  cardiovascular magnetic resonance (in small animals), 835
  fish meat, 964
  heart, 769
  integral membrane protein phospholamban, 313
  liver, 781
  metabolic profiling of biofluids, 781
  multinuclear, 845
  murine models of disease and, 769, 776
  muscle, 780
  phospholamban, 313
MUFA, 915
multi-configuration self-consistent field, 64, 82
multiconfigurational self-consistent field (MCSCF) theory, 63
multiconfigurational self-consistent field linear response (MCLR), 82
multidimensional NMR, 347
  filter diagonalization method, 347
  Hadamard encoding, 349
  of calmodulin, 505
  projection–reconstruction, 351
  spatially encoded single-scan NMR, 349
multidrug resistance protein, 339
multi-H-bonded systems
  H-transfer motions detection in, 431, 432
multi-H-transfer motions
  in (chloranilic acid)(1,2-diazine) 16 molecular complex, 435
  in (chloranilic acid)(1,4-diazine) 16 molecular complex, 432
multinuclear MRS, 845
multiple sclerosis, 810
multiple spin system
  REDOR in, 719
multiple spin system, REDOR in
  obtaining accurate internuclear distances in, 721
multiple spin system, REDOR in, 719
  dipolar
    coupling aspects, 722
    dephasing of, 719, 723
    interactions with neighboring molecules, 721
  finite pulse length aspects, 721
  flip angle errors of π pulse, 721
  for I–Sn, 723
  I–Sn, 719
  natural abundant nuclei, dipolar coupling contribution from, 722
  rf
    inhomogeneity, 721
    power fluctuation aspects, 721
  sample spinning stability, 721
  simple alternative to REDOR, 722
  spin selection using improved REDOR, 724
multi-spin systems
  NOE in, 410
multivariate analysis
  marine microalgae, 943
murine models of disease
  adipose tissue, 777
  adipose tissue and, 775
  brain, 779
  brain and, 773
  heart, 776, 779
  in vivo MRI and MRS, 769
  liver, 781
  lungs and, 775
  magnetic resonance
    histology 769
    imaging, 769
    spectroscopy, 776
  metabolic profiling of biofluids, 781
  muscle, 780
  phenomics, 771
  whole body phenome, 771
muscle
  MRS, 780
  murine models of disease, 780
mutants. *See* DNA-binding activities (hTRF1 and hTRF2 with hTRF2 mutants)
mutual orientation of anisotropic interactions
  torsion angle measurements, secondary structure analysis (proteins), 738
myocardial tissue contractility, 842
myocardium after infarction, manganese-based contrast in determining, 766
myosin light chain kinase, 503

N

^{15}N
  chemical shieldings, 63, 64
  labeled PLAs, 603
  positive labeling, 218
^{15}N NMR chemical shift, 35
^{23}Na-MRS, 847
nano cavities, polymer media with, 125
natural fibrous proteins
  ^{1}H CRAMPS NMR applications to, 597
  conformation study of, 597
  silk fibroins, 597
navigation surgery, 175
negative labeling. *See also* positive labeling
  ^{2}H, use of, 218
negative temperatures, 445
nematic echo, 120
Nephila clavipes Dragline silk, 104
nerve tracking, manganese chloride for, 765
net chain mobility, 22
networks, polymer. *See* polymer networks structure
neurodegenerative disorders, 809
  Alzheimer's disease, 810
  Huntington's disease, 810
  Parkinson's disease, 810
neuroimaging
  hemodynamic-based functional, 856
neuronal activation, manganese chloride for, 759
neuronal activity, 855
N–H bond length, 601
N–H bond length, polypeptides and, 600
NMR
  ^{13}C, 567, 570
  ^{19}F NMR study of b-type haemoproteins, 532
  ^{1}H, 432
  2D, 640
  ^{2}H, 642
  ^{3}H applications, 395
  Alzheimer's Aβ amyloid fibrils, polymorphism, 19
  and molecular size, 487
  and NQR in zero magnetic field, 446
  atlantic Salmon (Salmo salar), 904
  calcium-binding lysozyme, 497
  calmodulin investigation, 503
  chemical shift map, 37
  crystalline polymers, 615
  dioxygen in solution, 475
  dry or swollen polymer structure, 541
  dynamic NMR, 421
  fast multidimensional, 347
  field-cycling, 445

  fish feed, compositional analysis of, 893
  fish meat, 964
  fish oils
    and lipids, 915
    fatty acid composition and oxidation in, 921
  high-sensitivity NMR probe systems, 353
  LC with. *See* on-line SEC–NMR
  LCCAP–NMR, 404
  ligands and membrane-embedded receptors interactions (NMR study), 319, 321, 324
  lipid oxidation study (fish and fish products), 929
  lipids, 313
  low-field, 904
  mobile. *See* mobile NMR
  on-line SEC–NMR, 399
  organoboron chemistry, 455
  oriented bilayer systems, 241
  photosynthetic antennae and reaction centers, 327, 330
  PMMA stereocomplex, 403
  polymer
    blends, 631, 632
    microstructure, conformation and, 567
    networks structure, 583
    stereoregularity aspects, 557
    structure, 541, 542
  polypeptides, 591
  polypeptides dynamics, 621
  probe systems, 353
  REDOR, 713
  rheo-NMR, 383
  sensitivity issues, 353
  signal assignments and multi-dimensional, 472
  signal for
    DNA, 671
    RNA, 671
  silk
    fibroins structural analysis, 101
  solution NMR methods, 320
  spatially encoded single-scan, 349
  SSNMR, 695
  structural
    biology and, 657
  time domain, 893
  torsion angle determination, 727
  zero field, 444
NMR and NQR
  limitations of, 445
  zero field, 445
NMR chemical shielding tensors, 66
NMR chemical shift
  ^{13}C, 31
  ^{15}N, 32
  ^{17}O, 33
  ^{1}H, 32
  ^{2}H, 34
  band theory based, 43
  chemical shielding theory and, 54
  hydrogen-bonded structure and, 231
  modeling, 53
  solid polymers, 43
NMR diffusion, 135
  applications, 136
  association constants, 140
  data processing, 136
  pulse sequences for PFG, 135
  size and shape determination by, 137
  theoretical aspects, 135
NMR diffusometry, 109
  background gradients, 111
  complications, 110
  convection, 111
  diffusion in complex systems, 112
  Eddy currents and gradient mismatch, 112
  finite gradient pulses, 110
  gradient-based, 109
  gradient constancy, 111
  ligand binding and aggregation, 113
  radiation damping, 111
  restricted diffusion, 113
  solution dynamics and surfactants, 112
NMR imaging, 129
  encoding principles, 157
  field of view aspects, 157
  flow and acceleration mapping, 157
  in situ, 163
  pulse sequences, 157
NMR imaging (NMRI), 179
NMR imaging, biomedical
  biomedical, 173
  cellular tracking, 176
  H-1 detection, 173
  in vivo 13C, 173
  metabolites tracking, 173
  physiological properties, 174
  temperature image and navigation surgery, 175
NMR measurements
  using field gradients and spatial information, 129
NMR shielding constants, ab initio calculation and, 66
NMR studies of ion-transporting biological channels, 286
NMR, field gradient
  for polymer systems with cavities, 125
  liquid crystals, 117
NMR, site-directed
  membrane proteins, 291
NMR, solid-state. *See* soild-state NMR
NO·molecule
  EPR principles, 441
NOE
  applications, 411
  calmodulin study, 505
  heteronuclear, 411
  in multi-spin systems, 410
  intermolecular NOEs, 414
  intramolecular NOEs, 413, 414
  relaxation aspects, 409
  solute–solvent interactions and, 413, 414
  theoretical background, 409
  time dependence of, 411
  TROSY and, 493
NOESY, 411
  nucleic acid structures refinement and, 667
NQR
  and NMR in zero magnetic field, 445
  high sensitivity in 4-chlorobenzoic acid, 431
NQR measurements
  ^{35}Cl, 431
nuclear magnetic interactions, anisotropic, 736
nuclear Overhauser effect. *See* NOE
nuclear quadrupole interaction
  EPR principles, 443
nuclear quadrupole resonance
  low-γ, 446
  sensitivity enhancement and, 446
nuclear shielding
  configuration aspects, 46
  conformation aspects, 45
  solid polymers, 43
  TB method for interpreting, 45
nuclear spin–spin couplings
  coupled Hartree–Fock approximation (triplet instability), 82
  electron correlation effects, 82
  origin of indirect, 80
nuclear Zeeman interaction
  EPR principles, 439
nucleic acid structures refinement, 665, 667
  loop B RNA, 666
  residual dipolar coupling and, 665
  structural restraints, 666
nucleic acids
  TROSY, applications to, 493
nucleosides
  conformation of, 673
  structural analysis, 673
nucleotides
  conformation, 671
nucleotides triphosphates (NTPs), 673
  ^{17}O MQMAS NMR
  2D, 695
  data processing aspects, 695
  organic solids, 695
  pulse sequence, 695
  sensitivity, 698
  spectral analysis, 695

O

^{17}O NMR
  chemical shift, 33
O$_2$ migration pathways, 481 offset
  compensation by BB-SEMA, 704
  effects, 703
oils and lipids, fish, 915
oligonucleotides
  conformation, 674
oligosaccharides
  RDC and, 661
omega-3 fatty acid content of intact muscle of farmed atlantic Salmon
  gas chromatography, 937
  material and sample preparation, 937
  NMR spectroscopy experiments, 937
oncogene function, 827
oncology (MR contrast agents applications)
  gadolinium agents in evaluating tumor angiogenesis, 766
  targeted SPIO in detecting tumor necrosis (apoptosis), 766
ONIOM-NMR approach, 69
ONIOM-NMR construction, 68
on-line SEC–NMR, 399, 402
  coupling of LC and NMR, 399
  instrumentation, 399
  LCCAP–NMR and, 404
  molecular weight dependence
    coplymer composition, 401
    of tacticity, 402
  molecular weight determination (polymers), 400
  PMMA stereocomplex, 400
optimization, MRI contrast, 759
optimized detection coil design, 357
order parameters, lipid membranes, 252
organic free radicals
  EPR and, 440
organic host, 149. *See also* host–guest chemistry
organic solids
  2D ^{17}O MQMAS NMR, 695
organo metallic chemistry
  organogermanium, 459
organoboron chemistry, 455
organogermanium chemistry, 459
organometallic chemistry, 137
organotin chemistry, 461
oriented bilayer systems
  bicelle, 243
  DMPC, 246
  magic angle-oriented, 244
  magnetically oriented, 241, 246
  magnetically oriented vesicle systems, 243
  MAOSS, 244
  MAS experiment, 244
  mechanically oriented
    bilayer systems, 243
    on glass plates, 243
  membrane associated peptides,
    structure determination, 246
  NMR of, 241
  orientation dependence of
    chemical shift interaction, 244
    dipolar interaction, 245
  PISA, 245
  PISEMA, 245
  spontaneous magnetic orientation, 241
oriented biomembranes, solid state 19F-NMR analysis, 261
oxidation
  fish oil, 923
  in fish oils, 921
oxidation products (fish oils and lipids), 918
oxidation-reductive amination, 883

P

^{31}P
  chemical shift affecting factors, 133
^{31}P NMR
  of lipids, 309
  spectroscopy, 271
^{31}P-MRS, 846
PARAFAC, 912
paraffinic hydrocarbons, ^{13}C NMR study of, 568
paramagnetic agents for cell tracking, 880
paramagnetic effects
  dioxygen in solution NMR, 475
  under very fast magic angle spinning, 467
paramagnetic systems
  ^{13}C VFMAS SSNMR for, 469
  of ^{1}H MAS NMR spinning speed dependence and sensitivity, 467
parathyroid hormone receptor, 338
Parkinson’s disease, 809
partial least squares (PLS), 912
PBLG, 593
  gel, 125
  side chain of, 623
PEMA, 404
penumbra, 810
peptides
  19F-labeling, 263
  antimicrobial, 271
    gramicidin S, 265
    K3, 266
    PGLa, 265
  backbone torsion angle analysis, 735
  from helices, 335
  fusogenic peptide B18, 264
  membrane
    associated, 246, 263, 271
    permeating, 882
  structure, 336
peptides, elastin, 93
perfusion during ischema (animal model), 803. *See also* diffusion during ischemia (animal model)
perfusion imaging, 794
  arterial spin labeling, 795
  bolus tracking, 794
PFG. *See* pulsed field gradients
PGSE. *See* pulsed gradient spin-echo method
pH, NMR imaging and, 174
pharaonis, 295
pharmacodynamic markers, 829, 830
pharmacokinetic markers, 829
pharmacokinetic modeling, 864
phase encoding, 159
phase separation
  polymer blends, 575
phase transitions
phenomics, 771
  in vivo MRI and MRS, 769
  murine models of disease, 769
  whole body phenome, 771
phenyl ring, 622. *See also* polypeptides dynamics
phMRI, 855
  absence of signal changes, 872
  anesthesia effects, 872
  anesthetics and, 861
  BOLD
    imaging, 856
    phMRI studies, 857
    response to drugs, 864
  changes in physiological measures, 869
  considerations particular to, 859
  data analysis, 862, 865
  dopamine receptor agonists for animal phMRI, 865
  drug effects on cerebral blood vessels, 869
  future aspects of, 873
  global effects and fluctuating baseline signal intensity, 873
  hemodynamic-based functional neuroimaging, 856
  image acquisition strategies for preclinical, 858
  image pre-processing, 862
  imaging protocol, 865
  in awake animals, 862
  inhalation anesthetics, 861
  injectable anesthetics, 861
  magnetic field strength effects, 858
  MRI measures of rCBV, 856
  SE and GE BOLD imaging, 858
  statistical analysis, 864
  use of, 873
  validating phMRI experiments, 860

phMRI behavioral modeling, 866
phMRI pharmacokinetic modeling, 865
phosphatidylglycerophosphate synthase, 339
phospholamban (PLB), 314
  AFA-PLB monomer, 316
  integral membrane protein, 313
  MRS study of, 313
  solid-state NMR, 314
phospholipase C-δ1 (PLC-δ1), 299
phospholipid metabolism in tumors, 826
phosphorus MRS. *See* ^{31}P MRS
phosphorus signals
  RNA and DNA, 672
phosphorylation, 314
photosynthetic antennae and reaction centers, 327
  structure–function studies of, 327
pHtrII, 295
physical structure, polymer, 586
physiological origins of BOLD signal, 857
PISA, 245
  oriented bilayer systems, 245
  protein structure determination, 518
PISA wheel, protein structure determination, 518
PISEMA, 245
  oriented bilayer systems, 245
PISEMA experiments
  biological solids structural studies, 703
  low RF power experiments, 707
  offset compensation by BB-SEMA, 704
  offset effects, 703
  SEMA, 704
  SIn, 707
  SLF sequence, 703
  TANSEMA, 707
  very high RF power requirement, 706
PISEMA spectra, protein structure determination, 517, 518
PLC-δ1 PH domain, 300
PLF-d5, 622
PMAA, 631
PMAA/PVAc blends, 631
PMLA-d3, 631
PMMA stereocomplex, on-line SEC–NMR of, 403
point-resolved spectroscopy. *See* PRESS
polarity index slant angle, protein structure determination, 518
polarization transfer
  cross-correlated relaxation-induced, 494
  distortionless enhancement by polarization transfer, 354
  high-sensitivity NMR probe systems and, 353
poly(ethylene glycol), 123
poly(ethylene terephthalate), 566
poly(l-leucines), 591
poly(methyl methacrylate), 557
poly(styrene), 583
poly(γ-benzyl l-gultamate), 125
polyacetylene, 46
polyethylene-cobutene, 639
polyglycine, 593, 626
polyglycine I, 591
polymer blends, 631
  ^{1}H CRAMPS experiment, 638
  2D exchange NMR, 640
  ^{2}H NMR, 642
  absorbed xenon gas NMR, 639
  blend system, choice of, 639
  configurational entropy, 637
  experimental NMR methods, 638
  interaction in, 631
  MAS experiment, 638
  miscibility, 632, 637
  phase separation process, 634
  probe slow-chain reorientation, 640
  simulations, 642
  solid-state NMR, 638
polymer dynamics
  crystalline polymers, 616
  polypeptides, 621
polymer gel systems
  CLEAR gels, 124
  diffusion in, 123
  diffusional behavior of linear molecules in channels, 126
  inhomogeneities characterization, 123
  PBLG gel, 125
  polymer media with nano cavities, 125
  smart gels with regular structure, 125
polymer interfaces characterization
  interfacial dynamics, 579
  solid-state
    heteronuclear studies, 578
    NMR for, 575
    proton NMR studies, 575
polymer microstructure. *See also* polymer structure
  ^{13}C NMR, 567
  conformational connnection to NMR, 567
  γ-Gauche-Effect, 568, 569
polymer networks structure, 583
  chemical structure, 583
  crosslinked polyolefins, 584
  effect on NMR linewidths, 583
  physical structure, 586
  poly(styrene), 583
  residual dipolar coupling and, 587
  T_2 relaxation times, changes in, 586
  thermosetting resins, 586
polymer research
  electron spin resonance imaging in, 179
polymer stereoregularity
  methyl acrylate (A)/methyl methacrylate (B) copolymer, 558
  poly(methyl methacrylate), 557
polymer structure
  calibrated polymeric networks, 543
  chain diffusion and, 542
  cross-linked long chains, 542
  crystalline structure, 545
  dry or swollen, 541
  ethylene copolymers, 545
  local friction effect on, 541
  NMR structural parameter, 542
  polymeric dynamics, 541
  spin–lattice relaxation effect on, 541
  spin–spin relaxation and, 542
  statistical, 542
  stereoregularity aspects, 557
  temporary or permanent networks, 541
  temporary or permanent polymer networks study, 541
polymer systems with cavities
  field gradient NMR for, 123
polymeric dynamics, 541
polymers
  amorphous polymers, 607
  conformations study of disordered, 563
  crystalline polymers, 615
  miscibility, 632
  molecular weight determination, 400
  solid, 570
  solid state NMR applications of, 572
polymorphism
  ethylene copolymers, 543
polymorphism, Alzheimer's Aβ amyloid fibrils, 19
polyolefins, crosslinked, 583
polypeptide chains, 520
polypeptides, 97
  ^{15}N labeled PLAs, 602
  ^{1}H CRAMPS NMR, 591
  2D ^{1}H–^{13}C HETCOR NMR, 597, 602
  amide ^{1}H signals, 601
  amide proton chemical shift, 599
  amino acid residues in
    solid state, 595
    solution, 595
  conformational study, 591
  cyclic, 595
  deuterium-labeled, 595
  dipolar spinning sideband pattern of, 601
  in solid state, 591
  natural fibrous proteins, 597
  N–H bond length, 602
  N–H bond length determination, 601
  synthetic, 601
  α-amino-acid crystals, structural studies of, 602
  α-proton chemical shifts, 587

- polypeptides dynamics
  - main chain dynamics, 626
  - methyl group and, 621
  - phenyl ring, 622
  - side chain of of PBLG, 623
  - solid state 2H NMR, 621
- polyproline I, 593
- polysaccharide structure study, marine microalgae, 949
- polyunsaturated fatty acid. *See* PUFA
- pore spaces probing, host–guest chemistry, 150
- position component, 157
- positive labeling. *See also* negative labeling
  - ^{13}C and ^{15}N, use of, 215
- positron emission tomography (PET), 855
- potassium channel, voltage-gated, 339
- potassium ion channel, 339
- PP stereosequences, ^{13}C NMR, 570
- ppR, 294
- preclinical drug discovery and development, 855
- PRESS, 776
- principal axis system (PAS), 306
- probe and receiver requirements (CRAMPS), 367
- probe slow-chain reorientation, polymer blends, 631
- probe systems
  - high-sensitivity, 353
  - NMR, 353
- probes
  - brain disease, experimental models (MRI-based), 787
- profiling
  - intensity (from 1D ESRI), 180
  - line shape (from 2D ESRI), 181
- projection–reconstruction, 351, 355
- protein 3D structure determination
  - applications, 528
  - MAS NMR for, 527
  - sample preparation and methodology, 527
- protein backbone resonances
  - TROSY for, 491
- protein folding mechanism, 497
- protein NMR spectroscopy
  - stable-isotope-aided methods for, 215
- protein side-chain resonances
  - TROSY for, 491
- protein structure
  - isotope labeling and, 489
  - RDC and, 659
  - TROSY NMR for, 487, 489
- protein structure determination
  - 3D structure determination
    - applications, 528
    - MAS NMR for, 527
    - sample preparation and methodology, 527
  - analytical framework for, 517
  - chemical shift anisotropy, 517
  - formal geometric properties of polypeptide chains, 520
  - heteronuclear
    - correlation experiment (HETCOR), 517
    - dipolar couplings, 517
  - quadratic forms observables, 519
  - solid-state NMR, 517
  - spherical-basis treatment of
    - experimental angular constraints for, 519
  - structural fitting
    - algorithm, 521
    - examples, 521
- protein, multidrug resistance, 339
- protein–protein interactions
  - dioxygen in solution and, 481
- proteins. *See also* membrane proteins
  - unfolded denatured, 657
- proteins, secondary structure analysis of, 735
  - angle measurements, 736
  - angle-dependent interactions and, 735
  - anisotropic nuclear magnetic interactions, 736
  - backbone torsion angles, 736
    - analysis of peptides, 739
  - chemical shifts dependence, 735
  - distance measurements, 736
  - J coupling dependence, 736
  - NMR, 735
  - structure characterization, 735
  - torsion angle measurements, 738
- proton NMR
  - fish oils and lipids, 915
- proton positions refinement, 70
- proton signal (imino), telomeric DNA bound to hTRF2 and, 745
- pseudocontact shifts (PCS), 660
- pseudocontact shifts, RDC and, 660
- pseudo-forces
  - BPT, 74
  - chemical shift, 73
- pseudo-pure states, QIP and, 647
- PUFA, 915
- pulse field gradient (PFG) NMR method, 123
- pulse impurities (CRAMPS), 365
- pulse sequences
  - ^{17}O MQMAS NMR, 695
  - CRAMPS, 363
  - NMR imaging and, 163
- pulsed ASL (PASL), 795
- pulsed ENDOR, 647
- pulsed field gradients (PFGs), 129
  - NMR diffusion and, 135
- Pulsed Gradient Spin-Echo method, 109
- PVME, 631
- PWI. *See* perfusion-weighted MR Imaging

Q

- QC-ENDOR, 649
  - molecular ENDOR based, 648
  - molecular entity preparation of, 648
- QED. *See* quantum electrodynamics
- QM/MM framework, 67, 68
- QM/MM mechanics, 68
- quadratic forms observables, protein structure determination, 517
- quadrupolar coupling, 152, 249
- quadrupolar coupling constant. *See also* hydrogen-bonded structure
  - ^{17}O, 31
  - ^{2}H, 31
- quadrupolar effects, 148
- quadrupole interaction, nuclear, 443
- quadrupole resonance, nuclear, 446
- quantum computer
  - molecular ENDOR based, 648
  - molecular entity preparation of, 648
- quantum computer, molecular ENDOR based, 648
- quantum electrodynamics (QED), 81
- quantum information processing
  - ENDOR spectroscopy, 647
  - molecular ENDOR based quantum computer, 648
  - pseudo-pure states, 647
  - pulsed ENDOR, 647
  - quantum entanglements, 647
- quantum mechanics/molecular mechanics. *See* QM/MM framework
- QUEDOR, 150

R

- radiation damping, 111
- radiochemical facilities and radiation safety, 395
- rat angiotensin II AT1A receptor, 339
- rCBF, 856
  - MRI measures of, 856
- rCBV, 856
  - MRI measures of, 856
- RDC. *See* residual dipolar couplings
- reaction centers (RC). *See* photosynthetic antennae and reaction centers
- REAPDOR, 150
- receiver requirements (CRAMPS), 363
- receptors
  - bradykinin B2, 338
  - human cannabinoid, 338
  - human cholecystokinin-2, 338
  - parathyroid hormone, 338

- rat angiotensin II AT1A, 339
- *Saccharomyces cerevisiae* α-factor, 338
- tachykinin NK-1, 339
- β-adrenergic, 339

reconstitution technique, ^{19}F NMR study of b-type haemoproteins and, 537

recoupling
- dipolar, 713

REDOR, 150
- dipolar dephasing of, 715
- for I–Sn, 723
- in multiple spin system, 723
- obtaining accurate internuclear distances in, 721

REDOR NMR, 713
- dipolar recoupling aspects, 713
- practical details, 714

region of interest, 759

regional cerebral blood flow. *See* rCBF

regional cerebral blood volume. See rCRV

relaxation
- cross-relaxation, 410
- defined in NOE, 409
- dipolar, 409
- intermolecular cross-relaxation, 414
- spin relaxation (amorphous polymers dynamics), 607
- spontaneous, 421
- stimulated, 409

relaxation contrast during ischemia, 804

relaxation-induced polarization transfer, cross-correlated, 490

residual dipolar coupling
- application in protein, 491
- DNA and, 654, 661
- oligosaccharides and small organic molecules and, 661
- polymer networks structure and, 583
- protein structures and, 658
- pseudocontact shifts, 660
- restraints in nucleic acid structures refinement, 661
- RNA and, 649, 659, 660
- structural biology and, 657
- theory, 657
- unfolded denatured proteins and, 661

resins, thermosetting, 583

resolution maximization (CRAMPS), 364

resonance assignments in large molecules
- protein backbone resonances, 491
- protein side-chain resonances, 491

resonances
- nuclear quadrupole, 443

restricted diffusion, NMR diffusometry and, 109

rf coils

rheo-NMR, 383

Rhodobacter sphaeroides, 327

Rhodopseudomonas acidophila, 327

ribosome entry site, 666

RNA. *See also* DNA
- 3D structure determination, 674
- conformations, 671
- imino proton signals, 671
- immobile proton signals, 671
- loop B RNA, 656
- NMR signal for, 671
- phosphorus signals, 672
- residual dipolar couplings and, 656, 657, 675
- signal assignment aspects, 671
- stable isotopic labeling, 673

robotics
- rotational diffusion, 135

rotational isomeric state (RIS), 570

rotational-echo, double-resonance NMR. *See* REDOR NMR

S

S = 1/2 systems, 440

S > 1/2 systems, 443

Saccharomyces cerevisiae α-factor receptor, 338

Salmon. *See also* atlantic Salmon (Salmo salar), low-field NMR studies
- salt and fat distribution, 968
- salt interaction in smoked, 967

salt
- analysis, cod fillets, 960, 961
- and fat distribution in smoked Salmon, 968
- interaction in smoked Salmon, 967

salty, 967

Samia cynthia ricini, *See also Bombyx mori*
- silk, 97
- structure before spinning, 101

saturated fatty acids. *See* SFA

saturation transfer difference (STD), 319, 505
- across hydrogen bonds, TROSY for obeserving, 489

scaling factors (CRAMPS), 369

scaling under pulse sequences (CRAMPS), 366

scanning transmission electron microscopy. *See* STEM

SCULPTOR package, 666

SDC implementation by pulsed ENDOR, 647

SE and GE BOLD imaging, 858

SEC–NMR. *See* on-line SEC–NMR

second order polarization propagator approximation, 64

secondary structure, 335
- bacteriorhodopsin, 336
- bovine rhodopsin, 337
- human erythrocyte glycophorin, 336
- lactose permease, 338

secondary structure analysis (proteins)
- angle measurements, 736
- anisotropic nuclear magnetic interactions, 736
- backbone torsion angle analysis of peptides, 739
- backbone torsion angles, 735
- characterization of, 735
- chemical shifts dependence, 735
- distance measurements, 736
- J coupling dependence, 735
- NMR for, 735
- torsion angle measurements, 736

SEDOR. *See* spin-echo double resonance

seeds. *See* plant seeds

seizures
- generalized, 807
- simple partial, 807

selective solute interactions in mixed solvent systems, 417

SEMA
- BB-SEMA, 704
- very high RF power requirement, 703

semiconductors, organic. *See* organic semiconductors

sensitivity,
- ^{17}O MQMAS NMR, 695
- issues in NMR, 353

sensitivity enhancement
- by cross-polarization, 469
- low-γ nuclear quadrupole resonance, 446

separated local field (SLF) experiment, 703

SERCA, 313

SFA, 915

SGP condition, 109

shielding constants, ab initio calculation and, 63

shielding tensor, 63, 390

ship-in-a-bottle type synthesis, 148

short gradient pulse condition, 109

side chain of PBLG, 623

signal assignments, SSNMR, 468

signal-to-noise. *See* SNR

silanols, hydrogen-bonded, 197

silica gels, 199

silicates, 199

silk fibroins
- ^{1}H CRAMPS NMR, 595
- 2D^{1}H–^{13}C HETCOR NMR, 599
- 2D NMR, 611
- HETCOR NMR, 597
- *Bombyx mori*, 101
  - structure after spinning, 101
  - structure before spinning, 101
- conformation study of, 593
- *Nephila clavipes* Dragline, 104

- silk fibroins (*cont.*)
  - *Samia cynthia ricini*, 101
    - structure before spinning, 101
  - structural analysis, 101
- simple partial seizures, 807
- simulation
  - polymer blends, 638
- simultaneous frequency amplitude modulation (SFAM), 722
- SIn, PISEMA experiments of, 703
- single photon emission computed tomography (SPECT), 855
- site-directed
  - ^{13}C NMR, membrane proteins (monomers), 285
  - assignment,13C NMR signals, 291
  - NMR studies on membrane proteins, 291
  - size exclusion chromatography (SEC), 399
- SLICING, 902
- slow exchange, 421. *See also* chemical exchange
- small molecule
  - interactions
    - small molecule-organic solvent interactions, 409
  - small molecule–water interactions, 416
- small molecule-organic solvent interactions, 409
- small molecule–water interactions, 416
- small organic molecules
  - RDC and, 657
- smart contrast agents, 792
- smart gels characterization, 125
- SNR, 759, 760, 761
  - brain disease, experimental models (MRI-based), 787
  - MRI contrast optimization, 759
- sodium hydrous silicates, layered, 200
- solid polymers
  - ^{13}C NMR, 567
  - NMR chemical shifts, 43
  - nuclear shielding, 43
- solid state
  - polypeptides in, 591
- solid state ^{2}H NMR
  - polypeptides dynamics, 621
- solid-state ^{19}F-NMR
  - analysis of oriented biomembranes, 261
  - experimental aspects, 261
- solid-state deuterium
  - coupling tensors observation, 249
  - membrane lipids atudy and, 249
  - NMR spectroscopy of, 246
- solid-state heteronuclear NMR
  - polymer interfaces characterization and, 575
- solid-state MAS NMR
  - crystalline polymers, 615
- solid-state multiple-quantum NMR
  - disordered polymers, conformations study of, 563
- solid-state NMR, 87
  - ^{13}C, 567
  - ^{1}H and ^{13}C, 467
  - analytical
    - and numerical tools for experiment design, 679
    - aspects of, 389
    - tools, 679
  - average Hamiltonian theory (AHT), 679
  - cross-polarization (CP) MAS, 89
  - effective Hamiltonian Theory (EHT), 679
  - experimental aspects, 473
  - heterogeneous catalysts study, 205
  - high-resolution, 467
  - in host–guest chemistry, 147
  - isotropic shielding uses in, 389
  - ligands and membrane-embedded receptors interactions, 319, 321
  - membrane-active proteins and peptides, 287
  - membrane-associated peptides, 263
  - membrane-binding proteins structure and, 299
  - numerical tools, 679
  - phospholamban, 313
  - PLC-δ1 PH domain and, 300
  - polymer blends, 631, 633
  - polymer interfaces characterization, 575
  - polymer, applications of, 575
  - protein structure determination, 517
  - quadrupolar coupling, 391
  - quantification with, 392
  - signal assignments and multi-dimensional, 472
  - structure determination and, 392
  - systematic design of, 682
  - tools for systematic experiment design, 679
  - torsion angle determination, 727
- solid-state proton NMR
  - polymer interfaces characterization and, 575
- solute–solvent interactions, NOE and, 409, 410
  - biomolecule–water interactions, 418
  - cross-relaxation
    - intermolecular, 412
  - intermolecular cross-relaxation, determination of, 413
  - micelle–water interactions, 416
  - selective solute interactions in mixed solvent systems, 417
  - small molecule-organic solvent interactions, 417
  - small molecule–water interactions, 416
  - xenon–solvent interactions, 416
- solution dynamics, NMR diffusometry and, 109
- solution NMR methods
  - ligands and membrane-embedded receptors interactions (NMR study), 319
- solvent systems, mixed, 417
- SOPPA. *See* second order polarization propagator approximation
- SOS-DFPT. *See* sum-over-states-density functional perturbation theory
- spatial information
  - NMR measurements and, 129
- spatially encoded single-scan NMR, 347, 349
- spatially-resolved degradation, ESR imaging and, 179
- specific enrichment, 349
- spectral analysis
  - ^{17}O MQMAS NMR, 695
- spectral assignments
  - polymer microstructure and, 567
- spectral densities, lipid membranes, 254
- spectral-spatial ESRI, 179
- spectrometer requirements (CRAMPS), 367
- spherical-basis treatment, protein structure determination, 517
- SPI methods, 168
- spin 1/2 nuclei, structural information, 148
- spin counting, 150
- spin density map, 159
- spin diffusion, 410, 548
- spin Hamiltonian
  - EPR principles, 439
- spin relaxation
  - amorphous polymers dynamics, 607
- spin space
  - average Hamiltonians in, 363
- spin system, multiple, 719
  - of cod liver oil, 930
- spin-echo double resonance, 150
- spin–lattice relaxation
  - dioxygen in solution, paramagnetic effects of, 467
  - polymer structure, 539
- spin–lattice relaxation times, 607
  - deuterium, 249
- spinning sidebands, dipolar, 595
- spinning speed dependence
  - ^{13}C MAS spectra, 469
- and sensitivity, ^{1}H MAS NMR, 467
- spin–orbit interaction
  - EPR principles, 439
- spin–spin couplings, nuclear. *See* nuclear spin–spin couplings
- spin–spin relaxation polymer structure and, 539

spin–spin relaxation times, 607
spin–spin terms, higher order, 443
  SPIO
  and gadolinium chelates, in brain perfusion images, 765
  in detecting tumor necrosis (apoptosis), targeted, 766
spontaneous magnetic orientation, oriented bilayer systems and, 241
spontaneous relaxation, 409
spreading depression (SD), 806
SPRITE methods, 168
SQUIDs, 449
SSNMR. *See* solid-state NMR
stable isotope labeling
  glycoproteins, 285
stable isotopic labeling
  RNA and DNA, 671
stable-isotope-aided methods for protein NMR spectroscopy, 215
stable-isotope-assisted NMR spectroscopy
  structural glycobiology, 223
static tensor correlation techniques, 727
statistical analysis
  phMRI, 855
STEAM, 776, 777
steel-making process
  NMR imaging, 163
STEM
  Alzheimer's Aβ amyloid fibrils, polymorphism, 19
stem cells tracking
  CNS, 886
  heart, 885
stereoregularity, polymeric, 541, 542
stereoregularity, polymers
  methyl acrylate (A)/methyl methacrylate (B) copolymer, 558
  poly(methyl methacrylate), 608
stereosequences, PP, 567
stimulated relaxation, 409
STMAS
Stokes–Einstein equation, 135
structural analysis
  biomembranes, 261
  ligands and membrane-embedded receptors interactions (NMR study), 319
  membrane-associated peptides, 263
  nucleosides, 668
  of silk fibroins, 101
  secondary structure (proteins), 731
structural biology
  DNA, 658
  NMR in, 653
  oligosaccharides and small organic molecules, 661
  protein structures, 658
  residual dipolar couplings and, 657
  RNA, 658, 659
  unfolded denatured proteins, 661
structural characterization (inorganic materials), 197
structural fitting algorithm, protein structure determination, 517
structural fitting, protein structure determination, 517
  fitting to 2D spectra, 576
  fitting to 3D spectra, 517
structural glycobiology
  stable-isotope-assisted NMR spectroscopy, 218
structural stability
  of calcium-binding lysozyme, 497
structural studies
  biological solids, 700
structure determination
  DNA and RNA, 671
  solid-state NMR and, 389
sugar chains, *in vitro* labeling, 213
sum-over-states-density functional perturbation theory (SOS-DFPT) approach, 67
superparamagnetic agents for cell tracking, 880
superparamagnetic iron oxide (SPIO), 880
surface acidity
  heterogeneous catalysts, 205
surface coils
  surface structures
    membrane proteins, 289
surfactants, NMR diffusometry and, 109
swelling process, 187. *See also* hygrogels, NMR imaging of
synthetic polypeptides, 591

T

T_1 and T_2 contrast, 761
T_1 relaxation behavior, 13C, 546
T_1 vs. T_2 contrast agents, 764
T_1-weighted dynamic contrast enhanced MRI (brain disease), 790
T_1-weighted imaging, 787
$T_{1}\rho$-weighted imaging, 789
T_2 relaxation times
  polymer networks structure, 584
T_2^*-weighted imaging, 788
T_2-weighted imaging, 788
tachykinin NK-1 receptor, 339
tacticity, molecular weight dependence of, 401
TANSEMA, 704
  low RF power experiments, 704
targeted SPIO in detecting tumor necrosis (apoptosis), 766
TB MO methods, 45
  configuration aspects, 46
  conformation aspects, 45
  crystal structure aspects, 48
telomeric DNA, 743
telomeric DNA bound to hTRF2, 745
temperature imaging, 169
temporal resolution, 759
tensor correlation techniques
  MAS, 727
tensor correlation techniques, static, 727
tensor, shielding, 65
tensors
  chemical shielding, 67
  NMR chemical shielding, 66
  shielding, 390
tetramethylsilane, 140
thermosetting resins, 583
thermotropic applications, liquid crystals, 120
tight-binding (TB) molecular orbital (MO) theory. *See* TB MO methods
time dependence of NOE, 411
time domain NMR, 893
tissue signature modeling, 805
tissue-specific contrast agents, 764
TOAC, 316
TORQUE experiments, 199
torsion angle analysis
  backbone, 736, 739
  peptides, 739
torsion angle determination
  distance methods, 732
  MAS tensor correlation techniques, 727
  simultaneous (φ,ψ) determination, 731
  solid-state NMR, 727
  static tensor correlation techniques, 727
  φ angle techniques, 729
  ψ angle techniques, 730
torsion angle measurements, secondary structure analysis (proteins), 738
  mutual orientation of anisotropic interactions, 738
torsion angles, 277
transfection agents, 881
transformation, crystalline polymers, 615
trans–gauche isomerizations, 253
transient NOE, 299
translational diffusion, 135
translational motion, 152
transmembrane helices, 338
transmembrane protein, 338
transverse aortic constriction (TAC), 835
transverse relaxation-optimized spectroscopy, 489
transverse relaxationoptimized spectroscopy (TROSY) technique, 218
TRAPDOR, 150
traumatic brain injury (TBI), 812

triplet instability, 82
triplet instability of CHF, 82
tritiation procedures, 395
tritium NMR spectroscopy, 396
TRNOE measurement, 299
tropoelastin, 93
TROSY
  [^{13}C,^{1}H] correlation experiments, 491
  2D [^{15}N,^{1}H], 491
  and CRINEPT, 494
  and CRIPT, 494
  applications to nucleic acids, 493
  for large biological macromolecules study, 490
  for observation of scalar couplings across hydrogen bonds, 493
  for RDCs measurements, 493
  for resonance assignments in large molecules, 491
  for studies of dynamic processes, 493
  in NOE, 493
  protein backbone resonances, 491
  protein side-chain resonances, 491
T-Stimulus, 190
tumor angiogenesis, gadolinium agents in evaluating, 766
tumor necrosis (apoptosis), targeted SPIO in detecting, 766
tumors
  biology and physiology, 823
  cell-based tumor therapy, 888
  hypoxia, 823
  lipid metabolism in, 827
  pH, 826
  phospholipid metabolism in, 826

U

ultra small superparamagnetic iron oxide (USPIO), 880
unfolded denatured proteins, RDC and, 657
USPIO, 880, 881

V

vascular MRI, 848
velocity component, 159
velocity component mapping sequences, 160
very fast MAS
  paramagnetic effects under, 475
very large structures, cross-correlated relaxation-induced polarization transfer for studies of, 494
vesicle systems, magnetically oriented, 243
VFMAS. *See* very fast MAS
viable myocardium after infarction, manganese-based contrast in determining, 768
voltage-gated potassium channel, 339
volume phase transition, 187
vulcanization, 584

W

water analysis
  atlantic Salmon (*Salmo salar*), 903
    muscle after heating, 902, 904
    low-field NMR studies, 901
  atlantic salmon fillets, 960, 961
  cod fillets, 960, 961
water and solute interactions
  biomolecule–water, 418
  micelle–water, 416
  small molecule–water, 416
water diffusion inside gels, 192
water holding capacity, 913
waterLOGSY technique, 320
WAXD, 563
weighted imaging
  T$_1$, 787
  T$_{1}\rho$, 790
  T$_2$, 788
  T$_2^*$, 788
whole body phenome, 771
wide line separation spectroscopy (WISE), 580
wide-angle X-ray diffraction, 563

X

xenon gas, absorbed, 639
xenon–solvent interactions, 416. *See also* solute–solvent interactions, NOE and
XPLOR package, 657

Z

Zeeman interaction
  EPR principles, 439
Zeeman interaction, nuclear, 439
Zeeman splitting, 353
zeolites, 125
zero field NMR, 445
  demagnetization and initiation of evolution, 446
  experimental aspects, 446
  extensions of, 450
  NMR and NQR, 450
  NMR and NQR, limitations of, 482
  signal evaluation, 445
  zero field signal detection, 448
zero field spin Hamiltonian, 444
zero magnetic field
  NMR and NQR in, 445
zero-quantum experiments, disordered polymers study, 563
zeutmatography, 179

Modern Magnetic Resonance

Part 2

Part 1: Applications in Chemistry, Biological and Marine Sciences

Part 2: Applications in Medical and Pharmaceutical Sciences

Part 3: Applications in Materials Science and Food Science

Modern Magnetic Resonance

Part 2: Applications in Medical and Pharmaceutical Sciences

Graham A. Webb (Ed.)
Royal Society of Chemistry, London, UK

Springer

A C.I.P. Catalogue record for this book is available from the Library of Congress.

ISBN 978-1-4020-3894-5 (HB)
ISBN 978-1-4020-3910-2 (e-book)

Published by Springer,
P.O. Box 17, 3300 AA Dordrecht, The Netherlands.

www.springer.com

Printed on acid-free paper

First published in 2006
Reprinted with corrections in 2008

All rights reserved.
© 2008 Springer
No part of this work may be reproduced, stored in a retrieval system, or transmitted in any form or by any means, electronic, mechanical, photocopying, microfilming, recording or otherwise, without written permission from the Publisher, with the exception of any material supplied specifically for the purpose of being entered and executed on a computer system, for exclusive use by the purchaser of the work.

Contents

List of Section Editors VII
Preface IX
Color Plate Section XI

APPLICATIONS IN MEDICAL SCIENCES

Foreword 975
Abbreviations 977
Glossary of Terms 981

Acquiring Neurospectroscopy in Clinical Practice, *Alexander P. Lin* 985
Application of Magnetic Resonance for the Diagnosis of Infective Brain Lesions, *Uwe Himmelreich and Rakesh K. Gupta* 1005
Application of 2D Magnetic Resonance Spectroscopy to the Study of Human Biopsies, *Edward J. Delikatny and June Q.Y. Watzl* 1015
Correlation of Histopathology with Magnetic Resonance Spectroscopy of Human Biopsies, *Carolyn Mountford, Ian C.P. Smith, and Roger Bourne* 1027
Functional MRI, *Graeme D. Jackson, Regula S. Briellmann, Anthony B. Waites, Gaby S. Pell, and David F. Abbott* 1037
High Resolution Magic Angle Spinning (HRMAS) Proton MRS of Surgical Specimens, *Leo L. Cheng, Melissa A. Burns, and Cynthia L. Lean* 1051
Intraoperative MRI, *Isabelle Latour and Garnette R. Sutherland* 1065
***In Vivo* Magnetic Resonance Spectroscopy in Breast Cancer,** *Uma Sharma and N.R. Jagannathan* 1077
***In Vivo* Molecular MR Imaging: Potential and Limits,** *Mathias Hoehn and Uwe Himmelreich* 1087
***In vivo* ^{13}C MRS,** *Stefan Bluml* 1099
Magnetic Resonance Spectroscopy and Spectroscopic Imaging of the Prostate, Breast, and Liver, *Mark G. Swanson, Susan M. Noworolski, and John Kurhanewicz* 1113
MR-Mammography, *W.A. Kaiser* 1127
Phosphorus Magnetic Resonance Spectroscopy on Biopsy and In Vivo, *Geoffrey S Payne, Nada Al-Saffar, and Martin O Leach* 1143
Radio Frequency Coils for Magnetic Resonance Spectroscopy, *Boguslaw Tomanek* 1163
Spatially Resolved Two-Dimensional MR Spectroscopy in vivo, M. *Albert Thomas, Amir Huda, Hyun-Kyung Chung, Nader Binesh, and Talaignair Venkatraman* 1171

APPLICATIONS IN PHARMACEUTICAL SCIENCE

Foreword 1187
Key Terms 1189

Overview of NMR in the Pharmaceutical Sciences, *Horst Joachim Schirra and David J. Craik* 1195

Instrumentation 1203

Applications of Cryogenic NMR Probe Technology for the Identification of Low-Level Impurities in Pharmaceuticals, *Gary E. Martin* 1205
Flow NMR Techniques in the Pharmaceutical Sciences, *Paul A. Keifer* 1213
Developments in NMR Hyphenation for Pharmaceutical Industry, *Manfred Spraul* 1221
LC-NMR in Dereplication and Structure Elucidation of Herbal Drugs, *Gloria Karagianis and Peter G. Waterman* 1229

Techniques 1237

New Approaches to NMR Data Acquisition, Assignment and Protein Structure Determination: Potential Impact in Drug Discovery, *Antonio Pineda-Lucena* 1239
Transferred Cross-Correlated Relaxation: Application to Drug/Target Complexes, *T. Carlomagno and C. Griesinger* 1247
Novel Uses of Paramagnets to Solve Complex Protein Structures, *R. Andrew Byrd, C. Andrew Fowler, Robert L. McFeeters, and Vadim Gaponenko* 1255
Fast Assignments of ^{15}N-HSQC Spectra of Proteins by Paramagnetic Labeling, *Guido Pintacuda, Thomas Huber, Max A. Keniry, Ah Young Park, Nicholas E. Dixon, and Gottfried Otting* 1263
Phospholipid Bicelle Membrane Systems for Studying Drug Molecules, *Jianxin Guo, Xiaoyu Tian, Spiro Pavlopoulos, and Alexandros Makriyannis* 1271
Partial Alignment for Structure Determination of Organic Molecules, *Burkhard Luy and Horst Kessler* 1279
Measurement of Residual Dipolar Couplings and Applications in Protein NMR, *Keyang Ding and Angela M. Gronenborn* 1287
Using Chemical Shift Perturbations to Validate and Refine the Docking of Novel IgE Antagonists to the High-Affinity IgE Receptor, *Melissa A. Starovasnik and Wayne J. Fairbrother* 1293
Dual-Region Hadamard-Encoding to Improve Resolution and Save Time, *Ronald Crouch* 1299
Nonuniform Sampling in Biomolecular NMR, *Mark W. Maciejewski, Alan S. Stern, Glenn F. King, and Jeffrey C. Hoch* 1305

Applications 1313

Structural Characterization of Antimicrobial Peptides by NMR Spectroscopy, *Leonard T. Nguyen, Elmar J. Prenner, and Hans J. Vogel* 1315
Pharmaceutical Applications of Ion Channel Blockers: Use of NMR to Determine the Structure of Scorpion Toxins, *Muriel Delepierre and Lourival D. Possani* 1325
Structure and Dynamics of Inhibitor and Metal Binding to Metallo-β-Lactamases, *Christian Damblon and Gordon C.K. Roberts* 1331
NMR Spectroscopy in the Analysis of Protein–Protein Interactions, *David A. Gell and Joel P. Mackay*.. 1339
Identification and Characterization of Ternary Complexes Using NMR Spectroscopy, *Robert E. London* 1347
The Transferred NOE, *Mike P Williamson* 1357
NMR Kinetic Measurements in DNA Folding and Drug Binding, *Mark S. Searle, Graham Balkwill, Huw E.L. Williams, and Evripidis Gavathiotis* 1363
The Use of NMR in the Studies of Highly Flexible States of Proteins: Relation to Protein Function and Stability, *Søren M. Kristensen, Marina R. Kasimova, and Jens J. Led* 1369
NMR-based Metabonomics Techniques and Applications, *John C. Lindon, Elaine Holmes, and Jeremy K. Nicholson* 1377
Protein Misfolding Disease: Overview of Liquid and Solid-State High Resolution NMR Studies, *Harald Schwalbe and Julia Wirmer* 1387
^{19}F NMR Spectroscopy for Functional and Binding High-Throughput Screening, *Marina Veronesi and Claudio Dalvit* 1393
Applications of Receptor-Based NMR Screening in Drug Discovery, *Philip J. Hajduk* 1401
NMR SHAPES Screening, *Christopher A. Lepre and Jonathan M. Moore* 1409
NMR-Based Screening Applied to Drug Discovery Targets, *Jennifer J. Gesell, Mark A. McCoy, Mary M. Senior, Yu-Sen Wang, and Daniel F. Wyss* 1419
NMR and Structural Genomics in the Pharmaceutical Sciences, *Maša Čemažar and David J. Craik* 1429

Author Index
Subject Index

List of Section Editors

Subject	Name	Type of Editor
	Graham A. Webb	Editor-In-Chief
Chemistry	Hazime Saitô Himeji Institute of Technology and QuLiS, Hiroshima University Japan e-mail: hsaito@siren.ocn.ne.jp	Section Editors
	Isao Ando Department of Chemistry and Materials Science Tokyo Institute of Technology, Ookayama, Meguro-ku Tokyo 152-0033 Japan e-mail: iando@polymer.titech.ac.jp	
	Tetsuo Asakura Department of Biotechnology Tokyo University of Agriculture and Technology Koganei, Tokyo 184-8588 Japan e-mail: asakura@cc.tuat.ac.jp	
Biological Sciences	Jimmy D. Bell Molecular Imaging Group, MRC Clinical Sciences Centre Hammersmith Hospital Campus, Imperial College London London, W12 OHS UK e-mail: jimmy.bell@csc.mrc.ac.uk	Section Editor
Marine Science	M. Aursand SINTEF Fisheries and Aquaculture Ltd N-7465 Trondheim Norway e-mail: marit.aursand@sintef.no	Section Editor
Medical Science	Carolyn Mountford Institute for Magnetic Resonance Research, and Department of Magnetic Resonance in Medicine University of Sydney, PO Box 148, St Leopards, 1590, NSW Australia email: caro@imrr.usyd.edu.au	Section Editor
	Uwe Himmelreich, PhD Max-Planck-Institute for Neurological Research In vivo NMR Group, Gleueler Str 50, Cologne, D-50931 Germany email: himmelreich@mpin-koeln.mpg.de	
	Deborah Edward Pageturner (Editing & Research Services)	Assistant Editor

Subject	Name	Type of Editor
Pharmaceutical Science	David Craik Institute for Molecular Bioscience University of Queensland Brisbane 4072, Queensland Australia e-mail: d.craik@imb.uq.edu.au	Section Editor
Materials Science	Marcel Utz University of Connecticut, 97 N Eagleville Rd Storrs CT 06269-3136 e-mail: marcel.utz@uconn.edu	Section Editor
Food Science	Peter Belton School of Chemical Sciences and Pharmacy University of East Anglia Norwich NR4 7TJ, UK e-mail: p.belton@uea.ac.uk	Section Editor

Preface

It is a great pleasure for me to Introduce the handbook of Modern Magnetic Resonance, MMR. The various techniques which comprise MMR derive essentially from three sources, all of which were produced by physicists. Today they are widely used by scientists working in many diverse areas such as chemistry, biology, materials, food, medicine and healthcare, pharmacy and marine studies.

The first source of MMR studies is nuclear magnetic resonance, NMR. This provides details on the relative positions of nuclei, i.e. atoms, in a molecule. Consequently NMR provides structural information on samples which may be in the solid, liquid or gaseous state. Nuclear relaxation data yield dynamic information on the sample and the topology of the dynamic processes if the sample is undergoing a molecular change. Thus high and low resolution NMR studies provide information on all interesting aspects of molecular science. The protean nature of NMR is reflected in its many applications in chemistry, biology and physics which explore and characterize chemical reactions, molecular conformations, biochemical pathways and solid state materials, to name a few examples.

Magnetic resonance imaging, MRI, is the second source of MMR data. MRI provides a three-dimensional image of a substance, and is consequently widely employed to assess materials both *in vitro* and *in vivo*. The importance of MRI studies in many areas of science and medicine is shown by the recent award of the Nobel Prize to Lauterbur and Mansfield.

The third source of MMR results is due to electron spin resonance, ESR. This is a technique for detecting unpaired electrons and their interactions with nuclear spins in a given sample. Thus ESR data are often used to complement the results of NMR experiments.

Taken together NMR, MRI and ESR comprise the field of MMR, recent years have witnessed the fecundity of these techniques in many scientific areas. The present three volumes cover applications in most of these areas. Part 1 deals with Chemical Applications, Biological and Marine Sciences. Medical and Pharmaceutical Sciences are covered in Part 2. Part 3 provides examples of recent work in the Materials Science and Food Science.

I wish to express my gratitude to all of the Section Editors and their many contributors for their hard work and dedication in the creation of MMR. My thanks also go to Emma Roberts and the production staff at Springer, London, for their assistance in the realization of these volumes.

G.A.WEBB
February 2005

Royal Society of Chemistry
Burlington House
Piccadilly
London, W1J OBA

Please note that authors used either British or American English spelling depending on the language of their choice for individual papers.

Graham A. Webb (ed.), Modern Magnetic Resonance, IX.
© 2008 *Springer.*

Color Plate Section

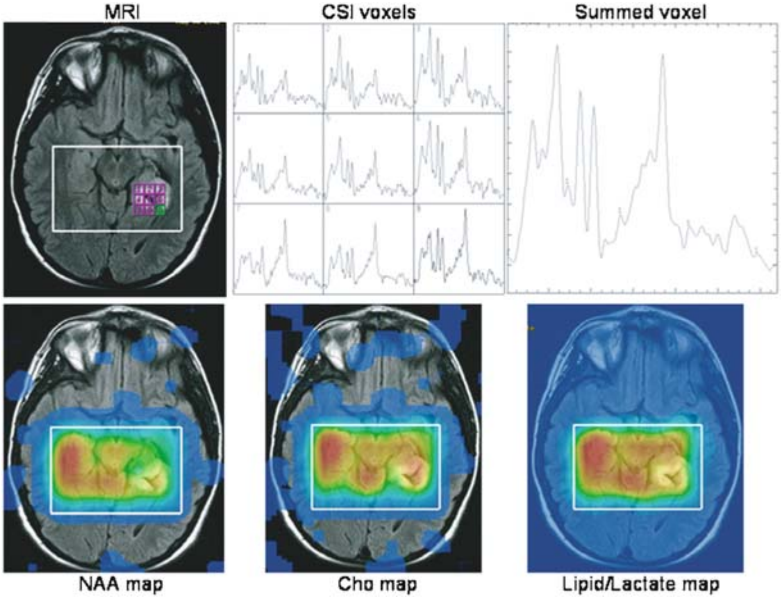
MRI
CSI voxels
Summed voxel
NAA map
Cho map
Lipid/Lactate map

Plate 82. See also Figure 15 on page 1002.

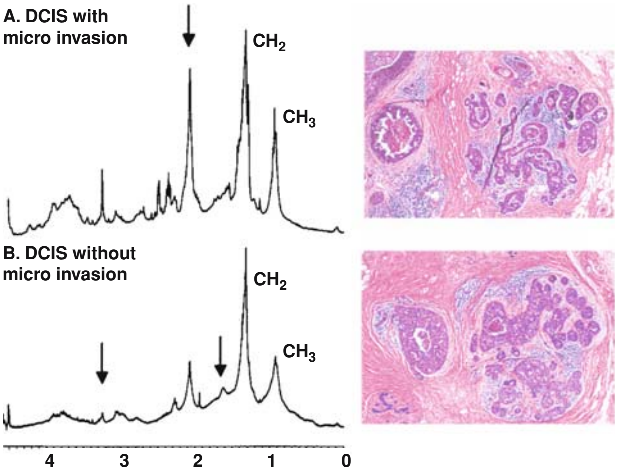

Plate 83. See also Figure 2 on page 1031.

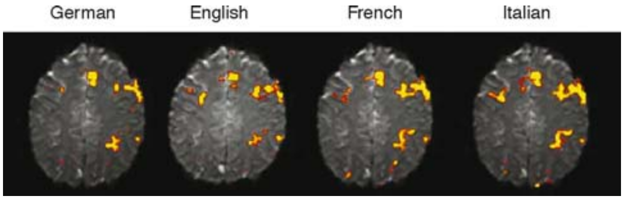
German
English
French
Italian

Plate 84. See also Figure 3 on page 1043.

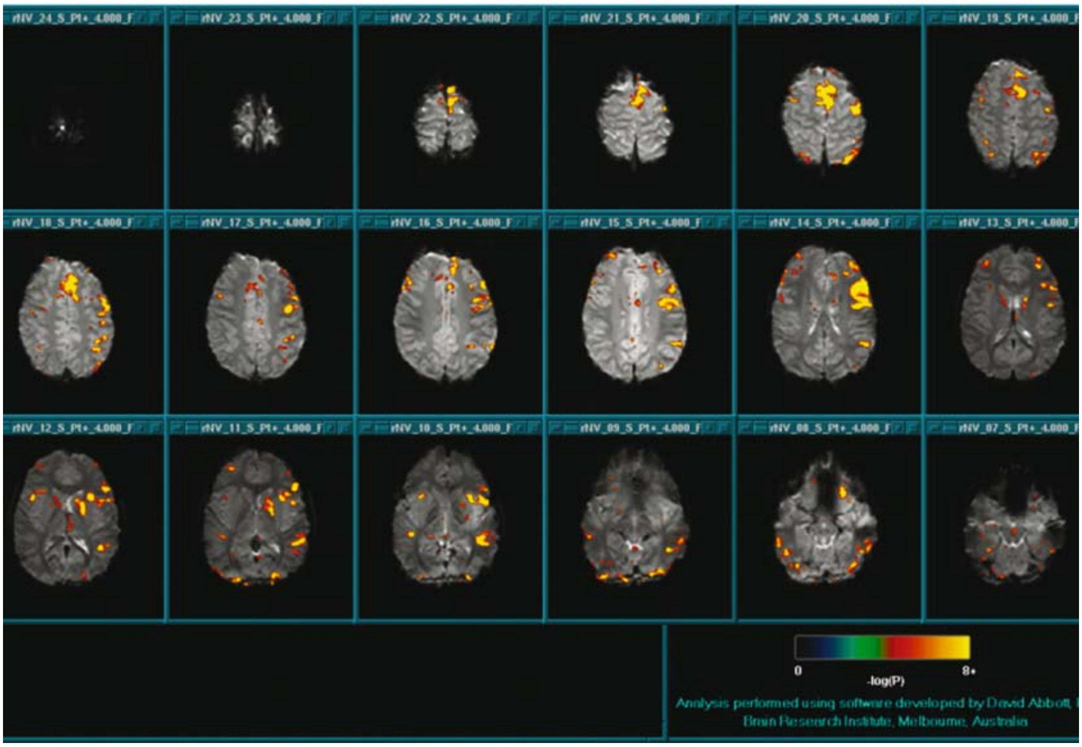
rNV_24_S_Pt+_4.000_F
rNV_23_S_Pt+_4.000_F
rNV_22_S_Pt+_4.000_F
rNV_21_S_Pt+_4.000_F
rNV_20_S_Pt+_4.000_F
rNV_19_S_Pt+_4.000_
rNV_18_S_Pt+_4.000_F
rNV_17_S_Pt+_4.000_F
rNV_16_S_Pt+_4.000_F
rNV_15_S_Pt+_4.000_F
rNV_14_S_Pt+_4.000_F
rNV_13_S_Pt+_4.000_
rNV_12_S_Pt+_4.000_F
rNV_11_S_Pt+_4.000_F
rNV_10_S_Pt+_4.000_F
rNV_09_S_Pt+_4.000_F
rNV_08_S_Pt+_4.000_F
rNV_07_S_Pt+_4.000_
0
-log(P)
8+

Analysis performed using software developed by David Abbott,
Brain Research Institute, Melbourne, Australia

Plate 85. See also Figure 6 on page 1045.

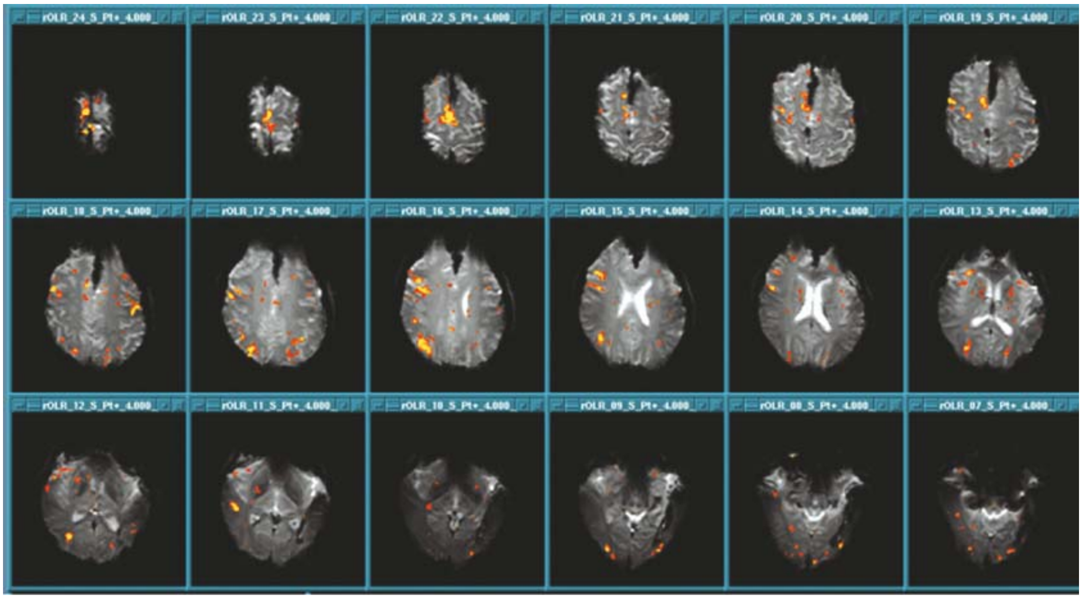
rOLR_24_S_Pt+_4.000_
rOLR_23_S_Pt+_4.000_
rOLR_22_S_Pt+_4.000_
rOLR_21_S_Pt+_4.000_
rOLR_20_S_Pt+_4.000_
rOLR_19_S_Pt+_4.000_
rOLR_18_S_Pt+_4.000_
rOLR_17_S_Pt+_4.000_
rOLR_16_S_Pt+_4.000_
rOLR_15_S_Pt+_4.000_
rOLR_14_S_Pt+_4.000_
rOLR_13_S_Pt+_4.000_
rOLR_12_S_Pt+_4.000_
rOLR_11_S_Pt+_4.000_
rOLR_10_S_Pt+_4.000_
rOLR_09_S_Pt+_4.000_
rOLR_08_S_Pt+_4.000_
rOLR_07_S_Pt+_4.000_

Plate 86. See also Figure 8 on page 1046.

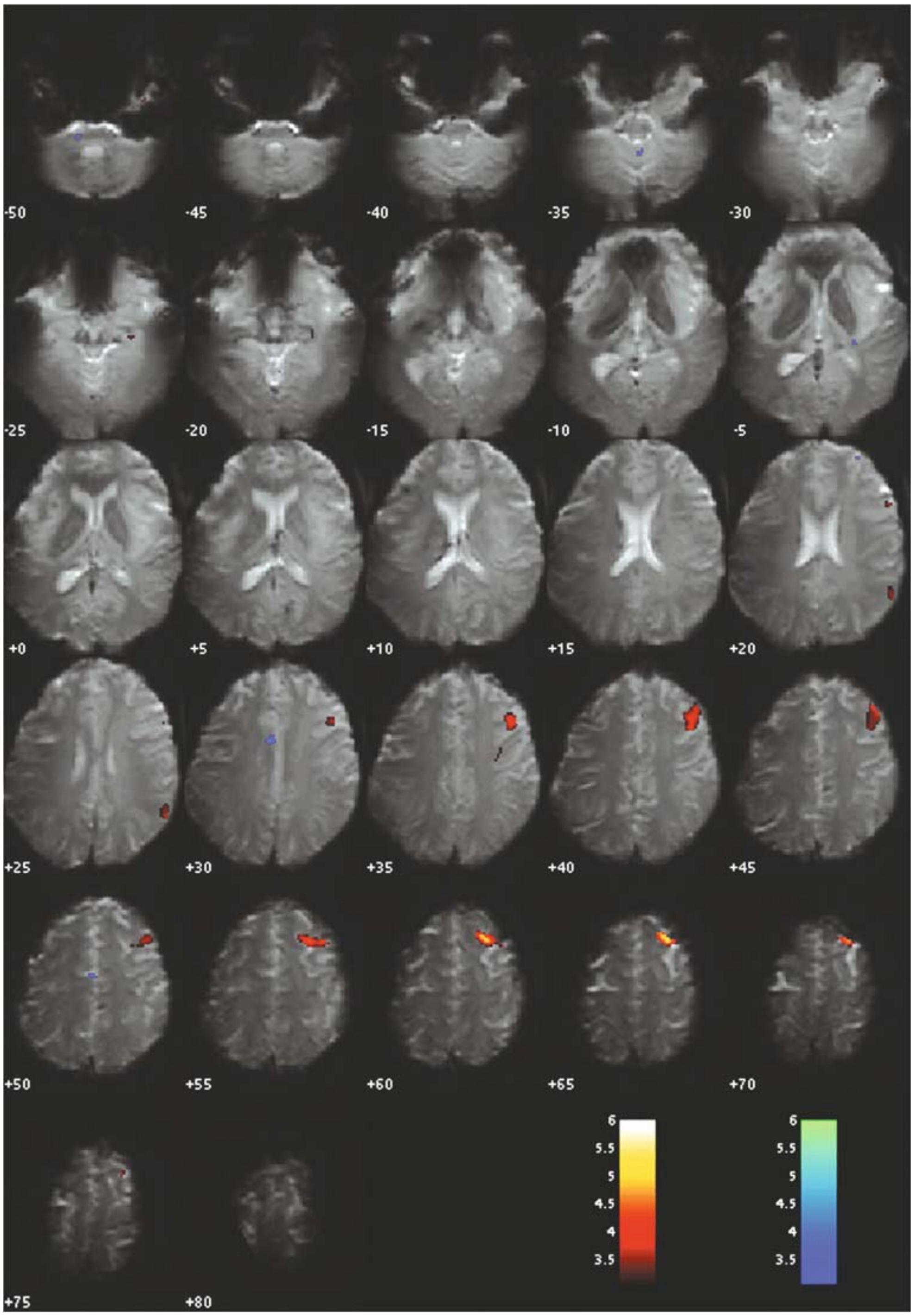
-50
-45
-40
-35
-30
-25
-20
-15
-10
-5
+0
+5
+10
+15
+20
+25
+30
+35
+40
+45
+50
+55
+60
+65
+70
+75
+80
6
5.5
5
4.5
4
3.5
6
5.5
5
4.5
4
3.5

Plate 87. See also Figure 10 on page 1048.

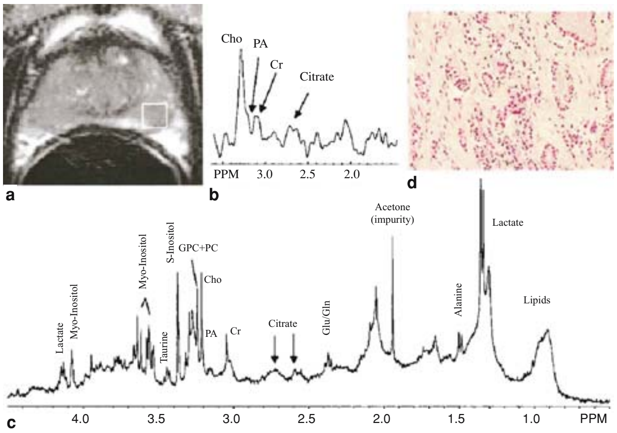
a
b
Cho
PA
Cr
Citrate
PPM
3.0
2.5
2.0
d
c
Lactate
Myo-Inositol
Myo-Inositol
Taurine
S-Inositol
GPC+PC
Cho
PA
Cr
Citrate
Glu/Gln
Acetone
(impurity)
Alanine
Lactate
Lipids
4.0
3.5
3.0
2.5
2.0
1.5
1.0
PPM

Plate 88. See also Figure 6 on page 1059.

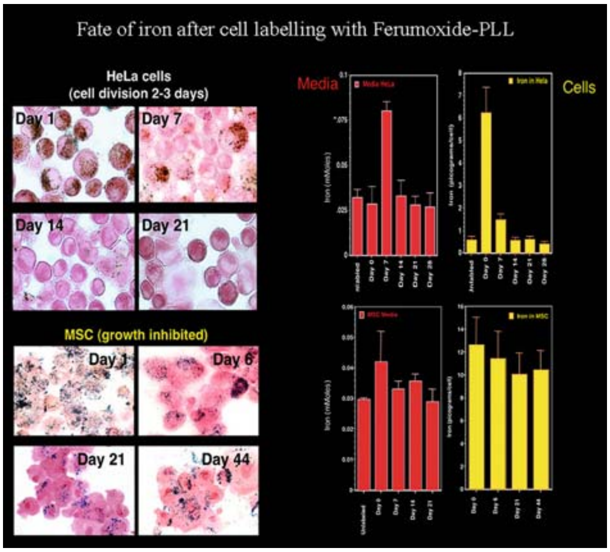

Plate 89. See also Figure 3 on page 1094.

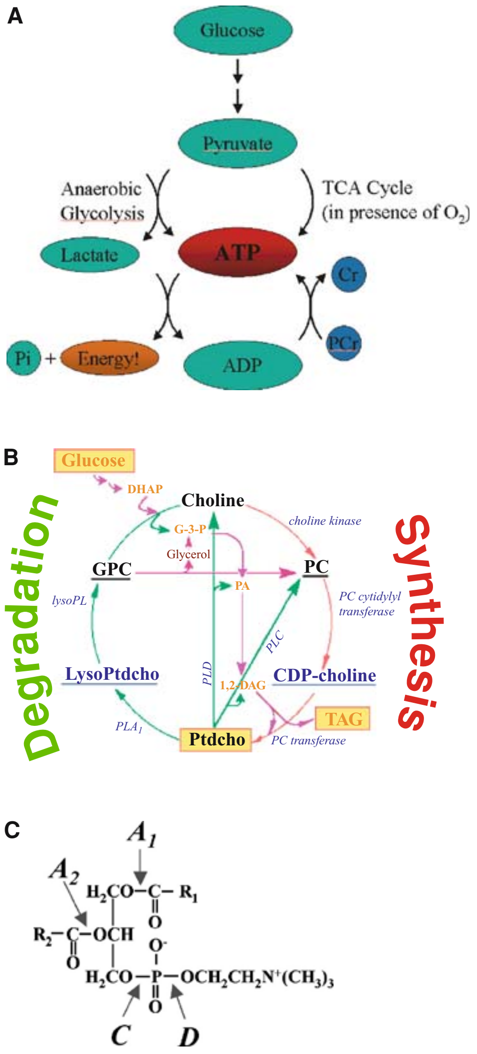
A
Glucose
Pyruvate
Anaerobic
Glycolysis
TCA Cycle
(in presence of O2)
Lactate
ATP
Cr
PCr
Pi
+
Energy!
ADP
B
Glucose
DHAP
Choline
G-3-P
Glycerol
choline kinase
GPC
PC
PA
lysoPL
PC cytidylyl transferase
PLC
PLD
LysoPtdcho
CDP-choline
1,2-DAG
PLA1
Ptdcho
TAG
PC transferase
Degradation
Synthesis
C
A1
A2
H2CO–C–R1
O
R2–C–OCH
O
O-
H2CO–P–OCH2CH2N+(CH3)3
O
C
D

Plate 90. See also Figure 3 on page 1146.

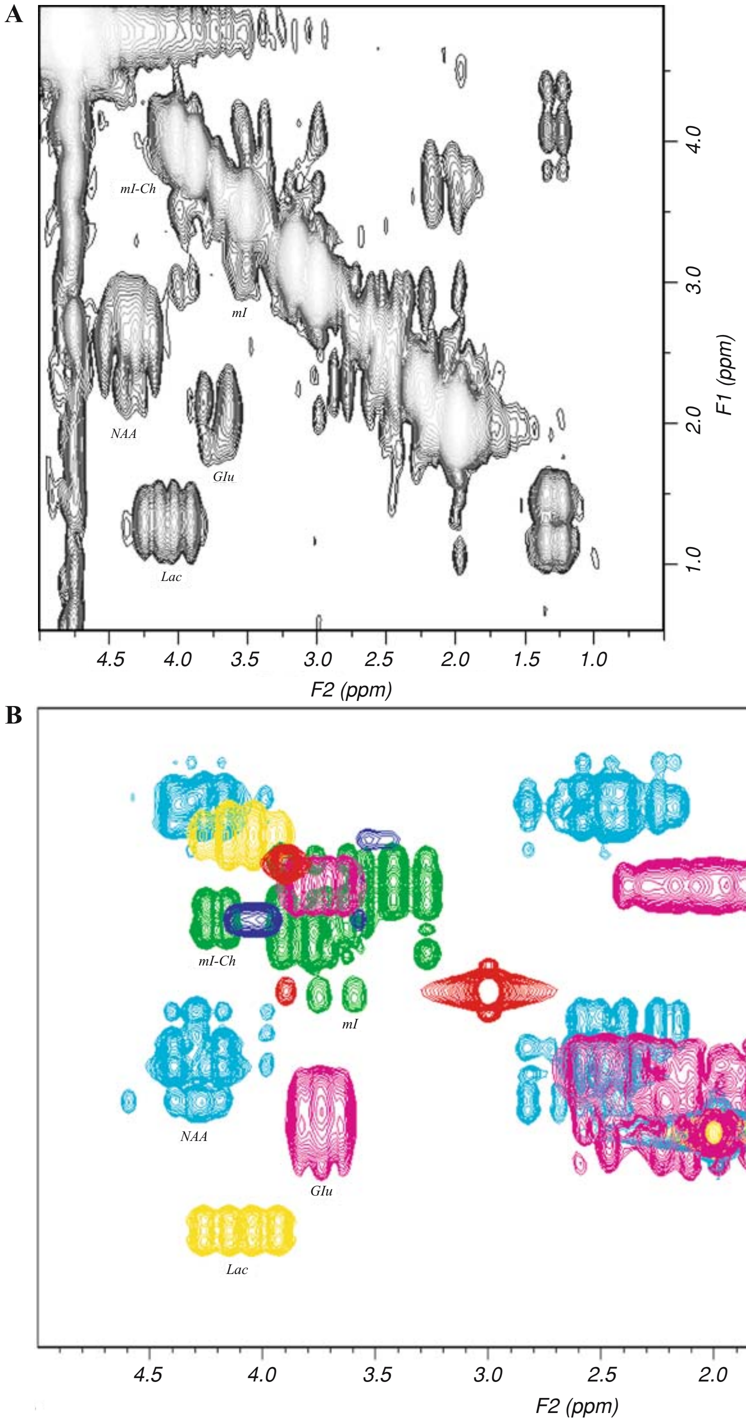
A
mI-Ch
mI
NAA
Glu
Lac
4.5
4.0
3.5
3.0
2.5
2.0
1.5
1.0
F2 (ppm)
4.0
3.0
2.0
1.0
F1 (ppm)
B
mI-Ch
mI
NAA
Glu
Lac
4.5
4.0
3.5
3.0
2.5
2.0
1.5
1.0
F2 (ppm)
4.0
3.0
2.0
1.0
F1 (ppm)

Plate 91. See also Figure 11 on page 1181.

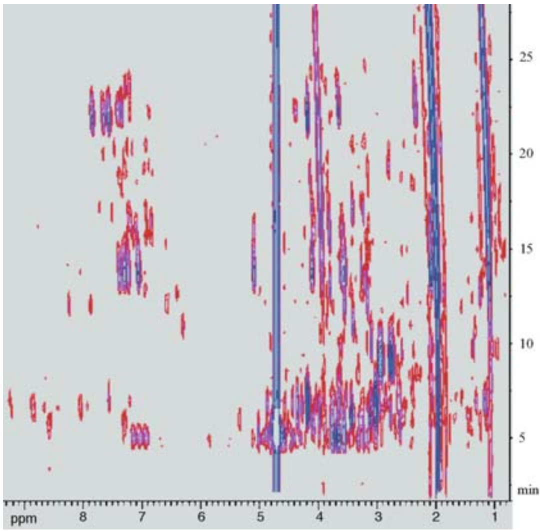

Plate 92. See also Figure 2 on page 1223.

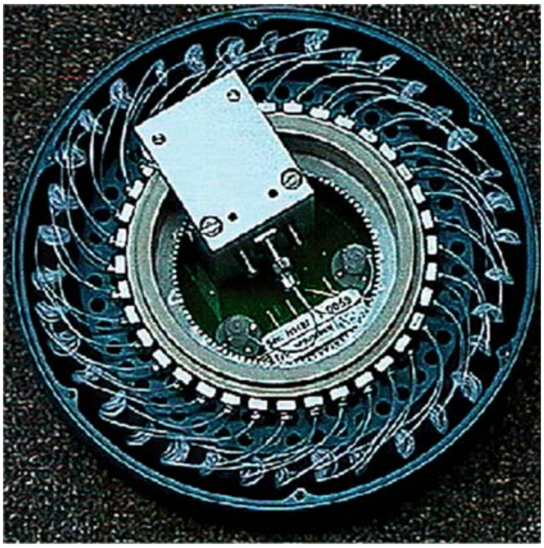

Plate 93. See also Figure 4 on page 1225.

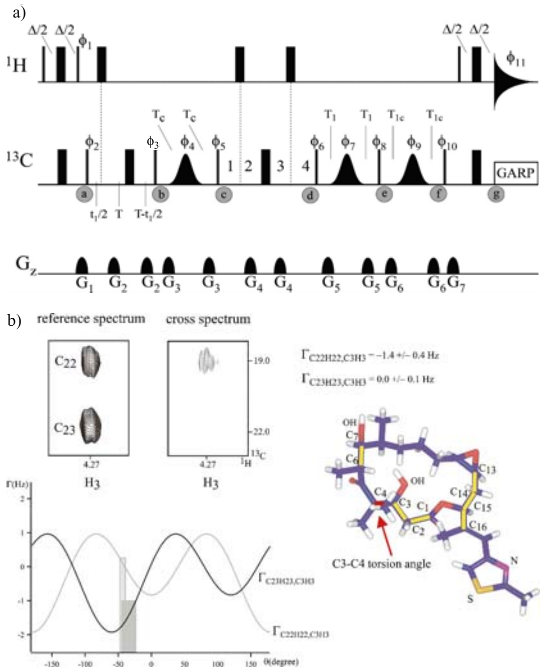
a)
Δ/2
Δ/2
ϕ_1
^{1}H
Δ/2
Δ/2
ϕ_{11}
T_c
T_c
T_1
T_1
T_{1c}
T_{1c}
^{13}C
ϕ_2
ϕ_3
ϕ_4
ϕ_5
1
2
3
4
ϕ_6
ϕ_7
ϕ_8
ϕ_9
ϕ_{10}
GARP
a
b
c
d
e
f
g
$t_1/2$
T
$T-t_1/2$
G_z
G_1
G_2
G_2
G_3
G_3
G_4
G_4
G_5
G_5
G_6
G_6
G_7
b)
reference spectrum
cross spectrum
C22
C23
4.27
H3
4.27
H3
19.0
22.0
^{13}C
^{1}H
$\Gamma_{C22H22,C3H3}$ = −1.4 +/− 0.4 Hz
$\Gamma_{C23H23,C3H3}$ = 0.0 +/− 0.1 Hz
Γ(Hz)
2
1
0
-1
-2
-150
-100
-50
0
50
100
150
θ(degree)
$\Gamma_{C23H23,C3H3}$
$\Gamma_{C22H22,C3H3}$
OH
C7
C6
OH
C4
C3
C1
C2
C13
C14
C15
C16
N
S
C3-C4 torsion angle

Plate 94. See also Figure 3 on page 1251.

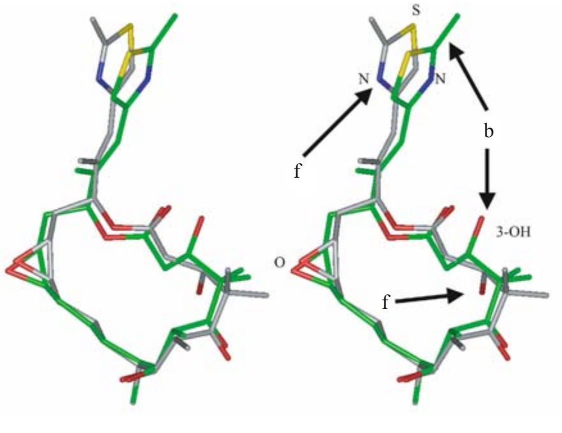
S
N
N
f
b
3-OH
O
f

Plate 95. See also Figure 4 on page 1253.

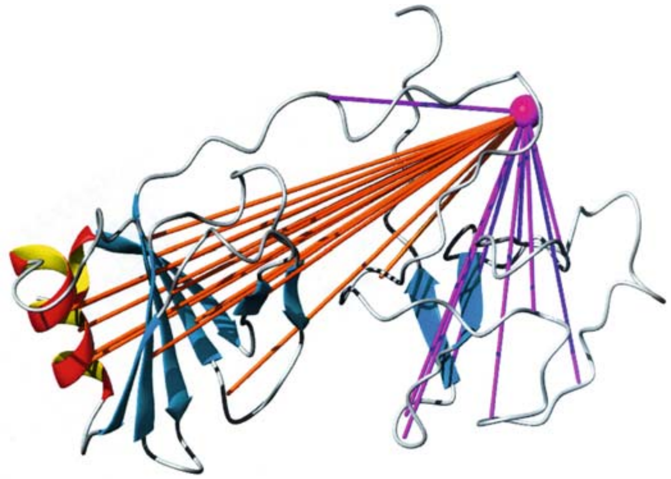

Plate 96. See also Figure 3 on page 1260.

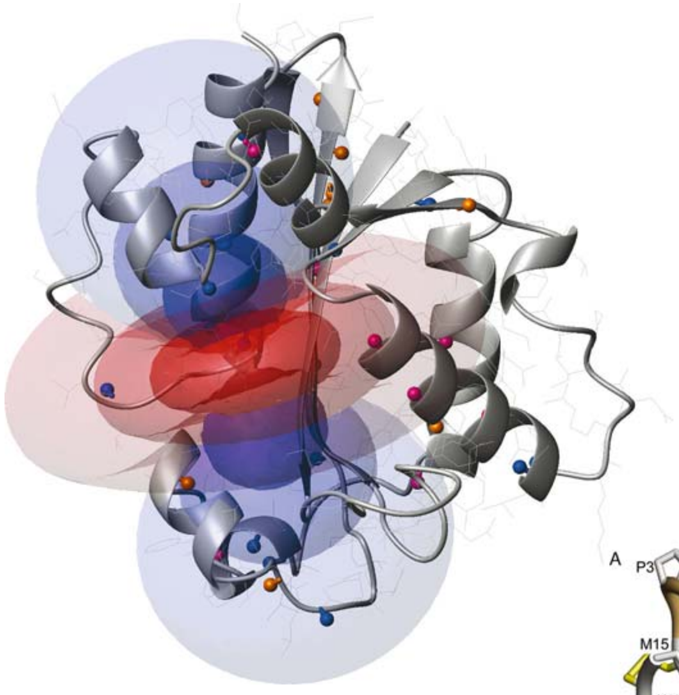

Plate 97. See also Figure 4 on page 1266.

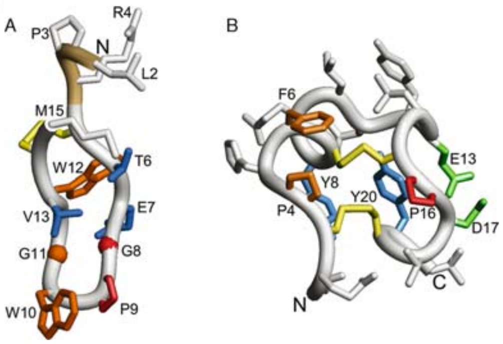
A
R4
P3
N
L2
M15
T6
W12
E7
V13
G8
G11
W10
P9
B
F6
E13
Y8
Y20
P4
P16
D17
N
C

Plate 98. See also Figure 1 on page 1294.

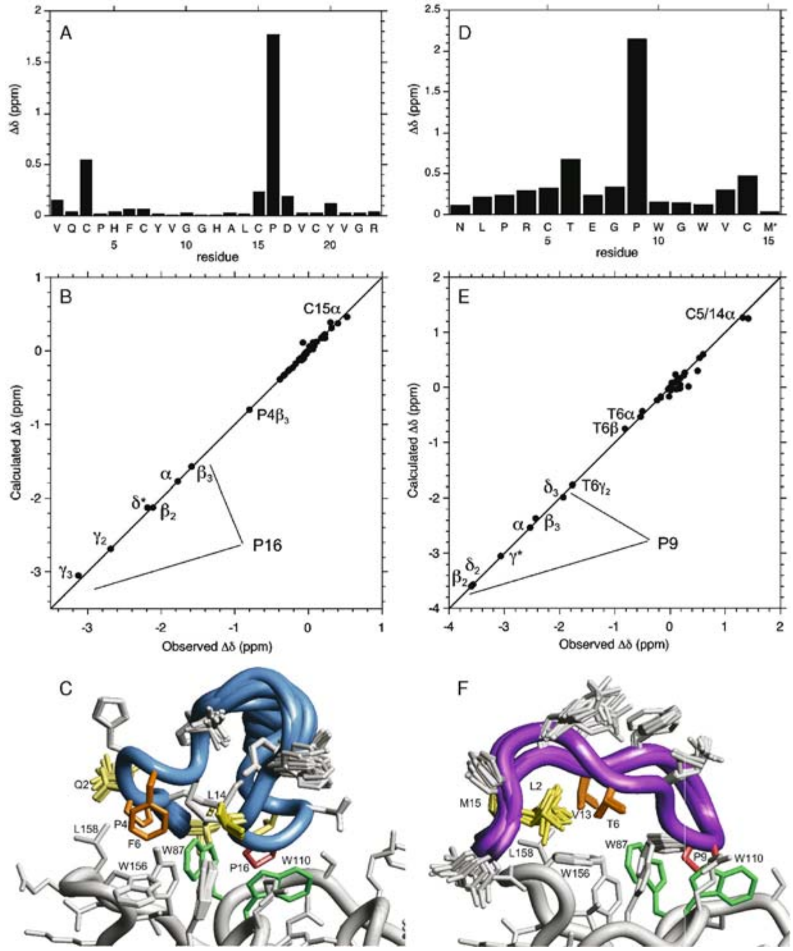

Plate 99. See also Figure 3 on page 1296.

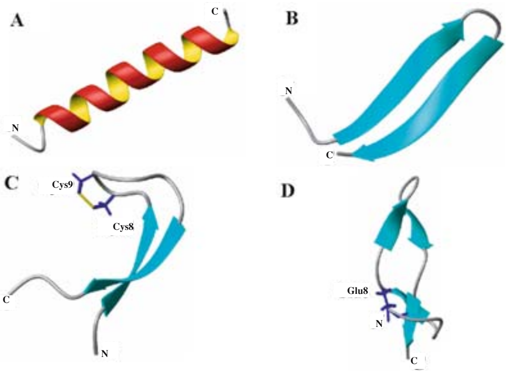
A
C
N
B
N
C
C
Cys9
Cys8
C
N
D
Glu8
N
C

Plate 100. See also Figure 1 on page 1317.

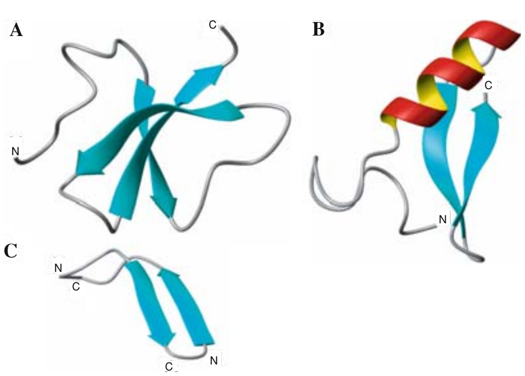
A
C
N
B
C
N
C
N
C
C
N

Plate 101. See also Figure 2 on page 1317.

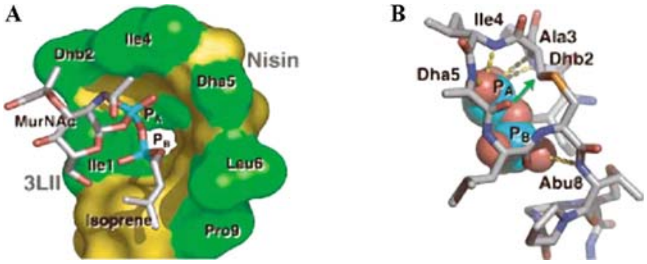
A
Dhb2
Ile4
Nisin
Dha5
MurNAc
P_A
P_B
Ile1
Leu6
3LII
Isoprene
Pro9
B
Ile4
Ala3
Dhb2
Dha5
P_A
P_B
Abu8

Plate 102. See also Figure 3 on page 1318.

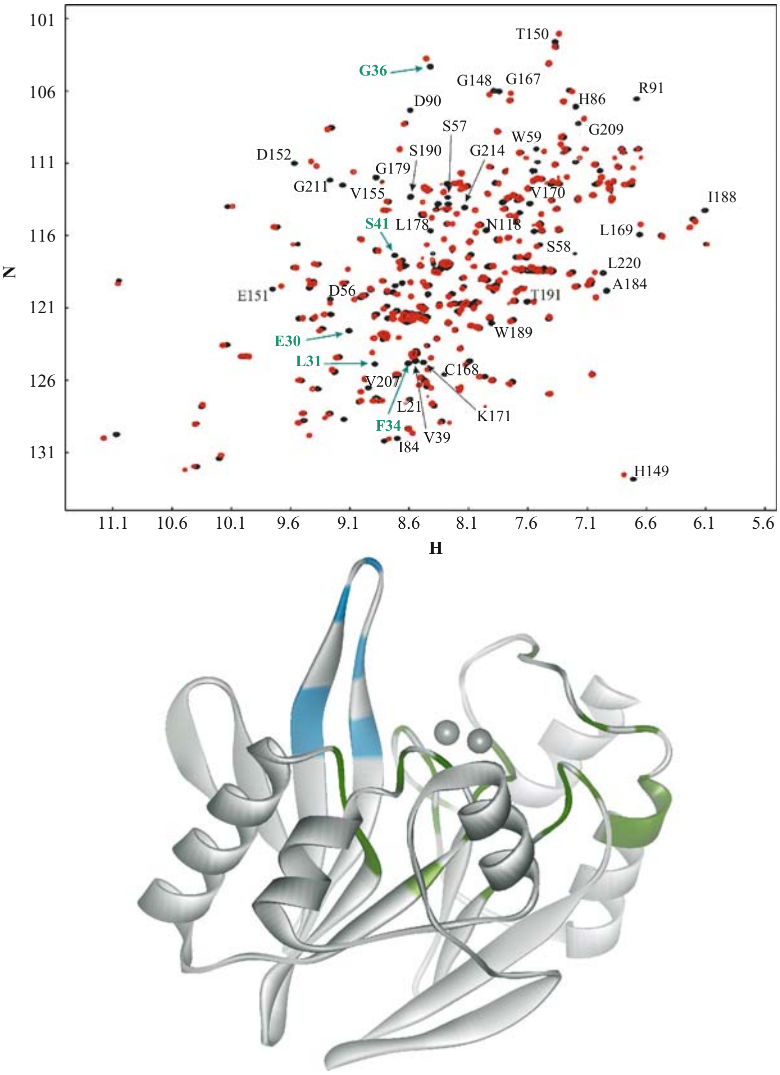

Plate 103. See also Figure 1 on page 1333.

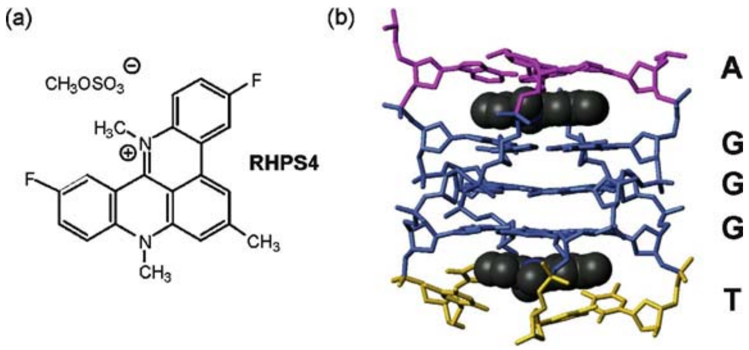
(a)
CH3OSO3
H3C
N
F
F
RHPS4
N
CH3
CH3
(b)
A
G
G
G
T

Plate 104. See also Figure 1 on page 1364.

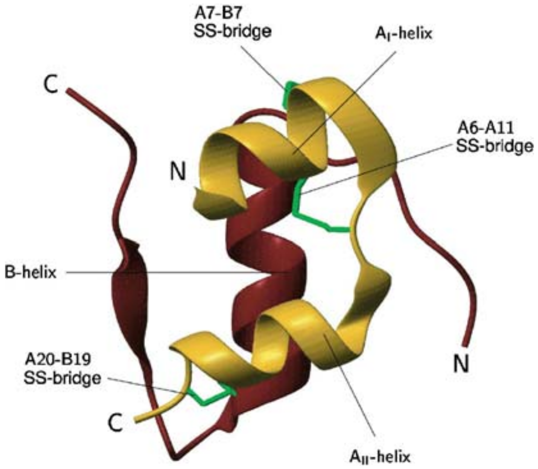
A7-B7
SS-bridge
AI-helix
C
N
A6-A11
SS-bridge
B-helix
N
A20-B19
SS-bridge
C
AII-helix

Plate 105. See also Figure 1 on page 1370.

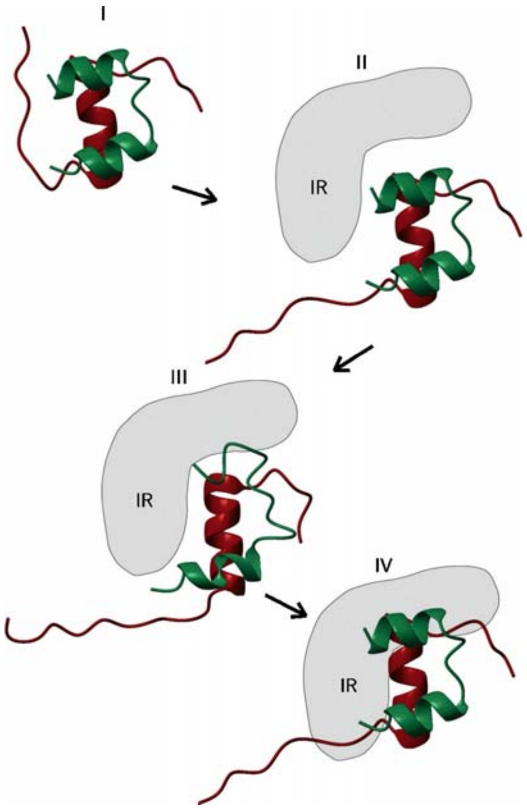
I
II
IR
III
IR
IV
IR

Plate 106. See also Figure 3 on page 1372.

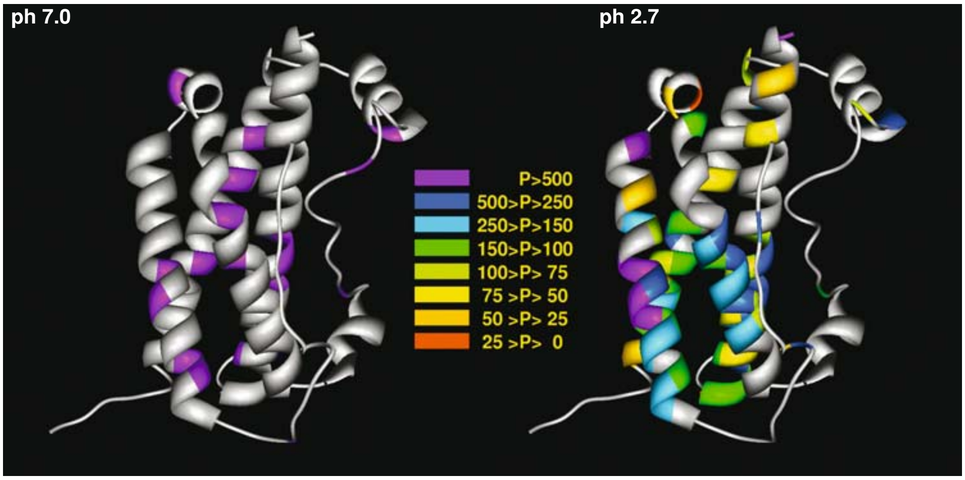
ph 7.0
ph 2.7
P>500
500>P>250
250>P>150
150>P>100
100>P> 75
75 >P> 50
50 >P> 25
25 >P> 0

Plate 107. See also Figure 4 on page 1373.

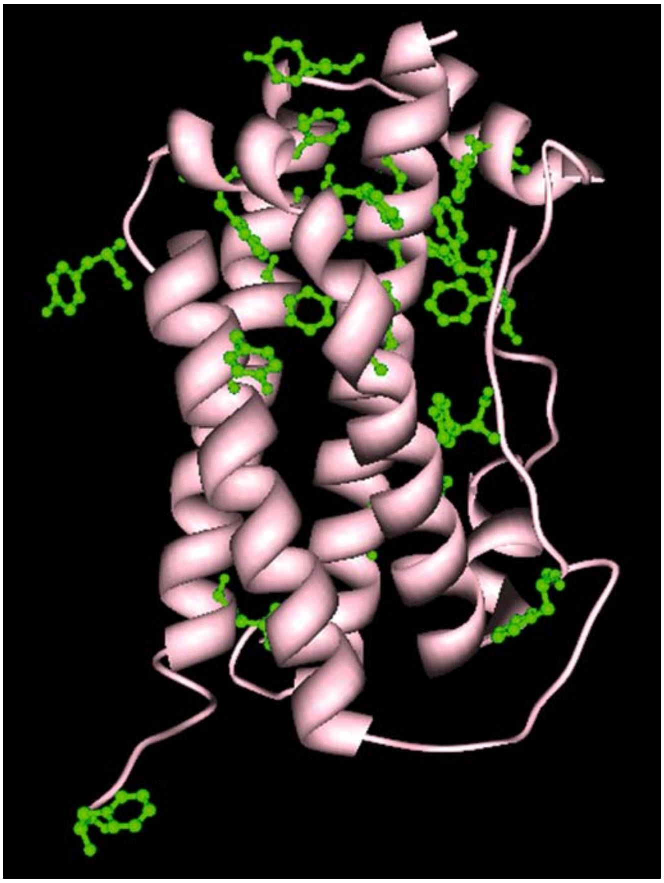

Plate 108. See also Figure 6 on page 1374.

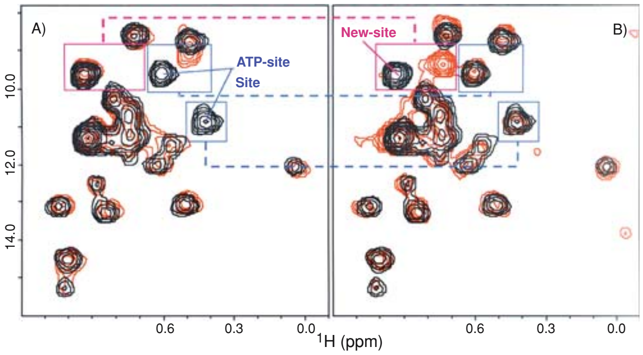

Plate 109. See also Figure 2 on page 1403.

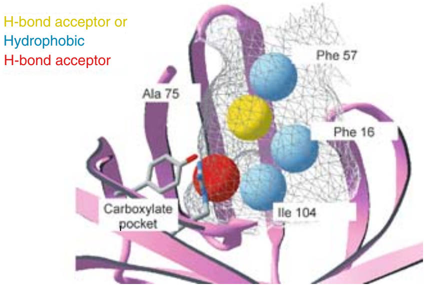
H-bond acceptor or
Hydrophobic
H-bond acceptor
Phe 57
Ala 75
Phe 16
Carboxylate pocket
Ile 104

Plate 110. See also Figure 4 on page 1413.

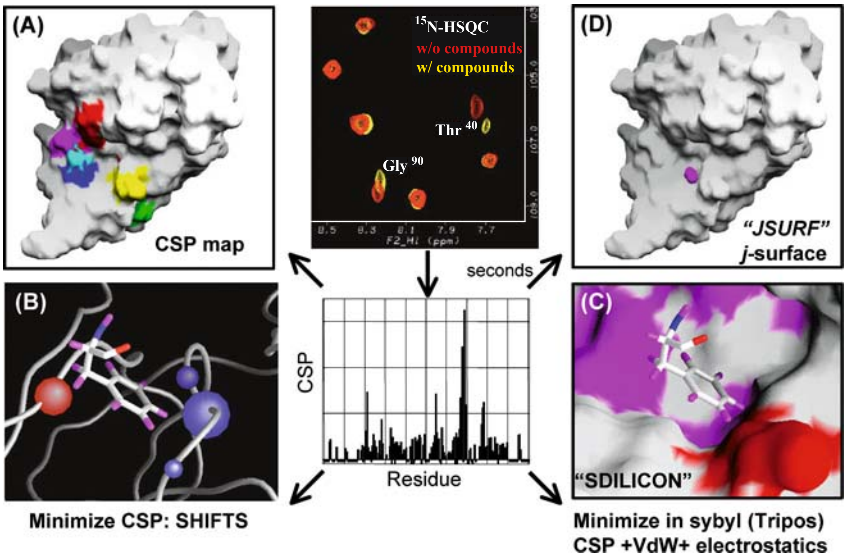
(A)
CSP map
^{15}N-HSQC
w/o compounds
w/ compounds
Thr 40
Gly 90
8.5
8.3
8.1
7.9
7.7
F2_H1 (ppm)
(D)
"JSURF"
j-surface
seconds
(B)
CSP
Residue
(C)
"SDILICON"
Minimize CSP: SHIFTS
Minimize in sybyl (Tripos)
CSP +VdW+ electrostatics

Plate 111. See also Figure 1 on page 1420.

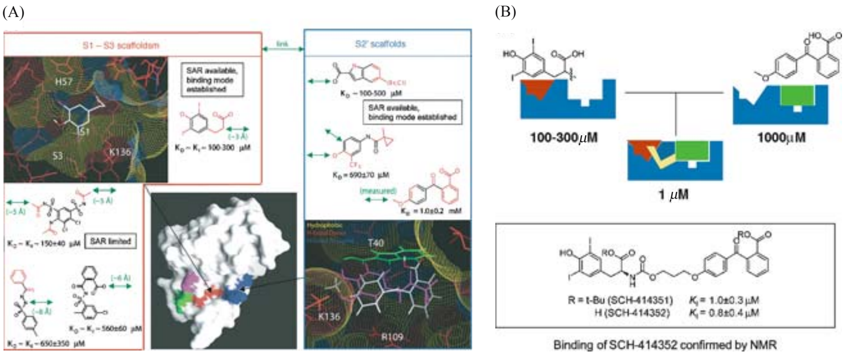
(A)
S1 – S3 scaffoldsm
link
S2' scaffolds
H57
S1
S3
K136
SAR available, binding mode established
$K_D \sim K_I \sim 100\text{-}300$ μM
(~3 Å)
$K_D \sim 100\text{-}500$ μM
SAR available, binding mode established
$K_D = 690 \pm 70$ μM
(measured)
$K_D = 1.0 \pm 0.2$ mM
(~5 Å)
(~5 Å)
$K_D \sim K_I \sim 150 \pm 40$ μM
SAR limited
(~6 Å)
(~8 Å)
$K_D \sim K_I \sim 560 \pm 60$ μM
$K_D \sim K_I \sim 650 \pm 350$ μM
T40
K136
R109
(B)
100-300μM
1000μM
1 μM
R = t-Bu (SCH-414351) $K_i = 1.0 \pm 0.3$ μM
H (SCH-414352) $K_i = 0.8 \pm 0.4$ μM
Binding of SCH-414352 confirmed by NMR

Plate 112. See also Figure 3 on page 1425.

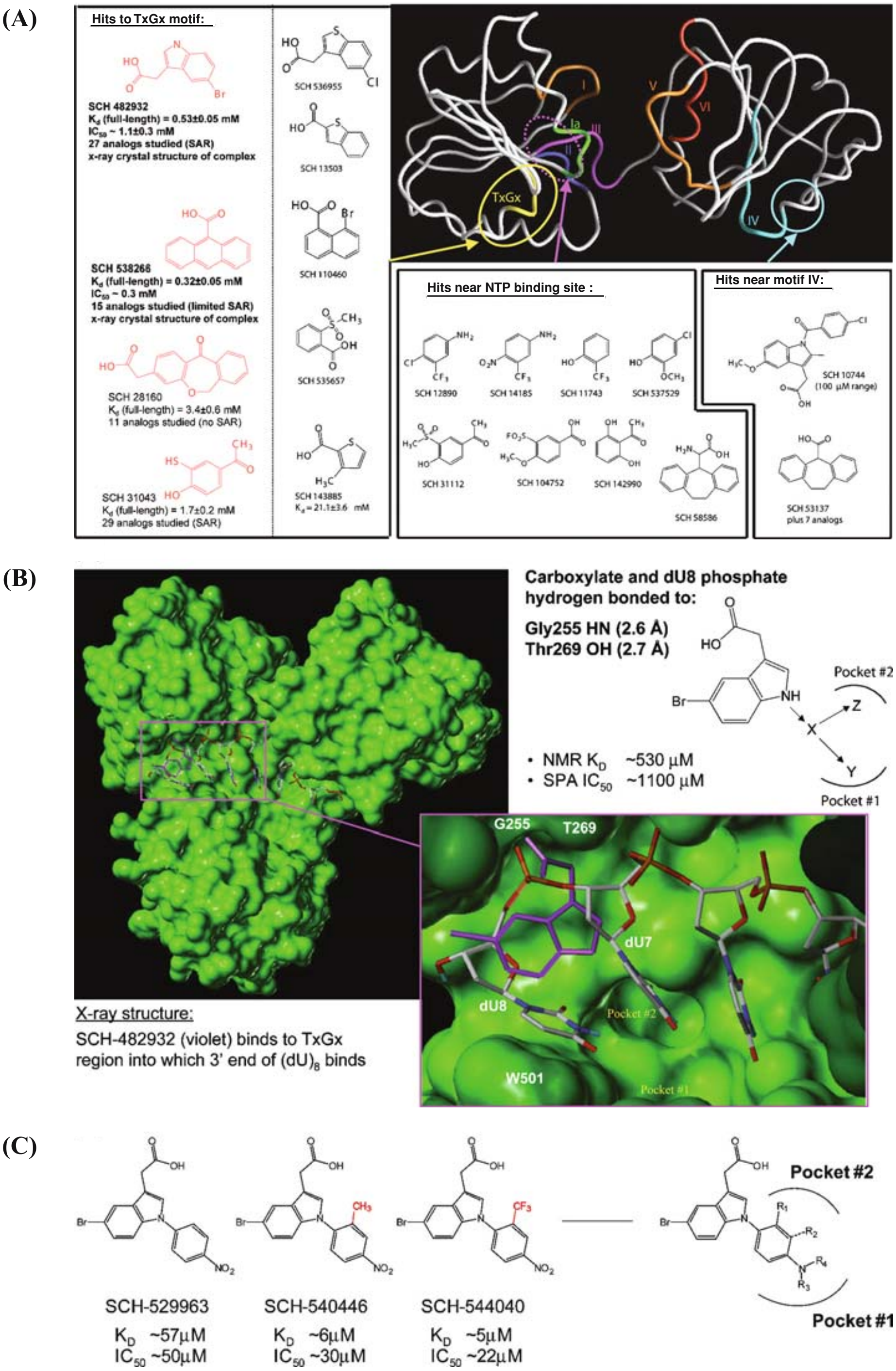
(A)
Hits to TxGx motif:
SCH 482932
Kd (full-length) = 0.53±0.05 mM
IC50 ~ 1.1±0.3 mM
27 analogs studied (SAR)
x-ray crystal structure of complex
SCH 538266
Kd (full-length) = 0.32±0.05 mM
IC50 ~ 0.3 mM
15 analogs studied (limited SAR)
x-ray crystal structure of complex
SCH 28160
Kd (full-length) = 3.4±0.6 mM
11 analogs studied (no SAR)
SCH 31043
Kd (full-length) = 1.7±0.2 mM
29 analogs studied (SAR)
SCH 536955
SCH 13503
SCH 110460
SCH 535657
SCH 143885
Kd = 21.1±3.6 mM
I
Ia
II
III
TxGx
V
VI
IV
Hits near NTP binding site :
SCH 12890
SCH 14185
SCH 11743
SCH 537529
SCH 31112
SCH 104752
SCH 142990
SCH 58586
Hits near motif IV:
SCH 10744
(100 µM range)
SCH 53137
plus 7 analogs
(B)
Carboxylate and dU8 phosphate hydrogen bonded to:
Gly255 HN (2.6 Å)
Thr269 OH (2.7 Å)
Pocket #2
Pocket #1
• NMR KD ~530 µM
• SPA IC50 ~1100 µM
X-ray structure:
SCH-482932 (violet) binds to TxGx region into which 3' end of (dU)8 binds
G255
T269
dU7
dU8
Pocket #2
W501
Pocket #1
(C)
SCH-529963
KD ~57µM
IC50 ~50µM
SCH-540446
KD ~6µM
IC50 ~30µM
SCH-544040
KD ~5µM
IC50 ~22µM
Pocket #2
Pocket #1

Plate 113. See also Figure 4 on page 1426.

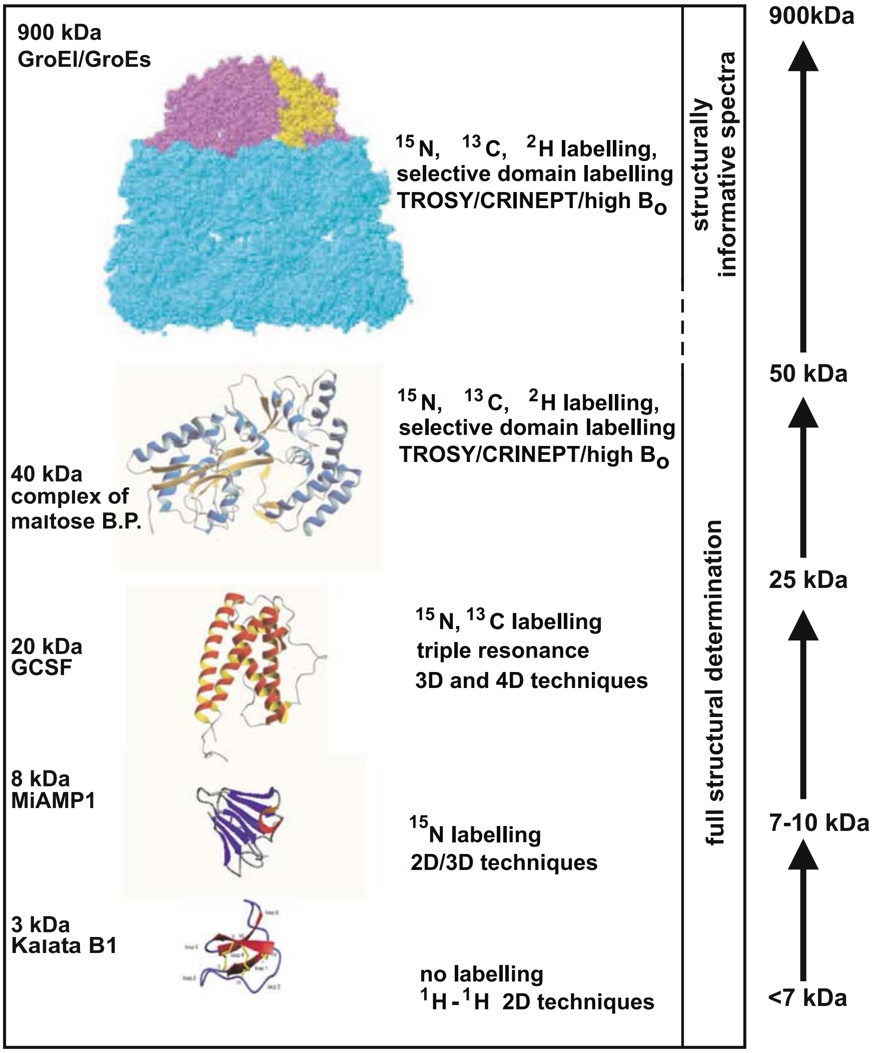
900 kDa
GroEl/GroEs
^{15}N, ^{13}C, ^{2}H labelling,
selective domain labelling
TROSY/CRINEPT/high B_o
40 kDa
complex of
maltose B.P.
^{15}N, ^{13}C, ^{2}H labelling,
selective domain labelling
TROSY/CRINEPT/high B_o
20 kDa
GCSF
^{15}N, ^{13}C labelling
triple resonance
3D and 4D techniques
8 kDa
MiAMP1
^{15}N labelling
2D/3D techniques
3 kDa
Kalata B1
no labelling
^{1}H-^{1}H 2D techniques
structurally informative spectra
full structural determination
900kDa
50 kDa
25 kDa
7-10 kDa
<7 kDa

Plate 114. See also Figure 1 on page 1432.

Part II, Section 1:
Applications in Medical Science

Foreword to Applications in Medical Science

Magnetic resonance (MR) remains an emerging trend in technological innovation. In support is the award of four Nobel Prizes since 1991. Magnetic resonance has provided a paradigm shift in medical diagnosis and treatment planning and now plays an ever increasing role in health and medical research. Magnetic resonance imaging (MRI) is used worldwide with magnetic resonance spectroscopy (MRS), functional MRI and intraoperative MRI increasingly used in the clinic and for medical research purposes.

Each is technically difficult and requires a determined effort by those who develop, and use, the methods to obtain reproducible output at multiple sites. In the case of medical applications multidisciplinary teams are needed to develop, test and implement the method for routine clinical use in a controlled environment.

In this volume the authors, researchers from around the globe, have documented their technology in a way that will allow others to implement the methods for either research or clinical use. They share their many years of experience with the readers. We would like to thank them for taking the time to write their contributions with the end-user in mind.

We hope that the field of magnetic resonance in medicine will benefit from this volume by sharing the various experimental protocols and details. This will ultimately translate into improved medical care.

We would like to thank Professors Robert Lenkinski, Brian Tress, Drs Roger Bourne, Peter Malycha, Alan McLaughlin, Saadallah Ramadan, Robert Savoy and Peter Stanwell for their assistance reviewing the chapters.

Our special thanks to Dr Deborah Edward for the large amount of time and effort she put into editing and collating the Chapters. Thanks also to Sinead Doran for assistance with the diagrams.

Carolyn Mountford D. Phil (Oxon)
Uwe Himmelreich Ph.D.

Abbreviations

(HR)MAS: (High Resolution) Magic Angle Spinning

(S)SB: (shifted) sine bell

1D: One-Dimensional

^{1}H: MRS Proton Magnetic Resonance Spectroscopy

2D: Two Dimensional

31P MRS: phosphorus magnetic resonance spectroscopy

3D: Three-dimensional

Ac: Acetate

ADC: apparent diffusion coefficient

AQ: acquisition time

Asp: Aspartate

B1: Magnetic Field of RF Coil

BASING: Band Selective Inversion with Gradient Dephasing

BIR: B1-Insensitive Rotation

BISTRO: B1-Insensitive Train to Obliterate Signal

BPH: Benign Prostatic Hyperplasis

CABINET: Coherence transfer based spin-echo spectroscopy

CE-MRI: contrast enhanced magnetic resonance imaging

CHESS: chemical shift selective

CHESS: Chemical Shift Selective Saturation

CHESS: Chemical Shift Selective Suppression

COSY: correlated spectroscopy

CSF: Cerebral Spinal Fluid

CSI: Chemical Shift Imaging

CT-COSY: Constant time-based COSY

CT-PRESS: Constant time-based PRESS

DCIS: Ductal Carcinoma In Situ

DQF: double-quantum filtered

DWI: diffusion weighted imaging

EPI: echo planar imaging

EPSE: Echo-Planar Spin-Echo

FDA : Federal Drug Administration

FID: Free Induction Decay

fMRI: functional magnetic resonance imaging

FNAB: Fine Needle Aspiration Biopsy

FOV: Field of View

FWHM: full width at half maximum

GABA: γ-amino butyric acid

GAMMA: General Approach to Magnetic Resonance Mathematical Analysis

GB: Lorentzian-Gaussianlineshape transformation fraction

GBM : Glioblastoma Multiforme

Glc: Glucose

Gln : Glutamine

Glu: Glutamate

GM: grey matter

HCA: Hierarchical Cluster Analysis

HCO3-: Bicarbonate

HDR: haemodynamic response function

HMQC: heteronuclear multiple-quantum correlation

HPLC: High Pressure Liquid Chromatography

HR-MAS: High Resolution Magic Angle Spinning

HSQC: heteronuclear single-quantum correlation

ISI: inter-stimulus interval

ISIS: Image Selected In Vivo Spectroscopy

J: scalar coupling constant

KD: Ketogenic Diet

LASER: Localization by Adiabatic Selective Refocusing

LB: Lorentzian line broadening

LCModel: Linear Combination of Model Spectra

L-COSY : Localized Correlated Spectroscopy

LDA: Linear Discriminant Analysis

LG: Lorentzian Gaussian

MAS: magic angle spinning

MM: magnitude mode

MR: magnetic resonance

MR(S): magnetic resonance (spectroscopy)

MRI: magnetic resonance imaging

MRS: Magnetic Resonance Spectroscopy

MRSI: magnetic resonance spectroscopic imaging

NAFLD: Non-Alcoholic Fatty Liver Disease

NASH: Non-Alcoholic Steatohepatitis

NE: number of experiments

NOE: Nuclear Overhauser Effect

NOE: Nuclear Overhauser Enhancement

NS: number of transients

NVG: Noun Verb Generation

OLR: Orthographic Lexical Retrieval

OSIRIS: outer volume suppressed ISIS

OVS: Outer Volume Suppression

PA: Polyamines

PCA: Principal Component Analysis

PCG: posterior cingulated gyrus

PDE: phosphodiester

PME: phosphomonoester

PPM: Parts-Per-Million

PRESS: Point Resolved Spectroscopic Sequence

PRESS: Point Resolved Spectroscopy

PRESSCSI: Multi-voxel based PRESS

PRESSSV: single-voxel based PRESS

PS: phase-sensitive

PTC: Phosphatidylcholine

PWI: Perfusion Weighted Imaging

RF: Radio Frequency

SAR: Specific Absorption Rate

SCS: Statistical Classification Strategy

SECSY: Spin-echo Correlated Spectroscopy

SI: Spectroscopic Imaging

SNR: Signal-to-Noise Ratio

SPM: statistical parametric mapping

SS: Slice-Selective

SSB: Spinning Side Bands

STEAM: STimulated Echo Acquisition Mode

STEAMCSI: Multi-voxel based STEAM

STEAMSV: single-voxel based STEAM

STIR: Short Time Inversion Recovery

SVS: single voxel spectroscopy

T_1: spin-lattice or longitudinal relaxation time

T1: Longitudinal (Spin-Lattice) Relaxation Time

T_2: spin-spin or transverse relaxation time

T2 : Transverse (Spin-Spin) Relaxation Time

TCA: Tricarboxylic Acid

T_E: echo-time

TOCSY: total correlated spectroscopy

TPPI: time-proportional phase incrementation

T_R: repetition time

TRUS: Transrectal Ultrasound

U-FLARE: Ultra-fast Low Angle Rapid Acquisition with Relaxation Enhancement

VOI: Volume Of Interest

VOSY: Volume Localized Spectroscopy

VSS: Very Selective Suppression

WALTZ: Broadband Decoupling Scheme

W-F: water-to-fat ratio

WM: white matter

Metabolite Abbreviations

Ala: Alanine

ATP: Adenosine Triphosphate

Cho: Choline

Cr: Creatine

Eth: Ethanolamine

Glx: Glutamine/Glutamate

GPC: Glycerophosphocholine

GPE: Glycerophosphoethanolamine

Lac: Lactate

MI: Myo-Inositol

NAA: N-acetyl aspartate

NTP: Nucleotide Triphosphate (e.g., ATP)

PC: Phosphocholine

PCr: Phosphocreatine

PE: Phosphoethanolamine

Pi: Inorganic Phosphate

SI: Scyllo-Inositol

Tau: Taurine

UDP: Uridine Diphosphate

Glossary of Terms

Abscess: Focal infection that consists of an abscess capsule, containing fibrous material and chronic inflammation cells, and a central cavity filled with pus.

Absolute quantitation: Determination of concentrations of metabolites in mMoles per kg of tissue or volume.

Astrocytoma: The most common type of brain tumor in adults; astrocytomas, known for their marked potential for malignant progression and infiltrative nature, can be classified histopathologically into three grade of malignancy: WHO grade II astrocytoma, WHO grade III anaplastic astrocytoma, and WHO grade IV GBM.

B_0: Strong magnetic field, constant in time and space, generated by the superconducting magnet.

B_1: Radiofrequency (RF) magnetic field generated by *radiofrequency coils*.

Benign Prostatic Hyperplasia: Enlargement of the prostate and more specifically, overgrowth of the epithelium and fibromuscular tissue of the transition zone and periurethral area.

Bifunctional contrast agent: Contrast agent that increases the intrinsic contrast for two different imaging modalities.

calar coupling: See *J-coupling*

Contrast agent : Chemical compound that increases the intrinsic contrast in an image.

Δf: bandwidth (in Herz) of the receiver

Dendrimers: Large and complex polymers of a consistent size and a regular and highly branched architecture. They are often used for the encapsulation of smaller molecules.

Ductal Carcinoma In Situ: Noninfiltrative lesions composed of malignant epithelial cells that are confined to the mammary ducts and lobules.

Endocytosis : In endocytosis, the cell engulfs some of its extracellular medium including material dissolved or suspended in it. A portion of the plasma membrane is invaginated and pinched off forming a membrane-bound vesicle called an endosome.

Endosome : Vesicle formed during endocytosis.

η: filling factor

F: noise figure of the preamplifier

Focal infection: Infection that is results in the formation of lesions. Can be caused by bacteria, fungi, parasites or viruses.

Glioblastoma Multiforme: Highly malignant tumour with a low overall survival time for most patients. They are histologically characterised by a dense cellularity, high endothelial proliferation, and often the presence of focal tissue necrosis. These tumours are can occur in a cystic form.

Glioblastoma Multiforme: The most malignant grade of astrocytoma (WHO grade IV), which has an overall survival time of less than two years for most patients. These tumors are histopathologically characterized according to their dense cellularity, high proliferative indices, endothelial proliferation, and most importantly the presence of focal tissue necrosis.

Hetero-nuclear J-coupling: *J-coupling* between different species of spins, e.g. proton and carbon.

Homo-nuclear J-coupling: *J-coupling* between the same species of spins, e.g. proton and proton.

ISIS: **I**mage-**s**elected ***in vivo*** **s**pectroscopy is based on a cycle of eight acquisitions which need to be added and subtracted in the right order to get a single volume. ISIS is considerably more susceptible to motion then *STEAM* or *PRESS* and is mostly used in heteronuclear studies, where its advantage of avoiding *T2-relaxation* is valuable.

J-coupling (or scalar coupling): Many resonances split into multiplet components. This is the result of an internal indirect interaction of two spins via the intervening electron structure of the molecule. The coupling strength is measured in Hertz (Hz) rather than *ppm* because it is independent of the external B_0 field strength.

k: Boltzman constant

K: numerical factor depending on the coil geometry

Lipoma: Commonly diagnosed benign tumors of adipose tissue that can develop anywhere in the body where fat is normally found.

Liposarcoma: A commonly diagnosed soft tissue sarcoma in adults which be found anywhere in the body and for which there exists several types with varying clinical outcomes.

Meningioma: Intracranial tumors that arise in the meninges and compress the underlying brain. In general, many of these tumors are benign, however, others are malignant with the capability to metastasize, both locally and distally.

Metabolite Profiling: The study of small molecules, such as lipids, peptides, amino acids and carbohydrates, which represent steady state concentrations of intermediate products or end products of cellular processes and as a result can be thought of as the ultimate response to genetic and environmental stimuli.

Mo: Magnetization

μo: Permeability of free space

Molecular imaging: Non-invasive, *in vivo* visualization of cellular and molecular events in normal and pathological processes.

Necrosis: Tissue and/or cell death.

Neoplasm: Literally meaning "new growth". An abnormal growth of tissue which may be benign or malignant.

NOE: Nuclear Overhauser effect, the magnetization of protons dipolar-coupled to ^{13}C nuclei can be used to enhance the ^{13}C signal. While the term NOE is mainly associated with ^{13}C MRS, NOE enhancement can also be observed in ^{31}P MRS and with other nuclei.

ω0**:** Larmor frequency

Oncogenomics: The study of genes, gene sequences, and the underlying genetic alterations that appear to be involved in oncological pathways.

Polarization transfer: Many interesting nuclei like ^{13}C suffer from low inherent sensitivity compared with proton MR. Techniques like DEPT (**d**istortionless **e**nhancement by **p**olarization **t**ransfer) and INEPT (**i**nsensitive **n**uclei **e**nhanced by **p**olarization **t**ransfer) improve the ^{13}C sensitivity by transferring the higher polarization of coupled protons to the carbon nuclei. Special hardware with two RF channels is needed for polarization transfer experiments. A modification of DEPT and INEPT is reverse DEPT and inverse INEPT where the polarization is transfered back to utilize the higher sensitivity of the protons for observation (inverse detection).

PRESS: Point-resolved spectroscopy, utilizes three 180° slice selective pulses along each of the spatial directions and generates signals from the overlap in form of a spinecho.

Pus: Content of an infective lesion. It consists of dead and dying polymorphous cells (leucocytes), living and dead microorganisms, tissue debris and other components of inflammation (oedema fluid and fibrin).

Q: Quality factor of the coil

Reactive Nodes: Lymph nodes that have been immunologically challenged.

Responsive contrast agent: Contrast agent that conditionally increases the intrinsic contrast (depending on the change of environmental conditions like enzyme activation, pH change, change in ion concentration and others).

SAR: Specific absorption rate. Due to inductive and dielectric losses energy from radiofrequency pulses is absorbed by tissue and mainly transferred into rotational and translational movements of water molecules which causes an increase of tissue temperature. Limits for the human brain are established by FDA guidelines.

Schwannoma: Benign tumors that arise on peripheral nerves in general and on cranial nerves in particular, especially on the vestibular portion of the eighth cranial nerve.

Sensitivity: The term relating to the percentage of people with disease who test positive for the disease, i.e. the percentage of patients with cancer who have positive biopsy results.

SNR: Signal to noise ratio

Specificity: The term referring to the percentage of people without disease who test negative for the disease, i.e. patients without cancer with cancer negative biopsy results.

STEAM: Stimulated **e**cho **a**cquisition **m**ode, localization method utilizing three 90° slice selective pulses, along each of the spatial directions. Signal, in form of a *stimulated echo*, from the overlap is generated in a "single shot" experiment. In contrast to *PRESS*, only half of the possible signal is recovered when the same *echo time* is used.

Stem cell: Cell with broad differentiation potential that retains the capacity for unlimited self-renewal. A totipotent stem cell has the ability to differentiate to all cell types of an organism, whereas a pluripotent stem cell produces many but not all cell types.

T1-relaxation, T1-relaxation time: After the *magnetization* vector has been flipped into the transverse plane, new magnetization builds up along the z-axis. The time after 63% (1-1/e) of the equilibrium magnetization has built up is called the T1-relaxation time. T1 and T2 relaxation is caused by time-dependent fluctuations of local magnetic fields arising mostly from the motion of molecules with electric or magnetic dipoles at the site of the spins. For accurate *absolute quantitation* the relaxation times of all metabolites must be known in order to correct peak intensities appropriately.

T1-saturation: The repetition times *TR* are usually in the range of the *T1-relaxation* times. As a consequence of this, not all the *magnetization* has recovered, for example when TR = T1 only 63% of the equilibrium magnetization can be used for each scan (with the exception of the first scan) when 90° flip angles are used for excitation. This effect is called T1-saturation. The extreme case of saturation occurs when several *RF pulses* are applied within a very short time followed by dephasing *gradients*. This technique is used in localized ^{1}H MRS to remove the dominant water signal (see *water suppression*).

T2-relaxation, T2-relaxation time: The *magnetization* vector can be flipped into the transverse plane by using an *RF pulse*. The so generated transverse magnetization undergoes an exponential decay. The time after the magnetization has relaxed to 37% (1/e) of its amplitude is called the T2 or transverse or spin-spin relaxation time. See also *T1- relaxation*

.

Tc: probe temperature

TR (repetition time): The time between each initial excitation of the magnetization is called the repetition time.

Transfection: A method by which experimental DNA (or in our case contrast agents) can be incorporated into mammalian cells after interaction of the encapsulating transfection agent and the cell membrane.

Vc: volume of the coil

Acquiring Neurospectroscopy in Clinical Practice

Alexander P. Lin

Huntington Medical Research Institutes, Rudi Schulte Research Institute, Pasadena, CA 91105, USA

Part I: Seven Secrets to Successful Spectroscopy

Neurospectroscopy or magnetic resonance spectroscopy (MRS) has moved from the realm of academic research into that of the clinical world. All major MR manufacturers have aided in the endeavor by automating neurospectroscopy so that it no longer requires an MR physicist and is a push-button technique that can be run by technologists just as a typical MR sequence. Thousands of papers have demonstrated the clinical efficacy of neurospectroscopy and there are a dozens of medical reviews of how this technique can be applied across a wide range of neurological disorders. However, few papers address the practical issue of acquiring neurospectroscopy in a clinical practice. Based on over a decade of clinical experience on our 1.5 T scanner and applications training for technologists and radiologists at our international clinical neurospectroscopy courses, this chapter was developed to demonstrate proven protocols for clinical diagnosis and outline the strategies involved in acquiring successful clinical spectra.

Introduction

While the goals of the MR technologist are not very different between imaging and spectroscopy, the terminology and approach are slightly different. Imagers desire clear and detailed images without motion artifacts. Spectroscopists want spectra with well-defined peaks and few artifacts as well. The composition of a peak can be broken down to two parameters: (1) peak height or how readily discernible the metabolites are from noise; this in turn is governed by the principles of signal-to-noise ratio (SNR) and (2) line width or how narrow the peaks are, which is governed by magnetic field homogeneity. It is the goal of the spectroscopist to therefore maximize these two principles using a variety of different parameters discussed in this chapter. Using the same analogy, imagers use different sequences such as T_2w or FLAIR to investigate certain pathological properties; spectroscopists use different protocols to diagnose different disorders. These protocols can be broadly categorized into focal and global protocols, each of which will require a different approach to these parameters.

When we began developing and growing a clinical spectroscopy program, we soon discovered that the "secret" to a successful spectroscopy service was CONSISTENCY. Once a methodology of acquisition or guideline is established, it must be maintained. In any clinical MR unit, all technologists must follow that guideline in order to guarantee spectral reliability from patient to patient. Worldwide, the same consistency is essential to ensure "universality" of clinical diagnosis.

Signal and Homogeneity

In the following sections, we will be discussing different parameters that can be changed to optimize your spectroscopy. There are two components to optimization, namely: SNR and homogeneity. With a high SNR, the metabolite peaks (signal) are very easy to distinguish from the smaller peaks that surround it (noise) as you can see in Figure 1. High SNR is critical to the interpretability of spectra by both the radiologist and the automated processing software. Maintaining high SNR throughout all your acquisitions is a prime responsibility for spectroscopy quality control. The factors that affect SNR are (in order of impact): voxel size, number of averages, echo time (T_E), localization sequence, and repetition time (T_R).

Homogeneity refers to the uniformity of the magnetic field present in the voxel of interest (VOI: a voxel is the box which defines the area you wish to examine). A very homogeneous field has very little change in the magnetic field throughout the VOI (Figure 2B). A heterogeneous field has differing magnetic properties throughout the VOI (Figure 2A). A "sharp" spectrum at 1.5 T reflects both consistent and relatively thin line widths (<3 Hz) as shown in Figure 2D. The reason why spectroscopy is performed primarily in the brain is that the magnetic field is remarkably homogeneous throughout it. A severe example of inhomogeniety would be the magnetic field as dental braces affect it. By having a homogeneous field in your VOI, you reduce the chances of artifacts that would make the spectrum unreadable. These artifacts can affect the entire spectrum or affect just a certain area of chemical shift, however, you would like to avoid them if at all possible. The elements that cause homogeneity problems will be discussed in voxel positioning.

Graham A. Webb (ed.), Modern Magnetic Resonance, 985–1003.
© 2008 *Springer.*

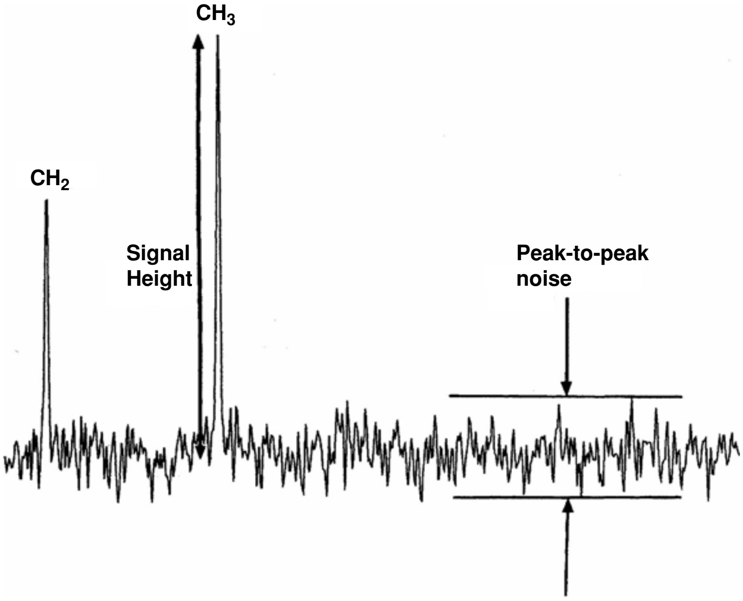

Fig. 1. Definition of signal-to-noise ratio. The large peak labeled as CH_3 is the signal and the peak-to-peak noise is indicated. Signal-to-noise ratio is simply the dividend of the height of the two measurements.

Acquisition Paradigms

As you will see throughout this chapter, there are essentially two methods of acquiring spectra: FOCAL vs. GLOBAL. The definition in terms of spectroscopic applications is as follows:

- *Focal:* Acquiring spectra from specific regions of interest that are variable from patient to patient. For example: in brain tumor spectroscopy, the location, size, and homogeneity of the tumor will differ from patient to patient. It is therefore critical to understand the underlying concepts behind each parameter such that you can use it to your advantage in different situations.
- *Global:* Acquiring spectra from a specific region of interest that is the same in all patients. A well-defined protocol is used for this type of spectroscopy. For example, in diagnosing Alzheimer's disease, the technologist will always place the voxel in the posterior cingulate gyrus (PCG) in the posterior parietal lobe of the brain. In this paradigm, very little changes from patient to patient. Therefore, great care must be taken to ensure that the protocol is followed to the letter.

Patient Positioning

Patient positioning plays a key role in maintaining consistency from patient to patient as well as from exam to exam. This is critical in use of spectroscopy for monitoring treatment or determining medication efficacy. More and more clinicians are turning to spectroscopy as a noninvasive tool to help determine how the patient is progressing in a quantitative way through neurospectroscopy. If the patient's head is not in the same position from his/her first MRS exam before treatment, it makes it all the more difficult to compare the results of the MRS exam after treatment.

- Landmark the patient at a consistent anatomical location. The eyebrow is a good location that is easily determined in each patient (Figure 3). By routinely landmarking in the same location, you can ensure that you are achieving maximum homogeneity within the magnet bore.
- Make sure the patient's head is centered. The left and right halves of the patient head should be symmetrical. This is critical for exams that compare the contralateral areas of the brain.
- Try to place the center of the coil at the landmark position. This ensures that the most homogeneous part of the coil is at the area of the brain where you will be acquiring your spectra. Depending on the anatomy of the patient, this may be difficult (i.e. short neck); however, try to do your best!
- Reduce patient movement by securing the head. Foam inserts or rolled up towels to the left and right side of the head help to reduce the chance of the patient moving their head after imaging (Figure 3). Using a strap around the forehead can also be useful but difficult to employ in claustrophobic patients.

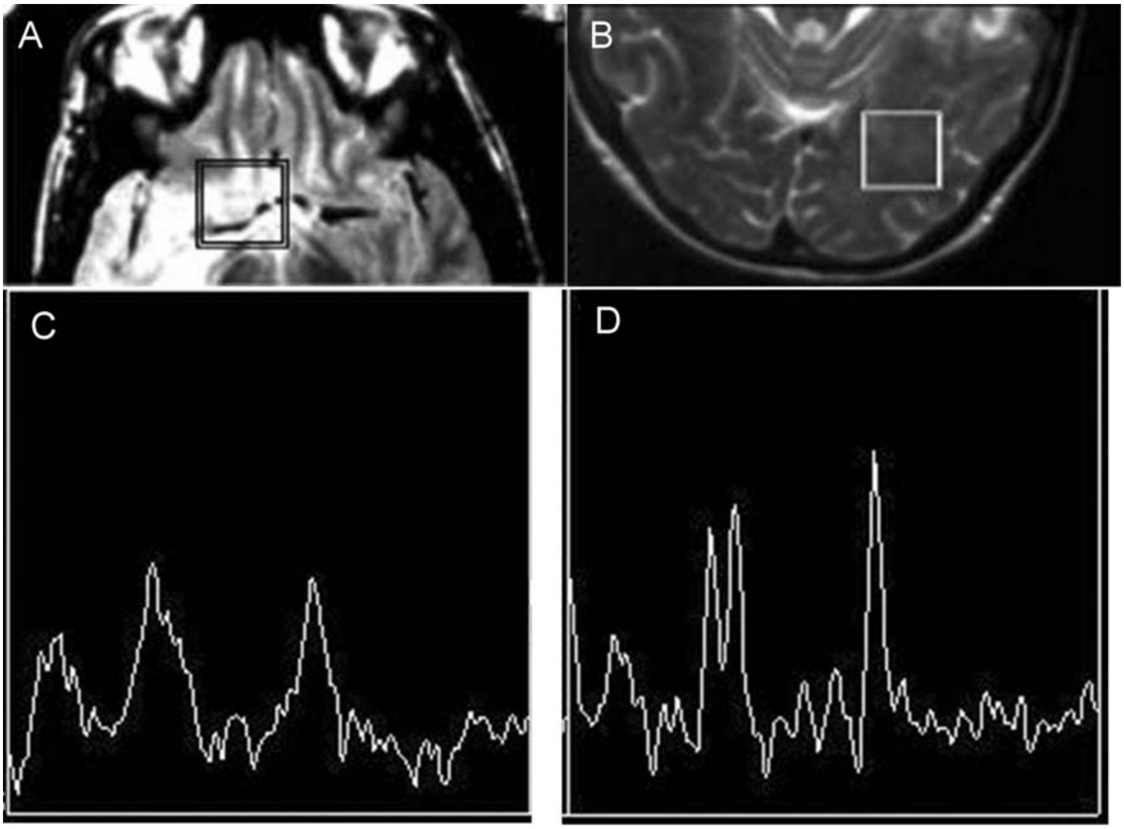

Fig. 2. Example of poor and good homogeneity. (A) This MRI image on the left demonstrates a voxel (indicated by the square) that contains different types of tissue as well as arteries. This is a very heterogeneous region. (B) The image on the right contains a voxel (square) from a very homogeneous region. (C) The long echo spectrum that was the result of the heterogeneous voxel in image A on the left has low signal as well as poor homogeneity as evidenced by the lack of splitting between Cho and Cr. (D) The long echo spectrum on the right, the result of the homogeneous voxel indicated in image B, although not of excellent quality, has enough signal to be interpreted.

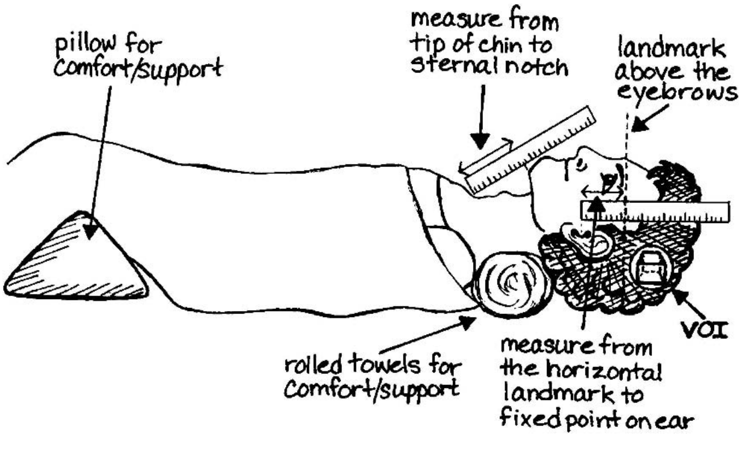
pillow for Comfort/support
measure from tip of chin to sternal notch
landmark above the eyebrows
VOI
rolled towels for Comfort/support
measure from the horizontal landmark to fixed point on ear

Fig. 3. Good positioning is achieved by a proper landmark, increased patient comfort, and additional measurements that can be used for repeat exams. Pillows and rolled towels provide comfort and support that prevents the patient from squirming about. Measurements such as those shown can dramatically improve spectral reproducibility.

Sequences

Manufacturers have greatly improved upon the localization sequences used in diagnostic spectroscopy. PRESS can reliably acquire spectra at short echo times and gives an almost doubled SNR advantage over STEAM. It is clearly the localization sequence of choice.

However, in many of the protocols described in available clinical texts, STEAM localization was utilized to acquire the spectra at 1.5 T. It is important to note that there are significant differences between metabolite ratio values for STEAM and PRESS that go beyond a simple scalar increase in SNR. For example, in exactly the same voxel in the same patient STEAM will give an NAA/Cr of 1.35, whereas PRESS will give a value of 1.71! Therefore, in order to use the spectra presented in other textbooks and papers as a comparison, you MUST use the exact methods described in the protocol. To avoid errors in diagnosis and in order to compare against those results, it is imperative not to mix STEAM and PRESS sequences. It is best to rigorously adhere to ONE sequence.

Echo Time

The greatest advantage of short echo neurospectroscopy is that the shorter the echo time, the greater the signal. Of course there is a practical limit to how short an echo time can be acquired. In general, echo times of 21–35 ms are used for neurospectroscopy. Another advantage of short echo times is that metabolites with short T_2 relaxation times such as *myo*-inositol, glutamate, glutamine, *scyllo*-inositol, etc. can be observed as shown in Figure 4. This adds to the diagnostic power of neurospectroscopy. For example, the diagnosis of Alzheimer's disease is less sensitive with NAA alone; the addition of mI allows neurospectroscopy to achieve excellent sensitivity and specificity. Initially, short echo neurospectroscopy was more prone to artifacts, however, at this time PRESS is robust. Because of another property of brain metabolites, termed *J* coupling, even small differences in T_E are critical: while using 27 ms may not give significantly different results, using 45 ms will!

So why use long echo time ($T_E = 135$, 144, 270, 288 ms)? Initially, it reduced the baseline "artifacts" observed sometimes with short echo spectroscopy. Also at long echo, lipid signals are significantly reduced, allowing other metabolites to be observed originally obscured by lipid. At $T_E = 135$ or 144 ms, lactate is easily observed as an inverted doublet (an admirable use of *J* coupling as described above), whereas in short echo it can often be hidden within the lipid resonance. This is all at the sacrifice of SNR of at least 40% as well as the reduction in the number of diagnostic markers. Typically, echo times of 135 or 144 ms are used. If you do decide to employ long echo times, be sure to recognize that the normal spectra heights are dramatically different in long echo than they are in short echo simply due to different intrinsic metabolite T_2 relaxation times. It is therefore imperative to stick with just ONE choice of echo time to save yourself from confusion and misdiagnosis.

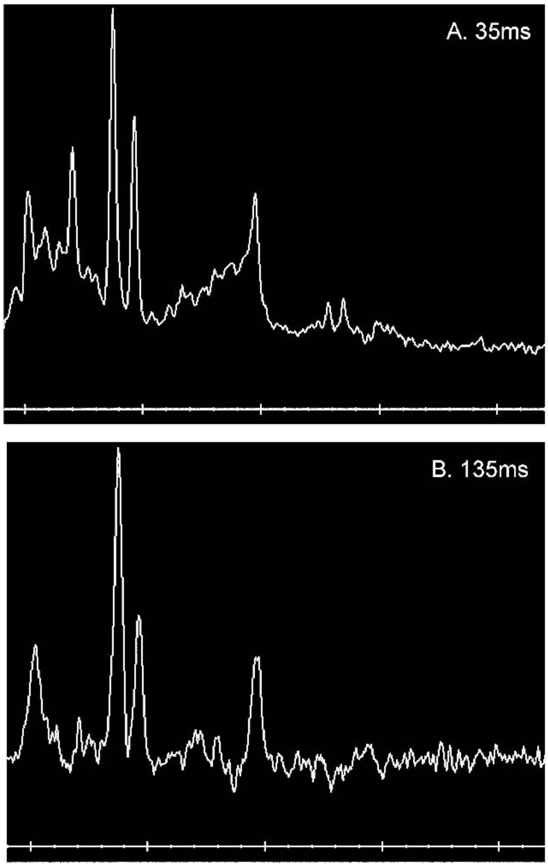

Fig. 4. Both of these spectra were acquired from the same exam using the same voxel position, voxel size, and number of averages using PRESS in a patient with recurrent brain tumor. The spectrum on top was acquired with an echo time of 35 ms, the bottom spectrum at 135 ms. Note that the Cho/Cr is vastly different and mI is absent in the bottom spectrum. Although the abnormal choline that is diagnostic of brain tumor is evident in both spectra, additional information, such as the significantly elevated mI that may indicate low-grade glioma, is missing from the long echo spectrum. It is difficult to tell the amount of signal loss since both spectra are scaled to the highest peak. However, the noise is much greater at long echo when compared to short echo to the extent that the small amount of lactate, which is diagnostic in the short echo spectrum, is not observed in the long echo spectrum.

Voxel Size

SNR is highly dependent on your voxel size. The typical voxel size of 2.0 × 2.0 × 2.0 cm (8 cc) is standard on most 1.5 T scanners. This is also an optimal voxel size for most 1.5 T applications (except notably in neonatal neurospectroscopy where smaller voxels may be required). In global diseases, the voxel sizes are well established and should not change from patient to patient. In some protocols, the default of 8 cc may not be used due to location-specific optimization; nonetheless, all patients examined with that particular protocol must have the same voxel size.

However, with focal neurospectroscopy, 8 cc may not be suitable to obtain enough partial volume of the lesion or may be too small for a large lesion. For lesions that are smaller than 8 cc, we recommend that you first obtain a spectrum from the larger volume to guarantee that you receive signal at all. A common mistake is to shrink your voxel to too small a volume as shown in Figure 5. In that case, there will not be enough signal to generate a readable spectrum. If the first voxel is successful, then at the very least the radiologist has some data to review. For a more accurate reflection of the metabolites within the lesion, after obtaining a successful first voxel, one can

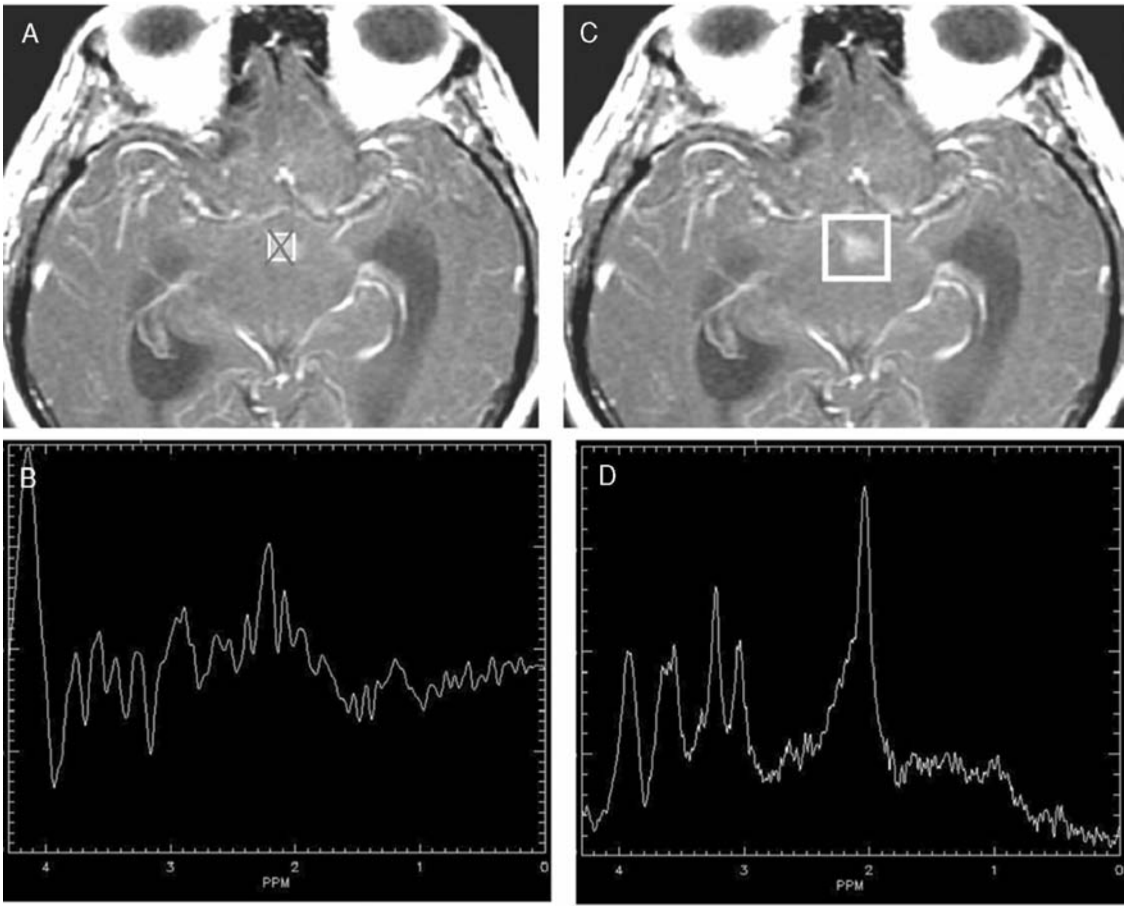

Fig. 5. Example of how voxel size affects spectral quality. In this patient case, a small hyperintense signal was discovered in the MRI that was too dangerous for surgical biopsy. Furthermore, MRI was indeterminate for neoplasm or stroke. It is therefore imperative for neurospectroscopy to provide an answer. When trying to acquire signal from a small lesion, it is common to try to shrink the voxel size to as small as possible. The result of such a small voxel (A) results in an uninterpretable spectrum (B). Although the larger voxel (C) has a small partial volume of the lesion, it produces (D) a good quality spectrum that gives a diagnostic result (high Cho) that proved to be a brain tumor.

then shrink the voxel to increase the partial volume. A good rule of thumb is that if the lesion occupies greater than 40% partial volume, there will be enough signal from tumor to generate an abnormal spectrum.

If the lesion is greater than 8 cc, then it would most likely make more sense to increase your voxel to match that volume. However, the larger the voxel, the greater the chances of observing inhomogeneity effects (such as artifacts and eddy current problems) in the volume. We recommend not obtaining a voxel larger than 30 cc. It is best to use a volume between 8 and 27 cc and change the voxel position instead of trying a larger voxel. This will be further discussed in the section regarding voxel position.

Another option when dealing with partial volume is to not assume that the voxel volume must be cubic. The advantages of using a different shape would be to maximize partial volume or minimizing the artifacts that one may get. For example, in trying to obtain a spectrum from the basal ganglia, we have observed that by using a rectangular voxel shape one can obtain a greater partial volume of the basal ganglia as well as minimizing the chances of the voxel being affected by other structures, such as the ventricles. However, it is best to keep the shape of the voxel as close to a square as possible since manufacturers most likely optimized their hardware to a cubic volume.

Number of Averages

The number of averages is directly proportional to SNR. This implies that the longer the acquisition, the more signal one can get. Obviously there are limits to the amount of time one can spend for each voxel. This is dependent not only on the patient's limits of tolerance but also due to the number of acquisitions required in a certain protocol. The total time for the scan is the prescan plus the number of averages in the scan multiplied by the repetition time.

In the global paradigm where you already have a defined size and location, it is best to set the number of averages the same for every acquisition as it does not need to be adjusted for signal and homogeneity effects. The data from the defined size and location should also always be acquired with the same number of averages.

In the focal paradigm, adjustments are dependent on the size of the voxel. Generally an 8 cc voxel requires 128 averages for a high quality spectrum. If you reduce the volume to half, you must increase the number of averages to 256 in order to maintain the same spectral quality. Therefore, if you use a very small volume such as 2 cc, you would require 512 averages, which at $T_R = 1.5$ ms would take nearly 13 min! This implies that small volumes are NOT the place to start acquiring data, hence why we recommend first acquiring data from an 8 cc volume and then reduce size accordingly. Homogeneity within the voxel should also factor into your determination of number of averages. By averaging for longer time, you reduce the artifacts that can occur in a heterogeneous acquisition.

Voxel Position

Voxel position is an inherent part of optimizing your ability to collect interpretable spectra. More importantly, the position plays a key role in the diagnostic power of the spectra. The diagnosis of diseases with neurospectroscopy is dependent on differences in metabolite peak heights as compared to normal values. If the difference you observe in a certain pathology is 15%, the reproducibility of that voxel must be 10% or better. In order to optimize reproducibility, the voxel parameters must be the same in every patient. All other parameters can be set as part of a protocol, leaving voxel position as the only factor that can affect reproducibility.

For example, in the diagnosis of Alzheimer's disease, an increase of mI/Cr of 10% is considered "significant." How does one determine if this change is significant? Utilize the standard deviation in a cohort of spectra from normal, healthy adults. In this case, the standard deviation is 5%; therefore the physician can rightly assume that the 10% change in mI/Cr is due to pathology and not due to normal variation in the human brain. In order to ensure that the standard deviation in all measurements was 5%, one must maintain reproducibility of the spectra. The voxel is placed and landmarked in the same position in every patient. The greater the reproducibility of the voxel, the less likely that the change observed has come from a different voxel location.

As with voxel size, changing voxel position can greatly alter your results when dealing with global spectroscopy. Gray and white matters contain different Cho/Cr ratios, therefore a shift in voxel position, causing it to contain more white than gray matter could lead the reader of the spectra to believe that there is a higher Cho/Cr in the voxel that he/she will attribute to pathology. This is the wrong conclusion to draw if the voxel position is incorrect and the observed change is due to greater partial volume of white matter. Although not all brains are exactly the same, using anatomical landmarks, such as the ventricles, will allow for a high measure of reproducibility. Positions for each diagnostic test will be described in detail with accompanying figures in the following section.

When dealing with the focal spectroscopy paradigm, the concerns of acquiring exact voxel position from patient to patient is disregarded because by definition, the key location will NOT be the same from patient to patient. In this case, it is more important to optimize the position such that you increase homogeneity as well as

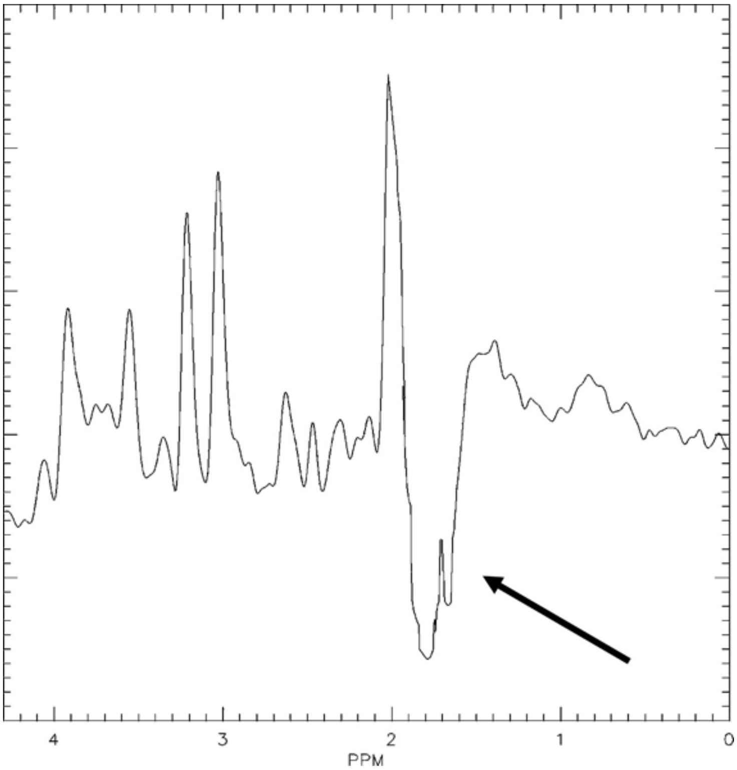

Fig. 6. Example of out-of-volume lipid artifact. The artifact is indicated by the arrow. This artifact comes about as a result of the voxel being to close to the back of the brain. The danger of this artifact is that it may impact upon the NAA signal that results in an artificially low NAA/Cr reading that would impact on spectral interpretation. This artifact is the reason why with voxel placements described in Protocols 1, 2, and 3 in Part II of this text it is critical to stay away from the skull.

signal. While in each pathology, different techniques in determining voxel position can be used; there are some areas of the brain or pathology you want to avoid:

- *Skull:* Stay away from the surfaces of the brain. The lipids that lie in the meninges of the brain, within the bones of the skull, or in the scalp can contaminate your spectra in two ways: (1) By creating an overriding lipid signal that can be misinterpreted or can dominate the entire spectra thus hiding the spectra; (2) an artifact that can result is "out-of-volume lipid artifact" (Figure 6) which is a large broad negative resonance or "dip" in the spectra around 1.8 ppm which can cause the resonance for NAA that resides at 2.0 ppm to be "dragged" down. Be sure to check all slices of the image that your voxel is located to ensure you have not come too close to the skull.
- *Necrosis:* As described above, lipids can cause severe problems with spectra. One major problem is domination of the spectra as shown in Figure 7. The spectra displayed on the scanner are scaled based on the highest peak. If there is a huge amount of lipid in the spectra, the scanner will scale the remainder of the peaks to the height of the lipid peaks. If the lipid peaks are very tall, the remaining peaks will be reduced and therefore become unreadable. In certain pathologies this is an important factor and therefore the strategy is to move away from the necrosis to the edge of the lesion.
- *Blood:* Blood contains heme-iron which is paramagnetic and will destroy signal coming from brain tissue. Post-surgical locations or highly necrotic centers can pool blood which makes spectra unobtainable or at the very least very difficult to read due to decrease in SNR.
- *Open space:* Within the brain there can be areas of open space such as in air sinuses adjacent to the temporal lobes. In cases of resection, there can be areas of the brain "missing." These should be avoided not only because of the possibility of blood; the large air spaces cause field inhomogeneity problems. You must be sure to check through all slices of the images to ensure that your voxel does not contain any of the air space.
- *Cerebral spinal fluid (CSF):* While having some CSF in the voxel can be unavoidable, it is important not to have CSF occupy more than 40% of the voxel. CSF has no brain metabolite signal, therefore, if CSF comprises

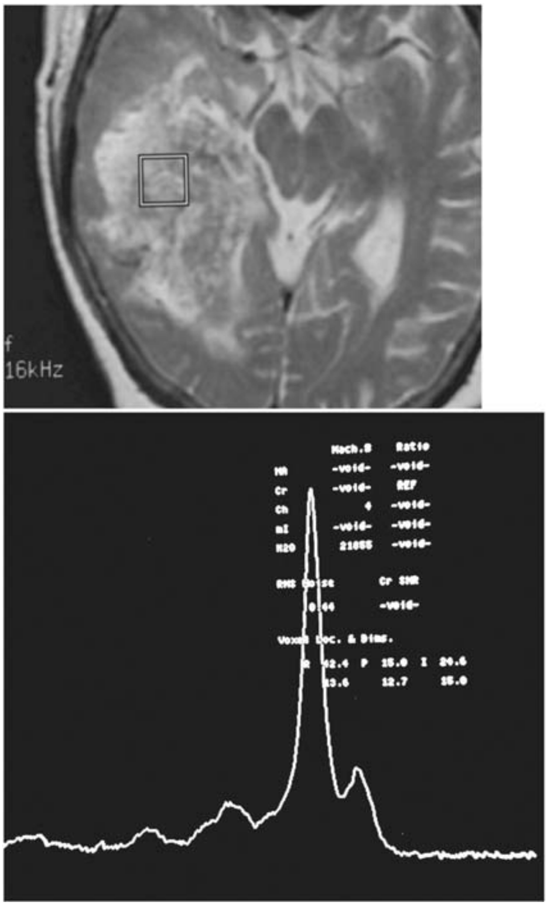

```
         Mech.B   Ratio
NA       -void-   -void-
Cr       -void-   REF
Ch            4   -void-
mI       -void-   -void-
H2O       21055   -void-

RMS Noise       Cr SNR
     0.44       -void-

Voxel Loc. & Dims.
     R 42.4  P 15.0  I 24.6
       13.6    12.7    15.0
```

Fig. 7. Example of lipid overwhelming the spectrum. With the lipid peaks overwhelming the spectrum, it is very difficult to ascertain if there is an increase in Cho for diagnosis. Although this is a short echo acquisition, enough lipid within the voxel can negatively impact a long echo neurospectroscopy exam as well. This is a common problem when dealing with focal neurospectroscopy where the voxel is often placed in the center of a necrotic lesion as shown in the MRI at the top. The necrosis contains a great deal of lipid which would overwhelm the spectra, reducing its diagnostic value. The key to avoiding this artifact is to move the voxel to the edge of the lesion where there is not as much lipid signal from necrosis.

a large part of your voxel, the total signal is reduced causing a very "noisy" spectrum. CSF does, however, contain lactate (1–2 mM) and glucose, which could be misinterpreted as an indicator of pathology. Nevertheless, it is better to include CSF in your voxel if it helps avoid the four areas listed above.

As described in the section dealing with voxel size, partial volume is one of the attributes of focal spectroscopy that can be optimized with voxel position. This is especially the case in large areas of interest that should not or cannot be acquired with a single large voxel. In this case, one must use a smaller voxel that brings into question where to place the voxel: In the middle of the area of interest or at the edge? Studies have shown that in cases such as brain tumors, it is better to obtain spectra from the edge of the lesion away from the brain. This is due to the necrotic centers often found in tumors which as described above, can cause serious problems with your acquisition. By obtaining spectra from the edge you may not have complete partial volume but you guarantee yourself a more interpretable spectra. You should choose a voxel that has the highest partial volume while avoiding the areas stated above.

A frequently asked question is whether it is necessary to obtain a second spectrum that is contralateral to the focal voxel. This is obviously quite useful to the radiologist so that there is a comparable "normal" spectrum with which to compare the pathological one. The danger of blindly trusting such a spectra is that in some pathologies, the changes in metabolism are not limited to the region of interest. For example, when trying to distinguish radiation necrosis from tumor, it is assumed that the contralateral region to the tumor is "normal." However, studies have shown that radiation therapy itself causes global changes to the brain and therefore would affect the metabolite ratios of "normal" spectra. We recommend that one use this technique for the first generation of cases. As the radiologist becomes more familiar with the spectral patterns in different areas of the brain, it will not be necessary to provide a so-called normal contralateral spectrum.

Consistency

Once again we would like to reemphasize the importance of being consistent and reliably following protocol. When training our own technicians, we follow a set pattern that has allowed us over the course of a decade to acquire spectra with a high degree of reproducibility and very low variability. For example, one patient who has been examined every year for the past 6 years has demonstrated spectra with a reproducibility of less than 5% despite several upgrades and different technologists running each exam (Figure 8). The goal in mind is to try to achieve this level of consistency. This way, any biochemical changes can be attributed to pathology and not to changing acquisition parameters.

With the global paradigm, it is essential to be consistent. By following the protocol, you can ensure that your results will be comparable to published data utilizing the same technique. With the focal paradigm, it is not quite

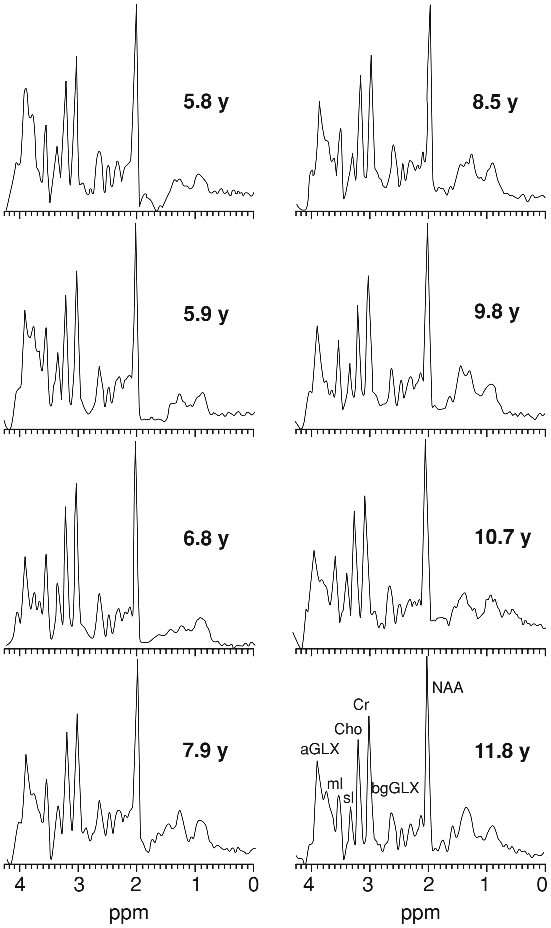

Fig. 8. Sequential neurospectroscopy: Monitoring the effects of treatment over a period of six years. Despite several system upgrades and different technologists, the consistent normal spectra obtained in a child with x-linked adrenoleukodystrophy has convinced physicians to keep the patient on Lorenzo oil treatment rather than the highly dangerous bone marrow transplantation he would have otherwise received. These spectra were all acquired with the gray matter protocol described in Protocol 1.

as simple: all of these parameters do interact with one another. In particular, voxel size and number of averages are very dependent on one another and will require adjustments if either is altered. If you decrease your voxel size by a factor of two (one-half) you increase the number of averages (to obtain the same level of SNR) by a factor of four! This in turn causes the exam to last longer which, in turn, can jeopardize the exam as a whole because the patient may become restless and move the head (moving your voxel to an entirely different location!) or worse, demand to be released from the scanner. How do you balance all of these elements?

We recommend starting with a "basic" protocol for all exams (this of course does not apply to global protocols which should not be changed) and then adjust the parameters according to the situation. Factors such as sequence and echo time should NOT be changed unless absolutely required. This is critical in maintaining consistency of spectra from patient to patient. Voxel size should be set at a default size: 8 cc is generally system's default size on most 1.5 T scanners. If you can acquire good quality spectra with 128 averages at 8 cc, then simply adjust averages according to size. Voxel position does not necessarily negatively affect the other parameters unless positioned incorrectly. Therefore, take special care in choosing the best area possible.

Multivoxel Spectroscopy

All of the rules described above also apply to multivoxel spectroscopy (a.k.a. Chemical Shift Imaging (CSI), Metabolite Maps, Spectroscopic Imaging, etc), the main difference being that instead of just an excitation volume (voxel) you must also consider the number of phase and frequency encoding steps as well as the field of view (FOV). The approach to multivoxel neurospectroscopy is more similar to imaging. It is easiest to imagine the FOV defining the image area as shown in Figure 9. The frequency and phase encode steps then divide the FOV into smaller boxes which can be reproduced as individual spectra. The increased number of encoding steps and the smaller the FOV, the higher the resolution you will have for each individual spectra. For example, a 16 × 16 cm FOV using 16 frequency and 16 phase encode steps will provide a volume of 1 cc per voxel when using a thickness of 1 cm. The same FOV, with the number of encoding steps increased to 24 will then give a resolution of 0.44 cc. This of course comes with the time penalty of increasing scan time approximately from 5 to 10 min. However, there is a signal gain by increasing the encoding steps. Depending on the resolution you require, you want to set your protocol accordingly. We give our standard protocol at the end of the next section.

The excitation volume is therefore equivalent to the voxel where the same rules in voxel positioning apply as shown in Figure 9. However, the number of averages and voxel size are no longer correlated since scan time is completely dependent on the number of encoding steps. It is a common mistake to try to use the largest volume possible (since there is no impact on time and all of the data from that region is acquired anyways), however, we have found that this affects the line width of the scan. We

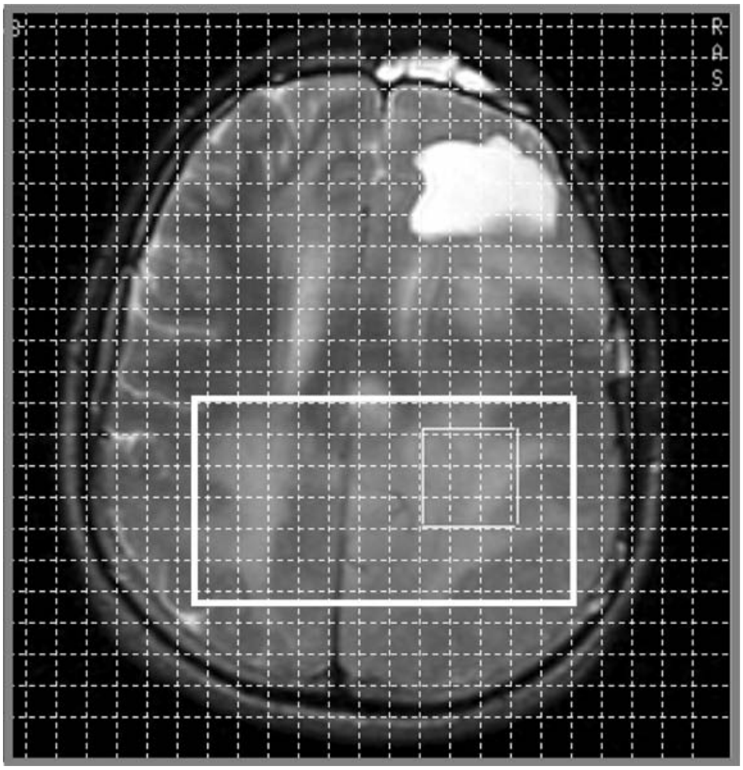

Fig. 9. Multivoxel neurospectroscopy. This is an example of short echo multivoxel neurospectroscopy in a patient with acute disseminated encephalomyelitis. The FOV is the entire image as indicated by the thick gray box. The FOV is then split into smaller voxels by phase and frequency encode steps as represented by the dotted line boxes. The excitation volume, or the voxel, is indicated by the thick white box. Note that the voxel does not acquire excitation from the entire brain but rather just from the region that is clinically relevant which are the hyperintense areas in the posterior aspect of the brain.

therefore recommend that the voxel only encompasses the region that you are interested in and no larger.

The third aspect of multivoxel neurospectroscopy that is different is the display of the data. Initially, multivoxel had the great promise of eliminating the need for interpreting spectra by using "metabolite maps"—color maps that correspond to the peak height of the metabolite over the area of excitation. However, we found that not only are the metabolite maps not reliable, they could be actually misleading. This has to do with the fact that it does not correct for overall signal strength. In other words, the high choline observed may not be due to increased Cho in the region but simply due to an increase in all MR signals from a homogeneous region. We therefore rely on the individual spectra for analysis. This presents a problem in itself since the radiologist will not want to comb over hundreds of spectra generated by each multivoxel exam. Instead we describe a "speed reading" technique where only select regions (those that are most clinically relevant) of the spectra are displayed. The region of interest is displayed with a summed spectrum and the individual spectra, usually in an easy-to-read 3 × 3 grid. This also has the benefit of providing quality assurance by generating a summed spectrum from the same voxel region as the single voxel exam. In this way, we find the most efficacious exams to include both single and multivoxel neurospectroscopy both using the same echo time.

Part II: Neurospectroscopy Protocols

Clinical Protocol Decision Matrix

All of the following protocols have been time-tested and proven to provide all of the necessary information required for the accurate diagnosis of disease. They are based on peer-reviewed published studies demonstrating efficacy with these techniques. In addition, the protocols are designed to be practical for the demands of a clinical practice.

The first step in applying these protocols is to know which diagnostic test is most efficacious for a disease process. With that in mind, the following section details a decision matrix for deciding which protocols should be used in each patient case. Although the list is not all inclusive, it provides a framework from which exam planning

Table 1: Clinical protocol decision matrix

Diagnosis	Protocol
Dementia, memory loss	Standard GM/WM
Frontal lobe Lewy body dementia	+Frontal GM
Focal Lesion (tumor, recurrence)	Focal SV-MRS, CSI
+Contrast	+T_1w, T_1w + c, MRS OK after Gad
vs. Stroke	+DWI, voxel in center of lesion and rim
vs. Abscess	Voxel in the center of lesion, maximize PV
Radiation necrosis vs. recurrence	Voxel at the edge of the lesion
Demyelinating disease, white matter disease	Standard WM
Multiple sclerosis w/o lesions	Standard WM
Multiple sclerosis w/ lesions	Lesion if >3 cc, CSI if <3 cc L or R WM in normal appearing WM
Epilepsy	Standard GM/WM
Mesial temporal lobe epilepsy	+L/R temporal lobe
Known focus	Focal SV (bilateral)
Parkinson's/Huntington's disease	Standard GM/WM, L/R BG
Hepatic encephalopathy	Standard GM/WM (earliest changes in WM)
Global hypoxia	Standard GM/WM
Trauma	SV MRS away from blood/lesions
Possible hypoxia	GM
No hypoxia	WM
Systemic diseases, unknown not focal	Standard GM/WM

can be initiated. The decision matrix also provides a basis for dynamic decision making at the time of the exam. For example, discoveries made at the time of the exam may necessitate additional tests to be run. It is important to note, however, that input from the managing physician at the time of the exam provides the greatest diagnostic precision.

Protocol 1: Standard Gray Matter (GM) or Posterior Cingulate Gyrus (PCG)

1. Position the patient in the scanner as indicated in Section 1 (Figure 3).
2. Acquire localization images for spectroscopy
   a. For single-plane acquisition scanners:
      i. Slice thickness + Interspace = 5.0 mm. That way you can place your voxel on the center slice and check two slices up and two slices down to ensure that your voxel does not fall into any bad areas.
      ii. For ease of landmarks, we suggest using the axial plane.
   b. For three-plane acquisition scanners:
      i. Choose a sequence that shows the best contrast between gray and white matters. We generally use a T_2w image.
3. Set up your neurospectroscopy scan parameters:
   a. Pulse sequence: PRESS
   b. $T_E = 35$ ms
   c. $T_R = 1500$ ms
   d. Voxel size = 20 × 20 × 20 mm
   e. Number of averages = 128
4. Place your voxel using the following landmarks:
   a. Center across falx at level 1 cm above posterior commissures of corpus callosum.
   b. Start inferior one slice (5 mm) above the slice with the (a) internal capsule, (b) angular artery in sylvian fissure, (c) occipitoparietal fissure, (d) vein of Galen, (e) internal cerebral vein, and (f) frontal horn of lateral ventricle. *Note:* If the head is tilted not all of these landmarks may be visible.
   c. By choosing a voxel shape of 20 mm in A/P and 20 mm in R/L, most of the tissue within the voxel is GM.
   d. Review above and below center position at least two slices (for 5 mm MRI slice thickness and 20 mm voxel slice thickness) for single-plane acquisitions. Check all three planes to ensure that you stay away from the skull, white matter (particularly the corpus callosum), and ventricles (Figure 10).
5. *Prescan routine:* this is different on different platforms. What is performed, however, remains the same:

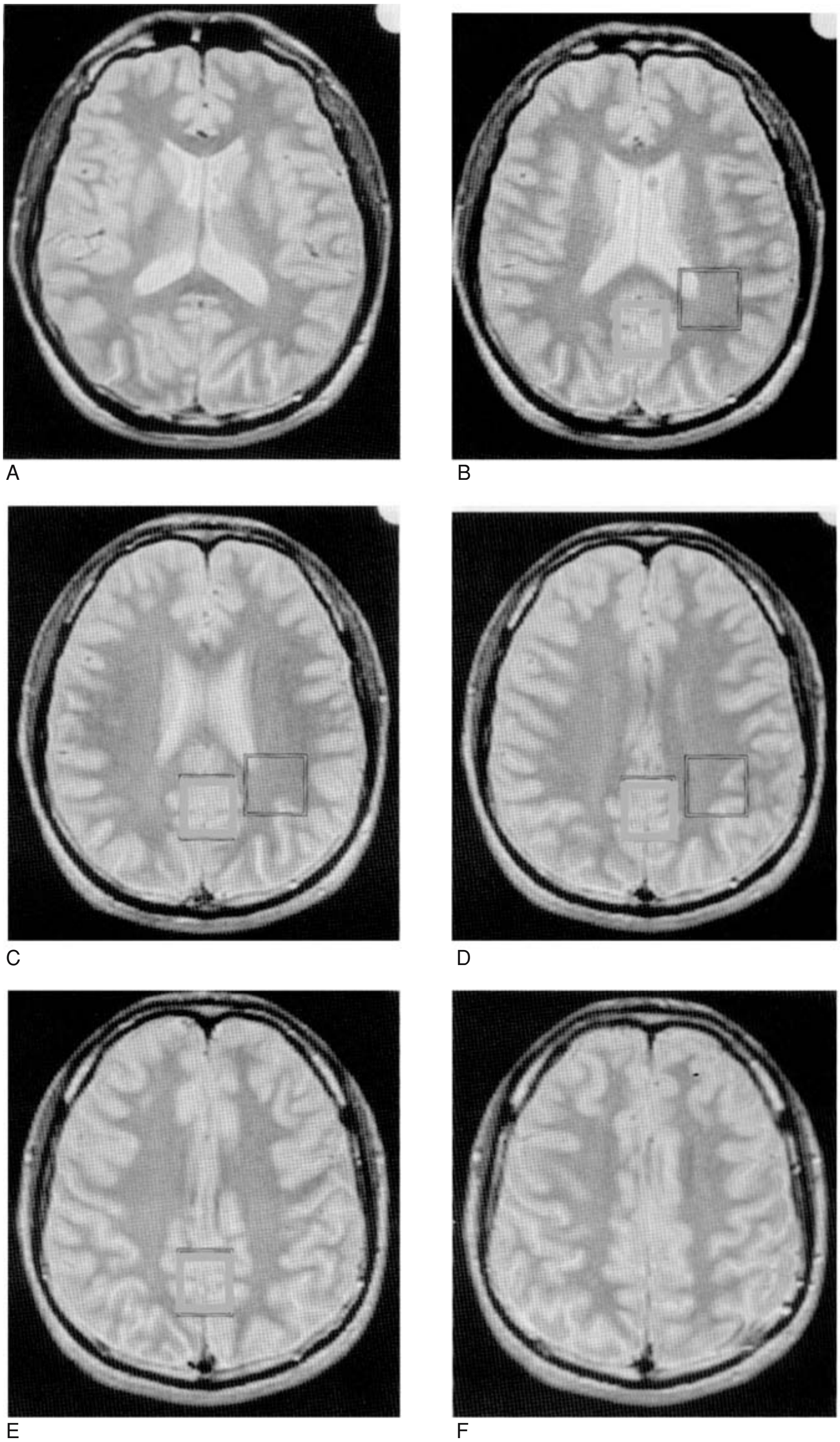

Fig. 10. Gray matter voxel position. Note that you should not only have a well-placed center slice but keep in mind all other slices as well.

   a. *TG optimization:* Optimize for the greatest amount of signal.
   b. *Water suppression:* You are better off to slightly under-suppress than to over-suppress.
   c. *Shim:* This is the most critical factor, the line width (sometimes represented as FWHM, full width half max of the water peak) should be less than 7 Hz at 1.5 T.
6. Acquire the scan.
7. Reconstruct the data. Generally this is automated, however, the routines include spectral apodization, fast Fourier transform, baseline corrections, and peak fitting.
8. Filming the data:
   a. Show the voxel location in three dimensions—"3D"
      i. Three-plane localizers, that is fairly straightforward. You simply place a voxel in each plane as shown.
      ii. For single-plane localizers, you will need to prescribe the center slice and then two slices above and below to demonstrate the voxel position in 3D.
   b. Show the reconstructed spectra. Label as GM or PCG.

Protocol 2: Standard White Matter

Repeat Protocol 1 with just a modification to step 4:

4. Place your voxel using the following landmarks:
   a. Stay in largely white matter, but allow up to 25% of GM.
   b. Landmarks are the
      i. Center posterior rim of left (right) lateral ventricle
      ii. 1–1.5 cm above posterior commissures of corpus callosum.
   c. Review above two and below at least two slices (for 5 mm MRI slice thickness and 20 mm voxel slice thickness).
   d. The S/I center position should be not more than 0–5 mm (superior) off from the GM center (Figure 11).

Protocol 3: Frontal GM

Repeat Protocol 1 with the following modifications:

4. For placement of the frontal GM voxel, use the axial T_2w MRI as shown in Fig. 12 (FGM is the box with the dotted lines, ignore the posterior boxes).
   a. Place the single voxel neurospectroscopy in the frontal GM just as you would for the PCG.
   b. You must tuck it in between the anterior skull and the anterior corpus callosum.
   c. Avoid being close to the nasal sinuses as well as CSF space.
   d. Try not to include the frontal white matter.

On GE systems: change FreqDIR to L/R instead of A/P. This is an important step as it reverses the gradient order which allows for better shims (Figure 12).

Protocol 4: Hippocampus/Temporal Lobe

1. For scanners that utilize the true coronal plane, make sure that the patient head is as straight as possible. If the head is tilted to the left or right, it will make voxel placement and/or comparison more difficult.
2. Acquire coronal localizers that can easily differentiate the hippocampal GM and temporal lobe white matter.
3. Set up the following parameters:
   a. Pulse sequence: PRESS
   b. $T_E = 35$ ms
   c. $T_R = 1500$ ms
   d. Voxel size = 15 × 15 × 30 mm (30 mm thick in the S/I direction)
   e. Number of averages = 256
4. Find the slice where the brainstem is apparent (as shown in Fig. 13) and place the voxel in the hippocampus. Try to capture as much of the GM of the hippocampus as possible. This will be your center slice.
   a. Check three slices up and three slices down—you may have to shift the center slice to capture as much of the hippocampus as possible.
   b. Make sure to not fall outside of the temporal lobe! Check your bottom left corner of the voxel for the left-sided voxel and bottom right corner for the right.
   c. Try not to include any of the inferior ventricles (Figure 13).
5. Prescan routine: It is absolutely essential that the line widths are less than 7 Hz. In many cases, you may need to check the line width and move the voxel to try to obtain a better line width. This is the most challenging aspect of hippocampal spectroscopy and why measurements from this region have a high variation.
6. Acquire data.
7. Prescribe a voxel that is exactly contralateral to the previously acquired voxel. This is also difficult but you must be absolutely precise in order to ensure comparability between the two spectra.
   a. Remember to take into account any tilt of the patient to ensure that the same regions are measured.
   b. For single-plane scanners, you may have to prescribe your center slice on a different slice if the patient's head is tilted to the left or right (reference the eye balls to check for head tilt).

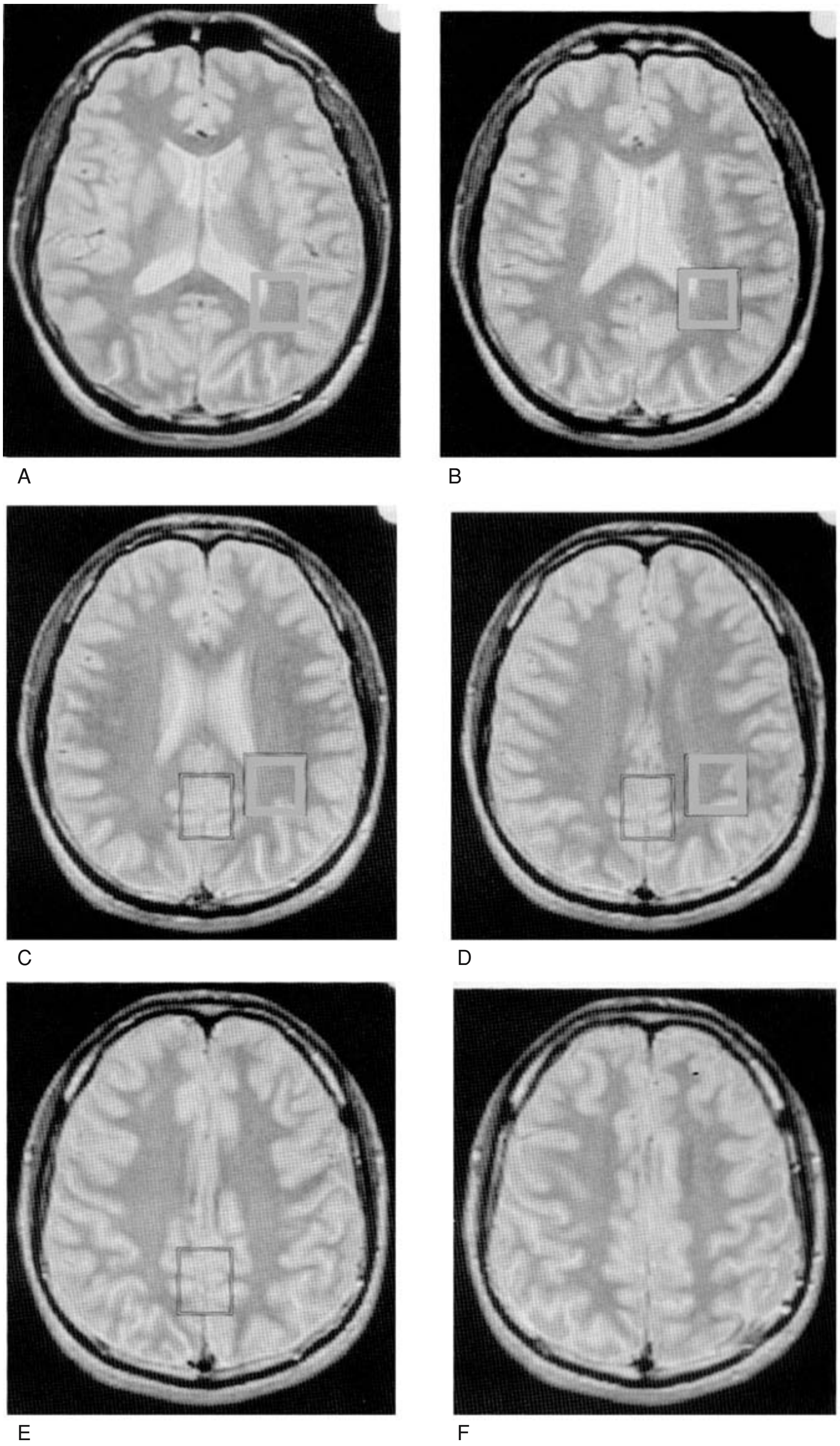

Fig. 11. White matter voxel position.

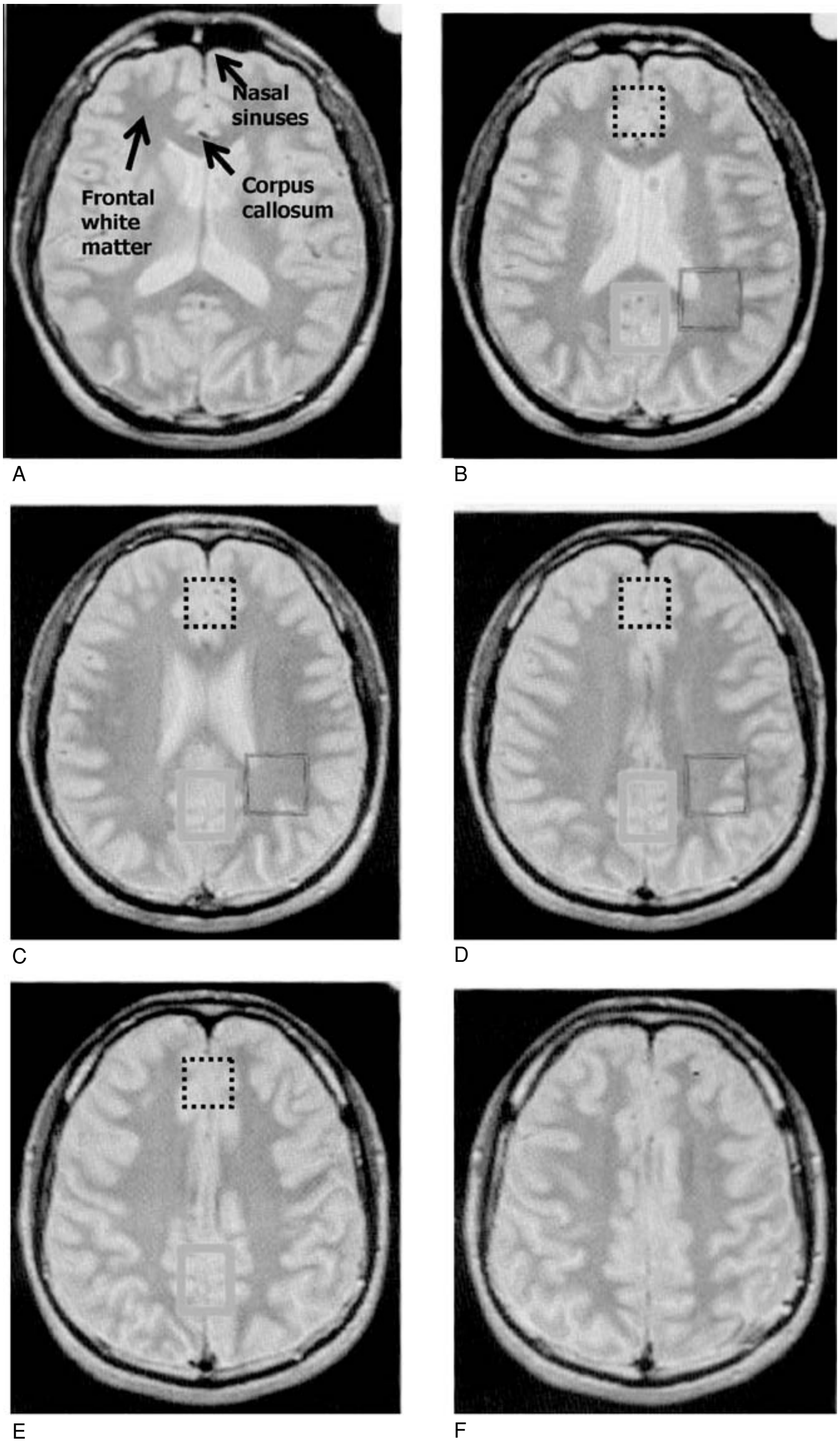
Nasal sinuses
Frontal white matter
Corpus callosum
A
B
C
D
E
F

Fig. 12. Frontal gray matter voxel position. The frontal gray matter voxel is indicated in the dotted black lines. The posterior gray matter voxel is shown for reference. Be careful to avoid too much frontal white matter and corpus callosum in your voxel but at the same time stay away from the nasal sinuses.

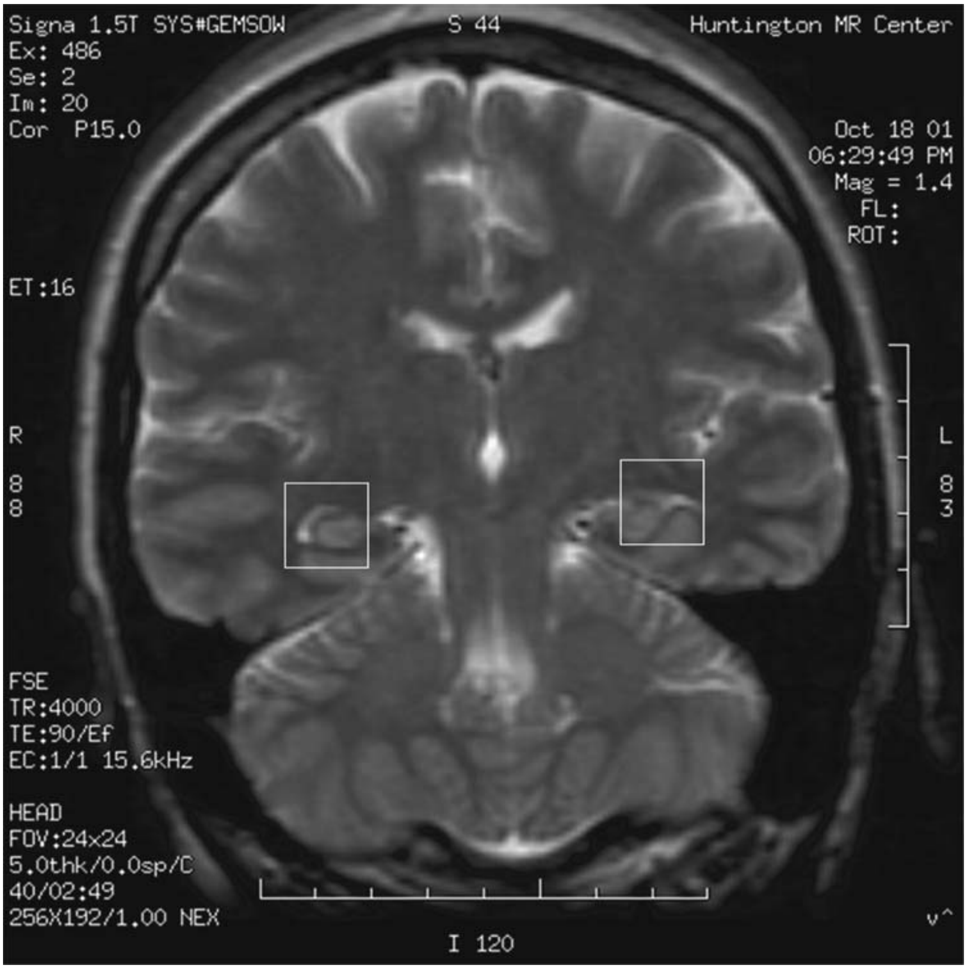
Signa 1.5T SYS#GEMSOW
S 44
Huntington MR Center
Ex: 486
Se: 2
Im: 20
Cor P15.0
Oct 18 01
06:29:49 PM
Mag = 1.4
FL:
ROT:
ET:16
R
8
8
L
8
3
FSE
TR:4000
TE:90/Ef
EC:1/1 15.6kHz
HEAD
FOV:24x24
5.0thk/0.0sp/C
40/02:49
256X192/1.00 NEX
I 120

Fig. 13. Left and right hippocampal voxel position. Note how the voxel may not be on the same S/I level due to some minor head tilt. Not shown are the other slices that are 15 mm above and below this center slice.

Protocol 5: Multivoxel Neurospectroscopy (For Focal Use Only)

1. Position the patient in the scanner as indicated in Section 1 (Figure 3).
2. It is recommended that a single voxel exam precedes the multivoxel exam for the most efficacious exam. Proceed with focal techniques described in the first section.
3. Acquire localization images for spectroscopy
   - c. For single-plane acquisition scanners:
     - i. Slice thickness + Interspace = 5.0 mm. That way you can place your voxel on the center slice and check two slices up and two slices down to ensure that your voxel does not fall into any bad areas.
     - ii. For ease of landmarks, we suggest using the axial plane.
   - d. For three-plane acquisition scanners:
     - i. Choose a sequence that shows the best contrast between gray and white matters. We generally use a T_2w image.
4. Set up your neurospectroscopy scan parameters:
   - e. Pulse sequence: PRESS-CSI
   - f. $T_E = 35$ ms
   - g. $T_R = 1000$ ms

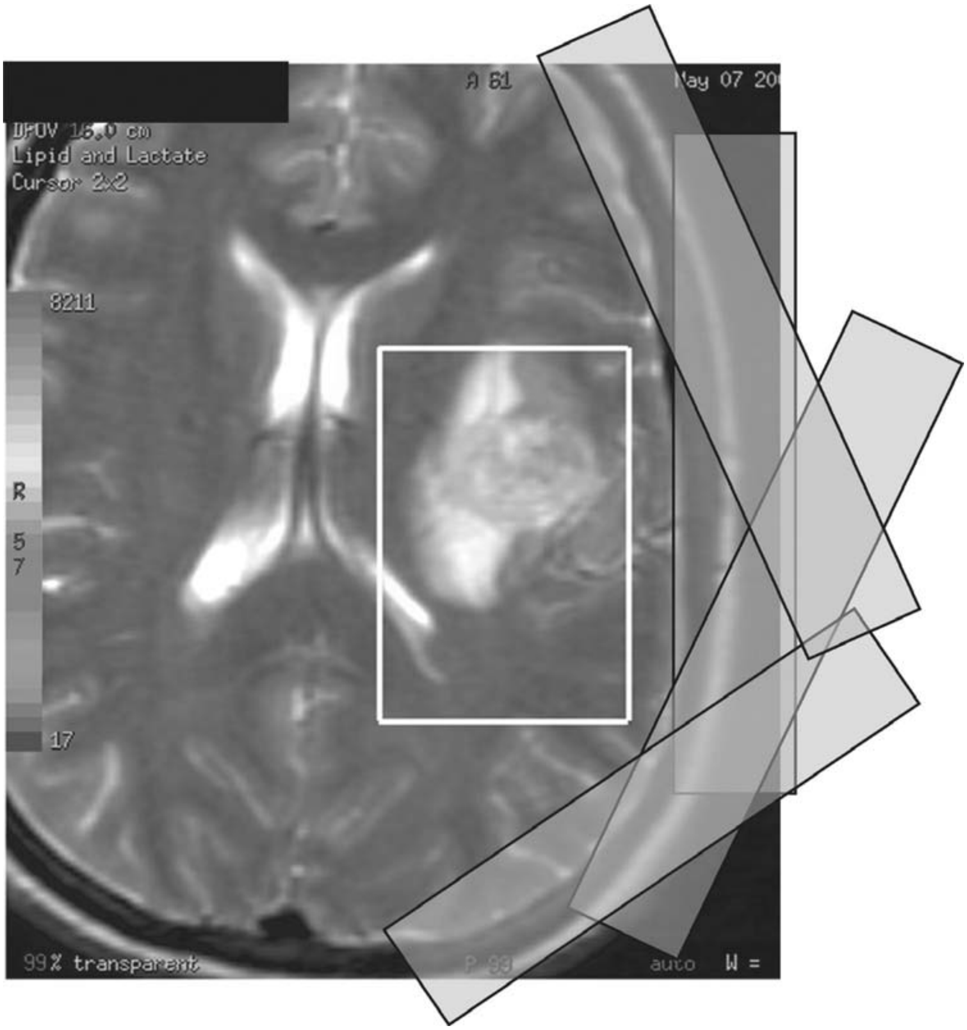

Fig. 14. Saturation band and excitation volume placement. If available on your scanner, additional saturation bands can be placed to regions close to the excitation volume to avoid lipid contamination from the skull.

   h. Phase encode = 24
   i. Frequency encode = 24
   j. FOV = 24 × 24 cm
   k. Slice thickness = 10 mm
   l. NEX = 1
5. Prescribe the excitation volume voxel around the area of interest (i.e. lesion) and a bit more. Make the size relevant to what you are looking for. Use the same center slice as that of the single voxel exam. Use the same care described above in not placing the excitation volume too close to the skull and other areas of inhomogeneity.
6. If they are available on your scanner system, place saturation bands over skull closest to the voxel in order to avoid any lipid contamination. Make sure that the saturation bands do not intersect with the excitation volume. The saturation bands are used to cut out the residual water and any lipids surrounding the skull (Figure 14).
7. Prescan routine: In the case of multivoxel neurospectroscopy, since the volumes are larger, the line widths will not be as low as those for single voxel. Generally, a line width of <11 Hz is acceptable.
8. Acquire the data.

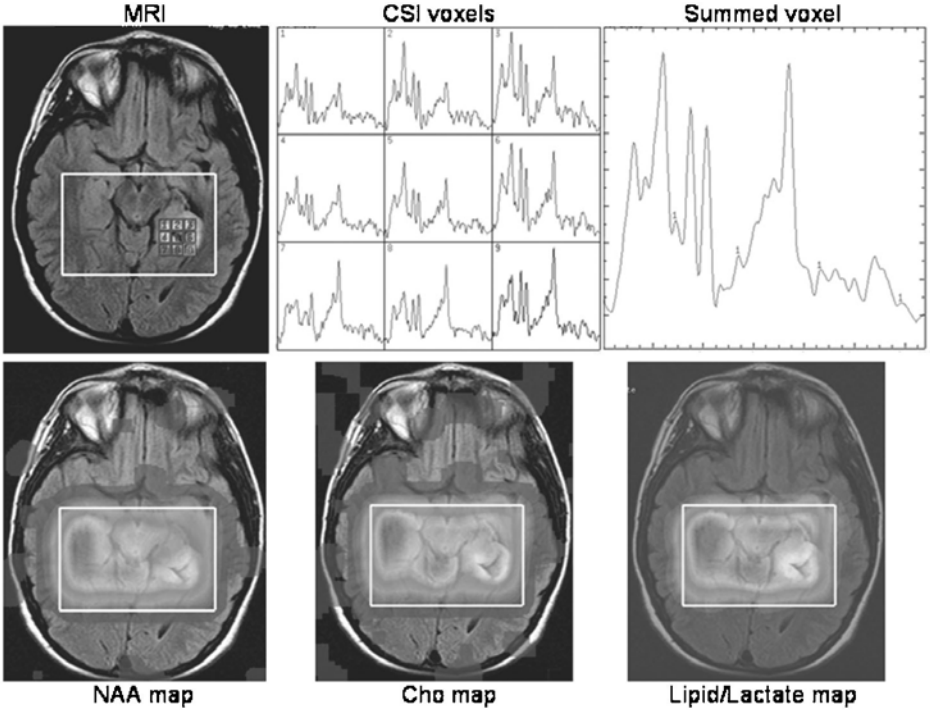

Fig. 15. Filming multivoxel neurospectroscopy for "Speed Reading." This case of a temporal lobe lesion demonstrates the value of multivoxel short echo neurospectroscopy. The region of interest is indicated on the images (top left) from which the summed spectrum is shown (top right). To benefit from the fine resolution of multivoxel neurospectroscopy without the obfuscation of hundreds of spectra, the individual spectra from the region of interest are also shown (top middle). The bottom row demonstrates the metabolite maps generated from this same exam. They are not particularly diagnostic despite excellent spectral quality as demonstrated in the top row. These spectra demonstrate a high mI signal which indicates a low-grade tumor which would have been missed if it had been acquired with long echo TE or relying on high Cho alone. The results were confirmed by autopsy. (See also Plate 82 on page XIII in the Color Plate Section.)

9. Data analysis: it is best to visualize the multivoxel as soon as possible. Users will want to check for quality first and then use the multivoxel results for planning a confirmatory single voxel exam. The reasons why a second single voxel result is recommended are a) it provides confirmation of multivoxel results, and b) the single voxel technique is much more robust and not prone to artifacts that could mislead the diagnosis.
10. When filming the multivoxel results, the "speed reading" technique is used where multiple regions from the excitation volume are selected and summed as well as individual spectra from that region are shown (Figure 15, top row). This allows for quick yet detailed inspections of multiple data points. It is important to also film the regions from which single voxel were acquired to provide quality assurance of your multivoxel data.

Summary

Once the above routines are well established, they can be enshrined in a protocol on your scanner. This limits the number of variables—and hence sources of error—as well as greatly speeding the diagnostic scan. In our clinical practice, technologists must go through a training routine before they are allowed to run patients. Initially they run "phantom" studies: acquiring spectra on a container with different concentrations of chemicals similar to those found in the brain. This can be purchased from the manufacturer or the Spectroscopy Institute (http://www.spectroscopy.org). This will enable the technologist to become familiar with the controls and the protocols. Secondly, they acquire several spectra from volunteers. This allows the new technologist to build up a working knowledge of different brain regions and their biochemistry as well as providing the group with a larger base of their own "normal values." If this is not possible, then close supervision of the acquisition on patients is necessary. Quality control is essential at this stage. Ensure that they are following protocol religiously. At the end, you will have a well-trained technologist in spectroscopy.

This chapter was written with the assumption that the reader will have a basic familiarity with clinical applications of neurospectroscopy. Recommended reading would include "Magnetic Resonance Spectroscopy Diagnosis of Neurological Diseases" by Else Danielsen and Brian D. Ross (Marcel Dekker, 1999). Additional resources include the Clinical MR Spectroscopy Course offered annually by Dr. Brian Ross and his staff at Huntington Medical Research Institutes (http://www.hmri.org) as well as on-site technologist training course offered by the Spectroscopy Institute available throughout the year (http://www.spectroscopy.org). The manufacturers such as General Electric Healthcare, Siemens Medical Systems, and Philips also offer applications training and courses that cover spectroscopy throughout the United States, Asia, and Europe.

Acknowledgments

All of the experiences detailed above would not have been possible without the guidance and support of Dr. Brian D. Ross at Huntington Medical Research Institutes. He and the many scientists that have been under his tutelage have truly brought the science to the bedside by developing neurospectroscopy as a clinical diagnostic tool. Drs. Stefan Bluml, Else Danielsen, Thomas Michaelis, Thomas Ernst, and Roland Kreis are among the many that have contributed to the clinical practice of neurospectroscopy.

Suggested Reading List for "Clinical Neurospectroscopy Protocols"

1. Danielsen E, Ross BD. Magnetic Resonance Spectroscopy Diagnosis of Neurological Diseases. Marcel-Dekker: New York, 1999.
2. Salibi NM, Brown MA. Clinical MR Spectroscopy: First Principles. Wiley-Liss: New York, 1997.
3. Mountford CE, Doran S, Lean CL, Russell P. Proton MRS can determine the pathology of human cancers with a high level of accuracy. Chem. Rev. 2004;104(8):3677–704.
4. Lin A, Bluml S, Mamelak AN. Efficacy of proton magnetic resonance spectroscopy in clinical decision making for patients with suspected malignant brain tumors. J. Neurooncol. 1999;45(1):69–81.
5. Preul MC, Caramanos Z, Collins DL, Villemure JG, Leblanc R, Olivier A, Pokrupa R, Arnold DL. Accurate, noninvasive diagnosis of human brain tumors by using proton magnetic resonance spectroscopy. Nat. Med. 1996;2(3):323–5.
6. Ricci PE, Pitt A, Keller PJ, Coons SW, Heiserman JE. Effect of voxel position on single-voxel MR spectroscopy findings. AJNR Am. J. Neuroradiol. 2000;21(2):367–74.
7. Chang L, Miller BL, McBride D, Cornford M, Oropilla G, Buchthal S, Chiang F, Aronow H, Beck CK, Ernst T. Brain lesions in patients with AIDS: H-1 MR spectroscopy. Radiology. 1995;197(2):525–31. Erratum in: Radiology 1996; 198(2):586.
8. Shonk TK, Moats RA, Gifford P, Michaelis T, Mandigo JC, Izumi J, Ross BD. Probable Alzheimer disease: diagnosis with proton MR spectroscopy. Radiology. 1995;195(1):65–72.
9. Kantarci K, Jack CR Jr, Xu YC, Campeau NG, O'Brien PC, Smith GE, Ivnik RJ, Boeve BF, Kokmen E, Tangalos EG, Petersen RC. Regional metabolic patterns in mild cognitive impairment and Alzheimer's disease: a 1H MRS study. Neurology. 2000;55(2):210–7.
10. Ashwal S, Holshouser BA, Shu SK, Simmons PL, Perkin RM, Tomasi LG, Knierim DS, Sheridan C, Craig K, Andrews GH, Hinshaw DB. Predictive value of proton magnetic resonance spectroscopy in pediatric closed head injury. Pediatr. Neurol. 2000;23(2):114–25.
11. Lee PL, Yiannoutsos CT, Ernst T, Chang L, Marra CM, Jarvik JG, Richards TL, Kwok EW, Kolson DL, Simpson D, Tang CY, Schifitto G, Ketonen LM, Meyerhoff DJ, Lenkinski RE, Gonzalez RG, Navia BA, HIV MRS Consortium. A multicenter 1H MRS study of the AIDS dementia complex: validation and preliminary analysis. J. Magn. Reson. Imaging. 2003; 17(6):625–33.
12. Ross B, Bluml S. Magnetic resonance spectroscopy of the human brain. Anat. Rec. 2001;265(2):54–84.

Application of Magnetic Resonance for the Diagnosis of Infective Brain Lesions

Uwe Himmelreich[1] and Rakesh K. Gupta[2]

[1] *Institute for Magnetic Resonance Research and Centre for Infectious Diseases and Microbiology, Westmead Hospital at the University of Sydney, Sydney, Australia; and*
[2] *Department of Radiodiagnosis, Sanjay Gandhi Postgraduate Institute of Medical Sciences, Lucknow, India*

Abbreviations: ADC, apparent diffusion coefficient; DWI, diffusion-weighted imaging; GBM, glioblastoma multiforme; MRI, magnetic resonance imaging; MRS, magnetic resonance spectroscopy; PCA, principal component analysis; PWI, perfusion-weighted imaging; PRESS, point-resolved spectroscopy; SCS, statistical classification strategy; SNR, signal-to-noise ratio; STEAM, stimulated echo acquisition mode; TE, echo time; TR, repetition time; VOI, volume of interest

Introduction

Brain infections are often acute and potentially life-threatening diseases of immunocompromised and healthy hosts. Rapid, accurate, and safe diagnostic methods are essential to initiate optimal treatment and reduce mortality from brain infections. We will focus here on focal brain infections as an example of the diagnostic potential and limitations of magnetic resonance imaging (MRI) and spectroscopy (MRS) methods. Particular attention will be paid to distinguishing between tumors and infective lesions. Different types of infections will be discussed.

Brain lesions are usually diagnosed after biopsies are taken. A definitive diagnosis is still typically established by culture of bacteria from pus obtained after neurosurgical biopsy, or inferred by culture of infected material from other body sites. Computerized tomographic (CT) and MRI methods have reduced mortality by improving the detection and localization of brain lesions over the last decades [1,2]. Typically, necrotic or cystic tumors, tumorfactive demyelinating lesions, and cerebral abscesses show similar appearances using conventional radiological methods. The use of diffusion-weighted images, perfusion MRI and MRS have been suggested for differential diagnosis of these pathologies [3–5]. However, differential diagnosis of post-contrast ring-enhancing cerebral lesions continues to be a challenge, as such lesions include glioblastoma, metastasis, pyogenic abscess, subacute ischemic infarction, resolving hematoma, and demyelinating disease [3,6–8]. This becomes a particular problem when other indications of infections (like fever) are missing and microbial culture from body fluids is negative, as can be the case in up to 50% of infective lesions [2]. In addition, case reports are relatively sporadic and the microbial spectrum is diverse.

Pathological, clinical, and diagnostic aspects of brain infections, and their diversity, have been addressed in a number of reviews and are beyond the scope of this review [1,2,6,9]. Although detailed descriptions of the fundamentals of MR techniques have been addressed elsewhere [6,10], essential methods will be discussed and their application will be demonstrated, using the example of focal brain infections.

Scenarios that need to be addressed by non-invasive diagnostic tools include: (1) the differentiation between infective lesions and other pathologies like glioma and (2) the identification of the infection-causing microorganisms.

Magnetic Resonance Techniques

The physical basis of MRI and MRS has been reviewed by numerous authors (for example Ref. [10]). In order to access the most appropriate MR techniques one has to consider the physical nature of an infective brain lesion. A "true" abscess consists of an abscess capsule, containing fibrous material and chronic inflammation cells, and a central cavity filled with pus. Pus is of variable viscosity and consists of dead and dying polymorphous cells (leucocytes), living and dead microorganisms, tissue debris, and other components of inflammation (edema fluid and fibrin) [1,2]. In contrast to "true" abscesses, some focal infections (parasitic, fungal) lack an abscess wall. In order to distinguish between abscesses and other focal brain diseases and to distinguish between various types of focal infections the following properties are of interest for diagnosis: proton density, spin–lattice relaxation time (T_1), spin–spin relaxation time (T_2), flow, diffusion, chemical composition, and variation in uptake of contrast agents. For clinical diagnosis, it is important to select protocols that are rapid, as some of these patients are critically ill. Short protocols increase patient comfort, allow

Graham A. Webb (ed.), Modern Magnetic Resonance, 1005–1013.
© 2008 *Springer.*

additional studies, and decrease motion artifacts. It is also important to suggest protocols that can be implemented on various hardware platforms, including older MR systems that are common in developing countries where the cohort of abscess patients is large.

At present, two-dimensional (2D) multislice images are commonly used in routine diagnosis. The most widely used pulse sequences are based on spin-echo sequences. The main drawback of the spin-echo sequence is a relatively long acquisition time. Alternatively to spin-echo T_1-weighted images, inversion recovery results in stronger T_1 weighting due to an initial 180° pulse followed by an evolution time, during which the inverted spins relax back to $+Z$ according to T_1. By choosing a specific evolution time that suppresses lipid resonances, T_1-weighted images can be acquired with inversion recovery spin-echo sequences that suppress lipid signals. Combining inversion recovery with T_2-weighted spin-echo sequences can be used to attenuate otherwise hyperintense signals from fluids [fluid-attenuated inversion recovery (FLAIR)]. FLAIR permits the detection of CNS lesions that are adjacent to regions containing fluids (e.g. CSF). Significant improvement of lesion-to-CSF contrast has been achieved using FLAIR [11].

Reduction of repetition times (TR) is possible with gradient echo imaging. Gradient echo images are particularly sensitive to field inhomogeneities. Instead of 180° pulses, gradients are used to refocus the signal. Adjustment of pulses is therefore less critical than in spin-echo sequences. Spin-echo sequences are sensitive to T_2 effects, gradient echo sequences are sensitive to T_2^* effects. Due to the sensitivity to field inhomogeneity, the quality of gradient echo imaging is usually lower compared with spin-echo sequences.

A more rapid version of spin-echo sequences is fast-spin-echo or turbo-spin-echo imaging [12]. The total scan time is hereby reduced by traversing through several phase-encoding levels during each TR. Thus, several echoes are collected during each TR. Fast-spin-echo methods require rapid switching of gradients, imposing considerable strain on the hardware. The large refocusing angles make constraining RF power a challenge. Nutation angles of much less than 180° can overcome this problem [13]. Other rapid acquisition methods include gradient echo fast-low-angle-shot (FLASH) [14] and echo planar imaging (EPI) [15,16]. In EPI the entire matrix is acquired in one excitation with multiple phase-encoding gradient echoes. The penalty of the rapid data acquisition is a relatively low image quality. EPI is of great importance for applications that do not necessarily require a high resolution such as functional MRI or diffusion-weighted imaging (DWI) [17]. The drawback of EPI is image distortion, dropout, blurring, and signal loss [18]. EPI quality and resolution can be improved by reducing the readout time (parallel imaging or half-Fourier techniques) [19].

Acquisition time gained by the application of rapid pulse sequences can be reinvested in improving the quality of the image. This applies to increasing the signal-to-noise ratio (SNR) by averaging more transients, increasing the resolution to reduce partial volume effects by acquiring a larger data matrix or by applying stronger T_2 weighting using longer TR and TE values.

Differences in tissue molecular self-diffusion due to translational motion can be monitored by application of strong magnetic field gradients. Molecular motion between the application of these gradients results in dephasing of the MR signal. Diffusion-weighted images can be acquired by varying either the gradient strength (G), the gradient length (δ), or the separation (Δ) between two read out gradients (dephasing and rephasing of water protons) [20]. The so-called b value ($b = (\gamma G \delta)^2 [\Delta - \delta/3]$) describes these variables in comparable form. In diffusion-weighted images, regions of hyperintensity represent restricted diffusion. Maps of apparent diffusion coefficients (ADC) can be calculated by acquisition of a number of images in which either G, δ or Δ have been incremented systematically. Due to time constraints for the acquisition of a series of images, diffusion-weighted EPI is usually used to obtain ADC maps. It has become common practice to use only two b values for the calculation of ADCs. However, in order to avoid an overestimation of the ADC, multiple points (b) should be used for more accurate calculations [4,21].

Perfusion-weighted MR imaging (PWI) exploits signal changes following the passage of a contrast agent or labeled spins through the cerebrovascular system. A series of images is acquired in short intervals from which relative cerebral blood volume (rCBV) maps are calculated. The CBV is proportional to the area under the contrast agent concentration–time curve. Fast acquisition methods are required for PWI (rapid gradient echos, EPI).

Magnetization transfer (MT) has been used to increase tissue specific contrast in various diseases [22,23]. Selective saturation of signal contributions from protons with very low T_2 values (broad lines due to decreased mobility) can be achieved by off-resonance irradiation. MT from the saturated protons to mobile protons results in decreased signal intensity and produces substantial changes in contrast [24].

Localized *in vivo* MRS is probably the most powerful tool for determining the chemical composition of an object of interest non-invasively. In contrast to MRI methods, chemical shift information for the acquisition of metabolite profiles is acquired from a volume of interest (VOI), suppressing unwanted signals from outside the VOI. Although, ^{31}P and other nuclei like ^{13}C are increasingly studied (for example [25–27]), the most commonly used method for clinical diagnosis is ^{1}H MRS. From the relatively large number of MRS protocols [28], single VOI spectroscopy is most useful when studying lesions that are magnetically distinct from surrounding tissue. Although, chemical shift imaging (CSI) provides a matrix of spectra over relatively large regions within a short time, it is less suitable for the acquisition of high-quality spectra of focal lesions due to difficulties of shimming over a heterogeneous region. The two main pulse sequences used for single VOI MRS are point-resolved spectroscopy (PRESS) [29] and stimulated echo acquisition mode (STEAM) [30]. PRESS uses an excitation pulse ($\pi/2$) and a double echo and STEAM uses stimulated echoes. In general, PRESS results in higher SNRs but requires more precise pulse calibrations to suppress signal from outside the defined VOI. It can be distinguished between localized MRS that has been acquired with relatively short echo times (TE $<$ 35 ms) and with long echo times (TE $>$ 130 ms). The latter has the advantage of suppressing contributions from compounds with short T_2 relaxation times like lipids and macromolecules that would otherwise mask resonances from small metabolites in low concentrations. On the other hand, those compounds may be of diagnostic value. MR spectra can be applied for the quantification of metabolites [31,32].

More recently, methods from high-resolution (*ex vivo*) MR spectroscopy like ^{1}H, ^{1}H COSY and J-resolved MRS have been applied to *in vivo* assignment of resonances [33,34].

Contrast Enhancement

MR contrast agents modulate T_1 and T_2 relaxation times of water molecules inside the organism. Intravenous administration of gadolinium (Gd)-based contrast agents results in signal enhancement in T_1-weighted images in areas of accumulation of the substance. In the case of brain lesions, this most commonly reflects an increase in blood volume or a breakdown of the blood–brain barrier. Post-contrast hyperintensity of a perilesional ring is common in cerebral abscesses in the capsule stage as well as cystic and necrotic brain tumors [most commonly glioblastoma multiformes (GBMs)]. This makes differentiation between abscess and tumor difficult based on conventional contrast agents.

Most recently, responsive contrast agents have become more and more important. These contrast agents are usually responsive to chemical modification or specific binding to receptors, resulting in an activation or accumulation of the contrast agents at the targeted site [35,36]. One example in cancer diagnosis is the combination of iron oxide particles with ligands that bind to transferin receptors, resulting in accumulation of contrast agent in glioma cells [36]. Similarly, antibody–polylysine Gd chelates or Gd chelates targeting cell surface molecules have been suggested for specific visualization of tumor cells [37–39].

Ultra-small paramagnetic iron oxide particles (USPIOs) generate large susceptibility effects in surrounding tissue. This results mainly in shortening of T_2 and T_2^* relaxation times and subsequent hypointensity in respectively weighted MR images [40,41]. Labeling of phagocytes with USPIOs has been used for cell tracking *in vivo* [42]. Krieg *et al.* suggested the use of USPIOs for the detection of inflammatory processes as they result in the accumulation of large numbers of phagocytes [43]. This hypothesis has been proven by the utilization of *in vitro* labeled neutrophils in an animal model of induced abscesses. Intravenous administration of USPIOs was subsequently shown to differentiate between normal tissue and abscess [44]. Phagocytosis of USPIOs by macrophages and neutrophils partly contributed to a persistent signal decrease in interstitial spaces of the abscess wall and perifocal granulation tissue. It remains to be seen if the use of USPIOs is useful in clinical diagnosis of abscesses, as other diseases such as stroke also result in inflammatory response and subsequent accumulation of iron labeled macrophages [42,45].

The utilization of iron or Gd-based contrast agents linked to antigens specific for particular pathogenic microorganisms is still an unexplored, potentially useful tool for the diagnosis and etiological characterization of brain infections.

Conventional MRI of Infective Brain Lesions

Pyogenic bacterial abscesses are the most common focal brain infections. Radiologically, a brain abscess appears in CT and MRI as a mass surrounded by edema, similar to brain tumors [9]. They are hypointense on T_1- and hyperintense on T_2-weighted MR images (Figure 1). The mature abscess often has a rim that is slightly hyperintense on T_1- and hypointense on T_2-weighted images. This has partly been attributed to accumulation of macrophages [9]. Post-contrast ring enhancement in T_1-weighted MRI is common in brain abscesses (Figure 1).

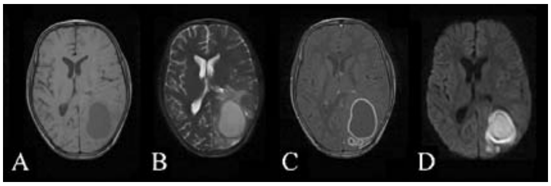

Fig. 1. Transverse MR images of a mixed bacterial abscess (*Streptococcus milleri* and *Bacteroides fragilis*). Images were acquired on a 1.5 T human MR scanner. (A) Hypointensity on T_1-weighted MR image (TR/TE = 660/15), (B) Hyperintensity and perifocal edema on T_2-weighted MR image (2200/80), (C) post-Gd contrast enhancement of a perilesional ring in T_1-weighted MR image (660/15) and (D) hyperintensity in a DWI ($b = 1000$ s/mm^{-2}) indicating restricted diffusion.

Features similar to pyogenic abscess were seen in intracranial tuberculoma [46,47] and focal infections caused by higher bacteria like *Nocardia* spp. [48,49].

Focal brain infections caused by fungi are less common. These infections can be caused by filamentous fungi (*Aspergillus* spp., *Mucor* spp.) or yeast and yeast like organisms (*Cryptococcus neoformans*, *Blastomyces dermatitides*, *Candida* spp., *Histoplasma capsulatum*). They differ from pyogenic abscesses as they do not necessarily form an abscess wall. The MR appearance of infections by filamentous fungi is often consistent with infarcts. Their hyphal elements lodge in intracerebral blood vessels, causing occlusions which result in microinfarcts and thrombosis. The actual infective lesions are not necessarily well defined. They show inhomogeneous hyperintensity on T_2-weighted images, surrounded by edema [50–53]. Hypointense peripheral rims have been reported due to blood products [51]. T_1-weighted images are often consistent with hemorrhages (hyperintense). Ring enhancement after administration of Gd contrast agent has been reported in some cases. The center of the lesion is often necrotic. Pituitary lesions due to *Aspergillus* spp. result in similar features to pituitary bacterial abscesses: a hypo- or isointense mass on T_1-weighted images, a hyperintense mass on T_2-weighted images and a peripheral contrast enhancing rim, which may also be features of pituitary tumor [54].

Similarly, yeast infections are characterized by isointensity [53,55] or hypointensity [9,53,56] on T_1-weighted images, hyperintensity on T_2-weighted images [9,52,53,55,56], and absence [53,56] or presence [52,53] of ring enhancement after Gd contrast. Some lesions show hypointense rings on T_2-weighted images due to the presence of macrophages [9].

Parasitic infections are caused by organisms that live part of their life cycle in a host. Parasites that cause focal brain infections in humans are most commonly *Taenia solium* larvae (causing cysticercosis), *Toxoplasma gondii* (toxoplasmosis), *Paragonimus* spp. (paragonimiasis), *Echinococcus* larvae (echinococcosis), amoebic infections, and others [57]. The appearance of lesions may change with development of the parasite and treatment. Many parasites can cause multiple lesions. They appear hypointense on T_1-weighted images, hyperintense on T_2-weighted images and show often no ring enhancement post-contrast [57–64]. Toxoplasmosis shows usually variable signal intensity on T_2-weighted images due to different amount of necrotic tissue, and post-contrast ring enhancement [64]. Later stages of paragonimiasis result in calcification and subsequent hypointense T_1- and T_2-weighted images [60]. Treatment of cysticercosis results in increased fluid content and immune response resulting in increased signal intensity on T_1, DW, and PW images and contrast enhancement [62].

Other MRI Methods

Diffusion

DWI provides unique information about translational molecular diffusion of water protons, which is also affected by the presence of cellular substructures [65]. Restricted diffusion within the cavity of a brain abscess, as opposed to the increased diffusion observed in cystic or necrotic tumors, was reported by Ebisu *et al.* [5]. This phenomenon was correlated with the high viscosity and cellularity of the respective pus samples. Further studies confirmed restricted diffusion in abscesses (Figure 1) [3,4,66]. However, the ADC values between and within these studies varied widely. Increased or unchanged ADCs have been reported for a number of abscesses [7,67,68]. Similar to these pyogenic abscesses, toxoplasmosis also resulted in increased ADCs [69]. These findings are not surprising as the viscosity of pus varies widely with the amount of inflammatory cells and microorganisms, the etiology and the age of the infective lesion (data not shown). In addition, restricted diffusion has also been found in cystic metastasis [7]. While decreased ADCs are highly suggestive of abscesses, they are not pathognomonic. A definite diagnosis of infective brain lesions cannot be based solely on DWI.

Perfusion

The main pitfall of PWI for the detection of brain lesions is that it can be inaccurate, where there is breakdown of the blood–brain barrier, which is the case in GBM and many infections [70]. In a low number of studies, it has been reported that intracranial infections resulted in a variable appearance in PWI, depending on the type of infection [71–73]. Pyogenic abscesses showed areas of increased rCBV in regions adjacent to the capsular rim in one study [71], suggesting that this may distinguish abscesses from solid tumors with areas of high vascularity, like high-grade GBMs and metastases [74]. Other studies have reported significantly lower rCBVs in abscesses compared to tumors, with lower rCBVs of the walls in abscesses compared to cystic/necrotic tumors [73]. However, these tumors can still be mistaken for abscesses based on PWI. Heterogeneous, hypervascular appearance of a significant number of tuberculomas has been reported, making differentiation between these lesion and tumors difficult [72].

This clearly indicates that more data are required to draw robust conclusions about the diagnostic value of PWI and DWI in distinguishing between subgroups of infective brain lesions and other pathological processes.

Magnetization Transfer

MT MRI for the diagnosis of infections is based on exchange of magnetization of protons from proteins with protons from water [22,75]. Pre-contrast MT spin-echo imaging was used for assessment of disease load in CNS tuberculosis and other infections due to better visualization of the lesions. Tuberculous lesions showed significantly lower MT ratios compared to pyogenic abscesses. Quantitative MT imaging was suggested in order to distinguish between various types of infective lesions [22]. A larger number of cases need to be evaluated in order to assess the influence of variable protein concentrations in abscesses.

Magnetic Resonance Spectroscopy

Although sophisticated MRI techniques are able to distinguish between certain infective lesions and tumors, cystic and necrotic gliomas can still be difficult to differentiate from abscesses. MRI methods are not able to distinguish between different infection-causing microorganisms. Microorganisms have diverse metabolite profiles that are distinct from mammalian metabolites [76]. This makes MR spectroscopy a suitable method for determining the etiology of an infection.

MRS chemotypes living microbial and mammalian cells by providing information on their chemical constituents rapidly and simultaneously. Studies on cell suspensions have shown that even closely related bacteria and fungi could be distinguished when MR spectra were analyzed by pattern recognition techniques [77,78]. Metabolites identified by MRS in cell cultures were also found in body fluids and biopsies from infective tissue [68,79–81]. If typical marker metabolites are present infection-causing microorganisms can be identified or at least classified without isolation and cultivation. In cases where spectroscopic patterns are similar to those from other pathologies, such as the presence of large concentrations of lipids and lactate in *Staphylococcus aureus* or *Streptococcus milleri* abscesses as well as necrotic GBMs, diagnostic "marker" metabolites can be masked. Analysis of MR spectra by statistical classification methods is still powerful enough to distinguish between such similar spectroscopic patterns [68,82,83].

In vivo MRS has been reported to distinguish the broad group of pyogenic abscesses from malignant gliomas and tuberculoma non-invasively [8,48,75,84–90]. A selection of *in vivo* MR spectra from brain abscesses is shown in Figure 2. While highly necrotic and cystic tumors and pyogenic abscesses contain both, large amounts of lipids and lactate, other organic acids like acetate and succinate have been identified in cerebral abscesses in humans and utilized as bacterial "marker metabolites" for non-invasive diagnosis by MRS. Diverse profiles of organic acids are mainly characteristic for hetero-fermentative bacteria [76]. In addition, elevated concentrations of amino acids have been found in pyogenic abscesses [86,88]. This could not always be confirmed, as MRS of abscesses caused by microaerophilic bacteria like *S. milleri* and *S. aureus* did not consistently show elevated resonances from amino acids [8,68]. A remaining diagnostic problem is the differentiation between abscesses caused by exclusively

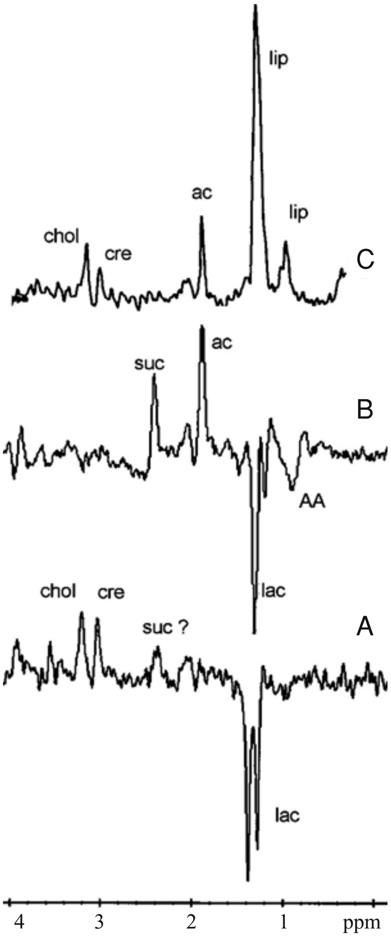

Fig. 2. MR spectra of bacterial abscesses with different etiological composition. Spectra were acquired from an 8 cm^3 VOI placed in the center of the lesion on 1.5 T human MR scanners (TR/TE = 3000/135). Bacteria causing the infections were: (A) *Streptococcus milleri*, (B) *Streptococcus milleri* and *Bacteroides fragilis* (same patient as in Figure 1), and (C) *Staphylococcus aureus, Proteus mirabilis*, and *Escherichia coli*.

Table 1: Choline to creatine ratio determined by integration of the resonances at 3.2 and 3.0 ppm, respectively. Ratios were determined for cystic GBMs, abscesses with growth of *Streptococcus aureus* and sterile abscesses

	Cases	Mean ± SD	Range of choline:creatine ratio
Cystic GBM	11	1.8 ± 0.8	0.4–4.2
S. aureus abscess	9	0.9 ± 0.4	0–1.4
Sterile pus	5	0.2 ± 0.1	0–0.4

microaerophilic bacteria, sterile cysts, and cystic glioma. MR spectra of these lesions contain only resonances from lipids, lactate, and choline containing compounds. Attempts were made to distinguish between these groups based on increased choline levels in gliomas [8]. As Table 1 indicates, substantial overlap exists between the choline to creatine ratio in these lesions. However, statistical analysis of MRS from animal models has indicated that classification is feasible [68].

MR spectroscopy was also able to identify a characteristic pattern for parasitic infections (cysticercus and hydatid cysts) [91,92] as well as yeast infection (cryptococcoma) [56,80]. Relatively non-specific MR spectra were acquired from cerebral aspergillosis [53], nocardidosis [48], and tuberculomas [75,93].

Treatment of brain abscesses was monitored in animal models as well as humans. It was noticed that characteristic metabolites of hetero-fermentative bacteria like acetate and succinate disappeared completely [8,85,94]. Only lactate remained in these cases. These results indicate that the spectral specificity is only valid for untreated abscesses or soon after the start of treatment and that success of antibiotic treatment can be monitored by MRS.

In general, MR spectra acquired with long echo times are most informative as potentially masking intense resonances of lipids are suppressed and phase modulation due to J-coupling supports resonance assignment (lactate, amino acid residues). Unequivocal resonance assignment is currently not possible *in vivo*. First attempts to utilize localized *in vivo* ^{1}H, ^{1}H-COSY spectra for clinical diagnosis are promising and might further improve diagnostic accuracy when applied to abscesses [33,34]. It remains to be seen if the currently unsuitably long acquisition times can be reduced.

Considering the diversity of microorganisms causing brain lesions and the sparseness of cases for some of them, more MRS data are required to evaluate the whole potential of MR spectroscopy and to suggest robust strategies for its application to *in vivo* diagnosis. Based on small numbers, distinction between abscess causing microorganisms seems to be feasible [8,86,87]. This was confirmed for animal models in which a relatively large number of reproducible lesions can be evaluated by MRS [68,80].

Data Analysis

Diagnosis in radiological practice is based on interpretation of images by individuals. Using various MRI methods, this is feasible by following flow charts in the decision making process. Although the diagnostic value of MRS is established, it is little used for medical diagnosis, since interpretation of spectra is complex and few clinicians are trained to use this method. Diagnosis of abscesses is relatively easy in the presence of anaerobe microorganisms that produce unique “marker” metabolites like acetate or succinate [6,84,86,90]. However, focal infections caused by other microorganisms may result in MR spectra that appear similar to those acquired from other pathologies [8,68,86].

Metabolite assignment and quantification can be assisted by utilization of fitting routines like LCModel and other programs [32,95,96]. These semi-automated spectral evaluation tools have the disadvantage that some prior knowledge is required for data fitting, as only metabolites that are in the base set of LCModel can be quantified. Although, the latest versions of LCModel contain a relatively large set of metabolites or can be extended by additional model metabolites [32,97], this would always require prior knowledge and the accumulation of MR spectra from metabolites that are expected to be of value for the diagnosis of infections. The list of such metabolites could include organic acids like acetate, succinate, butyrate, propionate, and carbohydrates/polyols like trehalose, and mannitol. It remains to be seen if fitting routines are still reliable if extended by such a large number of metabolites.

The project International Network for Pattern Recognition of Tumours Using Magnetic Resonance (INTERPRET) aims to develop a decision support system that automates the analysis of multimodal MR data (MRI and MRS) for clinical diagnosis [98,99]. The objective of this multicenter study is the classification of brain tumors. It was demonstrated that, based on a large set of MR spectra for training and various pathologies, fully automated processing and analysis of test spectra by pattern recognition techniques was relatively robust and accurate [98].

Similarly, Poptani *et al.* were able to distinguish between tumors and non-neoplastic disorders using neural networks for the classification of MR spectra [100]. However, neural networks tend to be over-optimistic in cases of relatively small data sets.

A more robust approach was successfully used for the identification of microorganisms and classification of brain abscesses in animal models [8,68,77]. A statistical classification strategy (SCS) of MR spectra that consisted of: (1) automated processing of the spectra, (2) feature reduction by a genetic algorithm-based optimal region selection [101] and (3) the development of a set of linear discriminant analysis-based classifiers was robust and highly accurate. The validation of a classification system containing five classes of closely related pathogens resulted in less than 2% misclassifications [77]. As SCS was successful for the diagnosis of abscess animal models [68] and *in vivo* MRS data to classify human diseases, this seems to be a promising approach for the development of a multiclass classification system for the non-invasive diagnosis of focal brain infections that does not rely on the operator's ability to interpret MRS data. The limiting factor is the sparseness of data to make such a system robust.

Summary

A definitive diagnosis of infective lesions is still typically established by culture of bacteria from invasively obtained samples. Further reduction of mortality from brain abscesses requires more rapid, accurate, and safe diagnostic techniques. It is currently possible with conventional MRI to distinguish infective lesions from a broad range of other pathologies that are indistinguishable by other radiological modalities. Conventional MRI methods of typical abscesses result in hypointense lesions on T_1-weighted images, hyperintense lesions on T_2-weighted images, and ring enhancement in T_1-weighted images after administration of Gd-based contrast agents. The remaining indistinguishable pathologies (necrotic and cystic tumors, tumorfactive multiple sclerosis, and other demyelinating lesions) can be distinguished from infective lesions with relatively high probability by using DWI, PWI, MT MRI combined with MRS. DWI results typically in a reduction of ADCs in abscesses. However, variability in viscosity of pus in abscesses causes a large variability of ADCs, resulting in unchanged or even increased ADCs for some cases. MRS is the most promising method to distinguish between different etiologies of brain infections due to its ability to identify bacterial "marker" metabolites. MRS has also demonstrated its potential to assess the success of treatment. With increasing computerized data analysis and statistical data interpretation, an objective, automated data interpretation is feasible for clinical diagnosis. However, MRS fails if lesions are small (<1 mm) or if only a small cohort of cases is available. Animal models can overcome the limitations of small case numbers. Correlation between models and clinical cases has been successfully demonstrated.

Glossary of Terms

Abscess—Focal infection that consists of an abscess capsule, containing fibrous material and chronic inflammation cells; and a central cavity filled with pus.

Focal infection—Infection that is results in the formation of lesions. Can be caused by bacteria, fungi, parasites, or viruses.

Glioblastoma Multiforme—Highly malignant tumor with a low overall survival time for most patients. They are histologically characterized by a dense cellularity, high endothelial proliferation, and often the presence of focal tissue necrosis. These tumors are can occur in a cystic form.

Pus—Content of an infective lesion. It consists of dead and dying polymorphous cells (leucocytes), living and dead microorganisms, tissue debris, and other components of inflammation (edema fluid and fibrin).

References

1. Mathisen GE, Johnson JB. Clin. Infect. Dis. 1997;25:763.
2. Calfee DP, Wispelway B. Semin. Neurol. 2000;20:353.
3. Leuthardt EC, Wippold FJ, Oswood MC, Rich KM. Surg. Neurol. 2002;58:395.
4. Desbaratsa LN, Herlidoua S, de Marcoa G, Gondry-Jouetb C, Le Garsc D, Deramondb H, Idy-Peretti I. Magn. Reson. Imaging. 2003;21:645.
5. Ebisu T, Tanaka C, Umeda M. Magn. Reson. Imaging. 1996;14:1113.
6. Gupta RK, Lufkin RB. MR Imaging and Spectroscopy of Central Nervous System Infection. Kluwer Academic, Plenum Publishers: New York, 2001.
7. Hartmann M, Jansen O, Heiland S. Am. J. Neuroradiol. 2001;22:1738.
8. Himmelreich U, Dorsch N, Gomes L, Jones N, Brown G, Taylor J, Mountford CE, Sorrell TC. MAGMA. 2003;17(S7):106.
9. Haimes AB, Zimmerman RD, Morgello S, Weingarten K, Becker RD, Jennis R, Deck MDF. Am. J. Neuroradiol. 1989;10:279.
10. Young IR. Methods in Biomedical Magnetic Resonance Imaging and Spectroscopy. John Wiley and Sons: New York, 2000.
11. Rydberg JN, Hammond CA, Grimm RC, Erickson BJ, Jack CR Jr, Huston J, Riederer SJ. Radiology. 1994;193:173.
12. Hennig J, Nauerth A, Friedburg H. Magn. Reson. Med. 1986;3:823.
13. Hennig J. J. Magn. Reson. 1988;78:397.
14. Haase A, Frahm J, Matthaei D, Hänicke W, Merboldt KD. J. Magn. Reson. 1986;67:258.
15. Mansfieldv P. J. Phys. C. Solid State Phys. 1977;10:L55.
16. Stehling MK, Turner R, Mansfield P. Science. 1991;254:43.
17. DeYoe EA, Bandettini P, Neitz J, Miller D, Winans P. J. Neurosci. Methods. 1994;54:171.
18. Fischer H, Ladebeck P. Echo-planar imaging. Image artifacts. In: MS Schmitt, FR Turner (Eds). Echo-Planar

Imaging. Springer-Verlag: Berlin, Heidelberg, 1998, p 179.

19. Jesmanowicz A, Bandettini PA, Hyde JS. Magn. Reson. Med. 1998;40:754.
20. Stejskal EO, Tanner JE. J. Chem. Phys. 1965;43:3579.
21. Burdette J, Elster A, Ricci P. J. Comput. Assist. Tomogr. 1998;22:792.
22. Gupta RK, Kathuria MK, Pradhan S. Am. J. Neuroradiol. 1999;20:867.
23. Mehta RC, Pike BG, Haros PS, Enzmann DR. Radiology. 1995;195:41.
24. Tanttu JI, Sepponen RE, Lipton MJ, Kuusela T. J. Comput. Assist. Tomogr. 1992;16:19.
25. Bluml S, Moreno A, Hwang JH, Ross BD. NMR Biomed. 2001;14:19.
26. Gruetter R, Adriany G, Choi IY, Henry PG, Lei HX, Oz GL. NMR Biomed. 2003;16:313.
27. Payne GS, Al-Saffar N, Leach MO. Phosphorus magnetic resonance spectroscopy on biopsy and in vivo. In: GA Webb (Ed). Handbook of Modern Magnetic Resonance. Kluwer Academic Publisher: New York, 2006, pp 1125–43.
28. Ross B, Bluml S. Anat. Rec. 2001;265:54.
29. Bottomley PA. Ann. N.Y. Acad. Sci. 1987;508:333.
30. Frahm J, Merboldt KD, Hänicke W. J. Magn. Reson. 1987;72:502.
31. Kreis R. Prog. Nucl. Magn. Reson. Spectrosc. 1997;31:155.
32. Provencher SW. Magn. Reson. Med. 1993;30:672.
33. Thomas MA, Hattori N, Umeda M, Sawada T, Naruse S. NMR Biomed. 2003;16:245.
34. Ryner LN, Sorenson JA, Thomas MA. J. Magn. Reson. 1995;B107:126.
35. Aime S, Cabella C, Colombatto S, Crich SG, Gianolio E, Maggioni F. J. Magn. Reson. Imaging. 2002;16:394.
36. Weissleder R, Moore A, Mahmood U, Bhorade R, Benveniste H, Chiocca EA, Basilion JP. Nat. Med. 2000;6:351.
37. Gohr-Rosenthal S, Scmitt-Willich H, Ebert W, Conrad J. Invest. Radiol. 1993;28:789.
38. Sipkins DA, Cheresh DA, Kazemi MR, Nevin LM, Bednarski MD, Li KCP. Nat. Med. 1998;4:623.
39. Lemieux GA, Yarema KJ, Jacobs CL, Bertozzi CR. J. Am. Chem. Soc. 1999;121:4278.
40. Thomassen T, Wiggen UN, Gundersen HG, Fahlvik AK, Aune O, Klaveness J. Magn. Reson. Imaging. 1991;9:255.
41. Weissleder R, Elizondo G, Wittenberg J, Lee AS, Josephson L, Brady TJ. Radiology. 1990;175:489.
42. Rausch M, Baumann D, Neubacher U, Rudin M. NMR Biomed. 2002;15:278.
43. Krieg FM, Andres RY, Winterhalter KH. Magn. Reson. Imaging. 1995;13:393.
44. Gellissen J, Axmann C, Prescher A, Bohndorf K, Lodemann KP. Magn. Reson. Imaging. 1999;17:557.
45. Ramsay SC, Weiller C, Myers R, Cremer JE, Luthra SK, Lammertsma AA, Frackowiak RS. Lancet. 1992;339:1054.
46. Kioumehr F, Dadsetan MR, Rooholamini AA. Neuroradiology. 1994;36:93.
47. Gupta RK, Jena A, Sharma A, Guha DK, Khushu S, Gupta AK. J. Comput. Assist. Tomogr. 1998;12:280.
48. Murray RJ, Himmelreich U, Gomes L, Ingham NJ, Sorrell TC. Clin. Infect. Dis. 2002;34:849.
49. Pyhtinen J, Paakko E, Jartti P. Neuroradiology. 1997;39:857.
50. Ashdown BC, Tein RD, Feisberg GJ. Am. J. Roentgenol. 1994;162:155.
51. Mikhael MA, Rushovish AM, Ciric I. Comput. Radiology. 1985;9:85.
52. Stave GM, Heimberger T, Kerkering TM. Am. J. Med. 1989;86:115.
53. Kathuria MK, Gupta RK. Fungal infections. In: RK Gupta, RB Lufkin (Eds). MR Imaging and Spectroscopy of Central Nervous System Infection. Kluwer Academic, Plenum Publishers: New York, p 177.
54. Iplikcioglu AC, Bek S, Bikmaz K, Ceylan D, Gökduman CA. Acta Neurochir. 2004;146:521.
55. Kelly WM, Brandt-Zawadzki M. Radiology. 1983;149:485.
56. Himmelreich U, Sorrell TC, Dzendrowskyj T, Malik R, Mountford CE. Mircobiol. Aust. 2002;23:31.
57. Gupta RK, Chang KH. Parasitic infections. In: RK Gupta, RB Lufkin (Eds). MR Imaging and Spectroscopy of Central Nervous System Infection. Kluwer Academic, Plenum Publishers: New York, p 205.
58. Turgut M, Benli K, Eryilmaz M. J. Neurosurg. 1997;86: 714.
59. Nurchi G, Floris F, Montaldo C, Mastio F, Peltz T, Coraddu M. Neurosurgery. 1992;30:436.
60. Chang KH, Cha SH, Han MH. J. Korean Radiol. Soc. 1993;29:345.
61. Dietz R, Schanen S, Kramann B, Erpelding J. J. Comput. Assist. Tomogr. 1991;15:168.
62. Jena A, Sanchetee P, Tripathi R, Jain R, Gupta AK, Sapra M. Magn. Reson. Imaging. 1992;10:77.
63. Chang KH, Lee JH, Han MH. Am. J. Neuroradiol. 1991;12:501.
64. Post MJD, Sheldon JJ, Hensley GT, Solia K, Tobias JA, Chan JC, Quencer RM, Moskowitz LB. Radiology. 1986;158:141.
65. Hajnal JV, Doran M, Hall AS. J. Comput. Assist. Tomogr. 1991;15:1.
66. Tomczak R, Wunderlich A, Görich J, Brambs HJ, Rilinger N. Radiologe. 2003;43:661.
67. Krabbe K, Gideon P, Wagn P, Hansen U, Thomsen C, Madsen F. Neuroradiology. 1997;39:483.
68. Himmelreich U, Accurso R, Malik R, Dolenko B, Somorjai RL, Gupta RK, Gomes L, Mountford CE, Sorrell TC. Radiology. 2005;236:261.
69. Camacho DLA, Smith JK, Castillo M. Am. J. Neuroradiol. 2003;24:633.
70. Bruening R, Wu RH, Yousry TA. J. Comput. Assist. Tomogr. 1998;22:104.
71. Cha S, Knopp EA, Johnson G, Wetzel SG, Litt AW, Zagzag D. Radiology. 2002;223:11.
72. Batra A, Tripathi RP. J. Comput. Assist. Tomogr. 2003;27:882.
73. Chan JH, Tsui EY, Chau LF. Comput. Med. Imaging Graph. 2002;26:19.
74. Harting I, Hartmann M, Bonsanto MM, Sommer C, Sartor K. Neuroradiology. 2004;46:189.
75. Gupta RK, Vatsal DK, Husain N, Chawla S, Prasad KN, Roy R, Kumar R, Jha D, Husain M. Am. J. Neuroradiology. 2001;22:1503.
76. Schlegel HG. Allgemeine Mikrobiologie. Georg Thieme Verlag: Stuttgart, 1992.

77. Himmelreich U, Somorjai RL, Dolenko B, Lee OC, Daniel HM, Murray R, Mountford CE, Sorrell TC. Appl. Environ. Microbiol. 2003;69:4566.
78. Bourne R, Himmelreich U, Sharma A, Mountford CE, Sorrell TC. J. Clin. Microbiol. 2001;39:2916–23.
79. Himmelreich U, Allen C, Dowd S, Malik R, Shehan BP, Mountford CE, Sorrell TC. Microbiol. Infect. 2003; 5:285.
80. Himmelreich U, Dzendrowskyj T, Allen C, Dowd S, Malik R, Shehan BP, Russell P, Mountford CE, Sorrell TC. Radiology. 2001;220:122.
81. Garg M, Misra MK, Chawla S, Prasad KN, Roy R, Gupta RK. Eur. J. Clin. Invest. 2003;33:518.
82. Torri GM, Torri J, Gulian JM, Vion-Dury J, Viout P, Cozzone PJ. Clin. Chim. Acta. 1999;279:77.
83. Dzendrowskyj T, Dolenko B, Sorrell TC, Somorjai RL, Malik R, Mountford CE, Himmelreich U. Diagn. Infect. Dis. Microbiol. 2005;52:101.
84. Remy C, Grand S, Lai ES, Belle V, Hoffmann D, Berger F, Esteve F, Ziegler A, Le Bas JF, Benabid AL. Magn. Reson. Med. 1995;34:508.
85. Dev R, Gupta RK, Poptani H, Roy R, Sharma S, Husain M. Neurosurgery. 1998;2:37.
86. Garg M, Gupta RK, Husain M, Chawla S, Chawla J, Kumar R, Rao SB, Misra MK, Prasad KN. Radiology. 2004;230: 519.
87. Himmelreich U, Dzendrowskyj T, Bourne R, Mountford CE, Sorrell TC. MAGMA. 2000;11(S1):197.
88. Grand S, Passaro G, Ziegler A, Esteve F, Boujet C, Hoffman D, Rubin C, Segebarth C, Decorps M, LeBas JF, Remy C. Radiology. 1999;213:785.
89. Kim SH, Chang KH, Song IC, Han MH, Kim HC, Kang HS, Han MC. Radiology. 1997;204:239–245.
90. Chang KH, Song IC, Kim SH. Am. J. Neuroradiol. 1998;19:401.
91. Agarwal M, Chawla S, Husain M, Jaggi RS, Husain M, Gupta RK. Neuroradiology. 2004;46:211.
92. Garg M, Chawla S, Prasad KN, Roy R, Sikora SS, Kumar R, Husain M, Khetrapal CL, Gupta RK. NMR Biomed. 2002;15:320.
93. Gupta RK, Raja R, Dev R, Husain M, Poptani H, Pandey R, Kishore J, Bhaduri AP. Magn. Reson. Med. 1996; 36:829.
94. Burtscher IM. Holtas S. Am. J. Neuroradiol. 1999; 20:1049.
95. De Graaf AA, Bovee WMMJ. Magn. Reson. Med. 1990;15:305.
96. Mierisova S, van den Boogaart A, Tkac I, van Hecke P, Vanhamme L, Liptaj T. NMR Biomed. 1998;11:32.
97. Seeger U, Klose U, Mader I, Grodd W, Nägele T. Magn. Reson. Med. 2003;49:19.
98. Tate AR, Majos C, Moreno A, Howe FA, Griffiths JR, Arus C. Magn. Reson. Med. 2003;49:29.
99. Tate AR, Julia-Sape M, Ladroue G, Murphy M, Loosemore A, Bell B, Wilkins P, Capdevila A, Majos C, Moreno A, Howe FA, Arus C, Griffiths JR. Proc. Int. Soc. Magn. Reson. Med. 2002;10:572.
100. Poptani H, Kaartinen J, Gupta RK, Niemitz M, Hiltunen Y, Kauppinen RA. J. Cancer Res. Clin. Oncol. 1999; 125:343.
101. Nikulin AE, Dolenko B, Bezabeh T, Somorjai RL. NMR Biomed. 1998;11:209.

Application of 2D Magnetic Resonance Spectroscopy to the Study of Human Biopsies

Edward J. Delikatny[1] and June Q.Y. Watzl[2]
[1]*Molecular Imaging Laboratory, Department of Radiology, University of Pennsylvania School of Medicine, Philadelphia, PA 19104, USA; and*
[2]*Department of Diagnostic Radiology, School of Medicine, Yale University, New Haven, CT 06519, USA*

Abbreviations: 2D, two-dimensional; AQ, acquisition time; COSY, correlated spectroscopy; DQF, double-quantum filtered; FID, free induction decay; GB, Lorentzian–Gaussian lineshape transformation fraction; J, scalar coupling constant; LB, Lorentzian line broadening; LG, Lorentzian–Gaussian; HMQC, heteronuclear multiple-quantum correlation; HSQC, heteronuclear single-quantum correlation; MAS, magic angle spinning; MM, magnitude mode; MRI, magnetic resonance imaging; MR(S), magnetic resonance (spectroscopy); NE, number of experiments; NS, number of transients; PS, phase-sensitive; (S)SB, (shifted) sine-bell; T_1, spin–lattice or longitudinal relaxation time; T_2, spin–spin or transverse relaxation time; TOCSY, total correlated spectroscopy; TPPI, time-proportional phase incrementation

Introduction

Proton magnetic resonance spectroscopy (^{1}H MRS) provides detailed information on cellular metabolites in whole cells and tissues enabling a non-invasive assessment of the chemical composition of these samples and the changes that occur with a disease process. As such, ^{1}H MRS can be used as an adjunct method for the pathological staging of human biopsy tissues [1–3]. Single pulse or one-dimensional (1D) proton spectra are rich with information, containing overlapping resonances from a number of mobile intracellular and extracellular metabolites and present in millimolar and submillimolar quantities. As a result of this overlap, information from metabolically important or potentially diagnostic resonances can be obscured, affecting both peak assignment and quantitative estimation of metabolite levels. One method of overcoming this problem has been the development and application of two-dimensional (2D) magnetic resonance (MR) spectroscopic methods to deliver additional chemical information than that available from 1D spectra.

2D magnetic resonance spectroscopy (MRS), from its initial proposal by Jeener in 1971 (reprinted in [4]), and first applications in the late 1970s [5] has developed into a major tool in organic and inorganic chemistry for spectral assignment and structural determination [6,7]. 2D spectroscopy relies on the collection of multiple free induction decays (FIDs) with the systematic incrementation of a delay time separating one or more pulses in the time domain of a pulse sequence. This results in a variable time-dependent evolution of spin interactions during this delay, thus effectively encoding information in a second frequency domain. 2D Fourier transformation is used to convert the 2D time-domain data into two frequency domains, which is often displayed as a contour plot with two frequency axes representing the primary spin properties of interest (e.g. chemical shift, J-coupling) and cross peaks joining regions of the spectra where spin interactions have occurred. A number of excellent review articles and textbooks have been published on 2D MRS, and the interested reader is referred to them for a detailed theoretical framework and practical information on pulse sequence design and implementation [6–11].

The most common 2D MR experiment used on biological specimens to date has been homonuclear ^{1}H–^{1}H magnitude mode correlated spectroscopy (MM-COSY). The additional chemical information obtained from the COSY experiment arises from protons that are linked or coupled through covalent bonds in a molecule, appearing in the 2D spectra as a pair of intersected resonant frequencies or cross peaks [6]. In principle, however, any homonuclear or heteronuclear 2D MRS experiment can be applied to biological samples, limited only by the imagination of the investigators. In practice, however, there are a number of limitations that arise when dealing with samples of biological material, including the stability of cells or tissues, restricted metabolite motion leading to the presence of multiple and short T_2 relaxation values, and the detection of low concentration metabolites. There are also issues associated with the low natural abundance and sensitivity of some nuclei [12].

In this chapter, we will address the practical issues associated with sample preparation, data acquisition, data processing, and interpretation of 2D spectra, concentrating primarily on the application of 2D spectroscopy to the

Graham A. Webb (ed.), Modern Magnetic Resonance, 1015–1025.
© 2008 *Springer.*

study of human biopsy material. We will place the subject in perspective by briefly reviewing the literature, followed by a presentation of some theoretical aspects relevant to 2D spectroscopy of tissues, and then discuss the technical aspects of sample preparation, 2D data acquisition, and strategies for data processing.

Application of 2D NMR Spectroscopy to Cells and Tissues

Although the technique of 2D NMR spectroscopy was first introduced in the late 1970s, it was not applied to the study of biological materials until the 1980s. The first published study used MM-COSY to identify fatty acyl chain resonances in a packed suspension of rat mammary adenocarcinoma cells [13]. It was soon recognized that the fatty acyl chains and head groups, that constituted the most intense cross peaks in many 2D spectra, arose from mobile lipid resonances, predominantly neutral lipids such as triglycerides and cholesteryl esters [14–16]. However, a number of other cross peaks were also observed in 2D spectra of cells [14–16]. The assignment of these cross peaks in 2D spectra were facilitated by the applications of techniques such as T_2 filters to selectively observe resonances with long T_2 [17], and 2D J-resolved spectra to assist in resonance assignment [18]. It was recognized that in biological samples containing metabolites with a range of T_2 relaxation values, the size of the acquisition domains and the window functions applied in processing could have dramatic effects on cross peak appearance and structure in COSY spectra [12]. As a result of these advances, over 40 cross peaks were identified in COSY spectra from intracellular metabolites. A comprehensive table of resonance assignments of lipids, amino acids, and sugars present in colorectal cancer cells was published in 1992 [19], and a similar table showing resonances observed in thyroid tissue biopsies [20], is presented in Table 1.

Around the same time, COSY and 2D J-spectroscopy were applied to investigate animal tissues such as rat brain *ex vivo* [18,21,22]. One of these studies showed one of the first 2D COSY spectra on dead rat brain *in situ* [18], thus demonstrating the feasibility for the later development of 2D MRS *in vivo* [23–27]. In another study, lactate COSY cross peak intensities were shown to be linearly correlated with lactate concentration in muscle thus providing a potential method of estimating relative metabolite concentrations [28]. The first application of total correlation spectroscopy (TOCSY) on frog muscle was published in 1990 [28]. Since these initial studies, 2D spectroscopy has become a standard spectroscopic tool for the study of cells and animal tissues, including the activation of immune cells [29–32], detection of changes associated with tumor development and progression [33,34], and the study of the actions of antitumor drugs on cultured cancer cell lines [35–37].

The first application of 2D COSY to human tissue was on a human ovarian biopsy specimen [38]. An initial study demonstrated that *ex vivo* 2D spectroscopy might be useful in discriminating the pathology of human cervical punch biopsies [39]. This was followed by the first major clinical study using 1D and 2D spectroscopy on 159 cervical biopsy specimens that showed consistently increased lipid cross peaks in malignant relative to premalignant specimens [40]. Subsequent studies were published demonstrating the usefulness of 2D COSY as an adjunct to 1D MRS and histopathology on brain tumors [41,42], colon adenomas and carcinomas [43], draining lymph nodes [44], and in samples from ovarian cancer [45] and thyroid cancer [20]. TOCSY and 2D J-resolved spectra have also been used to study smooth muscle tumors [46], myosarcomas [47], and liposarcomas [48]. The use of ^{1}H MRS on human biopsies as an adjunct to histopathology is discussed in detail elsewhere in this issue and in a number of review articles [1,2,49].

There has recently been a renaissance in 2D spectroscopy of human and animal tissues because of two innovations, reviewed elsewhere in this issue: the application of magic angle spinning (MAS) and the development of techniques for obtaining *in vivo* 2D spectra. *In vivo* 2D spectroscopy has the potential to permit the detailed examination of metabolites of diagnostic or metabolic interest *in situ* [23–25], and may extend 2D methods into the realm of true non-invasive detection of disease. MAS has allowed MR spectra of biopsy tissue to be obtained with extremely high resolution. Of particular relevance to this chapter is the application of 2D MAS experiments for high-resolution resonance assignment in animal and human tissues. MAS analogs of the homonuclear COSY, TOCSY, and J-resolved experiments have been developed for the evaluation of metabolite profiles characteristic of human disease in breast [50,51], kidney [52] and prostate tumors [53], liposarcomas [48], and draining lymph nodes [54]. Further, MAS analogs of the heteronuclear ^{1}H–^{13}C heteronuclear multiple-quantum correlation (HMQC) and heteronuclear single-quantum correlation (HSQC) experiments have been employed to assist in resonance assignment in human tissues and in animal model studies [52,55–58].

2D MR Spectroscopy

The major advantage of 2D MRS is the separation of resonances that overlap in 1D spectra. 2D spectroscopy collects data in two time domains, t_1 and t_2, which can be converted to two frequency domains, F_1 and F_2, by double Fourier transformation. The t_2 is the direct or acquisition dimension that consists of the FIDs collected in the 2D experiment, and t_1 is the orthogonal, or indirect, dimension defined by the number of FIDs acquired in the 2D

Table 1: Assignment of major cross peaks in 2D ^1H–^1H COSY MR spectra of thyroid biopsy tissue*

Molecules	Abbreviation	Coupling partners (bold face)	Cross peak coordination (ppm)
Lipid			
Fatty acyl chains	A	$-(CH_2)_n-C\mathbf{H}_2-C\mathbf{H}_3$	1.27, 0.87
	B	$-CH=CH-C\mathbf{H}_2-C\mathbf{H}_2-$	2.01, 1.30
	C	$-CH_2-C\mathbf{H}_2-C\mathbf{H}=CH-$	2.00, 5.31
	D	$=CH-C\mathbf{H}_2-C\mathbf{H}=CH-$	2.82, 5.32
	E	$-O-C(O)-CH_2-C\mathbf{H}_2-C\mathbf{H}_2$	1.58, 1.27
	F	$-O-C(O)-C\mathbf{H}_2-C\mathbf{H}_2$	2.23, 1.57
Glycerol backbone	G′ (geminal, J_{AB})	$RO-C\mathbf{H}_A\mathbf{H}_B-CH(OR)-C\mathbf{H}_A\mathbf{H}_B-OR$	4.07, 4.27
Amino acids			
Alanine	Ala (α, β)	$-C\mathbf{H}-C\mathbf{H}_3$	3.77, 1.47
Glutamate/glutamine	Glu/Gln	$-CH-C\mathbf{H}_2-C\mathbf{H}_2-COO^-/-CONH_2$	2.14, 2.45
Glutamate	Glu	$-C\mathbf{H}-C\mathbf{H}(NH_3^+)-COO^-$	2.14, 3.78
Isoleucine	Ile (β, γ)	$-CH-C\mathbf{H}(CH_3)-C\mathbf{H}_2-CH_3$	2.04, 0.95
Leucine	Leu (γ, δ)	$-C\mathbf{H}-(C\mathbf{H}_3)_2$	1.71, 0.95
Lysine/polyamines	Lys (δ, ε)	$-CH_2-C\mathbf{H}_2-C\mathbf{H}_2-NH_3^+$	1.67, 3.00
Threonine	Thr (β, γ)	$-CH-C\mathbf{H}(OH)-C\mathbf{H}_3$	4.26, 1.31
Tyrosine	Tyr (γ, δ)	o, m Protons on p-substituted ring	6.89, 7.19
Valine	Val (β, γ)	$-C\mathbf{H}-(C\mathbf{H}_3)_2$	2.28, 1.01
Phospholipid metabolism			
Choline	Cho	$(CH_3)_3-N^+-C\mathbf{H}_2-C\mathbf{H}_2-OH$	3.51, 4.05
Glycerophosphocholine	GPC	$(CH_3)_3-N^+-C\mathbf{H}_2-C\mathbf{H}_2-OPO_2-CH_2-$	3.67, 4.33
Phosphocholine	PC	$(CH_3)_3-N^+-C\mathbf{H}_2-C\mathbf{H}_2-OPO_3^{2-}$	3.56, 4.17
Phosphoethanolamine	PE	$H_3N^+-C\mathbf{H}_2-C\mathbf{H}_2-OPO_3^{2-}$	3.22, 3.98
Other			
Inositol	Inos	$-C\mathbf{H}(OH)-C\mathbf{H}(OH)-$	3.28, 3.64
Lactate	Lac	$-C\mathbf{H}(OH)-C\mathbf{H}_3$	4.10, 1.30
Taurine	Tau	$H_3N^+-C\mathbf{H}_2-C\mathbf{H}_2-OSO_3^-$	3.25, 3.42
Unique to thyroid†	Th1		5.10, 2.05
	Th2		5.10, 1.60

*Cross peak assignments obtained from follicular thyroid tissues ^1H–^1H MM-COSY spectra at 37 °C (table adapted from Refs. 20 and 36).

†Cross peaks unique to thyroid.

experiment. The 2D pulse sequence is often divided into four time periods: the preparation, evolution, mixing, and detection periods (Figure 1). The preparation period consists of a delay time during which equilibrium is attained and/or solvent suppression is performed, followed by a radio frequency (rf) pulse or series of pulses to prepare transverse magnetization. The evolution period consists of a variable delay time $t_1 + \Delta t_1$ during which magnetization evolves. The mixing period includes at least one rf pulse or a series of pulses and delays, to induce mixing of states and magnetization coherence transfer. The detection period is the time of FID acquisition, t_2. The indirect dimension is sampled by systematically incrementing the delay time in the evolution period, thus modulating the available magnetization during the mixing period. The size of the increment, or sampling period, in the t_1 dimension is inversely proportional to the spectral width in F_1 [59].

Choice of Pulse Sequence

In principle, any 2D pulse sequence can be applied to studies of human biopsy tissue, within the constraints defined by the stability of the sample. These time constraints make heteronuclear experiments more difficult to perform, especially for nuclei of low natural abundance. Many of these problems have been overcome using gradient-enhanced techniques with inverse detection and ^1H–^{13}C HMQC and HSQC MAS experiments have been

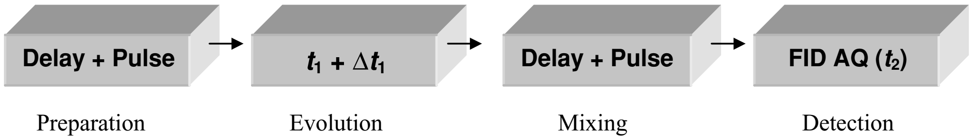

Fig. 1. The four basic periods of a 2D experiment.

reported for resonance assignment in human and rat tissues [52,55–58]. To date, however, the majority of 2D studies have been performed using ^{1}H–^{1}H homonuclear 2D spectroscopy, with COSY, 2D J-resolved and TOCSY experiments being by far the most common. Different and complementary information is available from these experiments, such that they may be usefully applied alone or in tandem to tissues of different origins.

The COSY sequence is the simplest and one of the most useful 2D experiments. The basic MM-COSY pulse sequence (Figure 2A) consists of two 90° pulses, the first to create magnetization in the transverse plane and the second to mix spin states, transferring coherence between scalar coupled spins. A variable delay $t_1 + \Delta t_1$ separating these pulses is incremented systematically during the evolution time and the FID is acquired during the detection time, t_2. After Fourier transformation the 2D spectrum consists of a diagonal representing spins that did not exchange magnetization during the mixing period and cross peaks or off-diagonal peaks for nuclei exchanging magnetization through scalar coupling. Since MM-COSY spectra are collected with no phase discrimination in F_1, a magnitude calculation must be performed after Fourier transformation.

Phase-sensitive double-quantum filtered COSY (PS DQF-COSY, Figure 2B) is an analog of the COSY experiment. The data are collected using time-proportional phase incrementation (TPPI) [60], in which the phase of the first pulse is incremented by 90° in successive FIDs resulting in phase discrimination in F_1. This obviates the need for the MM calculation, leading to improved apparent spectral resolution. However, the phase discrimination in the t_1 dimension means that twice as many FIDs need to be collected to achieve the same resolution. The signal to noise (S/N) is unchanged because S/N is proportional to the product of the number of transients (NS) and the number of FIDs acquired [6]. Thus, the total acquisition time (AQ) can remain constant by reducing the equivalent number of scans by a factor of two.

In the DQF pulse sequence, the first and second pulses act as in the MM-COSY. The third pulse in the DQF-COSY pulse sequence converts double-quantum magnetization into observable single-quantum magnetization, with phase cycling or gradients used to cancel unwanted single- and multiple-quantum magnetizations. This results in the diagonal signals of uncoupled nuclei, arising from single-quantum magnetization, being severely reduced as well as the conversion of the dispersive diagonal peaks into pure antiphase absorptive signals. This is useful for biological samples, since cross peaks resulting from the coupling of nuclei with similar chemical shift appearing near the diagonal can be resolved [61].

The 2D J-resolved sequence (Figure 2C) consists of a 90° preparation pulse, followed by the incremented delay

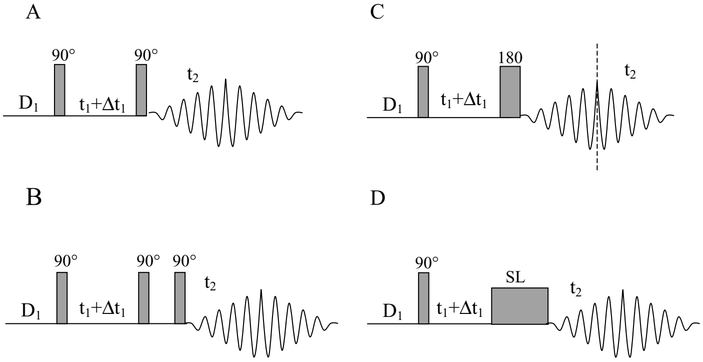

Fig. 2. Four basic 2D homonuclear pulse sequences routinely used in the study of human tissues. (A) ^{1}H–^{1}H MM-COSY, (B) ^{1}H–^{1}H DQF-PS COSY, (C) ^{1}H–^{1}H 2D J-resolved, and (D) ^{1}H–^{1}H TOCSY.

time and a 180° mixing pulse. The 180° pulse reverses linear spin interactions, such as chemical shift, such that at time $2(t_1 + \Delta t_1)$, chemical shift is refocused, leaving only interactions from J coupling in t_1. This results in a 2D spectrum with chemical shift on the F_2 axis and J coupling only on the F_1 axis. J-resolved spectroscopy has proven to be valuable for resonance assignment, especially in regions of the spectrum with substantial overlap.

One of the more useful methods in the 2D spectroscopic arsenal is the TOCSY (Figure 2D). In the TOCSY experiment, the mixing pulse is replaced with a spin lock field or series of pulses, often an MLEV-17 pulse train [62]. This allows coherence transfer between all coupled spins simultaneously, which ideally gives rise to cross peaks between all spins in a spin system. One advantage to the TOCSY experiment is that the coherence transfer results from in phase rather than antiphase magnetization, leading to in phase cross peaks that are not subject to cross peak cancelation.

Sample Preparation

A general harvest procedure that we have found acceptable is to collect unfixed, surgically removed tissue specimens from the operating theatre. To prevent sample decomposition, these specimens are placed immediately into vials containing phosphate-buffered saline in D_2O (PBS/D_2O), snap frozen in liquid nitrogen and stored at −70 °C. Samples can generally be stored this way for several weeks, without serious deterioration. Samples for MR experiments are cut frozen into tissue plugs of wet weight 20–50 mg and washed in PBS/D_2O, although this washing may lead to depletion or removal of certain metabolites [63]. Positioning of the sample in a standard NMR tube can be performed by placing the tissue on top of a glass susceptibility plug in a susceptibility-matched MR tube, or by suspending the tissue either in buffer or on the surface of glass wool plug. The NMR tube need not be filled with tissue to obtain reasonable spectra. Smaller cylindrically shaped samples are easier to shim and the presence of deuterated buffer is advantageous for locking purposes. Sample preparation for MAS is dealt with elsewhere in this issue.

Data Acquisition

A 2D data set consists of a series of FIDs, which are acquired and stored consecutively in a file as a 2D matrix of points. A number of operator controlled factors affect the total experiment time of the 2D data set: most notably the total repetition time, which is pulse sequence dependent, the NS collected per FID in the t_2 dimension, including dummy scans (DS) performed to put the spin system in a steady state before data accumulation, and number of experiments (NE), the number of FIDs to be collected in the t_1 dimension. The repetition time includes parameters such as the relaxation/equilibrium delay, the incrementation delay during the evolution period, and the t_2 AQ.

The relaxation delay in the preparation period is dependent on the T_1 relaxation values of the sample. Ideally, five times the longest T_1 should be used to ensure that all spins are fully relaxed before the experiment begins. In practice, a 3-h time constraint allows only about 8000 transients (for example 250 FIDs of 32 transients) to be acquired before viability drops below an acceptable level. This requires acquisition parameters that are less than ideal: a repetition time of about 1.4 s is an absolute minimum for establishing an optimal steady-state magnetization and avoiding spurious coherences and instabilities due to the presence of residual transverse magnetization before the excitation pulse [12]. In general, the AQ should be at least 3 T_2 and the repetition time have a minimum value of 1.3 T_1. For lipid resonances, T_2 and T_1 relaxation values in cells have been reported to be in the range of 120–300 and 200–600 ms, respectively [41,48,64–66].

The transmitter offsets for both t_1 and t_2 time domains should be set to the center of the spectrum. For ^1H–^1H spectra, the transmitter offsets can conveniently be set to the water frequency, which lies approximately in the center of the spectrum with spectral widths, sw_1 and sw_2 equal to 10 ppm. The size of the time increment, Δt_1, is related to the spectral width, for MM-COSY Δt_1 is equal to $1/sw_1$, and for PS-COSY to $0.5/sw_1$. The NS to be collected for each FID is generally a multiple of eight if full phase cycling is used. Gradient-assisted sequences, such as the G-COSY [67–69] can be used to reduce the number of scans in the phase cycle, but in small biopsy specimens of 20–40 mg wet weight, S/N is sufficiently limited such that often 32 or more scans must be collected to obtain 2D spectra with reasonable S/N ratios.

One major consideration in the acquisition of 2D spectra of human tissues is the time allocated to collect experimental data. This is important for two reasons, the first is that metabolite levels can change over time due to sample degradation, especially if the data are collected at temperatures above ambient. Neutral amino acids resonances from proteolytic breakdown will often appear as sharp peaks on the downfield side of the methyl resonance in 1D spectra [63]. In the case where the total experiment time is sufficiently long, the contribution of these resonances to the 2D cross peaks will almost certainly be variable over time. Secondly, it may be necessary or desirable to have histopathology performed on the same piece of tissue that was used to acquire the spectrum, in the case where only small pieces of tissue are available, or where direct comparison of spectral properties and histological diagnosis is required. This is a more stringent condition, since the tissue must remain in good enough shape for a pathologist to make a reasonable diagnosis. In cervical biopsy tissue, we found that colposcopically obtained punch biopsies kept at 37 °C for 1.5 h, remained suitable for histopathological analysis. Although these parameters may vary for different tissue types, for punch biopsy sized tissue (5–10 mg) this is not enough time for anything but the detection and assignment of major metabolite cross peaks.

The limited time available for data collection means that acquisition parameters must be established to achieve an optimum S/N ratio in the limited time available. In practice, this generally means restricting the number of FIDs collected in t_1, balancing the desired or necessary spectral resolution against S/N and sample viability [12]. For equal resolution in F_1 and F_2 in COSY or TOCSY spectra, a square 2D data set of complex data points must be collected (e.g. 512 × 2K for MM; 1024 × 2K for PS mode). In small biopsy specimens of 20–40 mg, a reasonable S/N ratio can be obtained in a total experiment time of 2–3 h. For COSY and TOCSY spectra, the collection of 200 FIDs of 32 transients will give reasonable S/N and resolution for most specimens in about 3 h. Recall that for PS data, the phase discrimination in F_1 dictates that twice the number of FIDs be collected, with half the number of scans for equivalent resolution and S/N [6]. For ^{1}H–^{1}H J-resolved spectra, where the detection of scalar coupling requires a spectral width in F_1 on the order of about 100 Hz, the number of FIDs accumulated in t_1 can be correspondingly reduced to 100–150 [55,70]. For heteronuclear MAS experiments, t_1 domains of around 200 FIDs have frequently been used to obtain reasonable resolution in human and animal tissues [55–57].

Data Processing

2D data processing converts a 2D time-domain data set to a 2D frequency domain spectrum. The general steps involved are zero filling, apodization by multiplication with a window function, and Fourier transformation. This is followed by phase correction for data collected in PS mode or magnitude calculation for MM collection. Zero filling is the procedure of supplementing the time-domain data points with a string of data points with zero amplitude prior to Fourier transformation to improve digital resolution [6]. In 2D MRS, zero filling is also used when the collected matrix of data points is not square or incomplete. In general, time constraints dictate that the number of increments collected in the t_1 domain be as few as possible. As a result zero filling of at least one level is recommended to improve resolution in t_1 [6].

Apodization and the Use of Window Functions

Since a wide range of T_2 relaxation values are encountered in biological samples, additional considerations and flexibility are required for processing 2D spectra. Different window functions may be applied to the data set to extract relevant information from different peaks [12]. A window function is a time-dependent analytical mathematical function that shapes or filters the signal envelope, providing apodization to avoid truncation artifacts created by zero filling, or when acquisition is terminated before signal has fully decayed. Window functions are also used to maximize S/N and resolution, minimize line widths or to convert the frequency domain lineshape into a more desirable form [6,7,71]. Windowing is achieved by point-by-point multiplication of the window function with each data point of the FID in the time domain, which results in a convolution of the window function with the data set in the frequency domain.

In coherence transfer 2D spectra, where the desired information is often contained in an echo not centered at the beginning of the time domain, window functions are chosen that have the form of a pseudoecho, with small initial values, peaking later in the time domain and decaying smoothly to zero. Three commonly used window functions for 2D data processing are the Lorentzian–Gaussian (LG), sine-bell (SB), and shifted sine-bell (SSB) window functions.

The unshifted SB function begins at an initial value of zero rising to a normalized value of 1 halfway through the data set (at the time point $t_i = t_m =$ AQ/2), decaying smoothly to zero in both the t_1 and t_2 time domains. The unshifted SB function emphasizes sine dependent cross peaks relative to cosine dependent diagonal peaks and removes broad wings (dispersive components) from MM lineshapes. SB window functions optimize the presentation of high-resolution cross peaks from spins with long relaxation times, but spins with shorter relaxation times, those with $T_2 <$ AQ may exhibit substantial signal loss [6,12]. The SSB function is similar to the sine and can be used on samples with $T_2 >$ AQ. The initial value of the SSB function is not zero but (π/n), with $n \geq 2$. However, the SSB is not as effective at canceling out dispersive wings in MM spectra [6]. The application of SB windows to a complete symmetrical 2D data set can result in a 2D spectrum in which only cross peaks from a number of free amino acids and low molecular weight metabolites appear.

The LG window function is commonly used as a window function in t_2. The LG function has two adjustable parameters, which offer increased flexibility in the position and shape of the window function within the time domain and allows optimum detection of short T_2 species such as lipids. The LG function is controlled by two parameters: a Lorentzian broadening (LB), expressed as a negative number in Hz, and a Gaussian lineshape transformation fraction (GB). GB is a decimal fraction, which positions the LG maximum at GB × AQ, scaled such that $\mathrm{LG}_{\max} = 1$. The position of the LG window is controlled by adjusting GB, while adjustment of the LB parameter controls the initial and final values and width of the window function in the time domain, but not independently of GB.

The detection of compounds with short T_2 requires that the length of the time domains be reduced before performing the 2D F T, which can be achieved either by applying the LG function with the maximum shifted to a shorter time, or by reducing the number of data points used for processing and using symmetrical window functions such as the SB. There is no particular advantage to the LG over the SB window if the maximum in the SB window is positioned by adjusting the number of time-domain points. In fact, reduction of the number of t_1 points is often the condition set by sample viability and can be achieved by reducing the number of FIDs acquired or used in processing. If short T_2 species are of most interest, the efficiency of data acquisition can be significantly improved by acquiring fewer FIDs with correspondingly more transients per t_1 value. The analysis of cross peaks from both long and short T_2 species in a single data set can only be performed by acquiring conventional data sets with long AQs and performing several transforms with processing time domains and window functions optimized for the T_2 and J values of the cross peak of interest.

Quantitation

Although 2D spectroscopy can reveal numerous differences in the metabolite profiles in normal and diseased tissues, absolute quantitation of changes in metabolite levels, as in all forms of MR, can prove to be problematic, and must be performed with care. One method of quantifying 2D coherence transfer (e.g. COSY and TOCSY) spectra is by integrating the volume enclosed by a cross peak above the base plane (noise level) of the 2D spectra. However, there are a number of factors, besides the concentration of the species that influence both the appearance and the intensities of cross peaks in 2D spectra. These factors include the molecular weight and the T_2 relaxation value of the coupling partners, the MR pulse program being used and the chosen acquisition and processing parameters. In the case of COSY spectra, cross peak intensities can be further decreased due to cross peak cancelation arising from antiphase signal components [7,59]. Cross peak cancelation is more serious for resonances with short T_2 relaxation values, or small J-couplings since the degree of cancelation depends on the ratio of J/T_2. For COSY spectra, the problem is further complicated since the sum of the integrated area for any antiphase cross peak is zero. Therefore, any non-zero cross peak volumes have to be obtained either from spectra in which a MM calculation has been performed or from the sum of positive and negative antiphase components in PS spectra. TOCSY cross peaks appear as pure absorption mode, not antiphase, and hence and are not subject to problems arising from cross peak cancelation.

As a result, of these limitations it is difficult to compare absolute concentrations of two species in the same 2D spectrum, as well as difficult to estimate the concentrations relative to internal or external standards. However, if collected and processed under identical conditions, the same cross peaks from two different 2D spectra can be compared. Assuming that the experimental treatment does not change the T_2 of the cross peak of interest, it is possible to estimate the relative concentration from cross peak integrals.

It is worth noting that the volumes of cross peaks in COSY spectra have been shown to be linearly proportional to metabolite concentrations in standard solutions [28]. We have confirmed the linear dependence of cross peak volume on concentration in samples of mixed amino acids, and find that the linear relationship holds regardless of cross peak coupling partner (Watzl and Delikatny, unpublished data). Absolute concentration estimates of lipid and lipid metabolite concentrations in activating immune cells have been obtained by comparing metabolite cross peak volumes to those of paramagnetic-doped standards of similar T_2 and known concentrations [29,30]. Quantitation of heteronuclear correlation cross peaks has been reported in bacterial supernatants [72].

Factors Affecting Cross Peak Volumes

In order to improve the diagnostic potential of 2D ^{1}H MRS, it is necessary to understand the factors controlling the resolution and intensity of cross peaks in complex 2D spectra with multiple T_2 relaxation times [12]. As discussed above, window functions commonly used to improve the spectral resolution can selectively enhance cross peaks with different T_2 relaxation times [6,12]. Moreover, in unsymmetrized COSY spectra, significant asymmetries in cross peak intensities for methyl groups (for example those from alanine, lactate, and threonine) have been observed with peaks above the diagonal being generally more intense even when time domains and windows were equal. At higher fields this effect can be quite pronounced and can lead to substantial reduction in certain cross peaks upon symmetrization [12]. For this reason, quantitation should always be performed on unsymmetrized spectra.

In Figure 3, we present two MM-COSY 2D spectra of follicular thyroid tissue, acquired from the same sample, but processed using different parameters. In the t_2 dimension, 32 transients of 2048 data points were collected, and in the t_1 dimension, 512 FIDs (NE) were collected. The spectra were processed with a LG window in t_2 and a SB window function in t_1; an NE of either

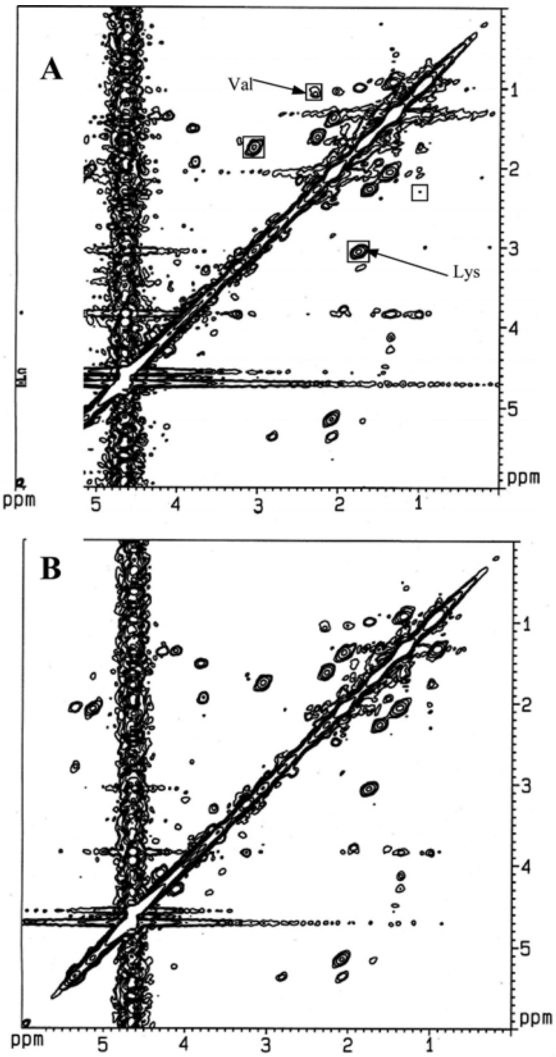

Fig. 3. Two-dimensional MM-COSY spectra of follicular thyroid tissue processed using (A) 200 and (B) 512 FIDs. In the t_2 domain, 2048 data points were collected and 512 FIDs consisting of 32 transients were collected in t_1. Data processing was performed with a sine-bell window applied in t_1 and a Lorentz-Gauss window in t_2 ($LB_2 = -30$, $GB_2 = 0.12$) before Fourier transformation. Cross peaks chosen for analysis are indicated with arrows.

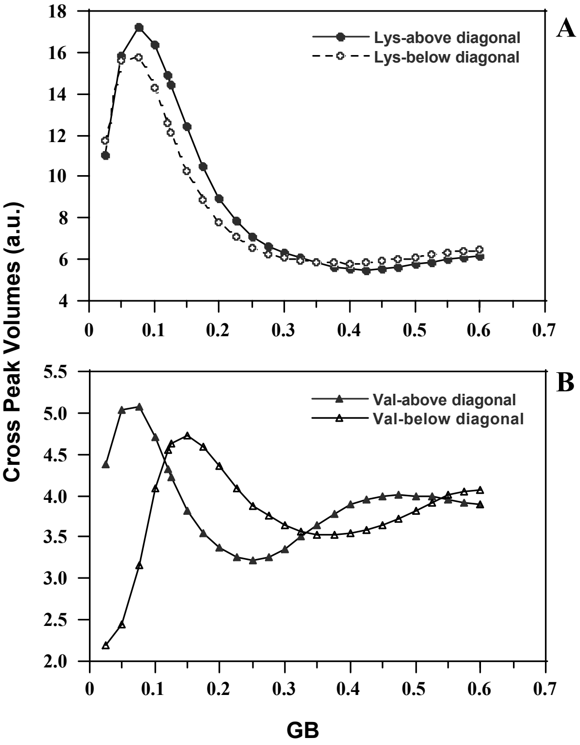

Fig. 4. Variation of (A) Lys $\mathbf{CH}_2$–$\mathbf{CH}_2$–NH_2 (1.67 and 3.00 ppm) and (B) Val $\mathbf{CH}_3$–$\mathbf{CH}$ (1.01 and 2.28 ppm) cross peak volumes as a function of GB in the t_2 time domain in magnitude-mode COSY spectra of follicular thyroid tissue processed with 200 FIDs. A sine-bell window was applied in t_1 and a Lorentz-Gauss window in t_2.

200 or 512 FIDs was used to produce Figures 3A and 3B, respectively. The volumes of two sets of amino acid cross peaks were selected from this data set (Lys, from the CH_2–$\mathbf{CH}_2$–$\mathbf{CH}_2$–NH_3^+ coupling of lysine at 1.67 and 3.00 ppm, and Val, from the $(\mathbf{CH}_3)_2$–$\mathbf{CH}$–CH coupling of valine at 1.01 and 2.28 ppm; arrows in Figure 3A), and the integrated cross peak volumes on the top and bottom of the diagonal and plotted relative to systematic changes in the processing parameter GB. Figure 4 demonstrates that cross peak volumes from COSY spectra vary significantly as a function of GB. The volumes measured for the pair of symmetrically matched cross peaks on either side of the diagonal are very close in value throughout the profile for the Lys cross peak whereas for the Val pair, they are substantially different. In contrast, cross peak volume profiles generated by varying LB resulted in strict monotonic increases in cross peak volume regardless of cross peak chosen (Figure 5).

Volumes measured from cross peaks at the same chemical shifts in different spectra display similar variation with respect to processing parameters, regardless of

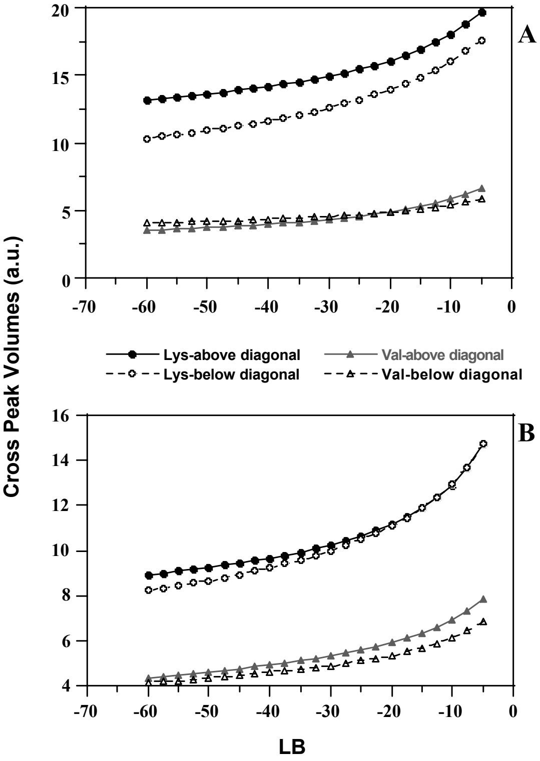

Fig. 5. Variation of cross peak volumes as a function of LB in the t_2 time domain in magnitude-mode COSY spectra of follicular thyroid tissue. A sine-bell window was applied in t_1 and a Lorentz-Gauss window in t_2. $GB_2 = 0.12$. Figure 5A and B were processed with 200 and 512 FIDs, respectively.

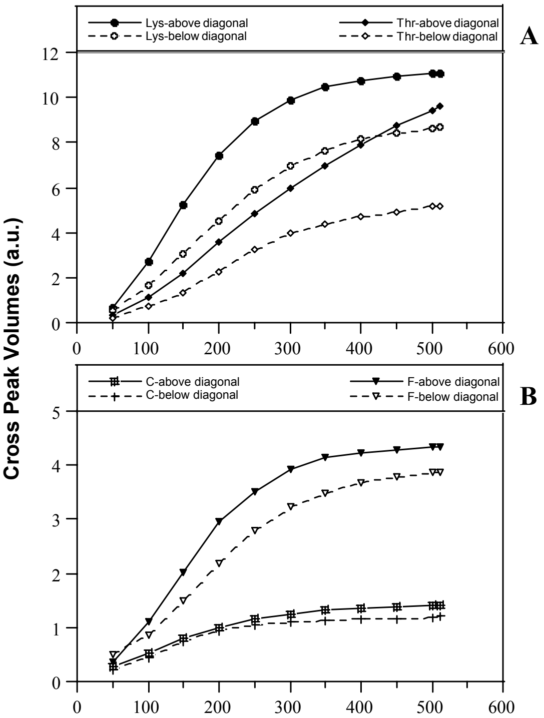

Fig. 6. Variation of cross peak volumes as a function of FIDs processed in the t_1 time domain in phase-sensitive double-quantum filtered COSY spectra of the malignant human colorectal cell line LIM 1215. A $\pi/4$ shifted sine-bell window was applied in t_1 and a Lorentzian–Gaussian window in t_2. $LB_2 = -30$, $GB_2 = 0.3$. (A) lysine and threonine, (B) F (–O–C(O)–$\mathbf{CH}_2$–$\mathbf{CH}_2$; 2.23, 1.57 ppm), and C (–CH_2–$\mathbf{CH}_2$–$\mathbf{CH}$=CH–; 2.00 and 5.31 ppm) resonances from mobile fatty acid chains.

whether the sample is a tissue specimen, cultured cells or a chemical standard [73]. Moreover, the comparison of cross peak volumes from either MM- or PS DQF-COSY spectra show similar patterns of oscillation, although they are dampened in samples with shorter T_2 relaxation values, such as tissue specimens. Similar analyses have not been performed on data obtained from other pulse sequences, e.g. TOCSY. However, this observation indicates that these processing dependent variations in cross peak volumes depend on the spin systems rather than the environment. As a general observation, cross peaks arising from symmetric AB and A_2B_2 spin systems show similar processing dependent volumes above and below the diagonal, whereas those from asymmetric A_2B, A_3B, or A_3B_2 show variation in cross peak volumes on either side of the diagonal [73].

Changing Parameters in t_1

The time constraints imposed by biological sample degradation restricts the number of t_1 increments collected during 2D experiments. The shortened t_1 time domain often leads to a restricted choice of window functions in t_1, and for COSY spectra the shifted or unshifted SB are most often used. Modulation of the phase shift of a SB window in t_1 leads to little variation in cross peak volumes for a constant number of FIDs processed (data not shown). However, for samples where large data sets have been collected, increasing the number of FIDs processed leads to increases in volumes for all cross peaks in all samples (Figure 6).

In summary, acquisition and processing parameters may be tailored to maximize the apparent S/N ratio of a cross peak and to affect the quality of 2D spectra. The disparity between volumes above and below the diagonal is controlled by the spin systems present in the sample. An understanding of the response of the spin systems and judicious choice of acquisition and processing windows allows an optimization of S/N ratio in cross peaks in 2D spectra, and allows better comparison of cross peaks between tissue samples of differing pathologies.

Concluding Remarks

2D MRS remains a powerful tool for the *in vivo* and *ex vivo* study of human cancer and other pathologies. The ability to separately identify numerous metabolites in human tissue non-invasively in a single experiment, allows a high degree of metabolic profiling to be performed that can be correlated with various disease states. The ability to assess multiple parameters through different pulse sequences gives 2D MRS extreme flexibility in experimental design. The limitations imposed by the time constraints inherent in dealing with tissue samples can be dealt with through careful experimental practice and attention to acquisition and processing details. The linking of modern 2D MR pulsed spectroscopic techniques with sophisticated technologies, such as MAS and *in vivo* spectroscopy, addressed elsewhere in this issue, hold great promise for the unraveling of metabolic parameters associated with the onset and progression of human disease.

Acknowledgments

EJD wishes to acknowledge the support of the Leo and Jenny Leukaemia Foundation, the University of Sydney Cancer Research Foundation, the University of Pennsylvania Research Foundation, the National Institutes of Health (NIH grants R21-CA-79718 and R21-EB-002537), and the Small Animal Imaging Resource Program at the University of Pennsylvania (R24-CA-83105).

JQYW wishes to thank the University of Sydney Medical Foundation for a Postgraduate Scholarship.

References

1. Mountford CE, Mackinnon WB, Delikatny EJ, Russell P. In: JD de Certaines, WMMJ Bovee, F Podo (Eds). Text of Magnetic Resonance Spectroscopy in Biology and Medicine: Functional and Pathological Tissue Characterization. Pergamon Press, Oxford 1992, p 507.
2. Mountford CE, Lean CL, Mackinnon WB, Russell P. Ann. Rep. NMR Spectrosc. 1993;27:173.
3. Mountford CE, Doran S, Lean CL, Russell P. Chem. Rev. 2004;104:3677.
4. Jeener J. In: M Goldman, M Porneuf (Eds). NMR and More in Honour of Anatole Abragam, Les editions de physique. Les Ulis cedex A: France, 1994.
5. Aue WP, Bartholdi E, Ernst RR. J. Chem. Phys. 1976;64:2229.
6. Hull WE. In: WR Croasmun, Carlson RMK (Eds). Two-Dimensional NMR Spectroscopy: Applications for Chemists and Biochemists, 2nd ed. VCH Publishers Inc.: New York, 1994, p 67.
7. Ernst RR, Bodenhausen G, Wokaun A. Principles of Nuclear Magnetic Resonance in One and Two Dimensions, Vol. 14. Clarendon Press: Oxford, 1987, p 610.
8. Croasmun WR, Carlson RMK (Eds). Two-Dimensional NMR spectroscopy. Application for Chemists and Biochemists, 2nd edition. VCH Publishers Inc.: New York, 1994.
9. Dyson H. In: W Croasman, R Carlson (Eds). Two-Dimensional NMR Spectroscopy—Applications for Chemists and Biochemists, 2nd ed. VCH Publishers: New York, 1994, p 655.
10. Bax A. Two-Dimensional Nuclear Magnetic Resonance in Liquids. Delft University Press: Delft, Holland, 1982, p 200.
11. Ziegler A, Izquierdo M, Rémy C, Decorps M. J. Magn. Reson. B. 1995;107:10.
12. Delikatny EJ, Hull WE, Mountford CE. J. Magn. Reson. 1991;94:563.
13. Cross KJ, Holmes KT, Mountford CE, Wright PE. Biochemistry. 1984;23:5895.
14. May GL, Wright LC, Holmes KT, Williams PG, Smith ICP, Wright PE, Fox RM, Mountford CE. J. Biol. Chem. 1986;261:3048.
15. Wright LC, May GL, Dyne M, Mountford CE. FEBS Lett. 1986;203:164.
16. Holmes KT, Mountford CE. J. Magn. Reson. 1991;93:407.
17. Williams PG, Saunders JKS, Dyne M, Mountford CE, Holmes KT. Magn. Reson. Med. 1988;7:463.
18. Behar KL, Ogino T. Magn. Reson. Med. 1991;17:285.
19. Lean CL, Mackinnon WB, Delikatny EJ, Whitehead RH, Mountford CE. Biochemistry. 1992;31:11095.
20. Mackinnon WB, Delbridge L, Russell P, Lean CL, May GL, Doran S, Dowd S, Mountford CE. World J. Surg. 1996;20:841.
21. Gillet B, Mergui S, Beloil J-C, Champagnat J, Fortin G, Jacquin T. Magn. Reson. Med. 1989;11:288.
22. Remy C, Arus C, Ziegler A, Lai ES, Moreno A, Le Fur Y, Decorps M. J. Neurochem. 1994;62:166.
23. Thomas MA, Binesh N, Yue K, DeBruhl N. J. Magn. Reson. Imaging. 2001;14:181.
24. Ryner LN, Sorenson JA, Thomas MA. Magn. Reson. Imaging. 1995;13:853.
25. Brereton IM, Galloway GJ, Rose SE, Doddrell DM. Magn. Reson. Med. 1994;32:251.
26. Ryner LN, Sorenson JA, Thomas MA. J. Magn. Reson. B. 1995;107:126.
27. Dreher W, Leibfritz D. Magn. Reson. Imaging. 1999;17:141.
28. Alonso J, Arus C, Westler WM, Markley JL. Magn. Reson. Med. 1989;11:316.
29. Dingley AJ, Veale MF, King NJC, King GF. Immunomethods. 1994;4:127.
30. Dingley AJ, King NJC, King GF. Biochemistry. 1992;31:9098.

31. Wright LC, Groot Obbink KL, Delikatny EJ, Santangelo RT, Sorrell TC. Eur. J. Biochem. 2000;267:68.
32. King NJC, Delikatny EJ, Holmes KT. Immunomethods. 1994;4:188.
33. Mackinnon WB, Huschtscha L, Dent K, Hancock R, Paraskeva C, Mountford CE. Int. J. Cancer. 1994;59:248.
34. Ferretti A, Knijn A, Iorio E, Pulciani S, Gaimbenedetti M, Molinari A, Meschini S, Stringaro A, Calcabrini A, Freitas I, Strom R, Arancia G, Podo F. Biochim. Biophys. Acta. 1999;1438:329.
35. Delikatny EJ, Roman SK, Hancock R, Jeitner TM, Lander CM, Rideout DC, Mountford CE. Int. J. Cancer. 1996;67:72.
36. Roman SK, Jeitner TM, Hancock R, Cooper WA, Rideout DC, Delikatny EJ. Int. J. Cancer. 1997;73:570.
37. Cooper WA, Bartier WA, Rideout DC, Delikatny EJ. Magn. Reson. Med. 2001;45:1001.
38. Mountford CE, Saunders JK, May GL, Holmes KT, Williams PG, Fox RM, Tattersall MHN, Barr JR, Russell P, Smith ICP. Lancet. 1986;i:651.
39. Mountford CE, Delikatny EJ, Dyne M, Holmes KT, Mackinnon WB, Ford R, Hunter JC, Truskett ID, Russell P. Magn. Reson. Med. 1990;13:324.
40. Delikatny EJ, Russell P, Hunter JC, Hancock R, Atkinson K, van Haaften-Day C, Mountford CE. Radiology. 1993;188:791.
41. Kuesel AC, Sutherland GR, Halliday W, Smith ICP. NMR Biomed. 1994;7:149.
42. Kuesel AC, Donnelly SM, Halliday W, Sutherland GR, Smith ICP. NMR Biomed. 1994;7:172.
43. Lean CL, Newland RC, Ende DA, Bokey EL, Smith ICP, Mountford CE. Magn. Reson. Med. 1993;30:525.
44. Mountford CE, Lean CL, Hancock R, Dowd S, Mackinnon WB, Tattersall MHN, Russell P. Invasion Metastasis. 1993;13:57.
45. Mackinnon WB, Russell P, May GL, Mountford CE. Int. J. Gynaecol. Oncol. 1995;5:211.
46. Sivaraja M, Turner C, Souza K, Singer S. Cancer Res. 1994;54:6037.
47. Singer S, Sivaraja M, Souza K, Millis K, Corson JM, J. Clin. Invest. 1996;98:244.
48. Millis K, Weybright P, Campbell N, Fletcher JA, Fletcher CD, Cory DG, Singer S. Magn. Reson. Med. 1999;41:257.
49. Smith IC, Blandford DE. Biochem. Cell Biol. 1998;76:472.
50. Sitter B, Sonnewald U, Spraul M, Fjosne HE, Gribbestad IS. NMR Biomed. 2002;15:327.
51. Cheng LL, Chang IW, Smith BL, Gonzalez RG. J. Magn. Reson. 1998;135:194.
52. Moka D, Vorreuther R, Schicha H, Spraul M, Humpfer E, Lipinski M, Foxall PJ, Nicholson JK, Lindon JC. J. Pharm. Biomed. Anal. 1998;17:125.
53. Cheng LL, Wu C, Smith MR, Gonzalez RG. FEBS Lett. 2001;494:112.
54. Cheng LL, Lean CL, Bogdanova A, Wright SC Jr, Ackerman JL, Brady TJ, Garrido L. Magn. Reson. Med. 1996; 36:653.
55. Bollard ME, Garrod S, Holmes E, Lindon JC, Humpfer E, Spraul M, Nicholson JK. Magn. Reson. Med. 2000; 44:201.
56. Garrod S, Humpfer E, Spraul M, Connor SC, Polley S, Connelly J, Lindon JC, Nicholson JK, Holmes E. Magn. Reson. Med. 1999;41:1108.
57. Griffin JL, Williams HJ, Sang E, Nicholson JK. Magn. Reson. Med. 2001;46:249.
58. Chen JH, Enloe BM, Weybright P, Campbell N, Dorfman D, Fletcher CD, Cory DG, Singer S. Magn. Reson. Med. 2002;48:602.
59. Derome AE. Modern NMR Techniques for Chemistry Research. Pergamon Press: Oxford, 1989.
60. Marion D, Wuthrich K. Biochem. Biophys. Res. Commun. 1983;113:967.
61. Gray AG. In: Croasmun WR, Carlson RMK (Eds). Two-Dimensional NMR Spectroscopy: Applications for Chemists and Biochemists, 2nd ed. VCH: New York, 1994, p 1.
62. Bax A, Davis DG. J. Magn. Reson. 1985;65:355.
63. Bourne R, Dzendrowskyj T, Mountford C. NMR Biomed. 2003;16:96.
64. Mountford CE, Mackinnon WB, Bloom M, Burnell EE, Smith ICP. J. Biochem. Biophys. Methods. 1984;9:323.
65. Kotitschke K, Jung H, Nekolla S, Haase A, Bauer A, Bogdahn U. NMR Biomed. 1994;7:111.
66. Deslauriers R, Somorjai R, Geoffrion Y, Kroft T, Smith ICP, Saunders JK. NMR Biomed. 1988;1:32.
67. Hurd RE. J. Magn. Reson. 1990;87:422.
68. Brereton IM, Crozier S, Field J, Doddrell DM. J. Magn. Reson. 1991;93:54.
69. Keinlin M, Moonen CT, van der Toorn A, van Zijl PC. J. Magn. Reson. 1991;93:423.
70. Garrod S, Humpher E, Connor SC, Connelly JC, Spraul M, Nicholson JK, Holmes E. Magn. Reson. Med. 2001; 45:781.
71. Wider G, Macura S, Kumar A, Ernst RR, Wuthrich K. J. Magn. Reson. 1984;56:207.
72. Bubb WA, Wright LC, Cagney M, Santangelo RT, Sorrell TC, Kuchel PW. Magn. Reson. Med. 1999;42:442.
73. Watzl, JQY. Ph.D. thesis, Sydney University, 2001.

Correlation of Histopathology with Magnetic Resonance Spectroscopy of Human Biopsies

Carolyn Mountford[1], Ian C.P. Smith[2], and Roger Bourne[1]
[1] *Institute for Magnetic Resonance Research, Department of Magnetic Resonance in Medicine, University of Sydney, St Leonards 1590, NSW, Australia; and*
[2] *Institute for Biodiagnostics, National Research Council of Canada, Winnipeg, Manitoba, Canada R3B 1Y6*

Introduction

The pathology of human tissue can be determined by magnetic resonance spectroscopy (MRS) but it was a controversial field for over 20 years. Now MRS on human biopsies identifies disease processes, neoplastic status, and prognostic variables with high accuracy. The MRS databases were compared with careful and specialized histology [1,2]. The MR method is fast, accurate, and robust and for most organs complements routine histopathological diagnosis. For some organs such as the thyroid and esophagus it can provide information not available using a light microscope. However, rigorous procedures and quality control are required to ensure this level of accuracy and are the basis of this chapter.

The reason the MRS method is so precise is that it monitors changes to cellular chemistry during the development and progression of a disease process. This is also the reason that it was controversial. Unless the pathology was undertaken with care there were discrepancies. An early experiment, undertaken in 1978, demonstrated that MRS could identify sequential alterations in cells before they manifested frank malignancy by light microscopy [3,4]. This was an exciting step forward but it also meant that correlation with both pathology and clinical outcome was essential. Twenty-five years on the MRS method is confirmed to show pathological categories which are not documented by light microscopy, due to the absence of architectural differences. The cells do, however, have a different chemical make-up consistent with clinical outcomes [5,6].

The basis of the MRS method for identifying tumor pathology is the increase in MR visible chemical species with the onset and the development of the disease. This was clearly seen in the first clinical study on human cervix biopsies [7]. Cancer of the uterine cervix was chosen for the first clinical ^{1}H MRS study as, histologically, the distinction between the presence and the absence of malignancy is made with a high level of accuracy. As seen in Figure 1, invasive specimens are characterized by an intense MR resonance at 1.33 ppm, primarily from the methylene protons of lipid acyl chains, with additional contributions from the methyl protons of lactate and threonine. There are also methyl, choline, and olefinic resonances at 0.90, 3.2, and 5.32 ppm, respectively (Table 1). The spectrum from human papilloma virus infected tissue (Figure 1B) lacks the intense resonance at 1.33 ppm. Other visible spectral differences include increases in the broad resonances between 3.4 and 4.2 ppm in the pre-invasive specimens compared with their invasive counterpart. It can be seen by comparing these three spectra that there is a gradual increase in the MR visible chemistry associated with the development of disease. In this study, the accuracy of the MRS method was 98% [8].

It is now established that the MRS-detectable chemical information present in the primary tumor is reporting on cellular chemistry associated with tumor development and progression, as well as cellular proliferation, immunosuppression, and metastasis. For a review see Mountford *et al.* [2].

Histopathology—Strengths and Limitations

Histopathology is the gold standard of the 20th century, providing diagnostic and prognostic information for human diseases. It is a very mature discipline that draws upon the experience of medical specialists who rely on visual pattern recognition in human tissues and cells using light microscopy. Its major limitation is the restrictive range of morphological changes that tissues express. The changes are often in a continuum and from this the pathologists are expected to identify patterns for individual diseases. These patterns often overlap making it necessary to make a subjective assessment.

Of importance to the development of MRS as a mature discipline are the sampling errors inherent at several levels in routine diagnostic services. Routine hospital pathology will often examine only one or two sections per sample of tissue. This is at least partly due to the time cost of examining multiple sections of tissue. A study of prostate biopsies by Swindle *et al.* [9] demonstrated that routine hospital histopathology (i.e. one or two slices) failed to

Graham A. Webb (ed.), Modern Magnetic Resonance, 1027–1036.
© 2008 *Springer.*

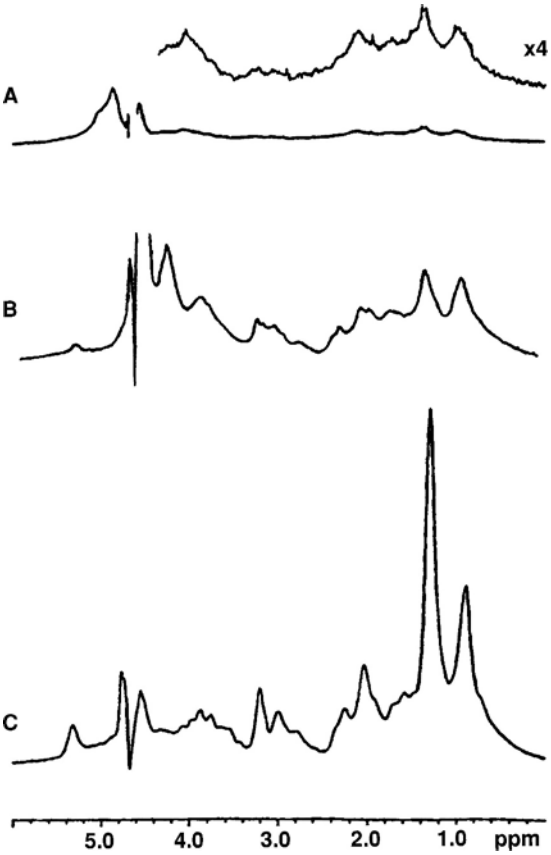

Fig. 1. ^{1}H MR spectra of cervical biopsy specimens. The histological assessment of each specimen is as follows: (A) Nonspecific chronic inflammatory disease. The inset shows the region 4.5–0 ppm with the vertical gain increased fourfold, NE = 400. (B) HPV infection but no significant dysplasia observed, 512 accumulations. (C) Cervical carcinoma, 40 accumulations. Spectra were recorded on a Bruker WM 400 (9.4 T) spectrometer at 37 °C. The water peak was suppressed by gated irradiation, sweep width 4000 Hz, acquisition time 1.024 s, and a line broadening of 3 Hz was applied in each case. *Source:* Reprinted from Magnetic Resonance in Medicine 1990;13:324–31. Mountford CE, Delikatny EJ, Dyne M, Holmes KT, Mackinnon WB, Ford R, Hunter JC, Truskett ID, Russell P. Uterine Cervical Punch Biopsy Specimens Can Be Analyzed by 1H MRS. With permission from Wiley-Liss, Inc., a subsidiary of John Wiley & Sons, Inc.

identify a number of cancers that have been detected by MRS. In order for the MRS method to achieve its potential and provide accuracies approaching 100% detailed non-routine histopathological analysis of the same piece of tissue examined by MRS is needed for correlation.

A good example of the need for serial sectioned histopathological analysis is seen in Figure 2. The spectra from breast ductal carcinoma *in situ* with and without microinvasion present are compared. Tissue sections of DCIS taken 100 μm apart are shown with microinvasion present and without microinvasion. The chemical activity seen in the MR spectrum of the cells with microinvasion is far greater. It should be noted that when both pathologies are present in a single specimen the most active chemical profile will normally be seen. The MRS method can also determine the percentage of each type of pathology but this requires a mathematical pattern recognition method. See the section on regression analysis below.

Finally, in contrast to histopathology, the MRS method has the advantage that it examines the entire piece of tissue that is placed between the transmit-receive coils thus removing any sampling errors associated with histopathological examination of only a fraction of the tissue sample.

Collection and Storage of Biopsy Specimens for Analysis

This is possibly the most important point of this chapter. If the biopsy specimens are not handled appropriately the tissue will start to degenerate and the important chemical species that have diagnostic and prognostic capabilities will alter.

For each tissue type reported to date handling protocols have been individually determined and reported [2]. Biopsy specimens can be a piece of tissue or a fine-needle aspirate biopsy (FNAB). The specimen must be immediately placed in a vial containing PBS/$D_2$0 after the biopsy is obtained and the vial placed without delay in a dewar containing liquid nitrogen. The polypropylene vials must have been tested for leakage of minute levels of chemicals which leach from the plastics and can cause cell death. This can be time consuming and often requires a number of batches of plastics to be tested. Similarly, the barrels of syringes used for FNAB need to be tested. Each tissue type, for example cervix, lung, kidney, has a finite time in which it can be stored in a freezer before the MRS examination is undertaken. It is unacceptable to store specimens for longer than 6 weeks.

The accuracy of the MRS method is dependent upon tissues and cellular pools of chemicals retaining integrity. In some of the earlier studies, tissue delivered to the pathology laboratory after surgery was then sent for MRS examination [10,11]. These spectra often displayed metabolite profiles characteristic of tissue degradation (e.g. increased lactate levels and depleted glucose). The predictive accuracy of such analyses was much lower than where the tissue was snap frozen immediately after collection.

Table 1: Resonances in one-dimensional ^{1}H MR spectra

Molecules	Abbreviation	Species	Chemical shift (ppm)
Amines			
Choline, phosphocholine, glycerophosphocholine	Chol	$-\mathrm{N}(\mathbf{CH}_3)_3$	3.2
Spermine, spermidine, polyamines	PA	$-\mathrm{NC}\mathbf{H}_2$	3.1
Creatine, phosphocreatine	Cr	$-\mathrm{NC}\mathbf{H}_3$	3.0
Lipids			
Triaclglycerol (fatty acyl chain)	Lip	$\mathbf{CH}_3-\mathrm{CH}_2-\mathrm{CH}_2-$	0.90
	Lip	$\mathrm{CH}_3-\mathbf{CH}_2-\mathrm{CH}_2-$	1.33
	Lip	$-\mathrm{OOC}-\mathrm{CH}_2-\mathbf{CH}_2$	1.6–1.7
	Lip	$\mathrm{CH}_3-\mathbf{CH}_2-\mathrm{CH}_2-$	2.02
	Lip	$\mathrm{CH}{=}\mathrm{CH}-\mathbf{CH}_2-$	2.08
	Lip	$-\mathrm{OOC}-\mathbf{CH}_2-\mathrm{CH}_2$	2.3
	Lip	$\mathbf{CH}{=}\mathrm{CH}-$	5.32
Amino Acids			
Alanine	Ala	$-\mathbf{CH}_3-\mathrm{CH}-$	1.49
Glutamate, glutamine	Glu, Gln	$-\mathrm{CH}-\mathbf{CH}_2-\mathrm{CH}_2-\mathrm{COO}-/\mathrm{NH}_{3+}$	2.2
Glutamate, glutamine	Glu, Gln	$-\mathrm{CH}-\mathbf{CH}_2-\mathrm{CH}_2-\mathrm{COO}-/\mathrm{NH}_{3+}$	2.6
Isoleucine	Ile	$-\mathbf{CH}_3$	0.97
Leucine	Leu	$-\mathbf{CH}_3$	0.97
Lysine	Lys	$\mathrm{H}_3\mathrm{N}^+-\mathrm{CH}_2-\mathbf{CH}_2-\mathrm{CH}_2$	1.7
Lysine	Lys	$\mathrm{H}_3\mathrm{N}^+-\mathrm{CH}_2-\mathbf{CH}_2-\mathrm{CH}_2$	3.03
Threonine	Thr	$\mathbf{CH}_3-\mathrm{CHOH}-$	1.33
Fucose	Fuc	$-\mathrm{CH}_2-\mathbf{CH}_3$	1.33
Threonine	Thr	$\mathbf{CH}_3-\mathrm{CHOH}-$	4.25
Valine	Val	$-\mathbf{CH}_3$	1.03
Other			
Lactate	Lac	$-\mathbf{CH}_3-\mathrm{CH}^-$	1.33
Citrate	Cit	$-\mathrm{OOC}-\mathbf{CH}_\mathrm{A}\mathbf{H}_\mathrm{B}-\mathrm{C(OH)}$	2.4–2.7
Taurine	Tau	$\mathrm{H}_3\mathrm{N}^+-\mathbf{CH}_2-\mathrm{CH}_2-\mathrm{SO}_3-$	3.25
Taurine	Tau	$\mathrm{H}_3\mathrm{N}^+-\mathbf{CH}_2-\mathrm{CH}_2-\mathrm{SO}_3-$	3.43

Care is needed to reduce or eliminate any minor and variable contamination of the sample. However, contamination with preparative agents (e.g. ultrasound gel, skin preparations) is inevitable during collection of biopsies of some tissue types. A robust pattern recognition method should be insensitive to such contamination.

Collection of a FNAB

A FNAB, which can be obtained from lymph nodes or any accessible lesion, usually comprises individual cells. It is important that for adequate signal-to-noise levels between one and five times 10^6 cells are obtained. To perform FNABs a 21/23 G needle is fitted to a 2, 5, or 10 ml syringe. After insertion of the needle tip into the tissue to be sampled the syringe plunger is withdrawn to about 1 ml to apply suction and the tip of the needle is pushed back and forth up to 20 times throughout the volume of the mass to be sampled without removal of the needle tip from the mass. The needle is withdrawn from the tissue, and the tip immersed in 300 μl PBS/D_2O in a prepared vial and the suction is then released. The buffer is aspirated into the tip of the syringe only and expelled back into the vial to wash out from the tip of the syringe and needle the cells aspirated from the tissue. No cells or liquid should be taken into the barrel of the syringe at any time. Gross contamination of the sample with blood should be noted as this may affect the quality of MR spectra. The vial is immediately placed in an upright position into liquid nitrogen and snap frozen.

Table 2: Summary of classifiers and spectral regions using SCS

Biopsy type (n)	Classification	Spectral regions (ppm)	Accuracy	References
Thyroid ($n = 107$)	Normal vs. malignant	Spectral identity not retained	99.0%	[22]
Brain ($n = 206$)	Control vs. malignant	23/55 Subregions	94.4%	[27]
Astrocytoma ($n = 91$)	High vs. low grade	0.81–0.85, 1.71–1.75, 2.16–2.20, 2.46–2.50, 2.54–2.58, 3.02–3.06, 3.51–3.55	95.7%	[28]
Breast FNA ($n = 140$)	Benign vs. malignant	1: 0.87–0.92, 1.20–1.25, 1.63–1.67, 1.79–1.82, 1.95–1.98, 2.85–2.87, 2.95–2.97, 3.19–3.33 2: 1.19–1.23, 1.32–1.38, 1.79–1.82, 1.96–2.00, 2.13–2.15, 2.70–2.76,2.92–2.94, 2.97–2.99	96.1%	[20]
	Lymph node involvement	1: 0.43–0.51, 0.64–0.77, 1.10–1.20, 1.56–1.59 2: 0.44–0.51, 0.67–0.71, 1.13–1.19, 1.56–1.60, 1.86—1.96	95.0%	[20]
Prostate ($n = 87$)	Benign vs. malignant	3.46–3.52, 3.40–3.46, 2.50–2.56, 2.14–2.20, 1.84–1.90, 1.12–1.18	96.6%	[21]
	Residual cancer after radiotherapy	0.77–0.82, 0.94–1.00, 1.32–1.37, 1.59–1.71, 2.24–2.27, 3.19–3.28	91.4%	[29]
Liver ($n = 122$)	Normal vs. HCC	1.34–1.37, 2.28–2.33, 2.83–2.85	100%	[30]
	Cirrhotic vs. HCC	3.00–3.03, 3.56–3.60, 3.66–3.68	98.4%	[30]
	Normal vs. cirrhotic	1.52–1.57, 2.03–2.08, 3.63–3.67	92.1%	[30]
Ovary ($n = 56$)	Normal vs. cancer	1.47, 1.68, 2.80, 2.97, 3.17, 3.34	98%	[31]
Esophagus ($n = 105$)	Normal vs. cancer	3.49–3.57, 3.23–3.28, 0.92–1.12	100%	[5]
	Normal vs. Barretts	3.50–3.54, 1.93–2.06, 1.37–1.43	100%	[5]
	Barretts vs. cancer	3.05–3.13, 2.51–2.57, 1.45–1.49, 1.21–1.29	98.6%	[5]
Melanoma	Metastatic vs. benign	Not yet available		[32]

Preparation of Specimens for MRS

Fine-needle Biopsy

Before ^{1}H MRS each fine-needle biopsy specimen is thawed at room temperature, then transferred to a 5 mm susceptibility-matched Shigemi MR tube. The volume is increased to 300 μl with fresh PBS/D_20 when necessary.

Tissue Specimens Can Be Handled in One of Two Ways

(A) The specimen is thawed and transferred together with the storage buffer directly to a 5 mm susceptibility-matched Shigemi MR tube.

(B) The sample is suspended in a constrained environment by means of insertion into a capillary tube [12]. This tube is then placed in a Shigemi 5 mm MR sample tube containing buffer and a reference standard. The goal here was to quantify the amount of each chemical with the weighed tissue.

It is important to note that freezing, storage, and thawing of tissue biopsies collected and stored in PBS/D_2O results in very significant and unpredictable leakage of metabolites into the storage buffer immediately upon thawing [13]. Leakage of metabolites is most exaggerated in small tissue samples such as needle core biopsies. For this reason the common practice of washing thawed tissue biopsies in D_2O is not recommended for biochemical characterization of tissue. Instead, biopsies should be collected, frozen, and thawed in a small volume (e.g. 400 μl) of buffer. With efficient water suppression techniques, such as Double Watergate [14], it is not necessary to attempt to replace any of the tissue water with D_2O prior to spectroscopy.

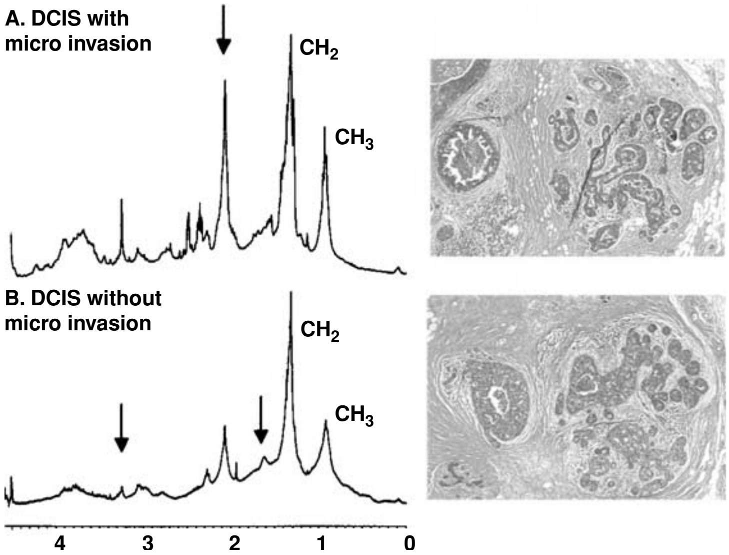

Fig. 2. ^{1}H MR spectra (8.5 T, 37° C) of fine-needle biopsy specimens obtained from breast ductal carcinoma *in situ*: (A) With microinvasion present and (B) without micro invasion. Tissue sections of DCIS are shown in (A) With microinvasion present and (B) without microinvasion. Spectra were acquired over a sweep width of 3597 Hz, 8192 data points, 256 accumulations, and relaxation delay of 2 s. *Source:* Reprinted from J. Women. Imaging. 2000;2:19–30. Lean CL, Russell P, Mountford CE. Magnetic Resonance Spectroscopy: A New Gold Standard for Medical Diagnosis. With permission from Lippincott Williams &Wilkins. (See also Plate 83 on page XIII in the Color Plate Section.)

All of the tissue and buffer should be within the sensitive region of the rf coils of the probe head so that diffusion of metabolites out of the tissue during the spectroscopy measurement does not result in loss of detected signal. This can be achieved by the use of Shigemi susceptibility-matched sample tubes. The maximum sample volume (tissue + buffer) that will fit within the sensitive region of the probe head will be specific to the particular probe head used. Care should be taken that all sample tubes are appropriately positioned in the probe head prior to measurement. The sample of tissue in buffer is spun at 20 Hz and shimmed optimally. In most cases a line width of 10 Hz for the residual water peak should be easily achievable. In a few cases, when examined with heterogeneous tissue samples, better shims can be obtained in the absence of sample spinning by adjustment of the *x* and *y* axis shims.

Experimental Temperature

There are several schools of thought on the appropriate temperature at which to run biopsy specimens. Much of the reported literature has MRS data collected at 37° C in an attempt to obtain data that can be correlated with *in vivo* spectroscopy. Clearly, at body temperature, the tissues degrade faster. Some groups have attempted studies at 4° C in order to reduce tissue degradation. However, it should be remembered that tissue and cell specimens contain a significant amount of lipid molecules. These lipid molecules undergo several phase transitions between 4 and 44° C [15]. It is imperative that the spectra that make up each database are collected at the same temperature.

Magnetic Field Strength

The majority of reported biopsy studies have been undertaken at the frequency of 360 MHz (8.5 T) [2]. There are some reports at 400 MHz (9.4 T) [16–18]. However, earlier work, predominantly on cultured cells, demonstrated that many of the diagnostic and prognostic spectra were frequency-dependent and thus care is needed.

MR Spectroscopy Methods

The most commonly performed measurement used for biopsy tissue characterization is a simple one-dimensional (1D) water suppressed ^{1}H spectrum. For a typical 50–100 mg (wet weight) tissue sample a spectrum of adequate signal-to-noise (SNR) ratio should be obtainable in 2–3 min. With manual sample changeover total preparation, spectrometer setup, and measurement time should be around 10 min per sample. Typical acquisition parameters for a 1D water suppressed ^{1}H MRS measurement are as follows.

Pulse angle 90° (6–7 μs), acquisition time 1 s, recycle delay 1 s, 8K data points, 128 transients, spectral width 3600 Hz, total acquisition time ca. 5 min. Water suppression can be effected by low power saturation during the recycle delay (presaturation) or, more effectively and selectively, by a selective excitation field gradient method (e.g. DPFGSE [14]).

As noted above, spectra acquired at different magnetic field strengths cannot be directly compared because, although proton resonance frequency is directly proportional to field strength, coupling constants are independent of field strength. Maximum SNR for a particular resonance of specific T_1 and T_2 is obtained under conditions of partial magnetic saturation with a specific flip angle and interpulse delay. In general, such conditions of maximum SNR will apply to, at best, a few resonances in the spectrum. It may be advantageous to choose flip angle and recycle delay to optimize SNR for specific resonances if these can be identified in advance of measurement. Flip angle, acquisition time, and recycle delay should be maintained constant for all measurements so that relative amounts of partial saturation are constant for samples with similar physical properties. For simplicity of data processing the spectral width and time domain should be maintained constant for all measurements. For samples of low cellularity the number of scans/acquisitions may be increased to obtain adequate SNR without detriment to the comparison of spectra from different samples.

After MR Spectroscopy

It is important to note that the correlation of tissue metabolite profiles by MR spectroscopy is critically dependent on rigorous histopathological assessment of the actual tissue examined by spectroscopy. To this end tissue should be transferred to fixative immediately after MR measurements are complete. The assumption that the histopathologic status of a tissue sample taken adjacent to the spectroscopy sample will be identical to that of tissue used for spectroscopy may be erroneous, especially in heterogeneous tissue types (e.g. prostate). As described earlier, routine preparation and examination of tissue for histopathological reporting may fail to detect the presence of prostate cancer in the spectroscopy sample [9]. Note that for the long-term goal of MRS-based tissue analysis to provide more rapid and sensitive diagnosis than routine histopathology it is necessary for the acquired spectra to be correlated with a more rigorous histopathological examination protocol than usual. Specifically, examination of 5×5 μm slices taken every 100 μm through the prostate tissue sample will ensure that all acini in the tissue sample are examined.

Assignments and Visual Inspection of the Data

The resonances of common chemical species found in the 1D ^{1}H MR spectra from human tissues are summarized in Table 1. These assignments have been made by different groups over 15 years. For review see [2]. Two-dimensional (2D) correlated spectroscopy has been used to make and confirm assignments [19]. See chapter on 2D methods in this Handbook. Many chemical species have been correlated with biological, diagnostic, and prognostic markers.

Typical spectra from malignant and benign breast cells obtained by aspirating the primary lesion are shown in Figure 3. The choline (3.25 ppm) to creatine (3.05 ppm) ratio clearly distinguishes the malignant and benign spectra (Figure 4). This ratio discriminates malignant and benign samples with an accuracy of 96% [20]. The four false positives, seen in Figure 4, are correctly classified when a more sophisticated pattern recognition analysis is performed [20].

The Complexity of Tumor Development and Progression

Another example of the complex and varying spectra that can occur during tumor development and progression is seen in Figure 5 where spectra from different types and pathologies of prostate tissue are seen. The simple resonance intensity ratio analysis described above for breast results in 80–90% accuracy for predicting malignancy [9]. For prostate the amount of data, spectroscopic, histological, and clinical, is considerable and difficult to analyze collectively by simple methods. Thus, a multivariate analysis method was developed [21,22] which formed the basis of the statistical classification strategy (SCS) described below.

Pattern Recognition Methods

A typical 1D MRS data set will have 4096 data points across the frequency spectrum. In contrast to simple resonance intensity ratio analysis described above where ratios of resonance intensities are compared, automated pattern recognition methods offer a more accurate and robust method with which to correlate MRS and clinicopathological characteristics. A method which combines a variety of pattern recognition procedures has been developed by Somorjai *et al.* [22] and is known as a "statistical classification strategy". The SCS method has been applied to a large number of systems and has been described in detail in a recent review [23] (see Table 1 for a summary).

The first stage of the SCS method uses an optimal region selector (ORS) to determine a small number of spectral regions that are most discriminatory [24]. To develop a robust classifier, the number of regions used to develop the classifier must be at least 5–10 times smaller than the number of spectra. The second stage uses these optimal regions and linear discriminant analysis (LDA)

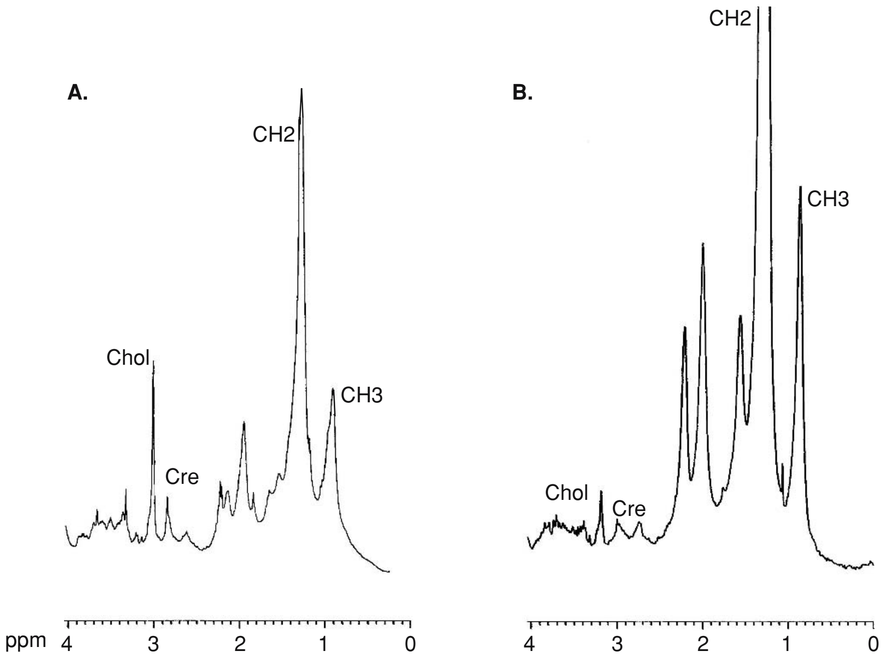

Fig. 3. ^{1}H MR spectra (8.5 T, 37° C) of breast FNABs with SNR >10: (A) Malignant and (B) Benign. Spectra were acquired over a sweep width of 3597 Hz, 8192 data points, 256 accumulations, and a relaxation delay of 2 s. *Source:* Reprinted from the Br. J. Surg. 2001;88:1234–40. Mountford CE, Somorjai RL, Malycha P, Gluch L, Lean C, Russell P, Barraclough B, Gillett D, Himmelreich U, Dolenko B, Nikulin AE, Smith IC. Diagnosis and Prognosis of Breast Cancer by Magnetic Resonance Spectroscopy of Fine-Needle Aspirates Analyzed Using a Statistical Classification Strategy, with permission from John Wiley & Sons Ltd on behalf of the British Journal of Surgery Society Ltd.

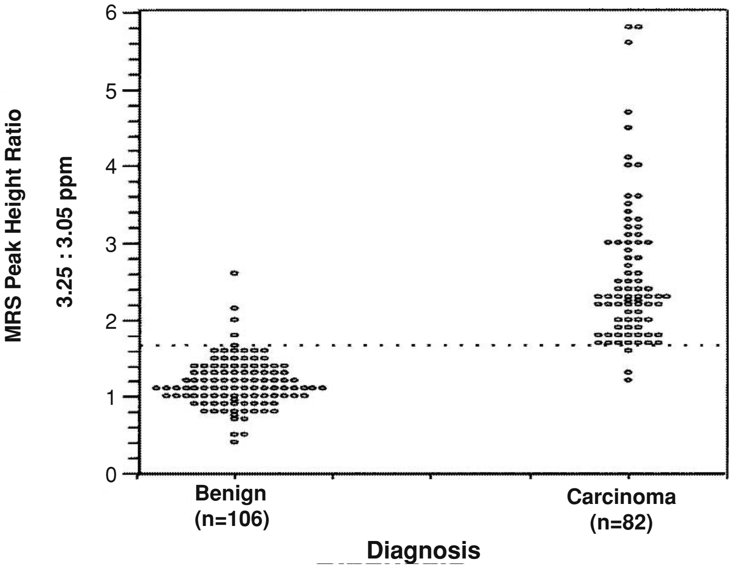

Fig. 4. Breast fine-needle biopsy MR spectroscopic (MRS) findings of unequivocally benign vs. infiltrating carcinoma. Data are grouped on the basis of the final histopathologic findings in tissue specimens from the aspiration site. *Source:* Reprinted from Radiology, 1997;204:661–6. Mackinnon WB, Barry B, Malycha P, Gillett D, Russell P, Lean CL, Doran S, Barraclough B, Bilous M, Mountford CE. Fine Needle Biopsy of Benign Breast Lesions Distinguished from Invasive Cancer by Proton Magnetic Resonance Spectroscopy, with permission from the Radiological Society of North America.

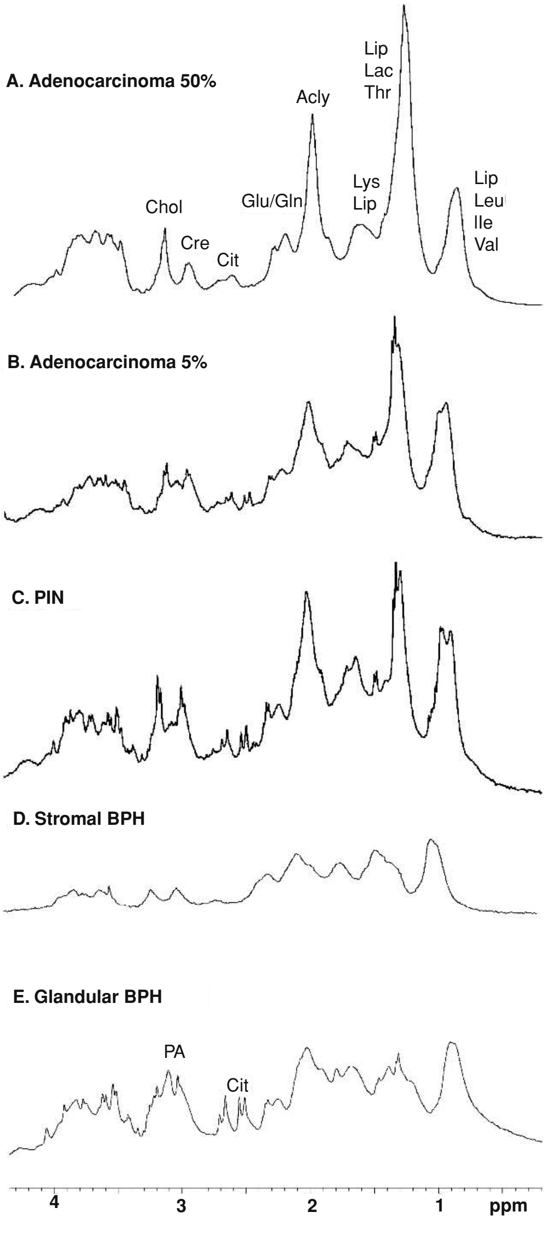

Fig. 5. ^{1}H MR (8.5 T, 37° C) spectra of prostate biopsy specimens, 256 acquisitions, sweep width 3597 Hz, and a pulse repetition time of 2.14 s. The water peak was suppressed by selective gated irradiation. (A) adenocarcinoma (50% of the tissue made up of malignant tissue), (B) adenocarcinoma (5% of the tissue made up of malignant tissue), (C) Prostatic intraepithelial neoplasia (PIN), (D) stromal BPH (95% stromal, 5% glandular), and (E) glandular BPH (85% glandular, 15% stromal) are compared. *Source:* Reprinted from Radiology 2003;228:144–151. Swindle P, McCredie S, Russell P, Himmelreich U, Khadra M, Lean CL, Mountford CE. Pathologic Characterization of Human Prostate Tissue with Proton Magnetic Resonance Spectroscopy, with permission from Radiological Society of North America.

to develop a classifier. Data are divided into training and test sets. The classifier is developed from the training set and then applied to the test set to see how well it does on data with which it has not trained. The original data are then mixed again and a different training and test set used to perform the same analysis. This is done up to 10,000 times to develop up to 10,000 different classifiers. This we call bootstrapping. The 10,000 classifiers are then used in combination to produce a final classifier. If at the end of stage 2 the accuracy of the final classifier is not sufficient, stage 3 of the SCS method is employed. Here other representations of the spectra, such as first or second derivatives, are used to make separate classifiers using stages 1 and 2. All stage 2 classifiers are then combined to yield a meta-classifier of increased accuracy [22].

In a study of FNAB from the breast, the data were subdivided into women with cancer with ($n = 29$) and without ($n = 32$) lymph node involvement [20]. Applying the SCS yielded classification of nodal involvement or not with sensitivity and specificity of 97 and 96%, respectively. Similar classification of patients with and without tumor vascular invasion yielded sensitivity and specificity of 84 and 100%. These classifications should be of great value in determining the therapeutic path for patients. More recent data from the same authors show great promise in calculating the tumor grade and estrogen and progesterone receptor status of breast tumors, also very important in planning therapy [25].

Regression Analysis

Routine histopathological reporting commonly includes a semi-quantitative description (e.g. "occasional foci," "extensive infiltration") of the amount of structural abnormality observed microscopically. Although imprecise, such semi-quantitative descriptions of observed disease burden are a factor in treatment planning. However, correlation of the MRS characteristics of tissue with histopathological characterization of the same tissue has largely been based on a simple two-class analysis in which tissue samples are classified according to the presence or absence of a single specific characteristic such as cancer. Diagnostic interpretation of the spectra from such mixed tissue voxels would ideally report not only the presence of disease, but also the extent or partial volume of disease within the volume of interest (VOI).

To address these two problems a linear regression analysis was undertaken on spectra acquired from 82 cancer-containing prostate tissue specimens. MR spectra were correlated with serial section histopathological examination of each tissue specimen for which the volume fraction of cancer tissue was estimated in 5% increments. A classifier based on five spectral features developed from a training set of 45 randomly chosen spectra was used to predict from spectra the volume fraction of cancer in a validation set of 37 tissue samples. The overall accuracy of predicted cancer volume, measured as the average accuracy of all cancer volume estimates, was 96% [26].

Future Challenges

Putting magnets into a pathology environment is a new concept. The challenge is to move this technology into a routine clinical environment. This was achieved by Liposciences for serum lipoprotein analysis of serum (www.liposcience.com). Serum specimens are easier to transport and the test is for screening purposes.

Clinical acceptance testing is required and is currently being undertaken in Sydney by a group of endocrine and urology surgeons. They need to verify that the tests provide additional information that is necessary for the management of the patient.

Automation of the software to drive the system and to allow comparison of spectra with classifiers will see the spectroscopy method for analyzing human pathology move into a new age.

Acknowledgments

We thank Deborah Edward, Brooke O'Donnell, Sinead Doran, and Raquel Baert for assistance in preparing this manuscript. Our thanks go to all present and past collaborators in particular Professor Peter Russell and Dr. Ray Somorjai, without whom none of this would have been possible.

References

1. Mountford CE, *et al.* Lancet. 1986;1(8482):651–3.
2. Mountford C, *et al.* Chem. Rev. 2004;104:3677–704.
3. Metcalf D. Recent Result Cancer Res. 1966;5:5.
4. Mountford CE, *et al.* Br. J. Cancer. 1980;41(6):1000–3.
5. Doran S, *et al.* Am. J. Surg. 2003;185(3):232–8.
6. Russell P, *et al.* Am. J. Med. 1994;96(4):383–8.
7. Mountford CE, *et al.* Magn. Reson. Med. 1990;13(2):324–31.
8. Delikatny EJ, *et al.* Radiology. 1993;188(3):791–6.
9. Swindle P, *et al.* Radiology. 2003;228:144–51.
10. Ende D, *et al.* Proc. Soc. Magn. Reson. Med. 1993;2:273.
11. Mackinnon WB, *et al.* Int. J. Gynaecol. Cancer. 1995;5:211–21.
12. Kuesel AC, *et al.* Magn. Reson. Med. 1992;27(2):349–55.
13. Bourne R, Dzendrowskyj T, Mountford C. NMR Biomed. 2003;16(2):96–101.
14. Braun S, Kalinowski HO, Berger S. 2nd ed. 150 and More Basic NMR Experiments: A Practical Course. Weinheim: Wiley-VCH, 1998, pp 473–5.
15. Baenziger JE, Jarrell HC, Smith ICP. Biochemistry. 1992;31:3377–85.
16. Cheng LL, *et al.* FEBS Lett. 2001;494(1–2):112–6.
17. Leemans CR, *et al.* Cancer. 1994;73:187–90.
18. Tzika AA, *et al.* J. Neurosurg. 2002;96(6):1023–31.
19. Cross KJ, *et al.* Biochemistry. 1984;23(25):5895–7.
20. Mountford CE, *et al.* Br. J. Surg. 2001;88(9):1234–40.
21. Hahn P, *et al.* Cancer Res. 1997;57(16):3398–401.
22. Somorjai RL, *et al.* Magn. Reson. Med. 1995;33(2):257–63.
23. Lean CL,*et al.* In: G Webb (Ed). Annual Reports NMR Spectroscopy. Guildford, UK: Academic Press, 2002, pp 71–111.
24. Nikulin A, *et al.* NMR Biomed. 1998;11:209–17.
25. Doran S, *et al.* Proc. ISMRM. Kyoto, Japan, 2004, p 2495.
26. Bourne R, *et al.* Proc. ISMRM. Toronto, Oral, 2003.

27. Somorjai RL, *et al*. J. Magn. Reson. Imaging. 1996;6(3): 437–44.
28. Somorjai RL, *et al*. J. Med. Biochem. 1999;3:17–24.
29. Menard C, *et al*. Int. J. Radiat. Oncol. Biol. Phys. 2001;50(2):317–23.
30. Soper R, *et al*. Pathology. 2002;34:417–22.
31. Wallace JC, *et al*. Magn. Reson. Med. 1997;38(4):569–76.
32. Bourne R, *et al*. Proc. ISMRM. Toronto, Canada, 2003, p 1302.

Functional MRI

Graeme D. Jackson, Regula S. Briellmann, Anthony B. Waites, Gaby S. Pell, and David F. Abbott
Brain Research Institute, Melbourne, Victoria, 3081, Australia

Principles of fMRI

In recent years, it has been demonstrated that MRI is capable of detecting changes in cerebral blood volume, flow, and oxygenation that accompany a change in neuronal activity. MRI techniques that observe these activation-induced signal changes are termed "functional MRI" (fMRI).

The most common contrast mechanism in fMRI is known as blood oxygenation level dependent (BOLD) contrast, first described by Ogawa *et al*. This contrast mechanism relies on the relationship between local changes in oxygenation and blood flow that occur with neuronal activation. The sequence of events is as follows:

1. The neuronal cells fire.
2. The small amount of energy used is recovered via oxygen metabolism, resulting in a small increase in deoxyhemoglobin in the first second or two after cell firing.
3. A vascular response also occurs, being a local increase in blood flow (perfusion).
4. In the next few seconds, the delivery of oxygen via the vascular response is far in excess of that depleted to meet the local energy demands. Therefore, paradoxically, there is a local *decrease* in the concentration of deoxyhemoglobin of a much greater magnitude than the initial increase.

BOLD contrast relies on the sensitivity of MRI to detect the changing concentration of deoxyhemoglobin. The initial small increase in deoxyhemoglobin has been observed by some groups as a very small "initial dip" in the time course of the BOLD MR signal; however, it is the subsequent larger decrease in deoxyhemoglobin concentration that provides the substantial and robust signal increase that makes the method most useful. The signal change arises because deoxygenated hemoglobin is paramagnetic, whereas oxygenated hemoglobin is diamagnetic. Paramagnetic molecules are especially visible in MRI since they exert a strong enhancing effect on the relaxation rate of the water in the vascular environment. The transverse relaxation times, T_2 and T_2^* are reduced by this mechanism. These are the contrast dependencies of spin echo and gradient echo images, respectively. Both these basic imaging techniques can therefore be used to detect BOLD contrast. Differences between these two techniques exist with regard to the extent of sensitivity to the environmental change. The T_2^* relaxation time is uniquely sensitive to the intravascular changes of water environment and therefore BOLD contrast is magnified in gradient echo images. Currently, the most commonly applied imaging technique for BOLD fMRI is echo planar imaging (EPI). It allows very rapid imaging, allowing for whole brain coverage with standard paradigms.

Another more recently developed contrast mechanism for fMRI is that of perfusion. This utilizes imaging methods that are sensitive to detecting the local change in blood flow which is the initial response to the neuronal firing. This technique acts as a more direct means of detecting the activation site. However, the perfusion imaging methods suffer from limitations in signal-to-noise ratio (SNR) in comparison with the simpler BOLD imaging techniques.

Design of fMRI Trials

One of the most important parts of an fMRI experiment is the designing of the appropriate paradigm that will allow identification of brain voxels involved in a particular cognitive or sensory–motor function. In this chapter, we will discuss two commonly used approaches, the "block design" and the "event-related design." For both approaches, it is important to keep in mind that the vascular response (which is what we can measure with BOLD) follows the neuronal activity (which is what we would like to know) with a delay of several seconds.

Block Design

The simplest form of a design for fMRI experiments is called a block design. This comprises alternating cycles of periods of task and rest conditions (Figure 1). Each task and rest period should not be too short, as the BOLD signal takes around 5–10 s to reach a maximum after a neuronal event. Shorter periods will lead to a reduced contrast between task and rest states. Very long periods also have a drawback, as they may resemble the low frequency fluctuations or drift in the scanner signal. Such a design would lead to confusion between the cognitive variation, which we wish to measure, and artifactual changes, which we

Graham A. Webb (ed.), Modern Magnetic Resonance, 1037–1050.
© 2008 *Springer.*

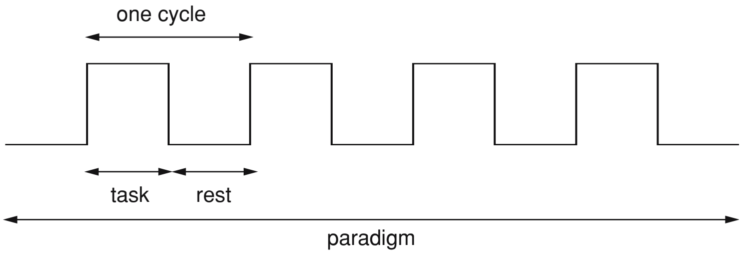

Fig. 1. Scheme of a block design paradigm with alternating block and task periods of identical length.

wish to minimize. The ideal design allows the BOLD signal to reach a steady state within each condition in order to maximize contrast. In practice, a 40 s to 1 min cycle time (i.e. 20–30 s task then 20–30 s rest) with about 5–8 cycles, giving a total experiment time of 4–10 min is suitable for many experiments. With more robust tasks (such as visual stimulation, which leads to large neuronal response) and higher magnetic field strengths, such as 3 T, the total experiment time may be reduced. Longer experiment times increase the chance of motion artifacts due to subject discomfort, as well as loss of concentration on the task.

Block design experiments allow maximization of SNR, but also have some disadvantages. Repeating the same task may lead to the subject anticipating the task and sometimes even the response. This may considerably confound the results. A randomized design avoids this issue since the occurrence of a particular task type is unpredictable. Further, not all cognitive studies can be adapted to a block design. For example, experiments assessing the cognitive effect of an unexpected stimulus within another task, known as an oddball paradigm, cannot be performed in a block. Similarly, studies assessing unpredictably occurring physiological events, such as myoclonic jerks, cannot be performed as block designs. Block designs also do not provide information on the shape of the blood flow change in response to the task. This vascular response to a neuronal event is referred to as the hemodynamic response function (HDR). The HDR is used in event-related designs.

Event-Related Designs

Event-related designs are a more flexible approach, and involve the placement of single events within a train of “rest state” conditions. The order of the events is often randomized, preventing anticipation of the task. Events with varying periods of rest allow measurement of different parts of the hemodynamic response, allowing the HDR to be identified. This can be useful in understanding the different response from different brain regions, which may be a result of either the different vasculature of the region, or the differences in cognitive dynamics in the different regions.

The disadvantage of such designs is the low SNR. This is due to the fact that the task state is not sustained for long periods, leading to a less intense vascular response. This can be partially overcome by using “clustered” random presentation of events, where the random pattern of task events is chosen so that there are clumps of task and clumps of rest, albeit with some variability. This is a compromise, giving some increase in SNR whilst maintaining the benefits of a random design.

Event-related analysis techniques can also be applied to data from a block-designed study. This can either take the form of modeling the block of task as a series of events, or performing a *post hoc* analysis of the data. The *post hoc* analysis involves identifying events within a block, such as correct responses to a stimulus, and comparing them to for example incorrect responses.

Inter-Stimulus Interval Selection for Event-Related Designs

It is important to consider the inter-stimulus interval (ISI) carefully. One must first decide whether a sparse or rapid event-related design is to be used. Sparse designs have a long ISI such that the hemodynamic response returns to baseline before the next event is encountered. More common are rapid event-related designs where the minimum ISI is often as little as 2 s. These designs have the advantage that they are more efficient (many more events are captured in a given period of time), and they are therefore the preferred choice if the nature of the task allows it. One must be more careful with these designs, however, as analysis methods usually rely on the assumption that the BOLD response to multiple events adds linearly. This is not always the case (especially if the ISI is much less than 2 s), and one must be careful when interpreting results in brain areas where the linearity of the BOLD response is not well known.

Other issues should also be considered when choosing the ISI. The use of an ISI equal to an integer multiple of the repetition time (TR) can lead to a missed peak in the HDR. This occurs because the stimulus and measurement are synchronized, and measurements may repeatedly occur before or after the peak of the HDR. Making matters worse, there would be a systematic difference in the time each individual slice in a single volume is acquired relative to the event, so that some slices may always be more sensitive to the event than others. If synchronous timing is to be used, it is therefore best to choose an ISI that differs from the TR such that measurements of the HDR occur at different times for many successive events. For example, if events were timed to occur each 1.3 × TR, the HDR would be effectively sampled at nine different time points before the sampling pattern began to repeat. This would be better than 1.5 × TR, for example, where only two different time points would ever be sampled. Another approach is to use jittering. Jittering involves randomly varying the ISI slightly for each event, which again leads to measurements at different points throughout the HDR.

Modeling the Hemodynamic Response in an Even-Related Study

Analysis of an event-related study requires a specific model for the HDR. If the primary goal of the experiment is to determine the precise form of the HDR, a flexible basis set is usually chosen such as a set of sine and cosine waves (a Fourier set), or a set of Gamma functions. On the other hand, if the goal is to determine where and when an event occurred, a canonical HDR is typically used. The canonical HDR is an empirically determined shape found to fit experimental data. One can improve the canonical model by including the temporal derivative (which allows flexibility in the delay of the HDR) and a dispersion term to allow a broader than typical response. This can accommodate some regional and inter-subject variation in response. The canonical model is the most powerful at detection, since it has the fewest parameters, and thus preserves the highest number of degrees of freedom. Conversely, the basis function approaches will be more sensitive if the response differs significantly from the canonical form. A combination of approaches is possible. For example, a portion of a study can be dedicated to eliciting the regional shape of the HDR in an individual (perhaps with a stimulus known to yield a large signal change), and this can then be used as a more accurate model for detection of subtle stimuli in that individual.

Principles of Experimental Design

Where to Start?

There are many factors that affect detection power including the type of experimental design, the scanner, the population, and the nature of the task being imaged. In order to identify the optimal task, a clear hypothesis will aid greatly in designing the experiment. Such a hypothesis may be based on theoretical background of a particular function, or more commonly, is an extension of an observation made outside the scanner. The development of an appropriate task for fMRI scanning is often based on published, somewhat similar paradigms. A protocol can then be further refined after a few pilot studies have been undertaken. Typically, the durations of the final protocol should be a little longer than the estimated optimum, as the subjects used for pilot studies are often highly motivated individuals who will give better results than the average study population.

Block or Event-Related Design?

The block design is optimal for determining the location of activity, but cannot readily be used to determine the nature of the HDR time course. Event-related designs could be optimized to efficiently determine the nature of the HDR time course; however they generally offer much less power to prove that a response actually exists at a particular location. There are many subtleties to possible designs, including hybrid block and event-related designs. In general a block design is preferred if there are no contraindications, as it gives higher statistical power. Alternative approaches should be taken only for questions that cannot be answered using a block design.

Baseline Considerations

Choosing the appropriate baseline is as important as choosing the optimal task. Commonly, the baseline consists of "rest," during which the subject is asked to do "nothing." This is a very poorly defined state, and some paradigms improve with a more defined, engaging baseline. Contrast in fMRI arises from a measured *change* in signal, and it is therefore important to know from what baseline state the signal changed. Our brains are always "on," so one must be careful when interpreting signal change related to a task. All we can really say about significant activation is that there is greater signal whilst a subject is performing a task of interest than when they are performing the baseline task. Rest can and should be considered as just a different task than the task of interest. Similarly, if signal decreases during the task of interest, one can regard this as an increase in activity during rest. Importantly, signal decrease or "deactivation" is not the same as inhibition, since inhibition is itself an active process that can contribute to an increase in signal. If inhibitory processes are involved, the reduction of activity that is observed may have been signaled from an active inhibitory process adjacent to or some distance from the site of "deactivation."

Performance Measures

Proper interpretation of fMRI results generally relies on knowledge of the tasks subjects were performing during the imaging session. One common assumption is that the subjects are doing what they are told. Ideally performance measures should be undertaken concurrently with the imaging, but this is not always practical. For example, in a commonly used language paradigm subjects may be asked to generate as many words as they can that begin with a provided letter. To avoid problems associated with subject motion, this task is normally performed covertly (i.e. without vocalization). This task performance cannot be directly verified. To minimize the possibility of incorrect interpretation, one should obtain some measure of task performance. This is often the measurement of a subject's performance on a similar task out of the scanner. Subjects should also be asked after their scan whether or not they encountered any difficulty in performing the task in the scanner.

Improved interpretation of functional imaging results can often be made when performance of aspects other than the task of interest are also measured. For example, it is known that changes in physiological measures such as cardiac and respiratory rates can affect the cerebral circulation, and breath-holding especially can result in very large changes in the BOLD response that can potentially confound interpretation. Measures of skin conductance and eye tracking are also possible, and these and other measures can be used to remove variance in the data that may be unrelated to the task of interest, or to explicitly model effects that may be related to the task of interest.

Principles of Analysis

There are a number of steps involved in taking raw fMRI data and turning it into colored maps of activity that can be readily interpreted. The processing pipeline contains procedures to minimize artifact, maximize signal, and aid interpretation. We will describe here a commonly used imaging pipeline for BOLD fMRI.

Data Preparation

Often the first step in an analysis pipeline is extraction of the imaging data from the scanner and conversion into a format suitable for further processing. Whilst scanner manufacturers are slowly introducing functional image analysis tools into their standard software, at the present time such software is often rudimentary and inflexible.

Pre-Processing

Pre-processing steps are those performed prior to statistical image analysis. Depending upon the type of acquisition they can include:

- *Correction for signal drop out near magnetic susceptibility inhomogeneities.* The variation in magnetic susceptibility especially near tissue–air boundaries can cause extensive areas of signal loss in typical EPI acquisitions due to the inability of scanners to shim to a uniform field in these regions. Various methods have been devised to overcome this problem, including the z-shim method that involves acquiring two or more sequential acquisitions with different imposed corrective gradients that effectively image separately the areas of drop out. A post-processing step is required to combine these multiple acquisitions.
- *Correction for geometric distortion*, e.g. Measured B_0 phase maps can be used to calculate and correct for geometric distortions that plague EPI fMRI images.
- *Slice timing correction.* Acquisition volumes most commonly consist of a series of sequentially acquired slices. Slice timing correction methods generally resample the temporal response of a voxel, applying interpolation to estimate what the response would be at the time of commencement of each acquisition volume. Of course this correction should not be used in conjunction with imaging methods that involve acquisition of an entire volume in one imaging shot.
- *Gross motion rejection and/or realignment.* The deleterious effects of subject motion can be reduced with these steps. Gross motion rejection can also remove data contaminated by acquisition failures such as a gradient misfire.
- *Global intensity normalization*. This step is necessary with some scanners that are not able to provide a stable signal from one acquisition to the next. If one assumes that the BOLD signal change due to the task is small relative to the mean signal of all within-brain voxels, one can normalize the global signal to a common value (proportional scaling). Unfortunately, the BOLD signal change is not always negligible in relation to the mean global signal, so there is a risk that this processing step will do more harm than good (for example by reducing the apparent size of real activation). If the MRI system is reasonably stable, then global intensity normalization should usually be avoided.
- *Spatial normalization.* This step involves registration of the imaging data of each subject in a study to a common template, to enable voxel-wise statistical analysis of group data and/or to allow reporting of activation locations relative to a standard atlas. In the case of a single subject analysis, the derived transformation may

be applied to the statistical result instead of the raw imaging data, so as to avoid resampling artifact. If this is done, nearest-neighbor resampling is used to preserve the fidelity of the statistical result.

- *Smoothing.* Spatial and temporal smoothing with a Gaussian kernel is often performed to improve the SNR of imaging data. This pre-processing step also ensures that the variance distribution is Gaussian, allowing the valid application of Gaussian random field theory in statistical analysis. To achieve this, the smoothing kernel should have a full width at half maximum (FWHM) of at least twice the voxel size.
- *Linear de-trending.* This is a controversial processing step as the underlying assumption that a linear trend in a voxel time course is "noise" is unlikely to be valid. There are other ways to deal with this later when statistically analyzing the images.

It is important to note that the order in which these processing steps are performed can have a substantial effect on results. The order listed above is a typical scenario, however, it may not always be the best arrangement.

Statistical Analysis

Statistical analysis of fMRI data is necessary because the signals of interest are usually of a similar magnitude to the noise in the data. By collecting many images and applying statistical analysis, one can enumerate the voxels that have an acceptable probability of being associated with the task of interest. The most common method of analysis is a general linear model based approach. The signal is assumed to comprise a linear combination of effects of interest, confounding effects, and a random noise term. The effect of interest in the model usually consists of a function representing the time course of tasks performed convolved with an estimate of the brain's HDR. Confounding effects are also often included in the model, such as the realignment parameters determined in the motion correction pre-processing stage (these are often included to model any residual motion effects such as changes in the magnetization experienced by protons that are not corrected by realignment). The statistical analysis determines, for each voxel independently, the proportion of included model terms that best fit the measured data, and provides an estimate of the probability that the coefficient of the effect of interest is non-zero (implying the effect is present). Gaussian random field theory is often used to estimate a probability corrected for the multiple comparisons made in this massively univariate data.

Other statistical analyses are also possible, including data driven approaches where no assumptions are made about the tasks performed. Rather the data are interrogated in such a way as to extract structured components that are able to describe the data in some way. Such methods include principle components analysis and independent components analysis, the latter generally being more useful in the neuroimaging context. Detailed descriptions of these approaches are beyond the scope of the current discussion. However, it is worth noting that these approaches are beneficial when the nature of the expected response is not known. Results of data driven analyses can be difficult to interpret however, and model based approaches are generally more powerful when a good estimate of the expected response is available.

Software Packages

There are now a number of software packages available to assist with functional imaging analysis. Probably the package in most widespread use is SPM, a powerful and flexible package for performing "statistical parametric mapping." A comprehensive competitor with some unique advantages is FSL. Both of these packages are available free of charge. There are many other packages that are also worth considering, including several specialized utilities that have been designed to perform particular aspects of processing, analysis, and/or visualization. Often the best analysis approach will take advantage of several packages. Selection can often be a matter of determining the packages that are already in use in your geographical area, since an experienced user is often the best source of help for inexperienced users.

Artifacts and Pitfalls

Since fMRI studies usually require a relatively long series of scans in order for the activation-induced signal changes to build up to a detectable level, gross subject motion may occur. Image processing techniques exist to at least partially correct for motion, as we discussed earlier, however prevention is better than cure. For example, head immobilization via straps, vacuum-bean bags, and/or use of bitebars can help minimize head motion. Immobilizing the upper part of the extremities during sensory–motor tasks can help minimize task-related motion. A further confounding factor can be task-associated physiological effects resulting in changes in brain activation, such as subconscious breath-holding during challenging tasks. Such artifacts may lead to misinterpretation of the study results, and every effort should be undertaken to minimize their occurrence and to monitor for their presence.

Another common problem with fMRI is geometric distortion. The most common rapid imaging technique for fMRI is EPI. With this technique, images of the brain can be acquired in times of 100 ms or less; however the technique is particularly prone to exhibit geometric distortion.

This is especially severe in areas of high susceptibility differences such as the air–tissue boundary in the temporal lobes. Correct interpretation and detection of fMRI changes in these areas is often difficult. Even in relatively susceptibility-free regions of the brain, EPI images will display subtly different distortions in comparison with slower structural scans and this complicates the overlay of function and structure that is a necessary for interpretation of results.

Even when all these problems are minimized, and an appropriate activation map has been generated, one has to be careful in the interpretation of the fMRI results. A common pitfall in group studies is an inadequate number of participants, leading to group results that do not survive correction for multiple comparisons. Whereas such results may be important pilot data, directing further experiments, one has to consider that they are at best a "trend" and provide no statistical proof of an effect greater than noise. A further common problem is the interpretation that a significant "activation" is equivalent to preserved function. There are many examples in the literature, demonstrating that the degree of activation does not linearly follow performance of a function. A very poor performer and an excellent performer may both activate relatively few areas, whereas a moderate performer may show a relatively higher degree of activation. Task-related activation in a particular area may not represent "the site" of a particular function, but rather represent part of a network of areas used to perform this task, or even an associated function, such as attention to the task or eye movements in relation to the paradigm. Furthermore, just because an area is active does not necessarily mean that it is essential for the performance of the task.

Practical Applications

All the fMRI examples shown here were acquired on a GE Signa 3 Tesla MR scanner (GE Medical Systems). Higher magnetic field strength is associated with a higher SNR, which can be translated into shorter imaging times for a given resolution, or higher resolution for a given imaging time, or combination of both. At the time of writing 1.5 T scanners are most common. Compared to 1.5 T, at 3 T the same fMRI paradigm could be run for a shorter period of time, or paradigms evoking typically a very small response may give sufficient signal, whereas they may not be useful at lower field strength. However, the higher field strength has also some disadvantages. There is the potential for greater energy deposition into tissue and increased susceptibility-related artifacts.

Functional images are always acquired together with other sequences. The T_2^*-weighted sequence used for fMRI has a low resolution, so T_1 or T_2-weighted images are usually acquired in the same planes as the T_2^*-weighted images. Further, angiogram/venogram images are often acquired to localize vessels in the brain, in order to avoid confusion of a signal arising from a vessel with the BOLD response. fMRI in the examples below was performed using a whole brain (22 slices) gradient EPI technique (TE = 40 ms, TR = 3600 ms, acquisition matrix = 128 × 128, flip angle = 60°, and 4 mm thick slices, 1 mm gap).

Language fMRI

Language is a cognitive brain function that involves a network of brain areas. In the majority of healthy subjects, these language-related brain areas are predominantly in the left hemisphere. Since the first reported use of fMRI for the study of language in 1993 by McCarthy *et al.*, fMRI has become established for the purpose of assessing language lateralization. The determination of "language dominance" is an important investigation step in patients undergoing brain surgery. Many different language fMRI tasks have been developed. Some are designed to activate particular parts of the language network. In our Institute, we have developed and validated two language paradigms, both performed as a block designs.

For the orthographic lexical retrieval (OLR) paradigm a letter is presented visually, and the subject asked to retrieve silently as many words as possible beginning with that letter. After 18 s a second letter is presented, giving a 36-s task period. For the noun–verb generation (NVG) paradigm, the subject is visually presented with a common noun (e.g. fish) and is asked to generate an appropriate verb (e.g. swim). A new noun is presented every 4 s, with a task period of 36 s. For both tasks the baseline consists of visual fixation of a cross hair, this rest period also has a duration of 36 s (Figure 1). Both paradigms have four cycles with an additional rest period at the start of the paradigm; the total duration of the paradigm is 5.4 min.

Determination of Language Lateralization

Image processing, as described above, will result in maps of activation; these can be used to quantify the lateralization of a function. The laterality index (LI) is based on the number of activated pixels in language-associated areas. The LI is calculated using the following equation: LI = (left-hemispheric pixel count—right-hemispheric pixel count)/(left-hemispheric pixel count + right-hemispheric pixel count).

Examples of fMRI Language in Controls

We recently performed a study in multilingual subjects using a NVG task in four different languages. For reference to this publication, see figure legend. We hypothesized that the degree of proficiency in each language would be related to the extent of functional activity measured in a region of interest analysis. Therefore, the degree of

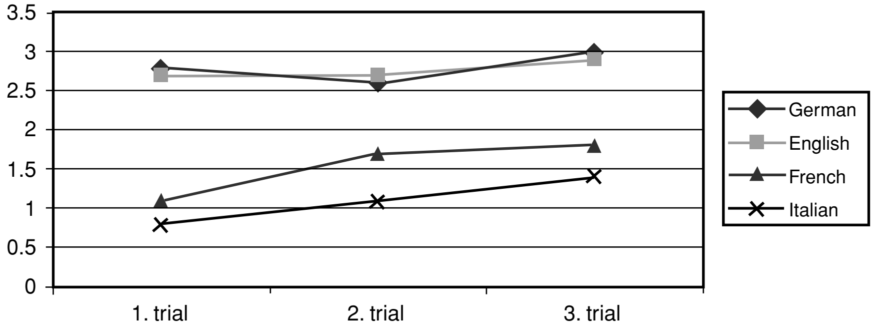

Fig. 2. This diagram shows an example of an out-of-scanner performance test in a quadrilingual subject. The subject was given a cartoon with a word-free story, and was asked to produce a discourse based on this cartoon. This was repeated three times, and then a new cartoon was given to assess the discourse in another language. Results are given for the words/second produced at all three trials. Note the overall increase in word production, particularly noticeable for languages with poorer proficiency. This subject had two "good" and two "poor" languages. *Source:* Adapted from Briellmann RS, Saling MM, Connell AB, Waites AB, Abbott DF, Jackson GD. A high-field functional MRI study of quadri-lingual subjects. Brain Lang. 2004;89:531–42.

proficiency in each language had to be quantified in detail. We used several tests, including a discourse test, in which the subjects were asked to produce a story based on a cartoon, which displayed a word-free story. Figure 2 shows the results in one subject, demonstrating a clear difference between languages with good performance (in this subject German and English), and languages with poor performance (Italian and French). The fMRI showed that all four languages activated overlapping brain areas, corresponding to the major language regions (Figure 3). Interestingly, the number of activated voxels correlated with proficiency, so that the activated volume increased for languages in which a subject had poorer proficiency. This observation highlights an important issue in the design and interpretation of fMRI experiments. In some cases better performance is associated with more brain activity, whilst in others the reverse is true. Correct interpretation of a novel task therefore requires some independent measure of subject performance or response.

Examples of fMRI Language in Patients

Atypical language lateralization is more frequently found in patients with epilepsy and some other focal and chronic brain disorders. In a series of 30 healthy controls and 30 epilepsy patients, we confirmed the increased frequency of atypical language in epilepsy patients (Figure 4). Such atypical lateralization may represent reorganization due to early disturbances of the left hemisphere, such as a perinatal vascular event. fMRI is not only used to determine language lateralization, it has been used to assess the

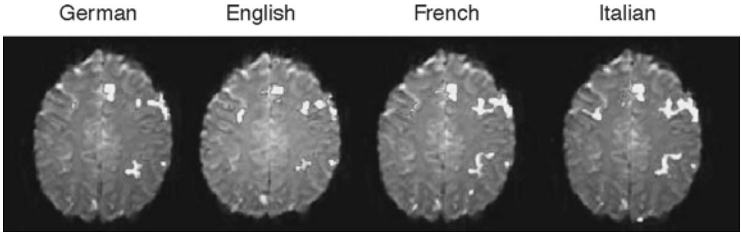

Fig. 3. Functional MRI of language of a quadrilingual subject. The subject performed the NVG task in four different languages. The figure shows the activation during task in comparison to rest in all four languages. Note that all languages activate similar brain areas, however, there is a subtle increase in the amount of activation in poor compared to good languages. *Source:* Image taken from Briellmann RS, Saling MM, Connell AB, Waites AB, Abbott DF, Jackson GD. A high-field functional MRI study of quadri-lingual subjects. Brain Lang. 2004;89:531–42. (See also Plate 84 on page XIII in the Color Plate Section.)

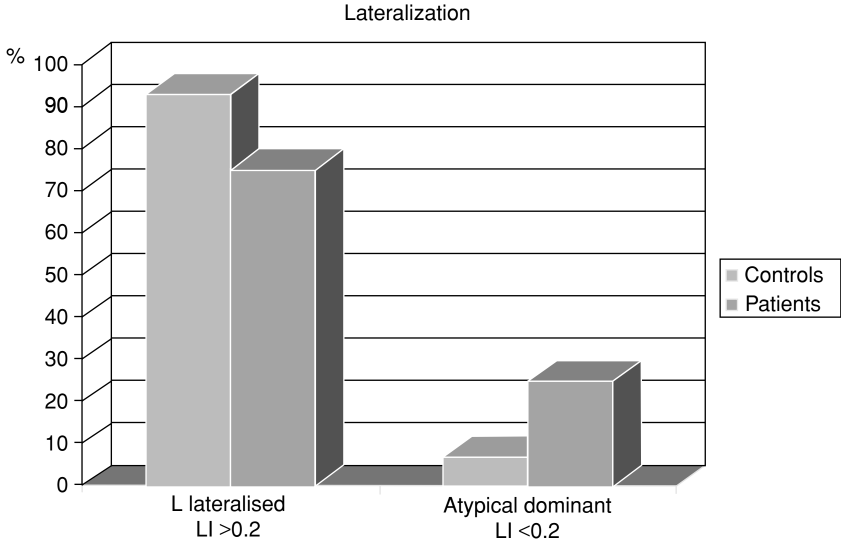

Fig. 4. This diagram shows the distribution of typical and atypical language lateralization in a group of 30 healthy controls and 30 patients with refractory partial epilepsy. Note the predominance of left-lateralized language in both groups, but the relatively higher proportion of atypical language in the patient population.

spatial relationship between the seizure focus and brain function (for review see Sunaert and Yousry 2001). This is of particular interest in the planning of neurosurgical resection.

Figures 5 and 6 show findings of a 9-year-old girl who was investigated for possible epilepsy surgery. Her epilepsy was first noted at the age of 5 years, when she developed complex partial seizures, occurring in clusters, often out of sleep. Her structural MR investigation showed a left mesial temporal lesion, suggestive of a low-grade tumor (Figure 5). Her language fMRI shows clear left-lateralized language dominance (Figure 6). Therefore, in this case language and seizure focus were co-lateralized to the same hemisphere.

A different situation is present in the patient described in Figures 7 and 8. These figures show the findings of a 35-year-old woman, who is left-handed. Her epilepsy started at the age of 12 years. Her EEG showed two independent, left-hemispheric epileptogenic foci, one in the occipital region, the other in the mesial temporal lobe. Her structural MR shows a left occipital lesion, suggestive of an old hemorrhagic lesion (Figure 7).

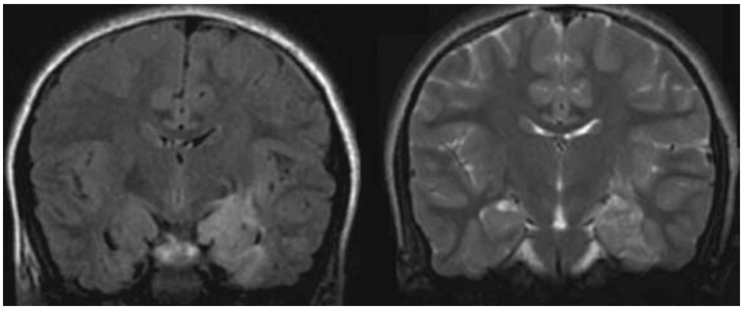

Fig. 5. This figure shows the structural MR examination in a 9-year-old girl with temporal lobe epilepsy. Representative coronal slices in the area of the mesial temporal lesion are shown. On both the FLAIR (left) and T_2-weighted (right) scans, the lesion is characterized by heterogeneously increased signal intensity, affecting mainly the mesial temporal area, but also partially involving the stem of the temporal lobe. This pattern is indicative for a low-grade tumor, such as dysembryoplastic neuroepithelial tumor.

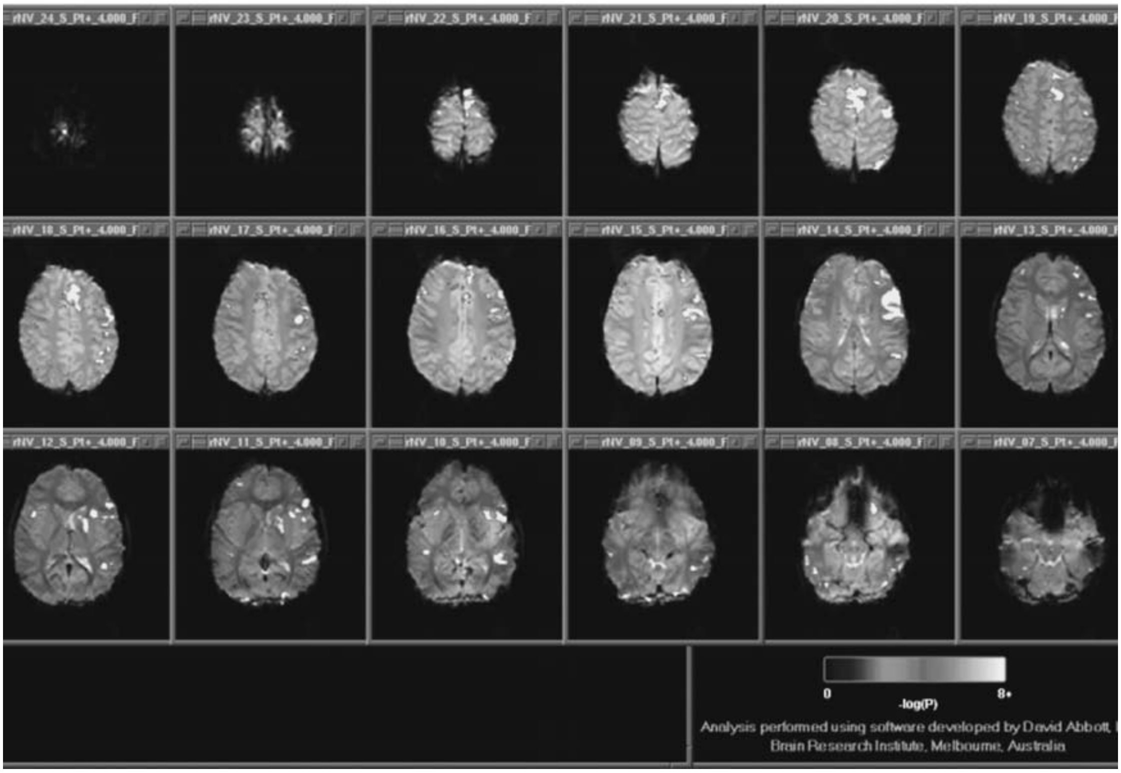
rNV_24_S_Pt+_4.000_F
rNV_23_S_Pt+_4.000_F
rNV_22_S_Pt+_4.000_F
rNV_21_S_Pt+_4.000_F
rNV_20_S_Pt+_4.000_F
rNV_19_S_Pt+_4.000_F
rNV_18_S_Pt+_4.000_F
rNV_17_S_Pt+_4.000_F
rNV_16_S_Pt+_4.000_F
rNV_15_S_Pt+_4.000_F
rNV_14_S_Pt+_4.000_F
rNV_13_S_Pt+_4.000_F
rNV_12_S_Pt+_4.000_F
rNV_11_S_Pt+_4.000_F
rNV_10_S_Pt+_4.000_F
rNV_09_S_Pt+_4.000_F
rNV_08_S_Pt+_4.000_F
rNV_07_S_Pt+_4.000_F
0
-log(P)
8+
Analysis performed using software developed by David Abbott,
Brain Research Institute, Melbourne, Australia

Fig. 6. Language fMRI in the same patient as shown in Figure 5. There is strong left-lateralized language dominance, with particularly strong activation in the frontal lobe language areas (middle frontal gyrus and inferior frontal gyrus). There is also activation in the superior temporal gyrus, which is not involved in the lesion. Therefore, language and seizure focuses were co-localized to the same hemisphere. Note: the subject's left is displayed on the image right (i.e. radiological convention). (See also Plate 85 on page XIV in the Color Plate Section.)

Based on the clinical symptomatology, this lesion was considered the primary seizure focus. Additionally, there were also signs of ipsilateral hippocampal sclerosis, suggestive for secondary damage. Her fMRI of language shows right-lateralized language dominance (Figure 8). Therefore, in this case language and seizure focus were in different hemispheres, and given the suspected early left-hemispheric damage, shift of the language function to the undamaged right hemisphere may have taken place.

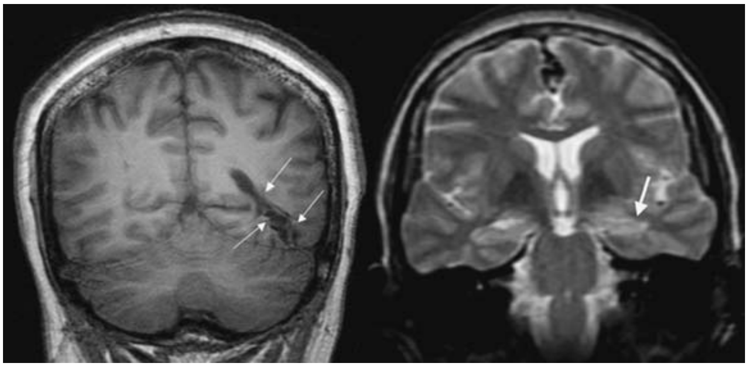

Fig. 7. Structural MRI of a 35-year-old women with refractory partial epilepsy. The image on the left shows a T_1-weighted, coronal slice at the level of the left occipital abnormality (highlighted by thin arrows). The image on the right shows a T_2-weighted, coronal slice at the level of the hippocampus (highlighted by thick arrow). There is increased T_2-weighted signal in the body of the hippocampus (114% of mean normal value, whereas the empirically determined cutoff indicating an abnormally increased value is 105% of mean normal value).

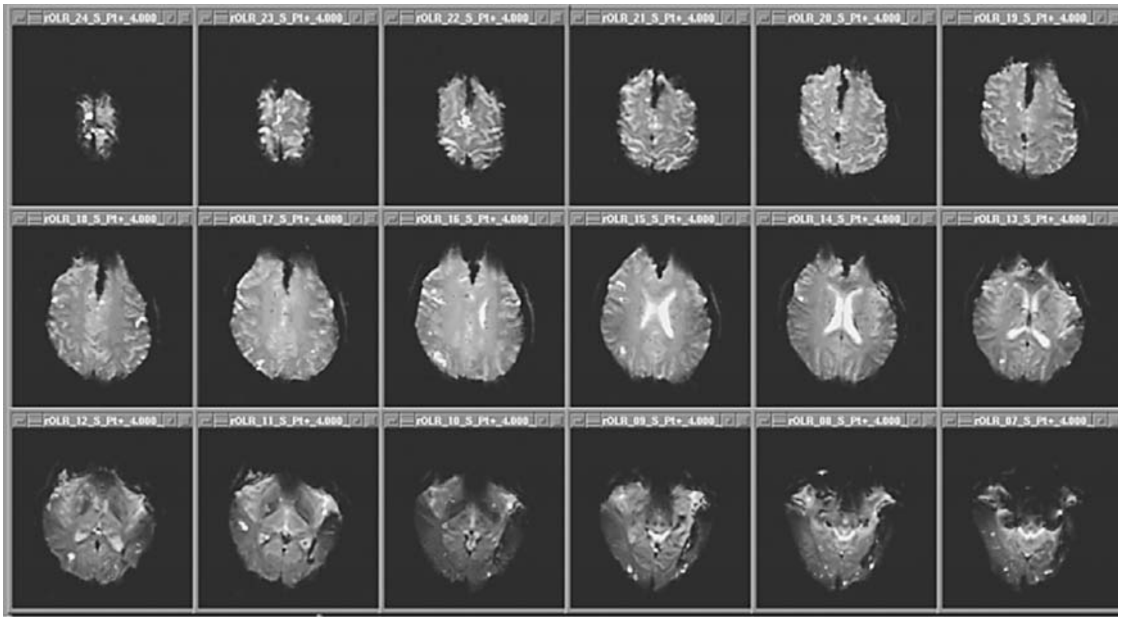

Fig. 8. Language fMRI in the same patient as shown in Figure 7. There is strong right-lateralized language dominance, involving both frontal and temporal lobe areas. In this left-handed patient, language and seizure focus were not co-localized (see text for more details). Note: the subject's left is displayed on the image right (i.e. radiological convention). (See also Plate 86 on page XIV in the Color Plate Section.)

FMRI/EEG

Some neurological diseases are associated with changes on the electroencephalogram. Probably the best-known example is the epileptiform discharge in patients with epilepsy. These discharges can occur without associated clinical symptomatology, and are termed interictal discharges. These discharges can be used as "events-of-interest" in an fMRI paradigm. This technique has a great practical potential for the investigation of patients with focal epilepsy. Interictal focal discharges typically originate from around the seizure focus, and can therefore be used as a localization indicator. However, whereas the EEG gives excellent temporal information on when these discharges occur, it has rather poor spatial resolution. The combination of EEG and fMRI overcomes this limitation. Until relatively recently, recording of EEG within the bore of the magnet has been regarded as too difficult since the EEG signal is impaired due to factors including induced currents from slight movement of leads in a large static magnetic field, changing magnetic field gradients during the scanning procedure and the radio frequency (RF) energy emitted by the transmitter coil. The MR image itself can be further impaired by RF interference from conductors and electrical devices within the magnet. However, these problems have been gradually overcome, and an increasing number of centers are reporting successful EEG recording within the scanner. This approach allows studying fMRI activation in association with subclinical events.

The quality of the EEG during scanning is of crucial importance for the fMRI/EEG analysis. Our system is now of a quality that allows discrimination of the interictal discharges during continuous fMRI scanning. Figure 9A demonstrates the high quality of the EEG obtained during scanning and Figure 9B shows further improvement of the EEG using post-processing methods (Figure 9). In suitable patients, fMRI/EEG can show focal activation in the area of the presumed seizure focus, as demonstrated in Figure 10.

Conclusion

fMRI is a relatively young investigation method. Nevertheless, it has proven to be a very useful diagnostic and research tool. fMRI is safe, non-invasive and can be repeated as many times as needed. Due to the need for active participation of the subject it can, however, only be applied to cooperative subjects. Typically, this is difficult to achieve

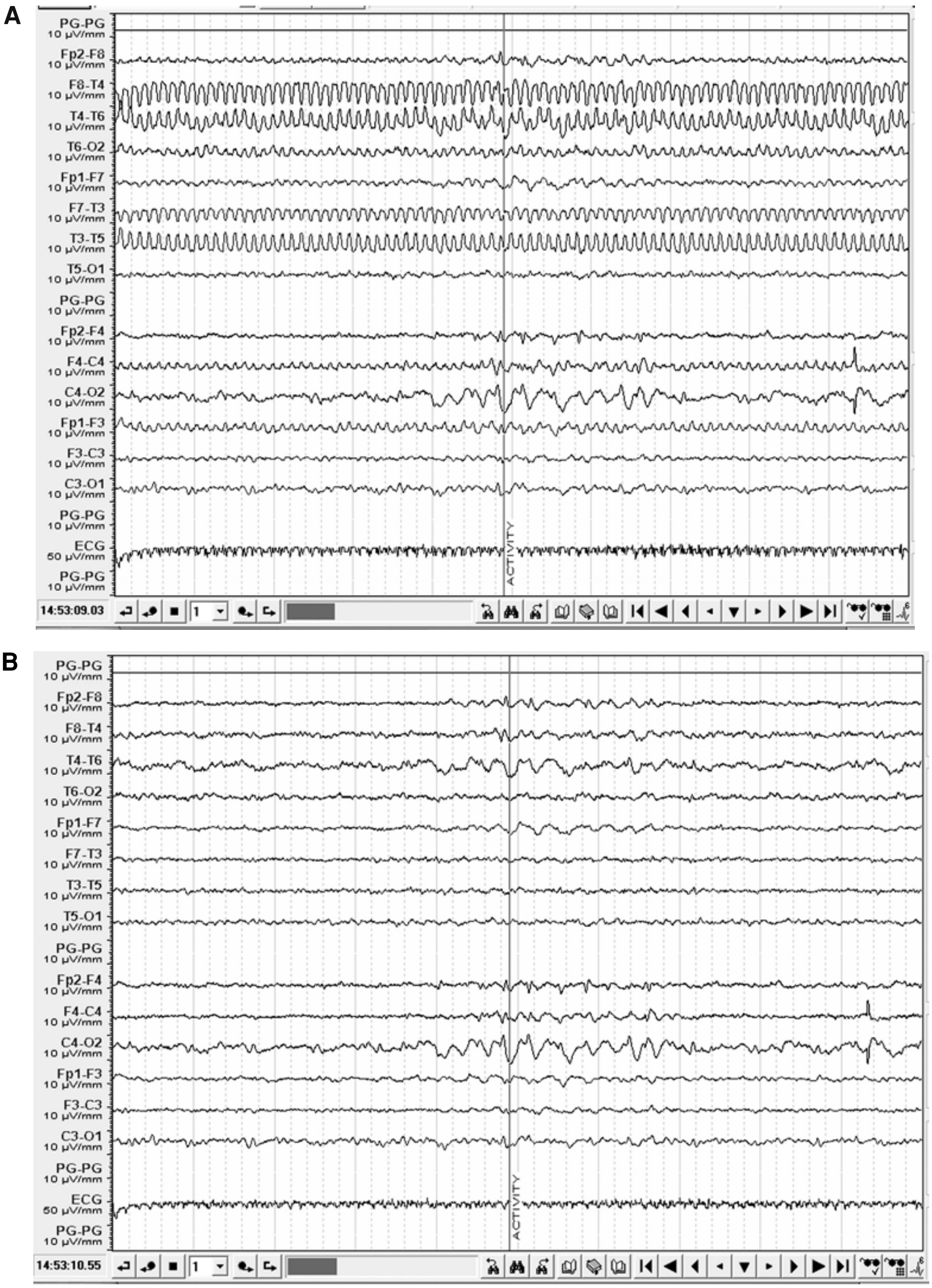
A
PG-PG 10 µV/mm
Fp2-F8 10 µV/mm
F8-T4 10 µV/mm
T4-T6 10 µV/mm
T6-O2 10 µV/mm
Fp1-F7 10 µV/mm
F7-T3 10 µV/mm
T3-T5 10 µV/mm
T5-O1 10 µV/mm
PG-PG 10 µV/mm
Fp2-F4 10 µV/mm
F4-C4 10 µV/mm
C4-O2 10 µV/mm
Fp1-F3 10 µV/mm
F3-C3 10 µV/mm
C3-O1 10 µV/mm
PG-PG 10 µV/mm
ECG 50 µV/mm
PG-PG 10 µV/mm
ACTIVITY
14:53:09.03
B
PG-PG 10 µV/mm
Fp2-F8 10 µV/mm
F8-T4 10 µV/mm
T4-T6 10 µV/mm
T6-O2 10 µV/mm
Fp1-F7 10 µV/mm
F7-T3 10 µV/mm
T3-T5 10 µV/mm
T5-O1 10 µV/mm
PG-PG 10 µV/mm
Fp2-F4 10 µV/mm
F4-C4 10 µV/mm
C4-O2 10 µV/mm
Fp1-F3 10 µV/mm
F3-C3 10 µV/mm
C3-O1 10 µV/mm
PG-PG 10 µV/mm
ECG 50 µV/mm
PG-PG 10 µV/mm
ACTIVITY
14:53:10.55

Fig. 9. Example of EEG recording during scanning, at the time of an epileptiform discharge. (A) The image shows the EEG before post-processing, demonstrating the quality of our EEG during scanning. A run of rhythmic theta is seen with maximum over C4. (B) The image shows the same trace after filtering. Note the disappearance of residual gradient artifact after filtering, allowing one to appreciate the sharp transients associated with the theta waves. For the analysis of this study, see Figure 10.

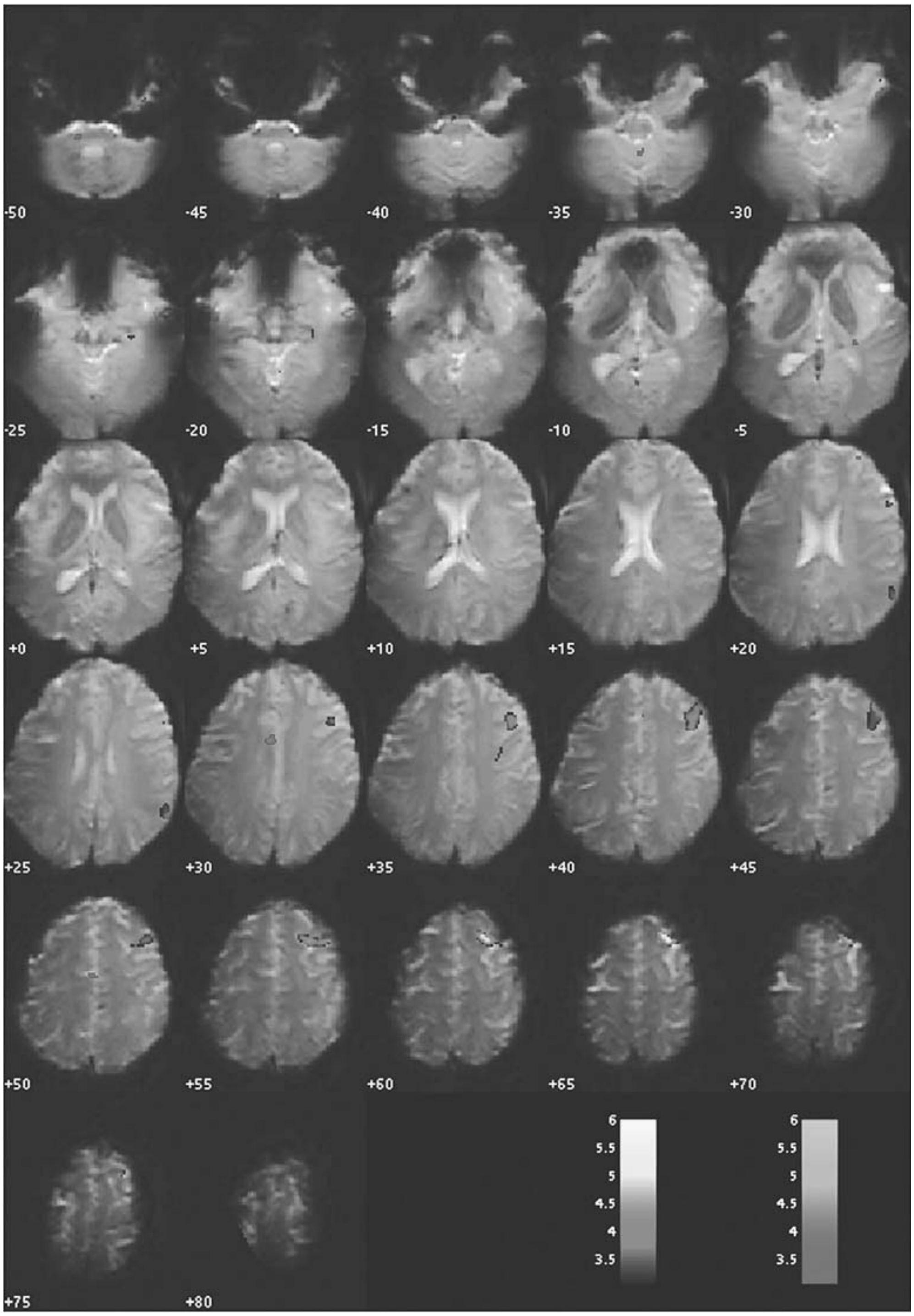

Fig. 10. This figure shows the analysis of an fMRI/EEG study in a 39-year-old woman with refractory partial seizures, arising from a small dysplastic lesion in the right frontal lobe. The figure shows positive BOLD response associated with six interictal discharges, captured during 35 min of fMRI acquisition. The fMRI analysis was performed using SPM99. The areas of activation are shown in warm colors, and the areas of deactivation in cold colors. The threshold was set at $p = 0.001$, uncorrected for multiple comparisons. There is a focal signal increase in the right frontal lobe in close proximity to the suspected seizure focus. Note: Here the subject's left is displayed on the image left (i.e. neurological convention). (See also Plate 87 on page XV in the Color Plate Section.)

in children younger than 6 years (although we have occasionally successfully performed fMRI in 5-year-olds), or in the severely ill or disabled patient. If applied and interpreted correctly, fMRI has the great promise to further improve our knowledge of the function of the human brain, by many applications in brain research. It is beginning to simplify patient investigation and monitoring, and in some centers is already replacing some of the more invasive investigation techniques.

Abbreviations

fMRI, functional magnetic resonance imaging; BOLD, blood oxygenation level dependent; EPI, echo planar imaging; SNR, signal-to-noise ratio; HDR, hemodynamic response function; ISI, inter-stimulus interval; TR, repetition time; FWHM, full width at half maximum; SPM, statistical parametric mapping; OLR, orthographic lexical retrieval; NVG, noun–verb generation.

Further Reading

1. Abbott D, Jackson GD. iBrain®—Software for analysis and visualisation of functional MR images. NeuroImage. 2001;13:59.
2. Abbott DF, Opdam HI, Briellmann RS, Jackson GD. Brief breath-holding may confound functional magnetic resonance imaging studies. Human Brain Mapping. 2005;24(4):284–90.
3. Aghakhani Y, Bagshaw AP, Benar CG, *et al*. fMRI activation during spike and wave discharges in idiopathic generalized epilepsy. Brain. 2004;127(Pt 5):1127–44.
4. Al-Asmi A, Benar CG, Gross DW, *et al*. fMRI activation in continuous and spike-triggered EEG–fMRI studies of epileptic spikes. Epilepsia. 2003;44(10):1328–39.
5. Baxendale S. The role of functional MRI in presurgical investigation of temporal lobe epilepsy patients: a clinical perspective and review. J. Clin. Exp. Neuropsychol. 2002; 24:664–76.
6. Binder JR, Swanson SJ, Hammeke TA, *et al*. Determination of language dominance using functional MRI: a comparison with the Wada test. Neurology. 1996;46:978–84.
7. Boxerman JL, Hamberg LM, Rosen BR, Weiskoff RM. MR contrast due to intravascular magnetic susceptibility perturbations. Magn. Reson. Med. 1995;34:555–66.
8. Constantine G, Shan K, Flamm SD, Sivananthan MU. Role of MRI in clinical cardiology. Lancet. 2004;363(9427): 2162–71.
9. Dale AM. Optimal experimental design for event-related fMRI. Hum. Brain Mapp. 1999;8:109–14.
10. Desmond JE, Glover GH. Estimating sample size in functional MRI (fMRI) neuroimaging studies: statistical power analyses. J. Neurosci. Methods. 2002;118:115–28.
11. Detre JA, Wang J. Technical aspects and utility of fMRI using BOLD and ASL. Clin. Neurophysiol. 2002;113(5): 621–34.
12. Frackowiak R, Friston K, Frith C, Dolan R, Price C, Ashburner J, Penny W, Zeki S (Ed). Human Brain Function, 2nd ed. Academic Press: London, 2004.
13. Friston KJ, Zarahn E, Josephys O, Henson RNA, Dale AM. Stochastic designs in event-related fMRI. Neuroimage. 1999;10:607–19.
14. Fujiwara N, Sakatani K, Katayama Y, Murata Y, Hoshino T, Fukaya C, Yamamoto T. Evoked-cerebral blood oxygenation changes in false-negative activations in BOLD contrast functional MRI of patients with brain tumors. Neuroimage. 2004;21(4):1464–71.
15. Gaillard WD, Hertz-Pannier L, Mott SH, Barnett AS, LeBihan D, Theodore WH. Functional anatomy of cognitive development: fMRI of verbal fluency in children and adults. Neurology. 2000;54:180–5.
16. Glover GH. Deconvolution of impulse response in event-related BOLD fMRI. Neuroimage. 1999;9(4):416–29.
17. Golay X, Hendrikse J, Lim TC. Perfusion imaging using arterial spin labeling. Top Magn. Reson. Imaging. 2004; 15(1):10–27.
18. Gusnard DA, Raichle ME. Searching for a baseline: functional imaging and the resting human brain. Nat. Rev. Neurosci. 2001;2:685–94.
19. Hampson M, Peterson BS, Skudlarski P, Gatenby JC, Gore JC. Detection of functional connectivity using temporal correlations in MR images. Hum. Brain Mapp. 2002;15: 247–62.
20. Himberg J, Hyvarinen A, Esposito F. Validating the independent components of neuroimaging time series via clustering and visualization. Neuroimage. 2004;22(3): 1214–22.
21. Jackson GD, Connelly A, Cross JH, Gordon I, Gadian DG. Functional magnetic resonance imaging of focal seizures. Neurology. 1994;44:850–856.
22. Lazeyras F, Zimine I, Blanke O, Perrig SH, Seeck M. Functional MRI with simultaneous EEG recording: feasibility and application to motor and visual activation. J. Magn. Reson. Imaging. 2001;13:943–8.
23. Lemieux L, Salek-Haddadi A, Josephs O, *et al*. Event-related fMRI with simultaneous and continuous EEG: description of the method and initial case report. Neuroimage. 2001;14(3):780–7.
24. Logothetis NK, Pauls J, Augath M, Trinath T, Oeltermann A. Neurophysiological investigation of the basis of the fMRI signal. Nature. 2001;412(6843):150–7.
25. Logothetis NK. The neural basis of the blood-oxygen-level-dependent functional magnetic resonance imaging signal. Philos. Trans. R. Soc. Lond. B. Biol. Sci. 2002;357 (1424): 1003–37.
26. McKeown MJ, Hansen LK, Sejnowsk TJ. Independent component analysis of functional MRI: what is signal and what is noise? Curr. Opin. Neurobiol. 2003;13(5):620–9.
27. Menon RS. Imaging function in the working brain with fMRI. Curr. Opin. Neurobiol. 2001;11:630–6.
28. Ogawa S, Lee TM, Kay AR, Tank DW. Brain magnetic resonance imaging with contrast dependent on blood oxygenation. Proc. Natl. Acad. Sci. U.S.A. 1990;87:9868–72.
29. Prichard JW, Rosen BR. Functional study of the brain by NMR. J. Cereb. Blood Flow Metab. 1994;14:365–72.

30. Rosen BR, Buckner RL, Dale AM. Event-related functional MRI: past, present, and future. Proc. Natl. Acad. Sci. 1998;95:773–80.
31. Schenck JF. MR safety at high magnetic fields. Magn. Reson. Imaging Clin. N. Am. 1998;6:715–30.
32. Schlosser R, Hutchinson M, Joseffer S. Functional magnetic resonance imaging of human brain activity in a verbal fluency task. J. Neurol. Neurosurg. Psychiatry 1998;62: 492–8.
33. Springer JA, Binder JR, Hammeke TA, *et al*. Language dominance in neurologically normal and epilepsy subjects: a functional MRI study. Brain. 1999;122:2033–45; Sunaert S, Yousry TA. Clinical applications of functional magnetic resonance imaging. Neuroimaging Clin. N. Am. 2001;11:221–36.
34. Wilke M, Holland SK, Myseros JS, Schmithorst VJ, Ball WS Jr. Functional magnetic resonance imaging in pediatrics. Neuropediatrics. 2003;34(5):225–33.

High Resolution Magic Angle Spinning (HRMAS) Proton MRS of Surgical Specimens

Leo L. Cheng[1,2], Melissa A. Burns[1] and Cynthia L. Lean[3,4]
[1]*Departments of Pathology;*
[2]*Departments of Radiology Massachusetts General Hospital, Harvard Medical School Boston, Massachusetts 02114, USA;*
[3]*Institute for Magnetic Resonance Research, NSW 1590, Australia; and*
[4]*Department of Magnetic Resonance in Medicine, University of Sydney, NSW 2006, Australia*

List of Abbreviations

BPH	Benign prostatic hyperplasis
DCIS	Ductal carcinoma *in situ*
FNAB	Fine needle aspiration biopsy
GBM	Glioblastoma multiforme
HCA	Hierarchical cluster analysis
^{1}H MRS	Proton magnetic resonance spectroscopy
HPLC	High pressure liquid chromatography
(HR)MAS	(High resolution) Magic angle spinning
NAA	N-acetyl aspartate
PA	Polyamines
PC	Phosphocholine
PCA	Principal component analysis
PTC	Phosphatidylcholine
SCS	Statistical classification strategy
SSB	Spinning side bands

Introduction

Over the last two decades, a large body of *ex vivo* work and some *in vivo* work has demonstrated the utility of proton magnetic resonance spectroscopy (^{1}H MRS) in detecting and monitoring cellular chemical alterations associated with the development and progression of human malignant diseases [1–3]. Reports of conventional *ex vivo* ^{1}H MRS studies of human tissues, i.e. analysis of intact tissues with liquid-state MRS probes, have demonstrated that diagnosis, and for some organs, prognosis of malignant disease using metabolite ratios measured from spectra may reach 95% for both sensitivity and specificity. The accuracy can further be improved using an objective pattern recognition technique, statistical classification strategy (SCS) [2]. While tissue conventional MRS is fast and has shown the ability to diagnose accurately various human malignancies, it is limited by poor spectral resolution caused by the magnetic susceptibility effects of heterogeneous structures of the sample, and therefore detailed identification of individual metabolites is difficult. Metabolite profiling involving the measurement and quantification of tissue metabolites [4] is of increasing interest in the era of genomics and proteomics due to the direct involvement of tissue metabolites in tumor development and progression. High-resolution magic angle spinning (HRMAS) was developed to improve the spectral resolution of MR spectra of intact tissue by the reduction of susceptibility induced broadening such that individual metabolites may be identified and correlated with disease states.

Characterization of Human Malignancies

A malignant lesion exhibits unregulated growth characteristics both at primary and secondary (metastatic) sites. Initial attempts to characterize and understand tumor development and progression hinged therefore on lesion morphology and, as such, on histopathology using the light microscope, which has been the medical diagnostic “gold standard” for much of the 20th century. With the discovery of DNA and the advent of molecular genetics it became evident that tumor morphology represented only a single variable in the characterization of malignancies and could not report on risk factors or on the biological potential of a lesion. Predicting tumor behavior is essential for determining optimal disease management protocols and it is proteomics and spectroscopic metabolite profiling that have the potential to provide the information necessary for this endeavor. Metabolite profiling data, thus far, has been generated predominantly by studies involving MR spectroscopy and mass-spectrometry.

Specific Limitations of Histopathology

The principal limitation of histopathology is the restricted range of morphological changes that tissues can express. Pathologists attempt to extract a sophisticated pattern specific for an individual disease process from a continuum of morphological changes. These patterns overlap,

Graham A. Webb (ed.), Modern Magnetic Resonance, 1051–1064.
© 2008 *Springer.*

are susceptible to subjective assessment, and may be altered by sampling error. Patient assessment involves histological grading and clinicopathological staging. Tumor grading attempts to establish the aggressiveness of the tumor based on the degree of differentiation, or anaplasia, of tumor cells. However, such a distinction is subjective and often inconclusive. Staging of cancer determines the extent and spread of the disease, but it is unable to distinguish between recent but aggressive primary tumors and older but more slowly growing ones since clinical presentation of patients does not usually reveal how long a neoplasm has been present. Adequate staging of disease is often problematic. For instance, histopathological assessment of lymph nodes is subject to observer and sampling errors due to the large volumes of tissue to be assessed and the time and resource constraints that prevent thorough and complete examination. A retrospective study revealed that: "Serial sectioning of lymph nodes judged to be disease-free after routine examination revealed micrometastases in an additional 83 (9%) of 921 breast cancer subjects" [5].

Current histopathology has shown both conceptual and procedural inadequacies in providing optimal medical diagnosis. The development of new modalities capable of improving the accuracy of disease diagnosis is needed.

Cancer Pathology Determined by Conventional ^{1}H MRS

Conventional MRS measures cellular chemicals that are mobile on the MR time scale and their variations with changes in physiological or pathological function [6]. Although restricted by achievable spectral resolutions due to susceptibility induced broadening of resonances, many promising results have been obtained from conventional proton MRS studies of human malignant tissue and fine needle aspiration biopsies. The potential for diagnoses of malignant diseases in many organs has been demonstrated and more importantly, metabolic changes have been reported that were not morphologically manifested [7,8]. A study of aspiration biopsies from primary breast tumors not only determined diagnosis, but also reported on nodal involvement and tumor vascularization [9]. The sensitivity of MRS was demonstrated in a study using a rat model for lymph node metastasis where malignant cells in lymph nodes were detected with a greater sensitivity than histology. Micrometastases were detected that were not apparent even when the entire node was serially sectioned for examination by histology. The MR diagnoses were confirmed to be correct by xenografting nodal tissue into nude mice [10].

Historically, the limitation in spectral resolution of conventional proton MRS of tissue samples was realized as an obstacle to the identification of detailed cellular metabolism. A number of procedures, including sample packing and chemical extraction of tissue were investigated as ways to improve spectral resolution [11]. While solutions of tissue extracts did produce high-resolution spectra, the process was destructive and was found to alter the spectroscopic results to an unknown degree, depending on the procedure used and the thoroughness of extraction. Therefore, neither broad-line tissue analyses nor high-resolution measurements of extracts have been able to successfully evaluate malignant disease or exemplify the advantages of proton MRS in metabolite identification.

Methodology

Limited spectral resolution is a common problem in solid-state MRS for which many techniques have been proposed and tested. Among these magic angle spinning (MAS), a line-narrowing technique, was invented after the realization of the angle-dependent characteristics of the so-called "solid effects" that broaden the resonance lines [12,13]. These "effects" classically include dipolar coupling and chemical shift anisotropy, which always exist in solids. It was later shown that MAS could also reduce resonance line-broadenings caused by bulk magnetic susceptibility [14]. Specifically, in solids, spectral broadening due to these effects follows $(3\cos^2\theta - 1)$, where θ is the angle between the static magnetic field and the internuclear vector. Therefore, if a sample is spun mechanically at the "magic angle ($54°44'$, i.e. $3\cos^2(54°44') - 1 = 0$)," and at a rate faster than the broadening originating from these effects, the contribution of these effects to the spectral broadening can be reduced [15].

The HRMAS Method

The term HRMAS is currently used to refer to proton MRS of non-solution samples, such as biological tissues and cells, obtained with the application of MAS. It is important to note, however, that there are conceptual differences between classical MAS and tissue HRMAS used with proton spectroscopy [16]. The targets of MAS in classical proton solid-state studies are chemical shift anisotropies and dipolar couplings that are in ordinary solids >50 kHz. The application of MAS in solid-state studies has involved the use of high spinning rates and strong radio-frequency pulses in an attempt to decouple these homonuclear interactions. This is not the case, however, for the MAS study of cellular metabolites in biological tissues. Here, water-soluble molecules reside in the cytoplasm wherein their motion is restricted by magnetic susceptibilities caused by various interfaces with other cell structures and by inherent viscosity. Although classical "solid-effects" exist, for instance within cell membranes, they would contribute only to an almost invisible spectral background that is too broad (~50 kHz) to be measurable in a typical HRMAS spectrum of metabolites (~5 kHz, or 10 ppm on a 500 MHz spectrometer). Overall, the magnitude of line-broadenings due to magnetic susceptibility is approximately 10^3 less than that caused by "solid-effects," and can be greatly reduced by MAS.

Experimental

Sample Preparation

Fresh and previously frozen samples may be measured directly with HRMAS MRS [17–21]. For the purpose of preserving the metabolite concentrations within tissues, samples should not be collected or stored in any liquid medium. In cases where the size of frozen tissue exceeds the sample size required for HRMAS MRS analysis, samples must be cut on a frozen surface to avoid multiple freezing and thawing. Such a surface can be made with a thin metal plate, covered with gauze and placed on top of dry ice.

Tissue samples may be washed briefly with D_2O prior to spectroscopy if they contain visible amounts of blood. However, exposure to D_2O should be brief to minimize the possible loss of cellular metabolites [22]. We have observed complete depletion of metabolites for human prostate samples (~10 mg blocks) submerged in ~2 ml D_2O for approximately 10 min.

As always, when working with human materials of potential biohazard, universal precautions need to be practiced at all times. In particular, tissue samples will undergo spinning and even at "slow spinning speeds" of less than 1 kHz, tissue fluid can leak from the rotor cap if the cap is not in tight-fit with the rotor (Figure 1). Thus the compatibility and seal between rotor and cap should be tested using a D_2O solution prior to tissue analysis. The test can be done by comparing the weights of the rotor with solution before and after HRMAS using the same experimental conditions (temperature and spinning speed) used for tissue analysis.

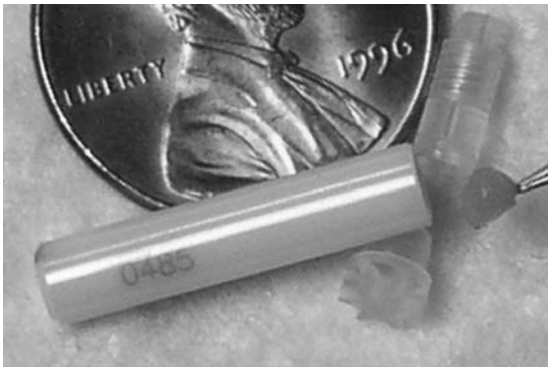

Fig. 1. Photograph of the rotor and a typical biopsy tissue sample that will be placed in the rotor using the tweezers for HRMAS MRS analysis.

To maximize spectral resolution, tissue samples should be limited to the physical boundaries of the receiving coils; for example by using Kel-F inserts to create a spherical sample when measuring samples on a Bruker spectrometer (Bruker BioSpin Corp., Billerica, MA). The use of a spherical sample is recommended for it minimizes shimming efforts as well as reduces the effect of the magnetic field inhomogeneity on the broadening of spectral lines.

Spectrometer Settings

Before tissue measurements, the HRMAS probe should be adjusted for its magic angle with potassium bromine (KBr) following the manufacturer's protocol for solid-state MRS. Ideally, measurements should be made at a low temperature (e.g. 4 °C) to reduce tissue degradation during acquisition.

The optimal spinning rate should be decided after consideration of several factors, including tissue type, metabolites of interest, and the plan for the tissue after HRMAS MRS analysis. Generally, the higher the spinning rate, up to 10 KHz as reported in the literature, the better the spectral resolution [23]. However, since high spinning rates can function as a centrifuge that can potentially disrupt tissue structures, if subsequent histopathological evaluation of the tissue is critical to the study, spinning rates must be reduced to limit any structural damage of the tissue that may interfere with histopathology. It is important to note that different tissue types endure different levels of stress. For instance, for the same spinning rate, skin tissue may be perfectly preserved in structure, while brain tissue can be completely destroyed. On the other hand, if less mobile metabolites such as lipids are the focus of HRMAS MRS evaluation, faster spinning rates may be necessary. The preservation of tissue architectures during HRMAS MRS is often critical and, as such, a number of studies have explored HRMAS MRS tissue analysis using moderate to slow spinning conditions [24–27]. These studies aimed to suppress spinning side bands (SSB) that overlapped with metabolite spectral regions of interest, using spinning rates that were not fast enough to "push" the 1st SSB beyond these regions. Interested readers should test these reported techniques for applicability to their specific tissue systems.

Optimal probe shimming is another critical factor that directly affects achievable spectral resolution. We have found that shimming on the lock or tissue water signal was not as sensitive as shimming on the splitting of the lactate doublet at 1.33 ppm, which fortunately presents in most excised biological tissues. However, in order to shim interactively on the degree of splitting, it is necessary to work with the frequency domain. This should not present a challenge to most current spectrometers. Furthermore, it should be possible to establish autoshimming protocols based on this criterion.

It is now accepted that malignancy related cellular marker metabolites may not present simply as present or absent, but rather as continuous changes in intensity throughout disease development and progression. Quantification of these metabolites can be extremely important if they are to accurately diagnose and characterize stages of disease. Metabolite concentrations may be estimated from HRMAS MR spectra by using either the intensity of tissue water signals or an external standard (e.g. a small piece of silicone rubber) permanently attached to the inside of the rotor or attached to the rotor inserts. Such an external standard can be calibrated with known compounds of known concentrations. Interested readers can make such compounds by dissolving known amounts of relevant metabolites in agarose gel.

HRMAS MR spectra may be acquired with or without water suppression, depending on whether water intensities are required for the estimation of metabolite concentrations. A rotor-synchronized CPMG sequence may be applied to achieve a flat spectral baseline if there are undesired broad resonances from the probe background.

Histopathology

The clinical utility of high-resolution tissue metabolite profiles obtained with HRMAS MRS needs to be investigated and validated by means of accurate and detailed correlation with serial-section tissue pathologies. Such correlations are particularly important for studies of human malignancies due to the heterogeneity that may be inherent in the disease. Tissue pathology can vary greatly from region to region within a single tumor, and intertumor differences may be even more pronounced. An obvious advantage of HRMAS MRS is its preservation of tissue for subsequent histopathological analyses, allowing the establishment of correlations between metabolite profiles and quantitative pathologies [28–30].

Routine clinical histopathology data is most often inadequate. Routine histopathology, in particular 5 micron slices of the tissue biopsy, provides information about the presence or absence of certain features. These features may vary from slice to slice and therefore information from a small percentage of the tissue may not correlate with the spectral profile, which consists of the weighted sum of the profiles from all tissue slices or indeed the entire piece of tissue. Hence, for certain types of tissues, particularly neoplasm samples with known heterogeneities, histopathology needs to be evaluated quantitatively. This can be achieved laboriously by the histopathologist's examining serially sectioned tissue slices or possibly with the assistance of computer image analysis of these same sections. The sectioning frequency differs with tissue type and should be determined in consultation with the pathologist. For instance, the optimal sectioning frequency for human prostate was found to be between 200 ∼ 400 μm.

Data Analysis

Histopathological analysis in cancer diagnosis relies on the observation of variations in colors and shapes using a light microscope. Importantly, to suspect disease the pathologist must observe widespread rather than isolated changes in color and/or shape, a process requiring keen pattern recognition. Similarly, pattern recognition methods are most often required to allow the diagnosis of malignancy from MRS tissue metabolite profiles. Development and progression of malignant disease involves the simultaneous evolution of many metabolic processes. Therefore, although some individual metabolites have been reported to correlate with disease types and stages [1,2] it is more likely that the overall metabolite profile rather than changes in single metabolites will be sensitive and specific for disease diagnosis [31,32]. Sophisticated statistical classification strategies (SCS) have been developed and applied to the analysis of conventional MRS of malignant tissues [33]. To date, however, principal component analysis (PCA) using readily available statistical programs has been sufficient for revealing accurate diagnostic information from HRMAS MRS data [34,35]. However, the application of SCS may further improve these accuracies.

HRMAS MRS of Human Surgical Specimens

Over recent years, HRMAS MRS has been applied biomedically to the analysis of human surgical samples, research animal tissues, and cultured cells. The scope of the methodology presented in this section will be limited to HRMAS MRS studies of human tissues and will be presented where possible in context with preceding studies of the same tissues using conventional MRS. Although presented in this context, comparison of the sensitivities and specificities obtained using conventional and HRMAS MRS are not at this stage warranted as unlike the mature discipline of conventional MRS, HRMAS MRS is still in its infancy and has reported only studies with restricted patient numbers. Although the capability of HRMAS has been clearly demonstrated in generating high-resolution spectra from which individual metabolites can be measured and such measurements were impossible with conventional methods, studies of large patient populations, as with conventional MRS studies, that allow evaluation of the sensitivity and specificity of the method have not yet appeared in literature. Similarly, it is not as yet possible to provide the reader with one concise and optimal method for undertaking HRMAS MRS. Detailed methods are provided for each of the studies presented and these methods discussed in terms of the study aims. In an emerging discipline such as HRMAS MRS care must be taken to rigorously address methodological variables with respect to the type of tissue being analyzed and the specific information required. Increased spectral quality will most often be obtained with higher spinning speeds but this will be at the expense of tissue preservation allowing subsequent histopathological assessment of the tissue. Some tissues are less easily destroyed than others by high spinning speeds and thus preliminary experiments need to be undertaken to determine optimal parameters.

MRS analyses on tissue extracts have been studied for many years on many diseases, and have formed a large body of literature. Results from these studies are worthy of close examination and review but will not, however, be included in this review due to the following: the pathology of the tissue samples most often remains incomplete and/or the degree of extraction cannot be certain.

Brain

Human brain was the first study reported using proton HRMAS MRS to determine tissue pathology. Due to the relative motion stability and homogeneity compared to other organs, brain has dominated the development of *in vivo* MRS, and accordingly has inspired many *ex vivo* studies, primarily including neurodegenerative diseases and tumors, aimed at understanding metabolism and defining brain tissue chemistry.

The first HRMAS MRS human studies on brain tissues from autopsies described semi-quantitative evaluation of the pathology of a neurodegenerative disease, specifically Pick disease [36]. Through MRS measurements and traditional neurohistopathology, direct and semi-quantitative correlations were found to exist between the levels of N-acetyl aspartate (NAA) and the amount of surviving neurons in varying regions of examined brain as seen in Figure 2. The study also, for the first time, demonstrated that the spectral resolution of HRMAS proton MRS was comparable with that measurable with conventional proton MRS of tissue

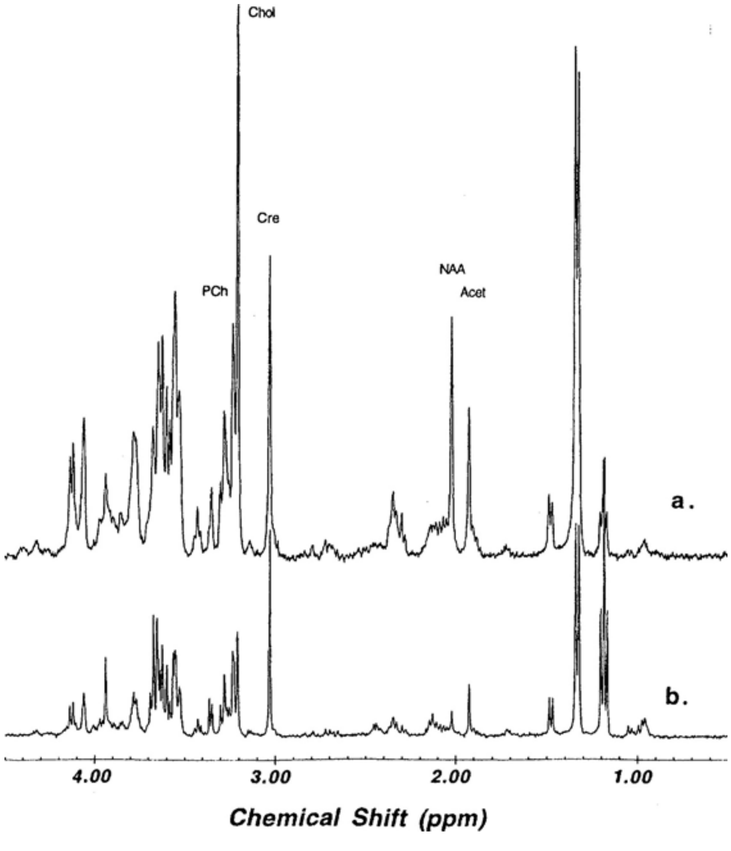

Fig. 2. Comparison of HRMAS MR spectra of brain tissue from the relatively unaffected primary visual cortex region (a) and the severely Pick disease affected rostral inferior temporal gyrus region (b), showing a marked decrease in NAA concentration, 8.48 μmol/g for spectrum a and 4.96 μmol/g for spectrum b. This decrease in NAA was found to correlate with an average neuronal count decrease of 33 neurons per 0.454 mm^2. The spectra were acquired at 2 °C, and were scaled according to concentration of creatine at 3.03 ppm for enhanced visualization. *Figure 4 from ref. [36]*

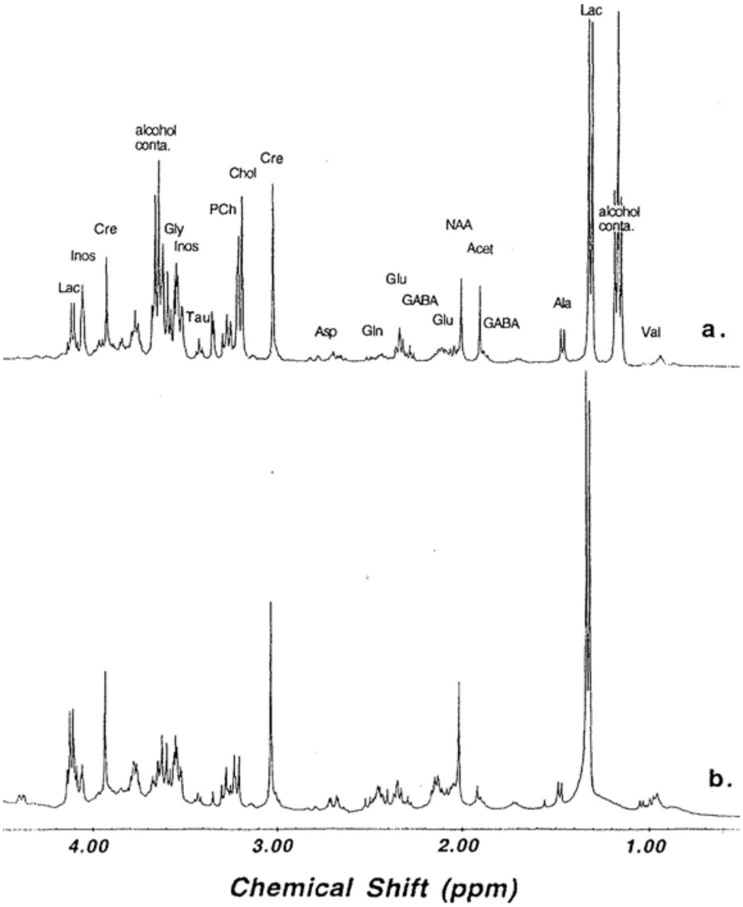

Fig. 3. Comparison of human brain proton MRS acquired with (a) HRMAS on intact tissue and (b) conventional method on extract solution. The spectral resolution was comparable while relative intensities for certain metabolites varied.

extracts (Figure 3), and superior to that obtained using conventional MRS of intact tissue (Figure 4). Another early study, also on autopsy brain tissues, correlated MRS data and stereological pathology for Alzheimer's disease and confirmed NAA concentration to be proportional to neuronal density (Figure 5). In this study, 7 human brains were examined, 3 of which were Alzheimer diseased and 4 which presented as normal human control brains. Figure 5 demonstrates the quantitative nature of the NAA and neuronal count relationship, as the correlation intercepted at zero (–0.29 ± 1.15 μmol/g) [37].

The MRS study of brain tumor intact tissues using conventional MRS suggested the diagnostic importance of lipid and lipid metabolites. Kuesel and colleagues reported correlations between MR lipid signal intensities and the amount of necrosis in astrocytomas [38]. With 42 cases, they showed that the intensity of the mobile fatty acyl –CH=CH- resonance at 5.3 ppm, differentiated 0, 1–5 and 10–40% of necrosis with statistical significance [39]. These results represented a great potential use for *ex vivo* MRS for astrocytoma diagnosis, in particular for differentiating Grade III and Grade IV tumors, which have radically different prognoses. The technique also ensured that necrotic foci often missed by clinical pathology were identified. Working with conventional MR spectra of brain tumor tissues, Rutter *et al.* attempted to categorize tumors according to 1D peak ratios (3.1–3.4 vs. 1.1–1.5 ppm), T_2 values of peaks at 1.3 ppm and cross-peaks on 2D COSY spectra (0.9 ppm with 1.35 ppm, representing methyl-methylene couplings; and 1.3 ppm with 2.05 ppm for couplings between methylene groups in fatty acids) [40]. With 38 samples studied from 33 subjects (including normal tissue, astrocytoma, GBM, meningiomas, and metastases), they were able to use peak ratios to

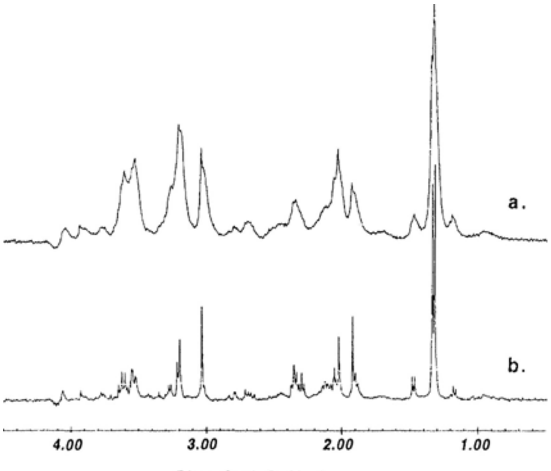

Fig. 4. Comparison of human brain proton MRS acquired with (a) conventional MRS and (b) HRMAS MRS. *Figure 2 from ref. [36].*

differentiate GBM from astrocytomas and normal tissues. They also found that the T_2 of the 1.3 ppm peak could be fitted by a double exponential function and that the long fraction of T_2 values could be used to group both GBM and metastasis from normal tissue. However, tissue spectra measured with conventional method of low resolution prevented these studies from observation of individual brain metabolites other than identification of broad lipid peaks.

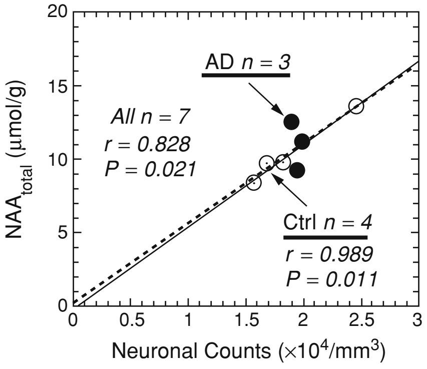

Fig. 5. A statistically significant linear correlation was found to exist between the number of neurons and the concentration of $\mathrm{NAA_{total}}$, measured from 3 Alzheimer diseased and 4 normal control brains (the dotted line, $r = 0.828$, $P = 0.021$). The solid line represents the linear correlation obtained when only normal control brains were included ($r = 0.989$, $P = 0.011$). *Figure 3 from ref. [37].*

HRMAS MRS of brain tumors allowed for the first-time detailed profiles of water-soluble metabolites and lipids to be obtained from the same spectra [31]. In a study of 19 brain tumors, including astrocytomas, GBM, meningiomas, Schwannomas, and normal brain, metabolite concentrations both in absolute units and relative ratios normalized to the creatine resonance at 3.03 ppm were reported and T_2 values for these metabolites were measured *ex vivo* for the first time (Table 1). Metabolite concentrations from intact tissues and tissue extracts from the same tumors were compared to each other and to the literature values. While the concentrations for some metabolites, measured by HRMAS MRS, were similar to those in extracts, others showed much higher concentrations in tissue than in extracts. Metabolite concentrations and T_2 values accurately differentiated tumor types based on clinical data, but detailed histopathology of the tissue samples was not performed due to the false belief at the time that HRMAS MRS damaged tissue such that subsequent histopathological analysis was not possible.

The important fact that accurate histopathological evaluation of tissue samples after HRMAS MRS is possible and the necessity of performing quantitative pathology on the same tissues after MRS was reported by Dr. Anthony and colleagues [28]. Tissue pathologies from both HRMAS MRS analyzed tissue and adjacent tissue that had not undergone HRMAS MRS before histopathological evaluation were analyzed semi-quantitatively for each region of the brain tumor. The quantitative histopathological data obtained from the study showed that adjacent specimens from the same tumor region shared similar histopathological features. Although quantitative differences were noted, these differences were most likely due to extensive tumor microheterogeity and not the result of the HRMAS MRS procedure. Futhermore, correlations between the amount of tumor necrosis and the concentrations of mobile lipids ($R^2 = 0.961$, $p < 0.020$) and lactate ($R^2 = 0.939$, $p < 0.032$), as well as between the numbers of glioma cells and the ratio of phosphocholine (PC) to choline resonances ($R^2 = 0.936$, $p < 0.033$) were observed. The strong linear correlation between tissue necrosis (%area) and lipids (mM) indicated that the amount of tissue necrosis can be estimated using the measured concentration of lipids from HRMAS MRS, and that according to the long T_2s these lipids are relatively mobile consistent with them being products of cell membrane degradation. Additionally, the results of the correlation obtained between the number of glioma cells and the phospocholine to choline resonances suggested the importance of measuring and quantifying these two resonances separately, which is difficult with both *in vivo* and *ex vivo*

Table 1: Matrix of selected brain metabolite concentrations measured with HRMAS MRS for differentiation between different pathological specimens NAA, in the table, includes both measured resonances of NAA at 2.01ppm and acetate at 1.92 ppm (see text for details); Numbers in parentheses represent resonance chemical shift in ppm. The resonance at 3.93 is tentatively assigned to the Cr metabolite. As an example of the use of this matrix, the Chol resonance can be used to differentiate low-grade/anaplastic astrocytomas from GBMs with a significance of $p < 0.05$. Similarly, the glycine resonance (Gly) can be used to distinguish GBMs from Schwannomas with a $p < 0.005$

	Normal	LG and AA[a]	GBMs	Schwannomas	Meningiomas
Normal		NAA[b] Lac (1.33)[c]	Cr (?, 3.93)[c] Gly (3.55)[d] Chol (3.20)[b] Cr (3.03)[b] NAAf Lac (1.33)[b]	Chol (3.20)[b] NAA[b] Lac (1.33)[d]	Cr (?, 3.93)[b] Chol (3.20)[e] Glu (2.35)[d] Ala (1.48)[b]
LG&AA			Chol (3.20)[e]		Glu (2.35)[b]
GBMs				Gly (3.55)[d]	Gly (3.55)[b]
Schwannomas					
Meningiomas					

[a] LG and AA, low-grade/anaplastic astrocytomas

[b] $p < 0.05$, two-tailed student's t test.

[c] $p < 0.0005$, two-tailed student's t test.

[d] $p < 0.005$, two-tailed student's t test.

[e] $p < 0.05$, calculated according to one-tailed student's t test, based on the hypothesis that chol increases in tumors.

[f] $p < 0.00005$, two-tailed student's t test.

conventional MRS methods, but readily achievable with MAS.

It is expected that HRMAS MR spectra of tissue rather than MRS of tissue extracts will provide metabolite information more closely related to that in the *in vivo* brain. However, cautions should be exercised when comparing *in vivo* MRS and HRMAS MRS data, as *in vivo* MRS will always be broad-line in nature. Nevertheless, a number of studies, both in adult [41] and pediatric [42] brain tumors, have concluded that there is good agreement between *in vivo* and *ex vivo* tissue MR spectra with high-resolution *ex vivo* results providing both insight into which metabolites reside within the broad resonances observed *in vivo* and a link between *in vivo* MRS evaluations and neuropathologies.

Prostate

The search for marker metabolites of prostate cancer has been inspired by the current state of prostate cancer pathology, wherein more than 70% of newly diagnosed cases are categorized with similar Gleason scores (6 or 7), but for which individual patient outcomes within these tumors are drastically different and unpredictable.

Hahn and colleagues reported the first intact prostate tissue conventional MRS study of 66 benign prostatic hyperplasia (BPH) and 21 prostate cancer samples from 50 patients [43]. They divided the proton spectral region between 0.5 and 3.55 ppm into 50 equal subregions, and applied multivariate linear-discriminant analysis to the point-reduced spectra. The study found six spectral regions including those containing citrate, glutamate, and taurine to be sensitive in differentiating BPH from cancer with an overall accuracy of 96.6%. This algorithm was tested by the same research group on another group of 140 samples from 35 patients after radiotherapy to test for the sensitivity of spectroscopy analysis in differentiating cancer positive vs. cancer negative samples [44]. After eliminating 24 samples that did not have sufficient signal-to-noise ratios, they reported, with the remaining 116 spectra, the sensitivity and specificity of tissue spectra in identifying cancer samples to be 88.9 and 92%, respectively.

Van der Graaf and colleagues presented another interesting study of intact prostate tissue combining conventional MRS and high-pressure liquid chromatography (HPLC) analysis to measure the relationship between polyamines (PA) and prostate cancer [45]. Although they observed PA in the proton spectra and measured statistically significant drops of PA in cancer samples with HPLC, no correlation between PA levels measured by MRS and those determined by HPLC were presented for the same cases due to very limited number of samples analyzed. Nevertheless, the study suggested the existence

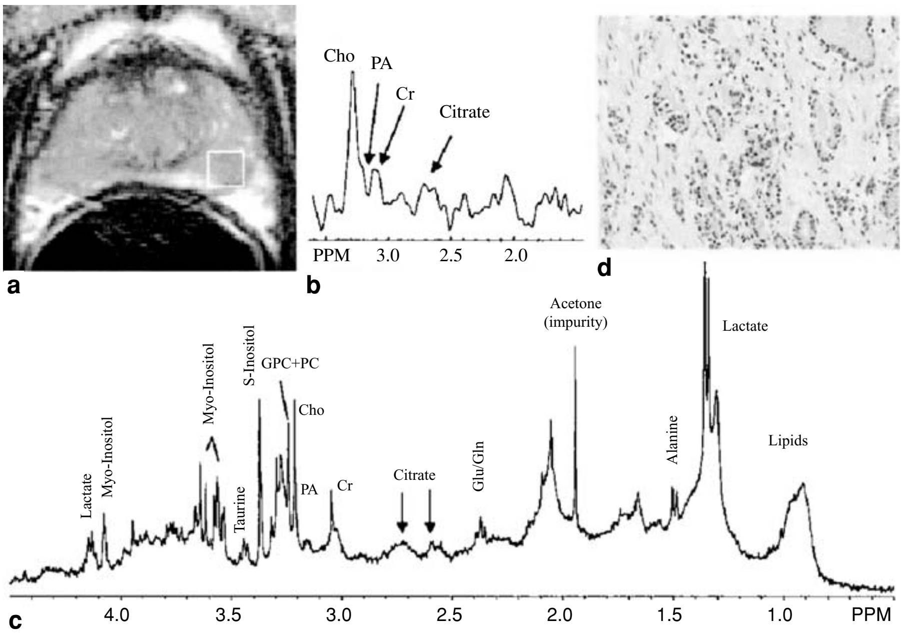

Fig. 6. Results from a presurgical 3D-MRSI of a 56-year-old prostate cancer patient were concordant with histopathologically classified malignancy of H and E stained tissue samples of excised tissue with Gleason 3 + 4 prostate cancer, **d**. Spectrum **b**, shows elevated levels of choline and low levels of citrate and polyamines relative to creatine in the 0.24 cm3 voxel of **a**. The postsurgical HRMAS MR spectrum (c) confirms the 3D-MRSI results with enhanced resolution that also identifies elevated levels of GPC + PC relative to choline. *Figure 2 from ref. [30].* (See also Plate 88 on page XVI in the Color Plate Section.)

of a potential prostate biomarker that MRS may be able to quantify, as well as a direction for future studies. More recently, Mountford *et al.* reported a conventional MRS study of 71 prostate samples from 41 patients who underwent both cancer and non-cancer prostate surgeries [46]. By using peak ratios 3.2/3.0 ppm (choline-to-creatine) and 1.3/1.7 ppm (lipid-to-lysine), they were able to differentiate malignant from benign tissues with 97% sensitivity and 88% specificity.

Tomlins and colleagues experimented with proton HRMAS MRS analysis on human prostate tissues with both 1D and 2D MR spectroscopy. In their qualitative report, they confirmed the usefulness of HRMAS MRS in producing high-resolution spectra from intact human prostate tissues [47]. A second HRMAS MRS study of human prostate tissues from 16 patients was the first to include quantitative pathology on the MRS specimens and to include multiple subjects [29]. The results of the study proved the validity of HRMAS MRS for the accurate determination of tissue histopathology. Both citrate and spermine were quantified from the tissue HRMAS MR spectra and shown to be linearly correlated with the amounts of prostate normal epithelium. In 2003, Swanson and colleagues reported an interesting study of HRMAS MRS of tissues from 26 patients harvested post surgically under the guidance of 3D-MRSI from lesions that had been analyzed using *in vivo* MRS prior to prostatectomy. Figure 6 shows the resulting spectra from a 56-year-old prostate cancer patient [30]. By combining the MRS results with quantitative pathology of the same tissue after spectroscopy, metabolite discriminators (i.e. ratios of citrate, polyamine, and choline compounds to creatine) were found to differentiate normal prostate epithelial tissue from cancer and stromal tissue. Furthermore, a correlation between the intensity of MIB-1 immunohistochemical staining and the ratio of choline to creatine resonances was reported, supporting their findings *in vivo*. These results were dependent on the assumption that the creatine concentration did not alter during the disease process, which awaits verification.

Breast

Human breast tissue was difficult to analyze using conventional proton MRS due to high lipid content. As pioneers of this work, Mountford and colleagues noted that to acquire a spectrum that was diagnostically meaningful, fine-needle aspiration biopsy (FNAB) instead of regular tissue samples had to be utilized [48]. In a study of 218 FNAB samples from 191 patients with benign lesions, ductal carcinoma *in situ* (DCIS), and invasive carcinoma, they found that by using the resonance peak height ratio threshold of 1.7 (3.25 vs. 3.05 ppm; or choline-compounds vs. creatine), benign lesions could be differentiated from carcinoma with 95% sensitivity and 96% specificity. However, this single ratio identifier only worked if the signal-to-noise ratio, particularly for choline peaks at 3.25 ppm, was above 10. To extend the MRS differentiation capability below this limit, and more importantly to search for a more robust diagnostic protocol of computerized spectral analysis, Mountford *et al.*, along with Smith *et al.* at the NRC, Canada, used a pattern recognition method, SCS, developed to utilize the entire MR spectrum instead of only the aforementioned two peaks for the purpose of analysis [9]. From measurements conducted on 140 samples, they reported an overall accuracy of 93% in distinguishing benign from malignant tumors using SCS. Furthermore, they reported that using SCS classifiers, lymph node involvement and tumor vascular invasion could be predicted with 95 and 94% overall accuracies, respectively. The advantage of SCS in relating proton FNAB spectra with breast cancer diagnosis and possibly prognosis is evident and its potential in clinical usage is apparent. However, the more advanced the SCS, the less evident were the direct connections with individual metabolites.

HRMAS MRS overcame many of the limitations of conventional MRS32. Even with such lipid-rich tissue, HRMAS MRS successfully produced high-resolution proton spectra. Results from a study at 400 MHz of 19 cases of ductal carcinomas showed that both the high fat contents and individual cellular metabolites could be measured from the same spectrum. Particularly, from these spectra, PC could be quantified separately from choline; and the ratio between PC and choline was found to correlate with tumor grades, as shown in Figure 7.

A more recent detailed HRMAS MRS study at 600 MHz of 10 ductal carcinomas by Sitter *et al.* compared HRMAS MR spectra with those obtained using conventional MRS of perchloric acid tissue extracts [20]. The study concluded that for breast tissue, HRMAS MRS was able to achieve spectral resolutions approaching those obtained using conventional MRS of extracts. 2D J-resolved and COSY MRS was used to accurately assign metabolites.

Cervix

Mountford and colleagues began analysis of human cervical biopsies with conventional proton MRS in the early 1990s [49]. Broad-line resonances at 0.9 ppm (CH3), 1.3 ppm (CH2), and 3.8–4.2 ppm (CH) were found to distinguish invasive from pre-invasive epithelial malignancy [50].

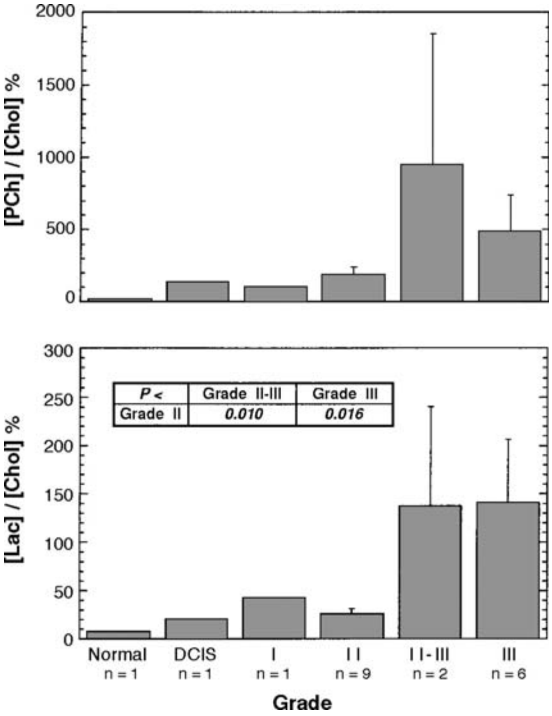

Fig. 7. Examples of observed correlations between histopathological grades of breast ductal carcinomas and the means for metabolic intensities, particularly PC over choline (A) and lactate over choline (B) measured with HRMAS MRS. Of note, the HRMAS method provided a means to differentiate PC from choline in the such a lipid-rich tissue. *Figure 4 from ref. [32].*

More recently, Sitter and colleagues reported the use of HRMAS MRS of cervical tissue from eight cancer and eight non-cancer patients [.35]. In addition to their presentation of detailed resonance assignments for cervical metabolites, they were able to use PCA to separate cancer from non-cancer samples with the first principal component (PC1). This principal component was comprised primarily of lactate, the methyl, and methylene groups of lipids, and, to a lesser extent, the choline-containing compounds. This component represented 63% of the variations in the spectra.

Kidney

HRMAS MRS analysis of kidney tissue has been shown to diagnose renal cell carcinoma based on an increased intensity of lipid resonances in malignant compared to

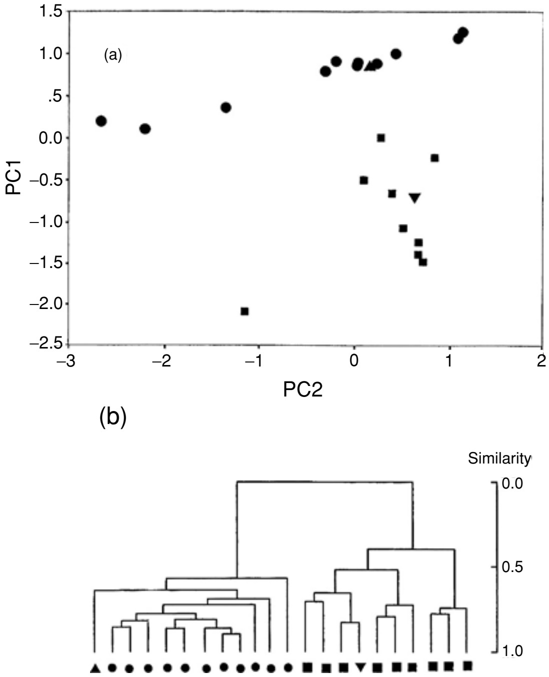

Fig. 8. Using PCA (a) and HCA (b), tumor samples can be differentiated from non-tumor samples. Key: (•) normal tissue; (■) renal cell carcinoma; (▲) sample from bladder metastasis in renal collecting duct; and (▼) lung metastasis in renal cortex. *Figure 3 from ref. [.35].*

control tissues [51,52]. These studies were not designed to test the utility of HRMAS MRS in the diagnosis of renal cell carcinoma, but rather to illustrate the feasibility of HRMAS MRS for assignment of resonances and identification of metabolites as well as to develop two-dimensional HRMAS MRS techniques for the assessment of intact tissues.

Later, a study of 22 paired control and tumor samples of human renal cortex used computer-based pattern recognition techniques to show that using PCA and hierarchical cluster analysis (HCA), tumor samples were differentiated from non-tumor samples, as shown in Figure 8 [34].

Sarcoma

HRMAS MRS has been shown to be a useful technique in the analysis of human sarcoma tissue. Singer and colleagues reported a comparison of 2D TOCSY spectra with and without HRMAS MRS, which demonstrated the superior resolution of the MAS technique by revealing less intense cross peaks that were not observed when the sample was not spun [53,54]. For this initial study, spectra of liposarcoma and lipoma were dominated by signals from lipids, interfering with the ability to observe resonances from other metabolites. More recently, Chen and colleagues have developed a double pulsed field gradient selective echo (DPFGSE) technique in combination with HRMAS MRS to selectively excite spectral regions that contain less abundant non-lipid metabolites [23]. With their new technique they were able to observe and quantify phosphatidylcholine (PTC), PC and choline, and found, using six paired samples from six patients, that the ratio of PTC/PC differentiated normal fat from lipoma-like well-differentiated liposarcoma with statistical significance ($p < 0.001$).

Lymph Nodes

Accurate detection of metastatic deposits in lymph nodes is often the most important predictor of cancer patient prognosis. Histopathology is subject to sampling and observer error and thus there is a real need for a new, rapid, and cost-effective method with high accuracy for this purpose.

An early study identifying malignant cells in lymph node tissue using 1D ^{1}H MRS was limited by high fat content of the tissue and the low spectral resolution obtained. Two-dimensional (2D) techniques successfully resolved resonances and allowed the complex spectra from lymph nodes to be assigned and correlated with detailed histopathology [10]. Choline and lactate were found to be key metabolites diagnostic of the presence of metastases in lymph nodes using the 2D method. However, these 2D MR experiments require long acquisition times (4–5 h) during which sample degradation may occur, potentially compromising the outcome of the measurement. In addition, conventional 1D and 2D techniques cannot address the problem of resonance broadening directly and thus useful diagnostic information may be missed.

Alternatively, MRS of FNAB of lymph node tissues has been used to diagnose the presence of metastases in lymph nodes from melanoma patients [55]. Spectra of node tissue containing metastatic melanoma were characterized by the presence of a distinct resonance from choline-containing metabolites at 3.2 ppm. The ratio of the integrals of resonances from lipid and metabolites (1.8–2.5 ppm region) and "choline" (3.1–3.3 ppm region) distinguished benign nodes (38.8 ± 34.3) from melanoma containing nodes (7.2 ± 6.8) with $p < 0.012$ (separate t-test) [55]. This method assumes the chemistry of the node detectable by MRS changes immediately upon the node being infiltrated by metastatic cells. This is supported by studies in a rat lymph node metastasis model where MRS detected the presence of malignant cells prior to clusters of metastatic cells being identified by histopathology.

Instead, single malignant cells were observed unclustered throughout the node, the presence of which was confirmed by growing these nodes in nude mice, which subsequently developed tumors. Datasets in the study of MRS on FNAB as a method of diagnosing lymph node metastases remain, however, small and until larger databases confirm these findings the possibility that the method introduces a sampling error cannot be excluded.

The application of HRMAS MRS to intact tissue analysis was in fact initiated from the proton MR detection of lymph node metastases in a rat model for breast cancer metastasis. Since then, HRMAS MRS has also been successfully applied to the proton MR analyses of human lymph nodes from breast cancer patients. Malignant nodes were distinguished from reactive nodes based on the peak height ratio of the smallest to largest peaks resolved in the 0.9 ppm resonance multiplied by the peak height ratio of the choline and creatine resonances at 3.2 and 3.0 ppm, respectively (Figure 9). Three of four axillary nodes from breast cancer patients that were clinically suspicious but diagnosed cancer free on routine histopathology had an HRMAS MRS ratio consistent with reactive nodes. The fourth node in this category was, by HRMAS MRS criteria, malignant. Review of the histology of these nodes using increased magnification and immunohistochemical staining identified malignancy in the fourth node missed during routine examination.

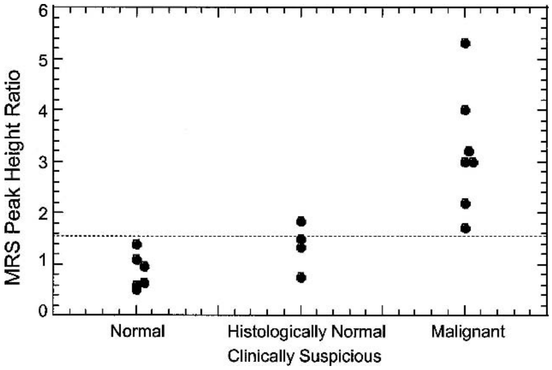

Fig. 9. HRMAS MRS of Human Lymph Nodes: Malignant nodes were distinguished from normal (reactive) nodes based on the MRS Peak Height Ratio (ratio of the smallest to largest peaks resolved in the 0.9 ppm resonance multiplied by the ratio of the choline and creatine resonances at 3.2 and 3.0 ppm). One of four axillary nodes that were clinically suspicious but cancer free on routine histopathology had an HRMAS MRS ratio consistent with malignancy. Review of the histology for all four nodes identified malignancy in this one node missed by routine histopathology.

Future Developments and Conclusions

The development of proton HRMAS MRS for tissue analysis has not only drastically simplified the procedure of obtaining high resolution cellular metabolite spectra directly from intact tissue, but more importantly allows quantitative pathology to be conducted on the same tissue after MRS measurements for correlation with individual metabolite concentrations or collective alterations in overall metabolite profiles. The high-resolution spectra generated by HRMAS MRS contain many more resonance peaks for analysis than conventional MRS. This greatly improves the likelihood that sophisticated data analysis methods can accurately distinguish between differing pathologies. However, the increased discriminatory power of the method relies on precise histopatholgical information about the tissue assessed by HRMAS MRS being available. This is only possible when detailed serial section histopathological methods are undertaken to substantially increase the precision of the information currently obtained from clinical pathology.

Glossary of Terms

Astrocytoma—The most common type of brain tumor in adults; astrocytomas, known for their marked potential for malignant progression and infiltrative nature, can be classified histopathologically into three grade of malignancy: WHO Grade II astrocytoma, WHO Grade III anaplastic astrocytoma, and WHO Grade IV GBM.

Benign Prostatic Hyperplasia—Enlargement of the prostate and more specifically, overgrowth of the epithelium and fibromuscular tissue of the transition zone and periurethral area.

Ductal Carcinoma *In Situ*—Noninfiltrative lesions composed of malignant epithelial cells that are confined to the mammary ducts and lobules.

Glioblastoma Multiforme—The most malignant grade of astrocytoma (WHO Grade IV), which has an overall survival time of less than 2 years for most patients. These tumors are histopathologically characterized according to their dense cellularity, high proliferative indices, endothelial proliferation, and most importantly the presence of focal tissue necrosis.

Lipoma—Commonly diagnosed benign tumors of adipose tissue that can develop anywhere in the body where fat is normally found.

Liposarcoma—A commonly diagnosed soft tissue sarcoma in adults which be found anywhere in the body and for which there exists several types with varying clinical outcomes.

Meningioma—Intracranial tumors that arise in the meninges and compress the underlying brain. In general, many of these tumors are benign, however, others are malignant with the capability to metastasize, both locally and distally.

Metabolite Profiling—The study of small molecules, such as lipids, peptides, amino acids, and carbohydrates, which represent steady-state concentrations of intermediate products or end products of cellular processes and as a result can be thought of as the ultimate response to genetic and environmental stimuli.

Necrosis—Tissue and/or cell death.

Neoplasm—Literally meaning "new growth." An abnormal growth of tissue which may be benign or malignant.

Oncogenomics—The study of genes, gene sequences, and the underlying genetic alterations that appear to be involved in oncological pathways.

Reactive Nodes—Lymph nodes that have been immunologically challenged.

Schwannoma—Benign tumors that arise on peripheral nerves in general and on cranial nerves in particular, especially on the vestibular portion of the eighth cranial nerve.

Sensitivity—The term relating to the percentage of people with disease who test positive for the disease, i.e. the percentage of patients with cancer who have positive biopsy results.

Specificity—The term referring to the percentage of people without disease who test negative for the disease, i.e. patients without cancer with cancer negative biopsy results.

Acknowledgments

The authors thank their former and present staff, students, and collaborators involved in the research presented in this review whom have all worked diligently towards developing MRS and HRMAS MRS for determining tissue pathology. We also thank our colleagues and friends from around the world for allowing us to describe their work and for their many interesting discussions and contributions to this review. Particular thanks to Carolyn Mountford, Peter Russell, and Peter Malycha for their encouragement and support. We thank Sinead Doran and Deborah Edward for helping prepare the manuscript. LLC and MAB acknowledge grant supports from PHS/NIH CA095624 and from DOD W81XWH-04-1-0190.

References

1. Mountford C, Doran S, Lean C, Russell P. Chem. Rev. 2004;104:3677.
2. Lean C, Somorja R, Smith I, Russell P, Mountford C. In: AG Webb (Ed). Accurate Diagnosis and Prognosis of Human Cancers by Proton MRS and A Three Stage Classification Strategy. Guildford, UK, 2002.
3. Pomper MG. In VT DeVita Jr, S Hellman, SA Rosenberg (Ed). Functional and Metabolic Imaging. Philadelphia, 2001.
4. Nicholson JK, Lindon JC, Holmes E. Xenobiotica 1999;29:1181.
5. Bettelheim R. Price K, Gelber R, Davis B, Castiglione M, Goldhirsch A, Neville A, Lancet 1990;335:1565.
6. Mountford CE, Lean CL, Mackinnon WB, Russell P. In GA Webb (Ed). The Use of Proton MR in Cancer Pathology in Annual Reports on NMR Spectroscopy. Academic Press. London 1993;27:173.
7. Russell P, Lean C, Delbridge L, May G, Dowd S, CE Mountford Am. J. Med. 1994;96:383.
8. Doran ST, Falk GL, Somorjai RL, Lean CL, Himmelreich U, Philips J, Russell P, Dolenko B, Nikulin AE, Mountford CE. Am. J. Surg. 2003;185:232.
9. Mountford CE, Somorjai RL, Malycha P, Gluch L, Lean C, Russell P, Barraclough B, Gillett D, Himmelreich U, Dolenko B, Nikulin AE, Smith IC. Br. J. Surg. 2001;88:1234.
10. Mountford C, Lean C, Hancock R, Dowd S, Mackinnon W, Tattersall M, Russell P. Invasion and Metastasis, 1993;13:57.
11. Kuesel A, Kroft T, Saunders J, Prefontaine M, Mikhael N, Smith I. Magn. Reson. Med. 1992;27:340.
12. Andrew E, Bradbury A, Eades R. Nature 1958;182:1695.
13. Lowe I. Phy. Rev. Lett. 1959;2:285.
14. VanderHart D, Earl W, Garroway A. J. Magn. Reson. 1981;44:361.
15. Maricq M, Waugh J. J. Chem. Phys. 1979;70:3300.
16. Cheng LL, Lean CL, Bogdanova A, Wright SC Jr, Ackerman JL, Brady TJ, Garrido L. Magn Reson Med. 1996;36:653.
17. Middleton DA, Bradley DP, Connor SC, Mullins PG, Reid DG, Magn. Reson. Med. 1998;40:166.
18. Garrod S, Humpfer E, Spraul M, Connor SC, Polley S, Connelly J, Lindon JC, Nicholson JK, Holmes E. Magn. Reson. Med. 1999;41:1108.
19. Waters NJ, Garrod S, Farrant RD, Haselden JN, Connor SC, Connelly J, Lindon JC, Holmes E, Nicholson JK. Anal. Biochem. 2000;282:16.
20. Sitter B, Sonnewald U, Spraul M, Fjosne HE, Gribbestad IS. NMR Biomed. 2002;15:327.
21. Wu CL, Taylor JL, He WL, Zepeda AG, Halpern EF, Bielecki A, Gonzalez RG, Cheng LL. Magn. Reson. Med. 2003;50:1307–1311.
22. Bourne R, Dzendrowskyj T, Mountford C. NMR Biomed. 2003;16:96.
23. Chen JH, Enloe BM, Fletcher CD, Cory DG, Singer S. J. Am. Chem. Soc. 2001;123:9200.
24. Wind RA, Hu JZ, Rommereim DN. Magn. Reson. Med. 2001;46:213.
25. Hu JZ, Rommereim DN, Wind RA. Magn. Reson. Med. 2002;47:829.
26. Hu JZ, Wind RA. J. Magn. Reson. 2003;163:149.
27. Taylor JL, Wu CL, Cory D, Gonzalez RG, Bielecki A, Cheng LL. Magn. Reson. Med. 2003;50:627.
28. Cheng LL, Anthony DC, Comite AR, Black PM, Tzika AA, Gonzalez RG, Neuro-oncol. 2000;2:87.
29. Cheng LL, Wu C, Smith MR, Gonzalez RG. FEBS Lett. 2001;494:112.
30. Swanson MG, Vigneron DB, Tabatabai ZL, Males RG, Schmitt L, Carroll PR, James JK, Hurd RE, Kurhanewicz J. Magn. Reson. Med. 2003;50:944.

31. Cheng LL, Chang IW, Louis DN, Gonzalez RG. Cancer Res. 1998;58:1825.
32. Cheng LL, Chang IW, Smith BL, Gonzalez RG. J. Magn. Reson. 1998;135:194.
33. Somorjai R, Dolenko B, Nikulin A, Pizzi N, Scarth G, Zhilkin P, Halliday W, Fewer D, Hill N, Ross I, West M, Smith I, Donnelly S, Kuesel A, Briere K. J. Magn. Reson. Imaging. 1996;6:437.
34. Tate AR, Foxall PJ, Holmes E, Moka D, Spraul M, Nicholson JK, Lindon JC. NMR Biomed. 2000;13:64.
35. Sitter B, Bathen T, Hagen B, Arentz C, Skjeldestad FE, Gribbestad IS. MAGMA. 2004;16:174.
36. Cheng LL, Ma MJ, Becerra L, Ptak T, Tracey I, Lackner A, Gonzalez RG. Proc. Natl. Acad. Sci. U.S.A. 1997;94:6408.
37. Cheng LL, Newell K, Mallory AE, Hyman BT, Gonzalez RG. Magn. Reson. Imag. 2002;20:527.
38. Kuesel A, Donnelly S, Halliday W, Sutherland G, Smith I. NMR Biomed. 1994;7:172.
39. Kuesel AC, Briere KM, Halliday WC, Sutherland GR, Donnelly SM, Smith ICP. Anticancer Res. 1996;16:1485.
40. Rutter A, Hugenholtz H, Saunders J, Smith I. J. Neurochem. 1995;64:1655.
41. Barton SJ, Howe FA, Tomlins AM, Cudlip SA, Nicholson JK, Bell BA, Griffiths JR. Magma 1999;8:121.
42. Tzika AA, Cheng LL, Goumnerova L, Madsen JR, Zurakowski D, Astrakas LG, Zarifi MK, Scott RM, Anthony DC, Gonzalez RG, Black PM. J. Neurosurg. 2002;96:1023.
43. Hahn P, Smith I, Leboldus L, Littman C, Somorjai R, Bezabeh T. Cancer Res. 1997;57:3398.
44. Menard C, Smith IC, Somorjai RL, Leboldus L, Patel R, Littman C, Robertson SJ, Bezabeh T. Int. J. Radia. Oncol. Biol. Phys. 2001;50:317.
45. van der Graaf M, Schipper RG, Oosterhof GO, Schalken JA, Verhofstad AA, Heerschap A. Magma 2000;10:153.
46. Swindle P, McCredie S, Russell P, Himmelreich U, Khadra M, Lean C, Mountford C. Radiology 2003;228:144.
47. Tomlins A, Foxall P, Lindon J, Lynch M, Spraul M, Everett J, Nicholson J. Analy. Common. 1998;35:113.
48. Mackinnon WB, Barry PA, Malycha PL, Gillett DJ, Russell P, Lean CL, Doran ST, Barraclough BH, Bilous M, Mountford CE. Radiology, 1997;204:661.
49. Mountford CE, Delikatny EJ, Dyne M, Holmes KT, Mackinnon WB, Ford R, Hunter JC, Truskett ID, Russell P. Magn. Reson. Med. 1990;13:324.
50. Delikatny E, Russell P, Hunter J, Hancock R, Atkinson K, van Haaften-Day C, Mountford C. Radiology, 1993;188:791.
51. Moka D, Vorreuther R, Schicha H, Spraul M, Humpfer E, Lipinski M, Foxall P, Nicholson J, Lindon J. Analy. Common. 1997;34:107.
52. Moka D, Vorreuther R, Schicha H, Spraul M, Humpfer E, Lipinski M, Foxall PJ, Nicholson JK, Lindon JC. J. Pharm. Biomed. Anal. 1998;17:125.
53. Millis KK, Maas WE, Cory DG, Singer S. Magn. Reson. Med. 1997;38:399.
54. Millis K, Weybright P, Campbell N, Fletcher JA, Fletcher CD, Cory DG, Singer S. Magn. Reson. Med. 1999;41:257.
55. Lean CL, Bourne R, Thompson JF, Scolyer RA, Stretch J, Li LX, Russell P, Mountford C. Melanoma Res. 2003;13:259.

Intraoperative MRI

Isabelle Latour and Garnette R. Sutherland
Division of Neurosurgery, Seaman Family MR Research Centre, Foothills Hospital, Calgary, AB, Canada T2N 1N4

> *Nothing is certain and everything changes*
> ——Leonardo da Vinci

Contemporary neurosurgeons depend on precise lesion localization to maximize surgery and clinical outcome. Advances in neurosurgical technique and instrumentation evolved as surgical corridors became more precise. Magnetic resonance imaging (MRI) has considerably improved the diagnosis, treatment, and follow-up of patients with neurological disease. With the widespread use of MRI, it is difficult to conceive that, before the introduction of imaging technology, neurosurgery relied on precarious tools.

Historical Milestones in Neurology

Cranial trephination was used thousands of years ago by Neolithic man to liberate individuals thought to be possessed by evil spirits [1,2]. It resurfaced as a treatment for infantile convulsions and was still performed as late as the mid-19th century for both trauma and epilepsy [3]. Franz Joseph Gall proposed that intellectual faculties are highly compartmentalized in the brain and that examination of the surface of the skull reflects the extent to which an aptitude is developed [4]. The use of scientific evidence to determine cortical compartmentalization of function was first initiated by Paul Broca [5]. The development of imaging techniques began with the discovery of X-rays by Wilhelm Röntgen in 1895. In 1918, Walter Dandy made the serendipitous discovery of intraventricular air in a patient who had suffered cranial trauma [6]. This observation led to the development of pneumoencephalography (Figure 1) as a method for localizing intracranial pathology, based on ventricular displacement by cerebral mass lesions. A decade later, Moniz introduced cerebral angiography, a method still used to visualize vascular abnormalities [7]. Ultrasound was subsequently developed as a non-invasive method of localizing central nervous system (CNS) pathology [8]. Originating from ideas of Cormack [9] and Hounsfield [10], brain imaging was revolutionized in the mid-1970s by the invention of computerized tomography (CT). This discovery significantly enhanced diagnostic accuracy and improved surgical planning and outcome. The subsequent development of MRI by Lauterbur [11] and Mansfield [12] provided enhanced tissue contrast and remains the best imaging modality for diagnosis and determining the effect of treatment on both the lesion and the brain.

Principles of Intraoperative Imaging

Intraoperative imaging allows acquisition of near real-time images in the operating room (OR). As surgery often disrupts the brain environment, acquiring instant images at any time during and after completion of the surgery represents a considerable advantage. CT imaging was introduced into the OR in 1982 [13]. The first report of intraoperative MRI (iMRI), by Black *et al.* was in 1997 [14]. The use of intraoperative CT declined following the introduction of iMRI, in part due to lower tissue contrast and image artifact due to surgery and instrumentation. MR technology confers non-invasive, radiation-free, multiplanar, real-time, high-resolution images of the nervous system. MRI systems that include magnets of $\geq$1.5 T and high performance gradients provide a unique method for the evaluation of diffusion and perfusion tensor imaging, as well as a way to assess brain function. Diffusion images measure the mobility of water molecules in tissue. As pathological states can disrupt barriers that normally restrict water motion, diffusion imaging reveals information about tissue integrity [15]. Perfusion images represent the rate at which blood is delivered to the tissue, and can therefore be used to identify areas displaying an increase or decrease in blood flow [16]. Functional MRI allows in a non-invasive way the precise identification of brain areas undergoing a sharp increase in oxygen supply induced by a certain cognitive process or task [17]. Essential components of an iMRI system are the magnet, gradients, radio frequency (RF) coil designs, the operating table, and the RF shielding. Real-time, three-dimensional (3D) navigation software allows the neurosurgeon to localize surgical instruments and intracranial targets in 3D space. This improves localization of intracranial pathology from which more minimalist approaches may be directed.

Hardware and Configuration

Three different types of magnets can be used for MRI: permanent, resistive, and superconducting. iMRI has utilized

Graham A. Webb (ed.), Modern Magnetic Resonance, 1065–1076.
© 2008 *Springer.*

Fig. 1. Coronal (A) and lateral (B) pneumoencephalography. The lateral ventricles are visible and show no evidence of displacement.

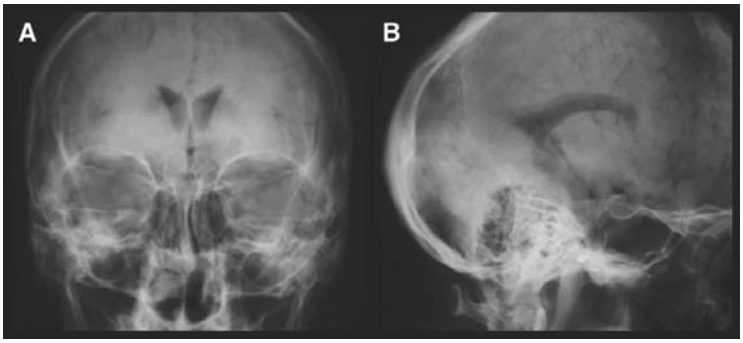

magnets of 0.12–1.5 T, with gradient strength ranging from 12 to 33 mT/m (Table 1). Gradient strength and performance is important for rapid imaging sequence, in particular echo-planar imaging (EPI), diffusion, perfusion, and fMRI. For iMRI, inductively coupled [18] or volume coils [19] can be used. The full spectrum of imaging sequences including T_1, T_2, MR angiography, diffusion, perfusion, and fluid attenuated inversion recovery (FLAIR) have been applied to the evaluation of the utility of iMRI as an adjunct to surgery. The first iMRI system, manufactured by General Electric, consisted of a 0.5 T vertical, biplanar double doughnut magnet configuration [14]. A significant advantage of this setup is that real-time images can be acquired frequently, without interrupting surgery nor having to move the patient or the magnet. Although this initial system represented a major advance in intraoperative imaging technology, it has limitations. The system requires positioning the patient and surgeon between two magnetic poles. This results in a constrained working environment, restricted patient positioning, and the requirement for MR-compatible instrumentation. Furthermore, the magnetic field strength and gradient performance are below that needed for contemporary EPI. To partly overcome these issues, 0.2 and 0.3 T, horizontal, biplanar imaging systems were produced by Siemens and Hitachi, respectively [20,21]. For these, the surgical area is located outside of the magnetic field and the patient is moved into the magnet for image acquisition. Physically separating surgery and imaging resolved the problem of operating within a magnetic field. However, this requires interruption of surgery and moving the anesthetized, monitored patient from the surgical site to the magnet. In need of better image resolution and to maintain a patient focused environment, a movable, ceiling-mounted wide bore 1.5 T magnet was developed and manufactured by IMRIS [22–24]. With this system, conventional neurosurgical procedures are maintained and the magnet is moved to the patient for imaging (Figure 2). The higher magnetic field and improved gradient performance provides high-resolution and rapid imaging including echo planar. The system includes a versatile MR-compatible OR table accommodating various patient positioning including prone, supine, and lateral. Philips and Siemens have recently developed and installed 1.5 T iMRI systems based on stationary magnets. In the Siemens configuration, surgery takes place in the fringe field and, for imaging, the OR

Table 1: iMRI systems with main advantage and disadvantage

Manufacturer	Magnet strength	Gradient performance	Main advantage	Main disadvantage
Odin	0.12	25 mT/m	Portable	Image resolution
Siemens	0.2	20 mT/m	Unrestricted instrumentation	Image resolution
Hitachi	0.3	21 mT/m	Unrestricted instrumentation	Need to move patient for imaging
General Electric	0.5	12 mT/m	Real-time imaging	Requires MR-compatible tools
Philips	1.5	33 mT/m	Image resolution	Need to move patient for imaging
Siemens	1.5	30 mT/m	Image resolution	Need to move patient for imaging
IMRIS	1.5	20 mT/m	Image resolution	Interruption of surgery for imaging

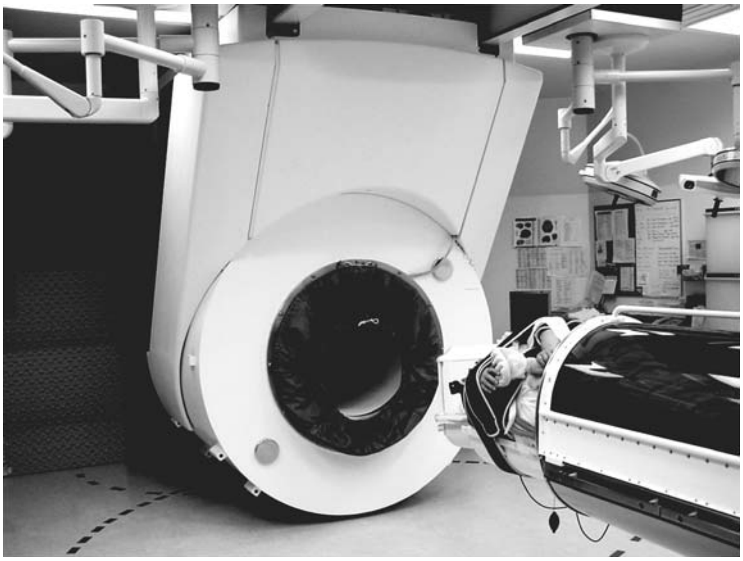

Fig. 2. Ceiling-mounted 1.5 T magnet being moved into the surgical field, together with the OR table and local RF shielding.

table is rotated to the magnet [25]. Philips designed a 1.5 T interventional/neurosurgery suite where the patient is moved by a floating tabletop from the operative table to the imaging platform for image acquisition [26]. Using the Philips system, surgeons have performed stereotaxy by reaching into the magnet, using iMRI for accurate instrument placement. To decrease the impact of iMRI in the OR environment, a small highly portable 0.12 T iMRI system, positioned under the OR table, was developed by Odin [27]. While this represented a unique innovation, imaging quality, and patient positioning are compromised by the low magnetic field and close opposition of the two magnetic poles.

Clinical Applications of iMRI

The development of iMRI has been driven by neurosurgical desire to have intraoperative imaging of CNS pathology following the induction of anesthesia and patient positioning, at various stages of the surgical dissection and as a measure of quality assurance prior to reversal of anesthesia. Despite these advantages, instrument size, weight, magnetic field, RF interference, and cost continue to pose significant challenges for widespread acceptance. Also, there has been no randomized controlled trial demonstrating superiority of iMRI-assisted neurosurgery over standard neurosurgical procedures. This in part reflects traditional education bias, the difficulty of recruiting patients for trials, crossover, and the relatively recent introduction of iMRI technology. Nevertheless, case studies and existing databases of patients who underwent iMRI procedures represent important sources of information to assess potential efficacy. Non-randomized retrospective studies matching patients based on prognostic factors are considered valuable. Examples where the use of iMRI led to modifications of the surgical procedure are also accepted as supportive evidence of utility. To fully evaluate the benefit of iMRI, randomized clinical trials, with blinded outcome assessment and long-term follow-up, are needed. At the University of Calgary, iMRI has been used to study surgery in 530 patients, 61 of which were pediatric (4 months to 18 years), with various CNS pathologies (Table 2). For each condition, surgical planning iMRI was performed after induction of anesthesia and patient positioning; interdissection iMRI was performed at various stages of the resection and quality assurance iMRI was acquired after wound closure, but before emergence from anesthesia. On average, an imaging session required 30 min. This included re-registration of surgical navigation. A total of 1930 MR studies were performed (Table 3). In 225 patients, trajectories were established by coupling surgical planning images with frameless stereotaxy (BrainLAB, Heimstetten, Germany). Time required for imaging depended on the specific MRI sequences used. Scout images (field of view 30 cm; $T_R = 35$ ms; $T_E = 15$ ms; matrix size 128×256; slice thickness 10 mm; one average) were obtained in 15 s. T_1-weighted images were obtained with spin-echo sequences (field of view 26 cm; $T_R = 400$ ms; $T_E = 12$ ms;

Table 2: Patient characteristics grouped by pathological finding

	Number, gender	Mean	SD	Age range	Total
Neoplasia					
Low-grade glioma	47 F, 64 M	36	17	3–77	111
High-grade glioma	30 F, 47 M	43	16	6–80	77
Meningioma	33 F, 15 M	57	16	24–84	48
Pituitary adenoma	13 F, 26 M	52	15	15–80	39
Metastatic tumor	5 F, 5 M	49	14	26–63	10
Schwannoma	3 F, 2 M	38	20	14–59	5
Vascular					
AVM	9 M, 9 F	35	14	8–56	18
Cavernoma	16 M, 11 F	35	14	24–69	27
Aneurysm	10 F, 2 M	55	13	37–76	12
ECIC bypass	2 M, 1 F	74			3
Epilepsy					
Temporal lobe	34 M, 30 F	36	12	8–55	64
Corpus callosotomy	1 F–1 M	13		13–28	2
Miscellaneous					
Abscess	1	27			1
Angiofibroma	2 M	16	1		2
Central neurocytoma	1 F, 1 M	20	1	19–20	2
Chondromyxoid fibroma	F	22			1
Choroid plexus carcinoma	F	15			1
Colloid cyst	2 F, 2 M	48	11	34–49	4
Cortical dysplasia	5 F, 4 M	19	14	1–35	9
Craniopharyngioma	3 M, 3 F	23	25	13–51	6
Cysticercosis	M	32			1
Dermoid cyst	1 F,1 M	36			2
DNT tumor	1 F,1 M	10			2
Hydrocephalus	2 M	20			2
Ganglion cell tumor	M	41			1
Germinoma	M	12			1
Glomus jugular tumor	M	60			1
Hamartoma	M	32			1
ICH	M	38			1
Lymphoma	2 F–3 M	45	24	10–62	5
Medulloblastoma	6 F, 1 M	26	13	5–35	7
Optic nerve biopsy	M	40			1
Osteoma	1 F, 1 M	67			2
Pachymeningitis	F	34			1
Parotid adenoma	2 M	29			2
Plasmacytoma	2 F				2
Rathke's cleft cyst	F	17			2
Sarcoma	M	67			1
Tubularsclerosis					2
Other					14
Spine	13 F, 8 M	45	21	23 months–81	21
Liver resection	5 M, 2 F	68		58–83	7

Table 3: Number and type of intraoperative MR imaging sequences

	Patients	MR studies	MR technique T_1	T_1-Gd	T_2	MRA
Surgical planning	503	923	425	255	243	7
Interdissection	300	550	278	126	146	3
Quality assurance	298	457	253	103	101	4
Total number		1930	956	484	490	14

matrix size 192 × 256; slice thickness = 4 mm; two or three averages) in ~4 min. T_2-weighted images with fast spin-echo sequences (field of view 26 cm; $T_R = 4000$ ms; $T_E = 90$ ms; matrix size 256 × 256; slice thickness 4 mm; two averages) and FLAIR fast spin-echo sequences (field of view 26 cm; T_R, 6000 ms; T_E, 96 ms; matrix size 192 × 256; slice thickness 4 mm; two averages) were obtained in ~4 min. The following sections summarize the impact of iMRI on various neuropathologies.

Neoplasia

CNS neoplasia represented the largest group of patients ($n = 337$) undergoing iMRI-assisted neurosurgery. Similarly to other iMRI units, we have observed a case selection of patients with low-grade glioma, pituitary adenoma, and childhood tumors. This in part reflects the growing body of knowledge that outcome for these patients correlates to the extent of resection. iMRI application to tumor resection was beneficial for many reasons. Assessment of the lesion immediately prior to surgery may show progression or regression of the lesion, as compared to the diagnostic study. In some cases, this dramatically changed the planned procedure and occasionally led to the decision not to proceed, as in four of the cases (Figure 3). Surgical planning iMRI resulted in more accurate, smaller craniotomies, and narrower surgical corridors (Figure 4). Such precise operative procedures are thought to have resulted in improved outcome. Interdissection iMRI, in addition to correcting for intraoperative brain shift for frameless stereotaxy, provided an ideal method for resection control (Figure 5). This was advantageous when tumor borders were difficult to identify during microdissection, such as in many of the patients with low-grade glioma. Unsuspected residual neoplasm was observed in 9% high-grade glioma, 20% low-grade glioma, 33% pituitary adenoma, and 2% meningioma. Quality assurance iMRI, at the end of the procedure, confirmed the lack of acute surgical complications such as postoperative hemorrhage, obstructive hydrocephalus, or cerebral edema. This knowledge facilitated early postoperative care.

Spreading enhancement, particularly in patients with malignant neoplasms, was observed (Figure 6). While the nature of this phenomenon needs to be determined, it is likely to be multifactorial, reflecting disrupted blood–brain barrier, surgical manipulation, and extension of neoplasm outside borders visible with diagnostic or iMRI. This spreading enhancement was not observed in patients with meningioma, a benign encapsulated tumor, despite considerable gadolinium (Gd) tumor enhancement, and extensive surgical manipulation, including, in many cases, disruption of the arachnoid and pia. In selected cases, biopsy of the area of spreading enhancement confirmed the presence of tumor. Based on these observations, we now limit, in patients with suspected malignant neoplasms, the administration of Gd until late in the surgical dissection.

Randomized clinical trials, where patients are randomly assigned to undergo either iMRI-assisted or traditional surgery for neoplasia, are essential to assess the efficacy of iMRI over standard procedures. Patients with low-grade glioma would be ideal for such a study, as surgical resection is often incomplete and outcome may well correlate with gross resection. While the primary outcome for such a study would be the interval before tumor recurrence, other secondary outcome measures could include: accuracy of craniotomy placement, extent of tumor resection, operative complications, and length of hospital stay. A positive study would establish iMRI as *the standard of care*. Apart from surgery, iMRI can be useful to track biopsy needle and to monitor probe placement at the tumor site for brachytherapy [28], delivering viral vectors, chemotherapeutics, or heat (thermal ablation therapy) [29].

Epilepsy

The surgical management of epilepsy is based on a number of variables including the type of epilepsy, location of the epileptogenic focus, patient wishes, and expertise of the surgeon. The immediate goal of surgery is maximal safe resection of the epileptogenic tissue or

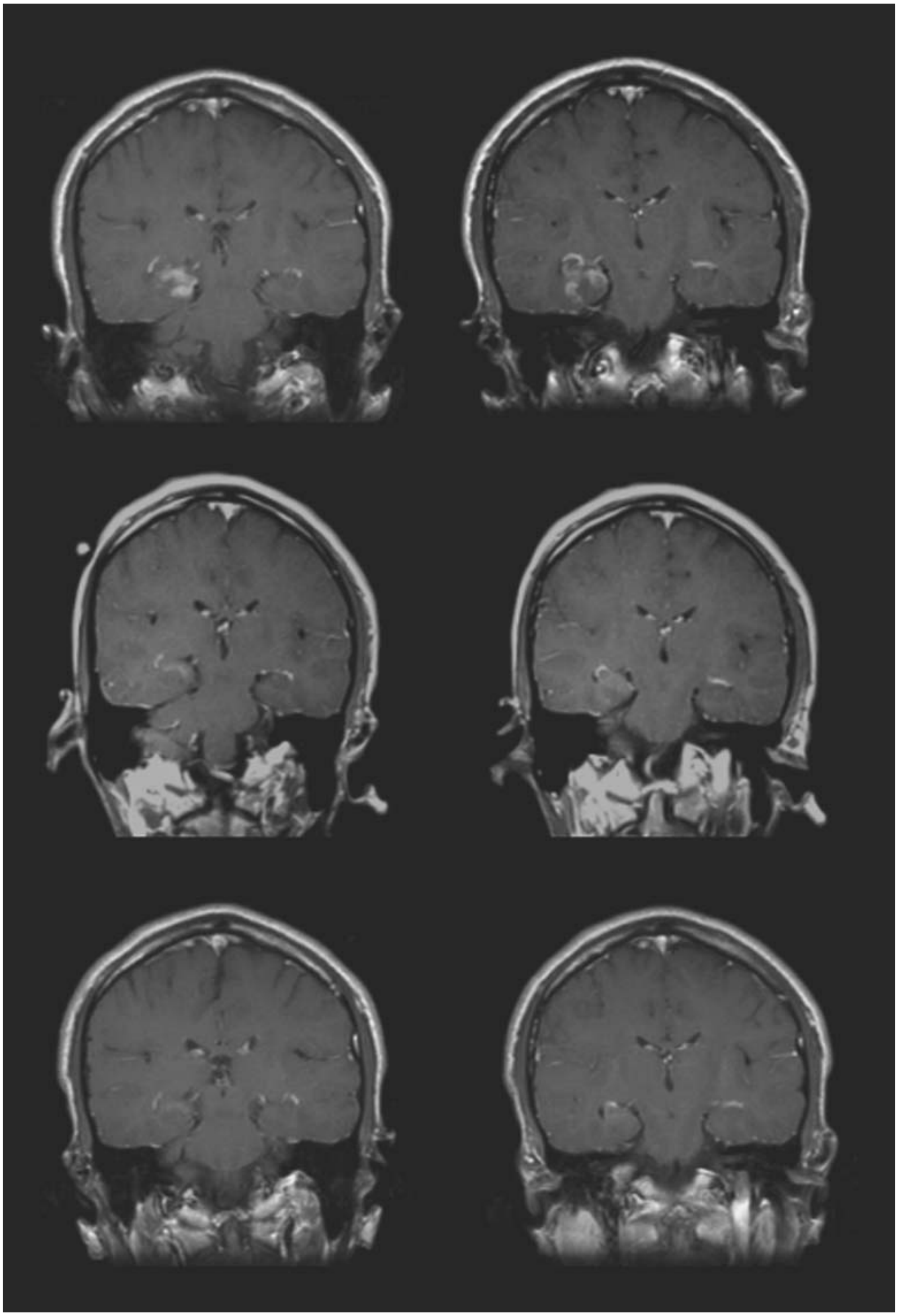

Fig. 3. T_1-Gd coronal 1.5 T MR images obtained at diagnosis (upper), surgical planning iMRI (middle) and 3-month follow-up (lower). At the time of surgical planning iMRI, the lesion had virtually disappeared and the procedure was aborted.

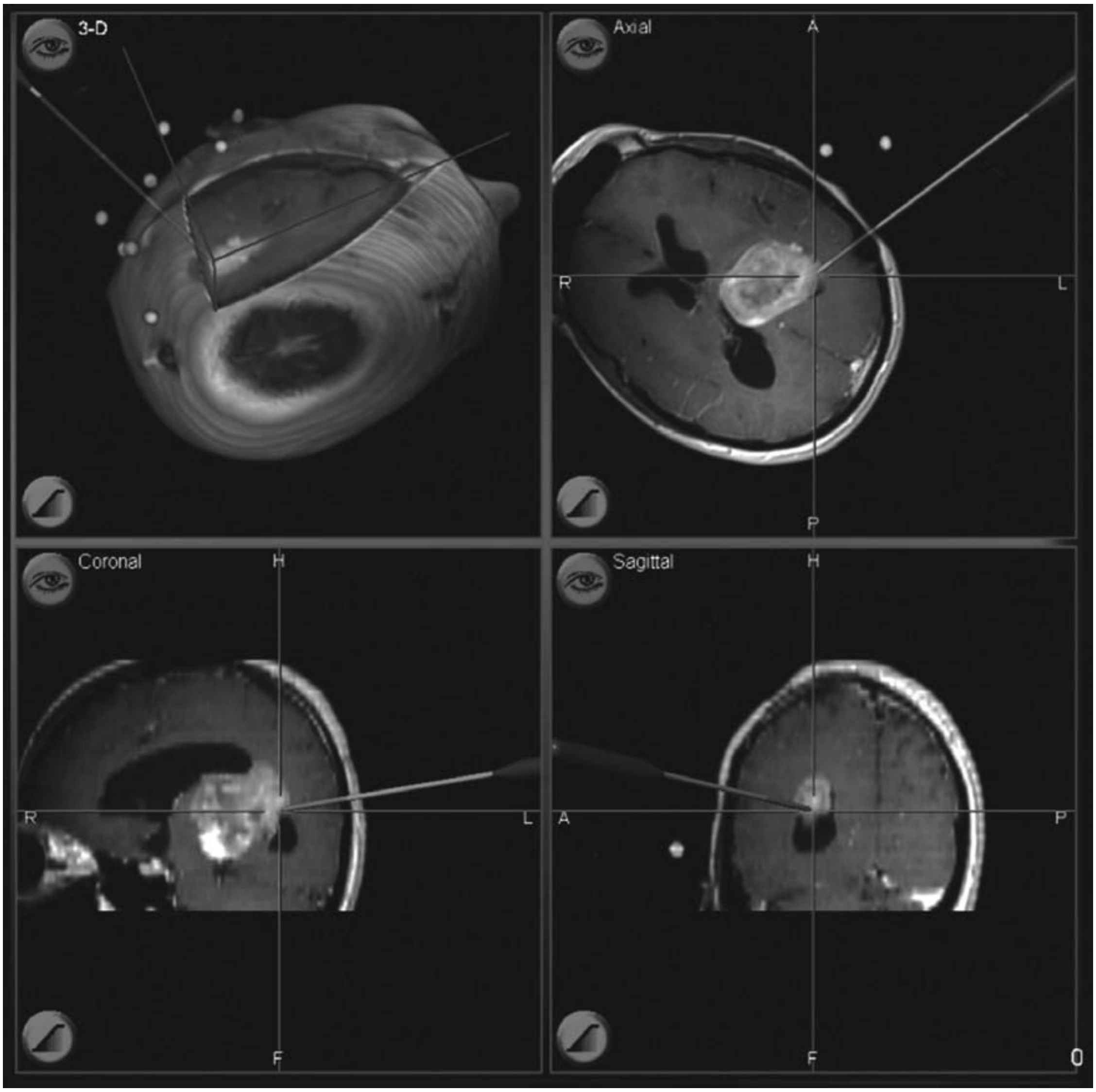

Fig. 4. Surgical planning T_1-Gd iMRI showing a large intraventricular lesion, together with registration for surgical navigation (BrainLAB, Heimstetten).

anatomical and functional disconnection, to eliminate or reduce the number of clinically significant seizures without causing major deficit. Of the 530 patients, 75 presented with intractable epilepsy. iMRI provided precise identification of abnormal tissue such as cortical dysplasia or medial temporal lobe sclerosis. When coupled to surgical navigation technology, targeting epileptogenic structures, in particular the medial temporal lobe, was optimized. As the magnet can be moved from the operative site, iMRI did not interfere with the use of surgical adjuncts such as electrocorticography, cortical mapping, and Cavitron Ultra-Sonic Aspirator (CUSA, Valleylab, Boulder, CO, USA). Selective amygdalohippocampectomy was performed in 36 of our 64 patients with temporal lobe epilepsy. We and others have found this to be as effective as temporal lobectomy for seizure control

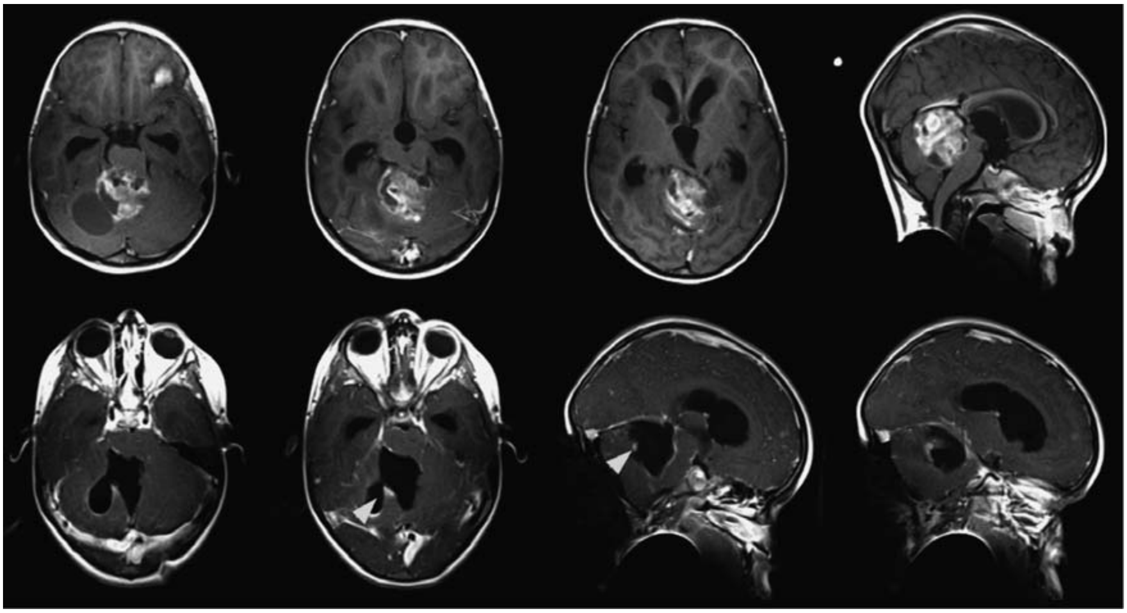

Fig. 5. Surgical planning T_1-Gd iMRI obtained from a 5-year-old boy with pilocytic astrocytoma show the large tumor with associated brain shift (upper). Interdissection images (lower) revealed unsuspected residual tumor (arrows).

[30]. Despite the fact that this procedure is routinely performed, anatomical targets can become unclear during microdissection. When approaching through the mid temporal gyrus, the amygdala may be hard to define, while with trans-sylvian dissections, it is often difficult to determine the extent of hippocampal removal. In 19% of patients with temporal lobe epilepsy, interdissection iMRI, showed unsuspected residual tissue, which was then removed (Figure 7). Notwithstanding these encouraging results, a randomized trial is necessary to both confirm the observations and determine the impact of iMRI on clinical outcome.

The assessment of cortical dysplasia requires the signal-to-noise ratio of 1.5 T or higher-field MR systems. In 4 patients with cortical dysplasia, extent of the abnormality was well assessed with the 1.5 T iMRI system, enhancing craniotomy placement and resection control.

Vascular disorders

Surgical planning iMRI significantly improved craniotomy placement for patients with arteriovenous malformation (AVM) and cavernous angioma, making lesion exposure relatively straightforward. Among the 60 patients with cerebral vascular pathology, 18 had AVM and 27 had cavernous angioma. We have, as of yet, not used diffusion/perfusion MR imaging to evaluate the effect of resecting AVM on the adjacent brain. The literature suggests that AVM resection may result in hyperperfusion of the adjacent brain. It is this consequence that is thought to contribute to the relatively high frequency (10%) of postoperative hemorrhage [31]. There were 12 patients with aneurysm and 3 had extracranial carotid occlusion. For all vascular procedures, interdissection iMRI and quality assurance iMRI confirmed complete resection of the target or treatment of the abnormality.

For patients with aneurysm, intraoperative MR angiography accurately revealed vascular anatomy and clip placement. However, clip-induced susceptibility and/or eddy current artifact interfered with evaluation of the aneurysm neck. Intraoperative assessment of the aneurysm neck will require the development of MR-invisible clips. EPI was used to identify diffusion/perfusion abnormality in the distribution of distal vascular branches, including perforators. The presence of such abnormalities would allow clip repositioning prior to irreversible brain injury (Figure 8). We have not encountered such changes and none of the aneurysm patients have suffered deficit.

Patients with carotid occlusion were symptomatic with recurrent transient ischemic attacks, and diagnostic MRI showed diffusion/perfusion mismatch. Extracranial to intracranial bypass resulted in immediate correction of the

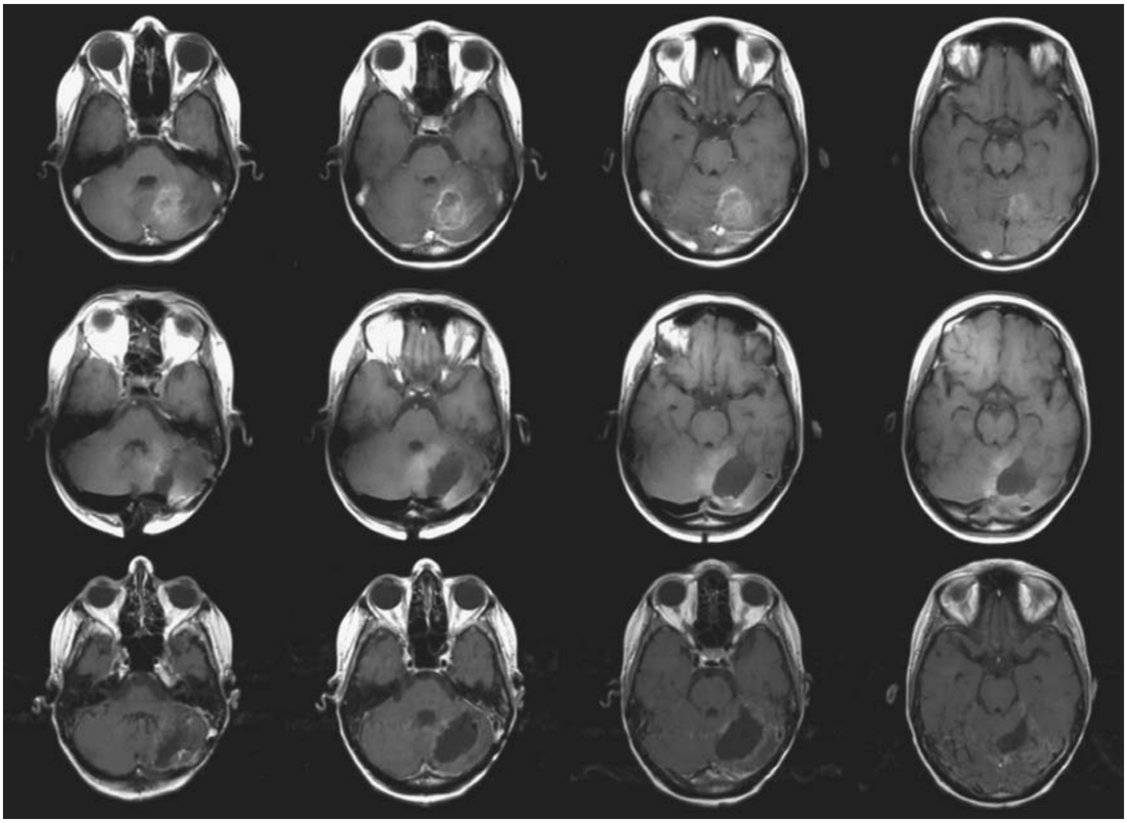

Fig. 6. Surgical planning (upper), interdissection (middle), and day 2 postoperative (lower) T_1-Gd iMRI of a patient with recurrent medulloblastoma. Diffusion of contrast well beyond the suspected tumor margin can be observed on interdissection but not on follow-up images.

perfusion deficit as shown with iMRI. Diffusion-weighted EPI quality requires a homogenous magnetic field, excellent eddy current compensation, strong gradients with fast switching times, and excellent shimming [32].

Spine

iMRI was used as an adjunct to spine surgery in 21 patients. The procedures included anterior cervical discectomy, cervical corpectomy with instrumentation, and the transoral resection of various C1/2 pathologies. iMRI with surgical navigation provided precise targeting of spinal pathology particularly lesions involving the C1/2 region, that are difficult to visualize through surgical corridors designed to limit trauma associated with extensive exposure. Interdissection images accurately determined the extent of decompression and showed the relationship of the surgical dissection to neural vascular structures (Figure 9). Extending iMRI capability to the thoracic and lumbar spine will be increasingly important as spinal surgery becomes reliant on microsurgical technique including restricted surgical corridors. The modified phased array spine RF coils are used to maximize images of the spine. The volume coil is used to transmit the RF power while the phased array coils work in the receive only mode.

Future Directions

Technology

While imaging techniques have greatly enhanced diagnostic accuracy and improved surgical outcomes, technical limitations necessitate further iMRI improvement. Increasing the magnetic field would further enhance image

Fig. 7. Surgical planning T_1-weighted iMRI from a patient with intractable temporal lobe epilepsy, showing the targeted amygdala and hippocampus (upper). Interdissection images (middle) indicate unsuspected residual amygdala (arrow). Quality assurance iMRI reveals complete dissection of the target (bottom).

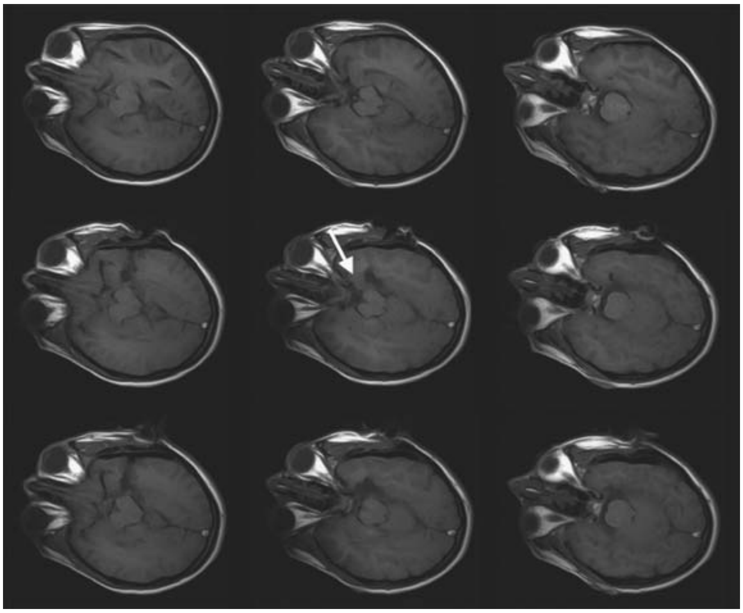

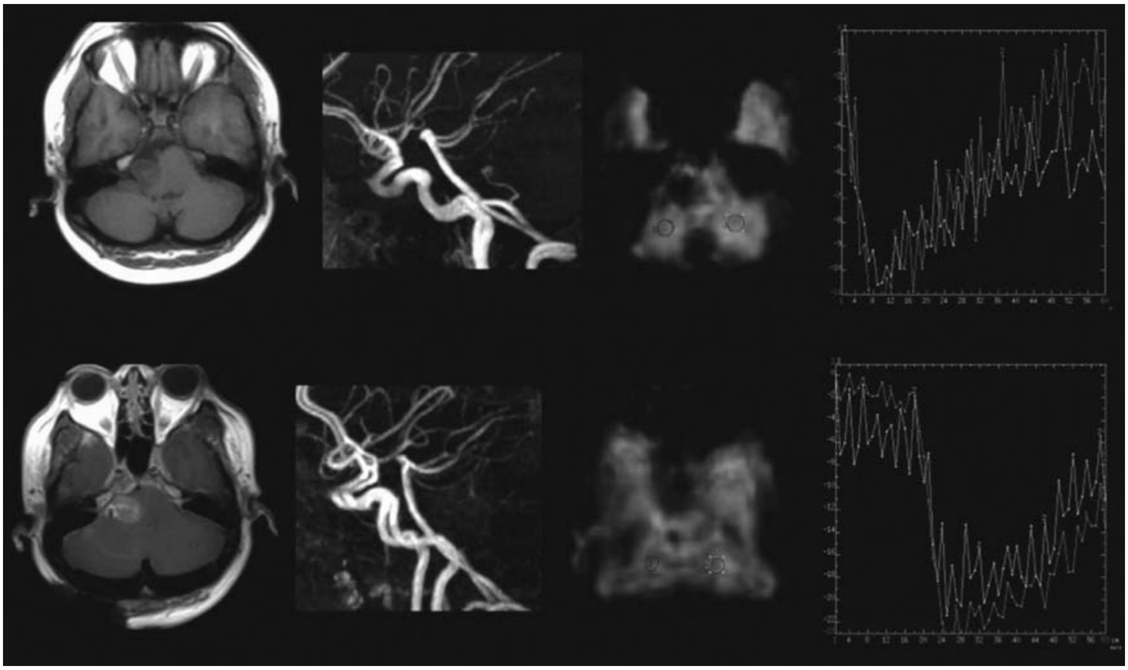

Fig. 8. Surgical planning (upper) and interdissection (lower) T_1-weighted, MR angiography, diffusion, and perfusion iMRI studies obtained from a patient with a giant left PICA aneurysm. Interdissection studies obtained 5–10 min following clip ligation of PICA show flow change within the aneurysm, parent vessel occlusion, aneurysm obliteration, and no diffusion or perfusion abnormality.

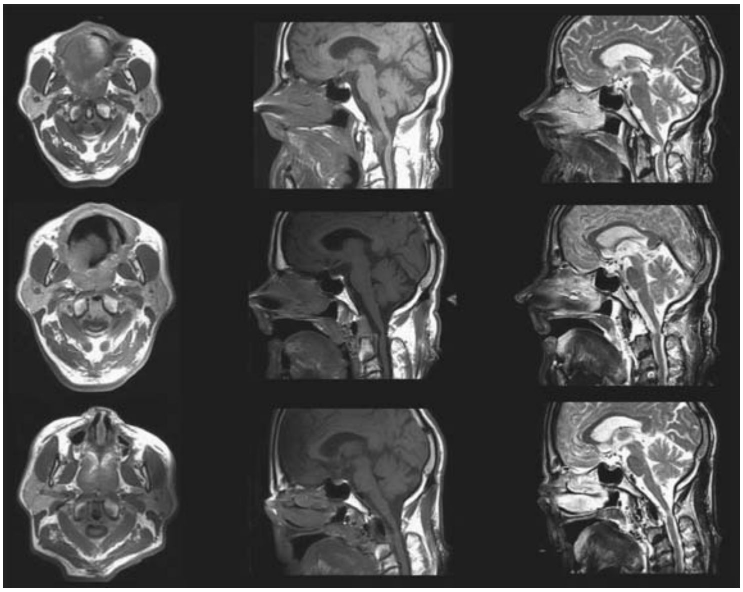

Fig. 9. T_1- and T_2-weighted iMRI from patient with retro-odontoid synovial cyst. Surgical planning iMRI (upper) show significant spinal cord compression. Interdissection iMRI show unsuspected residual spinal cord compression at the C2 level (middle). Quality assurance iMRI show optimal decompression (lower).

resolution by improved signal-to-noise ratio, although this might also lead to an amplification of susceptibility artifacts in certain areas. Improvements in RF coil design need to take advantage of improved technology while not limiting surgery. Larger RF coils, not restricting access to the operative field, would be an asset. Additional reduction in total acquisition time could be achieved by the application of phased array technology that allows the acquisition of parallel images. Enlarging the magnet bore facilitates patient positioning and the introduction of surgical technologies. To take full advantage of an iMRI system and maximize its use, the magnet should ideally be movable and sited for use in two or more rooms.

Bioinformatics

Software development has made possible 3D reconstruction of iMRI including lesion segmentation. 3D reconstruction augments lesion localization, diagnosis, and surgery planning. MRI and spectroscopic characteristics may correlate with outcome [33,34]. Multimodal fusion of MR images provides information as to the relationship of eloquent brain and vasculature to the planned surgical corridor and target.

Robotics

The introduction of iMRI has provided an imaging adjunct to surgery. Despite this and other technologies, such as microscopy, surgeons operate much like they did 100 years ago, depending to a large extent on hand–eye coordination. Robotic advances, such as tremor filtration and motion scaling permit maximal use of magnification and enable precise, tremor-free tool manipulation during surgery. Integrating robotic technology with iMRI would allow surgeons to manipulate images in real time and reduce limitations imposed by iMRI, particularly those related to a restricted working environment (GE double doughnut configuration) and disruptions in surgery related to image acquisition (1.5 T IMRIS, Siemens or Philips systems).

At the University of Calgary, we are developing an MRI-compatible, image-guided, ambidextrous robot called neuroArm [35]. Our industrial collaborator, MD Robotics (Brampton, Ontario, Canada), has successfully developed safety-critical robotic systems for the space shuttle and International Space Station. NeuroArm consists of a neurosurgical robot, main controller, and a workstation. The robot has two MR-compatible articulated arms with dextrous mechanical manipulators that grasp and move surgical tools. Each arm has 8 degrees of freedom (DOF) and are small enough to work within the 68 cm working diameter of the 1.5 T IMRIS magnet and capable of 30 μm precision (Figure 10). A 3-DOF strain gauge sensor system was integrated to provide haptic feedback to the surgeon. The workstation incorporates a computer processor, two hand controllers to manipulate the robot arms, a controller for positioning the microscope and lights, and three types of display and data recorders.

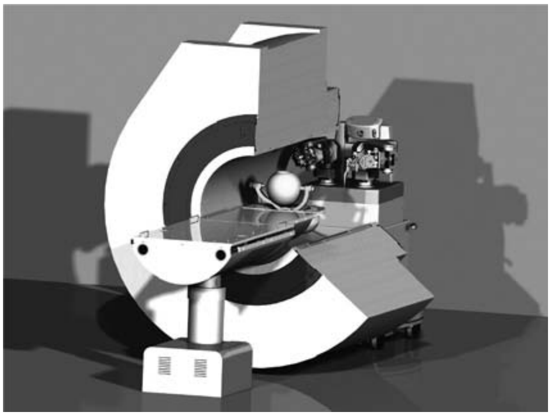

Fig. 10. NeuroArm in position for stereotaxy. The base is equipped with an extension platform (not shown), allowing the manipulator arms to reach inside the magnet bore.

The interface maximizes ergonomic comfort and minimizes surgeon fatigue.

The robotic platform and imaging environment include surgical simulation capability. This will be of increasing importance as advances in surgical technologies and associated techniques increase case complexity and produce a tyranny of choice. Risk-free rehearsal and development of patient specific interventional recipes will allow surgeons to safely take full advantage of iMRI and robotic technologies.

Acknowledgments

The authors would like to thank Boguslaw Tomanek and John Saunders for their kind suggestions. The iMRI program has been supported by a grant from the Canadian Foundation for Innovation. The iMRI system is being marketed by IMRIS (info@IMRIS.com).

References

1. Clower WT, Finger S. Neurosurgery. 2001;49:1417.
2. Piek J, Lidke G, Terberger T, von Smekal U, Gaab MR. Neurosurgery. 1999;45:147.
3. Barker FG II. J. Neurosurg. 1993;79:948.
4. Gall FJ. Sur les fonctions du cerveau et sur celles de chacune de ses parties avec des observations sur la possibilité de reconnaitre les instincts, les penchans, les talens, ou les dispositions morales et intellectuelles des hommes et des animaux, par la configuration de leur cerveau et de leur tête, Vol 1. J.B. Baillière: Paris, 1822.
5. Broca P. Bull. Soc. Anat. Paris. 1861;6:398.
6. Dandy WE. Ann. Surg. 1919;70:397.
7. Moniz E. Rev. Neural. 1927;2:72.
8. Fry WJ, Fry FJ. IRE Trans. Med. Electron. 1960;ME-7:166.
9. Cormack AM. Phys. Med. Biol. 1973;18:195.
10. Hounsfield GN. Br. J. Radiol. 1973;46:1016.
11. Lauterbur PC. Philos. Trans. R. Soc. Lond. B. Biol. Sci. 1980;289:483.
12. Mansfield P, Maudsley AA. Br. J. Radiol. 1977;50:188.
13. Lunsford LD. Appl. Neurophysiol. 1982;45:374.
14. Black PM, Moriarty T, Alexander E III, Stieg P, Woodard EJ, Gleason PL, Martin CH, Kikinis R, Schwartz RB, Jolesz FA. Neurosurgery. 1997;41:831.
15. Le Bihan D, Mangin JF, Poupon C, Clark CA, Pappata S, Molko N, Chabriat H. J. Magn. Reson. Imaging. 2001; 13:534.
16. Keston P, Murray AD, Jackson A. Clin. Radiol. 2003;58:505.
17. Le Bihan D. J. Neuroradiol. 1996;23:1.
18. Hoult DI, Saunders JK, Sutherland GR, Sharp J, Gervin M, Kolansky HG, Kripiakevich DL, Procca A, Sebastian RA, Dombay A, Rayner DL, Roberts FA, Tomanek B. J. Magn. Reson. Imaging. 2001;13:78.
19. Steidle G, Graf H, Schick F. Magn. Reson. Imaging. 2004;22:171.
20. Steinmeier R, Fahlbusch R, Ganslandt O, Nimsky C, Buchfelder M, Kaus M, Heigl T, Lenz G, Kuth R, Huk W. Neurosurgery. 1998;43:739.
21. McPherson CM, Bohinski RJ, Dagnew E, Warnick RE, Tew JM. Acta Neurochir. Suppl. 2003;85:39.
22. Sutherland GR, Kaibara T, Louw DF, Hoult DI, Tomanek B, Saunders J. J. Neurosurg. 1999;91:804.
23. Kaibara T, Saunders JK, Sutherland GR. Neurosurgery. 2000;47(1):131.
24. Sutherland GR, Kaibara T, Wallace C, Tomanek B, Richter M. Intraoperative assessment of aneurysm clipping using magnetic resonance angiography and diffusion-weighted imaging: technical case report. Neurosurgery. 2002;50(4): 893.
25. Nimsky C, Ganslandt O, von Keller B, Fahlbusch R. Acta Neurochir. Suppl. 2003;88:21.
26. Hall WA, Liu H, Martin AJ, Truwit CL. Top. Magn. Reson. Imaging. 2000;11:203.
27. Schulder M, Jacobs A, Carmel PW. Stereotact. Funct. Neurosurg. 1998;76:151.
28. Susil RC, Camphausen K, Choyke P, McVeigh ER, Gustafson GS, Ning H, Miller RW, Atalar E, Coleman CN, Menard C. Magn. Reson. Med. 2004;52:683.
29. Dick EA, Joarder R, de Jode M, Taylor-Robinson SD, Thomas HC, Foster GR, Gedroyc WM. Clin. Radiol. 2003; 58:112.
30. Olivier A. Can. J. Neurol. Sci. 2000;27(Suppl 1):S68.
31. Schaller C, Urbach H, Schramm J, Meyer B. Neurosurgery. 2002;51(4):921.
32. Fischer H, Ladebeck R. Echo-Planar Imaging: Theory, Technique and Application. Springer: New York, 1998, pp 179–200.
33. Ekinci G, Akpinar IN, Baltacioglu F, Erzen C, Kilic T, Elmaci I, Pamir N. Eur. J. Radiol. 2003;45(2):99.
34. Wu WC, Chen CY, Chung HW, Juan CJ, Hsueh CJ, Gao HW. Am. J. Neuroradiol. 2002;23(10):1775.
35. Louw DF, Fielding T, McBeth PB, Gregoris D, Newhook P, Sutherland GR. Neurosurgery. 2004;54(3):525.

In Vivo Magnetic Resonance Spectroscopy in Breast Cancer

Uma Sharma and N.R. Jagannathan
Department of NMR, All India Institute of Medical Sciences, New Delhi 110029, India

Abbreviations: MR, magnetic resonance; MRI, magnetic resonance imaging; MRS, magnetic resonance spectroscopy; ^{1}H MRS, proton magnetic resonance spectroscopy; ^{31}P MRS, phosphorus magnetic resonance spectroscopy; CE-MRI, contrast-enhanced magnetic resonance imaging; VOI, volume of interest; CSI, chemical shift imaging; MRSI, magnetic resonance spectroscopic imaging; STEAM, stimulated echo acquisition mode; PRESS, point resolved spectroscopy; CHESS, chemical shift selective; W–F, water-to-fat ratio; PME, phosphomonoester; PDE, phosphodiester; PCr, phosphocreatine; SV, single-voxel.

Introduction

Breast cancer is the most common cancer affecting women and is a significant health care problem, worldwide [1–3]. Breast cancer is classified as either ductal or lobular, depending on its morphological origin and similarities to the normal cellular components. Considerable heterogeneity among breast tumors demands highly accurate diagnostic techniques. Methods like X-ray mammography, ultrasound, and physical examination are often limited in sensitivity and specificity, especially in young women [4–6]. Magnetic resonance (MR) mammography and contrast-enhanced magnetic resonance imaging (CE-MRI) methodologies have greatly improved the ability to differentiate malignant from benign breast tumors [7–11] (see chapter by Kaiser). However, the reported specificity of the above studies is widely variable [8] and does not provide any metabolic information.

Recently, there has been an increasing interest in augmenting breast MRI with magnetic resonance spectroscopy (MRS) investigations by using the biochemical information to increase the specificity in differentiating benign from malignant tumors. Results of *in vivo* proton (^{1}H) [12–25] and phosphorus (^{31}P) [26–28] MRS, *ex vivo* and *in vitro* [29–32], and cell line [33,34] studies reported to date suggest that malignant breast tumors exhibit elevated levels of choline-containing compounds (total choline, TCho). In the case of MRS applied to fine needle aspiration biopsies (FNAB), the creatine to choline ratio can provide the pathological diagnosis with accuracies in the late 90th percentile [32,35]. This chapter reviews the potential of *in vivo* MRS (both ^{1}H and ^{31}P) in breast cancer especially in relation to the various methodological issues involved, technical limitations, diagnostic specificity, clinical applications, and future directions.

In vivo Localization in MRS

The basic requirement of *in vivo* localized MRS is to acquire the signal from a particular volume of interest (VOI) with optimal sensitivity. In the last 20 years, the availability of gradients has led to the development of localization techniques to obtain spectra from specific VOI. Magnetic field gradients in either the B_0 field as in imaging or the B_1 (radio frequency) field are used for localization of a particular volume. *In vivo* MRS began with the analysis of isolated tissues and surface regions. Most ^{31}P studies on breast cancer use surface coils, which are one of the earliest methods of localization. Surface coils provide rough localization. However, spatial selectivity can be achieved by varying the radio frequency pulse length. The disadvantages include extremely inhomogeneous transverse magnetic field, difficulty in assessing VOI that is below the surface, and contamination of signals from extraneous tissues. For these reasons, surface coils are used with other techniques like depth resolved spectroscopy, DRESS [36], which uses B_0 magnetic field gradients and a frequency selective pulse for localization. Depth resolved spectroscopy is also possible by using B_1 changes [37].

Currently employed image guided localization methods use proton images acquired in three orthogonal planes (transverse, sagittal, and coronal) to guide the placement of VOI. The magnetic field gradients spatially encode the resonance frequencies and the frequency selective pulse excites the spin distribution within the sample. Position, size of VOI, and the actual shape depend on the slice profile of the selective pulses. Localization methods acquire spectra either as single-voxel (SV) or as multivoxel [chemical shift imaging (CSI) or magnetic resonance spectroscopic imaging (MRSI)]. MRSI offers many advantages over SV techniques, such as localized spectra from many locations and small VOIs can be acquired simultaneously which can be used to obtain the metabolite

Graham A. Webb (ed.), Modern Magnetic Resonance, 1077–1086.
© 2008 *Springer.*

images. The pixel intensity in these images is proportional to the relative concentrations of the metabolites which is useful in visually assessing the spatial variation in the metabolite concentrations. However, the technique suffers from some disadvantages, such as signal from a voxel is prone to contamination from outside the VOI. This contamination occurs due to discrete and finite sampling, since the number of phase-encoding steps is typically more limited than normal imaging acquisitions. In addition, shimming the magnetic field over large volume especially in breast due to heterogeneity of tissues and long acquisition times are other disadvantages. In recent times, echo-planar imaging-based MRSI sequences which offer less image acquisition times have also become available. The most commonly used pulse sequences in breast cancer MRS are image selected *in vivo* spectroscopy (ISIS) [38], stimulated echo acquisition mode (STEAM) [39,40], point resolved spectroscopy (PRESS) [41], and CSI or MRSI [42,43]. In breast ^{1}H MRS, detection of resonances from metabolites with lower concentration in the presence of a large water and lipid signals is a major problem. Chemical shift selective (CHESS) radio frequency pulses that excite a limited narrow band (~60 Hz) of frequencies corresponding to the water signal are used to suppress the water signal [44]. Sequences that simultaneously suppress both water and lipid resonances are also being developed (*vide infra*).

^{31}P MR Spectroscopy

^{31}P MR spectra provide information on cellular metabolism by measuring various phosphorus metabolites and have been reviewed recently [26,27]. Most studies were carried out at 1.5 T with the patient positioned either supine or prone with a dual ^{1}H/^{31}P surface coil covering the area of the tumor. Shimming is carried out at ^{1}H frequency. The measurement methodology adopted by different groups varies in relation to the use of repetition time, size of coil used, and other experimental parameters. Figure 1A shows the ^{31}P MR spectrum obtained from a normal volunteer, and reflects the level of various

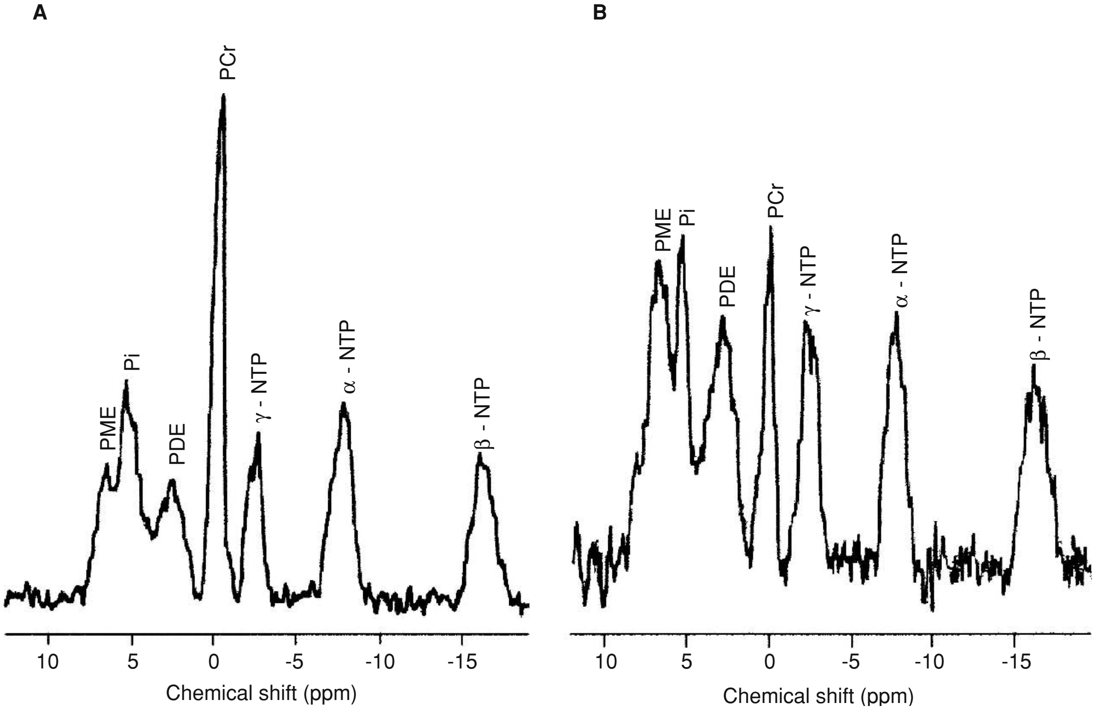

Fig. 1. (A) ^{31}P MR spectrum from normal breast tissue of a volunteer. Peak assignment corresponds to adenosine triphosphate (ATP), phosphodiesters (PDE), phosphomonoesters (PME), phosphocreatine (PCr), and inorganic phosphate (Pi). (B) ^{31}P MR spectrum from a patient suffering from infiltrating duct carcinoma of the breast. Spectra were obtained using a 10 cm surface coil with a single RF pulse.

phosphorus containing metabolites. In general, considerable variations in the ^{31}P metabolite profile of the normal breast were observed during the menstrual cycle [45,46]. Pre-menopausal women showed a rise in phosphomonoester (PME) signal at the late follicular stage of the menstrual cycle and less signal at the early luteal phase [46]. Phosphodiester (PDE) was maximal at the early follicular phase, and minimal at the late follicular stage. Twelves *et al.* [45] have reported lower PME and a high PDE/PME ratios during the second week of menstrual cycle. It is also reported that PME is increased in lactating breast compared with non-lactating post-menopausal women [45,47]. In general, ^{31}P MR signals are lower in post-menopausal women compared with pre-menopausal women [45,46].

Figure 1B shows the ^{31}P MR spectrum of a patient suffering from infiltrating duct carcinoma with elevated levels of PME and PDE, similar to that reported by other researchers [26,28,48–51]. In general, breast tumors have higher total phosphate content compared to the normal breast tissues of non-menstruating women [26,48]. The potential of ^{31}P MRS in distinguishing benign lesions from malignant has also been reported on the basis of elevated PME [49,50]. Biopsy results demonstrate that carcinomas contain three times more adenosione triphosphate and PME than benign breast lesions [29]. Recently, the utility of *in vivo* ^{31}P MRS for patients with various malignant and benign diseases has been evaluated [28]. Significant differences in PME and the ratio of PDE to phosphocreatine in malignant tumors were observed compared to normal breast tissue. However, no difference was observed between malignant and benign tumors suggesting that ^{31}P MRS is not helpful in differential diagnosis between benign and malignant lesions [28]. The use of ^{31}P MRS to monitor the response of breast tumors to chemotherapy has also been reviewed [26]. Serial measurements of localized ^{31}P MRS of breast cancer patients using the image guided *in vivo* spectroscopy sequence [26] was carried out both before and after chemotherapy showing decreased PME that was found to be associated with the response of the disease, while an increase in PME was associated with the disease progression [12,45,51–53].

Even though ^{31}P MRS studies were promising, they gave diverse results [28]. Moreover, its use in characterizing the tumors *in vivo* is hampered by lower MR sensitivity for detecting ^{31}P signals (sensitivity 1/10 of ^{1}H MRS). To achieve a similar signal-to-noise ratio of metabolites detected by ^{1}H MRS, a ^{31}P MRS study requires a voxel that is about 10 times larger than that used in ^{1}H MRS and hence can be performed only on large sized tumors. In addition, ^{31}P MRS requires special hardware that may not be available with all clinical scanners. By contrast, ^{1}H MRS examination can easily be integrated into a routine MRI examination. In view of this, considerable interest has been shown in recent years in evaluating the role of *in vivo* ^{1}H MRS in breast cancer.

^{1}H MR Spectroscopy of Breast

Presently seven groups are involved in breast *in vivo* ^{1}H MRS [12–25]. Katz-Brull *et al.* [54] have reviewed these reports and carried out pooled analysis of the existing ^{1}H MRS data. However, several methodological issues need to be addressed and these are outlined below.

Methodological Issues Related to Proton *in vivo* Breast MRS

Most *in vivo* ^{1}H MRS of human breast cancer studies reported to date were performed at 1.5 T except for the work of two groups [24,55,56]. The patient is usually positioned prone and this has some technical advantages, in that a tumor may be relatively distant from other structures that provide a substantial signal, such as chest wall muscle. However, positioning a surface coil is difficult in prone position and thus, a relatively large volume coil is often employed which has the disadvantage of potentially reducing the signal-to-noise ratio. In the supine position, a surface coil can be used, but contamination from chest wall and motion artifacts may increase. An additional disadvantage is the loss of signal from lesions that are not close to the surface coil of the breast.

A dedicated single or bilateral surface receive coil (custom/commercial make) is used for optimal signal reception with the body coil as transmitter. Automatic tuning and electronic decoupling is used for optimal signal reception. Some groups have used a transmit–receive breast coil (usually custom made) for their study [15,23,24]. Patients are positioned prone with the breast fitting into the cup of the coil. Followed by localizer images, T_1-weighted images in sagittal plane are obtained using a spin-echo sequence. To identify precisely the full extent of the irregular, speculated border of malignant tumors, lipid saturated proton MR images in the transverse, and coronal planes are acquired. Some centers use CE-MRI to localize the tumor region. Kvistad *et al.* used non-contrast MRI, when the tumor was easy to localize, otherwise CE-MRI was used for positioning the voxel [16]. Caution should be exercised when MRS is performed after using contrast agents to identify the tumor, since gadolinium has been reported to influence the *in vivo* detection of TCho [57]. Depending on the tumor size, voxels of appropriate dimension are chosen and positioned well within the tumor area.

Magnetic field shimming must be carried out both globally and over the voxel region to optimize the field homogeneity and for good water-suppression. In our experience, the line width after voxel shimming typically should correspond to 10–25 Hz for the lipid peak in case of normal breast tissue and 5–20 Hz for the water peak in patients with breast tumors. If this is not achieved, the quality of water-suppression will be poor leading to broad or no detectable choline signal. Solvent suppression pulses can be optimized to have narrow bandwidth excitation to minimize spectral perturbations outside the desired area. Water-suppressed and un-suppressed localized spectra with an adequate number of scans are acquired using an appropriate echo time (TE = 30/135/270/350 ms). Chemical shifts are reported using water as the internal standard at 4.7 ppm. The total study time per patient ranges between 60 and 75 min including MRI and MRS. Table 1 summarizes details of the pulse sequence, acquisition parameters, etc. used in various studies reported in the literature.

Table 1: Summary of experimental details used in various ^{1}H MRS studies

Study and reference	Patients, number of cases studied, and other details	Sequence used and SV/MRSI	Water or lipid suppression sequence used	Field, coil used, methods, acquisition parameters, sensitivity, and specificity
Roebuck *et al.* [13]	Malignant, $n = 10$ (pre-therapy); benign, $n = 7$	STEAM; SV	Water; CHESS	1.5 T; single breast multicoil receive; CE-MRI; TR = 2 s; TE = 31, 270 ms; voxel size = 0.7–9.8 ml; sensitivity = 70%; specificity = 86%
Jagannathan *et al.* [14,17]	Malignant, $n = 17$ (pre-therapy); $n = 34$ (post-therapy); benign, $n = 2$; controls, $n = 14$	STEAM; SV	Water; CHESS	1.5 T; bilateral surface receive coil; non-CE-MRI; TR = 3 s; TE = 135 ms; voxel size = 1–8 ml
Kvistad *et al.* [16]	Malignant , $n = 11$ (pre-therapy); $n = 1$ (post-therapy); benign, $n = 11$; control, $n = 11$; lactating, $n = 7$	PRESS; SV	Water frequency selective inversion	1.5 T; single breast receive coil; non-CE and CE-MRI; TR = 2 s; TE = 135, 350, 450 ms; voxel size = 1–25.2 ml; sensitivity = 82%; specificity = 82%
Jagannathan *et al.* [22]	Malignant, $n = 46$ (pre-therapy); $n = 35$ (post-therapy); benign, $n = 14$; control, $n = 16$; lactating, $n = 1$	STEAM; SV	Water; CHESS	1.5 T; bilateral surface receive coil; non-CE-MRI; TR = 3 s; TE = 135 ms; voxel size = 1–27 ml; sensitivity = 78%; specificity = 86%
Cecil *et al.* [18]	Malignant, $n = 23$ (pre-therapy); benign, $n = 15$	STEAM; SV	Water; CHESS	1.5 T; phased array multicoil receive; non-CE and CE-MRI; TR = 2 s; TE = 31, 270 ms; voxel size = 1–3.4 ml; sensitivity = 83%; specificity = 87%
Yeung *et al.* [19]	Malignant, $n = 24$ (pre-therapy); benign, $n = 6$	PRESS; SV	Water frequency selective inversion recovery	1.5 T; double breast receive coil; CE-MRI; TR = 2 s; TE = 38, 135, 270 ms; voxel size = 1–95 ml; sensitivity = 92%; specificity = 83%
Gribbestad *et al.* [15]	Malignant, $n = 12$ (pre-therapy); control, $n = 10$	PRESS; SV	Water frequency selective inversion	1.5 T; double breast transmit-receive coil; non-CE-MRI; TR = 2 s; TE = 136 ms; voxel size = 8–27 ml
Gribbestad *et al.* [61]	Malignant, $n = 6$ (pre-therapy)	PRESS; SV	Water and lipid using MEGA	1.5 T; standard coil; CE-MRI; TR = 1.6 s; TE = 270 ms; voxel size = 3.4 ml
Stanwell *et al.* [23]	Malignant, $n = 21$ (pre-therapy); control, $n = 43$; lactating , $n = 3$	PRESS; SV	VSS and CHESS	1.5 T; single breast transmit–receive coil; non-CE-MRI; TR = 2 s; TE = 135, 350 ms; voxel size = 3.4 ml

Table 1: (*Continued*)

Study and reference	Patients, number of cases studied, and other details	Sequence used and SV/MRSI	Water or lipid suppression sequence used	Field, coil used, methods, acquisition parameters, sensitivity, and specificity
Bolan *et al.* [24]	Malignant, $n = 86$ (pre-therapy); $n = 14$ (post-therapy); control, $n = 5$	LASER; SV	VAPOR	4 T; single breast transmit–receive coil; CE-MRI; TR= 3 s; TE = 45–196 ms; voxel size = 0.4–6 ml
Thomas *et al.* [66]	Malignant, $n = 8$; control, $n = 9$	2D, SV CABINET	No suppression	1.5 T; phased array coil; TR = 2 s; TE = 30 ms; voxel size = 1 ml
Jacobs *et al.* [25]	Malignant, $n = 8$ (pre-therapy); benign, $n = 7$	PRESS; MRSI	Water and lipid; CHESS and STIR	1.5 T; phased array coil; TR = 2 s; TE = 272 ms; voxel size = 1 ml
Meisamy *et al.* [56]	Malignant, $n = 16$; MRS both pre- and post-therapy	SV, localization with adiabatic selective refocusing	VAPOR	4 T; single breast quadrature transmit–receive coil; TR = 3 s; TE = 45–196 ms; voxel size = variable dimensions according to tumor size

Note: TR = time for repetition; TE = time for echo; LASER = localization by adiabatic selective refocusing; STIR = short inversion time recovery; VAPOR = variable pulse power and optimized relaxation; CABINET = coherence transfer based spin-echo spectroscopy; MEGA = MEscher GArwood (named after the authors); VSS = very selective suppression.

In our work, the observation of TCho was based on strict experimental criteria [22], namely: (i) the line width of the un-suppressed water peak to be around 5–20 Hz and (ii) the ratio of the water-suppression factor ≥ 20. If these criteria were not met, the data were discarded [22]. It is our experience that these criteria are essential since the observation of choline may be affected by poor shimming, the relative position of the voxel in relation to the surface coil, coil loading, and partial volume effects [22,24,54]. Moreover, SV-MRS of breast is sensitive to the size and placement of the voxel because of the heterogeneous distribution of TCho in the breast [24].

In addition, quantification of metabolite levels in breast is more difficult because of the heterogeneous distribution of the glandular and adipose tissues. Absolute concentration of TCho in breast lesions has also been reported using a phantom containing 1 mmol/l solution of choline placed in the multicoil array [13]. Recently, Bolan *et al.* used water as an internal reference peak for quantification of TCho [24]. This approach compensates for the partial volume of adipose tissue in the voxel and leads to a molal (mol/kg) concentration of water-soluble metabolites. Use of an appropriate echo time in breast *in vivo* spectroscopy involves a trade-off between signal intensity (high with short echo time) and signal contrast (the ability to resolve the composite choline signal from the lipid signal, which is higher with long echo time). The use of long echo times (≥ 135 ms) is preferred, despite the loss of signal intensity, for improved visibility of TCho signal because of a decreased overlap with the lipids [13,19,22]. Recently, Stanwell *et al.* have demonstrated the importance of referencing and optimized post-acquisitional data processing to improve the spectral resolution of MR spectra [23]. This allows the resolution of the composite choline resonance into its constituent components and helps in improving the specificity of *in vivo* MRS method [23]. In addition, water-to-fat (W–F) (lipid) ratio can also be calculated using the respective peak areas (using area under the water and the major lipid peak) from the un-suppressed MR spectra [12,14,17].

Interpretation of ^{1}H and ^{31}P spectra should include the age and the menopausal status of the patient. Postmenopausal women have more adipose tissue compared to glandular tissue. In pre-menopausal women, glandular tissue can give an adequate signal, and this needs to be considered both in the measurement strategies as well as in interpreting the spectra obtained. In a study by Stanwell *et al.* composite choline signal was observed in three non-lactating normal volunteers [23]. The chemical shift of this resonance was found to differ from that recorded from patients with malignant disease. When ^{1}H MRS on two of these volunteers was repeated once a week for a period of 8 weeks [23], in one volunteer the choline resonance was absent at different stages throughout the menstrual cycle but re-appeared in the next cycle. In the other volunteer, the resonance was always detectable but appeared to fluctuate during the 8-week period. However, long-term follow-up of these individuals has revealed no disease.

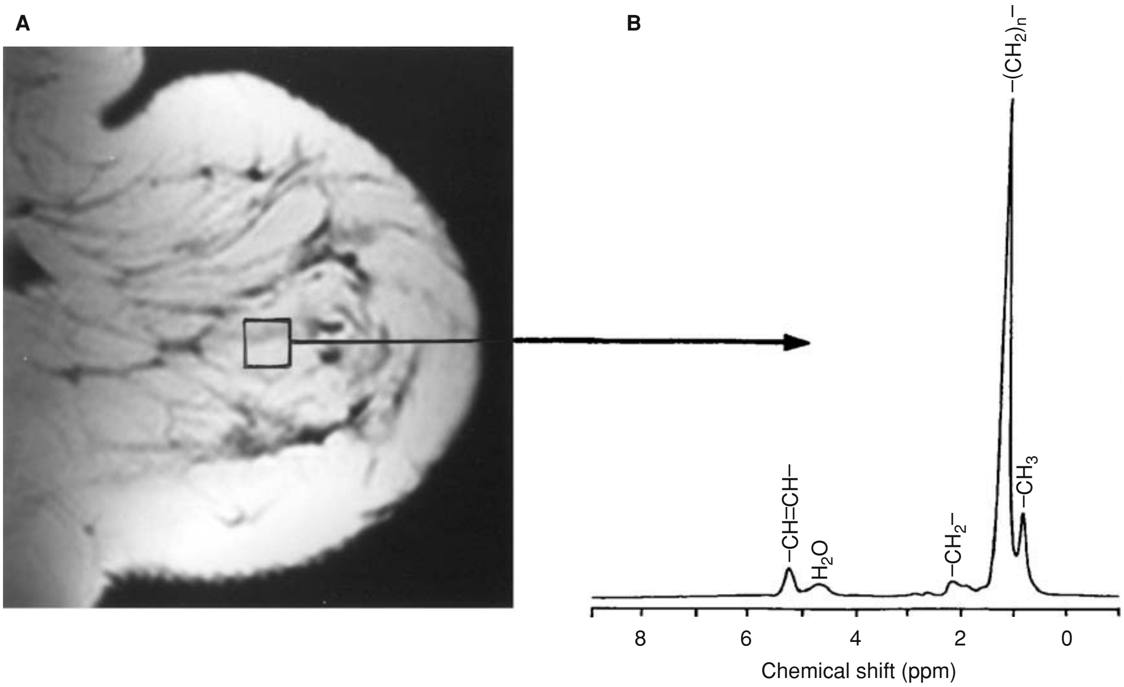

Fig. 2. (A) T_1-weighted axial image from a volunteer using spin-echo sequence with the following parameters: TR = 600 ms, TE = 15 ms, and slice thickness = 4 mm. (B) ^{1}H MR spectrum acquired from an 8 ml voxel localized in the normal breast tissue at TE = 135 ms using PRESS sequence.

Comparison of ^{1}H MRS of Normal and Malignant Breast Tissues

Water-to-Fat Ratio

A typical ^{1}H MR spectrum obtained from our laboratory using STEAM sequence (without water-suppression) from the normal breast tissue of a volunteer is shown in Figure 2B while the corresponding voxel location in Figure 2A. Lipid resonance dominates and the assignment of the various lipid resonance peaks are as shown. A ^{1}H spectrum without water-suppression from the tumor of a patient suffering from infiltrating duct carcinoma is shown in Figure 3B and the voxel location in Figure 3A. In tumor spectrum, the water peak dominates with low contributions from protons of the fatty acid chains in comparison to the normal breast tissue of controls and from the unaffected contralateral breast of the patient. Elevated W–F ratio characterizes the breast tumor. Similar findings have been documented by several others [12,14,17]. Observation of elevated W–F ratio in breast cancer patients is in agreement with the generally established trend that tumors have considerably higher water content [12,58,59]. Mackinnon *et al.* [60] reported changes in lipid content with tumor development and progression. In patients receiving chemotherapy, resulting in the reduction of primary tumor size, the W–F ratio showed a statistically significant ($p < 0.01$) decrease compared with the pretherapy value, thus providing a non-invasive indicator of favorable clinical outcome of chemotherapy [14,17]. The method thus provides the potential for non-invasively monitoring and assessing the response of breast cancer to chemotherapy. However, due to overlap of W–F values between benign and malignant lesions it has limited utility [59] and hence a search for other biochemical/s, which can be used as marker for malignancy, was undertaken.

Choline Signal

Water-suppressed ^{1}H MR spectra of breast tumor showed, in addition to the residual water and lipid peak, a peak at 3.2 ppm due to TCho as shown in Figure 3C. In general, the observation of TCho from breast tumors is hampered by the presence of huge water and lipid signals. However, if the strict experimental criteria outlined earlier are followed, then the observation of TCho is feasible. Evaluation of a pulse sequence to suppress simultaneously both the water and lipid signals to improve the detection

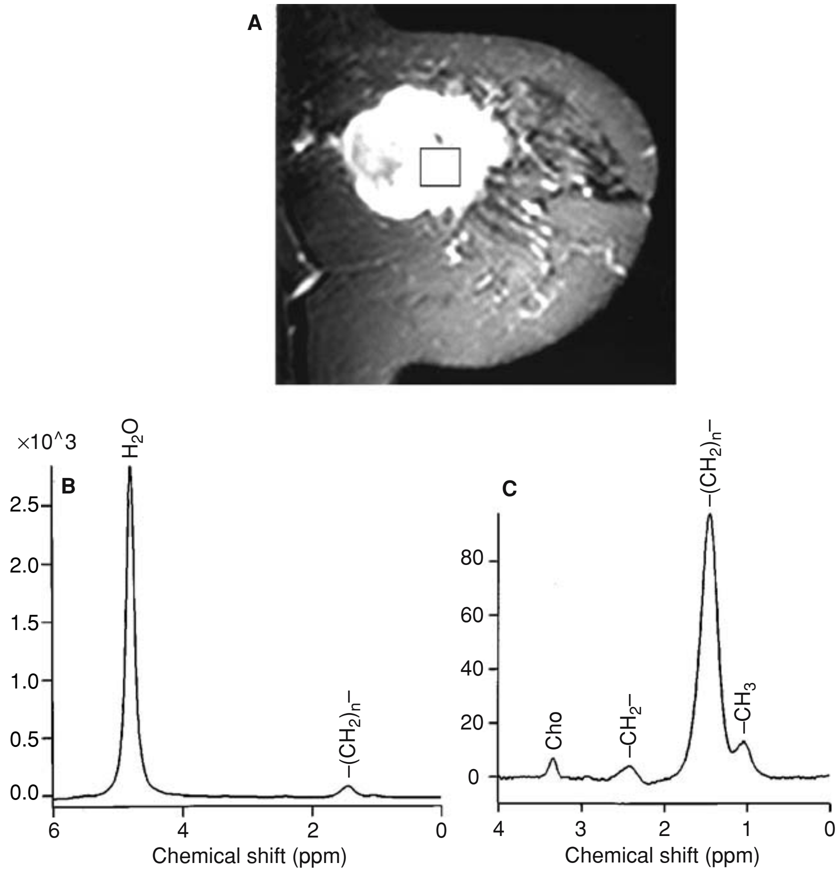

Fig. 3. (A) T_2-weighted lipid-suppressed sagittal MR image of a patient suffering from infiltrating duct carcinoma of the right breast, the tumor is seen as hyper-intense area. ^{1}H MR spectrum from an 8 ml voxel positioned in the tumor of the same patient obtained at TE = 135 ms using PRESS sequence: (B) without water-suppression and (C) with water-suppression.

of choline resonance is currently underway in our laboratory (see Figure 4). Lipid/water signal reduction is obtained using the spectral saturation method, by which transverse magnetization is dephased selectively before and after the second slice selective 180° spin-echo pulse. This dephasing is defined to affect both the water and lipid signals from 0.7 to 2 ppm, following the procedure of Mescher *et al.* [61]. Recently, Gribbestad *et al.* have also used a similar sequence to suppress the signals from water and lipid [62].

Of the various TCho (Cho, glycerophosphocholine, and phosphocholine) that contribute to the *in vivo* peak at 3.2 ppm, an increase in phosphocholine has been documented [23,33,63]. Elevation of TCho levels in malignant breast tumors compared to benign cases from *in vitro* MRS of FNAB and tissue has also been reported [30,31,32]. Results of ^{1}H *in vivo* breast MRS investigations to date have shown that the TCho resonance is specific to malignant tissue and can be used to differentiate cancerous from benign tissue. Combined analysis of the published reports reveal that the overall sensitivity and specificity of MRS is 83 and 85%, respectively [54]. The details are as presented in Table 1. In younger women, differentiation of benign from malignant lesion is important since the incidence of benign breast disease in young women is high [64,65] and mammography examination has lower sensitivity. Results from Cecil *et al.* [18], Yeung *et al.* [19], and Roebuck *et al.* [13] show that in younger patients ($\leq$40 years of age), ^{1}H MRS has a sensitivity of 100% and a specificity of 89–100% in detecting malignancy.

Several factors that limit the sensitivity of ^{1}H MRS were discussed earlier and the false negative results reported in many studies are ascribed mainly to technical limitations. For example, if the tumor size is small,

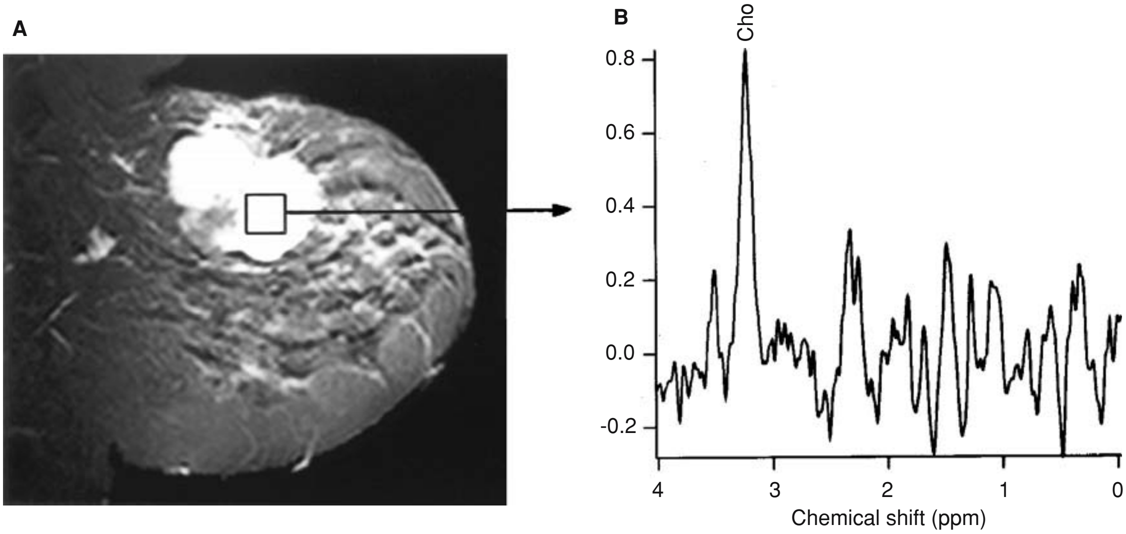

Fig. 4. (A) T_2-weighted lipid-suppressed sagittal MR image of a patient suffering from infiltrating duct carcinoma. (B) ^{1}H MR spectrum from an 8 ml voxel positioned in the tumor of the same patient obtained at TE = 270 ms using PRESS sequence with both the water and the lipid peak simultaneously suppressed.

relatively long acquisition time is required resulting in the patient becoming restless leading to movement artifacts. This also could lead to incorrect sampling of the tumor, thereby leading to contributions from surrounding fatty tissue. Moreover, movement of a patient would also lead to incorrect sampling and hence to false diagnosis. Incorrect sampling may also play a role in the detection of the choline signal. Few benign cases also showed TCho signal [16,18,19,22]. Detection of choline from the normal breast tissue of lactating women has also been reported [16,22,23]. This observation implies that the interpretation of spectra from such patients needs to be evaluated with caution and also points out the limitation of using TCho as a marker of malignancy. Stanwell *et al.* have documented that the main contribution to the TCho resonance observed in lactating breast is from the glycerophosphocholine [23]. They have documented that optimized post-processing of the spectra resolved a resonance at 3.22 ppm, consistent with phosphocholine, in patients with cancer. In contrast, the spectra recorded for three false positive volunteers and the three lactating mothers had a resonance centered at 3.28 ppm (possibly taurine, *myo*-inositol, or glycerophosphocholine).

Recently Jacobs *et al.* [25] have reported on a proton MRSI of breast cancer patients; their results show that TCho from malignant tissue was significantly elevated compared to benign breast tissue. The potential advantages of MRSI over SV-MRS include the ability to assess multiple lesions and tissues with normal appearance, as well as to distinguish lesion borders and infiltration into the surrounding tissue. Another major concern of *in vivo* breast MRS is the spectral overlap, in particular the dominant peaks due to lipids. To address this issue, Thomas *et al.* have carried out localized two-dimensional correlation spectroscopy experiments [66] and have shown that the W–F ratio can be calculated using two-dimensional spectral peak volumes. In addition, peaks due to unsaturated fatty acids can also be differentiated from saturated fatty acids. The TCho signal can also be used to monitor tumor response to different therapeutic regimens [22,56]. In a study carried out in our laboratory on 44 infiltrating duct carcinoma patients, the TCho peak was either reduced or absent after the third and/or sixth cycle of neoadjuvant chemotherapy [22].

Future Directions and Conclusions

Results obtained to date indicate that the sensitivity of MRS may be limited by various technical factors rather than by intrinsic properties of the tumors. Therefore, any improvement in signal-to-noise ratio that will effectively enhance the detection of TCho resonance may increase the sensitivity and improve the diagnostic potential especially in relation to ^{1}H MRS. Moreover, the detection of choline signal can be increased by performing MRS at higher fields [24,55]. Use of special radio frequency pulse sequences, like simultaneous suppression of water and lipid signals that are specifically optimized for detection of the signal at 3.2 ppm, would also improve the sensitivity of detection of TCho. Use of respiratory-gated radio frequency sequences would improve motion related artifacts. In addition, advances in the design of MR coils should improve detection of TCho. Use of metabolic imaging will also allow exploration of tumor heterogeneity and characterization.

Currently, breast MRS is not routinely performed as part of a breast MRI examination in many centers, in part because it is technically challenging and time consuming. More research focusing on early diagnosis with improved sensitivity and specificity and evaluation of response to chemotherapeutic agents in breast cancer patients would be clinically useful. Presently, MRS and MRI are complementary tools to histology, mammography, and other accepted techniques. Increasing use of these methods is expected for basic research, clinical investigations, and ultimately for patient diagnosis. The sensitivity and specificity of *in vivo* MR particularly for small lesions needs to be improved before MRS can be incorporated into clinical practice.

Acknowledgments

The financial grant (SP/S0/B27/95 and SP/S0/B21/2001) to NRJ from the Department of Science and Technology, Government of India, is gratefully acknowledged. We wish to thank Prof. G. Govil for critical evaluation of the manuscript and for many useful suggestions. The authors thank Drs. Mahesh Kumar, V. Seenu, O. Coshic, S.N. Dwivedi, Profs. A. Srivastava, P. K. Julka, G.K. Rath, Dr. Stefan Roell, and Mr. Virendra Kumar for their support and help.

References

1. Greenlee RT, Hill-Harmon MB, Murray T, Thun M. CA Cancer J. Clin. 2001;51:15.
2. National Cancer for Health Statistics. SEER Cancer Statistics Review (1973–1995). Bethesda, MD: US National Cancer Institute, 1998.
3. National Cancer Registry Programme (NCRP): Consolidated Report (1990–1996). An Incidence and Distribution of Cancer. Indian Council of Medical Research, New Delhi, 2001.
4. Stavros AT, Thickman D, Rapp CL, Dennis MA, Parker SH, Sisney GA.Radiology. 1995;196:123.
5. Fenlon HM, Phelan N, Tierney S, Gorey T, Ennis JT. Clin. Radiol. 1998;53:17.
6. Birdwell R, Ikeda D, O'Shaughnessy KF, Sickles EA. Radiology. 2001;219:192.
7. Schnall MD, Orel SD. Magnetic Resonance Imaging Clinics of North America: Breast MR Imaging, Vol. 9. WB Saunders Co.: Philadelphia, 2001.
8. Orel SG, Schnall MD. Radiology. 2001;220:13.
9. Sinha S, Sinha U. Ann. N. Y. Acad. Sci. 2002;980:95.
10. Kneeshaw PJ, Turnbull LW, Drew PJ. Br. J. Cancer. 2003;13:4.
11. Schnall MD. Radiol. Clin. N. Am. 2003;41:43.
12. Sijens PE, Wijrdeman HK, Moerland MA, Bakker CGJ, Vermeulen JW, Luyten PR. Radiology. 1988;169:615.
13. Roebuck JR, Cecil KM, Schnall MD, Lenkinski RE. Radiology. 1998;209:269.
14. Jagannathan NR, Singh M, Govindaraju V, Raghunathan P, Coshic O, Julka PK, Rath GK. NMR Biomed. 1998;11:414.
15. Gribbestad IS, Singstad TE, Nilsen G, Fjosne HE, Engan T, Haugen OA, Rinck PA. J. Magn. Reson. Imaging. 1998;8:1191.
16. Kvistad KA, Bakken IJ, Gribbestad IS, Ehrnholm RJB, Steiner L, Fjosne HE, Haraldseth O. J. Magn. Reson. Imaging. 1999;10:159.
17. Jagannathan NR, Kumar M, Raghunathan P, Coshic O, Julka PK, Rath GK. Curr. Sci. 1999;76:777.
18. Cecil KM, Schnall MD, Siegelman ES, Lenkinski RE. Breast Cancer Res. Treat. 2001;68:45.
19. Yeung DKW, Cheung HS, Tse GMK. Radiology. 2001;220:40.
20. Lee JK, Tsai SC, Ho YJ, Chanclai SP, Kao CH. Anticancer Res. 2001;21:1481.
21. Bakken IJ, Gribbestad IS, Singstad TE, Kvistad KA. Magn. Reson. Med. 2001;46:189.
22. Jagannathan NR, Seenu V, Coshic O, Dwivedi SN, Julka PK, Srivastava A, Rath GK. Br. J. Cancer. 2001;84:1016.
23. Stanwell P, Gluch L, Clark D, Tomanek B, Baker L, Giuffre B, Lean C, Malycha P, Mountford CE. Eur. Radiol. 2005;15:1037.
24. Bolan PJ, Meisamy S, Baker EH, Lin J, Emory T, Nelson M, Everson LI, Yee D, Garwood M. Magn. Reson. Med. 2003;50:1134.
25. Jacobs MA, Barker PB, Bottomley PA, Bhujwalla Z, Bluemke DA. J. Magn. Reson. Imaging. 2004;19:68.
26. Leach MO, Varrill M, Glaholm J, Smith TAD, Collins DJ, Payne GS, Sharp JC, Ronen SM, McCready VR, Powles TJ, Smith IE. NMR Biomed. 1998;11:314.
27. Ronen SM, Leach MO. Breast Cancer Res. 2001;3:36.
28. Park JM, Park JH. Korean J. Radiol. 2001;2:80.
29. Degani H, Horowitz R, Itzchak Y. Radiology. 1986;161: 53.
30. Gribbestad IS, Fjosne HE, Haugen OA, Nilsen G, Krane J, Petersen SB, Kvinnsland S. Anticancer Res. 1993;13: 1973.
31. Gribbestad IS, Petersen SB, Fjosne HE, Kvinnsland S, Krane J. NMR Biomed. 1994;7:181.
32. Mackinnon WB, Barry PA, Malycha PL, Gillett DJ, Russell P, Lean CL, Doran ST, Barraclough BH, Bilous M, Mountford CE. Radiology. 1997;204:661.
33. Glunde K, Jie C, Bhujwalla ZM. Cancer Res. 2004;15:4270.
34. Ting YT, Sherr D, Degani H. Anticancer Res. 1996;16:1381.
35. Mountford CE, Somorjai RL, Malycha P, Gluch L, Lean C, Russell P, Barraclough B, Gillett D, Himmelreich U, Dolenko B, Nikulin AE, Smith ICP. Br. J. Surg. 2001;88:1234.
36. Bottomley PA. U.S. Patent 4. 1984;480:228.
37. Bendall MR, Gordon RE. J. Magn. Reson. 1983;53:365.
38. Ordidge RJ, Connelly A, Lohman JAB. J. Magn. Reson. 1986;66:283.
39. Frahm J, Merboldt KD, Hanicke W. J. Magn. Reson. 1987;72:502.

40. Frahm J, Bruhn H, Gyngell ML, Merboldt KD, Hanicke W, Sauter R. Magn. Reson. Med. 1989;9:79.
41. Orididge RJ, Bendall MR, Gordon RE, Connelly A. Volume selection for *in vivo* biological spectroscopy. In: G Govil, CL Khetrapal, A Saran, AS Tata (Eds). Magnetic Resonance in Biology and Medicine. McGraw Hill: New Delhi, 1985, p 387.
42. Brown TR, Kincaid BM, Ugurbil K. Proc. Natl. Sci. U.S.A. 1982;79:3523.
43. Maudsley AA, Hilal SK, Perman WH, Simon HE. J. Magn. Reson. 1983;51:147.
44. Haase A, Frahm J, Hanicke W, Matthei D. Phys. Med. Biol. 1985;30:341.
45. Twelves CJ, Porter DA, Lowry M, Dobbs NA, Graves PE, Smith MA, Rubens RD, Richards MA. Br. J. Cancer. 1994;69:1151.
46. Payne GS, Dowsett M, Leach MO. Breast. 1994;3:20.
47. Twelves CJ, Lowry M, Porter DA, Dobbs NA, Graves PE, Smith MA, Richards MA. Br. J. Radiol. 1994;67:36.
48. Ng TC, Grundfest S, Vijaykumar S, Baldwin NJ, Majors AW, Karalis I, Meaney TF, Shin KH, Thomas FJ, Tubbs R. Magn. Reson. Med. 1989;10:125.
49. Merchant TE, Gierke LW, Meneses P, Glonek T. Cancer Res. 1988;48:5112.
50. Merchant TE, Meneses P, Gierke LW, Otter WD, Glonek T. Br. J. Cancer. 1991;63:693.
51. Kalra R, Wade KE, Hands L, Styles P, Camplejohn R, Greenall M, Adams GE, Harris AL, Radda GK. Br. J. Cancer. 1993;67:1145.
52. Glaholm J, Leach MO, Collins DJ, Mansi J, Sharp JC, Madden A, Smith IE, Mc Cready VR. Lancet. 1989;1:1326.
53. Redmond OM, Stack JP, O'Connor NG, Carney DN, Dervan PA, Hurson BJ, Ennis JT. Magn. Reson. Med. 1992;25: 30.
54. Katz-Brull R, Lavin PT, Lenkinski RE. J. Natl. Cancer Inst. 2002;94:1197.
55. Roebuck JR, Lenkinski RE, Bolinger L, Schnall MD. Proc. Int. Soc. Magn. Reson. Med. 1996;4:1246.
56. Meisamy S, Bolan PJ, Baker EH, Bliss RL, Gulbahce E, Everson LI, Nelson MT, Emory TH, Tuttle TM, Yee D, Garwood M. Radiology. 2004;233:424.
57. Sijens PE, vander Bent MJ, Nowak PJ, van Dijk P, Oudkerk M. Magn. Reson. Med. 1997;37:222.
58. Bakker CJG, Vriend J. Phys. Med. Biol. 1983;28:331.
59. Jagannathan NR, Seenu V, Kumar M. Radiology. 2002; 223:281.
60. Mackinnon WB, Huschtscha L, Dent K, Hancock R, Paraskeva C, Mountford CE. Int. J. Cancer. 1994;59: 248.
61. Mescher M, Tannus A, Johnson MO'N, Garwood M. J. Magn. Reson. 1996;A123:226.
62. Gribbestad IS, Singstad TE, Kristofferson A, Kvistad KA, Johnson IT, Lundgren S, Roell S. Proc. Int. Soc. Magn. Reson. Med. 2004;11:2044.
63. Katz-Brull R, Margalit R, Bendel P, Degani H. MAGMA 1998;6:44.
64. Johnstone PA, Moore EM, Carrillo R, Goepfert CJ. Cancer. 2001;91:1075.
65. Wang J, Shih TT, Hsu JC, Li YW. Clin. Imaging. 2000;24: 96.
66. Thomas MA, Binesh N, Yue K, DeBruhl N. J. Magn. Reson. Imaging. 2001;14:181.

In Vivo Molecular MR Imaging: Potential and Limits

Mathias Hoehn and Uwe Himmelreich
In-vivo-NMR-Laboratory, Max-Planck-Institute for Neurological Research, Cologne, Germany

Introduction

The recent years have seen dramatic progress in molecular imaging across the board of various techniques. Molecular imaging, in the context of the authors' goals in this chapter, is termed as the non-invasive, *in vivo* visualization of cellular and molecular events in normal and pathological processes. In particular, optical and *in vivo* bioluminescence imaging (BLI) techniques [1,2] but also positron emission tomography (PET) [3,4] have set the pace. All these high-resolution imaging modalities are based on the same general idea that the presence of specific contrast agents, incorporated or intracellularly induced by cellular activities, will provide the necessary contrast of the cells or compartments of interest against the background of the host tissue [1,5].

For the purpose of specific contrast generation, either tracers or contrast agents are incorporated in cells or attached via selective antigen–antibody bindings. Alternatively, cells are, in close cooperation with molecular biologists, transfected with the goal of expressing selected markers. These markers are considered "reporter genes," as the genes responsible for the marker expression are coupled to other predefined genetic expression patterns. Thus, the reporter genes can be chosen to be expressed constitutively (i.e. permanently) or conditionally (i.e. dependent on specific gene activities, linked to particular cellular dynamics or functional activity).

Magnetic resonance imaging (MRI) has joined this group of imaging modalities with cellular/molecular focus only very recently. The reason for this "late appearance" as a player in the field of molecular imaging, despite its high spatial three-dimensional (3D) resolution, is based on the fact that labeling strategies of cells for this imaging technique are not as intuitively available and not directly accessible. For example, optical techniques exploit very successfully the existence of naturally occurring chromophores, genetic code of which is transfected in a selected group of cells. The most successful single chromophore to date is probably the green fluorescent protein "GFP," originally found in certain jellyfish.

For MRI applications of microscopic resolution and for the study of cellular dynamical processes, cells can be effectively loaded with iron oxide nanoparticles. This cell loading generates a pronounced contrast in T_2^*-weighted images. This approach is by now well established and has already led to a variety of applications in diverse medical but also in developmental biological areas. In the latter field, individual cells of an embryo have been labeled [6,7] and, consequently, the fate of the labeled cells during further cell division and selective cell migration was followed *in vivo*. In the medical arena, there are two major application fields: one dealing with the monitoring of macrophage activity during inflammatory processes in various organs including liver [8,9] as well as brain [10–12] and another field dealing with stem cell implantation in the hope of successful tissue regeneration [13–16] (Figure 1).

This chapter is not aiming to review the broad application field. For this purpose, the reader is referred to a couple of excellent recent reviews [17,18]. The basis for the success of these applications in animal models rests in all cases on fundamental considerations concerning the reliable detectability of the cells of interest and the monitoring of their fate in space and time. The present chapter will review the methodological and technical aspects of the ultrahigh-resolution MRI technique, and, most of all, the key tool of this strategy: cell labeling. The goal of the present chapter is to provide the reader with an insight into the methodological requirements for successful *Molecular MRI*, and to prepare an overview of the various strategies from which the reader is then free to determine an optimal strategy for particular applications.

Detectability

Intrinsic contrast is in most cases insufficient to monitor cells *in vivo*. Cell-specific contrast must be generated in order to distinguish between targeted cells and other tissue or cells. Generation of sufficient contrast depends on (a) the availability of high-affinity contrast agents, (b) the ability of these contrast agents to overcome biological delivery barriers (e.g. cell membranes; blood–brain barrier), (c) minimal disturbance of the cellular microenvironment (low toxicity), (d) amplification strategies that result in appropriate concentrations, and (e) the availability of sensitive, high-resolution imaging techniques. Cells can be labeled *in vivo* or by pre-labeling, *ex vivo*.

Paramagnetic MRI contrast agents modulate the spin–lattice relaxation time (T_1) of rapidly exchanging water

Graham A. Webb (ed.), Modern Magnetic Resonance, 1087–1098.
© 2008 *Springer.*

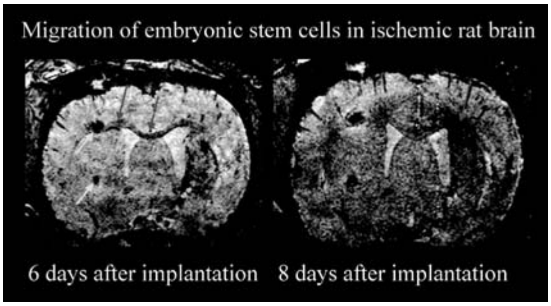
Migration of embryonic stem cells in ischemic rat brain
6 days after implantation
8 days after implantation

Fig. 1. Coronal sections through a rat brain at 6 and 8 days following implantation of embryonic stem cells into the left hemisphere, contralateral to the induced transient 60 min focal cerebral ischemia. 3D data sets were recorded with isotropic spatial resolution of 78 μm with a scan time of approximately 70 min. The primary implantation sites in the cortex and the striatum are indicated by white arrows. Note at 6 days, the discrete dark line (dark arrow) along the corpus callosum between the cortical implantation site and the ventricular wall showing cells migrating toward the lesioned hemisphere. At 8 days postimplantation, a dark region becomes visible in the dorsal part of the lesioned territory reflecting the first arrival of USPIO-labeled cells.

molecules and alter the local homogeneity of the magnetic field (T_2 and T_2^* relaxation times). Cells labeled with contrast agents generate *hypo*intense contrast in T_2-weighted (T_2w) images (labeled e.g. with iron oxide particles) or *hyper*intense contrast in T_1-weighted (T_1w) images (labeled e.g. with Mn or lanthanide chelates). These contrast agents most commonly consist of nanoparticles (iron oxide, T_2w), inorganic chelates (Gd, Eu, and Mn chelates; T_1w), or particles contained in a polymer sphere (iron oxide microspheres).

A precondition for a contrast agent is that the relaxivity of exchanging/surrounding protons is sufficiently modified. The large magnetic susceptibility of small paramagnetic particles can affect much larger regions of the image than is suggested by the actual size of the particle [19]. The limits of cell detectability are defined by the spatial resolution, the signal-to-noise ratio (SNR), and the contrast-to-noise ratio (CNR).

Contrast Agents for Molecular Imaging

The suitability of magnetic markers for molecular MR imaging is influenced by the change of the MR signal caused by alterations in the magnetic susceptibility and expressed by the relaxivity (R). Contrast agents for molecular imaging must provide a high relaxivity *in vivo* without compromising the cellular microenvironment. This sets certain limitations for the concentrations of contrast agents. The choice of contrast agents also depends on the intrinsic background signal of the respective application.

Dextran coated superparamagnetic iron oxide particles (SPIOs) [20] and ultrasmall SPIOs (USPIOs) have magnetic moments more than three orders of magnitude larger than those of clinically applied contrast agents [21]. Iron oxide particles can be used for T_1- [22], T_2- [12], and T_2^*- [23] weighted imaging. Due to the large magnetic moment of (U)SPIOs, the relaxivities R_2 and R_2^* are several thousand times larger than R_1 [24]. (U)SPIOs are well suited for cell tracking because of the long-range susceptibility effects. Relaxivity (R_2/R_2^*) of iron particles can easily be tested *in vitro* by comparison of signal quench in the presence of respective contrast agents. R_2^* relaxivity increases with increasing concentrations of the iron oxide particles but will be saturated (complete quench of signal) [24–26]. Saturation of magnetization occurs once the mass of iron per cell exceeds a certain threshold [24]. When normalized to iron content, larger particles greatly decrease T_2^* and enhance the susceptibility effect when compared to smaller particles [27].

The T_2^* effect of iron oxide based contrast agents is also larger than T_1 effects of Mn- and lanthanide-chelates because water molecules must be in close proximity of the paramagnetic center to generate T_1 contrast [28]. Crich *et al.* estimated the minimum detectable number of Gd-HPDO3A labeled cells in a phantom at approximately 10^3 cells [29]. Visualization is attainable when cellular concentrations of Gd-contrast agents are in the order of 10^{-4}–10^{-5} molar [30,31].

Magnetic properties that are most commonly modified for the design of contrast agents that predominantly increase R_1 relaxivity (hyperintensity in T_1w MR images) include:

(a) hydration number (q)—water bound to agent
(b) exchange rate of water molecules (τ_m)
(c) rotational correlation time of complex (τ_r).

In order to achieve sufficient contrast with T_1w contrast agents *in vivo*, accumulation of contrast agent to millimolar concentrations is usually required [32]. A system that entraps several units of a Gd chelate is apoferritin, resulting in an increase of relaxivity by almost 20 times compared to the free contrast agent [33,34]. Other approaches to concentrate Gd chelates at the site of interest include self-assembling aggregates [30,35,36]. It was suggested in recent studies that even picomolar binding is sufficient to achieve detectable CNR if high loads of particles were delivered to the cell [37].

The rotational correlation time of a contrast agent can be altered by changing the viscosity of the environment or by interaction with large molecules [38]. The latter has resulted in the design of contrast agents that specifically bind to certain proteins [39,40].

Resolution

Low image resolution can attenuate the relaxation effects through partial volume effects and thereby reduce detectability of labeled cells. The spatial resolution is limited by the strength of the gradients and the matrix size. The acquisition of MR images with a resolution in the order of tens of microns is currently possible within a reasonable time frame. The trade-off of high resolution is a reduced SNR.

A precondition for detection of single labeled cells by MRI is that the number of voxels is higher than the number of individual cells in the respective volume. Dodd *et al.* have demonstrated a good correlation of individual cell distribution between MRI and microscopic methods, proving the detectability of single cells by MRI [41]. Larger susceptibility effects, like for micron-size iron oxide particles, result in higher contrast and permit detection at lower resolution [27,42,43]. These microspheres can be considered a point source that creates a localized field larger than the field created by the evenly distributed, smaller (U)SPIOs, resulting in detectability of single cells with a spatial resolution as low as 200 µm [42].

Signal- and Contrast-to-Noise Ratio

The dilemma of cell tracking in animal models is that acquisition time is limited and resolution has to be as high as possible in order to meet the requirements set by working with anaesthetized animals and being able to detect small numbers of cells *in vivo*. This limits the options to maximize SNR and CNR. Apart from longer acquisition times, the SNR can be increased by stronger magnetic fields, smaller RF coils, and cryoprobes [44,45]. Pulse sequences, repetition time (T_R), echo time (T_E), and pulse length have to be chosen carefully and adjusted for each animal model. Optimization of MR parameters has been reviewed extensively [46,47]. The CNR is influenced by the efficiency of the labeling strategy. Visually apparent contrast is defined as $\mathrm{CNR} \geq 5$, with $\mathrm{CNR} = |(I_A - I_B)N^{-1}|$ (I_A, I_B—signal intensities of the two adjacent regions, N—noise level). Using the relaxivity of the respective contrast agents and T_1/T_2—values of the tissue, acquisition parameters (T_R, T_E) can be optimized to maximize CNR [31,37].

It was demonstrated that detection of single cells *in vitro* is feasible [41,42,48].

Quantification

Cells can be quantified *in vitro* by the construction of simple gelatin phantoms [25,49] (Figure 2). If a sufficient spatial resolution is provided in 3D MR images and homogeneous phantoms are utilized individual cells labeled with iron oxide particles can be counted in high dilutions [49].

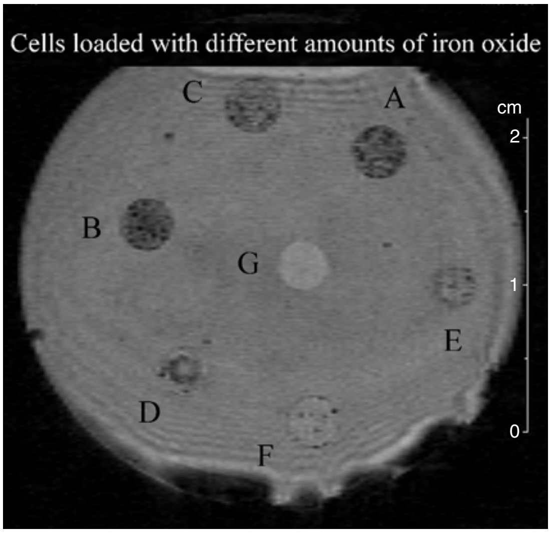

Fig. 2. Agarose gel phantom containing embryonic stem cells transfected with iron oxide particles. The holes A–E and G contain approximately 10^4 cells and the hole F contains 5×10^2 cells, which were suspended in 50 µl agarose. Cells were incubated with different concentrations of iron oxide nanoparticles prior to suspension (amount of iron oxide per 5×10^5 cells: A, 40 mg; B, 18 mg; C and F, 5 mg; D, 1 mg; E, 0.2 mg; and G, no iron oxide particles). The 3D gradient-echo MR image (FLASH) was acquired with the following parameters: field strength = 7 T, matrix = 256K × 128K × 64K data points; $T_R = 250$ ms, $T_E = 20$ ms, FOV = 4 cm × 4 cm).

Bowen *et al.* have addressed the quantification of iron oxide concentrations in cell suspensions based on relaxivities [24]. Relaxation rates of compartmentalized (U)SPIOs correlated with predicted values using the static dephasing theory [50]. Best correlations were achieved using (R_2^*–R_2) under the dilute pertuber assumption, indicating the suitability for quantification for cases where volume fractions of cells containing iron oxide are relatively small, as is the case, e.g. for implanted cells *in vivo* [24]. This model has only been tested *in vitro*. Experimentally, detection of cell clusters of tens to hundreds of (U)SPIO-labeled cells was demonstrated in animal models [14,51]. It was suggested that the utilization of micron-size iron oxide particles are suitable to detect single cells *in vivo* [52]. An additional advantage of these latter particles is that single particles or cells can be detected *in vitro* even with relatively low resolution (due to the large diameter and magnetic moment), and that the label is not diluted beyond the minimum observable threshold by cell division but remains within the cell for up to 1 year [27,43,52].

If the relaxivity of lanthanide contrast agents is known model-based predictions of local concentrations of T_1 contrast agents can be reliably performed by measurement of T_1 values [31,37]. If particle loading of cells and relaxivity of the contrast agent remain constant after implantation this could result in quantitative MRI in *in vivo* models. Contrary to these results, Crich *et al.* have found that cell pellets with variable Gd-chelate loading show a decrease of R_1 relaxivity if concentrations exceed 0.1 μmol/mg protein [29]. Possible explanations include competing T_2^* effects, resulting in signal broadening.

Cell Labeling

Route of Uptake

Conventional MR cell labeling relies on surface attachment of contrast agents to the cell [53–56]. Contrast agents are often chemically modified so that they bind unspecifically or to specific cell types. A common strategy involves linking a contrast agent with a monoclonal antibody that is recognized by receptors on the cell surface [55]. For review see Ref. [30]. These strategies are generally not suitable for *in vivo* applications, where interactions with other cells have to be avoided, as for stem cell tracking. Extracellular labeling may result in detachment of the label or transfer to other cells. We will therefore focus on strategies to internalize contrast agents.

Probably the most effective route to internalize compounds into cells is by endocytosis. Hereby, intracellular vesicles (endosomes) are formed after introflection of portions of the cell membrane and fusion of its extremities. The endosomes contain compounds that are either bound to the membrane or present in the extracellular medium. Endocytosis is most effective in phagocytic cells (also called phagocytosis). Paramagnetic iron oxide particles but also Gd chelates have been successfully internalized into macrophages, monocytes, mononuclear T-cells, and oligodendrocyte progenitors [13,26,29,57–61]. In order to internalize high quantities of a contrast agent, receptor-mediated endocytosis is sometimes the method of choice. Hereby, the substrate in the extracellular medium interacts with receptor molecules on the membrane (like contrast agents linked with a monoclonal antibody) and are internalized in high concentrations [26,62].

Hinds and co-workers [27,43] have demonstrated that even micron-scale particles (0.9–2.8 μm) of an aggregate of iron oxide magnetite that is encapsulated in a polymer, are incorporated into perinuclear endosomes by stem and progenitor cells [48]. This labeling strategy has been highly efficient (almost 100%). It was also found that concentrating (U)SPIOs into cells increases the relative R_2^* sensitivity, compared to uniformly distributed particles [26,63].

In order to increase the uptake of contrast agents that do not spontaneously accumulate in endosomes, magnetoliposomes [64], and lectins [65] have been used in several experiments. A method developed in molecular biology for transfection of oligonucleotides, lipofection has been successfully adopted for labeling of cells with contrast agents [14]. Commercially available polycationic transfection agents encapsulate (U)SPIOs through electrostatic interaction [66]. The transfection agents shuttle the (U)SPIOs into the cell and form endosomes that finally merge into liposomes. This procedure has successfully been applied for labeling T-cells, stem cells, and other mammalian cells [14,66–69]. A similar approach is the labeling of cells with magnetodendrimers, which consist of (U)SPIOs coated with carboxylated dendrimers [51]. These compounds are also used as transfection agents and result in the formation of endosomes [70]. A broad range of cells has been labeled with dendrimers [15,51,71,72].

Others have produced transgenic cells expressing, for example, the transferrin receptor and are thus susceptible to the uptake of conjugates of transferrin and monocrystalline iron oxide nanoparticles [73,74].

Many larger probes are membrane impermeable and fail to attain intracellular concentrations required for MRI. Peptides or proteins mediating membrane translocation signals (MTS) have been coupled with contrast agents for internalization. MTS from the HIV tat peptide have been linked to SPIOs and lanthanide chelates for transport into several cell types [75–78]. Hereby, the contrast agents most likely accumulate in the cytoplasm [77]. Allen and Meade have suggested a relatively simple system for internalization that consists of a polyarginine-modified Gd DOTA system [79].

Microinjection of contrast agents was used in embryology for cell tracking [6,7]. Increased contrast was detectable in the developed embryo compared to controls, indicating sufficient contrast with cell division. However, this method has only applications limited to injection of large single cells in developing embryos. It is not practical for tracking populations of cells due to its labor-intensive preparation and the dilution of the label with cell division [7].

Zhang *et al.* adopted another method from molecular biology, where so-called biolistic "gene-guns" are used to introduce oligonucleotides into cells [80,81]. Biolistic labeling was performed with ferromagnetic particles and resulted in a labeling efficiency of 95% of surviving cells. Similarly to microinjection, cell labeling remained stable.

Electroporation is a process that permeabilizes cell membranes by exposure to an external electric field. Rapid resealing of the membrane pores traps internalized compounds inside the cell. Widely used to introduce foreign DNA into cells, it has also been used for drug delivery [82]. Paturneau-Jouas *et al*. have used electroporation for the uptake of low-molecular weight Gd chelates *in vivo* [83]. It remains to be seen how efficient this labeling method is and how stressful it proves for the respective cells.

In vivo and *ex vivo* Labeling

In vivo labeling of cells is possible if phagocytes take up contrast agents that were administered either intravenously or after injection in the targeted organ. This labeling strategy is based on naturally occurring or targeted, mediated endocytosis (mainly macrophages). Hereby, macrophages accumulate the iron oxide particles from the blood, whereas the remaining iron oxide in the blood (or other organs) is washed out. It was first introduced for hepatic imaging [84]. Subsequent development of clinically approved USPIOs have resulted in labeling strategies to distinguish between normal tissue and tumor metastases in lymph nodes [85] and bone marrow [86] based on the uptake of these particles by macrophages in those organs.

The uptake of iron oxide by macrophages has also been utilized in some disease models to highlight increased macrophage activity in areas of inflammation. Such applications include visualization of atherosclerotic plaques [87], visualization of increased macrophage activity in the kidney after injury and organ rejection [88,89], and macrophage infiltration in brain lesions following ischemia [10,90].

Direct injection of micron-size iron oxide particles into various regions of the sub-ventricular zone of the rat brain resulted in *in vivo* labeling of neuronal stem cells by endocytosis, allowing their migration to be tracked along the rostral migratory stream to the olfactory bulb [52]. Coupling of MTS peptides with nanoparticles and antibody or receptor binding ligands has been suggested as a possible targeted *in vivo* labeling strategy [91]. Paturneau-Jouas *et al*. have used electroporation after intraperitoneal injection of Gd chelates for internalization into muscle cells *in vivo* [83].

So far, targeted *in vivo* labeling was mainly demonstrated for phagocytes. In all other cases, pre-labeling of cells according to the procedures listed above is necessary. Hereby, *in vitro* pre-labeled cells are transferred to the targeted organ or tissue by injection.

Responsive Contrast Agents

Contrast agents have been developed with the aim of reporting on the physiological status and metabolic activity of cells [30,92]. Most of these contrast agents are Gd based chelates with one or more potential coordination sites blocked in the inactive state, preventing free access of exchanging water molecules to the paramagnetic ion.

Lowe *et al.* synthesized an MR contrast agent that is responsive to changes in pH, generating no contrast at high pH but high contrast at low pH [93]. The Gd DO3A derived agent contains a sulfonamide nitrogen, which is protonated at low pH. Therefore, it cannot coordinate at low pH and provides free access to exchanging water molecules. Meade and co-workers developed a probe that is responsive to intracellular changes in calcium concentrations [94,95]. Similarly, two carboxyl groups of the chelate coordinate either to the Gd^{3+} ion (inactive) or to the Ca^{2+} ion (active). Probes responsive to enzyme activity (e.g. β-galactosidase) have been developed [96] and applied for cell visualization *in vivo* [6]. Contrast agents responsive to pO_2 were developed on the basis of the BOLD effect [97] and coupling an increase in τ_r with and redox switch [98].

Other contrast agents utilize the so-called chemical exchange saturation transfer (CEST) agents to be responsive to variable concentrations of targeted molecules [99,100]. Aime *et al*. have suggested an insoluble contrast agent that is activated by intracellular enzymatic solubilization [30]. However, the effective incorporation of the contrast agent in its insoluble state is still an unresolved issue.

In vivo MRI Experiments

Cell tracking *in vivo* requires the acquisition of isotropic 3D MR images of living animals at near-cellular resolution in order to minimize partial volume effects. Temporal constraints are set by working with live animals so that spatial resolution is typically in the range of tens up to a hundred of microns. The principle challenge is to obtain sufficient SNR. Hardware improvements often target the reduction of thermal noise voltages from the sample by using small surface RF coils [101]. Design of the receiver coil aims for low coil resistance. This can be achieved by cryo-cooled probes [102], which have been applied to micro-imaging in animal models [44,45]. RF coils made of high temperature superconducting material have also been demonstrated to reduce coil loss substantially *in vitro* and in animal models [103,104].

Animal models require usually anaesthetized animals. Apart from the obvious associated disadvantages, it has the advantage of decreasing movement artifacts in MR images as the animal can be firmly fixed in an animal holder.

MRI of animal models is usually performed at a high field strength (>4 T). While this is an advantage for improving the SNR it has the disadvantage of an increase in the T_1/T_2 ratio, resulting in an increase in the acquisition time and in a loss of intrinsic contrast in the brain. The increase in the magnetic field strength, compared to clinical systems, also results in more pronounced magnetic susceptibility effects. While this can lead to unwanted artifacts in the MR images, it has also the advantage that magnetically labeled cells can be more easily visualized. Gradient-echo sequences tend to be more susceptible to those artifacts than spin-echo experiments.

Data acquisition methods utilized for cell tracking are similar to those employed for clinical MRI (spin-echo, gradient-echo, diffusion-weighted imaging, inversion recovery, and magnetization transfer sequences). Rapid acquisition methods are commonly used for animal models, namely gradient-echo fast-low-angle-shot (FLASH) [105] and echo planar imaging (EPI) [106]. The utilization of MR microscopy for animal models was reviewed by Ahrens *et al.* [107].

Pulse sequences that emphasize signal loss due to field inhomogeneities are beneficial for (U)SPIOs. Cell tracking in animals is usually performed using 3D gradient-echo sequences (FLASH) for T_2/T_2^* effects [14,51,62] and two-dimensional (2D) multi-slice or 3D spin-echo sequences for T_1 effects [6,29,57]. Unless very strong T_1 weighting is used with T_Rs of approximately 100 ms, spin-echo sequences are not fast enough to permit the acquisition of a high-resolution 3D image within the time frame required for anaesthetized animals. 2D multi-slice images have the disadvantage of strong partial volume effects. A resolution of 100 to 200 μm is usually sufficient for the visualization of small cell clusters. The detection of single cells is not realistic as naturally occurring movements like breathing and muscle twitching are in the order of hundreds of microns, resulting in blurring effects. Additional blurring effects are caused by diffusion [41]. The acquisition of 3D data sets is, at any rate, a requirement for the co-registration of data sets in longitudinal studies and for the co-registration with independently recorded, non-MR data sets.

The effects of gradient strength, T_R and T_E to optimize SNR and CNR in MRI have been studied extensively [41,46,47]. For conditions of large magnetic moments due to (U)SPIOs loaded cells in animal models, the greatest sensitivity was observed with R_2^*, rather than R_2 or R_1[24]. Low gradient strengths through the use of low acquisition bandwidths will enhance susceptibility effects. This is also beneficial in terms of SNR, due to reduced diffusion loss.

An intrinsic problem for tracking iron oxide labeled cells in animal models are other areas of susceptibility induced field inhomogeneities (signal loss in T_2/T_2^*w images), namely from airspaces, but more importantly, from blood clots/hemorrhages and tissue interfaces. Seppenwoolde *et al.* have developed a technique that exploits the natural dipolar field surrounding paramagnetic markers by introducing a dephasing gradient on the slice-select axis to spoil signal across all the sample except in regions where the local gradients surrounding the paramagnetic marker are of the right amplitude and orientation to combine constructively with the added dephasing gradient to result in refocusing of the lost signal [108]. Coristine *et al.* have applied this "white-marker" technique to distinguish iron oxide labeled cells from other sources of field inhomogeneities [109].

The optimal acquisition parameters need to be determined for each combination of cell type, animal model, and contrast agent.

Biological Aspects of Cell Labeling

Reproducible and efficient visualization of cells with MRI does not only require optimized MR properties of contrast agents but also biological properties that result in stable labels without affecting other cellular processes.

Toxicity

Many contrast agents are administered in coated (polymer coating) or chelated (in particular the lanthanides) form, in order to reduce toxicity. Commercially available and clinically tested contrast agents are often used for molecular imaging, for which short and medium term toxicity is minimal. However, one has to consider that contrast agents for molecular imaging are often applied for longitudinal labeling, and in concentrations much higher than clinically applied. Immediate toxic effects can easily be tested by growth and viability studies in cell suspensions. It is more difficult to assess long-term stability (and toxicity) of coated contrast agents and the effect of contrast agents on cellular processes like differentiation.

It has been reported that very high concentrations of (U)SPIOs for cell labeling (up to 2 mg iron/ml) can cause decreased proliferation and even cell death [110]. This is in particular true after the formation of reactive oxygen species [111]. Some dextran coatings for iron oxide particles are biodegradable [112]. Released iron enters into the cellular iron metabolic pathways. Iron in high concentrations is known to interact with a number of other metabolic pathways [113,114]. Overloading can result in increased oxidative stress. Although iron oxide can be released by biodegradation, one has to consider that this will occur gradually resulting in non-toxic free iron concentrations. Stroh *et al.* have found that decomposition of the coating of iron oxide particles does not affect cell growth but causes oxidative stress [113]. These authors have suggested the application of antioxidants or iron chelators to prevent toxic effects of leaking iron.

T-cells labeled with SPIOs by endocytosis retain their function [58,115]. Sapiro *et al.* have shown in longitudinal studies that even large iron oxide loaded microspheres do not influence cell proliferation and differentiation at low concentrations [48,52]. Hill *et al*. found a dose-dependent alteration in cell proliferation but not in differentiation for mesenchymal stem cells [43]. Also, magnetodendrimers and (U)SPIOs did not cause differences between labeled and unlabeled cells in terms of proliferation, viability, and differentiation of neural stem cells in short term *in vitro* experiments [14,51,71]. Frank and co-workers have studied the effect of superparamagnetic iron oxide nanoparticles and transfection agents extensively [67–69,116]. No long-term effect on cell viability, rate of apoptosis, phenotype, proliferation, activation, and differentiation was found.

The toxicity of lanthanide contrast agents has also been studied extensively [38]. As lanthanides are known to be highly toxic, stable chelates are required for protection. Gd-HPDO3A is one of the best tolerated contrast agents with an $LD_{50} > 10$ mmol/kg in rats [38]. Although well tolerated in clinical applications, high dose toxicity for molecular imaging application requires further investigations. Several studies have confirmed that Gd-dextrans remain intact in cells [29] and are tolerated by cells in culture and *in vivo* after implantation [13,29,57].

In addition to metal ions, the interactions of chelates, transfection agents, or antibodies have to be considered for the assessment of toxicity. Although concern has been raised about potential release of reactive iron species from tat-labeled cells [67], functional tests with and without HIV tat peptide based contrast agents have shown no difference between labeled and unlabeled cells [77]. When used alone, some transfection agents are reported to be toxic [116]. However, iron oxide complexed with transfection agents does not affect viability, differentiation, or proliferation [68,69,116]. It was found in one study that the differentiation of stem cells can be influenced by transfecting agents [117]. This highlights the need to study possible biological side effects for each labeling system and cell type.

In addition to toxicological aspects of the contrast agent, one has to consider that labeling procedures like electroporation, microinjection, or biolistic "gene-guns" can cause mechanical damage to cells.

Assessment and Stability of Label

It is crucial for *in vivo* cell tracking to estimate the efficiency of cell labeling, the internalization of the label, and for how long these cells are detectable (i.e. dilution of the label; Figure 3). Various approaches have been taken to assess *in vitro* labeled cells by using agar or gelatin based phantoms (Figure 2).

It was found that uptake of (U)SPIOs as well as Gd chelates by endocytosis is linear with dose [24,29]. Linearity was also shown for (U)SPIO uptake with incubation time [24,118]. Interestingly, uptake is increased with particle size [118], which also explains the excellent uptake of micron-size microspheres [27,48].

The labeling efficiency can be assessed by NMR relaxometry [29,30,7,78] or by other techniques like atomic absorption spectroscopy to determine the iron content of USPIO-labeled cells [14]. Internalization of contrast agents (Figure 3) can also be verified by staining techniques in combination with (electron) microscopy.

The visibility of cells with time depends primarily on the dilution of the contrast agent due to cell proliferation and on degradation processes of the coating of contrast agents. Stem cells labeled with iron oxide particles have been monitored *in vivo* for up to 7 weeks in rat brains [14] and for up to 3 months in a spinal cord implantation model [72]. Embryonic stem cells were detectable, with contrast condition comparable to the originally labeled culture, after 20 cycles of cell division, which is an increase of cell numbers by a factor of 10^6 [14,25,49]. In another study, the complete disappearance of iron particles has been observed due to dilution after proliferation within 2–3 weeks [69].

An advantage of large micron-size particle is that a single particle per cell may result in sufficient contrast. Hill *et al*. were able to detect mesenchymal stem cells for up to 3 months [43]. Shapiro and co-workers monitored microsphere labeled cells for 1 year [52].

Cell labeling with lanthanide chelates is more affected by dilution after cell division due to its lower sensitivity. Modo and co-workers were able to visualize stem cells for up to 7 days after labeling with a Gd chelate [13].

Histological evaluation at the endpoint of longitudinal MR studies is necessary to evaluate MR tracking of cells *in vivo*. Other causes for loss of label are exocytosis (Figure 3) and immune reaction with a subsequent transfer of contrast agents to macrophages. Co-location can be estimated by co-registration of MR images with stained histological sections. Due to the invasiveness of histological methods, co-registration with MR images will always be problematic due to swelling, distortion, etc. Possible approaches include corroboration of MRI detection of labeled cells by using Prussian blue staining against iron [62], validation with X-gal staining [51], or electron-dense inclusions for visualization by electron microscopy [61]. In addition, dual staining detects co-localization of contrast agent with certain cell types. An example is the Prussian blue and $ED1^+$ staining to discriminate USPIO-labeled macrophages [10,119].

The use of bifunctional contrast agents allows co-registration of histology and MRI without recourse to other methods. Dual labeling strategies can be classified in methods that use dual contrast agents and methods that utilize cells that can be visualized by specific modalities (e.g. cells that express certain proteins). Modo labeled stem cells with a Gd-Rhodamine dextran (GRID) that is

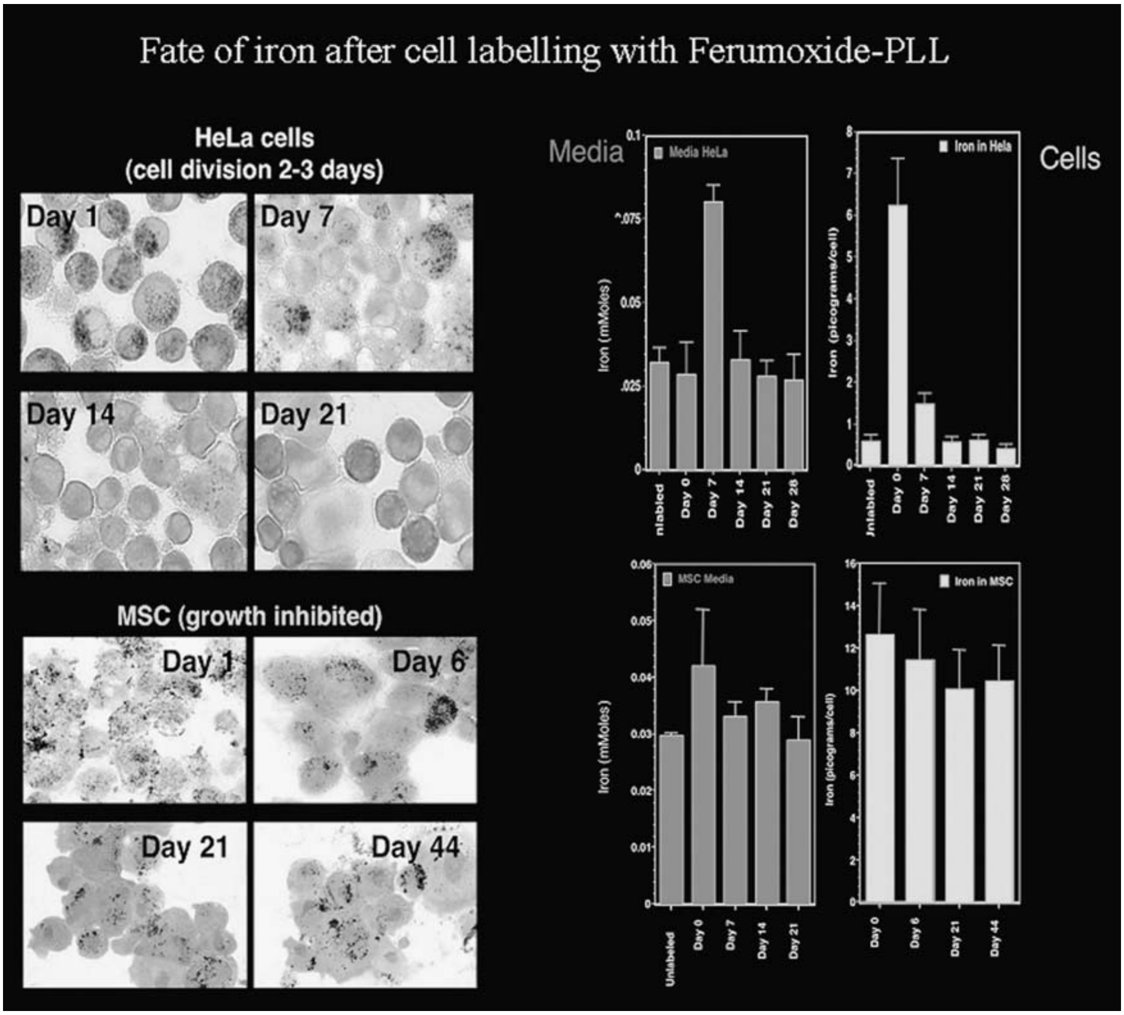

Fig. 3. Investigation into the persistence of iron oxide label after incorporation into HeLa cells or mesenchymal stem cells (MSC). On the left side, Prussian blue staining of cell cultures is depicted at various times after cell labeling. It is clear that the blue stain reflecting the iron content is rapidly lost in the heavily proliferating HeLa cells, while dark blue stains are still detected in the (very little proliferating) MSCs even after 44 days. The bar diagrams on the right show the iron content as determined in the cell culture medium (red) and in the cells (yellow), with the situation for the HeLa cells above, and the MSCs below. Again, the iron content remains quite stable for the MSCs, both in the cytosol and in the media. The HeLa cells have a maximum of iron directly following labeling, which is rapidly lost again (by leakage). This is reflected in the medium where the iron content transiently increases during the phase when the cells lose their iron content. Modified with permission from Ref. [69]. (See also Plate 89 on page XVI in the Color Plate Section.)

both magnetically and fluorescently detectable [13,57]. Hereby, MRI results can be assessed by subsequent fluorescence microscopy on histological sections. In addition, fluorescence microscopy allows additional staining to detect co-localization with markers for cell differentiation [13].

Similarly, labeling with Mn^{2+} as contrast agent allows validation by an independent method. Mn^{2+} has been used as an *in vivo*, trans-synaptic, MRI-detectable neuronal tract tracer that enters selectively neurons via Ca^{2+} channels [120–122]. The fate of Mn^{2+} can be verified by independent fluorescent dye staining.

Similar approaches, combining iron oxide particles with fluorophores were taken to track stem cells *in vivo* [27,43]. In contrast to dual contrast agents, co-localization can also be achieved by labeling stem cells that express fluorescence properties with USPIO [14]. These genetically modified stem cells express the GFP that can be detected on histological sections. In contrast to the other approaches, only those cells show fluorescence that is still viable at the time of termination. Hereby, dead cells and cells whose label had been transferred to macrophages can be distinguished from the targeted cells.

Summary

In summary, the successful design of a molecular imaging study of cells by MRI depends on a series of methodological evaluations and optimizations. As several of these optimization steps will prove to be dependent on the particular circumstances of the investigation, a checklist of aspects to be assessed before *in vivo* experiments are started can be compiled and is given here.

1. Select contrast agent dependent on intrinsic background (e.g. signal loss vs. signal gain),
2. optimize internalization of contrast agent,
3. check residence duration of contrast agent in cells/dilution of label,
4. check toxicity of label/labeling procedure,
5. consider independent/dual (e.g. in combination with optical) labeling options, generated by cells or co-localized on contrast agent,
6. relaxivity of labeled cells *in vitro,*
7. MRI sensitivity, and
8. hardware optimization for scan-time minimization.

As some of these considerations and tests will vary very much with cell type, disease model, etc. it is always advisable to perform the respective assessments anew when new cell lines or animal models or contrast agent is considered for use.

Outlook

With a more widespread application of cell labeling, the above discussed procedures will become more routine and established for a broad range of cell lines and applications. An integrative view on sensitivity improvement of MRI systems will most likely lead to voxel sizes reflecting a handful of cells, under true *in vivo* conditions, compatible with scan times that result in anesthesia periods tolerable for weakened animals of various disease models, in longitudinal investigations.

A close interaction between specialists of three different disciplines is seen as the basis for the exciting contributions of *in vivo* molecular MRI in the future. Expertise in *in vivo* MRI, including the understanding of animal physiology and pathophysiology, is a central prerequisite. The second partner will contribute expertise in contrast agent chemistry to design and synthesize the new generation of so-called “smart contrast agents.” These could be agents that are activated or deactivated under external control or under control of the cell status. Finally, the third discipline is molecular biology to design transgenic cells, so-called “smart cells.” These cells will be able to activate or deactivate added smart contrast agents according to the selected reporter gene. Alternatively, such transgenic cells may even produce their own intracellular contrast agent, as has recently been shown in an impressive investigation by the laboratory of Neeman [123], where cells under TET-on/TET-off switches could be shifted between modes where they either produced a strong T_2 contrast or not. In the activated mode, these cells upregulated the intracellular iron depot ferritin, resulting in (non-toxic) massive accumulation of iron in the cell.

The use of MR reporter genes that are genetically expressed and generate contrast coupled to the regulation of genes or by the presence/absence of exogenous substrates opens new doors for the non-invasive analysis of cell functions in various animal models under true *in vivo* conditions. In conclusion, with the synergy of the above-described three complementary disciplines, molecular MR imaging is only beginning to explore its own potential for future biomedical studies on cellular and molecular levels.

Acknowledgment

Financial support of the Hertie-Foundation and of the German-Israeli Cooperation project by the German Ministry of Education and Research (BMBF) is gratefully acknowledged. UH gratefully acknowledges an international reintegration grant (#013080) by the European Commission.

Glossary of Terms

Contrast agent—Chemical compound that increases the intrinsic contrast in an image.

Bifunctional contrast agent—Contrast agent that increases the intrinsic contrast for two different imaging modalities.

Responsive contrast agent—Contrast agent that conditionally increases the intrinsic contrast (depending on the change of environmental conditions like enzyme activation, pH change, change in ion concentration, and others).

Dendrimers—Large and complex polymers of a consistent size and a regular and highly branched architecture.

They are often used for the encapsulation of smaller molecules.

Endocytosis—In endocytosis, the cell engulfs some of its extracellular medium including material dissolved or suspended in it. A portion of the plasma membrane is invaginated and pinched off forming a membrane-bound vesicle called an endosome.

Endosome—Vesicle formed during endocytosis.

Molecular imaging—Non-invasive, *in vivo* visualization of cellular and molecular events in normal and pathological processes.

Stem cell—Cell with broad differentiation potential that retains the capacity for unlimited self-renewal. A totipotent stem cell has the ability to differentiate to all cell types of an organism, whereas a pluripotent stem cell produces many but not all cell types.

Transfection—A method by which experimental DNA (or in our case contrast agents) can be incorporated into mammalian cells after interaction of the encapsulating transfection agent and the cell membrane.

References

1. Weissleder R, Mahmood U. Radiology. 2001;219:316.
2. Edinger M, Cao YA, Hornig YS, Jenkins DE, Verneris MR, Bachmann MH, Negrin RS, Contag CH. Eur. J. Cancer. 2002;16:2128.
3. Blasberg R, Tjuvajev JG. Mol. Imaging. 2002;1:160.
4. Gambhir SS. Nat. Rev. Cancer. 2002;9:683.
5. Weissleder R, Ntziachristos V. Nat. Med. 2003;1:123.
6. Louie AY, Hüber MM, Ahrens ET, Rothbächer U, Moats R, Jacobs RE, Fraser SE, Meade RJ. Nat. Biotechnol. 2000;18:321.
7. Jacobs RE, Fraser SE. Science. 1994;263:681.
8. Weissleder R. Radiology. 1994;193:593.
9. Stark DD, Weissleder R, Elizondo G, Hahn PF, Saini S, Todd LE, Wittenberg J, Ferrucci JT. Radiology. 1988;168:297.
10. Saleh A, Wiedermann D, Schroeter M, Jonkmanns C, Jander S, Hoehn M. NMR Biomed. 2004;17:163.
11. Saleh A, Schroeter M, Jonkmanns C, Hartung HP, Mödder U, Jander S. Brain. 2004;127:1670.
12. Dousset V, Delalande C, Ballarino L, Quesson B, Seilhan D, Coussemacq M, Thiaudiere E, Brochet B, Canioni P, Caille JM. Magn. Reson. Med. 1999;41:329.
13. Modo M, Cash D, Mellodew K, Williams SCR, Fraser SE, Meade TJ, Price J, Hodges H. Neuroimage. 2002;17:803.
14. Hoehn M, Küstermann E, Blunk J, Wiedermann D, Trapp T, Wecker S, Föcking M, Arnold H, Heschler J, Fleischmann BK, Schwindt C, Bührle C. Proc. Natl. Acad. Sci. U.S.A. 2002;99:16267.
15. Bulte JWM, Ben-Hur T, Miller BR, Mizrachi-Kol R, Einstein O, Reinhartz E, Zywicke HA, Douglas TD, Frank JA. Magn. Reson. Med. 2003;50:201.
16. Veizovic T, Beech JS, Stroemer RP, Watson WP, Hodges H. Stroke. 2001;32:1012.
17. Bulte JWM, Modo M, Hoehn M. Mol. Imaging. 2005;4:143.
18. Bulte JWM, Duncan ID, Frank JA, Cereb. J. Blood Flow Metab. 2002;22:899.
19. Lauterbur PCM, Bernardo ML Jr, Mendonca Dias MH, Hedges LK. Proc. Int. Soc. Magn. Reson. Med. 1986;5:229.
20. Fahlvik AK, Klaveness J, Stark DD. J. Magn. Reson. Imaging. 1993;3:187.
21. Bulte JWM, Brooks RA, Moskowitz BM, Bryant LH Jr, Frank JA. Magn. Reson. Med. 1999;42:379.
22. Moore A, Marecos E, Bogdanov A Jr, Weissleder R. Radiology. 2000;214:568.
23. Furman-Haran E, Margalit R, Grobgeld D, Degani H. J. Magn. Reson. Imaging. 1998;8:634.
24. Bowen CV, Zhang X, Saab G, Gareau PJ, Rutt BK. Magn. Reson. Med. 2002;48:52.
25. Küstermann E, Wiedermann D, Bührle C, Arnold H, Föcking M, Trapp T, Hoehn M. Proc. Int. Soc. Magn. Reson. Med. 2002;10:1255.
26. Weissleder R, Cheng HC, Bogdanowa A, Bogdanow A Jr. J. Magn. Reson. Imaging. 1997;7:258.
27. Hinds KA, Hill JM, Shapiro EM, Laukkanen MO, Silva AC, Combs CA, Varney TR, Balaban RS, Koretsky AP, Dunbar CE. Blood. 2003;102:867.
28. Lauffer RB. Chem. Rev. 1987;87:901.
29. Crich SG, Biancone L, Cantaluppi V, Duo D, Esposito G, Russo S, Camussi G, Aime S. Magn. Reson. Med. 2004;51:938.
30. Aime S, Cabella C, Colombatto S, Crich SG, Gianolio E, Maggioni F. J. Magn. Reson. Imaging. 2002;16:394.
31. Ahrens ET, Rothbächer U, Jacobs RE, Fraser SE. Proc. Natl. Acad. Sci. U.S.A. 1998;95:8443.
32. Wickline SA, Lanza GM. J. Cell Biochem. 2002;39:90.
33. Harrison PM, Arosio P. Biochim. Biophys. Acta. 1996;1275:161.
34. Aime S, Crich SG, Frullano L. Angew. Chem. Int. Ed. Engl. 2002;114:1059.
35. Aime S, Botta M, Fedeli F, Gianolio E, Terreno E, Anelli PL. Chem. Eur. J. 2001;7:5261.
36. Bogdanov A, Matuszewski L, Bremer C, Petrovsky A, Weissleder R. Mol. Imaging. 2002;1:16.
37. Morawski AM, Winter PM, Crowder KC, Caruthers SD, Fuhrhop RW, Scott MJ, Robertson JD, Abendschein DR, Lanza GM, Wickline SA. Magn. Reson. Med. 2004;51:480.
38. Caravan P, Ellison JJ, McMurry TJ, Lauffer RB. Chem. Rev. 1999;99:2293.
39. Nivorozhkin AL, Kolodziej AF, Caravan P, Greenfield MT, Lauffer RB, McMurry TJ. Angew. Chem. Int. Ed. Engl. 2001;40:2903.
40. De Leon-Rodriguez LM, Ortiz A, Weiner AL, Zhang S, Kovacs Z, Kodadek T, Sherry T. J. Am. Chem. Soc. 2002;124:3514.
41. Dodd SJ, Williams M, Suhan JP, Williams DS, Koretsky AP, Ho C. Biophys. J. 1999;76:103.
42. Sapiro EM, Skrtic S, Hill JM, Dumbar CE, Koretsky AP. Proc. Int. Soc. Magn. Reson. Med. 2003;11:229.
43. Hill JM, Dick AJ, Raman VK, Thompson RB, Yu ZX, Hinds KA, Pessanha BSS, Guttman MA, Varney TR, Martin BJ, Dunbar CE, McVeigh ER, Lederman RJ. Circulation. 2003;108:1009.
44. Wecker S, Küstermann E, Radermacher B, Hoehn M. Proc. Int. Soc. Magn. Reson. Med. 2002;10:878.

45. Wright AC, Song HK, Wehrli FW. Magn. Reson. Med. 2000;43:163–169.
46. Vinitski S, Griffey R, Fuka M, Matwiyoff N, Prost R. Magn. Reson. Med. 1987;5:278.
47. Haacke EM. Magn. Reson. Med. 1987;4:407.
48. Shapiro EM, Koretsky AP. Proc. Int. Soc. Magn. Reson. Med. 2004;12:1734.
49. Wiedermann D, Küstermann E, Blunk J, Wecker S, Bührlez C, Schwindt W, Trapp T, Föcking M, Hescheler J, Hoehn M. Proc. Int. Soc. Magn. Reson. Med. 2002;10:1257.
50. Yablonskiy DA, Haacke EM. Magn. Reson. Med. 1994;32:749.
51. Bulte JWM, Douglas T, Witwer B, Zhang SC, Strable E, Lewis BK, Zywicke H, Miller B, van Gelderen P, Moskowitz BM, Duncan ID, Frank JA. Nat. Biotechnol. 2001;19: 1141.
52. Shapiro EM, Skrtic S, Koretsky AP. Proc. Int. Soc. Magn. Reson. Med. 2004;12:166.
53. Safarik I, Safarikova M. J. Chromatogr. 1999;B722:33.
54. Högemann D, Basilion JP. Eur. J. Mol. Med. 2002;29:400.
55. Sipkins DA, Cheresh DR, Kazemi MR, Nevin LM, Bednarski MD, Li KCP. Nat. Med. 1998;4:623.
56. Lemieux GA, Yarema KJ, Jacobs CL, Bertozzi CR. J. Am. Chem. Soc. 1999;121:4278.
57. Modo M, Mellodew K, Cash D, Fraser SE, Meade TJ, Price J, Williams SCR. Neuroimage. 2004;21:311.
58. Yeh TC, Zhang W, Ildstad ST, Ho C. Magn. Reson. Med. 1993;30:617.
59. Sipe JC, Filippi M, Martino G, Furlan R, Rocca MA, Rovaris M, Bergami A, Zyrozz J, Scotti G, Comi G. Magn. Reson. Imaging. 1999;17:1521.
60. Moore A, Weissleder R, Bogdanov A Jr. J. Magn. Reson. Imaging. 1997;7:1140.
61. Franklin RJM, Blaschuk KL, Mearchell MC, Prestoz LLC, Setzu A, Brindle KM, ffrench-Constant C. Neuroreport. 1999;10:3961.
62. Bulte JWM, Zhang SC, van Gelderen P, Heryneki V, Jordan EK, Duncan ID, Frank JA. Proc. Natl. Acad. Sic. U.S.A. 1999;96:15256.
63. Majumdar S, Zoghbi SS, Gore JC. Magn. Reson. Med. 1989;10:289.
64. Bulte JWM, Ma LD, Magin RL, Kamman RL, Hulstaert CE, Go KG, The TH, de Leij L. Magn. Reson. Med. 1993;29:32.
65. Bulte JWM, Laughlin PG, Jordan EK, Tran VA, Vymazal J, Frank JA. Acad. Radiol. 1996;3:S301.
66. Kalish H, Arbab AS, Miller BR, Lewis BK, Zywicke HA, Bulte JWM, Bryant LH, Frank JA. Magn. Reson. Med. 2003;50:275.
67. Frank JA, Miller BR, Arbab AS, Zywicke HA, Jordan EK, Lewis BK, Bryant LH Jr, Bulte JWM. Radiology. 2003;228:480.
68. Arbab AS, Yocum GT, Kalish H, Jordan EK, Anderson SA, Khakoo AY, Read EJ, Frank JA. Blood. 2004.
69. Arbab AS, Bashaw LA, Miller BR, Jordan EK, Lewis BK, Kalish H, Frank JA. Radiology. 2003;229:838.
70. Zhang ZY, Smith BD. Bioconjug. Chem. 2000;11:805.
71. Walter GA, Cahill KS, Huard J, Feng H, Douglas T, Sweeney HL, Bulte JWM. Magn. Reson. Med. 2004;51:273.
72. Lee IH, Bulte JWM, Schweinhardt P, Douglas T, Trifunovski A, Hofstetter C, Olson L, Spengera C. Exp. Neurol. 2004;187:509.
73. Moore A, Josephson L, Bhorade RM, Basilion JP, Weissleder R. Radiology. 2001;221:244.
74. Weissleder R, Moore A, Mahmood U, Bhorade R, Benveniste H, Chiocca EA, Basilion JP. Nat. Med. 2000;6:351.
75. Bhorade R, Weissleder R, Nakakoshi T, Moore A, Tung CH. Bioconjug. Chem. 2000;11:301.
76. Lewin M, Carlesso N, Tung CH, Tang XW, Cory D, Scadden DT, Weissleder R. Nat. Biotechnol. 2000;18:410.
77. Dodd CH, Hsu HC, Chu WJ, Yang P, Zhang HG, Mountz JD Jr, Zinn K, Forder J, Josephson L, Weissleder R, Mountz JM, Mountz JD. J. Immunol. Methods. 2001;256:89.
78. Josephson L, Tung CH, Moore A, Weissleder R. Bioconjug. Chem. 1999;10:186.
79. Allen MJ, Meade TJ. J. Biol. Inorg. Chem. 2003;8:746.
80. Zhang RL, Zhang L, Zhang ZG, Morris D, Jiang Q, Wang L, Zhang LJ, Chopp M. Neuroscience. 2003;116:373.
81. Zhang ZG, Jiang Q, Zhang R, Zhang L, Wang L, Zhang L, Arniego P, Ho KL, Chopp M. Ann. Neurol. 2003; 53:259.
82. Rols MP, Delteil C, Golzio M, Dumond P, Cros S, Teissie J. Nat. Biotechnol. 1998;16:168.
83. Paturneau-Jouas M, Parzy E, Vidal G, Carlier PG, Wary C, Vilquin JT, de Kerviler E, Schwartz K, Leroy-Willig A. Radiology. 2003;228:768.
84. Stark DD, Weissleder R, Elizondo G, Hahn PF, Saini S, Todd LE, Wittenberg J, Ferrucci JT. Radiology. 1988; 168:297.
85. Weissleder R, Heautot JF, Schaffer BK, Nossiff N, Papisov MI, Bogdanov A Jr, Brady TJ. Radiology. 1994;191:225.
86. Seneterre E, Weissleder P, Jaramillo D, Reimer P, Lee AS, Brady TJ, Wittenberg J. Radiology. 1991;179:529.
87. Ruehm SG, Corot C, Vogt P, Kolb S, Debatin JF. Circulation. 2001;103:415.
88. Beckmann N, Cannet C, Fringeli-Tanner M, Baumann D, Pally C, Bruns C, Zerwes HG, Andriambeloson E, Bigaud M. Magn. Reson. Med. 2003;49:459.
89. Zhang Y, Dodd SJ, Hendrich KS, Williams M, Ho C. Kidney Int. 2000;58:1300.
90. Rausch M, Baumann D, Neubacher U, Rudin M. NMR Biomed. 2002;15:278.
91. Wunderbaldinger P, Josephson L, Weissleder R. Bioconjug. Chem. 2002;13:264.
92. Meade TJ, Taylor AK, Bull S. Curr. Opin. Neurobiol. 2003;13:597.
93. Lowe MP, Parker D, Reany O, Aime S, Botta M, Castellano G, Gianolio E, Pagliarin R. J. Am. Chem. Soc. 2001;123:7601.
94. Li WH, Parigi G, Fragai M, Luchinat C, Meade TJ. Inorg. Chem. 2002;41:4018.
95. Li WH, Fraser SE, Meade TJ. J. Am. Chem. Soc. 1999;121:1413.
96. Moats RA, Fraser SE, Meade TJ. Angew. Chem. Int. Ed. Engl. 1997;36:726.
97. Burai L, Scopelliti R, Toth E. Chem. Commun. 2002;20:2366.
98. Aime S, Botta M, Gianolio E, Terreno E. Angew. Chem. Int. Ed. Engl. 2002;39:747.
99. Aime S, Castelli DD, Terreno E. Angew. Chem. Int. Ed. Engl. 2002;41:4334.
100. Aime S, Botta M, Mainero V, Terreno E. Magn. Reson. Med. 2001;47:10.

101. Hoult DI, Lauterbur PC. J. Magn. Reson. 1979;34:425.
102. Styles P, Soffe NF, Scott CA, Cragg DA, Row F, White DJ, White PCJ. J. Magn. Reson. 1984;60:397.
103. Black RD, Early TA, Roemer PB, Mueller OM, Mogro-Campero A, Turner LG, Johnson GA. Science. 1993;259:793–795.
104. Miller JR, Hurlston SE, Ma QY, Face DW, Kountz DJ, MacFall JR, Hedlund LW, Johnson GA. Magn. Reson. Med. 1999;41:72.
105. Haase A, Frahm J, Matthaei D, Hnicke W, Merboldt KD. J. Magn. Reson. 1986;67:258.
106. Stehling MK, Turner R, Mansfield P. Science. 1991;254:43.
107. Ahrens ET, Narasimhan PT, Nakada T, Jacobs RE. Prog. Nucl. Magn. Reson. Spectrosc. 2002;40:275.
108. Seppenwoolde JH, Viergever MA, Bakker CJG. Magn. Reson. Med. 2003;50:784.
109. Coristine AJ, Foster P, Deoni SC, Heyn C, Rutt BK. Proc. Int. Soc. Magn. Reson. Med. 2004;12:163.
110. van den Bos EJ, Wagner A, Mahrholdt H, Thompson RB, Morimoto Y, Sutton BS, Judd RM, Taylor DA. Cell Transpl. 2003;12:743.
111. Emerit J, Beaumont C, Trivin F. Biomed. Pharmacother. 2001;55:333.
112. Weissleder R, Stark DD, Engelstad BL. Am. J. Roentenol. 1989;152:167.
113. Stroh A, Zimmer C, Gutzeit C, Jakstadt M, Marschinke F, Jung T, Pilgrimm H, Grune T. Free Radiat. Biol. Med. 2004;36:976.
114. Pouliquen D, le Jeune JJ, Perdrisot R, Ermias A, Jallet P. Magn. Reson. Imaging. 1991;9:275.
115. Yeh TC, Zhang W, Ildstad ST, Ho C. Magn. Reson. Med. 1995;33:200.
116. Arbab AS, Yocum GT, Wilson LB, Parwana A, Jordan EK, Kalish H, Frank JA. Mol. Imaging. 2004;324.
117. Kostura L, Mackay D, Pittenger MF, Kraitchman DL, Bulte JWM. Proc. Int. Soc. Magn. Reson. Med. 2004;12:167.
118. Pratten MK, Lloyd JB. Biochim. Biophys. Acta. 1986;881:307.
119. Schroeder M, Saleh A, Wiedermann D, Hoehn M, Jander S. Magn. Reson. Med. 2005;52:403.
120. Pautler RG, Silva AC, Koretsky AP. Magn. Reson. Med. 1998;40:740.
121. Saleem KS, Pauls JM, Augath M, Trinath T, Prause BA, Hashikawa T, Logothetis NK. Neuron. 2002:34:685.
122. van der Linden A, Verhoye M, van Meir V, Tindemans I, Eens M, Absil P, Balthazart J. Neuroscience. 2002;112:467.
123. Cohen B, Dafni H, Meir G, Neeman M. Proc. Int. Soc. Magn. Reson. Med. 2004;11:1707.

In vivo ^{13}C MRS

Stefan Bluml
Childrens Hospital Los Angeles, Department of Radiology, USC Keck School of Medicine Los Angeles, CA

Abbreviations: MRS = Magnetic Resonance Spectroscopy; MRI = Magnetic Resonance Imaging; SNR = Signal-to-noise ratio; RF = Radiofrequency; FDA = federal drug administration; SAR = specific absorption rate; B_1 = magnetic field of RF coil; NOE = nuclear Overhauser effect; VOI = volume of interest; LCModel = linear combination of model spectra; TCA = tricarboxylic acid; Glc = glucose; Glu = glutamate; Gln = glutamine; Asp = aspartate; NAA = N-acetylaspartate; GABA = γ-amino butyric acid; Lac = lactate; Ala = alanine; HCO_3^- = bicarbonate, Ac = acetate; KD = ketogenic diet.

Introduction

The application of ^{13}C Magnetic Resonance Spectroscopy (MRS) for basic research/medical applications is challenging and, despite being available for more than 25 years, only a few groups have attempted ^{13}C MRS *in vivo*. However, the few studies undertaken illustrate the great promise of *in vivo* ^{13}C MRS. Interest in ^{13}C MRS has grown considerably in recent years. The potential of ^{13}C arises from its biggest handicap: Low natural abundance [and the compromised sensitivity (≈1/50 of ^{1}H)] renders ^{13}C spectroscopy *in vivo* very difficulty due to the inherently very low signal-to-noise ratio (SNR). This low natural abundance, on the other hand, is the key to new, exciting applications of *in vivo* MRS: Investigation of metabolic pathways and the measurement of flux rates *in vivo* in animal and humans after ^{13}C enriched substrate infusion. The interested reader is referred to a recent issue of *NMR in Biomedicine* [1] exclusively dedicated to the application of ^{13}C MRS to study biological systems for a more detailed update on progress in ^{13}C MRS than given below. Instead, in this chapter, basic experimental procedures of *in vivo* ^{13}C MRS, with emphasis on experimental work in humans, are illustrated and discussed for the researcher interested in conducting similar experimental work in the future.

Methods

Equipment

A list of additional equipment needed beyond that required for MR imaging or ^{1}H MRS is provided in Table 1.

Radiofrequency (RF) Coils

Even for “niche” manufacturers, ^{13}C RF coils are too “exotic” and most groups conducting *in vivo* ^{13}C research have built their own coils. Volume coils are more flexible and have a special advantage when quantitation of cerebral metabolites is the goal. Nevertheless, surface coils have exclusively been used for ^{13}C MRS since they furnish the much-needed extra signal required for *in vivo* ^{13}C MRS. Because all ^{13}C methods either apply direct detection with proton-decoupling, polarization transfer, or heteronuclear editing, dual-tuned coils (^{1}H and ^{13}C frequencies) are required. Two concentric circular surface coils, a small ^{13}C coil and a larger ^{1}H coil, have been used by several investigators. However, the need to block the ^{1}H flux of the inner ^{13}C coil resulted in poor performance of the ^{1}H coil in the sensitive volume of the ^{13}C coil. A much improved assembly of two semi-orthogonal surface ^{1}H coils, operated in quadrature mode, and a single linear ^{13}C coil (Figure 1) was first introduced by Adriany and Gruetter [2] and has since been adopted by other groups [37]. The quadrature ^{1}H coil assembly offers twofold improved efficiency over linear-polarized coils in the power requirement. This is important to avoid excessive power RF absorption by tissue during *proton-decoupling* (see below).

Broadband Excitation/Detection

Even if dual-tuned RF coils are available, not all magnetic resonance imaging (MRI) scanners can progress beyond ^{1}H excitation and detection. Broadband amplifiers covering the frequency of ^{13}C are essential. Similarly, RF receivers tuned to the ^{13}C resonance frequency must be provided along with several other hardware features.

Graham A. Webb (ed.), Modern Magnetic Resonance, 1099–1112.
© 2008 *Springer.*

Table 1: Equipment needed for ^{13}C MRS beyond that required for standard MR imaging

Hardware	Purpose	Specifications/comments
RF Coil	^{13}C and ^{1}H excitation, receive, editing, decoupling	Dual-tuned ^{13}C-1H coil, ^{13}C surface coil/surface coil assembly, quadrature ^{1}H coil for efficient decoupling
Broadband capabilities		
Broadband receiver	To digitalize, filter, and store RF signal at ^{13}C frequency	Low noise figure
Transmit/receive switch for ^{13}C with pre-amp	Protects ^{13}C receiver from high power RF during excitation, boosts the gain of the ^{13}C signal during receive	Low noise figure ($<$0.60 dB), high gain ($\sim$35 dB) pre-amp. May be supplemented with a simple gain block to provide further enhancement of the signal. A proton trap or filter (for ^{13}C a low-pass design is acceptable) placed directly before the pre-amp to limit saturation of the device and subsequent reduction in ^{13}C SNR.
Broadband exciter[a]/amplifier	Create/amplify RF pulses at ^{13}C frequency	Minimum output power to drive the ^{13}C coil described above is 2 kW and 8 kW at 1.5 T and 3.0 T, respectively. 4 kW amplifiers on some 3.0 T systems may be barely adequate.
2nd RF channel or "Stand-alone" decoupler		
^{1}H exciter, ^{1}H amplifier[b]	Proton-decoupling	The decoupling amplifier should be capable of delivering $>$50 W of CW RF power. The output of the amplifier should be high-pass filtered to suppress ^{13}C frequencies.
RF source and modulation capabilities	Generation of a decoupling sequence at the ^{1}H frequency	Typical operating requirements: e.g. WALTZ-4 sequence with a 90 degree pulse range from 0–9.9 ms (in steps of 0.1 ms), bilevel (NOE/decoupling) operation, and manual control of the WALTZ-4 pulse width, attenuation control of output RF power over a 50 dB range in 1 dB steps.
Power meter	Power monitoring	Able to measure forward/reflected RF power. Values (in Watts or dB) should be displayed in real-time, e.g. on a computer screen. In normal operations, hard power limits should force the automatic shutdown of the amplifier if the output exceeds the limits. In addition, it should be possible to establish soft limits that generate warning signals or messages.
Miscellaneous		
Phantom	System/sequence performance evaluation	A spherical phantom containing one or more ^{13}C compounds suitable to test system performance/demonstrate decoupling.

[a] The manufacturers all have specifications for exciter output levels, linearity, phase stability, etc.— the specs for broadband are always a little lower than those for the narrow band imaging exciter.

[b] With amplifiers capable of high CW output, it is advisable that some safety interlock is available to insure that a power limit, e.g. 100 W, cannot be exceeded in normal operation. Typical amplifier specifications: 1000 W (peak)/100 W (CW) into a 50 Ohm load. The RF power amplifier should be electrically connected to the MR scanner so that all automatic, emergency electrical power shutdown procedures apply.

Proton-Decoupler and Power Monitoring

Along with the capability to perform heteronuclear (other than ^{1}H) MRS comes the need to enhance sensitivity and specificity of chemical analyses by *proton-decoupling* and *heteronuclear polarization transfer* and *editing*. This involves excitation at different frequencies, and accordingly requires a second RF channel and amplifier. Since it appears that there is a renewed interest in advanced multinuclear spectroscopy, the major manufacturers of clinical MR scanners are all offering broadband capabilities and second RF channels. There are two basic options for decoupling; a fully integrated, second RF exciter channel

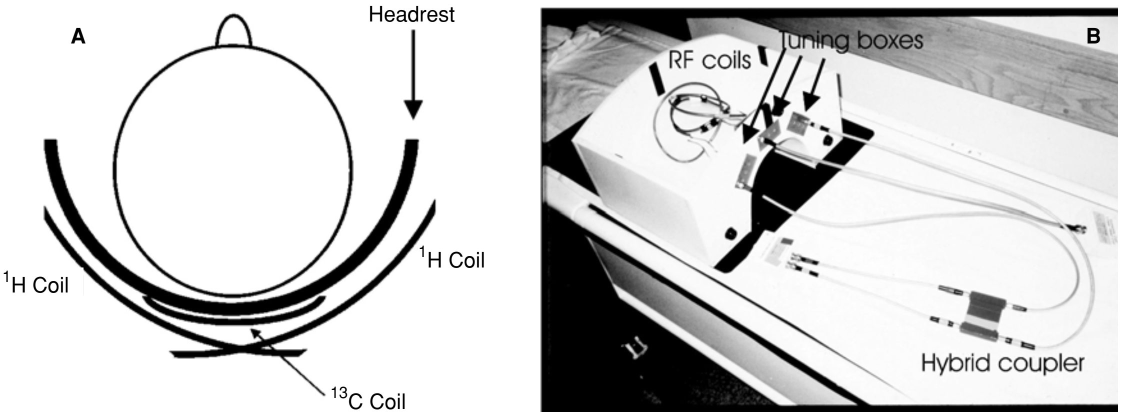

Fig. 1. Dual-tuned RF coil for in vivo ^{13}C MRS of human brain. (**A**) Schematic of the "half-volume" coil assembly as originally proposed by Adriany and Gruetter [2] and since then adopted by other groups. The two orthogonal ^{1}H coils can be used for MRI, ^{1}H MRS, as well as for proton-decoupling during ^{13}C signal reception. A single ^{13}C surface coil is mounted immediately adjacent to the head rest. The overlap of the ^{1}H coils and the position of the individual coils needed to be adjusted to minimize interaction between the different coils. It is also important to minimize the distance between ^{13}C coil and the region of interest to optimize SNR. (B) Picture of the coil assembly used at Huntington Medical Research Institutes, Pasadena, California. A hybrid coupler is necessary to operate the two ^{1}H coils 90° out of phase for quadrature excitation and detection. "Tune and match" is accomplished for each coil individually with three separate tuning boxes. Coils, cables, and connectors are "color-coded" to avoid mistakes when connecting the coil assembly with the MR scanner.

that is part of the MR scanner, or an independent or "Stand-alone" sequence generator with simple timing signals provided by the MR scanner. The fully integrated channel requires pulse sequence programming but gives the user direct access to the decoupling sequence and parameters. Standalone decouplers exist in several flavours, ranging from simple pre-programmed decoupling sequences with hardware control of all parameters to more complex signal generating devices under computer control.

Excessive RF power deposition during decoupling can result in potentially damaging heating of tissue. Federal drug administration (FDA) guidelines limit the deposited energy below levels which are considered to be of any risk [8,9]. Manufacturers have developed decouplers with built-in power monitoring and automatic shutdown should a certain threshold for the average power be exceeded. It should be noted that since for decoupled ^{13}C MRS ^{1}H surface coils are being used, the *local* specific absorption rate (SAR) may vary with the magnetic field profile of the proton coils (B_1). It is possible that the *average* SAR over the whole sensitive volume is below the FDA approved limit, whereas the *local* SAR of tissue adjacent to the ^{1}H decoupling coils may be above that threshold [2,10].

Proton-Decoupling and NOE

Proton-decoupling and the nuclear Overhauser effect (NOE) are essential tools for ^{13}C MRS. It is not advised to attempt ^{13}C MRS without decoupling/NOE. Even the simplest application, such as measuring the lipid profile of a human leg [11], would be quite demanding without the improved SNR and resolution facilitated by decoupling and NOE.

Proton-Decoupling

Heteronuclear scalar couplings between ^{1}H and ^{13}C nuclei result in a splitting of ^{13}C resonance lines in to multiplets. The goal of *proton-decoupling* is to suppress these couplings and to collapse multiplets into singlets, simplifying the spectrum and improving the signal intensity. This is achieved by irradiation of decoupling proton RF pulses during the readout of ^{13}C signal over the whole range of the spectrum (= *broadband* decoupling). The most commonly used proton-decoupling RF sequence for *in vivo* ^{13}C MRS is WALTZ [12–15]. Several WALTZ decoupling schemes have been developed named WALTZ-4, WALTZ-8, and WALTZ-16 and they all appear to work well for *in vivo* applications.

NOE—The NOE is based on changes in the polarization, which occur in coupled systems when the population of one of the systems is manipulated. In contrast to *scalar* coupling, which is facilitated indirectly by the electron bond, it is the *dipolar* coupling between ^{13}C and ^{1}H nuclei, which generates the NOE. In fluids, dipolar coupling does not result in a line splitting due to "Motional Narrowing," however, it is still an effective relaxation mechanism resulting in changes of signal intensities. While it was necessary to irradiate at the proton frequency *during* the readout of ^{13}C signal for proton decoupling, NOE enhancement is generated by irradiation at the proton frequency *before* the ^{13}C signal is detected. Excitation of protons coupled to ^{13}C has an impact on the polarization of ^{13}C. In particular, if the protons are saturated an increase of the polarization of ^{13}C can be observed. Since the maximum NOE enhancement for two nuclei A and B in fluids is given by, $\text{NOE} = 1 + \frac{1}{2}\,\gamma_B/\gamma_A$, a threefold signal enhancement can be achieved for ^{13}C MRS ($\gamma_{1H} \approx 4\gamma_{13C}$). To have maximum NOE enhancement for all resonances it is necessary to irradiate RF over the full chemical shift range of dipolar coupled protons. As for proton decoupling, a WALTZ-*n* cycle can be employed, however, it is usually sufficient to irradiate at a much lower power levels ($\approx$1/10 of decoupling power). The optimum choice for the center frequency and the bandwidth for NOE may be different from what works best for decoupling.

Pulse Sequences for *in vivo* ^{13}C MRS

More detailed discussions of pulse sequences and data acquisition strategies than provided below can be found elsewhere [16,17] and in references therein.

^{13}C Excitation and ^{13}C Detection

Direct detection ^{13}C MRS is the *least sensitive* method and spectra with sufficient quality can only be acquired from very large volumes [18] or without any localization [3]. *Gradient localized* direct ^{13}C MRS is further compromised by considerable chemical shift displacement errors due to the large chemical shift dispersion of ^{13}C spectra. On the other hand, spectra acquired with this method offer high spectral resolution and an impressive number of ^{13}C resonances, all measured simultaneously under identical conditions (Figure 2). In particular when a simple "pulse and acquire" sequence is used, the impact of acquisition parameters on the spectral pattern is small and sequence parameter adjustment is quick. These features may be important in a clinical setting where experimental simplicity is important [19,20]. Direct ^{13}C excitation and detection requires proton-decoupling and NOE to improve the spectral quality.

Polarization Transfer

A better SNR can be achieved with heteronuclear polarization transfer. The basic concept of polarization transfer is to excite protons coupled to ^{13}C and, as the polarization is transferred to the adjacent ^{13}C nucleus during the evolution period, to detect the signal at the ^{13}C frequency. Because the heteronuclear J-coupling constants between ^{1}H and ^{13}C nuclei are very similar ($\approx$120 Hz for methyl groups, $\approx$160 Hz for aromatic groups), sequence parameters, in particular the delay for coupling evolution, can be adjusted to the optimum detection of all signals. There are two distinct features of this method. (i) Proton excitation can be combined with *localization* such as image-selected *in vivo* spectroscopy (ISIS) [21] greatly reducing the chemical shift displacement error [4,22]. (ii) ^{13}C detection retains the large dispersion and thus spectral resolution of ^{13}C (Figure 3). This method also allows recovering the maximum fourfold sensitivity gain due to the higher magnetization of protons. During detection at the ^{13}C frequency, proton decoupling is applied to generate a simplified spectrum for better interpretation. Polarization transfer becomes less advantageous in situations where the resonance of interest has a very short T_2 (e.g. glycogen). If T_2 is short relative to the time delay necessary to facilitate polarization transfer, a substantial loss of signal can occur [17].

Indirect Detection

Indirect detection can improve greatly the sensitivity by detecting protons attached to ^{13}C utilizing heteronuclear scalar couplings. In the simplest case, protons coupled to a ^{13}C nucleus will form two resonances symmetrically placed around the center of the singlet generated by a proton attached to a ^{12}C nucleus. In practice however, the ^{1}H spectra of chemicals such as glutamate and glutamine are complex because of home- and heteronuclear couplings and resonances overlap due to the small chemical shift dispersion of ^{1}H MRS. This renders the detection of ^{13}C coupled protons difficult. It is therefore necessary to apply *editing* pulses at the ^{13}C frequency, which will result in a modulation of a spectrum, e.g. an inversion of the signal from ^{13}C bound protons relative to ^{12}C bound protons. When unedited and edited spectra are analyzed, the difference spectra will represent protons attached to ^{13}C while the added spectrum represents protons bound to ^{12}C. This approach is referred to as *proton-observed, carbon-edited* (POCE) [23]. Indirect detection offers the highest SNR among the methods discussed here and has the advantage of localization at the proton frequency, reducing chemical shift displacement artifacts. Another advantage of indirect detection is that only hardware for the *transmission* of RF at the ^{13}C frequency is required and that the proton channel of MR systems, used for signal detection, is usually well engineered, guaranteeing good performance (Figure 4). A disadvantage is that the high spectral resolution of ^{13}C is sacrificed. While this is acceptable for simple spectra with selective isotopic enrichment, it may

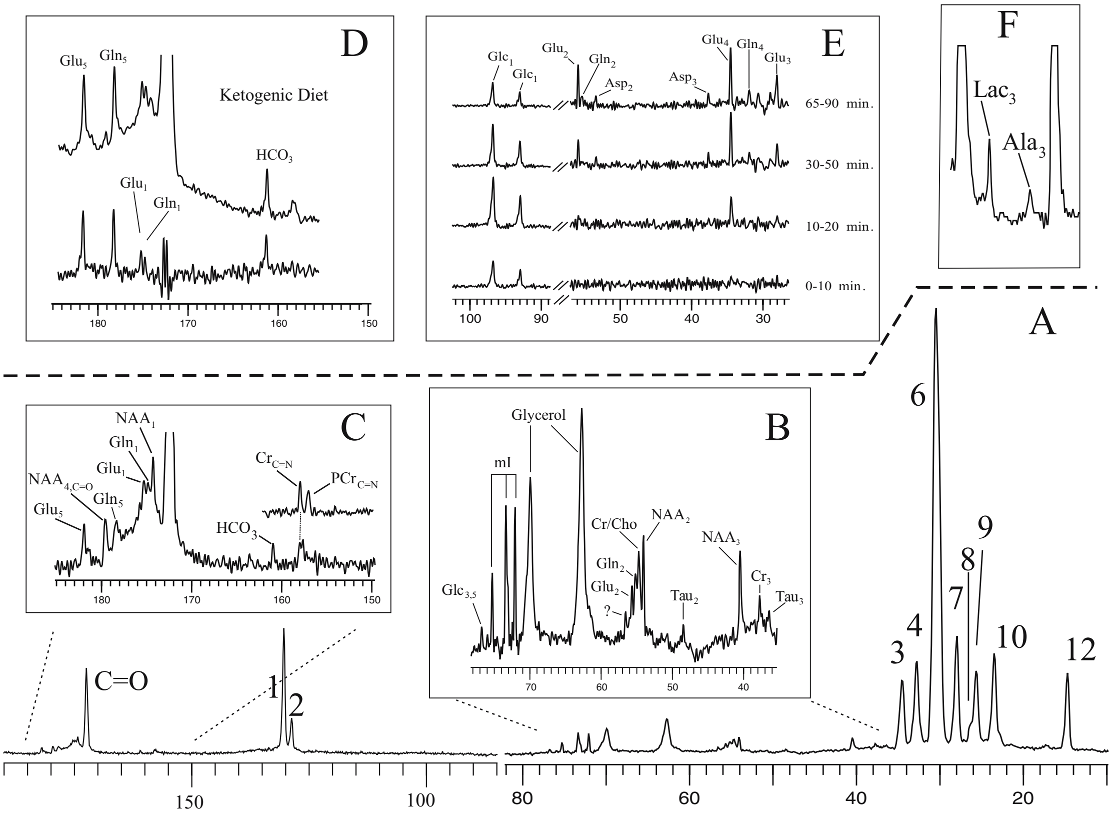

Fig. 2. *In vivo* natural abundance and ^{13}C MR spectra after substrate infusion of the human brain acquired with "pulse-and-acquire" and direct ^{13}C detection. (A–C) Shown is a natural abundance ^{13}C MR spectrum of a patient with Canavan disease. B + C are expansions of A to allow a more detailed inspection. Lipid signal originating from the skull and subcutaneous fat dominates the spectrum due to non-localized acquisition. (D) ^{13}C spectrum (upper trace) obtained from ketogenic diet (KD) patients 30–80 min after infusion [1-^{13}C] acetate. The lower trace is the difference spectrum computed by subtraction of the baseline spectrum, acquired before infusion start, (not shown) to directly illustrates ^{13}C label accumulation. ^{13}C label incorporation into bicarbonate (HCO_3), Glu C_5 and Gln C_5 and, Glu C_1 and Gln C_1 can be observed. (E) The time course of glucose uptake and metabolism to glutamate and other products in the brain in a normal adult subject after i.v. [1-^{13}C] glucose infusion. Difference spectra were calculated to subtract prominent lipid peaks. ^{13}C enriched peaks of Glu $C_{1,2,3,4}$, Gln $C_{1,2,3,4}$, Asp $C_{2,3}$, NAA $C_{2,3}$ can be observed [36]. (F) Although lactate (Lac) and alanine (Ala) concentrations are too low to be detected with natural abundance ^{13}C MRS in normal brain, ^{13}C enriched resonances are readily observed after [1-^{13}C] glucose infusion. All spectra were acquired with the dual-tuned half-volume head coil shown in Figure 1 on a GE, 1.5 T clinical scanner.

be more problematic when high resolution of complex spectra with many components is the goal.

Checking System Performance

Once the required hardware is installed and an MR sequence developed, the next essential step is the thorough evaluation of the system performance.

Low SNR

Low overall SNR of ^{13}C MRS may be caused by several reasons. A poorly designed or tuned ^{13}C coil will not provide adequate SNR. Also, poor SNR may be caused by site specific factors. RF noise at ^{13}C frequency may be generated by other MR equipment used for MRI and not filtered appropriately. Also, equipment not related with MR may emit RF at the frequency of ^{13}C and adversely

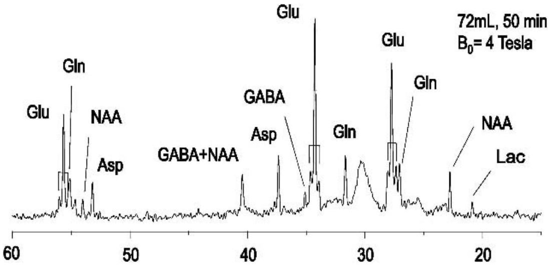

Fig. 3. Localized ^{13}C MR spectrum of the human occipital lobe The spectrum was acquired from 72-ml volume 60–110 min after start of [1-^{13}C] glucose infusion on a 4 T system using polarization transfer, proton excited carbon detected, for improved SNR and localization (Figure provided by Rolf Gruetter, Ph.D. and reproduced with permission from Dev Neurosci 1998 S. Karger AG).

interfere with the quality of a spectrum. There are many tests that can be performed to isolate the cause for insufficient SNR, however, the questions the new investigator faces first are: "How does a good spectrum look like?" "Is the performance of my system the best possible?" For that reason, it is recommended that the investigator should team-up with a reference site with experience with ^{13}C MRS. The coil, a phantom, and specific instruction on how to perform a test should be sent to a collaborating site with the request to acquire data for comparison. Even better, a new investigator may want to visit an established site for ^{13}C MRS to witness a quality scan and to ensure that scans at the reference site and at the local site are performed under identical conditions. Once a problem has been identified or narrowed down, the manufacturer of the MR system or the RF coil can be approached with a specific request to fix a problem.

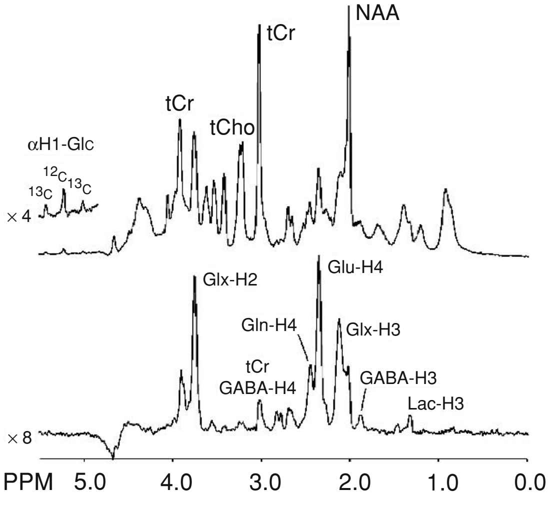

Fig. 4. Indirect detection of ^{13}C label accumulation The spectrum was acquired from rat brain at 9.4 T (180 ul volume, T_R = 4000 ms, T_E = 8.5 ms, 512 averages). It was acquired between 110 and 140 min following the intravenous infusion of [U-^{13}C6]-glucose (i.e. uniformily labelled glucose). The upper trace is the regular ^{1}H spectrum, while the bottom spectrum is the ^{1}H-[^{13}C] edited fraction (i.e. it only shows resonances from protons attached to ^{13}C). The sequence is described in de Graaf *et al.* [37] (figure provided by Robin de Graaf, Ph.D. and reproduced with permission from Wiley-Liss. Inc., 2004).

Crosstalk

Crosstalk between ^{1}H and ^{13}C coils during decoupling is caused by the transmission of RF at the proton frequency with relatively high power while the small ^{13}C signal is received. It can cause two unwanted effects. (i) Although, the ^{1}H signal is suppressed by subsequent filtering, the ^{13}C pre-amplifier usually placed immediately after the ^{13}C coil, sees both ^{13}C and ^{1}H signal. Both signals may be amplified. Since the ^{1}H signal is much larger than the ^{13}C signal it may *saturate* the pre-amplifier. This results in an overall scaling (down) of the decoupled ^{13}C spectrum. It may not affect the SNR but is nevertheless unwanted since an absolute comparison of scans becomes very difficult. (ii) Unacceptable artifacts are caused when decoupling causes spikes at the ^{13}C frequency. Detecting of these two problems is relatively straightforward. If the maximum amplitude of decoupled spectra becomes smaller after further increasing decoupling power, saturation may have occurred. Spikes are readily detectable in the spectrum because of the dramatic adverse impact on the SNR. The problems caused by crosstalk of coils can be minimized by additional filtering of the ^{13}C signal and by using coil assemblies with efficient built-in proton traps. Reducing the decoupling power is useful only when it does not result in incompletely decoupled spectra.

Incomplete Decoupling

Insufficient decoupling power results in a "hybrid" spectrum, partially non-decoupled and partially decoupled. These spectra are not quantifiable and should not be interpreted.

Instabilities

Scanner and coil instabilities are often another concern. Electronic components may heat-up during a pro-longed acquisitions and change the tuning of a coil, an amplifier may not deliver the same power over an extend period of time, etc. Usually these variations are small, however, in particular when difference spectroscopy is attempted or the time course of a signal is observed over a long time, the quality of the results and the accuracy of the interpretation may be compromised. Scanner and coil instabilities can readily be checked in vitro by scanning phantoms.

Reproducibility

The nature of a study defines when insufficient reproducibility (= different results from the same subject on different occasions) is a problem. Hardware imperfections can cause insufficient reproducibility. However, often the positioning of a subject, selection of region of interest, adjustment of acquisition parameters, shimming, etc. is not consistent thus limiting the reproducibility. These problems can be minimized/avoided by generating macros (if possible), dedicated protocols, and clear written instruction on how to conduct a scan. Macros, protocols, and instructions should be tested by scanning different phantoms. Sequence parameters should not be "guessed" when starting an acquisition. Ideally, good and reproducible spectra should be obtained without the need to "manually" adjust scan parameters in each cause. If the lack of reproducibility is small compared with the postulated differences between two groups of subjects, it only complicates the study by the need to examine more individuals in order to reach significance. It is always a good strategy to conduct several studies in the same subject to investigate this matter. There are of course limitations to that when a study is very complex such as a lengthy examination with substrate infusion.

Data Processing

High quality spectra are of no use if the information they contain is not or incorrectly extracted. Therefore appropriate data processing is as important as the acquisition of the spectra. In general, data processing should be as *user independent* as possible to prevent unavoidable operator bias.

Since the signal generated by a specific nucleus is proportional to the number of equivalent nuclei in the volume of interest (VOI), *in vivo* concentrations of a metabolite M (in mmol/kg tissue or mmol/l) can be determined by $[M] = C_{\mathrm{MRS}} A_{\mathrm{M}}$, where C_{MRS} comprises all correction factors (T_1 saturation, T_2 relaxation, VOI, number of equivalent nuclei, receiver gains, etc.) and A_{M} is the total area under a curve. Resonances in decoupled ^{13}C spectra are usually well resolved and line fitting of individual resonances is relatively straightforward. However, when quantifying spectra of low SNR (^{13}C spectra are compromised by low SNR), the investigator may want to keep in mind that not all parameters of a curve are measured with the same accuracy. In particular the determination of the position of a resonance on the chemical shift axis and the amplitude can be measured with a much higher accuracy than the width (or area). Therefore, most of the time, it is advantageous to measure peak amplitudes instead of areas. On the other hand, the amplitude is affected by the homogeneity whereas the area is not. Nevertheless, in a well-designed study, spectra are acquired from comparable regions of interest and the variation of the homogeneity across subjects should be very small and there should be no correction necessary. In cases where small systematic variations could be expected (e.g. when a comparison of spectra from different brain region is attempted), it is still better to perform an adjustable lineshape correction (see below) and to measure amplitudes rather than areas. If due to the nature of a study, large systematic differences of the field homogeneity is expected then areas rather than amplitudes should be evaluated.

Lineshape Transformation

For spectra of low SNR and partially overlapping peaks it is generally advisable to perform a lineshape transformation. A common lineshape transformation is the Lorentzian-to-Gaussian transformation. The first step is a negative Lorentzian linebroadening to create a spectrum with a standardized linewidth. E.g. a spectrum with resonances with 4 Hz linewidth will be corrected by −3 Hz whereas a spectrum with resonances with 4.5 Hz linewidth will be corrected by −3.5 Hz to result in standardized spectra with a 1 Hz linewidth. The second step is a positive Gaussian linebroadening to improve SNR. Although this lineshape transformation is not linear (= the relative areas of peaks with different linewidths are not the same after transformation), in practice, this imperfection is more than compensated for by the fact that Gaussian lines can be fitted much easier than Lorentzian lines because of the reduced overlap of adjacent resonances.

LCModel for ^{1}H MRS

^{13}C spectra are usually well resolved and fitting of the individual resonances can be achieved relatively straightforward. Should the user decide to use inverse detection, proton spectra need to be processed. Proton spectra suffer from the narrow chemical shift range, complex pattern due to homonuclear couplings, and a broad baseline due to macromolecules. On the other hand, good processing software for ^{1}H MRS is commercially available. LCModel (Linear combination of model spectra, Stephen Provencher Inc., Oakville, Ontario, Canada) is a well-developed, robust, and at the same time flexible software package [24]. LCModel fits the *in vivo* data by finding the best linear combination of spectra obtained from phantoms with known concentrations. LCModel is most suited for standard ^{1}H MRS as carried out in a clinical environment (e.g. 1.5 T, 2.0 T, 3.0 T, PRESS, STEAM) with pre-measured basis spectra available from the vendor. For applications with complex acquisition sequences and unusual sequence parameters the user may need to prepare his/her own phantoms to acquire the appropriate model spectra the specific experimental conditions. Although this can be tedious when many metabolites are being analyzed, it is time well spent.

Modeling and Determination of Flux Rates

Infusion of a ^{13}C labeled substrate allows the metabolism of the substrate to be followed by sequential ^{13}C MRS. A *mathematical model*, basically a set of differential equations, of the metabolism is then needed to determine the *in vivo* flux rates (Figure 5). It needs to be pointed out that the formulation of the differential equations for a biological model is the easy part—finding the right model is the tricky part. Assumptions and simplifications are necessary, even if the correct model is known [e.g. for the tricarboxylic acid (TCA) cycle] because only a limited number of metabolites can be measured with sufficient SNR. E.g. the measurement of the TCA-cycle rate after [1-^{13}C] labeled glucose infusion is based to a large extent on the time course of the glutamate C_4 enrichment. However, glutamate is NOT a metabolite of the TCA-cycle. Only because the pool sizes of TCA-cycle intermediates are small and the exchange rate between α-ketoglutarate and glutamate is fast (there are some controversies in the literature on how fast "fast" is), it is reasonable to assume that glutamate C_4 acts as a trap for ^{13}C label entering

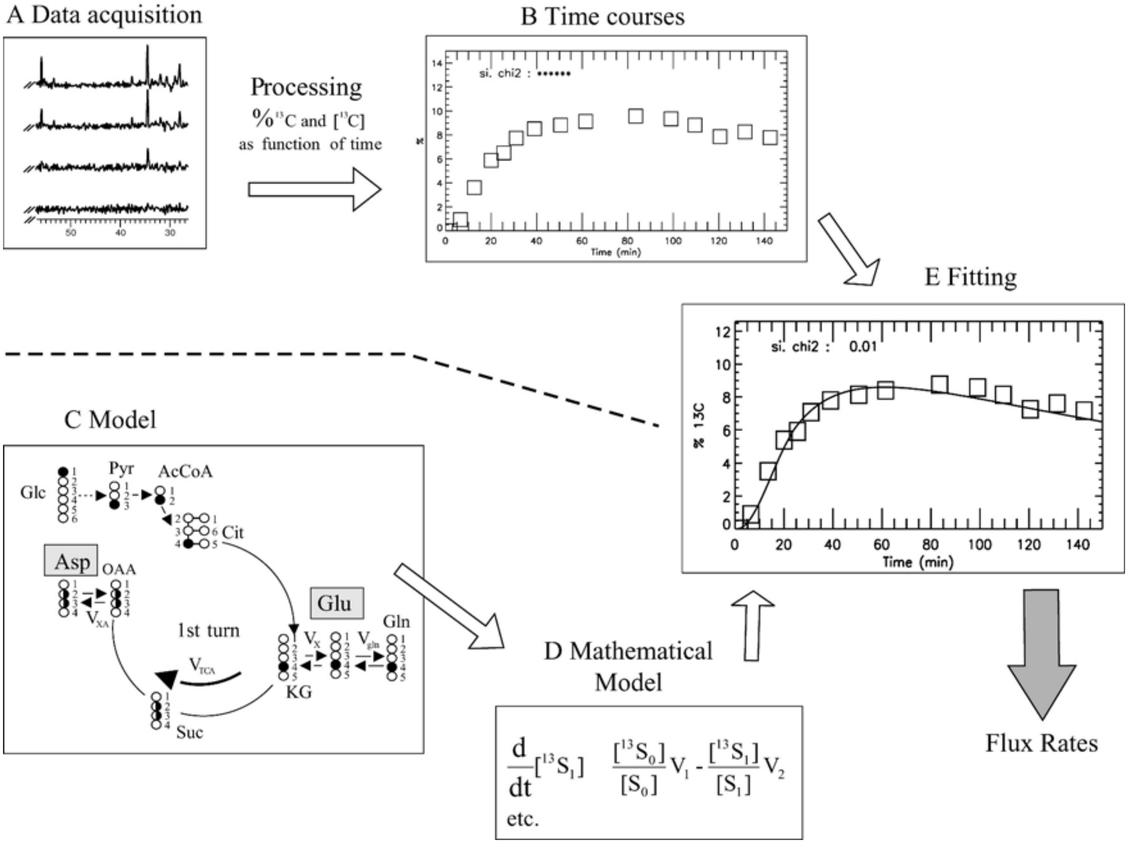
A Data acquisition
50
40
30
Processing
%^{13}C and [^{13}C]
as function of time
B Time courses
si. chi2 : ••••••
%
0
2
4
6
8
10
12
14
0
20
40
60
80
100
120
140
Time (min)
E Fitting
si. chi2 : 0.01
% 13C
0
2
4
6
8
10
12
0
20
40
60
80
100
120
140
Time (min)
C Model
Glc
Pyr
AcCoA
Cit
Asp
OAA
V_{XA}
1st turn
V_{TCA}
Glu
V_x
V_{gln}
Gln
KG
Suc
D Mathematical Model
$\frac{d}{dt}[^{13}S_1]$ $\frac{[^{13}S_0]}{[S_0]}V_1 - \frac{[^{13}S_1]}{[S_1]}V_2$
etc.
Flux Rates

Fig. 5. (A) Dynamic ^{13}C MRS involves the sequential acquisition of ^{13}C spectra after substrate infusion to ^{13}C label accumulation. (B) The next step is the processing and quantitation of spectra to generate time courses of ^{13}C concentration (or ^{13}C enrichment). (C + D) A set of differential equations is derived from the metabolic model applied for an experiment. (E) By iteratively varying flux parameters (and pool concentrations) of the mathematical model to optimize the fit with experimental data, flux rates (and pool concentrations) can be determined.

the TCA-cycle at acetyl-Coa [25]. It is beyond the scope of this chapter to get involved in the discussion of current complex models of glucose and acetate metabolism in animal and human brain and it is recommended that the interested reader studies recently published articles [1]. Sometimes it is possible to simplify the mathematical model considerably to answer very specific questions. Examples are the determination of the N-acetyl-asparate synthesis rate in humans *in vivo*, the glutamine synthesis rate in human hepatic encephalopathy, or the measurement of the astro-glial TCA-cycle rate after [1-^{13}C] acetate infusion [20,26,27].

A simple two Compartment Model—Mathematical Description

$$S_0 \xrightarrow{V_1} S_1 \xrightarrow{V_2} S_2$$

In this model S_0 is the initial substrate and S_1, S_2 are intermediates of S_0 metabolism. $[^{13}S_0]$, $[^{13}S_1]$, $[^{13}S_2]$ are the ^{13}C enriched pools; e.g. before infusion $[^{13}S_1] = 1.1\%$ $[S_1]$. V_1 and V_2 are the fluxes from S_0 to S_1 and from S_1 to S_2. Assuming that the total concentration of S_1 remains constant ($V_1 = V_2$), the ^{13}C flux into and out of pool S_1 is described by:

$$\frac{d}{dt}[^{13}S_1] = \frac{[^{13}S_0]}{[S_0]}V_1 - \frac{[^{13}S_1]}{[S_1]}V_2. \qquad (1)$$

In the special case that the fractional enrichment of substrate S_0 is constant ($[^{13}S_0]/[S_0] = E_0 =$ constant), the ^{13}C enrichment of S_1 will exponentially approach that of the precursor:

$$[^{13}S_1](t) = E_0[S_1] \times \left(1 - \exp V_1 t \big/ [S_1]\right) \qquad (2)$$

Since the time constant for the pool to turn over is the ratio of pool size and flux rate ($[S_1]/V_1$), large metabolic pools take longer to turn over whereas small pools will quickly have the same enrichment as the precursor. For this hypothetical model, the concentration of ^{13}C enriched S_1, would be measured by sequential MRS. Once the total pool size is known (e.g. from literature, quantitative natural abundance ^{13}C, or ^{1}H MRS), the flux rate V_1 can be obtained by fitting an exponential function to the measured time course for $[^{13}S_1]$.

Real biological systems, although analytical differential equations for each metabolic pool can be written readily, are too complex for analytical solutions and numerical solutions need to be found by a step-by-step integration. Software (CWave, Graeme Mason, Ph.D., Yale University) for the design of models and analysis of ^{13}C-labeling studies is available after signing a license agreement [28]. To obtain a copy contact Graeme Mason, Ph.D., at the Magnetic Resonance Center, Yale University, School of Medicine.

Miscellaneous

Even when all technical obstacles have been resolved, the investigator still needs to plan any study very carefully. *In vivo* ^{13}C studies, in particular of human requiring large amounts of ^{13}C labeled substrates, are expensive, lengthy, and the subsequent data analysis requires a considerable effort. To avoid frustration and jeopardizing the success of a ^{13}C experiment, all "peripheral" steps of a study need to be planned with equal due diligence than the acquisition of the ^{13}C spectra. Depending on the biological question asked, it needs to be decided what substrate should be infused for how long and in what fashion. For some applications oral administration may be appropriate [29,30,26] which would simplify the procedure considerably because one inter-venous (i.v.) infusion line could be eliminated. In particular for studies of humans, i.v. administered substrates should be prepared with care, kept refrigerated, and used within a couple of days. It is usually necessary to determine fractional ^{13}C enrichment of the substrate in plasma. Therefore the drawing, storage, and analysis of blood samples need to be planned. A new investigator is advised to carefully read the "Methods" sections of previous publications [22,25,28] and references therein.

Applications

Although there are undoubtedly applications for *in vivo* natural abundance ^{13}C MRS, to harvest the full potential of ^{13}C MRS, enrichment of metabolites with ^{13}C via intravenous or oral administration of ^{13}C labeled substrates is necessary. Glucose is the principal substrate for energy metabolism for both neurons and glia cells in the brain and also facilitates the *de novo* synthesis of many neurochemicals. In normal human adults, i.v. infused [1-^{13}C] labeled glucose (Glc) passes the blood-brain barrier and is readily metabolized. ^{13}C enrichment of individual carbon atoms of glutamate (Glu), glutamine (Gln), aspartate (Asp), N-acetylaspartate (NAA), γ-amino butyric acid (GABA), lactate (Lac), alanine (Ala), and bicarbonate (HCO_3^-) follows [5,19,20,22,25,31]. From repeated ^{13}C MR spectra acquired during studies over 2–3 h, the *in vivo* rates of several of the principal bioenergetic pathways of normal adult brain have been determined [22,25,4].

The role of ^{13}C glucose MRS in *diseased brain* remains a matter of speculation as there are only a few studies

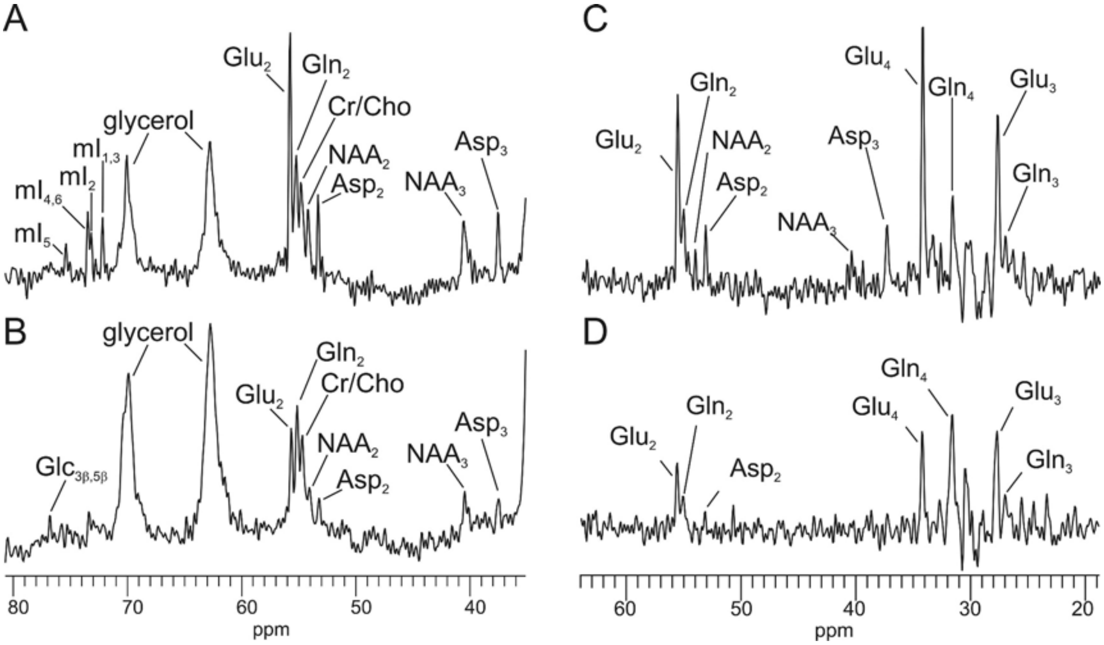

Fig. 6. ^{13}C MRS of human hepatic encephalopathy (HE) Hepatic encephalopathy is a metabolic brain disorder caused by liver dysfunction and incomplete removal of ammonia and other neurotoxins from the blood. (**A+B**) Spectra acquired over a period of 60–120 min after a 20 min infusion of $[1-^{13}C]$ glucose of an adult control (A) and a patient with severe chronic HE (grade III–IV) are shown. ^{13}C enrichment of Glu C_2, Asp C_2, Asp C_3 is reduced while ^{13}C accumulation in Gln C_2 is comparable to the control. Note the absence of natural abundance *myo*-inositol (mI) signal in HE. (**C+D**) Difference spectra, to enable inspection of ^{13}C accumulation in Glu C_4, Gln C_4, Glu C_4, and Gln C_4, of a control and a chronic HE patient (grade I-II) acquired 80–100 min after infusion start, are shown. Spectra were scaled to represent absolute concentrations. Note the apparent reduction of ^{13}C incorporation into Glu C_4, C_2, Asp C_2,3 in HE. Even though affected by the subtraction analysis to a larger extent in HE than in control, the Gln C_4 resonance appears strikingly prominent in spectra of the patient. Label accumulation in NAA C_2,3 observed in the control was not detected in HE. The pattern of label accumulation in HE is consistent with an overall reduction of glucose oxidation and altered glutamate/glutamine cycling.

conducted. Striking abnormalities in glucose metabolism and glutamate and glutamine label accumulation were observed in patients with chronic hepatic encephalopathy (Figure 6). Glucose oxidation was also reduced in a juvenile with hypoxic injury and in a premature infant. Abnormalities were also detected in pediatric patients with leukodystrophies and in children with mitochondrial disorders [19,20]. The information obtained from following the fate of ^{13}C labeled glucose goes beyond that of providing a rate for energy production. A tight coupling between cerebral glucose metabolism and glutamate neurotransmitter flux in humans has been proposed by Magistretti *et al.* [32]. Aspartate, (a neurotransmitter?), can be studied *in vivo* in humans by its ^{13}C label accumulation. The role of NAA in mammalian brain, a neuronal/axonal marker which is central for its diagnostic power in ^{1}H MRS, is incompletely understood. NAA synthesis can be measured with ^{13}C MRS after glucose infusion in a clinical setting [26] (Figure 7).

The application of ^{13}C MRS after substrate infusion is by no means limited to glucose. Glucose is convenient because of its rapid oxidation and the fast appearance of ^{13}C label in its metabolites and its non-toxicity even at extremely high concentrations. However, the use of other substrates may further enhance the potential of ^{13}C MRS as a research and diagnostic tool in human brain disease. The candidate next best to glucose appears to be acetate [7,27]. Acetate (Ac) is metabolized to acetyl-CoA only in the glial compartment [33]. Using the same MR technique as for $[1-^{13}C]$ glucose, glial acetate metabolism can be investigated in normal and diseased brain. ^{13}C label accumulation in HCO_3, in Glu C_5 and Gln C_5 (first turn of the TCA-cycle), and in Glu C_1 and Gln C_1 (second turn) can be observed after $[1-^{13}C]$ Ac in fusion. The rate of Ac

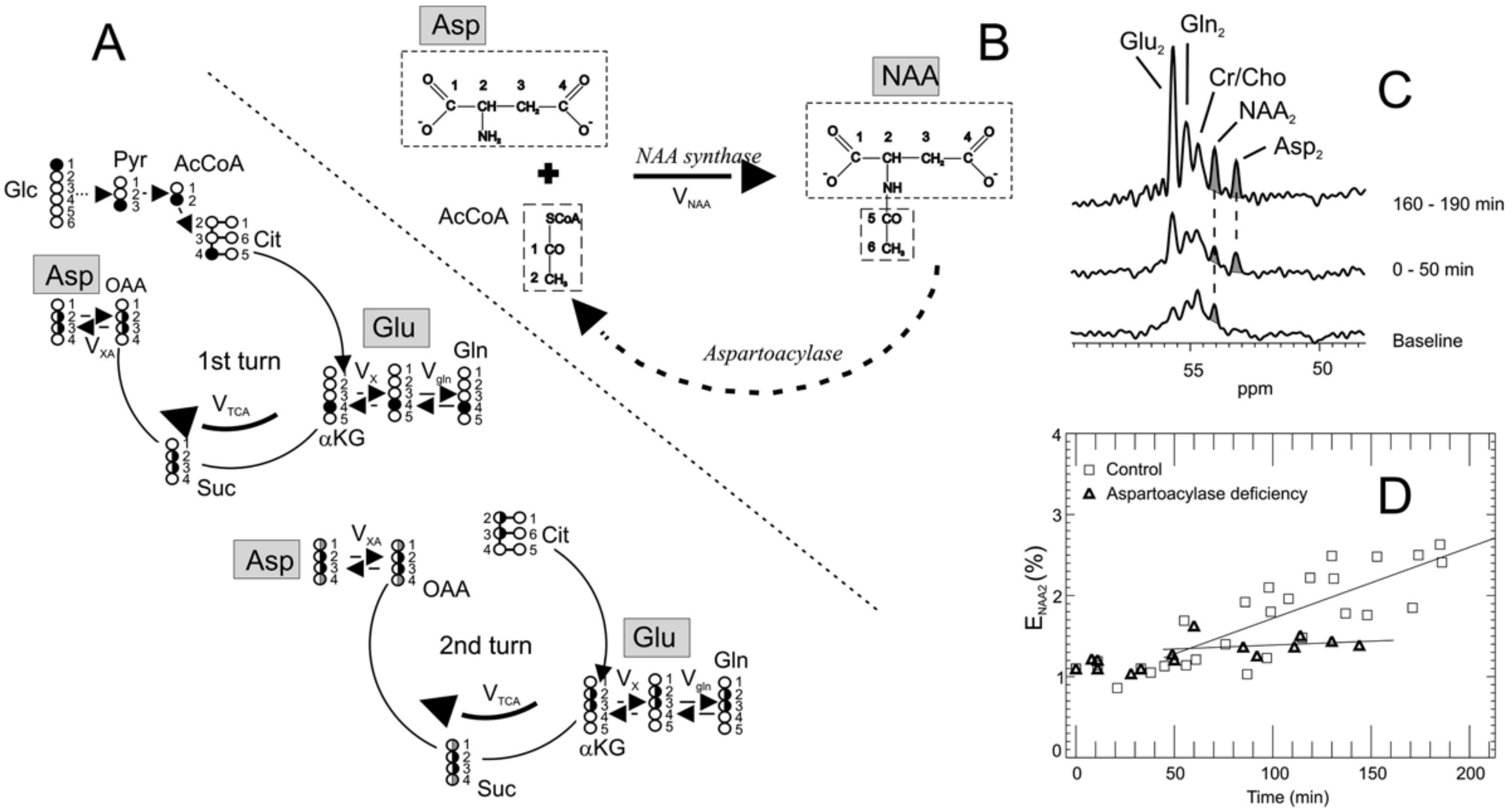
A
Glc
Pyr
AcCoA
Cit
Asp
OAA
V_{XA}
1st turn
V_{TCA}
Suc
αKG
Glu
V_x
V_{gln}
Gln
2nd turn
B
Asp
AcCoA
NAA synthase
V_{NAA}
NAA
Aspartoacylase
C
Glu₂
Gln₂
Cr/Cho
NAA₂
Asp₂
160 - 190 min
0 - 50 min
Baseline
55
50
ppm
D
Control
Aspartoacylase deficiency
E_{NAA2} (%)
Time (min)
0
1
2
3
4
0
50
100
150
200

Fig. 7. Determination of N-acetyl-aspartate synthesis rate, V_{NAA}, in humans *in vivo* (A) ^{13}C labeling scheme used to predict the transfer of ^{13}C label from Glu$_4$ to Asp$_{2,3}$. Only relevant TCA-cycle intermediates are shown (B). N-acetyl-aspartate (NAA) synthesis by condensation of aspartate and Acetyl CoA. (C) Human brain natural abundance (baseline) and ^{13}C enriched spectra after [1-^{13}C] glucose infusion. The time intervals indicate the time of acquisition relative to the commencement of [1-^{13}C] glucose infusion. Peak intensities of Asp$_2$ and NAA$_2$ (as well as Glu C$_2$ and Gln C$_2$) increased progressively as ^{13}C label accumulates. (D) Fractional ^{13}C enrichment of NAA (E_{NAA2}) versus time was lower in patients with aspartoacylase deficiency (Canavan Disease) than in control subjects. Linear regression lines are superimposed on data points $t > 50$ min in each group. The calculated mean rate of *in vivo* NAA synthesis in normal subjects was 9.2 ± 3.9 nmol/min/g. In patients with Canavan Disease statistically significant reductions of [Asp] and [Glu] were observed. NAA pool size was increased and V_{NAA} was significantly lower (3.6 ± 0.1 nmol/min/g, $p < 0.001$) than in controls. V_{TCA} = TCA-cycle rate, V_{x} = α-ketoglutarate/glutamate exchange rate. V_{gln} = glutamine synthesis rate, V_{xa} = oxaloacetate/aspartate exchange rate, Cit = citrate, Suc = succinate, Pyr = pyruvate, AcCoA = Acetyl CoA.

oxidation in human brain was estimated to be ≈20% of the total neuronal/glial TCA-cycle rate in fasted human brain [7,27]. Recently it was demonstrated that Glu C_5 and Gln C_5, which are primarily derived from acetate in the glial compartment, accumulated more in patients on ketogenic diet (KD) than in controls, whilst accumulation of bicarbonate was similar [34] (Figure 8). These results are consistent with altered glutamate-glutamine neutrotransmitter cycling and adaptation to ketogenic diet with up-regulation of acetate oxidation relative to glucose oxidation. KD is a treatment option for epileptic patients, which is particularly effective in children. The biochemical mechanisms why KD improves seizure activity are incompletely understood. *In vivo* ^{13}C MRS may elucidate a possibly biochemical basis for reduction in seizures during KD therapy. These studies indicate that ^{13}C MRS is an appropriate tool to investigate diseases which are believed to originate in glial cells. Together with data from glucose infusion experiments this could result in a more complete understanding of cerebral metabolism in normal and diseased human brain.

Hyperpolarized ^{13}C Compounds

Recently, dynamic nuclear polarization was used to obtain highly polarized ^{13}C nuclei in endogenous substances such as isotopically enriched ^{13}C urea [35]. Methods have been developed to perform the polarization process outside the body and a nuclear polarization of 50% for ^{13}C appears to be possible [35]. This polarization corresponds with an enhancement of 500,000 (!) compared with the thermal equilibrium polarization at 1.5 T for ^{13}C. Hyperpolarization vanishes due to longitudinal relaxation (T_1) and spectroscopy studies with the goal to investigate metabolic pathways face two major obstacles. (i) The hyperpolarized substrate needs to reach the organ of interest quickly and (ii) turnover rates need to be sufficiently fast to allow the observation of metabolites of a hyperpolarized substrate. Therefore, the application of hyperpolarized substrates to study normal and abnormal metabolism depends mainly on the capability to prepare metabolically active, non-toxic substrates with long T_1-times. Once that is achieved, the promise of ^{13}C MRS with endogenous substances is enormous. Already, Golman *et al.* [35] report a T_1-time of 20 s for ^{13}C urea *in vivo*. The polarization of such a substrate would still be ≈10 times higher than the thermal equilibrium polarization 4 min after injection. A hyperpolarized compound with a T_1 of 40 s would have a ≈1000 (!) higher polarization and a hypothetical 12 day acquisition time could be shortened to 1 s without compromising SNR! As these compounds become available, detailed studies of chemicals of low concentrations in tissue, first in animals and then in humans, may be feasible. In particular, the study of neurotransmitters, until now out of reach for spectroscopist may become a reality.

Acknowledgments

The author likes to thank Thomas Raidy, Ph.D. and Mark Albers, BS for discussions and for using their expertise with MR hardware. The author also likes to thank Rolf Gruetter, Ph.D. and Robin A. de Graaf, Ph.D. for providing figures.

Glossary

Absolute quantitation—Determination of concentrations of metabolites in mMoles per kg of tissue or volume.

***B*₀**—Strong magnetic field, constant in time and space, generated by the superconducting magnet.

***B*₁**—Radiofrequency (RF) magnetic field generated by *radiofrequency coils*.

Hetero-nuclear J-coupling—*J-coupling* between different species of spins, e.g. proton and carbon.

Homo-nuclear J-coupling—*J-coupling* between the same species of spins, e.g. proton and proton.

ISIS—**I**mage-**s**elected *in vivo* **s**pectroscopy is based on a cycle of eight acquisitions which need to be added and subtracted in the right order to get a single volume. ISIS is considerably more susceptible to motion then *STEAM* or *PRESS* and is mostly used in heteronuclear studies, where its advantage of avoiding T_2*-relaxation* is valuable.

J-coupling (or scalar coupling)—Many resonances split into multiplet components. This is the result of an internal indirect interaction of two spins via the intervening electron structure of the molecule. The coupling strength is measured in Hertz (Hz) rather than *ppm* because it is independent of the external B_0 field strength.

NOE—Nuclear Overhauser effect, the magnetization of protons dipolar-coupled to ^{13}C nuclei can be used to enhance the ^{13}C signal. While the term NOE is mainly associated with ^{13}C MRS, NOE enhancement can also be observed in ^{31}P MRS and with other nuclei.

Polarization transfer—Many interesting nuclei like ^{13}C suffer from low inherent sensitivity compared with proton MR. Techniques like DEPT (**d**istortionless **e**nhancement by **p**olarization **t**ransfer) and INEPT (**i**nsensitive **n**uclei **e**nhanced by **p**olarization **t**ransfer) improve the ^{13}C sensitivity by transferring the higher polarization of coupled protons to the carbon nuclei. Special hardware with two RF channels is needed for polarization transfer experiments. A modification of DEPT and INEPT is reverse DEPT and inverse INEPT where the polarization is transfered back to utilize the higher sensitivity of the protons for observation (inverse detection).

PRESS—Point-resolved spectroscopy, utilizes three 180° slice selective pulses along each of the spatial directions

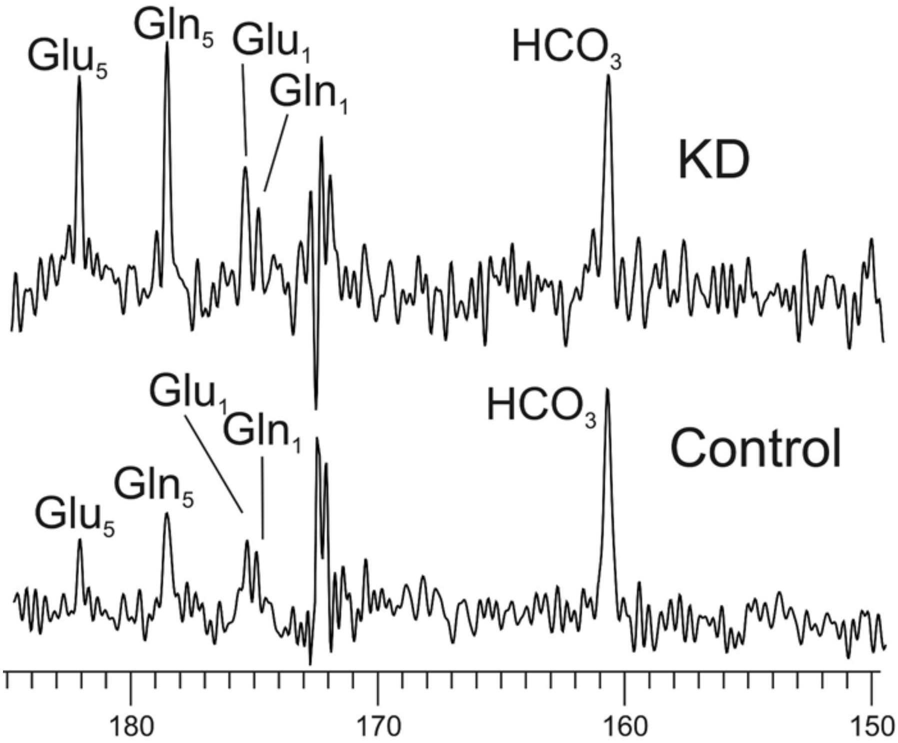

Fig. 8. Impact of ketogenic diet (KD) on astroglial acetate oxidation (A) ^{13}C difference spectra obtained from ketogenic diet patients (average of three) and (B) controls after infusion of [1-^{13}C] acetate. ^{13}C label incorporation into Glu C_5 and Gln C_5 was more pronounced in patients. In addition, Glu C_1 and Gln C_1 enrichment was more prominent, whereas equivalent production of HCO_3 was observed.

and generates signals from the overlap in form of a spinecho.

SAR—Specific absorption rate. Due to inductive and dielectric losses energy from radiofrequency pulses is absorbed by tissue and mainly transferred into rotational and translational movements of water molecules which causes an increase of tissue temperature. Limits for the human brain are established by FDA guidelines.

Scalar coupling—See *J-coupling*

STEAM—Stimulated **e**cho **a**cquisition **m**ode, localization method utilizing three 90° slice selective pulses, along each of the spatial directions. Signal, in form of a *stimulated echo*, from the overlap is generated in a “single shot” experiment. In contrast to *PRESS*, only half of the possible signal is recovered when the same *echo time* is used.

T_1-relaxation, T_1-relaxation time—After the *magnetization* vector has been flipped into the transverse plane, new magnetization builds up along the z-axis. The time after 63% (1-1/e) of the equilibrium magnetization has built up is called the T_1-relaxation time. T_1 and T_2 relaxation is caused by time-dependent fluctuations of local magnetic fields arising mostly from the motion of molecules with electric or magnetic dipoles at the site of the spins. For accurate *absolute quantitation* the relaxation times of all metabolites must be known in order to correct peak intensities appropriately.

T_1-saturation—The repetition times T_R are usually in the range of the T_1*-relaxation* times. As a consequence of this, not all the *magnetization* has recovered, for example when $T_R = T_1$ only 63% of the equilibrium magnetization can be used for each scan (with the exception of the first scan) when 90° flip angles are used for excitation. This effect is called T_1-saturation. The extreme case of saturation occurs when several *RF pulses* are applied within a very short time followed by dephasing *gradients*. This technique is used in localized ^{1}H MRS to remove the dominant water signal (see *water suppression*).

T_2-relaxation, T_2-relaxation time—The *magnetization* vector can be flipped into the transverse plane by using an *RF pulse*. The so generated transverse magnetization undergoes an exponential decay. The time after the magnetization has relaxed to 37% (1/e) of its amplitude is called the T_2 or transverse or spin-spin relaxation time. See also T_1- *relaxation*.

T_R (repetition time)—The time between each initial excitation of the magnetization is called the repetition time.

References

1. NMR in Biomed, 2003;16(6–7):301–457. Special issue: ^{13}C NMR studies of cerebral metabolism.
2. Adriany G, Gruetter R. J. Magn. Reson. 1997;125(1):178.
3. Bluml S. J. Magn. Reson. 1999;136(2):219.
4. Shen J, Petersen KF, Behar KL, Brown P, Nixon TW, Mason GF, Petroff OA, Shulman GI, Shulman RG, Rothman DL. Proceedings of the National Academy of Sciences of the United States of America. 1999;96(14), 8235.
5. Pan JW, Stein DT, Telang F, Lee JH, Shen J, Brown P, Cline G, Mason GF, Shulman GI, Rothman DL, Hetherington HP. Magn. Reson. Med. 2000;44(5):673.
6. Chhina N, Kuestermann E, Halliday J, Simpson LJ, Macdonald IA, Bachelard HS, Morris PG. J. Neurosci. Res. 2001;66(5):737.
7. Lebon V, Petersen KF, Cline GW, Shen J, Mason GF, Dufour S, Behar KL, Shulman GI, Rothman DL. J. Neurosci. 2002;22(5):1523.
8. FDA. Federal Register, 1988;53:7575.
9. FDA. US Department of Health and Human Services, Food and Drug Administration, http://www.fda.gov/cdrh/ode/mri340.pdf(http://www.fda.gov/cdrh/ode/mri340.pdf) (1998).
10. van den Bergh AJ, van den Boogert HJ, Heerschap A. Magn. Reson. Med. 1998;39(4):642.
11. Hwang JH, Bluml S, Leaf A, Ross BD. NMR Biomed. 2003;16(3):160.
12. Levitt MH, Freeman R. J. Magn. Reson. 1981;43:502.
13. Levitt MH. J. Magn. Reson. 1982;48:234.
14. Shaka AJ KJ, Frenkiel AJ, Freeman R. J. Magn. Reson. 1983;52:335.
15. Shaka AJ KJ, Freeman R. J Magn Reson, 1983;52:313.
16. de Graaf RA, Mason G, Pantel AB, Behar KL, Rothman DL. NMR Biomed. 2003;16:339.
17. Gruetter R, Adriany G, Choi IY, Henry P-G, Lei H, Oz G. NMR Biomed. 2003;16:313.
18. Gruetter R, Rothman DL, Novotny EJ, Shulman RG. Magn. Reson. Med. 1992;25(1):204.
19. Bluml S, Moreno A, Hwang JH, Ross BD. NMR in Biomed. 2001;14(1):19.
20. Bluml S, Moreno-Torres A, Ross BD. Magn. Reson. Med. 2001;45(6):981.
21. Ordidge RJ, Connelly A, Lohman JAB. J. Magn. Reson. 1986;66:283.
22. Gruetter R, Seaquist ER, Kim S, Ugurbil K. Dev. Neurosci. 1998;20(4–5):380.
23. Rothman DL, Behar KL, Hetherington HP, den Hollander JA, Bendall MR, Petroff OA, Shulman RG. Proc. Natl. Acad. Sci. U.S.A. 1985;82:1633.
24. Provencher SW. Magn. Reson. Med. 1993;30(6):672.
25. Mason GF, Gruetter R, Rothman DL, Behar KL, Shulman RG, Novotny EJ. J. Cereb. Blood. Flow. Metab. 1995;15(1):12.
26. Moreno A, Ross BD, Bluml S. J. Neurochem. 2001;77(1):347.
27. Bluml S, Moreno-Torres A. Shic F, Nguy CH, Ross BD. NMR Biomed. 2002;15(1):1.
28. Mason GF, Falk Petersen K, de Graaf RA, Kanamatsu T, Otsuki T, Shulman GI, Rothman DL. Brain Res. Brain Res. Protoc. 2003;10(3):181.
29. Watanabe H, Umeda M, Ishihara Y, Okamoto K, Oshio K, Kanamatsu T, Tsukada Y. Magn. Reson. Med. 2000;43(4):525.
30. Moreno A, Bluml S, Hwang JH, Ross BD. Magn. Reson. Med. 2001;46(1):39.
31. Beckmann N, Turkalj I, Seelig J, Keller U. Biochemistry. 1991;30(26):6362.
32. Magistretti PJ, Pellerin L, Rothman DL. Shulman RG. Science. 1999;283(5401):496.
33. Muir D, Berl S, Clarke DD. Brain Res. 1986;380(2):336.
34. Bluml S, Shic F, Lai L, Yahya K, Lin A, Ross BD. In Proceedings, 10th International Society of Magnetic Resonance in Medicine, Honolulu, 417 (2002).
35. Golman K, Ardenkjaer-Larsen JH, Petersson JS, Mansson S, Leunbach I. Proc. Natl. Acad. Sci. U.S.A. 2003;100(18):10435.
36. Bluml S, Hwang JH, Moreno A, Ross BD. J. Magn. Reson. 2000;143(2):292.
37. de Graaf RA, Brown PB, Mason GF, Rothman DL, Behar KL. Magn. Reson. Med. 2003;49(1):37.

Magnetic Resonance Spectroscopy and Spectroscopic Imaging of the Prostate, Breast, and Liver

Mark G. Swanson, Susan M. Noworolski, and John Kurhanewicz
Center for Molecular and Functional Imaging, Department of Radiology, University of California, San Francisco, CA 94107, USA

Metabolite Abbreviations: Ala, Alanine; ATP, Adenosine triphosphate; Cho, Choline; Cr, Creatine; Eth, Ethanolamine; Glx, Glutamine/Glutamate; GPC, Glycerophosphocholine; GPE, Glycerophosphoethanolamine; Lac, Lactate; MI, *myo*-Inositol; NAA, N-acetyl aspartate; NTP, Nucleotide triphosphate (e.g. ATP); PC, Phosphocholine; PCr, Phosphocreatine; PE, Phosphoethanolamine; Pi, Inorganic phosphate; SI, *scyllo*-Inositol; Tau, Taurine; UDP, Uridine diphosphate.

Introduction

In this chapter, we describe the current and potential role of magnetic resonance spectroscopy (MRS) and magnetic resonance spectroscopic imaging (MRSI) in organs of the body with an emphasis on the technical aspects of applications in prostate and breast cancer, and diseases of the liver. In contrast to anatomical magnetic resonance imaging (MRI), which detects changes in the relaxivity or density of bulk tissue water, spectroscopy detects small molecular weight metabolites within the cytosol of cells or within extracellular spaces such as glands or ducts. The addition of spectroscopy has been shown to improve the ability (i.e. sensitivity, specificity, and accuracy [1]) of conventional MRI to detect and stage prostate and breast cancer [2–4] and has shown promise in the evaluation of primary and metastatic liver tumors [5] and other liver diseases [6,7]. However, the potential of spectroscopy is even greater because multiple metabolic markers may be combined to provide an independent assessment of disease state, cancer aggressiveness, and therapeutic response [8–10]. The clinical use of spectroscopy as an adjunct to MRI has expanded dramatically over the past several years. This has been due to both the need to answer clinically relevant questions and recent technical advances in hardware and software that have provided improvements in the spatial and time resolution of the spectral data and have resulted in the incorporation of this technology on commercial MR scanners. These breakthroughs have allowed the routine addition of spectroscopy sequences to clinical MRI exams, and have led to spectroscopy being factored into the clinical decision process.

Historically, ^{31}P and ^{1}H have been the nuclei of choice for *in vivo* MRS in the body and each has distinct advantages and disadvantages. The major advantage of ^{1}H spectroscopy is its high sensitivity, which is necessary to achieve high spatial resolution (< 1 cm^3) in a clinically reasonable amount of time. Because the sensitivity of ^{31}P is only 6.6% that of ^{1}H, much larger voxel sizes (typically >8 cm^3) must be used to achieve the same sensitivity in the same amount of time. ^{31}P MRS also suffers from long T_1 and short T_2 relaxation times relative to ^{1}H. The inherently low sensitivity of ^{31}P MRS can be improved by broadband ^{1}H decoupling (e.g. WALTZ) during the acquisition, which sharpens signals by collapsing multiplets and produces a large nuclear overhauser enhancement (NOE) [11], and through the use of higher magnetic field clinical MR scanners. The major advantages of ^{31}P MRS are that no water or lipid suppression is needed and there is less spectral overlap because a relatively small number of metabolites are dispersed over a large spectral window ($\sim$25 ppm[1]). However, both ^{1}H and ^{31}P spectroscopy require additional hardware, software, and post-processing and display tools, much of which can now be purchased in the form of spectroscopy packages from the major MR manufacturers General Electric, Siemens, and Philips.

Several metabolites are present in high enough concentrations (>1 mM) to be detected by ^{1}H or ^{31}P MRS, although many have not yet been detected or fully exploited *in vivo* in the body. The ^{1}H MR spectrum spans a frequency range of about 10 ppm and is centered around water at 4.8 ppm. To date, the resonances

---

[1] Parts-per-million (ppm) is a dimensionless unit used to describe differences (usually from zero) in chemical shift (δ) independent of the applied frequency (B_0). Frequencies in Hertz (Hz) are converted to ppm by dividing the value by the carrier frequency in MHz and multiplying by 10^6. For example, a magnetic field strength of 1.5 T corresponds to a ^{1}H carrier frequency of $\sim$63 MHz, such that 1 ppm $\approx$ 63 Hz, whereas at 3.0 T, 1 ppm $\approx$ 126 Hz.

Graham A. Webb (ed.), Modern Magnetic Resonance, 1113–1125.
© 2008 *Springer.*

upfield of water have received the most attention, including lactate (Lac, $\delta = 1.33$ and 4.12 ppm), alanine (Ala, $\delta = 1.48$ and 3.78 ppm), glutamine/glutamate (Glx, $\delta = 2.04, 2.11, 2.35$, and 3.76 ppm), taurine (Tau, $\delta = 3.26$ and 3.43 ppm), *myo*-inositol (mI, $\delta = 3.28, 3.54, 3.60$, and 4.05 ppm), *scyllo*-inositol (sI, $\delta = 3.35$ ppm), creatine/phosphocreatine (Cr/PCr, $\delta = 3.04$ and 3.93 ppm), the choline containing compounds choline (Cho, $\delta = 3.21, 3.55$, and 4.07 ppm), phosphocholine (PC, $\delta = 3.23$, 3.62, and 4.18 ppm) and glycerophosphocholine (GPC, $\delta = 3.24, 3.68$, and 4.34 ppm), and the ethanolamine containing compounds ethanolamine (Eth, $\delta = 3.15$ and 3.80 ppm), phosphoethanolamine (PE, $\delta = 3.22$ and 3.99 ppm), and glycerophosphoethanolamine (GPE, $\delta = 3.30$ and 4.12 ppm). Healthy prostate tissue is unique in that citrate ($\delta = 2.55$ and 2.71 ppm) [12] and polyamines (predominantly spermine, $\delta = 3.11, 2.09$, and 1.78 ppm) [13] are also present in very high concentrations and can be readily observed by ^{1}H MRS. There is also much interest in observing glucose (3.43, 3.80, and 5.23 ppm) and uridine diphosphate (UDP) sugars (5.5–6.1 ppm), which resonate very close to water, because of the role of increased glycolysis in cancer [14]. It has also been demonstrated that amide proton transfer from the downfield exchangeable amide protons of proteins and peptides ($\sim 7.8-8.8$ ppm) to water can improve sensitivity by several orders of magnitude and provide a novel imaging mechanism [15].

The major contributors to the ^{31}P MR spectrum include inorganic phosphate (Pi, $\delta = 2.26$ ppm), phosphocreatine (PCr, $\delta = -2.89$ ppm), the phosphomonoesters (PC and PE, $\delta = 3.76$), the phosphodiesters (GPC and GPE, $\delta = 0.11$ and 0.74 ppm), diphosphodiesters (e.g. UDP sugars, $\delta = -11.07$ and -12.76 ppm), and nucleotide phosphates [e.g. adenosine triphosphate (ATP), $\delta = -5.24, -10.37$, and -19.02 ppm] [16]. ^{31}P chemical shifts are typically referenced to either *in vivo* PCr or external 85% H_3PO_4 (as listed here). It should be noted that when ^{31}P chemical shifts are reported with PCr set to 0.00 ppm, the values are 2.89 ppm greater than the corresponding values referenced with H_3PO_4 set to 0.00 ppm. It is also widely believed that ^{13}C spectroscopy, which to date has been primarily limited to the brain [17,18], will play a major role in the future of body MRS as higher field human scanners, ^{13}C labeled substrates (e.g. glucose, acetate, and pyruvate), and commercial ^{13}C hyperpolarizers [19] become more widely available and approved for human studies. However, because ^{13}C MRS is described elsewhere in this book, it will not be further discussed in this chapter.

Previous MR studies on prostate, breast, and liver tumors have identified elevated levels of phosphomonoesters and phosphodiesters (detected by ^{31}P MRS) [5,16,20–24] and elevated levels of the composite Cho resonance (detected by ^{1}H MRS) relative to normal healthy tissues [4,12,20,25–29]. Although the *in vivo* ^{1}H signal that is attributed to Cho contains contributions from Cho, PC, GPC, Eth, PE, GPE, Tau, *m*I, and *s*I, the Cho head group contains nine equivalent protons; consequently, a small increase in concentration results in a large increase in signal intensity. In cancer, the observed increases in Cho and Eth containing compounds have been primarily associated with increased cell membrane synthesis and degradation [24]. However, changes in cell density and altered phospholipid metabolism with cancer evolution and progression also contribute to the observed changes in phospholipid metabolites [27,30].

In spectroscopy it is also very important to identify markers for healthy or normal tissue that can be used for quantitation purposes. In ^{31}P MRS, metabolite ratios are often calculated relative to Pi, PCr, or NTP. In studies of cancer, before and after therapy, the phosphomonoester to phosphodiester ratio is particularly useful because it compares markers of proliferation (PC and PE) to markers of cellular breakdown or apoptosis (GPC and GPE). ^{1}H MRS has been highly successful in the prostate and brain because, in addition to increased Cho, there are unique markers for healthy tissue that decrease in cancer [31]. Consequently, the ratios of Cho to citrate in the prostate and Cho to N-acetyl aspartate (NAA) in the brain are significantly greater in regions of cancer compared to surrounding healthy tissues [2,32]. However, because citrate and NAA are not observed in any other tissues of the body, novel markers for healthy tissue, which may or may not change with malignancy or disease, are needed.

Techniques for Spectroscopy and Spectroscopic Imaging of the Body

Spatial Localization

The most common localization schemes for single voxel spectroscopy are image selected *in vivo* spectroscopy (ISIS) [33], stimulated echo acquisition mode (STEAM) [34], and point resolved spectroscopy (PRESS) [35]. ISIS consists of a series of selective inversion (i.e. 180°) pulses, which are turned on and off according to an eight-step encoding scheme, in the presence of magnetic field gradients. Because the magnetization remains along the "z" axis prior to the read pulse, ISIS is relatively insensitive to T_2 relaxation, and therefore has historically been popular for ^{31}P MRS. However, ISIS is particularly sensitive to motion because the eight transients must be added and subtracted to achieve spatial localization. Consequently, STEAM and PRESS, which are capable of three-dimensional (3D) localization in a single acquisition, are preferred for ^{1}H MRS studies in the body.

The STEAM radio frequency (rf) pulse sequence can be represented as $90^\circ - t_1 - 90^\circ - t_2 - 90^\circ - t_1-$ acquire, where t_1 and t_2 are inter-pulse delay times. STEAM generates three FIDs, four spin echoes, and one "stimulated echo" at distinct temporal positions, depending on t_1 and t_2, and the unwanted coherences are removed by applying crusher gradients. The desired stimulated echo appears at time $2 \times t_1 + t_2$ and corresponds to the signal from the volume of interest. The PRESS rf pulse sequence can be represented as $90^\circ - t_1 - 180^\circ - t_1 - t_2 - 180^\circ - t_2-$ acquire, where t_1 and t_2 are inter-pulse delay times. When the first 180° pulse is applied after time t_1, a spin echo forms at time $2 \times t_1$. When a second 180° pulse is applied after time t_2, the spin echo formed at $2 \times t_1$ is refocused into a second spin echo at time $2 \times t_1 + 2 \times t_2$, producing the signal that corresponds to the volume of interest. As in STEAM, crusher gradients are used in PRESS to remove the unwanted coherences.

Although STEAM can be used with shorter echo times for the observation of short T_2 metabolites, PRESS offers a factor of two times greater signal-to-noise, is less sensitive to motion and diffusion, and is not susceptible to the effects of multiple quantum coherence [36]. The use of longer echo times with PRESS also improves water and lipid suppression, but with improved gradient technology, echo times of the PRESS sequence can be reduced to that of STEAM to exploit the increased chemical information that can be obtained at shorter echo times. Recently, modified PRESS sequences for single voxel MRS and MRSI with very short echo times have been described using asymmetric rf pulses as well as optimized design and timing of the PRESS sequence [37].

Improved Volume Selection and Outer Volume Suppression

Spectroscopy studies in the body are critically dependent on accurate volume selection, since the region of interest is often adjacent to regions of lipid or air-tissue interfaces, which can significantly impair spectral quality. A recent technical advance for ^{1}H MRS has been the substitution of optimally shaped rf pulses, e.g. Shinnar-Le Roux pulses [38], in place of conventional sinc-shaped pulses for improved volume selection in PRESS acquisitions. Although low tip angle pulses can produce reasonably good slice profiles, optimized pulses are essential for 90° and especially 180° excitations [38]. Water saturation performance can also be improved using shaped pulses; however, due to the imperfect excitation profiles of the PRESS spin-echo pulses, even with Shinnar-Le Roux pulses, significant contamination from lipids outside the PRESS selected region can still occur. Several groups have used outer volume suppression (OVS) sequences to better conform the volume of interest [39–43]. These sequences utilized optimized pulses or special excitation schemes to shape the excitation volume to the region of interest. However, due to the non-rectangular suppression profiles of these pulses residual unsuppressed water and lipid signals at the band edges often rendered large portions of the spectral array unusable.

Quadratic phase pulse designs, e.g. very selective suppression (VSS) pulses [44], can provide excellent spatial selectivity, high effective bandwidths, and improved B_1 and T_1 insensitivity compared to conventional OVS pulses. VSS pulses can be inserted just before the PRESS excitation pulses and are used to better define the edges of the PRESS box. Additional VSS pulses can also be graphically prescribed in order to shape the selected volume to the region of interest to exclude regions of lipid or air tissue interfaces. Because of the imperfect PRESS excitation profile, the effects of chemical shift misregistration and the rounded edges of the PRESS selected volume can be dramatically reduced by overprescribing the PRESS selection by $\sim$20–30% and applying the VSS pulses to define the desired dimensions of the box as shown in Figure 1. The use of graphical VSS pulses to exclude periprostatic lipids in the prostate is illustrated in Figure 2A and B.

Water and Lipid Suppression

In order to detect the resonances of biological interest, the 110 molar water resonance must be suppressed by approximately 1000–10,000 fold and spectral contamination from lipids outside the volume of interest must be minimized as much as possible. Good shimming is absolutely essential for water and lipid suppression. Although automated shimming routines are often adequate and should be used as a starting point, it is well worth the extra time to manually shim and visually assess the shape of the water resonance and the FID. The ability to obtain a narrow water line width ($<$10 Hz) is also dependent upon the proper placement of the PRESS or STEAM box. When there are large differences in magnetic susceptibility, which can be caused by air-tissue or bone-tissue interfaces or the presence of radioactive seeds, it may be impossible to obtain adequate shim. If an adequate shim cannot be obtained in less than 5 min, the volume of interest should be re-prescribed and shimmed again, or the spectroscopy exam should be aborted. Prior to starting the MRS sequence, the water and lipid suppression pulses should be turned on in the pre-scan window to ensure that adequate suppression is being achieved.

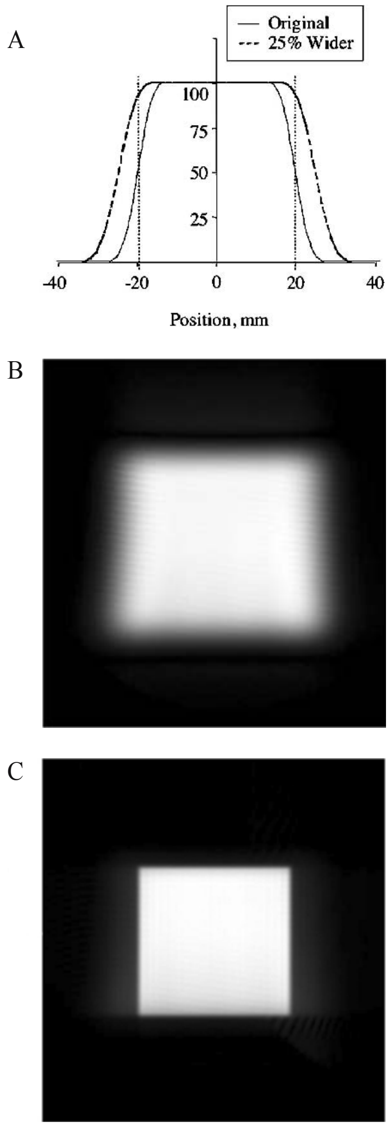

Fig. 1. Imperfect excitation profiles and compensation strategies. (A) Modeled excitation profile based upon the General Electric 90-PRESS excitation pulse, designed for a 40 mm width (solid line) and an identical pulse profile overprescribed by 25% (dashed line) at 1.5 T. An ideal pulse would be perfectly rectangular with 100% excitation at the edges (dotted lines at ±20 mm); however as prescribed the edges are only 50% excited at ±20 mm. For the overprescribed pulse, the edges are 93% excited at ±20 mm. (B) Image of a 40 × 40 × 40 mm^3 PRESS selected volume, overprescribed 20%. (C) Image of the PRESS selected volume shown in (B) with six VSS pulses added, yielding a very uniform excitation profile.

Techniques for water suppression have usually involved frequency selective saturation pulses (e.g. CHESS) [45]. Lipid suppression can be achieved by the selective excitation of a region of interest or by a combination of frequency and/or spatially selective pulses and selective inversion (STIR) [46]. These approaches require optimization for each individual study and often demonstrate inadequate water and lipid suppression, resulting in baseline artifacts and difficulty in quantifying metabolites. Recently, band selective inversion with gradient dephasing (BASING) pulses have been developed for combined water and lipid suppression, and have demonstrated suppression factors over 100 times greater than CHESS and STIR [47].

Spectral-Spatial Pulses

Spectral-spatial echo-planar spin-echo (EPSE) pulses simultaneously excite a selected frequency range and a selected volume, with the added advantage of reducing the chemical shift dependence of the PRESS volume [48]. Water and lipid suppression are not needed since their frequency ranges are simply not excited. Schricker *et al.* recently developed dual band spectral-spatial pulses which completely exclude lipid but allow for a partially excited water resonance for phase and frequency referencing [48]. This partial water signal can also be used to distinguish the absence of detectable metabolites due to therapy or atrophy from a technically failed study.

Chemical Shift Imaging

Single voxel MR studies are limited in the information they can provide and often suffer from improper or imprecise localization because their location is determined from MR images that cannot differentiate between tissue types. Furthermore, it is very difficult to attain perfect placement of the localized volume without spectral contamination from adjacent tissues, even when the region of interest is the same size or even slightly larger than the selected voxel size. Another limitation of single voxel studies is the inability to assess the spatial distribution of the metabolic changes. For heterogeneous or multi-focal lesions, particularly in prostate cancer, the exact choice of voxel size and position has a critical impact on the spectra acquired and their interpretation. To overcome the limitations of single voxel techniques, 3D phase encoding techniques have been added to PRESS or STEAM localization schemes [49,50] to provide localized spectra from arrays of multiple contiguous voxels with improved signal-to-noise. These techniques are referred to interchangeably as chemical shift imaging (CSI) or MRSI.

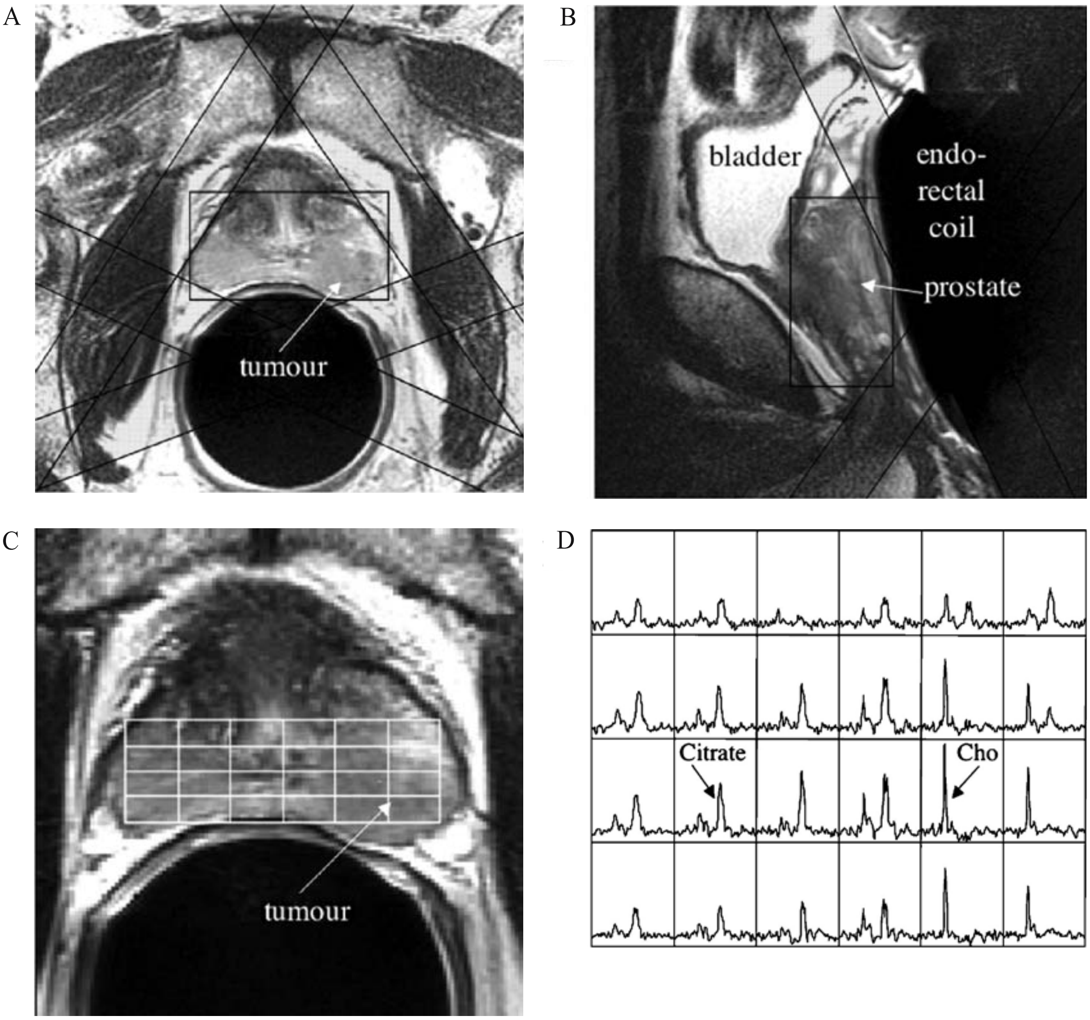

Fig. 2. Combined MRI/3D-MRSI of the prostate at 1.5 T. (A) Axial and (B) sagittal T_2-weighted images of the prostate showing the locations of the PRESS box and graphically prescribed VSS bands. (C) Axial T_2-weighted image and 3D-MRSI spectral grid which has been zero-filled in the anterior–posterior dimension. (D) Corresponding 3D-MRSI spectral array showing the presence of an aggressive appearing tumor (very elevated Cho and reduced citrate) on the left side of the gland (right side of the image). *Note:* Spectral array is one out of typically seven or eight acquired throughout the prostate.

Surface Coils

The ability to achieve high sensitivity, specifically high signal-to-noise, in the body is often impeded by the deep location of the organs within the body. While in principal body coils provide uniform excitation, they are not sensitive enough to be used for signal reception. Consequently, surface coils have been developed for signal reception, and for ^{31}P MRS applications, both transmission and reception. For prostate spectroscopy, a rigid or inflatable endorectal probe is essential to achieve the necessary sensitivity and to reduce peristaltic motion. For other organs, larger arrays of coils are typically placed over the torso or abdomen. These arrays include rigid frames of coils that are placed anteriorly and posteriorly, flexible coils which can be molded to the body allowing closer placement to regions of interest, and specialized breast coil arrays which circle the breasts and extend into the axilla for the supine patient. Many surface coils are now commercially available from a number of vendors (e.g. USA Instruments Inc., MRI Devices Corporation, and Medrad Inc.).

While surface coils and phased arrays of surface coils can provide much better sensitivity than the body coil, their sensitivity varies with position and decreases with increasing distance from the coil. If interpretation of spectra is to be based on ratios of resonance intensities or areas then the inhomogeneous reception profile of the surface coil can generally be neglected. However, the absolute amplitudes of individual metabolite peaks cannot be directly compared without taking into account the surface coil reception profiles. Like MR images, spectra can be at least partially corrected for inhomogeneous reception profiles by numerical evaluation of the Biot–Savart law [51]. Simplistically, the coil is modeled as a series of finite elements of various lengths from which a theoretical reception profile is calculated and the spectra are then divided by the theoretical profile. In practice, such correction algorithms need to take into account the anatomical location of the coil with respect to the location of the voxels to be corrected. The quality of the coil correction can then be evaluated by applying the same algorithm to the corresponding MR images, and by comparing the corrected images to the coil map. If the location of the coil map is incorrect, the images will contain very distinct hypointense (dark) or hyperintense (bright) spots, and the position of the coil should be re-determined and the algorithm reapplied. An alternative approach is to acquire proton density weighted images, which demonstrate the sensitivity profile of the coil, and use these to correct the data [52].

In heteronuclear and high field (e.g. 4 and 7 T) MRS, combined transmit/receive surface coils are required and inhomogeneous excitation profiles become a major issue. Specifically, an inhomogeneous excitation profile results in different locations experiencing different nutation (flip) angles, which causes poor or inadequate spatial selection and chemical shift misregistration. One way of overcoming problems associated with inhomogeneous excitation profiles is to excite with a much larger surface coil than that used for signal reception. Another way to overcome the problems with inhomogeneous excitation profiles of surface coils is to use adiabatic rf pulses, such as B_1 insensitive rotation (e.g. BIR-4) pulses [53]. Adiabatic pulses produce a uniform flip angle, typically 90° or 180°, across a region of interest despite variations in B_1, provided that the rf power is above a minimum threshold value. Adiabatic pulses are highly versatile and can be exploited for spatial localization [e.g. localization by adiabatic selective refocusing (LASER) [54]], as well as water suppression and OVS [e.g. B_1-insensitive train to obliterate signal (BISTRO) [43,55]].

Motion

Respiratory and peristaltic motion can also be major problems in body spectroscopy. In the prostate, peristaltic motion is reduced by the use of an inflatable endorectal coil. Because the prostate is directly beneath the bladder, as shown in Figure 2B, additional motion may be caused by the bladder filling up during the course of the examination. To minimize this, patients are asked to refrain from drinking (especially caffeinated beverages) for 2–3 h prior to the exam. In the breast, motion is reduced by having the patient lay supine on a breast coil, supported by the chest, resulting in the breasts remaining relatively free of respiratory motion. Nonetheless, one study showed that in 20 breast and abdominal tumors, 30% moved 6–23 mm, while the diaphragm and fatty tissues of the gut typically moved $\sim$15–20 mm [56]. Recently, it has been reported that breathheld MRS can significantly reduce phase and frequency shifts and outer voxel contamination due to respiratory motion [57], while the use of navigator echoes can aid with retrospective motion correction [58].

Data Processing and Display

Single voxel MRS data can often be processed and displayed using commercial software packages designed for conventional NMR spectroscopy, provided that the header can be interpreted or removed. Basic data processing involves Lorentzian and/or Gaussian apodization of the FID to enhance resolution and/or signal-to-noise, baseline correction, zero-filling, and Fourier transformation of the data. Phasing and frequency referencing are then performed manually on the resulting spectra. Because MRSI data may contain hundreds of useable spectra, completely automated and robust data processing algorithms are essential. In addition to the basic data processing steps just described, the data must be reconstructed to correctly reproduce the spatial dependence of the data [59] and can also be spatially zero filled as shown in Figure 2C and D. After the spectra have been Fourier transformed, automated baseline, phase, and frequency corrections can then be applied using water as a reference or by using prior knowledge of the approximate relative positions of the major peaks in the spectrum. Peak areas may be estimated by integration across fixed frequency ranges, by fitting baseline subtracted data as a sum of components with particular lineshapes [60–63], or using linear combinations of model *in vitro* spectra [64].

Several different approaches have been used to display the information from multi-dimensional localized spectra and to correlate spatial variations in metabolites with the anatomy [50,65–68]. These include superimposing a grid on the MR image and plotting the corresponding arrays of spectra, and calculating images of the spatial distribution of metabolites to overlay on the corresponding MR images. These formats provide an excellent summary of the spatial distribution of different metabolites enabling rapid identification of regions of suspected abnormal signal and facilitating correlation with the anatomy. Additionally, since 3D volume MRI and MRSI data are collected, the data can be viewed in any plane (axial, coronal, or sagittal), and the spatial position of spectroscopic voxels can be selected retrospectively via "voxel-shifting," using the appropriate mathematical weighting of the raw data based upon the translation property of the Fourier transform [69,70]. This method of interactive analysis will be the way that MRI/MRSI data is used in the future and should reduce interpretative errors associated with the overlap of normal and abnormal tissues.

Data Interpretation

Interpretation of spectroscopy and spectroscopic imaging data requires both knowledge of what constitutes a clinically interpretable spectrum and an understanding of the underlying biochemistry and morphology that result in the observed changes. ^{1}H spectra are considered clinically interpretable if they are not contaminated by insufficiently suppressed water or lipid and have resolvable metabolite peaks with peak area to noise ratios of greater than 5 to 1. Metabolic criteria must then be established to distinguish abnormal from normal metabolism and then validated using a pathologic "gold standard." In the prostate, the (Cho + Cr)/Cit ratio discriminates prostate cancer from benign glandular tissues with high specificity [12]. In the other organs of the body, similar metabolic criteria must still be established. *Ex vivo* high-resolution magic angle spinning (HR-MAS) spectroscopy and quantitative pathologic analysis of intact surgical or biopsy tissues can aid in understanding the relationship between metabolism and tissue composition [71] and thereby help with the identification of the appropriate metabolic criteria. Finally, the metabolic criteria used to identify residual or recurrent disease often change following therapy [8]. Treatment effects typically result in an overall reduction in the signal-to-noise of all metabolites, which underscores the need to be able to distinguish an absence of metabolites (termed "metabolic atrophy") from a technically failed study.

Applications in the Prostate, Breast, and Liver

To date, *in vivo* MRS has been applied to the prostate [12,22], breast [4,25,72,73], liver [74,75], kidney [76,77], colon [78], heart [79–81], skeletal muscle [82–84], sarcomas [85,86], and non-Hodgkin's lymphomas [10,87,88]. In the following sections, specific applications in the prostate, breast, and liver are described and ^{1}H MRS examples are shown.

Prostate Cancer

The earliest MRS studies of the human prostate involved ^{31}P spectroscopy using a dual tuned (^{31}P/^{1}H) transmit/receive endorectal probe [22,89,90]. The proton frequency was used to image the location of the coil and obtain a homogeneous field of view, prior to performing phosphorus spectroscopy. These studies demonstrated the ability of ^{31}P MRS to detect metabolic differences between normal, hyperplastic, and malignant prostate tissues. Specifically, the ^{31}P MR spectra taken from regions of prostate cancer were characterized by increases in the phosphomonoester to β-NTP ratio and decreases in the PCr to β-NTP ratio relative to healthy prostate tissues [22,89,90]. Additional studies using murine models of prostate cancer also identified ^{31}P spectral characteristics that may be related to the hormone sensitivity, radiation sensitivity, and metastatic potential of the cancer [16]. However, these early ^{31}P MRS studies of the prostate were limited by coarse spectral localization and spatial resolution due to the inherent insensitivity of ^{31}P MRS. Therefore, most of the clinical prostate studies performed to date have utilized a combination of high spatial resolution MRI and ^{1}H MRSI.

High-resolution T_2-weighted imaging, using combined endorectal and pelvic phased array coils, has demonstrated good sensitivity but relatively poor specificity for identifying prostate cancer, because numerous other conditions, including prostatitis, benign prostatic hyperplasia, and treatment effects can all mimic cancer. Prior to therapy, the addition of 3D-MRSI to anatomical MRI has been shown to improve the localization [2] and staging [3] of prostate cancer, provide a measure of prostate tumor volume [91], and provide an assessment of prostate cancer aggressiveness [92]. The ability of combined MRI/MRSI to identify residual or recurrent prostate cancer after hormone deprivation [8,9] and radiation therapy [93,94] has also been described.

Healthy glandular prostate tissue demonstrates two unique metabolic markers, citrate and spermine, that are produced by highly specialized epithelial cells and secreted into the prostatic ducts that empty into the ejaculate. Both citrate and spermine are reduced or absent in regions of prostate cancer, due to both biochemical changes and a loss of the prostate's normal ductal morphology [95–98]. Although the citrate resonance is completely resolved, its detection is complicated due to strong coupling. At 1.5 T, under good shimming conditions, polyamines are seen as a hump resonating between Cho and creatine, while in regions of cancer, the reduction or loss of polyamines is observed as an increase in the discrimination between Cho and creatine.

At our institution, axial high-resolution T_2-weighted images (3 mm slice thickness, no intersection gap) are used to select a PRESS volume (typically 50–100 cm^3) that encompasses the entire prostate, but excludes periprostatic lipids, the seminal vesicles which contain very high levels of GPC, and the air tissue interface of the rectum. The PRESS box is overprescribed by 20–30% in all three dimensions and then six VSS pulses are used to define the desired edges of the PRESS box. Six additional VSS pulses are graphically prescribed to eliminate contamination from surrounding lipids (Figure 2A and B). With a typical voxel size of ∼7 mm on a side (0.34 cm^3), $16 \times 8 \times 8$ step phase encoding ($112 \times 56 \times 56\ \text{mm}^3$ field of view) is performed with a 1 s repetition time for a total acquisition time of ∼17 min.

Spectral data from a MRI/MRSI staging exam acquired under these conditions are shown in Figure 2. Figures 2A and B show the location of the PRESS box and the locations of the graphical VSS bands. Figure 2C shows a portion of the 3D spectral grid, which has been zero filled in the anterior/posterior direction, and Figure 2D shows the corresponding MRSI spectral data. As can be seen, the right side of the gland (left side of the image/array) demonstrates fairly normal metabolism with high levels of citrate and low levels of Cho. However, the left side of the gland (right side of the image/array) demonstrates very elevated levels of Cho and in some areas a complete absence of citrate, consistent with the presence of an aggressive prostate tumor. The patient subsequently went on for a transrectal ultrasound (TRUS) guided biopsy and was diagnosed with Gleason 4 + 3 prostate cancer.

The interpretation and utility of prostate MRSI can be complicated by the presence of chronic inflammation (prostatitis) [99], which appears metabolically similar to prostate cancer. Additionally, post-biopsy hemorrhage can persist for 6–8 weeks or more after biopsy and demonstrates a reduction or absence of citrate and polyamines due to the disruption of prostatic ducts, and in worse cases results in a complete absence of all prostatic metabolites [100]. Regions of hemorrhage are usually identified as bright areas, and less frequently dark areas, on axial T_1-weighted images and these can be used to exclude suspected regions from the MRSI data analysis. Following therapy, the time course of treatment-induced metabolic changes must be taken into account when interpreting the data. For example, hormone deprivation has a very fast impact on prostate metabolism and often results in a total loss of citrate and polyamines within 16 weeks [8]. Conversely, radiation therapy has a much slower impact on prostate metabolism and may take 1–3 years to achieve metabolic atrophy. In either case, the presence of elevated Cho relative to creatine appears to be the best current indicator of recurrent prostate cancer.

Breast Cancer

For breast cancer, one of the critical clinical questions is whether the lesion detected on screening is benign or malignant. About 75% of the breast lesions detected by mammography and about 50% of the enhancing lesions detected by contrast-enhanced MRI are pathologically benign [101]. Sonographic classification of benign and malignant tumors has low specificity (about 30%) as well [102]. Recent advances in contrast-enhanced MRI methodology and interpretation have greatly improved the ability to differentiate malignant from benign breast tumors. However, there still remains a clinical need for improved specificity [103,104], which spectroscopy may be able to provide [4].

Breast spectroscopy has lagged behind prostate and brain spectroscopy because of the presence of mobile lipids and a lack of multiple metabolic markers. Early ^{31}P MRS studies typically observed increased phosphomonoester, phosphodiester, and sometimes PCr levels in breast cancer vs. normal tissues [105]. However, because of the poor sensitivity of ^{31}P MRS combined with the decreasing size of breast tumors due to early detection, ^{1}H MRS is now being primarily used. Typical breast MRS studies use a single voxel ($\sim 1 - 27\ \text{cm}^3$) [4] localization technique such as STEAM or PRESS with the intent of selecting signals from the lesion of interest and excluding signals from the surrounding adipose tissue and normal parenchyma [4]. However, due to the magnitude of lipid resonance in the breast, gradient induced sidebands of the lipid resonance can cause both positive and negative artifacts in the Cho region of the spectrum. Recently, a technique called "T_E-averaging," based upon oversampled 2D J-resolved spectroscopy [106], has demonstrated the ability to separate lipid induced sidebands and provide increased sensitivity for the study of small or irregularly shaped lesions [72]. An example of the spectral improvement provided by T_E-averaging is shown in Figure 3.

Currently, the interpretation of breast ^{1}H MRS data is relatively simple and mainly involves determining whether Cho is present (malignant) or absent (benign) [4]. This observation is consistent with the high PC content of human breast cancer cells, which is 10-fold higher than that of normal human mammary epithelial cells [107]. However, Stanwell *et al.* found that 20% of normal volunteers also demonstrated detectable Cho, leading to an overall sensitivity and specificity of 80 and 86%, respectively, when Cho presence alone is used to define cancer [108]. Additionally, smaller tumors tend to be diagnosed as benign (false–negative) because of the lack of a detectable composite Cho signal [4]. Other complications in the interpretation of breast spectra have primarily been technical and associated with poor spectral quality [4,109]. The utility and robustness of breast spectroscopy can be improved by increasing the Cho signal-to-noise

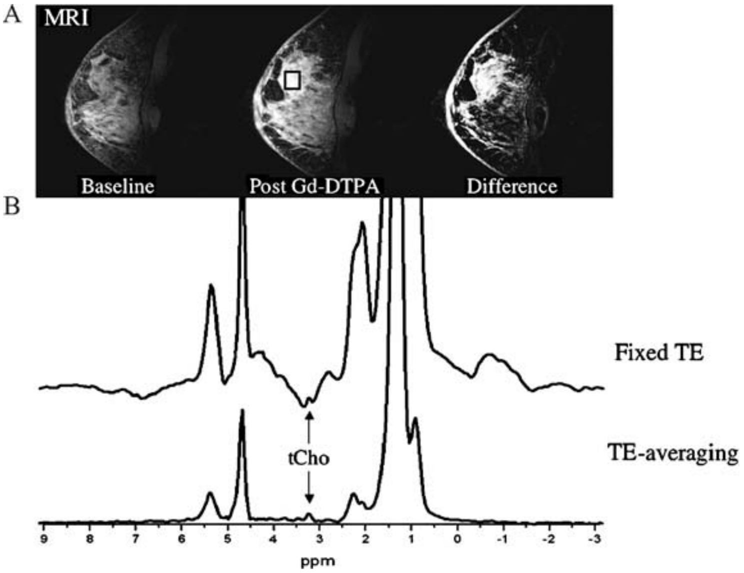

Fig. 3. (A) T_1-weighted image, dynamic contrast-enhanced image, and difference image of a poorly differentiated adenocarcinoma of the breast acquired at 4.0 T. (B) Single voxel ^{1}H MR spectra localized using LASER, demonstrating the improvement in lipid sideband suppression obtained by T_{E}-averaging (data acquired at 4.0 T). Figure courtesy of Drs Patrick J. Bolan and Michael Garwood, University of Minnesota School of Medicine.

through the use of higher sensitivity coils, the addition of new metabolic markers, and the use of improved pulse sequences and higher field human scanners.

MRS of the Liver

The liver is the most biochemically complex organ in the human body, and in addition to being the second most common site of cancer metastasis (after lymph nodes) [110], the liver is subject to a variety of non-malignant diseases including inflammation, hepatitis, cirrhosis, and fatty liver disease. The majority of liver MRS studies have looked at fat content and have shown that proton MRS of liver fat correlates well with *ex vivo* liver fat measurements [111]. Lipid levels have been shown to change with cancer [28,29], metabolism [112,113], and non-alcoholic fatty liver disease (NAFLD) and non-alcoholic steatohepatitis (NASH) [7,114,115]. Example single voxel ^{1}H MR spectra from a healthy individual and from a patient with fatty liver disease are shown in Figure 4. While the body mass index of these two individuals were similar (26 vs. 27, respectively), the lipid to water ratio is much greater in the subject with fatty liver disease.

Because of the problem of motion in the abdomen, liver MRS is typically performed as a single voxel technique, with a surface coil phased array used for reception. In the case of diffuse disease (e.g. fatty liver disease), where the location within the organ is not critical, the voxel should be placed at least 1 cm from all edges of the liver to reduce the chance of contamination from signals outside the liver. In the superior/inferior direction, the voxel should be placed such that it will remain in the liver throughout respiration. This can be ascertained by comparing breathheld images acquired at end-expiration to those at end-inspiration. During pre-scanning, the signal amplitude should also remain relatively constant from pulse to pulse. To account for small shifts in position over time, MR spectra can be saved individually before averaging. These individual MR spectra can then be phase and frequency aligned before summation to account for some respiratory motion.

Summary

MR spectroscopy and spectroscopic imaging are promising techniques for the metabolic assessment of cancer and other diseases in the body. However, spectroscopy in the body is challenging due to motion and the deep location of many organs. The critical considerations when performing spectroscopy in the body include the choice of: nucleus (^{1}H is preferred at 1.5 T due to high sensitivity, but ^{31}P and ^{13}C may be valuable at higher field); single voxel vs. multi-voxel (CSI or MRSI) approach; localization scheme (e.g. PRESS, STEAM, LASER); water and lipid suppression (e.g. BASING, CHESS, STIR) and OVS techniques (e.g. VSS pulses); surface coils; and data display and analysis tools. Proper spectral interpretation based upon a pathologic “gold standard” and knowledge of the impact of therapy on metabolism are both critical for evaluating the clinical utility of new MRS applications in the

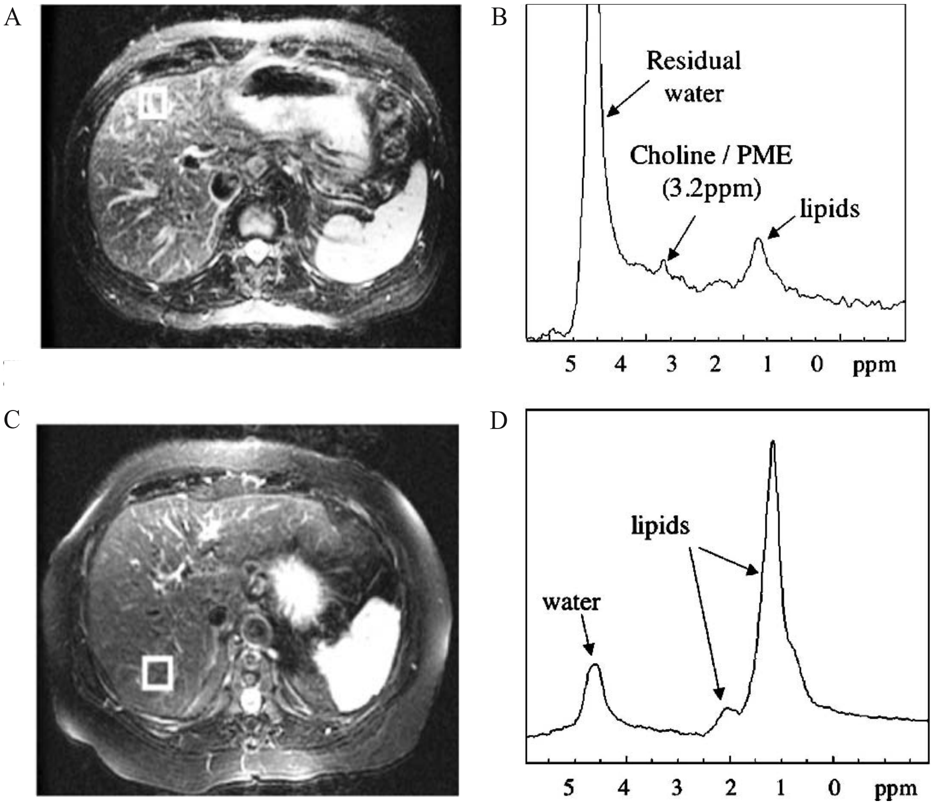

Fig. 4. Axial T_2-weighted image and $2 \times 2 \times 2$ (8 cm^3) single voxel ^1H spectra acquired from the liver of a normal volunteer (A and B) and a patient with NAFLD (C and D). Data were acquired at 1.5 T using PRESS with VSS pulses and CHESS water suppression (no lipid suppression), with 128 transients, $T_R = 2500$ ms, and $T_E = 35$ ms. Voxels were prescribed >1 cm from the edges of the liver, avoiding vessels, and spectra were individually phased and frequency shifted before averaging.

body. The increased sensitivity provided by higher field MR scanners, improved pulse sequences and technology, and the ability to include additional metabolic markers will also have a major impact on the clinical potential of body spectroscopy in the future.

Acknowledgments

The authors wish to acknowledge and thank Drs. Michael Garwood and Patrick J. Bolan, Center for Magnetic Resonance Research, University of Minnesota School of Medicine, Minneapolis, for providing the breast figure presented in this chapter, and Dr. Aliya Qayyum, Department of Radiology, University of California, San Francisco, for providing the liver figures presented in this chapter.

Glossary of Terms

BASING	Band selective inversion with gradient dephasing
BIR	B_1-insensitive rotation
BISTRO	B_1-insensitive train to obliterate signal
CHESS	Chemical shift selective saturation
CSI	Chemical shift imaging
EPSE	Echo-planar spin-echo
FID	Free induction decay
HR-MAS	High-resolution magic angle spinning
ISIS	Image selected *in vivo* spectroscopy
LASER	Localization by adiabatic selective refocusing
MRI	Magnetic resonance imaging
MRS	Magnetic resonance spectroscopy

MRSI	Magnetic resonance spectroscopic imaging
NAFLD	Non-alcoholic fatty liver disease
NASH	Non-alcoholic steatohepatitis
NOE	Nuclear overhauser enhancement
OVS	Outer volume suppression
PPM	Parts-per-million
PRESS	Point resolved spectroscopy
STEAM	Stimulated echo acquisition mode
STIR	Short time inversion recovery
T_1	Longitudinal (spin–lattice) relaxation time
T_2	Transverse (spin–spin) relaxation time
TRUS	Transrectal ultrasound
VSS	Very selective suppression
WALTZ	Broadband decoupling scheme

References

1. Obuchowski NA. Radiology. 2003;229:3.
2. Scheidler J, Hricak H, Vigneron DB, Yu KK, Sokolov DL, Huang LR, Zaloudek CJ, Nelson SJ, Carroll PR, Kurhanewicz J. Radiology. 1999;213:473.
3. Yu KK, Scheidler J, Hricak H, Vigneron DB, Zaloudek CJ, Males RG, Nelson SJ, Carroll PR, Kurhanewicz J. Radiology. 1999;213:481.
4. Katz-Brull R, Lavin PT, Lenkinski RE. J. Natl. Cancer. Inst. 2002;94:1197.
5. Bell JD, Bhakoo KK. NMR Biomed. 1998;11:354.
6. Cho SG, Kim MY, Kim HJ, Kim YS, Choi W, Shin SH, Hong KC, Kim YB, Lee JH, Suh CH. Radiology. 2001;221:740.
7. Heiken JP, Lee JK, Dixon WT. Radiology. 1985;157:707.
8. Mueller-Lisse UG, Swanson MG, Vigneron DB, Hricak H, Bessette A, Males RG, Wood PJ, Noworolski S, Nelson SJ, Barken I, Carroll PR, Kurhanewicz J. Magn. Reson. Med. 2001;46:49.
9. Mueller-Lisse UG, Vigneron DB, Hricak H, Swanson MG, Carroll PR, Bessette A, Scheidler J, Srivastava A, Males RG, Cha I, Kurhanewicz J. Radiology. 2001;221:380.
10. Arias-Mendoza F, Smith MR, Brown TR. Acad. Radiol. 2004;11:368.
11. van Sluis R, Payne GS, Leach MO. Magn. Reson. Med. 1995;34:893.
12. Kurhanewicz J, Vigneron DB, Hricak H, Narayan P, Carroll P, Nelson SJ. Radiology. 1996;198:795.
13. Cheng LL, Wu CL, Smith MR, Gonzalez RG. FEBS Lett. 2001;494:112.
14. Stubbs M, Bashford CL, Griffiths JR. Curr. Mol. Med. 2003;3:49.
15. Zhou J, Lal B, Wilson DA, Laterra J, van Zijl PC. Magn. Reson. Med. 2003;50:1120.
16. Kurhanewicz J, Dahiya R, Macdonald JM, Jajodia P, Chang LH, James TL, Narayan P. NMR Biomed. 1992;5:185.
17. Ross B, Lin A, Harris K, Bhattacharya P, Schweinsburg B. NMR Biomed. 2003;16:358.
18. Morris P, Bachelard H. NMR Biomed. 2003;16:303.
19. Ardenkjaer-Larsen JH, Fridlund B, Gram A, Hansson G, Hansson L, Lerche MH, Servin R, Thaning M, Golman K. Proc. Natl. Acad. Sci. U.S.A. 2003;100:10158.
20. Cornel EB, Smits GA, Oosterhof GO, Karthaus HF, Deburyne FM, Schalken JA, Heerschap A. J. Urol. 1993;150:2019.
21. Kalra R, Wade KE, Hands L, Styles P, Camplejohn R, Greenall M, Adams GE, Harris AL, Radda GK. Br. J. Cancer. 1993;67:1145.
22. Kurhanewicz J, Thomas A, Jajodia P, Weiner MW, James TL, Vigneron DB, Narayan P. Magn. Reson. Med. 1991;22:404.
23. Ronen SM, Leach MO. Breast Cancer Res. 2001;3:36.
24. Daly PF, Lyon RC, Faustino PJ, Cohen JS. J. Biol. Chem. 1987;262:14875.
25. Cecil KM, Schnall MD, Siegelman ES, Lenkinski RE. Breast Cancer Res. Treat. 2001;68:45.
26. Kurhanewicz J, Dahiya R, Macdonald JM, Chang LH, James TL, Narayan P. Magn. Reson. Med. 1993;29:149.
27. Aboagye EO, Bhujwalla ZM. Cancer Res. 1999;59:80.
28. Kuo YT, Li CW, Chen CY, Jao J, Wu DK, Liu GC. J. Magn. Reson. Imaging. 2004;19:598.
29. Soper R, Himmelreich U, Painter D, Somorjai RL, Lean CL, Dolenko B, Mountford CE, Russell P. Pathology. 2002;34:417.
30. Schiebler ML, Tomaszewski JE, Bezzi M, Pollack HM, Kressel HY, Cohen EK, Altman HG, Gefter WB, Wein AJ, Axel L. Radiology. 1989;172:131.
31. Kurhanewicz J, Vigneron DB, Nelson SJ. Neoplasia. 2000;2:166.
32. Vigneron D, Bollen A, McDermott M, Wald L, Day M, Moyher-Noworolski S, Henry R, Chang S, Berger M, Dillon W, Nelson S. Magn. Reson. Imaging. 2001;19:89.
33. Ordidge RJ, Connelly A, Lohman JAB. J. Magn. Reson. 1986;66:283.
34. Frahm J, Merboldt KD, Hanicke W. J. Magn. Reson. 1987;72:502.
35. Bottomley PA. Ann. N.Y. Acad. Sci. 1987;508:333.
36. Moonen CT, von KM, van ZP, Cohen J, Gillen J, Daly P, Wolf G. NMR Biomed. 1989;2:201.
37. Geppert C, Dreher W, Leibfritz D. MAGMA. 2003;16:144.
38. Pauly J, Le Roux P, Nishimura D, Macovski A. IEEE Trans. Med. Imaging. 1991;10:53.
39. Shungu DC, Glickson JD. Magn. Reson. Med. 1993;30:661.
40. Posse S, Tedeschi G, Risinger R, Ogg R, Le Bihan D. Magn. Reson. Med. 1995;33:34.
41. St Lawrence K, Lee TY, Henkelman M. Magn. Reson. Med. 1998;40:944.
42. Le Roux P, Gilles RJ, McKinnon GC, Carlier PG. J. Magn. Reson. Imaging. 1998;8:1022.
43. Luo Y, de Graaf RA, DelaBarre L, Tannus A, Garwood M. Magn. Reson. Med. 2001;45:1095.
44. Tran TK, Vigneron DB, Sailasuta N, Tropp J, Le Roux P, Kurhanewicz J, Nelson S, Hurd R. Magn. Reson. Med. 2000;43:23.
45. Haase A, Frahm J, Hanicke W, Matthaei D. Phys. Med. Biol. 1985;30:341.
46. Bydder GM, Young IR. J. Comput. Assist. Tomogr. 1985;9:659.
47. Star-Lack J, Nelson SJ, Kurhanewicz J, Huang LR, Vigneron DB. Magn. Reson. Med. 1997;38:311.

48. Schricker AA, Pauly JM, Kurhanewicz J, Swanson MG, Vigneron DB. Magn. Reson. Med. 2001;46:1079.
49. Brown TR, Kincaid BM, Ugurbil K. Proc. Natl. Acad. Sci. U.S.A. 1982;79:3523.
50. Maudsley AA, Hilal SK, Simon HE, Wittekoek S. Radiology. 1984;153:745.
51. Moyher SE, Vigneron DB, Nelson SJ. J. Magn. Reson. Imaging. 1995;5:139.
52. Liney GP, Turnbull LW, Knowles AJ. J. Magn. Reson. Imaging. 1998;8:994.
53. DeGraaf RA, Nicolay K. Concepts Magn. Reson. 1997;9:247.
54. Garwood M, DelaBarre L. J. Magn. Reson. 2001;153:155.
55. de Graaf RA, Luo Y, Garwood M, Nicolay K. J. Magn. Reson. B. 1996;113:35.
56. Schwarz AJ, Leach MO. Phys. Med. Biol. 2000;45:2105.
57. Katz-Brull R, Rofsky NM, Lenkinski RE. Magn. Reson. Med. 2003;50:461.
58. Tyszka JM, Silverman JM. Magn. Reson. Med. 1998;39:1.
59. Nelson SJ. Magn. Reson. Med. 2001;46:228.
60. Spielman D, Webb P, Macovski A. Magn. Reson. Med. 1989;12:38.
61. Nelson SJ, Brown TR. J. Magn. Reson. 1987;75:229.
62. Nelson S, Brown T. J. Magn. Reson. 1989;84:95.
63. Derby K, Hawryszko C, Tropp J. Magn. Reson. Med. 1989;12:235.
64. Provencher SW. NMR Biomed. 2001;14:260.
65. Tropp JS, Sugiura S, Derby KA, Suzuki Y, Hawryszko C, Yamagata H, Klein JE, Ortendahl DA, Kaufman L, Acosta GF. Radiology. 1988;169:207.
66. Twieg DB, Meyerhoff DJ, Hubesch B, Roth K, Sappey MD, Boska MD, Gober JR, Schaefer S, Weiner MW. Magn. Reson. Med. 1989;12:291.
67. Lenkinski RE, Holland GA, Allman T, Vogele K, Kressel HY, Grossman RI, Charles HC, Engeseth HR, Flamig D, MacFall JR. Radiology. 1988;169:201.
68. Vigneron DB, Nelson SJ, Murphy BJ, Kelley DA, Kessler HB, Brown TR, Taylor JS. Radiology. 1990;177:643.
69. Bracewell RN. The Fourier Transform and Its Applications. McGraw-Hill: New York, 1978, p 104.
70. Marcei TH, Booker HR. J. Magn. Reson. 1984;57:157.
71. Swanson MG, Vigneron DB, Tabatabai ZL, Males RG, Schmitt L, Carroll PR, James JK, Hurd RE, Kurhanewicz J. Magn. Reson. Med. 2003;50:944.
72. Bolan PJ, DelaBarre L, Baker EH, Merkle H, Everson LI, Yee D, Garwood M. Magn. Reson. Med. 2002;48:215.
73. Bolan PJ, Meisamy S, Baker EH, Lin J, Emory T, Nelson M, Everson LI, Yee D, Garwood M. Magn. Reson. Med. 2003;50:1134.
74. Li CW, Negendank WG, Murphy-Boesch J, Padavic-Shaller K, Brown TR. NMR Biomed. 1996;9:141.
75. Gonen O, Murphy-Boesch J, Li CW, Padavic-Shaller K, Negendank WG, Brown TR. Magn. Reson. Med. 1997;37:164.
76. Dixon RM, Frahm J. Magn. Reson. Med. 1994;31:482.
77. Kim DY, Kim KB, Kim OD, Kim JK. J. Korean Med. Sci. 1998;13:49.
78. Kasimos JN, Merchant TE, Gierke LW, Glonek T. Cancer Res. 1990;50:527.
79. Bottomley PA, Hardy CJ, Roemer PB. Magn. Reson. Med. 1990;14:425.
80. Deslauriers R, Kupriyanov VV. Biochem. Cell. Biol. 1998;76:510.
81. Neubauer S, Horn M, Hahn D, Kochsiek K. Mol. Cell. Biochem. 1998;184:439.
82. Kreis R, Boesch C. J. Magn. Reson. B. 1996;113:103.
83. Boska MD, Nelson JA, Sripathi N, Pipinos II, Shepard AD, Welch KM. Magn. Reson. Med. 1999;41:1145.
84. Meyerspeer M, Krssak M, Moser E. Magn. Reson. Med. 2003;49:620.
85. Li CW, Kuesel AC, Padavic-Shaller KA, Murphy-Boesch J, Eisenberg BL, Schmidt RG, von Roemeling RW, Patchefsky AS, Brown TR, Negendank WG. Cancer Res. 1996;56:2964.
86. Sijens PE. NMR Biomed. 1998;11:341.
87. Negendank WG, Padavic-Shaller KA, Li CW, Murphy-Boesch J, Stoyanova R, Krigel RL, Schilder RJ, Smith MR, Brown TR. Cancer Res. 1995;55:3286.
88. Griffiths JR, Tate AR, Howe FA, Stubbs M. Eur. J. Cancer. 2002;38:2085.
89. Narayan P, Vigneron DB, Jajodia P, Anderson CM, Hedgcock MW, Tanagho EA, James TL. Magn. Reson. Med. 1989;11:209.
90. Narayan P, Jajodia P, Kurhanewicz J, Thomas A, MacDonald J, Hubesch B, Hedgcock M, Anderson CM, James TL, Tanagho EA *et al.* J. Urol. 1991;146:66.
91. Coakley FV, Kurhanewicz J, Lu Y, Jones KD, Swanson MG, Chang SD, Carroll PR, Hricak H. Radiology. 2002;223:91.
92. Kurhanewicz J, Swanson MG, Nelson SJ, Vigneron DB. J. Magn. Reson. Imaging. 2002;16:451.
93. Pickett B, Ten Haken RK, Kurhanewicz J, Qayyum A, Shinohara K, Fein B, Roach M. Int. J. Radiat. Oncol. Biol. Phys. 2004;59:665.
94. Coakley FV, Qayyum A, Swanson MG, Lu Y, Roach M, Pickett B, Shinohara K, Vigneron DB, Kurhanewicz J. Radiology. 2004;233:441.
95. Costello LC, Franklin RB. Prostate. 1991;18:25.
96. Costello LC, Franklin RB. Prostate. 1991;19:181.
97. Heby O. Differentiation. 1981;19:1.
98. Heston WD. Cancer Surv. 1991;11:217.
99. Shukla-Dave A, Hricak H, Eberhardt SC, Olgac S, Muruganandham M, Scardino PT, Reuter VE, Koutcher JA, Zakian KL. Radiology. 2004;231(3):717.
100. Kaji Y, Kurhanewicz J, Hricak H, Sokolov DL, Huang LR, Nelson SJ, Vigneron DB. Radiology. 1998;206(3):785.
101. Orel SG, Schnall MD. Radiology. 2001;220:13.
102. Buchberger W, Niehoff A, Obrist P, DeKoekkoek-Doll P, Dunser M. Semin. Ultrasound CT MR. 2000;21:325.
103. Degani H, Gusis V, Weinstein D, Fields S, Strano S. Nat. Med. 1997;3:780.
104. Esserman L, Hylton N, George T, Weidner N. Breast J. 1999;5:13.
105. Leach MO, Verrill M, Glaholm J, Smith TA, Collins DJ, Payne GS, Sharp JC, Ronen SM, McCready VR, Powles TJ, Smith IE. NMR Biomed. 1998;11:314.
106. Hurd RE, Gurr D, Sailasuta N. Magn. Reson. Med. 1998;40:343.
107. Gribbestad IS, Petersen SB, Fjosne HE, Kvinnsland S, Krane J. NMR Biomed. 1994;7:181.

108. Stanwell P, Gluch L, Clark D, Tomanek B, Baker L, Giuffre B, Lean C, Malycha P, Mountford C. Eur. Radiol. 2005;15:1037.
109. Star-Lack J, Vigneron DB, Pauly J, Kurhanewicz J, Nelson SJ. J. Magn. Reson. Imaging. 1997;7:745.
110. Pickren J, Tsukada Y, Lane WW. In: L Weiss, HA Gilbert (Eds). Analysis of Autopsy Data. GK Hall and Company: Boston, 1982, p 2.
111. Thomsen C, Becker U, Winkler K, Christoffersen P, Jensen M, Henriksen O. Magn. Reson. Imaging. 1994;12:487.
112. Ryysy L, Hakkinen AM, Goto T, Vehkavaara S, Westerbacka J, Halavaara J, Yki-Jarvinen H. Diabetes. 2000;49:749.
113. Sutinen J, Hakkinen AM, Westerbacka J, Seppala-Lindroos A, Vehkavaara S, Halavaara J, Jarvinen A, Ristola M, Yki-Jarvinen H. AIDS. 2002;16:2183.
114. Rosen BR, Carter EA, Pykett IL, Buchbinder BR, Brady TJ. Radiology. 1985;154:469.
115. Szczepaniak LS, Babcock EE, Schick F, Dobbins RL, Garg A, Burns DK, McGarry JD, Stein DT. Am. J. Physiol. 1999;276:E977.

MR-Mammography

W. A. Kaiser

Institute for Diagnostic and Interventional Radiology, Friedrich Schiller University, Jena, Germany

Introduction

MR-Imaging (MRI) of the breast, or MR-Mammography (MRM), has probably been one of the most controversially discussed indications for MRI in the last 20 years. Whereas MRI of the brain and spine or of the musculoskeletal system was rather quickly accepted as a valuable and helpful tool to detect diseases, descriptions of MRM initially ranged from "probably not useful" to "unclear" to "wait and see". However, in the last 5 years or so a striking wave of publications has underlined the significant additional information provided by MRM.

In this chapter a brief overview about the history of MRM is followed by a description of the pathophysiological basics and the present status and indication. An overview of the different techniques follows and the description of future challenges will finalize this report.

History of MRM

The development of MRM included several phases:

MR-Tomography in general had first to be developed, then special *breast coils* (single breast coils, followed by double breast coils later combined imaging/interventional coils) built and optimized. *Contrast media* were used at first in spin–echo sequences, later in sophisticated the so-called "*dynamic*" *techniques* using gradient echo sequences for a better differential diagnosis.

1. By 1971 different relaxation times in tumor tissue in comparison to normal tissue were measured using *in vitro* experiments [1]. However, MRI of the human body was possible only after the application of local gradient fields [2]. First, tissue samples of the breast were published by Mansfield *et al*. [3]. These tissue samples were taken about 90 min after operation. First, *in vivo* images of the breasts from 65 patients (128 breasts) including seven cancers was undertaken using whole-body MR-machines in 1982 [4]. In these reports a whole-body scanner with a field strength of 0.045 T was used and patients imaged in a supine position providing two proton-density-weighted images and six T_1-relaxation-time measurements per patient. In 1983, El Yousef *et al*. [5] published results from 2 patients using an experimental surface coil in a field strength of 0.03 T and reported a reduced signal intensity of both cancers. In a following publication of the same group [6] in 1984, images of 10 volunteers and 45 patients were reported describing a reduced signal intensity of breast lesions in spin echo and inversion-recovery sequences.
2. From 1983, onwards special breast coils were developed which were used only for breast imaging and later sold commercially. Until 1986 only single breast coils were available [7,8]. After first-disappointing trials in a supine position the examinations were performed in a prone position to minimize movement and artefacts caused by breathing. However, at that time the available spin-echo- and inversion-recovery sequences did not allow a definite detection and differentiation of small lesions in all cases, yet the advantage of imaging in thin slices in any orientation in a variable soft tissue contrast without X-rays was already clear [9–12]. Further progress was made with the development and introduction of the MR-contrast-medium Gadolinium-DTPA [13]. Experiments were possible in analogy to computer tomographic results using ionized X-ray contrast medium and radioactive iodine uptake from the mid seventies [14,15]. The first group to acquire and use contrast medium was Heywang *et al*. [16]. Initially spin-echo sequences in relatively long examination times and high contrast dosages were applied and reported; however, the uptake of contrast medium of cancers, normal tissue, and proliferative changes could not be differentiated sufficiently. After the introduction of fast echo gradient sequences [17] the first dynamic examinations using repetitive measurements of the same slices before and, in short time intervals, after contrast injection were established [18,19]. However, how to achieve better differentiation between benign and malignant lesions was a major issue amongst scientists [20]. The following development of a double breast coil [21] allowed routine measurements of both breasts of a patient in a single examination in a good signal-to-noise (SNR) ratio. These initial steps were followed by a phase of evaluation of dynamic techniques using different measurement sequences and dosages, which was mainly performed in Europe. The result of the enormous variety of measurement techniques was, at

Graham A. Webb (ed.), Modern Magnetic Resonance, 1127–1141.
© 2008 *Springer.*

first, Babylonian confusion and a broad range of opinions about the usefulness of MRM [22–72], especially before 1995.

3. Using MRM small lesions of a few millimeters could be detected, which were often not seen by X-ray or ultrasound. Therefore, a need for the development of interventional MR procedures was rising, at first for positioning of markers, later for biopsy and therapeutic removal [73–80]. These techniques currently require an additional MR image to be taken later, i.e. a second measurement and a repeated use of the MR-device and contrast injection. At present single breast biopsy coils in the so-called "closed" as well as in "open" MR-devices are tested. A bilateral coil for combined imaging and simultaneous intervention has been used in clinical tests since 1997 [81].

Pathophysiological Background of MRM

The secret of the very high sensitivity of MRM for the detection of breast lesions is the detection of tumor-based angiogenesis [82–84]. It is well-established that any tumor of more than 2 mm needs an increased perfusion to selectively direct nutrients towards the malignant tumor. Fifty years ago it was found that the implantation of breast cancer cells induces new micro-vessels after 3 days post implantation. Meanwhile numerous publications especially from Judah Folkman, have clarified that human breast cancers, like other malignant tumors, possess the angiogenentic power as well [85–91]. Over 20 years ago [92] it was established that, in a "far" distance of 3 cm from the cancer, an increased concentration of tumor angiogenetic factors can be measured. Probably induced by

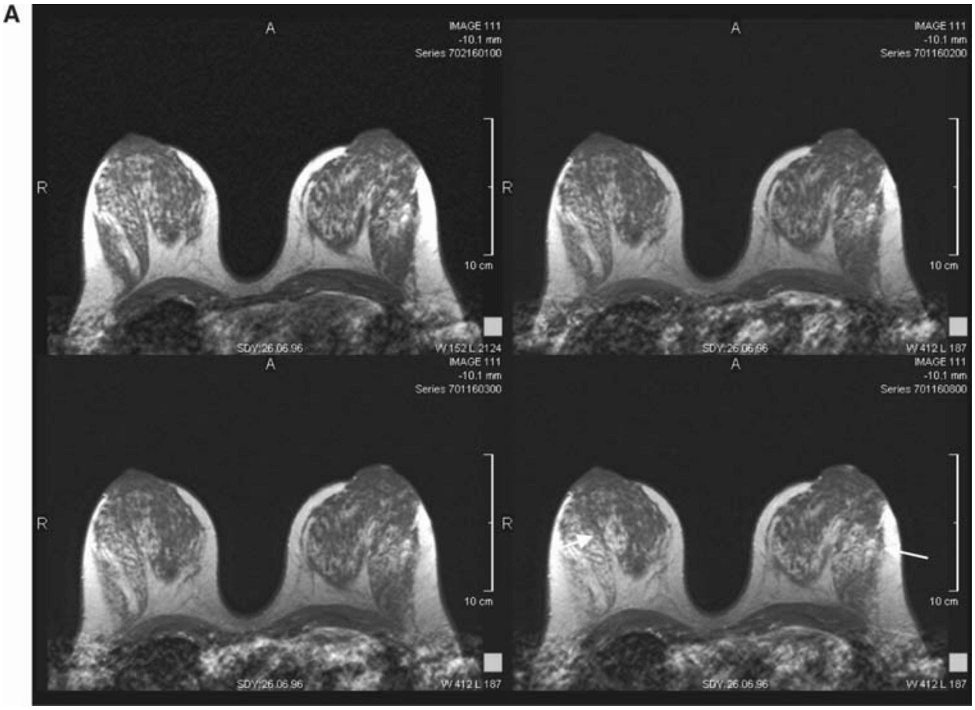

Fig. 1. Normal enhancement, Inflow-phenomenon (40-year-old patient, dense breast) (A) Original dynamic scans showing the uptake of contrast over 7 min (upper left = precontrast, upper right = 1-min-postcontrast, lower left = 2-min-postcontrast, lower right = 7 min postcontrast), slow progressive enhancement especially in the outer portions of the parenchyma, bilateral, symmetric enhancement. The contrast usually arrives via lateral thoracic artery in the outer upper quadrant at first (inflow phenomenon) (arrows). (The left breast is displayed on the right side of the image, the right breast is displayed on the left side of the images.) (B) The inflow phenomenon is best delineated in the corresponding subtraction images (arrows) (upper left = subtraction 1-min-postcontrast minus precontrast, upper right = subtraction 2-min-postcontrast minus precontrast, lower left = subtraction 3-min-postcontrast minus precontrast, lower left = subtraction 7-min-postcontrast minus precontrast). (C) So-called "mosaic-image" (upper left = precontrast, upper right = 1-min-postcontrast, lower left = subtraction 1-min-postcontrast minus precontrast, lower left = T_2w-TSE image; all images in identical sclice positions).

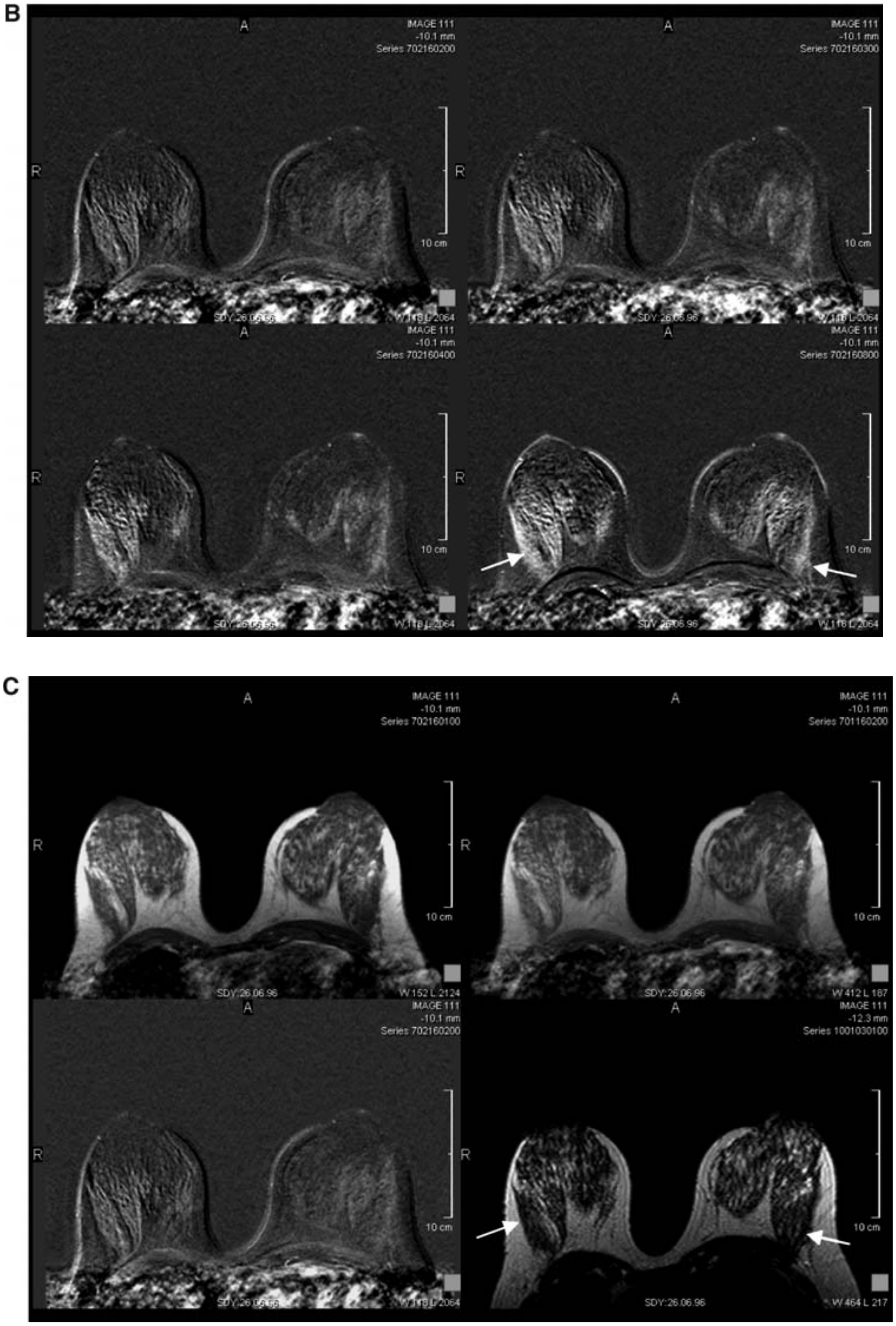
B
A
IMAGE 111
-10.1 mm
Series 702160200
R
10 cm
SDY:26.06.96
W 118 L 2064
A
IMAGE 111
-10.1 mm
Series 702160300
R
10 cm
SDY:26.06.96
W 118 L 2064
A
IMAGE 111
-10.1 mm
Series 702160400
R
10 cm
SDY:26.06.96
W 118 L 2064
A
IMAGE 111
-10.1 mm
Series 702160800
R
10 cm
SDY:26.06.96
W 118 L 2064
C
A
IMAGE 111
-10.1 mm
Series 702160100
R
10 cm
SDY:26.06.96
W 152 L 2124
A
IMAGE 111
-10.1 mm
Series 701160200
R
10 cm
SDY:26.06.96
W 412 L 187
A
IMAGE 111
-10.1 mm
Series 702160200
R
10 cm
SDY:26.06.96
W 118 L 2064
A
IMAGE 111
-12.3 mm
Series 1001030100
R
10 cm
SDY:26.06.96
W 464 L 217

Fig. 1. (*Continued*)

hypoxia, acidosis, and many tumor angiogenetic factors, and eventually combined by an inactivation of the p53 suppressor gene, the so-called "tumor angiogenetic switch" is induced and new vessels arise through the sprouting of capillaries from pre-existing micro-vessels. Host capillaries dilate and become hyperpermeable, fibrin exudes through the leaky capillaries, proteinases, and collagenases break basal membranes, endothelial cells migrate across ruptures, form loops and canalize and finally a "functional neovasculature" called "tumor angiogenesis" is built.

Unique properties of tumor vessels are increased tumor blood volume, increased arterio-venous shunt formation, altered capillary bed transit time, increased interstitial pressure, and increased capillary permeability.

Among more than fifty so-called "tumor-angiogenetic factors" the vascular permeability factor (VPF), vascular endothelial growth factor (VEGF), and basic fibroblastic growth factor (bFGF) are most important.

Various pharmacokinetic models revealed that, in particular, differences in tumor vessel permeability are the

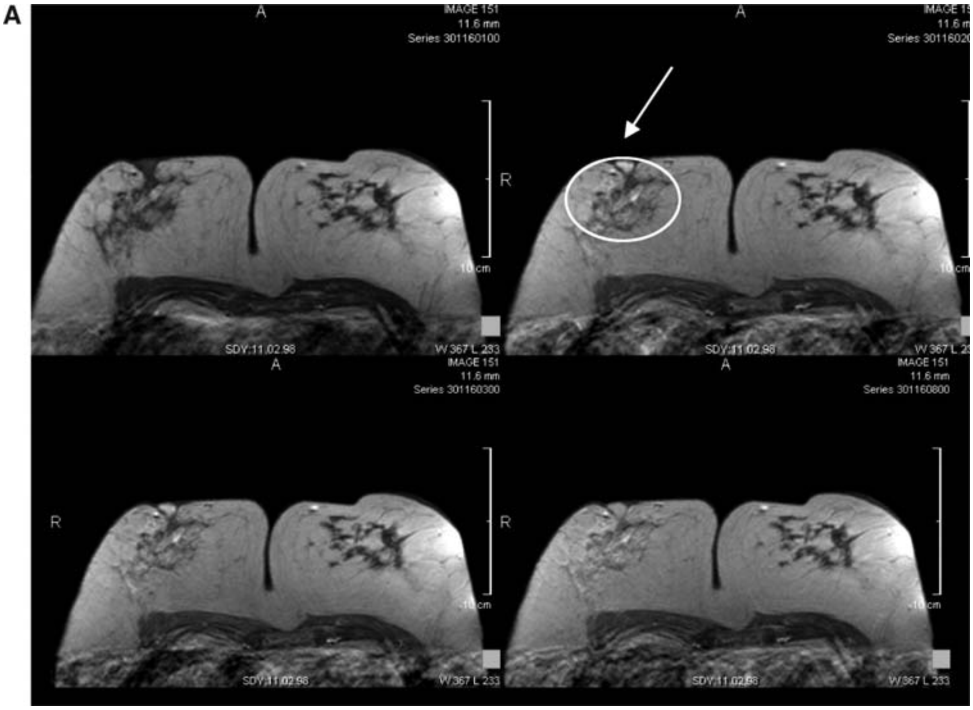

Fig. 2. Invasive lobular cancer and Lobular cancer in situ (LCIS, 78-year-old patient). (A) Original dynamic scans showing the uptake of contrast over 7 min (upper left = precontrast, upper right = 1-min-postcontrast, lower left = 2-min-postcontrast, lower right = 7 min postcontrast), strikingly enhancing area in a diameter of 1.3 cm behind the nipple in the right breast (arrow) with a maximum signal rise within the first minute after the injection of contrast followed by a decrease of signal intensity ("washout-phenomenon") which is very typical for a cancer. In addition to that, nearly the complete right parenchyma shows a reticular, network-like enhancement compared to the other non-affected left breast (ellipse). (B) This reticular enhancement (ellipse) can clearly be detected in the corresponding subtraction images besides the focal mass enhancement of the invasive cancer (arrow). Most of this network-loke enhancement representing LCIS is steadily continuously enhancing with confluent irregular lesions in late scans (upper left = subtraction 1-min-postcontrast minus precontrast, upper right = subtraction 2-min-postcontrast minus precontrast, lower left = subtraction 3-min-postcontrast minus precontrast, lower left = subtraction 7-min-postcontrast minus precontrast). (C) The "mosaic-image" (upper left = precontrast, upper right = 1-min-postcontrast, lower left = subtraction 1-min-postcontrast minus precontrast, lower left = T_2w-TSE image in identical sclice positions) shows the invasive cancer dark in T_2w-scans (arrow), whereas the LCIS is unspecific in T_2w-signal intensity (ellipse). The main hallmark for invasive cancer is a striking "washin" in a typical range for cancers followed by a "washout-phenomenon;" the main hallmark for non-invasive cancer is the asymmetric enhancement in relation to the opposite breast (both the invasive and the non-invasive cancer had not been described by X-ray mammography and ultrasound in this case).

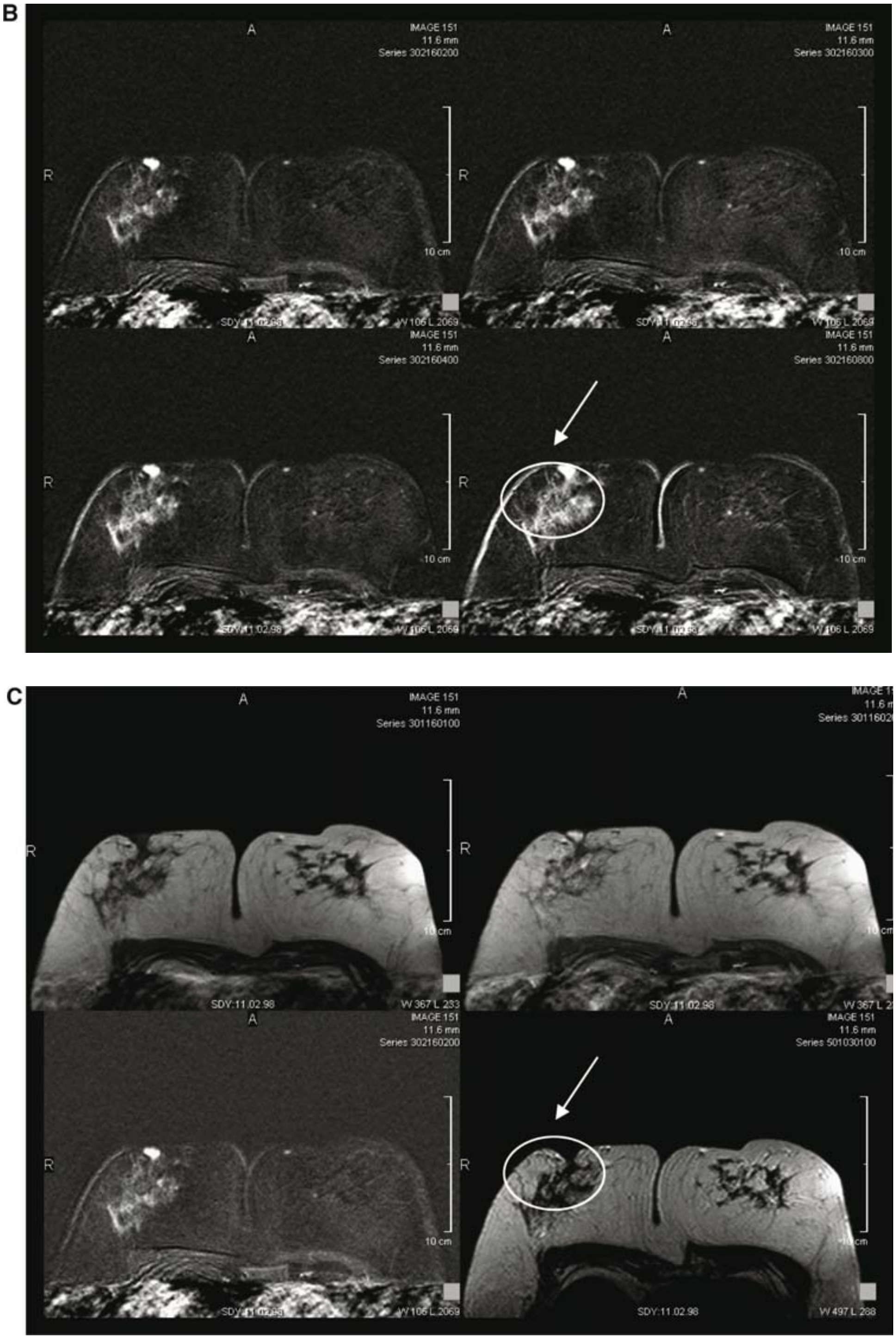
B
A
IMAGE 151
11.6 mm
Series 302160200
R
10 cm
W 106 L 2069
A
IMAGE 151
11.6 mm
Series 302160300
R
10 cm
W 106 L 2069
A
IMAGE 151
11.6 mm
Series 302160400
R
10 cm
SDY:11.02.98
W 106 L 2069
A
IMAGE 151
11.6 mm
Series 302160800
R
10 cm
W 106 L 2069
C
A
IMAGE 151
11.6 mm
Series 301160100
R
10 cm
SDY:11.02.98
W 367 L 233
A
SDY:11.02.98
A
IMAGE 151
11.6 mm
Series 302160200
R
10 cm
W 106 L 2069
A
IMAGE 151
11.6 mm
Series 501030100
R
10 cm
SDY:11.02.98
W 497 L 288

Fig. 2. (*Continued*)

defining feature of tumor angiogenetically based uptake of contrast medium in breast cancer [93–96].

As a consequence of this pathophysiological basis MRM is looking for the type, the amount and the morphology of enhancement within the neighborhood of, and in, a lesion [97–102]. As mentioned above, malignant lesions are characterized by a tumor angiogenetic network of tumor-specific micro-vessels; thus, they show a rapid initial increase of signal intensity in T_1-weighted images (T_1w-images) after the injection of contrast medium within the first 1–2 min after injection, followed by a plateau, or the so-called "washout" effect, i.e. a decrease of signal intensity. This "washout" effect is probably caused by the arterio-venous-shunts within the angiogenetic network. Most benign tumors show a significantly different type of enhancement, either a slow progressive uptake or a very rapid increase with a further signal rise after the initial enhancement. However, about 20% of benign lesions (especially myxoid fibro-adenomas) might also show a strong initial enhancement followed by a plateau or a washout effect.

It is vital that the kinetic analysis is drawn only from the non-necrotic part of the tumor and that the maximum signal increase is used; a tumor contains all types of cells and compartments including haemorrhage, necrosis, and fibrosis besides vital malignant tumor cells. The so-called "wash-in"-phenomenon (i.e. the initial enhancement before the bending of the curve) is the most sensitive

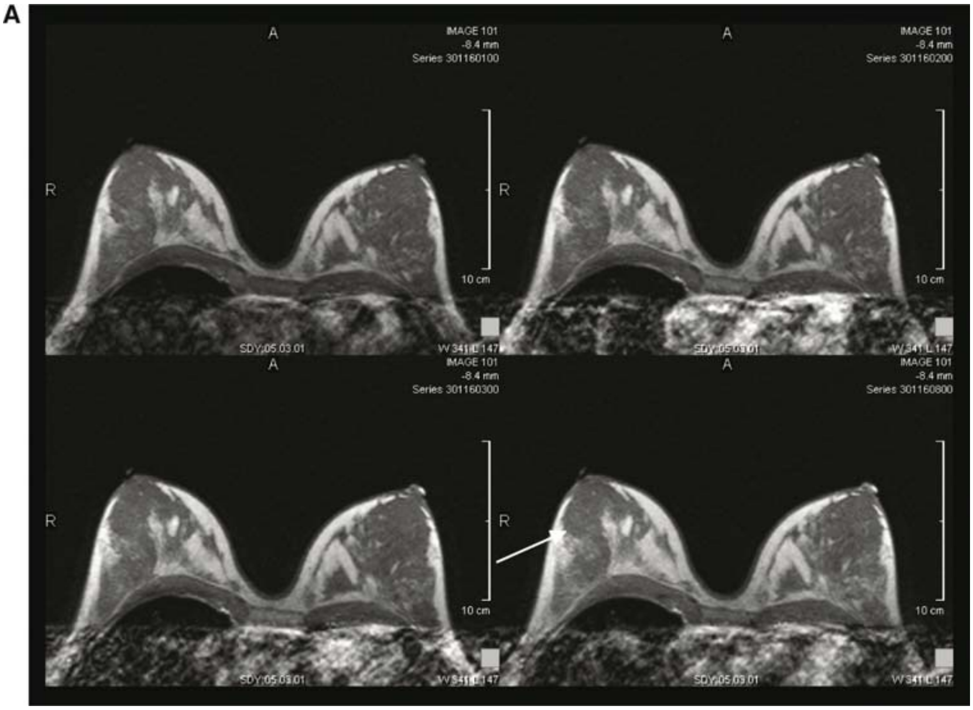

Fig. 3. Fibrous fibroadenoma (41-year-old patient with a lump in the lateral part of the right breast. The left breast is displayed on the right side of the image, the right breast is displayed on the left side of the image). (A) The original dynamic scans show a slow steady area of enhancement in the lateral portion of the right breast (arrow) without any cancer-like washin or washout-phenomenon. (upper left = precontrast, upper right = 1-min-postcontrast, lower left = 2-min-postcontrast, lower right = 7 min postcontrast). (B). The corresponding subtraction images (upper left = subtraction 1-min-postcontrast minus precontrast, upper right = subtraction 2-min-postcontrast minus precontrast, lower left = subtraction 3-min-postcontrast minus precontrast, lower left = subtraction 7-min-postcontrast minus precontrast) display this slow enhancement (arrow) better than the original images. In addition a slight motion artefact in the left breast. (C) The "mosaic-image" (upper left = precontrast, upper right = 1-min-postcontrast, lower left = subtraction 1-min-postcontrast minus precontrast, lower left = T_2w-TSE image in identical sclice positions). The T_2w-scan show the lesion in a dark signal intensity (arrow). Typical signal change of a fibrous fibroadenoma, i.e. a slow, steady enhancement without cancer signs, dark in precontrast and dark in T_2w-scans.

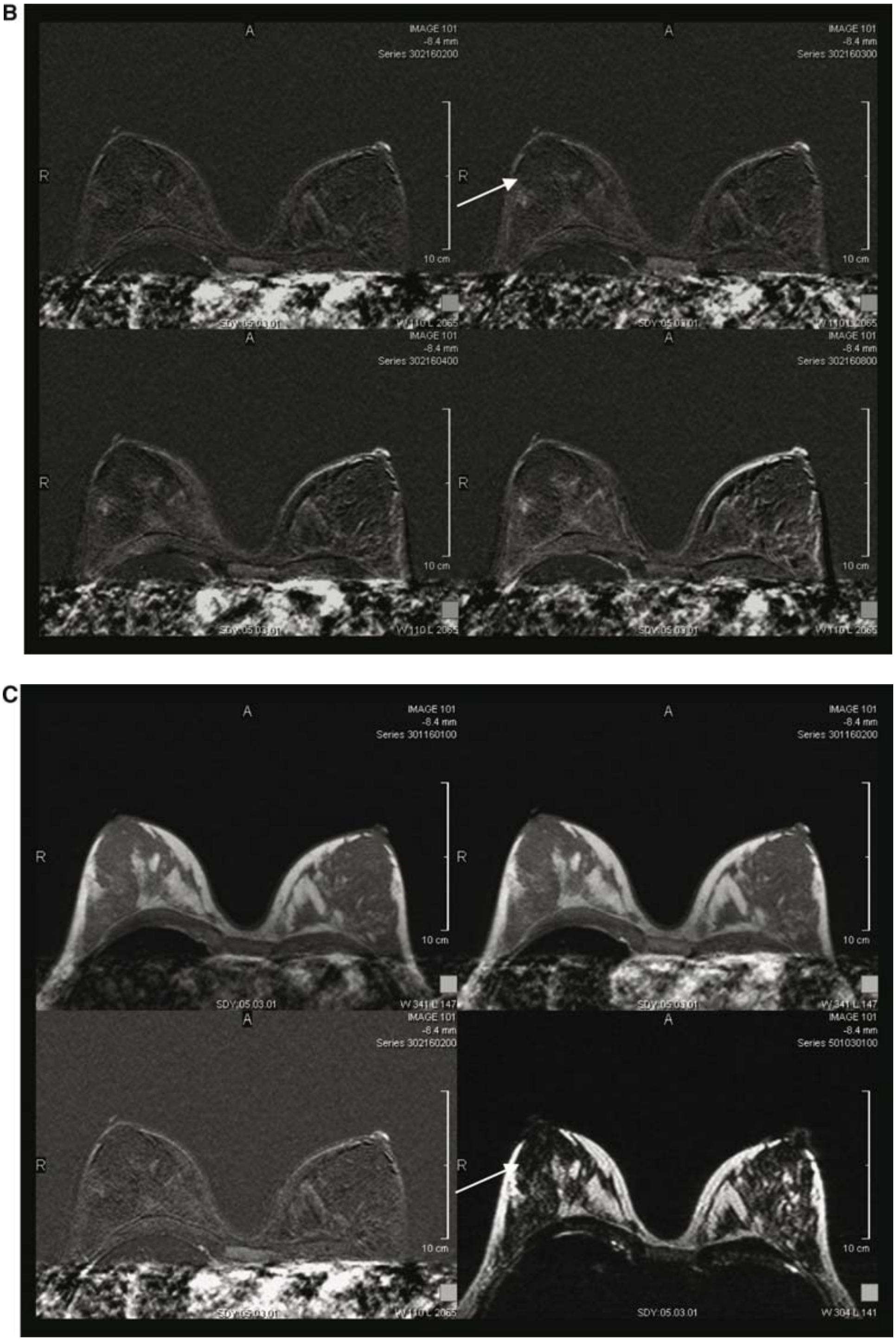
B
A
IMAGE 101
-8.4 mm
Series 302160200
R
10 cm
SDY:05.03.01
W 110 L 2065
A
IMAGE 101
-8.4 mm
Series 302160300
R
10 cm
SDY:05.03.01
W 110 L 2065
A
IMAGE 101
-8.4 mm
Series 302160400
R
10 cm
SDY:05.03.01
W 110 L 2065
A
IMAGE 101
-8.4 mm
Series 302160800
R
10 cm
SDY:05.03.01
W 110 L 2065
C
A
IMAGE 101
-8.4 mm
Series 301160100
R
10 cm
SDY:05.03.01
W 341 L 147
A
IMAGE 101
-8.4 mm
Series 301160200
R
10 cm
SDY:05.03.01
W 341 L 147
A
IMAGE 101
-8.4 mm
Series 302160200
R
10 cm
SDY:05.03.01
W 110 L 2065
A
IMAGE 101
-8.4 mm
Series 501030100
R
10 cm
SDY:05.03.01
W 304 L 141

Fig. 3. (*Continued*)

parameter; the "washout" effect (i.e. the late signal decrease following the initial signal increase at the "cancer-corner") is the most specific parameter to diagnose a malignant tumor.

In addition to kinetic data, morphological signs have to be included for the distinction between benign and malignant lesions. As malignant tumors often show a "rim-enhancement" (i.e. the most enhancing vital tumor areas are in the outer rim of the lesions, because the centre consists mostly of necroses). In contrast to this, benign lesions usually enhance within the centre as well as, and as early as, in the border areas. Malignant tumors often show irregular borders and spiculation, whereas most benign lesions have sharply delineated, often polylobulated margins. Benign lesions might show clear, non-enhancing septations. The vast majority of cancers (98%) show low signal-intensities in the T_2-weighted-Turbo-Spin-Echo-images (T_2w-TSE-images), whereas the strongly enhancing myxoid fibroadenomas are more or less brighter than parenchyma in T_2w-TSE-images.

Malignant lesions often show the so-called "blooming-sign", i.e. an increasing enhancement in the neighborhood outside the lesion [100].

Meanwhile more than 20 different signs in the combined morphological and kinetic analysis enable a highly reliable discrimination between a benign and malignant

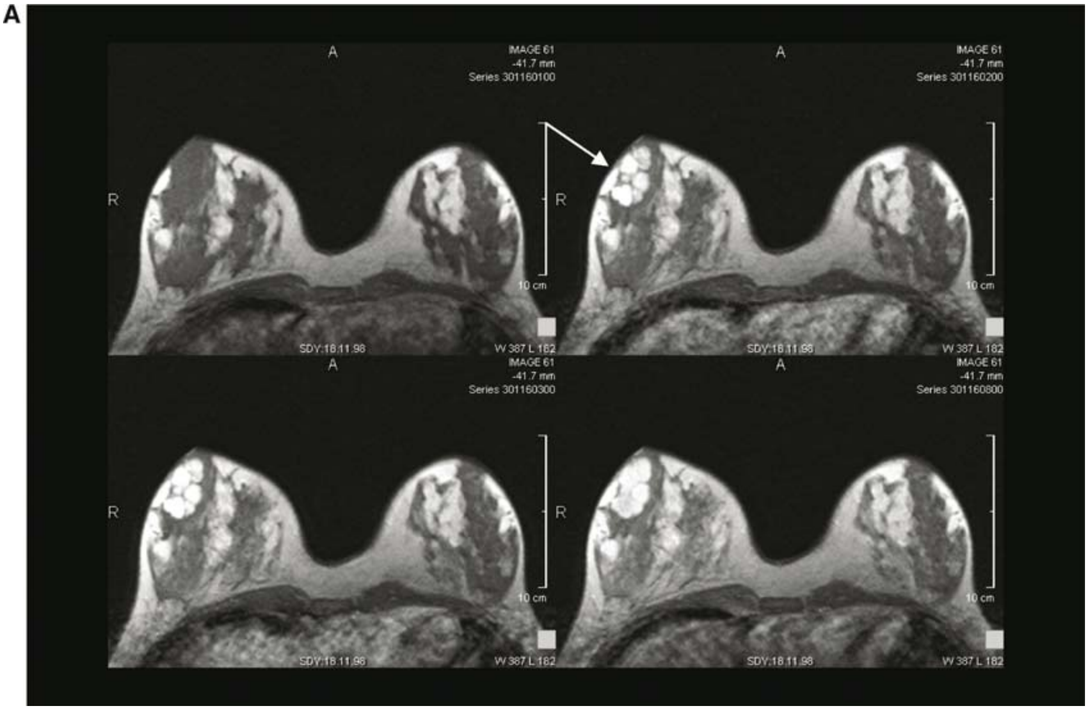

Fig. 4. Myxoid or "hyaline" fibroadenoma (22-year-old patient with a lump in the lateral part of the right breast. (The left breast is displayed on the right side of the image, the right breast is displayed on the left side of the images). (A) The original dynamic scans show a 3 × 4 cm multicompartmental area in the right breast; some compartments enhance suddenly and more intensively than cancers, some compartments enhance slower, some compartments show a plateau-phenomenon or even a washout-effect (upper left = precontrast, upper right = 1-min-postcontrast, lower left = 2-min-postcontrast, lower right = 7 min postcontrast). (B) In the corresponding subtraction images (upper left = subtraction 1-min-postcontrast minus precontrast, upper right = subtraction 2-min-postcontrast minus precontrast, lower left = subtraction 3-min-postcontrast minus precontrast, lower left = subtraction 7-min-postcontrast minus precontrast) the partially very strong signal increase after contrast injection is delineated. (C) In the "mosaic-image" (upper left = precontrast, upper right = 1-min-postcontrast, lower left = subtraction 1-min-postcontrast minus precontrast, lower left = T_2w-TSE image in identical sclice positions) some components of this multicompartmenatal lesion are brighter (arrow) than parenchyma in the T_2w-scan, some are dark. Note the typical behavior of myxoid fibroadenomas: Sharp borders and intact septations throughout the dynamic scans, partially very striking enhancement, often much stronger than the range of cancer-like enhancement, no "blooming-effect" and partial brightness in T_2w-images.

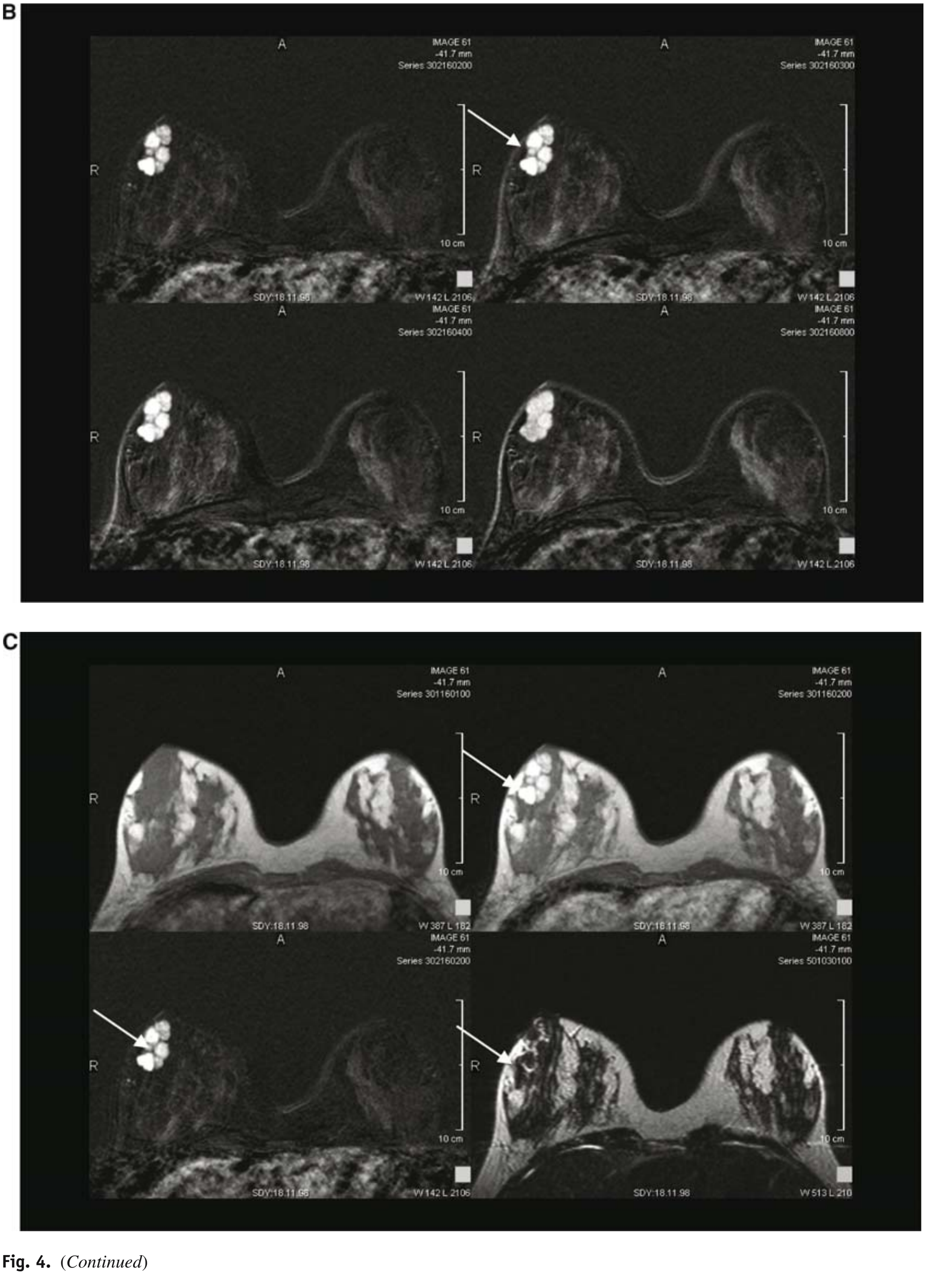
B
A
IMAGE 61
-41.7 mm
Series 302160200
R
10 cm
SDY:18.11.98
W 142 L 2106
A
IMAGE 61
-41.7 mm
Series 302160300
R
10 cm
SDY:18.11.98
W 142 L 2106
A
IMAGE 61
-41.7 mm
Series 302160400
R
10 cm
SDY:18.11.98
W 142 L 2106
A
IMAGE 61
-41.7 mm
Series 302160800
R
10 cm
SDY:18.11.98
W 142 L 2106
C
A
IMAGE 61
-41.7 mm
Series 301160100
R
10 cm
SDY:18.11.98
W 387 L 182
A
IMAGE 61
-41.7 mm
Series 301160200
R
10 cm
SDY:18.11.98
W 387 L 182
A
IMAGE 61
-41.7 mm
Series 302160200
R
10 cm
SDY:18.11.98
W 142 L 2106
A
IMAGE 61
-41.7 mm
Series 501030100
R
10 cm
SDY:18.11.98
W 513 L 210

Fig. 4. (*Continued*)

lesion. After more than 20 years of clinical research a significant number of publications describe a very high sensitivity for MRM for detecting malignant lesions in the range of more than 95–100%. Even indications which had previously been described as "difficult", like the identification of Ductal carcinoma *in situ* (DCIS), are now accepted indications for MRM [99].

Technique

High temporal and spatial resolution is important for the detection and distinction between benign and malignant lesions. Today high-resolution dynamic techniques, i.e. the repeated imaging of the same slices before and in short time intervals after injection of contrast are used. The patient is placed in a prone position with the breasts hanging into a bilateral phased-array double breast coil after an iv-cannula had been placed in the cubital vein. The series of sequences in a dynamic MRM examination at 1.5 T includes (further technical details about the MRM examination are described elsewhere [101]:

1. a scout sequence (to clarify the position of the patient and breasts)
2. a coronal T_1-weighted Gradient-Echo-Sequence (T_1w-GRE-sequence) in a large field-of-view (FOV) including the axillary region and the neck region (to detect enlarged lymph nodes)
3. a transversal T_2w-TSE sequence.
4. a transversal T_1w-GRE sequence (i.e. the precontrast scan)
5. an iv injection of contrast (0.1 mmol/kg Gd-DTPA)
6. a sevenfold repetition of the precontrast scan (=nr. 4, in identical imaging parameters) every minute for the next 7 min
7. an automatic image subtraction
8. a coronal post-contrast scan (identical scan as nr. 2, so that any lesion in the breasts or the lymph nodes can be evaluated in two pre- and post-contrast orientations)
9. in the case of a breast implant, a silicone-selective sequence is added (focusing on the resonance frequency of silicone, which is 100 Hz lower than the resonance frequency of fat at 1.5 T.

The important T_1-weighted dynamic gradient-echo-sequences before and in short time intervals after the injection of contrast are performed as two dimensional-(2D) gradient-echo-sequences (TR/TE/flip-angle = 100 ms/4.7 ms/80°) in our institution. The FOV for scan nr. 4 is 350 mm, the slice thickness 3 mm for 36 slices in a matrix of 512 × 512 in a parallel imaging data aquisition. The aquisition time for sequence nr. 4 is 60 s.

Alternatively a dynamic three dimensional-(3D) gradient-echo-sequence can be performed which allows a better spatial resolution with thinner slices. However, the homogeneity of 3D-sequences in some machines is limited and artefacts caused by inhomogeneity deteriorate the kinetic data evaluation.

Another alternative is a dynamic fat-saturation-sequence (fat-sat-sequence) which usually also requires a following subtraction.

After the measurements, the kinetic data evaluation (signal-intensity-time-curves) in addition to the morphological analysis is made.

Modern MR-machines are able to acquire images in 512 × 512 matrices in time distances of each minute. Today parallel imaging techniques in fast gradient-echo-sequences (FLASH, FFE, GRASS) fulfill these prerequisites. Some teams prefer the so-called "fat-sat"-techniques by applying saturation pulses towards fat signal; these techniques suffered from signal inhomogeneities, longer measurement times and often single-breast examinations in the past and therefore could not be successfully applied in Europe [101].

Indications for MRM

The scientific results gained so far recommend MRM for the following indications:

1. The definite identification and/or exclusion of breast cancer in cases of unclear mammographic or sonographic breasts.
2. Clarification of number, size, and location of breast lesions, i.e. clarification of multifocality and/or multicentricity; thus enabling more precise planning for treatment.
3. Differentiation between scars and/or recurrent/residual tumors after previous operation/radiation.
4. Delineation of implants, implant-ruptures, and/or lesions around implants like inflammations or benign or malignant tumors.
5. Detection of primary tumors in the case of an unknown primary tumor following a positive lymph node.
6. Delineation of diseases in the contralateral breast before operation/radiation.
7. Detection of the early effect of chemotherapy after the first doses of anticancer drugs.
8. Examination of high-risk patients (family history, genetic risk like BRCA1 and BRCA2).

Discrepancies and Pitfalls

Despite striking results for the sensitivity the value of MRM is still in question because of variations in specificity, the high cost of the machine and examination, its inability to detect micro-calcifications, its role in detecting DCIS, questions about different dosages of contrast etc. As with other MR-examinations, patients with ferromagnetic particles, pacemakers, and operations that have taken place within the weeks prior to the examination, and patients undertaking hormone-replacement-therapy should not be included.

The major pitfalls consist of the following:

1. Signal-inhomogeneities in the image due to the rf-profile of the double-breast coil.
2. Signal-inhomogeneities and saturation artefacts in fat-sat images
3. Application of an inappropriate dose and type of contrast medium.
4. Measurement in an inappropriate ("opposed") echo-time where fat and water protons are oriented in different directions.
5. Inappropriate positioning of the breast using high compression of the breast and/or bent arms and lack of control of contrast uptake.
6. Incomplete injection of contrast medium and/or no detection of incomplete injection.
7. Movement of patient during the examination due to insufficient information.
8. Lack of kinetic analysis.
9. No inclusion of T_2-weighted-scans (T_2w-scans)
10. False data evaluation
11. Susceptibility artefacts due to small bleedings because of previous punctures and/or biopsies.
12. Omittance of normal enhancements and "inflow" effects.

Since the time intensity curve is (in addition to morphological evaluations) very important for the diagnosis, the signal intensity in the first post-contrast images, in particular, is absolutely crucial for diagnosis. This critical first contrast signal intensity image depends on exact measurement parameters. Injection time, injection site, sodium chloride bolus, length of plastic tube, arm position, tuning parameters are some of the major factors affecting this critical image signal intensity.

In our experience an increase of more than 90% in the first 90 s after the beginning of contrast injection ("90–90 rule") is a typical threshold for a malignant enhancement at 1.5T-2D-dynamic MRM. To reach this critical threshold measurement using a region of interest procedure (ROI) has to be performed carefully: Only the "vital" tumor areas show a critical initial enhancement followed by a plateau phenomenon or a washout effect. The inclusion of necrotic areas of the tumor or surrounding normal glandular or fatty tissue will deteriorate and falsify the effect of kinetic data evaluation. It is necessary to look for the fastest enhancing portion of the lesion.

It is also important not to include any enhancing focus and to describe it as malignant. Vessels are cut in different orientations in the slice and are therefore displayed in a round, oval or comet shaped manner. The detection of inflow phenomenon, the delineation of further vessels in other slices or other orientations or, if you have still any doubts, an additional MR angiography sequence clarifies the tiny enhancing area as a vessel or not.

Fat saturation techniques are in relatively widespread use in the United States. They allow a high spatial resolution, but have a limited value for kinetic data evaluation. Since a pre-pulse in a low bandwidth is necessary, the adjustment parameters in pre- and post-contrast scans are not identical. Current fat-sat techniques usually have a relatively high signal inhomogeneity, so that a quantitative evaluation is difficult and subtractions are difficult, though often necessary. The measurement time is in most cases longer than in non-fat saturation techniques and the "diagnostic window" for the detection of differences between benign and malignant enhancement criteria is restricted.

Fat suppression methods may be by temporal subtraction, which is ideal for fat suppression, since only enhancing structures are delineated as high signal intensity lesions. An alternative is fat suppression by pre-pulses with the above-mentioned limitations.

The injection of contrast medium is made in a bolus (3 ml/s) either manually or by an automatic injector followed by a post-contrast bolus of physiological sodium chloride of 20 ml (cubital vein) or 30 ml (lower arm/hand). The procedure should be explained to the patient before positioning in the machine. No movement of, or discussion with, the patient is recommended during injection. The dosage of contrast medium should not be higher than 0.1 mmol/kg. A higher dosage shortens the already short "diagnostic window", i.e. the time difference of only 1–2 min where the contrast uptake between malignant and benign lesions is sufficiently different in order to enable a differential diagnosis.

The evaluation begins by examining fatty tissue on both breasts to assess if the signal intensity of fat is constant. If this signal intensity of fatty tissue as an "internal standard" varies, consider changing receiver adjustment or field inhomogeneity effects or artefacts. In these cases a quantitative evaluation is difficult or impossible, since the technical problems overlap any morphological information.

Dynamic MRM should be performed in transversal scans, because in this orientation the identification of vessels, nipple, posterior borders of implants, fatty layer between parenchyma and muscle, signal homogeneity of the coil, and signal correlation with the aorta is possible. However, if the lateral border of the parenchyma towards the axillary region and/or lymph nodes is especially important, a dynamic MRM in coronal scans is advantageous. A sagittal orientation should be avoided because of doubled measurement time and the lack of correlation with the other breast, and the difficulty of detecting inflow phenomenon and hormone effects. This image orientation might be acceptable if sagittal images can be acquired simultaneously from both breasts.

If only the axillary region is important, the rotation of the phase encoding direction towards a dorso-ventral orientation is recommended to keep the lateral axillary region free of phase encoding artefacts.

It is of crucial importance to use echo times where fat and water protons are in “in-phase” conditions, because Gd has a signal-*increasing* effect on the water protons in the voxel only in these echo times. Particularly tiny reticular structures like DCIS or lobular cancers can be imaged only in these “in-phase” images. “In-phase” conditions for 1.5 T are even numbers of 2.4 ms, i. e. 4.8, 9.6 ms etc. Odd numbers of 2.4 ms, for example 7.2 ms are “forbidden” because of the “opposed effect” of water and fat protons. This effect is field-strength dependent and should be adjusted according to the field strength which is used.

During the dynamic examination it is essential not to change tuning parameters between scans and to guarantee identical pulses in pre- and post-contrast scans. No change of pulses should be allowed between pre- and postcontrast scans. Only under these conditions is a correct signal intensity/time evaluation possible.

The pre-contrast signal intensity of parenchyma should be in a typical range for this sequence. If it is too low, this may be caused by an inappropriate receiver adjustment or inappropriate coil design; try to repeat the receiver adjustment. If this pre-contrast signal intensity is too high, it could also be an inappropriate receiver adjustment or a medical/biological reason (bleeding after puncture/biopsy, hormone effect, pregnancy, previous operation, and/or radiation).

Diagnosis of breast lesions in MRM is always made by a combined morphological and kinetic analysis. It is the main feature of MRM that tumor typical “tumor-angiogenesis” can be detected by signal-intensity-time-curves. A typical malignant lesion shows the striking initial increase (wash-in phenomenon) within the first 1–2 min followed by either a constant signal (plateau phenomenon) or—more specifically—a decrease in signal intensity (washout effect). The sudden increase and the following constancy or washout effect make the “cancer-corner” of the signal-time-curve. Benign lesions normally show a slower initial increase which is continuously rising over the complete dynamic examination. The distribution of a lesion is described as regional or patchy or diffuse or symmetric; the lesion itself is morphologically described as a focal mass with sharp or non-sharp margins, linear, linear-branched or segmental aspects. The initial and late enhancement is described as being homogeneous, heterogeneous, rim enhancement, bright or dark septations after contrast and centripetal or centrifugal filling effect over time. A centrifugal filling (from inside to outside) is directed mainly towards a benign lesion, a centripetal filling (from outside to inside) towards a malignant lesion.

Another major mistake is the inclusion of patients under hormone-replacement-therapy for MRM, because hormone effects cause bilateral, patchy, continuously enhancing spots which are confluent on late scans [103] and thus might be difficult to separate from bilateral DCIS or lobular cancers. However, in most patients DCIS and lobular cancers show unilateral enhancements and, in two-thirds, also a cancer-like wash-in and washout effect.

Future Challenges

At present MRM is classified as an additional diagnostic tool in all cases of unclear mammographic and sonographic situations. The medical community needs teaching, training, increased experience, and consensus. MRM will allow a precise detection of cancers in a size as small as 3 mm. For this purpose special techniques providing high spatial and temporal resolution are needed.

New specific contrast agents might enable a selective display of specific cancers and differentiate them from other lesions in the breast and in the whole body as well.

The combination of MRI and MR-spectroscopy will probably increase the overall accuracy of MRM.

Today modern “high-field MR-devices” (high-field for imaging means above 1.0 T) do not allow direct access to the breast during data acquisition. The patient has to be in the isocenter of the magnet field during imaging and must be moved outside the machine for a following intervention. The position of a wire marker, a core biopsy or a laser fibre has to be checked by a following MR-image, thus increasing measurement time, artefacts, and pitfalls. A MR-compatible robotic system for simultaneous imaging and immediate biopsy/intervention at high field strength is in clinical testing.

Combining MRI and therapy in one session—at least for lesions smaller than 2 cm—might enable a “one-stop-shop” procedure of detection and simultaneous removal in one single examination [104–105]. Preliminary tests applying laser therapy, radio frequency therapy, or cryotherapy have been promising so far [106–107] as has receptor-specific near-infrared-imaging *in vitro* [108].

References

1. Damadian R. Science 1971;171:1151–1153.
2. Lauterbur PC. Nature 1973;242:190–191.
3. Mansfield P, Morris PG, Ordidge R. *et al.* Brit. J. Radiol. 1979;52:242–243.
4. Ross RJ, Thompson JS, Kim K, Bailey RA. Radiology 1982;143:195–205.
5. El Yousef SJ, Alfidi RJ, Duchesneau RH. J. Comput. Assist. Tomogr. 1983;7:215–218.
6. El Yousef SJ, Duchesneau RH, Alfidi RJ, Haaga JR, Bryan PJ, LiPuma JP. Radiology 1984;150:761–766.
7. Kaiser W. Arch. Int. de Physiol. et de Biochim. 1985;93:67–76.
8. Fritschy P, Müller E, Sauter R, Kaiser W. Radiology 1984;153(P):243–244.
9. Stelling CB, Wang PC, Lieber A, Mattingly SS, Griffen WO, Powell DE. Radiology 1985;154:457–462.
10. Kaiser W, Zeitler E, Fortschr. Röntgenstr. 1986;144.5:459–465.
11. Kaiser W, Zeitler E, Fortschr. Röntgenstr. 1986;144.5:572–579.
12. Heywang SH, Fenzl G, Edmaier M, RÖFO 1985;143:207–212.
13. Weinmann HJ, Laniado M, Mützel W. Physiol. Chem. Phys. Med. NRM. 1984;16:167–172.
14. Eskin BA, Parker JA, Bassett JG, George DL. Obstet. Gynecol. 1974;44:398–492.
15. Chang CHJ, Sibala JL, Lin F, Fritz SL, Gallagher JH, Dwyer-ill SJ, Templeton AW. Am. J. Roentgenol. 1978;131:459–464.
16. Heywang SH, Hahn D, Schmidt H, Krischke I, Eiermann W, Bassermann RJ, Lissner J. J. Comput. Assist. Tomogr. 1986;10:199–204.
17. Haase A, Frahm J, D Matthaei *et al.* J. Magn. Res. 1986;67:258–268.
18. Kaiser WA, Oppelt A, KST der Mamma mit Schnellbildverfahren. MR'87, 2. Internationales Kernspintomographie Symposium, 29.1.–1.2.87, Garmisch-Partenkirchen, Referateband, 303–310, Schnetztor-Verlag, Konstanz (1987).
19. Kaiser WA, Zeitler E. Radiology 1989;170:681–686.
20. Heywang SH, Wolf A, Pruss E, Hilbertz T, Eiermann W. Radiology 1989;171:95–103.
21. Kaiser WA, Kess H. Fortschr. Röntgenstr. 1989;151:103–105.
22. Kaiser WA. Eur. Front. Radiol. 1990;7:39–68.
23. Ercolani P, Giovagnoni A, Giuseppetti G, Radiol. Med. Torino. 1991;82:422–426.
24. Hachiya J, Seki T, Okada M, Radiat. Med. 1991;9:232–240.
25. Hess T, Knopp MV, Brix G, Zentralbl. Radiol. 147, 969 (1993).
26. Stack JP, Redmond OM, Codd MB. Radiology, 1990;174:491–494.
27. Boetes C, Strijk SP, Holland R, Barentsz JO, Van Der Sluis RF, Ruijs JH. Eur. Radiol. 1997;7:1231–1234.
28. Bone B, Aspelin P, Bronge L, Isberg B, Perbeck L, Veress B, Acta. Radiol. 1996;37(2):208–213.
29. Buadu LD, Murakami J, Murayama S *et al.* Radiology 1996;200:639–649.
30. Daldrup HE, Roberts TP, Muhler A, Gossmann A, Roberts HC, Wendland M, Rosenau W, Brasch RC, Radiologe 1997;37(9):733–740.
31. DeAngelis GA, de Lange EE, Miller LR, Morgan RF. Radiographics 1994;14:783–94.
32. el Kwae EA, Fishman JE, Bianchi MJ, Pattany PM, Kabuka MR. J. Digit. Imaging. 1998;11(2):83–93.
33. Farria DM, Gorczyca DP, Barsky SH, Sinha S, Bassett LW. Am. Roentgenol. J. 1996;167(1):187–189.
34. Fischer U, von-Heyden D, Vosshenrich R, Vieweg I, Grabbe E. Rofo. 1993;158(4):287–292.
35. Fobben ES, Rubin CZ, Kalisher L, Dembner AG, Seltzer MH, Santoro EJ, Radiology 1995;196(1):143–152.
36. Frankel SD, Sickles EA, Radiology 1997;202(3):633–634.
37. Gilles R, Guinebretiere JM, Lucidarme O *et al.* [published erratum appears in Radiology 1994 Oct;193(1):285], Radiology 1994;191:625–631.
38. Gilles R, Guinebretiere JM, Shapeero LG *et al.* Radiology 1993;188:473–478.
39. Gilles R, Zafrani B, Guinebretiere JM *et al.* Radiology 1995;196:415–419.
40. Gorczyca DP, DeBruhl ND, Ahn CY, Hoyt A, Sayre JW, Nudell P, McCombs M, Shaw WW, Bassett LW. Radiology 1994;190(1):227–232.
41. Gorczyca DP. Radiology 1993;186(3):906–907.
42. Graham RA, Homer MJ, Sigler CJ *et al.* Am. J. Roentgenol. 1994;162:33–36.
43. Gribbestad IS, Nilsen G, Fjosne HE, Kvinnsland S, Haugen OA, Rinck PA. J. Magn. Reson. Imaging 1994;4(3), 477–480.
44. Harms SE, Flamig DP. Magn. Reson. Imaging. Clin. Am. N. 1994;2(4):573–584.
45. Hochman MG, Orel SG, Powell CM, Schnall MD, Reynolds CA, White LN. Radiology 1997;204:123–129.
46. Hoffmann U, Brix G, Knopp MV, Hess T, Lorenz WJ, Magn. Reson. Med. 1995;33(4):506–514.
47. Hylton NM, Frankel SD, Magn. Reson. Imaging. Clin. Am. N. 1994;2(4):511–525.
48. Knopp MV, Brix G, Junkermann HJ, Sinn HP, Magn. Reson. Imaging. Clin. Am. N. 1994;2(4):633–658.
49. Kuhl CK, Kreft BP, Hauswirth A, Elevelt A, Steudel A, Reiser M, Schild HH. Rofo. 162(5):381–389 (1995).
50. Kuhl CK, Seibert C, Sommer T, Kreft B, Gieseke J, Schild HH. Rofo. 1995;163(3):219–224.
51. Kuwabara M, Nippon Igaku Hoshasen Gakkai Zasshi, 1991;51(11):1366–1374.
52. Morris EA, Schwartz LH, Dershaw DD, van Zee KJ, Abramson AF, Liberman L. Radiology 1997;205(2):437–440.
53. Muller RD, Barkhausen J, Sauerwein W, Langer R, J. Comput. Assist. Tomogr. 1998;22(3):408–412.
54. Muller-Schimpfle M, Ohmenhauser K, Stoll P, Dietz K, Claussen CD. Radiology 1997;203(1):145–149.
55. Mumtaz H, Hall-Craggs MA, Davidson T *et al.* Am. Roentgenol. J. 1997;169:417–424.

56. Nunes LW, Schnall MD, Siegelman ES *et al.* Am. J. Roentgenol. 1997;169:409–415.
57. Orel SG, Hochman MG, Schnall MD, Reynolds C, Sullivan DC, Radiographics 1996;16:1385–1401.
58. Orel SG. Semin Ultrasound MCT R. 1996;17(5):476–493.
59. Pedevilla M. Radiology 1997;205(2):580–581.
60. Peller M, Stehling MK, Sittek H, Kessler M, Reiser M, MAGMA 1996;4(2):105–113.
61. Piccoli CW. Magn. Reson. Imaging. Clin. Am. N. 1994;2(4):557–571.
62. Pierce WB, Harms SE, Flamig DP, Griffey RH, Evans WP, Hagans JE. Radiology 1991;181(3):757–763.
63. Rieber A, Zeitler H, Rosenthal H, Gorich J, Kreienberg R, Brambs HJ, Tomczak R. Br. Radiol. J. 1997;70(833):452–458.
64. Rodenko GN, Harms SE, Pruneda JM *et al.* Am. Roentgenol. J. 1996;167:1415–1419.
65. Seki T, Hachiya J, Nitatori T, Yokoyama K, Fukushima H, Uchigasaki S, Nippon Geka Gakkai Zasshi 1996;97(5): 347–56.
66. Soderstrom CE, Harms SE, Copit DS, Evans WP, Savino DA, Krakos PA, Farrell RS Jr, Flamig DP. Radiology 1996; 201(2):427–432.
67. Soo MS, Kornguth PJ, Walsh R *et al.* J. Magn. Reson. Imaging. 1997;7:724–730.
68. Stelling CB. Radiol. Clin. North. Am. 1995;33(6):1187–11204.
69. Van Goethem M, Van Breusegem L, Ceulemans R, De Schepper A, de Moor J. J. Belge. Radiol. 1995;78(1):6–10.
70. Weinreb JC, Newstead G, Controversies in Breast MRI 1994;10(2):67–83.
71. Weinreb JC, Newstead G. Radiology 1995;196(3):593–610.
72. Kaiser WA, Fortschr. Röntgenstr. 1996;165(5):425–427 (Editorial).
73. Hussman K, Renslo R, Phillips JJ, Fischer HJ, Khalkhali I, Braslau DL, Sinow RM. Work in Progress, Radiology. 1993;189:915–917.
74. Kuhl CK, Elevelt A, Leutner CC, Gieseke J, Pakos E, Schild HH. Radiology. 1997;204:667–675.
75. Thiele J, Schneider JP, Franke P, Lieberenz S, Schmidt F. Fortschr Röntgenstr. 1998;168:374–379.
76. Doler W, Fischer U, Metzger I, Harder D, Grabbe E. Radiology 1996;200:863–864.
77. Mahfouz AE, Rahmouni A, Zylbersztejn C, Mathieu D, Am. Roentgenol. J. 1996;167:167–169.
78. Wurdinger S, Noras H, Straube K, Michaelsen S, Kaiser WA, ECR'97, Eur. Congr. Radiol. 2–7. March 1997, European Radiology 1997;7. S243.
79. de Souza NN, Kormos DW, Krausz T, Coutts GA, Hall AS, Burl M, Schwieso JE, Puni R, Vernon C. J. Magn. Reson. Imaging. 1995;5:525–528.
80. Silverman SG, Collick BD, Figueira MR, Khorasani R, Adams DF, Newman RW, Topulos GP. Radiology. 1995;197:175–182.
81. Pfleiderer SO, Reichenbach JR, Azhari T, Marx C, Wurdinger S, Kaiser WA, Invest. Radiol. 2003;Jan 38(1):1–8.
82. Knopp MV, Weiss E, Sinn HP, Mattern J, Junkermann H, Radeleff J, Magener A, Brix G, Delorme S, Zuna I, G van Kaick. J. Magn. Reson. Imaging. 1999;Sep 10(3):260–266.
83. Brix G, Schreiber W, Hoffmann U, Guckel F, Hawighorst H, Knopp MV. Radiologe 1997;Jun 37(6):470–480.
84. Buckley DL, Drew PJ, Mussurakis S, Monson JR, Horsman A. J. Magn. Reson. Imaging. 1997;May to Jun 7(3):461–664.
85. Algire GH. J. Int. Chir. 1953;Jul to Aug 13(4):381–384 (includes translations).
86. Gimbrone MA Jr, Leapman SB, Cotran RS, Folkman J. J. Exp. Med. 1972;Aug 1, 136(2):261–276.
87. Folkmann J, Long DM Jr, Becker FF. 1963;Apr 16:453–467.
88. Ottinetti A, Sapino A. Breast Cancer Res. Treat. 1988;Jul 11(3):241–248.
89. Samejima N, Yamazaki KA. Jpn. J. Surg. 1988;May 18(3):235–242.
90. Folkman J. Adv. Cancer. Res. 1985;43:175–203.
91. Weidner N, Semple JP, Welch WR, Folkman J, Engl N. Med J. 1991;Jan 3, 324(1):1–8.
92. Jensen HM, Chen I, DeVault MR, Lewis AE. Science 1982;Oct 15, 218(4569):293–295.
93. Port RE, Knopp MV, Brix G. Magn. Reson. Med. 2001;Jun, 45(6):1030–1038.
94. Lucht RE, Knopp MV, Brix G. Magn. Reson. Imaging 2001;Jan 19(1):51–57.
95. Knopp MV, Himmelhan N, Radeleff J, Junkermann H, Hess T, Sinn HP, Brix G. Radiologe 2002 Apr ;42(4):280–290.
96. Buckley DL, Drew PJ, Mussurakis S, Monson JR, Horsman A. J. Magn. Reson. Imaging 1997;May to Jun 7(3), 461–464.
97. Kaiser WA. Magnetic-Resonance-Mammography (MRM), Springer-Verlag, 1993.
98. Kaiser WA. In: PL Davis (Ed). MRI-Clinics of North America, Vol 2.4, Saunders, Philadelphia, 1994, pp 539–555.
99. H Neubauer, Li M, Kuehne-Heid R, Schneider A, Kaiser WA. Br. Radiol. J. 2003 Jan;76(901):3–12.
100. Fischer DR, Baltzer P, Malich A, Wurdinger S, Fresmeyer MG, Marx C, Kaiser WA. Eur. Radiol. 2004 Mar; 14(3):394–401, Epub 2003 Sep 27 (2004).
101. Kaiser WA. Breast, Unit 21. In: EM Haake, W Lin, NYC Cheng, CP Ho, WA Kaiser, JS Lewin, ZP Liang, SK Mukhery, RC Semelka, KR Thulborn, PK Woodard (Eds). Current Protocols in Magnetic Resonance Imaging. Wiley & Sons: New York, 2004.
102. Ikeda DM, Hylton NM, Kinkel K, Hochman MG, Kuhl CK, Kaiser WA, Weinreb JC, Smazal SF, Degani H, Viehweg P, Barclay J, Schnall MD. J. Magn. Reson. Imaging 2001;Jun 13(6):889–895.
103. Pfleiderer SO, Sachse S, Sauner D, Marx C, Malich A, Wurdinger S, Kaiser WA. Breast Cancer Res. 6(3):R232–238, Epub, Mar 16 (2004).
104. Kaiser WA, Selig M, Jung R, Vagner J, S Schönherr: Patentanmeldung: Manipulator für einen geschlossenen Magnetresonanztomographen (MRT). Patent Application Nr. 19941019.4; 28.08.1999, German Patent Office.
105. Pfleiderer SO, Reichenbach JR, Azhari T, Marx C, Malich A, Schneider A, Vagner J, Fischer H, Kaiser WA. 2003 Apr;17(4):493–498.

106. Pfleiderer SO, Freesmeyer MG, Marx C, Kuhne-Heid R, Schneider A, Kaiser WA. Eur. Radiol. Dec 12(12):3009–3014, Epub 2002 Jun 21.
107. Jeffrey SS, Birdwell RL, Ikeda DM, Daniel BL, Nowels KW, Dirbas FM, SM Griffey. Arch. Surg. 1999 Oct.;134(10): 1064–1068.
108. Hilger I, Leistner Y, Berndt A, Fritsche C, Haas KM, Kosmehl H, Kaiser WA. Eur. Radiol. 2004 Jun 14(6); 1124–1129, Epub 2004, Apr 30.

Internet Resources

http://www.mediteach.de: List of detailed courses in MRM.
http://www.mrisafety.com: List of safe or unsafe materials for a quick overview.

Phosphorus Magnetic Resonance Spectroscopy on Biopsy and *In Vivo*

Geoffrey S Payne, Nada Al-Saffar, and Martin O Leach
Cancer Research UK Clinical Magnetic Resonance Research Group, Royal Marsden Hospital and the Institute of Cancer Research
SUTTON, Surrey, SM2 5PT, UK

Features of ^{31}P MRS in Tissues

General Properties of ^{31}P

^{31}P is one of the most sensitive of the NMR nuclei. It has spin ½, a gyromagnetic ratio of 1.083×10^8 rad/s/T, and a natural abundance of 100%, giving a sensitivity of 6.63% relative to ^{1}H. Since many metabolites of biochemical interest are phosphorylated, ^{31}P MRS is a useful probe of tissue biochemistry. Spectra *in vivo* are relatively uncrowded as the number of ^{31}P-containing metabolites of sufficient concentration are relatively few. Properties of the individual metabolites of major interest are given below, while the abbreviations used for the various metabolites referred to in this chapter are given in Table 1. Note that there are nucleoside triphosphates (NTP) in addition to adenosine triphosphate (ATP), so in general we have followed the convention of referring to the corresponding peaks as NTP rather than as ATP.

Spectral Dispersion. In general ^{31}P gives rise to spectral peaks covering a wide range of frequencies. However in tissues most peaks of interest lie within a 30 ppm range (see Figure 1). Chemical shift is often referenced relative to phosphocreatine (PCr) at 0 ppm *in vivo*, or to H_3PO_4 in tissue extracts *in vitro*.

Dependence of Chemical Shift on pH. Many ^{31}P metabolites have a pKa in the range that makes the chemical shift dependent on tissue pH. The classic example of this is the equilibrium between the two forms of inorganic phosphate (Pi) in tissue [1];

$$H_2PO_4^- \Leftrightarrow HPO_4^{2-} + H^+ \qquad pKa \cong 6.7$$

Since this is a dynamic equilibrium between two forms of phosphate with different chemical shifts, the net shift of the observed Pi peak depends on the relative concentrations of the two species and hence on the hydrogen ion concentration (pH). Measurement of the chemical shift of the Pi peak relative to a peak that does not shift significantly with pH (usually PCr is used) provides a non-invasive way to measure intracellular pH, as most phosphate is intracellular. Some other ^{31}P metabolites also demonstrate sensitivity to pH, in particular phosphocholine (PC) and phosphoethanolamine (PE) (see Figure 2).

Other Factors Affecting Chemical Shift. Chemical shift is also affected by factors such as ionic strength and metal ion binding. In particular the β and γ peaks of ATP are sensitive to the magnesium concentration in the tissue [2,3].

Homonuclear J-Coupling. The main example of homonuclear coupling is found in NTP. In ATP this leads to α- and γ-ATP being observed as doublets, while β-ATP is a triplet, with a coupling constant of about 16 Hz. Homonuclear decoupling is not generally required. However, allowance for coupling is necessary when measuring the T_2 of coupled metabolites, such as ATP [4].

Heteronuclear J Coupling. The phosphomonoesters (PE, PC) have weak (6–7 Hz) 3-bond coupling to ^{1}H nuclei, forming a triplet, while the phosphodiesters couple to two-proton pairs, producing quintets (Table 1). Nearly all preclinical systems and a few of the more advanced clinical scanners have the facility to perform ^{1}H-decoupling to collapse these multiplets back to singlets (see below). A few research systems can also perform more complex double resonance measurements for further sensitivity enhancement.

Metabolites Observed in Tissues

Most of the metabolites detectable with ^{31}P MRS in tissues can be seen in Figure 1, while the structures are shown in Table 1. Metabolites are involved in either energy production (high energy phosphates—ATP, PCr, sugar phosphates; NADH) or in membrane metabolism (phosphomonoesters—PC, PE; phosphodiesters—GPC, GPE; membrane phospholipids). The reactions involved are summarized in Figure 3. For more details a biochemistry textbook should be consulted [5,6].

Graham A. Webb (ed.), Modern Magnetic Resonance, 1143–1161.
© 2008 *Springer.*

Table 1: Summary of main metabolites detected by ^{31}P MRS *in vivo*

Metabolite	Abbreviation	Structure	Chemical shift relative to PCr (ppm)	*J* coupling[a] (Hz)
Phosphoethanolamine	PE	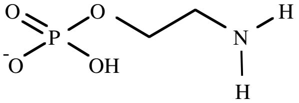	5–7	7.19
Phosphocholine	PC	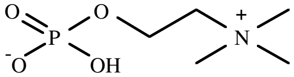	4.2–6.5	6.25
Inorganic phosphate	Pi	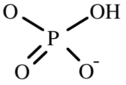	3.5–5.5	Singlet
Glycerophosphoethanolamine	GPE	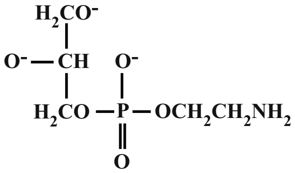	3.6	b
Glycerophospocholine	GPC	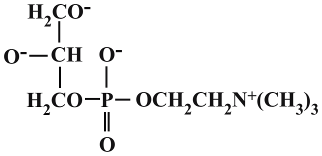	2.96	6.03
Phosphocreatine	PCr	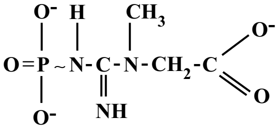	0	Singlet
Adenosine triphosphate	ATP	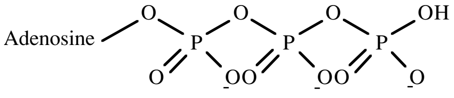	α-7.5 ppm β-16–19[c] γ-2–7.5[c]	

Notes: [a]The coupling quoted is the main $^{3}J_{PH}$ coupling. Additional J_{HH} couplings are often present. [138]; [b]This was not measured. It will be similar to that of GPC. [c]Depends on magnesium concentration.

Additional Notes on Specific Metabolites

Phosphomonoesters—phosphocholine and phosphoethanolamine. These metabolites are involved in membrane synthesis and degradation (Figure 3B [7]). PC is also involved in cell signalling [8,9]. The chemical shifts of both are pH sensitive (Figure 2).

Phosphodiesters—glycerophosphocholine (GPC) and glycerophosphoethanolamine (GPE). These are produced by the action of phospholipases A_1 and A_2, or phospholipase B on the corresponding phospholipids (Figure 3C). The chemical shift does not depend on pH. When interpreting a "PDE" peak one must be careful to distinguish phosphodiesters from the peak of the broader phospholipid component (see below).

Broad Resonances from Phospholipids and Bone. In unlocalized spectra of brain a large broad (~750 Hz

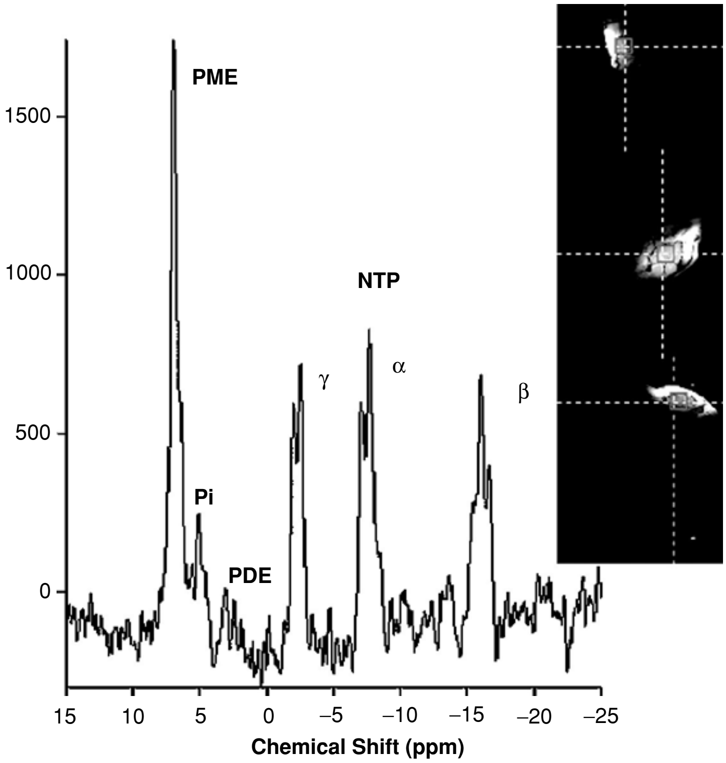

Fig. 1. Example of a ^{31}P MR spectrum from a non-Hodgkins lymphoma in the groin of a patient, measured at 1.5 T. Note the absence of PCr at 0 ppm.

width) symmetric resonance is observed due to immobile phosphates in bone [10]. In localized spectra of brain, liver, and kidney a broad asymmetric resonance is observed that decreases in amplitude with increasing magnetic field strength, and therefore suggesting a strong influence of chemical shift anisotropy. It has been demonstrated that the peak is produced by membrane lipid bilayers and that it may be eliminated by off-resonance presaturation [11].

Nucleoside Triphosphates. In most systems the dominant contribution is from ATP. As mentioned above, the chemical shifts of the β and γ peaks are sensitive to magnesium concentration.

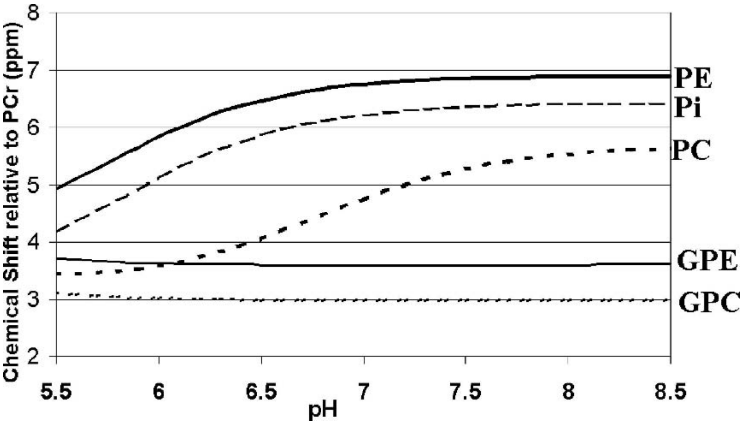

Fig. 2. Chemical shift of several metabolites relative to PCr as a function of pH (calculated from .[137]).

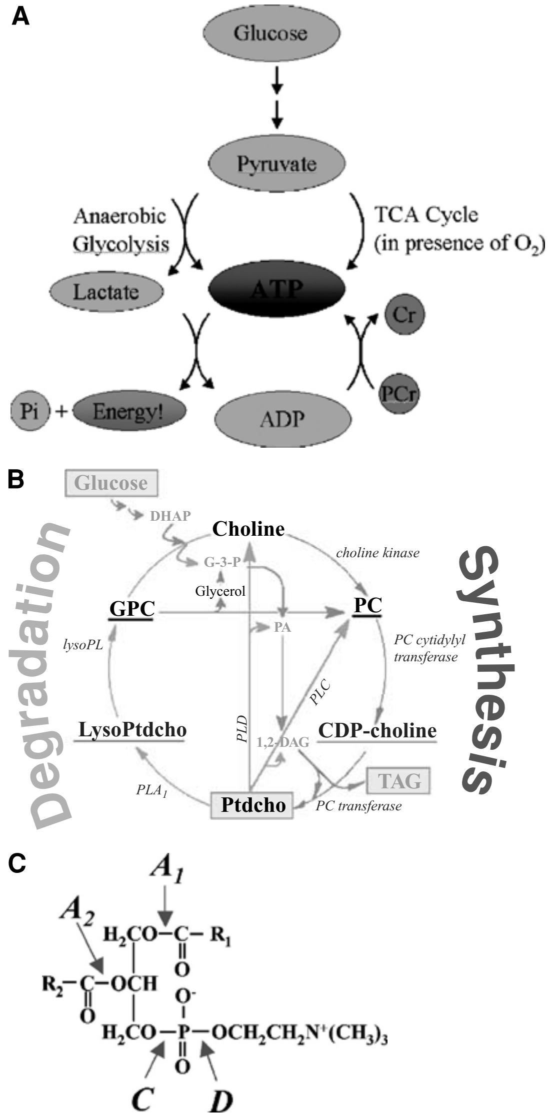
A
Glucose
Pyruvate
Anaerobic Glycolysis
TCA Cycle (in presence of O2)
Lactate
ATP
Cr
PCr
Pi
+
Energy!
ADP
B
Glucose
DHAP
Choline
choline kinase
G-3-P
Glycerol
GPC
PC
PA
lysoPL
PC cytidylyl transferase
PLC
PLD
LysoPtdcho
1,2-DAG
CDP-choline
TAG
PLA1
Ptdcho
PC transferase
Degradation
Synthesis
C
A1
A2
H2CO−C−R1
O
R2−C−OCH
O
O-
H2CO−P−OCH2CH2N+(CH3)3
O
C
D

Fig. 3. Simplified biochemical pathways of main compounds visualized by ^{31}P MRS in tissues. (A) Metabolism of high energy phosphates. (B) Synthesis and degradation pathways of main membrane phospholipid. (C) Sites of action of the phospholipases on phosphatidylcholine. Phospholipase B can also bring about the successive removal of both fatty acids. (See also Plate 90 on page XVI in the Color Plate Section.)

Adenosine Diphosphate (ADP). The concentration measured by NMR is much lower than that measured biochemically after freeze-clamping of the tissue. This suggests that much of the ADP is tightly bound to larger structures leading to rapid transverse relaxation such that the peaks become invisible by NMR.

Metabolite Concentrations and Relaxation Times

Some published measurements of concentrations and relaxation times of various metabolites in different tissues are summarized in Tables 2 and 3.

^{31}P MRS of Tissue Biopsy Samples

Methods

Extraction Methods

The type of extraction method to be selected depends greatly on the nature of the investigation and the analytical methods involved. To analyze cellular lipids and/or their water-soluble metabolites, it is necessary to use extraction procedures that quantitatively recover the metabolites of interest. Currently available methods include the following.

Perchloric Acid (PCA). This is widely used for extraction of water-soluble cell components [12].

Modified Folch's Method. The extraction of cellular lipids using organic solvents, usually chloroform and methanol [12].

A Combined Extraction Technique. The above two methods performed on the same cell batch [13].

The Dual Phase Extraction Method (DPE). The recovery of both the lipid and water-soluble fractions from the same biological sample by a single extraction method [12].

Chemical Shift and Concentration Referencing for ^{31}P MRS

The separation of resonance frequencies from an arbitrary chosen reference frequency is termed the "chemical shift", and is expressed in terms of the dimensionless unit parts per million (ppm). Depending on the phase of the extracts and the type of nucleus detected, different solvent systems and references (internal or external) are used.

Aqueous Fraction. An example of stock solution used is D_2O with 10 mM ethylenediaminetetraacetate (EDTA) adjusted to pH 8.2 with tris (hydroxymethyl)-methylamine (Tris) (0.5 M, pH 10.4), and methylene-diphosphonic acid (MDPA) ($\delta = 16.8$ ppm) calibrated against GPC ($\delta = 0.49$ ppm @ pH 7.2) for referencing.

Table 2: Some measured concentrations of metabolites detected by ^{31}P MRS in different human tissues (units of mM)

Tissue	Meth	PE	PC	PME	Pi	GPE	GPC	PDE	MP	PCr	ATP (NTP)	Reference
Kidney	NMR			2.32 ± 0.50	0.66 ± 0.25			2.14 ± 0.91		None	1.6 ± 0.26	[95]
Kidney	NMR			2.6	1.6			4.9		None	2.0	[67]
Brain cerebrum	NMR			3.2 ± 0.3	1.0 ± 0.2			10.8 ± 2.0		2.9 ± 0.3	2.9 ± 0.2	[71]
Brain—cerebellum				4.0 ± 0.6	1.0 ± 0.2			9.4 ± 3.4		3.9 ± 0.4	2.6 ± 0.2	[71]
Brain cortical GM	NMR			3.1 ± 0.4	1.0 ± 0.2			10.1 ± 2.5		3.1 ± 0.3	2.9 ± 0.2	[71]
Brain cortical WM	NMR			4.3 ± 0.8	1.3 ± 0.3			14.2 ± 2.6		2.9 ± 0.4	2.9 ± 0.3	[71]
Brain	NMR			3.6 ± 0.8	1.5 ± 0.5			10.2 ± 1.9		3.8 ± 0.7	2.1 ± 0.5	[139]
Brain	NMR			2.3 ± 0.4	1.2 ± 0.2			7.0 ± 0.8		3.1 ± 0.5	2.3 ± 0.2	[140]
Brain tumor	NMR			0.9 ± 0.3	0.9 ± 0.1			2.3 ± 0.4		1.2 ± 0.1	1.3 ± 0.2	[140]
Brain (left parieto-occipital cortex)		.81 ± .21	.46 ± .14			.74 ±. 30	1.15 ±. 43		1.54 ± .95			[141]
Brain (right parieto-occiptal cortex)		.94 ± .16	.46 ±. 17			.83 ± .22	1.14 ± .40		1.26 ± .78			[141]
Left thalamus		.69 ±. 18	.42 ± .16			.63 ± .20	1.05 ± .42		0.93 ± .56			[141]
Right thalamus		.68 ±. 24	.34 ±. 18			.60 ± .23	1.09 ± .36		.74 ±. 48			[141]
Muscle	Bioch									17.4	5.5	[142]
Muscle	Bioch									17.3	5.4	[143]
Muscle	Bioch				10					17.4	5.5	[144]
Muscle	NMR				2.7					25.6	5.5	[145]
Muscle	NMR				2.6					23.9	(5.5)	[146]
Muscle	NMR			2.5	3.6					24.7	(5.5)	[147]
Muscle	NMR				2.9					17.7	8.2	[148]
Muscle	NMR			2.2	4.7			4.2		32.0	6.3	[149]
Muscle	NMR				3.8					24.5	4.9	[150]
Muscle	NMR			2.0	2.9			3.8		22.0	5.7	[67]
Liver	NMR			0.9	2.1			5.4			2.2	[69]
	NMR			3.3	1.9			8.4			2.9	[67]
Liver (alcoholic hepatitis)	NMR			0.6 ± 0.3	1.4 ± 0.4			2.9 ± 1.1			1.5	[151]
Liver (alcoholic cirrhosis)	NMR			0.7 ± 0.5	1.1 ± 0.3			3.3 ± 1.8			1.65	[151]
Liver (viral hepatitis)	NMR			1.9 ± 0.6	2.1 ± 0.5			5.4 ± 2.0			2.8	[151]
Heart	NMR									8.82 ± 1.30	5.69 ± 1.02	[119]
Heart	NMR									9.0 ± 1.2	5.3 ± 1.2	[173]

Table 3A: Published values of T_1 relaxation times in different human tissues

Tissue	Field strength	PME	Pi	PDE	PCr	γ-NTP	α-NTP	β-NTP	Reference
Brain	1.9 T				4.0 ± 0.4	1.2 ± 0.2			[152]
Brain	2.0T	4.0	2.5	2.0	3.0	0.7	0.7	1.0	[56]
Brain (neonate)	2.35	4.9 ± 1.0	1.8 ± 0.6	1.7 ± 0.4	4.4 ± 1.2	1.3 ± 0.3	1.5 ± 0.4	1.6 ± 0.5	[153]
	2.35	6.4 ± 1.0	3.4 ± 1.1	2.1 ± 0.7	3.9 ± 1.0	2.2 ± 0.6	2.7 ± 1.0	1.7 ± 0.6	[153]
Brain (infants)	2.35	2.9 ± 0.6	1.8 ± 0.5	1.6 ± 0.2	3.2 ± 0.3	1.5 ± 0.3	1.7 ± 0.3	1.3 ± 0.4	[153]
Brain (infants)	2.35	4.9 ± 0.6	2.2 ± 0.6	2.0 ± 0.6	3.7 ± 1.1	2.2 ± 0.6	2.3 ± 0.8	2.5 ± 0.7	[153]
Muscle	1.5	3.20.5	3.3 ± 0.2	3.6 ± 0.4	4.6 ± 0.2	2.9 ± 0.4	2.2 ± 0.3	2.7 ± 0.3	[67]
Muscle	1.5		3.5 ± 0.4		5.0 ± 0.6	4.1 ± 0.4	2.9 ± 0.5	3.6 ± 0.3	[154]
Muscle	1.5		4.2 ± 0.5		6.1 ± 0.3	4.6 ± 0.3	3.2 ± 0.5	3.7 ± 0.6	[155]
Muscle	1.5		4.0 ± 0.5		5.6 ± 0.5	4.5 ± 0.4	3.4 ± 0.6	3.8 ± 0.8	[155]
Muscle	2.0		5.4 ± 1.7		6.0 ± 0.5	3.5 ± 1.0	3.9 ± 0.8	3.9 ± 0.8	[156]
Muscle	2.0		4.6 ± 0.5		6.5 ± 1.1	4.8 ± 0.6	3.5 ± 0.6	3.6 ± 0.8	[156]
Muscle	1.5		4.0 ± 0.4		6.5 ± 0.1	4.3 ± 0.5	3.2 ± 0.2	4.1 ± 0.3	[157]
	1.5		4.7 ± 0.3		6.5 ± 0.7	3.9 ± 1.3	4.2 ± 0.6	4.1 ± 1.3	[158]
	1.5		4.1 ± 0.5		6.6 ± 0.5	5.0 ± 0.7	3.8 ± 0.5	3.0 ± 0.5	[150]
	1.5		5.3 ± 0.5		6.9 ± 0.6	5.0 ± 0.5	3.2 ± 0.5	4.1 ± 0.4	[159]
	1.5		4.0 ± 0.8		5.5 ± 0.2	4.8 ± 0.5	3.6 ± 0.5	4.3 ± 0.6	[160]
Muscle	1.5	3.7 ± 1.6	3.9 ± 1.9	3.1 ± 1.9	5.8 ± 0.7	3.4 ± 0.1	2.8 ± 0.3	2.8 ± 0.4	[161]
Rhabdo Myosarcoma	1.5	5.2 ± 3.9	2.9 ± 1.3	2.0 ± 0.3	1.3 ± 0.3	1.3 ± 0.4	2.1 ± 0.4	1.6 ± 1.1	[161]
Muscle	3T		5.2 ± 1.0		6.4 ± 0.2	4.5 ± 0.3	2.6 ± 0.9	3.5 ± 1.1	[162]
Heart	1.5T			5.0 ± 1.0	6.1 ± 0.5	5.4 ± 0.5	5.0 ± 0.5	5.8 ± 1.0	[163,164]
Liver	1.5		0.41 ± 0.1	1.4 ± 0.13	none	0.43 ± 0.18	0.68 ± 0.09	0.40 ± 0.13	[158]
Liver	1.5	1.6 ± 0.4	0.8 ± 0.2	1.9 ± 0.4	none	0.5 ± 0.2	0.9 ± 0.3	0.5 ± 0.1	[67]
Liver	2.0	0.84 ± 0.26	0.97 ± 0.25	1.36 ± 0.37	none	0.35 ± 0.06	0.46 ± 0.09	0.35 ± 0.05	[69]
Liver	1.9	0.74 ± 0.1	0.44 ± 0.06			0.33 ± 0.04			[165]

Table 3B: Published values of T_2 relaxation times in different human tissues.

Tissue	Field strength	PME	Pi	PDE	PCr	γ−NTP	α−NTP	β−NTP	NTP	Reference
Muscle	1.5		240 ± 48		425 ± 21	93 ± 3	74 ± 1	75 ± 2		[4]
Muscle	1.5				61^a	66^a	69^b			[166]
Muscle	1.5				95^b	74^b	75^b			[4]
Muscle	1.5		205 ± 14		424 ± 21	$(16 \pm 5)^c$	$(22 \pm 6)^c$	$(8 \pm 2)^c$		[167]
Muscle	3T		148 ± 17		334 ± 30	78 ± 13	55 ± 7	55 ± 10		[162]
Brain	1.5					89 ± 9	84 ± 6	62 ± 3		[168]
Brain	2.0	70	80	20	150	30^c	30^c	20^c		[56]

Notes: ^{a}Spin echo with $T_E = 1/J$; ^{b}Selective echo 90-T_E/2-2(6)6(2)-Te/2-acquire; ^{c}These measurements have not allowed for modulation owing to homonuclear J coupling.

Lipid Fraction. A 2:1 mixture of $CDCl_3$ and 40 mM methanolic EDTA (200 mM EDTA in water adjusted to pH 6.0 with CsCl, and further diluted fivefold with absolute methanol) [14]. Examples of internal references are: GPC ($\delta = -0.13$ ppm) which is soluble in chloroform solutions, although it can be extracted with water and triphenylphosphine oxide ($\delta = 33.5$ ppm when PtdCho $\delta = 0.0$ ppm) or phosphocholine ($\delta = 3.5$ ppm when PtdCho $\delta = 0.0$ ppm) which is used as an external reference.

In all cases, metabolic contents are quantified by integration, normalized relative to the reference peak, and corrected for the number of live cells extracted and cell size in cases when treatment is expected to modify cellular size.

Acquisition Hardware and Condition

Measurements are usually performed in vertical superconducting magnets, with field strengths in the range 7–14 T. Manufacturers provide a wide range of RF probes, that are usually equipped with a deuterium lock to ensure the field does not drift over the time of the measurement, and with a separate ^{1}H coil in order to perform ^{1}H decoupling. Most measurements will use 5 mm NMR tubes, although 2.5 mm and even 1 mm tubes are becoming available.

Acquisition conditions will depend to some extent on the system and concentration being studied. The following conditions are an example of those used for cellular extracts of $0.5 - 2.0 \times 10^8$ cells measured on a 500 MHz spectrometer [15,16]. Some example spectra are given in Figure 4.

Spectra are acquired at room temperature with proton broad-band decoupling to eliminate ^{1}H-^{31}P NMR multiplets (decoupler power "on" during acquisition and "off" during the interpulse delay in order to prevent the building of NOE enhancement), spectral width of 100 ppm (aqueous) and 20 ppm (lipid), 32K data points and 4K transients accumulation. The sample spinning rate is 20 Hz. Exponential multiplication to give a line-broadening of 1–2 Hz is applied before Fourier transformation.

Spectral Analysis

Most spectrometers include software for processing and analysis of data. For off-line processing several packages are available, such as MestRe-C software (available free from Javier Sardina Research Group, University of Santiago de Compostela, Spain (http://qobrue.usc.es/jsgroup/MestRe-C/MestRe-C.html)). In addition to the measurement of peak areas directly, when large numbers of samples are available it is possible to look for patterns characteristic of different sample groups using automated pattern recognition techniques [17].

MRS of Intact Tissue Samples

While virtually all MRS measurements of biopsy samples are performed on tissue extracts, it has recently become possible to perform high resolution MRS directly on samples of intact tissue using the technique of magic angle spinning [18]. While most studies have used ^{1}H MRS, high resolution ^{31}P MR spectra may also be obtained [19]. Unlike extract studies the enzymes are still active, so it is necessary to perform measurements at low temperature (usually about 4° C). The high-energy phosphates are usually not visualized, but the metabolites involved in membrane metabolism (phosphomonoesters and phosphodiesters) are found to be reasonably stable.

Applications using ^{31}P MRS of Tissue Extracts

In practice, ^{31}P MRS of biopsy samples *ex vivo* is not as widely used as ^{31}P MRS *in vivo*, owing to the wide variety of alternative analytical techniques available for evaluating tissue samples. However the high resolution permits the identification of many more metabolites than is possible *in vivo*, for example, 14 different phospholipids were identified in a study of malignant breast tumors, several of which (sphingomyelin, PtdCho, PtdSer, phosphatidic

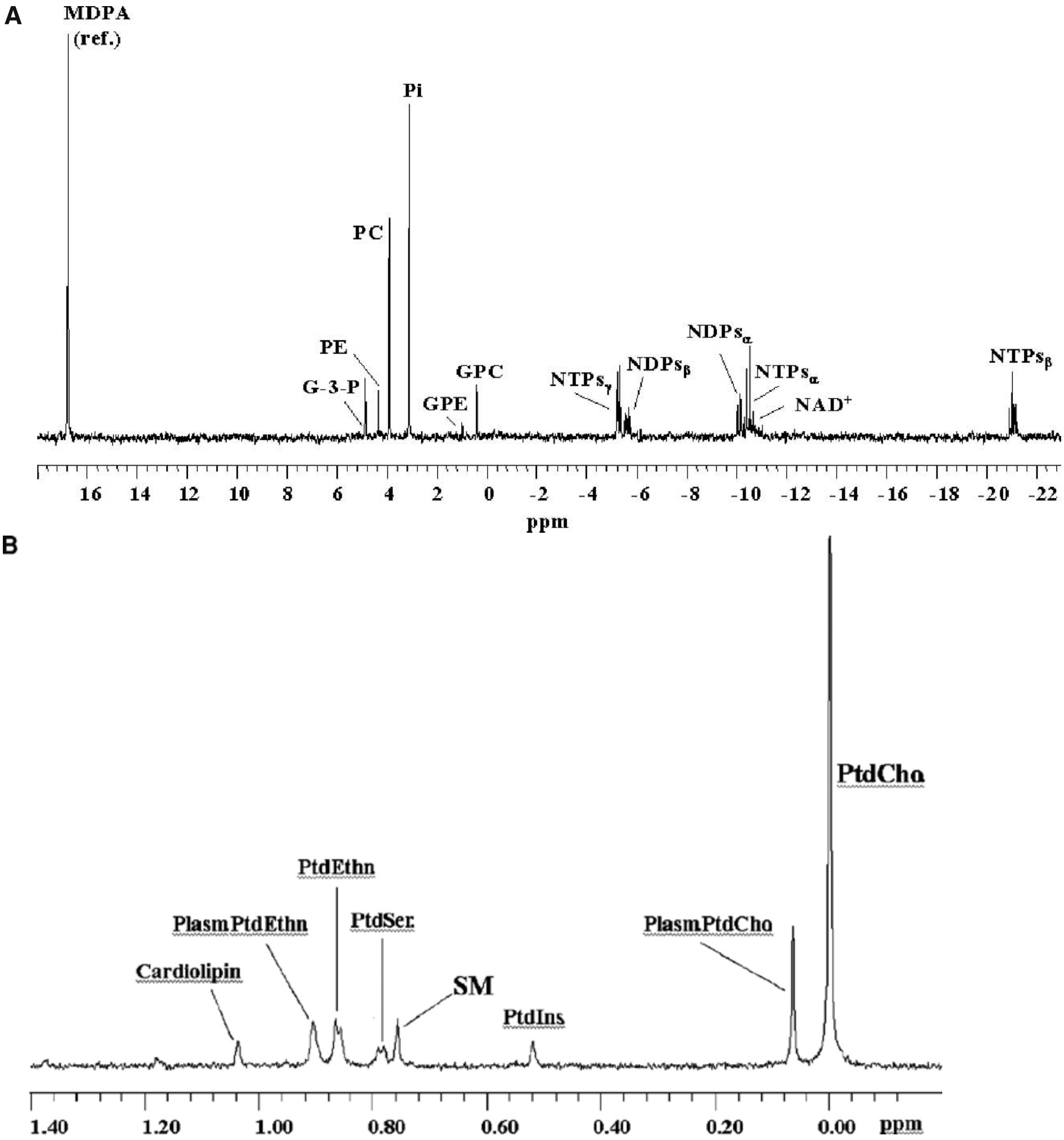

Fig. 4. Example spectra from cell extracts. All measurements were performed at 9.4 T. Spectra were plotted and analyzed using MestRe-C version 1.5.1 software. (A) ^{1}H decoupled ^{31}P MR spectrum of the water soluble fraction of Jurkat T-cell extracts (*G-3-P* = glycerol-3-phosphate, PE = phosphoethanolamine, PC = phosphocholine, Pi = inorganic phosphate, GPE = glycerol-3-phosphoethanolamine, GPC = glycerol-3-phosphocholine, NDPs = nucleotide diphosphates, NTPs = nucleotide triphosphates. NAD$^+$ = nicotinamide adenine dinucleotide). Spectrum is the result of 1280 scans plotted with line broadening of 2 Hz. (B) ^{1}H decoupled 31P MR spectrum of the lipid fraction of Jurkat T-cell extracts. Spectrum is the result of 1280 scans plotted with line broadening of 0.1 Hz and zero filling to 64 K data points (Plasm.PtdEthn = plasmalogen phosphatidylethanolamine, PtdIns = phosphatidylinositol, Plasm.PtdCho = plasmalogen phosphatidylcholine, SM = sphingomyelin, PtdCho = phosphatidylcholine, PtdEthn = phosphatidylethanolamine).

Table 4: Relative merits of tissue extracts and *in vivo* ^{31}P MRS measurements

	Tissue Extracts	*In vivo*
Tissue biopsy required?	Yes	No
Sample preparation required?	Yes	No
Max measurement time	Unlimited	Approx. 1 h
Measurement co-registered with anatomical image?	Not usually	Yes
System disturbed?	Yes	No
Capacity to follow kinetics	No	Yes
Spectral resolution	∼0.01ppm	∼0.1 ppm
Sensitivity to motion	N/A	Depends on tissue and method
Complexity of NMR sequence	Decoupled pulse-acquire	Requires localization
Field strength generally available	7–14 T	1.5–3 T
Coil design / availability	Good range of commercial coils	Few commercial coils; most need to be custom-built
Safety issues	Biopsy	MR Hazards (esp. RF heating from surface coils)

acid, phosphatidylglycerol and alkylacylphosphatidylcholine) predicted tumor characteristics such cellular infiltration, lymphatic invasion and necrosis [20].

In other studies biopsy specimens from patients with chronic ductopenic rejection [21] and liver cirrhosis [22] showed elevated PE and PC, and reduced GPE and GPC, reflecting altered phospholid metabolism [21]. In malignant hyperthermia-susceptible patients PCA extracts of vastus medialis muscle showed elevated GPC/(PCr+Pi) but no histological differences, suggesting GPC could be a marker of impairment [23]. PCA extracts of transurethral prostate samples show statistically different ratios of PE/totP, PC/totP and GPC/totP in prostate cancer samples compared with those from patients with benign prostatic hyperplasia [24]. In extracts of breast tumors no correlation was found between levels of GPC, GPE, PC, and PE and with indices of tumor proliferation, but higher PC levels were found in high grade tumors [25].

PCA and lipid extracts from kidney show that oncocytomas (benign tumors) have a biochemical composition between healthy and malignant tissue [26].

Blood samples are easier to obtain than tissue samples. One application is in thyroid cancer, where plasma levels of sphingomeylin and PtdCho have been found to be reduced in patients with remnants of thyroid tissue, and are even lower in patients with metastatic thyroid cancer, compared with patients in remission [27].

^{31}P MRS *In Vivo*

Introductory Comments

Given the difficulty and limited patient acceptance of obtaining tissue biopsy samples, the option to perform the spectroscopy measurements on the tissue *in vivo* is clearly very welcome. While the sensitivity and spectral resolution can never approach those obtained *in vitro*, the possibility of obtaining biochemical information from tissues non-invasively, repeatedly if necessary, provides the opportunity to monitor aspects of tissue biochemistry and response to treatment. Table 4 lists some of the main differences between measurements *in vivo* and *ex vivo*. A direct comparison of spectra of breast tumors from extracts and *in vivo* is given in [28].

Magnets

Most ^{31}P MRS studies on human subjects are performed in clinical NMR systems using horizontal bore superconducting magnets at a field strength of between 1.5 and 3T. Since sensitivity increases with field strength even higher fields would be advantageous but are not yet widely available. Since clinical scanners are normally designed for operation at a single frequency (for ^{1}H MR imaging) it is necessary to add or modify the RF hardware (coils, frequency source, transmit amplifier, receiver preamplifier, filters etc.) to permit operation at the ^{31}P resonant frequency.

RF Coils for *In Vivo* Studies (see also Chapter "Radiofrequency Coils for Magnetic Resonance Spectroscopy")

Appropriate RF coils of high sensitivity are essential for acquiring good ^{31}P MRS data. Because *in vivo* ^{31}P MRS is largely a research activity, with users having different specifications and applications, at present the choice of commercial coils is very limited. Unlike ^{1}H coils, for which the vendors of the MR systems provide a good range of options, commercial ^{31}P coils are often supplied by specialist coil companies, while many researchers design and build their own. Some good reviews on coil design principles can be found in [29–32]. Again in contrast to ^{1}H coils, almost all ^{31}P coils are used in transmit/receive mode—principally because there is no ^{31}P body resonator to provide a uniform transmit field. Occasionally a small surface coil receiver (to optimize sensitivity) is used together with a larger transmit coil (to optimize transmit field uniformity).

Surface Coils

Apart from studies in the brain, ^{31}P MRS measurements are usually performed with surface coils because of their superior sensitivity in superficial tissues [33]. There is a huge variety of designs, with the main differences being shape (e.g. circular or rectangular; mounting on a flat or curved surface), number of turns, material for construction (e.g. wire or foil), type of tuning network (e.g. simple LC circuit or balanced match), and whether there is a complementary ^{1}H coil to provide imaging and dual resonance capability. Surface coils are characterized by a spatial variation in the RF field. During transmit this leads to non-uniform excitation within the field of view of the coil. For small regions of interest that are not too close to the coil conventional amplitude-modulated RF pulses are often used, calibrated to give the required flip angle at the centre of the volume. However larger volumes are often of interest. In this case it is necessary to use adiabatic RF pulses to achieve uniform excitation over the region of interest (see below).

The non-uniform transmit field of surface coils also leads to non-uniform RF power deposition, which can be very high close to the coil itself. This is hard to measure experimentally, so sophisticated models (e.g. using finite element analysis) are required to calculate the expected power deposition [34]. International guidelines specify limits to RF power deposition for local and whole-body irradiation [35]. In practice the high RF power deposition near surface coils does limit the minimum repetition time or pulse amplitude in some studies, especially where double-resonant techniques are being used (see below).

Volume Coils

Volume coils are characterized by a more uniform RF field than surface coils, but usually at the expense of lower sensitivity. The most common designs for clinical studies are co-axial pairs of surface coils (often loosely called "Helmholtz pairs" but in fact having a separation larger than the radius), or birdcage coils [36]. Birdcage coils can be circularly polarized (which reduces RF power and improves receive sensitivity) and also double-resonant ($^{1}H/^{31}P$) [37].

Double-Resonance Coils

When performing ^{31}P MRS studies a ^{1}H capability is also usually required to obtain localization MR images, to shim, and sometimes to acquire complementary ^{1}H MR spectra (sequential or interleaved) or for double resonance studies (NOE, decoupling, polarization transfer). The hardware required depends on whether both ^{1}H and ^{31}P need to be used simultaneously.

Double Resonance Coil Options

(a) Two separate coils—such as ^{1}H body coil and ^{31}P surface coil or co-axial surface coils [38,39]. It is necessary to ensure they do not interact, in particular that ^{1}H transmit fields do not induce currents in the ^{31}P coil (leading to signal drop-out and local heating).
(b) Single coil, either with wide tuning range to permit sequential tuning to ^{1}H and then ^{31}P (e.g. 63 MHz and 25 MHz at 1.5 T), or that has two independent tuning networks may be switched to tune to each frequency.
(c) Single dual-resonant coil, for which the tuning circuit has resonances at both ^{1}H and ^{31}P. Depending on the design, the ^{1}H and ^{31}P connections may be on the same input [40] or different ones [31].

System Options

(a) Single channel with wide frequency range to permit transmit and receive operation at ^{1}H followed by ^{31}P in separate measurements. Some systems permit operation at specific frequencies only (e.g. at ^{1}H and ^{31}P). No double resonance experiments are possible.
(b) As (a) but with rapid switching of the transmit frequency. This permits irradiation at the ^{1}H frequency during the recovery time of ^{31}P measurements, and hence ^{31}P signal enhancement by the nuclear overhauser effect (NOE).
(c) Two-channel system that is able to transmit at one frequency (e.g. ^{1}H) while receiving on another (e.g. ^{31}P). Such systems can perform ^{1}H -decoupling (see below) as well as NOE studies.
(d) Two-channel system with full transmit and receive capability on two channels simultaneously. This permits both sequential acquisition at different frequencies [41–43] and also more complex double-resonance measurements such as polarization transfer [44,45].

Other Hardware for Double Resonance Studies

If there are no transmit pulses during signal acquisition then the only requirement is that the coils and frequencies do not interact. However for decoupling studies, where ^{1}H irradiation is applied during ^{31}P receive, it is necessary to apply a high level of isolation (~80 dB) between the channels. If this is not done the main problems are (1) saturating the receiver, leading to lower receiver gain, and (2) introducing extra noise into the receive channel, which again reduces the signal-to-noise ratio. Isolation is normally achieved in three steps, (i) use a coil that has a sharp resonance at the frequency of interest (e.g. ^{31}P) and negligible response at the other frequency (e.g. ^{1}H) (ii) a narrow band-width ^{31}P preamplifier, to minimize impact of ^{1}H irradiation, (iii) narrow bandwidth filters on both ^{1}H transmit and ^{31}P receive paths.

Adiabatic RF Pulses for *In Vivo* Studies with Surface Coils

Adiabatic RF pulses have the useful property that once a threshold transmitter amplitude is exceeded they produce uniform excitation over the sensitive region of the RF coil. In general they are characterized by a modulation of the frequency (or phase) as well as of the amplitude. For example the sech/tanh pulse ("hyperbolic secant pulse") widely used for slice-selective inversion [46] is described by

$$\mathrm{Amp} = \Omega_0 \,\mathrm{sech}(\beta t)$$

$$\mathrm{Freq} = \mu\beta \tanh(\beta t)$$

A variety of adiabatic pulses have been developed. Helpful reviews are available [47]. Other useful pulses include the tanh/tan pulse for 90° excitation [48] and the BIR4 or BIRP pulses for excitation by smaller flip angles to reduce partial saturation effects [48,49]. While there are adiabatic pulses suitable for many purposes some applications are particularly difficult, for example slice-selective excitation (for which the subtraction of two measurements is required [50]) and spin-refocusing [51].

The major disadvantages of adiabatic RF pulses compared with conventional amplitude-modulated pulses is that they are often (but not always) longer and/or requiring of a higher peak or total power.

Localization Methods for *In Vivo* Studies

For most studies *in vivo* it is necessary to select signal from a specified volume, usually identified from MR images acquired on the same occasion. A schematic representation of the three classes of technique is shown in Figure 5. An ideal acquisition method would have a sharp edge profile matching the requested target volume on the MR images, acquire signal from the selected volume with 100% efficiency, and include no contamination at all from elsewhere. The relative merits of the different acquisition strategies available are discussed briefly below.

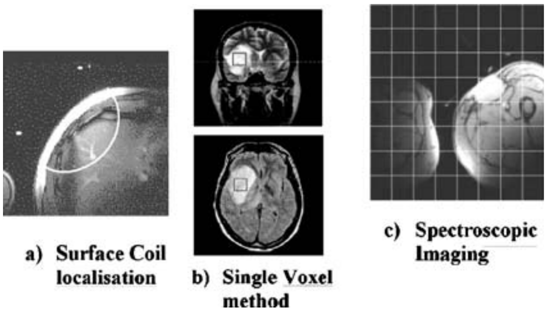
a) Surface Coil localisation **b) Single Voxel method** **c) Spectroscopic Imaging**

Fig. 5. Schematic illustrating the different methods of spectral localization.

Surface-Coil Localization

The relative sensitivity of an RF coil in receive mode at a particular point in space is proportional to the relative RF field produced at the same position by the coil in transmit mode [52]. Thus the sensitivity falls away with distance from a surface coil, limiting the sensitive volume. An indication of this region is shown in Figure 5, although in practice the boundary is not well defined. However, the localization method is simple and has the maximum available sensitivity for a given coil. It is normally only used alone (i.e. without further localization) when the sensitive region is almost entirely occupied with the target tissue, and when the signal losses associated with additional forms of localization cannot be tolerated.

Single Voxel Localization Methods

Single voxel methods make use of a series of frequency-selective RF pulses in combination with slice-selective B_0 field gradients. These define three intersecting slices that are usually but not necessarily orthogonal. Of the wide range of strategies that have been developed over the years, only three are in widespread use—PRESS [53], STEAM [54] and ISIS [55]. ^{31}P MRS has been demonstrated to work with STEAM [56] but ISIS has been the method of choice. While PRESS and STEAM have the great advantage of achieving localization in a single measurement, they both include echo times during which significant losses occur for nuclei which are characterized by short transverse time constants, such as are observed in most ^{31}P metabolites. As technology advances and shorter minimum echo times become possible this will become less of a problem.

PRESS and STEAM. PRESS is conceptually the simplest single voxel method and uses a $90° - 180° - 180°$ double spin echo sequence (Figure 6A). The first 90° RF pulse excites a slice of spins (e.g. transverse). The first 180° refocus pulse affects an intersecting slice (e.g. sagittal), so that only spins with the column defined by the intersection

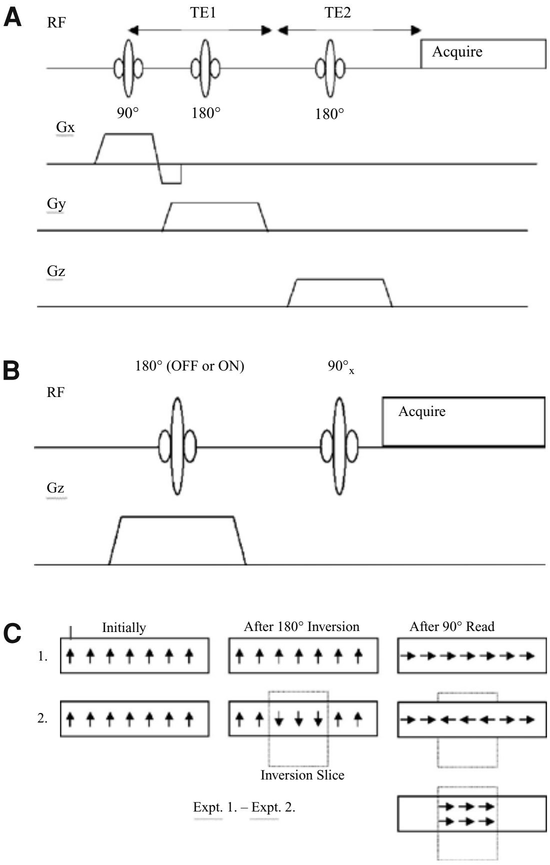

Fig. 6. (A) The PRESS localization sequence. (B) The ISIS localization sequence in 1 dimension (C) Schematic illustrating the effect on spins inside and outside the selected slice in the two measurements when performing ISIS localization in one dimension. The difference of the two measurements leads to signal addition within the slice and signal cancellation outside the slice.

of the two slices are refocused. The second 180^o pulse affects a third slice that intersects the other two, so that spins within the intersecting cuboid are refocused while other spins are dephased.

The STEAM sequence is similar to PRESS except that it uses a $90^\circ - 90^\circ - 90^\circ$ stimulated echo sequence instead of a double spin echo, with corresponding changes in timings and gradient patterns. It also localizes in a single measurement. However the maximum signal obtainable is 50% of the available magnetization.

ISIS. Localization with ISIS in one dimension requires two acquisitions (Figure 6B). In the first, a broadband RF pulse excites signal from the whole sample. In the second measurement the excitation pulse is preceded by a slice-selective inversion pulse. Subtraction of the two measurements causes cancellation of signal from outside the slice, but addition of signal from spins within the slice (Figure 6C). Three dimensional (3D)-Localization requires the appropriate addition/subtraction of eight separate measurements with all possible on/off permutations of slice-selective inversion pulses in the three intersecting slices.

Table 5: A summary of the relative merits of STEAM, PRESS, and ISIS for single voxel acquisition of ^{31}P MR spectroscopy data.

	STEAM	PRESS	ISIS
Surface coils	Poor	Poor	Good
Volume coils	Good	Good	Poor
Short T_2 metabolites	Moderate	Poor	Good
Single-shot	Yes	Yes	No
Edge definition	Good	Improving	Good
Sensitivity	<50%	Good	Good
Use use for shimming	Yes	Yes	Need other method

Relative Merits of the Different Single Voxel Localization Schemes for ^{31}P Acquisition. A summary of the relative merits of the three main single-voxel sequences is given in Table 5. The main advantage of the PRESS and STEAM schemes is that they are single-shot, thus reducing the problems of subtraction artefacts. However because the spins spend significant time in the transverse plane these methods are sensitive to signal loss from T_2 relaxation. With ISIS all magnetization is longitudinal till the final read pulse, thus reducing this problem. ISIS also has the advantage that it can be used easily with transmit surface coils by incorporating adiabatic RF pulses (usually hyperbolic secants); both STEAM and PRESS require slice-selective RF pulses, for which good adiabatic pulses are not available.

Spectroscopic Imaging (Chemical Shift Imaging)

Spectroscopic imaging (SI, also known as Chemical Shift Imaging—CSI) produces spectra for each member of a 2d or 3d grid, using a single excitation RF pulse followed by phase-encoding gradients [57]. For 2D-SI a slice-selective RF pulse is required, while for 3D-SI a non-selective pulse is used, which is better for use with surface coils. In principle it is possible to measure peak areas for a given metabolite in each cell and create a metabolite map. However with the voxel sizes often used for ^{31}P SI (e.g. 3 cm) this is not always useful.

Unlike single-voxel techniques the grid can be shifted after acquisition to make a cell line up with a target tissue

Table 6: Comparison of CSI and Single voxel techniques

	Single voxel	CSI
Specification of VOI		
Number of volumes	1	Typically ~512 (i.e. 8 × 8 × 8)
Voxel specification	Must be specified before measurement	1. Many voxels available 2. Grid shift can be performed retrospectively
Voxel shape	Dimensions adjustable; also tilt	(Usually) orthogonal grid e.g.$(2\text{cm})^3$ voxels
Voxel Integrity		
Edge definition	That of slice	Point spread function effects
Chemical shift displacement artefact	Yes (in each direction)	No
Sensitivity		
Relaxation losses	T_2 (STEAM, PRESS)	Negligible (basic implementation)
Other losses	Imperfect RF pulse profiles and flip angles. STEAM loses 50%.	Phase-encoding loses 13% in each dimension
Conformation to target	Usually good	Sometimes poor. Addition of small voxels does not recover SNR of the larger corresponding voxel.
Other aspects		
Minimum number of acquisitions	1	Many
Use with Tx/Rx surface coils	ISIS OK; STEAM and PRESS not good	OK with adiabatic excitation pulse

of interest. However the edges of the cells are blurred by a process known as Fourier bleed, which leads to signal leakage into adjacent voxels [58]. In the presence of motion this can cause leakage into quite distant voxels [59,60]. Some of these effects can be mitigated by suitable apodisation before the spatial Fourier transform [61] or by weighting of the number of acquisitions for each phase-encoding step [62].

For an N × M array it is necessary to acquire N × M individual transients into a data matrix, from which the spatial information is recovered by a 2D (or 3D) Fourier transform. Thus the minimum number of transients for an 8 × 8 × 8 matrix is 512, giving an acquisition time of about 8.5 minutes if TR = 1s.

A summary of the relative merits of single voxel methods and spectroscopic imaging for ^{31}P acquisition is given in Table 6.

Double-Resonance Acquisition Schemes

Double resonance methods excite spins of a different species (e.g. ^{1}H) in addition to those that are being detected (^{31}P) within the same measurement sequence. In the context of *in vivo* spectroscopy the aim is usually to improve the signal-to-noise ratio, although they can also be used for spectral editing. Not all scanners are capable of performing these studies. The main classes of sequence are outlined in Table 7; the references should be consulted for a more detailed description.

Table 7: Features of double resonance techniques

Name of technique	Method	References	Mechanism	Result
Nuclear overhauser effect	Saturation of ^{1}H spins during ^{31}P recovery	[169,170]	Dipolar coupling	Signal enhancements of up to 50%
Decoupling	Saturation of ^{1}H spins during ^{31}P acquisition	[171,172]	*J* coupling	Collapse multiplets to singlets e.g. phosphocholine improves resolution and sensitivity
Polarization transfer	Simultaneous pulsing of ^{1}H and ^{31}P (large range of different schemes, e.g. INEPT, DEPT, cross-polarization etc.)	[44,45]	*J* coupling	Signal enhancements on coupled spins

Spectral Analysis

Chemical Shift Referencing

For measurements *in vivo* it is necessary to have an internal peak as a chemical shift reference. Historically PCr was used (defined to be 0 ppm), as the pKa is 4.3, and therefore the chemical shift change is very small in the range of pH values found in tissue. Many of the early *in vivo* ^{31}P MRS studies were performed in muscle in which PCr is a dominant peak. For tissues that do not contain PCr (for example liver, and many tumors) alternatives include the phosphodiester peaks (GPE at 3.6 ppm and GPC at 2.96 ppm), and α-NTP (-7.5 ppm). Where ^{1}H spectra are also acquired, the signal from tissue water can also be used as a reference [63].

Measuring of Peak Areas

A large range of methods have been suggested for the measurement of the peak areas in MR spectra. In the early days both cutting-and-weighing and "triangulation" (approximating the peak as a triangle, and calculating the area from measured base and height) were used. When used consistently these gave quite reasonable results. However, both these methods perform poorly in the presence of overlapping peaks or broad bases to the peaks. Today it is more usual to model the spectrum as a series of peaks of particular shapes, and to fit such a model to the data. This approach can be performed both in the frequency domain and in the time domain. Most scanners are supplied with some frequency-domain fitting routines. A series of time domain methods have been evolving under the umbrella of MRUI (magnetic resonance user interface [64,65]) of which a Java version of the Amares algorithm is the current implementation of choice. This method can utilize quite a large amount of prior knowledge, thus reducing the number of free variables and improving the results of a fit.

A totally different approach, LC Model, uses spectra obtained from real solutions at a given pH and temperature rather than simulated spectra [66]. While principally used for ^{1}H spectral analysis it may also be used for ^{31}P.

Estimating Metabolite Concentrations

For many purposes it is sufficient to measure the area of one peak relative to another. This is simple and avoids the errors introduced by trying to obtain absolute values of the concentration. However it does not define which peak has changed, requires good agreement on acquisition conditions before results acquired at different institutions may be compared, and does not permit comparison with results of biochemical measurements.

Calculation of absolute concentrations requires

1. knowledge of the peak area relative to the area from a compound of known concentration;
2. correct values of T_1 and T_2 of both compounds to correct for relaxation effects during the sequence;
3. knowledge of the relative spatial distribution of both compounds and of the sensitivity of the RF coil, to correct for differences in excitation and receive efficiency.

In practice this is far from straightforward [67–72]. The known compound may be an external sample measured in the same study, or a test object measured in the same location as the tissue of interest in a subsequent measurement. Endogenous compounds (e.g. concentration of NTP) are also sometimes used, although one can never be quite sure that the concentration or relaxation times have not changed. Measurements with surface coils are particularly problematic owing to the spatial variation of the RF field, although in principle it is possible to correct for this [73].

Examples of ^{31}P MRS *In Vivo*

Some measured values of metabolite concentrations in different tissues are given in Table 2.

Skeletal Muscle

Muscle is characterized by high PCr, NTP and Pi. ADP is largely bound to macromolecules and is therefore largely MR-invisible.

One particular feature of ^{31}P MRS studies of muscle is that by exercising the muscle (usually within the magnet) dynamic measurements are possible. Thus many protocols measure resting metabolite levels, followed by exercise and recovery to permit measurement of fluxes in the metabolic pathways involved. Exercise is sometimes performed with cuff ischaemia to evaluate non-oxidative phosphorylation. Reviews are available in [74,75].

^{31}P MRS has been used to study many factors influencing muscle metabolism. These include,

- obesity [76] and level of fitness [77];
- age (Pi/PCr increases, ATP/totalP falls) [78];
- gender—the energy cost of contraction is twice as large in untrained women as men [79]; females have lower resting pH [78];
- creatine supplementation leads to increased muscle PCr but there with no change in recovery rates of ATP, Pi, pH, PCr, or muscle strength and endurance [80];
- muscle fibre distribution by analysis of Pi width at end of exercise [81];
- muscular dystrophy—less acidic than controls, pointing to deficit in glycolytic lactate production (perhaps owing to reduced glucose availability) [82];
- evaluation of reported weakness and fatigue, e.g. in juvenile variant of dermatomyositis significant metabolic abnormalities were observed—mean ATP and PCr

35–40% below normal, suggesting defective oxidative phosphorylation in mitochondria of diseases muscles [83];

- Studies of muscle energy metabolism, including coupling of ADP levels to glycogenolysis to regenerate ATP [84], non-oxidative ATP metabolism and acidosis [85];
- McArdles syndrome, a lack of phosphorylase activity in skeletal muscle that prevents the production of lactic acid under ischaemic exercise, and is therefore elegantly demonstrated by an absence of acidification with 31P MRS [86];
- peripheral vascular disease—showing larger changes in PCr utilization owing to reduced oxygen supply, and correlation between PCr and NIRS recovery rate constants [87], but that there may be defective metabolism in mitochondria of claudicating calf muscle [88].

Kidney

A major interest of ^{31}P MRS studies in kidney relate to evaluation of renal transplants. Pretransplant assessment of renal viability found a correlation of PME/Pi with clinical kidney function [89]. Storage may be monitored by effect on intracellular pH [90]. The ATP/Pi ratio has been used to evaluate success of implantation; a ratio of ATP/Pi greater than >1.2 has good sensitivity (92.8%) and specificity (100%) for predicting 3-year (5-year) survival, while a ratio >2.5 predicts for 5-year survival [91]. ^{31}P MRS is also used in experimental studies to improve the transplant technique, for example combined pretreatment with lipid-soluble and water-soluble antioxidants has been shown to lead to better restoration of energy phosphates in kidney subjected to ischaemia-reperfusion [92].

Cardiovascular disease is common in patients with chronic renal failure. Measurements have been performed of the phosphorylation potential of heart in renal dialysis patients and show that the PCr/ATP ratio is significantly reduced [93]. Exercise tolerance of CRF patients in muscle has also been performed [94].

^{31}P MRS permits measurements of metabolite concentrations in normal and diseased kidneys *in vivo* [95]. In advanced renal cell carcinoma it has been found that plasma levels of lysophosphatidylcholine are significantly lower than in control subjects [96].

Renal stone patients have low potassium and magnesium status. ^{31}P MRS has been used to assess the effect on intracellular pH, cytosolic magnesium and phosphorylation potential (PCr/ATP) in muscle [97]. Renal stones have also been analyzed with *ex vivo* ^{31}P MAS [98].

Liver

Liver is characterized by absence of PCr but the presence of a large number of sugar phosphates in the PME region [99].

In liver ^{31}P MRS has been used to assess severity of hepatitis C virus-related liver disease without biopsy [100]; the PME/PDE ratio can distinguish between mild, moderate and cirrhosis disease with specificity and sensitivity of 80% [100]. In addition cirrhosis is characterized by altered hepatic gluconeogenesis [101].

Energy metabolism and phospholipid biochemistry has been studied in the liver of patients with obstructive jaundice. Without treatment patients PME/total phosphate ratio is increased by 50% compared with controls [102].

Lung cancer patients have been found to have elevated PME in the liver, reported to reflect increased glucose flux and gluconeogenesis from alanine [103]. ATP infusion restores hepatic energy levels in patients with advanced lung cancer [104].

^{31}P MRS has also been used to evaluate changes in liver metabolism after surgery [105,106].

Studies in experimental models include hypothermia to reduce hepatic failure under hypoxia, progression of chronic liver disease to cirrhosis, and models to assess damage in acute liver failure.

Brain

A wide range of brain disorders have been investigated using ^{31}P MRS. Elevated GPC, GPE and high energy phosphate (PCr) have been observed in the anterior cingulate of brains of patients with first-episode schizophrenia [107,108], while parts of the brain of patients with bipolar disorder are characterized by reduced pH [109].

Lithium, used to treat depression, changes levels of ATP and of PME [110,111]. The pH is also observed to be reduced, but this may be the effect of disease rather than lithium [112]. Lithium is presumed to reduce intracellular *myo*-inositol, and increase levels of inositol monophosphate precursors (included in PME but not resolved).

In alcoholics lower concentrations and enhanced transverse relaxation of white matter phospholipids is observed, reflecting changes in membrane composition and rigidity [113].

While most studies look at resting levels of metabolites, some studies are now looking at the effects of visual activation on high-energy phosphates and pH in normal volunteers and in patients, for example those with mitochondrial disease [114].

A few studies have looked at spectral changes with age. In particular, it has been found that PE dominates in neonate, falling with age (as does PC). GPE, GPC, and PCr increase in concentration with postnatal age [115].

Heart

For review see [116]. In patients with haemachromatosis, often associated with cardiomyopathy, the PCr/ATP ratio in the left ventricle is significantly reduced compared with healthy volunteers, possibly reflecting mitochondrial impairment due to iron overload [117].

PCr/ATP is reported to be reduced with age [118], dilated cardiomyopathy [119], multiple sclerosis [120] and aortic stenosis [119]. The PCr/ATP ratio recovers towards control values in the latter group following surgical valve replacement [121]. In hypertensive patients the unstressed PCr/ATP ratio is variously reported as being normal [119] or reduced [122]. No reduction in PCr/ATP is observed in the non-infarcted septal myocardium of patients compared with controls [123]. Heart transplant patients studied within 24 h of a biopsy showed reduced PCr/ATP compared with controls, but with no strong correlation either with biopsy scores or with subsequent biopsies [124].

Stress tests show that cardiac patients with some forms of ischaemia showed a decrease in PCr/ATP even under light exercise, while no decrease was observed in patients whose hearts were non-ischaemic [122]. (*Note:* ^{31}P MRS measurements in the heart are often contaminated by signal from blood. In particular signal from 2,3 diphosphoglycerate overlaps with Pi signal making it hard to quantify.)

Tumors

A good review of the use of ^{31}P MRS in cancer is given by Negendank [125]. In particular ^{31}P MRS has been important in demonstrating that, contrary to expectation, the intracellular space of many cancers is alkaline [125]. In addition PE and PC have been shown to be elevated in many cancers. The ratio of PME/NTP is now being evaluated as an early indicator of response. There is also increasing evidence that both PME/NTP [126] and NTP/Pi [127] in the pretreatment spectrum may be able to predict response to treatment. Separate studies in patients with non-resectable soft tissue sarcoma have shown that changes in PME/ATP predict response to isolated limb perfusion to permit limb sparing [128].

Patients with non-small cell lung cancer have infusion of ATP to restrict weight loss; an increase in liver ATP (8.8 → 12.2%) is observed [104]. PME levels have also been observed to be higher in the weight-loss patients [129].

In breast cancer, there is an association between transformation and an increase in the phosphomonoesters (PMEs), while a decrease in PME content after treatment is associated with response to treatment as assessed by tumor volume [130]. In normal premenopausal breast a consistent pattern of changes is seen in the ^{31}P MR spectrum during the menstrual cycle, suggesting a potential application in assessing effects of exogenous hormones such as contraceptives or hormone replacement therapy which may increase breast cancer risk [131].

^{31}P MRS can also be used as marker of drug action (based on results of model systems and leading into clinical trials, e.g. 17-AAG [132]).

^{31}P MRS has been used extensively in experimental studies on effects of drugs, optimization strategies (reversing pH gradient, carbogen breathing), radiation etc. on cell systems.

Drug Detection

While ^{31}P MRS is normally used for study of endogenous compounds it also has the potential for monitoring uptake and metabolism *in vivo* of drugs that contain ^{31}P nuclei. The sensitivity is much lower than that of radionuclide labels, but the method has the advantages of being able to follow the metabolism of the drug, is not limited by a radioactive half-life, and makes use of the native compound without further chemistry required to perform the measurement. One example application has been the investigation of the alkylating agent ifosfamide. ^{31}P MRS studies have examined ifosfamide metabolites in body fluids [133], preclinical model systems [134,135], and in patients [136].

References

1. Moon R, Richards J. J. Biol. Chem. 1973;248:7276.
2. Gadian DG. Nuclear Magnetic Resonance and Its Applications to Living Systems. Oxford University Press, 1995.
3. Cohn M, Hughes TR Jr. J. Biol. Chem. 1962;237:176.
4. Jung WI, Straubinger K, Bunse M, Schick F, Kuper K, Dietze G, Lutz O. Magn. Reson. Med. 1992;28:305.
5. Cox M, Nelson DL. Lehninger Principles of Biochemistry. Palgrave Macmillan, New York, 2004.
6. Stryer L, Berg JM, Tymoczko JL. Biochemistry W H Freeman, New York, 2002.
7. Podo F. NMR Biomed. 1999;12:413.
8. Cuadrado A, Carnero A, Dolfi F, Jimenez B, Lacal JC. Oncogene. 1993;8:2959.
9. Jimenez B, del Peso L. Montaner S. Esteve P. Lacal JC. J. Cell. Biochem. 1995;57:141.
10. Gonzelez-Mendez R, Litt L, Koretsky AP, Voncolditz J, Weiner MW, James TL. J. Magn. Reson. 1984;57:526.
11. Murphy EJ, Rajagopalan B, Brindle KM, Radda GK. Magn. Reson. Med. 1989;12:282.
12. Tyagi RK, Azrad A, Degani H, Salomon Y. Magn. Reson. Med. 1996;35:194.
13. Henke J, Willker W, Engelmann J, Leibfritz D. Anticancer Res. 1996;16:1417.
14. Meneses P, Glonek T. J. Lipid. Res. 1988;29:679.
15. Al-Saffar NM, Titley JC, Robertson D, Clarke PA, Jackson LE, Leach MO, Ronen SM. Br. J. Cancer. 2002;86:963.
16. Ronen SM, DiStefano F, McCoy CL, Robertson D, Smith TA, Al-Saffar NM, Titley J, Cunningham DC, Griffiths JR, Leach MO, Clarke PA. Br. J. Cancer 1999;80:1035.
17. Tate AR, Griffiths JR, Martinez-Perez I, Moreno A, Barba I, Cabanas ME, Watson D, Alonso J, Bartumeus F, Isamat F, Ferrer I, Vila F, Ferrer E, Capdevila A, Arus C. NMR Biomed. 1998;11:177.
18. Cheng LL, Lean CL, Bogdanova A, Wright SC, Ackerman JL, Brady TJ, Garrido L. Magn. Reson. Med. 1996;36:653.

19. Payne GS, Chung Y-L, Vaidya SJ, Leach MO. In International Society for Magnetic Resonance in Medicine: Twelth Annual Meeting. Kyoto, Japan, 2004, p 68.
20. Merchant TE, Kasimos JN, Vroom T, de Bree E, Iwata JL, de Graaf PW, Glonek T. Cancer Lett. 2002;176:159.
21. Taylor-Robinson SD, Sargentoni J, Bell JD, Thomas EL, Marcus CD, Changani KK, Saeed N, Hodgson HJ, Davidson BR, Burroughs AK, Rolles K, Foster CS, Cox IJ. Gut. 1998;42:735.
22. Taylor-Robinson SD, Sargentoni J, Bell JD, Saeed N, Changani KK, Davidson BR, Rolles K, Burroughs AK, Hodgson HJ, Foster CS, Cox IJ. Liver. 1997;17:198.
23. Payen JF, Fouilhe N, Sam-Lai E, Remy C, Dupeyre R, Mezin P, Halsall J, Stieglitz P. Anesthesiology. 1996;84: 1077.
24. Cornel EB, Smits GA, Oosterhof GO, Karthaus HF, Deburyne FM, Schalken JA, Heerschap A. J. Urol. 1993;150:2019.
25. Smith TA, Bush C, Jameson C, Titley JC, Leach MO, Wilman DE, McCready VR. NMR Biomed. 1993;6:318.
26. Tosi MR, Tugnoli V, Bottura G, Lucchi P. Applied Spectroscopy 2001;55:908.
27. Moka D, Dietlein M, Raffelt K, Hahn J, Schicha H. Am. J. Med. 2002;112:634.
28. Smith TA, Glaholm J, Leach MO, Machin L, Collins DJ, Payne GS, McCready VR. Br. J. Cancer. 1991;63:514.
29. Schnall M. In: P Diehl, E Fluck, H Gunther, R Kosfeld, J Seelig (Eds). NMR Basic Principles and Progress 26. Springer-Verlag: Berlin Heidelberg, 1992, p 33.
30. Link J. In: P Deihl, E Fluck, H Gunther, R Kosfeld, J Seelig (Eds). NMR Basic Principles and Progress 26. Springer-Verlag: Berlin Heidelberg, 1992, p 1.
31. Hoult DI. Prog. NMR Spec. 1978;12:41.
32. Jin J. Electromagnetic Analysis and Design in Magnetic Resonance Imaging. CRC Press LLC, London, 1999.
33. Ackerman JJ, Grove TH, Wong GG, Gadian DG, Radda GK. Nature. 1980;283:167.
34. Prock T, Collins DJ, Leach MO. Phys. Med. Biol. 2002;47: 1805.
35. IEC. In: International Electrotechnical Commission (IEC), 2002.
36. Hayes CE, Edelstein WA, Schenck JF, Mueller OM, Eash M. J. Magn. Reson. 1985;63:622.
37. Murphy-Boesch J, Srinivasan R, Carvajal L, Brown TR. J. Magn. Reson. Series B 1994;103:103.
38. Klomp DW, Collins DJ, van den Boogert HJ, Schwarz A, Rijpkema M, Prock T, Payne GS, Leach MO, Heerschap A. Magn. Reson. Imaging. 2001;19:755.
39. Murphy-Boesch J, He L, Elsasser C, Brown TR. In: International Society for Magnetic Resonance in Medicine: Forth Annual Meeting. New York, USA 1996, p 1430.
40. Collins DJ, Prock T, Leach MO. In: International Society for Magnetic Resonance in Medicine: Eighth Annual Meeting, 2000, p 1417.
41. Yongbi NM, Payne GS, Leach MO. Magn. Reson. Med. 1994;32:768.
42. Arias-Mendoza F, Javaid T. Stoyanova R, Brown TR, Gonen O. NMR Biomed. 1996;9:105.
43. Gonen O, Hu J, Murphy-Boesch J, Stoyanova R, Brown TR. Magn. Reson. Med. 1994;32:104.
44. Gonen O, Mohebbi A, Stoyanova R, Brown TR. Magn. Reson. Med. 1997;37:301.
45. Payne GS, Leach MO, Magn. Reson. Med. 2000;43:510.
46. Silver MS, Joseph RI, Hoult DI. Physical Review A 1985; 31:2753.
47. Garwood M, Ugurbil K. In: P. Diehl, E. Fluck, H. Gunther, Kosfeld R, Seelig J (Eds). NMR: Basic Principles and Progress, Springer-Verlag, Berlin Heidelberg, 1992, p 109.
48. Garwood M, Ke Y. J. Magn. Reson. 1991;94:511.
49. Bottomley PA, Ouwerkerk R. J. Magn. Reson. Series A 1993;103:242.
50. Johnson AJ, Garwood M, Ugurbil K. J. Magn. Reson. 1989;81:653.
51. Ugurbil K, Garwood M, Rath AR, Bendall MR. J. Magn. Reson. 1988;78:472.
52. Hoult DI, Richards RE. J. Magn. Reson. 1976;24:71.
53. Bottomley P. Ann. NY Acad. Sci. 1987;508:333.
54. Frahm J, Merboldt K-D, Hanicke W. J. Magn. Reson. 1987;72:502.
55. Ordidge R, Connelly A, Lohman J. J. Magn. Reson. 1986; 66:283.
56. Merboldt KD, Chien D, Hanicke W, Gyngell ML, Bruhn H, Frahm J. J. Magn. Reson. 1990;89:343.
57. Brown T, Kincaid B, Ugurbil K. Proceedings of the National Academy of Sciences U.S.A. 1982;79:3523.
58. Koch T, Brix G, Lorenz WJ. J. Magn. Reson. Series B 1994;104:199.
59. Doyle VL, Howe FA, Griffiths JR. Phys. Med. Biol. 2000; 45:2093.
60. Schwarz AJ, Leach MO. Phys. Med. Biol. 2000;45:2105.
61. de Graaf RA, In vivo NMR spectroscopy, John Wiley & Sons, 1998.
62. Pohmann R, von Kienlin M. Magn. Reson. Med. 2001; 45:817.
63. Madden A, Leach MO, Collins DJ, Payne GS. Magn. Reson. Med. 1991;19:416.
64. Knijn A, de Beer R, van Ormondt D. J. Magn. Reson. 1992; 97:444.
65. ven den Boogaart A, Van Hecke P, Van Huffel S, Graveron-Demilly D, de Beer R. In: European Society for Magnetic Resonance in Medicine and Biology: 13th Annual Meeting, Prague, p. 318, 1996.
66. Provencher SW. Magn. Reson. Med. 1993;30:672.
67. Buchli R, Meier D, Martin E, Boesiger P. Magn. Reson. Med. 1994;32:453.
68. Tofts PS, Wray S. NMR Biomed 1988;1:1.
69. Meyerhoff DJ, Karczmar GS, Matson GB, Boska MD, Weiner MW. NMR Biomed 1990;3:17.
70. Buchli R, Martin E, Boesiger P. NMR Biomed. 1994;7:225.
71. Buchli R, Duc CO, Martin E, Boesiger P. Magn. Reson. Med. 1994;32:447.
72. Murphy -Boesch J, Jiang H, Stoyanova R, Brown TR. Magn. Reson. Med. 1998;39:429.
73. Doyle VL, Payne GS, Collins DJ, Verrill MW, Leach MO. Phys. Med. Biol. 1997;42:691.
74. Argov Z, Lofberg M, Arnold DL. Muscle Nerve 2000;23: 1316.
75. Heerschap A, Houtman C, in 't Zandt HJ, van den Bergh AJ, Wieringa B. Proc. Nutr. Soc. 1999;58:861.
76. Newcomer BR, Larson -Meyer DE, Hunter GR, Weinsier RL. Int. J. Obes. Relat. Metab. Disord. 2001;25:1309.

77. Tartaglia MC, Chen JT, Caramanos Z, Taivassalo T, Arnold DL, Argov Z. Muscle Nerve 2000;23:175.
78. Schunk K, Pitton M, Duber C, Kersjes W, Schadmand-Fischer S, Thelen M. Invest. Radiol. 1999;34:116.
79. Mattei JP, Bendahan D, Roussel M, Lefur Y, Cozzone PJ. FEBS Lett. 1999;450:173.
80. Smith SA, Montain SJ, Matott RP, Zientara GP, Jolesz FA, Fielding RA. J. Appl. Physiol. 1999;87:116.
81. Schunk K, Losch O, Kreitner KF, Kersjes W, Schadmand-Fischer S, Thelen M. Invest. Radiol. 1999;34:348.
82. Lodi R, Kemp GJ, Muntoni F, Thompson CH, Rae C, Taylor J, Styles P, Taylor DJ. Brain 122 (Pt 1) 121 (1999).
83. Park JH, Niermann KJ, Ryder NM, Nelson AE, Das A, Lawton AR, Hernanz-Schulman M. Olsen NJ. Arthritis Rheum 2000;43:2359.
84. Hsu AC, Dawson MJ. Magn. Reson. Med. 2003;49:626.
85. Roussel M, Mattei JP, Le Fur Y, Ghattas B, Cozzone PJ, Bendahan D. J. Appl. Physiol. 2003;94:1145.
86. Ross BD, Radda GK, Gadian DG, Rocker G, Esiri M, Falconer-Smith J, Engl N. J. Med. 1981;304:1338.
87. Kemp GJ, Roberts N, Bimson WE, Bakran A, Harris PL, Gilling-Smith GL, Brennan J, Rankin A, Frostick SP. J. Vasc. Surg. 2001;34:1103.
88. Pipinos, II, Shepard AD, Anagnostopoulos PV, Katsamouris A, Boska MD. J. Vasc. Surg. 2000;31:944.
89. Niekisch MB, Von Elverfeldt D, Saman AE, Hennig J, Kirste G. Transplantation 2004;77:1041.
90. Moller HE, Gaupp A, Dietl K, Buchholz B, Vestring T. Magn. Reson. Imaging. 2000;18:743.
91. Seto K, Ikehira H, Obata T, Sakamoto K, Yamada K, Kashiwabara H, Yokoyama T, Tanada S. Transplantation 2001;72:627.
92. Jonsson O, Lindgard A, Fae A, Gondalia J, Aneman A, Soussi B. Scand J. Urol. Nephrol. 2003;37:450.
93. Ogimoto G, Sakurada T, Imamura K, Kuboshima S, Maeba T, Kimura K, Owada S. Mol. Cell. Biochem. 2003;244:135.
94. Sala E, Noyszewski EA, Campistol JM, Marrades RM, Dreha S, Torregrossa JV, Beers JS, Wagner PD, Roca J. Am. J. Physiol. Regul. Integr. Comp. Physiol. 280 R1240 (2001).
95. Kugel H, Wittsack HJ, Wenzel F, Stippel D, Heindel W, Lackner K. Acta Radiol. 2000;41:634.
96. Sullentrop F, Moka D, Neubauer S, Haupt G, Engelmann U, Hahn J, Schicha H. NMR Biomed. 2002;15:60.
97. Mairiang E, Hanpanich P, Sriboonlue P. Magn. Reson. Imaging. 2004;22:715.
98. Bak M, Thomsen JK, Jakobsen HJ, Petersen SE, Petersen TE, Nielsen NC. J. Urol. 2000;164:856.
99. Bell JD, Bhakoo KK. NMR Biomed. 1998;11:354.
100. Lim AK, Patel N, Hamilton G, Hajnal JV, Goldin RD, Taylor-Robinson SD. Hepatology 2003;37:788.
101. Changani KK, Jalan R, Cox IJ, Ala-Korpela M, Bhakoo K, Taylor-Robinson SD, Bell JD. Gut 2001;49:557.
102. Mann DV, Lam WW, Magnus Hjelm N. So NM, Yeung DK, Metreweli C, Lau WY. Gut 2002;50:118.
103. Leij-Halfwerk S, Dagnelie PC, Van Den Berg JW, Wilson JH, Sijens PE. Clin. Sci. (London) 2000;98:167.
104. Leij-Halfwerk S, Agteresch HJ, Sijens PE, Dagnelie PC. Hepatology 2002;35:421.
105. Mann DV, Lam WW, Hjelm NM, So NM, Yeung DK, Metreweli C, Lau WY. Ann. Surg. 2002;235:408.
106. Mann DV, Lam WW, Hjelm NM, So NM, Yeung DK, Metreweli C, Lau WY. Hepatology 2001;34:557.
107. Jensen JE, Miller J, Williamson PC, Neufeld RW, Menon RS, Malla A, Manchanda R, Schaefer B, Densmore M, Drost DJ. Br. J. Psychiatry. 2004;184:409.
108. Bluml S, Tan J, Harris K, Adatia N, Karme A, Sproull T, Ross B. J. Comput. Assist. Tomogr. 1999;23:272.
109. Hamakawa H, Murashita J, Yamada N, Inubushi T, Kato N, Kato T. Psychiatry. Clin. Neurosci. 2004;58:82.
110. Yildiz A, Demopulos CM, Moore CM, Renshaw PF, Sachs GS. Biol. Psychiatry. 2001;50:3.
111. Silverstone PH, Rotzinger S, Pukhovsky A, Hanstock CC. Biol. Psychiatry. 1999;46:1634.
112. Kato T, Murashita J, Kamiya A, Shioiri T, Kato N, Inubushi T. Eur. Arch. Psychiatry Clin. Neurosci. 1998;248:301.
113. Estilaei MR, Matson GB, Payne GS, Leach MO, Fein G, Meyerhoff DJ. Alcohol Clin. Exp. Res. 2001;25:1213.
114. Rango M, Bozzali M, Prelle A, Scarlato G, Bresolin N. J. Cereb. Blood. Flow. Metab. 2001;21:85.
115. Bluml S, Seymour KJ, Ross BD. Magn. Reson. Med. 1999;42:643.
116. von Kienlin M, Beer M, Greiser A, Hahn D, K Harre, H Kostler, W Landschutz, T Pabst, Sandstede J, Neubauer S. J. Magn. Reson. Imaging. 2001;13:521.
117. Schocke MF, Zoller H, Vogel W, Wolf C, Kremser C, Steinboeck P, Poelzl G, Pachinger O, Jaschke WR, Metzler B. Magn. Reson. Imaging. 2004;22:515.
118. Schocke MF, Metzler B, Wolf C, Steinboeck P, Kremser C, Pachinger O, Jaschke W, Lukas P. Magn. Reson. Imaging. 2003;21:553.
119. Beer M, Seyfarth T, Sandstede J, Landschutz W, Lipke C, Kostler H, von Kienlin M. Harre K, Hahn D, Neubauer S. J. Am. Coll. Cardiol. 2002;40:1267.
120. Beer M, Sandstede J, Weilbach F, Spindler M, Buchner S, Krug A, Kostler H, Pabst T, Kenn W, Landschutz W, von Kienlin M, Toyka KV, Ertl G, Gold R, Hahn D. Rofo Fortschr Geb Rontgenstr Neuen Bildgeb Verfahr 2001;173:399.
121. Beer M, Viehrig M, Seyfarth T, Sandstede J, Lipke C, Pabst T, Kenn W, Harre K, Horn M, Landschutz W, von Kienlin M, Neubauer S, Hahn D. Radiologe. 2000;40:162.
122. Butterworth EJ, Evanochko WT, Pohost GM. Ann. Biomed. Eng. 2000;28:930.
123. Beer M, Sandstede J, Landschutz W, Viehrig M, Harre K, Horn M, Meininger M, Pabst T, Kenn W, Haase A, von Kienlin M, Neubauer S, Hahn D. Eur. Radiol. 2000;10:1323.
124. Buchthal SD, Noureuil TO, den Hollander JA, Bourge RC, Kirklin JK, Katholi CR, Caulfield JB, Pohost GM, Evanochko WT. J. Cardiovasc. Magn. Reson. 2000;2:51.
125. Negendank W. NMR Biomed. 1992;5:303.
126. Arias-Mendoza F, Smith MR, Brown TR. Acad. Radiol. 2004;11:368.
127. Zakian KL, Shukla-Dave A, Meyers P, Gorlick R, Healey J, Thaler HT, Huvos AG, Panicek DM, Koutcher JA. Cancer Res. 2003;63:9042.
128. Kettelhack C, Wickede M, Vogl T, Schneider U, Hohenberger P. Cancer 2002;94:1557.
129. Leij -Halfwerk S, van den Berg JW, Sijens PE, Wilson JH, Oudkerk M, Dagnelie PC. Cancer Res. 2000;60:618.

130. Ronen SM, Leach MO. Breast Cancer Res. 2001;3:36.
131. Payne GS, Dowsett M, Leach MO. The Breast 1994;3:20.
132. Chung YL, Troy H, Banerji U, Jackson LE, Walton MI, Stubbs M, Griffiths JR, Judson IR, Leach MO, Workman P, Ronen SM. J. Natl. Cancer Inst. 2003;95:1624.
133. Martino R, Crasnier F, Chouini-Lalanne N, Gilard V, Niemeyer U, De Forni M, Malet-Martino. J. Pharmacol. Exper. Therap. 1992;260:1133.
134. Rodrigues LM, Maxwell RJ, McSheehy PMJ, Pinkerton CR, Robinson SP, Stubbs M, Griffiths JR, Br. J. Cancer 1997;75:62.
135. Mancini L, Payne GS, Dzik-Jurasz AS, Leach MO. Magn. Reson. Med. 2003;50:249.
136. Payne GS, Pinkerton CR, Bouffet E, Leach MO. Magn. Reson. Med. 2000;44:180.
137. Robitaille P-M, Robitaille P, Brown GJ,. Brown G. J. Magn. Reson. 1991;92:73.
138. Govindaraju V, Young K, Maudsley AA. NMR Biomed. 2000;13:129.
139. Deicken RF, Calabrese G, Raz J, Sappey-Marinier D, Meyerhoff D, Dillon WP, Weiner MW, Fein G. Biol. Psychiatry 1992;32:628.
140. Hubesch B, Sappey-Marinier D, Roth K, Meyerhoff DJ, Matson GB, Weiner MW. Radiology 1990;174:401.
141. Jensen JE, Drost DJ, Menon RS, Williamson PC. NMR Biomed. 2002;15:338.
142. Harris RC, Hultman E, Nordesjo LO. Scand. J. Clin. Lab. Invest. 1974;33:109.
143. Bylund-Fellenius AC, Walker PM, Elander A, Holm S, Holm J, Schersten T. Biochem. J. 1981;200:247.
144. Dawson M, Allan RJ, Watson TR. Br. J. Clin. Pharmacol. 1982;14:453.
145. Taylor DJ, Styles P, Matthews PM, Arnold DA, Gadian DG, Bore P, Radda GK. Magn. Reson. Med. 1986;3:44.
146. Rees D, Smith MB, Harley J, Radda GK. Magn. Reson. Med. 1989;9:39.
147. Newham DJ, Cady EB. NMR Biomed. 1990;3:211.
148. Venkatasubramanian PN, Mafee MF, Barany M. Magn. Reson. Med. 1988;6:359.
149. Cady EB. J. Magn. Reson. 1990;87:433.
150. Roth K, Hubesch B, Meyerhoff DJ, Naruse S, Gober JR, Lawry TJ, Boska MD, Matson GB, Weiner MW, J. Magn. Reson. 1989;81:299.
151. Meyerhoff DJ, Boska MD, Thomas AM, Weiner MW. Radiology. 1989;173:393.
152. Blackledge MJ, Styles P. J. Magn. Reson. 1989;83:390.
153. Gruetter R, Fusch C, Martin E, Boesch C. Magn. Reson. Med. 1993;29:7.
154. Brown TR, Stoyanova R, Greenberg T, Srinivasan R. Murphy-Boesch J. Magn. Reson. Med. 1995;33:417.
155. Newcomer BR, Boska MD. Magn. Reson. Med. 1999;41:486.
156. Bottomley PA, Ouwerkerk R. J. Magn. Reson. Series B 1994;104:159.
157. Yongbi NM, Leach MO, Payne GS, Collins DJ. NMR Biomed. 1992;5:95.
158. Buchthal SD, Thoma WJ, Taylor JS, Nelson SJ, Brown TR. NMR Biomed. 1989;2:298.
159. Luyten PR, Groen JP, Vermeulen JW, den Hollander JA. Magn. Reson. Med. 1989;11:1.
160. Thomsen C, Jensen KE, Henriksen O. Magn. Reson. Imaging. 1989;7:231.
161. Moller HE, Vermathen P, Rummeny E, Wortler K, Wuisman P, Rossner A, Wormann B, Ritter J, Peters PE. NMR Biomed. 1996;9:347.
162. Meyerspeer M, Krssak M, Moser E. Magn. Reson. Med. 2003;49:620.
163. Schindler R, Krahe T, Neubauer S, Hillenbrand H, Entzeroth C, Horn M, Lackner K, Ertl G. Rofo Fortschr Geb Rontgenstr Neuen Bildgeb Verfahr 1992;157:452.
164. Neubauer S, Krahe T, Schindler R, Hillenbrand H, Entzeroth C, Horn M, Bauer WR, Stephan T, Lackner K, Haase A *et al.* Magn. Reson. Med. 1992;26:300.
165. Blackledge MJ, Oberhaensli RD, Styles P, Radda GK. J. Magn. Reson. 1987;71:331.
166. Straubinger K, Jung WI, Bunse M, Lutz O, Kuper K, Dietze G. Magn. Reson. Imaging. 1994;12:121.
167. Thomsen C, Jensen KE, Henriksen O. Magn. Reson. Imaging. 1989;7:557.
168. Jung WI, Widmaier S, Bunse M, Seeger U, Straubinger K, Schick F, Kuper K, Dietze G, Lutz O. Magn. Reson. Med. 1993;30:741.
169. Noggle JH, Schirmer RE. The Nuclear Overhauser Effect, Academic Press: New York and London, 1971.
170. Bachert P, Bellemann ME. J. Magn. Reson. 1992;100:146.
171. Murphy-Boesch J, Stoyanova R, Srinivasan R, Willard T, Vigneron D, Nelson S, Taylor JS, Brown TR. NMR Biomed. 1993;6:173.
172. Luyten PR, Bruntink G, Sloff FM, Vermeulen JW, van der Heijden JI, den Hollander JA. Heerschap A. NMR Biomed. 1989;1:177.
173. Meninger M, Landschutz W, Beer M, Seyfarth T, Horn V, Pabst T, Haase A, Hahn D, Neubauer S, von Kienlin M. Magn. Reson. Med. 1999:41:657.

Radio Frequency Coils for Magnetic Resonance Spectroscopy

Boguslaw Tomanek
Institute for Biodiagnostics, Winnipeg, Manitoba, Canada

The Requirements

Localized magnetic resonance spectroscopy (MRS) as well as magnetic resonance imaging (MRI) require both maximal signal-to-noise ratio (SNR) and radio frequency (rf) field (B_1) homogeneity. While MRI allows the application of post-processing methods, such as correction of image intensity to correct B_1 inhomogeneities, MRS is more demanding from this point of view leaving very little opportunity for post-processing and requiring mostly hardware improvement. In addition, due to the smaller volume of interest (VOI) and particularly low metabolite concentration, there is less signal available in MRS than in MRI. The time required to obtain good spectra is long pushing the SNR requirements to the limits.

The Issues

Unfortunately, when considering rf probe construction the requirements of high SNR and good B_1 homogeneity usually conflict. The SNR depends on many factors such as the strength of the magnetic field, geometry, resistance and quality factor (Q) of the coil, sample size, filling factor of the coil, type of the reception (linear or circular), etc. The B_1 field distribution depends on the geometry of the coil, its type (transmit and receive or transmit/receive), and the material used for the coil construction.

When designing an rf coil all of these factors plus patient access to the coil and the direction of the magnetic field relative to B_1 must be considered. Therefore whilst a coil may work very well, providing good SNR and B_1 homogeneity, at a low frequency (say 1.5 T) it may not work so well (or even not at all) at a higher frequency (say 3 T). A trade-off amongst all these factors is inevitable and there is no simple, consistent recipe for making a perfect rf coil that fulfills all the requirements for MRS.

With this knowledge of the problems we shall consider some of the requirements for the MRS coil: SNR, B_1 distribution, coil geometry, method of reception as well as some other factors. For this discussion we will be ignoring other potential problems associated, for example, with relaxation times, pulse parameters or even eddy currents induced in the coil, gradients coil, or in the cryostat due to the short TE (fast gradient switching) required frequently in MRS.

The first expression describing the NMR signal was derived by Abragam [1], who showed that the electromagnetic force (emf) induced by the nuclear magnetization in the receiving coil can be expressed as:

$$\Psi_{\mathrm{rms}} \propto K\eta M_0\,(\mu_0 Q\omega_0 V_{\mathrm{c}}/4FkT_{\mathrm{c}}\Delta f)^{1/2} \qquad (1)$$

where K is numerical factor depending on the coil geometry; η is the filling factor, i.e. a measure of the fraction of the rf field volume occupied by the sample; M_0 is the magnetization (proportional to the magnetic field strength); μ_0 is the permeability of free space; Q is the quality factor of the coil; ω_0 is the Larmor frequency; V_{c} is volume of the coil; F is the noise figure of the preamplifier; k is Boltzmann constant; T_{c} is the probe temperature; Δf is the bandwidth (in Hertz) of the receiver. As one can notice, the SNR is proportional to the 3/2 power of the magnetic field ($M_0 \sim \omega_0$). This is true assuming that other factors are independent of frequency. This is an important statement that will be analyzed in detail later.

The above revelation explains the historical tendency to introduce stronger and stronger magnets in an effort to increase SNR. Therefore, magnets generating a magnetic field of 20 T were produced for *ex vivo* MRS, while whole body MRI systems have reached 7 T, and even higher field magnets are under construction.

However, a closer analysis of the dependence of noise mechanism with frequency reveals a less favorable SNR relationship. The rule of thumb is a linear relationship between the SNR and the magnetic field strength. While the Equation (1) gives a reasonable estimate of the SNR, it does not consider other factors such as rf coil shape, preamplifier noise, and other electronic components whose performance depends on, and usually degrades with, the frequency. Thus, innocent engineers constructing rf coils for MRI systems are often blamed for insufficient increase in SNR as expected from MR theory.

Probably the most comprehensive summary of the SNR and its relationship with MR hardware was given by Hoult *et al.* [2,3], who applied reciprocity theory and

Graham A. Webb (ed.), Modern Magnetic Resonance, 1163–1170.
© 2008 *Springer.*

considering the sources of noise they obtained:

$$\psi_{\mathrm{rms}} = \frac{K(B_1)_{xy} V_s N \gamma \bar{\lambda}^2 I(I+1)}{7.12 k T_{\mathrm{s}}} \cdot \left(\frac{p}{F k T_{\mathrm{c}} l \zeta \Delta f} \right)^{1/2} \times \frac{\omega_0^{7/4}}{[\mu \mu_0 \rho(T_{\mathrm{c}})]^{1/4}} \qquad (2)$$

where $K(B_1)_{xy}$ is the effective field over the sample volume produced by unit current flowing in the receiving coil, p is the perimeter of the conductor, l is the length of the conductor. The above factors are dependent only on coil geometry. T_{c} is the temperature of the coil, $\rho(T_{\mathrm{c}})$ is the resistivity of the material from which the coil is made, ζ is the proximity factor, F is the quality of the preamplifier.

From the above equation one can see that SNR seems to be proportional to $\omega_0^{7/4}$. However, in the above equation Q and η have been replaced by a function ζ, that is also ω_0 dependent. Hence, SNR is not always proportional to the 7/4 power of the frequency. A careful reader will also notice that SNR depends on the type and geometry of the coil (factors: K, l, ρ).

The Solenoid Coil and Saddle-Shape Coil

As seen from Equation (1) SNR can be improved by an increase of the Q factor, which depends on the coil resistance and inductance. The Q of a solenoidal coil is proportional to $\omega_0^{1/2}$ only well below self-resonance frequency of the coil, but when approaching the self-resonance frequency the Q drops away from the $\omega^{1/2}$ line and prevents further increase of the SNR as one could expect from Equation (2). The only solution is then to decrease the self-resonance frequency of the coil by the reduction of the coil inductance or/and resistance. This can be achieved by reducing the number of turns for a solenoidal coil. A detailed analysis of solenoidal and saddle-shape coils [2], the most common coils producing very homogenous rf field, yield to the conclusion that the solenoidal coil performance is about three times better that the saddle-shape coil with comparable dimensions. As shown above, a solenoidal coil would be a very good candidate for the rf probe providing good B_1 homogeneity and good sensitivity within a reasonable range of frequencies. However, further consideration should be given when the direction of the main magnetic field is considered. To produce the NMR phenomenon (to flip the magnetization), the direction of the rf field must be perpendicular to the main magnetic field. This creates additional constraints when selecting an rf coil for MRS and MRI. Unfortunately, the direction of the rf field produced by the solenoidal coil (along its long axis) prevents almost all applications for horizontal bore magnets. Such a coil could not be made for a human head, for example, since it would require the head to bend by 90°.

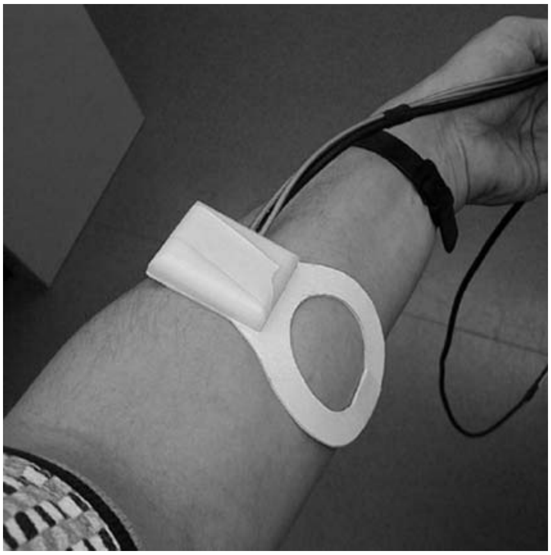

Fig. 1. Surface coil for 3 T MR system (National Research Council, Institute for Biodiagnostics, Winnipeg, Canada).

However, a single loop solenoidal probe, namely a surface coil (Figures 1 and 2), overcomes this obstacle. In addition, in MRS we are interested in small voxels to detect small abnormalities. Thus a volume coil is usually not required or even not welcome. A surface coil (Figure 2A) provides a very good SNR produces but also a very inhomogenous B_1 field (Figure 2B). Along the axis the B_1 field can be calculated, neglecting interaction of the tissue with the rf field, based on Bio-Savart law:

$$B_1(x) = \frac{\mu_0 I}{2} \frac{a^2}{\sqrt{(a^2 + x^2)^3}} \qquad (3)$$

where a is the radius of the coil, x is the axial distance from the center of the coil and I is the current flowing through the coil.

Surface Coil

So far we have concluded that the best solution from the point of view of the SNR is the application of the surface coil. Further improvement in SNR by up to $\sqrt{2}$ can be achieved by the application of the quadrature surface coil [4,5]. However, the perfect quadrature rf coil requires the creation of equal and orthogonal B_1 fields (Figure 3), which is difficult to achieve for a surface coil. The most common configuration for the quadrature surface coil [so-called circular polarized (CP) coil] is the use of a shaped butterfly coil and a standard surface coil to

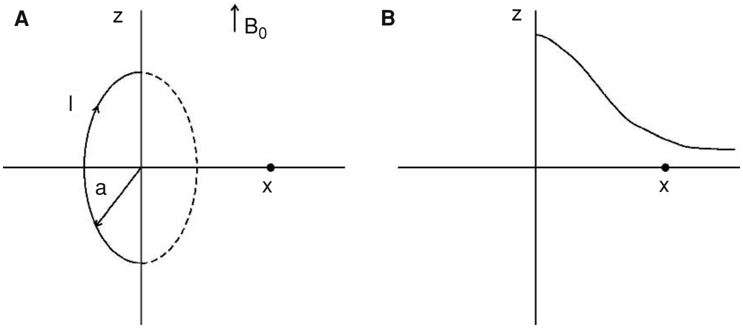

Fig. 2. (A) Geometrical model of the surface coil: A current I flows in the ring of a radius. (B) The B_1 field magnitude generated by the surface coil along the x-axis.

create two orthogonal or, more often—nearly orthogonal rf fields. While such a coil provides larger field of view (FOV) it gives only modest (less than $\sqrt{2}$) increase in SNR due to the lack of perfect perpendicularity or/and unequal amplitude of B_1 fields. The quadrature surface coil requires, however, less power when compared to the linear coil (LP coil). Let us now answer a question: what is the optimum diameter of the surface coil to maximize SNR within the specific VOI? In attempt to find the answer we will take a closer look at the sources of noise. Neglecting radiation losses, the noise picked up by the receiver (N) is proportional to the sum of the effective resistance of the sample (R_s) and the resistance of the coil itself (R_c):

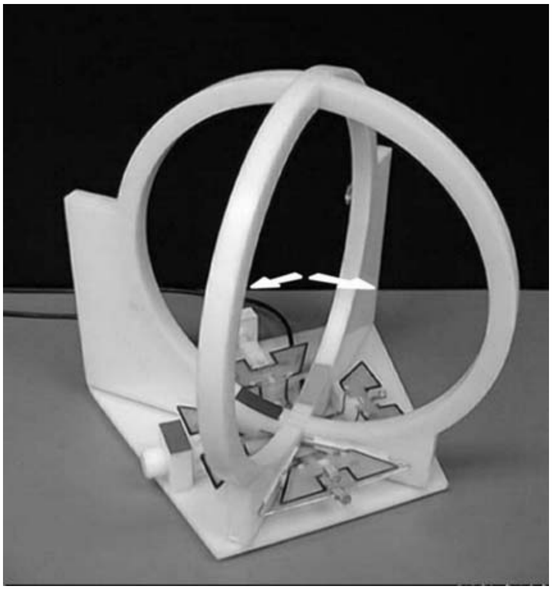

Fig. 3. Two surface coils assembled into the quadrature probe. The two perpendicular B_1 fields are marked with arrows (National Research Council, Institute for Biodiagnostics, Winnipeg).

$$N \propto \sqrt{R_s + R_c} \tag{4}$$

The resistance of the sample comes from two sources: dielectric losses (that can be minimized using distributed capacitance and proper capacitor shielding) and inevitable inductive losses associated with rf induced eddy currents within the sample. Hoult and Lauterbur [3] showed that

$$R_s \propto \omega_0^2 B_1 b^5 \tag{5}$$

where ω_0 is the Larmor frequency, B_1 is the rf field produce by unit current, b is the sample radius.

One can see that the sample losses increase with frequency and become predominant at a higher frequency. It can be shown [5,6] that in such a case SNR per unit volume depends on the surface coil radius a as:

$$SNR \propto 1/a \tag{6}$$

This equation, as explained in detail by Hayes and Axel [6] is exact only at the surface of the coil, however, it gives a good estimate of the dependence of the SNR of the coil radius. Thus, the smaller the coil the higher SNR hence surface coils which are so popular in MRS. The diameter of a surface coil may be chosen to give maximum SNR at a particular point within the sample. If sample loses are dominant (above 1T), maximum SNR can be obtained for $a = d/\sqrt{5}$ where a is the coil radius and d is the distance from the coil center [7,8]. When the coil losses are dominant [9] then the optimum SNR occurs for the coil radius $a = d\sqrt{2}$. The exact optimum diameter depends on the frequency and the sample. For example, at 3T and 1 cm^3 VOI placed at $d = 2.5$ cm from the coil the maximum SNR occurs, as found experimentally, when the coil diameter is 4.0 cm. This diameter lies between the coil loss dominant case (7.1 cm) and the sample loss dominant case (2.25 cm).

Superconducting rf Coils

The noise in NMR comes also from the coil and depends on the temperature:

$$R_c \propto \sqrt{\mu\mu_0\omega_0\rho(T_c)} \tag{7}$$

This equation could be used to decrease noise thus increase SNR by decreasing the coil resistance. The recent introduction of high-temperature superconductive materials [10] allowed new possibilities for this increase of SNR. This new technology, however, brings new technical challenges, such as cryocooling devices, high-temperature superconducting material, patient safety, etc., and has not yet found clinical applications. It is mostly used in micro-MRI research[10,11] and in chemistry MR labs.

Phased Array

The success of the surface coils in producing high SNR also, unfortunately, reduces FOV. To rectify this limitation a phased array technology was introduced to extend the FOV over the sample [12]. Each element of the array, coupled to an independent receiver channel, works as an independent surface coil maximizing SNR and increasing FOV (Figure 4). Recently, the so-called parallel imaging techniques using phased array have been introduced into MRI reducing the total acquisition time [13,14]. Despite the costs and complexity of the electronics 8, 16, or even 32-channel phased array coils are become a clinical standard. Because complexity of the MRS experiment (e.g. requirements of the phase control of rf pulses) the phased array technology is only slowly being introduced into MRS.

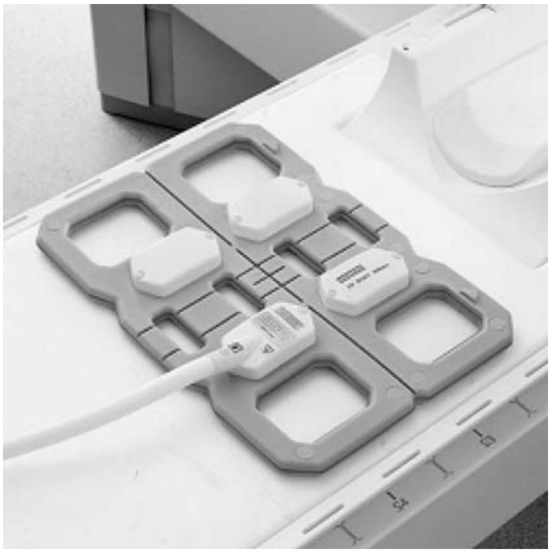

Fig. 4. Phased array (Siemens, Germany).

B_1 Homogeneity Vs. SNR

In quantitative MRS, metabolite concentration cannot be properly evaluated when the rf coil produces an inhomogenous B_1 field. Even excellent MRS techniques [15,16] require homogenous transmit and receive rf fields. The inhomogenous B_1 field causes a variety of inconveniences, such as imperfect spatial localization [17,18], poor water suppression [19], and contamination from outside the voxel of interest [20]. B_1 inhomogeneity also prevents the quantification of metabolites concentration as the spectra would then depend on the tissue–coil orientation. This would cause different spectra from the same tissue, which is of particular concern for heterogenous tissues such as tumors. Therefore, the application of rf coils producing spatially uniform B_1 field is preferred. This conclusion contradicts the previous one we recorded, i.e. that the best SNR is produced by a surface coil, which unfortunately produces a very inhomogenous rf field. Volume coils, such as the saddle coil, the solenoidal coil, the Adelman-Grant, the Helmholtz pair, and birdcage (Figure 5), etc. produce very homogenous field. Unfortunately, they suffer from low sensitivity and

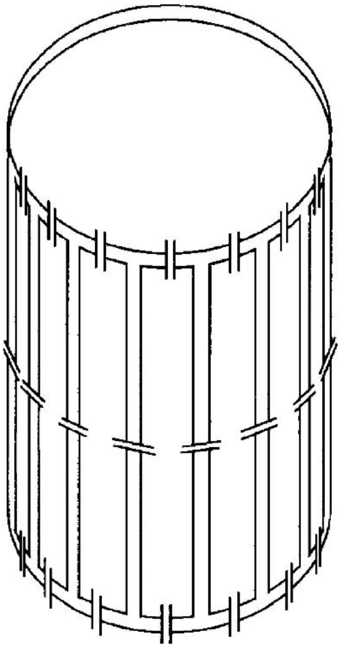

Fig. 5. Geometrical model of the 16-element birdcage rf coil.

high power requirements compared to the surface coil. Because the surface coil, as stated before, generates a very inhomogenous rf field, it provides spatially dependent flip angles, which is particularly inconvenient when more than one pulse is used—as is common in MRS.

There are few methods, none of these being perfect, that try to deal with this problem. One of them is the application of adiabatic rf pulses [21,22], that, however, are suitable only for a single-shot techniques. They also require high power [thus increased specific absorption ratio (SAR)], strong gradients, and they also limit echo time (TE). A very elegant solution was proposed by Bendall [23] who proposed the application of multiple inhomeogenous rf coils, that take advantage of the spatial dependence of flip angles to increase the localization and allow a larger FOV.

Transmit-Only and Receive-Only Coils

So far we have only considered coils that are transmit and receive (T_x/R_x). In this case the excitation and receive rf profiles are identical. However, in most clinical systems the standard configuration is volume coil—transmit-only (T_x), local coil—receive-only (R_x). This arrangement comes mostly from manufacturer convenience, since in this case the sample is excited always with the same, usually body rf coil and SAR is calculated for this one coil only. This configuration allows also easy attaching other receive coils dedicated for any particular body part. The set-up also avoids problems with inhomogenous excitation, yet reception remains non-uniform. Other difficulties with separate T_x and R_x coils are associated with SAR limits: the large body coil requires a lot of rf power (typically for 3 T clinical systems up to 30 kW) due to the unnecessary excitation of organs outside the VOI. The coupling between the coils [24–26] is yet another problem. All these challenges increase rapidly with the field strength.

Leaving aside SAR issues (which is particularly a pulse sequence issue) we will consider decoupling. The decoupling of the coils is needed to avoid any current being generated in the receive coil during the transmission. The problem here is that, during the transmission, mutual inductance between coils current is induced in the receiving coil, which generates an opposing B_1 field. During the receiving period the noise currents produced by the larger T_x coil are also induced in the receive coil. Both effects cause the degradation of the SNR and artifacts in MRI. To separate transmit and receive coils, crossed diodes (Figure 6) are used in series with the T_x coil as well as in parallel with the tuning capacitor of the receive coil. The solution as proposed by Bendall and Edelstein *et al.* [24] is to detune the receive coil during the power transmission and detune the T_x coil during the receiving period. The cross diodes in the T_x coil conduct during the transmit (high voltage) thus the coil is resonating at the Larmor frequency; during the receive period, when the current is small, the open diodes prevent the current from flowing in the T_x coil. An alternative to using active switching may also be used: the receive coil is actively decoupled using externally driven PIN diodes. The diodes are placed at a certain distance from the capacitance so the cable creates an inductance between the diodes and the capacitance. During the transmission the diodes are switched on and create a short-circuit. This way the R_x coil is not active. The same assembly could also be used without an external drive (passive mode): during transmission the small current, induced in the R_x coil by T_x coil turns the diodes on and such a circuit has a high impedance and prevents current flow in the R_x coil. During the reception the current is low the diodes are by-passed by the signal. In addition the T_x and $R_x$coils can be design to be electrically orthogonal each to other if the space allows.

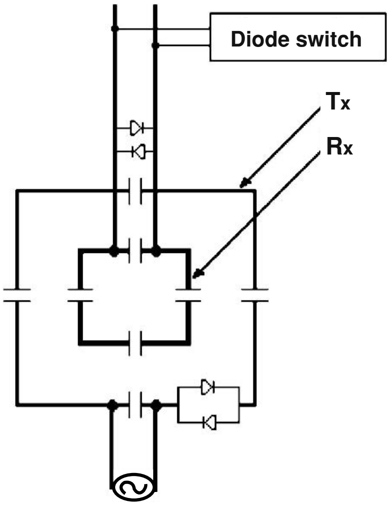

Fig. 6. Decoupling model of the transmit and receive coils. The cross diodes in the transmit coil conduct during the transmission while diodes in the receive coil are open during the receiving. The receive coil is actively decoupled using externally driven PIN diodes during the transmission.

At higher magnetic fields (>3T), when the rf wavelength within the sample becomes comparable with the sample size, and a body rf coil is used for the excitation, a new problem arises: the complex interaction between the body tissue and the rf field. This problem is discussed in detail by Hoult [27].

The other problem when using the separate transmit and receive coils is that the relative direction of B_1 field may be different for transmit and receive coils. This may also degrade the signal [28–30] as well efficacy of the shimming procedures [31,32].

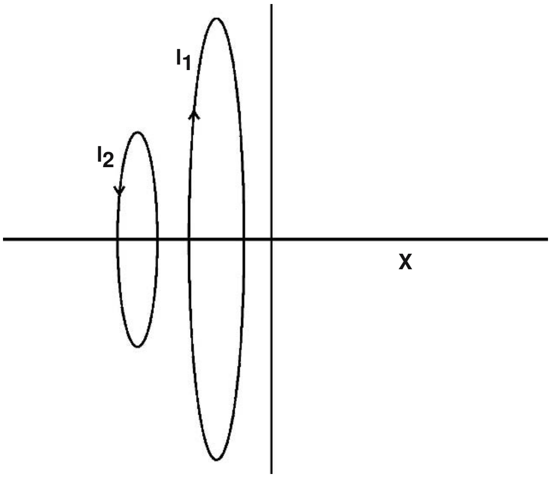

Fig. 7. Multi-ring surface coil assembly. Currents I_1, I_2 flow in opposite directions to compensate B_1 inhomogeneity of each separate surface coil.

Local rf Coils with Improved B_1 Homogeneity and SNR

An interesting solution [33,34] to generate identical fields for both excitation and receiving periods was proposed: the combination of surface coil sensitivity with volume coil homogeneity. This idea uses two or more inductively coupled rings of different diameter, carrying current in opposite directions (Figure 7). Such an assembly produces homogenous, identical excitation and receiving B_1 in the desired region of interest while providing SNR comparable with the surface coil. While this coil seems to be perfect for MRS its major disadvantage is fixed VOI, what in practice means that for each VOI another rf coil should be constructed. The possible applications of this coil include skin or thyroid MRS, where the VOI varies little between subjects.

Another solution to increase SNR is the application of rf shields [35]. This concept works particularly well for breast MR imaging and spectroscopy. If the B_1 field is perpendicular to the chest wall, a Helmholtz pair probe gives good field homogeneity over the breast and good chest penetration, but significant chest power dissipation with concomitant loss of SNR. Weak B_1 fields covering the large volume could generate substantially larger losses than bigger fields confined to a smaller volume. Thus, the combination of the Helmholtz pair with the rf shielding of the chest wall away from the breast brought a substantial improvement of up to a factor of two when compared with the standard breast rf coil.

Implanted rf Coils

For imaging of some small, deeper organs, for example, the spinal cord, the rf surface coils are used but due to their field drop with the distance from the coil, they bring even more challenges in the coil design. Because of that the SNR within the VOI is compromised due to the low and inhomogenous B_1 field. The noise source from the "disturbing" tissue (e.g. fat) between the coil and the VOI, where the B_1 is strong, is yet another source of noise. One of the possible ways of dealing with this problem is the application of implanted rf coils [36,37]. Briefly, the implanted coil consists of a loop of wire (the "actual" coil generating and receiving rf signal) tuned to the Larmor frequency, and a matching ring inductively coupled to the loop. Thus, no electrical connections between the implanted coil and the external matching network are required. Such an implanted rf coil provides better SNR than the surface coils, thanks to their close proximity to the VOI. It also brings some disadvantages: the procedure can no longer be considered non-invasive, and as such its application to human MRS becomes questionable. In addition, implanted coils are vulnerable to various failure modes including mechanical and electrical. The blood and body fluids can change the coil loading or even its position, thus SNR during the MRS experiment. In some cases matching also becomes difficult due to the restricted access of the matching coil and the loop.

Microcoils

When using ultra-high fields and ultra-low samples ($\sim$1 μl) new challenges arise such as susceptibility, low filling factors, increased coil noise, skin depth, etc. As shown [38,39] for the coils of diameter of order of millimeters or less the major source of the noise comes from the coil. Therefore, special attention must be placed to the resistance of the coil. A so-called single and multilayer rf microcoil, using metallic foil rather than wires was used to enable very high field *ex vivo* MRS [40].

The performance of the standard rf surface coil can also be surpassed by a microstrip rf surface coil for extremely high-field MRI as reported by Zhang *et al.* [41]. This design is based on the microstrip transmission line concept that does not require the use of lumped elements. The microstrip surface coil can be used up to 500 MHz. Such a coil gives about 20% better SNR when compared to the standard surface coil [41]. This concept can also be used with any other configurations such as quadrature volume or phase array rf coils. Such an assembly resonates at the frequency $f = c/2L\sqrt{\varepsilon_{\text{eff}}}$ where c is the speed of light, L length of the coil, ε_{eff} dielectric constant of the material. This concept has not yet found a clinical use but may be promising.

Dual Frequency rf Coils

Quantification of the tissue metabolites by heteronuclear MRS can be achieved using dual frequency rf coils. The dual frequency coils allow simultaneous measurement of two nuclei frequencies, without disruptions associated with exchanging coils for imaging and spectroscopy examinations. One is usually ^{1}H while the other is phosphorus (^{31}P), sodium (^{23}Na), or other nuclei (^{23}Na). The proton frequency is often used for high-resolution imaging that allows lesion localization while the other frequency is used for spectroscopic lesion analysis. The proton frequency also provides the sensitivity needed for shimming. Dual frequency coils have to deliver SNR of the single frequency rf coil as well as produce homogenous rf field over the sample volume. To achieve these needs double-tuned quadrature birdcage coils were developed. One example is a design based on two coaxial birdcage coils resonating at ^{31}P and ^{1}H frequencies each. Such a coil provides excellent ^{31}P performance although lower SNR for ^{1}H when compared to a single frequency ^{1}H coil. This design allows altering the ^{31}P coil length thus can provide better SNR sacrificing however B_1 [42]. Another solution is to use the same sized coils and tune every other leg of the coil to the desired frequency, using trap circuits and inductive matching to optimize the coil [43,44].

An elegant design based on transmission line resonators for a volume quadrature, double-tuned coil was also proposed by Vaughan [45]. In our work to even further increase SNR for two or more frequencies, a dual frequency surface coil was designed using frequency splitting circuitry [46]. This construction allows concurrent ^{1}H and ^{31}P MRS and provides the same B_1 homogeneity for both frequencies almost without reducing SNR when compared to the single frequency rf coils. Such a design was further improved by combining a multi-ring coil concept [47] with a splitting circuit. This coil provides better SNR than a volume coil within the specified VOI, but about 70% of the SNR of the single frequency surface coil, however, it creates homogenous and identical B_1 fields for both frequencies over the desired VOI. The dual frequency coils require dual frequency receive and transmit channels, which are still not standard in clinical MRI systems, hence their limited application.

Summary

This chapter describes the most common rf coils for MRS as well as possible methods of improving SNR and B_1 homogeneity. As concluded, there is no perfect rf coil for MRS. Compromises must be made among SNR, B_1 homogeneity, voxel size, total experiment time, size, and position of VOI. The choice of the coil depends on the application, field strength, available MRI system, and the patient position. The volume coil—transmit and surface or local coil receive-only seem to be the most effective, yet not perfect rf coil configuration.

Glossary of Terms

SNR	signal-to-noise ratio
B_1	rf field
M_0	magnetization
μ_0	permeability of free space
Q	quality factor of the coil
K	numerical factor depending on the coil geometry
η	filling factor
ω_0	Larmor frequency
V_c	volume of the coil
F	noise figure of the preamplifier
k	Boltzmann constant
T_c	probe temperature
Δf	bandwidth (in Hertz) of the receiver

References

1. Abragam A. The Principles of Nuclear Magnetism. Clarendon Press: Oxford, 1961, p 82.
2. Hoult DI, Richards RE. J. Magn. Reson. 1976;24:71.
3. Hoult DI, Lauterbur, PC. J. Magn. Reson.1979;34:425.
4. Chen CH, Hoult DI, Sank VJ. J. Magn. Reson. 1983;54: 324.
5. Hyde JS, Jesmianowicz A, Grists TM, Froncisz W, Kneeland JB. Magn. Reson. Med. 1987;4:179.
6. Hayes CE, Axel L. Med. Phys. 1985;12(5):604.
7. Edelstien WA, Foster TH, Schenk JF. The relative sensitivity of surface coils to deep lying tissue. Proceedings of the SMRM 4th Annual Meeting, London, 1985, p 964.
8. Wang J, Reykowski A, Dickas J. IEEE Trans. Biomed. Eng. 1995;42:908.
9. Chen CN, Hoult DI. Biomedical Magnetic Resonance Technology. Adam Hilger: Bristol, 1989, p 161.
10. Hill HDW. Solid State Commun. 1997;102:169.
11. Darrasse L, Ginefri JC. Biochemie. 2003;85:915.
12. Roemer PB, Edelstein WA, Hayes CE, Souza SP, Mueller OM. Magn. Reson. Med. 1990;16:192.
13. Sodickson DK, Manning WJ. Magn. Reson. Med. 1997;38: 591.
14. Pruessmann KP, Wieger M, Scheidegger MB, Boesiger P. Magn. Reson. Med. 1999;42:952.
15. Bottomley PA. Selective volume method for performing localized NMR spectroscopy. US Patent 4,480,228, 1984.
16. Frahm J, Merboldt KD, Hanicke W. J. Magn. Reson. 1987;72:502.
17. van Zijl PCM, Moonen CTW, Alger JR, Cohen JS, Chesnick SA. Magn. Reson. Med. 1989;10:256.
18. Lawry TJ, Kaczmar GS, Weiner MW, Matson GB. Magn. Reson. Med. 1989;9:299.
19. Moonen CTW, van Zijl PCM. J. Magn. Reson. 1990;88:28.
20. Lawry TJ, Kaczmar GS, Weiner MW, Matson GB. Magn. Reson. Med. 1989;9:299.

21. de Graaf RA, Nicolay K, Garwood M. Magn. Reson. Med. 1996;35:652.
22. de Graaf RA, Nicolay K, Garwood M. J. Magn. Reson. B. 1996;113:35.
23. Bendall MR. Chem. Phys. Lett. 1983;99(4):310.
24. Edelstein WA, Hardy CJ, Mueller OM. J. Magn. Reson. 1986;67:156.
25. Haase A. J. Magn. Reson. 1985;61:130.
26. Barberi EA, Gati JS, Rutt BK, Meonon RS. Magn. Reson. Med. 2000;43:284.
27. Hoult DI. J. Magn. Reson. Imaging. 2000;12:46.
28. Crowley MG, Evelhoch JL, Ackerman JJH. J. Magn. Reson. 1985;64:30.
29. Styles P, Smith MB, Briggs RW, Radda GK. J. Magn. Reson. 1985;62:397.
30. Chen CH, Hoult DI. Biomedical Magnetic Resonance Technology. Adam Hilger: Bristol, 1989, p 157.
31. van Zijl PCM, Moonen CTW, Alger JR, Cohen JS, Chesnick SA. Magn. Reson. Med. 1989;10:256.
32. Crozier S, Field J, Brereton IM, Moxon LN, Shannon GF, Doddrell DM. J. Magn. Reson. 1991;94:123.
33. Tomanek B, Ryner L, Hoult DI, Kozlowski P, Saunders JK. Magn. Reson. Imaging. 1997;15: 1199.
34. King S, Ryner L, Tomanek B, Sharp J, Smith I. Magn. Reson. Med. 1999;42:655.
35. Tomanek B, Hoult DI, Chen X, Gordon R. Magn. Reson. Med. 2000;43:917.
36. Silver X, Xu W, Mercer EV, Beck BL, Bossart EL, Inglis B, Mareci TH. Magn. Reson. Med. 2001;46:1216.
37. Arnder LL, Shattuck MD, Black RD. Magn. Reson. Med. 1996;35:727.
38. Cho Z, *et al*. Med. Phys. 1998;15:815.
39. Peck T, Magin R, Lautenbur P. J. Magn. Reson. B. 1995;108: 114.
40. Grant SC, Murhpy LA, Magin RL, Friedman G. IEEE Trans. Magn. 2001;37(4).
41. Zhang X, Ugurbil K, Chen W. Magn. Reson. Med. 2001;46: 443.
42. Fitzsimmons JR, Beck BL, Brooker HR. Magn. Reson. Med. 1993;30:107.
43. Matson GB, Vermathen P, Hill TC. Magn. Reson. Med. 1999;42:173.
44. Shen GX, Boada FE, Thulborn KR. Magn. Reson. Med. 1997;38:717.
45. Vaughan JT, Hetherington HP, Out JO, Pan JW, Pohost GM. Magn. Reson. Med. 1994;32:206.
46. Schnall MD, Subramanian H, Leigh JS, Chance B. J. Magn. Reson. 1985;65:122:
47. Volotovskyy V, Tomanek B, Corbin I, Buist R, Tuor UI, Peeling J. Magn. Reson. Eng. Concepts in Magnetic Resonance, Part B 2003;17B:11.

Spatially Resolved Two-Dimensional MR Spectroscopy *in vivo*

M. Albert Thomas[1], Amir Huda[1,2], Hyun-Kyung Chung[1], Nader Binesh[1], Talaignair Venkatraman[1], Art Ambrosio[1], and Shida Banakar[1]

[1] *Department of Radiological Sciences, University of California, Los Angeles, CA 90095, USA; and*
[2] *Department of Physics, California State University, Fresno, CA 93740, USA*

Introduction

Acquisition of three-dimensional (3D) spatially localized, water-suppressed one-dimensional (1D) ^{1}H MR spectra has been optimized in human tissues over the last two decades [1–6]. Introduction of automated MRS a decade ago has enabled a 1–2 min pre-scan to calibrate the flip-angle using the transmitter power, to adjust the static field homogeneity (B_0) using the linear gradient shim coils, and to optimize water suppression, which used to be an at least 15 min operation, facilitating the integration of clinical MRS protocols into routine MRI examinations [7]. In ^{1}H MR spectroscopy of human brain, spectral resonances due to methyl, methylene, and methine protons of N-acetylaspartate (NAA), glutamate/glutamine (Glx), creatine (Cr), choline (Ch), *myo*-inositol (mI), GABA, aspartate (Asp), N-acetylaspartyl-glutamate (NAAG), and other metabolites have been identified in the region of 0–4.5 ppm [2–12].

One-dimensional MRS *in vivo* is hampered by the fact that it is difficult to resolve a multitude of peaks existing over a small spectral range of approximately 300 Hz at 1.5 T. Spectral overlap of macromolecules, GABA, and glutathione with the methyl resonances of NAA, Cr, NAAG, and methylene resonances of Glx has also been reported [8,14–15]. Attempts have been made to quantify Glx [16], glucose [17], and other metabolites with only minimal success due to the difficulty in extracting this information from a region with many overlapping resonances. Using spectral-editing techniques, it is possible to select a particular J-coupled metabolite [2,14,18–20]. However, one major drawback of editing techniques is that only one metabolite is optimized at a time assuming that the multiplets of the J-coupled metabolites are well separated. Using the LC-Model post-processing algorithm, quantification of several metabolites in human brain *in vivo* has been reported recently using a basis-set of 10–20 different metabolite spectra *in vitro* [21–23].

Unlike the spectral editing techniques, which target one metabolite at a time, two-dimensional (2D) MRS can unambiguously resolve many overlapping peaks nonselectively *in vitro* as shown by Ernst and co-workers two decades ago using the vertical bore NMR spectrometers [24–25]. 2D-MR spectroscopy enables converting a crowded overlapping 1D MR spectrum to a better-resolved 2D spectrum through the addition of a spectral dimension. Instead of a standard 1D spectrum plotting intensity vs. a single-axis (i.e. chemical shift), 2D MR spectroscopy techniques produce a 2D spectrum plotting intensity vs. two axes, the dimensions of which depend on the specific 2D MR technique [25]. Better dispersion of several metabolite peaks and improved spectral assignment make the proposed technique more attractive. It seems natural to explore the clinical potentials of 2D MRS techniques of human tissues *in vivo*.

There have been several attempts during the last 15 years in the implementation and evaluation of 2D NMR spectroscopy on *in vivo* MRI scanners and MR spectrometers [26–30]. The aim of this chapter is to discuss the recent progress on the implementation of selected localized 2D MRS sequences on the whole body 1.5 T and higher field MRI scanners. This includes a summary of 1D spectroscopy with and without chemical shift imaging (CSI), followed by single- and multi-voxel based 2D spectroscopy dealing with coherent interactions such as chemical shift and J-coupling. A brief overview of potential artefacts in 2D spectroscopy and simulation is also included.

Single- and Multi-voxel Based 1D ^{1}H MR Spectroscopy

Clinical 1D MR spectroscopy has some important differences and challenges compared to MR imaging. Often how the challenges are resolved define the particular technique of spectroscopy with its limitations and advantages. Some of these basic challenges are pertinent to water and lipid suppression, spatial localization of the volume of interest (VOI) including single vs. multiple volume elements (voxel) as shown in Figure 1.

Graham A. Webb (ed.), Modern Magnetic Resonance, 1171–1183.
© 2008 *Springer.*

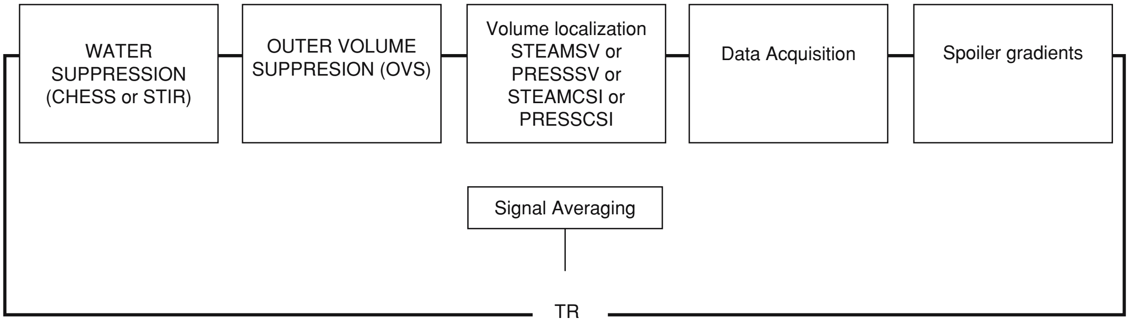
WATER SUPPRESSION (CHESS or STIR)
OUTER VOLUME SUPPRESION (OVS)
Volume localization STEAMSV or PRESSSV or STEAMCSI or PRESSCSI
Data Acquisition
Spoiler gradients
Signal Averaging
TR

Fig. 1. Different modules of 1D MRS protocol.

Water and Lipid Suppression

What makes MR imaging quite sensitive is the large concentration of water in biological tissue. However, the dominance of water limits spectroscopy since the metabolites are tens of thousands of times lower in concentration than water. Thus, in order to obtain a visible signal from the metabolites, MRS techniques must incorporate ways of minimizing or eliminating the water signals. This water suppression can be extended from changes in hardware for data acquisition (digitizers), pulse sequences, to post-processing software. The primary contribution stems from an addition of three frequency selective (water as the target frequency) radio frequency (rf) pulses with arbitrary flip-angles followed by a dephasing gradient to the pulse sequence. These pulses are commonly called the chemical shift selective saturation (CHESS) pulses [5,31]. Instead of water saturation using CHESS, an inversion recovery scheme can also be employed with a 180° frequency selective pulse on water such that excitation of the metabolites can be prolonged until the crossing of the water signal at the null point with known T_1 values [32].

Quite often the lipid signals from either within the VOI or outside of the VOI hold a similar challenge like water. In order to suppress the lipids, the same two approaches utilized in water suppression in terms of pulse sequence modification can also be applied here [33]. The most common approach is the use of frequency selective (targeted at lipids) pulses in conjunction with spatial selection around the edges of the brain called the outer volume saturation or suppression (OVS) slabs. Of course, post-processing software can also contribute to elimination of lipid signals.

Spatial Localization of the Volume

There is a fundamental difference between the localization done in imaging and spectroscopy. Imaging relies on acquisition of the entire proton signal (primarily water and fat) and the differences in frequencies of the signal are attributed to the spatial shifts introduced *via* the application of the frequency encoding gradients during signal sampling to reproduce the selected slice within a plane or a data point in volumetric MRI. A frequency encoding gradient cannot be used in spectroscopy during sampling because the differences in frequencies of metabolites sought after are due to the small chemical shifts and a frequency encoding gradient would corrupt this basic information. However, the demand for volume definition remains, whether single voxel or multiple voxel spectroscopy is done since the metabolite concentration information is sought from a particular voxel and not the whole brain. The most common localization procedure is the use of slice selection and phase encoding gradients. These serve to demarcate the dimensions of the voxel and are operated for a very short duration. The spins then return to the influence of the external magnetic field.

Single Voxel Spectroscopy

The two most popular pulse sequences for defining a small (ranging from 1 cm^3 to 8 cm^3) volume within the anatomy are termed as STEAM and PRESS [3,9,34]. Both PRESS ($90°_{ss}-180°_{ss}-180°_{ss}$) and STEAM ($90°_{ss}-90°_{ss}-90°_{ss}$) use frequency selective RF pulses along with magnetic field gradients to isolate a single volume, called STEAMSV and PRESSSV; however, the timing and the sequence of the pulses has consequences on the sensitivity and the strength of the signal [35].

Multivoxel Spectroscopy or Chemical Shift Imaging

This technique known as spectroscopic imaging (SI) or CSI is challenged with distilling both chemical shift as well as spatial information from the acquired region of interest [36–37]. The data processing in this case requires both spatial and chemical shift dimensions. For CSI, the

PRESS and STEAM sequences described above can be used including the field gradients modified for spatial encoding (STEAMCSI and PRESSCSI). The phase encoding gradients are repeated several times between the remainder of the rf pulses each time repeating the entire sequence but with the phase encoding gradient amplitude changing slightly. This successive change is done in a stepwise fashion with the gradient amplitude changing; thus, several samples of a frequency are produced. The data can then be Fourier transformed to allocate signal intensities of different frequencies to appropriate voxels.

Single Volume Localized 2D ^{1}H MR Spectroscopy

For MR spectroscopy of a particular nucleus, namely hydrogen (^{1}H), one counts on the differences in internal spin interactions which are due to different inter- and intra-molecular environments. These differences in the molecular environment are of several types and are, hence, responsible for different features of a spectrum or an image. For example, the translational molecular motion is exploited in a diffusion weighted image. While the chemical shift expresses the local electronic environment and is predominantly an intra-molecular property, molecular motion also influences this shift significantly. A primary manifestation and measure of the chemical bonds between the nuclear spins, i.e. the indirect spin-spin coupling communicated through the covalent bonds, is the exclusively intra-molecular J-coupling, which is independent of the applied magnetic field. The motive for introducing the 2D MRS sequences to whole body MR spectroscopy is simple—the extraction of more information out of the MR spectrum to aid in the biochemical analysis of human tissue *in vivo*. 2D spectroscopy can do this by converting a crowded, overlapping 1D MR spectrum to a better-resolved 2D spectrum through the addition of a spectral dimension [24,25]. The problems due to the overlap in the 1D spectrum introduced by the multiplicity of various peaks due to J-coupling could be removed by separating the interactions due to chemical shift and indirect spin-spin coupling (J) along the two dimensions in 2D MR spectroscopy. Instead of a standard 1D spectrum plotting intensity vs. a single-axis (i.e. chemical shift), 2D NMR spectroscopy techniques produce a 2D spectrum plotting intensity vs. two axes, the dimensions of which depend on the specific 2D NMR technique.

The Nobel prizes were awarded to Prof. Richard Ernst in 1991 and Prof. Kurt Wuthrich in 2002 for their innovative contributions focused on coherent and incoherent intra- and inter-molecular interactions using multidimensional MR spectroscopy *in vitro* [38]. Exploitation of this interaction is the crucial link to the molecular chemistry of the metabolites in human tissues. Before applying these multidimensional MR techniques in human tissues, each sequence needs to be converted first into localizing a VOI using three orthogonal slice-localizing rf pulses. A second task is to minimize the number of rf pulses essential for creation of Hahn's spin-echo or coherence transfer echoes. Similar to the 1D MRS protocol, shown in Figure 2 are different compartments of 2D MRS protocol. In addition to repeated spectral acquisition for signal averaging, the sequence has to be repeated multiple times for encoding the second spectral dimension.

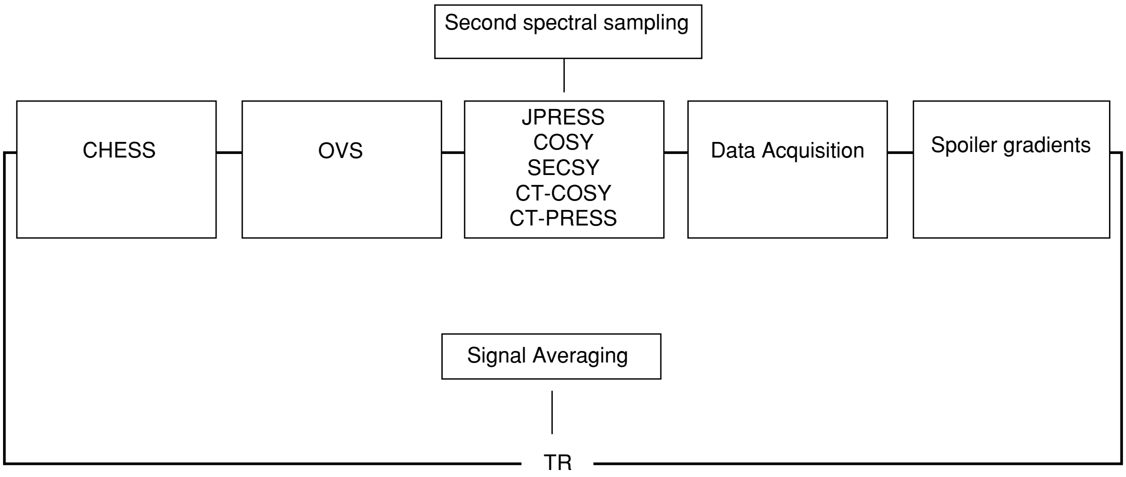

Fig. 2. Different modules of 2D MRS protocol.

2D J-Resolved MR Spectroscopy (JPRESS)

As discussed earlier, the conventional PRESS sequence uses three slice-selective rf pulses (90°, 180°, and 180°) along three orthogonal directions with the second spin-echo originating from a voxel at the intersection of three orthogonal slices. The original 2D J-resolved homonuclear MR spectroscopic sequence is a modified Hahn spin-echo sequence [90°-t_1/2-180°-t_1/2-acquire(t_2)], where signal is acquired during t_2 and the incremental period t_1 is the additional time domain to sample the second spectral dimension of a 2D MR spectrum [25]. In 1995, Ryner *et al.* coded the first 3D-localized 2D J-resolved sequence (JPRESS) by modifying the PRESS sequence to allow simultaneous incrementation of the two periods before and after the last 180° rf pulse [39,40] as shown in Figure 3. The localized 2D JPRESS sequence has been implemented on both GE and Siemens 1.5 and 3 T MRI scanners [39–46]. Shown in Figure 4 are 2D JPRESS spectra of a 100 mM Lac phantom using a Siemens 3T Trio MRI scanner before and after rotating the entire 2D dataset by 45°. A voxel size of 27 ml and a head transmit/receive coil were used. The time period Δ was kept to the minimum necessary to play out rf and gradient pulses. The evolution time (t_1) was incremented in 10-ms steps in order to achieve a spectral window of ±50 Hz that is well within the range of homonuclear (^{1}H–^{1}H) J-coupling. A digital resolution of 1024 complex points along t_2 over a sweep width of 2000 Hz and T_R of 2000 ms was used. The total duration was 4.3 min using two averages per t_1 and 64 increments. However, a longer acquisition time of 17 min will be necessary for signal averaging the metabolite signals at the physiological concentrations. Water suppression was achieved using CHESS. The refocusing of the chemical shift by the last 180° RF pulse resulted in only J-coupling information along the F_1 dimension. A 45° rotation of the 2D data matrix results in J-couplings and chemical shifts along orthogonal axes F_1 and F_2as shown in Figure 4B. As reported earlier [40,41], additional cross peaks due to strong coupling have been observed even at 3 T.

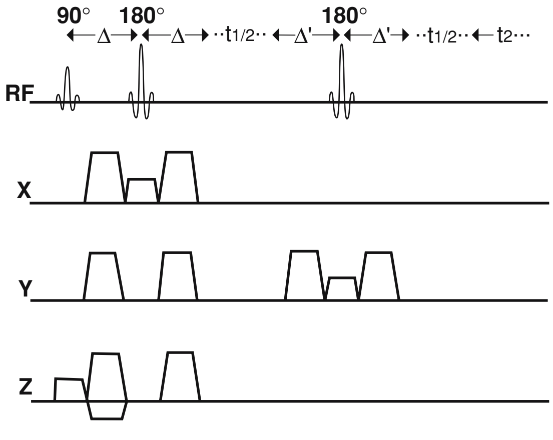

Fig. 3. Localized 2D J-resolved MRS sequence (JPRESS) consisting of three slice-selective rf (90°, 180°, 180°) pulses.

The peaks due to the non-coupled spins are also retained in the 2D J-resolved spectrum unlike the 1D edited spectra. Another advantage of this sequence is that 100% of the available magnetization is retained, neglecting losses caused by T_2 relaxation and spin diffusion. Hence, it is more advantageous than some of the filtered spectral editing techniques, in which 50% or more of the available magnetization is lost. The 2DJ-resolved pulse sequence is versatile such that it can be used for the acquisition of a standard 1D PRESS spectrum by simply removing the incrementation of the t_1-period. A homonuclear broadband decoupled ^{1}H spectrum can also be retrieved after projecting the 2D JPRESS cross peaks onto the F_2 dimension as demonstrated in Figure 4B. This technique has been further extended to human brain and prostate tumours recently to select certain metabolites [42–43]. An over-sampled 2D J-resolved sequence without any water suppression has also been demonstrated [44–46].

Chemical Shift Correlated MR Spectroscopy (L-COSY)

Figure 5 shows a localized 2D correlated spectroscopy (L-COSY) sequence [47]. Similar to JPRESS, the VOI was localized in ‘one-shot’ by a combination of three slice-selective rf pulses (90°-180°-90°), a new MRS volume localization sequence called CABINET (coherence transfer based spin-echo spectroscopy). The last slice-selective 90°RF pulse acts also as a coherence transfer pulse for the 2D spectrum

In addition to the slice-selective 180° rf pulse, there are B_0 gradient crusher pulses before and after the last 90° rf pulses. The incremental period for the second dimension can be inserted at two different locations: first, immediately after the formation of the Hahn spin-echo (t_1) and second, after the last gradient crusher column (k^*t_1), where k^*t_1 can be 4 μs or minimum allowed by the scanner hardware. The L-COSY sequence can be considered a single-shot technique in terms of simultaneous volume localization and coherence transfer. In contrast to PRESS, the CABINET sequence retains only 50% net signal from the localized volume due to a selection of only N-type echo, enabled by the B_0 gradient crusher pulses [47]. If a surface coil is used for both transmission/reception, one has to consider the influence of flip-angle errors due to the delivery of the inhomogeneous rf pulses delivered by a surface coil. In the CABINET sequence with the

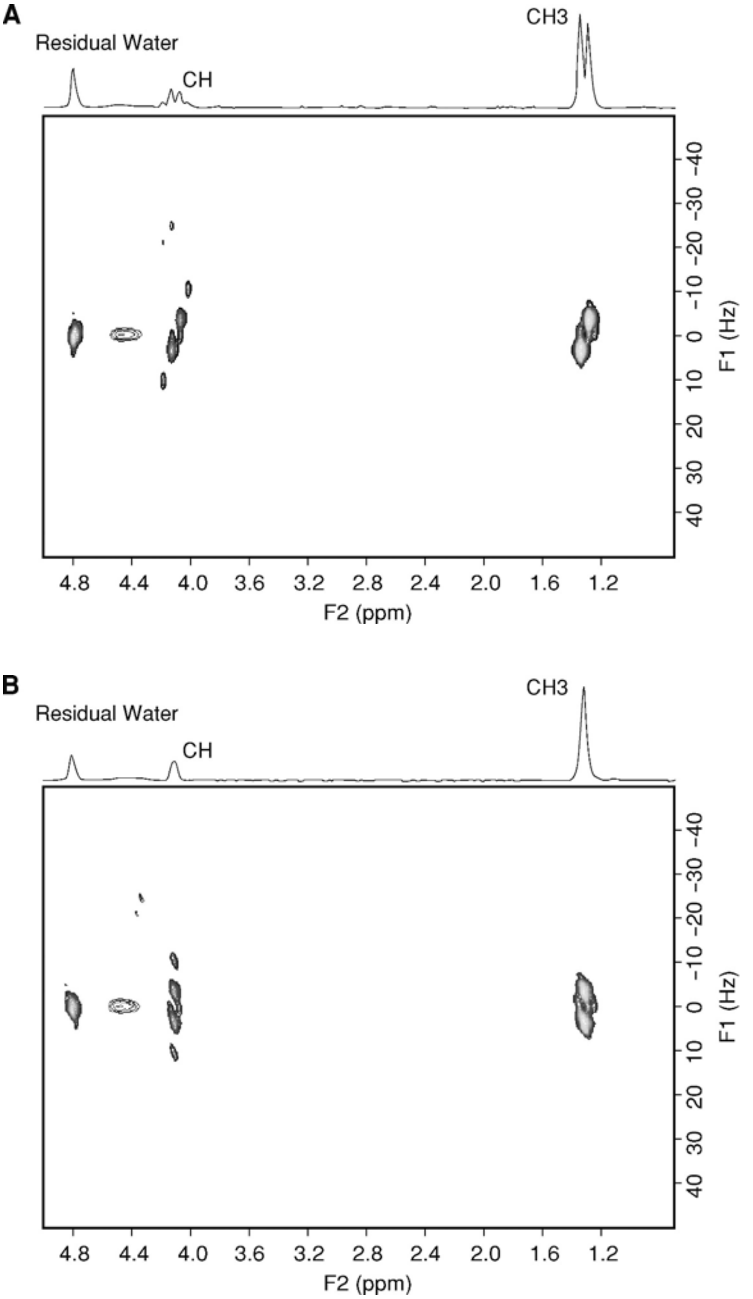

Fig. 4. Localized 2D JPRESS spectra of 100 mM Lac phantom. (A) before and (B) after 45° rotation of the 2D data matrix.

flip-angle distribution of (φ°, $2\varphi^\circ$, φ°), the total signal amplitude from the VOI will be scaled by a factor of $\sin 4\varphi$. The maximum attenuation coefficient for the PRESS sequence (φ°, $2\varphi^\circ$, $2\varphi^\circ$) will be $\sin 5\varphi$. The diagonal and cross peaks of an L-COSY spectrum have mixed phases along the F_1 axis. In contrast to the amplitude modulation in conventional COSY, the phase modulation in L-COSY is caused by the evolution during the B_0 gradient pulse before the last 90° rf pulse. Pure phase L-COSY spectra can be recorded using a quadrature detection method along the

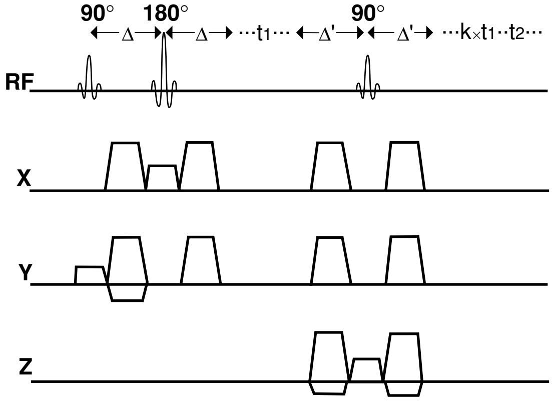

Fig. 5. The 2D L-COSY sequence consisting of three slice-selective rf (90°, 180°, 90°) pulses.

F_1 axis described by Doddrell and co-workers [48,49] that will require two separate P- and N- type spectral acquisition and recombination of the two datasets. Relaxation during the gradient pulses before the last 90° rf pulse will cause further losses in signal intensities.

Two-dimensional L-COSY has been implemented recently on GE and Siemens 1.5 and 3 T MRI scanners [41,47,50] and the test-retest reliability has been demonstrated *in vitro* as well as *in vivo* [41,51]. Shown in Figure 6 are the L-COSY spectra recorded in a) a grey matter brain phantom using a Siemens 3 T MRI scanner and b) the occipito-parietal white matter region of a 38-year-old healthy human subject using a GE 3 T MRI scanner. The brain phantom had the following metabolites at physiological concentrations: 8.9mM NAA, 0.7 mM GABA, 2.1 mM Asp, 0.9 mM Ch, 7 mM Cr, 1 mM Glc, 12.5 mM Glu, 2.5 mM Gln, 2 mM GSH, 4.4 mM mI, 0.4 mM Lac, 3.6 mM PCr, 0.6 mM PCh, 1.8 mM Tau, 0.3 mM Thr, 1 mM PE, and 1 mM DSS in a phosphate buffer solution to maintain pH of 7.2. 2D L-COSY spectra were recorded using the following parameters: 27 ml voxel, $T_E = 20–30$ ms, $T_R = 2$ s, total number of scans = 768 (96 Δt_1 increments and 8NEX/Δt_1). The total duration for each 2D scan with water suppression was approximately 24 min. Typical experimental parameters used for 2D L-COSY are listed in Table 1. Applications of this technique in brain and breast tumours, and brain disorders have also been reported recently [52–54]. Other researchers have also reported the implementation of different versions of 2D COSY [30,49,55–57]. A gradient enhanced COSY in combination with volume localized spectroscopy (VOSY) used the steam sequence for volume localization [49]. Due to additional signal losses, a human brain 2D COSY spectrum recorded in a gross occipital volume of $5 \times 6 \times 8$ cm^3 using a 2 T MRI scanner took a total sampling duration of 1 h and 42 min.

Simultaneous acquisition of COSY from multiple volumes of interest was proposed by Delmas and co-workers (55) and two-voxel localized COSY spectra of rat brain were recorded in a total duration of 42 min using a Bruker 4.7 T MRI scanner. A different pulse-sequence (ISIS-COSY) was also proposed by Welch *et al.* (57), where the volume was localized by outer-volume suppressed ISI (OSIRIS). Two major drawbacks of ISIS-COSY compared to L-COSY were: (1) eight shots are necessary to achieve the VOI and (2) five rf pulses are necessary to record the single voxel localized COSY leading to more dependence on the B_1-field inhomogeneity.

Spin-Echo Correlated MR Spectroscopy (SECSY)

A second variation of COSY, namely spin echo correlation spectroscopy (SECSY) was originally reported by Nagayama *et al.* [58]. Localized SECSY works the same way as L-COSY as shown in Figure 3 except the second incremental period (k^*t_1) should be kept the same as the first period with $k = 1$. Compared to L-COSY, the diagonal peaks of SECSY lie on ($F_2 = F_1 = 0$) and the J-cross peaks are symmetrically disposed above and below the diagonal. A localized SECSY spectrum recorded in the anterior cingulate of a 24-year-old healthy subject is shown in Figure 7. 1024 complex points along the t_2 dimension, 64 points along the t_1 dimensions, a 27 ml voxel and 16 averages per t_1 were acquired. The resultant 2D spectrum was displayed in the magnitude mode. Typical experimental parameters for 2D SECSY are included in Table 1. An advantage of SECSY over COSY is that a smaller sweep width is needed along F_1, however there is additional T_2^*-weighting during the second incremental period.

Constant-Time Based Point Resolved Spectroscopic Sequence (CT-PRESS)

Constant time (CT)-PRESS based on constant time (T_c) chemical shift encoding was recently implemented by Dreher*et al.* [59]. In addition to three rf pulses required for PRESS, an additional 180° rf pulse was used. 2D CT-PRESS spectra were recorded in rat brain with improved spectral resolution using a Bruker 4.7 T MRI scanner. Two different versions of modified CT-PRESS were recently implemented on a whole body 1.5 T MRI scanner including only three-slice selective (90° – 180° – 180°) rf pulses for volume localization and the CT chemical shift encoding as an integral part of volume localization [60]. In the first version, CT was inserted prior to the first spin-echo and in the second version, prior to the second spin-echo. A 2D CT-PRESS spectrum recorded in a phantom containing six metabolites, namely 12.5 mM NAA, 10 mM Cr, 3 mM Ch, 7.5 mM mI, 12.5 mM Glu and 5 mM Lac at pH = 7.3 using a GE 1.5 T MRI scanner is shown

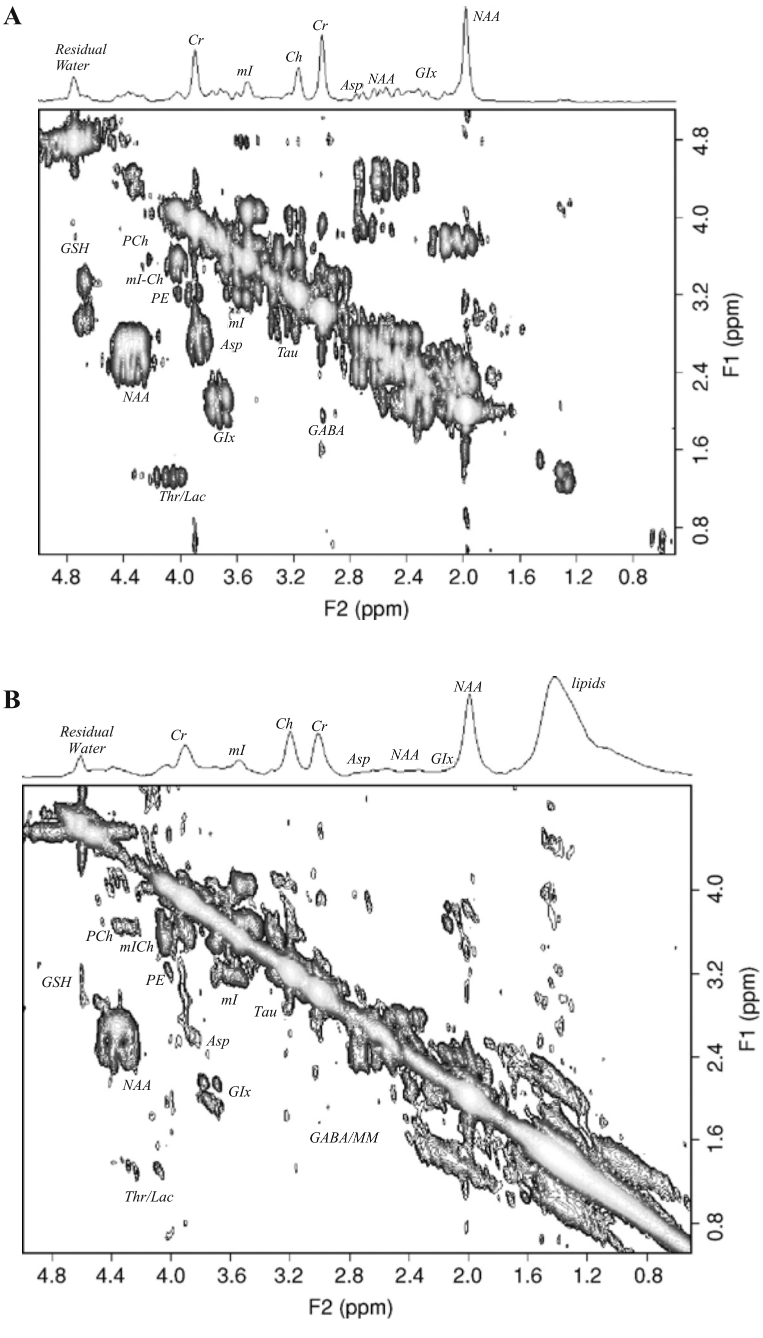

Fig. 6. 2D L-COSY spectra of (A) a grey-matter brain phantom (Siemens) and (B) occipito-parietal white matter region of a 38-year-old healthy human brain (GE) using 3 T MRI scanners.

Table 1: Experimental parameters for 2D MRS

T_R/T_E	2000/20–30 ms
Number of averages/Δt_1	8–16
Number of increments (Δt_1)	64–128
RF pulse widths (90°/180°)	3.2/5.2 ms
Digital resolution (t_2)	Complex 1024–2048
Voxel size	18–27 ml
Duration of crusher gradients	4–6 ms
Spectral width (F_2/F_1)	(2000–5000)/(625–1250) Hz

in Figure 8. Global water suppression was achieved using CHESS.

One major advantage of 2D CT-PRESS is that a homonuclear broadband-decoupled COSY-type spectrum along the F_1-dimension.can be recorded without a second rf-channel for decoupling. Also, compared to the basic localized COSY spectra, a further increase in SNR was obtained by CT-PRESS for coupled resonances since there was no coherence transfer of magnetization between the J-coupled protons leading to disappearance of cross-peaks. Two major drawbacks of the optimized 2D CT-PRESS are: 1) The signal amplitude in CT-PRESS depends on T_c. 2) The spectrum has to be acquired in the 2D mode, which requires long acquisition time.

Constant-time Based Correlated MR Spectroscopy (CT-COSY)

Constant time (CT)-COSY can be easily derived from CT-PRESS by converting the last 180° into 90° rf pulse [61]. Four versions of CT-COSY sequence with the following slice-selective (ss) rf pulses can be easily conceived as described below: (A) $90^\circ_{ss} - (T_c - \Delta t_1) - 180^\circ_{ss} - \Delta t_1 - 90^\circ_{ss}-$Acquire ($t_2$), (B) $90^\circ_{ss}-$ $(T_c + \Delta t_1)/2 - 180^\circ_{ss}-(T_c - \Delta t_1)/2 - 90^\circ_{ss} -$ Acquire(t_2), (C) $90^\circ_{ss} - \Delta t_1 - 180^\circ_{ss} - (T_c - \Delta t_1) - 90^\circ_{ss} -$ Acquire (t_2), and (D) $90^\circ_{ss} - (T_c - \Delta t_1)/2 - 180^\circ_{ss} - (T_c + \Delta t_1)/2 - 90^\circ_{ss} -$ Acquire (t_2), where T_c is defined as the constant time between the 90°_{ss} pulses.

Shown in Figure 9 is a localized 2D CT-COSY spectrum recorded in a phantom containing six metabolites, namely 12.5 mM NAA, 10 mM Cr, 3 mM Ch, 7.5 mM mI, 12.5 mM Glu, and 5 mM Lac at pH = 7.3. The following parameters were used: $T_R = 2$ s, $T_E = 132$ ms, $T_c = 125$ ms, $\Delta t_1 = 0.8$ ms, $\Delta t_2 = 0.8$ ms, spectral widths of 2500 Hz and 625 Hz along the two spectral axes (F_2 and F_1); 1024 complex points along t_2 and 128 points along t_1 dimensions; the number of excitations (NEX) per Δt_1between 8.

Compared to L-COSY, a fixed interval of T_c ($> t_1^{\max}$) separating the preparation and mixing periods is chosen to be of the order of ($1/2J$). The precession under J-coupling is not affected by the 180° rf pulse during T_c. Hence, a

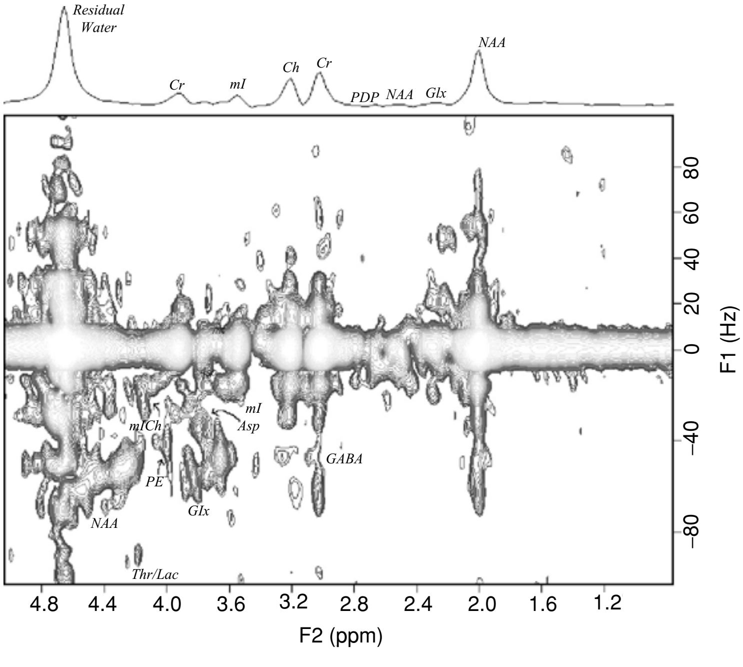

Fig. 7. 2D localized SECSY spectrum of recorded in the occipito-parietal grey matter region of a 24-year-old healthy volunteer using a 1.5 T GE MRI scanner.

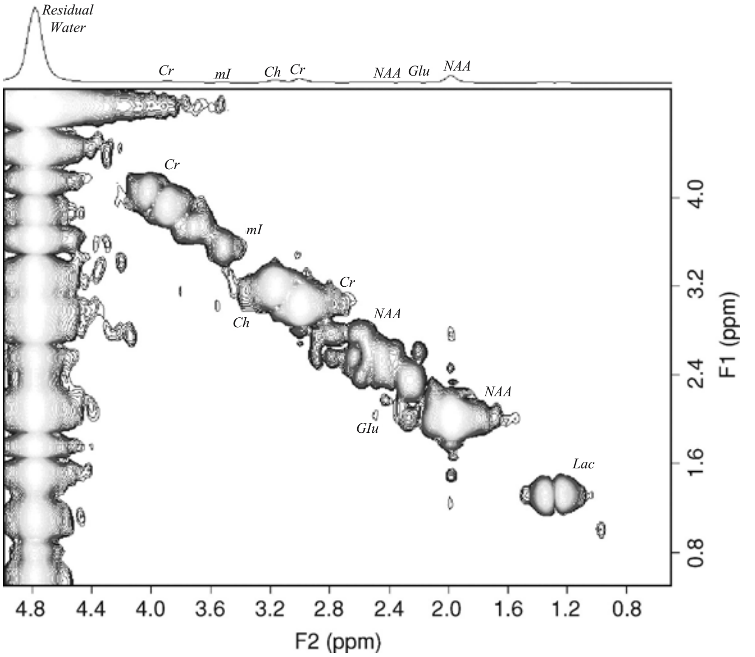

Fig. 8. A CT-PRESS spectrum of recorded in a phantom containing six metabolites using a 1.5 T GE MRI scanner.

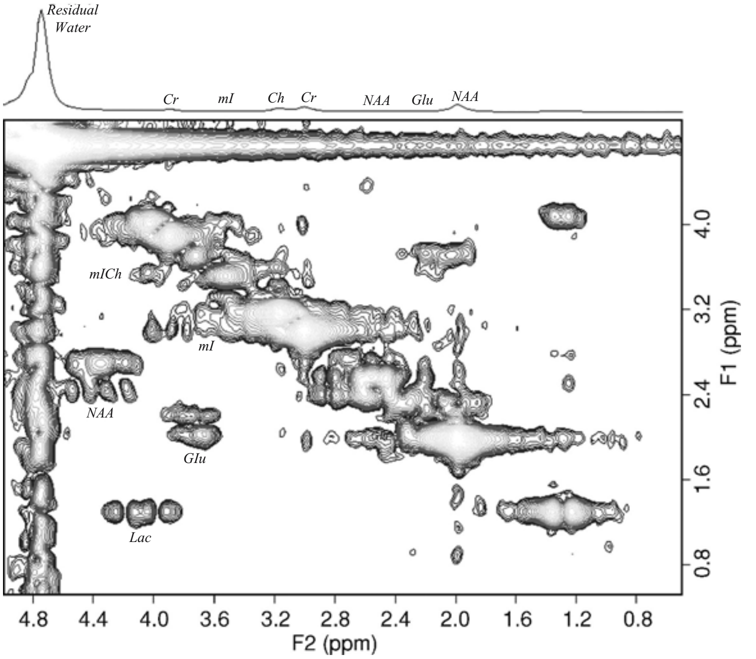

Fig. 9. A CT-COSY spectrum of recorded in a phantom containing six metabolites using a 1.5 T GE MRI scanner.

further increase in SNR was obtained by CT-PRESS for coupled resonances since there was no coherence transfer of magnetization between the J-coupled protons. Secondly, collapse of multiplets along the second dimension was evident without using a second rf channel to achieve broadband decoupling.

Artefacts in Localized 2D MRS and Simulation

In this section, a brief discussion of the commonly observed artefacts in localized 2D MR spectra in presented. First, the flip-angle errors such as an imperfect 180° rf pulse, can lead to ghost artefacts in 2D JPRESS. A four-step phase-cycling scheme, namely EXORCYCLE can eliminate such artefactual peaks [25]. Second, strong coupling effect also complicates 2D JPRESS as discussed by Ryner *et al.* [40]. These artefacts can also impact CT-PRESS and CT-COSY. Third, the asymmetric cross peaks of L-COSY/SECSY are disposed on both sides of the diagonal peaks. The asymmetry has been reported to be more severe with the upper cross peaks of NAA at ($F_2 =$ 2.5 ppm, $F_1 = 4.35$ ppm) above the diagonal [47].

A GAMMA (general approach to magnetic resonance mathematical analysis) software package can be used to simulate different metabolite spectra [62]. The GAMMA library [62] uses a density matrix description of the spin system and provides the simulation of MRS experiments. Density matrices can be calculated for each metabolite using the reported chemical shifts and J-coupling [10]. The GAMMA codes have been extended to simulate the JPRESS, L-COSY/SECSY, CT-COSY, and CT-PRESS spectra including water suppression. As shown in Figure 10, The first 90° rf pulse of the L-COSY pulse sequence is replaced by a binomial rf pulse ($1\,\bar{3}\,3\,\bar{1}$) to mimic the water suppression pulse sequence [63]; where the numerals give the relative pulse lengths, the bars indicate a 180° phase shifted pulse and equal delays τ between pulses. Thus $1\bar{3}\ 3\bar{1}$ corresponds to $11.25°(x)\text{-}\tau\text{-}33.75°(\text{-}x)\text{-}\tau\text{-}33.75°(x)\text{-}\tau\text{-}11.25°(-x)$, $\tau = 1/2\Delta f$, and Δf is the offset frequency [63]. The phase shift is optimized based on the target a null at the water frequency.

Shown in Figure 11 are (A) experimental 2D L-COSY spectrum of a phantom containing NAA, Cr, Ch, mI, Lac, and Glu and (B) simulated composite 2D COSY spectra of the same metabolites using GAMMA [64]. The parameters used for simulation were identical to that of experiments (T_E of 30 ms for L-COSY, 1024 complex points along $F_2$and 128 points along F_1). Another type of water-suppression artefact is due to the t_1-ridge running vertically at $F_2 = 4.8$ ppm as evident in the experimental COSY spectrum shown in Figure 11A. This is mainly due to the scanner hardware fluctuations during the acquisition of the 2D raw matrix [25]. Also, more artefacts can arise due to wrong choice of post-processing parameters and one needs to use caution in selecting optimal apodization filters along both F_2 and F_1 dimensions during post-processing the 2D data.

Multi-Voxel Based 2D ^{1}H MR Spectroscopy

Long data acquisition has been one of the major drawbacks of single-voxel localized 2D MRS. There will be a further increase of time when conventional SI is added to 2D MRS [36–37]. In contrast to reconstructing metabolite images from the 2D spatial and 1D spectral data, the metabolite images can be reconstructed from the 2D spatial and 2D spectral data projecting the cross peak volumes into the corresponding spatial images. This methodology was termed as "cross peak imaging" (CPI) by Metzler and co-workers [65–66]. An obvious drawback of CPI is extended total acquisition time. For example, a combination of 16 × 16 spatial, 64 spectroscopic encoding steps and T_R of 1 s will result in a total duration of 4.6 h [66]. Recently, implementation of circular sampling combined

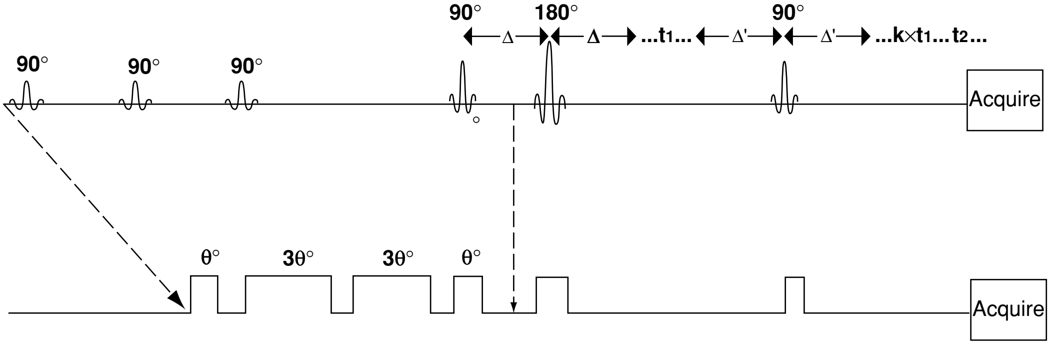

Fig. 10. A 2D COSY sequence used for simulation.

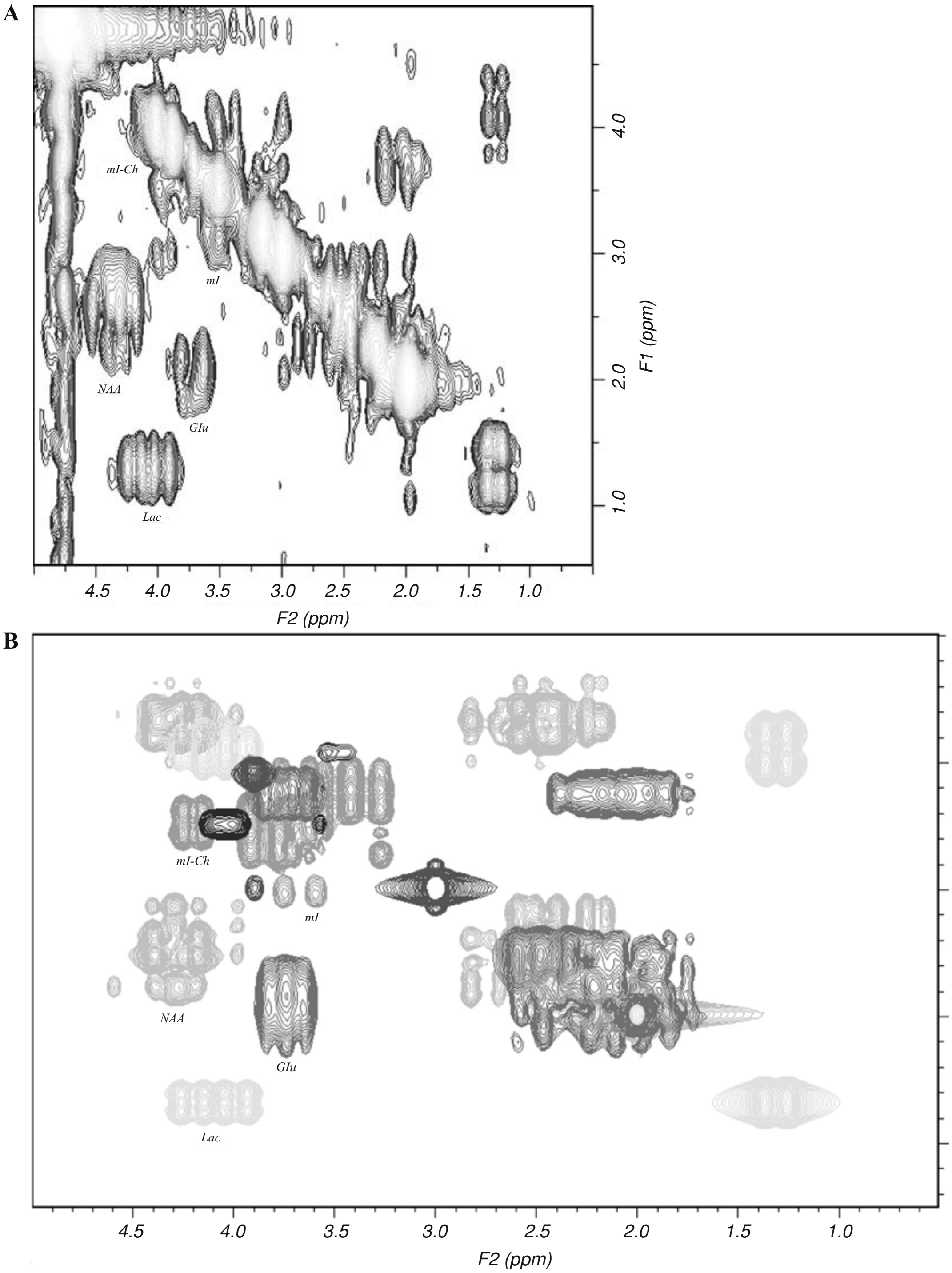

Fig. 11. 2D L-COSY spectra of (A) a brain phantom containing six metabolites and (B) simulated spectra for the same metabolites (Reproduced with permission from Banakar *et al.* [64]). (See also Plate 91 on page XVII in the Color Plate Section.)

with 2D J-resolved spectroscopy was demonstrated by Renshaw and co-workers using a 4 T whole body MRI scanner with a total duration of 2 h [67].

A drastic reduction of total duration has been proposed by two different multidimensional MRS sequences. First, Adalsteinsson and Spielman introduced the first application of time-varying gradients during the read-out time to acquire multi-voxel based 2D J-resolved spectral data in phantom solutions containing lactate and ethanol using a 1.5 T MRI scanner [68]. Spiral-based k-space trajectories were used in conjunction with a 2D J-resolved sequence. By preceding the spiral read-out with a 2D preparation scheme, 128 spectral encoding with T_R of 2 s resulted in a total duration of 17 min.

An asymmetric variant of echo-planar spectroscopic imaging (EPSI) consisting of a train of trapezoidal read-out gradients, each followed by short refocusing pulse was implemented by Meyer *et al.* [69]. A constant-time based COSY was used and the total acquisition was 34 min. Application of this technique was demonstrated in rat brain using a 4.7 T MRI scanner and the cross peak images of mI and Tau were recorded only. In an alternative approach, COSY was combined with spectroscopic ultra-fast low angle rapid acquisition with relaxation enhancement (U-FLARE) [70]. CT along the two spectral dimensions (evolution and detection) facilitated complete effective homonuclear decoupling. A spiral imaging combined CT-PRESS was also recently proposed [71].

Summary

Localized 2D MRS is still at its infancy and different techniques discussed earlier need further improvements in terms of voxel sizes, coil design, etc. Non-selective excitation of the J-coupled metabolites is facilitated by different 2D MRS techniques. 2D cross peaks of more than ten J-coupled metabolites have been observed using L-COSY recorded in the frontal and occipital regions of human brain [41,47,54]. In contrast to ISIS-COSY [57], the 2D techniques discussed in this chapter are one-shot based. Even though it has been shown recently that 1D MR spectra processed using the LC-Model algorithm [21], 2D L-COSY shows the unambiguous presence of 2D cross peaks originating from several J-coupled metabolites. However, further work is necessary in order to ascertain the superiority of 2D L-COSY over the other methodology. Due to the differential T_2^*-weighting during the incremental duration of 2D L-COSY, absolute quantitation of several metabolites is further complicated by lack of T_2 and T_1 values in the literature for different proton groups (methyl, methylene, methine, etc.) in any given metabolite. Regarding the application of these multidimensional MRS techniques in different pathologies, targeting a specific metabolite or selected metabolites in different pathologies may be more advantageous than non-selective excitation/detection of several metabolites. Another major concern is that the 2D spectra are complicated by artefacts contributed by strong coupling of various metabolite protons unavoidable at both 1.5 and 3 T MRI scanners. As discussed earlier, the artefacts in these multi-voxel based 2D MRS sequences need to be further evaluated. Further work is necessary to demonstrate the clinical potential of both single and multi-voxel based multidimensional MR SI methods.

Acknowledgment

This work was supported by the grants from the National Institute of Health (NIH) and the US Army Breast and Prostate Cancer Research Programs. Authors acknowledge the scientific support of Drs. Kenneth Yue and Lawrence Ryner in the earlier implementation of 2D MR sequences, and Ashwin Thomas and Tai Dou during the preparation of the chapter.

References

1. Gadian DG. Nuclear Magnetic Resonance and Its Applications to Living Systems. Oxford University Press: New York, 1982.
2. Rothman DL, Behar KL, Hetherington HP, Shulman RG. Proc. Natl. Acad. Sci. U.S.A. 1984;81:6430.
3. Moonen CTW, Kienlin MV, van Zijl PCM *et al.* NMR Biomed. 1989;2:201.
4. Kreis R, Ross BD, Farrow N, Ackerman Z. Radiology 1982;182:9.
5. Michelis T, Merboldt KD, Bruhn H *et al.* Radiology 1983;187:219.
6. Gruetter R, Weisdorf SA, Rajanayagan V *et al.* J. Magn. Reson., 1998;135:260.
7. Webb PG, Sailasuta N, Kohler SJ *et al.* Magn. Reson. Med. 1994;31:365.
8. Rothman DL, Petroff OAC, Behar KL, Mattson RH. Proc. Natl. Acad. Sci. U.S.A. 1993;90:5662.
9. Bruhn H, Frahm J, Gyngell ML *et al.* Magn. Reson. Med. 1989;9:126.
10. Govindaraju V, Young K, Maudsley AA. NMR Biomed. 2000;13:129.
11. Renshaw PF, Lafer B, Babb SM *et al.* Biol. Psych. 1997;41:837.
12. Pouwels PJW, Frahm J. Magn. Reson. Med. 1998;39:53.
13. Barker PB, Hearshen DO, Boska MD. Magn. Reson. Med. 2001;45:765.
14. Trabesinger AH, Weber OM, Duc CO, Boesiger P. Magn. Reson. Med. 1999;42:283.
15. Prichard JW. Curr. Opin. Neur. 1997;10:98.
16. Pan JW, Stein DT, Telang F *et al.* Magn. Reson. Med. 2000;44:673.
17. Choi IY, Lei H, Gruetter R. J. Cereb. Blood Flow Metab. 2002;22:1343.
18. Hardy DL, Norwood TJ. J. Magn. Reson. 1998;133:70.

19. de Graaf AA, Luyten PR *et al.* Single and Double Quantum Lactate Imaging of the Human Brain at 1.5 T. 9th SMRM, New York 1990, p 138.
20. Crozier S, Brereton IM *et al.* Magn. Reson. Med. 1990;16:492.
21. Ith M, Bigler P, Scheurer E, *et al.* Magn. Reson. Med. 2002;48:915.
22. Kumar A, Thomas MA, Lavretsky H *et al.* Am. J. Psych. 2002;159:630.
23. Pfeuffer J, Tkac I, Provencher SW, Gruetter R. J. Magn. Reson. 1999;141:104.
24. Aue WP, Bartholdi E, Ernst RR. J. Chem. Phys. 1976;64:2229.
25. Ernst RR, Bodenhausen G, Wokaun A. Principles of NMR Spectroscopy in One and Two Dimensions. Oxford Publications: Oxford, 1987, pp 283–489.
26. Crozier S, Brereton IM *et al.* Magn. Reson. Med. 1990;16:492.
27. Sotak CH, Freeman DM, Hurd RE. J. Magn. Reson., 1988;78:355.
28. Desmoulin F, Seelig J. Magn. Reson. Med. 1990;14:160.
29. van Zijl PCM, Chesnick AS, Despres D. *et al.* Magn. Reson. Med. 1993;30:544.
30. Kreis R, Boesch C. J. Magn. Reson. 1996;B113:103.
31. Ogg RJ, Kingsley PB, Taylor JS. J. Magn. Reson. 1994;B103:1.
32. Patt SL, Sykes BD. J. Chem. Phys. 1972;56:3182.
33. Tran TK, Vigneron DM, Sailasuta N *et al.* Magn. Reson. Med. 2000;43:23.
34. Bottomley PA. Ann. NY. Acad. Sci. 1987;508:333.
35. Salibi N, Brown MA. Clinical MR Spectroscopy: First Principles. Wiley-Liss: New York, 1998, p 75.
36. Brown TR, Kincaid BM, Ugurbil K. Proc. Natl. Acad. Sci. U.S.A. 1982;79:3523.
37. Maudsley AA, Hilal SK, Perman WH, Simon HE. J. Magn. Reson. 1983;51:147.
38. Boesch C. J. Magn. Reson. Imag. 2004;16:177.
39. Ryner LN, Sorenson JA, Thomas MA. J. Magn. Reson. 1995;B107:126.
40. Ryner LN, Sorenson JA, Thomas MA. Magn. Reson. Ima. 1995;13:853.
41. Thomas MA, Hattori N, Umeda M, *et al.* NMR Biomed. 2003;16:245.
42. Thomas MA, Ryner LN, Mehta MP *et al.* J. Magn. Reson. Imag. 1996;6:453.
43. Yue K, Binesh N, Marumoto N *et al.* Magn. Reson. Med. 2002;47:1059.
44. Hurd RE, Gurr D, Sailasuta N. Magn. Reson. Med. 1998;40:343.
45. Swanson MG, Vigneron DB, Tran TK *et al.* Magn. Reson. Med. 2001;45:973.
46. Adalsteinsson E, Hurd RE, Mayer D *et al.* Neuroimage 2004;22:381.
47. Thomas MA, Yue K, Binesh N *et al.* Magn. Reson. Med. 2001;46:58.
48. Brereton IM, Crozier S, Field J, Doddrell DM. J. Magn. Reson. 1991;93:54.
49. Brereton IM, Galloway GJ, Rose SE, Doddrell DM. Magn. Reson. Med. 1994;32:251.
50. Binesh N, Thomas MA. Proc. Intl. Soc. Magn. Reson. Med. Kyoto, Japan, 2004, p 2303.
51. Binesh N, Yue K, Fairbanks L, Thomas MA. Magn. Reson. Med. 2002;48:942.
52. Prescot AP, Leach MO, Saran F, Collins DJ. Proc. Intl. Soc. Magn. Reson Med. 2004, p 2493.
53. Thomas MA, Yue K, Binesh N, Debruhl N. J. Magn. Reson. Imag. 2001;14:181.
54. Binesh N, Bugbee M, Fairbanks L *et al.* Proc. Intl. Soc. Magn. Reson. Med. Hawaii, 2002, p 699.
55. Delmas F, Beloeil JC, van der Sanden BPJ *et al.* J. Magn. Reson. 2001;149:119.
56. Ziegler A, Gillet B, Beloeil JC *et al.* Magn. Reson. Mat. Phys. Biol. Med. 2002;14:45.
57. Welch JWR, Bhakoo K, Dixon RM *et al.* NMR Biomed. 2003;16:47.
58. Nagayama K, Wuthrich K, Ernst RR. Biochem. Biophys. Res. Commun. 1979;90:305.
59. Dreher W, Leifbritz D. Magn. Reson. Imag. 1999;17:141.
60. Chung HK, Banakar S, Thomas MA. Proc. Intl. Soc. Magn. Reson. Med., Kyoto, Japan, 2004, p 687.
61. Chung HK, Banakar S, Thomas MA. Proc. Intl. Soc. Magn. Reson. Med. Toronto, 2003, p 1143.
62. Smith SA, Levante TO, Meier BH, Ernst RR. J. Magn. Reson. A 1994;106:75.
63. Hore PJ. J. Magn. Reson. 1983;55:283.
64. Banakar S, Venkatraman TN, Yue K *et al.* Proc. Int. Conf. Math. Engg. Tech. Med. and Biol. Sci., Las Vegas, 2002, Vol II, p 500.
65. Metzler A, Izquierdo M, Ziegler A *et al.* Proc. Natl. Acad. Sci. U.S.A. 1995;92:11912.
66. Ziegler A, Metzler A, Kockenberger W *et al.* J. Magn. Reson. 1996;B112:141.
67. Jensen JE, Frederic BD, Wang L *et al.* Proc. Intl. Soc. Magn. Reson. Med. 2004, p 2301.
68. Adalsteinsson E, Spielman DM. Magn. Reson. Med. 1999;41:8.
69. Mayer D, Dreher W, Leibfritz D. Magn. Reson. Med. 2000;44:23.
70. D. Mayer, Dreher W, Leibfritz D. Magn. Reson. Med. 2003;49:810.
71. Mayer D, Kim DH, Adalsteinsson E, Spielman DM. Proc. Intl. Soc. Magn. Reson. Med., Kyoto, Japan, 2004, p 678.

Part II, Section 2:
Applications in Pharmaceutical Science

Foreword to Applications in Pharmaceutical Science

NMR has a long history of applications in the pharmaceutical sciences. Initially it was almost exclusively used for the study of small molecules, i.e., drug leads or drugs themselves. As NMR technology developed and became amenable for the study of macromolecules and their complexes NMR has become an increasingly valuable as a tool in the drug discovery process. The 30 articles comprising this section of the Handbook of Modern Magnetic Resonance reflect the major contributions that NMR is making in this field. The articles cover the broad spectrum of activities that NMR encompasses, ranging from the early phases of drug discovery to lead optimization and even to the monitoring of drug effects within organisms in the newly emerging field of metabonomics.

The chapters are written by leading experts in their respective fields, who have highlighted specific applications with examples from their own laboratories. In keeping with the concept of a Handbook, most of the articles focus on a particular NMR technique. However several of the articles cover broad fields of application, as exemplified by the chapters on antimicrobial peptides and toxin structures. Both classes of molecules have obvious applications in the pharmaceutical sciences.

In the short space available in this introduction it is not possible to give a detailed overview of all of the articles. I would just like to highlight one area where I think NMR has shown particularly exciting potential and has had a major impact in the pharmaceutical sciences over the last few years. That area is NMR-based screening. There are now a number of complementary NMR approaches that can be used to discover new ligands by using NMR as the detector in screening assays. Reflecting the importance of this field four chapters that address various aspects of NMR screening are included in this Handbook and many of the other chapters also address the area.

David Craik
October 2004

Key Terms for Applications in Pharmaceutical Science

Overview of NMR in the Pharmaceutical Sciences

Drug design

LC NMR

Ligand based screening

Metabonomics

Receptor based screening

SAR by NMR

Screening

Structure-based design

Structural genomics

Applications of Cryogenic NMR Probe Technology for the Identification of Low-Level Impurities in Pharmaceuticals

Correlation experiments

Cryogenic NMR probes

Degradation products

Metabolite identification

Metabonomic studies

Natural products

Pharmaceutical impurities

Protein characterization

Small volume NMR probes

Structure characterization

Flow NMR Techniques in the Pharmaceutical Sciences

Cold probes

DI-NMR

Direct injection NMR

FIA-NMR

Flow injection analysis NMR

Flow NMR

Flow probe

LC-NMR

LC-NMR-MS

Microcoil NMR

Developments in NMR Hyphenation for Pharmaceutical Industry

Cryogenic probes

Drug impurity profiles

LC-NMR

LC-NMR/MS

Natural product screening

Solid phase extraction

Stop flow LC-NMR

LC-NMR in Dereplication and Structure Elucidation of Herbal Drugs

Crude plant extracts

Dereplicaion

HMBC

HSQC

LC-NMR

Structure elucidation of natural products

WET pulse sequence

New Approaches to NMR Data Acquisition, Assignment and Protein Structure Determination: Potential Impact in Drug Discovery

Automated structure determination

Assignment

Computer-assisted sequential assignment

Fast multidimensional NMR

Transferred Cross-Correlated Relaxation: Application to Drug/Target Complexes

Bound conformations

Cross-correlated relaxation

Drug receptor complexes

Epothilone/tubulin complex

Transferred cross-correlated relaxation

Transferred NOE

Novel Uses of Paramagnets to Solve Complex Protein Structures

Domain orientation

J-modulation

Long-range restraints

Paramagnetic labelling

Protein structure

Pseudocontact shift

Residual dipolar coupling

Fast Assignments of ^{15}N-HSQC Spectra of Proteins by Paramagnetic Labeling

HSQC spectrum

Ligand binding

Paramagnetic labelling

PLATYPUS

Proteins

Pseudocontact shift

Resonance assignment

Phospholipid Bicelle Membrane Systems for Studying Drug Molecules

Bicelles

Conformation

Drug membrane-interactions

Model membranes

Orientation

Partial Alignment for Structure Determination of Organic Molecules

Liquid crystal phase

Partial alignment

Organic molecules

Residual dipolar couplings

Stretched polymer gels

Measurement of Residual Dipolar Couplings and Applications in Protein NMR

Aligned proteins

Conformational substrates

Echo-anti-echo manipulation

Protein folding

Protein NMR

Residual dipolar coupling

Using Chemical Shift Perturbations to Validate and Refine the Docking of Novel IgE Antagonists to the High-Affinity IgE Receptor

Chemical shift

Docking

High-affinity binding

IgE receptor

Peptides

Simulated annealing

Dual-Region Hadamard-Encoding to Improve Resolution and Save Time

Adiabatic gHMBC

Cyclosporine-A

HMBC

Hadamard spectroscopy

Region-selection

Resolution enhancement

Sensitivity enhancement

Nonuniform Sampling in Biomolecular NMR

Maximum entropy reconstruction

Nonuniform data acquisition

Sensitivity

Spectrum analysis

Resolution

Structural Characterization of Antimicrobial Peptides by NMR Spectroscopy

Antimicrobial peptides

Diffusion NMR

Disulfide cross-linking

Membrane-peptide interactions

Membrane insertion of peptides

Peptide solution structure

Solid-state NMR

Pharmaceutical Applications of Ion Channel Blockers: Use of NMR to Determine the Structure of Scorpion Toxins

Low abundance samples

Nano probes

Scorpion toxins

Small sample probes

Toxin structure

Structure and Dynamics of Inhibitor and Metal Binding to Metallo-β-Lactamases

Cadmium NMR

Cooperativity

Imidazole

Metallo-β-lactamases

Minimum chemical shift approach

Mono-cadmium

Tautomer

Thiomandelate

NMR Spectroscopy in the Analysis of Protein–Protein Interactions

Chemical exchange

Cross saturation

Deuterium labelling of proteins

Mapping protein interfaces

Large proteins

Protein complexes

Paramagnetic nuclei

Protein-protein interactions

Protein structure

Residual dipolar coupling

Titrations

TROSY NMR

Identification and Characterization of Ternary Complexes Using NMR Spectroscopy

Borate

Dihydrofolate reductase

Inorganic ions

Interligand NOE

Nuclear Overhauser Effect

Transferred NOE

Trypsin

The Transferred NOE

Fast exchange

Non-specific binding

Off rate

On rate

Saturation transfer difference (STD)

Slow exchange

Spin diffusion

Transferred NOE

NMR Kinetic Measurements in DNA Folding and Drug Binding

DNA hairpin

DNA quadruplex

Drug binding kinetics

Fast chemical exchange

Line shape analysis

Magnetisation transfer NMR

Quadruplex-ligand interactions

Slow conformational equilibria

The Use of NMR in the Studies of Highly Flexible States of Proteins: Relation to Protein Function and Stability

Amide exchange rates

Flexibility

Growth hormone

Insulin

Order parameters

Protein dynamics

Trifluoroethanol

NMR-based Metabonomics Techniques and Applications

Atherosclerosis

Biofluids

Clinical trials

Diagnosis

Drug safety

Efficacy

Genomics

Metabonomics

Pharmaceutical attrition

Physiological variation

Proteomics

Transcriptomics

Protein Misfolding Disease: Overview of Liquid and Solid-State High Resolution NMR Studies

Amyloid

Alzheimers disease

Intrinsically unstructured proteins

Non-native states of proteins

Natively unfolded proteins

Prion proteins

Protein misfolding disease

Structural biology

^{19}F NMR Spectroscopy for Functional and Binding High-Throughput Screening

Competition binding experiments

Drug discovery

^{19}F NMR spectroscopy

3-FABS

FAXS

High-throughput screening

IC_{50} measurement

K_D measurement

Ligand libraries

Protein binding

Screening

Applications of Receptor-Based NMR Screening in Drug Discovery

Core replacement

Drug discovery

Fragment-based screening

Lead validation

Receptor-based screening

NMR SHAPES Screening

Compound libraries

Drug scaffolds

High-throughput screening

Lead optimisation

SHAPES screening

NMR-Based Screening Applied to Drug Discovery Targets

Chemical shift perturbations

Competition STD NMR

Fragment-based screening

HSQC

Lead discovery

NMR-based screening

SAR-by-NMR

STD NMR

NMR and Structural Genomics in the Pharmaceutical Sciences

High throughput structure determination

HSQC

Structural genomics

X-ray crystallography

Overview of NMR in the Pharmaceutical Sciences

Horst Joachim Schirra and David J. Craik*
Institute for Molecular Bioscience, University of Queensland, Brisbane 4072, Australia

Abbreviations: 3-FABS, Fluorine atoms for biochemical screening; CRINEPT, cross relaxation-enhanced polarization transfer; D, deuterium; DFT, discrete Fourier transformation; DI-NMR, direct injection NMR; FIA-NMR, flow injection analysis NMR; FAXS, Fluorine chemical shift anisotropy and exchange for screening; FT, Fourier transformation; GFT, G-matrix Fourier transformation; HSQC, heteronuclear single quantum coherence; ILOE, inter-ligand NOE; INEPT, insensitive nuclei enhanced by polarization transfer; LC, liquid chromatography; ME, maximum entropy reconstruction; MS, mass spectrometry; NMR-SOLVE, structurally-oriented library valency engineering; NOE, nuclear Overhauser effect; PR-NMR, projection-reconstruction NMR; RDC, residual dipolar coupling; SAR, structure-activity relationship; SEA-TROSY, solvent-exposed amides with TROSY; STD, saturation transfer difference spectroscopy; TROSY, transverse-relaxation optimised spectroscopy; Water-LOGSY, Water-ligand observed via gradient spectroscopy

Abstract

NMR spectroscopy has a wide range of applications in the pharmaceutical sciences. This chapter gives an overview of these applications and attempts to draw together information from the specialist articles on individual topics covered in this handbook of modern magnetic resonance.

Introduction

Since its inception NMR has been an important tool for the characterization of molecules that have relevance in the pharmaceutical sciences. Initial interest focused on small organic molecules that were either drugs themselves or were leads in the drug discovery process. As the technology developed over the last few decades molecules of increasing complexity have been examined and it is now possible to study not only small-molecule drugs, but also their macromolecular targets, including proteins and nucleic acids. NMR spectroscopy is now a powerful tool for the study of structure, dynamics, and interactions of biomolecules. In particular, the study of protein–ligand interactions forms the basis for the use of NMR spectroscopy in the process of drug design and discovery, ranging from the simple identification of whether a particular compound binds to a target protein on the one hand to the full determination of a protein–ligand complex's three-dimensional structure on the other.

An outline of the general process of structure-based drug design is given in Figure 1. The iterative cycle is generally started by determining the three-dimensional structure of a target protein or the structure of a complex between the target protein and a ligand, identified through screening a library of compounds. This structural information is then used to design new ligands, which are subsequently synthesized and screened for binding to the target protein and/or for biochemical activity. The structures of promising ligands are then determined in complex with the target protein and used to suggest improvements during further iterations of the design cycle. The cycle is repeated until suitable lead molecules with the desired affinity, specificity, activity, and pharmacokinetic properties have been identified.

NMR spectroscopy is ideally suited to provide critical information at several points of this iterative cycle. Together with X-ray crystallography it is the second major experimental technique used for determining the three-dimensional structures of proteins and protein–ligand complexes in atomic detail, thus providing accurate and detailed descriptions of the regions of a protein involved in ligand binding, the conformation of the bound ligand and the key interactions between the two molecules that determine binding affinity and specificity. By contrast with X-ray crystallography NMR is typically carried out in solution (for an overview on solid-state NMR spectroscopy applications see the related section of Handbook of Modern Magnetic Resonance), thus removing the need for suitable crystals. In addition, NMR spectroscopy is unique in providing crucial information about dynamics of the target protein as well as the bound ligand. Molecular motion is important in determining the kinetics of protein–ligand complex formation and dissociation. Upon binding of a ligand, the dynamics of the reactive site of the target protein is usually perturbed. In addition, the mobility of the active site also determines the range of ligands that can be bound and whether multiple conformations of the ligand can exist. Furthermore, NMR spectroscopy can be used to study solvent accessibility and study and identify

Graham A. Webb (ed.), Modern Magnetic Resonance, 1195–1202.
© 2008 *Springer.*

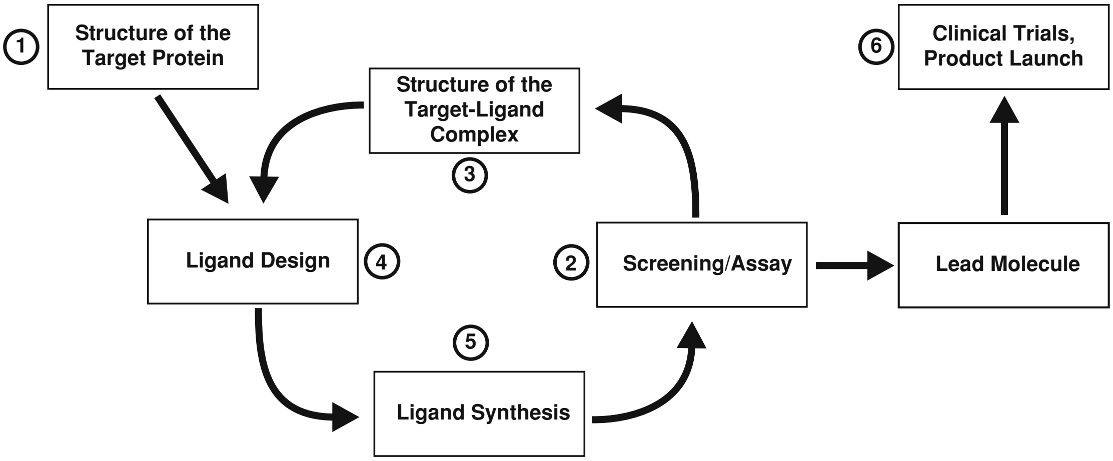
① Structure of the Target Protein
Structure of the Target-Ligand Complex
③
⑥ Clinical Trials, Product Launch
Ligand Design ④
② Screening/Assay
Lead Molecule
⑤
Ligand Synthesis

Fig. 1. Schematic outline of the process of structure-based drug design and discovery. In an iterative cycle the structures of protein targets and/or protein-ligand complexes are determined, ligands are designed using the structural information, screened for binding to the target and assayed for activity. The interactions of suitable ligands with the target proteins are structurally investigated and the information is used for improving the ligands in further iterations of this cycle until a suitable lead compound has been generated. NMR spectroscopy is involved in all aspects of this cycle: (1) Protein structure determination; (2) ligand screening; (3) structural analysis of protein ligand-complexes; (4) ligand design (as a conformational analysis tool); (5) ligand synthesis (as a structure verification tool); and (6) quality control of the pharmaceutic production process and metabonomic studies during clinical trials and after release of the drug.

bound water molecules. Finally, NMR spectroscopy can be used to determine binding constants and other thermodynamic data as well as ionization states of the protein and/or ligand.

In this overview article we will briefly discuss the applications of NMR spectroscopy techniques in drug design and discovery. More detailed discussions are presented in the individual chapters of this section of the Handbook of Modern Magnetic Resonance. A number of other review articles covering various aspects of the application of NMR spectroscopy in drug design and discovery have been published in recent years [1–8] and in addition to the specialist articles contained in this edition of Handbook of Modern Magnetic Resonance the reader is referred to these publications.

The review is divided into four sections. In the first section, we review the latest technical developments in NMR spectroscopy, ranging from hardware developments such as the use of cryoprobes and coupled techniques like LC-NMR to improvements in the acquisition and measurement of NMR spectra. The second section deals with the structural characterization of target molecules and ligands and discusses labeling strategies, NMR experiments suited for large molecules (TROSY) and the use of non-NOE-based NMR data such as residual dipolar couplings (RDC) and paramagnetic labels. The third section is dedicated to applications of NMR spectroscopy in the screening of ligands, and reviews target-based methods as well as ligand-based methods. While the first three sections focus on applications of NMR to obtain structural information, the fourth section focuses on NMR applications unique to pharmacy and pharmacology, from drug monitoring, quality control, and pharmacokinetics to the new field of metabonomics. The chapter finishes with a short section on future developments and directions.

Technical Developments

Several significant technical developments have been made in NMR in hardware, software, and experimental techniques in recent years. The most significant development in terms of NMR hardware is the introduction of cryoprobes. Cryoprobes reduce the thermal noise in the detection circuit by cooling the receiver coil and electronic parts of the probe (but not the sample) with liquid helium. Consequently, the sensitivity of a cryoprobe is two to four times higher than conventional room-temperature probes [9,10]. This sensitivity improvement benefits pharmaceutical applications in two ways: on one hand, the improved sensitivity can be utilized to investigate samples of much lower concentration than before, which is especially useful in natural product discovery or screening for low-concentration impurities in pharmaceutical samples during quality control, as reviewed in more detail in Chapter 2 by Martin [11]. On the other hand, the improved sensitivity can be utilized to acquire data of the same quality in a much shorter time—up to 16 times faster—which is especially useful in high-throughput screening applications.

Other developments on the hardware side include the integration of NMR spectroscopy with other analytical techniques such as liquid chromatography (LC) or mass spectrometry (MS) to yield techniques such as LC-NMR [12] or LC-NMR-MS [13,14]. In addition, developments such as direct-injection NMR (DI-NMR) [15] and flow-injection analysis NMR (FIA-NMR) [16] aim at utilizing NMR spectroscopy in support of pharmaceutical applications. DI-NMR has already become a routine technology in pharmaceutical laboratories and in other industrial applications [17–21]. These techniques are reviewed in Chapters 3–5 [22–24].

The most significant advance with respect to new experimental techniques is the development of transverse-relaxation optimized spectroscopy (TROSY) by Pervushin *et al.* [25], in which the line-broadening effects of transverse relaxation are eliminated by selecting specifically the line of a heteronuclear multiplet for which the effects of dipole–dipole relaxation and chemical shift anisotropy compensate each other, yielding improved spectral resolution and sensitivity. However, TROSY is applied only during evolution periods in NMR experiments, and transverse relaxation, which is still active during periods of magnetization transfer, becomes a limiting factor for molecular weights beyond 100 kDa when magnetization is transferred via spin-spin couplings with the insensitive nuclei enhanced by polarization transfer (INEPT) technique [26]. This limitation can be overcome by replacing INEPT steps with cross relaxation-enhanced polarization transfer (CRINEPT) [27], which combines INEPT with cross-correlated relaxation-induced polarization transfer [28], a highly effective transfer mechanism for molecules with a molecular weight above 200 kDa. Thus, TROSY and CRINEPT represent complementary techniques that have revolutionized NMR spectroscopy within a short period of time by making it applicable to proteins larger than the "traditional" 30 kDa limit [29]—reports of NMR data on a 900 kDa complex have been widely cited [30]. In addition, modifications of the TROSY experiment, like solvent-exposed amides with TROSY (SEA-TROSY), have been developed [31] that are specifically geared towards screening studies as part of structure-based drug design approaches. Techniques for improving the study of large proteins and protein complexes with NMR spectroscopy are reviewed in more detail in Chapter 19 [32].

Other developments with respect to experimental NMR techniques focus on modifying and speeding up data acquisition. In general, they involve replacing the uniform sampling of time-space with other sampling schedules and consequently replacement of the discrete Fourier-transformation (DFT) with other transformations. One approach is multiplexing, by encoding more than one resonance frequency in one dimension, as realized in G-matrix FT (GFT) [33,34] or Hadamard encoding [35,36]. Other approaches are projection-reconstruction NMR (PR-NMR) [37] and maximum entropy reconstruction (ME) [38]. These techniques are discussed in more detail in Chapters 6, 14, 15 [39–41].

Structure-based Design

As already outlined, the first step in the cycle of structure-based drug design is the structural characterization of the target receptor molecule. Table 1 shows a collection of

Table 1: NMR technologies used for structural characterization of receptors, ligands, and ligand–receptor complexes

Target	Technique	Information
Receptor	2-4D NMR	3D structure
	RDC	3D structure
	Relaxation	Macromolecular dynamics
Ligand	1D/2D NMR	Solution conformation
	RDC	Solution conformation
	Chemical shift	Charge/tautomeric state
	Lineshape/relaxation analysis	Solution dynamics
	Transfer NOE	Bound conformation
Receptor–ligand complex	3D/4D NMR	3D structure of complex
	RDC	Ligand orientation in complex
	Shift perturbation (HSQC)	Mapping of binding site, Stoichiometry of complex, K_D
	Line width	Binding kinetics
	Relaxation	Dynamics of complex

NMR techniques that can be employed for this purpose as well as for the structure determination of protein–ligand complexes.

Isotopic labeling is essential for the structure determination of target proteins that are not small in NMR terms (i.e. larger than 10 kDa). Labeling is also a prerequisite to harvest the benefits of the TROSY effect. The stable isotopes most commonly used for labeling are ^{15}N, ^{13}C, and ^{2}H (deuterium), and they can be employed in different labeling schemes [42,43]. Uniform labeling with ^{15}N and ^{13}C allows for sequential assignment and structure determination of the target protein with multidimensional triple resonance experiments [44]. For larger proteins, additional substitution of non-exchangeable protons with deuterium ameliorates relaxation effects. In this case, TROSY experiments are usually employed to obtain spectral information. In large multidomain proteins individual domains can be labeled by segmental labeling thereby simplifying the information in the NMR spectrum [45]. Another method of simplifying spectral information, which is especially useful for screening studies with large proteins, is the selective labeling of individual amino acids or of amino acid types [46,47]. The former approach can also be achieved with amino-acid specific pulse sequences [48,49].

After NMR spectra have been recorded, and all resonances have been assigned, the three-dimensional structure of the target protein is determined mostly from information based on NOE connectivities and dihedral restraints [50]. Recently, additional sources of structural information have been made accessible, most important among them RDCs [51] and shift and relaxation changes associated with paramagnetic nuclei [52,53]. Both methods have the distinct advantage of providing long-range constraints, which is a useful complementation for the short-range information derived from NOEs and dihedral restraints. Furthermore, they are able to provide structural information in the case of large proteins that have been extensively labeled with deuterium and thus have a reduced number of observable proton-proton NOEs. Labeling, RDC and paramagnetic methods are discussed in more detail in Chapters 8, 9, 11, 12, and 19 [32,54–57].

Similar methods can be employed to determine the three-dimensional structures of ligand molecules. Although ligand molecules are easier to examine because of their small size and can generally be studied by standard homonuclear NMR methods, the use of more advanced techniques such as RDCs has been demonstrated to be beneficial e.g. for obtaining structural information on sugars and small organic molecules as reviewed in Chapter 11 [56]. Other examples of the application of NMR spectroscopy for structure determination of small organic molecules are antimicrobial peptides and scorpion toxins as discussed in Chapters 16 and 17 [58,59].

A major milestone in structure-based drug design is a detailed determination of the three-dimensional structure of a ligand-target protein complex. If the structure of the target protein has been solved, but the ligand binding site is unknown then a quick determination of the binding site can be obtained by chemical shift mapping: a labeled sample of the target protein is titrated with the ligand, and due to the change in chemical environment associated with ligand binding amide proton resonances at, or close to, the binding site change their position in a HSQC spectrum. Mapping of the shift perturbations on the structure of the target protein reveals the ligand binding site. Similarly, in the case of a small ligand protein binding to a large receptor the binding face of the ligand can be determined by titrating labeled ligand with unlabeled receptor and chemical shift mapping.

To determine the detailed nature of protein–ligand interactions the observation of intermolecular NOEs between target protein and ligand is crucial. The aforementioned combination of labeled protein and unlabeled ligand (or vice versa) is helpful here, and for example, “filtered” experiments can be used to selectively observe NOE signals either within the protein, within the ligand, or most importantly the desired intramolecular signals between protein and ligand [60].

RDCs offer an alternative approach for determining the orientation of ligands within the target protein’s binding site. Upon binding, the ligand adopts the alignment tensor of the target protein, and thus a comparison of ligand RDCs in the free and bound state makes it possible to determine the conformation of the ligand in the bound state in the complete absence of ligand-protein or ligand–ligand NOEs [61–63]. A further discussion of techniques for determining the structures of protein–ligand complexes, including some case examples, is given in Chapters 13, 18, 19, and 20 [32,64–66]. Transferred NOE and cross-correlated relaxation methods are also particularly important for determining the conformation of bound ligands, provided certain kinetic conditions are met. These approaches are described in Chapters 7 and 21 [67,68].

One of the distinct advantages of NMR spectroscopy is the possibility of obtaining information about the dynamics of a protein or a protein–ligand complex. The dynamics of the binding site is of fundamental importance in determining affinities and binding kinetics. In addition, it is a not an uncommon observation that the binding site of a protein exhibits considerable flexibility, but becomes more rigid upon binding of the ligand [69,70]. Phenomena like this can be readily investigated with NMR relaxation experiments, which can determine molecular motions on a nanosecond up to millisecond timescale [71]. In addition, lineshape analysis offers an avenue into further determining events on the millisecond timescale like chemical exchange, including the measurement of rate constants of the exchange process [72]. Finally, NMR titrations can be used to determine dissociation constants of a protein–ligand complex. These topics are further reviewed in Chapters 18, 21, 22, and 23 [66,68,73,74].

NMR Screening

The screening of libraries of compounds is becoming an increasingly useful adjunct to structure-based drug design. Table 2 gives an overview of the different screening strategies that can be employed. In general, screening techniques can either be target-based—i.e. changes in the macromolecular target protein upon ligand binding are observed, or ligand-based—i.e. changes in NMR properties of the ligand upon binding are observed.

In general target-based screening techniques are based on monitoring chemical shifts with a HSQC spectrum. For large target proteins specific labeling strategies and TROSY experiments are employed, but the principle stays the same. A recent modification of the TROSY experiment specifically geared for application in screening programs with large target proteins is the SEA-TROSY experiment [31]. The experiment is based on the concept that only groups on the solvent-exposed surface of the protein are likely to be involved in ligand binding, while residues in the protein interior are unlikely to be in contact with the ligand. SEA-TROSY observes by magnetization transfer from the bulk water only solvent-exposed amide protons in fully deuterated and ^{15}N-labeled proteins that are dissolved in water. Thus the SEA-TROSY spectrum contains significantly fewer signals than conventional spectra, alleviating the problem of spectral overlap for large target proteins.

Table 2: NMR technologies used for high-throughput screening of ligand–receptor complexes

Target	Technique	Reference
Receptor-based	SAR by NMR	[75]
	SEA-TROSY	[31]
	NMR-SOLVE	[47]
Ligand-based, Direct	Relaxation	[78,79]
	Diffusion coefficients	[78]
	STD	[83]
	ILOE	[65,85]
	Transfer NOE	[68,80]
	NOE pumping	[81,82]
	Water-LOGSY	[84]
	SHAPES	[87]
Ligand-based, Indirect	FAXS	[86]
	3-FABS	[96]
	STD with spy-molecule	[86]

The by now “classic” strategy employed in NMR target-based screening is structure–activity relationships (SAR) by NMR [75]. It aims at the identification of two ligands with moderate binding affinities that bind to two different but adjacent binding sites on the target protein. Crosslinking of the two ligands via chemical synthesis then produces a first-generation lead molecule with substantially improved binding affinity. It has been responsible for the development of numerous novel drug leads, as outlined in the article by Hajduk in this Handbook [76].

NMR-Structurally orientated library valency engineering (NMR-SOLVE) is a new target-based screening approach that has been developed specifically for the postgenomic era to provide guidance for the construction of libraries against multiple related target proteins [47]. One key element of NMR-SOLVE is to use highly selective isotopic labeling (e.g. ^{13}C-^{1}H labeled CH_3 groups in otherwise uniformly deuterated proteins) to observe only a small number of key resonances in a binding site, thus yielding information in the absence of complete assignments. The NMR-SOLVE strategy is based on the fact that several enzyme families have multiple binding sites—one that is common for all family members, and one that is specific for each protein. In a first-step NMR-SOLVE uses a known reference ligand that binds to the common binding site to map and identify the specifically labeled groups that are around this binding site. In the next steps mimics of the reference ligand that could bind to the common binding site of most family members of the protein family are investigated. Finally, in an act of core-expansion structural information is used to design a linker that could connect the core of ligand-mimetic fragments binding in the common binding site with additional ligand fragments that would bind to the secondary binding sites, unique to each protein. Thus, a library of bivalent ligands is obtained that is specifically geared towards a given protein family. The NMR-SOLVE strategy has been demonstrated with target proteins as large as 170 kDa [47]. Further discussion on target-based screening approaches can be found in Chapters 27 and 29 [76,77].

A plethora of ligand-based screening methods has been developed targeting a wide variety of observable NMR parameters, as indicated in Table 2. Parameters that have been utilized include longitudinal, transverse, and double-quantum relaxation [78,79], diffusion coefficients [78], and intramolecular and intermolecular transfer of magnetization, such as transfer NOE [68,80], NOE pumping, and reverse NOE pumping [81,82], saturation transfer experiments [83], Water-ligand observed via gradient spectroscopy (water-LOGSY) [84] and inter-ligand NOEs (ILOE) [65,85]. Individual techniques are discussed in detail in Chapters 21, 26, and 29 [68,77,86] and are reviewed here only briefly.

The main advantage of monitoring the small ligands is that there is no need for isotopic labeling of the target protein, and thus limitations of protein yields in minimal media or molecular size of the target protein do not apply. Furthermore, the identity of a binding ligand in a mixture can be readily established, and screening methods based on 1D-NMR experiments are generally faster than a 2D-HSQC spectrum. However, ligand-based methods provide no direct information about ligand binding sites, and generally require the ligand to be in fast or medium exchange with the target protein.

Ligand-based screening methods can be divided in two classes: direct methods, in which the NMR signals of the ligand are observed directly, and indirect methods, where signals of a "reporter" or "spy" molecule that binds weakly to the target protein are observed. The indirect methods are especially suitable for the investigation of strongly binding ligands that are not in fast exchange with the target protein. As the ligand binds competitively to the protein, it replaces the reporter molecule, and the changes in the NMR signal of the reporter molecule are observed.

A broadly applicable approach that utilizes ligand-based screening is SHAPES [87]. This drug design strategy is based on a diverse library of small organic fragment molecules, whose molecular shapes represent those most commonly found in the structures of established drugs. Unlabeled target proteins are screened against this library of weakly binding water-soluble library, and hits are used to construct more complex, high-binding lead compounds. The strategy is discussed in more detail in Chapter 28 [88].

Studies of Drug Effects

NMR spectroscopy has not only applications within the iterative cycle of structure-based drug design, as outlined in the previous section, but can also be applied in later stages once a lead molecule has been identified. One obvious example is the use of NMR spectroscopy as a routine analytic technique for the quality control during synthesis and production. This includes the profiling of drug impurities or the analysis of drug stability. Another application is pharmacokinetics and the screening for drug metabolites in biological fluids or extracts. The use of coupled analytical techniques such as LC-NMR and new technical developments such as cryoprobes have already been mentioned and are reviewed in more detail in Chapters 2, 3, and 4 [11,22,23].

A most exciting development in this respect is the application of NMR spectroscopy in metabonomics [89]. Metabonomics is formally defined as the quantitative measurement of the dynamic multiparametric metabolic response of living systems to pathophysiological stimuli or genetic modification [90]. In other words, in metabonomics biofluids and tissues are monitored with various analytical techniques, chiefly among them 1D-NMR spectroscopy, for changes in the levels of metabolites. These changes can occur as a consequence of disease (vs. healthy state) or after administering of a drug. The immense value of metabonomics in all stages of drug development from first assessments of pharmacology, through clinical trials and later on for monitoring of patients and epidemiological studies is becoming increasingly apparent. NMR-based metabonomic techniques and applications are discussed in detail in Chapter 24 [90].

Future Directions

A remaining frontier for both NMR spectroscopy and X-ray cystallography is the structure elucidation of membrane proteins. Membrane proteins are often involved in signal transduction and consequently many targets of pharmaceutical interest involve membrane-bound or membrane-associated proteins. Recent developments in the field of solid-state NMR have made it possible to study the structure of membrane proteins [91,92]. Similar progress has been made in solution NMR spectroscopy with the development of phospholipid bicelle systems that mimic the environment of the cell membrane and are mobile enough to allow the study of drug-membrane or protein-membrane interactions with solution NMR. These developments are further detailed in Chapter 10 [93].

Another challenge/opportunity for NMR spectroscopy in the pharmaceutical sciences comes from structural genomics programs. In the postgenomic era it is becoming increasingly important to obtain information about ligand-target protein interactions not just for one target protein, but for whole classes of related proteins. More often than not, full assignments of the target protein(s) are not available or cannot be obtained within the constraints of time. Thus the development of techniques, such as NMR-SOLVE [47], that can provide information about ligand–protein interactions without full NMR characterization of the target protein is very important. A discussion of NMR applications in structural genomics is provided in Chapter 30 [94]. One of the interesting features that is emerging from such programs is that the average size and amino acid composition of genomically encoded proteins is substantially different from folded proteins in the PDB. There are many proteins now being discovered that are intrinsically unfolded and hence unsuitable for structure determination. Chapter 25 [95] describes NMR approaches to the study of such proteins and to the related issue of protein misfolding in disease.

Acknowledgments

DJC is an Australian Research Council Professorial Fellow. HJS is an Australian Research Council Postdoctoral Fellow.

References

1. Pellecchia M, Sem DS, Wüthrich K. Nat. Rev. Drug Discov. 2002;1:211.
2. Homans SW. Angew. Chem. Intl. Ed. 2004;43:290.
3. Heller M, Kessler H. Pure Appl. Chem. 2001;73:1429.
4. Meyer B, Peters T. Angew. Chem. Intl. Ed. 2003;42:864.
5. Stockman BJ. Prog. Nuc. Mag. Reson. Spectrosc. 1998;33:109.
6. Roberts GCK. Drug Discov. Today. 2000;5:230.
7. Craik DJ, Scanlon MJ. Annu. Rep. NMR Spectrosc. 2000;42:115.
8. Stockman BJ, Dalvit C. Prog. Nuc. Mag. Reson. Spectrosc. 2002;41:187.
9. Styles P, Soffe NF, Scott CA, Cragg DA, Row F, White DJ, White PCJ. J. Magn. Reson. 1984;60:397.
10. Styles P, Soffe NF, Scott CA. J. Magn. Reson. 1989;84:376.
11. Martin GE. In: Webb GA (Ed). Modern Magnetic Resonance, Springer, The Netherlands, 2006, pp 1179–1192.
12. Dorn HC. In: DM Grant, RK Harris (Ed). Encyclopedia of Nuclear Magnetic Resonance, John Wiley & Sons, Ltd: West Sussex, England, 1996, p 2026.
13. Burton KI, Everett JR, Newman MJ, Pullen FS, Richards DS, Swanson AG. J. Pharm. Biomed. Anal. 1997;15:1903.
14. Corcoran O, Spraul M. Drug Discov. Today 2003;8:624.
15. Keifer PA, Smallcombe SH, Williams EH, Salomon KE, Mendez G, Belletire JL, Moore CD. J. Comb. Chem. 2000;2:151.
16. Keifer PA. Magn. Reson. Chem. 2003;41:509.
17. Keifer PA. Curr. Opin. Chem. Biol. 2003;7:388.
18. Lewis K, Phelps D, Sefler A. Am. Pharm. Rev. 2000;3:63.
19. Kalelkar S, Dow ER, Grimes J, Clapham M, Hu H. J. Comb. Chem. 2002;4:622.
20. Stockman BJ, Farley KA, Angwin DT. Methods Enzymol. 2001;338:230.
21. Kraus WE, Houmard JA, Duscha BD, Knetzger KJ, Wharton MB, McCartney JS, Bales CW, Henes S, Samsa GP, Otvos JD, Kulkarni KR, Slentz CA. N. Engl. J. Med. 2002;347:1483.
22. Keifer PA. In: Webb GA (Ed). Modern Magnetic Resonance, Springer, The Netherlands, 2006, pp 1187–1193.
23. Spraul M. In: Webb GA (Ed). Modern Magnetic Resonance, Springer, The Netherlands, 2006, pp 1195–1202.
24. Karagianis G, Waterman PG. In: Webb GA (Ed). Modern Magnetic Resonance, Springer, The Netherlands, 2006, pp 1203–1209.
25. Pervushin K, Riek R, Wider G, Wüthrich K. Proc. Natl. Acad. Sci. U.S.A 1997;94:12366.
26. Morris GA, Freeman R. J. Am. Chem. Soc. 1979;101:760.
27. Riek R, Wider G, Pervushin K, Wüthrich K. Proc. Natl. Acad. Sci. U.S.A 1999;96:4918.
28. Brüschweiler R, Ernst RR. J. Chem. Phys. 1992;96:1758.
29. Riek R, Pervushin K, Wüthrich K. Trends Biochem. Sci. 2000;25:462.
30. Fiaux J, Bertelsen EB, Horwich AL, Wüthrich K. Nature. 2002;418:207.
31. Pellecchia M, Meininger D, Shen AL, Jack R, Kasper CB, Sem DS. J. Am. Chem. Soc. 2001;123:4633.
32. Gell DA, Mackay JP. In: Webb GA (Ed). Modern Magnetic Resonance, Springer, The Netherlands, 2006, pp 1313–1320.
33. Kim S, Szyperski T. J. Am. Chem. Soc., 2003;125:1385.
34. Ding K, Gronenborn AM, J. Magn. Reson. 2002;156:262.
35. Kupce E, Freeman R. J. Magn. Reson. 2003;163:56.
36. Kupce E, Freeman R. J. Magn. Reson. 2003;162:300.
37. Kupce E, Freeman R. J. Am. Chem. Soc. 2003;125:13958.
38. Wernecke SJ, Daddario LR. IEEE Transact. Comput. 1977;26:351.
39. Crouch R. In: Webb GA (Ed). Modern Magnetic Resonance, Springer, The Netherlands, 2006, pp 1273–1278.
40. Maciejewski MW, Stern AS, King GF, Hoch JC. In: Webb GA (Ed). Modern Magnetic Resonance, Springer, The Netherlands, 2006, pp 1279–1285.
41. Pineda-Lucena A. In: Webb GA (Ed). Modern Magnetic Resonance, Springer, The Netherlands, 2006, pp 1213–1220.
42. Kay LE, Gardner KH, Curr. Opin. Struct. Biol. 1997;7:722.
43. Goto NK, Kay LE. Curr. Opin. Struct. Biol. 2000;10:585.
44. Kay LE, Ikura M, Tschudin R, Bax A. J. Magn. Reson. 1990;89:496.
45. Xu R, Ayers B, Cowburn D, Muir TW. Proc. Natl. Acad. Sci. U.S.A 1999;96:388.
46. Griffey RH, Redfield AG, Loomis RE, Dahlquist FW. Biochemistry. 1985;24:817.
47. Pellecchia M, Meininger D, Dong Q, Chang E, Jack R, Sem DS. J. Biomol. NMR 2002;22:165.
48. Schubert M, Smalla M, Schmieder P, Oschkinat H. J. Magn. Reson. 1999;141:34.
49. Schubert M, Oschkinat H, Schmieder P. J. Magn. Reson., 2001;148:61.
50. Wüthrich K. NMR of Proteins and Nucleic Acids. John Wiley & Sons: New York, 1986.
51. Bax A, Kontaxis G, Tjandra N. Methods Enzymol. 2001; 339:127.
52. Ubbink M, Worrall JA, Canters GW, Groenen EJ, Huber M. Annu. Rev. Biophys. Biomol. Struct. 2002;31:393.
53. Pintacuda G, Keniry MA, Huber T, Park AY, Dixon NE, Otting G. J Am. Chem. Soc. 2004;126:2963.
54. Byrd RA, Fowler CA, McFeeters RL, Gaponenko V. In: Webb GA (Ed). Modern Magnetic Resonance, Springer, The Netherlands, 2006, pp 1229–1235.
55. Ding K, Gronenborn AM. In: Webb GA (Ed). Modern Magnetic Resonance, Springer, The Netherlands, 2006, pp 1261–1265.
56. Luy B, Kessler H. In: Webb GA (Ed). Modern Magnetic Resonance, Springer, The Netherlands, 2006, pp 1253–1259.
57. Pintacuda G, Huber T, Keniry MA, Park AY, Dixon NE, Otting G. In: Webb GA (Ed). Modern Magnetic Resonance, Springer, The Netherlands, 2006, pp 1237–1243.
58. Delepierre M, Possani LD. In: Webb GA (Ed). Modern Magnetic Resonance, Springer, The Netherlands, 2006, pp 1299–1304.
59. Nguyen LT, Prenner EJ, Vogel HJ. In: Webb GA (Ed). Modern Magnetic Resonance, Springer, The Netherlands, 2006, pp 1289–1297.
60. Otting G, Wüthrich K. J. Magn. Reson. 1989;85:586.
61. Shimizu H, Donohue-Rolfe A, Homans SW. J. Am. Chem. Soc. 1999;121:5815.
62. Bolon PJ, Al-Hashimi HM, Prestegard JH. J. Mol. Biol. 1999;293:107.
63. Al-Hashimi HM, Bolon PJ, Prestegard JH. J. Magn. Reson. 2000;142:153.

64. Starovasnik MA, Fairbrother WJ. In: Webb GA (Ed). Modern Magnetic Resonance, Springer, The Netherlands, 2006, pp 1267–1272.
65. London RE. In: Webb GA (Ed). Modern Magnetic Resonance, Springer, The Netherlands, 2006, pp 1321–1330.
66. Damblon C, Roberts GCK. In: Webb GA (Ed). Modern Magnetic Resonance, Springer, The Netherlands, 2006, pp 1305–1311.
67. Carlomagno TMR, Griesinger C. In: Webb GA (Ed). Modern Magnetic Resonance, Springer, The Netherlands, 2006, pp 1221–1228.
68. Williamson MP. In: Webb GA (Ed). Modern Magnetic Resonance, Springer, The Netherlands, 2006, pp 1331–1336.
69. Hodsdon ME, Cistola DP. Biochemistry 1997;36:1450.
70. Hodsdon ME, Cistola DP. Biochemistry 1997;36:2278.
71. Palmer 3rd AG. Curr. Opin. Struct. Biol. 1997;7:732.
72. Nieto PM, Birdsall B, Morgan WD, Frenkiel TA, Gargaro AR. Feeney J. FEBS Lett. 1997;405:16.
73. Kristensen SM, Kasimova MR, Led JJ. In: Webb GA (Ed). Modern Magnetic Resonance, Springer, The Netherlands, 2006, pp 1343–1350.
74. Searle MS, Balkwill G. Williams HEL, Gavathiotis E. In: Webb GA (Ed). Modern Magnetic Resonance, Springer, The Netherlands, 2006, pp 1337–1341.
75. Shuker SB, Hajduk PJ, Meadows RP, Fesik SW. Science 1996;274:1531.
76. Hajduk PJ. In: Webb GA (Ed). Modern Magnetic Resonance, Springer, The Netherlands, 2006, pp 1375–1381.
77. Gesell JJ, McCoy MA, Senior MM, Wang Y-S, Wyss DF. In: Webb GA (Ed). Modern Magnetic Resonance, Springer, The Netherlands, 2006, pp 1393–1402.
78. Hajduk PJ, Olejniczak ET, Fesik SW. J. Am. Chem. Soc. 1997;119:12257.
79. Dalvit C, Bohlen JM. Annu. Rep. NMR Spectrosc. 1999; 37:203.
80. Ni F. Prog. Nuc. Mag. Reson. Spectrosc. 1994;26:517.
81. Chen A, Shapiro MJ. J. Am. Chem. Soc. 1998;120: 10258.
82. Chen AD, Shapiro MJ. J. Am. Chem. Soc. 2000;122:414.
83. Mayer M, Meyer B. Angew. Chem. Intl. Ed. 1999;38: 1784.
84. Dalvit C, Pevarello P, Tato M, Veronesi M, Vulpetti A, Sundstrom M. J. Biomol. NMR 2000;18:65.
85. Li D, DeRose EF, London RE. J. Biomol. NMR 1999;15: 71.
86. Dalvit C, Veronesi M. In: Webb GA (Ed). Modern Magnetic Resonance, Springer, The Netherlands, 2006, pp 1367–1373.
87. Fejzo J, Lepre CA, Peng JW, Bemis Ajay GW, Murcko MA, Moore JM. Chem. Biol. 1999;6:755.
88. Lepre CA, Moore JM. In: Webb GA (Ed). Modern Magnetic Resonance, Springer, The Netherlands, 2006, pp 1383–1391.
89. Nicholson JK, Lindon JC, Holmes E. Xenobiotica. 1999;29:1181.
90. Lindon JC, Holmes E, Nicholson JK. In: Webb GA (Ed). Modern Magnetic Resonance, Springer, The Netherlands, 2006, pp 1351–1359.
91. Watts A. Curr. Opin. Biotech. 1999;10:48.
92. Opella SJ. Nat. Struct. Biol. 1997;4:845.
93. Guo J, Tian X, Pavlopoulos S, Makriyannis A. In: Webb GA (Ed). Modern Magnetic Resonance, Springer, The Netherlands, 2006, pp 1245–1251.
94. Cemazar M, Craik DJ. In: Webb GA (Ed). Modern Magnetic Resonance, Springer, The Netherlands, 2006, pp 1403–1408.
95. Schwalbe H, Wirmer J. In: Webb GA (Ed). Modern Magnetic Resonance, Springer, The Netherlands, 2006, pp 1361–1365.
96. Dalvit C, Ardini E, Fogliatto GP, Mongelli N, Veronesi M. Drug Discov. Today. 2004;9:595.

Instrumentation

Applications of Cryogenic NMR Probe Technology for the Identification of Low-Level Impurities in Pharmaceuticals

Gary E. Martin
Pfizer Global Research & Development, Michigan Structure Elucidation Group, Kalamazoo, MI 49001-0199

Abstract

Following the detection of low-level impurities in pharmaceuticals, structural characterization of these components represents a continuing challenge. Irrespective of whether the impurity in question arises from side reactions of the chemical processes being employed for the synthetic elaboration of the active pharmaceutical, through degradation chemistry processes, or through accidental contamination, the identification of low-level impurities is a mandatory component of the preparation and marketing of pharmaceuticals. The development of cryogenic NMR probes and the corresponding increases in sensitivity that they provide has significantly impacted this phase of pharmaceutical development. The role of cryogenic NMR probe technology in the characterization of low-level impurities from pharmaceuticals is discussed.

Introduction

Multiple creative approaches have been utilized in the quest for improved NMR sensitivity. NMR spectroscopy, despite the wealth of chemical structure information that it can provide, has always had an Achilles' heel in the form of the low inherent sensitivity of the technique. Approaches that have been used to improve sensitivity have included the development of new pulse sequences, such as the proton- or "inverse"-detected heteronuclear 1D-, 2D-, and 3D-NMR experiments that are now in wide use. Another approach that has been heavily exploited has been that of "shrinking" the size of NMR probes and hence the required sample [1,2]. Although small volume probes have been known for a considerable period of time, contemporary small volume probe development effectively began in 1991 with the first reports of 3 mm NMR probe applications, followed shrinking of probe diameters to 1.7 mm, then 1 mm, and finally μ-coil probes with sample volumes as small as a few μl. This area was the subject of a recent review and the interested reader is referred there for more details [3]. Cooling the rf coils of an NMR probe to cryogenic temperatures to reduce noise, thereby improving sensitivity, is also a well-established approach to enhancing NMR performance [4–7].

Unlike conventional NMR probe developments, which were commercially realized after prototype design and testing, the commercial manufacture of cryogenic NMR probes proved to be a more daunting task requiring a number of years for even the first prototypes to be delivered to customer laboratories. In part this was due to design considerations necessary to cool the internal components to temperatures for the rf coil in the range of 10–25 K and preamps housed in the probe body to temperatures near 50 K without destroying those components during thermal cycling that the probe must occasionally be subjected to. Nevertheless, numerous commercial cryogenic NMR probes have been delivered and have begun to have a significant impact on the way in which various disciplines perform NMR-based chemical structure investigations.

Cryogenic NMR Probes

Commercial examples of cryogenic NMR probes have been developed in a limited number of configurations. Typically, they have been 3 or 5 mm diameter probes and most commonly, inverse-detection triple resonance gradient designs, although a cryogenic probe for direct carbon detection has also been developed. Cryogenic NMR probes have also been developed for flow applications. Perhaps one of the most interesting of these is the interchangeable flow cell (IFC) design by Varian, which allows the user to change between NMR tubes and a flow cell without having to remove the cryoprobe from the magnet. Although some early cryogenic probes were developed and tested using an open configuration of a liquid helium dewar, to the best of the author's knowledge, all commercial examples use a closed loop system to deliver the helium refrigerant to the probe at temperatures in the vicinity of 8–10 K. The helium refrigerant is used to cool the rf coils to their operating temperature as well as the associated electronic circuitry housed in the probe body such as preamps, after which the helium refrigerant is cycled back and re-chilled. Typically,

Graham A. Webb (ed.), Modern Magnetic Resonance, 1205–1212.
© 2008 *Springer.*

the rf coil temperature for cryogenic probe installations is 25 K although in the author's laboratory 500 and 600 MHz cryogenic gradient triple resonance inverse probes are both operated at 20 K to provide improved sensitivity. From a serviceability standpoint, the closed loop helium chillers perform reliably for intervals ranging from 10 to 14 months in the author's experience before requiring a rebuild. This type of required "annual" maintenance, and the associated expense, should be taken into consideration when any NMR laboratory weighs the sensitivity advantages of a cryogenic NMR probe installation vs. a high sensitivity small volume conventional NMR probe.

Sample Preparation

In the author's experience, one factor that has a considerable impact on cryogenic NMR probe performance is the uniformity of sample preparation. While conventional NMR probes are very forgiving in terms of sample-to-sample variation in column height, etc. the same cannot be said for cryogenic NMR probes. Figure 1 shows an example of the variability of performance that can be seen simply by varying column height in a conventional NMR tube over the range from 35 to 20 mm. Given that the utilization of cryogenic NMR probes will generally be in those cases where time or sample are scarce, the impact of sample preparation on the quality of the data generated should receive adequate attention.

Another less obvious factor associated with sample preparation when using a cryogenic NMR probe is the selection of tube size. While it would seem to make sense to use a 5 mm NMR tube for samples to be run in a 5 mm cryogenic NMR probe, thereby avoiding filling factor losses, reality is quite the opposite. Almost counterintuitively, substantially better performance can be obtained with extremely scarce samples by preparing them carefully in a 3 mm NMR tube. An illustration of attainable s/n ratios for a limited quantity of the simple antibiotic clindamycin in 3, 4, and 5 mm NMR tubes is presented in Figure 2. These results can be explained when the noise sources in a cryogenic NMR probe are considered. In reality, the sample is the single largest source of noise in a cryoprobe NMR experiment. Hence, as the diameter of the NMR sample itself is decreased in going from 5 to 4 and then 3 mm sample tubes, the noise contributed to the experiment correspondingly diminishes as the isolation of the rf coil from the noise source improves with smaller diameter NMR tubes [8]. Thus, despite potential filling factor losses associated with smaller diameter NMR tubes run coaxially in a 5 mm probe, performance still improves since the impact of the sample noise is larger than filling factor losses.

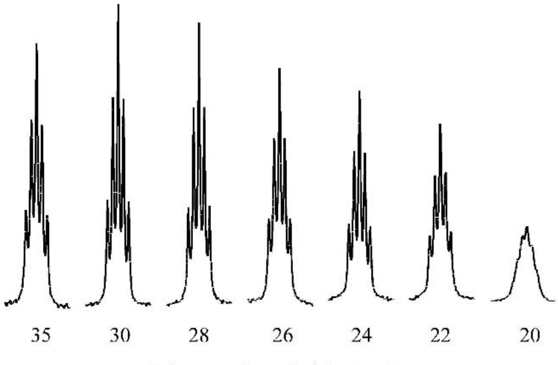

Fig. 1. The effect of solvent column height on lineshape and s/n characteristics for a 4 mm NMR tube with a sample of d_4-methanol. The spectra of the solvent multiplet were acquired in a Varian 5 mm 500 MHz triple resonance gradient-inverse detection Cold Probe^{TM}. Each column height was first gradient and then manually shimmed to afford the best possible lineshape and sensitivity.

Identification of Degradants

To illustrate what would be a typical pharmaceutical industry application of cryogenic NMR probe sensitivity, a sample of a complex alkaloid studied more than a decade ago that was kept in a sealed 5 mm NMR tube was used as a model system. The sample consisted of 2.5 mg of the complex spiro nonacyclic indoloquindoline alkaloid cryptospirolepine (**1**) that was stored in DMSO-d_6 (Scheme 1). During the life of the sample, the color changed from an initial red-orange to a dark brown. When the sample tube was cut open and the sample subjected to HPLC analysis, the chromatogram shown in Figure 3 was obtained. By LC/MS methods, there was no trace of the starting alkaloid left in the sample among the 26 degradant peaks observed in the chromatogram. An investigator dealing with a typical pharmaceutical would not be faced with total degradation. Instead, most of the drug would be intact and impurity peaks ranging from a few tenths of a percent to a few percent would be observed in the chromatogram. Nevertheless, this still affords a useful example of the capabilities engendered in cryogenic NMR probe technology.

The two largest chromatographic peaks in the HPLC of the degraded sample of **1** were identified as cryptolepinone (**2**) and cryptoquindolinone (**3**). Cryptolepinone (**2**) is a simple molecule and was readily identified from just a COSY and ^{1}H–^{13}C GHSQC spectra. Cryptoquindolinone (**3**) is a more complex molecule and required considerably more effort to characterize. Approximately 100 μg of **3** was isolated chromatographically and, using a 600 MHz spectrometer with a state-of-the-art 3 mm triple resonance gradient inverse-detection NMR probe afforded a good ^{1}H–^{13}C HSQC spectrum overnight (18 h). Given the relative differences in sensitivity of the HSQC

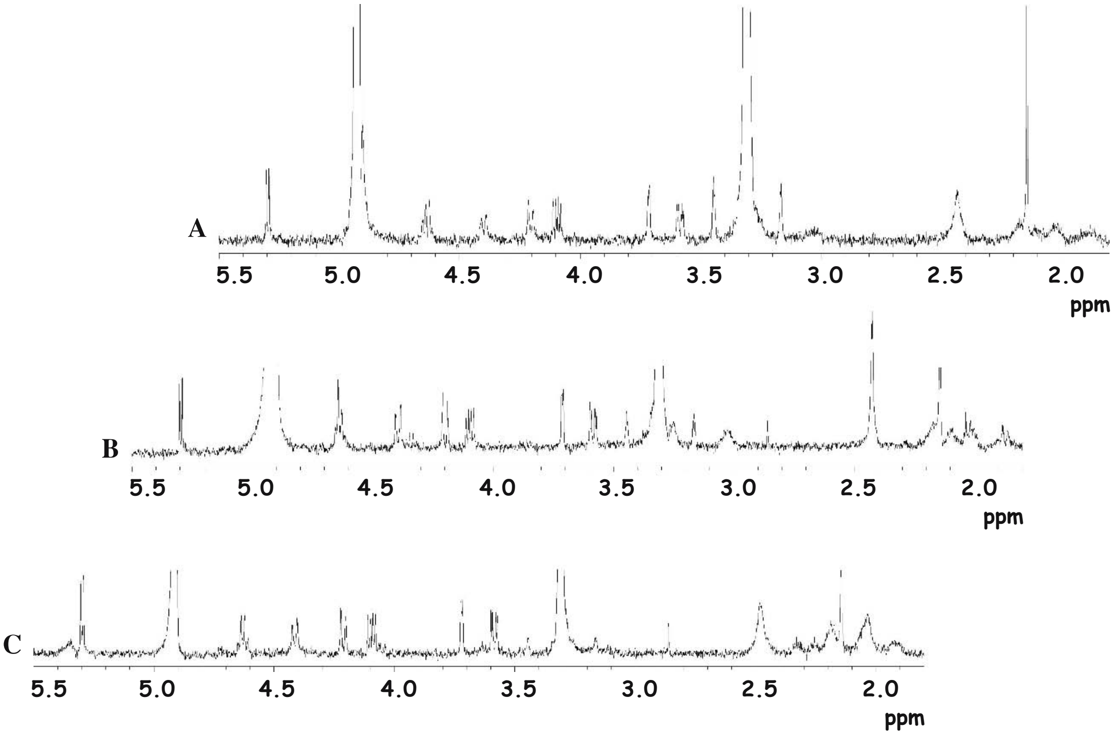

Fig. 2. Comparison spectra of 11.6 μg samples (0.0027 μmoles) of the simple antibiotic clindamycin prepared: (A) 500 μl solve in a 5 mm NMR tube; (B) 292 μl solvent in a 4 mm NMR tube; or (C) 163 μl of solvent in a 3 mm NMR tube (identical column heights of 30 mm). Each sample was gradient and then hand shimmed to afford optimum lineshape and performance, after which a spectra was recorded using 8 transients. The s/n ratio was then measured using the anomeric proton of the sugar with a 200 Hz standard "noise" window downfield of the lowfield anomeric proton doublet. The measured s/n for three samples in this limited sample scenario was: (A) 14.4:1 s/n; (B) 20.8:1; and (C) 21.5:1.

and HMBC experiments, a long-range ^{1}H–^{13}C spectrum was anticipated to require from 3 to 4 days. In contrast, using the available sample, the 6 Hz optimized HMBC [9] shown in Figure 4 was acquired overnight at 500 MHz using a 5 mm triple resonance gradient inverse-detection cryogenic NMR probe. These data were necessary to assemble the structure of the degraded molecule. Using the same sample, it was also possible over a weekend to acquire a 3–6 Hz optimized long-range ^{1}H–^{15}N CIGAR-HMBC spectrum of **3** in which correlations to three of the four nitrogens in the structure were observed, including a correlation to the N10 resonance at 230 ppm, which confirmed the presence of the C=N double bond as shown in Scheme 1. Without where indicated access to a cryogenic NMR probe, long-range ^{1}H–^{15}N data for a sample of this size would consume a week or more of spectrometer time, precluding the acquisition of these data in most laboratories.

The example just described is typical of many encountered within the pharmaceutical industry. While it is certainly possible to isolate larger samples and solve impurity and degradant structures using conventional NMR probe technology there are several disadvantages to doing so. First the chromatography required to isolate larger samples generates large volumes of chromatographic mobile phase that must be disposed of or recycled. Second, the time required to isolate larger samples for conventional spectroscopy is proportionally longer and undesirable whenever tight timelines are imposed on a pharmaceutical development effort for whatever reason.

Applications of Cryogenic NMR Probe Technology

There are several possible ways to break down applications of cryogenic NMR probe technology that have appeared in the literature thus far. One logical subdivision would be to separate applications on the basis of the type

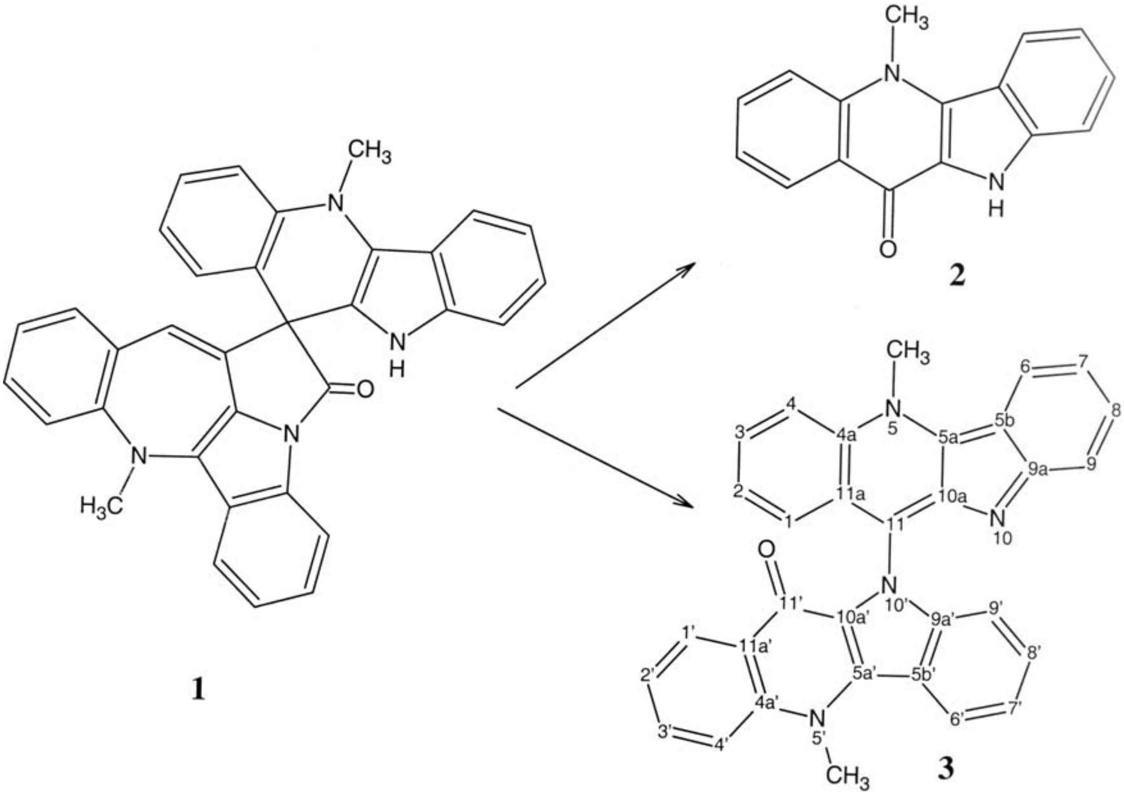

Scheme 1.

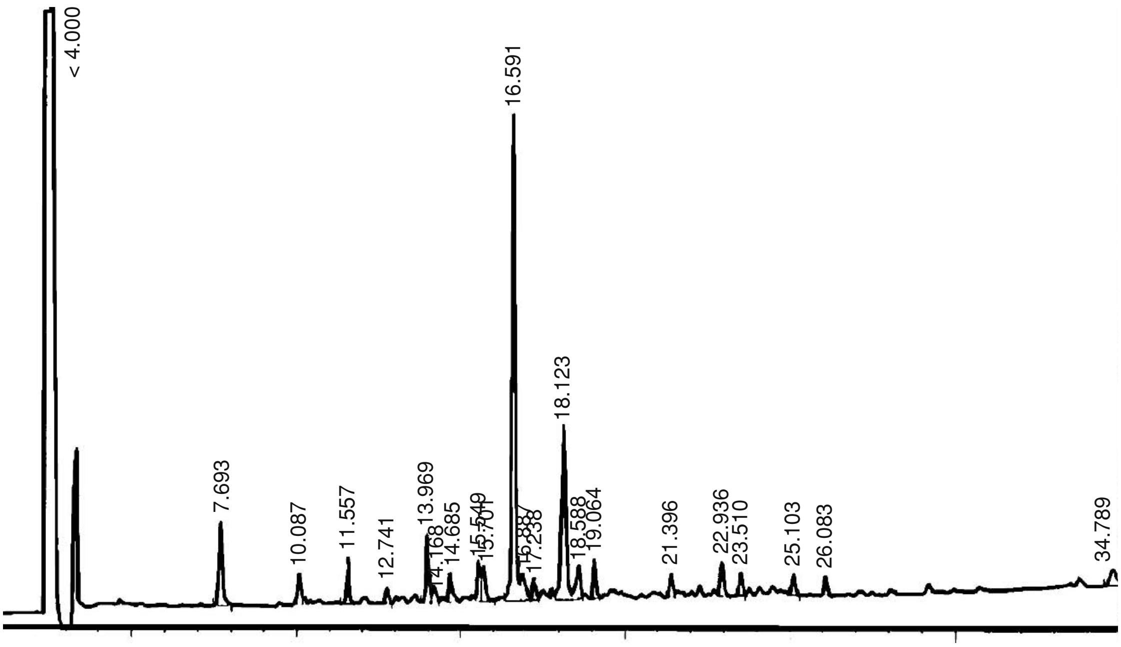

Fig. 3. HPLC chromatograph showing the result obtained after chromatographing a 2.5 mg sample of cryptospirolepine (**2**) stored in DMSO-d_6 for more than 10 years. Based on LC/MS measurements, none of the starting alkaloid remained in the sample.

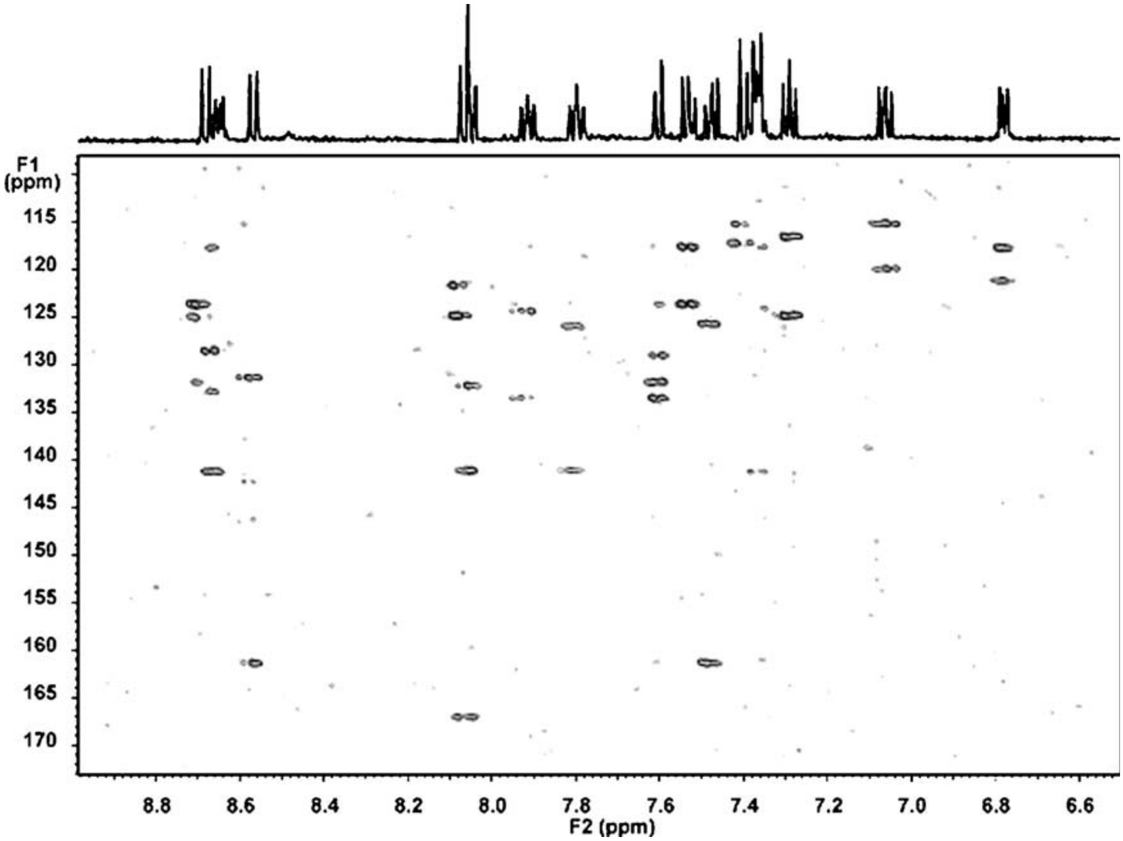

Fig. 4. Phase-sensitive 6 Hz optimized non-gradient HMBC spectrum of a sample of ∼100 μg of cryptoquindolinone (**4**) dissolved in 150 μl DMSO-d_6 in a 3 mm NMR acquired overnight using a Varian 500 MHz 5 mm triple resonance gradient inverse-detection cryogenic NMR probe.

of cryoprobe employed. However, the vast majority of applications utilize inverse-detection cryogenic probes so subdivision on the basis of probe type is not particularly informative. A more logical way of sorting applications is on the basis of the type of study reported. It is this basis that will be used for this final segment of this contribution. Reports that have appeared in the literature will be subgrouped into small molecule applications, which include both natural products and pharmaceuticals; metabolic and metabonomic studies; and finally protein and biochemical applications, in which NMR screening is included.

Small Molecule Applications

Among the earliest of the small molecule applications reported in the literature was a report by Logan and co-workers in 1999 that demonstrated the results that could be obtained with a 5 mm ^{1}H cryogenic probe in the acquisition of NOE difference spectra on small samples of the natural product taxol [10]. In 2000, the author and co-workers reported a comparative study using conventional and cryogenic 3 mm gradient inverse NMR probes using a 40 μg sample of the indole alkaloid strychnine [11]. This comparison demonstrated an improvement in performance for the cryogenic probe relative to the conventional 3 mm probe by approximately a factor of 3.5X. Liu and co-workers presented the results of their application of cryogenic NMR probe capabilities in the study of several mass-limited pharmaceutical samples [12]. With samples ranging from 10 to 80 μg this group of authors was able to record data that allowed the characterization of the samples. In an example that utilized a ^{13}C detection cryogenic NMR probe, Bringmann and co-workers [13] reported the results of a study of the biosynthetic pathway leading to acetogenic isoquinoline alkaloids. The ^{13}C-^{13}C INADEQUATE experiments employed to study the incorporation of [$^{13}C_2$] acetate were greatly facilitated by the enhanced sensitivity provided by the cryoprobe.

The significant performance advantage of cryogenic NMR probes for the acquisition of long-range ^1H–^{15}N correlation data was demonstrated using the small oxazolidinone antibiotic eperezolid by the author and co-workers in 2001 [14]. Using a 2 mg sealed sample, data were acquired in both a conventional 3 mm gradient inverse triple-resonance probe and a 5 mm cryogenic probe. Data with a s/n ratio of ~100:1 were acquired in less than 30 min using the cryogenic NMR probe while it took ~4 h to achieve only half that s/n ratio in the conventional 3 mm probe.

In 2002, Gustafson and co-workers reported the elucidation of the complex polyketide-derived macrolactam pecillastrin A from a deep water Caribbean sponge [15]. It was necessary for these authors to resort to a 500 MHz gradient inverse triple resonance cryogenic probe to acquire the necessary long-range correlation data on the 800 μg sample of the C_{82} natural product to complete the structure elucidation. Later in 2002, the author and co-workers [16] reported the utilization of a 500 MHz gradient triple resonance cryoprobe in the acquisition of long-range ^1H–^{13}C and ^1H–^{15}N correlation data in the characterization of one of the isolated degradants, **3**, shown in Scheme 1. Cook and co-workers put the sensitivity enhancement of cryogenic NMR probe technology to excellent use in their study of the Boreal forest fulvinic acid [17]. This group of authors acquired both ^1H–^{13}C HSQC and HMBC on this complex mixture, which gave >300 direct correlation responses in the HSQC spectrum. In a study that represents an interesting potential technique for natural products characterization, Griesinger and co-workers reported the measurement of long-range ^1H–^{13}C coupling constants of natural products at natural abundance using orienting media [18]. Sandvoss and co-workers, exploited the sensitivity of a cryoprobe to facilitate the acquisition of HSQC-TOCSY data for limited samples of two complex new asterosaponins from the starfish *Asterias rubens* [19]. Cryogenic NMR probe capabilities were also of importance in the acquisition of HSQC-TOCSY and ^1H–^{15}N long-range data acquired during the characterization of the complex indoloquinoline dimeric alkaloid quindolinocryptotackieine, which relied on Computer-Assisted Structure Elucidation (CASE) methods because of the extensive overlap in both the proton and carbon frequency domains [20]. Another example of the use of cryogenic NMR probe capabilities for small molecules is found in the work of Exarchou and co-workers [21] who used a combination of solid phase extraction (SPE) and cryoprobe technology for the identification of constituents present in Greek oregano. Further applications are surveyed in a recently published review [8].

Metabolic and Metabonomic Applications

In the first application of cryogenic NMR probe technology of which the author is aware, Pease and co-workers reported the results obtained with a 2.5 mm cryoprobe in the characterization of several metabolites [22]. Using a spectrometer equipped with a ^{13}C detection cryogenic NMR probe, Keun and co-workers investigated the applicability of ^{13}C spectral data as a compliment to routinely utilized ^1H data for metabonomic studies [23]. Griffin [24] reported an overview of ongoing metabonomic studies of xenobiotic toxicity and disease states that relied on cryoprobe data. Corcoran and co-workers [25] characterized the sensitivity advantages afforded by cryogenic NMR flow probes in LC-NMR-MS applications in a study of acetaominophen metabolites in urine. Stöckigt and co-workers [26] described the results of an interesting study in which alkaloid metabolism in hybrid *Rauwolfia* plant cell cultures was followed using a 500 MHz cryogenic NMR probe. The authors contrast the cryoprobe results with conventional 800 MHz NMR data on the same samples. Cryogenic NMR probe capabilities were also utilized by Bertini and co-workers [27] to study the degradation of aromatic compounds by *Pseudomonas putida*. More recent applications are surveyed in a recent review [8].

Protein and Biochemical Applications

In an early application in the field of protein NMR, Dötsch and co-workers [28] reported the development of several new ^{13}C detected protein NMR experiments designed to exploit the sensitivity of a ^{13}C detection cryoprobe. Wand and co-workers [29] described their efforts in the optimization of the application of cryogenic NMR probe technology in the study of proteins. In one of the early applications of cryoprobe technology involving proteins used in NMR-based screening of pharmaceuticals, Fesik and co-workers [30] compared the results obtained in NMR screening studies using specifically ^{13}C labeled amino acids in proteins with the more traditionally employed ^1H–^{15}N HSQC NMR screening methods. The authors demonstrated that with cryogenic NMR probes, this approach gave ~3X the sensitivity of the more traditional proton-nitrogen based screening approach.

After the initial flurry of cryoprobe applications in the field of protein NMR, there was somewhat of a gap before papers again began to appear. This interval corresponds to initial vendor-investigator collaborations during the early development of cryogenic NMR probes and when they began to appear in the laboratories of the investigators. Cowburn and co-workers [31] communicated the results that they obtained for triple resonance NMR experiments of proteins using a cryogenic NMR probe in 3–4 h that would typically require 1–2 days using conventional NMR probe technology. Bertini and co-workers [32] employed ^{13}C direct detection cryoprobe capabilities to facilitate a study of broad lines in paramagnetic metalloproteins in late 2003. Another application of the use of a ^{13}C detection cryogenic probe was the early 2004 report by Bertini and colleagues [33] in the acquisition of ^{13}C–^{13}C NOESY spectra of large macromolecules. In a departure from most other cryogenic NMR probe applications, Shu and Frieden [34] described the application of a ^{19}F cryogenic NMR probe in a study of the urea-dependent unfolding of murine adenosine deaminase by measuring sequential destabilization of ^{19}F NMR. Petros and co-workers [35] employed a 500 MHz cryogenic NMR probe in a study to define the p53 DNA-binding domain/Bcl-X_L binding interface. The cryoprobe data were used to monitor perturbations in the ^{13}C shifts of labeled substrate to the unlabeled p53 DNA-binding domain. Germann and co-workers [36] used the sensitivity of a 500 MHz cryoprobe to acquire F_2-coupled ^{1}H–^{13}C HSQC spectra of a DNA duplex containing an α-anomeric adenosine as a part of a study to explore substrate recognition by endonuclease IV. Further examples are again found in a recent review [8]. Armengod and co-workers [37] utilized a 500 MHz cryoprobe to facilitate multinuclear NMR assignments for the 18.7 kDa GTPase domain of *E. coli* MnmE protein. The enhanced sensitivity of the cryoprobe was necessary to provide adequate signal-to-noise for the assignments of the low solubility and unstable protein sample.

Conclusions

Cryogenic NMR probes are continuing to go through what will probably be a long series of iterative design improvements that should move sensitivity incrementally higher. At present, cryogenic probes offer a very significant gain in sensitivity over conventional NMR probes, typically threefold or higher at observation frequencies ranging from 500 to 900 MHz. The pharmaceutical industry is already heavily invested in cryogenic NMR probes, which have significant reduced sample isolate requirements for the characterization of impurities and degradants of pharmaceuticals in the possessive author's—laboratories. Similar advantage has been gained in laboratories devoted to the characterization of metabolites of pharmaceuticals. As investigator access to cryogenic NMR probe-equipped spectrometers continues to improve, there will undoubtedly be many new applications reported in the literature in the fields of natural product characterization, biosynthesis, forensic sample identification, and many other disciplines.

References

1. Claridge TDW. High Resolution NMR Techniques in Organic Chemistry. Pergammon Press: Amsterdam, 1999, pp 221–58.
2. Martin GE, Hadden CE, Russell DJ. In: G Gauglitz, T Vo-Dinh (Eds). Handbook of Spectroscopy, Vol. 1. Wiley-VCH: New York, 2003, pp 234–54.
3. Martin GE. In: DM Grant, RK Harris (Eds). Encyclopedia of Nuclear Magnetic Resonance, Vol. 9. Wiley and Sons: Chichester, 2002, pp 98–112.
4. Styles P, Soffe NF, Scott CA, Cragg DA, Row F, White D, White PCJ. J. Magn. Reson. 1983;60:397.
5. Styles P, Soffe NF, Scott CA. J. Magn. Reson. 1989;84: 376.
6. Anderson WA, Brey WW, Brooke AL, Cole B, Delin KA, Fuks LH, Hill HDW, Johanson ME, Kotsubo VY, Nast R, Withers RS, Wong WH. Bull. Magn. Reson. 1995;17:98.
7. Hill HDW. IEEE Trans. Appl. Superconduct. 1997;7: 3750.
8. Martin GE. In: GA Webb (Ed). Annual Reports on NMR Spectroscopy, Vol. 56. Elsevier: Amsterdam, 2005, pp 1–99.
9. These data were acquired without gradients. In the author's experience, for ^{1}H–^{13}C long-range correlation experiments with very small samples, i.e. <50 μg, the benefits of using gradients are overshadowed by the signal losses from the experiment. Our observations have been confirmed by the work of Reynolds WF, Enriquez RG. Magn. Reson. Chem. 2001;39:531.
10. Logan TM, Murali N, Wang G, Jolivet C. Magn. Reson. Chem. 1999; 37:762. Note—this paper appears twice during 1999, an earlier version in the same journal on p 512 contained errors that were corrected in the republished form cited.
11. Russell DJ, Hadden CE, Martin GE, Gibson AA, Zens AP, Carolan JL. J. Nat. Prod. 2000;63:1047.
12. Liu Y, Pease J, Potts B, Deese A, Liu YD, O'Neil-Johnson M, Withers R, Nast R. Poster 21, SMASH meeting, Argonne National Laboratory, July 16–19, 2000.
13. Bringmann G, Wohlfarth M, Rischer H, Grüne M, Schlauer J. Angew. Chem. Intl. Ed. 2000;39:1464.
14. Crouch RC, Llanos W, Mehr K, Hadden CE, Russell DJ, Martin GE. Magn. Reson. Chem. 2001;39:555.
15. Rashid MA, Gustafson KR, Crouch RC, Groweiss A, Pannell LK, Van QN, Boyd MR. Org. Lett. 2002;4:3293.
16. Martin GE, Hadden CE, Russell DJ, Kaluzny BD, Guido JE, Duholke WK, Stiemsma BA, Thamann TJ, Crouch RC, Blinov K, Elyashberg M, Martirosian ER, Molodtsov SG, Williams AJ, Schiff PL, Jr. J. Heterocyclic Chem. 2002;39:1241.
17. Cook RL, McIntyre DD, Langford CH, Vogel HJ. Environ. Sci. Technol. 2003;37:3935.
18. Verdier L, Sakhaii P, Zweckstetter M, Griesinger C. J. Magn. Reson. 2003;163:353.
19. Sandvoss M, Preiss A, Levsen K, Weisemann R, Spraul M. Magn. Reson. Chem. 2003;41:949.

20. Blinov K, Elyashberg M, Martirosian ER, Molodtsov SG, Williams AJ, Tackie AN, Sharaf MHM, Schiff PL, Jr, Crouch RC, Martin GE, Hadden CE, Guido JE, Mills KA. Magn. Reson. Chem. 2003;41:577.
21. Exarchou V, Godejohann M, van Beek TA, Gerothanassis IP, Vervoot J. Anal. Chem. 2003;75:6288.
22. Pease J, Withers R, Nast R, Deese A, Calderon P, Mehtas S, Kelly T, Laukien F. Poster W&Th P202, 40th Experimental NMR Conference, Orlando, Florida, February 28–March 5, 1999.
23. Keun HC, Beckonert O, Griffin JL, Richter C, Moskau D, Linden JC, Nicholson JK. Anal. Chem. 2002;74: 2588.
24. Griffin JL. Curr. Opin. Chem. Biol. 2003;7:648.
25. Spraul M, Freund AS, Nast RE, Withers RS, Mass WE, Corcoran O. Anal. Chem. 2003;75:1546.
26. Hinse C, Richter C, Provenzani A, Stöckigt J. Bioorg. Med. Chem. 2003;11:3913.
27. Bertini I, Provenazni A, Viezzoli MS, Pieper DH, Timmis KN. Magn. Reson. Chem. 2003;41:615.
28. Serber Z, Richter C, Moskau D, Böhlen J-M, Gerfin T, Marek D, Häberli M, Baselgia L, Laukien F, Stern SA, Hoch JC, Dötsch V. J. Am. Chem. Soc. 2000;122:3554.
29. Flynn PF, Mattiello DL, Hill HDW, Wand AJ. J. Am. Chem. Soc. 2000;122:4823.
30. Hajduk PJ, Augeri DJ, Mack J, Mendoza R, Yang J, Betz SF, Fesik SW. J. Am. Chem. Soc. 2000;122:7898.
31. Goger MJ, McDonnell JM, Cowburn D. Spectroscopy. 2003;17:161.
32. Bermel W, Bertini I, Felli IC, Kümmerle R, Pieratelli RB. J. Am. Chem. Soc. 2003;125:16423.
33. Bertini I, Felli IC, Kümmerle R, Moskau D, Pierattelli R. J. Am. Chem. Soc. 2004;126:464.
34. Shu Q, Frieden C. Biochemistry. 2004;43:1432.
35. Petrso AM, Gunasekera A, Xu N, Olejniczak ET, Fesik SW. FEBS Lett. 2004;559:171.
36. Aramini JM, Cleaver SH, Pon RT, Cunningham RP, Germann MW. J. Mol. Biol. 2004;338:77.
37. Monleón D, Yim L, Martínez-Vicent M, Armengod ME, Celda B. J. Biomol. NMR. 2004;28:307.

Flow NMR Techniques in the Pharmaceutical Sciences

Paul A. Keifer
University of Nebraska Medical Center, Eppley Institute, 986805 Nebraska Medical Center, Omaha, NE 68198-6805, USA

Introduction

Flow NMR [1,2] is a rapidly growing subset of solution-state NMR, which itself is commonly used in the pharmaceutical sciences. Flow NMR is defined here as any solution-state NMR technique in which the sample is introduced into the NMR probe as a flowing stream. The sample may—or may not—be flowing during the time of actual data acquisition. In contrast, conventional solution-state NMR uses static samples contained in glass tubes.

All known flow NMR techniques can be separated into two categories, depending upon the primary purpose of the flow. The first category uses a separation technique, such as chromatography or electrophoresis, prior to the NMR analysis (Figure 1A). The standard examples are LC-NMR and LC-NMR-MS [3]. The second category uses the liquid flow primarily as a means of transport; as a way to conveniently move solution-state samples in and out of the NMR analysis coil (Figure 1C and 1D). The standard examples of this category are direct-injection NMR (DI-NMR) [4] and flow-injection NMR (FIA-NMR) [5].

Flow NMR has both advantages and disadvantages when compared to non-flow NMR techniques. As such, although flow NMR complements non-flow NMR, it will never replace it. One advantage of flow NMR is that it allows samples to be moved quickly and easily in and out of the flow cell in the NMR probe. One disadvantage is that some flow hardware can be prone to contamination (or even clogging), because the NMR probe's flow cell is often used for hundreds of different samples.

LC-NMR

Complex mixtures are normally analyzed by fractionation, followed by an examination of the individual components one at a time. The traditional method of doing this consists of running a chromatographic separation off-line, collecting the individual fractions, evaporating them to dryness (to remove the mobile phase), and re-dissolving them in deuterated solvents. This is followed by examination with conventional NMR methods (using specialized microprobes, submicroprobes, Nanoprobes, or microcells, as needed) [6].

LC-NMR is an alternative to this method. It combines the separation and analysis steps, and because the analysis immediately follows the separation, it is especially useful if the solutes are volatile, unstable, or air-sensitive [7].

LC-NMR was first developed in 1978 [8], but during the 1980s it was more of an academic curiosity than a robust analytical tool. It became more popular during the mid-1990s as high-sensitivity flow probes became more readily available, better solvent-suppression techniques were developed [9], and the overall robustness increased. LC-NMR is now considered to be an almost routine technique [3].

The hardware for LC-NMR, including the NMR flow probe, is shown in Figure 1A. LC-NMR experiments can be run either in an on-flow mode, in which the mobile phase moves continuously during acquisition, or in a stopped-flow mode, in which the peaks of interest are stopped in the NMR flow probe for as long as is needed for NMR data acquisition. On-flow data are more useful for preliminary or survey-mode analyses, while stopped-flow data are more useful for careful examinations of individual components, using either 1D or 2D NMR techniques.

There are at least four ways to acquire stopped-flow data. First, the chromatographic peaks of interest can be stopped in the flow probe (directly as they elute from the chromatography column) and analyzed one at a time, for as long as necessary. Second, the LC pump may be programmed to "time slice" through a chromatographic peak, stopping every few seconds to acquire a new spectrum (or pumping very slowly). This is useful both for resolving multiple components (by NMR) from within a peak that is not fully resolved chromatographically, or for verifying the purity of a chromatographic peak. A third method involves collecting the chromatographic peaks of interest into loops of tubing (off-line) and then flushing the intact fractions into the NMR flow probe (one at a time) as needed. A fourth method involves trapping the eluted peaks onto another chromatographic column and then re-eluting them with a stronger solvent into the flow probe. This method (called SPE-NMR; Figure 1B) is discussed below.

Graham A. Webb (ed.), Modern Magnetic Resonance, 1213–1219.
© 2008 *Springer.*

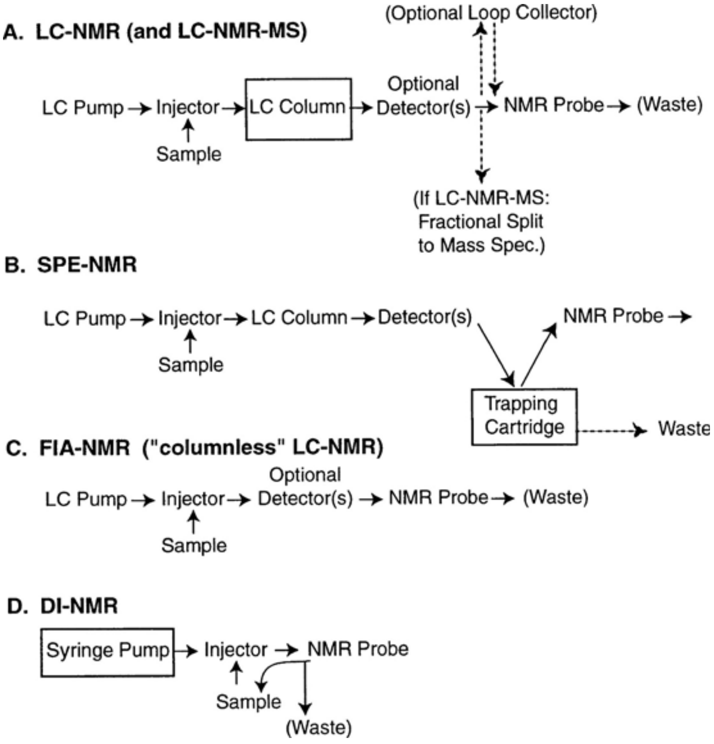
A. LC-NMR (and LC-NMR-MS)
(Optional Loop Collector)
LC Pump
Injector
LC Column
Optional Detector(s)
NMR Probe
(Waste)
Sample
(If LC-NMR-MS: Fractional Split to Mass Spec.)
B. SPE-NMR
LC Pump
Injector
LC Column
Detector(s)
NMR Probe
Sample
Trapping Cartridge
Waste
C. FIA-NMR ("columnless" LC-NMR)
Optional
LC Pump
Injector
Detector(s)
NMR Probe
(Waste)
Sample
D. DI-NMR
Syringe Pump
Injector
NMR Probe
Sample
(Waste)

Fig. 1. Flow NMR fluid paths for: (A) LC-NMR and LC-NMR-MS, (B) SPE-NMR, (C) FIA-NMR, and (D) DI-NMR. Boxes show highly significant differences of each technique. The fluid pumps in LC-NMR and SPE-NMR are typically piston pumps capable of producing solvent gradients. The pumps in DI-NMR are typically syringe pumps. The pumps in FIA-NMR can be either (solvent gradients are not typically used nor required). The optional detectors in LC-NMR, SPE-NMR, and FIA-NMR may be any type of single (or multiple) in-line non-destructive chromatography detectors (i.e., UV, RI, radiochemical, ELSD, fluorescence). In LC-NMR, SPE-NMR, and FIA-NMR, the fluid flow is always uni-directional through the probe. In DI-NMR the flow of sample fluid is usually bi-directional (unless the flow cells are made of only uniform capillary tubing), but the additional rinsing steps may be either bi-directional or uni-directional.

The acquisition of LC-NMR data can be difficult for several reasons. First, the mobile phases in LC-NMR are solvent mixtures, and because the solvents are often non-deuterated there are usually one or more solvent resonances that need to be suppressed. Second, the resonances of the organic solvents within the mobile phase contain ^{13}C satellites, which complicate the NMR spectrum and also need to be suppressed. Third, the pulse sequences of many solvent suppression schemes (like presaturation) do not work well on samples that are flowing through the probe. Fourth, during the commonly used gradient elution, the solvent resonances that need to be suppressed are constantly changing frequency (because the solvent composition changes during the experiment). In reversed-phase LC-NMR (which uses water), the chemical shift of water can move up to 3 ppm during a gradient run. Fifth, if the mobile phase is fully protonated (non-deuterated) there will be no ^{2}H lock to keep the frequencies constant. All of these problems are solved by using WET solvent suppression combined with the SCOUT-scan technique [9]. WET uses a combination of shaped-pulse selective excitation, multi-frequency SLP pulses, PFG, and indirect-detection-style ^{13}C decoupling during the shaped pulses to properly suppress multiple solvent resonances using only a two-channel spectrometer. The FIA-NMR and DI-NMR techniques (discussed below) also benefit from using SCOUT and WET [4,5].

LC-NMR-MS

Although LC-NMR is a powerful analytical tool, it can be made even more powerful by adding mass spectrometry to create on-line LC-NMR-MS [10]. This is usually done by splitting off a fraction of the chromatographic effluent (prior to the NMR flow cell) and sending it to a mass spectrometer. Numerous papers and reviews have shown how LC-NMR-MS runs one-step analyses on problems that were either sample limited or that proved to be tough structural problems [3,11,12]. LC-NMR-MS has now been fully adopted for pharmaceutical problems that are both urgent and important. Both LC-NMR and LC-NMR-MS are now commercially available (Bruker—www.bruker.com, Varian—www.varianinc.com, and JEOL—www.jeol.com).

One advantage of incorporating a mass spectrometer into the detector chain is that the mass spectrometer output provides a selective and sensitive signal that can be used to stop the fluid flow to allow NMR signal averaging (to increase the NMR signal-to-noise). This is especially useful for drug-metabolism studies where mass information about the parent compound is already known [13].

Other Detectors in LC-NMR

In LC-NMR, although the NMR serves as one detector, additional in-line detectors (connected in series) can also be used. One or more additional detectors—such as UV, fluorescence, radiochemical, refractive index, or evaporative light scattering detectors—are commonly added (Figure 1), either to get more data or to trigger the HPLC pump to stop the flow on a specific chromatographic peak (for NMR signal averaging).

Other Chromatography in LC-NMR

Other types of chromatography (besides reversed-phase HPLC) were coupled to NMR flow probes starting around 1994. Examples include capillary electrophoresis NMR (CE-NMR), capillary electrochromatography NMR (CEC-NMR), capillary HPLC (CapLC-NMR or CHPLC-NMR), supercritical fluid chromatography (SFC-NMR), and supercritical fluid extraction NMR (SFE-NMR) [3,14–16]. Additionally, size-exclusion chromatography NMR (SEC-NMR) is used to analyze polymers [17–19], and ion-exchange chromatography NMR is used to analyze both protein mixtures [20] and polar metabolites [21].

Other Plumbing Schemes: Loop-Collection LC-NMR and Solid-Phase Extraction NMR (SPE-NMR)

As mentioned above, chromatographic peaks are sometimes collected in loops (i.e. in loops of capillary tubing controlled by a loop-collection system) prior to NMR analysis. The contents of each loop can then be individually flushed into the NMR probe as needed.

A variation upon loop collection is SPE-NMR (solid phase extraction LC-NMR), which attempts to increase solute concentration (to increase NMR sensitivity) by reversing the sample dilution that inevitably occurs during loop collection and analysis [22,23]. In SPE-NMR, the HPLC peaks that elute from the column are individually diverted to in-line solid-phase extraction cartridges (Figure 1B). Water is added to the mobile phase so that the solutes are retained on this small cartridge. Once the column trapping is complete, the solutes are eluted with a stronger solvent (which can be deuterated to ease the NMR analysis) into a concentrated plug that is pumped directly into the NMR flow cell. SPE-NMR has been used for the analysis of microsomal incubate metabolites [24] and natural products [25].

Applications of LC-NMR

LC-NMR has been readily embraced by numerous fields in pharmaceutical research, as evidenced by hundreds of research publications. LC-NMR and LC-NMR-MS are now essentially routine techniques for groups studying drug metabolism [26,27]. They are proving useful for drug-manufacturing and quality-control groups [28], for the analysis of drug impurities [29], for the analysis of drug stability [30], for identifying unstable compounds [31–33] or volatile compounds [34], for metabonomics [35,36], and for evaluating the environmental fate of pharmaceuticals [37]. LC-NMR is being used for natural product drug discovery [38–41] as well as for determining the chirality of natural products [42]. LC-NMR was also evaluated for monitoring reactions within production facilities [43] and has proven useful in evaluating compounds that do not contain UV chromophores [44]. Numerous reviews of the applications of LC-NMR and LC-NMR-MS are in the literature [3,11].

Limitations of LC-NMR

Although LC-NMR and LC-NMR-MS techniques are very powerful analytically, they tend to be slow (1–24 h) compared to LC-MS [45] or other high-throughput analysis methods (2–5 min) because of two limitations. First, NMR is less sensitive than many other techniques (i.e., mass spectrometry) and the need for signal averaging consumes time. Second, although LC-NMR can handle solvent gradients, samples for NMR need to have a “uniform magnetic susceptibility,” which means that LC-NMR is not easily adaptable to ultra-fast “turbo” solvent gradients that ramp from 0 to 100% in just a few minutes. These two limitations, combined with the higher cost of an LC-NMR system (as compared to LC-MS), mean that LC-NMR and LC-NMR-MS are best suited to solving the toughest problems on the most expensive samples that cannot be solved in other ways.

Flow-Injection Analysis NMR (FIA-NMR)

The second category of flow NMR methods uses the liquid flow primarily as a means of transport to and from the NMR probe, and does not use any separation technique. This category consists of two basic techniques that differ in the type of fluid flow used: flow-injection analysis NMR (FIA-NMR) [5] and direct-injection NMR (DI-NMR) [4].

Like classical flow injection analysis [46], classical FIA-NMR [5] injects the sample as a plug into an unbroken stream of fluid (an "isocratic mobile phase"), and the resulting sample plug is pushed into the NMR detector coil (and then stopped) by the controlled motion of the fluid (Figure 1C). The fluid serves three purposes. First, it serves as a conveyer belt to carry the sample into the NMR probe. Second, it rinses out the flow cell at the end of the analysis. Third, it allows samples smaller than the volume of the flow cell to be analyzed. (The intact liquid stream reduces the NMR line broadenings caused by the magnetic-susceptibility distortions that would arise from air bubbles in a non-filled NMR flow cell, although this also causes sample dilution when small sample volumes are injected. Unlike other variants of FIA, conventional FIA does not use any air bubbles (or other devices) as separators in the liquid stream [46].)

As in all other flow NMR techniques, once the sample is placed within the NMR flow cell, the NMR acquisition itself can be readily automated. This can consist of PFG gradient shimming (if desired), automated receiver gain adjustment (if desired), and SCOUT scans (to find the solvent frequencies and create the appropriate WET-shaped pulse), followed by the acquisition of 1D or 2D NMR spectra using WET solvent suppression. The whole process (injection and acquisition), for entire queues of samples, is normally controlled by automation software running on the NMR spectrometer.

The first hyphenation of FIA and NMR was published in 1997 [47,48], where it was called "column-less LC-NMR." More recent papers have since demonstrated its viability as an analytical method [5,49,50], and it has been the subject of several reviews [6,51]. Note that there are entire books [46] and journals [52] dedicated to the technique of FIA.

Direct Injection NMR (DI-NMR)

In contrast to FIA-NMR, DI-NMR [4] injects the sample solution directly into an empty flow cell in the NMR probe (Figure 1D). The sample is not injected into a stream of liquid (because no "mobile phase" is present), which generates the maximum NMR sensitivity (because there is no sample dilution) and allows the sample to be recovered intact if desired. Sample recovery is normally accomplished by pulling the analyzed samples back out the way they went in (Figure 1D). The flow cell is then rinsed by pushing clean solvent in and out as many times as is needed to remove traces of solute. Residual rinse solvents can be a source of sample dilution, although the flow cell is emptied each time, so the dilution is usually minimal. Although samples could instead be recovered by pushing them on through the detector coil, this is usually inefficient and requires additional inefficient rinsing steps, unless the NMR flow cell has a capillary (non-standard) geometry.

Although the solvents used in LC-NMR are usually simple mixtures of water and either acetonitrile or methanol, DI-NMR has been run with a wider range of solvents and solvent mixtures, including $CHCl_3$, dimethylsulfoxide (DMSO), tetrahydrofuran (THF), biofluids, and water, as well as HPLC mobile phases. NMR software has evolved so much that it is now relatively easy to automatically acquire NMR data on samples dissolved in even complex solvent mixtures when using WET solvent suppression and the SCOUT-scan technique [9].

One disadvantage of DI-NMR is that the volume of the injected samples must be bigger than the volume of the NMR flow cell or the NMR resonances will be broadened (due to magnetic-susceptibility distortions arising from the air pockets within the flow cell). The other disadvantage of DI-NMR is that the sample cell can become contaminated from repeated contact with "raw" samples, or the connecting capillary tubing can become plugged. Both of these issues can be addressed in FIA-NMR, although FIA-NMR does not readily allow sample recovery, and does not generate the maximum possible NMR sensitivity. Note that FIA-NMR and DI-NMR are complementary, in that their advantages and disadvantages are the opposite of each other.

The injection in DI-NMR is typically performed using a robotic liquid handler controlled by the NMR spectrometer. The normal liquid handlers used for DI-NMR allow samples to be stored in a wide range of containers, including disposable vials or microtiter plates (vs. the precision glass sample tubes required in conventional solution-state NMR). DI-NMR is now commercially available [as systems called VAST (from Varian—www.varianinc.com) and BEST (from Bruker—www.bruker.com)]. These systems are normally capable of analyzing samples ranging in size from 150 to 350 ml (or more), with concentrations ranging from 1–50 mM, and stored in multiple 96-well microtiter plates. A typical analysis time may range from 2 to 7 min, depending upon the viscosity of the solvent, the concentration and volume of the sample, and the amount of rinsing desired. A complete description of DI-NMR was published in 2000 [4], which included a description of the use of DI-NMR in the analysis of combinatorial chemistry libraries, and numerous examples of different data-presentation formats.

The technique of DI-NMR was first published in 1997 [47,48], followed quickly by publications describing its use for analyzing chemical libraries [4,53–58], for analyzing biological fluids (including the commercial analysis of human plasma) [59,60], and for the screening of ligand binding with proteins and other biomolecules [36,61–63]. DI-NMR has spurred further developments in flow probes

[64], NMR pulse sequences [65], and reference standards [66,67]. The development of DI-NMR has also been the subject of several reviews [2,6,36,47,48,51,63].

Complementary Technologies

Numerous developments in other fields of NMR are proving useful to flow NMR. One important area is in probe development. "Normal" flow probes have active volumes of 30–60 ml. (Conventional flow cells require sample volumes of at least twice the active volume to obtain reasonable NMR lineshapes.) Some applications may require probes that have different volumes, to analyze either smaller-volume or lower-concentration samples. For the latter application, a larger volume (120-ml) flow probe was optimized for "SAR-by-NMR" (NMR-screening) assays that use DI-NMR to acquire ^{15}N HSQC data [64].

Microcoils

Even more interest is being generated by the work on smaller-volume "microcoil" flow probes [3,15,68–71]. The RF coils of microcoil probes are wound around capillary tubing and this produces probes with active volumes of typically 1–5 ml. These probes are usually filled using a flow technique, but not always [72,73]. There are dozens of articles now describing the use of microcoil flow probes to analyze effluents from on-line capillary HPLC, capillary electrophoresis (CE), and capillary isotachophoresis (cITP-NMR) [74–79]. As evidence of their sensitivity, a microcoil was used to analyze the 540 pmol of compound cleaved from a single 160-micron-diameter solid-phase resin bead [80]. A microcoil flow probe was also used to identify members of a natural products library using 5–50 micrograms of compound dissolved in 3 microliters of solvent [57]. Microcoil probes have now been interfaced with automated capillary liquid handlers, and are commercially available (from the MRM division of Protasis; www.protasis.com).

Interchangeable Flow Cells

Another limitation of flow NMR, particularly DI-NMR, is that repetitive injections of "raw" samples can eventually contaminate (or clog) the NMR flow cell. (LC-NMR samples have been "filtered" through the HPLC column, and FIA-NMR can incorporate in-line filters, but DI-NMR cannot easily do so.) This limitation has been addressed with the development of user-changeable flow cells to form the interchangeable flow cell (IFC) probe, which has been discussed in the literature [6,51]. User-changeable flow cells are designed to minimize instrument downtime.

Cold Probes

NMR users always need better spectral signal-to-noise. The conventional solution is to increase the signal intensity, but another way is to decrease the noise. This has been accomplished by cooling the electronics of the NMR probe (but not the sample) so as to reduce thermal noise. The resulting probe, called a cold probe, a cryogenic probe, or a cryoprobe, is usually operated at a temperature of 25 K, which provides a signal-to-noise improvement of about fourfold [81]. This technology has since been incorporated into flow probes [11,82,83].

Parallel NMR: Multiplex NMR

The goal for any high-throughput technique is to run the analyses in parallel. NMR has historically been only a serial technique, but this is changing, as ways are being developed to acquire NMR data in parallel—by placing multiple sample chambers, each with their own dedicated detection (RF) coil, all within one NMR probe (within one magnet) [84,85]. The multiple coils are usually designed so they can analyze one sample while other samples are being loaded into different coils (to reduce the percentage of analysis time lost to shuttling samples into the NMR magnet) [86,87]. Other functions of multiple-coil (multiplex) probes are to measure rapid-reaction kinetics (by placing multiple coils at different points along a flowing sample) [88], to acquire capillary electrophoresis data using solenoidal microcoils [89], or to acquire the difference spectrum between two samples in a "difference probe" [90,91].

Alternative Ways to Acquire nD-NMR Data

The filter diagonalization method (FDM) [92] is a way to rapidly acquire nD-NMR data rapidly, and store the resulting data in a much smaller space. Although the development of FDM is still in its infancy, if it can rapidly acquire 2D ^{1}H{^{13}C} or ^{1}H{^{15}N} heteronuclear correlation (HSQC) data, this could help DI-NMR either to characterize combinatorial chemistry libraries or to screen proteins for ligand binding. It may also benefit LC-NMR.

Frydman *et al.* have developed another method for rapidly acquiring nD-NMR data [93]. They have proposed using this technique in combination with LC-NMR [94]. Although its sensitivity limitations make it currently impractical for LC-NMR, it may prove useful in the DI-NMR analyses of compound libraries.

DOSY: A Possible Alternative to LC-NMR

Diffusion-ordered spectroscopy (DOSY) [95] can separate the 1D NMR spectrum of a mixture into individual 1D sub-spectra based upon the diffusion rates of the individual components. DOSY is already being used now for NMR screening (determining which compounds bind to large-molecule receptors) [96], although not in a flow mode. (It easily could be because other kinds of NMR screening are being performed using flow NMR.) DOSY has also been proposed as a possible alternative to LC-NMR [97]. The *combined* use of DOSY on LC-NMR fractions is interesting, but it is unlikely to be a practical technique due to the typically low NMR signal-to-noise in LC-NMR. DOSY should prove useful within DI-NMR, however, to verify compound purity in a chemical library.

Conclusions

A variety of different flow NMR techniques are currently being used in the pharmaceutical sciences, each with their own unique advantages and disadvantages. LC-NMR techniques offer separation capabilities, and are powerful, but are often slow. FIA-NMR is well suited to fast, repetitive, destructive analyses that do not need chromatographic separations, where carryover must be minimized, and which do not require much NMR time-averaging. DI-NMR is best suited to repetitive, non-destructive analyses that do not need chromatographic separations, where the sample needs to be recovered, where slight carryover is not a problem, and which may need time-averaging of the NMR data.

References

1. Dorn HC. In: DM Grant, RK Harris (Eds). Encyclopedia of Nuclear Magnetic Resonance. John Wiley & Sons Ltd.: West Sussex, England, 1996, p. 2026.
2. Keifer PA. Curr. Opin. Chem. Biol. 2003;7:388.
3. Albert K. On-Line LC-NMR and Related Techniques. Wiley: Chichester, 2002.
4. Keifer PA, Smallcombe SH, Williams EH, Salomon KE, Mendez G, Belletire JL, Moore CD. J. Comb. Chem. 2000;2:151.
5. Keifer PA. Magn. Reson. Chem. 2003;41:509.
6. Keifer PA. In: E Jucker (Ed). Progress in Drug Research, Vol. 55. Birkhauser Verlag: Basel, 2000, p. 137.
7. Schlotterbeck G, Tseng LH, Haendel H, Braumann U, Albert K. Anal. Chem. 1997;69:1421.
8. Watanabe N, Niki E. Proc. Jpn. Acad. Ser. B 1978;54:194.
9. Smallcombe SH, Patt SL, Keifer PA. J. Magn. Reson. A 1995;117:295.
10. Bendel P, Lai CM, Lauterbur PC. J. Magn. Reson. 1980;38:343.
11. Corcoran O, Spraul M. Drug Discov. Today 2003;8:624.
12. Wilson ID. J. Chromatogr. A 2000;892:315.
13. Dear GJ, Plumb RS, Sweatman BC, Ayrton J, Lindon JC, Nicholson JK, Ismail IM. J. Chromatogr. B Biomed. Sci. Appl. 2000;748:281.
14. Albert K. J. Chromatogr. A 1995;703:123.
15. Olson DL, Lacey ME, Sweedler JV. Anal. Chem. 1998;70:257A.
16. Gfrorer P, Schewitz J, Pusecker K, Bayer E. Anal. Chem. 1999;71:315A.
17. Ute K, Niimi R, Hongo SY, Hatada K. Polym. J. 1998;30:439.
18. Kramer I, Pasch H, Handel H, Albert K. Macromol. Chem. Phys. 1999;200:1734.
19. Ludlow M, Louden D, Handley A, Taylor S, Wright B, Wilson ID. J. Chromatogr. A 1999;857:89.
20. Ruckert M, Wohlfarth M, Bringmann G. J. Chromatogr. A 1999;840:131.
21. Dear GJ, Plumb RS, Sweatman BC, Parry PS, Roberts AD, Lindon JC, Nicholson JK, Ismail IM. J. Chromatogr. B Biomed. Sci. Appl. 2000;748:295.
22. Griffiths L, Horton R. Magn. Reson. Chem. 1998;36:104.
23. de Koning JA, Hogenboom AC, Lacker T, Strohschein S, Albert K, Brinkman UAT. J. Chromatogr. A 1998;813:55.
24. Bao D, Thanabal V, Pool WF. J. Pharm. Biomed. Anal. 2002;28:23.
25. Nyberg NT, Baumann H, Kenne L. Magn. Reson. Chem. 2001;39:236.
26. Tugnait M, Lenz EM, Hofmann M, Spraul M, Wilson ID, Lindon JC, Nicholson JK. J. Pharm. Biomed. Anal. 2003;30:1561.
27. Mortensen RW, Corcoran O, Cornett C, Sidelmann UG, Lindon JC, Nicholson JK, Hansen SH. Drug Metab. Dispos. 2001;29:375.
28. Jiang T, Phelan M. J. Pharm. Sci. Technol. 2003;57:287.
29. Sharman GJ, Jones IC. Magn. Reson. Chem. 2003;41:448.
30. Segmuller BE, Armstrong BL, Dunphy R, Oyler AR. J. Pharm. Biomed. Anal. 2000;23:927.
31. Fischer H, Gyllenhaal O, Vessman J, Albert K. Anal. Chem. 2003;75:622.
32. Wolfender JL, Verotta L, Belvisi L, Fuzzati N, Hostettmann K. Phytochem. Anal. 2003;14:290.
33. Stintzing FC, Conrad J, Klaiber I, Beifuss U, Carle R. Phytochemistry 2004;65:415.
34. Elipe MVS, Huskey SE, Zhu B. J. Pharm. Biomed. Anal. 2003;30:1431.
35. Gavaghan CL, Nicholson JK, Connor SC, Wilson ID, Wright B, Holmes E. Anal. Biochem. 2001;291:245.
36. Stockman BJ. Curr. Opin. Drug. Discov. Dev. 2000;3:269.
37. Cardoza LA, Williams TD, Drake B, Larive CK. ACS Symp. Ser. 2003;850:146.
38. Hostettmann K, Marston A. Phytochem. Rev. 2003;1:275.
39. Wolfender JL, Ndjoko K, Hostettmann K. J. Chromatogr. A 2003;1000:437.
40. Bobzin SC, Yang S, Kasten TP. J. Chromatogr. B Biomed. Sci. Appl. 2000;748:259.
41. Sandvoss M, Weltring A, Preiss A, Levsen K, Wuensch G. J. Chromatogr. A 2001;917:75.
42. Queiroz EF, Wolfender JL, Raoelison G, Hostettmann K. Phytochem. Anal. 2003;14:34.
43. Maiwald M, Fischer HH, Kim YK, Albert K, Hasse H. J. Magn. Reson. 2004;166:135.
44. Petritis K, Gillaizeau I, Elfakir C, Dreux M, Petit A, Bongibault N, Luijten W. J. Sep. Sci. 2002;25:593.

45. Yurek DA, Branch DL, Kuo MS. J. Comb. Chem. 2002;4:138.
46. Ruzicka J, Hansen EH. Flow Injection Analyses, John Wiley and Sons: New York, NY, 1988.
47. Keifer PA. Drug Discov. Today 1997;2:468.
48. Keifer PA. Drugs Future 1998;23:301.
49. Lenz E, Taylor S, Collins C, Wilson ID, Louden D, Handley A. J. Pharm. Biomed. Anal. 2002;27:191.
50. Louden D, Handley A, Taylor S, Lenz E, Miller S, Wilson ID, Sage A. Analyst 2000;125:927.
51. Keifer PA. In: H-Y Mei, AW Czarnik (Ed), Integrated Drug Discovery Technologies. Marcel Dekker Inc.: New York, NY, 2002, p. 485.
52. Segundo MA, Rangel AOSS. J. Flow Injection Anal. 2002;19:3.
53. Hamper BC, Snyderman DM, Owen TJ, Scates AM, Owsley DC, Kesselring AS, Chott RC. J. Comb. Chem. 1999;1:140.
54. Lewis K, Phelps D, Sefler A. Am. Pharm. Rev. 2000;3:63.
55. Combs A, Rafalski M. J. Comb. Chem. 2000;2:29.
56. Kalelkar S, Dow ER, Grimes J, Clapham M, Hu H. J. Comb. Chem. 2002;4:622.
57. Eldridge GR, Vervoort HC, Lee CM, Cremin PA, Williams CT, Hart SM, Goering MG, O'Neil-Johnson M, Zeng L. Anal. Chem. 2002;74:3963.
58. Leo GC, Krikava A, Caldwell GW. Anal. Chem. 2003;75:1954.
59. Potts BCM, Deese AJ, Stevens GJ, Reily MD, Robertson DG, Theiss J. J. Pharm. Biomed. Anal. 2001;26:463.
60. Robertson DG, Reily MD, Sigler RE, Wells DF, Paterson DA, Braden TK. Toxicol. Sci. 2000;57:326.
61. Gmeiner WH, Cui W, Konerding DE, Keifer PA, Sharma SK, Soto AM, Marky LA, Lown JW. J. Biomol. Struct. Dyn. 1999;17:507.
62. Ross A, Schlotterbeck G, Klaus W, Senn H. J. Biomol. NMR 2000;16:139.
63. Stockman BJ, Farley KA, Angwin DT. Methods Enzymol. 2001;338:230.
64. Haner RL, Llanos W, Mueller L. J. Magn. Reson. 2000;143:69.
65. Spitzer T, Sefler AM, Rutkowske R. Magn. Reson. Chem. 2001;39:539.
66. Gerritz SW, Sefler AM. J. Comb. Chem. 2000;2:39.
67. Pinciroli V, Biancardi R, Colombo N, Colombo M, Rizzo V. J. Comb. Chem. 2001;3:434.
68. Wolters AM, Jayawickrama DA, Sweedler JV. Curr. Opin. Chem. Biol. 2002;6:711.
69. Lacey ME, Subramanian R, Olson DL, Webb AG, Sweedler JV. Chem. Rev. 1999;99:3133.
70. Webb AG. Prog. Nucl. Magn. Reson. Spectrosc. 1997;31:1.
71. Li Y, Logan TM, Edison AS, Webb A. J. Magn. Reson. 2003;164:128.
72. Griffin JL, Nicholls AW, Keun HC, Mortishire-Smith RJ, Nicholson JK, Kuehn T. Analyst 2002;127:582.
73. Schlotterbeck G, Ross A, Hochstrasser R, Senn H, Kuehn T, Marek D, Schett O. Anal. Chem. 2002;74:4464.
74. Lacey ME, Tan ZJ, Webb AG, Sweedler JV. J. Chromatogr. A 2001;922:139.
75. Kautz RA, Lacey ME, Wolters AM, Foret F, Webb AG, Karger BL, Sweedler JV. J. Am. Chem. Soc. 2001;123:3159.
76. Wolters AM, Jayawickrama DA, Larive CK, Sweedler JV. Anal. Chem. 2002;74:2306.
77. Krucker M, Lienau A, Putzbach K, Grynbaum MD, Schuler P, Albert K. Anal. Chem. 2004;76:2623.
78. Lacey ME, Webb AG, Sweedler JV. Anal. Chem. 2002;74:4583.
79. Wolters AM, Jayawickrama DA, Larive CK, Sweedler JV. Anal. Chem. 2002;74:4191.
80. Lacey ME, Sweedler JV, Larive CK, Pipe AJ, Farrant RD. J. Magn. Reson. 2001;153:215.
81. Anderson WA, Brey WW, Brooke AL, Cole B, Delin KA, Fuks LF, Hill HDW, Johanson ME, Kotsubo VY, Nast R, Withers RS, Wong WH. Bull. Magn. Reson. 1995;17:98.
82. Spraul M, Freund AS, Nast RE, Withers RS, Maas WE, Corcoran O. Anal. Chem. 2003;75:1536.
83. Exarchou V, Godejohann M, Van Beek TA, Gerothanassis IP, Vervoort J. Anal. Chem. 2003;75:6288.
84. Webb AG, Sweedler JV, Raftery D. On-Line LC-NMR and Related Techniques. John Wiley & Sons Ltd.: West Sussex, England, 2002, p. 259.
85. Raftery D. Anal. Bioanal. Chem. 2004;378:1403.
86. Macnaughtan MA, Hou T, Xu J, Raftery D. Anal. Chem. 2003;75:5116.
87. Zhang X, Sweedler JV, Webb AG. J. Magn. Reson. 2001;153:254.
88. Ciobanu L, Jayawickrama DA, Zhang X, Webb AG, Sweedler JV. Angew. Chem. Int. Ed. Engl. 2003;42:4669.
89. Wolters AM, Jayawickrama DA, Webb AG, Sweedler JV. Anal. Chem. 2002;74:5550.
90. Macnaughtan MA, Hou T, Macnamara E, Santini RE, Raftery D. J. Magn. Reson. 2002;156:97.
91. Macnaughtan MA, Smith AP, Goldsbrough PB, Santini RE, Raftery D. Anal. Bioanal. Chem. 2004;378:1520.
92. Mandelshtam VA. Prog. Nucl. Magn. Reson. Spectrosc. 2001;38:159.
93. Frydman L, Scherf T, Lupulescu A. Proc. Natl. Acad. Sci. U.S.A. 2002;99:15858.
94. Shapira B, Karton A, Aronzon D, Frydman L. J. Am. Chem. Soc. 2004;126:1262.
95. Johnson CS Jr. Prog. Nucl. Magn. Reson. Spectrosc. 1999;34:203.
96. Hodge P, Monvisade P, Morris GA, Preece I. Chem. Commun. 2001;3:239.
97. Huo R, Wehrens R, Van Duynhoven J, Buydens LMC. Anal. Chim. Acta 2003;490:231.

Developments in NMR Hyphenation for Pharmaceutical Industry

Manfred Spraul

Bruker BioSpin GmbH, Silberstreifen, D-76287 Rheinstettan, Germany

Introduction

First introduced in 1978 [1], LC-NMR since the early 1990s has grown into a standard analytical method in pharmaceutical industry with an increasing number of publications every year [2–24].

This has been enabled by improved magnet design, dedicated NMR flow probes, automatic multiple solvent suppression, and full automation. The typical application areas for LC-NMR in the pharmaceutical industry are:

- screening for drug metabolites in biofluids or extracts;
- drug impurity profiling;
- drug stability profiling;
- detection of new biomarkers of toxicity or disease;
- combinatorial chemistry and parallel synthesis to investigate product mixtures;
- natural product screening.

The following operation modes have evolved and can be executed in an automated fashion on a modern hyphenated system which will be explained in more detail later and include:

- on-flow LC-NMR;
- direct stop-flow;
- loop collection [17];
- post-column solid phase extraction (SPE) [14,23];
- time slicing.

To be able to perform the stop-flow, loop collection, or post-column SPE, a non-NMR detector is needed to locate LC peaks of interest for the NMR transfer. UV detection was used exclusively in early LC-NMR experiments. Currently, DAD and MS are used for LC peak detection in most cases. Refractive index detectors are less suitable for LC-NMR due to the gradient LC methods that are required to keep the eluting peaks as sharp as possible to preserve the NMR sensitivity.

In the following sections, the operation modes mentioned above will be explained and the required hardware discussed.

On-Flow LC-NMR

In this mode, the flow from the chromatographic column is guided through a flow cell in a dedicated NMR flow probe. Repeated NMR measurements are performed in a pseudo-two-dimensional (2D) acquisition mode; however in contrast to real 2D experiments, there is no incremented evolution time and timing stays constant over the whole experiment. The time for one measurement is defined by the flow rate of the chromatographic separation and typically lies between 8 and 20 s for standard analytical columns. The flow cells used in the NMR probe head typically have an active volume of 120 or 60 μl, with the active volume defined by the detection coil dimensions. The total volume of such a flow cell is about 200 or 100 μl, respectively.

The possible accumulation time in one experiment of an on-flow run is defined not only by the flow rate, but also by the steepness of the LC gradient. Normally in reversed phase separations, water is replaced by D_2O for locking purposes. In addition to the locking advantage, the need for solvent suppression on two signals is also reduced. If water is used, the signal can be very broad, especially when methanol is used as the cosolvent through exchange with the methanol-OH. The suppression power required for such a system would be large and would also reduce desired signals in the vicinity of the water resonance. When D_2O is used, non-deuterated methanol or acetonitrile are added for the LC gradient. The dynamic range of the NMR detection system is limited by the large concentration difference between the compounds of interest and the organic solvent signal, which is orders of magnitude larger. Suppression of the solvent signals therefore is mandatory in order to achieve the optimized detection of the weak solute signals of interest.

A further complication arises through the fact that the chemical shifts of the NMR signals are strongly dependent on the composition of the solvent mixture and the pH. This means in an LC-gradient run, the relative position of the organic solvent signal to the water frequency constantly moves. If one has to suppress the solvent, one has to follow this change in frequency constantly. Within one experiment the suppression frequencies can be defined

Graham A. Webb (ed.), Modern Magnetic Resonance, 1221–1228.
© 2008 *Springer.*

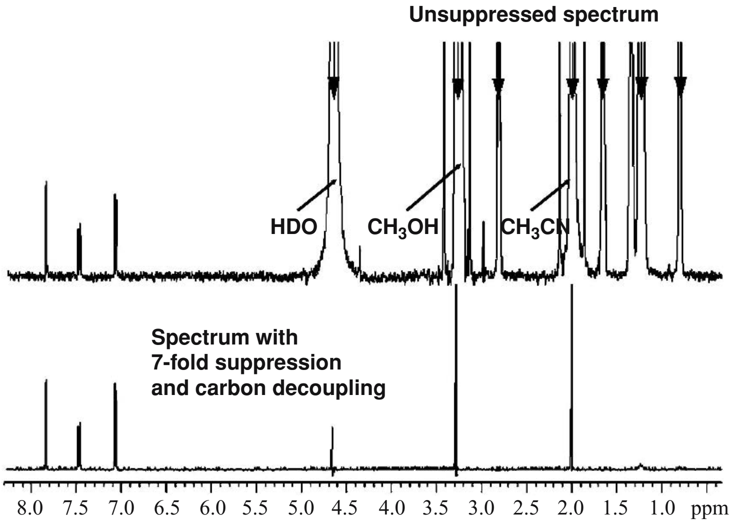

Fig. 1. The effect of automatic solvent suppression in LC-NMR on a solvent system containing acetonitrile, methanol, water, and ion-pair reagent, the signals marked with an arrow are selected for suppression automatically.

automatically by a short preparation experiment, which only takes a few seconds and delivers the correct frequencies that are then loaded for the experiment with suppression. In order not to lose suppression quality, the length of one accumulation is restricted due to the steepness of the LC gradient. Solvent signals like acetonitrile or methanol show a single resonance line, which is easy to suppress. However, at the 0.5% level of this signal, a doublet is visible. This is due to the fact that 1% of the carbon atoms are not carbon-12, but carbon-13, which are NMR active and cause the splitting of the resonance line to a doublet. These carbon satellite lines, as they are called, are still large compared to the solute signals and also increase the disturbed area in the spectrum. Therefore it is advantageous to remove the doublet by also irradiating the carbon frequencies at the same time; by this action the doublet collapses into the singlet line of the C12-based solvent, which is already suppressed. The automation control of a modern NMR spectrometer allows the suppression of as many solvent lines as needed, by using phase-shifted-shaped radio frequency pulses and carbon decoupling. However, it is obvious that the observable region in a spectrum can be diminished seriously when suppressing too many solvent or buffer lines.

Figure 1 shows the typical effect solvent suppression, comparing the non-suppressed spectrum with the result of the automatic solvent suppressed spectra. In this case, an ion-pair reagent separation was performed and the signals of acetonitrile, methanol, residual water, and octane-1-sulfonic acid were suppressed.

The lines to be suppressed are indicated by arrows in the upper spectrum. The solute in this case was 5-hydroxysalicylic acid.

A typical on-flow experiment is shown in Figure 2, along the horizontal axis the proton-NMR chemical shift is shown, along the vertical axis the retention time of the chromatogram is increasing from bottom to top. The lines at 2 and 4.7 ppm are due to the suppressed acetonitrile and water signals. A 100 µl of urine, obtained 4 h after ingestion of 500 mg of paracetamol (male adult) was injected onto a 150 × 4.6 mm RP-18 column using a flow rate of 0.8 ml/min and a time resolution on the NMR detection of 16 s. The acetonitrile signal shows the change in frequency due to the LC gradient, it moves to higher ppm values with increasing amount of acetonitrile. Some paracetamol metabolites can be identified through the aromatic signals between 6.8 and 7.3 ppm. The anomeric protons of the glucuronides show resonances at $\sim$5.2 ppm.

Taking a horizontal row out of the on-flow spectrum generates the ^{1}H-spectrum at a given retention time.

Due to the short residence time in the flow cell and by this the limited number of scans per row, sensitivity in this operation mode of LC-NMR is limited to the microgram range of detection. Therefore the need for stopped flow measurements emerged, especially for pharmaceutical applications, where often impurities or low concentration metabolites have to be identified.

Direct Stop-Flow

To be able to stop the flow exactly when the maximum of an LC peak of interest has reached the center of the flow cell, fast detection of the LC peaks is needed. NMR is too slow and not sensitive enough, therefore other analytical tools are needed. UV detection is most often used as a

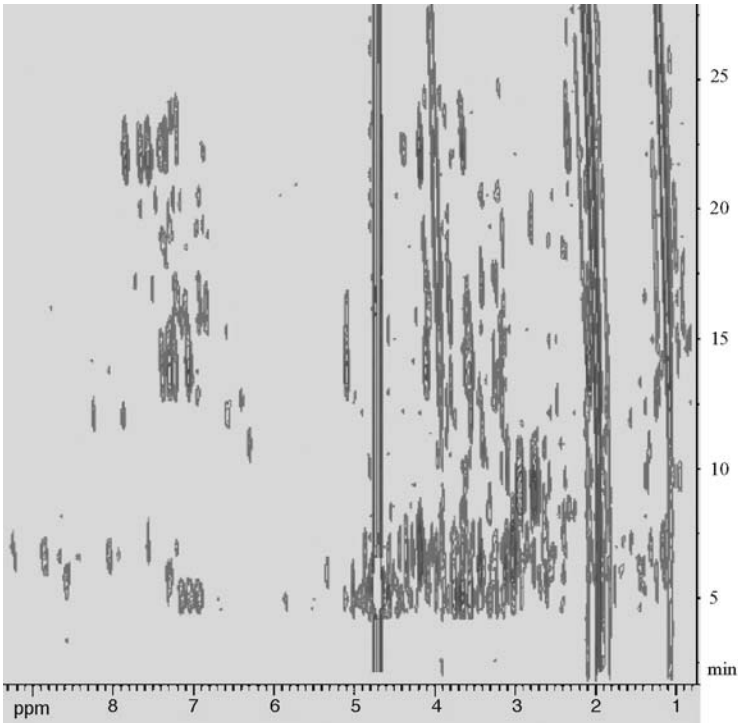

Fig. 2. On-Flow LC-NMR spectrum of a reversed phase separation after injection of a human urine obtained 4 h after ingestion of 500 mg of paracetamol (150 × 4.6 mm RP-18 column using a flow rate of 0.8 ml/min). (See also Plate 92 on page XVIII in the Color Plate Section.)

chromatographic detector and it is much more sensitive compared to NMR. Therefore a UV cell has to be positioned between the LC column outlet and the NMR flow cell. An additional valve is needed to switch the NMR flow cell off-line when an LC peak has reached the flow cell. Knowing the capillary length and diameter, as well as the flow rate, the time for an LC peak to the NMR flow cell can be calculated. In order to perform automatic stop-flow, software is needed that monitors the UV signal and stops the pump at the correct time. Since the pump flow is not stopped immediately, the valve mentioned, will turn on the stop command, to isolate the NMR flow path and prevent all movement of the LC peak inside the NMR flow cell.

In this mode of operation, long-term NMR acquisitions can be executed, also allowing fully quantitative measurements, impossible in the on-flow mode. This is also the mode to execute 2D experiments to get further structural information.

The direct stop-flow mode has limitations, if multiple stops are needed to look to all LC peaks of interest. All peaks still residing in the column or on the way to the NMR when a stop occurs will undergo diffusion. The longer the stop, the more diffusion will lead to LC peak broadening by this degrading the chromatographic resolution. After a restart, the peaks still on the column will be partly refocused; however, an effect is clearly visible. Broadening of LC peaks leads to loss of NMR sensitivity due to a smaller fraction of the peak fitting into the flow cells active region. Pump control also has to assure, that after a restart, the gradient ratio is the same as when the flow stopped.

Figure 3 shows a comparison of a chromatographic separation on an RP-18 column at 1 ml/min flow with injection of a mixture of four *p*-hydroxy benzoic acid esters. The left side shows the run with stop-flow on every peak, and the right side shows the on-flow result. The degradation of the chromatographic separation is clearly visible; even so only four short stops to acquire a one-dimensional (1D) NMR spectrum were done. The problem of the multiple stop-flow degradation can be overcome by the use of a loop collection system, which is explained in the next section.

An extension of the direct stop-flow experiment is the so-called time slicing, in this case the flow is stopped for example every 30 s, independent of LC peak positions. This allows a pseudo on-flow experiment to be obtained with reduced time resolution along the chromatographic axis and improved NMR sensitivity due to the longer acquisition time. It is also possible to do the time slicing

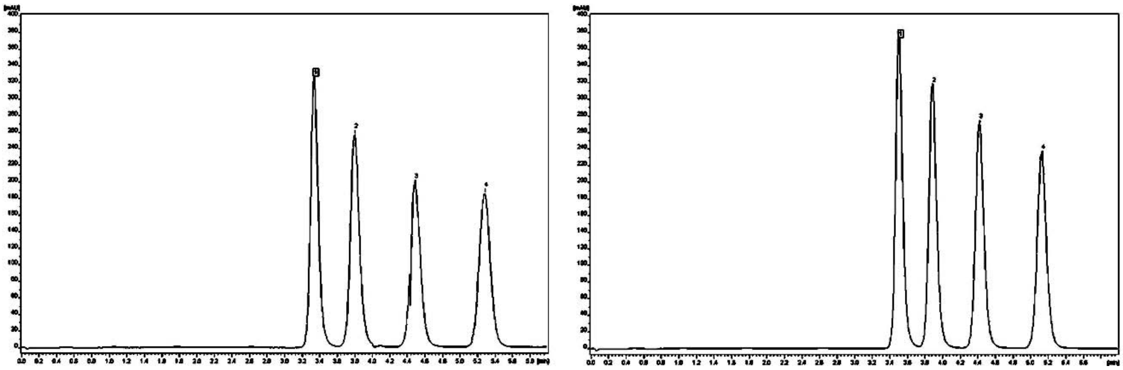

Fig. 3. Visualization of the effect of multiple stop-flow on the separation quality of a reversed phase separation after injection of a mixture of four *p*-hydroxy benzoic acid esters (methyl- to *n*-butyl-ester, 5 μg each on column) 150 × 4.6 mm RP 18 column, flow rate 0.8 ml/min).

into loops (see "Loop Collection" section) or solid phase extraction cartridges (see "Post-Column Solid Phase Extraction" section).

Loop Collection

If LC peaks are cut out of the running separation into small capillaries, where the LC peak shape is retained, the separation quality does not suffer. In order to achieve this, another valve system is needed, that allows the connection multiple capillaries allowing the collection of multiple LC peaks into the loop capillaries. In this mode, the flow is uninterrupted, only valves are turned to redirect the individual peaks into the capillaries. The first model introduced had 12 fixed loops. The next generation of loop collection systems had 36 loops housed in a removable cartridge, which is placed in a temperature-controlled environment, allowing the loop contents to be cooled, to further reduce diffusion inside the capillaries. Such a loop collection system allows the collection of LC peaks outside the NMR laboratory by transferring the cartridge after collection. To allow clear identification of the loop contents, such cartridges are equipped with an on board memory, carrying all of the information about the LC peaks in the capillaries. By using capillaries with small internal diameter (i.d.), the LC peak shape is maintained and can be transferred to the NMR flow cell to retain the sensitivity.

During a separation, multiple LC peaks can be collected and after the separation, the peaks are sequentially transferred to the NMR flow cell. This procedure also guarantees minimized back mixing between LC peaks close in retention time, which is a problem with direct stop-flow due to the stopping and restarting of the pump.

Using high-pressure valves in the loop collection device allows operation with small capillary i.d., e.g. 0.15 mm. The NMR sensitivity of the system can be improved by blowing the transfer pathway and the NMR flow cell dry using nitrogen gas before the transfer. In this operation mode, there is no dilution of the LC peak by preceding solvent.

Figure 4 shows an exchangeable loop cartridge with 36 capillaries with the top cover removed. The individual loop positions are connected to the flow path by turning the cartridge.

Since the NMR flow cells are restricted in size, typically 60 or 120 μl active volume, it is essentially impossible to place a complete LC peak inside the NMR flow cell and sensitivity is lost. In a typical analytical LC column (e.g. 150 × 4.6 mm) peaks eluting after 15–20 min, for example, would show an eluting volume above 200 μl. This problem applies to direct stop-flow and loop collection. It does not apply to on-flow operation, as there the peak is flowing through the cell completely. A way to reduce the sensitivity loss is described in the following section.

Post-Column Solid Phase Extraction

SPE is a well-known technology in LC and LC-MS to concentrate or pre-clean the sample before injection. If the SPE device is placed after the LC column, several advantages are obtained for LC-NMR operation. In this case, the SPE operates like the loop collection system, sitting after the LC peak detection (UV cell) and a valve to direct the flow into the SPE cartridges. To be able to trap LC peaks in reversed phase mode also at high organic solvent ratios, addition of water is needed before the trap cartridges. This also allows the trapping of peaks multiple times, by repeated injection and trapping of the same peaks to the same trap cartridge.

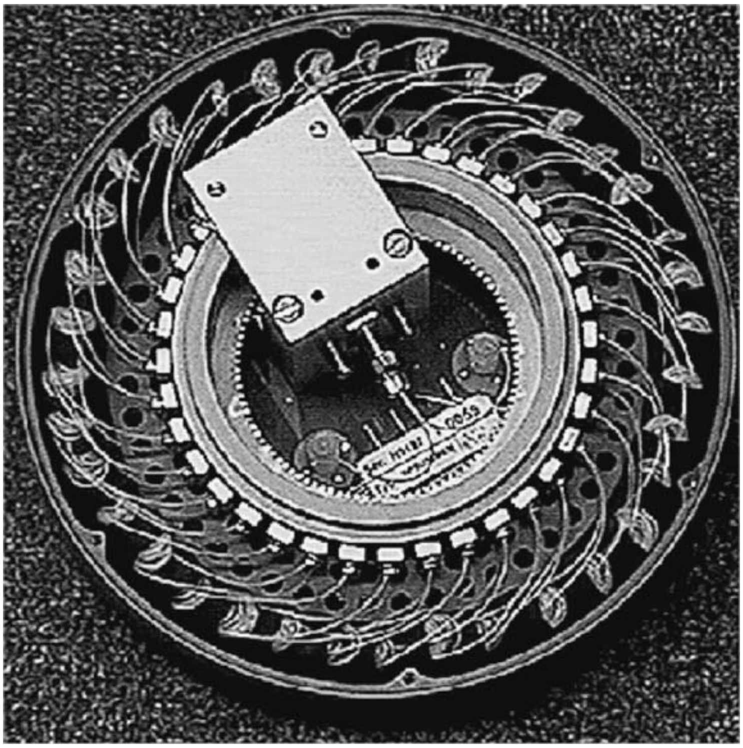

Fig. 4. Loop collection cartridge with 36 loops for LC peak collection in LC-NMR. (See also Plate 93 on page XVIII in the Color Plate Section.)

The advantages obtained are as follows:

- Higher NMR sensitivity (up to a factor four for single SPE) by up-concentration of the LC peaks.
- Use of non-deuterated solvents in the trapping process reduces cost and does not lead to deuterium exchange as is observed with MS detection when using D_2O.
- Free choice of solvents and buffers independent of their NMR signals as solvents are removed before the NMR measurement by drying with nitrogen.
- Elution of the peaks trapped with pure deuterated solvent, typically only 200 μl of solvent are needed, which is less than half compared to the solvent amount in a 5 mm NMR tube.
- Multiple trapping allows a linear increase of the NMR S/N until the trap cartridge holding capacity is reached.

To control break through of a peak from the trap cartridge, it is advisable to place a second UV detection device in the outflow after the trap cartridge. The amount of trap cartridges needed depends on the automation possibilities. With an autosampler, multiple samples can be injected, and for each sample multiple peaks can be trapped. It is also possible to run time slicing experiments. In this case, the flow would be guided through a trap cartridge for a certain time period (e.g. 30 s), before the next cartridge is switched in line. In this mode, the goal is to work toward a total analysis of a sample. A typical example would be in urine analysis. To allow a large number of SPE cartridges, a system has been introduced, placing trap cartridges in 2 well plates of 96 cartridges each. A gripper transfers the cartridges from the well plate to the flow lines. Since it must be possible to trap LC peaks close to each other in retention time, two flow lines are used. So when one cartridge is exchanged, trapping occurs on a second cartridge. Such an SPE device consists of a high-pressure double dilutor, nitrogen gas supply, two well plates with trap cartridges, two flow lines, and a gripper to transfer the trap cartridges.

Trap cartridges can have an inner diameter of either 1 or 2 mm and are 10 mm long. The eluting volume of an LC peak is approximately 10 or 25 μl respectively. To preserve the sensitivity gain from using trap cartridges, an NMR probe head with 30 μl active volume is best suited.

SPE operation under reversed phase conditions will not allow the trapping of very polar compounds, therefore the optimal LC-NMR system is equipped with the SPE device and a loop collection system and allows the switching of targets during a chromatographic run: polar compounds are collected into the loops, later eluting peaks are trapped on the SPE cartridges.

A further possibility to increase NMR sensitivity, namely the use of cryogenic probes is described in "Cryogenic Probes for LC-NMR" section. SPE allows 2D experiments or even carbon direct detection to be obtained, whereas under standard LC-NMR conditions, only proton 1D spectra can be measured in reasonable time frame.

Cryogenic Probes for LC-NMR [24]

Cryogenic probes use the noise reduction afforded by low coil temperature to enhance the NMR sensitivity by up to a factor of 4 compared to a conventional room temperature probe. A rapidly growing number of such probes can be found in NMR laboratories. While the first probes of this type were for tube applications only, dedicated cryoflow probes were introduced in 2002 and have been optimized for the LC-SPE application, with active volumes of 30 μl. Since a cryogenic probe is not as readily changed as the room temperature equivalent, probes were introduced that allow rapid conversion of a tube cryoprobe into a flow probe without compromising on signal to noise. A further improvement of sensitivity could also be obtained by cooling the pre-amplifier system.

Combining a single SPE step with cryoprobe detection allows the enhancement of LC-NMR sensitivity by more than a factor of 20 compared to conventional LC-NMR.

Figure 5 shows a comparison of NMR sensitivity obtained with the injection of 5 μg of *p*-hydroxy benzoic acid esters onto a reversed phase column (100 × 2 mm). Doing standard LC-NMR detection at 500 MHz with 24 scans, an S/N of about 9:1 is achieved for the aromatic protons. Doing post-column SPE allows an S/N of about 23:1 with a room temperature flow probe. Adding a cryoflow device brings up the sensitivity to 170:1 as shown in the figure. Doing fourfold trapping increases the S/N to 660:1. In this example, the S/N gain of going from LC-NMR to SPE was not a factor of 4, as an example was used where the peak of interest had a retention time less than 4 min. Higher S/N gain can be obtained for later eluting LC peaks, where the eluting volume is substantially increased and the concentration factor is higher.

Using flow inserts into tube-based cryoprobes allows compensation for another disadvantage of a dedicated flow probe: the flow cell size can be adjusted to the eluting peak volume. While the 30 μl flow cell is optimized for 2 mm SPE cartridges, a 10 μl cell is better suited for SPE with 1 mm cartridges, where the eluting volume is further reduced. Larger flow cells are needed for conventional LC-NMR with 4.6 or 2 mm LC columns. In this case, the eluting peak volume is substantially larger and the small detection volume of the probe would reduce sensitivity of the NMR experiment in direct stop-flow or loop collection mode.

If the cell volume of a flow cell is changed, it also changes the inner diameter of the connection capillaries. Doing SPE with 1 mm cartridges produces an eluting peak of around 10 μl. Having standard LC-NMR capillaries with an i.d. of 0.25 mm would broaden the peak eluting from the SPE cartridge considerably. Normal LC-NMR with analytical columns, however, needs this inner diameter to allow standard flow rates.

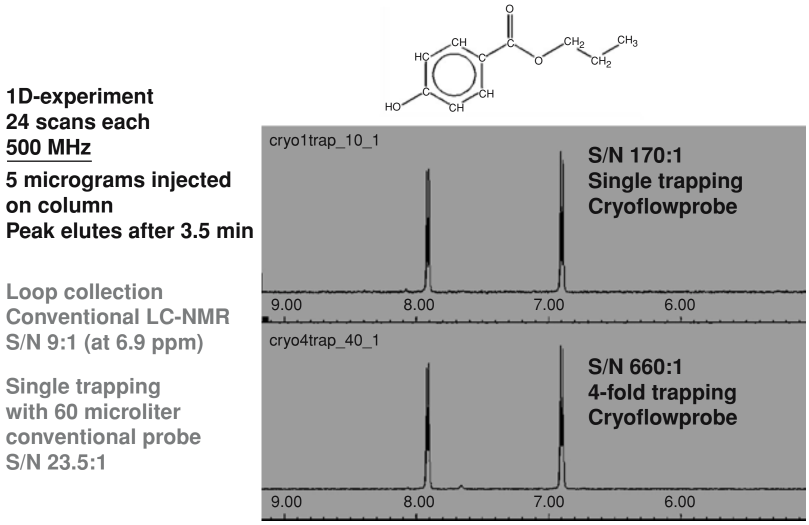

Fig. 5. Result of LC-SPE-NMR signal to noise using a cryogenic probe with single trapping of *p*-hydroxy-benzoic acid-*n*-propyl ester after an injection of 5 μg and fourfold trapping.

Improvements in the LC Peak Detection by Integrating Mass Spectroscopy into the LC-NMR Setup [13,25–36]

LC peak detection as described so far has mostly used UV detection. UV is a sensitive detector, but lacks structural specificity and cannot detect compounds without chromophores. A typical situation is the search for drug metabolites in biofluids. Such compounds often have aromatic rings and will of course give rise to UV signals; however in biofluids there are also many naturally occurring compounds giving UV signal, therefore it is difficult to find out which are the drug metabolite peaks. This leads to the situation that all peaks giving UV signals have to be measured by NMR. Doing this, peaks of no interest will also be acquired and expensive NMR time is lost. This situation can be improved, using mass spectroscopic detection, especially if high resolution MS can be used in conjunction with LC-NMR. In many cases, possible metabolite structures can be predicted, and their masses can be specifically sought out. Combining UV and MS detection provides a safety net to prevent LC peaks of interest being overlooked. The simplest way to do LC-NMR/MS is to implement a splitter into the flow path after the column and the UV detector. Obviously, only a small fraction of the flow has to be guided to the mass spectrometer, due to its much higher intrinsic sensitivity. Typically split ratios of 20:1 or higher are used. Since the MS information has to be searched for peaks of interest, the transfer to the MS electrospray interface must be completed before the NMR fraction reaches the valve. The position of the valve determines the fate of the peak fraction for the NMR, whether it goes to the flow cell directly, to a loop, to SPE, or to waste. Due to the lower NMR sensitivity, much larger sample amounts are typically injected than needed for MS detection, even considering the split ratio. This can lead to contamination of the detector if appropriate measures not are taken.

Keeping this in mind, a dedicated LC-NMR/MS interface was developed (as shown in Figure 6) that consists of a splitter, a T-piece, a double dilutor, and valve with a delay loop allows the length of transfer to the MS interface to be changed.

Having a double dilutor and a T-piece allows dilution of the flow to the MS further, to readjust the polarity of the solvent system as needed for ionization, or to add ionization helping agents that are not wanted in the NMR component of the LC peak fraction. The valve with the delay loop allows the transfer timing into the electrospray interface of the MS to be changed. This is used if a peak that went into loop collection is transferred from the loop system into the NMR. During the transfer, the NMR/MS interface is passed again and MS spectra can be run. This valve position guides the MS fraction through the delay loop, which enhances the transfer pathway in such a way, that after the NMR fraction is positioned in the flow cell, the MS fraction is still in the delay loop. When the NMR fraction reaches the flow cell, the main pump stops. The double dilutor in the NMR/MS interface can then be used to transfer the MS peak fraction in the delay loop slowly into the electrospray interface of the mass spectrometer. In doing so, a time frame of several minutes can be obtained, where MS spectra can be measured from this peak. Having minutes for measurement allows time for experiments such as multiple fragmentation, switching from positive to negative ionization, or the acquisition of high-resolution MS spectra. Such information can be obtained to help in structure identification. Together with 1D and 2D NMR spectra, an unknown structure can be solved. Therefore the NMR/MS interface allows the enhancement of the LC peak selection for the NMR and the attainment of important structural information.

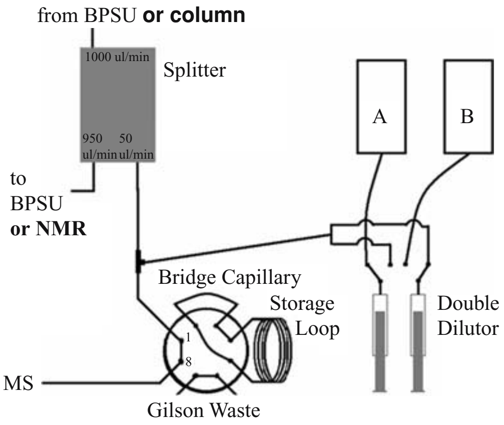

Fig. 6. Dedicated LC-NMR/MS interface, consisting of a flow splitter, a T-piece connected to a double dilutor and a valve with delay loops. The unit is positioned after the LC column or can be switched in line after a loop collection unit (BPSU).

To allow even more selectivity in the decision of which peaks proceed to the NMR, multiple decision-making channels can be defined that use UV or other analogue information together with various MS decision-making channels. MS decisions are possible based on total ion current, selected ions, an ion range, and/or MS/MS information, if the mass spectrometer used allows this.

Conclusion and Outlook

Over the last few years, the performance of LC-NMR has been improved substantially by the addition of tools that allow an increase in the NMR sensitivity by up to two orders of magnitude using post-column SPE, cryogenic probes and shielded magnets with improved homogeneity. Adding mass spectroscopy as an integral part of the process has allowed an increase in the selectivity of the LC peak selection and at the same time obtaining more information for structure elucidation. In the years to come, downscaling will play an important role in further improving the performance of LC-NMR. This is true for the columns used, the SPE cartridges and as a consequence of those, the active volume of the NMR flow cell will have to shrink. This means that the detection coils will have to shrink equally in order not to lose filling factor. With further reduction in the size of the NMR probes, techniques such as CE or CEC will be interfaced with the NMR successfully and such open the area to new applications.

References

1. Watanabe N, Niki E. Proc. Jpn. Acad. Ser. B. 1978;54:194.
2. Görög S, Balogh G, Gazdag M. J. Pharm. Biomed. Anal. 1991; 9:829.
3. Spraul M, Hofmann M, Dvortsak P, Nicholson JK, Wilson ID. J. Pharm. Biomed. Anal. 1992;10(8):601.
4. Spraul M, Hofmann M, Wilson ID, Lenz E, Nicholson JK, Lindon JC. J. Pharm. Biomed. Anal. 1993;11(10):1009.
5. Spraul M, Hofmann M, Dvortsak P, Nicholson JK, Wilson ID. Anal. Chem. 1993;65(4):327.
6. Spraul M, Hofmann M, Lindon JC, Farrant RD, Seddon MJ, Nicholson JK, Wilson ID. NMR Biomed. 1994;7:295.
7. Roberts JK, Smith RJ. J. Chromatogr. Ser. A. 1994;677:385.
8. Mutlib AE, Strupczewski JT, Chesson SM. Drug Metab. Dispos. 1995;23(9):951.
9. Sidelmann UG, Gavaghan C, Carless HAJ, Spraul M, Hofmann M, Lindon JC, Wilson ID, Nicholson JK. Anal. Chem. 1995;67:4441.
10. Sidelmann UG, Gavaghan C, Carless HAJ, Farrant RD, Lindon JC, Wilson ID, Nicholson JK. Anal. Chem. 1995;67(19): 3401.
11. Lenz EM, Greatbanks D, Wilson ID, Spraul M, Hofmann M, Troke J, Lindon JC, Nicholson JK. Anal. Chem. 1996;68:2832.
12. Sidelmann UG, Braumann U, Hofmann M, Spraul M, Lindon JC, Nicholson JK, Hansen SH. Anal. Chem. 1997;69:607.
13. Holt RM, Newman MJ, Pullen FS, Richards DS, Swanson AG. J. Mass Spectrosc. 1997;32(1):64.
14. Griffiths L, Horton R. Magn. Reson. Chem. 1998;36:104.
15. Peng SX, Borah B, Dobson RLM, Liu YD, Pikul S. J. Pharm. Biomed. Anal. 1999;20(1):75.
16. Bringmann G, Rückert M, Saeb W, Mudogo V. Magn. Reson. Chem. 1999;37:98.
17. Tseng LH, Braumann U, Godejohann M, Lee SS, Albert K. J. Chin. Chem. Soc. 2000;47:1231.
18. Wolfender JL, Terreaux C, Hostettmann K. Pharm. Biol. 2000;38(Suppl.):41.
19. Vogler B, Spring O. Recent Res. Dev. Phytochem. 2000;4: 207.
20. Mortensen RW, Corcoran O, Cornett C, Sidelmann UG, Troke J, Lindon JC, Nicholson JK, Hansen SH. J. Pharm. Biomed. Anal. 2001;24:477.
21. Tugnait M, Lenz EM, Phillips P, Hofmann M, Spraul M, Lindon JC, Nicholson JK, Wilson ID. J. Pharm. Biomed. Anal. 202;28:875.
22. Elipe MVS, Huskey S-EW, Zhu B. J. Pharm. Biomed. Anal. 2003;30(5):1431.
23. Corcoran O, Wilkinson PM, Godejohann M, Braumann U, Hofmann M, Spraul M. Am. Lab. Perspect. Chromatogr. 2002;34:18.
24. Spraul M, Freund AS, Nast RE, Withers RS, Maas WE, Corcoran O. Anal. Chem. 2003;75:1546.
25. Shockcor JP, Unger ES, Wilson ID, Foxall PJD, Nicholson JK, Lindon JC. Anal. Chem. 1996;68(24):4431.
26. Scarfe GB, Wilson ID, Spraul M, Hofmann M, Braumann U, Lindon JC, Nicholson JK. Anal. Comm. 1997;34:37.
27. Scarfe GB, Wright B, Clayton E, Taylor S, Wilson ID, Lindon JC, Nicholson JK. Xenobiotica. 1998;28(4):373.
28. Taylor SD, Wright B, Clayton E, Wilson ID. Rapid Commun. Mass Spectrom. 1998;12:1732.
29. Clayton E, Taylor S, Wright B, Wilson ID. Chromatographia. 1998;47(5/6):264.
30. Scarfe GB, Wright B, Clayton E, Taylor S, Wilson ID, Lindon JC, Nicholson JK. Xenobiotica. 1999;29(1):77.
31. Wilson ID, Morgan ED, Lafont R., Shockcor JP, Lindon JC, Nicholson JK, Wright B. Chromatographia. 1999; 49(7/8):374.
32. Sandvoss M, Pham LH, Levsen K, Preiss A, Mügge C, Wünsch G. Eur. J. Org. Chem. 2000;1253.
33. Lommen A, Godejohann M, Venema DP, Hollman PCH, Spraul M. Anal. Chem. 2000;72:1793.
34. Sandvoss M, Weltring A, Preiss A, Levsen K, Wünsch G. J. Chromatogr. A. 2001;917:7.
35. Schrader W, Geiger J, Godejohann M, Warscheid B, Hoffmann T, Angew. Chem. Int. Ed. 2001;40(21):3998.
36. Duarte IF, Godejohann M, Braumann U, Spraul M, Gil A. J. Agric. Food Chem. 2003;51:4847.

LC-NMR in Dereplication and Structure Elucidation of Herbal Drugs

Gloria Karagianis and Peter G. Waterman
Centre for Phytochemistry and Pharmacology, Southern Cross University, PO Box 157,
Lismore, NSW 2480, Australia

Abstract

The direct on-line ^{1}H NMR analysis of HPLC eluates from plant extracts using a flow probe offers the opportunity to gather structural information on individual plant metabolites without the often time-consuming preliminary purification of each metabolite. Two examples are discussed. Firstly, resolution of the major flavonoid constituents in "skullcap herb" in the absence of "standard compounds" can be achieved by a single pass experiment and interpretation of 1D ^{1}H spectra. Secondly, the potential of the technique to allow a full structure elucidation of an unknown compound using a full range of 1D and homo- and inverse detected heteronuclear 2D experiments will be examined using extracts of *Aloe* species from South Africa.

Introduction

The coupling of high performance liquid chromatography with nuclear magnetic resonance (LC-NMR) spectroscopy represents a powerful analytical technique for detailed on-line structure and composition analysis of plant extracts. It has been more than 25 years since the first paper on LC-NMR was published [1]. Since then the technique has rapidly advanced, particularly over the last decade, with the introduction of higher field magnets, pulse field gradients, and efficient solvent suppression techniques, which are now standard in modern NMR instruments. For a detailed account on the historical development of LC-NMR, the reader is referred to the recent review by Elipe [2].

In principle, LC-NMR is based on the separation of organic mixtures by reversed-phase HPLC, followed by direct on-line NMR analysis of each eluting peak. In a typical LC-NMR setup, the HPLC instrument is connected to a UV detector and the chromatographic outlet passes through a special interface, comprised of switching valves, which connects to the LC-NMR flow probe via PEEK capillary. The HPLC system must be located ca. 2–3 m away from a conventional spectrometer in order to avoid interferences to its operation from the stray magnetic field produced by the cryomagnet. However, with shielded cryomagnets, this distance is reduced to less than 0.5 m.

There are basically three different modes of operation available in LC-NMR: (1) on-flow; (2) stop-flow; and (3) loop-collection. The simplest of these is on-flow as the HPLC and NMR systems can operate independently and no HPLC detector is required. Proton NMR spectra are acquired continuously while the eluate is flowing through the detection cell of the NMR flow probe. While this mode has the advantage of maintaining good HPLC resolution, it suffers in having the lowest sensitivity because of the very short dwell time in the NMR flow cell (3.6 s at 1 ml/min flow rate for a flow cell with 60 μl detection volume). Therefore, its application is limited to 1D proton acquisitions on mixtures containing major components.

The stop-flow mode is the most versatile and is significantly more sensitive than the on-flow mode and allows the measurement of 2D NMR correlation experiments, which are important techniques in the structure determination of unknown compounds. In this mode, the user sets predefined HPLC peak thresholds and UV detector parameters so that the LC pump stops on each chromatographic peak that meets these criteria, and the NMR collects the required data. This operation requires dedicated chromatographic software to control the synchronization between the HPLC and NMR systems. The chromatographic separation is triggered to stop on the peak after a calibrated time delay, which is the time required for the peak to travel from the UV detector to the NMR flow cell, and is determined during installation procedures. Once the peak is positioned in the NMR, the sample remains static in the flow cell and the conditions remain stable during the course of the NMR acquisition. This allows precise adjustments to the field homogeneity and solvent suppression parameters to be made so as to give optimized NMR measurements. In our laboratory, we routinely use the stop-flow mode for the analysis

Graham A. Webb (ed.), Modern Magnetic Resonance, 1229–1235.
© 2008 *Springer.*

of plant extracts that give good chromatographic separation. We have found this mode to be highly efficient, particularly in situations where the plant metabolites are present at relatively high levels, as rapid structural information can be obtained from a single chromatographic run.

In the third mode, loop collection, the eluting chromatographic peaks are first captured into separate capillary loops and later transferred to the NMR for analysis. This mode is useful for the analysis of complex extracts that contain closely eluting peaks, and where large differences in metabolite concentrations are observed. Another useful aspect of this technique is that the chromatographic separations are performed independently of the NMR measurements, which means the NMR spectrometer can be used for other purposes during the preparation of the LC-NMR samples.

For LC-NMR analysis, the choice of mobile phase solvents is limited typically to mixtures of deuterium oxide:methanol or deuterium oxide:acetonitrile with 0.1% deuterated trifluoroacetic acid commonly added to the aqueous phase to help improve the resolution of the chromatographic peaks. As the NMR signals arising from the HPLC solvents are much larger than those of the analyte, they need to be suppressed. Solvent suppression techniques, such as the presaturation or WET pulse sequences, are therefore required for acquisition of LC-NMR spectra. One drawback to the use of solvent suppression is that any analyte signals residing underneath those of the solvent will also be suppressed, causing a loss in structural information. This can be a major disadvantage when dealing with mixtures containing unknown compounds. However, this problem may be overcome by carrying out the LC-NMR analysis in two independent solvent systems as exemplified in the study by Ndjoko *et al.* [3] on pyrrolizidine alkaloids.

In theory, LC-NMR should be of great value in natural products chemistry where one is often dealing with mixtures of structurally allied compounds that can be resolved by HPLC. This has been confirmed in a number of studies [4–7], but the technique has not become popular for a number of reasons including cost and the amount of instrument time required for a comprehensive NMR investigation. In this paper, we demonstrate both the very rapid use of LC-NMR to confirm the major flavone glycoside present in a plant extract and a comprehensive 1D and 2D homo- and hetero-nuclear study for structure elucidation of an unknown compound.

Dereplication of Skullcap Herb

Problems can arise with the identification of herbal drugs and their constituents, most notably in cases such as skullcap (*Scutellaria* species), where a number of different species are being used with similar, but different suites of compounds. A traditional phytochemical approach involving isolation, purification, and structure elucidation was initially used to establish that the flavone glucuronide baicalin (**1**) rather than its congener scutellarin (**2**) was the major flavonoid in samples of *Scutellaria lateriflora* (Figure 1). This is expensive and time consuming and we were able to overcome the need for isolation through use of LC-NMR.

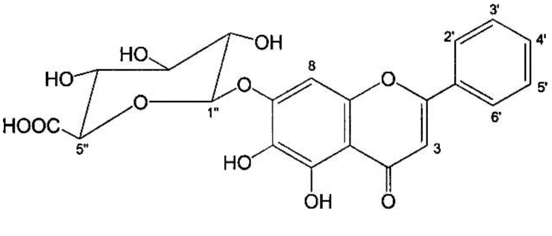

1 Baicalin
2 Scutellarin = 4'-OH
3 Ikonnikoside = 2'-OH

Fig. 1. Chemical structure of flavonoids from *Scutellaria lateriflora*.

Figure 2A shows a typical C_{18} reversed-phase chromatogram for *S. lateriflora* exhibiting five peaks attributable to major flavonoid components. For each of the five flavonoids 1D ^{1}H NMR spectra were obtained, the total time required for this exercise being about 2 h. Figure 2B shows the spectrum for the major flavone glycoside. From an analysis of the signals for each proton, making the presumption that the compound under analysis is a flavone, it is possible to identify two singlets attributable to H-3 and a single A-ring proton (H-8 in this case). The presence of glucuronic acid is established by the two doublets that can be attributed to H-1″ and H-5″ with coupling constants that require both protons to be axial. The remaining aromatic signals integrate for five protons and are made up of a doublet (2H) and two triplets (1H and 2H—shown in expanded form in Figure 2C), which are typical for an unsubstituted flavonoid B-ring. All these features are supportive of the structure of baicalin, and establish that the major constituent in this extract is baicalin. Figure 2D shows the spectrum for the first small peak that eluted from the extract (R_t 8.07 min, Figure 2A). While the resolution is not as good as for baicalin, proton resonances are clearly defined. Once again H-3, H-8 of the flavone, and H-1″ and H-5″ of

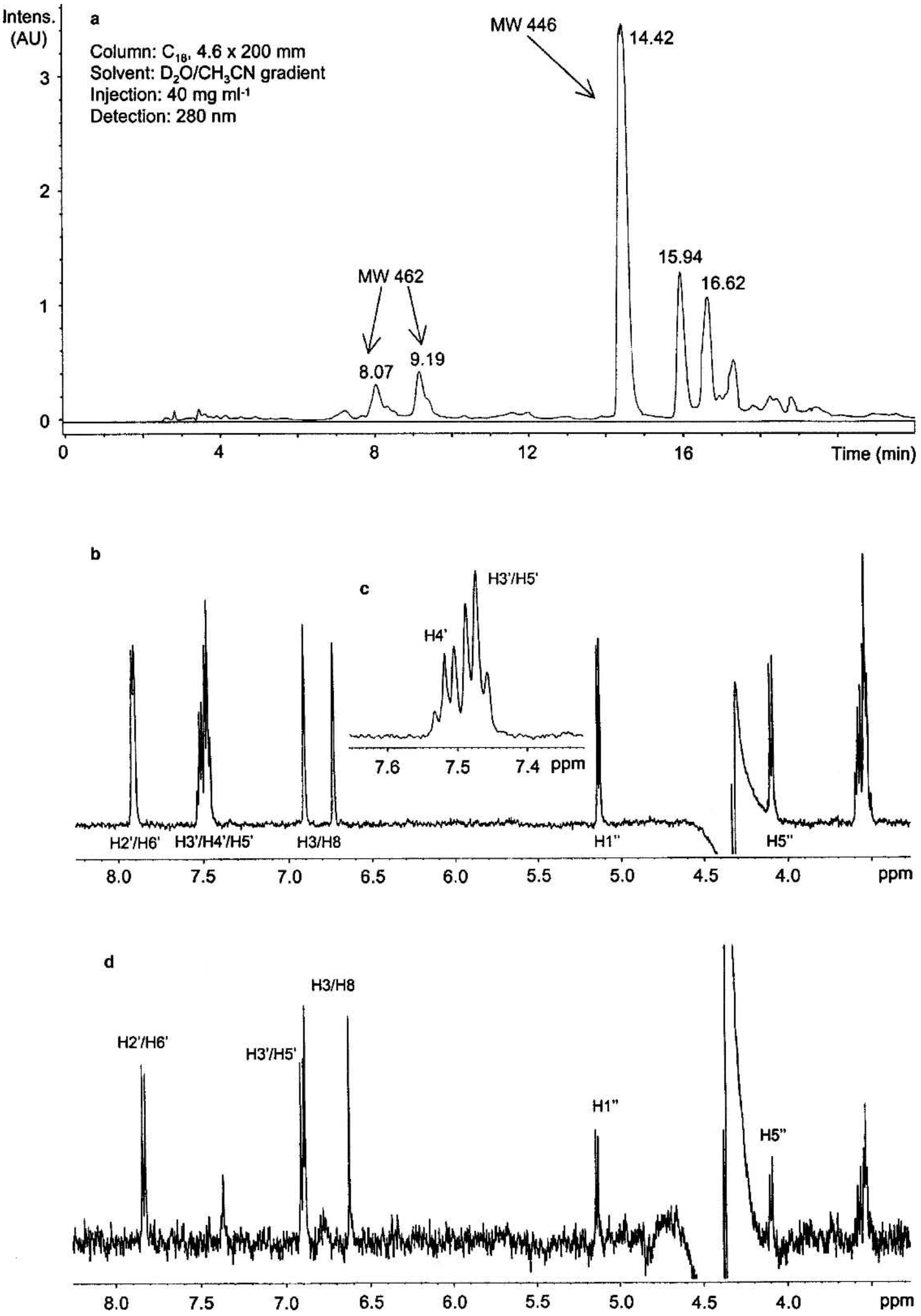

Fig. 2. Analysis of skullcap extract by LC-NMR. (a) LC trace; (b) stop-flow LC-^{1}H NMR spectrum of baicalin (**1**) (14.42 min peak, 512 scans); (c) expansion of H-3′ to H-5′ spin-system of baicalin; (d) stop-flow LC-^{1}H NMR spectrum of scutellarin (**2**) (8.07 min peak, 512 scans).

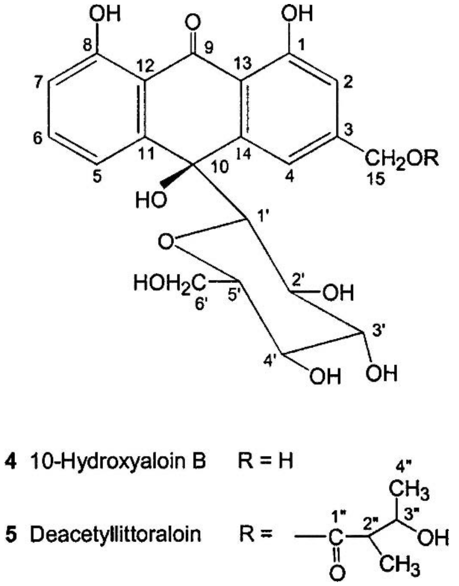

Fig. 3. Chemical structure of oxanthrones from *Aloe littoralis*.

the glucuronide can be identified. But in this case, the signals attributable to the B-ring have changed. The pattern has simplified to two doublets (2H each) which requires a *para* di-substituted aromatic ring. This, coupled with the 16-mass unit increase in molecular weight in comparison with baicalin identified the minor component as scutellarin.

In the same manner, it was possible to identify the other three components such as ikonnikoside (**3**, R_t 9.19 min as shown in Figure 2A; with the four B-ring protons now in an ABCD splitting pattern), a methyl ether of ikonnikoside (R_t 15.94 min), and 2,3-dihydrobaicalin (R_t 16.62 min).

Structure Elucidation of *Aloe* Metabolites

The genus *Aloe* contains numerous species with very localized distributions and populations that can comprise fewer than 100 individuals. The pioneering work undertaken on using LC-NMR to identify compounds from small amounts of exudates [8] has established that we can determine the identity of individual *Aloe* secondary metabolites on weights of as little as 40 μg. Using the crude leaf exudate of *Aloe littoralis*, we were able to obtain 1D proton, 2D homonuclear (COSY, TOCSY) and 2D heteronuclear (HSQC, HMBC) NMR data on the two major metabolites, 10-hydroxyaloin B (**4**), and deacetyllittoraloin (**5**) (Figure 3).

Figure 4 shows the 2D COSY spectrum of **4** and 2D TOCSY spectrum of **5.** The coupling pattern observed in these two experiments, along with the 1D proton NMR data, indicate that the two metabolites are structurally similar. Both show connectivities consistent with an aromatic ABC spin-system and a hexose moiety, which can be identified as glucopyranose. In addition, the resonance and large coupling constant of the shielded doublet corresponding to the anomeric proton H-1′ in each metabolite, indicate a C-linkage and β-configuration for the sugar group.

Figure 5 shows the 2D HSQC and 2D HMBC spectra of **4**. All C-H connectivities are clearly visible in the 2D HSQC. From an analysis of the long-range couplings observed in the 2D HMBC, the position of the hydroxymethyl group and the C-glucopyranosyl group on the oxanthrone ring system could be determined. These long-range couplings are illustrated in Figure 6. The combined data from these two inverse ^{1}H, ^{13}C correlation experiments allowed the unambiguous assignment of the ^{13}C resonances of 20 of the 21 carbons in **4**. Similarly, the 2D HSQC and 2D HMBC data obtained on **5** allowed the unambiguous assignment of the ^{13}C resonances of 25 of the 26 carbons present. The HMBC long range couplings observed for **5** were similar in pattern to those shown by **4**, and confirmed the presence of a 10-hydroxyaloin skeleton in **5** (Figure 6). Additional long-range correlations observed for **5**, in particular from the oxymethylene protons (H-15) to the ester carbonyl at C-1″, confirmed along with 2D COSY and 2D TOCSY data the assignment of the nilate (3-hydroxy-2-methylbutanaote) moiety at position C-15. The only carbon resonance that could not be assigned in both metabolites was that of the ketone group at position C-9. This carbon is situated more than $^3J_{HC}$ from the nearest proton, making its detection out of the scope of a conventional HMBC experiment.

This last example clearly indicates the considerable capacity of LC-NMR as a direct tool for structure elucidation. Unfortunately with current technology the cost, in terms of instrument time, remains prohibitive. However, with new probe technology and improved sample handling in the LC phase this should change over the next few years. At that point LC-NMR, we believe, will be used widely to ascertain novelty prior to large-scale natural product isolation studies being undertaken. Among other advantages this will allow us to undertake analysis of the increasing number of species that are critically endangered without the need for destructive harvesting.

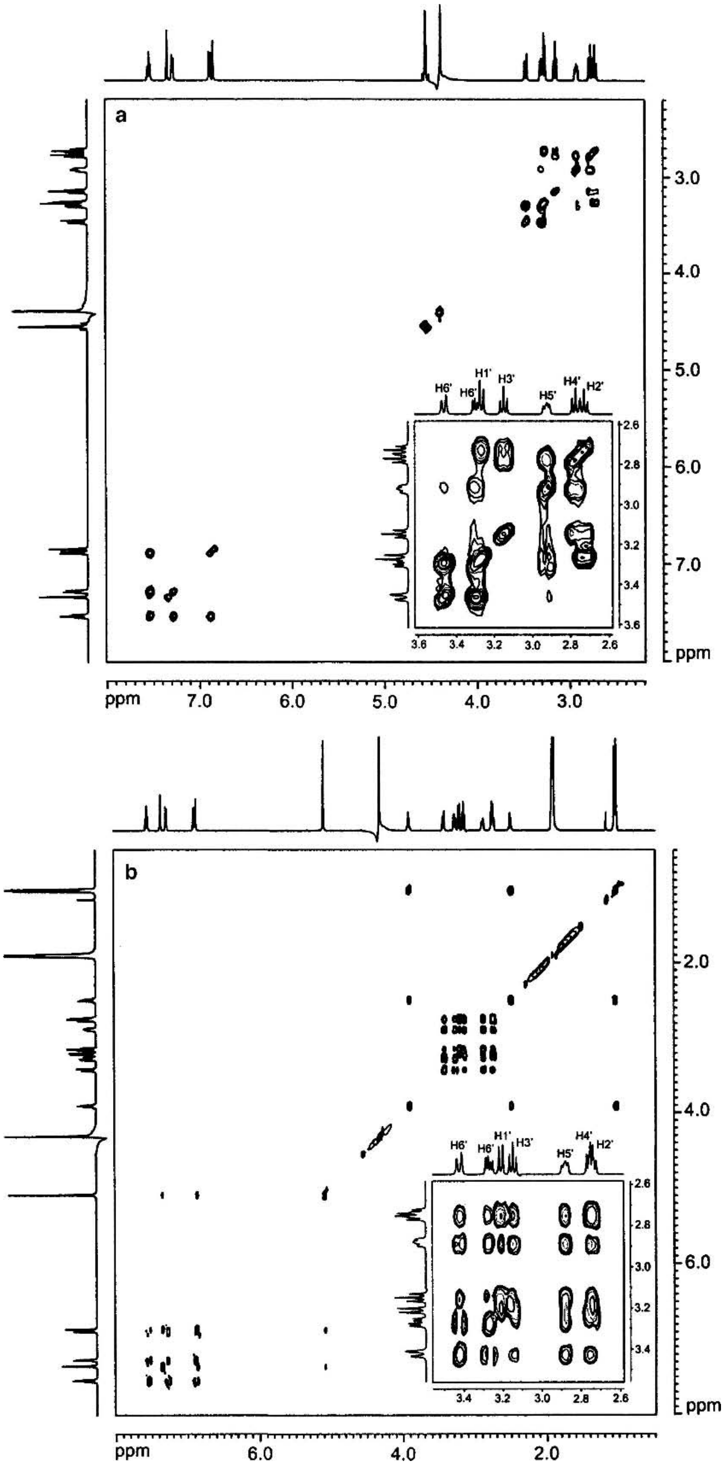

Fig. 4. (a) Stop-flow 2D LC-COSY spectrum of 10-hydroxyaloin B (**4**); (b) stop-flow 2D LC-TOCSY spectrum of deacetyllittoraloin (**5**) with a mixing time of 65 ms. Expansion of the region containing cross-peaks from the glucose moiety is shown in both spectra.

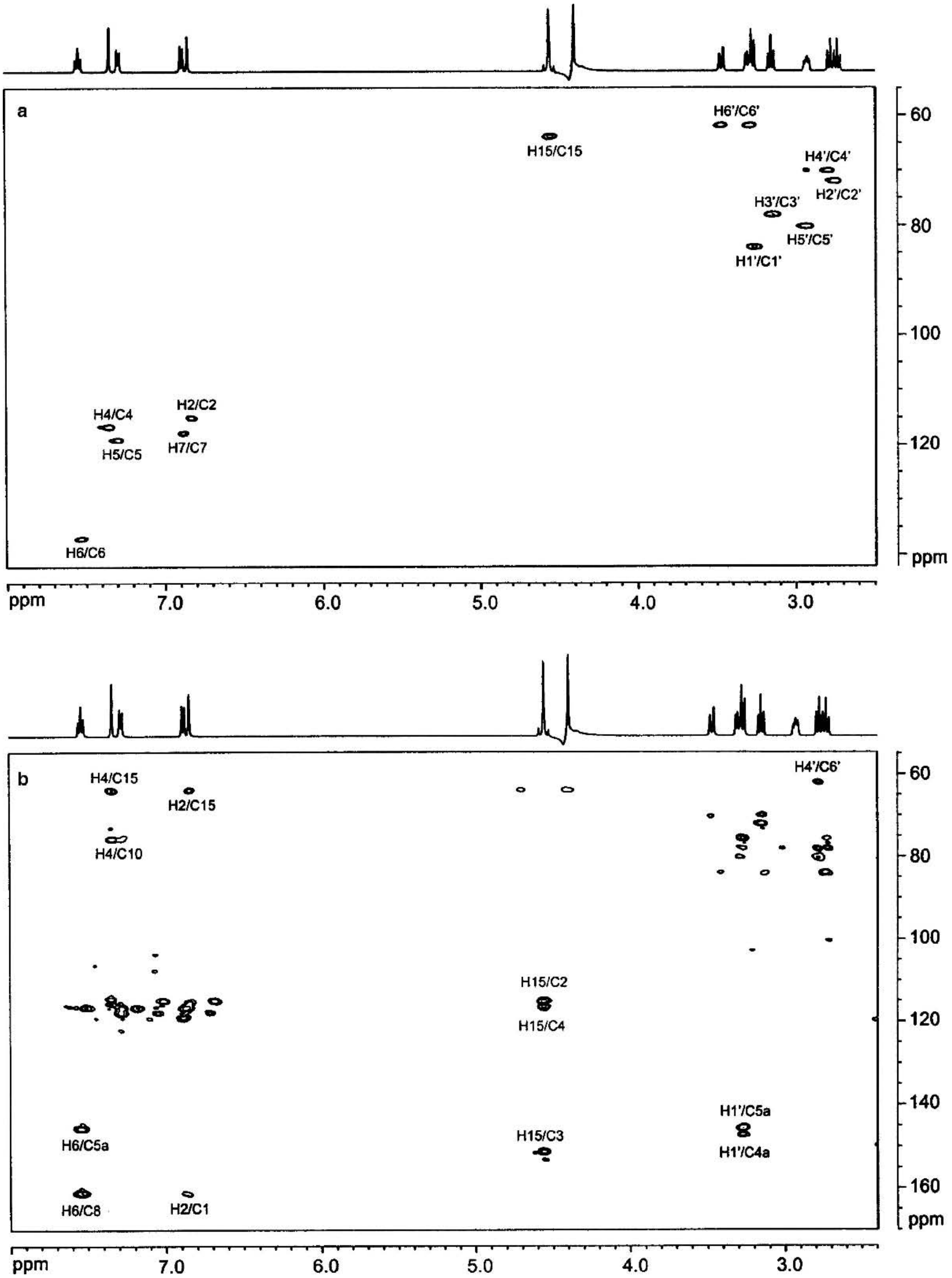

Fig. 5. (a) Stop-flow 2D LC-HSQC spectrum of 10-hydroxyaloin B (**4**); (b) stop-flow 2D LC-HMBC spectrum of **4** with some of the long-range couplings labeled.

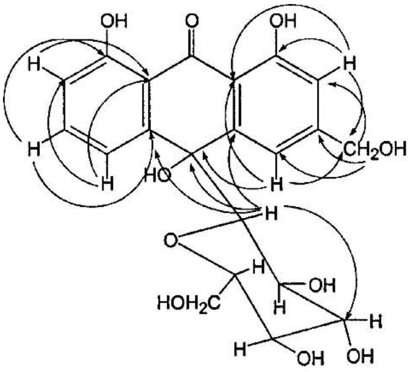

4

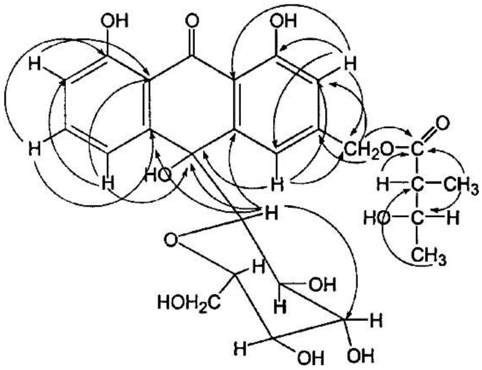

5

Fig. 6. Long-range couplings observed in the 2D LC-HMBC spectra of 10-hydroxyaloin B (**4**) and deacetyllittoraloin (**5**). In order to reduce the complexity of the above diagrams, the correlations for the anomeric proton (H-1′) of the glucose moiety only are illustrated.

References

1. Watanabe N, Niki E. Proc. Jpn. Acad. Ser. B 1978;54:194.
2. Elipe MVS. Anal. Chim. Acta 2003;497:1.
3. Ndjoko K, Wolfender J-L, Röder E, Hostettmann K. Planta Med. 1999;65:562.
4. Setzer WN, Vogler B, Bates RB, Schmidt JM, Dicus CW, Nakkiew P, Haber WA. Phytochem. Anal. 2003;14:54.
5. Andrade FDP, Santos LC, Datchler M, Albert K, Vilegas W. J. Chromatogr. A 2002;953:287.
6. Hölscher D, Schneider B. Phytochemistry 1999;50:155.
7. Renukappa T, Roos G, Klaiber I, Vogler B, Kraus W. J. Chromatogr. A 1999;847:109.
8. Karagianis G, Viljoen A, Waterman PG. Phytochem. Anal. 2003;14:275.

Techniques

Part II

New Approaches to NMR Data Acquisition, Assignment and Protein Structure Determination: Potential Impact in Drug Discovery

Antonio Pineda-Lucena
Associate Principal Scientist, Protein NMR Laboratory, AstraZeneca Pharmaceuticals, Macclesfield Cheshire England

Introduction

The majority of drugs available today were discovered either from chance observations or from the screening of synthetic or natural product libraries. The chemical modification of lead compounds, on a trial-and-error basis, typically led to compounds with improved potency, selectivity, bioavailability, and reduced toxicity. However, this approach is labor- and time-intensive, and researchers in the pharmaceutical industry are constantly developing methods with a view to increasing the efficiency of the drug discovery process. One of these relatively new approaches is the so-called rational drug design that relies heavily in the determination, either by X-ray crystallography or nuclear magnetic resonance (NMR) spesctroscopy, of the three-dimensional structures of the targets and the ligand-target complexes.

NMR spectroscopy is a biophysical technique with wide applicability in drug discovery research, particularly for the detection and characterization of molecular interactions. NMR can also be used as a tool for the determination of structure and dynamics of proteins, and protein-ligand complexes. In drug design, NMR can be used to validate or invalidate hits from high-throughput-screening (HTS) and can also generate lead compounds by a fragment-based approach. Thus, NMR is not only a technique for structure-guided drug design, but can also be integrated with HTS and combinatorial chemistry. Being so versatile, NMR can be applied to all phases of a drug discovery program, including target selection, lead generation, and lead optimization [1].

To most pharmaceutical companies structural information is an important contributor to drug discovery programs, and this information is sought and utilized whenever a target appears structurally feasible. For structure determination of large proteins, or the complex of a large protein with a tightly bound inhibitor, structure determination by X-ray crystallography is generally faster. On the contrary, smaller proteins sometimes do not readily crystallize and can be more rapidly solved by NMR. Furthermore, NMR can be applied to the structure determination of weakly bound ligands. The two methods are complementary, and each has its own strengths and weaknesses.

From a practical point of view, the main challenges NMR faces in the pharmaceutical world are the costs associated with the production of large amounts of labeled material for screening and structural studies, and, more importantly, the speed with which data are generated. Only when these issues are resolved, will NMR be able to fully exploit its potential in the drug discovery field. This chapter will review some of the methodologies recently developed to increase the efficiency of strategies for data acquisition, analysis, and protein structure calculation by NMR.

Fast Multidimensional NMR Spectroscopy

Data acquisition for multidimensional NMR spectra is not optimal in terms of speed. Systematic exploration of the indirect evolution dimensions one step at a time has the advantage that no signal frequencies are overlooked, but this is not the fastest mode of data acquisition for relatively sparse spectra. In a traditional three-dimensional NMR experiment, the evolution of the signal is followed as a function of t_1, t_2, and t_3 independently. On the contrary, a variety of methods [2] introduced in the last few years seek to simplify this process by cutting down the number of individual measurements, either in the time domain or in the frequency domain. Two of the most promising approaches are described below.

In GFT-NMR, the speed problem of multidimensional NMR is tackled by incrementing several evolution periods jointly, either exactly in step with one another or with suitable scaling factors between them. In a three-dimensional case where the evolution rates are all equal, this is equivalent to exploring the body diagonal of a cube representing the time-domain data space. This is clearly much quicker than incrementing these time dimensions independently. The chemical shifts appear in the experimental time-domain data set as linear combinations, but if several scans are carried out with the radiofrequency

Graham A. Webb (ed.), Modern Magnetic Resonance, 1239–1246.
© 2008 *Springer.*

mixing pulses systematically phase-shifted in 90° steps, a separation can be achieved by a procedure based on a G-matrix [3].

The reduction in measurement time improves exponentially as the number of locked dimensions increases, despite the increase in mandatory scans. However, the technique sacrifices sensitivity for each stage of dimensionality reduction, and higher-dimensional experiments necessarily incur increased signal loss through relaxation. Eventually a point is reached where the sensitivity, rather than the duration, becomes the limiting factor. Thus, the strength of the GFT method lies in the possibility of reducing the dimensionality of high-dimensional spectra, and the limitations of the GFT method might be expected to become evident in cases of severe overlap and in situations where sensitivity is a problem.

Another strategy aims to use projection-reconstruction (PR) techniques to recreate the full three-dimensional NMR experiments. This approach is related to that used in the X-ray tomography field [4] where it is employed to study complex systems. PR-NMR [5,6] reduces the time required to perform a three-dimensional experiment by an order of magnitude, and four-dimensional spectra by two orders of magnitude, by replacing the slow exploration of the evolution dimensions one-by-one by the acquisition of a relatively small number of plane projections.

If F_1 and F_2 are the evolution dimensions and F_3 the direct acquisition dimension of a three-dimensional NMR experiment, then the projections onto the orthogonal F_1F_3 and F_2F_3 are readily recorded by setting $t_2 = 0$ and $t_1 = 0$, respectively. These are the first planes of the three-dimensional spectrum and can be measured quite quickly. In an ideal situation where not too many peaks contribute to the intensity of a single response in the projection, and where the measured NMR intensities in both projections are reliable, the entire three-dimensional spectrum can be extracted from information on these two planes. In actual practice, ambiguities are to be expected and must be resolved if the three-dimensional spectrum is to be recovered. One solution is to measure a skew projection intermediate between the F_1F_3 and F_2F_3 planes by incrementing t_1 and t_2 jointly, with a suitable scaling factor. Skew projections are obtained by replacing the normal evolution time increments, t_1 and t_2, with $t_1\cos\alpha$ and $t_2\sin\alpha$, where α is the desired projection angle (Figure 1). The projection method relies on a Fourier transform theorem [7,8] which states that a section through the origin of a two-dimensional time domain signal $S(t_1, t_2)$, subtending an angle α with respect to the t_1 axis, transforms as the projection onto a line through the origin of the two-dimensional frequency-domain signal $S(F_1,F_2)$, subtending the same angle α with respect to the F_1 axis. By extension, a three-dimensional NMR experiment where the evolution parameters t_1 and t_2 are incremented simultaneously in the ratio $\Delta t_2/\Delta t_1 = \tan\alpha$, projects the three-dimensional NMR spectrum onto a plane tilted through an angle α with respect to the F_1F_3 plane. With the usual hypercomplex Fourier transformation, where real and imaginary signal components are acquired in both evolution dimensions [9] and suitably combined [10], projections are obtained for both $+\alpha$ and $-\alpha$, providing two independent views of the three-dimensional array of NMR peaks.

Although the sensitivity per unit time is the same as that of the conventional mode, it is reduced overall in proportion to the square root of the experimental time. Consequently, PR can realize its full theoretical speed advantage only if the inherent sensitivity of the sample is already adequate. Fortunately, modern high-field NMR spectrometers have improved in sensitivity, particularly those equipped with a cryoprobe receiver coil. As opposed to other methods of simultaneous incrementation of two evolution parameters [3,9,11], PR-NMR uses a simple and transparent method for data processing, providing a direct comparison with the traditional three-dimensional spectrum.

The inverse Radon transform can be used to reconstruct a three-dimensional NMR spectrum from a small number of different plane projections [12,13]. The Radon procedure calculates multiple line integrals of the absorption along parallel paths through the sample, and repeats the process for a set of different angles of incidence arranged around a circle. The Radon transform converts these line integrals into a related set of projections at right angles to the original beams. In practice, it is the inverse Radon transform that is of particular interest.

The reconstruction treatment aims to use the unique multidimensional array of NMR peaks compatible with all the measured plane projections. Projections involve the integration of the absorbed intensity along a series of parallel beams through the sample, and the Radon transform calculates these line integrals. The actual approach followed to find a density function compatible with all the measured projections depends on the quality of the NMR spectra. Thus, spectra with good sensitivity favor a processing scheme based on only a few projections. In this case, a three-dimensional array $S(F_1, F_2, F_3)$ is reconstructed by processing one F_1F_2 plane at a time. In a typical F_1F_2 plane, the raw experiment data for $\alpha = 0°$ and $\alpha = 90°$ are one-dimensional absorption spectra, representing the projections of NMR intensity onto the F_1 and F_2 axes, and a provisional map defining all the possible cross-peak coordinates can be derived easily. This provisional map is obtained by a two-dimensional convolution of the one-dimensional F_1 and F_2 traces. Some of these locations correspond to actual peaks, and others will later, after acquisition of additional projections at $\pm\alpha$, turn out to be unoccupied. Once all F_1F_2 planes have been processed, the three-dimensional spectrum is complete and can be displayed in any of the usual formats.

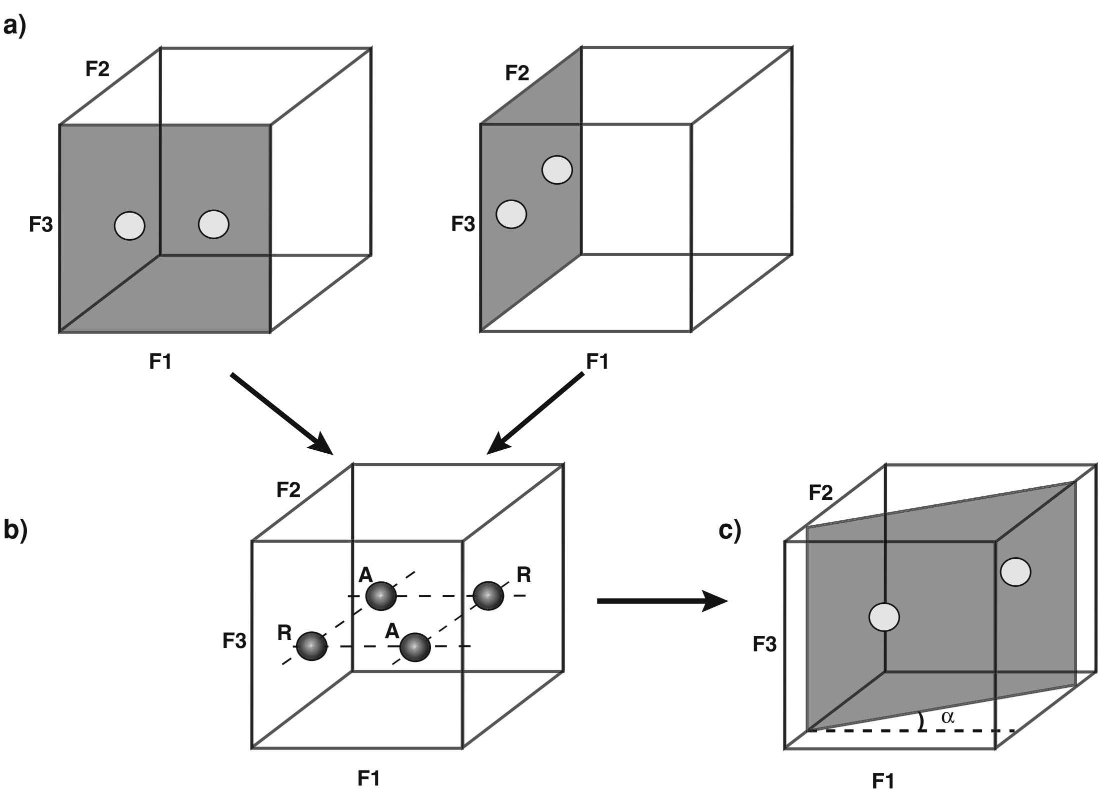

Fig. 1. Reconstruction of a three-dimensional NMR spectrum based on PR NMR techniques. First plane projections obtained for F_1F_3 and F_2F_3 at $t_2 = 0$ and $t_1 = 0$, respectively (a) cannot define unambiguously the positions of the signals in the three-dimensional spectrum (b), but this uncertainty can be resolved by measuring the projection onto a plane tilted by an angle α with respect to the F_1F_3 plane. "A" indicates artefact signals generated when the only information used for the reconstruction are first planes, and "R" indicates real signals that only become apparent when the tilted projection is measured.

For spectra with poor sensitivity, it is an advantage to record a larger number of different projections, usually spaced uniformly around a circle as in the Radon transform methodology. In this case, reconstruction is achieved by adding the contributions from the many different back-projections. There is a strong reinforcement of intensity at positions of genuine NMR peaks, enhancing the sensitivity in proportion to the number of different projections. This is an advantage as long as the number of projections remains smaller than the number of evolution increments in the conventional mode. This additive approach is preferred in situations where the intrinsic signal-to-noise is poor because each new projection enhances the final signal intensities, and the weak artefacts tend to disappear below the general noise level. Under these circumstances, it is better to enhance the signal-to-noise ratio by sampling the time-domain signals at more closely spaced angles of incidence, than to employ multiscan averaging.

In summary, provided that sensitivity is not a limiting factor, it is clear that multidimensional NMR spectroscopy can be sped up by linking the evolution periods together, rather than by varying them independently.

Speeding Up the Assignment Process

A crucial step in determining solution structures of proteins using NMR spectroscopy is the process of sequential assignment, which correlates backbone resonances to corresponding residues in the primary sequence of the protein. It has been recognized for some time that many of the interactive tasks carried out by an expert during the process of spectral analysis, could be carried out more efficiently and rapidly by computational systems. With the advent of triple-resonance and multidimensional strategies for determining resonance assignments and 3D structures, it became increasingly clear that the quality and information content of protein NMR spectra could allow largely automated analyses of assignments.

Successful automated spectral analysis is normally preceded by high-quality (manual or automatic) peak picking. Several high-quality peak-picking programs have been described over the last few years. For example, AUTOPSY [14] is a comprehensive program for automating peak picking with facilities for determining noise level, segmenting the spectra into peak-containing regions, identifying well-separated peaks, resolving spectral overlap and integrating peaks. In this context, SAMPA [15] is the only program attempting to automatically assign proteins in the absence of peak picking. As input, the module uses processed 2D and/or 3D spectra from XWIN-NMR (Bruker Biospin GmbH) and the amino acid sequence of the investigated protein. The result is a sequential assignment of the backbone atoms.

The algorithm is based on the consecutive comparison and analysis of 2D and 3D NMR-spectra whereby 2D spectra of selective experiments and 3D spectra of triple resonance experiments may be included. The program uses basic principles of pattern recognition theory and numerical recipes of mathematical analysis. The main idea is the search for characteristic patterns in different 2D and 3D spectra. A pattern is derived from the relationship of the amino acid type itself and its neighbors in the spectra.

A considerable amount of effort has been devoted in the last few years towards the automated analysis of resonance assignments [16–21] using triple-resonance NMR data. As described in Moseley and Montelione [22], most automation programs use the same general analysis scheme which includes filtering of peaks and referencing resonances from different spectra, grouping resonances into spin systems, identifying the amino acid type of the spin system (typing), linking sequential spin systems into segments, and, finally, mapping the spin-system segments onto the primary sequence of the protein. Linking and mapping can be achieved by two main methods: deterministic best-first methods [18–20,23] that require a one-time, all-to-all, full comparison between every spin system, and optimization algorithms [17,21] that use a pseudo-energy function with simulated annealing to evaluate potential connections between nearest neighbor spin systems. Best-first approaches establish criteria to select the best candidate from several potential connectivities. Unfortunately, wrong choices made early in the assignment process can lead to solutions which can be substantially incorrect [20]. On the other hand, the optimization algorithms are generally rather slow and can be susceptible to becoming trapped in local minima that correspond to incorrect assignment configurations.

Although the development of automated approaches for sequential assignment has facilitated the analysis of triple-resonance experiments, the performance of these programs is usually less satisfactory for large proteins, especially in the cases of missing connectivity or severe chemical shift degeneracy. In addition, successful algorithms must be able to address missing peaks, extra peaks from impurity or multiple conformers, uncertainty in the amino acid type determinations, and broken connectivities due to the uncertainty of resonance positions caused by the distortion or overlap of peaks.

An interesting approach to solve these problems have been proposed by Coggings and Zhou with the introduction of PACES [24], an interactive program for Protein Sequential Assignment by Computer-Assisted Exhaustive Search. The program conducts an exhaustive search of all spin systems both for establishing sequential connectivities and then for assignment. By running the program iteratively with user intervention after each cycle, ambiguities can be eliminated efficiently and backbone resonances can be assigned rapidly. PACES establishes sequential assignment based on the sequential connectivity and residue type information derived from C^{α}, C^{β}, CO, and H^{α} triple-resonance data, or any subset of these data. Additional information derived from other experiments, such as residue types or NOESY constraints, can also be introduced as PACES input. PACES anchors the resonances of a spin system to its HSQC peak, and subsequently refers to spin systems by HSQC peak numbers. The identification of residue type information is done by comparing C^{α}, C^{β}, CO shifts to the statistical chemical shift distribution of each amino acid type derived from the BioMagResBank (BMRB). If the protein under study is perdeuterated, PACES can be directed to adjust its amino acid ranges accordingly [25,26]. The mapping process involves aligning a connectivity fragment at the beginning of the protein sequence, and then moving it down the sequence, one residue at a time. When the C-terminus of the protein is encountered, spin systems are looped back to align with the N-terminus of the protein, until every spin system in the fragment has been examined at every position of the protein sequence. If at any position, the list of possible amino acid types for a spin system includes the amino acid type of the paired residue in the sequence, that pairing is considered a match. If multiple sequentially connected spin-systems match, the algorithm identifies the resulting segment as a matching fragment. Short matching fragments are filtered out unless they contain a spin system with less than five possible amino acid types. The chemical shift data and additional constraints are provided by the user on a properly formatted Excel worksheet, in a text file or from XEASY peak lists. Results are also presented on a formatted Excel worksheet, with one column for each residue. In summary, PACES is based on the methods used by NMR spectroscopists to assign proteins manually, but taking advantage of the abilities of a computer to work through all of the possibilities for connecting peaks and mapping them to the protein sequence.

Another strategy has been proposed by Reed *et al.* [27] for the semi-automated assignment of PGK (394 amino acids) based on a simulated annealing Monte Carlo technique using the following experiments as input: 2D ^{15}N-TROSY, 3D TROSY ct-HNCA, ct-HN(CO)CA, HN(CA)CB, HN(COCA)CB, HNCO, and HN(CA)CO. The program attempts to reorder the spin systems and place them in the amino acid sequence of the protein, by minimising an energy function based on both matching up the chemical shift data for adjacent residues, and on characteristic chemical shift ranges for resonances in particular residue types. Carbonyl chemical shifts are only used at the end of the process to confirm the assignments. After the initial peak picking and one run of the assignment program, a 60–80% complete assignment was obtained for this protein. The final 20–40% of the assignment took up the majority of the assignment time. Improving the level of assignment to 94% and then to 95% involved two further periods of 5 days each.

Finally, Lagnmead and Donald have published a new algorithm [28] that performs Nuclear Vector Replacement (NVR) by Expectation/Maximization (EM) to compute assignment using a combination of experimentally measured residual dipolar couplings, chemical shifts (2D H^N-N HSQC), H^N-H^N NOEs and amide exchange rates to a given *a priori* whole-protein 3D structural model. The authors proposed that this algorithm could form the basis for Molecular Replacement by NMR because of its resemblance with the technique used in X-ray crystallography to solve the phase problem using a close or homologous model. NVR adopts a minimalist approach [29], demonstrating the large amount of information available in a few key spectra. So far, NVR have been only tested on models with both high sequence and structural homology. Consequently, the present form of the algorithm may best be applied to scenarios where a crystal structure of the same protein is available, as may be the case in an SAR by NMR study. Models with significantly less homology will likely have somewhat different networks of hydrogen bonds and NOEs, as well as different amide bond-vector orientations.

Automated Protein Structure Determination

Until very recently, NMR protein structure determination has remained a laborious undertaking that occupied a trained spectroscopist over several months for each new protein structure. It has been recognized that many of the time-consuming interactive steps carried out by an expert during the process of spectral analysis could be accomplished by automated computational approaches [22]. Today automated methods for NMR structure determination are playing a more prominent role and will most likely supersede the conventional manual approaches to solving three-dimensional protein structures in solution [30].

The assignment of NOESY cross peaks requires as a prerequisite a knowledge of the chemical shifts of the spins from which nuclear Overhauser effects (NOEs) are arising. In *de novo* three-dimensional structure determination of proteins in solution by NMR spectroscopy, the key conformational data are upper distance limits derived from NOEs [31–34]. In order to extract distance constraints from a NOESY spectrum, its cross peaks have to be assigned. The NOESY assignment is based on previously determined chemical shift values that result from the chemical shift assignment. Because of the limited accuracy of chemical shift values and peak positions many NOESY cross peaks cannot be attributed to a single unique spin pair, but have an ambiguous NOE assignment comprising multiple spin pairs. Once available, a preliminary three-dimensional structure may be used to resolve ambiguous NOE assignments. Obtaining a comprehensive set of distance constraints from a NOESY spectrum is thus by no means straightforward, but becomes an iterative process in which preliminary structures, calculated from limited numbers of distance constraints, serve to reduce the ambiguity of cross peak assignments. In addition to this problem of resonance and peak overlap, considerable difficulties may arise from spectral artefacts and noise, and from the absence of expected signals because of fast relaxation.

Automated procedures follow the same general scheme but do not require manual intervention during the assignment/structure calculation cycles. Two main obstacles have to be overcome by an automated approach starting without any prior knowledge of the structure. First, the number of cross peaks with unique assignment based on chemical shifts is, in general, not sufficient to define the fold of the protein. Therefore, the automated method must have the ability to make use also of NOESY cross peaks that cannot yet be assigned unambiguously. Second, the automated program must be able to cope with the erroneously picked or inaccurately positioned peaks and with the incompleteness of the chemical shift assignment of typical experiment data sets.

In NOAH [35,36], an automated NOESY assignment routine present in the programs DIANA [37] and DYANA [38], the multiple assignment problem is treated by temporarily ignoring cross peaks with too many assignment possibilities, and instead generating independent constraints for each of the assignment possibilities of the remaining low-ambiguity cross peaks. In order to reduce the impact of these incorrect constraints on the structure, an error-tolerant target function is used [35,36]. NOAH requires a high accuracy of the input chemical shifts and peak positions, and makes use of the fact that only a set of correct assignments can form a self-consistent network.

In the initial assignment cycle with NOAH, all peaks with one or two assignment possibilities are included into the structure calculation. In view of the large number of erroneous conformational constraints that are likely to be included at this stage, it seems non-trivial that the NOAH/DIANA approach may ultimately converge to the correct structure. The explanation is related to the fact that the structure calculation algorithm attempts to satisfy a maximum number of conformational constraints simultaneously. The correctly assigned constraints form a large subset of self-consistent constraints, whereas, in contrast, the erroneously assigned constraints are randomly distributed in space, generally contradicting each other. As a consequence, erroneously assigned constraints may distort the structure, but will not lead to a distinctly different protein fold. One must keep in mind that the elimination of erroneously assigned constraints through contradiction with correct constraints will in general be less efficient in regions of low NOE density than in the well-defined protein core. Another peculiarity of the randomly distributed erroneously assigned constraints is that they are more likely to be long-range than short-range or intra-residual. This contrasts with the overall constraint distribution of a correctly assigned NOESY spectrum, where more than 50% of all cross peaks are from short-range NOEs [39].

Another widely used automated NOESY assignment procedure is ARIA [40–43] that was originally interfaced with XPLOR [44] and later with the program CNS [45]. ARIA introduced many new concepts, most importantly the use of ambiguous distance constraints [46,47] for handling ambiguities in the initial, chemical shift-based NOESY cross peak assignments. Prior to the introduction of ambiguous distance constraints, in general only unambiguously assigned NOEs could be used as distance constraints in a structure calculation. Since the majority of NOEs cannot be assigned unambiguously from chemical shift information alone, this lack of a general way to directly include ambiguous data into the structure calculation considerably hampered the performance of automatic NOESY assignment algorithms.

When using ambiguous distance constraints, each NOESY cross peak is treated as the superposition of the signals from each of its multiple assignments, using relative weights proportional to the inverse sixth power of the corresponding inter-atomic distance. ARIA starts from lists of peaks and chemical shifts in the format of the common spectral analysis programs, and proceeds in cycles of NOE assignment and structure calculation. The experimental peak lists can in practice not be assumed to be completely free of errors, especially in the early stages of a structure determination or if they originate from automatic peak picking. In addition, if the chemical shift assignment is incomplete, even the most carefully prepared peak list will contain peaks that cannot be assigned correctly, namely those involving unassigned spins, because the ARIA algorithm does not attempt to extend or modify chemical shift assignments provided by the user. When building a three-dimensional structure from NOE data, most erroneous distance constraints will be inconsistent with each other and with the correct ones. The erroneous constraints can therefore be identified by analyzing the violations of constraints with respect to the bundle of three-dimensional structures from the previous cycle of calculation. The only drawback with this program could be obtaining a correct fold at the outset of a *de novo* structure determination because the powerful structure-based filters used for the elimination of erroneous cross peak assignments are not yet operational at that stage.

The CANDID algorithm [48] in the program CYANA [49] combines features from NOAH and ARIA, such as the use of three-dimensional structure-based filters and ambiguous distance constraints, with the new concepts of network-anchoring and constraint combination that further enable an efficient and reliable search for the correct fold in the initial cycle of *de novo* NMR structure determination. Network-anchoring exploits the observation that the correctly assigned constraints form a self-consistent subset in any network of distance constraints that is sufficiently dense for the determination of a protein 3D structure. On the other hand, the concept of constraint combination aims to reduce the effect of spurious distance constraints that may arise from misinterpretation of noise and spectral artefacts. It is used in the first two CANDID cycles, and consists of generating distance constraints with combined assignments from different, in general unrelated, cross peaks. Constraint combination is applied only to the long-range peaks because in case of error their effect on the global fold of a protein is more pronounced than that of erroneous short- and medium-range constraints.

The automated CANDID method proceeds in iterative cycles of ambiguous NOE assignment followed by structure calculation with the CYANA torsion angle dynamics algorithm. Between subsequent cycles, information is transferred exclusively through the intermediary three-dimensional structures, in that the molecular structure obtained in a given cycle is used to guide the NOE assignments in the following cycle. Otherwise, the same input data are used for all cycles, that is, the amino acid sequence of the protein, one or several chemical shift lists from sequence-specific resonance assignment, and one or several lists containing the positions and volumes of cross peaks in 2D, 3D, or 4D NOESY spectra.

A CANDID cycle starts by generating for each NOESY cross peak an initial assignment list containing the hydrogen atom pairs that could, based on the chemical shift lists, contribute to the peak. Subsequently, for each cross peak these initial assignments are weighted with respect to several criteria (agreement between the values of the chemical shift list and the peak positions, and compatibility, if available, with the three-dimensional structure from the previous cycle), and initial assignments with low overall scores discarded. For each cross peak, the retained assignments are interpreted in the form of an upper distance limit derived from the cross peak volume. Thus, a conventional distance constraint is obtained for cross peaks with a single retained assignment. Otherwise an ambiguous distance constraint is generated that embodies several assignments. The structure calculations typically comprise seven cycles. Since the precision of the structure determination improves with each subsequent cycle, the criteria for accepting assignments and distance constraints are tightened in more advanced cycles of the CANDID calculation. In the final CANDID cycle, an additional filtering step ensures that all NOEs have either unique assignments to a single pair of hydrogen atoms, or are eliminated from the input for the structure calculation. This allows for the direct use of the NOE assignments in subsequent refinement and analysis programs that do not handle ambiguous distance constraints.

A very different strategy has been proposed by Kuszweski *et al.* [50] with the development of PASD, a new highly error-tolerant Probabilistic Assignment algorithm for Automated Structure Determination. The PASD algorithm which has been incorporated into the molecular structure determination package XPLOR-NIH [51], is conceptually and philosophically different from previously implemented algorithms in that it has been expressly designed with the aim of ensuring that the results from successive iteration cycles are not biased by the global fold of structures calculated in the preceding cycles. No NOE assignment is ever removed permanently, and consequently the likelihood of becoming trapped in a false minimum of NOE assignment space is significantly reduced.

Finally, although it is universally assumed that a protein structure determination by NMR requires sequence-specific resonance assignments, the chemical shift assignment by itself has no biological relevance. It is required only as an intermediate step in the interpretation of the NMR spectra. Several attempts have been made to devise a strategy for NMR protein structure determination that circumvents the tedious chemical shift assignment step. There is an analogy between these approaches and the direct phasing methods in X-ray crystallography [52].

The underlying idea of assignment-free NMR structure calculation methods is to exploit the fact that NOESY spectra provide distance information even in the absence of any chemical shift assignments. This proton-proton distance information can be exploited to calculate a spatial proton distribution. Since there is no association with the covalent structure at this point, the protons of the protein are treated as a gas of unconnected particles. Provided that the emerging proton distribution is sufficiently clear, a model can then be built into the proton density in a manner analogous to X-ray crystallography in which the structural model is constructed into the electron density. The most recent approach to NMR structure determination without chemical shift assignment is the CLOUDS protocol [53,54]. For the first time, the feasibility of the method has been demonstrated using experimental data rather than simulated data sets.

Conclusion

This review has presented some of the new tools available to improve data acquisition, analysis, and protein structure calculation by NMR. Given its wide applicability, NMR ought to play a very important role, in biomedical research and in the development of drugs for novel targets, during the post-genomic era. From the drug discovery perspective, an environment where a fast turnover of structural information is required, NMR will be competitive, if it is able to increase the speed with which assignments and protein structures are generated. This is particularly true if we consider that the sequencing of the human genome suggests that there are between 600 and 3000 genes that code for potential drug targets for human diseases [55]. About 400 of these gene products are currently in the research portfolio of pharmaceutical companies, and marketed drugs target only 120 of them. Therefore, the identification and characterization of new targets is of high interest for pharmaceutical research. NMR can contribute to this effort by determining the solution structure of a potential new target, particularly for monomeric proteins under 40 kDa or oligomeric proteins under 60 kDa [56–58], and in the characterization of proteins that do not have a defined three-dimensional structure [59]. Furthermore, NMR can also be used downstream of the drug discovery process in the identification of new compounds with biological activity against particular targets by fragment-based screening approaches [60], and in the three-dimensional characterization of the ligand-target complexes.

References

1. Widmer H, Jahnke W. Cell. Mol. Life Sci. 2004;61(5):580.
2. Freeman R, Kupce E. J. Biomol. NMR. 2003;27(2):101.
3. Kim S, Szyperski T. J. Am. Chem. Soc. 2003;125(5):1385.
4. G. Hounsfield N. Br. J. Radiol. 1973;46(552):1016.
5. Kupce E, Freeman R. J. Biomol. NMR. 2003;27(4):383.
6. Kupce E, Freeman R. J. Am. Chem. Soc. 2004;126(20):6429.
7. Bracewell RN. Aust. J. Phys. 1956;9:198.
8. Nagayama K, Bachmann P, Wuthrich K, Ernst RR. J. Magn. Reson. 1978;31:133.
9. Brutscher B, Morelle N, Cordier F, Marion DJ. J. Magn. Reson. B. 1995;109:338.
10. Ottiger M, Delaglio F, Bax A. J. Magn. Reson. 1998;131:373.
11. Ding K, Gronenborn A. J. Magn. Reson. 2002;156:262.

12. Dean SR. The Radon Transform and Some of Its Applications. John Wiley and Sons: New York, 1992.
13. Kupce E, Freeman R. Concepts Magn. Reson. 2004;22A(1): 4.
14. Koradi R, Billeter M, Engeli M, Güntert P, Wüthrich K. J. Magn. Reson. 1998;135:288.
15. Labudde D, Leitner D. personal communication.
16. Bartels C, Güntert P, Billeter M, Wüthrich K. J. Comput. Chem. 1997;18:139.
17. Buchler NEG, Zuiderweg ERP, Wang H, Goldstein RA. J. Magn. Reson. 1997;125:34.
18. Li K-B, Sanctuary BC. J. Chem. Inform. Comput. Sci. 1997;37:467.
19. Lukin JA,Grove AP, Talukdar SN, Ho C. J. Biomol. NMR. 1997;9:151.
20. Zimmerman DE, Kulikowski CA, Huang Y, Feng W, Tashiro M, Shimotakahara S, Chien C-Y, Powers R, Montelione GT. J. Mol. Biol., 1997;269:592.
21. Leutner M, Gschwind RM, Liermann J, Schwarz C, Gemmecker G, Kessler H. J. Biomol. NMR, 1998;11:31.
22. Moseley HN, Montelione GT. Curr. Opin. Struct. Biol. 1999;9(5):635.
23. Szyperski T, Baneck B, Braun D, Glaser RW. J. Biomol. NMR, 1998;11:387.
24. Coggins BE, Zhou P. J. Biomol. NMR. 2003;26(2):93.
25. Venters RA, Farmer 2nd BT, Fierke CA, Spicer LD. J. Mol. Biol. 1996;264(5):1101.
26. Farmer 2nd BT, Venters RA. Biol. Magn. Reson. 1999;16:75.
27. Reed MA, Hounslow AM, Sze KH, Barsukov IG, Hosszu LL, Clarke AR, Craven CJ, Waltho JP. J. Mol. Biol. 330(5):1189 (2003).
28. Langmead CJ, Donald BR. J. Biomol. NMR. 2004;29(2):111.
29. Bailey-Kellogg C, Widge A, Kelley III JJ, Berardi M, Bushweller J, Donald B. J. Comput. Biol. 2000;7: 537.
30. Guntert P. Prog. Nucl. Mag. Res. 2003;43:105.
31. Solomon I. Phys. Rev. 1955;99:559.
32. Macura S, Ernst RR. Mol. Phys. 1980;41:95.
33. Kumar A, Ernst RR, Wüthrich K. Biochem. Biophys. Res. Commun. 1980;95:1.
34. Neuhaus D, Williamson MP. The Nuclear Overhauser Effect in Structural and Conformational Analysis, VCH, 1989.
35. Mumenthaler C, Güntert P, Braun W, Wüthrich K. J. Biomol. NMR. 1997;10:351.
36. Mumenthaler C, Braun W. J. Mol. Biol. 1995;254:465.
37. Güntert P, Braun W, Wüthrich K. J. Mol. Biol. 1991;217:517.
38. Güntert P, Mumenthaler C, Wüthrich K. J. Mol. Biol. 1997;273:283.
39. Wüthrich K. NMR of Proteins and Nucleic Acids, Wiley, 1986.
40. Nilges M, Macias MJ, O'Donoghue SI, Oschkinat H. J. Mol. Biol. 1997;269:408.
41. Nilges M, O'Donoghue SI. Prog. NMR Spectrosc. 1998;32:107.
42. Linge JP, O'Donoghue SI, Nilges M. Methods Enzymol. 2001;339:71.
43. Linge JP, Habeck M, Rieping W, Nilges M. Bioinformatics 2003;19:315.
44. Brünger AT. X-PLOR Version 3.1. A system for X-ray crystallography and NMR. Yale University Press, 1993.
45. Brünger AT, Adams PD, Clore GM, DeLano WL, Gros P, Grosse-Kunstleve RW,Jiang JS, Kuszewski J, Nilges M, Pannu NS, Read RJ, Rice LM, Simonson T, Warren GL. Acta Crystallogr. 1998;54:905.
46. Nilges M. Proteins. 1993;17:297.
47. Nilges M. J. Mol. Biol. 1995;245:645.
48. Herrmann T, Güntert P, Wüthrich K. J. Mol. Biol. 2002;319: 209.
49. CYANA version 1.0, www.guentert.com.
50. Kuszewski J, Schwieters CD, Garrett DS, Byrd RA, Tjandra N, Clore GM. J. Am. Chem. Soc. 2004;126(20):6258.
51. Schwieters CD, Kuszewski JJ, Tjandra N, Marius Clore G. J. Magn. Reson. 2003;160(1):65.
52. Drenth J. Principles of Protein X-ray Crystallography, Springer, 1994.
53. Grishaev A, Llinás M. Proc. Natl Acad. Sci. U.S.A. 2002;99: 6707.
54. Grishaev A, Llinás M. Proc. Natl Acad. Sci. U.S.A. 2002;99: 6713.
55. Hopkins AL, Groom CR. Nat. Rev. Drug Discov. 2002;1(9): 727.
56. Clore GM, Gronenborn AM. Curr. Opin. Chem. Biol. 1998;2(5):564.
57. Staunton D, Owen J, Campbell ID. Acc. Chem. Res. 2003;36(3):207.
58. Montelione GT, Zheng D, Huang YJ, Gunsalus KC, Szyperski T. Nat. Struct. Biol. 2000;7:982.
59. Wright PE, Dyson HJ. J. Mol. Biol. 1999;293(2):321.
60. Huth JR, Sun C. Comb. Chem. High Throughput Screen. 2002;5:631.

Transferred Cross-Correlated Relaxation: Application to Drug/Target Complexes

T. Carlomagno and C. Griesinger
Max Planck Institut for Biophysical Chemistry, 37077 Göttingen, Germany

Introduction

The NMR spectra of biomolecules without and especially with isotopic labeling provide a wealth of information about interatomic distances and angular geometries that can be used as conformational restraints in structure determination. In this review we will focus on the application of cross-correlated relaxation rates to obtain structural information on a small-molecule/protein complex that has pharmaceutical implications. Cross-correlated relaxation complements information derived from NOEs. The chosen complex: epothilone/tubulin could not be subjected to X-ray crystallography. Electron microscopy can only be performed on tubulin sheets induced with Zn ions, which show an assembly of the tubulin dimers that is not found under physiological conditions. A structure of epothilone when bound to tubulin has been determined by electron crystallography. However, the resolution is too low to deduce the conformation of epothilone in a unique way. Thus, NMR constitutes a unique tool for the investigation of this drug/protein complex to obtain a high-resolution structure of the drug molecule in the bound state.

Cross-Correlated Relaxation for the Measurement of Projection Angles between Tensors [1]

Angular information on molecules is not only encoded in through-bond scalar or through-space dipolar couplings, but can also be derived from measurements of relaxation rates. Relaxation is caused by the correlation of two tensorial interactions. If these interactions are different, then relaxation caused by the cross-correlation of the two interactions is called cross-correlated relaxation. The cross-correlated relaxation rate depends on the strengths of the tensorial interactions as well as on the projection angle between the two tensors. To be effective the time-dependence of the tensorial interactions must be similar. Such a situation exists, e.g. between dipolar interactions of two proximate spin pairs within well-structured parts of the molecule, which display the same time-dependence due to overall tumbling. The most important tensorial interactions are the dipolar coupling and the chemical shift anisotropy. The dipole tensor between two spins I_k and I_l (I_m and I_n) is axially symmetric and the main axis is collinear with the respective internuclear bond vectors.

The cross-correlated relaxation rate observed for double- or zero-quantum coherence involving I_k or I_l and I_m or I_n for two dipolar interactions takes the following form:

$$\Gamma^c_{kl,mn} = \frac{\gamma_k \gamma_l}{(r_{kl})^3} \frac{\gamma_m \gamma_n}{(r_{mn})^3} \left(\frac{\mu_0}{4\pi}\hbar\right)^2 \frac{1}{5}(3\cos^2\theta_{kl,mn} - 1) \times \tau_c \tag{1}$$

The characterization of the angular dependence of the interaction of two nuclear dipoles $I_k I_l$ and $I_m I_n$ is therefore straightforward, namely it depends on the projection angle of the two bonds between I_k and I_l and between I_m and I_n. As can be seen from the equation for the cross-correlated relaxation rates, they depend on the correlation time of the molecule. Therefore, cross-correlated relaxation rates will increase with increasing size of the biomolecule under investigation as opposed to J coupling or dipolar coupling constants whose size does not depend on the molecular weight of the molecule. A second application lies in the fact that in analogy to the transferred NOESY experiment, in which distances are measured for ligands when bound to large target molecules, a transferred cross-correlated relaxation (trCCR) experiment allows to measure projection angles of weakly bound ligands when bound to large molecules.

Effects of Cross-Correlated Relaxation on Spectra

In two pairs of nuclei $I_k I_l$ and $I_m I_n$, projection angle dependent cross-correlated relaxation rates $\Gamma^c_{kl,mn}$ due to two dipolar couplings of double- and zero-quantum coherences between nuclei I_k and I_m leads to differential relaxation of the four submultiplet lines as indicated in Figure 1. The cross-correlated relaxation rate leads to

Graham A. Webb (ed.), Modern Magnetic Resonance, 1247–1254.
© 2008 *Springer.*

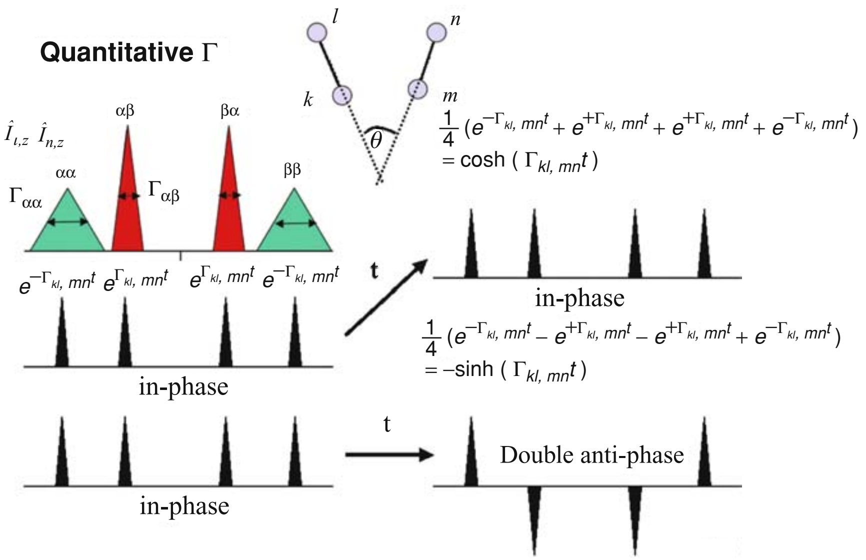
Quantitative Γ
$\hat{I}_{l,z}\ \hat{I}_{n,z}$
αβ
βα
αα
ββ
$\Gamma_{\alpha\alpha}$
$\Gamma_{\alpha\beta}$
$e^{-\Gamma_{kl,mn}t}$ $e^{\Gamma_{kl,mn}t}$ $e^{\Gamma_{kl,mn}t}$ $e^{-\Gamma_{kl,mn}t}$
l
n
k
m
θ
$\frac{1}{4}(e^{-\Gamma_{kl,mn}t}+e^{+\Gamma_{kl,mn}t}+e^{+\Gamma_{kl,mn}t}+e^{-\Gamma_{kl,mn}t})$
$=\cosh(\Gamma_{kl,mn}t)$
t
in-phase
in-phase
$\frac{1}{4}(e^{-\Gamma_{kl,mn}t}-e^{+\Gamma_{kl,mn}t}-e^{+\Gamma_{kl,mn}t}+e^{-\Gamma_{kl,mn}t})$
$=-\sinh(\Gamma_{kl,mn}t)$
t
Double anti-phase
in-phase

Fig. 1. Differential relaxation of the four submultiplet lines of a double-quantum coherence. The splitting originates from the J-couplings, while the line broadening originates from the cross-correlation of the two dipole–dipole couplings between k and l, as well as m and n, respectively. The differential relaxation can be expressed by the indicated product operators with evolutions that are sums and differences of exponential decays amounting to cosh and sinh dependencies.

additional line broadening of the outer lines (αα and ββ for the double-quantum coherence and αβ and βα for the zero-quantum coherence), while the inner lines (αβ and αβ for the double-quantum coherence and αα and ββ for the zero-quantum coherence) narrow by the same amount. This statement is true if the cross-correlated relaxation rate is positive ($3\cos^2\theta_{kl,mn}-1>0$) and thus the angle θ is between 0 and the magic angle θ^{magic} or between 180° and $180^\circ-\theta^{\text{magic}}$. In case that θ lies in the remaining region ($3\cos^2\theta_{kl,mn}-1<0$) the outer lines become narrower and the inner lines become broader. The case for positive cross-correlated relaxation rate $\Gamma^c_{kl,mn}$ is represented in Figure 1.

Often, line width measurements suffer from inaccuracies, especially since there are many contributions to the line width. Therefore, it is desirable to perform product operator transformations that create operators exclusively based on cross-correlated relaxation that otherwise could not be created. For that, we write down the product operator transformations that are effected by dipole/dipole cross-correlated relaxation. As pictorially demonstrated in Figure 1, we then find [2]:

$$I_{k,x}I_{m,y}\xrightarrow{\Gamma^c_{kl,mn}t}I_{k,x}I_{m,y}\cosh\Gamma^c_{kl,mn}t-4I_{k,x}I_{m,y}I_{l,z}I_{n,z}\sinh\Gamma^c_{kl,mn}t \tag{2}$$

Similarly we obtain for the evolution of an antiphase operator:

$$2I_{k,x}I_{m,y}I_{l,z}\xrightarrow{\Gamma^c_{kl,mn}t}2I_{k,x}I_{l,z}I_{m,y}\times\cosh\Gamma^c_{kl,mn}t-2I_{k,y}I_{m,x}I_{n,z}\times\sinh\Gamma^c_{kl,mn}t \tag{3}$$

Obviously, operators are formed due to the evolution of cross-correlated relaxation that would not be formed without. The trick to perform now quantitative Γ experiments lies in the observation that the simultaneous evolution of the J_{kl} and J_{mn} couplings will lead to the same transformation as in Equation (3) but with known transfer amplitude provided the size of the coupling constants is known:

$$2I_{k,x}I_{m,y}I_{n,z}\xrightarrow{J_{kl},J_{mn}}2I_{k,x}I_{m,y}I_{l,z}\sin\pi J_{kl}t\sin\pi J_{mn}t-2I_{k,y}I_{m,x}I_{n,z}\cos\pi J_{kl}t\cos\pi J_{mn}t+\text{additional terms} \tag{4}$$

Thus, two experiments can be performed, one that transforms the operator $2I_{k,x}I_{m,y}I_{l,z}$ into $2I_{k,y}I_{m,x}I_{n,z}$ with $\sinh\Gamma^c_{kl,mn}t$ in a so-called quantitative Γ cross experiment and a second experiment, the reference experiment, in which this transformation is effected by evolution of J

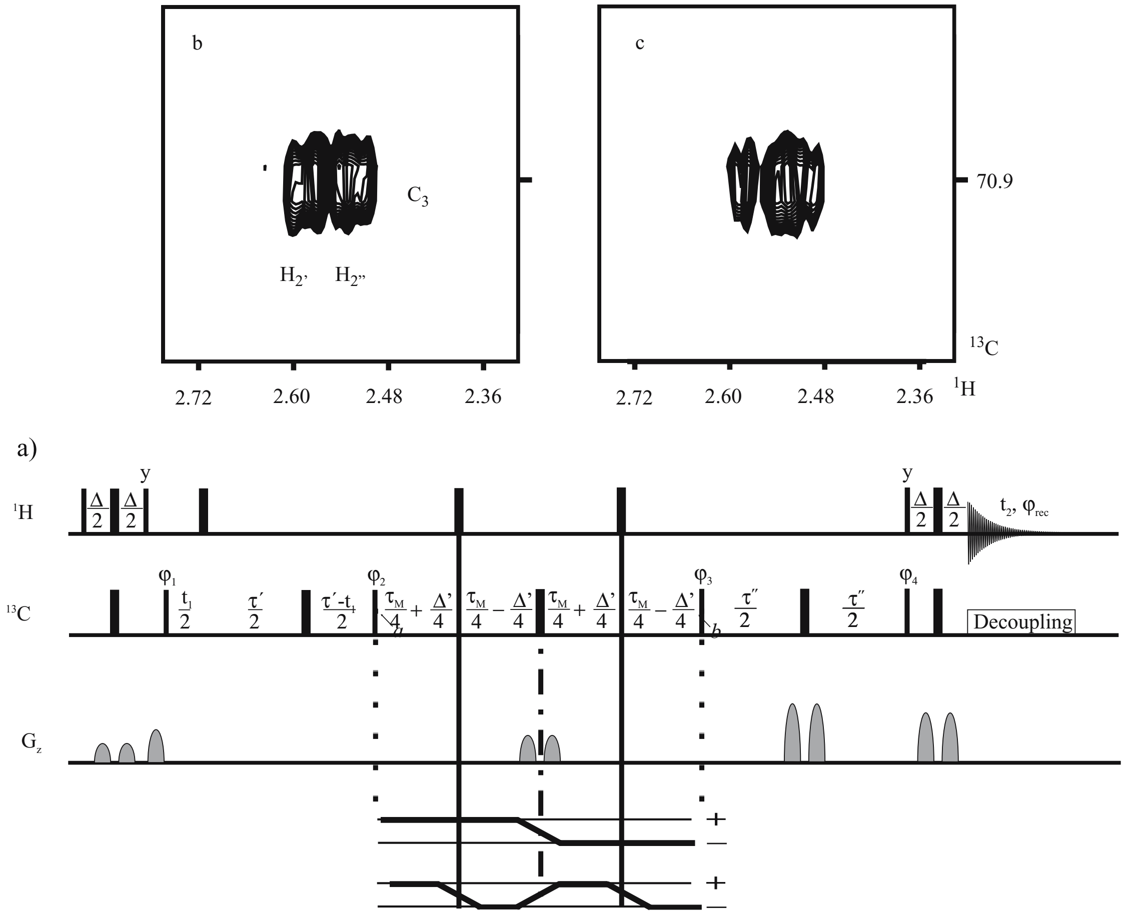

Fig. 2. Quantitative $\Gamma^{c}_{\mathrm{CH,CH}}$HCCH experiment (a) and spectra from reference (b) and cross experiments (c) applied to the H2′(H2″)C2C3H3 moiety of epothilone when bound to tubulin. From the comparison of the peak intensities of the respective peaks the cross-correlated relaxation rates ($\Gamma^{\mathrm{DD,DD}}_{\mathrm{C2H2',C3H3}}) = 2.1. + / - 0.3$ and $\Gamma^{DD,DD}_{C2H2",C3H3} = 3.8 + / - 0.4$) can be derived and related to the torsional angle C1–C2–C3–C4 of −146°.

couplings with the efficiency: $\sin\pi J_{kl}t \sin\pi J_{mn}t$. Provided the coupling constants are known or can be measured by well-known methodology, it is possible by comparing the intensities of a cross peak in the cross to the reference experiment to determine the cross-correlated relaxation rate.

Measurement and Application of the Quantitative Γ Method for Cross-Correlated Relaxation Rates

Quantitative Γ methods have been introduced originally by Felli *et al.* [3] and Pelupessy *et al.* [4] for dipole–dipole cross-correlated relaxation by transferring an initial operator to another operator by the evolution of the desired cross-correlated relaxation rate. Figure 2 shows the quantitative Γ sequence that measures the $\Gamma^{c}_{\mathrm{CH,CH}}$ cross-correlated relaxation rate. In this Γ HCCH experiment, which has been applied to aliphatic side chains or to sugars to measure the pseudorotation phase cross-correlated relaxation $\Gamma^{c}_{\mathrm{C}_i\mathrm{H}_i,\mathrm{C}_j\mathrm{H}_j}$ of the double- and zero-quantum coherence (DQ/ZQ) $4\mathrm{H}_{iz}\mathrm{C}_{ix}\mathrm{C}_{jy}$ generated at time point *a* creates the DQ/ZQ operator $4\mathrm{H}_{jz}\mathrm{C}_{jx}\mathrm{C}_{iy}$. In the second part of the experiment, the operator $4\mathrm{H}_{jz}\mathrm{C}_{jx}\mathrm{C}_{iy}$ is transferred via a 90° *y*-pulse applied to ^{13}C nuclei further to the proton H_j to give rise to a cross peak at $(\omega_{\mathrm{H}_j}, \omega_{\mathrm{C}_i})$. $\Gamma^{\mathrm{CSA,DD}}_{\mathrm{C}_i,\mathrm{C}_j\mathrm{H}_j}$ and $\Gamma^{\mathrm{CSA,DD}}_{\mathrm{H}_i,\mathrm{C}_j\mathrm{H}_j}$ cross-correlated relaxation are refocused by application of the 180° carbon and proton pulses during the mixing time τ_M. The following transfers are achieved in the sequence of Figure 2:

$$\begin{aligned}4H_{iz}C_{ix}C_{jy} \to 4H_{iz}C_{ix}C_{jy}&\left[\cosh\left(\Gamma^{c}_{C_iH_i,C_jH_j}\tau_M\right)\right.\\ &\times\cos^2\left(\pi J_{CH}\Delta'\right)-\sinh\left(\Gamma^{c}_{C_iH_i,C_jH_j}\tau_M\right)\\ &\left.\times\sin^2\left(\pi J_{CH}\Delta'\right)\right]-4H_{jz}C_{jx}C_{iy}\\ &\times\left[\sinh\left(\Gamma^{c}_{C_iH_i,C_jH_j}\tau_M\right)\cos^2\left(\pi J_{CH}\Delta'\right)\right.\\ &\left.+\cosh\left(\Gamma^{c}_{C_iH_i,C_jH_j}\tau_M\right)\sin^2\left(\pi J_{CH}\Delta'\right)\right]\end{aligned} \tag{5}$$

The last term produces a cross peak at $(\omega_{C_i}, \omega_{H_j})$ due to coherence transfer between $4H_{iz}C_{ix}C_{jy}$ and $4H_{jz}C_{jx}C_{iy}$, while the first term produces a cross peak at $(\omega_{C_i}, \omega_{H_i})$ and can therefore be distinguished. In the experiment with $\Delta' = 0$, the intensity of the cross peak (I^{cross}) is proportional to $\sinh(\Gamma^{c}_{C_iH_i,C_jH_j}\tau_M)$ whereas for $\Delta' = 1/2J_{CH}$, the intensity of the cross peak (I^{ref}) is proportional to $\cosh(\Gamma^{c}_{C_iH_i,C_jH_j}\tau_M)$. By comparing the intensity of the cross peak measured in the two experiments one can determine:

$$\frac{I^{\text{cross}}}{I^{\text{ref}}} = \tanh\left(\Gamma^{c}_{C_iH_i,C_jH_j}\tau_M\right) \tag{6}$$

This is applied in Figure 2B and C to the torsion angle defined by C1–C2–C3–C4 of epothilone and an angle of −143° is obtained.

An extension of this method is the measurement of cross-correlated relaxation between a methyl group and a remote HC moiety in a $C^1H_3C^2C^3H$ fragment [5] which yields the torsion angle about the C^2C^3 bond. The pulse sequence used for the measurement of the $\Gamma_{CH,CH}$ rate between the C^3H vector and the C^1H_3 vectors is shown in Figure 3A. Two experiments are recorded, yielding a *cross* and a *reference* spectrum similarly as for the HCCH case except for the fact that the transfer requires one further transfer step and the double-quantum and zero-quantum coherence is excited between geminal instead of directly bound carbons. The CCR rate is extracted from the ratio of peak intensities in the *cross* and *reference* experiment. The pulse sequence is optimized for maximum sensitivity of the cross experiment: the $8H^1_zC^1_yC^2_zC^3_y$ coherence present at point *c* is transformed by $\Gamma^{DD}_{C^1H,C^3H}$ into $8C^1_xC^2_zC^3_xH^3_z$ with efficiency equal to $3\sinh(\Gamma^{DD}_{C^1H,C^3H}\mathrm{T}_{rel})\cosh^2(\Gamma^{DD}_{C^1H,C^3H}T_{rel})$. For the reference experiment, the same operator transformation is achieved with the efficiency: $3\sin(\pi J_{C^1H}\Delta/2)\ \sin(\pi J_{C^3H}\Delta/2)\ \cosh^2(\pi J_{C^1H}\Delta/2)\cosh^3(\Gamma^{DD}_{C^1H,C^3H}T_{rel})$. The last term stems from the fact that the cross-correlated relaxation is active also in the reference experiment. It is obvious that a comparison of the relative intensities based on the knowledge of the respective coupling constants yields the cross-correlated relaxation rate. The $8C^1_xC^2_zC^3_xH^3_z$ term is then transformed into H^3_x for detection. The delays are optimized for optimal refocusing and defocusing of the couplings. Selective π pulses on the carbons prevent loss of magnetization to other passively coupled carbons. The complete coherence transfers are given in the following:

$$\begin{aligned}&\boxed{a}\,2H^1_zC^1_y \xrightarrow[\pi/2(C)]{{}^1J_{C^1C^2}} \boxed{b}\,4H^1_zC^1_yC^2_x \xrightarrow[\pi/2(C)]{{}^1J_{C^2C^3}} \boxed{c}\,8H^1_zC^1_yC^2_zC^3_y\\ &\xrightarrow[{}^1J_{CH}(\text{reference})]{\text{CCR(cross)}} \boxed{d}\,8C^1_xC^2_zC^3_xH^3_z \xrightarrow{\pi/2(C)} 8C^1_zC^2_xC^3_zH^3_z\\ &\xrightarrow[\pi/2(C)]{{}^1J_{C^1C^2}} \boxed{e}\,4C^2_zC^3_yH^3_z \xrightarrow{{}^1J_{C^2C^{23}}} \boxed{f}\,2C^3_xH^3_z \xrightarrow{\text{INEPT}} \boxed{g}\,H^3_x\end{aligned} \tag{7}$$

Transferred Cross-Correlated Relaxation

Due to the fact that cross-correlated relaxation depends linearly on the correlation time it can be used to determine the conformation of ligands when bound to target molecules, provided the off rate is fast enough to enable detection of the cross-correlated relaxation rate via the free ligand [6, 7]. The conditions, under which such an experiment can be performed, are similar to those found for transferred NOEs [8] and for K_ds normally exceeding 10^{-6}M, ligands are in an equilibrium between a protein-bound and a free form. The period during which the molecule is in the bound conformation will contribute to relaxation to the largest extent and hence will heavily weight experiments that are based on relaxation. The population-averaged cross-correlated relaxation rate for dipole, dipole cross-correlated relaxation between two sites with fractions p_L of the free ligand and $p_{ML} = (1 - p_{ML})$ of the bound ligand is given in Equation (8):

$$\begin{aligned}\left\langle\Gamma^{DD,DD}_{C_mH_m,C_nH_n}\right\rangle = \frac{2}{5}\,&\frac{\gamma_C^2\gamma_H^2\mu_0{}^2\hbar^2}{(4\pi)^2 r^3_{C_mH_m} r^3_{C_nH_n}}\\ &\times\left[S^2_{mn,L}\,p_L\frac{3\cos^2\theta_{mn,L}-1}{2}\tau_{c,L}\right.\\ &\left.+S^2_{mn,ML}\,p_{ML}\frac{3\cos^2\theta_{mn,ML}-1}{2}\tau_{c,ML}\right]\end{aligned} \tag{8}$$

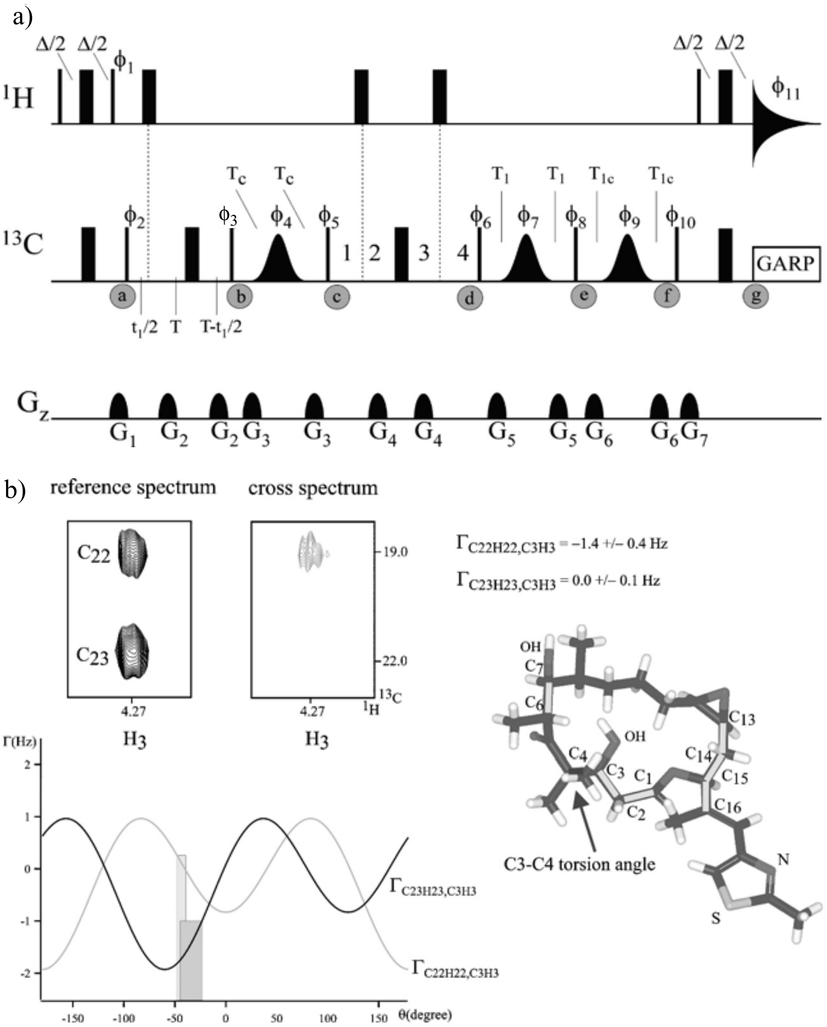
a)
Δ/2 Δ/2
ϕ1
1H
Δ/2 Δ/2
ϕ11
Tc Tc
T1 T1 T1c T1c
ϕ2 ϕ3 ϕ4 ϕ5 1 2 3 4 ϕ6 ϕ7 ϕ8 ϕ9 ϕ10
13C
GARP
a b c d e f g
t1/2 T T-t1/2
Gz
G1 G2 G2 G3 G3 G4 G4 G5 G5 G6 G6 G7
b) reference spectrum cross spectrum
C22
C23
4.27
H3
4.27
1H
H3
19.0
22.0
13C
ΓC22H22,C3H3 = −1.4 +/− 0.4 Hz
ΓC23H23,C3H3 = 0.0 +/− 0.1 Hz
Γ(Hz)
2
1
0
-1
-2
-150 -100 -50 0 50 100 150 θ(degree)
ΓC23H23,C3H3
ΓC22H22,C3H3
OH
C7
C6
OH
C4
C3
C1
C2
C13
C14
C15
C16
N
S
C3-C4 torsion angle

Fig. 3. (A) Pulse sequence for the measurement of dipolar–dipolar cross-correlated relaxation between the $(CH)^{22/23}_{ave.}$ vector and the $(CH)^3$ vector in epothilone. $\Delta = 1/(2^1J_{CH})$; $T = 1/(4^1J_{CC}) = 7$ ms; $T_c = 1/(4^1J_{CC}) = 7$ ms; $T_1 = 1/(8^1J_{CC}) = 3.5$ ms; $T_{1c} = T_c$. Delays 1–4 are equal to $T_{rel}/4$ ($T_{rel} = 1/^1J_{CC} = 28$ ms) in the cross experiment; in the reference experiment delay 1 $= T_{rel}/4 + \Delta/8 =$ delay 3 and delay 2 $= T_{rel}/4 - \Delta/8 =$ delay 4. $\phi_1 = y$; $\phi_2 = x, -x$; $\phi_3 = 2(y), 2(-y)$; $\phi_5 = 4(x), 4(-x)$; $\phi_6 = 8(y), 8(-y)$; $\phi_8 = x$; $\phi_{10} = y$.; $\phi_{11} = 2(x,-x), 4(-x,x), 2(x,-x)$; $\phi_4 = \phi_7 = \phi_9 = x$. The pulses with phase ϕ_4 and ϕ_9 are Q3 pulses of 768 ms duration, centered at 63 ppm, to selectively invert the C^3 and C^4 (C^3 resonates at 70.9 ppm and C^4 at 53.0 ppm); the pulse with phase ϕ_7 is a Q3 pulse of 512 ms duration centered at 37 ppm, to selectively invert the $C^{22/23}$ and C^4 (C^{22} resonates at 19.1 ppm and C^{23} at 21.7 ppm). The proton carrier was at 4.78 ppm and the carbon carrier at 37 ppm; spectral widths were 4807.69 Hz for proton and 8333.33 Hz for carbon. Carbon decoupling in acquisition consisted of a GARP modulated pulse train at 2.38 kHz field strength. *Reference* (b) and *cross* (c) spectra acquired with the sequence in (a). The peaks visible in the reference spectrum are at the chemical shift of C^{22} (19.1 ppm) and C^{23} (21.7 ppm) in the carbon dimension and at the chemical shift of H^3 (4.27 ppm) in the proton dimension. The *cross* experiment was four times longer than the *reference* experiment. 1024 and 64 complex points were acquired in t_2 and t_1, respectively. The final matrices were 2048 × 128 points. The gray lines represent negative contours. The sample contained 0.5 mM epothilone A and 5 μM tubulin dissolved in D_2O. (D) Dependence of cross-correlated relaxation rates on the torsion angle about the C3–C4 bond. The two cross-correlated relaxation rates determine the angle to be −45°. (E) Numbering scheme of epothilone A and location of the torsion angles studied (indicated by bars drawn along the relevant bonds. (See also Plate 94 on page XVIII in the Color Plate Section.)

If the correlation time of the free ligand $\tau_{c,L}$ is much smaller than the correlation time of the bound ligand $\tau_{c,ML}$, the observed averaged cross-correlated relaxation rate $\left\langle \Gamma^{\mathrm{DD,DD}}_{\mathrm{C}_m\mathrm{H}_m,\mathrm{C}_n\mathrm{H}_n} \right\rangle$ is dominated by the bound conformation and therefore, precise information on the conformation of a bound ligand can be obtained. This concept has been introduced on the determination of the conformation of a phosphotyrosine peptide weakly bound to STAT-6 [7] []and of a tRNA analog bound to EF-Tu· GDP complex [6]. Here we will show the power of the method on the determination of the epothilone conformation in the tubulin-bound state.

Application to the Epothilone/Tubulin Complex

In this review, we describe the application of trCCR measurements for the determination of the conformation of epothilone when bound to tubulin. Epothilones are microtubule stabilizers and inhibit cell proliferation through a mechanism of action which is analagous to that of the renowned clinical anti-cancer drug Taxol® (paclitaxel).[9] Epothilones exhibit extraordinary antiproliferative activity in vitro and they efficiently induce cell death in paclitaxel-resistant tumor cell lines at up to 5000-fold lower concentrations than paclitaxel [9–11]. In addition, they possess higher water solubility than paclitaxel [10,12] which allows delivery *in vivo* with non cremaphor-containing formulation vehicles, thus eliminating formulation-based side effects [major hypersensitivity reactions (HSR)] [13] The potential clinical utility of epothilones is supported by *in vivo* experiments with epothilone B in a variety of nude mouse human tumor models [10,14].

Fortunately, the kinetic and thermodynamic properties of the complex between epothilone A and tubulin are in the desirable range for trNOE and trCCR experiments. Indeed, the trNOE and trCCR data are found in agreement with a dissociation constant K_d in the range of 10–100 μM. Evidence of *specific* binding of epothilone A to tubulin is provided by the restoration of the NOE spectrum of free epothilone A upon addition of epothilone B to the mixture, which proves the quantitative displacement of epothilone A from tubulin by the tighter binder epothilone B (not shown). The existence of specific and transient binding of epothilone A to tubulin enables the structural analysis of the active conformation of the epothilones by NMR.

The tubulin-bound conformation of epothilone A was calculated from 46 inter-proton distance restraints and seven torsion angle restraints measured for a 0.5 mM solution of epothilone A in water in the presence of 5 μM tubulin. The distance restraints were derived from transferred NOE experiments. To filter out spin-diffusion mediated peaks, only those signals were taken into account which were present with opposite sign to the diagonal peaks in a transferred ROESY experiment. The dihedral angle restraints were obtained by measuring CH–CH dipolar–dipolar and CH–CO dipolar-CSA transferred CCR rates for 60–70% ^{13}C labeled epothilone A. The trCCR experiments [6,7] were indispensable to obtain a unique description of the bound conformation, as more than one structure of the macrolide ring is compatible with the same H–H distance set (NOE intensities). Seven trCCR rates defined the torsion angles C1–C2–C3–C4, C5–C6–C7–C8, C12–C13–C14–C15, C13–C14–C15–O11, and C14–C15–C16–C17 were all determined using the quantitative Γ HCCH. The C2–C3–C4–C5 was determined from the ratio of the cross-correlated relaxation rates between the $\mathrm{C}^{22}\mathrm{H}_3$ and $\mathrm{C}^{23}\mathrm{H}_3$, respectively, with the $\mathrm{C}^3\mathrm{H}$ dipole. The O11–C1–C2–C3 was determined from CSA/DD trCCR (not described here) [15]. Figure 3B and C shows a representation of the methyl group experiment with the cross and reference experiments, respectively. In the cross spectrum the $\mathrm{C}^{23}(\omega 1)$–$\mathrm{H}^3(\omega 2)$ peak is missing, indicating that the dipolar–dipolar CCR between the $(\mathrm{CH})^{23}_{\mathrm{ave.}}$ vector and the $(\mathrm{CH})^3$ vector is close to zero. The quantitative value for the two CCR rates can be extracted according to the equation:

$$I_{\mathrm{cross}}/I_{\mathrm{ref}} = \tanh(\Gamma T_{\mathrm{rel}})/\sin^2(\pi J_{\mathrm{CH}}\Delta/2)\cos^2 \times (\pi J_{\mathrm{CH}}\Delta/2) \quad (9)$$

where I_{cross} and I_{ref} are the intensities of the peaks in the cross and reference experiment, respectively and Γ indicates the cross-correlated relaxation rate. The measured CCR rates between the $(\mathrm{CH})^3$ vector and the $(\mathrm{CH})^{23}_{\mathrm{ave.}}$ and $(\mathrm{CH})^{22}_{\mathrm{ave.}}$ vectors are 0.1 ± 0.1 and -1.4 ± 0.4, respectively. The dihedral angle θ that complies with the ratio between the two CCR rates is $-45° \pm 5°$. We used the ratio of the two CCR rates, instead of the rates themselves, to determine the dihedral angle because this approach is independent from both the τ_c and the internal motion order parameter S^2, if equal internal reorientation of all the CH vectors is assumed. The change in the θ dihedral angle from the gauche + conformation in the free form to the gauche—conformation in the bound form is corroborated by transfer-NOE data.

The tubulin-bound conformation of epothilone A [15] is shown in green in Figure 4 and is compared with the free (unbound) conformation of epothilone A determined by X-ray crystallography, [15,16] which is shown in gray. We choose to compare the tubulin-bound conformation of epothilone with the X-ray structure and not with the solution structure available in $\mathrm{CD_2Cl_2}$, because of the extensive flexibility of epothilone in solution in absence of tubulin [17]. However, the most populated conformer in

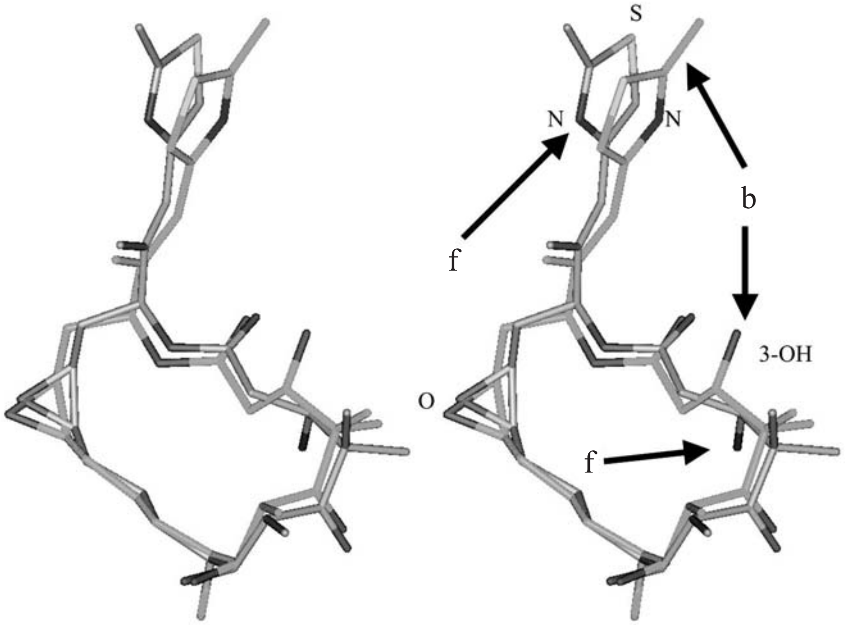

Fig. 4. Comparison of the conformations of epothilone as a stereoview. Arrows indicate free epothilone A (f: X-ray) and epothilone A bound to tubulin (B). Note the inversion of the orientation of the thiazole ring as well as the change in position of the 3-OH group. (See also Plate 95 on page XVIII in the Color Plate Section.)

solution is indeed very similar to the X-ray conformer. The position of the thiazole nitrogen (blue in Figure 4) and 3-OH (red in Figure 4), which are important for the delineation of a pharmocophore model, change significantly upon binding.

The structure of epothilone as derived from transferred NOE and cross-correlated relaxation is not identical with the structure derived from an electron crystallography study on Zn induced tubulin sheets [18]. The difference may be due to differences between the conformation of tubulin when assembled in Zn induced flat sheets as opposed to soluble tubulin or the low resolution of the electron crystallography that required extensive modeling of the epothilone conformation.

Conclusion

In conclusion, we have shown that transfer NOE and tr-CCR rates can be used for the determination of the conformation of epothilone when bound to tubulin in physiological conditions. So far, it has not been possible to obtain crystal structures of tubulin or microtubules. The structure differs from the one proposed from electron crystallography on Zn induced tubulin sheets which could be due to differences in the preparation of the samples under investigation or due to the low resolution of the electron crystallography structure.

References

1. Reif B, Hennig M, Griesinger C. Science. 1997;276:1230–3; Reif B, Diener A, Hennig M, Maurer M, Griesinger C. J. Magn. Reson. 2000;143:45–68.
2. Schwalbe H, Carlomagno T, Junker J, Hennig M, Reif B, Richter C, Griesinger C. Methods Enzymol. 2001;338:35–81.
3. Felli IC, Richter C, Griesinger C, Schwalbe H J. Am. Chem. Soc. 1999;121:56–7.
4. Pelupessy P, Chiarparin E, Ghose R, Bodenhausen G. J. Biomol. NMR. 1999;13:375–80.
5. Carlomagno T, Sánchez V, Blommers MJJ, Griesinger C. Angew. Chem. 2003;115:2619–21; Angew. Chem. Int. Ed. 2003;42:2515–7
6. Carlomagno T, Felli IC, Czech M, Fischer R, Sprinzl M, Griesinger C. J. Am. Chem. Soc. 1999;121:1945–8.
7. Blommers MJJ, Stark W, Jones CE, Head D, Owen CE, Jahnke W. J. Am. Chem. Soc. 1999;121:1949–53.
8. Clore GM, Gronenborn AM. J. Magn. Reson. 1982;48:402–17; Clore GM, Gronenborn AM. J. Magn. Reson. 1983;53:423–42; Ni F. Prog. NMR Spectrosc. 1994;26:517; Lian LY,

Barsukov IL, Sutcliffe MJ, Sze KH , Roberts GCK. Methods Enzymol. 1994;239:657–707

9. Bollag DM, McQueney PA, Zhu J, Hensens O, Koupal L, Liesch J, Goetz M, Lazarides E, Woods CM. Cancer Res. 1995, 55, 2325–33.
10. Altmann K-H, Wartmann M, O'Reilly T. BBA-Rev. Cancer 2000;1470:M79–91.
11. Kowalski J, Giannakakou P, Hamel E. J. Biol. Chem. 1997;272:2534–41.
12. Höfle G, Bedorf N, Steinmetz H, Schomburg D, Gerth K, Reichenbach H. Angew. Chem. 1996;108:1671–2; Angew. Chem. Int. Ed. 1996;35:1567–9.
13. Rowinsky EK. Ann. Rev. Med. 1997;48:353–74.
14. Altmann K-H, Bold G, Caravatti G, End N, Florsheimer A, Guagnano V, O'Reilly T, Wartmann M, Chimia 2000;54:612–21.
15. Carlomagno T, Blommers MJJ, Meiler J, Jahnke W, Schupp T, Petersen F, Schinzer D, Altmann K-H, Griesinger C. Angew. Chem. 2003;115:2615–9, Angew. Chem. Int. Ed. 2003;42:2511–5.
16. Rihs G, Walter HR. unpublished results.
17. Taylor RE, Zajicek J. J. Org. Chem. 1999;64:7224–8.
18. Nettles JH, Li H, Cornett B, Krahn JM, Snyder JP, Downing KH. Science 2004;305:866–69

Novel Uses of Paramagnets to Solve Complex Protein Structures

R. Andrew Byrd, C. Andrew Fowler, Robert L. McFeeters, and Vadim Gaponenko
Structural Biophysics Laboratory; Center for Cancer Research; National Cancer Institute; Frederick, MD 21702-1201, USA

Abbreviations: PCS, pseudocontact shift; RDC, residual dipolar coupling; pmiRDC, paramagnetic induced residual dipolar coupling; PRE, paramagnetic relaxation enhancement; PAS, paramagnetic anisotropic susceptibility.

Introduction

NMR is a critical tool in current structural biology, and plays a significant role in the understanding of pharmacologically significant proteins, as well as the development of modulators for these proteins. The general approach for structure determination has been well established; however, as the systems of interest become larger (e.g. >25 kDa) and less well behaved in solution (e.g. solubility limits of 50–200 μM), new approaches are required to enable NMR to remain a key player. The introduction of cryogenic probes has dramatically impacted our ability to study lower concentration and/or lower stability proteins. Nevertheless, there has been a need to develop new approaches to provide long-range structural restraints to solve structures of highly deuterated proteins and to determine the orientation of domains in multidomain proteins, or in multimeric complexes. This article will focus on our recent efforts in this area of research, specifically the introduction of paramagnetic metal ions into non-metalloproteins and the unique and powerful structural restraints that can be obtained from this approach.

The ability of paramagnetic centers to provide valuable structural information for proteins has been recognized for a long time [1,2]. The principal significance of this information is the long-range distance (10–40 Å) or global (distance and orientation) nature of the restraints. By augmenting traditional short-range, scalar restraints (such as NOEs) with long-range restraints, more accurate protein structures can be obtained. The relative proximity and/or orientation of protein domains or proteins within a complex can also be investigated. There are three main types of data that are obtainable: paramagnetic relaxation enhancement (PRE), pseudocontact shifts (PCSs), and residual dipolar couplings (RDCs).

Paramagnetic relaxation enhancements provide long-range distance information [3–6]; however, while relaxation enhancement is a powerful tool, we will focus our discussion here on the use of PCSs and RDCs. Paramagnetic induced residual dipolar couplings (pmiRDCs) and cross-correlation rates between dipolar and Curie relaxation pathways offer unique ways for obtaining orientational information on bond vectors in protein molecules [7–10]. PCSs provide both distance and orientational information that is very important for protein structure determination [11–14]. However, until recently, observation of these valuable structural parameters was limited to naturally metal binding proteins. Investigators have now begun to examine ways to introduce paramagnetic centers into non-metal binding proteins. We will illustrate two different approaches to achieve paramagnetic tagging and discuss new methods that enhance this general approach by providing more precise measurements of RDCs. Finally, we will demonstrate the impact of PCSs and pmiRDCs on solving difficult protein structures (>25 kDa) and on defining domain orientation in two pharmacologically significant proteins, STAT4 and hepatocyte growth factor (HGF).

Methods to Bind Paramagnets to Non-Metalloproteins

One way to introduce paramagnetic probes into non-metalloproteins is through chemical modification that introduces a metal-chelating site. A facile modification site is either a unique, natural cysteine residue or an engineered cysteine residue within the protein of interest. Two early examples of this type of protein modification with paramagnetic agents involved the attachment of nitroxide spin labels to lysozyme and bovine pancreatic trypsin inhibitor [15,16], allowing the measurement of relaxation enhancements. One limitation of this approach is evident for proteins with multiple, structurally important cysteine residues, wherein complications due to cross-linking, aggregation or refolding of the unmodified protein may occur. In this case, alternative approaches to attachment of the metal binding ligand can be utilized (*vide infra*). More recently, EDTA based ligands were successfully employed for paramagnetic labeling of macromolecules. Proteins modified with

Graham A. Webb (ed.), Modern Magnetic Resonance, 1255–1261.
© 2008 *Springer.*

S-(2-pyridylthio)-cysteaminyl-EDTA have been shown to bind Co^{2+} and allow measurement of PCSs and pmiRDCs. This approach has been demonstrated on barnase and the N-terminal domain of STAT4 [17,18]. Other paramagnetic ions, e.g. lanthanides, can be bound to the EDTA ligands and yield a wealth of PCS and pmiRDC data. It has been shown that under some conditions the EDTA-metal complex can exist in two forms, believed to be stereoisomers. The two forms result in two different paramagnetic ansisotropic susceptibility (PAS) tensors and two sets of shifted resonances, as observed for two proteins, trigger factor and ArgN [19,20]. Further inspection indicates that the multiple forms may be due to the protonation state of the EDTA moiety at the time of complexation (Gaponenko *et al.*, to be published). Additionally, a different cysteine-ligation paramagnetic tagging reagent has been proposed [21]; however, multiple isomers were observed and the reagent may prove problematic. To address the problem of multiple forms, a slightly modified and enantiometrically pure EDTA-derived tag has been proposed [19]. This new ligand is anticipated to facilitate broader use of the cysteine-ligation approach, and it is clear that further advances in ligand design will be forthcoming soon. A related approach employed cysteaminyl-EDTA-derivatized 4-thio-deoxythymidine incorporated into DNA that was subsequently used to form a protein-DNA complex. By binding Mn^{2+} to the EDTA moiety, long-range intermolecular distances were derived from PREs of protein resonances [22,23].

Since PCSs are dependent on the distance and orientation of nuclei from the paramagnet, it is likely that not all segments of a molecule will reveal PCS data using a single ligation site. However, it is straightforward to serially engineer multiple ligand attachment sites, thereby obtaining PCS data for all segments of secondary structure (Figure 1) [17]. The multiple ligand attachment sites also yield separate, distinct alignment tensors, relative to the molecular coordinate system. This is particularly attractive, since it is often difficult to reduce the degeneracy for RDC solutions with one alignment [24,25], while multiple alignments can be difficult to achieve due to protein interactions with the alignment media or correlation of the tensor orientations (C.A. Fowler *et al.*, in preparation).

A second method of achieving paramagnetic binding to proteins is through the use of chelating peptide tags. Several peptides that can be cloned at either terminus of an expressed protein have been reported to bind paramagnetic metals. ATCUN (amino terminal Cu^{2+}(Ni^{2+}) binding) motifs [26] with bound Cu^{2+} have been used to provide distance restraints by PRE in both ubiquitin [27] and several calmodulin-peptide complexes [28]. Another short peptide tag, HHP (His-His-Pro), has been cloned at the N-terminus of thioredoxin [29], allowing the measurement of PRE in the presence of Ni^{2+}. Longer peptides can also chelate metals. A 17 residue lanthanide binding peptide tag has been cloned at the N-terminus of ubiquitin and used to obtain partial orientation and observe pmiRDCs [30]. Finally, chelated metals can be bound using a combination approach. A 26 residue, calmodulin binding peptide was attached via a short linker to the C-terminus of dihydrofolate reductase (DHFR) and Tb^{3+}-saturated calmodulin was added and observed to bind to DHFR, transferring a degree of paramagnetic alignment and allowing the measurement of pmiRDCs [31].

We have proposed a simpler, common peptide tag that is used in immobilized metal affinity chromatography (IMAC) [32–35]. IMAC is a technique generally used to purify recombinant proteins expressed with a chelating peptide tag. The tag binds to partially chelated metal ions in the column resin, allowing contaminants to be washed away followed by elution of the purified protein. One of the most common tags used for IMAC is hexahistidine (the so called his-tag) [36,37], which can be added at either the N- or C-terminus of a protein. Since his-tags can bind resin-associated metal ions, it follows that they can also bind free metal ions in solution.

It has recently been shown that several his-tagged proteins are capable of binding free cobalt ions in solution. The paramagnetic anisotropy of the cobalt-his-tag complex allows measurement of PCSs and also leads to partial alignment of the sample in a magnetic field, allowing the observation of pmiRDCs. The PCSs and pmiRDCs measured from the protein-his_6-Co^{2+} species

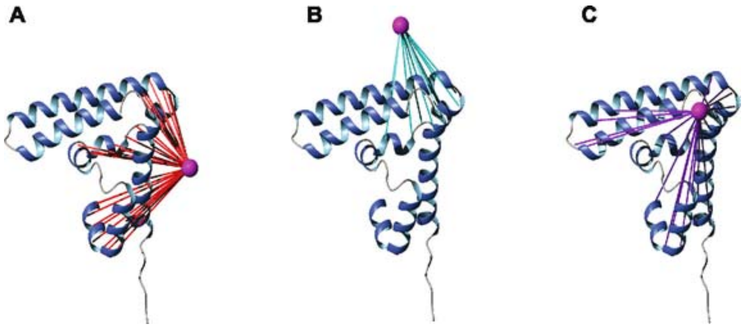

Fig. 1. Co^{2+} ligation at three distinct sites on $STAT4_{NT}$. (A) wt-C107, (B) T50C, and (C) K92C. The vectors illustrate the PCSs observed for H^N protons.

Table 1: Magnitudes of pmiRDCs observed for various protein-metal complexes

Protein and chelating tag	Metal or metal chelate	Largest magnitude ^{1}H-^{15}N RDC (Hz)
NK1-his$_6$	Co^{2+}	−3.0
Ubiquitin-his$_6$ (N-terminus)	Co^{2+}	−2.5
Ubiquitin-his$_6$ (C-terminus)	Co^{2+}	−0.7
Ubiquitin-LBP	Tb^{3+}	−7.6
Ubiquitin-LBP	Dy^{3+}	−6.6
Ubiquitin-LBP	Tm^{3+}	+4.5
DHFR-CBP	calmodulin(Tb^{3+})$_4$	−7.4
YmoA-his$_6$	Co^{2+}	+2.0
NusB-his$_6$	Co^{2+}-NTA	+2.0
STAT4-EDTA	Co^{2+}	−4.0
Trigger factor-EDTA-carbonic acid	Dy^{3+}	+8.0

LBP, lanthanide binding peptide; DHFR, dihydrofolate reductase; CBP, calmodulin binding peptide; NTA, nitrilotriacetic acid

have been shown to be relatively small; however, they are structurally significant and readily obtained (*vide infra*). Table 1 lists the magnitudes of observable pmiRDCs for several different chelating tags and conditions.

PCS Assignment and Use of PCSs and pmiRDCs as Structural Restraints

First, we will consider the PCSs. The presence of a metal ion introduces a PAS that results in the observation of PCSs for the NMR resonances. PCSs are measured as differences ($\Delta\delta_{pc}$) in chemical shift between the paramagnetic and diamagnetic species. Such differences are readily measured in the metal-free and metal-bound states. PREs can degrade the sensitivity of NMR experiments for sites close to the metal. For this reason, we have chosen to use Co^{2+}, which provides less relaxation enhancement than lanthanides or Mn^{2+}. Assignment of PCSs can be achieved using traditional NMR assignment strategies [38]. An alternative assignment strategy utilizes a preliminary structure of the macromolecule to estimate the PAS tensor orientation from several unambiguous PCSs [11], which have been assigned by inspection of HSQC spectra. The subsequent assignment of the remaining PCSs is accomplished by an iterative procedure of predicting the PCS values, using the PAS tensor orientation and the preliminary structure coordinates, and then re-optimizing the PAS based on new assignments. We have found that this procedure can assign all observable PCSs, including shifts up to 650 ppb, which were not previously assignable by inspection or other methods (Gaponenko *et al.* in preparation, 2005).

If the metal is chelated only by the EDTA or His$_6$ ligand, then there is no Fermi-contact contribution to $\Delta\delta_{\text{pc}}$, since there is no direct overlap of the molecular orbitals of the paramagnetic center with the protein atoms [2,12]. The pseudocontact shift is described by the following equation:

$$\Delta\delta_{\text{pc}} = \frac{P_{\text{ax}}}{r^3}\left(3\cos^2\theta - 1\right) + \frac{P_{\text{rh}}}{r^3}\sin^2\theta\cos(2\varphi). \quad (1)$$

where P_{ax} and P_{rh} are the axial and rhombic components of the PAS, r is the distance between the unpaired electron and the observed nucleus, and θ and ϕ are the polar angles describing the orientation of the electron-nucleus vector in the PAS tensor frame. PCSs follow the same functional form as RDCs and the structural restraints are very similar to homonuclear dipolar couplings [39]. However, the PCS restraints are more useful than homonuclear dipolar couplings because the sign information is readily available.

It is a straightforward procedure to incorporate PCS restraints into structure calculation programs, e.g. Xplor-NIH, that already have utilities for RDC refinement. The restraint is expressed in terms of the actual PCS and does not have an explicit input distance or orientation. Since many PCS restraints are included (for each tagged site) and combined with other NOE and torsion-angle restraints, a unique solution can be obtained. The distance of the atom, corresponding to the PCS, from the paramagnetic center is determined from the final structures. The corresponding distances range from 10 to 40 Å for the two cases described below.

The use of RDCs in protein structure determinations has become very significant and has been recently reviewed [40]. In the present application, partial alignment of the protein arises due to the paramagnetic susceptibility of the tagged protein. The alignment is known to be small [9]; nevertheless, the pmiRDCs are readily obtained without the need for steric alignment media, and have shown to be extremely valuable, both in terms of structure determination and domain orientation (*vide infra*). The pmiRDCs obtained from paramagnetic alignment are used in structure calculations exactly as has been described for steric alignment induced RDCs. They have also been useful for cross-validation.

New Approaches to Measurement of Small, Paramagnetically Induced RDCs

Paramagnetic alignment can induce relatively small RDCs (±2 to ±8 Hz for H^N-N), and it is important to have accurate methods to measure these couplings. Typical procedures for measuring RDCs involve the use of direct frequency measurements of resolved multiplet components, often augmented with the IPAP procedure [41]. These methods can suffer from measurement precision for small couplings. We have recently introduced a suite of experiments, based on the principal of J-modulation, that facilitate the measurement of H^N-N, H^{α}-C^{α}, C^{α}-C', and C^{α}-C^{β} RDCs [58]. The experiments encode the coupling of interest into peak modulation within familiar two-dimensional H^N-N (equivalent to HSQC spectra) or HN-C' correlation spectra.

Briefly, J-modulation can be incorporated into a pulse sequence in several different forms (see Figure 2), and the underlying principal remains that the coupling of interest is evolved for an amount of time, Δ, which can be varied. The observed resonance intensity is modulated by the coupling of interest in a sinusoidal manner dependent on Δ. Different types of J-modulation can be introduced into pulse sequences and result in different modulation functions of the coupling of interest. Simple, non-constant time J-modulation (Figure 2A) measures coupling for a total time 2Δ, but the intensity is a composite of J-modulation and I-spin relaxation, which complicates data analysis. Constant-time J-modulation incorporates the J-modulation delay into a constant time period, keeping relaxation effects constant and providing a means to decouple a third spin (Figure 2B). Chemical shift evolution can be reintroduced to constant time J-modulation rather easily (Figure 2C), thus expanding the repertoire of experiments that can be designed. Acquiring a series of spectra in which Δ is incremented allows the coupling of interest to be extracted from a plot of resonance intensity vs. total evolution time (Figure 2D). Examples of simple J-modulation [42–45], and constant-time J-modulation [46] have appeared, and we have extended these concepts and developed a suite of experiments to facilitate the rapid and precise measurement of a complete set of RDCs. With adequate signal-to-noise and a sufficient number of data, the precision of J-modulated couplings can exceed those of direct and E.COSY measurements. For a detailed discussion of these methods and the overall suite of experiments see McFeeters *et al.* [58].

In general, the precision of RDC measurement using the J-modulation experiments can be of the order of ±0.1 Hz and is significantly improved compared to IPAP methods or three-dimensional methods used to decrease spectral overlap. The convenience of spectral analysis for the familiar HSQC-like H^N-N 2D spectra facilitates a rapid, accurate measurement of multiple RDCs for samples with even weak alignment, such as found for paramagnetic induced alignment. These advances ensure that the maximum amount of structural data can be obtained from the paramagnet-tagged protein system.

Structural Applications of PCSs and pmiRDCs

We have addressed two difficult problems in protein structure determination: (1) improving structural accuracy for large, perdeuterated proteins, and (2) orientation of protein domains (or separate molecules) without the use of interdomain/intermolecular NOEs. Each of these problems reflects the use of NMR methods in larger, more biologically and pharmacologically significant proteins. The use of deuteration and selective methyl-protonation to enable structural studies of proteins $\geq$25 kDa is becoming common and has been reviewed [47].

Structural accuracy can be significantly improved by combining observed H^N (Figure 1) and methyl-^{1}H PCSs with the limited NOE-restraints available from an ILV-labeled protein to calculate the three-dimensional structure, as demonstrated for the N-terminal domain of STAT4 [17]. When PCSs were included in structure calculations the RMSD for backbone atoms in secondary structure elements between the solution structure and the crystal structure decreased from 2.9 to 2.0 Å, while the quality factor, Q [48], calculated from pmiRDCs *not used* in structure refinement decreased from 0.6 to 0.2. Furthermore, PCSs restraints for methyl groups of Ile, Leu, and Val afforded improvement in accuracy of the sidechain positions for these residues. The RMSD values for all heavy atoms in Ile, Leu, and Val sidechains relative to the crystal structure decreased from 2.97 to 2.43 Å, while the precision within the ensemble improved from 2.37 to 1.66 Å. Using the N-terminal domain of STAT4, we have also demonstrated that it is possible to break magnetic symmetry in homodimers, including the difficult case of head-to-head dimers, thus yielding unique structural information for each monomeric domain within the dimer [38] By binding subequimolar amounts of the paramagnet, only one monomer was tagged with paramagnet, and the PCSs to otherwise symmetric residues rendered the two sites magnetically inequivalent. The asymmetric system provided structural restraints, in the form of PCSs and pmiRDCs for each monomer, which enabled the

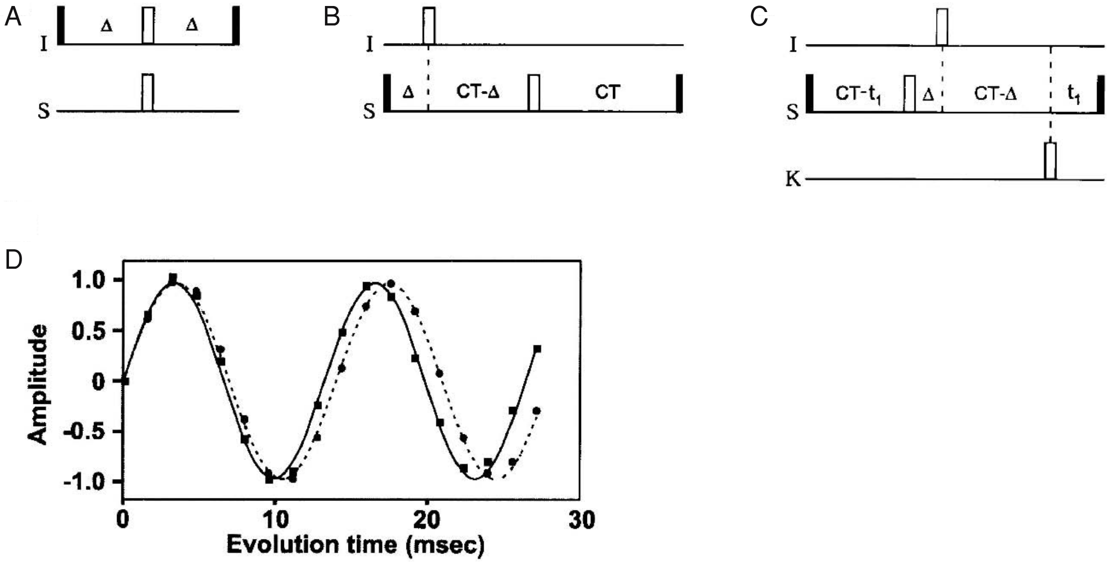

Fig. 2. Improved measurement of RDCs via J-modulation. (A) Basic pulse sequence element for non-constant time J-modulation. Intensity as a function of Δ, is a composite of both relaxation and modulation according to $\sin(2\pi J_{IS}\Delta)\bullet\exp(-R2\Delta)$. (B) Constant-time J-modulation removes relaxation damping resulting in modulation by $\sin(2\pi J_{IS}\Delta)$. (C) Frequency labeling can be reintroduced into constant-time J-modulation with no alteration in the form of modulation. (D). Typical modulation data, H^{α}-C^{α} couplings in an isotropic (solid line with squares) and aligned (dashed with circles) sample.

positioning of the two monomers with respect to one another (Gaponenko, unpublished). The improvements in structure calculations derive directly from the fact that PCSs, unlike one-bond RDCs, contain translational (distance) information in addition to orientational information. This fact heightens the value and future impact of using PCS restraints in general for protein structure determinations.

The second problem that we address is the ability to orient domains relative to one another within a multidomain protein or complex in the absence of traditional, NOE-based distance restraints, which is especially pertinent where deuteration is employed. This is a general form of the problem relating to the positioning of monomers within a homodimer structure (see above). The general approach assumes that any relatively rigid molecular fragments can be oriented relative to one another, provided enough data can be measured to determine the alignment tensor for each fragment. If the overall molecule is determined to behave as a single rigid unit, then each fragment must experience the same degree of alignment. Superimposing the alignment tensors allows the fragments to be correctly oriented with respect to one another. This technique has been successfully applied to fragments as small as a few residues [49,50], as well as to the problem of orienting entire protein domains. Recent examples of domain orientation using RDCs include the B and C domains of barley lectin [51], the domains of maltodextrin binding protein [52], and sequential domains in polyubiquitin chains [53–55]. The tensorial information may also be obtained from relaxation analyses [56,57]; however, we will focus on the use of RDCs and PCSs in this discussion.

Although useful, domain orientation using RDCs poses two significant challenges. The first of these is overcoming the well known “inversion problem” [25]. Although an alignment tensor can be determined using as few as five RDCs, it is impossible to determine which direction along each axis is positive and which is negative. This leads to four degenerate orientations, and additional independent data is required to overcome this inversion problem. A second problem is that while domains can be properly oriented, RDCs provide no translational (or distance) information and additional data must be used to position the two domains relative to one another.

We have recently combined PCSs with RDCs to orient the two domains in the NK1 fragment of HGF (C.A. Folwer *et al.*, in preparation, 2005). RDCs for the two domains were measured in phospholipid bicelles, yielding four possible domain orientations. Several additional alignment media were screened to find a second, independent alignment tensor; however, the protein either interacted with the media or the alignment tensor was

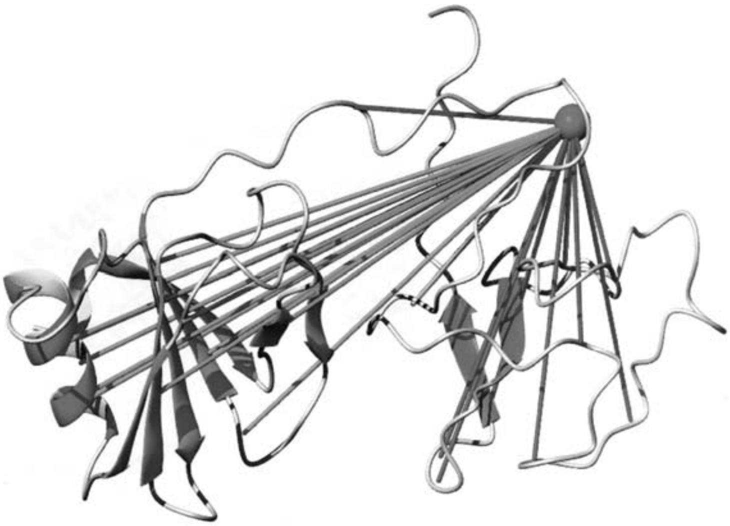

Fig. 3. Solution structure of NK1 refined against bicelle RDCs and cobalt PCSs (PCSs illustrated as orange and purple vectors to the N and K1 domains, respectively). (See also Plate 96 on page XIX in the Color Plate Section.)

not sufficiently different to solve the inversion problem. The protein was then re-cloned with a his-tag at the C-terminus, and shown to bind cobalt specifically to the his-tag. A saturating amount of cobalt was added to the sample, resulting in the observation of PCSs (±80 ppb) for amide protons in both domains. Furthermore, partial alignment of NK1 in the magnetic field, due to paramagnetic anisotropy, allowed the observation of H^N-N pmiRDCs on the order of ±3 Hz. The alignment tensor determined from the pmiRDCs was unique relative to the steric alignment tensors and was used to resolve the inversion problem, leading to a unique orientation of the two domains. The observed H^N PCSs for both domains were subsequently used as restraints and combined with RDCs measured from bicelle alignment, in a structure calculation to position the two domains of NK1 with respect to each other. The PCSs provided the requisite translational (distance) restraints to achieve a unique structural solution, and the significance is clearly seen in the long-range distances (10–40 Å) that correspond to the PCS restraints (Figure 3). The cobalt pmiRDCs were withheld from the structure calculations and subsequently used for cross-validation, which confirmed the structure. The final structure was obtained without the use of *any* intermolecular NOEs, and it is currently being analyzed to improve our understanding of the interaction of HGF with the cMet receptor.

Conclusion

We have summarized some of the exciting new applications of paramagnets in non-metalloprotein systems. The structures generated using the newly accessible restraints are of high quality and hold the potential for more accurate structures, access to larger structures, and more rapid structure determinations. While, to date, a limited number of applications of paramagnetic labeling have been described in the literature, it is already clear that this approach offers a wealth of valuable structural information. Improved tagging techniques and better software for data analysis should further enhance the advantages offered by this methodology for NMR structure determination and studies of molecular dynamics.

References

1. La Mar GN, Overkamp M, Sick H, Gersonde K. Biochem. 1978;17:325.
2. Bertini I, Luchinat C, Piccioli M. Meth. Enzymology. 2001;339:314.
3. Gillespie JR, Shortle D. J. Mol. Biol. 1997;268:170.
4. Gillespie JR, Shortle D. J. Mol. Biol. 1997;268:158.
5. Battiste JL, Wagner, G. Biochem. 2000;39:5355.
6. Gaponenko V, Howarth JW, Columbus L, Gasmi-Seabrook G, Yuan J, Hubbell WL, Rosevear PR. Prot. Sci. 2000;9:302.
7. Hus JC, Marion D, Blackledge M. J. Mol. Biol. 2000;298:927.
8. Ghose R, Prestegard JH. J. Magn. Reson. 1997;128:138.
9. Tolman JR, Flanagan JM, Kennedy MA, Prestegard JH. Proc. Natl. Acad. Sci. USA. 1995;92:9279.
10. Banci L, Bertini I, Huber JG, Luchinat C, Rosato A. J. Am. Chem. Soc. 1998;104:12903.
11. Allegrozzi M, Bertini I, Janik MBL, Lee YM, Liu G, Luchinat C. J. Am. Chem. Soc. 2000;122:4154.
12. Gochin M. J. Biomol. NMR. 1998;12:243.
13. La Mar GN, Del Gaudio J, Frye JS. Biochim. Biophys. Acta. 1977;498:422.

14. Ubbink M, Ejdeback M, Karlsson BG, Bendall DS. Structure. 1998;6:323.
15. Schmidt PG, Kuntz ID. Biochem. 1984;23:4261.
16. Kosen PA, Scheek RM, Naderi H, Basus VJ, Manogaran S, Schmidt PG, Oppenheimer NJ, Kuntz ID. Biochem. 1986;25:2356.
17. Gaponenko V, Sarma SP, Altieri AS, Horita DA, Li J, Byrd RA. J. Biomol. NMR. 2004;28:205.
18. Dvoretsky A, Gaponenko V, Rosevear PR. FEBS Lett. 2002;528:189.
19. Ikegami T, Verdier L, Sakhaii P, Grimme S, Pescatore B, Saxena K, Fiebig KM, Griesinger C. J. Biomol. NMR. 2004;29:339.
20. Pintacuda G, Moshref A, Leonchiks A, Sharipo A, Otting G. J. Biomol. NMR. 2004;29:351.
21. M. Prudencio, Rohovec J, Peters JA, Tocheva E, Boulanger MJ, Murphy ME, Hupkes HJ, Kosters W, Impagliazzo A, Ubbink M. Chemistry. 2004;10:3252.
22. Iwahara J, Schwieters CD, Clore GM. J. Am. Chem. Soc. 2004;126:5879.
23. Iwahara J, Anderson DE, Murphy EC, Clore GM. J. Am. Chem. Soc. 2003;125:6634.
24. Ramirez BE, Bax A. J. Am. Chem. Soc. 1998;120:9106.
25. Al-Hashimi HM, Valafar H, Terrell M, Zartler ER, Eidsness MK, Prestegard JH. J. Magn. Reson. 2000;143:402.
26. Harford C, Sarkar B. Acc. Chem. Res. 1997;30:123.
27. Donaldson LW, Skrynnikov NR, Choy WY, Muhandiram DR, Sarkar B, Forman-Kay JD, Kay LE. J. Am. Chem. Soc. 2001;123:9843.
28. Mal TK, Ikura M, Kay LE. J. Am. Chem. Soc. 2002;124:14002.
29. Jensen MR, Lauritzen C, Dahl SW, J. Pedersen, Led JJ. J. Biomol. NMR. 2004;29:175.
30. Wöhnert J, Franz KJ, Nitz M, Imperiali B, Schwalbe H. J. Am. Chem. Soc. 2003;125:13338.
31. Feeney J, Birdsall B, Bradbury AF, Biekofsky RR, Bayley PM. J. Biomol. NMR. 2001;21:41.
32. Ueda EKM, Gout PW, Morganti L. J. Chromatogr. A. 2003;988:1.
33. Lindner P, Guth B, Wülfing C, Krebber C, Steipe B, Müller F, Plückthun A. Methods. 1992;4:41.
34. Porath J, Carlsson J, Olsson I, Belfrage G. Nature. 1975;258:598.
35. Kågedal L. In: J-C Janson and L Rydén (Eds). *Protein Purification: Principles, High-Resolution Methods, and Applications*, 2nd ed. Wiley-VCH, Inc.: New York, 1998, p. 311.
36. Hochuli E. In: JK Setlow (Ed.). *Genetic Engineering*; *Vol. 12*, Plenum Press: New York, 1990, p. 87.
37. Hochuli E, Bannwarth W, Döbeli H, Gentz R, Stüber D. Biotechnology. 1998;6:1321.
38. Gaponenko V, Altieri AS, Li J, Byrd RA. J. Biomol. NMR. 2002;24:14S3.
39. Tjandra N, Marquardt J, Clore GM. J. Magn. Reson. 2000;142:393.
40. Bax A. Protein Sci. 2003;12:1.
41. Ottiger M, Delaglio F, Bax A. J. Magn. Reson. 1998;131:373.
42. Tjandra N, Grzesiek S, Bax A. J. Am. Chem. Soc. 1996;118:6264.
43. Wirmer J, Schwalbe H. J. Biomol. NMR. 2002;23:47.
44. Evenas J, Mittermaier A, Yang DW, Kay LE. J. Am. Chem. Soc. 2001;123:2858.
45. Mittermaier A, Kay LE. J. Am. Chem. Soc. 2001;123:6892.
46. Hitchens TK, McCallum SA, Rule GS. J. Magn. Reson. 1999;140:281.
47. Kay LE, Gardner KH. Curr. Opin. Struct. Biol. 1997;7:722.
48. Ottiger M, Bax A. J. Biomol. NMR. 1999;13:187.
49. Fowler CA, Tian F, Al-Hashimi HM, Prestegard JH. J. Mol. Biol. 2000;304:447.
50. Delaglio F, Kontaxis G, Bax A. J. Am. Chem. Soc. 2000;122:2142.
51. Fischer MWF, Losonczi JA, Weaver JL, Prestegard JH. Biochem. 1999;38:9013.
52. Skrynnikov NR, Goto NK, Yang D, Choy WY, Tolman JR, Mueller GA, Kay LE. J. Mol. Biol. 2000;295:1265.
53. Fushman D, Varadan R, Assfalg M, Walker O. Prog. Nucl. Magn. Reson. Spectrosc. 2004;44:189.
54. Varadan R, Walker O, Pickart C, Fushman D. J. Mol. Biol. 2002;324:637.
55. Varadan R, Assfalg M, Haririnia A, Raasi S, Pickart C, Fushman D. J. Biol. Chem. 2004;279:7055.
56. Bruschweiler R, Liao X, Wright PE. Science. 1995;268: 886.
57. Fushman D, Xu R, Cowburn D. Biochem. 1999;38:10225.
58. McFeeters RL, Fowler CA, Gaponenko VV, Byrd RA. J. Biomol. NMR. 2005;31:35.

Fast Assignments of ^{15}N-HSQC Spectra of Proteins by Paramagnetic Labeling

Guido Pintacuda[1,2], Thomas Huber[3], Max A. Keniry[1],
Ah Young Park[1], Nicholas E. Dixon[1], and Gottfried Otting[1]
[1]*Research School of Chemistry, Australian National University, Canberra ACT 0200, Australia*
[2]*Karolinska Institute, Tomtebodavägen 6, S-17177 Stockholm, Sweden*
[3]*Departments of Mathematics and Biochemistry, The University of Queensland, Brisbane QLD 4072, Australia*

Abstract

^{15}N-HSQC spectra of ^{15}N-labeled proteins are widely used to identify ligand-binding sites on protein surfaces, providing a way to assess protein–protein interactions as well as to screen for the binding of small chemical compounds. The method is particularly powerful if the cross peaks in the ^{15}N-HSQC spectrum have been sequence-specifically assigned. The present article reviews the use of paramagnetic labeling to obtain these resonance assignments quickly with the use of ^{15}N-labeled protein, provided the crystal structure of the protein is known and the protein can be labeled with a paramagnetic ion. The method also yields the anisotropy tensor of the magnetic susceptibility, which can be used to model the orientation of the ligand with respect to the protein.

Introduction

^{15}N-HSQC spectra of uniformly ^{15}N-labeled proteins play a unique role in pharmaceutical research by providing a two-dimensional fingerprint of the protein, where each amino acid residue, except proline, is represented by a peak from its backbone amide proton [1,2]. The cross peaks serve as sensitive reporters of ligand binding, as changes in the local chemical environment affect their chemical shifts and line widths, providing positive evidence of binding and information about the location of interacting surfaces. The binding of small molecules and interactions with macromolecular partners can both be assessed in this way. The method presents a tool for target validation (e.g. where do natural interaction partners bind?) but is even more attractive for the screening of chemical compound libraries (which compounds bind?) [3,4], since weak and strong binding can be detected equally well.

Assignment of the spectral changes observed in ^{15}N-HSQC spectra to specific binding sites (where does the compound bind?) requires the assignment of the cross peaks to the individual amino-acid residues in the protein. Traditional ways of assigning the ^{15}N-HSQC spectrum of a protein of molecular weight above 15 kDa require the preparation of doubly- (^{15}N and ^{13}C) or triply labeled (^{15}N, ^{13}C, and ^{2}H) samples and the recording of three-dimensional NMR spectra. These experiments are much less sensitive and more time consuming than recording of a ^{15}N-HSQC spectrum. Although uniformly labeled protein samples can, in principle, readily be prepared by expressing the protein in cell cultures grown in isotope-labeled media, labeling with isotopes other than ^{15}N proves prohibitively expensive in many cases. Therefore, resonance assignments are restricted to proteins which can be expressed in high yields and which are sufficiently soluble to record the NMR spectra necessary for resonance assignment. As a result, NMR resonance assignments seem to be out of reach for many target proteins of pharmaceutical interest, even when crystal structures and ^{15}N-HSQC spectra may be available.

The present article describes a different strategy for assigning ^{15}N-HSQC spectra of ^{15}N-labeled proteins. It requires prior knowledge of the three-dimensional protein structure and a lanthanide-binding site in the protein. The strategy has been demonstrated for the 30 kDa complex of the subunits ε (N-terminal segment with residues 2–186) and θ of *Escherichia coli* DNA polymerase III, where ε had been selectively labeled in three separate samples with ^{15}N-labeled Leu, Val, and Phe [5]. Resonance assignments are obtained from the comparison of two highly sensitive ^{15}N-HSQC spectra, recorded with and without a paramagnetic lanthanide ion bound to the complex.

ε186–θ Complex

The crystal structure of the N-terminal domain of ε (ε186) has been solved by X-ray crystallography [6]. The same fragment has been studied by NMR spectroscopy, both free and in complex with θ, using doubly and triply

Graham A. Webb (ed.), Modern Magnetic Resonance, 1263–1269.
© 2008 *Springer.*

isotope-labeled samples [7,8]. Two Mn^{2+} ions are bound to the active site of the enzyme in the crystal structure. In analogy to the related domain of DNA polymerase I, these two ions can be replaced by a single lanthanide [9].

Paramagnetic Restraints Derived from ^{15}N-HSQC Spectra of Paramagnetic and Diamagnetic ε186–θ Complexes

^{15}N-HSQC spectra of the complex between ε186 and θ with a Dy^{3+} ion bound (the paramagnetic complex) and of the complex without an ion bound or with La^{3+} bound (the diamagnetic complex) were recorded at a ^{1}H NMR frequency of 600 MHz. Spectra recorded in the presence or absence of La^{3+} were very similar; either spectrum provided an adequate diamagnetic reference for the measurement of paramagnetic restraints.

The cross peaks recorded for the paramagnetic complex are strongly shifted with respect to those of the diamagnetic spectrum (Figure 1). The chemical shift difference between the paramagnetic and diamagnetic spectrum presents the pseudocontact shift (PCS). The PCS values, measured in ppm, are almost the same in the ^{15}N and ^{1}H dimension of the spectrum. Consequently, the paramagnetic signals are shifted along approximately parallel lines, enabling the pairwise association of diamagnetic and paramagnetic cross peaks. Ambiguities resulting from situations of cross-peak overlap (Figure 1) can often be resolved by the assignment algorithm discussed below.

The ^{15}N-HSQC spectra are best recorded without decoupling during the acquisition time [5], resulting in a shorter pulse sequence and hence, reduced loss of magnetization by relaxation. More importantly, analysis of the doublet fine structure provides access to paramagnetic parameters, which would not be observable in a decoupled spectrum (Figure 2). For example, differential line broadening of the doublet components reflects the cross-correlated relaxation (CCR) between dipole–dipole (with the amide proton and amide nitrogen as the dipolar-coupled spin system) and Curie relaxation of the paramagnetic center [10–12]. In addition, the coupling constant displayed by the doublet contains the residual dipolar coupling (RDC) which arises from the partial alignment of the paramagnetic molecule with the magnetic field [13,14]. Finally, the overall broadening of the doublet components reflects the paramagnetic relaxation enhancement (PRE) by the paramagnetic center. The PRE effect is a function of the distance from the Dy^{3+} ion [15,16]. In practice, cross peaks from amide protons closer than 14 Å from the metal ion were broadened beyond detection.

PCS, RDC, CCR, and PRE effects [17] present four paramagnetic parameters arising from different structural information (Figure 3). Of these four effects, PCS data of protons are most easily measured with high accuracy. Their dependence on the anisotropy of the magnetic

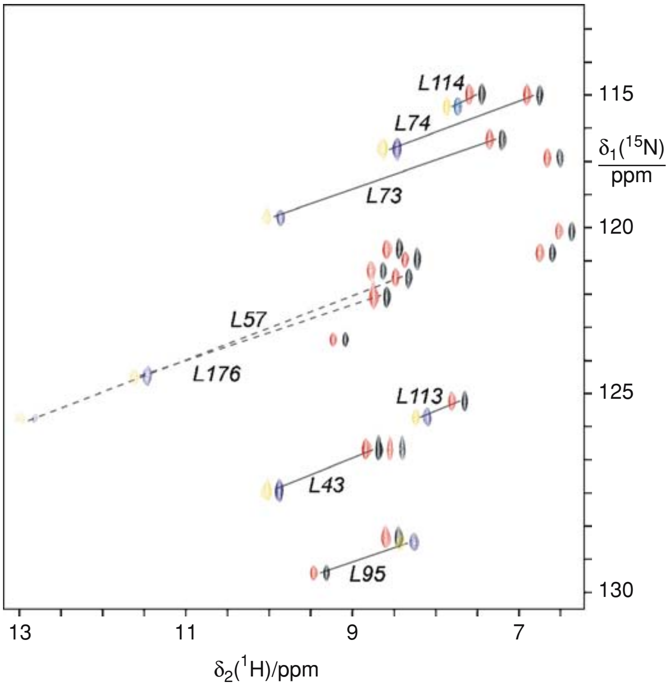

Fig. 1. ^{15}N-HSQC spectra of ^{15}N-Leu labeled ε186 complexed to unlabeled θ. Two spectra are superimposed, one recorded with paramagnetic Dy^{3+} and the other with diamagnetic La^{3+} complexed to ε186. No decoupling was applied during the acquisition time. The cross peaks appear as antiphase doublets split by the one-bond ^{1}H–^{15}N coupling constant. Positive and negative contours are plotted, respectively, with blue and yellow lines for the spectrum of the paramagnetic complex and black and red lines for the spectrum of the diamagnetic complex. Straight lines connect pairs of diamagnetic and paramagnetic cross peaks. Dashed lines identify the two most strongly shifted paramagnetic cross peaks for which the diamagnetic partners could not be identified by simple visual inspection. The spectra were recorded with 0.5 mM solutions of the complex at 25°C and pH 7.0, using total recording times of 5 and 16 h for the diamagnetic and paramagnetic samples, respectively, on a Varian Inova 600 MHz NMR spectrometer. Reproduced with permission from Ref. [5]. © 2004 Am. Chem. Soc.

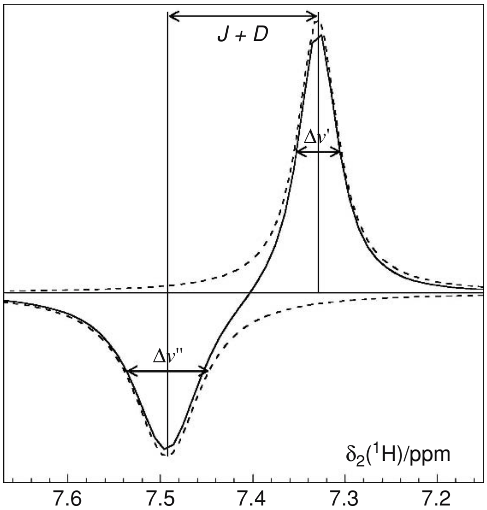

Fig. 2. Cross section through a cross peak from the spectrum of Figure 1 with two Lorentzian lineshapes fitted to the doublet components (dashed lines). The fit provides the accurate chemical shift of the doublet, the line widths of the individual doublet components, and the coupling constant of the doublet. Reproduced with permission from Ref [5]. © 2004 Am. Chem. Soc.

susceptibility tensor also provides stringent geometric restraints that are relatively insensitive with respect to local structural variations. In contrast, in our experience PRE effects yield the least accurate data, partly because line widths can vary between samples due to aggregation effects and chemical exchange phenomena [5]. The values of all four paramagnetic effects can be predicted provided that the three-dimensional structure of the protein, the position of the metal ion, and the susceptibility anisotropy tensor are known (Figure 4) [17].

PLATYPUS Algorithm for Resonance Assignments from Paramagnetic Restraints

In our assignment strategy, the resonance assignment is obtained from a comparison of the experimentally measured paramagnetic data with the data predicted from the three-dimensional structure of the protein. An exhaustive evaluation of all $n!$ possible assignments, however, is not viable when the number of cross peaks, n, is large. Consequently, a novel algorithm named PLATYPUS (paramagnetic labeling for assignment with terrific yields of proteins using their structures) was developed to derive the resonance assignments from the paramagnetic data automatically (Figure 5). Since the parameters defining the susceptibility anisotropy tensor are not known a priori, the algorithm employs a grid search with a large number of different tensors. A target function, defined as the sum of the squared deviations between experimentally measured and back-calculated paramagnetic data, is minimized to determine the best-fitting resonance assignment. Starting from each grid point, PLATYPUS uses the "Hungarian method for minimal cost assignment" [18] to arrive at resonance assignments that are continuously updated, while the tensor parameters and rotational correlation time are optimized by gradient minimization of the target function (Figure 5).

In principle, the grid search over different possible susceptibility anisotropy tensors is five-dimensional, since five parameters are required to define the shape and orientation of the tensor. In practice, the algorithm

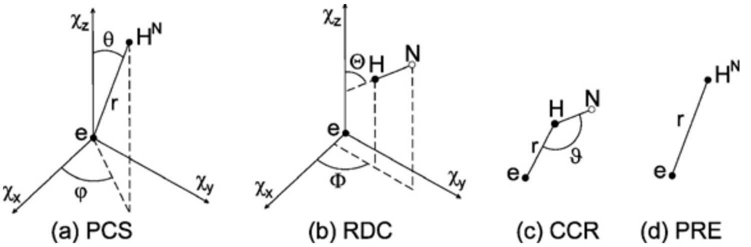

(a) PCS (b) RDC (c) CCR (d) PRE

Fig. 3. Dependence of paramagnetic effects on local geometry. (a) Pseudocontact shifts (PCS) depend on the location of the nuclear spin with respect to the susceptibility anisotropy tensor. They result in chemical shift changes of the NMR signal. (b) Residual dipolar couplings (RDC) depend on the angle formed between the vector connecting the coupled spins and the axes of the alignment tensor resulting from alignment of the paramagnetic protein in the magnetic field. They are manifested in altered multiplet splittings. (c) Cross-correlated relaxation (CCR) between the Curie spin of the paramagnetic protein and the dipole–dipole interaction between two nuclear spins depends on the angle between the internuclear vector and the vector between the nuclear and electronic spins. This relaxation mechanism results in different line widths of the two doublet components. (d) Paramagnetic relaxation enhancements (PRE) depend on the distance from the paramagnetic center. The relaxation enhancement results in equal line broadening of both doublet components.

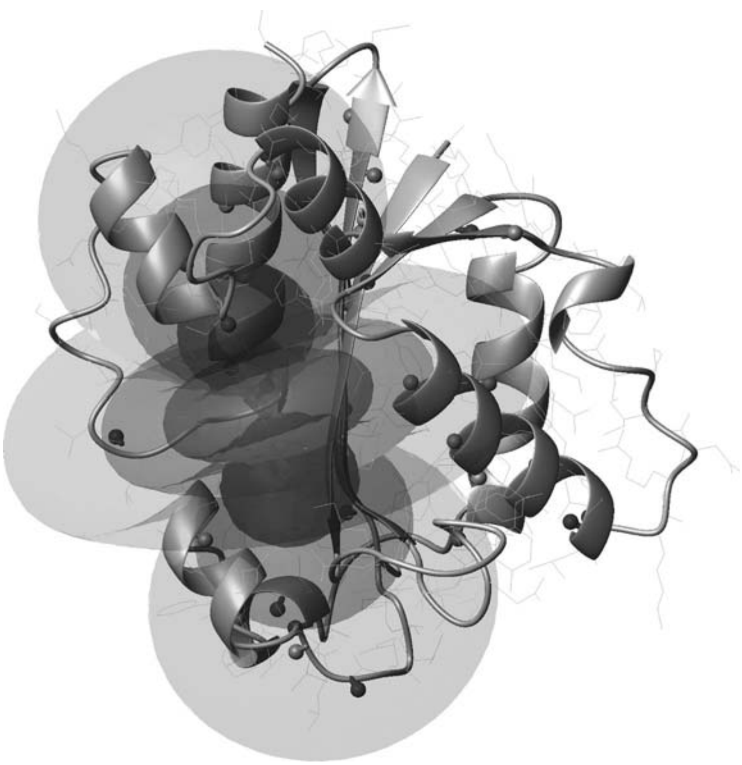

Fig. 4. Iso-surfaces indicating pseudocontact shifts of ±1, ±0.5, and ±0.2 ppm, respectively, superimposed onto the crystal structure of ε186 (drawn in a ribbon representation). Blue and red colors identify positive and negative pseudocontact shifts, respectively. The N–H groups of Leu (blue), Phe (pink), and Val (orange) residues are displayed in a ball-and-stick representation. The figure was plotted with Molmol [39]. Reproduced with permission from Ref. [5]. © 2004 Am. Chem. Soc. (See also Plate 97 on page XIX in the Color Plate Section.)

converges even when starting from any plausible combination of axial and rhombic components of the tensor and using increments as large as 20° between different tensor orientations.

PLATYPUS presents a very fast algorithm because the search space is limited to the optimization of the assignments initially suggested for each of the grid points. Its efficiency allows the extension of the search to test in a systematic way all conceivable pairings of diamagnetic and paramagnetic cross peaks, even in cases where the pairings are ambiguous due to cross-peak overlap (Figure 1). For those cross peaks, minimization of the target function yields not only the resonance assignment of the paramagnetic cross peaks but also the identification of their diamagnetic partners.

Results Obtained with Selectively Labeled ε186–θ Complexes

ε186 contains 17 leucine residues. All their ^{15}N-HSQC cross peaks were observable in the diamagnetic ε186–θ complex containing selectively ^{15}N-Leu labeled ε186. In the presence of Dy^{3+}, however, the ^{15}N-HSQC cross peaks of only eight of them could be observed; the other leucine residues were too close to the paramagnetic center and their resonances were broadened beyond detection. Despite the limited number of cross peaks which could be evaluated and ambiguities in pairing some of the paramagnetic cross peaks with diamagnetic partners (Figure 1), PLATYPUS yielded assignments in complete agreement with those determined previously in the conventional manner with triply isotope-labeled protein preparations [8]. This result is particularly remarkable, since the description of the shape and orientation of the susceptibility anisotropy tensor alone requires five independent variables, i.e. information from at least five different ^{15}N–^{1}H cross peaks. The assignment of ^{15}N-HSQC cross peaks broadened beyond detection in the presence of Dy^{3+} can be achieved by the use of a different, less strongly paramagnetic lanthanide ion. In the case of the ε186–θ complex, all 17 leucine residues yielded observable cross peaks in the presence of Ce^{3+}. Paramagnetic effects from Ce^{3+} are limited to the closer vicinity of the metal ion, providing complementary data to those obtained with Dy^{3+} [5].

Besides resonance assignments, PLATYPUS also provides a measure of the reliability of the individual assignments by checking for their resilience against variations of the three-dimensional structure. This is achieved by

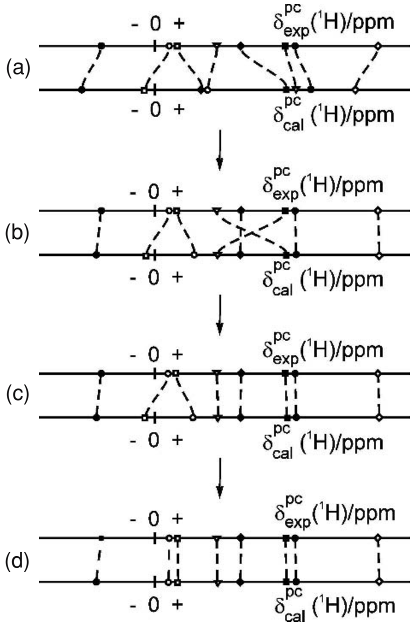
(a)
(b)
(c)
(d)
- 0 +
$\delta^{pc}_{exp}(^{1}H)$/ppm
$\delta^{pc}_{cal}(^{1}H)$/ppm

Fig. 5. Pictorial representation of progressing assignments in PLATYPUS. Different orientations and shapes of the susceptibility anisotropy tensor are systematically varied in a grid search. The figure illustrates the procedure for the case of pseudocontact shifts only. For each grid point the paramagnetic effects are calculated and the back-calculated paramagnetic data sorted by magnitude (lower lines). Comparison with experimental values, also sorted by magnitude (top lines), generates an assignment (a). The tensor parameters are subsequently optimized by gradient minimization. Recalculation of the predicted paramagnetic effects with the new tensor parameters may require some reassignments to maintain the match of predicted versus experimental data when sorted by magnitude (b and c). The assignment with the lowest residual target function (the sum of the squared differences between experimental and back-calculated data) obtained from any of the starting grid points is presented as the correct assignment (d). The Hungarian method for minimal cost assignment [18] is used to perform the sorting and minimization in the *m*-dimensional space spanned by *m* different paramagnetic parameters.

the deliberate addition of structural noise to the coordinates of the protein structure, including variations in the orientations of chemical bonds and changes in the locations of protein atoms and of the paramagnetic ion, followed by repetition of the assignment procedure. As expected, availability of more than a single selectively ^{15}N-labeled sample improves the reliability of the resonance assignment.

Alternative Methods

Two other protocols have been reported [19,20] which use a similar approach to determine NMR resonance assignments with the help of an available three-dimensional protein structure. These protocols back-calculate residual dipolar couplings and diamagnetic chemical shifts from the structure and use combinatorial optimization algorithms for the assignment. However, they require doubly ^{15}N/^{13}C-labeled samples and the time-consuming measurement of two or three residual dipolar couplings per amino acid residue.

Paramagnetic data are much easier to evaluate from straightforward ^{15}N-HSQC spectra. Furthermore, PCSs are less sensitive than residual dipolar couplings to small differences between protein structures in solution and in single crystals. Finally, PLATYPUS yields the magnetic susceptibility anisotropy tensor simultaneously with the resonance assignment (Figure 4). With Dy^{3+}, sizable PCSs can be observed for distances up to 40 Å from the metal ion [21]. This opens unique opportunities for the study of intermolecular complexes with ligands.

Outlook

The assignment strategy outlined here provides access to resonance assignments with unprecedented speed. For comparison, 56 days of NMR spectrometer time were used to assign the resonances of ε186 in complex with θ[7,8]. Although our strategy provides resonance assignments of only a few ^{15}N-HSQC cross peaks for each selectively labeled sample, complete resonance assignments of all cross peaks observable for a uniformly ^{15}N-labeled protein are often not necessary in pharmaceutical applications.

The main drawback of the method is the requirement of a lanthanide-binding site. Most proteins are diamagnetic and do not possess a specific lanthanide-binding site. In principle, lanthanide-complexing reagents have been reported which can be covalently attached to side-chain amine, carboxylate, or sulfhydryl groups on the protein surface [22,23]. The most generally applicable technique for site-specific attachment of a lanthanide-complexing reagent may be via formation of a disulfide bond with a single Cys residue on the protein surface. A suitable reagent needs to have a short linker [24] to avoid poorly defined positioning of the lanthanide ion with respect to the protein surface [25,26]. Furthermore, formation of different diastereomeric complexes must be suppressed which would otherwise increase the number of NMR signals [27–29]. Corresponding reagents are not yet commercially available.

It has been demonstrated that fusion proteins can be designed with lanthanide-binding peptide motifs

[30–34]. Lanthanide-binding peptide motifs avoid the generation of different diastereomers, but restrict the choice of attachment sites to the terminal ends of the protein. Furthermore, many of the paramagnetic effects are reduced when the linker to the lanthanide-binding peptide is flexible.

A paramagnetic tag attached to a selected site on the protein surface offers a powerful tool for the detection and structural characterization of ligand binding. The attachment of TEMPO spin labels has been shown to enhance the sensitivity of NMR methods for the screening of compound libraries by several orders of magnitude [35]. TEMPO spin labels have also been shown to provide long-range structural information in large biomolecules as well as access to the study of transient interactions in partially or completely unfolded proteins. The relaxation enhancement effect of TEMPO spin labels is, however, governed by a $1/r^6$ distance dependence, whereas PCSs induced by lanthanide ions follow a $1/r^3$ distance law, resulting in effects observable over longer distances. Furthermore, the isotropic nature of the magnetic susceptibility tensor in TEMPO prohibits the observation of the PCS, CCR, and RDC effects that contain the most valuable structural information (Figure 3). Therefore, more information can be obtained from site-specifically attached lanthanides. In addition, lanthanide ions could not only detect the presence of ligand binding, but also provide a detailed picture of the relative orientation of the ligand with respect to the magnetic susceptibility anisotropy tensor and hence, with respect to the protein. This information could be obtained with a minimal number of resonance assignments of the protein.

The present version of PLATYPUS was designed for the assignment of selectively ^{15}N-labeled proteins. For some proteins, cell-free protein expression systems offer a cost-effecitve and fast route to protein samples with selectively labeled amino acids [36–38]. Selective labeling of proteins becomes expensive when the proteins cannot be expressed in high yields. For those situations, a modified strategy would be desirable, which provides reliable cross-peak assignments for uniformly ^{15}N-labeled proteins. Work towards this goal is in progress.

Acknowledgments

Complete resonance assignments of ε186 or ε186 in complex with θ were not available at the time we published the ^{15}N-HSQC assignments of Leu, Val, and Phe labeled ε186 in complex with θ. We thank Drs. Eugene F. DeRose and Robert E. London for making their resonance assignments available to us afterwards to confirm the correctness of the assignments. G.P. thanks the EU for a postdoctoral fellowship within the Research Training Network on Cross Correlation (HPRN-CT-2000-00092). G.O. thanks the Australian Research Council for a Federation Fellowship. Financial support by the Australian Research Council is gratefully acknowledged.

References

1. Pellecchia M, Sem DS, Wüthrich K. Nat. Rev. Drug Discov. 2002;1:211.
2. van Dongen M, Weigelt J, Uppenberg J, Schultz J, Wikström M. Drug Discov. Today 2002;7:471.
3. Shuker SB, Hajduk PJ, Meadows RP, Fesik SW. Science 1996;274:1531.
4. Hajduk PJ, Meadows RP, Fesik SW. Q. Rev. Biophys. 1999;32:211.
5. Pintacuda G, Keniry MA, Huber T, Park AY, Dixon NE, Otting G. J. Am. Chem. Soc. 2004;126:2963.
6. Hamdan S, Carr PD, Brown SE, Ollis DL, Dixon NE. Structure 2002;10:535.
7. DeRose EF, Li D, Darden T, Harvey S, Perrino FW, Schaaper RM, London RE. Biochemistry 2002;41:94.
8. DeRose EF, Darden T, Harvey S, Gabel S, Perrino FW, Schaaper RM, London RE. Biochemistry 2003;42:3635.
9. Brautigam CA, Aschheim K, Steitz TA. Chem. Biol. 1999; 6:901.
10. Boisbouvier J, Gans P, Blackledge M, Brutscher B, Marion D. J. Am. Chem. Soc. 1999;121:7700.
11. Pintacuda G, Hohenthanner K, Otting G, Müller N. J. Biomol. NMR 2003;27:115.
12. Ghose R, Prestegard JH. J. Magn. Reson. 1997;128:138.
13. Tolman JR, Flanagan JM, Kennedy MA, Prestegard JH. Proc. Natl. Acad. Sci. USA 1995;92:9279.
14. Barbieri R, Bertini I, Cavallaro G, Lee YM, Luchinat C, Rosato A. J. Am. Chem. Soc. 2002;124:5581.
15. Guéron M. J. Magn. Reson. 1975;19:58.
16. Vega AJ, Fiat D. Mol. Phys. 1976;31:347.
17. Bertini I, Luchinat C, Parigi G. Solution NMR of Paramagnetic Molecules: Applications to Metallobiomolecules and Models. Elsevier: Amsterdam, 2001.
18. Kuhn HW. Nav. Res. Logist. Q. 1955;2:83.
19. Hus JC, Prompers JJ, Brüschweiler R. J. Magn. Reson. 2002;157:119.
20. Zweckstetter M. J. Biomol. NMR 2003;27:41.
21. Allegrozzi M, Bertini I, Janik MBL, Lee YM, Lin GH, Luchinat C. J. Am. Chem. Soc. 2000;122:4154.
22. Liu S, Edwards DS. Bioconjugate Chem. 2001;12:7–34.
23. Caravan P, Ellison JJ, McMurry TJ, Lauffer RB. Chem. Rev. 1999;99:2293.
24. Selvin PR. Annu. Rev. Biophys. Biomol. Struct. 2002;31: 275.
25. Voss J, Wu J, Hubbell WL, Jacques V, Meares CF, Kaback HR. Biochemistry. 2001;40:3184.
26. Purdy MD, Ge P, Chen J, Selvin PR, Wiener MC. Acta Crystallogr. D. 2002;58:1111.
27. Dvoretsky A, Gaponenko V, Rosevear PR. FEBS Lett. 2002;528:189.
28. Ikegami T, Verdier L, Sakhaii P, Grimme S, Pescatore B, Saxena K, Fiebig KM, Griesinger C. J. Biomol. NMR, 2004;29:339.

29. Pintacuda G, Moshref A, Leonchiks A, Sharipo A, Otting G. J. Biomol. NMR, 2004;29:351.
30. Ma C, Opella SJ. J. Magn. Reson. 2000;146:381.
31. Biekofsky RR, Muskett FW, Schmidt JM, Martin SR, Browne JP, Bayley PM, Feeney J. FEBS Lett. 1999;460:519.
32. Feeny J, Birdsall B, Bradbury AF, Biekofsky RR, Bayley PM. J. Biomol. NMR 2001;21:41.
33. Wohnert J, Franz KJ, Nitz M, Imperiali B, Schwalbe H. J. Am. Chem. Soc. 2003;125:13338.
34. Caravan P, Greenwood JM, Welch JT, Franklin SJ., Chem. Commun. 2003;20:2574.
35. Jahnke W, Rudisser S, Zurini M. J. Am. Chem. Soc. 2001;123:3149.
36. Kigawa T, Muto Y, Yokoyama S. J. Biomol. NMR 1995;6:129.
37. Guignard L, Ozawa K, Pursglove SE, Otting G, Dixon NE. FEBS Lett. 2002;524:159.
38. Yabuki T, Kigawa T, Dohmae N, Takio K, Terada T, Ito Y, Laue ED, Cooper JA, Kainosho M, Yokoyama S. J. Biomol. NMR 1998;11:295.
39. Koradi R, Billeter M, Wüthrich K. J. Mol. Graph. 1996;14:51.

Phospholipid Bicelle Membrane Systems for Studying Drug Molecules

Jianxin Guo[1], Xiaoyu Tian[1], Spiro Pavlopoulos[2], and Alexandros Makriyannis[1]
[1]*Center for Drug Discovery, Bouve College of Health Sciences, Northeastern University, 360 Huntington Avenue, Boston, MA 02115, USA; and*
[2]*Department of Pharmaceutical Sciences, University of Connecticut, U-3092, 69 North Eagleville Road, CT 06269, USA*

Abbreviations: NMR, nuclear magnetic resonance; DSC, differential scanning calorimetry; DPPC, 1,2-dipalmitoyl-*sn*-glycero-3-phosphocholine; DMPC, 1,2-dimyristoyl-*sn*-glycero-3-phosphocholine; DHPC, 1,2-dihexanoic-*sn*-glycero-3-phosphocholine; CHAPSO, 3-(cholamidopropyl) dimethylammonio-2-hydroxy-1-propanesulfonate; SDS, sodium dodecyl sulfate; DPC, dodecylphosphocholine; Δ^8-THC, $(-)$-Δ^8-tetrahydrocannabinol; Me-Δ^8-THC, $(-)$-O-methyl-Δ^8-tetrahydrocannabinol

Introduction

The design of drugs that modulate membrane bound receptors has always been of prime importance to the pharmaceutical industry. It is increasingly being recognized that the cellular membrane plays an important role in drug action and that understanding the manner in which drug molecules interact with lipid bilayers can enhance our abilities to design and develop improved medications. It has been proposed that lipophilic drugs reach their sites of action through cell membrane penetration and lateral diffusion within the membrane leaflet [1–4]. The protein supporting lipid membranes may be capable of a high degree of structural discrimination by positioning the ligand in a proper location, orientation, and active conformation for a productive interaction with the receptor. Therefore, acquiring detailed knowledge of drug and ligand physical properties that underlie their interaction profiles with the cellular membrane is of great interest in the discovery, design, and delivery of novel therapeutic agents. Information related to drug–membrane interactions, however, can rarely be derived directly from experiments with complex and labile natural membranes. Thus, various membrane models with different levels of complexity have been developed in order to exploit all the biophysical techniques available [5–7]. Whether it is in the form of liposomes, micelles, or other membrane mimetics, the interplay between the ligand and membranes is central to many aspects in pharmaceutical research.

Liposomes (in most cases, multilamellar vesicles) have been extensively utilized to study the manner in which drug molecules perturb cellular membranes as well as the location, conformation, and preferred orientation of a drug molecule within the membrane bilayer using differential scanning calorimetry (DSC), nuclear magnetic resonance (NMR) spectroscopy, and small angle X-ray diffraction [3,8–15]. Among these techniques, NMR spectroscopy holds a prominent place by being particularly sensitive to the fine structural and dynamic details of drug molecules within the bilayer system. However, liposomes are not suitable model membrane systems for exploring the conformational properties of embedded ligands since even the smallest lipid vesicles are too large to yield a quality high-resolution NMR spectrum [16]. Alternatively, fast tumbling micelles consisting of various detergents have been widely used to mimic the membrane environment in high-resolution NMR conformational analysis [5,17–19], even though it has long been a concern that micelles may not accurately represent cellular membrane bilayers [20,21]. Recently, phospholipid bilayered-micelles (often referred to as bicelles) have received much attention as promising membrane-mimetic systems [22–27]. Work in our laboratory has demonstrated that bicelle systems can serve as excellent bilayer membrane models for studying drug–membrane interactions using high-resolution NMR. We have developed an isotropic bicelle system for studying the conformational properties of small- and medium-sized ligands without the need of isotopic labeling [21]. We also used magnetically oriented bicelles to determine the preferred orientations of several lipophilic drugs from deuterium NMR experiments [28].

In this chapter, we briefly review the commonly used model membrane systems for studying drug–membrane interactions using NMR with an emphasis on phospholipid bicelles. To highlight the advantages of using bicelle systems for such work, we have sought to determine the conformational properties as well as the preferred orientation of two lipophilic ligands in different membrane-mimetic systems. A comparison of the ligand spectra in

Graham A. Webb (ed.), Modern Magnetic Resonance, 1271–1277.
© 2008 *Springer.*

the different media clearly demonstrates the value of phospholipid bicelles in such studies.

Membrane Systems for NMR Studies

Cell membranes consist of a variety of glycerolphospholipids, sphingolipids, and cholesterol with local heterogeneities and segregated microdomains. Although much work has been dedicated to understand their structural and dynamic properties, many questions still remain unanswered [29]. Opportunities for studying the drug–membrane interactions with native membranes are presently confined to the use of solid-state NMR methods. Only few published examples can be found of the interactions between small- or medium-sized molecules with native membranes where the ligand is isotopically labeled in specific positions for effective NMR observation [30,31]. Simplified model membranes composed of certain synthetic or native lipids have become the most commonly used systems for such work.

It can be argued that notwithstanding their great functional diversity, membranes share the common features of an anisotropic bilayer system consisting of a hydrophobic interior and a hydrophilic headgroup region. This fundamental structure defines many of the key structural and functional properties of biological membranes. For this reason, it is possible to use simplified lipid systems as legitimate mimics of the cellular membrane.

Liposomes

Liposomes are the most used and best-characterized model membrane system. They can be produced in a variety of sizes and lipid compositions including multilamellar vesicles and small or large unilamellar vesicles [32,33]. Liposomes are generally prepared from glycerolphospholipids, mainly phosphatidycholines such as DPPC, DMPC, and POPC, while cholesterol and charged lipids can also be added. Because multilamellar vesicles are relatively easy to prepare and multilayering makes it possible to incorporate larger amounts of drug, they have been extensively employed for studying drug–membrane interactions using various solid-state NMR techniques, such as stationary ^{2}H, ^{31}P, and ^{13}C NMR as well as the cross polarization magic angle spinning (CP/MAS) experiments [11,34,35]. Liposomes in the L_α liquid crystalline phase have been used to determine the preferred orientations of native and xenobiotic molecules and the effects of these ligands on the membrane system [8,9,11,12,14,36–39]. Liposomes are usually not suitable for studying the conformation of a ligand using solution NMR because of the relatively slow tumbling rates resulting from their large size. For such applications, other model membrane systems consisting of much smaller aggregates must be used.

Organic Solvent Mixtures

The simplest membrane-mimetic environment resembling the membrane interior and interfacial regions can be obtained by carefully mixing two organic solvents of low and intermediate polarity [40]. However, such systems are overly simplified membrane models and are of limited value.

Micelles

The most commonly used spherical micelle preparations can be obtained from SDS, DPC, or DHPC. Because of effective motional averaging, the small and uniformly sized micelles can yield satisfactory high-resolution NMR spectra of an enclosed ligand. Micelles have been extensively utilized as membrane-mimetic media for studying the conformational properties of small molecules and peptides [18,19]. However, as micelles do not consist of natural cell membrane lipids and have a highly curved surface, their value as a reliable model membrane system is somewhat reduced [21,26].

Phospholipid Bicelles

An optimal membrane-mimetic system for solution NMR experiments should consist of a relatively smaller lipid aggregate with a bilayer structure. With a short correlation time, such a membrane preparation enables more detailed structural studies of drugs in a bilayer environment. In order to form such a lipid aggregate, the mean chemical potential μ_N^0 must initially decrease and reach its minimum at a certain aggregation number N. If there were no free energy contributions, such small lipid aggregates would be entropically favored. However, because of the large cohesive binding energies of lipid molecules, discrete planar bilayer systems have never been observed when only one type of lipids is present. For a hypothetical planar bilayer disc, the free energy for molecules sequestered along the rim is expected to be much higher than that of molecules in the planar center. The mean free energy per molecule in such a planar bilayer disc is [41]:

$$\mu_N^0 = \mu_\infty^0 + \alpha kT/N^{1/2}$$

where μ_∞^0 is the mean free energy in an aggregate of infinite size, k is the Boltzmann constant and T is the temperature. As μ_N^0 decreases monotonically with N, the expectation is that an infinite number of lipid molecules will aggregate spontaneously at critical micelle concentrations while single component lipid bilayers with exposed edges are not favored.

However, discrete planar bilayer disc assemblies can be obtained if detergents are added to stabilize the energetically unfavorable edges [23,26]. Such systems,

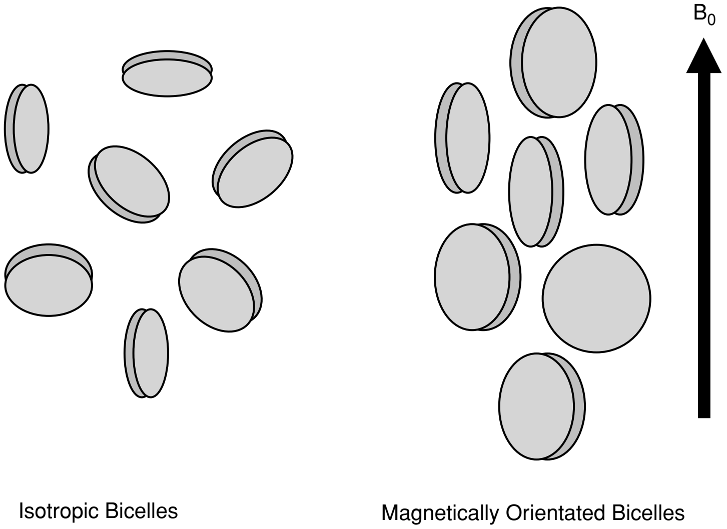

Fig. 1. Isotropic (left) and magnetically oriented bicelles (right).

commonly referred to as phospholipid bicelles, are typically composed of DMPC with either DHPC or a bile-salt derivative CHAPSO in 0.1 M KCl solution [26]. Above the phase transition temperature (T_m), the DMPC-rich domain resembles the liquid crystalline L_α phase multilamellar membrane bilayers [22,42]. Phospholipid bicelles combine the attractive structural and dynamic properties of both micelles and lipid vesicles and maintain most of the key bilayer properties that are absent in the micellar systems. Additionally, compared to the liposome preparations, bicelles are relatively small, noncompartmentalized, effectively monodisperse and ideally suited for high-resolution NMR studies.

Phospholipid bicelles (Figure 1) are a versatile model membrane system whose morphology and dynamic properties can be adjusted over wide ranges of lipid to detergent ratio (q), total lipid concentration, buffer pH, and temperature [26]. With appropriate manipulation, bicelles can provide isotropic membrane systems suitable for studying the conformational properties of embedded ligands using high-resolution NMR [21,43]. Alternatively, bicelles can serve as anisotropic membrane preparations capable of orienting in an applied magnetic field [23,25].

Optimizing Isotropic Bicelles for Drug Conformational Studies

At a DMPC to DHPC molar ratio (q) of 0.5 and an overall lipid concentration of 15% (w/v), the bicelle system has been shown to be at the isotropic state and the bicelles are small enough for high-resolution experiments NMR [43]. This is promising in that without isotopic labeling, such a preparation can be used to explore the conformational properties of incorporated drugs. However, such bicelles may not serve as an ideal membrane environment for studying our lipophilic drugs. As the diameter of the bicelle is estimated to be approximately 80 Å [44], the embedded drugs may have much higher chances of interacting with the stabilizing detergents rather than with the lipids. In addition, small bicelles are incapable of incorporating adequate quantities of lipophilic drugs and precipitation has been frequently observed in our research.

For these reasons, we have sought to develop larger isotropic bicelles that would better represent cellular membrane bilayer systems. Our approach to maximizing bicelle size while maintaining isotropic conditions was to systematically adjust the lipid to detergent ratio (q) as well as the overall lipid concentration. Additionally, preparations free of KCl allow us to use higher values of q and the stability of bicelles can be significantly improved by adding trace amount of amphiphiles. We found that a preparation of a much higher DMPC/DHPC ratio ($q = 2.0$) and an overall lipid concentration of 8% (w/v) is optimal for not only allowing effective drug incorporation, but also providing an isotropic system suitable for high-resolution NMR studies. In such a preparation, no precipitation of either the drug or lipid was observed over the course of several days. Well-resolved proton resonances reflect the isotropic nature of the optimized bicelle membrane media within the NMR time scale. This can be attributed to the ample spacing between the individual bicelles, which allow for faster motional averaging [25]. Although a certain degree of broadening in the ^{1}H resonances is still observed, the spectral resolution is adequate for standard 2D-NMR experiments such as DQF-COSY

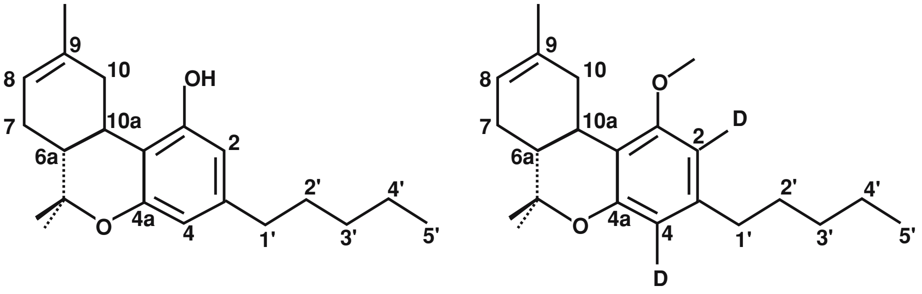

Fig. 2. The structure of Δ^8-THC (left) and Me-Δ^8-THC (right).

and NOESY from which ligand conformational properties can be obtained.

To evaluate the experimental benefits of our isotropic bicelle preparation, we compared the ^{1}H spectra of Δ^8-THC (Figure 2) in chloroform, SDS micelles, and two different isotropic bicelle preparations with $q = 0.5$ and $q = 2.0$, respectively. Figure 3 shows the NOE patterns observed between the aromatic ring protons and protons of the pentyl tail. In chloroform, only two NOEs were observed between the H2, H4 aromatic protons, and the pentyl tail H1′ protons. Additional NOEs were observed between the aromatic H4 resonance and resonances due to protons beyond H1′ of the pentyl sidechain with their relative intensities varying depending on the membrane

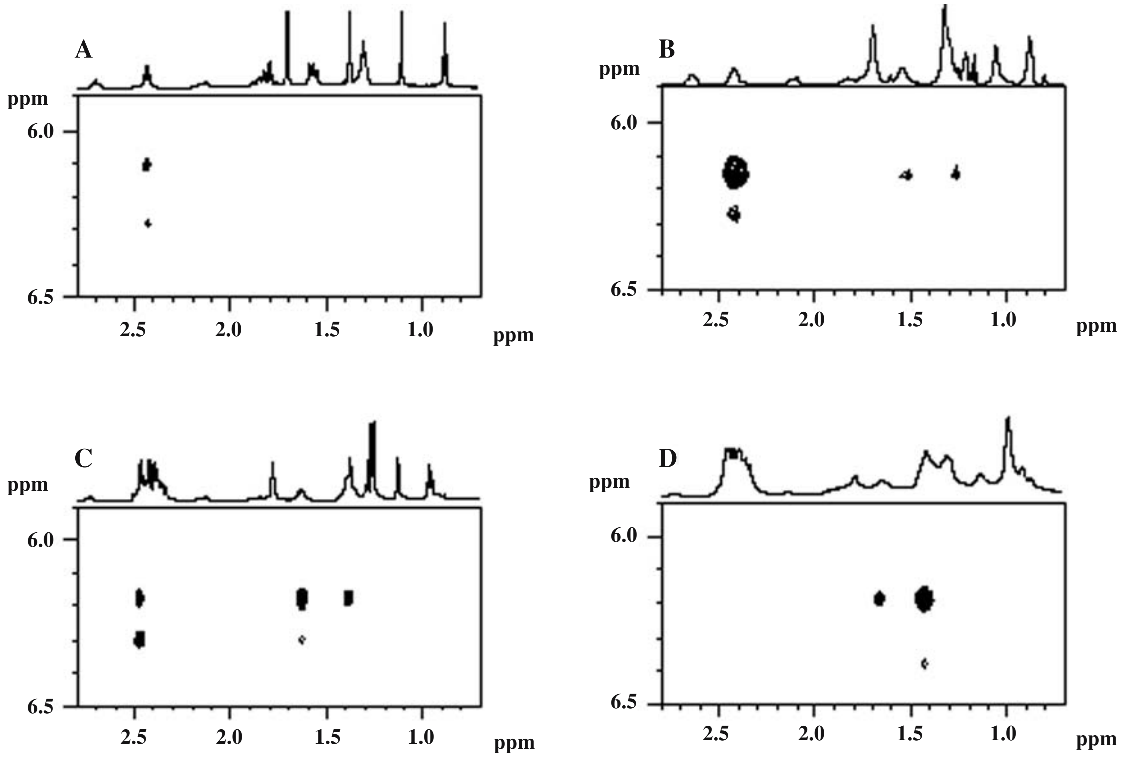

Fig. 3. Expansions of NOESY spectra showing NOEs between the aromatic ring and the pentyl-tail of Δ^8-THC in (A) $CDCl_3$; (B) SDS micelles; (C) $q = 0.5$ bicelle, and (D) $q = 2.0$ bicelle.

preparations used. In SDS micelles, the NOESY spectrum from Δ^8-THC is comparable to that observed in chloroform where strong NOEs were observed between the H2, H4 aromatic protons, and the H1′ protons in the pentyl group. Two weak NOEs were also observed between H4 and H2′, and H3′, H4′ overlapping protons, suggesting a conformational preference for orientation of the pentyl chain towards the H4 side of the tricyclic ring system. In the $q = 0.5$ bicelle solution, the H4–H2′ and H4–H3′/H4′ NOEs are similar in intensity to the H4–H1′, H2–H1′ NOEs; while in the $q = 2.0$ solutions, the former set of NOEs are significantly stronger than the latter. This observation shows that higher proportions of DMPC within the bicelle lead to an increased preference for an "amphipathic" conformation of the pentyl sidechain towards the H4 side of the tricyclic ring system.

The above results indicate that the choice of model membrane systems can greatly influence the structural and dynamic properties of the incorporated drugs. It is also worth noting that in both the SDS micelle and the $q = 0.5$ bicelle preparations, Δ^8-THC was observed to precipitate over 3–6 h whereas it was well solubilized in the $q = 2.0$ bicelle solution. Our results obtained from the $q = 2.0$ bicelle preparation are congruent with previous studies using DPPC multilamellar membrane bilayers [11,14,15], which we attribute to the more bilayer-like morphology of the $q = 2.0$ lipid bicelles compared to the SDS micelle and $q = 0.5$ bicelle solutions. Therefore, the $q = 2.0$ bicelles represent a satisfactory membrane bilayer system suitable for high-resolution NMR conformational studies.

Magnetically Aligned Bicelles for Studying Drug Orientation

The formation of magnetically oriented phospholipid bicelles under various conditions and the corresponding properties of the bicelles have been reviewed [22,45]. By using a series of titration studies, it has been found that the liquid crystalline L_α DMPC/DHPC bicelles with q ranging from 2.0 to 3.5 are well aligned in the applied magnetic field as indicated by their ^{31}P and ^{2}H NMR spectra, while addition of KCl can drastically improve the degree of orientation.

The orientation may be explained by the anisotropy of the diamagnetic susceptibility tensor χ of the lipid molecule. If we assume an axis of rotational symmetry, the diamagnetic anisotropy $\Delta\chi$ will be the difference between the susceptibilities parallel and perpendicular to this axis. For the bicelle forming long acyl chain lipid DMPC in the L_α phase, $\Delta\chi$ was found to be $(-1.0 \pm 0.1) \times 10^8$ erg cm^{-3} G^{-2} [46]. Since the magnetic potential energy ΔU can be expressed by:

$$\Delta U = -N \Delta\chi B_0^2$$

where N is the number of long acyl chain DMPC lipids within one bicelle disc, and B_0 is the external magnetic field, when $\Delta\chi$ is less than zero, the energically favorable orientation of a bicelle aggregate will be with its principal axis perpendicular to the applied magnetic field.

In earlier work, we have described how the preferred orientation of a drug molecule within the membrane bilayer system can be obtained from the quadrupolar splittings ($\Delta\nu_Q$) of ^{2}H-labels introduced in specific sites of the molecule [9,11]. We have, thus, sought to explore whether such data could be obtained in a magnetically oriented bicellar system. Figure 4 compares three deuterium spectra of 2,4-D_2-Me-Δ^8-THC (Figure 2) obtained in DHPC micelles, DPPC multilamellar vesicles, and magnetically oriented DMPC/DHPC bicelle preparations, respectively. The spectrum acquired in a DHPC micelle solution displays a single isotropic deuterium peak, while that from the DPPC multilamellar vesicles corresponds to two pairs of overlapping Pake patterns from which the quadrupolar splittings can be extracted. Conversely, in magnetically oriented bicelles, the spectrum is reduced to two pairs of doublets representing the two and four deuterium atoms in Me-Δ^8-THC. The sharp deuterium resonances indicate that the bicelles are completely aligned in the magnetic field. Due to the fact that the bicelles with the incorporated drug molecules are magnetically oriented with their

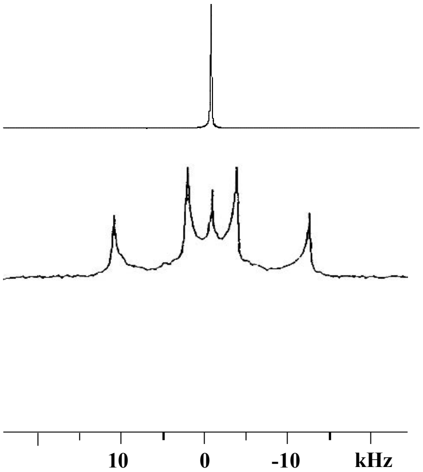

Fig. 4. A comparison of deuterium spectra of 10% 2,4-D_2-Me-Δ^8-THC in DHPC micelles (top), DPPC multilamellar bilayers (middle), and magnetically oriented DMPC/DHPC bicelles (bottom).

bilayer normal perpendicular to the external magnetic field, the observed splittings in the ^{2}H spectrum correspond to the 90° edges of the respective Pake patterns from the semi-solid hydrated DPPC sample. However, the $\Delta\nu_Q$ values are much reduced in the bicelle system, reflecting a lower order parameter (S_{mol}) when compared to that from the multilamellar preparations. The calculated orientation of Me-Δ^8-THC (to be reported elsewhere) closely matches our result from the multilamellar vesicles, thus attesting to the reliability of the bicelle system as a model membrane.

In contrast to micelle preparations where quadrupolar couplings are completely averaged out due to fast isotropic tumbling, magnetically oriented bicelles can serve as an alternative to multilamellar membrane preparations for studying the orientation of a ligand in an anisotropic membrane system. In addition, the experiment described above was carried out under solution NMR conditions and offers the advantages of higher sensitivity and more accurate direct measurement of the $\Delta\nu_Q$ values from the sharp ^{2}H doublets.

Conclusion

Bicelles can serve as satisfactory membrane systems for isotropic and anisotropic NMR experiments aimed at studying the conformational properties and preferred orientation of lipophilic drug molecules in the cell membrane. Using the lipophilic Δ^8-THC as an example, we have demonstrated that high-resolution NOESY spectra of this ligand in optimized isotropic bicelles can be obtained without the need for isotopic labeling. Our results clearly showed that isotropic bicelle systems are better membrane bilayer models than the commonly used micelles. Arguably, the specific "amphipathic" conformation of Δ^8-THC obtained in the optimized bicelles may be necessary for a productive interaction with its receptor. We also demonstrated that the preferred orientation of the embedded cannabinoids can be determined by adjusting bicelle conditions to produce larger bicelle aggregates capable of aligning in the magnetic field.

Phospholipid bicelles offer many opportunities for use as successful membrane mimetics. The preparation may be further improved by using lipids with certain negative charges and some degree of unsaturation, and by incorporating appropriate amounts of cholesterol to more closely resemble native cell membranes. A most recent application of bicelles is for determining the relative stereochemistry of multiple stereocenters [47]. Also, crystallization of membrane proteins has been achieved from bicelle-forming lipid/detergent mixtures [48], an experiment which may be extended to study the drug/membrane–protein complex.

References

1. Herbette LG, Chester DW, Rhodes DG. Biophys. J. 1986;49: 91–3.
2. Mason RP, Rhodes DG, Herbette LG. J. Med. Chem. 1991;34: 869–77.
3. Makriyannis A. In: RG Pertwee (Ed). Cannabinoid Receptors. Academic Press: London, UK, 1995, pp 87–115.
4. Xie XQ, Melvin LS, Makriyannis A. J. Biol. Chem. 1996;271: 10640–7.
5. Henry GD, Sykes BD. Bull. Can. Biochem. Soc. 1987;24:21–6.
6. Scrimin P, Tecilla P. Curr. Opin. Chem. Biol. 1999;3:730–5.
7. Milhaud J. Biochem. Biophys. Acta 2004;1663:19–51.
8. Makriyannis A, Banijamali A, Van Der Schyf C, Jarrell H. NIDA Res. Monogr. 1987;79:123–133.
9. Makriyannis A, Banijamali A, Jarrell HC, Yang DP. Biochem. Biophys. Acta 1989;986:141–5.
10. Mavromoustakos T, Yang DP, Charalambous A, Herbette LG, Makriyannis A. Biochim. Biophys. Acta 1990;1024:336–44.
11. Yang DP, Banijamali A, Charalambous A, Marciniak G, Makriyannis A. Pharmacol. Biochem. Behav. 1991;40:553–7.
12. Makriyannis A, Yang DP, Mavromoustakos T. NIDA Res. Monogr. 1991;112:106–28.
13. Yang DP, Mavromoustakos T, Makriyannis A. Life Sci. 1993;53:117–22.
14. Makriyannis A, Yang DP. In: BN Dhawan, RC Sirmal, R Raghubir, RS Rapaka (Ed). Recent Advances in the Study of Neurotransmitter Receptors. Central Drug Research Institute: Lucknow, India, 1994, pp 329–48.
15. Mavromoustakos T, Yang DP, Makriyannis A. Biochim. Biophys. Acta 1995;1237:183–8.
16. Henry GD, Sykes BD. Methods Enzymol 1994;239:515–35.
17. Opella SJ, Kim Y, McDonnell P. Meth Enzymol 1994;239:536–60.
18. Mavromoustakos T, Theodoropoulou E, Yang DP, Lin SY, Koufaki M, Makriyannis A. Chem. Phys. Lipids 1996;84:21–34.
19. Naito A, Nishimura K. Curr. Top. Med. Chem. 2004;4:135–45.
20. Sanders CR, Oxenoid K. Biochem. Biophys. Acta 2000;1508: 129–45.
21. Guo J, Pavlopoulos S, Tian X, Lu D, Nikas SP, Yang DP, Makriyannis A. J. Med. Chem. 2003;46:4838–46.
22. Sanders CR, Schwonek JP. Biochemistry 1992;31:8898–905.
23. Sanders CR, Hare BJ, Howard KP, Prestegard JH. Prog. Nucl. Magn. Reson. Spectrosc. 1994;26:421–44.
24. Howard KP, Prestegard JH. J. Am. Chem. Soc. 1996;118: 3345–53.
25. Tjandra N, Bax A. Science 1997;278:1111–4.
26. Sanders CR, Prosser RS. Structure 1998;6:1227–34.
27. Glover KJ, Whiles JA, Wu G, Yu N-J, Deems R, Struppe JO, Stark RE, Komives EA, Vold RR. Biophys. J. 2001;81:2163–71.
28. Guo J. Ph.D. Thesis. University of Connecticut, Storrs, 2004.

29. Dowhan W, Bogdanov M. In: DE Vance, JE Vance (Ed). Biochemistry of Lipids, Lipoproteins and Membranes. Elsevier Press: Amsterdam, 2002, pp 1–35.
30. Watts A, Ulrich AS, Middleton DA. Mol. Membr. Biol. 1995;12:233–46.
31. Kisselev OG, Kao J, Ponder JW, Fann YC, Gautam N, Marshall GR. Proc. Natl. Acad. Sci. USA 1998;95:4270–5.
32. Bloom M, Evans E, Mouritsen OG. Q. Rev. Biophys. 1991;24:293–397.
33. Bangham AD. Chem. Phys. Lipids 1993;64:275–85.
34. Tang P, Yan B, Xu Y. Biophys. J 1997;72:1676–82.
35. Gutierrez ME, Garcia AF, Africa de Madariaga M, Sagrista ML, Casado FJ, Mora M. Life Sci. 2003;72:2337–60.
36. Davis J. Biochim. Biophys. Acta 1983;737:117–71.
37. Makriyannis A, Rapaka RS. Life Sci. 1990;47:2173–84.
38. Bechinger B. Biochem. Biophys. Acta 1999;1462:157–83.
39. Yamaguchi S, Huster D, Waring A, Lehrer RI, Kearney W, Tack BF, Hong M. Biophys. J. 2001;81:2203–14.
40. Girvin ME, Rastogi VK, Abildgaard F, Markley JL, Fillingame RH. Biochemistry 1998;37:8817–24.
41. Israelachvilli JN, Mitchell DJ, Ninham BW. J. Chem. Soc. Faraday Trans. II 1976;72:1525–68.
42. Sanders C. Biophys. J. 1993;64:171–81.
43. Vold RR, Prosser RS, Deese AJ. J. Biomol. NMR 1997;9:329–35.
44. Vold RR, Prosser RS. J. Magn. Reson. B 1996;113:267–71.
45. Sternin E, Nizza D, Gawrisch K. Langmuir 2001;17:2610–6.
46. Scholz F, Boroske E, Helfrich W. Biophys. J. 1984;45:589–92.
47. Yan J, Delaglio F, Kaerner A, Kline AD, Mo H, Shapiro MJ, Smitka TA, Stephenson GA, Zartler ER. J. Am. Chem. Soc. 2004;126:5008–17.
48. Faham S, Bowie JU. J. Mol. Biol. 2002;316:1–6.

Partial Alignment for Structure Determination of Organic Molecules

Burkhard Luy and Horst Kessler
TU München, Department Chemie, Lehrstuhl für Organische Chemie II, Lichtenbergstrasse 4, D-85747 Garching, Germany

Introduction

NMR spectroscopy is the most important method for structure elucidation in solution. Once the atomic connectivity is established (constitution of the molecule) the proof of stereochemistry is the next step. NMR as an achiral method provides only relative stereochemical information unless chiral environments (solvents, interaction with shift reagents, chemical modification via chiral auxiliaries) are used. For determining the relative stereochemistry, the classical parameters are NOE effects and J coupling constants. Only recently, two different new sources of stereochemical information have been introduced for biomolecules: cross-correlated relaxation [1] and residual dipolar couplings (RDCs) [2,3]. We will here consider the application of RDCs for small molecules such as drugs or drug-like molecules.

Residual Dipolar Couplings

Magnetically active nuclei in molecules interact through space, as they are magnetic dipoles. These couplings, which depend on the relative orientation of the dipoles and their distance, are on the order of several kHz and cause immense numbers of splittings in solid-state NMR. In solution, the rapid isotropic molecular tumbling averages out all dipolar couplings, resulting in the narrow line width of high-resolution NMR spectroscopy. With the removal of all anisotropic interactions, however, there is also a significant loss in potential structural information. Therefore, an intermediate state between solid and liquid is desirable in which the narrow line width is maintained, but anisotropic interactions are re-established and measurable. In general, there are two ways to reach this intermediate state: if the sample of interest is available in a microcrystalline phase, high-speed magic angle spinning can effectively reduce the dipolar interactions to give resolved resonances similar to the liquid state; in contrast, a sample in solution can be transferred into a directional molecular lattice, which then partially aligns the molecule to have measurable anisotropic interactions. For example, if the molecules are oriented to a low percentage, let us say on the order of 0.1%, the dipolar coupling is also reduced to ~0.1% of its original size. A molecule containing a CH fragment, which would normally exhibit a $^1J_{\mathrm{CH}}$ coupling of about 130 Hz in isotropic solution will give rise to an additional RDC that adds or subtracts to this coupling depending on the tiny preferred orientation. If one measures the $^1J_{\mathrm{CH}}$ coupling constant with and without partial orientation, the difference directly yields the RDC.

The Alignment Tensor

In the following section, a very brief and handwavy introduction to the alignment tensors is given and includes only basic equations. For a more detailed and exact derivation of key equations, we refer to [4].

In the static case, the dipolar coupling constant is given by [5]

$$D = \frac{\kappa}{R^3}\left(\cos^2\theta - \frac{1}{3}\right), \tag{1}$$

where θ is the angle between an internuclear vector and the magnetic field B_0. The term

$$\kappa = -\frac{3}{8\pi^2}\gamma_I\gamma_S\mu_0\hbar \tag{2}$$

only depends on physical constants [5]: the gyromagnetic ratios γ_{I} and γ_{S} of the two vector-spanning spins I and S, respectively, the Planck constant $\hbar = h/2\pi$ and the permeability of vacuum μ_0. For example, for ^{1}H–^{1}H and ^{13}C–^{1}H spin pairs, $\kappa = -360.3$ and -90.6 kHz Å^3, respectively. However, in the case of a tumbling molecule, the dipolar coupling is further averaged in the way that

$$\bar{D} = \frac{\kappa}{R^3}\left(\overline{\cos^2\theta} - \frac{1}{3}\right) \tag{3}$$

represents the so-called RDC constant between the two spins, which depends on the average alignment of the molecule.

In the case of isotropic tumbling as in conventional liquid-state NMR, $\overline{\cos^2\theta} = 1/3$ in all three dimensions

Graham A. Webb (ed.), Modern Magnetic Resonance, 1279–1285.
© 2008 *Springer.*

and the dipolar interaction is quenched. In a partially oriented molecule instead, the term $\overline{\cos^2\theta}$ generally is a three-dimensional tensor. This tensor is equivalent to the probability tensor **P** to find the axis of the magnetic field $B_0(t)$ along the internuclear vector **r** expressed in a reference frame, which is fixed to the molecule. This (3×3) probability tensor is symmetric with respect to the diagonal and the diagonal elements must fulfill the condition $P_{xx} + P_{yy} + P_{zz} = 1$, which implicitly leads to five independent tensor components. In reverse, this implies that in an arbitrary case a minimum of five non-identical RDCs have to be measured to unambiguously identify a probability tensor of a given sample.

Although the concept of the probability tensor **P** is very intuitive and sufficient to completely describe RDCs in rigid molecules, it is more common in the NMR literature to express the partial orientation of a molecule by the so-called alignment tensor **A**. This tensor is related to the probability tensor **P** via

$$\mathbf{A} = \mathbf{P} - \frac{1}{3}\mathbf{1} \tag{4}$$

and is therefore proportional to the anisotropy of the magnetic field distribution in the molecular frame. The eigenvalues of **A** are usually denoted as A_{xx}, A_{yy}, and A_{zz} and fulfill the condition $A_{xx} + A_{yy} + A_{zz} = 0$. For further definitions like the axial and rhombic components of an alignment tensor of the Saupe matrix, we refer to the appendix of [4].

Alignment Media

So far, we have not discussed how to partially orient the molecules. When a molecule has considerable magnetic susceptibility anisotropy, the molecule orients partially under the strong magnetic field. But this effect—although already observed in the eighties [6]—is normally too small to be observed. On the other hand, orientation can also be induced by an oriented molecular lattice, which then partially aligns the molecule of interest via steric or electrostatic interactions. All known alignment media can basically be assigned to one of two classes: liquid crystalline phases and stretched polymer gels.

Liquid Crystalline Phases

In 1963, the first spectrum of benzene partially oriented in the nematic mesophase of 4,4′-di-*n*-hexyloxyazoxybenzene was reported, a spectrum with at least 30 resonances and a width of the multiplet pattern of approximately 2500 Hz [7]. Following this result, a large number of liquid crystals for partially aligning small molecules was found in the sixties and seventies (see, for example, reviews [8–10]), but it turned out that the orientation introduced by liquid crystalline phases generally is very strong, yielding numerous large splittings by RDCs that can hardly be interpreted for more complex organic molecules. Poly-γ-benzyl-L-glutamate, dissolved in solvents like dichloromethane, chloroform, or dimethylformamide, was introduced by Panar and Phillips [11]. It was one of the least orienting liquid crystals known at that time and was used for the first successful measurements of RDCs in an organic solvent to obtain structural information of a small molecule [12–14]. Currently, new liquid crystalline phases for organic solvents have been developed that can achieve lower degrees of anisotropies. 4-*n*-Pentyl-4′-cyanobiphenyl [15] and poly-γ-ethyl-L-glutamate [16] seem to be two promising candidates for the measurement of RDCs in small molecules. The existence of liquid crystalline phases with very low induced anisotropies was proven in the last 7 years in the field of biomolecular NMR. Several lipid/detergent mixtures [2,3], filamentous phage [17], and other liquid crystalline phases [18,19] were used to successfully measure RDCs for structure refinement of proteins and nucleic acids. These alignment media are, of course, also applicable to small molecules in aqueous solutions [20–26].

Stretched Polymer Gels

Deloche and Samulski showed in their pioneering work in 1981 that partial alignment can also be achieved by stretching polymer gels [27], usually mechanically. This technique now is a standard approach in polymer NMR to obtain information about polymer properties. Not until 2000 was the use of these stretched polymer gels for aligning molecules dissolved inside the gel to obtain RDCs for structural investigations realized. The new approach is called “strain-induced alignment in a gel” and is demonstrated on stretched polyacrylamide [28–31] and polyacrylamide/acrylate [32] copolymers. Several ways of aligning by using a shigemi plunger [28], teflon funnels [33], or glass capillaries [32] have been developed and successfully applied to proteins as well as small molecules.

Recently, we were able to show that stretched polymers can also be used to partially align small molecules in organic solvents [34]. Cross-linked polystyrene (PS) sticks were simply swollen in NMR tubes, where they are automatically stretched by the boundaries of the glass walls (cf. Figure 1). In the meantime, the approach was successfully applied to a number of other cross-linked polymers like polymethylmethacrylate (with no polymer signals in the aromatic region, unpublished results) and polydimethylsiloxane (with strongly improved spectral quality [35]). Very recently, the gap of alignment media for polar

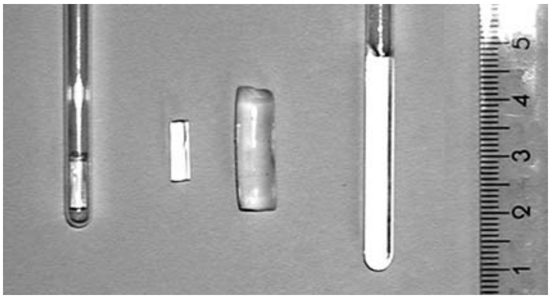

Fig. 1. Photographs of a cross-linked PS stick designed for partial alignment in different states of swelling. From left to right: unswollen polymer stick in standard 5-mm NMR tube, polymer stick directly after polymerization, free polymer stick completely swollen, and polymer stick swollen in the NMR tube.

solvents was closed by stretched gels that swell in DMSO [36,37] and other solvents like methanol, acetonitrile, or acetone [36]. The main advantage of stretched polymer gels compared to liquid crystalline phases is that no lower limit of alignment is imposed because an unstretched gel principally does not show any alignment. The induced anisotropy is generally field independent, but as in liquid crystals, a significant temperature dependence is observed (35,72). Despite the microheterogeneity of the gels, line widths below 1 Hz can be achieved. Very importantly, the strength of alignment can be adjusted in many ways, like changing the diameter of the polymer sticks, the amount of cross-linking agent, or the polymerization conditions [34–36]. Of course, swelling properties and thus the strength of alignment are different in different solvents. It is also interesting to note that the orientation and overall form of the alignment tensor not only depends on the polymer chosen but also on the solvent used [36, 72].

RDC Measurement

NMR experiments on partially aligned samples are special with respect to some details in the setup. The lock, for example, is usually split by the quadrupolar coupling of the deuterium nuclei. As a consequence, the spectrometer might lock on one or the other half of the doublet and built-in spectrometer frequency references that are based on the defined lock signal typically lead to wrongly referenced chemical shifts. Also, shimming is affected: since the lock signal is split, it cannot be used for shimming purposes. Instead, it is necessary to shim on the integral of the FID. Having learned how to deal with these specialties, the acquisition of NMR experiments is straightforward. Some general considerations concerning the practicability of measuring certain RDCs should, however, be taken into account. We therefore have a quick look at the relative size of different types of RDCs before we give an overview of a number of available experiments.

Relative Size of RDCs

Equations (1) and (2) contain all the information necessary to estimate the relative size of different types of RDCs. The dipolar coupling is proportional to the gyromagnetic ratios γ_I and γ_S and to the inverse cube of the internuclear distance r of an arbitrary pair of spins. Since the RDCs also depend on the angle θ, their size generally cannot be predicted without knowing the alignment tensor. Nevertheless, the maximum possible RDC values can be estimated and we will concentrate on these maximum values in the following text. In Figure 2, the relative size of maximum ^{1}H-X-RDCs is shown for different nuclei with respect to the internuclear distance r. It turns out that typical D_{HH} RDCs over two or three bonds and one bond D_{CH} RDCs show the strongest couplings, while long-range D_{CH} or direct D_{CC} RDCs (one-fourth of the D_{CH} couplings for a given distance r) are one order of magnitude smaller in size. Because of potential line broadening and to avoid strong coupling or second order effects in NMR spectra, the largest occurring RDCs should be ideally limited to be $\leq\sim 30$ Hz by adjusting the alignment medium. In this range, one bond D_{CH} and D_{HH} couplings can be accurately measured and provide valuable structural information. All other RDCs to carbon nuclei, however, are very small in size and require highly accurate techniques to obtain structural information. Therefore, the goal must be to measure as many strong RDCs as possible and only in cases where the easily obtained information is not sufficient, more advanced techniques should be used to measure the weaker RDCs, which generally have a larger relative error. In addition to proton and carbon bound RDCs, one bond D_{NH} couplings should provide useful structural information with RDCs of intermediate size. Whenever present, D_{HF} and D_{FF} RDCs behave very similar to D_{HH} RDCs. Although having a high gyromagnetic ratio and 100% natural abundance, RDCs involving ^{31}P nuclei are usually small because of the large internuclear distance to the next NMR-active nucleus.

Experimental Methods

After having the assignment, RDCs are in principle measurable in 1D experiments. Proton-coupled ^{13}C spectra provide useful information in this regard. In fact, if the alignment is so strong that RDCs are on the order of $^1J_{CH}$ coupling constants, one-dimensional experiments provide the only viable way to measure RDCs [12]. However, if the largest RDCs are in the desired range of ±30 Hz

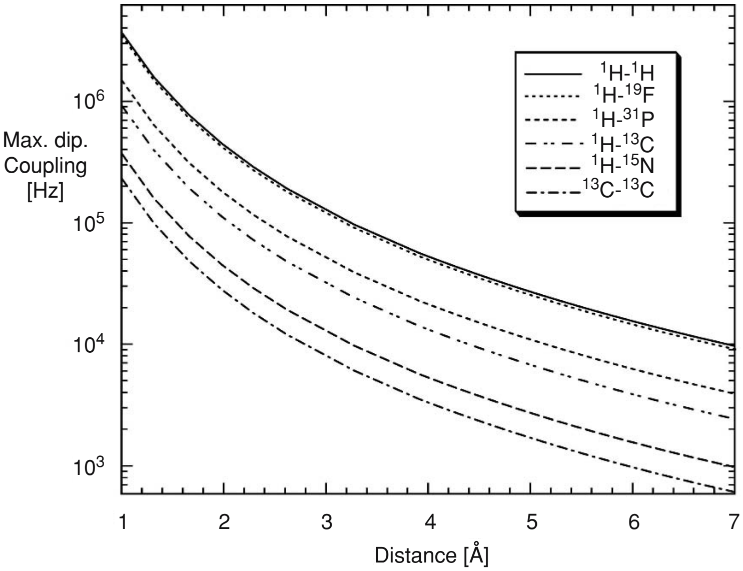

Fig. 2. Relative size of maximum dipolar couplings for protons for various NMR-active nuclei with respect to the internuclear distance *r* [see Equations (1) and (2)]. ^{13}C–^{13}C dipolar couplings are one-fourth of the ^{1}H–^{13}C dipolar couplings.

more advanced NMR experiments with high sensitivity and better resolution can be applied. The most easily measurable RDCs are one bond D_{CH} couplings, which can be measured using standard coupled HSQC or HMQC experiments [12–14,25,26,31,34–36] (cf. Figure 3, for example, spectra of strychnine in PS/CDCl$_3$ gel). Because of the variation in ($^1J_{\mathrm{CH}} + D_{\mathrm{CH}}$)-effective couplings, a procedure in which every multiplet component is phased separately should be applied to get reliable coupling constants [25].

If the resolution of standard HSQC/HMQC experiments is not sufficient, a large number of specialized techniques developed in the field of biomolecular NMR spectroscopy are available to accurately measure one bond D_{CH} and D_{NH} couplings. Spin-state selective excitation [38,39] and coherence transfer [40], IPAP [41],

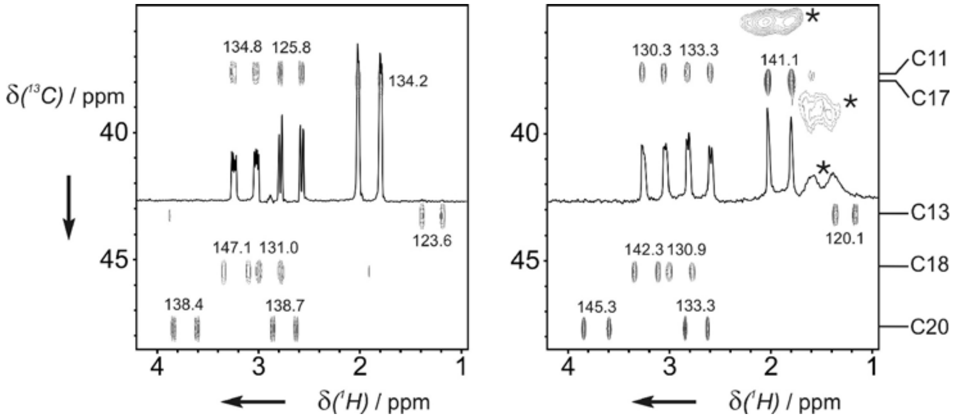

Fig. 3. Region of the ^{1}H,^{13}C-correlation spectra (HSQC) acquired on ~50 mg strychnine in CDCl$_3$ (left) and in a PS gel swollen in CDCl$_3$ (right) at 300 K. $^1J_{\mathrm{HC}}$ and $^1J_{\mathrm{HC}} + D_{\mathrm{HC}}$ couplings, respectively, are given next to the corresponding cross peaks. As can be seen from the 1D slice at 37.8 ppm D_{CH} RDCs are easily measured. The broad signals of the PS polymer are indicated with an asterisk (*).

J modulation [42], JE-TROSY [43], and quantitative J [44] experiments are some useful examples. For methylene groups, the so-called SPITZE-HSQC provides a separation of multiplet components in four spectra that allow RDC determination in more crowded regions [45]. It should also be mentioned that in almost all experiments, the use of BIRD filtering techniques can further improve spectra by selectively decoupling long-range C–H couplings [46–48]. The experiments designed for measuring D_{CH} RDCs should also be easily adaptable to the D_{NH} case. Due to the fast averaging D_{CH} RDCs of methyl groups cannot be used directly as structural information. However, they can be converted to D_{CC} RDCs to the attached carbon via the formula $D_{CC} = D_{CH_3}(-3\gamma_C/\gamma_H)(r^3_{CH}/r^3_{CC})$ [13].

The measurement of D_{HH} couplings is more difficult: in simple cases $(J + D)$ splittings can be measured directly in a one-dimensional experiment. However, since the sign of the splitting is not known and J and D are of comparable size, two possible RDC values must be considered (e.g. $J = 5$ Hz, $|J + D| = 7$ Hz leads to either $D = 2$ or -12 Hz). A sign-sensitive measurement of coupling constants is therefore highly desirable, which can be achieved in principle by E-COSY [49–51] and S^{3}E-E-COSY [39,52] methods. Unfortunately, the applicability of at least the homonuclear E-COSY methods might be strongly reduced because of the broadened lines of partially aligned samples. A more sophisticated homonuclear approach to accurately measure RDCs is the SIAM-TOCSY [53,54], which uses in-phase and anti-phase components in TOCSY-type experiments in combination with the Keeler–Titman fitting procedure [55]. Integration-based techniques like the CT-COSY [56,57] or even the integration of conventional COSY cross peaks [58] offer an alternative for measuring the size of RDCs. The sign of couplings might then be determined with additional pulse sequences that use recently developed Hartmann–Hahn like multiple pulse elements [59]. The sign of the dipolar coupling might also be measurable by slightly changing the strength of alignment in the same alignment medium. The difference in measured RDCs should then lead to the sign of the dipolar coupling relative to the scalar coupling.

Long range D_{CH} couplings can basically obtained in two ways: if the carbon atom has a proton attached, S^{3}E-E-COSY type methods [52,60] provide an efficient, sign-sensitive procedure; in the case that the carbon of interest does not have a proton attached, recently developed HMBC-based methods can be applied that use a sophisticated fitting procedure to obtain the size of the coupling [13,61,62].

Methods for measuring D_{CC} couplings at natural abundance are the well-known INADEQUATE [63,64] and ADEQUATE [65,66] experiments, which inherently have very low sensitivity. RDCs to ^{31}P nuclei have been measured in nucleic acids [67,68]. Fluorine with its high gyromagnetic ratio and 100% natural abundance is perfectly suited for RDC measurements. D_{CF} couplings should be measurable the same way as D_{CH} RDCs. In the case when a rather strong J_{HF} coupling is present, specially designed E-COSY and S^{3}E-E-COSY type experiments allow the very sensitive measurement of D_{HF}, D_{HH}, and D_{FF} couplings [69,70].

Applications

The first applications to obtain structural information from RDCs for sugars were reported in 2000 and for medium-sized molecules in organic solvents in 2003. Considering this short time-span, the demonstrated uses of RDCs are quite remarkable.

Maybe the most elegant application of RDCs is found in six-membered chair-like rings, where RDCs can be used directly to distinguish axial and equatorial protons without having the need to derive an alignment tensor [25]. The method uses the fact that all axial C–H vectors are oriented in the same direction and therefore must have virtually identical D_{CH} couplings. The assignment then simply can be achieved by looking at the occurrence of identical RDCs: all protons with very similar D_{CH} RDCs are axial while all others are equatorial (cf. Figure 4).

But even for arbitrary molecules the prochiral assignment of methylene groups can be achieved in most cases without having to rely on NOE connectivities as long as the alignment tensor is known [12,13]. This is especially important for isolated CH$_2$ groups, which have few neighbors for NOE identification.

A major application can also be found in the determination of Z/E configurations [14] and the determination of the relative chirality of stereochemical centers [26,35] even in different parts of a molecule that might be spatially distant. For this technique, structural models of all possible configurations have to be built first. The measured RDCs are then compared with RDCs backcalculated from the different structures. The quality of the fits expressed in

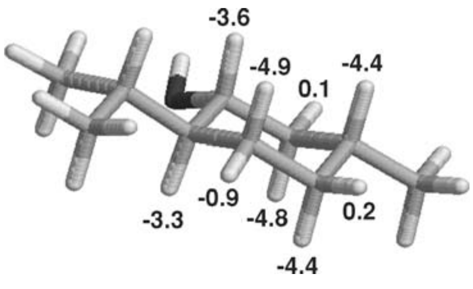

Fig. 4. Measured D_{CH} RDCs for menthol in a PS/CDCl$_3$ gel. Axial and equatiorial protons can easily be distinguished without knowing the alignment tensor.

χ^2 or the correlation factor R^2 leads to the best structural model.

A challenging application is the determination of the sugar pucker with RDCs. Freedberg [24] has shown that the RDCs measured for sucrose cannot be explained by a single conformation. On the other hand, a large number of potential sugar puckers can be ruled out, giving more insight into the population of structures and the dynamic behavior of sugars.

Dynamic regions in molecules are generally difficult to handle and there is no exception in the case of RDCs. RDCs in dynamic regions are averaged over all populated states and might lead to misinterpretations if the populated structures differ significantly. However, the use of several different alignment media should make it possible to unambiguously identify flexible regions in a molecule and together with the improved prediction of alignment tensors [71], the determined RDCs might be fitted to a small ensemble of structures in the future.

A potential application of RDCs as upper distance restraints surprisingly has not yet been reported. RDCs over distances larger than 7Å have been measured. For a given measured RDC, an upper distance restraint can be immediately specified, as long as the axial component of the alignment tensor is known.

Conclusion

The development of partial alignment media over the last years allows for the first time the broad use of anisotropic parameters like RDCs or residual chemical shift anisotropy in high-resolution NMR spectroscopy. Liquid crystalline phases and stretched polymer gels with scalable alignment properties for practically all useful NMR solvents are available. The RDCs of these samples can be measured by simply calculating the difference of couplings measured in isotropic solution and couplings measured in aligned samples. So far mostly solutes in aqueous solutions have been studied. Recently developed alignment techniques in stretched polymer gels will open the measurement of RDCs to structural studies in all NMR relevant solutions. Quite a number of applications with small organic molecules have been demonstrated, including the assignment of axial/equatorial or prochiral methylene protons, and the determination of relative stereochemistry and configuration. The method significantly widens the potential of modern liquid-state NMR spectroscopy and it will be interesting to see new developments in this promising young field.

References

1. Reif B, Hennig M, Griesinger C. Science. 1997;276:1230.
2. Tjandra N, Bax A. Science. 1997;278:1111.
3. Prestegard JH. Nat. Struct. Biol. 1998;5:517.
4. Kramer F, Deshmukh MV, Kessler H, Glaser SJ. Concepts Magn. Reson. Part A 2004;21A:10.
5. Ernst RR, Bodenhausen G, Wokaun A. Principles of Nuclear Magnetic Resonance in One and Two Dimensions. Oxford University Press: New York, 1987.
6. Bothnerby AA, Domaille PJ, Gayathri C. J. Am. Chem. Soc. 1981;103:5602.
7. Saupe A, Englert G. Phys. Rev. Lett. 1963;11:462.
8. Emsley JW, Lindon JC. NMR Spectroscopy Using Liquid Crystal Solvents. Pergamon Press: Oxford, 1975.
9. Diehl P, Henrichs PM. Specialist Report on NMR Spectroscopy. Chemical Society, Vol. 1, 1972.
10. Diehl P, Niederberger W. Specialist Report on NMR Spectroscopy. Chemical Society, Vol. 3, 1974.
11. Panar M, Phillips WD. J. Am. Chem. Soc. 1968;90:3880.
12. Thiele CM, Berger S. Org. Lett. 2003;5:705.
13. Verdier L, Sakhaii P, Zweckstetter M, Griesinger C. J. Magn. Reson. 2003;163:353.
14. Aroulanda C, Boucard V, Guibe F, Courtieu J, Merlet D. Chem. Eur. J. 2003;9:4536.
15. Bendiak B. J. Am. Chem. Soc. 2002;124:14862.
16. Thiele CM. J. Org. Chem. 2004;69:7403.
17. Hansen MR, Mueller L, Pardi A. Nat. Struct. Biol. 1998; 5:1065.
18. Rückert M, Otting G. J. Am. Chem. Soc. 2000;122:7793.
19. Fleming K, Gray D, Prasannan S, Matthews S. J. Am. Chem. Soc. 2000;122:5224.
20. Martin-Pastor M, Bush CA. Abstracts of Papers of the Am. Chem. Soc. 2000;220:U117.
21. Martin-Pastor M, Bush CA. J. Biomol. NMR 2001;19: 125.
22. Neubauer H, Meiler J, Peti W, Griesinger C. Helvetica Chim. Acta. 2001;84:243.
23. Azurmendi HF, Bush CA. Carbohydr. Res. 2002;337:905.
24. Freedberg DI. J. Am. Chem. Soc. 2002;124:2358.
25. Yan JL, Kline AD, Mo HP, Shapiro MJ, Zartler ER. J. Org. Chem. 2003;68:1786.
26. Yan JL, Delaglio F, Kaerner A, Kline AD, Mo HP, Shapiro MJ, Smitka TA, Stephenson GA, Zartler ER. J. Am. Chem. Soc. 2004;126:5008.
27. Deloche B, Samulski ET. Macromolecules. 1981;14:575.
28. Tycko R, Blanco FJ, Ishii Y. J. Am. Chem. Soc. 2000; 122:9340.
29. Ishii Y, Markus MA, Tycko R. J. Biomol. NMR 2001;21:141.
30. Sass HJ, Musco G, Stahl SJ, Wingfield PT, Grzesiek S. J. Biomol. NMR 2000;18:303.
31. Mangoni A, Esposito V, Randazzo A. Chem. Commun. 2003; 154.
32. Meier S, Haussinger D, Grzesiek S. J. Biomol. NMR 2002;24: 351.
33. Chou JJ, Gaemers S, Howder B, Louis JM, Bax A. J. Biomol. NMR 2001;21:377.
34. Luy B, Kobzar K, Kessler H. Angew. Chem. Int. Ed. 2004; 43:1092.
35. Freudenberger C, Spitteler P, Bauer R, Kessler H, Luy B. J. Amer. Chem. Soc. 2004;126:14690.
36. Freudenberger C, Kobzar K, S. Knör, Heckmann D, Paululat T, Kessler H, Luy B. Angew. Chem. Int. Ed. 2005;44:423.
37. Haberz P, Farjon J, Griesinger C. Angew. Chem. Int. Ed. 2005;44:427.

38. Meissner A, Duus JO, Sørensen OW. J. Biomol. NMR 1997;10:89.
39. Meissner A, Duus JO, Sørensen OW. J. Magn. Reson. 1997;128:92.
40. Sørensen MD, Meissner A, Sørensen OW. J. Biomol. NMR 1997;10:181.
41. Ottiger M, Delaglio F, Bax A. J. Magn. Reson. 1998;131:373.
42. Tjandra N, Bax A. J. Magn. Reson. 1997;124:512.
43. Luy B, Marino JP. J. Magn. Reson. 2003;163:92.
44. Vuister GW, Bax A. J. Am. Chem. Soc. 1993;115:7772.
45. Carlomagno T, Peti W, Griesinger C. J. Biomol. NMR 2000;17:99.
46. Garbow JR, Weitekamp DP, Pines A. Chem. Phys. Lett. 1982;93:504.
47. Uhrin D, Liptaj T, Kover KE. J. Magn. Reson. Ser. A 1993;101:41.
48. Feher K, Berger S, Kover KE. J. Magn. Reson. 2003;163:340.
49. Griesinger C, Sørensen OW, Ernst RR. J. Am. Chem. Soc. 1985;107:6394.
50. Griesinger C, Sørensen OW, Ernst RR. J. Chem. Phys. 1986;85:6837.
51. Griesinger C, Sørensen OW, Ernst RR. J. Magn. Reson. 1987;75:474.
52. Meissner A, Sørensen OW. Magn. Reson. Chem. 2001;39:49.
53. Prasch T, Gröschke P, Glaser SJ. Angew. Chem. Int. Ed. 1998;37:802.
54. Möglich A, Wenzler M, Kramer F, Glaser SJ, Brunner E. J. Biomol. NMR 2002;23:211.
55. Titman JJ, Keeler J. J. Magn. Reson. 1990;89:640.
56. Tian F, Bolon PJ, Prestegard JH. J. Am. Chem. Soc. 1999;121:7712.
57. Wu ZR, Bax A. J. Magn. Reson. 2001;151:242.
58. Delaglio F, Wu ZR, Bax A. J. Magn. Reson. 2001;149:276.
59. Kramer F, Jung A, Brunner E, Glaser SJ. J. Magn. Reson. 2004;169:49.
60. Meissner A, Sørensen OW. Chem. Phys. Lett. 1997;276:97.
61. Edden RAE, Keeler J. J. Magn. Reson. 2004;166:53.
62. Schulte-Herbrüggen T, Meissner A, Papanikos A, Meldal M, Sørensen OW. J. Magn. Reson. 2002;156:282.
63. Bax A, Freeman R, Kempsell SP. J. Am. Chem. Soc. 1980;102:4849.
64. Meissner A, Sørensen OW. Concepts Magn. Reson. 2002;14:141.
65. Reif B, Köck M, Kerssebaum R, Kang H, Fenical W, Griesinger C. J. Magn. Reson. Ser. A 1996;118:282.
66. Reif B, Køck M, Kerssebaum R, Schleucher J, Griesinger C. J. Magn. Reson. Ser. B 1996;112:295.
67. Wu ZR, Tjandra N, Bax A. J. Biomol. NMR 2001;19:367.
68. Carlomagno T, Hennig M, Williamson JR. J. Biomol. NMR 2002;22:65.
69. Luy B, Marino JP. J. Biomol. NMR 2001;20:39.
70. Luy B, Barchi JJ, Marino JP. J. Magn. Reson. 2001;152:179.
71. Zweckstetter M, Bax A. J. Am. Chem. Soc. 2000;122:3791.

Measurement of Residual Dipolar Couplings and Applications in Protein NMR

Keyang Ding and Angela M. Gronenborn

Laboratory of Chemical Physics, National Institute of Diabetes and Digestive and Kidney Diseases, National Institutes of Health, Bethesda, MD 20892

Abstract

Residual dipolar couplings (RDCs) provide important constraints for the determination and refinement of protein NMR structures. Based on echo–anti-echo manipulation or IPAP principle, a suite of sensitivity enhanced experiments are described for measuring backbone $^1H^N$–^{15}N, ^{15}N–$^{13}C'$, $^1H^N$–$^{13}C'$, $^{13}C'$–$^{13}C^\alpha$, $^{13}C^\alpha$–$^1H^\alpha$, $^{15}N(i)$–$^{13}C^\alpha(i)$, $^1H^N(i)$–$^{13}C^\alpha(i)$, $^{15}N(i)$–$^{13}C^\alpha(i-1)$, and $^1H^N(i)$–$^{13}C^\alpha(i-1)$ dipolar couplings in proteins. The accuracy of the measured couplings can be assessed by comparing the experimentally obtained values with those predicted based on high resolution structures. Even for very small RDCs, such as the $^{15}N(i)$–$^{13}C^\alpha(i-1)$ couplings that are smaller than 0.3 Hz, a correlation coefficient of 0.83 is obtained, attesting to the accuracy of couplings obtained with these sensitivity-enhanced IPAP experiments. We also present a novel application for the use of RDCs. Under certain conditions, the folded state of a protein comprises detectable, conformational sub-states. Such sub-states at local sites, so-called melting hot spots, are characterized by re-orienting bond vectors. Determination of RDCs allows for efficient and easy detection of such hot spots.

Introduction

The importance of being ordered has been highly recognized in the field of protein NMR spectroscopy [1]. When a protein is placed into a magnetic field, it will experience a small degree of alignment. This causes any pair of spins within the protein to exhibit a dipolar interaction in addition to the scalar interaction that is manifested in the J coupling. It was noted earlier [2,3] that these small dipolar couplings are a direct reflection of the protein structure, since they provide a measure of the distance and the orientation of the vector connecting the two nuclei. Most proteins lack sufficient intrinsic magnetic susceptibility anisotropies for practical alignment purposes, however, alignment of any biological macromolecule can be achieved using liquid crystalline media. Generally, there are two major aspects that need to be addressed in the residual dipolar coupling (RDC)-related techniques: selection and optimization of the alignment media to yield measurable dipolar couplings and the development of accurate methods for measuring these small couplings.

Any alignment medium should be inert to the solutes (proteins) under investigation and needs to be stable over reasonably wide pH and temperature ranges. In addition, it should not cause any adverse effects on the NMR line widths, so that the NMR spectra in the alignment media remain at comparable resolution to those in the isotropic aqueous solution. The first alignment medium ever used was a lyotropic liquid crystal consisting of binary mixtures of dihexanoyl phosphatidylcholine and dimyristoyl phosphatidylcholine [3]. At present, a large variety of different alignment media are in use, including suspensions of charged, rod-shaped viruses, such as tobacco mosaic virus and filamentous bacteriophages fd/M13 and Pf1, quasi-ternary systems of surfactant/salt/alcohol or aqueous alkyl-poly(ethylene glycol)/alcohol mixtures, known to form stacked lamellar phases, and vertical or radial strained polyacrylamide gels [4–10]. Such gels are generally believed to be the most inert media for proteins. The degree of alignment can be tuned by adjusting the concentration of the liquid crystalline materials or the degree of strain/compression in case of the polyacrylamide gels. A suitable degree of alignment results in RDC values for $^1D_{NH}$ between 15 and 25 Hz.

The most commonly investigated dipolar couplings for proteins are the five backbone one-bond ^{15}N–$^1H^N$, ^{15}N–$^{13}C'$, $^{13}C'$–$^{13}C^\alpha$, and $^1H^\alpha$–$^{13}C^\alpha$ and two-bond $^1H^N$–$^{13}C'$ RDCs [11]. In addition, one-bond $^{13}C^\alpha$–$^{13}C^\beta$ and $^1H^\beta$–$^{13}C^\beta$, and one-bond ^{13}C–^{13}C and ^1H–^{13}C couplings in methyl groups are also of interest [12,13]. Long-range ^1H–^1H RDCs of protons close in space or connected via multiple bonds may yield important information with respect to quantitative NOE connectivity or local conformation [14].

Accurate measurement of these small dipolar couplings is still a challenge in protein NMR spectroscopy. Generally, all presently available methods for RDC determination can be classified into two major categories.

Graham A. Webb (ed.), Modern Magnetic Resonance, 1287–1291.
© 2008 *Springer.*

Fig. 1. Schematic representation of the echo–anti-echo manipulation. The upper left box displays the normal area of a 2D ^{15}N–^{1}H^{N} HSQC spectrum. Only one ^{15}N–^{1}H^{N} cross peak is shown, split by the coupling J_{NX} and J_{HX} along the ^{15}N and ^{1}H dimensions, respectively. Using echo–anti-echo manipulation, a spectrum such as shown in the right box is obtained. One peak of the pair remains at its original position, while the other one is flipped around the zero ^{15}N frequency line. In this manner, coupled ^{15}N–^{1}H^{N} cross peaks are separated. The splitting J_{NX} and J_{HX} can be the active coupling J_{NH}, or the passive coupling from a third spin X.

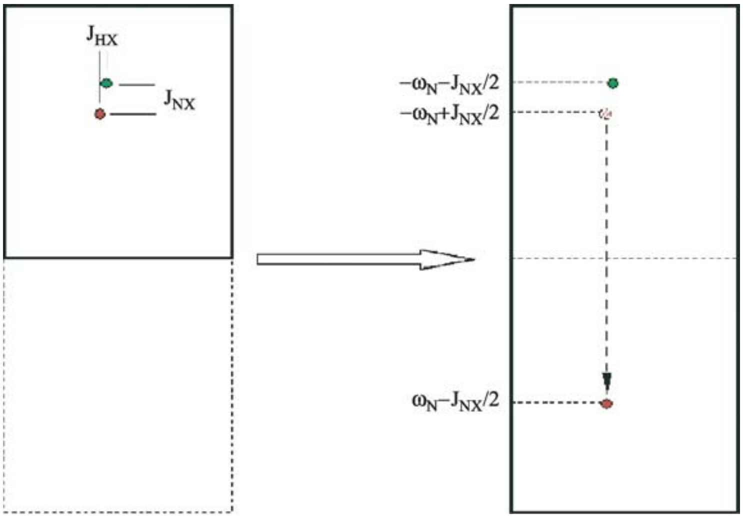

One methodology is called the quantitative J correlation and is based on intensity analysis [15]. Here, the coupling constant is often estimated from two points in the period during which this coupling evolves. If the measurement is based on a series of points, the resulting experiment is equivalent to a three-dimensional (3D) experiment. The accuracy of quantitative J correlation experiments relies critically on the uniqueness of the selected magnetization transfer pathways and the model employed to de-convolute the coupling from all other complex relaxation processes. The second methodology for the determination of dipolar couplings involves measuring the corresponding splitting directly from coupled multidimensional spectra. In these spectra the number of peaks is doubled due to coupling splitting, resulting in a reduction of resolution in these coupled spectra compared to their decoupled counterparts. In some cases, the splitting may actually be too small to be resolved with respect to the digital resolution of the spectra. It therefore is highly desirable to separate the two peaks within a split doublet.

In the following section, we describe techniques for separating the two peaks within a coupled doublet. They result in a suite of sensitivity-enhanced experiments for accurately and efficiently measuring backbone RDCs in proteins [16–20]. In addition, we describe some of the applications with respect to using RDCs to study protein folding and unfolding [21].

Measurement of Backbone Residual Dipolar Couplings in Proteins

Generally, there are two methods to separate the couplings within a split pair of resonances in a coupled spectrum: echo–anti-echo manipulation [16–18] and spin-state-selective technique [22–24]. The echo–anti-echo manipulation is schematically represented in Figure 1. The two peaks within a doublet are manipulated into P-type and N-type peaks [18], respectively. In a series of FIDs, the t_1-modulation alternates between echo and anti-echo for one peak and between anti-echo and echo for the other peak within the doublet. In this way, sensitivity enhancement is achieved naturally and directly. The loss in resolution of such coupled spectra, when compared to the decoupled spectra, can be easily compensated for by setting the spectral width in the ^{15}N dimension to twice the chemical shift range and by implementing TPPI [25,26] to shift the carrier frequency to the edge of the ^{15}N chemical shift range. In special cases, either J_{NX} or J_{HX} may be zero. Based on the echo–anti-echo manipulation, four sensitivity-enhanced experiments [16,17] were devised for measuring one-bond ^{1}H^{N}–^{15}N dipolar couplings and one sensitivity-enhanced experiment [18] for simultaneously measuring one-bond ^{15}N–^{13}C′ and two-bond ^{1}H^{N}–^{13}C′ dipolar couplings. We demonstrated the accuracy of the developed experiments using the protein GB1 aligned in liquid crystalline Pf1 (15 mg/ml) in 95% H_2O/5% D_2O at pH 7 and 25 °C and measured a large set of RDCs. Comparing the experimentally obtained RDCs with those calculated from a previously obtained high resolution model structure [27] (PDB code: 3GB1), excellent agreement between these values can be noted [16–18]. For one-bond ^{15}N–^{1}H^{N}, ^{15}N–^{13}C′ and two-bond ^{1}H^{N}–^{13}C′ RDCs the correlation coefficients are 0.998, 0.98, and 0.96, respectively. Interestingly, the presence of cross-correlated relaxation between ^{15}N–^{1}H^{N} and ^{1}H^{N}–^{1}H$^{\alpha}$ dipolar interactions causes one-bond ^{15}N–^{1}H^{N} couplings measured in the ^{15}N dimension to be different from those measured in

Table 1: Modulation of the coupling J_{MX} evolution and ^{15}N chemical shift frequency ω_{N} to the raw and manipulated FIDs in the 2D series for values of n from 1 to $\mathrm{TD}_1/2$

2D series number	Real part	Imaginary part
Raw dataset		
$4n-3$	$\cos(\pi kJ_{\mathrm{MX}}t_1)\cos(\omega_{\mathrm{H}}t_2-\omega_{\mathrm{N}}t_1)$	$-\cos(\pi kJ_{\mathrm{MX}}t_1)\sin(\omega_{\mathrm{H}}t_2-\omega_{\mathrm{N}}t_1)$
$4n-2$	$\sin(\pi kJ_{\mathrm{MX}}t_1)\sin(\omega_{\mathrm{H}}t_2-\omega_{\mathrm{N}}t_1)$	$\sin(\pi kJ_{\mathrm{MX}}t_1)\cos(\omega_{\mathrm{H}}t_2-\omega_{\mathrm{N}}t_1)$
$4n-1$	$\cos(\pi kJ_{\mathrm{MX}}t_1)\cos(\omega_{\mathrm{H}}t_2+\omega_{\mathrm{N}}t_1)$	$-\cos(\pi kJ_{\mathrm{MX}}t_1)\sin(\omega_{\mathrm{H}}t_2+\omega_{\mathrm{N}}t_1)$
$4n$	$-\sin(\pi kJ_{\mathrm{MX}}t_1)\sin(\omega_{\mathrm{H}}t_2+\omega_{\mathrm{N}}t_1)$	$\sin(\pi kJ_{\mathrm{MX}}t_1)\cos(\omega_{\mathrm{H}}t_2+\omega_{\mathrm{N}}t_1)$
New dataset 1		
$(2n-1)=(4n-3)+(4n-2)$	$\cos[\omega_{\mathrm{H}}t_2-(\omega_{\mathrm{N}}+\pi kJ_{\mathrm{MX}})t_1]$	$-\sin[\omega_{\mathrm{H}}t_2-(\omega_{\mathrm{N}}+\pi kJ_{\mathrm{MX}})t_1]$
$2n=(4n-1)+(4n)$	$\cos[\omega_{\mathrm{H}}t_2+(\omega_{\mathrm{N}}+\pi kJ_{\mathrm{MX}})t_1]$	$-\sin[\omega_{\mathrm{H}}t_2+(\omega_{\mathrm{N}}+\pi kJ_{\mathrm{MX}})t_1]$
New dataset 2		
$(2n-1)=(4n-3)-(4n-2)$	$\cos[\omega_{\mathrm{H}}t_2-(\omega_{\mathrm{N}}-\pi kJ_{\mathrm{MX}})t_1]$	$-\sin[\omega_{\mathrm{H}}t_2-(\omega_{\mathrm{N}}-\pi kJ_{\mathrm{MX}})t_1]$
$2n=(4n-1)-(4n)$	$\cos[\omega_{\mathrm{H}}t_2+(\omega_{\mathrm{N}}-\pi kJ_{\mathrm{MX}})t_1]$	$-\sin[\omega_{\mathrm{H}}t_2+(\omega_{\mathrm{N}}-\pi kJ_{\mathrm{MX}})t_1]$

the ^{1}H dimension [17]. Therefore, it is in general preferable to measure the amide RDCs in the ^{15}N dimension in these spectra, although the orientational information is identical in both dimensions.

The spin-state-selective technique combined with sensitivity enhancement and interleaved data acquisition is summarized in Table 1 [19]. This approach is especially useful for the cases where the coupling is to be measured and the ^{15}N chemical shift evolve during different time periods. In these cases, it is often necessary to record a 3D experiment, which in turn is reduced in dimensionality from 3 to 2 [28–30] using the accordion principle [31,32]. Generally, a scaling factor of k can be introduced to scale the J_{MX} coupling evolution. By carefully setting the t_1-modulation according to Table 1, sensitivity-enhanced experiments were implemented for measuring one-bond ^{13}C′–^{13}C$^\alpha$ and ^{1}H$^\alpha$–^{13}C$^\alpha$ dipolar couplings [19]. In this way, two sub-spectra with resolution comparable to the decoupled spectra are obtained and the corresponding peak displacement along the ^{15}N dimension provides a direct measure of the one-bond ^{13}C′–^{13}C$^\alpha$ and ^{1}H$^\alpha$–^{13}C$^\alpha$ dipolar couplings. Again, the applicability of these experiments was demonstrated for protein GB1 aligned in liquid crystalline Pf1 (15 mg/ml) in 95% H_2O/5% D_2O at pH 7 and 25 °C. Excellent correspondence between measured and calculated one-bond ^{13}C′–^{13}C$^\alpha$ and ^{1}H$^\alpha$–^{13}C$^\alpha$ dipolar couplings was found [19], with correlation coefficients of 0.96 and 0.96, respectively.

In a further application of the spin-state-selective techniques, sensitivity-enhanced experiments for measuring ^{15}N(i)–^{13}C$^\alpha$(i), ^{1}H$^{\mathrm{N}}$(i)–^{13}C$^\alpha$(i), ^{15}N(i)–^{13}C$^\alpha$($i-1$), and ^{1}H$^{\mathrm{N}}$(i)–^{13}C$^\alpha$($i-1$) dipolar couplings were also developed [20]. Since the ^{15}N(i)–^{13}C$^\alpha$(i) and ^{15}N(i)–^{13}C$^\alpha$($i-1$) coupling evolution and the ^{15}N chemical shift evolution are in a common time period, there is no need for the accordion principle. Every cross peak in the two sub-spectra exhibits E.COSY splittings from the intra-residue ^{13}C$^\alpha$ spin. Because one-bond ^{15}N–^{13}C$^\alpha$ J couplings are small, ranging from 8.5 to 13.5 Hz, very high digital resolution in ^{15}N dimension is necessary for resolving the E.COSY doublet. Consequently, the application of this type of experiment is limited to small proteins with an apparent ^{15}N line width $\leq$8.5 Hz. The comparison between measured and calculated one-bond and two-bond ^{15}N–^{13}C$^\alpha$, as well as two-bond and three-bond ^{1}H$^{\mathrm{N}}$–^{13}C$^\alpha$ RDCs for the protein GB1 aligned in liquid crystalline Pf1 (15 mg/ml) in 95% H_2O/5% D_2O at pH 7 and 25 °C, yields correlation coefficients of 0.983, 0.833, 0.976, and 0.944, respectively. We wish to point out that the two-bond ^{15}N–^{13}C$^\alpha$ RDCs are extremely small, namely ≤ 0.3 Hz, still yielding a remarkable correlation coefficient of 0.833 [20]. This implies that the experimentally measured values have to be highly accurate and that the quality of the model structure is also very good.

Applications of Residual Dipolar Couplings in Proteins

The most direct application of RDCs in protein NMR is their use as orientational constraints for 3D structure determination. For a rigid molecule, the orientations of all the two-spin vectors are fixed with respect to the molecular frame. Therefore, the corresponding RDC is proportional to the scalar product between a 3 × 3 traceless order tensor, global to any pair of spins, and the second-order tensor of the two-spin vector [33]. It is this relationship between the order tensors that is the basis for using RDCs in NMR structure determination. If, however, the directions of some two-spin vectors reorient with respect to the molecular frame, the proportionality to the scalar product is broken and the corresponding RDCs cannot

Fig. 2. Characterization of melting hot spots in a destabilized mutant of GB1 (S14) by RDC measurement. The measured D_{NH} for S14 against the predicted values are shown in (A) and (B), and data points associated with local melting hot spots are displayed as filled triangles (T11, L12, K13) and filled circles (A24, T25). (C) Measured D_{NH} of S14 in the molten state vs. those predicted from the folded structure. (D) Correlation between measured D_{NH} of folded S14 at 25 °C in a stretched gel at pH 5.5 and at pH 3.0. (Data points for the residues comprising the melting hot spots are excluded.)

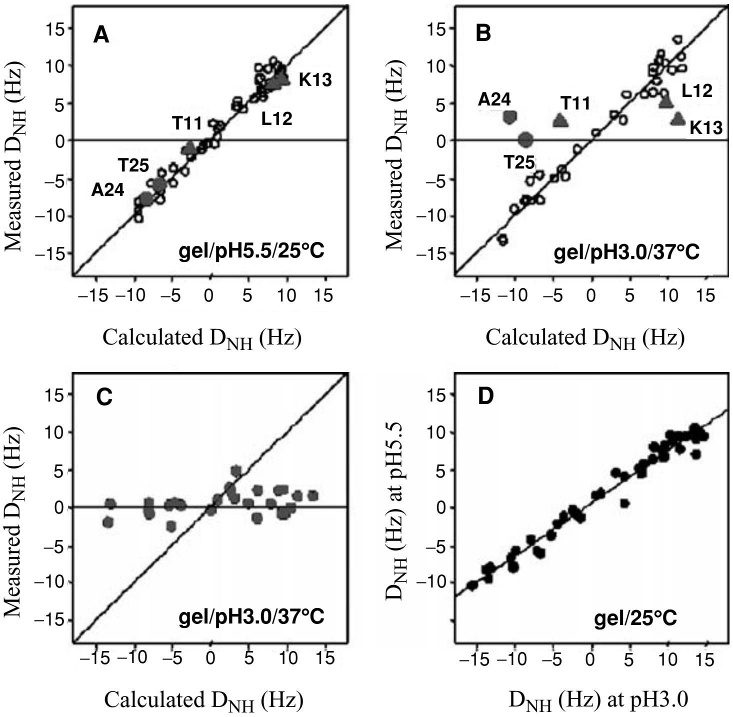

provide meaningful structural constraints. They can, on the other hand, reveal important information about motions, either relating to inter-domain motions [34] or local melting events [21]. Local melting hot spots are easily identified since local order tensor parameters will be different from the global tensor, caused by the local reorientation motion at this site. For example, we examined the structure and dynamics of a series of core mutants of the protein GB1. For one of these, S14, local melting was discovered under destabilizing conditions based on RDC measurements. The identification of the melting hot spots is illustrated in Figure 2 [21]. RDCs were measured in a stretched polyacrylamide gel at temperatures between 25 and 37 °C and at pH 5.5 they correlate well (Pearson correlation coefficient = 0.99) with calculated values based on the refined NMR structure of wild-type GB1 (PDB code: 3GB1). However, at pH 3.0 and 37 °C, the data points for residues T11, L12, K13, A24, and T25 deviate from the diagonal correlation line and are scattering along a horizontal line (Figure 2B). Under those experimental conditions S14 exists in a folded and unfolded state, as evidenced by a second set of resonances, not belonging to native state. For the unfolded protein, no correlation with the native, folded structure is preserved and all experimental RDCs scatter along the same horizontal line (Figure 2C) as noted before for the outliers of the folded state. We also established that the changes in RDCs are not caused by a pH change on the gel, since the couplings of the folded GB1 at pH 3.0 and 5.5 are in excellent agreement (Figure 2D).

In conclusion, our application of RDC measurements to the GB1 folding landscape clearly demonstrates their power for identifying melting hot spots in proteins.

Discussion

There is now ample data available (see above) that indicate the importance of RDC derived constraints for NMR structure determination of proteins as well as for identifying local areas of mobility. Proteins are also rich in ^{1}H–^{13}C spin pairs in the side chains. Therefore long-range ^{1}H–^{1}H RDCs will probably attract more and more attention since they will be able to provide quantitative distance constraints. Once accurate and efficient methods are developed for measuring these side-chain ^{1}H–^{13}C and the long-range ^{1}H–^{1}H dipolar couplings, NMR structural biology will move into a new area again.

Acknowledgments

This work was supported in part by the Intramural AIDS Targeted Antiviral Program of the Office of the Director of the National Institutes of Health to AMG.

References

1. Gronenborn AM. C. R. Biol. 2002;325:957–66.
2. Tolman JR, Flanagan JM, Kennedy MA, Prestegard JH. Proc. Natl. Acad. Sci. U.S.A. 1995;92:9279–83.
3. Tjandra N, Bax A. Science. 1997;278:1111–4.
4. Clore GM, Starich MR, Gronenborn AM. J. Am. Chem. Soc. 1998;120:10571–2.
5. Hansen MR, Mueller L, Pardi A. Nat. Struct. Biol. 1998;5:1065–74.
6. Prosser RS, Losonczi JA, Shiyanovskaya IV. J. Am. Chem. Soc. 1998;120:11010–1.
7. Barrientos LG, Dolan C, Gronenborn AM. J. Biomol. NMR. 2000;16:329–37.
8. Ruckert M, Otting GJ. Am. Chem. Soc. 2000;122:7793–7.
9. Tycko R, Blanco FJ, Ishii Y. J. Am. Chem. Soc. 2000;122:9340–1.
10. Sass HJ, Musco G, Stahl SJ, Wingfield PT, Grzesiek SJ. Biomol. NMR. 1998;18:303–9.
11. deAlba E, Tjandra N. Prog. Nucl. Magn. Reson. Spectrosc. 2002;40:175–97.
12. Ottiger M, Bax A. J. Am. Chem. Soc. 1999;121:4690–5.
13. Chou JJ, Bax A. J. Am. Chem. Soc. 2001;123;3844–5.
14. Wu Z, Bax A. J. Am. Chem. Soc. 2002;124:9672–3.
15. Bax A, Vuister GW, Grzesiek S, Delaglio F, Wang AC, Tschudin R, Zhu G. Methods Enzymol. 1994;239:79–105.
16. Ding K, Gronenborn AM. J. Magn. Reson. 2002;158:173–7.
17. Ding K, Gronenborn AM. J. Magn. Reson. 2003;163:208–14.
18. Ding K, Gronenborn AM. J. Am. Chem. Soc. 2003;125:11504–5.
19. Ding K, Gronenborn AM. J. Magn. Reson. 2004;167:253–8.
20. Ding K, Gronenborn AM. J. Am. Chem. Soc. 2004;126:6232–3.
21. Ding K, Louis JM, Gronenborn AM. J. Mol. Biol. 2004;335:1299–307.
22. Ottiger M, Delaglio F, Bax A. J. Magn. Reson. 1998;131:373–8.
23. Cordier F, Dingley AJ, Grzesiek S. J. Biomol. NMR. 1999;13:175–80.
24. Lerche MH, Meissner A, Poulsen FM, Sorensen OW. J. Magn. Reson. 1999;140:259–63.
25. Drobny G, Pines A, Sinton S, Weitekamp D, Wemmer D. Faraday Div. Chem. Soc. Symp. 1979;13:49.
26. Bodenhausen G, Vold RL, Vold RR. J. Magn. Reson. 1980;37:93–106.
27. Kuszewski J, Gronenborn AM, Clore GM. J. Am. Chem. Soc. 1999;121:2337–8.
28. Szyperski T, Yeh DC, Sukumaran DK, Moseley HNB, Montelione GT. Proc. Natl. Acad. Sci. U.S.A. 2002;99:8009–14.
29. Ding K, Gronenborn AM. J. Magn. Reson. 2002;156:262–8.
30. Kozminski W, Zhukov I. J. Biomol. NMR. 2003;26:157–66.
31. Bodenhausen G, Ernst RR. J. Magn. Reson. 1981;45:367–73.
32. Bodenhausen G, Ernst RR. J. Am. Chem. Soc. 1982;104:1304–9.
33. Tolman JR, Al-Hashimi HM, Kay LE, Prestegard JH. J. Am. Chem. Soc. 2001;123;1416–24.
34. Braddock DT, Cai ML, Baber JL, Huang Y, Clore GM. J. Am. Chem. Soc. 2001;123:8634–5.

Using Chemical Shift Perturbations to Validate and Refine the Docking of Novel IgE Antagonists to the High-Affinity IgE Receptor

Melissa A. Starovasnik and Wayne J. Fairbrother
Department of Protein Engineering, Genentech Inc., South San Francisco, CA 94080, USA

The binding of IgE to its high-affinity receptor, FcεRI, is fundamental to allergic disease. Molecules that block this interaction could therefore act as useful therapeutics for the treatment of asthma, allergic rhinitis, and other forms of atopy. To this end, binding selections using the extracellular portion of the α-chain of FcεRI (FcεRIα) and polyvalent peptide-phage libraries have yielded two distinct classes of peptide ligands that antagonize IgE binding to its receptor and prevent downstream IgE-mediated signaling events in basophils [1,2]. NMR spectroscopy has been used to characterize the structures of these peptide antagonists and their modes of binding to FcεRIα.

Structure determination of the ~32-kDa peptide/receptor complexes by NMR methods was not feasible for these systems because the heavily glycosylated receptor protein could not be bacterially expressed and thus could not be isotopically labeled (at least not readily). The high carbohydrate content of the receptor also makes these systems challenging for structure determination using X-ray crystallography. As described below, however, large ^{1}H chemical shift perturbations observed for the isotopically labeled peptide ligands upon binding to the receptor protein in solution could be used qualitatively to validate hypothesis-driven models of ligand binding, and quantitatively to refine these models. The resulting structural models will be useful in the development of novel IgE antagonists.

Hairpin Peptide Structure

The first family of peptides identified by phage display have the general form $X_4CX_2GPX_4CX_4$ and bind FcεRIα with affinities in the 1–10 μM range [1]. Analysis of one of these peptides, IGE06, by NMR spectroscopy revealed that the peptide has a well-defined three-dimensional (3D) structure in solution comprising two β-strands (residues 5–8 and 11–14) connected by a type I β-turn centered at residues Pro9 and Trp10 (Figure 1A). The three N-terminal residues are not as well defined by the NMR data and appear to be more flexible in solution than residues Cys5-Cys14. Residues required for structure and/or function were identified by analysis of peptide variants using both NMR and activity measurements. Importantly, NMR analysis of peptides having alanine substitutions for Gly8, Pro9, and Trp10 indicate that these substitutions do not disrupt the hairpin structure even though they have a significant impact on FcεRIα-binding affinity (Figure 1A).

Zeta Peptide Structure

Using an expanded set of peptide-phage libraries, a second family of peptides with a simpler motif, X_2CPX_2CYX, was identified [2]. When synthetic peptides were assayed for inhibition of IgE binding to cell-surface FcεRI, however, IC_{50} values of 250 μM or greater were obtained. Surprisingly, this activity improved over time and stabilized at 64 μM when assayed similarly 10 days after solubilization. One-dimensional (1D) and two-dimensional (2D) NMR analysis of a freshly prepared nine-residue monomeric disulfide-bonded peptide demonstrated at least four conformationally distinct forms, with the major form showing no evidence of stable structure (Figure 2). Analysis of 1D NMR spectra over time showed changes in the relative populations of the different forms (Figure 2), and after 7 days at room temperature ~90% of the peptide had converted to a single new form that also showed significantly longer retention time than the original sample in an analytical HPLC run. This form had a stable structure in solution as evidenced by significant chemical shift dispersion relative to "random coil," and extreme values for backbone and side chain ^3J coupling constants. Mass spectra of the new peptide form showed it to be a covalent disulfide-linked dimer. Comparison of analytical HPLC chromatograms and NMR spectra of synthetic parallel or antiparallel dimeric peptides confirmed that the active state of the phage-derived peptide was an antiparallel dimer with two intermolecular disulfide bonds. Subsequent linking of the monomeric peptides with a three-residue linker sequence to make a 21-residue "single-chain dimer" species, and further optimization on phage, resulted in a 32 nM-affinity peptide antagonist (e131).

Graham A. Webb (ed.), Modern Magnetic Resonance, 1293–1298.
© 2008 *Springer.*

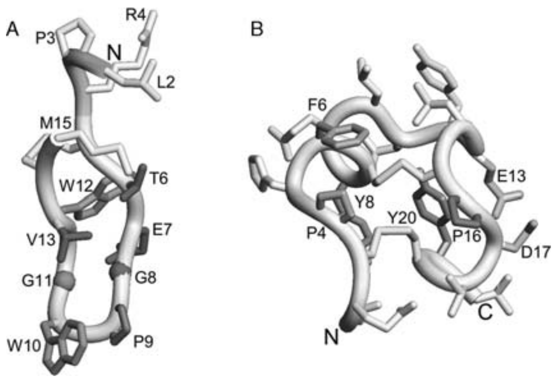

Fig. 1. Solution structures of representative (A) hairpin and (B) zeta peptides. Shown are ribbon diagrams of the first structure from the ensembles in PDB files 1JBF (hairpin) [1] and 1KCO (zeta) [2]. Side chains are colored to indicate those residues that are important for maintaining the structure of the peptide (green; disulfide bonds in yellow), and those that are important for receptor binding, but are not important for maintaining a stable structure of the peptide (from most important to least, red > orange > blue). The backbone of residues 2–4 of the hairpin peptide is colored to indicate that truncation of this region results in significant loss in receptor-binding affinity. (See also Plate 98 on page XIX in the Color Plate Section.)

NMR structural analysis of e131 showed that the peptide adopts a stable structure comprised of two small antiparallel 3_{10} helices connected by two disulfide bonds and a flexible linker region (Figure 1B). The helical backbone conformation is stabilized by packing of two Tyr side chains (Tyr8 and Tyr20) "below" the disulfide bonds, with each Tyr hydroxyl donating a hydrogen bond across the "dimer interface" to the carbonyl oxygen of a Cys residue. The backbone structure is pseudo-symmetric with residues 1–9 adopting essentially the same conformation as residues 13–21. Peptides of this class were designated "zeta" peptides due to a resemblance between the structurally conserved regions and the Greek letter zeta (ζ). As with the hairpin class of peptides, residues in the zeta peptide required for structure and/or function were identified from analysis of peptide analogs both by NMR and activity measurements. Again, the most important residue for high-affinity receptor binding was found to be a proline (Pro16) (Figure 1B).

Receptor Binding

Despite their significantly different structures, the two-peptide classes were shown to compete for binding at the same site on the receptor. Alanine-scanning mutagenesis of FcεRIα demonstrated further that the peptides bind to a region of the receptor that had been shown previously to contact IgE. This aromatic-rich IgE interaction site is centered around two tryptophan residues on the receptor (Trp87 and Trp110), between which Pro426 of bound IgE is buried [3]. In order to characterize further the receptor-binding modes of the different peptide classes, ^{13}C/^{15}N-labeled peptides were obtained by expression of protein A Z-domain fusion proteins [4] in *Escherichia coli* using a previously described alkaline phosphatase induction system [5], followed by cleavage (using trypsin or CNBr for the zeta or hairpin peptide, respectively) and purification of the peptides [6]. Isotopic labeling of FcεRIα was not practical because the heavily glycosylated extracellular domain (average molecular mass ~30 kDa) could be produced only via baculoviral infection of insect cells [6].

NMR Analysis of Zeta Peptide/Receptor Complex

The 23-residue zeta peptide selected for NMR structural studies (e117) was shown previously to bind FcεRI and block IgE binding with an IC_{50} of 80 nM [2]. The resonances of the free zeta peptide were assigned readily by standard analysis of 2D ^{1}H/^{15}N-HSQC, 3D ^{1}H/^{15}N-TOCSY-HSQC, 2D ^{1}H/^{13}C-HSQC, 2D CBCA(CO)NH, and 2D ^{1}H/^{13}C-HCCH-TOCSY spectra [7]. Resonance assignments of the receptor-bound zeta peptide were complicated, however, by the overall reduced sensitivity of J-correlated spectra for the ~32 kDa complex, and by large variations in line widths, with those residues at the peptide termini and in the GGH "linker" being sharper and more intense than those from the rest of the peptide. Nevertheless, unambiguous assignments were obtained for a majority of the zeta peptide resonances based on analysis of 3D ^{15}N-edited and ^{13}C-edited NOESY spectra.

Comparison of the resonance assignments of the free and receptor-bound peptide showed that many of the peaks from residues within the "disulfide-bonded core" of the peptide experienced significant chemical shift perturbations; the most dramatic chemical shift changes upon receptor binding were seen for the ^{1}H resonances of Pro16 (Hα, Hβ, Hγ, and Hδ all shifted upfield by 1.7–3.1 ppm; Figure 3A). Shifts of this magnitude observed for all proton resonances within the proline side chain can be explained if the proline is packed between aromatic rings in the protein/peptide complex, in much the same way as Pro426 of IgE is found "sandwiched" between two tryptophan residues in the crystal structure of the Fc fragment of IgE in complex with FcεRIα [3]. By contrast, the sharper peaks from the bound state of the zeta peptide underwent only minimal changes in chemical shift relative to the free state (Figure 3A), consistent with this group of residues being of minimal importance for receptor binding [2].

In addition to the chemical shift perturbations indicating that the zeta peptide binds proximal to aromatic residues on the receptor, ^{13}C-edited/^{12}C-filtered NOESY

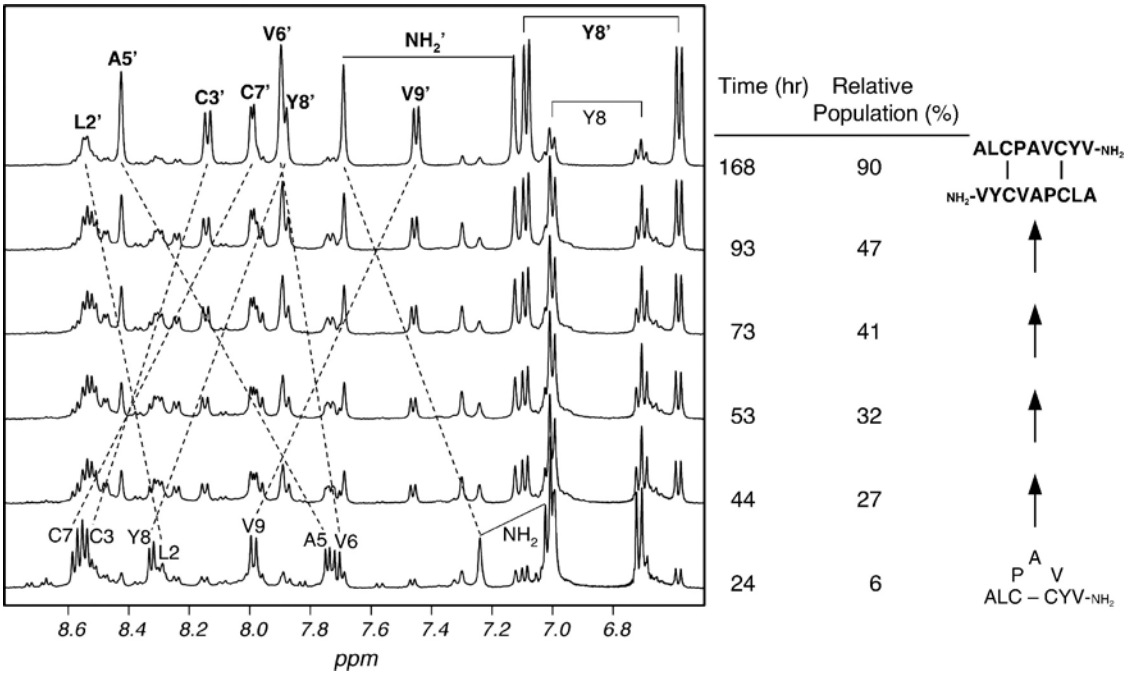

Fig. 2. Spontaneous rearrangement of a monomeric 9-mer peptide into a covalent disulfide-linked dimer monitored by 1D NMR spectroscopy. Amide and aromatic region of a series of 1D ^{1}H NMR spectra acquired at 500 MHz, 25 °C, on a sample of peptide e101 (ALCPAVCYV-NH$_2$), originally synthesized and purified as a monomeric peptide with an intramolecular disulfide bond. Lyophilized peptide was resuspended in water and spectra were acquired intermittently over the course of a week, with the time after resuspension indicated. The population of well-folded dimeric peptide present over time is estimated based on the relative intensities of the two most upfield peaks shown, corresponding to the Tyr8 ^{1}H$^\varepsilon$ resonance in the ordered dimeric state and in the monomeric or intermediate states. Note that if the peptide existed in a single conformation in solution, that no more than 11 peaks would be expected in this region of the spectrum.

spectra [8] showed NOE correlations between at least two distinct aromatic groups on the receptor and peptide residues Val1, Leu14, and Val18. Peptide residues Val1, Gln2, and Pro4 also had NOE correlations with a pair of peaks resonating at 0.75 and 0.73 ppm that were assigned tentatively to a pair of methyl groups on the receptor based on resonance intensity and frequency. No NOE correlations were observed from Pro16 of the peptide, despite the large chemical shift changes observed for this residue, due to the increased line widths in the receptor-bound state. The resonance broadening is most likely due to the large chemical shift gradient in which the proline is located; even small changes in the orientation of Pro16 with respect to the aromatic residues on the surface of the receptor would cause chemical shift changes resulting in the observed resonance broadening.

Receptor contacts involving aromatic and methyl-containing side chains are consistent with the zeta peptide binding to the IgE-binding site as identified by receptor mutagenesis. The peptide was therefore docked manually into the IgE-binding site of FcεRIα using coordinates of the free peptide and the previously published crystal structure of the IgE/FcεRIα complex [3]. The initial peptide placement was based on the assumption that the functionally important proline residue, Pro16, which experienced the most significant ^{1}H chemical shift perturbations upon receptor binding (Figure 3A), would bind between Trp87 and Trp110 of the receptor, in approximately the same way as observed for Pro426 of IgE. The resulting peptide orientation appeared consistent with the observed intermolecular NOE correlations; in particular, intermolecular NOE correlations between zeta peptide residues Val1, Gln2, and Pro4 and the unidentified pair of receptor methyl groups could be assigned tentatively to Leu158 of the receptor because these are the only methyl groups in this region of the receptor.

The aliphatic ^{1}H chemical shifts of the manually docked peptide were calculated using the program SHIFTS 4.1 (X. Xu and D.A. Case, The Scripps Research Institute, La Jolla, CA; http://www.scripps.edu/case/

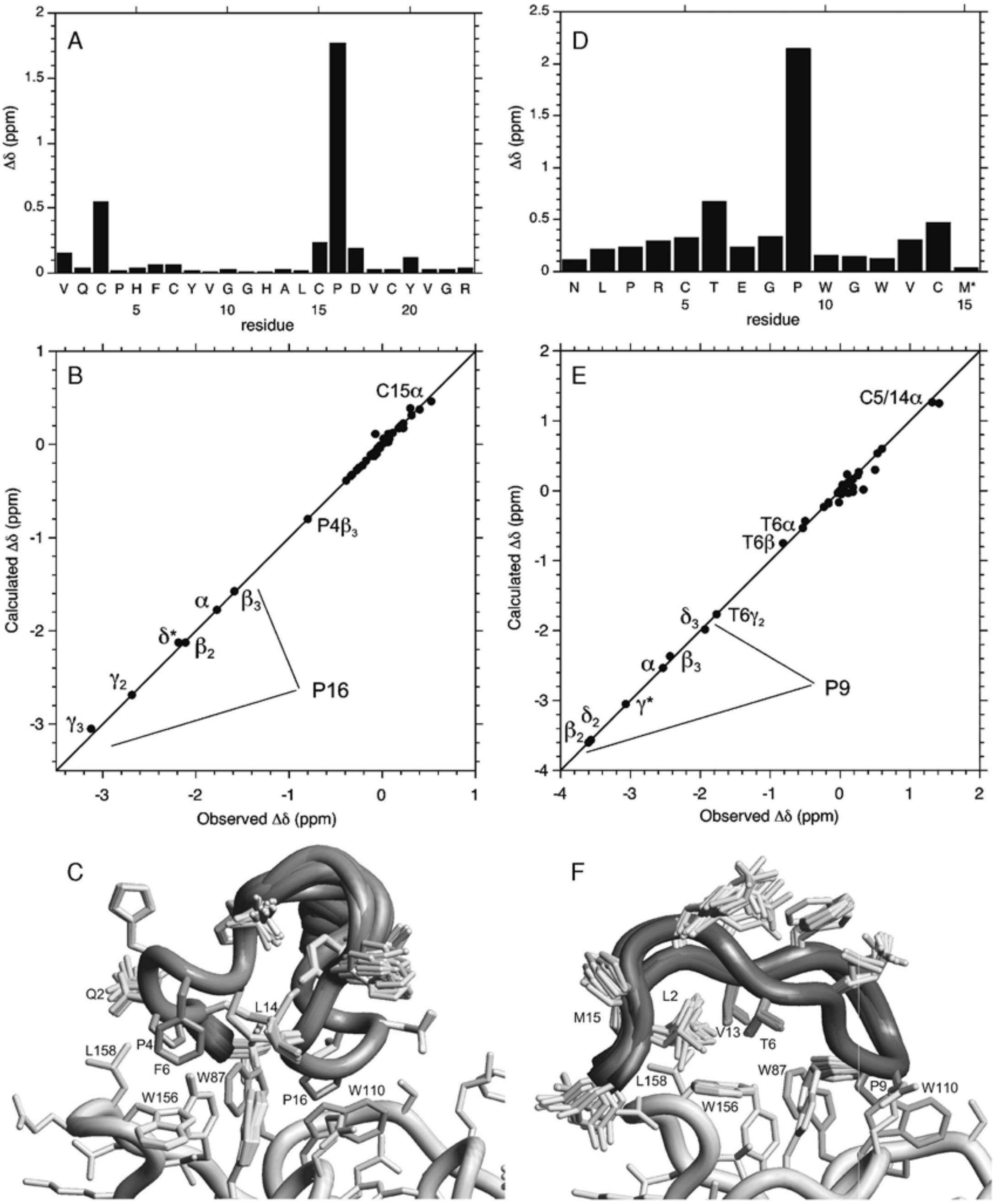

Fig. 3. (A) Plot of the net change in zeta peptide ^{1}H$^\alpha$ chemical shifts upon binding FcεRIα ($\Delta\delta = [\Delta\delta^2_{^1\mathrm{H}^\alpha}]^{1/2}$). (B) Correlation between observed and calculated chemical shifts ($\Delta\delta = \delta_{\mathrm{total}} - \delta_{\mathrm{random\ coil}}$) following refinement of the zeta peptide/FcεRIα complex structure using AMBER 6.0 (rms error = 0.038 ppm, $R^2 = 0.9978$). (C) Superposition of 20 models of the zeta peptide/FcεRIα complex structure obtained by docking and refinement against the ^{1}H chemical shifts of the peptide (average rms error = 0.041 ± 0.005 ppm). (D) Plot of the net change in hairpin peptide ^{1}H$^\alpha$ chemical shifts upon binding FcεRIα. (E) Correlation between observed and calculated chemical shifts following refinement of the hairpin peptide/FcεRIα complex structure using AMBER 6.0 (rms error = 0.090 ppm, $R^2 = 0.9954$). (F) Superposition of 20 models of the hairpin peptide/FcεRIα complex structure obtained by docking and refinement against the ^{1}H chemical shifts of the peptide (average rms error = 0.12 ± 0.02 ppm). (See also Plate 99 on page XX in the Color Plate Section.)

qshifts/qshifts.htm), in which the "structural" effects on chemical shifts due to contributions of ring currents of aromatic groups [9,10], magnetic anisotropy from peptide groups [11], and electrostatic effects arising from charges and dipoles [12], are calculated using empirical functions [13–15]. The total chemical shift of a given resonance is defined as the sum of the "random coil" value, as observed in short disordered linear peptides [16,17], and the conformation-dependent contributions ($\Delta\delta$). The conformation-dependent contribution to the total chemical shift, as calculated by SHIFTS 4.1, is thus defined as:

$$\Delta\delta = \delta_{\text{total}} - \delta_{\text{random coil}} \approx \sum \delta_{\text{rc}} + \sum \delta_{\text{m}} + \sum \delta_{\text{el}} + \delta_{\text{const}} \qquad (1)$$

where rc, m, and el, refer to ring current, magnetic anisotropy, and electrostatic contributions, respectively. The δ_{const} term is an empirical "fitting" parameter that includes contributions from δ_{m} and δ_{el} that are present in the random coil state [14]. Good general agreement was found between the calculated and experimentally observed chemical shifts, although differences suggested that the manually docked model could be refined further.

The docked model was therefore refined by optimizing the agreement between the calculated and observed ^{1}H chemical shifts of the receptor-bound peptide using functionally equivalent code within the molecular modeling package AMBER 6.0 (http://amber.scripps.edu/doc6/). All the unambiguously assigned aliphatic ^{1}H chemical shifts were incorporated as restraints (force constant = 25 kcal/·mol/·ppm) in a simple simulated annealing protocol. For initial rounds of refinement the chemical shifts of prochiral methylene and methyl protons were averaged. The chemical shifts of all peptide protons were subsequently back-calculated using SHIFTS 4.1 and compared to the experimentally determined chemical shifts. In some cases the chemical shifts of prochiral proton pairs were sufficiently different, and the agreement between the calculated and experimentally observed values was sufficiently close, to allow for stereospecific assignments that could be incorporated into subsequent rounds of refinement. In this way stereospecific assignments were possible for Pro4 ^{1}H$^\beta$, Leu14 ^{1}H$^\beta$, and Pro16 ^{1}H$^\beta$ and ^{1}H$^\gamma$.

In addition to the chemical shift restraints, distance and dihedral angle restraints derived from those used to calculate the solution structure of the free peptide were incorporated into the refinement to ensure that the peptide structure was maintained. The coordinates of the receptor were restrained to be nearly fixed during the simulated annealing and subsequent restrained minimization calculations using a harmonic potential with a force constant of 5 kcal/·mol. A weak harmonic potential (force constant = 0.5 kcal/·mol) was also used to restrain the disulfide-bonded core (residues Cys3-Tyr8 and Ala13-Tyr20) of the zeta peptide. Finally, tentatively assigned intermolecular NOE distance restraints were incorporated iteratively into the refinement calculations as upper-bound distance restraints of 5.8 Å, only if they were clearly satisfied in the current models; in total, 17 intermolecular distance restraints were included in the final simulated annealing calculation. Importantly, the intermolecular distance restraints were not required for convergence of the refined models. Indeed, trial calculations in which the starting zeta peptide and receptor molecules were separated by ~20 Å still converged to essentially the same peptide/receptor orientation as those starting from manually docked models, even in the absence of intermolecular distance restraints (W.J. Fairbrother, unpublished results).

The resultant agreement between the calculated and experimentally observed ^{1}H chemical shifts was excellent (Figure 3B), suggesting that the refined model of the zeta peptide/receptor complex (Figure 3C) represents a good approximation of the structure. In this model Pro16 packs between Trp87 and Trp110 on the receptor, and the N-terminal region of the peptide makes additional hydrophobic contacts near Leu158. A subsequent 3 Å-resolution X-ray crystal structure of the complex between a closely related zeta peptide (e131) and FcεRIα was in very close agreement with the NMR-based model [6], confirming the validity of the approach.

NMR Analysis of Hairpin Peptide/Receptor Complex

Resonances of the free 15-residue hairpin peptide, IGE32, were assigned by analysis of 2D ^{1}H/^{13}C-HSQC, 2D CBCA(CO)NH, and 2D ^{1}H/^{13}C-HCCH-TOCSY spectra [7]. Assignments of the receptor-bound state were obtained by analysis of 2D ^{1}H/^{13}C-HSQC and 3D ^{13}C-edited NOESY spectra. However, as observed for Pro16 of the zeta peptide, the resonances of the functionally important Pro9 were broad and did not show observable cross peaks in the ^{13}C-edited NOESY spectrum; assignment of these resonances was thus confirmed by analysis of a 2D ^{1}H/^{13}C-HSQC spectrum of a sample prepared with ^{13}C-Pro9 specifically labeled hairpin peptide generated by chemical synthesis.

Similar dramatic chemical shift changes to those found for the zeta peptide were observed when the hairpin peptide was added to FcεRIα (Figure 3D). In particular the ^{1}H resonances of residues Thr6 and Pro9 were shifted upfield by 1.7–3.2 ppm upon binding the receptor. As for the zeta peptide, these large chemical shift changes imply that the hairpin peptide packs closely with aromatic rings in the complex. In this case, a total of 40 intermolecular NOE correlations involving peptide residues Asn1, Leu2, Pro3, Thr6, Val13, and Met15, were identified. These included NOE correlations between peptide residues Val13 and Met15 and a pair of methyl groups on the receptor; as with the zeta peptide complex, the receptor methyl resonances could be assigned tentatively to Leu158. This assignment allowed for manual docking of the hairpin peptide so that the C-terminal residues were proximal to Leu158 on the receptor while, at the same time, Pro9 packs between Trp87 and Trp10 in the IgE-binding site. The resulting docked model was refined in a similar fashion to the refinement of the zeta peptide complex, as outlined above. In the case of the hairpin peptide calculations, however, the weak harmonic potential (force constant = 0.25 kcal/·mol) used to restrain the peptide structure was applied only during the initial iterations, and was never applied to peptide residues Asn1, Leu2, Thr6, Trp10, or Trp12. Conformational freedom of these residues was found to be necessary in order to satisfy the ^{1}H chemical shift restraints; in particular the side chain conformation of Trp10 changed significantly during the refinement. Stereospecific ^{1}H resonance assignments were possible for Pro9 $^1H^\beta$ and $^1H^\delta$, and Val13 $^1H^\gamma$, and using the same criteria as for the zeta peptide complex a total of 22 intermolecular distance restraints could be included in the final simulated annealing calculations.

The final correspondence between the calculated and observed ^{1}H chemical shifts was again excellent (Figure 3E) indicating that the resulting model (Figure 3F) is a good approximation of the structure of the hairpin peptide/receptor complex. As was found for the zeta peptide complex, and consistent with original assumptions, the functionally important Pro9 is sandwiched between Trp87 and Trp110 on the receptor. Thr6 is proximal to Trp156 on the receptor, which accounts predominantly for the upfield shifts observed for resonances of this residue.

Comparison of the zeta and hairpin peptide/FcεRIα complex models reveals that even though the phage-derived peptides are structurally distinct they make remarkably similar contacts with the receptor. For instance, in addition to the zeta peptide Pro16 and the hairpin peptide Pro9 being "sandwiched" between Trp87 and Trp110 of the receptor, Pro4 and Phe6 of the zeta peptide occupy essentially the same space on the receptor as Val13 and Thr6, respectively, of the hairpin peptide (Figure 3C and F). Interestingly, the latter interactions are not utilized by the natural ligand, IgE, and thus, together with the proline pocket defined by Trp87 and Trp110, represent a novel binding epitope for IgE antagonists.

Conclusion

In the examples presented above the readily obtained ^{1}H chemical shifts of peptide ligands were used to validate docked models of the peptide/receptor complexes that were based originally on assumption and limited experimental data, such as mutational analysis. More extensive data, such as receptor chemical shift assignments, and consequently assigned intermolecular NOE correlations, were not available. The ^{1}H chemical shifts of the bound peptides, and in particular the large upfield shifts of ^{1}H resonances observed for some of the peptide residues, could be accounted for quantitatively by directly refining the models against the observed chemical shifts.

Some caveats of the approach are worth mentioning. First, this is not a *de novo* docking method, but rather a docking validation method, and thus requires some degree of independent data in order to localize the binding site. Starting models could come from *de novo* docking algorithms, or could be based on experimental data such as obtained from mutational analysis, as used here. Secondly, reasonably accurate structural models of the ligand and receptor are necessary and conformational changes upon binding should be minimal (although as noted in the hairpin peptide example some degree of conformational flexibility can be accommodated and might be necessary in order to obtain a good fit). Finally, the most sensitive restraints of ligand orientation are the ring current contributions of aromatic groups. Thus, the presence of aromatic groups that cause significant perturbations in the ligand chemical shifts is likely a prerequisite for successful application of this approach.

References

1. Nakamura GR, Starovasnik MA, Reynolds ME, Lowman HB. Biochemistry. 2001;40:9828.
2. Nakamura GR, Reynolds ME, Chen YM, Starovasnik MA, Lowman HB. Proc. Natl. Acad. Sci. U.S.A. 2002;99:1303.
3. Garman SC, Wurzburg BA, Tarchevskaya SS, Kinet JP, Jardetzky TS. Nature. 2000;406:259.
4. Dennis MS, Roberge M, Quan C, Lazarus RA. Biochemistry. 2001;40:9513.
5. Reilly D, Fairbrother WJ. J. Biomol. NMR. 1994;4:459.
6. Stamos J, Eigenbrot C, Nakamura GR, Reynolds ME, Yin J, Lowman HB, Fairbrother WJ, Starovasnik MA. Structure. 2004;12:1289.
7. Cavanagh J, Fairbrother WJ, Palmer AG III, Skelton NJ. Protein NMR Spectroscopy: Principles and Practice. Academic Press: San Diego, 1995.
8. Zwahlen C, Sébastien PL, Vincent JF, Greenblatt J, Konrat R, Kay LE. J. Am. Chem. Soc. 1997;119:6711.
9. Johnson CE, Bovey FA. J. Chem. Phys. 1958;29:1012.
10. Haigh CW, Mallion RB. Prog. NMR Spectrosc. 1980;13:303.
11. McConnell HM. J. Chem. Phys. 1957;27:226.
12. Buckingham AD. Can. J. Chem. 1960;38:300.
13. Ösapay K, Case DA. J. Am. Chem. Soc. 1991;113:9436.
14. Ösapay K, Case DA. J. Biomol. NMR. 1994;4:215.
15. Dejaegere AP, Bryce RA, Case DA. In: JC Facelli, AC de Dios (Eds). Modeling NMR Chemical Shifts. American Chemical Society: Washington, 1999, p 194.
16. Bundi A, Wüthrich K. Biopolymers. 1979;18:285.
17. Merutka G, Dyson HJ, Wright PE. J. Biomol. NMR. 1995;5:14.

Dual-Region Hadamard-Encoding to Improve Resolution and Save Time

Ronald Crouch
Varian NMR Systems, NC 27513, USA

The advent of indirect detection has revolutionized the world of NMR spectroscopy in all areas of chemistry. For the purpose of assembling fragments of moieties as defined by NMR resonances into meaningful structural fragments or even complete structures, HMBC [1] is one of the most powerful tools available to the modern NMR spectroscopist. In situations of low sensitivity brought about most commonly by the availability of vanishingly small amounts of sample to analyze, direct observation of ^{13}C resonances can be difficult or impossible. Accordingly, the sensitivity afforded by indirect detection with HMBC and variants provides a tool that has the potential to access the key and difficult quaternary ^{13}C atoms while at the same time assembling the puzzle pieces into a coherent structure.

The strength of ^{1}H detection, thereby casting the ^{13}C chemical shift information into the indirect dimension, is also the weakness of HMBC. This is especially true in the more difficult situations where there are a large number of ^{13}C resonances spread out over a large chemical shift range. At a ^{1}H observe frequency of 500 MHz, 225 ppm of ^{13}C chemical shift represents nearly 28,000 Hz of frequency space. Resolving two ^{13}C resonances separated by10 Hz would require $\sim$2800 t1 increments (or $\sim$1000 t1 increments with high enough signal to noise to allow reliable linear prediction) in F1! Region selection in the ^{13}C dimension with HMBC is a very old idea [2–3]. Utilization of excitation sculpting [4–5] added considerable robustness to the method. Combination of excitation sculpting with a simple Hadamard-encoding step [6] provides a simple and reliable methodology to greatly reduce the number of t1 increments required for a needed resolution. This encoding methodology affords a mean to either record lower resolution HMBC information in less time or much higher resolved spectra in equivalent time relative to traditional sampling methods.

Consider the simplest two-element Hadamard matrix $+,+$ and $+,-$. Addition of the two elements leads to one enhanced signal to noise in one region, whereas subtraction results in cancelation of the first region and enhanced signal to noise in the second region. Bear in mind that with modern NMR spectrometers, given an actual ^{13}C spectrum from which to build the needed shaped ^{13}C pulses, a Hadamard matrix can automatically be created to record and construct a complete 2D HMBC spectrum in *n* increments, where *n* represents the number of ^{13}C resonances [7–10]. A major advantage of using a simple two-element matrix is that the regions can be quite wide and general and not require a precise understanding of carbon chemical shifts. It is quite reasonable to simply divide the carbon regions by half, and immediately obtain a time saving of a factor of two, because by employing Hadamard-encoding, the number of t1 increments is cut in half to maintain exactly the same digital resolution as in a full single-region HMBC. The magic is in the encoding pulses and it is quite practical to create whatever is needed on the fly to obtain the two required pulses for a simple two-element matrix. Alternatively, a pair of pulses appropriate for a routine experiment with any desired frequency bounds can be created, and the pulse width and power parameters remembered for future use. A pulse sequence optimized for long-range ^{1}H–X correlation spectroscopy with an option for single or multiple X-band selection is presented in Figure 1 [11].

As an introduction to the illustration of the method, consider the gHMBC spectrum acquired with a sample of cyclosporine-A shown in Figure 2. The F1 window required to observe all ^{13}C resonances is not particularly large. A ^{13}C chemical shift range from 0 to 190 ppm is more than enough. Inspection of the data in Figure 2 reveals that is quite practical to consider splitting the F1 window into two $\sim$80 ppm regions; 0–80 and 105–185 ppm. Simply acquiring a simultaneous dual F1 region-selected long-range ^{1}H/^{13}C chemical shift correlation experiment with the pulse sequence shown in Figure 1, immediately affords a time saving of a factor of two over the full single-region data set, simply because the number of t1 increments for equivalent digital resolution in the ^{13}C dimension can be cut in half.

A direct comparison of a single-region gHMBC and the simultaneous dual F1 region-selected gHMBC variant is presented in Figure 3, panels A–D. The two data sets

Graham A. Webb (ed.), Modern Magnetic Resonance, 1299–1304.
© 2008 *Springer.*

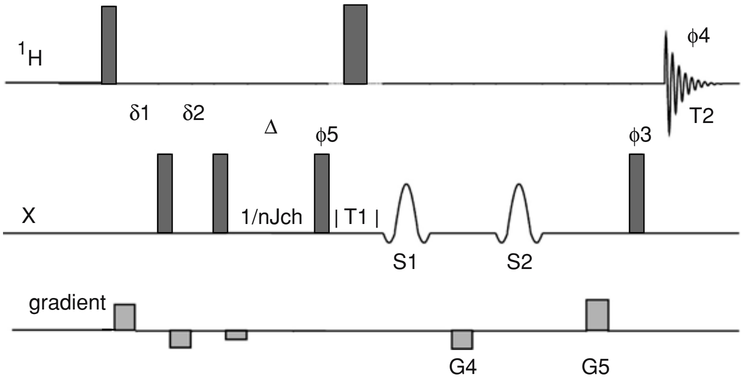

Fig. 1. Gradient coherence-selected pulse sequence for HMBC with adiabatic swept refocusing. Narrow bars denote 90° pulses. The wide bar and two selective pulses (S1 and S2) are 180° pulses with the t1 evolution time split by the ^{1}H 180. All of the data presented in this note were acquired with a constant adiabaticity cosine^2 (WURST2i) 180° pulse [12–13]. Gradients G4 and G5 are for coherence selection and can be in ratios of −3/5 or 5/−3 for N or P type selection of $^{13}CH_n$ resonances. The $\delta 1$ and $\delta 2$ delays in the low pass filter are optimized for $^1J_{\max}$ of 165 Hz and $^1J_{\min}$ of 130 Hz, as described by Sorensen and co-workers [14]. The delay for long-range XH coherence selection (Δ) can be set as desired. The gradients in the low pass filter are in the ratios of 9, −6, and −3. The basic phase cycling is as follows: $\phi 3 = x, x, -x, -x$; $\phi 5 = x, -x$; $\phi 4 = x, -x, -x, x$. Pulses S1 and S1 are adiabatic shaped pulses with downfield to upfield inversion sweep.

were obtained in precisely the same time with 128 t1 increments in each. The dual-region data (panels B and D) were acquired with two scans per t1 increment (with the two required band-selected shapes) and the single-region data (panels A and C) used four scans. Clearly the digital resolution and overall quality of data are improved for the dual-region Hadamard-encoded data presented in Figure 3, panels B and D.

A simple single-region band-selected experiment can be performed with the pulse sequence shown in Figure 1 to obtain extremely high digital resolution with efficient selection of the desired F1 region and rejection of other responses. Figure 4 shows a very high ^{13}C resolution long-range ^{1}H–^{13}C correlation experiment wherein the correlations between the protons and only the carbonyl ^{13}C resonances have been selected. The time to acquire the data was once again ~20 min. Comparison with the data in Figure 2 (or Figure 3, panel C) reveals the much higher digital resolution afforded by confining the F1 sampling solely to the carbonyl region of the ^{13}C spectrum.

At this point, it is useful to address the details of the experiment in terms of the requirements imposed by the band-selected pulses. A good means for illustration would be to graphically compare the pulses required for the acquisition of the single-region data presented in Figure 4, with those required to acquire the simultaneous dual-region data presented in the Figure 3 panels. This comparison is shown in Figure 5. Application of a very narrow band ^{13}C inversion pulse pair, as illustrated in Figure 5A, affords the possibility of quite high ^{13}C digital resolution with relatively few t1 increments precisely because only the portion of the ^{13}C frequency space refocused by the narrow band pulse is detected.

For simultaneous dual-region selection, it is necessary to interleave data acquisition using the two pulses graphically presented in Figure 5B and C. After data acquisition, 2DFT sum of the two interleaved data sets would result in full signal to noise for the upfield region of the ^{13}C frequency space, whereas 2DFT difference would give full signal to noise for the downfield ^{13}C frequency space. It is important to understand that the upfield and downfield regions are the result of two separate data processing steps that are graphically represented in Figure 5D and E.

The method presented here is both robust and simple to implement. It is the author's feeling that the full Hadamard-encoded techniques outlined in Refs. [7–10] may well represent the beginnings of a major revolution in the general approach to multi-dimensional NMR spectroscopy typically used in support of the elucidation of chemical structure in the pharmaceutical industry. It is hoped that the presentation of this simple two-step procedure serves to illustrate the general concepts.

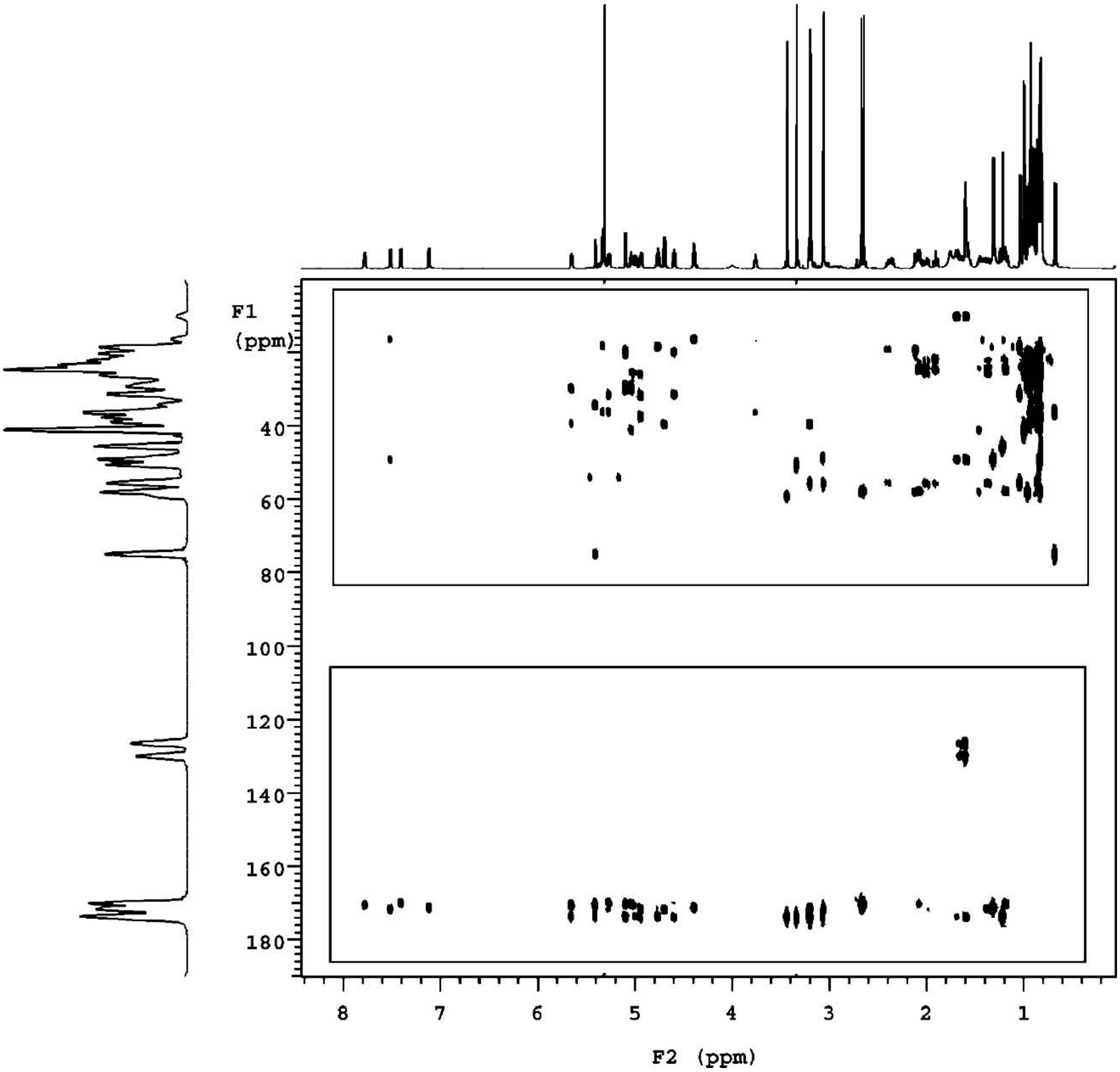

Fig. 2. Plot of the full single-region gHMBC acquired with a 2 mg sample of cyclosporine-A using an INOVA 600 with HCN Cold Probe. Data were acquired with four scans in each of 128 t1 increments in 22 min. A normal ^{1}H spectrum is on top and a projection showing the detected ^{13}C resonances is shown on the side. The boxed areas denote the regions to be selected in subsequent dual Hadamard-encoded experiments.

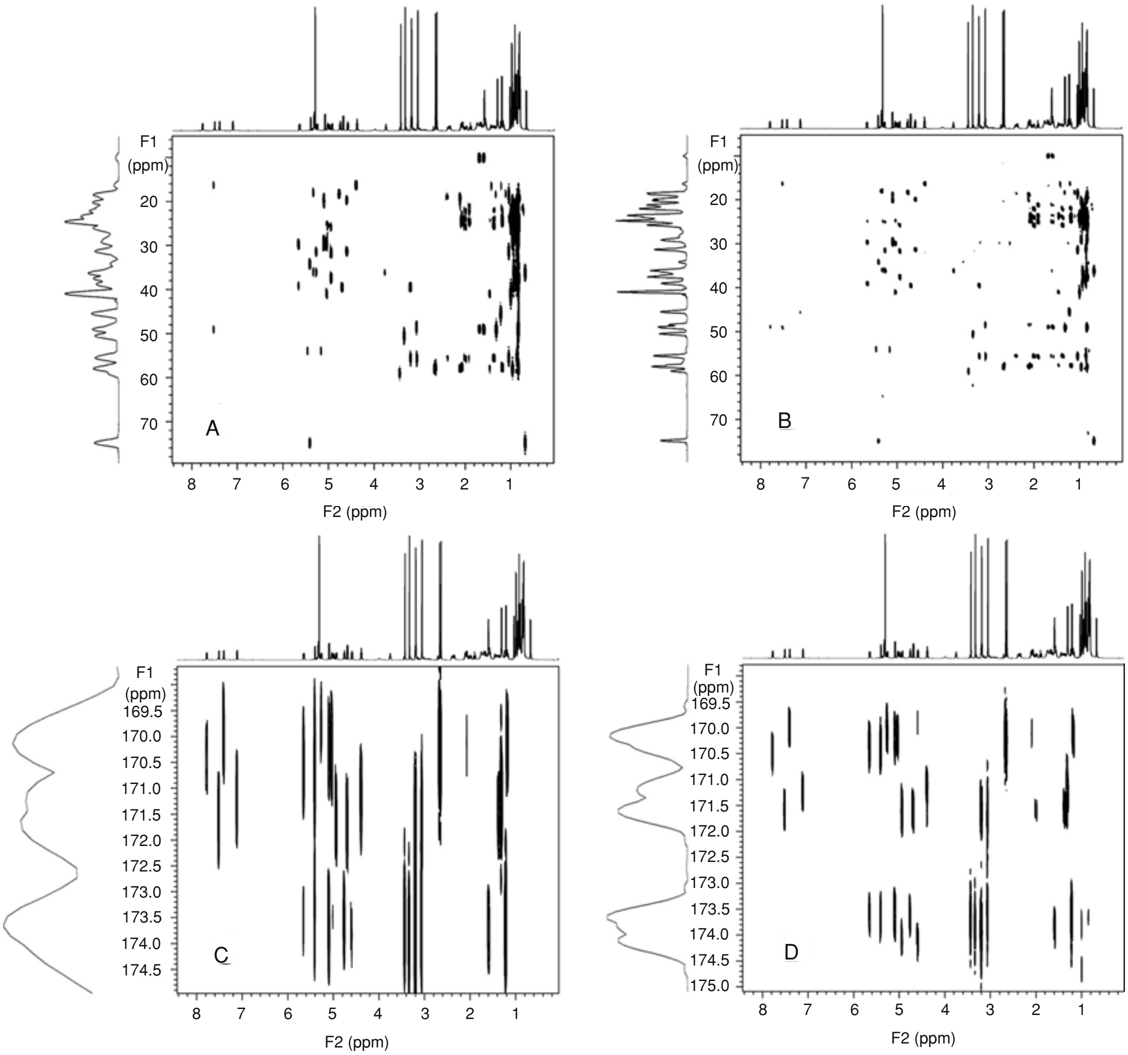

Fig. 3. Panels A–D compare regions from both traditional gHMBC and simultaneous dual-region Hadamard-encoding using the pulse sequence described in Figure 1. Panels A and C are simply expansions from the normal gHMBC depicted in Figure 2, whereas panels B and D are the result of 2DFT sum or difference of Hadamard-encoded data acquired in a single experiment in exactly the same experimental time as the gHMBC data shown in panels A and C. The data in panels A and C (gHMBC) were acquired with four scans/t1 increment. The Hadamard-encoded data in panels B and D were acquired with two scans per increment for both of the region-selected encoding ^{13}C pulses.

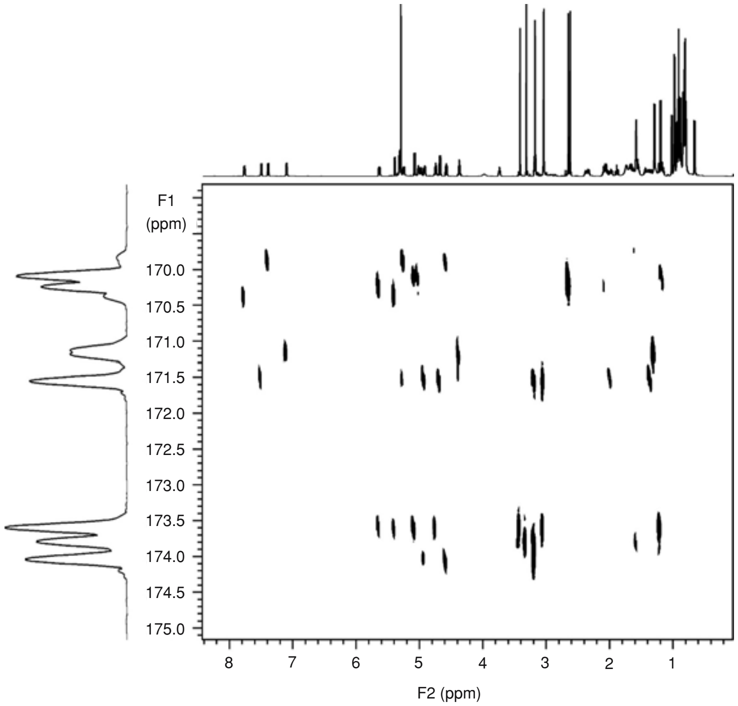

Fig. 4. Single C=O region-selected data acquired with the 2 mg sample of cyclosporine-A in 20 min. Data were acquired with two scans for each of the 256 t1 increments. The data were acquired and processed as a single phase with sine-bell window functions.

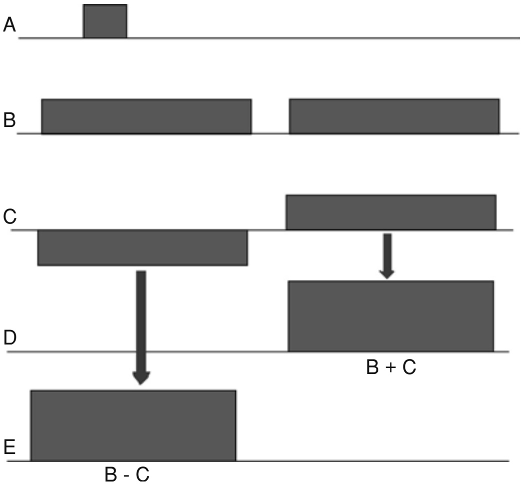

Fig. 5. Graphical representation of band-selection pulses required to acquire data in a two-step Hadamard matrix to generate the results shown in Figure 3. (A) For the single-region band-selection of carbonyl ^{13}C resonances described in Figure 4 only a very narrow refocusing of the ^{13}C carbonyl resonances is required. Figure 5B and C illustrate the pair of band-selected inversion pulses required for Hadamard-encoding. The anti-echo refocusing shown in the inverted portion of Figure 5C is achieved by application of a 90° phase shift for the band-selection of that π pulse portion of the ^{13}C frequency window. In Figure 5D and E the effect of processing the two encoded data sets, respectively, as sum and difference is illustrated. Figure 5D depicts 5B plus 5C, whereas Figure 5E depicts 5B minus 5C.

References

1. Bax A, Summers MF. J. Am. Chem. Soc. 1986;108:2093.
2. Crouch RC, Martin GE. J. Magn. Reson. 1991;92:189.
3. Crouch RC, Spitzer TD, Martin GE. Magn. Reson. Chem. 1992;30:595.
4. Stott K, Stonehouse J, Keeler J, Hwang T-L, Shaka AJ. J. Am. Chem. Soc. 1995;117:4199.
5. Gaillet G, Lequart C, Debeire P, Nuzillard J-M. J. Magn. Reson. 1999;139:454.
6. Krishnamurthy K. J. Magn. Reson. 2001;153:144.
7. Kupce E, Nishida T, Freeman R. Prog. NMR Spectrosc. 2003;42:95.
8. Kupce E, Freeman R. J. Magn. Reson. 2003;162:158.
9. Kupce E, Freeman R. J. Magn. Reson. 2003;163:56.
10. Kupce E, Freeman R. J. Magn. Reson. 2003;163:158.
11. Crouch RC, Boyer R, Johnson R, Krishnamurthy K. Magn. Reson. Chem. 2003;42:301.
12. Kupce E, Wagner G. J. Magn. Reson. 1995;109B:329.
13. Kupce E, Freeman R. J. Magn. Reson. 1996;118A:299.
14. Meissner A, Moskay D, Nielson NC, Sorensen OW. J. Magn. Reson. 1997;124:245.

Nonuniform Sampling in Biomolecular NMR

Mark W. Maciejewski[1], Alan S. Stern[2], Glenn F. King[1], and Jeffrey C. Hoch[1]
[1]Department of Molecular, Microbial and Structural Biology, University of Connecticut Health Center, CT, USA
[2]Rowland Institute at Harvard, Cambridge, MA, USA

Abstract

The twin challenges of biomolecular NMR spectroscopy are sensitivity and resolution. Nonuniform sampling, in which data collection is tailored to meet the requirements of sensitivity or resolution, enables new approaches to meet these challenges. We describe the use of nonuniform sampling in biomolecular NMR and the use of maximum entropy reconstruction to process the data. Data collected using nonuniform sampling cannot be processed using conventional methods such as the discrete Fourier transform or linear prediction, because these methods require data sampled at uniform intervals. A two- to three-fold reduction in acquisition time can routinely be realized for each indirect time dimension that employs nonuniform sampling, making this approach a valuable complement to cryogenic probes and high-field magnets for the most demanding biomolecular NMR applications. The approach is especially well suited for high-throughput applications of NMR spectroscopy in drug discovery.

The development of Fourier transform (FT) NMR spectroscopy by Ernst and Anderson [1] in the late 1960s set the stage for the subsequent development of multidimensional experiments [2–4]. By resolving individual nuclear coherences, these experiments enable systematic determination of the structure of biological macromolecules in solution. However, the need to avoid spectral aliasing when using the discrete FT (DFT) to compute frequency spectra from the time domain data imposes substantial data collection requirements; it is not unusual for each additional dimension to increase the amount of data that must be collected, and the time required to complete the experiment, by two orders of magnitude. The Nyquist theorem places a lower bound on the sampling rate, or time between samples (the dwell time), needed to avoid aliasing. This rate is inversely proportional to the width of the spectrum. Frequency resolution comparable to the natural line widths of the resonances is needed to exploit the dispersion of resonances at a given magnetic field, and high-resolution requires data collected at long acquisition times, in essence because the closer two resonances are in frequency, the longer it takes for a detectable difference in their signals to evolve. Since the DFT requires samples collected at uniformly spaced intervals, acquiring data at long acquisition times requires collecting samples at all of the intervening multiples of the dwell time. The data collection requirements increase with increasing magnetic field, because the increased dispersion of resonances necessitates shorter dwell times.

In the 1980s, linear prediction (LP) extrapolation of NMR data beyond the sampled interval was introduced [5,6], and it remains in common use today. LP extrapolation dramatically reduces the need for aggressive apodization when working with short data records, providing improvements in both sensitivity and resolution in favorable situations. However, LP has drawbacks; it has recently been shown that LP extrapolation generates false-positive peaks when applied to noisy data or when used to extrapolate too far beyond the measured interval [7]. A more subtle but insidious defect is that LP extrapolation can cause slight frequency shifts of real signals in these situations. These shifts are not apparent on casual inspection but have potentially serious consequences, such as improper resonance assignments. Furthermore, the extent to which NMR data can be extrapolated using LP depends mainly on the signal-to-noise (S/N) ratio, and consequently additional LP extrapolation is not a general solution to increased data requirements imposed by the increased spectral dispersion at higher magnetic fields.

Conventional approaches employing the DFT, including LP extrapolation, require acquisition times that can be prohibitively long, especially for biomolecules that are fleetingly stable or for data collected at very high magnetic field. Thus, there is considerable impetus for developing alternative methods that can produce high-resolution multidimensional spectra in less time. A wide variety of different approaches are actively being developed. One approach involves multiplexing, resulting in coherence frequencies that encode more than one resonance frequency in a single dimension. These include "reduced dimensionality" experiments such as G-matrix FT (GFT) [8,9] and Hadamard encoding [10]. A drawback of these approaches is that they require special radiofrequency pulse sequences as well as additional post-processing steps to disentangle the multiplexed

Graham A. Webb (ed.), Modern Magnetic Resonance, 1305–1311.
© 2008 Springer.

frequencies. A different approach to multiplexing has been developed by Frydman and colleagues [11], which utilizes orthogonal magnetic field gradients to partition the sample into "subsamples," each reporting a different part of the spin response. This approach is not practical when sensitivity is already a limiting factor for measuring the response of the entire sample, but as advances in probe technology continue to improve sensitivity and gradient strength (which determines the resolution), it will likely find increasing application in biomolecular NMR. Parametric methods that model the NMR signal as a sum of exponentially decaying sinusoids, such as LP singular value decomposition [12], Hankel SVD [13], filter diagonalization method (FDM) [14], maximum likelihood [15], and Bayesian [16] methods are in principle capable of producing high-resolution spectra from very short data records. These methods often exhibit "spontaneous splitting," resulting in multiple sinusoids for a single resonance when applied to noisy or nonideal (non-Lorentzian) data, complicating the parametric interpretation. Indeed the regularized resolvent transform [17], in which an FDM-like approach is used to extrapolate the signal, rather than compute a parametric decomposition, was developed to avoid this problem.

Another class of methods utilizes symmetries or redundancy in multidimensional spectra to avoid acquiring all combinations of the evolution times for the different dimensions. An approach inspired by the methods used in medicine to reconstruct images in computerized axial tomography exploits the relationship between line projections in the frequency domain and linear cross sections in the time domain. Called back-projection reconstruction [18], this approach can, in favorable circumstances recover a complete two-dimensional spectrum from a small number of cross sections through the full time domain data matrix. However, it has been pointed out that in the general case *n* cross sections are needed to unambiguously resolve *n* peaks in multiple dimensions [19], and for complex biomolecules, this may not result in significant time savings. Another approach, called three-way decomposition [20], exploits the fact that line shapes in multiple dimensional spectra can be decomposed into products of one-dimensional line shapes.

Back-projection reconstruction and three-way decomposition are special cases of nonuniform sampling in the time domain. In principle, any method that approaches spectrum reconstruction as an inverse problem, that is, computes spectra and inverts the spectrum to obtain "mock" data that are then compared with the empirical data for consistency, can be used with nonuniformly sampled time domain data. A very general method that makes no assumptions regarding the nature of the signals, and imposes no particular constraints on the subset of the time domain data matrix that must be collected, is maximum entropy (MaxEnt) reconstruction [21]. It has been shown recently to be particularly robust, yielding fewer false positives and more accurate frequencies than LP extrapolation [7]. It is also versatile: it can be used to construct spectra from the same data utilized by back-projection reconstruction, or can be used in combination with other methods, such as GFT (Jim Sun and Gerhard Wagner, personal communication). In principle, it can be used with any pulse sequence, and the computed spectra are compatible with conventional analysis tools developed for Fourier spectra. In this chapter, we describe the use of nonuniform sampling and MaxEnt reconstruction in multidimensional NMR experiments and its application to biomolecules. In practice, factors of two to three savings in data acquisition time per indirect time dimension are readily achieved. The robustness and versatility of MaxEnt reconstruction make it a powerful tool for improving sensitivity and resolution, and saving time in biomolecular NMR experiments.

MaxEnt Reconstruction

The MaxEnt reconstruction of the spectrum of a complex-valued time series **d** is the spectrum **f** which maximizes the entropy $S(\mathbf{f})$, subject to the constraint that the mock data **m**, given by the inverse DFT of the spectrum, is consistent with the time series **d**. Consistency is defined by the condition

$$C(\mathbf{f}, \mathbf{d}) \leq C_0 \tag{1}$$

where $C(\mathbf{f}, \mathbf{d})$ is the unweighted chi-squared statistic,

$$C(\mathbf{f}, \mathbf{d}) = \sum_{i=0}^{M-1} |m_i - d_i|^2 = \sum_{i=0}^{M-1} |\mathrm{IDFT}(\mathbf{f})_i - d_i|^2, \tag{2}$$

and C_0 is an estimate of the noise level; IDFT is the inverse DFT. A definition of the entropy $S(\mathbf{f})$ applicable to complex-valued spectra can be derived from consideration of the entropy of an ensemble of spin-1/2 particles [22] or by extending the Shannon information formula to the complex domain along with suitable differentiability conditions [23]. The two approaches yield equivalent formulations for the entropy of a complex spectrum

$$S(\mathbf{f}) = -\sum_{n=0}^{N-1} \frac{|f_n|}{def} \log\left(\frac{|f_n|/def + \sqrt{4 + |f_n|^2/def^2}}{2}\right) - \sqrt{4 + |f_n|^2/def^2}, \tag{3}$$

where *def* is a scale factor. In principle, the quantum-mechanical derivation prescribes the value of *def* (it depends on the sensitivity of the spectrometer and the number of spins in the sample), but it is more convenient to treat *def* as an adjustable parameter. Essentially, it determines the scale at which the nonlinearity of MaxEnt becomes pronounced. The MaxEnt solution is found by maximizing the objective function

$$O = S(\mathbf{f}) - \lambda C\left(\mathbf{f}, \mathbf{d}\right), \qquad (4)$$

where the value of the Lagrange multiplier λ is adjusted to obtain $C = C_0$. The value of λ depends on the values of the parameters *def* and C_0, and on the data. Practical guidelines for choosing the values of *def* and C_0 are described elsewhere [24].

The formulas for entropy and constraint readily generalize to multidimensional data. However, because MaxEnt reconstruction is nonlinear, MaxEnt must be the last time-to-frequency transformation applied. So if MaxEnt is to be used in t_1, then the t_2 dimension must be transformed to the frequency domain first. And if MaxEnt is to be used for both t_1 and t_2, then it must be applied to both dimensions simultaneously, rather than one at a time. The IDFT operation appearing in Equation (2), and the corresponding sums in Equations (2) and (3), can be applied along as many dimensions as one likes.

Applying MaxEnt to reconstruct separately each t_1 row, or each t_1–t_2 plane, of a three-dimensional spectrum raises another problem. The extent of the nonlinearity of the reconstructions can vary from row to row (or from plane to plane), resulting in distorted peak shapes. One way to avoid this is to process the entire data set as a single unit, extending the sums in Equations (2) and (3) to cover the entire spectrum, rather than working on a single row or plane at a time. Of course, such an approach will entail drastically increased data storage requirements. A simpler solution is to use a fixed value of λ rather than iterating to attain $C = C_0$ [25]. The correct value for λ can be determined by choosing a representative row, then computing the normal MaxEnt reconstruction with an appropriate value for C_0. In quantitative applications, it is important to use one of these methods—full data set MaxEnt reconstruction or constant λ reconstruction—to assure that the nonlinearity is uniform across the spectrum, and thus it can be calibrated in a reliable way.

The nature of the nonlinearity of MaxEnt reconstructions is fairly well understood—in general, MaxEnt reconstruction tends to scale intensities down, compared to the DFT, with small amplitudes scaled down more than large amplitudes [26]. In addition to requiring calibration when used for quantitative applications, such as measuring nuclear Overhauser effects, the nonlinearity of MaxEnt reconstruction heightens the distinction between sensitivity, which is the ability to distinguish peaks from noise, and signal-to-noise ratio (S/N). For MaxEnt reconstruction, S/N is not a reliable indicator of sensitivity.

Nonuniform Sampling

The matched filter is a function that follows the decay envelope of the FID; multiplying the FID by the matched filter results in optimal S/N in the DFT spectrum [27]. In essence, the matched filter places more emphasis on the portion of the data where the S/N (in the time domain) is highest. The same idea can be applied to sampling in the time domain: instead of sampling at uniform intervals, the signal can be sampled more frequently when it is strong, and less frequently when it is weak [28–32]; we call this nonuniform sampling. Nonuniform sampling prevents the use of LP or the DFT, since they require data sampled at uniform intervals, but MaxEnt handles such data because the chi-squared statistic in Equation (2) can be computed from just the collected samples. Nonuniform sampling provides additional flexibility in balancing the trade-offs between acquisition time, resolution, and sensitivity. The potential for time saving accrues in the indirect time dimensions of multidimensional experiments, since the relaxation delay between transients renders the total acquisition time insensitive to the number of samples acquired in the direct time dimension. In contrast, the total experiment time increases in direct proportion to the number of indirect time samples.

A list of evolution times for which data are acquired is called a sampling schedule. Examples of nonuniform sampling schedules are depicted in Figure 1. A uniform grid is used to signify evenly spaced points in the various time dimensions. A large dot indicates a sampled time interval and small dots indicate times not sampled. Panel A illustrates an exponential sampling schedule in one indirect dimension (t_1), and panel B illustrates an exponential sampling schedule in two indirect dimensions. Panel C also illustrates a schedule employing randomly selected points chosen from a two-dimensional exponential distribution; this helps to suppress coherent artifacts that can be introduced by schedules that use exactly the same time values for successive rows or columns (such as the schedule in panel B). Panel D illustrates a schedule appropriate for reduced sampling of constant-time dimensions, where there is no decay. For COSY-type spectra, an optimal sampling schedule can be constructed from a sine-modulated exponential distribution. In principle, it is possible to construct more complex sampling schedules that make explicit consideration of the dimensionality of the experiment or the distribution of expected frequencies, for example, along the lines of the samples used for back-projection reconstruction.

Example Applications

Comparisons of spectra obtained using conventional linear sampling and nonuniform sampling applied to two

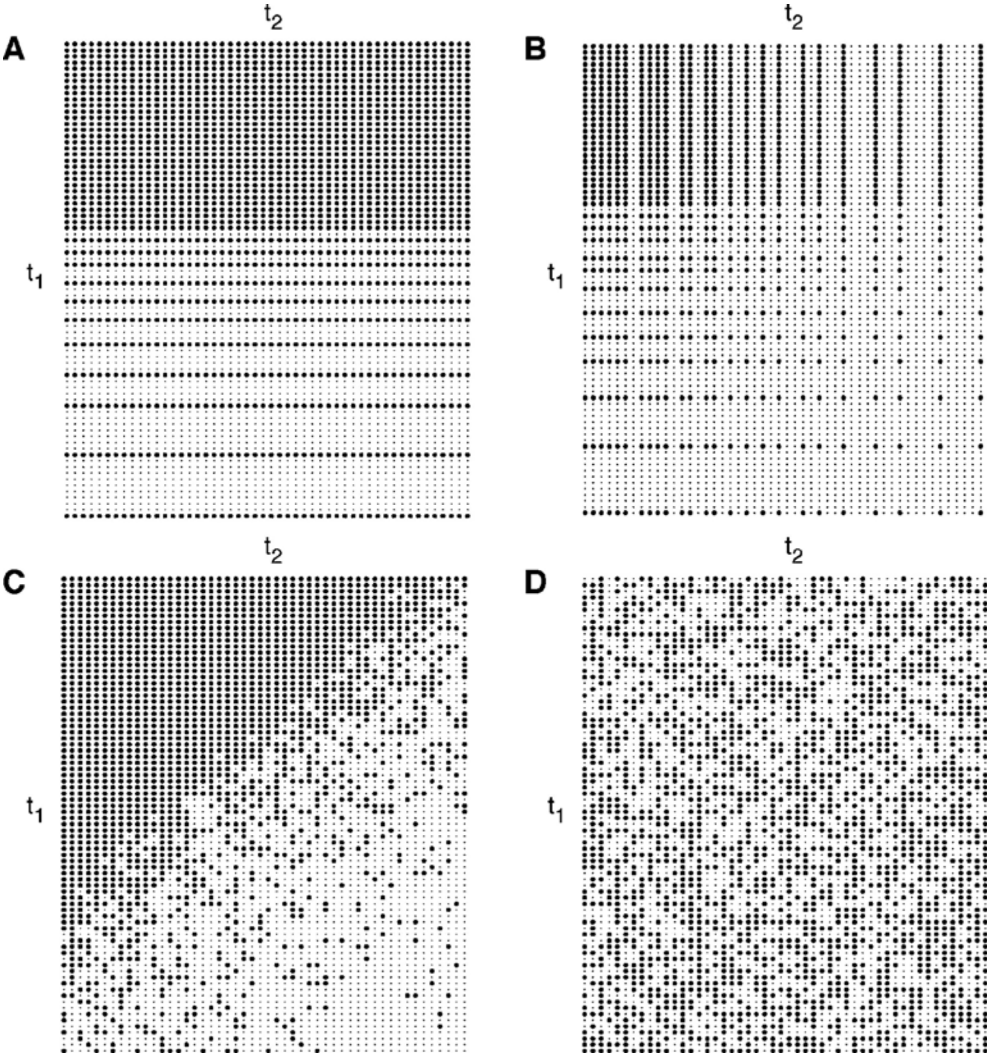

Fig. 1. Nonuniform sampling schedules in one and two indirect time dimensions. Large and small dots indicate times for which samples are collected and not collected, respectively. The schedules depicted are (A) exponential in t_1 and linear in t_2, (B) exponential in both t_1 and t_2, (C) randomly sampled from an exponential distribution in t_1 and t_2, and (D) random in t_1 and t_2.

experiments important for pharmaceutical applications of protein NMR are shown in Figures 2 and 3. Figure 2 shows ^{15}N–^{1}H HSQC spectra of a 42-residue atracotoxin from the Australian funnel-web spider *Hadronyche versuta*. Panel A is the spectrum computed using LP extrapolation, shifted sine-bell windowing, and DFT to produce a 1024-point spectrum in f_1 from 512 uniformly spaced samples in t_1. Panel B was computed in the same fashion and to the same size in f_1, using 64 samples in t_1. The spectrum in panel C was computed using MaxEnt reconstruction, using 64 t_1 samples with exponentially increasing time between samples. Panels D, E, and F show an expanded region of panels A, B, and C, respectively. The resolution obtained from 64 t_1 samples using MaxEnt reconstruction and nonuniform sampling is comparable to that obtained using uniform sampling and conventional processing; however, data acquisition required a factor of eight less time. This time saving can be important for high-throughput applications such as screening compound libraries for molecules that bind to a protein target.

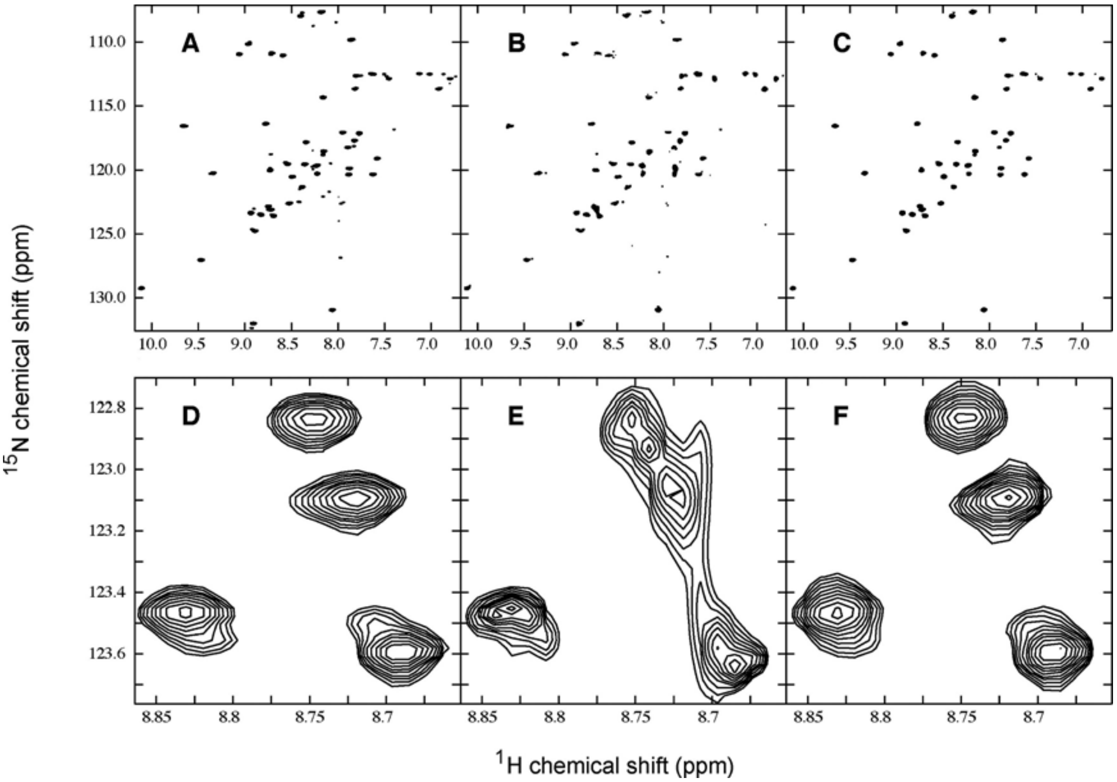

Fig. 2. ^{15}N–^{1}H HSQC spectra for a 42-residue atracotoxin. (A) Computed using LP extrapolation and DFT from 256 linearly spaced samples in t_1, (B) using LP extrapolation and DFT from 64 linearly spaced samples in t_1, and (C) using MaxEnt reconstruction from 64 exponentially spaced samples in t_1. Panels D, E, and F depict an enlarged region from panels A, B, and C, respectively.

Extension of nonuniform sampling and MaxEnt reconstruction to two indirect time dimensions is straightforward, enabling the acquisition of triple resonance spectra for sequential assignment of proteins in 1 day [33]. Experiments in which the signals of interest span a wide range of intensities (such as those involving nuclear Overhauser effects) remain a challenge. The very nature of the nonlinearity of MaxEnt reconstruction, which is to scale down weak signals more than strong signals, makes it more difficult to choose parameters of the reconstruction (*def* and C_0) that enable weak signals to be distinguished from noise. Nonuniform sampling can introduce additional nonlinearities. An example is shown in Figure 3, in which exponential nonuniform sampling and MaxEnt reconstruction have been applied to the two indirect dimensions of a 3D ^{15}N–^{1}H HSQC-NOESY experiment. Panels A and B shows f_1–f_3 cross sections at the f_2 frequency 120.27 ppm, close to the amide ^{15}N chemical shift of residue Cys 21 (120.24 ppm); A is from the linearly sampled DFT spectrum and B is computed using MaxEnt reconstruction from data containing one-eighth fewer samples. Remarkably, the MaxEnt spectrum exhibits resolution superior to the spectrum computed from the larger linearly sampled data set. This is evidenced by the disappearance of resonances at the f_3 frequencies of 8.69 and 8.22 ppm, which correspond to residues with amide ^{15}N chemical shifts of 120.53 and 120.30 ppm, respectively, which have maxima in adjacent f_2 planes. However, the nonlinearity (which depends on the values chosen for *def* and C_0, as well as the sampling schedule) in this instance makes it difficult to observe several weak peaks. Panels C and D are linear cross sections from panels A and B at the f_3 frequency of the amide proton of Cys 21, scaled vertically to the height of the maximum in each panel. While the noise level is greatly reduced, so are the weak peaks, making clear the difficulty caused by high dynamic range.

While careful choice of the nonuniform sampling schedule and parameters of the MaxEnt reconstruction can in principle permit observation of the missing weak

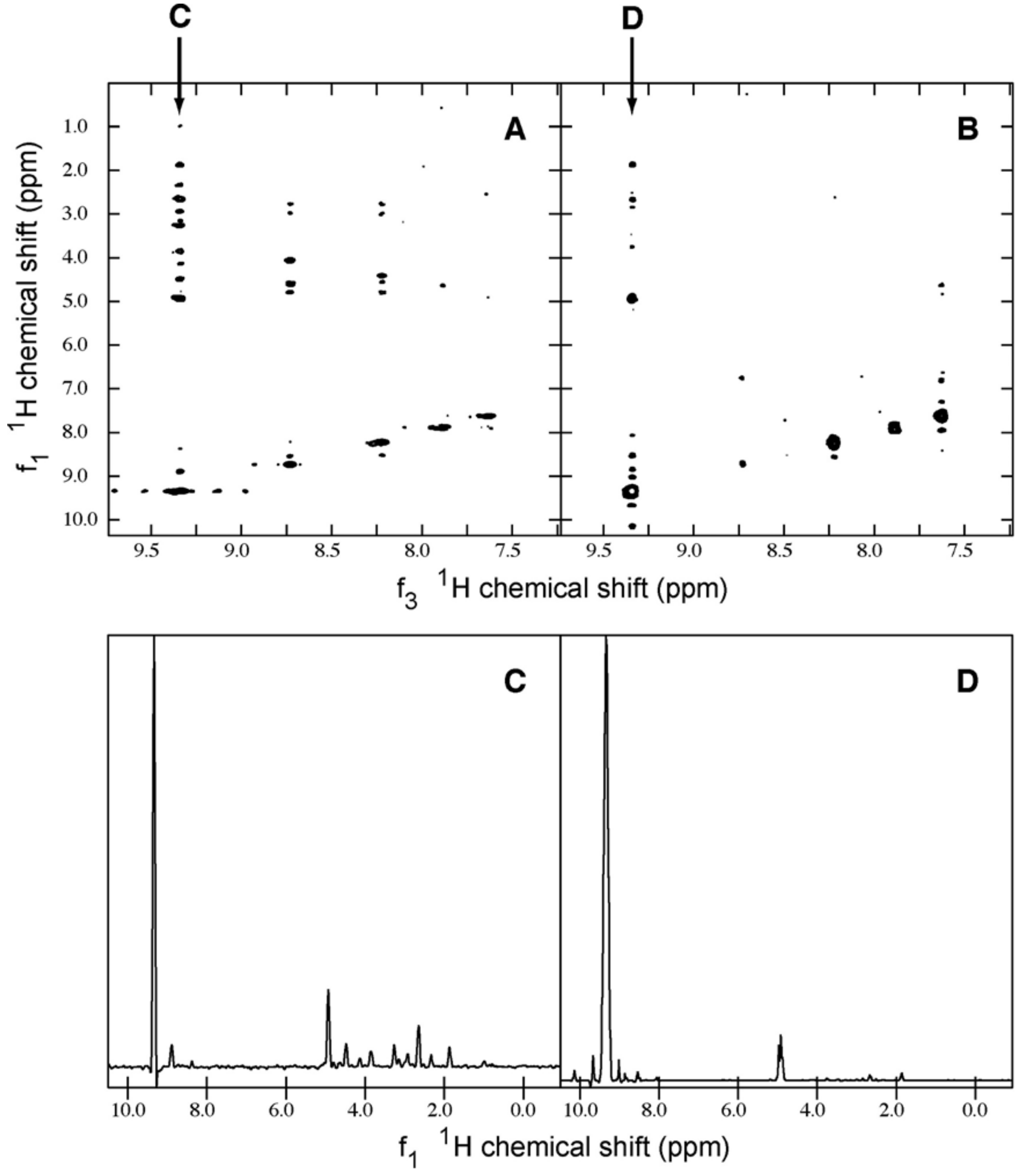

Fig. 3. Two-dimensional cross sections at $f_2 = 120.27$ ppm from 3D ^{15}N–^{1}H HSQC-NOESY spectra of a 42-residue atracotoxin. (A) Computed using LP extrapolation and DFT, (B) using nonuniform sampling in t_1 and t_2 and MaxEnt reconstruction. (C) and (D) are linear cross sections from panels A and B at the f_3 frequency of the amide proton of Cys 21 (9.34 ppm).

peaks (for example, using a small value for C_0 decreases the nonlinearity of the reconstruction), determination of the appropriate values is by no means straightforward, and remains the subject of active research [34]. Regardless of the application, the nonlinearities make error analysis an important adjunct to nonuniform sampling and MaxEnt reconstruction.

Concluding Remarks

MaxEnt reconstruction is a particularly versatile method of spectrum analysis, capable of providing high-resolution spectral estimates from short data records. Its ability to determine spectra from data sampled at arbitrary times enables the use of nonuniform sampling to improve resolution or reduce data acquisition time. Model-based methods, such as Bayesian analysis or FDM, offer many of the same capabilities but are not suited to the computation of spectra containing non-Lorentzian lines. The availability of efficient algorithms and powerful computers has removed what were once perceived as significant barriers to the widespread application of MaxEnt reconstruction in NMR. The ability to collect high-resolution spectra in substantially less time not only enables more efficient use of expensive spectrometers, but also enables investigation of biomolecular systems that are fleetingly stable. These capabilities are particularly well suited to the demands of applications of NMR in drug discovery, including high-throughput screening and rapid assignment of protein spectra.

Acknowledgments

We thank Drs. Peter Schmieder, David Rovnyak, and Gerhard Wagner for sage advice. Financial support was provided by the US National Institutes of Health (GM47467), the US National Science Foundation (MCB 9316938 and MCB 0234638), and The Rowland Institute at Harvard.

References

1. Ernst RR, Anderson WA. Rev. Sci. Instrum. 1966;37:93–102.
2. Jeener J. Oral Presentation, Ampere International Summer School: Yugoslavia, 1971.
3. Aue WP, Bartholdi E, Ernst RR. J. Chem. Phys. 1976; 64: 2229–46.
4. Oschkinat H, Griesinger C, Kraulis PJ, Sorensen OW, Ernst RR, Gronenborn AM, Clore GM. Nature. 1996;332:374–6.
5. Zeng Y, Tang J, Bush CA, Norris JA. J. Magn. Reson. 1989;83:473–83.
6. Ni F, Scheraga HA. J. Magn. Reson. 1986;70:506–11.
7. Stern AS, Li K-B, Hoch JC. J. Am. Chem. Soc. 2002;124: 1982–93.
8. Kim S, Szyperski T. J. Am. Chem. Soc. 2003;125:1385–93.
9. Ding K, Gronenborn AM. J. Magn. Reson. 2002;156:262–8.
10. Kupce E, Freeman R. J. Magn. Reson. 2003;162:300–10.
11. Frydman L, Scherf T, Lupulescu A. Proc. Natl. Acad. Sci. USA 2002;99:15858–62.
12. Barkhuijsen H, de Beer R, Bovee WM, Creyghton JH, van Ormondt D. Magn. Reson. Med. 1985;2:86–9.
13. de Beer R, van den Boogaart A, van Ormondt D, Pijnappel WW, den Hollander JA, Marien AJ, Luyten PR. NMR Biomed. 1992;5:171–8.
14. Mandelshtam VA, Taylor HS, Shaka AJ. J. Magn. Reson. 1998;133:304–12.
15. Chylla RA, Markley JL. J. Biomol. NMR 1995;5:245–58.
16. Kotyk JJ, Hoffman NG, Hutton WC, Bretthorst GL, Ackerman JJH. J. Magn. Reson. 1995;A116:1–9.
17. Chen J, Shaka AJ, Mandelshtam VA. J. Magn. Reson. 2000; 147:129–37.
18. Kupce E, Freeman R. J. Am. Chem. Soc. 2003;125:13958–9.
19. Coggins BE, Venters RA, Zhou P. J. Am. Chem. Soc. 2004; 126:1000–1.
20. Orekhov VY, Ibraghimov I, Billeter M. J. Biomol. NMR 2003; 27:165–73.
21. Wernecke SJ, D' Addario LR. IEEE Trans. Comp. 1977;26: 351–64.
22. Daniell GJ, Hore PJ. J. Magn. Reson. 1989;84:515–36.
23. Hoch JC, Stern AS, Donoho DL, Johnstone IM. J. Magn. Reson. 1990;86:236–46.
24. Hoch JC, Stern AS. Methods Enzym. 2001;338:159–78.
25. Schmieder P, Stern AS, Wagner G, Hoch JC. J. Magn. Reson. 1997;125:332–9.
26. Donoho DL, Johnstone IM, Stern AS, Hoch JC. Proc. Natl. Acad. Sci. USA 1990;87:5066–8.
27. Ernst RR. Adv. Magn. Reson. 1966;2:1–135.
28. Barna JCJ, Laue ED. J. Magn. Reson. 1987;75:384–9.
29. Barna JCJ, Laue ED, Mayger MR, Skilling J, Worrall SJP. J. Magn. Reson. 1987;73:69–77.
30. Schmieder P, Stern AS, Wagner G, Hoch JC. J. Biomol. NMR 1993;3:569–76.
31. Schmieder P, Stern AS, Wagner G, Hoch JC. J. Biomol. NMR 1994;4:483–90.
32. Robin M, Delsuc MA, Guittet E, Lallemand JY. J. Magn. Reson. 1991;92: 645–50.
33. Rovnyak D, Frueh DP, Sastry M, Sun Z-Y, Stern AS, Hoch JC, Wagner G. J. Magn. Reson., 2004;170:15–21.
34. Rovnyak D, Hoch JC, Stern AS, Wagner G. J. Biomol. NMR. 2004;30:1–10.

Applications

Structural Characterization of Antimicrobial Peptides by NMR Spectroscopy

Leonard T. Nguyen, Elmar J. Prenner, and Hans J. Vogel
Structural Biology Research Group, Department of Biological Sciences, University of Calgary Alberta, Canada T2N 1N4

Introduction

Antimicrobial peptides are ubiquitous in nature and they aid in host defenses against bacterial infections. While initial discoveries of bacterial peptides go as far back as the 1950s, the 1990s saw an explosion in research to isolate novel peptides from all kingdoms of life. Out of the more than 800 eukaryotic peptides reported in the Antimicrobial Sequences Database (found at www.bbcm.units.it/∼tossi/pag1.htm), more than 700 entries were reported since 1990. The rapid growth of this field is fueled by the potential of these compounds to be used in a clinical setting [1,2] and replace commonly used antibiotics. The latter are losing potency against disease-causing bacterial strains that are increasingly becoming resistant. The unique qualities of the various antimicrobial peptides make them an incredibly diverse family in terms of sequence, structure and by extension, mechanism of action [3].

Typically shorter than 50 amino acid residues, antimicrobial peptides are prime candidates for structural study by NMR spectroscopy. Cyclic and disulfide cross-linked peptides usually have a stable structure in aqueous solution. However, many of the linear peptides do not form defined structures in aqueous solution and do so only in a membrane mimetic environment [4]; this finding supports the idea that peptide-lipid interactions are critical for antimicrobial action and/or insertion [5]. In addition to solution structures calculated mostly from standard two-dimensional TOCSY and NOESY ^{1}H experiments [6], much progress has been made to characterize the insertion and orientation of the peptides in membrane bilayers through solid-state NMR measurements [7]. This chapter will examine the progress in structural studies of antimicrobial peptides by NMR. Recent reviews have described the solution structures of antimicrobial peptides in an attempt to elucidate general themes and mechanisms [8,9]. Therefore to avoid overlap in this chapter we will highlight the versatility of NMR as a tool to characterize the solution structures of antimicrobial peptides which possess some unique features. In addition, we will describe some solid-state NMR studies which focus on several well known peptides.

Solution Structures of Antimicrobial Peptides

To date, more than 100 unique three-dimensional structures of antimicrobial peptides have been solved by NMR. The complete list consists of more than 80 parent peptides and roughly 20 synthetic peptide derivatives, resulting in great variability. Table 1 summarizes the information for selected solution structures of peptides that have been studied because of their potential as bactericidal agents. In order to be useful, such peptides cannot have high toxicity toward mammalian cells. Some representative structures are shown in Figures 1 and 2. Well-characterized antimicrobial peptides include magainin 2 from the skin of the African clawed frog (Figure 1A) [10], protegrin-1 from mice (Figure 1B) [11], and several members of the defensin family (Figure 2). Some rather distinct antimicrobial peptides have been included in Table 1 as well: These are human hepcidin (Figure 1C) [12], which is better known as a peptide involved in the regulation of iron absorption [13], three gramicidin S derivatives [14], which are listed in spite of the fact that the parent gramicidin S compound, which is secreted from a Bacillus species [15], possesses significant hemolytic activity, and a completely synthetic peptide, combi-1 [16], that was obtained by screening from a library of hexa-peptides produced by combinatorial chemistry.

Various structural classification schemes have been used in the past ([8] for example). However, given the wide diversity of the peptides, a satisfactory organization scheme can misrepresent the properties of certain peptides. Nevertheless, the eukaryotic cationic peptides are often classified into broad groups according to the secondary structure of the parent peptide. As such researchers often talk about helical, β-sheet, turn or extended peptides. This nomenclature can be somewhat misleading at times as some of the larger peptides should really be considered as mini-proteins with various types of secondary structure. For example, insect defensin A [17], as a defensin, is grouped as a β-sheet peptide even though there is an α-helix present in the structure in addition to several β-strands. It should also be noted that sometimes the structure of a synthetic derivative deviates from that of the parent peptide. This is seen for a shortened derivative of

Graham A. Webb (ed.), Modern Magnetic Resonance, 1315–1323.
© 2008 *Springer.*

Table 1: Examples of NMR derived high-resolution solution structures of antimicrobial peptides

Peptide	Class	Membrane Mimetic[a]	Source	Ref.
Cecropin A	α-helix	HFIP	*Hyalophora cecropia*	[87]
Cecropin A-Magainin 2 hybrid (CA-MA) (4)[b]	α-helix	DPC, None	Synthetic	[88]([89])c
Cecropin A-Melittin hybrid (CA-ME)	α-helix	DPC	Synthetic	[88]
Magainin 2 (1)	α-helix	DPC, SDS,TFE	*Xenopus laevis*	[10]([90])
Ovispirin-1 (2)	α-helix	TFE	Synthetic (from *Ovis aries*)	[91]([91])
PGLa	α-helix	DPC	*Xenopus laevis*	[92]
Sheep myeloid antimicrobial peptide (SMAP-29)	α-helix	TFE	*Ovis aries*	[93]
Bovine lactoferricin (1)	β-sheet	None	*Bos taurus*	[19]([18])
Drosomysin	β-sheet	None	*Drosophila melanogaster*	[41]
γ-1-H thionin	β-sheet	None	*Hordeum vulgare*	[42]
Hepcidin-20 and -25	β-sheet	None	*Homo sapiens*	[12]
Human β defensin-3 (HBD-3)	β-sheet	None	*Homo sapiens*	[44]
Human neutrophil protein-1 (HNP-1)	β-sheet	None	*Homo sapiens*	[39]
Insect defensin A/Phormicin	β-sheet	None	*Protophormia terraenovae*	[17]
NaD1 floral defensin	β-sheet	None	*Nicotiana alata*	[94]
Protegrin-1 (2)	β-sheet	None, DMSO	*Sus scrofa*	[11]([95,96])
Rabbit kidney defensin 1 (RK-1)	β-sheet	None	*Oryctolagus cuniculus*	[97]
Rhesus θ defensin-1 (RTD-1)	β-sheet	Acetonitrile	*Macaca mulatta*	[47]
Tachyplesin I (3)	β-sheet	None	*Tachypleus tridentatus*	[98]([98])
Tachystatin A	β-sheet	None	*Tachypleus tridentatus*	[99]
Ac-RRWWRF-NH2 (Combi-1)	Extended	SDS	Synthetic	[16]
Indolicidin (1)	Extended	SDS, DPC	*Bos taurus*	[21]([20])
Tritrpticin	Turn	SDS	Synthetic (from *Sus scrofa*)	[100]
NK-lysin	Loop	None	*Homo sapiens*	[101]
Thanatin	Loop	None	*Podisus maculiventris*	[102]
Bacteriocins				
Carnobacteriocin B2	α-helix	TFE	*Carnobacterium piscicola*	[103]
Gramicidin S derivatives (3)	Loop	None	Synthetic (from *Bacillus brevis*)	([14])
Microcin J25	Loop	None	*Escherichia coli*	[36,61,62]
Nisin A	Turn	DPC, SDS	*Lactococcus lactis*	[30]

[a] Abbreviations used for membrane mimetic present are as follows: TFE, trifluoroethanol; DPC, dodecylphosphocholine micelles; HFIP, hexafluoroisopropanol; SDS, sodium dodecyl sulfate micelles, and DMSO, dimethyl sulfoxide.

[b] Number in parentheses denotes the number of derivatives from a parent peptide for which structures are available.

[c] Number in parentheses in the reference column refers to the structures of the derivatives.

bovine lactoferricin [18] which forms an extended peptide structure even though intact bovine lactoferricin itself [19] adopts a β-sheet conformation. Also, a cyclized derivative [20] of indolicidin [21] has quite a different structure than its parent compound.

The prevalent theme among all eukaryotic cationic peptides is a structure with an amphipathic character. Thus the vast majority of the peptides have a preponderance of basic and hydrophobic amino acids, yet they have no sequence homology. The cationic side of the structure is responsible for electrostatic interactions with the bacterial membranes, which have a high abundance of negatively charged phosphatidylglycerol phospholipids head groups. The charge-charge interactions are thought to be an important factor in providing long-range attraction between the peptide and bacterial membranes [3]. This mechanism allows for broad specificity in target cells while retaining low toxicity to eukaryotic membranes, which mostly have

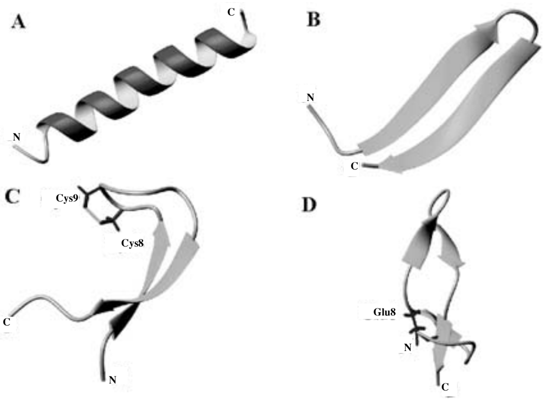

Fig. 1. Representative solution structures of antimicrobial peptides presented as ribbon diagrams: (A) magainin 2 (PDB ID 2MAG) in TFE solution, (B) protegrin-1 (PDB ID 1PG1), (C) hepcidin-20 showing the vicinal disulfide link between Cys8 and Cys9 (PDB ID 1M4E), and (D) microcin J25 showing the amide link between the sidechain of Glu8 and the N-terminal amino group (PDB ID 1Q71). These figures were prepared using MOLMOL [104]. (See also Plate 100 on page XX in the Color Plate Section.)

zwitterionic phosphatidylcholine head groups. However, a few anionic peptides from eukaryotic sources have been identified, for example in human lungs where Zn^{2+} chelation is required for activity [22], or from the toad *Bombina maxima* where the activity does not require the presence of cations [23]. The hydrophobic portion of the antimicrobial peptides allows them to interact with the acyl chain region of membrane bilayers. The amphipathicity that balances both facets of the peptides plays a key role in target selectivity, as peptides that have greater hydrophobicity usually act as general toxins, such as the bee venom melittin [24].

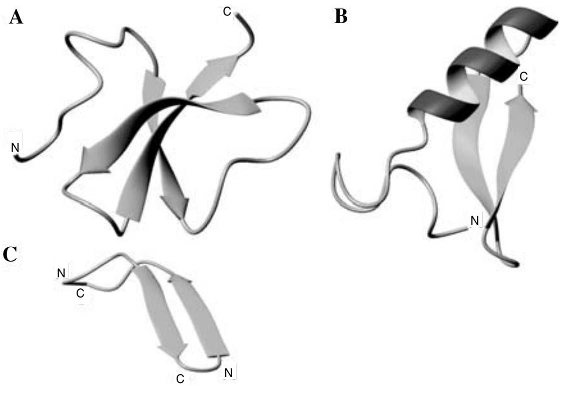

Fig. 2. Solution structures of some defensin peptides in ribbon diagram: (A) bovine neutrophil β-defensin-12 (BNBD-12) (PDB ID 1BNB), (B) insect defensin A (PDB ID 1ICA), and (C) rhesus θ-defensin (RTD-1) (PDB ID 1HVZ). These figures were prepared using MOLMOL [104]. (See also Plate 101 on page XX in the Color Plate Section.)

Almost all α-helical linear peptide structures were solved using either a micelle suspension or an organic co-solvent environment because the vast majority does not form a defined structure in aqueous solution. Highly represented in this category are the peptides obtained from the skins of frog or toad species. β-sheet peptides meanwhile, which encompass the mini-protein defensin family, come from a variety of plants and animals and are known for their characteristic disulfide linkages between cysteine residues [25,26]. Highly disulfide bridged peptides quite frequently act as antimicrobial peptides because the crosslinking would reduce their flexibility and promote stability against proteolytic enzymes. In contrast to the α-helical peptides, structures of the β-sheet peptides have mostly been solved in an aqueous environment and in fact, binding of protegrin-1 to lipid bilayers resulted in aggregation, which prevented detailed structural analysis [27,28]. Highly oligomerized peptides on membrane-mimetic surfaces, while possibly more representative of *in vivo* behavior, unfortunately pose difficulties in structure elucidation.

Also included in Table 1 are a few antimicrobial peptides from bacterial origin. Bacteria use these to protect themselves from unrelated microbes in their ecological niche. These “biological warfare” peptides contain many unusual amino acids which are either the result of extensive post-translational modifications of ribosomally synthesized peptides (e.g. lantibiotics and microcins) or they are synthesized non-ribosomally on large peptide synthesis complexes (e.g. peptaibols). These peptides, often referred to as bacteriocins [29], have been the focus of many studies and nisin A [30] from *Lactococcus lactis* particularly has received a lot of attention to date, because this peptide is currently widely used as a food preservative [32]. Moreover, it is active at lower concentrations than the cationic antimicrobial peptides. The more potent activity could be explained when it was discovered that nisin, and related lantibiotics, form a specific complex with phospholipid II, a precursor for bacterial cell wall biosynthesis [33,34]. Very recently, an NMR paper was published showing the complex structure of nisin with lipid II (Figure 3) [35]. This is a unique contribution as lipid/peptide interactions are usually too transient to experimentally capture their complex structures. The reader is encouraged to read this intriguing paper describing the “pyrophosphate cage” structure for the nisin/lipid II complex. The solution structure of microcin J25 (Figure 1D) [36], another bacterial peptide with uncommon biochemical properties, will be discussed later in this chapter.

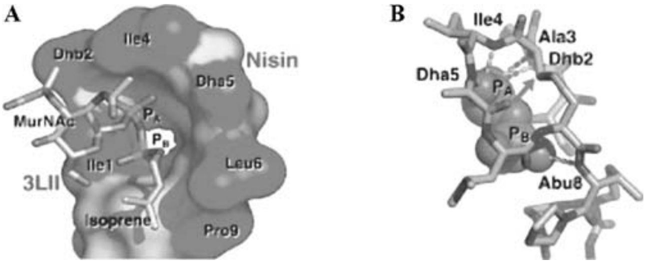

Fig. 3. The contact region between nisin and 3LII, a lipid II variant, as determined from the NMR solution structure of the complex in dimethyl sulfoxide. (A) The N-terminal part of nisin (shown in van der Waals surface) encages the two phosphate groups (P_A and P_B) of 3LII, which also contains the amino sugar N-acetylmuramic acid (MurNAc) and an isoprene tail. The side chains of nisin are labeled, with the dehydrated residues dehydroalanine, Dha, and dehydrobutyrine, Dhb. (B) The intermolecular hydrogen bond network between the nisin backbone and the 3LII pyrophosphate group (in spheres). Hydrogen bonds with high occurrence in the ensemble of structures are indicated by dashed lines, with corresponding residues labeled (with Abu representing α-aminobutyric acid). An arrow indicates the position of Ala3-Cβ, at which bioactivity is disrupted by the addition of a methyl group. The figures were taken with permission from Hsu *et al.* [35]. (See also Plate 102 on page XXI in the Color Plate Section.)

Defensins; Structure Determination and Dimerization Properties

The defensins (Figure 2) are cationic antimicrobial miniproteins that play a key role in the innate immune defense of organisms. Major families are found in plants, insects, and vertebrates including humans. They are distinguished by the position and cross-linking patterns of six disulfide-bonded cysteine residues. A three-stranded β-sheet structure is found in most of the defensins. Plant and insect defensins have their own distinct disulfide connectivity patterns while the disulfides of the mammalian defensins [26] are separated into three major classes: the α- and β-defensins and the more recently discovered θ-defensins. Along with the cathelicidins [37], the defensins make up the major family of antimicrobial peptides produced in humans. They are of great biological importance as they can also play a key role in stimulating the adaptive immune response, substituting for chemokines [28]. They are found on the skin and other epithelial linings and in phagocytic neutrophils [26].

Defensins are of a small enough size (30–50 amino acids) that their proton NMR spectra can be fully assigned by regular TOCSY and NOESY NMR spectroscopy [6]. The first structures solved were those of rabbit neutrophil defensin-5 (NP-5) [38], NP-2 [39], and human neutrophil protein-1 (HNP-1) [38]. These early studies revealed a typical monomeric defensin structure with an amphipathic triple stranded antiparallel β-sheet. The structure was further characterized by hairpin formation and several other tight turns which appear to be stabilized by the disulfide bonds. The structure of the bovine neutrophil β-defensin-12 (Figure 2A) was also shown to be similar to the previously studied α-defensins [40]. While the structure of insect defensin A (Figure 2B) has similar features to the mammalian defensins, it contains an additional "cysteine-stabilized α-helix" (CSH) motif where the α-helix is stabilized by disulfide bridging to the nearby antiparallel β-sheet [17]. This CSH motif is also found in other insect defensins such as in drosomycin from *Drosophila melanogaster* [41] as well as in a few plant defensins such as the γ-1-H and γ-1-P thionins from *Hordeum vulgare* and *Triticum turgidum*, respectively [42].

While the majority of the structures of the defensins show monomeric molecules, a few human peptides are thought to dimerize at low concentrations in aqueous solution. The rationale for this is unclear but it may be a first-step toward oligomerization which is required for pore formation in membranes. For example, the crystal structure of human neutrophil protein-3 (HNP-3) [43] showed an amphipathic symmetrical dimer of peptides. Diffusion NMR and dynamic light scattering, which were used to estimate the approximate size of human β-defensin-3 (HBD-3) in solution, also suggest the presence of a dimeric complex for this peptide, but not for other β-defensins [44]. Distinct chemical shifts for a region within the first β-strand of HBD-3 indicate that it is likely involved in intermolecular β-sheet formation. However, unambiguous NOE crosspeaks in the spectra could not be found to identify the exact dimerization contacts between the two β-defensin molecules in the dimer. Diffusion NMR, using the PG-SLED approach [45], is a facile technique to study the dimerization and multimerization properties of peptides and small proteins in solution [12,44,46].

A recently solved structure of interest is that of the cyclic θ defensin-1 (RTD-1) [47] from rhesus macaque leukocytes. The biosynthesis of RTD-1 involves the translation of two α-defensin-related nonapeptides which are combined by head-to-tail backbone ligation of the peptides and the formation of three disulfide bridges between these two molecules [48]. The resulting NMR-derived structure (Figure 2C), determined in 10% acetonitrile, shows an antiparallel β-sheet with very well defined turns but an overall flexible structure as judged from the poor superposition of the final 10 structures. The lack of a well-defined structure was attributed to bending motions at the center of the cyclic peptide [47].

Hepcidin; Identification of Disulfide Cross-Linking

The structure determination of the liver-synthesized peptide hepcidin presented a challenge in establishing the correct disulfide bond connectivities. Hepcidin was originally discovered in human urine [49] and plasma ultrafiltrate [50] in two forms of 20 and 25 amino acid residues long. The peptide plays an important role in the control and regulation of iron uptake; in addition, hepcidin has also been found to have antimicrobial and antifungal properties [50]. As observed with several antimicrobial peptides, there is a high proportion of Cys in hepcidin. All eight of its Cys residues are involved in disulfide bonds [50], but the specific connectivities between the residues could not be determined by conventional proteolysis methods [51]. Therefore, the solution structure determination of the two peptides by 2D ^{1}H NMR was used to establish the connectivities [12]. As done previously for the 51-residue pheromone Er-23, where the disulfide bond pattern could also not be determined by chemical methods [52], initial structure calculations incorporated only NOE restraints and bond angle constraints, without the disulfide bonds or the hydrogen bonds being included. The initial NOE patterns of the hepcidins themselves only clarified two out of the four unambiguous disulfide links. Hydrogen exchange experiments in D_2O helped to establish the position of some hydrogen bonds, and once these were introduced all the disulfide cross-links could be assigned in further rounds of the structure calculations. This approach resulted in a highly unusual vicinal cysteine bridge between the adjacent Cys residues 8 and 9. Support for this unexpected connectivity was obtained from other NMR parameters, such as a lack of amide proton correlations in the fingerprint regions for these two residues in the TOCSY and NOESY spectra, as well as broad peaks for their α and β-protons, indicating a conformational exchange process on the NMR timescale. The role of this unique structural feature in the hepcidins is still unclear. Vicinal disulfides have been observed in a few enzymes where they were found to be critical for enzyme function [53]. They have not yet been found in any other antimicrobial peptide. The overall structure of the hepcidins is a distorted two-stranded β-sheet where the vicinal disulfide bridge is found at the turn of the hairpin. In a similar manner, disulfide connectivities have been determined on the basis of NMR experiments alone for other peptides such as the antifungal Alo-3 [54] and the insecticidal pea albumin 1, subunit b [55]. These authors used ambiguous disulfide restraints and reduced charges on the sulfur groups in the early stages of the structure calculation, with the ARIA software [56] to establish the correct connectivities.

Microcin J25; Characterization of Unusual Linkages

The bacteriocin microcin J25 is secreted by certain strains of *Escherichia coli*; its antibacterial mechanism of action has been suggested to involve cell membrane disruption [57]. However, several bacterial strains with specific mutations in the β-subunit of RNA polymerase have been found to be resistant to the peptide [58], suggesting another mode of action. The original solution structure determined for the peptide [59] revealed a distorted, highly compact β-sheet structure with the main chain N- and C-termini joined together by an amide bond.Unexpectedly, microcins with their circular backbone cleaved by thermolysin retained their antimicrobial activity as well as the core structure [60]. Subsequent NMR analysis of chemically synthesized linear and head-to-tail cyclic peptides revealed that the spectra of these synthetic peptides were different from those of the natural compound [36]. A reanalysis of the original NMR data for native microcin J25 revealed that the expected sequential NOEs linking the glycines of both termini were absent. Nevertheless, mass spectrometry of the native peptide showed that there was one extra link present in the peptide, which had been formed through a dehydration reaction. A careful NMR analysis of microcin J25 revealed that the compact peptide did not have a head-to-tail cyclized backbone, but rather a novel side chain-to-backbone ring structure (Figure 1D). This linkage involves an amide link between the amino terminus of the peptide and the carboxyl side chain of Glu 8, with an overall knot structure where the C-terminal end is threaded through the ring in a rigid conformation. In fact, this noose-shaped structure was simultaneously reported in two other independent NMR studies [61,62]. The internal cross-link found in microcin J25 has been found in other bacterial proteins, such as small peptide inhibitors [63], where it is believed to contribute to a greater resistance to proteolytic degradation.

Solid-State NMR Experiments: Peptide Orientation in Bilayers

Magainin 2

As a classical example of amphipathic α-helical antimicrobial peptides, magainin, and its natural and synthetic analogues have been intensively studied [64]. Membrane pore formation is thought to be at the center of its mechanism of action, given that magainin has been shown to disrupt the electrochemical gradient across cell membranes [65]. Hence, recent NMR studies have focused on characterizing its interactions with membrane bilayers. Residue-specific ^{15}N labeling of a series of synthetic magainin 2 peptides has been used in solid-state NMR measurements of oriented membrane samples. This work conclusively showed that the helix formed by magainin, and the related PGLa peptide, lie in an orientation that is parallel to the membrane surface of oriented bilayer samples [66], in agreement with fluorescence quenching experiments [67]. The cationic side of the magainin helix is exposed to the aqueous environment and interacts with the surrounding polar lipid head groups, while the hydrophobic half of the peptide is embedded into the membrane and interacts with the fatty acyl chains in the bilayer. Additionally, a recent hydrogen/deuterium exchange NMR experiment confirms this parallel arrangement in SDS micelles [68], with lower exchange factors associated with the hydrophobic residues and higher exchange rates seen for the polar residues.

These findings have helped in explaining the mechanism of pore formation for these peptides by excluding the “barrel-stave” model of pore formation in favor of the “toroidal” pore model [5] (shown in a schematic in Figure 4). In the barrel-stave model, lytic peptides oligomerize at very low peptide:lipid ratios on the membrane and then form peptide-lined pores by orienting perpendicularly to the membrane plane. A good example of such a barrel-stave pore is provided by alamethicin [9], a peptide that is inhibitory of prokaryotic as well as eukaryotic cells. In the toroidal pore model, after reaching a high peptide:lipid threshold, the peptides associate loosely with each other to form transmembrane pores that are lined with peptides separated by lipid head groups. This lipid-peptide rearrangement has been supported in the case of magainin 2 through fluorescence experiments showing rapid flip-flop of the lipids from one side of the bilayer leaflet to the other upon addition of the peptide [70]. Solid-state ^{31}P NMR studies of lipid bilayers showed that upon addition of MSI-78, a synthetic analogue of magainin, the temperature-dependent transition from the fluid lamellar to the hexagonal phase was inhibited [71]. This means that the peptide induced a positive curvature strain in the membrane which is consistant with toroidal pore formation.

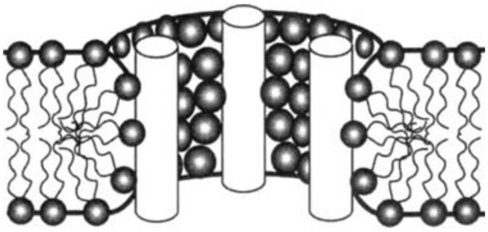

Fig. 4. The toroidal pore model as originally proposed for magainin 2. After a threshold concentration is reached, the peptides change their conformation from a parallel orientation on the bilayer plane. The peptides transiently cross the membrane to adopt a conformation perpendicular to the bilayer plane. Contacts with the phospholipid head groups remain because the pore is lined with peptides intercalated with lipids.

Recently, TRNOE experiments [72] of magainin 2 transiently bound to dilaurylphosphatidylcholine (DLPC) vesicles suggested that the peptide formed an antiparallel dimer structure; this interpretation was based on numerous long-range NOE crosspeaks that were not compatible with the peptide being in a monomeric state [73]. This study contests that solid-state NMR studies of magainin 2 missed this dimer formation because the ^{15}N labeling only provides information for the main chain conformation. Meanwhile, side chain conformations and therefore oligomerization contacts are harder to determine. The impact of this dimer formation on the currently accepted model of pore formation by magainin is presently unclear.

Protegrin-1

Solid-state NMR measurements with protegrin-1, a β-sheet peptide, showed different results compared to magainin 2. Chemical shifts of ^{13}CO and ^{15}N labels on Val-16 of the peptide were measured, and the two-stranded hairpin was calculated to be rotated by 48 ± 5° from the bilayer normal of the DLPC bilayers [74]. This orientation and the length of the peptide still allow for the positively charged arginine side chains to protrude out of the hydrophobic core of the membrane and interact with the lipid head groups. Three of the six Arg’s are near the termini of the peptide and the other three are adjacent to each other near the hairpin turn, while the residues on the strands are hydrophobic to allow for favorable interactions with the acyl portion of the membrane. In a related solid-state NMR experiment, relatively low concentrations of paramagnetic Mn^{2+} were used to induce distance-dependent dipolar relaxation to investigate the depth of insertion of specific residues of protegrin-1 bound to DLPC bilayers [75]. This was accomplished through specific labeling of four selected residues with

^{13}C, and the order of penetration of the residues was in agreement with the tilted model for protegrin-1 insertion. While these experiments shed an interesting light on the arrangement of protegrin-1 in bilayers, it should be recognized that the DLPC lipids used have shorter acyl chains by 4–6 carbons than physiologically relevant phospholipids.

Solid-state NMR studies making use of the magic-angle-spinning (MAS) technique to obtain higher resolution have also been reported. These allowed the study of protegrin-1 bound to palmitoyloleoylphosphatidylcholine (POPC) bilayers, a more relevant membrane system [27]. However, the ^{13}C signals of the isotopically labeled protegrin-1 indicated a high level of aggregation in these bilayers; therefore proper characterization of the bound peptides could not be achieved. Be that as it may, information about the lipid arrangement could be obtained by studying ^{2}H NMR spectra of deuterium-labeled POPC with increasing concentrations of protegrin-1. The results clearly showed a greater proportion of unordered lipids in the lamellar phase [74]. These findings support the toroidal pore mechanism in the case of the protegrin-1 peptide where the membrane is under positive curvature stress and the lipids can move between the inner and outer leaflets.

Conclusions and Future Directions

Standard 2D proton NMR spectroscopy remains the primary method to obtain reliable and detailed structural information about antimicrobial peptides in solution or bound to micelles. As we have discussed, when performing structure calculations based on NMR data alone, one must carefully consider at what stage of the process it is justified to include hydrogen bonding, disulfide bridging or special features such as the knot motif in microcin J25 [36,61,62] as a constraint in the calculations. As the population of easily solvable peptide structures decreases, new NMR strategies will be necessary to fully characterize antimicrobial peptides in a more realistic membrane environment, where many are thought to exert their antimicrobial effects [3]. To this end solid-state NMR has already started to provide a snapshot of such peptides in a membrane bilayer. In the future, it should be possible to use fully isotope-labeled and deuterated peptides and TROSY NMR approaches to study these antimicrobial peptide in small vesicles, as is already being done for some membrane proteins [76,77,78]. Vesicles are a better membrane mimetic than the frequently used micelles.

The development of lipid bicelles, bilayers composed of lipids with different chain lengths forming small discoidal shapes [79], could also prove useful in determining more accurate membrane-bound solution structures. Multimerization of the peptides presents difficulties in data analysis and yet, the oligomerization states could be more reflective of biologically relevant conditions. Also, the structural data coming from solution NMR studies should be supplemented by dynamic information to gain further insights. Novel approaches using homonuclear NMR are now available [80].

Additionally, a multitude of other aspects of the mechanism of action of antimicrobial peptides remain to be characterized. In particular, studies of their interactions with the lipopolysaccharides of the outer membrane of Gram negative bacteria need to be done. Although many peptides exert their cytotoxicity through membrane disruption, in the case of peptides that do not act on the membrane, interaction studies with their intracellular targets will need to be pursued.

In addition to being bactericidal, other useful properties are starting to emerge for many of these peptides [81]. A fair number of them also selectively exhibit toxicity toward tumor cells [82], fungi [83], and viruses [84]. Interaction studies with relevant receptors can lead to an understanding of a peptide's role in the anti-inflammatory response [85], cell signaling pathways [86], or its capacity to stimulate the adaptive immune response [28]. These alternate properties present further directions in which research in this field can go.

Great strides have been made in the characterization of the solution structures of antimicrobial peptides by high-resolution NMR. In addition, solid-state NMR is beginning to provide valuable insights into the positioning of these peptides in membrane environments. Such information will be crucial for the design and development of novel classes of powerful pharmaceuticals to combat bacterial infections.

Acknowledgments

The authors would like to thank Drs. David Schibli, Howard Hunter, and Weiguo Jing for many insightful discussions. This research is supported by the Canadian Institute for Health Research and the Alberta Heritage Foundation for Medical Research.

References

1. Hancock RE. Expert. Opin. Investig. Drugs. 2000;9:1723.
2. Boman HG. J. Intern. Med. 2003;254:197.
3. Epand RM, Vogel HJ. Biochim. Biophys. Acta. 1999;1462:11.
4. Marassi FM, Opella SJ. Curr. Opin. Struct. Biol. 1998;8:640.
5. Matsuzaki K. Biochim. Biophys. Acta. 1999;1462:1.
6. Wuthrich K (Ed). NMR of Proteins and Nucleic Acids, John Wiley and Sons: New York, 1986.
7. Bechinger B. Biochim. Biophys. Acta. 1999;1462:157.
8. Hwang PM, Vogel HJ. Biochem. Cell Biol. 1998;76:235.

9. Powers JP, Hancock RE. Peptides. 2003;24:1681.
10. Gesell J, Zasloff M, Opella SJ. J. Biomol. NMR 1997;9:127.
11. Fahrner RL, Dieckmann T, Harwig SS, Lehrer RI, Eisenberg D, Feigon J. Chem. Biol. 1996;3:543.
12. Hunter HN, Fulton DB, Ganz T, Vogel HJ. J. Biol. Chem. 2002;277:37597.
13. Leong WI, Lonnerdal B. J. Nutr. 2004;134:1.
14. Lee DL, Hodges RS. Biopolymers. 2003;71:28.
15. Ando S, Nishikawa H, Takiguchi H, Lee S, Sugihara G. Biochim. Biophys. Acta. 1993;1147:42.
16. Jing W, Hunter HN, Hagel J, Vogel HJ. J. Pept. Res. 2003;61:219.
17. Cornet B, Bonmatin JM, Hetru C, Hoffmann JA, Ptak M, Vovelle F. Structure. 1995;3:435.
18. Schibli DJ, Hwang PM, Vogel HJ. FEBS Lett. 1999;446:213.
19. Hwang PM, Zhou N, Shan X, Arrowsmith CH, Vogel HJ. Biochemistry. 1998;37:4288.
20. Rozek A, Powers JP, Friedrich CL, Hancock RE. Biochemistry. 2003;42:14130.
21. Rozek A, Friedrich CL, Hancock RE. Biochemistry. 2000;39:15765.
22. Fales-Williams AJ, Gallup JM, Ramirez-Romero R, Brogden KA, Ackermann MR. Clin. Diagn. Lab. Immunol. 2002; 9:28.
23. Lai R, Liu H, Hui LW, Zhang Y. Biochem. Biophys. Res. Commun. 2002;295:796.
24. Matsuzaki K, Yoneyama S, Miyajima K. Biophys. J. 1997;73:831.
25. White SH, Wimley WC, Selsted ME. Curr. Opin. Struct. Biol. 1995;5:521.
26. Ganz T. Science 2002;298:977.
27. Buffy JJ, Waring AJ, Lehrer RI, Hong M. Biochemistry 2003;42:13725.
28. Roumestand C, Louis V, Aumelas A, Grassy G, Calas B, Chavanieu A. FEBS Lett. 1998;421:263.
29. Riley MA, Wertz JE. Annu. Rev. Microbiol. 2002;56:117.
30. Van Den Hooven HW, Doeland CC, Van De KM, Konings RN, Hilbers CW, Van De Ven FJ. Eur. J. Biochem. 1996;235: 382.
31. Breukink E, de Kruijff B. Biochim. Biophys. Acta. 1999; 1462:223.
32. Cleveland J, Montville TJ, Nes IF, Chikindas ML. Int. J. Food Microbiol. 2001;71:1.
33. Twomey D, Ross RP, Ryan M, Meaney B, Hill C, Antonie Van Leewenhoek 2002;82:165.
34. Breukink E, Wiedemann I, van Kraaij C, Kuipers OP, Sahl H, Kruijff B. Science 1999;286:2361.
35. Hsu ST, Breukink E, Tischenko E, Lutters MA, de Kruijff B, Kaptein R, Bonvin AM, van Nuland NM. Nat. Struct. Mol. Biol. 2004;11:963.
36. Rosengren KJ, Clark RJ, Daly NL, Goransson U, Jones A, Craik DJ. J. Am. Chem. Soc. 2003;125:12464.
37. Zanetti M, Gennaro R, Scocchi M, Skerlavaj B. Adv. Exp. Med. Biol. 2000;479:203.
38. Pardi A, Zhang XL, Selsted ME, Skalicky JJ, Yip PF. Biochemistry 1992;31:11357.
39. Pardi A, Hare DR, Selsted ME, Morrison RD, Bassolino DA, Bach AC. J. Mol. Biol. 1988;201:625.
40. Zimmermann GR, Legault P, Selsted ME, Pardi A. Biochemistry 1995;34:13663.
41. Landon C, Sodano P, Hetru C, Hoffmann J, Ptak M. Protein Sci. 1997;6:1878.
42. Bruix M, Gonzalez C, Santoro J, Soriano F, Rocher A, Mendez E, Rico M. Biopolymers. 1995;36:751.
43. Hill CP, Yee J, Selsted ME, Eisenberg D. Science 1991;251:1481.
44. Schibli DJ, Hunter HN, Aseyev V, Starner TD, Wiencek JM, McCray PB Jr, Tack BF, Vogel HJ. J. Biol. Chem. 2002;277:8279.
45. Wilkins DK, Grimshaw SB, Receveur V, Dobson CM, Jones JA, Smith LJ. Biochemistry. 1999;38:16424.
46. Weljie AM, Yamniuk AP, Yoshino H, Izumi Y, Vogel HJ. Prot. Sci. 2003;12:228.
47. Trabi M, Schirra HJ, Craik DJ. Biochemistry. 2001;40:4211.
48. Tang YQ, Yuan J, Osapay G, Osapay K, Tran D, Miller CJ, Ouellette AJ, Selsted ME. Science. 1999;286:498.
49. Park CH, Valore EV, Waring AJ, Ganz T. J. Biol. Chem. 2001;276:7806.
50. Krause A, Neitz S, Magert HJ, Schulz A, Forssmann WG, Schulz-Knappe P, Adermann K. FEBS Lett. 2000;480:147.
51. Creighton TE. In: TE Creighton (Ed). Protein Structure, A Practical Approach. IRL Press Ensyham: Oxford, 1989, p 155.
52. Zahn R, Damberger F, Ortenzi C, Luporini P, Wuthrich K. J. Mol. Biol. 2001;313:923–931.
53. Wang X, Connor M, Smith R, Maciejewski MW, Howden ME, Nicholson GM, Christie MJ, King GF. Nat. Struct. Biol. 2000;7:505.
54. Barbault F, Landon C, Guenneugues M, Meyer JP, Schott V, Dimarcq JL, Vovelle F. Biochemistry. 2003;42:14434.
55. Jouvensal L, Quillien L, Ferrasson E, Rahbe Y, Gueguen J, Vovelle F. Biochemistry. 2003;42:11915.
56. Nilges M, O'Donoghue SI. Prog. NMR Spec. 1992;32:107.
57. Rintoul MR, de Arcuri BF, Salomon RA, Farias RN, Morero RD. FEMS Microbiol. Lett. 2001;204:265.
58. Delgado MA, Rintoul MR, Farias RN, Salomon RA. J. Bacteriol. 2001;183:4543.
59. Blond A, Cheminant M, Segalas-Milazzo I, Peduzzi J, Barthelemy M, Goulard C, Salomon R, Moreno F, Farias R, Rebuffat S. Eur. J. Biochem. 2001;268:2124.
60. Blond A, Cheminant M, Destoumieux-Garzon D, Segalas-Milazzo I, Peduzzi J, Goulard C, Rebuffat S. Eur. J. Biochem. 2002;269:6212.
61. Wilson KA, Kalkum M, Ottesen J, Yuzenkova J, Chait BT, Landick R, Muir T, Severinov K, Darst SA. J. Am. Chem. Soc. 2003;125:12475.
62. Bayro MJ, Mukhopadhyay J, Swapna GV, Huang JY, Ma LC, Sineva E, Dawson PE, Montelione GT, Ebright RH. J. Am. Chem. Soc. 2003;125:12382.
63. Katahira R, Uosaki Y, Ogawa H, Yamashita Y, Nakano H, Yoshida M, J. Antibiot. (Tokyo) 1998;51:267.
64. Matsuzaki K. Biochim. Biophys. Acta. 1998;1376:391.
65. Westerhoff HV, Juretic D, Hendler RW, Zasloff M. Proc. Natl. Acad. Sci. U.S.A. 1989;86:6597.
66. Bechinger B, Zasloff M, Opella SJ. Protein Sci. 1993;2: 2077.
67. Matsuzaki K, Murase O, Tokuda H, Funakoshi S, Fujii N, Miyajima K. Biochemistry 1994;33:3342.
68. Veglia G, Zeri AC, Ma C, Opella SJ. Biophys. J. 2002;82:2176.

69. Laver DR. Biophys. J. 1994;66:355.
70. Matsuzaki K, Murase O, Fujii N, Miyajima K. Biochemistry. 1996;35:11361.
71. Hallock KJ, Lee DK, Ramamoorthy A. Biophys. J. 2003;84:3052.
72. Post CB. Curr. Opin. Struct. Biol. 2003;13:581.
73. Wakamatsu K, Takeda A, Tachi T, Matsuzaki K. Biopolymers 2002;64:314.
74. Yamaguchi S, Hong T, Waring A, Lehrer RI, Hong M. Biochemistry 2002;41:9852.
75. Buffy JJ, Hong T, Yamaguchi S, Waring AJ, Lehrer RI, Hong M. Biophys. J. 2003;85:2363.
76. Fernandez C, Hilty C, Wider H, Guntert P, Wuthrich K. J. Mol. Biol. 2004;336:1211.
77. Hwang PM, Choy WY, Lo EI, Chen L, Forman-Kay JD, Raetz CR, Prive GG, Bishop RE, Kay LE. Proc. Natl. Acad. Sci. U.S.A. 2002;99:13560.
78. Arora A, Abildgaard J, Bushweller JH, Tamm LK. Nat. Struct. Biol. 2001;8:334.
79. Glover KJ, Whiles JA, Wu G, Yu N, Deems R, Struppe JO, Stark RE, Komives EA, Vold RR. Biophys. J. 2001;81:2163.
80. Schleucher J, Wijmenga SS. J. Am. Chem. Soc. 2002;124:5881.
81. Kamysz W, Okroj M, Lukasiak J. Acta. Biochim. Pol. 2003;50:461.
82. Lichtenstein A, Ganz T, Selsted ME, Lehrer RI, Blood. 1986;68:1407.
83. Lupetti A, Danesi R, van 't Wout JW, van Dissel JT, Senesi S, Nibbering PH. Expert. Opin. Investig. Drugs. 2002;11:309.
84. Cole AM, Lehrer RI. Curr. Pharm. Des. 2003;9:1463.
85. Murphy CJ, Foster BA, Mannis MJ, Selsted ME, Reid TW. J. Cell Physiol. 1993;155:408.
86. Charp PA, Rice WG, Raynor RL, Reimund E, Kinkade JM Jr, Ganz T, Selsted ME, Lehrer RI, Kuo JF. Biochem. Pharmacol. 1988;37:951.
87. Holak TA, Engstrom A, Kraulis PJ, Lindeberg G, Bennich H, Jones TA, Gronenborn AM, Clore GM. Biochemistry 1988;27:7620.
88. Shin SY, Kang JH, Hahm KS. J. Pept. Res. 1999;53:82.
89. Oh D, Shin SY, Kang JH, Hahm KS, Kim KL, Kim Y. J. Pept. Res. 1999;53:578.
90. Hicks RP, Mones E, Kim H, Koser BW, Nichols DA, Bhattacharjee AK. Biopolymers 2003;68:459.
91. Sawai MV, Waring AJ, Kearney WR, McCray PB Jr, Forsyth WR, Lehrer RI, Tack BF. Prot. Eng. 2002;15:225.
92. Bechinger B, Zasloff M, Opella SJ. Biophys. J. 1998;74:981.
93. Tack BF, Sawai MV, Kearney WR, Robertson AD, Sherman MA, Wang W, Hong T, Boo LM, Wu H, Waring AJ, Lehrer RI. Eur. J. Biochem. 2002;269:1181.
94. Lay FT, Schirra HJ, Scanlon MJ, Anderson MA, Craik DJ. J. Mol. Biol. 2003;325:175.
95. Lai JR, Huck BR, Weisblum B, Gellman SH. Biochemistry 2002;41:12835.
96. Shankaramma SC, Athanassiou Z, Zerbe O, Moehle K, Mouton C, Bernardini F, Vrijbloed JW, Obrecht D, Robinson JA. Chembiochem. 2002;3:1126.
97. McManus AM, Dawson NF, Wade JD, Carrington LE, Winzor DJ, Craik DJ. Biochemistry. 2000;39:15757.
98. Laederach A, Andreotti AH, Fulton DB. Biochemistry. 2002;41:12359.
99. Fujitani N, Kawabata S, Osaki T, Kumaki Y, Demura M, Nitta K, Kawano K. J. Biol. Chem. 2002;277:23651.
100. Schibli DJ, Hwang PM, Vogel HJ. Biochemistry. 1999;38:16749.
101. Andersson M, Gunne H, Agerberth B, Boman A, Bergman T, Olsson B, Dagerlind A, Wigzell H, Boman HG, Gudmundsson GH. Vet. Immunol. Immunopathol. 1996;54:123.
102. Mandard N, Sodano P, Labbe H, Bonmatin JM, Bulet P, Hetru C, Ptak M, Vovelle F. Eur. J. Biochem. 1998;256:404.
103. Wang Y, Henz ME, Gallagher NL, Chai S, Gibbs AC, Yan LZ, Stiles ME, Wishart DS, Vederas JC. Biochemistry. 1999;38:15438.
104. Koradi R, Billeter M, Wuthrich K. J. Mol. Graph. 1996;14:29.

Pharmaceutical Applications of Ion Channel Blockers: Use of NMR to Determine the Structure of Scorpion Toxins

Muriel Delepierre[1] and Lourival D. Possani[2]
[1] *Unité de Résonance Magnétique Nucléaire des Biomolécules, CNRS URA 2185, 75 724 Paris Cedex 15, France*
[2] *Department of Molecular Medicine, Institute of Biotechnology, National Autonomous University of Mexico, Cuernavaca 62210, Mexico*

Introduction

Animal venoms, such as those from snakes, scorpions, cone snails, sea anemones, spiders and honeybees, are rich sources of different classes of ligands that affect the function of eukaryotic cells and tissues by blocking ion channels [1]. These ligands recognize membrane bound proteins with different specificities and affinities, thus providing scientists with unique tools to investigate diverse areas of neuroscience, protein chemistry and evolution, including the ionic channels of excitable membranes, the phylogeny of proteins and structure–function relationships of proteins [2,3]. It is unclear why toxins with similar structures display such different functions, for example why do they show specific affinities for ion channels from a particular animal? Specific recognition of a wide range of ion channel types allows the use of their pharmacological properties.

A given toxin can act on several different channels, of which only one may be of therapeutic interest [4], rendering its use as a therapeutic agent dangerous [5]. Nevertheless, successful approaches have been developed for the production of immunosuppressive agents from toxins and structural analogs [4] for the treatment of chronic pain [6] and for the treatment of various human disorders such as multiple sclerosis [7], cancer, diabetes, cardiovascular, and neurological diseases [1,8]. The fact that animal toxins are built around limited disulfide bonded frameworks, makes them resistant to degradation and permissive to mutations, meaning that they can be used as templates for protein engineering [9,10]. Before the detailed structure of a potassium channel was solved by X-ray crystallography [11], animal toxins were mainly used to map the channel-binding site and to identify the structural attributes that make a channel unique [12]. With present knowledge, the use of these toxins can be switched to the design or identification of new compounds that compete or interfere with their action upon ion channels. Unfortunately, for Na^+ channels no high-resolution structural model is yet available [13]. Therefore, further structure–activity relationship studies are required on animal toxins to determine the molecular basis of the toxin–ion channel interaction in order to engineer molecules with novel biological functions and/or therapeutic potential [1].

This chapter will focus on toxins extracted from scorpion venoms that are active on sodium and potassium channels. Sodium channel toxins are much more abundant in scorpion venom than potassium channel toxins, which account for less than 0.1% of total venom. In addition, toxins affecting potassium channels usually make only a minor contribution to the effects of envenomation on humans. It is therefore not surprising that the first toxin structure to be solved was that of a sodium channel-specific toxin, the *Centruroides sculpturatus* variant-3 toxin [14].

Use of NMR to Determine the Structure of Rare Components

It is essential to solve the three-dimensional structure of a toxin to determine how it interacts with its receptors. NMR and X-ray crystallography are the two most powerful tools available for structural determination and have been extensively used to obtain structural information on toxins. X-ray crystallography is limited by the necessity to obtain crystals, whereas NMR is limited by the size of the molecule and the low sensitivity of the method, making these two techniques complementary. NMR, which is particularly useful for determining the structure of small molecules, can also be used to obtain information on the dynamics of macromolecules over a wide timescale range and to study molecular interactions [15,16]. However, NMR is inherently less sensitive than almost all other analytical methods as a result of the small energy gap between ground and excited states. Indeed, the minimal quantity that can be analyzed by NMR is usually in the

Graham A. Webb (ed.), Modern Magnetic Resonance, 1325–1330.
© 2008 *Springer.*

nanomolar range or higher, precluding its routine use in trace analysis.

Nevertheless, the sensitivity of NMR has been improved considerably in the last decade by increasing the field strength—900 MHz is now available—and by increasing probe performance [17]. The use of cryogenic probes increases the coil quality factor, improving sensitivity by four- or fivefold compared to conventional 5 mm probes [18]. Sensitivity can be also improved by optimizing the sample volume as a function of the specific availability or solubility of a given sample.

Three types of small sample volume probes have been developed:

(i) Microprobes that use small diameter (3 mm) vertical sample tubes with volumes ranging from 120 to 150 µl. These probes, designed to couple HPLC with NMR, use saddle-type radio frequency (RF) coils. They were initially used in the pharmaceutical industry and are now becoming more widely used in academic laboratories for the characterization of small volumes of natural products and other rare samples [19]. The sample volume can be further reduced to 70–80 µl by using 3 mm Shigemi tubes. In this case, the bottom of the tube that is not in the receiver coil is filled with glass with the same dielectric properties as the solvent used. The amount of material necessary and/or the experimental time can be decreased further by using a 3-mm cryogenic probe [20]. Finally, 1.7 mm submicro inverse-detection gradient NMR probes first described in 1998 are compatible with sample volumes of just 20–30 µl [21].

(ii) The nano-NMR probe was first developed to characterize molecules covalently attached to solid-phase synthesis beads [22]. It uses a 40 µl observable volume that does not need to be filled without compromising the line widths [23] and identical concentrations to standard probes. High detection efficiency is achieved by placing the entire sample in the receiver coil. Magnetic susceptibility contributions to the line width around or within the sample are removed by spinning samples very rapidly (1–4 kHz) at the magic angle. This produces a very narrow water lineshape even at the base of the water signal (Figure 1). However, the spinning of samples in the presence of both RF and magnetic field inhomogeneities modulates the effective field, dramatically reducing the performance of isotropic mixing in TOCSY experiments when conventional composite-pulse mixing sequences are used. Adiabatic mixing sequences are less susceptible to such modulations [24] and perform considerably better in TOCSY experiments at the magic angle [25].

(iii) Microcoil NMR probes were first described in 1994 [26]. Their capillaries can contain nanoliter to microliter volumes and the probes are built with a solenoid coil of about 1 mm. They were developed to couple capillary HPLC or electrophoresis to NMR [27]. Although impressive results have been obtained [28], most of these microprobes are still in the prototype phase.

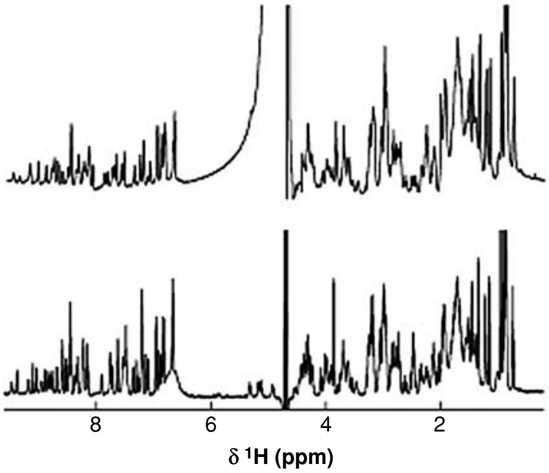

Fig. 1. One-dimensional spectra of the Pi4 toxin [56]. The lower spectrum corresponds to natural ($CONH_2$) Pi4 toxin at 380 µM 15% D_2O obtained at 500 MHz with a nano-NMR probe (Varian INNOVA) while top spectrum corresponds to synthetic (COO^-) Pi4 toxin at 100 µM 15% D_2O, 3 mm Shigemi tube obtained at 600 MHz with a cryoprobe (Varian INNOVA). In both cases 80 µg of protein was dissolved in 5 mM pH 4.0 CD_3COONa buffer. The water was suppressed with presaturation (courtesy of Inaki Guijarro).

The small volume probes make it possible to collect spectra with excellent resolution, sensitivity, and lineshape with small amounts of product, making this technique a promising option when sample size is a real limitation. The combined use of small volume probes—3 mm and below—cryogenic technology, and Shigemi tubes makes it possible to determine chemical structures at unprecedented low concentrations. The use of these technological improvements has allowed the reduction of sample amounts to less than 2% of the initial quantity required. This is evidenced by the fact that for the first scorpion toxin solved by NMR, the sodium channel-specific insect toxin AaHIT, about 12 mg was needed [29], whereas for the first potassium channel-specific scorpion toxin, charybdotoxin (ChTX) 8 mg was required [30]. Nowadays, as little as 200 µg is necessary to obtain structure of potassium channel-specific toxin with a reasonable precision, i.e. with an average of 8–14 constraints per residue [31,32].

NMR Structures of Toxins Active on Sodium Channels

Sodium channel toxins typically contain 60–70 amino acid residues. Two classes of toxin were initially described based on their pharmacological properties and their ability to bind to two different sites on the extracellular surface of the sodium channel [33,34]. Alpha scorpion toxins (α-ScTxs) slow down sodium channel inactivation by binding to receptor site 3 in a voltage-dependent manner. These have been mostly found in the venom of Asian and African scorpions. Beta scorpion toxins (β-ScTxs) bind to receptor site 4 of sodium channels and alter the mechanism of activation of the channel. They were initially found in the New World scorpion (North and South America). This rule is not absolute, because α-ScTxs have been found in the New World and conversely β-ScTxs in the Old World. Displacement experiments on excitable tissues have shown that the two binding sites are not related.

In addition to channel specificity, the sodium channel toxins also display species specificity, for example some α-like toxins are active on insects and mammals [33]. Based on toxicity tests, binding experiments and electrophysiological experiments, sodium channel toxins can be divided into peptides that are specifically toxic to either one or combinations of groups of animals. In this context, the term specific does not mean “exclusively effective” but refers to low toxicity or affinity in one group and/or higher toxicity or affinity in another.

The three-dimensional structures of several sodium channel toxins have been determined by NMR or X-ray crystallography. All toxins (α, β, and α-like) have the same overall structure based on a conserved scaffold with different insertions, deletions, and mutations. Inserted fragments are named loops J, M, B, and F and correspond, respectively, to loop 1 between β strand 1 and the α-helix, loop 2 between the α-helix and the β strand 2, loop 3 between β strands 2 and 3 and finally the C-terminal end. The α-ScTxs have a short J loop and a long B loop, while the β-ScTxs have a long J loop and a short B loop. Excitatory toxins have short J and B loops. An example of such insertion is the excitatory insect toxin from *Buthotus judaicus* (BjxtrIT) in which a five-amino acid insertion occurs just before the α-helix in loop 1 and a short α-helix is inserted in the C-terminal part of the molecule [35]. The α-ScTxs contain an insertion at around residue 42 of the B loop that is believed to play a key role in the modulation of toxic activity [36].

Based on experimental evidence, three criteria appear to be important for sodium channel specificity, namely: (i) the presence of a positively charged residue at the N-terminus (usually lysine and sometimes arginine), immediately followed by a negatively charged residue such as glutamic acid or aspartic acid at position 2; (ii) a conserved aromatic cluster; and (iii) a positively charged group (e.g. lysine or arginine) at position 13 in β-type toxins or position 58 in α-type toxins.

Most of the scorpion toxin structures that have been reported so far have been assigned to the α-type group or are weakly toxic to mammals. In North and South America, two of the most dangerous scorpions for mammals are *Centruroides noxius* and *Tityus serrulatus*, respectively. In each case, the most toxic components for mammals are β-type toxins active on sodium channels, respectively Ts1 and Cn2. Ts1 is a β-ScTxs and is the major component of the venom of *T. serrulatus*. The structure of Ts1, also known as Ts-γ or toxin VII, has been determined by X-ray diffraction to a resolution of 1.7 Å [37] while the structure of Cn2 has been determined by NMR [38]. Cn2 is composed of one α-helix and three β strands. It contains 10 aromatic residues, several of which are located on the same face of the molecule, face A, as is generally observed for sodium channel toxins. This face was thought to be the determinant for the sodium channel specificity. The orientation of the C-terminal region differs between α- and β-toxins as do the sizes of the J loop and B loop regions. The unique orientation of the Cn2 C-terminal region stems from a proline in a *cis* conformation. Interestingly Ts1 C-terminal orientation is similar to that of Cn2 but here the *cis*-proline is replaced by a helix turn. Whereas binding of β toxins to a common site on the sodium channel may be explained by the same recognition pattern on face A (i.e. the face containing the hydrophobic cluster), the difference in their toxicities may be related to the distribution of residues on the opposite face (face B). In Cn2 and Ts1, this face, formed by loop 1 and the C-terminal end, displays a large number of basic amino acid residues, whereas in weakly active toxins these residues are replaced by neutral amino acids.

The fact that the first crustacean-specific toxin for which a structure was solved came from a scorpion of the same genus as Cn2 (*Centruroides limpidus limpidus*) revealed structural features that might be responsible for the species specificity: mammals versus crustaceans. Whether a particular toxin of the genus *Centruroides* is specific towards mammals or arthropods depends on the nature of a few residues clustered in two well-defined regions (mainly loops between secondary structure elements). Mutational analyses in which the two regions are exchanged or point mutations introduced at these residues are required to corroborate these results.

NMR Structures of Toxins Active on Potassium Channels

Potassium channel toxins also vary considerably in terms of sequence and specificity, and can act on a wide range of potassium channels. Although potassium channel toxins from scorpions of the family Buthidae are mostly present as minor components of the venom, the increasing interest in venom constituents has led to efforts to improve the separation and identification of all venom compounds. So far, more than 120 different K^+ channel toxins have been found in scorpion venoms [39,40]. They have been divided into three subfamilies based on their primary structures and functions: α-, β- and γ-KTxs. The α-KTx family is the largest one, containing more than 80 members in 18 subfamilies active on Kv, BK_{Ca}, or SK_{Ca} channels. They are short-chain toxins, consisting of 23–41 amino acids and three or four disulfide bridges [41]. The four members of the β-Ktxs family identified so far are long-chain toxins composed of 60–64 amino acids and containing only three disulfide bridges [42]. Twenty-six members of the γ-Ktxs family have been identified. Members of this family are HERG channel blockers consisting of 36–47 amino acids and three or four disulfide bridges [43].

With the exception of the κ-Hefutoxins [44], all the K^+ channel-specific toxins isolated from scorpion venoms are structurally related. They are characterized by the cysteine-stabilized α/β motif (CS-αβ) in which Ci–Cj and $Ci+4$–$Cj+2$ disulfide bridges link the α-helix to the second strand of the β-sheet. κ-Hefutoxin 1 adopts a unique three-dimensional fold, consisting of two parallel helices linked by two disulfide bridges and without any β-sheets [44].

The first potassium channel toxin to be identified was noxiustoxin in 1982 [45]. Its three-dimensional structure was solved in 1995 [46]. The first potassium channel for which the structure was solved was charybdotoxin [47] discovered in 1985 [48]. The structures of several potassium channel toxins have been elucidated in the last 15 years either by X-ray or by NMR. This was made possible by following developments including: (i) chemical synthesis associated with efficient refolding, (ii) recombinant methods allowing uniform ^{15}N and ^{13}C labeling of these toxins, (iii) advances in methods for the extraction and purification, and (iv) recent developments in highly sensitive NMR methodology allowing structure determination with just a few hundred micrograms of compound [49, and references therein].

Among the 120 K^+ channel toxins the α-Ktx6 subfamily, which now comprises five different members, is characterized by the presence of an additional disulfide bridge that, in most members, fixes the C-terminus to the turn following the α-helix. Two different arrangements of disulfide bonds have been described for members of this subfamily. Pi1 [50], Pi4 [51], Pi7 [32,51] and HsTX1 [52] show half-cystine pairing of C1–C5, C2–C6, C3–C7, C4–C8, whereas MTX displays a different S–S bond topology C1–C5, C2–C6, C3–C4, C7–C8 [53]. The different S–S bonds in MTX link contiguous regions in the sequence; however MTX displays the characteristic structure of a small scorpion toxin [54]. Interestingly, no target has yet been found for toxin Pi7 despite it having a similar overall fold to all potassium channel toxins [32]. Another toxin containing four disulfide bridges has also been purified from *T. serrulatus*, TXT α-KTx17, but the additional disulfide is on the N-terminal end and the structure of this toxin has not yet been solved [55].

The three-dimensional structures of the three *Pandinus imperator* toxins have been determined using nanomolar amounts of the natural compounds and the nano-NMR probe approach and/or 3 mm Shigemi tubes [31–32,56]. The structures of HsTX1 [57] and MTX [54] were determined using synthetic molecules. The structure of Pi4 was determined using both the natural and synthetic toxins, showing that both have the same fold and disulfide pairing [56].

Disulfide bridges can be identified from the spatial interactions observed between Hα and Hβ and between Hβ and Hβ of cysteines involved in the disulfide bridge. However, in cysteine-rich proteins, such as scorpion venom toxins, it is not always possible to obtain conclusive results, as connections between Hβ protons can involve more than two cysteines. S–S bonds have been successfully assigned by NMR and modeled using different methodologies for several proteins [57,58]. Structures are calculated using NMR data only, with no disulfide bridges, to propose topologies compatible with NMR restraints for all possible combinations of disulfide bridges. Given that the bond between the sulfur atoms can only be formed if the distance between the two sulfur atoms is 2.03 Å, the structures with lowest experimental energies are analyzed in terms of the statistical distribution of distances between cystine sulfur atoms [32]. Even when other experimental data are available, NMR and structure calculations offer the possibility of testing the disulfide bridge pattern determined by other techniques and can be routinely used to locate the S–S bonds of proteins of unknown structures.

The structures of only two members of the γ-KTx family have been solved: BeKm-1 [59] and CnErg1 [60]. They have different disulfide bridging patterns and do not share any significant homology in primary structure, but both block the turret region of the HERG channel [61,62]. Their structure was solved using the recombinant toxin [59], the synthetic toxin [63] and the native toxin in the case of CnErg1 [64]. They adopt the α-KTx CS-αβmotif; however the turn of helix observed in the N-terminal part of CnErg1 is unique to the family of potassium channel toxins [63,64]. BeKm-1 and CnErg1 share similar interaction surfaces with the HERG channel. Evolutionary [65] and structural analyses demonstrated the presence of two important functional residues that are mainly located in two patches—one hydrophobic and the other hydrophilic—located at the two opposite heads of the toxin molecules [40,54,61,62]. Therefore, scorpion γ-KTx toxins seem to share the same interaction mode regardless of their primary structures.

Conclusion

The structures determined so far for scorpion toxin acting on ion channels seem to converge to a unique global fold CS-αβmotif even though they exert a wide range of biological functions. It is therefore reasonable to expect that molecular modeling will be enough to establish reasonable structural models. However, it is probably the unique fine details of structure (i.e. subtle changes in secondary structure elements and/or the relative orientation of side chains and/or the dynamic properties of the molecule) that are important for channel recognition and species specificity. Two recent findings emphasize how fine structure can help to elucidate the structure–function relationships of scorpion toxins. The first one concerns the finding that a α-KTx toxin, BmTx3, isolated from the venom of the scorpion *Buthus martensi* Karsch, can display dual activity, blocking HERG activity and A-type potassium currents [66]. The second is the finding of the inhibitor cystine knot (ICK) [67] fold among scorpion toxins [68]. Furthermore, preliminary results on venom proteomics [39] seem to suggest that a large number of toxins from the venom of various animal species remain to be structurally characterized, thus it is reasonable to expect that new folds and new potent molecules will be discovered.

References

1. Lewis RJ, Garcia ML. Nat. Rev. Drug Discov. 2003:2;790.
2. Menez A. Toxicon. 1998:36;1557.
3. Mouhat S, Jouirou B, Mosbah A, De Waard M, Sabatier J-M. Biochem. J. 2004:378;717.
4. Kem W, Pennington MW, Norton RS. Drug Discov. Des. 1999:15/16;111.
5. Kalman K, Pennington MW, Lanigan MD, Nguyen A, Rauer H, Mahnir V, Paschetto K, Kem WK, Grissmer S, Gutrman GA, Christian EP, Cahalan MD, Norton RS, Chandy KG. J. Biol. Chem. 1998:273;32697.
6. Nielsen K, Schroeder T, Lewis RJ. J. Mol. Recognit. 2000:13;55.
7. Beeton C, Wulff H, Barbaria J, Clot-Faybesse O, Pennington M, Bernard D, Cahalan MD, Chandy KG, Béraud E. Proc. Natl. Acad. Sci. U.S.A. 2001:98;13942.
8. Chandy KG, Wulff H, Beeton C, Pennington M, Gutman GA, Chalan MD. Trends Pharmacol. Sci. 2004:25;280.
9. Vita C, Roumestand C, Toma F, Menez A. Proc. Natl. Acad. Sci. U.S.A. 1995:92;6404.
10. Mer G, Kellenberger E, Lefevre JF. J. Mol. Biol. 1998:281;235.
11. Doyle DA, Morais Cabral JM, Pfuetzner RA, Kuo A, Gulbis JM, Cohen SL, Chait BT, MacKinnon J. Science. 1998:280;69.
12. Aiyar J, Withka JM, Rizzi JP, Singleton DH, Andrews GC, Lin W, Boyd J, Hanson D, Simon M, Dethlefs B, Lee CL, Hall JE, Gutman GA, Chandy G. Neuron. 1995:15;1169.
13. Blumenthal KM, Seibert AL. Cell Biochem. Biophys. 2003:38;1.
14. Fontecilla Camp JC, Almassy RJ, Suddath FL, Watt DD, Bugg CE. Proc. Natl. Acad. Sci. U.S.A. 1980:77;6496.
15. Wolff N, Guenneugues M, Gilquin B, Drakopoulou E, Vita C, Ménez A, Zinn-Justin S. Eur. J. Biochem. 2000:267;6519.
16. Cui M, Shen J, Briggs JM, Fei W, Wu J, Zhang Y, Luo X, Chi Z, Ji R, Jiang H, Chen K. J. Mol. Biol. 2002:318;417.
17. Hoult D, Richards RE. J. Magn. Reson. 1976:24;71.
18. Styles P, Soffe NF, Scott CA, Cragg DA, Row F, White DJ, White PCJ. J. Magn. Reson. 1984:60;397.
19. Crouch RC, Martin GE. J. Nat. Prod. 1992:55;1343.
20. Russel DJ, Hadden CE, Martin GE, Gibson AA, Zen AP, Cavolan JL. J. Nat. Prod. 2000:63;1047.
21. Subramanian R, Lam MM, Web AG. J. Magn. Reson. 1998:133;227.
22. Keifer PA. Drug Discov. Today 1997:2;468.
23. Delepierre M, Roux P, Chaffotte A-F, Goldberg ME. Magn. Reson. Chem. 1998:36;645.
24. Kupce E, Freeman R. J. Magn. Reson. A. 1995:115;273.
25. Kupce E, Keifer PA, Delepierre M. J. Magn. Reson. 2001:148;115.
26. Wu N, Peck TL, Webb AG, Magin RL, Sweedler JV. Anal. Chem. 1994:66;3849.
27. Olson DL, Peck TL, Webb AG, Magin RL, Sweedler JV. Science. 1995:270;1967.
28. Martin GE, Guido JE, Robins RH, Sharaf MHM, Tackie AN, Schiff PL Jr. J. Nat. Prod. 1998:61;555.
29. Darbon H, Weber C, Braun W. Biochemistry. 1991:30;1836.
30. Bontems F, Roumestand C, Boyot P, Gilquin B, Doljansky Y, Menez A, Toma F. Eur. J. Biochem. 1991:196;19.
31. Delepierre M, Prochnicka-Chalufour A, Possani LD. Biochemistry. 1997:36;2649.
32. Delepierre M, Prochnicka-Chalufour A, Boisbouvier J, Possani LD. Biochemistry. 1999:38;16756.
33. Gordon D, Savarin P, Gurevitz M, Zinn-Justin S. J. Toxicol. Toxin Rev. 1998:17;131.
34. Possani LD, Becerril B, Delepierre M, Tytgat J. Eur. J. Biochem. 1999:264;287.
35. Oren DA, Froy O, Amit E, Kleinberger-Doron V, Gurevitz M, Shaanan B. Structure. 1998:6;10995.
36. Fontecilla-Camps JC, Habersetzer-Rochat C, Rochat H. Proc. Natl. Acad. Sci. U.S.A 1988:85;7443.
37. Polikarpov I, Matilde MS Jr, Marangoni S, Toyama MH, Teplyakov A. J. Mol. Biol. 1999:290;175.
38. Pintar A, Possani LD, Delepierre M. J. Mol. Biol. 1999:287;359.
39. Tytgat J, Chandy KG, Garcia ML, Gutman GA, Martin-Eauclaire M-F, van der Walt JJ, Possani LD. Trends Pharmacol. Sci. 1999:20;444.
40. Rodriguez de la Vega RC, Merino E, Becerril B, Posan LD. Trends Pharmacol. Sci. 2003:24;222.
41. Batista CVF, del Pozo L, Zamudio FZ, Contreras S, Becerril B, Wanke E, Possani LD. J. Chromatogr. B. 2004:803; 55.
42. Legros C, Ceard B, Bougis PE, Martin-Eauclaire MF. FEBS Lett. 1998:431;375.
43. Corona M, Zurita M, Possani LD, Becerril B. Toxicon. 1996:34;251.
44. Srinivasan KN, Sivaraja V, Huys I, Sasaki T, Cheng B, Kumar TKS, Sato K, Tytgat J, Yu C, Cheng San BC, Ranganathan

S, Bowie HJ, Kini RM, Gopalakrishnakone P. J. Biol. Chem. 2002:277;30040.
45. Possani LD, Martin BM, Svendsen I. Carlsberg Res. Commun. 1982:47;285.
46. Dauplais M, Gilquin B, Possani LD, Gurrola-Briones G, Roumestand C, Menez A. Biochemistry. 1995:34; 16563.
47. Bontems F, Roumestand C, Gilquin B, Menez A, Toma F. Science. 1991:254;1521.
48. Miller C, Moczydlowski E, Latorre R, Philipps M. Nature. 1985:313;316.
49. Possani LD, Becerrill B, Tytgat J, Delepierre M. In: Lopatin A, Nichols CG (Eds). Ion Channel Localization Methods and Protocols. Humana Press Inc., Totowa, NJ, 2000, pp 145–66.
50. Olamendi-Portugal T, Gomez-Lagunas F, Gurrola GB, Possani LD. Biochem. J. 1996:315;977.
51. Olamendi-Portugal T, Gomez-Lagunas F, Gurrola GB, Possani LD. Toxicon. 1998:36;759.
52. Lebrun B, Romi-Lebrun R, Martin-Eauclaire M-F, Yasuda A, Ishiguro M, Oyama Y, Pongs O, Nakajima T. Biochem. J. 1997:328;321.
53. Kharrat R, Mabrouk KP, Crest M, Darbon H, Oughideni R, Martin-Eauclaire M-F, Jacquet G, El Ayeb M, Van Rietschoten J, Rochat H, Sampieri F. Eur. J. Biochem. 1996:242;491.
54. Blanc E, Sabatier JM, Kharrat R, Meunier S, El Ayeb M, Van Rietschoten J, Darbon H. Proteins Struct. Funct. Genet. 1997:29;321.
55. Becerril B, Marangoni S, Possani LD. Toxicon. 1997:35; 821.
56. Guijarro IJ, M'Barrek S, Olamendi-Portugal T, Gomez-Lagunas F, Garnier D, Rochat H, Sabatier J-M, Possani LD, Delepierre M. Protein Sci. 2003:12;1844.
57. Savarin P, Romi-Lebrun R, Zinn-Justin S, Lebrun B, Nakajima T, Gilquin B, Ménez A. Protein Sci. 1999:8;2672.
58. Nilges M, Macias MJ, O'Donoghue SI, Oschkinat H. J. Mol. Biol. 1997:269;408.
59. Boisbouvier J, Albrand J-P, Blackledge M, Jaquinod M, Schweitz H, Lazdunski M, Marion D. J. Mol. Biol. 1998:283;205.
60. Korolkova YV, Bocharov EV, Angelo K, Maslennikov IV, Grinenko OV, Lipkin AV, Nosyreva ED, Pluzhnikov KA, Olesen SP, Arseniev AS, Grishin EV. J. Biol. Chem. 2002:277;43104.
61. Gurrola GB, Rosati B, Rocchetti M, Pimienta G, Zaza A, Arcangeli A, Olivotto M, Possani LD, Wanke E. FASEB J. 1999:13;953.
62. Zhang M, Korolkova YV, Liu J, Jiang M, Grishin EV, Tseng GN. Biophys. J. 2003:84;3022.
63. Pardo-Lopez L, Zhang M, Liu J, Jiang M, Possani LD, Tseng GN. J. Biol. Chem. 2002:277;16403.
64. Torres AM, Bansal P, Alewood PF, Bursill JA, Kuchel PW, Vandenberg JI. FEBS Lett. 2003:539;138.
65. Frenal K, Xu C-Q, Wolff N, Wecker K, Gurrola G, Zhu S-Y, Chi C-W, Possani LD, Tytgat J, Delepierre M. Proteins Struct. Funct. Bioinform. 2004:56(2);367–75.
66. Huys I, Xu C-Q, Wang C-Z, Vacher H, Martin-Eauclaire M-F. Biochem. J. 2004:378;745.
67. Craik DJ. Toxicon. 2001:39;1809.
68. Zhu S, Darbon H, Dyason K, Verdonk F, Tytgat J. Faseb J. 2003:17;1765.

Structure and Dynamics of Inhibitor and Metal Binding to Metallo-β-Lactamases

Christian Damblon and Gordon C.K. Roberts

Biological NMR Centre, Department of Biochemistry, University of Leicester, Leicester LE1 7RH, UK

Introduction

The β-lactam antibiotics are among the most useful antibacterial chemotherapeutic agents, for both human and animal use, but their efficiency is continuously being challenged by the emergence of resistant strains of pathogenic bacteria. Production of β-lactamases, which inactivate these antibiotics by hydrolyzing their endocyclic amide bond, is the most important resistance mechanism [1]. β-Lactamases have been divided into four classes on the basis of their amino acid sequences and catalytic mechanisms [2]. Class B enzymes, the metallo-β-lactamases (MBLs), are ∼30 kDa metallo-proteins which require one or two zinc ion(s) for their activity [3]. In the last 20 years, MBL-mediated resistance has appeared in several pathogenic strains including *Bacteroides fragilis*, *Aeromonas hydrophila, Stenotrophomonas maltophilia*, and *Serratia marcescens* [4], and some MBL genes are being disseminated rapidly by horizontal transfer, involving both plasmid and integron-borne genetic elements [5–9]. The spread of MBL-mediated bacterial resistance to β-lactams is thus a matter of concern, particularly in view of the very wide substrate profile displayed by many MBLs, which can hydrolyze almost all the known β-lactam antibiotics, including the carbapenems such as imipenem [10].

The MBLs share a small number of conserved motifs, but otherwise show significant sequence diversity. Crystal structures have been determined for the MBLs from *B. cereus* [11,12], *B. fragilis* [13–15], *Chryseobacterium meningosepticum* [16] and *S. maltophilia* [17], and for the IMP-1 enzyme from *Pseudomonas aeruginosa* [18]. These structures reveal a unique “αββα sandwich” characteristic of this family of enzymes and distinct from other zinc-dependent amide hydrolases such as thermolysin and carboxypeptidase A. It has subsequently become apparent that the metallo-β-lactamase fold is a widespread one [19–21]. Two zinc cations are present in the active site of the MBLs for which crystal structures are available. For example, in site I of the *B. cereus* enzyme, the zinc is co-ordinated by the imidazole rings of three histidine residues, H86, H88, and H149 (H116, H118, and H196 according to the standard numbering of MBLs [22]) and one water molecule. This water (or hydroxide) bridges to the zinc in site II, which is also co-ordinated by a histidine (H210 in *B. cereus*), a cysteine, an aspartate and a second water (or a carbonate ion). The zinc ligands are not absolutely conserved among MBLs, some enzymes having an Asn in place of a His in position 116 (site I ligand) and others having an Asp in place of the Cys in site II. These differences may contribute to some of the observed differences in substrate profiles and zinc affinities between different MBLs.

The precise role of the two metals in catalysis is still unclear (e.g. [3,23–26]); mechanisms have been proposed in which only the zinc in site I is involved in catalysis [23], and in which both zinc cations play essential catalytic roles [3,26]. In fact, it remains unclear whether the mononuclear or binuclear enzyme is the more physiologically relevant; recent measurements suggest that at physiological metal ion concentrations most MBLs may exist as the apoenzyme, and that the presence of substrate leads to enhanced zinc binding in the mononuclear form of the enzyme [27]. It is notable that, while the presence of the second zinc does seem to be necessary for obtaining the maximum catalytic efficiency in MBLs, most of them can catalyze substrate hydrolysis with only one zinc cation bound [28–30]. Indeed, catalytic activity of the *A. hydrophila* MBL is actually inhibited by the binding of a second zinc cation [30]. It has been proposed that the observed conservation of the ligating residues at site II may be explained if a translocation of the metal ion between the two metal sites is involved in catalysis, and that this might explain the observation of catalytic activity with only one zinc per molecule of enzyme.

The range of active site architectures for the MBLs makes the discovery of useful broad-spectrum inhibitors a challenging task, although compounds of several different chemical classes which inhibit the enzyme *in vitro* have been described [15,18,23,31–44]. Structural information, from crystallography or NMR, is available for the binding of a biphenyl tetrazole, which binds to the zinc in site II [31], and for a number of mercaptocarboxylates [18,41,44,45]. We recently demonstrated that a simple mercaptocarboxylate, thiomandelic acid

Graham A. Webb (ed.), Modern Magnetic Resonance, 1331–1337.
© 2008 *Springer.*

(β-mercapto phenylacetic acid), is a reasonably potent (sub-micromolar) inhibitor for most MBLs, except for the enzyme from *A. hydrophila* [45]. The kinetic data for thiomandelic acid fitted a competitive pattern of inhibition, and no evidence was obtained for irreversible binding of thiomandelic acid, at least to the *B. cereus* enzyme. Such a wide spectrum of activity against MBLs is unprecedented in previously published data concerning MBL inhibitors. For instance, thiomandelic acid is only about 25-fold less potent as an inhibitor of the enzyme from *B. fragilis* than of the IMP-1 enzyme from *P. aeruginosa*. This is in marked contrast to the reported thioester inhibitors, which are very much poorer inhibitors of the *B. fragilis* enzyme [37,38,43].

To obtain structural information to guide the design of improved broad-spectrum MBL inhibitors, we have used NMR to study the interaction of thiomandelic acid with the *B. cereus* MBL, BcII, particularly with its metal ions. The approaches we have used are described below.

Effect of Inhibitor Binding on the Backbone Amide Resonances

A two-dimensional proton–nitrogen correlation spectrum (^{1}H-^{15}N HSQC) of ^{15}N-labelled BcII allows the rapid observation of most of the backbone amide ^{1}H and ^{15}N resonances. We have assigned these resonances to individual residues in the free protein [45], and monitoring changes in these resonances thus provides a convenient method for identifying the regions of the enzyme affected by inhibitor binding—the "chemical shift mapping" approach has become a widely used method for the initial characterization of protein–ligand and protein–protein interactions.

Figure 1 shows a comparison of the ^{1}H-^{15}N HSQC spectra of the free enzyme and of the enzyme in the presence of *R*-thiomandelic acid (*R*-TM). Most of the spectrum remains essentially unaffected, but some significant changes are observed, generally involving residues which are close to the zinc binding sites. Only very few residues in the secondary structure elements of the core of the protein are affected by the inhibitor; some 90 residues in this part of the structure which give well-resolved resonance signals are unaffected by the addition of inhibitors. While the resonance assignment for the free enzyme is complete, the resonances in the complex are not yet assigned, so that the magnitude of the shifts of individual resonances cannot be accurately determined. We have thus used the "minimum chemical shift" approach [46–48], in which the chemical shift difference from a given cross-peak in the free protein to the closest cross-peak in the complex is calculated, to identify the residues most affected by inhibitor binding; these are indicated on the structure in Figure 1. As would be expected for a competitive inhibitor, many of the residues showing significant changes in chemical shift are in the active-site region of the structure, near the zinc ions. Only two or three residues in the structural core of the enzyme show significant changes.

Substantial amide chemical shift perturbations are, however, observed for residues in the "flexible-flap" region (the β_3–β_4 loop, residues 30–40), which in the absence of inhibitor is some distance from the active site (Figure 1). Shift changes are seen for E30, L31, F34, and V39 in this loop. (A significant shift perturbation is also observed for W59, which is located at the beginning of a loop on the top of the cavity; since the side-chain of W59 extends towards the β_3–β_4 loop, this could result from a movement of the loop.) There is good evidence that this loop plays a role in ligand binding and catalytic activity [18,41,44,45,49,50]. Loop deletion and loop swapping experiments with the *B. fragilis, B. cereus* and IMP-1 MBLs [49,50] have shown that the loop influences not only the K_i of inhibitors but also both the K_M and k_{cat} of substrates, suggesting that it plays a role in the catalytic mechanism. In the structure of the complex of IMP-1 MBL with a large mercaptocarboxylate inhibitor [18], there are clear hydrophobic contacts between the inhibitor and residues of the β3–β4 loop. These interactions might stabilize the loop, which is flexible in the absence of the inhibitor [44], in a "closed" position. However, our own studies with the *B. cereus* enzyme have shown that the residues of this loop are affected by the binding of much smaller inhibitors, not only thiomandelic acid [45] but even the simple mercaptoacetic acid [Kumar, S. unpublished work]. This clearly shows that hydrophobic interactions with the bound ligand cannot be the origin of the loop movement; there must be a "trigger" mechanism related to the coordination of the metal ions.

Effect of Inhibitor Binding on the Imidazole Resonances of the Metal Ligands

In examining the effect of inhibitor binding on the active site of the *B. cereus* enzyme, the imidazole resonances of the metal-binding histidine residues (H86, H88, and H149 in site I, H210 in site II) provide valuable probes. The imidazole N*H* resonances appear between 12 and 15 ppm (Figure 2). They have been assigned to individual residues by using ^{1}H-^{15}N HMQC spectra optimized for observation of the long-range ^{1}H-^{15}N couplings in the imidazole ring [29], which allow one to connect the N*H* resonances to those of the two nitrogens and the two C*H* protons in each imidazole. At pH 6.4, 298K, in the absence of inhibitors, relatively sharp resonances are observed for H86 and H88, and a broad resonance for H210, but no signal is apparent for H149. At lower pH or temperature, the H210 resonance sharpens and a signal for H149 appears. These differences in linewidth reflect the

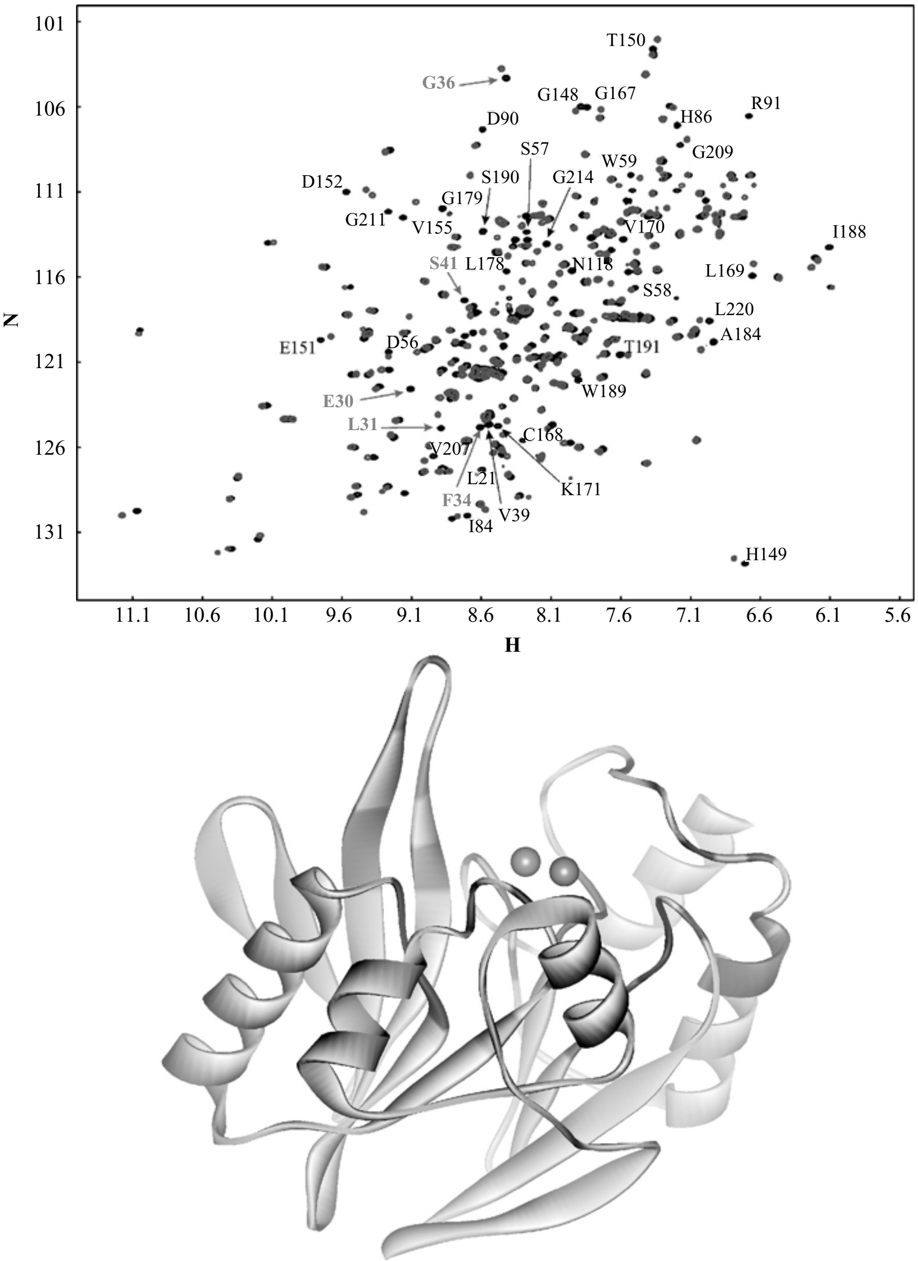

Fig. 1. ^{1}H-^{15}N HSQC spectra of *B. cereus* MBL BcII alone in black, and in its complex with *R*-TM in red. Assignments of residues affected by ligand binding are labelled on the HSQC spectra and are displayed on the X-ray structure of the free BcII. Residues affected in the flexible β3-β4 loop are labelled in blue on the HSQC and on the structure. Other residues affected by the presence of the inhibitor are coloured in green on the structure. (See also Plate 103 on page XXI in the Color Plate Section.)

Fig. 2. Part of the ^{1}H NMR spectrum of *B. cereus* MBL BcII in the presence and absence of *R*-TM, showing the imidazole N*H* resonances of the metal-binding histidine residues.

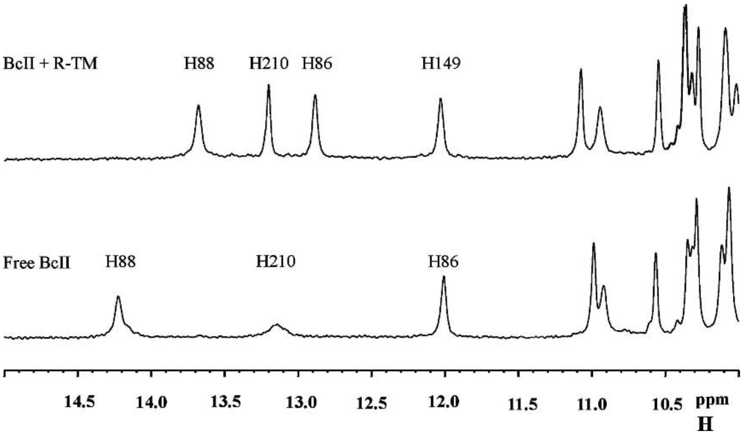

differences in accessibility of the histidine imidazole N*H*s for exchange with the solvent. Gradual addition of *R*-thiomandelic acid to the enzyme results in a progressive decrease in the intensity of the imidazole N*H* signals from the free enzyme, and a progressive increase in a new set of signals attributable to the enzyme-inhibitor complex. The changes are complete at a 1:1 ratio of inhibitor to enzyme, and the spectrum of the fully formed complex is shown in Figure 2. It is clear that the imidazoles in both metal binding sites are markedly affected by inhibitor binding. In site I, both H86 and H88 show large (>0.5 ppm) changes in N*H* chemical shift on inhibitor binding. In addition, inhibitor binding clearly tends to decrease the rate of exchange with water of the imidazole N*H*s of the metal-binding histidines, thus sharpening their resonances, although the magnitude of this effect varies significantly from one residue to another. Thus, the resonances of H86 and H88 are reasonably sharp in the spectrum of the free enzyme, and their linewidths are little affected by inhibitor binding, while the resonance of H210 is broad in the spectrum of the free enzyme and is markedly sharpened by the binding of *R*-thiomandelic acid so that in the complex it has approximately the same linewidth as H86 and H88. The N*H* resonance of H149, on the other hand, is too broad to see in the spectrum of the free enzyme; only the binding of the inhibitor decreases the imidazole N*H* exchange rate of this residue sufficiently to yield an observable resonance—in fact one as sharp as those of the other three active site histidines in this complex. The binding of *R*-thiomandelic acid thus changes not only the time-average environment of the zinc-ligating residues, as reflected in their chemical shifts, but also their dynamics, as reflected in the rate of exchange of their N*H* protons with water.

Direct Observation of the Active-Site Metals

In the majority of MBLs, zinc can be exchanged with cadmium to yield catalytically active enzymes [51], and in the case of CcrA, the structure of the cadmium-substituted enzyme has been shown to be essentially identical to that of the zinc enzyme [52]. Isotopes of cadmium provide very convenient spectroscopic probes, allowing direct studies of the co-ordination and dynamics of the metal ion. We have used NMR and, in collaboration with Prof. R. Bauer (Copenhagen), perturbed angular correlation of γ-rays (PAC) spectroscopy [29,45,53,54] to make detailed studies of metal binding to the *B. cereus* MBL. The enzyme with two cadmium ions bound gives a ^{113}Cd NMR spectrum containing two distinct resonances at ~140 and ~260 ppm [29]. We have assigned these two signals to the two metal binding sites of the enzyme by using a variety of multinuclear NMR experiments, particularly ^{113}Cd-edited ^{1}H and ^{1}H-^{15}N HSQC experiments, which allow us to connect the ^{113}Cd signals to assigned ^{1}H and ^{15}N resonances from the metal ligands (see Figure 3; [29,45,53,54]).

Analysis of the ^{1}H-^{15}N HSQC spectra of the *B. cereus* MBL enzyme with only one cadmium ion bound demonstrates the existence of a mononuclear cadmium enzyme, which is distinct from the apoenzyme, and from the species with two cadmiums bound. This mononuclear enzyme shows one single broad ^{113}Cd NMR signal at ~175 ppm, suggesting at first sight that cadmium occupies only one of the two sites under these conditions; however, two well defined cadmium PAC signals are observed [53]. The only explanation for these observations comes from considering the dynamics of metal binding and the different time regimes monitored by the two methods.

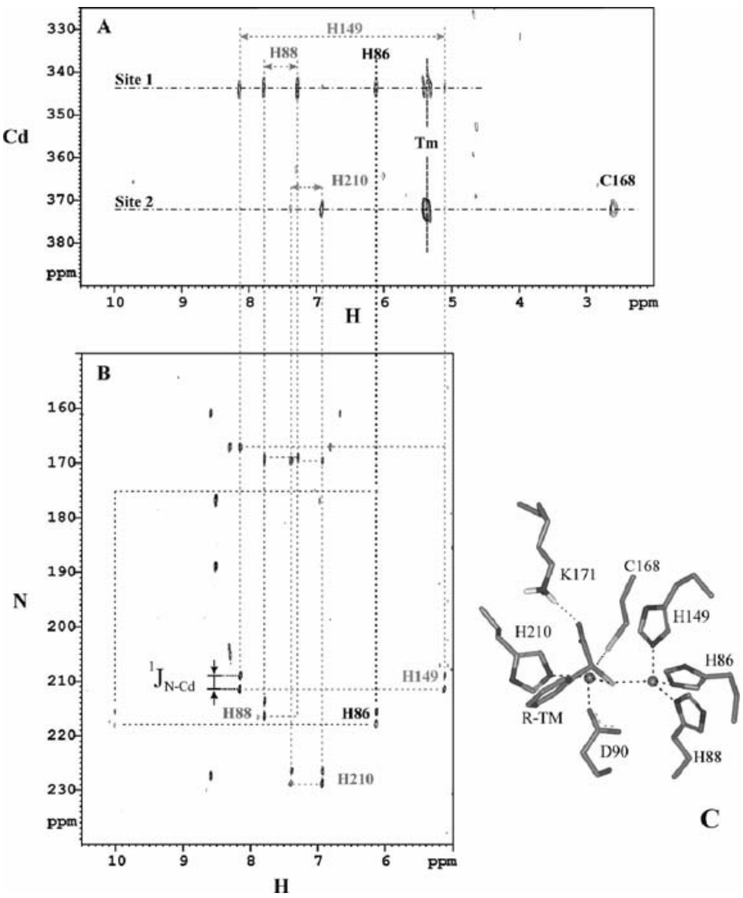

Fig. 3. NMR spectra of di-cadmium BcII in the presence of one equivalent of *R*-TM. (A) ^{1}H-^{113}Cd HMQC spectrum; (B) ^{1}H-^{15}N HMQC spectrum of the imidazole resonances, allowing assignment of the imidazole cross-peaks in A. Signal splittings in the nitrogen dimension due to the N-Cd coupling are observed for the four active site histidines. (C), Model of the binding of *R*-TM to the active site of BcII [49].

The timescales to which the two methods are sensitive are quite different: ^{111m}Cd-PAC experiments can monitor dynamics in a time regime from about 0.1 ns to 100 ns, whereas chemical exchange effects in ^{113}Cd NMR, with large chemical shift differences arising from differences in coordination, can typically monitor dynamics from 0.01 to 10 ms. The most straightforward explanation consistent with both the NMR data and the PAC data at [Cd(II)]/[E] ratios ≤ 1, is that a single cadmium bound to the enzyme jumps between the two binding sites on a time scale between 100 ns and 0.01 ms. Thus, the long-held assumption that the two different macroscopic dissociation constants for metal ion binding to the enzyme, reflecting a higher affinity of the metal for site I was shown to be wrong; they in fact reflect negative co-operativity in metal binding [53]. Recent studies of the wild-type and mutant enzyme by optical spectroscopy and EXAFS experiments indicated that there is a similar negative co-operativity in the binding of zinc and cobalt [55].

Effects of Thiomandelate Binding on the ^{113}Cd Spectrum

The BcII gives a ^{113}Cd NMR spectrum containing two distinct resonances at ~140 and ~260 ppm [29,53]. Addition of one molar equivalent of *R*-thiomandelic acid to the *B. cereus* MBL with two cadmium ions bound leads to a substantial downfield shift of both the ^{113}Cd resonances, to ~343 and ~372 ppm (Figure 3). Addition of 0.5 molar equivalent of thiomandelate leads to a spectrum containing both resonances corresponding to the free enzyme, and those corresponding to the complex, with approximately equal intensities, indicating that thiomandelate binding is in slow exchange on the ^{113}Cd NMR timescale. Further addition of the inhibitor from one to two molar equivalents does not change the NMR spectra. The direction and magnitude of the inhibitor-induced change in chemical shift is consistent with that expected for the co-ordination of a sulphur atom to each of the cadmium ions, and hence with the idea that the inhibitor binds directly to both metal sites.

Direct evidence for this, and the assignment of the two ^{113}Cd resonances in the inhibitor complexes, can be obtained from the combination of ^{1}H-^{113}Cd HMQC spectra and ^{1}H-^{15}N HSQC spectrum optimized for observation of imidazole resonances [29], shown in Figure 3. In the ^{1}H-^{113}Cd HMQC spectrum, cross-peaks are observed from the 343 ppm ^{113}Cd resonance for three imidazoles, His88, His86, and His149. The His88 can easily be assigned because it is the only metal-bound histidine which is in the N_{ε}H tautomeric form, and thus readily recognized in the ^{1}H-^{15}N HSQC spectrum[1]. The 343 ppm ^{113}Cd resonance can thus be unambiguously assigned to the cadmium in site I. There is also a strong cross-peak to a signal at 5.36 ppm, which can be assigned to the CαH (benzylic proton) of the bound *R*-thiomandelate (*R*-TM). This inhibitor resonance also gives a strong cross-peak to the low-field ^{113}Cd resonance (Figure 3), which in turn shows cross-peaks to the imidazole protons of His210 and the β-proton(s) of Cys168, and can thus be assigned to the metal in site II. The observation that, in a complex containing one molar equivalent of inhibitor, the *R*-TM resonance at 5.36 ppm gives a cross-peak in the ^{1}H-^{113}Cd HMQC spectrum to both ^{113}Cd resonances, is clear evidence that *R*-TM co-ordinates through its sulphur atom to both cadmium ions.

As described above, the ^{113}Cd spectrum of the enzyme having one cadmium equivalent bound contains a single resonance, reflecting a rapid intramolecular exchange of the single metal between the two sites. Addition of one molar equivalent of *R*-TM to the mono-cadmium enzyme led to a ^{113}Cd spectrum having two resonances at the same chemical shifts as those observed for the complex of the di-cadmium enzyme. Furthermore, the ^{113}Cd-edited ^{1}H spectra of the *R*-TM complex demonstrated that the thiomandelate CαH resonance at 5.35 ppm showed ^{1}H-^{113}Cd scalar coupling to two cadmium nuclei, just as observed for the di-cadmium enzyme, demonstrating that the thiomandelate-enzyme complex contains two cadmium ions. These observations clearly demonstrate that addition of thiomandelate to a sample of enzyme containing cadmium at a [Cd]/[E] ratio of one, leads to the formation of the *R*-TM complex of the di-cadmium enzyme together with a corresponding amount of apoenzyme [54]. This was confirmed by analysis of the backbone amide ^{1}H-^{15}N HSQC spectrum. The presence of the inhibitor, which binds to both metal ions, thus induces positive co-operativity in metal binding, in marked contrast to the negative co-operativity in cadmium binding observed in the absence of inhibitor [29].

Conclusion

The power of NMR in determining the three-dimensional structure of proteins and their complexes in solution is well-established. Full structure determination of course provides the most detailed picture of a drug–protein complex, and in the present case the determination of the structure of the complex of *R*-thiomandelic acid with the *B. cereus* MBL is in progress. However the experiments described here demonstrate some of the range of NMR experiments which can provide very valuable structural and dynamic information on ligand binding short of a full structure; others are reviewed elsewhere [56,57]. Experiments of this kind, which can be carried out rapidly, have considerable value in understanding drug–protein interactions and in comparing the binding of related compounds to a target, and promise to have a continuing place in structure-based drug design.

References

1. Frere JM, Mol. Microbiol. 1995;16(3):385.
2. Matagne A, Dubus A, Galleni M, Frère JM. Nat. Prod. Rep. 16,1 (1999).
3. Wang Z, Fast W, Valentine AM, Benkovic SJ. Curr. Opin. Chem. Biol. 1999;3(5):614.
4. Payne DJ. Med J. Microbiol. 1993;39(2):93.
5. Laraki N, Franceschini N, Rossolini GM, Santucci P, Meunier C, de Pauw E, Amicosante G, Frere JM, Galleni M. Antimicrob. Agents Chemother. 1999;43(4):902.
6. Riccio ML, Franceschini N, Boschi L, Caravelli B, Cornaglia G, Fontana R, Amicosante G, Rossolini GM. Antimicrob. Agents Chemother. 2000;44(5):1229.
7. Iyobe S, Kusadokoro H, Ozaki J, Matsumura N, Minami S, Haruta S, Sawai T, O'Hara K. Antimicrob. Agents Chemother. 2000;44(8):2023.
8. Chu YW, Afzal-Shah M, Houang ET, Palepou MF, Lyon DJ, Woodford N, Livermore DM. Antimicrob. Agents Chemother. 2001;45(3):710.
9. Yano H, Kuga A, Okamoto R, Kitasato H, Kobayashi T, Inoue M. Antimicrobial. Agents and Chemother. 2001;45(5): 1343.
10. Livermore DM, Woodford N. Curr. Opin. Microbiol. 2000; 3(5):489.
11. Fabiane SM, Sohi MK, Wan T, Payne DJ, Bateson JH, Mitchell T, Sutton BJ, Biochemistry 1998;37(36):12404.

---

[1] The other two histidines have not been individually assigned in the cadmium-substituted enzyme, but can be tentatively assigned by comparison with the assigned resonances in the zinc enzyme [45].

12. Carfi A, Du Eée, Galleni M, Frère JM and Dideberg O. Acta Cryst. 1998;D54:313.
13. Carfi A, Duee E, Paul-Soto R, Galleni M, Frere JM, Dideberg O, Acta Crystallogr. D. Biol. Crystallogr. 1998;54(Pt 1):45.
14. Concha NO, Rasmussen BA, Bush K, Herzberg O. Structure 1996;4(7):823.
15. Fitzgerald PM, Wu JK, Toney JH. Biochemistry 1998; 37(19):6791.
16. Garcia-Saez I, Hopkins J, Papamicael C, Franceschini N, Amicosante G, Rossolini GM, Galleni M, Frere JM, Dideberg O. J. Biol. Chem. 2003;278(26):23868.
17. Ullah JH, Walsh TR, Taylor IA, Emery DC, Verma CS, Gamblin SJ, Spencer J. Mol. J. Biol. 1998;284(1):125.
18. Concha NO, Janson CA, Rowling P, Pearson S, Cheever CA, Clarke BP, Lewis C, Galleni M, Frere JM, Payne DJ, Bateson JH, Abdel-Meguid SS, Biochemistry. 2000;39(15):4288.
19. Aravind L. In Silico Biol. 1999;1(2):69.
20. Daiyasu H, Osaka K, Ishino Y, Toh H. FEBS. Lett. 2001; 503(1):1.
21. Melino S, Capo C, Dragani B, Aceto A, Petruzzelli R. Trends Biochem. Sci. 1998;23(10):381.
22. Galleni M, Lamotte-Brasseur J, Rossolini GM, Spencer J, Dideberg O, Frere JM. Antimicrob. Agents Chemother. 2001; 45(3):660.
23. Bounaga S, Laws AP, Galleni M, Page MI. Biochem. J. 1998; 331(Pt 3):703.
24. Rasia RM, Vila AJ. Biochemistry. 2002;41(6):1853.
25. Wang ZG, Fast W, Benkovic SJ. Biochemistry. 1999;38(31): 10013.
26. Cricco JA, Orellano EG, Rasia RM, Ceccarelli EA, Vila AJ. Coordination Chem. Rev. 192,519 (1999).
27. Wommer S, Rival S, Heinz U, Galleni M, Frere JM, Franceschini N, Amicosante G, Rasmussen B, Bauer R, Adolph HW. J. Biol. Chem. 2002;277(27):24142.
28. Paul-Soto R, Hernadez-Valladares M, Galleni M, Bauer R, Zeppezauer M, Frère JM, Adolph HW. FEBS Lett. 1998;438: 137.
29. Damblon C, Prosperi C, Lian LY, Barsukov I, Paul-Soto R, Galleni M, Frère JM, Roberts GCK. J. Am. Chem. Soc. 1999;121:11575.
30. Hernandez Valladares M, Felici A, Weber G, Adolph HW, Zeppezauer M, Rossolini GM, Amicosante G, Frere JM, Galleni M. Biochemistry. 1997;36(38):11534.
31. Toney JH, Fitzgerald PM, Grover-Sharma N, Olson SH, May WJ, Sundelof JG, Vanderwall DE, Cleary KA, Grant SK, Wu JK, Kozarich JW, Pompliano DL, Hammond GG. Chem. Biol. 1998;5(4):185.
32. Nagano R, Adachi Y, Imamura H, Yamada K, Hashizume T, Morishima H, Antimicrob. Agents Chemother. 1999;43(10): 2497.
33. Walter MW, Felici A, Galleni M, Paul-Soto R, Adlington RM, Baldwin JE, Frère JM, Gololobov M, Schofield CJ. Bioorg. Med. Chem. Lett. 1996;6(20):2455.
34. Walter MW, Hernandez Valladres M, Adlington RM, Amicosante G, Baldwin JE, Frère JM, Galleni M, Rossolini GM, Schofield CJ. Bioorg. Chem. 1999;27:35.
35. Toney JH, Hammond GG, Fitzgerald PMD, Sharma N, Balkovec JM, Rouen GP, Olson SH, Hammond ML, Greenlee ML, Gao YD, J. Biol. Chem. 2001;276(34):31913.
36. Goto M, Takahashi T, Yamashita F, Koreeda A, Mori H, Ohta M, Arakawa Y. Biol. Pharm. Bull. 1997;20(11):1136.
37. Payne DJ, Bateson JH, Gasson BC, Proctor D, Khushi T, Farmer TH, Tolson DA, Bell D, Skett PW, Marshall AC, Reid R, Ghosez L, Combret Y, Marchand-Brynaert J. Antimicrob. Agents Chemother. 1997;41(1):135.
38. Payne DJ, Bateson JH, Gasson BC, Khushi T, Proctor D, Pearson SC, Reid R, Fems. Microbiol. Lett. 1997;157: 171.
39. Payne DJ, Bateson JH, Gasson BC, Khushi T, Proctor D, Pearson SC, Reid R. FEMS Microbiol. Lett. 1997;157(1):171.
40. Page MI, Laws AP. Chem. Commun. 1998;16:1609.
41. Scrofani SDB, Chung J, Huntley JJA, Benkovic SJ, Wright PE, Dyson HJ. Biochemistry. 1999;38(44):14507.
42. Greenlee ML, Laub JB, Balkovec JM, Hammond ML, Hammond GG, Pompliano DL, Epstein_Toney JH. Bioorgan. Med. Chem. Lett. 1999;9(17):2549.
43. Hammond GG, Huber JL, Greenlee ML, Laub JB, Young K, Silver LL, Balkovec JM, Pryor KD, Wu JK, Leiting B, Pompliano DL, Toney JH. FEMS Microbiol. Lett. 1999;179(2):289.
44. Huntley JJA, Scrofani SDB, Osborne MJ, Wright PE, Dyson HJ. Biochemistry. 2000;39(44):13356.
45. Mollard C, Moali C, Papamicael C, Damblon C, Vessilier S, Amicosante G, Schofield CJ, Galleni M, Frere JM, Roberts GCK. J. Biol. Chem. 2001;276(48):45015.
46. Lian LY, Barsukov I, Golovanov AP, Hawkins DI, Badii R, Sze KH, Keep NH, Bokoch GM, Roberts GCK. Structure 2000;8(1):47.
47. Farmer BT. Nat. Struct. Biol. 1996;3(12):995.
48. Williamson RA, Carr MD, Frenkiel TA, Feeney J, Freedman RB. Biochemistry. 1997;36(45):13882.
49. Yang Y, Keeney D, Tang X, Canfield N, Rasmussen BA, J. Biol. Chem. 1999;274(22):15706.
50. Moali C, Anne C, Lamotte-Brasseur J, Groslambert S, Devreese B, Van Beeumen J, Galleni M, Frere JM. Chem. & Biol. 2003;10(4):319.
51. Paul-Soto R, Bauer R, Frere JM, Galleni M, Meyer-Klaucke W, Nolting H, Rossolini GM, de Seny D, Hernandez-Valladares M, Zeppezauer M, Adolph HW. Biol. J. Chem. 1999;274(19):13242.
52. Concha NO, Rasmussen BA, Bush K, Herzberg O, Protein Sci. 1997;6(12):2671.
53. Hemmingsen L, Damblon C, Antony J, Jensen M, Adolph HW, Wommer S, Roberts GCK, Bauer R, Amer. J. Chem. Soc. 2001;123:10329.
54. Damblon C, Jensen M, Ababou A, Barsukov I, Papamicael C, Schofield CJ, Olsen L, Bauer R, Roberts GCK, J. Biol. Chem. 2003;278(31):29240.
55. de Seny D, Heinz U, Wommer S, Kiefer M, Meyer-Klaucke W, Galleni M, Frere JM, Bauer R, Adolph HW. Biol. J. Chem. 2001;276(48):45065.
56. Roberts GCK, Curr. Opin. Biotech. 1999;10(1):42.
57. Roberts GCK. Drug Discov. Today. 2000;5(6):230.

NMR Spectroscopy in the Analysis of Protein–Protein Interactions

David A. Gell and Joel P. Mackay
School of Molecular and Microbial Biosciences, University of Sydney, Sydney, NSW 2006, Australia

Introduction

Specific interactions between pairs or larger sets of proteins are central to all processes that take place within an organism, and many of these interactions may prove to be suitable targets for therapeutic intervention. In order to target such complexes effectively, detailed structural information is highly desirable, and NMR spectroscopy is one of the methods of choice for providing this information.

Recent methodological advances have enabled full structure determination for increasingly large proteins and protein complexes. These methods include TROSY pulse sequences, sample deuteration, and the use of additional long-range structural restraints derived from residual dipolar couplings (RDCs) and paramagnetic effects to complement traditional NOE-based methods. For protein–protein complexes, filtered/edited NOE experiments with differentially labeled samples greatly reduce spectral complexity through selecting only intra- or intermolecular NOEs.

While NMR cannot currently compete with X-ray crystallography in the determination of the structures of huge macromolecular machines such as the ribosome, it has many advantages for the study of more transient protein complexes, for which crystals are less likely to form. Relatively weak or transient interactions (high μM–mM dissociation constants) allow cells to respond dynamically to rapidly changing conditions; for example, many cell surface receptor interactions [1] and electron transport processes [2] rely on transient interactions. Likewise, transcription factor complexes are often formed from combinations of low-affinity interactions [3], facilitating exchange of factors that alter the transcriptional activity of the complex [4]. For weak protein complexes full structure determination by NMR may be prevented by exchange processes, but protein–protein interfaces and association constants may still be determined using chemical shift perturbation experiments. In such cases, shift perturbation data or long-range conformational restraints can be used to drive the docking of a complex, based on known structures of subunit components.

This chapter will outline the approaches mentioned above, together with experimental difficulties that are likely to be encountered. Examples both from our own work and from that of others will be used for illustration.

Tackling the Size Issue for Larger Protein Complexes

In general, the study of protein complexes involves dealing with larger species. Unfortunately, the slower tumbling (measured by τ_c, the molecular correlation time) of larger species leads to increased transverse relaxation rates. Faster transverse relaxation reduces the efficiency with which magnetization can be transferred through scalar couplings. As a consequence, the experiments used to make resonance assignments perform more poorly as τ_c increases. This has effectively placed a rough upper limit of ~30 kDa on the size of a system that can be solved using standard triple resonance methods [5]. However, several recently developed approaches have opened the door to the analysis of much larger proteins and protein complexes.

Deuteration

The first strategy involves the preparation of protein samples in which some percentage of protons is substituted by deuterons. This can be achieved by protein over-expression in cells grown on deuterated media [6]. Two advantages are conferred by the incorporation of ^{2}H. Firstly, the relaxation of ^{13}C nuclei is brought about primarily through the dipolar interaction with their attached proton(s). Because the magnitude of the dipolar interaction is directly proportional to the gyromagnetic ratios of the nuclei involved, substitution of ^{1}H for ^{2}H ($\gamma_H/\gamma_D = 6.5$) reduces the magnitude of this interaction significantly. With the addition of ^{2}H decoupling that removes the line broadening effects that arise from scalar coupling to a quadrupolar nucleus, ^{13}C line widths are dramatically reduced. Secondly, the general reduction in

Graham A. Webb (ed.), Modern Magnetic Resonance, 1339–1346.
© 2008 *Springer.*

proton density reduces spin diffusion significantly, resulting in narrower ^1H line widths.

Growth medium for protein deuteration is made up in ^2H_2O, and cells often require acclimatization on this media to grow well [7]. To achieve complete deuteration (perdeuteration), labeled carbon sources are required in addition to ^2H_2O (e.g. ^2H, ^{13}C-glucose or acetate). The extent of deuteration aimed for will depend on the goal of the study. Perdeuteration, followed by back exchange of labile backbone and side chain amide deuterons for protons, as will generally occur during protein purification in ^1H_2O, will yield the greatest improvements in sensitivity and resolution for backbone triple resonance experiments and chemical shift perturbation experiments (see below). However, lower levels of deuteration, down to ~50% [8], are required if side chain NOEs are to be detected. Alternatively, several groups have pioneered the use of biosynthetically directed labeling strategies that can be used to produce, for example, ^2H-, ^{13}C-, and ^{15}N-labeled proteins that bear protonated methyl groups on Leu, Val, and the $\delta 1$ methyl of Ile [9]. Such protein samples allow NOEs to be detected between methyl groups, which often lie in the protein core and provide a substantial number of structural constraints. Indeed, H^N–H^N, H^N–methyl, and methyl–methyl NOEs alone may be sufficient to define the global fold of a large protein [6].

TROSY

The other recent breakthrough that is revolutionizing the analysis of large systems is transverse relaxation optimized spectroscopy (TROSY) [10]. Transverse relaxation of amide ^1H and ^{15}N spins at high field strengths is dominated by two main mechanisms: dipole–dipole (DD) interactions and chemical shift anisotropy (CSA). Amide protons additionally experience significant relaxation (~40% of T_2 [11]) from remote ^1H spins, but this latter term can be largely eliminated by perdeuteration, as described above. Interference between DD and CSA relaxation (cross-correlation) has the effect of enhancing the relaxation of one component of the H^N doublet while slowing the relaxation of the other; the two doublet components thus display different line widths. The same is true for the ^{15}N doublet, and an undecoupled 2×2 multiplet in an HSQC has one component that is considerably narrower in both dimensions. The degree of relaxation interference changes with field strength, because CSA but not DD relaxation is field dependent, and at ~1 GHz the two relaxation mechanisms essentially cancel each other in the narrow component. The line width of this component consequently becomes relatively insensitive to the rotational correlation time of the protein, and the TROSY pulse sequence element (a simple modification of the HSQC pulse sequence) selects this signal. TROSY promises a great deal for the analysis of large systems and high-quality TROSY-HSQC spectra have already been recorded of systems up to ~900 kDa (a GroEL–GroES complex [12]). The TROSY element has been incorporated into a number of triple resonance experiments, and in combination with deuteration these sequences have been used to make massive strides in the size of systems that are amenable to solution NMR analysis. Backbone assignments of malate synthase, a 723-residue monomer [13], and aldolase, a 110-kDa octamer [14], have been reported recently. Perhaps even more excitingly, the structures of several integral membrane proteins solubilized in lipid micelles have been determined [15–17]. These latter studies hold substantial promise for the analysis of interactions between receptors and effector proteins.

The benefits of TROSY and deuteration have already been applied to map the interaction surfaces of large protein complexes using chemical shift perturbation experiments. Complexes formed between Ras and Byr2 [18], calreticulin and Erp57 [19], p53 and Hsp90 [20], and FimC and FimH [21] have all been characterized in this fashion.

Reducing Complexity: Differential Isotope Labeling

An additional issue that arises in NMR studies of protein complexes is the increase in the number of resonances. A simple method to alleviate this problem involves preparing complexes in which individual subunits carry different isotope labeling patterns. Most commonly, one protein will be ^{15}N- and ^{13}C-labeled, while its partner will be unlabeled. This arrangement has two advantages. First, HSQC spectra show signals from only the labeled partner, simplifying chemical shift titration experiments. Second, heteronuclear filters can be incorporated into pulse programs to either select or filter out magnetization from protons attached to specific nuclides, and hence select specific subsets of inter- or intramolecular resonances. The double half-filtered NOESY spectrum comprises four sub-spectra that are created by the linear combination of four data sets recorded with different phase cycles [22]. The most useful of these sub-spectra contain only NOEs between protons attached to different nuclides. For example, the $^{13}C(\omega_1)$-filtered/$^{13}C(\omega_2)$-selected sub-spectrum of a $^{13}C(\omega_1, \omega_2)$ double half-filtered NOESY will display NOEs between protons not bound to ^{13}C in ω_1 and protons exclusively bound to ^{13}C in ω_2. Figure 1 shows such a sub-spectrum from a data set recorded on a complex of two zinc finger domains [23] in our laboratory, and many other studies have utilized this technique to gather NOE constraints for structure determination.

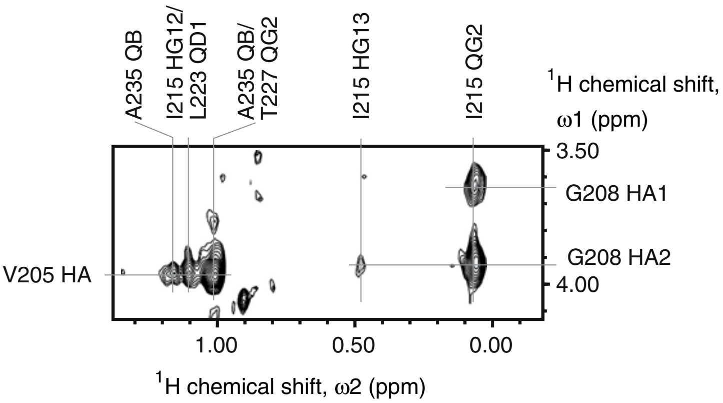

Fig. 1. Heteronuclear filtered/selected NOESY data. A portion of a two-dimensional ^{13}C-filtered, ^{13}C-edited NOESY spectrum of a 1:1 complex formed from ^{15}N and ^{13}C-labeled GATA-1 N-finger and unlabeled U-shaped finger 1, highlighting a number of intermolecular NOEs (Liew *et al.* (2005) PNAS 102, 583–8). This sub-spectrum contains only NOEs between protons attached to ^{12}C (ω2) and protons attached to ^{13}C (ω1).

Obtaining Long-Range Structural Information

A recent innovation has been the use of long-range structural information to supplement the conventional NOE data. Two methods for deriving long-range structure calculation restraints are described below; these methods have particular significance for protein complexes as they provide information about the relative orientation of subunits.

Line ‘em Up—Residual Dipolar Couplings

In NMR spectra of species that do not undergo rotational motion, resonances are split not only by scalar couplings (J), but also by dipolar couplings (D) involving nuclei that are nearby in space. These dipolar couplings can be extremely large (thousands of Hz), but average to zero if the molecule tumbles rapidly in solution. Because the magnitude of a dipolar coupling is dependent on the orientation of each internuclear vector relative to the static field, couplings between different pairs of nuclei reveal the orientation of those vectors relative to a common frame of reference (and therefore relative to each other). This represents valuable structural information, not least because it reports on the relative orientations of distant parts of a molecule or complex, in contrast to the more usual NOEs and scalar coupling constants [24].

The trick in creating a useful structural tool from this concept has been to create a physical environment where a protein exhibits a small degree of preferential alignment. Too much alignment results in the observation of many dipolar couplings that render spectra un-interpretable, but a small amount yields RDCs of up to ~10–20 Hz that are observed only for spin pairs that are strongly coupled: generally one-bond interactions. Solutions containing low concentrations of a highly aligned and asymmetric component provide suitable environments for these experiments. Bacteriophage, disc-shaped lipid bicelles (both of which align completely in a magnetic field) and compressed polyacrylamide gels have all been used [24], and in such media, the reorientation of a protein becomes slightly non-isotropic. The magnitudes of the RDCs can be tuned by altering the concentration of the alignment medium.

These splittings (e.g. $^1D_{\mathrm{HNN}}$, $^1D_{\mathrm{H}\alpha\mathrm{C}\alpha}$) can be measured directly in simple 2D and 3D NMR experiments such as undecoupled HSQC and HNCO spectra, and methodologies have been developed to incorporate these data into standard structure calculation programs [25]. It should be noted that there is some degeneracy in the derived data, with more than one possible relative orientation of a vector leading to the same RDC. This fact, together with issues with the energy landscapes generated by dipolar couplings in simulated annealing protocols, have somewhat hindered the widespread use of such data to date [24].

Dipolar coupling data have been demonstrated to be beneficial in a number of scenarios, including validation of NMR structures [26] and DNA structure determination [27]. One of their most powerful uses may prove to be in defining the relative orientations of domains in a multi-domain proteins [28–30] or of protein subunits in a complex [31,32].

Paramagnetic Nuclei

Paramagnetic species cause a multitude of effects on the relaxation and chemical shifts of neighboring nuclei [33]. Paramagnetics induce both T_1 and T_2 relaxation in nearby nuclei through a number of mechanisms, and traditionally cause problems in the structure determination of metalloproteins such as copper(II) plastocyanin. However, these effects show predictable distance and angle dependence, and can therefore provide useful structural information [33,34]. Pseudocontact shifts (PCSs) are chemical shift changes induced through the interaction of nuclei with the anisotropic susceptibility tensor χ of the paramagnetic center. These changes are dependent on the position of the nucleus relative to the χ tensor and fall off with the third power of distance, thereby providing useful long-range structural information [35]. Furthermore, interaction between the χ tensor and the strong static magnetic field can lead to preferential orientation of the protein, generating RDCs.

Because PCSs are long-range effects, chemical shift changes can be induced across protein–protein interfaces and the information can therefore be used to orient protein complexes. This approach has been successful for complexes containing cytochromes [36–38] as well as for a DNA polymerase III complex [34]. Many proteins contain metal sites that can accommodate paramagnetic ions. For example many Ca^{2+} binding sites can bind paramagnetic lanthanide ions, which due to their highly anisotropic paramagnetic susceptibilities are good choices for PCS and RDC studies [39]. In the absence of natural metal binding sites, spin-labels, such as gadolinium-EDTA [40], cobalt-EDTA [35], and TEMPO (which contains a stable nitroxide radical [41]), can be attached to proteins by chemical cross-linking.

Mapping Protein–Protein Interfaces

Chemical Shift Perturbation Experiments

The chemical shift of a nuclear spin is extremely sensitive to the physical and chemical environment of the spin, and has been used extensively to map the amino acids in a protein that directly contact a binding partner. Figure 2A shows ^1H, ^{15}N HSQC data from the titration of a solution of unlabeled α-hemoglobin into uniformly ^{15}N-labeled alpha hemoglobin stabilizing protein (AHSP [42]). ^1H, ^{15}N HSQC spectra are generally used in such titrations because of their high sensitivity and excellent resonance dispersion. It can be seen that a subset of the signals shift significantly upon the addition of α-hemoglobin, and it can be inferred that the amino acids that correspond to these signals (Figure 2B) either reside on the α-hemoglobin binding surface of AHSP, or are involved in a conformational change upon α-hemoglobin binding Feng *et al.* (2004) CELL 119, 629–40. Because of this latter possibility, care must be taken in interpreting the results of chemical shift titrations; complementary data from mutagenesis studies are often extremely useful [23,43]. Identification of binding surfaces is potentially an

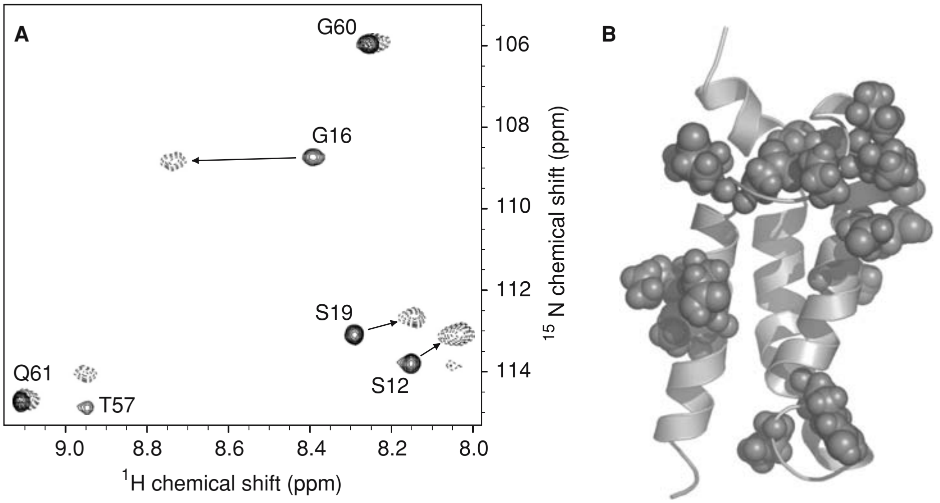

Fig. 2. Chemical shift perturbation experiment. (A) Sections of ^1H, ^{15}N HSQC spectra of ^{15}N-labeled AHSP are shown in the absence (solid lines) and the presence (dashed line) of 1.2 molar equivalents of unlabeled α-hemoglobin. Resonance assignments are indicated for several residues that undergo significant chemical shift changes (indicated by arrows), as well as several that remain unperturbed. (B) A ribbon representation of the AHSP NMR structure, highlighting the residues that undergo significant chemical shift changes upon titration with α-hemoglobin (space-fill). These residues constitute the major portion of the α-hemoglobin binding surface of AHSP (Feng *et al.* (2004) CELL 119, 629–40).

important early step in the design of targeted therapeutics, and chemical shift titrations have been used extensively in the screening of small molecule libraries to find lead compounds that bind a target protein [44]. Chemical shift titration data can also be used to determine equilibrium constants (for $K_A \sim 10^3$–10^6 M^{-1}).

Cross-saturation

Recently, a new method for mapping protein interfaces, called cross-saturation [45], has been employed to map interaction interfaces of a number of protein complexes [46–48]. In this approach, the protein whose interaction surface is to be mapped is ^{2}H- and ^{15}N-labeled and mixed with its unlabeled partner. Saturation of high-density ^{1}H nuclei of the unlabeled protein spreads to the back-exchanged amide protons on the interaction surface of the double-labeled protein by spin diffusion and can be detected through quenching of signals in a ^{1}H, ^{15}N TROSY-HSQC. Because this technique relies on through-space proximity of the interaction surfaces, conformational changes would not be expected to affect the results as they do with chemical shift mapping studies.

Protein–Protein Interactions and Chemical Exchange

The phenomenon of chemical exchange is observed in many different guises in NMR spectra. In the examination of protein–protein interactions, the rate of exchange between free and bound protein forms can lead to poor NMR spectra if the timescale of the binding process compared to the chemical shift timescale is inappropriate.

As is well known, slow and fast exchange regimes exist [49]. Consider a single proton at a protein–protein interface. In slow exchange, the lifetimes of both the bound and free states are sufficiently long ($>\sim$1 s) that a separate signal is observed for each. In fast exchange ($\sim$µs or shorter lifetimes), a single signal at an averaged chemical shift (determined by the populations of the bound and free states) is observed. At the extremes of these regimes, no signal broadening occurs. However, in between lies the intermediate exchange regime, where substantial line broadening and non-Lorentzian lineshapes can occur.

In the situation where two species with equal populations interconvert in a unimolecular reaction ($A \leftrightarrow B$), the maximum amount of line broadening occurs when the rate of exchange (k_{ex}) is given by:

$$k_{ex} = \frac{\pi \Delta \nu}{\sqrt{2}} \tag{1}$$

where $\Delta \nu$ is the frequency difference for a spin between two states. For bimolecular reactions ($A + B \leftrightarrow C$), the mathematics is more complex, but analogous expressions, albeit approximate, can be derived. In cases of intermediate exchange, the degree of line broadening depends on several parameters, namely the off-rate for the complex (k_d), the equilibrium constant (K_A), the line widths of the free and bound species, and the concentrations of each component. For typical frequency changes that might be observed in the formation of a protein complex ($\sim$10–600 Hz for ^{1}H), and assuming diffusion controlled on-rates for complex formation, equilibrium constants in the range 10^3–10^6 M^{-1} are most likely to give rise to NMR spectra exhibiting intermediate exchange. As noted above, regulatory interactions of this strength are common in cells.

Chemical shift titration data can be used to determine interaction affinities. For systems in fast exchange, non-linear least squares fitting of the population averaged chemical shift to a simple hyperbolic binding function can be carried out. For slow exchange, disappearance and/or reappearance of signals from the free or bound protein states can be used to generate a binding curve. In the case of intermediate exchange, where significant line broadening occurs, the analysis is more complex, but binding constants may still be calculated [50] (Figure 3).

Line widths often increase substantially during the course of such a titration as a result of exchange broadening, but then decrease toward the end as the fraction of labeled protein in the complexed state nears one. If the

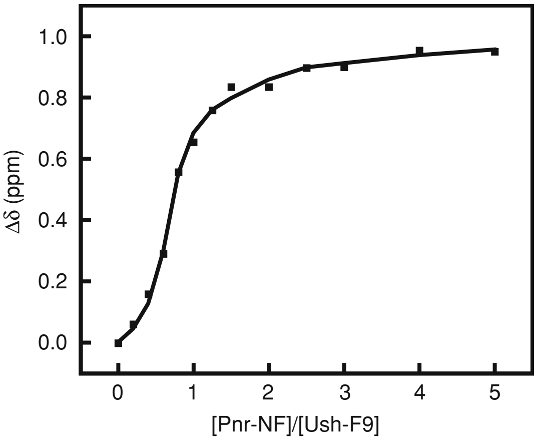

Fig. 3. Deriving binding affinity from NMR data. Plot of the change of ^{15}N chemical shift ($\Delta\delta$) for residue V21 of U-Shaped finger 9 (Ush-F9) upon binding to the N-finger of Pannier (Pnr-NF). The analysis [62] was based using a model of intermediate exchange [50] and reveals an association constant of 2.5×10^4 M^{-1}.

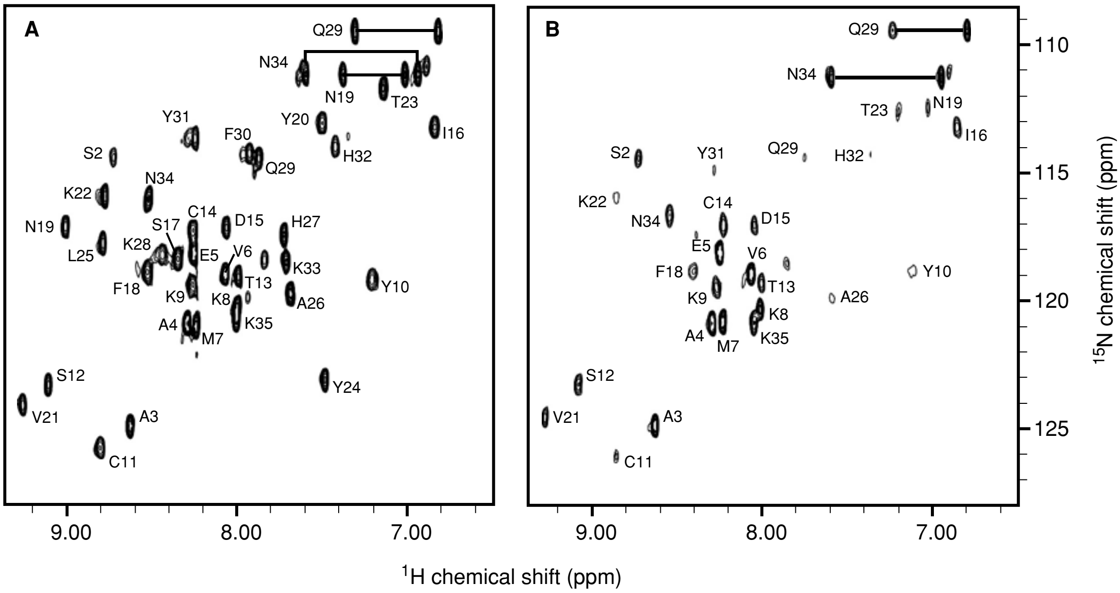

Fig. 4. The effect of intermediate chemical exchange on NMR spectra. ^{1}H, ^{15}N HSQC spectra of a point mutant (C32H) of zinc finger 9 from U-shaped, in the absence (left) and presence (right) of 5 molar equivalents of its binding partner, the N-terminal zinc finger from GATA-1 [62].

binding is relatively weak, however, it may be impractical to reach this point, preventing assignment of the complex and determination of a structure. In the titration shown in Figure 4, the signals that disappear correspond to residues that are known to lie at the protein–protein interface from mutagenesis studies [23], but it can be seen that they do not reappear even following the addition of 5 molar equivalents of unlabeled binding partner.

In principle, manipulation of solution conditions might allow one to move from intermediate to fast or slow exchange; however, in practice, the narrow range of conditions under which protein structural studies can be carried out often precludes this possibility. Protein complexes that exhibit unfavorable chemical exchange properties therefore often remain difficult to characterize by NMR.

Stitching Up Proteins for Improved Stability

In many cases, the preparation of protein complexes for structural studies is hindered by the instability of one or both components. In such cases, it may prove advantageous to either co-express the two partners [51] or to express engineered fusions of the interacting proteins. For example, the LIM domain proteins LMO2 and LMO4 are extremely unstable in isolation, which hampered studies in our laboratory of their structures and their interaction with the co-regulator ldb1. In contrast, single-chain LMO2-ldb1 and LMO4-ldb1 fusion proteins [52] could be readily purified and their structures determined [53]. Volkman *et al.* used an identical strategy in their analysis of the N-WASP:WIP complex [11]: the EVH1 domain from N-WASP was poorly expressed and insoluble, but these problems were alleviated in a N-WASP:WIP fusion protein.

A similar approach may hold promise for the analysis of weak protein complexes in which chemical exchange prevents the acquisition of high-quality data. By constraining diffusion of the two components, it may be possible to shift the system to a more favorable exchange regime. Indeed, covalent end-to-end ligation of two individually expressed recombinant proteins could potentially be achieved using intein technology (self-splicing protein modules [54]), thus permitting differential labeling of the two components as described above.

Docking Protein Complexes

An interesting new development is the use of NMR data to guide docking of protein–protein complexes, given the known 3D structures of the subunits. The *in silico* docking of two proteins in the absence of direct experimental data has generally been unsuccessful because of the large

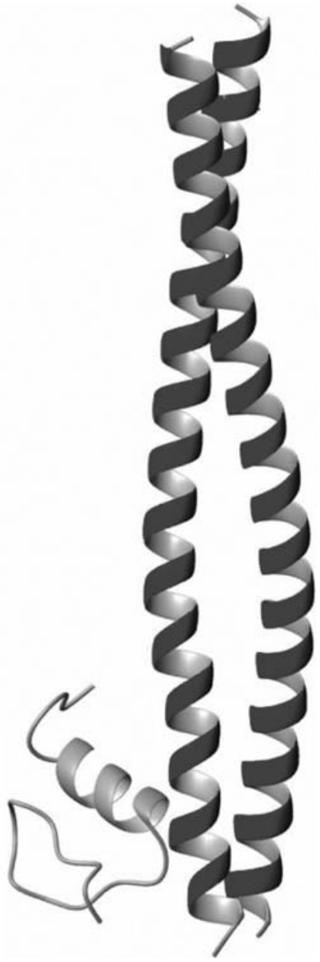

Fig. 5. HADDOCK derived structure of a complex formed between TACC3 and the third zinc finger of FOG. The TACC3 dimeric coiled-coil (dark) and the FOG zinc finger (light). The model was generated using the known structure of FOG finger 3, a homology model of the TACC3 coiled-coil, and a combination of alanine scanning mutagenesis and chemical shift perturbation data (Simpson *et al.* (2004) J Biol Chem 279, 39789–97).

number of degrees of freedom presented by two protein surfaces. However, long-range structural information derived from RDCs or paramagnetic effects, along with limited intermolecular NOEs, can be used to orient protein subunits in docking routines. For example, the N-terminal domain of enzyme I (EIN) and the histidine phosphocarrier, HPr were successfully docked using 231 ${}^{1}D_{\mathrm{HNN}}$ RDC restraints and only nine intermolecular NOEs. The final docked complex was within 1.3 Å of the previously solved NMR structure of the complex [55]. Such approaches can equally be employed to determine the domain packing of multi-domain proteins [56].

The identification of intermolecular NOEs requires the time-consuming assignment of side chain resonances. A number of approaches have been recently described for docking protocols that do not rely on NOE data [57–59]. These methods utilize chemical shift perturbation, mutagenesis and RDC data, which require only backbone assignments. HADDOCK [58] docks two proteins of known structure in the CNS-based ARIA protocol [60,61]. The use of ARIA allows the introduction of ambiguous interaction restraints (AIRs) derived from a wide range of NMR and other biophysical data. Chemical shift titration data are introduced by defining AIRs between each amino acid on the identified interaction surface of one protein and all of the residues on the surface of the partner protein. Mutagenesis data can be included in a similar fashion. We recently used this procedure to generate a model of the complex formed between a zinc finger from the transcriptional regulator FOG and a coiled-coil domain from TACC3 (Figure 5). One limitation of docking approaches is that they rely on the assumption that the structures of the bound and complexed proteins remain unchanged.

Summary

In this chapter, we have outlined the major approaches to characterizing protein–protein complexes using solution NMR spectroscopy, with a particular emphasis on recently developed experimental techniques. Essentially all of these approaches are applicable to other macromolecular complexes, and it is likely that we will see a substantial increase in both the number and the complexity of the systems analyzed over the next 5 years.

References

1. van der Merwe PA, Barclay AN, Trends Biochem. Sci. 1994;19(9):354.
2. Crowley PB, Ubbink M. Acc. Chem. Res. 2003;36(10):723.
3. Ptashne M, Gann A. Curr. Biol. 1998;8(22):R812.
4. Naar AM, Lemon BD, Tjian R. Annu. Rev. Biochem. 2001; 70:475.
5. Sattler M, Schleucher J, Griesinger C. Prog. NMR Spectrosc. 1999;34:93.
6. Gardner K, Lay L. Annu. Rev. Biophys. Biomol. Struct. 1998; 27:357.
7. Venters RA, Huang CC, Farmer BT 2nd, Trolard R, Spicer LD, Fierke CA. J. Biomol. NMR. 1995;5(4):339.
8. Nietlispach D, Clowes RT, Broadhurst RW, Ito Y, Keeler J, Kelly M, Ashurst J, Oschkinat H, Domaille PJ, Laue ED. J. Am. Chem. Soc. 1996;118(2):407.
9. Gardner K, Kay L. J. Am. Chem. Soc. 1997;119:7599.

10. Pervushin K, Riek R, Wider G, Wüthrich K. Proc. Natl. Acad. Sci. U.S.A. 1998;94:12366.
11. Volkman BF, Prehoda KE, Scott JA, Peterson FC, Lim WA. Cell. 2002;111(4):565.
12. Fiaux J, Bertelsen EB, Horwich AL, Wuthrich K. Nature. 2002;418(6894):207.
13. Tugarinov V, Muhandiram R, Ayed A, Kay LE. J. Am. Chem. Soc. 2002;124(34):10025.
14. Salzmann M, Pervushin K, Wider G, Senn H, Wuthrich K. J. Am. Chem. Soc. 2000;122:7543.
15. Fernandez C, Adeishvili K, Wuthrich K. Proc. Natl. Acad. Sci. U.S.A. 2001;98(5):2358.
16. Arora A, Abildgaard F, Bushweller JH, Tamm LK. Nat. Struct. Biol. 2001;8(4):334.
17. Hwang PM, Choy WY, Lo EI, Chen L, Forman-Kay JD, Raetz CR, Prive GG, Bishop RE, Kay LE. Proc. Natl. Acad. Sci. U.S.A. 2002;99(21):13560.
18. Gronwald W, Huber F, Grunewald P, Sporner M, Wohlgemuth S, Herrmann C, Kalbitzer HR. Structure. 2001;9(11):1029.
19. Frickel EM, Riek R, Jelesarov I, Helenius A, Wuthrich K, Ellgaard L. Proc. Natl. Acad. Sci. U.S.A. 2002;99(4):1954.
20. Rudiger S, Freund SM, Veprintsev DB, Fersht AR. Proc. Natl. Acad. Sci. U.S.A. 2002;99(17):11085.
21. Pellecchia M, Sebbel P, Hermanns U, Wuthrich K, Glockshuber R. Nat. Struct. Biol. 1999;6(4):336.
22. Otting G, Wüthrich K. J. Magn. Reson. 1989;85:586.
23. Liew CK, Kowalski K, Fox AH, Newton A, Sharpe BK, Crossley M, Mackay JP. Structure. 2000;8:1157.
24. Bax A, Kontaxis G, Tjandra N. Methods Enzymol. 2001; 339:127.
25. Tjandra N, Omichinski JG, Gronenborn AM, Clore GM, Bax A. Nat. Struct. Biol. 1997;4(9):732.
26. Clore GM, Garrett D. J. Am. Chem. Soc. 1999;121:9008.
27. Ramos A, Grunert S, Adams J, Micklem DR, Proctor MR, Freund S, Bycroft M, St Johnston D, Varani G. EMBO J. 2000;19(5):997.
28. Fisher M, Losonczi J, Prestegard J. Biochemistry. 1999; 38:9013.
29. Walters KJ, Lech PJ, Goh AM, Wang Q, Howley PM. Proc. Natl. Acad. Sci. U.S.A. 2003;100(22):12694.
30. Tsui V, Zhu L, Huang TH, Wright PE, Case DA. J. Biomol. NMR. 2000;16(1):9.
31. Garrett DS, Seok YJ, Peterkofsky A, Gronenborn AM, Clore GM. Nat. Struct. Biol. 1999;6(2):166.
32. Wang G, Louis JM, Sondej M, Seok YJ, Peterkofsky A, Clore GM. EMBO J. 2000;19(21):5635.
33. Ubbink M, Worrall JA, Canters GW, Groenen EJ, Huber M. Annu. Rev. Biophys. Biomol. Struct. 2002;31:393.
34. Pintacuda G, Keniry MA, Huber T, Park AY, Dixon NE, Otting G. J. Am. Chem. Soc. 2004;126(9):2963.
35. Gaponenko V, Sarma SP, Altieri AS, Horita DA, Li J, Byrd RA. J. Biomol. NMR. 2004;28(3):205.
36. Ubbink M, Ejdeback M, Karlsson BG, Bendall DS. Structure. 1998;6(3):323.
37. Guiles RD, Sarma S, DiGate RJ, Banville D, Basus VJ, Kuntz ID, Waskell L. Nat. Struct. Biol. 1996;3(4):333.
38. Worrall JA, Liu Y, Crowley PB, Nocek JM, Hoffman BM, Ubbink M. Biochemistry. 2002;41(39):11721.
39. Barbieri R, Bertini I, Cavallaro G, Lee YM, Luchinat C, Rosato A. J. Am. Chem. Soc. 2002;124(19):5581.
40. Arumugam S, Hemme CL, Yoshida N, Suzuki K, Nagase H, Berjanskii M, Wu B, Van Doren SR. Biochemistry. 1998;37(27):9650.
41. Jain NU, Venot A, Umemoto K, Leffler H, Prestegard JH. Protein Sci. 2001;10(11):2393.
42. Kihm AJ, Kong Y, Hong W, Russell JE, Rouda S, Adachi K, Simon MC, Blobel GA, Weiss MJ. Nature. 2002; 417(6890):758.
43. Schmiedeskamp M, Rajagopal P, Klevit RE. Protein Sci. 1997;6(9):1835.
44. Shuker SB, Hajduk PJ, Meadows RP, Fesik SW. Science. 1996;274(5292):1531.
45. Takahashi H, Nakanishi T, Kami K, Arata Y, Shimada I. Nat. Struct. Biol. 2000;7(3):220.
46. Lane AN, Kelly G, Ramos A, Frenkiel TA. J. Biomol. NMR. 2001;21(2):127.
47. Nishida N, Sumikawa H, Sakakura M, Shimba N, Takahashi H, Terasawa H, Suzuki EI, Shimada I. Nat. Struct. Biol. 2003;10(1):53.
48. Shao W, Im SC, Zuiderweg ER, Waskell L. Biochemistry. 2003;42(50):14774.
49. Sanders J, Hunter B. Modern NMR Spectroscopy. Oxford University Press: Oxford, 1987.
50. Feeney J, Batchelor J, Albrand J, Roberts G. J. Magn. Reson. 1979;33:519.
51. Demarest SJ, Martinez-Yamout M, Chung J, Chen H, Xu W, Dyson HJ, Evans RM, Wright PE. Nature. 2002;415(6871): 549.
52. Deane JE, Sum E, Mackay JP, Lindeman GJ, Visvader JE, Matthews JM. Protein Eng. 2001;14:493.
53. Deane J, Mackay J, Kwan A, Sum E, Visvader J, Matthews J. EMBO J. 2003;22:2224.
54. Hofmann RM, Muir TW. Curr. Opin. Biotechnol. 2002;13(4): 297.
55. Clore GM. Proc. Natl. Acad. Sci. U.S.A. 2000;97(16):9021.
56. Dosset P, Hus JC, Marion D, Blackledge M. J. Biomol. NMR. 2001;20(3):223.
57. Dobrodumov A, Gronenborn AM. Proteins. 2003;53(1):18.
58. Dominguez C, Boelens R, Bonvin AM. J. Am. Chem. Soc. 2003;125(7):1731.
59. Fahmy A, Wagner G. J. Am. Chem. Soc. 2002;124(7):1241.
60. Brunger AT, Adams PD, Clore GM, DeLano WL, Gros P, Grosse-Kunstleve RW, Jiang JS, Kuszewski J, Nilges M, Pannu NS, Read RJ, Rice LM, Simonson T, Warren GL. Acta. Crystallogr. D. Biol. Crystallogr. 1998;54(Pt 5):905.
61. Nilges M. J. Mol. Biol. 1995;245(5):645.
62. Kowalski K, Liew CK, Matthews JM, Gell DA, Crossley M, Mackay JP. J. Biol. Chem. 2002;277:35720.

Identification and Characterization of Ternary Complexes Using NMR Spectroscopy

Robert E. London

Laboratory of Structural Biology, National Institute of Environmental Health Sciences, Research Triangle Park, NC 27709, USA

Introduction

The complex macromolecules that have evolved to serve a broad range of biological functions present surfaces with highly variable topological, electrostatic, and hydrogen bonding properties. These surfaces provide the basis for interactions that play critical roles in catalysis and signal transduction, and offer a limitless landscape of potential targets for chemical agents designed to interfere with these functions. A broad range of analytical techniques has been developed to exploit this topological information when it is available, but it is clear that flexible ligands can interact in unanticipated ways with their theoretical targets, and often with unintended targets as well. Substitution of an amino group for a single oxygen substituent to convert folate to aminopterin results in a potent antifolate drug which, unexpectedly, adopts a dramatically different conformation in the complex with the target enzyme, dihydrofolate reductase [1,2]. Studies of the inhibition of alpha-chymotrypsin by a series of 1-acetamidoboronic acids unexpectedly revealed that when the side chain of the inhibitor was altered from a *p*-chlorophenyl to a 1-naphthyl group, the enzyme reversed its usual preference for L-enantiomers, which more closely resemble the natural substrates, and bound more tightly to the D-enantiomer [3].

The sensitivity of NMR spectroscopy to ligand–macromolecule interactions makes it of considerable value for the process of ligand identification and modification, and a broad range of approaches have been described that involve direct observations of either the target macromolecule [4] or the ligand [5]. The use of any particular approach is generally strongly dependent on the particular problem under study, however direct NMR studies of biologically important macromolecules are limited by the size and complexity of the macromolecule, its solubility, the general requirement for isotopic labeling, and the more extensive analysis which may be required. Alternatively, observations of ligands have been demonstrated to be useful for selecting lead compounds from complex mixtures [6] and for obtaining insight into the conformation of bound ligands [7], and are often more straightforward to interpret.

One approach for the analysis of ligand–macromolecule interactions involves the identification of ternary complexes formed from pairs of ligands in the presence of a macromolecule. In some cases, biologically interesting complexes have formed from adventitious inorganic ions such as aluminum or beryllium fluorides [8]. The presence of adventitious zinc ions led to the identification of a trypsin-Zn^{2+}-bis(5-amidino-2-benzimidazolyl)methane ternary complex, which formed a basis for the further development of serine protease inhibitors [9]. Arsenate and borate complexes have been identified due to the use of cacodylate and borate buffers [10,11]. Vanadate complexes have been identified in toxicological and bioinorganic studies [12–14]. These complexes have been detected based on their biochemical effects, or by structural methods including X-ray crystallography and NMR spectroscopy. Arsenate complexes often mimic phosphate complexes, both structural and biochemically, while vanadate complexes often form pentavalent structures that mimic the transition state involved in nuclease and phosphatase biochemistry [12–15]. Vanadate, and aluminum and beryllium fluorides are all capable of mimicking the terminal phosphate group of nucleotides, e.g. turning ADP into the ADP-VO_4 analog of ATP [16–18]. Boronate and borate complexes most frequently mimic the tetrahedral transition state of serine proteases and mechanistically related enzymes [19–21]. Alternatively, enzymatic catalysis frequently involves the formation of ternary complexes that include two, and occasionally more, organic ligands. For example, many enzyme-catalyzed redox reactions involve ternary enzyme-substrate–cofactor complexes. Formation of transient complexes involving macromolecules and organic ligands can be studied using transferred interligand Overhauser effects (ILOEs) [22–27]. A brief outline of NMR approaches used to study ternary complexes is described in the present article.

Borate Complexes and Their Study by NMR Spectroscopy

Studies of ternary and higher order complexes formed from inorganic ions have provided insights into the

Graham A. Webb (ed.), Modern Magnetic Resonance, 1347–1356.
© 2008 *Springer.*

toxicological properties of these ions, valuable structural information, insight into catalytic mechanisms, as well as fundamental information of use for the design of inhibitors. In some cases, these ions interact with active site residues of enzymes in ways that mimic transition state structures. A comprehensive review of this area is beyond the scope of the present article, but our recent studies of borate complexes illustrate many of the features of these studies.

Boric acid (pK = 9.0) is a convenient buffer for high pH assays of enzymes or other biochemical phenomena. The use of borate buffers has led to a number of unanticipated observations that resulted from the presence of borate–ligand complexes. For example, borate has been found to inhibit pyridine nucleotide and flavin-requiring enzymes as a result of complex formation with these cofactors [28,29]. A more dramatic effect is observed in studies of the membrane protein γ-glutamyl transpeptidase (γ-GT), an enzyme important for glutathione metabolism that transfers γ-linked glutamyl groups between peptides, amino acids, or other acceptors. For this enzyme, serine and borate, which individually exert little effect on the enzyme, exhibit a dramatic inhibitory synergy [11]. This inhibitory synergy apparently results from the stabilization of a ternary γ-GT–serine–borate complex, in which the borate adopts a tetrahedral, anionic form that is esterified to both an enzyme threonine hydroxyl group, as well as to the hydroxyl group of the serine ligand [20,21]. This ternary complex thus mimics a putative transition state in which the threonine hydroxyl group of the active site binds to the γ-carbon of the glutamyl group in glutathione or another substrate, creating a transition state with tetrahedral geometry.

Although direct NMR observations of membrane associated enzymes such as γ-GT are difficult, the general features of such ternary complexes have been observed for the serine protease trypsin [30–32]. In these studies, several cationic alcohols with presumed affinity for the trypsin S1 specificity binding pocket were studied. The molecules were selected so that the alcohol function would be appropriately positioned to interact with a borate bound to the active site serine-195. Boron-11 spectra of samples containing borate, trypsin, and 4-aminobutanol (4AB) are characterized by a resonance with a chemical shift that corresponds to the boric acid–borate equilibrium at the pH used for the study, as well as an upfield shifted resonance corresponding to a tetrahedral borate which is now in slow exchange with the free boric acid/borate species (Figure 1). Binary mixtures of borate–trypsin or borate–4AB, or a ternary mixture of borate, trypsin, and 3-aminobutanol do not show the upfield shifted resonance. The resonance observed at −17.3 ppm can therefore be assigned to a ternary trypsin–borate–4AB complex.

Analogous complexes have now been observed in the crystalline state [31,32]. Interestingly, the crystallographic studies demonstrate that the nature of the borate complex formed at the active site is significantly influenced by lattice contacts, so that a ternary trypsin–borate–4AB complex analogous to that observed in solution could be observed in $P3_121$ crystals [32], while only quaternary trypsin–borate–4AB–ethylene glycol complexes were observed in $P2_12_12_1$ crystals [31]. In the $P2_12_12_1$ crystals, formation of the active site borate complex was found to be correlated with a 4% expansion of the crystal along the *b*-axis. These results were interpreted to indicate that the additional stability of the quaternary complex was required to overcome crystal packing effects. This study therefore illustrates the significant effect that lattice contacts can have on crystallographic screening for enzyme ligands.

Most of the inorganic complexes which have been studied by NMR, involve nuclei with spin >1/2, and hence are subject to quadrupolar relaxation. For quadrupolar nuclei bound to very large molecules such that $\omega\tau \gg 1$, where ω is the Larmor frequency of the nucleus and τ its rotational correlation time, the relaxation behavior is multiexponential. For nuclei with half-integral spin in this limit, the central $1/2 \leftrightarrow -1/2$ transition can give rise to a relatively narrow signal, while the remaining transitions are very broad and generally unobserved [33–36]. Subject to the above assumptions, the linewidth of the central transition is then inversely related to $\omega^2\tau$, i.e. the linewidth actually narrows as the rotational correlation time of the complex τ increases:

$$\Delta\nu_{1/2} = \frac{1}{\pi T_2} = \frac{2s+3}{\pi s^2(2s-1)}\Big(2J_1^Q(\omega_S) + ((s+3/2) \times (s-1/2)-1)\Big(J_2^Q(2\omega_S)\Big)\Big) \quad (1)$$

where

$$J^Q(\omega) = \frac{3\chi^2}{160}\left(\frac{\tau}{1+\omega^2\tau^2}\right) \quad (2)$$

χ is the quadrupole coupling constant, nucleus S has spin s and Larmor frequency ω_S, τ is the rotational correlation time, and isotropic motion is assumed. In the limit $\omega\tau \gg 1$, we obtain:

$$\Delta\nu_{1/2} = \frac{1}{\pi T_2} \approx \left(\frac{2(2s+3)}{\pi s^2(2s-1)}\right)\left(1+\frac{1}{8}((s+3/2) \times (s-1/2)-1)\right)\frac{3\chi^2}{160}\frac{1}{\omega^2\tau} \quad (3)$$

This inverse dependence on τ contrasts with the linewidth predictions based on other relaxation mechanisms such as the dipolar interaction and chemical shift anisotropy, which predict $\Delta\nu_{1/2} \sim J(0) \sim \tau_c$. Exchange

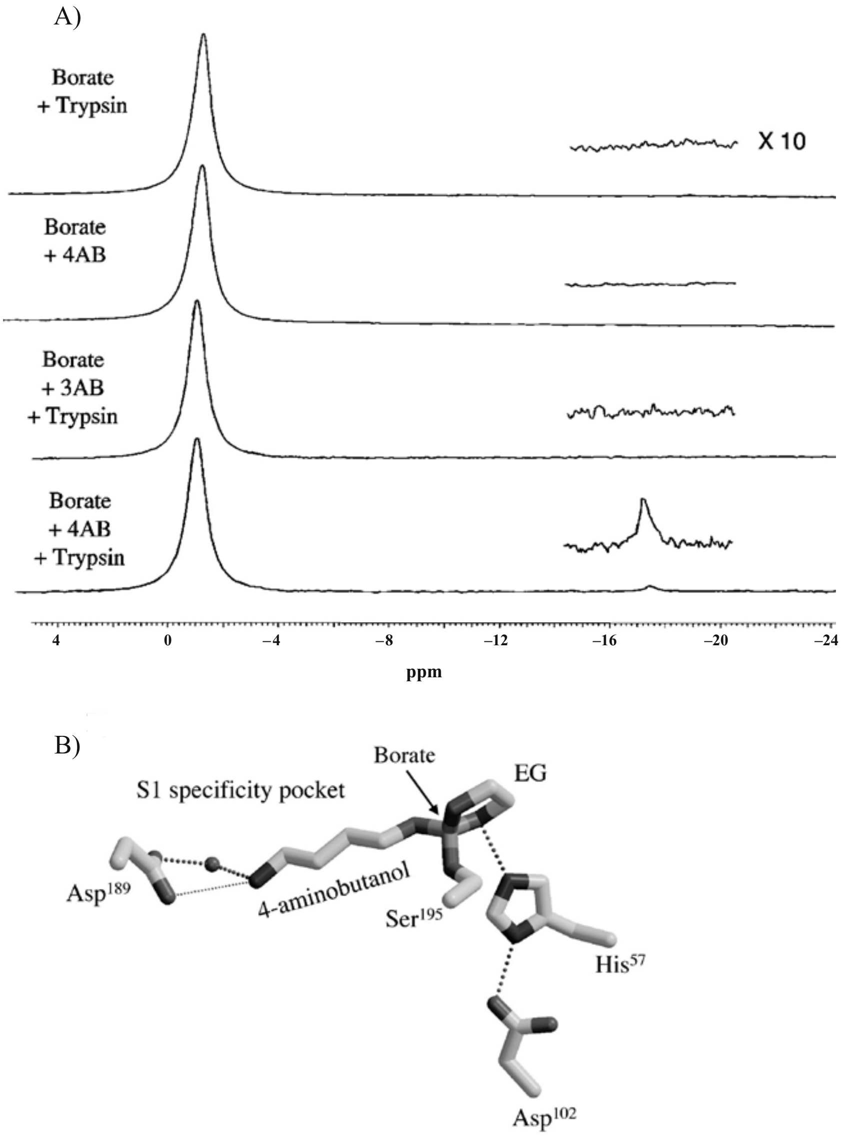

Fig. 1. (A) Boron-11 NMR spectra obtained at 160.6 MHz, 25°C on samples containing (top to bottom) 5 mM borate and 2 mM porcine pancreatic trypsin; 25 mM borate and 250 mM 4-aminobutanol; 5.0 mM borate, 50 mM 3-aminopropanol, and 2 mM trypsin; 5.0 mM borate, 50 mM 4-aminobutanol, and 2 mM trypsin. Insets show a 10-fold vertical expansion. All samples contained 20 mM HEPES, pH 8.0 (based on Figure 1 of Ref. [30]). (B) Active site of trypsin showing complex formed with borate, 4-aminobutanol, and ethylene glycol (EG) (based on Figure 1F of Ref. [31]). A similar ternary complex without the EG has also been observed for crystals in the $P3_{1}21$ space group [32].

broadening due to the chemical exchange between uncomplexed and variously complexed forms of the ion also can make significant contributions. The observation of narrow resonances for quadrupolar nuclei in macromolecules is illustrated by the ^{11}B NMR spectrum of 4-fluorobenzeneboronic acid (FBBA) in the presence of a small ligand, sorbitol, and the enzyme subtilisin Carlsberg (MW = 27.3 kD), shown in Figure 2. As

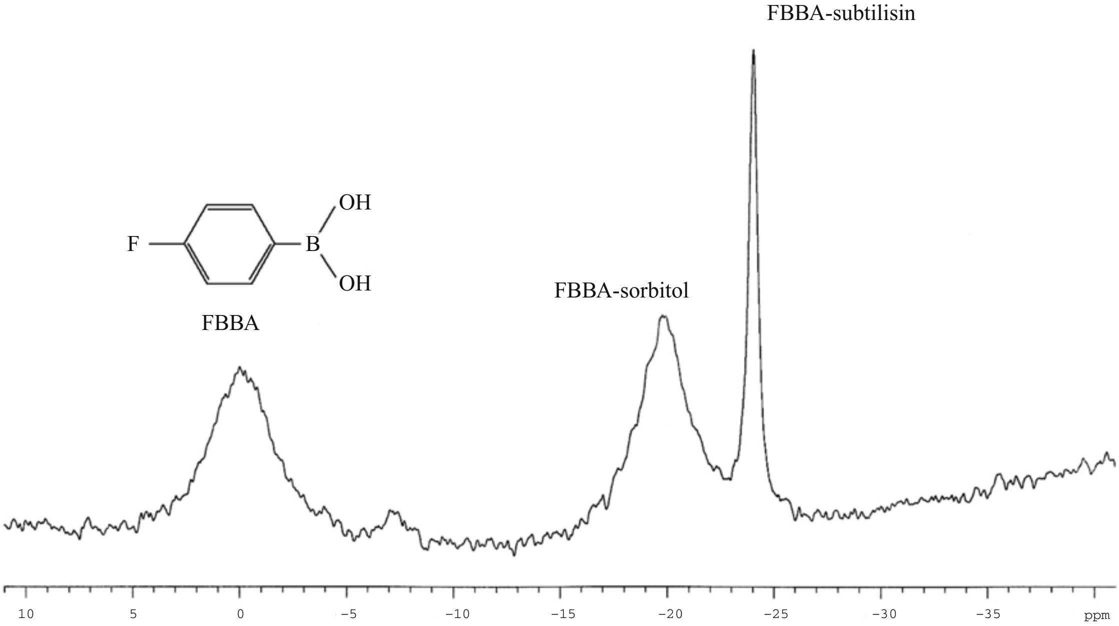

Fig. 2. Boron-11 NMR spectrum of 5 mM 4-fluorobenzeneboronic acid, 1.5 mM sorbitol, 2 mM subtilisin Carlsberg (MW = 27.3 kD) in 50 mM HEPES, pH 7.5 obtained at 11.75 T (160.6 MHz ^{11}B frequency), 5°C.

predicted above, the resonance arising from the boronate–subtilisin complex is significantly narrower than the resonances for either free boronate or for the boronate–sorbitol complex. The ^{11}B linewidth of the uncomplexed FBBA is determined by quadrupolar relaxation of the ^{11}B nucleus (spin = 3/2) and by boronic acid–boronate exchange, while the linewidths of the FBBA–sorbitol and FBBA–subtilisin complexes are probably determined primarily by quadrupolar ^{11}B relaxation. In addition to this unintuitive dependence of linewidth on rotational correlation time, the quadrupolar nuclei are also subject to a second-order dynamic frequency shift which is also inversely correlated with ω (i.e. B_0) [35,36]:

$$\delta = \frac{8s(s+1)-6}{s^2(2s-1)^2}\Big(L_1^Q(\omega_S) - L_2^Q(2\omega_S)\Big) \qquad (4)$$

where

$$L^Q(\omega) = \frac{3\chi^2}{160}\left(\frac{\omega\tau^2}{1+\omega^2\tau^2}\right) \qquad (5)$$

so that

$$\delta \approx \frac{4s(s+1)-3}{s^2(2s-1)^2}\left(\frac{3\chi^2}{160}\right)\left(\frac{1}{\omega}\right) \quad \text{for } \omega\tau \gg 1 \qquad (6)$$

Expression of the shift in ppm results in a ω^{-2} dependence. Observations on the relaxation behavior of various metal ion complexes with transferrin have verified the predicted linewidth and shift behavior [37–39].

In summary, ^{11}B NMR studies provide a useful way of characterizing transient complexes that may form involving borate esters. The exchange behavior among various complexes is often sufficiently slow on the NMR time scale to allow observation of separate resonances. Similar complexes can be observed in the crystalline state, however in this case, lattice contacts can significantly alter the observation of these weak complexes. The observation of such complexes can provide useful insight into the development of boronated as well as non-boronated ligands.

Ternary Complexes Involving Organic Molecules

Although ternary complexes formed from inorganic ions can provide a useful basis for the development of high affinity ligands, it is desirable to generalize this approach by removing the restriction to inorganic ions. The observation of ILOEs provides one basis for obtaining information on the spatial proximity and relative orientation of two (or potentially more) ligands that form a relatively weak complex with a macromolecular binding site. Nuclear Overhauser effect (NOE) interactions involving

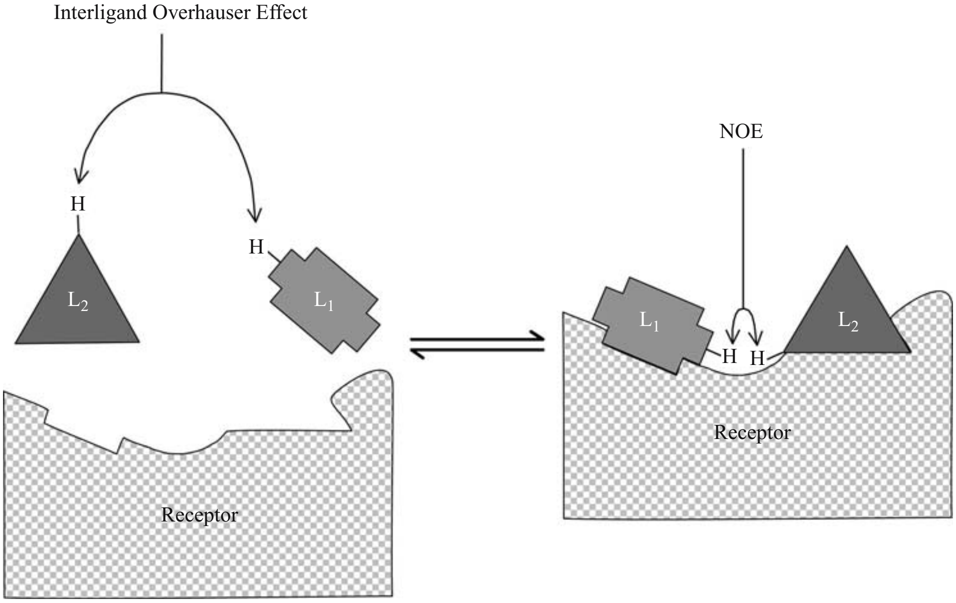

Fig. 3. Schematic illustration of the interaction of two ligands, L$_1$ and L$_2$, with a macromolecule. NOE interactions between the protons on the two different ligands can be transferred to the free ligands due to dissociation of the complex.

protons on the two ligands are transferred to the pair of uncomplexed ligands much as the intramolecular NOE information is transferred to the free ligand in a transferred NOE experiment (Figure 3). As in the transferred NOE experiment, these experiments are typically performed using a significant excess of ligand concentration, i.e. [L$_1$], [L$_2$] $\gg$ [E], where L$_1$ and L$_2$ are the two ligands and E is the enzyme or other macromolecule forming the complex. Since this approach involves direct observation of the ligand resonances, but not the resonances of the macromolecule, it does not require complex resonance assignment strategies. Further, as with the transferred NOE experiment, it works well on macromolecules that are too large for direct structural determination using currently available NMR methodology. However, in contrast with the transferred NOE experiment, this experiment is considerably less subject to misinterpretation resulting from non-specific binding, ligand aggregation, or ligand misbinding. The latter effect arises because ligand binding is essentially an exploratory process in which a ligand may become transiently lodged in an enzyme cleft in a non-productive conformation such that the structural constraints will not allow it to readily adopt a productive conformation. It then becomes most probable for the ligand to dissociate, and subsequently it may reassociate in a conformation which can lead to a productive complex. If the misbound ligand remains associated with the macromolecule for a time that is on the order of the rotational correlation time, it is then able to develop an NOE characteristic of the bound state, and this NOE information characteristic of the misbound complex will be transferred to the free ligand, along with the NOE information from the correctly bound ligand.

For both transferred NOE and interligand NOE studies to provide useful information, the exchange rates for both ligands must be reasonably fast compared with the T_1 time scale of the protons that are under observation. This allows NOE interactions characteristic of the bound ligand(s) to be observed regardless of whether the exchange is fast or slow on the chemical shift time scale, although in general, slow exchange on the shift time scale is less likely to satisfy the T_1 time scale constraint noted above, and leads to non-linear NOE build-up curves. The long T_1 values for the uncomplexed ligand allow it to be used as a "magnetic storage device" for NOE information that is formed in the macromolecular complex. The kinetic behavior of such a system is described using eight rate constants, seven of which are independent, as shown in Scheme 1. The fractional populations of the uncomplexed enzyme/macromolecule, pE, the two binary complexes pEL$_1$ and pEL$_2$, and the ternary complex pEL$_1$L$_2$, can be expressed as a function of the concentrations and rate constants, as described previously [24]. From a practical standpoint, we have generally found that

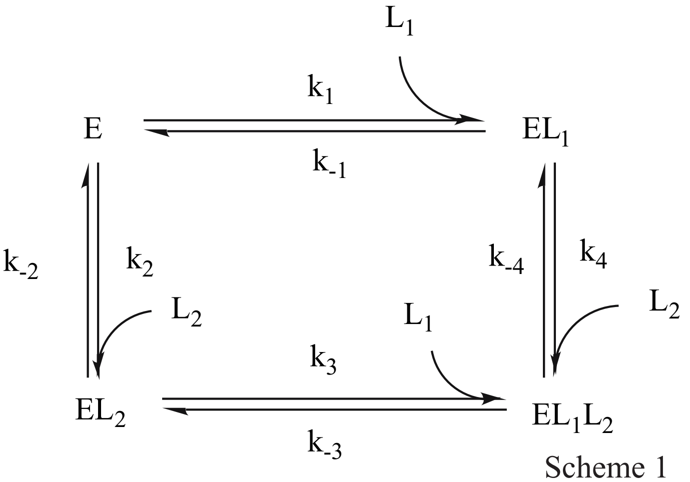

Scheme 1

association rate constants of ~10^8/M/s and dissociation rate constants of 10^3/s that correspond to equilibrium dissociation constants of ~10 μM produce strong effects that are readily observed under typical sample conditions.

An illustrative 2D NOESY spectrum for a system with two spins is shown in Figure 4. The 1D spectrum for this system consists of two sets of three resonances: for spin 1 on L_1, the shift will generally be dependent on whether the ligand is free, in a binary complex with E, or in a ternary complex with E and L_2. The diagonal peaks are shown as open circles. The exchange cross peaks which connect specific spins interconverting among the free, binary, and ternary complexed forms are in black. The NOE cross peaks connecting spins 1 and 2 on the ternary complex are shown in light gray. Of course, since the spins are postulated to be on different ligands, the values for the binary complexes and the free ligands will be zero in the absence of exchange. Finally, the dark gray cross peaks are exchange-mediated NOE interactions which become non-zero when both chemical exchange and NOE interactions are present. For example, such cross peaks can connect spin 1 in a ternary complex with spin 2 in the free state. When the exchange is sufficiently rapid compared with the relevant spin lattice relaxation rates, the sets of nine cross peaks in each of the four boxes shown in the figure exhibit the same time dependence, differing only in a magnitude. When this condition is not met, the elements in each box can exhibit different dependences on the mixing time. In a typical experiment of this type, one observes only a single resonance for each spin due to the fact that the concentrations of the binary and ternary complexes are much lower than the free ligand concentrations, or, more typically, due to fast exchange on the chemical shift time scale. If the latter condition is met, it is appropriate to sum the NOE build-up curves for the nine peaks in each of the indicated boxes. This represents the optimal condition for the transferred NOE and interligand NOE observations. In this case, the sum of the nine NOE cross peaks, A_{ij}, can be represented by another matrix, C_{ij} [24].

Simulations of the dependence of the interligand NOE (ILOE) on mixing time have been performed for a range of geometric structures and kinetic rate constants [24]. In general, the ILOE curves exhibit a dependence on mixing time which is similar to the transferred NOE curves, characterized by an initial build up and a subsequent decay as relaxation effects become dominant. Calculations corresponding to the intensities of the NOESY cross peaks, A_{ij}, and to the sums of elements, C_{ij}, have been performed for a model system that contains two ligands with three spins arranged linearly and separated by 2.5 Å. A ternary complex was modeled in which all six nuclei of both ligands are also arranged in a line, with nucleus 3 on ligand 1 and nucleus 4 on ligand 2 also separated by 2.5 Å, as shown below:

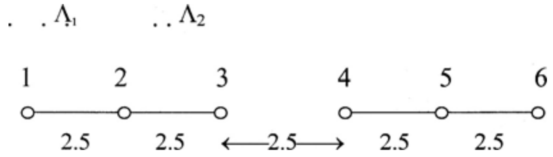

Using parameters: [E] = 0.4 mM, $[L_1] = [L_2] = 5$ mM, $\tau_{1F} = \tau_{2F} = 10^{-10}$ s; $\tau_B = 10^{-7}$ s, $k_1 = k_2 = k_3 = k_4 = 10^8$/M/s, $k_{-1} = k_{-2} = k_{-3} = k_{-4} = 10^{-3}$/s, and other parameters as given in Ref. [24], curves showing

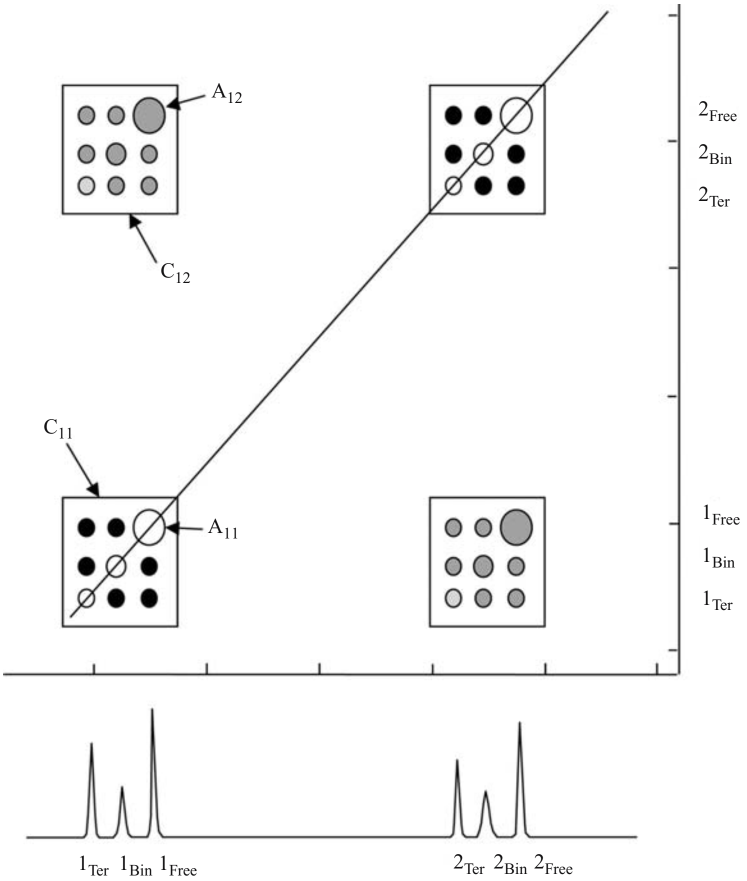

Fig. 4. Schematic representation of a 2D NOESY spectrum for a system containing a macromolecule, E, and two ligands, L_1 and L_2, which can form binary or ternary complexes with E. Nucleus 1 is assumed to be positioned on L_1, and nucleus 2 on L_2. The observation of separate resonances for each spin in the free, binary, and ternary complexes would only be possible under slow exchange conditions on the chemical shift time scale, but is useful for illustrative purposes. The exchange peaks which interconvert nucleus 1 (or 2) between free, binary, and ternary complexes are shown in black. Cross peaks arising from NOE interactions between nuclei 1 and 2 in the ternary complex are shown in light gray. Note that if spins 1 and 2 are on different ligands, there will be no cross peaks for the uncomplexed ligands and for either binary complex. Cross peaks that arise due to a combination of exchange and NOE interactions are shown in dark gray. Under conditions of fast exchange, only the sums of the peaks in each square, i.e. the C_{ij} matrix elements, are observed (based on Figure 1 of Ref. [24]).

the dependence of C_{12}, C_{56}, and C_{34} on the mixing time are shown in Figure 5A. Note that the initial slopes of the C_{12}, C_{56}, and C_{34} curves are identical, consistent with the equal r_{12}, r_{56}, and r_{34} internuclear distances in the model ternary complex which, based on the above parameters, corresponds to 0.996 of the total enzyme concentration available. Most of the difference that can be observed between C_{12} and C_{34} arises due to the faster decay of the C_{34} NOESY interaction, which arises primarily from the presence of two nearest neighbor spins in the ternary complex, compared with one nearest neighbor spin for nucleus 1. Thus, a comparison of the C_{23} with C_{34} curves shows greater similarity (not shown).

In a typical transferred NOE experiment, the internuclear distances of the complexed ligand can be calibrated by comparing the initial slope of the NOE build-up curves with that obtained for a pair of nuclei that have a fixed internuclear distance. For example, in a study involving NADPH, the calibration curve could correspond to the H5–H6 protons on the nicotinamide ring. For the interligand NOE, the analysis becomes more complex if the two ligands have significantly different kinetic parameters. If the fraction of the ternary complex pEL_1L_2 becomes significantly less than one and the fraction of one binary complex, e.g. pEL_1 becomes significant, ligand 1 will be subject to greater transferred NOE effect than ligand 2. In general, the ILOE will scale with the weaker binding ligand. As shown in Figure 5B, increasing the off rates for L_2 to 10^5/s results in a relatively modest increase in pEL_1 and decreased initial slopes for the C_{56} and C_{34} build-up curves. Further increasing the off rate of L_2 to 10^6/s lowers the fraction of E in the ternary complex to 1/3, resulting in a significantly greater initial slope for C_{12} than for C_{56} or C_{34}, which exhibit similar values (Figure 5C). Increasing $k_{-2} = k_{-4}$ to 10^7/s largely eliminates the binding of ligand 2, giving $pEL_1 = 0.95$ (Figure 5D). Interestingly, the initial slope calculated

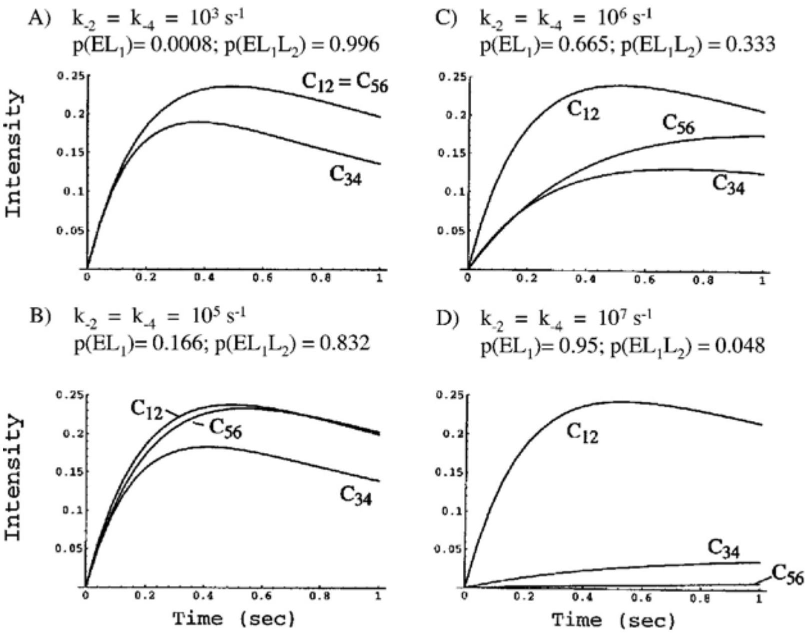

Fig. 5. Sensitivity of interligand Overhauser effects to weaker binding. The set of simulations shown above illustrates the effect of increasing the dissociation rate constant of L$_2$, while leaving that of L$_1$ fixed, with $k_{-1} = k_{-3} = 10^3$/s. All association rate constants are set at 10^5/M/s. The calculated fractions of E involved in the ternary (pEL$_1$L$_2$) and binary (pEL$_1$) complexes are shown for the corresponding dissociation rate constants above each figure. (A) $k_{-1} = k_{-2} = k_{-3} = k_{-4} = 10^3$/s; (B) $k_{-2} = k_{-4} = 10^5$/s; (C) $k_{-2} = k_{-4} = 10^6$/s; (D) $k_{-2} = k_{-4} = 10^7$/s. Other parameters as given in Ref. [24] (based on Figure 6 in Ref. [24]).

for C_{34} is greater than that calculated for C_{56}, and no significant transferred NOEs are predicted for ligand 2. This results because for these parameters, L$_2$ is largely free, and free L$_2$ experiences an NOE of opposite sign to the bound ligand. Hence, the presence of free L$_2$ reduces the observed build-up. However, no such subtraction effect arises for the interaction between nuclei 3 and 4, since these do not interact when L$_2$ is not bound to E.

ILOE Observations—Type II Dihydrofolate Reductase

Interligand Overhauser effects have been observed in several systems of interest [22,23,25–27]. In general, such effects can be observed in non-productive ternary enzyme complexes that involve inhibitors or other molecules that are not substrates for the enzyme under study. Ternary complexes involving enzyme substrates can be observed if the enzyme has been inactivated by mutagenesis. Alternatively, enzymes involved in redox chemistry can be studied if the pair of ligands are both in the oxidized or reduced state, rather than the reduced–oxidized combination that functions as a substrate–cofactor pair. Of course, binding to other types of macromolecules can also be studied, and in this case, there are no concerns about ligand tur over.

Dihydrofolate reductase catalyzes the NADPH-dependent reduction of dihydrofolate to tetrahydrofolate. Type II dihydrofolate reductase is a plasmid-encoded enzyme that is structurally unrelated to the extensively studied type I enzyme, and confers antifolate drug resistance on bacteria containing the plasmid. The enzyme is a symmetric tetramer that binds the substrate and cofactor in a central pore [27]. Figure 6 illustrates portions of a NOESY experiment for a sample containing 0.1 mM R67 DHFR, 5 mM folate, and 5 mM NADP [25]. The region of the spectrum including the CH$_2$ protons of folate (at the F9 position) are shown in Figure 6. Transferred NOE cross peaks to the folate F7, proton, and to the folate F12/16 and F13/15 protons on the *p*-aminobenzoyl group are readily observed. ILOE peaks connecting the folate F9 protons to the nicotinamide NH-4 and NH-5 protons on the NADP also can be observed in the spectra. All of these peaks exhibit time-dependent build-up curves expected for the

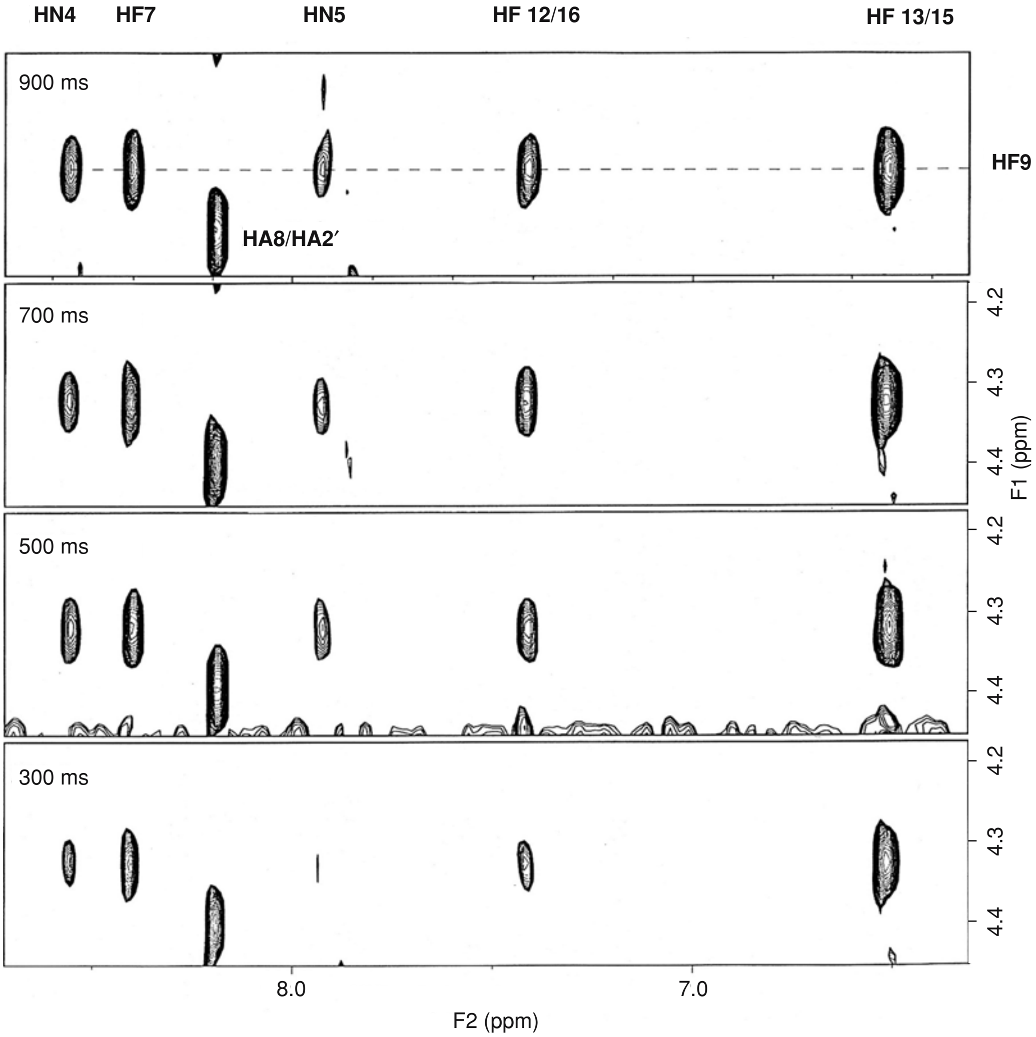

Fig. 6. A portion of the NOESY spectrum illustrating the cross peaks connecting the folate H-9 protons with the aromatic protons of folate and NADP$^+$, obtained on a sample containing 0.1 mM R67 DHFR, 5 mM folate, and 5 mM NADP$^+$ in 100 mM Tris-d11, pH 8.0 in D_2O. The spectra correspond to mixing times of 300, 500, 700, and 900 ms, as indicated (based on Figure 2 of Ref. [25]).

NOE experiment. The results obtained in this study are intuitive since the ILOE peaks are observed near the positions (NH-4 on NADPH, C-6 on folate) at which redox chemistry occurs. The very weak ILOE peaks involving the folate F-7 were also useful for determining the relative positions of the two ligands.

The potential application of ILOE studies for ligand discovery has been demonstrated in experiments on alcohol dehydrogenase, in which a sample contained NADH and an inhibitor, *m*-methylbenzamide, as well as a reducing agent, sodium cyanoborohydride, included in order to maintain the NADH in the reduced state [26]. In this study, unanticipated cross peaks were observed between the BH_3 protons on the cyanoborohydride and the methylbenzamide protons. It was concluded that the methylbenzamide binds primarily to a hydrophobic pocket in the active site that is involved in binding larger substrates, such as benzyl alcohol, while the cyanoborohydride formed a transient complex with the active site Zn^{2+} ion [26].

Summary

The identification and characterization of ternary complexes involving organic molecules and inorganic ions should provide a useful basis for the further development of targeted ligands. Although the example of borate discussed above involved the serine protease trypsin, recent structural data indicate that borate complexes can form outside of the active site, supporting the possibility of targeting protein–protein interactions in a more general way. Comparisons with crystallographic analyses of the same complexes indicate that crystal screening approaches, while generally very useful, are subject to potentially significant influences that result from lattice contacts. ILOEs can provide useful insight into the relative binding and orientation of ligands that reversibly form ternary complexes. The presence of unanticipated complexes has been observed in some studies, supporting the potential application of this approach to the design of novel ligands.

References

1. Charlton PQ, Young DW, Birdsall B, Feeney J, Roberts GCK. J. Chem. Soc. Chem. Commun. 1979;922.
2. Bystroff C, Oatley SJ, Kraut J. Biochemistry 1990;29:3263.
3. Stoll VS, Eger BT, Hynes RC, Martichonok V, Jones JB, Pai EF. Biochemistry 1998;37:451.
4. Shuker SB, Hajduk PJ, Meadows RP, Fesik SW. Science 1996;274:1531.
5. Meyer B, Peters T. Angew. Chem. Int. Ed. 2003;42:864.
6. Mayer M, Meyer B. Angew. Chem. Int. Ed. 1999;38:1784.
7. Post CB. Curr. Opin. Struct. Biol. 2003;13:581.
8. Sternweis PC, Gilman AG. Proc. Natl. Acad. Sci. U.S.A. 1982;79:4888.
9. Katz BA, Clark JM, Finer-Moore JS, Jenkins TE, Johnson CR, Ross MJ, Luong C, Moore WR, Stroud RM. Nature 1998;391:608–12.
10. Boyle FA, Cook ND, Peters TJ. Clin. Chim. Acta 1988;172:291–6.
11. Revel JP, Ball EG. J. Biol. Chem. 1959;254:577.
12. Lindquist RN, Lynn JL Jr, Lienhard GE. J. Am. Chem. Soc. 1973;95:8762.
13. Borah B, Chen C-W, Egan W, Miller M, Wlodawer A, Cohen JS. Biochemistry 1985;24:2058.
14. Crans DC, Smee JJ, Gaidamauskas E, Yang L. Chem. Rev. 2004;104:849.
15. Davies DR, Interthal H, Champoux JJ, Hol WGJ. J. Med. Chem. 2004;47:829.
16. Goodno CC. Proc. Natl. Acad. Sci. U.S.A. 1979;76:2620.
17. Maruta S, Henry GD, Sykes BD, Ikebe M. J. Biol. Chem. 1993;268:7093.
18. Fisher AJ, Smith CA, Thoden JB, Smith R, Sutoh K, Holden HM, Rayment I. Biochemistry 1995;34:8960.
19. Walker B, Lynas JF. Cell. Mol. Life Sci. 2001;58:596.
20. Tate SS, Meiser A. Proc. Natl. Acad. Sci. U.S.A. 1978;75:4806.
21. London RE, Gabel SA. Arch. Biochem. Biophys. 2001;385:250.
22. Barsukov IL, Lian LY, Ellis J, Sze KH, Shaw WV, Roberts GCK. J. Mol. Biol. 1996;262:543.
23. Li D, DeRose EF, London RE. J. Biomol. NMR 1999;15:71.
24. London RE. J. Magn. Reson. 1999;141:301.
25. Li D, Levy LA, Gabel SA, Lebetkin MS, DeRose EF, Wall MJ, Howell EE, London RE. Biochemistry 2001;40:4242–52.
26. Li D, London RE. Biotechnol. Lett. 2002;24:623–9.
27. Pitcher WH III, DeRose EF, Mueller GA, Howell EE, London RE. Biochemistry 2003;42:11150.
28. Roush A, Norris ER. Arch. Biochem. 1950;29:345.
29. Smith KW, Johnson SL. Biochemistry 1976;15:560.
30. London RE, Gabel SA. Biochemistry 2002;41:5963.
31. Transue TR, Krahn JM, Gabel SA, DeRose EF, London RE. Biochemistry 2004;43:2829.
32. Babine RE, Rynkiewicz MJ, Jin L, Abdel-Maguid SS. Lett. Drug Des. Discov. 2004;1:35.
33. Bull TE, Forsen S, Turner DL. J. Chem. Phys. 1979;70:3106.
34. Werbelow LG. J. Chem. Phys. 1979;70:5381.
35. Werbelow LG, Pouzard G. J. Phys. Chem. 1981;85:3887.
36. Werbelow LG. In: DM Grant (Ed). Encyclopedia of Nuclear Magnetic Resonance, Vol. 6. John Wiley & Sons: New York, 1995, p 4092.
37. Aramini JM, Vogel HJ. J. Am. Chem. Soc. 1993;115:245.
38. Aramini JM, Germann MW, Vogel HJ. J. Am. Chem. Soc. 1993;115:9750.
39. Aramini JM, McIntyre DD, Vogel HJ. J. Am. Chem. Soc. 1994;116:11506.

The Transferred NOE

Mike P Williamson

Department of Molecular Biology and Biotechnology, University of Sheffield,
Firth Court, Western Bank, Sheffield S10 2TN, UK

Abstract

The transferred NOE allows NOE information to be obtained on a bound ligand, but appearing on the resonances of the free ligand. It is thus a very useful method for gaining information on the bound ligand. Its major limitation is that it only works well in a range of dissociation constants between 1 mM and 10 nM. A key negative control experiment is to demonstrate the absence of NOEs arising from nonspecific binding, by addition of competitor ligands. A second is to measure NOEs in the absence of protein. For quantitative work, it is also necessary to minimize spin diffusion, by using relatively short mixing times. Recent work has shown that spin diffusion in TR-NOE is no worse than spin diffusion in standard NOE spectra of proteins. With care, TRNOE can thus provide powerful quantitative information on bound conformation.

Affinities and Timescales

The appearance and information content of an NMR spectrum of a protein/ligand mixture depend strongly on the rates of binding and tumbling of the components. This is why it is important to think about these rates, and understand their implications.

The binding of a ligand to a protein can be written

$$L + P \underset{k_{\text{off}}}{\overset{k_{\text{on}}}{\rightleftharpoons}} L \cdot P \tag{1}$$

The overall on-rate is k_{on}[L][P], and the off-rate is k_{off}[L.P]. At equilibrium, these are by definition equal. The dissociation constant K_d is [L][P]/[LP], which is therefore also equal to $k_{\text{off}}/k_{\text{on}}$. The association constant K_a is simply $1/K_d$.

For most ligand/protein interactions, binding happens as fast as ligand and protein can come together: in other words, the on-rate is diffusion controlled. The on-rate (k_{on}) is usually assumed to have a value of around 10^8 M^{-1}s^{-1}, and will only be significantly slower if the protein binding site is somehow buried or hidden (which is unusual, particularly for inhibitors as compared to substrates). We can therefore get a good estimate of the off-rate if we know the dissociation constant, since $k_{\text{off}} \approx 10^8 K_d$. A good drug often has a K_d in the low nM range, and therefore has a k_{off} of around 1 s^{-1} or less. By contrast, initial targets derived from screening programes will typically have K_d values in the high μM or low mM range, and will therefore have off-rates of around 10^5 s^{-1}. This leads to very different NMR behavior.

We also need to consider that the concentrations of samples in NMR are comparable to some of these numbers, and therefore the fraction of ligand bound is strongly dependent on K_d. It is easily shown that for the simple binding equilibrium shown above, the concentration of free ligand is given by

$$[\text{L}] = 0.5([\text{L}_0] - [\text{P}_0] - K_d + \{([\text{L}_0] - [\text{P}_0] - K_d)^2 + 4[\text{L}_0]K_d\}^{1/2}) \tag{2}$$

where [L$_0$] and [P$_0$] are the total concentrations of ligand and protein respectively. So for example, if the total protein concentration is 50 μM, K_d is 10 nM, and there is a 1:1 ratio of ligand to protein, then almost all the ligand is bound (only ca. 1.4% is free); if there is a 10-fold excess of ligand over protein, then to a good approximation one equivalent is bound and the other 9 are free. By contrast, with the same protein concentration, a 10-fold ligand excess and a much weaker K_d of 1 mM, the concentration of bound ligand is only 16 μM (i.e. only one-third of the protein is bound), and 97% of the ligand is free. Thus, the amount of bound complex depends strongly on K_d. This will be important when we come to think about what the NMR spectrum looks like.

The off-rate is important for another reason, namely because it defines whether exchange processes are in "fast" or "slow" exchange [1]. Confusingly, there are different definitions of what is meant by fast and slow, depending on what we are interested in. The most obvious is the chemical shift timescale: whether we see one signal or two. This depends on $\Delta\nu$, the difference in resonance frequency between the two signals, expressed in Hz. Fast exchange is when $k_{\text{off}} \gg \Delta\nu$. Thus if for example we are considering a ^{1}H spectrum at 500 MHz, in which free and bound signals are 0.3 ppm different, $\Delta\nu = 150$ Hz, so k_{off} must be 1000 s^{-1} or greater for fast exchange (corresponding to a K_d of 10 μM or weaker). Slow exchange requires k_{off} <30 s^{-1} and K_d 0.3 μM or

Graham A. Webb (ed.), Modern Magnetic Resonance, 1357–1362.
© 2008 *Springer.*

stronger. Thus, almost all initial leads and screening hits are in or close to fast exchange, while strong ligands are in slow exchange. Intermediate off-rate values give broadened signals. It is however worth noting that intermediate exchange looks different when the amounts of the two species are unequal, which would happen if for example there were an excess of free over bound ligand. In this situation, the appearance of the free signal is almost unaffected, while the bound signal is broadened so much that it is frequently unobservable [2]. It is therefore not easy to tell whether the ligand is in fast exchange on the chemical shift timescale simply by looking at the appearance of the signal.

A ligand undergoing exchange can of course be in slow exchange for some signals and fast exchange for others, depending on the chemical shift differences involved. Going to higher magnetic field pushes the system toward slower exchange, as does cooling the sample. A typical chemical shift change could be 0.3 ppm or 150 Hz in ^{1}H, as illustrated above, but 0.5 ppm or 25 Hz in ^{15}N and 0.3 ppm or 38 Hz in ^{13}C. Thus, a spectrum in slow exchange for ^{1}H could be in fast or intermediate exchange for ^{15}N or ^{13}C. Since the biggest difficulty for carrying out TRNOE experiments on many "interesting" (i.e. tight binding) ligands is that their off-rate is too slow, it is worth noting that better results can often be obtained by increasing the temperature and sometimes by going to lower field.

The other exchange rates that affect the spectra obtained are relaxation rates, and in particular the spin-lattice relaxation rate and the cross-relaxation rate. The spin-lattice relaxation rate R_1 is the inverse of the more familiar spin-lattice relaxation time T_1, and is the ultimate entropic sink: if the off-rate is much slower than R_1 (and in particular, R_1 of the bound state) then there is no way that any information on the bound state (such as an NOE) can ever be transferred over into the free state, because it is lost to relaxation before it can be seen. R_1 is typically around 10 s^{-1}, and therefore off-rates slower than 1 s^{-1} (i.e. K_d values stronger than 10 nM) usually mean that no information can be obtained about the bound state by observation of the free state. We will see an example of this below. The cross-relaxation rate is the rate responsible for the NOE (and a similar relaxation rate is responsible for cross-correlated relaxation), and it is typically slower than k_off, being around 1–10 s^{-1}. The important consequence of this is that NOEs can build up in one state, for example the bound state, and be transferred across to the free state by chemical exchange without significant loss of magnetization from spin-lattice relaxation: hence its name of transferred NOE or TRNOE. (Some authors have suggested that the abbreviation TRNOE can be confused with the transient NOE, and prefer other terms, such as exchange-transferred NOE (et-NOE) [3].) The TRNOE has recently been reviewed [3]. However, before we can consider the transferred NOE, we need to clarify a few things about the NOE.

The NOE

The NOE is a very useful technique for measuring distance in NMR, because the rate of buildup of the NOE (the cross-relaxation rate) is proportional to the inverse sixth power of the internuclear distance. In a homonuclear two-spin system, the cross-relaxation rate is given by [1]

$$\sigma = \left(\frac{\mu_0}{4\pi}\right)^2 \frac{\hbar^2\gamma^4}{10}\left(\frac{6\tau_c}{1+4\omega^2\tau_c^2} - \tau_c\right) \tag{3}$$

where $\mu_0/4\pi$ is a conversion factor, γ is the gyromagnetic ratio, τ_c is the correlation time of the internuclear vector, and ω is the spectrometer frequency (in rad s^{-1}, i.e. 2π times larger than the more conventional value in Hz). The correlation time is the time it takes for the relevant internuclear vector to rotate by approximately one radian. The crucial factor here is the term involving τ_c, which in practice means that the cross-relaxation rate scales with the correlation time, except for a hiatus around $\omega\tau_\mathrm{c} = 1$, where the cross-relaxation rate passes from positive to negative (Figure 1). The important point is that the cross-relaxation rate is much faster for large τ_c, i.e. for large proteins.

In principle, the relationship between NOE intensity and distance makes the NOE a very precise measure of distance. However, there are several factors that in practice make it much less precise than it should be, of which the most important are spin diffusion and internal mobility.

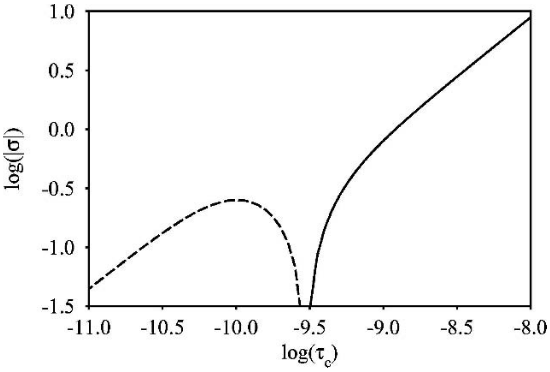

Fig. 1. Variation of the cross-relaxation rate with correlation time, calculated for two protons 2 Å apart for a 600 MHz spectrometer. For $\omega\tau_\mathrm{c} < 1.12$, σ is positive (dashed line), and for $\omega\tau_\mathrm{c} > 1.12$, it is negative (solid line).

Spin Diffusion

This is a process analogous to heat diffusion, whereby an NOE from one proton to another can subsequently diffuse to other protons throughout the protein. There are thus several pathways for NOE transfer, and therefore any spin diffusion immediately renders distance information less useful. This can be illustrated with a simple three-spin example (Figure 2), which shows that a third proton that bridges between the two protons being measured can reduce the apparent distance between them if it is significantly closer to both of them than they are to each other. Clearly, this is much more of a problem when trying to measure long internuclear distances. It is hard to detect the presence of spin diffusion (except using ROESY experiments, as described below), and therefore spin diffusion is normally handled by using rather wide ranges for NOE distance calibration and short mixing times. This clearly makes structure calculation less precise.

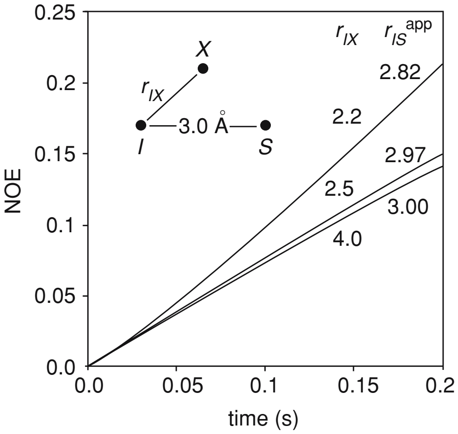

Fig. 2. Spin diffusion. Protons *S* and *I* are 3.0 Å apart, and there is a third spin *X* equidistant between *S* and *I*. The figure shows results for three positions of *X* with distances $r_{IX} = r_{XS}$ of 2.2 Å (dashed line), 2.5 Å (dotted) and 4.0 Å (solid line). The time course of *IS* NOESY crosspeak buildup is shown, calculated for a smallish protein with a correlation time of 5 ns on a 500 MHz spectrometer. It can be seen that whereas for $r_{IX} = 4$ Å the *IS* NOE builds up smoothly, for $r_{IX} = 2.2$ Å there is a "lag time" of about 30 ms, during which spin *X* has little effect on the NOE, but then the *IS* NOE buildup rate increases because of spin diffusion via *X*. The initial buildup over 200 ms was fitted by hand and converted to an apparent distance by taking the sixth root of the buildup rate. Spin diffusion reduces the apparent distance r_{IS} from 3.0 to 2.82 Å when proton *X* is close to both *I* and *S*. In most cases, such a reduction in apparent distance would have little effect on the calculated structure.

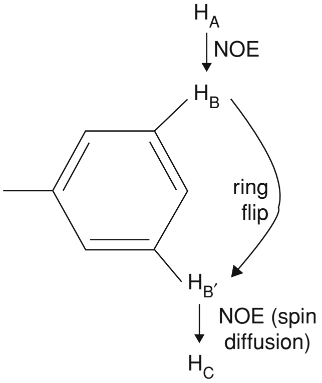

Fig. 3. The effect of ring flipping on NOEs. Proton *A* generates an NOE at *B*. If the phenylalanine ring flips 180°, then *B* ends up at *B′*, and can pass an NOE on to *C* by spin diffusion. This will be significant as long as the flip rate is greater than the NOE cross-relaxation rate, which is almost always the case. The buildup rate of NOE at proton *C* suggests it is close to *A*, when in fact it can be easily 8–10 Å away.

Internal Mobility

Internal mobility can affect the NOE in several ways. The main result, as for spin diffusion, is to make the relationship between NOE and distance less precise. Any mobility will cause the protons to have a range of distance separations. Because of the r^{-6} averaging, this almost always results in an apparent shortening of the distance. Very close protons cannot be brought any closer together, and so the distance averaging effect is more significant with more distant protons. In practice, this often makes the r^{-6} effect end up looking more like a r^{-5} or even r^{-4} effect. Potentially the most severe effect of motion is when there is an NOE to an aromatic proton. Flipping of the ring can lead to the NOE then being passed on by spin diffusion to protons on the other side of the ring (Figure 3). This will have a marked effect on apparent distances in the vicinity of the ring.

The Transferred NOE

The transferred NOE makes use of a particularly useful phenomenon, namely that the rate of buildup of the NOE is approximately proportional to the correlation time (Figure 1). The average cross-relaxation rate in a ligand exchanging between free and bound states is given by

$$<\sigma> = N_F\sigma_F + N_B\sigma_B \tag{4}$$

where N_F and N_B are the fractions of free and bound ligand. The cross-relaxation rate of bound ligand, σ_B, is much greater than the cross-relaxation rate of free ligand, σ_F. It is therefore easy to produce a situation where the observed NOE is dominated by cross-relaxation in the bound state. Depending on the exact values of σ_B and σ_F (which depend on the tumbling rate of bound and free ligand), ligand:protein ratios of 10–40 can be and are often used, and give useful quantitative results. A further helpful aspect of this high ligand:protein ratio is that one can use protein concentrations in the low μM range and still measure NOEs. An NOE measurement (almost always run as a NOESY experiment) then produces NOEs characteristic of the bound state. In the usual situation in which the off-rate is fast on the chemical shift timescale, the only signals observed are sharp and virtually identical to those of free ligand, and consequently are easily assigned. We therefore observe NOEs characteristic of the bound state, but seen on the signals of the free state. The experiment has a characteristic unusual for NMR spectra of proteins, that the experiment actually gets better as the protein gets bigger, because σ_B increases, and therefore the NOE is dominated more and more by the cross-relaxation rate in the bound state.

For many ligands, σ_F is so small as to be insignificant. It can (and should) always be checked by running a control NOE experiment in the absence of protein. For intermediate sized ligands, such as peptides, there is a particularly advantageous situation, in that the cross-relaxation rate goes through zero at $\omega\tau_c \approx 1$; as it happens, this is where many peptides come. This greatly reduces the need to worry about NOEs in the free peptide.

There have been a number of detailed simulations carried out on the TRNOE [4–7]. Figure 4 shows simulation results of a closely similar experiment, the STD experiment (discussed later), which show a complex dependence on K_d [8]. At K_d values weaker than 1 mM (right-hand side of Figure 4), the TRNOE falls off to zero because there is not enough ligand bound to give rise to an NOE. Conversely, at K_d values stronger than about 10 nM (left-hand side of Figure 4), the off-rate is so slow that bound ligand hardly ever dissociates from the complex, and the TRNOE again goes to zero. There is thus in this simulation a "window" of K_d of between 10 nM and 100 μM where the TRNOEs are not greatly affected by exchange rates and can be related simply to distance (see however the discussion in the figure legend). For really quantitative results (i.e. an NOE that is related *only* to the distance in the complex and is not affected by exchange), it is necessary to have k_{off} much greater than the cross-relaxation rate. An approximate guide to estimating cross-relaxation rates in proteins has been suggested: [3] $\sigma \approx -24 \times \text{MWt (kDa)}/r^6$ (Å). Protons cannot get much closer than 2 Å apart, which means that the largest possible cross-relaxation rate is approximately 0.375 × MWt, or 19 s^{-1} for a "typical" 50 kDa protein. This implies that k_{off} should be at least 100 s^{-1}, or alternatively K_d should be 1 μM or weaker. Of course, for protons at more realistic distances, this limit can be relaxed somewhat. As the molecular weight of the protein increases, the limitations on K_d become more stringent, such that for example for a 500 kDa protein, K_d should be 10 μM or weaker. This implies that for properly quantitative results, the window of K_d is very small, being only between 1 μM and 100 μM. Fortunately this is a range that includes a good proportion of ligands of interest, and one can go at least a factor of 10 to either side without losing much quantitative information. It should also be added that TRNOEs have been observed and used even with much more tightly bound ligands. Useful TRNOEs were for example observed for a ligand with a K_d of 30 nM [9].

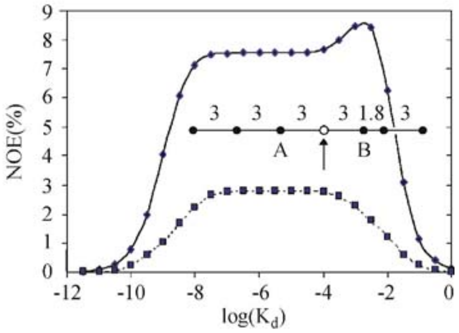

Fig. 4. The effect of irradiating a protein resonance (open circle) on ligand signal intensity, shown for two ligand signals, A (diamonds, solid line) and B (squares, dashed). The effect calculated is STD, which is closely similar to what would be measured in a TRNOE experiment. All distances are 3 Å except for the distance from ligand proton B to its nearest neighbor which is 1.8 Å. This near neighbor causes a rapid loss of NOE from B by spin diffusion: this loss (and the consequent reduction in the NOE measured at B) is not as severe in the case of TRNOE. A 10:1 excess of ligand over protein is used in the calculation, with $k_{on} = 10^9\ s^{-1}M^{-1}$, $\tau_c = 10^{-7}$ s, a 600 MHz spectrometer and a uniform leakage relaxation rate of 0.3 s^{-1} on all protons. The free ligand is assumed to have zero NOE. Using data from Jayalakshmi and Krishna [8].

Some of the early work on TRNOEs was overly precise and optimistic in the power of TRNOE to produce structural information. The pendulum therefore later swung in the opposite direction, with dire warnings about the dangers of over-interpreting TRNOE spectra [1]. More recent work has brought the pendulum back towards its proper position, and has shown that with proper controls, TRNOEs can give distance information that is very nearly as accurate as from conventional structure calculations. Apart from the problems discussed below, the main limitation is simply that ligands often bind in fairly extended geometries on protein surfaces, which means that most of the distances measurable by NOE are already close in terms of the covalent structure, and thus there are relatively few informative NOEs that can be measured. It is worth looking at the two most important pitfalls, as listed below:

1. Spin Diffusion. This has already been described above, but in the TRNOE there is a further problem, that there could be spin diffusion from one ligand proton to another, going *via* a protein proton [10]. Such a transfer would be very hard to detect, and would seriously affect measured distances. Recent simulations have shown that in practice, this very seldom happens, basically because most ligands bind on the exposed surfaces of proteins and therefore are not close enough to the protein for this to happen (cf. Figure 2) [11,12]. In particular, if the ligand has a reasonably high density of protons (for example, a peptide) it would be uncommon for ligand-protein-ligand spin diffusion to affect a distance measurement. The spin diffusion problem is less severe if a short presaturation time is used [12]. However, the large excess of free ligand effectively dilutes the buildup of NOE on the bound ligand by exchanging with it, with the consequence that one can use longer mixing time for TRNOE experiments than for conventional NOE experiments on proteins: mixing times of 100–200 ms are common, even with very large proteins. (It should also be added that the large number of TRNOEs that can be measured also means that one inaccurate TRNOE is less likely to perturb the structure.) This does not remove the problem of spin diffusion within the ligand, which is as bad as it is in a conventional NOE measurement, and still implies a need for caution in interpreting NOEs as distances.

It has been noted that spin diffusion (of any kind) can be detected using a transferred ROESY experiment, in which spin diffusion gives rise to smaller NOEs of opposite sign to direct NOEs. Bax and co-workers have provided an elegant example of a TRNOE that disappeared on using a transferred ROESY experiment, and was thereby shown to be due to spin diffusion [13]. However, this experiment typically requires a low peptide:protein ratio (and more careful control experiments in the absence of protein), because the ratio of σ_B to σ_F is not as great as for NOESY. It is also more prone to artifacts, and has not proved as popular as one might expect. Where used, it tends to be used as a check that measured NOEs are genuine, rather than as a stand-alone method.

2. Nonspecific Binding. Usually, one uses something like a 30-fold excess of ligand over protein. Under these circumstances, a ligand that binds specifically, but in addition binds nonspecifically but 100-fold more weakly, will be fully bound at the tight binding site and almost fully bound at the weaker site, Equation (2). It will thus give equally strong TRNOEs from its strongly and weakly bound conformations (indeed, if it binds very strongly at the more specific site, these TRNOEs will be small for reasons shown in Figure 4, and thus almost all the TRNOE will in fact come from nonspecific binding!). This gives rise to averaged TRNOEs, which, if not spotted, will produce misleading distance information. This is best detected using a control experiment, in which a strong competitive ligand is added [7]. This will displace the ligand from the binding site, and any remaining TRNOEs must therefore arise from nonspecific binding. Nonspecific binding appears to be very common, and therefore a control experiment is extremely valuable: indeed, for quantitative results such an experiment is crucial.

Practical Implementation

One of the beauties of TRNOE is that it is simple to do: one just needs to carry out a conventional NOESY experiment (in conjunction with a control using a tight inhibitor, to rule out nonspecific binding). It is common

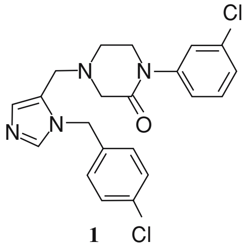

1

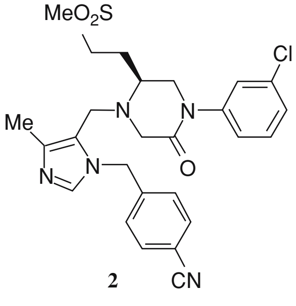

2

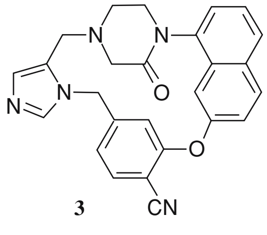

3

to add a relaxation filter to the experiment, often in the form of a T_2 or $T_{1\rho}$ filter, to reduce broad signals from the protein and therefore make the baseline flatter and reduce integration problems. As an example, compound **1** is a lead compound as an inhibitor of farnesyltransferase (FTase), and therefore a potential antitumor agent. It binds to FTase with an IC_{50} of 2 nM, and its off-rate is therefore too slow to give TRNOEs. However, an analogue **2** has an IC_{50} of only 475 nM and is therefore suitable for TRNOE experiments. Measurements were carried out using 64 μM enzyme and 2 mM **2** (ca. 1:30), a typical concentration for such experiments. TRNOE experiments were carried out using several mixing times, going up to 300 ms. Secondary binding was identified by addition of an excess of a competitive ligand. Measurement of TRNOEs revealed an NOE between the cyanophenyl ring and the piperazinone ring, which prompted the authors to design a cyclised ligand **3** that resembled the bound conformation and has an IC_{50} of 0.1 nM.

Related Experiments

The TRNOE is closely related to two other experiments described in this volume, namely saturation transfer difference (STD) and transferred cross-correlated relaxation. The only difference between TRNOE and STD is that in STD one saturates the protein and transfers magnetization from protein to bound ligand, whereas in TRNOE one uses intramolecular NOEs in the bound ligand. (It is also true that STD is normally run as a steady-state NOE experiment, with irradiation of the protein resonance for several seconds, while TRNOE is normally run as a 2D transient experiment.) The dependence on off-rate and molecular size is the same, and it is therefore applicable in the same circumstances. This of course means that STD does not produce a signal for very tightly bound ligands. A neat method has been devised to get around this limitation, using competition experiments—for example, an STD seen to a relatively weakly binding ligand disappears on addition of a much tighter binding competitor, thus allowing the tight binding competitors to be identified in high-throughput screens. The same would hold with the TRNOE also, but it would of course be a less useful result. A combination of STD and TRNOE experiment is particularly valuable in screening strategies [14,15].

References

1. Neuhaus D, Williamson MP. The Nuclear Overhauser Effect in Structural and Conformational Analysis, 2nd ed. Wiley-VCH: New York, 2000.
2. Sandström J. Dynamic NMR Spectroscopy. Academic Press: Paris, 1982.
3. Post CB. Curr. Op. Struct. Biol. 2003;13:581–588.
4. Clore GM, Gronenborn AM. J. Magn. Reson. 1982;48:402–417.
5. Campbell AP, Sykes BD. Annu. Rev. Biophys. Biomolec. Struct. 1993;22:99–122.
6. Lippens GM. Cerf C, Hallenga K. J. Magn. Reson. 1992;99:268–281.
7. Ni F. Prog. Nucl. Magn. Reson. Spectrosc. 1994;26:517–606.
8. Jayalakshmi V, Krishna NR. J. Magn. Reson. 2002;155:106–118.
9. Weimar T, Petersen BO, Svensson B, Pinto BM. Carbohydr. Res. 2000;326:50–55.
10. Jackson PL. Moseley HNB, Krishna NR. J. Magn. Reson. Ser. B 1995;107:289–292.
11. Eisenmesser EZ. Zabell APR, Post CB. J. Biomol. NMR, 2000;17:17–32.
12. Zabell APR, Post CB. J. Biomol. NMR, 2002;22:303–315.
13. Arepalli SR. Glaudemans CPJ. Daves GD. Kovac P, Bax A. J. Magn. Reson. Ser. B 1995;106:195–198.
14. H. Kogelberg, Solis D, Jimenez-Barbero J. Curr. Op. Struct. Biol. 2003;13:646–653.
15. Stockman BJ, Dalvit C. Prog. Nucl. Magn. Reson. Spectrosc. 2002;41:187–231.

NMR Kinetic Measurements in DNA Folding and Drug Binding

Mark S. Searle[1], Graham Balkwill[1], Huw E.L. Williams[1], and Evripidis Gavathiotis[2]
[1]*Centre for Biomolecular Sciences, School of Chemistry, University Park, Nottingham NG7 2RD, UK; and*
[2]*Laboratory of Molecular Biophysics, The Rockefeller University, New York, NY 10021, USA*

Drug–Quadruplex Interactions Studied by NMR

DNA quadruplex structures have been of considerable interest as supramolecular self-assembling systems [1] and because of their potential biological importance in the regulation of a variety of processes within the cell cycle including replication, transcription, and recombination [2]. The observation that the telomeric repeats at the ends of chromosomes (5′-TTAGGG in humans) are able to assemble in the presence of monovalent cations into folded structures containing stacked G-tetrads has bought them into focus as a drug target, notably to interfere with telomere maintenance in immortalized human tumor-derived cell lines by inhibiting the enzyme telomerase [1–6]. The novel fluorinated polycyclic quinoacridinium cation RHPS4 (Figure 1a) shows enhanced binding to higher-ordered DNA structures (triplex/quadruplex) and is a potent inhibitor of telomerase function [7,8]. To investigate the drug–quadruplex interaction, as part of a rational ligand design approach, we have studied by NMR the structure (Figure 1b) and dynamics of the RHPS4 complex with the intermolecular parallel-stranded quadruplex d(TTAGGGT)$_4$, formed from the human telomeric repeat [9,10].

Exchange Rates for Drug Binding to Quadruplex DNA

Fluorescence quenching studies have established that RHPS4 interacts with d(TTAGGGT)$_4$ with a binding affinity of 2.2×10^5 M [7]. NMR lineshape analysis during drug titration studies shows that the drug is in fast exchange between free and bound states with the quadruplex accommodating drug molecules at both the 5′-AG and 5′-GT steps at the ends of the core G-quadruplex structure [10]. Drug complexation was monitored using the downfield guanine imino proton resonances between 10 and 12 ppm. These initially shift upfield due to ring current effects from the drug, broadening significantly at a bound drug:DNA ratio of ~0.3, but subsequently sharpen as the fully bound state is reached.

For a ligand-binding interaction where free and bound states are in fast exchange [11,12], the observed chemical shift δ_{obs} is given by,

$$\delta_{\text{obs}} = \delta_{\text{f}} p_{\text{f}} + \delta_{\text{b}} p_{\text{b}} \tag{1}$$

The parameters δ_{f} and δ_{b} are the chemical shifts for the free DNA and the fully bound DNA:ligand complex, and p_{f} and p_{b} are the fractional populations of these species ($p_{\text{f}} + p_{\text{b}} = 1$), enabling the chemical shift change to be used to determine p_{b} as a function of drug concentration. The observed line width (LW$_{\text{obs}}$) is related to the populations of free and bound states with an additional exchange contribution given by the expression,

$$\text{LW}_{\text{obs}} = p_{\text{f}}\text{LW}_{\text{f}} + p_{\text{b}}\text{LW}_{\text{b}} + [p_{\text{b}}(1 - p_{\text{b}})^2 4\pi(\Delta\nu)^2]/k_{\text{off}} \tag{2}$$

where k_{off} is the off-rate (per second) and $\Delta\nu$ the chemical shift difference (Hz) between the *free* and fully *bound* states, and LW$_{\text{f}}$ and LW$_{\text{b}}$ the line widths in the free and bound states. The exchange contribution, and hence the off-rate, can be determined by monitoring LW$_{\text{obs}}$ as a function of the fraction bound (p_{b}) at each site. Selected 1D NMR spectra from the RHPS4 titration study at 303 K are shown in Figure 2a, with line width changes as a function of the p_{b} shown in Figure 2b. Data for the guanine imino proton resonances G5 and G6 were fitted to Equation (2) using values of $\Delta\nu$ of 205 and 415 Hz, giving estimated values for k_{off} of 1814 (±170)/s and 3812 (±250)/s. Given the uncertainty in line width measurements at values of p_{b} close to ~0.3 (Figure 2), the factor of ~2 difference in exchange rates measured using the two different probes probably represents a more realistic estimate of possible errors, at least in this context, and hence we report a mean value for k_{off} of 2800 (±1000)/s.

Thus, despite the fact that RHPS4 is a potent inhibitor of telomerase its interaction with quadruplex DNA is highly dynamic. Structural analysis reveals that the drug is not able to intercalate between the G-tetrads since the core structure is highly stabilized by K$^+$ ions which are

Graham A. Webb (ed.), Modern Magnetic Resonance, 1363–1367.
© 2008 *Springer.*

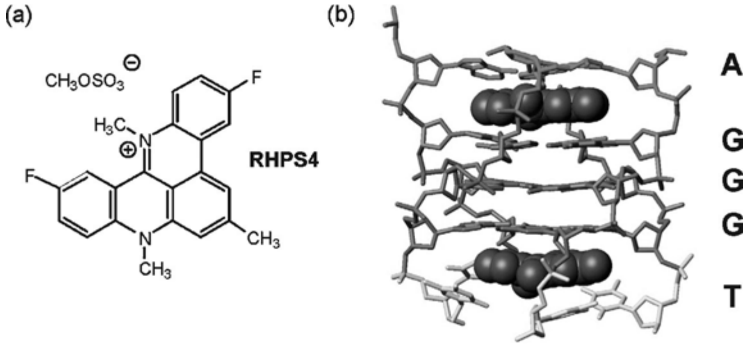

Fig. 1. (a) Chemical structure of the telomerase inhibitor RHPS4; (b) NMR structure of the 2:1 complex of RHPS4 bound at the 5′-AG and 5′-GT sites in the intermolecular parallel-stranded quadruplex formed from the human telomeric repeat d(TTAGGGT)$_4$. Only the core AGGGT structure is shown (5′-terminal thymines are relatively disordered). From Ref. [10]. (See also Plate 104 on page XXII in the Color Plate Section.)

octahedrally co-ordinated to the O6 carbonyl of guanine bases in adjacent tetrads. Displacement of these ions is energetically costly. Consequently, quadruplex-binding ligands appear to associate with the terminal G-tetrads, binding at the 5′-AG and 5′-GT steps within the sequence 5′-TTAGGGT (Figure 1b), where the adjacent nucleotides are less well structured [9,10]. As we have shown, small energy barriers to binding and dissociation permit fast kinetics at these sites.

DNA Hairpin Folding and Slow Exchange Eqilibria

The mechanisms and pathways by which biomolecules fold to their native structures is well developed in the protein folding arena; however, the folding of DNA and large RNA assemblies is still poorly understood [13]. The process is likely to be just as complex, involving multiple pathways and kinetic traps originating from misfolded structures and non-native interactions [13]. DNA and RNA hairpins, consisting of a double stranded stem region and connecting loop, occur naturally in single stranded nucleotide sequences and serve a range of important biological functions. A number of DNA mini-hairpin sequences have been identified with extraordinary stability containing GNNA and GNA loop sequences (N = any nucleotide) where the purine bases fold back to form a G–A wobble base pair. In the most stable hairpin structures, the G–A pair preferentially stacks on an adjacent C–G base pair in the adjoining double stranded stem region [14,15]. We have exploited the 5′-C*GNA*G mini-hairpin motif (with a 5′-GAA loop) in the design of hairpins with mismatched or extrahelical bases for studies of drug recognition and binding [16]. We recently identified a 13-mer sequence (5′-GCTACGTAGTCGC) that folds in solution to form a hairpin with C–T mismatch (Figure 3a). In the presence of 100 mM NaCl (10 mM sodium phosphate, pH 7.0) the folded state is in slow exchange with the unstructured single strand with two sets of resonances assignable in 2D NMR spectra. The observation of two distinct species in slow exchange is unusual and indicative of a large activation energy barrier between folded and unfolded conformations. Significant chemical shift differences are observed between resonances in the two conformers (up to ~0.3 ppm), making this an ideal system for characterizing the folding kinetics via magnetization transfer experiments.

Slow Exchange Between Two Conformers

In the general case, two conformers A and B are in slow exchange when the first order rate constants k_A and k_B for interconversion are $\ll \Delta\nu_{AB}$, where $\Delta\nu_{AB}$ is the chemical shift difference in Hz between a nucleus X in the two structural environments A and B. Selective perturbation of one signal can result in magnetization transfer to the other due to the exchange between environments. Assuming that the longitudinal relaxation rates in the two conformers are not considerably faster than the exchange rate, the time-dependent change in intensity after the perturbation can enable the rate of exchange to be measured [11,17]. Selective inversion of nucleus X in conformation A results in the recovery of the magnetization of A via a double exponential process,

$$M_A(t) = C_1 e^{\lambda 1 t} + C_2 e^{\lambda 2 t} + M_A^{\infty} \qquad (3)$$

Similarly, inversion of A leads to transfer of magnetization to B with recovery of the magnetization of B also

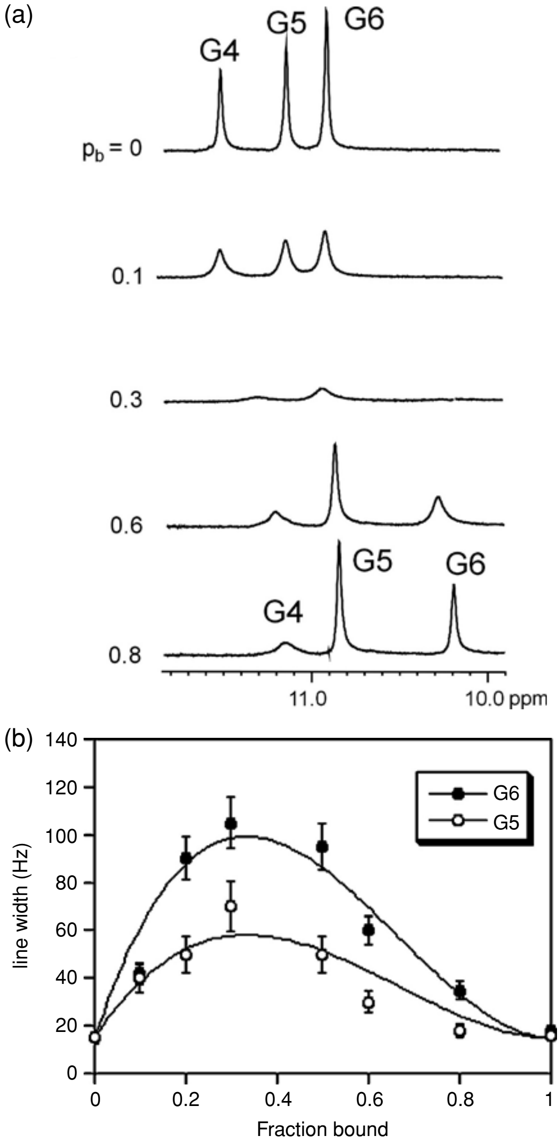

Fig. 2. (a) Selected 600 MHz 1D NMR spectra at 303 K showing the guanine imino proton resonances of the G-quadruplex structure d(TTAGGGT)$_4$ as a function of the fraction of drug bound (p_b); resonances are shifted upfield by ring current effects from the bound drug and initially broaden (maximum line width at $p_b \sim 0.3$) before again sharpening as the binding sites are filled. From Ref. [10]. (b) Measured line width (LW_{obs}) as a function of the fraction of drug bound showing the best fit to Equation (2).

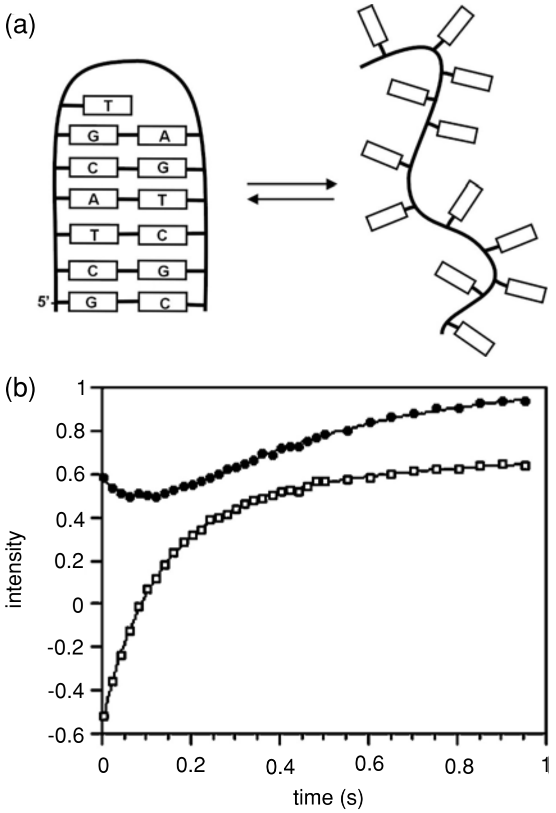

Fig. 3. (a) Proposed equilibrium between the hairpin conformation of the 13-mer d(GCTACGTAGTCGC) and the disordered single strand with interconversion rates k_A and k_B. (b) Magnetization transfer data showing the recovery of magnetization after selective inversion of the A4 H8 signal for the single stranded conformation at 8.23 ppm (open squares), and the change in intensity of A4 H8 (hairpin conformation) due to magnetization transfer (black dots); 600 MHz data collected at 308 K. Both data sets were analyzed using a double exponential fit [see Equations (3) and (4)]. The experimental parameters obtained are as follows (open squares): $C_1 = 0.458$, $\lambda_1 = 2.787$, $C_2 = 0.765$, $\lambda_2 = 9.892$, $M_A^\infty = 0.677$, and $M_A^0 = 0.521$; (black dots) $C_3 = 0.895$, $\lambda_1 = 2.572$, $C_4 = 0.455$, $\lambda_2 = 10.014$, $M_B^\infty = 1.022$, and $M_B^0 = 0.582$.

following a double exponential decay,

$$M_B(t) = C_3 e^{\lambda 1t} + C_4 e^{\lambda 2t} + M_B^\infty \tag{4}$$

where M_A^∞ and M_B^∞ are the equilibrium longitudinal magnetization of X in the two conformations A and B. The various parameters have the following relationships as solutions of McConnell's equations [18]:

$$\lambda_1 = \{-(k_{1A} + k_{1B}) + [(k_{1A} - k_{1B})^2 + 4k_A k_B]^{1/2}\}/2 \tag{5}$$

$$\lambda_2 = \{-(k_{1A} + k_{1B}) - [(k_{1A} - k_{1B})^2 + 4k_A k_B]^{1/2}\}/2 \tag{6}$$

$$C_1 = [(\lambda_2 + k_{1A})(M_A^\infty - M_A^0) - k_B(M_B^\infty - M_B^0)]/(\lambda_1 - \lambda_2) \tag{7}$$

$$C_2 = [-(\lambda_1 + k_{1A})(M_A^\infty - M_A^0) + k_B(M_B^\infty - M_B^0)]/(\lambda_1 - \lambda_2) \tag{8}$$

$$C_3 = [-k_A(M_A^\infty - M_A^0) - (\lambda_1 + k_{1A})(M_B^\infty - M_B^0)]/(\lambda_1 - \lambda_2) \tag{9}$$

$$C_4 = [k_A(M_A^\infty - M_A^0) + (\lambda_2 + k_{1A})(M_B^\infty - M_B^0)]/(\lambda_1 - \lambda_2) \tag{10}$$

where k_{1A} and k_A, and k_{1B} and k_B are related by

$$k_{1A} = k_A + R_{1A} \tag{11}$$

$$k_{1B} = k_B + R_{1B} \tag{12}$$

where k_A and k_B are the required rate constants (Figure 3), R_{1A} and R_{1B} the longitudinal relaxation rates, and M_A^0 and M_B^0 are proportional to the initial intensities immediately after the perturbation to the magnetization of A. Since conformers A and B are in equilibrium, the following relationship must also hold:

$$k_A M_A^\infty = k_B M_B^\infty \tag{13}$$

The double exponential nature of the time-dependence of the magnetization means that λ_1 and λ_2 can only be determined independently with any certainty if they differ by more than a factor of 3, otherwise only the combination $C_1\lambda_1 + C_2\lambda_2$ can be determined, as discussed in detail elsewhere [11,17]. This is remedied by repeating the experiment by selectively inverting signal B to provide another pair of independent combinations.

DNA Hairpin Folding Kinetics by Magnetization Transfer

Inversion transfer experiments were used to characterize the hairpin to single strand equilibrium at 308 K where the two conformers are significantly populated ($M_A^\infty/M_B^\infty = k_B/k_A = 0.662$). Selective inversion was achieved using a 180° Gaussian-shaped pulse with the excitation bandwidth optimized to give the desired selectivity. Perturbation of the A4 H8 signal at 8.23 ppm in the single strand conformation results in transfer of magnetization to the resonance of the folded hairpin at 8.28 ppm. The recovery curves for both resonances are illustrated in Figure 3b. A double exponential fit resolves two rate constants which differ by a factor >3. Making use of Equation (13) to substitute into Equations (11) and (12), and subsequent substitutions into Equations (5)–(10) using experimentally determined values for λ_1, λ_2, and C_1–C_4, enables all of the unknown rate constants in Equations (11) and (12) to be determined, from which we deduce that $k_A = 3.3/\mathrm{s}$ and $k_B = 2.1/\mathrm{s}$ at 308 K. Rate constants were similarly determined from the reverse experiment (inversion of the hairpin signal at 8.28 ppm), and from inversion of other resonance pairs, with all the data in very close agreement.

We have chosen experimental conditions under which the two conformations are of similar stability (at 308 K, $K_{eq} = 1.6$) with the slow rate of interconversion indicating that the two states are separated by a large activation barrier. Recent thermodynamic investigations involving mutation of residues in various mini-loop sequences, including 5′-C*GNA*G, suggest that stacking interactions are highly co-operative with base substitutions or functional group mutations leading to large changes in stability [19,20]. Thus, a significant kinetic barrier may originate from the requirement for a highly structured loop region in the transition state which may have many of the interactions of the fully folded state. Our investigations have shown that the introduction of the destabilizing C–T mismatch has enabled the equilibrium to be sufficiently perturbed to be able to detect both folded and disordered species simultaneously in slow exchange. Magnetization transfer methods are ideally suited to measuring the kinetics of such systems, and have similarly been employed in characterizing coiled-coil transitions in the folding of GCN4 leucine zipper peptides [21].

Acknowledgments

We acknowledge our collaborators Professor Malcolm Stevens and Dr. Robert Heald on the drug–quadruplex studies, and the support from the EPSRC of the UK and the School of Chemistry, University of Nottingham.

References

1. Neidle S, Parkinson G. Nat. Rev. Drug Discov. 2002;1:383.
2. Wheelhouse RT, Sun D, Han H, Han FX, Hurley LH. J. Am. Chem. Soc. 1998;120:3261.
3. Mergny J-L, Mailliet P, Lavelle F, Riou J-F, Laoui A, Helene C. Anticancer Drug Des. 1999;14:327.
4. Davies JT. Angew. Chem. Int. Ed. 2004;43:668.

5. Haider SM, Parkinson GN, Neidle S. J. Mol. Biol. 2003;326:117.
6. Schouten JA, Ladame S, Mason SJ, Cooper MA, Balasubramanian S. J. Am. Chem. Soc. 2003;125:5594.
7. Heald RA, Modi C, Cookson JC, Hutchinson I, Laughton CA, Gowan SM, Kelland LR, Stevens MFG. J. Med. Chem. 2002;45:590.
8. Gowan SM, Heald RA, Stevens MFG, Kelland LR. Mol. Pharmacol. 2001;60:981.
9. Gavathiotis E, Heald RA, Stevens MFG, Searle MS. Angew. Chem. Int. Ed. 2001;40:4749.
10. Gavathiotis E, Heald RA, Stevens MFG, Searle MS. J. Mol. Biol. 2003;334:25.
11. Lian L-Y, Roberts GCK. In: GCK Roberts (Ed). NMR of Macromolecules. IRL Press, Oxford, 1993, p 152.
12. Craik DJ, Pavlopoulos S, Wickham G. NMR in Drug Design. CRC Press Inc., New York, 1996, p 423.
13. Pan J, Thirumalai D, Woodson SA. J. Mol. Biol. 1997;273:7.
14. Hirao I, Kawai G, Yoshizawa S, Nishimura Y, Ishido Y, Watanabe K, Miura K. Nucleic Acids Res. 1994;22:576.
15. Yoshizawa S, Kawai G, Watanabe K, Miura K, Hirao I. Biochemistry. 1997;36:4761.
16. Colgrave ML, Williams HEL, Searle MS. Angew. Chem. Int. Ed. 2002;41:4754.
17. Led JJ, Gesmar H, Abildgaard F. Methods Enzymol. 1989;176:311.
18. McConnell HM. J. Chem. Phys. 1958;28:430.
19. Moody EM, Bevilacqua PC. J. Am. Chem. Soc. 2003;125:2032.
20. Moody EM, Bevilacqua PC. J. Am. Chem. Soc. 2003;125:16285.
21. d' Avignon DA, Bretthorst GL, Holtzer ME, Holtzer A. Biophys. J. 1998;74:3190.

The Use of NMR in the Studies of Highly Flexible States of Proteins: Relation to Protein Function and Stability

Søren M. Kristensen[1], Marina R. Kasimova[2], and Jens J. Led[1]
[1]*Department of Chemistry, University of Copenhagen, DK-2100 Copenhagen, Denmark; and*
[2]*Optics and Fluid Dynamics Department, Risø National Laboratory, DK-4000 Roskilde, Denmark*

Introduction

The power of NMR as a method for characterizing the solution state of proteins stems from the highly specific way that NMR reports on protein structure and dynamics. This is due to the fact that NMR parameters, such as chemical shifts, relaxation rates and exchange-rate parameters report specifically about the local environment around the investigated nuclei. This obviously requires that the relevant NMR resonances have been assigned to the individual nuclei of the protein structures, which with present day techniques for isotope labeling and multidimensional NMR methods is possible for proteins with molecular weights higher than 30 kDa. After the resonances have been assigned, the overall three-dimensional structure of a protein can be determined from distance and angular constraints derived from additional spectral information.

However, a detailed NMR determination of the three-dimensional solution structure of proteins may be hampered by the dynamics of the protein molecules. At the same time, a detailed characterization of the flexible regions in the protein is highly interesting due to the functional importance of these regions, as shown by several NMR studies in recent years [1–4]. To solve this immediate conflict, that is, to alleviate the impact of the dynamics on the NMR structure determination of proteins, while at the same time obtaining important information on their dynamics and flexibility, several approaches can be used. Here we illustrate some of the approaches that have been used in the studies of the structure and function of two flexible insulin mutants and a flexible state of human growth hormone (hGH).

One of the approaches concerns the determination of the relatively fast exchanging amide protons involved in weak intra- and intermolecular hydrogen bonds. This approach is useful in cases where the exchange rates of the amide protons are relatively fast while separate amide proton signals can still be observed, that is, the exchange takes place within an hour or less. This approach is illustrated using a monomeric insulin mutant that, although flexible, still forms a well-defined structure in water.

Another approach focuses on the use of the helix-promoting solvent 2,2,2-trifluoroethanol (TFE) to stabilize helices inherently encoded in the amino acid residue sequence of the protein. This approach is illustrated in the study of a highly flexible insulin mutant without a well-defined structure in water. TFE strengthens helical structures in peptides and proteins and induces helical structures in segments which have the propensity for forming helices [5,6]. It has also been found that TFE stabilizes β-turns and β-hairpins in proteins [7,8]. On the other hand, TFE disrupts the quaternary structure of proteins and reduces interactions between non-polar residues [9,10].

However, a complete assignment of the resonances may not always be possible. In particular, resonances in highly flexible regions in proteins may be broadened beyond detection and thereby preventing an assignment of these resonances. Still, NMR can provide valuable information about the structure and dynamics of such highly flexible proteins, despite an incomplete assignment. Here, this is exemplified by the study of hGH. A partial assignment can be used to track structural changes caused by variations in the solution conditions. Changes in pH, for instance, may result in alterations in the charge distribution on the protein surface, which may modulate both intra- and intermolecular coulombic interactions and hydrogen bond interactions. This, in turn, may give rise to changes in NMR parameters such as chemical shifts, relaxation rates and exchange rates of labile protons. Similarly, changes in the salt concentration and the buffer composition can modulate structure and stability of specific regions in proteins, as well as intermolecular interactions, while changes in temperature are likely to influence the stability of the structure of a protein and to affect exchange phenomena. Hence, by measuring the NMR parameters for a protein at different solution conditions, it is possible to obtain information about non-native and destabilized structural states, even if only a partial assignment is available.

Graham A. Webb (ed.), Modern Magnetic Resonance, 1369–1376.
© 2008 *Springer.*

Insulin Flexibility and Activity

Insulin is a 5.8-kDa peptide hormone with two chains, a 30-residue long A-chain and a 21-residue long B-chain, and with a three-dimensional structure as shown in Figure 1. Native insulin forms well-defined dimers and higher aggregates thereof in water solution, and in the presence of Zn^{2+} it forms a well-defined hexamer complexed with two zinc ions. However, the active form of insulin is the monomer. Therefore, the structure of several monomeric insulin mutants have been determined by NMR, and their *in vivo* activities have been compared, in order to elucidate the function of insulin and the mechanism of its interaction with the receptor, through the correlation between its structure and flexibility and its activity. However, active monomeric mutants are often highly flexible, making it necessary to use special NMR techniques to extract the dynamical and structural information. Here we describe the NMR investigations of two monomeric mutants, the des-[Phe(B25)] mutant, that is, an insulin mutant in which Phe in position B25 has been removed, and the T(B27)P, P(B28)T mutant (PT insulin), where Thr(B27) and Pro(B28) of the native insulin have been interchanged. In both cases, a hydrophobic patch that is surface exposed in native insulin is turned toward the inside of the molecule, resulting in intramolecular hydrophobic interactions that eliminate the aggregation propensity. Both mutants have a biological activity that is higher than that of native insulin. However, they also have flexible structures. In the case of des-[Phe(B25)]insulin this results in increased exchange rates of the H-bonded amide protons involved in the stabilization of the α-helices, while in the case of PT insulin the structure is too unstable in water solution to be determined by NMR.

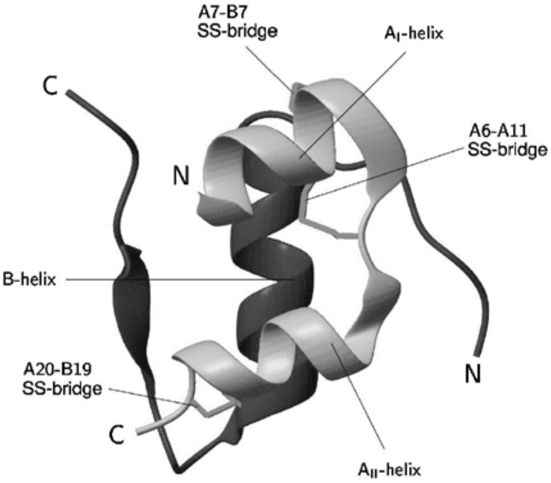

Fig. 1. The native insulin monomer consists of a 21-residue long A-chain (yellow) and a 30-residue long B-chain (red). Two disulfide bridges (SS bridge), CysA7-CysB7 and CysA20-CysB19, tie the two chains together, while a third disulfide bridge connects CysA6 and CysA11. The N- and C-terminal ends of the A-chain form α-helices ($A_{\rm I}$: A2–A8 and $A_{\rm II}$: A13–A20) connected by a loop. The central part of the B-chain forms a third helix (B10–B19). The C-terminal end of the B-chain forms an extended structure, while the N-terminal end is unstructured. (See also Plate 105 on page XXII in the Color Plate Section.)

Des-[Phe(B25)] Insulin: Quantitative Exchange Rates of Weakly H-bonded Amide Protons in Proteins from a Single 2D Experiment

To get more detailed information about the structure of the des-[Phe(B25)] mutant, the relatively fast exchange rates of the H-bonded amide protons were determined quantitatively using the two-dimensional (2D) NMR method for measuring exchange rates of the order of reciprocal hours (h^{-1}). This method is based on a single two-dimensional NOESY or TOCSY spectrum of the protein. It exploits the line broadening of the amide cross-peaks in the indirect dimension, caused by the hydrogen/deuterium exchange of the amide proton during the indirect evolution period when the protein is dissolved in D_2O. The method is described in detail in Ref. [11]. It allows the determination of amide proton exchange rates that are considerably faster than those, which can be measured by the conventional 2D approach based on series of NOESY spectra [12]. Furthermore, it is far less time consuming than the conventional 2D approach, since it is based on a single 2D experiment. At the same time, the accuracy of the rates determined by the method is high because data points from all the slices in the indirect dimension of the 2D experiment contribute to the determination of the rates. The accuracy can be further improved if the method is combined with a spectral analysis base on linear prediction. Moreover, the range of exchange rates covered by the method can be further expanded using the linear prediction model method described previously [13].

Using this method together with standard methodologies for NMR structure determination of proteins, it was found [14] that, although the des-[Phe(B25)] mutant has the normal insulin structure in water (Figure 1), the exchange rates of the H-bonded amide protons are relatively fast. Thus, the rates are about an order of magnitude faster than those of an insulin mutant where the hydrophobic patch is surface exposed, namely the B9(Asp) or S(B10)D mutant where Ser in position B9 has been substituted by Asp [15,16]. This clearly indicates that the structure of the des-[Phe(B25)] mutant is considerably less stable than that of the B9(Asp) mutant. Most importantly, the absence in the des-[Phe(B25)] insulin of

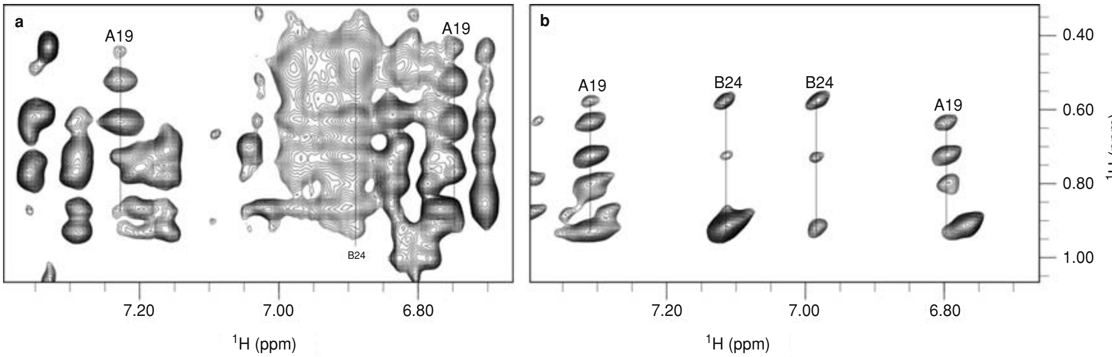

Fig. 2. The amide/aromatic region of an 800 MHz ^1H–^1H NOESY spectra of PT insulin showing the correlations between the aromatic side chain protons and aliphatic side chain protons (a) in pure water and (b) in 35% TFE-d_3. The broadening of the signals in the spectrum recorded in water reflects the high flexibility of the side chains. (Reproduced with permission from Ref. [17].)

slow exchanging amide protons, corresponding to the intermolecular hydrogen bonds associated with the dimer formation, show unambiguously that the mutant does not form a dimer in water solution. This is in contrast to the B9(Asp) mutant that forms a well-defined dimer in water, as reflected by the slow exchange of amide protons involved in intermolecular hydrogen bonds that stabilize the dimer.

PT Insulin: Stabilizing the Structure of an Unstructured Protein by 2,2,2-trifluoroethanol

In the case of proteins that are sufficiently flexible in water to escape any NMR structure determination, secondary or tertiary, the helix-promoting solvent TFE may stabilize the structure [10], allowing the determination of a sufficient number of NOE constraints for a regular NMR structure determination. This was demonstrated in a study of the structure and folding propensity of the highly flexible PT insulin mutant [17].

PT insulin is biologically active with an activity that is 50% higher than that of native insulin [18]. It can, therefore, adapt the conformation necessary for its binding to the insulin receptor (IR). However, it is also unusually flexible with a poorly defined structure in water. This is indicated by the broad NOESY cross-peaks between the side chain protons observed for the mutant dissolved in water (Figure 2a). Moreover, only a few slowly exchanging amide protons can be detected in the protein dissolved in water, and only at low temperature (15 °C). The slowly exchanging amide protons are all involved in weak hydrogen bonds associated with very loose secondary or tertiary structure elements. The strength of a hydrogen bond can be measured by the protection factor, P, of the amide proton involved in the H bond [19]. A more detailed description of the protection factor is given below together with the studies of hGH. Suffice it to mention here that a normal hydrogen bond corresponds to a protection factor of ≥ 25 [20], while the protection of the observed slow exchanging amide protons in PT insulin in water solution are in the range from 2.1 to 18.7.

When dissolved in a mixture of 35% TFE and water, PT insulin assumes a more stable structure, as shown by the relatively sharp and well-defined NOESY cross-peaks between the side chain protons observed for the mutant dissolved in this solvent (Figure 2b). Thus, a sufficient number of NOE-derived distance constraints and slowly exchanging amide protons could be identified to allow a regular NMR structure determination using the program X-PLOR [21]. Moreover, the structure that PT insulin assumes is identical to the structure of native insulin shown in Figure 1. That is, even though PT insulin does not have a well-defined structure in water, it has the propensity to form the native fold.

Model for the Insulin–Receptor Interaction

It is well established that the flexibility of the insulin molecule is important for its function. Thus, it was found [22] that an insulin mutant, where the N-terminal end of the A-chain was tied to the C-terminal end of the B-chain by a short peptide link, was biologically inactive even though it has a three-dimensional structure similar to that of native insulin (Figure 1). Also NMR studies of insulin mutants in which the C-terminal end of the B-chain is turned away from the rest of the molecule [23,24] indicate that such a structural change is required for insulin to interact with its receptor.

In the light of these findings, the concomitant high flexibility and biological activity of PT insulin is interesting.

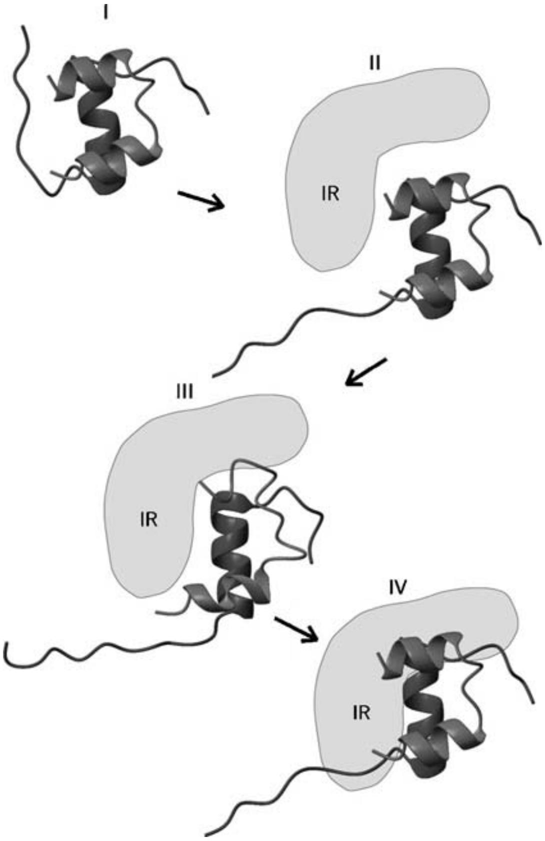

Fig. 3. Model of the interaction of native insulin with the insulin receptor (IR). I, free insulin in solution; II, detachment of the C-terminal part of the B-chain (vertical helix) from the rest of the molecule; III, unfolding of the A_I-helix; IV, refolding of the A_I-helix after navigating into the binding site of receptor (gray) and binding to the receptor. The enhanced biological activity of the PT insulin mutant could result from the fact that the A_I-helix of PT insulin is very loose or non-existing in water, yet it has the propensity to form the helix (see text). Therefore, PT insulin does not need to go through a genuine unfolding before navigating into the active site of the receptor. (Reproduced with permission from Ref. [17].) (See also Plate 106 on page XXII in the Color Plate Section.)

Together with the observation that the mutant has the propensity to form the native fold, these characteristics led to the suggestion of the mechanism for the binding of insulin to its receptor (IR) shown in Figure 3. This mechanism also includes a detachment of the C-terminal end of the B-chain from the rest of the molecule before the interaction with the receptor can take place, as suggested in previous studies [23,24].

The Acid State of Human Growth Hormone

In order to rationalize a rather puzzling study of hGH, the so-called acid state that occurs at pH 2.7, we shall compare this state with the native state of hGH at pH 7.0. hGH is a 191-residue four-helix bundle protein with a classical up-up-down-down cytokine topology [25]. The native state is characterized by a high thermal and chemical stability, similar to most native states of globular proteins. The acid state of hGH is more difficult to categorize, because it has characteristics of both the molten globule and the native state. Similar to the native state, the acid state has a high stability toward both chemical [26] and thermal denaturation and shows a cooperative unfolding behavior [27]. These features are contradictory to a classic definition of molten globules as defined by Ptitsyn [28]. They also differ from the behavior of other four-helix bundle proteins at similar solution conditions. Thus, the two cytokines, interleukin-2 and interleukin-4, were reported to adopt a classical molten globule state [29] and a “highly ordered molten globule” state [30], respectively, at low pH. In accordance with the stability data, far-UV CD measurements indicate that the structural properties of the acid state of hGH are very similar to those of its native state, suggesting that the helical content of the two states are similar. However, the near-UV CD spectrum of the acid state deviates from the spectrum of the native state and is more similar to the spectrum of denatured hGH [26]. This indicates that the aromatic side chains in the acid state are disordered, just like in the denatured state or a molten globule state. It is puzzling how it is possible to have a structural state with both a high stability toward denaturation and, at the same time, a disordered and flexible protein core.

Using standard three-dimensional triple-resonance techniques combined with uniform ^{13}C- and ^{15}N-labeling, only partial assignments of the hGH molecule were obtained [31]. In total, 60% and 75% of the backbone resonances were assigned for the native and acid states, respectively. Complete resonance assignment was not possible because of severe resonance overlap and line broadening effects [31].

However, even without access to the solution structure of hGH, NMR investigations of the protein allow a detailed comparison of the native and the acid states. The investigation includes analyses of the backbone chemical shifts, the amide and indole hydrogen/deuterium exchange rates, and backbone amide ^{15}N relaxation rates. Backbone C^{α} and H^{α} chemical shifts contain information about the secondary structure, and provide means for accessing the structural integrity of a protein under a particular set of experimental conditions. This information is derived by calculation of secondary chemical shifts and a subsequent comparison with reference values for helix,

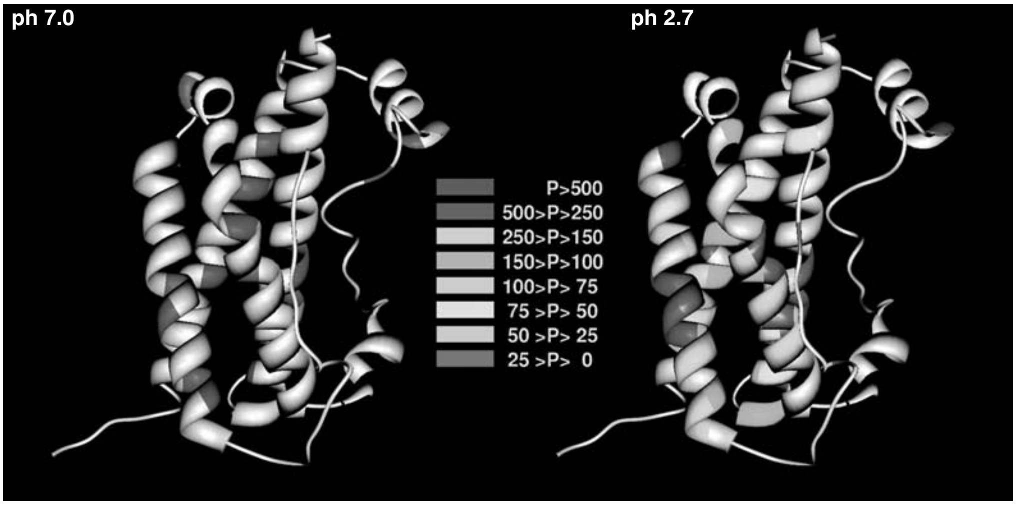

Fig. 4. Distribution of measured protection factors (P) for the native state (pH 7) and the acid state (pH 2.7) of human growth hormone. The protection factors are color mapped onto the three-dimensional structure as indicated in the figure. Structural parts colored in gray correspond to regions where the amide proton exchange rates could not be quantified. The figure was created with UCSF chimera [40]. (See also Plate 107 on page XXIII in the Color Plate Section.)

sheet, and extended structure [32]. Exchange-rate constants of labile protons report directly on solvent accessibility and in particular on the protection of labile protons by hydrogen bonds [33]. Sequence-related differences in intrinsic exchange-rate constants, k_{intr}, and their dependencies upon pH, are taken into account by calculation of protection factors $P = k_{\mathrm{ex}}/k_{\mathrm{intr}}$ [19], where k_{ex} is the experimentally derived exchange-rate constant. Measurement of ^{15}N longitudinal (R_1) and transverse (R_2) relaxation rates, and [^1H]–^{15}N heteronuclear NOE for each assigned amide ^1H–^{15}N pair, and analysis within the framework of the Lipari–Szabo model-free formalism [34,35]

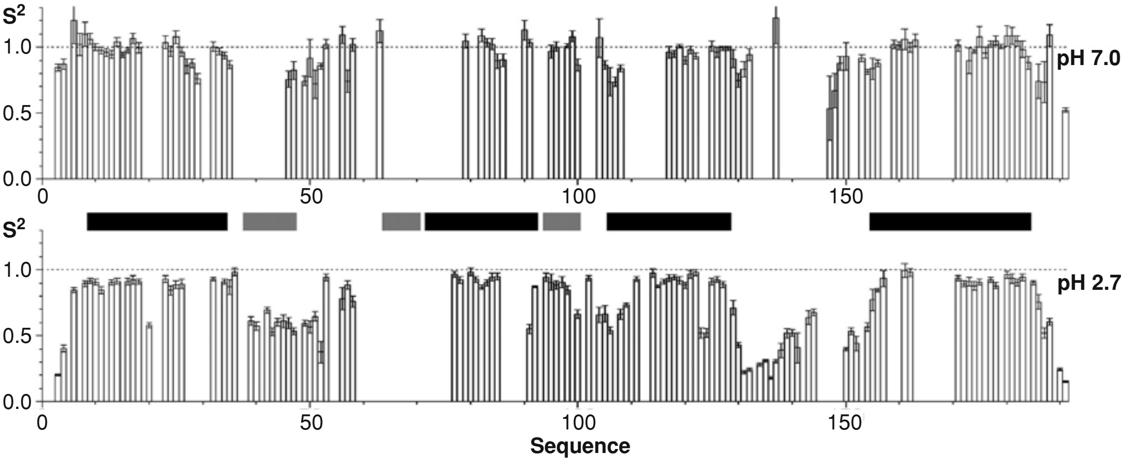

Fig. 5. Squared generalized order parameters (S^2) for the native state (pH 7.0) and the acid state (pH 2.7) of human growth hormone mapped as a function of the amino acid sequence. The black horizontal bars indicate the position of the four central helices A, B, C, and D forming the helix bundle (residues 9–34, 72–97, 106–128, and 155–184, respectively) and the gray horizontal bars indicate the position of the minor helices observed in the crystal structure of the hormone–receptor complex (PDB entry 3HHR).

provide a structural mapping of the so-called generalized order parameters, which reflect the restriction of the N–H bond vector on the pico- to nanosecond dynamics on a scale from zero to one. The ^{15}N relaxation measurements also provide information about exchange processes on the micro- to millisecond timescale as reflected in line broadening effects, and finally, information about the overall molecular tumbling rate and rotational diffusion anisotropy [36,37].

Backbone C^{α} and H^{α} assignments for the two states form the basis for a chemical-shift-based prediction of secondary structure [32]. This provides secondary structural data for the protein at the level of the individual residues without *a priori* knowledge of the overall structure. A comparison with the crystal structures of the free hormone (PDB entry 1HGU) and of the hormone bound to the extracellular domain of the receptor (PDB entry 3HHR) shows a high degree of similarity between the solution-state predictions at high and low pH and the two crystal structures [31]. The general conclusion that can be drawn from the NMR data is that the helix bundle scaffold is preserved at both high and low pH. However, subtle differences exist, including evidence for a helical propensity from residue 102 to 107 in the native solution state at neutral pH, which is not seen in the acid state. Also, the secondary chemical shifts indicate that the mini-helix from residue 94 to 100, observed in the crystal structure of the hGH–receptor complex but not in the crystal structure of free hGH, is present in the solution states.

The partial assignment of hGH gives access not only to structural information. NH exchange and backbone ^{15}N relaxation report on the flexibility of a molecule, and hence can help in the understanding of molecular stability.

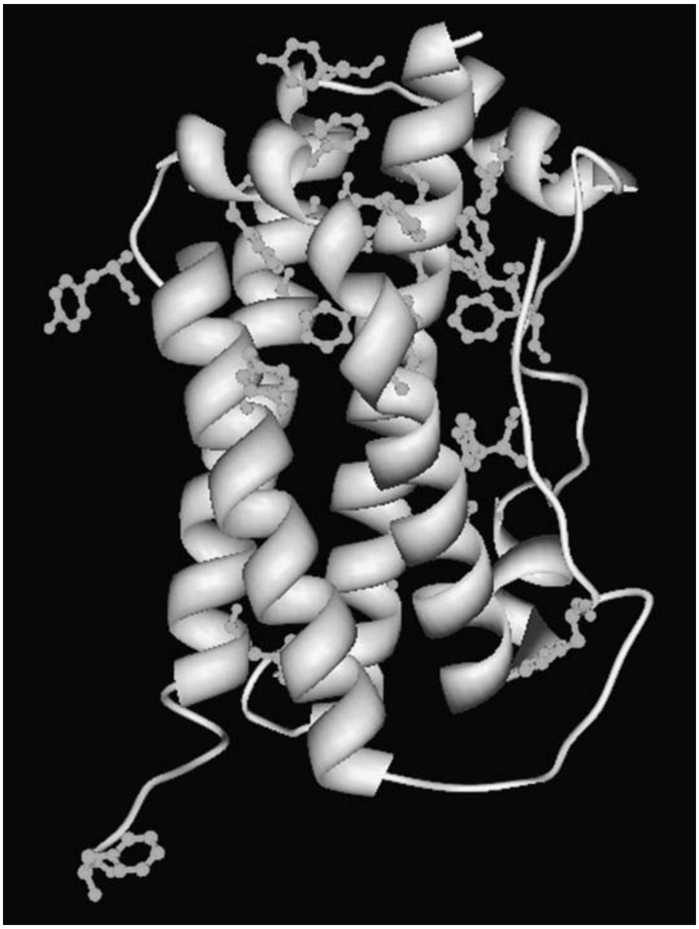

Fig. 6. Mapping of the aromatic residues in ball-and-stick representation on the ribbon diagram of human growth hormone shows a high density of aromatic groups in the north end of the molecule and a low density of aromatic groups in the south end of the molecule. The figure was created with UCSF chimera [40]. (See also Plate 108 on page XXIII in the Color Plate Section.)

For the native state of hGH, protection factors were determined for 22 backbone amide proton and despite the scarcity of the data, it is apparent that the protection factors are high throughout the helix bundle with values in the range 6×10^3 to 1×10^6. Furthermore, the indole NH of tryptophan 86 shows a high degree of protection ($P \sim 1 \times 10^6$) consistent with the hydrogen bond to $O^{\delta 1}$ of Asp169 first suggested by Bewley and Li [38] and later verified in the crystal structures. In the acid state, the backbone protection factors are orders of magnitude smaller than in the native state, and are in the range from 9×10^3 to 2×10^3, with the highest protection factors in the south end of the molecule. Figure 4 graphically illustrates the distribution of protection factors in the two solution states. Also, the Trp86 indole NH is exhibiting fast exchange with the solvent consistent with absence of the hydrogen bond to $O^{\delta 1}$ of Asp169 observed in the native state.

The backbone ^{15}N order parameters, S^2, for the native state are uniformly high throughout the sequence, corresponding to a highly rigid globular protein. This is in agreement with the high protection factors observed for this state. The acid state, on the other hand, displays increased flexibility throughout the sequence, but most pronounced in the long loop regions between the four main helices, as shown in Figure 5. In particular, the loop between helices C and D display order parameters as low as ~0.2, which is comparable to what is expected for an unfolded state [39]. Thus, the acid state of hGH is characterized by a preserved helix bundle structure with slightly increased overall flexibility as compared to the native state, but with highly mobile inter-helical loop regions.

The notion of the acid state as a well-defined, though more flexible, helix bundle with flexible loop regions is consistent with the high stability of the acid state toward denaturation. Also the native-like far-UV CD spectrum is indicative of a helix bundle structure with largely preserved inter-helical stabilizing interactions. On the other hand, the similarity of the near-UV CD spectrum with that of the denatured state of the protein suggests a certain degree of disorder of the aromatic groups, and seems to contradict the picture of a native-like helix bundle with preserved inter-helix stabilizing interactions. As shown in Figure 6, the majority of the aromatic side chains are located in the north end of the molecule. Thus, a unified picture is emerging, where the north end of the helix bundle is opening up resulting in a disorder of aromatic groups and an increased solvent access to amide groups—in agreement with near-UV CD and NH exchange data. At the same time, inter-helix interactions in the south end of the molecule are preserved, which can account for the high stability toward denaturation.

All taken together, the NMR investigation of hGH shows that important and detailed information about the structure and stability of proteins can be obtained from a multitude of available NMR data, despite an incomplete assignment of the NMR spectra.

Acknowledgement

The 800 MHz spectra were acquired at The Danish Instrument Center for NMR Spectroscopy of Biological Macromolecules.

References

1. Feher VA, Cavanagh J. Nature. 1999;400:289.
2. Eisenmesser EZ, Bosco DA, Akke M, Kern D. Science. 2002; 295:1520.
3. Ma LX, Hass MAS, Vierick N, Kristensen SM, Ulstrup J, Led JJ. Biochemistry. 2003;42:320.
4. Hansen DF, Hass MAS, Christensen HM, Ulstrup J, Led JJ. J. Am. Chem. Soc. 2003;125:6858.
5. Buck M, Radford SE, Dobson CM. Biochemistry. 1993;32: 669.
6. Hamada D, Kuroda Y, Tanaka T, Goto Y. J. Mol. Biol. 1995; 254:737.
7. Blanco FJ, Ortiz AR, Serrano L. Fold. Des. 1997;2:123.
8. Mabrouk K, Vanrietschoten J, Rochat H, Loret EP. Biochemistry. 1995;34:8294.
9. Albert JS, Hamilton AD. Biochemistry. 1995;34:984.
10. Buck M. Q. Rev. Biophys. 1998;31:297.
11. Olsen HB, Gesmar H, Led JJ. J. Am. Chem. Soc. 1993;115: 1456.
12. Wagner G, Wüthrich K. J. Mol. Biol. 1982;160:343.
13. Moss R, Gesmar H, Led JJ. J. Am. Chem. Soc. 1994;116: 747.
14. Jørgensen AMM, Olsen HB, Balschmidt P, Led JJ. J. Mol. Biol. 1996;257:684.
15. Kristensen SM, Jørgensen AMM, Led JJ, Balschmidt P, Hansen FB. J. Mol. Biol. 1991;218:221.
16. Jørgensen AMM, Kristensen SM, Led JJ, Balschmidt P. J. Mol. Biol. 1992;227:1146.
17. Keller D, Clausen R, Josefsen K, Led JJ. Biochemistry. 2001;40:10732.
18. Clausen R, Jørgensen TG, Jørgensen KH, Johnsen AH, Led JJ, Josefsen K. Eur. J. Endocrinol. 2002;147:227.
19. Bai YW, Milne JS, Mayne L, Englander SW, Proteins Struct. Funct. Genet. 1993;17:75.
20. Mori S, Abeygunawardana C, Berg JM, Vanzijl PCM. J. Am. Chem. Soc. 1997;119:6844.
21. Brunger AT. X-PLOR: A system for X-ray Crystallography and NMR. Yale University Press: New Haven, Connecticut, 1992.
22. Derewenda U, Derewenda Z, Dodson EJ, Dodson GG, Bing X, Markussen J. J. Mol. Biol. 1991;220:425.
23. Hua QX, Shoelson SE, Kochoyan M, Weiss MA. Nature. 1991; 354:238.
24. Ludvigsen S, Olsen HB, Kaarsholm NC. J. Mol. Biol. 1998;279:1.
25. de Vos AM, Ultsch M, Kossiakoff AA. Science. 1992;255: 306.

26. DeFelippis MR, Kilcomons MA, Lents MP, Youngman KM, Havel HA. Biochim. Biophys. Acta-Prot. Struct. Mol. Enzymol. 1995;1247:35.
27. Kasimova MR, Milstein SJ, Freire E. J. Mol. Biol. 1998; 277:409.
28. Ptitsyn OB. J. Protein Chem. 1987;6:273.
29. Dryden D, Weir MP. Biochim. Biophys. Acta. 1991;1078:94.
30. Redfield C, Smith RAG, Dobson CM, Nat. Struct. Biol. 1994;1:23.
31. Kasimova MR, Kristensen SM, Howe PWA, Christensen T, Matthiesen F, Petersen J, Sørensen HH, Led JJ. J. Mol. Biol. 2002;318:679.
32. Wishart DS, Sykes BD, Methods Enzymol. 1994;239:363.
33. Englander WS, Downer NW, Teitelba H. Annu. Rev. Biochem. 1972;41:903.
34. Lipari G, Szabo A. J. Am. Chem. Soc. 1982;104:4546.
35. Lipari G, Szabo A. J. Am. Chem. Soc. 1982;104:4559.
36. Tjandra N, Feller SE, Pastor RW, Bax A. J. Am. Chem. Soc. 1995;117:12562.
37. Tjandra N, Wingfield P, Stahl S, Bax A. J. Biomol. NMR. 1996;8:273.
38. Bewley TA, Li CH. Arch. Biochem. Biophys. 1984;233:219.
39. Farrow NA, Zhang OW, Formankay JD, Kay LE. Biochemistry. 1997;36:2390.
40. Huang CC, Couch GS, Pettersen EF, Ferrin TE, Pac. Symp. Biocomput. 1996;1:724.

NMR-based Metabonomics Techniques and Applications

John C. Lindon, Elaine Holmes, and Jeremy K. Nicholson
Biomedical Sciences Division, Imperial College London, Sir Alexander Fleming Building, South Kensington, London SW7 2AZ, UK

Introduction

Since the decoding of the human genome, there has been much interest in using changes in gene expression to discover the basis of disease and for the identification of new drug targets. However to date, the promise of the approach is yet to be comprehensively realized and there remains a difficulty in relating such changes to real conventional end points used in diagnosis and pharmaceutical development. The simultaneous measurement of many gene expression changes is termed transriptomics, and is usually carried out in an automatic fashion using so-called gene microarrays. The relevance of such gene changes is not always clear, which has led subsequently to efforts focused on the consequent protein level changes (a subject termed proteomics), but again it is not always possible to relate such changes directly to pathological events.

On the other hand, metabonomics, a whole systems approach for evaluating metabolite changes and pathway analysis through study of biofluids and tissues [1] offers a process whereby real end points can be obtained. In complex organisms, these three levels of biomolecular organization and control are highly interdependent, but they can have very different time scales of change. All of the technologies, which rely on analytical chemistry methods, result in complex multivariate data sets that require a variety of chemometric and bioinformatic tools for interpretation. The aim of such procedures is to extract biochemical information that is of diagnostic or prognostic value, and that reflects actual biological events. The areas where metabonomics impacts pharmaceutical R&D are:

- validation of animal models of disease, including genetically modified animals;
- preclinical evaluation of drug safety and ranking of compounds;
- assessment of safety in clinical trials and after product launch;
- quantitation, or ranking, of the beneficial effects of pharmaceuticals both in development and clinically;
- improved understanding of idiosyncratic toxicity;
- improved, differential diagnosis and prognosis of clinical diseases;
- better understanding of environmental population effects through epidemiological studies;
- patient stratification (pharmaco-metabonomics);
- nutrition, interactions between drugs, and between drug and diet;
- studies in environmental science.

Importantly, metabonomics also allows time-dependent patterns of change in response to stimuli to be measured. In multi-cellular organisms, there are a broad variety of time scales, varying widely according to gene, protein, pathway, and tissue. One important potential role for metabonomics therefore is to direct the timing of proteomic and genomic analyses in order to maximize the probability of observing “omic” biological changes that are relevant to functional outcomes.

Metabonomics, formally defined as the quantitative measurement of the dynamic multi-parametric metabolic response of living systems to pathophysiological stimuli or genetic modification, thus provides an approach which leads to real world end points. Metabolites can be identified and quantified, and changes can be related to health and disease, and are changeable by therapeutic intervention. The subject of metabonomics has been reviewed recently [2–4].

Metabonomics Analytical Technologies

The two principal methods that can produce metabolic profiles of biomaterials, comprise ^{1}H NMR spectroscopy [2] and mass spectrometry (MS) [5], the latter usually including a separation stage such as GC or LC. NMR has the advantages of being non-destructive, also applicable to intact tissues using magic angle spinning (MAS) methods [6], and provides detailed information on molecular structure, especially in complex mixture analysis. In addition, NMR can also be used to probe molecular dynamics as well as concentrations. MS is inherently considerably more sensitive than NMR, but it is necessary generally to employ different separation techniques for different classes of substances. Quantitation in MS can also be impaired by variable ionization effects, such that derivatization may be necessary. Most published mammalian studies have used NMR spectroscopy, but LC–MS is increasing in usage.

Graham A. Webb (ed.), Modern Magnetic Resonance, 1377–1385.
© 2008 *Springer.*

Typically metabonomics is carried out on biofluids that provide an integrated view of the whole systems biology. The biochemical profiles of the main diagnostic fluids, blood plasma, cerebrospinal fluid (CSF), and urine, reflect both normal variation and the impact of drug effects or disease on single or multiple organ systems [7]. Urine and plasma are obtained in a non- or minimally invasive fashion, and hence are appropriate for clinical trials monitoring and disease diagnosis. Different biofluids have characteristically different metabolic profiles (Figure 1). Although urine and plasma are the main diagnostic fluids, others have also been used in special cases. These include CSF, seminal fluids, digestive fluids, pathological fluids such as cyst fluid, and administered fluids such as dialysis fluids. A standard ^{1}H NMR spectrum of urine typically contains thousands of sharp lines from predominantly low molecular weight metabolites. Plasma contains low and high molecular weight components, which give a wide range of signal line widths. Protein and lipoprotein signals dominate ^{1}H NMR spectra of plasma, with small molecule fingerprints superimposed on them. Standard editing experiments based on T_1, $T_{1\rho}$, T_2, or diffusion coefficients can be used to select only the contributions from proteins, and other macromolecules and micelles, or alternatively to select only the signals from the small molecule metabolites. Each biofluid yields a characteristic ^{1}H NMR

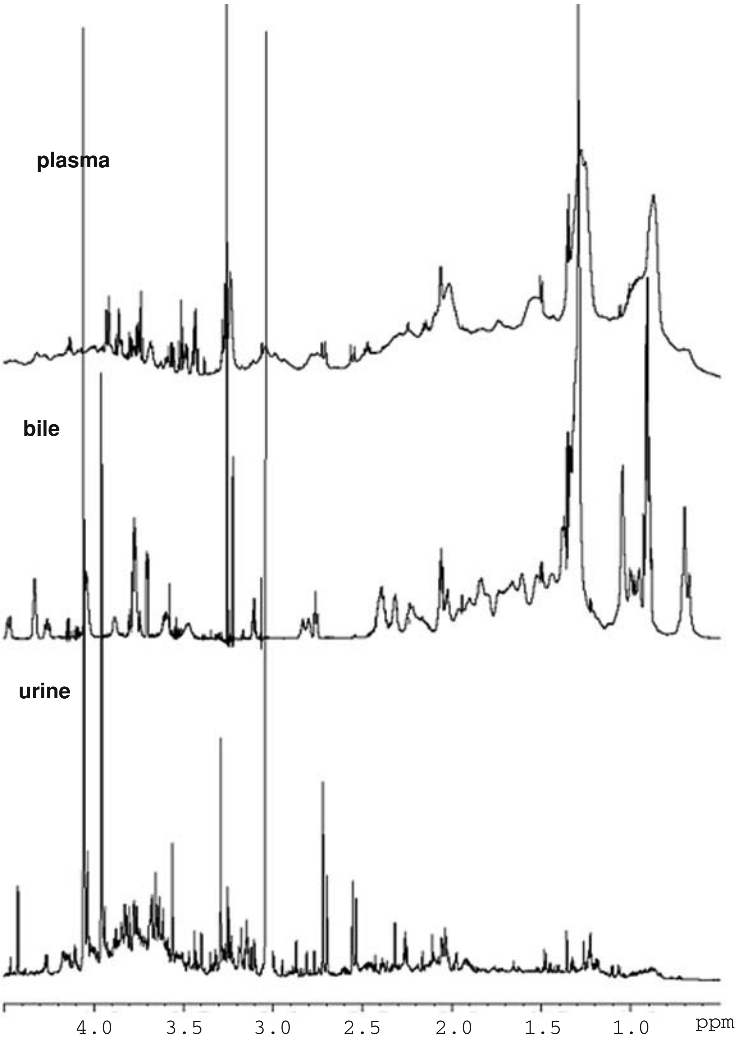

Fig. 1. 800 MHz ^{1}H NMR spectra with water peak suppression of control human biofluids, urine, gall bladder bile, and blood plasma showing characteristically different biochemical profiles.

spectroscopic fingerprint in which the spectral intensity distribution is determined by the relative concentrations of solutes, and in some cases by their intermolecular interactions. Standard spectra typically take only a few minutes to acquire using robotic flow injection methods. These entail robotic sample preparation involving buffering, addition of a chemical shift and quantitation standard such as TSP, and addition of D_2O as a magnetic field lock signal for the spectrometer. The large interfering NMR signal arising from water in all biofluids is easily eliminated by use of appropriate NMR solvent suppression methods such as NOESY presaturation or WET. Using NMR flow probes, the capacity for NMR analysis has increased enormously and now up to 200–300 samples per day can be measured.

Identification of the biomarkers (i.e. metabolites that change in level as a consequence of the pathology) detected in a biofluid NMR spectrum can involve the application of a number of other NMR techniques including two-dimensional (2D) experiments [2]. Although ^{1}H NMR spectra of urine and other biofluids are very complex, many resonances can be assigned directly based on their chemical shifts, signal multiplicities, and by adding authentic material and remeasuring the spectrum. 2D NMR spectroscopy can also be useful for spreading the signals out and for working out the connectivities between signals, thereby enhancing the information content and helping to identify biochemical substances. These include the ^{1}H–^{1}H J-resolved experiment, which reduces the contribution of macromolecules and yields information on the multiplicity and coupling patterns of resonances. Other 2D experiments such as COSY and TOCSY provide ^{1}H–^{1}H spin–spin coupling connectivities. Use of other nuclei can be important to help assign NMR peaks and here inverse-detected heteronuclear correlations, usually ^{1}H–^{13}C, can also be obtained by use of sequences such as HSQC or HMBC.

A major improvement in the scope of metabonomics has been made possible by the commercialization of miniaturized NMR probes. Now it is possible to study metabolic profiles by NMR using as little as 2–20 μl of sample, and examples have been published using CSF and blood plasma [8,9].

Cryogenic NMR probe technology, whereby the NMR detector coil and preamplifier are cooled to about 20 K, is now commercially available and provides an improvement in spectral signal–noise ratios of up to 500%. This improvement permits the routine use of natural abundance ^{13}C NMR spectroscopy of biofluids, such as urine or plasma, with acquisition times that enable a high throughput of samples. Information-rich ^{13}C NMR spectra of urine can be obtained using appropriately short acquisition times suitable for biochemical samples when using a cryogenic probe [10].

For metabolite identification, directly coupled chromatography–NMR spectroscopy methods can be used. The most powerful of these "hyphenated" approaches being HPLC–NMR–MS, [11] which can provide the full array of NMR and MS-based molecular identification tools. These include MS–MS for fragment ions and Fourier transform (FT)-MS or time-of-flight (TOF)-MS for accurate mass measurement and hence derivation of molecular empirical formulae.

Within the last few years, the development of high-resolution ^{1}H MAS NMR spectroscopy has had a substantial impact on the ability to analyze intact tissues [12]. Rapid spinning of the sample (∼4–6 kHz typically) at an angle of 54.7° relative to the applied magnetic field serves to reduce line broadening effects caused by sample heterogeneity, residual dipolar couplings, and residual chemical shift anisotropy. Thus, it is possible to obtain very high quality NMR spectra of whole tissue samples with no sample pretreatment. Such experiments indicate that diseased or toxin-affected tissues have substantially different metabolic profiles to those taken from healthy organs [13]. In addition, MAS NMR spectroscopy can be used to access information regarding the compartmentalization of metabolites within cellular environments. Such MAS NMR-based metabonomics can also be applied to *in vitro* systems such as tissue extracts [14], Caco-2 cells [15], or spheroids [16].

The NMR spectrum of a sample can be thought of as an object in a multi-dimensional set of metabolic coordinates, the values of which could be the spectral intensity at every data point. Similarity or differences between samples can then be evaluated using multivariate statistical methods or other pattern recognition approaches. One simple approach that has been widely used is to effect a dimension reduction from the typically 32K or 64K NMR intensity points describing each spectrum, down to a few dimensions to visualize similarities and differences between samples. This can be accomplished using principal components analysis (PCA). This constructs latent variables from linear combinations of the original descriptors to describe as much variation as possible in the data set, with first principal component (PC) explaining the maximum variation and successive components explaining decreasing amounts of variance with the constraint that all PCs are orthogonal to each other. The approach gives rise to two matrices based on the data, a scores and a loadings matrix. A plot of the PC scores shows the relationships between the samples (each point on the plot comprises one sample) and the PC loadings provide information on those variables, which contribute to the position of the samples in the scores plot. This is illustrated in Figure 2 for rat urine NMR spectra. The scores plot shows three clusters of samples, those of NMR spectra of control urine and those of NMR spectra of urine from animals dosed with two different liver toxins, hydrazine and a substance known as ANIT. These cause different biochemical changes and produce the separate clusters (Figure 2a). Examination of

Fig. 2. Classification of rat urine samples based on their ^{1}H NMR spectra using principal components (PC) analysis. Animals were dosed with hydrazine or ANIT, two model liver toxins operating by different biochemical mechanisms, or with dosing vehicle alone (controls). (a) PC scores plot where each spectrum is reduced to a single point and samples with similar metabolic profiles appear close to each other. (b) PC loadings plot where each point corresponds to the signal intensity a single NMR spectral region of width 0.04 ppm and the position of a spectral region point determines which regions are responsible for the corresponding clustering in the scores plot [17].

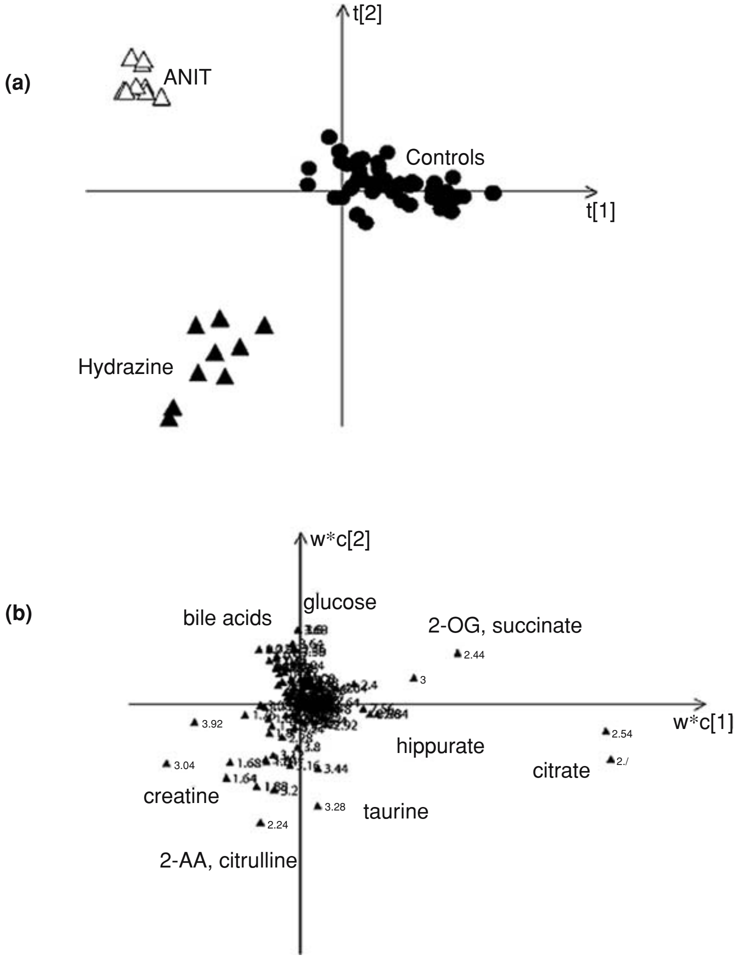

the loadings plot, Figure 2b, gives information on which NMR spectral regions are responsible for the clustering in the scores plot, i.e. a cluster with a low PC1 and a low PC2 score (such as hydrazine) will appear in the bottom left hand quadrant and the corresponding loadings or altered NMR spectral regions will be in the same quadrant.

In the real world, biochemical changes caused by disease, nutrition, lifestyle, drug therapy, or drug toxicity develop and recover in real time and there can be complex, time-related changes in NMR spectra of biofluids. Hence, in order to develop automatic classification methods, it has proved efficient to use advanced chemometrics and bioinformatics approaches, known as supervised methods, that also take time into account. In general, these methods allow the quantitative description of the multivariate boundaries that characterize and separate each class of sample in terms of their metabolic profiles, some providing a level of probability for the classification. By using a variety of chemometric methods, it is possible to use such models to provide classification probabilities or even quantitative response factors for a wide range of sample types. It is important to build and test such chemometric models using independent training data and validation data sets.

Subtle biochemical changes in ^{1}H NMR spectroscopic profiles of biofluids can be obscured in such analyses by interfering factors such as variations in pH, which can cause changes in NMR chemical shifts because of differences in ionization state of some molecules. In NMR spectroscopy of urine, one means of limiting the effects of pH on the chemical shift of sensitive moieties is to add a standard amount of buffer to the sample prior to NMR spectroscopic analysis. Alternatively, mathematical algorithms can be used to realign the chemical shifts of resonances from protons near ionizable groups displaced by pH effects [18]. Some spectral regions, such as those containing water or urea, are very variable due to water NMR peak suppression effects. In addition, many drug compounds or their metabolites are excreted in biofluids and these can obscure significant changes in the concentration of endogenous components. Therefore, it is usual to remove these redundant spectral regions prior to chemometric analysis.

One example of a robust automatic data reduction method that has been widely used is the division of the NMR spectrum into regions of equal chemical shift ranges followed by signal integration within those ranges [19]. Automatic data reduction of 2D NMR spectra can be performed using a similar procedure, in which the spectrum is divided by a grid containing squares or rectangles of equal size, and the spectral integral in each volume element is calculated.

Selected Applications of Metabonomics

Preclinical Drug Candidate Safety Assessment

There is evidence through the recurring need to withdraw drugs from the market place that drug safety assessment approaches used in the pharmaceutical industry can still fail. There is a need for methodologies that can pick up potential problems earlier, faster, more cheaply, and more reliably. A recent survey of market withdrawals during the period 1960–1999 has identified hepatotoxicity as the most common reason for withdrawal [20]. Minimizing attrition caused by drug adverse effects is therefore one of the most important aims of pharmaceutical R&D, and metabonomics has been used extensively in evaluating the adverse effects of candidate drugs.

In this application, NMR-based metabonomics can be used for (i) definition of the metabolic hyperspace occupied by normal samples, (ii) rapid and simple classification of the sample as normal or abnormal (this enables spectrometer automation for data acquisition), (iii) classification of target organ toxicity, (iv) site and mechanism of action within the organ, (v) identification of biomarkers of toxic effect, and (vi) evaluation of the time course of effect, e.g. the onset, evolution, and regression of toxicity. The role that metabonomics has in the evaluation of xenobiotic toxicity has been comprehensively defined by the Consortium for Metabonomic Toxicology (COMET) formed between five pharmaceutical companies and Imperial College, London, UK [21]. The aim of this project is to define methodologies and to apply metabonomic data generated using ^{1}H NMR spectroscopy of urine and blood serum for preclinical toxicological screening of candidate drugs. This has been achieved by generating databases of spectral and conventional results for a wide range of model toxins (147 in total) that serve as the raw material for computer-based expert systems for toxicity prediction. The project goals of the generation of comprehensive metabonomic databases (now around 35,000 NMR spectra) and multivariate statistical models for prediction of toxicity (initially for liver and kidney toxicity in the rat and mouse) have completely been achieved.

A study operated to the same detailed protocol and using the same model toxin was carried out over seven sites in the companies and contract research organizations. This was used to probe both the analytical and biological variation that could both arise through the use of metabonomics. The inter-site NMR analytical reproducibility revealed a high degree of robustness where split samples were analyzed both at Imperial College and at various company sites, giving a coefficient of variation of about 1.6%. The biological variability was evaluated by a detailed comparison of the ability of the companies to provide consistent urine and serum samples with all samples measured at Imperial College. There was a high degree of consistency between samples from the various companies, and the differences between samples were small compared to the biochemical effects of the toxin, where dose-related effects could be distinguished [22]. Following this successful start, metabonomic models have been constructed for urine from control rats and mice, enabling identification of outlier samples and the metabolic reasons for the deviation. Building on this, and with the completion of all planned studies, and the development of new chemometrics methodology to meet the challenges thrown up by this project, workable expert systems for prediction of liver and kidney toxicity have been generated.

To achieve this goal, a new approach to the classification of a large data set of COMET samples has been developed, termed—Classification Of Unknowns by Density Superposition (CLOUDS)—a novel non-neural implementation of a classification technique developed from probabilistic neural networks [23]. Modeling the urinary NMR data according to organ of effect (control, liver, kidney, or other organ), using a model training set of 50% of the samples and predicting the other 50%, over 90% of the test samples were classified as belonging to the correct group with only a 2% misclassification rate between the classes. This work showed that it is possible to construct predictive and informative models of metabonomic data, delineating the whole time course of toxicity—the ultimate goal of the COMET project.

Genetic Differences and other Physiological Effects by Metabonomics

In order to determine therapeutic effects, it is necessary to understand any underlying physiological variation and to this end, metabonomics can be used to separate classes of experimental animals such as mice and rats according to a number of inherent and external factors based on the endogenous metabolite patterns in their biofluids [24]. Such differences may help explain differential toxicity of drugs between strains and inter-animal variation within a study.

Metabonomics is also being used for the phenotyping of mutant or transgenic animals and the investigation of the consequences of transgenesis such as the transfection process itself [25]. This suggests that the method may be appropriate for following treatment regimes such as gene therapy. It is important to differentiate often-seen unintended consequences of the genetic engineering process from the intended result, because pharmaceutical companies are developing genetically engineered animal models of disease using transfection procedures. Metabonomic approaches can give insight into the metabolic similarities or differences between mutant or transgenic animals and the human disease processes that they are intended to simulate and their appropriateness for monitoring the efficacy of novel therapeutic agents.

The importance of gut microfloral populations on urine composition has been highlighted by a study in which axenic (germ-free) rats were allowed to acclimatize in normal laboratory conditions and their urine biochemical composition was monitored for 21 days [26].

Many other effects can be distinguished using metabonomics, including male/female differences, age-related changes, estrus cycle effects in females, diet, diurnal effects, and interspecies differences and similarities [24].

Integrated Metabonomic Studies

The value of obtaining multiple NMR data sets from various biofluid samples and tissues of the same animals collected at different time points has been demonstrated. This procedure has been termed "integrated metabonomics," [13,14] and can be used to describe the changes in metabolic chemistry in different body compartments affected by exposure to toxic drugs. Such timed profiles in multiple compartments are themselves characteristic of particular types and mechanisms of pathology and can be used to give a more complete description of the biochemical consequences than can be obtained from one fluid or tissue alone. An example is given in Figure 3 that shows ^{1}H NMR spectra from intact liver tissue, tissue extracts, and blood plasma from a mouse after administration of a toxic dose of paracetamol. Building on this, it has also been possible to integrate data from transcriptomics and metabonomics to find common metabolic pathways implicated by both gene expression changes and changes in metabolism [27].

Disease Diagnosis

Many examples exist in the literature on the use of NMR-based metabolic profiling to aid human disease diagnosis, including the use of plasma to study diabetes, CSF for investigating Alzheimer's disease, synovial fluid for osteoarthritis, seminal fluid for male infertility and urine in the investigation of drug overdose, renal transplantation, and various renal diseases. Most of the earlier studies have been reviewed [7].

Some studies have been undertaken in the area of cancer diagnosis using perchloric acid extracts of various types of human brain tumor tissue.[28] The spectra were classified using neural network software giving ∼85% correct classification. Tissues themselves can be studied by metabonomics using the MAS technique and published examples include prostate cancer [29] and renal cell carcinoma [30]. Other recent studies include an NMR-based urinary metabonomic study of multiple sclerosis in humans and non-human primates [31].

Currently, the only reliable diagnostic method for coronary heart disease (CHD) is the injection of X-ray opaque dye into the blood stream and visualization of the coronary arteries using X-ray angiography. This is both expensive and invasive with an associated 0.1% mortality and 1–3% of patients experiencing adverse effects. Recently metabonomics has been applied to provide a method for diagnosis of CHD non-invasively through analysis of a blood serum sample using NMR spectroscopy [32]. Patients were classified into two groups, those with normal coronary arteries and those with triple coronary vessel disease, as based on an angiographic examination. Around 80% of the NMR spectra were used as a training set to provide a two-class model after appropriate data filtering techniques had been applied and the samples from the two classes were easily distinguished. The remaining 20% of the samples were used as test set and their class was then predicted based on the derived model with a sensitivity of 92% and a specificity of 93% based on a 99% confidence limit for class membership.

It was also possible to diagnose the severity of the CHD that was present by employing serum samples from patients with stenosis of one, two, or three of the coronary arteries. Although this is a simplistic indicator of disease severity, separation of the three sample classes was evident even though none of the wide range of conventional clinical risk factors that had been measured was significantly different between the classes.

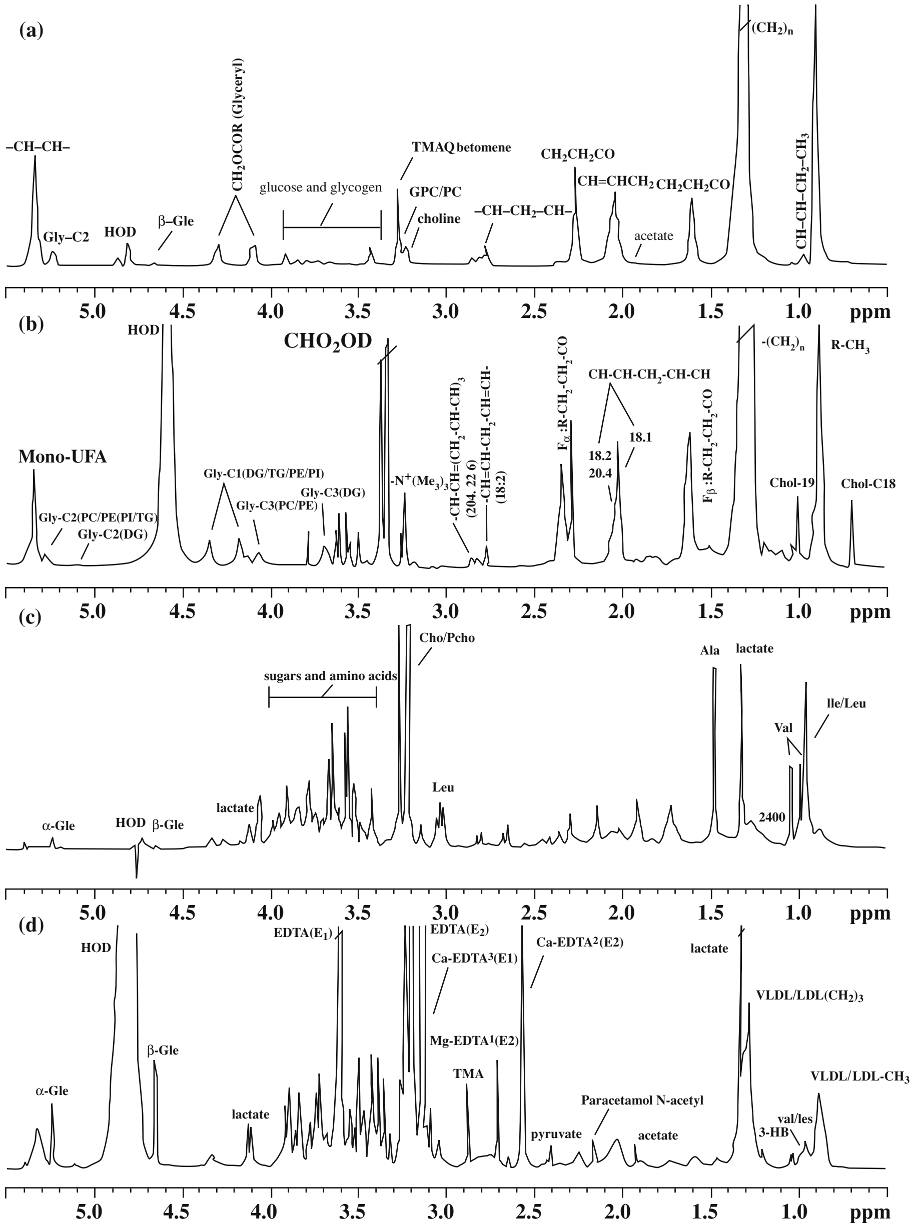

Fig. 3. (a) 600 MHz ^1H MAS NMR CPMG spin-echo spectrum of intact liver tissue; (b) 600 MHz standard ^1H NMR spectrum of a lipid-soluble liver tissue extract; (c) 600 MHz solvent suppressed ^1H NMR spectrum of an aqueous-soluble liver tissue extract; (d) 500 MHz ^1H NMR CPMG spectrum of blood plasma. All spectra are from animals treated with a toxic dose of paracetamol (500 mg/kg) and sacrificed at 240 min after dosing. Key: 3HB, 3-D-hydroxybutyrate; Cho, choline; Chol, cholesterol; Glu, glucose; GPC, glycerophosphorylcholine; Gly, glycerol; LDL, low-density lipoprotein; P Cho, phosphocholine; TMAO, trimethylamine-*N*-oxide; VLDL, very low-density lipoprotein.

Conclusions

Although there continues to be a need for advances in metabonomic analytical technologies both in NMR and MS, NMR is likely to remain the method of choice for a broad impartial survey of metabolic profiles, especially given recent gains in sensitivity through the use of cryoprobe detectors. MS coupled to a separation stage is always likely to yield better detection limits for specific classes of metabolite, but is inherently less general.

NMR-based metabonomics is now recognized as an independent and widely used technique for evaluating the toxicity of drug candidate compounds, and it has been adopted by a number of pharmaceutical companies into their drug development protocols. For drug safety studies, it is possible to identify the target organ of toxicity, derive the biochemical mechanism of the toxicity, and determine the combination of biochemical biomarkers for the onset, progression and regression of the lesion. Additionally, the technique has been shown to be able to provide a metabolic fingerprint of an organism (metabotyping) as an adjunct to functional genomics, and hence has applications in the design of drug clinical trials and for evaluation of genetically modified animals as disease models. The potential and real impact of metabonomics on all stages of pharmaceutical R&D is encapsulated in Figure 4.

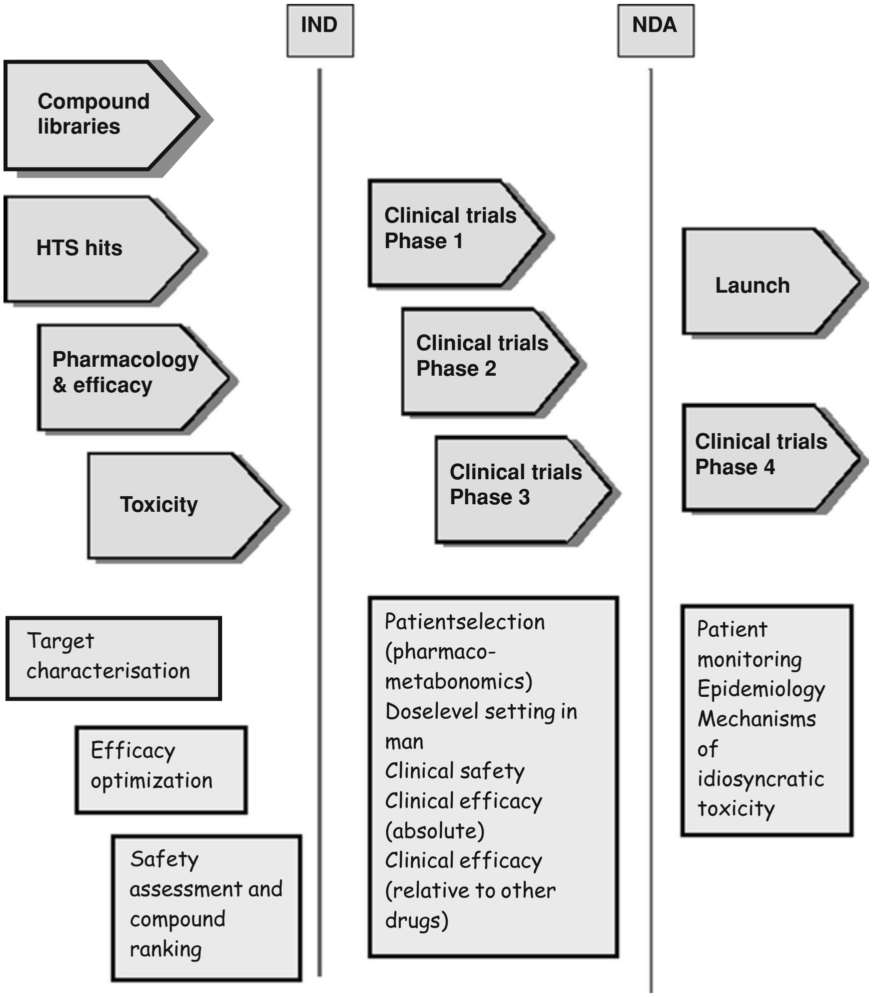
IND
NDA
Compound libraries
HTS hits
Pharmacology & efficacy
Toxicity
Clinical trials Phase 1
Clinical trials Phase 2
Clinical trials Phase 3
Launch
Clinical trials Phase 4
Target characterisation
Efficacy optimization
Safety assessment and compound ranking
Patientselection (pharmaco-metabonomics)
Doselevel setting in man
Clinical safety
Clinical efficacy (absolute)
Clinical efficacy (relative to other drugs)
Patient monitoring
Epidemiology
Mechanisms of idiosyncratic toxicity

Fig. 4. The role of metabonomics in the various stages of pharmaceutical R&D. IND—Investigational new drug application—required before administration to man is permitted. NDA—new drug application—required before a new product launch.

Using metabonomics, it has proved possible to derive new biochemically based assays for disease diagnosis and to identify combination biomarkers for disease, which can then be used to monitor the efficacy of drugs in clinical trials. Thus, based on differences observed in metabonomic databases from control animals and from animal models of disease, diagnostic methods and biomarker combinations might be derivable in a preclinical setting. Similarly, the use of databases to derive predictive expert systems for human disease diagnosis and the effects of therapy, require compilations from both normal human populations and patients before, during, and after therapy. In human studies, metabonomics also has the potential for disease diagnosis and possibly even prognosis.

References

1. Nicholson JK, Lindon JC, Holmes E. Xenobiota. 1999;29: 1181.
2. Lindon JC, Nicholson JK, Holmes E, JR Everett. Concepts Magn. Reson. 2000;12:289.
3. Nicholson JK, Connelly J, Lindon JC Holmes E. Nat. Rev. Drug Discov. 2002;1:153.
4. Lindon JC, Holmes E Nicholson JK. Anal. Chem. 2003;75: 384A.
5. Plumb RS, Stumpf CL, Gorenstein MV, Castro-Perez JM, Dear GJ, Anthony M, Sweatman BC, Connor SC Haselden JN. Rapid Commun. Mass Spectrom. 2002;16:1991.
6. Moka D, Vorreuther R, Schicha H, Spraul M, Humpfer E, Lipinski M, Foxall PJD, Nicholson JK Lindon JC. Anal. Commun. 1997;34:107.
7. Lindon JC, Nicholson JK Everett JR. Annu. Rep. NMR Spectrosc. 1999;38:1.
8. Khandelwal P, Beyer CE, Lin Q, McGonigle P, Schechter LE, Bach C. J. Neurosci. Methods. 2004;133:181.
9. Griffin JL, Nicholls AW, Keun HC, Mortishire-Smith RJ, Nicholson JK, Kuehn T. Analyst. 2002;127:582.
10. Keun HC, Beckonert O, Griffin JL, Richter C, Moskau D, Lindon JC, Nicholson JK. Anal. Chem. 2002;74:4588.
11. Lindon JC, Nicholson JK, Wilson ID. J. Chromatogr. B. 2000;748:233.
12. Garrod SL, Humpfer E, Spraul M, Connor SC, Polley S, Connelly J, Lindon JC, Nicholson JK, Holmes E. Magn. Reson. Med. 1999;41:1108.
13. Waters NJ, Holmes E, Williams A, Waterfield CJ, Farrant RD, Nicholson JK. Chem. Res. Toxicol. 2001;14:1401.
14. Coen M, Lenz EM, Nicholson JK, Wilson ID, Pognan F, Lindon JC. Chem. Res. Toxicol. 2003;16:295.
15. Lamers RJAN, Wessels ECHH, van der Sandt JJM, Venema K, Schaafsma G, van der Greef J, van Nesselrooij JHJ. J. Nutr. 2003;133:3080.
16. Bollard ME, Xu JS, Purcell W, Griffin JL, Quirk C, Holmes E Nicholson JK. Chem. Res. Toxicol. 2002;15:1351.
17. Lindon JC, Holmes E, Nicholson JK. Prog. NMR Spectrosc. 2001;39:1.
18. Brown TR, Stoyanova R. J. Magn. Reson. 1996;112:32.
19. Farrant RD, Lindon JC, Rahr E, Sweatman BC. J. Pharm. Biomed. Anal. 1992;10:141.
20. Fung M, Thornton A, Mybeck K, Wu JH-H, Hornbuckle K, Muniz E. Drug Inf. J. 2001;35:293.
21. Lindon JC, Nicholson JK, Holmes E, Antti H, Bollard ME, Keun H, Beckonert O, Ebbels TM, Reily MD, Robertson D, Stevens GJ, Luke P, Breau AP, Cantor GH, Bible RH, Niederhauser U, Senn H, Schlotterbeck G, Sidelmann UG, Laursen SM, Tymiak A, Car BD, Lehman-McKeeman L, Colet JM, Loukaci A, Thomas C. Toxicol. Appl. Pharmacol. 2003;187:137.
22. Keun HC, Ebbels TMD, Antti H, Bollard M, Beckonert O, Schlotterbeck G, Senn H, Niederhauser U, Holme E, Lindon JC, Nicholson JK. Chem. Res. Toxicol. 2002;15:1380.
23. Ebbels T, Keun H, Beckonert O, Antti H, Bollard M, Holmes E, Lindon J, Nicholson J. Anal. Chim. Acta. 2003;490:109.
24. Lindon JC, Holmes E, Bollard ME, Stanley EG, Nicholson JK. Biomarkers. 2004;9:1–31.
25. Griffin JL, Sang E, Evens T, Davies K, Clarke K. FEBS Lett. 2002;530:109.
26. Nicholls AW, Mortishire-Smith RJ, Nicholson JK. Chem. Res. Toxicol. 2003;16:1395.
27. Coen M, Nicholson JK, Lindon JC, Lenz EM, Wilson ID, Ruepp SU, Pognan F. J. Pharm. Biomed. Anal. 2004;35:93.
28. Maxwell RJ, Martinez-Perez I, Cerdan S, Cabanas ME, Arus C, Moreno A, Capdevila A, Ferrer E, Bartomeus F, Aparicio A, Conesa G, Roda JM, Carceller F, Pascual JM, Howells SL, Mazucco R, Griffiths JR. Magn. Reson. Med. 1998;39:869.
29. Tomlins A, Foxall PJD, Lindon JC, Lynch MJ, Spraul M, Everett JR, Nicholson JK. Anal. Commun. 1998;35:113.
30. Moka D, Vorreuther R, Schicha H, Spraul M, Humpfer E, Lipinski M, Foxall PJD, Nicholson JK, Lindon JC. J. Pharm. Biomed. Anal. 1998;17:125.
31. 't Hart BA, Vogels JTWE, Spijksma G, Brok HPM, Polman C, van der Greef J. J. Neuro. Sci. 2003;212:21.
32. Brindle JT, Antti H, Holmes E, Tranter G, Nicholson JK, Bethell HWL, Clarke S, Schofield PM, McKilligin E, Mosedale DE, Grainger DJ. Nat. Med. 2002;8:1439.

Protein Misfolding Disease: Overview of Liquid and Solid-State High Resolution NMR Studies

Harald Schwalbe and Julia Wirmer

Institute for Organic Chemistry and Chemical Biology, Center for Biomolecular Magnetic Resonance, Johann Wolfgang Goethe-Universität, Marie-Curie-Strasse 11, D-60439 Frankfurt/M, Germany

Protein Misfolding Diseases

The failure of proteins to fold into their functional forms can occasionally lead to "protein misfolding" or "protein conformational" diseases. Many among the most common and debilitating of these diseases are associated with the formation of protein amyloid, an insoluble material that is deposited as fibrils or plaques in different tissues and organs of the body. Amyloid formation is known to be accelerated by a variety of cellular factors, including metal ions, such as copper and zinc, and interactions with other species, such as lipids and RNA. It is implicated in many medical conditions including Alzheimer's disease and the transmissible prion disorders. It is becoming increasingly recognized that the switch from a normal to a diseased state of the cell in protein misfolding diseases is induced by a shift in the equilibrium between different conformational and aggregation states of a polypeptide chain that are present under normal conditions. The native state [N] of a protein can be investigated in great detail using X-ray crystallography and NMR-spectroscopy. Our understanding of states other then the native one, however, is only now emerging. Liquid and solid-state high-resolution NMR spectroscopy are the major structural techniques to determine structure and dynamics of the polypeptide chain under a variety of different conditions. They describe proteins in their native state [N], in unfolded states [U], in transient intermediates [I], and in their fibrillar and prefibrillar states (Figure 1).

Natively Unfolded Proteins Involved in Protein Misfolding Diseases

Non-native and unfolded states of proteins have also come into interest recently from the observation that an axiomatic linking of the function of a protein to a persistent fold might not be general, because a number of proteins have been identified that lack intrinsic globular structure in their normal functional form [1–3]. The expressions "intrinsically unstructured" and "natively unfolded" are being used synonymously, the latter being coined by Schweers *et al.* in 1994 in the context of structural studies of the protein tau [4]. Intrinsically unstructured proteins are extremely flexible, non-compact, and reveal little if any secondary structure under physiological conditions. In 2000, the list of natively unfolded protein comprised 100 entries [5]. Natively unfolded proteins are implied in the development of a number of neurodegenerative diseases including Alzheimer's disease (deposition of amyloid-β, τ-protein, α-synuclein), Down's syndrome and Parkinson disease to name a few [5]. They are predicted to be ubiquituous in the proteome [6,7] and algorithms available as a web-program (http://dis.embl.de/) have been developed to predict protein disorder [8]. According to the predictions, 35–51% of eucaryotic proteins have at least one long (>50 residues) disordered region and 11% of proteins in Swiss-Prot and between 6 and 17% of proteins encoded by various genomes are probably fully disordered [6]. Proteins predicted to be intrinsically unstructured show low compositional complexity. These regions sometimes correspond to repetitive structural units in fibrillar proteins. Therefore, it does not seem unlikely that lack of structure of the polypeptide chains in some states of a protein plays an important role in the development of fibrillar states and this further supports the importance for detailed structural and dynamic investigations of non-native states of proteins. It has also been noted by Gerstein that the average genomially encoded protein is significantly different in terms of size and amino acid composition from folded proteins in the PDB [9]. This difference would indicate that the structures deposited in the PDB are not random and in turn that they cannot be taken as representative for the entire structural diversity of polypeptide chains.

Brief Background in NMR Parameters

NMR is able to provide both dynamic and structural information about proteins in a variety of different states at atomic resolution. NMR has the potential for probing residual structure, the size of aggregating molecules, and variation in the internal dynamical properties on the basis of diffusion-weighted NMR spectroscopy, heteronuclear relaxation measurements, paramagnetic enhancement of

Graham A. Webb (ed.), Modern Magnetic Resonance, 1387–1391.
© 2008 *Springer.*

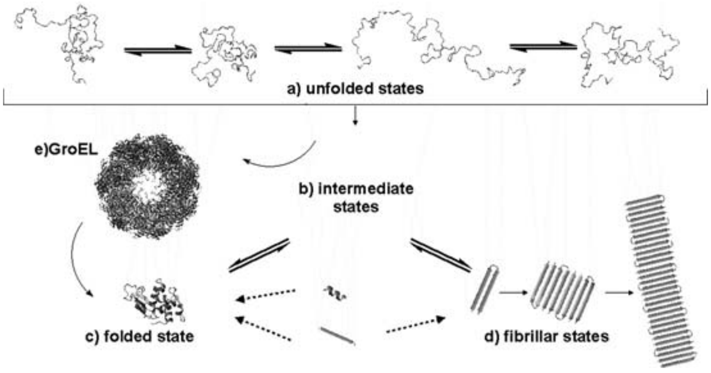

Fig. 1. The characteristics of states accessible to a protein differ widely in their structural and kinetic properties. The different conformations adopted by a polypeptide chain can range from the native, often monomeric state (c), in which a single conformation exists and which is built up from secondary structure elements and their specific arrangements, to the ensemble of conformers representing the random coil state of a protein (a). The individual members of this ensemble have widely different compaction, dynamics, local, and non-local conformations. Protein folding preceeds via formation of folding intermediates (b) whose structure and dynamics may be modulated by protein–protein interactions with molecular chaperones such as GroEL (scaled down by a factor of 2) (e) shown in the figure. At the other extreme of conformational states, proteins can aggregate and form oligomeric states called fibrils (d). Liquid and solid-state NMR spectroscopy can provide detailed information on structure and dynamics in all of these states.

relaxation induced by paramagnetic spin labels, and residual dipolar couplings (summarized in Table 1). More recently, NMR techniques have been developed to characterize the structural transitions from unfolded states of protein, via low molecular oligomers to fibrils. Such studies include both static and time-resolved experiments.

Proteins Involved in Misfolding Diseases Studied by NMR

Two proteins intimately linked to neurodegenerative illnesses seem to have a possible function in copper homeostasis: the amyloid precursor protein (APP) of Alzheimer's disease, and the prion protein (PrP), which causes transmissible spongiform encephalopathies (TSE). APP gives rise to the amyloid Aβ peptide and the prion protein PrP^c can convert to the variant isoform PrP^{Sc} of Creutzfeldt-Jakob's disease (CJD). The protein Cu,Zn dismutase (SOD) is a metalloprotein for which familial mutants are linked to familial amyotrophic lateral sclerosis (FALS). The three proteins are known to interact: The prion protein specifically binds copper and native PrP charged with copper has superoxide dismutase (SOD1) activity. In turn, overexpression of APP alters brain copper content and attenuates SOD1. On the other hand,

Table 1: Overview of NMR parameters and their conformational dependence

NMR parameter	Conformational dependence
Chemical shift δ (ppm)	Multiple torsion angles: ϕ, ψ, ω, χ_1
Scalar couplings ^nJ (Hz)	Single torsion angles via Karplus equations
Homonuclear NOEs (a.u.)	Distances, dependence on correlation time, and motional properties
Heteronuclear relaxation (Hz)	Motional properties, dependence on τ_c, S^2, τ_e[a]
Residual dipolar couplings RDC (Hz)	Overall shape, dynamics, S[b]
H/D exchange	Exchangeable H^N
Diffusion	Radius of hydration (R_h)
Photo CIDNP	Accessible Trp, Tyr, His

[a] τ_c correlation time for overall rotational tumbling, S^2 order parameter of local dynamics, τ_e correlation time for local dynamics
[b] S order parameter for local dynamics

for the other systems discussed here, α-synuclein and transthyretin, no metal induced misfolding is currently being discussed in the literature.

Amyloid Precursor Protein

Cleavage of APP by β- and γ-secretases results in amyloid forming peptides containing 39–43 residues referred to as the Amyloid β-peptide (Aβ). The Aβ is the major constituent of the plaques in the brains of Alzheimer patients. The presence of copper inhibits Aβ production and stimulates the non-amyloidogenic pathway of APP in cells and in transgenic animals overexpressing APP. The soluble and the fibrillar form of various peptides of Aβ have been studied using liquid and solid-state NMR spectroscopy: conformations in the soluble form range from α-helical conformations via random coil to β-sheet conformations, depending on solvent condititions, pH values and peptide concentration. In membrane mimicking environments such as SDS, the N-terminus is unstructured (residues 1–14) while α-helical conformation is found from residue 15–36 with a kink from residues 25–27 [10–13]. A high propensity for aggregation is found in solution and the conformation in solution is often found to be in an equilibrium between random coil conformation [14] and β-sheet conformers [15] with increased β-sheet propensity at high concentration, high temperature and high salt conditions. However, at very low concentrations and at 0 °C, a conformational equilibrium between a left handed 3(10) helix and random coil conformations is found [16]. Solid-state NMR studies revealed the structure of the amyloid fibrils formed by Aβ (1−40): approximately the first 10 residues of the peptide are disordered in the fibril, residues 12–24 and 30–40 adopt β-strand conformations and form parallel β-sheets through intermolecular hydrogen bonding. The two β-sheets within a single peptide unit form an antiparallel sheet [17]. The structural model found for the Aβ(1–40) is very similar to structural models of smaller (11–25, 16–22) and larger (1–42) peptides [18,19].

Prion Protein

Prion protein (PrP^c) is a glycosyl-phosphatidyl-inositol (GPI) anchored membrane protein of 35 kD. Its conformational altered scrapie form (PrP^{Sc}) is associated with neurodegenerative diseases. Cellular PrP^c is synthesized in three topologic forms, secreted ^{sec}PrP and the single-spanning membrane proteins of opposite orientations ^{Ntm}PrP, and ^{Ctm}PrP. Increases in ^{Ctm}PrP are associated with the development of neurodegenerative disease. The conformational properties of a protein are generally thought to be determined by specific elements in the sequence; for the prion protein these are the N-terminal sequence, a hydrophobic stretch around residue 100, a putative transmembrane domain, and the C-terminus for GPI anchor addition. The signal sequence plays a decisive role in determining the membrane orientation of the PrP. ^{Ctm}PrP contains an uncleaved N-terminal signal peptide.

NMR solution structures have been reported for PrP^c from several species [20–31]. Interestingly, it was shown that only few of the disease related mutations lead to reduced stability of N [26]. Residues 23–121 comprise a flexibly disordered tail in contrast to the well-ordered 125–228 core part. Cu^{2+} binding to histidines located in the flexible part of the protein (high affinity octarepeat regions are found between residues 51–90 and low affinity binding sites are formed by His96 and His111) induces a shift towards β-sheet conformation as shown by liquid-state NMR [32–36]. In particular, the conformational shift induced by binding of His96 and His111 is remarkable, as these residues are part of the infectious region (residues 90–231) [24]. β-sheet conformation has also been observed by liquid and solid-state NMR studies on fibrillar states: a hydrogen exchange study of the fibrillar form of the 106–121 peptide revealed 50% β-sheet structure, which is located in the center portion of the peptide [37]. Complete β-sheet structure was found by solid-state NMR investigation on the fibrillar state of a peptide corresponding to the infectious P101L mutant of residues 89–143 [38].

α-Synuclein

α-synuclein is associated with Parkinson's disease, a neurodegenerative disorder affecting some five million people worldwide. This disease is characterized by the formation of proteinaceous inclusions called Lewy bodies that are known to be composed primarily of aggregated α-synuclein. There is mounting evidence that the oligomeric species that are formed during the process of aggregation of the monomeric α-synuclein are at the origin of the pathology. In solution, α-synuclein can be either found in a monomeric, substantially unfolded conformation, or it can form several morphologically different types of aggregates, including oligomers, amorphous aggregates, and amyloid-like fibrils. Its normal function is poorly understood, but it is believed that it includes transient or reversible lipid interactions [39]. NMR studies of the lipid bound form of α-synuclein revealed that the C-terminus of the protein remains free in solution, while the N-terminus of the protein binds to the lipids in a helical conformation [40–43]. This helical conformation in the lipid bound state remains nearly unchanged in the early onset mutations (A30P, A53T) [43]. More interesting results were found by NMR studies on the natively unfolded monomeric form free in solution: the protein is more compact than expected for a highly denatured protein [44] and residual helical structure is present in the N-terminal part of α-synuclein (residues 18–31) [40,45,46]. This residual helical structure is diminished in one of the early onset mutants A30P, while enhanced β-sheet propensity around the mutation site in the other early onset mutant A53T is observed [45]. Changes in these parts of the sequence (residues 22–93) were also observed upon binding of aggregation promoting polyamines at the C-terminal part (residues 109–140) [47]. Taking all NMR investigations on the monomeric form in solution together, clearly the N-terminal part of the protein is the aggregation nucleus.

Cu-Zn-Superoxide Dismutase

Mutations in the gene for cytosolic SOD are linked with familial FALS. The active site of each monomer of SOD (153 residues) contains one copper and one zinc ion. The enzyme catalyzes the dismutation of superoxide to dioxygen and hydrogen peroxide. FALS-related mutations are concentrated either in the metal-binding loop or in loops III (38–40) and V (90–93). In this protein, metal ions have a fundamental role for protein stabilization, correct folding, and in increasing protein rigidity. Binding of the metal ions is of fundamental importance to stabilize its secondary structure and to define the tertiary interactions relevant for the relative orientation of the two sheets forming as can be shown by a comparison of the NMR strucutures in the presence and the absence of metal ions [48,49]. A comparison of WT SOD and the FALS-related mutant G93A based on NMR dynamics revealed that indeed a in the β-barrel loops III and V are a lot more dynamic and thus less stable in the mutant than in the wild type proteins [50].

Transthyretin

Transthyretin (TTR) is a homotetrameric protein that is involved in the transport of thyroid hormones and retinol in human serum. A large number of mutations (more than 80 different ones) have been found that lead to misfolded forms of the protein. These misfolded forms are implicated in amyloid diseases such as familial amyloidotic polyneuropathy and senile systemic amyloidosis. A combination of hydrogen exchange experiments coupled with NMR detection have compared WT TTR under native conditions and under conditions that are known to promote amyloid formation: These studies revealed that amyloidogenic behavior is linked to destabilization of one half of the β-sandwich structure of TTR [51]. These findings were further confirmed by additional NMR studies of some of the amyloidogenic mutants [52,53]. Liquid-state NMR studies of amyloidogenic peptides (TTR10–20 and TTR105–115) showed that the peptides are unstructured in solution [54,55]. In contrast, the TTR105–115 peptide in its fibrillar state is in an extended β-sheet conformation, with its backbone and side chain torsion angles close to their optimal values for this secondary structure element. In addition, long-range order could be detected that is generally associated with crystalline materials by solid-state NMR [56,57].

References

1. Dyson HJ, Wright PE. Curr. Opin. Struct. Biol. 2002;12:54.
2. Wright PE. Dyson HJ. J. Mol. Biol. 1999;293:321.
3. Uversky VN. Eur. J. Biochem. 2002;269:2.
4. Schweers O, Schonbrunn-Hanebeck E, Marx A, Mandelkow E. J. Biol. Chem. 1994;269:24290.
5. Uversky VN, Gillespie JR, Fink AL. Proteins. 2000;41: 415.
6. Tompa P. Trends Biochem. Sci. 2002;27:527.
7. Uversky VN. Protein Sci. 2002;11:739.
8. Linding R, Jensen LJ, Diella F, Bork P, Gibson TJ, Russell RB. Structure (Camb.) 2003;11:1453.
9. Gerstein M. Fold Des. 1998;3:497.
10. Coles M, Bicknell W, Watson AA, Fairlie DP, Craik DJ. Biochemistry 1998;37:11064.
11. Shao H, Jao S, Ma K, Zagorski MG. J. Mol. Biol. 1999;285: 755.
12. D'Ursi AM, Armenante MR, Guerrini R, Salvadori S, Sorrentino G, Picone D. J. Med. Chem. 2004;47:4231.
13. Crescenzi O, Tomaselli S, Guerrini R, Salvadori S, D'Ursi AM, Temussi PA, Picone D. Eur. J. Biochem. 2002;269: 5642.
14. Riek R, Guntert P, Dobeli H, Wipf B, Wuthrich K. Eur. J. Biochem. 2001;268:5930.
15. Jarvet J, Damberg P, Bodell K, Eriksson LEG, Graslund A. J. Amer. Chem. Soc. 2000;122:4261.
16. Jarvet J, Damberg P, Danielsson J, Johansson I, Eriksson LE, Graslund A. FEBS Lett. 2003;555:371.
17. Petkova AT, Ishii Y, Balbach JJ, Antzutkin ON, Leapman RD, Delaglio F, Tycko R. Proc. Natl. Acad. Sci. U.S.A. 2002; 99:16742.
18. Petkova AT, Buntkowsky G, Dyda F, Leapman RD, Yau WM, Tycko R. J. Mol. Biol. 2004;335:247.
19. Antzutkin ON, Leapman RD, Balbach JJ, Tycko R. Biochemistry. 2002;41:15436.
20. Riek R, Hornemann S, Wider G, Billeter M, Glockshuber R, Wuthrich K. Nature, 1996;382:180.
21. Glockshuber R, Hornemann S, Riek R, Wider G, Billeter M, Wuthrich K. Trends Biochem. Sci. 1997;22:241.
22. Billeter M, Riek R, Wider G, Hornemann S, Glockshuber R, Wuthrich K. Proc. Natl. Acad. Sci. U.S.A. 1997;94:7281.
23. Riek R, Hornemann S, Wider G, Glockshuber R, Wuthrich K. FEBS Lett. 1997;413:282.
24. James TL, Liu H, Ulyanov NB, Farr-Jones S, Zhang H, Donne DG, Kaneko K, Groth D, Mehlhorn I, Prusiner SB, Cohen FE. Proc. Natl. Acad. Sci. U.S.A. 1997;94:10086.
25. Donne DG, Viles JH, Groth D, Mehlhorn I, James TL, Cohen FE, Prusiner SB, Wright PE, Dyson HJ. Proc. Natl. Acad. Sci. U.S.A. 1997;94:13452.
26. Riek R, Wider G, Billeter M, Hornemann S, Glockshuber R, Wuthrich K. Proc. Natl. Acad. Sci. U.S.A. 1998;95:11667.

27. Liu H, Farr-Jones S, Ulyanov NB, Llinas M, Marqusee S, Groth D, Cohen FE, Prusiner SB, James TL. Biochemistry. 1999;38:5362.
28. Zahn R, Liu A, Luhrs T, Riek R, von Schroetter C, Lopez Garcia F, Billeter M, Calzolai L, Wider G, Wuthrich K. Proc. Natl. Acad. Sci. U.S.A. 2000;97:145.
29. Lopez Garcia F, Zahn R, Riek R, Wuthrich K. Proc. Natl. Acad. Sci. U.S.A. 2000;97:8334.
30. Calzolai L, Lysek DA, Guntert P, von Schroetter C, Riek R, Zahn R, Wuthrich K. Proc. Natl. Acad. Sci. U.S.A. 2000;97:8340.
31. Zahn R, Guntert P, von Schroetter C, Wuthrich K. J. Mol. Biol. 2003;326:225.
32. Stockel J, Safar J, Wallace AC, Cohen FE, Prusiner SB. Biochemistry. 1998;37:7185.
33. Viles JH, Cohen FE, Prusiner SB, Goodin DB, Wright PE, Dyson HJ. Proc. Natl. Acad. Sci. U.S.A. 1999;96:2042.
34. Jackson GS, Murray I, Hosszu LL, Gibbs N, Waltho JP, Clarke AR, Collinge J. Proc. Natl. Acad. Sci. U.S.A. 2001;98:8531.
35. Jones CE, Abdelraheim SR, Brown DR, Viles JH. J. Biol. Chem. 2004;279:32018.
36. Belosi B, Gaggelli E, Guerrini R, Kozlowski H, Luczkowski M, Mancini FM, Remelli M, Valensin D, Valensin G. Chembiochem. 2004;5:349.
37. Kuwata K, Matumoto T, Cheng H, Nagayama K, James TL, Roder H. Proc. Natl. Acad. Sci. U.S.A. 2003;100:14790.
38. Laws DD, Bitter HM, Liu K, Ball HL, Kaneko K, Wille H, Cohen FE, Prusiner SB, Pines A, Wemmer DE. Proc. Natl. Acad. Sci. U.S.A. 2001;98:11686.
39. Clayton DF, George JM. Trends Neurosci. 1998;21:249.
40. Eliezer D, Kutluay E, Bussell R Jr, Browne G. J. Mol. Biol. 2001;307:1061.
41. Bussell R Jr, Eliezer D. J. Mol. Biol. 2003;329:763.
42. Chandra S, Chen X, Rizo J, Jahn R, Sudhof TC. J. Biol. Chem. 2003;278:15313.
43. Bussell R Jr, Eliezer D. Biochemistry. 2004;43:4810.
44. Morar AS, Olteanu A, Young GB, Pielak GJ. Protein Sci. 2001;10:2195.
45. Bussell R Jr, Eliezer D. J. Biol. Chem. 2001;276:45996.
46. Yao J, Chung J, Eliezer D, Wright PE, Dyson HJ. Biochemistry. 2001;40:3561.
47. Fernandez CO, Hoyer W, Zweckstetter M, Jares-Erijman EA, Subramaniam V, Griesinger C, Jovin TM. Embo. J. 2004;23:2039.
48. Assfalg M, Banci L, Bertini I, Turano P, Vasos PR. J. Mol. Biol. 2003;330:145.
49. Banci L, Bertini I, Cramaro F, Del Conte R, Viezzoli MS. Biochemistry. 2003;42:9543.
50. Shipp EL, Cantini F, Bertini I, Valentine JS, Banci L. Biochemistry. 2003;42:1890.
51. Liu K, Cho HS, Lashuel HA, Kelly JW, Wemmer DE. Nat. Struct. Biol. 2000;7:754.
52. Liu K, Kelly JW, Wemmer DE. J. Mol. Biol. 2002;320:821.
53. Niraula TN, Haraoka K, Ando Y, Li H, Yamada H, Akasaka K. J. Mol. Biol. 2002;320:333.
54. Jarvis JA, Craik DJ. J. Magn. Reson. B. 1995;107:95.
55. Jarvis JA, Kirkpatrick A, Craik DJ. Int. J. Pept. Protein. Res. 1994;44:388.
56. Jaroniec CP, MacPhee CE, Astrof NS, Dobson CM, Griffin RG. Proc. Natl. Acad. Sci. U.S.A. 2002;99:16748.
57. Jaroniec CP, MacPhee CE, Bajaj VS, McMahon MT, Dobson CM, Griffin RG. Proc. Natl. Acad. Sci. U.S.A. 2004;101:711.

^{19}F NMR Spectroscopy for Functional and Binding High-Throughput Screening

Marina Veronesi and Claudio Dalvit
Chemistry Department, Nerviano Medical Sciences, 20014 Nerviano, Milan, Italy

NMR screening has emerged as a powerful and reliable approach for identification of potential drug candidates [1]. The technique is now recognized for its impact on the drug discovery process and has become an important tool for lead identification, lead validation, and lead optimization in many pharmaceutical companies and universities [2–17]. A plethora of different NMR experiments has been proposed in the literature for performing these tasks. Two of these approaches, recently introduced, use fluorine NMR spectroscopy. FAXS (fluorine chemical shift anisotropy and exchange for screening) [18,19] and 3-FABS (three fluorine atoms for biochemical screening) [20] allow one to perform binding and functional high-throughput screening (HTS), respectively, and determine the dissociation binding constant (K_D) and the 50% mean inhibition concentration (IC_{50}) of the identified binders and inhibitors, respectively. This chapter provides an insight into the theory and practical aspects of these two experiments and presents applications to the screening of different biomolecular targets.

FAXS

Competition ligand-based NMR screening experiments were introduced for overcoming all the limitations associated with ligand-based NMR screening experiments [21–23]. The screening of chemical mixtures or single compounds against the biomolecular target of interest is performed in the presence of a weak- to medium-affinity ligand of known binding constant referred to in its role as the spy or reporter. Changes in the transverse or selective longitudinal relaxation rates of the spy resonances are monitored. Signals from the molecules screened are not utilized. Often the screening is performed in the presence of an additional molecule that does not interact with the receptor and referred to in its role as the control molecule. This compound represents an internal reference. Competition NMR-based screening, originally proposed with proton detection experiments, was subsequently extended to fluorine detection experiments [18,19]. For these experiments it is sufficient to have a spy molecule containing either a CF or a CF_3 moiety. This approach offers some unique advantages. (i) Absence of overlap permits the screening of large chemical mixtures and automated analysis of the spectra. (ii) Protonated solvents, buffers, or detergent do not interfere with the measurements thus allowing, for example, the screening against membrane proteins. (iii) The ^{19}F transverse relaxation rate R_2, given by Equation (1), is a sensitive parameter of binding events since it contains spectral densities calculated at zero frequency for both the heteronuclear ^{19}F–^{1}H dipolar interactions and the ^{19}F chemical shift anisotropy (CSA) interaction [24]:

$$
\begin{aligned}
R_2^{F} = {} & \frac{\gamma_F^2\gamma_H^2\hbar^2\tau_c}{20}\sum_{H_i}\frac{1}{r_{FH_i}^6}\left\{4+\frac{1}{1+(\omega_F-\omega_H)^2\tau_c^2}\right. \\
& +\frac{3}{1+\omega_F^2\tau_c^2}+\frac{6}{1+\omega_H^2\tau_c^2} \\
& \left.+\frac{6}{1+(\omega_F+\omega_H)^2\tau_c^2}\right\} \\
& +\frac{2}{15}\Delta\sigma^2\left(1+\frac{\eta_{CSA}^2}{3}\right)B_0^2\gamma_F^2\tau_c \\
& \times\left\{\frac{2}{3}+\frac{1}{2(1+\omega_F^2\tau_c^2)}\right\} \qquad (1)
\end{aligned}
$$

The H_i correspond to all the protons of the spy compound and of the protein close in space to the fluorine atom and r_{FH_i} is the internuclear distance between proton H_i and the fluorine atom of the spy molecule. $\Delta\sigma$ is the CSA of the ^{19}F atom and is given by $\Delta\sigma = \sigma_{zz} - (\sigma_{xx} + \sigma_{yy})/2$ where the different σs are the components of the chemical shift tensor. The asymmetry parameter η_{CSA} is given by $\eta_{CSA} = (3/2)(\sigma_{xx} - \sigma_{yy})/\Delta\sigma$, B_0 is the strength of the magnetic field, γ_H and γ_F are the proton and fluorine gyromagnetic ratios, respectively, ω_H and ω_F are the proton and fluorine Larmor frequencies, respectively, and τ_c is the correlation time.

Owing to the large CSA of ^{19}F (as much as few hundreds ppm) it will contribute significantly, according to Equation (1), to the transverse relaxation of the fraction of bound spy molecule [18,25–28]. CSA contribution to

Graham A. Webb (ed.), Modern Magnetic Resonance, 1393–1399.
© 2008 *Springer.*

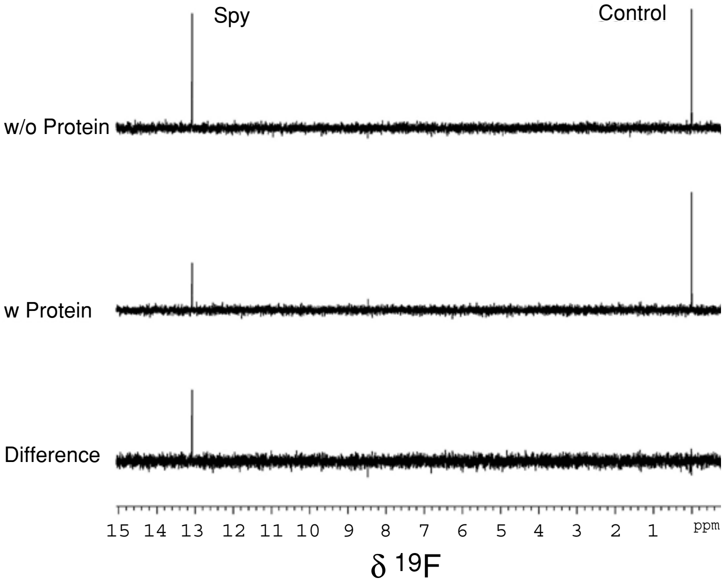

Fig. 1. One-dimensional ^{19}F NMR spin-echo ($n2\tau = 100$ ms) spectra recorded for the identification of a spy and control molecule required for FAXS. The two molecules are the weak-affinity ligand PHA-739917 and the non-interacting trifluoroacetic acid (TFA) molecule and the protein is the p21 activated kinase. The chemical shifts are referenced to TFA. The concentration of PHA-739917 and TFA was 50 and 15 μM, respectively. The spectra were recorded in the absence (top) and the presence of 1.5 μM of the protein (middle). In the difference spectrum (bottom) only the signal of the spy molecule is visible. Reprinted with permission from Dalvit *et al*. [18]. © 2002 Bentham Science Publishers.

transverse relaxation is directly proportional to the square of the magnetic field thus resulting in a more pronounced effect at stronger magnetic fields.

For a weak-affinity spy molecule the observed transverse relaxation $R_{2,\text{obs}}$ is given by [29,30]:

$$R_{2,\text{obs}} = \frac{[\text{EL}]}{[\text{L}_{\text{TOT}}]} R_{2,\text{bound}} + \left(1 - \frac{[\text{EL}]}{[\text{L}_{\text{TOT}}]}\right) R_{2,\text{free}} + \frac{[\text{EL}]}{[\text{L}_{\text{TOT}}]}\left(1 - \frac{[\text{EL}]}{[\text{L}_{\text{TOT}}]}\right)^2 \times \frac{4\pi^2(\delta_{\text{free}} - \delta_{\text{bound}})^2}{K_{-1}} \quad (2)$$

where $[\text{EL}]/[\text{L}_{\text{TOT}}]$ and $(1 - [\text{EL}]/[\text{L}_{\text{TOT}}])$ are the fraction of bound and free ligand, respectively, $R_{2,\text{bound}}$ and $R_{2,\text{free}}$ are the transverse relaxation rate constants for the ligand in the bound and free states, respectively. The last term in Equation (2) is the exchange term where δ_{bound} and δ_{free} are the isotropic chemical shifts of the fluorine resonance of the spy molecule in the bound and free states, respectively, and $1/K_{-1}$ is the residence time τ_{res} of the spy molecule bound to the protein.

Typically, a Carr–Purcell–Meibom–Gill (CPMG) spin-echo scheme [31,32] with a long 2τ interval between the train of 180° pulses (where $2\tau > 5\tau_{\text{res}}$) [33,34] is used in these experiments before the acquisition time. This is possible because the evolution with the heteronuclear ^{1}H–^{19}F scalar couplings is refocused at the end of the scheme. However, the 2τ period should not be very long in order to minimize signal attenuation originating from the spatial diffusion of the spy molecule.

The steps required for the screening with FAXS are described below:

1. A library of ^{19}F (CF or CF_3) containing molecules well characterized, chemically stable, and with high aqueous solubility is tested in mixtures against the receptor of interest for the identification of the potential spy and control molecules. STD [35], WaterLOGSY [36], or spin-echo ^{19}F experiments [18,19,37], as the example of Figure 1, are used for the identification of the two molecules.
2. The K_D of the identified spy molecules are determined with either ITC or fluorescence spectroscopy. The spy molecule is then selected on the basis of its K_D and the presence of only one binding site.
3. After the selection of the spy and control molecules, titration experiments as a function of the protein concentration are recorded and the intensity ratio of the two fluorine signals is plotted as a function of the fraction of protein-bound spy molecule [21], as shown in the example of Figure 2. The fraction of bound compound is calculated by using its K_D value and the equation:

$$\frac{[\text{EL}]}{[\text{L}_{\text{TOT}}]} = \frac{[\text{E}_{\text{TOT}}] + [\text{L}_{\text{TOT}}] + K_D}{2[\text{L}_{\text{TOT}}]} - \frac{\sqrt{([\text{E}_{\text{TOT}}] + [\text{L}_{\text{TOT}}] + K_D)^2 - 4[\text{E}_{\text{TOT}}][\text{L}_{\text{TOT}}]}}{2[\text{L}_{\text{TOT}}]} \quad (3)$$

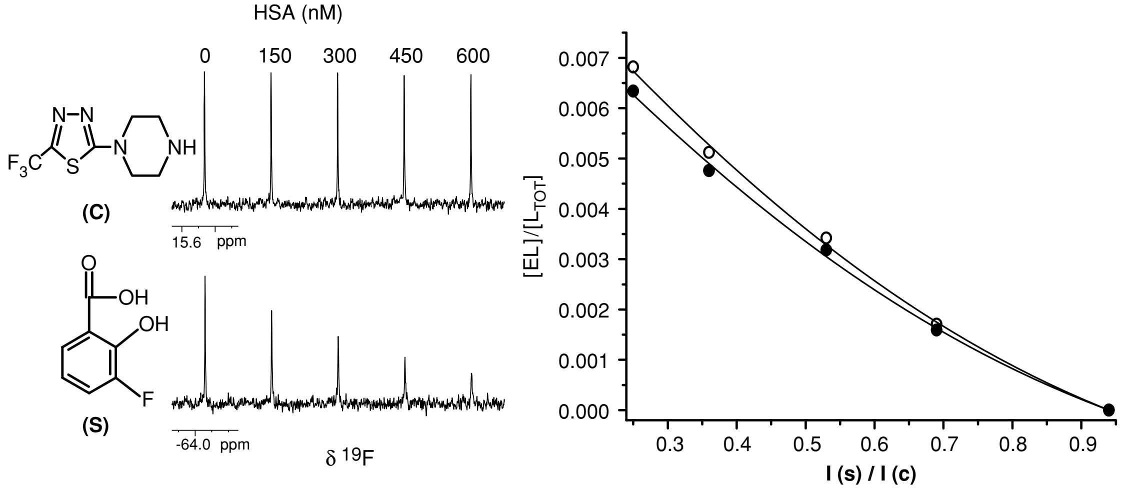

Fig. 2. (Left) One-dimensional ^{19}F NMR spin-echo spectra ($n2\tau = 80$ ms) recorded for the spy molecule 2-hydroxy 3-fluorobenzoic acid (**s**) and the control molecule 1-[5-(trifluoromethyl)1,3,4-thiadiazol-2-yl]piperazine(**c**) as a function of HSA concentration. The concentration of (**s**) and (**c**) was 50 and 25 μM, respectively. (Right) Plot of the signal intensity ratio (x-axis) of the two ^{19}F signals of (**s**) and (**c**) as a function of the fraction of bound spy molecule ([EL]/[L_{TOT}]) (y-axis). The last point on the right corresponds to the value in the absence of the protein. Two ratios ([EL]/[L_{TOT}]) were calculated using the limits of the ITC-derived K_D value of 41 ± 3.3 μM for (**s**) and using Equation (3). Values indicated by open circles were calculated with a K_D of 44.3 μM, values indicated by filled circles were calculated with a K_D of 37.7 μM. The curves represent the best fits of the experimental points. Reprinted with permission from Dalvit *et al.* [19]. © 2003 American Chemical Society.

where [E_{TOT}] and [L_{TOT}] are the total concentration of enzyme and ligand, respectively, and [EL] is the concentration of bound ligand.

4. The experimental conditions for the FAXS are then selected according to the graph of Figure 2. Compounds are tested in mixtures or as a single compound in the presence of the two molecules. Displacement of the spy molecule results in a shift of the R_2 parameter toward the intrinsic of the free state. When mixtures are used, deconvolution is then performed for the identification of the active compound. The screening with FAXS against human serum albumin (HSA) is shown in Figure 3. For screening, a total spin-echo period ($2n\tau$) is selected for which the signal of the spy molecule is approaching zero. The presence in the mixture of 5-CH_3 D, L Trp, and sucrose, known as non-binders, do not alter the spectrum of the spy molecule. In contrast, the presence in the mixture of the warfarin derivative 4-hydroxy-3-[1-(*p*-iodophenyl)-3-oxobutyl] coumarin (PNU-24009) results in the reappearance of the signal of the spy molecule thus identifying the NMR-hit.
5. The extent of displacement of the spy molecule is then used to calculate the binding constant K_I of the NMR-hit. Since [L_{TOT}] in the NMR screening experiments is known and fixed, the concentration of [EL] in the presence of the competing molecule can be calculated from the titration curve of Figure 2. The knowledge of [L_{TOT}], [EL], and [E_{TOT}] permits determination of the apparent dissociation binding constant K_D^{app} of the spy molecule in the presence of the competing molecule according to the equation:

$$K_D^{app} = \frac{[E_{TOT}][L_{TOT}] - [E_{TOT}][EL] + [EL]^2 - [L_{TOT}][EL]}{[EL]} \tag{4}$$

In the assumption of a simple competitive mechanism, the K_D^{app} is then used to extract the binding constant K_I of the NMR-hit according to the equation:

$$K_I = \frac{[I]K_D}{K_D^{app} - K_D} \tag{5}$$

where [I] is the concentration of the NMR-hit. The NMR-derived K_I values obtained with a single experimental point compare favorably with the values derived from full titration fluorescence or ITC measurements [18,21,38]. A major advantage of NMR applied to these measurements is the direct determination of the concentration of the NMR-hits thus providing reliable K_I values.

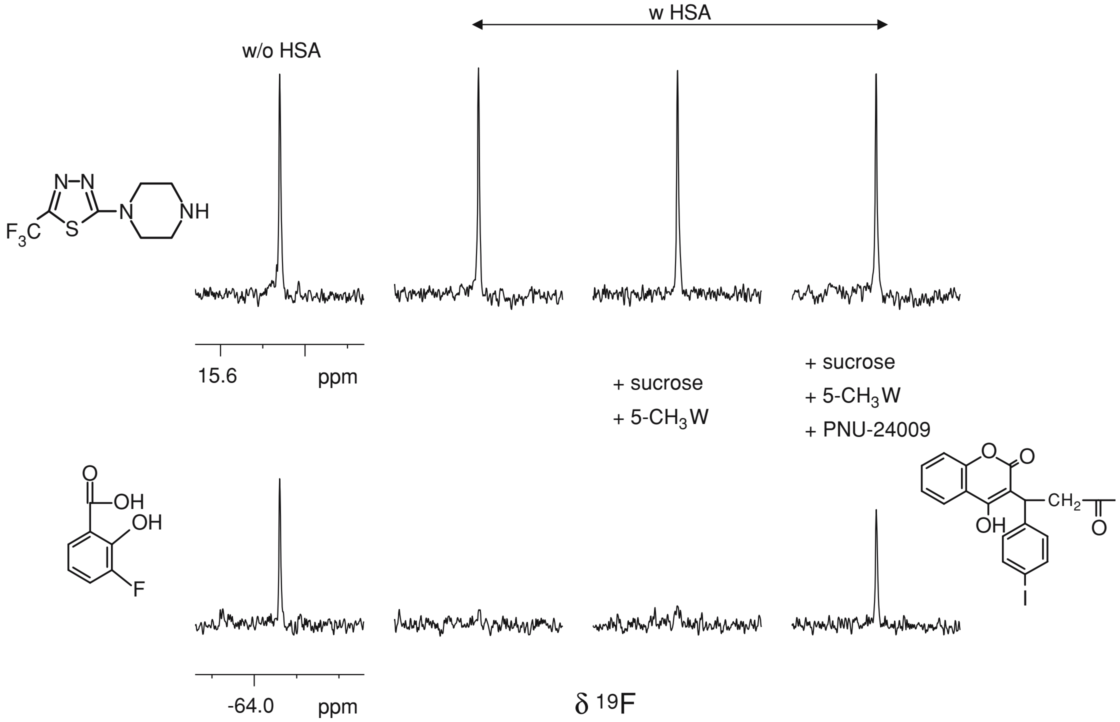

Fig. 3. FAXS performed with **(c)** (top) and **(s)** (bottom). The spectra were recorded with a total spin-echo period of 160 ms with an interval between the 180° pulses (2τ) of 40 ms. The concentration of **(s)** and **(c)** was 50 and 25 μM, respectively. The spectra on the left were recorded in the absence of protein while all the other spectra were recorded in the presence of 600 nM HSA. Reprinted with permission from Dalvit *et al.* [19]. © 2003 American Chemical Society.

3-FABS

NMR has been extensively used for characterizing the product or products of an enzymatic reaction and for gaining insight into the kinetics of the reaction (see, for example, Refs. [39,40]). A high substrate concentration was necessary for these studies due to the low sensitivity of the NMR technique. The required high concentration represents a major hurdle for the utilization of this approach to functional screening purposes, since only the very strong inhibitors would be detected. The goal in a primary screening is the identification also of weak- and medium-affinity inhibitors derived from a diversity of chemical classes.

A way to overcome the sensitivity limitation is to tag the substrate with a CF_3 moiety and use ^{19}F NMR (with proton decoupling) as the method of detection. The principle of this approach named 3-FABS [20] is described in Figure 4. The high receptivity of ^{19}F NMR spectroscopy, the 100% natural abundance of the isotope ^{19}F and the presence of three fluorine atoms result in ^{19}F NMR signals of high intensity. Modification of the substrate through the enzymatic reaction results in changes of the fluorine chemical shift tensor components even when the CF_3 moiety is distant from the reaction site. Therefore, distinct ^{19}F signals for the substrate and product (or products) are observed. The process involved with 3-FABS requires the following steps [20]:

1. Determination of the linear range (first-order region) of the enzymatic reaction. This is achieved by monitoring the course of the reaction within the NMR tube. ^{19}F spectra at different intervals are recorded and the ^{19}F signal integral of the substrate or product (products) is plotted as a function of the time elapsed from the beginning of the reaction. Screening and K_M measurements are then performed in an end point format. The reaction is quenched with either a strong inhibitor, a denaturating or a chelating molecule after a delay for which the reaction is still linear and sufficient product is formed.

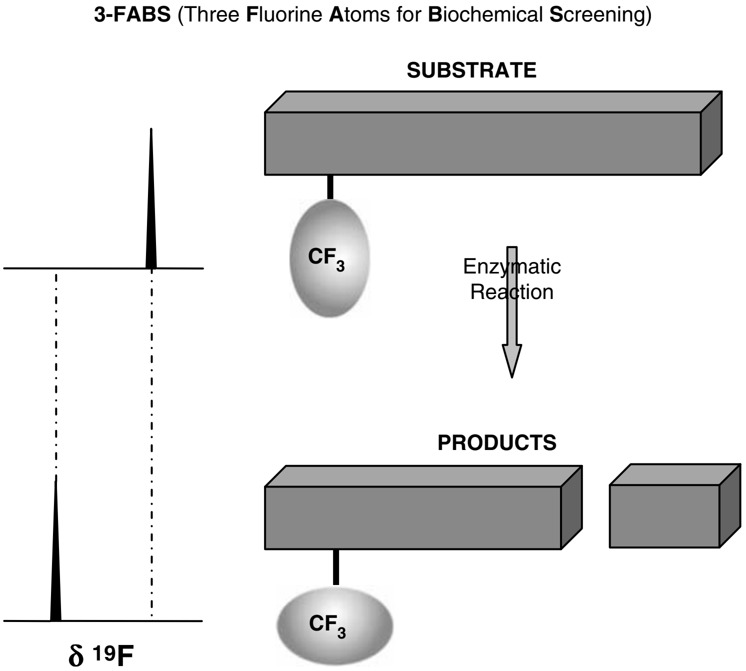

Fig. 4. Schematic diagram of the 3-FABS method. The enzyme in the example is a protease that cleaves the peptide bond with the formation of two products.

2. Determination of the K_M of the substrate and cosubstrate. This is achieved by performing the reaction at different substrate or cosubstrate concentrations. The K_M is measured using the following equation [41]:

$$V = \frac{[S]}{K_M + [S]} V_{max} \tag{6}$$

   where V is the initial speed of the reaction and V_{max} is the maximum speed that would be observed if all the enzyme $[E_{TOT}]$ is complexed with the substrate ($V_{max} = K_{cat}{*}[E_{TOT}]$, where K_{cat} is the catalytic rate constant) and [S] is the substrate concentration. V is obtained experimentally by measuring the integral of the ^{19}F NMR signal of the product divided by the incubation time of the reaction. A plot of these values as a function of [S] permits the determination of K_M and V_{max}.
3. Screening, as shown in Figure 5, is performed in an end point format using either chemical mixtures or single compound at a substrate concentration in the range 2–5 K_M. In every screening run a sample without test molecules is recorded. This sample represents the reference with 0% inhibition. Deconvolution of the active mixtures is then performed for the identification of the inhibitors.
4. The IC_{50} value of the detected inhibitor is obtained by simply recording experiments at different inhibitor concentration and by monitoring the integral of the product or substrate ^{19}F NMR signal as shown in Figure 5. A plot of these values as a function of the inhibitor concentration allows the determination of IC_{50} according to the equations:

   a) monitoring the substrate signal

$$[S_w] = \frac{[S_{w/o}] - [S_{TOT}]}{1 + ([I]/IC_{50})^n} + [S_{TOT}] \tag{7}$$

   b) monitoring the product signal

$$[P_w] = \frac{[P_{w/o}]}{1 + ([I]/IC_{50})^n} \tag{8}$$

   where $[S_w]$ and $[S_{w/o}]$ are given by the integrals of the substrate signal in the presence and absence of the inhibitor, respectively, $[P_w]$ and $[P_{w/o}]$ are given by the integrals of the product (or products) signal in the presence and absence of the inhibitor, respectively, and $[S_{TOT}] = [P_{w/o}] + [S_{w/o}] = [P_w] + [S_w]$. $[S_{TOT}]$ is the substrate concentration used for the experiments and it represents an internal reference, [I] is the concentration of the inhibitor, IC_{50} the concentration of the inhibitor

Fig. 5. Screening and deconvolution (top) and IC_{50} measurement (bottom) for compound H89 [43] performed with 3-FABS. The substrate is the N-terminal trifluoracetylated AKTide [44], the enzyme is the Ser/Thr kinase AKT1. The five compounds are (2-amino-6 methylquinazolin-4 ol, ethyl 2-quinoxalinecarboxylate, 5-methylbenzimidazole, methyl isoquinoline-3-carboxylate, and N-(2-{[(2E)-3-(4-bromophenyl)prop-2-enyl]amino}ethyl, known as H89). The activated enzyme AKT1, peptide, ATP, and compound concentrations were 25 nM, 30 μM, 131 μM (~2 K_M), and 10 μM, respectively. S and P represent the CF_3 signal of the peptide and the phosphorylated peptide, respectively. IC_{50} was measured with Equation (7), but the same value was obtained with Equation (8). The asterisks indicate the tiny amount of phosphorylated peptide in the presence of H89. Reprinted with permission from Dalvit *et al.* [20]. © 2003 American Chemical Society.

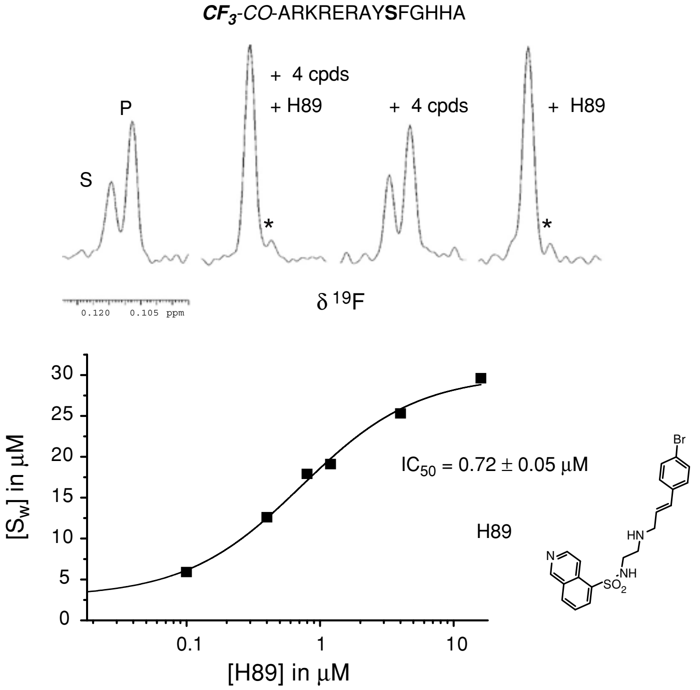

at which 50% inhibition is observed and n is the cooperativity factor (known also as Hill slope). In the absence of allosteric effects (i.e. $n = 1$) a meaningful value for IC_{50} can be derived with a single experimental point. This is possible because the values for both plateaus are known. These are $[S_{w/o}]$ and $[S_{TOT}]$ if Equation (7) is used and $[P_{w/o}]$ and the 0 value if Equation (8) is used.

Typically, enzyme concentration in the low nanomolar is used, but if the reaction is fast (substrates with large K_{cat}/K_M) and the enzyme is stable at room temperature for few hours the concentration can be further reduced [42]. This can be appreciated in the example of Figure 6 where the screening against the protease trypsin is performed with only 50 pM enzyme concentration. With cryoprobe technology optimized to fluorine NMR detection it will be possible, in some fortunate cases, to perform 3-FABS at enzyme concentration in the femtomolar range.

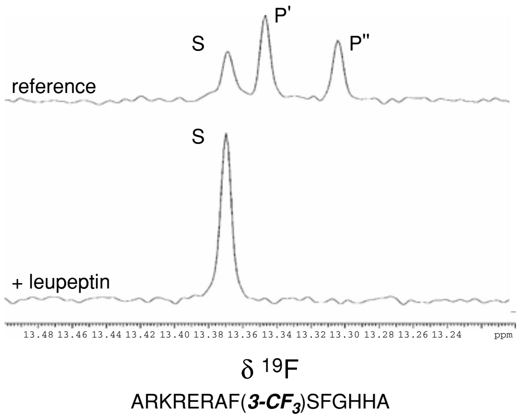

Fig. 6. 3-FABS performed with the protease trypsin (Roche Molecular Biochemical Cat. No. 1418475) at an enzyme concentration of only 50 pM. The substrate concentration was 30 μM. The reaction was performed in 50 mM Tris pH 7.5 and 0.03% Triton X-100 (Sigma X-100) at 20 °C and quenched after 6:40 hours with 0.5 mM phenylmethylsulfonyl fluoride (PMSF). S is the original peptide and P′, P″ are two different products of the enzymic hydrolysis. In the presence of 20 μM leupeptin no product formation is observed. Reprinted with permission from Dalvit *et al.* [42]. © 2004 Elsevier Science Ltd.

Conclusion

The fluorine NMR approaches FAXS and 3-FABS represent powerful tools for performing HTS and determining the K_D and IC_{50} values of the identified hits. The low protein consumption required by these methodologies compares favorably with the concentration used with the other techniques used in HTS. In addition, the two NMR techniques have some important advantages. Their simplicity together with the possibility of directly monitoring the real concentration, purity, stability, and solubility of the screened compounds results in reliable lead molecule detection and precise quantification of their strength. It is envisioned that the speed and easy set-up of FAXS and 3-FABS together with their broad range of applications will play a major role in the drug discovery process for discovering potent, bioavailable, and safe clinical candidates.

References

1. Shuker SB, Hajduk PJ, Meadows RP, Fesik SW. Science. 1996;274:1531.
2. Moore JM. Biopolymers (Peptide Science). 1999;51:221.
3. Hajduk PJ, Meadows RP, Fesik SW. Q. Rev. Biophys. 1999;32:211.
4. Roberts GCK. Drug Discov. Today. 2000;5:230.
5. Ross A, Senn H. Drug Discov. Today. 2001;11:583.
6. Peng JW, Lepre CA, Fejzo J, Abdul-Manan N, Moore JM. Methods Enzymol. 2001;338:202.
7. Diercks T, Coles M, Kessler H. Curr. Opin. Chem. Biol. 2001;5:285.
8. Pellecchia M, Sem DS, Wüthrich K. Nat. Rev. Drug Discov. 2002;1:211.
9. Van Dongen M, Weigelt J, Uppenberg J, Schultz J, Wikström M. Drug Discov. Today. 2002;7:471.
10. Wyss D, McCoy MA, Senior MM. Curr. Opin. Drug Discov. Dev. 2002;5:630.
11. Stockman BJ, Dalvit C. Prog. NMR Spectrosc. 2002;41:187.
12. Zartler ER, Yan J, Mo H, Kline AD, Shapiro MJ. Curr. Top. Med. Chem. 2003;3:25.
13. Fielding L. Curr. Top. Med. Chem. 2003;3:39.
14. Meyer B, Peters T. Angew. Chem. Int. Ed. 2003;42:864.
15. Coles M, Heller M, Kessler H. Drug Discov. Today. 2003;8:803.
16. Salvatella X, Giralt E. Chem. Soc. Rev. 2003;32:365.
17. Jahnke W, Widmer H. Cell. Mol. Life Sci. 2004;61:580.
18. Dalvit C, Flocco M, Veronesi M, Stockman BJ. Comb. Chem. HTS. 2002;5:605.
19. Dalvit C, Fagerness PE, Hadden DTA, Sarver RW, Stockman BJ. J. Am. Chem. Soc. 2003;125:7696.
20. Dalvit C, Ardini E, Flocco M, Fogliatto GP, Mongelli N, Veronesi M. J. Am. Chem. Soc. 2003;125:14620.
21. Dalvit C, Flocco M, Knapp S, Mostardini M, Perego R, Stockman BJ, Veronesi M, Varasi M. J. Am. Chem. Soc. 2002;124:7702.
22. Jahnke W, Floersheim P, Ostermeier C, Zhang X, Hemmig R, Hurth K, Uzunov DP. Angew. Chem. Int. Ed. 2002;41:3420.
23. Siriwardena AH, Tian F, Noble S, Prestegard JH. Angew. Chem. Int. Ed. 2002;41:3454.
24. Canet D. Nuclear Magnetic Resonance Concepts and Methods. John Wiley & Sons: Chichester, 1996.
25. Hull WE, Sykes BD. J. Mol. Biol. 1975;98:121.
26. Gerig JT. Methods Enzymol. 1989;177:3.
27. Gerig JT. Prog. NMR Spectrosc. 1994;26:293.
28. London RE, Gabel SA. J. Am. Chem. Soc. 1994;116:2570.
29. Lian LY, Barsukov IL, Sutcliffe MJ, Sze KH, Roberts GCK. Methods Enzymol. 1994;239:657.
30. Craik DJ, Wilce JA. In: DG Reid (Ed). Protein NMR Techniques. Humana Press Inc.: New Jersey, 1997, pp 195–232.
31. Carr HY, Purcell EM. Phys. Rev. 1954;94:630.
32. Meiboom S, Gill D. Rev. Sci. Instrum. 1958;29:688.
33. Luz Z, Meiboom S. J. Chem. Phys. 1963;39:366.
34. Allerhand A, Gutowsky HS. J. Chem. Phys. 1964;41:2115.
35. Mayer M, Meyer B. Angew. Chem. Int. Ed. 1999;38:1784.
36. Dalvit C, Pevarello P, Tatò M, Veronesi M, Vulpetti A, Sundström M. J. Biomol. NMR. 2000;18:65.
37. Tengel T, Fex T, Emtenas H, Almqvist F, Sethson I, Kihlberg J. Org. Biomol. Chem. 2004;2:725.
38. Doerr AJ, Case MA, Pelczer I, McLendon GL. J. Am. Chem. Soc. 2004;126:4192.
39. Percival MD, Withers SG. Biochemistry. 1992;31:505.
40. Evans JNS. Biomolecular NMR Spectroscopy. Oxford University press, New York, USA, 1995, pp 237–340.
41. Segel IH. Biochemical Calculations. John Wiley & Sons, New York, USA, 1976.
42. Dalvit C, Ardini E, Fogliatto GP, Mongelli N, Veronesi M. Drug Discov. Today. 2004;9:595.
43. Reuveni H, Livnah N, Geiger T, Klein S, Ohne O, Cohen I, Benhar M, Gellerman G, Levitzki A. Biochemistry. 2002;41:10304.
44. Obata T, Yaffe MB, Leparc GG, Piro ET, Maegawa H, Kashiwagi A, Kikkawa R, Cantley LC. J. Biol. Chem. 2000;46:36108.

Applications of Receptor-Based NMR Screening in Drug Discovery

Philip J. Hajduk
Global Pharmaceutical Research and Development, Abbott Laboratories, Abbott Park, IL 60064, USA

Introduction

High-throughput screening (HTS) of large corporate compound libraries has become the primary strategy for lead generation in the pharmaceutical industry. However, despite the advances in screening and chemistry technologies over the last decade, there has been little increase in the rate of discovery of quality drug leads [1,2]. One of the primary reasons for this problem is the nature of the hits that come from traditional HTS campaigns. Most hits tend to look "drug-like," with molecular weights <500 and $C\log P$ values <5, but the optimization process tends to increase both size and hydrophobicity—leading to compounds with significantly poorer drug-like properties [3]. An additional problem is the large numbers of false positives that potentially come from HTS campaigns, confounding lead triage and the identification of quality leads that act via the intended mechanism of action [4].

Recently, NMR-based screening has become a powerful complement to traditional HTS technologies to identify lead compounds that have high potential for further optimization. Unlike conventional HTS, most NMR-based screening applications focus on the identification of low molecular weight, low-affinity compounds from which high-affinity drug candidates can be constructed. In addition, NMR screening has been particularly successful when closely integrated with other drug discovery technologies, including HTS, X-ray crystallography, and high-throughput organic synthesis. There have been many excellent reviews on the applications as well as the theoretical and experimental aspects of NMR-based screening [5–14]. In this review, the rationale, advantages, and applications of fragment-based screening will be presented, with particular emphasis on receptor-based methods for NMR screening.

Fragment-Based Screening: Identifying "Hot Spots" on Protein Surfaces

Over the last decade, it has become widely recognized that the interaction energy of a protein with its natural ligand or receptor is not necessarily evenly distributed over the binding surface, but instead can be highly localized to specific regions of the protein surface called "hot spots." This was first recognized in mutational analyses of protein–protein interactions [15], but has also been extended to the study of protein–ligand interactions [16]. These studies imply that there are relatively small regions of the protein surface that impart the majority of the free energy of binding with the ligand, while additional interaction surface primarily serves to modulate specificity. This has significant implications for drug design, in that the rapid identification and optimal utilization of the energetic focal point of the binding site can accelerate the discovery of potent molecules with good lead-like or drug-like properties [2]. Unfortunately, the large compounds that come from typical HTS campaigns tend to interact sub-optimally with the hot spot, while gaining potency by interacting with peripheral sites in the binding pocket that have little potential for further optimization (Figure 1a). This can confound subsequent optimization, as the region of the compound that interacts with the hot spot (which has the greatest potential for increasing binding affinity) is initially unknown and must be discovered through several rounds of blind chemical modification. Unfortunately, even after this "core" piece is discovered, it is often difficult to modify in the context of the lead molecule without incurring unacceptable losses in potency.

As an alternative to pursuing relatively high molecular weight, sub-optimal leads, fragment-based screening is becoming a powerful tool in the drug discovery arena. In fragment-based screens, low molecular weight (typically 100–300 Da) compounds that interact optimally with the hot spot of the active site are initially pursued. By targeting only a small region of the binding site, the chances of identifying a compound that interacts optimally in the pocket are increased dramatically [17]. In addition, because of the reduced complexity of the protein–ligand interface, the number of compounds that need to be screened is drastically reduced. Typical fragment libraries reported in the literature tend to be on the order of 10^3–10^4 compounds, compared to the 10^6 compounds typically evaluated in HTS assays. There are a variety of ways to utilize fragment leads in drug design efforts, as will be described

Graham A. Webb (ed.), Modern Magnetic Resonance, 1401–1407.
© 2008 *Springer.*

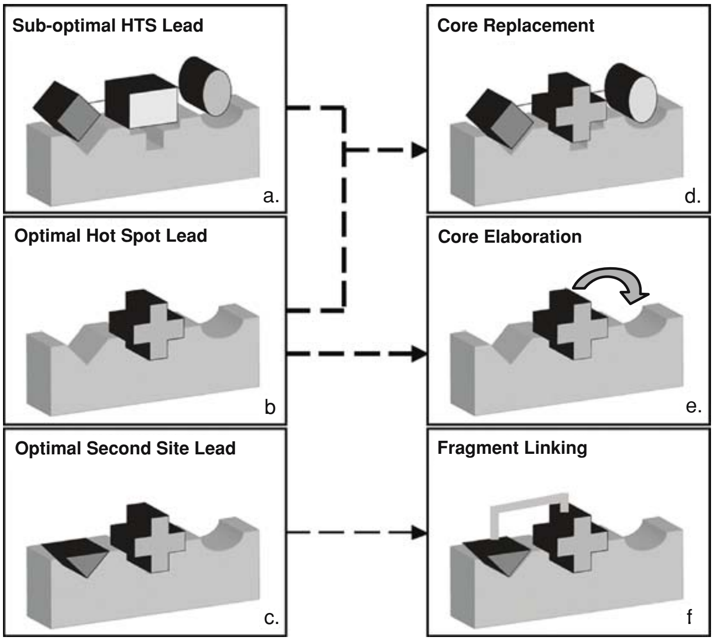

Fig. 1. Fragment-based strategies for the design of novel drug leads. (a) Representation of a high-throughput screening lead (connected shapes) binding sub-optimally to the protein target (gray surface). Sub-optimal binding is depicted by poor packing and shape complementarity. (b) Identification of a fragment lead (cross) that interacts optimally with the protein, indicated by close packing and good shape complementarity. (c) Identification of two ligands (cross and triangles) that bind to proximal subsites on a protein surface. (d) Core replacement strategy for lead design, in which the fragment identified in (b) is incorporated into the lead compound depicted in (a). (e) Core elaboration strategy, in which the fragment identified in (b) is directionally modified via high-throughput synthetic means to produce large libraries of compounds that can access neighboring subsites. (f) Fragment-linking strategy, in which the two fragments identified in (c) are linked to produce a high-affinity ligand.

below. However, these leads first need to be reliably identified. While attractive starting points for design, these fragment leads tend to bind with low affinity to the target (e.g. K_D values of 10–1000 μM)—which can complicate biochemical means of detection. As a result, a host of new technologies have been developed or elaborated for the express purpose of enabling fragment-based drug design. Such methodologies include NMR-based screening (both target-based and ligand-based) [10,11], high-throughput X-ray crystallography (e.g. CrystaLEAD) [2,18], mass spectroscopy [19], surface plasmon resonance [20], fragment tethering [21], and dynamic combinatorial chemistry [22]. This review will focus on receptor-based methods for fragment-based screening. The reader is referred to other sections in this handbook for more thorough discussions of other aspects on NMR-based screening in drug discovery and design.

Receptor-Based NMR Screening

Receptor-Based NMR screening monitors the perturbations in the protein signals upon addition of a test compound. The target is isotopically labeled and two-dimensional $^{15}N/^{1}H$- or $^{13}C/^{1}H$-correlation spectra are collected. Screening is typically performed against mixtures of 10–30 compounds, and the mixtures that produce the largest chemical shift perturbations are deconvoluted to identify the leads. NMR screening based on chemical shift perturbations of the resonances of the protein target is a profoundly reliable method for detecting protein–ligand interactions, and has significant advantages over other screening methods. The observation of discrete, stable chemical shift perturbations is strong evidence for a specific, well defined binding event. As a result, target-based NMR screening is essentially immune to false positives that can arise from non-specific binding or compound aggregation [23]. In addition, the spectral editing essentially eliminates the ligand signals, enabling the experiments to be performed even at very high ligand concentrations. Finally, the unique chemical shift perturbation "fingerprint" induced by ligand binding can be used not only to detect binding, but also to identify the ligand-binding site. This is shown in Figure 2 for $^{13}CH_3$-labeled protein kinase A (PKA) (mutant form). Addition of adenosine gives rise to characteristic chemical shift perturbations, and all screening hits that shift these same peaks can be classified as ATP-site ligands (Figure 2A). However, ligands can be identified that bind to alternative pockets on the protein (Figure 2B). These pockets can potentially be independently exploited for the development of therapeutics or ligands for these sites can be reliably classified and safely ignored if it is determined that the site is therapeutically irrelevant. In either case, this unique feature of receptor-based NMR screening makes it a powerful tool in the discovery and characterization of ligands for protein targets.

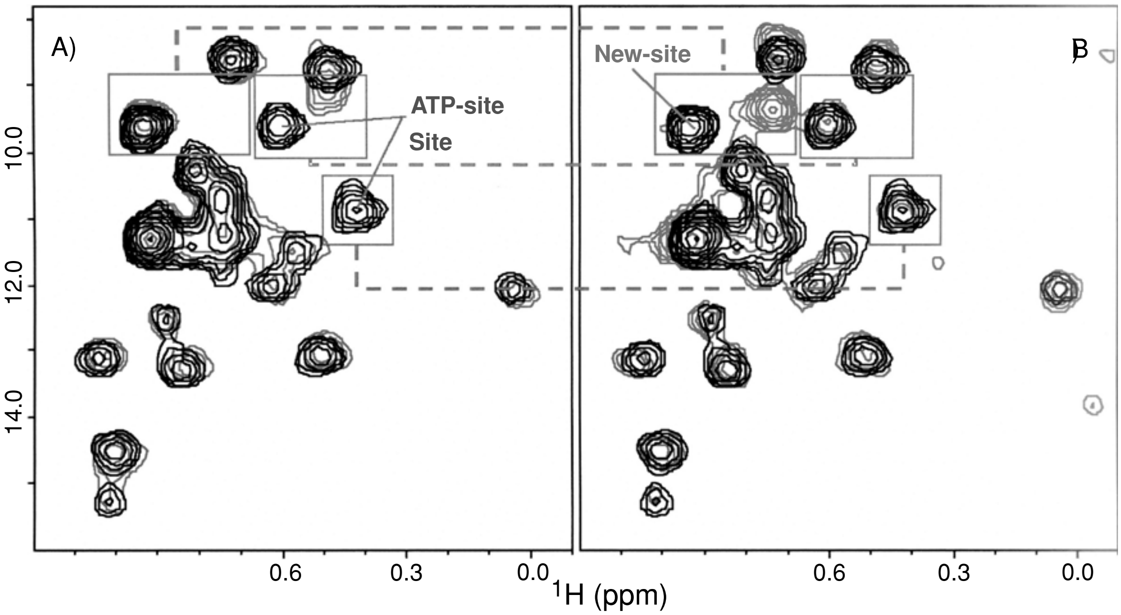

Fig. 2. Expanded section of $^1H/^{13}C$-HSQC spectra (showing isoleucine-δ signals) acquired on a mutant form of protein kinase A (PKA) in the absence (black contours) and presence (red contours) of (A) ATP-γS and (B) a test compound that binds to a site on PKA other than the ATP-binding site. The unique chemical shift fingerprint for each binding site can be used to classify new compounds as ATP- or non-ATP-site ligands. (See also Plate 109 on page XXIV in the Color Plate Section.)

With the advance of cryogenic probes [24] and cost-effective ^{13}C-methyl labeling [25], target-based NMR screening utilizing ^{15}N- or ^{13}C-labeling can now routinely be applied to targets with MW in excess of 40 kDa. For larger targets, extensive deuteration and the use of TROSY pulse sequences can significantly increase this MW limit [25,26], although the high cost associated with extensive deuteration usually limits these applications to lead validation and characterization. Another limitation of receptor-based screening is that cost-effective and efficient labeling can currently only be achieved in bacterial systems. While isotopic labeling in insect cell systems has recently been reported [27], such methods are still in their infancy. Thus, for high MW targets or those that can only be produced in baculovirus or mammalian cells, the ligand-based NMR methods described elsewhere in this volume should be explored.

Utilization of Fragment Leads in Drug Design

Receptor-based NMR screening has been quite successful at its desired objective: the identification of low MW leads that bind to hot spots on protein surfaces and that would be difficult or impossible to detect using any other method. Figure 3 shows the molecular weight and pK_D values for more than 750 NMR leads that we have derived from receptor-based screens against more than 20 protein targets. By intentional library design, the leads are small (average MW of 234 ± 56 Da), and this results in leads that are quite weak (average pK_D of 2.7, which translates to a K_D value of 500 μM). The key question is how to utilize these hits in drug design. Three strategies for utilizing NMR-derived fragments in drug design will be briefly described: (1) core replacement, (2) high-throughput core elaboration, and (3) fragment linking.

Core Replacement

As mentioned above, most leads from HTS interact sub-optimally with the hot spot of the binding site. In contrast, as shown in Figure 1b, fragment-based screening attempts to identify a low molecular weight fragment that takes full advantage of the available binding interactions. One approach to exploiting these fragments is to incorporate the optimized core back into the lead molecule. This strategy is called core replacement and is shown schematically in Figure 1, where the optimized core (Figure 1b) is synthetically incorporated into the lead molecule (Figure 1a) to produce a compound with improved interactions with the target (Figure 1d). This approach can be especially

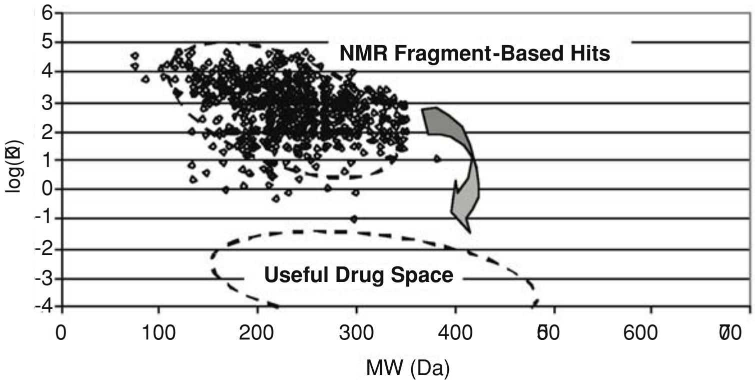

Fig. 3. Plot of molecular weight (in Da) vs. affinity [expressed in terms of log(K_D), where K_D is in μM units] for more than 750 leads derived from receptor-based NMR screens against more than 20 protein targets.

useful in breaking out of existing structural classes to address unanticipated safety, pharmacological, or intellectual property issues.

Core replacement strategies have been effectively used to address non-drug-like properties of several leads (Table 1). For example, reported inhibitors of both the SH2 domain of Lck and protein tyrosine phosphatase 1B (PTP-1B) contain highly charged phosphotyrosine (pTyr) mimetics that can severely limit cellular permeability and oral bioavailability. Receptor-based screening was able to identify singly charged moieties that could serve as superior pTyr replacements for these targets [28,29]. Significantly, in the case of PTP-1B, a class of isoxazole leads were incorporated back into the lead series, resulting in potent compounds that exhibited increased Caco-2 permeability and dose-dependent cellular activity [29]. A core replacement strategy was also implemented in the design of inhibitors of urokinase, in which the highly basic phenylguanidine group was successfully replaced with a more neutral aminobenzimidazole moiety [30].

High-Throughput Core Elaboration

While the leads from NMR-based screening are only of low molecular weight and affinity, they can be viewed as small molecule scaffolds that can be rapidly elaborated through combinatorial chemistry or high-throughput parallel synthesis. While many scaffolds have been utilized in the design of combinatorial libraries [31,32], it is typically unknown whether any scaffold possesses inherent binding affinity for any given target. In this sense, it is significant to note that an NMR-derived lead with a K_D value of only 1 mM represents more than 4 kcal/mol of binding energy. Thus, such leads are ideal for use in target-directed library design. The design of such libraries is

Table 1: Published examples of receptor-based fragment approaches in the design of novel drug leads

Target	Fragment approach	Result	References
Lck-SH2	Core replacement	Novel pTyr mimetics	[28]
UK	Core replacement	Novel, sub-μM inhibitors	[30]
PTP-1B	Core replacement	Novel, cell permeable inhibitors	[29]
Erm-AM	Core elaboration	Novel, μM inhibitors	[34]
PTP-1B	Core elaboration	Novel, selective, nM inhibitors	[35]
Oxidoreductases	Core elaboration	Novel, selective, nM inhibitors	[36]
FKBP	Linked fragment	Novel, nM ligands	[39]
Stromelysin	Linked fragment	Novel, nM ligands	[40]
Stromelysin	Linked fragment	Improved bioavailability	[41]
AK	Linked fragment	Structural diversity	[42]
LFA	Linked fragment	Improved solubility	[43]
PTP-1B	Linked fragment	Novel, nM inhibitors	[44]
DHPR	Linked fragment	Novel, nM inhibitors	[36]
HCV protease	Linked fragment	Non-peptidic, μM inhibitors	[50]

significantly enhanced when structural information on the protein–ligand complex can be obtained either from NMR or X-ray crystallography. The process of core elaboration is shown schematically in Figure 1, where the optimized fragment lead (Figure 1B) is synthetically modified to produce libraries of compounds in the expectation of accessing a neighboring pocket to increase both binding affinity and target specificity. A wide range of chemistries is available for the elaboration of suitable scaffolds. In particular, polymer assisted solution phase (PASP) synthesis is rapidly emerging as a method of choice for library preparation via parallel synthesis [33].

High-throughput core elaboration has been effectively utilized in the design of targeted libraries for ErmAM [34], PTP-1B [35], and various oxidoreductases (Table 1) [36]. In the case of ErmAM, a millimolar lead derived from receptor-based screening was rapidly elaborated at multiple positions, resulting in a more than 200-fold gain in potency [34]. For PTP-1B, a library of 76 compounds was prepared around an NMR-based lead resulting in compounds with K_I values <100 nM—representing a 30-fold gain over the parent compound [35]. Most significantly, members of this library exhibited moderate selectivity over highly homologous phosphatases, suggesting that such selectivity could be achieved with a small molecule inhibitor. NMR-SOLVE [37] was implemented to target the oxidoreductase family by first identifying a low molecular weight ligand that inhibited multiple members of the family, and then rapidly elaborating this core to increase affinity and specificity. From a library of 300 compounds, nM inhibitors of three oxidoreductases (LDH, DHPR, and DOXPR) were identified. Significantly, while the initial core was essentially non-selective with respect to these oxidoreductases, the resulting inhibitors exhibited 10- to 100-fold selectivity.

Fragment Linking

By far the most powerful utilization of fragment-based screening in drug design is the linked fragment approach. As depicted in Figure 1, a linked fragment strategy involves identifying not simply one (Figure 1B) but two fragments that bind simultaneously to the protein at neighboring sites (Figure 1C). The two fragments are then linked together (maintaining their spatial geometry) to produce high-affinity, highly optimized leads (Figure 1F). One of the most significant advantages of the linked fragment approach is that the amount of chemical space that is sampled increases exponentially with the size of the fragment library [38]. For instance, an NMR screen in which 10,000 compounds are tested for independent binding to two subsites on a protein covers as much chemical space as screening ~100 million single compounds. The linked fragment strategy has been utilized in two related approaches: (1) the *de novo* construction of high-affinity ligands and (2) the optimization of existing leads by identification of new substituents. The construction of high-affinity ligands from pieces that have been identified via NMR has been described for FKBP [39], stromelysin [40,41], adenosine kinase [42], LFA [43], PTP-1B [44], and DHPR [36]. In all of these cases, screens were performed to identify ligands for peripheral sites that bound simultaneously with a first-site ligand, and nM ligands were produced after linking. The strategies for *de novo* construction vs. lead optimization differ only in the sense of the desired end: generation of a novel structural series vs. improved physicochemical properties of an existing series.

Receptor-Based Methods for Lead Validation and Characterization

In addition to their use as screening tools, receptor-based NMR Methods are being increasingly utilized as lead validation tools. Often, HTS yields tens or even hundreds of compounds that modulate the biochemical response with apparent IC_{50} values on the order of 10 μM or less. As many assays utilized by HTS can be complex, multi-component systems, some number of the hits will actually disrupt or inhibit an assay component other than the target of interest. In addition, false positives can result from the method of detection (e.g. interference from fluorescent or colored compounds), or mechanisms such as non-specific binding, compound aggregation [23], or compound reactivity [45]. Thus, it is extremely valuable to identify false positives as early as possible in the hit evaluation process in order to focus resources on those hits that have the highest potential to become bonafide leads.

Typically, complex, target-specific secondary assays are used to eliminate false positives from the original primary screening hits. However, NMR is a universal tool that has been successfully applied in the evaluation of leads from a variety of screening formats, including activity assays, ligand competition assays, whole-cell screens, affinity-based screens, and virtual ligand screening (VLS) [4,46,47]. It has also been demonstrated that, using specific labeling strategies, multiple protein targets can be simultaneously evaluated for binding to test compounds—opening the door for monitoring compound selectivity in a single experiment [48]. Table 2 shows results on published targets for which NMR follow-up of HTS or VLS hits was employed. In all of the cases listed, ligands were confirmed that could be prioritized for further follow-up. However, the majority of compounds derived even from HTS or affinity-based screens did not form a stable complex with the target of interest. In fact, it is our experience that, on average, <20%

Table 2: Examples of receptor-based NMR methods for the validation of leads derived from HTS, affinity screening, and virtual ligand screening campaigns

Target	Discovery technology	No. of hits tested	No. of hits confirmed	Ultimate result	References
LFA	HTS	2	2	Clinical candidate	[43]
Bcl-xL	HTS/affinity	55	23	Novel structural series	[53]
MurF	Affinity	11	2	Novel, nM lead series	[51]
RGS4	Affinity	50	1	Validated lead series	[46]
FBP	VLS	100	1	Novel structural series	[54]
IGFPB-1	VLS	3	1	Novel structural series	[52]
DNA gyrase	VLS	14	7	Novel structural series	[20]

of all leads from HTS campaigns are suitable for further evaluation [4]. Thus, a combination of the inherent strengths of both HTS and NMR represents a powerful strategy for the identification of lead compounds that bind with high affinity to and specificity for the protein target. Such compounds have high potential for further optimization through medicinal chemistry and/or structure-based design approaches.

Summary

In summary, receptor-based NMR methods for fragment lead identification have been used in a number of design strategies. Significantly, these design strategies can be used throughout the entire course of pre-clinical drug discovery—including initial lead identification, potency optimization, and even modulation of physicochemical properties to aid in candidate selection. Even more significant, however, is the fact that compounds from several programs employing receptor-based NMR screening and fragment design have already gone beyond the pre-clinical setting into the clinic (e.g. matrix metalloproteinase inhibitors [49] and inhibitors of the LFA–ICAM interaction [43]). This is ample validation that the methods described in this review can be used to produce ligands not only with high affinity, but also with the appropriate drug-like properties for use in therapeutic intervention in man.

References

1. Campbell SJ. Clin. Sci. 2000;99:255–60.
2. Carr R, Jhoti H. Drug Discov. Today. 2002;7:522–7.
3. Oprea TI, Davis AM, Teague SJ, Leeson PD. J. Chem. Inf. Comput. Sci. 2001;41:1308–15.
4. Hajduk PJ, Burns DJ. Comb. Chem. High Throughput Screen. 2002;5:613–22.
5. Hajduk PJ, Meadows RP, Fesik SW. Q. Rev. Biophys. 1999; 32:211–40.
6. Peng JW, Lepre CA, Fejzo J, Abdul-Manan N, Moore JM. Methods Enzymol. 2001;338:202–30.
7. Stockman BJ, Farley KA, Angwin DT. Methods Enzymol. 2001;338:231–46.
8. Huth JR, Sun C. Comb. Chem. High Throughput Screen. 2002;5:631–44.
9. Lepre CA, Peng JW, Fejzo J, Abdul-Manan N, Pocas J, Jacobs M, Xie X, Moore JM. Comb. Chem. High Throughput Screen. 2002;5:583–90.
10. Stockman BJ, Dalvit C. Prog. NMR Spectrosc. 2002;41:187–231.
11. Meyer B, Peters T. Angew. Chem. Int. Ed. 2003;42:864–90.
12. Coles M, Heller M, Kessler H. Drug Discov. Today. 2003;8:803–10.
13. Jahnke W, Florsheimer A, Blommers MJJ, Paris CG, Heim J, Nalin CM, Perez LB. Curr. Top. Med. Chem. 2003;3:69–80.
14. Jahnke W, Widmer H. Cell. Mol. Life Sci. 2004;61:580–99.
15. DeLano WL. Curr. Opin. Struct. Biol. 2002;12:14–20.
16. Kuntz ID, Chen K, Sharp KA, Kollman PA. Proc. Natl. Acad. Sci. 1999;96:9997–10002.
17. Hann MM, Leach AR, Harper G. J. Chem. Inf. Comput. Sci. 2001;41:856–64.
18. Nienaber VL, Richardson PL, Klinghofer V, Bouska JJ, Giranda VL, Greer J. Nat. Biotechnol. 2000;18:1105–8.
19. Swayze EE, Jefferson EA, Sannes-Lowery KA, Blyn LB, Risen LM, Arakawa S, Osgood SA, Hofstadler SA, Griggey RH. J. Med. Chem. 2002;45:3816–9.
20. Boehm H-J, Boehringer M, Bur D, Gmuender H, Huber W, Klaus W, Kostrewa D, Kuehne H, Luebbers T, Meunier-Keller N, Mueller F. J. Med. Chem. 2000;43:2664–74.
21. Erlanson DA, Braisted AC, Raphael DR, Randal M, Stroud RM, Gordon EM, Wells JA. Proc. Natl. Acad. Sci. 2000;97:9367–72.
22. Ramstrom O, Lehn J-M. Nat. Rev. Drug Discov. 2002;1:26–36.
23. McGovern SL, Caselli E, Grigorieff N, Shoichet BK. J. Med. Chem. 2002;45:1712–22.
24. Hajduk PJ, Gerfin T, Boehlen J-M, Häberli M, Marek D, Fesik SW. J. Med. Chem. 1999;42:2315–7.
25. Hajduk PJ, Augeri DA, Mack J, Mendoza R, Yang J, Betz SF, Fesik SW. J. Med. Chem. 2000;122:7898–904.
26. Fernandez C, Wider G. Curr. Opin. Struct. Biol. 2003;13:570–80.

27. Strauss A, Bitsch F, Cutting B, Fendrich G, Graff P, Liebetanz J, Zurini M, Jahnke W. J. Biomol. NMR. 2003;26:367–72.
28. Hajduk PJ, Zhou M-M, Fesik SW. Bioorg. Med. Chem. Lett. 1999;9:2403–6.
29. Liu G, Xin Z, Pei Z, Zhao H, Hajduk PJ, Abad-Zapatero C, Hutchins CW, Lubben TH, Ballaron SJ, Haasch DL, Kaszubska W, Rondinone CM, Trevillyan JM, Jirousek MR. J. Med. Chem. 2003;46:4232–5.
30. Hajduk PJ, Boyd S, Nettesheim D, Nienaber V, Severin J, Smith R, Davidson D, Rockway T, Fesik SW. J. Med. Chem. 2000;43:3862–6.
31. Fecik RA, Frank KE, Gentry EJ, Menon SR, Mitscher LA, Telikepalli H. Res. Rev. 1998;18:149–85.
32. Fauchere JL, Boutin JA, Henlin JM, Kucharczyk N, Ortuno JC. Chemom. Intell. Lab. Sys. 1998;43:43–68.
33. Hinzen B. Methods Princ. Med. Chem. 2000;9:209–37.
34. Hajduk PJ, Dinges J, Schkeryantz JM, Janowick D, Kaminski M, Tufano M, Augeri DJ, Petros A, Nienaber V, Zhong P, Hammond R, Coen M, Beutel B, Katz L, Fesik SW. J. Med. Chem. 1999;42:3852–9.
35. Xin A, Oost TK, Abad-Zapatero C, Hajduk PJ, Pei Z, Szczepankiewicz BG, Hutchins CW, Ballaron SJ, Stashko MA, Lubben T, Trevillyan JM, Jirousek MR, Liu G. Biorg. Med. Chem. Lett. 2003;13:1887–90.
36. Sem DS, Bertolaet B, Baker B, Chang E, Costache AD, Coutts S, Dong Q, Hansen M, Hong V, Huang X, Jack RM, Kho R, Lang H, Ma C-T, Meininger D, Pellecchia M, Pierre F, Villar H, Yu L. Chem. Biol. 2004;11:185–94.
37. Sem DS, Yu L, Coutts SM, Jack R. J. Cell. Biochem. 2001;S37:99–105.
38. Hajduk PJ, Meadows RP, Fesik SW. Science. 1997;278:497–9.
39. Shuker SB, Hajduk PJ, Meadows RP, Fesik SW. Science. 1996;274:1531–4.
40. Hajduk PJ, Sheppard G, Nettesheim DG, Olejniczak ET, Shuker SB, Meadows RP, Steinman DH, Carrera GM, Marcotte PA, Severin J, Walter K, Smith H, Gubbins E, Simmer R, Holzman TF, Morgan DW, Davidsen SK, Fesik SW. J. Am. Chem. Soc. 1997;119:5818–27.
41. Hajduk PJ, Shuker SB, Nettesheim DG, Xu L, Augeri DJ, Betebenner D, Craig R, Albert DH, Guo Y, Meadows RP, Michaelides M, Davidsen SK, Fesik SW. J. Med. Chem. 2002; 45:5628–39.
42. Hajduk PJ, Gomtsyan A, Didomenico S, Cowart M, Bayburt EK, Solomon L, Severin J, Smith R, Walter K, Holzman TF, Stewart A, McGaraughty S, Jarvis MF, Kowaluk ES, Fesik SW. J. Med. Chem. 2000;43:4781–6.
43. Liu G, Huth JR, Olejniczak ET, Mendoza R, DeVries P, Leitza S, Reilly EB, Okasinski GF, Fesik SW, von Geldern TW. J. Med. Chem. 2001;44:1202–10.
44. Szczepankiewicz BG, Liu G, Hajduk PJ, Abad-Zapatero C, Pei Z, Xin Z, Lubben T, Trevillyan JM, Stashko MA, Ballaron SJ, Liang H, Huang F, Hutchins CW, Fesik SW, Jirousek MR. J. Am. Chem. Soc. 2003;125:4087–96.
45. Rishton GM. Drug Discov. Today. 1997;2:382–4.
46. Moy FJ, Haraki K, Mobilio D, Walker G, Powers R, Tabei K, Tong H, Siegal MM. Anal. Chem. 2001;73:571–81.
47. Rudisser S, Jahnke W. Comb. Chem. High Throughput Screen. 2002;5:591–603.
48. Zartler ER, Hanson J, Jones BE, Kline AD, Martin G, Mo H, Shapiro MJ, Wang R, Wu H, Yan J. J. Am. Chem. Soc. 2003;125:10941–6.
49. Wada CK, Holms JH, Curtin ML, Dai Y, Florjancic AS, Garland RB, Guo Y, Heyman HR, Stacey JR, Steinman DH, Albert DH, Bouska JJ, Elmore IN, Goodfellow CL, Marcotte PA, Tapang P, Morgan DW, Michaelides MR, Davidsen SK. J. Med. Chem. 2002;45:219–32.
50. Wyss DF, Arasappan A, Senior M, Wang Y-S, Beyer BM, Njoroge FG, McCoy MA. J. Med. Chem. 2004;47:2486–98.
51. Gu Y-G, Florjancic AS, Clark RF, Zhang T, Cooper CS, Anderson DD, Lerner CG, McCall O, Cai Y, Black-Schaefer CB, Stamper GF, Hajduk PJ, Beutel BA. Bioorg. Med. Chem. Lett. 2004;14:267–70.
52. Kamionka M, Rehm T, Beisel H, Lang K, Engh R, Holak T. J. Med. Chem. 2002;45:5655–60.
53. Qian J, Voorbach MJ, Huth JR, Coen ML, Zhang H, Ng S-C, Comess KM, Petros AM, Rosenberg SH, Warrior U, Burns DJ. Anal. Biochem. 2004;328:131–8.
54. Huth JR, Yu L, Collins I, Mack J, Mendoza R, Isaac B, Braddock DT, Muchmore SW, Comess KM, Fesik SW, Clore GM, Levens D, Hajduk PJ. J. Med. Chem. 2004;47: 4851–7.

NMR SHAPES Screening

Christopher A. Lepre and Jonathan M. Moore
Vertex Pharmaceuticals, Inc., Cambridge, MA 02139-4242, UK

Introduction

The SHAPES strategy is a process that employs nuclear magnetic resonance (NMR) spectroscopy to screen small, drug-like molecules in a directed search for novel (or improved) medicinal chemistry leads. This strategy typically integrates NMR screening experiments with other enabling methods in drug discovery such as enzymatic assays, high-throughput screening (HTS), X-ray crystallography, molecular modeling, and combinatorial chemistry. There are three components of any NMR-based lead discovery strategy: (1) a carefully selected library of screening compounds, (2) a NMR screening method that is well-suited to the target of interest, and (3) effective use of the information obtained through screening to generate or optimize drug leads for that target. Each of these aspects will be discussed in this chapter to provide an overview of how NMR SHAPES screening may be used in drug discovery. For additional reading, we have recently published more detailed treatments of each of these components, i.e. NMR screening library design [1,2], experimental approaches [3–5], and examples of SHAPES applications [6,7].

Principles of SHAPES Screening

The SHAPES screening strategy was developed based on two assumptions. The first assumption is that information about molecules that bind to a target with relatively low affinities may be used to direct the design of more potent inhibitors of that target. Any biophysical method that is capable of detecting weak interactions between ligands and macromolecules can be used, however, NMR methods are particularly well suited for this purpose. In many cases, NMR methods are capable of identifying inhibitors of a target that are beyond the limits of detection by traditional enzyme assays. The second assumption inherent in the SHAPES strategy is that compounds containing molecular fragments found in successful drugs are more likely to possess desirable, drug-like properties (such as good oral bioavailability, low toxicity, metabolic stability, and good synthetic accessibility) than random molecules. Thus, the SHAPES method uses simple NMR techniques to detect binding of a relatively small but diverse library of low molecular weight, soluble compounds to a drug target. The resulting SHAPES screening hits are then used to guide molecular modeling efforts, synthesize combinatorial libraries, and bias the choice of compounds selected to undergo high throughput enzymatic screening (Figure 1). Integration of the SHAPES strategy with iterative ligand structure determination has proven to be very useful for deriving pharmacophore models and rapidly achieving dramatic improvements in inhibitor potency with minimal synthetic effort.

Design of the SHAPES Compound Library

The design of an NMR screening library based on molecules derived from known drugs evolved from a modeling study carried out at Vertex Pharmaceuticals [8]. In this study, 5120 drugs covering a spectrum of therapeutic indications were selected from the Comprehensive Medicinal Chemistry database and computationally reduced to graph frameworks (i.e. unadorned rings and linkers). The authors found that only 32 simple frameworks described approximately half of the drugs in the database. When atom type and bond order were included in the analysis, only 41 "complex" frameworks, or scaffolds, described about a quarter of the known drugs. These findings implied that a relatively small number of molecular "shapes" could be used in a screening library for a wide variety of therapeutic targets.

Although many of the factors responsible for the failure of clinical candidates are not well understood, it was believed that commonly recurring drug scaffolds are predisposed to having favorable clinical properties. Therefore, the original SHAPES library was built with compounds containing the most common scaffolds found in known drugs, combined with commonly occurring drug side chains (identified in a later study [9] (Figure 2). Subsequently, the library has been expanded to incorporate drug-like and "lead-like" [10] compounds that contain linkages amenable to combinatorial chemistry, are targeted against targets from a particular gene family, or exhibit diverse pharmacophores [1,2].

The SHAPES library has been designed to satisfy stringent criteria for compound solubility, drug-likeness (or lead-likeness), and synthetic accessibility. Details of the compound selection process and overall library design have been described previously [1,2]. More generally, starting from a database of over 1 million commercially

Graham A. Webb (ed.), Modern Magnetic Resonance, 1409–1417.
© 2008 *Springer.*

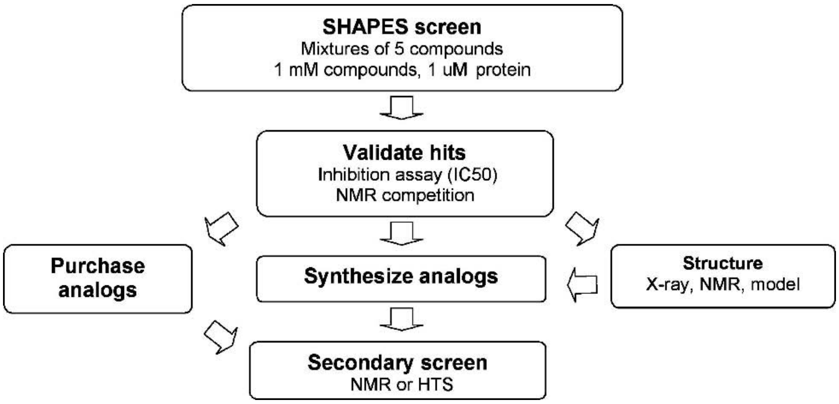

Fig. 1. Flow diagram of the SHAPES process.

available compounds, computational filters were applied to remove compounds predicted to have poor solubilities or other physicochemical properties (using "Rule of 5" [11] and other criteria [1]), as well as to eliminate compounds possessing undesirable functional groups [12]. Candidates surviving the filtering process were then clustered using the Jarvis–Patrick method [13], and individual compounds were picked manually from the centroids of the clusters. Mixtures of compounds were then chosen with NMR considerations in mind, i.e. to minimize NMR resonance overlap and avoid interactions between the components. Prior to screening, the mixtures were checked for aggregation by recording 2D NOESY experiments.

NMR Methods for Screening Compound Libraries

Because the molecules in the SHAPES screening library are typically small (<350 MW) and unelaborated, they are expected to have lower average affinities than most compounds screened by HTS. To enable the broadest possible range of affinities for detection, we use well-known NMR-based methods capable of identifying molecules that bind with dissociation constants ranging from low micromolar (and lower for some methods [14,15]) to millimolar in a single experiment.

We have recently reviewed and compared these methods in detail [4,5]. Although protein-based detection methods [16,17] are very useful for mapping the binding sites of hits on protein targets, ligand-detected methods for primary screening consume less reagents, do not require isotopic labeling, and may be used for many types of targets with no limit to molecular mass.

Many approaches have been proposed that monitor differences in ligand NMR parameters in the free vs. bound states. These approaches have used transverse relaxation rates, selective longitudinal relaxation rates, exchange-transferred NOE, and translation diffusion coefficients as probes of interactions between small molecules and a macromolecular target. In these experiments, a small molecule binder will transiently assume the much slower rotational and translational mobility of the much larger receptor, exhibiting changes in the aforementioned relaxation and diffusion parameters.

A second class of experiments does not rely on differences between ligand free and bound state parameters, but rather takes advantage of ^{1}H magnetization transfer from the target to the ligand. These experiments have distinct advantages, because binders to the target experience the magnetization transfer, while non-binders do not. This phenomenon results in significant simplification of spectra and identification and deconvolution of hits. The two most commonly used of this latter class of experiments are the Saturation Transfer Difference (STD) [18] and WaterLOGSY [19,20] methods. In the STD experiment, the target is saturated via a train of radiofrequency pulses. Upon saturation, spin diffusion occurs throughout the protein matrix to the binding site, and is transferred to ligands during the ligand residence time. WaterLOGSY relies similarly on initial saturation of the receptor, however the mechanism for saturation differs, in that either saturation or inversion of solvent water molecules is the initial step, followed by transfer of that magnetization to sites on the target via multiple pathways, and subsequently to the binding ligand. A more rigorous physical treatment of magnetization transfer processes in both the STD and WaterLOGSY classes of experiments may be found elsewhere [5].

Our preferred method for detection of ligand binding to protein targets is saturation transfer difference spectroscopy [18], which offers high sensitivity, low

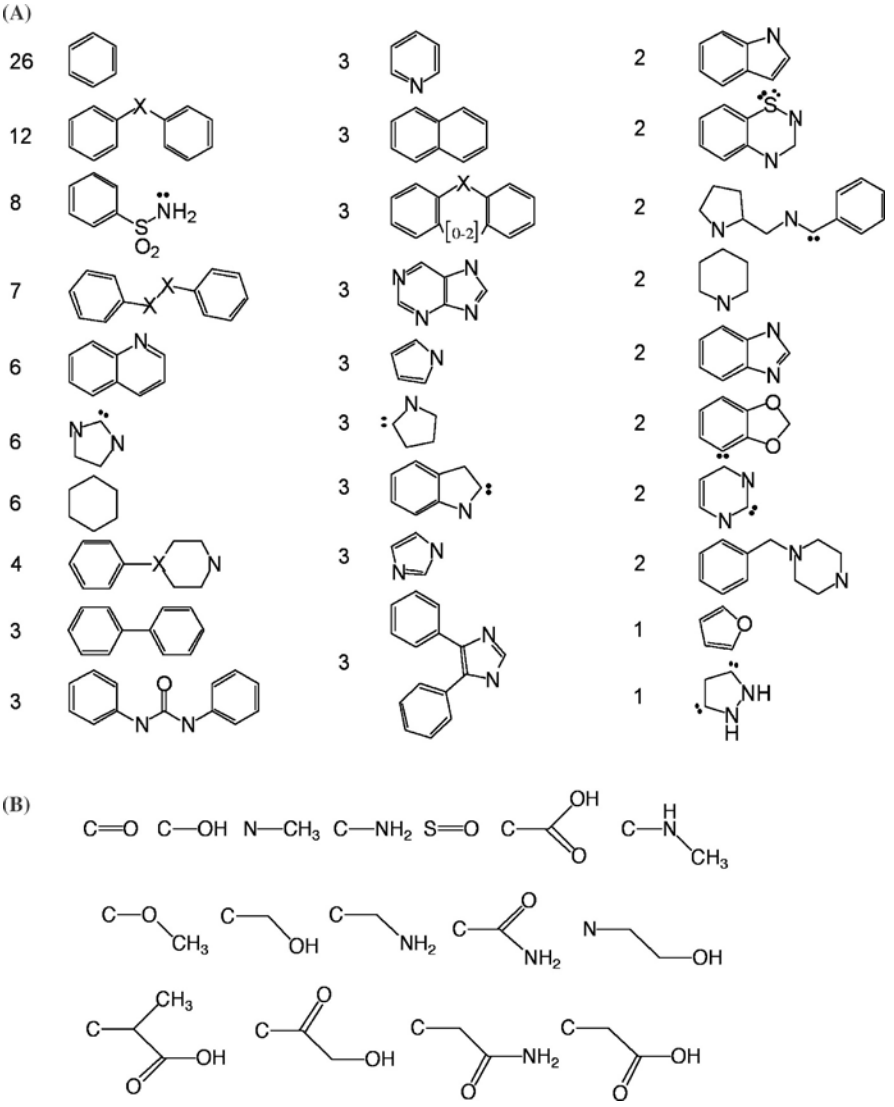

Fig. 2. (A) Molecular frameworks used in the SHAPES library. The numbers denote the frequency of occurrence of each framework. Side chain positions are indicated by lone pairs. "X" denotes a C, N, O, or S atom. Frameworks representing less common classes of drug scaffolds are not shown. (B) Common drug side chains used in the SHAPES library. The left-most atom indicates the point of attachment to the framework. *Source:* Reproduced with permission from ref. [3].

protein consumption, and the ability to tune the detection range of the experiment [3,5]. SHAPES screening hits are validated by detection of inhibition (e.g. by enzymatic assay), competition with a known inhibitor (e.g. by NMR displacement experiment), or localization to the active site (e.g. by NMR chemical shift mapping experiments or crystallographic soaking studies). An example of STD spectra for a mixture of ligands is shown in Figure 3. For nucleic acid targets, WaterLOGSY is the method of choice, as the multiple sites for interaction of water molecules with the nucleic acid molecules compensate for the reduced proton

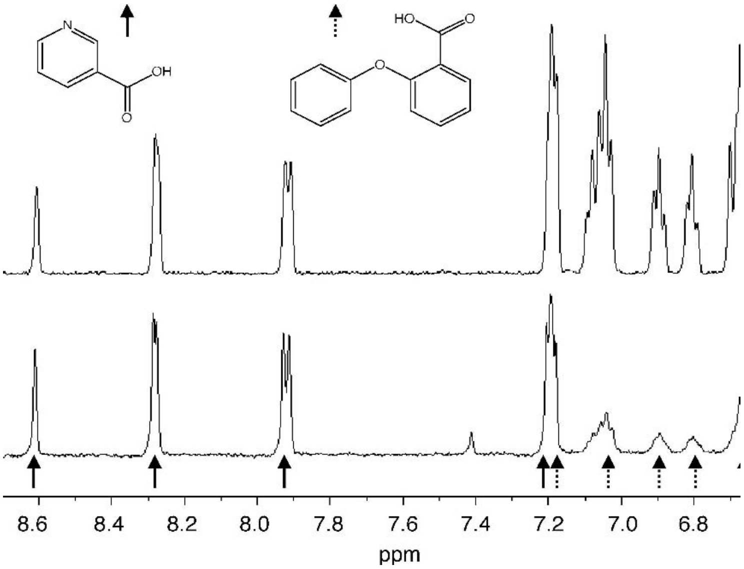

Fig. 3. Comparison of (top) the 1D ^{1}H NMR spectrum of two potential small molecule ligands in the absence of target and (bottom) the STD [18] spectrum of the same mixture in the presence of p38 MAP kinase. Resonances from nicotinic acid and 2-phenoxy benzoic acid are marked with asterisks and diamonds, respectively. Only peaks from the ligand that binds to p38, 2-phenoxybenzoic acid, appear in the STD spectrum. The sample contained 35 μM p38 MAP kinase, 1 mM ligands, 100 mM deutero-Tris, 10% deutero-glycerol, 20 mM deutero-DTT at pD* = 8.4. Experiments were carried out at 278 K. The 1D spectrum was collected using a standard NOESY pulse sequence with 16K data points, 128 transients and a relaxation delay of 3 s. 2K data points were collected with 256 transients each for the on and off resonance spectra. Internal subtraction was achieved via phase cycling. On resonance irradiation was at $\delta = 0.74$ and off-resonance at $\delta = -20$ ppm. A pulse train of 60 Gaussian selective pulses of 50 ms duration separated by a 1 ms delay was used to saturate the protein. *Source:* Reproduced with permission from ref. [3].

density in this class of macromolecule vs. protein targets [6,21].

Implementation of SHAPES Screening

SHAPES screening has been implemented at Vertex at several stages of drug discovery projects: very early in the life cycle, before a conventional enzymatic screen is run to find leads (pre-HTS); in the mid-life of a discovery project, in the event that HTS has not produced viable leads (post-HTS); and late in a project, when mature leads are undergoing final optimization to become preclinical candidates (lead optimization). Effective use of information from SHAPES screens is essential for successful implementation of the method. SHAPES hits are followed up using one or more of three strategies [2,5]: (1) primary hits are combined or linked together into larger, more potent molecules; (2) the scaffolds from primary hits are systematically elaborated by adding functional groups to make more complex molecules; and (3) portions of primary hits or a lead molecule are systematically varied. We present here examples that illustrate these three follow-up strategies applied to each of the three principal implementations of the SHAPES method.

Pre-HTS Screening

SHAPES screening is most commonly applied at the pre-HTS stage of a project, when a new protein first becomes available and the HTS screen is still under development. Because NMR screening requires no assay development and only a few milligrams of protein, it is possible to find SHAPES hits, then purchase analogs or synthesize a combinatorial library around these hits quickly enough to be included in an initial HTS run, thereby enriching the HTS library with scaffolds known to bind to the protein.

Validated hits from pre-HTS SHAPES screens are most often followed up by purchasing more elaborate analogs, as has been described elsewhere [1,7]. Retrospective analysis of HTS screening results has shown that compounds containing SHAPES scaffolds (those shown to bind by NMR) typically have hit rates about tenfold higher than general screening compounds that do not contain those scaffolds [6]. Higher enhancements are possible by designing combinatorial libraries around SHAPES scaffolds. For example, SHAPES screening of regulatory erythroid kinase (REDK) identified a novel class of ATP-competitive inhibitors with IC50s of 100–200 μM. A 64 compound combinatorial library was synthesized around this scaffold, 14 of which (22%) had IC50s better than 5 μM (including several that were sub-micromolar) when subsequently included in the HTS screen. This small, focused combinatorial follow-up library thus improved upon the potency of the primary SHAPES hits by two orders of magnitude and enhanced the HTS hit rate by around 170-fold. The observation of such enhancements validates the assumption that binding information from compounds with weak affinities can lead to discovery of significantly (e.g. several orders of magnitude) more potent inhibitors.

SHAPES screening has also been applied to targets for which high throughput enzymatic assays are unavailable, and can identify reagents for use in developing such assays. These targets include RNA [6,21] and non-enzymatic proteins, such as molecular transport proteins and receptors. For example, SHAPES screening was used as a primary screen to find leads for human adipocyte lipid binding protein (ALBP), a putative therapeutic target for treating type II diabetes [22–26] for which a HTS assay was unavailable. Using a prototype 100-compound SHAPES library, thirteen ligands were found with affinities ranging from 0.3 μM to 800 μM. A fluorimetric assay and chemical shift (^{1}H and ^{15}N) perturbation studies confirmed that these ligands bind in the lipid-binding pocket. Several fluorescent analogs of the SHAPES hits bound avidly in the ALBP lipid-binding pocket, including 1-anilinonapthlalene-8-sulfonic acid (1,8-ANS), which exhibits an apparent dissociation constant of 0.4 μM. These analogs were later used to develop a high-throughput fluorescence-based competition assay.

In order to identify more potent binders, two primary SHAPES hits were soaked into crystals of apo-ALBP and the structures of the complexes solved by crystallography. This structural information, along with molecular models of other hits, was used to identify likely protein interaction sites. Twelve commercially available analogs were screened in order to explore variations at positions predicted to make favorable protein contacts. All of the analogs inhibited lipid binding to ALBP and the bound structures of several were subsequently determined by crystallography. This information was used to design a second-generation follow-up library of 134 commercially available compounds that was calorimetrically screened, yielding nine leads with sub-micromolar affinities, including a compound class with Kd values of 80–100 nM.

Fatty acid binding proteins, unlike most enzymes, have considerable space in the lipid binding pocket that can accomodate a variety of fatty acid substrates as well as bound water molecules. Understanding the binding modes of different ligands by solving multiple crystal structures allows one to derive a pharmocophore model describing key interactions in the binding pocket that may be accessed to achieve higher affinity and selectivity. A pharmacophore model for ALBP based on eight different crystal structures is shown in Figure 4.

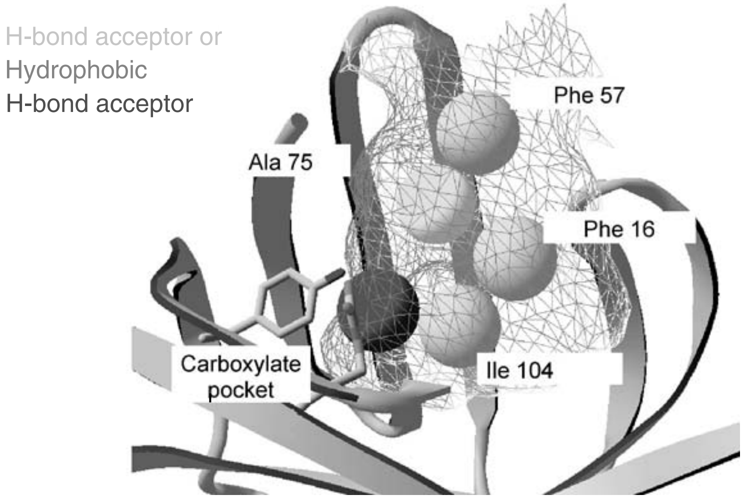

Fig. 4. Pharmacophore model for ALBP derived from ligand binding and crystallographic studies. (See also Plate 110 on page XXIV in the Color Plate Section.)

This example demonstrates that by combining NMR-based screening, computational methods, and X-ray crystallography, it is possible to rapidly converge upon multiple sub-micromolar lead classes (in this case, by testing only ~250 compounds), using modest resources and without requiring chemical synthesis or a HTS assay. The information derived from this work serves as an excellent starting point for a structure-based drug design program for this unique class of drug target.

Post-HTS Screening

We have also applied SHAPES screening to targets for which conventional HTS and medicinal chemistry have failed to produce viable leads. For example, the c-Jun N-terminal kinase Jnk3, a potential target for the treatment of stroke and Parkinson's disease [27,28], was one of the first targets screened by the SHAPES method, after extensive medicinal chemistry efforts to adequately improve the potency of the HTS hits. NMR screening of a 100 compound prototype SHAPES library yielded 17 hits with very weak (approximately millimolar) affinities, 13 of which were confirmed to target the ATP site [7].

Attempts to soak the SHAPES hits into crystals of apo-Jnk3 for crystallographic studies were unsuccessful (presumably due to their low affinity). In the absence of structural information about the bound hits, two approaches were taken to design follow-up libraries. First, approximately 200 analogs containing combinations of binding fragments were chosen by using substructure-matching and similarity based searches of a database of commercially available compounds.

Second, compounds were selected using a virtual screening procedure. The SHAPES screening hits were computationally docked into the ATP site of the crystal structure, and four produced distinct, energetically reasonable bound orientations. A substructure search for commercially available analogs was then carried out using the four preferred molecules, followed by filtering for drug-like character [12], to give a starting set of 1647 compounds. These candidates were then docked into the ATP site and the best 171 conformers from the consensus of four scoring functions [29] were then manually reduced to 94 top picks.

These procedures selected approximately 300 compounds that were then screened in an enzymatic assay, yielding 8 inhibitors with potency better than 20 μM, a hit rate tenfold higher than was observed in the original HTS screen of Jnk3 using a random compound library. Interestingly, none of the SHAPES-derived inhibitor classes were found in the original HTS screen of Jnk3, even though compounds containing those scaffolds were present in the random HTS library. The compounds representing those scaffolds in the HTS library are more highly elaborated, which presumably reduces the likelihood of binding. The unelaborated SHAPES scaffolds are more likely to bind, albeit with affinities too weak to detect reliably by enzymatic methods. These results support the idea that NMR screens of weakly binding scaffolds can be used to direct HTS to novel classes of compounds that might otherwise be missed.

The SHAPES leads were followed up by medicinal chemistry after efforts to develop the leads from the original HTS screen were unsuccessful. Several hundred compounds were prepared (mostly in combinatorial libraries) based on four SHAPES-derived leads, producing three sub-micromolar classes of compounds, shown in Figure 5. X-ray structures of examples from each class of compounds complexed to Jnk3 suggested routes for improving the potency of these inhibitors. By incorporating substituents to access all available binding pockets in the active site, a number of compounds were synthesized which were able to inhibit Jnk3 activity with potencies better than 10 nM.

Lead Optimization

NMR screening of molecular fragments has been used by other laboratories to selectively optimize portions of existing lead molecules for the purpose of improving potency, novelty, or ADME properties [30,31]. A recent example from our own laboratory combines virtual screening and NMR screening to selectively optimize a portion of an ATP site inhibitor of a protein kinase involved in inflammation. The original lead molecule consisted of three fragments (depicted schematically in Figure 6): a central scaffold, a group that hydrogen-bonds to the protein backbone of the inter-domain hinge and a group that forms an unusual salt bridge with nearby charged side chains. The latter group was of particular interest because optimizing this novel interaction offered a potential means to improve the selectivity for this kinase vs. other kinases.

An NMR screening library of fragments targeting the salt bridging site was selected using virtual screening. The ATP-site conformation derived from the crystal structure of the lead compound bound to an analogous kinase was used as a template for computationally docking 20,000 small, commercially available compounds, which were pre-selected for their putative salt bridging ability. Twenty-four compounds were then manually chosen from the best-scoring 0.8% of docked compounds; these were purchased and screened by NMR. Fourteen of these compounds (58%) bound to the kinase with potencies in the millimolar range. The hit rate with this virtual screening-derived library was approximately fivefold higher than that measured for a comparable NMR screen that used the diverse SHAPES library. The binding site of the NMR hits was determined by using a double

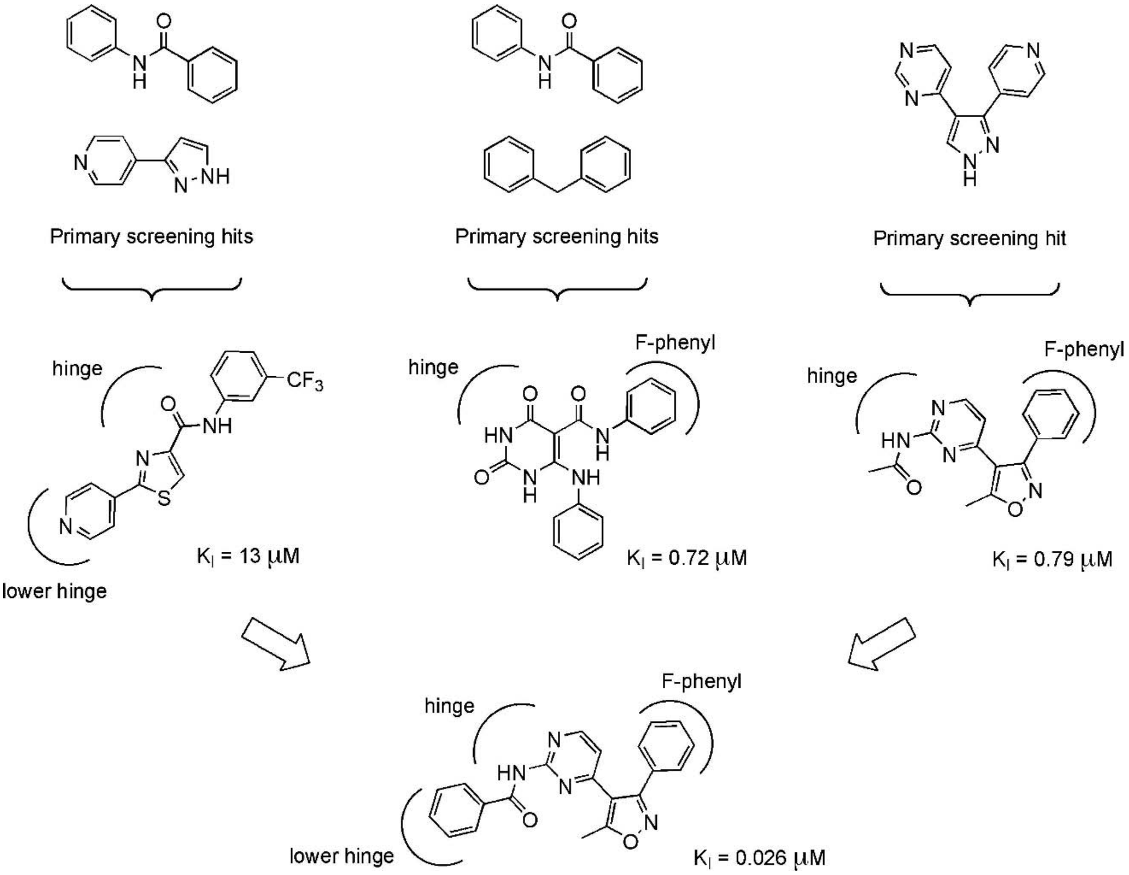

Fig. 5. Evolution of Jnk-3 SHAPES screening hits into potent leads. The SHAPES hits (top row) were followed up by screening commercially available compounds containing random combinations (left and center columns) and variations (right column) of scaffolds found in the primary hits. Crystal structures of the three lead classes (center row) revealed three ATP site subsites (hinge, fluorophenyl pocket, and lower hinge pocket) that were occupied by functional groups on the lead molecules. Each lead molecule contacts two of the three subsites, leading to synthesis of a third generation molecule (bottom row) that contacts all three. *Source*: Reprinted with permission form ref. [5].

knockoff filter (Figure 6), a two-step competition binding experiment that first uses a moderate-affinity inhibitor that binds only to the core and hinge sites, followed by a high-affinity inhibitor that binds to all three sites. Ten of the 14 hits (71%) behaved as expected in the double knockoff filter, indicating that they bound at the salt bridge site.

This example demonstrates that the combination of virtual and NMR screening can be used not only to enrich a library with active compounds, but also to preferentially discover compounds that bind to a desired site. Intermolecular NOEs or chemical shift perturbation data can then be used to determine the relative proximity and orientation of the bound fragments, enabling the design of more potent linked compounds. In this manner, thousands of putative replacement fragments can be efficiently screened prior to carrying out chemical synthesis.

Conclusion

NMR SHAPES screening can be an extremely useful tool for the identification of drug leads. Even in the absence of HTS hits, the SHAPES screening process is capable of identifying chemically accessible, drug-like fragments that can be rapidly translated into potent lead compounds. As illustrated in the examples, the unique ligand-binding data derived from NMR SHAPES screening and subsequent integration with other enabling technologies (such

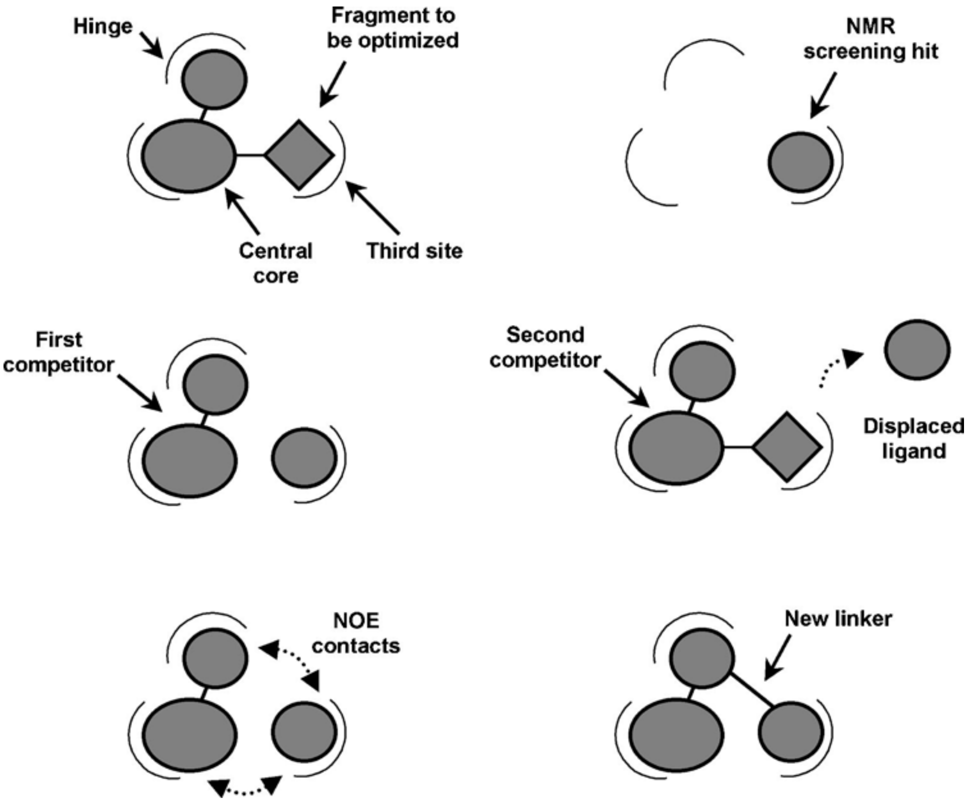

Fig. 6. Fragment optimization process. The original lead molecule (top left) consists of a hinge-binding motif, central scaffold, and a functional group (diamond) to be optimized in the third subsite. A library of fragments is selected by virtual screening and the binding fragments are identified by NMR screening (top right). The binding site of a NMR screening hit with low (e.g. millimolar) affinity is determined using a double knockoff competition experiment. The binding (or displacement) of the NMR hit at each step is measured using the same NMR method as was used for the screen. First, the sample is spiked with a moderate (e.g. micromolar) affinity competitor compound that occupies only the hinge and central sites (center left); if the NMR hit is in the third site it will not be displaced. The sample is then spiked (center right) with a second competitor compound (i.e. the original lead molecule) that occupies all three sites and has an affinity, high enough (nanomolar) to displace the first competitor; if the NMR hit is in the third s site it will be displaced as well. A new, higher concentration sample containing the first competitor and the NMR is then used to determine the relative orientations of the two bound molecules by means of intermolecular NOEs (lower left). Using this information, a linked compound is designed, possibly even incorporating a novel linkage site (lower right).

as X-ray crystallography, computational chemistry, and other biochemical and biophysical techniques) can greatly accelerate the discovery of lead molecules, as well as aid in optimization of existing leads.

References

1. Lepre CA. Drug. Discov. Today 2001;6:133.
2. Lepre CA. In: O Zerbe (Ed). Strategies for NMR Screening and Library Design. Wiley-VCH: Weinheim, 2003, p 1349.
3. Peng JW, Lepre CA, Fejzo J, Abdul-Manan N, Moore JM. Methods Enzymol. 2001;338:202.
4. Peng JW. Prog. Nucl. Mag. Reson. Spectrosc. 2004;44: 225.
5. Lepre CA, Moore JM, Peng JW. Chem. Rev. 2004;104: 3641.
6. Lepre CA, Peng J, Fejzo J, Abdul-Manan N, Pocas J, Jacobs M, Xie X, Moore JM. Comb. Chem. High Throughput Screen. 2002;5:583.
7. Fejzo J, Lepre, C, Xie, X. Curr. Top. Med. Chem. 2002;2: 1349.
8. Bemis GW, Murcko MA. J. Med. Chem. 1996;39:2887.

9. Bemis GW, Murcko MA. J. Med. Chem. 1999;42:5095.
10. Teague SJ, Davis AM, Leeson PD, Oprea T. Angew. Chem. Int. Ed. 1999;38:3743.
11. Lipinski CA, Lombardo F, Dominy BW, Feeny PJ. Adv. Drug Deliv. Rev. 1997;23:3.
12. Walters WP, Stahl MT, Murcko MA. Drug. Discov. Today. 1998;3:160.
13. Jarvis RA, Patrick EA. IEEE Trans. Comput. 1973;C-22:1025.
14. Dalvit C, Fasolini M, Flocco M, Knapp S, Pevarello P, Veronesi M. J. Med. Chem. 2002;45:2610.
15. Dalvit C, Flocco M, Knapp S, Mostardini M, Perego R, Stockman BJ, Veronesi M, Varasi M. J. Am. Chem. Soc. 2002;124:7702.
16. Shuker SB, Hajduk PJ, Meadows RP, Fesik SW. Science 1996;274:1531.
17. Pellecchia M, Meininger D, Dong Q, Chang E, Jack R, Sem DS. J. Biomol. NMR 2002;22:165.
18. Mayer M, Meyer B, Angew. Chem. Int. Ed. 1999;38:1784.
19. Dalvit C, Pevarello P, Tato M, Veronesi M, Vulpetti A, Sundstr Möm. J. Biomol. NMR 2000;18:65.
20. Dalvit C, Fogliatto G, Stewart A, Veronesi M, Stockman B. J. Biomol. NMR. 2001;21:349.
21. Johnson EC, Feher VA, Peng JW, Moore JM, Williamson JR. J. Am. Chem. Soc. 2003;125:15724.
22. Hotamisligil GS, Johnson RS, Distel RJ, Ellis R, Papaioannou VE, Spiegelman BM. Science. 1996;274:1377.
23. Scheja L, Makowski L, Uysal KT, Wiesbrock SM, Shimshek DR, Meyers DS, Morgan M, Parker RA, Hotamisligil GS. Diabetes 1999;48:1987.
24. Uysal KT, Scheja L, Wiesbrock SM, Bonner-Weir S, Hotamisligil GS. Endocrinology 2000;141:3388.
25. Layne MD, Patel A, Chen YH, Rebel VI, Carvajal IM, Pellacani A, Ith B, Zhao D, Schreiber BM, Yet SF, Lee ME, Storch J, Perrella MA. FASEB J. 2001;15:2733.
26. Makowski L, Boord JB, Maeda K, Babaev VR, Uysal KT, Morgan MA, Parker RA, Suttles J, Fazio S, Hotamisligil GS, Linton MF. Nat. Med. 2001;7:699.
27. Bruckner SR, Tammariello SP, Kuan CY, Flavell RA, Rakic P, Estus S. J. Neurochem. 2001;78:298.
28. Xia XG, Harding T, Weller M, Bieneman A, Uney JB, Schulz JB, Proc. Natl. Acad. Sci. U.S.A. 2001;98:10433.
29. Charifson PS, Corkery JJ, Murcko MA, Walters WP. J. Med. Chem. 1999;42:5100.
30. Hajduk PJ, Gomtsyan A, Didomenico S, Cowart M, Bayburt EK, Solomon L, Severin J, Smith R, Walter K, Holzman TF, Stewart A, McGaraughty S, Jarvis MF, Kowaluk EA, Fesik SJ. J. Med. Chem. 2000;43:4781.
31. Hajduk PJ, Burns DJ, Comb. Chem. High Throughput Screen. 2002;5:613.

NMR-Based Screening Applied to Drug Discovery Targets

Jennifer J. Gesell, Mark A. McCoy, Mary M. Senior, Yu-Sen Wang, and Daniel F. Wyss
Schering-Plough Research Institute, Department of Structural Chemistry, Kenilworth, NJ 07033, USA

Abstract

While conventional bioassay-based high-throughput screening (HTS) remains a mainstream approach for lead discovery, its limitations have driven the development of alternative and complementary tools. In this regard, novel NMR-based approaches that have emerged over the last few years show great promise. We have used NMR-based screening approaches for a variety of drug targets to identify low molecular weight (MW) small molecule hits from customized libraries, which subsequently could be optimized into leads through focused, structure-guided chemistry. Focus was placed on targets for which HTS failed to identify suitable leads. This report discusses different NMR-based screening techniques and follow-up strategies for lead discovery and illustrates their application to the NS3 protease and NS3 helicase domains of the hepatitis C virus (HCV).

NMR for Lead Discovery

NMR methods are solidly established for studying molecular interactions [1]. In the last few years various NMR approaches have been developed to aid in lead discovery [2–13]. They involve different NMR screening methods [14–34] to identify initial compounds which often bind only weakly, in the μM–mM range, to the drug target. Intelligent and focused follow-up strategies enable their development into potent, sub-μM inhibitors for use as leads in drug discovery projects [35–46]. An interesting NMR-based biochemical screening method was also recently introduced [47]. NMR-based screening has several advantages over more traditional screening methods which are important for lead discovery: (1) it can reliably detect site-specific ligand binding even for compounds with very weak affinities which are typically missed in HTS (dissociation constants (K_D) up to $\sim 10^{-2}$–10^{-1} M); (2) it is a universal screening technique that unlike bioassays, requires no prior knowledge of a protein's function and therefore, does not require the development of specific assays for each target; (3) it allows the concomitant determination of K_D (or K_I) values over a large affinity range and thus, provides structure-activity relationship (SAR); information (4) it can provide crucial structural information for both the target and the ligand with atomic resolution for the subsequent optimization of weak initial hits into strongly binding lead candidates; (5) it can report on the quality of either the target or the ligand during the NMR screen which reduces the rate of false positives; (6) it is less prone to false positives due to trace contaminants; (7) the final lead does not need to be present in the initial screening library and because affinity is built up progressively, it is derived from a large virtual library. Despite these advantages, once higher affinity ligands are produced, it is always prudent to verify that they show the desired activity in a functional bioassay. Although NMR screening is, in principle, slower than conventional HTS, it can provide good, reliable starting points for focused chemistry to produce leads.

NMR-Based Screening Techniques

Many NMR observables can be used to monitor small molecule-protein interactions as a consequence of either global effects or local effects which occur upon complex formation [6,7,20]. Because the small molecule ligand adopts motional properties in the bound state that are similar to those of the drug target (slow motion), but very different from those in its unbound state (fast motion), observation of ligand binding based on global effects is restricted to the small molecule ligand where the effects are most pronounced. On the other hand, local NMR effects of complex formation such as intermolecular magnetization transfer or chemical shift perturbations (CSP) may be observed on the protein target and/or the small molecule ligand. In addition, structural information may be available as effects are mostly localized at the intermolecular binding sites.

NMR methods for detecting ligand-binding fall into two main categories that are based on whether signals from the protein target or the ligand are monitored (see also the reports by P.J. Hajduk and J.M. Moore in this volume). Methods within each category have inherent limitations, such as sample availability, solubility, stability, and molecular size, which dictate the choice of the NMR

Graham A. Webb (ed.), Modern Magnetic Resonance, 1419–1428.
© 2008 *Springer.*

screening approach taken to discover hits for a particular drug target.

Target-Detected 2D Heteronuclear NMR-Based Screening

We have used 2D heteronuclear NMR-based screening, in which the protein target is isotopically labeled with ^{15}N or ^{13}C, to assist lead discovery in several programs. HSQC-based screening detects ligand-binding based on chemical shift changes of protein signals which occur near the ligand-binding site. HSQC-based screening is simple (a single tube experiment with only the target and compound), robust (isotopic editing ensures that only the protein target is observed), and information-rich. The NMR correlation spectra not only give detailed information about whether the compound binds, with virtually no limit on the K_D value, but also yield a distinct pattern of CSP that serves as a fingerprint for binding to a specific region of the protein target. Thus, compounds that bind at the active site can be readily distinguished from those that bind outside the active site, or that, for one reason or another, do not bind to the target of interest at all. If CSP of the protein target are analyzed in a more quantitative manner, often the exact ligand-binding site can be determined rapidly [7,48]. In addition, the detailed binding orientation of the ligand with respect to the protein surface may be available, especially if good quality CSP data of closely related ligands are available [7,49] (Figure 1 and see below).

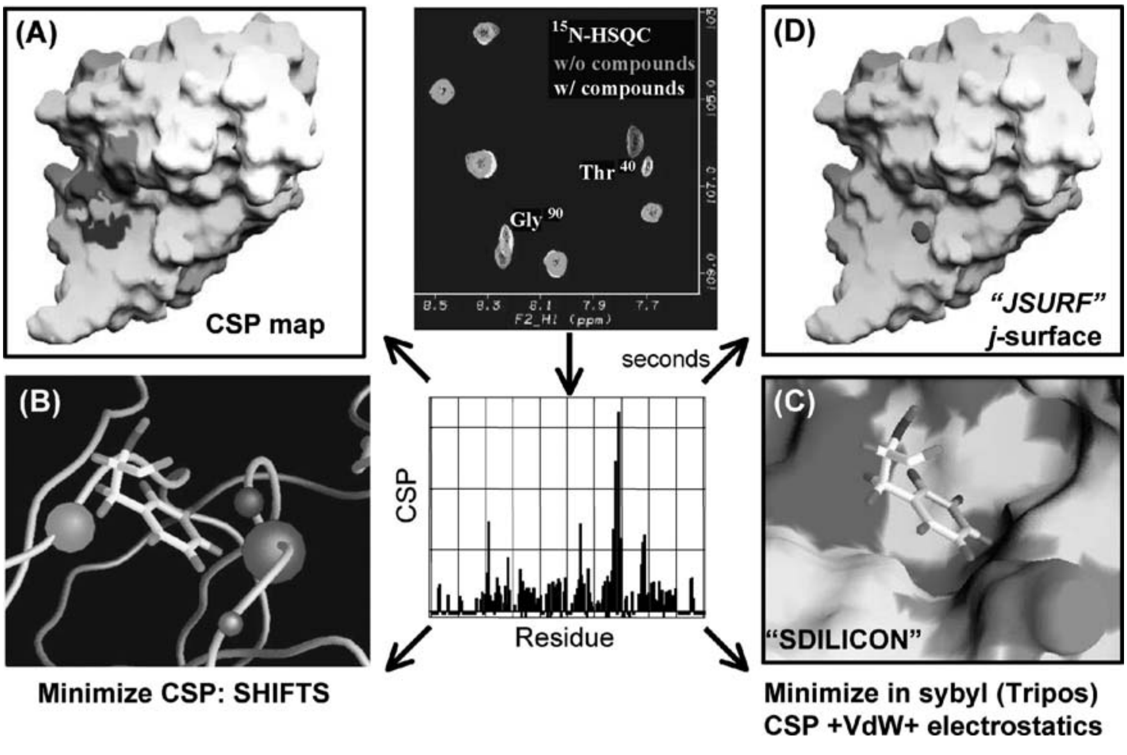

Fig. 1. New tools to determine structures of protein-small molecule ligand complexes using NMR chemical shift perturbation. (A) A CSP map is used to approximate the interaction site of an aromatic ligand binding to the HCV NS3 protease domain [7]. This map was created by coloring protein residues for which significant CSP (center) were observed in ^{15}N-^{1}H HSQC spectra; each color represents a different residue. The resulting map is diffuse; it suggests that the ligand binds the unprimed side of the substrate channel but no particular site is suggested by this data. (B) Ring location and orientation is determined on an atomic level by minimizing the difference between experimental and simulated CSP [49]. (C) Ring location and orientation when energy minimized against van der Waals and CSP [7]. (D) A ligand j-surface (magenta), created from the same data used in Figure 1A localizes the ligand-binding site to the S$_1$-pocket [48]. Recently, these procedures have been implemented into two programs, "SDILICON" and "JSURF" (http://tonga.usip.edu/gmoyna/sdilicon/index.html). (See also Plate 111 on page XXIV in the Color Plate Section.)

HSQC spectra can also reveal if the protein target was folded during the screen or if addition of the compound mixture caused the drug target to aggregate, unfold or precipitate. The verification of the chemical structure of NMR-detected hits by NMR and mass spectrometry and the determination of their aqueous solubility under the screening conditions using NMR, make this type of screen very reliable. Moreover, HSQC-based NMR titrations can be used to determine accurate K_Ds for weakly interacting ligands which are in fast exchange on the NMR time scale between their bound and free states (typically $K_D >\sim 10\mu$M).

However, efficient application of HSQC-based screening requires large amounts of isotope-labeled protein and is typically limited to smaller proteins (MW >~40–60 kDa). This restricts its application to a subset of proteins which do not aggregate at concentrations around 100 μM in an aqueous buffer, and to those that can be overproduced in high isotope-labeled yields (mg/l cell culture). Therefore, several ligand-detected 1D NMR screening methods have emerged over the last few years [7,8,15,17,18,20,30–33] which require no isotope labeling of the target, use significantly less target (micrograms vs. milligrams), and are for proteins of almost any MW.

Ligand-Setected 1D NMR-Based Screening

The saturation transfer difference (STD) [15] and water-ligand observed via gradient spectroscopy (WaterLOGSY) [17,18] experiments are the most sensitive methods in this category. The STD method relies on transfer of saturation to detect ligand binding; only STD signals from compounds in a mixture which directly interact with the drug target are observed. STD NMR is based on the intermolecular transfer of saturation from the protein to the bound small molecule ligands which in turn, by fast chemical exchange between their bound and unbound states, is moved into solution where it is detected. For high-affinity ligands, the saturation cannot effectively be transferred further to the free state of the small molecule ligands due to slow chemical exchange resulting in no observable STD effect, that is, ligand peaks are not observed in the difference spectrum. WaterLOGSY is a related experiment that is based on the transfer of magnetization from bulk water to the protein binding site and onto a bound ligand. The concentrations of both the protein and the compound mixture can be adjusted to adjust the sensitivity of such screens.

Because the ligand-detected methods usually require no isotope labeling of the protein, use less protein (~10–1000× less) than the target-detected approaches, can be applied to protein targets of almost any MW (even perform best for large proteins), and are useful when no 3D structure of the drug target is available, they are widely used in the pharmaceutical industry. However, these methods do not reveal the ligand-binding site on the drug target and any structural information available is limited to the binding epitope of the small molecule ligand. In general, these methods are only for weaker ligands ($K_D \sim 10^{-7}-10^{-3}$ M) and compounds must be soluble in an aqueous buffer solution at concentrations of at least ~50–200 μM, which prevents the detection of ligands with high affinity and/or low solubility. In our experience, these screening methods are less robust and produce more false positives than 2D heteronuclear NMR screening for reasons such as non-specific binding and compound aggregation. However, many of these drawbacks can be overcome by combining ligand-observed NMR screening methods with competition binding experiments [24–28]. Therefore, we recently implemented a competition STD NMR method which can be used to identify ligands that bind to the same site as, for example, a natural substrate, a cofactor or a known inhibitor of a protein drug target [50].

STD NMR in Combination with Competition Experiments

A site-specific affinity marker is used in this experiment which binds weakly to an interesting subsite of the drug target (K_D typically in the tens-to-hundreds of μM range) and produces strong STD signals. Reduction or disappearance of the STD signal of the site-specific affinity marker upon addition of a compound mixture suggests the presence of at least one ligand in the mixture which competes with the marker for binding to the active site (Figure 2A). We have used this approach to screen a kinase-directed library of novel, chemically accessible cores against a variety of kinases. An example is shown in Figure 2B, in which we used ATP as a site-specific affinity marker in competition experiments (c-STD[ATP]). ATP binds this particular kinase with a K_D of ~30 μM and produces an STD signal for the H-2 proton of ATP at 8.30 ppm when 200 μM ATP are added to 5 μM of this kinase target. Addition of a sub-μM ligand which competes for binding to the ATP site completely removes the STD signal of ATP and this high-affinity binder does not produce an STD epitope itself. Addition of a ligand in the μM range still effectively competes with ATP, but now generates an STD epitope due to increased exchange between its bound and unbound states. A weaker binder in the tens of μM range only partially competes with ATP and produces an even stronger STD epitope due to increased exchange. This example illustrates that c-STD[ATP] can be used to (1) rapidly rank-order the affinity of ATP-competitive binders and (2) detect high-affinity ligands which would be missed in the simple STD NMR experiment.

This method can also be used to determine K_I's of high-affinity ligands which are in slow chemical exchange

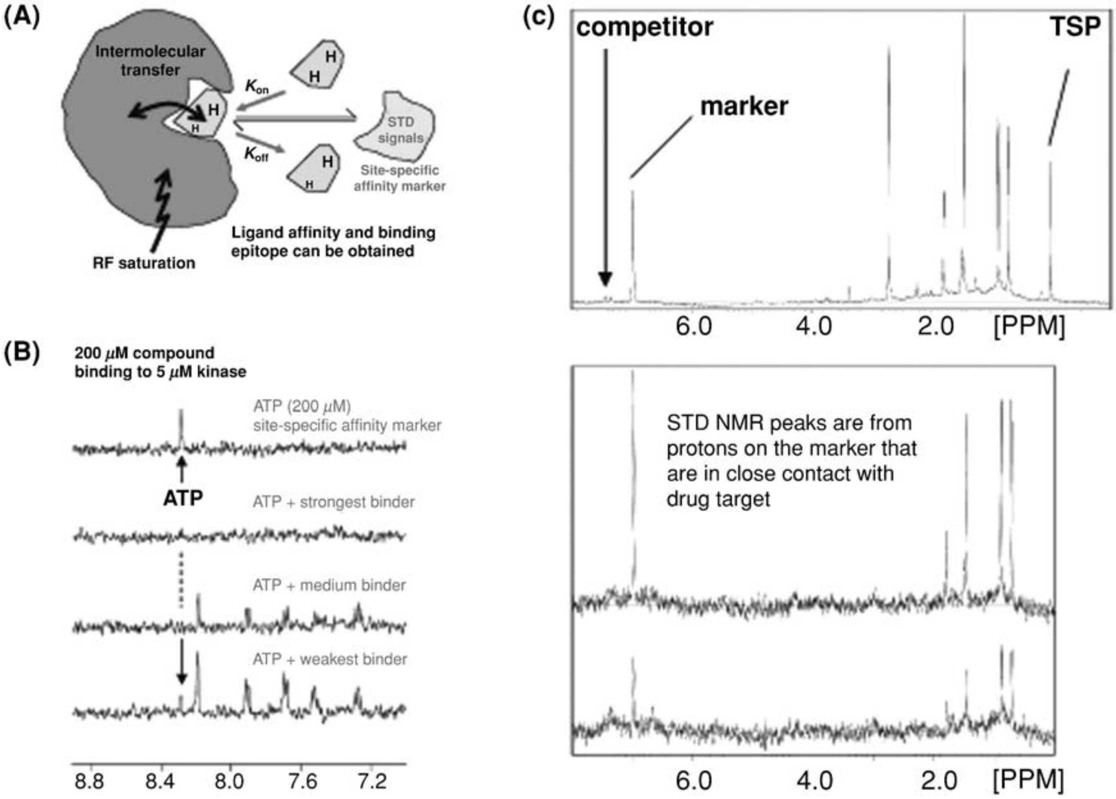

Fig. 2. 1D competition STD NMR [50].(A) A ligand which binds weakly to an interesting subsite of the drug target weakly (K_D typically in the tens-to-hundreds of μM range) and produces strong STD signals is used as a site-specific affinity marker. Reduction or disappearance of the STD signal of the site-specific affinity marker upon addition of a compound mixture suggests the presence of at least one ligand in the mixture which competes with the marker for binding to the same subsite. (B) c-STD[ATP] NMR spectra of a kinase (from top to bottom) in the absence of ligand and in the presence of a strong, medium and weak ATP-competitive binder at a concentration of 200 μM each (see text), illustrating its use to rapidly rank-order the affinity of ATP-competitive binders including high-affinity ligands which do not produce STD signals. (C) K_I's of high-affinity ligands which are in slow chemical exchange on the NMR time scale (K_D typically sub-μM) can also be determined with this method (see text). Addition of 140 μM of an active site-specific affinity marker (K_D[^{15}N-HSQC] = 60 μM) to 5.6 μM kinase produces strong STD signals in a reference spectrum (middle). Addition of 6.1 μM high-affinity inhibitor reduces the STD signals of the site-specific affinity marker (bottom). Based on this reduction and the experimentally determined ligand concentration relative to an internal standard TSP (top) yielded a K_I of 330 nM for the high-affinity ligand.

on the NMR time scale; this cannot be achieved with HSQC-based NMR titration experiments. Recently, we used this method in a drug discovery program to determine the K_I's of sub-μM NMR-derived lead inhibitors. An active site-specific affinity marker with a K_D[^{15}N-HSQC NMR] of 60 μM was used which produced strong STD signals in a reference spectrum (Figure 2C). Addition of small amounts of the high-affinity inhibitor then reduced the STD signals of the site-specific affinity marker. Based on this reduction and the experimentally determined ligand concentration relative to an internal standard (TSP) yielded a K_I of 330 nM for the high-affinity ligand. A second experiment with a different site-specific affinity marker (K_D of 120 μM) gave a similar K_I of 360 nM for the high-affinity ligand (data not shown), which was in good agreement with the IC_{50} of 500 nM from a homogenous time-resolved fluorescence (HTRF)-based enzymatic assay.

NMR–Based Screening Applied to Drug Targets

We have used NMR to assist lead generation in a number of difficult drug discovery programs in which HTS of large chemical libraries identified either no, or only a few, suitable leads for chemical optimization (Table 1) [51]. NMR-based screening (previous section) of customized libraries containing several hundred to several thousand small molecules identified multiple weak hits to active-site regions of these drug targets in the μM–mM range. Some of these initial hits were followed-up through the evaluation of analogs by a combination of NMR, X-ray crystallography and bioassays to derive SAR and 3D structural data. Interesting scaffolds were subsequently either linked, or further optimized by the parallel synthesis of a large number of analogs, or used as templates for structure-based inhibitor design to develop novel lead series against a variety of these targets.

A critical step in these fragment-based methods [2,3,10], which take a modular approach to drug design, is the optimization of weak NMR hits ($K_D \sim \mu$M–mM range) into potent leads ($K_D < \mu$M) using chemistry guided by 3D structural data. However, such information cannot always be obtained easily. We have, therefore, developed novel tools, which utilize protein CSP data, generated in HSQC-based NMR screens, to rapidly provide an accurate structural representation of protein-ligand complexes under conditions unfavorable for traditional structural work using X-ray crystallography and/or solution NMR [48,49]. These tools use the CSP data in a more quantitative manner than the traditional “chemical shift perturbation mapping” widely used to qualitatively map

Table 1: NMR-based screening applied to drug discovery targets

Drug targets	MW (kDa)	# HTS leads	# compounds screened	# NMR hits to active site(s) [affinity range]	# NMR hit-to-lead [affinity/activity range]	# sub-sites	X-ray structure with NMR hit	Chemistry approach [lead activity]
CNS	46	0	10,100 HSQC	10 [30 μM–mM]	6 series [15–100 μM]	3	yes	• structure-based • directed libraries on-going [<0.03 μM]
Cancer	13	0	6750 HSQC	62 [<700 μM]	3 series [1–100μM]	4	no	• link • directed libraries [<0.05 μM]
Cancer	37–40	1	Hundreds (in progress) HSQC/STD	>20 [5–500 μM]	4 series (in progress)	1	One	• Directed libraries on-going [<0.6 μM]
HCV NS3 protease—NS4A	20	0	3639 HSQC	16 [100 μM–10 mM]	5 series [100 μM–mM]	3–5	No	• Directed libraries • Link [0.8 μM]
HCV NS3 helicase	15/30/49	0	6006 HSQC	19 [mM range]	5 series [100 μM–mM]	3	Yes	• Structure-based • Directed libraries [3.0 μM]
Anti-viral	64	0	Hundreds STD	Few [<500 μM]	1 series [400 μM]	1	Yes	• Directed libraries [20 μM]
Cancer	42	Few	Hundreds (in progress) c-STD [ATP]	>60 [0.4–500 μM]	7 series (in progress)	>2	One	Being initiated
Cancer	48	Few	Hundreds (in progress) c-STD [ATP]	>60 [<0.7–500μM]	Not initiated	>2	No	Not initiated
Anti-infective	41	0	3647 HSQC	13 [~mM]	3 series [50 μM–mM]	3	Yes	Not initiated

molecular interfaces, and hence, they allow rapid determination of the ligand-binding site with much higher precision [7] (Figure 1). By carefully comparing CSP data of closely related analogs, these methods also often enable an unambiguous determination of the binding mode of a small molecule ligand.

The following sections describe our application of target-detected NMR approaches to assist the discovery of leads against the HCV NS3 protease [46] and HCV NS3 helicase [51] domains. Table 1 lists additional programs in which target- or ligand-detected NMR-based screening was used as a primary assay and the chemistry approaches that were applied to develop leads from the NMR-derived hits [51].

NMR-Derived Competitive Non-Peptide Inhibitors of the HCV NS3 Protease

The RNA virus hepatitis C (HCV) has chronically infected an estimated 170 million people worldwide, of whom 10–20% will ultimately develop cirrhosis and 1–5% will develop liver cancer [52]. The HCV NS3 protein is a 631 amino acid residue bifunctional enzyme with a serine protease localized to the N-terminal 180 residues and an RNA helicase located in the C-terminal 451 residues [53], and represents an attractive molecular target for drug development [54]. Both protease and helicase domains retain their *in vitro* activity [55] and structural integrity [56] when expressed separately. Due to the importance of the NS4A cofactor for efficient catalytic activity and structural integrity [57] of the NS3 protease domain, we used a single chain HCV NS3 protease/NS4A complex (ns4a-ns3p) [58] for our NMR-based screens.

From a customized small molecule library, 3639 compounds were screened against uniformly ^{15}N-labeled ns4a-ns3p protein using 2D ^{15}N-^{1}H HSQC NMR identifying sixteen small molecule hits that bound weakly ($K_D \sim$ 100 μM–10 mM) to substrate binding sites of the NS4A-bound HCV NS3 protease. Analogs for five classes of NMR hits were evaluated by a combination of NMR and biochemical data yielding SAR and, in most cases, optimized hits with improved potencies ($K_D \sim K_I \sim 40\ \mu$M–1 mM). However, we were unsuccessful in determining X-ray crystal structures of complexes between the optimized NMR hits and ns4a-ns3p. Therefore, we used NMR CSP data to establish the binding location and orientation of the active site directed scaffolds in these five analog series (Figure 3A). Based upon the NMR-derived binding mode we produced models of linked molecules in which the S2' binding NMR hits were tethered with the S1-S3 binding NMR hits through various linkers.

Two of these scaffolds, which bind the enzyme at the proximal S1-S3 and S2' substrate binding sites, were linked together producing competitive inhibitors of the HCV NS3 protease with potencies in the μM range (Figure 3B). The linked molecule, SCH-414352, and its diester derivative (SCH-414351) showed competitive inhibition with K_I values in the μM range when tested in the biochemical assay. Thus, the linked compounds are approximately 200-fold and 1000-fold more potent than the individual unlinked NMR-derived scaffolds. This shows that much more potent inhibitors against the HCV protease can be obtained by linking weaker NMR hits based on the NMR data, which was first demonstrated by Fesik and co-workers in their pioneering work on stromelysin [35]. Moreover, SCH-414352 showed sufficient solubility in the aqueous NMR buffer for NMR binding studies. The pattern of CSP values observed for the linked compound was consistent with the proposed model. However, the complex between SCH-414352 and ns4a-ns3p was unstable over a period of days to weeks (slow complex precipitation out of solution) precluding attempts to determine its 3D structure by NMR and/or X-ray crystallography. This example illustrates that the low MW scaffolds discovered from NMR-based screening can be optimized with focused structure-guided chemistry to produce potent non-peptidic small molecule inhibitors of the HCV NS3 protease.

NMR-Derived Lead Inhibitors of the HCV NS3 Helicase

The HCV NS3 helicase is an enzyme which unwinds double-stranded RNA in a NTP-dependent fashion. *In vitro* this activity is stimulated by the addition of single-stranded (ss) nucleic acid. Most RNA helicases are grouped into two major superfamilies based on the occurrence of 7–8 conserved motifs which are implicated in the function of the enzyme. Residues in those motifs contribute to either NTP or RNA binding or couple the energy of NTP hydrolysis to dsRNA unwinding activity. These conserved motifs are localized within the two N-terminal subdomains and line the interfaces between the three subdomains of the HCV NS3 helicase domain. To simplify structural work and target-based NMR screening we optimized the 49 kDa HCV NS3 helicase domain as well as truncated protein versions containing subdomains 1 and 2 either linked or separated as individual subdomains [59]. Because the NS4A-bound protease may affect helicase activity [60], we used the bifunctional enzyme in complex with NS4A co-factor peptide in functional assays to test the inhibitory activity of NMR derived inhibitors.

Using 2D ^{15}N-^{1}H HSQC NMR we screened 6006 compounds from a custom-built small molecule library against an engineered ~30 kDa protein construct containing subdomains 1 and 2 ($d_{1,2\Delta}$–HCVh) in which the NTP binding site, part of the nucleic acid binding surface and all the sequence motifs conserved between SFI and SFII helicases are retained. Nine, eight and two small molecule NMR hits were identified which bound weakly

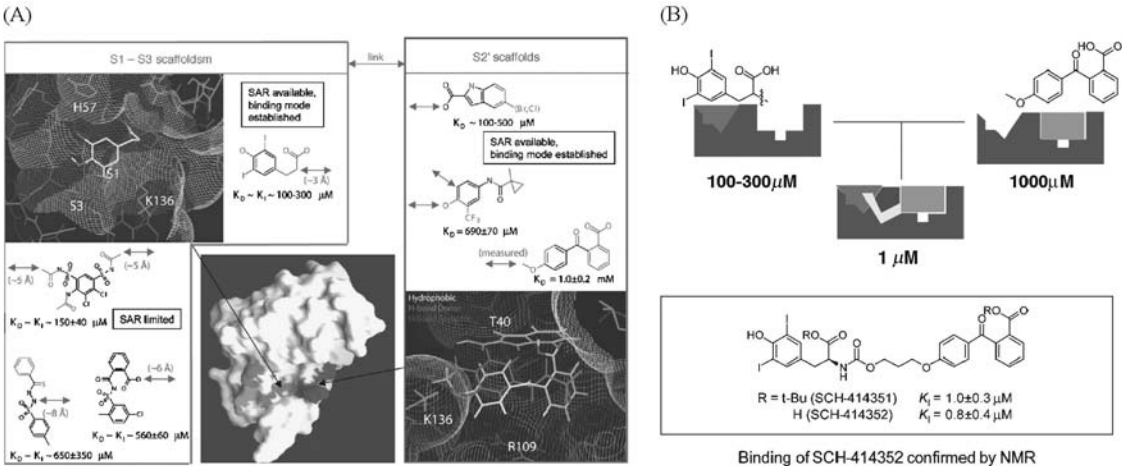

Fig. 3. NMR-derived competitive non-peptide inhibitors of the HCV NS3 protease. (A) NMR-derived binding orientation of optimized NMR hits to proximal substrate binding sites of the ns4a-ns3p [46]. Shown in green parentheses are the approximate distances which would have to be spanned by an appropriate linker in order to connect the S1-S3 scaffolds with the S2′ scaffolds at the respective sites (indicated with green arrows). Red highlights indicate those parts of the chemical structures for which detailed SAR is available. (B) Linking of two NMR-derived scaffolds which weakly bind the enzyme at the proximal S1-S3 and S2′ substrate binding sites yields competitive inhibitors with approximately 200- to 1000-fold increased potencies. (See also Plate 112 on page XXIV in the Color Plate Section.)

($K_D \sim 100\ \mu$M–10 mM) to $d_{1,2\Delta}$–HCVh near the TxGx motif, the NTP binding site, and motif IV, respectively, as judged by the induced protein CSP (Figure 4A). Binding of the NMR hits to the various motifs was confirmed by interaction with the full-length HCV NS3 helicase domain. Four NMR hits to the TxGx motif were followed-up by evaluating related compounds to derive SAR and 3D structural information. Hits to this site were targeted to potentially develop specific and selective HCV helicase inhibitors, since residues in and near this motif are implicated in the function of the enzyme [61,62], involved in ssDNA binding [63], highly conserved across all HCV genotypes, but nevertheless unique to a subgroup of SFII helicases [64].

Two of the NMR-detected hits could be soaked into crystals of the HCV helicase (Figure 4A). The x-ray crystal structure of SCH-482932 in complex with the enzyme (Figure 4B) was used as a starting point in the structure-guided design of lead inhibitors and the construction of focused chemical libraries using high-throughput synthesis methods. NMR-derived SAR showed that the carboxylate is required for binding of SCH-482932 to the HCV helicase domain, the 3-acetic acid and the 5-bromine are optimal, and the framework can be extended at the indole nitrogen to gain affinity. The 3D structure of the SCH-482932/HCV helicase complex suggested that this chemotype could be extended at the N1-position into two nearby conserved binding pockets through a suitable linker X (Figure 4B). Twenty-eight compounds were synthesized based on the 5-bromo-indole-3-actic acid scaffold which contained extensions at the indole nitrogen using either flexible alkyl linkers (3), or more rigid linkers such as amide (3), benzyl (3), benzoyl (1), urea (2), and phenyl (16). Several of these compounds showed K_D and IC_{50} values in the single digit μM range. Interestingly, the phenyl intermediate, SCH-529963, showed ~10-fold improvement in potency over the starting fragment, SCH-482932, and simple substituents at the *ortho* position on the phenyl ring increased its affinity another ~10-fold (Figure 4C). Importantly, the resulting compounds are small, lead-like [65] and suitable for high-throughput chemical library construction to efficiently explore the two nearby binding pockets of the HCV helicase domain.

Conclusion

We have used NMR-based screening as a reliable primary assay which provides chemists with good starting points for the structure-guided development of viable leads that are active-site directed and validated using fragment-based approaches. Focus was placed on targets for which HTS failed to identify suitable leads. NMR-based screening was carried out on a diverse set of targets to identify and optimize novel scaffolds, which subsequently were either linked, or further optimized by the parallel synthesis of a large number of analogs, or used as templates for structure-based inhibitor design. A critical step in these fragment-based methods, which take a

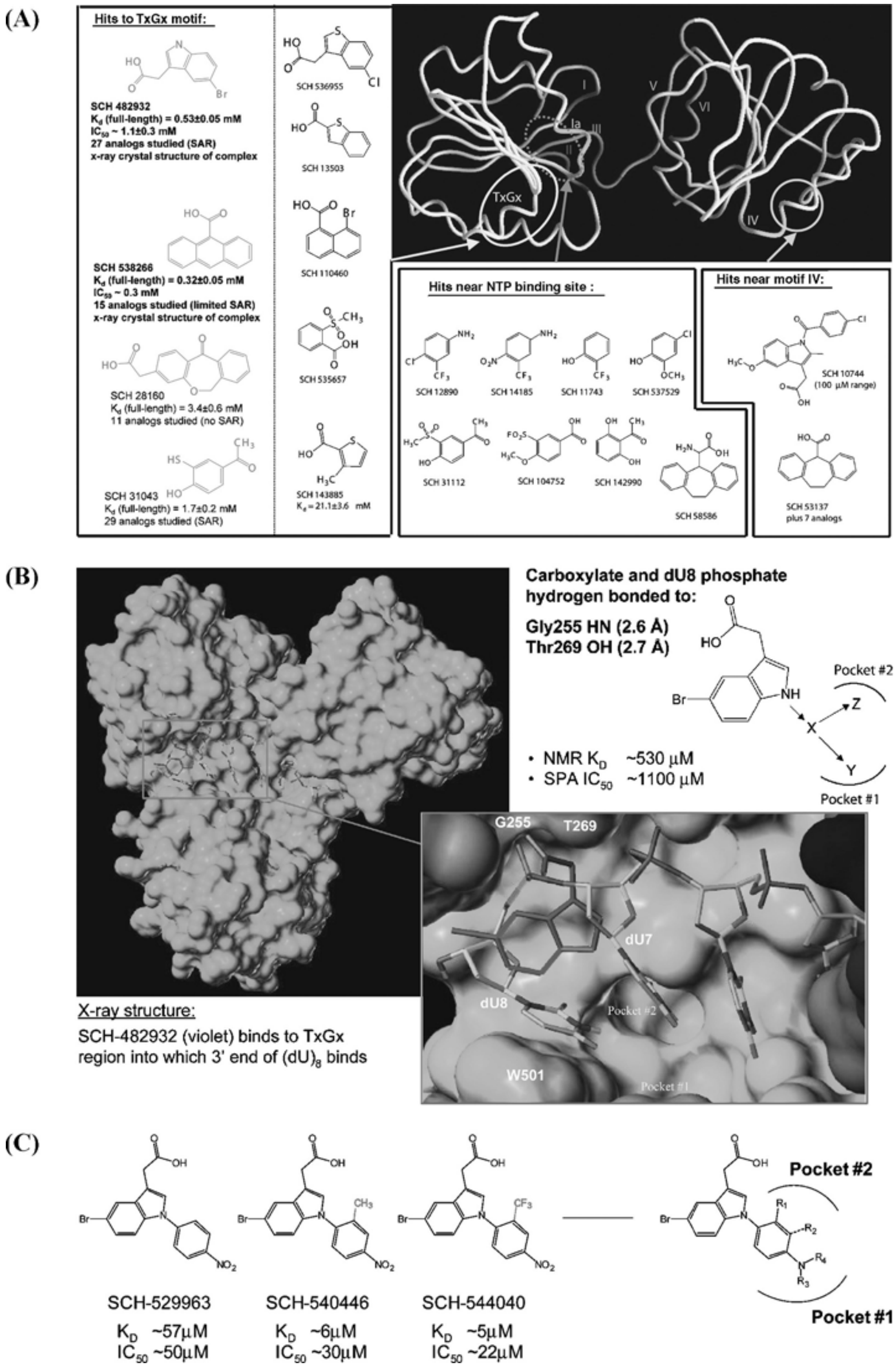
(A)
Hits to TxGx motif:
SCH 482932
Kd (full-length) = 0.53±0.05 mM
IC50 ~ 1.1±0.3 mM
27 analogs studied (SAR)
x-ray crystal structure of complex
SCH 538266
Kd (full-length) = 0.32±0.05 mM
IC50 ~ 0.3 mM
15 analogs studied (limited SAR)
x-ray crystal structure of complex
SCH 28160
Kd (full-length) = 3.4±0.6 mM
11 analogs studied (no SAR)
SCH 31043
Kd (full-length) = 1.7±0.2 mM
29 analogs studied (SAR)
SCH 536955
SCH 13503
SCH 110460
SCH 535657
SCH 143885
Kd = 21.1±3.6 mM
I
Ia
II
III
V
VI
TxGx
IV
Hits near NTP binding site :
SCH 12890
SCH 14185
SCH 11743
SCH 537529
SCH 31112
SCH 104752
SCH 142990
SCH 58586
Hits near motif IV:
SCH 10744
(100 µM range)
SCH 53137
plus 7 analogs
(B)
Carboxylate and dU8 phosphate
hydrogen bonded to:
Gly255 HN (2.6 Å)
Thr269 OH (2.7 Å)
Pocket #2
Pocket #1
• NMR KD ~530 µM
• SPA IC50 ~1100 µM
G255
T269
dU7
dU8
Pocket #2
W501
Pocket #1
X-ray structure:
SCH-482932 (violet) binds to TxGx
region into which 3' end of (dU)8 binds
(C)
SCH-529963
KD ~57µM
IC50 ~50µM
SCH-540446
KD ~6µM
IC50 ~30µM
SCH-544040
KD ~5µM
IC50 ~22µM
Pocket #2
Pocket #1

Fig. 4. NMR-derived lead inhibitors of the HCV NS3 helicase. (A) Validated active-site directed NMR hits identified by 2D ^{15}N-^{1}H HSQC-based NMR screening of 6006 compounds from a customized library against $d_{1,2\Delta}$-HCVh. Four NMR hits (red) to the TxGx motif were followed-up by evaluating related compounds to derive SAR and 3D structural information. (B) Binding orientation of SCH-482932 (in-house crystal structure) relative to bound ssDNA (PDB accession code 1A1V) illustrating that this NMR hit binds to the same subsite as the 3′ end of $(dU)_8$. (C) Simple phenyl extensions at the indole nitrogen of SCH-482932 yields mM HCV helicase lead inhibitors that are amenable to high throughput chemical synthesis. (See also Plate 113 on page XXV in the Color Plate Section.)

modular approach to drug discovery, is the optimization of the often weak NMR hits ($K_D \sim \mu$M–mM) into potent leads ($K_D < \mu$M) using chemistry guided by 3D structural data and SAR. We have implemented a number of NMR-based tools which are designed to facilitate this process.

In addition, we have used the NMR methods described in this report in several programs to validate hits from other sources and rapidly assist the project team chemists in selecting candidate leads for synthetic efforts. In this respect, NMR-derived information often helps to eliminate false positives hits early in the drug discovery process.

References

1. Zuiderweg ERP. Biochemistry. 2002;41:1.
2. Shuker SB, Hajduk PJ, Meadows RP, Fesik SW. Science 1996;274:1531.
3. Hajduk PJ, Meadows RP, Fesik SW. Q. Rev. Biophys. 1999;32:211.
4. Fejzo J, Lepre CA, Peng JW, Bemis GW, Ajay Murcko MA, Moore JM, Chem. Biol. 1999;6:755.
5. Peng JW, Lepre CA, Fejzo J, Abdul-Manan N, Moore JM. Methods Enzymol. 2001;338:202.
6. Pellecchia M, Sem DS, Wüthrich K. Nat. Rev. Drug Discov. 2002;1:211.
7. Wyss DF, McCoy MA, Senior MM. Curr. Opin. Drug Discov. Devel. 2002;5:630.
8. Stockman BJ, Dalvit C. Prog. NMR Spectrosc. 2002;41:187.
9. Hajduk PJ, Burns DJ. Comb. Chem. High Throughput Screen. 2002;5:613.
10. Huth JR, Sun C. Comb. Chem. High Throughput Screen. 2002;5:631.
11. Jahnke W, Flörsheimer A, Blommers MJJ, Paris CG, Heim J, Nalin CM, Perez LB. Curr. Top. Med. Chem. 2003;3:69.
12. Fejzo J, Lepre C, Xie X. Curr. Top. Med. Chem. 2003;3:81.
13. Jahnke W, Widmer H. Cell. Mol. Life Sci. 2004;61:580.
14. Hajduk PJ, Gerfin T, Boehlen JM, Häberli M, Marek D, Fesik SW. J. Med. Chem. 1999;42:2315.
15. Mayer M, Meyer B, Angew. Chem. Int. Ed. Engl. 1999;38:1784.
16. Hajduk PJ, Augeri DJ, Mack J, Mendoza R, Yang J, Betz SF, Fesik SW. J. Am. Chem. Soc. 2000;122:7898.
17. Dalvit C, Pevarello P, Tatò M, Veronesi M, Vulpetti A, Sundström M. J. Biomol. NMR 2000;18:65.
18. Dalvit C, Fogliatto G, Stewart A, Veronesi M, Stockman B. J. Biomol. NMR 2001;21:349.
19. Ross A, Senn H. Drug Disc. Today 2001;6:583.
20. Diercks T, Coles M, Kessler H. Curr. Opin. Chem. Biol. 2001;5:285.
21. Weigelt J, van Dongen M, Uppenberg J, Schultz J, M. Wikström, J. Am. Chem. Soc. 2002;124:2446.
22. Weigelt J, Wikström M, Schultz J, van Dongen MJP. Comb. Chem. High Throughput Screen. 2002;5:623.
23. Jahnke W. Chem. Bio. Chem. 2002;3:167.
24. Dalvit C, Fasolini M, Flocco M, Knapp S, Pevarello P, Veronesi M. J. Med. Chem. 2002;45:2610.
25. Dalvit C, Flocco M, Knapp S, Mostardini M, Perego R, Stockman BJ, Veronesi M, Varasi M. J. Am. Chem. Soc. 2002;124:7702.
26. Jahnke W, Floersheim P, Ostermeier C, Zhang X, Hemmig R, Hurth K, Uzunov DP. Angew. Chem. Int. Ed. 2002;41:3420.
27. Siriwardena AH, Tian F, Noble S, Prestegard JH. Angew. Chem. Int. Ed. 2002;41:3454.
28. Dalvit C, Flocco M, Veronesi M, Stockman BJ, Comb. Chem. High Throughput Screen. 2002;5:605.
29. Dalvit C, Fagerness PE, Hadden DTA, Sarver RW, Stockman BJ. J. Am. Chem. Soc. 2003;125:7696.
30. Meyer B, Peters T. Angew. Chem. Int. Ed. 2003;42:864.
31. Zartler ER, Yan J, Mo H, Kline AD, Shapiro MJ, Curr. Top. Med. Chem. 2003;3:25.
32. Zartler ER, Hanson J, Jones BE, Kline AD, Martin G, Mo H, Shapiro MJ, Wang R, Wu H, Yan J. J. Am. Chem. Soc. 2003;125:10941.
33. Coles M, Heller M, Kessler H, Drug Discov. Today 2003;8:803.
34. Tengel T, Fex T, Emtenas H, Almqvist F, Sethson I, Kihlberg J. Org. Biomol. Chem. 2004;2:725.
35. Hajduk PJ, Sheppard G, Nettesheim DG, Olejniczak ET, Shuker SB, Meadows RP, Steinman DH, Carrera GM Jr, Marcotte PA, Severin J, Walter K, Smith H, Gubbins E, Simmer R, Holzman TF, Morgan DW, Davidsen SK, Summers JB, Fesik SW. J. Am. Chem. Soc. 1997;119:5818.
36. Hajduk PJ, Dinges J, Mikins GF, Merlock M, Middleton T, Kempf DJ, Egan DA, Walter KA, Robins TS, Shuker SB, Holzman TF, Fesik SW. J. Med. Chem. 1997;40:3144.
37. Hajduk PJ, Dinges J, Schkeryantz JM, Janowick D, Kaminski M, Tufano M, Augeri DJ, Petros A, Nienaber V, Zhong P, Hammond R, Coen M, Beutel B, Katz L, Fesik SW. J. Med. Chem. 1999;42:3852.
38. Hajduk PJ, Zhou MM, Fesik SW, Bioorg. Med. Chem. Lett. 1999; 9:2403.
39. Hajduk PJ, Boyd S, Nettesheim D, Nienaber V, Severin J, Smith R, Davidson D, Rockway T, Fesik SW. J. Med. Chem. 2000;43:3862.
40. Hajduk PJ, Gomtsyan A, Didomenico S, Cowart M, Bayburt EK, Solomon L, Severin J, Smith R, Walter K, Holzman TF, Stewart A, McGaraughty S, Jarvis MF, Kowaluk EA, Fesik SW, Med J. Chem. 2000;43:4781.
41. Liu G, Huth JR, Olejniczak ET, Mendoza R, DeVries P, Leitza S, Reilly EB, Okasinski GF, Fesik SW, von Geldern TW. J. Med. Chem. 2001;44:1202.
42. van Dongen M, Weigelt J, Uppenberg J, Schultz J, Wikström M. Drug Discov. Today 2002;7:471.
43. Szczepankiewicz BG, Liu G, Hajduk PJ, Abad-Zapatero C, Pei Z, Xin Z, Lubben TH, Trevillyan JM, Stashko MA, Ballaron SJ, Liang H, Huang F, Hutchins CW, Fesik SW, Jirousek MR, J. Am. Chem. Soc. 2003;125:4087.
44. Liu G, Xin Z, Pei Z, Hajduk PJ, Abad-Zapatero C, Hutchins CW, Zhao H, Lubben TH, Ballaron SJ, Haasch DL, Kaszubska W, Rondinone CM, Trevillyan JM, Jirousek MR. J. Med. Chem. 2003;46:4232.
45. Yu L, Oost TK, Schkeryantz JM, Yang J, Janowick D, Fesik SW, J. Am. Chem. Soc. 2003;125:4444.
46. Wyss DF, Arasappan A, Senior MM, Wang Y-S, Beyer BM, Njoroge FG, McCoy MA. J. Med. Chem. 2004;47:2486.
47. Dalvit C, Ardini E, Flocco M, Fogliatto GP, Mongelli N, Veronesi M, J. Am. Chem. Soc. 2003;125:14620.

48. McCoy MA, Wyss DF. J. Am. Chem. Soc. 2002;124:11758.
49. McCoy MA, Wyss DF, J. Biomol. NMR 2000;18:189.
50. Wang Y-S, Liu D, Wyss DF. Magn. Reson. Chem. 2004;42: 485.
51. Wyss DF. Cambridge Healthtech Institute's 4th Ann. Struct.-Based Drug Design. Boston (2004).
52. Lauer GM, Walker BD. Engl N., J. Med. 2001;345:41.
53. Reed KE, Rice CM. Curr. Top. Microbiol. Immunol. 2000;242:55.
54. Tan SL, Pause A, Shi Y, Nat. Rev. Drug Discov. 2002;1:867.
55. Levin MK, Patel SS, J. Biol. Chem. 277, 29377 2002.
56. Yao N, Reichert P, Taremi SS, Prosise WW, Weber PC. Structure 1999;7:1353.
57. Bartenschlager R. J. Viral Hepat. 1999;6:165.
58. McCoy MA, Senior MM, Gesell JJ, Ramanathan L, Wyss DF. J. Mol. Biol. 2001;305:1099.
59. Gesell JJ, Liu D, Madison VS, Hesson T, Y-S Wang, Weber PC, Wyss DF, Protein Eng. 2001;14:573.
60. Howe AY, Chase R, Taremi SS, Risano C, Beyer B, Malcolm B, Lau JY, Protein Sci. 1999;8:1332.
61. Lin C, Kim JL. J. Virol. 1999;73:8798.
62. Tai CL, Pan WC, Liaw SH, Yang UC, Hwang LH, Chen DS. J. Virol. 2001;75:8289.
63. Kim JL, Morgenstern KA, Griffith JP, Dwyer MD, Thomson JA, Murcko MA, Lin C, Caron PR, Structure. 1998;6:89.
64. Pause A, Sonenberg N, EMBO J. 1992;11:2643.
65. Oprea TI, Davis AM, Teague SJ, Leeson PD. J. Chem. Inf. Comput. Sci. 2001;41:1308.

NMR and Structural Genomics in the Pharmaceutical Sciences

Maša Čemažar and David J. Craik*
Institute for Molecular Bioscience, University of Queensland, Brisbane 4072, Queensland, Australia

Introduction

Structural genomics (or more correctly structural proteomics) involves the high-throughput determination of protein structures on a genome-wide scale. It is a new field of research that has the potential to add substantial value to the sequence information becoming available from genome projects. The purpose of structural genomics is to accelerate protein structure determination so as to obtain structural examples of all available protein folds. The derived information will be essential in providing new insights into relationships between protein sequence, structure, and function.

There have been a large number of structural genomics consortia established in recent years in many countries. In addition to their primary purpose of generating large numbers of protein structures many of these consortia are developing and improving techniques for high-throughput structure determination. Together with X-ray crystallography, NMR is one of the two main structure determination methods. The two techniques are complementary and have advantages over one another in the specific ways that they can be applied to the problem of structure determination. In the pharmaceutical sciences structural genomics is beginning to play an important role in drug design strategies. This chapter reviews current progress and trends in structural genomics, with an emphasis on NMR structure determination.

Strategies and Targets in Structural Genomics

The present stage of structural genomics has been referred to as the "low-hanging fruit" phase [1]. Presently the proteins that are being tackled mostly express well in *E. coli* in a soluble form, can be purified easily, and either crystallize readily or give high-quality NMR spectra. The structure determination of these proteins does not require any conceptual or technical advances, although such advances are being made and will accelerate progress. The reason for the choice of the "low-hanging fruit" is that researchers in the field are still seeking to improve the downstream technology, i.e. high-throughput data collection, processing, and structure determination, and to develop automated procedures for many of the steps before embarking on more extensive programs involving more challenging targets.

Table 1 lists some of the major structural genomics initiatives around the world that are using X-ray crystallography or NMR spectroscopy or, in a majority of cases, both techniques. There are several resources on the World Wide Web where links to the details of these initiatives can be found, including for example http://www.rcsb.org/pdb/strucgen.html#Worldwide. Many targets chosen by these initiatives are either from model organisms such as *E. coli*, *S. cerevisiae*, *C. elegans*, or are human proteins that have important functions in essential cell processes such as signal transduction or nucleic acid binding.

Sequence alignment strategies are frequently used to predict the folds of proteins from related families with high sequence homology from across different genomes. However, sometimes even though the homology between two sequences is rather low, they might have a high similarity in their folds and vice versa, so at the moment predictive methods have not replaced the need for experimental structure determination. Even in cases where the predictions of the fold work well, the atomic resolution of the predicted structures may not be sufficient for some applications. In particular, for pharmaceutical applications there is still often a need to experimentally determine the high-resolution structure of a particular target to be able to predict and study the interactions of this protein with ligands for drug design.

Advantages and Disadvantages of NMR for Structural Genomics

From a structural proteomics perspective, NMR studies are mostly limited because of the size of the proteins that can be successfully tackled and by the lengthy data collection and analysis steps. Even with recent developments in the field, complete structure determination of monomeric proteins has still not been pushed beyond the

---

[*] To whom correspondence hould be addressed.

Graham A. Webb (ed.), Modern Magnetic Resonance, 1429–1434.
© 2008 *Springer.*

Table 1: Summary of global structural genomics initiatives[*]

Initiative	Full name	Location	Target genomes and/or proteins	Techniques used
BIGS	Bacterial targets Informatiom Genomique et Structurale	France	*Escherichia coli,* rickettsia, gram-positive, and gram-negative bacteria	X-ray crystallography
BSGC	Berkley Structural Genomics Centre	USA	Genomes of *Mycoplasma genitalium* and *M. pneumoniae*	NMR and X-ray crystallography
BSGI	Bacterial Structural Genomics Initiative	Canada	*E. coli*	NMR and X-ray crystallography
CESG	Centre for Eukaryotic Structural Genomics	USA	Eukaryotic proteins, arabidopsis	NMR and X-ray crystallography
ISPC	Israel Structural Proteomics Centre	Israel	Human health and disease-related proteins	X-ray crystallography
JCSG	Joint Centre for Structural Genomics	USA	Prokaryote *Thermotoga maritima* and eukaryote *Caenorhabditis elegans*	X-ray crystallography
MCSG	Midwest Centre for Structural Genomics	Worldwide	Unknown folds and proteins from disease-causing organisms	X-ray crystallography
MSGP	Marseilles Structural Genomics Program	France	Bacterial, viral, and human ORFs of (un)known function	X-ray crystallography
NESG	Northeast Structural Genomics Consortium	USA, Canada	*S. cerevisiae, C. elegans*, and *D. melanogaster* as well as homologs from the human genome	NMR and X-ray crystallography
NYSGRC	New York Structural Genomics Research Consortium	USA	Proteins from humans and model organisms	X-ray crystallography
OCSP	Ontario Centre for Structural Proteomics	Canada	*E. coli*, *Methanobacterium thermoautotrophicum*, *T. maritima*, *S. cerevisiae*	NMR and X-ray crystallography
OPPF	Oxford Protein Production Facility	UK	Human proteins and those of human pathogens	X-ray crystallography
PSF	Protein Structure Factory	Germany	cDNA clones from German Human Genome Project	NMR and X-ray-crystallography
RIKEN	RIKEN Structural Genomics Initiative	Japan	Human, mouse, and plant proteins	NMR and X-ray crystallography
S2F	Structure to Function	USA	*Haemophilus influenzae*	
SECSG	Southeast Collaboratory for Structural Genomics	USA	Eukaryotic *C. elegans*, *Homo Pyrococcus furiosus*	NMR and X-ray crystallography
SGPP	Structural Genomics of Pathogenic Protozoa	USA	*Leishmania major*, *Trypanosoma brucei*, *Trypanosoma cruzi*, and *Plasmodium falciparum*	X-ray crystallography
SPINE	Structural Proteomics in Europe	Europe	Bacterial pathogens, viral pathogens, and human proteins from fundamental processes and disease	NMR and X-ray crystallography
TB	Tuberculosis Structural Genomics Consortium	Worldwide	*Mycobacterium tuberculosis*	NMR and X-ray crystallography
YSG	Yeast Structural Genomics	France	*S. cerevisiae*	NMR and X-ray crystallography
SGC	Structural Genomics Consortium	UK, Canada	Chemical transformation of human metabolites, signal transduction, membrane receptor/channel signaling, and human parasitic disease	NMR and X-ray crystallography

[*] A selection of the largest structural genomics initiatives is shown, with their abbreviated name, main focus and/or target organisms and the preferred structural determination technique(s) used.

molecular mass limit of around 50 kDa. On the other hand, NMR has a great advantage over X-ray crystallography because it does not require crystals and the experiments are conducted in aqueous solution. Thus NMR can complement X-ray crystallography in providing structural determination for proteins that do not crystallize. Disordered and flexible regions within a protein may limit its "crystallizability", but a thorough NMR analysis using relaxation techniques and heteronuclear NOE measurements can detect and quantify the motions in flexible regions. Membrane proteins are particularly hard to crystallize and although NMR still has some major technical barriers to overcome, there have been some recent positive developments in the field of NMR structure determination of membrane proteins [2,3]. An approach that has been particularly successful is the use of detergent micelles to solubilize membrane proteins, as exemplified by recent studies on the structures of a series of *E. coli* outer membrane proteins, including OmpX, OmpA, and PagP in DHPC, DPC, and *n*-octyl-β-D-glucoside micelles, respectively. The micelle complexes of these β-barrel proteins are in the size range 50–70 kDa [3].

In X-ray crystallography the screening for suitable samples represents a real bottleneck as there is still no predictability about whether the sample will crystallize and if so, how fast. NMR has an advantage in that it can be used as a fast screening method for suitable samples that can be later subjected to structural determination. After successful purification, ^{15}N labeled protein samples can be screened using ^{1}H-^{15}N HSQC spectroscopy, in which exactly one backbone amide peak is expected for each of the non-proline residues, providing a diagnostic fingerprint of the protein. Since there may be correlations between the "foldedness" of a protein and its crystallizability, data from such an NMR screen can support efforts to make samples for a successful crystallographic analysis [4].

Although the acquisition of preliminary screening data can be quite fast in NMR, for example 10–30 min for a 2D HSQC spectrum on a 50 μM sample, the time for collection of an entire set of data is still slow (2–4 weeks) compared to crystallography, where the time from a diffracting crystal to structure can be sometimes hours. Whereas crystallography continues to struggle with the unpredictable rate-determining step of producing diffracting crystals, NMR struggles with months-long periods of more or less manual assignment and structural determination. This timescale is not compatible with many structural genomics initiatives objectives, which for example aim for 100–200 structures per year from each of the NIH-sponsored pilot centers [5].

As already mentioned, the size of proteins that can be studied by NMR is one of its greatest limitations. An analysis of the sizes of the proteins in the Protein Data Bank (PDB, http://www.rcsb.org/pdb/) shows that until now the median size of all proteins solved by NMR was approximately 7 kDa [6], which is substantially less than the median size of proteins solved by X-ray crystallography. Although NMR has solved many proteins larger than 7 kDa, the PDB statistics provide a clear reminder of where the "market" for NMR structures has been in the past.

Figure 1 summarizes the way the size limit has been pushed higher over recent years by the development of novel NMR techniques and improvements in the sensitivity of spectra by technological advances in NMR instrumentation. Proteins larger than 7–10 kDa need to be isotopically labeled with ^{15}N and/or ^{13}C and subjected to 3D or 4D experiments, whereas proteins below approximately 7 kDa can be structurally characterized using traditional 2D homonuclear (^{1}H–^{1}H) techniques based on NOE distance restraints, torsion angles, and inferred H bonds. Transverse relaxation optimization techniques (TROSY) have been a major development in pushing the limit of protein sizes to about 50 kDa when combined with appropriate labeling strategies [7]. It seems likely that this limit will be pushed higher still in coming years, at least from the perspective of deriving structurally informative data from spectra, if not full three-dimensional structures. In an exciting recent development informative solution spectra of a GroEl/GroEs protein complex of about 900 kDa [8] were obtained using TROSY/CRINEPT methods at high magnetic field. Another approach that has been successfully used in recent years is the domain-targeted approach that overcomes the size problem when the structural determination of the whole protein is not feasible. [9]. The average domain size of encoded proteins is approximately 150–175 amino acids, which is well within the NMR size limit [4,10]. Large, multidomain proteins sometimes exhibit interdomain flexibility, which complicates or prevents crystallization, so NMR can be particularly suitable for their structure determination, especially if specific domains can be selectively labeled in turn using intein technology [11,12].

An example of an ongoing structural genomics project on non-membrane proteins of the archeon *M. thermoautotrophicum* provides some typical numbers for the success rates of a high-throughput approach that involves the complementary use of NMR and X-ray crystallography [13]. At target selection, proteins are divided into larger/smaller molecular weight categories (>20 kDa or <20 kDa) that are earmarked for X-ray or NMR, respectively. Interestingly the statistics for successful expression rates hardly differed for them, at 93 and 94%, respectively. At the purification stage, small proteins had a better success rate, 32% vs. 21% for larger proteins. In the end, however, NMR provided an overall success rate for structures of smaller proteins of 5%, whereas X-ray crystallography was successful with 3% of larger proteins and an additional 0.5% of smaller proteins that had HSQC

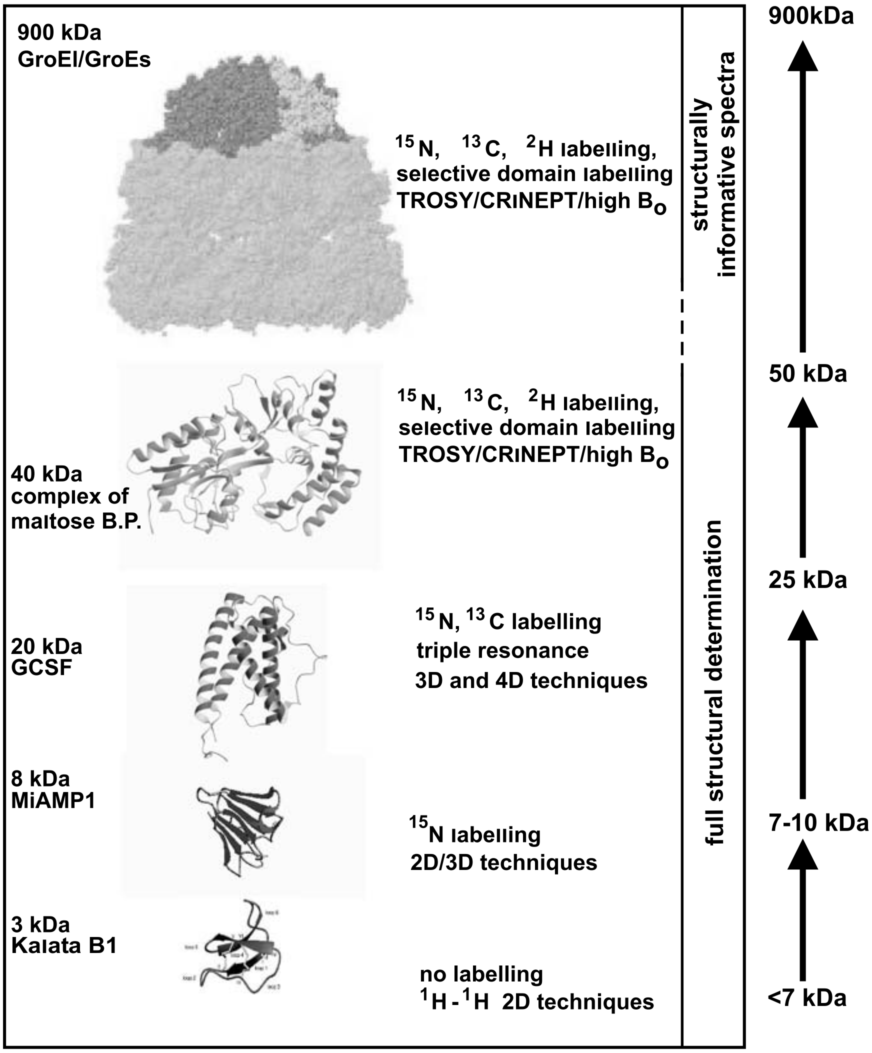
900 kDa
GroEl/GroEs
^{15}N, ^{13}C, ^{2}H labelling,
selective domain labelling
TROSY/CRINEPT/high B_o
40 kDa
complex of
maltose B.P.
^{15}N, ^{13}C, ^{2}H labelling,
selective domain labelling
TROSY/CRINEPT/high B_o
20 kDa
GCSF
^{15}N, ^{13}C labelling
triple resonance
3D and 4D techniques
8 kDa
MiAMP1
^{15}N labelling
2D/3D techniques
3 kDa
Kalata B1
no labelling
^{1}H-^{1}H 2D techniques
structurally
informative spectra
full structural determination
900kDa
50 kDa
25 kDa
7-10 kDa
<7 kDa

Fig. 1. NMR structural information and biomolecular size limits. A schematic representation of the relationship between various NMR structural determination techniques and biomolecular size limits. For each size range an example of a protein structure is given: 3 kDa macrocyclic peptide kalata B1, 8 kDa antimicrobial protein MiAMP1 from the nut kernel of *Macadamia integrifolia* [32], 20 kDa granulocyte colony stimulating factor [33], the 40 kDa complex of maltodextrin binding protein with β-cyclodextrin [34], and the 900 kDa complex of GroEl/GroEs [14]. On the right hand side of the figure the NMR techniques that can be applied to the specific mass range are summarized. So far full 3D structures have been determined up to the size limit of ~50 kDa, but this limit is set to expand over the coming years. (See also Plate 114 on page XXVI in the Color Plate Section.)

spectra that were judged too poor to allow NMR structure determination. It is useful to point out just what a central role HSQC spectra play in structural genomics programs. For proteins that are soluble and purifiable, HSQC spectra can be categorized as good, promising, or poor (or “none” for those where protein had been lost during the concentration procedure) and appropriate decisions made as to whether to proceed with structure determination [13]. A graphic representation of the distribution of spectral types is shown in Figure 2. The exact distribution varies for different organisms but the result is illustrative of general findings. It shows that almost half of the small (<20 kDa)

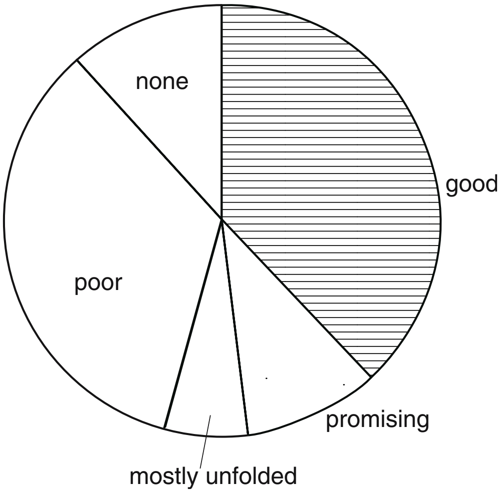

Fig. 2. Distribution chart for the HSQC classification of soluble, purifiable proteins. Spectra can be classified as good, promising, mostly unfolded, poor, or none (for those cases where no HSQC could be obtained). The chart shows the distribution obtained for the archeon *M. thermoautotrophicum*. Data are taken from Yee *et al.* [13].

proteins have potential for NMR structure determination. A key downstream application of NMR in structural genomics with particular relevance to the pharmaceutical sciences is in screening for ligand interactions, especially for those ligands that bind weakly to the protein target, an area where many conventional screening methods fail. In the same way, NMR is useful in screens for protein–protein interactions. Perturbations of specific peaks in an HSQC spectrum identify regions of contact, whereas recently developed residual dipolar coupling (RDC) methods [14,15] can be used to define the relative orientation of associated proteins, including the relative orientation of loosely associated domains in multidomain proteins [16,17]. Compared to conventional approaches, NMR significantly reduces the time for identification and optimization of novel ligands. As noted above, this is usually done by studying changes in ^{15}N/^{1}H chemical shifts of the protein resonances to identify binding ligands from a library of compounds [18].

Advances in NMR Instrumentation and Methodology

In recent years there have been a number of technological improvements in NMR that are being driven in part by structural genomics initiatives. The pharmaceutical sciences will particularly benefit from these advances. As targets move from well-studied and conventional systems to the more challenging systems that are usually more relevant as medicinal targets, high-throughput techniques in NMR will become increasingly important. The advances in NMR in recent years can be divided into advances in instrumentation, methods, data analysis, and sample preparation, as described below.

In terms of instrumentation, the introduction of cryogenic probes probably represents the greatest quantum leap in technology. In these, the traditionally low sensitivity of NMR has been improved by using radio frequency coils that are cooled to about 25 K [19]. This is an important advantage for structure genomics high-throughput methods as cryogenic probes decrease the time of data sampling by factors from 4 to 16. In addition to this new probe technology, the trend towards developing magnets of higher fields has continued incrementally, resulting in further improvements in the sensitivity and resolution of NMR spectra. As of 2004, 900 MHz is the highest commercially available field strength. 800 MHz systems are widely used in structural genomic programs and 900 MHz systems are beginning to come on-line in such programs.

New methods play an important and complementary role to new instrumentation. As already mentioned, the TROSY technique has been developed to be used with higher magnetic fields to give better spectral resolution so that large protein complexes can be tackled [20]. A development that might be especially important for future high-throughput analysis in structural genomics involves the collection of a single set of triple-resonance data from ^{15}N-, ^{13}C-labeled samples in isotropic and liquid crystalline media to provide a rapid low-resolution view of a protein fold [21].

The bottleneck of structural genomics with NMR is still the analysis of NMR data and there is much effort currently been directed towards automation. These efforts have produced several programs [22–26] that can successfully assign well-resolved spectra, but there is scope for future improvement in this area for more robust peak-peaking algorithms that can better distinguish artifacts and noise from real peaks. Another recent development in data analysis has been to include restraints other than the short range ones, particularly RDCs, in the calculation of structures, providing information about long-range order in macromolecules [21,27,28].

Several developments on the protein expression side also have important impacts on high-throughput structural analysis. Especially important are cell-free or *in vitro* expression systems, which now produce yields suitable for structural studies (mg/ml) [29]. These approaches have several advantages over the traditional *in vivo* expression systems, amongst them the fact that some proteins, that are prone to aggregation in the cell or have toxic properties, may now be produced without the need of cloning genes into expression systems. Another advantage of this approach is that labeling of specific amino acids can be introduced because they are additionally supplemented to the reaction mixture. Other resolution-enhancing methods such as encapsulation of proteins in inverted micelles in low-viscosity solvents lead to rapid tumbling and hence to narrower resonances in the spectra [30].

Outlook and Conclusions

From an analysis of current structural genomics initiatives, it has been estimated that on average about 4.7 out of 100 cloned proteins are expected to yield crystal structures and about 5 out of 100 protein NMR structures [31]. These statistics however do not reflect the number of solved structures in a given time frame, since X-ray crystallography is substantially faster. Overall only about 17% of all deposited protein structures in the PDB have so far been determined by NMR methods. On the other hand, NMR can tackle a number of proteins that might are not accessible for crystallization, and about 75% of NMR structures in the PDB do not have corresponding crystal structures. Overall, it is clear that NMR is a viable and economic strategy for structural genomics and will continue to be successfully used for drug design and screening strategies.

References

1. Edwards AM, Arrowsmith CH, Christendat D, Dharamsi A, Friesen JD, Greenblatt JF, Vedadi M. Nat. Struct. Biol. 2000;7(Suppl):970.
2. Castellani F, van Rossum B, Diehl A, Schubert M, Rehbein K, Oschkinat H. Nature. 2002;420:98.
3. Fernandez C, Wuthrich K. FEBS Lett. 2003;555:144.
4. Montelione GT, Zheng D, Huang YJ, Gunsalus KC, Szyperski T. Nat. Struct. Biol. 2000;7(Suppl):982.
5. Norvell JC, Machalek AZ. Nat. Struct. Biol. 2000;7(Suppl): 931.
6. Wuthrich K. NMR studies of structure and function of biological macromolecules (Nobel Lecture). J. Biomol. NMR. 2003;27:13.
7. Wider G. Biotechniques. 2000;29:1278.
8. Fiaux J, Bertelsen EB, Horwich AL, Wuthrich K. Nature. 2002;418:207.
9. Campbell ID, Downing AK. Nat. Struct. Biol. 1998; 5(Suppl):496.
10. Burley SK. Nat. Struct. Biol. 2000;7(Suppl):932.
11. Xu R, Ayers B, Cowburn D, Muir TW. Proc. Natl. Acad. Sci. U.S.A. 1999;96:388.
12. Otomo T, Teruya K, Uegaki K, Yamazaki T, Kyogoku Y. J. Biomol. NMR. 1999;14:105.
13. Yee A, Pardee K, Christendat D, Savchenko A, Edwards AM, Arrowsmith CH. Acc. Chem. Res. 2003;36: 183.
14. Bax A. Protein Sci. 2003;12:1.
15. Bolon PJ, Al-Hashimi HM, Prestegard JH. J. Mol. Biol. 1999;293:107.
16. Bewley CA, Clore GM. J. Am. Chem. Soc. 2000;122: 6009.
17. Skrynnikov NR, Goto NK, Yang D, Choy WY, Tolman JR, Mueller GA, Kay LE. J. Mol. Biol. 2000;295:1265.
18. Hajduk PJ, Meadows RP, Fesik SW. Q. Rev. Biophys. 1999;32:211.
19. Styles P, Soffe N, Scott C. J. Magn. Reson. 1989;84:376.
20. Riek R, Pervushin K, Wuthrich K. Trends Biochem. Sci. 2000;25:462.
21. Zweckstetter M, Bax A. J. Am. Chem. Soc. 2001;123: 9490.
22. Duggan BM, Legge GB, Dyson HJ, Wright PE. J. Biomol. NMR. 2001;19:321.
23. Mumenthaler C, Braun W. J. Mol. Biol. 1995;254:465.
24. Atreya HS, Sahu SC, Chary KV, Govil G. J. Biomol. NMR. 2000;17:125.
25. Zimmerman DE, Kulikowski CA, Huang Y, Feng W, Tashiro M, Shimotakahara S, Chien C, Powers R, Montelione GT. J. Mol. Biol. 1997;269:592.
26. Helgstrand M, Kraulis P, Allard P, Hard T. J. Biomol. NMR. 2000;18:329.
27. Clore GM, Gronenborn AM. Proc. Natl. Acad. Sci. U.S.A. 1998;95:5891.
28. Tjandra N, Bax A. Science. 1997;278:1111.
29. Kigawa T, Yabuki T, Yoshida Y, Tsutsui M, Ito Y, Shibata T, Yokoyama S. FEBS Lett. 1999;442:15.
30. Wand AJ, Ehrhardt MR, Flynn PF. Proc. Natl. Acad. Sci. U.S.A. 1998;95:15299.
31. O'Toole N, Grabowski M, Otwinowski Z, Minor W, Cygler M. Proteins. 2004;56:201.
32. McManus AM, Nielsen KJ, Marcus JP, Harrison SJ, Green JL, Manners JM, Craik DJ. J. Mol. Biol. 1999;293: 629.
33. Werner JM, Breeze AL, Kara B, Rosenbrock G, Boyd J, Soffe N, Campbell ID. Biochemistry. 1994;33:7184.
34. Mueller GA, Choy WY, Yang D, Forman-Kay JD, Venters RA, Kay LE. J. Mol. Biol. 2000;300:197.

Author Index

Abbott, D.F., 1037
Al-Saffar, N., 1143
Ambrosio, A., 1171

Balkwill, G., 1363
Banakar, S., 1171
Binesh, N., 1171
Bluml, S., 1099
Bourne, R., 1027
Briellmann, R.S., 1037
Burns, M.A., 1051
Byrd, R.A., 1255

Carlomagno, T., 1247
Čemažar, M., 1429
Cheng, L.L., 1051
Chung, H.-K., 1171
Craik, D.J., 1195
Craik, D.J., 1429
Crouch, R., 1299

Dalvit, C., 1393
Damblon, C., 1331
Delepierre, M., 1325
Delikatny, E.J., 1015
Ding, K., 1287
Dixon, N.E., 1263

Fairbrother, W.J., 1293
Fowler, C.A., 1255

Gaponenko, V., 1255
Gavathiotis, E., 1363
Gell, D.A., 1339
Gesell, J.J., 1419
Griesinger, 1247
Gronenborn, A.M., 1287
Guo, J., 1271
Gupta, R.K., 1005

Hajduk, P.J., 1399
Himmelreich, U., 1005, 1087
Hoch, J.C., 1305
Hoehn, M., 1087
Holmes, E., 1377
Huber, T., 1263
Huda, A., 1171

Jackson, G.D., 1037
Jagannathan, N.R., 1077

Kaiser, W.A., 1127
Karagianis, G., 1229
Kasimova, M.R., 1369
Keifer, P.A., 1213
Keniry, M.A., 1263
Kessler, 1279
King, G.F., 1305
Kristensen, S.M., 1369
Kurhanewicz, J., 1113

Latour, I., 1065
Leach, M.O., 1143
Lean, C.L., 1051
Led, J.J., 1369
Lepre, C.A., 1409
Lin, A.P., 985
Lindon, J.C., 1377
London, R.E., 1347
Luy, B., 1279

Maciejewski, M.W., 1305
Mackay, J.P., 1339
Makriyannis, A., 1271
Martin, G.E., 1205
McCoy, M.A., 1419
McFeeters, R.L., 1255
Moore, J.M., 1409
Mountford, C., 1027

Nguyen, L.T., 1315
Nicholson, J.K., 1377
Noworolski, S.M., 1113

Otting, G., 1263

Park, A.Y., 1263
Pavlopoulos, S., 1271
Payne, G.S., 1143
Pell, G.S., 1037
Pineda-Lucena, A., 1239
Pintacuda, G., 1263
Possani, L.D., 1325
Prenner, E.J., 1315

Roberts, G.C.K., 1331

Schirra, H.J., 1195
Schwalbe, H., 1387
Searle, M.S., 1363
Senior, M.M., 1419
Sharma, U., 1077
Smith, I.C.P., 1027
Spraul, M., 1221
Starovasnik, M.A., 1293
Stern, A.S., 1305
Sutherland, G.R., 1065
Swanson, M.G., 1113

Thomas, M.A., 1171
Tian, X., 1271
Tomanek, B., 1163

Venkatraman, T., 1171
Veronesi, M., 1393
Vogel, H.J., 1315

Waites, A.B., 1037
Wang, Y.-S., 1419
Waterman, P.G., 1229
Watzl, J.Q.Y., 1015
Williams, H.E.L., 1363
Williamson, M.P., 1357
Wirmer, J., 1387
Wyss, D.F., 1419

Subject Index

A

- α-synuclein, protein misfolding disease and, 1389
- Γ method, quantitative, 1249
- ε186–θ complex, 1263, 1266
  - diamagnetic, 1264
  - paramagentic, 1264
- 1D ^{1}H MRS
  - single- and multi-voxel based, 1161
- 1D NMR
  - based screening, 1393
- 2,2,2-trifluoroethanol. *See* TFE
- 2D ^{1}H MRS, 1173
- 2D heteronuclear NMR-based screening, 1420
- 2D j-resolved MRS, 1174
- 2D MAS experiments, 1016
- 2D MRS, 1015, 1024
  - advantages in human biopsies, 1016
  - artefacts in localized, 1180
  - CT-COSY, 1173
  - CT-PRESS, 1173
  - JPRESS, 1173
  - L-COSY, 1174
  - multi-voxel based, 1180
  - SECSY, 1173
  - single volume localized, 1175
- 2D NMR, 1015
  - applications to cells and tissues, 1016
- 2D TOCSY, 1242
- 3-FABS
  - high-throughput screening and, 1393
- *A. hydrophila*, 1341, 1342
- abscess, 1021
- absolute quantitation, 1021, 1110
- acquiring spectra method
  - global, 986
  - local, 986
- active-site metals, 1334
- adenosine diphosphate (ADP), 1146
- adsorption, gas. *See* gas adsorption
- *Aeromonas hydrophila*, 1331
- alignment media
  - organic molecules structure determination, 1280
- alignment tensor, 1279
- aloe metabolites, 1232
- amide protons, H-bonded, 1369
- amide resonances, backbone, 1332
- amyloid precursor protein, 1388
- antimicrobial peptides, structural
  - characterization of defensins, 1315
  - dimerization properties, 1318
  - disulfide cross-linking, 1319
  - hepcidin, 1319
  - microcin J25, 1319
  - NMR for, 1315
  - NOESY, 1319
  - NOESY NMR, 1318
  - orientation in bilayers (magainin 2), 1320
  - protegrin-1, 1320
  - solid-state NMR experiments, 1320
  - solution structures of, 1315
  - TOCSY, 1315, 1318
  - unusual linkages characterization, 1317
- apodization, human biopsies and, 997
- aqueous fraction, 1146
- ARIA, 1244
- arteriovenous malformation (AVM), 1072
- *Aspergillus spp*, 1008
- assignments
  - human biopsies, 1032
  - pharmaceutical sciences, NMR in, 1239
- astrocytoma, 1030, 1056
- ATP, 1143
- automated protein structure determination, 1243
- AUTOPSY, 1242

B

- B0 field, 1077
- B1 field, 1163
- B1 homogeneity and SNR
  - local rf coils, 1170
- B1 homogeneity versus SNR, 1166
- backbone amide resonances, 1332
  - inhibitor binding and, 1332
- backbone RDC
  - protein NMR and, 1287
- backbone torsion angle
- *Bacteroides fragilis*, 1331
- basic fibroblastic growth factor (bFGF), 1130
- benign prostatic hyperplasia, 1051, 1058
- bicelle
  - isotropic, 1273
  - magnetically aligned, 1275
  - membrane systems, phospholipid, 1271
  - phospholipid, 1272
- bifunctional contrast agent, 1093, 1095
- bilayer systems
  - magainin 1315
  - peptide orientation in, 1320
- binding activities, DNA. *See* DNA-binding activities (hTRF1and hTRF2 with hTRF2 mutants)
- biochemical applications (cryogenic NMR probe technology), 1207
- bioinformatics, intraoperative MRI and, 1075
- biomolecular NMR, 1305
- biopsy
  - ^{31}P MRS and, 1077, 1078
  - human. *See* human biopsies
  - tissue, 1078
- *Blastomyces dermatitides*, 1008
- blood oxygen level dependent. *See* BOLD imaging
- BMRB, 1242
- BOLD contrast, 1029. *See also* contrast agents
- BOLD imaging 1037. *See also* functional MRI phMRI
- *Bombina maxima*, 1317
- bone, 1115
- borate complexes, 1347
- brain. *See also* infective brain lesions
  - HRMAS MAS analysis, 1051
  - surgical specimens, 1051
- breast. *See also* MR-mammography
  - HRMAS MAS of, 1061
  - MRS, 1127
- breast cancer
  - MRS and, 1077
- breast cancer, in vivo MRS, 1077
  - ^{1}H MR spectroscopy, 1079
  - ^{1}P MR spectroscopy, 1078
  - future aspects, 1084
  - localization in MRS, 1077
  - methodological issues related to proton in vivo MRS, 1079
  - normal and malignant, 1082
- broadband decoupling, 1101
- Bruker single-sided NMR device, 1873

C

- ^{13}C excitation and detection, in vivo^{13}C MRS, 1102
- ^{13}C NMR
  - in vivo, 1099
- ^{113}C spectrum, thiomandelate binding effect, 1335
- CABINET, 1174

calar coupling, 1015
cancer pathology determination, 1038
CANDID, 1244
CANDID algorithm, 1244
Candida spp, 1008
CCPPA. *See* coupled-cluster polarization propagator
cell labeling
  biological aspects, 1092
  in vivo molecular MRI, 1087
cellular and tissue systems
  2D NMR spectroscopy applications, 1016
Centruroides limpidus limpidus, 1327
Centruroides noxius, 1327
cervix
  HRMAS MAS of, 1060
chemical change
  protein–protein interactions and, 1343
chemical exchange saturation transfer, 1091
chemical shift, 1015
  ^{31}P, 1143
  ^{31}P MRS, 1146
chemical shift correlated MRS, 1174
chemical shift imaging, 993, 1007, 1116, 1172
  ^{31}P MRS, 1146
  MRS and, 1108
  IgE antagonists and, 1293
  protein–protein interactions, 1339
chemical shift referencing
  ^{31}P MRS, 1156
CHESS, 1097, 1172
CHF. *See* coupled Hartree–Fock approximation
chromatography
  in LC-NMR, 1213
Chryseobacterium meningosepticum, 1331
CLOUDS, 1381
coils
  double-resonance, 1152
  rf coils, 1151, 1163. *See also under* rf coils
  surface (MRS), 1117
  surface coils, 1152, 1153, 1156
  volume, 1152
cold probes. *See also* probes
  flow NMR techniques, 1209
computer-assisted structure elucidation (CASE) methods, 1206
computerized tomographic, 1005
contrast agents, 1007, 1079. *See also* brain disease, MRI contrast mechanism for bifunctional, 1093
  for in vivo molecular MRI, 1095
  in vivo molecular MRI, 1092
contrast enhancement, 1007
contrast-to-noise ratio (CNR)
  in vivo molecular MRI, 1095
core elaboration
  high-throughput, 1404
core replacement, 1403
coronary heart disease (CHD)
  metabonomics techniques, 1377
COSY, 1015
  2D, 1232
  spectra, 1010
coupling
  hetero-nuclear J-coupling, 1102
  heteronuclear scalar couplings, 1101
  homo-nuclear J-coupling, 1102
  J-coupling, 1102
  scalar, 1102
Creutzfeldt-Jakob's disease (CJD), 1388
CRINEPT, 1195
  method, 1429
  structural genomics and, 1429
CRINEPT. *See* cross-correlated relaxation-enhanced polarization transfer
CRIPT. *See* cross-correlated relaxation-induced polarization transfer
cross peak imaging (CPI), 1180
cross peak volumes, factors affecting, 1025
cross polarization, 1435
cross spectrum, 1252
cross-correlated relaxation, 1247
  15N-HSQC spectra of proteins, 1263
  effect on spectra, 1247
  project angles between tensors, measurement of, 1247
  quantitative method, 1249
  transferred, 1250
  transferred (epothilone/tubulin complex), 1252
cross-linking
  disulfide, 1315
cross-saturation
  protein–protein interactions, 1343
crosstalk
  in vivo 13C MRS, 1099
cryogenic NMR probe technology, 1206
  applications, 1205
  identification of degradants, 1206
  metabolic and metabonomic applications, 1210
  protein and biochemical applications,1202
  sample preparation, 1206
  small molecule applications, 1209
cryogenic probes for LC-NMR, 1216
Cryptococcus neoformans, 1008
CT-COSY, 1173
CTOCD. *See* continuous transformation of the origin of the current density
CT-PRESS, 1173
  2D, 1173
Cu-Zn-superoxide dismutase, 1390
CYANA, 1244
cyclic θ defensin-1, 1319
cysteine-stabilized α-helix (CSH), 1318

D

dairy products. *See also* foods
data acquisition, human biopsies and, 1015
data analysis, 1002
  infective brain lesions and, 1005
  surgical specimens, 1051
data interpretation
  MRS, 1119
data preparation
  functional MRI, 1037
data processing
  human biopsies and, 1016
  in vivo ^{13}C MRS, 1099
  MRS, 1118
decoupling. *See also* residual dipolar couplings
  broadband decoupling, 1101
  incomplete (in vivo ^{13}C MRS), 1099
  proton-decoupling, 1101
defensins, 1314
degradants identification (cryogenic NMR probe technology), 1206
dendrimers, 1090
density functional theory. *See* DFT
des-[phe(B25)] insulin, 1384
detectability (in vivo molecular MRI), 1087
deuteration, 1339
DFT, 1300
diamagnetic ε186–θ complex, 1263
differential isotope labeling, 1340
diffusion-weighted imaging, 1005
dihydrofolate reductase (DHFR), 1256
  type II, 1354
dimerization properties, antimicrobial peptides, 1318
DI-NMR, 1213
direct stop-flow, 1221
disease diagnosis
  metabonomics techniques, 1382
disulfide cross-linking, 1319
DNA
  quadruplex DNA, 1363

DNA folding
  hairpin folding
    and slow exchange equilibria, 1364
    by magnetization transfer, 1364
  NMR and, 1363
DNA quadruplex structures, 1363
docking protein complexes, 1364
docking, IgE, 1293
DOQSY
  flow NMR techniques, 1218
double resonance studies, 1152
double-resonance acquisition schemes, 1155
double-resonance coils, 1152
  single coil, 1152
  single dual-resonant coil, 1152
  two separate coils, 1152
Drosophila melanogaster, 1318
drug binding
  NMR and, 1363
  to quadruplex DNA, 1363
drug conformational studies, phospholipid bicelle membrane systems and, 1273
drug detection (in vivo 31P MRS), 1158
drug discovery
  fragment leads utilization, 1403
  fragment linking and, 1405
  NMR and, 1239
  receptor-based NMR screening in, 1402
drug discovery targets
  NMR
    based screening and, 1419
    for lead discovery, 1419
  target-detected 2D heteronuclear, 1420
drug effects
  pharmaceutical sciences (NMR), 1200
drug molecules, phospholipid bicelle membrane systems and, 1271
drug orientation
  phospholipid bicelle membrane systems and, 1275
drug targets
  lead inhibitors, 1424
  NMR-based screening applied to, 1423
  NMR-derived
    competitive non-peptide inhibitors, 1424
drug/target complexes, 1247
drug–quadruplex interactions study, 1363
DSC
  phospholipid bicelle membrane systems, 1285
dual frequency rf coils, 1169
dual phase extraction method (DPE), 1146
dual-region Hadamard-encoding, 1299
ductal carcinoma in situ, 1028, 1051
DWI. *See* diffusion-weighted imaging

E

Echinococcus larvae, 1008
echo planar imaging (EPI), 1006, 1037 1092
echo time, 985. *See also* neurospectroscopy
EDTA, 1255-1257
EEG, 1044. *See also* functional MRI
electroporation, 1090
endocytosis, 1090, 1091
endosome, 1090, 1091
EPI. *See* echo planar imaging
epilepsy
  intraoperative MRI, 1065
epothilone/tubulin complex, 1252
EPSE, 1116
EPSI, 1182
even-related study (functional MRI), 1039, 1040
ex vivo labeling, 1091. *See also* labeling
exchange rates
  for drug binding to quadruplex DNA, 1363
expectation/maximization (E/M), 1243
extraction methods
  modified Folch's method, 1146
  perchloric acid, 1146
extraction methods (^{31}P MRS)
  dual phase extraction method, 1146

F

19F NMR
  for high-throughput screening, 1393
F noise figure, 1169
fast multidimensional NMR
  data acquisition, 1239
  pharmaceutical sciences and, 1231
fast-low-angle-shot, 1006
FAXS, 1393
  high-throughput screening and, 1393
fFLASH. *See* fast-low-angle-shot
FIA-NMR
  flow NMR techniques, 1213, 1215
field of view (FOV), 993
fine-needle aspirate biopsy (FNAB), 1028
fine-needle biopsy, 1030
FLAIR. *See* fluid attenuated inversion recovery
FLASH, 1092
flow NMR techniques, 1213
  chromatography in LC-NMR, 1215
  cold probes, 1217
  complementary technologies, 1217
  detectors in LC-NMR, 1215
  DI-NMR, 1216
  DOSY, 1218
  FIA-NMR, 1213, 1215
  interchangeable flow cells, 1217
  LC-NMR, 1215
  LC-NMR
    applications, 1215
    limitations, 1215
  LC-NMR-MS, 1214
  microcoils, 1217
  multiplex NMR, 1217
  nD-NMR data, 1217
  parallel NMR, 1217
  plumbing schemes, 1215
  SPE-NMR, 1215
fluid attenuated inversion recovery, 998, 1066
flux rates
  in vivo 13C MRS, 1099
fMRI. *See* functional MRI
FNAB
  collection of, 1029
  focal (acquiring spectra method), 986
  focal infection, 1005, 1008
Folch's method, modified, 1146
folding, DNA
  hairpin folding
    and slow exchange equilibria, 1364
    by magnetization transfer, 1366
  NMR and, 1363
FOV. *See* field of view
fragment leads use in drug design, 1401
fragment linking, 1403
fragment screening, 1401
fragment-based screening, 1401
  hot spot indentifcation on protein surfaces, 1401
free induction decay (FID), 1015
freezing in glassy crystals, 1485
frontal GM protocol, 997
functional MRI, 1037. *See also* BOLD imaging; intraoperative MRI
  advantages and disadvantages, 1041
  baseline considerations, 1039
  block design, 1037, 1039
  correction for
    geometric distortion, 1040
    signal drop, 1040
  data preparation, 1040
  design, 1037
  even-related
    design, 1038
    study, 1039
  FMRI/EEG, 1046
  global intensity normalization, 1040
  gross motion rejection, 1040
  hemodynamic response modeling, 1039
  inter-stimulus interval selection for event-related designs, 1038
  language
    fMRI, 1042

- language (*cont.*)
  - in controls, 1042
  - in patients, 1043
  - lateralization, determination of, 1042
- linear de-trending, 1041
- performance measures, 1040
- practical applications, 1042
- pre-processing, 1040
- principles, 1037
  - of analysis, 1040
  - of experimental design, 1039
- repetition time, 1038
- slice timing correction, 1040
- smoothing, 1041
- software packages, 1041
- spatial normalization, 1040
- statistical analysis, 1041

G

- gadolinium (Gd)-based contrast agents, 1007
- G-COSY, 1019
  - stretched polymer, 1280
- genomics, structural. *See* structural genomics, NMR and
- GFT-NMR, 1253
- glioblastoma multiforme, 1007, 1011, 1051, 1062
- global (acquiring spectra method), 985. *See also* local (acquiring spectra method)
- glycerophosphocholine (GPC), 1144
- glycerophosphoethanolamine (GPE), 1144
- gray matter (GM) protocol, 993

H

- ^{1}H MRS
  - 2D, 1180
  - breast cancer, 1077
  - breast tissues, normal and malignant, 1082
  - cancer pathology determination by, 1052
  - human biopsies, 1016
  - LCModel for, 1105
  - single- and multi-voxel based, 1171
- ^{2}H NMR
  - antimicrobial peptides, structural characterization of, 1315
- Hadamard encoding
  - dual-region, 1299
- hairpin folding
  - kinetics by magnetization transfer, 1364
  - slow exchange equilibria and, 1366
- hairpin peptide structure, 1293
- hairpin peptide/receptor complex, 1297
  - NMR analysis of, 1297
- H-bonded amide protons
  - in proteins from a single 2D experiment, 1370
- HCV NS3 helicase, 1424
- hemodynamic response function, functional MRI, 1038, 1039
- hepcidin, 1315
- herbal drugs, LC-NMR in, 1229
  - dereplication of skullcap herb, 1230
  - structure elucidation of aloe metabolites, 1232
- hetero-nuclear J-coupling, 981
  - 31P, 1147
- heteronuclear multiple-quantum correlation, 1015
- heteronuclear NMR based screening, 2D, 1420
- heteronuclear polarization transfer, 1100
- heteronuclear scalar couplings, 1101
- heteronuclear single-quantum correlation, 1016
- high-affinity IgE receptor, 1307
- high-resolution MAS, 1051
  - surgical specimens, 1051, 1052
- high-resolution MAS NMR
  - marine microalgae, 951, 957
- high-resolution MAS MRS
  - cancer pathology determination, 1052
  - future developments, 1062
  - human surgical specimens, 1054
  - of brain, 1055
  - of breast, 1059
  - of cervix, 1060
  - of kidney, 1060
  - of lymph nodes, 1061
  - of prostate, 1058
  - of sarcoma, 1061
- high-throughput core elaboration, 1404
- high-throughput screening (HTS), 1239, 1393
  - 19F NMR for, 1393
  - 3-FABS and, 1396
  - FAXS and, 1393
  - post-HTS screening, 1414
  - pre-HTS screening, 1418
- hippocampus/temporal lobe protocol, 997
- histopathology
  - limitations, 1027, 1051
  - MRS of human biopsies and, 1027
  - surgical specimens, 1054
  - strengths, 1027
- Histoplasma capsulatum, 1008
- HMBC, 1299
- homogeneity, neurospectroscopy and, 985
- homonuclear j-coupling, 981. *See also* heteronuclear j-coupling
  - ^{31}P, 1143
- *Hordeum vulgare*, 1318
- hot spots identification on protein surface, 1401
- HR MAS NMR. *See* high-resolution MAS NMR
- HR solid state NMR. *See* high-resolution solid-state NMR
- HRMAS. *See* high-resolution MAS
- HSQC
  - based screening, 1420
- HTS screening. *See* high-throughput screening
- human biopsies, 1027
  - 2D MR spectroscopy, 1016
  - 2D NMR spectroscopy, 1016
  - after MRS, 1032
  - apodization, 1020
  - assignments and visual inspection of data, 1023
  - changing parameters in t1, 1023
  - choice of pulse sequence, 1027
  - collection and storage of specimen, 1028
  - cross peak volumes factors, 1021
  - data acquisition aspects, 1019
  - data processing, 1020
  - experimental temperature aspects, 1031
  - fine-needle aspirate biopsy, 1028, 1029
  - fine-needle biopsy, 1030
  - future challenges, 1035
  - histopathology correlation with MRS and, 1027
  - magnetic field strength and, 1031
  - MRS and, 1027
    - 2D, 1016
    - applications in, 1015
    - methods, 1031
  - pattern recognition methods, 1032
  - quantitation aspects, 1021
  - regression analysis, 1035
  - sample preparation, 1019
  - tissue specimens preparation, 1030
  - tumor development and progression, 1032
  - Window functions, 1020
- human growth hormone (hGH), 1369
  - acid state of, 1372
- human malignancies characterization, 1051
- human neutrophil protein-3, 1318
- human specimens
  - breast, 1059
  - cervix, 1060
  - prostate, 1058
- human surgical specimens
  - HRMAS MRS of, 1053
- hyperpolarized^{13}C compounds, 1110
- hyphenation, NMR, 1221
  - cryogenic probes for LC-NMR, 1226
  - direct stop-flow, 1222

  - LC-NMR, integration of MS and, 1227
  - loop collection, 1224
  - on-flow LC-NMR, 1221
  - post-column solid phase extraction, 1224

I

- IgE
  - hairpin peptide structure, 1293
  - hairpin peptide/receptor complex, 1297
  - receptor binding and, 1294
  - zeta peptide/receptor complex, 1294
- IgE antagonists, 1293
  - chemical shift perturbations and, 1293
- IgE receptor, 1293
  - high affinity, 1293
- ILOEs, 1347
  - ternary complexes identification and characterization, 1347, 1349
- image-selected *in vivo* spectroscopy, 981
- imidazole resonances of metal ligands inhibitor binding and, 1332
- implanted rf coils, 1168
- improved volume selection, 1115
- iMRI. *See* intraoperative MRI
- in silico docking, 1344
- *in vitro* MRS, 1173
- *in vivo* ^{13}C MRS, 1099
  - ^{13}C excitation and detection, 1102
  - applications, 1107
  - broadband
    - decoupling, 1101
    - excitation/detection, 1099
  - crosstalk, 1104
  - data processing, 1105
  - equipment, 1099
  - flux rates, 1106
  - heteronuclear scalar couplings, 1101
  - hyperpolarized 13C compounds, 1110
  - incomplete decoupling, 1104
  - indirect detection, 1102
  - instabilities aspects, 1104
  - lineshape transformation, 1105
  - low SNR, 1103
  - polarization transfer, 1102
  - proton-decoupler and power monitoring, 1100
  - proton-decoupling, 1101
  - proton-decoupling and NOE, 1101
  - pulse sequences for, 1102
  - reproducibility aspects, 1105
  - simple two compartment model, 1107
  - system performance, checking of, 1103
- *in vivo* ^{1}H MRS
  - LCModel for, 1105
- *in vivo* 2D MRS, 1171
- *in vivo* 2D spectra, 1016
- *in vivo* ^{31}P MRS, 1143
  - adiabatic rf pulses, 1153
  - chemical shift referencing, 1156
  - double-resonance acquisition schemes, 1156
  - drug detection, 1158
  - examples of, 1156
  - localization methods, 1153
  - metabolite concentrations estimation, 1156
  - peak areas measurement, 1156
  - single voxel localization methods, 1153
  - skeletal muscle, 1156
  - spectral analysis, 1156
  - surface-coil localization, 1153
- *in vivo* bioluminescence (BLI), 1087
- *in vivo* labeling, 1091
- *in vivo molecular MRI*, 1087
  - cell labeling, 1090
    - biological aspects of, 1092
  - contrast agents, 1088
  - contrast-to-noise ratio, 1089
  - detectability, 1087
  - *ex vivo* labeling and, 1091
  - experiments, 1091
  - label assessment and stability, 1093
  - quantification, 1089
  - resolution, 1089
  - responsive contrast agents, 1091
  - SNR, 1089
  - toxicity, 1092
- *in vivo* MR spectra, infective brainlesions and, 1005
- *in vivo* MRS, 1171
  - ^{31}P MRS, 1120, 1143
  - breast cancer, 1077, 1079
- INEPT, 1191
- infective brain lesions
  - contrast enhancement aspects, 1007
  - conventional MRI of, 1007
  - data analysis aspects, 1010
  - diffusion method, 1008
  - in vivo MR spectra, 1009
  - magnetic resonance spectroscopy, 1009
  - magnetization transfer, 1009
  - MRI for, 1005
  - perfusion method, 1008
- inhibitor binding, 1332
  - backbone amide resonances and, 1332
  - imidazole resonances of metal ligands and, 1332
- inhibitors
  - NMR-derived competitive non-peptide inhibitors, 1424
  - NMR-derived laed inhibitors, 1424
- insulin
  - des-[phe(B25)] insulin, 1370
  - flexibility and activity, NMR study of, 1370
  - insulin–receptor interaction, 1371
  - PT insulin, 1371
- intact tissue samples, MRS of, 1149
- interchangeable flow cell (IFC), 1217
  - flow NMR techniques, 1217
- interligand Overhauser effects, 1347
- internal mobility
  - NOE, 1358
- INTERPRET, 1010
- inter-stimulus interval selection, 1038. *See also* functional MRI
- intraoperative MRI, 1065. *See also* functional MRI
  - bioinformatics, 1075
  - clinical applications, 1067
  - epilepsy, 1069
  - future aspects, 1073
  - hardware and configuration, 1065
  - neoplasia, 1069
  - neurology and, 1065
  - principles, 1056
  - robotics, 1075
  - spine, 1073
  - vascular disorders, 1072
- inverse Radon transform, 1240
- ion channel blockers, 1325
- ISIS, 1110
  - ^{31}P MRS, 1153, 1154
- isotope labeling differential, 1340
- isotropic bicelles, 1273

J

- J-coupling, 981, 1010
  - hetero-nuclear, 981
  - homo-nuclear, 981
- JPRESS, 1173
- j-resolved MRS, 2D, 1173

K

- human specimens, 1061
- kidney
  - HRMAS MAS of, 1061

L

- labeling
  - assessment and stability (in vivo molecular MRI), 1093
  - cell, 1090
  - cell labeling, 1092
  - differential isotope, 1340
  - *ex vivo*, 1091
  - *in vivo*, 1091
  - paramagnetic, 1255

Lactococcus lactis, 1316
language fMRI, 1042
language lateralization determination (functional MRI), 1042
LC-NMR
  applications, 1210
  chromatography in, 1210
  cryogenic probes for, 1226
  detectors in, 1210
  flow NMR techniques, 1208
  herbal drugs and, 1229
  limitations, 1210
  MS and, 1227
  on-flow LC-NMR, 1221
  pharmaceutical sciences, 1195, 1196
  post-column solid phase extraction, 1221
LC-NMR-MS, 1215
  flow NMR techniques, 1218, 1219
L-COSY, 1178
  2D, 1178
lead discovery
  NMR for, 1413
lead optimization, NMR screening and, 1414
lesions, brain. *See* infective brain lesions, 1005
ligand-based screening
  pharmaceutical sciences (NMR), 1195
linear de-trending, 1041
linear discriminant analysis (LDA), 1032
linear prediction extrapolation, 1305
lineshape transformation
  in vivo ^{13}C MRS, 1105
lipid fraction, 1149
lipid suppression
  MRS, 1113
  water and, 1171
lipoma, 1061, 1062
liposarcoma, 1061, 1062
liposomes, 1271
  phospholipid bicelle membrane systems, 1271
liquid crystalline phases
  organic molecules structure determination, 1279
liver
  MRS, 1132, 1113
local rf coils, 1168
localization, 1102
  schemes in MRS, 1114
localization methods
  ^{31}P MRS, 1154
  single voxel, 1154, 1155
  surface-coil, 1154
localized *in vivo* MRS, 1006
loop collection
  NMR hyphenation and, 1225
Lorentzian–Gaussian (LG) function, 1020
low-level impurities in pharma, 1215
lymph nodes
  HRMAS MAS of, 1061

M

magnetic field strength
  human biopsies and, 1031
magnetic resonance
  for infective brain lesions diagnosis, 1005
  infective brain lesions, 1007
magnetic resonance techniques, 1005
magnetically aligned bicelles, 1275
magnetization transfer (MT), 1005
  DNA hairpin folding kinetics by, 1366
  infective brain lesions and, 1005
magnets
  ^{31}P MRS, 1151
MAS
  antimicrobial peptides, structural characterization of, 1315
  cancer pathology determination, 1052
  HRMAS, 1051
MaxEnt reconstruction, 1306
McArdles syndrome, 1157
meningioma, 991, 1056
metabolic and metabonomic applications (cryogenic NMR probe technology), 1210
metabolism and metabonomics,
metabolites
  aloe, 1232
  observed in tissues, 1143
  profiling, 991, 1057
metabonomics techniques
  analytical technologies, 1377
  disease diagnosis, 1382
  genetic differences and other physiological effect, 1382
  integrated metabonomic studies, 1382
  NMR-based, 1377
  preclinical drug candidate safety assessment, 1381
metal ligands
  imidazole resonances of, 1332
metallo-β-lactamases, 1323 , 1331
  active-site metals, observation of, 1334
  inhibitor binding
    and backbone amide resonances, 1332
    on imidazole resonances of metal ligands, 1332
  thiomandelate binding effect on 113Cd spectrum 1335
micelles, 1272
microcin J25, 1315, 1316
microcoils, 1154, 1326
  flow NMR techniques, 1213
microprobes, 1326
MM-COSY, 1015, 1016, 1018, 1019
MM-COSY 2D spectra, 1021
modified Folch's method, 1146
molecular imaging, 991, 1093
molecular MRI
  cell labeling, 1087
  contrast agents for, 1085
  contrast-to-noise ratio, 1086
  detectability, 1084
  experiments, 1088
  quantification, 1086
  resolution, 1086
  responsive contrast agents, 1088
  SNR, 1086
  toxicity, 1089
motion aspects of MRS, 1118
MRI, 977, 1005
  epilepsy, 1061, 1065
  functional MRI, 1037
  in vivo molecular, 1087
  intraoperative, 1065
  MR-mammography and, 1127
  neoplasia, 1065
  spine, 1073
  vascular disorders, 1072
  MR-mammography, 1127
  discrepancies and pitfalls, 1137
  future challenges, 1138
  history, 1119
  indications for, 1136
  pathophysiological background, 1120
  technique, 1136
MR-mammography (MRM), 1127
MRS, 977, 985, 1005
  2D, 1015
  2D j-resolved, 1174
  ^{31}P MRS, 1143
  applications, 1015
  artefacts in localized, 1175
  breast, 1113
  breast cancer, 1077, 1120
  cancer
    pathology determination by, 1052
  chemical
    shift correlated, 1174
    imaging, 1116, 1172
  CT-COSY, 1173
  CT-PRESS, 1176
  data interpretation, 1119
  data processing and display, 1118
  for human biopsies, 1015
  human biopsies after, 1032

  human biopsies and, 1027, 1030, 1031
  improved volume selection, 1115
  in vitro, 1175
  in vivo, 1077, 1171
  in vivo ^{13}C, 1099
  infective brain lesions and, 1005
  JPRESS, 1174
  L-COSY, 1174
  liver, 1113, 1121
  localization schemes, 1114
  motion aspects, 1118
  MR-mammography and, 1127
  multi-voxel based, 1180
  multivoxel spectroscopy, 1172
  outer volume suppression, 1115
  prostate, 1113
  prostate cancer applications of, 1119
  rf coils, 1163
  SECSY, 1173
  single- and multi-voxel based, 1171
  single voxel spectroscopy, 1172
  spatial localization of of volume, 1172
  spectral-spatial pulses, 1116
  surface coils, 1117
  surgical specimens, 1051
  water and lipid suppression, 1115, 1171
MS
  LC-NMR and, 1227
  LC-NMR-MS, 1213
Mucor spp., 1008
multidimensional NMR
  pharmaceutical sciences and, 1239
multiplex NMR, 1227
multi-voxel based 2D MRS, 1180
multi-voxel based MRS, 1171
multivoxel neurospectroscopy, 1000
multivoxel spectroscopy, 993, 1171
muscular dystrophy, 1156

N

^{15}N-HSQC spectra of proteins, 1263
  alternative methods, 1267
  cross-correlated relaxation, 1264
  paramagnetic restraints derived from, 1264
  PLATYPUS algorithm for, 1265
  PRE, 1264
  RDC, 1264
  ε186–θ complexes, 1263, 1264, 1266
nano-NMR probes, 1326
nD-NMR data
  flow NMR techniques, 1217
necrosis, 991, 1057
neoplasia
  intraoperative MRI, 1065
neoplasm, 991, 1057
neurology
  intraoperative MRI and, 1057
neurospectroscopy, 985
  acquisition paradigms, 986
  consistency aspects, 992
  echo time, 988
  Global acquisition paradigms, 986
  Local acquisition paradigms, 986
  multivoxel spectroscopy, 993
  number of averages, 990
  patient positioning aspects, 986
  sequences, 988
  signal and homogeneity aspects, 985
  voxel size, 989
neurospectroscopy protocols
  clinical protocol decision matrix, 994
  frontal GM, 997
  hippocampus/temporal lobe, 997
  multivoxel neurospectroscopy, 1000
  standard gray matter (GM) or posterior cingulate gyrus (PCG), 995
  standard white matter protocol, 997
NMR
  3-FABS, 1393
  analysis of hairpin peptide/receptor complex, 1297
  analysis of zeta peptide/receptor complex, 1294
  antimicrobial peptides, structural characterization of, 1315, 1320
  based screening, 1419
  biomolecular, 1305
  borate complexes study by, 1347
  DI-NMR, 1203
  DNA folding, 1363
  drug binding, 1363
  drug discovery targets and, 1419
  drug–quadruplex interactions study, 1363
  FAXS, 1393
  FIA-NMR, 1213
  flow NMR techniques, 1213
  for high-throughput screening, 1393
  GFT-NMR, 1239
  in pharmaceutical sciences, 1195
  insulin flexibility and activity, 1370
  LC-NMR, 1211, 1213
  LC-NMR-MS, 1212
  membrane systems for, 1272
  metabonomics techniques and, 1377
  multiplex NMR, 1213
  NMR hyphenation developments, 1221
  on-flow LC-NMR, 1221
  parallel NMR, 1213
  protein misfolding disease, 1387, 1388
  protein NMR, 1287
  protein structure determination, 1243
  protein–protein interactions, 1347
  RDC application in protein NMR, 1287
  screening, 1196
    receptor-based, 1402, 1403
  SHAPES screening, 1409, 1410
  SPE-NMR, 1213
  STD NMR, 1421
  structural
    genomics and, 1429
  ternary complexes identification and characterization, 1347
  toxins active on
    potassium channels, structure determination of, 1325
    sodium channels, structure determination of, 1325
NMR-derived competitive non-peptide inhibitors, 1422
NMR-derived lead inhibitors, 1422
NMR-SOLVE strategy, 1199
NOAH, 1243
NOAH/DIANA approach, 1244
Nocardia spp., 1008
NOE, 1111, 1362
  in vivo 13C MRS and, 1101
  internal mobility, 1367
  spin diffusion, 1367
  ternary complexes identification and characterization, 1350, 1351
  transferred, 1357, 1367
NOESY
  antimicrobial peptides, structural characterization of, 1316
NOESY NMR
  antimicrobial peptides, structural characterization of, 1315
non-alcoholic fatty liver disease (NAFLD), 1121
non-alcoholic steatohepatitis (NAS), 1121
non-metalloproteins, paramagnets binding to, 1255
nonspecific binding
  transferred NOE, 1357
nonuniform sampling in biomolecular NMR, 1297, 1299
  example applications, 1307
  MaxEnt reconstruction, 1306
noun–verb generation (NVG), 1042
NTP, 1143
nuclear Overhauser effect. *See* NOE
nuclear vector replacement (NVR), 1243
nucleoside triphosphates, 1143
number of averages, neurospectroscopy and, 985

O

oncogenomics, 982, 1063
on-flow LC-NMR, 1221
optimizing isotropic bicelles, 1273
organic molecules structure
  determination, 1279

- organic molecules structure (*cont.*)
  - alignment media, 1280
  - alignment tensor, 1280
  - applications, 1283
  - experimental methods, 1281
  - liquid crystalline phases, 1280
  - partial alignment for, 1279
  - RDC measurement, 1281
  - relative size of RDCs, 1281
  - residual dipolar couplings, 1279
  - stretched polymer gels, 1280
- organic solvent mixtures, 1272
- orthographic lexical retrieval (OLR), 1042
- OSIRIS, 1176
- outer volume saturation (OVS), 1172
- outer volume suppression (OVS), 1115

P

- ^{31}P
  - adenosine diphosphate, 1146
  - chemical shift affecting factors, 1143
  - dependence of chemical shift on pH, 1143
  - general properties of, 1143
  - heteronuclear j coupling, 1143
  - homonuclear j-coupling, 1143
  - metabolites, 1144
  - phosphodiesters, 1144
  - phospholipids and bone, 1144
  - phosphomonoesters, 1144
  - spectral dispersion aspects, 1143
- ^{31}P MRS, 1143
  - acquisition hardware and condition, 1149
  - adiabatic rf pulses, 1153
  - aqueous fraction, 1146
  - biopsy and, 1143
  - breast cancer, 1077
  - broad resonances from phospholipids and bone, 1144
  - chemical shift and concentration referencing, 1146
  - chemical shift imaging, 1154
  - chemical shift referencing, 1156
  - double-resonance acquisition schemes, 1155
  - double-resonance coils, 1152
  - drug detection, 1158
  - dual phase extraction method, 1146
  - examples of, 1156
  - extraction methods, 1146
  - hardware for double resonance studies, 1152
  - in vivo, 1151
  - intact tissue samples, 1149
  - ISIS, 1156
  - lipid fraction, 1149
  - localization methods, 1153
  - magnets, 1151
  - metabolite concentrations estimation, 1156
  - metabolites observed in tissues, 1143
  - modified Folch's method, 1146
  - nucleoside triphosphates, 1145
  - peak areas measurement, 1156
  - perchloric acid, 1146
  - rf coils, 1151
  - single voxel localization, 1154
  - skeletal muscle, 1156
  - spectral analysis, 1149, 1156
  - spectroscopic imaging, 1154
  - surface coils, 1152
  - surface-coil localization, 1153
  - system options, 1152
  - tissue biopsy samples, 1146
  - tissue extracts application of, 1149
  - tumors, 1158
  - volume coils, 1152
- PACES, 1242
- Pandinus imperator toxins, 1328
- *Paragonimus spp.*, 1008
- paramagnetic induced residual dipolar couplings (pmiRDC), 1245
- paramagnetic labeling, 1263
  - fast assignments of 15N-HSQC spectra of proteins by, 1263
- paramagnetic nuclei
  - protein–protein interactions, 1339
- paramagnetic relaxation enhancement (PRE), 1255
- paramagnetic restraints
  - derived from ^{15}N-HSQC spectra of ε186–θ complex, 1264
  - resonance assignments from, 1265
- paramagnets
  - binding to non-metalloproteins, 1255
- paramagnets use, protein structures and, 1255
- pattern recognition methods
  - human biopsies and, 1032
- PCS
  - assignment, 1257
  - structural applications of, 1258
- peptide orientation
  - in bilayers (magainin 2), 1320
- peptide structure
  - hairpin, 1293
  - zeta, 1293
- peptides
  - antimicrobial, 1315
- perchloric acid (PCA), 1146
- perfusion, 1008
  - infective brain lesions and, 1005
- perfusion-weighted MR imaging, 1006
- peripheral vascular disease, 1157
- phagocytosis, 1004
- pharmaceutical sciences, NMR in, 1195, 1429
  - assignment process, speeding up, 1241
  - cryogenic NMR probe technology, 1206
  - drug design and discovery, 1195
  - drug discovery, 1239
  - drug effects studies, 1200
  - drug/target complexes, 1247
  - epothilone/tubulin complex, 1252
  - fast multidimensional NMR, 1239
  - flow NMR techniques, 1213
  - future directions, 1200
  - herbal drugs, 1229
  - ion channel blockers, 1325
  - LC-NMR, 1196, 1197, 1229
  - ligands-based screening, 1197
  - low-level impurities, 1206
  - NMR
    - data acquisition, 1239
    - hyphenation developments, 1221
    - screening, 1221
    - -SOLVE strategy, 1221
  - phospholipid bicelle membrane systems, 1271
  - protein structure determination, 1239, 1243
  - protein–protein interactions, 1339
  - SEA-TROSY, 1221
  - structure-based design, 1197
  - technical developments, 1196
  - transferred cross-correlated relaxation application, 1250
- phased array, 1166
- phosphodiesters, 1143
- phospholipid bicelle membrane systems, 1271
  - for NMR, 1272
  - liposomes, 1272
  - magnetically aligned bicelles, 1275
  - micelles, 1272
  - optimizing isotropic bicelles, 1273
  - organic solvent mixtures, 1272
  - phospholipid bicelles, 1272
- phospholipids and bone, 1144
- phosphomonoesters, 1144, 1158
- phosphorus MRS. *See* ^{31}P MRS
- PLATYPUS algorithm, 1265
- pmiRDC, 1255, 1256
  - structural applications of, 1256
- point-resolved spectroscopy. *See* PRESS
- polarization transfer, 1099
  - in vivo ^{13}C MRS, 1099
- polymer gels
  - stretched, 1280
- POPC bilayers, 1321
- post-column solid phase extraction, 1221

posterior cingulate gyrus (PCG) protocol, 995
post-HTS screening, 1414
potassium channels active toxins, 1325
pre-processing
  functional MRI, 1037
Prescan routine, 995
PRESS, 988, 995, 1005, 1077, 1105, 1110
  2D CT-PRESS, 1176
  ^{31}P MRS, 1153, 1154
PRESSSV, 1172
principal component analysis (PCA), 1051
prion protein, 1388
probe technology
  cryogenic NMR, 1205
probes
  cold probes, 1217
  cryogenic, 1226
  microcoils, 1326
  microprobes, 1326
  nano-NMR probe, 1326
profiling
projection angles (between tensors) measurement, 1247
projection-reconstruction (PR) techniques, 1240
prostate
  MRS, 1113
prostate cancer
  MRS and, 1119
protegrin-1, 1320
protein complexes
  docking, 1344
protein misfolding disease, 1387
  amyloid precursor protein and, 1389
  CJD, 1388
  Cu-Zn-superoxide dismutase, 1390
  natively unfolded proteins involved in, 1387
  NMR parameters and, 1387
  prion protein, 1389
  proteins involved in, 1388
  transthyretin and, 1390
  TSE, 1388
  α-synuclein and, 1389
protein NMR, RDC application in, 1283, 1285
  measurement of backbone RDC, 1284
protein structure
  determination, automated, 1243
  NMR in, 1239
  NOESY, 1243
  paramagnets use, 1255
  PCS assignment and, 1257
  pmiRDCs and, 1257
  stabilization by TFE, 1371
  unsaturated protein, 1371
protein–ligand interactions, 1404
protein–protein interactions
  chemical exchange and, 1343
  chemical shift perturbation experiments, 1342
  cross-saturation, 1343
  deuteration, 1340
  differential isotope labeling, 1340
  docking protein complexes, 1344
  larger protein complexes (size issues),
  long-range structural information, 1341
  NMR and, 1341
  paramagnetic nuclei, 1341
  residual dipolar couplings, 1341
  stability improvement aspects, 1344
  TROSY, 1340
proteins. *See also* membrane proteins
  15N-HSQC spectra of, 1263
  cryogenic NMR probe technology applications, 1210
  des-[phe(B25)] insulin, 1370
  H-bonded amide protons, 1370
  hot spots on protein surfaces, 1402
  human growth hormone, 1372
  insulin flexibility and activity, 1370
  insulin–receptor interaction, 1371
  PT insulin, 1371
  ε186–θ complex, 1263, 1264
proton decoupling, 1100
proton-decoupler, 1100
proton-decoupling
  in vivo ^{13}C MRS, 1101
proton-observed, carbon-edited (POCE), 1102
PS-COSY, 1019
pseudocontact shifts (PCS), 1255, 1265
Pseudomonas aeruginosa, 1331
pulse sequences
  for in vivo ^{13}C MRS, 1089
  human biopsies and, 1018
pus, 985, 1005
PWI. *See* perfusion-weighted MR Imaging

Q

Q factor, 1164
quadruplex DNA
  exchange rates for drug binding to, 1363
quality factor
  rf coils, 1163
quantification
  in vivo molecular MRI, 1095
  quantitation, human biopsies and, 1015

R

Radon transform, inverse, 1240
reactive nodes, 982, 1062
receive-only coils, 1167
receptor binding
  IgE and, 1294
receptor-based NMR screening, 1401
  drug discovery and, 1393
  methods, 1393
regression analysis
  human biopsies and, 1027
relative cerebral blood volume (rCBV), 1006
relaxation
  T_1-relaxation, 982
  T_2-relaxation, 983
  transferred cross-correlated, 1247
relaxation times
  T_1-relaxation time, 982
  T_2-relaxation time, 983
repetition time
  functional MRI and, 1037
reproducibility
  in vivo ^{13}C MRS and, 1089
residual dipolar coupling, 1251
  backbone, 1287
  organic molecules structure determination, 1279, 1284
  protein–protein interactions, 1339
  relative size of, 1281
resolution
  in vivo molecular MRI, 1095
resonance assignments from paramagnetic restraints, 1264
resonances
  backbone amide, 1332
  imidazole, 1331
responsive contrast agent, 982, 1091
  in vivo molecular MRI, 1095
rf coils
  B1 homogeneity and SNR, 1168
  dual frequency rf coils, 1169
  implanted rf coils, 1168
  issues, 1163
  local rf coils, 1168
  microcoils, 1168
  MRS and, 1163
  phased array, 1166
  quality factor issues, 1163
  requirements, 1163
  saddle-shape coils, 1164
  SNR issues, 1163
  solenoid coils, 1164
  superconducting, 1166
  surface coil, 1165
  transmit-only and receive-only coils, 1167
robotics
  intraoperative MRI, 1065
R-thiomandelic acid, 1334

S

saddle-shape coils, 1164. *See also* rf coils
SAMPA, 1242
sample preparation
  cryogenic NMR probe technology, 1206
sample preparation, human biopsies and, 1015
Sampling
  nonuniform, 1305, 1306
sampling, nonuniform
  MaxEnt reconstruction, 1306
SAR (specific absorption rate), 1111
SAR limits, 1167
sarcoma
  HRMAS MAS of, 1052
saturation
  T1-saturation, 983
  NMR-based screening and, 1415
scalar coupling, 1015
schwannoma, 1057
scorpion toxins
  ion channel blockers and structure determination of, 1318
scorpion toxins structure, 1325
screening. *See also* high-throughput screening 1D NMR-based, 1421
  applied to drug targets, 1423
  core replacement strategy, 1402
  drug discovery targets and, 1419
  fragment linking, 1405
  fragment-based, 1401
  high-throughput core elaboration, 1404
  HSQC-based, 1420
  in drug discovery, 1393
  lead optimization aspects, 1414
  ligand-detected 1D NMR-based, 1421
  NMR SHAPES, 1409
  NMR-based, 1419
  post-HTS, 1414
  pre-HTS, 1412
  receptor-based methods for lead vaklidation and characterization, 1412
  receptor-based NMR, 1402, 1403
  STD NMR, 1421
Scutellaria lateriflora, 1230
SEA-TROSY, 1195
SECSY, 1176
sensitivity, 988
  defined, 1083
Serratia marcescens, 1331
SHAPES screening
  compound library, design of, 1404
  implementation, 1408
  NMR methods for screening compound libraries, 1410
  post-HTS, 1414
  pre-HTS, 1412
  principles, 1409
shifted sine-bell (SSB) function, 1020
signal and homogeneity, 985
signal-to-noise. *See* SNR
simulation
  2D MRS, 1171
sine-bell (SB) function, 1020
single coils, 1151
single dual-resonant coil, 1152
single volume localized 2D MRS, 1173
single voxel localization methods, 1153
single voxel spectroscopy, 1172
single-voxel based MRS, 1180
skeletal muscle (in vivo ^{31}P MRS), 1156
skullcap herb, 1229
slice timing correction, 1040
  between two conformers, 1364
slow exchange equilibria DNA hairpin folding and, 1364
small molecule
  applications
    cryogenic NMR probe technology, 1205
SNR
  B1 homogeneity versus, 1163
  dual frequency rf coils, 1169
  implanted rf coils, 1168
  in vivo ^{13}C MRS, 1099
  in vivo molecular MRI, 1095
  issues in rf coils, 1163
  local rf coils, 1168
  phased array, 1166
  principles, 985
  superconducting rf coils, 1166
  surface coils, 1156
sodium channels active toxins, 1327
solenoid coils, 1164. *See also* rf coils
solid phase extraction
  post-column, 1217
solid-state high resolution NMR
  protein misfolding disease, 1387
solid-state NMR
  protein misfolding disease, 1387
solution structures
  antimicrobial peptides, 1315
spatial localization of volume, 1166
spatial normalization, functional MRI, 1037
spatially resolved 2D MRS, 1171
specificity, 988
  defined, 1083
spectral analysis
  31P MRS, 1143
spectral dispersion, 1143
spectral-spatial pulses (MRS), 1116
spectroscopic imaging, 1154
  31P MRS, 1155
SPE-NMR
  flow NMR techniques, 1213
  NOE, 1339
  transferred NOE, 1351
spine
  intraoperative MRI, 1065
standard white matter protocol, 997
Staphylococcus aureus, 1009
statistical analysis
  functional MRI, 1037
statistical classification strategy (SCS), 1051
STD NMR, 1421
STEAM
  ^{31}P MRS, 1145, 1146
STEAMSV, 1172
stem cell, 1088, 1089
Stenotrophomonas maltophilia, 1331
Streptococcus aureus, 1010
Streptococcus milleri, 1009
stretched polymer gels
  organic molecules structure determination, 1279
structural characterization of antimicrobial peptides
  NMR for, 1294
structural genomics, NMR and, 1421
  advances in NMR instrumentation, 1431
  advantages and disadvantages of NMR, 1429
  CRINEPT, 1431
  strategies and targets in, 1429
  TROSY, 1431
structure elucidation of aloe metabolites, 1232
superconducting rf coils, 1166
superparamagnetic iron oxide particles, 1088
surface coils, 1099, 1101, 1117
surface-coil localization, 1153
surgical specimens
  brain, 1043
  breast, 1052
  cancer pathology determination, 1052
  cervix, 1060
  data analysis, 1054
  experimental aspects, 1053
  histopathology, 1051
  histopathology limitations, 1051
  HRMAS, 1051
  HRMAS method, 1052
  human malignancies characterization, 1051
  kidney, 1060
  methodology, 1052
  prostate, 1053
  proton MRS of, 1051
  sample preparation, 1053
  spectrometer settings, 1053

T

T$_1$-relaxation, 1111
T$_1$-relaxation time, 1111
T$_1$-saturation, 1112
T$_2$-relaxation, 1112
T$_2$-relaxation time, 1112
Taenia solium, 1008
TEMPO spin labels, 1268
tensors
  projection angles between, 1247
ternary complexes identification and characterization
  borate complexes, 1348
  complexes involving organic molecules, 1350
  ILOE observations, 1352, 1354
  NMR for, 1347
  NOE, 1351
  type II dihydrofolate reductase, 1354
TFE, 1369, 1371
TFE for protein structure stabilization, 1371
thiomandelate binding, 1335
thiomandelate binding effect on 113Cd spectrum, 1335
tissue biopsy
  ^{31}P MRS, 1146
tissues
  ^{31}P MRS features in, 1143
  extracts application of, 1149
  intact (MRS), 1149
  metabolites observed in, 1143
Tityus serrulatus, 1327
TOCSY, 1015, 1016
  2D, 1232
  antimicrobial peptides, structural characterization of, 1315, 1316
toxicity
  in vivo molecular MRI, 1092
toxins
  active on potassium channels, 1327
  active on sodium channels, 1327
  scorpion, 1325
Toxoplasma gondii, 1006
transfection, 1090, 1093
transferred cross-correlated relaxation, 1247
  epothilone/tubulin complex, 1247
transferred NOE, 1357, 1359
  affinities and timescales, 1357
  nonspecific binding, 1361
  practical implementation, 1361
  related experiments, 1362
  spin diffusion, 1361
transmissible spongiform encephalopathies (TSE), 1388
transmit-only coils, 1167
transthyretin, protein misfolding disease and, 1369
Triticum turgidum, 1318
TROSY, 1431
  pharmaceutical sciences, 1195, 1196
  protein–protein interactions, 1340
  structural genomics and, 1431
tumors
  ^{31}P MRS, 1158
  human biopsies and, 1032
type II dihydrofolate reductase, 1354

U

U-FLARE, 1182
ultra-small paramagnetic iron oxide particles, 1007
unstructured protein, 1371

V

vascular disorders
  intraoperative MRI, 1072
  vascular endothelial growth factor (VEGF), 1130
vascular permeability factor (VPF), 1130
very selective suppression (VSS), 1115
volume coils, 1152
volume of interest
  breast cancer, in vivo MRS, 1077
volume of interest (VOI), 1005
VOSY, 1176
voxel of interest, 985
voxel position, 986
  areas to be avoided (blood), 987
  areas to be avoided (cerebral spinal fluid), 987
  areas to be avoided (necrosis), 987
  areas to be avoided (open space), 987
  areas to be avoided (skull), 987
voxel position, neurospectroscopy and, 986
voxel size, 985. *See also* echo time

W

water and lipid suppression, 1172
  MRS, 1115
WaterLOGSY, 1410
Window functions, human biopsies and, 1016

Z

zeta peptide structure, 1293
zeta peptide/receptor complex
  NMR analysis of, 1293

Modern Magnetic Resonance

Part 3

Part 1: Applications in Chemistry, Biological and Marine Sciences

Part 2: Applications in Medical and Pharmaceutical Sciences

Part 3: Applications in Materials Science and Food Science

Modern Magnetic Resonance

Part 3: Applications in Materials Science and Food Science

Graham A. Webb (Ed.)
Royal Society of Chemistry, London, UK

Springer

A C.I.P. Catalogue record for this book is available from the Library of Congress.

ISBN 978-1-4020-3894-5 (HB)
ISBN 978-1-4020-3910-2 (e-book)

Published by Springer,
P.O. Box 17, 3300 AA Dordrecht, The Netherlands.

www.springer.com

Printed on acid-free paper

First published in 2006
Reprinted with corrections in 2008

All rights reserved.
© 2008 Springer
No part of this work may be reproduced, stored in a retrieval system, or transmitted in any form or by any means, electronic, mechanical, photocopying, microfilming, recording or otherwise, without written permission from the Publisher, with the exception of any material supplied specifically for the purpose of being entered and executed on a computer system, for exclusive use by the purchaser of the work.

Contents

List of Section Editors IX
Preface XI
Color Plate Section XIII

APPLICATIONS IN MATERIALS SCIENCE

Foreword 1437

- **Acoustically Stimulated NMR Relaxometry: Application to the Study of Molecular Dynamics in Liquid Crystalline Materials,** *E. Anoardo and F. Bonetto* 1439
- **Characterization of Elastomers Based on Monitoring Ultraslow Dipolar Correlations by NMR,** *Farida Grinberg* 1445
- **Correlating Molecular and Macroscopic Properties of Elastomers by NMR Relaxometry and Multi-pulse NMR Techniques,** *S. Stapf, S. Kariyo, and B. Blümich* 1455
- **Determining Structural and Dynamic Distribution Functions from Inhomogeneously Broadened NMR Spectra: The Conjugate Orthogonal Functions Approach,** *Marcel Utz and Magesh Nandagopal* 1463
- **Fluid Diffusion in Partially Filled Nanoscopic and Microscopic Porous Materials,** *I. Ardelean, G. Farrher, C. Mattea, and R. Kimmich* 1471
- **Gas Adsorption on Carbon Nanotubes,** *Tanja Pietraß* 1479
- **Magnetic Resonance Studies of the Heterogeneous Rotational and Translational dynamics in Disordered Materials,** *R. Böhmer, G. Diezemann, G. Hinze, K.R. Jeffrey, and M. Winterlich* 1487
- **Nuclear Magnetic Resonance in Ferromagnetic Multilayers and Nanocomposites: Investigations of Their Structural and Magnetic Properties,** *C. Mény and P. Panissod* 1493
- **^{1}H Solid-State NMR of Supramolecular Systems,** *Ingo Schnell and Hans Wolfgang Spiess* 1499
- **Quadrupolar NMR of Inorganic Materials: The Multiple-Quantum Magic Angle Spinning Experiment,** *Stephen Wimperis* 1507
- **Rheo-NMR Spectroscopy,** *Claudia Schmidt* 1515
- **Advances in Single-Sided NMR,** *J. Perlo, F. Casanova, and B. Blümich* 1523
- **Site-specific Characterization of Structure and Dynamics of Complex Materials by EPR Spin Probes,** *Dariush Hinderberger and Gunnar Jeschke* 1529
- **NMR of Organic Semiconductors,** *Magesh Nandagopal, Mathew Mathai, Fotios Papadimitrakopoulos, and Marcel Utz* 1539
- **Solid State NMR of Xerogels,** *J.L. Yarger, D.A. Buttry, and G.P. Holland* 1547
- **Solid-State ^{17}O NMR Spectroscopy of High-Pressure Silicates,** *Sharon E. Ashbrook* 1551
- **The Structure of Oxide Glasses: Insights from ^{17}O NMR,** *Philip J. Grandinetti and Ted M. Clark* 1563
- **Studies of the Local Structure of Silk Using Solid-State NMR,** *Jacco D. van Beek, Lilyane Beaulieu and Beat H. Meier* 1569
- **Velocity Imaging of Granular Materials,** *Siegfried Stapf, A. Khrapitchev, C. Heine and Bernhard Blümich* . 1581

APPLICATIONS IN FOOD SCIENCE

Foreword 1591
Glossary 1593

High Resolution Solution State Methods 1595

- **Characterization of the Chemical Composition of Beverages by NMR Spectroscopy,** *Jurkica Kidrič and Iztok Jože Košir* 1597
- **High Resolution NMR of Carrageenans,** *Fred van de Velde and Harry S. Rollema* 1605

Flavor–Food Compound Interactions by NMR Spectroscopy, *C. Moreau and E. Guichard* 1611
High-Resolution Nuclear Magnetic Resonance Spectroscopy of Fruit Juices, *Ana M. Gil and Iola F. Duarte* 1617
High-Resolution NMR Spectroscopy in Human Metabolism and Metabonomics, *Huiru Tang and Yulan Wang* 1623
High-Resolution NMR of Milk and Milk Proteins, *Josefina Belloque* 1631
High-Resolution ^{13}C Nuclear Magnetic Resonance in the Study of Oils, *Maria Antonietta Brescia and Antonio Sacco* 1637
High-Resolution ^{1}H Nuclear Magnetic Resonance in the Study of Oils, *Maria Antonietta Brescia and Antonio Sacco* 1645
SNIF-NMR—Part 1: Principles, *Gérard J. Martin, Serge Akoka, and Maryvonne L. Martin* 1651
SNIF-NMR—Part 2: Isotope Ratios as Tracers of Chemical and Biochemical Mechanistic Pathways, *Maryvonne Martin, Benli Zhang, and Gérard J. Martin* 1659
SNIF-NMR—Part 3: From Mechanistic Affiliation to Origin Inference, *Gérard J. Martin, Maryvonne L. Martin and Gérald Remaud* 1669
SNIF-NMR—Part 4: Applications in an Economic Context: The Example of Wines, Spirits, and Juices, *Eric Jamin and Gérard J. Martin* 1681
High-Resolution Nuclear Magnetic Resonance Spectroscopy of Wine, Beer, and Spirits, *Ana M. Gil and Iola F. Duarte* 1689

Relaxation Time Methods 1695

NMR Relaxation of Dairy Products, *F. Mariette* 1697
Characterization of Molecular Mobility in Carbohydrate Food Systems by NMR, *Pavinee Chinachoti, Elena Vittadini, Pathama Chatakanonda, and Yael Vodovotz* 1703
Diffusion and Relaxation in Gels, *Joachim Götz and Ruth Hinrichs* 1713
NMR Relaxation and Diffusion Studies of Horticultural Products, *B.P. Hills* 1721
Proton NMR Relaxometry in Meat Science, *Hanne Christine Bertram and Henrik Jørgen Andersen* 1729
Time-Domain NMR in Quality Control: More Advanced Methods, *Gisela Guthausen, Harald Todt, Wolfgang Burk, Dieter Schmalbein, and Andreas Kamlowski* 1735
Time-Domain NMR in Quality Control: Standard Applications in Food, *Harald Todt, Gisela Guthausen, Wolfgang Burk, Dieter Schmalbein, and Andreas Kamlowski* 1739
Nuclear Magnetic Relaxation in Starch Systems, *Huiru Tang and Yulan Wang* 1745

High Resolution Solid State Methods 1755

Magic Angle Spinning NMR of Flours and Doughs, *Maria Antonietta Brescia and Antonio Sacco* 1757
High-Resolution Magic Angle Spinning NMR Spectroscopy of Fruits and Vegetables, *Ana M. Gil and Iola F. Duarte* 1765
High-Resolution Solid-State NMR of Gluten and Dough, *Lucia Calucci and Marco Geppi* 1769
High-Resolution Solid-State NMR as an Analytical Tool to Study Plant Seeds, *Michel Bardet, Marie Françoise Foray, and Armel Guillermo* 1777
High-Resolution Solid-State NMR Spectroscopy of Starch Polysaccharides, *Huiru Tang and Yulan Wang* 1783

Imaging and Related Techniques 1793

NMR Imaging of Bread and Biscuit, *Lucas Tiphaine, M. Wagner, S. Quellec, and A. Davenel* 1795
NMR Imaging of Dairy Products, *F. Mariette* 1801
NMR Imaging of Dough, *Lucas Tiphaine, A. Grenier G. Collewet, and A. Davenel* 1807
MRI in Food Process Engineering, *Joachim Götz* 1813
Rheo-NMR: Applications to Food, *Joachim Götz and Klaus Zick* 1819
Temperature Measurements by Magnetic Resonance, *Kevin P. Nott and Laurance D. Hall* 1825

Statistical Methods 1831

Chemometric Analysis of NMR Data, *Nanna Viereck, Lars Nørgaard, Rasmus Bro, and Søren B. Engelsen* . 1833
Direct Exponential Curve Resolution by Slicing, *Søren B. Engelsen, Henrik T. Pedersen, and Rasmus Bro* 1847

ESR Methods 1853

ESR as a Technique for Food Irradiation Detectio, *Eric Marchioni* 1855
ESR Spectroscopy for the Study of Oxidative Processes in Food and Beverages, *Mogens L. Andersen and Leif H. Skibsted* 1861

Applications to Food Systems 1867

Magnetic Resonance Studies of Food Freezing, *William L. Kerr* 1869
Nuclear Magnetic Resonance Studies on the Glass Transition and Crystallization in Low Moisture Sugars, *Bill MacNaughtan* 1879
Probing the Sensory Properties of Food Materials with Nuclear Magnetic Resonance Spectroscopy and Imaging, *Youngsoo Lee, Soo-Yeun Lee, and Shelly J. Schmidt* 1889
Single-Sided NMR in Foods, *Gisela Guthausen, Harald Todt, Wolfgang Burk, Dieter Schmalbein, Andreas Guthausen, and Andreas Kamlowski* 1895
Applications of NMR in the Studies of Starch Systems, *Imad A. Farhat* 1899

Author Index
Subject Index

List of Section Editors

Subject	Name	Type of Editor
	Graham A. Webb	Editor-In-Chief
Chemistry	Hazime Saitô Himeji Institute of Technology and QuLiS, Hiroshima University Japan e-mail: hsaito@siren.ocn.ne.jp	Section Editors
	Isao Ando Department of Chemistry and Materials Science Tokyo Institute of Technology, Ookayama, Meguro-ku Tokyo 152-0033 Japan e-mail: iando@polymer.titech.ac.jp	
	Tetsuo Asakura Department of Biotechnology Tokyo University of Agriculture and Technology Koganei, Tokyo 184-8588 Japan e-mail: asakura@cc.tuat.ac.jp	
Biological Sciences	Jimmy D. Bell Molecular Imaging Group, MRC Clinical Sciences Centre Hammersmith Hospital Campus, Imperial College London London, W12 OHS UK e-mail: jimmy.bell@csc.mrc.ac.uk	Section Editor
Marine Science	M. Aursand SINTEF Fisheries and Aquaculture Ltd N-7465 Trondheim Norway e-mail: marit.aursand@sintef.no	Section Editor
Medical Science	Carolyn Mountford Institute for Magnetic Resonance Research, and Department of Magnetic Resonance in Medicine University of Sydney, PO Box 148, St Leopards, 1590, NSW Australia email: caro@imrr.usyd.edu.au	Section Editor
	Uwe Himmelreich, PhD Max-Planck-Institute for Neurological Research In vivo NMR Group, Gleueler Str 50, Cologne, D-50931 Germany email: himmelreich@mpin-koeln.mpg.de	
	Deborah Edward Pageturner (Editing & Research Services)	Assistant Editor

Subject	Name	Type of Editor
Pharmaceutical Science	David Craik Institute for Molecular Bioscience University of Queensland Brisbane 4072, Queensland Australia e-mail: d.craik@imb.uq.edu.au	Section Editor
Materials Science	Marcel Utz University of Connecticut, 97 N Eagleville Rd Storrs CT 06269-3136 e-mail: marcel.utz@uconn.edu	Section Editor
Food Science	Peter Belton School of Chemical Sciences and Pharmacy University of East Anglia Norwich NR4 7TJ, UK e-mail: p.belton@uea.ac.uk	Section Editor

Preface

It is a great pleasure for me to Introduce the handbook of Modern Magnetic Resonance, MMR. The various techniques which comprise MMR derive essentially from three sources, all of which were produced by physicists. Today they are widely used by scientists working in many diverse areas such as chemistry, biology, materials, food, medicine and healthcare, pharmacy and marine studies.

The first source of MMR studies is nuclear magnetic resonance, NMR. This provides details on the relative positions of nuclei, i.e. atoms, in a molecule. Consequently NMR provides structural information on samples which may be in the solid, liquid or gaseous state. Nuclear relaxation data yield dynamic information on the sample and the topology of the dynamic processes if the sample is undergoing a molecular change. Thus high and low resolution NMR studies provide information on all interesting aspects of molecular science. The protean nature of NMR is reflected in its many applications in chemistry, biology and physics which explore and characterize chemical reactions, molecular conformations, biochemical pathways and solid state materials, to name a few examples.

Magnetic resonance imaging, MRI, is the second source of MMR data. MRI provides a three-dimensional image of a substance, and is consequently widely employed to assess materials both *in vitro* and *in vivo*. The importance of MRI studies in many areas of science and medicine is shown by the recent award of the Nobel Prize to Lauterbur and Mansfield.

The third source of MMR results is due to electron spin resonance, ESR. This is a technique for detecting unpaired electrons and their interactions with nuclear spins in a given sample. Thus ESR data are often used to complement the results of NMR experiments.

Taken together NMR, MRI and ESR comprise the field of MMR, recent years have witnessed the fecundity of these techniques in many scientific areas. The present three volumes cover applications in most of these areas. Part 1 deals with Chemical Applications, Biological and Marine Sciences. Medical and Pharmaceutical Sciences are covered in Part 2. Part 3 provides examples of recent work in the Materials Science and Food Science.

I wish to express my gratitude to all of the Section Editors and their many contributors for their hard work and dedication in the creation of MMR. My thanks also go to Emma Roberts and the production staff at Springer, London, for their assistance in the realization of these volumes.

Royal Society of Chemistry
Burlington House
Piccadilly
London, W1J OBA

G.A.WEBB
February 2005

Please note that authors used either British or American English spelling depending on the language of their choice for individual papers.

Graham A. Webb (ed.), Modern Magnetic Resonance, XI.
© 2008 *Springer.*

Color Plate Section

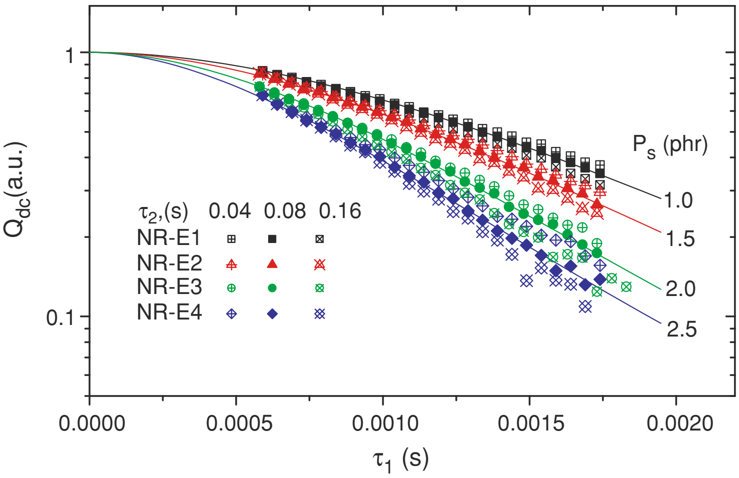

Plate 115. See also Figure 1 on page 1448.

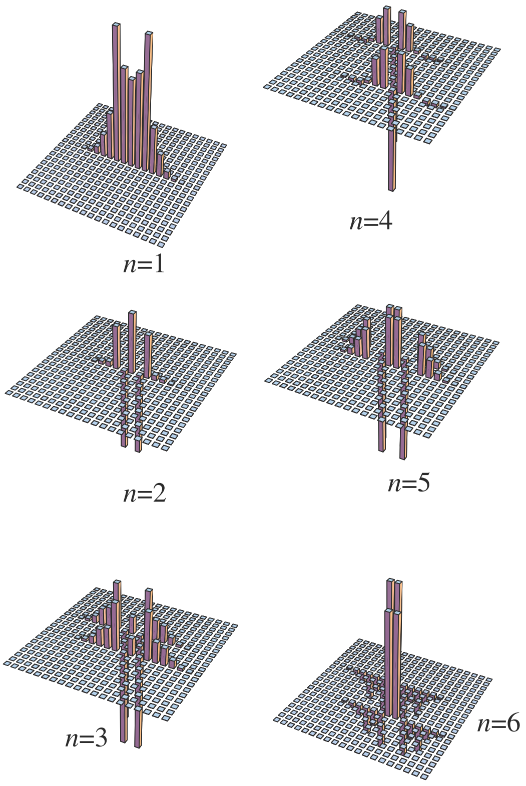

Plate 116. See also Figure 3 on page 1467.

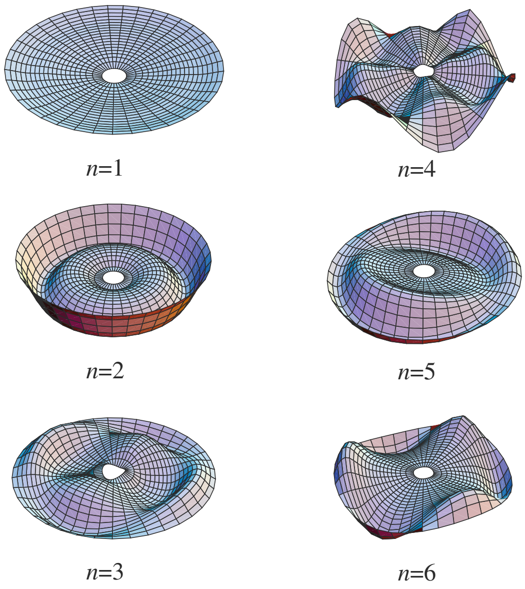
n=1
n=4
n=2
n=5
n=3
n=6

Plate 117. See also Figure 4 on page 1467.

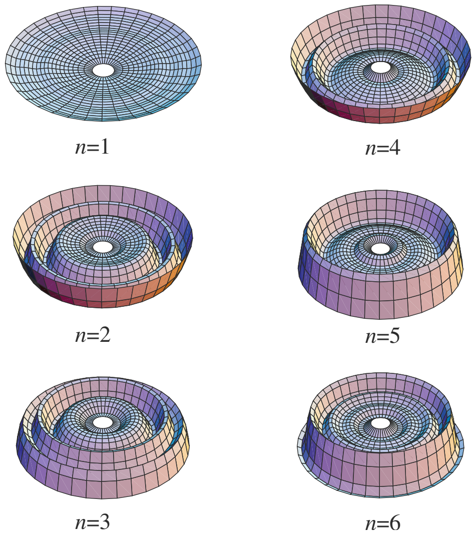
n=1
n=4
n=2
n=5
n=3
n=6

Plate 118. See also Figure 5 on page 1468.

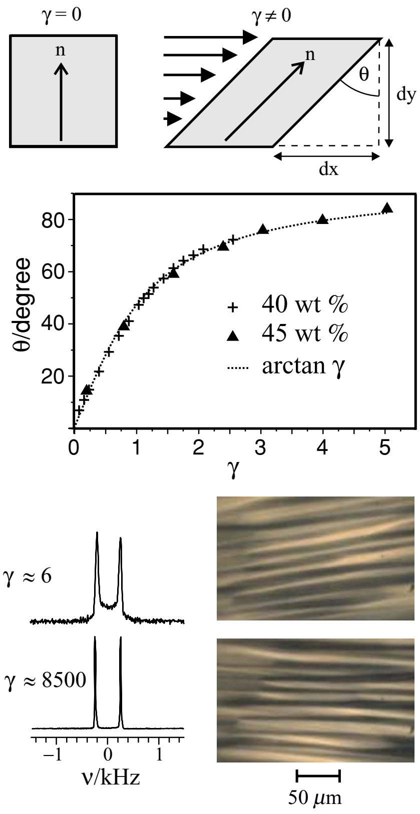

Plate 120. See also Figure 3 on page 1518.

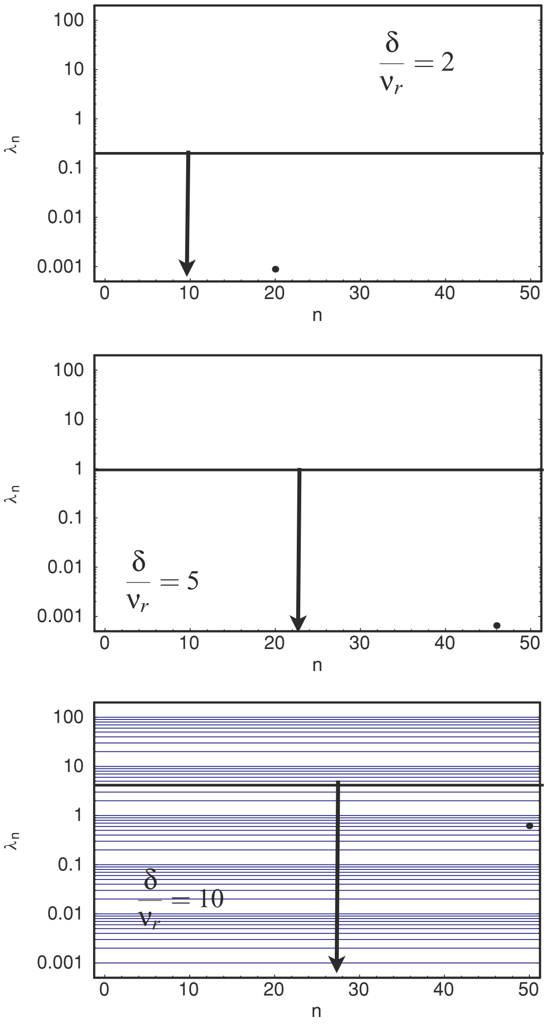

Plate 119. See also Figure 6 on page 1468.

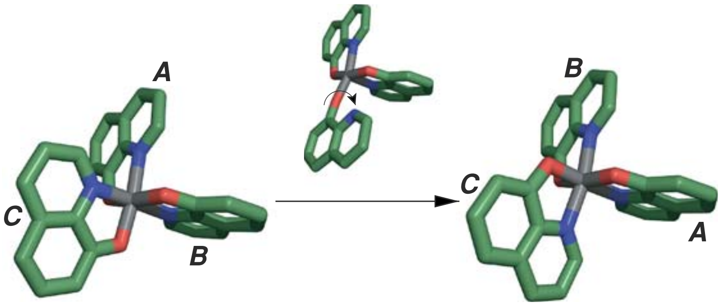

Plate 121. See also Figure 3 on page 1543.

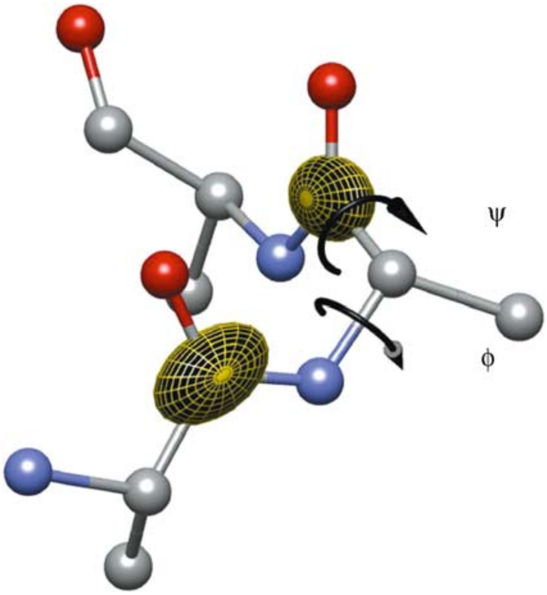

Plate 122. See also Figure 1 on page 1570.

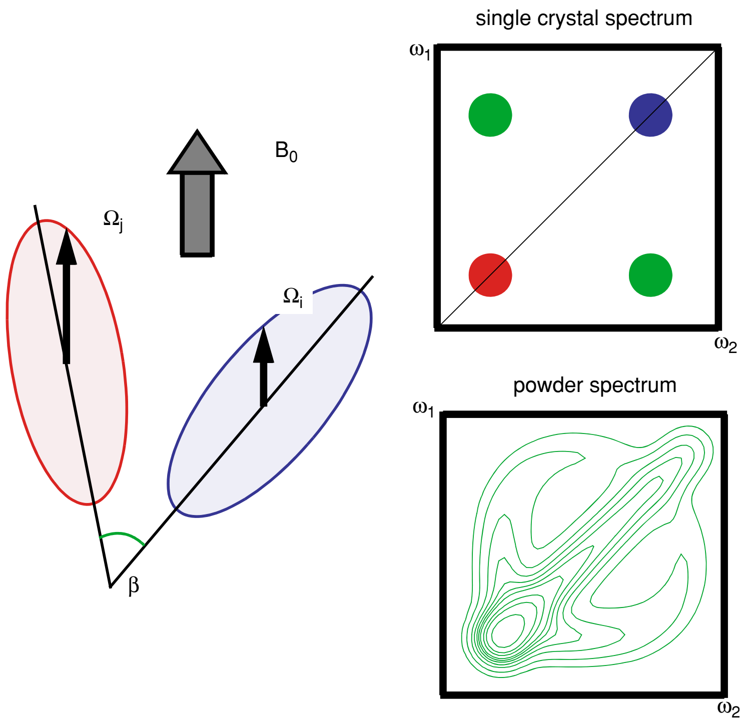
single crystal spectrum
ω1
ω2
B0
Ωj
Ωi
β
powder spectrum
ω1
ω2

Plate 123. See also Figure 2 on page 1571.

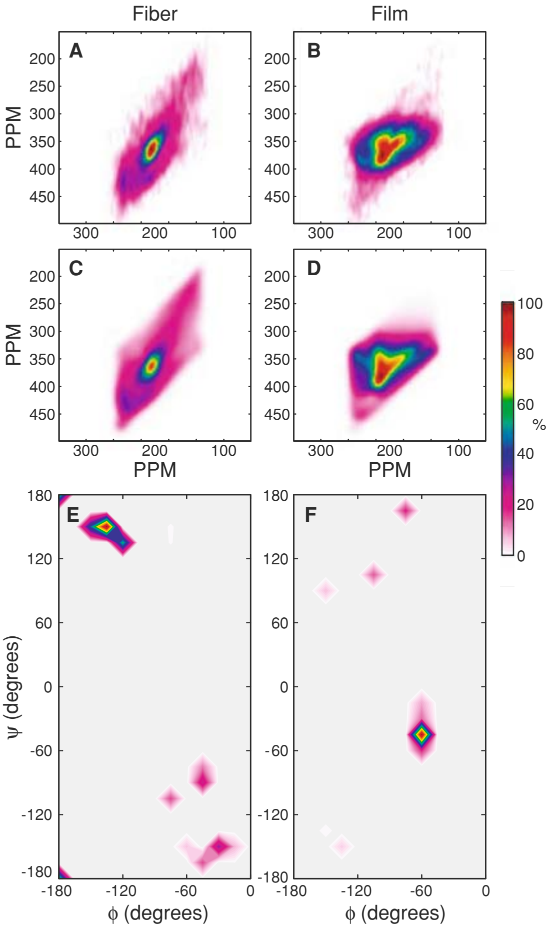

Plate 124. See also Figure 3 on page 1572.

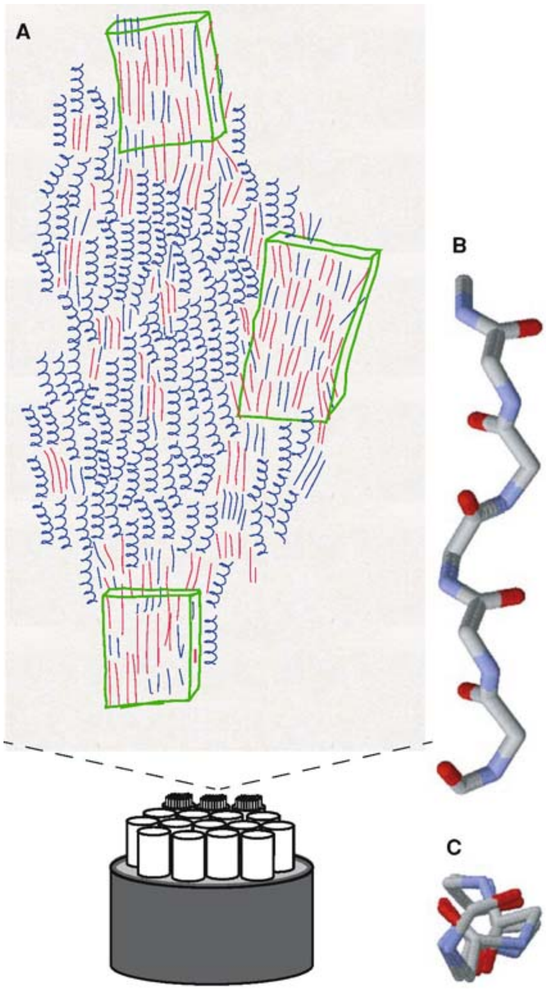

Plate 125. See also Figure 4 on page 1572.

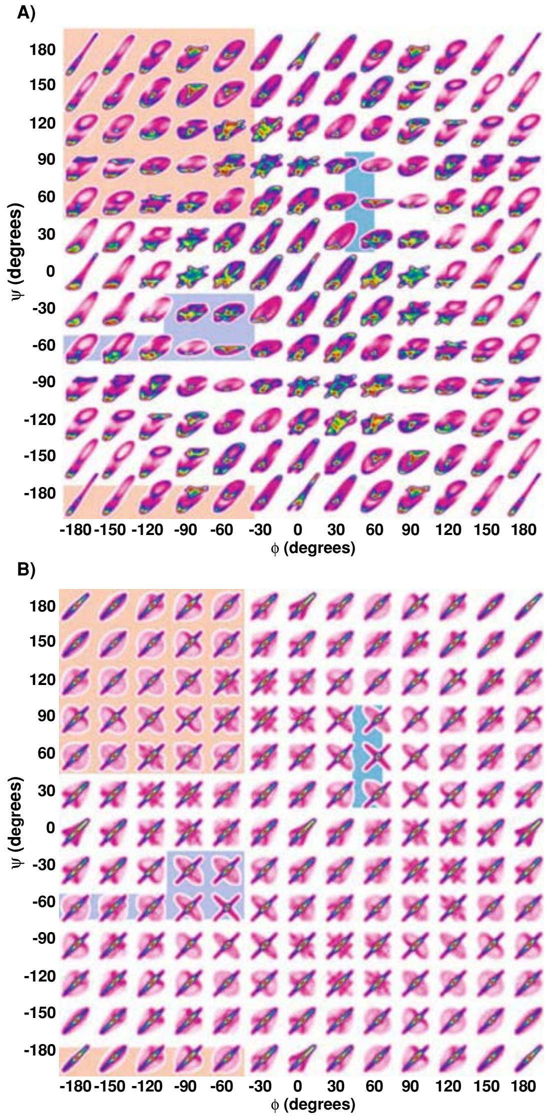

Plate 126. See also Figure 5 on page 1573.

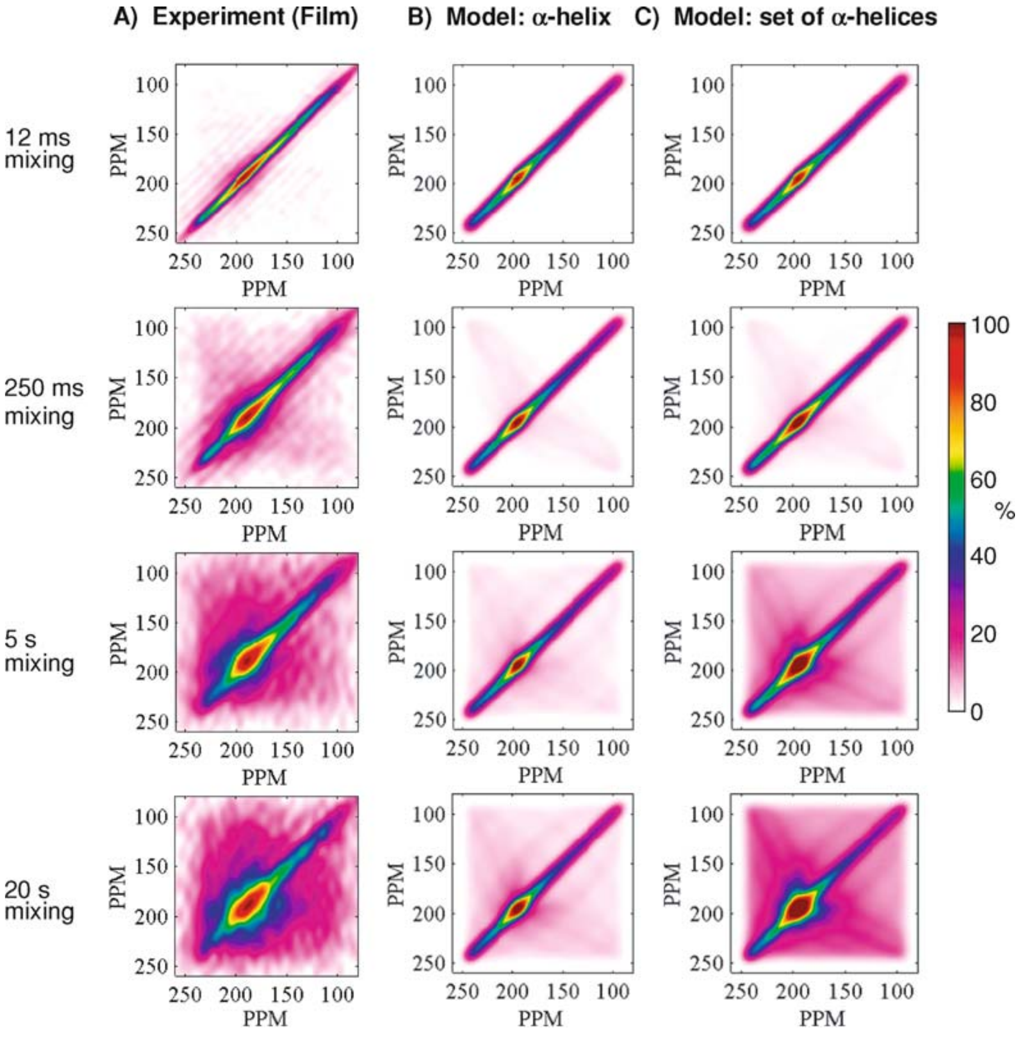

Plate 127. See also Figure 7 on page 1575.

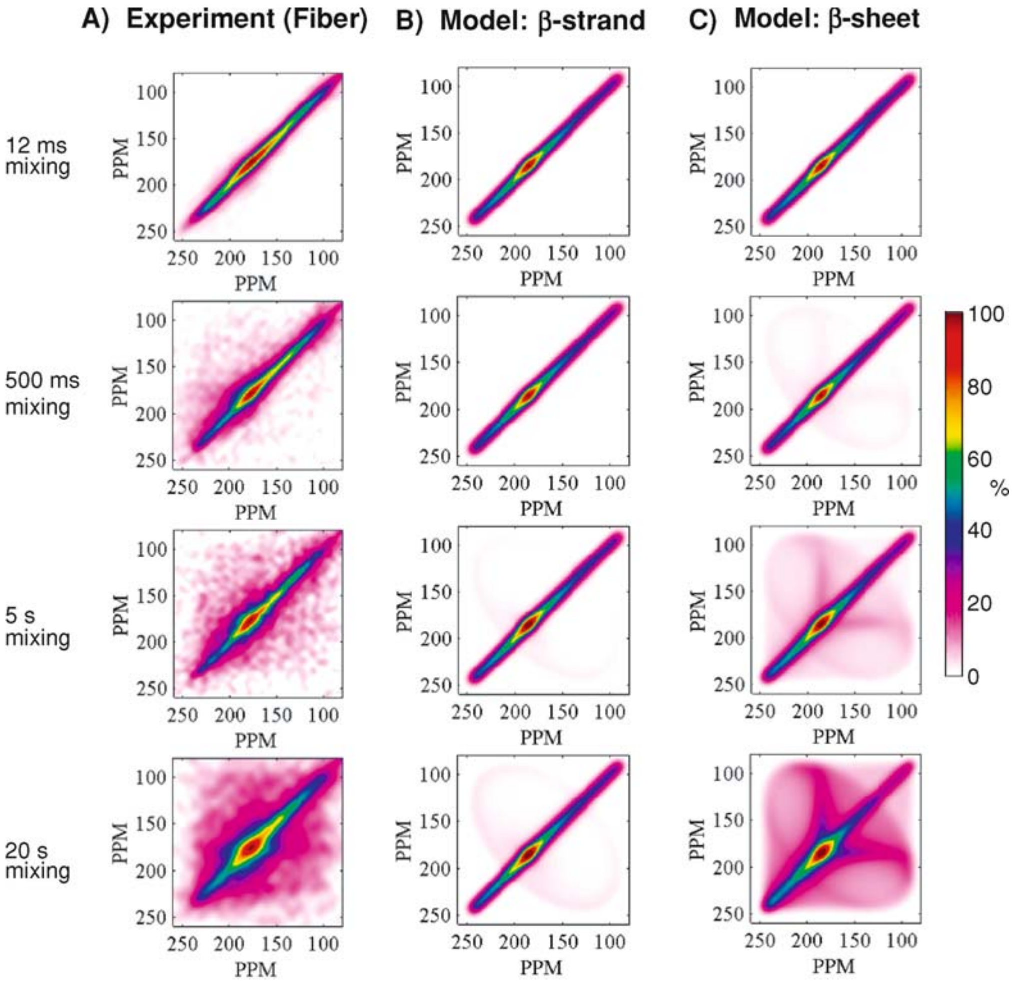

Plate 128. See also Figure 8 on page 1576.

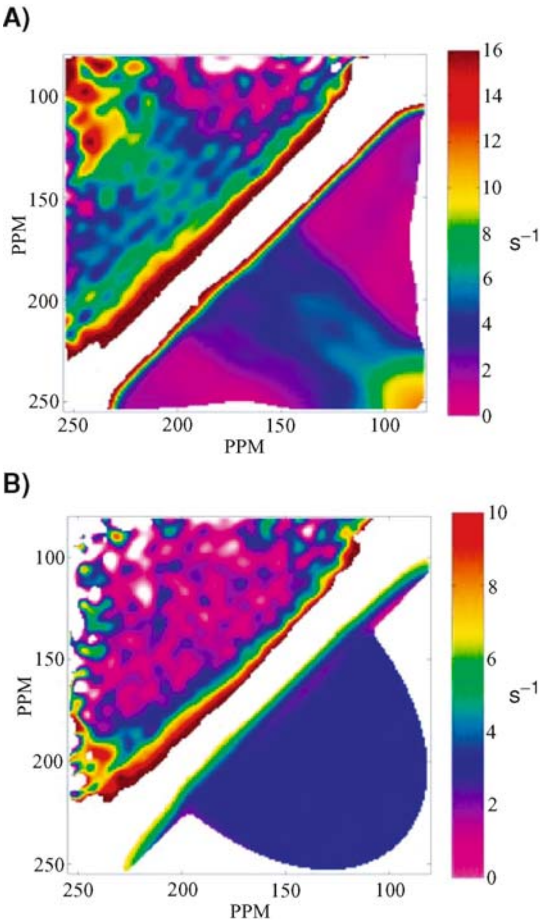

Plate 129. See also Figure 9 on page 1577.

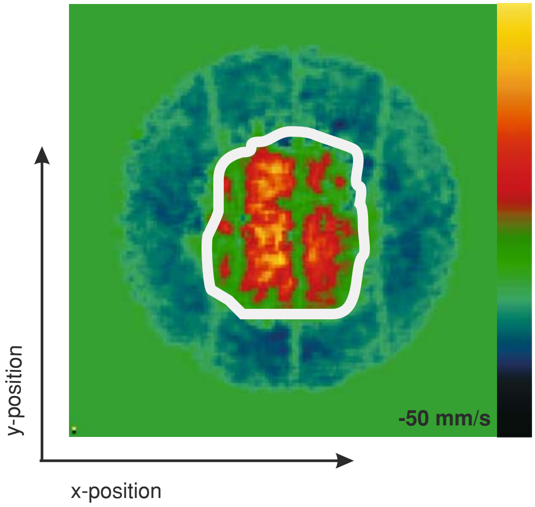
y-position
x-position
-50 mm/s

Plate 130. See also Figure 4 on page 1585.

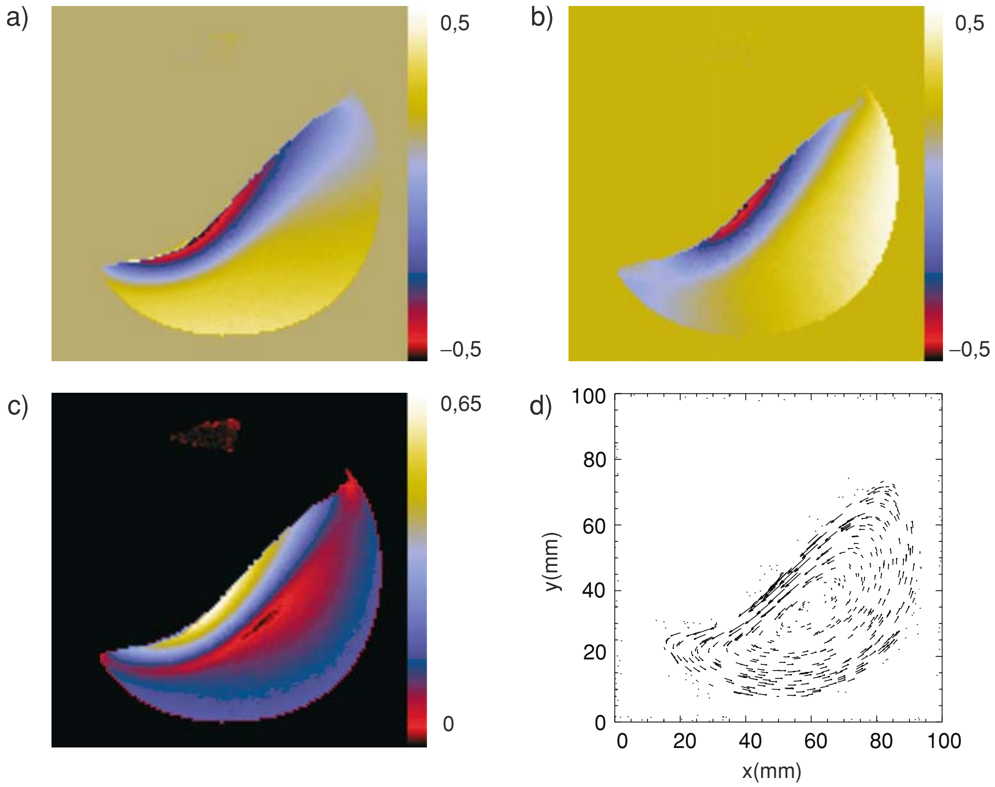

Plate 131. See also Figure 5 on page 1586.

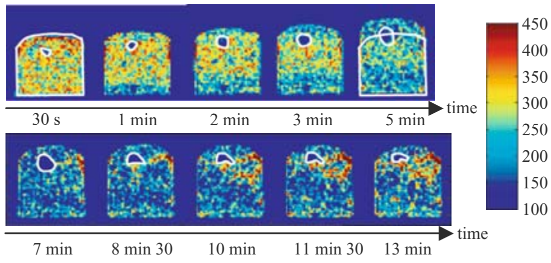

Plate 132. See also Figure 2 on page 1796.

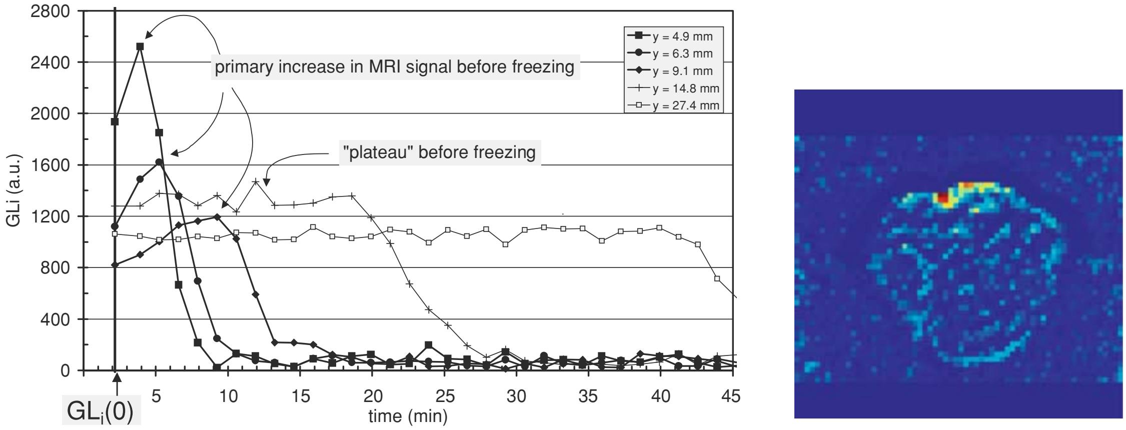

Plate 133. See also Figure 3 on page 1798.

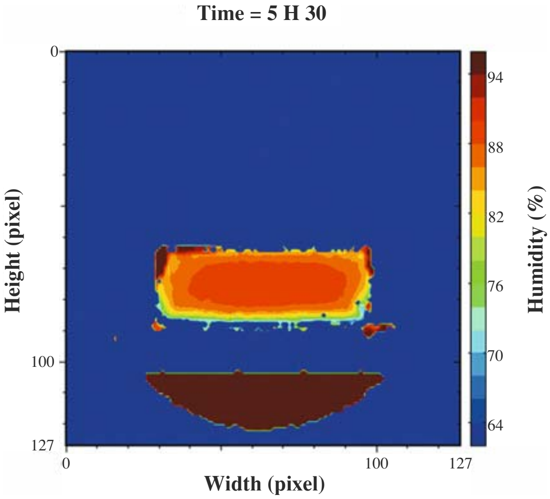

Plate 134. See also Figure 1 on page 1802.

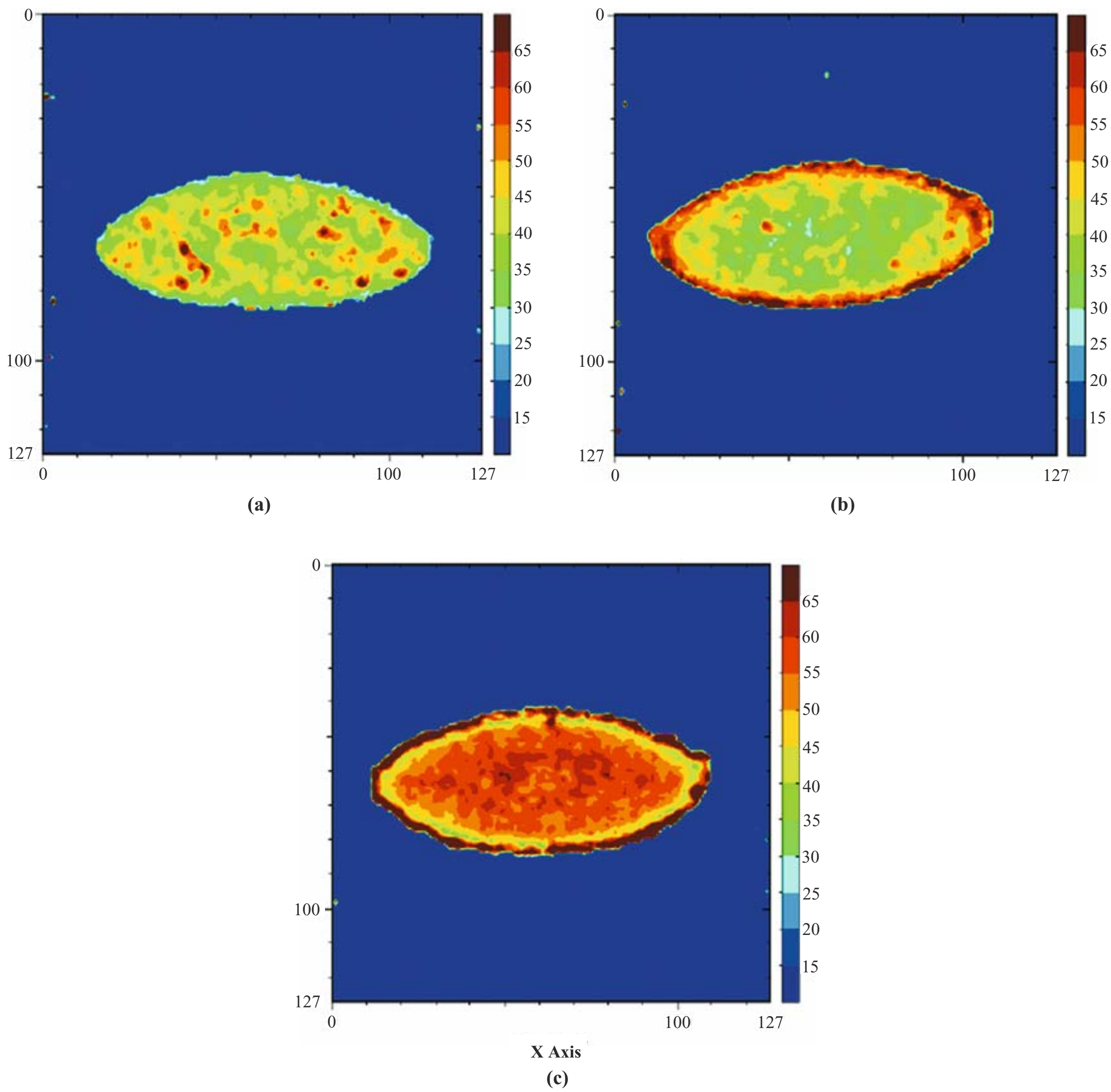

Plate 135. See also Figure 2 on page 1803.

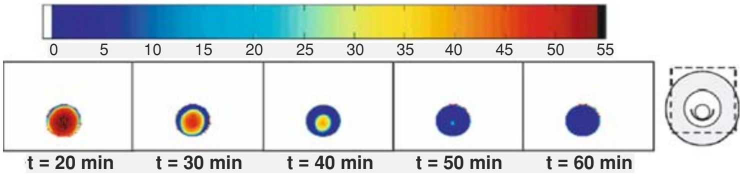

Plate 136. See also Figure 3 on page 1809.

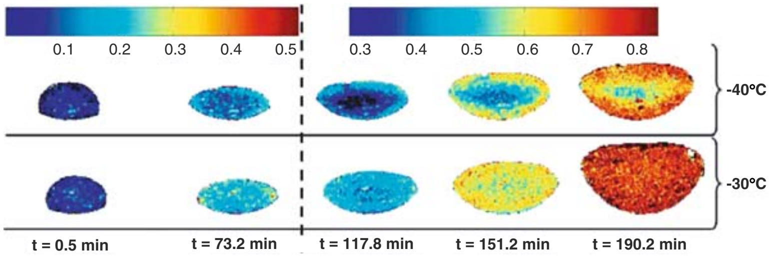
0.1
0.2
0.3
0.4
0.5
0.3
0.4
0.5
0.6
0.7
0.8
-40°C
-30°C
t = 0.5 min
t = 73.2 min
t = 117.8 min
t = 151.2 min
t = 190.2 min

Plate 137. See also Figure 5 on page 1811.

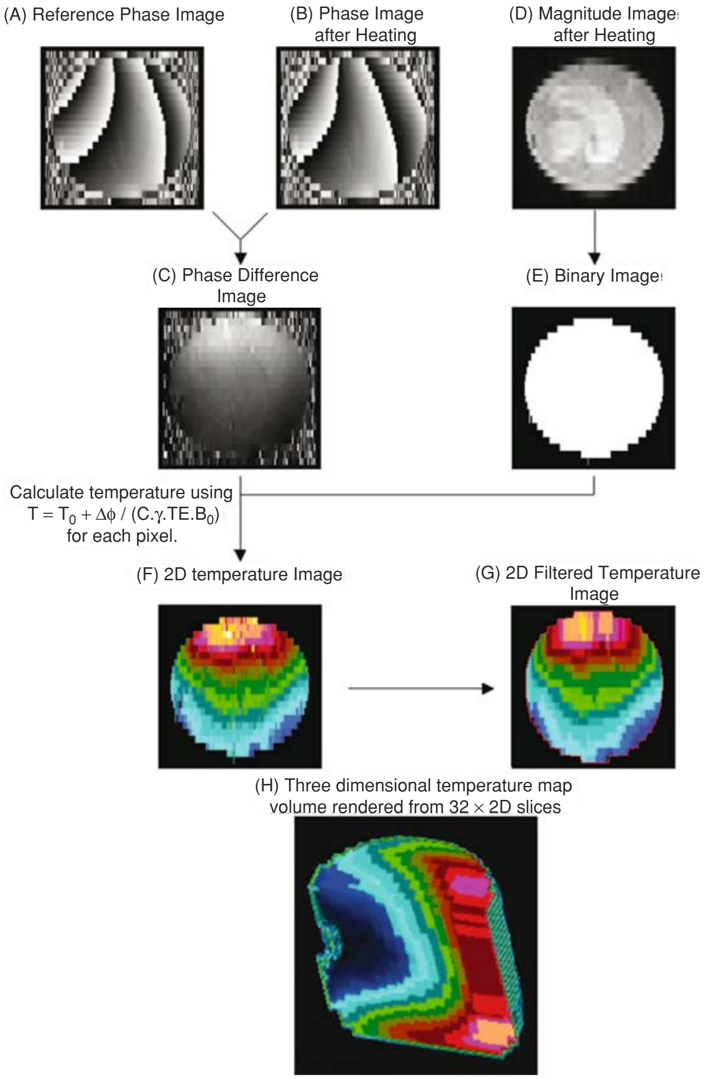
(A) Reference Phase Image
(B) Phase Image after Heating
(D) Magnitude Image after Heating
(C) Phase Difference Image
(E) Binary Image
Calculate temperature using
$T = T_0 + \Delta\phi / (C.\gamma.TE.B_0)$
for each pixel.
(F) 2D temperature Image
(G) 2D Filtered Temperature Image
(H) Three dimensional temperature map volume rendered from 32 × 2D slices

Plate 138. See also Figure 1 on page 1828.

Plate 139. See also Figure 1 on page 1896.

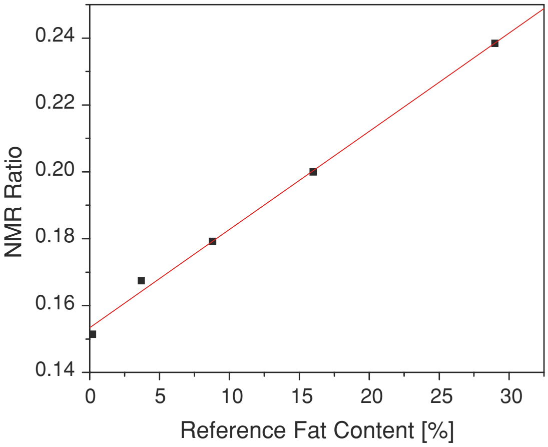

Plate 140. See also Figure 3 on page 1896.

Part III, Section 1: Applications in Materials Science

Foreword to Applications in Materials Science

After unsuccessful experiments by Gorter in the early 1930s, the principle of magnetic resonance was first applied experimentally to atomic nuclei in 1938 by Rabi and coworkers in a molecular beam experiment. Their purpose was to determine the magnitude and, in particular, the sign of the nuclear gyromagnetic ratio [1]. It is noteworthy that none of their papers of that period mention the possibility to use magnetic resonance to study anything but the magnetic properties of atomic nuclei. This situation did not change 10 years later with the work in the groups of Purcell [2] and Bloch [3,4] who, thanks to advances of radio-frequency electronics during World War II, were able to directly detect the induction signal due to magnetic resonance in bulk condensed samples. It was only the discovery of the chemical shift around 1950 by Gutowsky and Hoffmann [5], that opened the door for wider applications, forming the basis for the success of nuclear magnetic resonance as a tool of chemistry, biology, medicine and materials science. In parallel, electron paramagnetic resonance became available after 1945 [6–8]. Its wider benefits were more immediately clear, due to the direct involvement of the electrons in the formation of chemical bonds.

Chemistry and biology have benefitted greatly from advances in solution-state NMR spectroscopy (and imaging), whereas the development of high-resolution solid-state NMR spectroscopy has been particularly important for materials science. While the analytical power of solid state NMR spectroscopy rests on many incremental improvements and discoveries, too numerous to list exhaustively, a few noteworthy milestones should not go unmentioned. These include the introduction of magic angle spinning by Andrew *et al.* [9], the discovery of cross-polarization by Hartmann and Hahn [10], and the combination of the two to study low-gamma, low-abundance nuclei [11,12]. The development of multi-pulse homonuclear decoupling sequences [13], combined with multi-dimensional NMR [14] has made it possible to separate different nuclear spin interactions in different spectral dimensions. More recently, the multiple-quantum magic angle spinning methods first introduced by Medek and coworkers [15] have greatly facilitated high-resolution spectroscopy of half-integer quadrupolar nuclei, which represent the majority of elements in the periodic table. This success story provides a striking example for the importance of free research, solely driven by the challenge of the unknown and the quest for fundamental understanding.

The present volume is dedicated to the application of magnetic resonance techniques in the context of materials science. Bridging fundamental concepts of condensed matter physics with problems of engineering and technology, materials science plays a crucial role in reaping practical benefits from scientific advances. Throughout human history, technological progress has been intimately linked to the availability of materials with favorable combinations of properties. While the 19th and early 20th centuries have seen great advances in the quality and availability of metallic materials, the focus of innovation has shifted towards “soft” materials in the more recent past. Their properties in many ways resemble those of structural substances found in plants and animals: they are often based on organic compounds, processed at relatively low temperatures, and integrate themselves well into living environments. A particularly striking example of what is ultimately possible in this direction is provided by spider silk, which is an amazing material, admirably adapted to its application: It exhibits a very high ultimate tensile strength, combined with enormous toughness, to withstand wind forces and the attempts of caught prey to escape, and resists air humidity and rain water without deterioration of its properties. In addition, depending on the particular application either as tangential or radial net thread, or as drag line, its surface is modified to provide the right amount of tackiness. All of this is achieved with a small number of amino acids as building blocks, which are not specific to this application, but form the basis of all known forms of life. The silk is synthesized and processed by the spider on demand, in real time, in a gland that is only a few hundred μm in size, at ambient temperature. Contrast to this with the production of aramid fibers, which are the only man-made material to rival the mechanical properties of spider silk: They are synthesized using toxic precursor compounds, and processed by high-temperature spinning with concentrated mineral acids as solvents. Obviously, there are still many things that human technology can learn from nature.

This, however, requires experimental tools that provide structural and dynamic information on all length scales, down to atomic dimensions. The development of metallic and ceramic materials has benefitted enormously from experimental techniques that rely on diffraction to provide structural information, such as electron microscopy or X-ray scattering. Although such techniques are extremely powerful in crystalline solids, they are much less useful in the context of soft organic materials, where crystalline order is the exception rather than the rule. For this rapidly evolving class of materials, magnetic resonance provides an extremely flexible and powerful tool of investigation, as is amply illustrated in the articles of this volume.

Given the growing diversity of modern materials, the flexibility of magnetic resonance techniques is a major asset. It is difficult to find two contributions in the present volume that utilize the same pulse sequences and data acquisition techniques. Similarly, the materials that are investigated vary widely, including synthetic and natural polymers, organic semiconductors, inorganic glasses, glass-forming fluids, magnetic materials and xerogels, to just name a few. Finally, the information provided by magnetic resonance is diverse also, ranging from structural data to relaxation times and transport properties.

On the one hand, the flexibility to taylor the experimental approach to the research question to be answered is a great strength of magnetic resonance techniques. On the other hand, the resulting complexity of experimental techniques and data interpretation makes it unlikely that magnetic resonance spectroscopy will evolve into a "black box" tool that the materials scientist will be able to apply without thoroughly understanding its inner workings. Therefore, it will remain necessary for materials scientists to work closely with spectroscopists in order to generate meaningful results. On each part, this requires a certain level of understanding of the other field. It is my sincere hope that the present volume will facilitate this interaction.

I am grateful to the main editor, Professor Graham Webb, for the opportunity to serve as section editor, and for his patience, support and guidance. This volume, of course, would not have been possible without the authors of the individual articles, and it is a great pleasure to acknowledge their contributions.

Marcel Utz, Section Editor,
Storrs, CT, December 2004.

References

1. Rabi I, Zacharias JR, Millman S, Kusch P. Phys. Rev. 1938;53:318.
2. Purcell EM, Torrey HG, Pound RV, Phys. Rev. 1946;69:37.
3. Bloch F, Phys. Rev. 1946;70:460.
4. Bloch F, Hansen W, Packard ME, Phys. Rev. 1946;69:127.
5. Gutowsky HS, Hoffman CH, Phys. Rev. 1950;80:110.
6. Gorter CJ, Physica. 1936;3:503.
7. Zavoisky E, J. Phys. U.S.S.R. 1945;9:211.
8. Cummerow RL, Halliday D, Phys. Rev. 1946;70:433.
9. Andrew ER, Bradbury A, Eades RG, Nature. 1958;182:1659.
10. Hartmann SR, Hahn EL, Phys. Rev. 1962;128:2042.
11. Pines A, Gibby M, Waugh J, J. Chem. Phys. 1973;59:569.
12. Maricq MM, Waugh JS, J. Chem. Phys. 1979;70:3300.
13. Waugh JS, Huber LM, Haeberlen U, Phys. Rev. Lett. 1968; 20:180.
14. Aue WP, Bartholdi E, Ernst RR, J. Chem. Phys. 1976; 64:2229.
15. Medek A, Harwood JS, Frydman L, J. Am. Chem. Soc. 1995; 117:12779.

Acoustically Stimulated NMR Relaxometry: Application to the Study of Molecular Dynamics in Liquid Crystalline Materials

E. Anoardo and F. Bonetto

Facultad de Matemática, Astronomía y Física, Universidad Nacional de Córdoba—Ciudad Universitaria,
X5016LAE Córdoba, Argentina

Introduction

Field-cycling NMR relaxometry represents a powerful approach for investigating the spin–lattice relaxation times within the lowest Larmor frequency window. With sophisticated electronic manipulation, i.e. precise control of the current through non-mobile, very special electromagnets, magnetic field switching rates may be made as fast as 0.5 T/ms, allowing to extend relaxation experiments involving relaxation times of the order of 1 ms within a typical proton Larmor frequency range starting from local field frequencies up to 20 MHz. In this particular case, we refer to fast-field-cycling (FFC) [1, 2, 3]. The technique was successfully applied in recent years mainly for the study of the molecular dynamics in polymer and liquid crystals (LCs) [4], confined LCs [5], in the development of contrast agents for magnetic resonance imaging [6] and the study of biomolecules containing paramagnetic centers [7].

By comparing the characteristic Larmor frequency (ν) relaxation dispersions, FFC allows to gain a better understanding of the involved molecular dynamics. This can be interpreted as a superposition of different contributions, provided that in some cases a time scale separation may be applied. For instance, collective contributions due to order fluctuations in a nematic LC specimen can be usually separated from fast individual molecular motions. Therefore, a clear limitation of the FFC technique appears when both, collective and individual motions, contribute to the dispersion with similar frequency dependences. In this case, unless one of these processes can be filtered or enhanced, the mentioned discrimination becomes impossible. In this brief chapter we deal with this problem, particularizing the discussion to smectic organizations.

Why Field-Cycling Experiments in Liquid Crystals?

Relaxation features due to order director fluctuations (ODF) were first worked out for the nematic phase by Pincus [8]. His model predicted a characteristic $\nu^{1/2}$ Larmor frequency dependence for the spin–lattice relaxation time T_1. In the following years, several attempts were reported insinuating the finding of this frequency dependence by using standard non-cycled magnetic field apparatus within the MHz frequency range. However, it was not until 1975 when Wölfel *et al.* [9], using the FFC method, clearly showed for the first time that Pincus' prediction was correct. The ODF mechanism is usually manifested predominantly within the kHz frequency range, absolutely inaccessible by conventional methods (including rotating frame relaxation, see ref. [10] for a better understanding), where a concomitant degradation of the signal-to-noise ratio limits the quality of the experiments. Since then, FFC relaxometry was applied to the study of many different bulk and confined liquid crystalline compounds, mainly in the isotropic (I), nematic (N) and smectic A (SmA) phases.

Distinguishing features of FFC as a unique NMR tool for the study of LC, polymers and confined systems are: (a) the noticeable T_1-relaxation dispersion shown by these materials, (b) the strong differences shown-up by the corresponding T_1 dispersions in different mesophases, and (c) the remarkable sensitivity to a minimum spatial confinement. On these grounds, a further development of the technique is mandatory.

Relevant Properties of Liquid Crystals

In the following, we briefly discuss relevant properties of the nematic and smectic phase that are important for the interpretation of relaxation dispersion experiments. For further details the reader can refer to some of the specialized books about the matter [11, 12, 13].

The nematic phase is characterized by a molecular orientational correlation over macroscopic distances, while lacking molecular positional order. The orientational order defines a director field $\widehat{n}\left(\vec{r},t\right)$ that indicates the molecular average orientation within a certain region [14]. The free energy of the N phase due to elastic distortions

Graham A. Webb (ed.), Modern Magnetic Resonance, 1439–1444.
© 2008 *Springer.*

of the media can be expressed as:

$$F = \int \frac{d^3r}{2}\left[K_1\,(\nabla.n)^2 + K_2\,(n.\nabla \times n)^2 \right.$$
$$\left. + K_3\,(n \times \nabla \times n)^2\right], \tag{1}$$

where K_1, K_2 and K_3 are the elastic constants associated with the splay, bend and twist deformations, respectively. The elastic constants strongly depend on temperature and, as the elastic free energy is small compared with thermal energy, relatively weak external forces can easily distort the molecular arrangement.

In addition to the orientational order present in nematics, smectic phases exhibit layered structures. In the SmA phase, no long range positional order is shown inside each layer and the director is perpendicular to the smectic planes.

The order parameter for the SmA phase is defined as the amplitude of a one-dimensional density wave whose wave vector points along the director [12,15]:

$$\rho\left(\overrightarrow{r}\right) = \rho_o\left[1 + \frac{1}{2}\,|\Psi|\cos(q_o z + \varphi)\right], \tag{2}$$

where $|\Psi|$ is a measure of the strength of the smectic order, ρ_o is the average density, $q_o = 2\pi/d$ is the wave vector of the density wave (being d the interlayer distance), φ is an arbitrary phase, and z is the coordinate perpendicular to the planes.

For an ideal SmA phase, twist and bend elastic distortions are forbidden [15]. For an undistorted smectic, only the splay term of the nematic elastic free energy survives. Besides this term, the smectic free energy term f_{sm} and the corresponding one to the smectic–nematic interaction should be included in the free energy density expression [12,16]. Then:

$$f = f_{\text{nem}} + f_{\text{sm}} + f_I, \tag{3}$$

where,

$$f_{\text{sm}} = \alpha(T)\,|\psi|^2 + \beta(T)\,|\psi|^4 + \ldots$$
$$f_I = \left(\nabla + iq_s\overrightarrow{\delta n}\right)\psi * \frac{1}{2M}\left(\nabla - iq_s\overrightarrow{\delta n}\right)\psi, \tag{4}$$

here, α and β are coefficients in the f_{sm} expansion in powers of ψ. M is a mass tensor with two main components, along ($M_{//}$) and normal ($M_\perp$) to the layers, and $\overrightarrow{\delta n} = \widehat{n}\left(\overrightarrow{r}\right) - \widehat{n}_o$, being $\widehat{n}_o$ the unperturbed director.

Order Director Fluctuations

Due to the long range orientational order characteristic of liquid crystals, the molecules around a given spatial position (defined by $\overrightarrow{r}$) tend to align parallel to an average direction defined by an unitary vector $\widehat{n}\left(\overrightarrow{r}\right)$ called "director". The existence of thermal fluctuations cause the director to fluctuate around $\widehat{n}_0\left(\overrightarrow{r}\right)$, turning it dependent on the time t. These fluctuations of collective nature are called order director fluctuations (ODF), being effective to scatter light (a reason for the turbid appearance of the nematic phase) [17].

NMR relaxation due to ODF originates in the modulation of the dipolar interaction between spin pairs due to the presence of hydrodynamic modes [8,18–20]. In the following, we briefly discuss the basic arguments of this theory.

Let us consider a nematic sample in presence of a magnetic field along the z direction. Then $\widehat{n}(\overrightarrow{r}, t) = \widehat{n_0} + \overrightarrow{\Delta n}(\overrightarrow{r}, t)$, with $\overrightarrow{\Delta n}(\overrightarrow{r}, t) = n_x(\overrightarrow{r}, t)\widehat{i} + n_y(\overrightarrow{r}, t)\widehat{j}$. and $\widehat{n_0}$ the average director parallel to the z direction.

According to equation (1), the change in the free energy caused by these distortions will be (neglecting the magnetic term):

$$F = \frac{1}{2}\int\left\{K_1\left(\frac{\partial n_x}{\partial x} + \frac{\partial n_y}{\partial y}\right)^2 + K_2\left(\frac{\partial n_y}{\partial x} - \frac{\partial n_x}{\partial y}\right)^2\right.$$
$$\left. + K_3\left[\left(\frac{\partial n_x}{\partial z}\right)^2 + \left(\frac{\partial n_y}{\partial z}\right)^2\right]\right\}. \tag{5}$$

Expanding in Fourier series and rotating the coordinate system, it is possible to write the last equation in terms of two uncoupled modes (n_1, n_2):

$$F = \frac{1}{2}\sum_{\overrightarrow{q}}\sum_{\beta=1}^{2} K_\beta\left(\overrightarrow{q}\right)\left|n_\beta\left(\overrightarrow{q}\right)\right|^2 \tag{6}$$

where $K_\beta(\overrightarrow{q}) = K_\beta q_\perp^2 + K_3 q_{\backslash\backslash}^2$, $\langle|n_\beta(\overrightarrow{q})|^2\rangle = \frac{K_B T V}{K_\beta(\overrightarrow{q})}$, K_B is the Boltzmann constant and T is the temperature.

It is well known from different relaxation theories [21–23] that spin lattice relaxation time T_1 due to dipolar coupling interaction is given by:

$$\frac{1}{T_1} = \frac{9}{8}\gamma^4\hbar^2\left[J_1(\omega_L) + J_2(2\omega_L)\right], \tag{7}$$

where $J_q(\omega) = \int_{-\infty}^{\infty} g_q(\tau)e^{-i\omega\tau}d\tau$, $q = 1, 2$, being $g_q(\tau)$ the correlation function for a given dynamic process, ω is the Larmor frequency, γ is the spin gyromagnetic ratio and $\hbar$ is the Planck constant over 2π.

For the ODF process, under the low angle approximation ($|\overrightarrow{\Delta n}(\overrightarrow{r}, t)| \ll |\widehat{n_0}|$), it can be demonstrated that

$J_2(2\omega_L) \ll J_1(\omega_L)$, and:

$$J_1(\omega) = 3\frac{K_B T}{16\pi^3}\sum_{\alpha=1}^{2}\int_q \frac{d^3q}{\left(K_\alpha\left(\overrightarrow{q}\right)\right)^2 + \eta_\alpha^2\omega^2}, \tag{8}$$

where η_α are viscosity constants. Due to the anisotropic nature of nematics, the integration should be made over a cylindrical or ellipsoidal volume. Considering that the minimum wavelength is associated with molecular dimensions:

$$\int_q d^3q \rightarrow \int_0^{2\pi} d\phi \int_0^{q_{zh}} dq_z \int_0^{q_{\perp h}\sqrt{1-\frac{q_z^2}{q_{zh}^2}}} q_\perp dq_\perp, \tag{9}$$

where q_{zh} and $q_{\perp h}$ are the parallel and perpendicular associated cut-off wavelength, and ϕ is the azimuthal angle.

Integration of equation (8) conduces to a general expression [24] that, in the simplified nematic one constant approximation (isotropic viscoelastic properties) and assuming $(K/\eta)\,q_h^2 = \omega_h \gg \omega$ (i.e. within a Larmor frequency window far below from the high frequency cut-off), the result reduces to the Pincus' law for nematic dispersion: $T_1^{ODF}(\omega) \propto \sqrt{\omega}$.

The SmA phase can be approximated from the nematic formalism assuming the extreme anisotropic condition $K_3 \ll K_1 = K_2$. Under this assumption, the model reduces to a linear frequency dependence [24] $T_1^{ODF}(\omega) \propto \omega$. The same frequency dependence may be obtained from the assumption that only the splay term and the local fluctuation of the layers are present in the SmA elastic free energy [25].

A more refined model for the SmA phase can be obtained by including all terms in the SmA free energy (see equation (3)). In this case [26]:

$$T_1^{DF}(\omega) \propto \left(\frac{\eta_1}{D^{1/2}K_1^{3/2}}Y_1 + \frac{\eta_2}{D^{1/2}K_3^{1/2}K_2}Y_2\right)^{-1}, \tag{10}$$

with

$$Y_1 = \frac{B}{D}\int_0^1 \frac{dx}{x\left(\frac{B}{D}\left(1-x^2\right)+\frac{K_3}{K_1}x^2\right)^{3/2}\sqrt{1+\sqrt{1+\frac{1}{x^4}\left(\frac{\omega}{\omega_{s1}}\right)^2}}},$$

$$Y_2 = \frac{1}{\sqrt{1+\sqrt{1+\left(\frac{\omega}{\omega_{s2}}\right)^2}}},\ B = \frac{\psi_0^2 q_s^2}{M_{//}},\ D = \frac{\psi_0^2 q_s^2}{M_\perp},$$

$$\omega_{s1} = \frac{D}{\eta_1}$$

and $\omega_{s2} = \frac{D}{\eta_2}$; being ψ_0 the equilibrium value of the smectic order parameter. In contrast with the simplified models conducing to a linear dependence, in this case the resulting dispersion ranges from ω^0 to $\omega^{1/2}$.

Self Diffusion

Self diffusion is a relevant intermolecular relaxation mechanism for mesomorphic materials [27]. The theory of translational diffusion for isotropic liquids [28] was directly used in the analysis of the relaxation dispersion in LCs [29,30]. Later, modified versions of Torrey's model were proposed for nematics [31] and SmA structures [32]. Both models predict a flat dispersion in a frequency range where $\omega\tau \ll 1$, being τ the correlation time associated with the self diffusion process.

Molecular Reorientations

The influence of molecular reorientations in the spin–lattice of isotropic liquids is well known [23]. In liquid crystals, the unique relevant difference remains in connection with the anisotropic nature of the media, which usually demands to consider more than one correlation time for a given process. Internal motions and configurational molecular fluctuations are mainly due to molecular flexibility and rotations of chain groups. These processes are in general fast and usually manifest in the relaxation dispersion at high frequencies. At the simplest case, these contributions may be represented by a sum of BPP-type terms with their associated correlation times [33]. In the SmA phase, free rotation of the whole molecule about the long molecular axis is less probable than in nematics due to the layered packing [34].

Proton FC Relaxometry in Liquid Crystals

Proton spin–lattice relaxation time in liquid crystals is basically determined by both, collective fluctuations and individual molecular motions like self diffusion or molecular reorientations. If a time scale separation is feasible at correlation function level, collective and individual molecular dynamics may be assumed statistically independent. This may not be the case between translational and rotational diffusion. In turn, such individual contributions may be hardly identifiable in the relaxation dispersion unless the explored frequency range is extended up to a Larmor frequency well above the inverse of the involved correlation times. Consequently, the effective relaxation rate can be, at least, considered as the sum of two different contributions: $(T_1)^{-1} = \left(T_1^{ODF}\right)^{-1} + \left(T_1^{IM}\right)^{-1}$, where T_1^{IM} stands for the individual molecular dynamics.

In nematics, the typical $\omega^{1/2}$ law was observed for the first time in p-azoxyanisole PAA [9]. This study was later extended to very low frequencies as well as other compounds [29,35–38]. However, the relevance of local magnetic fields and hardware setting was only better understood in recent times [4,39,40]. Summarizing these experimental results:

- The typical square root law (Pincus' model) is found to be dominant in the T_1 dispersion within the kHz frequency range.
- In the MHz range, individual molecular motions dominate T_1.
- The change in tendency of the dispersion within the kHz region depends on different parameters related to the hardware setting and the nature of the local fields.
- The low frequency plateau is mainly due to the unavoidable presence of the local fields.

In the SmA phase, the typical relaxation dispersion looks nearly flat till a minimum frequency of about 20 kHz, where a noticeable steep down dispersion appears up to a low frequency plateau. The steep dispersion was currently attributed to ODF through a ω^1 dispersion law, while the low frequency plateau, usually between 300–800 Hz, interpreted in terms of the cut-off of the ODF modes. At higher frequencies than the starting point of the steep decay (30 kHz–10 MHz), the T_1 frequency dependence is minor. This behavior was normally explained in terms of individual motions with a dominant role of the translational diffusion, although this interpretation is based on the ω^1 law for T_1 due to ODF.

By means of two independent experiments, it has been recently shown that the strong dispersion observed in the low frequency regime in the SmA phase is not due to ODF, but a conjunction of experimental pitfalls and the strong local fields present in smectic phases [41].

When equation (10) is used to explain the contribution of ODF in the SmA phase, the frequency dependence of T_1^{ODF} becomes very similar to the diffusive one, thus turning difficult the identification of each of them. Lately, studies of relaxation dispersions under sonication shed light on this topic [42].

Ultrasound Induced Relaxometry

When sound is applied to a mesomorphic specimen, the acoustic perturbation induces density fluctuations. A coupling is established between ODF and the acoustic field through this process. A new free energy term associated with molecular reorientation in uniaxial mesophases was recently proposed on experimental [43] and theoretical grounds [44]. In the following, the problem we will consider concerns how relaxation dispersions due to ODF can be modified under the influence of sonication. For the sake of simplicity, only ultrasonic waves parallel and perpendicular to the director will be treated. Henceforth, signs between parenthesis stand for perpendicular waves.

The interaction energy between an acoustic wave and the director $\widehat{n}$ is given by [43,44]:

$$f_a = \frac{1}{2} a^2 \left(\widehat{s}.\widehat{n}\right), \tag{11}$$

where a^2 depends on the acoustic intensity, the ultrasound velocity, the average of the sample density, the magnitude of the ultrasound wave vector and the director-density coupling. In the last equation, $\widehat{s}$ represents the ultrasound wave unitary vector and $\widehat{n}$ the director. The last equation results after averaging over fast oscillations of the ultrasonic waves [44].

If an ultrasound wave propagates across the liquid crystalline media parallel (perpendicular) to the magnetic field, the fluctuations of the local director decrease (increase) f_a by:

$$\Delta f_a = -(+)\frac{1}{2} a^2 \left(n_x^2 + n_y^2\right). \tag{12}$$

Adding this free energy term to the equation (5), a closed expression for the modified dispersion ($T_1^{ODF+S}(\omega)$) can be obtained [45]. In the simplified nematic one constant approximation, this result reduces to [43,45]:

$$T_1^{ODF+S}(\omega) \propto \frac{\sqrt{\sqrt{1+(\omega\tau_0)^2} - (+)\,1}}{\sqrt{\tau_0}}, \tag{13}$$

while for the smectic simplified case ($K_3 \ll K_1 = K_2$), the following expression is obtained:

$$T_1^{ODF+S}(\omega) \propto \sqrt{1+\frac{1}{(\omega\tau_0)^2}} \times \frac{\omega}{\pi + (-)\,2\arctan\left(\dfrac{\dfrac{1}{\omega\tau_0}}{\sqrt{1+\dfrac{1}{(\omega\tau_0)^2}}}\right)}. \tag{14}$$

In the last two equations, $\tau_0 \equiv \frac{\eta}{a^2}$.

When the acoustic term is considered in the model where the coupling between smectic order with director fluctuations is taken into account, the expression obtained for $T_1^{DF+S}(\omega)$ becomes very complex [42,45]. Main remarks about the results of the model are:

- In the limit of zero acoustic intensity ($a \to 0$, $\tau_0 \to \infty$), the three results tend, respectively, to the Pincus' model, the linear model and equation (10).
- Parallel sound waves enhance the relaxation by ODF, while the opposite behavior is observed for normal incidence.
- More remarkable changes (respect to the non-sonicated case) manifest at lower frequencies.
- Main assumptions of the model are (a) the existence of a preferential macroscopic orientational order induced by the magnetic field, (b) time averaging over fast oscillations of the density and (c) the sound power (in the case of parallel irradiation) is low enough to prevent a violation of the low angle approximation.

This model has already been successfully contrasted with experimental data in nematics [43,46] as well as in SmA compounds [42]. Typical results of relaxometry experiments using the field cycling technique under the simultaneous irradiation with ultrasonic waves can be observed in Figures 1 and 2. Experimental data and model fitting (or simulations) are shown for nematic and smectic compounds at both, in the presence and absence of sonication.

The ultrasound-induced changes in the T_1 dispersion observed in nematics can be characterized by:

- A decrement in the characteristic slope of the dispersion (as observed in the logarithmic plots). The effect is stronger within the lower frequency range and for higher ultrasonic powers.

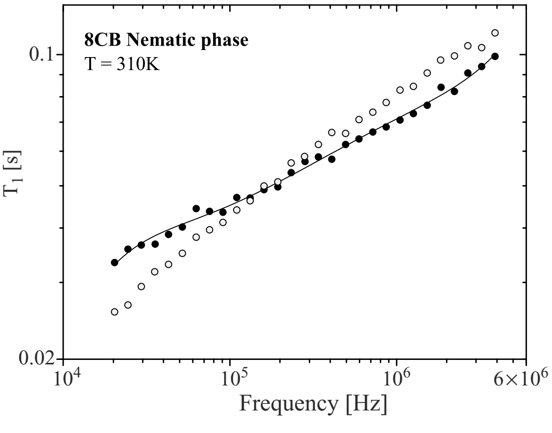

Fig. 1. Frequency dependence of T_1 in nematic 8CB at 310K in the absence (hollow circles) and the presence (filled circles) of ultrasonic waves. The fitting curve corresponding to the later case is also shown.

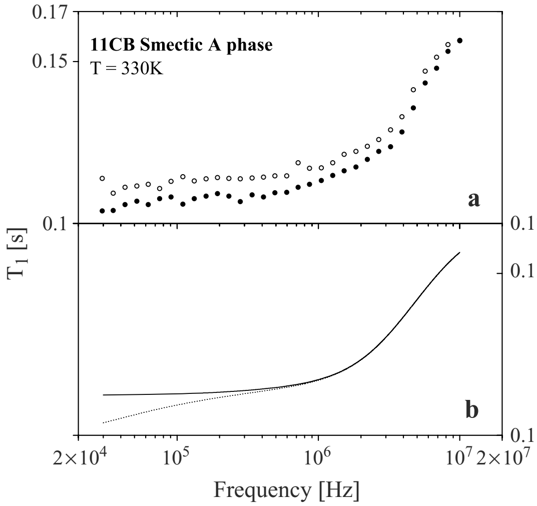

Fig. 2. T_1 dispersion experimental data (a) and simulated curves (b) for 11CB at the smectic temperature of 330K in the presence (filled circles and dotted line) and the absence (hollow circles and solid line) of ultrasonic waves.

- A nearly uniform relaxation enhancement within the whole observed Larmor frequency window.

Only the first effect is predicted by the model. The second effect may be a consequence of changes in the viscoelastic properties induced by the sound [46]. A similar behavior was encountered in the SmA phase.

Most notably, in cases where the smectic ODF relaxation model (and not the simplified versions) has to be considered, an enormous dilemma comes up [42]. The similitude between ODF frequency dependence with those contributions due to individual relaxation mechanisms has an ominous consequence for standard relaxometry: collective and individual processes cannot be identified in the dispersion. The matter can be fortunately circumvented by the fact that only ODF couple with the sonic field, allowing the selective enhancement of its relative contribution and changing the associated frequency dispersion. Consequently, both contributions can be separated. Unlike the nematic case, the T_1 relaxation dispersion in the SmA phase of cyanobiphenyls seems to be mainly driven by individual motions. For this reason, the observed sound-induced changes are less important than in nematics.

Outlook

The study of NMR relaxation with simultaneous sonication provides a new tool for the investigation of collective dynamics in mesomorphic systems. A topic of high interest is, for instance, how a sonic field can be used to influence an ordered molecular arrangement thus changing the rheological properties of the assembly. Within this picture, NMR relaxometry can be used to monitor sound-induced dynamical features that take place at microscopic level, as a means of achieving a comprehensive description of the involved processes. The main advantage of this newly proposed method relays in the possibility of disentangling between different mechanisms that cannot be identified in a simple T_1 dispersion experiment. From a technical standpoint, the evolution of this *acoustically stimulated relaxometry* technique encourages further instrumental development. A challenging task is, for instance, the design of special combined NMR and sonication probes, allowing to scan the acoustic frequency, while keeping a precise control of the involved acoustic parameters. On a different way, the study of other NMR relaxation parameters like T_{1D} or $T_{1\rho}$ under sonication looks appealing for many reasons. Firstly, it may allow to display the involved information in terms of a different spectral density set. Secondly, with a careful experimental management, individual and collective contributions may be selectively filtered out. A deeper discussion on this topic is left for future work as being matter of current active development.

Acknowledgment

The authors are indebted to Professor Rainer Kimmich (Ulm University, Germany) for fruitful discussions and for a successful scientific collaboration. Financial support from CONICET, Fundación Antorchas and ANPCYT (Argentina) and Alexander von Humboldt Foundation and DAAD (Germany) is also acknowledged.

References

1. Noack F. Prog. Nucl. Magn. Reson. Spectrosc. 1986;18:171.
2. Seitter R-O, Kimmich R. In J. C. Lindon, G. E. Tranter and J. L. Holmes (Eds.). "Enciclopedia of Spectroscopy and Spectrometry", Academic Press: London, pp. 2000–2008 (1999).
3. Anoardo E, Galli G, Ferrante G. Appl. Magn. Reson. 2001;20:365.
4. Kimmich R, Anoardo E. Progr. Nucl. Magn. Reson. Spectrosc. 2004;44:257.
5. Grinberg F, Vilfan M, Anoardo E, In Burnell EE, de Lange CA (Eds.). "NMR of Ordered Liquids", Kluwer Academic Publishers; Amsterdam, pp. 375–398,2003.
6. Aime S, Botta M, Fasano M, Terreno E. Chem. Soc. Rev. 1998 27:19.
7. Bertini I, Luchinat C. Coord. Chem. Rev. 1996;150:1.
8. Pincus P. Solid State Commun. 1969;7:415.
9. Wölfel W, Noack F, Stohrer M. Naturforsh Z. 1975;30a:437.
10. Anoardo E, Grinberg F, Vilfan M, Kimmich R. Chem. Phys. 2004;297:99.
11. Luckhurst GR, Veracini, CA (Eds.). *The Molecular Dynamics of Liquid Crystals*, Kluwer, 1994.
12. De Gennes PG, Prost J. *The Physics of Liquid Crystals*, 2nd ed., Clarendon Press: Oxford, 1994.
13. Demus D, Goodby J, Gray GW, Spiess HW, Vill V. *Physical Properties of Liquid Crystals*, Wiley-VCH: Weinheim, 1999.
14. Leslie FM. Quart. J. Mech. Appl. Math. 1966;19:357.
15. Schaetzing R, Litster J. Advances Liq. Cryst. 1979;4:147.
16. De Gennes PG. Solid State Commun. 1972;10:753.
17. Chatelain P. Acta Cryst. 1951;4:453.
18. Blinc R, Hogenbloom DL, OReilly DE, Peterson EM. Phys. Rev. Lett. 1969;23:969.
19. Doane JW, Visitainer JJ. Phys. Rev. Lett. 1969;23:1421.
20. Doane JW, Johnson DL. Chem. Phys. Lett. 1970;6:291.
21. Bloembergen N, Purcell EM, Pound RV. Phys.Rev. 1948;73:679.
22. Wangness RK, Bloch F. Phys. Rev. 1953;89:728.
23. Abragam A. Principles of Nuclear Magnetism, Clarendon Press: Oxford, 1961.
24. Vold RR, Vold RL. J. Chem. Phys. 1988;88:465.
25. Blinc R, Luzar M, Vilfan M, Burgar M. J. Chem. Phys. 1975;63:3445.
26. Vilfan M, Kogoj M, Blinc R. J. Chem. Phys. 1987;86: 1055.
27. Vilfan M, Blinc R, Doane JW. Sol. State Commun. 1972;11:1073.
28. Torrey HC. Phys. Rev. 1953;92:962.
29. Graf V, Noack F, Stohrer M. Naturforsch Z. 1977;32a:61.
30. Schweikert KH, Noack F. Naturforsch Z. 1989;44a:597.
31. Zumer S, Vilfan M. Phys. Rev. A. 1978;17:424.
32. Vilfan M, Zumer S. Phys. Rev. A. 1980;21:672.
33. Dong RY. Nuclear Magnetic Resonance of Liquid Crystals, Springer: New York, 1997.
34. Doucet J, Levelut AM. J. Phys. (Paris). 1977;38:1163.
35. Kimmich R. Bull. Magn. Reson. 1980;1:195.
36. Nagel G, Wölfel W, Noack F. Israel J. Chem. 1983;23:380.
37. Noack F, Notter M, Weiss W. Liq. Cryst. 1988;3:907.
38. Pusiol D, Noack F. Liq. Cryst. 1989;5:377.
39. Anoardo E, Kimmich R. XXXII National Congress on Magnetic Resonance GIDRM, Pavia, Italy (2002).
40. Anoardo E, Ferrante GM. Appl. Magn. Reson. 2003;24:85.
41. Anoardo E, Bonetto F, Kimmich R. Phys. Rev. E. 2003;68:022701.
42. Bonetto F, Anoardo E. J. Chem. Phys. 2004;121:554.
43. Bonetto F, Anoardo E, Kimmich R. Chem. Phys. Lett. 2002;361:237.
44. Selinger J, Spector M, Greanya V, Weslowsky B, Shenoy D, Shashidhar R. Phys. Rev. E. 2002;66:051708.
45. Bonetto F, Anoardo E. Phys. Rev. E. 2003;68:021703.
46. Bonetto F, Anoardo E, Kimmich R. J. Chem. Phys. 2003;118:9037.

Characterization of Elastomers Based on Monitoring Ultraslow Dipolar Correlations by NMR

Farida Grinberg
Universität Leipzig, LinnéStraße 5, D-04103 Leipzig, Germany

Introduction

Owing to enormous industrial use, elastomers remain an important field of intensive NMR studies [1–15] since more than three decades. The major goal is to establish a correlation between the molecular structure, molecular dynamics and the macroscopic mechanical properties of final materials. On this basis, material properties can be tailored using an optimization of the technological procedures and an application of cross-linking agents and special additives [16,17].

Undisputable advantage of NMR in comparison to other conventional methods of material characterization (like swelling or stress–strain measurements [16,17]) is that it is fully non-destructive and does not require any special sample treatment. Various NMR methods proposed as the characterization tools are based mainly on probing stochastic molecular motions via the measurements of the line shapes, nuclear magnetic relaxation rates and translational displacements.

At room temperatures, the NMR response of elastomers is predominantly determined by the so-called residual dipolar couplings (RDCs). Finite RDCs are characteristic of many "soft" materials like liquid crystals or polymers in which molecular motions are restricted by anisotropic molecular alignment or topological constraints [18,19]. In isotropic non-viscous liquids, in contrast, dipolar interaction are averaged out completely [20,21]. In polymers, restrictions to chain re-orientations arise owing to the excluded volume effects or "entanglements". The constraints of this art can also be produced artificially by confining polymeric materials in the nanoscopic pores [22,23]. In rubber, especially severe constraints on isotropic chain re-orientations are imposed by chemical cross-links. The consequence is that any fast chain fluctuations between the cross-links remain strongly anisotropic in the time scale of typical NMR experiments and cannot completely average out the secular part of the dipolar Hamiltonian. This feature is exploited in various experimental NMR approaches deployed in study of elastomers.

The influence of topological constraints on "residual" dipolar fluctuations was elaborated many years ago in works by Cohen-Addad [1–4]. In these works, a given chain is assumed to have a mean position in space which is determined by the cross-links and/or the constraints formed by the so-called chain entanglements. The chain is described in terms of N freely jointed Kuhn (or statistical) segments of length b. If chain meshes between the cross-links are not too long, an end-to-end vector $\boldsymbol{R}$ is determined mainly by the two adjacent cross-links. In the time scale of typical NMR pulse sequences, the mean orientation of the end-to-end vector can be considered as constant, whereas fast intrachain fluctuations tend to be anisotropically restricted in space. Averaging over fast fluctuations with respect to a local symmetry axis determined by the fixed vector $\boldsymbol{R}$ gives for the "residual" dipolar coupling constant in elastomers [4]:

$$\overline{\Omega}_d \approx \Omega_0 \frac{\boldsymbol{R}^2}{N^2 b^2}(1 - 3\cos^2\theta), \qquad |\boldsymbol{R}| = \boldsymbol{R} \ll Nb, \qquad (1)$$

where $\Omega_0 = 3\mu_0\gamma^2\hbar/(8\pi r_{kl}^3)$, r_{kl} and α_{kl} are polar coordinates of the internuclear vector, θ is the angle between the magnetic field and the vector $\boldsymbol{R}$.

Depending on the strength, the RDCs affect many measurable NMR variables in various ways. Interpretation in terms of RDCs was undertaken for experimental NMR line shapes and relaxation properties in cross-linked elastomers [5,24–26]. Later, a "sine" correlation echo function was suggested in Ref. [27] for monitoring weak residual dipolar interactions in stretched rubbers and "entangled" polymeric liquids [28]. Recently, elegant though more sophisticated approaches based on elucidation of multiple-quantum coherences were successfully explored both theoretically and experimentally for various elastomers [9,13]. A combination of frequency-dependent relaxometry with double quantum spectroscopy was elaborated in Ref. [15]. Some recent advances in studies of polymer chain dynamics with help of field-cycling NMR relaxometry and field-gradient NMR diffusometry were outlined in Ref. [22].

This review will concentrate on a simple efficient method usually referred to as the dipolar correlation effect (DCE) [29] and it's application to polymer elastomers [30–32]. The DCE arises in macro and microscopically

Graham A. Webb (ed.), Modern Magnetic Resonance, 1445–1453.
© 2008 *Springer.*

anisotropic liquids like liquid crystals, biological membranes, polymer melts and elastomers. Motions like ultra-slow orientational director fluctuations in liquid crystals [29,33,34] or reorientations of long chain backbones in polymer melts [35,36] can be probed via the DCE. In rubbers, molecular motions of this sort are associated with slow reorientations of long chain backbones spanned by the adjacent cross-links. The DCE proved to provide a valuable tool for materials characterization. In particular, it was shown to be sensitive to cross-link density in the series of synthetic elastomers and in natural rubber materials [30–32]. A new imaging procedure permitting one to directly visualize the mean squared dipolar fluctuation (MSDF) in spatially resolved maps [37] was developed on the basis of the DCE.

Background of the Dipolar Correlation Effect

The DCE [29,36] represents a specific relaxation mechanism produced essentially by modulations of RDCs due to ultra-slow anisotropic molecular motions. The relevant time scale of motions in question is that of the order of the interpulse spacings in the stimulated echo pulse sequence, that is, between a few microseconds and a few seconds in the case of protons. The upper limit is ultimately determined by spin–lattice relaxation and represents the longest time scale accessible to NMR techniques in general.

We consider systems where dipolar couplings of spin pairs represent dominating internal interactions. The aim is to monitor the effects of RDCs on the stimulated and primary echoes generated by a standard sequence of three 90°-radio frequency pulses [38,39]:

$$90^\circ - \tau_1 - 90^\circ - \tau_2 - 90^\circ. \tag{2}$$

The time intervals τ_1 and τ_2 denote the interpulse spacings between the first two and between the second and the third pulses, respectively.

A residual dipolar coupling constant (in angular-frequency units)

$$\Omega_d = \Omega_0 \langle (1 - 3\cos^2 \alpha_{kl}) \rangle \propto 1 - 3\cos^2 \theta, \tag{3}$$

remains after averaging pair dipolar interactions over motions fast on the time scale $t \ll \tau_1, \tau_2$. The brackets in Equation (3) denote the average with respect to the local symmetry axis of the system persisting on the much longer time scale. The quantity Ω_d in Equation (3) has then a finite value determined by an angle between an external magnetic field and that direction. In the case of elastomers, the local symmetry axis is determined by the vector connecting the two adjacent cross-links, so Ω_d becomes identical with $\overline{\Omega}_d$ in Equation (1).

In contrast to non-viscous liquids, where any dynamical motions are very fast, the RDCs in soft materials tend to additionally be modulated on the time scale of the interpulse intervals by much slower motions. Examples of such ultra-slow motions are given by orientational director fluctuations in liquid crystals [18], the "reorientaions mediated translational diffusion" mechanism in geometrically confined liquids [36] or cross-link fluctuations in rubber materials. The effects produced on echo amplitudes by this kind of motions is referred to as the DCE.

Experimentally, the DCE is elucidated by measuring the quotient of amplitudes of the stimulated, A_{st} and the primary, A_{pr}, echoes at the time points $2\tau_1 + \tau_2$ and $2\tau_1$ of their maximal refocusing, respectively. The quotient

$$\frac{A_{\mathrm{st}}(2\tau_1 + 2\tau_2)}{A_{\mathrm{pr}}(2\tau_1)} = Q_{\mathrm{dc}} \tag{4}$$

is then usually analyzed as a function of τ_1 for a constant value of τ_2. Varying τ_2 as a parameter then produces a set of the experimental curves $Q_{\mathrm{dc}}(\tau_1, \tau_2)$.

Equation (4) implies that ultra-slow dipolar fluctuations of interest are statistically (quasi)-independent of those due to fast internal molecular motions, that is, motions with correlation times short on the time scale determined by the pulse sequence (2). The parts of the transverse relaxation due to slow and fast types of fluctuations are then factorized. The attenuation factors associated with fast fluctuations (that is, "ordinary" relaxation dominating in non-viscous liquids) consequently cancel in the quotient since they are equal for both the primary and the stimulated echoes. The longitudinal relaxation depends only on the time interval τ_2 and does not affect $Q_{\mathrm{dc}}(\tau_1)$ normalized for $\tau_1 \to 0$. Equation (4) further anticipates a validity of quasi-static conditions for a coherence evolution due to single particle local resonance offsets. That is, spins are assumed to experience the same local resonance offsets during the initial and the final evolution intervals providing a complete refocusing of echoes at the times of their maximal amplitudes. This requires in practice that magnetic field inhomogeneities are sufficiently small in order to ignore effects of translational molecular or spin diffusion [40,41]. As mentioned above, pair dipolar couplings are assumed to dominate all other internal interactions, so that any cross-relaxation [21,42,43] processes between chemically in-equivalent local environments are also of negligible importance (or compensated otherwise).

The DCE manifests itself as an attenuation of the dipolar-correlation quotient $Q_{\mathrm{dc}}(\tau_1)$, Equation (4). Given a Gaussian distribution of resonance frequencies the latter takes a form [29]

$$Q_{\mathrm{dc}} = \exp\left\{-\frac{1}{4}\left\langle\delta\Omega_d^2\right\rangle C_1\right\} \left(1+\overline{\cos(\langle\Omega_d\rangle\tau_1)}\exp\left\{-\frac{1}{2}\left\langle\delta\Omega_d^2\right\rangle C_2\right\}\right). \quad (5)$$

Here $\delta\Omega_d$ is the part of "residual" dipolar coupling constant, Ω_d, fluctuating on the time scale of the experiment about its mean value, $\langle\Omega_d\rangle$,

$$\delta\Omega_d(t) \equiv \Omega_d(t) - \langle\Omega_d\rangle. \quad (6)$$

Coefficients C_1 and C_2 are functions of the time intervals τ_1 and τ_2 and of the characteristic times of dipolar correlations. In the case of an exponential correlation function

$$g(t) \equiv \frac{\langle\delta\Omega_d(0)\delta\Omega_d(t)\rangle}{\left\langle\delta\Omega_d^2\right\rangle} = e^{-|t|/\tau_c}, \quad (7)$$

with the correlation time, τ_c, these coefficients read [29]

$$C_1 = \tau_c^2\left(e^{-\tau_1/\tau_c}-1\right)^2\left(1-e^{-\tau_2/\tau_c}\right) \quad (8)$$

$$C_2 = \tau_c^2\left(e^{-\tau_1/\tau_c}-1\right)^2 e^{-\tau_2/\tau_c}. \quad (9)$$

The analytical expressions for C_1 and C_2 for other types of correlation functions can be found in the literature [29,35].

The mean coupling constant has a finite value proportional to the order parameter

$$\langle\Omega_d\rangle \propto \langle 1-3\cos^2\theta(t)\rangle. \quad (10)$$

The bar over the cosine term in Equation (5) denotes the average over all orientations of local directors. In macroscopically ordered uniform systems in which the order parameter does not vary over space, it can be omitted. The attenuation curves in such systems are then subject to oscillations [29] with a frequency proportional to the macroscopic order parameter. In non-stretched polymer systems like rubber, orientations of local "directors" with respect to the external magnetic field are distributed in space. For the most common spherical distribution, the average $\overline{\cos(\langle\Omega_d\rangle\tau_1)}$ vanishes and Equation (5) reduces to

$$Q_{\mathrm{dc}} = \exp\left\{-\frac{1}{4}\left\langle\delta\Omega_d^2\right\rangle C_1\right\}. \quad (11)$$

More complicated situations are observed in systems in which RDCs are still finite but relatively weak. If chemical shift differences are of the same order of magnitude, the situation becomes favorable for cross-relaxation processes. These processes then easily give rise to additional undulations of spin echo amplitudes as a function of τ_1 [44,45]. Two mechanisms then interfere and the quotient of the stimulated echo and the primary echoes takes the form [31,44]

$$\frac{A_{\mathrm{st}}(2\tau_1+\tau_2)}{A_{\mathrm{pr}}(2\tau_1)} = Q_{\mathrm{dc}}A_{\mathrm{off}}, \quad (12)$$

where Q_{dc} is given by Equation (5) and A_{off} is the factor modulating amplitudes of the stimulated echo due to spin exchange

$$A_{\mathrm{off}}(2\tau_1+\tau_2) = 1-2P_aP_b(1-\cos(\Delta\omega\tau_1)) \times\left(1-e^{-\frac{\tau_2}{\tau_{ex}}}\right). \quad (13)$$

Here $\Delta\omega$ is the total frequency (chemical shift) difference between two spin states, P_a and P_b are the relative spin fractions in these states ($P_a+P_b=1$), and τ_{ex}^{-1} is the exchange rate depending on the efficiency of "residual" dipolar interactions. Equation (13) anticipates a "two-site" exchange model.

Undulations of the attenuation curves according to Equations (12) and (13) complicate the evaluation of the quantitative parameters of the DCE. This problem, however, can be overcome using a special modified pulse program [30,31] with the additional 180°-pulses permitting one to refocus any single particle local field offsets and cancel the modulation effect of spin exchange.

The DCE in Elastomers

In elastomers, the DCE was experimentally illustrated for a series of cross-linked synthetic poly-(styrene-butadiene) (SBR) networks [30] and natural rubber (NR) [31,32] as a strong attenuation of the quotient $Q_{\mathrm{dc}}(\tau_1)$. The influence of the cross-link density, swelling degree and the carbon black content was examined.

Besides the DCE, attenuation curves $A_{\mathrm{st}}(2\tau_1+\tau_2)$ as a function of τ_1 were affected by an additional strong modulation mechanism. The undulations of echo amplitudes observed in dry SBR and NR series could not be ascribed to any (macroscopic) ordering effects predicted by Equation (5), see cosine term, since investigated non-stretched rubber samples were macroscopically disordered. The latter was easily proven by the absence of any dipolar splitting in the corresponding proton spectra of the investigated samples. This obviously means that the macroscopic average $\overline{\cos(\langle\Omega_d\rangle\tau_1)}$ in Equation (5) vanishes. The observed undulation mechanism in both investigated sample series was actually identified with the cross-relaxation (spin exchange) between chemically in-equivalent protons of polymer chains.

In the case of NR samples, the oscillating behavior of the stimulated echo could be described on the basis of a simple two-site exchange model, Equation (13). The comparison of fitted values of $\Delta\omega$ with the chemical shifts observed in spectra permitted one to conclude that spin exchange occurs between CH and CH_3 (and/or CH_2) groups of polyisoprene chains. The exchange time was fitted to approximately 0.04 s. At the same time, the attenuation curves in swollen NR were free of any undulations. This indicates that spin exchange in swollen samples slows down drastically compared to that in dry materials as RDCs become much weaker.

In order to separate the contributions due to the DCE and spin exchange, a second experiment was performed using the modified pulse sequence [30,31]. The modified pulse sequence contains two additional π-pulses inserted in the middle of each free-evolution τ_1 intervals. Provided that spin exchange in the short τ_1 intervals is negligible, π-pulses refocus the phase shifts produced by spin interactions except those having a bilinear form. Spin exchange in the long interval $\tau_2 \gg \tau_1$ then does not affect the formation of the stimulated echo so that undulations described by Equation (13) vanish. The remaining attenuation of the dipolar-correlation quotient is due to the DCE only. This permits one to evaluate its quantitative characteristics by fitting the theoretical expressions to the experimental attenuation curves. An alternative approach permitting one to avoid spin exchange effects implies performing the experiments in low magnetic fields (see below).

In SBR samples, the theory, Equation (11), based on a power–law dipolar correlation function [30] was proved to provide reasonable fits to the attenuation curves of $Q_{\rm dc}(\tau_1)$. Before forming the quotient, the long-time tails of the individual (primary and stimulated) echo attenuation curves had to be subtracted. The observed tails were attributed to free chain ends or low-molecular weight constituents with a maximum percentage of 20%. This type of long tails was not detected in dry NR samples but showed up again when these samples were let to swell. In fact, there could be several reasons for the appearance of “slow” components in elastomers, see for instance Ref. [46] and references cited therein. This components are irrelevant for the DCE caused by slow re orientations of chain meshes. In this context one only needs to remember that attenuation curves consisting of two components must be decomposed in individual components before the quotient is formed. Ignoring this circumstance may produce strong distortions of $Q_{\rm dc}(\tau_1)$.

The exponent of the power-law correlation function was fitted in SBRs to ≈ 1.5 in coincidence with the previous finding for a melt of linear high molecular weight poly(ethylene oxide) [35]. The existence of ultraslow dynamics was supported by the results of the field-cycling relaxometry [36,47]. This powerful method permits one to probe molecular motional modes on the shorter ($t \ll 10^{-3}$ s), however, complementary time scale and can favorably be combined with the DCE. In combination, these two methods probe molecular motions on the time scale covering eight orders of the magnitude.

In NR samples, the best fits of Equation (11) to experimental attenuation curves, $Q_{\rm dc}(\tau_1)$, were obtained when using an exponential correlation function, see Equations (7–9). The experimental curves together with their fits are shown for four differently cross-linked samples in Figure 1. The samples are differentiated using the values of added sulfur, P_s. The cross-link density defined as the inverse of the number of segments $\tilde{N}$ between the nearest

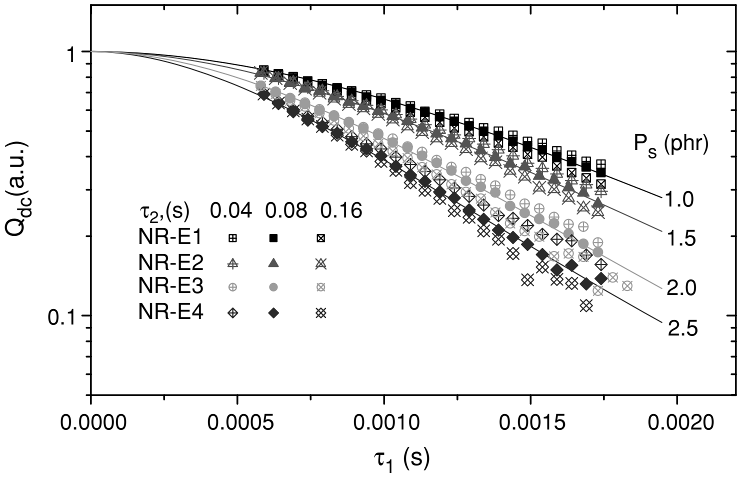

Fig. 1. Dipolar–correlation quotient, $Q_{\rm dc}$ of the stimulated and the primary echo amplitudes in samples of NR as a function of τ_1. The graph shows four sets of curves referring to the samples NR-E1—NR-E4 with different cross-link densities proportional to the sulfur content, P_s, as indicated. Each set contains three experimental curves measured at $\tau_2 = 0.04$, 0.08 and 0.16 s and fitted at one time. Solid lines are fits of Equations (11,8) to experimental data sets. Each solid line represents a corresponding set of three fitted curves which cannot be differentiated visually in a given graphic scale. The fit parameters were $\langle\delta\Omega_d^2\rangle$ and τ_c. The fitted values are listed in Table 1. All curves are normalized in the limit $\tau_1 \to 0$. (See also Plate 115 on page XV in the Color Plate Section.)

Table 1: Parameters of the Equations (11, 8) fitted to the experimental attenuation curves in dry and swollen samples of NR

	Dry	Dry	Swollen	Swollen
Sample	$\langle\delta\Omega_d^2\rangle$ $[10^6\text{rad}^2/\text{s}^2]$	τ_c[ms]	$\langle\delta\Omega_d^2\rangle$ $[10^6\text{rad}^2/\text{s}^2]$	τ_c[ms]
NR-E1	2.1 ± 0.4	4.2 ± 0.4	3.3 ± 0.2	1.3± 0.1
NR-E2	2.9 ± 0.2	3.3 ± 0.3	6.5 ± 0.3	1.3± 0.1
NR-E3	4.4 ± 0.3	2.6 ± 0.3	7.8 ± 0.5	1.5± 0.1
NR-E4	6.1 ± 0.8	2.0 ± 0.2	11.5 ± 0.1	1.2± 0.2

neighbour cross-links is proportional to added amounts of sulfur, P_s, [48], that is, $\tilde{N}^{-1} = \alpha P_s$ where α is the coefficient depending on a technological procedure and vulcanizing agents used. (Note that $\tilde{N}$ here refers only to the chemical cross-links and is not quite identical to N in Equation (1)). The four measured samples refer to different values of P_s equal to 1.0, 1.5, 2.0, and 2.5 given in mass fractions relative to the amount of polymer (or "rubber") used, that is, in "phr = parts per hundred rubber". In Table 1 these samples are denoted as NR-E1, NR-E2, NR-E3, NR-E4, respectively.

The curves in Figure 1 were measured using the modified pulse sequence and turned out to be completely free of any undulations. For each sample, a set of the curves was measured for several values of τ_2 ranging from 0.04 to 0.16 s. The fits were applied simultaneously to the whole set of the curves using just two fitting parameters, $\langle\delta\Omega_d^2\rangle$ and τ_c. The fitted values for dry and swollen samples are represented in Table 1.

The values of τ_c were fitted to a few milliseconds. This finding complies with the fact that the attenuation of the dipolar–correlation quotient tends to be independent of τ_2 since for $\tau_c \ll \tau_2$ the dependence of Q_{dc} on τ_2 in Equations (11,8) virtually vanishes. This is not true, as shown in Ref. [32], as soon as the measured range of τ_2 becomes shorter, below 10 ms, so that the condition $\tau_c \ll \tau_2$ does not hold. In this case a dependence of the dipolar–correlation quotient on τ_2 is distinct Ref. [32]. Again, the fits were applied simultaneously to the whole set of the curves using only two fitting parameters. This actually allowed one to confirm that a simple exponential correlation function complies indeed very well with the experimental data. Worth noting is that in materials in which a longitudinal relaxation is longer than a transverse one the application of the pulse sequence (2) has an essential advantage over the two pulse sequences. In the pulse sequence (2), two time variables τ_1 and τ_2 can be varied independently extending the overall time scale in which molecular motions can be probed.

The values of τ_c tend to decrease with increasing the cross-link density, that is, from sample NR-E1 to NR-E4. The correlation times in swollen samples were two to three times shorter than in dry rubber indicating much faster mesh chain fluctuations due to presence of small solvent molecules.

A strong dependence on the cross-link density was found for the second moment of the dipolar fluctuation $\langle\delta\Omega_d^2\rangle$. Both in dry and swollen samples, this quantity increases by a factor of ≈3 with increasing the cross-link density by a factor of 2.5. A similar effect was observed also for dry SBRs [30]. The carbon black used as a filler on the contrary does not seem to affect slow anisotropic chain modes in the elastomer: increasing of carbon black content by a factor of 2 did not produce any measurable effect on the attenuation of the dipolar–correlation quotient [31].

These findings comply with the results of Ref. [49]. In that work, effects of swelling, stretching and filling on molecular dynamics of NR samples were studied with help of the field-cycling relaxometry. It was shown that the dispersion curves of longitudinal relaxation rates alter significantly upon swelling and a uniaxial deformation. At the same time an addition of filler particles to the material was found to produce practiclly no effects on measured relaxation rates and thus underlying molecular dynamics at least at room temperatures.

As mentioned above, the DCE observed in elastomers is caused by the fluctuations of the chain meshes on the time scale exceeding $\approx 10^{-4}$s. It is reasonable to assume that on the time scale of the pulse sequence each given cross-link may undergo only small fluctuations around its mean position. The fluctuation of the residual coupling constant $\delta\Omega(t)$ then corresponds to the fluctuation of the mesh chain end-to-end vector around the average angle θ described in the "Introduction" Section. The characteristic time constant of this process in materials under consideration is thus estimated to be of the order of a few milliseconds.

The dependence of the MSDF, $\langle\delta\Omega_d^2\rangle$, on the number of segments between cross-links N can be estimated in two limits. If the meshes were completely stretched, that is, $|R| = R = Nb$, so that all Kuhn segments were parallel to R, the residual dipolar coupling constant and its mean squared fluctuation would be independent of N. The other limit is given by $R \ll Nb$. Using Equations (1) and (6) the mean squared fluctuation of the dipolar coupling constant reads [30]

$$\left\langle\delta\Omega_d^2\right\rangle \equiv \langle(\Omega_d(t) - \langle\Omega_d\rangle)^2\rangle \approx \Omega_0^2 \frac{R^4}{(N^2b^2)^2} \langle[(1 - 3\cos^2\theta) - \langle 1 - 3\cos^2\theta\rangle]^2\rangle. \quad (14)$$

If the dependence of $\langle[(1 - 3\cos^2\theta) - \langle 1 - 3\cos^2\theta\rangle]^2\rangle$ on N in Equation (1) is considered to be minor, the relation between $\langle\delta\Omega_d^2\rangle$ and N is determined simply by the function $R(N)$. The end-to-end distance of a random coil is distributed according to a Gaussian function. In the case of a freely jointed chain of Kuhn segments, the root mean square end-to-end distance is then given by $\sqrt{\bar{R^2}} \approx b\sqrt{N}$. In this case, the MSDF scales proportional to $1/N^2$, i.e.

$$\left\langle\delta\Omega_d^2\right\rangle \propto \frac{1}{N^2}. \tag{15}$$

The experimental findings in works [30,31] were compared to these limiting predictions. In the case of SBRs, the quantity $\langle\delta\Omega_d^2\rangle$ scales in the investigated cross-link density range as $\propto \frac{1}{N^{0.75}}$. For dry NR, the scaling exponent was considerably bigger, that is, $\langle\delta\Omega_d^2\rangle \propto \frac{1}{N^{1.3}}$ but still much smaller than that predicted by Equation (15). The conslusion was that mesh chains in both materials are more stretched than expected for a freely jointed mesh chain conformation. Scaling exponents observed for dry and swollen rubber appeared to be practically equal. This result was somewhat surprising considering that meshes in swollen rubber are expected to be more stretched than in dry.

The prediction for the MSDF as a function of the cross-link density was refined in Ref. [32]. It was demonstrated that the effects of topological constraints other than chemical cross-links must be taken into account. In Ref. [30,31] the comparison of the experimental findings with Equation (15) was done relying on the condition $P_s \propto \frac{1}{N}$, that is, only chemical cross-links were taken into account. Relevant for the DCE experiments, however, are not only chemical cross-links but also topological constraints that prevent a complete averaging of dipolar interactions on the experimental time scale.

The inverse value of N in rubber samples was tentatively decomposed into two contributions according to [50–52]

$$N^{-1} = \breve{N}^{-1} + \tilde{N}^{-1} = \breve{N}^{-1} + \alpha P_s \tag{16}$$

where $\breve{N}^{-1}$ is the density of the constraints other than chemical cross-links effective for the DCE. From Equations (15) and (16) it follows that

$$\sqrt{\left\langle\delta\Omega_d^2\right\rangle} \propto \breve{N}^{-1} + \alpha P_s = \sqrt{\left\langle\delta\Omega_d^2\right\rangle}_{P_s\to 0} + \tilde{\alpha} P_s \tag{17}$$

where $\tilde{\alpha}$ is a numerical coefficient, $\sqrt{\langle\delta\Omega_d^2\rangle}_{P_s\to 0}$ denotes $\sqrt{\langle\delta\Omega_d^2\rangle}(P_s)$ at $P_s \to 0$. Figure 2 shows the experimental results for $\sqrt{\langle\delta\Omega_d^2\rangle}$ as a function of $P_s \propto \frac{1}{N}$. A remarkable finding was that not only was the fitted value of $\sqrt{\langle\delta\Omega_d^2\rangle}_{P_s\to 0} = (1.65 \pm 0.3) \times 10^3$ rad/s finite but also it was approaching the value of $\sqrt{\langle\delta\Omega_d^2\rangle} = 1.97 \times 10^3$ measured for linear polyisoprene. In Figure 2 this value is represented by the point at $P_s = 0$. Linear highly viscous polyisoprene used in this study can be considered as a prototype of natural rubber at "zero" density of the chemical cross-links. The obtained results comply with the results obtained earlier for other linear polymer melts [28,35]. In that systems, the slow dipolar correlation effects are predominantly caused by the constraints due to topological constraints (excluded volume effects). The conclusion referring to rubber was that this kind of constraints is essential for slow dipolar fluctuations along with the chemical cross-links and that its contribution to the DCE is comparable to that in high molecular weight polymers.

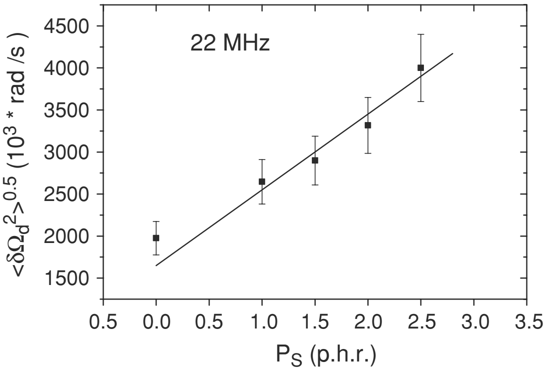

Fig. 2. Square root of the mean squared dipolar fluctuation, $\sqrt{\langle\delta\Omega_d^2\rangle}$, as a function of the amount of added sulfur, P_s. The cross-link density $1/\tilde{N}$ given by the number of segments per mesh is directly proportional to P_s. The solid line was fitted to the experimental data of rubber samples according to $\sqrt{\langle\delta\Omega_d^2\rangle} = K + \beta P_s$ with $K = (1.65 \pm 0.25) \times 10^3$ rad/sec and $\beta = (0.9 \pm 0.1) \times 10^3$ rad/(sec× phr).

A strong dependence of the DCE on the cross-link density of elastomers naturally suggests this method as a useful tool of a material characterization. On the other hand, the first works on the DCE in elastomers [30,31] were performed with a Bruker 300 and 400 MHz spectrometers not well suited for routine applications in industry because of high operating costs. Less expensive "mini"-spectrometers operating at much lower magnetic fields suggest a much better alternative for this purpose. Advantages and problems related with measuring the DCE in low magnetic fields was considered in Ref. [32]. One of the important issues that rises up in this context is the following. Although the DCE itself is virtually independent of the applied magnetic field, the relative contributions of other attenuation or undulation mechanisms may vary considerably with the external magnetic-flux density. This leads to certain peculiarities when performing the DCE experiment in low magnetic fields.

One of the findings of the study in Ref. [32] was that the low field DCE (at 0.52 T or 22 MHz) in dry NR measured using the standard pulse sequence (2) was not distorted by spin exchange modulations as it was the case with the high field measurements. The reason is that local resonance offsets due to chemical shifts scale linearly with the external magnetic-flux density. As a result, the corresponding period of modulations becomes much longer compared to the experimental range of τ_1 (limited by the transverse relaxation) and thus no modulation effects can be detected. Besides, this study revealed an advantage of having faster longitudinal relaxation compared to that in high magnetic fields. In NR for instance, the longitudinal relaxation time decreases from 800 ms at 400 MHz to 27 ms at 20 MHz. This permits one a reduction of the measuring time by more than one order of magnitude, which is greatly appreciated in the routine applications.

Imaging on the Basis of the DCE

NMR imaging is a well established tool in elastomer characterization [53–57]. An especially interesting application of the DCE in this context was demonstrated in Ref. [37], where the MSDF was used as a new parameter for NMR mapping.

The MSDF maps can be produced using the pulse sequence (2) combined with any scheme of the magnetic field gradients providing a spatial resolution (see, for instance, Refs. [53,36] or any other text books for NMR imaging). One of the appropriate pulse sequences is shown for example in Figure 3. The first 90°-pulse of the sequence might either be “hard” (if no slice selection is required) or “soft” (shaped) suited for selection of a particular sample slice.

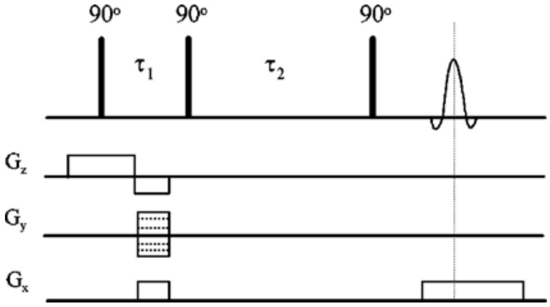

Fig. 3. Pulse sequence for measuring the MSDF maps. G_x, G_y and G_z denote the pulses of magnetic field gradients in X-, Y-, and Z- directions with Zeeman field applied along the Z-axis as usual. Signal amplitudes are acquired for the stimulated and primary echoes subject to maximal refocusing at $2\tau_1 + \tau_2$ and $2\tau_1$, respectively. In the case of the primary echo, τ_2 is set to zero and the third 90° pulse is omitted. The chemical-shift compensating version of the pulse sequence includes two additional 180°-pulses set in the middle of each τ_1-interval, that is, between the first two 90°-pulses and between the echo time and the preceding pulse.

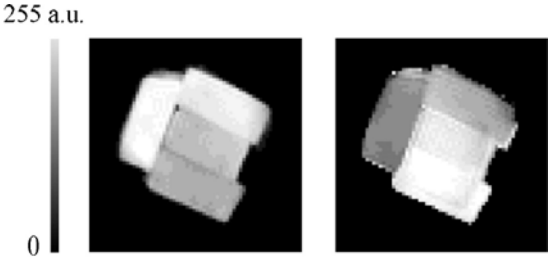

a) Relaxation weighted spin density image

b) $\langle \delta\Omega_d^2 \rangle$ - map

Fig. 4. RWSD image (a) and the MSDF map (b) of the sample consisting of four rubber stripes with different cross-link density. The RWSD image in (a) refers to the primary echo for $\tau_1 =$ 0.9 ms (echo time $2\tau_1 = 1.8$ ms). Each data matrix consists of 128×128 pixels. The in-plane pixel resolution is 78 μm in both directions. Field of view is 10 mm. The repetition time was 1 s. The range of the values measured for (a) the RWSD from 0 to 255 arbitrary units and for (b) $\langle \delta\Omega_d^2 \rangle$ from 1×10^6 to 5×10^6 rad^2/s^2 is displayed using the grey shade reference rulers shown on the left and on the right hand sides. The ruler assigns consistently decreasing grey shades (from black to white) to each of the 255 subsequent equidistant intervals covering the whole range of the measured values.

The primary and stimulated echo signals are acquired for a series of subsequently increasing τ_1-values, while τ_2 is kept constant. The dipolar–correlation quotients are formed to produce sets of values, $Q_{\mathrm{dc}}(\tau_1)$, for all pixels of the given map. The values of $\langle \delta\Omega_d^2 \rangle$ are evaluated for the individual pixels by fitting theoretical expressions, see Equation (5), to the obtained data sets. These values are then “visualized” in the grey shade or coloured MSDF maps.

Figure 4b demonstrates such an MSDF map of a composite sample consisting of the four rubber pieces with different cross-link density Ref. [37]. This sample models an inhomogeneous rubber object. The pixel values of the MSDF are “visualized” using grey shades related to the 255 equidistant intervals covering the whole range of the measured values. The values of $\langle \delta\Omega_d^2 \rangle$ evaluated for the corresponding areas of the map satisfactorily coincide with those found earlier for NR-E1—NR-E4 in the bulk measurements [31]. The regions with larger cross-link density (lower molecular mobility) are brighter according to their larger values of $\langle \delta\Omega_d^2 \rangle$, consider Equation (6). As it can easily be seen from Figure 4b, the MSDF map produces a clear contrast for the relevant regions.

Figure 4a shows for a comparison a conventional relaxation weighted spin density (RWSD) image of the same sample. It refers to the primary echo at echo time $2\tau_1 = 1.8$ ms. The RWSD images visualize the measured pixel signal intensity at this time point. It is proportional to initial magnetization attenuated by transverse relaxation. The contrast in the RWSD image in Figure 4(a) is obviously produced by the difference in the transverse relaxation rates of the different rubber stripes assuming that their initial magnetizations (proportional to proton density) are roughly equal. By the echo time, the corresponding magnetizations are attenuated stronger for the stripes with larger cross-link density resulting in darker regions. The contrast in the RWSD images depends on the experimental parameters (echo time in this case) as in any relaxation attenuated spin density images. On the contrary, single parameter MSDF maps enable one to visualize the areas with different orientational molecular mobility on the quantitative basis irrespective of the experimental parameters.

In studies of materials, the areas with reduced orientational mobility of molecules are quite often of a special interest. They may, for instance, indicate the aging processes in polymer elastomers. On the basis of the MSDF maps, the areas less mobile are favorably scaled up relative to more mobile regions. An additional advantage in the context of material characterization is that the DCE is not expected to be sensitive to the traces of low-molecular impurities or to motions like reorientations of the short free-end chains.

Worth noting is that in systems subject to slow correlated molecular motions, the overall transverse relaxation is generally not exponential [31]. Therefore, the conventional transverse-relaxation time (T_2) maps cannot be properly evaluated, as routinely done, on the basis of the Hahn echo attenuation curves. Mapping of the MSDF offers in such cases an alternative quantitative tool for the investigations of the heterogeneous objects exposed to ultraslow dipolar correlations.

Concluding Remarks

The experimental findings discussed in this paper suggest that the DCE represents an extremely useful tool of material characterization. In view of a strong dependence of the MSDF on the cross-link density of elastomers combined with the simplicity of performing the measurements with non-expensive low field NMR instruments, it can routinely be exploited for the determination of rubber cross-link density. The MSDF represents a new parameter of NMR mapping and can be used for visualizing material inhomogeneity and monitoring aging processes in rubber products. In studies of elastomer chain dynamics, the DCE is expected to be especially useful when favourably combined with other NMR methods like field-cycling relaxometry and field-gradient diffusometry.

References

1. Cohen-Addad J-P. J. Chem. Phys., 1974;60:2440.
2. Cohen-Addad J-P. J. Chem. Phys., 1975;63:4880.
3. Cohen-Addad J-P. J. Physique, 1982;43:1509.
4. Cohen-Addad J-P, Domard M, Herz JJ. Chem. Phys., 1982;76:2744.
5. Sotta P, Fuelber C, Demco DE, Blümich B, Spiess HW. Macromolecules, 1996;29:6222.
6. Demco DE, Hafner S, Fülber C, Graf R, Spiess HW. J. Chem. Phys. 1996;105:11285.
7. Kuhn W, Barth P, Denner P, Müller R, Solid State NMR, 1996;6:295.
8. Graf R, Demco DE, Hafner S, Spiess HW. Solid State NMR, 1998;12:139.
9. Schneider M, Gasper L, Blümich B, J. Chem.Phys. 1999;111:402.
10. Schneider M, Demco DE, Blümich B, J. Magn. Res. 1999;140:432.
11. Gasper L, Demco DE, Blümich B, Solid State NMR, 1999;14:105.
12. Malveau C, Pekely P, Canet D, Solid State NMR, 1997;7:271.
13. Saalwächter K, J. Chem. Phys. 2004;120:454.
14. Fechete R, Demco DE, Blümich B. J. Magn. Res. 2004;169:19.
15. Stapf S, Kariyo S, Blümich B, In: G. Webb (Ed), Handbook of Modern Magnetic Resonance, Kluwer, London, 2005.
16. Growther BG, Lewis PM, Metherell C. In: AD. Roberts (Ed), Natural Rubber Science and Technology, Oxford Press University, 1990, p. 363.
17. Sperling LH, Introduction to Physical Polymer Science, John Wiley & Sons: New York, 1986.
18. de Gennes PG, The Physics of Liquid Crystals, Clarendon Press: Oxford, 1974.
19. de Gennes PG. Scaling Concepts in Polymer Physics. Cornell University Press: Ithaca, 1979.
20. Slichter SP, Principles of Magnetic Resonance. Springer Verlag: Berlin, 1978.
21. Ernst RR, Bodenhausen G, Wokaun A. Principles of Nuclear Magnetic Resonance in One and Two Dimensions. Clarendon Press: Oxford, 1987.
22. Kimmich R, Fatkullin N. Adv. Polym. Sci. 2004;170:1.
23. Fatkullin N, Fischer E, Mattea C, Beginn U, Kimmich R. Chem Phys Chem. 2004;5:884.
24. Sotta P, Deloche B. J. Chem. Phys. 1994;100:4591.
25. Brereton MG, Macromolecules. 1993;26:1152
26. Lifshits MI, Polymer. 1987;28:454.
27. Callaghan PT, Samulski ET. Macromolecules. 1997;30:113.
28. Ball RC, Callaghan PT, Samulski ET. J. Chem. Phys. 1997;106:7352.
29. Grinberg F, Kimmich R. J. Chem. Phys. 1995;103:365.
30. Fischer E, Grinberg F, Kimmich R, Hafner S. J. Chem. Phys. 1998;109:846.
31. Grinberg F, Garbarczyk M, Kuhn W. J. Chem. Phys., 1999;111:11222.
32. Garbarczyk M, Grinberg F, Nestle N, Kuhn W. J. Polym. Sci., Part B: Polym. Phys. 2001;39:2207.

33. Grinberg F, Kimmich R, Möller M, Molenberg A. J. Chem. Phys. 1996;105:9657.
34. Grinberg F, Kimmich R. J. Chem. Phys. 1996;105: 3301.
35. Kimmich R, Fischer E, Callaghan P, Fatkullin N. J. Magn. Res. A 1995;117:53.
36. Kimmich R. NMR: Tomography, Diffusometry, Relaxometry, Springer: Berlin, 1997.
37. Grinberg F, Heidenreich M, Kuhn W. J. Magn. Reson. 2002;159:87.
38. Hahn E. Phys. Rev. 1950;80:580.
39. Fukushima E, Roeder S. Experimental Pulse NMR, Addison-Wesley Publishing Company: London, 1981.
40. Callaghan PT. Principles of Nuclear Magnetic Resonance Mi-croscopy, Clarendon Press: Oxford, 1991.
41. Fischer E, Kimmich R, Fatkullin N. J. Chem. Phys. 1997;106:9883.
42. Neuhaus D, Williamson M. The Nuclear Overhauser Effect in Structural and Conformational Analysis, VCH Publishers: New York, 1989.
43. Schmidt-Rohr K, Spiess HW. Multidimensional Solid-State NMR and Polymers, Academic press, London: San Diego, NY, Boston, Sydney, Tokyo, Toronto, 1994.
44. Grinberg F, Kimmich R, Stapf S. Magn. Reson. Imaging. 1996;14:883.
45. Isfort O, Geil B, Fujara F. J. Magn. Reson. 1998;130: 45.
46. Fedotov V, Schneider H. Structure and Dynamics of Bulk Polymers by NMR-Methods, Springer: Berlin, Heidelberg, N. Y., 1989.
47. Kimmich R, Anoardo E. Prog. Nucl. Mag. Res. Spectrose. 2004;44:257.
48. Kelm J, Tobisch K, Leisen J. KGK Kautschuk Gummi Kunststoffe, 1998;51:364.
49. Kariyo S, Stapf S. Solid State Nucl. Mag. 2004;25:64.
50. Lee SS, Pawlowski H-, Coran AY. Nat. Rubber Chem. Technol. 1994;67:854.
51. Langeley NR. Macromolecules. 1968;1:348.
52. Mullins L. J. Appl. Polym. Sci. 1959;2:1.
53. Blümich B. NMR imaging of materials, Oxford, Clarendon Press, 2000.
54. Knorgen M, Arndt KF, Richter S, Kuckling D, Schneider H. J. Molec. Struct. 2000;554:69.
55. Kuhn W, Barth P, Denner P, Müller R. Solid State Nucl. Magn. Reson. 1996;6:295.
56. Blümler P, Blümich B, Botto R, Fukushima E. (Eds.) “Spatially Resolved Magnetic Resonance. Methods, Materials, Medicine, Biology, Rheology, Geology, Ecology, Hardware” Wiley VCH, Weinheim, New York, Chichester, Brisbane, Singapure, Toronto, 1998.
57. “Magnetic Resonance Microscopy. Blümich B and Kuhn W. Eds., Methods and Application in Materials Science, Agriculture and Biomedicine” VCH, Weinheim, New York, Basel, Cambridge, 1992.

Correlating Molecular and Macroscopic Properties of Elastomers by NMR Relaxometry and Multi-pulse NMR Techniques

S. Stapf, S. Kariyo and B. Blümich
Lehrstuhl für Makromolekulare Chemie, ITMC, RWTH Aachen, Worringerweg 1, D-52074 Aachen, Germany

Introduction

Making use of NMR techniques for the characterization of elastomers poses the problem of identifying a connection between a parameter accessible to NMR and the material property of interest. Due to the origin of interactions affecting the NMR signal, this provides a link between the molecular level and the macroscopic scale. Understanding these links, and developing suitable experimental techniques for their investigation, also addresses the fundamental issue of the dynamics of macromolecules which is still a topic of extensive research with many open questions remaining. However, encoding these molecular properties within an NMR imaging sequence eventually allows the generation of parameter maps, which can be used for quality control of technical elastomers in the production process or under external constraints (deformation, aging, failure).

Spectra and relaxation times represent the simplest parameters with which material properties of elastomers can be correlated. They relate to either static or dynamic molecular properties, or combinations thereof. Considerably more information is contained in parameter sets which include one further dimension; this might be a second encoding leading to a 2D spectrum, or the dependence of the relaxation process on a certain time or frequency scale. The term "relaxometry", sometimes used in the general sense of providing any kind of relaxation information of a sample, was initially coined for the interrogation of the relaxation *spectrum*, i.e. the dependence of the longitudinal relaxation time on the Larmor frequency, and hence magnetic field strength [1]. The shape of such a relaxation dispersion curve contains information about molecular dynamics over the covered frequency scale. Related, but different, information is retrieved from measurements of the transverse relaxation time with a time-axis added, such as obtained by a CPMG sequence with variable pulse separations.

A different, less easily defined microscopic property is the concept of "order". It includes both static and dynamic aspects, because order, usually attributed to the relative orientation of atoms or molecules, depends on the time scale which is interrogated. It is thus less suitable to provide absolute and intuitively interpretable results, but can be equally powerful as a contrast parameter.

Published works highlight different aspects of the microscopic/macroscopic link in the investigation of elastomers, hereby employing a broad range of experimental techniques which go beyond the simple analysis of spectra and lineshapes:

The incomplete averaging of the dipolar interactions which is brought about by the presence of entanglements and cross-links can be quantified by exploiting the time dependence of a particularly encoded parameter in a multi-pulse sequence. Cohen-Addad [2] has proposed to extract quantitative information about couplings from combinations of solid echo and FID decays; Callaghan and Samulski have developed a related sequence that directly visualizes dipolar couplings and suppresses Zeeman effects [3,4]. Grinberg *et al.* determined the dipolar correlation effect for long evolution times based on stimulated echoes [5]. Multi-quantum encoded signals were correlated with elastomer properties [6,7] and were combined with imaging [8,9] and low-field realizations [10]. Measurements of the transverse and longitudinal relaxation times [11–14] of elastomers focussed on the dynamical aspects of the molecular motions, and correlations with material properties were established [15]. First results of relaxation dispersions in permanent and thermoreversible networks were presented [16,17], and recent investigations were carried out on elastomers employing the frequency dispersion of T_1 [18,19] and $T_{1,\rho}$ [20,21].

This overview is by no means complete, but provides some ideas of the "NMR toolbox" being available to cover" questions related to the behavior and quality of rubbery materials.

Theoretical Background

A general formulation of the dependence of the longitudinal relaxation time on Larmor frequency ω can be written

Graham A. Webb (ed.), Modern Magnetic Resonance, 1455–1461.
© 2008 *Springer.*

as follows:

$$T_1^{-1}(\omega) = C[\mathcal{I}(\omega) + 4\mathcal{I}(2\omega)] \tag{1}$$

where the constant C depends on the kind of interaction, e.g. dipolar or quadrupolar. The equation is correct for quadrupolar interactions, and in the case of like spins for dipolar relaxation. It has to be modified for dipolar coupling between unlike spins or for other types of coupling. Similar expressions are found for the transverse relaxation time T_2, and the longitudinal relaxation time in the rotating frame $T_{1,\rho}$.

The frequency dependence is introduced by the spectral density function $\mathcal{I}(\omega)$ describing reorientational motions which are responsible for the relaxation process. $\mathcal{I}(\omega)$, in turn, represents the Fourier transform of the autocorrelation function $G(t)$:

$$\mathcal{I}(\omega) = \int_{-\infty}^{\infty} G(t)e^{-i\omega t} \ . \tag{2}$$

For the most important case of dipolar relaxation, $G(t)$ is obtained from the time-dependence of fluctuating functions describing the orientational dependence of the spin-operator components in the dipolar Hamiltonian [1]. It should be kept in mind that "motion" of a polymer or an elastomer is parametrized via the reorientation of its segments, while other methods, e.g. PFG NMR diffusometry, use the lateral displacement as a parameter. This can explain method-dependent differences in the description of the time-dependence of motion.

Most models, which had been developed for the segmental reorientation, avoid a detailed analysis of the dynamics on an atomic scale and consider the motion of segments like the *Kuhn segment* as a whole. This is justified for two reasons. First, the molecular structure itself influences only the absolute value of the relaxation time and its frequency dependence in a range, which is not of interest for understanding the dynamics of the chain molecule, and also often inaccessible by the experiment. Second, the mechanism of spin diffusion leads to an averaging of the magnetization of individual protons in one segment, so that an average T_1 is found for a microscopically homogeneous sample, which is subject to ensemble averaged reorientations of the segment. This is no longer true for microscopically heterogeneous samples (e.g. block copolymers) or for relaxation of deuterons, where spin-diffusion is inefficient, resulting in multi-component relaxation decays.

The simplest case of an autocorrelation function is an exponential with an average correlation time τ_c, $G(t) = \exp(-t/\tau_c)$. It describes well the rotational contribution to relaxation in liquids. Its Fourier transformation is the Lorentzian, $\mathcal{I}(\omega) = \tau_c(1 + \omega^2\tau_c^2)^{-1}$, containing a frequency-dependent term which becomes much smaller than unity for liquids of low viscosity, hence the absence of a frequency dispersion. This is, of course, no longer true for polymers and elastomers which are known to show a wide spectrum of motion as found with many experimental techniques. The description of molecular motion in elastomers starts from models for polymer melts and solutions where several theories are available. Examples are the well-known reptation approaches by de Gennes [22,23], Doi and Edwards [24], and the mode-coupling ansatz by Schweizer [25]. In a nutshell, they all predict characteristic power–law dependences of the mean-squared displacement on time, and similar power-laws were proposed and indeed measured for the spectral density function of nuclear relaxation [16,26,27]. From these works, power-law relations of $T_1(\omega) \propto \omega^\gamma$ with $\gamma = 0.5$, $\gamma = 0.2 \ldots 0.25$ and $\gamma = 0.45 \ldots 0.5$ are expected in a succession from high to low frequencies.

A detailed discussion of these different regimes is beyond the scope of this article. The phenomenological description serves mainly as a starting point to demonstrate how these relations are affected in an elastomer, and how experimental results can be employed for a characterization of material properties. In this sense, the elastomer is regarded not as a "soft solid", but as a melt with additional geometrical constraints in the shape of permanent cross-links. The consistency of the experimental results supports this notion.

Relaxometry Experiments

The determination of relaxation times over a wide range of frequencies almost always requires the use of a magnetic field of variable strength. This is particularly true for the low-field region ($B_0 \ll 0.1$T), where signal intensity becomes critical. In a so-called *field-cycling* experiment, polarization and detection occur at (not necessarily equal) high fields, and the sample is exposed to the desired lower field for the relaxation period in between these two stages. In principle, either the sample can be moved mechanically between regions of different fields [28], or the current in the magnet is varied directly [29,30]. The latter method usually allows faster field changes and consequentially the determination of shorter relaxation times, which is often crucial for elastomers. For the studies presented here, relaxometry measurements were performed on a commercial Stelar Fast Field Cycling Relaxometer (Stelar s.r.l., Mede, Italy) which allowed the determination of longitudinal relaxation times at ^{1}H Larmor frequencies between 5 kHz and 20 MHz, providing field switching times of 1.3 ms. Signal decays were found to be monoexponential over more than one decade; the relaxation times were reproducible within 1%, the temperature stability was ±0.1 K.

Figure 1 demonstrates the principle shape of the dispersion curves for isoprene rubber and butadiene rubber

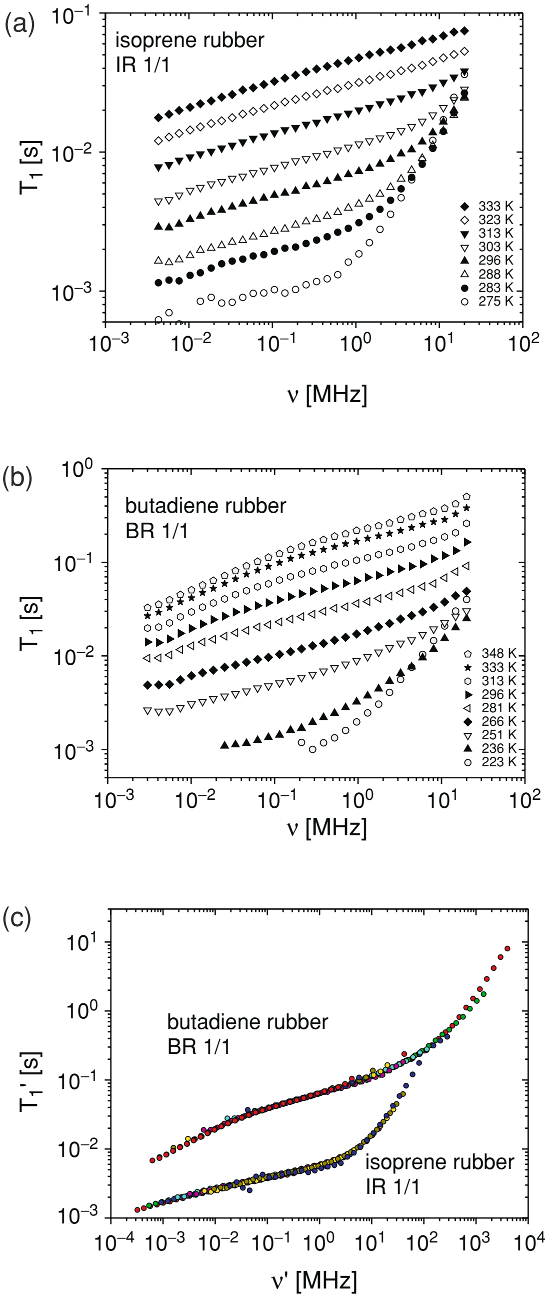

Fig. 1. Frequency-dependent relaxation times $T_1(\nu)$ for elastomers of low cross-link density as a function of temperature: (a) isoprene rubber; (b) butadiene rubber; (c) master curves relative to $T_0 = 296$ K derived from (a) and (b) applying shifts according to the WLF equation.

with low cross-link density (1 phr of sulfur and accelerator each, unfilled samples), and their dependence on temperature. It employs a double-logarithmic scale where a power–law relationship is identified by a line of constant slope γ. All dispersion curves can be approximated by a succession of power–laws. The changing shape of the curves with temperature can be explained by a shift along the frequency axis. Displacing the curves by empirically found shift parameters [31] according to the Williams–Landel–Ferry (WLF) equation

$$\log a_T = -C_1(T - T_0)/(C_2 + T - T_0) \,, \qquad (3)$$

where a_T is the shift factor relative to a reference temperature, T_0, one obtains *master curves* which cover a larger portion of the spectrum $\mathcal{I}(\omega)$. The master curves for the two different elastomers are compared in Figure 1c.

The data shown in Figure 1 for weakly cross-linked elastomers are qualitatively similar to those of the uncross-linked polymers (see [16,18]), only minor shifts relative to the melt relaxation curves are found but the exponents γ remain the same. One finds, in order from high to low frequencies, $\gamma \approx 1.15$, $\gamma = 0.24 \pm 0.01$ and $\gamma \approx 0.45$ for butadiene rubber (BR), and $\gamma = 1.23 \pm 0.07$ and $\gamma = 0.16 \pm 0.01$ for isoprene rubber (IR), respectively. The highest values are a consequence of semi-local (within the Kuhn segment) reorientations [18]; the small values observed for both elastomers describe frequency scales on which the fluctuation amplitude is sufficiently large to make geometrical constraints become effective for the individual chain; the lowest frequency range, only covered in part for BR (but reported for IR at higher temperatures [27,32]) denotes the onset to coherent chain motion. Only the latter is expected to be strongly affected by the presence of cross-links, but no clear evidence for such an effect has been found so far from the limited range of data of BR and polybutadiene melts. It should be noted that the particularly small value of $\gamma = 0.16$ found for IR is indeed a characteristic feature of the polyisoprene chain and has been investigated in some detail [18,19,33]. Like the other exponents, it is not changing due to cross-linking effects.

Note that the change of relaxation times in the low-frequency region is very sensitive to temperature changes, particularly so for IR. With the reproducibility of the data given above, this allows the indirect determination of temperature with a precision of 0.1–0.2 K from a single experiment, being improved by obtaining a full dispersion curve. This information is not available from high-field experiments where the temperature dependence of T_1 becomes much weaker. It is, however, accessible from T_2, and corresponding experiments of T_2 parameter images on rubber were suggested as a means of temperature mapping [34].

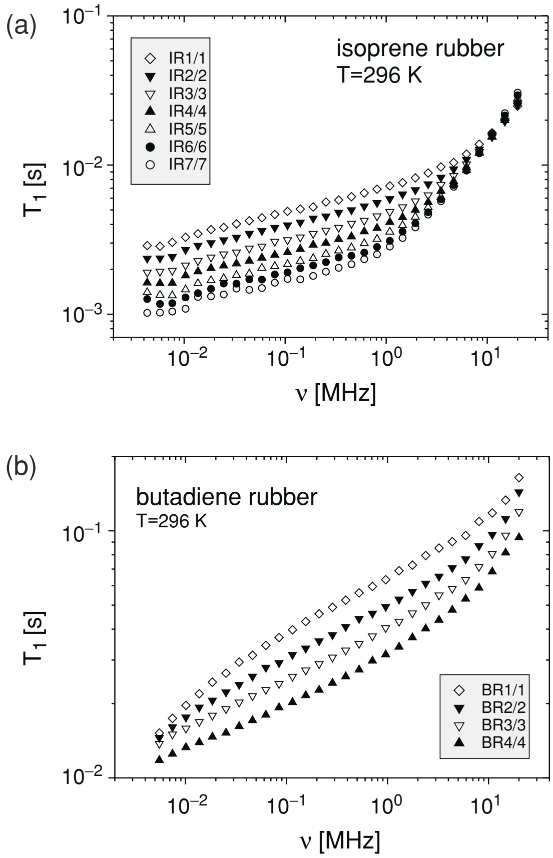

Fig. 2. Frequency-dependent relaxation times $T_1(\nu)$ at T $= 296$ K as a function of cross-link density (numbers indicate sulfur/accelerator content in phr): (a) isoprene rubber; (b) butadiene rubber.

The most important parameter for the characterization of elastomers is the cross-link density. Figure 2 shows the effect of increasing cross-link density at constant temperature for IR and BR. It is seen immediately that the relaxation times sharply decrease with increasing cross-link density. For IR, almost equidistant lines appear for relative sulfur concentrations between 1 and 7 phr. The dispersion curves, however, are not simply displaced vertically but follow the same WLF-type shift as observed from measurements at different temperatures. It is indeed possible to construct another master curve. The reason for this behavior is found in the dependence of the glass transition temperature, which enters into the WLF equation, on cross-link density. In a systematic investigation of several types of elastomers, Herrmann *et al.* have used the connection between glass temperature and T_2 at constant field for an estimation of cross-link densities [15]. From the dispersion data presented here and in [18,19], an estimated precision in the determination of the cross-linked sulfur of 0.1 phr or better seems feasible for IR. Regarding the absolute difference between T_1 values, the intermediate frequency range between 100 kHz and 1 MHz provides the best contrast as a function of cross-link density; this range is, in practice, only accessible by field-cycling relaxometry.

Once a correlation between relaxation times and cross-link density is established, one can continue with deforming the elastomer out of its equilibrium conformation. The first possibility is a static deformation experiment, i.e. stretching or compressing the sample. The deformation induces order on the molecular scale, which generates anisotropy in the spectral features. One can expect that relaxation itself also becomes angle-dependent, a fact that has been demonstrated for transverse relaxation times in stretched [10] and compressed samples [35]. Indeed, clear evidence for a possible angular dependence of T_1 was not found, but the dispersion curves obtained from IR samples deformed either parallel or perpendicular to the magnetic field axis show a surprising feature [18,19], see Figure 3. While T_1 values at high field remain indistinguishable, the curves diverge and stretching results in an increase in the value of the power–law exponent itself. The difference is small but significant, amounting to a change from $\gamma = 0.16$ to $\gamma = 0.24$ for IR stretched to $\lambda = 7$ and from $\gamma = 0.24$ to $\gamma = 0.28$ for SR for which extension was only obtained at $\lambda = 2$. The IR results indicate that the beginning of divergence is shifted to higher frequencies as temperatures are increased, making the difference more easily observable at low fields. From simple geometrical considerations, deformation of the local environment of the polymer chain should only affect the frequencies of transition between different power–law regimes, but not the statistical properties themselves. However, there are indeed strong indications that an actual change of the shape of the correlation function of reorientation, $G(t)$, can be made responsible for the observed effect.

Finally, the effect of the addition of solvents is demonstrated in Figure 4. Equilibrium swelling conditions have been reached for IR in different mixtures of a bad (ethanol-d6) and a good solvent (toluene-d8), being equivalent to weight increases between 4% and 439%. A gradual transition from a power–law behavior to Rouse dynamics, which is characterized by a logarithmic relation between T_1 and frequency [16], is found; the same qualitative observation has been made for polyisoprene melts with equivalent solvent contents (data not shown). Only at high degrees of swelling, the residual weak dispersion found for the elastomer becomes distinguishable from the solution where the frequency dependence of T_1 all but disappears. We present the results of Figure 4 mainly for pointing out the high sensitivity of the low-field relaxation

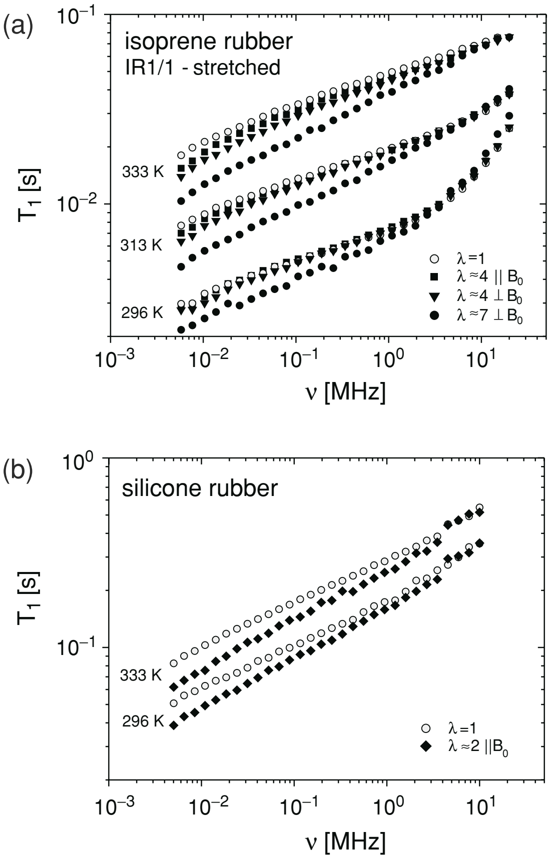

Fig. 3. Frequency-dependent relaxation times $T_1(\nu)$ at different temperatures for elastomer samples stretched parallel or perpendicular to B_0: (a) isoprene rubber IR1/1; (b) silicone rubber.

time to the presence of small amounts of solvent. Even for a weight increase of only 4%, T_1 increases for up to 30% at low fields so that the method allows, in principle, to determine solvent concentrations of well below 1%. A series of experiments with internal plasticizers as additives showed no measurable effect, but changed the behavior in T_2. The method can thus be useful for discriminating contaminants in elastomers at a low concentration.

Double Quantum Experiments

The determination of dipolar coupling constants provides further, and potentially complementary, information about the material properties of elastomers, and shall be presented briefly for comparison. Homonuclear (proton) dipolar couplings can be obtained, for instance, from double quantum (DQ) filtered spectra. The double-quantum coherences are encoded by at least two successive rf pulses and need to be reconverted into single-quantum (observable) coherences by a further pulse, with appropriate phase cycling selecting the correct coherence pathways to avoid "contamination" with unwanted signals. Apart from this basic three-pulse sequence [36,37], more advanced methods are in use which still consist of the basic scheme of encoding, evolution and reconversion (see, e.g. [7,9]). During the evolution period, the double quantum coherence builds up from the sum over proton spin pairs in the sample. For identical pairs, the dependence of the signal intensity is a well-defined quantity of the coupling strength expressed in frequency units, ω_D. In the presence of more than one possible combination of proton pairs, such as in IR, the interpretation is not as straightforward but the total evolution can be written in terms of an average coupling constant, $\overline{D}$. In order to obtain $\overline{D}$ from the experiment, the evolution time τ is varied and the initial slope of the resulting buildup curve is determined, which is proportional to $\overline{D}^2\tau^2$. For a more detailed description of the case of DQ encoding in elastomers, see [7].

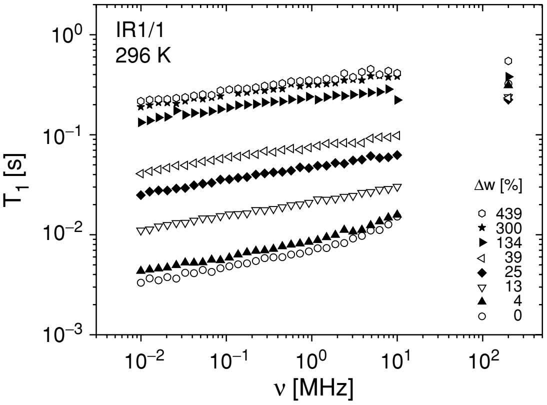

Fig. 4. Frequency-dependent relaxation times $T_1(\nu)$ as a function of weight increase (Δw) during swelling for isoprene rubber in a mixture of deuterated ethanol and toluene.

A complete averaging of dipolar couplings by fast and isotropic motion, such as in a low-viscosity liquid, does not allow the buildup of coherences between spin pairs. In a rigid solid, the coupling is strongest, and for substances such as elastomers, anisotropic motion of particular moieties and segmental motion add up to a reduced coupling strength which indicates an order parameter [6]. These residual couplings are employed as parameters to characterize the material properties on a microscopic level. In [7], it was already demonstrated that a strong correlation between $\overline{D}$ and the cross-link density exists. In [9],

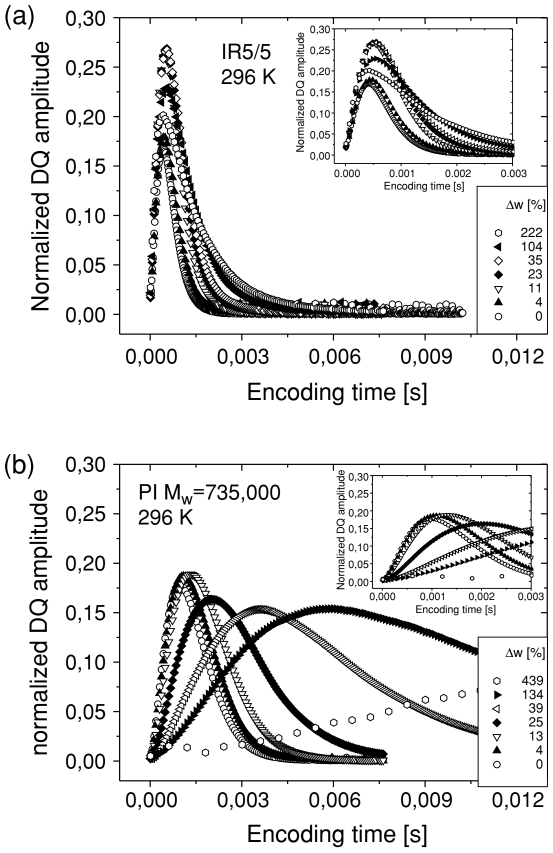

Fig. 5. Double quantum buildup curves as a function of encoding time τ for different weight increase Δw of solvent: (a) for isoprene rubber IR5/5, (b) for polyisoprene melt ($\overline{M_w} = 735000$).

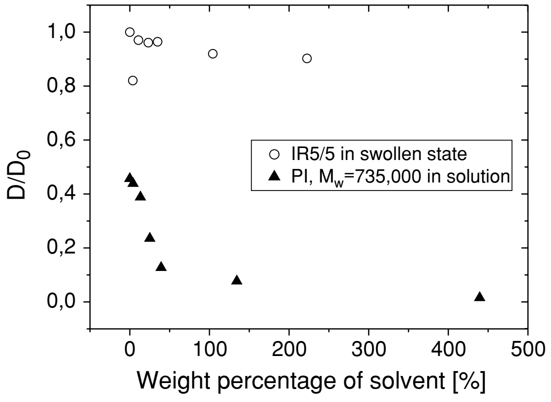

Fig. 6. Relative dipolar coupling constants obtained from the curves of fig. 5; data are normalized to the coupling constant for IR5/5 in the absence of solvent (D_0).

the dependence on the deformation ratio λ was shown, and indeed used in combination with imaging techniques to visualize the stress parameter distribution in a cut elastomer band. The increase of $\overline{D}$ with λ is intuitively understood from the preferential alignment of segments along the deformation axis, but it possesses the potential to quantify the affine or non-affine transformation of the macroscopic effect onto the molecular scale. Double-quantum experiments were performed for the stretched elastomers discussed above. However, we restrict ourselves to a demonstration of the effect of cross-links on the order parameter in the case of swelling. It becomes obvious by comparing the buildup curves of Figure 5 that the coupling behavior for cross-linked rubber changes only weakly even for the highest degree of swelling; the higher maximum value and the decaying part follow from a moderate increase in the transverse relaxation time, T_2 (data not shown). In contrast, uncross-linked polyisoprene in equivalent amounts of solvent shows a dramatic decrease of coupling strength, accompanied by a strong increase in T_2. A quantitative comparison between the coupling constants, determined as described above, is given in Figure 6. The effect of the cross-links is to maintain molecular order even under strong swelling. The order parameter in the uncross-linked melt is already lower by a factor of two, and drops significantly on addition of solvent. Thus, the presence of permanent cross-links has a pronounced influence on the order parameter as obtained from DQ experiments, but alters the longitudinal relaxation time dispersion only weakly. From a theoretical point of view, this can be explained by the different time scales and length scales involved: the change of the orientation of an internuclear vector affects relaxation but not necessarily the value of the coupling constant. By practical considerations, DQ encoding is demonstrated to be very sensitive to the detection of cross-links in general, but particularly in swollen samples. Its relatively simple use allows straight forward combinations with imaging techniques, thus providing spatially resolved maps of the order parameter.

Summary

The use of frequency-dependent relaxometry in combination with double quantum spectroscopy for the characterization of elastomers subject to different constraints has been presented. Relaxation dispersion master curves can be reconstructed from experiments performed in a limited frequency range, and feature a sequence of power–law regimes characteristic to the elastomer type. The exponents of this dispersion are the same for melts and corresponding elastomers; the dependence of the glass transition temperature is reflected in the shift of the dispersion curves. Both effects point to the high sensitivity of the low-field relaxation measurements to either temperature or cross-link density. At the same time, internal plasticizers or high concentrations of fillers hardly affect the relaxation behavior, making the method insensitive to these properties. Deformation, on the other hand, was shown probably to change the spectrum of segmental motions itself. A similar, but much stronger effect is observed for swelling of the elastomer, making only small amounts of solvents indirectly detectable via the elastomer relaxation. Finally, double quantum encoding is likewise sensitive to the cross-link density, and even more so in the presence of mobile components such as solvents. Provided that a sufficiently precise calibration has been established, a comparison of the experimental results for samples of different properties facilitates the choice of experimental conditions for achieving optimal contrast. The large potential of low field (<0.1 T) NMR in general, and low field imaging in particular, for the investigation of elastomer properties and their spatial distribution in heterogeneous samples has been demonstrated.

Acknowledgments

The authors are grateful to Dr. V. Herrmann, Dunlop GmbH, for kindly providing the IR and BR samples, and to M. Adams, K. Kupferschläger and G. Schroeder for continuous support throughout this study. Financial support from the Deutsche Forschungsgemeinschaft DFG (Sta 511/3) is gratefully acknowledged.

References

1. Kimmich R., NMR: Tomography—Diffusometry—Relaxometry, Springer Verlag: Berlin, 1997.
2. Cohen-Addad J. P., J. Chem. Phys. 1975;63:4880.
3. Callaghan PT, Samulski ET. Macromolecules. 1997;30:113.
4. Callaghan PT, Samulski ET. Macromolecules. 1998;31:3693.
5. Grinberg F, Garbarczyk M, Kuhn W. J. Chem. Phys. 1999;111:11222.
6. Graf R, Demco DE, Hafner S, Spiess H.-W. Solid State Nucl. Magn. Reson. 1998;12:139.
7. Schneider M, Gasper L, Demco DE, Blümich B. J. Chem. Phys. 1999;111:402.
8. Schneider M, Demco DE, Blümich B. J. Magn. Reson. 1999;140:432.
9. Schneider M, Demco DE, Blümich B. Macromolecules. 2001;34:4019.
10. Wiesmath A, Filip C, Demco DE, Blümich B. J. Magn. Reson. 2002;154:60.
11. Sotta P, Deloche B, Herz J, Lapp A, Durand D, Rabadeux J-C. Macromolecules. 1987;20:2769.
12. Brereton MG. Macromolecules. 1990;23:1119.
13. Cohen-Addad JP. Prog. NMR Spectrosc. 1993;25:1.
14. Menge H, Hotopf S, Schneider H. Polymer 2000;41:4189.
15. Herrmann V, Unseld K, Bohner T, Blümich B. Kautschuk Gummi Kunststoffe. 2004;57:22.
16. Weber HW, Kimmich R. Macromolecules. 1993;26:2597.
17. Kimmich R, Gille K, Fatkullin N, Seitter R, Hafner S, Müller M. J. Chem. Phys. 1997;107:5973.
18. Kariyo S, Stapf S. Macromolecules. 2002;35:9253.
19. Kariyo S, Stapf S. Solid State Nucl. Magn. Reson. 2004;25:64.
20. Chaumette H, Grandclaude D, Tekely P, Canet D, Cardinet C, Verschave E. J. Phys. Chem. A. 2001;105:8850.
21. Chaumette H, Grandclaude D, Boubel JC, Canet D. Chem. Phys. Lett. 2003;374:252.
22. de Gennes PG. J. Chem. Phys. 1971;55:572.
23. de Gennes P.-G. Scaling Concepts in Polymer Physics. Cornell University Press: Ithaca, NY, 1979.
24. Doi M, Edwards SF, *The Theory of Polymer Dynamics*. Clarendon: Oxford, England, 1986.
25. Schweizer KS. J. Chem. Phys. 1991;91:5802 and 5822.
26. Kimmich R, Weber HW. J. Chem. Phys. 1993;98:5847.
27. Fatkullin N, Kimmich R, J. Chem. Phys. 1994;101:822.
28. Redfield AG. Magn. Reson. Chem. 2003;41:753.
29. Noack F. Prog. NMR Spectrosc. 1986;18:171.
30. Anoardo E, Galli G, Ferrante G, Appl. Magn. Reson. 2001;20:365.
31. Ngai KL, Plazek DJ. In Ed: Physical Properties of Polymers Handbook, edited by JE Mark, American Institute of Physics: Woodbury, New York, 1996.
32. Kimmich R, Fatkullin N, Weber HW, Stapf S. J. Non-Cryst. Solids. 1994;172:689.
33. Kariyo S, Stapf S, Blümich B. Macromol. Chem. Phys. 2005;206:1300.
34. Hauck D, Blümler P, Blümich B. Macromol. Chem. Phys. 1997;198:2729.
35. Litvinov VM, Macromolecules. 2001;34:8468.
36. Ernst RR, Bodenhausen G, Wokaun H. *Principles of Nuclear Magnetic Resonance in One and Two Dimensions*, Clarendon Press, Oxford (1987).
37. Munowitz M, Pines A, Adv. Chem. Phys. 1987;66:1.

Determining Structural and Dynamic Distribution Functions from Inhomogeneously Broadened NMR Spectra: The Conjugate Orthogonal Functions Approach

Marcel Utz and Magesh Nandagopal
Department of Physics, Institute of Materials Science, University of Connecticut, Storrs CT 06269,USA

Introduction

The structure and dynamics of amorphous solids are difficult to characterize. On the one hand, the absence of structural coherence makes most experimental techniques, such as X-ray scattering and NMR spectroscopy more challenging due to line broadening effects, which degrade the available signal to noise ratio. On the other hand, the presence of structural and dynamic inhomogeneity means that a complete characterization of the sample involves the determination of distributions of structural and dynamic parameters [1,2].

Many NMR techniques exist that map a distribution of parameters such as molecular orientation [3–9], dihedral angles [1,10–12], bond distances and angles [13,14], or reorientation flip angles and rates [15–19], as well as structural relaxation times [20,21] onto an inhomogeneously broadened NMR spectrum. In all of theses cases, the underlying disorder is reflected in the intensity distribution in the resulting spectrum, whereby each molecular segment makes an additive contribution both the distribution to be determined and to the spectrum.

In most cases, the relationship between the structural or dynamic parameter under study and the resulting contribution to the observed NMR spectrum is not straightforward. This leads to an inverse problem, which is often ill-posed, particularly in the presence of experimental noise.

In this article, a general approach to inverse problems of this type is discussed. It is based on the representation of the mapping of the distribution function onto the observable spectrum as a linear integral operator. This leads to two conjugate sets of orthogonal functions, one in the distribution domain, and one in the spectral domain, which can be used to decompose the experimental data. The orthogonal functions in the distribution domain emerge as eigenfunctions of the linear integral operator associated with the spectral technique. As shown in the following, the corresponding eigenvalues provide useful information on the sensitivity of the experimental method to noise.

The problem of finding the distribution function from experimental data can be cast in the form of a Fredholm integral equation of the first kind. A large number of other physical inverse problems also lead to equations of this type, e.g. diffraction-limited imaging [22], the determination of particle size distributions from elastic [23] and inelastic [24] light scattering, measurement of radial distribution functions from EXAFS spectra [25], or the determination of potential energy surfaces from time-resolved probing of chemical reactions [26], just to name a few. As is well known, Fredholm equations of the first kind are ill-posed, and special care is required in order to ensure the stability of their solutions. McWhirter and Pike have discussed the extraction of information from Laplace transforms and similar integral equations using an eigenfunction analysis of the Laplace operator [27].

In the following, the theoretical framework for the conjugate orthogonal functions (COF) approach will be briefly reviewed, and its application to the determination of orientational distribution functions by rotor-synchronized magic angle spinning spectroscopy will be discussed as an example. A more complete discussion of the COF theory can be found in Ref. [1].

Conjugate Orthogonal Functions

Under the assumption that each structural element in the sample makes an additive contribution to both the spectrum $S(\omega)$ and the distribution $P(\Gamma)$, the spectroscopic method can be represented by a linear operator $\mathcal{S}$, and we can formally write

$$\mathcal{S}P(\Gamma) \mapsto S(\omega). \tag{1}$$

It should be noted that both Γ and ω need not be single scalars, but may represent, e.g. a set of Euler angles and a set of spectral frequency domains, respectively. The (hypothetical) spectra associated with single structural elements, for which Γ has a unique value, are called elementary spectra. They are obtained by applying $\mathcal{S}$ to Dirac

Graham A. Webb (ed.), Modern Magnetic Resonance, 1463–1469.
© 2008 *Springer.*

delta functions, such that

$$S_{\Gamma_0} = \mathcal{S}\delta(\Gamma - \Gamma_0). \tag{2}$$

The set of N elementary spectra $\{S_\Gamma\}$ can be viewed as a complete representation of $\mathcal{S}$. If $S_\Gamma(\omega)$ is known for all Γ, the spectrum that results from distribution function $P(\Gamma)$ can be calculated as

$$S(\omega) = \int_{\mathcal{D}_{\Gamma'}} P(\Gamma')\ S_{\Gamma'}(\omega)\ \mathrm{d}\Gamma', \tag{3}$$

In practice, one has measured a spectrum $S(\omega)$ and would like to calculate $P(\Gamma)$. It will become clear in the following that this problem is equivalent to finding the solution of a Fredholm integral equation of the first kind [28]. Its inversion is an ill-posed problem, since the information that is contained in the distribution function may not entirely be transferred to the experimentally accessible spectrum. Typically, infinitely many distribution functions provide approximate solutions to the inverse problem within experimental precision. Thus, the determination of a distribution function P from spectral data must be done in two steps. The first, which can be done rigorously, consists in finding the space of distribution functions that are compatible with the experimental data. Then, a decision must be made which function inside this space is a reasonable estimate of the "true" distribution function. This second step invariably involves the use of heuristic arguments or *a priori* information.

By multiplying Equation (3) with an elementary spectrum $S_\Gamma(\omega)$ and integrating over the frequency domain, one obtains

$$A(\Gamma) = \int_{\mathcal{D}_\Gamma} G(\Gamma, \Gamma')\ P(\Gamma')\ \mathrm{d}\Gamma', \tag{4}$$

where we have used the abbreviations

$$G(\Gamma, \Gamma') := \int_\omega S_\Gamma(\omega)\, S_{\Gamma'}(\omega)\ \mathrm{d}\omega \tag{5}$$

and

$$A(\Gamma) := \int_\omega S(\omega)\, S_\Gamma(\omega)\ \mathrm{d}\omega. \tag{6}$$

The kernel G defines a compact symmetric integral operator $\mathcal{G}$ acting on $P(\Gamma)$. $\mathcal{G}$ is a complete representation of the spectroscopic method. Unlike $\mathcal{S}$, it is symmetric, which allows it to be decomposed into a set of eigenfunctions $\phi_n(\Gamma)$ and real eigenvalues λ_n [28,29]:

$$\int_{\Gamma'} G(\Gamma, \Gamma')\phi_n(\Gamma')\ d\Gamma' = \lambda_n\ \phi_n(\Gamma). \tag{7}$$

In the following we will make use of the customary conventions that the eigenvalues λ_n be arranged in decreasing order and repeated according to their multiplicity. Moreover, for degenerating eigenvalues $\lambda_k \cdots \lambda_{k+m}$, the eigenfunctions $\phi_k \cdots \phi_{k+m}$ shall be chosen such that the ϕ_n form a complete orthonormal set.

It can be shown that the operator $\mathcal{G}$ is bounded, which means that its largest eigenvalue must be finite. In addition, $\mathcal{G}$ is positive semi-definte [1], i.e. all its eigenvalues are positive or zero. Furthermore, it follows from the theory of linear integral operators that $\lim_{n\to\infty} \lambda_n = 0$. The eigenvalues λ_n therefore decay monotonously from the largest value λ_1 to zero. The rate of decay of the λ_n provides a valuable measure of the sensitivity of the spectroscopic method under study.

Due to the linearity of $\mathcal{S}$, the mean square deviation between two spectra that corresponds to two different distribution functions P_1 and P_2 depends only on the difference $p = P_2 - P_1$. It is easily shown that the deviation can be obtained from the correlation kernel G as

$$\chi^2[p] = \int_{\Gamma,\Gamma'} p(\Gamma)G(\Gamma, \Gamma')p(\Gamma')\,\mathrm{d}\Gamma'\,\mathrm{d}\Gamma. \tag{8}$$

This simple relation is very useful when discussing the sensitivity of the spectroscopic method to experimental error.

The *eigenspectra* $\psi_n(\omega)$ result from application of $\mathcal{S}$ to the eigenfunctions $\phi_n(\Gamma)$:

$$\psi_n(\omega) = \mathcal{S}\phi_n = \int_\Gamma \phi_n(\Gamma)S_\Gamma(\omega)\,\mathrm{d}\Gamma. \tag{9}$$

They are orthogonal in the sense that

$$\int_{\mathcal{D}_\omega} \psi_n\, \psi_m\, \mathrm{d}\omega = \lambda_n \delta_{mn}. \tag{10}$$

The diagonalization of the kernel G thus leads to a set of orthogonal basis functions, not only in the structural domain $\mathcal{D}_\Gamma$, but also in the spectral domain $\mathcal{D}_\omega$. With the eigenspectra ψ_n known, the analysis of measured data becomes very simple. It is sufficient to decompose the measured spectrum into the set of eigenspectra $\{\psi_n\}$ in order to find the expansion coefficients p_n:

$$p_n = \frac{1}{\lambda_n} \int_{\mathcal{D}_\omega} S(\omega)\psi_n(\omega)\,\mathrm{d}\omega. \tag{11}$$

In practice, any spectroscopic measurement produces data that is contaminated with noise. Therefore, two measured spectra can only be regarded to be *significantly* different if their spectral deviation exceeds the threshold

$$\xi^2 = F\ \left(\chi^2_{\min} + W\sigma^2\right) \tag{12}$$

where $\chi^2_{\min}$ is the spectral deviation between the experimental spectrum and the best possible representation by an infinite number of eigenspectra, accounting for systematic errors. σ^2 represents the mean square noise spectral density, and W is the relevant spectral area. F is a statistical significance factor of order unity. It is easily shown that a change in a particular expansion coefficient, Δp_n, is detectable if it satisfies the condition

$$\Delta p_n^2 \geq \frac{\xi^2}{\lambda_n}. \tag{13}$$

Hence, the error margins associated with the expansion coefficients p_n of a distribution function P that has been measured spectroscopically are given by $\Delta p_n = \pm \xi \lambda_n^{-1/2}$.

The expansion coefficients p_n represent moments of the distribution function $P(\Gamma)$ with respect to the eigenfunctions of the spectroscopic mthod, and one can formally write $p_n = \langle \phi_n \rangle$. Since their error margins are well defined, they can be compared to the same moments resulting from a theoretically predicted distribution. This provides a rigorous, "model-free" approach to decide whether experimental results contradict or support a given theory.

As an illustration, consider a hypothetical spectroscopic method sensitive to a single scalar structural parameter $\gamma \in [0,1]$. The elementary spectra consist of a single normalized Gaussian peak, centered at $\omega_0 = \alpha\gamma$. The width of the elementary spectra, and thus the spectral resolution of the method, is given by a parameter β. The eigenvalues of the correlation kernel associated with these elementary spectra, $\mathcal{G}$, calculated numerically for different values of β, are plotted in Figure 1. The larger the width of the elementary spectra β, the faster the eigenvalues decay. As expected, the information content, measured by the number of eigenvalues above a certain threshold, increases with spectral resolution. However, the *type* of information is almost independent of β, as the eigenfunctions, some of which are shown in Figure 2, are very similar for all values of β.

In practice, due to the fact that the eigenvalues λ_n decay rapidly towards zero, the error bars Δp_n diverge for large values of n. Mathematically, this reflects the ill-posed nature of the inversion of Fredholm equations of the first kind. If a representation of the full distribution $P(\Gamma)$ is desired, rather than just its moments $\langle \phi_n \rangle$, *a priori* information and heuristic arguments must be used in order to select from the infinitely large space spanned by the set of coefficients $\{p_n \pm \Delta p_n\}$ a point which is a plausible approximation to the "true" underlying distribution function, a process is often referred to as regularization. In the simplest case, only the coefficients p_n up to a limit $n_{\max}$, are used, and the solution is given as a truncated series [30]

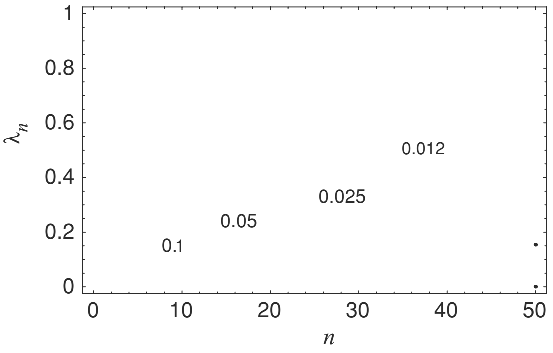

Fig. 1. The first 50 eigenvalues of the operator $\mathcal{G}$ corresponding to a hypothetical spectroscopic method. It is assumed that the elementary spectra consist of a single Gaussian peak whose position depends linearly on a structural parameter. Four different cases are shown, corresponding to elementary spectra with widths β indicated in the figure. The better the spectral resolution of the spectroscopic method, the slower the eigenvalues decay.

$$P(\Gamma) \approx \widetilde{P}(\Gamma) = \sum_{n=1}^{n_{\max}} p_n \, \phi_n(\Gamma). \tag{14}$$

As the eigenfunctions become more and more oscillatory for larger n, this is equivalent to restricting the solution to be smooth, which is a reasonable assumption in many cases. As a method of regularization of the solution of Fredholm equations, truncation of the eigenfunction expansion has been shown to be equivalent to weighting the residual with a smoothness functional [27,30], such as the Tikonov functional [31] or the entropy functional [32].

It must be noted, though, that any finite series approximation of $P(\Gamma)$ cannot be guaranteed to be positive. In particular, sharply peaked distribution functions typically have ripples in their truncated series approximations. If a sufficient number of coefficients p_n can be determined to good precision, $\widetilde{P}(\Gamma)$ will nevertheless be a useful approximation to the "true" distribution function $P(\Gamma)$.

Several numerical strategies can be employed to find a distribution function that is both positive, and compatible with the measured moments $p_n \pm \Delta p_n$. One possibility is to do a Monte Carlo optimization of the functional $\int (P - |P|)^2 d\Gamma$. This is easily implemented in the space of the expansion coefficients p_n.

Orientational Order

As an illustration for the COF approach, we discuss its application to the determination of orientational order in

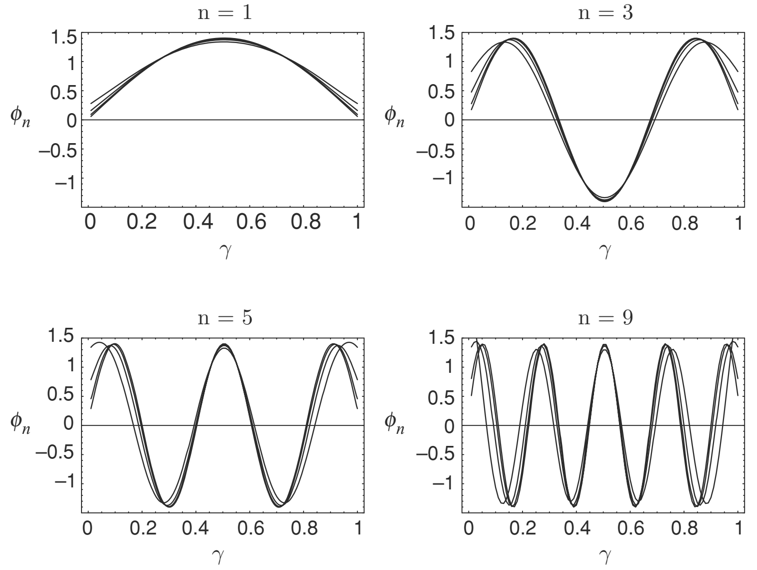

Fig. 2. The eigenfunctions associated with hypothetical elementary Gaussian spectra with line widths $\beta = 0.1$, 0.05, 0.025, 0.012.

amorphous solids. It has been shown by Harbison *et al.* that the orientational distribution function in disordered polymers can be quantified by a two-dimensional rotor synchronized magic angle spinning (MAS) experiment [5,9]. This method makes use of the fact that the spinning sidebands associated with a chemical shielding anisotropy (CSA) tensor are phase-modulated depending on the relative orientation of the principal axes frame of the CSA tensor with respect to the magnetic field and the spinner axis at the beginning of the acquisition. If many transients are added without rotor synchronization, this modulation is lost, and a purely absorptive sideband manifold results. The same happens if the orientational distribution of the molecular segments is isotropic, even if the acquisition is rotor-synchronized. By acquiring a series of transients with different rotor orientations at the beginning of the acquisition and taking the Fourier transform with respect to the rotor phase, Harbison *et al.* obtained a pure-phase two-dimensional sideband manifold, which quantitatively reflects the deviation of the orientational distribution from isotropy.

In the following, we consider a variant of this experiment that makes use of the Deuterium quadrupolar splitting, instead of the ^{13}C chemical shift. This has a number of advantages: the anisotropy of the ^{2}D quadrupolar coupling is usually large compared to the spin–spin relaxation rate, which allows a very sensitive measurement of orientation. In addition, the orientation of the principal axes of the quadrupolar interaction with respect to the molecular frame is usually known quite well. Of course, a major drawback lies in the necessity of isotopic labeling.

The expression given by Harbison *et al.* for the intensity of the sideband of order M, N (where N denotes the order with respect to the free evolution domain, and M is the order with respect to the rotor phase) is easily adapted to the quadrupolar interaction of ^2D. One finds

$$I_{M,N}(\beta,\gamma) \propto e^{iN\gamma}\left[\int_0^{2\pi} e^{i(N-M)\psi}F(-\gamma-\psi)\mathrm{d}\psi \int_0^{2\pi} e^{-iN\theta}F(\theta)\mathrm{d}\theta + \int_0^{2\pi} e^{i(N-M)\psi}F(\gamma+\psi)\mathrm{d}\psi \int_0^{2\pi} e^{iN\theta}F(\theta)\mathrm{d}\theta\right], \qquad (15)$$

where

$$F(\theta) = \exp(iA_2 \sin 2\theta + iA_1 \sin\theta); \qquad (16)$$

with

$$A_1 = -\frac{\sqrt{2}}{\omega_r}\delta \sin\beta\cos\beta;$$

$$A_2 = -\frac{1}{4\omega_r}(3\cos^2\beta - 1)\delta, \qquad (17)$$

where δ denotes the aniosotropy of the axially symmetric quadrupolar coupling tensor, and $\omega_r = 2\pi\nu_r$ is the angular velocity of the rotor. The relation between the

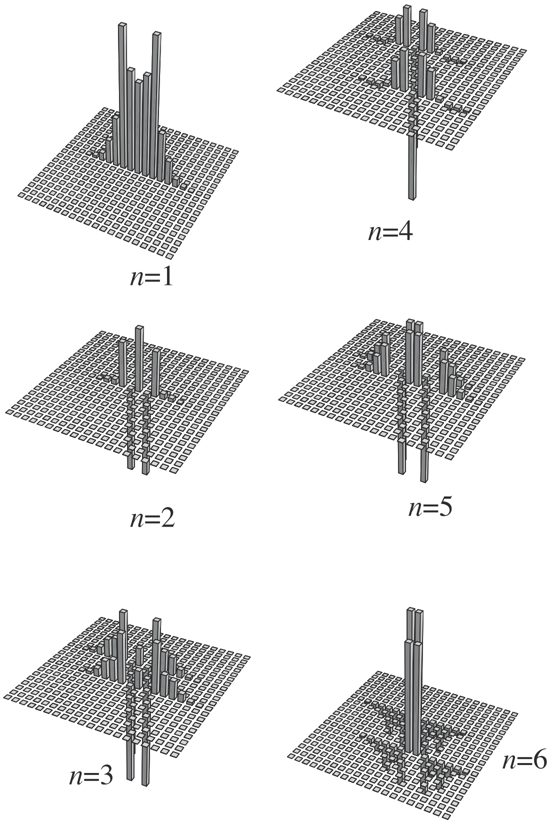

Fig. 3. Eigenspectra of a rotor-synchronized MAS experiment. The sideband intensities are indicated by the height of the bars; the main sideband index N increases to the right, whereas the secondary index (associated with the rotor phase) M increases to the back. The ratio of the quadrupolar anisotropy to the rotor speed was $2\pi\delta/\omega_r = 5$. (See also Plate 116 on page XV in Color Plate Section.)

orientation of a molecular segment (represented by the two polar angles β and γ orienting the unique axis of the quadrupolar tensor in the rotor frame) and the contribution to the spectrum $I_{M,N}$ is not straightforward at all. However, as will be shown in the following, COF analysis makes it easy to get a feel for the information content of the method.

As an example, the first six eigenspectra and eigenfunctions of this method are shown in Figures 3 and 4. As in the hypothetical Gaussian line example above, the first eigenfunction is almost a constant, whereas higher eigenfunctions are increasingly oscillatory.

The sideband intensities depend on the ratio between the quadrupolar anisotropy δ and the rotor speed ω_r. Slower rotor speeds lead to a larger number of sidebands. One would therefore intuitively expect that slower rotation speeds provide more information on the orientational distribution function. As will become clear in the following, this is not entirely true, since the total spectral intensity remains the same: more sidebands also mean a lower signal/noise ratio. An optimum value for ω_r can easily be found through the COF framework.

Figure 5 shows the eigenfunctions if only sidebands with $M = 0$ are taken into account. This corresponds to taking a conventional, one-dimensional spectrum without rotor synchronization. In this case, the anisotropy with respect to the circumferential polar angle γ is averaged out by the sample rotation. However, the distribution of polar angles β between the axes of the quadrupolar tensor and the rotor still influences the intensity distribution in the sideband pattern. This is directly seen in the eigenfunctions in Figure 5: they only depend on β (radial variation), but are symmetric with respect to rotation around the spinner axis.

While the eigenfunctions provide details of the *kind* of information provided by the spectroscopic method under study (e.g. its symmetry), the eigenvalues are useful to quantify *how much* of this information is contained in a spectrum with a given signal to noise ratio. As an

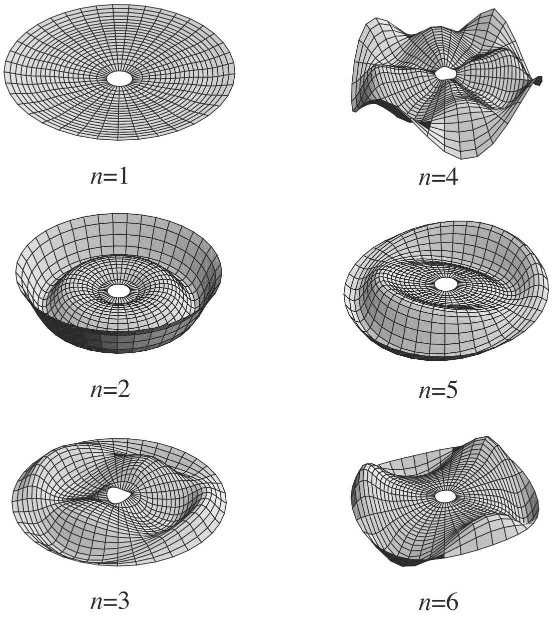

Fig. 4. Eigenfunctions $\phi_n(\beta, \gamma)$ of the rotor-synchronized MAS experiment with $\delta/\nu_r = 5$. The functions are shown in a stereographic projection, with the angle β varying from 0 to $\pi/2$ from the center to the outside of the graphs. The center point corresponds to the rotor axis direction. (See also Plate 117 on page XV in the Color Plate Section.)

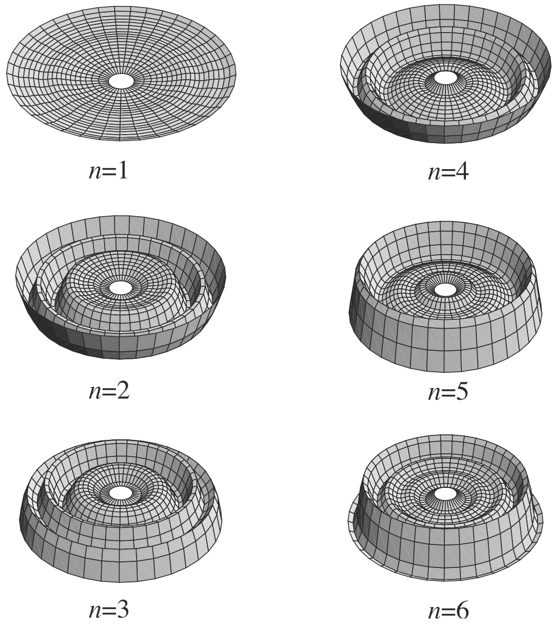

Fig. 5. Eigenfunctions $\phi_n(\beta, \gamma)$ of the rotor-synchronized MAS experiment, with only sidebands with $M = 0$ taken into account. The method is insensitive to the polar angle γ, but remains sensitive to the first polar angle β (cf. text). (See also Plate 118 on page XVI in the Color Plate Section.)

example, consider the eigenvalues of the ^{2}D rotor-sync MAS method shown in Figure 6 depending on the ratio between the quadrupolar anisotropy and the rotor speed δ/ν_r. This ratio essentially corresponds to the number of observable sidebands in a one-dimensional MAS spectrum, while the number of sidebands that can in principle be observed in a rotor-synchronized MAS experiment are proportional to $(\delta/\nu_r)^2$. As Figure 6 shows, the eigenvalues λ_n decay exponentially as a function of n. As expected, more observed sidebands lead to a slower decay.

Which spinning speed should be chosen in order to maximize the information content of the method? Answering this question requires consideration of the amount of noise that is included in the analysis. Assuming a constant spectral density of noise, the total mean-square noise introduced into the projections of the experimental spectra is proportional to the number of sidebands considered. The absolute limit of detection, given by the maximum tolerable error bar, is obviously a matter of choice. Setting the limit (arbitrarily) to $\lambda_n \geq 1$ for a ratio $\delta/\nu_r = 5$ (center panel in Figure 6), the first 22 coefficients are detectable. Decreasing the rotor speed to $\delta/\nu_r = 10$ results in a increase of the number of sidebands by a factor of 4. Therefore, at the same spectral noise density, the limit of detection increases to $\lambda_n \geq 4$. The bottom panel in Figure 6 shows that the first 26 coefficients can be detected in this case. The increase in information content over the faster rotor speed is therefore quite modest. By contrast, increasing the rotor speed to $\delta/\nu_r = 2$ (which is unrealistic in practice, since δ is of the order of 150 kHz) would lead to a very rapid decay of the eigenvalues, as seen in the top panel of Figure 6. In spite of the corresponding decrease in the limit of detection, the information content would be reduced to less than 10 coefficients.

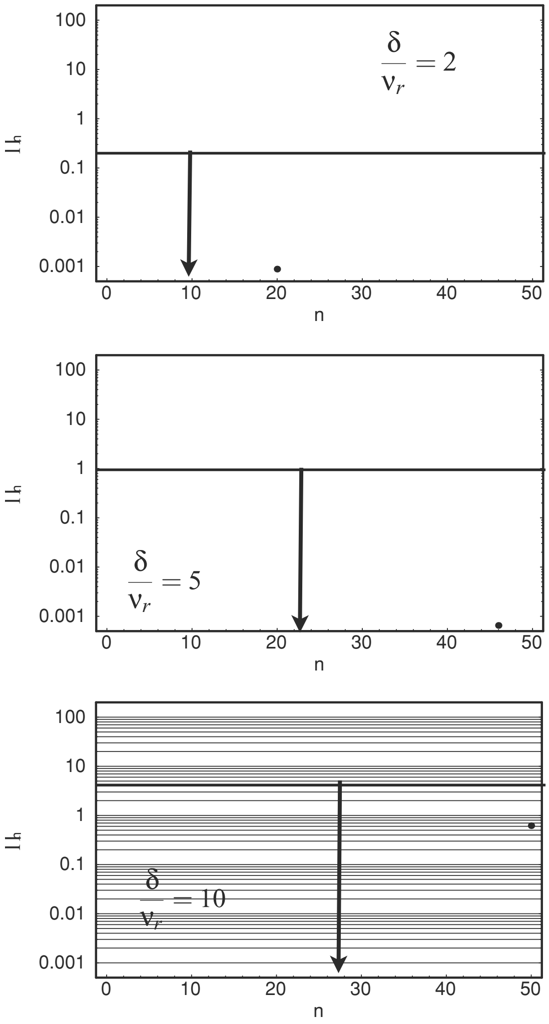

Fig. 6. Eigenvalues of the ^{2}D rotor-synchronized MAS experiment for different ratios between the quadrupolar anisotropy δ and the rotor speed ν_r. (See also Plate 119 on page XVI in the Color Plate Section.)

Conclusions

The conjugate orthogonal function approach provides a coherent framework for dealing with the inverse problem of extracting structural or dynamic distributions from inhomogenously broadened NMR spectra. It provides a rigorous and convenient method to obtain moments of the desired distribution with respect to a set of orthogonal eigenfunctions. Experimental spectra are decomposed by projection onto a conjugate set of orthogonal eigenspectra, rather than by an iterative fitting procedure. The experimental errors of the resulting moments depend on the spectral noise density in a well-defined manner. The set of moments $\langle \phi_n \rangle \pm \Delta p_n$ represents *all* the information on the distribution that is contained in an experimental spectrum with a particular signal-to-noise ratio. If a sufficient number of the moments $\langle \phi_n \rangle$ can be determined, they may be used to reconstruct the underlying distribution function.

The orthogonal eigenfunctions and eigenspectra also provide useful information on the spectroscopic method, and can be used to optimize experimental parameters for maximum sensitivity, as well as to compare the merits of alternative experimental approaches.

Acknowledgments

The support of the National Science Foundation, in the form of a CAREER award to MU (DMR-0094290), is gratefully acknowledged.

References

1. Utz MJ. Chem. Phys. 1998;109:6110.
2. van Beek JD, Meier BH, Schäfer H. J. Magn. Reson. 2003;162:141.
3. Hentschel R, Schlitter J, Sillescu H, Spiess H. J. Chem. Phys. 1978;68:56.
4. Hentschel R, Sillescu H, Spiess HW. Polymer 1981;22:1516..
5. Harbison GS, Spiess HW. Chem. Phys. Lett. 1986;124:128.
6. Schmidt-Rohr K, Hehn M, Schaefer D, Spiess HW. J. Chem. Phys. 1992;97:2247.
7. Chmelka BF, Schmidt-Rohr K, Spiess HW. Macromolecules. 1993;26:2282.
8. Utz M, Eisenegger J, Suter UW, Ernst RR. J. Magn. Reson. 1997;128:217.
9. Harbison GS, Vogt V-D, Spiess HW. J. Chem. Phys. 1987;86:1206.
10. Schmidt-Rohr K. J. Am. Chem. Soc. 1996;118:7601.
11. Schmidt-Rohr K. Macromolecules. 1996;29:3975.
12. Tomaselli M, Robyr P, Meier B, Grob-Pisano C, Ernst RR, Suter UW. Mol. Phys. 1996;89:1663.
13. Mauri F, Pasquarello A, Pfrommer BG, Yoon Y-G, Louie SG. Phys. Rev. B 2000;62:4786.
14. Clark TM, Grandinetti PJ, Florian P, Stebbins JF. Phys. Rev. B 2004;70:064202.
15. Zemke K, Chmelka BF, Schmidt-Rohr K, Spiess HW. Macromolecules. 1991;24:6874.
16. Shaefer D, Hansen M, Blümich B, Spiess HW. J. Non-Cryst. Solids. 1991;130:777.
17. Schmidt C, Blümich B, Spiess HW. J. Magn. Reson. 1988;79:269.
18. Hansen MT, Blümich B, Boeffel C, Spiess H, Morbitzer L, Zembrod A. Macromolecules. 1992;25:5542.
19. Zhao J, Chin YH, Liu Y, Jones AA, Inglefield PT, Kambour RP, White DM. Macromolecules. 1995;28:3881.
20. Heuer A, Tracht U, Spiess HW. J. Chem. Phys. 1997;107:3813.
21. Böhmer R, Diezemann G, Hinze G, Rössler E. Progr. NMR Spectrosc. 2001;31:191.
22. Pike ER, McWhirter JG, Bertero M, deMol C. IEE Proc. 1984;131:660.
23. Spänkuch D. App. Optics 1972;11:2844.
24. Ostrowsky N, Sornette D, Parker P, Pike ER. Optica Acta 1981;28:1059.
25. Babanov YA, Shvetsov VR. Phys. Stat. Sol. B. 1985;131:K1.
26. Lu Z-M, Rabitz H. Phys. Rev. A. 1995;52:1961.
27. McWirther JG, Pike ER. J. Phys. A: Math. Gen. 1978;11:1729.
28. Hochstadt H. *Integral Equations*, Wiley Interscience, 1973.
29. Kanwal RP. *Linear Integral Equations*, second ed. Birkhäuser: Boston, 1997.
30. Baker CTH, Fox L, Mayers DF, Wright K. Comput. J. 1964;7:141.
31. Tikonov AN. Sov. Math. 1963;4:1035.
32. Amato, U, Hughes W. Inverse Probl. 1991;7: 793.

Fluid Diffusion in Partially Filled Nanoscopic and Microscopic Porous Materials

I. Ardelean[1], G. Farrher[2], C. Mattea[2], and R. Kimmich[2]
[1]*Physics Department, Technical University of Cluj-Napoca, 400020 Cluj-Napoca, Romania; and*
[2]*Sektion Kernresonanzspektroskopie, Universität Ulm, 89069 Ulm, Germany*

Abstract

The contribution of the vapor phase to molecular diffusion in porous silica glasses with nanometer (Vycor) and micrometer (VitraPor #5) pores partially filled with water (polar) or cyclohexane (nonpolar) was investigated with the aid of field-gradient NMR diffusometry. The effective diffusion coefficient of water in nanometer pores (Vycor) decreases with decreasing filling factor, whereas that of cyclohexane increases due to the vapor phase contribution without exceeding its bulk liquid value. On the other hand, the effective diffusion coefficient of cyclohexane in micrometer pores (VitraPor #5) was up to ten times larger than the bulk liquid value. This is in contrast to the effective diffusion coefficient in water which first decreases and then increases upon reduction of the pore space filling factor. A general two-phase liquid/vapor exchange model is presented that is accounting well for all experimental diffusion features. The dependence of the effective diffusion coefficient on the pore filling factor is strongly related to the pore dimension and the polar character of the fluids.

Introduction

Field-gradient NMR diffusometry studies of fluids partially filling porous materials suggested effective self-diffusion coefficients enhanced due the vapor phase contribution relative to the bulk liquid phase [1–7]. The explanation is the exchange between the liquid and vapor phases. The bulk diffusivity at room temperature in the gas phase is four orders of magnitude larger than in the liquid phase. Consequently, the root mean squared displacement of a molecule entering the gas phase will be two orders of magnitude bigger than in the liquid phase for a given diffusion time. In some experimental situations, this can compensate for the three orders of magnitude smaller density in the vapor phase as compared with the liquid phase. The exchange between the two phases on the time scale of the experiment thus leads to an average diffusivity enhanced by the vapor phase whereas the NMR signal is still dominated by the liquid phase.

In the following, the contribution of the vapor phase to molecular diffusion in silica glasses with nanometer (Vycor; mean pore diameter 4 nm) and micrometer (VitraPor #5: mean pore diameter 1 μm) pores partially filled with water (polar) or cyclohexane (nonpolar) is investigated with the aid of the field-gradient NMR diffusometry technique represented by the pulse scheme shown in Figure 1A. The experimental results will be discussed in the frame of a general two-phase exchange model [6] that is based on a two-region approximation [8]. The general results of the theoretical model will be further analyzed into “fast” and “slow” molecular exchange limits between the liquid and vapor phases.

The Two-Phase Exchange Model in NMR Diffusometry

In completely filled pore spaces, the transport properties of filling fluids are predominantly affected by the geometrical restriction, i.e. the tortuosity and the interaction with the surface. According to Archie’s law, $D = \Phi_{\mathrm{t}}^{m} D_0$, the effective diffusion coefficient in the pore space, D, is reduced by tortuosity effects by a factor Φ_{t}^{m} relative to its bulk value, D_0 [2,9]. The quantity $\Phi_{\mathrm{t}} = V_0/V_{\mathrm{t}}$ represents the total porosity of the sample. V_{t} is the total volume including the matrix and the pore space, V_0 is the pores space volume and m is an empirical exponent.

In an unsaturated porous sample with polar inner surfaces, the liquid and the vapor phase form two interpenetrating systems of different geometry and porosity. Polar and nonpolar adsorbates such as liquid water and cyclohexane, respectively, tend to be distributed in a different way in the pore space depending also on the imbibing degree [10]. In any case, the remainder of the pore volume is filled by air saturated with the respective vapor phase. In this case, we have to consider two interpenetrating pore systems of different effective porosities $\Phi_{\mathrm{l}} = V_{\mathrm{l}}/V_{\mathrm{t}}$ and $\Phi_{\mathrm{v}} = (V_0 - V_{\mathrm{l}})/V_{\mathrm{t}}$ for the liquid and vapor phases, respectively (the subscript l stands for liquid and v for vapor).

Graham A. Webb (ed.), Modern Magnetic Resonance, 1471–1477.
© 2008 *Springer.*

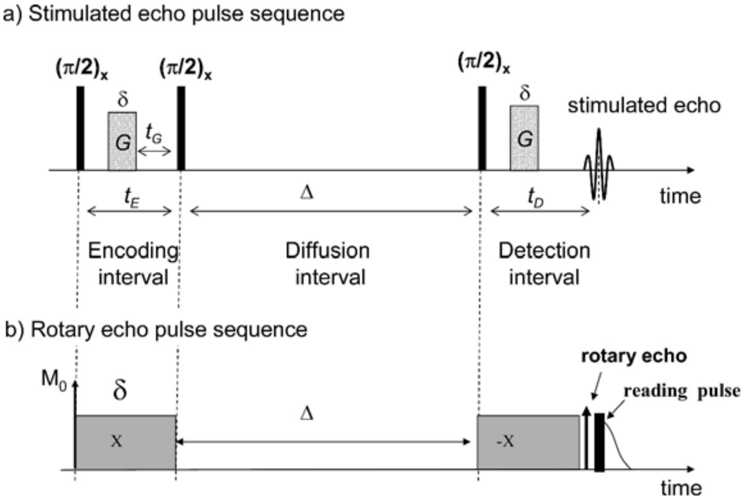

Fig. 1. (a) Schematic radio frequency (RF) and field-gradient pulse sequence for the stimulated echo variant of field-gradient NMR diffusometry. *G* represents the spatially constant field gradient along the *z* axis. (b) The rotary echo pulse sequence that was used in test experiments for the evaluation of internal gradient effects. The gradient of the RF amplitude B_1 was created with a conic coil [12].

Assuming Archie's law again, the reduced diffusion coefficient in the liquid phase can be written in the form [5]

$$D_\mathrm{l} = \Phi_\mathrm{l}^{m_\mathrm{l}} D_{\mathrm{l},0} = \Phi_\mathrm{t}^{m_\mathrm{l}} \left(\frac{V_\mathrm{l}}{V_0}\right)^{m_\mathrm{l}} D_{\mathrm{l},0} = \Phi_\mathrm{t}^{m_\mathrm{l}} f^{m_\mathrm{l}} D_{\mathrm{l},0}, \tag{1}$$

where $f = V_\mathrm{l}/V_0$ is the filling factor and m_l is an empirical exponent specific for the liquid phase and depends both on the sample geometry and the wetting properties of the liquid. The diffusion coefficient in bulk liquid is designated by $D_{\mathrm{l},0}$. Equation (1) thus links the porosity effective for the liquid phase, Φ_l, to the sample porosity, $\Phi_\mathrm{t} = \Phi_\mathrm{l} + \Phi_\mathrm{v}$.

Diffusion in the vapor phase is governed by collisions among the diffusing molecules themselves (Einstein diffusion) or with the pore walls (Knudsen diffusion). The term "wall" may refer both to liquid–vapor interfaces and to inner surfaces of the solid matrix. Taking Knudsen diffusion into account, the effective vapor diffusion coefficient inside a porous system can be derived by adding the diffusion resistances associated with these two types of collisions, i.e. molecule–wall and molecule–molecule [11]:

$$\frac{1}{D_\mathrm{v}} = \frac{1}{D_\mathrm{K}} + \frac{1}{D_\mathrm{E}} \tag{2}$$

D_K and D_E are the Knudsen and Einstein diffusivities, respectively. Note that D_v approaches D_K in the Knudsen limit, $D_\mathrm{K} \ll D_\mathrm{E}$, when molecule–wall collisions dominate. It becomes equal to D_E in the Einstein diffusion regime, $D_\mathrm{K} \gg D_\mathrm{E}$, where molecule–molecule collisions prevail [11].

Anticipating Archie's law again, the quantities D_K and D_E can be represented in terms of effective tortuosity factors as above, in order to relate the diffusivities in reduced pore spaces and in "bulk," i.e.

$$\begin{aligned} D_\mathrm{K} &= \Phi_t^{m_{\mathrm{v,K}}} (1-f)^{m_{\mathrm{v,K}}} D_{K,0}; \\ D_\mathrm{E} &= \Phi_t^{m_{\mathrm{v,E}}} (1-f)^{m_{\mathrm{v,E}}} D_{\mathrm{v},0}. \end{aligned} \tag{3}$$

The diffusivities in the "bulk" vapor phase are given by $D_{\mathrm{V},0}$ and $D_{\mathrm{K},0}$ in the Einstein and Knudsen diffusion limits, respectively. The exponents $m_{\mathrm{v,K}}$ and $m_{\mathrm{v,E}}$ account for tortuosity effects in the Knudsen and Einstein regimes and may consequently also deviate from each other [11].

If we assume that wetting liquids are distributed at the pore walls in the form of a hollow cylinder [2], the diameter of the vapor phase domains can be expressed as a function of the filling factor and the reference Knudsen diffusion coefficient can be written as [2,5]

$$D_{\mathrm{K},0}(f) = \frac{1}{3} d (1-f)^{\frac{1}{2}} \sqrt{\frac{8 k_\mathrm{B} T}{\pi M_0}}. \tag{4}$$

Here k_B is the Boltzmann constant, T is the absolute temperature, M_0 is the molecular mass, and d is the mean pore diameter. Note that the reference Knudsen diffusion coefficient is related to the pore shape but may also be different for different chemical species such as water and cyclohexane due to their different wetting properties.

In the following, we consider the pulse sequence in Figure 1A where we neglect diffusion, relaxation, and exchange phenomena during the encoding interval and assume the spoiling of the transverse magnetization component in the diffusion interval. The combined effect of diffusion, relaxation, and exchange on the modulated longitudinal magnetization in the diffusion interval can be evaluated on the basis of a set of "Bloch/Torrey/McConnell equations" (BTC) introduced in Ref. [6]:

$$\begin{aligned}\frac{\mathrm{d}M_{z,\mathrm{l}}(z,t)}{\mathrm{d}t} &= D_\mathrm{l}\frac{\mathrm{d}^2M_{z,\mathrm{l}}(z,t)}{\mathrm{d}z^2} - \frac{M_{z,\mathrm{l}}(z,t) - M_{0,\mathrm{l}}}{T_{1,\mathrm{l}}} \\ &\quad - \frac{M_{z,\mathrm{l}}(z,t)}{\tau_\mathrm{l}} + \frac{M_{z,\mathrm{v}}(z,t)}{\tau_\mathrm{v}}, \\ \frac{\mathrm{d}M_{z,\mathrm{v}}(z,t)}{\mathrm{d}t} &= D_\mathrm{v}\frac{\mathrm{d}^2M_{z,\mathrm{v}}(z,t)}{\mathrm{d}z^2} - \frac{M_{z,\mathrm{v}}(z,t) - M_{0,\mathrm{v}}}{T_{1,\mathrm{v}}} \\ &\quad - \frac{M_{z,\mathrm{v}}(z,t)}{\tau_\mathrm{v}} + \frac{M_{z,\mathrm{l}}(z,t)}{\tau_\mathrm{l}}. \end{aligned} \tag{5}$$

$T_{1,\mathrm{l}}$ and $T_{1,\mathrm{v}}$ are the longitudinal relaxation times in the liquid and vapor phase, respectively, in the absence of exchange. $M_{0,\mathrm{l}}$ and $M_{0,\mathrm{v}}$ are the corresponding equilibrium magnetizations. The mean lifetimes the adsorbate molecules spend in the liquid and vapor phases are denominated by τ_l and τ_v, respectively. Analogously, we allocate effective self-diffusion coefficients D_l and D_v to the two fluid phases, as given by Equations (1) and (2).

The first terms on the right-hand side of Equation (5) describe molecular transport inside the individual phase, the second terms are accounting for longitudinal relaxation in the absence of exchange, and the other terms represent molecular interphase exchange rates. As a strong simplification, the BTC equations anticipate that both phases are spread uniformly to the entire pore space. That is, mutual exchange between the two phases can occur at any position z without prior need to diffuse to an interface.

The mean lifetimes τ_l and τ_v are effective quantities determined by the extensions of the two-phase regions and the molecular mobilities therein. Additional transport resistances at the interfaces may also play a role. The mean lifetimes are related to the relative number (mass fraction) of molecules in the ith phase region, p_i, by

$$p_i = \frac{\tau_i}{\tau_\mathrm{l} + \tau_\mathrm{v}} \quad (i = \mathrm{l}, \mathrm{v}) \tag{6}$$

in a similar way as described in Ref. [8]. They can be expressed as a function of the filling factor $f = V_\mathrm{l}/V_0$ and of the respective mass densities, ρ_l and ρ_v, as follows:

$$p_l = \frac{f}{f + (1-f)(\rho_\mathrm{v}/\rho_\mathrm{l})} \quad \text{and} \quad p_\mathrm{v} = 1 - \rho_\mathrm{l}. \tag{7}$$

The general solution of BTC Equation (5) which can provide us the amplitude of the stimulated echo, has a generally complicated form (see Ref. [8]), and is not given here. It can be simplified in some experimental limits to be described in the following.

The General Liquid/Vapor Exchange Limit

For vapor/liquid phase systems we always have

$$p_\mathrm{v} \ll p_\mathrm{l}; \quad D_\mathrm{v} \gg D_\mathrm{l}; \quad T_{1,\mathrm{v}} \gg T_{1,\mathrm{l}}, \tag{8}$$

and the stimulated echo amplitude obeys [6]

$$\frac{A_\mathrm{STE}(k,\Delta)}{A_\mathrm{STE}(0,\Delta)} = \exp\left[-k^2\left(D_\mathrm{l} + \frac{p_\mathrm{v}D_\mathrm{v}}{k^2\tau_\mathrm{l}p_\mathrm{v}D_\mathrm{v} + 1}\right)\Delta\right]. \tag{9}$$

Here $k = \gamma G\delta$ represents the "wave number" of the modulated magnetization that is produced by the gradient pulses of strength G, and duration δ and γ is the gyromagnetic ratio. The relaxation term has been discarded in the above expression because in experiments with constant intervals but variable gradient strength, it does not affect the echo attenuation curve apart from a constant reduction factor. Note that the same expression was obtained by Kärger for the attenuation of the Hahn echo using a different approach [8]. An interesting feature of Equation (9) is that the mean lifetime, τ_l, the molecules spend in the liquid phase can be determined on this basis.

Equation (9) suggests that no effective diffusion coefficient can be defined since the term in parentheses depends on the wave number as a parameter varied in the experiments. However, for small gradient pulse areas complying with the limit $k^2\tau_l p_v D_v \ll 1$, one may define $D_\mathrm{eff} = D_\mathrm{l} + p_\mathrm{v}D_\mathrm{v}$ as an effective diffusivity with some similarity to the fast exchange version described below. The initial part of echo attenuation curves can be thus fitted by the monoexponential decay function

$$\frac{A_\mathrm{STE}(k,\Delta)}{A_\mathrm{STE}(0,\Delta)} = \exp\left[-k^2(D_\mathrm{l} + p_\mathrm{v}D_\mathrm{v})\Delta\right] \quad \text{for } k^2\tau_\mathrm{l}p_\mathrm{v}D_\mathrm{v} \ll 1. \tag{10}$$

The general liquid/vapor exchange limit implies two more limits concerning the exchange rates relative to the experimental time scale (the interval Δ in the pulse sequences shown in Figure 1).

The Fast Liquid/Vapor Exchange Limit ($\tau_1 \ll \Delta$ and $\tau_\mathrm{v} \ll \Delta$)

This limit was treated in the literature many times [1–5] and corresponds to large diffusion paths during Δ. The amplitude of the stimulated echo is thus attenuated by diffusive displacements according to [6]

$$\frac{A_\mathrm{STE}(k,\Delta)}{A_\mathrm{STE}(0,\Delta)} = \exp\left[-k^2D_\mathrm{eff}\Delta\right] \tag{11}$$

In this case, the effective diffusivity, D_{eff}, that characterizes the decay, is the weighted average between the diffusion coefficients in the two phases, i.e.

$$D_{\mathrm{eff}} = p_{\mathrm{l}} D_{\mathrm{l}} + p_{\mathrm{v}} D_{\mathrm{v}}. \tag{12}$$

The coefficients D_{l} and D_{v} are given by Equations (1) and (2), respectively, and are reduced relative to the bulk values due to the pore space confinement.

The Slow Liquid/Vapor Exchange Limit ($\tau_1 \gg \Delta$ and $\tau_{\mathrm{v}} \gg \Delta$)

In the slow exchange limit when molecular exchange can be neglected on the time scale of the experiment, the attenuation of the amplitude of the stimulated echo by diffusion is characterized by a superposition of two exponentials corresponding to the two phases:

$$\frac{A_{\mathrm{STE}}(k, \Delta)}{A_{\mathrm{STE}}(0, \Delta)} = p_{\mathrm{l}} \exp(-k^2 D_{\mathrm{l}} \Delta) + p_{\mathrm{v}} \exp(-k^2 D_{\mathrm{v}} \Delta). \tag{13}$$

The diffusion coefficients D_{l} and D_{v} in the liquid and vapor phase, respectively, are reduced due to the pore space confinement [see Equations (1) and (2)]. Due to the fact that the number of spins in the vapor phase is usually much smaller than in the liquid phase, $p_{\mathrm{v}} \ll p_{\mathrm{l}}$, the only component that will contribute to the signal is the liquid component and no contribution from the vapor phase is expected to be perceptible in this limit.

Experimental

Samples and Instrumentation

Vycor porous glass VPQ #7930 was purchased from Corning Ltd. It consists of 96% SiO_2. The nominal mean pore size is $d = 4$ nm (± 0.6 nm). The porosity is specified by manufacturer as $\Phi_{\mathrm{t}} = 0.28$. VitraPor #5 porous silica glass was purchased from ROBU Glasfilter-Geräte GmbH, Germany. The nominal mean pore size is $d = 1$ μm (± 0.6 μm). The porosity was measured as $\Phi_{\mathrm{t}} = 0.43$.

The samples were pretreated as suggested by the manufacturer. This includes 30 min of boiling in 30% H_2O_2. The samples were then washed with distilled water and left in vacuum for 24 h at 95 °C. After that, the samples are considered to be dry with a nominal filling factor of $f = 0$. The solvents were then filled into the porous glass with the aid of the bulk-to-bulk method resulting in a filling factor 1 for the corresponding solvent.

The solvents examined in this study were cyclohexane (nonpolar; nonwetting) and demineralized water (polar; wetting). Partial evaporation was then used for the adjustment of the desired filling factor. This was performed in a glove bag in a dry nitrogen atmosphere (for VitraPor #5 sample) in order to avoid any undesired contamination by water from the air humidity. The solvent content reached by this procedure was determined by weighing. The samples were placed in a sealed container with practically no empty space that would allow for further evaporation. All experiments were done only after about 1 h permitting the fluid to equilibrate with respect to phase distributions. After this annealing period, no changes were perceptible any longer.

All diffusion experiments were performed with a Bruker DPX 400 NMR spectrometer equipped with a microscopy gradient unit. The data were recorded at room temperature and at a proton resonance frequency of 400 MHz using the standard pulsed field-gradient-stimulated echo technique in Figure 1A [12]. The gradient calibration was done with the aid of diffusion measurements in bulk water.

Due to differences in the susceptibility between porous matrix and filling fluids, internal gradients may appear in partially field porous media. These gradients may influence the decay curves of the stimulated echo. In the case of Vycor porous sample, test experiments have been done with the "rotary echo" [13] method given in Figure 1B, which is not affected by the internal gradients. In the case of VitraPor #5 sample, the susceptibility induced gradients were estimated with the method described in Ref. [14]. The conclusion is that any influence of such gradients on the measurements with the stimulated echo technique can be excluded regarding the experimental parameters used.

Results

Figure 2a shows typical echo attenuation curves recorded for two filling factors of VitraPor #5 (1 μm pores). The decay for the partial filled pores with water (squares) and cyclohexane (circles) obviously cannot be described by monoexponential functions. The decay curves can only be described on the basis of Equation (9) by assuming the "general liquid/vapor exchange" model given above. Fits of this formalism to the experimental data are represented by the solid lines. As optimal parameters for fitting we found: $\tau_{\mathrm{l}}^{\mathrm{water}} = 0.7\ s$; $\tau_{\mathrm{l}}^{\mathrm{cyclohexane}} = 0.05$ s; $m_{\mathrm{v,E}}^{\mathrm{cyclohexane}} = m_{\mathrm{v,E}}^{\mathrm{water}} = 1.4$; $m_{\mathrm{v,K}}^{\mathrm{cyclohexane}} = 2.2$ and $m_{\mathrm{v,K}}^{\mathrm{water}} = 3.2$; $m_{\mathrm{l}}^{\mathrm{cyclohexane}} = 0.5$; $m_{\mathrm{l}}^{\mathrm{water}} = 0.87$ or 0.95 for $f = 1$ and 0.15, respectively. Other parameters used in these evaluations were taken from the literature [2,15] and are indicated in Table 1. Based on Equation (10), effective diffusion coefficients can be extracted from the "initial" slope of the attenuation curve (dashed lines) corresponding to the low wavenumber limit, $k^2 \tau_{\mathrm{l}} p_{\mathrm{v}} D_{\mathrm{v}} \ll 1$. The data for the effective

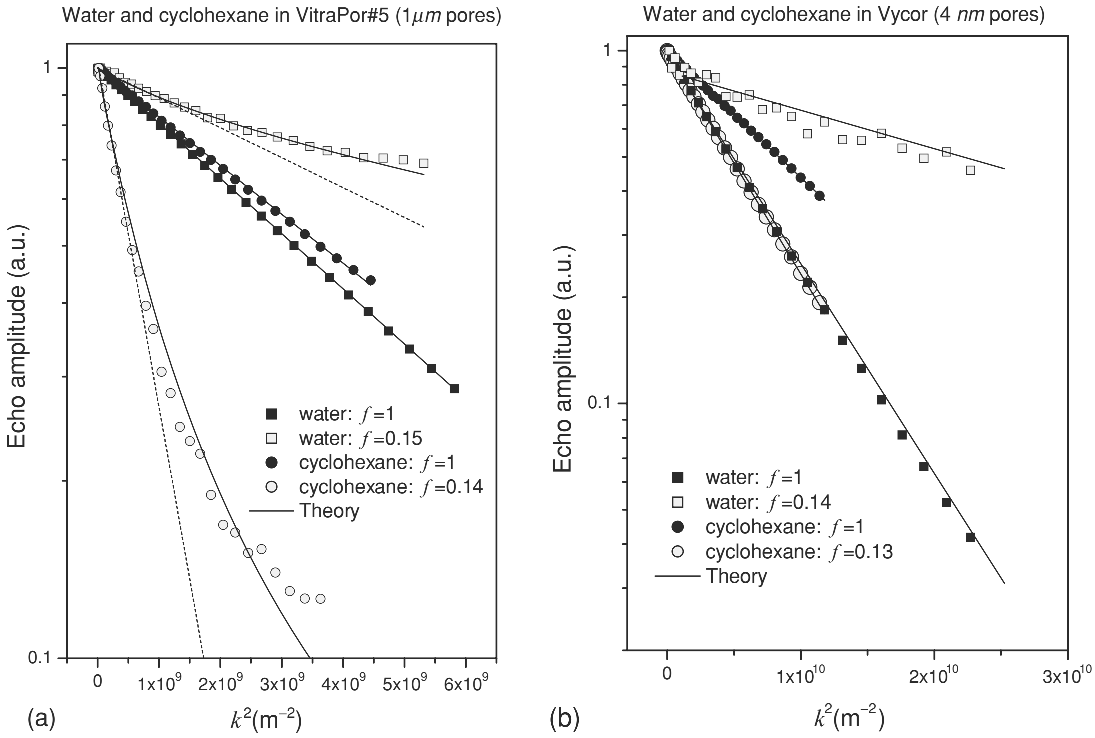

Fig. 2. (a) Echo attenuation curves for water (squares) and cyclohexane (circles) in VitraPor #5 for different filling degrees at room temperature. The experimental data are well reproduced by theoretical curves (solid lines) calculated on the basis of Equation (9) according to the "general liquid/vapor" exchange formalism. The fitting parameters (given in the text) were the mean residence time τ_l in the liquid phase and the exponents in Archie's law. All other parameters were preset by fixed literature values [2,15] as given in Table 1. (b) Echo attenuation curves for water (squares) and cyclohexane (circles) in Vycor for different filling degrees at room temperature. The theoretical curves (solid lines) are fits of Equation (11) to extract the effective diffusion coefficient corresponding to the "fast" exchange limit.

diffusion coefficients of water (squares) and cyclohexane (circles) are plotted in Figure 3 as a function of the filling factor. The theoretical curves are also indicated (solid lines). The different dependencies found for water and cyclohexane are attributed to the different vapor pressures [15] and the different surface interactions these two adsorbate species are subject to. The surface interaction is implied in the Knudsen term in Equation (2) which turned out to be important especially for water.

Table 1: The physical parameters of water and cyclohexane used in the fits of the theory to our experimental data [2,15]

	Water	Cyclohexane
ρ_v/ρ_l	2.5×10^{-5}	5.9×10^{-4}
$D_{l,0}$ (m^2/s)	2.3×10^{-9}	1.4×10^{-9}
$D_{v,0}$ (m^2/s)	2.4×10^{-5}	8.5×10^{-6}

The above results are in contrast with the measurements on Vycor (4 nm pores), where the echo decay (not shown) both for water and cyclohexane can be described by monoexponential functions (see Figure 2b). The conclusion is that "fast exchange" limit applies in this case and effective diffusion coefficients can be extracted as indicated in Figure 4. The fitting of the experimental results (solid lines) with an effective diffusion coefficient given by Equation (12) indicates different tortuosity effects on the Knudsen diffusion contribution in the case of water (squares) and cyclohexane (circles). The deviation of the theoretical curve, in the case of cyclohexane filled sample, from the experimental data can be due to residual water adsorbed from the air, which could not be removed by the procedure described above. Another possible

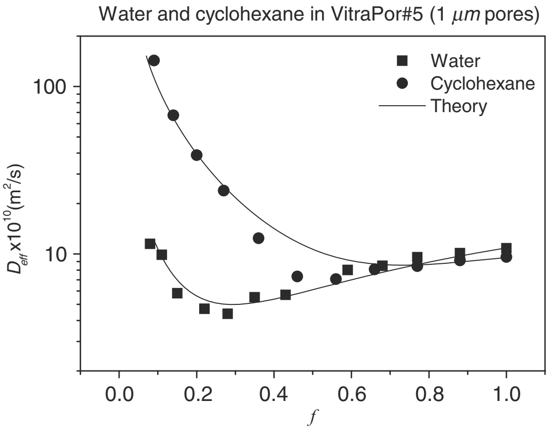

Fig. 3. Effective diffusion coefficients at room temperature for water (squares) and cyclohexane (circles) in VitraPor #5 as a function of the filling factor. The data have been extracted from the echo attenuation curves by fitting a monoexponential function [see Equation (10)] to the initial (low wave number) section. The solid lines represent fits of the effective diffusion coefficient $D_{\text{eff}} = D_l + p_{\text{v}} D_{\text{v}}$ to the data. The fitting parameters are: $m_{\text{v,E}}^{\text{cyclohexane}} = m_{\text{v,E}}^{\text{water}} = 1.4$; $m_{\text{v,K}}^{\text{cyclohexane}} = 2.2$; $m_{\text{v,K}}^{\text{water}} = 3.2$; $m_{\text{l}}^{\text{cyclohexane}} = 0.5$; $m_{\text{l}}^{\text{water}} = 0.87$.

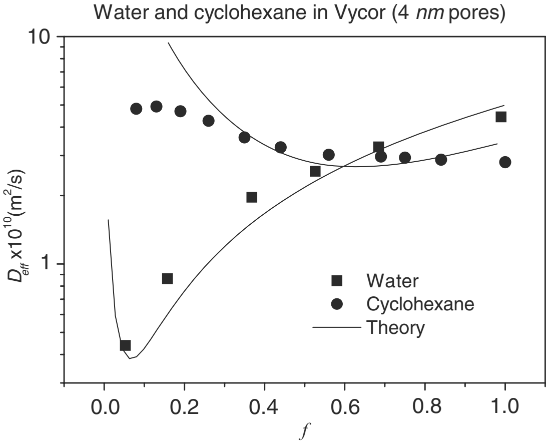

Fig. 4. Effective diffusion coefficients at room temperature for water (squares) and cyclohexane (circles) in Vycor as a function of the filling factor. The data have been extracted from the echo attenuation curves which were monoexponential functions corresponding to the "fast exchange" limit. The solid lines represent fits of the effective diffusion coefficient given by Equation (12) to the data. The fitting parameters are: $m_{\text{l}}^{\text{cyclohexane}} = m_{\text{v,E}}^{\text{cyclohexane}} = 1.1$; $m_{\text{v,K}}^{\text{cyclohexane}} = 0.01$; $m_{\text{l}}^{\text{water}} = m_{\text{v,E}}^{\text{water}} = 1.2$; $m_{\text{v,K}}^{\text{water}} = 2.0$.

explanation is the change of the vapor phase density introduced by the interactions with the surface for low filling factors [6].

Discussion and Conclusions

Translational diffusion of water and cyclohexane as polar and nonpolar solvent species was studied in porous silica glasses with nanometer (Vycor: mean pore diameter 4 nm) and micrometer pores (VitraPor #5: mean pore diameter 1 μm) using NMR diffusometry as a function of the filling factor. The general "two-phase exchange model" well describes all experimental features. The results can be further analyzed into "fast" and "slow" molecular exchange limits between the liquid and vapor phases.

In the case of Vycor (4 nm pores) a "fast exchange" between the liquid and vapor molecules is present both for water and cyclohexane filling fluids for a diffusion time of 300 ms. The data on VitraPor #5 sample (1 μm pores) can be interpreted in the frame of the "general liquid/vapor exchange" formalism, for an experimental time scale of 200 ms. One can conclude that the pore dimension plays an essential role for the applicable exchange limit. Extrapolating the pore size to larger and larger mean diameters, one can infer that this would finally lead to the slow exchange expected to be relevant for well separated liquid and vapor filled compartments independent of the filling fluid.

The vapor phase effect on diffusion as a function of the filling degree was clearly demonstrated in this way. Due to the molecular exchange, the values of the effective diffusion coefficient in the case of cyclohexane in VitraPor #5 sample (1 μm pores), exceed the bulk value by a factor of ten for low filling factors. Molecular exchange means that the solvent molecules are intermittently subject to diffusion features in either phase. Translational displacements in the vapor phase are much faster than in the liquid phase and contribute to the enhancement of the effective diffusion coefficient. For diffusion in the vapor phase, two mechanisms can be distinguished, namely ordinary ("Einstein") and Knudsen diffusion with, possible different, tortuosity effects from the sample structure. Finally, the mean residence time of the solvent molecules in the liquid phase can be evaluated from the fits of the theory to the experimental echo attenuation data.

Acknowledgments

This work was supported by the Alexander von Humboldt Foundation, the Deutsche Forschungsgemeinschaft, and the Romanian MEC by grant CNCSIS 411.

References

1. Kärger J, Pfeifer H, Riedel E, Winkler H. J. Coll. Interface Sci. 1973;44:187.
2. D'Orazio F, Bhattacharja S, Halperin WP, Gerhardt R. Phys. Rev. Lett. 1989;63:43.
3. Kimmich R, Stapf S, Callaghan P, Coy A. Magn. Reson. Imaging. 1994;12:339.
4. Kimmich R, Stapf S, Seitter RO, Callaghan P, Khozina E. Mater. Res. Soc. Symp. Proc. 1995;366:189.
5. Ardelean I, Mattea C, Farrher G, Wonorahardjo S, Kimmich R. J. Chem. Phys. 2003;119:10358.
6. Ardelean I, Farrher G, Mattea C, Kimmich R. J. Chem. Phys. 2004;120:9809.
7. Valiullin R, Kortunov P, Kärger J, Timoshenko V. J. Chem. Phys. 2004;120:11804.
8. Kärger J. Ann. Phys. (Leipzig). 1971;27:107.
9. Sahimi M. Rev. Mod. Phys. 1993;65:1393.
10. Allen SG, Stephenson PCL, Strange JH. J. Chem. Phys. 1997;106:7802.
11. Geier O, Vasenkov S, Kärger J. J. Chem. Phys. 2002;117: 1935.
12. Ardelean I, Kimmich R. Annu. Rep. NMR Spectrosc. 2003; 49:43.
13. Canet D, Prog. Nucl. Magn. Reson. Spectrosc. 1997;30: 101.
14. Kärger J, Pfeifer H, Rudtsch S. J. Magn. Reson. 1989;85: 381.
15. Landolt-Börnstein, Zahlenwerte und Funktionen aus Physik, Chemie, Astronomie, Geophysik und Technik, Vol. II, Part 5, Springer Verlag: Berlin, Heidelberg, New York, 1969, p 552.

Gas Adsorption on Carbon Nanotubes

Tanja Pietraß
Department of Chemistry, New Mexico Tech, Socorro, NM 87801, USA

Introduction

Since their discovery in 1991 [1], carbon nanotubes (CNTs) have attracted much attention due to their unique mechanical and electronic properties. Single-walled carbon nanotubes (SWNTs) can be envisioned as a single sheet of graphite rolled into a seamless tube. In multiwalled carbon nanotubes (MWNTs), several of these tubes are stacked inside each other in a concentric fashion. The length and direction of the roll-up vector determine the diameter and chirality of the tube. Statistically, one-third of tubes should be metallic, while the other two-thirds are semi-conducting [2]. Potential applications of CNTs range from field-emitting devices to gas sensors [3].

In 1997, CNTs were reported to store large amounts of hydrogen gas with uptake capacities in the range of 5–10% by weight (wt%) [4]. This result sparked intense research activity due to the potential to exceed the benchmark set by the Department of Energy of 6.5 wt% uptake capacity for an economically viable hydrogen storage medium [5]. The ensuing and continuing controversy about the uptake capacity and sorption mechanism has not yet been settled [10,11]. Results from experimental and theoretical studies indicate hydrogen storage capacities from less than 1 wt% to about 14 wt% [6–9]. A possible origin for these discrepancies may be due to the fact that a large number of production and purification methods are used, resulting in a wide variety of samples.

Experimental studies concerning gas adsorption on CNTs typically employ macroscopic techniques, such as temperature programmed desorption, thermal gravimetric analysis, or adsorption isotherms [6,9,12]. Spectroscopic tools, and in particular magnetic resonance techniques, have been rarely used for the study of gas adsorption. In this contribution, a summary of the literature will be provided together with a discussion of the data generated in our laboratory.

NMR Spectroscopy of CNTs

CNTs, and in particular SWNTs, are typically synthesized using a ferromagnetic catalyst, such as Fe, Co, or Ni. Residual catalyst particles in the sample often prohibit the application of NMR techniques. However, in these situations, ESR may still be able to provide useful information.

A review published in 2002 summarizes the application of ^{13}C NMR and ESR techniques to the structural investigation of CNTs which also includes a section on graphite and graphene [13]. In graphite, the susceptibility enhancement due to 3D stacking leads to strong shifts in the NMR spectra. The intrinsic isotropic shift of a single graphene sheet was deduced to be $\delta_{\mathrm{iso}} = +128$ ppm with an anisotropy of $\delta_{\mathrm{aniso}} = -163 \pm 5$ ppm [13].

A few attempts to record ^{13}C NMR data of CNTs have been undertaken. Maniwa *et al.* compared the ^{13}C NMR of different carbon forms, one of which is described as a bundle of nanotubes [14]. The ^{13}C NMR spectrum displays a line width on the order of 1000 ppm, which is attributed to the large diamagnetic susceptibility of the tubes, possibly in conjunction with the cylindrical structure [14]. A distribution of over 500 ppm centered at the graphene position is reported for MWNTs [13]. It has been suggested that such wide distributions could be due to residual catalyst particles, and the broadening could be reduced by annealing the samples at 1,600 K [15]. A subsequent theoretical study on perfect and isolated SWNTs indicates that high resolution ^{13}C NMR should be able to distinguish metallic and semiconducting tubes with a splitting of 11 ppm [16]. Experimental results have not yet confirmed this prediction, most likely due to a lack of a high-quality sample. Distributions on the order of 200 ppm were observed for SWNTs [13,17] that could be reduced upon MAS. It should be noted that ^{13}C spin-lattice relaxation time measurements indicated the existence of two components that were assigned to metallic and semiconducting CNTs, respectively [19].

We investigated nine different commercial MWNT and SWNT samples before and after subjecting them to an oxidative purification procedure [18]. Sample characteristics, as provided by the manufacturers, and metal contents from residual catalyst as determined by ICP-MS upon complete destruction of the carbon framework, are presented in Table 1 [19].

Recording ^{13}C NMR spectra proved difficult and only two of the samples (MRGC, NL1020) yielded analyzable data. A peak centered at 80 ppm and covering a range of about 160 ppm was obtained for unpurified NL1020, while MRGC displayed a broad peak around

Graham A. Webb (ed.), Modern Magnetic Resonance, 1479–1485.
© 2008 *Springer.*

Table 1: Sample characteristics.

Sample	Manufacturer	Prod. Method	Structure	Length [μm]	Diameter [nm]	Purification	Metal Imperities	ICP-MS	ICP-MS Purification
MRSW	Mer Corp.	CAD	Single-wall, open	up to 100	1.3	>90%	Co, Ni	0.32	0.15
CLex	Carbolex	CAD	Single-wall, closed	2–5	1.4, 50 tb./rope	50–70%	Ni, Yt	1.12	2.6
CNI	Carb. Nano.	HiPCo	Single-wall*	0.1–1	1	<72%	Fe 25%	1.69	0.20
CNI pur.	Carb. Nano.	HiPCo	Single-wall*	0.1–1	1	91%	Fe 9%	0.76	N/A
MRMWC	Mer Corp.	CVD	Multi-wall, closed	50	N/A	>95%	Fe < 0.1%	0.04	0.03
MRGC	Mer Corp.	CAD	Multi-wall, closed	N/A	50	N/A	none	0.01	0.003
NL15	Nanolab	CVD	Multi-wall, open	1–5	20–50	95%	Fe	0.12	0.13
NL1020	Nanolab	CVD	Multi-wall, open	10–20	20–50	95%	Fe	0.13	0.14
NLbamboo	Nanolab	N/A	Bamboo, open	N/A	N/A	95%	Fe	0.02	0.04

Carb. Nano. = Carbon Nanotechnologies, CAD = carbon arc discharge. ICP-MS data are given in $g_{\text{metal}}/g_{\text{raw material}}$; Met. Imp. = Metal Impurities, ICP-MS Pur. = ICP-MS results after purification.

* The manufacturer did not provide information about tube ends.

100 ppm. On purification, a large peak at about 22 ppm emerged.

ESR Spectroscopy of CNTs

The high conductivity of graphitic materials results in asymmetric Dysonian line shapes [13,20]. For CNTs, theoretical work predicts fundamental differences in the ESR spectra of SWNTs and MWNTs. While MWNTs are expected to exhibit only a single, narrow peak, spin-charge separation should lead to a splitting for SWNTs [21], which has not yet been confirmed experimentally. Kosaka *et al*. performed ESR studies of CNTs before and after purification [22]. The temperature dependence of the *g*-factor allowed for distinction between conduction electrons and defect sites, introduced in the oxidative purification procedure [22]. The same authors later concluded that annealing removed some types of defects [23]. A similar observation was made by Ishii *et al*. [24]. In contrast, Beuneu *et al.* observed a decrease in line width with irradiation of MWNTs due to a decrease in the *g*-factor anisotropy and in increase in motional narrowing [25]. Byszewski and Nabialek [26] and Kotonosov and Shilo [27] observed Dysonian line shapes with the ESR signal disappearing upon purification which they ascribed to a spin-angular momentum interaction [26]. Temperature dependent studies on MWNTs carried out by Bandow [28] showed the existence of conduction electrons with a largely temperature independent *g*-value, while the intensity of the resonance changed with temperature. The temperature independence of the *g*-factor in MWNTs was confirmed by Lee *et al.* [29] Petit *et al.* [30], however, found Dysonian line shapes at all temperatures for SWNTs, indicating that the metallic character persisted even at the lowest temperatures. Only slight asymmetries in the line shape were observed in solutions and suspensions of unpurified, purified, and shortened SWNTs [31]. The distinction between graphitic particles and MWNTs in solutions of various organic polymer hosts was reported by Coleman *et al.* [32].

For the multi-walled samples listed in Table 1, ESR spectra could only be obtained for MRGC and MRMWC. While MRGC gave rise to a Dysonian line shape, a symmetric line was observed for MRMWC. Purification removed one of the resonances in MRGC, which was assigned to graphitic particles, as suggested by TEM [19].

The high metal content of the SWNT samples resulted in ferromagnetic resonances which disappeared upon purification. A narrow, weak resonance was observed for CNI and MRSW upon acid purification, which was assigned to defects [19].

Gas Adsorption on MWNTs

To the best of our knowledge, Shen *et al.*'s [19] work is to date the only source for ESR data on gas exposure

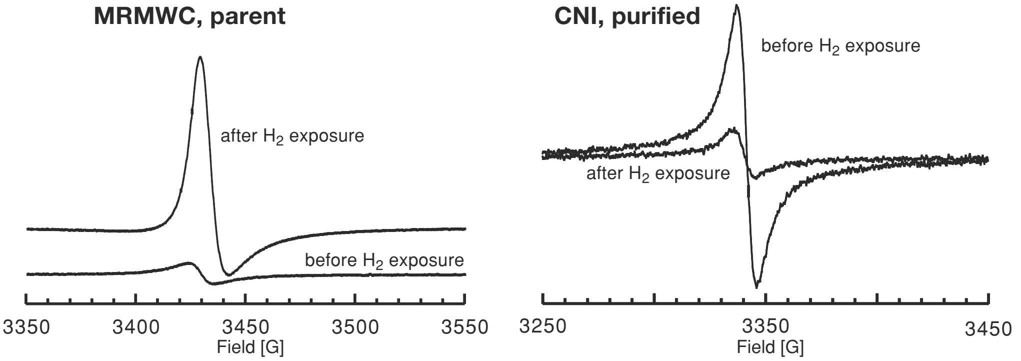

Fig. 1. ESR spectra of unpurified MRMWC and purified CNI before and after hydrogen adsorption. The data were collected at 4.2 K on a Bruker EMX spectrometer operating at a microwave frequency of 9.4 GHz. The samples were heated under vacuum before data acquisition, and exposed for 5 min at ambient temperature to a hydrogen (UHP grade, Matheson–Trigas) pressure of 136 kPa inside the sealed ESR tube.

of CNTs. Among the multi-walled samples described in Table 1, hydrogen exposure greatly increased the ESR signal intensity for MRMWC and MRGC. For the MRGC parent material, an increase of both signal components, assigned to graphitic particles and CNTs, was observed [19]. After purification, the line shape became Dysonian upon hydrogen exposure. It should be noted that MRGC was prepared without a metal catalyst, and the conduction electrons must therefore stem from metallic nanotubes or semiconducting tubes with a small band gap. A possible explanation for the observed increase is a decrease in band gap, such that semi-conducting tubes previously unobservable may become accessible to ESR [19]. Although this explanation is speculative, it is in agreement with theoretical work that shows that hydrogen adsorption on single-walled, radially deformed carbon nanotubes causes the energies of the valence band edge, and conduction band edge to change resulting in a decrease in band gap [33]. This effect is particularly pronounced for zigzag nano-tubes [34]. Hence, a similar increase in signal intensity is expected for other MWNTs, and in fact, was observed for MRMWC as shown in Figure 1.

NMR spectroscopy has been more widely used than ESR spectroscopy to analyze gas adsorption on carbon nanotubes. Early work discussed different carbon materials under a hydrogen pressure of 60 bar [35]. When compared to pure hydrogen gas, significant shifts and changes in line widths were observed for nanotubes, activated carbon, and nanofibers, due to the diamagnetic susceptibility of the carbon materials. Yu *et al.* [36] exposed unpurified MWNTs to hydrogen gas, and studied the ^{1}H NMR shifts and relaxation times as a function of pressure and temperature. At a hydrogen pressure of 300 kPa, the shift of the resonance was inversely proportional to temperature. At 250 K, the shift was about −5 ppm, and increased to about 60 ppm at 70 K. Spin–lattice and spin–spin relaxation times, T_1 and T_2, showed bi-exponential decay. One component was assigned to free hydrogen gas, while the longer T_1 component showed Korringa-type relaxation behavior, evidence of the metallic character of the tubes.

We used ^{1}H and ^{2}H NMR spectroscopy to study hydrogen and deuterium adsorption on the samples listed in Table 1, as a function of gas pressure. In our setup, the pressure could be varied without changing the sample position. After subjecting the samples to the highest gas pressure of 1,480 kPa, the samples were exposed to vacuum which led to the immediate and complete disappearance of the NMR signal. This is a clear indication of fast and reversible physisorption. None of our samples showed any sign of chemisorption.

^{1}H and ^{2}H NMR spectra for multi-walled (MRGC and MRMWC) and single-walled (MRSW and CNI) carbon nanotubes are presented in Figure 2. The ^{1}H NMR spectra for hydrogen exposed Nanolab samples gave rise to broad peaks that seemed to consist of a large number of components and were impossible to phase. These data will not be discussed.

The diminished signal intensity for both purified MWNT samples correlate with the smaller amount of sample weighed into the NMR tube. The ^{1}H NMR spectra of hydrogen exposed MRGC are composed of at least two components that shift downfield with increasing pressure. As shown in Figure 3, the component at −11 ppm (at 1,480 kPa) is dominant at lower pressures, indicating that the sites corresponding to this component are preferentially occupied. Considering that one ESR signal component disappeared upon purification, and that this component was identified as graphitic particles based on the TEM analysis [37], a similar conclusion can be drawn for the NMR data. The component at 2 ppm (at 1,480 kPa)

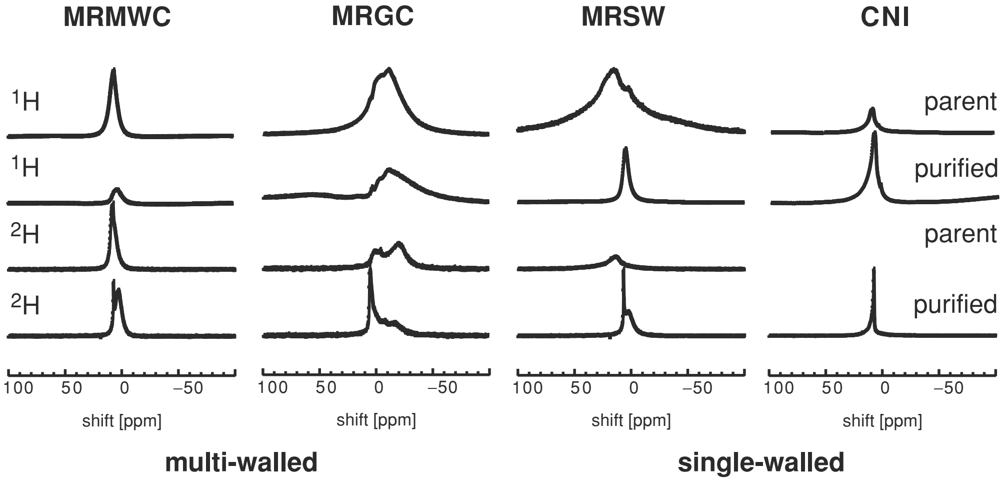

Fig. 2. ^{1}H and ^{2}H NMR spectra of parent and purified MWNTs and SWNTs after exposure to a hydrogen (UHP grade, Matheson–Trigas) or deuterium (D_2 99.6%, Cambridge Isotope Laboratories) pressure of 1,480 kPa. The narrow resonance discernible in the ^{2}H NMR spectra is due to free hydrogen gas. The data were recorded at ambient temperature on a Bruker MSL-400/Tecmag Apollo NMR spectrometer at a Larmor frequency of 400.13 and 61.42 MHz, respectively. Note that the signal component at 4 ppm, which is most obvious in the ^{1}H NMR spectra of purified MRGC, is due to probe background and also present when removing the sample.

is also diminished in intensity after purification, and is thus likely due to hydrogen adsorbed on graphitic particles. Therefore, the component at -11 ppm is tentatively assigned to hydrogen in contact with other carbon structures such as nano-onions or carbon nanotubes [37]. The line width of this peak component increases with pressure [38]. The large deviation from the typical chemical shift range for hydrogen is indicative of a Knight shift contribution due to interaction with metallic carbon nanotubes, and in agreement with the Dysonian line shapes observed with ESR [19].

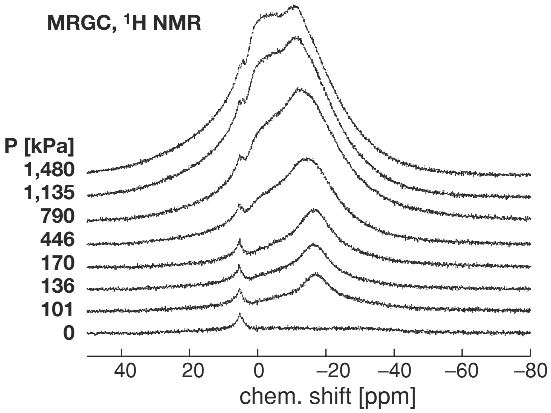

Fig. 3. ^{1}H NMR spectra of parent MRGC nanotubes after exposure to hydrogen (UHP grade, Matheson–Trigas) at a variety of pressures. Note that the signal observable at 0 kPa is due to probe background. The data were recorded at ambient temperature on a Bruker MSL-400/Tecmag Apollo NMR spectrometer at a Larmor frequency of 400.13 MHz.

^{2}H NMR data largely agree with the ^{1}H NMR results. The largest discrepancy lies in the different position of the -11 ppm resonance, which appears at -20 ppm in the ^{2}H NMR spectra. It remains to be resolved whether this effect can be attributed to differences in the two isotopes. When comparing the overall line width for the two isotopes, they scale with a factor of 6.5 which is remarkably close to the ratio of the gyromagnetic ratios, γ. Hence the most likely origin is susceptibility broadening. The narrower ^{2}H NMR line widths allow the resonances for free deuterium to be distinguished from adsorbed gas [38].

Both ^{1}H and ^{2}H NMR data for MRMWC reveal only a single resonance (Figure 2) due to adsorbed hydrogen. This is surprising given the fact that TEM data revealed the presence of nanofibers [37]. Moreover, the tube walls are severely damaged upon purification which is expected to cause the formation of defect sites as confirmed by ESR [19]. The much narrower NMR line widths and the line position suggests a much smaller contribution from conduction electrons, when compared to MRGC and a smaller number of sites accessible to hydrogen. These facts are in agreement with the hypothesis that MRMWC is predominantly made up of semiconducting nanotubes, and that nanofibers do not present preferred adsorption sites for hydrogen [38].

Gas Adsorption on SWNTs

Tang *et al.* [17] investigated electronic properties of CNTs under a variety of conditions using NMR spectroscopy. They found that oxygen exposure substantially affected the ^{13}C T_1, and suggested as the most probable mechanism the paramagnetic nature of the oxygen molecule. However, the authors indicated that changes in the electronic properties could contribute as well. Nevertheless, this observation underlines the necessity to carefully evacuate CNT samples before conducting any experiments. Schmid *et al.* [39] investigated hydrogen adsorption on fragmented SWNTs using ^{1}H NMR spectroscopy. The SWNTs were ball-milled at a hydrogen pressure of about 800 kPa, and then washed with hydrochloric acid. It was shown that both line width and spin-lattice relaxation were mainly affected by the paramagnetic impurities introduced via ball-milling. The authors quantitated the hydrogen uptake by comparison to an external reference of glycerine, and estimated an uptake of 5 wt%. Shiraishi *et al.* [40] observed a narrow resonance (less than 300 Hz) at 5.1 ppm. Due to the similarity of this shift to that of water, the authors exposed the sample to SO_2 gas. They observed no change in the resonance, concluding that it could not be due to water. The T_1 was measured at about 0.1–0.2 s, significantly longer than the ones we observed on our samples, which were all in the range of ms. In subsequent work, Schmid *et al.* [41] performed temperature dependent ^{1}H NMR studies on SWNTs synthesized with the non-magnetic catalysts rhodium and platinum, and subjected to a hydrogen pressure of about 2,300 kPa. They observed hydrogen desorption at about 150 K. The authors were not able to distinguish between different adsorption sites. Kleinhammes *et al.* [42] investigated the adsorption of ethane and methane on SWNTs using ^{1}H NMR spectroscopy. They concluded that the interior of the tubes became accessible to the gases upon cutting the tubes using an oxidative procedure. T_1 measurements revealed two components which were assigned to adsorbed and free gas. Co-exposure to oxygen gas did not affect the spectra which led the authors to conclude that oxygen did not enter the endohedral sites. Furthermore, the authors studied the effect of adsorbed gases on ^{13}C NMR relaxation times. These were strongly affected by oxygen due to its paramagnetism and, surprisingly, also by He. The authors argued that the small He can enter the interstitial sites and thus has access to the majority of the carbon atoms.

Unlike for MWNTs, we observed a reduction in ESR signal intensity when exposing SWNTs to hydrogen gas (Figure 1). The symmetric ESR line shapes indicate that the observed signal is due to isolated spins such as dangling bonds [19]. Hydrogen adsorbs preferentially on such defect sites as has been shown for mechanically prepared nanostructured graphite [43]. ^{1}H and ^{2}H NMR spectra are shown in Figure 2. The large metal content in CNI caused a low signal-to-noise ratio in the ^{1}H NMR spectra, so that no ^{2}H NMR was attempted. For the purified CNI sample, the ratio of the ^{1}H to ^{2}H line width is about 9, slightly larger than expected for pure susceptibility broadening. Additional contributions to the line width may arise from dipolar contributions.

TEM and ICP-MS showed that the MRSW sample was high quality despite the high metal content before purification (Table 1). Indeed, the ESR spectra revealed a ferromagnetic resonance as for CNI [19]. Correspondingly, the signal-to-noise ratio in the ^{1}H NMR spectra was low. After purification, only a single resonance was observed and the overall line width was reduced to 2.4 kHz from 16.1 kHz. ^{2}H NMR results mostly corroborated the ^{1}H NMR findings (Figure 2), although the line position for the main peak component changed. The ratio of the line widths for the two isotopes was about 20 at a pressure of 1,480 kPa, indicating significant contributions to the line width other than susceptibility broadening. Spectral hole burning and two-dimensional exchange experiments indicated that the line width is determined by a heterogeneity in adsorption sites. The same conclusion was drawn from ^{129}Xe and ^{131}Xe NMR spectroscopy [45]. Hole recovery experiments at different pressures suggest that exchange among these sites is diffusion limited [44].

Summary

Magnetic resonance spectroscopy as a tool to study gas adsorption in carbon nanotubes is an emerging field. The main difficulty encountered lies in the fact that CNTs are highly inhomogeneous. Careful characterization and possibly purification are necessary to minimize the interaction of adsorbates with impurities such as residual catalyst particles, other carbon nanostructures, graphitic, and amorphous carbon. The most pertinent questions, the nature of the adsorption and the gas storages capacities, have not yet been satisfactorily answered with magnetic resonance or any other technique.

However, all data seem to indicate that none of the samples investigated exhibited extraordinary gas sorption capacities in the pressure and temperature ranges investigated using magnetic resonance tools. We observed exclusively physisorption for our samples. The slopes of the ^{1}H NMR integrated signal intensities as a function of pressure for the samples listed in Table 1 were smaller by about a factor 2 than for pure hydrogen gas (Figure 4a). Even when taking into account that the available volume in the NMR pick-up coil was reduced due to the dead volume of the CNTs, we estimated an upper limit of the

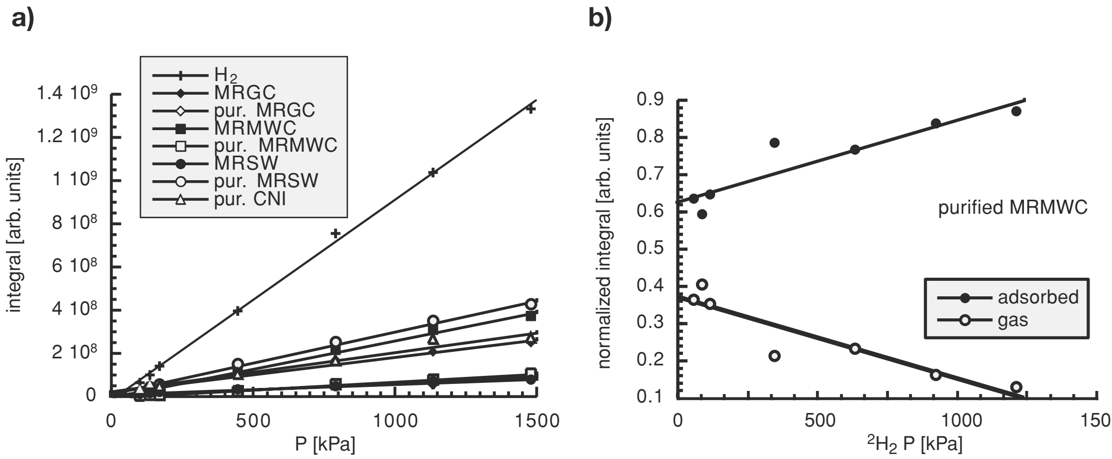

Fig. 4. (a) ^{1}H NMR integrated signal intensities as a function of pressure for different CNT samples. Pure hydrogen gas is included for comparison. (b) Integrated and normalized NMR signal intensities after decomposition into a gas and adsorbed component for purified MRMWC. Note that with increasing pressure, hydrogen is preferentially adsorbed on the CNTs.

uptake capacity of our samples to about 0.1% [38]. These findings were corroborated by ^{129}Xe and ^{131}Xe NMR experiments where adsorption (for unpurified MRMWC and MRSW) was observed only for temperatures below 200 K. Our data show that the distinction between free and adsorbed hydrogen is easier using ^{2}H due to decreased susceptibility broadening and dipolar interactions. In Figure 4b, the decomposed and normalized ^{2}H NMR signal intensities for purified MRMWC are plotted as a function of pressure. The difference in slopes clearly indicates that with increasing pressure, hydrogen preferentially enters the adsorbed phase. More data are needed to understand gas adsorption in these exciting materials, and magnetic resonance techniques are an ideal tool to study them.

Acknowledgments

This material is based upon work supported by the National Science Foundation under Grant No. 0107710. The contributions of K. Shen, CFM. Clewett, and D. Clewett are gratefully acknowledged.

References

1. Iijima S. Nature. 1991;354:56.
2. Ajayan PM, Ebbesen TW. Rep. Prog. Phys. 1997;60:1025.
3. Sinnott SB, Andrews R. Crit Rev. Solid State Mater. Sci. 2001;26:145.
4. Dillon AC, Jones KM, Bekkedahl TA, Klang CH, Bethune DS, Heben MJ. Nature. 1997;386:377.
5. Hynek S, Fuller W, Bentley J. Int. J. Hydrog. Energy. 1997;22:601.
6. Ding RG, Lu GQ, Yan ZF, Wilson MA. J. Nanosci. Nanotech. 2001;1:7.
7. Dresselhaus MS, Williams KA, Eklund PC. MRS Bull. Nov. 45 (1999).
8. Schlapbach L, Züttel A. Nature. 2001;414:353.
9. Cheng H-M, Yang Q-H, Liu C. Carbon. 2000;39:1447–1454.
10. Dagani R, C&EN. 2002;January 14:25.
11. Simonyan VV, Johnson JK. J. Alloys Compd. 2002;330–332:659.
12. Dillon AC, Heben MJ. Appl. Phys. A. 2001;72:133–142.
13. Goze-Bac C, Latil S, Lauginie P, Jourdain V, Conard J, Duclaux L, Rubio A, Bernier P. Carbon. 2002;40:1825.
14. Maniwa Y, Sato M, Kume K, Kozlov ME, Tokumoto M. Carbon. 1996;34:1287.
15. Goze-Bac C, Latil S, Vaccarini L, Bernier P, Gaveau P, Tahir S, Micholet V, Aznar R, Rubio A, Metenier K, Beguin F. Phys. Rev. 2001; B. 63:100302.
16. Latil S, Henrard L, Goze Bac C, Bernier P, Rubio A. Phys. Rev. Lett. 2001;86:3160.
17. Tang X-P, Kleinhammes A, Shimoda H, Fleming L, Bennoune KY, Sinha S, Bower C, Zhou O, Wu Y. Science. 2000;288: 492.
18. Dillon AC, Gennett T, Jones KM, Alleman JL., Parilla PA, Heben MJ. Adv. Mater. 1999;11:1354.
19. Shen K, Tierney DL, Pietraß T. Phys. Rev. 2003; B. 68: 165418.
20. Dyson FJ. Phys. Rev. 1955;98:349.
21. De Martino A, Egger R, Hallberg K, Balseiro CA. Phys. Rev. Lett. 2002;88:206402.
22. Kosaka M, Ebbesen TW, Hiura H, Tanigaki K. Chem. Phys. Lett. 1994;225:161.

23. Kosaka M, Ebbesen TW, Hiura H, Tanigaki K. Chem. Phys. Lett. 1995;233:47.
24. Ishii S, Aoki N, Miyamoto K, Oguri N, Horiuchi K, Ochiai Y. Physica. 2003; E. 17:386.
25. Beuneu F, l'Huillier C, Salvetat J-P, Bonard J-M, Forró L. Phys. Rev. 1999; B. 59:5945.
26. Byszewski P, Nabialek A. Europhys. Lett. 1996;34:31.
27. Kotosonov AS, Shilo DV. Carbon. 1998;36:1649.
28. Bandow S. J. Appl. Phys. 1996;80:1020.
29. Lee Y-H, Kim H, Kim D-H, Ju B-K. J. Electrochem. Soc. 2000;147:3564.
30. Petit P, Jouguelet E, Fischer JE, Rinzler AG, Smalley RE. Phys. Rev. 1997; B. 56:9275.
31. Chen Y, Chen J, Hu H, Hamon MA, Itkis ME, Haddon RC. Chem. Phys. Lett. 1999;299:532.
32. Coleman JN, O'Brien DF, Dalton AB, McCarthy B, Lahr B, Barklie RC, Blau WJ. J. Chem. Phys. 2000;113:9788.
33. Gülseren O, Yildirim T, Ciraci S. Phys. Rev. Lett. 2001;87:116802.
34. Gülseren O, Yildirim T, Ciraci S. Phys. Rev. 2002; B. 66:121401(R).
35. Schütz W, Klos H. AIP Proc. 1998;442:485.
36. Yu I, Lee J, Lee SG. Physica B. 2003;329–333:421.
37. Shen K, Pietraβ T. Carbon. 2004;42:2315.
38. Shen K, Pietraβ T. J. Phys. Chem. B. 2004;108:9937.
39. Schmid M, Krämer S, Mehring M, Roth S, Haluska M, Bernier P. AIP Proc. 2001;591:598.
40. Shiraishi M, Ata M. J. Nanosci. Nanotechnol. 2002;2: 463.
41. Schmid M, Krämer S, Goze C, Mehring M, Roth S, Bernier P. Synth. Metals. 2003;135–136:727.
42. Kleinhammes A, Mao S-H, Yang X-J, Tang X-P, Shimoda H, Lu JP., Zhou O, Wu Y. Phys. Rev. B. 2003;68: 075418.
43. Orimo S, Matsushima T, Fujii H, Fukunaga T, Majer G. J. Appl. Phys. 2001;90:1545.
44. Shen K, Pietraß T. Appl. Phys. Lett. 2004;84:1567.
45. Clewett CFM, Pietraß T. J. Phys. Chem. B 2005;109:17907.

Magnetic Resonance Studies of the Heterogeneous Rotational and Translational dynamics in Disordered Materials

R. Böhmer[1], G. Diezemann[2], G. Hinze[2], K. R. Jeffrey[3], M. Winterlich[1]
[1]*Experimentelle Physik III, Universität Dortmund, 44221 Dortmund, Germany*
[2]*Institut für Physikalische Chemie, Universität Mainz, 55099 Mainz, Germany*
[3]*Department of Physics, University of Guelph, Guelph, Ontario, Canada*

Introduction

The long-established method of distinguishing between heterogeneous and homogeneous *line shapes* was introduced in the seminal paper by Bloembergen *et al.* [1]. The differentiation between the two types of spectral lines is based on whether one can alter the shape or just the amplitude of a line by an external perturbation. This concept has been applied many times particularly in optical hole burning spectroscopy where the distribution of transition frequencies can often be traced back to structural inhomogeneities in the material under study. It is well known that the frequency of an electronic transition, for example, sensitively depends on the local symmetry. This technique has been successfully applied to the structural elucidation of glasses [2].

In condensed matter where there is a well-defined structural heterogeneity it is natural to expect that there will also be spatially non-uniform dynamics. The study of the recovery of spectral holes burnt into an inhomogeneously broadened line provides but one means of testing for such a scenario. However, for systems devoid of an evident structural heterogeneity, such as supercooled liquids, questions regarding possible dynamic disorder have for a long time been most prominently discussed in the field of dielectric spectroscopy rather than NMR. In this context, we mention the important works of Kohlrausch [3], Curie [4], and von Schweidler [5] on the one hand and papers by Wagner [6] and Cole and Cole [7] on the other. The approaches used in these works merely *assumed* that either a distribution of correlation times is present or that the correlation function itself decays non-exponentially. More systematic attempts to distinguish between these two scenarios experimentally using optical [8, 9] and dielectric techniques [10, 11] were carried out in the 1970s by various groups. In retrospect it can be stated that a well-established consensus as to whether the dynamics of disordered systems should be considered homogeneous or heterogeneous was *not* reached at this stage. Prior to the breakthrough achieved in the early 1990s there was very little activity in this area employing NMR techniques [12]. In their pioneering 1991 work Schmidt-Rohr and Spiess [13] resolved the homogeneity vs. heterogeneity issue for the structural relaxation, the so-called α-relaxation, which accompanies the vitrification transition of an amorphous polymer. To this end they introduced a reduced four-dimensional (4D) NMR technique which later was further reduced to an echo experiment employing four equally long evolution times. The nature of the secondary or β-relaxation in small-molecule glass-formers had been clarified previously by the observation of a non-exponential recovery in a deuteron spin–lattice relaxation experiment [14]. This work uses the theoretical statement that spin–lattice relaxation must be exponential for isolated deuterons in high field [15].

These experiments not only set the stage for numerous other NMR investigations but also stimulated the development of related optical [16], dielectric and magnetic spectroscopic techniques [17–19]. Since both theoretical [20, 21] and experimental work [16,20,22,23] in the field of dynamical heterogeneity has previously been reviewed, in the present chapter, we will focus on recent developments using NMR techniques and on aspects not widely appreciated in the glass community.

In this article we first discuss the spatial and dynamical heterogeneity in disordered materials as monitored via the rotational (Sections "Rotational Dynamics Near the Vitrification Transition" and "Freezing in Glassy Crystals") and translational (Section "Heterogeneous Transport in Ionic Conductors") degrees of freedom. The study of secondary relaxations using NMR techniques is then given separate consideration in the Section "Probing Secondary Relaxations." The concluding Section "Single-Molecule Spectroscopy" deals with some results and prospects arising from single-molecule spectroscopy for the investigation of dynamic heterogeneity.

Graham A. Webb (ed.), Modern Magnetic Resonance, 1487–1492.
© 2008 *Springer.*

Rotational Dynamics Near the Vitrification Transition

In the following we will use our previous definition of the term dynamic heterogeneity [24]: "we will call a system dynamically heterogeneous if it is possible to select a dynamically distinguishable subensemble by experiment or computer simulation." Using the reduced four-dimensional technique of Schmidt-Rohr and Spiess it is possible to implement such a selection experimentally. The technique is based on a sequence of seven radio frequency pulses which yields a four-time correlation function of the form

$$E_4(t_p, t_{m1}, t_{m2}, t_{m3}) \propto \langle \exp[i\varphi(0)] \exp[-i\varphi(t_{m1})] \times \exp[i\varphi(t_{m2})] \exp[-i\varphi(t_{m3})] \rangle \qquad (1)$$

Here the t_{mi} with $i = 1,2,3$ denote three mixing times and the phase angles φ are those acquired during the corresponding evolution times t_p. With appropriate phase cycling the sine and cosine contributions to the general four-time stimulated-echo (4t-SE) function can be mapped out separately [25].

A few degrees above the calorimetric glass transition temperature supercooled glasses and polymers exhibit a non-exponential structural relaxation. The 4t-SE functions in many of these materials have been measured using ^{2}H- and ^{13}C-NMR. Two important findings have emerged (for a compilation see Ref. [22]). First, it was generally observed that slow subensembles can be selected thus demonstrating the existence of dynamical heterogeneity of the primary relaxation. This conclusion was confirmed later by several other techniques [16,17,22] and furthermore a measure of the degree of heterogeneity was defined [24]. Second, the echo variant of the reduced 4D experiment provided evidence for a short-lived dynamic heterogeneity. The life-time of the heterogeneity τ_{het} relative to that of the typical structural relaxation time τ_α was characterized by a rate memory parameter $Q = \tau_{\text{het}}/\tau_\alpha$ [26]. While in neat samples typical Q-parameters were found to be close to one [27], experimental methods employing impurity probes give Q-parameters as large as 1000 [16,22].

A third parameter that has been used to characterize dynamic heterogeneity is its length scale ξ. The original four-time experiments were *not* designed to probe length scales directly. However, length scale determinations became possible by augmenting the original seven-pulse experiments with cross-polarization steps to an abundant species such as ^{1}H thus facilitating pronounced spin-diffusion effects [28]. A possible spatial heterogeneity for which ξ is well defined is sketched in Figure 1a. In reality, the spatial structure of the slow domains may be more complex than that depicted in the diagram and the definition of a unique length scale is often far from being unambiguous [20]. Nevertheless, given the fact that prior to these experiments, length scales could only be *estimated* using more or less well-accepted model assumptions, they marked a major step forward in the field of glass science.

Some results on the viscous liquid sorbitol are reproduced in Figure 1b [29]. Comparison of the dynamic selection experiments with calculations based on the assumption of slow spherical domains reveals evidence for length scales $\xi_{\text{het,NMR}}$ of 2.7 ± 1.2 nm. Results from the four glass-formers that have been studied so far using this type of experiment, indicate that $\xi_{\text{het,NMR}}$ is in the range of 1–4 nm, not too different from previous estimates, see e.g. [30, 31]. The relative error in $\xi_{\text{het,NMR}}$ which is typically about 30–50% has so far precluded the establishment of correlations with other properties characterizing the highly viscous state such as, e.g. measured by its fragility index [29].

Freezing in Glassy Crystals

A glass transition solely due to the freezing of the orientational degrees of freedom is sometimes exhibited by so-called plastic or glassy crystals. Well-known representatives of this family of (quasi-) monoatomic substances that were recently studied using NMR are C_{60} [32], cyanoadamantane [33, 34], and *ortho*-carborane (OCA) [35].

Four-time correlation functions have so far been only measured for OCA. By performing a detailed analysis of the experimental results the relatively complex reorientational geometry in this material was unraveled. Of particular importance in the present context was the finding that the molecular motion involves a sequence of small-angle tilts about locally preferred axes as well as symmetry adapted threefold jumps [35]. The rates for the tilt and for the jump motions were shown to be somewhat different. This difference is the source of the intrinsic non-exponential response which characterized this crystal. In addition, evidence for dynamic heterogeneity was obtained by measuring the 4t-SE function described above. As has been emphasized in more detail elsewhere [22], the geometry of the molecular motion enters into the interpretation of such experiments if the evolution time t_p is finite. Since it is impractical to let $t_p \to \infty$, the case $t_p \to 0$ has been analyzed both experimentally and theoretically [36]. If one uses the sin–sin–sin–sin correlation function for very small t_p then this amounts to studying the particularly simple form $L_4 \propto \langle \omega_1 \omega_2 \omega_3 \omega_4 \rangle$. Here ω_i denotes the perturbed NMR frequency during the evolution interval i. It turns out that this function can be decomposed into several parts one of which is independent of the rotational motion but sensitive to dynamic exchange. In particular it was found that, in the absence of dynamic

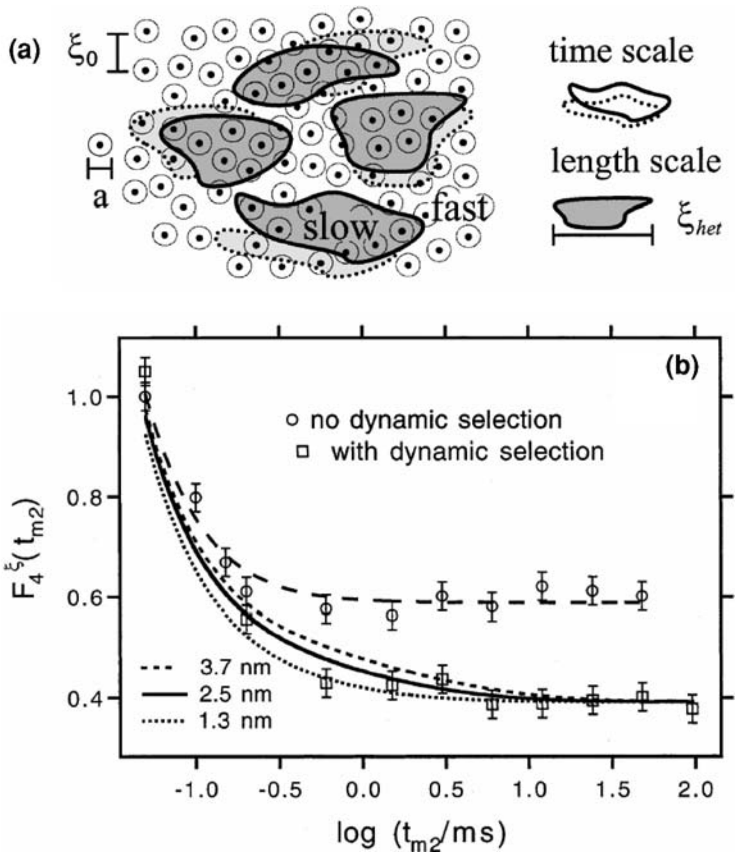

Fig. 1. (a) A sketch of the length scale of dynamic heterogeneities. The temporal "fluctuations" of the positions of the shaded areas are meant to indicate that the specified molecules or polymer segments switch between fast and slow states. Reproduced by permission from Ref. [28]. (b) Echo intensities for the 4D3CP experiment as a function of the mixing time t_{m2}. The data were recorded at 275 K on sorbitol with and without dynamic selection. The best fit to the data is obtained for $\xi_{\text{het}} = 2.5 \pm 1.2$ nm. Reproduced by permission from Ref. [29].

exchange, this part for isotropic motions does not become smaller than 7/15 of the initial value of L_4 [36,37]. This experiment seems well suited to the study of substances with a complex molecular motion geometry.

The experimental data, together with the results of calculations based on the anisotropic tilt and jump model recently obtained for L_4 in OCA [38] are shown in Figure 2. The effective evolution time used in the experiment is approximately given by the mean length of the radio frequency pulses; in this case about 3 µs. The calculations are therefore only shown for a small range of evolution times. It is seen that as $t_p \to 0$ the plateau value of 7/15 is not exactly met and for finite t_p a large variation in the plateau value is observed. The experimental data exhibit smaller values than the results from the theoretical computations and thus are compatible with the presence of dynamic exchange in harmony with earlier measurements for much longer evolution times [35].

In order to better approach the limit $t_p \to 0$, one could generate the transverse magnetization at the start of the four evolution intervals *not* by a single pulse but by a solid-echo sequence. This would add four more pulses to this multiple-pulse experiment. A similar replacement of a single $\pi/2$ pulse by a solid-echo sequence has been used in the context of multidimensional spectroscopy [39].

Heterogeneous Transport in Ionic Conductors

Dynamic heterogeneity has been intensively studied for organic glass-formers, but for inorganic materials such as ionic conductors the issue has been rarely addressed. One of the pioneering NMR works focused on the molten nitrate melt $2Ca(NO_3)_2 \cdot 3KNO_3$ [40] and exploited the non-exponential ^{15}N magnetization recovery to demonstrate that distinguishable subensembles can be selected. In a further study on the glassy state of this material dynamic heterogeneity was exhibited using non-resonant dielectric hole burning spectroscopy [41].

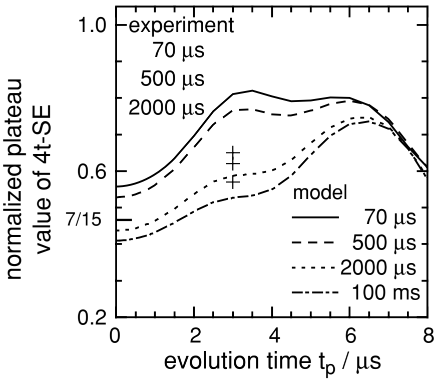

Fig. 2. The normalized plateau values ($t_{m2} \to \infty$) of the sin–sin–sin–sin correlation for OCA are shown as crosses for three different mixing times $t_{m1} = t_{m3}$. The corresponding two-time correlation function is characterized by a time constant of 720 µs. The assignment of the evolution time t_p takes the quadrupolar evolution during the pulses into account on an empirical level. The solid lines represent the computations of the evolution time dependence using the tilt and jump model [35] for the motion of the icosahedral molecules for several mixing times $t_{m1} = t_{m3}$. It seen that for the anisotropic tilt and jump model the isotropic limit of 7/15 is not met. Taken from Ref. [38].

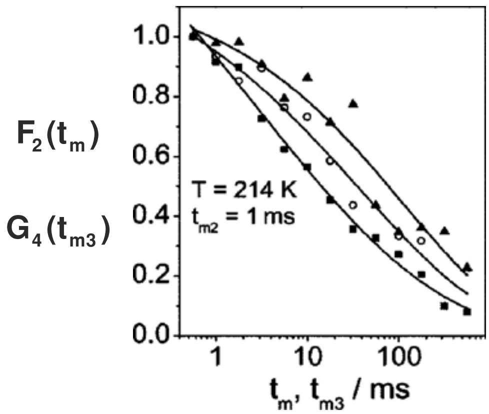

Fig. 3. The ^{109}Ag NMR data of a $(AgI)_{0.3}$–(1/3)$(2Ag_2O$–$P_2O_5)_{0.7}$ glass at T = 214 K shown here were normalized to the data points measured for the shortest mixing time. The two-time correlation function $F_2(t_\mathrm{m})$ (squares) is compared to the four-time correlation functions $G_4(t_\mathrm{m3})$. For the latter functions t_m2 was set to 1 ms and t_m1 was chosen as 1 ms (circles) or 7 ms (triangles). The solid lines represent fits using a stretched exponential function. For further details see Ref. [42] from which this figure was adapted.

The question whether dynamically distinguishable subensembles can be selected is of particular interest in the context of molten and solid electrolytes because it is not clear a priori how much the long-ranged ion–ion interactions homogenize the response of the mobile charge carriers. A question which has often been discussed in this context is whether there is an enhancement of forward-backward hops. In other words one wants to know whether a site memory effect exists. In order to address this question experimentally at least a three-time correlation function must be measured.

Measurements of higher-order correlation functions by stimulated-echo NMR techniques were recently carried out using the mobile ^{109}Ag species as the nuclear probe. Four-time correlation functions were first reported for silver phosphate glasses [42] and then also for related crystalline and amorphous silver ion conductors [43, 44]. As an example, in Figure 3 the two-time correlation function $F_2(t_{m2})$ [45] is compared with a low-pass filtered correlation function $G_4(t_{m3})$ of a $(AgI)_{0.3}$–(1/3)$(2Ag_2O$–$P_2O_5)_{0.7}$ glass. These are compared. These and related results [42–44] show that slow subensembles can be selected, demonstrating the dynamical heterogeneity of the translational degrees of freedom in these materials.

Light nuclear species such as ^{6}Li, ^{7}Li, and ^{9}Be or heavier spin ½ nuclei such as ^{77}Se or ^{125}Te would also seem to be suitable for such studies. For lithium in conducting glasses, the application of multiple-time correlation functions was considered from various perspectives [46, 47] but so far has not been exploited experimentally.

Probing Secondary Relaxations

The dynamics in a frozen structure that emerged from a dynamically heterogeneous melt are expected to be heterogeneous as well. In fact, in the previous paragraph we have discussed such a situation for the special case of ion conducting materials. The phenomenon is, however, more general and was, for instance, observed in two-dimensional "cross" spectra of mobile tracers in glassy hosts [48].

Several aspects of NMR studies concerning the secondary relaxation in glasses were reviewed earlier [49,22]. As mentioned above, one of the simplest methods to identify dynamic heterogeneity is to apply deuteron relaxometry and to check whether the longitudinal magnetization recovers in a non-exponential fashion [14,50,51]. If so, the difference between the mean relaxation rate, as measured via the initial slope of the magnetization recovery curve, and the mean relaxation time becomes very pronounced [52].

As demonstrated by Leisen *et al.* a dynamic low-pass filter can also be used to select subensembles out of a distribution of spin–lattice relaxation times [53]. It was found that by selecting the response of polystyrene segments with correlation times slower than about 10 ms, the subsequently measured magnetization recovery time, most sensitive to motions with rates near the Larmor frequency (of 45 MHz in that experiment) was slowed down somewhat. When investigating the dynamics of the methyl group of the supercooled liquid propylene carbonate it was found in a stimulated-echo experiment that the magnetization recovered faster than in the conventional T_1 experiment [54]. These and related effects were recently exploited and shed new light on the interplay between slow (i.e. primary) and fast (e.g. secondary) relaxation processes near and below the glass transition temperature [55].

Single-Molecule Spectroscopy

The concept of selecting particular subensembles is most uniquely implemented in single-molecule experiments. Mechanical and optical detection schemes with single-spin sensitivity have been developed. Most recently, a mechanical technique exploiting the sensitivity of the atomic force microscope was used to resolve the signal from a single unpaired electron spin in silicon dioxide [56]. Optical detection has also been achieved for a single electron as well as for single nuclear spins [57]. The cited experiments were all conducted at liquid helium temperatures. However, at room temperature single-spin detection has proven to be possible only in specific cases. For example Gruber *et al.* have studied a single paramagnetic nitrogen-vacancy (N-V) defect in diamond [58].

A particularly promising approach for the study of dynamic heterogeneity is the general capability of these techniques to record a time series for single molecules. Although *not* using single-*spin* detection but rather dielectric or optical single-molecule spectroscopy, such time series have been used, e.g. to characterize the spectral diffusion and switching of low-energy excitations in two-level systems [59]. As well, single-molecule techniques have been used to investigate dynamic heterogeneity in an amorphous polymer [19] and in the context of enzymology [60]. In the latter case, multiple-time correlation functions describing the chemical reaction kinetics were used to distinguish homogeneous from heterogeneous scenarios both of which could be implemented by changing the experimental conditions. In addition, polarization resolved recording of a single-molecule fluorescence time series [61] was used to probe dynamic heterogeneity in polymers [62] and simple organic glass-forming liquids [63].

Conclusion

The measurement of multiple-time correlation functions has emerged as an important tool for the elucidation of the nature of dynamical heterogeneities in disordered condensed matter. Relevant information comes from combining the results of various two-, three-, and particularly four-time NMR stimulated-echo experiments which are often used in conjunction with cross-polarization steps to a nuclear species characterized by spin-diffusion. The most important quantities observed in the context of the vitrification transition are the heterogeneity life-times and the associated length scales. A major limitation of these experiments arises because various relaxation times resulting from nuclear coupling constants, molecular correlation times, and spin-relaxation times impose severe restrictions on the time scales that can be investigated using these multiple-time correlation functions. Therefore, for a given material, measurements using these techniques can reasonably be obtained in a relatively narrow temperature range which typically is only a few degrees wide. As a result, other methods will certainly continue to play a major role in the selection of dynamically distinguishable subensembles. These include non-linear dielectric methods, nano-mechanical experiments using scanning microscopy and, probably most importantly, optical spectroscopies with sensitivities down to the single-molecule level.

References

1. Bloembergen N, Purcell EM, Pound RV. Phys. Rev. 1948;73:679.
2. Wang J, Angell CA. Glass-Structure by Spectroscopy. Dekker: New York, 1976.
3. Kohlrausch R. Pogg. Ann. Phys. 1854;91:179.
4. Curie J. Ann. Chim. Phys. 1899;18:20.
5. von Schweidler E, Handbuch der Elektrizität und des Magnetismus. Barth: Leipzig, 1918, p 286.
6. Wagner KW. Ann. Phys. (N.Y.) 1913;40:817.
7. Cole KS, Cole RH. J. Chem. Phys. 1941:9:341.
8. Austin RH, Beeson KW, Eisenstein L, Frauenfelder H, Gunsalus IC. Biochemistry 1975;14:5355. For more recent reviews see, e.g., Doster W, Post F, Settles M. In: R. Richert, A Blumen (Eds). Disorder Effects on Relaxational Processes. Springer: Berlin, 1994, p 615; Frauenfelder H, McMahon BH. In: R Rigler, M Orrit, T Basché (Eds). Single Molecule Spectroscopy (Nobel Conference Lectures. Springer: Berlin, 2001, p 257.
9. Barkatt A, Angell CA. J. Phys. Chem. 1975;71:2192.
10. Williams G, Cook M, Hains PJ. J. Chem. Soc. Faraday Trans. II 1972;2:1045.
11. Jonscher AK. Dielectric Relaxation in Solids. Chelsea: London, 1983.
12. Bjorkstam JL, Listerud J, Villa M. Solid State Ionics 1986;18&19:117.
13. Schmidt-Rohr K, Spiess HW. Phys. Rev. Lett. 1991;66:3020.
14. Schnauss W, Fujara F, Hartmann K, Sillescu H. Chem. Phys. Lett. 1990;166:381.
15. Diezemann G, Schirmacher W. J. Phys.-Condens. Matter 1990;2:6681.

16. Ediger MD, Annu. Rev. Phys. Chem. 2000;51:99.
17. Schiener B, Böhmer R, Loidl A, Chamberlin RV. Science. 1996;274:752.
18. Chamberlin RV. Phys. Rev. Lett. 1999;83:5134.
19. Russell EV, Israeloff NE. Nature. 2000;408:695.
20. Sillescu H. J. Non-Cryst. Solids. 1999:243:81.
21. See e.g. Vollmayr-Lee K, Kob W, Binder K, Zippelius A. J. Chem. Phys. 2002;116:5158; Lacevic N, Starr FW, Schrøder TB, Glotzer SC. J. Chem. Phys. 2003;119:7372 and references cited in these chapters.
22. Richert R. J. Phys.: Condens. Matter 2002;14:R703.
23. Böhmer R, Diezemann G, Hinze G, Rössler E. Prog. NMR Spectrosc. 2001;39:191.
24. Böhmer R, Chamberlin RV, Diezemann G, Geil B, Heuer A, Hinze G, Kuebler SC, Richert R, Schiener B, Sillescu H, Spiess HW, Tracht U, Wilhelm M. J. Non-Cryst. Solids 1998;235–237:1.
25. Hinze G, Böhmer R, Diezemann G, Sillescu H, J. Magn. Reson. 1998;131:218; Tracht U, Wilhelm M, Heuer A, Spiess HW. J. Magn. Reson. 1999;140:460.
26. Heuer A, Wilhelm M, Zimmermann H, Spiess HW. Phys. Rev. Lett. 1995;75:2851.
27. See, e.g. the compilation in Qi F, El Goresy T, Böhmer R, Döß A, Diezemann G, Hinze G, Sillescu H, Blochowicz T, Gainaru C, Rössler E, Zimmermann H. J. Chem. Phys. 2003;118:7431.
28. Tracht U, Wilhelm M, Heuer A, Feng H, Schmidt-Rohr K, Spiess HW. Phys. Rev. Lett. 1998;81:2727.
29. Qiu XH, Ediger MD. J. Phys. Chem. B. 2003;107: 459.
30. Donth E. J. Non-Cryst. Solids 1982;53:325.
31. Moynihan CT, Schroeder J. J. Non-Cryst. Solids 1993;160:52.
32. Pennington CH, Stenger VA. Rev. Mod. Phys. 1996;68:855 and references cited therein.
33. Affouard F, Cochin E, Decressain R, Descamps M. Europhys. Lett. 2001;53:611.
34. Lusceac SA, Roggatz I, Medick P, Gmeiner J, Rössler EA. J. Chem. Phys. 2004;121:4770.
35. Winterlich M, Diezemann G, Zimmermann H, Böhmer R. Phys. Rev. Lett. 2003;91:235504.
36. Hinze G, Diezemann G, Sillescu H. Europhys. Lett. 1998;44:565.
37. Additional discussion of this limit can be found in Böhmer R, Kremer F. In: F Kremer, A Schönhals (Eds). Broadband Dielectric Spectroscopy Springer: Berlin, 2002, p 625–84.
38. Winterlich M. Dissertation, Universität Dortmund, 2003; Winterlich M, Diezemann G, Zimmermann H, Böhmer R. J. Chem. Phys. 2003;123:094504.
39. Schaefer D, Leisen J, Spiess HW. J. Magn. Reson. A. 1995;115:60.
40. Sen S, Stebbins JF. Phys. Rev. Lett. 1997;78:3495.
41. Richert R, Böhmer R. Phys. Rev. Lett. 1999;83:4337.
42. Vogel M, Brinkmann C, Eckert H, Heuer A. Phys. Chem. Chem. Phys. 2002;4:3237.
43. Vogel M, Brinkmann C, Eckert H, Heuer A. Phys. Rev. B. 2004;69:094302 and references cited therein.
44. Berndt S, Jeffrey KR, Küchler R, Böhmer R. Solid State Nucl. Magn. Reson. 2005;27:122.
45. Vogel M, Brinkmann C, Eckert H, Heuer A. J. Non-Cryst. Solids 2002;307–310:971; Solid State Nucl. Magn. Reson. 2002;22:344.
46. Böhmer R. J. Magn. Reson. 2000;147:78.
47. Vogel M. Phys. Rev. B. 2003;68:184301.
48. Vogel M, Rössler E. J. Phys. Chem. A. 1999;102:2102.
49. Kudlik A, Benkhof S, Blochowicz T, Tschirwitz C, Rössler E. J. Mol. Struct. 1999;479:201.
50. Schnauss W, Fujara F, Sillescu H. J. Chem. Phys. 1992;97:1378.
51. Böhmer R, Hinze G, Jörg T, Qi F, Sillescu H. J. Phys.: Condens. Matter 2000;12:A383.
52. Geil B, Hinze G. Chem. Phys. Lett.1993;216:51.
53. Leisen J, Schmidt-Rohr K, Spiess HW. Physica. (Amsterdam) 1993;201A, 79.
54. Qi F, Böhmer R, Sillescu H. Phys. Chem. Chem. Phys. 2001;3:4022.
55. Geil B, Diezemann G, Böhmer R. Phys. Rev. E (submitted); Nowaczyk A, Winterlich M, Geil B, Hinze G, Böhmer R. Phys. Rev. E (submitted).
56. Rugar D, Budakian R, Mamin HJ, Chui BW. Nature 2004;430:329.
57. For a review see, e.g. Köhler J. Phys. Rep. 1999;310:261.
58. Gruber A, Dräbenstedt A, Tietz C, Fleury L, Wrachtrup J, von Borczyskowski C. Science. 1997;276:2012.
59. See, e.g. Th. Basché, WE Moerner, M Orrit, UP Wild. Single-Molecule Optical Detection, Imaging and Spectroscopy. VCH: Weinheim, 1996.
60. Lu HP, Xun L, Xie XS. Science. 1998;282:1877.
61. Ha T, Laurence TA, Chemla DS, Weiss S. J. Phys. Chem. B. 1999;103:6839
62. Deschenes LA, Vanden Bout DA. Science. 2001;292:255.
63. Deschenes LA, Vanden Bout DA. J. Chem. Phys. 2002;116:5850.

Nuclear Magnetic Resonance in Ferromagnetic Multilayers and Nanocomposites: Investigations of Their Structural and Magnetic Properties

C. Mény and P. Panissod
Institut de Physique et Chimie des Matériaux de Strasbourg UMR 7504 ULP-CNRS, 67034 Strasbourg Cedex, France

Introduction

In the past, nuclear magnetic resonance (NMR) studies have proved useful for structural investigations of magnetic multilayers in the direct space and at the atomic scale, complementing standard structural investigations [1]. Actually NMR provides with an original insight into the structural and magnetic characterization of composite nanostructured materials. Indeed the yield of NMR experiments is twofold. On one hand, the NMR spectrum, usually acquired in zero external field, reflects the distribution of hyperfine fields in the sample, and thus gives information about the different chemical configurations and site symmetries in the sample, the different phases, their structure, and their defects. On the other hand, the evolution of the spectral shape against the external field strength and orientation or against the radio frequency field strength probes the magnetic anisotropy or the magnetic stiffness of the electronic moments around the nucleus site, thus providing an information comparable to that given by ferromagnetic resonance (FMR) measurements. Therefore, combining both yields makes it possible to correlate the inhomogeneous magnetic properties of a composite sample to its different structural components [2]. The structural aspects of NMR studies are summarized in the first part of the chapter. Most of the chapter is devoted, though, to the analysis of NMR data in terms of local magnetic properties.

NMR and Atomic Structure

NMR probes primarily the hyperfine field (HF), arising from ordered local magnetic moments around the observed nuclei. HF determines the NMR resonance frequency. Since the moments depend on the local structure and chemical environment, specific structural regions correspond to specific frequency ranges in the NMR spectrum. The relationship between the hyperfine field and the local structure is usually inferred from studies of structurally well-known standard alloys and compounds [3] but theoretical calculations (although difficult) can be undertaken as well [4]. The analysis of the NMR lines yields the fractions of atoms involved in the various atomic configurations or structural components in a sample. For example, in a perfect Co/X multilayer, the spectrum should exhibit two narrow lines only, one for the bulk part of the Co layers (close to the frequency of bulk ferromagnetic Co) and one for Co atoms at the interfaces. An example Co NMR spectrum observed in a Co/Cu multilayer is shown in Figure 1. The layered structure is obviously far from perfect here. The spectrum can be coarsely separated into three parts: a main line at 215 MHz corresponding to bulk Co with fcc structure, a set of shoulders at higher frequencies corresponding to Co in hcp-like environments (bulk hcp Co at 225–228 MHz, stacking faults at 220–225 MHz), and a set of lines below 200 MHz corresponding to Co atoms with at least 1 Cu among their 12 nearest neighbors (Co atoms at the Co/Cu interfaces). The main line frequency is slightly lower than that of pure fcc Co (217 MHz), which is due to the expansive strains resulting from the difference between Co and Cu lattice constants [5]. The extended tail observed in the low frequency range is typical of diffuse interfaces, but a small fraction of sharp interface areas is evidenced by the well-defined peak at 165 MHz, which corresponds to Co with three Cu nearest neighbors at perfect ⟨1 1 1⟩ interfaces [1]. In samples with interface spectra extending over a spectral range corresponding to a spread of nearest neighbor (NN) configurations A_nB_{Z-n} around the probed nuclei (say B), modeling the spectral shape does provide more quantitative information about intermixing at the interfaces (short-range admixture). Simulated spectra consist of a sum of $Z+1$ lines ($Z = 12$ NN in compact structures), arising from B nuclei surrounded by $(Z-n)$ B atoms and (n) A atoms. The different lines are, in most cases, equally spaced [3]. Considering a model (topological and chemical) of the interface structure, configuration probabilities (line intensities) can be calculated, which are used to reconstruct the spectrum. The refined parameters obtained from the fitting procedure give a direct insight on the short-range order at the interfaces. Figure 2 illustrates

Graham A. Webb (ed.), Modern Magnetic Resonance, 1493–1498.
© 2008 *Springer.*

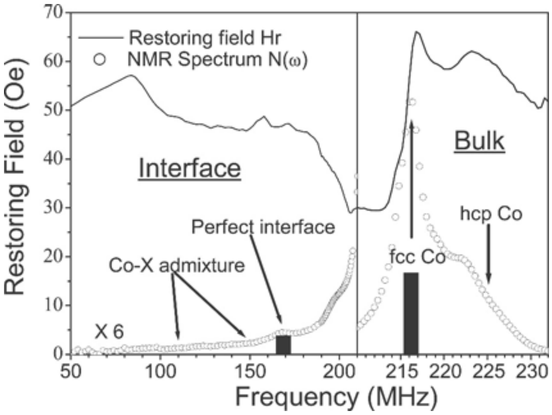

Fig. 1. Open circle: Co NMR spectrum recorded in a typical Cu/Co multilayer. The left part: interfacial components; right part: bulk components. The thick vertical bars represent the spectrum that should be observed for a perfect Co/Cu multilayer. Full line: Frequency dependence of the restoring field strength showing the magnetic softness of the interface (below 210 MHz) and the hardness of the bulk of the layers (above 210 MHz).

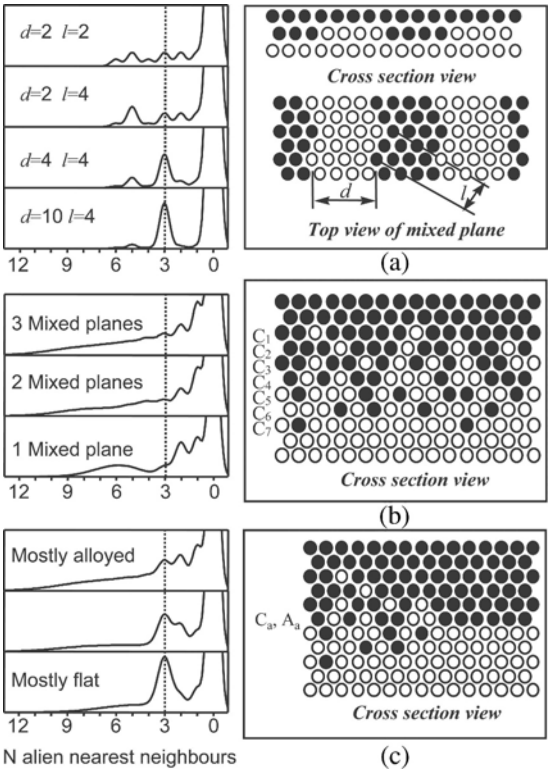

Fig. 2. Basic interface models for the simulation of buried interface spectra. (a) Monoatomic step defect model (d, the average distance between steps and l, the average distance between kinks are the parameters of the model, in atomic distance units) and (b) diffuse interface model with a linear concentration profile. (c) Pure Co and alloy patches—hybrid model consisting of clusters with sharp interfaces separated by diffuse areas. (C_a, concentration of the alloy in the atomic plane and A_a, area fraction of the alloy in the plane are the parameters of the model.)

some models that have been successfully used to describe the interface spectra of Co/X multilayers [1]. Note that the expected spectral shapes are quite different between the different models, which shows that the different types of interface structure can be easily discriminated (see Figure 2 legend for more details about the model parameters). For example, the interface spectrum of the sample in Figure 1 can be fitted with model C mostly alloyed.

Local Magnetic Moments—Hyperfine Field and Magnetization Profiles

The direct yield of an NMR experiment in magnetic materials is the hyperfine field produced by the spontaneous electron spin polarization at the observed nuclei. As such the measurement provides a direct insight, element and site specific, onto the electronic moment values and, possibly, the magnetic structure. This rather standard aspect is not developed here. Let us only mention that, in multilayers where there are several mixed planes at interfaces, the analysis of the interface concentration profile yields also the average HF for each atomic plane, which reflects the magnetization profile at the interfaces [2].

Zero-Field NMR—Local Restoring Field and Magnetic Stiffness

In magnetic materials, a DC external field is not necessary because the spontaneous magnetic moment creates a large internal field, the HF, at the nuclei. In addition, the nuclei are not directly excited by the external radio frequency field H_1 but by the oscillation of HF following the electronic moment response to H_1. The radio frequency field experienced by the nuclei ($B_\perp$) is therefore strongly enhanced compared to the external one (H_1). This enhancement, related to the transverse susceptibility of the samples (and therefore sample dependant), is often characterized by the so-called enhancement factor $\eta = B_\perp / H_1 = HF/H_r$, where H_r is the effective field that restores the equilibrium position of the electronic moments. When the NMR signal is recovered, the reverse process occurs: the precessing transverse nuclear magnetization exerts a torque on the electronic magnetization,

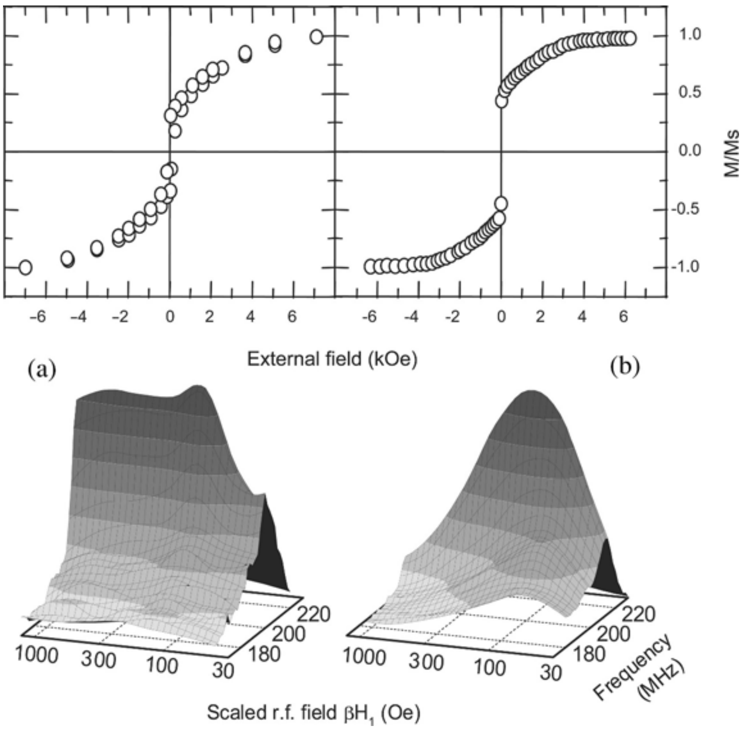

Fig. 3. Co/Cu multilayers with a large antiferromagnetic coupling showing similar magnetization loops (top panels) but very different degrees of coherence in their magnetization process (bottom panels). (a) Case of broad distribution of restoring field (inhomogeneous coupling). (b) Case of homogeneous magnetization process (homogeneous noncollinear coupling).

which is thus driven into rotation (or oscillation). Since the actual signal in the probe coil is mostly induced by the electronic magnetization, it is thus enhanced by the same factor η. Actually, there is a spread of enhancement factor values within a sample, which results from the distribution of magnetization orientation, demagnetizing field, etc. [6]. The resulting enhancement factor distribution is the convolution product of these distributions and tends to a lognormal distribution. Therefore, the spin-echo intensity in a single-phased magnetic material has a Gaussian dependence upon $\log(H_1)$ and can be expressed as a function of the external radio frequency field amplitude H_1 and frequency ω according to [7]:

$$S(H_1,\omega) \propto \langle\eta\rangle \exp[-\log^2(H_1/H_{\mathrm{opt}})/2\sigma^2]\omega^2 N(\omega)\gamma \times I(I+1)/T, \qquad (1)$$

where $\langle\eta\rangle$ is the average enhancement factor, $N(\omega)$ the nucleus density (the "true" NMR intensity), σ the width of the Gaussian distribution in $\log(H_1)$, and H_{opt} the radio frequency field value for which the signal is maximum. In a pulsed NMR experiment, the signal is maximum when the nuclear spins experience an effective radio frequency field strength such that, after the pulse sequence, the nuclear magnetization is perpendicular to HF: $\gamma\langle\eta\rangle H_{\mathrm{opt}}\tau = \pi/2$. Therefore, the radio frequency field strength for which the NMR signal is maximum measures directly the average sample enhancement factor. More recently, rather than using a dimensionless factor to characterize the sample stiffness, we have chosen to use the restoring field $H_{\mathrm{r}} = \mathrm{HF}/\langle\eta\rangle$. This restoring field is directly proportional to $H_{\mathrm{opt},}$ i.e. $H_{\mathrm{r}} = \beta H_{\mathrm{opt}}$ with β depending only on the probed nucleus (γ) and on the experimental setup. The restoring field has the advantage to be quantitatively comparable to macroscopic magnetic data (anisotropy field, coercive field, or exchange bias field) [2,8]; it is also the field that defines the resonance frequency in FMR experiments. In order to measure H_{r}, one has to record a set of spectra for several values of the radio frequency power. If the radio frequency field strength is scaled as βH_1, then H_{r} is directly read as the position of the maximum signal intensity on the βH_1 axis of the 2D NMR spectrum (Figure 3). Considering that each frequency range is associated with a specific region of a composite sample, such 3D plot images directly the structural inhomogeneities, along the frequency axis (NMR), and the magnetic inhomogeneities, along the radio frequency field axis. Therefore, the projection of the line of crest on the base plane yields the frequency, i.e. structural, dependence of the restoring field.

As an example, Figure 1 displays the 1D NMR spectrum $N(\omega)$ of a typical Co/Cu multilayer and the frequency dependence of the restoring field strength acting on Co moments. It can be observed that the interface moments (below 210 MHz) are magnetically softer than the bulk moments (210–230 MHz). This is a rather general observation in multilayers and shows that the magnetic moments rotate more easily in the interface planes than in bulk planes. This is a consequence of the lower number of magnetic neighbors and the reduction of the moment in the mixed interfaces. It is often observed that the coercive field of the layer corresponds to the value of H_r measured by NMR at the interfaces. As first noticed by Thomson *et al*. [8], this is a strong indication that the magnetization reversal is initiated at interfaces.

The restoring field of each frequency region can also be compared from sample to sample. For example, it is generally found in metallic multilayers that the coupling between the magnetic layers oscillates between ferromagnetic and antiferromagnetic as a function of the non-magnetic spacer thickness: this results from a Ruderman–Kittel–Kasuya–Yoshida (RKKY) like mechanism [9]. Such coupling strength oscillations are readily observed on the restoring field measured by NMR but, again, interface and bulk moments behave differently. For example, in Co/Ru multilayers, the oscillations of H_r resulting from the coupling have a larger amplitude at the interfaces than in the bulk [2]. The latter observation is readily explained by the fact that the antiferromagnetic coupling acts first between two interfaces through Ru. Therefore, its contribution to the restoring energy is expected to be larger at the interface planes than in the bulk of the Co layers.

The examples presented until now have pointed out the magnetic differences between different parts of the magnetic layers that are selected by their different NMR frequency range. Besides that the variation of the NMR signal with the RF field strength may evidence a more global magnetic inhomogeneity. Such inhomogeneity is revealed by the observation of very broad $S(H_1)$ curves with several peaks. The usefulness of the observation is illustrated by the example (Figure 3) of two Co/Cu multilayers. The magnetization loops of the two samples are similar (a rapid increase at low field followed by a slow saturation). Such curves can be interpreted as resulting from the inhomogeneity of the coupling strength, parts of layers being antiferromagnetically coupled and others being ferromagnetically coupled. Alternatively, one can interpret them in terms of homogeneous non-collinear coupling [10]. The NMR observation in the first multilayer shows a very broad distribution of restoring field in its 3D curve $S(\omega, H_1)$ that proves the inhomogeneous nature of the magnetization process (coupling inhomogeneities). On the contrary, the second multilayer exhibits a quite narrower distribution of H_r, which is consistent with a homogeneous magnetization process (non-collinear coupling).

Magnetic Phase Separation

If a material consists of several phases, more than one Gaussian distribution of $\log(\eta)$ is needed to describe the signal intensity as a function of the excitation field. In favorable cases, i.e. when the different phases in a sample have largely different structure and magnetic stiffness (by a factor of 3 at least), it is possible to separate the spectra arising from each of the phases and to determine their average restoring field and enhancement factor. The example shown in Figure 4 is that of a granular CoCu alloy [11]. Figure 4a shows the βH_1 dependence of the spin-echo intensity at two exemplary frequencies: 200 and 215 MHz. At both frequencies, two Gaussian distributions had to be used: a soft one: $H_r \sim 0.9$ kOe and a hard one: $H_r \sim 6.4$ kOe. Figure 4b displays the NMR spectrum recorded for $\beta H_1 = 2$ kOe as well as its hard and soft components that are deduced by fitting $S(H_1)$ with two η distributions at each frequency. The spectrum corresponding to the softer component is typical of a CoCu alloy (smooth and broad frequency spread of the NMR intensity), while

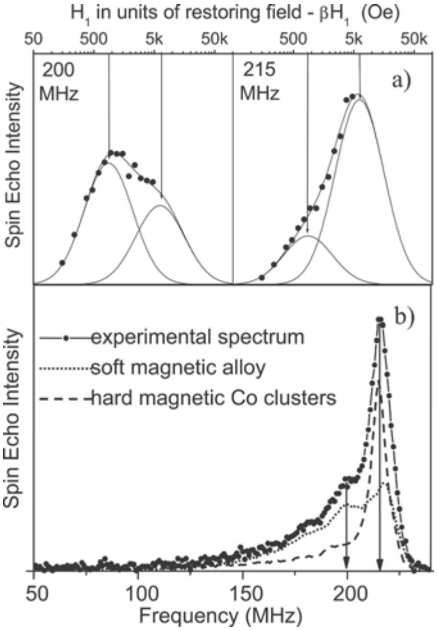

Fig. 4. CoCu melt spun granular alloy. (a) Spin-echo intensity vs. H_1 strength at two exemplary frequencies showing the existence of two magnetic phases (two restoring fields). (b) ^{59}Co spectrum and its decomposition into the spectra of the soft and hard phases.

the hard phase is dominated by a sharp pure fcc Co peak. The low frequency tail of this line is strikingly similar to the spectrum observed in Co/Cu multilayers with rough interfaces but limited interdiffusion. The interfacial intensity amounts to about 50% of the total intensity indicating that these Co clusters have a large surface to volume ratio, which can be understood if they are flat or needle like.

In Field NMR—Local Magnetic Anisotropy

Besides zero-field measurements, an external DC field is applied sometimes in order to saturate the magnetization. This is mostly used to remove domain walls or to perform standard, field swept, spectrum recording. In the experiments that are reported in this section, the external field dependence is used in a similar way as in standard magnetometric methods, i.e. in order to follow the magnetization process. However, all these measurements are, of course, analyzed at selected frequencies and, therefore, they probe the local magnetization process.

When the variation of the resonance frequency is studied vs. the external field orientation it allows the investigation of the anisotropic properties of the sample. This kind of in-field NMR experiment parallels closely torque magnetometry measurements. It must be performed on a single crystal, or at least, an oriented sample. Based on the fact that the resonance frequency is proportional to the vector sum of the external field and HF, the angles between HF, the moment, and the external field can be measured which yields quantitatively the magnetic anisotropy in frequency-selected components of the sample. The method has been employed by de Gronkel *et al.* [12] in order to determine the local magnetic anisotropy of the fcc and hcp components of mixed thin Co films.

When a small DC external field is applied to a multidomain ferromagnet, the resonance frequency does not shift immediately as expected. This is due to the compensation between the external field and the demagnetizing field that increases as the sample magnetizes. However, in small single domain particles the resonance line starts shifting from the smallest field values. The bimodal distribution of sizes of Co clusters embedded in silica has been demonstrated this way. As seen in Figure 5, the NMR spectrum observed in the samples consists in two main lines: at 217 MHz a standard line arising from large, multidomain, fcc Co clusters that does not shift with increasing field, and, at 223 MHz, another line that shifts exactly as $-\gamma_{\mathrm{Co}} H_{\mathrm{ext}}$ (a minus sign because in transition metals HF is antiparallel to the magnetization). Therefore, the 223 MHz line has to be attributed not to hcp Co but to small fcc Co spheres, the 6 MHz up shift being due to the 6 kOe demagnetizing field that adds to HF [13].

Finally, when the DC field strength is large enough to yield a single domain state, the restoring field is the vector sum of the external field H_{ext} and the anisotropy field H_{an}. Hence, when H_{ext} is applied along the easy magnetization axis, the enhancement factor is $\mathrm{HF}/(H_{\mathrm{ext}} + H_{\mathrm{an}})$ and the signal intensity varies as $1/(H_{\mathrm{ext}} + H_{\mathrm{an}})$ with the external field strength. Therefore, in a similar manner as through the measurement $S(\beta H_1)$, the local magnetic anisotropy can be measured through the variation of the signal intensity vs. the DC field strength. This has been applied by Thomson *et al.* [8] on Co/Cu Multilayers for bulk and interface Co atoms.

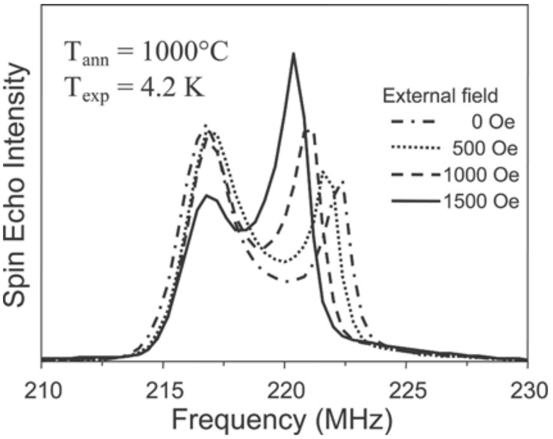

Fig. 5. ^{59}Co spectra of cobalt granules in silica showing two populations of sizes. At 217 MHz: large multidomain fcc Co clusters (do not shift under field). At 223 MHz: small single domain fcc Co clusters (shift under field). The spacing between the two lines in zero field is due to the demagnetizing field (6 kOe) in the single domain spheres.

Conclusions

In this paper, we have shown that NMR is a unique tool to correlate the nanostructure of composite magnetic materials and their magnetic properties. In summary, because they contribute to the NMR spectrum at different frequencies, different regions of the samples can be selected and their magnetic properties can be separately probed.

Besides the magnetic inhomogeneity that is expected from the composite design of the nanomaterials, such as the magnetization and magnetic stiffness profiles at multilayer interfaces, NMR can also image directly large inhomogeneities of interactions and/or anisotropy between the magnetic components. This may help to discriminate between various interpretations of the magnetization process of the composite structure.

Ultimately, such studies can help to identify the various magnetic phases that may be present in a composite sample, from both structural (topology and chemical nature) and magnetic (anisotropy and stiffness) viewpoints.

References

1. Panissod P, Jay JP, Mény C, Wójcik M, Jedryka E. Mat. Res. Soc. Proc. 1995;384:61; Panissod P, Jay JP, Mény C, Wojcik M, Jedryka E. Hyperfine Int. 1996;97–8:75; Riedi PC, Thomson T, Tomka G. In: KHJ Buschow (Ed). Handbook of Magnetic Materials. Elsevier, 1999;12:97–258.
2. Panissod P, Mény C, Wójcik M, Jedryka E. Mat. Res. Soc. Proc. 1997;475:157.
3. Mény C, Jedryka E, Panissod P. J. Phys. Condens. Matter 1993;5:1547.
4. Akai H, Akai M, Blügel S, Drittler B, Ebert H, Terakura K, Zeller R, Dederichs PH. Prog. Theor. Phys. 1990;(Suppl 101):11.
5. van Alphen EAM, de Velthuis SGE, de Gronckel HAM, Kopinga K, de Jonge WJM. Phys. Rev. B 1994;49: 17336.
6. Stearns MB. Phys. Rev. 1967;162:496.
7. Jay JP (1995) and Mény C (1994), PhD thesis, Université Louis Pasteur, Strasbourg; Panissod P, Mény C. Appl. Magn. Reson. 2000;19:447.
8. Thomson T, Kubo H, Lord JS, Riedi PC, Walker MJ. J. Appl. Phys. 1994;76:6504.
9. Bruno P. Phys. Rev. B. 1995;52:411.
10. Slonczewski JC. Phys. Rev. Lett. 1991;67:3172.
11. Malinowska M, Wojcik M, Nadolski S, Jedryka E, Mény C, Panissod P, Knobel M, Viegas ADC, Schmidt JE. J. Magn. Mater. 1999;198–9:599.
12. de Gronkel HAM, Bloemen PJH, van Alphen EAM, de Jonge WJM. Phys. Rev. B. 1994;49:11327.
13. Gossard AC, Portis AM, Rubinstein M, Lindquist RH. Phys. Rev. 1965;138:1415.

^{1}H Solid-State NMR of Supramolecular Systems

Ingo Schnell and Hans Wolfgang Spiess
Max Planck Institute for Polymer Research, Postfach 3148, 55021 Mainz, Germany

Introduction

Dipolar recoupling NMR experiments of protons and other spin-$\frac{1}{2}$ nuclei in solids, performed under fast magic-angle spinning (MAS), provide new and versatile spectroscopic tools, by use of which topics of general interest in materials science and bioscience can be addressed. For instance, in advanced synthetic as well as biological systems, self assembly of carefully chosen building blocks is of central importance [1–4]. Hydrogen bonding and aromatic π–π interactions are key features of supramolecular chemistry [5]. Despite being highly ordered on a local scale, such systems often do not crystallize. Therefore, their structures cannot be determined by conventional X-ray crystallography or neutron scattering. Hence, alternative characterisation methods are needed that provide information on molecular structure and dynamics, and preferably require only small amounts of as-synthesized samples without isotopic enrichment. Due to their high natural abundance of protons in organic solids, ^{1}H NMR spectroscopy meets these requirements [6–8] when fast MAS [9,10] ensures sufficient resolution of ^{1}H chemical shifts [11]. In case the selectivity provided by ^{1}H resonances is insufficient, a whole set of heteronuclear ^{1}H-X dipolar recoupling schemes (primarily with X = ^{13}C,^{15}N) has recently been developed [12–14], which combine information on ^{1}H chemical shifts or ^{1}H–X dipole–dipole couplings with the increased site resolution of X chemical shifts. These techniques take advantage of the significant simplification of the dipolar-coupled multispin network due to the decoupling performance of fast MAS [15].

Since MAS with spinning frequencies of 30 kHz and more became commercially available in 1998, the development of solid-state ^{1}H–^{1}H and ^{1}H–X dipolar recoupling methods has systematically been pursued by combining fast MAS and dipolar multiple-quantum (MQ) NMR spectroscopy [11,14], including in particular ^{1}H–^{1}H double-quantum (DQ) NMR spectroscopy. The latter method makes use of the homonuclear dipole–dipole coupling between the involved spins and thus inherently combines information on ^{1}H chemical shifts with the information on the mediating ^{1}H–^{1}H coupling. In studies of supramolecular systems, fast-MAS NMR methods have provided new insight into hydrogen-bonded structures in the solid state [16–20], columnar stacking and molecular dynamics of discotics [14,18,21,22], chain order and translational motion in polymer melts [23,24], and others. In this article, these new approaches for studying supramolecular organization will briefly be outlined, and their capabilties and advantages will be demonstrated on three examples.

High Resolution Solid-State NMR

Various aspects of solid-state NMR are subjects of other articles of this Handbook. For a full treatment of earlier work including multi-dimensional NMR techniques, please also refer to the extended monograph [25].

Magic Angle Spinning

A recent advance of particular importance to solid-state NMR is the availability of fast MAS with spinning frequencies of 25–60 kHz, as pioneered by Samoson [10]. For most organic solids, this means that the MAS frequency exceeds the strongest dipole–dipole couplings which are of the order of 20 kHz, e.g. in CH_2 groups with a proton–proton and proton–carbon distances of about 180 and 110 pm, respectively. Moreover, given such a strong coupling, the remaining spins are in most cases coupled over longer distances, so that the corresponding remote couplings are weaker and thus more efficiently averaged by MAS. In this way, MAS simplifies the complex behaviour of multispin coupled networks to a superposition of two-spin correlations which are dominated for each spin by its strongest coupling(s) to its closest-neighbour(s). This simple picture is indeed borne out in an elaborate theoretical treatment of multi-spin systems under fast MAS, combining Floquet theory and perturbation theory [15]. The higher-spin contributions are found to scale with increasing powers of the inverse rotor frequency and become less and less important at higher and higher MAS rates.

Thus, the dipolar decoupling effect of fast MAS has a two-fold implication for MAS-NMR experiments: Firstly, maximum spectral resolution is accomplished for densely coupled spins, such as ^{1}H, as soon as higher-spin correlations are efficiently suppressed, because the dominating two-spin correlations behave inhomogeneously under

Graham A. Webb (ed.), Modern Magnetic Resonance, 1499–1506.
© 2008 *Springer.*

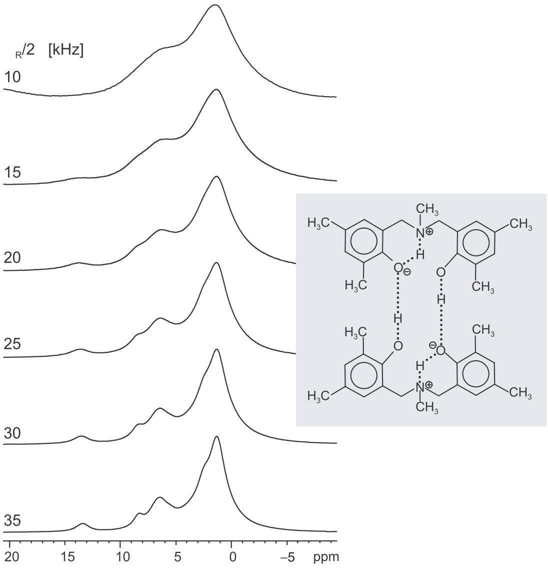

Fig. 1. Spectral resolution achievable at MAS frequencies between 10 and 35 kHz in the ^{1}H solid-state MAS spectrum of a crystalline hydrogen-bonded benzoxazine dimer, the chemical structure of which is depicted in the inset.

MAS, according to the terminology introduced by Maricq and Waugh [26], and therefore do not contribute to the width of the resonance line. Secondly, dipolar recoupling schemes will first re-introduce the dominating pair coupling and establish the respective pair correlation with relatively high selectivity before, at longer recoupling times, the whole multispin network forms again through multiple couplings. Consequently, the dominating coupling(s) can be measured by means of recoupling experiments with high accuracy.

Figure 1 shows ^{1}H NMR spectra recorded at different MAS frequencies on a crystalline benzoxazine dimer as an example [16] to illustrate the dipolar-decoupling and line-narrowing performance of MAS. It is obvious from Figure 1 that, for ^{1}H spectra of rigid solids, MAS needs to be applied at frequencies $\geq$ 25 kHz. At higher spinning frequencies, the resolution still increases very gradually, but the maximum resolution is not only determined by the technically available MAS frequencies, but also by the material itself. When the degree of crystallinity, i.e. the structural order, of a material is not perfect, the local distributions of electrons around the nuclei are affected by local disorder or variations of the packing structure. These phenomena give rise to dispersions of the chemical shifts and, thus, to an inherent line width, which cannot possibly be reduced by averaging techniques. Therefore, in amorphous samples, maximum ^{1}H resolution is often found to be achieved at MAS frequencies of about 30–35 kHz, and faster spinning would not further increase the spectral resolution.

Dipolar Recoupling Schemes

The fast-MAS NMR experiments considered in this article employ sequences of strong radio-frequency (RF) pulses separated by delays, during which the spin system evolves under the internal interactions. These pulse sequences are often referred to as “laboratory frame” sequences [27,28], because the quantisation axis is given by the static magnetic field B_0 along the laboratory z-axis. “Rotating frame” pulse sequences, in contrast, are characterised by a continuous application of RF fields, so that the spin system evolves no longer freely but in the presence of transverse RF fields. Levitt and coworkers have introduced a general and powerful concept by means of which the recoupling (and decoupling) properties and performances of pulse sequences can be analysed in terms of generalised symmetry properties [29]. Based on this concept, a number of pulse sequences have been proposed for various purposes, and a few of them are also applicable under fast MAS conditions, i.e. at spinning frequencies $\geq$25 kHz.

The principle of laboratory-frame recoupling pulse sequences is well established [27,28], and can easily be understood by considering the rotor modulations,which are introduced by the sample rotation. The spatial parts of the interaction Hamiltonians are modulated by the MAS frequency ω_R and twice the MAS frequency $2\omega_R$. For illustration, the respective oscillations are depicted in Figure 2b. By averaging—in other words: integrating—over a full rotor period, the modulated interactions vanish because positive and negative parts of the oscillations cancel each other. An obvious way to avoid this cancellation is to invert the sign of the spin part by a pulse sequence simultaneously to the sign changes imposed on the spatial part by MAS. Effectively, recoupling is accomplished by inducing a “counter-rotation” in spin space relative to MAS rotation in real space. As there are two modulation frequencies, ω_R and $2\omega_R$, the sign change in the spin part can be performed in intervals of either $\tau_R/2$ or $\tau_R/4$ [30].

The type of RF pulses required for this sign inversion depends on the nature of the spin part of the respective interaction. For interactions depending linearly on a spin (i.e. CSA and heteronuclear dipole–dipole couplings), the sign inversion is straightforwardly achieved by π pulses. The approach of utilizing π-pulse trains with pulse spacings of $\tau_R/2$ was first realised in the REDOR experiment, which was initially introduced by

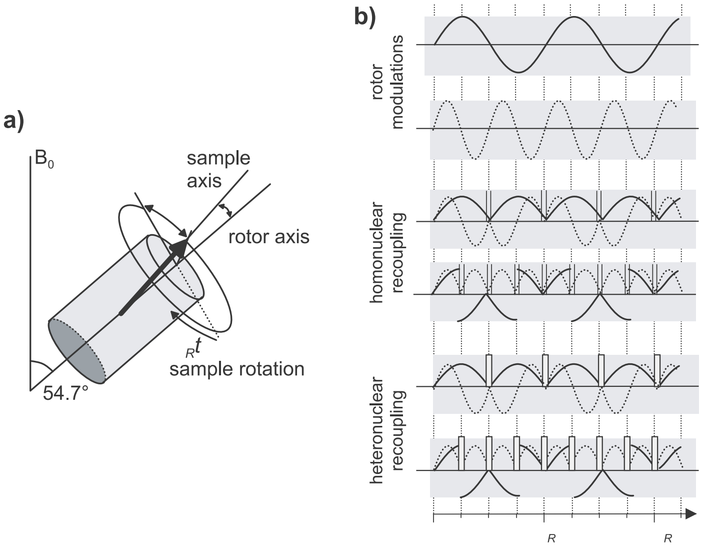

Fig. 2. (a) Geometric relations under MAS conditions, including the definition of the angles β and γ. They relate the main axis of a tensor representing a symmetric anisotropic interaction to the rotor and the magnetic field axes. (b) Modulations of an anisotropic interaction under MAS (top) and pulse sequences for recoupling interactions which depend on the nuclear spin in a bilinear (middle) or linear fashion (bottom). The pairs of $\pi/2$-pulses and the π-pulses (bottom) recouple homonuclear and heteronuclear dipole–dipole couplings, respectively.

Schaefer and Gullion [31,32] in order to recouple the heteronuclear dipole–dipole couplings between two kinds of low-γ nuclei. Interactions with a bilinear spin dependence (i.e. homonuclear dipole–dipole and quadrupole couplings) can be recoupled in an analogous fashion by the so-called Back-to-Back (BaBa) pulse sequence [11]. In this sequence, each π-pulse of REDOR-type recoupling is replaced by a pair of $\pi/2$-pulses with orthogonal phases. Effectively, these pairs of $\pi/2$-pulses invert the sign of the spin part of the homonuclear dipole–dipole and quadrupole coupling.

Rotor Encoding and Sideband Patterns

The ^{1}H–^{1}H DQ MAS experiments discussed in this article follow the principal scheme depicted in Figure 3a. While fast MAS is continuously applied, dipole–dipole couplings are recoupled by appropriate pulse sequences (BaBa) during two periods. These are separated by an indirect spectral dimension t_1, which is inserted to shift the phases of the two recoupling blocks relative to each other and/or to record a ^{1}H spectrum with DQ chemical-shift resolution. At the end of the pulse sequence, the ^{1}H signal is detected during the direct spectral dimension t_2. An efficient and sensitive way of measuring anisotropic interactions in general, and ^{1}H–^{1}H dipole–dipole couplings in particular, is the generation of spinning sideband patterns via rotor encoding (RE) of the recoupled interactions [11,33]. Such rotor encoding is accomplished by combining two recoupling blocks with different initial rotor phases, meaning that the second block is shifted with respect to the first by a time t_1, which is incremented in steps $\Delta t_1 < \tau_R$. The amplitude of the recoupled signal is then modulated according to [11]

$$S_{\sin}(t_1) \propto \sin(N_{\text{exc}}\Phi_{\omega_R}(0)) \cdot \sin(N_{\text{rec}}\Phi_{\omega_R}(t_1)) \qquad (1)$$

where the phase Φ_{ω_R} is determined by the dipole–dipole coupling constant D_{ij} and the orientation of the coupling vector relative to the rotor axis (angles β and γ):

$$\Phi_{\omega_R}(t) = \frac{3D_{ij}}{\omega_R} \cdot \sqrt{2}\sin 2\beta \cdot \sin(\omega_R t + \gamma) \qquad (2)$$

The time t_1 represents the delay between the two recoupling blocks, and N_{exc} and N_{rec} denote the numbers of rotor periods during which the first and second recoupling sequence is applied (referring to "excitation" and "reconversion", respectively). An example for sidebands arising from the recoupling of a ^{1}H–^{1}H dipole–dipole coupling is given in Figure 3b. The sideband patterns shown there correspond to the expression given in Equation 1.

^{1}H–^{1}H Double-Quantum Spectroscopy

Homonuclear DQ NMR spectroscopy is based on the generation of DQ coherences (DQCs) via homonuclear dipole–dipole couplings. Under MAS conditions, dipolar recoupling pulse sequences are applied to excite DQCs

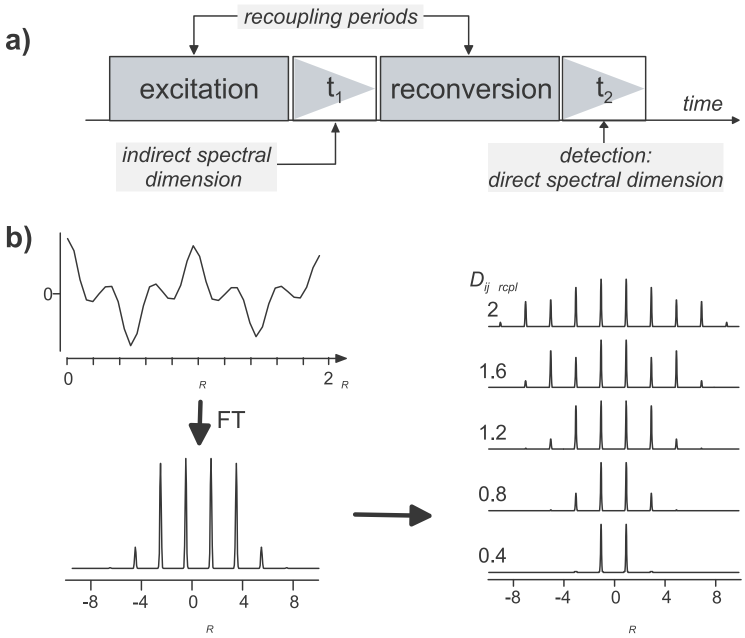

Fig. 3. (a) Schematic representation of the two-dimensional recoupling experiments described in this article. (b) Modulations of the t_1-signal arising from rotor-encoding in a dipolar ^{1}H–^{1}H DQ experiment performed under ω_R-recoupling conditions. The corresponding sideband patterns are shown below, together with the dependence of the sideband patterns on the product of the dipole–dipole coupling and the recoupling time (on the right).

and, subsequently, to reconvert them back into observable magnetisation. Accordingly, the overall recoupling time τ_{rcpl} can be split up into an excitation time τ_{exc} and a reconversion time τ_{rec}. The intensity of a DQ signal sensitively depends on the coupling D_{ij} between the respective pair of nuclei i and j. In the limit of short excitation/reconversion times, i.e. $D_{ij}\tau_{\text{exc/rec}} \ll 1$, the signal intensity is proportional to $D_{ij}^2\tau_{\text{exc}}\tau_{\text{rec}}$ [19]. Therefore, DQ signal intensities can be used as a qualitative and even semi-quantitative measure for internuclear distances [18] and molecular motions [23].

In most fast-MAS work on protons, the simple BaBa sequence is used for dipolar recoupling, as it proved to be extremely robust and easy to use. Two nested phase cycles consisting of four steps each are used to select the coherence transfer pathway $0 \rightarrow 2 \rightarrow 0 \rightarrow -1$ with an overall 16-step phase cycle. For ^{1}H–^{1}H DQ spectroscopy under fast MAS (30 kHz spinning with $\tau_{\text{exc}} = \tau_{\text{rec}} = \tau_R$), DQ signals are expected in a solid material for all proton pairs with a distance of less than approximately 0.4 nm [11,16]. In the DQ dimension, the chemical shift of the signals correspond to the sum of the chemical shifts of the two nuclei, A and B, involved in the DQC: $\omega_{AB} = \omega_A + \omega_B$. In the single-quantum (SQ) dimension, the signal splits up into the two single-spin resonances, ω_A and ω_B, so that for $\omega_A = \omega_B$ a single peak is found on the so-called DQ "diagonal", while for $\omega_A \neq \omega_B$ pairs of signals are located at either side of the DQ "diagonal".

Applications to Supramolecular Structures

Hydrogen Bonds in Bilirubin

Bilirubin is an unsymmetrically-substituted tetrapyrrole dicarboxylic acid, which is found in the body as a product of the metabolism of haemoglobin from red blood cells [18]. The involvement of the carboxylic acid groups in strong intramolecular hydrogen bonding renders bilirubin effectively insoluble in aqueous solution. In Figure 4a, the distances between the hydrogen-bonded protons as well as their geometrical arrangement are specified. Usually, the exact localisation of protons by X-ray scattering is very difficult. Indeed, in the first X-ray single-crystal study [34], the positions of the vital hydrogen-bonded protons were very poorly defined. Furthermore, although Le Bas *et al.* went to considerable trouble to obtain a single crystal of suitable quality to allow the location of the hydrogen-bonded protons, they were still forced to artificially calculate the position of one of the three hydrogen-bonded protons in each half of the bilirubin molecule [35]. Therefore, an alternative determination of the proton positions by solid-state NMR is of particular interest.

Figure 4b shows the region corresponding to the hydrogen-bonded protons of a rotor-synchronised ^{1}H–^{1}H DQ-MAS spectrum recorded on bilirubin at a MAS frequency of 30 kHz using one rotor period of BaBa recoupling to excite and reconvert the DQCs. Only the proton corresponding to the middle hydrogen-bonded peak at 10.8 ppm can then be seen to be in close proximity to both the other two hydrogen-bonded protons. By reference to the intramolecular hydrogen-bonded arrangement known from the single-crystal X-ray investigation, the peak at 10.8 ppm can be assigned to the lactam NH proton. From the DQ projection in Figure 4b, it is apparent that the pair of DQ peaks involving the SQ resonances at 10.8 and 9.1 ppm are significantly more intense than the other pair. Considering the intensities of the respective DQ peaks, the SQ resonances at 9.1 and 13.9 ppm can be assigned to the pyrrole NH and carboxylic acid OH protons, respectively.

The ^{1}H–^{1}H DQ MAS spinning-sideband pattern obtained for the lactam NH^1 resonance of bilirubin (at 10.8 ppm) is shown in Figure 4c, which was recorded at 30 kHz MAS using the BaBa sequence with $\tau_{\mathrm{exc/rec}} = 2\tau_R$. It is evident that the highest-order spinning sidebands are only observed for the NH^1–NH^2 pair. This immediately indicates, in agreement with the rotor-synchronised ^{1}H–^{1}H DQ MAS spectrum, that the dipolar coupling is the largest, and hence the proton–proton distance is the shortest, for NH^1–NH^2. Nevertheless, the longer recoupling time yields a meaningful sideband pattern also for the weaker OH–NH^1 coupling, so that both distances can be determined [18]. A sideband pattern, calculated assuming an isolated proton pair, is shown in Figure 4c as a dotted line with a slight displacement from the experimental peaks. A fitting procedure results in the coupling value and internuclear distance given in Figure 4c, which were also used for the calculated patterns. The determined proton–proton distance is accurate within an error margin of about ± 3 pm. From a detailed analysis of a set of spinning sideband patterns, the OH–NH^1 proton–proton distance as well as the H–H–H angle could also be determined as $r_{\mathrm{HH}} = 230$ pm and $122° \pm 4°$, respectively [18].

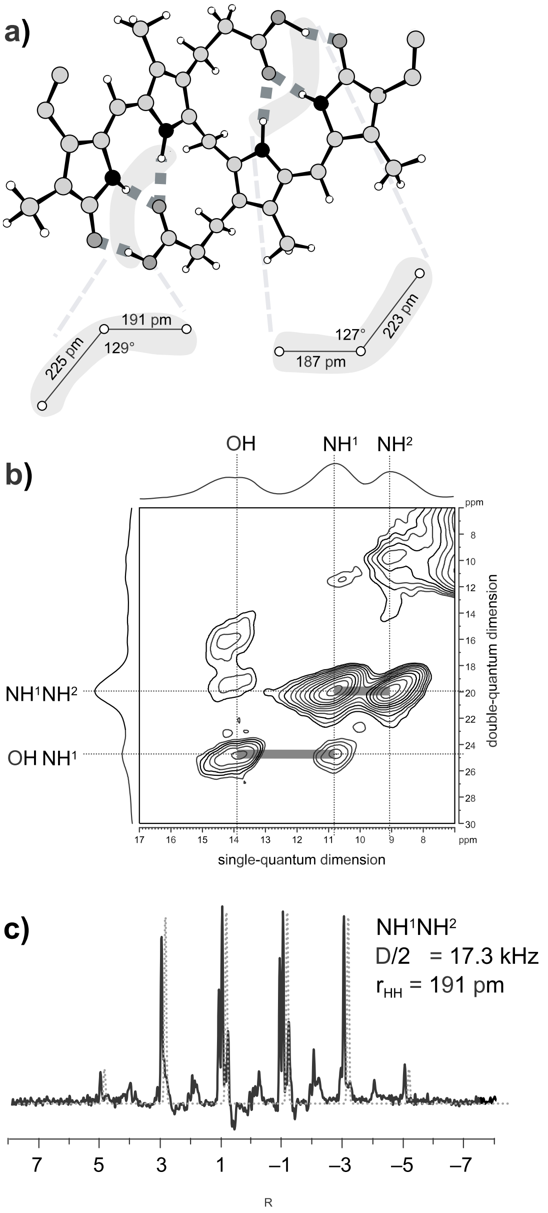

Fig. 4. (a) Chemical structure of bilirubin. The molecules form six intramolecular hydrogen bonds whose geometry is depeicted below. (b) Rotor-synchronised ^{1}H–^{1}H DQ MAS spectrum (700.1 MHz, 30 kHz MAS, BaBa recoupling, $\tau_{\mathrm{exc}} = \tau_R$) of bilirubin. The region of the hydrogen-bonded protons is shown, and the DQ peaks between hydrogen-bonded protons are highlighted. (c) ^{1}H–^{1}H DQ sideband pattern of the NH^1–NH^2 DQ signal (700.1 MHz, 30 kHz MAS, BaBa recoupling, $\tau_{\mathrm{exc}} = 2\tau_R$), indicating a proton–proton distance of 191 pm.

Packing Structures in Benzoxazines

Supramolecular structures influenced by self-assembly and hydrogen bonding are frequently observed in polymeric architectures, and polybenzoxazines are a classic example of such a structure [16]. They exhibit a number of unusual properties [36–39], which have been attributed to the unique intra- and intermolecular hydrogen bonding structure found in these materials, and therefore, this property has been the focus of recent investigation. In particular, extensive crystallographic, NMR and IR studies of the dimer precursors have provided much insight [40]. In particular, the *N*-alkyl subsituent was found to significantly influence the overall packing structure [16].

Consider first the ^{1}H–^{1}H DQ MAS spectrum of the methyl-substituted dimer in Figure 5. In the SQ dimension, the resonances of $\mathrm{N \cdots H \cdots O}$ (A), $\mathrm{O \cdots H \cdots O}$ (B) and aromatic protons (C) can be distinguished. The

Fig. 5. Hydrogen-bonded structures of *N*-methyl- (a) and *N*-ethyl-substituted (b) benzoxazine dimers and ^1H–^1H DQ spectra (700.1 MHz, 30 kHz MAS, BaBa recoupling, $\tau_{exc} = \tau_R$). The different DQCs formed by the hydrogen-bonded protons (A and B) provide evidence for the differences in the packing.

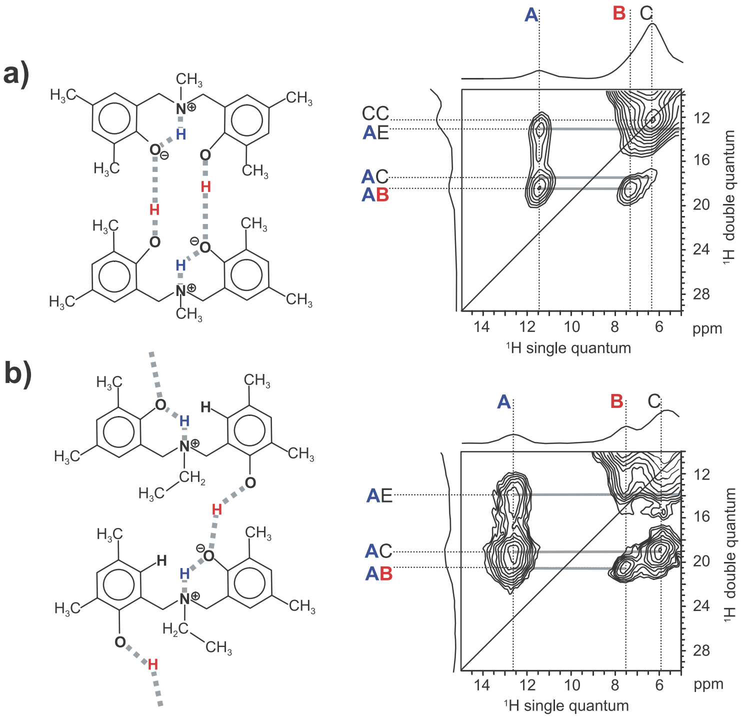

packing of the dimers in the solid-state structure is strongly influenced by the intra-molecular N···H···O and inter-molecular O···H···O hydrogen bonds which together form an extended N···H···O···H···O link. The two protons of these double hydrogen-bonds give rise to the intense AB cross peaks. In addition, there is some evidence of a weaker cross peak to the aromatic protons (AC), while there is no AA auto peak, which indicates that the nearest distance between two N···H···O protons is larger than about 0.4 nm. Moreover, the strong aromatic auto peak CC is due to the close proximity of two aromatic protons of two different hydrogen-bonded dimer pairs, and provides insight into the overall packing structure.

Although similar to that of the *N*-methyl dimer, the ^1H–^1H DQ MAS spectrum of the *N*-ethyl dimer exhibits some profound differences (Figure 5b). As for the methyl spectrum, clear AB cross peaks between the N···H···O and O···H···O protons can be identified, so providing evidence for the same type of extended N···H···O···H···O hydrogen-bonded link in both samples. The most striking differences between the methyl- and ethyl-dimer spectra are, while for the methyl dimer, there is a strong aromatic auto peak (CC) and only weak intensity corresponding to a DQC between a N···H···O and an aromatic proton (AC, see Figure 5a), the situation is reversed for the ethyl dimer (Figure 5b). These differences clearly indicate an alternative packing arrangement, which can be explained if one of the aromatic rings is flipped such that instead of pairs of hydrogen-bonded dimers there exist hydrogen-bonded chains as shown in Figure 5b. In addition, this arrangement gives rise to a close proximity of the O···H···O proton and the *N*-ethyl chain, and the resulting cross-peak between the O···H···O proton and the ethyl-chain CH_2 protons is, indeed, clearly seen in the ^1H–^1H DQ MAS spectrum of the ethyl dimer (see Ref. [16], not shown here). For the methyl dimer, where pairs of hydrogen-bonded dimers are believed to form, an analogous peak between the O···H···O proton and the *N*-methyl protons is neither predicted by the crystal structure nor apparent in the ^1H–^1H DQ spectrum.

Hence, the size of the *N*-alkyl substituent is responsible for the long-range packing of the benzoxazine dimers. For small methyl substituents, the dimers can form hydrogen-bonded pairs, while ethyl substituents (as well as larger alkyl substituents) force the molecules to twist about the central nitrogen and to arrange in an extended ladder-like hydrogen-bonded structure. Subsequent to the ^1H–^1H DQ NMR studies reviewed above, this finding could be confirmed by X-ray diffraction.

Columnar Stacking of Discotics

The solid phases and discotic mesophases of alkylated hexa-peri-hexabenzocoronenes (HBCs) represent striking examples of the wealth of information obtainable from fast-MAS ^{1}H–^{1}H DQ NMR experiments [14,17,21,22]. In the following, NMR findings about the packing of the HBC discs will briefly be discussed.

In the solid phases, HBC derivatives are found to adopt two different types of columnar stacking. In the "herringbone" arrangement, the aromatic cores are tilted relative to the columnar axis, while in the "planar" arrangement the disc planes are basically oriented perpendicular in the columns. The molecular tilt in the stacks is energetically preferred with respect to an optimised dense packing of the columns in the solid phase. The tilt can, however, be prevented by substituent effects on a molecular level, for example, by the steric requirements of phenylene (Ph) substituents, so that the HBC-Ph derivatives pack their columns in the material less densely. The two types of packing can readily be distinguished by means of ^{1}H NMR, because the ^{1}H resonance lines of the aromatic HBC protons are characteristically shifted due to ring-current effects which arise from the aromatic π-electron systems of adjacent HBC cores in the columns.

Considering a single molecule, the six-fold symmetry of a HBC core means that only one distinct aromatic ^{1}H resonance is expected, as is indeed found to be the case in the solution-state spectrum. However, as shown in Figure 6a, three aromatic resonances (A,B,C) are clearly identified in the solid-state ^{1}H spectrum of dodecyl-substituted HBC (HBC-C_{12}). This effect can be ascribed to the reduction of the six-fold molecular symmetry due to the packing arrangement in the crystal, as revealed by ^{1}H–^{1}H DQ spectra. In HBC-C_{12}, the six aromatic protons are grouped in pairs of "bay protons" with a proton–proton distance of approximately 200 pm, while the closest distance to another aromatic proton is >0.4 nm. Therefore, the aromatic region of the DQ MAS spectrum will be dominated, for short DQ excitation periods, by the dipole–dipole couplings within the three pairs. Strong CC auto and AB cross peaks are observed, which imply the presence of only two types of pairs of aromatic protons, H_A–H_B and H_C–H_C, in a ratio, as determined from the DQ peak intensities of ratio 2:1.

Assuming a "herringbone"-type of packing of the HBC cores [41], three different aromatic proton environments can be identified with respect to the degree to which the proton experiences the ring current of the adjacent layers. The least shielded resonance (highest ppm) belongs to protons which lie neither above nor below the π-orbitals of an adjacent layer. Protons situated close to an adjacent ring system are more shielded, and the highest shielding is found for protons which lie right above or below an adjacent aromatic core. Assigning these three differently

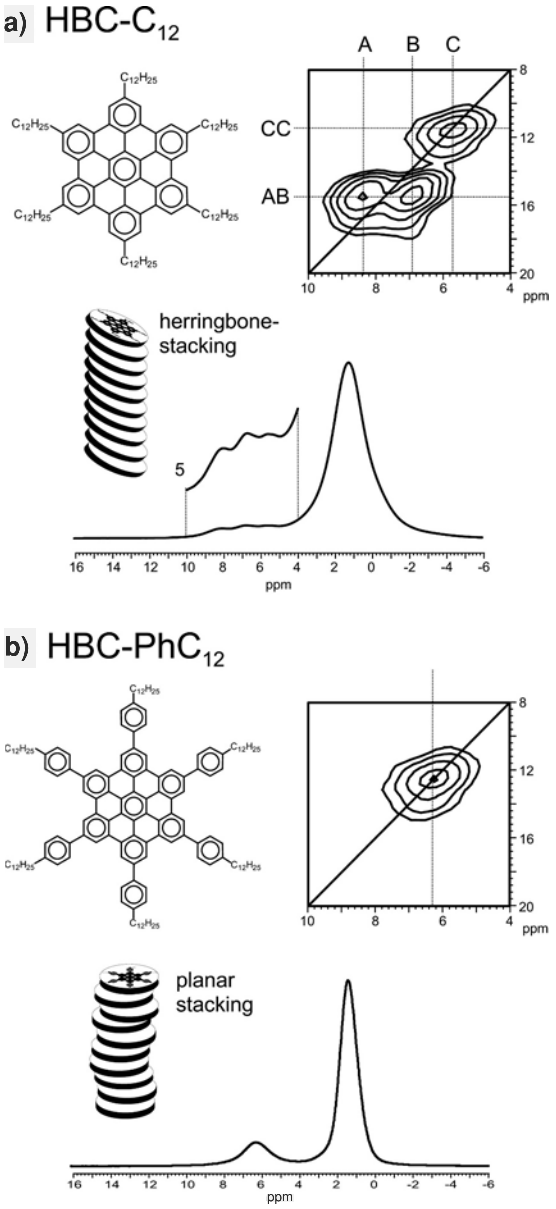

Fig. 6. Molecular structure, ^{1}H spectra (700.1 MHz, 30 kHz MAS) and ^{1}H–^{1}H DQ MAS spectra (700.1 MHz, 30 kHz MAS, BaBa recoupling, $\tau_{\mathrm{exc}} = \tau_R$) of two HBC derivatives: (a) HBC-C_{12} and (b) HBC-PhC_{12}. The ^{1}H NMR signals allow two types of molecular packing to be readily distinguished.

shielded types of aromatic protons to the A, B, and C resonances, respectively, the observed presence of only AB and CC pairs in the ratio 2:1, with the C resonance having the smallest chemical shift value (most shielded), can readily be explained. In this way, the characteristic ^{1}H–^{1}H DQ signal pattern provides a simple means of identifying the "herringbone" packing in the solid phases of HBC derivatives. This has also been confirmed in detail by quantum-chemical computations of the ^{1}H chemical shifts [42].

When instead a single aromatic ^{1}H resonance is observed in both, the ^{1}H fast-MAS spectrum and the ^{1}H–^{1}H DQ MAS spectrum (see Figure 6b), this serves as a strong indication for a planar stacking, i.e. with the HBC cores oriented perpendicular to the column axis [22]. In this case, the ring current effects caused by adjacent molecules are, on average, the same for all aromatic core protons, such that the aromatic ^{1}H line is shifted high-field, i.e. to lower ppm values, but no splitting is induced. The planar orientation is enforced in the solid phase of HBC-PhC$_{12}$ by the steric requirements of phenylene substituents at the aromatic core.

References

1. *Encyclopedia of Materials: Science and Technology* (Pergamon, Amsterdam,2001).
2. Lehn JM. Supramolecular Chemistry. Wiley-VCH: Weinheim,1995.
3. Müllen K, Wegner G. The Oligomer Approach. Wiley-VCH: Weinheim,1998.
4. Jeffrey GA, Saenger W. Hydrogen Bonding in Biological Structures. Springer-Verlag: New York,1991.
5. Atwood JL, Davies JED, MacNiol DD, Vgtle F. Comprehensive Supramolecular Chemistry. Elsevier:Oxford,1996.
6. Mehring M. High Resolution NMR of Solids. Springer-Verlag: Berlin,1983.
7. Taylor R E, Pembleton RG, Ryan LM, Gerstein BC. J. Chem. Phys. 1979;71:4541.
8. Scheler G, Haubenreisser U, Rosenberger H. J. Magn. Reson. 1981;44:134.
9. Jakobsen HJ. In: DM Grant, RK Harris (Eds). Encyclopedia of Nuclear Magnetic Resonance. Vol.1. p. 398, Wiley: Chichester,1996.
10. Samoson A, Tuherm T, Gan Z, Solid State Nucl. Magn. Reson. 2001;20:130.
11. Schnell I, Spiess HW.J. Magn. Reson./Adv. Magn. Opt. Reson. 2001;151:153.
12. Saalwächter K, Spiess HW.J. Chem. Phys. 2001;114:5707.
13. Saalwächter K, Schnell I. Solid State Nucl. Magn. Reson. 2002;22:157.
14. Brown SP, Spiess HW. Chem. Rev. 2001;101:4125.
15. Filip C, Hafner S, Schnell I, Demco DE, Spiess HW.J. Chem. Phys. 1999;110:423.
16. Schnell I, Brown SP, Low HY, Ishida H, Spiess HW.J. Am. Chem. Soc. 1998;120:11784.
17. Brown SP, Schnell I, Brand JD, Müllen K, Spiess HW. Phys. Chem. Chem. Phys. 2000;2:1735.
18. Brown SP, Zhu XX, Saalwächter K, Spiess HW. J. Am. Chem. Soc. 2001;123:4275.
19. Schnell I, Langer B, Söntjens SHM, van Genderen MHP, Sijbesma RP, Spiess HW.J. Magn. Reson. 2001;150:57.
20. Goward GR, Sebastiani D, Schnell I, Spiess HW , Kim H-D, Ishida H. J. Am. Chem. Soc. 2003;125:5792.
21. Brown SP, Schnell I, Brand JD, Müllen K, Spiess HW.J. Am. Chem. Soc. 1999;121:6712.
22. Fischbach I, Saalwächter K, Pakula T, Minkin P, Fechtenkötter A, Müllen K, Spiess HW. J. Phys. Chem. 2002;106:6408.
23. Graf R, Heuer A, Spiess HW. Phys. Rev. Lett. 1998;80: 5738.
24. Graf R, Demco DE, Hafner S, Spiess HW. Solid State Nucl. Magn. Reson. 1998;12:139.
25. Schmidt-Rohr K, Spiess HW. Multidimensional Solid-State NMR and Polymers. Academic Press:London,1994.
26. Maricq MM, Waugh JS. J. Chem. Phys. 1979;70:3300.
27. Bennett AE, Griffin RG, Vega S. In: Diehl P, Fluck E, Günter H, Kosfeld R, Seelig J(Eds). NMR Basic Principles and Progress. Vol. 33, pp. 1 –77, Springer-Verlag: Berlin, 1994.
28. Dusold S, Sebald A. Ann. Rep. NMR Spectr. 2000;41:185.
29. Jakobsen HJ. In: Grantand DM, Harris RK (Eds). Encyclopedia of Nuclear Magnetic Resonance. Vol. 9, p. 165, Wiley: Chichester,2002.
30. Fischbach I, Ebert F, Spiess HW, Schnell I. Chem. Phys. Chem. 2004;5:895–908.
31. Gullion T, Schaefer J. J. Magn. Reson. 1989;81:196.
32. Gullion T, Schaefer J. Adv. Magn. Reson. 1989;13:57.
33. Friedrich U, Schnell I, Brown S P, Lupulescu A ,Demco DE, Spiess HW. Mol. Phys. 1998;95:1209.
34. Bonnett R, Davies JR, Hursthouse MB. Nature 1976;262:326.
35. LeBas G, Allegret A, Mauguen Y,de Rango C, Bailly M. Acta Cryst. B. 1980;36:3007.
36. Ishida H, Allen DJ. J. Polym. Sci. Phys. Ed. 1996;34:1019.
37. Shen SB, Ishida H. Polym. Composites. 1996;17:5.
38. Ishida H, Low HY. Macromolecules. 1997;30:30.
39. Wirasate S, Dhumrongvaraporn S, Allen DJ, Ishida H. J. Appl. Polym. Sci. 1998;70:1299.
40. Dunkers J, Zarate EA, Ishida H. J. Phys. Chem. 1996;100:13512.
41. Goddard R, Haenel MW, Herndon WC, Krüger C, Zander M. J. Am. Chem. Soc. 1995;117:30.
42. Ochsenfeld C, Brown SP, Schnell I ,Gauss J, Spiess HW. J. Am. Chem. Soc. 2001;123:2527.

Quadrupolar NMR of Inorganic Materials: The Multiple-Quantum Magic Angle Spinning Experiment

Stephen Wimperis

Department of Chemistry and WestCHEM, University of Glasgow, Glasgow G12 8QQ, UK

Introduction

Over two-thirds of all NMR-accessible nuclides are quadrupolar with half-integer spin quantum numbers ($I = 3/2, 5/2, 7/2$, etc.). Far from being a minority interest, therefore, NMR of nuclei such as ^{7}Li, ^{11}B, ^{23}Na, ^{39}K, ^{71}Ga, ^{87}Rb ($I = 3/2$), ^{17}O, ^{25}Mg, ^{27}Al ($I = 5/2$), ^{45}Sc, ^{51}V, ^{59}Co ($I = 7/2$), and ^{93}Nb ($I = 9/2$) is central to the characterization and study of a wide range of minerals, glasses, novel oxide materials, and micro- and mesoporous solids, including zeolites. Although their quadrupolar coupling constants can be large (typically in the range 0–20 MHz), NMR of these nuclei is facilitated by the presence of a $|m_I = +1/2\rangle \leftrightarrow |-1/2\rangle$ "central transition" (CT) which, to a first-order approximation, is not broadened by the quadrupolar interaction. Figure 1a shows, however, that the ^{87}Rb central-transition NMR spectrum of polycrystalline RbNO$_3$, although relatively narrow, is still essentially a broad, almost featureless, "hump." The success of magic angle spinning (MAS) as a line-narrowing technique for spin $I = 1/2$ nuclei has encouraged its application to spectra of this type and yet, as the example in Figure 1b shows, despite achieving a significant narrowing of the ^{87}Rb lineshape, MAS still fails to resolve the three crystallographically distinct sites in RbNO$_3$.

The reason for the relative failure of MAS in this case is that the broadening of the CT spectrum in Figure 1a arises largely from a second-order quadrupolar interaction and this has second- and fourth-rank terms in its orientational dependence, with MAS capable of only fully averaging the former. In 1988, two methods were proposed for removing both the second- and fourth-rank quadrupolar broadening, and hence achieving truly high-resolution CT spectra. Both the double rotation (DOR) [1,2] and dynamic angle spinning (DAS) [2,3] experiments involve rapidly spinning the sample about two angles with respect to the magnetic field, either simultaneously in the case of DOR or sequentially in the case of DAS. Although these two techniques have been used with considerable success by a number of research groups, their use has neither become widespread nor commonplace, owing largely to the significant additional cost and mechanical complexity of the specialized NMR probe equipment that is required, but also to spinning rate limitations.

In this context, it is not surprising that the demonstration in 1995 by Frydman and Harwood of their novel multiple-quantum MAS (MQMAS) technique for removing the second-order quadrupolar broadening generated such instant and enormous interest [4,5]. Unlike DOR or DAS, this experiment is purely MAS based and can be performed on any NMR spectrometer that is equipped with a standard MAS probe. Figure 1c shows the success of the MQMAS technique in achieving a high-resolution ^{87}Rb NMR spectrum and resolving the three distinct Rb sites in RbNO$_3$.

The MQMAS experiment is now a well-established and popular method of obtaining high-resolution ^{17}O, ^{23}Na, or ^{27}Al NMR spectra of inorganic materials. The purpose of this article is to give a brief description of the technique as it is currently performed and to discuss how MQMAS NMR spectra of both crystalline and amorphous solids can be analyzed to yield chemical shift and quadrupolar parameters.

Multiple-Quantum MAS

For a spin $I = 3/2$ nucleus, the MAS-averaged ($\langle\ldots\rangle_{\text{MAS}}$) CT frequency can be written in a suitable rotating frame as

$$\langle\omega^{\text{CT}}\rangle_{\text{MAS}} = \delta_{\text{CS}}\omega_0 + \frac{2}{35}\frac{(\omega_Q^{\text{PAS}})^2}{\omega_0}\{-7 + 27 d^4_{0,0}(54.736^\circ) d^4_{0,0}(\beta)\}, \quad (1)$$

where δ_{CS} is the isotropic chemical shift, $\omega_0 = \gamma B_0$ the Larmor frequency, $\omega_Q^{\text{PAS}} = 3e^2qQ/(4I(2I-1)\hbar)$ a parameter describing the strength of the quadrupolar interaction, and $d^l_{m',m}(\theta)$ a reduced Wigner rotation matrix element. For simplicity, the quadrupolar axial asymmetry parameter, η, has been assumed to be zero. Thus, for a single crystallite spinning at the magic angle (54.736°) with respect to B_0, the CT has an isotropic frequency shift of $\delta_{\text{CS}}\omega_0 - 2(\omega_Q^{\text{PAS}})^2/5\omega_0$, as well as a rank $l = 4$ anisotropic shift that depends on the angle, β, between the sample

Graham A. Webb (ed.), Modern Magnetic Resonance, 1507–1514.

© 2008 *Springer.*

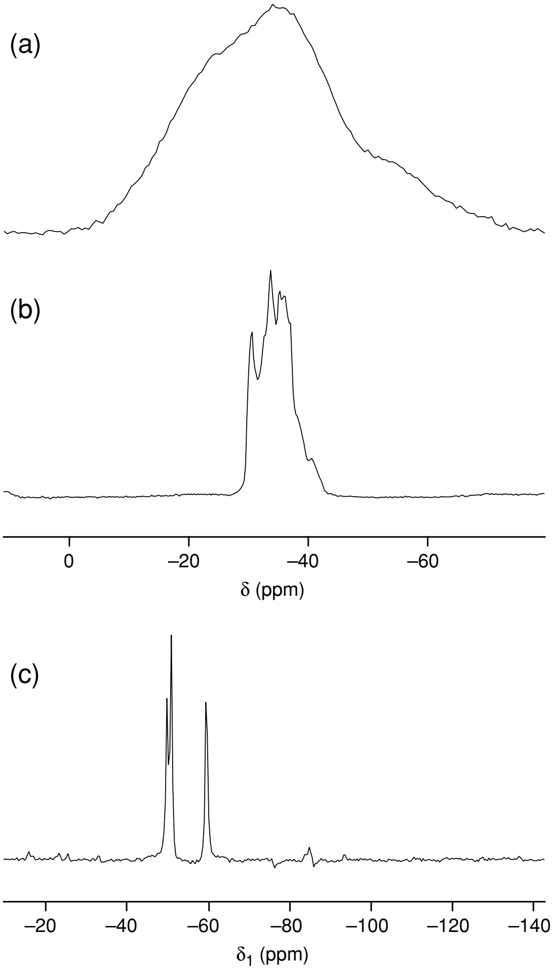

Fig. 1. ^{87}Rb ($\omega_0/2\pi = 130.9$ MHz) NMR spectra of $RbNO_3$. (a) Static; (b) MAS; and (c) isotropic triple-quantum MAS spectrum. The δ scales are referenced to the ^{87}Rb Larmor frequency and to 1 M $RbNO_3$ (aq). Adapted from J. McManus, Ph.D. thesis, University of Exeter, 2001.

rotation and quadrupole tensor axes. In a powdered solid, a spherical average over all orientations of the angle β must be considered and gives rise to the residual inhomogeneous second-order quadrupolar broadening observed in Figure 1b.

The key to the MQMAS experiment is that the residual fourth-rank quadrupolar broadening of the triple-quantum (TQ) transition ($|m_I = +3/2\rangle \leftrightarrow |-3/2\rangle$) under MAS conditions differs from that of the CT. For example, for a spin $I = 3/2$ nucleus:

$$\langle\omega^{\mathrm{TQ}}\rangle_{\mathrm{MAS}} = 3\delta_{\mathrm{CS}}\omega_0 + \frac{2}{35}\frac{(\omega_Q^{\mathrm{PAS}})^2}{\omega_0}\{21 - 21 d^4_{0,0}(54.736^\circ) d^4_{0,0}(\beta)\}, \tag{2}$$

Therefore, by performing a two-dimensional NMR experiment that correlates TQ coherences in the t_1 evolution period with CT coherences in the t_2 acquisition period, it is possible to refocus the residual fourth-rank quadrupolar broadening. If the time-domain signal, $s(t_1, t_2)$, in a two-dimensional triple-quantum MAS NMR experiment can be written as

$$s(t_1, t_2) = \exp\{-i\langle\omega^{\mathrm{TQ}}\rangle_{\mathrm{MAS}} t_1\}\exp\{-i\langle\omega^{\mathrm{CT}}\rangle_{\mathrm{MAS}} t_2\}, \tag{3}$$

then inspection of Equations (1) and (2) shows that the anisotropic fourth-rank terms cancel one another when $t_2 = (21/27)t_1 = (7/9)t_1$:

$$s(t_1, t_2 = (7/9)t_1) = \exp\{-i\omega^{\mathrm{MQMAS}} t_{1'}\}, \tag{4}$$

where $t_{1'} = (1 + (7/9))t_1 = (16/9)t_1$ and

$$\omega^{\mathrm{MQMAS}} = \frac{9}{16}\left(\left(3 + \frac{7}{9}\right)\delta_{\mathrm{CS}}\omega_0 + \frac{2}{35}\left(21 - 7\cdot\frac{7}{9}\right) \times \frac{(\omega_Q^{\mathrm{PAS}})^2}{\omega_0}\right) = \frac{17}{8}\delta_{\mathrm{CS}}\omega_0 + \frac{1}{2}\frac{(\omega_Q^{\mathrm{PAS}})^2}{\omega_0} \tag{5}$$

As expected, the frequency ω^{MQMAS} in Equation (5) consists of only isotropic terms and, hence, is identical for every crystallite orientation in the powder, regardless of the angle β. A spin $I = 3/2$ spectrum containing just the isotropic ω^{MQMAS} frequencies can be obtained by either Fourier transforming the cross-section through the time-domain signal defined by $t_2 = (7/9)t_1$ or, equivalently and more conveniently, projecting the full two-dimensional spectrum, $s(\omega_1, \omega_2)$, onto an axis with a gradient of 9/7, i.e. orthogonal to a gradient of $-21/27 = -7/9$.

Figure 2a shows the two-dimensional ^{87}Rb triple-quantum MAS spectrum of $RbNO_3$ recorded at $B_0 = 9.4$ T ($\omega_0/2\pi = 130.9$ MHz). The three “ridge” lineshapes (two are barely resolved) correspond to the three crystallographically distinct Rb sites in $RbNO_3$. The ratio of the fourth-rank broadening in the TQ dimension (δ_1) to that in the CT dimension (δ_2) is $-21{:}27 = -7{:}9$ (from Equations 1 and 2), and hence all three ridge lineshapes in Figure 2a lie on a gradient of $-7/9$. The isotropic spectrum shown in Figure 1c is obtained, as described above, by

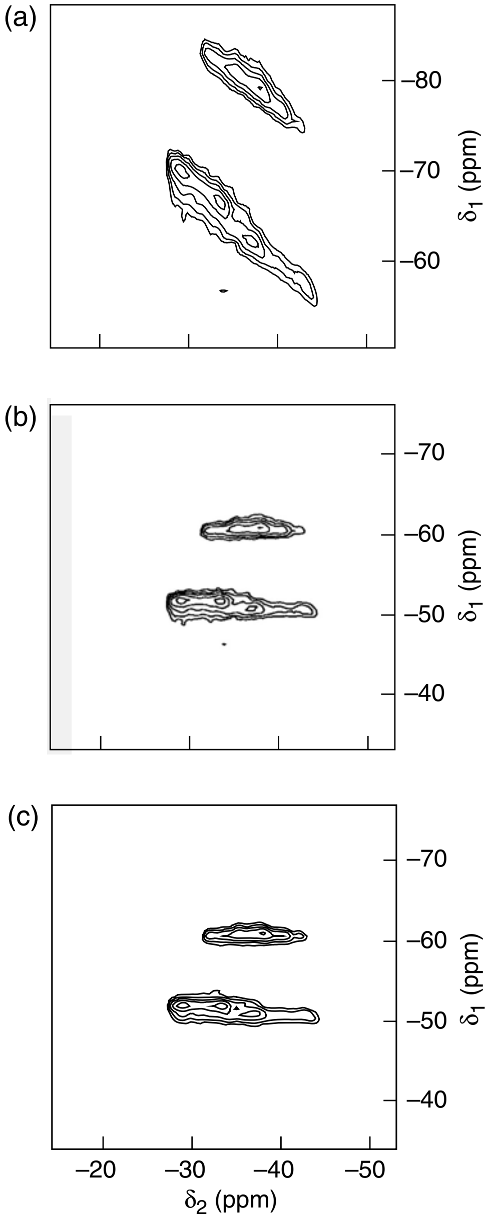

Fig. 2. Two-dimensional ^{87}Rb ($\omega_0/2\pi = 130.9$ MHz) triple-quantum MAS spectra of $RbNO_3$. (a) Nonsheared spectrum with ridge lineshapes at gradient of $-7/9$; (b) sheared version of (a) with ridge lineshapes parallel to δ_2; and (c) split-t_1 spectrum with ridge lineshapes parallel to δ_2. The δ scales are referenced to the ^{87}Rb Larmor frequency and to 1 M $RbNO_3$ (aq). Adapted from S. E. Ashbrook, D.Phil. thesis, University of Oxford, 2000.

projecting the two-dimensional spectrum onto an axis orthogonal to $-7/9$. This projection is most easily carried out by first "shearing" [6] the original two-dimensional spectrum, $s(\omega_1, \omega_2)$, to obtain the new spectrum $s(\omega_{1'}, \omega_2)$ where

$$\omega_{1'} = \frac{\omega_1 - \lambda\omega_2}{1 + |\lambda|}, \qquad (6)$$

and where λ is the gradient of the MQMAS ridge lineshapes, $-7/9$ in this case. As shown in Figure 2b, the ridge lineshapes in the sheared spectrum are parallel to the ω_2 axis and a purely isotropic spectrum is now easily obtained by projecting the sheared two-dimensional spectrum onto the $\omega_{1'}$ axis.

For half-integer nuclei with spin $I > 3/2$, triple-quantum MAS NMR spectra yield isotropic resolution of distinct crystallographic sites in a fashion similar to that shown for ^{87}Rb in Figure 2. The main difference is that the ridge gradient or "MQMAS ratio" is characteristic of each spin quantum number. For spin $I = 5/2$, for example, it is $+19/12$, while for spin $I = 7/2$ it is $+101/45$. For spin $I > 3/2$ nuclei, it is also possible to use MQ transitions of higher order than TQ to obtain high resolution, e.g. quintuple-quantum for spin $I = 5/2$ [7] and quintuple- and septuple-quantum for spin $I = 7/2$ [8], and these too will have their own characteristic MQMAS ratios, e.g. $-25/12$ for spin $I = 5/2$ quintuple-quantum. However, these higher order MQMAS experiments currently have very poor sensitivity compared with the TQ experiment and it seems unlikely that their use will ever become widespread.

Pulse Sequences for MQMAS

A typical MQMAS pulse sequence consists of the following steps: (i) excitation of MQ coherence, usually with a single radiofrequency pulse; (ii) time evolution of this coherence during the t_1 period of the two-dimensional experiment; (iii) application of a second pulse or group of pulses to convert the MQ coherence back into observable CT coherence; and (iv) detection of this coherence during the acquisition period, t_2.

Figure 3 shows probably the most popular pulse sequences for performing a TQ MAS experiment: the amplitude-modulated z-filter experiment [9] and two versions of the phase-modulated split-t_1 experiment [10,11]. The coherence pathway diagrams drawn below the pulse sequences are not merely decorative but specify the phase cycle that must be used with each experiment [12,13].

The phase cycle used in the z-filter experiment in Figure 3a retains coherences of order $p = +3$ and -3 during the t_1 period and these are combined to yield a signal

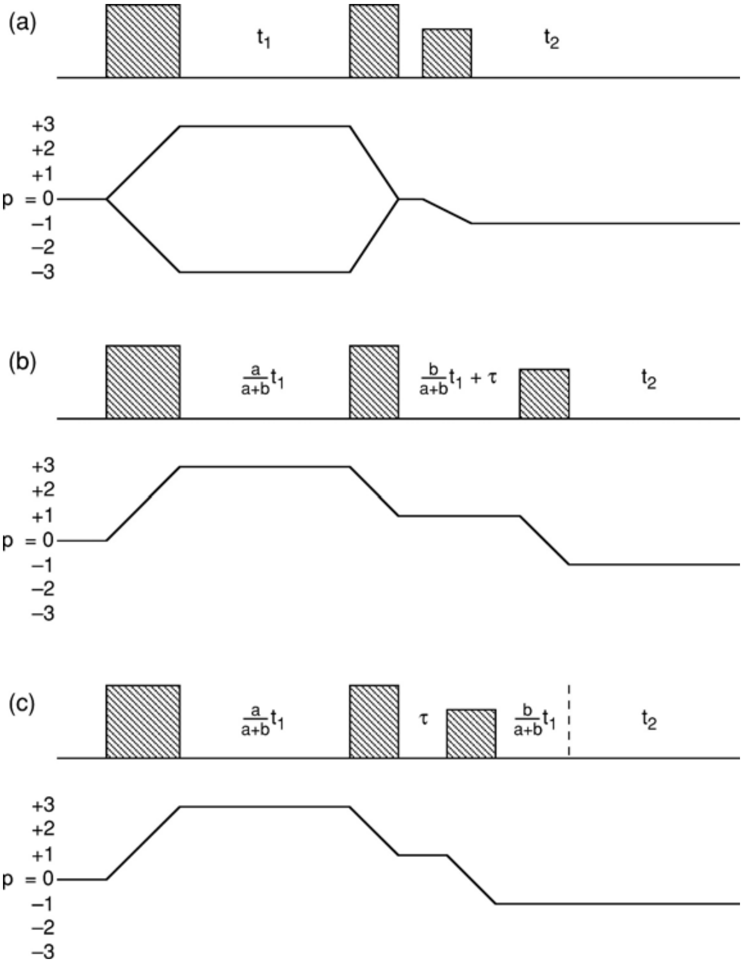

Fig. 3. Pulse sequences and coherence transfer pathway diagrams for three MQMAS experiments: (a) the amplitude-modulated *z*-filter experiment; (b) the phase-modulated split-t_1 experiment for negative MQMAS ratio (e.g. $-b/a = -7/9$ for spin $I = 3/2$ triple-quantum); and (c) the phase-modulated split-t_1 experiment for positive MQMAS ratio (e.g. $b/a = 19/12$ for spin $I = 5/2$ triple-quantum).

that is purely amplitude modulated in t_1 by first converting them into longitudinal (or z) magnetization (a state that has $p = 0$) before converting this into observable CT coherence (which has $p = -1$) with the final pulse. A two-dimensional NMR dataset that is amplitude modulated in t_1 should be Fourier transformed by the "hypercomplex" method if the desirable absorption-mode lineshape is to be obtained [6] and, in addition, either the States–Haberkorn–Ruben or TPPI method must be used when performing the experiment in order to determine the sense of coherence precession in t_1 [6].

In the experiments in Figure 3b and c, the t_1 period is split into two parts that mix TQ and CT evolution. This is done in such a way that the residual second-order quadrupolar broadening is refocused at the end of the t_1 period. Thus, these split-t_1 experiments yield spectra with ridge lineshapes already parallel to the ω_2 axis and that do not require shearing in order to extract an isotropic spectrum [10,11]. An example is shown in Figure 2c. The experiment in Figure 3b should be used where the MQMAS ratio is negative (e.g. $\lambda = -7/9 = -b/a$ for spin $I = 3/2$ triple-quantum), while that in Figure 3c is applicable where the MQMAS ratio is positive (e.g. $\lambda = +19/12 = b/a$ for spin $I = 5/2$ triple-quantum). The phase cycle retains only coherences of order $p = +3$ during the first part of the t_1 period and, hence, these experiments yield datasets that are phase modulated in t_1. Absorption-mode lineshapes are obtained in these experiments by virtue of using the final pulse to form a time-

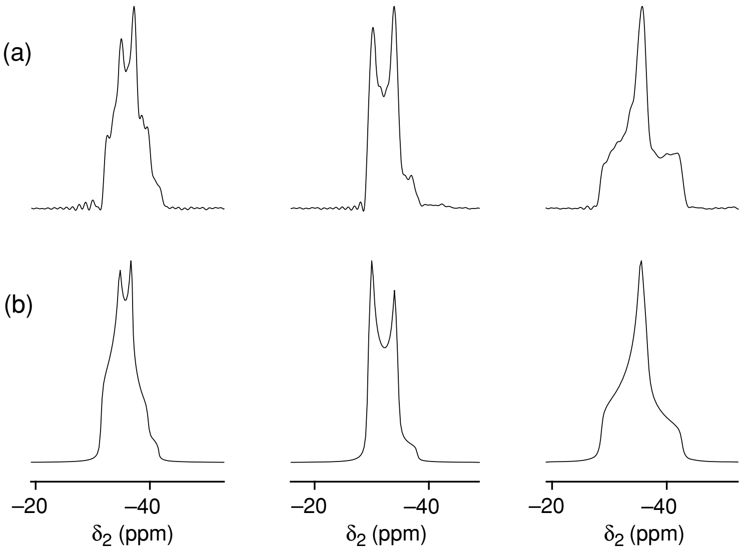

Fig. 4. (a) Cross-sections parallel to the ω_2 (or δ_2) axis through the three second-order broadened ridge lineshapes in the ^{87}Rb triple-quantum MAS spectrum in Fig. 2c. (b) The corresponding computer-fitted lineshapes, yielding values of δ_{CS}, C_Q, and η for each Rb site. Adapted from S. E. Ashbrook, D.Phil. thesis, University of Oxford, 2000.

symmetric spin-echo signal in the acquisition period t_2 [10,11,14,15]. After a suitable phase correction, the Fourier transform of a time-symmetric signal has no imaginary component and the basic two-dimensional complex (as opposed to hypercomplex) Fourier transform should be used. As the sense of coherence precession is already determined in a phase-modulated experiment, it would be quite wrong to apply either the States–Haberkorn–Ruben or TPPI method.

Both the *z*-filter and split-t_1 experiments are excellent methods of recording MQMAS spectra. The former is robust, requires little optimization, and has the virtue of familiarity in that it is similar to many other two-dimensional NMR experiments used for solids and liquids. The latter generally yield significantly higher sensitivity than the *z*-filter as $p = +3$ to $+1$ transfer is more efficient than $p = +3$ to 0 transfer [11], but require selection of a spin-echo interval τ that, inevitably, involves a degree of compromise when both broad and narrow lineshapes occur in the ω_2 dimension. With some experience, however, split-t_1 experiments become very easy to use and have the additional practical advantage that the signal does not shift in t_2 as the t_1 period is incremented, making application of weighting functions particularly straightforward [11].

Many alternatives to and variants of the pulse sequences in Figure 3 have been suggested. One class of experimental variants seeks to achieve greater isotropic resolution by utilizing higher order MQ coherences but, as mentioned above, currently it appears that the sensitivity of these is too poor to make them generally useful [7,8]. A second group seeks to improve the sensitivity of the triple-quantum MAS experiment by increasing the efficiency of the coherence transfer steps by substituting sophisticated pulse trains for the simple pulses in Figure 3 (e.g. the RIACT [16], FAM [17], SPAM [18], and, perhaps most interesting of all, DFS [19] sequences). However, although some impressive results have been shown on model systems, many of these results appear to have been achieved through extensive experimental optimization on spectra that already had high signal-to-noise ratios. It remains to be seen, therefore, whether such methods will have much use in real experimental practice on systems where the "ideal" forms of the spectra are not already known in advance.

Spectral Analysis

A full analysis of a peak in a two-dimensional MQMAS spectrum can yield the value of the isotropic chemical shift δ_{CS}, the quadrupolar coupling constant $C_Q = e^2qQ/h$ and asymmetry η, and, independently of the latter pair, a composite quadrupolar parameter $P_Q = C_Q(1 + \eta^2/3)^{1/2}$. All this information can be obtained from a single two-dimensional spectrum, without recourse to measurement at a second static magnetic field strength B_0, and it is this, just as much as the high resolution obtained in the isotropic dimension, that makes MQMAS such a useful spectroscopic tool [15,20,21]. Indeed, even in disordered or amorphous solids, where the increase in resolution over a conventional spectrum can be disappointing, this high information content still means that MQMAS spectra are worth recording.

The three parameters δ_{CS}, C_Q, and η can be obtained by fitting ω_2 cross-sections through the ridge lineshapes in a sheared or split-t_1 spectrum [15]. Figure 4 shows the three such cross-sections from the ^{87}Rb MQMAS spectrum in Figure 2c and the corresponding lineshape fittings. The values obtained for δ_{CS} are -31, -27, and -28 ppm, for C_Q are 1.7, 1.7, and 1.9 MHz, and for η are 0.6, 0.1, and 1.0, in order of increasing δ_1. Where applicable, this is the best method of extracting chemical shift and quadrupolar parameters. However, for it to be used, the signal-to-noise ratio must be good and a radiofrequency field strength, $\omega_1 = \gamma B_1$, that is reasonably strong compared with ω_Q^{PAS} must have been used in order to obtain undistorted lineshapes. Furthermore, this method may not be appropriate to disordered or amorphous solids (see below).

Alternatively, the two parameters δ_{CS} and P_Q can be obtained by measuring either the ω_1 and ω_2 or (in ppm, relative to the Larmor frequency and a reference peak) the δ_1 and δ_2 coordinates of the "center-of-mass" (c.o.m.) of a ridge lineshape [15,20,21]. For example, a straightforward generalization of Equation (1) to $\eta \neq 0$ shows that the shift of the center-of-mass of a ridge lineshape in the ω_2 dimension of a spin $I = 3/2$ triple-quantum MAS spectrum is given by

$$\delta_2^{\mathrm{c.o.m.}} = \delta_{\mathrm{CS}} - 7 \cdot \frac{2}{35}\frac{(\omega_Q^{\mathrm{PAS}})^2}{\omega_0^2}\left(1 + \frac{\eta^2}{3}\right). \qquad (7)$$

Similarly, Equation (2) indicates that the shift in the ω_1 dimension of a nonsheared spin $I = 3/2$ triple-quantum MAS spectrum is given by

$$\delta_1^{\mathrm{c.o.m.}} = 3\delta_{\mathrm{CS}} + 21 \cdot \frac{2}{35}\frac{(\omega_Q^{\mathrm{PAS}})^2}{\omega_0^2}\left(1 + \frac{\eta^2}{3}\right), \qquad (8)$$

while Equation (5) indicates that in a sheared or split-t_1 spectrum it is

$$\delta_{1'}^{\mathrm{c.o.m.}} = \frac{17}{8}\delta_{\mathrm{CS}} + \frac{1}{2}\frac{(\omega_Q^{\mathrm{PAS}})^2}{\omega_0^2}\left(1 + \frac{\eta^2}{3}\right). \qquad (9)$$

Thus, measurement of the two independent variables $\delta_1^{\mathrm{c.o.m.}}$ and $\delta_2^{\mathrm{c.o.m.}}$ allows determination of the parameters δ_{CS} and $(\omega_Q^{\mathrm{PAS}})^2[1 + (\eta^2/3)]$ (or, equivalently, δ_{CS} and P_Q). For the ^{87}Rb MQMAS spectrum in Figure 2c, the values obtained for δ_{CS} are -31, -27, and -29 ppm, and for P_Q are 1.9,1.7, and 2.3 MHz, in order of increasing δ_1. This method has the advantage of being easy to apply even when the signal-to-noise ratio is poor or the ridge lineshapes distorted but, as it relies upon determination of the center-of-mass of such a ridge lineshape, the limitations on its accuracy should be noted. It can also be applied to disordered or amorphous solids (see below).

Application to Disordered and Amorphous Solids

An MQMAS NMR spectrum of a disordered or amorphous solid does not usually yield discrete, well-defined ridge lineshapes such as those in Figure 2, which are typical of an ordered crystalline solid. Instead, rather featureless two-dimensional peaks tend to be observed that are significantly broadened in both frequency dimensions. These broad peaks arise as a result of a distribution of isotropic chemical shifts and quadrupolar parameters that reflect the underlying heterogeneity of the nuclear spin environments.

These distributions of NMR parameters correspond to broadening along characteristic gradients in the two-dimensional MQMAS spectrum. For example, in a nonsheared spin $I = 3/2$ triple-quantum MAS spectrum a distribution of δ_{CS} values corresponds, according to Equations (1) and (2), to a broadening along a gradient of 3 $\delta_{\mathrm{CS}}/\delta_{\mathrm{CS}} = +3$, while, from Equation (5), in the sheared or split-t_1 spectrum, it will be along $+17/8$. Similarly, Equations (1), (2), and (5) triple-quantum of P_Q values in a spin $I = 3/2$ triple-quantum MAS spectrum produces a broadening along a gradient of $+21/{-7} = -3$ in a nonsheared spectrum and $(1/2)/(-14/35) = -1/5$ in a sheared or split-t_1 spectrum. If present, these broadenings will, of course, be in addition to the basic anisotropic second-order quadrupolar broadening along the MQMAS gradient.

The effects of these distributions are shown for a spin $I = 5/2$ nucleus in the simulated nonsheared triple-quantum MAS spectra in Figure 5 [22]. Figure 5a shows the spectrum for a single crystallographic site with distinct δ_{CS} and P_Q values, as would be found in a crystalline solid. There is a well-defined ridge lineshape with a gradient equal to the spin $I = 5/2$ triple-quantum MQMAS ratio of $+19/12$. Figure 5b shows the same spectrum but with the addition of a distribution of δ_{CS} values leading to a broadening of the ridge lineshape along a $+3$ gradient. If, instead, a range of quadrupolar parameters were present the additional broadening would lie (for spin $I = 5/2$ triple-quantum MAS) along a gradient of $+3/4$, as shown in the simulated spectrum in Figure 5c. This lineshape looks quite different from that in Figure 5c because a change in P_Q not only shifts a ridge lineshape in the (in this case) $+3/4$ direction but also alters its width along $+19/12$.

Occasionally, as found in some studies of glasses, for example, the δ_{CS} distribution appears to be fully correlated with the distribution of quadrupolar parameters, C_Q and η, and ω_2 cross-sections through a broadened peak in a sheared or split-t_1 MQMAS spectrum still yield lineshapes, such as those in Figure 4, with the features characteristic of second-order quadrupolar broadening [23,24]. The analysis of such a spectrum, by fitting these cross-sections and extracting δ_{CS}, C_Q, and η, is highly

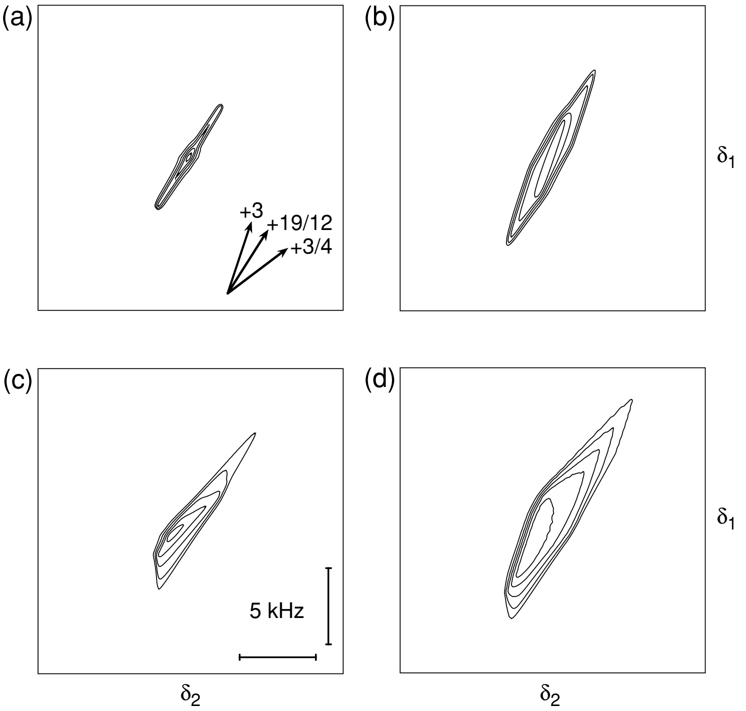

Fig. 5. Computer-simulated spin $I = 5/2$ lineshapes in nonsheared two-dimensional triple-quantum MAS spectra: (a) single ridge lineshape with $C_Q = 5$ MHz and $\eta = 1$; (b) same as (a) but includes a "boxcar" distribution of δ_{CS} of width 16 ppm; (c) same as (a) but includes a boxcar distribution of C_Q from 3 to 7 MHz; and (d) same as (a) but includes uncorrelated boxcar distributions of both δ_{CS} (of width 16 ppm) and C_Q (from 3 to 7 MHz). Simulations are for $\omega_0/2\pi = 104.3$ MHz and assume uniform excitation and conversion of triple-quantum coherences. Adapted from Ref. [22].

informative and has yielded valuable insight into the correlation of NMR parameters with the underlying structural ones, such as bond angles [23]. More commonly in amorphous solids, however, no apparent correlation can be observed between the distributions of chemical shift and quadrupolar parameters and cross-sections through the two-dimensional lineshape appear featureless. Such a case is simulated in Figure 5d, where uncorrelated distributions of both δ_{CS} and P_Q have been added to a spin $I = 5/2$ triple-quantum MAS lineshape [22]. In this case, it is still possible to use the center-of-mass of the two-dimensional lineshape to extract the mean values of the NMR parameters, $\langle\delta_{\mathrm{CS}}\rangle$ and $\langle P_Q\rangle$, while, if the shape of the distribution function is assumed, the widths of the distributions in δ_{CS} and P_Q can be estimated by fitting selected projections of the two-dimensional lineshape [22].

Figure 6a shows a peak from a ^{27}Al triple-quantum MAS spectrum of γ-Al$_2$O$_3$, recorded at $B_0 = 9.4$ T

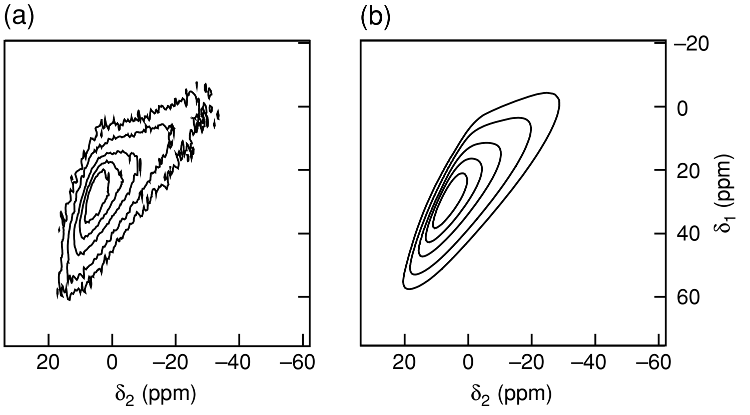

Fig. 6. (a) Peak (corresponding to the six-coordinate Al site) from nonsheared ^{27}Al ($\omega_0/2\pi = 104.3$ MHz) triple-quantum MAS spectrum of γ-Al$_2$O$_3$. (b) Computer-simulated lineshape with uncorrelated Gaussian distributions of δ_{CS} and P_Q (derived from fitting projections of lineshape in (a)). The δ scales are referenced to the ^{27}Al Larmor frequency and to 1 M Al(NO$_3$)$_3$ (aq). Adapted from J. McManus, Ph.D. thesis, University of Exeter, 2001.

($\omega_0/2\pi = 104.3$ MHz). This peak corresponds to the octahedrally coordinated Al site and exhibits features similar to the simulated lineshape in Figure 5d, characteristic of uncorrelated distributions of δ_{CS} and P_Q. The spectrum in Figure 6b was simulated using parameters derived from fitting projections of the lineshape in Figure 6a: $\langle\delta_{\mathrm{CS}}\rangle = 12$ ppm, $\Delta_{1/2}\delta_{\mathrm{CS}} = 5$ ppm (the half-width at half-height of a Gaussian distribution of δ_{CS} values), $\langle P_Q\rangle = 4.4$ MHz and $\Delta_{1/2}P_Q = 1.7$ ppm. The only fair agreement between the experiment and simulation is in part a consequence of the many assumptions made in the fitting and simulations, including uniform excitation and conversion of TQ coherences, $\eta = 1$, a complete absence of correlation between δ_{CS} and P_Q, and the Gaussian form of the distributions [22].

Summary

The MQMAS technique is one of the most powerful NMR methods for studying quadrupolar nuclei such as ^{17}O, ^{23}Na, and ^{27}Al in inorganic materials. This article has given a brief description of the experiment and outlined how MQMAS spectra can be analyzed to yield chemical shift and quadrupolar parameters. However, the reader is directed to the original literature, in particular Refs. [11,15], for more complete details on how to perform amplitude- and phase-modulated MQMAS experiments and on how to analyze spectra of nuclei of any spin quantum number.

Acknowledgments

I am grateful to the Royal Society for the award of a Leverhulme Trust Senior Research Fellowship, to EPSRC for funding our work on MQMAS from 1998 to 2003 (grants GR/M12209 and GR/N07622), and to Drs. Sharon E. Ashbrook and Jamie McManus for providing the spectra and simulations shown here.

References

1. Samoson A, Lippmaa E, Pines A. Mol. Phys. 1988;65:1013.
2. Chmelka BF, Mueller KT, Pines A, Stebbins J, Wu Y, Zwanziger JW. Nature 1989;339:42.
3. Llor A, Virlet J. Chem. Phys. Lett. 1988;152:248.
4. Frydman L, Harwood JS. J. Am. Chem. Soc. 1995;117:5367.
5. Medek A, Harwood JS, Frydman L. J. Am. Chem. Soc. 1995;117:12779.
6. Ernst RR, Bodenhausen G, Wokaun A, Principles of Nuclear Magnetic Resonance in One and Two Dimensions (Chapter 6). Clarendon Press: Oxford, 1987.
7. Fernandez C, Amoureux JP. Chem. Phys. Lett. 1995;242:449.
8. Pike KJ, Malde RP, Ashbrook SE, McManus J, Wimperis S. Solid State Nucl. Magn. Reson. 2000;16:203.
9. Amoureux JP, Fernandez C, Steuernagel S. J. Magn. Reson. A. 1996;123:116.
10. Brown SP, Wimperis S. J. Magn. Reson. 1997;124:279.
11. Brown SP, Wimperis S. J. Magn. Reson. 1997;128:42.
12. Bodenhausen G, Kogler H, Ernst RR. J. Magn. Reson. 1984;58:370.
13. Hore PJ, Jones JA, Wimperis S. NMR: The Toolkit (Chapter 6). Oxford University Press: Oxford, 2000.
14. Grandinetti PJ, Baltisberger JH, Llor A, Lee YK, Werner U, Eastman MA, Pines A. J. Magn. Reson. A. 1993;103:72.
15. Massiot D, Touzo B, Trumeau D, Coutures JP, Virlet J, Florian P, Grandinetti PJ. Solid State Nucl. Magn. Reson. 1996;6:73.
16. Wu G, Rovnyak D, Griffin RG. J. Am. Chem. Soc. 1996;118:9326.
17. Madhu PK, Goldburt A, Frydman L, Vega S. Chem. Phys. Lett. 1999;307:41.
18. Gan Z, Kwak HT. J. Magn. Reson. 2004;168:346.
19. Kentgens APM, Verhagen R. Chem. Phys. Lett. 1999;300:435.
20. Amoureux JP, Fernandez C. Solid State Nucl. Magn. Reson. 1998;10:211.
21. Brown SP, Ashbrook SE, Wimperis S. J. Phys. Chem. B. 1999;103:812.
22. McManus J, Ashbrook SE, MacKenzie KJD, Wimperis S. J. Non-Cryst. Solids. 2001;282:278.
23. Farnan I, Grandinetti PJ, Baltisberger JH, Stebbins JF, Werner U, Eastman MA, Pines A. Nature. 1992;358:31.
24. Xu Z, Stebbins JF. Solid State Nucl. Magn. Reson. 1998;11:243.

Rheo-NMR Spectroscopy

Claudia Schmidt
Department Chemie, Universität Paderborn, Warburger Str. 100, D-33098 Paderborn, Germany

Introduction

Rheology, the science of deformation and flow, is of practical importance for the preparation, processing or application of different materials such as plastics, paints, detergents, oil or food [1]. Besides this practical importance, there is a fundamental interest in understanding rheological phenomena, in particular, those of complex fluids [2]. Different types of complex fluids, for instance, polymer melts and solutions, micellar systems, and solutions of colloidal particles share the common feature of having a mesoscopic length, given by the size of macromolecules, aggregates, particles or superstructures, which is intermediate between the molecular and macroscopic scale [3]. Connected with this mesoscopic length scale is a characteristic relaxation time that is long enough to be important on the time scale of rheological experiments, defined, for example, by the shear rate. For a simple liquid of small molecules, which tumble on the time scale of 10^{-12} s, the application of shear at a rate of several hundreds or even thousands of s^{-1} is a slow disturbance not affecting the molecules, the fluid is made of. In this case Newtonian flow is observed. In complex fluids, however, the longest relaxation times can be several seconds and longer so that a shear rate of lower than 10 s^{-1} brings the experimental time scale and the intrinsic time scale of the system to match. In this case the rheology often becomes nonlinear [4].

In order to understand the rheology of complex fluids, it is important to investigate *in situ* how the structure of the fluid is affected by the flow. Many experimental techniques that provide structural information, for example, microscopy, birefringence measurements, and scattering of light, x-rays or neutrons, have been applied to flowing samples [2,5,6]. Among the newer ones of these “rheophysical” methods are magnetic resonance experiments. The term “rheo-NMR”, now widely used, was introduced by Nakatani *et al.* for their *in situ* NMR studies of sheared polymer melts [7]. Some earlier applications of NMR to sheared systems include the investigations by Vera and Grutzner [8,9] and by Lacelle [10].

There are two different approaches in rheo-NMR. The first one aims at the spatial mapping of the flow field, also known as velocity imaging. Besides the velocity other parameters such as particle concentration or diffusion constants can be mapped. This field of magnetic resonance is also known as dynamic imaging or, when high resolution is obtained, as dynamic NMR microscopy [11]. The imaging aspects of rheo-NMR have been reviewed frequently [12–17] and will not be considered here. The second approach in rheo-NMR uses simple spectroscopy, mostly without spatial resolution, to obtain information about a sample under flow. This article focusses on this spectroscopic approach of rheo-NMR. Only applications to flowing systems will be considered; the extensive work on solid-like systems, elastomers in particular, is not covered.

In liquid crystal research, rheological information, namely viscosity parameters and elastic constants of nematic phases, is often obtained through NMR spectroscopy by observing either the relaxation of the director from an out-of-equilibrium orientation back towards the magnetic field or the director orientation under continuous rotation [18–32]. For such experiments the term rheo-NMR has been applied as well.

Experimental Aspects

The most simple form of shear flow is planar Couette flow between two parallel plates as shown in Figure 1a [1]. With one plate at rest, the force per unit area that moves the other plate defines the shear stress, σ. The shear, $\gamma = dx/dy$, describes the deformation, and the shear rate, $\dot{\gamma} = d\gamma/dt$, equals the velocity gradient, dv/dy, where v is the velocity. The viscosity, η, defined by

$$\sigma = \eta\dot{\gamma} \qquad (1)$$

is constant for a Newtonian fluid. Complex fluids often show non-Newtonian flow, for example, shear thickening or shear thinning, that is, an increase or decrease of the viscosity, respectively, with increasing shear rate.

For practical reasons, such as limited amounts of sample material, rotational shear cells are used. The most common ones are the cylindrical Couette and the cone-and-plate geometry, shown in Figures 1b and c. In a cylindrical Couette system, the sample is contained in the annulus between two concentric cylinders and the shear is applied by rotating the inner or outer cylinder. If the inner cylinder is

Graham A. Webb (ed.), Modern Magnetic Resonance, 1515–1521.
© 2008 *Springer.*

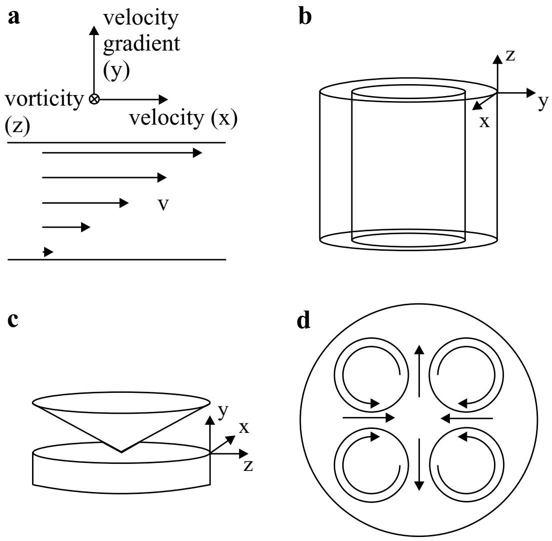

Fig. 1. Some flow geometries used in rheo-NMR experiments. (a) Planar Couette flow, the most simple type of shear flow, not used in experiments because of practical limitations. (b) Cylindrical Couette geometry. (c) Cone-and-plate geometry. (d) Four-roll-mill for extensional flow.

rotated inertia effects may cause a transition from laminar flow to Taylor vortex flow at high shear rates. Rheo-NMR experiments on Taylor vortices have been carried out, e.g., [9,33]. Compared to Couette systems, cone-and-plate devices have more uniform stress, provided the gap angle is small.

Shear occurs also in pipe or capillary flow. The stress varies across the radius and a parabolic velocity profile is observed for Newtonian liquids (Poisseuille flow). Rheo-NMR imaging of flow in cylindrical pipes or capillaries [34] and in more complex geometries with contractions and expansions [35] has revealed many interesting details.

Not only shear but also extensional flow has been studied by NMR. Callaghan and coworkers used a four-roll mill [36], shown in Figure 1d, where purely extensional flow occurs at the stagnation point in the center.

Since spin interactions are anisotropic, the orientation of the shear cell in the magnetic field is important. By aligning the symmetry axis of the shear device along the magnetic field direction spectral complexity due to different orientations of different parts of the sample is avoided. However, measurement at only one orientation with a single shear device does not provide complete information about the sample orientation in the locally biaxial shear field. Therefore, a cylindrical Couette system tilted at 90° to the magnetic field has been used, in combination with spatially selective excitation [36]. Nakatani *et al.* developed a motor-driven cone-and-plate insert for a sample tube that was used in the horizontal field of an electromagnet [7,37]. The cone-and-plate axis was perpendicular to the tube so that it could be oriented at arbitrary angles to the magnetic field. Alternatively, results obtained in axially aligned Couette and cone-and-plate systems can be combined [38].

The rotating part of the shear device can be driven by air, often using the spinner of a high-resolution NMR system [8–10,39], or by a mechanical motor [40–43]. In the latter case, samples of higher viscosity can be sheared. The motor drive can be mounted on top, which is the case in most laboratories, or below the superconducting magnet [42].

A rheo-NMR probe with a stress sensor was used by Grabowski and Schmidt [42,44]. Their cone-and-plate system consisted of a rotating plate, connected to a motor drive below the magnet, and a static cone fixed by a flexible spring. The steady-state position of the cone was measured optically. Calibration of the device with a fluid of known viscosity allowed for the determination of viscosities from the cone position.

The nuclei most commonly observed in flow experiments are ^{1}H [7,39,46–48] and ^{2}H [37,38,40,42,44–46,49–62] but also ^{13}C resonance has been used [63]. Despite the low sensitivity and the need for isotopic labeling ^{2}H has been used in the majority of experiments with spectral resolution because the single-site quadrupole interaction yields spectra that are easy to interpret. A few relaxation experiments have been carried out for protons with spectral resolution [39,47,48].

In the following, the application of ^{2}H rheo-NMR spectroscopy to liquid crystal polymers (LCPs) and surfactant solutions will be presented. Experiments were carried out with a Bruker MSL 300 spectrometer using a rotational shear device connected to a motor below the superconducting magnet with replacable tools of either cone-and-plate or cylindrical Couette geometry.

Nematic Liquid Crystals

The flow of nematic liquid crystals is described by the Leslie–Ericksen theory using six viscosity coefficients, α_i, five of which are independent [2]. Depending on the value of the flow-alignment parameter

$$\lambda = -\frac{\alpha_3 + \alpha_2}{\alpha_3 - \alpha_2} \tag{2}$$

two types of flow behavior can be distinguished. Flow-aligning nematics, characterized by $|\lambda| \geq 1$, show a stable director orientation in shear flow, whereas tumbling materials ($|\lambda| < 1$), exhibit a continuous rotation of the director. Below a critical shear rate, tumbling can be suppressed by a magnetic field.

The coupling between director and magnetic field in competition with the viscous torque is the basis for the measurement of viscosity parameters by a rheo-NMR-spectroscopic experiment [42]. In a cone-and-plate cell aligned parallel to the magnetic field, B_0, the angle between the nematic director and B_0, θ, is determined by the balance of the viscous and magnetic torques, yielding

$$\tan\theta = \mp\frac{\chi_a B_0^2}{2\mu_0|\alpha_3|\dot{\gamma}} \pm \sqrt{\left(\frac{\chi_a B_0^2}{2\mu_0\alpha_3\dot{\gamma}}\right)^2 \pm \left|\frac{\alpha_2}{\alpha_3}\right|}, \qquad (3)$$

where μ_0 is the magnetic susceptibility of the vacuum and χ_a is the anisotropy of the diamagnetic susceptibility. The upper and lower signs refer to flow-aligning materials and to tumbling systems below the critical shear rate, respectively. The critical shear rate is given by

$$\dot{\gamma}_c = \frac{\chi_a B_0^2}{2\mu_0\sqrt{-\alpha_2\alpha_3}}. \qquad (4)$$

For materials of sufficiently high viscosity such that moderate shear rates cause a substantial realignment of the director, a measurement of the director orientation θ as a function of $\dot{\gamma}$ yields α_2/χ_a and α_3/χ_a, according to equation 3 [42], and hence the flow-alignment parameter λ. The orientation angle θ is obtained from the quadrupole splitting of ^{2}H NMR spectra using

$$\Delta\nu = \frac{3}{4}\delta(3\cos^2\theta - 1). \qquad (5)$$

The motionally averaged quadrupole coupling constant, $\delta = e^2qQ/h$, is measured from the splitting at rest when $\theta = 0$. When the detection of the NMR spectra is combined with a simultaneous measurement of the viscosity, two additional viscosity parameters are obtained [42,44].

This rheo-NMR method has been applied to side-chain LCPs in bulk [42,45,49,50] and in solution [44]. Both flow-aligning and tumbling materials were identified. The onset of tumbling can be recognized qualitatively from line shapes that contain contributions from more than one angle θ.

In Figure 2, some results obtained for nematic polysiloxanes with different side chains are illustrated [45,50]. Homopolymers with only one type of side chain as well as random copolymers containing two different side chains, as shown on the top of Figure 2, were investigated. In the center of Figure 2, representative graphs of director orientation versus shear rate are depicted for the flow-aligning (PSi4) and the tumbling case (PSi6). Fitting equation 3 to the data yields the flow-alignment parameter λ. At the bottom of Figure 2, the λ values for three

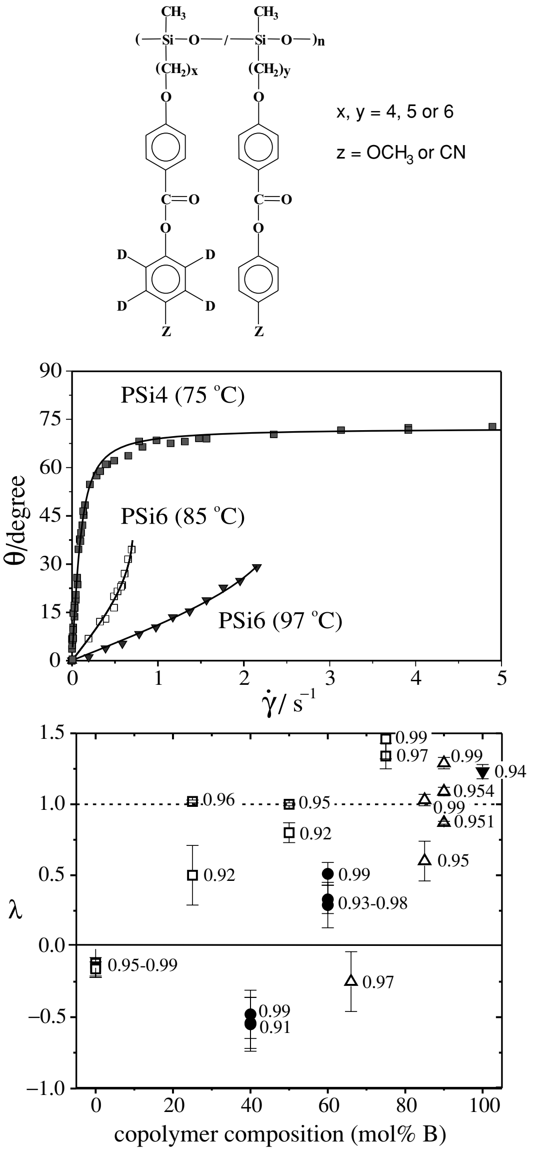

Fig. 2. Director alignment of LCPs in shear flow. Top: Chemical structure of the random copolymers ($n \approx 90$) studied by ^{2}H NMR spectroscopy in a cone-and-plate device. Center: Director orientation obtained from ^{2}H NMR spectra as a function of shear rate for the homopolymers with $z = \mathrm{OCH_3}$ and $x = 4$ (PSi4) or $x = 6$ (PSi6). Bottom: Flow-alignment parameters for different polymers (B: structural unit with $z = \mathrm{OCH_3}$ and $x = 4$, ▼: PSi4, □: $z = \mathrm{OCH_3}$, $x = 4$, $y = 6$, •: $z = \mathrm{OCH_3}$, $x = 4$, $y = 5$, △: $x = y = 4$, $z = \mathrm{OCH_3}$ or CN). The numbers next to the symbols represent the reduced temperatures T/T_{ni} (T_{ni}: clearing temperature). (From ref. [45]).

series of binary copolymers are compiled. The increase of λ with changing polymer composition can be correlated with a change of the phase structure from smectogenic to purely nematic [45,50]. In this respect, the investigated side-chain LCPs are similar to low-molar-mass nematics, for which flow tumbling is related to the existence of smectic clusters in the nematic phase.

Further investigations of nematic systems in shear flow by ^{2}H rheo-NMR spectroscopy include studies on a dimeric thermotropic material, for which the unusual observation of positive values for both α_2 and α_3 was made [51], and experiments on the calamitic and the discotic nematic phases of the surfactant system sodium dodecyl sulfate/decanol/D_2O, which were both found to be flow aligning and showed the different director orientations expected for rodlike and disklike aggregates [56]. Martins and coworkers studied the complex shear-induced reorientation behavior of lyotropic nematic solutions of polybenzylglutamate [64] and hydroxypropyl cellulose [43], which are both known tumbling LCPs.

In a recent publication, Cormier *et al.* reported on the extensional flow of the flow-aligning polymer PSi4 in a four-roll-mill [52]. By spatially selective excitation of the stagnation point the ^{2}H spectra of a protonated polymer sample containing a small amount of deuterated solvent were collected. Measurements at different strain rates show the expected flip from magnetic alignment to flow alignment along the axis of extension.

Hexagonal and Lamellar Lyomesophases

The shear-induced reorientation of the hexagonal mesophases of several nonionic surfactants was investigated by ^{2}H NMR spectroscopy [38,65–67]. Combined results from experiments in cone-and-plate and Couette geometry prove that the director aligns along the velocity axis. Log-rolling, an orientation along the vorticity axis, which was discussed initially on the basis of light scattering results, does not occur. Experiments at small shear rates below 10^{-2} s^{-1} starting from either disordered polycrystalline or magnetically aligned (by annealing at the isotropic-hexagonal phase transition) samples show that the reorientation is controlled by the strain and is independent of the shear rate. A simple model for the strain-controlled process of reorientation is shown on the top of Figure 3. The experimental data obtained for two solutions of $C_{12}E_5$ in D_2O (Figure 3, center) follow the predicted relationship between strain and orientation, $\gamma = \tan\theta$ [38].

The quadrupole doublets of both magnetically aligned and slightly sheared hexagonal samples exhibit a substantial linewidth, as shown in Figure 3 (bottom left). The detailed analysis of such line shapes using Tikhonov regularization [38,68] yielded a distribution of director orientations, which result from an undulation of the director. The undulation also causes the characteristic striated textures observed by polarizing microscopy [38,66] (cf. Figure 3 (bottom right)). However, when a sample is subjected to large shear at a small rate a substantial reduction of the linewidth is observed, indicating perfect alignment without undulations.

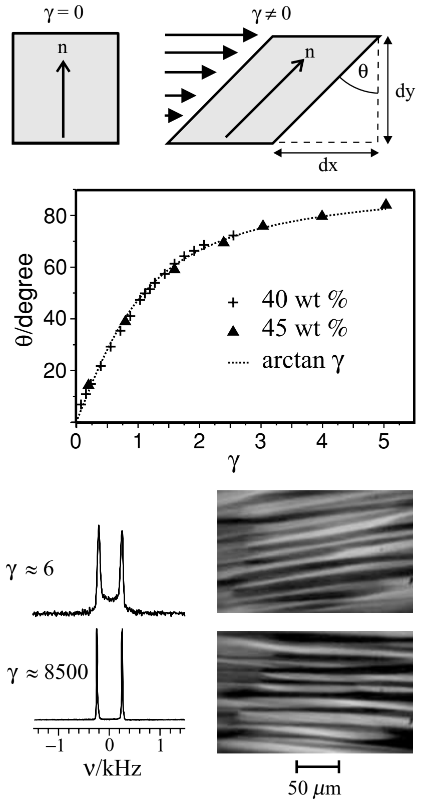

Fig. 3. Shear-induced alignment of the hexagonal phase of $C_{12}E_5/D_2O$. Top: Model of the realignment starting from an orientation of the director (**n**) along the velocity gradient axis. Center: Orientation angles in cone-and-plate geometry determined by ^{2}H NMR spectroscopy in dependence of the shear strain γ. Bottom: ^{2}H spectra at low and high strain (left) and micro-images of a sample sheared by a few strain units between crossed polarizers (right). The inversion of contrast upon inverting the angle between flow direction and polarizer axis indicates a director undulation (From Ref. [38]). (See also Plate 120 on page XVI in the Color Plate Section.)

First rheo-NMR experiments on lamellar phases were carried out on the nonionic surfactant system $C_{12}E_6/D_2O$ [53], confirming the shear-induced onion state, previously

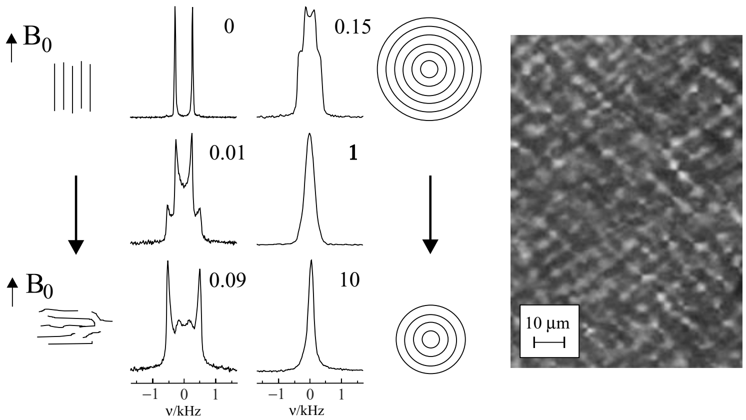

Fig. 4. Shear-induced formation of multilamellar vesicles (onions) in the lamellar phase of $C_{12}E_4/D_2O$ (35% w/w). Left: ^2H NMR spectra obtained in cone-and-plate geometry at increasing shear rates given in s^{-1} for each spectrum. At the beginning, the normal vectors of the layers (directors) are magnetically aligned in the velocity–vorticity plane. Shear at low rates leads to imperfect director alignment parallel to the velocity gradient. Increasing the shear rate induces the onion state. The vesicles get smaller upon increasing shear rate. Right: Microscopical image of the shear-induced onion texture between crossed polarizers (From Ref. [54]).

discovered [69]. This state of orientation is a metastable defect structure consisting of monodisperse, close-packed, multilamellar vesicles. Subsequently, the system $C_{12}E_4/D_2O$ was investigated by rheo-NMR as well as by conventional viscometry, rheo-light scattering and polarizing microscopy [54]. Like many other lamellar systems upon increasing shear rate, $C_{12}E_4/D_2O$ first shows an alignment of the layers in the velocity–vorticity plane accompanied by shear thinning. Further increase of the shear rate leads to shear thickening, indicating the formation of the onion structure. *In situ* NMR measurements, depicted in Figure 4, prove that the transition from aligned layers to onions is a gradual process that does not occur via a "two-phase" region. The decreasing linewidth is due to the decrease of the onion diameter from several micrometers down to about half a micrometer. Figure 4 (right) shows the characteristic onion texture as observed between crossed polarizers.

Rheo-NMR spectroscopy on other lamellar systems under shear has revealed further interesting details. Depending on the system, its components, concentration, and temperature, additional states of orientation may occur (cf. Figure 5). Besides the already mentioned alignment of layers in the velocity–vorticity plane (parallel orientation) and the onion state an alignment of layers in the velocity–velocity gradient plane (perpendicular orientation) is often found. The quadrupole splittings of one of the polymers, as shown in Figure 5, suggest such a perpendicular orientation at high shear rates [55], where the splitting is approximately the same as at rest.

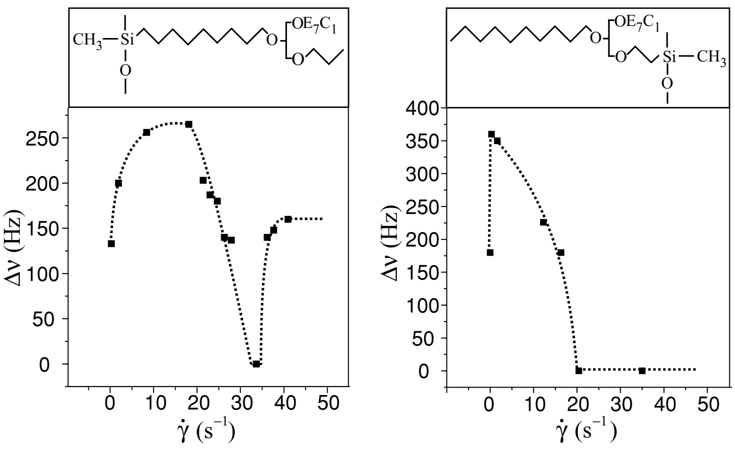

Fig. 5. Quadrupole splittings obtained for the lamellar phases of two different amphiphilic polymers in cone-and-plate geometry showing different states of shear orientation (From Ref. [55]).

Shear-Induced Phase Transitions

The sensitivity of NMR spectra to phase transitions was used for the investigation of the relaxation of shear-induced nematic order in an isotropic worm-like micellar system consisting of lecithin, D_2O, and cyclohexane [57]. When shear is stopped the nematic order disappears on the time scale of minutes. Time-resolved ^{2}H NMR spectra shows that the relaxation process is characterized by a continuous decrease of the measured quadrupolar splitting proportional to the nematic order parameter.

Conclusions

Rheo-NMR spectroscopy is a valuable addition to the stable of rheo-physical methods, yielding information complementary to other techniques. It is noninvasive and can be applied to opaque samples. Its future applications in material science will certainly provide more insight into the rheological phenomena of complex fluids.

References

1. Barnes HA, Hutton JF, Walters K. An Introduction to Rheology. Elsevier: Amsterdam, 1989.
2. Larson RG, The Structure and Rheology of Complex Fluids. Oxford University Press: New York, Oxford, 1999.
3. Gelbart WM, Ben-Shaul A. J. Phys. Chem. 1996;100:13169.
4. Malkin AY. Rheol. Acta 1995;34:27.
5. Søndergaard K, Lyngaae-Jørgensen J. (eds.). Rheo-Physics of Multiphase Polymer Systems. Characterization by Rheo-Optical Techniques. Technomic Publishing Company: Lancaster, 1995.
6. Fuller GG. Optical Rheometry of Complex Fluids. Oxford University Press: New York, 1995.
7. Nakatani AI, Poliks MD, Samulski ET. Macromolecules 1990;23:2686.
8. Vera M, Grutzner JB. Bull. Magn. Reson. 1986;8:181.
9. Vera M, Grutzner JB. J. Am. Chem. Soc. 1986;108:1304.
10. Lacelle S, Cau F, Tremblay L. J. Phys. Chem. 1991;95:7071.
11. Callaghan PT. Principles of Nuclear Magnetic Resonance Microscopy. Clarendon Press: Oxford, 1991.
12. Stepišnik J. Prog. Nucl. Magn. Reson. 1985;17:187.
13. Caprihan A, Fukushima E. Phys. Reports 1990;198:195.
14. Callaghan PT. Rep. Prog. Phys. 1999;62:599.
15. Fukushima E. Annu. Rev. Fluid Mech. 1999;31:95.
16. Callaghan PT. Encyclopedia of Magn. Reson. 2002;9:739.
17. Mantle MD, Sederman AJ. Prog. Nucl. Magn. Reson. Spectr. 2002;43:3.
18. Leslie FM, Luckhurst GR, Smith HJ. Chem. Phys. Lett. 1972;13:368.
19. Emsley JW, Lindon JC, Luckhurst GR, Shaw D. Chem. Phys. Lett. 1973;19:345.
20. Carr SG, Luckhurst GR, Poupko GR, Smith HJ. Chem. Phys. 1975;7:278.
21. Eastman MP, Freiha BA, Kessel B, Allen CC. Liq. Cryst. 1986;1:147.
22. Emsley JW, Khoo SK, Lindon JC, Luckhurst GR. Chem. Phys. Lett. 1981;77:609.
23. Khoo SK, Luckhurst GR. Liq. Cryst. 1993:15;729.
24. van der Putten D, Schwenk N, Spiess HW. Liq. Cryst. 1989;4:341.
25. Schwenk N, Boeffel C, Spiess HW. Liq. Cryst. 1992;12:735.
26. Schwenk N, Spiess HW. J. Phys. II 1993;3:865.
27. Gotzig H, Grunenberg-Hassanein S, Noack F, Z Naturforsch. 1994;49a:1179.
28. Martins AF, Esnault P, Volino F. Phys. Rev. Lett. 1986;57:1745.
29. Gonçalves LN, Casquilho JP, Figueirinhas J, Cruz C, Martins AF. Liq. Cryst. 1993;14:1485.
30. Martins AF, Gomes AE, Polimeno A, Orian L. Phys. Rev. E 2000;62:2301.
31. Ciampi E, Emsley JW. Liq. Cryst. 1997;22:543.
32. Ciampi E, Emsley JW, Luckhurst GR, Timimi BA, Kothe G, Tittelbach M. J. Chem. Phys. 1997;107:5907.
33. Seymour JD, Manz B, Callaghan PT. Phys. Fluids 1999;11:1104.
34. Xia Y, Callaghan PT. Macromolecules 1991;24:4777.
35. Xia Y, Callaghan PT, Jeffrey KR. AIChE J. 1994;38:1408.
36. Britton MM, Callaghan PT, Kilfoil ML, Mair RW, Owens K. Appl. Magn. Reson. 1998;15:287.
37. Nakatani AI, Samulski ET. Polym. Prep. (ACS) 1986;27:169.
38. Müller S, Fischer P, Schmidt C. J. Phys. II 1997;7:421.
39. Badiger MV, Rajamohanan PR, Suryavanshi PM, Ganapathy S, Mashelkar RA. Macromolecules 2002;35:126.
40. ter Beek LC, Linseisen FM. Macromolecules 1998;31:4986.
41. Rofe CJ, Lambert RK, Callaghan PT, J. Rheol. 1994;38:875.
42. Grabowski DA, Schmidt C. Macromolecules 1994;27:2632.
43. Godinho MH, van der Klink JJ, Martins AF. J. Phys.: Condens. Matter 2003;15:5461.
44. Siebert H, Grabowski DA, Schmidt C. Rheol. Acta 1997;36:618.
45. Siebert H, Becker P, Quijada-Garrido I, Grabowski DA, Schmidt C. Solid State Nucl. Magn. Reson. 2002;22:311.
46. Callaghan PT, Kilfoil ML, Samulski ET. Phys. Rev. Lett. 1998;81:4524.
47. Callaghan PT, Gil AM. Rheol. Acta 1999;38:528.
48. Callaghan PT, Gil AM. Macromolecules 2000;33:4116.
49. Quijada-Garrido I, Siebert H, Becker P, Friedrich C, Schmidt C. Rheol. Acta 1999;38:495.
50. Becker P, Siebert H, Noirez L, Schmidt C. Macromol. Symp. 2005;220:111.
51. Lukaschek M, Kothe G, Schmidt C, Gomes AE, Polimeno A. J. Chem. Phys. 2002;117:4550.
52. Cormier RJ, Schmidt C, Callaghan PT. J. Rheol. 2004; 48: 881.
53. Lukaschek M, Müller S, Hasenhindl A, Grabowski DA, Schmidt C. Colloid Polym. Sci. 1996;274:1.
54. Müller S, Börschig C, Gronski W, Schmidt C, Roux D, Langmuir 1999;15:7558.
55. Burgemeister D, Schmidt C. Prog. Colloid Polym. Sci. 2002;121:95.
56. Thiele T, Berret J-F, Müller S, Schmidt C. J. Rheol. 2001:45:29.
57. Angelico R, Burgemeister D, Ceglie A, Olsson U, Palazzo G, Schmidt C. J. Phys. Chem. B 2003;107:10325.
58. Kilfoil ML, Callaghan PT. Macromolecules 2000;33:6828.

59. Cormier RJ, Kilfoil ML, Callaghan PT. Phys. Rev. E 2001;64:051809.
60. Cormier RJ, Callaghan PT. J. Chem. Phys. 2002;116:10020.
61. Fischer E, Callaghan PT, Europhys. Lett. 2000;50:803.
62. Fischer E, Callaghan PT. Phys. Rev. E 2001;64:011501.
63. Fischer E, Callaghan PT, Heatley F, Scott JE. J. Mol. Struct. 2002;602–603:303.
64. Orian L, Feio G, Veron A, Polimeno A, Martins AF. Mol. Cryst. Liq. Cryst. 2003;394:63.
65. Lukaschek M, Grabowski DA, Schmidt C. Langmuir 1995;11:3590.
66. Schmidt G, Müller S, Lindner P, Schmidt C, Richtering W. J. Phys. Chem. B 1998;102:507.
67. Schmidt G, Müller S, Schmidt C, Richtering W. Rheol. Acta 1999;38:486.
68. Winterhalter J, Maier D, Grabowski DA, Honerkamp J, Müller S, Schmidt C. J. Chem. Phys. 1999;110:4035.
69. Diat O, Roux D, Nallet F. J. Phys. II 1993;3:1427.

Advances in Single-Sided NMR

J. Perlo, F. Casanova, and B. Blümich
Institut für Technische und Makromolekulare Chemie, RWTH Aachen D-52056, Germany

Introduction

Nuclear magnetic resonance (NMR) is an established powerful analytical tool widely used for structural and conformational analysis in chemistry, biology, medicine, and material science [1,2]. Material characterization is mainly carried out by measuring NMR parameters like the chemical shift, the nuclear spin relaxation times, the dipolar coupling, and the self-diffusion coefficient. Furthermore, NMR is employed to produce images contrasted by these parameters, and to characterize diffusive and coherent molecular motion in a non-invasive fashion. NMR methods have been initially developed to work in the homogeneous fields of strong magnets, but the limited working volume of these devices restricts the applications of NMR, in particular for *in situ* studies of large objects. But in addition to conventional NMR, where the sample is adapted to fit into the probe, there is inside-out NMR, which uses open magnet geometries specially adapted to the object under study. Such open magnets can be inexpensive and portable. They provide excellent versatility in accessing a large number of applications by NMR, which are inaccessible to closed magnet geometries. Historically the inside-out concept was developed for examining geological formations by lowering a full NMR spectrometer into a borehole to record signals from different formations [3]. Different tool geometries have been designed for well-logging [3,4] and water reservoir studies [5]. Later on the concept of single-sided NMR was extended to moisture detection in composites [6], medical diagnostics [7,8], and material analysis and quality control [9,10]

The price paid for non-invasiveness and access to arbitrarily large objects is the lack of high and homogeneous magnetic fields. This in turn limits the available experimental techniques, excluding for example high-resolution NMR spectroscopy methods, leaving for sample characterization mainly the measurement of signal amplitude, relaxation times T_1 and T_2, and the self-diffusion coefficient. Nevertheless, during the last years, the number of new methods especially developed to work in the inhomogeneous fields of single-sided sensors has considerably grown, so that, for example, multiple-quantum coherences [11], diffusion-relaxation correlation maps [12], images [13], and flow distributions can be measured [14]. Even the first steps to recover spectroscopic information in the presence of inhomogeneous fields have successfully been taken [15]. In the next sections, the state of the art in single-sided NMR is reported.

Material Characterization via Relaxometry by the NMR-MOUSE

A hand held single-sided NMR sensor that has extensively been used for non-destructive material testing is the so-called NMR-MOUSE® (mobile universal surface explorer) [9]. Its original magnet geometry combines two permanent magnets with opposite polarization placed on an iron yoke to form a U-shaped magnet. The open magnet defines a sensitive spot above its surface, from where the NMR signal is measured. Different regions of the object can be studied by simply repositioning the sensor. The main characterization procedure requires that a correlation between the relaxation times measured with the NMR-MOUSE and the material property of interest exists. An important example is the linear relationship between T_2 and the cross-link density of elastomers, which is explored to determine the homogeneity and the degree of vulcanization of intermediate and final products in the rubber manufacturing business [16].

The open geometry and mobility of the NMR-MOUSE are essential when investigating samples that cannot be moved, for example, specimens of Cultural Heritage, where the non-invasive and the non-destructive character are strict requirements for the safeguard of these objects. Examples of such applications are the analysis of historical building materials [17], and the degradation of antique paper, where, although only a small amount of paper (10–20 mg) is required, conventional NMR is destructive to the object under study [18].

As an example for single-sided NMR relaxometry, the use of the NMR-MOUSE is reported to study the water and oil absorption in polyethylene samples. This material is widely used in the construction of tanks and pipes used to store and transport different fluids. By simple molecular diffusion, the liquids penetrate the walls and sooner or later evaporate. Although the problem is well known, there are few experimental techniques to measure the degree of penetration *in situ*. The situation is even worse when

Graham A. Webb (ed.), Modern Magnetic Resonance, 1523–1527.
© 2008 *Springer.*

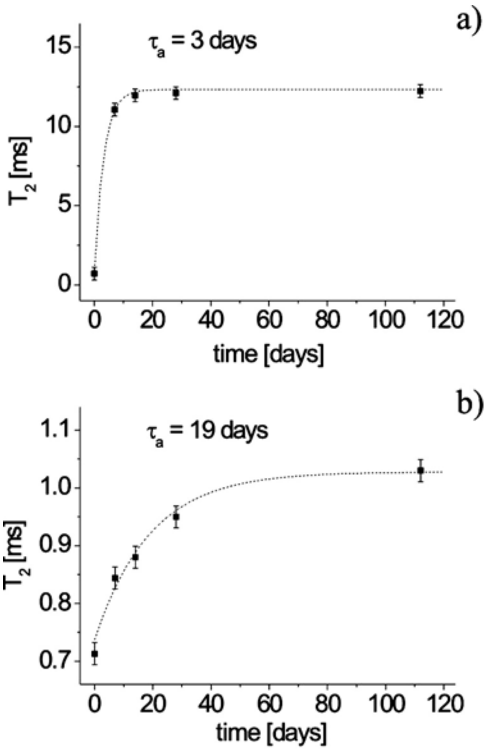

Fig. 1. Oil (a) and water (b) absorption in polyethylene. Samples with different contamination times were measured by applying a CMPG sequence. The decay of the echo envelope was fitted with a stretched exponential function to obtain T_2. The error bar corresponds to variations observed in a set of samples with the same contamination condition.

toxic substances are stored and already small evaporated quantities may give rise to relevant environmental damage.

A dedicated NMR-MOUSE sensor was set at the surface of polyethylene samples, and the presence of different contaminants was determined by measuring T_2 with a CMPG sequence. To study the characteristic absorption time of oil and water in polyethylene, different specimens were immersed in these solvents for 0, 7, 14, 28, and 112 days. Figure 1 shows the T_2 behavior as a function of the exposure time for both contaminants. The effect of the oil absorption is much larger than the one produced by the water, indicating that the oil strongly affects the material structure. Simply by correlating the dependence of T_2 with the weight of the sample as a function of the absorption, T_2 can be directly used to determine the amount of solvents inside polyethylene with good precision.

3D Imaging with a Single-Sided Sensor

Single-sided sensors are mainly used to characterize large size objects by measuring relaxation times and self-diffusion coefficients inside a spot near the surface. The complete object can be scanned by repositioning the sensor and an image with a typical resolution of about 1 cm can be obtained [19]. To obtain better spatial resolution, Fourier imaging techniques have been implemented with pulsed field gradients. In the presence of a strong static magnetic field gradient, only pure-phase encoding methods can be used to encode position across the selected sensitive volume [20]. Although long experimental times were initially required to produce 1D images, different methods have been proposed to improve the image quality and reduce the experimental time [21,22]. A milestone in the development of imaging methods for inhomogeneous fields was the design of a multi-echo acquisition scheme that reduces the experimental time up to two orders of magnitude [13]. The method has been implemented on a dedicated single-sided sensor, and different imaging experiments have been performed on objects with simple geometries to quantify the sensitivity enhancement and to test the performance of a 3D imaging multi-slice procedure. The multi-echo acquisition scheme has been also used to measure T_2 maps in heterogeneous objects, like samples from rubber with different cross-linking density across the object. The image contrast can be adjusted to relaxation time and diffusion weighting of the spin density.

In the following, applications of the open tomograph in medicine and in quality control of rubber products are demonstrated by two selected samples. A promising application of a mobile and low-cost single-sided tomograph is the diagnosis of arthritis, which produces deformation of the bones and joints. The multi-echo imaging sequence was implemented to produce cross-sections through a human finger at the positions marked in Figure 2A. Figure 2B shows two images of each slice reconstructed from the same experiment, but considering different parts of the acquired echo train. The first one possesses a low T_2 weight, while in the second one the T_2 contrast is increased to enhance the tissues with long T_2. The dimensions and shape of the bone and the bone marrow can be identified as well as the positions of vessels, arteries, and the tendon.

An application of the open tomograph to the quality control of rubber products is depicted in Figure 3 by example of slice-selective images of an air spring bellows from a shock absorber of a passenger car. The material is reinforced by two layers of textile fibers with perpendicular orientations. Figure 3b shows two 2D slice images, one for each fiber layer. The signal of the fibers is negligible compared to that of the rubber matrix, so that the fibers appear dark in the images. By projecting the 2D image

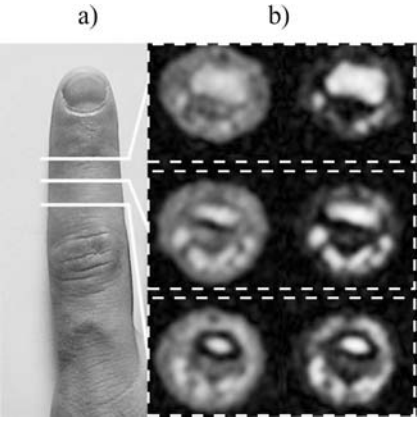

Fig. 2. (a) Human finger showing the position of the slices selected to be imaged. (b) Images obtained at three different positions along the fingertip. The image on the left shows the proton density while the one on the right possesses a strong T_2 contrast. For a slice thickness of 1 mm and lateral resolution of 1 mm^2, the imaging time was 9 min per slice.

along the fiber direction a 1D projection is obtained (Figure 3c). From the minima in the profile the position of the fibers can be determined with good precision, so that defects in the fiber layers can be identified.

Flow Characterization with a Single-Sided Sensor

Displacement or flow encoding is achieved by pulsed field-gradient techniques with pares of alternating gradients field pulses. Powerful sequences like the so-called 13-interval sequence have been designed to reduce distortions introduced by background gradients for displacement encoding in inhomogeneous fields [23], but they do not work in the highly inhomogeneous fields of single-sided sensors. The large off-resonance excitation in the static gradient field and the spatially inhomogeneous radio frequency field keep the radio frequency pulses from achieving uniform plane rotations for all the spins. The radio frequency pulses generate a large number of coherence pathways most of them being unfavorably encoded by the gradient pulses. Therefore, a new sequence to remotely measure the velocity distributions with a single-sided sensor was developed [14]. It consists of a 13-interval sequence and a suitable phase cycle to account for the signal from non-uniform rotations followed by a multi-echo acquisition scheme to overcome the sensitivity problem inherent to single-sided sensors. Moreover, the selective slice was moved along the depth direction, to spatially resolve the velocity distribution along the depth direction [24]. This method was used to measure the velocity profile of laminar flow through a rectangular pipe whose width is much larger than its height. For such an aspect ratio, the velocity

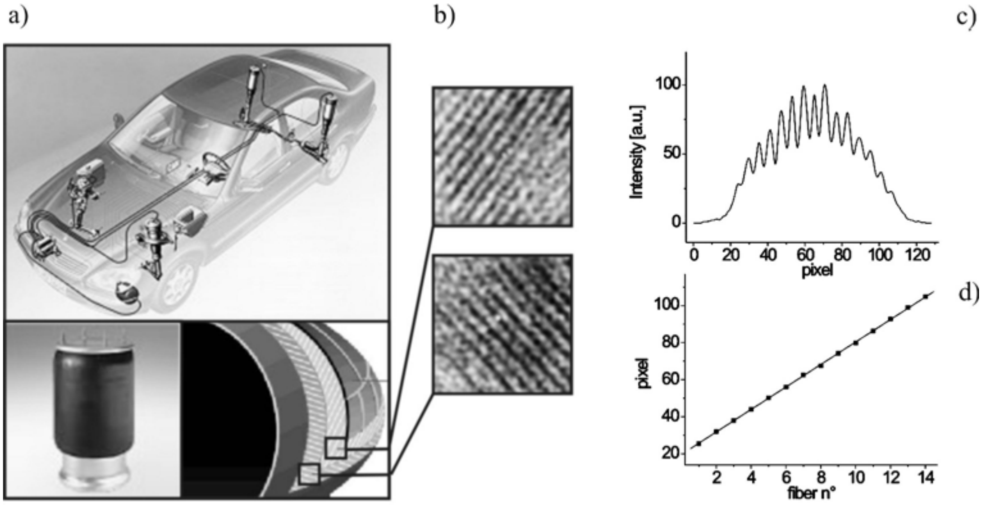

Fig. 3. (a) Airs springs are used in intelligent suspension systems that control the hardness of the shock absorber by adjusting the air pressure in the rubber bellows. The rubber matrix of the air spring bellows is reinforced by crossed layers of textile fibers. (b) Slice-selective 2D images of each fiber layer. The spatial resolution is about 200 μm, and the acquisition time of each image was 2 h. (c) Projection of one 2D image along the fiber direction. (d) Positions of the fibers determined from the 1D profile.

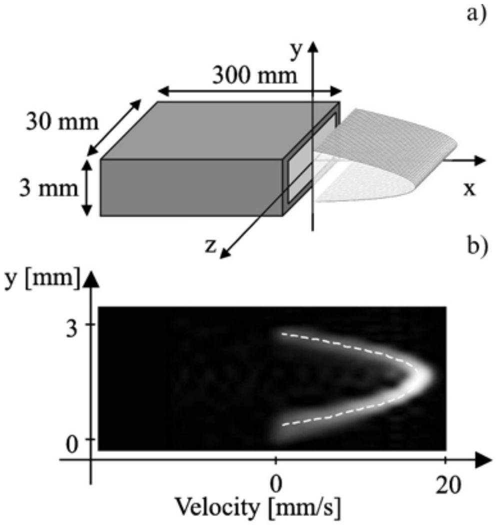

Fig. 4. (a) Laminar flow in a rectangular pipe. The velocity distribution is parabolic along the depth direction. (b) 1D velocity profile spatially resolved along the *y*-axis. The complete tube section was scanned in 10 slices, 0.3 mm thick. The measuring time was 5 min to obtain the velocity distribution in each slice with a resolution of 1 mm/s and a field of flow of 30 mm/s. The sensor used for these experiments is described in Ref. [13].

can be assumed to be constant along the long side, while it changes as a parabolic function along the short dimension (Figure 4a) [25]. Figure 4b shows the measured velocity distribution, which is in very good agreement with the predicted profile.

Conclusions and Remarks

Important advances in the development of dedicated single-sided sensors as well as pulse sequences suitable for their use have been reported during the last years. The conventional relaxation analysis has been combined with fast imaging methods to achieve a more detailed characterization of heterogeneous objects, and new sequences were developed to encode displacement, so that, for example, blood flow in vessels and arteries, and flow distributions in injectors and mixer can be analyzed non-destructively. The whole power of conventional NMR seems to become available to single-sided sensors, which are continuously finding new applications. The extreme versatility of such sensors to access immobile samples, in addition to the non-invasive character of the measurement identify this method as a unique tool to detect the presence of failures and defects in final products or at different stages during the production.

References

1. Callaghan PT. Principles of Nuclear Magnetic Resonance Microscopy. Clarendon Press: Oxford, 1991.
2. Blümich B. NMR Imaging of Materials. Clarendon Press: Oxford, 2000.
3. Kleinberg RL. Well logging. In: DM Grant, RK Harris (Eds). Encyclopedia of NMR. Wiley: New York, 1996, pp 4960–9.
4. Jackson JA, Burnett LJ, Harmon F. Remote (Inside-Out) NMR III: detection of nuclear magnetic resonance in a remotely produced region of homogeneous magnetic field. J. Magn. Reson. 1980;41:411–21.
5. Shushakov OA. Ground water NMR in conductive water. Geophysics 1996;61:998-1006.
6. Prado PJ. NMR hand-held moisture sensor. Magn. Reson. Imaging. 2001;19:505–8.
7. US Patent 5,959,454. Bruker Analytic. Magnet arrangement for an NMR tomography system, in particular for skin and surface examinations.
8. Haken R, Blümich B, Anisotropy in tendon investigated in vivo by a portable NMR scanner, the NMR-MOUSE. J. Magn. Reson. 2000;144:195–9.
9. Eidmann G, Salvelsberg R, Blümler P, Blümich B. The NMR-MOUSE, a mobile universal surface explorer. J. Magn. Reson. A. 1996;122:104–9.
10. Matzkanin GA. A review of non-destructive characterization of composites using NMR. In: Nondestructive Characterization of Materials. Springer: Berlin, 1998, p 655.
11. Wiesmath A, Filip C, Demco DE, Blümich B. NMR of multipolar spin states excitated in strongly inhomogeneous magnetic fields. J. Magn. Reson. 2002;144:60–72.
12. Hürlimann MD, Flaum M, Venkataramanan L, Flaum C, Freedman R, Hirasaki GJ. Diffusion-relaxation distribution functions of sedimentary rocks in different saturation states. Magn. Reson. Imaging. 2003;21:305–10.
13. Perlo J, Casanova F, Blümich B. 3D imaging with a single-sided sensor: an open tomograph. J. Magn. Reson. 2004;166:228–35.
14. Casanova F, Perlo J, Blümich B. Velocity distributions remotely measured with a single sided NMR Sensor. J. Magn. Reson. 2004;171:124–130.
15. Meriles CA, Sakellariou D, Heise H, A.Moulé J, Pines A. Approach to high-resolution ex situ NMR spectroscopy. Science. 2001;293:82–5.
16. Zimmer G, Guthausen A, Blümich B. Characterization of cross-link density in technical elastomers by the NMR-MUOSE. Solid State Nucl. Magn. Reson 1998;12:183–90.
17. Sharma S, Casanova F, Wache W, Segre A, Blümich B. Analysis of historical porous building materials by the NMR-MOUSE. Magn. Reson. Imaging. 2003;21:249–55.
18. Blümich B, Anferova S, Sharma S, A.Segre L, Federici C. Degradation of historical paper: nondestructive analysis by the NMR-MOUSE. J. Magn. Reson. 2003;161:204–9.
19. Guthausen A, Zimmer G, Eymaul R, Schitz U, Blümler P, Blümich B. Soft malter relaxation by the NMR mouse. In: Blümler P, Blümich B, Botto R, Fukushima E. (eds.) Spatially Resolved Magnetic Resonance. Wiley-VCH Publisher, Weinheim, 1998, pp. 195–209.
20. Prado P, Blümich B, Schmitz U. One-dimensional imaging with a palm-size probe. J. Magn. Reson. 2000;144:200–6.

21. Casanova F, Blümich B. Two-dimensional imaging with a single-sided NMR probe. J. Magn. Reson. 2003;163:38–45.
22. Casanova F, Perlo J, Blümich B, Kremer K. Multi-echo imaging in highly inhomogeneous magnetic fields. J. Magn. Reson. 2004;166:76–81.
23. Cotts RM, Hoch MJR, Sun T, Markert JT. Pulsed field gradient stimulated echo methods for improved NMR diffusion measurements in heterogeneous systems. J. Magn. Reson. 1989;83:252–66.
24. Perlo J, Casanova F, Blümich B. Velocity imaging by ex situ NMR. J. Magn. Reson. 2005;173:254–58.
25. Grondret P, Rakotomalala N, Rabaud M, Salin D, Watzky P. Viscous parallel flows in finite aspect ratio Hele-Shaw cell: analytical and numerical results. Phys. Fluids 1997;9:1841–3.

Site-specific Characterization of Structure and Dynamics of Complex Materials by EPR Spin Probes

Dariush Hinderberger and Gunnar Jeschke
Max-Planck-Institut für Polymerforschung, Postfach 3148, 55021 Mainz, Germany

Introduction

With the notable exceptions of magnetic materials and some transition metal catalysts most materials are diamagnetic and thus do not exhibit strong EPR signals. Occasionally, weak signals due to impurities and defects may be of significant interest, as for instance in semiconductors and optical materials, where such irregularities of the structure strongly influence those properties that have to be optimized for typical applications. The majority of materials, however, can be considered as EPR silent. This lack of background signals from the bulk of the sample provides the opportunity to apply EPR spectroscopy as a probe technique. Sites of interest in complex materials can thus be addressed with high specificity and a sensitivity corresponding to bulk concentrations of electron spins between 10 μM and 1 mM. Development of such approaches is strongly aided by similar work on biological systems [1]. Starting from the past decade several groups have focused on direct covalent attachment of stable free nitroxide radicals to interfacial sites in complex materials (spin-labeling) [2–5]. In an alternative concept, the electrostatic and hydrophobic interactions that govern self-assembly of supramolecular systems are utilized to direct spin probes with appropriate functionality to the site of interest [5–7]. Basic considerations about the choice of spin probes and the attachment of labels are discussed in Section "Addressing Specific Sites by Spin Probes and Spin Labels". Dynamics of such spin probes and labels on time scales between 10 ps and 1 μs can be characterized by the basic, fast and sensitive continuous-wave (CW) EPR experiment and is a rich source of information on both dynamics and structure of the materials themselves [6,8–10]. The most important approaches for analyzing such dynamics are discussed in Section "Detecting Supramolecular Interactions by Changes in Probe Dynamics".

Many materials of current interest exhibit structural features on length scales between 1 and 10 nm. Detailed structural information on this length scale is difficult to obtain by established characterization techniques unless the materials exhibit long-range order. Distance measurements between spin probes or spin labels [5,11–14] do not depend on such long-range order and can provide useful information even for conformational ensembles [14–17]. Measurements in the range between 1 and 2 nm are best performed with CW EPR measurements and have been reviewed in some detail before [5]. Therefore, Section "Characterization of Broad Distance Distributions" focuses on newer developments in the measurement of distance distributions in the range between 1.75 and 5 nm by pulse EPR techniques, while Section "Concatenated Macrocycles in Frozen Solution" demonstrates how such an approach can be used to characterize the coconformational ensemble of two concatenated macrocycles. Finally, Section "Polyelectrolytes: Probing Polyion-counterion . . . " illustrates application of a multitude of EPR techniques to a dianionic spin probe that interacts electrostatically with a cationic polyelectrolyte.

Addressing Specific Sites by Spin Probes and Spin Labels

Spin Probes as Tracers in Supramolecular Structures

Complex supramolecular structures are built from a number of different molecular constituents. Accordingly, characterization of their structure and dynamics is simplified if the constituents can be studied one by one. Such an approach requires spin probes that closely mimic certain constituents or have a strong preference for a certain domain in the material. In polymer films formed from collodial dispersions and the polymer dispersions themselves, we could selectively address polar and nonpolar sites and the head-group and tail-end regions of surfactant layers or surfactant aggregates [6,18]. Slightly polar probes in dispersions exhibited a stronger preference for the spherical polymer particles compared to the aqueous serum. For polymers above their glass transition temperature, they were found to diffuse from the serum into the particles on a timescale of several hours. By analyzing the diffusion kinetics of paramagnetic additive molecules, we could determine very small diffusion coefficients of less than $10^{-15}\,\mathrm{cm}^2\,\mathrm{s}^{-1}$ [8]. In general, spin probes can be selected or constructed that are

Graham A. Webb (ed.), Modern Magnetic Resonance, 1529–1537.
© 2008 *Springer.*

good tracers for constituent molecules whose size significantly exceeds 1 nm. The limit is given by the diameter of the nearly spherical nitroxide moiety that can be introduced as a five- or six-membered heterocycle (e.g., 2,2,5,5-tetramethyl-pyrrolidine-1-oxyl or 2,2,6,6-tetramethyl-piperidine-1-oxyl).

Principles of Spin Labeling

Nitroxide moieties are attached to macromolecules or surfaces via a linker group that has to be sufficiently long and flexible to avoid an influence of the label on the structure of the macromolecule [19]. On the other hand, the linker should be short enough to bring the label close to the intended site and rigid enough to couple it to the dynamics of the probed structure. As far as distance measurements on conjugated systems are concerned, the linker should break the conjugation pathway to avoid errors due to significant exchange coupling between the two spins [20]. Typically, the center of the nitroxide bond is thus separated by 0.6 to 1 nm from the point of attachment.

Detecting Supramolecular Interactions by Changes in Probe Dynamics

Continuous-wave EPR spectra of nitroxides are sensitive to rotational correlation times on time scales between 10 ps and 1 μs. In the range from 100 ps to 50 ns, the line shapes are a rich source of information on the specifics of the molecular reorientation process, e.g. on anisotropy of rotational dynamics or potentials that restrict reorientation. Rotational dynamics of spin labels attached to macromolecules is influenced by restricted sidegroup motion, local backbone fluctuations at the point of attachment, and global tumbling of the macromolecule. Successful line-shape simulations for such complex motion could be achieved in the context of site-specifically spin-labeled proteins by deriving a reorientation potential from molecular dynamics simulation and computing the EPR response from trajectories for Brownian rotational diffusion [22] in this potential [23]. A more abstract approach assumes that restricted sidegroup motion can be modeled by reorientation of the spin label in a cone and the combined effect of backbone fluctuations and global tumbling can be modeled by an axially symmetrical rotational diffusion tensor (slowly relaxing local structure model) [24]. At sufficiently high EPR frequencies, the latter slow processes do not significantly influence the line shape, as was demonstrated by a combined 250 and 9 GHz EPR study on membrane vesicles containing a chain and labeled phospholipid [25]. Detailed line-shape simulations based on a model of restricted rotational diffusion (microscopic order/macroscopic disorder) [26] were also successful for spin-labeled surfactant molecules in polymer dispersions [6].

In many cases, however, such detailed simulations are not feasible for material applications, either because the parameters for a complex reorientation process are distributed or the timescale of restricted motions in the temperature range of interest is too fast or too slow to resolve the details. Useful general information on the reorientation process can often be obtained nevertheless by *approximate* fits to a simple model of Brownian diffusion with an axially symmetric rotational diffusion tensor with principal values $R_{||}$ (unique axis) and $R_{\perp}$ (perpendicular to the unique axis) [6,10,18]. The sensitivity of CW EPR line shapes to the orientation of the unique axis in the molecular frame and to the rotational correlation time

$$\tau_r = \frac{1}{6\sqrt[3]{R_{\perp}^2 R_{||}}}. \tag{1}$$

is illustrated in Figure 1. Differences between isotropic rotational diffusion ($R_{||} = R_{\perp}$, left column) and preferential rotation about the z axis ($R_{||} = 10R_{\perp}$, second column from left) are best visible with high-frequency EPR (W-band, 94 GHz, bottom panel) as the difference is related to the g tensor, while preferential orientation about any other axis is easily recognized at X-band frequencies of 9.6 GHz, as it leads to significantly different averaging of the hyperfine tensor. The direction of the unique axis can provide information on the specifics of electrostatic attachment for ionic spin probes [6,10] (see also Section "Polyelectrolytes: Probing (Polyion-Counterion Interaction in Fluid and Frozen Solution") as well as on changes in the local environment of the spin probe due to changes in macromolecular structure or solvent conditions [27].

Characterization of Broad Distance Distributions

Many construction materials and most prospective functional materials derive their properties from a balance between flexibility and rigidity. This implies intermediate order on length scales beyond a few bond lengths (0.5 nm). In principle, such intermediate order can be detected by scattering techniques, but limited contrast, selectivity, and sensitivity restrict the complexity of the structures that can be characterized in detail. Distance measurements between site-specific spin probes or spin labels can overcome all these limitations and cover the distance range between 1 and 10 nm that is typical for such intermediate order. Moreover, distance measurements based on pulse EPR approaches [28] can provide not only just a single number for the average distance but also an estimate for the whole distance distribution [15]. Conversion of dipolar evolution functions to distance distributions is

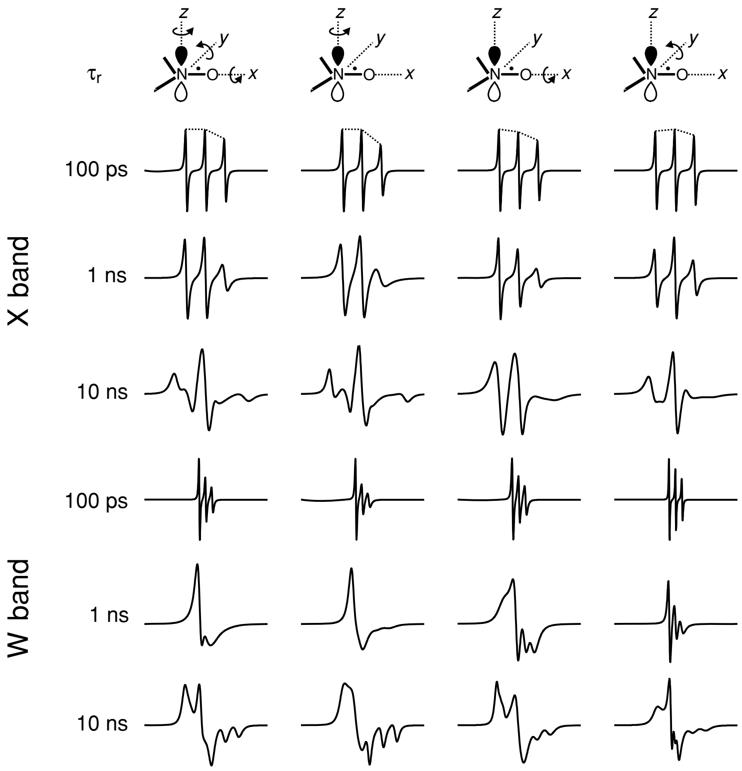

Fig. 1. Dependency of nitroxide spin probe spectra on rotational correlation time, preferential rotation axis, and EPR frequency. Panels from left to right correspond to isotropic rotational diffusion, and preferential rotation about the *z*, *x*, and *y* axis, respectively. Rotational diffusion about the preferred axis is assumed to be ten times faster than about other axes. X-band spectra are centered at 334.8 mT and are 10 mT wide, W-band spectra are centered at 3355 mT and are 30 mT wide. Simulations were performed with the Schneider/Freed suite of programs [21].

a (moderately) ill-posed problem, hence, some caution is advisable in the choice of data analysis procedures and in the interpretation of the results [17].

The main limitations of the method are illustrated in Figure 2. As the excitation bandwidth must cover the dipolar doublet (Pake doublet) of the two coupled spins, available microwave power and resonator bandwidth restrict the measurement to distances larger than 1.5–1.75 nm (blind volume around the observer spin, Figure 2A). The maximum observation time of the order of a few microseconds limits resolution in dipolar frequency domain and thus the maximum distances that can be measured. In most materials, distances up to 5 nm can be resolved quite nicely, while extension to distances up to 8 nm is possible in materials that are free of mobile protonated groups or are deuterated [17]. Spins at larger distances contribute a background signal with the general shape of a stretched exponential decay that must be removed by fitting the long-time decay and subtracting it (Figure 2B). The remaining dipolar evolution function is due to spins in the distance range of interest and can be converted to a distance distribution by an approximate Pake transformation [15], Tikhonov regularization, or fitting. A generalized and stable fitting procedure is obtained by defining the distribution by the amplitudes at sampling points and interpolating between the sampling points by Hermite polynomials [17]. The problem thus boils down to selecting a realistic resolution of the distance distribution, i.e. an appropriate number of sampling points. The broad asymmetric model distribution in Figure 2 cannot be approximated very well by only nine sampling points (C) so that a significant residual between experimental and fitted dipolar evolution function is found (arrows in D). A good fit is obtained with 17 sampling points (E and F). A further increase to 33 sampling points does not lead to a significant improvement of the fit residual (H) but introduces noise-induced features in the distance distribution (G). Generally, the minimum number of sampling points for which the residual is white noise provides the most realistic distance distribution. Distortions in this distribution increase more strongly than linear with an increase in noise amplitude.

Concatenated Macrocycles in Frozen Solution

In many cases, it is possible to construct a relatively simple approximate geometric model for the system under consideration. This considerably reduces the number of

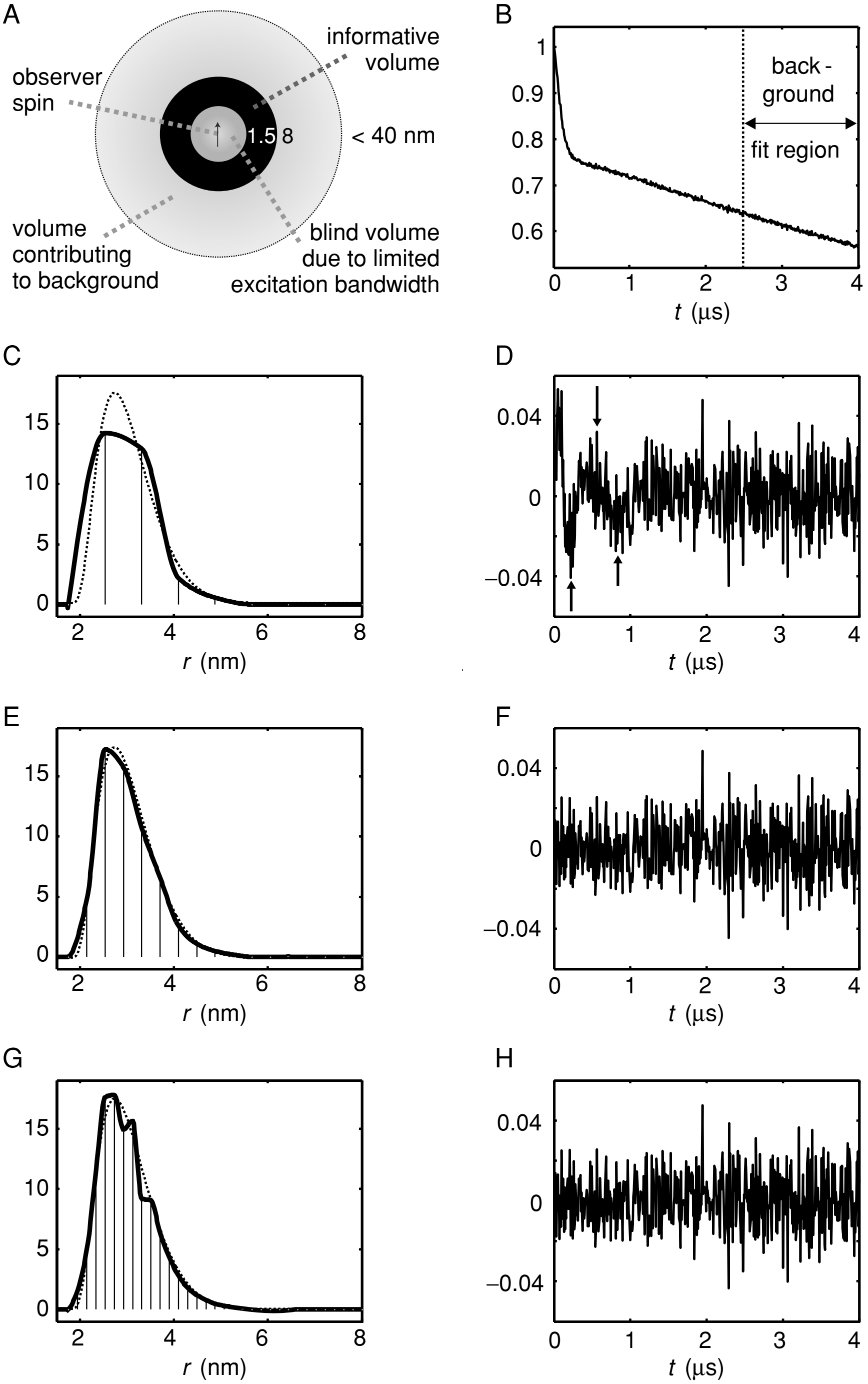

Fig. 2. Extraction of broad distance distributions from dipolar evolution functions. (A) Relevant length scales for the DEER experiment. (B) Simulated low-noise DEER data for an asymmetric distance distribution with a width of ≈ 2 nm. (C) Distance distribution fitted by variation of the amplitudes of nine sampling points (thin vertical lines) between 1.75 and 8 nm and Hermite polynomial interpolation in between sampling points. The dotted line is the theoretical distance distribution used in the simulation of the data in B. (D) Fit residual corresponding to the 9-point distance distribution shown in C. (E) Distance distribution fitted as in C, but with 17 sampling points. (F) Fit residual corresponding to E. (G) Distance distribution fitted as in C, but with 33 sampling points. (H) Fit residual corresponding to G.

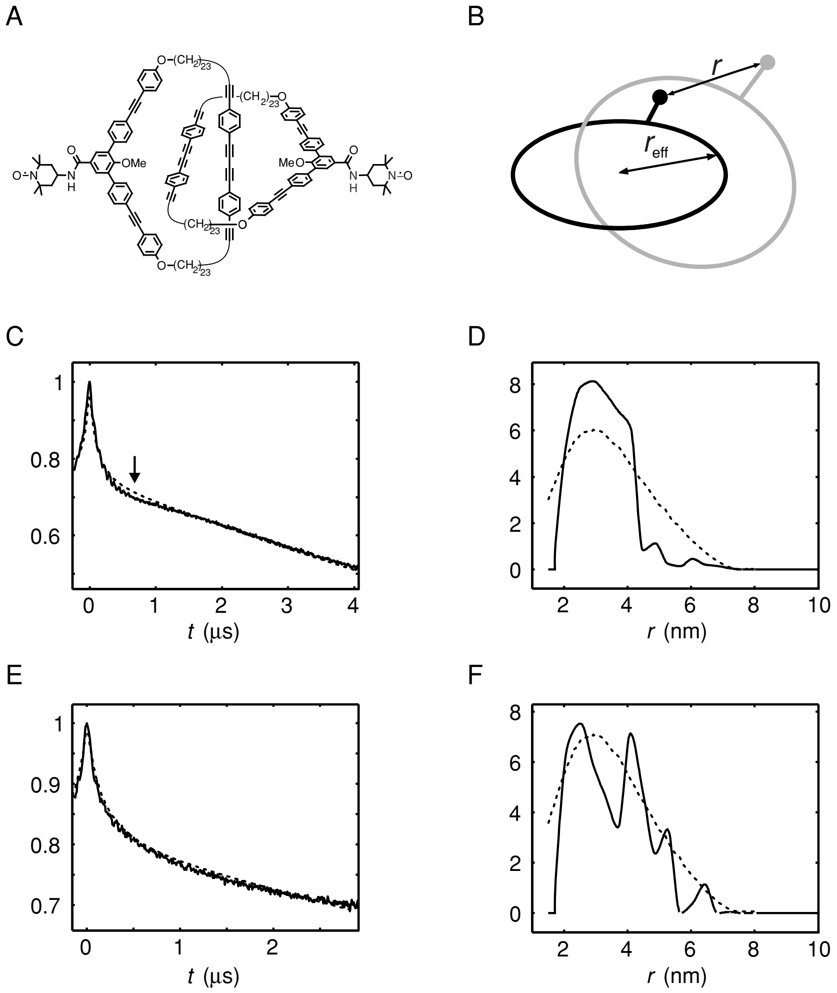

Fig. 3. Molecular shape of a nanosized [2]catenane. (A) Chemical structure. (B) Geometric model. (C) Experimental DEER data (solid line) and best fit by the geometric model (dotted line) for the catenane in shock-frozen o-terphenyl. The arrow marks the strongest deviation. (D) Experimental distance distribution corresponding to the data shown in C (solid line) and expected distance distribution (dotted line). (E) Experimental DEER data (solid line) and best fit by the geometric model (dotted line) for the catenane in shock-frozen chloroform. (F) Fit residual corresponding to E.

fit parameters and may circumvent the problem of ill-posedness of the conversion of dipolar evolution functions to distance distributions. For a nanosized [2] catenane (Figure 3A) consisting of two macrocycles with both rigid and flexible sections, we could thus answer the question whether the distribution of co-conformations is uniform, i.e. whether all possible relative orientations and inter-center distances of the macrocycles occur with the same probability [16]. Approximation of the macrocycles by circular rings and of the linker and spin label by a straight line (Figure 3B) results in a model with only one free parameter, namely, the effective radius r_{eff} of the rings. Moreover, a prediction of this parameter can be derived by equating the circumference of the ring with the contour length of the backbone of the macrocycle. For the medium-sized macrocycle discussed here, this approach predicts $r_{eff} = 1.75$ nm. For a glassy frozen solution of this [2] catenane in *o*-terphenyl, we find poor agreement of the shape of the distance distribution for this geometric model with the experimental distribution and a poor fit of the experimental dipolar evolution function (Figure 3C and D). In contrast, data for a frozen solution of the same [2] catenane in chloroform can be fitted rather nicely and provide an experimental value $r_{eff} = 1.50$ nm that is in reasonable agreement with theoretical predictions (Figure 3E and F). Similar results were obtained for a larger [2] catenane with nominal $r_{eff} = 2.99$ nm (experimental value $r_{eff} = 2.60$ nm). These results indicate that the flexible alkyl sections of the macrocycles are expanded in the good solvent chloroform but partially collapsed in the poor solvent *o*-terphenyl. In the former case, the simple geometric model provides a surprisingly good description of the distance distribution, suggesting that the distribution of co-conformations is indeed uniform.

Polyelectrolytes: Probing Polyion-Counterion Interaction in Fluid and Frozen Solution

Polyelectrolytes are a class of macromolecular substances that are mainly governed by electrostatic interactions. In water and other polar solvents they dissolve into charged polymer chains, called polyions, and many small ions of opposite charge, called counterions. Despite their obvious importance in molecular biology (e.g. DNA) and materials science, these complex many-particle systems belong to the least-understood classes of macromolecules.

Polyelectrolytes are often studied either using methods that probe macroscopic properties (such as conductivity) or scattering techniques (light-, X-ray and neutron scattering), which can only probe residual long-range order in solution [29]. Using these widely-employed methods it is therefore hardly possible to understand local polyion–counterion interactions and to obtain information on the distribution of counterions around polyion chains. The latter point is of particular importance in the theoretical description of these systems [29,30]. It is possible to obtain information on electrostatic interactions between polyions and counterions by use of charged spin probes [9,10,31] and the techniques described in Sections "Addressing Specific Sites by Spin Probes and Spin Labels", "Detecting Supramolecular Interactions by Changes in Probe Dynamics" and "Characterization of Broad Distance Distributions". The scope of this approach was explored in studies on cationic poly(diallyldimethylammonium chloride), (PDADMAC) to which small amounts of the dianionic nitroxide spin probe Fremy's salt, nitrosodisulfonate FS were added (see Figure 5 for structures). In these studies the concentration of the used spin probe was kept constant at $c = 0.5$ mM and the polyelectrolyte repeat unit concentration was varied between 4 and 140 mM. The data are presented as a function of the ratio of the concentrations $R = [\text{FS}]/[\text{PDADMAC}]$. In addition, solvent composition and the amount of added salt were varied and the effect on the EPR parameters was analyzed.

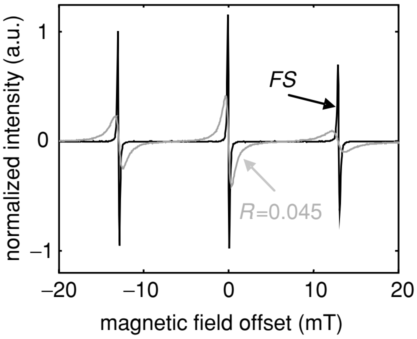

Fig. 4. X-band (9.79 GHz) EPR spectra in 66 wt.% glycerol/34 wt.% water at two different spin probe/PDADMAC ratios *R*. Black line: no polyelectrolyte, only FS; Gray line: $R = 0.045$. Spectra were normalized to equal double integral.

Figure 4 shows two CW EPR spectra (X-band) of FS in glycerol/water at room temperature with (gray line) and without (black line) added PDADMAC. On closer inspection of the line-shape it becomes apparent that the spectral changes are made up of two contributions: alterations of the relative amplitudes of the three individual hyperfine lines and non-Lorentzian broadening that affects all lines in the same way. Although the first contribution is indicative of a change in the rotational diffusion of the employed spin probes (see Figure 1), the deviation of the line shape from a derivative Lorentzian line could be assigned to spin-exchange broadening [32] due to enhanced intermolecular collisions of counterions situated close to the polyelectrolyte chain. Quantitative analysis requires a separation of both effects.

Using simulation programs by Schneider and Freed (see Figure 1; [21]), it was possible to reproduce the relative amplitudes of the three lines based on a model of Brownian rotational diffusion with an axially symmetric rotational diffusion tensor. However, even when spin–exchange interaction due to collisions with a *single* well-defined frequency was included in the Hamiltonian, the additional broadening and line shape changes could not be reproduced. Good fits were obtained by multiplying time-domain data $V_{\text{sim}}(t)$ corresponding to the simulated spectra with a stretched exponential decay function,

$$V(t) = V_{\text{sim}}(t)\exp(-(kt)^x), \qquad (2)$$

that accounts for heterogeneous exchange broadening in an empirical fashion (Figure 5A). Here, k is the characteristic decay constant and x is the stretch factor. The empirical broadening function accounts for a distribution

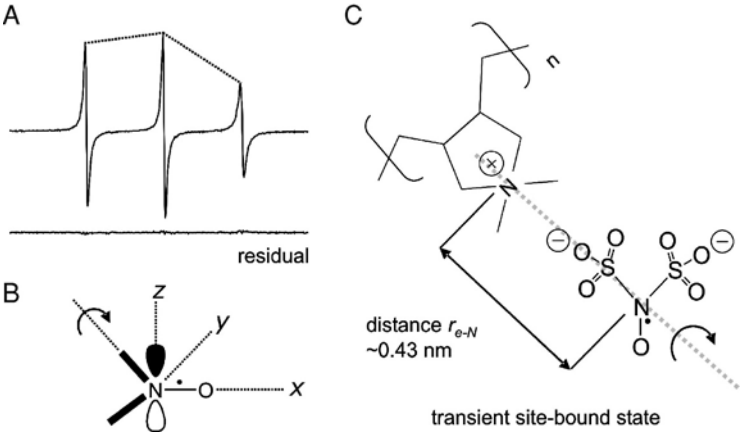

Fig. 5. Analysis of CW EPR (X-band, 9.79 GHz) spectra of FS ions in fluid solutions of PDADMAC. (A) CW EPR spectrum of FS at $R = 0.067$ in 50% ethanol/50% water and the residual after subtraction of a simulation according to Equation 2 with $k = 1.8 \times 10^{13}\ \mathrm{s}^{-1}$ and $x = 0.1$. (B) The rotational diffusion tensor used for this simulation. Rotation takes place preferentially along one of the nitrogen–sulfur bonds in FS, although both bonds are equivalent. The rotational rates are $R_{||} = 3.7 \times 10^9\ \mathrm{s}^{-1}$ and $R_\perp = 5.5 \times 10^7\ \mathrm{s}^{-1}$. (C) Illustration of the geometry and dynamics of the transient site-bound state derived from the analysis. The distance r_{e-N} was derived from ratio analysis of ESEEM data as explained in the text.

of spin–exchange frequencies which in turn is related to a distribution of local concentrations of spin probes close to the oppositely charged polyelectrolyte [9,10]. The detailed line-shape can also be reproduced in a more physically motivated picture by assuming that the radial counterion distribution around an individual polyion scales with the inverse square of the distance from the polyion [33]. Such scaling is suggested by a recent theoretical analysis of the charged cell model for polyelectrolyte chains and their counterions [34].

Irrespective of the solvent used, the CW EPR spectra could be fitted nicely by assuming an axially symmetric rotational diffusion tensor with the unique axis pointing along one of the sulfonate groups of the spin probe (Figure 5B and C). Rotation about the preferred axis was 15 (in water) to 100 (66 wt.% glycerol/34 wt.% water) times faster than rotation perpendicular to this axis [33]. Hence, the Coulombic interaction between the dianionic spin probes and the quaternary ammonium groups of the PDADMAC repeat units results in an attachment of FS that is transient and involves only one of the sulfonate groups at a time. During attachment, rotation about the axes perpendicular to the preferred axis requires reorientation of at least local segments of the polyion chain that causes the significant reduction of the rotational diffusion about these axes. Electrostatically, *site-bound* FS probes are in equilibrium with *territorially bound* probes, which are not directly attached but are located in the vicinity of the respective polyion chains and still interact with the electrostatic potential of larger segments of these chains. The lifetime of the site-bound state can safely be assumed to be shorter than 1 ns, since otherwise significant spectral components reflecting the slower motion would be expected (see Figure 1). This attachment–detachment process was termed as *dynamic electrostatic attachment* to stress its transient nature.

The site-bound state was further characterized by performing three-pulse electron spin echo envelope modulation (ESEEM) experiments [28] on glassy frozen solutions of the PDADMAC/FS samples. Ratio analysis of the decay provided a lower limit of the distance between electron spin and ^{14}N nuclear spin of the charge-bearing ammonium group of ≈ 0.43 nm for 20% of the spin probes (Figure 5C, [10,35]). This distance was found to be in excellent agreement with the distance in PDADMAC/FS contact ion pairs computed by a molecular force-field. The remaining 80% of the spin probes are presumably territorially bound.

Further details of the heterogeneous spin probe distribution were studied by applying the four-pulse version of the DEER experiment [36] to shock-frozen solutions of PDADMAC/FS in glycerol/water. The time trace of FS ions in PDADMAC ($R = 0.022$) obviously deviates from the exponential decay that would be expected for a homogeneous distribution of spin probes in three dimensions (Figure 6A). Variation of the concentration of PDADMAC reveals that the deviation increases with increasing R-values, i.e. with decreasing polyelectrolyte concentration. Due to the blind volume of the DEER experiment (see Section "Characterization of Broad Distance Distributions" and Figure 2) this heterogeneity cannot be attributed to the radial distribution that is observable with CW EPR, but must be related to the axial distribution along the chains. Indeed, the complete series of data can be analyzed using a two state model for the distribution of FS ions: FS ions are either distributed homogeneously in three dimensions (concentration c_{hom}) or along a one-dimensional linear object (linear spin density c_{lin}). The corresponding pair correlation function $G(r)$ for this model is given by:

$$G(r) = c_{\text{hom}} N_A + c_{\text{lin}}/r^2. \tag{3}$$

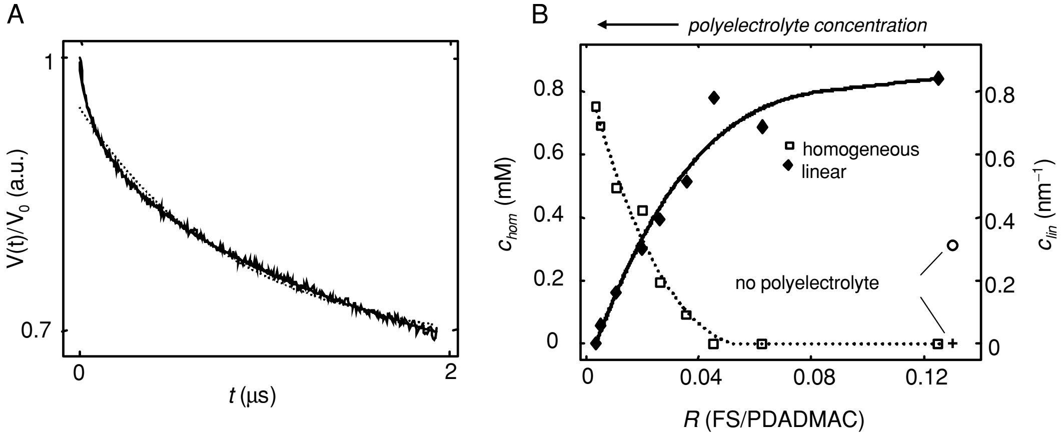

Fig. 6. Analysis of DEER time traces of FS in frozen solutions of PDADMAC in 66 wt.% glycerol/34 wt.% water. (A) Time trace at $R = 0.022$ (solid black line) with a single exponential decay (dotted black line) and a simulation according to Equation. 3 (solid gray line) overlaid. The extracted parameters for the latter simulation were $c_{hom} \approx 0.4$ mM and $c_{lin} \approx 0.3$ nm^{-1}. (B) Summary of the extracted parameters c_{hom} (open squares) and c_{lin} (filled diamonds) in the complete R-range investigated. The solid and dotted black lines are meant as guides to the eye.

where N_A is Avogadro's constant. Figure 6A shows that a simulation using $c_{\text{hom}} \approx 0.4$ mM and $c_{\text{lin}} \approx 0.3$ nm^{-1} (overlaid in gray) excellently reproduces the measured time trace. The two parameters are summarized for the complete series of measurements in Figure 6B. The homogeneously distributed component decreases with increasing R and is effectively zero for values larger than 0.05, whereas the component that is presumably distributed along one dimension follows an opposite trend and increases with R reaching a plateau value of $c_{\text{lin}} \approx 0.8$ nm^{-1} for $R > 0.05$. This behavior can be interpreted as a transition from a network of overlapping polyelectrolyte chains at high PDADMAC concentrations to a regime of isolated and locally extended polyelectrolyte chains at low polymer concentration. In the former regime, FS spin probes are distributed throughout the whole three-dimensional polyelectrolyte network, while with decreasing PDADMAC concentration, the single chain character increases and c_{lin} becomes larger. The plateau value of 0.8 nm^{-1} for c_{lin} is explained by the lower detection limit for electron spin distances of roughly 1.5 nm (see Section "Characterization of Broad Distance Distributions", [28]). As the DEER data are consistent with a picture of FS ions that are attached to a linear object one may indirectly conclude that the PDADMAC chains are in a locally elongated conformation with a persistence length of at least 5 nm, which is the range probed by a dipolar evolution function that is measured up to $t = 2\mu$s.

In conclusion, we find that for the complex structures formed by electrostatic self-assembly of polyelectrolytes and their counterions in solution, EPR spectroscopy on charged spin probes provide insights that are not accessible with other characterization methods. Similarly, the broad co-conformational ensemble of [2]catenanes, which is governed by the topological constraint that the two macrocycles must remain concatenated, would be difficult to elucidate with any other technique. These examples demonstrate that EPR spectroscopy is particularly well suited for characterizing the structure and dynamics of the materials that exhibit an intermediate degree of order on length scales between 0.5 and 10 nm.

References

1. Berliner L, (Ed), Biological magnetic resonance, Vol. 14, Plenum: New York, 1998.
2. Auteri FP, Belford RL, Robinson BH, Clarkson RB. Coll. Surf. A. 1993;81:25.
3. Hommel H, Adv. Colloid Interf. Sci. 1995;54:209.
4. Ottaviani MF, Turro NJ, Jockusch S, Tomalia DA, J. Phys. Chem. B. 2003;107:2046.
5. Jeschke G, Macromol. Rapid Commun. 2002;23:227.
6. Cramer SE, Jeschke G, Spiess HW, Macromol. Chem. Phys. 2002;203:182.
7. Dragutan I, Bokria JG, Vargese B, Szajdzinska-Pietek E, Schlick S, J. Phys. Chem. B. 2003;107:11397.
8. Cramer SE, Jeschke G, Spiess HW, Colloid Polym. Sci. 2002;280:569.
9. Hinderberger D, Jeschke G, Spiess HW, Macro molecules. 2002;35:9698.
10. Hinderberger D, Spiess HW, Jeschke G, J. Phys. Chem. B. 2004;108:3698.

11. Berliner L, Eaton S, Eaton G, (Eds), Biological magnetic resonance, Vol. 19, Plenum: New York, 2000.
12. Milov AD, Maryasov AG, Tsvetkov YD, Appl. Magn. Reson. 1998;15:107.
13. Borbat P, Freed J, Chem. Phys. Lett. 1999;313:145.
14. Jeschke G, Chem. Phys. Chem. 2002;3:927.
15. Jeschke G, Koch A, Jonas U, Godt A, J. Magn. Reson. 2002;155:72.
16. Jeschke G, Godt A , Chem. Phys. Chem. 2003;4:1328.
17. Jeschke G, Panek G, Godt A, Bender A, Paulsen H, Appl. Magn. Reson. 2004;26:223.
18. Cramer SE, Jeschke G, Spiess HW, Macromol. Chem. Phys. 2002;203:192.
19. Altenbach C, Marti T, Khorana HG, Hubbell WL, Science. 1990;248:1088.
20. Godt A et al., J. Org. Chem. 2000;65:7575.
21. Schneider DJ, Freed J, Biological magnetic resonance, Vol. 8, Chapter 1, Plenum: New York, 1989; pp. 1–75.
22. Robinson BH, Slutsky LJ, Auteri FP, J. Chem. Phys. 1992;96:2609.
23. Steinhoff HJ, Hubbell WL, Biophys. J. 1996;71:2201.
24. Liang Z, Freed JH, Keyes RS, Bobst AM, J. Phys. Chem. B. 2000;104:5372.
25. Lou Y, Ge M, and Freed JH, J. Phys. Chem. B. 2001;105:11053.
26. Budil DE, Lee S, Saxena S, Freed JH, J. Magn. Reson. 1996;120:155.
27. Vandermeulen GWM et al., Chem. Phys. Chem. 2004;5: 488.
28. Schweiger A, Jeschke G, Principles of Pulse Electron Paramagnetic Resonance, Oxford University Press: Oxford, 2001.
29. Manning GS, J. Chem. Phys. 1969;51: 924.
30. Dautzenberg H et al., Polyelectrolytes - Formation, Characterization and Application, Carl Hanser Verlag: München, 1994.
31. Hinderberger D, Spiess HW, Jeschke G, Macromol. Symp. 2004;211:71.
32. Molin Yu N, Salikhov KM, Zamaraev KI, Spin Exchange Principles and Applications in Chemistry and Biology, Springer-Verlag: Berlin, 1980.
33. Hinderberger D, Polyelectrolytes and Their Counterions Studied by EPR Spectroscopy, PhD thesis, Universität Mainz, 2004.
34. Deshkovski A, Obukhov S, Rubinstein M, Phys. Rev. Lett. 2001;86:2341.
35. Ichikawa T, Kevan L, Bowman MK, Dikanov SA, Tsvetkov YD, J. Chem. Phys. 1979;71:1167.
36. Pannier M, Veit S, Godt A, Jeschke G, Spiess HW , J. Magn. Reson. 2000;142:331.

NMR of Organic Semiconductors

Magesh Nandagopal[1], Mathew Mathai[1], Fotios Papadimitrakopoulos[2], Marcel Utz[3]
[1]*Institute of Materials Science, University of Connecticut, Storrs CT 06269, USA;*
[2]*Department of Chemistry,* [2] *Institute of Materials Science, University of Connecticut, Storrs CT 06269, USA; and*
[3] *Department of physics, Institute of Materials Science, University of Connecticut, Storrs CT 06269, USA*

Introduction

Organic semiconductors are conjugated molecules that act as charge carriers and are photo-active. Mainly due to their ease of processing, they offer great promise in replacing conventional semiconductors in optoelectronic devices, such as light-emitting diodes and photovoltaic cells [1]. In particular, organic light emitting diode (OLED) devices [2] have received considerable attention over the last 15 years. Their improved electro-optical properties, such as low operational voltage, high brightness, and luminescence efficiency combined with the ease of fabrication have made them very good candidates for flat panel displays.

The molecular structure and dynamics of organic semiconductors profoundly influence the transport of charge carriers and hence affect the performance of the devices in which they are used. As a group of materials, they offer an interesting blend of properties which are yet to be completely understood. Quantitative determination of the molecular structure and dynamics of the organic layer in OLEDs and other devices is a prerequisite to understand the properties of the devices and to optimize the processing parameters for maximum performance. This is complicated due the fact that the organic layers in OLEDs are generally amorphous, which greatly limits conventional diffraction-based techniques for structural investigation such as X-ray diffraction. NMR spectroscopy offers great potential in this regard, since it provides short-range structural information and does not depend on long-range structural coherence.

Several applications of solid-state and liquid-state NMR have been reported in the literature to study the structure and dynamics of organic semiconductors and the conducting polymers. The following list is not intended to be exhaustive, but illustrates the various possibilities of using NMR as an effective tool to study the organic semiconductors. For example, Yannoni and Clarke have conducted a structural study of polyacety-lene using solid-state nutation NMR spectroscopy [3]. There has been extensive use of NMR, as a tool, for studying the spin diffusion and electron conductivity in organic semiconductors [4]. ^{13}C and ^{2}H solid-state NMR has been used to study the structure and dynamics of polyanilines[5]. Also, the molecular geometry [6] and proton exchange [7] aspects of polyaniline have been probed by using NMR. The thermally-induced metal-semiconductor transition in organic salts has been studied using ^{13}C NMR. [8] The morphology and dynamics of lithium salt-based polyelectrolytes have been probed using ^{13}C and ^{6}Li NMR [9]. ^{2}H NMR has been used to characterize the phenylene ring flip motion in poly (*p*-phenylene vinylene) (PPV) films [10]. The structural aspects of nonconjugated polymers have been probed by ^{13}C NMR [11]. ^{129}Xe NMR has been used to study the microporous structure of polyacenic semiconductor [12].

In the present contribution, we focus on aluminum tris (8-hydroxyquinoline) (Alq$_3$), which is widely used as an electron transport and electron-hole recombination layer in OLED devices [2,13,14], A significant effort has been made to understand the properties, structure and dynamics of Alq$_3$, both in solution and in the solid state. In particular, fundamental studies directed towards the properties of the Alq$_3$ molecule, such as its electronic structure [15,16], dynamics [17–19], and crystal polymorphs [20–22], have been reported.

Alq$_3$ is an organometallic complex with the aluminum ion surrounded by three identical quinolinolate anions. In principle, both meridianal isomer, with the oxygen atoms forming meridian of the distorted coordination octahedron, and a facial isomer, with the oxygens forming a face of the octahedron, could exist. In the facial isomer, the three ligands are equivalent by symmetry, whereas in the meridianal isomer, they are distinct. As is well-known from earlier NMR studies [23], the meridianal isomer is the stable form in a solution at room temperature.

While the meridianal isomer of Alq$_3$ has so far been observed exclusively both in solvent-containing [23] crystals and in the pure α, β, and γ polymorphs [20] as well as in solution [23], a novel crystal polymorph [21], called the δ-phase, has been assigned tentatively to the facial isomer [21,22,24]. The δ polymorph exhibits a substantial blue shift of about 0.2 eV in its photoluminescence spectrum. This could lead to the development of Alq$_3$-based OLED devices which emit blue, rather than green, range of the spectrum.

Graham A. Webb (ed.), Modern Magnetic Resonance, 1539–1545.
© 2008 *Springer.*

In this paper, we review recent results on the internal dynamics of the Alq_3 molecule, studied using two-dimensional exchange NMR spectroscopy, the molecular structure in the α and δ polymorphs of crystalline Alq_3 by ^{27}Al NMR, as well as the structural disorder in amorphous films of Alq_3 as a function of the deposition rate.

OLEDs are fabricated by depositing the organic layer onto the device substrate from the vapor phase. The rate at which the organic layer is deposited on the substrate is known to influence the final device properties [25]. However, no fundamental explanation of this phenomenon based on the structure and morphology of Alq_3 has been forwarded yet. Our studies show that ^{27}Al solid-state NMR is a very useful tool to study amorphous Alq_3 deposits, and may therefore, lead to better understanding of the relationship between processing conditions, film structure, and device properties.

Ligand Dynamics in Alq_3

The internal dynamics of the Alq_3 molecule are crucial for the processing and long-time behavior of OLED devices. Current OLED devices use Alq_3 in the form of amorphous thin films. Both the deposition of these films and their gradual physical aging are kinetically controlled processes. In particular, significant effects of the deposition rate and conditions on the performance of Alq_3-based devices have been demonstrated recently [25–28].

As mentioned earlier, the Alq_3 molecule exists as two different isomers: facial and meridianal. The absence of an axis of symmetry in the meridianal form of Alq_3 leads to the three quinolinolate ligands being distinguishable. Their inequivalence becomes immediately apparent in the proton NMR spectrum in solution [23,29], where a separate set of resonances can be observed for each of the three ligands. It has been shown that the line shape of the proton resonances strongly depends on temperature, suggesting exchange dynamics between the ligands [23]. Two-dimensional NMR exchange spectroscopy is an ideal tool for the quantification of chemical exchange processes [30], provided the exchanging species are well resolved and the time scale of the process is shorter than the spin-lattice relaxation time. Both these conditions are met by Alq_3 in $CDCl_3$.

The two-dimensional exchange spectrum of Alq_3 in $CDCl_3$ solution at a temperature of 310 K and a mixing time of $\tau_m = 200$ ms is shown in Figure 1. There are two different kinds of off-diagonal peaks in the spectrum. One corresponds to the positive cross-peaks between protons of the same type on different ligands (inter-ligand peaks) and the other corresponds to the negative signals between protons of different type on the same ligand (intra-ligand peaks). While the former are indicative of the ligand exchange and the latter are caused by the nuclear Overhauser effect and are not of interest in the present context. By comparing the intensity of the inter-ligand peaks (H2 and H3, as they are better resolved compared to H4) with the peaks on the diagonal, we can get a measure of the ligand-exchange time-scale. This experiment was carried out at various temperatures (310, 300 and 283 K), to study the kinetics of ligand exchange. Under the conditions of Figure 1, the exchange is nearly complete, whereas at lower temperatures, the exchange was found to be much slower, reaching less than 10% and 50% for 283 and 300 K, respectively (at a mixing time of $\tau_m = 200$ ms).

No change in the relative cross-peak intensities was found upon changing the Alq_3 concentration from 13 to 6.5 mg/ml at a temperature of 300 K, which demonstrates that the exchange process follows first-order kinetics.

The observed data is consistent with a simple first-order kinetic model for the exchange mechanism, which involves breaking of the Al–N bond, creating a ligand that is free to rotate around the Al–O bond. It can reconnect either in the same orientation or rotate by 180° after overcoming a rotational energy barrier.

Due to the three-fold axis of symmetry, all three ligands in the facial isomer are identical. Flipping any of the ligands of the facial isomer converts the molecule to the meridianal form. Flipping of two out of the three ligands in the meridianal isomer, leads back to the meridianal isomer, with the ligand identities exchanged, as illustrated in Figure 3, whereas flipping the third one produces the facial isomer equalizing the three ligands.

The complete exchange model can therefore be formulated in terms of four independent reactions:

$$\begin{aligned} \mathrm{ABC} &\xrightarrow{k_1} \mathrm{ACB} \\ \mathrm{ABC} &\xrightarrow{k_2} \mathrm{BAC} \\ \mathrm{ABC} &\xrightarrow{k_3} \mathrm{FFF} \\ \mathrm{FFF} &\xrightarrow{k_4} \mathrm{ABC, ACB}\ldots, \end{aligned} \tag{1a}$$

where ABC *etc.* stands for different permutations of the meridianal and FFF for the facial isomer.

The integrated peak intensities of the H2 and the H3 protons as a function of mixing time τ_m at three different temperatures are shown in Figure 2. The symbols represent experimental values; the lines indicate the best fit of the data according to the above first-order kinetic model. Values for the reaction rates k_1, k_2, and k_3 have been obtained by least squares fitting of the above model to the experimental data, and are given in Table 1. All reaction rates are very sensitive to temperature, changing by up to a factor of 50 as the temperature is raised from 283 to 310 K.

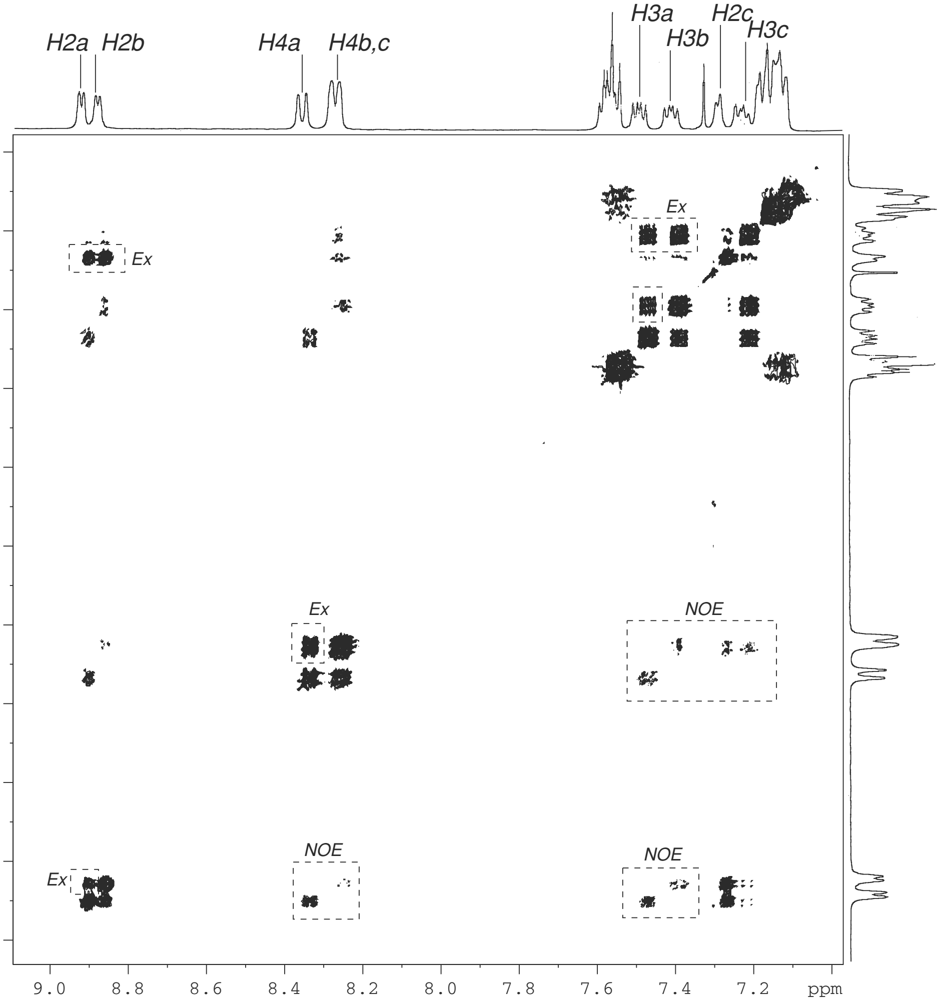

Fig. 1. Two-dimensional exchange NMR spectrum of Alq$_3$ in CDCl$_3$ solution at 300 K and a mixing time of $\tau_m = 200$ ms. Cross-peaks of two different types appear: exchange peaks appear with positive sign between corresponding protons on different ligands (Ex), whereas NOE peaks between different protons on the same ligand appear with negative sign (NOE).

As the rate constants have been determined at different temperatures, it is possible to estimate the activation parameters following Eyring's law

$$k = \frac{k_b T}{h} \exp \frac{\Delta S^{\ddagger}}{k_b} \exp - \frac{\Delta H^{\ddagger}}{k_b T}, \qquad (2)$$

where $\Delta S^{\ddagger}$ and $\Delta H^{\ddagger}$ represent the activation entropy and enthalpy, and k_b denotes Boltzmann's constant.

The activation parameters determined from the Eyring plot, given in Table 2, are of the order of 90 kJ/mol. Such large values would render ligand exchange in Alq$_3$ an exceedingly slow process at room temperature, if it were not for the large, positive activation entropies Δ S‡. The difference in energy between the meridianal and the facial isomer of Alq$_3$ has been determined by numerical simulation at about 20 kJ/mol [15]. The activation barrier is expected considerably above this value for the proposed reaction mechanism, as it involves the breakage of a coordination bond. The observed activation entropies range from 39 to 122 JK^{-1} mol^{-1}, suggesting a highly disordered transition state, which is again consistent with the proposed mechanism.

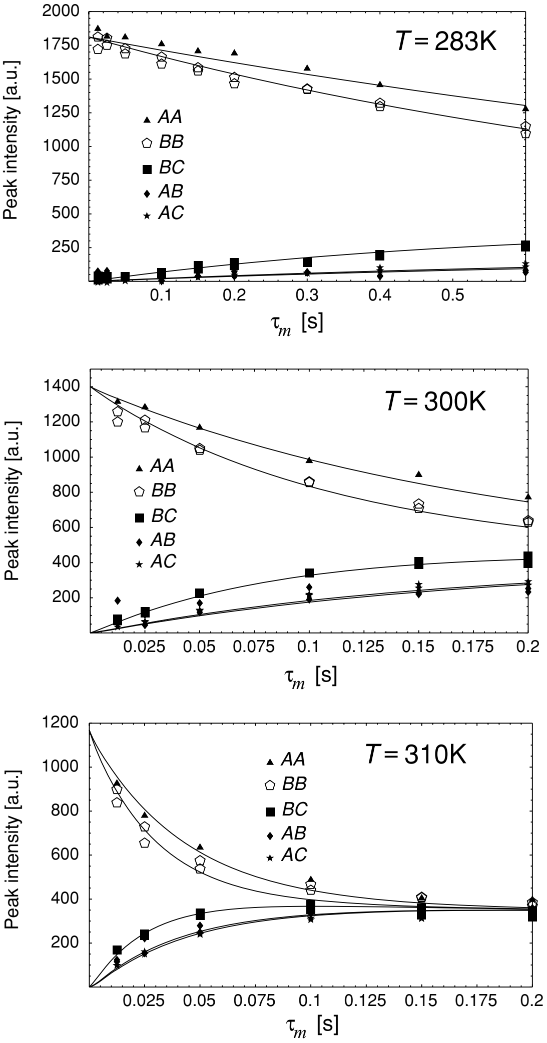

Fig. 2. Integrated peak intensities as a function of mixing time at three different temperatures. Data for both H2 and H3 are shown. The solid lines represent the first-order kinetic model described in the text. Note the different horizontal scale in the top panel ($T = 283$ K)

Table 1: Rate constants determined by least-squares fitting of the experimental H2 and H3 peak intensities. Error margins represent individual 95% confidence intervals.

T(K)	$k_1(s^{-1})$	$k_2(s^{-1})$	$k_3(s^{-1})$
283	0.29 ± 0.75	0.00 ± 1.00	0.39 ± 0.75
300	2.35 ± 0.60	0.14 ± 0.60	4.99 ± 0.60
310	6.68 ± 3.00	0.65 ± 6.00	22.01 ± 3.00

Characterizing the Isomers of Alq_3

^{27}Al, with a spin of $I = 5/2$, is the only stable isotope of aluminum. In most solids, the central magnetic transition of ^{27}Al is easily observed by NMR spectroscopy under MAS. As is common for half-integer nuclei, even though the quadrupolar interaction does not affect the frequency of the central transition within first-order perturbation theory, it causes a noticeable second-order broadening of the resulting line shape. This broadening is reduced, but not completely removed by magic angle spinning.

The quadrupolar coupling is due to the interaction of the nuclear electric quadrupole moment with the gradient of the electric field $\mathbf{V} = \nabla\mathbf{E}$, where $\mathbf{E}$ is the electric field caused by all charges in the system *except* the nucleus. In its principal axes frame (PAS), the EFG can be characterized in terms of the anisotropy δ and the asymmetry η, where $\delta = V_{zz}^{\mathrm{PAS}}$ and $\eta = (V_{yy}^{\mathrm{PAS}} - V_{xx}^{\mathrm{PAS}})/\delta$

The shape of the central line reflects both the quadrupolar interaction and the anisotropic chemical shift. Under MAS, the chemical shift anisotropy is averaged to zero, whereas the second-order quadrupolar coupling is only partly averaged. This leads to a narrowed powder pattern with a width controlled by the quadrupolar anisotropy (δ) and the Larmor frequency, and with a shape characteristic of the quadrupolar asymmetry (η). The shape of the central spectral line under MAS can therefore be used to characterize the EFG in crystalline polymorphs of Alq_3 or its distribution in amorphous Alq_3 deposits.

The values of δ and η are expected to substantially vary between the facial and the meridianal isomer. In the meridianal isomer, the three oxygen and the aluminum atoms lie approximately in a plane. Therefore, the EFG tensor at the aluminum site has to be approximately planar, leading to the expectation $\eta \approx 1$. In the facial isomer, due to the threefold symmetry, EFG tensor at the aluminum atom would be uniaxial with the expected value for $\eta = 0$.

Table 2: Activation parameters obtained from Eyring analysis of the rate constants given in Table 1. Standard errors of regression are indicated.

	k_1	k_2	k_3
$\Delta H^{\ddagger}$/(kJ/mol)	83.0 ± 1.7	95.0 ± 7.0	106.0 ± 2.3
$\Delta S^{\ddagger}$/(J/molK)	38.7 ± 5.9	56.8 ± 23.6	122.3 ± 7.0

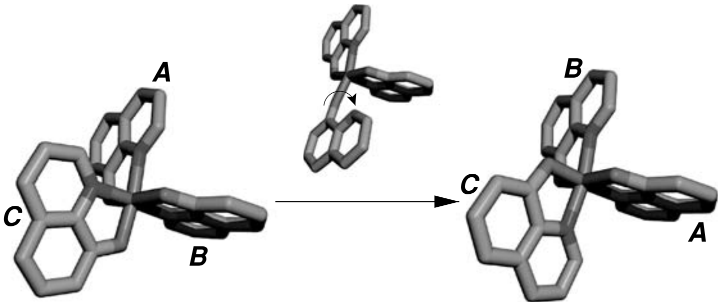

Fig. 3. Schematic representation of the elementary mechanism of exchange that forms the basis of the first-order kinetic model. Breaking the N–Al bond of the C-ligand isomer-Alq_3 allows it to rotate by 180° about the Al–O bond. This rotation leads to an interchange of A and B, whereas the rotating ligand C retains its identity. (See also Plate 121 on page XVII in the Color Plate Section.)

One-dimensional ^{27}Al MAS spectra of three solid modifications of Alq_3 are given in Figure 4. The α and δ polymorphs were obtained by train sublimation [21]. A highly disordered form of Alq_3 was also obtained by depositing the Alq_3 onto a cold substrate from the vapor phase at a very high rate.

The line shapes obtained from the α and δ phases closely correspond to theoretical powder patterns with values of $\eta = 1$ and $\eta = 0$, respectively. This result, therefore, provides a conclusive proof for the hypothesis that the recently discovered delta polymorph indeed does consist exclusively of the facial isomer.

By contrast, the spectrum obtained from the amorphous sample cannot be represented by a single set of (δ, η) values. Rather, the broadening reflects structural disorder in the amorphous packing. This observation has led us to systematically investigate amorphous Alq_3 deposits obtained at different vapor-deposition rates.

The NMR spectrum of the disordered Alq_3 phase shows that the line shape is much more rounded when compared to either of the crystalline phases. The broadening of the spectrum has been identified due to the inhomogeneity of the sample. This shows that in the rapidly deposited material, there is structural disorder at the molecular level.

Variable Deposition Rate Studies

It is known that varying the rate of thermal deposition of organic materials can influence the quality of the film deposited and thus influence the device performance [25]. This has been attributed to the homogeneity and defect density of the films. Slower evaporation rates are expected to produce films with lower defect density and higher homogeneity. These factors are in

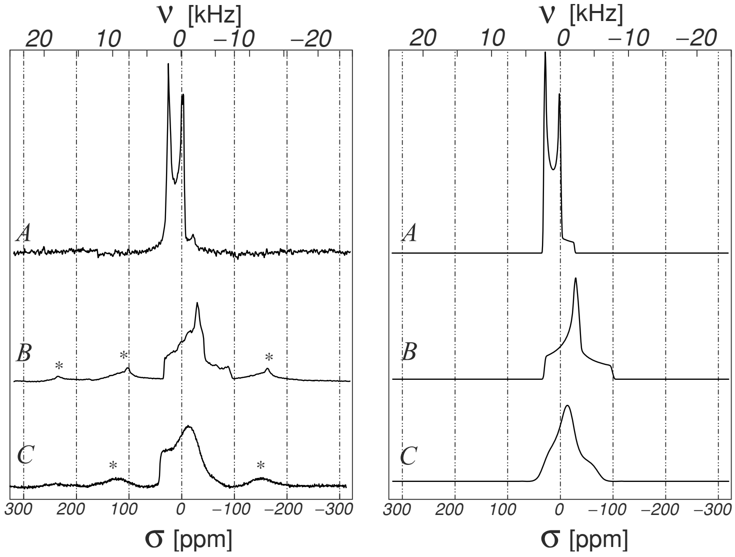

Fig. 4. One-dimensional ^{27}Al spectra under magic angle spinning of different modifications of solid Alq_3 at a field strength of $B_0 = 7.05$ T. Left: Experimental data; Right: Simulations with best-fit values for δ and η. (A) δ-Alq_3; (B) α-Alq_3; (C) dis-Alq_3 (disordered phase obtained by rapid vapor deposition onto a cold substrate, cf. text). The MAS speed was 10.1 kHz in all cases. All spectra were recorded under identical conditions. Spinning side bands are indicated by asterisks.

turn believed to affect carrier mobility of the resulting devices[25].

However, a complete understanding of the relation between the morphology of Alq$_3$ and the device performance has not been achieved yet. One obstacle in establishing this relationship lies the difficulty to characterize the molecular structure of such amorphous films. Due to the absence of long-range order, X-ray diffraction (XRD) yields only very little information. By contrast, our results show that considerable detail on the structural disorder at the molecular level can be extracted from the ^{27}Al MAS line-shape.

Samples for XRD and NMR were prepared by thermal evaporation of train sublimed Alq$_3$ in an Auto 306 Edwards vacuum coater at a pressure of 2.6 mPa. For the NMR measurement, films of 1 μm thickness of Alq$_3$ were deposited on glass substrates kept at room temperature with film growth rates of 0.03, 0.1 and 1 nm/s. At the same time, OLED devices were prepared at the same deposition rates.

The X-ray scattering patterns (not shown) consist of a single, very broad feature centered at $2\theta = 10$. There is little variation between the films obtained at 0.04 and 0.3 nm/s, while the 1 nm/s, film merely exhibits a slightly broader diffraction pattern.

1D ^{27}Al NMR spectra under MAS of the Alq$_3$ films obtained at different evaporation rates are shown in Figure 4. In contrast to the XRD patterns, the ^{27}Al spectra show clear differences. At slower evaporation rates, sharper features appear in the NMR spectra, indicative of a lesser degree of structural disorder.

The line shapes obtained at different deposition rates cannot be fitted using a single set of values of anisotropy (δ) and asymmetry (η) of the EFG tensor. Neither they can be fitted by combining the spectra obtained for the facial and meridianal isomer in different ratios. It must therefore be concluded that the amorphous packing leads to molecular distortions of Alq$_3$and a corresponding distribution of EFG tensors, which is reflected in the NMR line-shape.

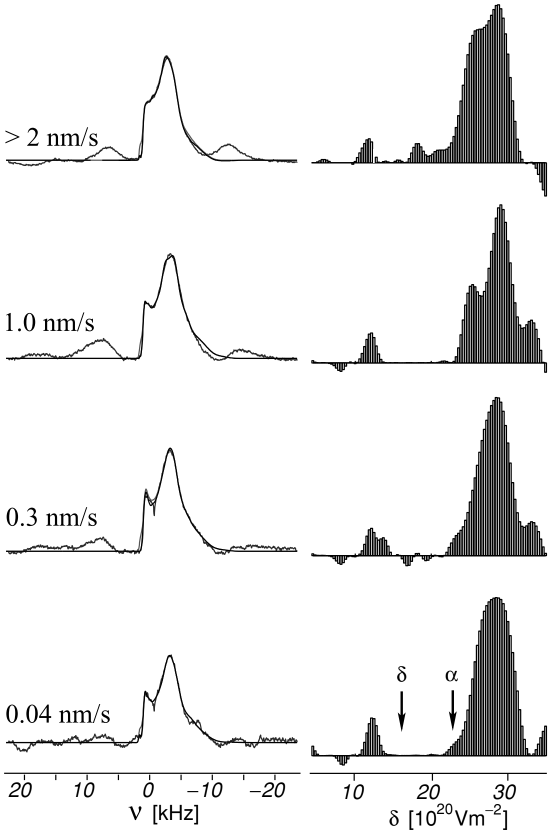

Fig. 5. COF fits of ^{27}Al MAS of amorphous Alq$_3$ obtained at different deposition rates. The insets show the distribution of the anisotropy parameter (δ) of the EFG tensor. The asymmetry parameter (η) is constant in all the fits.

Distributions of delta values were obtained from the measured spectra using the conjugate orthogonal function (COF) method [31]. The distribution of the anisotropy (δ) parameter was extracted assuming a fixed value of $\eta = 0.9$. In principle, a combined distribution $P(\delta,\eta)$ could be determined from the measured spectra. However, the COF analysis showed that the sensitivity and resolution of the current spectroscopic method are not sufficient for this. The COF fits for the various deposition rates are given in Figure 5. The resulting distribution of the quadrupolar anisotropy are bimodal, with a larger primary peak, and a much smaller secondary feature that appears at a smaller value of δ. There is a consistent shift in the position of the major peak to higher δ values with decreasing deposition rate. At the same time, the major peak narrows, indicating less disorder in the more slowly deposited samples. The bimodal distribution suggests the presence of two distinct conformations of the Alq$_3$ molecule. It is tempting to assign the small peak at a lower δ to the facial isomer, which exhibits a smaller EFG anisotropy than the meridianal form also in crystalline forms of Alq$_3$. This would allow us to estimate the content of facial isomer in the amorphous samples at $8\% \pm 4\%$. However, a more sensitive NMR technique, such as variable angle correlation, is necessary to confirm this. Such experiments are currently underway in our laboratory.

The observed dependence of the molecular order on the deposition rate correlates with changes in the charge transport properties. Figure 6 shows the variation of electroluminescence quantum efficiency with the current density of OLED devices prepared at different deposition rates. There is a significant difference in the performance

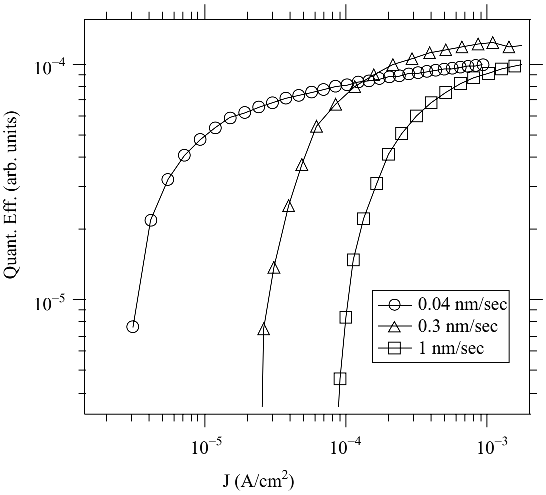

Fig. 6. Quantum Efficiency of the devices obtained by different thermal deposition rates(cf. text).

of the devices prepared at various evaporation rates. This must be due to structural changes at the molecular level, techniques such as XRD fails to pick up, in contrast to ^{27}Al NMR spectroscopy.

Conclusions

The kinetics of exchange between the inequivalent ligands in the meridianal isomer of Alq$_3$ have been studied at different temperatures by 2D exchange proton NMR spectroscopy. The ligands were found to exchange on a time scale of about 5 s^{-1} at room temperature, and the exchange pattern can be explained using a simple first-order mechanism based on 180° flips of the ligands. Using ^{27}Al solid-state NMR, it was found that the α polymorph consists of the meridianal isomer and the δ polymorph consists of the facial isomer. 1D ^{27}Al MAS NMR spectra of amorphous Alq$_3$ films obtained at different deposition rates have been studied. Our results show that ^{27}Al solid state NMR is a powerful tool to study the structure and morphology of Alq$_3$-based devices, capable of quantifying the molecular disorder in amorphous Alq$_3$ deposits.

Acknowledgments

Parts of the present work have been supported by the National Science Foundation through CAREER awards to both MU (DMR-0094290) and FP (DMR-970220), as well as by a type G grant from the Petroleum Research Fund administered by the American Chemical Society to MU (PRF-36246-G7). FP also gratefully acknowledges support of the Critical Technologies Program by Connecticut Innovations, Inc., and Trans-Lux Corp.

References

1. Cacialli F. Phil. Trans. R. Soc. Lond. A. 2000; 358:173.
2. Tang CW, Van Slyke SA. Appl. Phys. Lett. 1987; 51:913.
3. Yannoni CS, Clarke TC. Phys. Rev. Lett. 1983; 51:1191.
4. Mizoguchi K, Jpn. J. Appl. Phys., Part 1 1995; 34:1.
5. Kaplan S, Conwell EM, Richter AF, MacDiarmid AG. Synth. Met. 1989; 29:E235.
6. Stafström S, Sjögren B, Wennerström O, Hjertberg T. Synth. Met. 1986; 16:31.
7. Nechtschein M, Santier C. Physique J. 1986; 47:935.
8. Bernier P, Stein PC, Lenoir C, Physica B. C 1986; 143:494.
9. O'Gara J, Nazri G, MacArthur K. Solid State Ionics. 1991; 47:87.
10. Simpson JH, Rice DM, Karasz, FE. Polym. J. Sci. B. Polym. Phys. 1992; 30:11.
11. Cholli AL,Thakur M. Chem. J. Phys. 1989; 91:7912.
12. Ago H, Tanaka K, Yamabe T, Miyoshi T, Takegoshi K, Terao T, Yata S, Hato Y, Nagura S, Ando N, Carbon. 1997; 35:1781.
13. Tang CW, Van Slyke SA, Chen CH, Appl. J. Phys. 1989; 65:3610.
14. Farchioni R, Grosso G, (Eds). Organic Electronic Materials, Springer: Berlin, Heidelberg, 2001.
15. Curioni A, Boero M, Andreoni W. Chem. Phys. Lett. 1998; 294:263.
16. CurioniA, Andreoni W, Treusch R, Himpsel FJ, Haskal E, Seidler P, Heske C, Kakar S, van Buuren T, Terminello LJ. Appl. Phys. Lett. 1998; 72:1575.
17. Esposti A, Brinkmann M, Ruani G. Chem. J. Phys. 2002; 116:798.
18. Amati M, Lelj F. Chem. Phys. Lett. 2002; 363:451.
19. Utz, M Chen C Morton, Papadimitrakopoulos, M. F Am. J. Chem. Soc. 2003; 125:1371.
20. Brinkmann M, Gadret G, Muccini, M Taliani C, Masciocchi N, Sironi A. Am. J. Chem. Soc. 2000; 122:5147.
21. Braun M, Gmeiner J, Tzolov M, Coelle M, Meyer FD, Milius W, Hillebrecht H, Wendland O, von Schütz JU, Brütting W. Chem. J. Phys. 2001; 114:9625.
22. Cölle M, Gmeiner J, Milius W, Hillebrecht H, Brütting W. Adv. Funct. Mater. 2003; 13:108.
23. Schmidbaur H, Lettenbauer J, Wilkinson DL, Müller G, Kumberger O, Naturforsch Z. 1991; 46b:901.
24. Cölle M, Dinnebier RE, Brütting W. Chem. Comm. 2002; 2908.
25. Chen BJ, Lai WY, Gao ZQ, Lee CS, Lee ST, Gambling WA. Appl. Phys. Lett. 1999; 75:4010.
26. Cheng LF, Liao LS, Lai WY, Sun XH, Wong NB, Lee CS, Lee ST. Chem. Phys. Lett. 2000; 319:418.
27. Kim SY, Ryu SY, Choi JM, Kang SJ, Park SP, Im S, Whang CN, Choi DS. Thin Solid Films 2001; 398–399:78.
28. Qin DS, Li DC, Wang Y, Zhang JD, Xie ZY, Wang G, Wang LX. Appl. Phys. Lett. 2001; 78:437.
29. Baker BC, Sawyer DT. Analyt. Chem. 1968; 40:1945.
30. Jeener J, Meier BH, Bachmann T, Ernst RR. Chem. J. Phys. 1979; 71:4546.
31. Utz M. Chem. J. Phys. 1998; 109:6110.

Solid State NMR of Xerogels

J.L. Yarger,[1] D.A. Buttry[2] G.P. Holland[1]
[1] *Department of Chemistry and Biochemistry, Arizona State University, Tempe, AZ 85287-1604, USA*
[2] *Department of Chemistry, University of Wyoming, and Laramie, WY 82071, USA*

Xerogels, aerogels and other nanoporous solids are an important class of materials in electrochemical and catalytic process design. The preparation of these materials by sol–gel processing has become an important field in materials science [1]. In hydrolytic processes, the texture and structure of sol–gel-based materials largely depend on synthetic parameters, such as (i) solvent, (ii) temperature, (iii) monomer to water ratio, etc. Considerable work has been done to identify the relevant synthetic parameters in order to control the surface and porosity of xerogels (and aerogels). NMR spectroscopy has been extensively used to investigate the effect of these parameters in the sols, prior to gelation, or in the xerogels, after aging and drying [2–5].

Xerogels (*xero* means dry) are derived from sol–gel precursors by evaporative drying, while aerogels are supercritically (or hypercritically) dried. Both of these sol–gel-based materials typically have high porosity, low density, and therefore, high surface areas. Intercalation into xerogels is attractive, not only because of the high surface area, but also because of the small distances in the solid that must be penetrated by the guest ions [6]. Again, NMR spectroscopy has played a crucial role in structural and surface elucidation of xerogel-based intercalation materials as well as elucidation of transport properties and local environments of the guest ions or material [7,8].

While much of the NMR characterization of xerogels has been devoted to silicate based materials [9–12], we will focus our examples on the vanadate xerogel system [13–17]. We will use our NMR studies of lithium intercalated V_2O_5 xerogels as an extended example of several various solid-state NMR techniques that can be used to help elucidate the structure and dynamics of intercalated xerogel materials [18,19]. Because most of our NMR will focus on observation of the intercalating ions, the techniques presented are broadly applicable to other porous xerogel materials. Characterization of the host material is dictated strongly by the type of NMR nuclei present in specific xerogels. Hence, we will not focus on NMR characterization of the host xerogel, but rather the guest ions.

Vanadium pentoxide xerogels have attracted considerable attention as a next generation cathode for rechargeable lithium batteries [20,21]. NMR studies of vanadium pentoxide xerogels serve as an excellent example of the need for high resolution magic angle spinning (MAS) techniques to properly study such materials. Figure 1 (*left*) shows static ^{7}Li NMR spectra a several V_2O_5 samples prepared at different levels of lithiation. One can clearly see that as lithiation (i.e. reduction of vanadium (V) centers to vanadium (IV)) proceeds, the major resonance broadens and shifts. The peak asymmetry reveals that there may be more than one resonance, meaning that there may be more than one type of site for Li^+ in this high surface area material. However, the static spectrum offers limited possibility of learning details about these various lithium environments. In contrast, Figure 1 (*right*) shows a ^{7}Li MAS NMR spectra the same sample. In these spectra, one clearly resolves two sites. The sharper resonance corresponds to Li^+ at interfacial, ion-exchange sites and the broader resonance corresponds to Li^+ inserted within the sheets of the V_2O_5 layered lattice. In the context of battery materials, the availability of interfacial sites greatly increases the power density for a given material because of rapid and facile Li^+ access to those sites. Hence, high-resolution ^{7}Li solid-state NMR provides an excellent probe for testing the potential of new intercalation materials for the next generation of lithium battery cathodes.

In addition to identification and quantitation of Li^+ binding sites in such materials, solid-state techniques also provide information on dynamics, and, indirectly, on more subtle structural questions. For example, the T_1 (spin-lattice) relaxation time provides information on loss of NMR excitation energy into the surrounding material. For the case of lithiated V_2O_5 xerogels, we found that T_1 for the two sites described above was dominated by interactions between the ^{7}Li nuclear spins and nearby unpaired electrons at V(IV) sites (polaron hopping). Further, it was determined that the T_1 relaxation time for the Li^+ ions inserted within the lattice was substantially shorter than for those at the interfacial sites. This type of information reveals both the extent to which Li^+ interacts with electrons (polarons) within the material and provides information on the spatial relationship between Li^+ and the electron (i.e. the site geometry). In preliminary work, we have modeled these data based on the through-space coupling between unpaired electrons at V(IV) sites and Li^+ ions to determine the sites for the inserted Li^+.

Graham A. Webb (ed.), Modern Magnetic Resonance, 1547–1550.
© 2008 *Springer.*

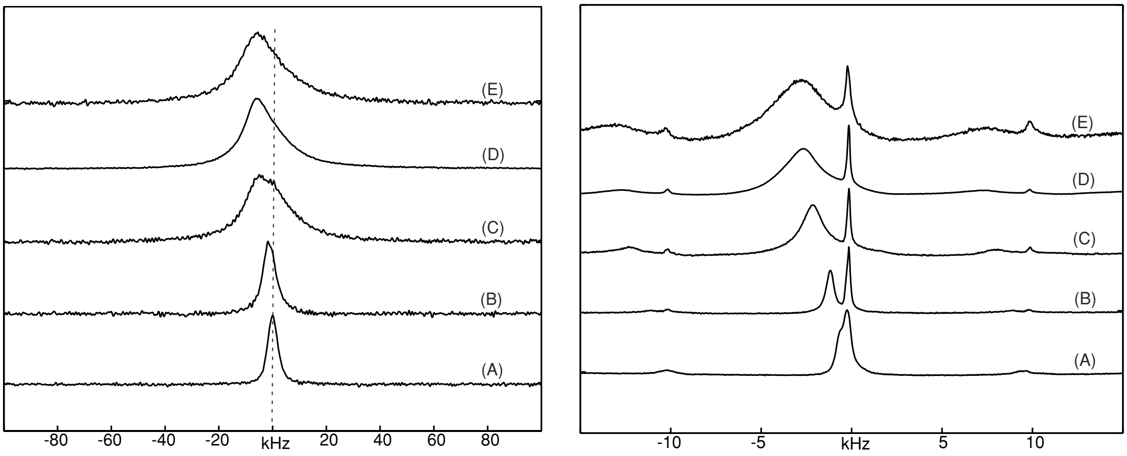

Fig. 1. Room temperature ^{7}Li static (left) and magic angle spinning (right). NMR spectra of lithium intercalated $V_2O_5 * nH_2O$ xerogel. The electrochemically lithiated $Li_xV_2O_5 * nH_2O$ xerogel, where x is 0.03 (A), 0.17 (B), 0.55 (C), 0.84 (D) and 0.98 (E). Spectra were collected on a 400 MHz NMR system with 4 mm MAS probe ($\omega_r = 10$ kHz).

A second issue of critical importance for cathode material design optimization relates to the interplay between ion motion and electron motion and how these depend on their relative locations. Figure 2 shows an example of how electron–nuclear dipole coupling can influence the T_1 relaxation time in lithiated vanadium pentoxide xerogels, $Li_xV_2O_5$. It is widely thought that the motion of Li^+ through a cathode material is often the rate-limiting process that controls power density. The NMR results associated with Figure 2 demonstrate a type of charge pinning in Li^+ insertion materials. This has also been observed in lithium vanadium phosphate cathode material, where it was shown that the extra unpaired electrons were ordered within the lattice and that the charge compensating Li^+ ions were pinned to this ordered unpaired electron sublattice [22]. This suggests that electron-ion pinning may be important in terms of understanding charge transport in such systems.

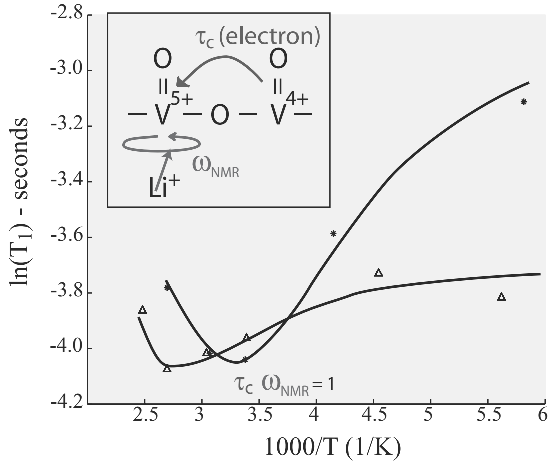

Fig. 2. The natural logarithm of T_1 versus inverse temperature for $x = 0.03$ (△) and $x = 0.17$ (●) $Li_xV_2O_5{\cdot}0.5H_2O$ xerogels. The solid lines represent the best spline fits to the experimental data and are included as a guide to the eye. The ^{7}Li static NMR T_1 was determined from a standard population inversion experiment ($\pi - \frac{\pi}{2}$). All measurements were performed on a 400 MHz NMR system ($\omega_{Li} = 155$ MHz).

Ionic mobility and binding in xerogel materials can further be explored to monitor ion-exchange processes. An example of this is displayed in Figure 3. In the ^{7}Li MAS NMR spectra of electrochemically lithiated V_2O_5 xerogels it was postulated that peak *A* represented interfacial, ion-exchangeable environments, while peak *B* corresponded to Li^+ intercalation sites. This was verified by exposing $Li_{0.2}V_2O_5$ xerogel to a $NaClO_4$ electrolyte solution, and monitoring the ^{7}Li MAS NMR response as a function of exposure time. These results provide strong evidence that peak *A* originates from an intrinsic ion-exchange site at the xerogel interface as it rapidly decays when the xerogel is exposed to Na^+ counter ions. This demonstrates that simple solid-state NMR spectroscopy can be effectively employed to follow charge compensation at surfaces in nanoporous solids like xerogels and further, that these types of environments can be distinguished from interlamellar intercalation sites in these materials.

Considerable effort has been made towards increasing the conductive properties in V_2O_5 xerogel materials by incorporating a conductive polymer within the xerogel matrix. It was shown with solid-state NMR that similar

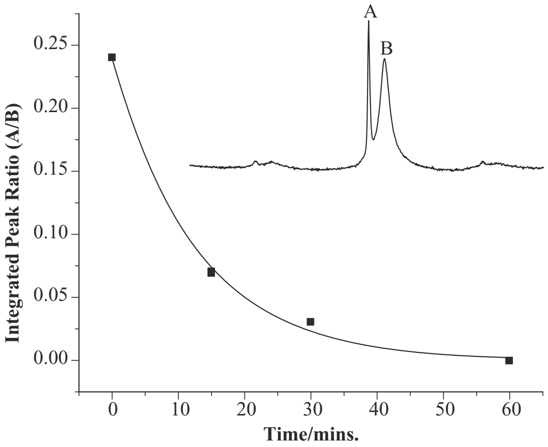

Fig. 3. Time dependence of ion-exchange in $Li_{0.2}V_2O_5$ xerogel exposed to 1 M $NaClO_4$ in propylene carbonate plotted as the integrated peak ratio ($\frac{A}{B}$) as a function of exposure time in minutes. Peaks *A* and *B* correspond to ion-exchangeable (interfacial) and intercalated (interlamellar) lithium sites, respectively.

ion-exchange processes are important in understanding how these V_2O_5 nanocomposites form and function. Two types of lithiated V_2O_5 nanocomposites containing polyaniline (PANI) and poly(aniline *N*-propane sulfonic acid) (PSPAN) have been studied with ^{7}Li MAS NMR [19]. In the ^{7}Li MAS spectra of the PANI/V_2O_5 nanocomposite essentially no ion-exchange site was observed, while the PSPAN/V_2O_5 composite displayed a significant ion-exchangeable component. PANI is cationic causing it to function as an anion exchange material. Therefore, the lack of Li^+ present in ion-exchange sites is interpreted to result due to PANI interacting with these sites during the synthetic process. In contrast, a significant ion-exchange resonance was observed in the PSPAN/V_2O_5 nanocomposite. This was attributed to the fact that PSPAN is a self-doped conducting polymer. It possesses pendent anionic groups that can inherently provide charge compensation during doping of the polyaniline-like groups in the main chains. The ^{7}Li NMR results of these composite materials not only provide information regarding the local Li environment in the material, but also indirectly provide some insight into how the conductive polymer and V_2O_5 xerogel host interact during the sol–gel synthetic process.

For quadrupolar nuclei ($I > \frac{1}{2}$), the quadrupole coupling constant and the asymmetry parameter carry valuable information about the nature of anisotropic interactions [23]. However, in the static and MAS ^{7}Li NMR ($I = \frac{3}{2}$) spectra of $Li_xV_2O_5$ xerogel the quadrupolar effects are masked by the paramagnetic broadening, especially at high V^{4+} concentrations (large Li^+ loadings). Two-dimensional separation techniques have been employed in solid-state NMR spectroscopy to separate competing interactions, such as, dipolar and chemical shift anisotropy interactions [24]. In our case, we use a 2D spin-echo experiment or a three-pulse sequence to separate out the contribution from quadrupolar and paramagnetic interactions of lithium-7 ($I = \frac{3}{2}$) in $Li_xV_2O_5$ xerogel. The 2D contour plot, together with the F_1 and F_2 projections, is shown in Figure 4. The two frequency dimensions are

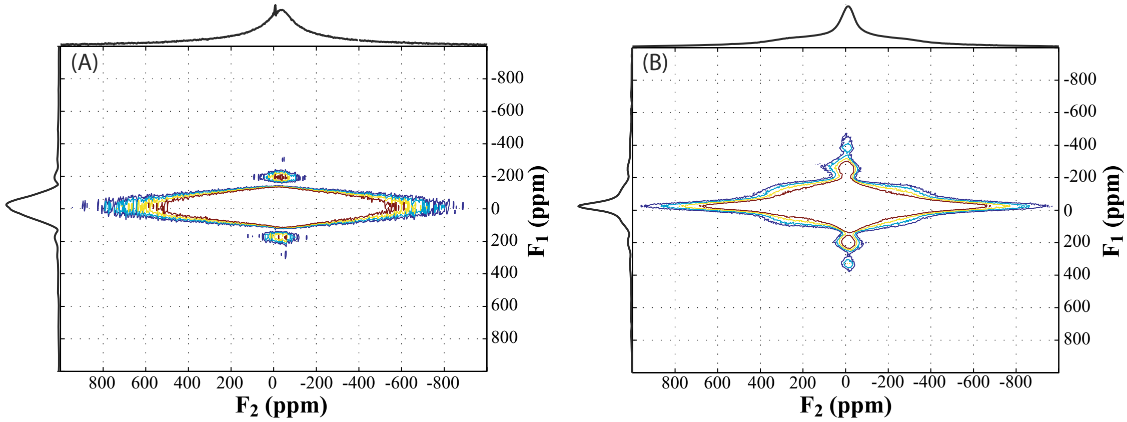

Fig. 4. ^{7}Li two-dimensional static spin-echo NMR spectrum of (A) LiV_2O_5 xerogel ($C_Q = 90$ kHz) and (B) γ-LiV_2O_5 crystalline material ($C_Q = 121$ kHz). F_2 dimension displays static spectrum affected by both quadrupolar and paramagnetic interaction. This method eliminates the paramagnetic interaction in the F_1 dimension allowing a model-free extraction of the ^{7}Li quadrupole coupling constant (C_Q) in this dimension.

asymmetrically correlated with respect to the diagonal. This is caused by the influence of the Li^+–V^{4+} paramagnetic dipolar interactions. From the resolvable satellite transitions ($\pm\frac{1}{2} \Leftrightarrow \pm\frac{3}{2}$) we can identify the paramagnetic frequency shift and the quadrupole coupling constant (C_Q).

The influence of paramagnetic dipolar interaction on the quadrupolar broadened ^{7}Li NMR spectrum of LiV_2O_5 materials is shown in Figure 4. The ^{7}Li quadrupole coupling constant was determined to be $C_Q = 90$ and 121 kHz for LiV_2O_5 xerogel and γ-LiV_2O_5 crystalline material, respectively. It is surprising to find that C_Q is smaller for the disordered xerogel, when compared to the ordered crystalline material. This indicates that though the host material is disordered, the lithium ions are in an ordered high-symmetry environment.

In summary, we show several NMR experiments used to elucidate the structural and dynamic environment of lithium ions in a xerogel host material. By using 2D separation, relaxation, high-resolution MAS, and exchange NMR experiments, we are able to completely characterize the motion and structural environment of lithium ions in vanadate xerogels. All the NMR techniques discussed can be used on any lithium host material.

Acknowledgments

Support provided from the National Science Foundation, the Department of Defense, the W.M. Keck Foundation and the Department of Energy.

References

1. Brinker C, Scherer G, Sol–Gel Science: The Physical and Chemical of Sol-Gel Processing. Academic Press; New York, 1990.
2. Cros F, Malier L, Korb J, Chaput F. J. Sol–Gel Sci. Technol. 1998;13:457.
3. Framery E, Mutin P. J. Sol–Gel Sci. Technol. 2002;24:191.
4. Okada K, Tomita T, Kameshima Y, Yasumori A, MacKenzie K, J. Mater. Chem. 1999;9:1307.
5. Pickup D, Mountjoy G, Holland M, Wallidge Newport G, Smith M. J. Mater. Chem. 2000;10:1887.
6. Faceelli J, de Dias A. Acs Symposium Series. American Chemical Society; Washington, D.C., 1999.
7. Babu P, Tong Y, Kim H, Wieckowski A. J. Electronal. Chem. 2002;524:157.
8. Lee Y, Wang F, Grey C. J. Am. Chem. Soc. 1998;120:12601.
9. Pickup D, Mountjoy G, Wallidge G, Newport R, Smith M. Phys. Chem. Chem. Phys. 1999;1:2527.
10. Brinker C, Keefer K, Schaefer D, Assink RKB, Ashley C. J. Non-Cryst. Solids 1984;63:45.
11. Klemperer W, Mainz V, Millar D. Mater. Res. Soc. Symp. 1986;73:15.
12. Franmery E, Mutin P, J. Sol–Gel Sci. Technol. 2002;24:191.
13. Bose M, Basu A. Solid State Ion. 1986;18/19:902.
14. Hirschinger J, Mongrelet T, Marichal C, Granger P, Savariault J-M, Déramond E, Galy J. J. Phys. Chems. 1993;97:10301.
15. Rozier P, Savariault J-M, Galy J, Marichal C, Hirschinger J, Granger P. Eur. J. Solid State Inorg. Chem. 1999;33:1.
16. Cocciantelli JM, Suh KS, Sénégas J, Documerc JP, Pouchard M. J. Phys. Chems. Solids 1992;53:57k.
17. Cocciantelli JM, Suh KS, Sénégas J, Documerc JP, Soubeyroux JL, Pouchard M. J. Phys. Chems. Solids 1992;53:51.
18. Holland G, Buttry D, Yarger J. Chem. Mater. 2002;14:3875.
19. Hollland G, Yarger J, Buttry D, Huguenin F, Torresi R. J. Electrochem. Soc. 2003;150:A1718.
20. Park HK, Smyrl WH, Ressler J, Owens BB, Smyrl WH. J. Electrochem. Soc. 1994;141:L25.
21. Le DB, Passerini S, Guo J, Ressler J, Owens BB, Smyrl WH. J. Elecrochem. Soc. 1996;143:2099.
22. Yin S, Grondey H, Strobel P, Huang H, Nazar L. J. Am. Chem. Soc. 2003;125:326.
23. Taylor P, Baugher J, Kriz H. Chem. Rev. 1975;75:591.
24. Ganapathy G, Rajamohanan R, Ganguly P, Venkatraman T, Kumar A. J. Phys. Chems. A. 2000;104:2007.

Solid-State ^{17}O NMR Spectroscopy of High-Pressure Silicates

Sharon E. Ashbrook

Department of Earth Sciences, University of Cambridge, Cambridge CB2 3EQ, UK
Present address: School of Chemistry, University of St. Andrews, St. Andrews, Fife KY16 9ST, UK

Introduction

Oxygen is the second most abundant element on Earth, constituting 30% by weight of the total Earth and 46% by weight of the Earth's crust. Given also the abundance of silicon (15% by weight) and the strength of the Si–O bond, it is perhaps no surprise that the majority of rocks are composed of silicates. The study of these materials, therefore, has an important role in the understanding of both the physical and chemical properties of the Earth. The vertical stratification of the Earth, into a largely aluminosilicate crust, oxide mantle, metallic liquid outer core, and metallic inner core is well known. As shown schematically in Figure 1, the mantle itself may be further subdivided, with the principal component of the upper mantle (down to a depth of 410 km) being olivine, $(Mg_{0.8}Fe_{0.1})_2SiO_4$, an iron-bearing form of forsterite (α-Mg_2SiO_4). A series of phase transitions occurs with increasing depth and pressure, resulting in the formation of the β- and γ-polymorphs of $(Mg,Fe)_2SiO_4$, wadsleyite, and ringwoodite, defining the transition zone [1,2]. At greater pressures still, in the lower mantle, disproportionation occurs forming $(Mg,Fe)SiO_3$ (perovskite) and magnesiowüstite, $(Mg,Fe)O$. The presence of less abundant phases in the mantle, such as garnets, pyroxenes, and high-pressure silica, is also of crucial importance in determining the physical properties of the deep Earth.

This simplified picture disguises a number of important questions within the Earth sciences, however. Although the compositions of the various mantle regions are somewhat constrained, we do not know the exact Si, Mg, Fe, Ca, or Al content of the various phases. We know about the interior of our planet only from secondary evidence, such as seismological measurements, meteorites, rocks brought to the crust from the mantle by geological processes, and the simulation of materials under extreme conditions [3]. In particular, there are many indications from these sources that the inner Earth contains many times the amount of hydrogen (colloquially termed water) than is present in the oceans, with estimates ranging from 200 to 600 ppm [4–7]. The presence of this water is of great interest owing to its influence on a range of physical and chemical properties such as mantle rheology and melting temperatures and pressures. It is now widely believed that nominally anhydrous minerals, such as olivine, wadsleyite, and ringwoodite can incorporate water within their structures [4–7]. The study of the structure and the dynamic behavior of high-pressure solid silicates and, in particular their hydration, is of vital importance.

Oxygen NMR

The study of solid silicates by oxygen NMR would appear to be a natural choice given the presence of oxygen in the minerals present in the crust and mantle and the sensitivity of NMR to the local environment. However, the only NMR active isotope of oxygen, ^{17}O ($I = 5/2$), has both a low sensitivity ($\omega_0/2\pi = 54.2$ MHz at 9.4 T) and an extremely low natural abundance (~0.037%). The additional problem of difficult experimental syntheses for high-pressure silicates, which produce only small amounts of material, results in a considerable sensitivity problem. Although samples may be synthesized with isotopic enrichment, sensitivity remains a crucial factor.

As ^{17}O has spin $I > 1/2$, spectra are broadened by the quadrupolar interaction, often over many megahertz [8]. Magic angle spinning (MAS) is able to remove the quadrupolar interaction to a first-order approximation but is unable to remove fully the second-order quadrupolar interaction [8] and resonances remain broadened. Much attention has been focused on the acquisition of high-resolution NMR spectra for quadrupolar nuclei. One approach is to use composite sample rotation techniques, such as dynamic angle spinning (DAS) [9] and double rotation (DOR) [10], which achieve resolution enhancement though rotation around two different angles. The introduction of the multiple-quantum (MQ) MAS technique [11] in 1995 revolutionized high-resolution NMR of quadrupolar nuclei, and this method has become widespread owing to the ease of its implementation. In 2000, Gan introduced an alternative method for obtaining high-resolution spectra of quadrupolar nuclei, the satellite-transition (ST) MAS experiment [12]. Although slightly more difficult to implement than MQMAS, its high inherent

Graham A. Webb (ed.), Modern Magnetic Resonance, 1551–1561.
© 2008 *Springer.*

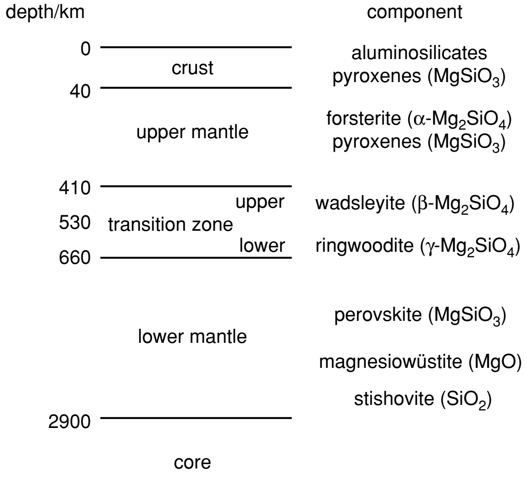

Fig. 1. Schematic diagram of the compositional variation of the Earth.

sensitivity has proved crucial in the study of high-pressure silicate phases, particularly in cases where sample volume is limited.

Despite the problems outlined above ^{17}O NMR has enormous potential in the study of silicate minerals. NMR enables investigation of both the local structure and the dynamic behavior of a system. Both ^{29}Si and ^{1}H NMR have been employed in the study of mantle phases [13–16], but neither can offer the flexibility of ^{17}O NMR. Silicon NMR provides information only on the local Si environment while, on its own, ^{1}H NMR is unable to identify specific O–H pairings, is insensitive to dynamic effects and suffers from problems with a large "background signal." In contrast, ^{17}O NMR (both single and double resonance techniques) provides information on the local O environment, can offer information on specific O–H pairings and often displays a sensitivity to dynamic behavior. Both the ^{17}O quadrupolar and chemical shift interactions are extremely sensitive to changes in the environment on a local scale [17], providing an excellent tool for studying silicates, a group of minerals with wide compositional diversity and structural modifications. Silicate structures tend to be dominated by the SiO_4 tetrahedron. These units can be isolated from each other, and coordinated to other cation polyhedra present in the structure. The nature of the cation has a significant effect upon the Si–O bond length and, hence, the ^{17}O chemical shift. It has been shown for many systems that an increase in ^{17}O chemical shift reflects an increased Si–O bond length. Alternatively, SiO_4 units can be connected to each other by corner sharing, forming Si_2O_7 groups or even long chains. Further polymerization results in silicate sheets and finally three-dimensional silicate frameworks. When corner-sharing tetrahedra are present, at least one oxygen species, denoted a "bridging oxygen," is bonded to two silicons simultaneously. This is reflected in considerable changes in chemical shift and, in particular, in quadrupolar coupling [17]. Bridging oxygen species exhibit C_Q values (~4–6 MHz) that are significantly higher than those for non-bridging species (~2–3.5 MHz). The largest quadrupolar couplings (~6–8 MHz), however, tend to be found for hydroxyl oxygens, providing an excellent opportunity to study hydration.

Sample Preparation

The low natural abundance of ^{17}O (0.037%) necessitates the use of isotopic enrichment in order to obtain good sensitivity. A wide range of enrichment schemes is possible, with both O_2 and H_2O readily available as isotopically enriched starting material. The exact enrichment level employed is usually a compromise between cost and sensitivity. For the high-pressure silicates considered here, the preparation method of choice is usually synthesis from ^{17}O-enriched oxides prepared from H_2O (l), with common enrichment levels between 10 and 75%. The ^{17}O is fixed by reaction of $H_2{}^{17}O$ with reagents such as $SiCl_4$, Mg_3N_2, Ca_3N_2, and AlN liberating a gas (HCl or N_2) and leaving a solid oxide or hydroxide product. These may then be mixed in appropriate stoichiometric amounts to prepare the silicate required. The elements O, Mg, Al, Ca, and Si represent the major components of an Fe-free crust and mantle and allow all major phases to be prepared. Mantle phases may be prepared by simulating the pressure and temperature conditions present in the mantle using either a piston cylinder or a multi-anvil apparatus. Piston cylinder devices produce only relatively moderate pressures (up to 4 GPa, corresponding to a depth of only 120 km) but allow large volumes of sample (~100 mg) to be produced. In comparison, multi-anvil devices allow access to a much greater pressure range (up to 22 GPa, or depths of >660 km) but the volume of material available is much reduced (often only 5–10 mg). Samples are quenched rapidly from the experimental high-pressure and high-temperature conditions as the high-pressure phases are usually kinetically stable at ambient conditions.

MQMAS NMR of Upper Mantle Silicates

Forsterite (or α-Mg_2SiO_4), is the Fe-free form of olivine, the principal component of the Earth's mantle to a depth of ~410 km. The crystal structure of forsterite (*Pbnm*) consists of isolated SiO_4^{4-} units with three distinct oxygen species (O1, O2, and two O3) [18]. Forsterite has become almost a "model" compound for ^{17}O NMR as: (i) isotopically enriched forsterite is relatively easily prepared at ambient pressures in reasonably large quantities [19]; (ii) olivine has a huge importance in the mantle; and

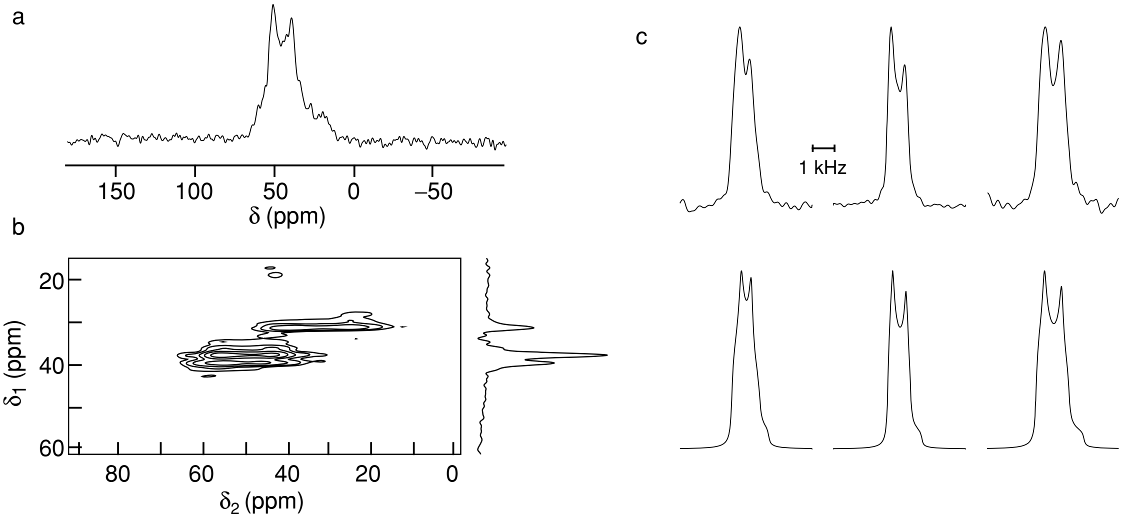

Fig. 2. ^{17}O (54.2 MHz) MAS NMR of 35% isotopically enriched forsterite (α-Mg_2SiO_4). (a) MAS NMR spectrum, (b) two-dimensional triple-quantum MAS NMR spectrum, recorded with a phase-modulated split-t_1 shifted echo sequence, and (c) cross sections parallel to δ_2, along the three second-order broadened ridge lineshapes and corresponding computer fits.

(iii) the non-bridging nature of the oxygen species results in only moderate quadrupolar couplings. As a result, a variety of NMR techniques have been employed in the study of forsterite. The extraction of information from the MAS spectrum alone, however, is hampered by the presence of second-order quadrupolar broadening [20], as shown in Figure 2a. This ^{17}O (54.2 MHz) MAS NMR spectrum of forsterite (enriched to 35% in ^{17}O) reveals a composite lineshape centered at ~50 ppm, with features characteristic of second-order broadening, but resulting from the overlap of three different lineshapes.

In order to obtain accurate chemical shift and quadrupolar information for the three oxygen species spectral resolution must be improved. Both DAS [21] and DOR [22] have been employed to obtain isotropic spectra of forsterite. However, a complete assignment of the ^{17}O high-resolution spectrum was first achieved using MQMAS [19]. Figure 2b shows the two-dimensional ^{17}O triple-quantum MAS NMR spectrum of forsterite (enriched to 35% in ^{17}O), recorded using a phase-modulated split-t_1 shifted echo experiment [23]. The spectrum consists of a series of ridge lineshapes, one for each crystallographically distinct species, lying parallel to the δ_2 axis. The high-resolution or isotropic spectrum, obtained from a projection onto δ_1, reveals three distinct resonances in the ratio 1:2:1. Although MQMAS efficiency varies as a function of the quadrupolar interaction [23], the small differences between the three distinct oxygen species enables the site populations to be determined directly from the relative intensities of the resonances. The position of the center of gravity of each lineshape in the two-dimensional spectrum (δ_1, δ_2) allows the extraction of the isotropic chemical shift, δ_{CS}, and the second-order quadrupolar shift, δ_Q [19]. From δ_Q, the quadrupolar product $P_Q = C_Q(1 + \eta^2/3)^{1/2}$ can be obtained. The individual quadrupolar parameters, the magnitude (C_Q) and asymmetry (η) of the quadrupolar interaction, may be determined from cross sections taken along each ridge, parallel to δ_2. The lineshapes obtained may be fitted using a computer fitting routine to obtain values for C_Q, η, and δ_{CS}, as shown in Figure 2c. The values of the chemical shift and quadrupolar parameters for the oxygen species in forsterite are given in Table 1 [19]. If the relative populations of the sites and the similarity in the coordination environment of O2 and O3 are considered a complete assignment of the resonances is possible, and is also shown in Table 1.

MQMAS has also been employed to study a series of pyroxenes, an important group of rock-forming minerals which occur in nearly all igneous rocks and comprise up to 25% of the upper mantle [24]. Pyroxenes have the general formula $M1M2Si_2O_6$ and consist of infinite chains of corner-sharing SiO_4 tetrahedra. Each tetrahedron contains both bridging and non-bridging oxygen species, providing a more challenging target for ^{17}O NMR. Perhaps the most relevant pyroxene for mantle chemistry is enstatite, $Mg_2Si_2O_6$, of which there are three stable or metastable polymorphs under ambient conditions. Orthoenstatite (*Pbca*) and protoenstatite (*Pbcn*) are orthorhombic [25,26], whilst

Table 1: ^{17}O isotropic chemical shifts (δ_{CS}), quadrupolar products (P_{Q}), quadrupolar coupling constants (C_{Q}), asymmetries (η), relative populations, and tentative assignments of the oxygen species a variety of silicate minerals.

Mineral	δ_{CS} (ppm)	P_Q/MHz	C_Q/MHz	η	Population	Assignment
Forsterite [19]	48(1)	2.8(1)	2.8(1)	0.3(1)	1	O1
	61(1)	2.4(1)	2.5(1)	0.2(1)	2	O3
	64(1)	2.6(1)	2.5(1)	0.4(1)	1	O2
Orthoenstatite [24]	42(1)	2.8(1)				O21
	46(1)	2.9(1)				O22
	52(1)	3.0(1)				O11
	54(1)	3.0(1)				O12
	64(3)	4.3(1)				O31
	73(3)	4.9(1)				O32
Clinoenstatite [24]	41(1)	2.8(1)				O21
	45(1)	2.8(1)				O22
	51(1)	3.0(2)				O11
	54(1)	3.0(2)				O12
	64(3)	4.3(3)				O31
	75(3)	4.8(3)				O32
Protoenstatite [24]	39(1)	2.7(1)				O2
	52(1)	2.8(1)				O1
	66(3)	4.3(2)				O3
Diopside [24]	63(1)	2.8(1)				O2
	72(2)	4.3(2)				O3
	84(2)	2.7(2)				O1
Wadsleyite [29]	38(1)	1.3(1)			1	O1
	65(1)	3.8(1)	3.8(1)	0.3(1)	4	O4
	66(1)	4.4(1)	4.4(1)	0.2(1)	2	O3
	76(1)	5.6(1)	4.9(2)	0.9(1)	1	O2
Ringwoodite [31]	63(1)	4.9(1)	4.9(2)	0.0(2)	1	O1
Chondrodite [37]	52(1)	2.7(1)	2.7(1)	0.2(1)	1	O4
	59(2)	2.3(2)	2.3(1)	0.3(1)	1	O2
	60(2)	2.3(2)	2.3(1)	0.2(1)	1	O3
	63(1)	2.6(1)	2.5(2)	0.3(1)	1	O1
	25(3)		6.6(1)	0.1(2)	1	O5
Clinohumite [37]	49(1)	2.7(1)	2.7(1)	0.2(1)	1	O1
	52(1)	2.7(1)	2.7(2)	0.2(2)	1	O5
	59(2)	2.4(2)	2.4(1)	0.2(1)	1	O8
	60(2)	2.3(2)	2.4(2)	0.2(1)	1	O7
	61(2)	2.3(2)	2.3(2)	0.1(2)	2	O3 + O4
	64(1)	2.5(1)	2.4(1)	0.2(1)	1	O6
	65(1)	2.5(1)	2.5(2)	0.3(1)	1	O2
	25(3)		7.0(1)	0.2(2)	1	O9

clinoenstatite ($P21/c$) is monoclinic [27]. The related mineral diopside, $MgCaSi_2O_6$, is also monoclinic ($C2/c$) [28]. In both orthoenstatite and clinoenstatite there are two types of silicate chains, whilst in protoenstatite and diopside the two chains are related by symmetry reducing the number of distinct O species. The polymorphs may be prepared from ^{17}O-enriched oxides either at ambient pressures or using a piston cylinder apparatus [24].

The ^{17}O MAS NMR spectra of the pyroxene minerals (shown in Figure 3) contain broad and complex resonances centered between 30 and 50 ppm, with little indication of the number and nature of crystallographically distinct oxygen species present [24]. MQMAS yields high-resolution isotropic spectra, as displayed in Figure 3, which reveal the presence of many distinct oxygen species [24]. Orthoenstatite and clinoenstatite exhibit very similar spectra with six distinct species present.

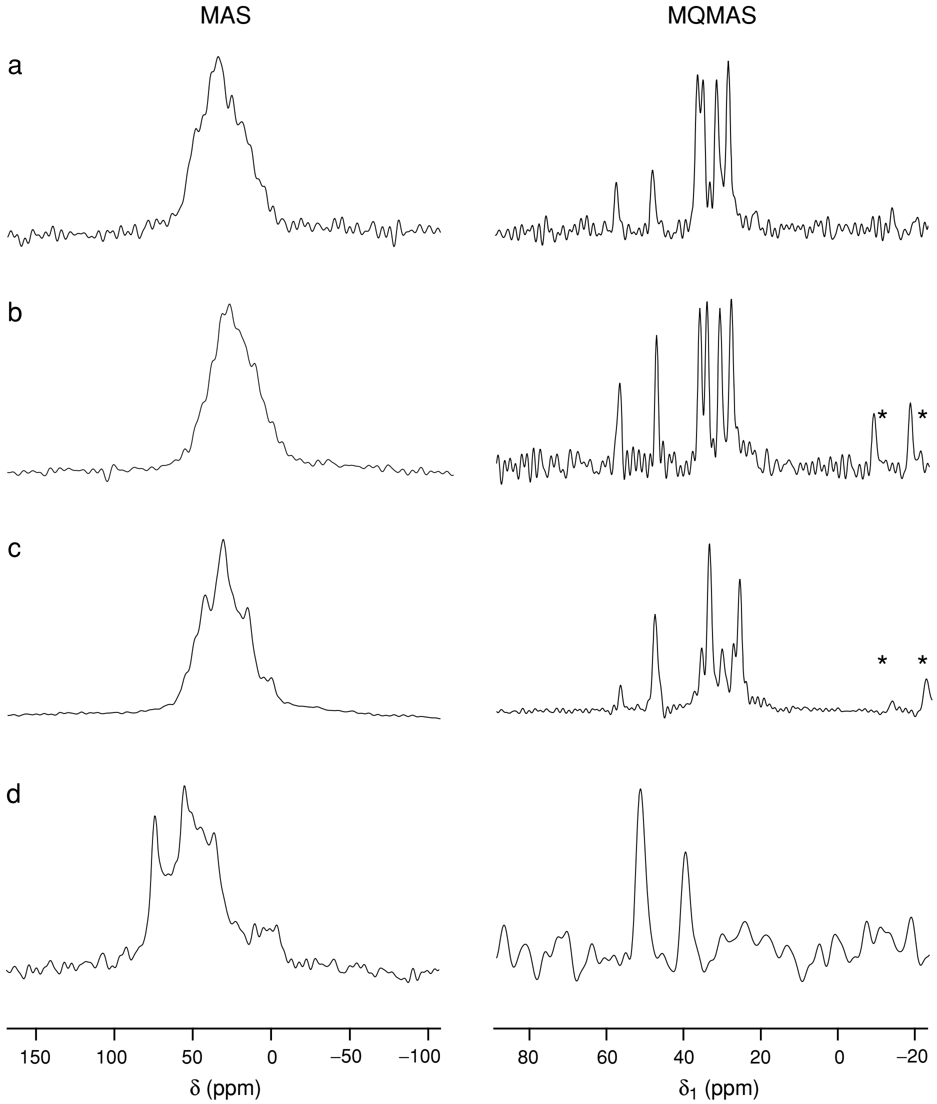

Fig. 3. ^{17}O (54.2 MHz) MAS and isotropic triple-quantum MAS NMR spectra of (a) orthoenstatite ($MgSiO_3$), (b) clinoenstatite ($MgSiO_3$), (c) protoenstatite ($MgSiO_3$), and (d) diopside ($CaMgSi_2O_6$). Nominal levels of isotopic enrichment are (a–c) 35% and (d) 29%.

In each case, four of the resonances possess small C_Q values indicative of non-bridging oxygens, whilst two have the increased chemical shift and quadrupolar interactions characteristic of bridging species. In protoenstatite, owing to the increased symmetry only three resonances are present, one bridging and two non-bridging, although an impurity phase of clinoenstatite is also detected. Diopside also displays three distinct oxygens species, but two are overlapped in the spectrum shown in Figure 3 (recorded at 9.4 T). Measurements at different field strengths allow these species to be separated. The values of the quadrupolar and chemical shift interactions for each species, along with their assignments are given in Table 1 [24]. The different chemical shifts observed in diopside are consistent with deshielding due to the increase in effective cation radius [17,24].

STMAS NMR of Dense Silicate Phases

While α-Mg_2SiO_4 in the form of olivine is the main component of the Earth's upper mantle, the increase in pressure at greater depths results in the formation of the β- and γ-polymorphs, wadsleyite, and ringwoodite. These minerals are thought to be the major constituents of the transition zone (as shown in Figure 1), with the α–β transition responsible for the seismic discontinuity observed at a depth of 410 km and the transition from γ-Mg_2SiO_4 to $MgSiO_3$ (perovskite) responsible for the discontinuity around 660 km [1,2]. The β–γ transition may well contribute to the less pronounced discontinuity around 520 km. These dense phases are of particular interest because of their potential as the repository for the largest reservoir of water in the Earth. Before studies of hydration can be undertaken, however, the anhydrous counterparts must be fully characterized.

Although high-resolution ^{17}O NMR spectra of forsterite were obtained easily using MQMAS [19], the sensitivity of this experiment, particularly at high MAS rates, is not sufficient for the study of wadsleyite and ringwoodite. These phases, found at much greater depths in the Earth, must be synthesized at much greater pressures (16 and 20 GPa) using a multi-anvil press, producing only 5–10 mg of material [29]. Furthermore, sample purity can also be a problem, with pressure or temperature gradients resulting in a mixture of phases, thereby reducing the sensitivity further. Recently, the introduction of the STMAS experiment [12], a method with inherently high sensitivity at both slow and fast MAS rates, has enabled the study of such small amounts of ^{17}O-enriched material on a reasonable timescale. Although of good sensitivity, STMAS does have stringent experimental requirements, such as a stable MAS rate (to within ±2 Hz) and an accurately adjusted spinning angle ($\chi = 54.736^\circ \pm 0.002^\circ$) [12,30].

STMAS has been successfully employed to obtain and assign high-resolution ^{17}O MAS NMR spectra of both wadsleyite and ringwoodite [29,31]. Figure 4a shows a ^{17}O MAS NMR spectrum of ~10 mg of 35% ^{17}O-enriched wadsleyite [29]. The broad complex lineshape results from the overlap of resonances from distinct oxygen species, which are resolved in the STMAS spectrum shown in Figure 4b. In addition to a diagonal resulting from the autocorrelation of the central transition, four ridge lineshapes are observed with relative intensities approximately 1:4:2:1 in order of increasing δ_1. As with MQMAS, the values of C_Q, η, δ_{CS} and P_Q may be extracted from either the position or shape of the ridge lineshapes, and are given in Table 1 [29]. Wadsleyite has a spinelloid structure (*Imma*) and contains Si_2O_7 groups, which results in both bridging (O2) and non-bridging (O3 and O4) oxygens, in addition to an oxygen (O1) coordinated by five Mg [32]. The quadrupolar and chemical shift information extracted from an STMAS spectrum of a sample of ~5 mg of 35% ^{17}O-enriched ringwoodite (with a substantial wadsleyite impurity) are also given in Table 1. Although ringwoodite has a spinel structure (*Fd3m*) with only a single non-bridging oxygen species [33], high-resolution NMR techniques were required to determine the exact nature of the impurity phases [31].

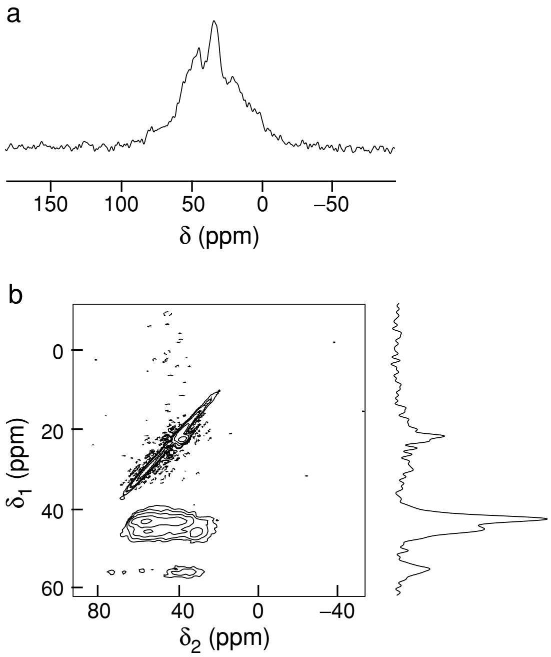

Fig. 4. ^{17}O (54.2 MHz) MAS NMR of ~10 mg of 35% isotopically enriched wadsleyite (β-Mg_2SiO_4). (a) MAS NMR spectrum, (b) two-dimensional STMAS NMR spectrum and corresponding isotropic projection, recorded with a phase-modulated split-t_1 shifted echo sequence.

NMR of Hydrous Magnesium Silicates: Humite Minerals

The suggestion that the mantle contains a large volume of water is supported by the potential of nominally anhydrous minerals, such as olivine and wadsleyite, to incorporate significant amounts of water into their structures [4–7]. The minerals of the hydroxyl-humite group, $n Mg_2SiO_4 \cdot Mg(OH)_2$, have been proposed as possible models of the defect sites accommodating water in olivine [34]. These minerals can be described (rather simplistically) as comprising of n forsterite-like layers alternating with brucite layers, and so may be viewed as hydrated forms of forsterite. Both chondrodite ($n = 2$)

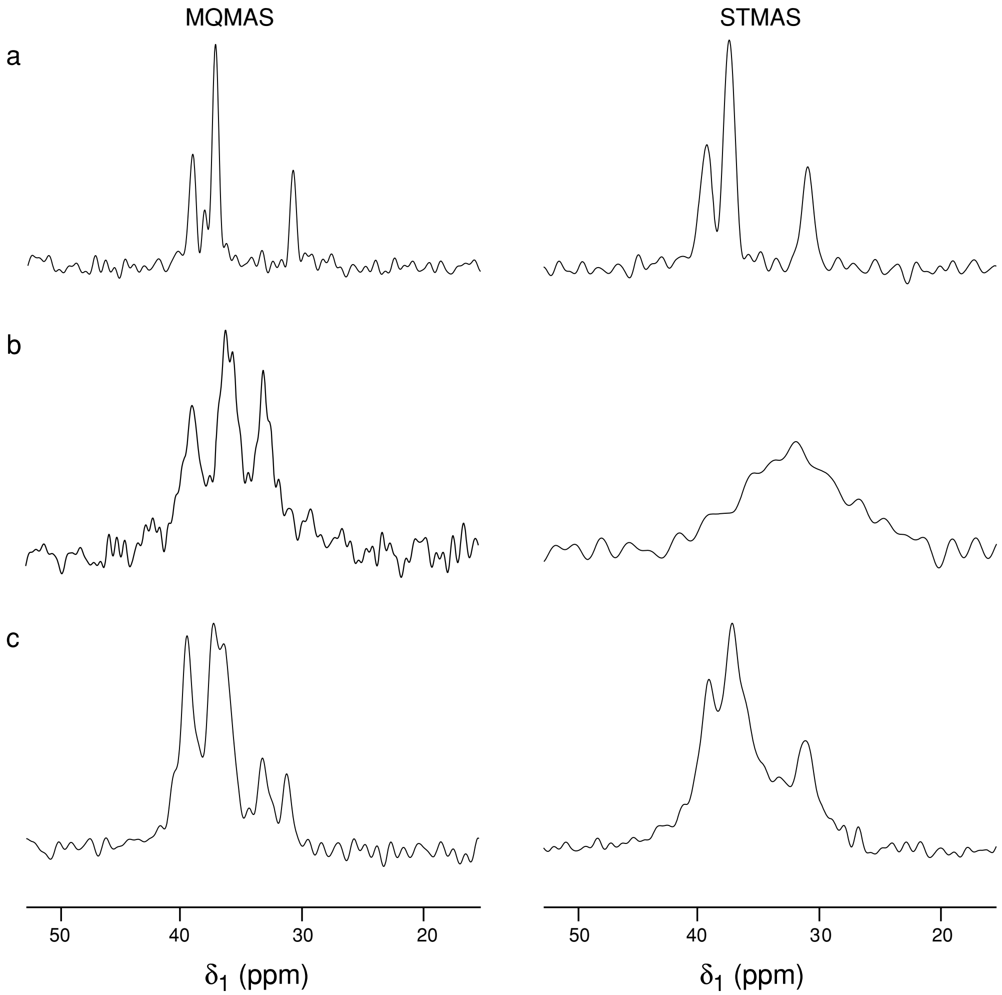

Fig. 5. ^{17}O (54.2 MHz) isotropic triple-quantum MAS and STMAS NMR spectra of (a) forsterite (Mg_2SiO_4), (b) chondrodite ($2Mg_2SiO_4 \cdot Mg(OH)_2$), and (c) clinohumite ($4Mg_2SiO_4 \cdot Mg(OH)_2$). Nominal levels of ^{17}O enrichment were 35% in all cases.

and clinohumite ($n = 4$) are monoclinic with space group $P21/c$, resulting in five (four non-bridging and one hydroxyl) and nine (eight non-bridging and one hydroxyl) distinct oxygen species, respectively [35,36]. Both minerals can be synthesized, isotopically enriched in ^{17}O, at pressures equivalent to the upper mantle using a piston cylinder apparatus [37].

The ^{17}O MAS NMR spectra of chondrodite and clinohumite are both extremely similar to that of forsterite, with a broad complex lineshape centered at ∼50 ppm [37]. Distinct oxygen species my be resolved, however, in MQMAS spectra, as shown in Figure 5, which displays isotropic ^{17}O triple-quantum MAS NMR spectra of 35% isotopically enriched forsterite, chondrodite, and clinohumite [37]. The spectrum of chondrodite is broadly similar to that of forsterite, with a shift of some resonances and the splitting of the central resonance ($\delta_1 =$ 36 ppm) into two as a result of the decrease in symmetry. This latter effect is clearer when a full two-dimensional spectrum is considered. The spectrum of clinohumite contains five peaks and can be clearly seen to resemble the summation of the spectra of forsterite and chondrodite, reflecting the (simplified) description of the crystal structure of clinohumite as layers of chondrodite and forsterite in equal proportion. The relative intensities of the peaks, 1:1:2:2:2, indicate that all eight non-bridging oxygens

Fig. 6. (a) Conventional and (b) cross-polarized ^{17}O (54.2 MHz) spin-echo NMR spectra of static samples of (a) chondrodite and (b) clinohumite.

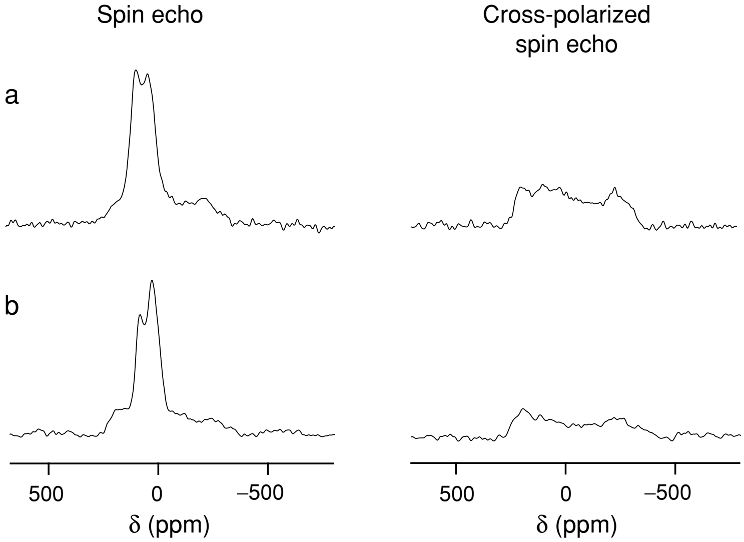

are observed, but that some are too similar to be resolved at this field strength. A high-resolution ^{17}O triple-quantum MAS NMR spectrum of clinohumite recorded at $B_0 = 16.4$ T was able to resolve seven of the eight distinct species [37], with O3 and O4 still too similar to be distinguished.

Although resolution of the non-bridging oxygen species in clinohumite and chondrodite was achieved with MQMAS, there is little evidence of the hydroxyl species in the brucite-like layer in these spectra. Hydroxyl oxygen species are predicted to possess much larger quadrupolar couplings [17] making their observation non-trivial at moderate B_0 fields, slow MAS rates and low ^1H decoupling strengths. However, the ^{17}O spin-echo NMR spectra of static samples of chondrodite and clinohumite shown in Figure 6 [37], display a composite lineshape with both a narrow feature and a broader component typical of an oxygen species with a much larger quadrupolar interaction. The use of cross-polarization, a technique which edits the NMR spectrum on the basis of spatial proximity to ^1H, retains only this broad species, confirming its assignment as the hydroxyl oxygen. The quadrupolar and chemical shift parameters for this species in both chondrodite and clinohumite, given in Table 1, are very similar to those observed for brucite [37].

Owing to the similarity of the two techniques, the isotropic spectra produced by MQMAS and STMAS are expected to be very similar in nature, and for many crystalline materials this is indeed the case [38]. However, the isotropic ^{17}O STMAS NMR spectra of 35% isotopically enriched forsterite, chondrodite, and clinohumite, shown in Figure 5, do show significant differences from the MQMAS spectra [38]. For forsterite, the two spectra are extremely similar with the small increase in line width in the STMAS spectrum attributed to a very small misset in the magic angle. However, the STMAS spectrum of chondrodite contains a very broad resonance, in contrast to the sharp peaks observed in the MQMAS spectrum. For clinohumite, some of the resonances observed in the MQMAS spectrum remain sharp whilst others appear significantly broadened. Both chondrodite and clinohumite contain a brucite-like layer with two distinct H sites, each of which is half occupied. The large isotropic displacement parameters associated with both sites suggest significant motion of H relative to the other atoms, either vibrational motion within a cavity or even exchange between the sites [39]. This motion of H modulates the electric field gradient experienced by the oxygens and, hence, the ^{17}O quadrupolar interaction. For the central transition (and indeed the multiple-quantum transition employed in MQMAS) this modulation is small. However for the satellite transitions, where a first-order quadrupolar interaction is present, the change in frequency may be significant and a “motional broadening” is observed in STMAS spectra [38]. In chondrodite, all oxygen species are within 3 Å of either H1 or H2, and will all most likely be involved in hydrogen bonding, producing a large effect in the spectrum. In clinohumite, the oxygens in the chondrodite-like layer are also to ^1H and display a significant motional broadening. However, those oxygens in the forsterite-like layer are sufficiently far from ^1H that they remain relatively unaffected by motional processes. It is possible to

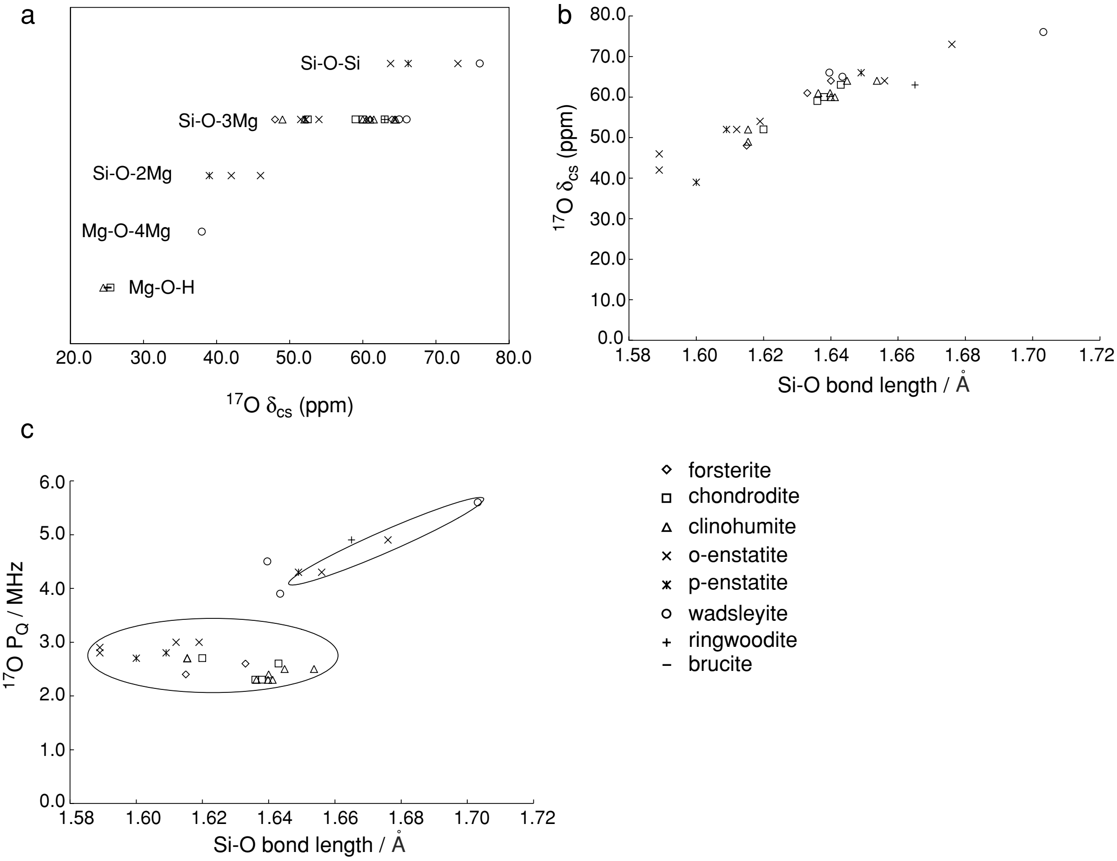

Fig. 7. (a) Variation of the ^{17}O isotropic chemical shift (δ_{CS}) with coordination environment, (b) plot of ^{17}O isotropic chemical shifts (δ_{CS}) against coordination environment, and (c) ^{17}O quadrupolar parameters (P_Q) against average Si–O bond length for a variety of silicate minerals.

observe changes in the line width of the resonances in STMAS spectra of both chondrodite and clinohumite by changing the temperature, confirming the motional origin of the broadening [38].

Discussion and Conclusions

Both MQMAS and STMAS may be employed to obtain isotropic ^{17}O NMR spectra with resolution of distinct oxygen species, and allow extraction of accurate quadrupolar and chemical shift parameters. These values, coupled with a comparison of isotropic spectra between like compounds often allows a complete assignment of the spectrum with reference to the suggested crystal structure. It is then possible to investigate any correlations between the NMR parameters and structural variables such as bond lengths or number and type of coordinating atoms. Figure 7a shows the ranges of the ^{17}O isotopic chemical shift (δ_{CS}) with the local coordination environment in the magnesium silicate minerals considered here. Oxygen species with different environments are reasonably well separated, with bridging species found between 65 and 80 ppm and non-bridging species between 40 and 67 ppm. Those non-bridging species coordinated to 1 Si and 2 Mg are found at significantly lower δ_{CS} than those with 1 Si and 2 Mg. A further decrease in chemical shift is observed for species with no Si bonds, the O coordinated only by 5 Mg atoms in wadsleyite (~38 pm) and Mg–O–H species (~25 ppm). The ^{17}O isotopic chemical shift can be linked directly to changes in the Si–O bond length (the average bond length for bridging oxygens) as shown in Figure 7b. A general positive correlation is observed with an increase in the Si–O bond length resulting in an increase in δ_{CS}. A linear regression analysis yields $\delta_{\mathrm{CS}}/dr_{\mathrm{Si-O}} = +325$ ppm/Å, with a correlation coefficient, R^2, of 0.816. A slightly better fit ($R^2 = 0.822$) can be obtained with a second-order polynomial regression. This increase in chemical shift with Si–O bond length appears general for both bridging and non-bridging oxygens. Figure 7c shows the variation of the ^{17}O quadrupolar parameter, P_{Q}, with Si–O bond length. Unlike the chemical shift, no real correlation is observed and the oxygen species tend to cluster into two distinct groups, non-bridging oxygens between 2 and 3.2 MHz and bridging species between 4 and 6 MHz, in general agreement with literature data for a range of different systems. However, it should be noted that the non-bridging oxygen species in the high-pressure polymorphs of Mg_2SiO_4, wadsleyite, and ringwoodite, show anomalously high P_{Q} values (between 3.8 and 4.8 MHz), much more similar to those expected for bridging species. Work is ongoing both experimentally and through *ab initio* computer simulations in order to gain a deeper understanding of the origin of these effects.

In conclusion, ^{17}O NMR offers great potential for the study of the silicate minerals that make up the Earth's crust and mantle as it is very sensitive to the local structural environment. The low natural abundance of ^{17}O (0.037%) may be overcome through the use of isotopic enrichment, and materials may be synthesized at mantle conditions using either piston cylinder or multi-anvil apparatus. Although the presence of second-order quadrupolar broadening hinders the extraction of information directly from conventional MAS NMR spectra, both MQMAS and STMAS methods can be used to obtain high-resolution spectra where distinct oxygen species are resolved. STMAS is a more sensitive technique and although technically difficult to implement is a vital tool in cases where sensitivity is limited or where only small amounts of material may be available. While removing the anisotropic quadrupolar broadening, both techniques retain the isotropic quadrupolar and chemical shift information enabling, in many cases, the full assignment of the spectra. The correlation of these interactions with local structural parameters, such as bond lengths or coordination environments, will help to provide information in cases where crystal structures are less well known, for example, in the investigation of hydrated minerals. The use of ^{17}O/^{1}H double resonance techniques, such as cross-polarization, are also of significant use in the determination and characterization of hydrated oxygen species. The observation of motional broadening in STMAS spectra offers indications that the combination of both MQMAS and STMAS may be able to provide information on the dynamic behavior of hydrated mineral phases. A combination of ^{17}O NMR methods, therefore, really does seem to offer an ideal opportunity to study mantle silicate minerals and their hydration processes.

Acknowledgments

I would like to thank Dr. Stephen Wimperis (University of Exeter, UK) and Dr. Andrew J. Berry (ANU, Canberra, Australia) who contributed considerably to much of the work described here and to Stefan Steuernagel (Bruker, Karlsruhe, Germany) for access to high-field NMR instruments. I also acknowledge the Royal Society for the award of a Dorothy Hodgkin Fellowship.

References

1. Ringwood AE. Composition and Petrology of the Earth's mantle. McGraw-Hill: New York, 1995.
2. Katsura T, Ito E. J. Geophys. Res. 1989;94:15663.
3. Navrotsky A. Physics and Chemistry of Earth Materials. Cambridge University Press: Cambridge, 1994.
4. Smyth JR. Am. Mineral. 1994;79:1021.
5. Bolfan-Casanova N, Keppler H, Rubie DC. Earth Planet. Sci. Lett. 2000;182:209.
6. Bell DR, Rossman GR. Science. 1992;255:1391.
7. Kohlstedt DL, Keppler H, Rubie DC. Contrib. Mineral. Petrol. 1996;123:345.
8. Ganapathy S, Schramm S, Oldfield E. J. Chem. Phys. 1982;77:4360.
9. Llor A, Virlet J. Chem. Phys. Lett. 1988;152:248.
10. Samoson A, Lippmaa E, Pines A. Mol. Phys. 1988;65:1013.
11. Frydman L, Harwood JS. J. Am. Chem. Soc. 1995;117:5367.
12. Gan Z. J. Am. Chem. Soc. 2000;122:3242.
13. Kohn SC. Am. Mineral. 1996;81:1523.
14. Kohn SC, Brooker RA, Frost DJ, Slesinger AE, Wood BJ. Am. Mineral. 2002;87:293.
15. Phillips BL, Burnley PC, Worminghaus K, Navrotsky A. Phys. Chem. Miner. 1997;24:179.
16. Stebbins JF, Kanzaki M. Science. 1991;251:294.
17. Kirkpatrick RJ. Spectroscopic Methods in Mineralogy and Geology. Reviews in Mineralogy, Volume 18. Mineralogical Society of America, Washington, 1988.
18. Hazen RM. Am. Mineral. 1976;61:1280.
19. Ashbrook SE, Berry AJ, Wimperis S. Am. Mineral. 1999;84:1191.
20. Schramm S, Oldfield E. J. Am. Chem. Soc. 1984;106:2502.
21. Mueller KT, Wu Y, Chmelka BF, Stebbins J, Pines A. J. Am. Chem. Soc. 1991;113:32.
22. Mueller KT, Baltisberger JH, Wooten EW, Pines A. J. Phys. Chem. 1992;96:7001.
23. Brown SP, Wimperis S. J. Magn. Reson. 1997;124:279.
24. Ashbrook SE, Berry AJ, Wimperis S. J. Phys. Chem. B. 2002;106:773.
25. Hawthorne FC, Ito J. Can. Mineral. 1977;15:321.
26. Murakami T, Takeuchi Y, Yamanaka T. Z. Kristallogr. 1982;160:299.
27. Ohashi Y, Finger LW. Carnegie Inst. Wash. Year Book. 1973;75:743.

28. Cameron M, Sueno S, Prewitt CT, Papike JJ. Am. Mineral. 1973;58:594.
29. Ashbrook SE, Berry AJ, Hibberson WO, Steuernagel S, Wimperis S. J. Am. Chem. Soc. 2003;125:11824.
30. Ashbrook SE, Wimperis S. Prog. NMR Spectrosc. 2004;45:53.
31. Ashbrook SE, Berry AJ, Hibberson WO, Steuernagel S, Wimperis S. Am. Mineral. 2005;90:1861.
32. Horiuchi H, Sawamoto H. Am. Mineral. 1981;66:658.
33. Sasaki S, Prewitt CT, Sato Y, Ito E. J. Geophys. Res. 1982;87:7829.
34. M. Kitamura, Kondoh S, Morimoto N, Miller GH, Rossman GR, Putnis A. Nature. 1987;328:143.
35. Taylor WH, West J. Proc. R. Soc. Lond. A1928;117:517.
36. Gibbs GV, Ribbe PH, Anderson CP. Am. Mineral. 1970;55:1182.
37. Ashbrook SE, Berry AJ, Wimperis S. J. Am. Chem. Soc. 2001;26:6360.
38. Ashbrook SE, Antonijevic S, Berry AJ, Wimperis S. Chem. Phys. Lett. 2002;364:634.
39. Berry AJ, James M. Am. Mineral. 2001;86:181.

The Structure of Oxide Glasses: Insights from ^{17}O NMR

Philip J. Grandinetti and Ted M. Clark
Department of Chemistry, Ohio State University, 100 West, 18th Avenue, Columbus, OH 43210 USA

As a probe of local structure in network forming oxide glasses, ^{17}O nuclear magnetic resonance (NMR) spectroscopy has been an invaluable tool [1–10]. The analysis of oxygen in these glasses is vital because their structure predominately consists of well-defined corner-sharing SiO_4 tetrahedra connected in a continuous infinite three-dimensional network lacking long-range order. The interconnection of two tetrahedra involves a Si–O–Si bond angle, and two dihedral angles, and the variation in these angles is considered to be one of the main sources of disorder in a conventional melt quenched silicate glass.

The best approach for measuring Si–O–Si bond angle distributions is to use methods that provide a detailed and direct measurement of the local environment around oxygen. Unfortunately, the information obtainable from X-ray absorption spectroscopies has been limited for light backscattering atoms like oxygen [11]. In contrast, solid-state ^{17}O NMR, specifically, the ^{17}O quadrupolar coupling and chemical shift parameters provide a simple and direct probe of electronic structure, and is well suited for measuring the local structure around bridging oxygen [12–21].

With the development of 2D NMR methods that separate and correlate anisotropic and isotropic lineshapes [22–24], it is becoming increasingly possible to obtain local structural information for glasses via ^{17}O NMR. In 1992, Farnan *et al.* [4] first demonstrated how the distribution of ^{17}O NMR parameters can be measured in a silicate glass using 2D dynamic-angle spinning (DAS) NMR without any assumptions about the shape of the NMR parameter distributions. Additionally, they demonstrated that the ^{17}O quadrupolar coupling parameter distribution can, in principle, be mapped into the Si–O–Si bond angle distribution in the glass.

A crucial aspect in these structural determinations is an understanding of the relationship between the measurable NMR parameters and the variations in local structure that influence the NMR parameters. The development of such relationships has been an ongoing task for oxygen in oxide glasses, with significant gains being made by the combination of computational methods and experimental investigation of a variety of oxygen environments in crystalline silicates.

For bridging oxygen, a number of structural features play a role in determining the ^{17}O quadrupolar coupling parameters, with the most significant features occurring in the first coordination sphere of the bridging oxygen. In the mid-1980's Oldfield and coworkers [25–27] clearly established on the basis of their ^{17}O magic-angle spinning (MAS) NMR measurements that the electronegativity of the cations coordinated to a bridging oxygen atom is a primary factor influencing the magnitude of the C_q-parameter for the bridging oxygen. In a series of *ab initio* calculations on model clusters focusing on the silicate bridging oxygen linkage Tossell and coworkers [12–14] predicted simple trends for the ^{17}O quadrupolar coupling parameters with Si–O–Si angle. These trends were later experimentally confirmed by Grandinetti *et al.* [17] in ^{17}O DAS measurements on coesite.

Vermillion *et al.* [19] and Clark *et al.* [20] further refined this understanding by examining the effect of additional coordination of the bridging oxygen by network modifier alkali cations. Their findings, obtained using *ab initio* methods on model clusters representing typical bridging oxygen environments in lithium, sodium, and potassium silicates, suggested that the previously established trend in ^{17}O C_q with Si–O–Si angle is systematically shifted to lower magnitudes with increasing number and field strength of coordinating alkali cations. They also found that the previously established trend [12–15] in ^{17}O quadrupolar coupling asymmetry parameter, η_q, with Si–O–Si angle is systematically shifted to higher values by the presence of one coordinating alkali cation, and only slightly shifted to higher values by the presence of two coordinating alkali cations.

In two related papers, Clark and Grandinetti [18, 28] used *ab initio* methods to study a number of clusters with the coordinating cations varied from Group III to Group VI and from Periods 2 to 4, while simultaneously varying the network forming cation–oxygen distance. A general trend, shown in Figure 1A, was observed that the magnitude of C_q increases linearly with increasing network forming cation–oxygen bond distance, and also increases with cation group number, as shown Figure 1B. These findings suggest that group number and cation-bridging oxygen distance can serve as a better predictor of the bridging oxygen quadrupole coupling constant than electronegativity differences [26, 27].

The observation that the magnitude of C_q increases linearly with increasing network forming cation–oxygen

Graham A. Webb (ed.), Modern Magnetic Resonance, 1563–1568.
© 2008 *Springer.*

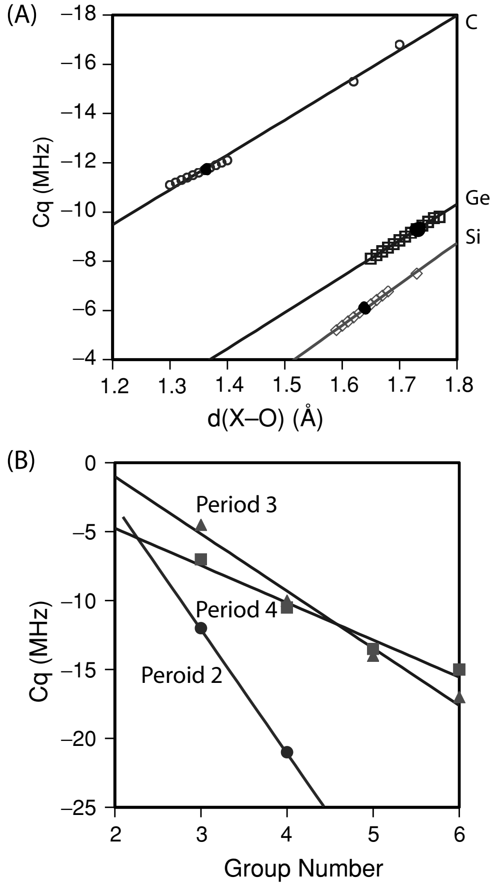

Fig. 1. (A) Comparison of bridging oxygen ^{17}O C_q values for the clusters (OH)$_3$T–O–T(OH)$_3$, where T = carbon, silicon, and germanium, as a function of d(T–O). (B) Bridging oxygen C$_q$ dependence on the group number of coordinating cations for each period. C$_q$ values are calculated for identical cation–oxygen distances and a bridging oxygen angle of 180°.

bond distance was investigated in more detail by Clark and Grandinetti for bridging oxygen atoms in silicates [21]. In this work, *ab initio* calculations were performed for model clusters to examine the dependence of ^{17}O quadrupolar coupling parameters on both Si–O distance and Si–O–Si angle. This work demonstrated that the ^{17}O quadrupolar coupling constant is dependent on both of these structural features, while η_q is primarily dependent on the Si–O–Si angle. Also, it is noteworthy that the strong linear dependence of C$_q$ on Si–O distance helped explain the rather different angular trends for C$_q$ found in coesite [17] and ferrierite [29], since the Si–O–Si angle and Si–O distance correlations for these two materials are quite different [21].

Relationships between ^{17}O quadrupolar coupling parameters and structure in silicates have also been examined using periodic density functional theory (DFT) calculations. These calculations, which are capable of describing quite accurately a system's electronic structure, have been performed for crystalline sodium silicates, the siliceous zeolite ferrierite, and also for plausible sodium silicate glasses that were generated using molecular dynamics [30, 31]. These calculations generally support the previously established trends, i.e. C$_q$ decreases in magnitude with decreasing Si–O–Si angle and Si–O distance, whereas η_q depends only on Si–O–Si angle. Additionally, these investigations found no dependence of the bridging oxygen C$_q$ upon the number of coordinating alkali cations, a finding in contrast to that reported using modeling clusters [19, 20].

Overall, it has become clear that first coordination sphere structural features that appear to be most important in determining the ^{17}O quadrupolar coupling parameters of the bridging oxygen are the nature of the two coordinating network forming cations, the T–O–T′ linkage angle, the T–O bond distances, and the nature and number of coordinating network modifier cations. Contributions from beyond the first coordination sphere of the bridging oxygen appear to be secondary in importance. For example, Xue and Kanzaki [16] performed *ab initio* calculations employing clusters expanded out to four coordination spheres to model each of the silicate bridging oxygen linkages in coesite and obtained a slightly improved agreement with the experimental trends, with corrections on the order of a few percent in the ^{17}O C_q and η_q values.

Equations proposed to summarize the important structural features for the determination of the ^{17}O quadrupolar coupling parameters are

$$C_q(\Omega, n_M) = a\left(\frac{1}{2}+\frac{\cos\Omega}{\cos\Omega-1}\right)^{\alpha} + n_M \Delta C_q^M + m_d(d_{TO} - d_{TO}^{o}) \qquad (1)$$

$$\eta_q(\Omega) = b\left(\frac{1}{2}-\frac{\cos\Omega}{\cos\Omega-1}\right)^{\beta} + \Delta\eta_q^M(n_M), \qquad (2)$$

where Ω is the Si–O–Si bond angle, d_{TO} is the average silicon–oxygen bond distance, and the terms $n_M \Delta C_q^M$ and $\Delta\eta_q^M(n_M)$ account for contributions from modifier cations coordinated to the bridging oxygen. These expressions are not unique in their ability to describe these relationships, and other expressions have been used previously [4,14,15].

Clark and Grandinetti [21] performed a least-squares fit of Equations (1) and (2) to the experimental values for coesite [17], cristobalite [32], and α-quartz [33] as

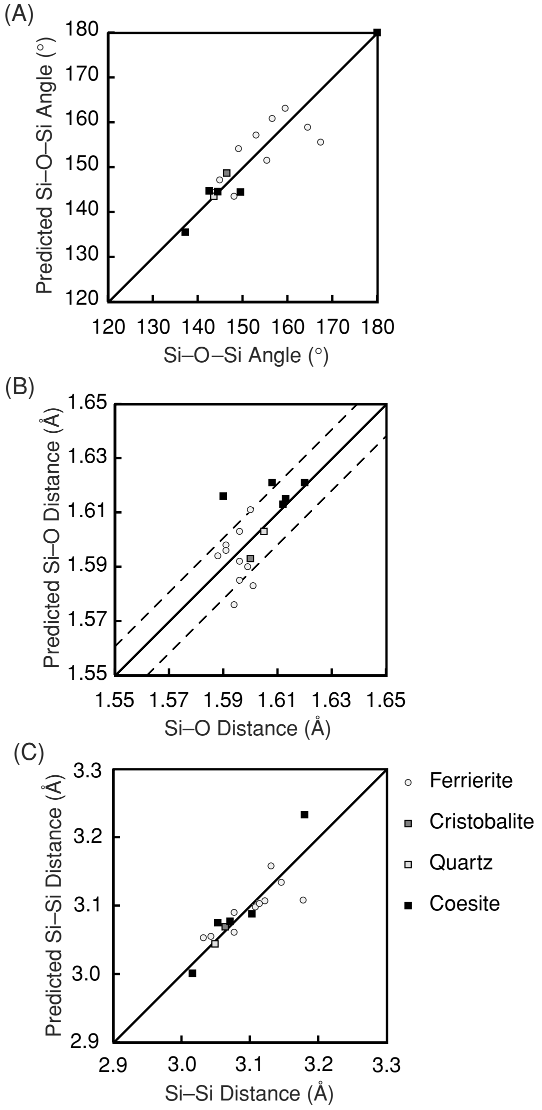

Fig. 2. Comparison between ^{17}O quadrupolar coupling predicted (A) Si–O–Si angle, (B) Si–O distance, and (C) Si–Si distance with corresponding quantities reported from X-ray crystallography [40–42]. Solid diagonal lines represent perfect agreement. Best fit parameters for Equations (1) and (2) are $a' = -6.53\,\text{MHz}, \alpha' = 1.80, m_d = -12.86\,\text{MHz/Å}, d^{\circ}_{TO} = 1.654\text{Å}$, $b = 4.73$, $\beta = 1.12$.

well as the *ab initio* predicted values for ferrierite [29] and obtained the parameter values given in the caption of Figure 2. The resulting parameterized equations describe the relationships between the ^{17}O quadrupolar coupling parameters and the relevant structural features in the first coordination sphere for a bridging oxygen atom in the absence of modifier cations. The precision of these relationships can be seen in Figure 2, where the Si–O–Si angles and Si–O distances predicted by these expressions are shown versus the actual values. Close agreement between predicted and reported values are demonstrated, even though only two structural variables are considered, i.e. the average bond distance and the bond angle. Here, the Si–O–Si angles in Figure 2A are predicted from η_q alone and, with the Si–O–Si angle determined, Equation (1) is used to predict the Si–O distance from C_q, as shown in Figure 2B. After having determined the Si–O distance for a given angle, it is also possible to determine the Si–Si distance.

It is noteworthy that not only the quadupolar coupling constant and asymmetry parameter can be used to measure the Si–O–Si angle and Si–O distance, but also the simultaneous measurement of C_q and η_q for each bridging oxygen site can be used to obtain the correlation between Si–O–Si angle and Si–O distance. This has significant impact for determining two-dimensional structural distributions around bridging oxygen in silicate glasses. This approach requires a good measurement of the quadrupolar asymmetry parameter, which has been historically been more difficult to measure than the quadrupolar coupling constant. Fortunately, this situation has been improved with the development of techniques such as Rotor Assisted Population Transfer (RAPT) [34–37] for enhancing the sensitivity of the MAS detected DAS [17,38,39]experiment, which allows overlapping anisotropic ^{17}O central transition lineshapes to be separated.

Figure 3A is the recently reported ^{17}O RAPT/MAS-detected DAS spectrum of silica glass [43]. From a least-square analysis of the ^{17}O 2D DAS spectrum a three-dimensional histogram, correlating the δ_{cs} (chemical shift), C_q, and η_q of ^{17}O, was obtained. A projection of this three dimensional histogram, showing the two-dimensional correlation between C_q and η_q for silica glass, along with corresponding one-dimensional projections is shown in Figure 3B. With the aid of Equations (1) and (2), the experimental C_q and η_q histograms were mapped into the two-dimensional histogram of the Si–O–Si angle versus the Si–O distance, shown in Figure 3C. This result is the first experimentally measured two-dimensional structural distributions in a glass, and illustrates nearly strong linear correlations between the Si–O–Si angle and Si–O distance in silica glass.

Significant insights into the structure of silicate glasses are now made possible by an analysis using this methodology. For example, in the case of silica glass, it is remarkable that a strong positive correlation is observed between Si–O distance and Si–O–Si bond angle. This trend was unexpected since it is *opposite* of that generally found in crystalline SiO_2 polymorphs, as shown in

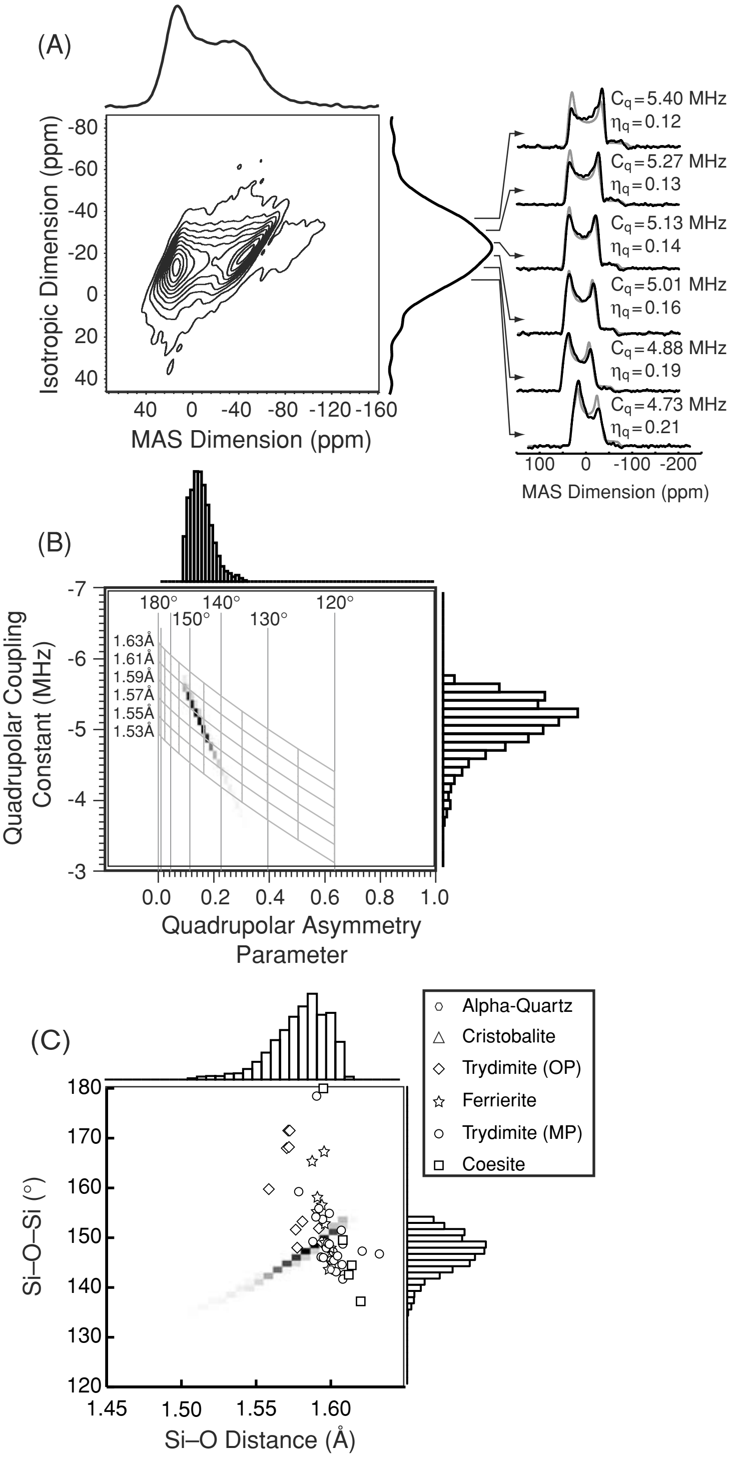

Fig. 3. (A) Experimental 2D ^{17}O RAPT/MAS-detected DAS spectrum of SiO_2 at 9.4 T along with experimental 1D projections onto the MAS and isotropic dimensions. Shown on the right are selected experimental cross sections along with best fit simulations. (B) Two-dimensional histograms along with the corresponding one-dimensional projection showing the correlation between C_q and η_q. Grid lines shown were obtained from Equations (1) and (2) by varying Si–O distance with Si–O–Si angle held constant and the Si–O–Si angle with the Si–O distance held constant. (C) 2D histograms of Si–O–Si angle versus Si–O distance for silica glass derived from NMR parameter distributions, and for various crystalline polymorphs.

Figure 3C. Also, the resulting Si–O–Si bond angle distribution, which peaks at 147° with a standard deviation of 3.8°, is noteworthy for its narrowness in comparison with distributions determined by diffraction or Si-29 NMR measurements [44–46].

In conclusion, ^{17}O NMR is proving to be an extremely robust probe of structure in silicate glasses. As the relationship between the ^{17}O NMR parameters and structure has become increasingly well-understood, it is now possible to apply this knowledge for the interpretation of the two-dimensional NMR spectra of disordered materials. This has led to the experimental determination of correlated structural distributions for oxygen sites in glasses, a significant achievement that is not presently possible by other experimental techniques. With the continued application of this methodology, it will be possible to gain a more complete understanding of many glasses of scientific and technological importance.

References

1. Jellison GE, Panek LW, Bray PJ, Rouse GB. Determinations of structure and bonding in vitreous B_2O_3 by means of ^{10}B, ^{11}B, and ^{17}O, NMR. J. Chem. Phys. 1977;66:802.
2. Geissberger AE, Bray PJ. Determinations of structure and bonding in amorphous SiO_2 using ^{17}O NMR. J. Non-Cryst. Solids. 1983;54:121.
3. Youngman RE, Haubrich ST, Zwanziger JW, Janicke MT, Chmelka BF. Short- and intermediate-range structural ordering in glassy boron oxide. Science. 1995;269:1416.
4. Farnan I, Grandinetti PJ, Baltisberger JH, Stebbins JF, Werner U, Eastman MA, Pines A. Quantification of the disorder in network-modified silicate glasses. Nature. 1992;358:31–5.
5. Wang S, Stebbins JF. On the structure of borosilicate glasses: A triple-quantum magic-angle spinning ^{17}O nuclear magnetic resonance study. J. Non Cryst. Solids. 1998;231:286–90.
6. Zhao P, Kroeker S, Stebbins JF. Non-bridging oxygen sites in barium borosilicate glasses: results from ^{11}B and ^{17}O NMR. J. Non-Cryst. Solids. 2000;276:122–31.
7. Florian P, Vermillion KE, Grandinetti PJ, Farnan I, Stebbins JF. Cation distribution in mixed alkali disilicate glasses. J. Am. Chem. Soc. 1996;118:3493–7.
8. Stebbins JF, Oglesby JV, Xu Z. Disorder among network-modifier cations in silicate glasses: New constraints from triple-quantum ^{17}O NMR. Am. Mineral. 1997;82:1116–24.
9. Stebbins JF, Lee SK, Oglesby JV. Al–O–Al oxygen sites in crystalline aluminates and aluminosilicate glasses: High-resolution oxygen-17 NMR results. Am. Mineral. 1999;84:983–6.
10. Lee SK, Musgrave CB, Zhao P, Stebbins JF. Topological disorder and reactivity of borosilicate glasses: Quantum chemical calculations and ^{17}O and ^{11}B NMR study. J. Phys. Chem. B. 2001;105:12583–95.
11. Elliott SR. Non-diffraction spectroscopic probes of the structure of amorphous solids. J. Non-Cryst. Solids. 1990;123:149.
12. Tossell JA, Lazzeretti P. *Ab Initio* calculations of oxygen nuclear quadrupolar coupling constants and oxygen and silicon NMR shielding constants in molecules containing Si–O bonds. Chem. Phys. Lett. 1987;112:205.
13. Tossell JA, Lazzeretti P. Calculation of NMR parameters for bridging oxygens in $H_3T–O–T'H_3$ linkages (T,T′ = Al, Si, P), for oxygen in SiH_3O^-, SiH_3OH and SiH_3OMg^+ and for bridging fluorine in $H_3SiFSiH_3^+$. Phys. Chem. Minerals. 1988;15:564.
14. Lindsay CG,Tossell JA. *Ab Initio* calculations of ^{17}O and ^{n}T NMR parameters (^{n}T = ^{31}P, ^{29}Si) in H_3TOTH_3 dimers and T_3O_9 trimeric rings. Phys. Chem. Minerals. 1991;18:191.
15. Sternberg U. The bond-angle dependence of the asymmetry parameter of the oxygen-17 electric field gradient tensor. Solid State NMR. 1993;2:181.
16. Xue X, Kanzaki M. An ab initio calculation of ^{17}O and ^{29}Si NMR parameters for SiO_2 polymorphs. Solid State NMR. 2000;16:245–259.
17. Grandinetti PJ, Baltisberger JH, Werner U, Pines A, Farnan I, Stebbins JF. Solid-state ^{17}O magic-angle and dynamic-angle spinning NMR study of coesite. J. Phys. Chem. 1995;99:12341–8.
18. Clark TM, Grandinetti PJ. Factors influencing the ^{17}O quadrupole coupling constant in bridging oxygen environments. Solid State NMR. 2000;16:55–62.
19. Vermillion KE, Florian P, Grandinetti PJ. Relationships between bridging oxygen ^{17}O quadrupolar coupling parameters and structure in alkali silicates. J. Chem. Phys. 1998;108(17):7274–7285.
20. Clark TM, Grandinetti PJ, Florian P, Stebbins JF. An ^{17}O NMR investigation of crystalline sodium metasilicate: Implications for the determinations of local structure in alkali silicates. J. Phys. Chem. B. 2001;105:12257–65.
21. Clark TM, Grandinetti PJ. Dependence of bridging oxygen O-17 quadrupolar coupling parameters on Si–O distance and Si–O–Si angle. J. Phys. Condensed Matter. 2003;15:S2387–95.
22. Bax A, Szeverenyi NM, Maciel GE. Correlation of isotropic shifts and chemical shift anisotropies by two-dimensional Fourier-transform magic-angle hopping NMR spectroscopy. J. Magn. Reson. 1983;52:147.
23. Terao T, Fujii T, Onodera T, Saika A. Switching-angle sample -spinning NMR spectroscopy for obtaining powder-pattern-resolved 2D spectra: Measurements of ^{13}C chemical-shift anisotropies in powdered 3,4-dimethoxybenzaldehyde. Chem. Phys. Lett. 1984;107:145.
24. Mueller KT, Sun BQ, Chingas GC, Zwanziger JW, Terao T, Pines A. Dynamic-angle spinning of quadrupolar nuclei. J. Magn. Reson. 1990;86:470.
25. Schramm S, Oldfield E. High-resolution oxygen-17 NMR of solids. J. Am. Chem. Soc. 1984;106:2502.
26. Timken HKC, Janes N, Turner GL, Lambert SL, Welsh LB, Oldfield E. Solid-state oxygen-17 nuclear magnetic resonance spectroscopic studies of zeolites and related systems. J. Am. Chem. Soc. 1986;108:7236.
27. Timken HKC, Schramm SE, Kirkpatrick RJ, Oldfield E. Solid-state oxygen-17 nuclear magnetic resonance spectroscopic studies of alkaline earth metasillicates. J. Phys. Chem. 1987;91:1054–8.

28. Clark TM, Grandinetti PJ. Relationships between bridging oxygen ^{17}O quadrupolar coupling parameters and structure in germanates. J. Non-Cryst. Solids. 2000;265: 75–82.
29. Bull LM, Bussemer B, Anupold T, Reinhold A, Samoson A, Sauer J, Cheetham AK, Dupree R. A high-resolution ^{17}O and ^{29}Si NMR study of zeolite siliceous ferrierite and ab initio calculations of NMR parameters. J. Am. Chem. Soc. 2000;122:4948–58.
30. Charpentier T, Ispas S, Profeta M, Mauri F, Pickard CJ. First-principles calculation of ^{17}O, ^{29}Si, ^{23}Na NMR spectra of sodium silicate crystals and glasses. J. Phys. Chem. B. 2004;108:4147–61.
31. Profeta M, Mauri F, Pickard CJ. Accurate first principles prediction of ^{17}O NMR parameters in SiO_2: Assignment of the zeolite ferrierite spectrum. J. Am. Chem. Soc. 2003;125:541–8.
32. Spearing DR, Farnan I, Stebbins JF. Dynamics of the alpha–beta phase transitions in quartz and cristobalite as observed by in situ high temperature Si-29 NMR and O-17 NMR. Phys. Chem. Miner. 1992;19(5): 307–21.
33. Dupree R. Nuclear magnetic resonance as a structural probe of SiO_2. In: R. Devine, JP. Durand, E. Dooryhee (Eds), Structure and Imperfections in Amorphous and Crystalline SiO_2, John Wiley, pp. 107–20, 2000.
34. Kwak H-T, Prasad S, Clark TM, Grandinetti PJ . Selective suppression and excitation of solid-state NMR resonances based on quadrupole coupling constants. J. Magn. Reson. 2003;160:107–13.
35. Yao Z, Kwak H-T, Sakellariou D, Emsley L, Grandinetti PJ. Sensitivity enhancement of the central transition NMR signal of quadrupolar nuclei under magic-angle spinning. Chem. Phys. Lett. 2000;327:85–90.
36. Kwak H-T, Prasad S, Yao Z, Grandinetti PJ, Sachleben JR, Emlsey L. Enhanced sensitivity in RIACT/MQ-MAS NMR experiments using rotor assisted population transfer. J. Magn. Reson. 2001;150:71–80.
37. Prasad S, Kwak HT, Clark T, Grandinetti PJ. A simple technique for determining nuclear quadrupole coupling constants using RAPT solid-state NMR spectroscopy. J. Am. Chem. Soc. 2002;124(18):4964–5.
38. Chmelka BF, Mueller KT, Pines A, Stebbins J, Wu Y, Zwanziger JW . Oxygen-17 NMR in solids by dynamic-angle spinning and double rotation. Nature. 1989;339:42–3.
39. Mueller KT, Wooten EW, Pines A. Pure-absorption-phase dynamic-angle spinning. J. Magn. Reson. 1990;92:620.
40. Geisinger KL, Spackman MA, Gibbs GV. Exploration of structure, electron density distribution, and bonding in coesite with fourier and pseudo atom refinement methods using single-crystal X-ray diffraction data. J. Phys. Chem. 1987;91:3237.
41. Downs RT, Palmer DC. The pressure behavior of alpha-cristobalite. Am. Mineral. 1994;79(1–2):9–14.
42. Kihara K. An X-ray study of the temperature dependence of the quartz structure. Eur. J. Mineral. 1990;2(1):63–77.
43. Clark TM, Grandinetti PJ, Florian P, Stebbins JF. Correlated structural distributions in silica glass. Physical Rev. B. 2004;70.
44. Mozzi RL, Warren BE. The structure of vitreous silica. J. Appl. Cryst. 1969;2:164–72.
45. Poulsen HF, Neuefeind J, Neuman H-B, Schneider JR, Zeidler MD. Amorphous silica studied by high energy X-ray diffraction. J. Non Cryst. Solids. 1995;188:63–74.
46. Mauri F, Pasquarello A, Pfrommer BG, Yoon Y-G, Louie SG. Si–O–Si bond-angle distribution in vitreous silica from first-principles ^{29}Si NMR analysis. Phys. Rev. B. 2000; 62(8):4786–9.

Studies of the Local Structure of Silk Using Solid-State NMR

Jacco D. van Beek, Lilyane Beaulieu and Beat H. Meier
Physical Chemistry, ETH Zurich, CH-8093 Zurich, Switzerland

Introduction

The focus of the present article is the description of some NMR methods that can be used to structurally characterize partially disordered biopolymers in solid phase. Silk is not only an attractive and important material of this class, but also it turns out to be a convenient compound to be studied by NMR spectroscopy because it is quite easy to obtain the relatively large sample amounts needed (in the order of 10 mg) with amino-acid specific isotope labelling, in particular with ^{2}H, ^{13}C and ^{15}N. In the following, we will give a short introduction to silks, followed by a description of selected NMR techniques and the results of their application to silks, in particular to the silk of the Eri silkworm *Samia cynthia ricini* (*S.c. ricini*).

Silks are fibrous proteins of considerable economic and scientific interest. They have found utility as textile fibre since thousands of years because of their strength, elasticity, luster, absorbency and affinity for dyes. The material is made by various animals for different biological purposes. Many silks exhibit interesting mechanical properties, e.g. a high toughness comparable to Kevlar combined with an extensibility of 30% or an extreme extensibility of more than 200% [1]. In our days, many new applications for these types of biopolymers are targeted [2–6].

The primary structure of silks is typically highly repetitive and rich in glycine and alanine [7–13]. Spider dragline silk and other silks like the one from the Eri silkworm, *S.c. ricini*, show a primary sequence of the silk protein with poly-alanine repeats of 6–12 monomers in between glycine-rich segments. In this article, we concentrate in particular on these types of silks and the spectra presented are all from *S.c. ricini*. The commercially most important silk from the domesticated silkworm *Bombyx mori* does not fall into this class and we refer the reader to a recent review of Zhao and Asakura [14].

Silks are partially disordered materials, and therefore, particularly interesting for solid-state NMR studies because there are few other methods for their structural characterisation. The linewidth in "high-resolution" magic-angle spinning (MAS) solid-state experiments turns out to be in the order of 5–10 ppm, which is typically an order of magnitude more than obtained with microcrystalline proteins [15–18] and amyloid fibres [19,20] with the corresponding loss in the signal-to-noise ratio. Therefore, not all the benefits of MAS spectroscopy, as obtained for more highly ordered materials, can be realised on silk samples. In particular, it is often not possible to make distance measurements to determine the local structure because the signals from different sites are not spectrally resolved, except for special pairs introduced by selective labelling [21–23]. However, the measurement of backbone torsion angles is an attractive alternative. The knowledge of the (ϕ, ψ) torsion angle pair for each residue in principle fully determines the backbone structure. In practice, however, only secondary structure information can be obtained due to the cumulative errors and long-range distance constraints are necessary to address higher-than-secondary structural questions.

In addition to the native fibres, we will also discuss studies of silk films. These films are formed when the liquid fibroin is directly casted from the posterior silk glands of the silkworm and can be used for immobilisation technology and especially as an immobilisation matrix for enzymes. Their functionality, including permeability, activity of entrapped enzymes and mechanical integrity depend on the orientation of the polymer chains and their conformation. Therefore, it is of interest to understand the relationship between the molecular structure and the diverse macroscopic particularities and utilities of this biopolymer.

The NMR Measurements of Torsion Angles

Torsion angles can be measured through the orientational correlation of spin interactions which have a known orientation of the principal axis of the spatial tensor with respect to the molecular coordinate system. As an example, we use the ^{13}C chemical-shift tensor of the backbone carbonyl functionality of selected amino acids. The orientation of this tensor with respect to the molecular frame at the carbonyl site is known to a precision of a few degrees and is indicated schematically in Figure 1. Therefore, if we are able to selectively transfer the magnetisation between a

Graham A. Webb (ed.), Modern Magnetic Resonance, 1569–1579.
© 2008 *Springer.*

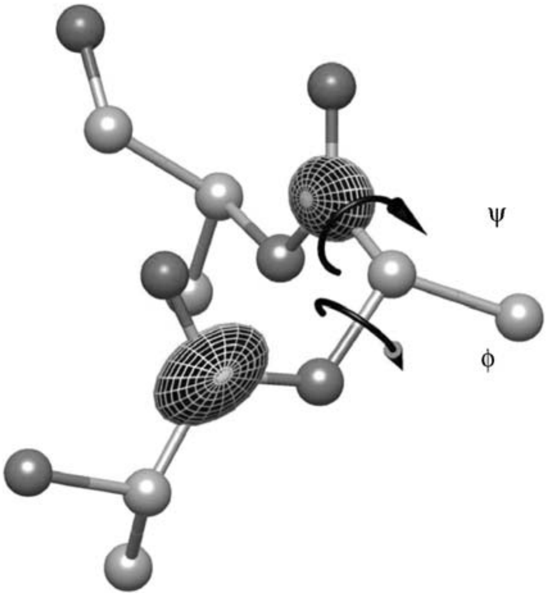

Fig. 1. Orientation of the carbonyl chemical-shielding tensor (yellow ellipses) with respect to the molecular coordinate system in a polypeptide and its relation to the backbone torsion angles. The following empirical rules apply [55–59]: The principal axis associated with the most shielded CSA principal value σ_{33} is perpendicular to the peptide plane. The principal axis associated with the intermediate component of the CSA tensor σ_{22} is almost colinear with the C=O vector. More precisely, for proteins, experimental determination of the angle between the bound direction and the principal axis σ_{22} falls into a range 0–12°. (See also Plate 122 on page XVII in the Color Plate Section.)

selected pair of carbon spins, or to excite double-quantum coherence involving the two selected spins, the two-dimensional CSA–CSA correlation spectrum would fully characterize the relative orientation of the two molecular segments described by the angle pair (ϕ, ψ), as schematically illustrated in Figure 2. The "selected" amino acids mentioned above are usually singled out by isotopic labelling schemes [24–27].

Obviously, a complex material like silk is not composed of isolated two-spin systems and the correlation spectrum will critically depend on the number of spins involved as well as on the experimental methods applied. Coherent ^{13}C–^{13}C polarization transfer experiments (e.g. rf-driven spin diffusion or double-quantum excitation/reconversion) typically favour the strongest coupling at the expense of weak coupling, not only through the inverse sixth power dependence of the spectral intensity from the intermolecular distance but also, in addition, through the effect of "dipolar truncation" [28]. They can in fact be set up, such that predominantly next–neighbour interactions are observed, which is particularly useful for double-quantum selection in the double-quantum–single-quantum correlation experiment (DOQSY) [29–32]. Nevertheless, even in this favourable situation, the evaluation of the structural parameters (ϕ,ψ) from the spectra is not trivial because of disorder in the material: there is no single angle-pair (ϕ,ψ) which could explain the spectra but there is a distribution of such angles which must be characterised. Notwithstanding these complications, a "model free" determination of the parameter distributions is often possible [30,31,33,34]. Alternatively, information about (ϕ,ψ) may also be obtained from the chemical-shift distribution of the ^{13}C resonances in a MAS spectrum using empirical rules [27,35–38] or from initial-rate studies in spin-diffusion spectra (vide infra) [39].

Experimental DOQSY spectra of alanine-labelled silk from *S.c. ricini* fibre and cast-film samples are presented in Figure 3 along with the simulated spectra and the distribution in (ϕ,ψ), which leads to the simulated spectrum [30]. The resulting distribution in (ϕ,ψ) allows for a relatively detailed characterisation of the alanine sites. Similar work for the glycine sites will is described elsewhere [31] and yielded results comparable to the measurements on spider dragline silk [40]. Therefore, *S.c. ricini* seems, in fibrous form, to have a similar structure to that observed for spider dragline silk depicted in Figure 4, while it adapts rather a different form in the cast film with α-helical structures for the alanine-rich parts [30] and with substantially disordered glycine-rich parts. [31]

Geometrical Information on the Molecular-to-Nanometer Scale

Proton-driven "incoherent" ^{13}C–^{13}C polarisation transfer is another option to probe the relative orientation of molecular segments. Proton-driven spin-diffusion (PDSD) on static samples is a well established technique for determining local structure (for a review see [41,42]). Because the length of the spin-diffusion period of the experiment is only limited by T_1 relaxation, it can be up to 10 s and the method allows to probe structures with sizes greatly exceeding a single bond length. The polarisation transfer follows a kinetic master equation in this experiment [43] and the dependence on the internuclear separation is between the inverse third and sixth powers of the distance, depending on the details of the experiment [42]. In the limit of quasi-equilibrium (QE), when the spectrum does not depend on the mixing time anymore, the spectrum becomes particularly easy to interpret as it reflects only the relative orientation of the CSA tensors of the spins that are correlated, and no longer the distances. Figure 5 shows a

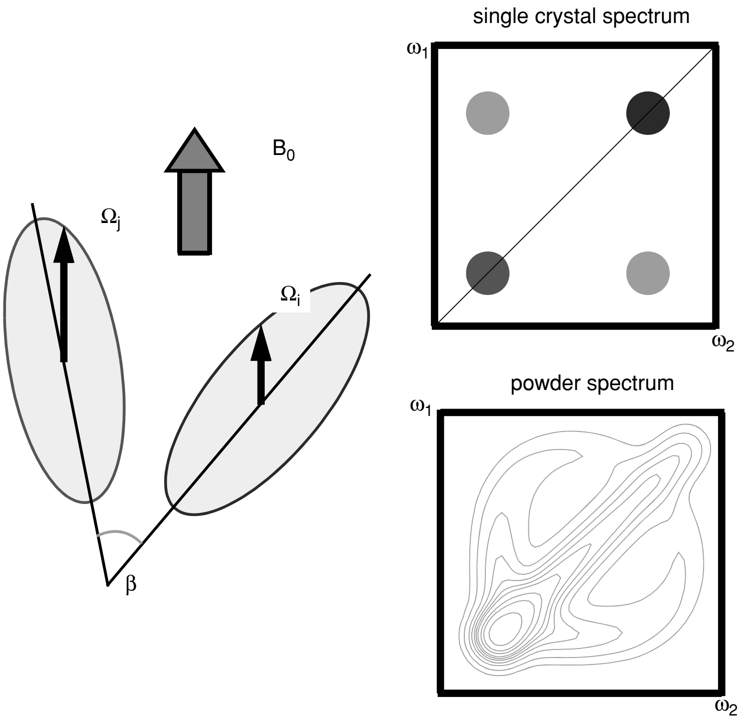

Fig. 2. Principles of two-dimensional CSA–CSA correlation spectroscopy using, e.g. PDSD. The single-crystal spectrum (B) depends on the relative orientation of the two CSA tensors symbolised in (A) and on the crystal orientation. For a static sample the powder spectrum (C) depends only on the relative tensor orientation (and, of course, on the principal values). The illustration uses the correlation of two axially symmetric tensors that yields only a single Euler angle β. For general tensors, all three Euler angles can be determined. (See also Plate 123 on page XVIII in the Color Plate Section.)

comparison of the DOQSY and PDSD experiments for the proposed labelling strategy, as a function of the backbone torsion angles (ϕ,ψ). In PDSD, spins not involved in magnetisation exchange processes on the time scale of the mixing time give rise to a (often dominant) diagonal signal in the 2D spectrum. This can overshadow the off-diagonal signal, which contains the structural information. In biological materials like silk, where the degree of isotopic labelling may be considerably less than 100% (e.g. our *S.c. ricini* examples are at around 15% for the enriched amino acid), this feature leads to a complication of the spectral interpretation and, if one is interested in determining structural information on a molecular scale (like torsion angles) it is beneficial to apply the DOQSY approach mentioned above. This method actively selects out the signals from close neighbours and suppresses the signals from spins not involved in a double-quantum coherence. Conversely, the PDSD experiment, is, for longer mixing times, sensitive to longer distances exceeding the ones probed by DOQSY by one or two orders of magnitude.

For fully disordered materials, the PDSD QE structure would be a pure "amorphous" spectrum where each cross section along t_1 as well as t_2 has the same shape (but not the same integral) [42]. In materials with sizeable domains (consisting of several monomers in each spatial dimension), the QE spectra can characterise both the local structure within a domain and the domain size [41]. If well-isolated domains exist, they can lead to a QE where the spectra do not change appreciably with the mixing time anymore. However, if the mixing time would be increased drastically, the "amorphous" spectra would again result.

A disadvantage to the PDSD experiment on static samples is the slow exchange of magnetisation coupled to a strong dependence on the frequency difference of the corresponding diagonal signals, which may lead to spectra difficult to interpret. The rate constant for the magnetisation exchange can be significantly enhanced, and made rather independent of the frequency-difference, if the sample is rotated slowly (10–100 Hz) during the mixing period of the experiment (slow magic-angle spinning (SMAS; [44]).

The SMAS-PDSD experiment can also be performed with short mixing times in the initial rate regime. In this approach the buildup of each point in the spectrum, as a function of the mixing time, is followed. The local structure can then be obtained by fitting a structural model to the data [39]. Since the isotopic labelling degree in

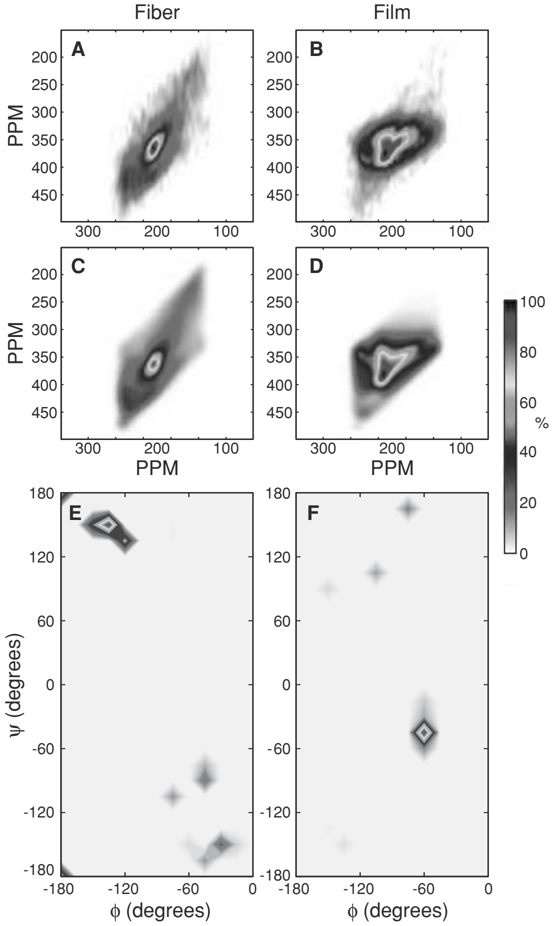

Fig. 3. Experimental 2D DOQSY spectra of (A–B) two different silk samples from the silkworm *S.c. ricini* with (C–D) corresponding to the best fits of these spectra and (E–F) to the distribution functions obtained from the fit. The samples were labelled with 1-^{13}C alanine and prepared either as a fibre or a cast film. The samples were measured a ^{13}C resonance frequency of 100 MHz. The grid resolution in (ϕ,ψ) was 15°. (See also Plate 124 on page XIX in the Color Plate Section.)

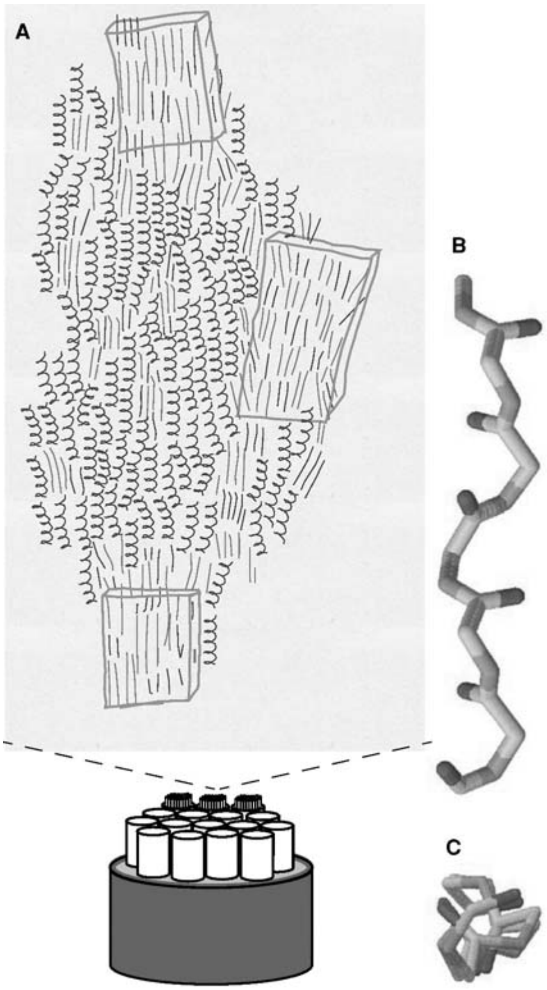

Fig. 4. Schematic model for the structure of spider dragline silk. Reproduced from Ref. [40], with permission. (See also Plate 125 on page XIX in the Color Plate Section.)

silk samples is often relatively low and non site-specific, i.e. all glycines or all alanines are labelled to a certain statistical degree, the intra- and inter-chain distances expected are comparable in length. This is in contrast to the DOQSY approach, where one, to good approximation, selectively filters out the signals from spin-pairs with the minimal possible distance. This distance is usually in fact the one between intramolecular neighbours. While a full 3D structural model is required to explain the data for the SMAS-PDSD experiments, the DOQSY Spectra can approximatively be described by two-spin systems. In our experience, the SMAS-PDSD spectra are often not sensitive enough towards the local structure in such samples, partly by the low signal-to-noise (SN) in the vital off-diagonal part of the spectrum in the initial rate regime, and partly by the large number of degrees of freedom of such a 3D model. While it is often possible to exclude certain packing models and torsion angles a unique solution is usually not available.

These statistical arguments do not hold, for site-selectively labelled peptides and good results have been obtained using PDSD on labelled model peptides at off-magic-angle spinning (OMAS) conditions [22,23,45–47].

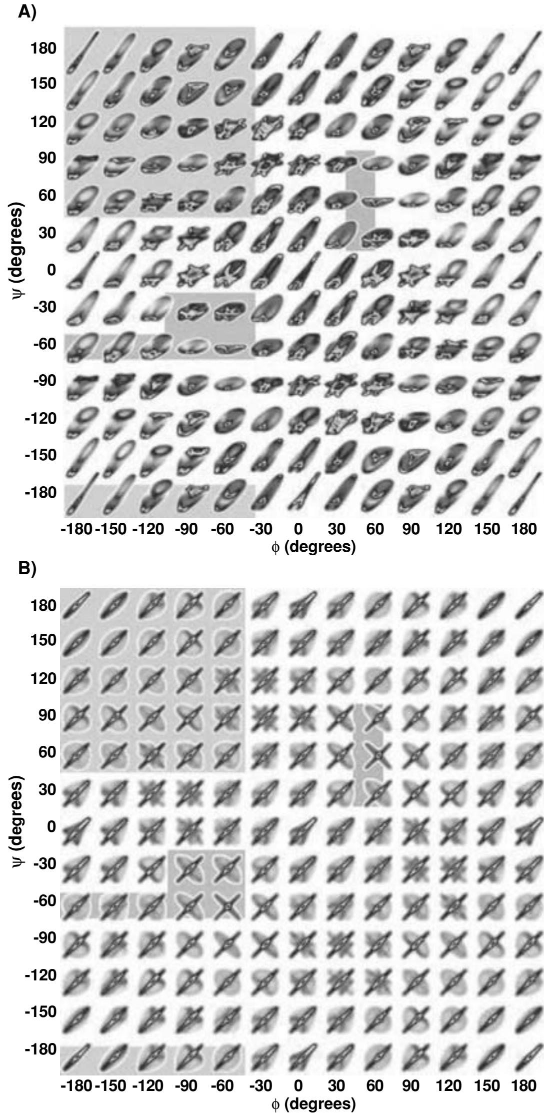

Fig. 5. Torsion-angle dependences of the (A) DOQSY and (B) PDSD experiments (at QE) when applied to ^{13}C=O labelled proteins, assuming an intra-chain contact between neighbouring amino acids. Typical β-sheet and right- and left-handed α-helical regions are marked by orange, dark blue and bright blue boxes, respectively. (See also Plate 126 on page XX in the Color Plate Section.)

Similar to SMAS, the OMAS experiment has a homogenous SD rate constant across the spectrum, but the spectrum is distributed over a smaller spectral area, which leads to a higher signal-to-noise ratio. Figure 6 shows an example of such spectra obtained in specifically labelled model peptides. In such systems QE may be quite easily reached and the analysis is comparatively simple (typically, a 2-spin simulation with only the torsion angles as variables).

The PDSD technique was first applied to static spider dragline silk samples by Kümmerlen et al. [26] and, by correlating ^{13}C=O labelled spins, an average value for (ϕ,ψ) was determined for alanine–alanine and glycine–glycine peptide segments. It was concluded that the segments were part of a β-sheet structure for the alanines and were close to a 3_1-helical arrangement for glycine. Whilst the main conclusions are identical to the ones obtained later using DOQSY [40], the PDSD results for both static [26] and slowly rotating [48] samples were less specific and would not support a similarly detailed analysis in terms of torsion-angle distributions.

SMAS-PDSD spectra from *S.c. ricini* silk are shown in Figures 7a and 8a for various mixing times for casted film and fibre samples, respectively. In the film (Figure 7a), significant cross peaks appeared at clearly shorter mixing times than for the fibre. After 20 s, the spectrum indicates the presence of substantial disorder in this sample on the nanometer length scale.

For the fibre (Figure 8a), the buildup of cross-peak intensity is slow, indicating that either the polarisation transfer between the alanines is very slow, because they are well separated in space, or that the alanines are highly ordered with all the 1-^{13}C CSA tensors close to parallel or anti-parallel to each other. The first explanation is improbable because the primary structure of *S.c. ricini* silk consists of alanine rich segments [47] and it is also incompatible with the DOQSY results discussed above. The second explanation is consistent with the DOQSY findings [30] and X-ray studies [49], which show the occurance of micro-crystalline domains with β-sheet structure. In contrast to the PDSD results of Kümmerlen et al. [26], the SMAS-PSDSD results of Figure 8 are able to detect some weak cross-peak intensity due to the enhanced efficiency of spin diffusion under SMAS.

A quantitative interpretation of the SMAS-PDSD spectra is rather involved but it is interesting to compare the measured spectra with the predicted spectra of simple model structures using numerical simulations. For the film sample, the spectrum at 250 ms shows the characteristic of a single α helix (b) or of an ordered bundle of helices (c). The spectra at longer mixing times indicate, that the cross-peaks cannot be explained by a single helix. The description by a bundle of biaxially ordered helices is better but still not fully convincing and further disorder is certainly present. Note that in the interpretation of the experimental and simulated data, the diagonal is usually not considered because it does not give information and is complicated by the presence of signals from nonexchanging spins.

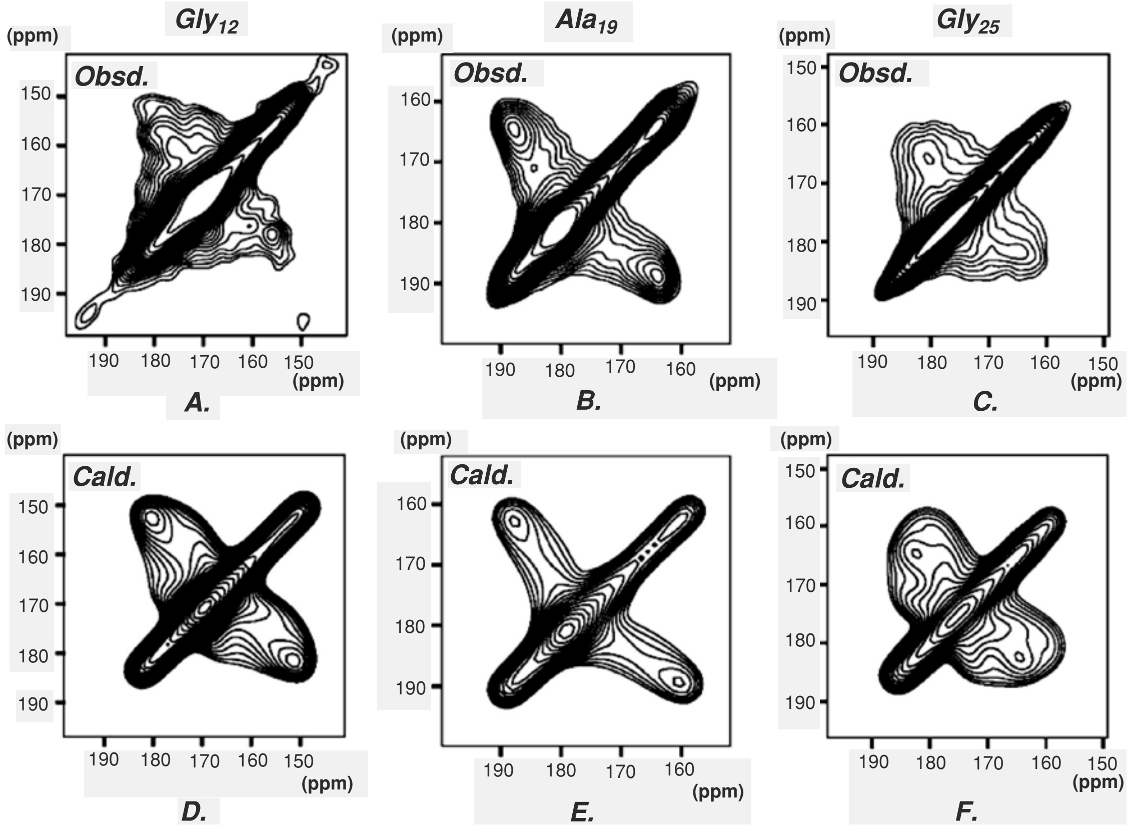

Fig. 6. 2D spin-diffusion NMR spectra of selectively doubly labelled model peptides, (A) GGAGGGYGGD[1-^{13}C]G$_{11}$[1-^{13}C]G$_{12}$(A)$_{12}$GGAGDGYGAG, (B) GGAGGGYGGDGG(A)$_5$[1-^{13}C]A$_{18}$[1-^{13}C]A$_{19}$ (A)$_5$GGAGDGYGAG, and (C) GGAGGGYGGDGG (A)$_{11}$[1-^{13}C]A$_{24}$ [1-^{13}C]G$_{25}$GAGDGYGAG, after TFA treatment, and their corresponding simulated spectra. Reproduced from Ref. [60], with permission.

For the fibrous sample, the simulations of a single β strand, or an idealised parallel β-sheet, indicate that very little cross-peak intensity is expected even if standard (ϕ,ψ) values for β-sheets are used instead of the more extended form postulated by Kümmerlen [26]. Again, the SMAS data are in good accordance with the DOQSY results. While the simulated spectra for a parallel or an anti-parallel arrangement of the β-sheets differ, it was not possible to determine the intermolecular arrangement from the spectra. The buildup rate of the cross-peaks in the SMAS spectra of both the film and fibre sample have been estimated from the initial rate regime and are reported in Figure 9, together with estimates from the simple models described above. Considering the approximations, the spectra represent a nice reconfirmation of the results extracted from the DOQSY spectra and they allow for the qualitative assessment of the disorder on a supramolecular scale.

Conclusions

To determine the local structure in partially disordered solid proteins, it is often attractive to perform NMR experiments without sample rotation. This reduces the signal-to-noise ratio in the experimental spectra, but on the other hand, there is often a much stronger dependence of the spectra on the parameters of interest and the increased spectral area typically yields a more strongly overdetermined problem in the data

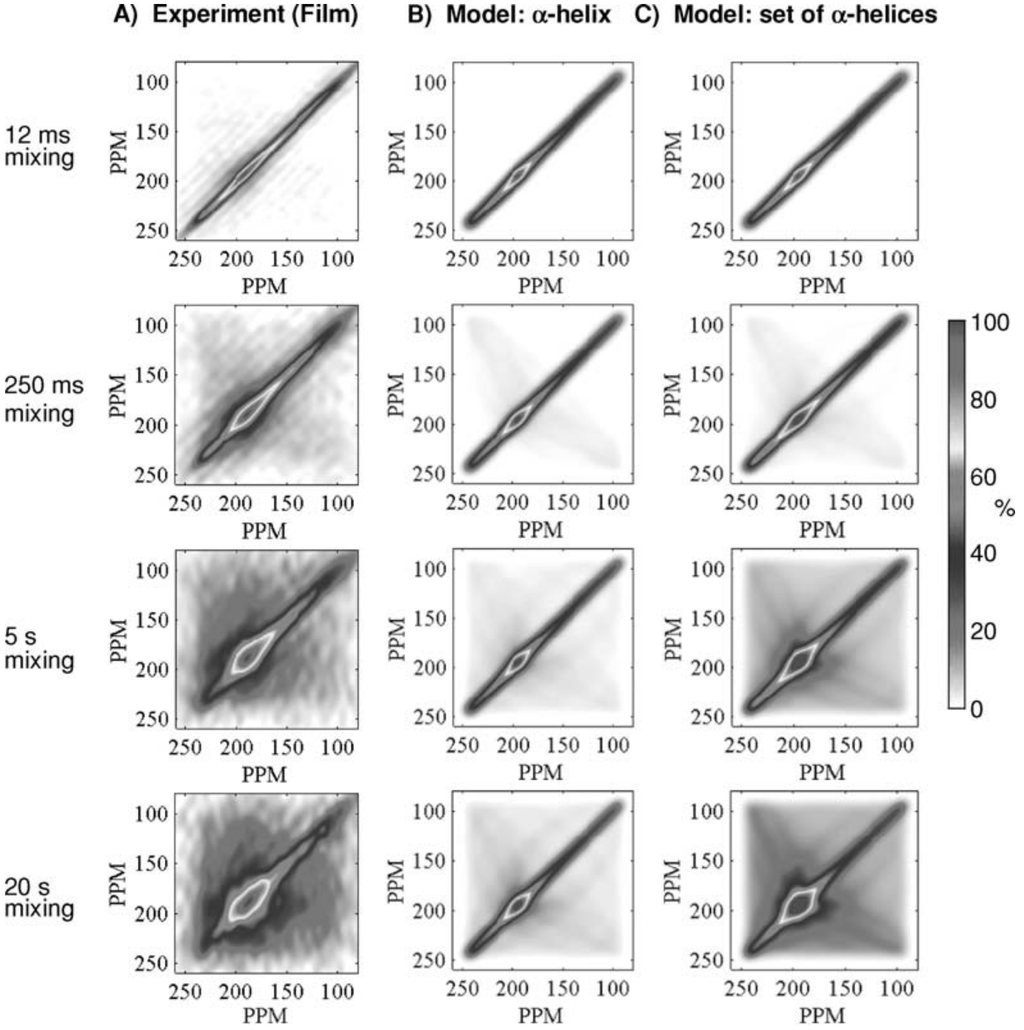

Fig. 7. (A) 2D ^{13}C PDSD spectra of *S.c. ricini* 1-^{13}C alanine labelled silk film recorded under SMAS using mixing periods of 12.5 ms, 250 ms, 5 s and 20 s. (B) Corresponding simulations for a $(\mathrm{Ala})_{100}$ segment organised in an α-helical structure. (C) Corresponding simulations for $(\mathrm{Ala})_{12}$ segments organised in an ordered array of α-helical structures. For a model peptide of poly(alanine)n ($n = 12$ or $n = 100$) arranged in an α-helix, the set of Euler angles used for the simulations was (-27.4°, 96.6°, -1.1°). As a first model (in B), one $\mathrm{poly(alanine)}_{100}$ helix has been considered. As a second model (C) 30 short α-helices ($n = 12$) have been taken into account: the helices were parallel and translationally symmetric to each other and the inter-helical distance between them has been set to 7 Å. (See also Plate 127 on page XXI in the Color Plate Section.)

analysis. In particular, for the case of less than 100% isotopic enrichment of the amino acid to be investigated, DOQSY experiments are best suited to give the backbone torsion angles connecting neighbours in primary sequence. The knowledge of these angles determines the secondary structure. Information about the further environment can be obtained by spin-diffusion experiment and by DECODER [50,51] type experiments on oriented silk samples, not discussed here [27,40,52–54]. The SD long-range information is, however, not specific enough to be able to construct an atomic model of the structure.

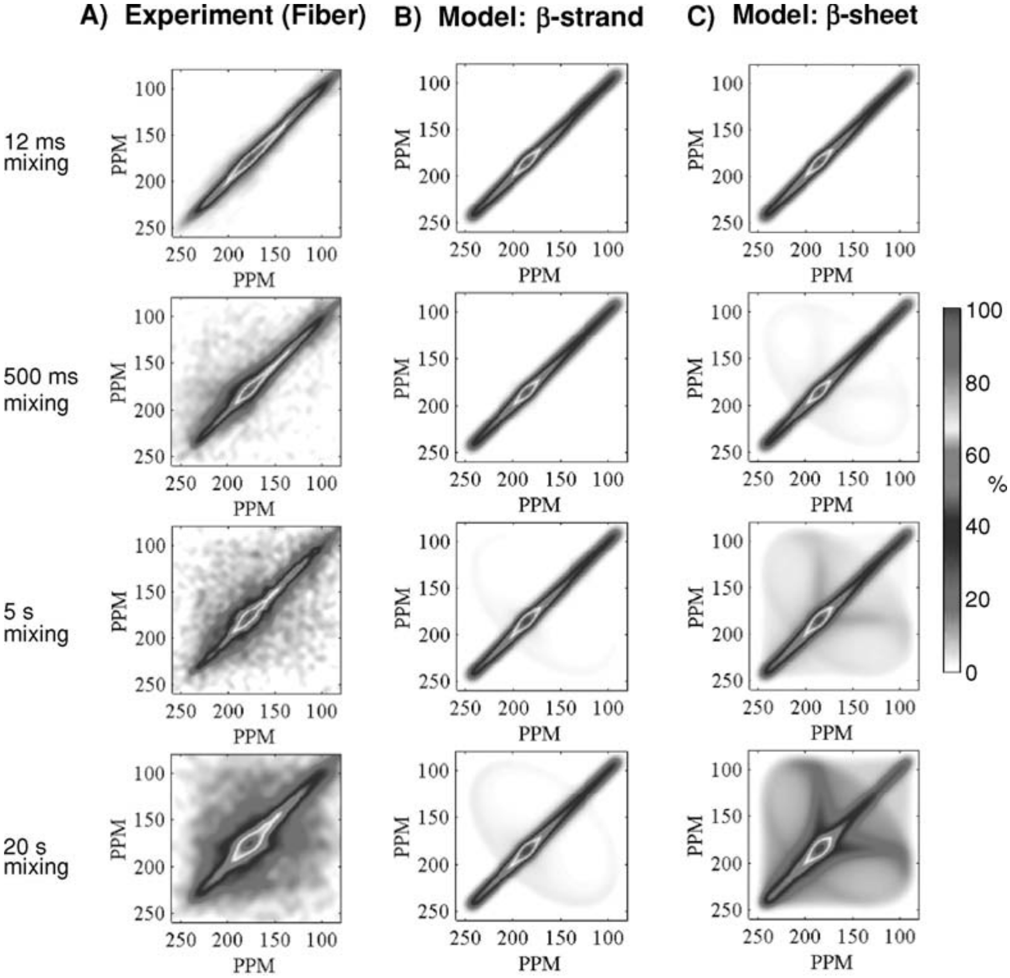

Fig. 8. (A) 2D ^{13}C PDSD spectra of *S.c. ricini* 1-^{13}C alanine labelled silk fibre recorded under SMAS using mixing periods of 12.5 ms, 500 ms, 5 s and 20 s. (B) Corresponding simulations for a $(Ala)_{100}$ segment organised as a β-strand structure. (C) Simulations corresponding to 30 strands of 12 residues each. The three Euler angles between neighbouring carbonyl tesnors used in the model were (173.2°, 120.5°, −12.4°). Two structures have been constructed. The first one is a long β-strand containing 100 alanine residues (B). As a second model, 30 β-strands containing 12 alanine residues have been taken into account (C). The relative orientation of all five layers is the same and the strands are anti-parallel. Such a model leads to a very ordered β-sheet. The inter-strand and inter-layer distances have been set to 6.10 and to 5.33 Å, respectively. (See also Plate 128 on page XXII in the Color Plate Section.)

The silk fibres of the Eri silkworm *S.c. ricini* were found to be structurally quite similar to spider dragline silk from *Nephila edulis:* the alanine residues are arranged in β-sheets, while the glycine residues form predominantly 3_1 helical structures. If cast films are produced, the alanine-rich domains adapt an α-helical form instead.

Acknowledgments

We acknowledge support by the Swiss National Science Foundation, the ETH Zurich, the Fonds pour la Formation de Chercheurs et l'Aide à la Recherche, Québec, Canada (FCAR) and the European Science Foundation through the Network: Silk, Properties and Production. We

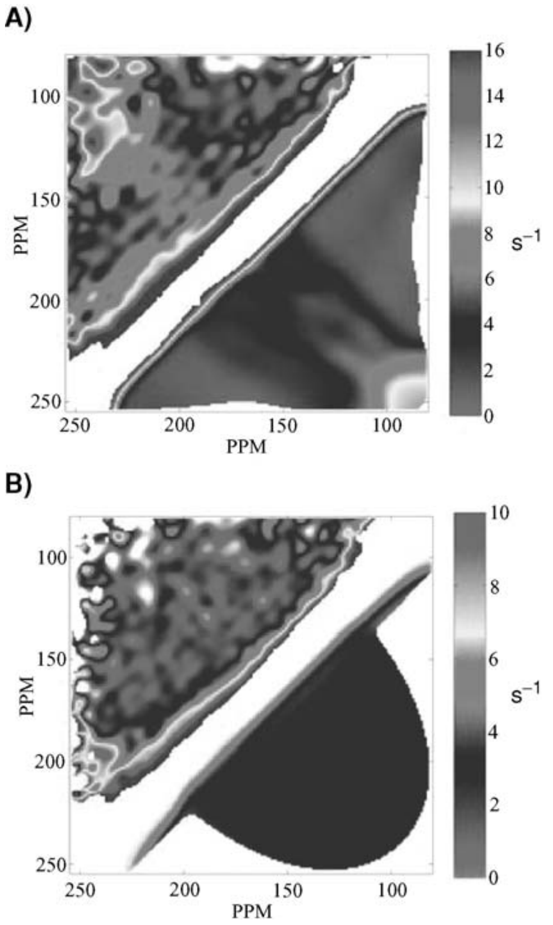

Fig. 9. Experimental average SD rate constants under SMAS between carbonyl-carbons in *S.c. ricini* 1-^{13}C alanine-labelled silk (A) film and (B) fibre as a function of the chemical shifts (upper part). The lower parts show corresponding simulations for (A) an $(Ala)_{100}$ segment organised in a α helix structure and (B) a set of parallel $(Ala)_{12}$ segments in a β sheet stucture. The off-diagonal region was fitted in the initial regime from four spectra with mixing times of 12.5, 75, 150 and 250 ms for the film and three spectra with mixing times of 12.5, 250 and 500 ms for the fibre. The fit determined the linear slope a in the equation $y = ax + bx^2$ used to approximate the initial regime of the buildup curve, where y are the data points, x the mixing times and a and b the coefficients. (See also Plate 129 on page XXIII in the Color Plate Section.)

thank Dr Pierre Robyr, Dr Edme Hardy, Kousuke Ohogo and Dr Phil. Williamson, Dr Aswin Verhoeven and Professor Michele Auger for constructive discussions. *S.c. ricini* silk samples were obtained from Professor Tetsuo Asakura.

References

1. Hinman MB, Jones JA, Lewis RV. Synthetic spider silk: a modular fiber. Trends Biotechnol. 2000;18:374–9.
2. Yao J, Asakura T. Synthesis and structural characterization of silk-like materials incorporated with an elastic motif. J. Biochem. (Tokyo) 2003;133:147–54.
3. Asakura T, Tanaka C, Yang M, Yao J, Kurokawa M. Production and characterization of a silk-like hybrid protein, based on the polyalanine region of *Samia cynthia ricini* silk fibroin and a cell adhesive region derived from fibronectin. Biomaterials. 2004;25:617–24.
4. Jin HJ, Park J, Valluzzi R, Cebe P, Kaplan DL. Biomaterial films of Bombyx mori silk fibroin with poly(ethylene oxide). Biomacromolecules. 2004;5:711–7.
5. Kim UJ, Park JY, Li CM, Jin HJ, Valluzzi R, Kaplan DL. Structure and properties of silk hydrogels. Biomacromolecules. 2004;5:786–92.
6. Nazarov R, Jin HJ, Kaplan DL. Porous 3-D scaffolds from regenerated silk fibroin. Biomacromolecules. 2004;5:718–26.
7. Mita K, Ichimura S, James TC. Highly repetitive structure and its organization of the silk fibroin gene. J. Mol. Evol. 1994;38:583–92.
8. Zhou CZ, Confalonieri F, Medina N, Zivanovic Y, Esnault C, Yang T, Jacquet M, Janin J, Duguet M, Perasso R, Li ZG. Fine organization of *Bombyx mori* fibroin heavy chain gene. Nucleic Acids Res. 2000;28:2413–9.
9. Yukuhiro K, Kanda T, Tamura T. Preferential codon usage and two types of repetitive motifs in the fibroin gene of the Chinese oak silkworm, *Antheraea pernyi*. Insect Mol. Biol. 1997;6:89–95.
10. Xu M, Lewis RV. Structure of a protein superfiber: spider dragline silk. Proc. Natl. Acad. Sci. USA. 1990;87:7120.
11. Hinman MB, Lewis RV. Isolation of a clone encoding a 2nd dragline silk fibroin—nephila-clavipes dragline silk is a 2-protein fiber. J. Biol. Chem. 1992;267:19320–4.
12. Guerette PA, Ginzinger DG, Weber BHF, Gosline JM. Silk properties determined by gland specific expression of a spider fibroin gene family. Science. 1996;272:112–5.
13. Hayashi CY, Lewis RV. Evidence from flagelliform silk cDNA for the structural basis of elasticity and modular nature of spider silks. J. Mol. Biol. 1998;275:773–84.
14. Zhao C, Asakura T. Structure of silk studied with NMR. Prog. Nucl. Magn. Reson. Spectrosc. 2001;39:301–52.
15. Böckmann A, Lange A, Galinier A, Luca S, Giraud N, Juy M, Heise H, Montserret R, Penin F, Baldus M. Solid state NMR sequential resonance assignments and conformational analysis of the 2×10^4 Da dimeric form of the Bacillus subtilis protein Crh. J. Biomol. NMR. 2003;27:323–39.
16. Pauli J, Baldus M, van Rossum B, de Groot H, Oschkinat H. Backbone and side-chain C-13 and N-15 signal assignments of the alpha-spectrin SH3 domain by magic-angle spinning solid-state NMR at 17.6 tesla. Chembiochem. 2001;2:272–81.
17. Castellani F, van Rossum B, Diehl A, Schubert M, Rehbein K, Oschkinat H. Structure of a protein determined by solid-state magic-angle-spinning NMR spectroscopy. Nature. 2002;420:98–102.

18. Igumenova TI, McDermott AE, Zilm KW, Martin RW, Paulson EK, Wand AJ. Assignments of carbon NMR resonances for microcrystalline ubiquitin. J. Am. Chem. Soc. 2004;126:6720–7.
19. Tycko R. Applications of solid state NMR to the structural characterization of amyloid fibrils: methods and results. Prog. Nucl. Magn. Reson. Spectrosc. 2003;42:53–68.
20. Jaroniec CP, MacPhee CE, Bajaj VS, McMahon MT, Dobson CM, Griffin RG. High-resolution molecular structure of a peptide in an amyloid fibril determined by magic-angle-spinning NMR spectroscopy. PNAS. 2004;101:711–6.
21. Michal CA, Jelinski LW. Rotational-echo double-resonance on complex biopolymers: a study of *Nephila clavipes* dragline silk. J. Biomol. NMR. 1998;12:231–41.
22. Asakura T, Ashida J, Yamane T, Kameda T, Nakazawa Y, Ohgo K, Komatsu K. A repeated beta-turn structure in poly(Ala-Gly) as a model for silk I of *Bombyx mori* silk fibroin studied with two-dimensional spin-diffusion NMR under off magic-angle-spinning and rotational echo double resonance. J. Mol. Biol. 2001;306:291–305.
23. Ashida J, Ohgo K, Komatsu K, Kubota A, Asakura T. Determination of the torsion angles of alanine and glycine residues of model compounds of spider silk (AGG)(10) using solid-state NMR methods. J. Biomol. NMR. 2003;25:91–103.
24. Hijirida DH, Do KG, Michal C, Wong S, Zax D, Jelinski LW. C-13 NMR of *Nephila clavipes* major ampullate silk gland. Biophys. J. 1996;71:3442–7.
25. Simmons AH, Michal CA, Jelinski LW. Molecular orientation and two-component nature of the crystalline fraction of spider dragline silk. Science. 1996;271:84–87.
26. Kümmerlen J, van Beek J, Vollrath F, Meier BH. Local structure in spider dragline silk investigated by two-dimensional spin-diffusion nuclear magnetic resonance. Macromolecules. 1996;29:2920–8.
27. Asakura T , Ito T, Okudaira M, Kameda T. Structure of alanine and glycine residues of *Samia cynthia ricini* silk fibers studied with 15N and 13C NMR. Macromolecules. 1999;32:4940–6.
28. Reif B, Griffin RG. 1H detected 1H,15N correlation spectroscopy in rotating solids. J. Magn. Reson. 2003;160:78–83.
29. Schmidtrohr K. A double-quantum solid-state NMR technique for determining torsion angles in polymers. Macromolecules. 1996;29:3975–81.
30. van Beek JD, Beaulieu L, Schafer H, Demura M, Asakura T, Meier BH. Solid-state NMR determination of the secondary structure of *Samia cynthia ricini* silk. Nature 2000;405:1077–9.
31. van Beek JD, Meier BH. A DOQSY approach for the elucidation of torsion angle distributions in biopolymers: application to silk. J. Magn. Reson. 2006;178:106–20.
32. Utz M, Robyr P, Suter UW. Solid-state NMR investigation of the structural consequences of plastic deformation in polycarbonate. 2. Local orientational order. Macromolecules. 2000;33:6808–14.
33. Utz M. Measurement of structural distribution functions in disordered systems: A general approach for sensitivity estimation. J. Chem. Phys. 1998;109:6110–24.
34. van Beek JD, Meier BH, Schafer H. Inverse methods in two-dimensional NMR spectral analysis. J. Magn. Reson. 2003;162:141–57.
35. Ando S, Yamanobe T, Ando I, Shoji A, Ozaki T, Tabeta R, Saito H. Conformational characterization of glycine residues incorporated into some homopolypeptides by solid-state 13C NMR spectroscopy. J. Am. Chem. Soc. 1985;107:7648–52.
36. Saito H, Iwanga Y, Tabeta R, Narita M, Asakura T. Chem. Lett. 1983;4:427.
37. Saito H, Tabeta R, Shoji a, Ozaki T, Ando I, Miyata T. A high-resolution 13C-NMR study of collagenlike polypeptides and collagen fibrils in solid-state studied by the cross-polarization magic angle-spinning method—manifestation of conformation-dependent C-13 chemical-shifts and application to conformational characterization. Biopolymers. 1984;23:2279–97.
38. Ishida M, Asakura T, Yokoi M, Saito H. Solvent- and mechanical-treatment-induced conformational transition of silk fibroins studies by high-resolution solid-state carbon-13 NMR spectroscopy. Macromolecules. 1990;23:88–94.
39. Robyr P, Tomaselli M, Grob-Pisano C, Meier BH, Ernst RR, Suter UW. Characterization of local order in atactic polystyrene using 2D NMR and atomistic simulations. Macromolecules. 1995;28:5320–4.
40. van Beek JD, Hess S, Vollrath F, Meier BH. The molecular structure of spider dragline silk: Folding and orientation of the protein backbone. Proc. Natl. Acad. Sci. USA. 2002;99:10266–71.
41. Schmidt-Rohr K, Spiess HW. Multidimensional Solid-State NMR and Polymers, Academic Press: London, 1994.
42. Ernst M, Meier BH. In: I. Ando, T. Asakura (Eds). Solid State NMR of Polymers. Elsevier, 1998.
43. Abragam A. The Principles of Nuclear Magnetism, Clarendon Press: Oxford, 1961.
44. Gan ZH, Ernst RR. Shift-independent nuclear spin diffusion by slow magic-angle sample spinning for the exploration of solids. Chem. Phys. Lett. 1996;253:13–9.
45. Asakura T, Yao JM, Yamane T, Umemura K, Ultrich AS. Heterogeneous structure of silk fibers from Bombyx mori resolved by C-13 solid-state NMR spectroscopy. J. Am. Chem. Soc. 2002;124:8794–5.
46. Nakazawa Y, Bamba M, Nishio S, Asakura T. Tightly winding structure of sequential model peptide for repeated helical region in *Samia cynthia ricini* silk fibroin studied with solid-state NMR. Protein Sci. 2003;12:666–71.
47. Nakazawa Y, Asakura T. Structure determination of a peptide model of the repeated helical domain in *Samia cynthia ricini* silk fibroin before spinning by a combination of advanced solid-state NMR methods. J. Am. Chem. Soc. 2003;125:7230–7.
48. van Beek JD. Methods for Studying Heterogeneous Solid Proteins and the Application to Silk, Diss. ETH No. 14637, ETH-Zurich, Zurich, 2002.
49. Warwicker JO. J. Mol. Biol. 1960;2:350–62.
50. Schmidt-Rohr K, Hehn M, Schaefer D, Spiess HW. Two-dimensional nuclear magnetic resonance with sample flip for characterizing orientation distributions, and its analogy to X-ray scattering. J. Chem. Phys. 1992;97:2247.

51. Chmelka BF, Schmidtrohr K, Spiess HW. Molecular-orientation distributions in poly(ethylene-terephthalate) thin-films and fibers from multidimensional decoder NMR-spectroscopy. Macromolecules. 1993;26:2282–96.
52. Demura M, Minami M, Asakura T, Cross TA. Structure of *Bombyx mori* silk fibroin based on solid-state NMR orientational constraints and fiber diffraction unit cell parameters. J. Am. Chem. Soc. 1998;120:1300–08.
53. Eles PT, Michal CA. Strain dependent local phase transitions observed during controlled supercontraction reveal mechanisms in spider silk. Macromolecules. 2004;37: 1342–5.
54. Eles PT, Michal CA. A DECODER NMR study of backbone orientation in *Nephila clavipes* dragline silk under varying strain and draw rate. Biomacromolecules. 2004;5: 661–5.
55. Saito H. Conformation-dependent 13C chemical shifts: A new means of conformational characterization as obtained by high-resolution solid state 13C NMR. Magn. Reson. Chem. 1986;24:835–52.
56. Hartzell CJ, Pratum TK, Drobny G. Mutual orientation of three magnetic tensors in a polycrystalline dipeptide by dipole-modulated nitrogen-15 chemical shift spectroscopy. J. Chem. Phys. 1987;87:4324–31.
57. Separovic F, Smith R, Yannoni CS, Cornell BA. Molecular sequence effect on the carbon-13 carbonyl chemical shift shielding tensor. J. Am. Chem. Soc. 1990;112:8324–8.
58. Teng Q, Iqbal M, Cross TA. Determination of the carbon-13 chemical shift and nitrogen-14 electric field gradient tensor orientations with respect to the molecular frame in a polypeptide. J. Am. Chem. Soc. 1992;114:5312–21.
59. Mehring M. Principles of High Resolution NMR in Solids, 2nd ed., Springer: Berlin, 1983.
60. Yao JM, Nakazawa Y, Asakura T. Structures of *Bombyx mori* and *Samia cynthia ricini* silk fibroins studied with solid-state NMR. Biomacromolecules. 2004;5:680–8.

Velocity Imaging of Granular Materials

Siegfried Stapf[1], A. Khrapitchev[1], C. Heine[1] and Bernhard Blümich[2]
[1]*RWTH Aachen, Lehrstuhl für Makromolekulare Chemie, Sammelbau Chemie, Worringer Weg 1, 52074 Aachen, Germany*
[2]*RWTH Aachen, Institut für Technische Chemie und Makromolekulare Chemie, (ITMC), Worringer Weg 1, D-52056 Aachen, Germany*

Introduction

Granular materials are a class of systems of widespread interest, touching fields as diverse as food and pharmaceutical production processes, storage and packing of agricultural products, waste disposal and recycling, or powder technology; but also natural phenomena of equal economic importance such as avalanches, sand transport by wind or water, and sedimentation. Motion of a granular substance frequently evokes the impression of chaotic behavior, but granular particles experience the same physical forces like any other moving object, in particular gravity, friction and interparticle forces. It is the correlated motions of a large number of particles which require their treatment as a coupled system, and therefore, a statistical description of the motion processes.

However, such a statistical description of motion is not restricted to granular materials. In fact, fluid dynamics uses the same type of formalism, describing the transport of finite fluid volume elements, while the trajectory of an individual molecule is ill-defined, with only time- and ensemble-averaged properties being available. In many senses, a granular medium can be considered as a close-up shot of a moving fluid, with a much reduced number of particles. The disadvantage of this could be that the particle number under some experimental conditions is not sufficient any longer for a proper averaging in the statistical sense; but at the same time, the observation of small numbers of particles, or even single ones, becomes feasible, at least in principle.

The resemblance of granular material dynamics to certain characteristics of phase behavior in "normal" matter (solids, liquids and gases) has quite naturally triggered much theoretical work attempting to find proper means to model and describe granular motion, but the ubiquity of granular media themselves and their huge economic importance have provided further impetus. Questions arising are either of everyday nature (the famous case of the shaken cornflakes box, an exercise in particle segregation), or comparatively far-fetched (much has been learnt by analyzing and modeling the shape of desert and underwater dunes that could be applied to understand the current and ancient atmospheric conditions on Mars and several moons in the solar system).

Many phenomena of interest in granular media are connected to transport properties. While transport through granular media, such as unconsolidated soils, falls into this category, it is similar to the well-covered field of flow in structured media, which has been investigated in great detail by NMR methods for a long time. In this article, we want to point out the difficulties and possibilities in NMR investigations of transport of granular media, i.e., the particle motion itself. Despite the large importance of such works, they remain scarce in the literature, one reason being the limited applicability of conventional NMR methods.

NMR of Transport in Granular Media—an Overview

The essential difficulty in tackling granular motion by NMR is the fact that the particles are very often solids in the NMR meaning of the word, i.e., their spectral features contain very broad lines, and sometimes sensitive nuclei like ^{1}H are even mostly absent, such as in dry sand grains. Provided that the sample indeed contains protons in sufficient quantity, pure *imaging* is still possible employing methods which had been specifically developed for solids (single-point acquisitions or multi-pulse line narrowing techniques). The encoding of *velocity* with pulsed field gradients (PFGs), however, consumes a minimum time of a few hundred μs in the best case, which is still one order of magnitude longer than the transverse relaxation time of solids. Only permanent-gradient techniques bear the potential to measure motion in some, but not all, solid granular particles directly, but no such effort has yet been made. The way out of this dilemma is either to obtain indirect information about the granular motion by measuring the transport of the surrounding fluid (which can be a liquid but frequently is a gas) or the particles have to be labeled with some narrow-line compound; this could be either a liquid imbibed into porous particles and held by capillary forces (particles made from a catalyst carrier material were used in [1]), or a liquid core covered by

Graham A. Webb (ed.), Modern Magnetic Resonance, 1581–1587.
© 2008 *Springer.*

a solid shell. Nature provides the latter particles in the shape of oil-filled seeds, such as mustard, sesame [2, 3] or poppy [1], which possess relatively even shapes and sizes. Liquid-filled hollow spheres are also manufactured for a wide range of pharmaceutical applications [4, 5].

Of the many conceivable geometries, research has been concentrated on only a few. Mueth *et al*. have looked into the velocity distribution of spherical particles inside a Couette cell [3, 6]. Shaken or vibrated beds were investigated by Kuperman *et al*. [7–9] and more recently by Yang *et al*. [10, 11]. Both segregation processes and localized velocities were measured for rotating horizontal cylinders half-filled with granular particles [2, 4, 5, 12, 13]. Finally, gas-fluidized beds were investigated because of their proximity to a common reactor type used in chemical engineering [1]. For a complete survey, see [14]. This contribution will focus on the latter two geometries as examples.

Gas-Fluidized Bed

A gas-fluidized bed consists of a granular system filled into a vessel which is subjected to a continuous gas stream. The intense exchange between the gas and the surface of the solid pellets favor gas phase reactions, hence its large industrial potential. The different stages of motion can be classified similar to phases in condensed matter [15, 16]. In the absence of flow, the medium behaves like a solid—if the whole array is tilted relative to the vertical axis, it will keep its overall shape until the angle of repose is reached. Above a certain threshold of gas flow rate, the bed becomes "fluidized", i.e. it will follow a tilt by liquid-like deformation so that the surface remains horizontal. In this stage, the particles have gained a slightly increased free volume, so that the total density of the bed is reduced. At higher flow rate, bubbles are formed, which drive those particles immediately above them upward, until dispersive components make them slide down around the bubble. The situation very much resembles a boiling liquid, the density is reduced further. Increasing the gas flow rate usually has the effect of increasing the average bubble size, which eventually reaches the diameter of the confining cell. Under these conditions, a pulsatile motion known as "slug phase" is observed. Depending on the cohesive forces and the inertia of the particles, they will eventually be driven out of the reactor cell. It is easy to imagine that boundary conditions, such as wall effects, even distribution of the air stream, but also particle size and shape, "stickiness" and size dispersion affect the transition between the phases.

Because optical methods can access only the vicinity of the container wall, where the unwanted wall effects are strongest, the advantage of NMR which can sample arbitrary volumes of the bed is obvious. The state and dynamics in the granular bed can then be characterized by the following approaches: (a) 1D imaging measures either the vertical extension of the bed or the signal intensity at any given layer, both being related to the particle density in the array; (b) the average particle mobility can be characterized by a number of parameters of increasing complexity, starting from dispersion coefficients via distribution functions of displacements within a given time (propagators) to higher-order information such as velocity changes, eventually leading to estimates of the collision time and the time-dependence of displacements; (c) velocity imaging combines both approaches and assigns average velocities or dispersion coefficients to the spatial position inside the bed.

In Figure 1, measurements of the average bed density normalized to the case in the absence of air flow are

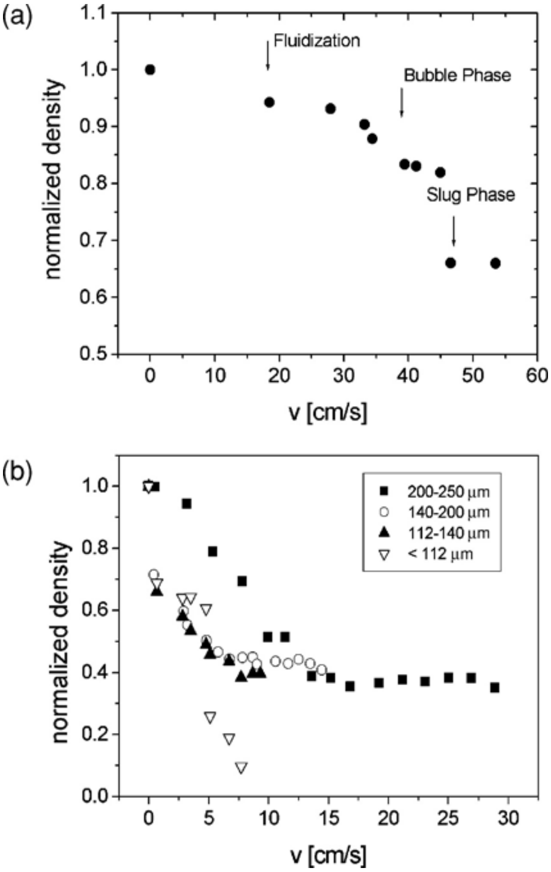

Fig. 1. Densities of gas-fluidized beds for different particle sizes, normalized by the density in the absence of flow. v indicates the average air velocity. (a) poppy seeds, (b) catalyst particles of different diameter ranges.

presented. As for all other experiments on fluidized beds, the measurements were taken out on a Bruker DSX 200 console equipped with a vertical 4.7 T magnet at MARC, RWTH Aachen, Germany.

A glass tube with an inner diameter of 21 mm was filled with either poppy seeds (diameter 500–800 μm but not spherical), or ground and sieved commercial catalyst pellets (Al_2O_3) saturated with acetone having size ranges given in the figure. The stepwise density changes are readily identified for the poppy seeds, but blurred for the smaller catalyst pellets. According to the categories given, e.g. in [16], the full spectrum of "phases" is not always expected; small particles with their relatively larger cohesive forces can be difficult to fluidize, while wall effects can become dominant for larger particles. Keeping these uncertainties in mind, all presented results must be regarded as somewhat imperfect states of granular flow which, however, are suitable for demonstrating the typical features of the dynamics.

It should be noted that, in order to obtain a value for the relative density, which is unbiased by relaxation effects, a single point acquisition technique had to be used which allowed signal acquisition during 10 μs following a low flip-angle pulse; the 1D profile was then reconstructed from 128 such encoding steps after sufficient averaging. A simple frequency-encoding sequence turned out to be unsuitable to provide a quantitative measure for the spin density; the relatively high particle velocities and short transverse relaxation times generate a combination which makes the use of a time-consuming velocity-compensated pulse sequence difficult, particularly for the catalyst pellets. From an experimental point of view, the adsorbate in these pellets was evaporating on a timescale of many hours. This is one example for experimental difficulties which require a careful consideration of the use of standard methods for moving samples when being applied to granular media.

The simplest motion-related quantity, which can be measured by NMR, is the dispersion coefficient. It is related to the velocity autocorrelation function (VACF) by

$$D(\Delta) = \int_0^\Delta \left(1 - \frac{\tau}{\Delta}\right) \langle \boldsymbol{v}(0)\boldsymbol{v}(\tau)\rangle d\tau \qquad (1)$$

if the VACF depends on the time differences τ only [5]. This condition can be violated, e.g. in the bubbling phase, when the system is macroscopically heterogeneous and each measurement probes a different particle distribution. It is assumed, however, that sufficient averaging does provide a reasonable approximation to the dispersion coefficient.

$D(\Delta)$ was determined using a standard diffusion encoding sequence, including a pair of pulsed field gradients of duration δ and strength $\boldsymbol{G}$, defining the wave vector $\boldsymbol{q} = (2\pi)^{-1}\gamma\delta\boldsymbol{G}$. Analyzing the initial slope of the normalized signal intensity, $\tilde{S}(q, \Delta) = S(q, \Delta)/S(0, \Delta)$, renders the dispersion coefficient [17]:

$$D(\Delta) \approx -(4\pi^2\Delta)^{-1} \lim_{q\to 0} \frac{\partial \ \ln|\tilde{S}(q, \Delta)|}{\partial q^2} \ . \qquad (2)$$

Figure 2a compares the increase of $D(\Delta)$ with air velocity for catalyst pellets with different size ranges. As expected, smaller and lighter particles are more affected by the driving air flow. By comparison with the density measurements in Figure 1, the sudden increase of the dispersion coefficient at an air velocity of 12 cm/s for the largest particles is indicative of the transition to the bubbling phase—when higher velocities begin to appear due

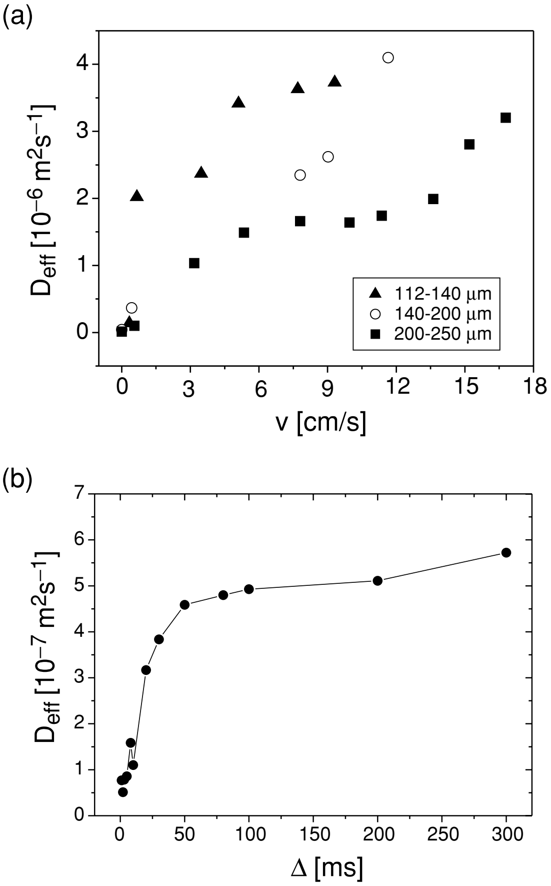

Fig. 2. (a) Dispersion coefficients for catalyst particles as a function of air velocity and particle size. (b) Dispersion coefficients for poppy seeds as a function of encoding time.

to the fast-moving bubbles—, this value being shifted to lower air velocities for the smaller particles. For the results of Figure 2a, encoding took place during a fixed interval $\Delta = 1.4$ ms, which is much longer than the average time between collisions, but short compared to the time required for an individual particle to sample a region with a statistical representation of all possible void structures and velocity distributions. Such a representative elementary volume had been identified as the characteristic structure beyond which dispersion processes become time-independent. The initial concept was formulated for fluid flow in fixed beds [18], but a similar volume can be defined for the fluidized bed, if wall effects can be neglected.

An example of the time-dependence of the dispersion coefficient is sketched in Figure 2b, which was obtained for poppy seeds, using a multi-PFG technique compensating for coherent motion contributions. It is this long-time limit, approached around $\Delta \approx 100$ ms for the case shown, which is of relevance for understanding processes that affect the efficiency of the fluidized-bed reactor as a whole. It is preceded by a regime which possesses some ballistic characteristics, where particles move in groups, for instance driven by an individual gas bubble; this regime shows an almost linear increase of $D(\Delta)$ with Δ. The truly ballistic regime would be observed on time scales much shorter than the time between collisions. Ongoing research attempts to access this time scale by reducing the encoding intervals to well below 1 ms and choosing the granular system appropriately.

The next, more complex function describing motion in the system is the so-called propagator [19]. It still represents an averaging over a large region or the whole bed, but provides the distribution of displacements $\boldsymbol{R}$ during a time Δ, and thus the velocities are averaged over this period. The propagator $\overline{P}(\boldsymbol{R}, \Delta)$ appears in the definition of the signal intensity as a function of encoding by wave vector $\boldsymbol{q}$:

$$\tilde{S}(\boldsymbol{q}, \Delta) = \int \overline{P}(\boldsymbol{R}, \Delta)\ \exp[i2\pi\boldsymbol{q} \cdot \boldsymbol{R}(\Delta)]\, d\boldsymbol{R}, \tag{3}$$

and is obtained via inverse Fourier transformation.

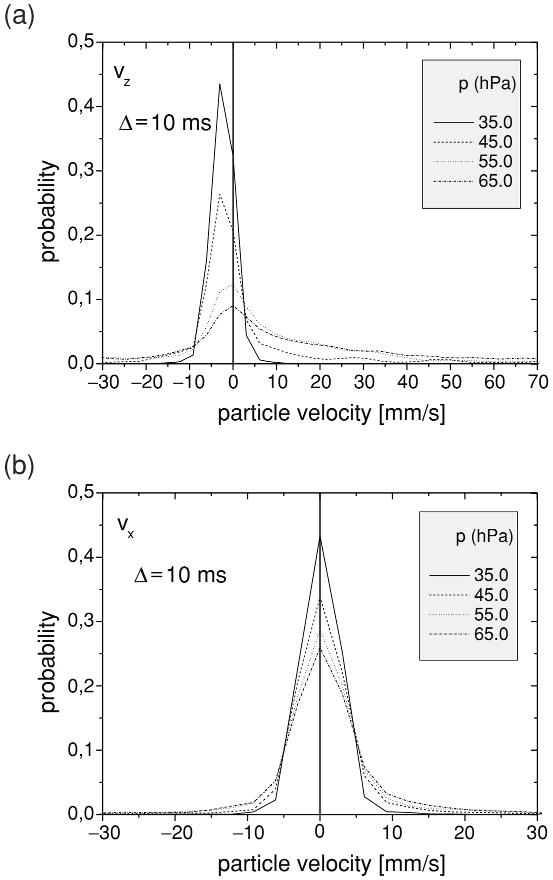

Fig. 3. Propagators for poppy seeds at different air pressure drops (a) parallel (Z) and (b) perpendicular (X) to the air flow direction.

Already the visual appearance of the bubbling phase in fluidized beds hints to a strongly asymmetric velocity distribution: a small number of fast particles moving upward is compensated by the remaining particles slowly moving downward. This impression is confirmed and quantified by the shape of the propagator averaged over the whole sample volume inside the resonator. Figure 3 demonstrates the influence of an increasing air flow rate on the propagator shapes for a bed of poppy seeds at a relatively short encoding time, $\Delta = 10$ ms. As expected, the distribution of vertical (Z) velocities is asymmetric, with a long tail of positive (upward) velocities gaining in weight for higher flow rates. For some conditions, the most probable velocity is actually negative, while mass balance requires the average to remain zero. The transverse velocities (X) have a symmetric distribution about zero because of the absence of a net transverse motion.

Finally, the combination of imaging sequences with a velocity-encoding module allows the local description of motion in terms of pixel-averaged velocities, or indeed propagators. One example, again for poppy seeds in the bubbling phase, is shown in Figure 4. Two-dimensional imaging (phase- and frequency-encoding) was combined with a preceding pair of velocity-encoding gradients at a separation of $\Delta = 4.7$ ms. Data were taken in a horizontal slice of 5 mm thickness near the center region of the bed of 27 mm height. For the chosen air flow

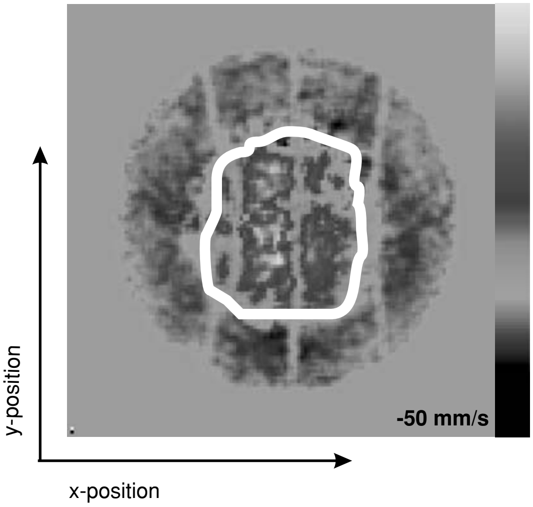

Fig. 4. Map of the vertical velocity v_z for a bed of poppy seeds of 44 mm diameter in the bubbling phase obtained in a horizontal slice of 5 mm thickness. The white line denotes zero vertical velocity. The vertical stripes are artifacts of the imaging reconstruction process. (See also Plate 130 on page XXIII in the Color Plate Section.)

rate, motion is characterized by a fountain-like behavior, where a relatively small fraction of particles in the central region is transported upwards with large velocities, while the particles further out and toward the cylinder wall move downward with smaller velocity values. The white line in Figure 4 separates the region with positive and negative velocities. The result was obtained from the difference of two differently encoded images to remove systematic phase errors; each image took 90 min. These results first demonstrate the feasibility of obtaining velocity images in a fluidized particle bed, but for the relatively small number of particles used in this particular case, the strong fluctuations in the velocity field, and therefore, the need for a large number of data accumulations becomes evident.

Rotating Drum

The first NMR measurements on granular flow in a partially filled rotating drum have been reported in 1993 [2]. Since then, continuous efforts have been made to either visualize the complex patterns arising from segregation effects between two types of particles distinguished by size and/or mass [12, 20, 21], or the actual velocity pattern by means of tagging sequences [13] or velocity encoding techniques [4, 5]. In particular, [5] uses the example of granular flow for a detailed demonstration of the experimental techniques and interpretations of the role of coherent and incoherent motion, providing maps of velocities, VACF correlation times and dispersion coefficients with spatial resolution.

As a demonstration of the essential features of granular flow in a rotating cylinder, Figure 5 presents velocity components in the two orthogonal directions normal to the rotation axis, being combined to a magnitude image and a vector plot. A PMMA cylinder of 88 mm inner diameter and 560 mm length has been filled to half its volume with mustard seeds (diameter 1.5 ± 0.2 mm) and was rotated at $\Omega/2\pi = 0.453$ per s. Experiments were performed on a horizontal 310 mm bore Oxford 1.9 T magnet at New Mexico Resonance, Albuquerque, NM. A double-echo pulse sequence consisting of one slice-selective $\pi/2$ pulse and two refocussing π hard pulses was used in order to compensate for background gradients [5]. The results were taken from [22].

The experimentally obtained velocity fields can be understood with the help of the theoretical interpretation given in Figure 6 [22] for an idealized situation. For small rotation angles, the granular bed will follow the motion like a solid object until the particles at the highest (top right in Figure 6) position will fall downward, generating an avalanche of other particles. Above a certain threshold rotation rate Ω, this series of individual avalanches will turn into a periodic process where the velocity field of all particles can reasonably be well described by average quantities which depend only on position. In Figure 6a, this situation is explained: all particles within the top layer of thickness r_0 (subset “1”, $r < r_0$) are sliding parallel to the surface, i.e. in direction d, with a velocity dependence

$$v_d(r) = v_{max}(1 - r/r_0)^2 - \Omega r \qquad (4)$$

while the particles in the bottom (subset “2”, $r > r_0$) rotate like a solid body with $v_d(r) = \Omega r$. An increase of Ω will lead to deviations from this ideal case, in particular the surface becomes curved [23]. The experimental results of Figure 5 can be interpreted by these different influences. The surface is clearly warped, but remains stationary during the course of the experiment. Figure 5a and b shows the expected smooth behavior of v_x and v_y in the bottom part of the granular bed. Figure 5c features the almost immobile region near the rotation axis and the strong dependence of velocities near the surface. Figure 5d finally visualizes the vectorial components of motion in the plane perpendicular to the rotation axis; the velocity vectors perfectly parallel to the surface can be easily identified, as the significant wall can slip, particularly at the bottom of the cylinder, where the column height of the granular material, normal to the cylinder wall, is largest.

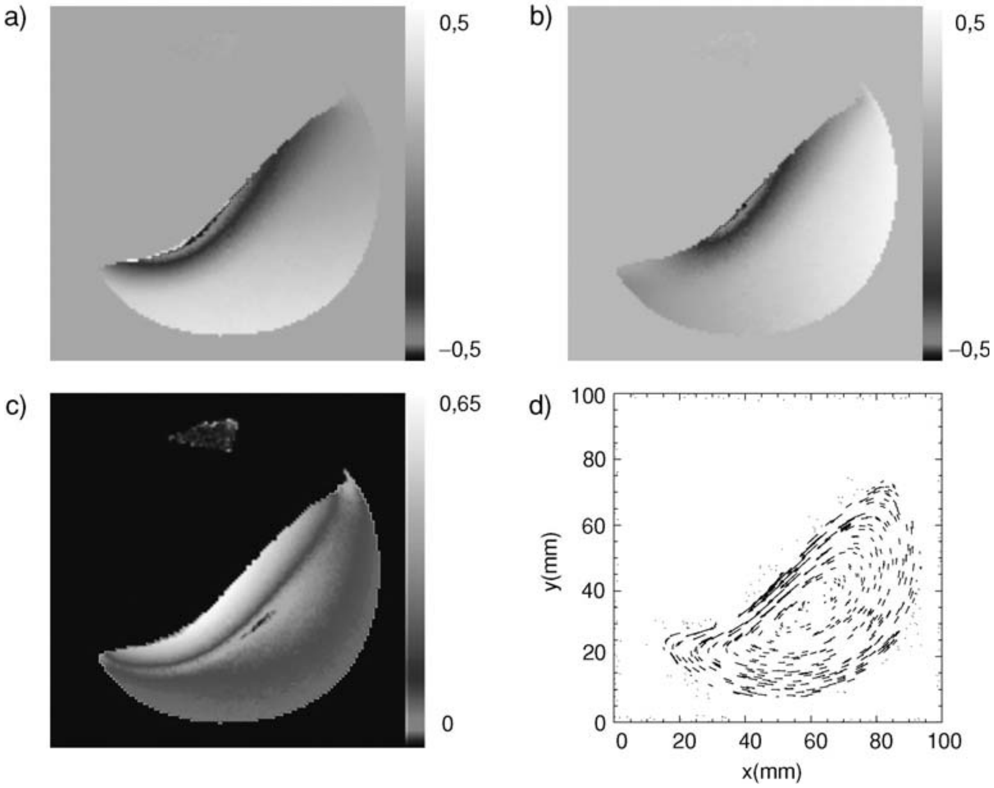

Fig. 5. Velocity maps of a bed of mustard seeds inside a cylinder of 88 mm inner diameter rotating at $\Omega/2\pi = 0.453$ per s; the images were taken from an axial slice of 20 mm width. (a) component v_x, (b) component v_y, (c) magnitude $(v_x^2 + v_y^2)^{1/2}$, (d) vector representation of the sum of (a) and (b). Numbers indicate velocities in m/s. (See also Plate 131 on page XXIV in the Color Plate Section.)

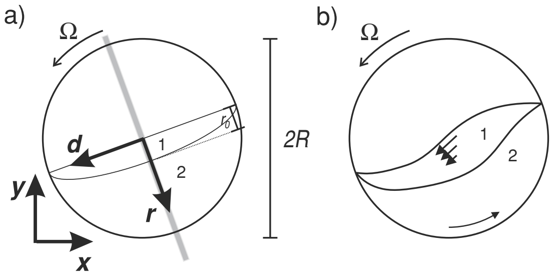

Fig. 6. Velocities for a granular bed inside a cylinder rotating with Ω. "1" denotes the region where granular flow occurs, "2" represents solid body rotation. (a) The surface orientation, which defines the vectors $\boldsymbol{d}$ and r relative to the gravity axis along $-y$, is determined by the angle of repose. (b) For larger Ω, the surface plane is deformed into a sinusoidal shape.

Summary

Granular systems in many ways still are a challenge for the theoretician, particulary if their dynamic behavior shall be understood. To develop and verify suitable methods, however, getting experimental evidence is inevitable. While this is feasible for averaged quantities, such as flow resistance or dispersion parameters, a more detailed knowledge of particle motion might become necessary. Most techniques are optical and are thus limited by the opacity of the granular medium and the presence of a large number of interfaces, restricting accessibility to the surface region of the granular array. NMR does not have this disadvantage and is, at least in principle, able to provide any kind of information about the dynamics of granular systems. It does, however, require systems containing a liquid-like marker component which has a relaxation time that is sufficiently long to allow all necessary manipulations of the spin system for making the encoding schemes applicable.

Such systems will frequently be of model character and are not identical to the real industrial application, but they are entirely sufficient to provide an extensive database with which theoretical descriptions can be developed.

Acknowledgments

We are grateful to R. Savelsberg for preparing and performing the first fluidized bed experiments, to E. Fukushima for helpful comments to this manuscript, and to M. Küppers for continuing support in the current part of this project. Part of this work was done during a productive stay of one of the authors (C.H.) at New Mexico Resonance, Albuquerque, and we would like to thank the whole team of NMR for their assistance and helpful contributions. Financial support by the DFG (Bl 231/25-2) is gratefully acknowledged.

References

1. Savelsberg R, Demco DE, Blümich B, Stapf S. Phys. Rev. E 2002;65:020301.
2. Nakagawa M, Altobelli SA, Caprihan A, Fukushima E, Jeong EK, Exp. Fluids. 1993;16:54.
3. Mueth DM, Debregeas GF, Karczmar GS, Eng PJ, Nagel SR, Jaeger HM, Nature. 2000;406:385.
4. Seymour JD, Caprihan A, Altobelli SA, Fukushima E, Phys. Rev. Lett. 2000;84:266.
5. Caprihan A, Seymour JD, Magn. J. Reson. 2000;144:96.
6. Mueth DM, Phys. Rev. E. 2003;67:011304.
7. Ehrichs EE, Jaeger HM, Karczmar GS, Knight JB, Kuperman VY, Nagel SR, Science. 1995;276:1632.
8. Kuperman V Yu, Phys. Rev. Lett. 1996;77:1168.
9. Knight JB, Ehrichs EE, Kuperman V Yu, Flint JK, Jaeger HM, Nagel SR, Phys. Rev. E. 1996;54:5726.
10. Yang XY, Huan C, Candela D, Mair RW, Walsworth RL, Phys Rev. Lett. 2002;88:044301.
11. Huan C, Yang X, Candela D, Mair RW, Walsworth RL, Phys. Rev. E. 2004;69:041302.
12. Hill KM, Caprihan A, Kakalios J, Phys. Rev. Lett. 1997;78:50.
13. Yamane K, Nakagawa M, Altobelli SA, Tanaka T, Tsuji Y, Phys. Fluids. 1998;10:1419.
14. Fukushima E, Adv. Complex Syst. 2001;4:503.
15. Davidson DF, Clift R, Harison D (Eds). Fluidization. Academic Press: London, 1985.
16. Geldart D (Ed). Gas Fluidization Technology. Wiley-Interscience: New York, 1986.
17. Callaghan PT, Stepišnik J, Adv. Magn. Opt. Reson. 1996;19:325.
18. Bear J, Dynamics of Fluids in Porous Media. American Elsevier: New York, 1972.
19. Kärger J, Heink W, Magn. J. Reson. 1983;51:1.
20. Nakagawa M, Chem. Eng. Sci. 1994;49:2540.
21. Hill KM, Caprihan A, Kakalios J, Phys. Rev. E. 1997;56:4386.
22. Heine C, NMR von rotatorischer und translatorischer Dynamik, PhD thesis, RWTH Aachen, Germany, 2001.
23. Nakagawa M, Altobelli SA, Caprihan A, Fukushima E. In: RB Behringer, JT Jenkins (Eds). Power & Grains' 97. AA Balkema: Rotterdam, 1997, p. 447.

Part III, Section 2:
Applications in Food Science

Foreword to Applications in Food Science

The range of chemicals, structures and materials represented by foodstuffs is enormous. At one extreme sugar is the purest mass produced chemical available. Beverages such as coffee, tea or wine are structurally homogeneous but may contain thousands of chemicals covering a vast range of concentration. Solid foods represent a higher level of complexity combining high levels of heterogeneity and chemical complexity. All these levels represent a challenge to magnetic resonance, and it is not surprising that in this section all available magnetic resonance methods are represented.

The challenge that foods represent to magnetic resonance have been amply exemplified in the biennial series of international conferences “Applications of Magnetic Resonance to Food Science”, the proceedings of which are a summary of state of the art of the subject [1–5]. However these books are summaries of work in progress they do not represent a review of the knowledge of particular areas.

Within this section the authors have been selected as authorities in their fields who are in a position to write an overview of their subjects. Given the scale of the field some selectivity and sharp focus has been required. However each time each author has produced an article which is complete in itself. Overlap, therefore, is inevitable, and a necessity, when each article is a comprehensive survey of its subject matter.

Whilst the entries have been divided by the magnetic resonance technique in the main, I have included section on the applications of a variety of techniques to specific systems. This is needed if the reader is to appreciate the range of problems that confront the spectroscopist and the way in which an approach using a range of techniques can tackle them.

Peter Belton

References

1. Belton PS, GA Webb and MJ McCarthy, ”Annual Reports on NMR Spectroscopy”, 1995;31.
2. Belton PS, I Delgadillo, AM Gil and GA Webb, ”Magnetic Resonance in Food Science”, RSC, Cambridge, 1995.
3. Belton PS, GA Webb, and BP Hills “Advances in Magnetic Resonance in Food Science” RSC, Cambridge, 1999.
4. Webb GA, PS Belton, AM Gil and I Delgadillo “Magnetic Resonance in Food Science A View to the Future” RSC, Cambridge, 2001.
5. Belton PS, AM Gil, GA Webb and D Rutledge “Magnetic Resonance in Food Science, Latest Developments” RSC, Cambridge, 2003.

Glossary

agar: A polysaccharide obtained form sea weeds containing galactose units

anthocyanins: Water soluble pigments occurring in many plants

Brix: A system of calculating sugar concentrations based on specific gravity

carrageenans: Sulphated polysaccharides derived from seaweeds

casein: General name for a group of proteins occurring in milk

catechins: generic name for a group of polyphenolic (QV) compounds

couette: A viscometer consisting on concentric cylinders

cutin: A waxy compound occurring in plants especially on leaves

cytoplasm: region within a cell in which the organelles are embedded

durum: Of wheat; a hard type of wheat used in making pasta

epicatechin: a member of the catechin group of compounds

extrusion: A thermomechanical process in which a screw system forces a product through a restricted opening

flavonoid: Polyphenolic (QV)compounds occurring in plants, thought to have role in protection against degenerative disease

galactomannans: A polysaccharide based on the sugar units galactose and mannose

gellan gum: A polysaccharide produced by bacterial fermentation

gliadins: A subset of gluten proteins soluble in ethanol water mixtures

gluten: A mixture of proteins which constitute the major storage proteins of wheat. The determining factor in the viscoelastic behaviour of dough

hemicelluloses: Complex carbohydrates occurring in plant cell walls

high molecular weight subunits: Protein subunits of gluten mainly responsible for the elasticity of dough

isoflavones: A sub group of the flavonoid group of compounds

kaempferol: One of the flavonoid group of compounds

lignins: A highly condensed polymer of phenolic compounds occurring in plants

lintnerization: Partial acid hydrolysis of starch

Maillard reaction: A non enzymic reaction between amino acids and sugars leading to brown colourations and complex chemical products

myofibril: The contractile unit of muscle fibre

myricetin: One of the flavonoid group of compounds

nutrigenomics: The study of how dietary chemicals interact with the genotype and gene expression

oleaginous: Of plants, oil bearing

organoleptic: The sensory properties of a food

pectin: A polysaccharide occurring in plants, widely used in food as thickener

phloretin: A flavonoid present in apples

polyphenols: Compounds consisting of a number of phenolic groups, most of which are thought to have antioxidant activity in vivo

quercetin: A compound belonging to the flavonoid group

renneting: Process of clotting of milk by enzymic action used in cheese making

resveratrol: a phenolic compound found in grape skins and wines

syneresis: separation of a liquid layer from gel

theaflavins: A complex molecule occurring in black tea formed by the oxidation of flavonoids

thearubigins: A group of chemicals similar to theaflavins also occurring in black tea

theophylline: A purine derivative which can act as muscle relaxant

trigonelline: A derivative of nicotinic acid present in green coffee

turgor: pressure within cells that contributes to the mechanical rigidity

vacuole: A sac within the cell that has functions of transport and storage, in plants it contributes to waste disposal and turgor (QV)

vanillin: The active principle in the flavour vanilla

water-holding capacity: The amount of water that may be held in a system without drip loss

High Resolution Solution State Methods

Characterization of the Chemical Composition of Beverages by NMR Spectroscopy

Jurkica Kidrič[1] and Iztok Jože Košir[1,2]
[1]National Institute of Chemistry, SI-1000 Ljubljana, Slovenia; and
[2]Slovenian Institute for Hop Research and Brewing, SI-3310 Žalec, Slovenia

Introduction

Characterization of the chemical composition of beverages is important for establishing their quality and authenticity and in connection with their organoleptic properties. It enables screening for the possible addition of toxic materials and the determination of compounds important for human health. A fine example of the latter are polyphenols found in wine, fruit juices, and tea; they have a wide range of biological and pharmacological effects, including anticarcinogenic, anti-inflammatory, and antioxidant activity [1,2].

Beverages are complex mixtures of different classes of compounds present at a broad range of concentrations. In the past, various analytical techniques have been used in the analysis of beverages, most frequently HPLC, GC, capillary electrophoresis, and conductometry. Because of the compositional complexity of beverages and the wide concentration range of components classical chemical analysis requires time consuming sample preparation. In the case of compounds at low concentration, separation, derivatizaion, and preconcentration are common steps in the procedure. To date, NMR has assumed an outstanding position in the field of chemical analysis of food products. Though NMR is less sensitive than the mentioned methods, sample preparation for NMR is simpler and less time consuming. NMR is nondestructive, selective, and capable of simultaneous detection of a great number of low molecular mass components in complex mixtures. The great advantage of NMR also is the possibility of detecting different nuclei in different spatial and electronic environments. As a consequence, it is the preferable technique for molecular structure determination and the study of molecular interactions in solution. With development of high-field (500–900 MHz) NMR spectrometers with superconducting magnets and the possibility of recording two- and multi-dimensional spectra, NMR has become a powerful method for analyzing at the molecular level complex mixtures like beverages. The use of 2D homo- and hetero-nuclear experiments, pulse sequences for the suppression of strong signals, and special probes, such as the so-called nano probe for μl quantities of samples, has enabled the characterization of minor compounds like anthocyanins [3]. The cold or cryogenic probe also is very promising. By cooling the key probe components to cryogenic temperature significant gains in sensitivity (up to 4 times in comparison to the room temperature probe) can be achieved and for a given amount of sample the experiment time is reduced by a factor of 16. The problems with signal overlapping and the limit detection may be overcome by the use of NMR hyphenation with techniques such as HPLC and MS spectrometry (LC-NMR, fully automated capillary scale LC-NMR, and LC-NMR/MS) [4–6]. Another way to overcome the problem of overlapping in NMR spectra of complex liquid mixtures is the application of diffusion-ordered spectroscopy (DOSY) [7].

NMR sensitivity can be further improved by combining hyphenated techniques with cryoprobe and by the incorporation of an online postcolumn solid-phase extraction (SPE) system for online preconcentration of analytes prior to transfer to NMR tube [4].

Alcoholic Beverages

Alcoholic beverages comprise a large group of beverages containing varying amounts of alcohol (ethanol). Large scale of production includes beer, wine and China rice wine, and distilled spirits such as brandy, whisky, rum, gin, cognac, vodka, and China distilled spirit. The components of alcoholic beverages are very complex and over 1300 compounds have been identified in various beverages. Using NMR for studying the chemical composition of beverages attention was paid mostly to wine and more recently to beer.

Wine

Water is the dominant component in wine. Ethanol, glycerol and other higher alcohols, sugars, organic acids, and various ions are present at high concentrations, while other aliphatic and aromatic alcohols, amino acids, phenolic compounds, and esters are present at much lower concentrations.

Graham A. Webb (ed.), Modern Magnetic Resonance, 1597–1603.
© 2008 *Springer.*

Already in 1976, it was demonstrated that NMR could be successfully used as a quick test for the determination of ethanol in wine, wine like beverages, and liquors [8]. Low-field (hence low cost) NMR spectroscopy has found application for the direct and rapid analysis of ethanol in wine and other alcoholic beverages [9]. A procedure to determine adulterations with diethylene glycol or methanol in natural wine has been described [10,11].

^{13}C NMR was introduced in wine analysis by Rapp *et al*. [11]. It has been shown that ^{13}C NMR can successfully be used for the detection of sugars, alcohols, organic acids, and amino acids [12,13], and that amino acids can be used as fingerprints for monitoring of European wines [14]. Spraul and Hofman have demonstrated the usefulness of LC-NMR for detecting sugars in wine concentrate, and for distinguishing α from β glucose [15]. ^{1}H and ^{13}C NMR spectra of wines of different variety, vintage, and geographical area differ in the intensity of particular signals and in the appearance of some signals [16]. This offers the possibility to follow the variability in their chemical composition on the ground of ^{1}H and ^{13}C NMR spectra. Use of 1D and 2D homo- and hetero-NMR experiments enables a reliable assignment of ^{1}H and ^{13}C resonances of some organic acids and alcohols normally present in wines in higher amounts. Using WET suppression for simultaneous suppression of strong signals ^{1}H and ^{13}C assignment of 17 amino acids and of γ-aminobutyric acid commonly present in wine has been possible [17] (Figure 1).

Brescia *et al*. have characterized the geographical origin of Italian red wines from Apulia using analytical and NMR data (^{1}H shifts) in combination with multivariate statistical methods. Heavy metals and amino acids seem to be the species most responsible for the discrimination of the analytical and the NMR data sets, respectively [18].

The NMR technique of high-resolution DOSY has been applied to the complex mixture of compounds that constitute Port wine in order to achieve improved interpretation of the composition changes between wines of different ages [19].

Wine polyphenols have attracted much attention in connection with the so-called “French Paradox” (i.e. despite of the fact that the French consume a high fat diet they have low rates of coronary heart disease). This has been attributed to the phenolic compounds found in red wine frequently consumed in France. SPE-^{1}H NMR in combination with chemometric analysis has been used for monitoring changes in phenolic composition of Cabernet Sauvignon produced in the Southern region of Brazil over 1986, 1987, and 1995 vintages in order to corroborate the standardization process of this beverage [20]. The combination of NMR with LC and MS methods enabled the characterization of phenolics in the phenolic extract from red wine of the variety Bordô [6].

Anthocyanins, the most important group of plant pigments, are responsible for the color of red wines. They are also considered to be safe color additives in the food industry. Considerable research efforts, concerning their stability, includes structural determinations, the studies of multiequilibria in solution, and the characterization of exchange processes among the different species by NMR

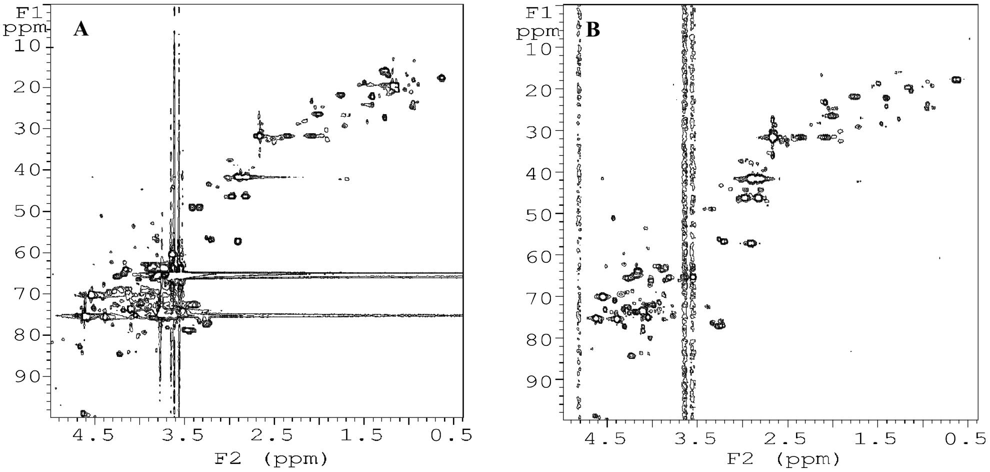

Fig. 1. Part of GHSQC (A) and WETGHSQC (B) spectra of wine in the region between 0.40 and 5.00 ppm in the ^{1}H dimension and between 0.00 and 100.00 ppm in the ^{13}C dimension. In the WETGHSQC experiment WET suppression was applied on water frequency at 4.80 ppm, on ethanol at 3.64 ppm, on glycerol at 3.62 ppm, and on unassigned signals at 3.55 and 3.53.

methods [21]. The identification of vitisin A, an anthocyanin occurring in some wines has been reported [22]. The anthocyanins in a particular LC fraction of red wines from the Coastal wine-growing region in Slovenia have been identified by NMR [3]. The structures of malvidin-derived wine pigments were determined by ^{1}H NMR and MS [23]. ^{1}H and ^{13}C analyses of anthocyanin-derived pigments isolated from red wine has been reported [24,25].

Special attention has been paid to resveratrol found in high content in some European and USA red wines, and particularly in Brazilian red wines. Resveratrol is known for its biochemical and pharmacological effects, including anticarcinogenic, antioxidant, and anti-inflammatory. *trans*-Resveratrol in commercial Brazilian red wines has been determined by ^{1}H NMR spectroscopy [26]. The assignment of ^{1}H and ^{13}C NMR spectra of resveratrol derivatives has been published [27].

The NMR studies of the structures of norisoprenoid glucosidic precursors of wine flavor have been reported [21].

The suitability of proton NMR for the quantitative determination of polydimethylsiloxanes (PDMS) in foodstuffs, particularly in wine, has been demonstrated [28]. PDMS are used in various stages of food processing as structure-shaping food additives and existing regulations of FDA and EU require the amount of added PDMS to be controlled.

The nature of undesirable insoluble deposits adhering to the inner glass surface of bottles of red wine has been investigated by solid-state ^{13}C NMR [29]. The deposit is composed of a phenolic polymer of anthocyanins, procyanidins, and proteins. Weekley *et al*. have extended high-resolution NMR spectroscopy to the analysis of full bottle wine samples [30]. In this work examples of full bottle ^{13}C NMR spectra are provided and the application of the method to the measurement of acetic acid content, the detection of complex sugars, phenols, and trace elements in wine is discussed.

It has been shown that using 5 mm diameter probehead with a 400 MHz spectrometer it was possible to measure fluorine-containing compounds directly in wine with a detection limit of 1.0 mg/l[31].

^{11}B NMR has been used for determining boric acid esters in wine [32]. Boron was found in at least three different molecular species that occur in variable proportions.

Troup and Hunter have discussed the achievements and uses of electron paramagnetic resonance in wine industry [33]. They presented the first observation of free radicals in red and white wines and found that the radical concentration, and therefore the antioxidant action, of white wines was increased by skin and oak wood exposure.

Beer

Beer is a fermented beverage made from malted grains (usually barley), hops, yeast, and water. Fruits, herbs, and spices may also be used to give beer a particular character. The different combination of ingredients, production processes, and storage conditions give rise to an enormous variety of beers [34]. There has been great interest in studying the chemical composition of beer as this information is valuable for the assessment of beer quality and the development of new products. Besides water and ethanol, the major components of beer are carbohydrates that comprise fermentable sugars (e.g. glucose, maltose, and maltotriose), glucose oligosaccharides (dextrins), and arabinoxylanes. Important components in beer also are iso-α- and β-acids responsible for the bitterness of beer and a range of polyphenols. The latter have an impact on foam stability, taste, and clearness of beer and, being antioxidants, also on human health.

The direct characterization of beer by NMR has been carried out by Duarte *et al*. [35]. With the aid of 1D and 2D NMR experiments about 30 compounds were identified. Many different metabolites such as adenosine, cystidine, histidine, phenylalanine, polyphenols, tryptophan, tyrosine, and uridine were also identified using 1D and 2D NMR experiments [6].

Since beer is a very complex mixture of a lot of different compounds occurring in a wide concentration range the signal overlapping and problems with the limit of detection may arise. These problems may be overcome by the use of LC-NMR/MS and DOSY technique. LC-NMR/MS has been used for the identification of dextrins with degree of polymerization up to nine monomers [36]. The preliminary application of DOSY technique to beer has been presented by Gil *et al*. [37]. It was found that this technique was useful mainly for aliphatic and aromatic compounds in beer.

HPLC-NMR has been used for the characterization of hop and beer bitter acids [38,39]. NMR data show clear distinction between cis and trans forms of the iso-α-acids, and unequivocally assign the structure of their acyl side chains.

Differentiation between different types of beer and the classification of different types of beer regarding different raw materials used in their production has become important since the final product should be clearly declared if it is not produced only from the malt originating from barley. For this purpose, NMR spectra can be used as fingerprints. Using the combination of ^{1}H NMR spectra and PCA method most ales, lagers, and alcohol-free samples could be distinguished based on their aromatic composition [35,40]. Also, it has been shown that the low-field NMR region is highly sensitive toward different types of beer fermentation [40].

SNIF-NMR method has been used in the studies of different stable isotope ratios to investigate their values in connection with raw materials from which the sugars used in the fermentation process have originated [41].

Nonalcoholic Beverages

The main difference in the chemical composition between alcoholic and nonalcoholic beverages is the absence of ethanol in nonalcoholic beverages. This simplifies the NMR characterization of composition since it is only the water signal that dominates in the spectra and should be suppressed by one of the suppression techniques.

Tea

Tea is made from the tender leaves of two varieties of the plant *Camellia sinensis*: *assamica* and *sinensis*. Tea was discovered in China where it has been consumed for its medicinal properties since 3000 BC. Tea was introduced to Europe in 17th century and, later, to America and Africa. Tea has become the most popular beverage after water throughout the world and has attracted more and more attention because of reported health benefits owing to its content of antioxidants and, particularly, for its potential for preventing cancer and cardiovascular diseases. Many kinds of tea are produced that can be classified principally into three types: green (unfermented), oolong (semifermented), and black (fully fermented). The important components of tea are the methylxanthine alkaloids, including caffeine and theophylline, polyphenols-flavonoids anthocyanins, catechins, quercetin, kaempferol and myricetin, and volatile and aromatic components. Aminoacids, carbohydrates, lipids, vitamins, minerals, and trace elements were also found. In the manufacture of black tea, catechins can be oxidized to form orange-colored theaflavins and brownish thearubigins. The overall chemical content of tea is influenced by genetic strain, climate, altitude of growth, type of soil, use of fertilizers, and even the processing of tea leaves.

The complete and unequivocal ^{1}H and ^{13}C assignments for a range of green tea polyphenols have been reported [42]. The same authors also assigned ^{1}H and ^{13}C resonances of theaflavin, theaflavin monogallate, and theaflavin digallate [43]. Using 2D NMR the structures of procyanidin and proanthocyanidin oligomers have been elucidated [44,45]. NMR has been used to clarify the antioxidative molecular mechanism of catechins [46]. It has been shown that NMR can be used to analyze simultaneously catechins, amino, organic, phenolic, and fatty acids, and sugars from a single green tea extract [47]. In this study, the data of just under 200 green teas from China, Japan, Vietnam, India, Indonesia, and Bangladesh were collected. It has been pointed out that the geographical origin may be indicated by the chemical composition of green teas provided that a representative number of samples for each population is available. Solution ^{1}H and ^{13}C spectra of commercial samples of green and black teas in acetone-d_6 and DMSO-d_6 and the solid-state NMR spectra have been recorded and ^{13}C chemical shifts of (+)-catechin in solution and in the solid state assigned [48]. Differences observed in chemical shifts are mainly due to the formation of stronger, intermolecularly hydrogen bonded species in the solid, with respect to those formed in solution.

Catechins have received considerable attention due to their diverse pharmacological activities, the commonly discussed mechanism of which is their antioxidative activity. ESR study on the structure-antioxidant activity relationship of tea catechins and their epimers has been performed [49]. Significant differences were found between the scavenging effects of the catechins and their epimers if their concentrations were low. The scavenging abilities of catechins were stronger than those of their corresponding epimers.

Tea infusions and dry tea leaves contain substantial amounts of aluminum, a powerful neurotoxicant that also has a potential for skeletal and hematopoietic toxicity. Hence, the consumption of large amounts of tea may significantly contribute to direct intake of aluminum. It has been shown that ^{27}Al NMR can be used nondestructively to determine aluminum at the ppm level in 0.5 cm^3 of complex matrices such as tea infusions and leaf digests [50]. ^{27}Al NMR has been used for characterization of aluminum complexes in tea extracts [51,52]. These studies provide evidence that Al forms complexes with catechins and organic acids.

Coffee

The beverage commonly called coffee is made from the roasted and ground beans of the coffee "tree"—a tropical evergreen shrub. There are three species of coffee "tree," arabica, originating from Ethiopia, liberica from West Africa, and robusta from the Congo. There are many different varieties of coffee beans due to the wide range of climatic differences in these areas. Coffee is composed of more than 700 compounds. Coffee's chemical composition is determined by a complex interaction of agricultural factors, roasting, blending, and brewing. In the order of abundance the water-soluble constituents ranging from 8% to 0.1% are phenolic polymers, polysaccharides, chlorogenic acids, minerals, water, caffeine, trigonelline, organic acids, sugars, lipids, and aroma compounds.

An extensive study using high-resolution ^{1}H NMR has been performed on expresso cups of two arabica and one robusta samples, and one water extract from ground green coffees and the chemical changes due to the roasting process have been followed [53].

^1H spectra of coffee in aqueous solution show a complicated pattern of signals. From the ^1H spectrum in H_2O/DMSO/HCL (HCL was added for better resolution and DMSO for dissolution of less hydrophobic molecules) it was possible to identify lactic, citric, free quinic, acetic, and formic acids whose concentration could be directly measured. The caffeine molecule was clearly identified as well as chlorogenic acids. The signals due to trigonelline and the signals of the methylene groups of the fatty acids were also observed. ^1H spectra of chloroform extracts are dominated by the signals from caffeine and triglycerides. Many other signals can be related to hydrophobic aromatic substances which were not detectable in the aqueous phase. Many aldehyde carbonyl signals from aldehydes were found. The signal found at 1.84 ppm seems to be a possible marker of the robusta variety. It was also possible to observe the resonances due to sterols.

The effect of roasting has been studied by observing the relative integrals of several selected resonances. The most pronounced is an increase of the concentration of free quinic acid during the roasting and a decrease of the concentrations of citric, chlorogenic, and formic acids. A decrease of the amount of trigonelline and an increase of the amount of its degradation product *N*-methyl pyridine is notable.

Significant differences in the relative intensities of signals originating in aldehydes from the three coffee samples have been observed. The Columbian sample, with a typical sweet and fruity taste, shows a higher content of aldehydes with respect to the Kenya sample.

The ^1H NMR spectra of a complex mixture such as coffee are difficult to interpret in details. Using multivariate statistical analysis it is possible to simplify the spectral data into a series of principal components that cover almost all the spectral variability. This allows for rapid comparison between many spectra, and the identification of differences within or between sample sets from the NMR data. The inherent ability of NMR to provide information about the chemical composition of a sample will allow the identification of source of variation. In this way the presence of inherent differences between coffees produced by different manufacturers and those produced by the same manufacturer has been demonstrated by identifying 5-(hydroxymethyl)-2-furaldehyde as a marker compound using the structural characteristics determined by NMR [54].

Using NMR and LC-MS it has been shown that antibacterial components in the coffee extract are protocatechuic acid (3,4-dihydroxy benzoic acid), chlorogenic acid, and caffeic acid [55].

Electron paramagnetic resonance has been used for the characterization of free radicals in soluble coffee [56]. Coffee solutions exhibit the strong free radical scavenging ability.

Fruit Juices

Fruit juices contain organic acids, sugars, amino acids, phenolics-particularly anthocyanins, vitamins, β-carotene, mineral salts, flavors originating from essential oils, and may contain some alcohol. The concentrations of organic acids, sugars, and amino acids are of comparable order of magnitude to those in wine. Composition and concentration of phenolics vary with the sort of the juice.

Rapp *et al*. have demonstrated the usefulness of ^{13}C NMR for the identification and quantification of amino acids in fruit juices and juice concentrates [12].

Belton *et al*. have assigned the ^1H NMR signals of different fruit juices to characterize several classes of compounds [57,58]. Significant spectral differences between cultivars were found. The results point to the usefulness of NMR in speciation and authentication studies and in the analysis of biochemical changes occurring in fruits and their juices. Vogels *et al*. have demonstrated the usefulness of NMR (peaks in the ^1H spectra) combined with PCA for detecting the adulteration in orange juices [59]. Colquhoun has studied the chemical composition of plum, raspberry, and strawberry purees/juices by ^1H NMR and chemometric methods [60]. For pure juices spectral differences are so great that visual identification is possible. To distinguish pure from adulterated juices (addition of small, fixed amount of plum, or apple juice to raspberry juices), multivariate analysis of NMR spectra is necessary.

Several quercetin and phloretin glycosides in an apple peel extract have been identified by HPLC-NMR/MS [61]. NMR provided the information on the identity of the compounds, the α and β conformations and the position of the glycosides on quercetin and phloretin. The paper by Gil *et al*. describes the application of NMR spectroscopy and LC-NMR/MS to the direct analysis of grape juice [6]. It has been shown that LC-NMR/MS can overcome the problems of signal overlap and the low peak intensity and aids significantly in the identification of aromatic compounds. DOSY NMR has been used for analyzing the composition of apple and grape juices [37]. Particularly useful is DOSY analysis in cases were NMR alone leads to ambiguous assignments. A series of compounds having uncoupled methyl signals but differing in size have been identified; the sugar region only allows interpretation in the anomeric region where signal overlap is reduced; in the aromatic region the larger compounds are identified by slower diffusivities.

Liquid- and solid-state NMR spectroscopy have been used to follow the compositional changes in mango juice and mango pulp during ripening [62]. It has been shown that NMR can aid in controlling postharvest quality and in developing appropriate technologies to enhance the marketable lifetime of the mango, one of the most important commercial fruit crops.

NMR with chemometrics has successfully been used in the discrimination between the orange juice and the pulp wash which is paler, more bitter, and regarded as a lower quality product [63]. It has been shown that dimethylproline is a marker compound for discrimination between two types of juice and can be used for orange juice adulteration.

References

1. Broustet JP. Heart. 1999;81:459.
2. Frémont L. Life Sci. 2000;66:663.
3. Košir IJ, Lapornik B, Andrenšek S, Golc Wondra A, Vrhovšek U, Kidrič J. Anal. Chim. Acta. 2004;513:277.
4. Corcoran O, Stone Wilkinson P, Godejohann M, Braumann U, Hofmann M, Spraul M. Am. Lab. 2002;34:18.
5. Smith JP, Hinson-Smith V. Anal. Chem. 2001;73:155A.
6. Gil AM, Duarte IF, Godejohann M, Braumann U, Maraschin M, Spraul M. Anal. Chim. Acta. 2003;488:35.
7. Barjat H, Morris GA, Smart S, Swanson AG, Williams SCR. J. Magn. Reson. B. 1995;108:170.
8. Anders U, Titgemeier F, Hailer G. Z. Lebensm. Unters. Forsch. 1976;162:21.
9. Guillou M, Tellier C. Anal. Chem. 1988;60:2182.
10. Rapp A, Spraul M, Humpfer E. Z. Lebensm. Unters. Forsch. 1986;182:419.
11. Rapp A, Markowetz A, Spraul M, Humpfer E. Dtsch. Lebensm. Rundsch. 1987;83:375.
12. Rapp A, Markowetz A, Niebergall H. Z. Lebensm. Unters. Forsch. 1991;192:1.
13. Rapp A, Spraul M, Humpfer E. In Vino Analytica Scientia, Bordeaux;359:1997.
14. Holland MV, Bernreuther A, Reniero F. In: PS Belton, I Delgadillo, AM Gil, G Webb (Eds). Magnetic Resonance in Food Science. The Royal Society of Chemistry: Cambridge, 1995, p 136.
15. Spraul M, Hofman M. In: PS Belton, I Delgadillo, AM Gil, G Webb (Eds). Magnetic Resonance in Food Science. The Royal Society of Chemistry: Cambridge, 1995, p 77.
16. Košir I, Kocjančič M, Kidrič J. Analusis. 1998;26:97.
17. Košir IJ, Kidrič J. J. Agric. Food Chem. 2001;49:50.
18. Brescia MA, Caldarola V, De Giglio A, Benedetti D, Fanizzi FP, Sacco A. Anal. Chim. Acta. 2002;458:177.
19. Nilsson M, Duarte IF, Almeida C, Delgadillo I, Goodfellow BJ, Gil AM, Morris GA. J. Agric. Food Chem. 2004; 52:3736.
20. Maraschin RP, Ianssen C, Arsego JL, Capel LS, Dias PF, Cimadon AMA, Zanus C, Caro MSB, Maraschin M. In: PS Belton, AM Gil, GA Webb, D Rutledge (Eds). Magnetic Resonance in Food Science. The Royal Society of Chemistry: Cambridge, 2003, p 255.
21. Ramos A, Santos H. In: GA Webb (Ed). Annual Reports on NMR Spectroscopy, Vol. 35. Academic Press: London, 1999, p 179.
22. Baker J, Timberlake CF. J. Agric. Food Chem. 1997; 45:35.
23. Fulcrand H, Cameira dos Santos P, Sarmi-Manchado P, Cheynier V, Favre-Bonvin J. J. Chem. Soc. Perkin Trans. 1996;1:735.
24. Mateus N, Silva AMS, Santos-Buelga C, Rivas-Gonzalo JC, De Freitas V. J. Agric. Food Chem. 2002;50:2110.
25. Mateus N, Carvalho E, Carvalho ARF, Melo A, González-Paramás AM, Santos-Buelga C, Silva AMS, De Freitas V. J. Agric. Food Chem. 2003;51:277.
26. Maraschin M, Passos R, Duarte da Silva JMO, Dias PF, Araujo PS, Oltramari J, Fontana JD, Caro MSB. In: G Webb, PS Belton, AM Gil, I Delgadillo (Eds). Magnetic Resonance in Food Science. The Royal Society of Chemistry: Cambridge, 2001, p 136.
27. Koh D, Park KH, Jug J, Yang H, Hun Mok K, Lim Y. Magn. Reson. Chem. 2001;39:768.
28. Mojsiewicz-Pieńkowska K, Jamrógiewicz Z, Lukasiak J. Food Addit. Contam. 2003;20:438.
29. Waters EJ, Peng Z, Pocock KF, Jones GP, Clarke P, Williams PJ. J. Agric. Food Chem. 1994;42:1761.
30. Weekley AJ, Bruins P, Sisto M, Augustine MP. J. Magn. Reson. 2003;161:91.
31. Mortimer AD, Dawson BA. J. Agric. Food Chem. 1995;39:1781.
32. Lutz O, Humpfer E, Spraul M. Naturwissenschaften. 1991;78:67.
33. Troup GJ, Hunter CR. Ann. N.Y. Acad. Sci. 2002;957:345.
34. Baxter ED, Hughes PS (Eds). An Overview of the Malting and Brewing Processes. In beer Quality, Safety and Nutritional Aspects. RSC: Cambridge, 2001, pp 1–13.
35. Duarte IF, Barros A, Belton PS, Righelato R, Spraul M, Humpfer E, Gil AM. J. Agric. Food. Chem. 2002;50:2475.
36. Duarte IF, Godejohann M, Braumann U, Spraul M, Gil AM. J. Agric. Food. Chem. 2003;51:4847.
37. Gil AM, Duarte I, Cabrita E, Goodfellow BJ, Spraul M, Kerssebaum R. Anal. Chim. Acta. 2004;506:215.
38. Nord LI, Sorensen SB, Duus JO. Magn. Reson. Chem. 2003;41:660.
39. Pusecker K, Albert K, Bayer E. J. Chromatogr. A. 1999;836:245.
40. Duarte IF, Barros A, Almeida C, Spraul M, Gil AM. J. Agric. Food. Chem. 2004;52:1031.
41. Rossmann A. Food Rev. Int. 2001;17:347.
42. Davis AL, Cai Y, Davies AP, Lewis JR. Magn. Reson. Chem. 1996;34:887.
43. Davis AL, Cai Y, Davies AP. Magn. Reson. Chem. 1995;33:549.
44. Balas L, Vercauteren J. Magn. Reson. Chem. 1994;32:386.
45. Balas L, Vercauteren J, Laguerre M. Magn. Reson. Chem. 1995;33:85.
46. Sawai Y, Sakata K. J. Agric. Food Chem. 1998;46:111.
47. Le Gall G, Colquhoun IJ, Defernez M. J. Agric. Food Chem. 2004;52:692.
48. Martinez-Richa A, Joseph-Nathan P. Solid State Nucl. Magn. Reson. 2003;23:119.
49. Guo Q, Zhao B, Shen S, Hou J, Hu J, Xin W. Biochim. Biophys. Acta. 1999;1427:13.
50. Koch KR. Analyst. 1990;115:823.
51. Nagata T, Hayatsu M, Kosuge N. Phytochemistry. 1992;31:1215.
52. Mhatre SN, Iyer RK, Moorthy PN. Magn. Reson. Chem. 1993;31:169.

53. Bosco M, Toffanin R, de Palo D, Zatti L, Segre A. J. Sci. Food Agric. 1999;79:869.
54. Charlton AJ, Farrington WHH, Brereton P. J. Agric. Food Chem. 2002;50:3098.
55. Dogasaki C, Shindo T, Furuhata K, Fukuyama M. Yakugaku Zasshi. 2002;122:487.
56. Pascual EC, Goodman BA, Yeretzian C. J. Agric, Food Chem. 2002;50:6114.
57. Belton PS, Delgadillo I, Holmes E, Nicholls A, Nicholson JK, Spraul M. J. Agric. Food Chem. 1996;44:1483.
58. Belton PS, Delgadillo I, Gil AM, Roma P, Casuscelli F, Colquhoun IJ, Dennis MJ, Spraul M. Magn. Reson. Chem. 1997;35:S52.
59. Vogels JTWE, Terwel L, Tas AC, van den Berg F, Dukel F, van der Greef J. J. Agric. Food Chem. 1996;44:175.
60. Colquhoun IJ. Spectrosc. Eur. 1998;10:1.
61. Lommen A, Godejohann M, Venema DP, Hollman PCH, Spraul M. Anal. Chem. 2000;72:1793.
62. Gil AM, Duarte IF, Delgadillo I, Colquhoun IJ, Casuscelli F, Humpfer E, Spraul M. J. Agric. Food Chem. 2000;48:1524.
63. Le Gall G, Puaud M, Colquhoun IJ. J. Agric. Food Chem. 2001;49:580.

High Resolution NMR of Carrageenans

Fred van de Velde[1,2], and Harry S. Rollema[2]
[1] *Wageningen Centre for Food Sciences, PO Box 557, 6700 AN Wageningen, The Netherlands; and*
[2] *NIZO Food Research, Kernhemseweg 2, 6710 BA Ede, The Netherlands*

Carrageenan Structure

Carrageenan is the generic name for a family of linear, sulphated galactans, obtained by extraction from certain species of marine red algae (Rhodophyta) [1]. They are composed of alternating 3-linked β-D-galactopyranose (G-units) and 4-linked α-D-galactopyranose (D-units) or 4-linked 3,6-anhydro-α-D-galactopyranose (DA-units), forming the disaccharide repeating unit of carrageenans (Figure 1). The sulphated galactans are classified according to the presence of the 3,6-anhydro-bridge on the 4-linked galactose residue and the position and number of sulphate groups. The most common types of carrageenan are traditionally identified by a Greek prefix indicating the major component of the sample. To describe more complex carrageenan structures a uniform letter code nomenclature has been developed by Knutsen *et al.* [2]. The three commercially most important carrageenans are called ι (iota)-, κ (kappa)-, and λ (lambda)-carrageenan, the corresponding letter codes are G4S-DA2S, G4S-DA, and G2S-D2S,6S. Two other types, called μ (mu)- and ν (nu)-carrageenan, which are the biological precursors of respectively κ- and ι-carrageenan, are often encountered in commercial carrageenan.

Experimental Setup

Sample Preparation

In general, carrageenan samples are sonicated prior to recording the spectra and the NMR experiments are carried out at elevated temperature to reduce the viscosity of the solution. Samples for ^{13}C NMR are prepared at relatively high concentrations (50–100 mg/ml in D_2O) as compared to ^{1}H NMR samples (5–10 mg/ml in D_2O). The solution is buffered by the addition of 20 mM Na_2HPO_4 to avoid hydrolysis at the elevated temperature used during the acquisition.

Sonicated carrageenan for ^{13}C NMR spectroscopy is preferably prepared according to the following procedure. A carrageenan solution (5 mg/ml in 20 mM Na_2HPO_4) is sonicated for at least three times 30 min in melting ice (Heat Systems XL 2020 sonicator, 12 mm tip, power 475 W, frequency 20 kHz). After centrifugation at elevated temperature, the sonicated solution is dialyzed against phosphate buffer (20 mM Na_2HPO_4) and water and lyophilized. ^{13}C NMR-samples are prepared by dissolving the sonicated carrageenans (70 mg/ml) in D_2O containing 20 mM Na_2HPO_4 and 10 mM internal standard (DSS). Sample preparation for the ^{1}H NMR experiments typically involves dissolving the carrageenan sample (5 mg/ml) at 80 °C in D_2O containing 1 mM DSS and 20 mM Na_2HPO_4, followed by sonication for at least 1 h in a sonicator bath (Branson 2510).

Internal Standards

The use of an appropriate internal standard is of importance to obtain valid chemical shift data. The IUPAC commission for molecular structure and spectroscopy recently recommended the use of 2,2-dimethyl-2-silapentane-3,3,4,4,5,5-d_6-5-sulfonate sodium salt (DSS) as the primary reference for both ^{1}H and ^{13}C NMR spectroscopy in polar solvents. For most purposes the difference between DSS and TMS when dissolved in the same solvent are negligible and, therefore, the data from DSS and TMS scales may be validly compared without correction [3]. Recently, the application of DSS as internal standard for NMR spectroscopy of carrageenans is studied and reported by Van de Velde *et al.* [4]. Moreover, this publication summarizes the chemical shift data of common internal standards, such as DMSO, MeOH, TSP, and acetone, relative to DSS and as a function of temperature and pD. Chemical shifts (δ) given throughout this chapter are relative to internal DSS standard ($\delta = 0.000$ ppm for both ^{1}H and ^{13}C according to the IUPAC recommendations [3]).

Methodology

^{1}H and ^{13}C NMR spectra are generally taken at 65 °C on a 500 or 600 MHz spectrometer. For ^{1}H NMR typically 64 scans are taken using 90° pulses with an interpulse delay of 5 s (T_1 values for the resonances of the anomeric protons of κ- and ι-carrageenan at 600 MHz are approximately 1.5 s [5]). ^{1}H decoupled ^{13}C NMR spectra are generally recorded using 90° pulses and interpulse delay

Graham A. Webb (ed.), Modern Magnetic Resonance, 1605–1610.
© 2008 *Springer.*

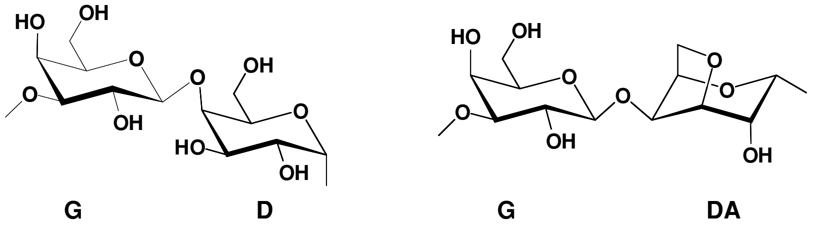

Carrageenan	3-linked	4-linked
μ (mu)	G4S	D6S
ν (nu)	G4S	D2S,6S
λ (lambda)	G2S	D2S,6S
ξ (ksi)	G2S	D2S

Carrageenan	3-linked	4-linked
κ (kappa)	G4S	DA
ι (iota)	G4S	DA2S
θ (tetha)	G2S	DA2S
β (beta)	G	DA

Fig. 1. Schematic representation of the repeating units of carrageenan. The letter codes refer to the nomenclature of Knutsen *et al.* [2].

of 1.5 s and acquiring 30,000 scans (T_1 values for the anomeric carbons of κ- and ι-carrageenan at 400 MHz are approximately 0.5 s [5]).

Quantitative applications of NMR techniques require a number of special precautionary measures. It is of paramount importance to ensure that the inter-pulse delay amounts to at least 4–5 times the longest T_1 value of the resonances used for the analysis [5,6]. For ^{1}H NMR of samples containing mono- or disaccharides relatively long inter-pulse delays have to be applied. On the other hand ^{13}C NMR spectra of carrageenans can be recorded using relatively short inter-pulse delays. An additional complicating factor for ^{13}C NMR is a possible variation of the NOE effects for the different carbons. However in the case of carrageenans all carbon atoms of the repeating unit have one proton attached. Based on this, one would expect little variance in the NOE effect for the different carbons. Experiments with a mixture of κ- and ι-carrageenan using continuous composite pulse decoupling and gated decoupling produced apart from signal to noise ratio (S/N), the same result for the intensity ratio of the anomeric carbon resonances [5].

Analysis of the Major Carrageenan Types

^{1}H-NMR Spectroscopy

Proton NMR spectroscopy is the preferred method to quantify the composition of carrageenan samples. ^{1}H NMR has the advantage of a relatively high sensitivity. Therefore, spectra of samples with low carrageenan concentration can be recorded in a couple of minutes. Generally, 5 mg sample is sufficient to record a ^{1}H NMR spectrum. Moreover, minor components can be detected at concentration down to 1%, due to the high S/N ratio. The quantification of different carrageenan types in a sample by ^{1}H NMR spectroscopy is based on the resonances of the α-anomeric protons (D- and DA-units) in the region from 5.0 to 5.7 ppm (Table 1 and Figure 2A) [4,6]. The signals for the β-anomeric protons (G-units) are less suitable for either identification or quantification purposes. This is the main drawback of proton NMR spectroscopy for carrageenan identification. Moreover, this limits this method to rather homogeneous samples,

Table 1: Chemical shifts (ppm) of the α-anomeric protons of carrageenans referred to DSS as internal standard at 0 ppm[a]

Carrageenan	Monosaccharide[b]	Chemical shift (ppm)
β (beta)	DA	5.07
ι (iota)	DA2S	5.29
κ (kappa)	DA	5.09
λ (lambda)	D2S,6S	5.55
ν (nu)	D2S,6S	5.50
μ (mu)	D6S	5.24

Source: van de Velde *et al.* [4].

[a] Carrageenan (30 mg/ml), DSS (10 mM) and Na_2HPO_4 (20 mM) in D_2O recorded at 65 °C.

[b] Codes refer to the nomenclature developed by Knutsen *et al.* [2].

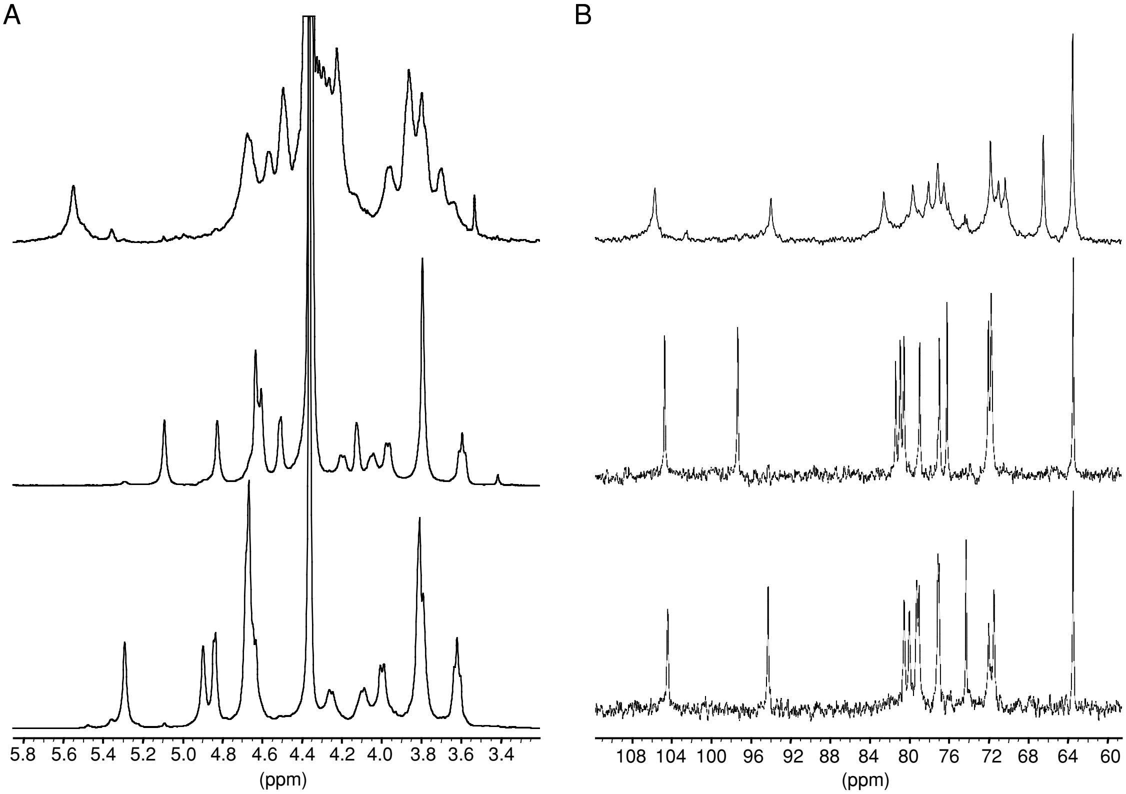

Fig. 2. ^{1}H NMR spectra (A) and ^{13}C NMR spectra (B) of the major carrageenan types from bottom to top: ι-carrageenan; κ-carrageenan and λ-carrageenan.

as resonances of some common additives and contaminants can interfere with the major carrageenan types (*vide infra*).

^{13}C-NMR spectroscopy

A typical ^{13}C NMR experiment takes approximately 12–18 h to reach a reasonable S/N. However, due to the high chemical shift dispersion in a ^{13}C NMR spectrum each carbon atom of the repeating unit of a carrageenan variant gives rise to one single signal and the various carrageenan variants show unique and characteristic patterns (Table 2 and Figure 2B). Therefore, ^{13}C NMR spectroscopy is needed for an unambiguous identification of carrageenan samples. The ^{13}C NMR spectra of gel forming κ- and ι-carrageenan have been interpreted, using studies on model synthetic monosaccharide derivatives [7] or oligomeric polysaccharide fragments [8,9]. A well-resolved spectrum of λ-carrageenan was obtained much later [10,11] due to some technical difficulties, which are usually explained by the high viscosity of λ-carrageenan solutions. It should be noted that the biological precursors (μ- and ν-carrageenan) and many other possible carrageenan diads given in Table 2 are usually found only as components of hybrid polymeric molecules.

Analysis of Minor Components

In addition to the common carrageenan repeating units, the NMR spectra of carrageenan samples may show resonances originating from minor constituents and/or contaminants. These signals can result from substituents of the carrageenan backbone, such as pyruvic acid acetals and *O*-methyl groups. Contaminants originate either from the red algal biomass, which were not removed in the carrageenan isolation procedure [1,12] or from compounds (inorganic salts, sucrose, galactomannans) added by manufacturers to improve and/or control some

Table 2: ^{13}C NMR chemical shifts for the most common carrageenan structural units[a]

		Chemical shift (ppm) relative to DSS as internal standard					
Carrageenan	Unit[b]	C-1	C-2	C-3	C-4	C-5	C-6
β (beta)	G	104.8	71.7	82.6	68.6	77.6	63.5
	DA	96.8	72.4	81.6	80.3	79.3	71.7
ι (iota)	G4S	104.4	71.5	79.1	74.3	77.0	63.5
	DA2S	94.3	77.2	80.0	80.6	79.3	72.0
κ (kappa)	G4S	104.7	71.7	81.0	76.3	77.0	63.5
	DA	97.3	72.1	81.4	80.5	79.1	71.7
λ (lambda)	G2S	105.6	79.6	78.0	66.4	76.5	63.5
	D2S,6S	93.9	77.0	71.8	82.6	70.9	70.3
μ (mu)	G4S	107.0	72.7	80.5	76.3	77.1	63.5
	D6S	100.3	70.7	72.8	81.4	70.5	69.9
ν (nu)	G4S	107.0	72.4	82.4	73.4	77.2	63.6
	D2S,6S	100.5	78.6	70.4	82.1	70.4	70.0
θ (tetha)	G2S	102.6	79.8	79.4	67.0	77.1	63.4
	DA2S	97.8	77.1	79.6	81.8	79.2	72.4
ξ (ksi)	G2S	105.4			66.9		
	D2S	94.9					

Source: van de Velde *et al.* [4].

[a] Carrageenan (30 mg/ml), DSS (10 mM) and Na_2HPO_4 (20 mM) in D_2O recorded at 65 °C.

[b] Codes refer to the nomenclature developed by Knutsen *et al.* [2].

functional properties of carrageenan samples (solubility, viscosity, gel strength, etc.). These additives are generally encountered in standardized commercial carrageenan samples. Low molecular weight contaminations and additives can be removed by dialysis, prior to recording the spectra. The identification of these components is described below and their chemical shifts are summarized in Table 3.

Carrageenan Substituents

NMR spectra of carrageenans may reveal the presence of *O*-methyl substitution of the carrageenan backbone. For example, as 3-linked 6-*O*-methyl-D-galactose residues in κ-carrageenan from *Kappaphycus alvarezii* [13] and in methylated ι-carrageenan from *Clavivlonium ovatum* [14]. These residues give specific signals for OMe at 61.0 ppm in ^{13}C NMR and 3.41 ppm in ^{1}H NMR relative to DSS [4,14]. Pyruvic acid is a common component of many complex carrageenans. It forms a cyclic acetal at positions 4 and 6 of 3-linked galactose residues. This substituent can be identified by characteristic signals of its carbons together with specific substitution effects on the corresponding carbon atoms of 3-linked D-galactose [15]. The ^{13}C NMR chemical shifts of these characteristic signals are 27.6, 103.6, and 178.0 ppm for, respectively, the methyl, acetal, and carboxyl carbon atoms. The pyruvic acid acetals are also detected in the ^{1}H NMR spectra by the methyl proton resonances with a chemical shift of 1.44 ppm relative to DSS [4]. In addition to the methyl

Table 3: NMR chemical shifts for minor components and additives observed in carrageenan samples

		Chemical shift (ppm) relative to DSS as internal standard	
Component/substituent	Observed unit	^{13}C NMR	^{1}H NMR
6-*O*-methyl-D-galactose	Methyl group	61.0	3.41
	C-6	73.9	
	C-5	79.4	
Pyruvic acid acetal	Methyl group	27.6	1.44
	Acetal	103.6	
	Carboxyl	178.0	
Floridean starch	C-1	102.6	
	C-1	74.3	
	C-5	74.0	
	H-1		5.35
iso-Propanol	Methyl group	26.4	1.17

signal, specific substition effects on the chemical shifts of the other protons are observed in the anomeric proton region of the ^{1}H-NMR spectra [15].

Contaminants

Floridean starch, a branched (1-4,1-6)-α-D-glucan structurally related to plant amylopectins, is a reserve polysaccharide of red seaweeds. It is soluble in water and can accompany carrageenans in the extraction and precipitation steps. Apart from the detection of glucose in an acid hydrolysate, the presence of floridean starch can be confirmed by the well-known set of signals of 4-linked α-D-glucopyranose residues in the ^{13}C-NMR spectrum (Table 3) [16]. In the ^{1}H NMR spectra, floridean starch is detected by the signal of the anomeric proton of the α(1 → 4)-linked D-glucopyranosyl at 5.37 ppm [16]. The resonance of the anomeric proton of the α(1 → 6)-linked D-glucopyranosyl appears at 4.98 ppm. Floridean starch can be removed by starch degrading enzymes or by any procedure of separation of acid and neutral polysaccharides. *iso*-Propanol is generally applied in industrial processing to precipitate carrageenans from the extraction liquid [1]. In the ^{1}H NMR spectra *iso*-propanol gives a characteristic triplet at 1.17 ppm and in the ^{13}C NMR spectra the methyl carbon is detected at 26.4 ppm.

Galactans of the agar group (differ from the carrageenan as the 4-linked units have the L-configuration) may be present in carrageenans, when mixed algal populations containing both agarophytes and carrageenophytes are used for carrageenan manufacture. The ^{13}C NMR spectral data of these so-called D/L-hybrids [6], may require complementary chemical analysis to unambiguously identify the agar-like structures. Some red algae contain water-soluble sulfated xylomannans and neutral xylans, but these polysaccharides are usually absent from the common carrageenophytes and only accidentally may be found in carrageenans. ^{13}C NMR spectra of both types of polysaccharides were published and may be used for their identification [17–19].

Additives

Commercial carrageenan preparations are often blended with additives such as sucrose and glucose to adjust their viscosity. In ^{13}C NMR spectroscopy, the anomeric signal of α-D-glucopyranose residue of sucrose may overlap with that of DA2S residue of ι-carrageenan at about 94 ppm. Nevertheless, the presence of sucrose can be unambiguously detected by its other signals in the ^{13}C-NMR spectrum of the mixture [6]. These additives do not disturb the NMR analysis and can in general be detected apart from the different carrageenan forms. Only the resonance of the anomeric proton of glucose overlaps with the resonance of μ-carrageenan in ^{1}H NMR. If necessary, glucose and sucrose together with inorganic salts can be removed by dialysis or ethanol precipitation.

The gelling properties of carrageenans can be considerably improved by addition of several galactomannans or mannans of some higher plants [20,21]. NMR studies were used to elucidate the possible modes of interaction between polysaccharide components in these blends [22]. Since the ^{13}C NMR spectra of galactomannans are well-known [23], the corresponding spectra of mixed preparations recorded at elevated temperatures (above the melting points of gels) can be used to detect the presence of galactomannan additives and to calculate their content relative to carrageenan. In ^{1}H NMR spectra the anomeric proton of the α-D-galactopyranose is observed at 5.0 ppm and that of the β-D-mannopyranose at 4.8 ppm [23].

References

1. Van de Velde F, De Ruiter AG. In: A Steinbüchel, S DeBaets, EJ VanDamme (Ed). Biopolymers Vol. 6. Polysaccharides II: Polysaccharides from Eukaryotes, Wiley-VCH: Weinheim, 2002, p 245.
2. Knutsen SH, Myslabodski DE, Larsen B, Usov AI. Bot. Mar. 1994;37:163.
3. Harris RK, Becker ED, CabralDeMenezes SM, Goodfellow R, Granger P. Pure Appl. Chem. 2001;73:1795.
4. Van de Velde F, Pereira L, Rollema HS. Carbohydr. Res. 2004;339:2309.
5. Van de Velde F, Peppelman HA, Rollema HS, Tromp RH. Carbohydr. Res. 2001;331:271.
6. Van de Velde F, Knutsen SH, Usov AI, Rollema HS, Cerezo AS. Trends Food Sci. Technol. 2002;13:73.
7. Usov AI. Bot. Mar. 1984;27:189.
8. Rochas C, Rinaudo M, Vincendon M. Int. J. Biol. Macromol. 1983;5:111.
9. Greer CW, Rochas C, Yaphe W. Bot. Mar. 1985;28:9.
10. Falshaw R, Furneaux R. Carbohydr. Res. 1994;252:171.
11. Stortz CA, Bacon CE, Cherniak R, Cerezo AS. Carbohydr. Res. 1994;261:317.
12. Rudolph B. In: RE Martin, EP Carter, LM Davis, GJ Flich (Ed). Marine and Freshwater Products Handbook. Technomic Publishing Company, Inc.: Lancaster, U.S.A., 2000, p 515.
13. Bellion C, Brigand G, Prome J-C, Bociek DWS. Carbohdr. Res. 1983;119:31.
14. Chiovitti A, Bacic A, Craik DJ, Kraft GT, Liao M-L. Carbohydr. Res. 2004;339:1459.
15. Chiovitti A, Bacic A, Craik DJ, Munro SLA, Kraft GT, Liao M-L. Carbohydr. Res. 1997;299:229.
16. Knutsen SH, Grasdalen H. Bot. Mar. 1987;30:497.
17. Kovac P, Hitsch J, Shashkov AS, Usov AI, Yarotsky SV. Carbohydr. Res. 1980;85:177.

18. Usov AI, Dobkina IM. Bioorg. Khim. 1991;17:1051.
19. Kolender AA, Pujol CA, Damonte EB, Matulewicz MC, Cerezo AS. Carbohydr. Res. 1997;304:53.
20. Therkelsen GH. In: RL Whistler, JN BeMiller (Ed). Industrial Gums: Polysaccharides and Their Derivatives. Academic Press Inc.: San Diego, 1993, p 145.
21. Imeson AP. In: GO Phillips, PA Williams (Ed). Handbook of Hydrocolloids. Woodhead Publishing Ltd.: Cambridge, 2000, p 87.
22. Rochas C, Taravel F-R, Turquois T. Int. J. Biol. Macromol. 1990;12:353.
23. Grasdalen H, Painter TJ. Carbohydr. Res. 1980;81:59.

Flavor–Food Compound Interactions by NMR Spectroscopy

C. Moreau and E. Guichard

Unité Mixte de Recherche sur les Arômes (UMRA, INRA-ENESAD), INRA, 17 rue Sully, BP 86510, 21065 Dijon, France

Interactions between flavor compounds and non-volatile food components (proteins, polyphenols, carbohydrates, polyolosides, etc.) could significantly affect their impact on flavor perception [1,2]. Indeed, the presence of protein or polysaccharides can decrease aroma intensity by forming complexes depending on the nature, the concentration, and the physicochemical properties of aroma compound [3].

Headspace or chromatographic methods have been extensively used to investigate the retention of aroma compounds in food matrices [4,5]. However, these techniques only give indirect information on aroma binding and no information at a molecular scale. Spectroscopic techniques have also been used to study interactions between small molecules and macromolecules since they can give information on the binding site localization and on the nature of the interactions [6–9]. Of all of the spectroscopic techniques, NMR spectroscopy is probably the most effective in investigating ligand–macromolecule interactions as protein–protein, drug–protein, DNA–protein, lipid–protein or small molecules–macromolecules [10–14]. Compared to other spectroscopic methods, NMR is a non-invasive technique and ligand–macromolecule complexes can generally be investigated in their natural environment (pH, temperature, buffer conditions) without spin labeling or fluorescent probe.

A wide range of NMR methods can be used to characterize macromolecule–ligand complexes and gives access to structural and dynamic information on both the ligand and macromolecule [13,15–17]. The choice of which of these NMR methods to use, depends on various factors such as macromolecule and ligand size and nature, equilibrium binding constant, and the complex dissociation rate (K_D). They depend on the facts that, after complex formation, mean perturbations are observed on NMR parameters such as chemical shifts, resonance broadening, relaxation constants, diffusion coefficients, or the nuclear Overhauser effect (NOE). The equilibrium constant, K, for the ML complex, where M is the macromolecule and L the ligand is defined as:

$$\mathrm{M} + \mathrm{L} \underset{k_{\mathrm{off}}}{\overset{k_{\mathrm{on}}}{\rightleftarrows}} \mathrm{ML}; \quad K = \frac{k_{\mathrm{on}}}{k_{\mathrm{off}}} = \frac{[\mathrm{ML}]}{[\mathrm{M}]\,[\mathrm{L}]}$$

The ligand binds to the macromolecule at a rate of k_{on}, the association rate, and leaves its binding site at a rate of k_{off}, the dissociation rate which depends on the ligand concentration, [L], and the interaction strength between the ligand and the binding site, K_D. The dissociation constant of the ML complex is defined as $K_D = k_{\mathrm{off}}/k_{\mathrm{on}} = [\mathrm{M}][\mathrm{L}]/[\mathrm{ML}]$. For such a ML complex, the appearance of the NMR spectrum depends principally on the exchange kinetic determined by the k_{off} rate, but also on the dissociation constant, K_D.

Depending on the NMR method used, the ligand and/or the macromolecule are observed and information on the dissociation constant and complex stoichiometry, binding site localization, and dynamic parameters (diffusion coefficient, relaxation times) can be obtained from the complex.

The most popular method of NMR used to investigate interactions of a specific ligand–macromolecule complex is based on the chemical shift changes (and/or on resonance broadening) of the macromolecule using 1D and/or 2D NMR spectroscopy. The spectrum of the macromolecule alone is recorded and is then compared to the one in the presence of the ligand. Chemical shift changes ($\Delta\delta$) of the macromolecule are induced by the presence of the ligand when it binds to the macromolecule. The observed spectral changes will depend on the exchange rate (τ) at which the complex is formed [18]. Three exchange regimes can be defined on the NMR timescale.

1. The slow exchange if $1/\tau \ll |\Delta\delta|$ in which two resonance sets are observed corresponding to the free and complex molecule resonances.
2. The rapid exchange if $1/\tau \gg |\Delta\delta|$ in which one set of resonances is observed but progressively shifted with the increase concentration of the ligand. Observed chemical shifts (δ_{obs}) of implicated groups in the complex are a weighted average of the free and bound molecule chemical shifts.
3. The intermediate exchange is observed if $1/\tau \approx |\Delta\delta|$ in which a broadening of resonances is observed.

For most of the studied systems, the rapid exchange is observed.

Graham A. Webb (ed.), Modern Magnetic Resonance, 1611–1615.
© 2008 *Springer.*

Other information can be obtained using this NMR method. Firstly, the chemical shift changes of specific chemical groups on the macromolecule provide information on the binding site localization. For example, ^1H–^1H TOCSY NMR spectra give information on short- and long-range coupling through chemical bonds and particularly for a protein, on signals of the NH–CHα region which is a fingerprint of the amino acid sequence. 1D and 2D NOE NMR experiments give information on proton coupling through space, thus showing which protons are spatially closed (<5 Å). The binding sites and the spatial position of the ligand can then be determined. 2D ^{15}N–^1H and ^{13}C–^1H HSQC/HMQC NMR experiments, which give proton–nitrogen or proton–carbon correlations, is also widely used in drug screening applications known as the "SAR-by-NMR" [12] but labeling of proteins is necessary.

Moreover, in the rapid exchange regime, information on ligand affinity and complex stoichiometry can be obtained by using NMR titration experiments. By progressively increasing the ligand concentration to the macromolecule solution (or inversely), and by recording spectra for each concentration, the dissociation constant, K_D, of a ligand–macromolecule complex can be calculated based on the chemical shift changes [18]. This method implies to previously assigned macromolecule resonances. However, proton spectra of macromolecules with high molecular weights such as proteins are complex and assignment of chemical shift resonances is difficult. Thus, nuclei such as ^2D, ^{13}C, and/or ^{15}N are generally used to label macromolecules in order to simplify the interpretation of NMR spectra [19]. Other nuclei can be observed in NMR and some works concern ^{19}F NMR spectra of small ligand molecules. However, few or no fluorined aroma compounds are present in food [20,21].

The effect of a ligand binding can also be demonstrated by following the changes of others NMR parameters such as diffusion coefficient or relaxation times. The main difference with the chemical shift method is that macromolecule with high molecular weights and with no labeling can be studied as the resonances of the ligand are preferentially visualized.

Differences in relaxation parameters, the transversal ($1/T1$) and the longitudinal ($1/T2$) relaxation rates, can be used to detect complex formation. Relaxation times characterize the dynamic movements of the molecules. A small molecule that tumbles rapidly in solution has a long relaxation time while a macromolecule has a shorter relaxation time since it tumbles more slowly. Thus, the complex formation will lead to a decrease in the relaxation times [22,23]. As in the chemical shift method, the relaxation parameter is observed in the spectrum of the ligand alone and compared to the spectrum of the complexed ligand and the K_D determination is calculated using NMR titration experiments.

As relaxation parameters, changes of the diffusion rate can be used to detect ligand interaction. Diffusion NMR method, or diffused-edited NMR, also known as affinity NMR in the drug design domain, is based on the diffusion coefficient of the ligand and the macromolecule [24]. A small molecule—free in solution—diffuses more rapidly than a large molecule such as a protein. If this small molecule interacts with the macromolecule, it will adopt the dynamic characteristics of the macromolecule and, then, its diffusion coefficient will decrease in comparison to the one of the free ligand. Diffusion NMR methods are based on the fact that translational diffusion depends inversely on the size of the molecule (Stokes–Einstein equation). Measuring the diffusion coefficient by NMR is based on pulsed field gradient impulsions [25–28]. Each molecule is firstly "coded" in its spatial position using a magnetic field gradient pulse, the "coding" gradient, the molecule then diffuses freely during the diffusion time, Δ, and after the application of a second field gradient, the diffusion information is obtained through signal attenuation. Two types of diffusion NMR experiments can be used. In the 1D NMR experiment, the diffusion parameters are chosen so as to suppress resonances of ligand which do not bind to the macromolecule (diffusion filter) and only resonances of bound ligands are observed [29]. The second experiment is a pseudo-2D NMR experiment (DOSY NMR) leading to spectra in which molecules are separated according to their diffusion coefficient. In the rapid exchange regime, the observed diffusion coefficient, D_{obs}, of the ligand is a time-weighted average of diffusion coefficients of free and bound ligands. By assuming that the diffusion constants of the complex and the free protein are the same, the fraction of the bound ligands can be obtained and the dissociation constant calculated.

Several other methods using NMR experiments are based on magnetization transfer from the macromolecule to the ligand (and inverse) such as transfer NOE [14], saturation transfer [30], and (inverse) NOE pumping [31,32]. More particularly, NOE pumping method combines a diffusion experiment and a classic NOE experiment. In the first step, a diffusion filter allows the suppression of all the NMR ligand signals while conserving the macromolecule signals. During this time, macromolecule magnetization is transferred to the bound ligands. In other words, only binding ligands adopt the magnetic properties of the macromolecule and this information is then detected during the NOE experiment. No signal is observed for free ligand molecules. Thus, using a mixture of different ligands, it is possible to differentiate between bound and free ligands. The first NOE pumping experiment has been applied to ligand–protein interactions and compared to diffusion NMR experiments [31]. The authors showed that diffusion experiments could not explain the interactions between salicylic acid and the L-ascorbic acid since the average diffusion rate (D_{obs}) is close to the diffusion rate of the free ligand. They demonstrated unambiguously the interaction using NOE pumping experiment.

Despite all the works using NMR to study ligand–macromolecule interactions, there are very few studies concerning the interactions of aroma compounds with food molecules. Two principal macromolecules have been studied to probe aroma-binding sites: wine phenolic compounds and β-lactoglobulin, a bovine whey protein. Phenolic compounds—the major components of plants—are able to complex proteins, metal ions, or aroma compounds. In wine, the polymerization degree and self-association of polyphenols and interactions of polyphenol–aroma compounds seem to have an effect on wine organoleptic properties. The β-lactoglobulin is found in various food preparations and since its structure is well established, this protein is widely used as a model in interaction studies. It is known to interact with different aroma compounds and two binding sites seem to exist (the central cavity and the external binding site), however, despite numerous studies, there is a lack of information on aroma biding site localization [2,33–35]. The investigation of the nature and strength of aroma compound–polyphenols or β-lactoglobulin interactions will allow us to better understand flavor perception in food and beverages.

Dissociation constants have been calculated for aromatic flavor and macromolecule complexes using different NMR methods.

^{1}H 1D NMR titrations of procyanidin monomers (catechin and epicatechin) have been realized using two aroma compounds—the benzaldehyde and the 3,5-dimethoxyphenol [36]. In order to investigate titration experiments, ^{1}H chemical shifts and scalar coupling constants (J) of proton rings of monomers have been previously assigned. Firstly, the authors have calculated self-association constants for each compound alone. With increasing concentration, all proton chemical shifts of polyphenol compounds were upfield shifted due to self-association. For the aroma compounds, benzaldehyde and 3,5-dimethoxyphenol were self-associated at concentrations up to saturation. Titration of phenolic compounds, kept at a constant concentration (5 mM), with increasing concentration of aroma compounds lead to an upfield shift of all the flavanol protons that it is characteristic of a rapid exchange on the NMR timescale. The observed chemical shift change, δ_{obs}, of phenolic resonance is a weighted average of the free (δ_{P}) and complex (δ_{PA}) phenolic species, and the chemical shift change, $\Delta\delta$, is defined as $\Delta\delta = \delta_{\text{P}} - \delta_{\text{obs}}$. The dissociation constant, K_{D}, can be calculated knowing $\Delta\delta$ and $\Delta\delta_{\max}$, with $\Delta\delta_{\max} = \delta_{\text{P}} - \delta_{\text{PA}}$ and assuming a 1:1 model. The benzaldehyde complex is stronger ($K_{\text{D}} = 0.0955$ M with catechin and 0.152 M with epicatechin) than the 3,5-dimethoxyphenol complex ($K_{\text{D}} = 0.194$ M with catechin and 0.169 M with epicatechin) whatever the polyphenol but these two aroma compounds have a different affinity for the two phenolic compounds. The increase of the scalar coupling for H_2 and H_3 protons of catechine in the presence of aroma compound also reveals a conformational change of the pyran ring. Moreover, the K_{D} values are higher than the self-association constants of the polyphenol monomers. These titrations were unsuccessful with limonene, isoamyl acetate, and ethylhexanoate due to their low solubility.

The inverse NMR titration, i.e. fixed aroma concentration in the presence of increasing concentration of catechine, has been carried out with all five aroma compounds. The binding affinity order of benzaldehyde and 3,5-dimethoxyphenol is similar to that in the first titration, but K_{D} values are two times larger. The authors underline the limitations of the method, however self-association of macromolecules has not been considered in this experiment. These NMR results suggest hydrophobic interactions between flavor and the polyphenol compounds.

In the same way, Jung *et al.* have investigated the binding of 2-methylpyrazine, vanillin, and ethylbenzoate with two phenolic compounds, gallic acid, and naringin [37]. Titrations were carried out at three temperatures with phenol/aroma molar ratio of 1:1, 1:2, and 2:1. Strong upfield shifts of specific resonances of phenolic and aroma compounds were observed for gallic acid with vanillin and 2-methylpyrazine whereas small chemical shift changes were observed in the presence of ethylbenzoate. Chemical shift changes are smaller with naringin than with gallic acid whatever the aroma concentration. The concentration equilibrium constant, K_{a}, for each complex was determined using NOESY titration experiments assuming a 1:1 stoichiometry and the thermodynamic parameters were calculated. As the temperature increases, K_{a} decreases for all the aroma compounds due to an increase of the kinetic energy of the molecules although the effect is greater for vanillin ($K_{\text{a}} = 51$ and 17 M^{-1} for vanillin and $K_{\text{a}} = 14$ and 12 M^{-1} for ethyl butyrate at 25 and 60 M^{-1}, respectively). Enthalpy and entropy values suggest that ethylbenzoate interacts more weakly than vanillin and 2-methylpyrazine.

The binding of aroma compound to proteins—bovine serum albumin (BSA) or β-lactoglobulin—has been studied by Jung *et al.* by 1D diffusion NMR method [38,39]. In the first study, diffusion coefficients of four aliphatic ketones (2-heptanone, 2-octanone, 2-nonanone, and 5-nonanone) have been measured alone in a phosphate buffer or in the presence of BSA with increasing concentrations of aroma compounds (molar ratio of 0.02 to 0.18) at 25 °C. For each aroma compound, the apparent diffusion coefficient strongly decreases after binding to protein and this decrease is more pronounced with the increase of BSA/aroma molar ratio. For example, the 2-nonanone diffuses at 630 μm^2/s in buffer solution while it diffuses at 140 μm^2/s in the presence of the protein. The association constant, K_a, the number of binding sites, and the free energy of association (ΔG) are measured from the experimental data of the apparent diffusion coefficient (D_{obs}). The association constant decreases as the aroma chain length increases (323 M^{-1} for the 2-heptanone to 833 M^{-1} for the 2-nonanone) as well as an increase in ΔG values for each additional methyl group suggests that there are hydrophobic interactions. Six to eight binding sites have been found for these ketones.

Jung *et al.* [38] have used the NOE pumping method to investigate interactions of aroma compounds to proteins or tannin extracts. From a mixture of three aroma compounds (benzaldehyde, vanillin, and 2-phenylethanol), specific interactions of benzaldehyde and vanillin to BSA have been shown using the same method. Moreover, the binding of ethylbenzoate to polyphenols of tannin extracts has been showed using this method. In another study, the interactions of α- and β-ionone to β-lactoglobulin at ligand–protein ratio of 0.25 to 5 and at different pH values were investigated [39]. The authors showed that binding affinities of two ionones are higher at pH 9 with a binding affinity of β-ionone higher than that of α-ionone. However, large aroma concentrations were used in this study (up to 10 mM) which could affect protein conformation and due to their low solubility, some aroma compounds could not be studied. And with this method, no information on binding site localization was obtained.

In order to determine the binding strength and how aroma compounds interact with polyphenols compounds, Jung *et al.* have realized NOESY (and ROESY) spectra in which the coupling between the hydroxyl groups of polyphenol and adjacent protons can be observed [37]. NOE experiments reveal interaction between protons of vanillin and 2-methylpyrazine and protons of hydroxyl and carboxyl groups of gallic acid. No intermolecular interactions for ethyl butyrate–gallic acid complexes and for aroma compounds–naringin were shown.

Lübke *et al.* have investigated the binding localization of aroma compounds, β-ionone, and γ-decalactone, to β-lactoglobulin using ^1H–^1H 2D NMR spectroscopy [40]. Experiments have been carried out in conditions for which the protein is in a monomeric state. In order to show these interactions, the authors compared the amino acid chemical shifts of 2D TOCSY and NOESY spectra of the protein alone with one of the protein after the addition of the aroma compound. The authors demonstrated the binding of the two aromas on the protein based on changes of cross-peak chemical shifts and, knowing the complete assignment of protein resonances they determined which amino acids were implicated in this interaction [41]. For the protein–γ-decalactone complex, all the amino acids located on the β-barrel which forms the wall of the central cavity are affected whereas for the protein–β-ionone complex, fewer amino acids are perturbed that concern different amino acids and region on the protein. Two cross-peaks are visible after the addition of aroma compound to the protein solution which seem to correspond to the aldehyde proton for the γ-decalactone and to the olefinic protons for the β-ionone. However, their exact assignment cannot be defined due to the crowed region of the protein resonances and further work is in progress.

Recently, DOSY NMR experiments have been performed on two aroma compounds—ethyl butyrate and linalool—in matrices containing a polysaccharide (1%, w/w), *iota*-carrageenan widely used in food as a texturing agent, with different amounts of salt at 30 °C [42]. Using this method, the authors showed that, based on their self-diffusion coefficients, aroma resonances are well distinguished to the polysaccharide peaks and they can directly measure the diffusion coefficients of the aroma compounds at concentrations used in food. By comparing the spectra of the aroma compounds alone and aroma compounds in different matrices, the authors showed that no interactions occurred between ethyl butyrate and the polysaccharide molecules but that sodium ions have an indirect influence on aroma diffusion, probably by acting on the matrix structure. At 30 °C, ethyl butyrate diffuses at 871 $\mu m^2/s$ into the matrix with 0.1% NaCl and at 1004 $\mu m^2/s$ in matrix with 0.5% NaCl. In matrix with 0.1% NaCl, linalool diffuses slightly slower than ethyl butyrate ($D = 669\ \mu m^2/s$). Other experiments are in progress to understand how the nature of the aroma compound and the salt content affect aroma diffusion. DOSY NMR is a powerful method as it can be applied to complex food matrices without labeling and with low concentrations of aroma compounds, however no information on binding site is available.

NMR spectroscopy is a powerful technique used to study weak interactions of small ligand–macromolecule (∼mM) and information on binding site localization and on dynamic parameters (relaxation times, diffusion coefficients) at atomic level. Using changes in NMR parameters, the stoichiometry of the complex, association or dissociation constant values, and enthalpic parameters can be calculated. All this information can be obtained for complexes in their natural environment without degradation or probe addition. Depending on the type of NMR method used, macromolecule or ligand resonances are observed. Firstly, 2D NMR experiments and isotope labeling for proteins with high molecular weights are often necessary, principally to determine binding sites. Methods based on the ligand visualization are suitable for non-labeled proteins with unlimited molecular weights. On the other hand, an excess in ligand concentration can be a main limitation for studying some aroma compounds due to their low solubility. This remark is available for all NMR titrations when concentration of the ligand is increased. Compared to the other techniques, the main advantage of NMR spectroscopy is that we can study molecules in natural conditions (pH, buffer, temperature, etc.) and its gives information on both the dissociation constant and the binding site localization. Moreover, the diversity and the improvement of the NMR methods can allow different approaches in studying ligand–macromolecule interactions.

References

1. Guichard E. Food Rev. Int. 2002;18:49.
2. Reiners J, Nicklaus S, Guichard E. Lait 2000;80:347.
3. Arvisenet G, Le Bail P, Voilley A, Cayot N. J. Agric. Food Chem. 2002;50:7088.
4. Jouenne E, Crouzet J. J. Agric. Food Chem. 2000;48:5396.
5. Lubbers S, Landy P, Voilley A. Food Technol. 1998;52:68.
6. Muresan S, van der Bent A, de Wolf FA. J. Agric. Food Chem. 2001;49:2609.
7. Le Thanh M, Goubet I, Le Quere JL, Voilley A. J. Am. Oil Chem. Soc. 1998;75:441.
8. Narayan M, Berliner LJ. Biochemistry 1997;36:1906.
9. Frapin D, Dufour E, Haertle T. J. Prot. Chem. 1993;12: 443.
10. Pellecchia M, Meininger D, Dong Q, Chang E, Jack R, Sem DS. J. Biomol. NMR 2002;22:165.
11. Zuiderweg ERP. Biochemistry 2002;41:1.
12. Stockman B, Dalvit C. Prog. Nucl. Magn. Spectrosc. 2002;41:187.
13. Hajduk PJ, Meadows RP, Fesik SW, Q. Rev. Biophys. 1999;32:211.
14. Lian LY, Barsukov IL, Sutcliffe MJ, Sze KH, Roberts GCK. Methods Enzymol. 1994;239:657.
15. Williamson MP, Kikuchi J, Asakura T. J. Mol. Biol. 1995;247:541.
16. Diercks T, Coles M, Kessler H. Curr. Opin. Chem. Biol. 2001;5:285.
17. Roberts GCK. Curr. Opin. Biotechnol. 1999;10:42.
18. Fielding L. Curr. Top. Med. Chem. 2003;3:39.
19. Wider G. BioTechniques 2000;29:1278.
20. Robillard KA, Wishnia A. Biochemistry 1972;11:3841.
21. Scheuring J, Fischer M, Cushman M, Lee J, Bacher A, Oschkinat H. Biochemistry 1996;35:9637.
22. Cui YF, Bai GY, Li CG, Ye CH, Liu ML. J. Pharm. Biomed. Anal. 2003;34:247.
23. Cui YF, Bai GY, Li CG, Ye CH, Liu ML. J. Pharm. Biomed. Anal. 2004;34:247.
24. Lucas LH, Larive CK. Concepts Magn. Reson. 2004;20A:24.
25. Antalek B. Concepts Magn. Reson. 2002;14:225.
26. Price WS, Elwinger F, Vigouroux C, Stilbs P. Magn. Reson. Chem. 2002;40:391.
27. Price WS. Concepts Magn. Reson. 1997;9:299.
28. Stilbs P. Prog. Nucl. Magn. Reson. Spectrosc. 1987;19:1.
29. Lin M, Shapiro MJ, Wareing JR. J. Am. Chem. Soc. 1997;119:5249.
30. Mayer M, Meyer B. Angew. Chem. Int. Ed. 1999;38:1784.
31. Chen A, Shapiro MJ. J. Am. Chem. Soc. 1998;120:10258.
32. Chen A, Shapiro MJ. J. Am. Chem. Soc. 2000;122:414.
33. Sawyer L, Kontopidis G. Biochim. Biophys. Acta 2000;1482:136.
34. Kontopidis G, Holt C, Sawyer L. J. Mol. Biol. 2002;318:1043.
35. Guichard E, Langourieux S. Food Chem. 2000;71:301.
36. Dufour C, Bayonove CL. J. Agric. Food Chem. 1999;47:678.
37. Jung DM, de Ropp JS, Ebeler SE. J. Agric. Food Chem. 2000;48:407.
38. Jung DM, de Ropp JS, Ebeler SE. J. Agric. Food Chem. 2002;50:4262.
39. Jung DM, Ebeler SE. J. Agric. Food Chem. 2003;51:1988.
40. Lübke M, Guichard E, Tromelin A, Le Quéré J-L. J. Agric. Food Chem. 2002;50:7094.
41. Uhrinova S, Uhrin D, Denton H, Smith M, Sawyer L, Barlow PN. J. Biomol. NMR 1998;12:89.
42. Gostan T, Moreau C, Juteau A, Guichard E, Delsuc M-A. Magn. Reson. Chem. 2004;42:496.

High-Resolution Nuclear Magnetic Resonance Spectroscopy of Fruit Juices

Ana M. Gil and Iola F. Duarte
Department of Chemistry, CICECO, University of Aveiro, 3810-193 Aveiro, Portugal

High-resolution nuclear magnetic resonance (NMR) spectroscopy has increasingly been used to provide direct and comprehensive compositional information on food complex mixtures. The ability of ^{1}H NMR to detect a wide type of compounds simultaneously and non-invasively makes it an important potential tool for the quality control of fruit juices. Such approach is distinct from the well-established Site-specific Nuclear Isotope Fractionation (SNIF)-NMR method which usually involves ^{2}H observation for the measurement of isotopic ratios and correlation with metabolite origins; this subject will not be described here since it justifies in itself a separate entry in this handbook. Furthermore, this entry will mostly deal with accounts of direct NMR analysis of whole juices, rather than of juice extracts, unless otherwise specified.

One of the earliest reports on NMR of fruit juices describes the characterisation of orange juice and apple juice using a water suppression method based on the selective effects of a paramagnetic agent on the transverse relaxation time (T_2) of water [1]. This resulted in spin-echo 270 MHz ^{1}H NMR spectra of improved sensitivity and resolution of solute resonances otherwise obscured by water. Ten years after this report, the enormous advances in NMR technology and software, leading to high magnetic field instruments and improved pulse sequences, have enabled high levels of water signal suppression and large dynamic ranges to be achieved. These improvements were first applied to the analysis of a selection of fruit juices (grape, apple, pineapple, grapefruit, and orange), at a field strength of 600 MHz, for which a wide range of compounds on the order of micromoles per millilitre were observed, with acquisition times of 7–14 min [2]. The qualitative analysis of fruit juices by high-resolution 1D and 2D NMR has, since then, benefited immensely from the available high-field NMR instrumentation ($>$500 MHz) [3] enabling comprehensive compositional information to be gathered for grape juice [2,4], apple juice [2,5], mango juice [6], orange juice [2,7], and tomato juice [8,9]. Figure 1 shows high-resolution 500 MHz ^{1}H NMR spectra of apple juice and grape juice, whereas Figure 2 shows an expansion of the ^{1}H-^{13}C heteronuclear single-quantum coherence (HSQC) spectrum of a Red Setter tomato juice. Due to the continuous need to detect low abundance compounds, often in crowded spectral, improvements in the qualitative analysis of juices by NMR have become increasingly necessary. Diffusion Ordered SpectroscopY (DOSY) has been explored in tomato juice (Figure 3) [9], apple juice and grape juice [10] as a potential tool to assign compounds with basis on their diffusivity values, in addition to NMR parameters. This method was found to be of value when identifying compounds in less overlapped spectral regions, the diffusivity information loosing resolution in the most crowded regions such as the carbohydrate region in juices. Hyphenated NMR involves the tandem use of NMR with liquid chromatography (LC) and mass spectrometry (MS), in the forms of LC-NMR or LC-NMR/MS. These methods achieve an extreme simplification of the full 1D NMR spectra as a result of chromatographic separation of compounds at the first stage of the experiment. Figure 4 shows an on-flow record obtained for grape juice, under conditions suitable for the analysis of aromatic compounds [4]. The lines shown correspond to spectra of single compounds or simple mixtures. The spread of NMR signals in the aromatic region as a function of retention time clearly shows the extension of spectral simplification achieved. In the case of grape juice, LC-NMR/MS enabled several cinnamic acids and their derivatives to be identified for the first time by direct analysis of the juice. The use of improved methods for qualitative analysis of fruit juices may, naturally, be explored with numerous aims in mind, including the study of biochemical changes with ripening [5,6] or with storage [5], detection of adulteration or contamination. However, the practical use of NMR in particular towards the latter applications necessarily involves vast numbers of samples and this brought about the tandem use of NMR with chemometrics. The potential of NMR for the authentication of orange juices was explored using 400 MHz 1D ^{1}H NMR together with Principal Component Analysis (PCA) and discriminant analysis [11]. In this way, authentic and non-authentic samples could be distinguished with basis on their NMR spectra, taking into account parallel measurements by alternative analytical methods [high-pressure liquid chromatography (HPLC) and atomic absorption spectroscopy]. As a result,

Graham A. Webb (ed.), Modern Magnetic Resonance, 1617–1621.
© 2008 *Springer.*

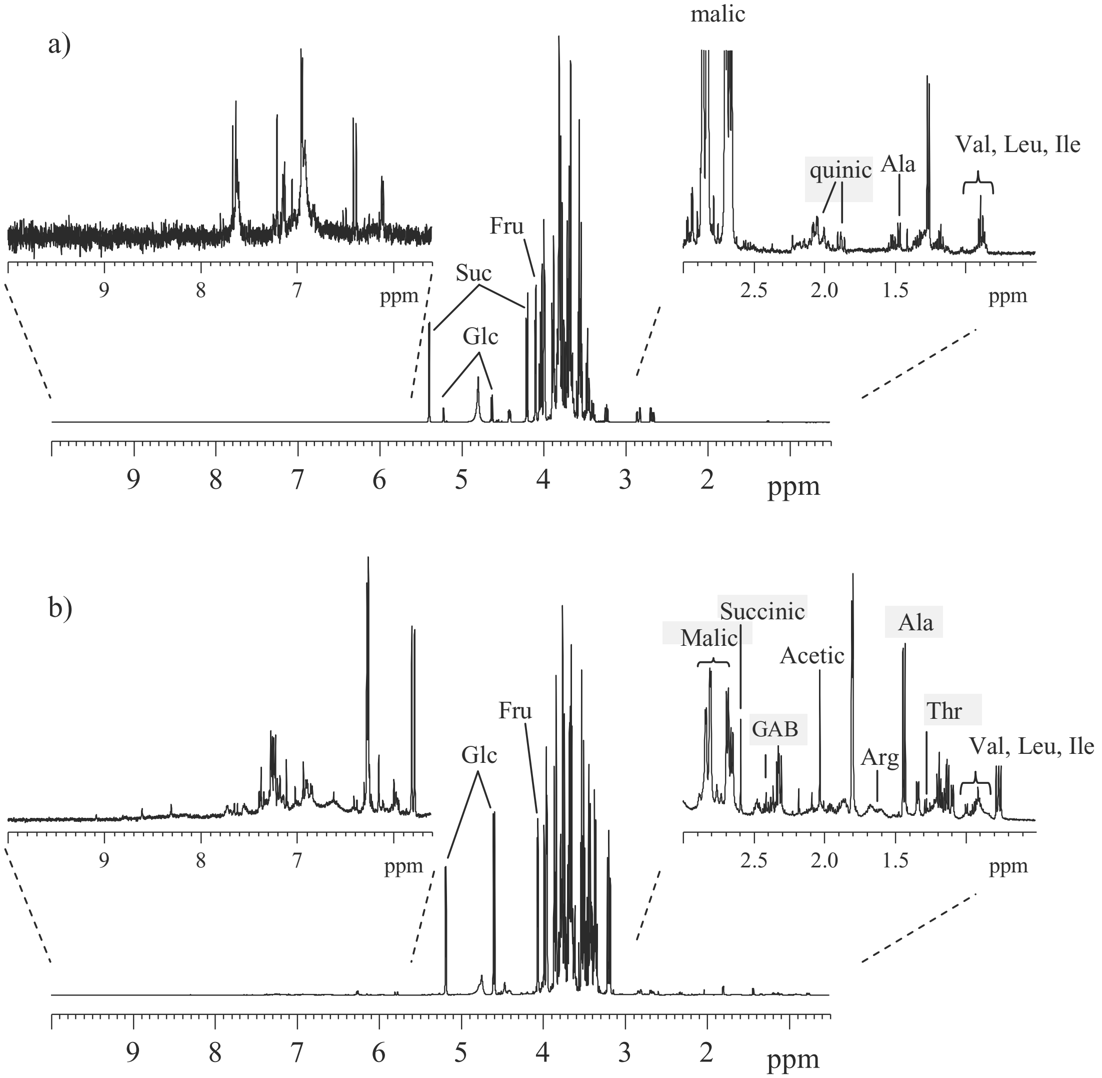

Fig. 1. High-resolution ^{1}H NMR spectra of (a) apple juice and (b) grape juice samples. Vertical expansions are shown for aliphatic and aromatic regions and some assignments are indicated. Reprinted with permission from Ref. [10]. © 2004 Elsevier.

additions of sucrose, beet medium invert sugar or sodium benzoate could be detected, as well as other deviations from authenticity requirements. The problem of orange juice adulteration with pulp wash is, at present, a pressing one in the fruit juice industry and this was addressed using PCA and discriminant analysis of ^{1}H NMR spectra of more than 300 orange and pulp wash juices [7]. It was shown that dimethylproline plays a key role in discriminating between the two sample types, with higher levels in pulp wash. In addition, at least 21 more peaks were identified in the spectra as potential markers of this type of adulteration. An additional study aimed at distinguishing apple juices of different varieties (Spartan, Bramley, and Russet) using PCA and discriminant analysis of their 500 and 600 MHz ^{1}H NMR spectra [12]. Samples were successfully separated in terms of variety, through the analysis of different subregions of the spectra. Different levels of malic acid and of sucrose were found

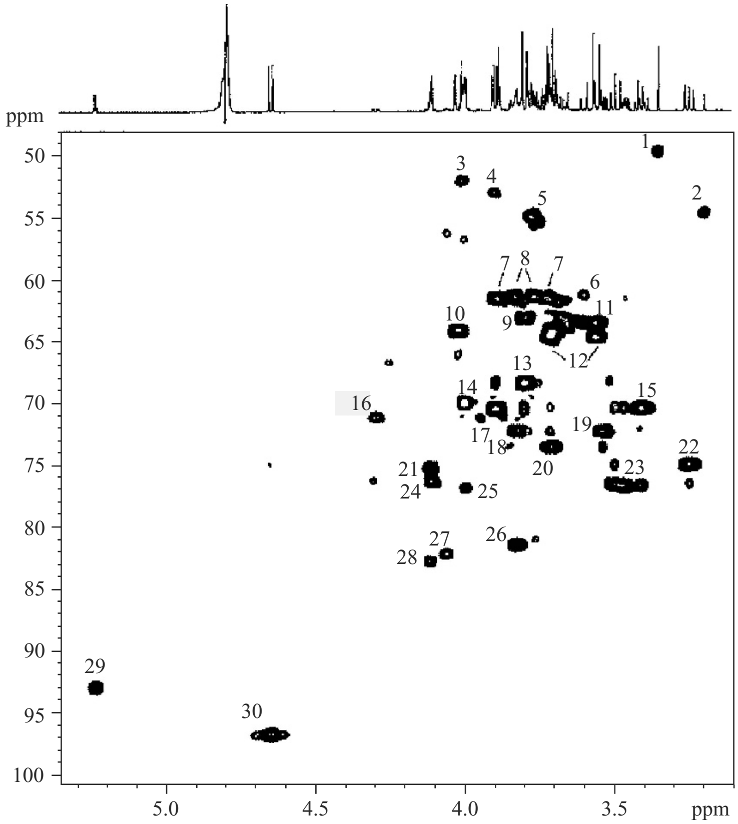

Fig. 2. Expansion of carbohydrates region of ^{1}H-^{13}C HSQC spectrum of a Red Setter tomato juice. Key: α-Glc, α-D-glucose; β-Glc, β-D-glucose; α-FF, α-D-fructofuranose; β-FF, β-D-fructofuranose; β-FP, β-D-fructopyranose; **1**, CH$_3$ of methanol; **2**, N(CH$_3$)$_3$ choline; **3**, α-CH asparagine; **4**, α-CH aspartate; **5**, α-CH glutamine and glutamate; **6**, α-CH threonine; **7**, C6 β-glc; **8**, C6 α-Glc; **9**, C6 β-FF; **10**, C6 β-FP; **11**, C1 β-FF; **12**, C1 β-FP; **13**, C3 β-FP; **14**, C5 β-FP; **15**, C4 α- and β-Glc; **16**, α-CH malate; **17**, C4, β-FP; **18**, C5 α-Glc; **19**, C2 α-Glc; **20**, C3 α-Glc; **21**, C4 β-FF; **22**, C2 β-Glc; **23**, C3 and C5 β-Glc; **24**, C3 β-FF; **25**, C4 α-FF; **26**, C5 β-FF; **27**, 5 α-FF; **28**, C3 α-FF; **29**, C1 α-Glc; **30**, C1 β-Glc. Reprinted with permission from Ref. [9]. © 2003 Wiley.

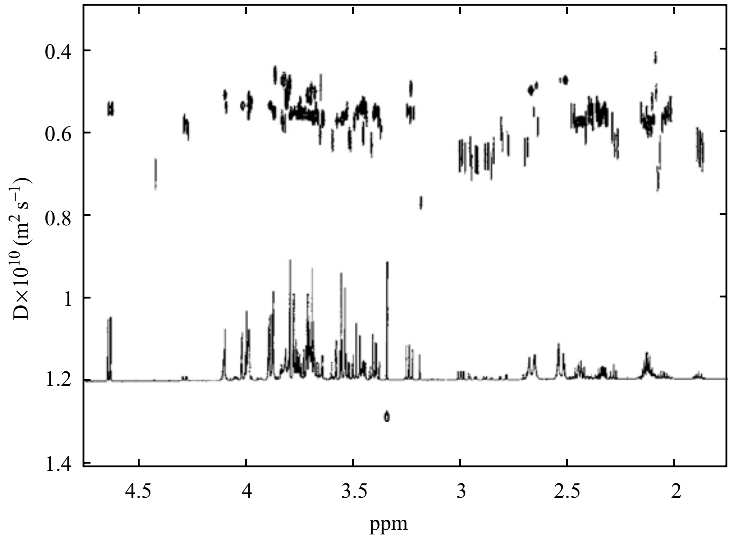

Fig. 3. DOSY spectrum of Red Setter tomato juice. Note that the error in the determination of diffusion coefficients was more substantial in the case of weaker resonances, which show spots stretched out along the f_1 direction in the DOSY map. Reprinted with permission from Ref. [9]. © 2003 Wiley.

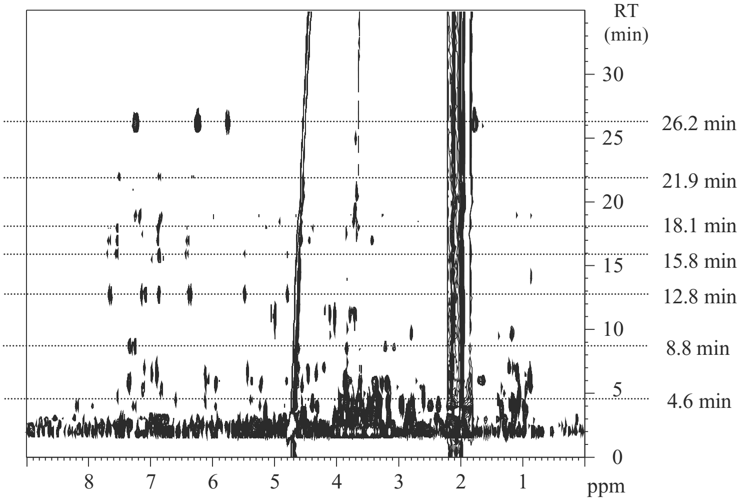

Fig. 4. On-flow NMR chromatogram obtained for a grape juice sample (flow rate 1.00 ml/min; injection volume 500 µl). Reproduced with permission from Ref. [4]. © 2003 Elsevier.

to be important discriminating variables, as well as some variations in minor constituents.

The potential of NMR to quantify and identify a large number of compounds makes it a leading technique in the emerging area of metabolomic studies. Within this area, a matter of present and increasing interest is the safety testing of genetically modified organisms (GMO) and their food derivatives. The NMR detection of possible unintended effects following a genetic modification has been significantly explored for tomato [8,13–15], a major transgenic crop. Such studies have involved mostly the analysis of tomato extracts and the methods used comprise combination of ^{1}H NMR and statistics [8,13,14] as well as off-line combination of LC and NMR[13,14]. The methodology proposed in ref. [13] and [14] is shown to enable the comparison of compositional alterations in a novel tomato crop with respect to related non-transgenic reference lines. The authors point out, however, that such differences must be statistically demonstrated to be significant compared to those arising from natural genetic and/or physiological variations [14]. The compositional effects of up-regulating flavonoid biosynthesis in tomato (*Lycopersicon esculentun*), in order to enhance its antioxidant capacity, was specifically investigated [8]. ^{1}H NMR of tomato extracts, in tandem with multivariate and univariate methods, was shown to distinguish between modified and non-modified tomatoes, not only with basis on the expected flavonoid increases but also on the levels of, at least, 15 additional compounds. Again, the authors point out that, although meaningful, such changes may fall into the same order of magnitude as natural variations observed in a field-grown crop. Further work along similar lines describes the application of ^{1}H NMR to the detection and quantification of metabolites related to the genetic origins of strawberry fruit quality and to tomato transformants overexpressing hexokinase [15]. In this study, absolute quantification of metabolites was performed by signal integration, with a synthesised electronic reference signal and validated by enzymatic or HPLC measurements.

Absolute quantitation by NMR usually involves signal integration, which is often not a straightforward subject due to extensive signal overlap and to possible intercomponent interactions that may affect visible signal areas. In spite of these difficulties, useful methods have been developed recently for the absolute quantitation of chlorogenic acid and of (-)-epicatechin in cider apple juices by NMR [16,17]. In both cases, 1,3,5-benzenetricarboxylic acid was added to the juice sample as an internal standard, allowing successful quantification of the selected metabolites by signal integration.

References

1. Eads TM, Bryant RG. J. Agric. Food Chem. 1986;34(5):834.
2. Belton PS, Delgadillo I, Holmes E, Nicholls A, Nicholson JK, Spraul M. J. Agric. Food Chem. 1996;44(6):1483.
3. Belton PS, Delgadillo I, Gil AM. Semin. Food Anal. 1998;3(3):223.
4. Gil AM, Duarte IF, Godejohann M, Braumann U, Maraschin M, Spraul M. Anal. Chim. Acta 2003;488(1):35.
5. Belton PS, Delgadillo I, Gil AM, Roma P, Casuscelli F, Colquhoun IJ, Dennis MJ, Spraul M. Magn. Reson. Chem. 1997;35:S52.
6. Gil AM AM, Duarte IF, Delgadillo I, Colquhoun IJ, Casuscelli F, Humpfer E, Spraul M. J. Agric. Food Chem. 2000;48(5):1524.
7. Le Gall G, Puaud M, Colquhoun IJ, J. Agric. Food Chem. 2001;49(2):580.

8. Le Gall G, Colquhoun IJ, Davis AL, Collins GJ, Verhoeyen ME. J. Agric. Food Chem. 2003;51(9):2447.
9. Sobolev AP, Segre A, Lamanna R. Magn. Reson. Chem. 2003;41(4):237.
10. Gil AM, Duarte I, Cabrita E, Goodfellow BJ, Spraul M, Kerssebaum R. Anal. Chim. Acta 2004;506(2):215.
11. Vogels JTWE, Terwel L, Tas AC, van den Berg F, Dukel F, van der Greef J. J. Agric. Food Chem. 1996;44(1): 175.
12. Belton PS, Colquhoun IJ, Kemsley EK, Delgadillo I, Roma P, Dennis MJ, Sharman M, Holmes E, Nicholson JK, Spraul M. Food Chem. 1998;61(1–2):207.
13. Lommen A, Weseman JM, Smith GO, Noteborn HPJM. Biodegradation 1998;9(6):513.
14. Noteborn HPJM, Lommen A, van der Jagt RC, Weseman JM. J. Biotechnol. 2000;77(1):103.
15. Moing A, Maucourt M, Renaud C, Gaudillere M, Brouquisse R, Lebouteiller B, Gousset-Dupont A, Vidal J, Granot D, Denoyes-Rothan B, Lerceteau-Kohler E, Rolin D. Funct. Plant. Biol. 2004;31(9):889.
16. Berregi I, Santos JI, del Campo G, Miranda JI, Aizpurua JM. Anal.Chim. Acta. 2003;486(2):269.
17. Berregi I, Santos JI, del Campo G, Miranda JI, Talanta 2003;61(2):139.

High-Resolution NMR Spectroscopy in Human Metabolism and Metabonomics

Huiru Tang[1,2] and Yulan Wang[3]

[1]*School of Chemical Science, Shaanxi University of Science and Technology, Xianyang, Shaanxi, P. R. China;*
[2]*State Key Laboratory of Magnetic Resonance and Molecular and Atomic Physics, Wuhan Institute of Physics and Mathematics, the Chinese Academy of Sciences, Wuhan 430071, P.R. China; and*
[3]*Biological Chemistry Section, Biomedical Sciences Division, Imperial College London, South Kensington, London SW7 2AZ, UK*

Introduction

Analysis of metabolites has always been an essential component in life science research since metabolites are the downstream and even endpoint products of a given biological process, thus carrying rich information about the process [1–8]. Whilst genes and proteins set the stage for what is likely to happen [1–8], metabolites indicate what has actually happened in the levels of proteins, transcriptions, and genes. Therefore, metabolite analyses will undoubtedly be vital to gain insights into life processes and to understand in greater depth the complexity of the whole organisms and their interactions with the environment. In the "post-genome" era, it is the total metabolite complement [3–8] (metabolome), not some parts of metabolites, that becomes the focus of attention. The changes of the metabolome, i.e., metabonomics [7], provide unique, dynamic, integrated, and holistic insights into the changes of the given biological process in metabolic level. These changes can be traced back, in turn, to the activities in the levels of proteins, transcriptions, and genes. The metabolomic studies of organisms (metabonomics or metabolomics) thus have increasingly become the inseparable part of the integrated systems biology strategy. The NMR-based metabonomics approach has become an established method and proven powerful for studying animal systems [7] by scrutinizing the changes of the metabolites in biofluids, such as blood plasma [8–12], urine [4–9,13] and cerebrospinal fluid [14–19], and biopsy tissues [9,20–26]. Since biofluids contain information about biochemistry status of human body as a whole, analysis of the metabolite compositions in biofluids provides information on the responses of human systems to the effects of the internal physiological changes and external stimuli, such as diets, drugs, and diseases. Furthermore, metabolome of tissue samples [20–24] provides information about what is happening *ex vivo* or *in situ* and sometimes can provide direct evidences *in vivo*.

Amongst biofluids, blood plasma consists of macromolecules, such as lipoproteins and immunoglobulin, and a range of low molecular weight metabolites such as amino acids, hydroxycarboxylic acids, and sugars [10–12]. In order to maintain consistency of the internal environments of human body, the content of blood plasma has to be kept reasonably stable until such homeostasis is perturbed by some "abnormal activities." Therefore, changes of the blood plasma metabolome offer a sensitive handle to monitor the changes in human physiology. On the other hand, some waste products have to be disposed for the same purpose of homeostasis and such wastes are excreted and disposed in the form of human urine. Urine contains small amount of proteins, amino acids, hydroxycarboxylic acids, considerable amount of salts, and metabolites of exogenous compounds such as those from diets and drugs [8,27]. Therefore, human urine contains information reflecting the superposition of many biochemical processes taking place in the human body. Urine analysis also provides embedded information about the functioning state of some organs such as kidneys [28], liver [29,30], and heart [31] as well. High-resolution ^{1}H NMR spectroscopy can be used to detect the signals of a wide range of low molecular weight metabolites simultaneously in the complex samples such as biofluids. These signals carry information about the identity, concentration, and interactions of metabolites in the samples. If required, the endogenous and exogenous metabolites detected in such samples can be related to the pathophysiological effects such as the state of health [31–33], dietary, and drug interventions.

Apart from analysis for human and animal samples, recently, high-resolution NMR spectroscopy have been employed to analyze food of plant origins [34–41]. Both liquid samples and tissues have been examined and metabolite resonances were assigned. Some plant extracts [42–46] were also examined for various purposes. Such concept can be easily extended to studies of the plant metabolites or metabolome.

Graham A. Webb (ed.), Modern Magnetic Resonance, 1623–1630.
© 2008 *Springer.*

Most of the metabolites are organic compounds and consist of the elements such as carbon, hydrogen, nitrogen, oxygen, and sometimes phosphorus. It is therefore conceivable that ^{1}H, ^{13}C, and ^{31}P are natural reporting probes for NMR studies of metabolism. Sometimes, ^{2}H, ^{13}C, and ^{15}N labeling are also used to provide probes with little or no background signals. ^{19}F NMR has also been used in drug metabolism studies for the similar reasons. However, high-resolution ^{1}H NMR methods are by far the most widely employed methods due to the high sensitivities and many reviews have been published already on ^{1}H NMR studies of biological samples [2–8]. Therefore, this chapter is not aimed to provide a comprehensive review of this literature. Instead, it is aimed to discuss problems related in such studies and possible solutions to them.

In almost all the biofluids and tissue samples, water is the nature's chosen solvent and accounts for more than 80% (w/w) of the whole samples. The concentration of water protons are therefore in the level of 100 M in contrast to that of the metabolites in 10^{-6}–10^{-3} M or even lower. For nuclei other than ^{1}H, NMR detection is not affected by the amount of water. For ^{1}H NMR and related correlation spectroscopy, however, such drastic difference in concentration becomes a huge dynamic range problem and water signals have to be suppressed even though in certain cases these signals also carries important information.

Water Suppression

For biological fluid samples, the ideal water suppression method should have (1) high effectiveness to suppress the water signals that are 10^{5}–10^{9} times more intense than metabolite signals, (2) high selectivity (or sharp suppression profile) to suppress the water signal without suppressing other signals close to water, and (3) high efficiency to suppress water signals within a short duration to minimize magnetization transfer with the exchangeable or interactive protons [12]. Besides, the method should be easy to be implemented in both 1D and multidimensional experiments. For the time being, the water suppression methods in use can be classified into three categories, spectral editing methods based on spin relaxation or translational diffusion properties between water and solutes, presaturation methods based on actively irradiating the water signals, and tailor-excitation methods by using the pulsed field gradient (PFG).

The relaxation- and diffusion-based methods take advantage of the difference between water and solutes in T_1, T_2, or self-diffusion rates. The T_1 and diffusion-based methods are only useful for solutes having T_1 and self-diffusion coefficients drastically different from these of water. For example, in aqueous solution of macromolecules, one can observe signals of macromolecules by the choice of an appropriate relaxation recovery time in the inversion-recovery experiment [47,48]. The gradient-HMQC/HSQC experiments [49] can also be used to saturate the water signals by repeating the (^{13}C or ^{15}N) experiment rapidly. In this case, the water signals can be saturated due to its long T_1 but can be done so only partially. The DRYCLEAN method [50] was based on the difference in diffusion coefficients between water and macromolecules by using a diffusion filter prior to detection. Whilst these methods are of some values for aqueous solution of macromolecules such as proteins, they are not useful for the biofluids (i.e. the solution of small metabolites) since the T_1 and diffusion rates of solutes and water are on the similar scale. A T_2 editing method has also been reported [51,52] and can be applied to some biofluids. This method, however, requires artificially shortening the T_2 of water by adding contaminants [51,52] to the sample, is thus invasive.

The irradiation methods are implemented by applying a secondary irradiation on resonance to the water peak. Amongst them, the simplest one is often referred to as "presaturation method," which combines a single pulse with a weak continuous wave (CW) irradiation on resonance to water signals [53] during recycle delays and necessary durations. The strength of such irradiation has to be controlled to a reasonable level to avoid heating-induced stability problems. Since the chemical shift of water is dependent on the sample temperature, the CW water suppression method requires good spectrometer stability, excellent magnetic field homogeneity and reasonable temperature controlling facilities. Generally, modern spectrometers can meet such demands. The presaturation method can be readily implemented in most pulse sequences and does not affect quantification of spectra with exception for the resonances close to water and interacting with water (via. NOE for instance).

The other variant, called 1D NOESY [54] or NOSEYPRESAT, is equivalent to the first increment of the NOESY experiment [54] (90°-t_1-90°-t_{mix}-90°-AQ-RD), where t_1 is set to about 3 μs, the mixing time, t_{mix}, to 0.1–0.15 s combined with irradiating the water resonance during both the t_{mix} and the recycle delay (RD). This method works well with systems where the exchange between water and metabolites is either slow or absent, resulting in much better suppression of the residual "hump" from the water signals [11,55]. However, unlike single-pulse version, this method is restricted to the flip angle of 90° and can only be used for quantitative work with an extremely long RD employed. Nevertheless, the FLIPSY (FLIP-angle adjustable one-dimensional NOESY) experiment [55] (θ-t_1-180-t_2-180-AQ-RD) can overcome the quantification problem by using a small flip angle ($\theta \sim$ 10–30°) and short t_1 and t_2 delays (~2 μs). It has to be noted that the water suppression efficiency is inferior to the 1D NOESY method. It is obvious that the above methods have only one suppressed region (or "null point") in the whole spectrum. These irradiation methods can be implemented on any spectrometers.

The other type of water suppression methods have been developed using PFGs in the form of so-called tailored excitation [56,57] or excitation sculpting [58] and therefore requires gradient facilities. Amongst them, WATERGATE (water suppression by gradient-tailored excitation) schemes are widely employed in the form of either three pairs [56] (W3) or five pairs [57] (W5) of symmetric pulses. The latter showed much improved (or narrower) suppression profiles [57]. However, such methods often employ lengthy pulse sequences and cause some phase distortions to multiplets with a large J couplings even with perfectly optimized spectrometers [58]. Furthermore, more than one "null points" are produced [57] and signals close to such points are attenuated. Another selective excitation sequence, WET [59–62], has also been reported, in particular for LC-NMR studies, with capability of suppressing several signals [61]. Whilst these sequences are reasonably efficient, elaborate optimization is often required posing a great hurdle for the non-specialists. On the other hand, a method called double PFG spin-echo (DPFGSE) have been reported [58] to suppress water resonance efficiently without causing any phase distortions and can be implemented in any sequences readily without elaborative optimization [58]. These gradient dependent methods require gradient facilities and often attenuate, to some extent, the broad signals such as those of lipids in plasma and tissues due to T_2 relaxation or J modulations in the spin-echo-based methods.

For all water suppression methods, the metabolite signals close to the "null points" (e.g. water resonance) will also be affected, if not suppressed completely. If these signals are essential for the purpose of studies, they can be recovered with magnetization transfer through scalar or dipolar coupling as in so-called RECUR-NMR methods [63]. RECUR-NMR methods also reduce, to some extent, the phase distortion caused by WATERGATE. From the above discussion, it becomes clear that the methods meet all criteria for an ideal method remains to be developed and in reality, the choice of water suppression method ought to be as simple as possible if the method is sufficient for the purpose of studies.

Assignments of the Metabolite Resonances

The water suppressed ^{1}H NMR spectra of biological samples, such as urine, blood plasma, and tissues, are information-rich but data complex owing to (1) large number of resonances and (2) superposition of the resonances from a multitude of different chemical entities in multiphase compartments. To make meaningful use of such spectra, the first step is often to assign as many resonances as possible. Normally, the assignments of metabolite signals rely on the positions (chemical shifts), multiplicity patterns (spin–spin coupling), and the intensity of the signals. However, extra care has to be taken when assigning the 1D ^{1}H NMR spectra since the NMR parameters can be affected by many factors such as pH, concentration, temperature, ionic strength, and interactions. To overcome the problems of resonance overlapping, 2D NMR experiments are normally employed to spread the resonances into greater space and to establish the atomic connectivity. Amongst them, ^{1}H–^{1}H 2D COSY [64], TOCSY [65], ^{1}H–^{13}C HSQC [66], HMQC [67], and HMBC [68] NMR experiments are useful for routine metabolite identification. Due to complex interactions the metabolites experiencing in the biological samples, "spiking" with the authentic compounds offers a simple but extremely useful way for unambiguous assignment.

In practice, however, the complexity of the spectra of the heterogeneous samples such as blood plasma [2–12,69] and tissues [20–23,70,71] are amplified by the presence of a large number of overlapping resonances resulting from a wide range of molecules, such as proteins, lipids, lipoproteins, and metabolites [2–12,20–23,69–73], which often have different NMR line shapes resulting from the biomolecules with a wide distribution of molecular weights and mobility. Consequently, the predominating peaks arising from the relatively high concentration molecules often obscure some substances at a low concentration. However, these low-concentration molecules can sometimes be extremely important for classifying toxicological or disease processes. For example, in blood plasma, the intense broad lipoprotein resonances often overwhelm the signals from small metabolites; in tissues, the dominant lipid resonances often obscure signals for the low-concentration metabolites. To overcome these problems, the hyphenated HPLC-NMR-MS can be employed to separate each component before spectroscopic detection. One can also use the non-invasive spectral editing methods to separate NMR signals without separating samples.

Spectral Editing in Biological NMR Spectroscopy

A number of NMR spectral editing methods have been developed based on the variation in spin relaxation [11,69], diffusion [74], and spin coupling properties. For molecules experiencing weak interactions, the diffusion rate measured as the apparent diffusion coefficients is inversely correlated with the molecular size. Therefore, larger molecules diffuse slowly whereas small ones diffuse fast (unless they are bound to macromolecules). Thus, the complex NMR spectra of biofluids can be edited by taking advantage of the differences in diffusivity (or size) of molecules. Diffusion-edited NMR spectroscopy can be implemented by inserting a "diffusion filter" to attenuate or even eliminate resonances from the fast-diffusing molecules [74–77] prior to the detection. Some 1D and 2D diffusion-edited NMR methods have been employed to aid the assignments of resonances arising from the lipoproteins [74–76] in human blood plasma.

Spin relaxation properties can also be exploited in spectral editing. For example, "relaxation-filters" can be inserted, before detection, to attenuate or eliminate the resonances selected according to their relaxation times. Such editing methods have been widely used in high-resolution NMR of biopolymers in the solid state [78–83] for many years and have proven useful. Three major spin relaxation phenomena can be encountered in high-resolution NMR of biological samples, spin–lattice relaxation characterized by T_1 and $T_{1\rho}$, and spin–spin relaxation described by T_2. Whilst the three relaxation times are identical for small molecules tumbling rapidly and isotropically, they can be different in multiphase, multicompartment systems, such as biofluids [12] and tissues [23,84].

To use T_1 editing, an inversion-recovery sequence ($180°_x$-τ_1-$90°_x$) is used to prepare spins in such a way that NMR signal intensities are dependent on the length of τ_1 relative to T_1. The 90° pulse can serve as a read-pulse in 1D experiments or the excitation pulse for the 2D experiments. One can purposefully make a choice of τ_1 to have a positive peak ($\tau_1 > T_1{*}\ln 2$), negative peak ($\tau_1 < T_1{*}\ln 2$), or no peak at all ($\tau_1 = T_1{*}\ln 2$). The T_1 editing has also been reported in 1D NMR as a method of solvent suppression [47,48]. Similarly, the magnetization can be prepared using a spin-locking sequence ($90°_x$-$\tau_{\mathrm{SP}y}$) such that resonances with different $T_{1\rho}$ can be separated by choosing an appropriate spin-lock time, τ_{SP}, and spin-lock power [12]. In the case of T_2 editing, the magnetization can be prepared using a spin-echo sequence, typically a CPMG sequence [85], [$90°_x$-(τ_{E}-$180°_y$-τ_{E})$_n$]. By choosing appropriate τ_{E} and n, the signals can be separated according to their T_2 (i.e. inverse of the line width). Generally, the broad NMR signals from macromolecules or bound small molecules are attenuated or even eliminated, leaving the sharper resonances from the mobile small molecules unaffected. The resonances having intermediate T_2 will be attenuated to an intermediate extent.

However, the T_1-, $T_{1\rho}$-, and T_2-edited 1D NMR spectra of biological samples can still be too complex [12], since NMR spectral peaks from the low concentration metabolites can still be severely overshadowed. Consequently, it is necessary to extend the relaxation-editing approach to multidimensional NMR spectra to establish atomic connectivity and to achieve resonance assignments unambiguously. Examples for T_1-, $T_{1\rho}$-, and T_2-edited 2D NMR methods have already been reported in studying blood plasma and biological tissues [12,86–90]. NMR spectra can also be edited according to the multiplicity using J-resolved spectroscopy or the nature of carbons (CH_3, CH_2, CH, or C) by using DEPT [91], INEPT [92] for ^{13}C NMR and MAXY [93–98] for ^{1}H NMR. These spectral editing techniques can be used in conjunction with most of 2D NMR sequences.

Other Useful Techniques

For most heterogeneous biological samples such as cells and tissues, ^{1}H NMR lines are broadened by residual dipolar interactions, chemical shift anisotropy and susceptibility [99,100]. With the magic angle spinning, these line-broadening effects can be eliminated and high-resolution magic-angle spinning NMR (HRMAS) [20,21,101] spectra can be obtained with similar quality to that of the solution state NMR. In addition, gradient is also available at the magic angle, allowing the gradient-enhanced NMR spectroscopy to be carried out effectively as well. However, automation in terms of shimming and sample exchanges is still in their infancy even though some automatic sample exchangers are commercially available. Therefore, throughput of the HRMAS NMR remains low (two to three samples per hour).

In contrast, high throughput facilities for solution state NMR are well developed and can be in the forms of either flow –injection [102] or automatic sample exchanger. Both methods can screen up to 400 samples per day with options of sample recovery. For flow NMR, the samples are handled with a liquid handler and a sample transfer system together with a flow NMR probe. The whole process can be automatically executed including sample preparation, delivering samples to the detection cells, matching and tuning of probe, pulse length calibration, shimming, data acquisition, and processing. The commercial flow probes include normal 5 mm probe which can handle 300–500 μl samples and micro-flow probes such as micro-capillary probes [103,104] that can handle samples with a volume as small as 3 μl. Automatic sample exchangers can also be used to handle samples in NMR tubes and, in this case, an exchanger, a lot of spinners, and NMR tubes are required, even though there is no need for a liquid handler, sample transfer systems, and Flow NMR probes.

NMR techniques are intrinsically insensitive and any attempts to improve the detection sensitivity have to consider ways to reduce noises (or increase signal-to-noise ratio). There are two types of "noises" in NMR spectroscopy, electronic noises, and chemical noises [8]. The chemical noises arise from the signal overlapping in particular in complex mixtures. To reduce the chemical noises, NMR has to be done with higher magnetic field to increase the chemical shift dispersion or with reduced complexity, ideally, in the form of a single compound by using separation techniques. Such separation can be done either separately or by hyphenating with NMR. The possible hyphenation between separation techniques and NMR detection now includes HPLC-NMR [105,106], HPLC-NMR-MS [107–109], HPLC-SPE-NMR-MS [110], CE-NMR or CEC-NMR [111,112], and SFC-NMR [113–115]. In these hyphenations, the purified fractions (peaks) from HPLC, capillary electrophoresis (CE), capillary electrochromatography (CEC), and supercritical fluid chromatography (SFC) can be measured with NMR or/and MS to obtain structural information. In LC-NMR-MS, the whole chromatogram can be detected in on-flow, direct stop-flow, or timed slice modes. One can also store interesting chromatographic peaks into separate loops and then carry out NMR/MS studies by transferring the loop content. Similarly, one also can store these peaks on a solid-phase extraction (SPE) cartridge and then elude the cartridges individually to determine the molecular characteristics of the peaks [110]. The SPE method offers higher detection sensitivity than loops due to much more compact peak elution and a great opportunity to trap the same peak several times to increase concentration of solutes, increasing detection sensitivity drastically. However, appropriate hardware is required and concentration of the solvent impurities will also be increased with multiple trapping. Hyphenated SFC and NMR and CE-NMR are less common but have enormous potentials for future applications.

On the other hand, in order to reduce the electronic noises, one has to reduce the temperature at which the detection electronic devices work. This involves cooling the detection electronics down to about 20K to increase the sensitivity for about fourfolds and such facilities are now available from almost all the major manufacturers. The latest cryogenic probe can also be used as a flow probe (for flow-injection and LC-NMR work) as well as a conventional tube probe. With a cryogenic probe on a moderate (say, 600 MHz) spectrometer, the detection limit can go down to the nanogram level. However, for the cryogenic probes, the radiation damping remains a massive problem especially when dealing with biological samples.

NMR-Based Metabonomics Techniques

The advantages of NMR spectroscopy include (1) detecting all the NMR visible molecules simultaneously, non-invasively, and non-destructively, (2) providing rich molecular information such as structure, dynamics, interactions, pH, and concentrations, and (3) making it possible to do *in vivo*, *in vitro*,*ex vivo*, and *in situ* studies. The molecular information so obtained includes that from both the endogenous and exogenous metabolites related to the human metabolisms. However, thousands of resonance signals so generated, e.g. from ^{1}H NMR of a urine sample, present a challenge to data interpretation. Such challenge is amplified even further by the requirements of multiple parallel sampling. For example, multiple samples are required for both controls and non-control samples in order to obtain statistically meaningful results. In such cases, visualizations of the spectra by conventional techniques (e.g. human naked eyes) are no longer adequate or possible at all for the data analysis. The large density of the NMR spectral data, nevertheless, can be regarded as fingerprints of the biological systems. Then multivariate data analysis can be readily applied on the NMR data to reduce the complexity and to visualize patterns inherent in the data. Such combination provided the basic methodology for the NMR-based metabonomics/metabolomics studies. In fact, the combination of NMR with the multivariate statistical data analysis, such as principal components analysis-and partial least square-based methods [30,116,117], has been extensively applied to study the human inborn errors of metabolism [118,119], the biochemical consequences of genetic strain differences in mice [120,121], and the responses of the biological systems to drugs [23,122] or other xenobiotics [123].

NMR detection strategies for studying the dietary effects on human metabolism are similar to that for drug effects and some results have already been reported using NMR-based metabonomics. For example, an elevation in urinal excretion of TMAO [124] is reported for subjects who consumed fish meals. Zuppi *et al.* [125] reported that the level of lipids and carbohydrates in diet profoundly affects the levels of urinary metabolites such as alanine, lactate, glycine, and hippuric acid. In another case, after 6 weeks of Atkins' diet containing high lipid, protein but no carbohydrate, a male subject showed elevation of citrate and ketobodies (e.g. β-hydroxybutyrate, acetoacetate) and depletion of alanine in his blood plasma compared to the same subject with normal diet. Furthermore, the level of the low-density lipoproteins (or bad cholesterols) was also elevated after Atkins's diet (Y.L. Wang, unpublished results).

The NMR-based metabonomics methods have also been used to monitor the human metabolomic changes following dietary intervention with soy isoflavones [126]. Substantial intersubject variations have been detected in the plasma metabolomes of five subjects [126]. Although the extent of metabolic responses to soy intervention, amongst volunteers, was subject dependent, the nature of such responses were consistent across subjects by showing changes in plasma lipoproteins, amino acids, and carbohydrates [126]. Similar observations were also obtained from a study of the effects of chamomile tea ingestion on human metabolism using metabonomics approach [127]. Clear differentiation between the samples obtained before and after chamomile ingestion was observed based on subtle changes in the spectral signature relating to increased excretion of hippurate, glycine, together with depletion in the levels of urinary creatinine. It was concluded that perturbation of the aromatic species might be indicative of altered intestinal microbial activity. Samples obtained in the 2-week period after daily chamomile ingestion formed an isolated cluster in the discriminant analysis map inferring that the metabolic effects of chamomile ingestion were not reversible during the 2-week post-dosing period. Such studies highlighted the potential for NMR-based metabonomics technology in the assessment of nutritional interventions, and demonstrated the sensitivity of the approach for characterizing subtle metabolomic changes in the presence of a high degree of variation from genetic and environmental sources.

Future Perspectives

It is clear that NMR-based metabonomics will be one of the most important applications of NMR spectroscopy in studies at the interface of chemistry and biology. Increasingly, our understandings to biological systems are required to treat such systems as an integrated entity or to use systems biology approaches. The information in the metabolism level is therefore essential to understand the functional aspects. In nutritional sciences, the NMR-based metabonomics, integrated together with nutrigenomics, nutritranscriptomics, and proteomics, will undoubtedly provides more complete understandings to the specificity of human responses to nutrients and assists the identification of surrogate tissues and biomarkers that can be used to predict a response. In such a revolutionary era, however, the shortcomings of NMR spectroscopy will have to be further addressed. From the hardware aspects, it is predictable that the NMR frequency will move beyond 1 GHz (1000 MHz) to further increase the chemical shift dispersion and to reduce the overlapping (or chemical noises). In addition, detection sensitivity will also be increased by developing the higher field spectrometers perhaps coupled with further reduction of the electronic noises of the detection circuits. For both aspects, the development of high temperature (e.g. liquid nitrogen or even room temperature) superconductors will be extremely helpful since not only the development of magnet production technology will benefit from such materials but also, when such materials are used for the detection circuits, the electronic noises will be drastically reduced. From the spectroscopy point of view, substantial efforts will be needed to overcome the radiation damping effects as the sensitivity increases. The other important area includes developing ultra-rapid methods to record the multidimensional NMR. Some recent reports of ultra-rapid multidimensional NMR spectroscopy are leading toward such progress already [128–135].

References

1. Fan WMT. Prog. NMR Spectr. 1996;28:161.
2. Nicholson JK, Wilson ID. Prog. NMR Spectr. 1989;21:449.
3. Lindon JC, Holmes E, Nicholson JK. Prog. NMR Spectr. 2001;39:1.
4. Nicholson JK, Connelly J, Lindon JC, Holmes E. Nat. Rev. Drug Discov. 2002;1:153.
5. Lindon JC, Nicholson JK, Holmes E, Everett JR. Concepts Magn. Reson. 2000;12:289.
6. Lindon JC, Holmes E, Nicholson JK. Curr. Opin. Mol. Ther. 2004;6:265.
7. Nicholson JK, Lindon JC, Holmes E. Xenobiotica. 1999;29:1181.
8. Lindon JC, Nicholson JK, Everett JR. Ann. Rep. NMR Spectr. 1999;38:1.
9. Nicholson JK. J. Anat. 1981;132:467.
10. Foxall PJD, Spraul M, Farrant RD, Lindon JC, Neild GH, Nicholson JK. J. Pharm. Biomed. Anal. 1993;11:267.
11. Nicholson JK, Foxall PJD, Spraul M, Farrant RD, Lindon JC. Anal. Chem. 1995;67:793.
12. Tang HR, Wang YL, Nicholson JK, Lindon JC. Anal. Biochem. 2004;325:260.
13. Keun HC, Ebbels TMD, Antti H, Bollard ME, Beckonert O, Schlotterbeck G, Senn H, Niederhauser U, Holmes E, Lindon JC, Nicholson JK. Chem. Res. Toxicol. 2002;15:1380.
14. Bloom M, Sternin E. Biochem. 1987;26:2101.
15. Sweatman BC, Farrant RD, Holmes E, Ghauri FY, Nicholson JK, Lindon JC. J. Pharm. Biomed. Anal. 1993;11:651.
16. Koschorek F, Offermann W, Stelten J, Braunsdorf WE, Steller U, Gremmel H, Leibfritz D. Neurosurg. Rev. 1993;16:307.
17. Lynch J, Peeling J, Auty A, Sutherland GR. Can. J. Neurol. Sci. 1993;20:194.
18. Wevers RA, Engelke U, Wendel U, DeJong JGN, Gabreels FJM, Heerschap A. Clin. Chem. 1995;41:744.
19. Nicoli F, VionDury J, ConfortGouny S, Maillet S, Gastaut JL, Cozzone PJ. Compt. Rend. Acad. Sci. III-Sci. Life Sci. 1996;319:623.
20. Moka D, Vorreuther R, Schicha H, Spraul M, Humpfer E, Lipinski M, Foxall PJD, Nicholson JK, Lindon JC. Anal. Commun. 1997;34:107.
21. Moka D, Vorreuther R, Schicha H, Spraul M, Humpfer E, Lipinski M, Foxall PJD, Nicholson JK, Lindon JC. J. Pharm. Biomed. Anal. 1998;17:125.
22. Garrod S, Humpfer E, Spraul M, Connor SC, Polley S, Connelly J, Lindon JC, Nicholson JK, Holmes E. Magn. Reson. Med. 1999;41:1108.
23. Wang YL, Bollard ME, Keun H, Antti H, Beckonert O, Ebbels TM, Lindon JC, Holmes E, Tang HR, Nicholson JK. Anal. Biochem. 2003;323:26.
24. Bollard ME, Garrod S, Holmes E, Lincoln JC, Humpfer E, Spraul M, Nicholson JK. Magn. Reson. Med. 2000;44:201.
25. Cheng LL, Chang IW, Smith BL, Gonzalez RG. J. Magn. Reson. 1998;135:194.
26. Cheng LL, Chang IW, Louis DN, Gonzalez RG. Cancer Res. 1998;58:1825.
27. Holmes E, Foxall PJD, Spraul M, Farrant RD, Nicholson JK, Lindon JC. J. Pharm. Biomed. Anal. 1997;15:1647.
28. Foxall PJD, Nicholson JK. Exp. Nephrol. 1998;6:409.
29. Sequeira S, So PW, Everett JR, Elcombe CR, Kelvin AS, Nicholson JK. J. Pharm. Biomed. Anal. 1990;8:945.
30. Holmes E, Nicholls AW, Lindon JC, Ramos S, Spraul M, Neidig P, Connor SC, Connelly J, Damment SJP, Haselden J, Nicholson JK. NMR Biomed. 1998;11:235.

31. Brindle JT, Antti H, Holmes E, Tranter G, Nicholson JK, Bethell HWL, Clarke S, Schofield PM, McKilligin E, Mosedale DE, Grainger DJ. Nat. Med. 2002;8:1439.
32. Nicholson JK, Sadler PJ, Bales JR, Juul SM, MacLeod AF, Sonksen PH. Lancet. 1984;2:751.
33. Foxall PJD, Mellotte GJ, Bending MR, Lindon JC, Nicholson JK. Kidney Int. 1993;43:234.
34. Belton PS, Delgadillo I, Gil AM, Roma P, Casuscelli F, Colquhoun IJ, Dennis MJ, Spraul M. Magn. Reson. Chem. 1997;35:S52–60.
35. Gil AM, Duarte IF, Delgadillo I, Colquhoun IJ, Casuscelli F, Humpfer E, Spraul M. J. Agric. Food Chem. 2000;48:1524.
36. Le Gall G, Colquhoun IJ, Davis AL, Collins GJ, Verhoeyen ME. J. Agric. Food Chem. 2003;51:2447.
37. Sobolev AP, Segre A, Lamanna R. Magn. Reson. Chem. 2003;41:237.
38. Ni QX, Eads TM. J. Agric. Food Chem. 1993;41:1035.
39. Defernez M, Colquhoun IJ. Phytochemistry. 2003;62:1009.
40. Belton PS, Colquhoun IJ, Kemsley EK, Delgadillo I, Roma P, Dennis MJ, Sharman M, Holmes E, Nicholson JK, Spraul M. Food Chem. 1998;61:207.
41. Belton PS, Delgadillo I, Holmes E, Nicholls A, Nicholson JK, Spraul M. J. Agric. Food Chem. 1996;44:1483.
42. Wang YL, Tang HR, Nicholson JK, Hylands PJ, Sampson J, Whitcombe I, Stewart CG, Caiger S, Oru I, Holmes E. Plant. Med. 2004;70:250.
43. Fan TWM, Lane AN, Pedler J, Crowley D, Higashi RM. Anal. Biochem. 1997;251:57.
44. Fan TWM, Lane AN, Shenker M, Bartley JP, Crowley D, Higashi RM. Phytochemistry. 2001;57:209.
45. Bailey NJC, Sampson J, Hylands PJ, Nicholson JK, Holmes E. Plant. Med. 2002;68:734.
46. Bailey NJC, Oven M, Holmes E, Zenk MH, Nicholson JK. Spectr. Int. J. 2004;18:279.
47. Benz FW, Feeney J, Roberts GCK. J. Magn. Reson. 1972;8:114.
48. Price WS, Hayamizu F, Arata Y. J. Magn. Reson. 1997;126:256.
49. Ruiz-Cabello J, Vuister GW, Moonen CTW, van Gelderen P, Cohen JS, and Van Zijl PCM. J. Magn. Reson. 1992;100:282.
50. Van Zijl PCM, Moonen CTW. J. Magn. Reson. 1990;87:18.
51. Connor S, Nicholson JK, Everett JR. Anal. Chem. 1987;59:2885.
52. Connor S, Everett J, Nicholson JK. Magn. Reson. Med. 1987;4:461.
53. Hoult DI. J. Magn. Reson. 1976;21:337.
54. Kumar A, Ernst RR, Wuthrich K. Biochem. Biophys. Res. Commun. 1980;95:1.
55. Neuhaus D, Ismail IM, Chung CW. J. Magn. Reson. A. 1996;118:256.
56. Piotto M, Saudek V, Sklenar V. J. Biomol. NMR. 1992;2:661.
57. Liu ML, Mao XA, Ye CH, Huang H, Nicholson JK, Lindon JC. J. Magn. Reson. 1998;132:125.
58. Hwang TL, Shaka AJ. J. Magn. Reson. A. 1995;112:275.
59. Crofton DJ, Pethrick RA. Polymer. 1981;22:1048.
60. Ogg RJ, Kingsley PB, Taylor JS. J. Magn. Reson. B. 1994;104:1.
61. Smallcombe SH, Patt SL, Keifer PA. J. Magn. Reson. A. 1995;117:295.
62. Zhang SM, Yang XB, Gorenstein DG. J. Magn. Reson. 2000;143:382.
63. Liu ML, Tang HR, Nicholson JK, Lindon JC. J. Magn. Reson. 2001;153:133.
64. Aue WP, Bartholdi E, Ernst RR. J. Chem. Phys. 1976;64:2229.
65. Bax A, Davis DG. J. Magn. Reson. 1985;65:355.
66. Bodenhausen G, Ruben DJ. Chem. Phys. Lett. 1980;69:185.
67. Bax A, Griffey RH, Hawkins BL. J. Magn. Reson. 1983;55:301.
68. Bax A, Summers MF. J. Am. Chem. Soc. 1986;108:2093.
69. Nicholson JK, Buckingham MJ, Sadler PJ. Biochem. J. 1983;211:605.
70. Griffin JL, Walker LA, Garrod S, Holmes E, Shore RF, Nicholson JK. Comp. Biochem. Physiol. B-Biochem. Mol. Biol. 2000;127:357.
71. Bollard ME, Holmes E, Lindon JC, Mitchell SC, Branstetter D, Zhang W, Nicholson JK. Anal. Biochem. 2001;295:194.
72. Foxall PJD, Parkinson JA, Sadler IH, Lindon JC, Nicholson JK. J. Pharm. Biomed. Anal. 1993;11:21.
73. Wevers RA, Engelke U, Heerschap A. Clin. Chem. 1994;40:1245.
74. Liu ML, Nicholson JK, London JC. Anal. Chem. 1996;68:3370.
75. Liu ML, Nicholson JK, Parkinson JA, Lindon JC. Anal. Chem. 2002;40:S83.
76. Liu ML, Tang HR, Nicholson JK, Lindon JC. Magn. Reson. Chem. 2002;40:S83–8.
77. Wu DH, Chen AD, Johnson CS. J. Magn. Reson. A. 1995;115:260.
78. Tang HR, Wang YL, Belton PS. Solid State NMR. 2000;15:239.
79. Tang HR, B. P. Hills in Webb GA, Belton PS, Gil AM, Delgadillo I (Eds). Magnetic Resonance in Food Science—A View to the Future. Royal Society of Chemistry: Cambridge, 2001, p 155.
80. Schmidtrohr K, Clauss J, Spiess HW. Macromolecules. 1992;25:3273.
81. Zumbulyadis N. J. Magn. Reson. 1983;53:486.
82. Tang HR, Hills BP. Biomacromolecules. 2003;4:1269.
83. Newman RH, Davies LM, Harris PJ. Plant Physiol. 1996;111:475.
84. Rooney OM, Troke J, Nicholson JK, Griffin JL. Magn. Reson. Med. 2003;50:925.
85. Meiboom S, Gill D. Rev. Sci. Instrum. 1958;29:688.
86. Williams PG, Saunders JK, Dyne M, Mountford CE, Holmes KT. Magn. Reson. Med. 1988;7:463.
87. Saunders JK, Stevens JD. Magn. Reson. Chem. 1986;24:1023.
88. Rabenstein DL, Fan S, Nakashima TT. J. Magn. Reson. 1985;64:541.
89. Trehout D, Desille M, Doan BT, Mahler S, Fremond B, Malledant Y, Campion JP, Desbois J, Beloeil JC, Certaines J, Clement B. NMR Biomed. 2002;15:393.
90. Rabenstein DL, Srivatsa GS, Lee RWK. J. Magn. Reson. 1987;71:175.
91. Doddrell DM, Pegg DT, Bendall MR. J. Magn. Reson. 1982;48:323.

92. Morris GA, Freeman R. J. Am. Chem. Soc. 1979;101:760.
93. Liu M, Farrant RD, Nicholson JK, Lindon JC. J. Magn. Reson. A. 1995;112:208.
94. Liu M, Farrant RD, Nicholson JK, Lindon JC. J. Magn. Reson. B. 1995;106:270.
95. Liu M, Nicholson JK, Lindon JC, Sanderson PN, Tranter GE. Magn. Reson. Chem. 1996;34:865.
96. Liu ML, Mao XA, Ye CH, Nicholson JK, Lindon JC. J. Magn. Reson. 1997;129:67.
97. Liu ML, Ye CH, Farrant RD, Nicholson JK, Lindon JC. Mol. Phys. 2001;99:1701.
98. Liu ML, Lindon JC. Curr. Org. Chem. 2001;5:351.
99. Mehring M. Principles of High Resolution NMR in Solids. Springer-Verlag: Berlin, 1983.
100. Fyfe CA. Solid State NMR for Chemists. C.F.C. Press: Guelph, ON, 1983.
101. Humpfer E, Spraul M, Nicholls AW, Nicholson JK, Lindon JC. Magn. Reson. Med. 1997;38:334.
102. Spraul M, Hofmann M, Ackermann R, Nicholls AW, Damment JP, Haselden JN, Shockcor JP, Nicholson JK, Lindon JC. Anal. Commun. 1997;34:339.
103. Webb AG. Prog. NMR Spectr. 1997;31:1.
104. Ciobanu L, Webb AG, Pennington CH. Prog. NMR Spectr. 2003;42:69.
105. Spraul M, Hofmann M, Dvortsak P, Nicholson JK, Wilson ID. J. Pharm. Biomed. Anal. 1992;10:601.
106. Spraul M, Hofmann M, Wilson ID, Lenz E, Nicholson JK, Lindon JC. J. Pharm. Biomed. Anal. 1993;11:1009.
107. Shockcor JP, Unger SE, Wilson ID, Foxall PJD, Nicholson JK, Lindon JC. Anal. Chem. 1996;68:4431.
108. Lenz EM, Greatbanks D, Wilson ID, Spraul M, Hofmann M, Troke J, Lindon JC, Nicholson JK. Anal. Chem. 1996;68:2832.
109. Lindon JC, Nicholson JK, Wilson ID. Prog. NMR Spectr. 1996;29:1.
110. Corcoran O, Spraul M. Drug Discov. Today. 2003;8:624.
111. Schewitz J, Gfrorer P, Pusecker K, Tseng LH, Albert K, Bayer E, Wilson ID, Bailey NJ, Scarfe GB, Nicholson JK, Lindon JC. Analyst. 1998;123:2835.
112. Pusecker K, Schewitz J, Gfrorer P, Tseng LH, Albert K, Bayer E, Wilson ID, Bailey NJ, Scarfe GB, Nicholson JK, Lindon JC. Anal. Commun. 1998;35:213.
113. Albert K, Braumann U, Tseng LH, Nicholson G, Bayer E, Spraul M, Hofmann M, Dowle C, Chippendale M. Anal. Chem. 1994;66:3042.
114. Albert K, Braumann U, Streck R, Spraul M, Ecker R. Fresen. J. Anal. Chem. 1995;352:521.
115. Albert K. J. Chromatogr. A. 1995;703:123.
116. Holmes E, Nicholson JK, Nicholls AW, Lindon JC, Connor SC, Polley S, Connelly J. Chemometr. Intel. Lab. Syst. 1998;44:245.
117. Tate AR, Foxall PJD, Holmes E, Moka D, Spraul M, Nicholson JK, Lindon JC. NMR Biomed. 2000;13:64.
118. Spraul M, Neidig P, Klauck U, Kessler P, Holmes E, Nicholson JK, Sweatman BC, Salman SR, Farrant RD, Rahr E, Beddell CR, Lindon JC. J. Pharm. Biomed. Anal. 1994;12:1215.
119. Holmes E, Foxall PJD, Nicholson JK, Neild GH, Brown SM, Beddell CR, Sweatman BC, Rahr E, Lindon JC, Spraul M, Neidig P. Anal. Biochem. 1994;220:284.
120. Gavaghan CL, Holmes E, Lenz E, Wilson ID, Nicholson JK. FEBS Lett. 2000;484:169.
121. Gavaghan CL, Wilson ID, Nicholson JK. FEBS Lett. 2002;530:191.
122. Holmes E, Nicholls AW, Lindon JC, Connor SC, Connelly JC, Haselden JN, Damment SJP, Spraul M, Neidig P, Nicholson JK. Chem. Res. Toxicol. 2000;13:471.
123. Azmi J, Griffin JL, Antti H, Shore RF, Johansson E, Nicholson JK, Holmes E. Analyst. 2002;127:271.
124. Alwaiz M, Mitchell SC, Ayesh R, Idle JR, Smith RL. Br. J. Clin. Pharmacol. 1987;23:614.
125. Zuppi C, Messana I, Forni F, Ferrari F, Rossi C, Giardina B. Clin. Chim. Acta. 1998;278:75.
126. Solanky KS, Bailey NJC, Beckwith-Hall BM, Davis A, Bingham S, Holmes E, Nicholson JK, Cassidy A. Anal. Biochem. 2003;323:197.
127. Wang YL, Tang HR, Holmes E, Nicholson JK. J. Agric. Food Chem. 2005;53:191.
128. Freeman R, Kupce E. J. Biomol. NMR. 2003;27:101.
129. Frydman L, Lupulescu A, Scherf T. J. Am. Chem. Soc. 2003;125:9204.
130. Shrot Y, Frydman L. J. Magn. Reson. 2004;167:42.
131. Mishkovsky M, Frydman L. Chemphyschem. 2004;5:779.
132. Kupce E, Nishida T, Freeman R. Prog. NMR Spectr. 2003;42:95.
133. Kupce E, Freeman R. J. Magn. Reson. 2003;162:300.
134. Kim S, Szyperski T. J. Am. Chem. Soc. 2003;125:1385.
135. Atreya HS, Szyperski T. Proc. Natl. Acad. Sci. USA. 2004;101:9642.

High-Resolution NMR of Milk and Milk Proteins

Josefina Belloque
Instituto de Fermentaciones Industriales, Consejo Superior de Investigaciones Cientficas (C.S.I.C.),
Juan de la Cierva 3, 28006 Madrid Spain

General Remarks

Milk contains basically water, carbohydrates, fat, proteins, and salts, in the form of a solution, a colloidal dispersion and an emulsion (Figure 1). There are excellent books that cover most aspects of milk and milk components [1,2]. High-resolution NMR has been applied to milk, and such studies include quali- and quantitative chemical analysis, the identification of isolated compounds, the *in vivo* monitoring of dairy bacterial metabolism, relaxometry studies, and structural studies of milk components, particularly proteins [3,4]. Initially, milk should be an ideal food product for NMR analysis because it is liquid. However, there are several considerations that have to be taken into account:

1. The presence of compounds in uneven proportions causes significant overlapping or masking of resonances. To solve this problem some components can be removed: fat can be removed by centrifugation in cold conditions, caseins can be precipitated by acidification to pH 4.6, both fat and caseins can be simultaneously removed by ultracentrifugation, whey proteins can be fractionated by ultrafiltration, and lactose can be partially removed by ethanol precipitation. Regular laboratory methods are found in specialized scientific publications, and official standard methods can be obtained from the web page of the International Dairy Federation (http://www.fil-idf.org).
2. The differences in size and mobility of milk components (Figure 1) leads to a wide range of relaxation times and mixed resonance line widths. Fat globules and casein micelles are large aggregates of variable sizes, with very low mobility compared with small soluble components, free in solvent, such as lactose. If better signal and resolution of the aggregated components is needed, and structural information is not required, it is convenient to disaggregate these large structures. For instance, since casein micelles are held together by calcium phosphate, and orthophosphate is partially in the form of insoluble calcium salts, chelation or removal of calcium, with EDTA or CHELEX resin, disaggregates both of them.
3. The natural composition changes significantly among species but, within the same species, there are also significant differences related to factors such as the breed, geographical location, stage of lactation, and even individuals. Bovine raw milk of a great mix of cows is available from dairy farms. Processed milk, purchased in supermarkets, comes from mixed milk, and has usually been subjected to a standardization process. However, differences can still be found among milks from different countries, farms, or milking seasons.
4. The different processing steps that milk undergoes along the processing chain leads to changes in composition and physico-chemical properties, for instance:

   - Storage: proteolysis, lipolysis, and other enzymatic reactions change the composition.
   - Heating: protein unfolding and aggregation, changes in phosphate distribution, and formation of products derived from the Maillard reaction. These alterations occur to different degrees as a function of the type and intensity of process (e.g. pasteurization, sterilization, UHT, drying).
   - Homogenization: Disruption of large structures, micelles and fat globules, into smaller ones, due to the pressure treatment.

NMR Spectra of Milk

Water, lactose, and wide lipid signals dominate the ^{1}H- and ^{13}C-spectra of whole milk, and little attention has been paid to these types of spectra. Recently, Hu and cols. [5] have applied 1D and field gradient HSQC and HMBC experiments to whole milk and milk extracts, and have assigned the observable resonances (Figure 2).

On the other hand, ^{31}P-spectra of milk are very clean (Figure 3) and the resonances assignments are available [3]. ^{31}P-NMR has the capability to distinguish among different forms of phosphate present naturally in milk (orthophosphate, casein SerP, phosphorylated carbohydrates, phosphoglycerydes, creatine-P, nucleotides), as well as diphosphates, added as stabilizers. Many of the phosphorylated compounds visible in the spectrum are

Graham A. Webb (ed.), Modern Magnetic Resonance, 1631–1635.
© 2008 *Springer.*

Fig. 1. Basic composition and structure of bovine milk.

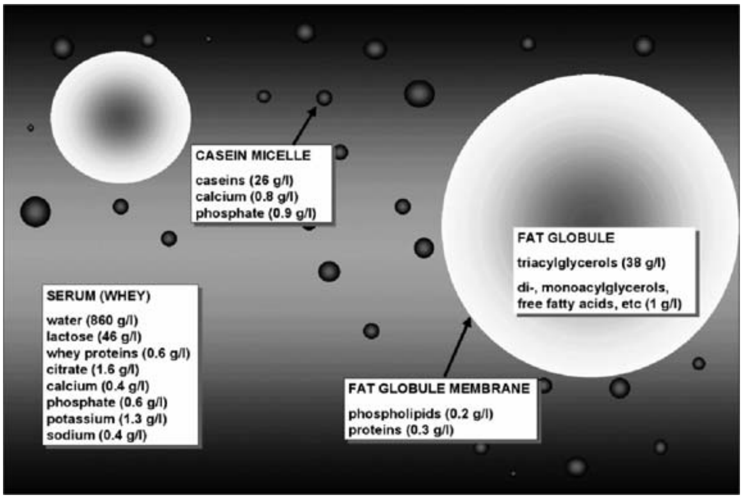
CASEIN MICELLE
caseins (26 g/l)
calcium (0.8 g/l)
phosphate (0.9 g/l)
FAT GLOBULE
triacylglycerols (38 g/l)
di-, monoacylglycerols, free fatty acids, etc (1 g/l)
SERUM (WHEY)
water (860 g/l)
lactose (46 g/l)
whey proteins (0.6 g/l)
citrate (1.6 g/l)
calcium (0.4 g/l)
phosphate (0.6 g/l)
potassium (1.3 g/l)
sodium (0.4 g/l)
FAT GLOBULE MEMBRANE
phospholipids (0.2 g/l)
proteins (0.3 g/l)

found in the serum, while most SerP, a significant proportion of phosphate, and diphosphate additives, are present in the micellar phase. ^{31}P-NMR spectra has allowed to analyse the distribution of phosphates between the micellar and the soluble phases, the evaluation of differences among species and during lactation, and has revealed new enzymatic reactions induced by pseudomonas. Quantitative analysis by ^{31}P-NMR is a good alternative to the classical spectrophotometric method, which is tedious and poorly informative. However, quantitation can be tricky, since the relaxation of the different compounds, even when disaggregated, can differ largely. For instance, in a 400 MHz spectrometer, ^{31}P spectra of a homogeneous sample, obtained from milk after fat and calcium removal, shows T_1 values of ~2 and ~12 s for casein SerP and orthophosphate, respectively. The use of the relative area to an internal standard can provide quantitative results, provided that full relaxation between transients is achieved,

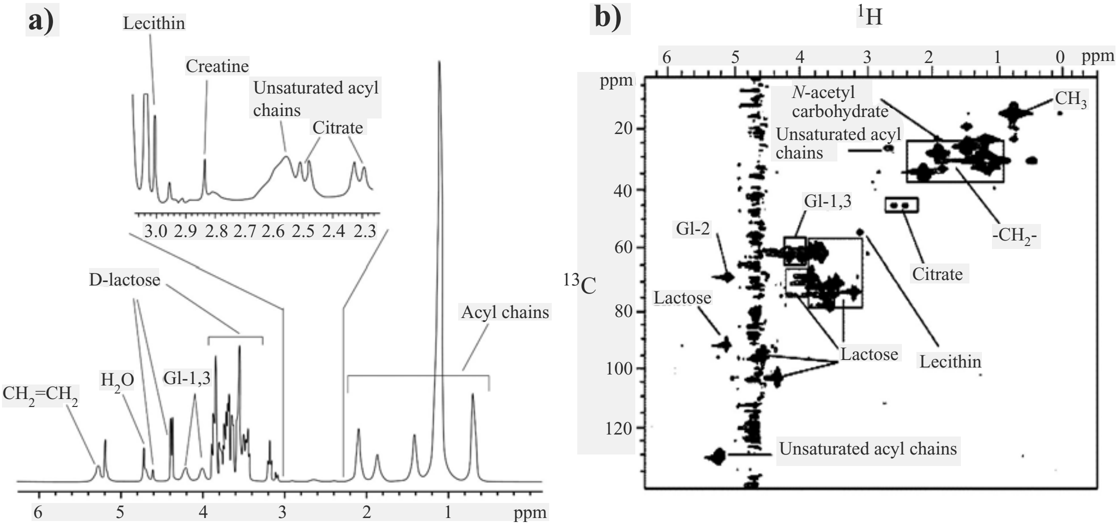

Fig. 2. (a) ^{1}H-NMR spectrum of whole milk. (b) ^{1}H-^{13}C HSQC spectrum of ethanol-extracted-milk. Reproduced from [5]. Gl: glycerol.

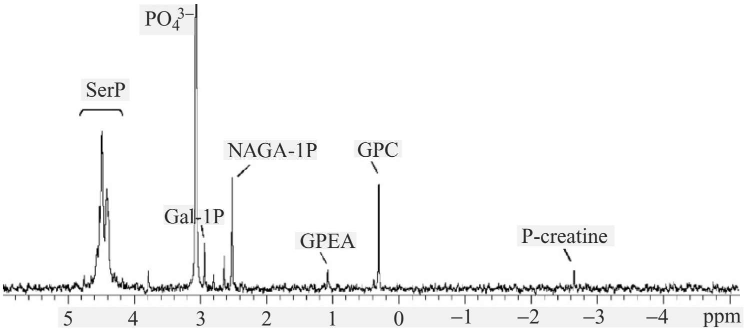

Fig. 3. ^{31}P-NMR spectrum of non-fat milk, pre-treated with CHELEX, at pH 9.5. SerP: casein phosphoserine, PO$_4^{3-}$: orthophosphate, Gal-1P: galactose-1-phosphate, NAGA-1P: N-acetylglucosamine-1-phosphate, GPEA: glycerophosphoethanolamine, GPC: glycerophosphocholine, P-creatine: phosphocreatine.

which may require a long time. If a shorter pulse (e.g. 45°) is used, relaxation is faster, thus shortening the experiment time. If the samples are homogeneous and relaxation times do not vary among samples, a 90° pulse and a short delay time (i.e. partial relaxation) can be used, obtaining reproducible spectra with good S/N (Figure 3). ^{31}P-NMR has also widely been applied to the study of the structure of caseins and casein micelles (see below).

In addition to proteins, the milk fat has become one of the most interesting fractions to study in milk. Quali- and quantitative NMR analysis of lipid components is being applied to develop methods for authentication of dairy products. The lipid analysis can discriminate among species [6], but also among different types of feeding and/or geographic origin [7], since the feeding of an animal modifies the milk fat composition. ^{13}C- is used to analyse the distribution of mono-, di- and unsaturated fatty acids, as well as the positional isomers of fatty acids in triacylglycerols. These compounds are fractionated from milk and dissolved in an organic solvent, usually $CDCl_3$. ^{31}P-NMR is used for the analysis of phospholipids, previously extracted from the fat globule membrane, and prepared in solvents such as dimethylformamide-triethylamine-guanidinum hydrochloride.

NMR Studies of Milk Proteins

The structure and structural changes of milk proteins have been a major research subject in the dairy field. First of all, the structure of milk is closely related to the structure of the casein micelles, which still remains a matter of controversy, although most accepted models agree that κ-casein is located on the surface of the micelle. Second, many milk proteins are allergens, and this activity is closely related to their structure and conformational stability. Third, the physiological and biological activities of peptides derived from milk proteins, that depend on the peptide structure, are a current matter of study. Fourth, the structural changes induced to milk proteins are related to their functional properties (e.g. gelling, foaming, emulsifying, thickening capabilities), that are used to improve dairy and non-dairy products. The 3D structure of milk proteins and peptides have been elucidated by NMR, X-ray diffraction and theoretical modelling, and have provided the basis for the study of induced structural changes. Whey proteins that are soluble and with well-defined structures, have been subjected to considerable research by NMR compared to caseins.

Caseins

They are difficult to study since their native form is the micelle. There is evidence to support that caseins are rheomorphic, i.e. they do not have a defined structure, and some authors have even further suggested that they are in an open/unfolded state [2,8]. Caseins are multiphosphorylated proteins that contribute to the solubilization and transport of calcium and phosphate, due to their ability to interact with calcium phosphate, through SerP residues, clustered in limited regions of their polypeptide chain. Phosphopeptides carrying these SerP residues are studied because they also bind calcium phosphate and are easier to study. NMR and structure models have been reported for phosphopeptides, such as β-CN f(1–25), α_{s2}CN f(2–20), casein macropeptide (κ-CN f(106–169) and, the most recent one, α_{s1}-CN f(59–79) [9].

Casein Micelles

Calcium phosphate, particularly the micellar calcium phosphate (MCP), plays an essential role in the stabilization of micelles, by cross-linking SerP residues of caseins, but at least part of the calcium phosphate is in equilibrium with serum (SCP). When casein micelles are subjected to ^{31}P-NMR, the observable resonances belong to casein SerP signals and the phosphate present in the micelle. Using liquid-state NMR, casein SerP appears as a broad peak providing little information, unless the micelles are disaggregated by calcium chelation. The use of solid-state magic angle spinning (MAS)-NMR provides higher resolution. ^{31}P single-pulse- and cross-polarization MAS NMR have been applied to casein micelles and milk powder. Using model compounds, and with the aid of simulation software, this technique has shown that phosphate is in the form of hydroxyapatite (HAP), has allowed the identification of mobile and immobile forms of HAP, and has made possible to identify Ca^{2+} binding SerP sites from different caseins [10].

Whey Proteins

Opposite to caseins, these are globular proteins that are soluble in the milk serum. The major proteins are β-lactoglobulin (BLG) and α-lactalbumin (ALA), although other proteins, such as BSA, lactoferrin, immunoglobulins and lysozime, are present in minor quantities. Even though many studies have been done with whey bovine proteins, the only structure that has been elucidated by NMR is that of BLG. This protein is easy to purify, it has a MW of 18 KDa, and gives reasonably sharp NMR signals, especially at pH 2–3 since, under these conditions, it is a monomer, and very stable. The structure has been solved by both X-ray crystallography and NMR (Protein DataBase (PDB) ID 1CJ5), and complete ^{1}H- and ^{13}C and ^{15}N assignments are available. The structure of bovine ALA was obtained from X-ray diffraction (PDB ID 1F6S), although ^{1}H, ^{13}C and ^{15}N NMR assignments are available from the BioMagRes data Bank (BMRB ID 4811 and 4332). Similarly, the structure of bovine lactoferrin comes from X-ray diffraction (PDB ID 1BLF). In some cases, such as BSA, lysozyme and immunoglobulin, crystal structures are available for other species different than bovine (e.g. human serum albumin (PDB ID 1BM0), or hen egg lysozyme (PDB ID 193L). Crystal structures can be very useful for partial NMR assignments of bovine whey proteins.

Peptides

Peptides present in milk are the result of proteolysis of caseins or whey proteins by enzymes, either indigenous in milk or from microorganisms. While proteolysis is, in general, detrimental to milk, it enhances the quality of some dairy products, particularly fermented milks and cheese. In the last years there has been an increased interest in the identification of milk peptides with antimicrobial, immunomodulant, ACE-inhibiting and other biological activities that can be used to improve the quality of fermented dairy products. NMR can contribute to the evaluation of the structure-function relationship. For instance, lactoferricin is a peptide derived from lactoferrin that has higher antimicrobial properties than its precursor. While this peptide has a helix shape in the native protein (PDB ID 1BLF), NMR studies have shown that, in solution, it has a hairpin conformation (PDB ID 1LFC), which is more effective for microbial membrane permeabilization.

Milk Protein Structural Changes

Because of the nature of caseins, structural changes studies have been limited to relaxation and diffusion measurements. However, whey proteins and, above all, BLG, has been subjected to detailed structural studies, analysing the influence of denaturing agents, heating, high pressure, lactosylation, site-directed mutagenesis, and ligand binding on its structure and/or stability [11].

One of the most interesting areas has been to elucidate the unfolding pathways of the protein under physical treatments. The knowledge of the unfolded intermediates helps to understand the nature of the interactions of the protein with other proteins, water and co-solutes. In the last years, there has been increasing evidence to support that protein folding is a hierarchical process that starts with the building of robust regions and allow the correct folding of the rest of the protein [12]. In the same manner, the unfolding of the protein is a stepwise process. In BLG, it can be observed that particularly robust regions, that seem to be the initiation-folding site, are the most resistant to unfolding [11]. ^{1}H-NMR coupled with deuterium exchange give very useful and detailed information about the unfolding process, by perturbing the protein, and observing the disappearance of backbone NH resonances. If the structure of the protein is known and the ^{1}H resonances are assigned, the unfolding process of precise regions of the protein can be followed by using 2D spectra (Figure 4). The effect of heat, cold and high pressures on BLG has been studied this way [13–16]. Some NMR probes allow performing experiments *in situ*, which provides the advantage of observing the real unfolding mechanism, avoiding the refolding of the protein and the re-equilibration of the system. However, if this is not available, an off-line scheme can be used, capturing different intermediate unfolded states by their degree of deuterium substitution (Figure 4). The recent progress on NMR techniques and the interest of researchers in the folding/unfolding processes have led to the development of methods that allow 2D spectra acquisition in real time.

Checking whether the structure is refolded after the physical treatment or, on the contrary, whether it shows changes from the original form, can be done by comparing the spectra taken before and after the treatment. If relaxation or diffusion parameters are measured before and after processing, information about aggregation can also be obtained.

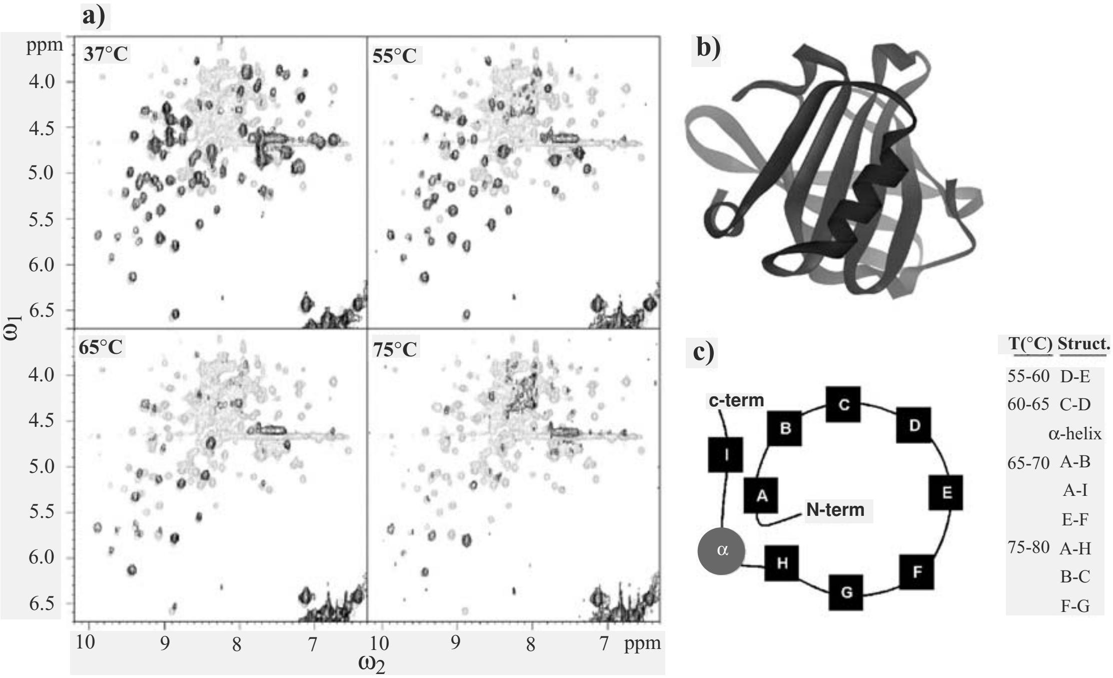

Fig. 4. Effect of heat on BLG. (a) Fingerprint region (NH-Hα) of TOCSY spectra of BLG heated at different temperatures in a D_2O solution. Grey contours are from a non-heated non-deuterium-exchanged BLG reference sample. Reproduced from [13]. (b) 3D structure of BLG. (c) Organization of β-strands (A-I) and the α-helix of BLG, and structural interactions that are lost at different temperatures [13].

References

1. Walstra P, Geurts TJ, Noomen A, Jellema A, Van Boekel MAJS, Dairy Technology. Principles of milk properties and processes. Marcel Dekker Inc. 1999.
2. Fox PF, McSweeney PLH (Eds). Advanced Dairy Chemistry, vol. 1: Proteins, Elsevier Applied Science, 2003.
3. Wahlgren NM, Drakenberg T. In: Webb GA, Belton PS, McCarthy MJ (Eds). Annual reports on NMR spectroscopy, vol. 31, Academic Press, London, 1995, p. 275
4. Belloque J, Ramos M. Tr. Food Sci. Tech. 1999;10:313.
5. Hu F, Furihata K, Ito Ishida M, Kaminogawa S, Tanokura M. Agric. J. Food Chem. 2004;52:4969.
6. Andreotti G, Lamanna R, Trivellone E, Motta A. J. Am. Oil Chem. Soc. 2002;79:123.
7. Renou JP, Deponge C, Gachon P, Bonnefoy JC, Coulon JP, Garel JP, Verité R, Ritz P. Food Chem. 2004;85:63.
8. Smyth E, Clegg RA, Holt C. Int. J. Dairy Tech. 2004;57:121–126.
9. Huq NL, Cross KJ, Reynolds EC. J. Dairy Res. 2004;71:28.
10. Bak M, Rasmussen LK, Petersen TE, Nielsen NC. J. Dairy Sci. 2001;84:1310.
11. Sawyer L, Barlow PN, Bol, MJ, Creamer LK, Denton H, Edwards PJB, Holt C, Jameson GB, Kontopidis G, Norris GE, Uhrinova S, Wu S-Y. Int. Dairy J. 2002;12:299.
12. Dinner R, Sali A, Smith LJ, Dobson CM, Karplus M. Tr. In Biol. Sci. 2000;25:331.
13. Edwards PJB, Jameson GB, Palmano KP, Creamer LK. Int. Dairy J. 2002;12:331.
14. Katou H, Hoshino M, Kamikubo H, Batt CA, Goto Y. J. Mol. Biol. 2001;310:471.
15. Kuwata K, Li H, Yamada H, Batt CA, Goto Y, Akasaka K. J. Mol. Biol. 2001;305:1073.
16. Belloque J, Smith G. J. Agric. Food Chem. 1998;46:1805.

High-Resolution ^{13}C Nuclear Magnetic Resonance in the Study of Oils

Maria Antonietta Brescia and Antonio Sacco
Dipartimento di Chimica, Università di Bari, via Orabona 4, 70126 Bari, Italy

Introduction

High-resolution ^{13}C NMR spectroscopy has been widely used in lipid and vegetable oil analysis [1,2]. This is due to the electronic configuration of ^{13}C nucleus, that makes the chemical shift spread over a wide range of frequencies (200 ppm), permitting a minor overlapping of the signals compared to proton spectra, and, consequently, the acquisition of structural information. The most important advantage of ^{13}C NMR spectroscopy is the possibility to determine the positional distribution of the acyl chains on the glycerol moiety. This determination cannot be done with ^{1}H NMR spectra due to the strong overlap of the peaks.

However, a limitation connected with the use of ^{13}C spectroscopy for the analysis of oils is due to low natural abundance of ^{13}C and small gyromagnetic ratio that results in its peculiar low sensitivity. As a consequence, longer analytical time is required for acquisition and only major components, like triacylglycerides can be analyzed and quantified. Quantitative information from ^{13}C NMR spectra can be acquired if resonances are not affected by the effect of nuclear Overhauser enhancement (NOE) that occurs during proton decoupling of ^{13}C, through the mechanism of dipole–dipole relaxation. NOE can be suppressed by using the inverse-gated proton-decoupled sequence, which gates the decoupler only for the acquisition time.

Analysis of the different regions of the ^{13}C NMR spectrum and/or the entire spectrum can provide useful insight on oil composition, enabling quality and authenticity controls.

Quantitative Determination of the Oils Major Components

Fatty Acids

The ^{13}C NMR spectrum of a virgin olive oil, dissolved in $CDCl_3$, is shown in Figure 1. Four signal regions can be recognized due to different types of carbons of triacylglycerides. The assignments were performed by comparing the signals of the ^{13}C spectrum with the chemical shift of standard glycerides. This procedure is generally followed [3–5] even though it has been recently demonstrated that a slight chemical shift of the signals in the ^{13}C NMR spectra of oils is a function of their concentration, especially in the carbonyl region [6].

Table 1 illustrates some case studies based on analytical applications of ^{13}C NMR spectroscopy. A quantitative determination of MUFA, linoleic, and linolenic acids of various vegetable oils from the resonances present in the methyl and methylene regions (14–35 ppm) of the ^{13}C NMR spectrum [7]was proposed. It was found that the optimization of the recovery delay was necessary in order to get data in agreement with those obtained by the classical gas chromatography method, in particular for the linoleic acid determination. It resulted that a total experimental time of 30 min per sample was required.

The areas of signals resonating in this region were also used for the determination of iodine value of palm oil [8].

An alternative method for the quantification of the major fatty acids (saturated, oleic, and linoleic) based on the analysis of the signals due to carbonyl and ethylenic carbons, resonating in the 195–105 ppm region was proposed for Greek olive oils [9]. This quantification procedure required the presence of an internal reference (pyrazine). The overlap of peaks in the carbonyl region was reduced applying a Lorentz Gaussian enhanced filter function to the FID and a peak deconvolution procedure to allow a precise integration. This methodology was extended investigating mixtures of virgin olive oils and seed oils. In this case, the quantitative analysis was performed only on signals resonating in the olefinic region, due to the minor overlapping presented [10]. A linear increase of linoleic acids contents was observed with increasing addition of seed oils to olive oils. This evidence allowed to construct reference curves, proposed as a diagnostic tool for the estimation of olive oil adulteration.

The adulteration of olive oil with soybean oil having high linoleic acid content was also examined by ^{13}C NMR distortionless enhancement by polarization transfer (DEPT). This technique employs a polarization transfer able to enhance signal intensities [11], and shorten the experimental times required when compared to ^{13}C NMR spectra. The signals of unsaturated carbons of

Graham A. Webb (ed.), Modern Magnetic Resonance, 1637–1643.
© 2008 *Springer.*

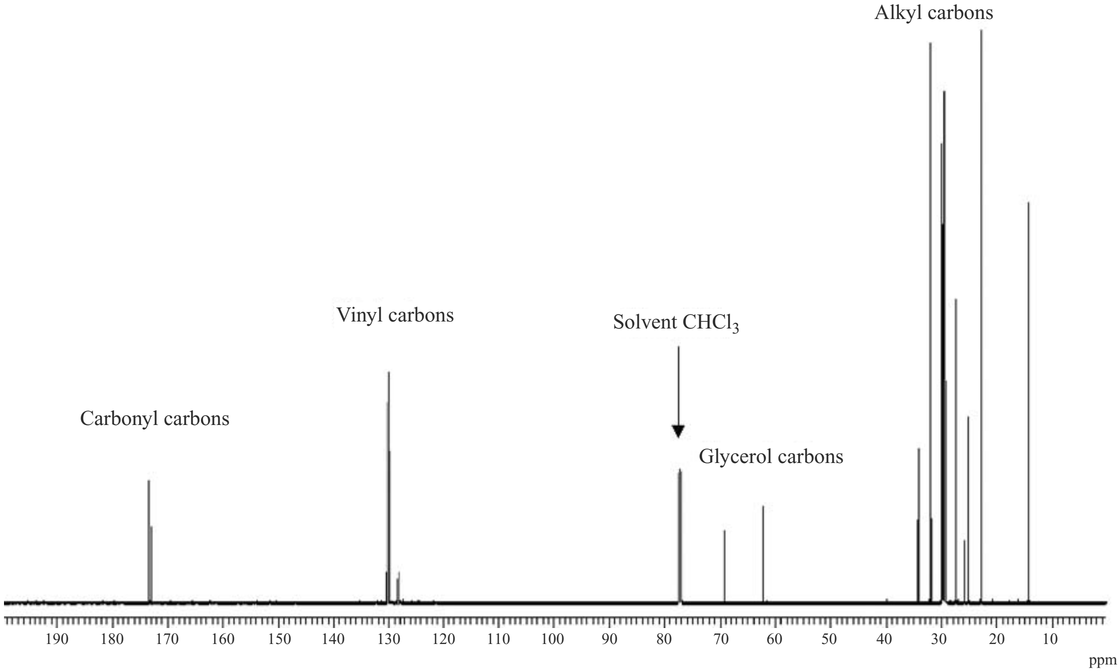

Fig. 1. ^{13}C NMR 500 MHz spectral pattern of an olive oil.

oleyl, linoleyl, and linolenyl chains, observed in the 132–127 ppm region, were found to give two resonances for each carbon signal, depending on the chain position on the glycerol backbone. Integrals of these resonances were used to calculate the calibration curves based on a linear relationship between resonance intensities and soybean concentration in olive oil.

The methylene, olefinic, and carbonyl regions in the ^{13}C NMR spectra were considered to obtain quantitative information about the fatty acid distribution of fish oils [12]. The addition of paramagnetic compounds to the analyzed samples was provided in order to decrease the experimental time for performing quantitative measurements.

Qualitative and quantitative determination of fatty acids in vegetable seeds is necessary to assess their value. Magic angle spinning ^{13}C NMR technique has shown to be very attractive in this case because it is a non-destructive

Table 1: Quantitative ^{13}C NMR determinations on oils

Samples	Parameters	Analyzed spectral region	Reference
Canola seeds	Fatty acids	29–20 ppm	12
Fish oils	Fatty acids	Entire spectrum	10
Fish oils	Fatty acids and positional distributions	178–172 and 75–50 ppm	25
Mixtures of olive and seed oils	Unsaturated fatty acids	130–127 ppm	9, 32
Olive oils	Free fatty acids and partial aylglycerols	176–173 and 75–60 ppm	16
Olive oils	Diglycerides	75–60 ppm	17
Palm oils	Iodine value	30–24 ppm	7
Palm oils	Free fatty acids and partial acylglycerols	174–172, 75–60, and 30–20 ppm	18
Vegetable oils	Unsaturated fatty acids	36–14 ppm	6
Vegetable oils	Fatty acids and positional distributions	173–127 ppm	8, 19–20, 22–24
Vegetable seeds	Unsaturated fatty acids	130–127 ppm	11

method, being applied directly on the seed, and because it permits to obtain a spectral resolution that approached that of liquid oils. However, it is worth to consider that for the analysis of seeds having a low oil content (like corn and rape seeds) or a complex unsaturated fatty acid composition, DEPT technique was necessary to increase the sensitivity [13]. From the analysis of the methylene region of canola seed oil spectrum, it was possible to detect trans olefins in oils [14] because allylic methylenes adjacent to cis double bonds are shifted by 5 ppm to frequency lower than that of trans isomer. This determination is advantageous respect to the classical chromatographic method, because it detects all trans isomers simultaneously, while in a chromatogram different isomers give rise to different small signals that are not accurately measurable. The detection of trans fatty acids can be extremely helpful to reveal the addition of refined oils to virgin olive oils. In fact, oil refining processes (bleaching and/or deodorizing) are carried out at high temperatures that favor the isomerization of oleic acid (cis) to elaidinic (trans). This acid is absent in virgin olive oils, while its content in olive and olive-pomace oils varies from 0.1 to 0.6%, therefore its presence in olive oil can be considered an index of adulteration [15]. The detection of the amount of trans and cis fatty acids is also important for the quality control of hydrogenated vegetable oils and to determine the effect of the experimental conditions of the hydrogenation process in double bonds isomerization and migration. Gunstone [16] and Miyake and Yokomizo [17] obtained important results on the position and configuration of double bonds by investigating the olefinic region of the ^{13}C spectrum.

Glycerol Esters

Glycerol can form mono-, di-, and triacylglycerols, resonating in the spectral region from 60 to 72 ppm (Figure 2). The symmetrical esters (2-monoacyl, 1,3-diacyl, and triacyl) give only two signals at 1:2 intensity ratio, while the asymmetrical esters give three separate signals of equal intensity. Assignments of standard glycerides were obtained using DEPT experiments [18]. The total amount of diacylglycerols and the ratio between 1,2 and 1,3-diacylglycerols can be evaluated in terms of molar ratios (%) through the analysis of the peaks intensities:

$$R1 = 100 \times \mathrm{DG}/(\mathrm{DG} + \mathrm{TG})$$

$$R2 = 1{,}2\text{-DG}/1{,}3\text{-DG}$$

$$R3 = \mathrm{MG} \times 100/(\mathrm{MG} + \mathrm{DG} + \mathrm{TG})$$

In the above-reported relationships, DG represents the sum of the intensities of the resonances due to carbons of 1,2- and 1,3-diacylglycerides; TG represents the sum of the intensities of carbons of triacylglycerides; MG indicates the intensities of signals due to α-monoglycerides (69.9 and 63.1) and β-monoglycerides (61.02 and 72.2) (signals not present in the spectrum shown in Figure 2). The spectrum must be acquired using appropriate relaxation delays and pulse widths in order to carry out the quantification procedure, since full recovery of magnetization between subsequent pulses is necessary.

This determinations can be useful to detect the freshness of the oils and to reveal the presence of partially neutralized oils to olive oils that are given out as "virgin". Diacylglycerols (mainly 1,2) can come either from incomplete triacylglycerols biosynthesis or from limited lipase action on triacylglycerols and their content, indicated by $R1$, should not exceed 2–3% in virgin olive oil. The glycerol content increases with olive oil acidity. Large amounts of diacylglycerols (mainly 1,3-diacylglycerols) are found in neutralized olive oils, produced from a starting material with a high level of free fatty acids and in oils obtained from overripe olives or after several months of oil storage due to lipolysis and 1,2- and 1,3-isomerization. In both the cases, $R2$ is always lower than 1. A quantitative ^{13}C NMR study carried out on olive oil showed that significant differences in diacylglycerols content occurred among cultivars [19], probably due to its relation with maturation stage. In fact, it was observed that lower total diacylglycerol content is characteristic of late maturing cultivars, whereas early maturing fruits produce higher levels of total diacylglycerides.

The determination of mono- and diacylglycerol content is also important, since they are commonly used as emulsifiers in the food industry. For this reason, the quantitative analysis of these compounds was performed on palm oil [20]. Since glycerol carbons are near the T_1 minimum for dipole–dipole relaxation mechanism, spectra were acquired at low magnetic fields (300 MHz) and at an elevated temperature (50 ˚C) to obtain narrow signals.

Fatty Acids Positional Distribution

In the low-field region of the spectrum, carbonyl carbons of the triacylglycerides resonate. Oil samples have two sets of carbonyl signals: the first, centered at ~173.2 ppm, includes the fatty acids esterified at 1,3-glycerol positions (α), while the second, centered at ~172.8 ppm, is due to fatty acids bonded to the 2-glycerol position (β). In olive oil, four signals were observed in the first group due to saturated (S), eicosenoic (E), oleic (O), polyunsaturated fatty acids (L), while in the second group there are two signals, respectively due to oleic and polyunsaturated acids (Figure 3). The analysis of this region enables the

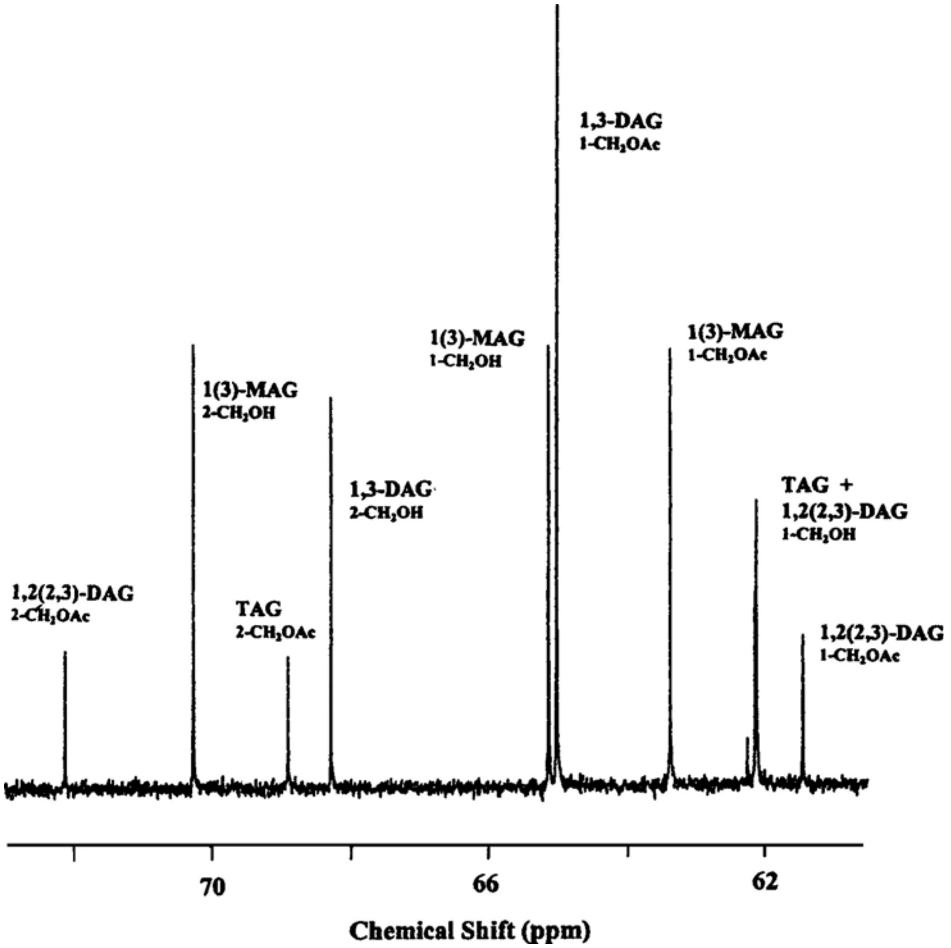

Fig. 2. The glycerol carbon region 60–72 ppm of the ^{13}C spectrum of a standard mixture of glycerides at different esterification degree. The resonances of glycerol carbons are labeled as $-CH_2OAc$ and $-CH_2OH$ in correspondence of an acylated and a non-acylated alcoholic group of the glycerol molecule (from Ref. [2]).

detection of addition of synthetic esterified oils, considered non-edible by the European Union, to virgin olive oils. Esterified oils show a random distribution of saturated fatty acids, leading the 15% of saturated acids in the 2-glycerol position. The biosynthesis of triacylglycerols in the vegetable oils leads to the preferential esterification of unsaturated fatty acids in the 2-glycerol position; therefore, the amount of oleic and linoleic acids in this position represents the 98–99% of the total fatty acid content. As a consequence, if the saturated fatty acids exceed 1.5% in this position, the analyzed oil contains a certain amount of esterified oils. The EU official analytical procedure for the analysis of esterified oils mixed with olive oils is based on an enzymatic method requiring several steps, while NMR making use of ^{13}C resonances yields immediate results, operating directly on the oil samples. In fact, in the carbonyl region of the ^{13}C NMR spectrum of virgin olive oil only one resonance is observed for the 2-glycerol position, corresponding to the unsaturated fatty acids, while in the same spectral region an esterified oil shows a minor peak due to saturated acids. This signal was quantified by means of a curve resolution program, enabling the detection of a 10% addition of esterified oils to olive oil [21].

The areas of the signals resonating in the carbonyl region of the spectrum were used to perform a regiospecific

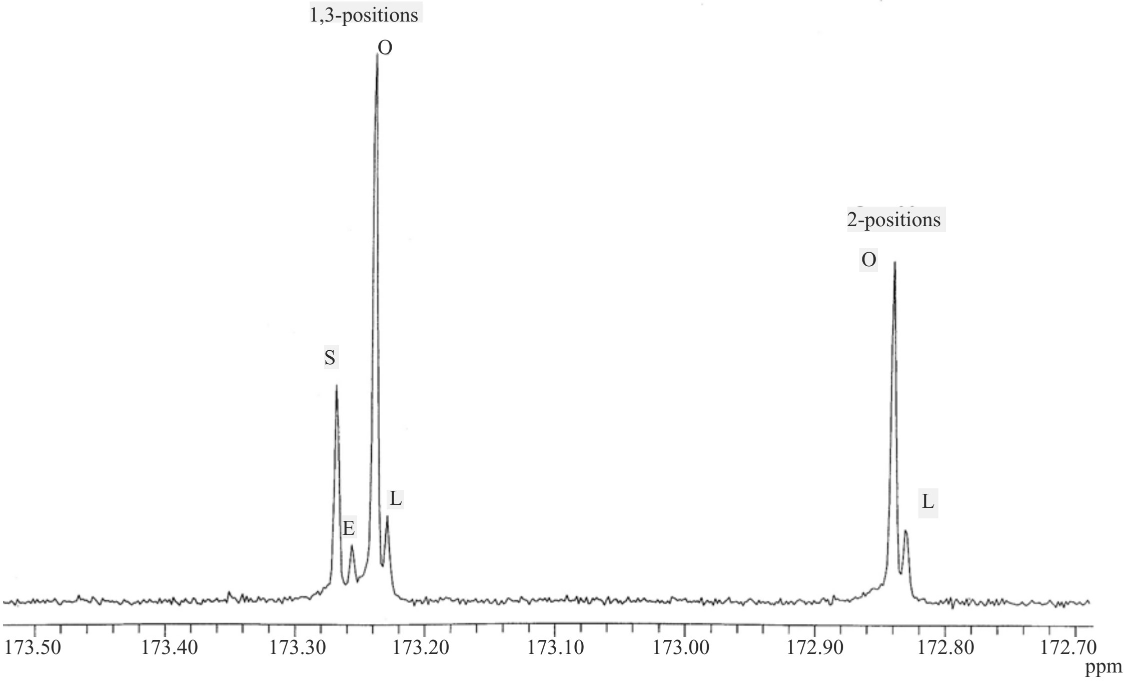

Fig. 3. 500 MHz ^{13}C NMR spectrum of the carbonyl region of an olive oil.

analysis of triacylglycerides of Italian monovarietal olive oils, calculating the distribution of saturated, oleyl, and linoleyl chains between 1,3 and 2 positions of glycerol [22]. Using the same approach, the fatty acid composition and distribution in triacylglycerols of other vegetable oils was determined [23–25].

The examination of acyl positional distribution in canola and other non-edible vegetable oils is more complex than for olive oil, due to the presence of eicosenoic and erucic acids, which signals result overlapping to those of linoleic acid in the carbonyl region. For this reason, the analysis of the olefinic region of the spectra was also necessary to obtain a qualitative and quantitative evaluation of these acids [26].

The study of the carbonyl region was also performed on the ^{13}C NMR spectra of fish oils revealing that glycerol β-position is esterified preferentially by docosahexaenoic acid [12].

In the ^{13}C NMR spectrum of an oil with high content of free fatty acids, the signals of free COOH groups appear at 176–178 ppm. The determination of free acidity can be easily performed by comparing the intensity of this signal to the sum of free and esterified carbonyl groups. This method was applied to quantify free fatty acids in olive oils [18] and in fish lipids [27]. Quantification of free fatty acids in palm oils was performed from the C3 peak of free fatty acids resonating in the region of aliphatic carbons [20].

Minor Oil Components

Among minor olive oil components, phenolic compounds play an important role in the sensory characteristics and in the oxidation stability of virgin olive oil (see Section 2.4 of "^{1}H NMR of oils"). In particular, it has been demonstrated that the esters of tyrosol (Ty) and hydroxytyrosol (OHTy) with elenolic acid contribute to the sensory characteristics of the oil, being responsible of the pungent taste, while OHTy and its derivatives are correlated with oil resistance to oxidation [14]. ^{13}C NMR spectroscopy of the polar fraction extracted from virgin olive oils permits to calculate the ratio of free and esterified Ty + OHTy comparing the intensities of C1 carbon of free Ty + OHTy (64.5 ppm) with the C1 signal of the corresponding esterified compounds (66.8 ppm).

The molar ratio between total (free and esterified) OHTy and Ty can be calculated by comparing the intensities of aromatic signals at 121.3 and 116.1 ppm and provides a useful parameter for oil stability.

^{13}C NMR Spectroscopy As a Discriminating for the Varietal, Geographical, and Botanical Origin of Vegetable Oils

Since olive oil is a product of high nutritional and commercial value, its adulteration with different quality and origin oils represents a big temptation. A rapid screening method is therefore requested to detect oil adulteration. Recently, methods based on ^{13}C NMR spectroscopy have been considered advantageous in this field because of compositional and structural information contained in the NMR signals. The proposed methods provide models which are obtained applying statistical methods of multivariate analysis to spectroscopic measurement of representative sets of samples.

Principal component analysis, principal component regression, and partial least squares were applied to 35 signals areas from the ^{13}C NMR spectra of six olive oil cultivars sampled in different Italian regions with variable selection methods of Fisher ratio and the ratio of inner variance to outer variance [28]. The classification of the oils by variety was found to be more successful than classification by region of origin. In order to improve the geographical origin discrimination, the potential of DEPT sequence was also investigated, since it permits to obtain better S/N ratio of ^{13}C NMR spectra. This approach was applied to olive oils coming from 13 Italian PDO areas [29] located in different regions, and to olive oils coming from three close PDO areas in Apulia region (Southern Italy) [30]. The acquisition and processing conditions were optimized in order to perform accurate and reproducible measurements. Multivariate statistical analysis was applied to the intensities of selected peaks present in the ^{13}C NMR spectra and permitted to distinguish the analyzed oils according to their origin. In both studies the cultivar factor seemed very important, since classification worked well especially when oils of different PDO where obtained from olives of different cultivars.

Cultivars differentiation of virgin olive oils coming from different PDO areas in Apulia region, was also explored with classical chromatographic analyses (fatty acid, sterol, and triacylglyceride composition) and with ^{13}C NMR spectroscopy, that was used for comparative purposes to official methods. Therefore, classical and NMR parameters were separately evaluated but the same statistical approach was used for both data sets. As far as NMR data are concerned, normalized heights of signals present in the ^{13}C NMR spectrum, selected with analysis of variance, were used as variables for statistical elaboration [31]. The models obtained from the application of discriminant analysis to the data sets of chromatographic and ^{13}C NMR results were found to be in a good agreement, being statistically similar. This study confirmed that ^{13}C NMR spectra contain the information about acyl composition and positional distribution of glycerol moiety; since for the analytical data, fatty acids and triacylglycerols were the most responsible for distinguishing oils' cultivars, and all the selected peaks for ^{13}C NMR were relevant. This technique could therefore be effectively used for classifying cultivars.

A combined ^{13}C NMR and GC approach was also successfully used to determine the cultivar effect on fatty acid composition of monovarietal Sicilian olive oils [32].

Some authors studied the potential of ^{13}C NMR analysis to distinguish oils from different cultivars, geographical and botanical origins, as well as mixtures of olive oils from different geographical origins and of hazelnut oil in olive oil [33]. The intensities of peaks most effective in the discrimination of the different types of oil were selected as variables by stepwise discriminant analysis (SDA). The difference between virgin olive oils and vegetable oils having a high content of linoleic and oleic acid was obtained. In addition, the statistical method classified, with 97% of classification ability, hazelnut oil samples and mixtures of hazelnut oil in olive oil.

^{13}C NMR of Olive Oil Minor Compounds to Determine Oil Authenticity

^{13}C NMR spectroscopy cannot be directly used for the analysis of minor compounds due to its low sensitivity. Nevertheless, the information acquired by ^{13}C NMR in the analysis of triacylglyceridic composition of oils have prompted some authors [34] to explore the unsaponifiable matter of virgin and refined olive and pomace oils, after previous separation from triacylglycerides by treatment with a potassium hydroxide solution. The low-field region of the spectra contained signals that were assigned to squalene that was the major component of the unsaponifiable matter of virgin olive oil and was present, in lower quantity, also in refined olive oils and in refined olive-pomace oils. Other signals were assigned to sterols, β-sitosterol, triterpenic, and long-chain monounsaturated alcohols. The heights of these peaks were evaluated by means of SDA permitting to achieve a discrimination between the different types of investigated oils.

However, the use of unsaponifiable matter requires a time-consuming preparation and does not hold information about triacylglycerols and other saponifiable components, which can also be related to oil quality. To overcome this limitation, a chromatographic method was used to isolate an oil fraction containing 15% of triacylglycerols and 85% of polar compounds [35]. ^{13}C NMR spectra of this fraction were obtained from 109 vegetable oils of different grade and various botanical and geographical origin. Moreover, mixtures of virgin olive oils from different geographical regions were analyzed. Spectra were similar to those obtained for olive oils but contained the double number of signals, since minor compounds like diacylglycerols, monoacylglycerols, sterols, and fatty alcohols were visible. The information contained in the spectra was employed to classify olive oils by using SDA and variable selection.

^{13}C NMR spectra of oil fractions obtained with the same method for 66 vegetable oils were also analyzed to evaluate the potential use of these fractions in predicting oil stabilities. A 0.99 correlation index was found by stepwise linear regression analysis between oil stability, determined by Rancimat method, and the heights of several signals present in the ^{13}C NMR spectra [36]. The statistical method selected the signals more correlated to oil stability. These signals were associated to fatty acid composition and to the presence of minor compounds with antioxidant characteristics.

References

1. Gunstone FD, Shukla VKS. Annu. Rep. NMR Spectrosc. 1995;31:219.
2. Vlahov G. Prog. Magn. Reson. Spectrosc. 1999;35:341.
3. Ng S. Lipids 1985;20:778.
4. Shaw AD, Di Camillo A, Vlahov G, Jones A, Bianchi G, Rowland J, Kell DB. Anal. Chim. Acta 1997;348:357.
5. Mannina L, Luchinat C, Emanuele MC, Segre AL. Chem. Phys. Lipids 1999;103:47.
6. Mannina L, Luchinat C, Patumi M, Emanuele MC, Rossi E, Segre AL. Magn. Reson. Chem. 2000;38:886.
7. Miyake Y, Yokomizo K, Matsuzaki N. J. Am. Oil Chem. Soc. 1998;75:1091.
8. Ng S, Gee PT. Eur. J. Lipid Sci. Technol. 2001;103:223.
9. Mavromoustakos T, Zervou M, Theodoropoulou E, Panagiotopulos D, Bonas G, Day M, Helmis A. Magn. Reson. Chem. 1997;35:S3.
10. Mavromoustakos T, Zervou M, Bonas G, Kolocouris A, Petrakis P. J. Am. Oil Chem. Soc. 2000;77:405.
11. Vlahov G. Magn. Reson. Chem. 1998;35:S8.
12. Aursand M, Rainuzzo JR, Grasladen H. J. Am. Oil Chem. Soc. 1993;70:971.
13. Wollenberg K. J. Am. Oil Chem. Soc. 1991;68:391.
14. Hutton WC, Garbow JR, Hayes TR. Lipids. 1999;34:1339.
15. Sacchi R, Addeo F, Paolillo L. Magn. Reson. Chem. 1997;33:133.
16. Gunstone FD. J. Am. Oil Chem. Soc. 1993;70:965.
17. Miyake Y, Yokomizo K. J. Am. Oil Chem. Soc. 1998;75:801.
18. Sacchi R, Addeo F, Giudicianni I, Paolillo L. Riv. Ital. Sost. Grasse. 1990;LXVII:245.
19. Vlahov G. Fett/Lipid. 1996;98:203.
20. Ng S. J. Am. Oil Chem. Soc. 2000;77:749.
21. Sacchi R, Addeo F, Giudicianni I, Paolillo L. Ital. J. Food Sci. 1992;2:117.
22. Vlahov G. J. Am. Oil Chem. Soc. 1996;73:1201.
23. Howarth OW, Vlahov G. Chem. Phys. Lipids. 1996;81:81.
24. Vlahov G. Phytochemistry. 1996;42:621.
25. Vlahov G, Chepkwony PK, Ndalut PK. J. Agric. Food Chem. 2002;50:970.
26. Wollenberg KF. J. Am. Oil Chem. Soc. 1990;67:487.
27. Sacchi R, Medina I, Aubbourg SP, Giudicianni I, Paolillo L, Addeo F. J. Agric. Food Chem. 1993;41:1247.
28. Shaw AD, di Camillo A, Vlahov G, Jones A, Bianchi G, Rowland J, Kell DB. Anal. Chim. Acta. 1997;348:357.
29. Vlahov G, Schiavone C, Simone N. Magn. Res. Chem. 2001;39:689.
30. Vlahov G, Del Re P, Simone N. J. Agric. Food Chem. 2003;51:5612.
31. Brescia MA, Alviti G, Liuzzi V, Sacco A. J. Am. Oil Chem. Soc. 2003;80:945.
32. Mannina L, Dugo G, Salvo F, Cicero L, Ansanelli G, Calcagni C, Segre AL. J. Agric. Food Chem. 2003;51:120.
33. Zamora R, Alba V, Hidalgo FJ. J. Am. Oil Chem. Soc. 2001;78:89.
34. Zamora R, Navarro JL, Hidalgo FJ. J. Am. Oil Chem. Soc. 1994;71:361.
35. Zamora R, Gómez G, Hidalgo FJ. J. Am. Oil Chem. Soc. 2002;79:267.
36. Hidalgo FJ, Gómez G, Navarro JL, Zamora R. J. Agric. Food Chem. 2002;50:5825.

High-Resolution ^{1}H Nuclear Magnetic Resonance in the Study of Oils

Maria Antonietta Brescia and Antonio Sacco
Dipartimento di Chimica, Università di Bari, via Orabona 4, 70126 Bari, Italy

Introduction

High-resolution NMR plays an important role in oil analysis. This is firstly due to the absence of sample pretreatment, since oils are simply added to a deuterated solvent before analysis. ^{1}H NMR studies of oils have increased because of the great amount of information that high field NMR instruments can provide with a single experiment and in a very short time. This entry is mainly focused on the qualitative and quantitative information that can be obtained from the oils ^{1}H NMR spectra regarding major and minor components. Some of the most interesting implications in the control of quality and authenticity will be also discussed.

Triglycerides

A typical ^{1}H NMR spectrum of an olive oil is reported in Figure 1. It shows 10 signals of significant intensity due to protons of triglycerides—the main oil components. These signals are also present in the spectra of other vegetable oils, but their shapes and intensities are different due to different fatty acid composition. These signals do not allow the complete discrimination of single fatty acid components, unlike the traditional gas chromatographic method, considering their overlapping in the spectral area of interest. Anyway, they can be used for various useful applications. For example, the oil unsaturation degree can be calculated by determining olefinic protons, resonating at 5.29 ppm (signal A in the spectrum), relative to the number of glyceride methylene protons (signal B in the spectrum) [1]. This parameter is an important indicator of the development of rancidity and was employed to monitor the lipid oxidation process in vegetable oils [2].

The traditional determination of the unsaturation degree of an oil consists in the quantitative reaction of iodine to fatty acids double bonds, giving as a result the iodine value (IV). It can be obtained directly from the NMR spectrum by means of the following equation:

$$\begin{aligned}\mathrm{IV} = {} & 253.8[(A - B/4)/2 + (E/4 + C/2)]/2/100 \cdot \\ & \text{average molecular weight,}\end{aligned}$$

where 253.8 is the molecular weight of iodine, and the average molecular weight of the considered oil is obtained as follows:

$$\begin{aligned}&\text{average molecular weight}\\ &\quad = 15.034(G + H)/3 + 14.026(C + D + E + F + I)/2\\ &\qquad + 173.100B/4 + 26.016(A - B/4)/2,\end{aligned}$$

where A–I are the integrals of the signals present in the spectrum in Figure 1. The IV was determined for several vegetable oils and coincided with that obtained by the conventional method [3].

The measurement of the ratio of olefinic to aliphatic protons was proposed to follow the oxidative deterioration of fish oils [4], since the common peroxide value is not easily measurable due to the high content of unstable polyunsaturated acids. A good correlation between the determined NMR index and peroxide value was also verified.

From the integrals of the signals A–I, the quantification of classes of fatty acids (saturated, monounsaturated, linoleic, and linolenic acids) [5] can also be carried out (Table 1). These data are well correlated with those obtained with the official chromatographic method, although they are less detailed, but these determinations are sufficient for preliminary quality and authenticity evaluations.

Recently, other procedures based on ^{1}H NMR spectra have been proposed for the quantification of fatty acids in prepared triacylglycerols mixtures [6] and in mixtures of methyl esters and triacylglycerols [7].

The methyl group of linolenic acid (signal G in Figure 1) can be used to quantify this acid but, in corn and olive oil, this signal is quite small, therefore accurate quantification through the formula given in Table 1 is precluded. A more suitable quantification method is based on the comparison of signal G and the nearby ^{13}C satellites of signal H, whose amount is exactly 0.57% of the intensity of signal H. This parameter is important because it permits to detect the adulteration of olive oil with seed oils as soybean and rapeseed oils, since they have a different linolenic acid content. Signal G can also be used to obtain a global measure of the ω-3 polyunsaturated fatty acids

Graham A. Webb (ed.), Modern Magnetic Resonance, 1645–1650.
© 2008 *Springer.*

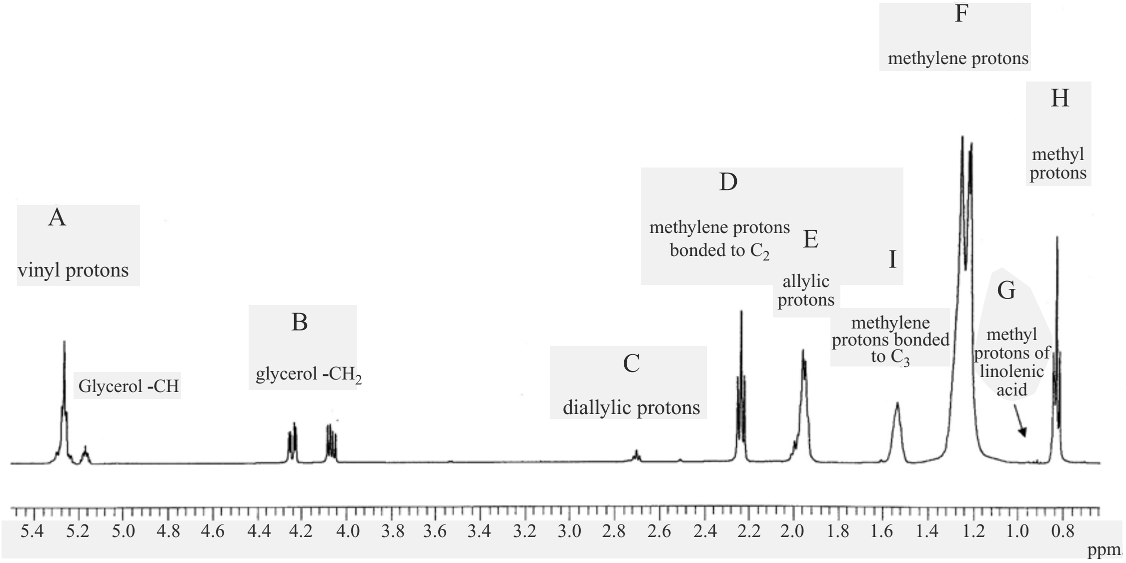

Fig. 1. ^{1}H NMR 500 MHz spectrum of an olive oil.

in fish oils [8]. In order to reduce errors in the quantitative determination, careful attention must be paid to avoid oxidative deterioration of sample oil, because oxidized oils may give signals interfering with measurements. Oils from 24 samples of raw, cooked, and canned albacore tuna were quantified and compared.

Since vegetable oils contain various proportions of saturated, oleic, and polyunsaturated acyl groups, the resulting signals have different chemical shifts and shapes depending on these proportions. A careful observation of the shape and number of peaks of each signal present in the spectra allows to find significant differences between vegetable oils of different composition [9,10]. For example, sunflower oil can be easily distinguished from olive oil due to its high linoleic acid content that is particularly evident in the intensity of the signal resonating at 2.76 ppm. Protons of linoleic acid give visible signals at 0.89 ppm, and at 2.06 ppm, due, respectively, to the terminal methyl group and to allylic protons of linoleic acid. A careful observation of the spectra can be also useful to distinguish oils of similar composition, such as olive and hazelnut oils. In fact, the presence of a very small proportion of linolenic acid in olive oil (∼1%) permits to distinguish it from hazelnut oil, whose amount of linolenic acid is much lower (∼0.1%). Moreover, the difference in saturated acids, higher in olive than in hazelnut oil, is evident also observing the shape of the signal due to methylene protons, that is formed by three signals, resonating at slightly different chemical shifts, due to saturated, oleic, and linoleic acids. These slight differences in unsaturated and polyunsaturated fatty acids content between olive and hazelnut oil become less remarkable when a real adulteration problem is concerned, and mixtures of hazelnut and olive oil have to be detected. In this case, pure and adulterated samples cannot be distinguished by a visual inspection of the spectra. To solve this problem, a multivariate statistical method was developed and evaluated first on a big number of pure and adulterated samples [11]. The integrals of peaks resonating at 5.29, 2.76, and 1.6 ppm were chosen as variables for statistical analysis, since they reflect, respectively, the amount of unsaturated, polyunsaturated fatty acids, and the total content of fatty acids. Moreover, the ratio of linolenic respect to linoleic acid and the ratio of linolenic to all other fatty acids were determined calculating ratios of suitable signal heights. Discriminant analysis was applied to these

Table 1: Calculations of fatty acid composition of oils by signal intensities in the ^{1}H NMR spectrum

Fatty acids (%)	Formula
Linolenic acid	$100[G/(G+H)]$
Linoleic acid	$100(3C-4G)/2(G+H)$
Unsaturated acids	$100(E/2D)$
MUFA	$100\{E/2D-[G(G+H)]-[(3C-4G)/2(G+H)]\}$
Saturated acids	$100[H/(G+H)-E/2D]$

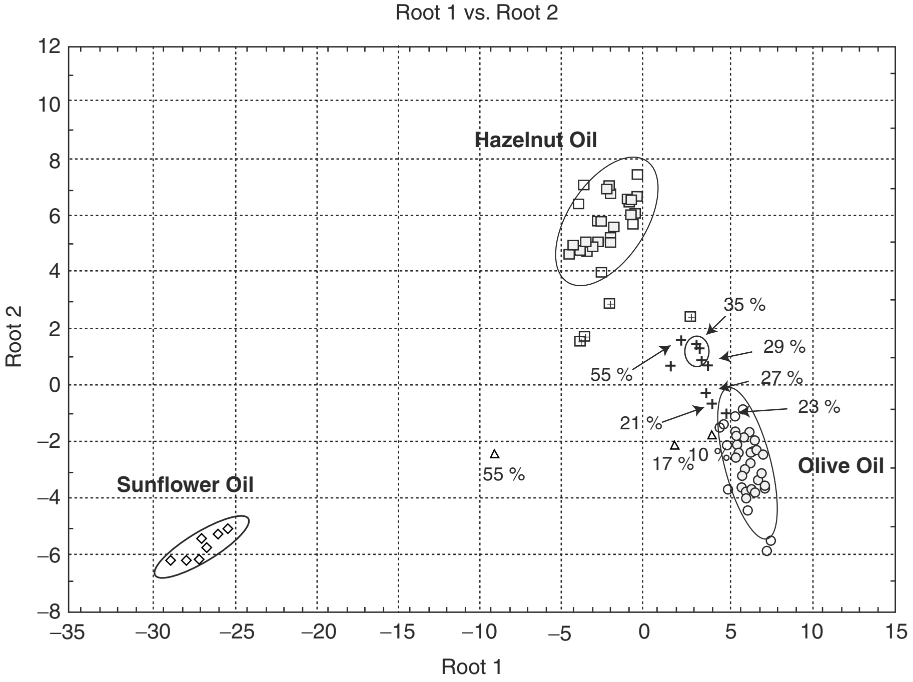

Fig. 2. Plot of discriminant functions determined by ^{1}H NMR parameters. Circles: olive oils; squares: hazelnut oils; rhombus: sunflower oils; crosses: mixtures (m/m%) of olive oil and sunflower oil; triangles: mixtures of olive oil and hazelnut oil. The ellipses display the 95% confidence range for each group of oils. The big cross indicates one olive oil which was repeated four times (from Ref. [11]).

variables permitting the detection of mixtures at a minimum level of 25% hazelnut oil (Figure 2).

Some analytical methods for the detection of mixtures of hazelnut oil in olive oil are based on the observation of the differences in δ and γ tocopherol and in β/δ tocopherol ratio [12], that are normally higher in hazelnut oil, and on LC/GC analysis of the esterified sterolic fraction [13]. These methods reveal the addictions of 5–10% of hazelnut oil, but need long times of sample preparation. ^{1}H NMR spectroscopy can be interesting as a screening method, because it allows much shorter times for sample preparation and analysis.

A statistical approach was also applied to the analysis of 13 types of vegetable oils and mixtures of virgin olive oil with seed oils (corn, sunflower, and soybean oil) in an attempt to establish the lowest possible detection level of adulteration. In this case, it was necessary to combine several oil compositional parameters obtained by two NMR approaches. 1,2-diglycerides, 1,3-dyglicerides, and sterols were determined by analysis of ^{31}P NMR spectra after derivatization of diglycerides with 2-chloro-4,4,5,5-tetramethyl dioxaphospholane. On the same phosphitylated samples, ^{1}H NMR spectra were carried out and fatty acids were quantified [14]. With this method, it was possible to detect olive oil adulteration at 5%.

The analysis of the ^{1}H NMR spectrum of fish oils permits the quantitative determination of docosahexaenoic acid (DHA), whose positive influence on human health has been emphasized. Its content depends on the fish species, on age, on storage and processing, due to the oxidative deterioration of the highly unsaturated lipids. Due to their proximity to a double bond, methylene C2 protons of DHA resonate downfield to C2 signals of other fatty acids. It was thus possible to determine the DHA content in mg/g in fish oils by comparing the signal areas of the C2 protons of DHA with those of other fatty acids, in the presence of an internal standard solution of ethylene glycol dimethyl ether and 1,4-dioxane [15].

Minor Compounds

Phenolic Compounds

Phenolic compounds play an important role in the nutritional characteristics and oxidation stability of edible vegetable oils. The majority of seed oils contains only traces of phenolic compounds, while virgin olive oil is particularly rich in these antioxidants. Moreover, these compounds contribute in a characteristic way to oil sensory qualities, since they are responsible for its bitter and pungent flavor. The bitter taste is particularly related to the presence of oleuropein glucoside and its aglycon. The content of phenolic compounds in olive oils is heavily affected by the variety, origin, and maturity degree of olives [16]. Phenyl acids and phenyl alcohols (like tyrosol and hydroxytyrosol) have been found prevalently in olives [17], but are also present in olive oil. The prevalent phenolic constituents of olive oil are secoiridoid derivatives, such as the dialdehydic form of the elenolic acid linked to hydroxytyrosol or to tyrosol (ligstroside) and the elenolic acid linked to hydroxytyrosol (oleuropein aglycon). Their structure has been identified using NMR [18], after extraction in absolute methanol and separation by HPLC. Other compounds detected in olive oil phenolic fraction, whose structure was elucidated with NMR, are demethyl-oleuropein, glucosides of hydroxytyrosol [19] and also two soluble lignans—pinoresinol and its derivative, 1-acetoxypinoresinol [20].

Aldehydes and Volatile Compounds

The aldehydic compounds are important in the evaluation of oil quality for two reasons: first of all they permit to follow the oils oxidative processes; secondly, due to their volatility, they play an important role in the sensory attributes of olive oils.

The first ^{1}H NMR studies regarding oxidation processes of edible oils have been conducted on pure triacylglycerols, like trilinolein, trilinolenin, and triolein. When these model systems were brought to 40 °C in presence of pure oxygen, they formed principally *mono*-hydroperoxides, together with *bis*-hydroperoxides and *tris*-hydroperoxides [21,22] that produce a characteristic signal at 8–8.9 ppm, due to the hydroperoxide group. Other authors [23,24] have directly monitored by ^{1}H NMR spectroscopy the deterioration process of edible oils submitted to thermal stressing, in order to study the nature and levels of potentially toxic products, which were produced during heating at frying temperature. They detected the presence of signals due to hydroperoxides and saturated, *mono*-unsaturated, *di*-unsaturated, and hydroxy *mono*-unsaturated aldehydes. While saturated and *mono*-unsaturated aldehydes were present in various vegetable oils, the last two were also detected in oils containing a high quantity of polyunsaturated fatty acids (as linseed oil). From these studies, it was concluded that the oxidation process occurs in two stages. In the first stage of thermal oxidation, the fatty acids take oxygen-forming hydroperoxides. When the hydroperoxide concentration reaches a certain level, and when the thermal process is intensified, second oxidation occurs with the formation of aldehydic compounds that are responsible of the undesirable rancid flavor. These aldehydes can be easily detected in the low-field region of the ^{1}H NMR spectrum [25] and can be used to follow the oxidation process of an oil and to evaluate its oxidative stability.

The composition of volatiles plays an important role in defining the sensory quality of virgin olive oils. Positive (green-fruity odor, etc.) and negative attributes (bitter tasting, etc.) have been correlated with the presence of aldehydes, alcohols, polyphenols, terpenes, and acetic acid. The very low concentration of these compounds in virgin olive oil makes possible their direct determination only by high field (500–600 MHz) ^{1}H NMR [26]. In order to observe these polar minor compounds, they should be soluble in the used solvent. For this reason, a trace of DMSO-d_6 is added to chloroform-d in the NMR tube. Moreover, a high number of scans (4000) is a necessary acquisition parameter to obtain these minor compounds with appreciable intensity (Figure 3).

Sterols

The signal due to methyl CH_3 in position 18 of the sterols resonates between 0.6 and 0.7 ppm. The signal due to methyl 18 signal of β-sitosterol, resonating at 0.62 ppm, has been clearly identified in virgin and refined olive oils. Its intensity can be compared with the resonance of ^{13}C satellites of the methyl group of fatty acids, permitting the quantification of β-sitosterol [5], that can be useful to distinguish seed and pomace oils from olive oils, since the former have shown a higher amount of β-sitosterol and other sterolic compounds.

Signals due to stigmasterol [26] and to cyclo-arthenol [27] have been also detected in olive oils.

Diglycerides

Diglyceride content and the ratio of 1,2-diglycerides and 1,3-dyglicerides represent an important index of olive oil quality and freshness. The quantitative evaluation of these compounds can be performed with medium field ^{1}H NMR (200–400 MHz) after oil derivatization with trichloroacetyl isocyanate that reacts with hydroxyl groups of diglycerides leading to the quantitative formation of trichloroacetyl carbamates [28]. After derivatization the CH_2 and CH glycerol resonances of 1,2-diacylglycerides are well resolved from the triacylglyceride multiplets, therefore an integration of the relative signal intensities is possible, permitting to evaluate the amounts of 1,2- and 1,3-diglycerides. In addition, the diglyceride proton is converted by derivatization in

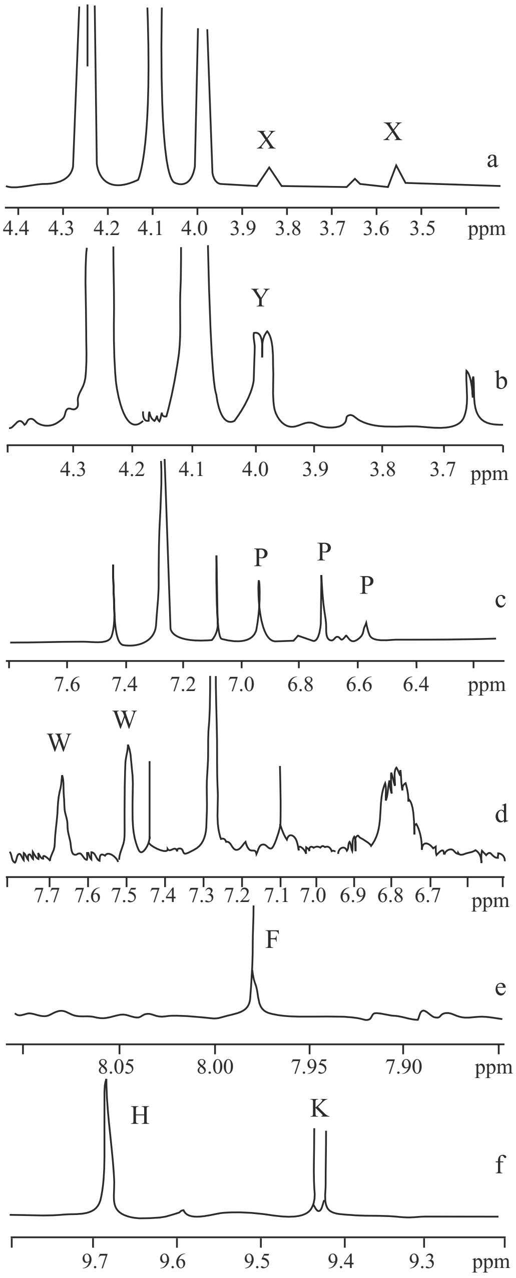

Fig. 3. ^{1}H NMR spectrum of olive oil. (a) X are the characteristic resonances of a bitter oil; (b) Y of a vinegary tasting oil; (c) and (d) P and W are soluble phenols; (e) F is formaldehyde present in pungent oils; (f) K and H are aldehydes in green-fruity olive oils (from Ref. [26]).

the NH proton, that resonates at 8.4 ppm and it can be integrated to give a quantitative measure of the free hydroxyl groups. The results obtained by this method agree with those obtained with ^{13}C NMR approach (see Section “Minor oil components” in “^{13}C NMR of oils”). Anyway, the same information can be achieved with 600 MHz ^{1}H NMR, since resonances of glyceryls protons of 1,2-diglycerides and 1,3-dyglicerides can be detected without the need of derivatization [5]. The same signals were also easily monitorable in the ^{1}H NMR spectra of encapsulated marine oil supplements [29].

Use of ^{1}H NMR Spectroscopy to Characterize Olive Oil Geographical Origin

Extra virgin olive oil is very valuable among edible oils due to its high nutritional value. Its characteristics are determined by a series of factors: nature of the soil, climate, variety of the plant, cultivation, and extraction techniques. In order to protect producers of high quality olive oils and ensure consumer awareness of product quality, European Community legislation has introduced the Protected Designation of Origin (PDO) mark that allows the labeling of virgin olive oils with the names of the areas where they are produced. This certification increases the oil value. Several studies, based on the combination of ^{1}H NMR data and multivariate statistical analysis, have been performed for the systematic characterization of olive oils composition. One of the first works was carried out on 55 olive oils coming from four Italian regions [30]. The samples were dissolved in a mixture of 0.7 ml of chloroform-*d* and 20 μl of DMSO-d_6 and the spectra were run on a 600 MHz spectrometer. The heights of 30 resonances present in the spectra were measured and normalized to the height of the signal due to the methylene resonance at 1.26 ppm, to give an index proportional to the molar ratio between each compound and the total amount of fatty acids. Afterwards, a variable selection method permitted to identify peaks which showed significant variations for oils of different geographical origins, that are due to β-sitosterol, saturated and unsaturated aldehydes, and volatile compounds. A cluster analysis was applied to the selected resonances permitting to discriminate the oils in relation to their geographical origin. This procedure demonstrated its reliability when applied on an enlarged data set formed by 216 oils collected in 3 years from different Italian regions, using the same set of selected resonances [31] (Table 2).

The question of geographical identification becomes more interesting when it regards small production areas, where high quality products are often obtained. Moreover, often there are several PDO oils in one region, produced in areas not far from each other, as it happens in some Italian regions, like Apulia and Tuscany, where four and three PDO were, respectively, designated for olive oil. For this

Table 2: Chemical shift assignment of the selected resonances used for geographical origin discrimination of olive oils (according to Ref. [31])

δ (ppm)	Group	Compound
9.70	−CHO	Hexanal
9.61	−CHO	Unsaturated aldehyde
9.54	−CHO	Unsaturated aldehyde
9.45	−CHO	*Trans*-2 hexenal
8.00	−CH	Formaldehyde
4.88	Nd	Cycloarthenol
4.65	Nd	Terpene
4.63	Nd	Terpene
4.53	Nd	Terpene
1.62	$-CH_3$	Squalene
0.62	$-CH_3$	β-sitosterol

reason, the same previously described statistical approach was used to discriminate 42 extra virgin olive oils from three different zones in Tuscany [32]. Several hierarchical clustering procedures and discriminant analysis were applied on the signal intensities confirming the potential of ^{1}H NMR in the differentiation of PDO oils. It was also interesting to notice that when oils differed in geographical origin and in cultivar, a better separation of the oils resulted, indicating that both cultivar and geographical origin contributed to the differentiation of oils.

A different approach consisted in the application of ^{1}H NMR to the phenolic extracts of olive oil samples coming from three close and restricted geographic areas. The peak intensities were determined and signals due to aldehydic, vinyl, and aromatic protons of the phenolic compounds were selected for the statistical analysis according to their capability of discriminating the origin of the samples. Discriminant analysis was applied to the selected intensities of the NMR signals [33] and permitted to separate the oils according to their geographical origin obtaining a predictive capacity of 88%.

References

1. Sacchi R, Addeo F, Giudicianni I, Paolillo L. Riv. Ital. Sostanze Grasse 1989;66:171.
2. Cengarle L, Carta A, Pranzetti P. Riv. Ital. Sostanze Grasse 1992;69:463.
3. Miyake Y, Yokomizo K, Matsuzaki N. J. Am. Oil Chem. Soc. 1998;75:15.
4. Saito H. Agric. Biol. Chem. 1987;51:3433.
5. Sacchi R, Patumi M, Fontanazza G, Barone P, Fiordiponti P, Mannina L, Rossi E, Segre AL. J. Am. Oil Chem. Soc. 1996;73:747.
6. Guillén MD, Ruiz A. Eur. J. Lipid Sci. Technol. 2003;105: 688.
7. Knothe G, Kenar JA. Eur. J. Lipid Sci. Technol. 2004;106: 88.
8. Igarashi T, Aursand M, Hirata Y, Gribbestad IS, Wada S, Nonaka M. J. Am. Oil Chem. Soc. 2000;77:737.
9. Guillén MD, Ruiz A. J. Sci. Food Agric. 2003;83:338.
10. Guillén MD, Ruiz A, Cabo N, Chirinos R, Pascual G. J. Am. Oil Chem. Soc. 2003;80:755.
11. Fauhl C, Reniero F, Guillou C. Magn. Res. Chem. 2000;38: 436.
12. Morchio G, Pellegrino A, Mariani C, Bellan G. Riv. Ital. Sostanze Grasse 1999;76:115.
13. Mariani C, Bellan G, Morchio G, Pellegrino A. Riv. Ital. Sostanze Grasse 1999;76:297.
14. Vigli G, Philippidis A, Spyros A, Dais P. J. Agric. Food Chem. 2003;51:5715.
15. Sacchi R, Medina I, Aubourg SP, Addeo F, Paolillo L. J. Am. Oil Chem. Soc. 1993;70:235.
16. Amiot MT, Fleuriet A, Macheix JT. J. Agric. Food Chem. 1986;34:823.
17. Gariboldi P, Jommi G, Verotta L. Phytochemistry 1986;24: 865.
18. Montedoro GF, Servili M, Baldioli M, Selvaggini R, Miniati E, Macchioni A. J. Agric. Food Chem. 1993;41:2228.
19. Bianco A, Mazzei RA, Melchioni C, Romeo G, Scarpati ML, Soriero A, Uccella N. Food Chem. 1998;63:461.
20. Brenes M, Hidalgo FJ, Garcia A, Rios JJ, Garcia P, Zamora R, Garrido A. J. Am. Oil Chem. Soc. 2000;77:715.
21. Neff WE, Frankel EN, Miyashita K. Lipids 1990;25:33.
22. Frankel EN, Neff WE, Miyashita K. Lipids 1990;25:40.
23. Moya Moreno MCM, Mendoza Olivares D, Amèzquita López FJ, Peris Martínez V, Bosch Reig F. J. Mol. Struct. 1999;482–483:557.
24. Schiller J, Süß R, Petković M, Arnold K. Eur. Food Res. Technol. 2002;215:282.
25. Sacchi R. In: GA Webb, PS Belton, AM Gil, I Delgadillo (Eds). Magnetic Resonance in Food Science. The Royal Society of Chemistry: Cambridge, 2001, p 213.
26. Mannina L, Segre A. Grasas y Aceites 2002;53:22.
27. Segre AL, Mannina L. Recent Res. Dev. Oil Chem. 1997;1:297.
28. Sacchi R, Paolillo L, Giudicianni I, Addeo F. Ital. J. Food Sci. 1991;4:253.
29. Siddiqui N, Sim J, Silwood CJL, Toms H, Iles RA, Grootveld M. J. Lipid Res. 2003;44:2406.
30. Sacchi R, Mannina L, Fiordiponti P, Barone P, Paolillo L, Patumi M, Segre AL. J. Agric. Food Chem. 1998;46:3947.
31. Mannina L, Patumi M, Proietti N, Bassi D, Segre A. J. Agric. Food Chem. 2001;49:2687.
32. Mannina L, Patumi M, Proietti N, Segre AL. Ital. J. Food Sci. 2001;1:53.
33. Sacco A, Brescia MA, Liuzzi V, Reniero F, Guillou C, Ghelli S, Van Der Meer P. J. Am. Oil Chem. Soc. 2000;77:619.

SNIF-NMR—Part 1: Principles

Gérard J. Martin[1], Serge Akoka[2], and Maryvonne L. Martin[1]
[1] *Eurofins Scientific, 44323 Nantes, France; and*
[2] *University of Nantes, LAIEM, 44322 Nantes, France*

Introduction

Applications of high resolution deuterium-NMR in organic and bioorganic chemistry have regularly expanded in the last decades, accompanying the development of high field spectrometers which are required to overcome, at least in part, the severe drawbacks resulting from the nuclear properties of deuterium. In the technological conditions of the seventies both the small gyromagnetic ratio (4.107×10^7 rad/s/T), responsible for poor intrinsic sensitivity (9.6×10^{-3} with respect to ^1H), and the very low natural abundance of deuterium (1.5×10^{-4}) were serious impediments to the study of natural abundance deuterium spectra. Fortunately, the predominance of quadrupolar relaxation avoids perturbations in signal intensities due to nuclear Overhauser effects. Since 1980, more than 300 articles have been published in the field of high resolution ^2H-NMR and, in this number, about 200 are concerned with quantitative determinations of isotope ratios, for which we have proposed the terminology SNIF-NMR (site-specific natural isotope fractionation studied by nuclear magnetic resonance). Both the first paper dealing with the NMR determination of non-random distributions of deuterium and the corresponding patent concerning applications appeared in 1981 [1,2].

Isotopic Abundances and Isotopic Ratios

In a closed system at equilibrium (chemical, plant, animal) the distribution of the different isotopes of a given atom may be described by overall and specific parameters which must satisfy mass and isotopic balance.

For a given atom, such as carbon or hydrogen, having both a heavy and a light stable isotope, the *isotopic abundance*, A, is the ratio of the number of heavy isotopes, H, to the number of heavy and light, L, isotopes:

$$A = H/(H + L) \tag{1}$$

The *isotope ratio*, R, is the ratio of the numbers of heavy and light isotopes:

$$R = H/L \tag{2}$$

A and R are related by the simple relations:

$$A = R/(R + 1) \tag{3a}$$

$$R = A/(1 - A) \tag{3b}$$

In principle, a given molecular species is composed of a large number of isotopomers containing one or several isotopes. Thus, for a given chemical species $C_xH_yO_z$, the theoretical number of isotopomers, N, is:

$$N = (XH_3 + 1)^a(XH_2 + 1)^b(XH_1 + 1)^c(2^x)(3^z) \tag{4}$$

where a, b, and c are the numbers of XH_3, XH_2, and XH_1 groups contributing respectively to 4, 3, and 2 isotopomeric possibilities. For example, vanillin, $C_8H_8O_3$, has 884,736 isotopomers.

In the case of hydrogen, owing to the low natural abundance of the deuterium isotope, the presence of bi-deuterated (and *a fortiori* multi-deuterated) molecules may be neglected at the usual precision of the NMR determinations and only mono-deuterated isotopomers are generally considered. In these conditions, the A and R values are equal. However, in the case of carbon for instance the A and R parameters should not be confused and bi-labeled molecules may no longer be ignored.

It may also be convenient to express the isotopic content in terms of the relative parameter, δ, commonly used in isotope ratio mass spectrometry (IRMS). The isotopic deviation, expressed in ‰, refers the isotopic content of the considered sample or molecule, i, to that of an international reference, ref:

$$\delta_i = 1000(R_i - R_{\text{ref}})/R_{\text{ref}} \tag{5}$$

The reference is a compound carefully calibrated by interlaboratory campaigns of measurements conducted by international organizations: IAEA (Vienna), IRMM (Geel), NIST (Washington, DC). The certified values of the isotopic ratio and isotopic abundance of the Vienna-Standard Mean Ocean Water (V-SMOW) [3] are 155.76 and 155.74 ppm, respectively. A secondary reference, the Standard Light Antarctic Precipitation (SLAP), exhibiting an isotope ratio of 89.0 ppm, is also available from IAEA in Vienna.

Graham A. Webb (ed.), Modern Magnetic Resonance, 1651–1658.
© 2008 *Springer.*

The site-specific isotope ratio, R_i, of a given molecular site, i, has been defined in the same way [4]:

$$(D/H)_i = D_i/H_i \tag{6}$$

where D_i is the number of deuterium atoms at site i. Since the presence of bi-deuterated molecules can usually be neglected D_i represents the number of isotopomers mono-deuterated at site i. H_i, the total number of hydrogen atoms of type i, is equal to $P_i N_H$ where P_i is the number of equivalent positions at site i and N_H the number of fully protonated molecules. The ^{2}H-NMR investigation of SNIF is presently the only way to access directly and simultaneously to hydrogen isotope ratios, $(D/H)_i$, associated with different positions, i, in a given molecule.

It is also convenient to define a relative parameter, $R_{i/j}$:

$$R_{i/j} = F_j S_i/S_j \tag{7}$$

where S is the intensity of signal i or j. $R_{i/j}$ represents the number of heavy isotopes at site i in a situation where site j is arbitrarily given its stoichiometric number of atoms, F_j. In principle, S is the area of the NMR signal. However, $R_{i/j}$ may be semi-empirically defined on the basis of signal heights which are usually measured with better precision than signal areas. Obviously, when computed from signal heights, the $R_{i/j}$ parameters measured in different samples of a given molecular species may be safely compared only on condition that constant transverse relaxation times are maintained by strictly identical preparation of the samples. In the case of ethanol, for instance, the line widths of the methyl and methylene deuterium signals being nearly equal, the ratio of signal heights is close to the ratio of signal area. When the methylene site, $i \equiv \mathrm{II}$, is compared to the methyl site, $j \equiv \mathrm{I}$, characterized by the stoichiometric number of hydrogens $F_{\mathrm{I}} = 3$, the value of $R_{\mathrm{II/I}}$ usually differs strongly from the statistical value 2 which would correspond to a random distribution of the deuterium atoms. Values of $R_{\mathrm{II/I}}$ higher than 2.7 are determined for instance in ethanol samples resulting from the fermentation of beet sugar.

Isotopic Fractionation

As discussed in Part 2, isotopic fractionation may occur at many steps of the elaboration of a product as a result of thermodynamic or kinetic isotope effects. The site-specific isotopic ratios of a molecule are therefore governed by the isotope contents in the precursor sites of the starting materials and by the subsequent individual fractionating events.

The Mass and Isotopic Balance

In a physical, chemical, or biochemical transformation the parameters of the starting and resulting compounds are connected by mass and isotopic balance relationships. Considering a complete transformation of a given compound, S, into two products P and Q, with mole fractions x and (1 - x), the mass and isotope balance requires that the isotopic abundances are related by:

$$A_S = xA_P + (1-x)A_Q \tag{8}$$

Denoting α_P and α_Q the fractionation factors of P and Q, the disproportionation of isotopes from S to P and Q is written:

$$A_S = \alpha_P A_P = \alpha_Q A_Q \tag{9}$$

More generally the overall isotopic abundances, A_S and A_Q of initial, S, and final, Q, states composed, respectively of $i = 1$ to n and $j = 1$ to m components are:

$$A_S = A_1x_1 + A_2x_2 + \ldots + A_ix_i + \ldots + A_nx_n \tag{10a}$$

$$A_Q = A_1x_1 + A_2x_2 + \ldots + A_jx_j + \ldots + A_mx_m \tag{10b}$$

Obviously, in a closed system where the S components have been completely transformed into Q: $A_Q = A_S$

Site-Specific Hydrogen Fractionation

If the deuterium isotope was randomly distributed within a given molecule, S, containing P hydrogen atoms, the molar fraction of isotopomer i would be equal to the statistical value $F_i = P_i/P$ where P_i denotes the number of equivalent hydrogen positions at site i. In fact, we have shown that most molecules exhibit strong deviations with respect to a statistical distribution of deuterium [1] and that the true molar fractions of the mono-deuterated isotopomers, denoted f_i, can be directly determined by quantitative ^{2}H-NMR. For a molecule with n different sites, the site-specific isotope ratio, R_i, is related to the overall isotope ratio, R, by:

$$R_i = f_i R/F_i \tag{11a}$$

$$R = \Sigma_i^n F_i R_i \tag{11b}$$

If we consider again the complete transformation of a set of starting materials, S, containing n sites, into products, Q, the deuterium content, R_j^Q, in every site, j, of an end product, Q, can be computed with a good approximation, from the deuterium contents, R_i^S, in the different sites, i, of the starting molecules [5]:

$$R_j^{\mathrm{Q}} = \sum\nolimits_i^n a_{ji} R_i^{\mathrm{S}} \tag{12a}$$

or, in matrix notation:

$$\mathbf{R}^{\mathrm{Q}} = [\mathrm{A}]\mathbf{R}^{\mathrm{S}} \tag{12b}$$

where $\mathbf{R}^{\mathrm{Q}}$ and $\mathbf{R}^{\mathrm{S}}$ are the column vectors of the deuterium contents in the end and starting molecules respectively and [A] is the matrix of the transfer coefficients, $a_{ji,}$ which connect selectively every site j of an end product to every site i of the reactants. These redistribution coefficients are powerful sources of mechanistic information (cf. Part 2). In particular, the a_{ji} value enables to determine whether a given hydrogen j of a reaction product is connected or not to hydrogen at position i of a starting compound. Intermolecular hydrogen exchanges occurring in the course of the reaction pathway for instance are thus detected [5].

Isotopic Fractionation in the Preparation of the Sample

Thermodynamic and kinetic isotope effects associated with physical transformations (cf. Part 2) have important repercussions on the reliability of the experimental isotopic parameters. Usually, a compound extracted from a chemical or natural medium has been subjected to various technological or chemical treatments, each of them being likely to be responsible for isotope effects. Consequently, the SNIF values measured on the extracted product may be considered as representative of the true isotopic parameters of the molecule only on condition that the compound has been completely recovered and that no hydrogen exchange with the medium has occurred [6]. In comparative studies of a given molecular species incompletely extractable from different materials it is therefore necessary either to elaborate a non-fractionating analytical chain or to define standardized analytical procedures in which isotopic fractionation is strictly controlled. In the last case, fractionation effects may be considered as reproducible and the experimental isotope ratios may be safely discussed on a relative basis.

Quantitative Deuterium-NMR

Experimental Parameters

Firstly it should be emphasized that, in a given magnetic field, the chemical shift discrimination expressed in frequency units is 6.5 times lower in ^{2}H-NMR as compared to proton NMR. With a spectrometer characterized by a proton nominal frequency of 400 MHz, for example, deuterium-NMR has therefore a resolution potential somewhat analogous to that of ^{1}H-NMR at 60 MHz. Consequently, in order to optimize peak separation it is advantageous to resort to high field equipments (11.4 T spectrometers are currently used). Neglecting small intrinsic isotope shifts, the deuterium chemical shifts expressed in ppm are identical to the corresponding proton chemical shifts. This property is very useful for assigning deuterium signals. However, differences in solvent shifts affecting the ^{1}H and ^{2}H spectra must be avoided or taken into account. In a first step, a complete analysis of the proton spectrum has therefore to be achieved by exploiting, if necessary, all resources of available one- and two-dimensional NMR sequences.

As previously noted, the relaxation of the deuterium nuclei (spin 1) is dominated by the relatively efficient quadrupolar mechanism. Consequently, nuclear Overhauser effects, which are mainly due to dipolar relaxation components, may usually be neglected. This property has important repercussions on the technical conditions of spectrum acquisition and on the methods of quantitative analysis. In particular, it is not necessary to resort to time-consuming gated decoupling sequences aimed to eliminate Overhauser enhancements. For simple organic molecules reorienting relatively rapidly, the quadrupolar longitudinal, T_1, and transversal, T_2, relaxation times are equal and relatively short. Short relaxation times are favorable from the sensitivity point of view since they authorize fast signal accumulation. However line widths increase when T_2 decreases. Fortunately, in the case of deuterium, the quadrupolar coupling constant is relatively small and the relaxation times of small molecules are frequently higher than 0.1 s. These values are convenient for efficient accumulation of signals with moderate line widths. For example, in the case of ethanol, accumulation of 90° pulses with an acquisition time At equal to 6.8 s fits conveniently the condition At $>6\ T_1$ required to recover at least 99.8% of the magnetization of the methyl isotopomer characterized by a relaxation time T_1 equal to 1 s. To recover the same proportion of the methylene isotopomer ($T_1 = 1.25$ s) an acquisition time $A_{\mathrm{t}} = 7$ s would be required. Moreover, the signal is sampled finely enough to ensure correct curve fitting. In order to minimize random fluctuations due to short-term instabilities of the spectrometer, each spectrum recorded with a given number of scans, N_{S}, is repeated N_{E} times, leading to a duration $N_{\mathrm{S}} \times N_{\mathrm{E}} \times A_{\mathrm{t}}$ of the experiment. For ethanol or vanillin studied at 11.75 T (500 MHz ^{1}H spectrometer) in a 10 mm OD cell with an acquisition time of 6.8 s, 2.4 and 5.8 h, respectively, are needed. At 7.05 T (300 MHz ^{1}H spectrometer) and in the same conditions the experimental times are, respectively, equal to 9.7 and 23.2 h. In order to weaken these drastic conditions the acquisition time for ethanol can be reduced from 6.8 to 3.4 s but at the price of a small decrease of the internal repeatability. As in most linear analytical techniques, the standard deviation of a series of measurements decreases with the number of repetitions, and obviously the precision increases with the signal-to-noise ratio.

From these properties, it is clear that the method is subjected to severe limitations when the compound to be investigated is available only in small quantity (<0.5 g) or when it is insufficiently soluble. In addition, since line widths increase rapidly when the size of the molecule increases, the spectra of large slowly reorienting molecules are hardly exploitable.

Signal Processing

Random and systematic errors occurring in quantitative treatments of NMR spectra have been fully documented [7–11]. They are attributed to instrumental instabilities, baseline distortions, phase corrections, imperfect algorithms for integrals estimation, etc. In particular, the manual phasing and fitting steps are responsible for operator dependent errors. Processing in the time domain was claimed to obviate artifacts arising after Fourier transformation. In this respect, interesting performances are exhibited by methods such as linear prediction and singular value decomposition which require no prior knowledge on behalf of the user [12,13]. However, in our case it is preferable to work in the frequency domain which offers the possibility of estimating the curve-fitting quality for every resonance. Quantitative analysis of deuterium spectra is fundamentally improved by a dedicated algorithm based on complex least-squares analysis of the NMR signal [14]. In the absence of truncation of the free induction decay, for reasonable values of the signal-to-noise ratio (>20), and in the hypothesis of Gaussian noise, this algorithm was theoretically proved to ensure optimum precision compared to all other exact and differentiable algorithms. The data are modeled as a sum of Gaussian noise, unphased Lorenztians, and zero-, first-, and second-order baseline distortions. The method, which is well suited for quantitative determination of spectra containing a limited number of signals (<30), rigorously manages all experimental parameters: frequencies, damping factors, intensities, phases, acquisition delay (described by specific intensity and phase parameters). The iteration time depends only on the number of signals since the number of sampling addresses is nearly the same whatever the molecule studied. In the pioneering times of bench top computers, 3 s were needed to compute a 10-signal spectrum but iteration is now instantaneous. Therefore, quantitative determination can be rapidly achieved in fully automatized conditions.

For identical acquisition conditions, the standard deviation, σ, on signal intensity computed from the complex least-squares treatment, is inversely proportional to the signal-to-noise ratio:

$$\mathrm{Log}(\sigma) = -\mathrm{Log}(S/N) + \mathrm{Cst} \tag{13}$$

A 10-fold increase in the signal-to-noise ratio increases the precision in the same proportion, but obviously at the price of a much longer acquisition time.

As illustrated in Figure 1, complex spectral residuals can be derived from a comparison of the real and simulated spectra. These residuals enable systematic components to be sorted out, such as isotopic satellite lines, and spectral distortions with respect to the Lorentzian model [14,15]. It was shown in particular that these distortions are mainly spectrometer dependent.

Referencing of Isotopic Parameters

For a given molecular species, the isotopic profile expressed in terms of molar fractions, f_i, of the different isotopomers is frequently sufficient for discriminating samples from different origins (cf. Part 3). Consequently, many problems can be solved without the need for isotopic referencing.

More generally, absolute values of the site-specific isotope ratios, $(D/H)_i$, of a compound, S, can be obtained either by using an intra- or intermolecular reference of known isotope content or by measuring independently the overall average isotope ratio of the compound, $(D/H)_{\mathrm{S}}$, by resorting to IRMS.

Referencing by Means of a Working Standard

This approach makes use of a working standard, WS, the $(D/H)_{\mathrm{WS}}$ value of which has been previously determined on the V-SMOW/SLAP scale. The working standard may be either weighed and dissolved into the sample or introduced into a hermetic cell coaxial to the sample cell [16].

In these methods the intensity, $I_{i\mathrm{S}}$, of the i signal in compound S is compared to that of the reference signal, I_{WS}:

$$(D/H)_{i\mathrm{S}} = (D/H)_{\mathrm{WS}}(I_{i\mathrm{S}}P_{\mathrm{WS}}N_{\mathrm{WS}})/(I_{\mathrm{WS}}P_{i\mathrm{S}}N_{\mathrm{S}}) \tag{14}$$

where P_{S} and P_{WS} are the stoichiometric numbers of hydrogen atoms in sites i and WS, and N_{S} and N_{WS} are the numbers of fully protonated molecules of S and WS in the active volume of the coil. When the coaxial arrangement is used, the isotope content in V-SMOW can also be referred to that of WS by using the same cell.

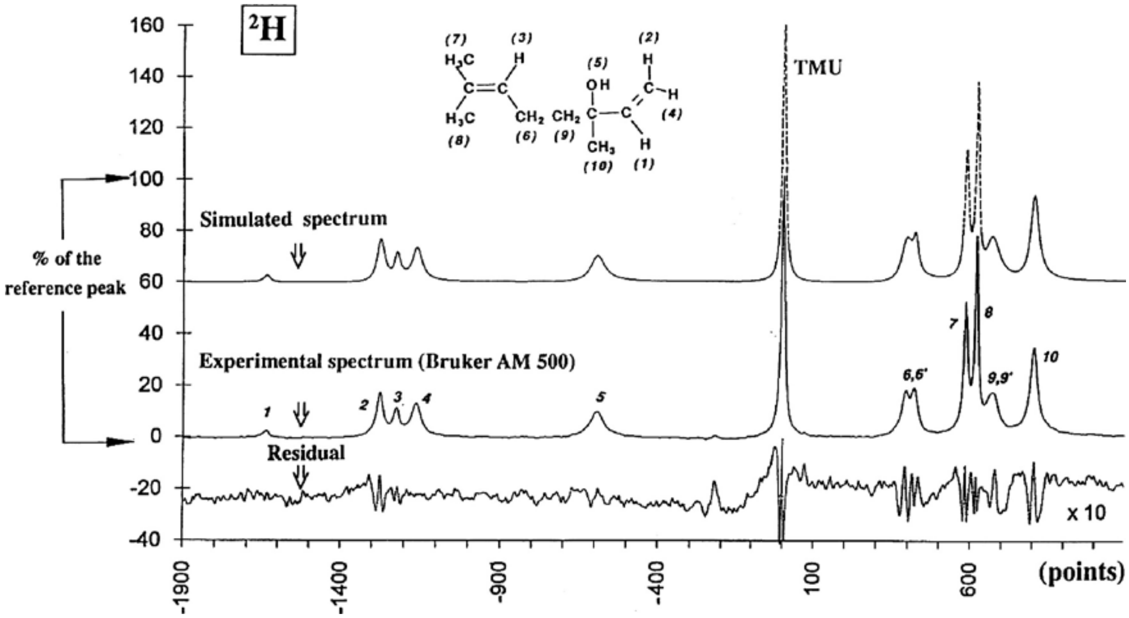

Fig. 1. Complex least-squares curve-fitting of the ^{2}H-NMR spectrum of linalool. The experimental spectrum has been obtained at 76.8 MHz with an AMX Bruker spectrometer equipped with the SNIF-NMR concept system [14]. The residual is represented on a 10 times expanded intensity scale. The isotopic reference is tetramethylurea.

It is necessary to select and calibrate carefully the working standard WS. Its NMR signals should not interfere with those of the target molecule and its volatility, chemical inertness, and solubility should be suitable. Moreover, its relaxation properties should conveniently fit those of the substrate. In this respect, *N*,*N* tetramethylurea, $[(CH_3)_2N]_2CO$ (TMU), was adopted in the study of ethanol used as a probe for investigating thousands of wines and fruit samples [17](Part 4). Samples of TMU with certified values of $(D/H)_{WS}$ are delivered by the Joint Research Centre of the E.U. at Geel, Belgium.

The error on $(D/H)_i$ depends on the quality of integration of the *i* and WS signals and on errors on the weights of S and WS. For simple mobile molecules, the cumulated relative error on mass and ^{2}H intensity, which is generally lower than 0.3×10^{-3}, induces an uncertainty of about 0.3 ppm on $(D/H)_i$. This value is in good agreement with results obtained in several interlaboratory comparison studies [18,19]. Equation (13) does not necessarily imply that the substrate S is chemically pure. If the amount of impurities can be determined with sufficient accuracy, by gas chromatography or proton NMR for instance, the corresponding purity ratio of S is then introduced into Equation (14).

SNIF-NMR has been fully investigated in terms of precision and accuracy. Precision is usually defined as repeatability, *r* (short-term repetition of measurements in the same laboratory, with the same instrument, by the same operator), and reproducibility, *R* (long interval of time between a series of repetitions involving different operators, different instruments, and different laboratories). Statistical expressions of *r* and *R* are derived from the notions of within, S_r^2, and between, S_L^2, variances of series of measurements [20,21]. Denoting *p* the number of laboratories (i) participating in the ring test and *n* the number of repetitions leading to an analytical result (in the case of SNIF-NMR, $n = N_E$ the number of replications of spectra for a given sample), S_r^2, S_R^2, and S_L^2 are given by:

$$S_r^2 = (1/p)\Sigma_1{}^p S_i^2 \tag{15}$$

$$S_L^2 = [1/(p-1)]\Sigma_1{}^p (x_i - X)^2 - S_r^2/n \tag{16}$$

$$S_R^2 = S_r^2 + S_L^2 \tag{17}$$

where x_i and S_i^2 are the mean and the standard deviation of the intensities resulting from *n* replications of spectra and *X* is the general mean.

The repeatability and reproducibility are:

$$r = 2.83\, S_r \text{ and } R = 2.83 S_R \tag{18}$$

The precision and accuracy performance has been reviewed in 1988 [17] but progress in instrumentation and data treatment in the last 15 years has helped to improve the quality of the determinations. In the case of ethanol, the presentation to the Office International de la Vigne et du Vin (OIV) of an up-to-dated version [22] of the UE regulation concerning the application of SNIF-NMR to wine analysis has brought to light the latest performance of the method for the measurement of $(D/H)_{\mathrm{I}}$ (I corresponds to CH_2DCH_2OH): $S_r = 0.29$ ppm, $S_R = 0.43$ ppm. For other types of products, r and R decrease with the size of the molecular probe. In the case of vanillin extracted from vanilla beans, S_r varies from 1 to 2% in relative values depending on the nature of the isotopomer.

Referencing by Combined Use of SNIF-NMR and Isotope Ratio Mass Spectrometry

This approach may be considered as a pseudo hyphenated technique since it uses IRMS to complement SNIF-NMR spectroscopy, according to the relationship:

$$(D/H)_{i\mathrm{S}} = (D/H)_{\mathrm{S}} f_{i\mathrm{S}}/F_{i\mathrm{S}} \tag{19}$$

where $f_{i\mathrm{S}}$ and $F_{i\mathrm{S}}$ are, respectively, the real and statistical molar ratio of isotopomer i and $(D/H)_{\mathrm{S}}$ is the overall isotope ratio of the substrate, S.

$f_{i\mathrm{S}}$ is determined by ^{2}H-NMR, in the absence of additional standard, and $(D/H)_{\mathrm{S}}$ is measured independently by IRMS. In this technique, which requires previous burning of the sample, only the overall isotope ratio of the molecule is directly accessible.

When large series of products involving the same molecular probe have to be studied, Equation (14) is certainly the best choice since it adapts satisfactorily to full automation. However, it should be emphasized that using internal referencing may induce serious biases when the aim is to compare deuterium contents in different chemical species. In this situation, the most accurate method to obtain site-specific isotope ratios is frequently to resort to Equation (19). However, this approach requires that both NMR and mass equipments are available.

Electronical Referencing

Finally, it is possible to refer the isotope ratio of an unknown product to that of a signal electronically generated [23]. The idea of the ERETIC$^{\mathrm{TM}}$ (ERETIC is a trademark of Bruker, France) method is to use as a reference, a pseudo-FID synthesized by an electronic device and transmitted inside the NMR probe during the reception of the NMR signal. If this electronic signal has the same shape and the same frequency as a FID, an additional peak is produced in the spectrum after Fourier transformation. Since all the parameters of this reference peak (half-height, magnitude, chemical shift, and phase) can be freely chosen from the spectrometer console, signal overlap, saturation of the receptor, and other drawbacks encountered with addition of referencing standards are avoided. Furthermore, the ERETIC signal has no T_1 relaxation time and does not introduce a limitation in experiment duration.

The ERETIC signal is obtained by multiplication of a sinusoidal signal (high frequency component) and an exponentially decreasing signal (low frequency component). The high frequency component is provided by one of the channels of the NMR spectrometer. It is derived just before the amplification stage. Most modern NMR spectrometers are equipped with hardware able to synthesize RF shaped pulses. An exponential shape can therefore be numerically defined and used as the low frequency component. In heteronuclear experiments with proton decoupling, as it is the case for isotopic NMR, the pseudo-FID can be transmitted through the proton coil, which is not tuned at the operating frequency (here the deuterium frequency) and acts therefore as a broadband antenna for the ERETIC signal. Because this coil is also used for decoupling, the ERETIC signal has to be mixed with the proton irradiation by an RF coupler placed just before the probe. There is no need for an additional electronic device to apply the method [24].

In the case of isotopic analyses, the intensity, $I_{i\mathrm{S}}$, of signal i in compound S is compared to the intensity, $I_{j\mathrm{C}}$, of site j in the spectrum of a calibration compound, C, run separately. The ERETIC signal is used to compensate for the variation of intensity that arises between the two experiments. By analogy with Equation (14):

$$(D/H)_{i\mathrm{S}} = (D/H)_{j\mathrm{C}}(I_{i\mathrm{S}} P_{j\mathrm{C}} N_{\mathrm{C}} I_{\mathrm{eS}})/(I_{j\mathrm{C}} P_{i\mathrm{S}} N_{\mathrm{S}} I_{\mathrm{ec}}) \tag{20}$$

where I_{eS} and I_{eC} are the intensities of the ERETIC signal measured on the spectra of compounds S and C, respectively. Ideally, the calibration molecule is the same as the studied molecule.

It must be noted that the ERETIC method uses a calibration compound located in a different tube from that of the sample measured. If the gravimetric method is employed to determine the ratio $N_{\mathrm{C}}/N_{\mathrm{S},}$ the volumes of the two samples have to be taken into account. Since it is technically difficult to measure the total volumes with the precision required, the relative concentrations may be more efficiently measured by ^{1}H-NMR [25,26]. Because the active volume is fully occupied by the sample, the ERETIC method is favorable from the sensitivity point of view. In the case of ethanol for instance, removing TMU from the sample improves the signal-to-noise ratio by a factor 1.6. With other molecules higher improvements may be obtained, in particular when solvent is needed to improve miscibility of the sample with the chemical reference.

It should be noted that reduced repetition times may be used. When the compound investigated and the calibration sample are identical in composition and concentration the relaxation times T_1 are the same. Therefore, partial saturation has the same magnitude and spectral distortions are identical for the two spectra. Consequently, it is not necessary to choose a repetition time, T_R higher than $6T_1$. For example, with $T_R = 1.5T_1$, the signal-to-noise ratio remains close to that obtained with $T_R = 6T_1$ and the same number of repetitions. Distortions are observed but differences between the D/H values are small.

Since the ERETIC method achieves quantification with the help of a reference which is not a real NMR signal, the limitations of the method are rather different from those of classical methods. The signal is transmitted by a broadband antenna to avoid quality factor variations. The method is therefore independent of coil variations both during emission, because the reference signal is transmitted by an additional probe, and during reception, because the reference and sample signals are collected from the same probe. The reference being stable in time, the calibration step does not need to be performed at every quantitative acquisition

Carbon SNIF-NMR

Although both the intrinsic sensitivity and the natural abundance of carbon-13 are much higher than those of deuterium the SNIF-NMR method is better suited to the determination of hydrogen isotope ratios than to that of carbon isotope ratios. This behavior is largely due to differences in the relaxation properties of the nuclei on one hand, and to differences in the extent of natural isotopic dispersions on the other hand. Whereas the fast quadrupolar relaxation of deuterium permits relatively short repetition times to be selected, signal accumulation in quantitative conditions is much less efficient in the case of carbon, which frequently exhibits relatively long relaxation times. Moreover, in the presence of broadband decoupling, dipolar contributions to the relaxation of ^{13}C are responsible for variable signal enhancements due to Nuclear Overhauser Effects. Consequently, long and precise sequences of NOE suppression must be carefully implemented [27,28]. In addition, whereas the large mass difference exhibited by the isotopes of hydrogen is associated with a wide range of hydrogen isotope ratios, the isotopic parameters of carbon vary in a relatively small range. In ‰ units [Equation (5)], the carbon isotopic range covers less than 40‰ as compared to about 500‰ in the case of hydrogen. Very high levels of relative experimental accuracy are therefore required in carbon SNIF-NMR.

Traditionally, carbon isotope ratios are measured by IRMS. However, since the compound must be combusted previously into carbon dioxide and water, the isotope ratio measured on CO_2 is an average over all carbon atoms of the sample. Site-specific values can be determined by IRMS but at the price of tedious degradations of the molecule aimed to isolate specific positions. In spite of its lower sensitivity, carbon SNIF-NMR provides a unique tool for directly comparing isotope contents at different molecular positions in a one-pot experiment. Thanks to continuous improvements in the technological performances, many instabilities, due in particular to filtering and field drifts can be eliminated.

Moreover, the reproducibility is improved by a rigorous complex least-squares treatment of the signal [14]. As mentioned above, this algorithm avoids, in particular, operator dependent errors associated with phase and baseline adjustment procedures.

The general principles discussed in the case of hydrogen (“Isotopic Abundances and Isotopic Ratios” section) also apply to carbon. However, since the natural abundance of carbon-13 (about 1.1%) is no longer negligible at the required precision of the measurements, the isotope ratio, R, may not be simply assimilated to the isotopic abundance, A.

On a relative basis, the site-specific abundances, A_i, can be calculated from the molar fractions, f_i, of the ^{13}C isotopomers mono-labeled at position i, and from the overall isotopic abundance, A_T, determined by IRMS, by means of Equation (20) [analogous to Equation (11)]:

$$A_i = A_T f_i / F_i \tag{21}$$

where F_i are the statistical molar fractions, which would characterize a random distribution of ^{13}C. The actual molar fractions, f_i, are determined from the signal area, S_i, of the mono-labeled isotopomers:

$$f_i = S_i / \Sigma_i S_i \tag{22}$$

This equation assumes, as a reasonable approximation, that the relative isotopic abundances of the bi-labeled species are analogous to those of the mono-labeled ones.

When integrating the signals of the mono-labeled isotopomers it is necessary to take into account possible contributions of the bi-labeled species. The corresponding satellite lines, situated at positions depending on the ^{13}C–^{13}C coupling constants and on small isotope effects, can be independently observed in INADEQUATE experiments. In glycerol, for instance [29], the molecule contains magnetically equivalent carbon atoms at positions 1, 3. In such a case, it is also necessary to correct the measured area, $S_{1,3}$, for the contribution of the degenerate single signal pertaining to the isotopomer bi-labeled at positions 1 and 3.

It has been checked that satisfactory repeatability and reproducibility performances of the SNIF-NMR analytical chain can be reached [28,29]. Results obtained on glycerol in particular are consistent with values derived from IRMS measurements carried out on derivatives of the same sample prepared by appropriate degradation reactions [29]. For a given molecular species it is now possible, once the experimental parameters have been optimized and standardized, to compare the carbon SNIF-NMR profiles of samples from different origins. Thus, the carbon fingerprint of glycerol originating from maize, olive, grape, or fossil sources are significantly different.

References

1. Martin GJ, Martin ML. Tetrahedron Lett. 1981;22:3525–8.
2. Martin GJ, Martin ML. Brevet France 1981;81–22710, pp 1–24.
3. Coplen TB. Pure Appl. Chem. 1994;66:273–6.
4. Martin ML, Martin GJ. In: P Diehl, E Fluck, H Günther, R Kosfeld, J Seelig (Eds). NMR Basic Principles and Progress. Springer-Verlag: Berlin, 1990;23, pp 1–61.
5. Martin GJ, Zhang BL, Naulet N, Martin ML. J. Am. Chem. Soc. 1986;108:5116–22.
6. Heck G, Mileham C, Martin GJ. Analusis 1997;25:202–6.
7. Martin ML, Delpuech JJ, Martin GJ. Practical NMR Spectroscopy, Heyden-Wiley: London, 1980 (Chapter 9).
8. Gesmar H, Led JJ, Abildgaard F. Prog. NMR Spectrosc. 1990;22:255–88.
9. Herring FG, Phillips PS. J. Magn. Reson. 1985;62:19–28.
10. Balacco G. J. Magn. Reson. Ser. A. 1994;110:19–25.
11. Rischel C. J. Magn. Reson. Ser. A. 1995;116:255–8.
12. Koehl P, Ling C, Lefevre JF. J. Magn. Reson. Ser. A. 1994;109:32–40.
13. Chen H, Van Huffel S, Decanniere C, Van Hecke P. J. Magn. Reson. Ser. A. 1994;109:46–55.
14. Martin YL. J. Magn. Reson. Ser. A. 1994;111:1–10.
15. Martin GJ, Martin ML, Martin YL. Bull. Magn. Reson. 1996;18:9–20.
16. Martin GJ, Sun XY, Guillou C, Martin ML. Tetrahedron. 1985;41:3285–96.
17. Martin G, Naulet N. Fresenius J. Anal. Chem. 1988;332:648–51.
18. Martin GJ, Trierweiler M, Ristow R, Hermann A, Belliardo JJ. BCR Inf. 1994, pp 1–58.
19. Martin GG, Wood R, Martin GJ. J. AOAC Int. 1996;79:917–28.
20. Martin GJ, Koziet J, Rossmann A, Dennis J. Anal. Chim. Acta. 1996;321:137–46.
21. AFNOR. Norme Française, 1987;1–49.
22. Off. J. Eur. Commun. 1990;2676, 2690.
23. Akoka S, Barantin L, Trierweiler M. Anal. Chem. 1999;71:2554–7.
24. Billault I, Robins R, Akoka S. Anal. Chem. 2002;74:5902–6.
25. Griffiths L. Magn. Reson. Chem. 2001;39:194–202.
26. Fauhl C, Wittkowski R. Lebensm. Unters. Forsch. 1996;203:541–5.
27. Caer V, Trierweiler M, Martin GJ, Martin ML. Anal. Chem. 1991;63:2306–13.
28. Zhang BL, Buddrus S, Trierweiler M, Martin GJ. J. Agric. Food Chem. 1998;46:1374–80.
29. Zhang BL, Trierweiler M, Jouitteau C, Martin G. J. Anal. Chem. 1999;71:2301–6.

SNIF-NMR—Part 2: Isotope Ratios as Tracers of Chemical and Biochemical Mechanistic Pathways

Maryvonne Martin[1], Benli Zhang[2], and Gérard J. Martin[1]
[1]*Eurofins Scientific, BP 42301, 44323 Nantes, France; and*
[2]*University of Nantes, LAIEM, BP 99208, 44322 Nantes, France*

Introduction

Isotope labeling is a privileged source of information on chemical and biochemical mechanisms. In this context, the SNIF-NMR approach, which quantifies non-random distributions of isotopes at the natural abundance level, can be considered as a labeling method devoid of the need for isotopic enrichment [1]. Consequently, in its fields of application, it benefits from specific advantages with respect to conventional labeling methods. In particular, it avoids time-consuming syntheses of selectively labeled precursors, enables all monolabeled isotopomers of a molecular species to be simultaneously compared in identical experimental conditions, and provides a unique strategy for investigating mechanistic pathways taking place in unperturbed conditions. The main limitations are due to the rather poor sensitivity and chemical shift resolution of ^{2}H-NMR (cf. Part 1), which preclude observation of complex metabolites present in very diluted media or available only at the submilligram level.

From a theoretical point of view, fractionation of isotopes occurring in the course of physical, chemical, or biochemical transformations is the result of kinetic and thermodynamic isotope effects. Consequently, in the case of a natural product, the hydrogen and carbon isotopic NMR profiles are expected to reflect the successive isotope effects which have actively presided to the elaboration of the molecule, starting from its ultimate parent precursors, water and carbon anhydride.

Influence of Phase Transitions and Transport Phenomena on the Isotopic Parameters

Phase transition phenomena are generally accompanied by fractionation of isotopes. An equilibrium liquid–vapor isotope effect, EIE, is defined as the quotient of the isotope ratios in the vapor state, R_V, and in the liquid state, R_L.

$$\alpha_e = R_V/R_L \tag{1}$$

In the case of water for instance, the vapor state at equilibrium is slightly depleted in deuterium with respect to the liquid state, and the value of the thermodynamic liquid/vapor isotope effect, α_e, is about 0.974 [2,3]. In general, the isotopic composition of environmental water is the result of many kinetic and thermodynamic isotope effects associated with evaporation and condensation events. In such transformations, the isotopic ratios follow simple kinetic equations of the Rayleigh type:

$$(R/R_0) = (N/N_0)^{(\alpha-1)} \tag{2}$$

where R_0 and R are the isotope ratios of the substrate at the beginning and at a given stage of the transformation and N/N_0 is the degree of conversion of the substrate. The nature of the fractionation factor, α, depends on the kind of transformation considered and may represent either thermodynamic, kinetic, or mixed mechanisms.

Since fractionation effects associated with phase transitions and transport phenomena depend on environmental parameters, the isotopic NMR profile is expected to reflect the climatic conditions that have prevailed during the period of plant growing. A first climatic influence is introduced by meteoric water used by the plant for its photosynthesis. In this respect, it has been shown by isotope ratio mass spectrometry that the deuterium and oxygen-18 contents of meteoric water are related by the so-called Craig equation [4]:

$$\delta^2\mathrm{H_w} = 8.08\delta^{18}\mathrm{O_w} + 9.57 \tag{3}$$

whose slope and intercept depend slightly on the geographical situation. A relationship of type 3 stands also for water accumulated in fruits but the slope is generally smaller.

The climatic dependency is transferred to leaves and then to sugars, cellulose, and other metabolites. Thus, the deuterium content of water of fruit berries is related to the climate of the region of production:

$$\text{Meteoric water}: \Delta\delta D_W(‰) = 0.086\,\Delta T - 0.0017\Delta P, \tag{4}$$

$$\text{Wine water}: \Delta\delta D_W(‰) = 0.20\,\Delta T - 0.0047\,\Delta P, \tag{5}$$

Graham A. Webb (ed.), Modern Magnetic Resonance, 1659–1667.
© 2008 *Springer.*

where $\Delta\delta D_W$ represents the change in deuterium content as a function of changes in temperature, T(°C), and precipitation, P (mm). For example, the difference in the deuterium contents of wine water in Vienna, Austria ($T = 10.3\,^\circ$C and $P = 612$ mm) and in Porto Allegre, Brazil ($T = 20.1\,^\circ$C and $P = 1212$ mm) is equal to 4.3‰ whereas the corresponding difference for meteoric water is equal to only 1.8‰. This behavior expresses the isotopic fractionation efficiency of leaves in vine.

Simultaneous Determination of Site-Specific Thermodynamic Isotope Effects

Since thermodynamic isotope fractionation effects in exchanging systems are important sources of information on chemical and biochemical mechanisms [5–8], many theoretical and experimental methods [9–12], including NMR chemical shift measurements [13–15], have been devoted to the investigation of these parameters. In contrast to most experimental procedures, which require the use of labeled compounds and only provide indirect access to equilibrium isotope effects, the SNIF-NMR method enables thermodynamic isotope effects at different molecular sites to be directly compared in many kinds of exchange equilibria [16,17].

Liquid–Vapor Fractionation Effects

The isotopomers of a given molecule may be affected differently by the liquid–vapor isotope effect defined in Equation (1). The site-specific values of α_e can be simultaneously measured by NMR through dedicated distillation experiments [16]. This one-pot determination is well suited to accurate comparisons of isotopomers. Thus, the results of distillation experiments, performed on alcohols, in technical conditions involving very high reflux and slow product rate, can be analyzed according to the Rayleigh-type model. For every isotopomer, the isotope ratios of the remaining material (L) and distillate (D) are expressed, as a function of the fraction of the transformation, ρ, by the following relationships:

$$R_L = R_S(1-\rho)^{\alpha-1} \tag{6a}$$

$$R_D = R_S(1/\rho)[1(1-\rho)^{\alpha}], \tag{6b}$$

where R_S is the isotope ratio of the starting material.

For a given site, the unit fractionation factor, α, depends on the constant number of theoretical plates of the distillation column and on the specific thermodynamic isotope effect, α_e. The accuracy of the determination is improved by performing a series of separate distillations stopped at different fractions of transformation, ρ. The unit fractionation factors can then be computed from nonlinear regression analyses carried out on the whole curves defined by Equations (6a) and (6b). However, since the intercept of the R_D curve at $\rho = 0$ verifies Equation (7), a first approximation of α can be rapidly deduced from a single experiment carried out for a value of ρ as low as possible [16,18].

$$\alpha = (R_D/R_S)_{\rho\to 0} \tag{7}$$

Some examples of results obtained on alcohols are given in Table 1.

Table 1: Site-specific unit fractionation factors, α, and thermodynamic isotope effects, α_e, for liquid–vapor phase transition of methanol and ethanol. The ^{13}C parameters are determined by isotope ratio mass spectrometry (IRMS) on the same distillate samples as those used in the hydrogen SNIF-NMR measurements

Molecule	T(K)	Factors	^{13}C (IRMS)	CH_2D	CHD	OD
CH_3OH	338	α	1.0020	1.0150		0.820
		α_e	1.00023	1.0017		0.977
CH_3CH_2OH	351	α	1.0035	1.0230	1.0180	0.819
		α_e	1.00043	1.0032	1.0024	0.975

Note: CH_2D denotes the CH_2DOH and CH_2DCH_2OH isotopomers, CHD the CH_3CHDOH isotopomer, and OD the CH_3OD and CH_3CH_2OD isotopomers.

It is interesting to note that the $\alpha_e(^{13}C)$, $\alpha_e(CH_2D)$, and α_e(CHD) values are higher than unity. This means that, in these cases, the heaviest isotopomers are more volatile than the lightest ones. This behavior differs from that of water and of the hydroxylic isotopomers which are usually characterized by α_e values [19] significantly smaller than unity, a situation corresponding to higher preference of the light isopomer for the vapor state.

These phase transition effects may be responsible for important isotopic fractionation in the preparation of samples. Thus, the site-specific isotope ratios measured on samples obtained by distillation depend on the rate of extraction. In case of insufficient recovery, the carbon-bound hydrogen atoms of alcohols for instance are significantly enriched in deuterium with respect to the starting material. Conversely, the occurrence of fractionation effects at phase transitions may be exploited to get information on rates of evaporation or concentration and more generally on technological treatments undergone by a given sample (cf. Part 4).

Isotope Effects in Chemically Exchanging Systems

Hydrogen exchange processes involving, in particular, water and exchangeable groups, such as OH, NH, SH, etc., are common in chemical and biological media and many experimental and theoretical methods have been devoted to the study of equilibrium isotope partitioning in such systems. In principle, at natural isotopic abundance, all isotopomers in an exchanging system at equilibrium, at given temperature and pressure values, can be simultaneously quantified by NMR [17]

$$\mathrm{AH}_i + \mathrm{BD}_j \xrightleftharpoons{} \mathrm{AD}_i + \mathrm{BH}_j (K).$$

Thus, when atoms i and j, pertaining, respectively, to species A and B containing P_i^{A} and P_j^{B} hydrogen atoms, exchange slowly on the NMR time scale, the thermodynamic isotope fractionation factor, α^*, corresponding to the equilibrium constant K, can be measured:

$$\alpha^* = (D/H)_i^{\mathrm{A}}/(D/H)_j^{\mathrm{B}} = K P_j^{\mathrm{B}}/P_i^{\mathrm{A}}, \tag{8}$$

where α^* is simply computed from the area of signals i and j in the deuterium spectrum and from the mole fractions of compounds A and B. Thus, in aqueous solutions of alcohols, deviations with respect to a statistical partitioning of deuterium between water and alcoholic hydroxyl groups are detected. It is directly shown, for instance, that deuterium exhibits a higher affinity for the hydroxyl bond of propanol or butanol than for water. Multiple hydrogen isotope partitioning can even be investigated in ternary mixtures.

Determination of Thermodynamic Isotope Effects in Tautomeric Equilibria

The SNIF-NMR method is particularly suited to the simultaneous determination of primary and secondary thermodynamic isotope effects in tautomeric equilibria [20]. Others methods [5] must usually face the complexity of multi-isotopomeric mixtures associated with the use of labeled substrates or deuterium enriched media and a limited number of exchanging systems is accessible to the existing techniques. In the keto–enol tautomeric exchange of acetylacetone for instance, several isotopomeric equilibria are simultaneously involved at natural isotopic abundance (Figure 1) and NMR can directly determine a set of four thermodynamic fractionation factors.

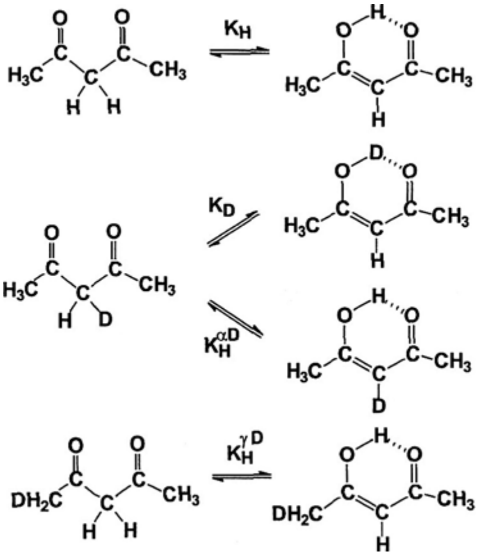

Fig. 1. Multi-isotopomeric exchanges simultaneously accessible in a SNIF-NMR investigation of acetylacetone tautomerism. In addition, a fast equilibrium (with respect to the NMR time scale) involves the two equivalent forms of the enol structure.

Thus, the fractionation factor $\alpha(=\mathrm{CH}^{\mathrm{e}}/\mathrm{OH}^{\mathrm{e}})$ relating the =CH and OH sites of the equivalent rapidly exchanging enol species is simply derived from the sole ^{2}H-NMR spectrum. More generally, a combination of ^{2}H- and ^{1}H-NMR experiments is used to determine the isotopic parameters that relate keto and enol tautomers in β-diketones. Thus the fractionation factor, $\alpha(\mathrm{CH}_2^{\mathrm{k}}/\mathrm{OH}^{\mathrm{e}})$, relating the hydroxyl group of the enol form and the methylene group of the keto form is

$$\alpha(\mathrm{CH}_2^{\mathrm{k}}/\mathrm{OH}^{\mathrm{e}}) = K_{\mathrm{H}}/2K_D^{\alpha\mathrm{H}} = S_{\mathrm{CHD}}^{k}(1-a)/2aS_{\mathrm{OD}}^{\mathrm{e}}, \tag{9}$$

where S_{CHD} and S_{OD} are the area of the keto CHD and enol OD signals measured on the deuterium spectrum and a is the molar fraction of the keto form determined on the proton spectrum. The measured primary equilibrium isotope effects illustrate a preference of deuterium for the methylene fragment of the keto form, with respect to both the hydroxylic or ethylenic positions of the enol tautomer. For instance, values $\alpha(\mathrm{CH}_2^{\mathrm{k}}/\mathrm{OH}^{\mathrm{e}}) = 1.09$ and $\alpha(\mathrm{CH}_2^{\mathrm{k}}/\mathrm{CH}^{\mathrm{e}}{=}) = 1.02$ are determined in acetylacetone. Secondary thermodynamic isotope parameters characterizing partner sites not directly involved in the exchange process (Figure 1) can also be simultaneously estimated.

Determination of Kinetic Isotope Effects

In the case of hydrogen, kinetic isotope effects (KIEs) are frequently the source of high values of the fractionation factors. This behavior results from the large difference in mass of the isotopes, which is itself responsible for significant differences in vibrational motions and in zero-point vibrational energies. KIEs are currently exploited to gain information on the mechanism of chemical or biochemical reactions and in particular to investigate the structure of transition states [8,21–25]. In conventional kinetic methods, determination of the KIE values requires the synthesis of selectively labeled reactants, which are then investigated in independent kinetic experiments. SNIF-NMR, which avoids the recourse to tedious labeling, enables primary and secondary KIEs at the different molecular positions to be compared in a one-pot experiment. Moreover, since the tracer is present in very small quantity in the substrate, the so-called Melander's kinetic equations become simpler [22].

The D/H ratios associated with the different isotopomers of a substrate, A, or of the reaction product, Y, can be expressed in terms of the primary and secondary KIEs, by taking into account the dilute isotopic conditions of the SNIF-NMR experiment and the type of the reaction [26]. For instance, in a closed system and in the absence of intramolecular competition, when a hydrogen atom AH is transferred to a product YH, the isotope ratios of the remaining reactant, R_A, and of the product, R_Y, depend on the primary isotope effect, $k_H/k_D = 1/\beta$ according to Equations (10a) and (10b) (Figure 2):

$$R_A = R_{0A}(1-\rho)^{(\beta-1)}, \qquad (10a)$$

$$R_Y = R_{0A}[1-(1-\rho)^{\beta}]/\rho, \qquad (10b)$$

where R_{0A} is the initial isotopic ratio and ρ is the degree of completion of the reaction.

It should be emphasized that, in this simple case, extrapolation of the kinetic Equation (10b) to $\rho = 0$, gives directly access to the KIE value.

$$\beta = k_D/k_H = 1/\mathrm{KIE} = (R_Y/R_{0A})_{\rho\to 0}. \qquad (11)$$

In addition, Equation (10a) shows that the ratio R_A/R_{0A} increases or decreases very rapidly in the vicinity of $\rho =$ 1. This means that the isotope ratio of the remaining reactant may differ strongly from that of the starting material at a high degree of completion. Then, R_A becomes very sensitive to the value of the KIE. This behavior can be exploited for improving the accuracy of the KIE determination [26–28].

If the site of reaction in AH is situated in a position α to the investigated bond the isotopic ratios depend on a secondary kinetic isotopic effect $k_H/k_H^{\alpha} = 1/\gamma$ and the same equations apply where β is replaced by γ.

Kinetic equations can be derived in the same way for more complex reactions, involving for instance hydrogen abstraction from a set of equivalent hydrogen atoms [26]. Thanks to the natural presence of tracer amounts of all types of monodeuterated isotopomers several primary and secondary isotope effects are simultaneously accessible from such equations. Some examples of the use of SNIF-NMR to determine KIE values and to elucidate chemical reaction mechanisms can be found in references [27–34].

Specific Connections Between SNIF Parameters of Reactants and Products

The sensitivity of site-specific isotope ratios to active equilibrium and KIEs intervening at various steps of product elaboration make them attractive sources of information on the mechanistic history of biological or chemical syntheses.

Isotope Effects and Affiliation Coefficients

It should be emphasized that high values of hydrogen primary KIEs are not necessarily accompanied by strong fractionation factors. In a simple open system where compound, S, present in unlimited quantity, is transformed into product Q, the values of the isotope ratios, $(D/H)_j^Q$ and $(D/H)_i^S$, are constantly related by the KIE proportionality coefficient. In contrast, in a closed system where S is totally transformed into Q, all deuterium and protium atoms, i, of the starting material are finally recovered in the product and the isotope ratios of Q and S are equal, whatever the value of the KIE. More generally, the influence of the KIE on the isotopic parameters depends on the rate of the transformation according to kinetic equations dictated by the mechanistic pathway.

As discussed in Part 1 (Equation 12), at the end of a transformation, the set of isotope contents in reaction products can be related to the initial set of isotope contents in reactants by a matrix of coefficients, [A], which describes the overall redistribution of the deuterium atoms governed by the reaction pathway [35]. A coefficient, a_{ji}, represents the individual degree of connection of a given site, j, in any product molecule, Q, to a specific site, i, of a starting material, S. Thus, whatever the complexity of the considered reaction, the SNIF parameters of the Q and S molecules provide a global isotopic balance representing the whole set of successive and competive reaction steps.

The SNIF-NMR profile of natural products is generally the result of complex chains of reactions. Many steps of the *in vivo* reactions are kinetically invisible because, in the absence of branching, they may be considered as taking place in closed systems and are devoid of isotopic fractionation whatever the values of possible KIEs. The final NMR profile is therefore conditioned by the genealogy of the atoms and is mainly governed by the site-specific isotope contents of the precursors, including water, and by the sole active fractionation effects introduced at isotopically sensitive branching points.

Determination of the Isotopic Redistribution Coefficients

For a given transformation, the a_{ji} coefficients can be determined by submitting starting materials characterized

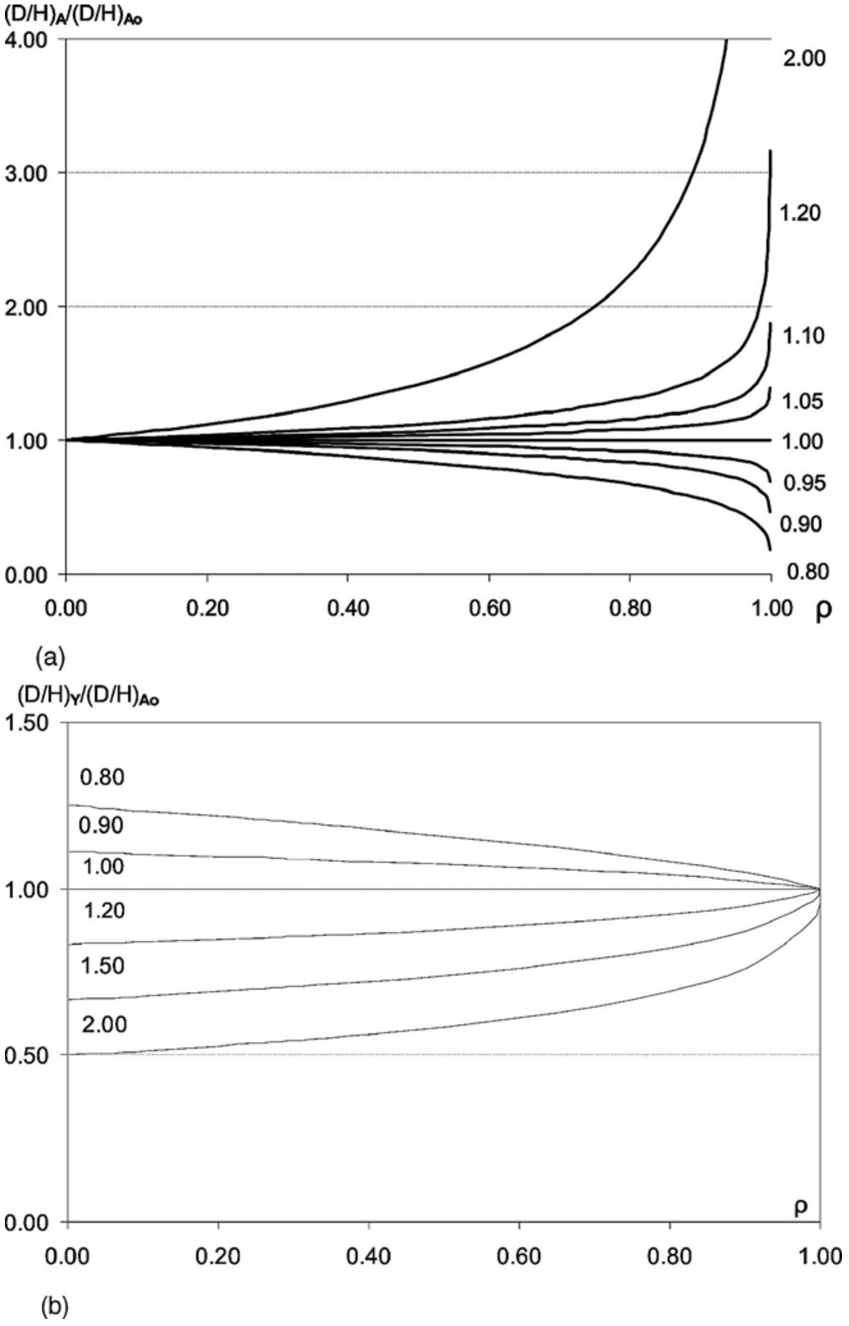

Fig. 2. Evolution of the isotope ratios, $(D/H)_A$ (Part a) and $(D/H)_Y$ (Part b) of reactant, A, and product, Y, as a function of the fraction of reaction, ρ, in a simple closed system where AH is transformed into YH with different values of the kinetic isotope effect k_H/k_D. The isotope ratios of A and Y are referred to $(D/H)_{A0}$ the isotope ratio of the starting reactant at $\rho = 0$. The region close to $\rho = 1$ corresponds to conditions of improved sensitivity for the determination of the KIE.

by different values of their SNIF parameters to a series of experiments carried out in strictly standardized conditions. When natural precursors with different isotopic NMR profiles are not available, molecules selectively labeled in deuterium at a level of enrichment close to natural abundance may be used.

Complete redistribution matrices can only be obtained when all deuterium signals of reactants and products are separated and correctly identified and quantified. Therefore, a limitation of the method is due to the relatively poor resolution potential of ^{2}H-NMR (cf. Part 1, Section "Quantitative deuterium-NMR"). Nevertheless, partial information may be usefully derived from coefficients relating signal clusters including several isotopomers. Moreover, when the spectrum of a molecular species is insufficiently resolved, it is often possible to synthesize derivatives exhibiting more exploitable NMR spectra. Care must obviously be taken in such derivatization procedures to preserve the initial isotopic values of the investigated molecule. This approach will be illustrated in the following section.

Elaboration of SNIF-NMR Probes: From Carbohydrates to Ethanol and Glycerol

Since glucose is a key compound in the biosynthesis of natural products, particular efforts have been devoted to the determination of its SNIF parameters and to the investigation of its glycolytic products.

Isotopic Parameters of Glucose and Photosynthetic Pathways

Due in particular to the presence of several hydroxyl groups engaged in exchange processes and hydrogen bonding, the glucose and fructose molecules themselves are not suitable NMR probes. Consequently, it has been necessary to synthesize derivatives exhibiting better-resolved spectra. Several glucose derivatives, such as 1,2:5,6-di-*O*-isopropylidene-α-D-glucofuranose, which are easily prepared, enable glucose isotopic profiles to be rapidly compared [36], but a better discriminating potential is reached by 3,6-anhydro-1,2-*O*-isopropylidene-α-D-glucofuranose prepared in good yield through three chemical steps [37]. Experimental conditions of the derivatizations were defined which minimize fractionation effects by maximizing the yields of the successive steps. However, since the transformation cannot be complete, the experimental procedures must be standardized in order to obtain isotopic parameters analyzable at least on a relative basis. Using this strategy, it could be shown that, despite the various exchange phenomena that occur in the course of photosynthetic pathways, deuterium is far from being randomly distributed in glucose [38]. Moreover, different SNIF-NMR profiles are exhibited by carbohydrates extracted from plants with different photosynthetic metabolism: C3, C4, or CAM. Even within a given metabolic family, physiological features of the plant introduce specific isotopic signatures. Taking into account the pivotal role of carbohydrates in natural biosyntheses, the NMR parameters may provide important sources of basic information in phytochemical studies.

From Carbohydrates to Ethanol: Hydrogen Isotope Redistribution in the Fermentation Reaction

When large numbers of samples have to be investigated the described strategy for isotopic characterization of glucose or fructose is excessively time consuming. Moreover, structurally different carbohydrate molecules cannot be directly compared. Fortunately, a common derivative, ethanol, well suited to ^{2}H-NMR (cf. Part 1, Section "Referencing of isotopic parameters") and easily obtained through fermentation experiments, could be proposed as a very sensitive probe, representative of sugars. Although the number of hydrogen sites in ethanol is strongly reduced with respect to the seven diastereotopic carbon-bound hydrogen positions of glucose, it was tempting to investigate to which extent, and in which conditions, isotopic properties of carbohydrates are transferred to glycolytic products and in particular to ethanol. Most investigations of glycolytic pathways have involved labeling experiments using either tritium or deuterium and a number of KIEs have been estimated for isolated enzymatic steps [39–42]. However, only a few of these KIEs are expected to participate actively in the resulting fractionation effects. Model fermentation experiments have been conducted in order to determine the a_{ji} coefficients characterizing the connection of specific hydrogen atoms in the products, ethanol and water, to their parent hydrogen atoms in the starting materials, glucose and water. For a given site j in the products, Equation (12) in Part 1 may be re-written as a function of the isotope ratio of a given site $i = k$ in a reactant, S, as:

$$(D/H)^{\mathrm{Q}}_j = a_{jk}(D/H)^{\mathrm{S}}_k + \textstyle\sum_{i\neq k} a_{ji}(D/H)^{\mathrm{S}}_i \qquad (12)$$

Values of the a_{ji} coefficients which relate sites $j = \mathrm{I}$ (methyl) and $j = \mathrm{II}$ (methylene) of ethanol to carbon-bound hydrogen sites i of glucose and to water are given in Table 2. Obviously, the complementary term of Equation (12), $C_i = \sum_{i\neq k} a_{ji}(D/H)^{\mathrm{S}}_i$, depends on the origin of the fermented carbohydrate and on the isotope ratio of the aqueous medium. The reported values hold for experiments carried out with maize samples and Nantes tap water.

Table 2: Isotopic redistribution coefficients, a_{ji}, relating reactants (water, W, and sites 1–6 of glucose) and products (water, W, and sites I—methyl and II—methylene of ethanol) in a fermentation reaction carried out with maize glucose and tap water [43].The coefficients a_{I3}, a_{I4}, a_{I5}, a_{II1}, a_{II2}, a_{II3}, a_{II5}, and a_{II6} are close to zero and a small connection between site II of ethanol and site 4 of glucose is detected. Slightly different values have been measured in other series of experiments [44–46]

a_{I1} C_1	a_{I2} C_2	a_{I6} C_6	a_{IW} C_W^{I}	a_{IIW} C_W^{II}
0.12112	0.08113	0.30114	0.2181	0.738

The a_{ji} values predicted for a situation where hydrogen i of glucose would be preserved from any kind of exchange with the medium in the course of the reaction pathway and would end at position j of the product are: $a_{Ii} = 1/6$ for the methyl site and $a_{IIi} = 1/4$ for the methylene site. Consequently, a first conclusion drawn from the results in Table 2 is that the methyl group of ethanol exhibits, a strong connection with the two hydrogen atoms at site 6, and a less tight connection with hydrogen at sites 1 and 2, of glucose, a moderate connection with water and no connection with sites 4 and 5 of glucose. In contrast, the methylenic hydrogen atoms are mainly derived from water and are only very slightly connected with site 4 of glucose. The deviations of a_{I1} and a_{I2} with respect to the theoretical value 1/6 are indicative of intermolecular hydrogen exchanges which can be further analyzed in mechanistic terms [43].

On the basis of this NMR isotopic strategy, it becomes possible to examine whether natural or experimental factors exert a significant influence on the mechanistic pathway. Thus, experiments performed with different yeasts, different concentrations of carbohydrates, and different yields of the transformation have demonstrated a remarkable mechanistic stability of the chain of reactions [44]. Although glycolysis is associated with overall fractionation effects that may exceed 40 ppm, the considered factors are responsible for variations limited to a few ppm. Similarly, it could be shown that, in spite of their strong influence on the rate of bioconversion, changes in the composition (natural or "synthetic") of the fermentation medium, exert only small effects, which can be interpreted, on the redistribution matrix and on the final isotopic values [45].

From Carbohydrates to Glycerol

Another example, the biosynthesis of glycerol through yeast fermentation of glucose, illustrates different kinds of information possibly derived from isotopic redistribution matrices [46]. Under its triacetate form, glycerol exhibits three ^{2}H-NMR signals stereochemically assigned in Figure 3.

The theoretical a_{ji} values corresponding to full hydrogen transfer from i to j are equal to 0.25. Through comparison with this limit, it is concluded that the experimental coefficients $a_{1A} \sim 0$, $a_{2A} = 0.16$, $a_{6A} = 0.23$, $a_{1B} = 0.22$, $a_{2B} \sim 0$, $a_{6B} = 0.22$, characterize high levels of intramolecular transfer from hydrogen atoms 6 pro-R and 2 of glucose to 3 pro-R of glycerol and from 6 pro-S and 1 of glucose to 3 pro-S of glycerol. Moreover, these results contain information on the *relative rates of certain reaction steps* and on the *stereospecificity of reaction*. Indeed the isotopic behavior is only compatible with a reversible isomerization of the triose phosphate intermediates, glyceraldehyde 3-phosphate and dihydroacetone phosphate (DHAP), and with a reduction of DHAP into glycerol slower than the isomerization step. In the reverse situation values of $a_{6(\text{pro-R})A}$ and $a_{6(\text{pro-S})B}$ equal to zero would be expected. In addition, values $a_{A2} \neq 0$ and $a_{B2} = 0$ are only compatible with a reduction of DHAP into glycerol operating through the *si*-face. A non-stereospecific reduction would require $a_{A2} \neq 0$ and $a_{B2} \neq 0$, whereas a reduction through the *re*-face would be characterized by $a_{A2} = 0$ and $a_{B2} \neq 0$. The method therefore provides attractive alternatives to experiments conducted with enriched materials [47].

When interpreting redistribution coefficients a_{ji} smaller than the theoretical value, it should be kept in mind that the percentage of deuterium transferred from i to j should not be assimilated to the percentage of transferred hydrogen unless active KIE can be excluded.

Access to Mechanistic Information on Enantiotopic Hydrogen Sites

Thanks to the diastereotopic character of geminal hydrogen atoms resulting from chirality, NMR is able to provide additional information about stereospecific mechanisms involving methylenic fragments. Thus, differences in isotope contents at the geminal positions of a methylene group indicate that stereospecificity has been preserved along the biosynthetic pathways. For instance, unequal *D/H* values have been determined at methylenic sites of D- and L-aspartic acids from biochemical origin, whereas equal values are exhibited by a D sample produced by chemical synthesis [48]. The method can be applied to the investigation of methylene groups in achiral molecules on condition that a suitable chiral derivative is synthesized by reacting the sample with an optically pure reactant capable of generating sufficient chemical shift discrimination. Thus, the genealogy of the pro-R and pro-S methylenic hydrogen atoms of ethanol can be separately

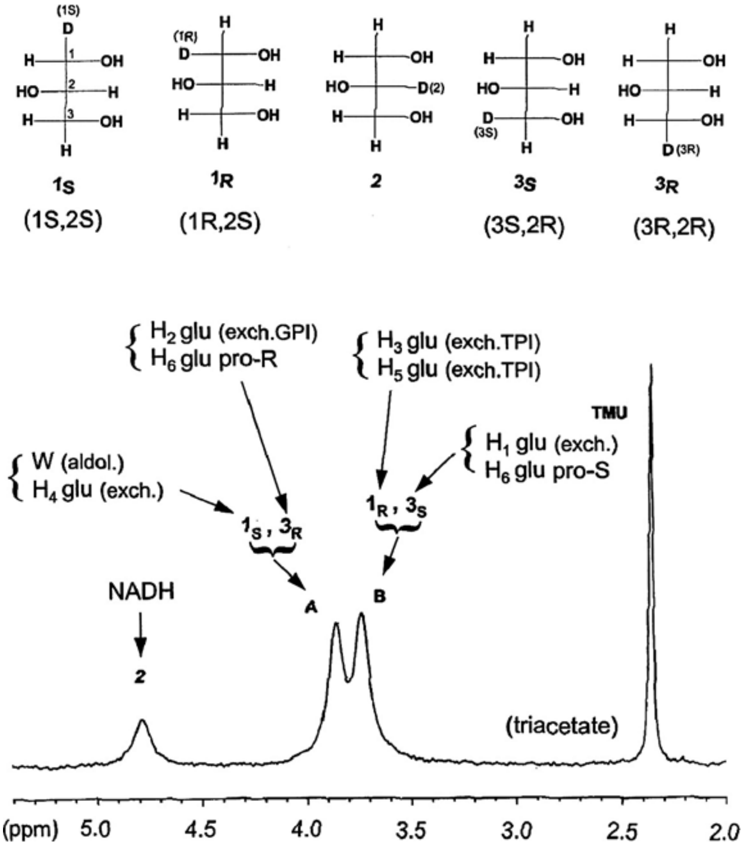

Fig. 3. ^{2}H-NMR spectrum (76.8 MHz) of the triacetate derivative of glycerol. The signals are stereochemically assigned to the monodeuterated isotopomers observable at natural abundance. TMU is the signal of tetramethylurea used as working standard. The described affiliation of the isotopomers to the glucose precursor has been deduced from the isotopic redistribution matrix [45]. Partial or total contributions of hydrogen atoms from the aqueous medium are mentioned. (glu = glucose, exch = exchange, GPI = glucose phosphate isomerization step, TPI = triosephosphate isomerization step, W = water, aldol = aldolization step).

investigated by reacting ethanol with L(–)-mandelic acid [49]. The enantiomeric resolution of the monodeuterated isotopomers thus achieved in optically active ethylmandelate can be used, in particular, to investigate yeast mediated stereospecific exchange of the pro-R hydrogen with water. Other illustrative examples in the field of terpenes will be discussed in Part 3.

References

1. Martin GJ, Martin ML, Mabon F, Michon MJ. JCS Chem. Commun. 1982:616–7.
2. Majoube M. J. Chim. Phys. 1971;68:625–36.
3. Merlivat L, Botter R, Nief G. J. Chim. Phys. 1963;60:56–9.
4. Craig H. Science 1961;133:1702–3.
5. Kresge AJ, More O'ferrall RA, Powell MF. In: E Buncel, CC Lee (Eds). Isotopes in Organic Chemistry, Vol. 7. Elsevier: Amsterdam, 1987;7, pp 177–273.
6. Cook PF, Blanchard JS, Cleland WW. Biochemistry 1980;19: 4853–8.
7. Cleland WW. Bioorg. Chem. 1987;15:283–302.
8. Cleland WW. Methods in Enzymology. Enzyme Kinetics and Mechanism. Part D Developments in Enzyme Dynamics. Academic Press: San Diego, 1995;249, pp 341–73.
9. Rolston JH, Gale KL. J. Phys. Chem. 1984;88:4394–7.
10. Fenby DV, Bertrand GL. Aust. J. Chem. 1982;35:237–45.
11. Jancso G, Van Hook WA. Chem. Rev. 1974;74:689–750.
12. Jancso G, Rebelo LPN, Van Hook WA. Chem. Rev. 1993;93: 2645–66.
13. Saunders M, Saunders S, Johnson CA. J. Am. Chem. Soc. 1984;106:3098–101.
14. Jarret RM, Saunders M. J. Am. Chem. Soc. 1985;107:2648–54.
15. Bolvig S, Hansen PE. Magn. Reson. Chem. 1996;34:467–78.
16. Moussa I, Naulet N, Martin ML, Martin GJ. J. Phys. Chem. 1990;94:8303–9.
17. Zhang BL, Martin ML. J. Am. Chem. Soc. 1992;114:7089–92.
18. Zhang BL, Jouitteau C, Pionnier S, Gentil E. J. Phys. Chem. (B) 2002;106:2983–2988.
19. Shirinsky Vg, Doronina OD. Geokhimiya 1984;10:1511–6.

20. Zhang BL, Mabon F, Martin ML. J. Phys. Org. Chem. 1993;6: 367–73.
21. Melander L, Saunders WH. Reaction rates of isotopic molecules, Wiley: New York, 1980.
22. Melander L. Isotope effects on reaction rates. The Ronald Press Company: New York, 1960.
23. Schowen RL. In: A Streitweiser, RW Taft (Eds). Progress in Physical Organic Chemistry. Wiley: New York, 1972;9, pp 275–330.
24. Cleland WW. In: DL Purich (Ed). Methods in Enzymology, Vol. 87, Part C. Academic Press: New York, 1982;87, pp 625–41.
25. Wolfsberg M. In: HL Schmidt, H Forstel, K Heinzinger (Eds). Stable Isotopes. Elsevier: Amsterdam, 1982, pp 3–14.
26. Martin ML, Martin GJ. In: P Diehl, E Fluck, H Günther, R Kosfeld, J Seelig (Eds). NMR Basic Principles and Progress. Springer-Verlag: Berlin, 1990;23, pp 1–61.
27. Singleton DA, Thomas AA. J. Am. Chem. Soc. 1995;117:9357–8.
28. Singleton DA, Merrigan SR, Thomas AA. Tetrahedron Lett. 1999;40:639–42.
29. Rabiller C, Maze F, Mabon F, Martin GJ. Analusis 1991;19:18–22.
30. Pascal RA, Baum MW, Wagner CK, Rodgers LR, Huang DS. J. Am. Chem. Soc. 1986;108:6477–82.
31. Zhang BL. Magn. Reson. Chem. 1988;26:955–9.
32. Zhang BL, Pionnier S. J. Phys. Org. Chem. 2001;14: 239–46.
33. De Rosa M, Shadle RG, Foster N. J. Chem. Soc. Chem. Commun. 1993:1757–8.
34. Meyer MP, Delmonte AJ, Singleton DA. J. Am. Chem. Soc. 1999;121:10865–74.
35. Martin GJ, Zhang BL, Naulet N, Martin ML. J. Am. Chem. Soc. 1986;108:5116–22.
36. Zhang BL, Quemerais B, Martin ML, Martin GJ, Williams JM. Phytochem. Anal. 1994;5:105–10.
37. Schleucher J, Vanderveer P, Markley JL, Sharkey TD. Plant Cell Environ. 1999;22:525–33.
38. Zhang BL, Billault I, Li X, Mabon F, Remaud G, Martin ML. J. Agric. Food Chem. 2002;50:1574–80.
39. Rieder SV, Rose IA. J. Biol. Chem. 1959;234:1007–10.
40. Rose IA, Kuo DJ, Warms JVB. Biochemistry 1991;30:722–6.
41. Malaisse WJ, Malaisse-Lagae F, Liemans V, Ottinger R, Willem R. Mol. Cell. Biochem. 1990;93:153–65.
42. London RE. In: LJ Berliner, J Reuben (Eds). Biological Magnetic Resonance. Plenum Press: New York, 1992;11, pp 277–306.
43. Zhang BL, Yunianta, Martin ML. J. Biol. Chem. 1995;270: 16023–9.
44. Vallet C, Said R, Rabiller C, Martin ML. Bioorg. Chem. 1996;24:319–30.
45. Zhang BL, Yunianta, Vallet C, Martin YL, Martin ML. Bioorg. Chem. 1997;25:117–29.
46. Zhang BL, Buddrus S, Martin ML. Bioorg. Chem. 2000;28:1–15.
47. Leichus BN, Blanchard JS. Biochemistry. 1994;33:14642–9.
48. Martin ML, Zhang BL, Martin GJ. FEBS Lett. 1983;158:131–3.
49. Rabiller C, Mesbahi M, Martin ML. Chirality. 1990;2:85–9.

SNIF-NMR—Part 3: From Mechanistic Affiliation to Origin Inference

Gérard J. Martin[1], Maryvonne L. Martin[1] and Gérald Remaud[2]
[1]*Eurofins Scientific, BP42301, F-44323 Nantes, France; and*
[2]*University of Nantes, LAIEM, BP 99208, F-44322 Nantes, France*

Introduction

In contrast to many other analytical parameters, which are mostly exploited on semi-empirical bases, the SNIF-NMR parameters rest on the well-established theoretical principles of isotope fractionation (Parts 1 and 2). Having shown how the isotopic ratios of end products can be quantitatively related to those of their starting materials, we shall illustrate now how isotopic profiles of natural or chemical products can be interpreted in terms of the mechanistic routes of their elaboration. On this basis, it will be shown that the NMR method provides a very powerful tool for inferring the origin of molecules in terms of different properties of the precursors such as—the natural or chemical nature, the type of plant, the region of plant growing, possibly the year of production, the technological treatments, etc.

SNIF Parameters as Witnesses of Individual Mechanistic Routes of Atoms

We have seen in Part 2 that model experiments conducted on a given chemical or biochemical reaction, enable the set of isotopic connections between individual atoms in starting materials and in products to be elucidated and quantified. The measured isotopic transfer coefficients describe, individually, the overall fate of every atom in the transformation, whatever its complexity. This experimental strategy is not always practicable but, fortunately, many mechanistic features of biosyntheses can be simply elucidated, from analyses of isotopic parameters carried out on appropriate selections of samples from known origin. Thanks to studies devoted to the isotopic characterization of carbohydrates and to the determination of the connectivity scheme in glycolytic reactions (Part 2), it is even possible to trace back the affiliation of many plant metabolites to their ultimate glucose precursor.

From a general point of view, since many kinetic isotope effects operating at various steps of a complex conversion are devoid of fractionating effects on the final products, the SNIF-NMR method is not expected fully to replace separate investigations of isolated reaction steps using selectively labeled precursors. However, in contrast to conventional experiments carried out in strongly deuterium-enriched media, where metabolic switching may occur, the NMR investigation, which operates at tracer isotopic abundance, faithfully describes the overall unperturbed metabolic pathway.

The typical example of monoterpene biosynthesis illustrates the potential of a SNIF analysis based on the sole end products to induce many properties of the biosynthetic pathway and in particular to eliminate incompatible mechanistic hypotheses. Isotopic distribution in natural terpenes is the result of complex chains of reactions starting from carbohydrates. In principle, the monoterpene isotopic profile, illustrated in Table 1, is related to that of geranyl diphosphate (GPP), which is generally considered as the common intermediate precursor [1]. In order to facilitate comparisons within the terpene family, the hydrogen atoms are numbered in Figure 1 according to mechanistic correspondences with the GPP precursor established, for every monoterpenic species, in the course of several decades of thorough biochemical studies [2–4].

Inasmuch as they exhibit consistent behavior when based on the retained schemes of hydrogen connections, the NMR results provide further checks for the whole set of biochemical pathways leading from GPP to the different terpenes.

The NMR approach, already applied in the 1980s, showed that α-pinene exhibits surprisingly large deviations with respect to a statistical distribution of deuterium and that exploitable differences exist in the isotope contents of enantiomers extracted from a given type of plant [5]. These results were incompatible with the mevalonate mechanism, universally admitted at that time for explaining GPP biosynthesis in plants. In particular, a strong deuterium depletion at site ex-2, associated with a much higher isotope ratio at site ex-6 (Table 1), could not be reconciled with the mevalonate mechanism in which both atoms would have the same origin. Unfortunately, at that time, specialists in the field of terpene chemistry suspected the reliability of the new isotopic approach rather than the accepted pathway [6]. The incompatibility of the

Graham A. Webb (ed.), Modern Magnetic Resonance, 1669–1680.
© 2008 *Springer.*

Table 1: Site-specific hydrogen isotope ratios, $(D/H)_i$ in ppm, of geraniol and α-pinene

Geraniol	C1	C2	C4	C5	C6	C8	C9	C10
C3	148	33.4	104	142.6	115.3	97.1	113.9	95.5
$N = 2$	4	2.3	4.4	0.7	2.9	1.5	6.8	0.2
C4	155.6	28.5	114.3	153.9	53.2	105.5	132	104.2
$N = 5$	8.8	6.8	3.9	6.1	4.7	6.7	6.4	4.2

α-pinene	C1	C1′	C2	C4	C5	C5′	C6	C8 (C9)	C9 (C8)	C10
1*R*,5*R* (+)	153.3	149.1	40.8	124.2	165.5	148.1	140.1	110.6	91.6	115.8
$N = 4$	2.3	4.6	4.1	10.4	6.5	4.9	6.5	2.9	4.1	1.7
1*S*,5*S* (−)	159.1	151	37.7	93.3	162.9	157.3	152.9	111.9	90.5	119.5
$N = 4$	3.3	4	7.7	1.2	7.9	7	5.1	3.8	4.8	5.9

The GPP numbering of the carbon-bound hydrogen atoms is specified in Figure 1. Geraniol has been extracted from plants with either C3 or C4 metabolism. Samples of α-pinene with strong and opposite enantiomeric enrichments have been investigated. Standard deviations are computed from determinations performed on N samples [10].

NMR results with the mevalonate pathway was recognized later on [7,8] when a new mechanism [9] was proposed for explaining terpenoid biosyntheses. The whole set of specific isotope ratios determined in a large selection of monoterpenes from different plant origins was fully analyzed recently [10], in light of the newly proposed DOXP pathway, which is no longer based on mevalonic acid but on glyceraldehyde 3-phosphate (G3P) and pyruvate precursors [11,12]. Several striking mechanistic properties may be deduced from the overall isotopic scheme. Thus, the remarkable consistency of the NMR isotopic profiles within the monoterpene family supports the existence of a common mechanistic origin and provides unambiguous one-pot checks for the stereochemical schemes of affiliation illustrated in Figure 1 on the examples of geraniol and pinene. The NMR results reveal that the type of photosynthetic metabolism, C3 or C4, exerts a significant influence on the isotopic parameters (Table 1). This behavior may be attributed to the possibility of direct or indirect origin of dimethylallyl diphosphate (DMAPP), one of the two building blocks of GPP. The isotopic profile suggests that, in C3 plants, both isopentenyl diphosphate (IPP), the other building blocks of GPP, and DMAPP are, in majority, synthesized directly through the DOXP pathway (Figure 2a), whereas GPP of C4 plants is largely synthesized through condensation of IPP with DMAPP resulting from isomerization of IPP (Figure 2b).

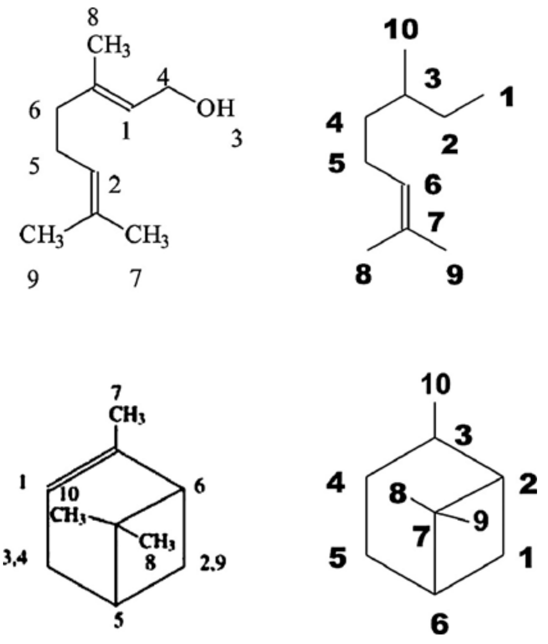

Fig. 1. Mechanistic correspondence between hydrogen positions in the geranyl and pinane skeletons (bold numbers) and corresponding assignments of the ^{2}H-NMR signals. The deuterium isotopomers of geraniol and α-pinene are numbered in the order of decreasing chemical shifts.

On this basis, the NMR method provides unique criteria for estimating the influence of physiological and environmental factors on the relative fluxes of directly and indirectly synthesized DMAPP in unperturbed natural environments. The NMR results also provide an order of magnitude of the kinetic isotope effects accompanying hydride and proton transfers at two steps of the DOXP pathway. Thus, a fractionation factor of the order of 5 with respect to water is determined at position ex-2 of a great variety of samples from the monoterpene family. This factor represents a minimum limit of the kinetic isotope effect accompanying the introduction of a proton

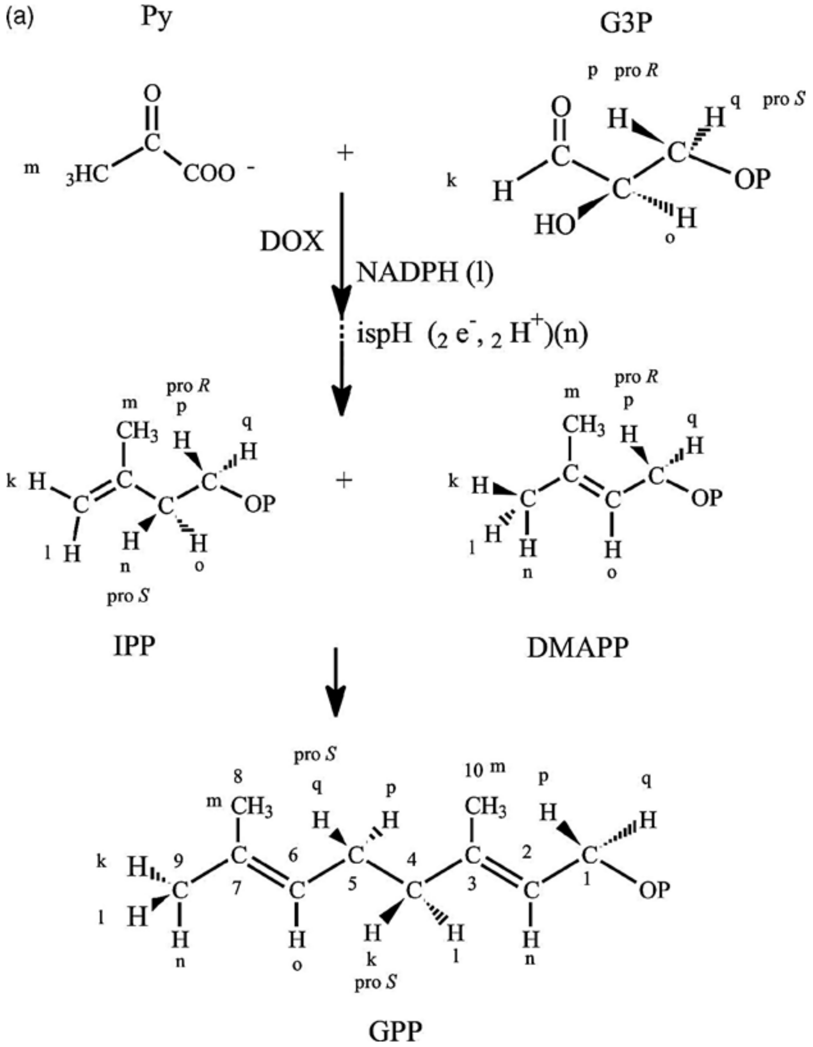

Fig. 2. Hydrogen affiliation of geranyl diphosphate (GPP) to its isopentenyl diphosphate (IPP) and dimethylallyl diphosphate (DMAPP) building blocks and formerly to the pyruvate (Py) and glyceraldehyde phosphate (G3P) precursors [10]. (a) The condensation involves IPP and DMAPP molecules independently biosynthesized through the DOXP pathway. (b) GPP results from condensation of IPP directly produced in the DOXP mechanism and of DMAPP obtained by isomerization of IPP.

(hydrogen denoted n) at a late step [13] of the DOXP sequence of reactions. It provides a reliable criterion for distinguishing the DOXP and mevalonate mechanisms, which may coexist in certain terpenoids [14].

Since transfer coefficients leading from carbohydrates to glycolytic products have been determined (Part 2, Section “Elaboration of SNIF-NMR probes: from carbohydrates to ethanol and glycerol”), it becomes possible to trace back selectively the hydrogen genealogy, going from the considered monoterpene to the key intermediate, GPP, then successively to the condensed couple IPP/DMAPP, then to the DOXP precursor couple pyruvate/G3P, and finally to the carbohydrate precursors (Figure 2).

Interestingly, the methylenic positions, which were enantiotopic in geraniol, become diastereotopic in chiral derivatives, and especially in cyclic monoterpenes. Consequently, they are, in principle, separately observable in the ^{2}H-NMR spectrum (Part 2, Section “Access to

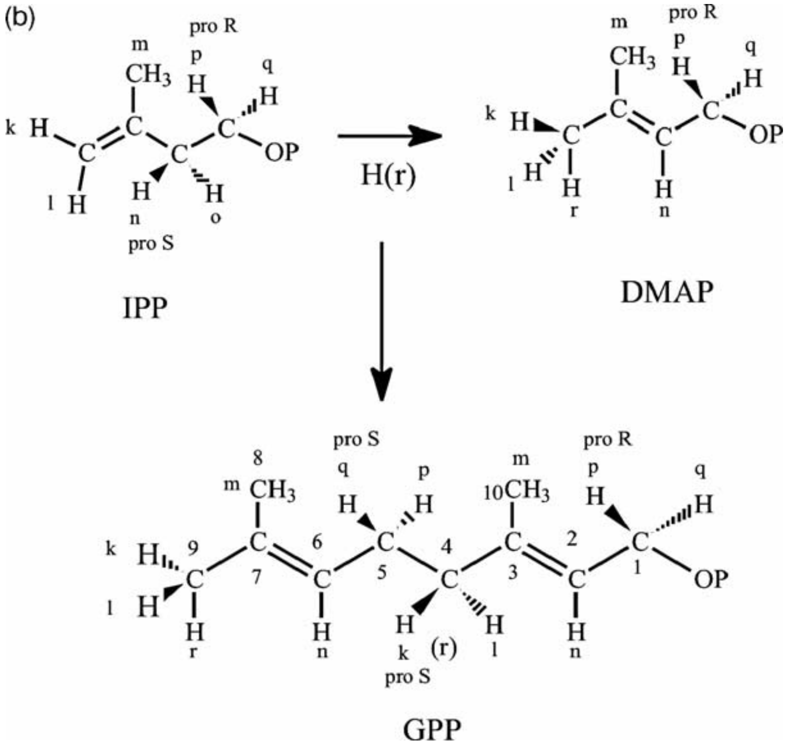

Fig. 2. (*Continued*)

mechanistic information on enantiotopic hydrogen sites"). The isotope contents at these positions may provide additional information [15] on the overall stereospecificity of the chain of reactions leading to GPP and then to terpenes, and, in particular, on the possible occurrence of scrambling steps. Thus, it was shown that all the geminal methylenic sites of GPP, are preserved from racemization. This behavior is demonstrated, for instance, by the existence of different deuterium contents at the diastereotopic methylenic positions ex-5 of optically active pinene samples (Table 1). Similarly, the strong difference in the $(D/H)_{\text{ex-4}}$ values of α-pinenes with opposite chirality proves that the two methylenic hydrogen atoms at site 4 of GPP have been stereospecifically transferred to the terpene. This behavior implies, in addition, that these two ex-4 hydrogen atoms have been stereospecifically introduced into GPP from different precursor atoms (one from the aldehydic site-k of G3P and the other from NADPH in the course of the DOXP pathway). These mechanistic properties provide the basis for an isotopic method of enantiomeric evaluation, applicable when optically pure enantiomers of opposite chirality are available as references. Once the maximum differences in the D/H values of the methylenic positions have been determined on the reference products, the corresponding differences measured on an unknown sample provide attractive criteria for estimating the rate of enantiomeric enrichment [5].

Many natural biosyntheses and biotechnological processes can be investigated in this way. Thus, information was obtained on cofactor recycling in asymmetric biocatalytic reduction of carbonyl compounds mediated by yeasts [16]. The situation is obviously more complicated for minor compounds issued from long biochemical pathways and/or for molecules insufficiently adapted to ^{2}H-NMR quantitative analysis. However, in this case, more exploitable spectra may often be obtained, as illustrated in the case of carbohydrates, through appropriate derivatizations. Thus, although the deuterium spectra of fatty acids suffer from drastic signal overlap, resorting to chemical degradations can individualize specific positions. Interesting information was derived in this way on enzyme mechanisms and in particular on the E-desaturation occurring in capsaicin [17,18].

The examples described above and in Part 2 are illustrative of the potential of isotopic NMR to elucidate different features of mechanistic pathways. They show that, either limited to the sole investigation of end products or possibly reinforced by determinations of isotopic redistribution coefficients through model experiments, the NMR method is particularly helpful (a) for eliminating inconsistent mechanistic hypotheses; (b) for detecting mechanistic changes and quantifying relative fluxes through different pathways; (c) for elucidating individual connections between hydrogen atoms of reactants and products and estimating the percentages of preserved affiliation; (d) for investigating stereochemical pathways in terms of stereospecificity and regioselectivity; (e) for detecting and even quantifying intermolecular exchanges and relative contributions of hydrogen atoms from the medium; (f) for identifying isotopically sensitive branching points; and (g) in certain circumstances, for estimating the value, or at least the order of magnitude, of active kinetic isotope effects.

Undoubtedly, this approach is able to spare considerable experimental time in the numerous labeling strategies usually implemented for elucidating biosynthetic pathways. Moreover, it provides a unique tool (a) for investigating *in vivo* metabolic responses to physiological characteristics of plants and, in particular, for estimating relative fluxes of intermediates in field conditions and for precising the role of different enzymic equipments, and finally for interpreting the influence of environmental factors on biosyntheses in unperturbed natural media. In this respect, natural isotopic abundance avoids the risk, inherent to enriched models, of perturbation of the biochemical pathway due to the effect of KIE in branched reaction steps.

Identification of Starting Materials: The Nature Laboratory

As discussed in Part 2, many mechanistic, physiological, environmental, and technological factors are likely to influence isotopic distribution in plant products. Moreover, hydrogen is reputed to be easily exchanged in the course of biochemical processes. A priori, the specific hydrogen isotope parameters were therefore not granted much future for precisely distinguishing chemically identical molecules biosynthesized in different plant species or grown in different environments. However, in spite of multiple sources of fractionation, the isotopic profile progressively appeared as an extremely powerful tool for precise origin inference. The aptitude of the SNIF-NMR parameters to elucidate the affiliation of a given type of molecule, both in terms of precursor and environment, rests on two important properties of isotope fractionation. Firstly, biosynthetic reactions operating in nature frequently exhibit remarkable mechanistic stability and reproducibility. Moreover, in contrast to many analytical methods, mostly based on hardly predictable compositional parameters [19], the NMR method exploits isotope fractionation effects which can be quantitatively appraised on theoretical bases. Consequently, as checked in the example of the fermentation reaction (Part 2), when a bioconversion is reproduced in strictly identical conditions, isotopic variations measured on products reflect solely differences in the isotopic parameters of their precursors [20].

In nature, a given molecular species is frequently synthesized in different plants species, different plant organs or different environments through the same complex chain of reactions and the kinetically fractionating steps are the same. Thanks to this mechanistic stability the NMR parameters of metabolites may be comparatively analyzed in terms of properties of the precursors. However, in this perspective of origin inference, the example of monoterpene biosynthesis discussed above (Section "SNIF parameters as witnesses of individual mechanistic routes of atoms," Table 1) draws attention on the importance of previously detecting and elucidating all possible changes in the reaction scheme.

The situation is somewhat different for products of animal origin, since the isotope ratios then reflect the diet rather than the animal species [21]. Thus, controlled feeding experiments have shown that lactose from cow's milk can be used for checking the type of diet given to the animal [22]. Similarly, isotope ratios measured on fish lipids are not efficient criteria for characterizing the fish species, a problem that is fairly well resolved by molecular biology, but they are able perfectly to classify wild salmon and salmon farmed in Norway and Scotland for instance [23].

Experimental Strategies for Origin Inference of Products

Taking into account the large price differences often exhibited by raw materials from different origins, it has always been tempting to substitute a cheap counterpart to an expensive molecular species. As illustrated in Part 4, being able to identify the origin of a given molecule is of great economical importance and a number of methodologies have been developed to this aim [19,24]. With the exception of isotope ratio mass spectrometry (IRMS), which measures overall isotope ratios, these methodologies are based on the detection of hardly predictable compositional differences resulting from the presence of molecules (minor components or impurities) structurally different from the adulterated species. When technically applicable, the NMR method of origin inference benefits from remarkable performances in terms of efficiency and reliability. Possibly combined with IRMS, it is often the only tool capable of identifying the origin of a pure molecular species.

Although it can be addressed to any product accessible to ^{2}H-NMR, the method has found a maximum number of applications in the field of food and aromas. In these domains, it has largely contributed to establishing the notion of authentication on quantitative bases.

General Methodology

In practice, many conclusions can be drawn from simple comparison of the $(D/H)_i$ values of the investigated sample with corresponding $(D/H)_i$ values determined, in the same experimental conditions, on samples from known origin. Official and private laboratories currently use this approach for controlling certain types of products (cf. Part 4). To operate in reliable conditions, it requires previous building up of reference databases composed of a great number of samples representing all possible different provenances. In addition, rigorous standardization of the whole experimental procedure is necessary. As a result of equilibrium and kinetic isotope effects accompanying physical treatments such as extraction, distillation, evaporation, etc. (cf. Part 2), isotopic values are likely to be spoilt by undesirable fractionation effects. It is therefore necessary to previously define, for every kind of molecule, standardized experimental conditions that optimize the yields. In a context of international regulation, it is recommended to organize dedicated collaborative studies.

For every type of molecule, this semi-empirical approach of origin inference should be secured by previous determination of the affiliation scheme and appraisal of possible sources of variation in the fractionation effects (cf. Part 2). This basic knowledge is of prime importance—to ensure correct interpretation of certain results, to detect anomalous values, to predict isotopic behavior when appropriate authentic reference samples are missing, and even to build properly a representative data bank.

Statistical Treatments

In order to improve the discriminating performances, numerous samples of a given type of product are usually investigated. Fortunately, integrated analyses of large numbers of data now benefit from computerized statistical methods, such as multidimensional analyses, developed in the course of the last decades. Thus, techniques of principal component analysis, hierarchical classification, or discriminant analysis are crucial help for classifying samples as a function of typical origins. Such statistical treatments of NMR isotopic variables provide interpretable graphical diagrams, which enable an unknown sample to be easily located in the appropriate group (cf. Section "Identification of plant precursors", Figure 4). Integration of multidimensional statistical treatments into automatized SNIF-NMR analytical chains, greatly improves the performance of authentication procedures. The discriminating parameters are retained according to their efficiency for both separating the considered origins and quantifying adulterations involving mixtures of species from different origins.

Natural or Synthetic Origin of Products

With the increasing interest of consumers for the natural status, it is desirable to dispose of methods capable of solving the problem of origin inference both for raw materials and for finished products [25]. In the case of flavors for instance, a distinct labeling may be claimed by food processors when using natural flavors. However, in many cases, the main molecules present in natural compounds can also be produced by chemical synthesis at a much cheaper price. Obviously, when flavors containing synthetic aroma chemicals are sold as natural ones, unfair competition destabilizes the market. Therefore, methods are required for detecting the addition of synthetic molecules to natural compounds. As discussed above, when two chemically identical molecules have been biosynthesized (or synthesized) through different reaction mechanisms, largely different isotopic profiles are expected. Therefore, in many cases, the SNIF-NMR method is particularly efficient for discriminating natural and synthetic origins and quantifying adulterations.

A typical example is that of the vanillin molecule which is nearly one hundred times more expensive when extracted from vanilla beans (4000 ˚ /kg) than when it comes out of the reactor. This gap in price has stimulated, for several decades, considerable research competition in view of alternatively developing and circumventing methods capable of recognizing the natural or synthetic origin of the molecule. Obviously, ^{14}C determination is a good tool for differentiating living pool products from fossil products devoid of radioactivity [26–28]. However, it is easy to "naturalize" synthetic samples through addition of ^{14}C-enriched materials. For a time, hope was placed on IRMS methods based on determination of the overall ^{13}C (and deuterium) content of the molecule [29–31]. Unfortunately, since the ^{13}C/^{12}C ratio of the natural species is higher than that of the synthetic one, the natural value was rapidly simulated through addition to the synthetic (or hemi-synthetic) species of a small quantity of vanillin enriched in ^{13}C on the methoxyl group. In reaction, chemists then developed cutting protocols aimed to isolate the methoxy group in order to detect abnormal enrichment. But since enrichment could also be directed to the carbonyl fragment, decarboxation procedures had to be defined. Finally, the skill of chemists in manipulating ^{13}C contents definitely compromised the chance of IRMS in solving the problem. The ^{2}H-NMR method, which simultaneously observes four isotopomers corresponding to non-exchangeable sites of vanillin, provides a highly discriminant fingerprint [32,33] which needs considerable labeling efforts to be efficiently simulated. Statistical analyses based on the four $(D/H)_i$ variables show that the group of vanillin ex-beans is unambiguously distinguished from synthetic origins [34]. The method enables about 5% addition of vanillin ex-guaiacol in vanillin ex-bean to be detected. Fortunately, research stimulation in this domain is still preserved, since the development of new sources of vanillin [35,36] has renewed the challenge! Whatever their official status, biotechnological vanillin samples obtained from different raw materials through different processes have now to be authenticated with respect to other origins [37].

We shall discuss a second example that of mustard oil. The major component of mustard oil is allyl isothiocyanate. When extracted from mustard seeds, this compound is much more expensive than when prepared by chemical synthesis. Therefore, there is substantial economic interest to reinforce the natural species by its synthetic counterpart. The ^{2}H-NMR signals of the four hydrogen isotopomers of allyl isothiocyanate, $SCN\text{–}CH_2\text{–}CH{=}CH_2$, are relatively thin and well separated [38]. The main difficulty of the experiment is due to the dangerous properties of this substance, which is toxic, flammable, corrosive, and strong lachrymator. Special techniques were therefore adapted to handle the relatively large amounts of sample required by NMR spectroscopy. In particular, Teflon tube liners were placed inside the NMR cell to prevent glass breaking and toxic leakages. Such configuration is detrimental to the shape of the peak but can be compensated for by appropriate signal processing [39]. A principal component analysis performed on the relative parameters R_{ij} (Part 1, Equation 7) shows that the natural samples are clearly distinguished from the synthetic ones. Adulteration of natural samples by the synthetic counterpart is detectable below 10%. Although the overall isotopic deviations, $\delta^{13}C$, $\delta^{15}N$, $\delta^{33}S$, measured by IRMS, are powerless to ensure this distinction, they are helpful, when combined with the NMR results, for improving the discrimination in terms of geographical origin (cf. Section "Climatic Effects and Geographical Origin") of the natural samples (India and Canada).

Many other examples demonstrating the potential of the NMR method for ascertaining the genuineness of flavors, perfumes, additives, etc., have been published. The following list, which is not exhaustive, illustrates the variety of molecular structures accessible to the isotopic NMR methodology: benzaldehyde [40,41], *p*-hydroxybenzaldehyde [34], phenylethanol [42], organic acids, in particular acetic acid from vinegar [43–45], esters [45], phenylacetic acids [46], raspberry ketone [47,48], (*R*)-δ-decanolide [49], camphor [50], squalene [51], hexenal and hexanol [52,53], resveratol and rhapontin [54], α-bisabolol [55], aminoacids [56,57], terpenes [58].... Appropriate degradations of the molecule are sometimes carried out in order to enhance the ^{2}H-NMR resolution potential [54]. In certain cases the NMR method is efficiently complemented by IRMS determinations of overall isotope ratios of carbon, hydrogen, oxygen, nitrogen... and hyphenated techniques such as gas chromatography-pyrolysis-IRMS are developed [59].

Characterization of Chemical Processes

Fractionation factors resulting from active kinetic isotope effects taking place in chemical processes may reach very high values and hydrogen isotope ratios of several hundreds of ppm are not rare. Different ^{2}H-NMR profiles are therefore expected for molecules synthesized through different chemical mechanisms and this property can be exploited for identifying chemical processes and therefore for controlling patent utilization.

Returning to the example of vanillin, the NMR method can be extended to the discrimination of synthetic samples produced by different chemical processes [60]. Electrophylic addition in position 4 of the benzene ring of guaiacol, the usual starting material of vanillin synthesis, generally involves formaldehyde or glyoxylic acid reagents. In the case of glyoxylic acid, two main industrial sources are available as shown in Figure 3. In process A, which starts from naphtha and maleic anhydride, glyoxylic acid is formed through a double bond oxidation step, whereas in process B, ionic oxidation of acetaldehyde is involved. In this last case, as in that of the oxidation of toluene into benzaldehyde [41], large fractionation factors due to kinetic isotope effects are expected. Consequently, the two processes may be identified from the well-distinct ranges of D/H values exhibited by the aldehydic hydrogen. More complete analyses of the NMR data provide complementary information on the nature of the raw materials, either biomass or oil, used in the synthesis.

Similarly, synthetic counterparts of benzaldehyde and cinnamaldehyde, the main active molecules of bitter almond and cinnamon oils, can be obtained either by direct oxidation of toluene or by hydrolysis of benzene chloride. These two chemical sources are easily distinguished on the basis of the NMR isotopic values [40,41]. Whereas the combination of primary and secondary kinetic isotope effects accompanying radical transfer in the chlorination of toluene result in fractionation factors <1.2, these factors may be on the order of 5 for proton elimination in the electrophylic oxidation. This behavior is responsible for very large differences in the hydrogen isotope ratio of the aldehydic fragment. Thus, whereas benzaldehyde resulting from hydrolysis of benzal is characterized by $(D/H)_{CHO}$ values of about 165 ppm, values up to

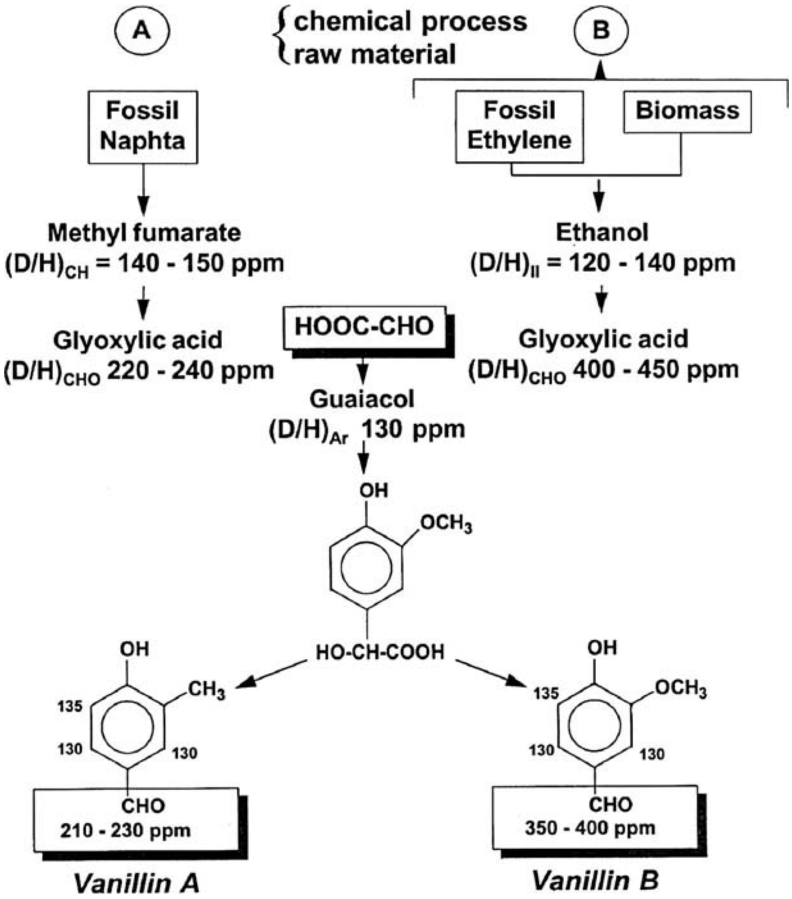
A
chemical process
raw material
B
Fossil Naphta
Fossil Ethylene
Biomass
Methyl fumarate
(D/H)CH = 140 - 150 ppm
Ethanol
(D/H)II = 120 - 140 ppm
Glyoxylic acid
(D/H)CHO 220 - 240 ppm
HOOC-CHO
Glyoxylic acid
(D/H)CHO 400 - 450 ppm
Guaiacol
(D/H)Ar 130 ppm
OH
OCH3
HO-CH-COOH
OH
CH3
135
130
130
CHO
210 - 230 ppm
Vanillin A
OH
OCH3
135
130
130
CHO
350 - 400 ppm
Vanillin B

Fig. 3. Schematic representations of the two main routes of synthesis of glyoxilic acid. The kinetic isotope effects involved in these reactions lead to very different contents of aldehydic isotopomers [60].

900 ppm are measured in benzaldehyde obtained through oxidation reactions. Thanks to this very large difference, even the overall deuterium content of the molecule determined by IRMS is sufficient for discriminating the two synthetic origins [61]. More generally statistical treatments have been carried out on the molar fractions, f_i, and the relative parameters, R_{ij} (Part 1, Equation 7) measured on 65 samples of benzaldehyde from four different origins: the two synthetic sources, natural benzaldehydes obtained through hydrolysis of amygdalin from bitter almond and kernels (apricots, peaches, plums, cherries, . . .), and semi-synthetic benzaldehyde obtained from cinnamaldehyde ex-cassia or ex-cinnamon through retroaldolization [41]. In the absence of any previous classification, a principal component analysis satisfactorily differentiates these four main origins (Figure 4).

This approach can be applied to both bitter almond oils and cinnamon oils. In the second case, previous derivatization of cinnamaldehyde into benzaldehyde is used for investigating the cinnamaldehyde molecule, which is not a suitable probe for ^{2}H-NMR due to signal overlap, even at high magnetic field.

Identification of Plant Precursors

As compared to the previous problems, which are concerned with the distinction of natural molecules from their synthetic counterparts or with the characterization of different chemical processes, the problem of discriminating molecules elaborated through the same type of biochemical pathway but in different plants species seems

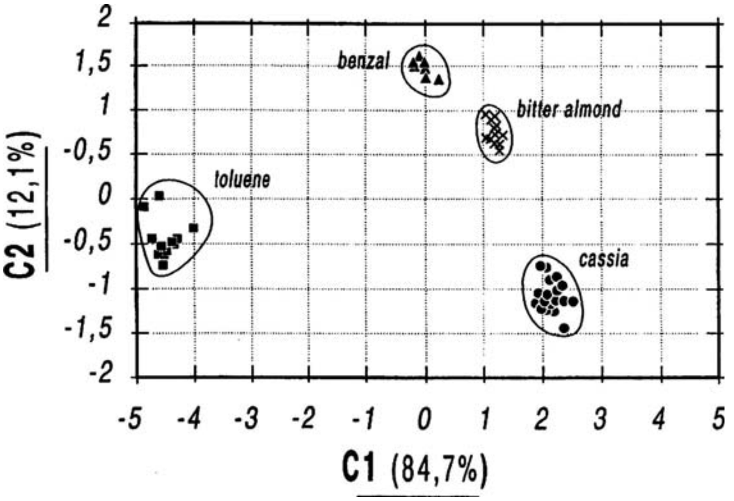

Fig. 4. Representation of benzaldehyde samples from different origins in the plane of the two first components of a principal component analysis based on the hydrogen isotopic variables [41].

less easy to solve. Nevertheless, one of the first papers concerning the method [62] enlightens, on the example of anethole, the capability of the ^{2}H-NMR spectrum to distinguish the three plant origins, fennel, star anise, or green anise [63].

The aptitude of site-specific parameters to discriminate different botanical origins of the precursor is particularly efficient in the case of sugars. Thanks to the reliability of the ethanol probe obtained through controlled fermentation of carbohydrates, many types of vegetal, and even animal species can be distinguished [64]. This strategy enables different chemical structures to be compared: polysaccharides from cereals, tubers, and leguminosae; glucose, fructose, and sucrose from fruits; sucrose from sugar plants; and lactose from milk [65]. Hierarchical clustering, based on hydrogen and carbon isotopic parameters, classifies the different precursor origins according to their degree of mutual dissimilarity. Firstly, sugars of C3 plants are discriminated from those of C4-CAM plants, then citrus are well distinguished from other C3 plants and the CAM pineapple is well identified with respect to the cane and maize C4 plants. Among C3 plants, beet then exhibits a good level of dissimilarity and, although more similar, many other plant species are satisfactorily distinguished [64]. These results provide the basis for the detection of adulteration of fruit juices by addition of exogeneous sugars from beet or cane for instance (cf. Part 4). Interestingly, citrus honey is distinguished, on the same basis, from honey obtained by feeding the bees with sucrose in seasons when they usually collect nectars [66]. A procedure, evaluated in a collaborative study, has also been defined for detecting added sugar in maple syrup [67].

A similar approach can be applied to lactic acid. Thus, the isotopic parameters of $D(-)$ or $L(+)$ enantiomers of lactic acid, produced in fermentation reactions with specific bacteria, are representative of the kind of fermented sugar [68]. As that of the methylene group of ethanol, the ^{2}H content of the CH(OH) group of lactic acid depends on the isotopic composition of the medium in which the fermentation took place.

Unfortunately, some important classes of products, such as lipids, exhibit poorly resolved ^{2}H-NMR spectra. In order to face the investigation of large numbers of samples, extracted from different types of plant or from fish oils, without resorting to time-consuming and fractionating separation and derivatization procedures, analytical strategies appropriate to the direct treatment of mixtures have been developed [69–72]. Thus, when exploited on a statistical basis, average isotopomeric compositions associated with clusters of signals originating from several chemical sites of one or of several fatty acids enable different kinds of plant precursors, in particular olive, to be distinguished. In this respect it should be mentioned that glycerol extracted from lipids also provides information on plant precursors, such as olive and sunflower [73].

Climatic Effects and Geographical Origin

Owing to thermodynamic and kinetic isotope effects associated with phase transition phenomena (Part 2, Section "Influence of phase transitions and transport phenomena on the isotopic parameters"), the hydrogen and oxygen isotope ratios of water are influenced by changes in climatic conditions. These parameters, measured by IRMS, have long been exploited in hydrogeology [74]. More generally, the overall isotope ratios of ice cores and of more or less complex materials such as sediments, wood or cellulose are currently used for paleoclimatic reconstruction [75,76]. However, owing to the complexity of the physicochemical and biochemical sources of isotope fractionation, the interpretation of overall IRMS parameters, which are averages over several molecular sites and, in many cases, over several molecular species, is not straightforward and often remains controversial.

By opening the possibility to investigate individual responses of hydrogen atoms to climatic variations, the SNIF-NMR method significantly decreases the level of complexity of the interpretation [77]. It was shown, for instance, that the ethanol probe obtained by standardized fermentation of fruits, enables successive climatic responses to be decoupled. As deduced from the values of the redistribution coefficients (Part 2, Section "Elaboration of SNIF-NMR probes: from carbohydrates to ethanol and glycerol"), the isotope ratio of the methyl site, $(D/H)_{\mathrm{I}}$, reflects the climatic sensitivity of the carbon-bound hydrogen atoms of sugars, whereas the isotope ratio of the methylene site, $(D/H)_{\mathrm{II}}$, varies with climatic effects on juice water. Consequently, these two parameters are influenced by climatic variations that occur at different periods of plant growth, generally characterized by different evapotranspiration intensities. The aptitude of site specific isotope ratios to convey reliable climatic information has been demonstrated by statistical analyses performed on isotopic variables measured on large numbers of grape (wines) or orange samples collected in different parts of the world. In the absence of previous classification, principal component analyses show that the samples are distributed according to the main climatic features of the regions of production [78,79]. Three main types of climate are roughly distinguished: cold and humid, hot and dry, and temperate. This climatic dependency implies that isotopic parameters can be exploited for inferring the region where the plant precursor has grown. Canonical correlation analyses performed on the basis of typical area of productions illustrate the surprisingly high discriminating potential of the isotopic variables. Not only samples from different countries may generally be identified, but even close regions with relatively similar climate, such as Alsace and the Loire Valley in France, can be distinguished. The performances of geographical inference can still be improved by combining NMR with trace element analysis, which provides soil criteria [80]. For a given plant grown in a given region, the climatic dependency of the isotope ratios may also be exploited for authenticating

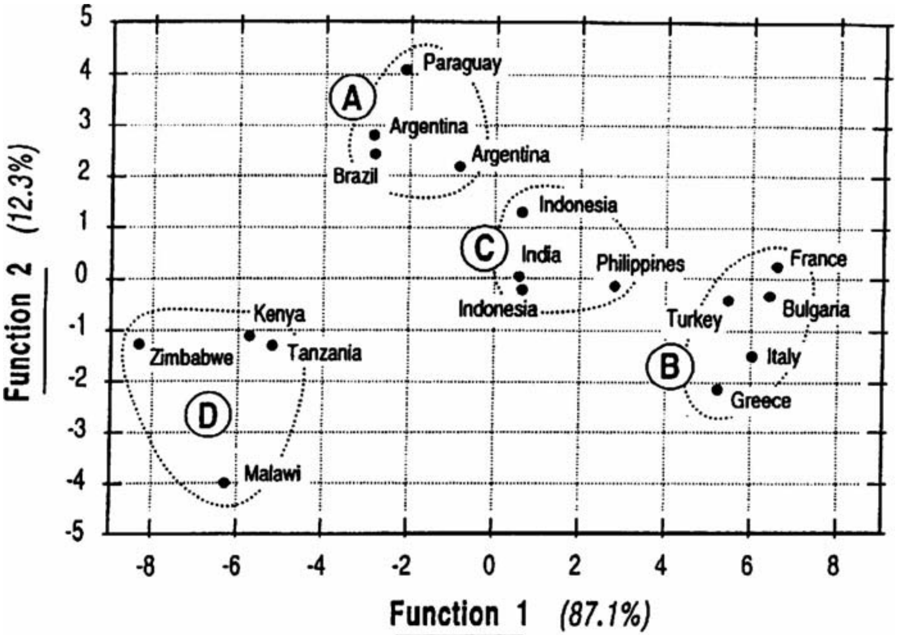

Fig. 5. Representation of nicotine samples extracted from tobacco grown in different countries, in the plane of the two first functions of a discriminant analysis based on site-specific isotope ratios. Four groups of countries characterized by relatively different climatic conditions are distinguished [84].

samples produced in years characterized by significantly different weather [81].

Whereas sugars, investigated through the ethanol probe, are particularly sensitive to climatic variations, the climatic influence is usually more slightly perceived by minor metabolites remote from the initial photosynthetic step. Nevertheless, caffeine from South America for instance can be authenticated with respect to caffeine from Africa [82]. Similarly, the NMR parameters may provide information on the geographical origin of heroin and cocaine [83]. It should also be emphasized that different sites in a given metabolite, do not necessarily exhibit the same sensitivity to climatic variables. In the case of nicotine for example [84], individual molecular sites exhibit different behavior but a canonical correlation analysis based on the site-specific variables enables several production areas of tobacco to be identified (Figure 5).

From a general point of view, it is concluded that different components of a plant and even different sites of a given molecular species may exhibit different isotopic responses to climatic variables. Consequently, care must be taken when interpreting variations in the overall IRMS parameters of complex materials, including cellulose, in terms of climate reconstruction.

References

1. Croteau RB. Biochem. In: ISI Atlas of Science 1988;1:182–8.
2. Croteau R, Gershenzon J, Wheeler CJ, Satterwhite DM. Arch. Biochem. Biophys. 1990;277:374–81.
3. Pyun HJ, Coates RM, Wagschal KC, Mcgeady P, Croteau RB. J. Org. Chem. 1993;58:3998–4009.
4. Wagschal KC, Pyun HJ, Coates RM, Croteau R. Arch. Biochem. Biophys. 1994;308:477–87.
5. Martin GJ, Janvier P, Akoka S, Mabon F, Jurczak J. Tetrahedron Lett. 1986;27:2855–8.
6. Arigoni D, Cane DE, Shim JH, Croteau R, Wagschal K. Phytochemistry 1993;32:623–31.
7. Rieder C, Jaun B, Arigoni D. Helv. Chim. Acta 2000;83:2504–13.
8. Schmidt HL, Werner RA, Eisenreich W. Phytochem. Rev. 2003;2:61–85.
9. Rohmer M, Knani M, Simonin P, Sutter B, Sahm H. Biochem. J. 1993;295:517–24.
10. Martin GJ, Lavoine-Hanneguelle S, Mabon F, Martin ML. Phytochemistry. 2004;20:2815–31.
11. Lichtenthaler HK, Schwender J, Disch A, Rohmer M. FEBS Lett. 1997;400:271–4.
12. Eisenreich W, Sagner S, Zenk MH, Bacher A. Tetrahedron Lett. 1997;38:3889–92.
13. Rohdich F, Zepeck F, Adam P, Hecht S, Kaiser J, Laupitz R, Gräwert T, Amslinger S, Eisenreich W, Bacher A, Arigoni D. Proc. Natl. Acad. Sci. USA 2003;100:1586–91.
14. Schuhr CA, Radykewicz T, Sagner S, Latzel C, Zenk MH, Arigoni D, Bacher A, Rohdich F, Eisenreich W. Phytochem. Rev. 2003;2:3–16.
15. Martin ML, Zhang BL, Martin GJ. FEBS Lett. 1983;158:131–3.
16. Zhang BL, Pionnier S. Chem. Eur. J. 2003;9:3604–10.
17. Billault I, Guiet S, Mabon F, Robins R. ChemBioChem. 2001;2:425–31.
18. Robins RJ, Billault I, Duan JR, Guiet S, Pionnier S, Zhang BL. Phytochem. Rev. 2003;2:87–102.
19. Martin ML, Lees M, Hanote V. In: C Ducauze (Ed). Fraudes Alimentaires. Tec. et Doc.: Paris, 2003, pp 281–315.
20. Sergeyev NM, Sergeyeva ND, Raynes WT. JCS Chem. Commun. 1994:485–6.
21. Peterson BJ, Fry B. Ann. Rev. Ecol. Syst. 1987;18:293–320.
22. Masud Z, Vallet C, Martin GJ. J. Agric. Food Chem. 1999;47:4693–9.
23. Aursand M, Mabon F, Martin GJ. JAOCS 2000;77:659–66.
24. Belton PS, Delgadillo I, Gil AM, Roma P, Casuscelli F, Colquhoun IJ, Dennis MJ, Spraul M. Magn. Reson. Chem. 1997;35:S52–60.
25. Martin GG, Remaud G, Martin GJ. Flavour Fragrance J. 1993;8:97–107.
26. Allen AB. Agric. Food Chem. 1961;9:294–5.
27. Drevon G, Marechal J, Marien G, Pachiaudi C. Riv. Ital. EPPOS 1980;62:211–2.
28. Hoffman PG, Salb MC. J. Assoc. Off. Anal. Chem. 1980;63:1181–3.
29. Bricout J, Fontes JC, Merlivat L. J. Ass. Off. Anal. Chem. 1974;57:713–5.
30. Hoffman PG, Salb M. J. Agric. Food Chem. 1979;27:352–5.
31. Krueger DA, Krueger HW. J. Agric. Food Chem. 1985;33:323–5.
32. Toulemonde B, Horman I, Egli H, Derbesy M. Helv. Chim. Acta. 1983;66:2342–5.
33. Maubert C, Guerin C, Mabon F, Martin GJ. Analusis. 1988;16:434–9.
34. Remaud GS, Martin YL, Martin GG, Martin GJ. J. Agric. Food Chem. 1997;45:859–66.
35. Walton NJ, Narbad A, Faulds CB, Williamson G. Curr. Opin. Biotechnol. 2000;11:490–6.
36. Walton NJ, Mayer MJ, Narbad A. Phytochemistry. 2003;63:505–15.
37. Bensaid FF, Wietzerbin K, Martin GJ. J. Agric. Food Chem. 2002;50:6271–5.
38. Remaud GS, Martin YL, Martin GG, Naulet N, Martin GJ. J. Agric. Food Chem. 1997;45:1844–8.
39. Martin YL. J. Magn. Res. Ser. A 1994;111:1–10.
40. Hagedorn ML. J. Agric. Food Chem. 1992;40:634–7.
41. Remaud G, Debon AA, Martin YL, Martin GG, Martin GJ. J. Agric. Food Chem. 1997;45:4042–8.
42. Fronza G, Fuganti C, Grasselli P, Servi S, Zucchi G. J. Agric. Food Chem. 1995;43:439–43.
43. Remaud G, Guillou C, Vallet C, Martin GJ. Fresenius J. Anal. Chem. 1992;342:457–61.
44. Hermann A. Eur. Food Res. Technol. 2001;212:683–6.
45. Rabiller A, Maze F, Mabon F, Martin GJ. Analusis. 1991;19:18–22.
46. Aleu J, Fronza G, Fuganti C, Serra S, Fauhl C, Guillou C, Reniero F. Eur. Food. Res. Technol. 2002;214:63–66.
47. Fronza G, Fuganti C, Guillou C, Reniero F, Joulain D. J. Agric. Food Chem. 1998;46:248–54.

48. Fronza G, Fuganti C, Pedrocchi-Fantoni G, Serra S, Zucchi G, Fauhl C, Guillou C, Reniero F. J. Agric. Food Chem. 1999;47:1150–1155.
49. Fronza G, Fuganti C, Grasselli P, Barbeni M, Cisero M. J. Agric. Food Chem. 1993;41:235–9.
50. Grant DM, Curtis J, Croasmun WR, Dalling DK, Wehrli FW, Wehrli S. J. Amer. Chem. Soc. 1982;104:4492–4.
51. Deiana M, Corongiu FP, Dessi MA, Scano P, Casu M, Lai A. Magn. Reson. Chem. 2001;39:29–32.
52. Fronza G, Fuganti C, Zucchi G, Barbeni M, Cisero M. J. Agric. Food Chem. 1996;44:887–91.
53. Joulain D. In: KAD Swift (Ed), Advances in Flavours and Fragrances. Royal Society of Chemistry: Cambridge, 2002, pp 84–91.
54. Fronza G, Fuganti C, Serra S, Cisero M, Koziet J. J. Agric. Food Chem. 2002;50:2748–54.
55. Carle R, Beyer J, Cheminat A, Krempp E. Phytochem. 1992;31:171–4.
56. Vallet C, Arendt M, Mabon F, Naulet N, Martin GJ. J. Sci. Food Agric. 1991;56:167–85.
57. Brenna E, Fronza G, Fuganti C, Pinciroli M. J. Agric. Food. Chem. 2003;51:4866–72.
58. Hanneguelle S, Thibault JN, Naulet N, Martin GJ. J. Agric. Food Chem. 1992;40:81–7.
59. Bilke S, Mosandl A. Eur. Food Res. Technol. 2002;214:532–5.
60. Martin GJ. In: JR Desmurs, Serge Ratton (Eds). The Roots of Organic Development, Industrial Chemistry Library, 1996;8, pp 506–27.
61. Butzenlechner M, Rossmann A, Schmidt HL. J. Agric. Food Chem. 1989;37:410–2.
62. Martin GJ, Martin ML, Mabon F, Bricout J. J. Amer. Chem. Soc. 1982;104:2658–9.
63. Martin GJ, Janvier P, Mabon F. Analusis. 1985;13:267–74.
64. Martin GJ, Danho D, Vallet C. J. Sci. Food Agric. 1991;56:419–34.
65. Vallet C, Masud Z, Martin ML. Food Chem. 1998;63:115–23.
66. Lindner P, Bermann E, Gamarnik B. J. Agric. Food Chem. 1996;44:139–40.
67. Martin YL. J. AOAC Intern. 2001;84:1509–21.
68. Zhang BL, Fallourd V, Role C, Martin GJ. Bioorg. Chem. 2003;31:227–36.
69. Quemerais B, Mabon F, Naulet N, M. G.J. Plant Cell Environm. 1995;18:989–98.
70. Lai A, Casu M, Saba G, Corongiu FP, Dessi MA. Magn. Res. Chem. 1995;33:163–6.
71. Aursand M, Mabon F, Martin GJ. Magn. Reson. Chem. 1997;35:S91–100.
72. Royer A, Naulet N, Mabon F, Lees M, Martin GJ. JAOCS 1999;76:365–73.
73. Zhang AL, Buddrus S, Trierweiler M, Martin GJ. J. Agric. Food Chem. 1998;46:1374–80.
74. Clark D, Fritz P. Environmental Isotopes in Hydrogeology, Lewis Publishers: New York, 1997.
75. Roden JS, Lin G, Ehleringer R. Geochim. Cosmochim. Acta. 2000;64:21–35.
76. Hatte C, Schwartz D. Phytochem. Rev. 2003;2:163–77.
77. Martin GJ, Martin ML. Phytochem. Rev. 2003;2:179–90.
78. Martin GJ, Guillou C, Martin ML, Cabanis MT, Tep Y, Aerny J. J. Agric. Food Chem. 1988;36:316–22.
79. Martin GJ, Martin GG. In: S Nagy, RL Wade (Eds), Methods to Detect Adulteration of Fruit Juice Beverages. . AG-Science: Florida, 1995;1, pp 1–27.
80. Day MP, Zhang BL, Martin GJ. J. Sci. Food Agric. 1995;67:113–23.
81. Martin GJ, Nicol L, Naulet N, Martin ML. J. Sci. Food Agric. 1998;77:153–60.
82. Danho D, Naulet N, Martin GJ. Analusis. 1992;20:179–84.
83. Hays PA, Remaud G, Jamin E, Martin YL. J. Forensic Sci. 2000:552–62.
84. Jamin E, Naulet N, Martin GJ. Plant Cell Environm. 1997;20:589–99.

SNIF-NMR—Part 4: Applications in an Economic Context: The Example of Wines, Spirits, and Juices

Eric Jamin and Gérard J. Martin
Eurofins Scientific, BP 42301, 44323 Nantes, France

Introduction

The direct access to site-specific natural isotope fractionation opened by the SNIF-NMR method [1,2] was immediately recognized, not only as a source of diversified information in a context of basic research, but also as a powerful technique for controlling the origin of commercial products. The method provides a unique tool for detecting whether a given main component of a food or beverage has been substituted or diluted by addition of a substance with the same molecular formula but from a different chemical, botanical, geographical origin (Part 3, Sections "Natural or Synthetic Origin of Products," "Characterization of Chemical Processes," "Identification of Plant Precursors," and "Climatic Effects and Geographical Origin"). In this respect, it has already largely contributed to establish the notion of *authenticity* of food products on rigorous bases. In order to illustrate the methodologies and performance of SNIF-NMR applied in official and industrial contexts, we have selected two examples of economically important products—wines and juices.

The world wine market has changed drastically in the last 10 years. In Europe—the largest production area—wine production is continually decreasing. Depending on the climatic conditions of the year, the production of the 15 countries of the EU has fallen from nearly 180 million to 155 million hectoliters. It is expected that in 2004 the admission in the EU of six countries whose wine production rose to 6 million hectoliters will just compensate the decrease of production of the 15 former state members. The cause is manifold but, roughly speaking, consumption switches from quantity to quality: for example, the share of quality wines produced in specific regions (QWPSR) which look like the French "Vins d'Appelation d'Origine Contrôlée" (AOC), overall production increases significantly. In France, Italy, and Spain, 46%, 23%, and 31% of the production is made up of QWPSR. However, in emerging Asian markets consumption is growing rapidly, mainly to the advantage of table wines, generally produced locally or imported from neighboring countries. Consequently, there is a greater pressure on the sensory and analytical properties of relatively expensive wines.

Insofar as fruit juices are concerned, the trend towards more quality and less quantity follows that observed for wines. Pure juices are frequently preferred to juices made from concentrates and to nectars, mainly based on the idea that fruit juice is "health in bottle," and in the EU and US, fruit juice markets are of a multi-billion ° magnitude. Orange juices represent more than 60% of the market.

Taking into account this economic context, it is of prime importance to be able to authenticate the origin of marketed products and to detect and estimate possible adulteration.

Current Regulations About Wines and Juices

In order to guarantee the quality of marketed products, very drastic requirements tend to be legally imposed. However, regulations are efficient only inasmuch as rigorous control methods can be implemented [3]. In the case of wines, spirits, and juices, important problems—still challenging in 1980s—are concerned with origin recognition of chemically identical molecules. By offering this possibility, the SNIF-NMR method has entered the field of official regulation and control.

Wines

The Commission of the EU subjects the common market of wines and wine products to very careful attention. The regulation of 1999 [4] resumes and completes regulations of 1987 and 1990 [5]. The principles behind the regulation may be explained in terms of three main vine growing zones A, B, and C (zone C being split into CI, CII, and CIII) rigorously defined according to the minimum alcoholic content of the natural must, *t*% min, the maximum enrichment, *c*% max, and the maximum alcoholic content, *t*% max, of the enriched wine (Table 1).

Men have always had an overactive imagination for transforming grapes into a number of beverages and food. Grape juice can be used as it stands, partly fermented,

Graham A. Webb (ed.), Modern Magnetic Resonance, 1681–1687.
© 2008 *Springer*.

Table 1: Conditions limiting the enrichment of musts in different regions A, B, and C. *t*% and *c*% are expressed in v/v of ethanol in wine and values into brackets correspond to red wines. For example, zone A includes the 15 State Members but France, Greece, Portugal, and Spain, zone B is composed of the Northern and Central France, Austria, and the Baden region in Germany, and zones C include Southern France, Greece, Portugal, and Spain

Area	A	B	CIa	CIb	CII	CIII
t% min	5	6	7.5	8	8.5	9
c% max	3.5 (4.5)	2.5 (3.5)	0 (2)	0 (2)	0	0
t% max	11.5 (12)	12 (12.5)	12.5	12.5	13	13.5

concentrated, rectified (grape sugar), caramelized, and so on. Fermented musts give table wines, quality wines, quality wines “psr” (provenance from specified region), liqueur wines, sparkling wines (aerated, semi-sparkling, etc.), wines lees, grape marc, piquette, wine vinegar, wine of overripe grapes, etc. The authorized oenological practices fill 12 A4 pages, printed in small characters, of the 1999 regulation but insofar as we are concerned with SNIF-NMR, only practices which can be enforced with the help of this technique will be discussed now. First of all, the problem of controlling wine enrichment was of great concern to the EU since the illegal increase of the alcoholic grade of wines by cheapest means, such as addition of sucrose into the fermenting must, is a heavy burden to the European budget. The surplus of wine produced by illegal enrichment should indeed be bought by the European Commission at a price that is significantly higher than that of the corresponding sugar. A second problem, less drastic for the European Treasury but severe for the consumer and the honest wine maker, is the fraud in quality wines “psr”: The geographical origin and the year of production of high priced wines (and spirits) should be ascertained in order not to entail the loss of confidence of the buyer. In the case of sparkling wines, the origin of the carbonic anhydride must be controlled.

Juices

In the European community, the Council directive 2001/112/EC defines several categories of fruit juices and the technology which can be used to produce them. The European industry, within the AIJN code of practice (http://www.aijn.org), provides more detailed guidelines of the expected composition of the most widely consumed fruit juices, including some isotopic parameters. At the world level, common definitions and guideline values of the main parameters are defined by the Codex committee for fruit juices (http://www.codexalimentarius.net). A fruit juice is defined as the fermentable but unfermented product obtained from the edible part of sound and ripe fruits using mechanical or physical means only. Two main categories are defined as follows:

- fruit juice: obtained directly from the fruit (only flavor, pulp, and cells lost during processing may be restored if necessary);
- fruit juice made from concentrate: obtained by replacing in a concentrated fruit juice the water extracted during concentration (plus flavor, pulp, and cells lost during processing).

The addition of sugars to fruit juices (for correcting the sugar/acid ratio) is authorized (except for grape and pear juice) up to 15 g/l, but this must be declared in the ingredients list. The addition of more sugar (up to a maximum of 150 g/l) implies labeling the product as “sweetened” (or “nectar,” when water is also added). The addition of lemon juice is also permitted up to 3 g citric acid per liter, but once again must be mentioned in the ingredients list. Moreover, the addition of both sugar and lemon juice is prohibited. No other ingredient not coming directly from fruit of the same kind is allowed. Especially, the restored flavor, pulp, and cells must be recovered during fruit juice processing.

Ethanol: A Reliable Isotopic NMR Probe for Characterizing Wines, Spirits, and Juices in an Industrial Context

Thanks to its favorable relaxation properties and its well-resolved signals, the ethanol molecule is well adapted to quantitative ^{2}H NMR (Part 2, Section “Elaboration of SNIF-NMR Probes—From Carbohydrates to Ethanol and Glycerol”) and high levels of repeatability and reproducibility are reached in standardized experimental procedures [6].

It is generally not obvious to consider that ethanol is a good probe for authenticating wines and still less evident for juices. In this last case, it is tempting to directly investigate carbohydrate molecules present in the juice. Unfortunately, the ^{2}H NMR spectra of polymeric and even simple carbohydrates are not suitable for estimating site-specific isotope ratios. Although the carbon-bound hydrogen parameters of glucose and fructose are accessible through appropriate chemical derivatizations [7], it is at the price of time-consuming experiments and degraded accuracy incompatible with analytical procedures applicable in an economic context. In contrast, ethanol obtained by fermenting sugars in strictly standardized conditions, provides an attractive probe that enables carbohydrates with

Table 2: Ranges of mean values exhibited by the isotopic ratios of ethanol samples obtained by fermenting different plant sugars, including grape, beet, and cane sugars. The carbon-13 deviation, $\delta^{13}C$ (%) (Part 1, Equation 5) has been measured by IRMS. $(D/H)_I$ (in ppm) is the isotope ratio of the methyl site of ethanol

Plant	$(D/H)_I$	$\delta^{13}C$
Beet	92.7	−26.6
Potato	96.7	−26.5
Red fruits	97.2	−26.6
Barley	98.2	−24.8
Wheat	99.7	−25.8
Apple	100.9	−25.0
Grape	101.8	−26.3
Citrus	105.0	−26.6
Pineapple	108.9	−14.5
Maize	110.7	−10.4
Cane	112.0	−12.2

different molecular structures, including polymers, to be easily compared in very accurate and precise conditions [8].

As discussed in Part 2 (Section "Elaboration of SNIF-NMR Probes—From Carbohydrates to Ethanol and Glycerol"), model fermentation experiments have established the quantitative scheme of site-specific connectivity between glucose and water reactants on one hand and ethanol and water products on the other hand. On this basis, it is concluded that the isotope ratio of the methyl site of ethanol, $(D/H)_I$ (and the overall carbon isotope ratio), reflects properties of sugars and, to a lesser extent, water whereas the methylene isotope ratio, $(D/H)_{II}$, is mainly representative of the aqueous medium. Since the natural abundance isotope ratios of the non-exchangeable hydrogen atoms of sugars depend on metabolic and physiological characteristics of the plant and on the environmental conditions of the photosynthesis [7,9], the isotopic distribution in the alcoholic fermentation products may reflect the origin of the carbohydrate precursors in terms of both plant species and geographical area of production (Part 3, Sections "Identification of Plant Precursors" and "Climatic Effects and Geographical Origin"). Table 2 illustrates several ranges of isotopic values exhibited by ethanol samples obtained through fermentation, in identical conditions, of sugars naturally present in fruit or possibly added to the juice.

Obviously, isotopic values measured on different ethanol samples may be safely interpreted in terms of properties of the sugar precursors only on condition that all mechanistic aspects of the fermentation reaction remain constant. In the case of wines, the fermentation parameters may significantly vary with the type of grapes and with oenological practices. Possible influence of the type of yeast strains and of changes in the composition of the medium had therefore to be investigated [10–12]. Only minor changes were observed in the percentages of intra- and inter-molecular transfer of hydrogen to the methyl site of ethanol as a function of the nature of the yeasts. More generally, a remarkable stability of the $(D/H)_I$ parameter was demonstrated. However, several factors responsible for marginal perturbations of the isotopic results were identified, providing helpful criteria for interpreting apparent anomalies observed in certain samples.

Origin Authentication and Data Banks

Aside from the illegal enrichment of must with sucrose, which has a considerable economic importance, other frauds only burden the wine market. For example, usurpation and abuse of origin affect wines from more or less prestigious estates. Apart from some renowned connoisseurs, very few people are able to precisely identify soil and vintage of a given wine and the consumer is forced to rely on the label. In such cases, isotopic analyses are very efficient tools to authenticate the origin of a wine.

According to the general principles described in Part 3 (Section "Climatic Effects and Geographical Origin"), the isotopic parameters of both water and ethanol are related to the humidity and temperature of the growing region of the plant. Therefore, consideration of meteorological data of the region and of the year helps to make a diagnosis. In the case of wine and fruits, the isotopic parameters of ethanol have been shown to respond even to subtle environmental variations and they efficiently characterize the region of production [13,14].

In practice, many types of wines have been investigated [15–21] and private and official data banks have been constructed in order to provide reference values. In the case of European wines, it was decided in 1991 to build an isotopic data bank concerning wines of all the Member States producing wine. At this time, the official laboratories of these States supply the data bank that is maintained in the Joint Research Centre of Ispra (Italy). The files contain several thousand entries for Austrian, French, German, Greek, Italian, Portuguese, Spanish, and even British and Luxembourg wines [22].

No official data are available for fruit juices, but many kinds of juices have now been isotopically characterized [23,24]. Producers organizations and private companies involved in food and beverage controls have collected authentic samples and built up specific data banks [25]. Since 1987, Eurofins laboratories have gathered data on several thousands of fruit samples. These have contributed in establishing some statistically defined confidence ranges for authentic fruits and guideline values for individual fruits included in the AIJN code of practice.

NMR Methodologies in an Official and Economic Context

Analytical requirements are very different for experiments carried out on limited numbers of samples in a research laboratory, and for measurements performed routinely in an economic context. In the second situation, the need for analyzing several thousands of samples a year and combining a variety of instrumental techniques appeals to rather sophisticated laboratory management systems. Moreover, conditions are placed on long-term reproducibility, reliability of the whole analytical chain, rapidity and minimum cost of the determination, and facility of interpretation.

In order to render the NMR method applicable at an industrial scale, much effort has been devoted to the elaboration of appropriate technological environments. Thus, through continuous collaboration between the Bruker firm and Eurofins laboratories in France, dedicated equipments and computerized programs were elaborated, commercialized, and maintained (SNIF-NMR Concept®). In particular, optimized NMR spectrometers have been fitted with specific probes and with fluorine locking devices, since the deuterium canal is used for observation. All parameters of signal adjustment have been released from any operator intervention through the development of a rigorous theoretical algorithm [26] which enables quantitative determinations to be fully automatized (Part 1, Section “Quantitative Deuterium NMR”).

Wines, juices, and even spirits cannot be directly studied as they stand and it is necessary to carry out a series of preliminary treatments. Since the measurements are done with ethanol and water, juices should be fermented in a first step and the resulting fruit wines must then be distilled. As a result of thermodynamic and kinetic isotope effects associated with phase transitions (Part 2, Sections “Simultaneous Determination of Site-specific Thermodynamic Isotope Effects” and “Determination of Kinetic Isotope Effects”), incomplete isolation of ethanol may induce isotopic fractionation of a few tenths of ppm for a yield of about 90%. The most critical point is therefore to extract ethanol from the product investigated with as high yield as possible and with the greatest alcoholic grade. For wines and spirits, a single distillation is sufficient but in any case, isotopic perturbations due to the process must be eliminated. Integrating the NMR detection into an information system, which routinely manages preparation of samples, NMR acquisition procedures, data handling, and diagnosis, optimizes the efficiency of the method. Moreover, detailed protocols have been defined and collaborative studies organized in order to check the accuracy performances.

Determination of Illegal Enrichments

According to the definitions given in Part 1, the isotopic composition of a mixture is a weighted mean of the parameters of the components. It is therefore required to know or to measure the isotopic ratios of the pure components in order to be able to compute the composition of the mixture. The first experimental description of the detection of chaptalization in wines appeared in 1983 [27]. It was published 4 years later as an official method of the “Office International de la Vigne et du Vin” (OIV) [28] and in 1990 it was included in the EU regulation concerning the control of wines [29,30]. If using only SNIF-NMR can determine wine chaptalization, the detection of other frauds is improved when the ^{2}H and ^{18}O isotopic ratios of the water contained in the product are measured. In this respect, although SNIF-NMR can be safely applied in determining the D/H of water, isotope ratio mass spectrometry (IRMS) is routinely preferred for this purpose. The precautions for eliminating adverse isotopic effects have been reviewed [21,29,31].

In the case of fruit juices, the SNIF-NMR and ^{13}C IRMS methods based on the isotopic analysis of ethanol resulting from fermentation have been officially recognized after international collaborative studies (AOAC Official Methods 995.17 and 2004.01, respectively).

The composition of a chaptalized wine or of an enriched juice is easily computed from the isotopic NMR ratio of site I of ethanol, providing that reference data are available. The molar fraction x of a mixture M containing two components A and B is given by Equation (1):

$$x = \left[(D/H)_{\mathrm{I}}^{\mathrm{A}} - (D/H)_{\mathrm{I}}^{\mathrm{M}}\right] \Big/ \left[(D/H)_{\mathrm{I}}^{\mathrm{A}} - (D/H)_{\mathrm{I}}^{\mathrm{B}}\right] \quad (1)$$

M may be either an unknown chaptalized wine or a fermented sugared orange juice for instance. A is the reference wine or juice and B is the sugar (beet or cane sucrose) added to the product [32]. Some more refined fraudsters use a mixture of beet and cane sucrose with the idea of circumventing SNIF-NMR, since it has been shown that an addition of beet sucrose in a must decreases the isotope ratio, $(D/H)_{\mathrm{I}}$, of the methyl site of wine ethanol, whereas addition of cane sucrose increases this parameter (Table 2). However, since two independent parameters can identify a ternary mixture containing grape, beet, and cane ethanol, combining ^{13}C IRMS determinations soon deterred this practice. To solve this system of equations, the knowledge of the isotopic parameters of authentic wines or juices is required. Geographical and annual variations may be taken into account by resorting to the up-to-date databases of authentic samples described in Section "Origin Authentication and Data Banks" [32]. On this basis, authenticity limits are defined as statistical confidence ranges of isotopic parameters, using either univariate or multivariate approaches.

Isotopic Characterization of Concentrated Juices

Commercial fruit juices are often made from concentrate. Similarly, concentrated grape juice may be used in wine production. Since the concentrated juices are prepared through low-temperature evaporation processes, the isotopic data of the final products, commercial juices and wines, depend not only on the botanical and geographical parameters but also on the fractionation factors associated with the physical transformation. Consequently, when isotopic analysis is used for sample authentication, the influence of the technological treatment must be estimated in order to isolate useful information about the original product. Model experiments of low-temperature evaporation processes have been carried out and analyzed [33], according to the principles discussed in Part 2 (Section "Simultaneous Determination of Site-specific Thermodynamic Isotope Effects"), on the basis of Equation (2):

$$R_C/R_S = N_C/N_S^{(\beta_{\text{eff}-1})} \tag{2}$$

where R_S and R_C are the hydrogen (or oxygen) isotope ratio of water in the starting juice and in the remaining concentrate respectively, and N_C/N_S is the molar ratio of residual water. β_{eff} is the effective fractionation factor which fits the kinetic contribution of the evaporation process. This parameter has been determined for ^{2}H and ^{18}O in experiments involving different sugar solutions and juices. At a temperature of 18 °C, the following values have been determined: $\beta_{\text{eff}}(^2\text{H}) = 0.923(\pm 0.003)$ and $\beta_{\text{eff}}(^{18}\text{O}) = 0.991(\pm 0.002)$. These results can be applied in two complementary ways. Firstly, in the case of orange concentrates suspected of containing sucrose, it is possible to infer the δ^2H (or δ^{18}O) value of the natural juice water before concentration from both the Brix value and the δ^2H (or δ^{18}O) value measured on water of the concentrate. The computed isotope contents of the original juice water are then used for evaluating the $(D/H)_I$ value of ethanol which would result from fermentation of the pure juice. These estimated parameters provide improved references for computing the amount of sucrose addition in concentrate and they significantly increase the sensitivity of detection of this practice. Conversely, when R_S is known, Equation (2) may be exploited for estimating the concentration rate. This procedure was successfully applied to the detection of added concentrated must in wine. The values of δ^2H and δ^8O of the wine water are then compared to the values of the same parameters measured in pure grape musts or natural wines from the same region and year.

Multi-component and Multi-isotope Strategies in the Detection of Adulterations

With the combined use of SNIF-NMR and ^{13}C IRMS, most of the economically profitable forms of adulteration, which are concerned with the addition of sugar from cheap sources such as beet, cane, or maize, can be detected. In some instances, however (e.g. when the geographical origin is unknown), it can be difficult to prove adulteration with certainty, and the use of other components as isotopic internal references is a way of improving the detection limits of adulterations. Such multi-component multi-isotope patterns may involve individual sugars [34], sugars and acids [35], or sugars and water [36]. Finally, some fractions like proteins can also be used as "absolute" internal references as they are not concerned by economic adulteration [37].

Thanks to the recent development of preparative HPLC procedures, organic acids can be routinely isolated from any kind of fruit juices and wine. Obviously, this requires complete recovery of each component at all stages of the purification to avoid any isotopic fractionation. Based on numerous results from a wide database of authentic fruits collected around the world, systematic isotopic correlations between individual organic acids or between organic acids and other components have been established. Reproducible relationships are observed for any given fruit species, which can be solely attributed to the metabolism of the fruit and remain independent from its geographical origin. The use of internal referencing based on such multi-component patterns significantly enhances the sensitivity of both NMR and IRMS isotopic methods for the detection of sophisticated adulterations [37–42].

To illustrate the increasing complexity of some problems, it should be mentioned that refined adulteration practices have been specially developed to bypass the isotopic methods based on sugar analysis via fermented ethanol. Thus, when addition of specifically designed sugar syrups, derived from starch or inulin from C3 plants is suspected, the only way to detect low levels of sugar addition is to use GC analysis of oligosaccharides profiles, which reveal the presence of marker peaks of these industrial syrups. Conversely, this method does not detect raw sucrose addition. Therefore, in order to fully control the absence of sophisticated adulteration of a fruit juice, it may be necessary to combine isotopic and conventional analyses.

Detection of Exogeneous Minor Components

In certain cases, adulteration by exogeneous minor components may also be suspected. Frequently this practice aims to mask illegal dilution or enrichment of the product.

The most abundant acids of fruit products (citric, L-malic, and L-tartaric acids) are solids that are insoluble in most organic solvents, which makes their SNIF-NMR analysis more difficult. Nevertheless, suitable derivatives such as esters provide access to the D/H ratios of non-exchangeable hydrogen atoms. For example the ^{2}H NMR spectrum of triethyl citrate enables the two original methylene sites of citric acid to be conveniently quantified. Looking at the affiliations of carbon and hydrogen atoms along the glycolysis pathway and in the Krebs cycle, it appears that citric acid carbon atoms derive from all glucose carbon atoms and that at least two-thirds of the non-exchangeable methylenic hydrogen atoms come from water of the medium. Since the industrial production of citric acid uses various cheap sugar sources, the ^{13}C deviations cover the whole range of values characterizing C3 and C4 plants. On the other hand, the deuterium enrichment in plant water versus ground water results in a significant shift of the deuterium content of fruit citric acid as compared to its artificial counterpart. Then, the combined use of global $^{13}C/^{12}C$ and site-specific $^{2}H/^{1}H$ ratios satisfactorily discriminates citric acid from fruits such as lemon from all commercial sources.

As a final example, we may consider the case of glycerol, usually produced in significant amounts (3–5%) in fermentation reactions. Its presence in wine has a noticeable influence on the sensory parameters. Forbidden addition of exogeneous glycerol is easily detected by SNIF-NMR since the isotopic profile of glycerol naturally present in wines can be differentiated from that of synthetic glycerol and also from that of glycerol derived from other plants [43,44].

References

1. Martin, G. J. and Martin, M.L., Tetrahedron Lett. 1981; 22:3525–8.
2. Martin GJ, Martin ML. Brevet France: 1981;81-22710:1–24.
3. Simpkins W, Harrison M. Trends Food Sci. Technol. 1995; 6:321–8.
4. Commission of the European Communities. Off. J. Eur. Commun. 1999;1–84.
5. Commission of the European Communities. Off. J. Eur. Commun. 1987;822:87 and 1990;2676:90.
6. Martin GG, Guillou C, Martin YL. Fruit Process. 1995;4:246–54.
7. Zhang BL, Billault I, Li X, Mabon F, Remaud G, Martin ML. J. Agric. Food Chem. 2002;50:1574–80.
8. Martin GG, Martin YL. Fruit Process. 1996;5:186–94.
9. Martin GJ, Danho D, Vallet C. J. Sci. Food Agric. 1991;56:419–34.
10. Vallet C, Said R, Rabiller C, Martin ML. Bioorg. Chem. 1996;24:319–30.
11. Zhang BL, Yunianta, Vallet C, Martin YL, Martin ML. Bioorg. Chem. 1997;25:117–29.
12. Fauhl C, Wittkowski R. J. Agric. Food Chem. 2000;48:3979–84.
13. Martin GJ, Guillou C, Martin ML, Cabanis MT, Tep Y, Aerny J. J. Agric. Food Chem. 1988;36:316–22.
14. Martin GJ, Martin ML. In: HF Linskens and JF Jackson (Eds). Modern Methods of Plant Analysis, Springer-Verlag, Berlin, 1988;6:258–75.
15. Monetti A, Reniero F, Versini GZ. Lebensm. Unters. Forsch. 1994;311–6.
16. Versini G, Monetti A, Reniero F. Wine: Nutritional and Therapeutic Benefits. In: TR Watkins (Ed). ACS Symposium Series 661. Washington, Amer. Chem. Soc. 1997, pp 113–30.
17. Gimenez-Miralles JE, Salazar DM, Solana I. J. Agric. Food Chem. 1999;47:2645–52.
18. Ogrinc N, Kosir IJ, Kocjancic M, Kidric J. J. Agric. Food Chem. 2001;49:1432–40.
19. Martin GJ, Mazure M, Jouitteau C, Martin YL, Aguile L, Allain P. Am. J. Enol. Vitic. 1999;50:409–17.
20. Christoph N, Rossmann A, Voerkelius S. Mitt. Klosterneuburg 2003;53:23–40.
21. Ogrinc N, Kosir IJ, Spangenberg JE, Kidric J. Anal. Bioanal. Chem. 2003;376:424–30.
22. Official Journal of the European Communities. Off. J. Eur. Commun. 1991;L214:39–43.
23. Pupin AM, Dennis MJ, Parker I, Kelly S, Bigwood T, Toledo MCF. J. Agric. Food Chem. 1998;46:1369–73.
24. Simpkins WA, Patel G, Collins P, Harrison M, Goldberg D. J. Agric. Food Chem. 1999;47:2606–12.
25. Guillou C, Jamin E, Martin GJ, Reniero F, Wittkowski R, Wood R. Bulletin OIV. 2001;74:26–36.
26. Martin YL. J. Magn. Res. Ser. A. 1994;111:1–10.
27. Martin GJ, Martin ML. J. Chim. Phys. 1983;80:293–7.
28. Martin GJ, Brun S. Méthodes d'Analyse de l'OIV. 1987;1–15.
29. Zhang BL, Fourel F, Naulet N, Martin GJ. Feuillet vert OIV. 1992 (1954/220792).
30. Martin GJ. Endeavour. 1990;14:137–43.
31. Martin GG, Wood R, Martin GJ. J. AOAC Int. 1996;79:917–28.
32. Martin GG, Hanote V, Lees M, Martin YL. J. AOAC Int. 1996;79:62–72.
33. Yunianta (*), Zhang BL, Lees M, Martin GJ. J. Agric. Food Chem. 1995;43:2411–7.
34. Day MP, Correia P, Hammond DA. J. AOAC Int. 2001;3:957–63.
35. Gonzalez J, Remaud G, Jamin E, Naulet N, Martin GG. J. Agric. Food Chem. 1998;46:2316–21.

36. Jamin E, Guerin R, Retif M, Lees L, Martin GJ. J. Agric. Food Chem. 2003;51:5202–6.
37. Jamin E, Gonzalez J, Bengoechea I, Kerneur G, Remaud G, Iriondo C, Martin GG. J. Agric. Food Chem. 1998;46:5118–23.
38. Jamin E, Gonzalez J, Remaud G, Naulet N, Martin GG. J. Agric. Food Chem. 1997;45:3961–7.
39. Jamin E, Gonzalez J, Remaud G, Naulet N, Martin GG, Weber D, Rossmann A, Schmidt HL. Anal. Chim. Acta. 1997;347:359–68.
40. Jamin E, Gonzalez J, Bengoechea I, Kerneur G, Remaud G, Naulet N, Martin GG. J. AOAC Int. 1998;81:604–9.
41. Gonzalez J, Jamin E, Remaud G, Martin YL, Martin GG, Martin ML. J. Agric. Food Chem. 1998;46: 2200–5.
42. Weber D, Rossmann A, Schwarz S, Schmidt HL. Z. Lebensm. Unters. Forsch. 1997;205:158–64.
43. Zhang BL, Buddrus S, Trierweiler M, Martin GJ. J. Agric. Food Chem. 1998;46:1374–80.
44. Weber D, Kexel H, Schmidt H. J. Agric. Food Chem. 1997;45:2042–6.

High-Resolution Nuclear Magnetic Resonance Spectroscopy of Wine, Beer, and Spirits

Ana M. Gil and Iola F. Duarte
Department of Chemistry, CICECO, University of Aveiro, 3810-193 Aveiro, Portugal

This text aims at presenting an account of the use of high resolution ^{1}H and ^{13}C Nuclear Magnetic Resonance (NMR) spectroscopy for the direct characterization of the composition of wine, beer, and spirits. This differs from the approach involved in the well established quality control method known as Site-specific Nuclear Isotope Fractionation (SNIF)-NMR, which usually involves ^{2}H observation for the measurement of isotopic ratios and correlation with product origin and which is described in a separate entry of this handbook. The application of high resolution NMR to the complex food mixtures mentioned above aims at detecting as many compounds as possible, including minor components, not only giving a compositional overview of the food, but also allowing the unexpected to be detected in a number of possible situations (biochemical studies, adulterations, contaminations). A vast number of studies have used NMR to identify particular compounds in sample extracts following specific separation and concentration steps. In wine, phenolic compounds are still the class of compounds more extensively studied due to their role in wine characteristics as well as interesting antimicrobial and antioxidant properties. However, the intention of this text is to account preferably for studies involving the direct NMR analysis of whole samples, rather than of their extracts, except where otherwise specified.

Wine has been, by far, the alcoholic beverage to which NMR has been most extensively applied. Direct NMR analysis of wine emerged in the mid 1980s, with the seductive advantages of avoiding lengthy separation and concentration steps prior to analysis of specific compounds or compound families. The first studies involved ^{13}C NMR for determination of several components: diethylene glycol [1], sugars, sugar alcohols and sugar acids [2], and amino acids [3]. However, the relative higher sensitivity and natural abundance of ^{1}H make it a preferred nucleus for practical uses where measurement rapidity is intended. In ^{1}H NMR, efficient suppression of solvent peaks (water and ethanol in the case of alcoholic drinks) is necessary and the significant technological advances in NMR instrumentation and software have played a key role in enabling good quality ^{1}H NMR spectra to be obtained. Comprehensive peak assignment in the ^{1}H NMR spectra of wines requires necessarily the combined use of 1D and 2D NMR experiments such as COrrelation SpectroscopY (COSY), Heteronuclear Single-Quantum Coherence (HSQC), and Heteronuclear Multiple-Bond Correlation (HMBC). Such techniques were used in a study of Slovenian wines, differing in variety, vintage, and geographical area, in tandem with comparison with the ^{1}H and ^{13}C NMR spectra of known compounds [4]. Many amino acids, alcohols and organic acids were detected and some spectral variations were correlated to the variables under study. Subsequent reports describe a similar approach for the identification of amino acids and anthocyanins in wine, compounds which play determinant roles in wine properties and quality [5,6]. Figure 1 shows regions of the ^{1}H and ^{13}C NMR spectra of the wine under study, without the use of suppression for the large signals. The incorporation of a WET (water suppression enhanced through T_1 effects) pulse sequence in the 1D and 2D experiments allowed simultaneous suppression of several large signals (water, ethanol, glycerol, and some unassigned signals) and significant improvement of the spectra. Unambiguous ^{1}H and ^{13}C assignment of many amino acids could then be achieved [5,6], together with that of several anthocyanins [6]. Improvements in NMR peak assignment may still be required, particularly in regions of strong signal overlap (even in 2D spectra) and/or of very low signal to noise ratio. Hyphenated NMR may be of help in future qualitative studies of wine, as shown by preliminary results obtained for a wine phenolic extract sample by the on-line combination of liquid chromatography, NMR, and mass spectrometry (LC-NMR/MS) [7]. This study reports the identification of catechin, epicatechin, *trans*-resveratrol, tyrosol and caffeic acid, compounds which could not be identified using NMR spectroscopy alone. An additional aid for peak assignment comes from Diffusion Ordered SpectroscopY (DOSY). Applied recently to Port wine (Figure 2) [8], DOSY makes use of information on compounds diffusivity, in addition to NMR parameters. Compositional differences between Port wines of different

Graham A. Webb (ed.), Modern Magnetic Resonance, 1689–1694.
© 2008 *Springer.*

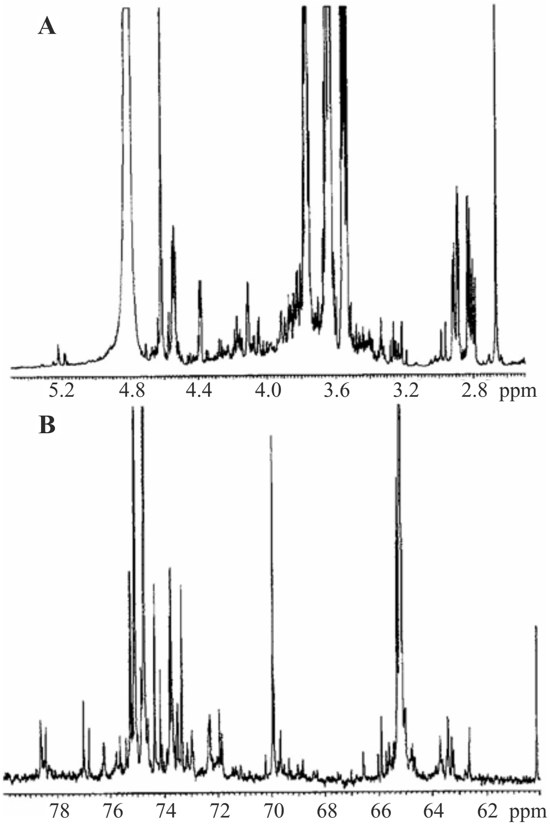

Fig. 1. Parts of ^{1}H (A) and ^{13}C NMR spectra (B) of wine (Sauvignon, Coastal wine-growing region, 1994) in the region where the signal overlapping due to the great difference in signal intensities is the most problematic. Both spectra were obtained without suppression of strong signals. Reprinted with permission from Košir and Kidric. Identification of amino acids in wine by one- and two-dimensional NMR spectroscopy. J. Agric. Food Chem. 2001;49:50–6. Copyright (2001) American Chemical Society.

ages were noted, including a significant decrease of the relative amount of high molecular weight aromatics in the oldest wine.

The possibility of using NMR spectroscopy to differentiate and classify different wine types was firstly explored by combining ^{1}H and ^{13}C NMR with pattern recognition techniques [9]. This approach is indeed necessary if large sample numbers are to be handled. The 1D NMR spectra of 53 German white wines from different regions were recorded and subjected to Principal Component Analysis (PCA). Small variations in peak positions, due to pH, concentration effects, and/or apparatus instabilities, were corrected by a specifically developed algorithm; this resulted in successful sample classification. A subsequent study addressed a set of Slovenian white wines differing in vine variety and geographical origin [6]. Multivariate analysis of some amino acids signals enabled wine varieties to be distinguished and the inclusion in the analysis of signals from glycerol, butylene glycol, and succinic acid allowed separation according to geographical origin. A classification study of Apulian Italian wines [10] involved the comparison of multivariate analysis of ^{1}H NMR spectra with that of data obtained by alternative methods, including high performance ion chromatography (HPIC), high performance ion chromatography exclusion (HPICE), and emission spectrometry. Results enabled wines from different geographical regions to be distinguished with basis on amino acids composition, as viewed by NMR, or on heavy metals composition, as viewed by the alternative methods. A similar approach was applied to a group of wine samples from Southern Italy and Slovenia, showing that the best prediction of the country of origin is achieved by multivariate analysis of the NMR data (Figure 3), rather than of data obtained by HPICE or inductively coupled plasma emission spectroscopy (ICP-OES) [11].

Additional interesting applications of NMR to wine include the elucidation of key metabolic traits of wine bacteria through the *in vivo* NMR analysis of cell suspensions [12] and the development of a method to study full intact wine bottles [13,14]. In the latter case, a new experimental setup was devised in order to use a horizontal bore magnetic resonance imaging magnet of 2.01 T to accommodate a full wine bottle. ^{1}H and ^{13}C NMR spectra were recorded for a selected wine and their use for quantifying acetic acid and detecting complex sugars, phenols, and trace elements was discussed.

The applications of high resolution NMR to beer and spirits are much more limited, compared to wine. One of the first reports of NMR of beer drew attention for the importance of characterizing the carbohydrate fraction of beer and for the complexity of the carbohydrate profile in the ^{1}H NMR spectrum, recorded at 600 MHz [15]. Chromatographic separation of the low molecular weight fraction of beer oligosaccharides was carried out, followed by fraction analysis by 1D and 2D NMR. In tandem with MS spectrometry and HPLC, NMR results enabled the identification of several isomaltooligosaccharides of degree of polymerization (DP) up to 10. More recent reports describe the use of NMR for the characterization of water soluble arabinoxylans from barley and barley malt [16] and a novel flavanol glucoside from barley and malt [17]. Hop bitter acids,

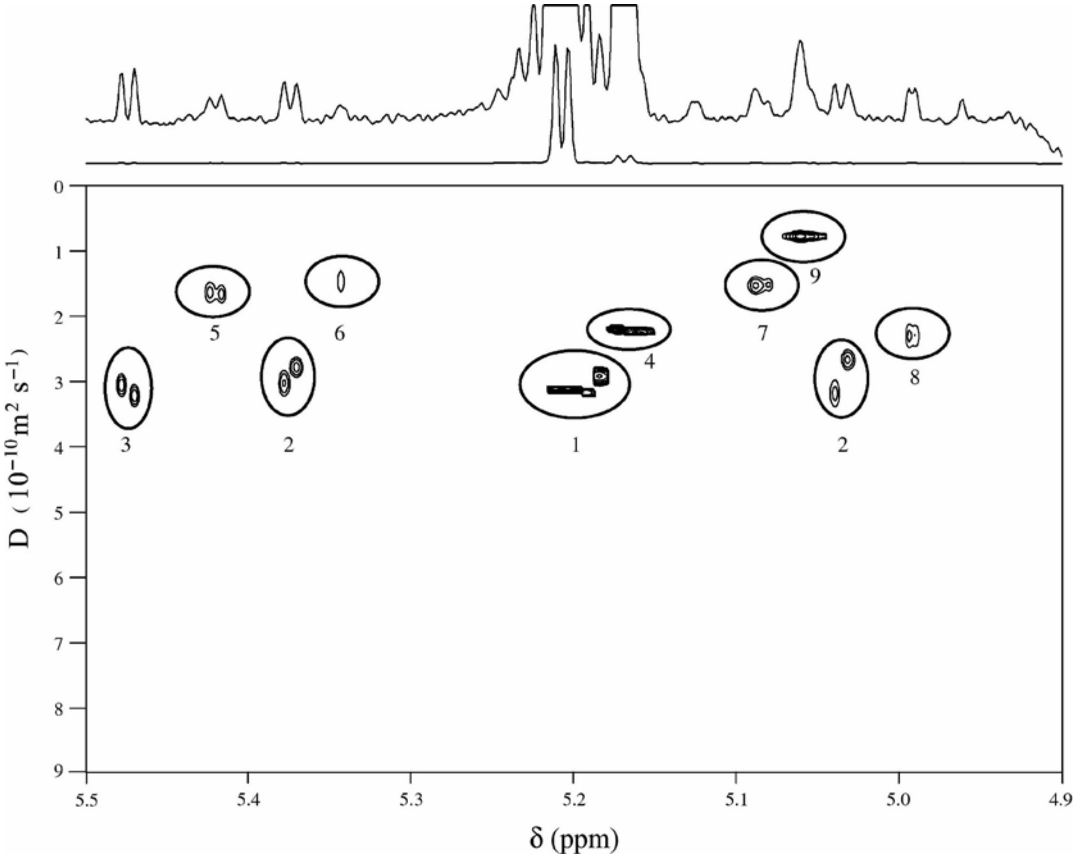

Fig. 2. DOSY spectrum of the anomeric proton region 4.9–5.5 ppm from a Port wine sample. Spectra were treated with digital filtration to reduce the residual water signal, Lorentz-Gauss resolution enhancement, and cubic spline baseline correction. Signals shown are (1) glucose, (2) ^{13}C satellites of glucose, (3) unidentified monosaccharide, (4) unidentified disaccharide, (5)–(8) unidentified disaccharide or larger species, and (9) unidentified larger species. Reprinted with permission from Nilsson *et al.* High resolution NMR and diffusion-ordered spectroscopy of port wine. J. Agric. Food Chem. 2004;52:3736–43. Copyright (2004) American Chemical Society.

which are important taste and flavor agents in beer, were analyzed by LC-NMR [18]. Several bitter acids such as humulones, isohumulones, dihydroisohumulones, and tetrahydroisohumulones, were successfully identified in hop extracts and their structures characterized by NMR. Particular attention has been given to hop isohumulones in a study which involved HPLC of hop extracts prior to NMR characterization of the fractions [19].

Some accounts of direct NMR analysis of whole beer may also be found. Overall qualitative analysis of beer has been carried out by standard 1D and 2D NMR methods [20], the only sample preparation involved being the ultrasonic degassing of the sample. Figure 4 shows regions of the 2D TOtal SpectroscopY (TOCSY) spectrum of a beer. About 30 compounds could be identified covering a range of chemical families. In subsequent work, use was made of LC-NMR/MS for the detailed characterization of beer aromatic compounds [21] and carbohydrates [22]. In the former case, tyrosol, 2-phenylethanol, and thryptophol could be identified for the first time by direct analysis of beer, whereas, in the latter case, detection of maltooligosaccharides of DP up to 9 was achieved. Figure 5 shows an on-flow NMR chromatogram obtained for beer. Preliminary DOSY results have also shown that the coupling of diffusivity information to NMR

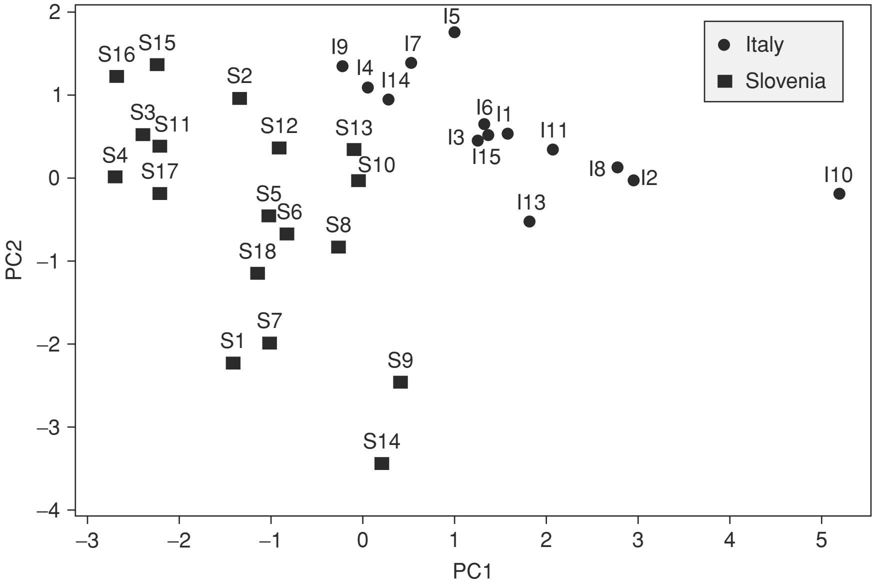

Fig. 3. Scatter plot of the scores from the first two principal components PC1 and PC2 obtained using NMR data. Reprinted with permission from Brescia *et al.* Chemometric classification of Apulian and Slovenian wines using ^{1}H NMR and ICP-OES together with HPICE data. J. Agric. Food Chem. 2003;51:21–6. Copyright (2003) American Chemical Society.

parameters may help significantly in the characterization of beer by NMR [23]. The subject of compound quantification in beer has been tackled very recently and in detail by ^{1}H NMR [24]. Organic acids and amino acids were quantified both by signal integration and by partial least squares (PLS) regression, comparing NMR data with amino acid analysis by HPLC and organic acid analysis by capillary electrophoresis. ^{1}H NMR is shown to be a rapid and satisfactorily accurate method to quantify compounds down to 10 mg/L in concentration. The use of PLS improves accuracy and enables compound quantification using partially overlapped signals. The issue of beer classification was addressed using NMR in tandem with PCA [20,25]. This work has shown that beers differing in types (lager, ale, alcohol-free) may be distinguished with basis on their dextrin content and composition, as well as on aromatic composition.

Reports on NMR of spirits include some accounts of SNIF-NMR analyses for detecting sugar addition in maple syrup [26], authentication of fruit spirits [27], dating of brandies and spirits [28], authentication of tequila [29], together with some studies involving the isolation of specific compounds followed by NMR characterization.

References

1. Rapp A, Spraul M, Humpfer E. Z. Lebensm. Unters. Forsch. 1986;182(5):419.
2. Rapp A, Markowetz A, Spraul M, Humpfer E. Z. Lebensm. Unters. Forsch. 1989;188(2):138.
3. Rapp A, Markowetz A, Niebergall H. Z. Lebensm. Unters. Forsch. 1991;192(1):1.
4. Kosir I, Kocjancic M, Kidric J. Analusis. 1998;26(2):97.
5. Kosir IJ, Kidric J. J. Agric. Food Chem. 2001;49(1):50.
6. Kosir IJ, Kidric J. Anal. Chim. Acta. 2002;458(1):77.
7. Gil AM, Duarte IF, Godejohann M, Braumann U, Maraschin M, Spraul M. Anal. Chim. Acta. 2003;488(1):35.
8. Nilsson M, Duarte IF, Almeida C, Delgadillo I, Goodfellow BJ, Gil AM, Morris GA. J. Agric. Food Chem. 2004;52(12):3736.
9. Vogels JTWE, Tas AC, van den Berg F, van der Greef J. Chemometr. Intell. Lab. 1993;21:249.
10. Brescia MA, Caldarola V, De Giglio A, Benedetti D, Fanizzi FP, Sacco A. Anal. Chim. Acta. 2002;458:177.
11. Brescia MA, Kosir IJ, Caldarola V, Kidric J, Sacco A. J. Agric. Food Chem. 2003;51(1):21.
12. Ramos A, Santos H. Annu. Rep. NMR Spectrosc. 1999;37:179.
13. Weekley AJ, Bruins P, Augustine MP. Am. J. Enol. Viticult. 2002;53(4):318.
14. Weekley AJ, Bruins P, Sisto M, Augustine MP. J. Magn. Reson. 2003;161(1):91.

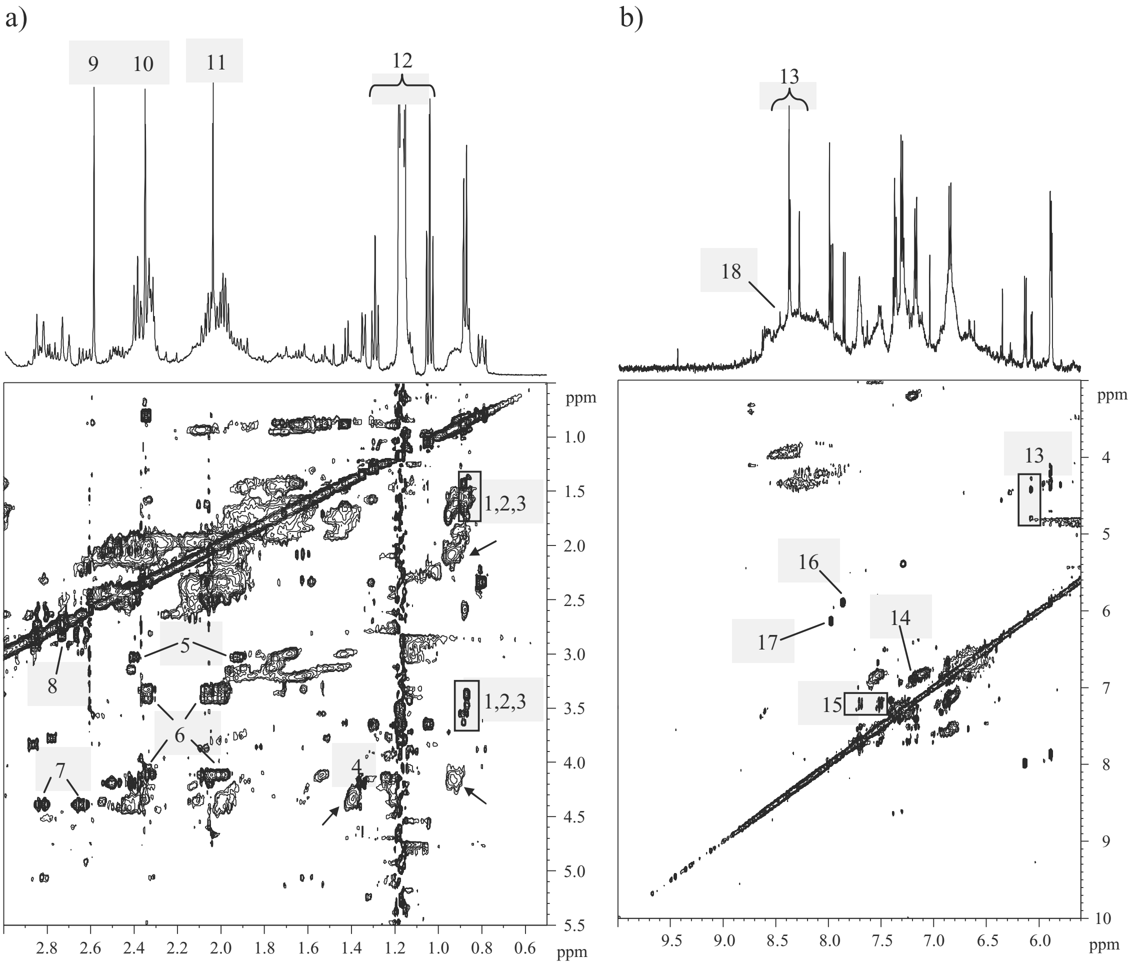

Fig. 4. Regions of the TOCSY spectrum of a beer sample, recorded at 500 MHz: (a) aliphatic region, (b) aromatic region. Some assignments are indicated: 1-propanol, 2-isobutanol, 3-isopentanol, 4-lactic acid, 5-GABA, 6-proline, 7-malic acid, 8-citric acid, 9-succinic acid, 10-pyruvic acid and/or diacetyl, 11-acetic acid and acetates, 12-ethanol and ^{13}C-satellites, 13- adenosine and/or inosine, 14-tyrosine, 15-tryptophane, 16-uridine, 17-cytosine, 18-formic acid. Reprinted with permission from Duarte *et al.* High resolution NMR spectroscopy and multivariate analysis for the characterization of beer. J. Agric. Food Chem. 2002;50:2475–81. Copyright (2002) American Chemical Society.

15. Vinogradov E, Bock K. Carbohydr. Res. 1998;309(1):57.
16. Dervilly G, Leclercq C, Zimmermann D, Roue C, Thibauls J-F, Saulnier L. Carbohydr. Polym. 2002;47:143.
17. Friedrich W, Galensa R. Eur. Food Res. Technol. 2002;214(5): 388.
18. Pusecker K, Albert K, Bayer E. J. Chromatogr. A. 1999;836 (2):245.
19. Nord LI, Sorensen SB, Duus JO. Magn. Reson. Chem. 2003; 41(9):660.
20. Duarte I, Barros A, Belton PS, Righelato R, Spraul M, Humpfer E, Gil AM. J. Agric. Food Chem. 2002;50(9): 2475.
21. Gil AM, Duarte IF, Godejohann M, Braumann U, Spraul M. Anal. Chim. Acta, 2003;488:35.
22. Duarte IF, Godejohann M, Braumann U, Spraul M, Gil AM. J. Agric. Food Chem. 2003;51:4847.
23. Gil AM, Duarte I, Cabrita E, Goodfellow B, Spraul M, KerssebaumR Anal. Chim. Acta. 2004;506:215.

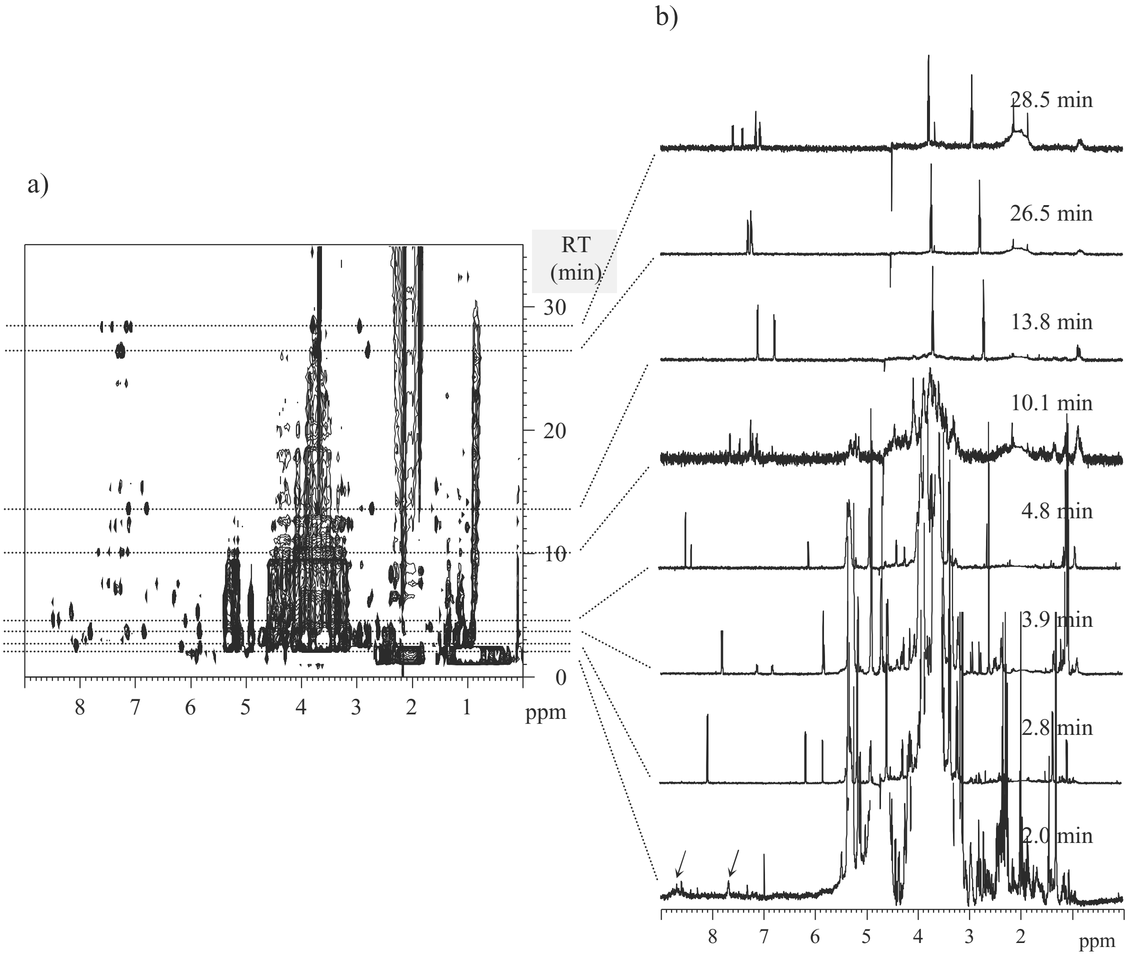

Fig. 5. (a) "Pseudo" on-flow NMR chromatogram, resulting from the elution of a beer sample (flow rate 1.00 mL/min; injection volume 500 μL), (b) selected rows from the on-flow diagram in (a). Reprinted from Gil *et al.* Characterization of the aromatic composition of some liquid foods by NMR spectrometry and liquid chromatography with NMR and mass spectrometric detection. Anal. Chim. Acta. 2003;488:35–51. Copyright (2003) with permission from Elsevier.

24. Nord LI, Vaag P, Duus JO. Anal. Chem. 2004;76(16):4790.
25. Duarte IF, Barros A, Almeida C, Spraul M, Gil AM. J. Agric. Food Chem. 2004;52:1031.
26. Martin GG, Martin YL, Naulet N, McManus HJD. J. Agric. Food Chem. 1996;44(10):3206.
27. Bauer-Christoph C, Wachter H, Christoph N, Rossmann A, Adam L. Z. Lebensm. Unters. Forsch. 1997;204(6):445.
28. Martin GJ, Nicol L, Naulet N, Martin ML. J. Sci. Food Agric. 1998;77(2):153.
29. Bauer-Christoph C, Christoph N, Aguilar-Cisneros BO, Lopez MG, Richling E, Rossmann A, Schreier P. Eur. Food Res. Technol. 2003;217(5):438.

Relaxation Time Methods

NMR Relaxation of Dairy Products

F. Mariette

CEMAGREF, Food Engineering research unit, CS64427, 35044 Rennes Cedex, France

Introduction

The applications of NMR to dairy products are numerous and can be divided into three groups. The first group comprises the use of high-resolution NMR spectroscopy for the molecular study of dairy compounds such as casein and whey protein [1,2]. The second group involves the use of Magnetic resonance imaging applied to dairy processing [3,4], and the third group concerns studies based on NMR relaxation measurements. This chapter will focus only on NMR relaxation applications, including pulsed field gradient NMR for the measurement of molecular diffusion. Relaxation measurements on dairy products have usually been performed at low field and the main aim was to propose a non-destructive technique to determine water or fat content [5] and solid fat content (SFC) [6]. These applications use NMR signal intensity and little attention has been paid to relaxation time values and their significance. We have therefore chosen to review this field of application specifically.

Water Relaxation

All possible water nuclei (^{1}H, ^{2}H, and ^{17}O) have been used in attempts to obtain information about molecular structure and water mobility. The interpretation of relaxation time parameters is quite difficult as relaxation involves several mechanisms such as chemical exchange, cross relaxation and diffusive exchange between different water populations. There has for many years been considerable controversy about the ways to interpret relaxation time parameters, especially the relative importance of chemical exchanges between protein protons and water protons [7] and cross relaxation between the longitudinal magnetization associated with water protons and protein protons [8]. ^{17}O Nuclear Magnetic Relaxation Dispersion (NMRD) studies recently demonstrated that relaxation dispersion is not due to a long-range hydrodynamic effect or to long-lived water molecules on the protein surface, but to small numbers of crystallographic water molecules buried inside the protein and exchanging with bulk water on a submicrosecond time scale [9,10]. ^{2}H dispersion includes an additional contribution from a labile proton, which dominates over the hydration water contribution for ^{1}H relaxation. It is therefore now clear that, in contrast to ^{17}O relaxation, ^{1}H and ^{2}H water relaxation does not provide any information about water mobility [11], and water relaxation measurements cannot be used to obtain detailed information about the protein structure. Nevertheless, water relaxation measurement is a very sensitive way to study the changes in the protein structure induced by chemicals and physical parameters [12]. Several studies have therefore investigated the water-casein interactions in milk and in milk powders [7,13–16]. Others have dealt with isolated milk components such as lactose [17,18], caseins [19,20], caseinate [8,13,17,21–27] bovine serum albumin [28,29–33], β lactoglobulin [34–36], α lactalbumin [34], and whey [17,34]. For example, ^{17}O NMR relaxation measurements have been used to investigate the effects of NaCl, $CaCl_2$, sucrose concentration, temperature, and pH on casein hydration [13,23–26]. Similar variations in water relaxation rate have been observed between ^{17}O and ^{1}H relaxation measurements according to milk pH. The structure of the micellar casein changes when the pH decreases due to release of the calcium–phosphate complex into the soluble phase. Release is maximal at pH 5.3 and both the ^{17}O and ^{1}H water relaxation rates are minimal [13]. For non-casein micelles such as sodium caseinate solution, the dependency of the water relaxation time on pH is negligible compared to variations observed with micellar casein dispersion.

The advantage of the NMR technique to monitor pH changes is that the method can be used for whole milk and skim milk [37], and for various experimental conditions such as high-pressure treatment of the milk [16] and allows study of effects of the pH kinetics on micellar destabilization [37]. The study of milk was also extended to concentrated casein samples. However, when the casein concentration increased, the variation in relaxation time to changes in pH decreased [4].

The use of water NMR relaxation time to quantify changes in casein micelle structure is not limited to processes involving changes in pH. For example, measurement of relaxation time has been used to study the effects of added salt on the hydration behavior of casein micelle powder [19]. Another study involved the effects of protein—fat interactions on the protein structure in emulsion. It was established that the extent of the structural

Graham A. Webb (ed.), Modern Magnetic Resonance, 1697–1701.
© 2008 *Springer.*

changes induced by adsorption at the interface varies according to the native structure of the protein. For example, variation in water relaxation time induced by formation of an emulsion was greater for β lactoglobulin than sodium caseinate [4].

Because of the sensitivity of water relaxation to protein structure changes, NMR relaxation studies of complex dairy products such as cheese, dairy mix, and ice cream have been reported. The major difficulty with such products from an NMR point of view is that the relaxation cannot be described by a single component and multi-exponential fitting has to be used. For example, a multi-exponential model with four relaxation components was used to fit the spin–spin relaxation decay curve with soft cheeses [38]. At 6 °C the two components with $T_2 < 100\,\mu$ were attributed to crystallized and amorphous fat protons and the two components with T_2 around 12 and 30 ms were attributed to liquid fat protons and water protons, respectively. Since the water relaxation can be distinguished from the liquid fat protons, the water relaxation time can be used to monitor casein structure changes. This has been well illustrated in experiments involving the ripening of soft cheeses [39], to predict the water content of cheese [40] and to provide information about viscoelastic properties [41]. Protein hydration changes during cheese aging were recently reported for the field cycling NMR technique [42].

Another example of multi-exponential behavior of relaxation has been reported with ice cream [43]. At –14 °C, the spin–spin relaxation consists of a Gaussian and two decreasing exponentials. The first component with T_2 close to 20 μs includes the relaxation of both the protons of the crystallized fat and of the ice. The second component with T_2 around 1 ms describes relaxation of the protons of the liquid fat and the non-exchangeable protons of the sugars, and the component with $T_2 > 5$ ms can primarily be attributed to the relaxation of the water protons. Variations in the water relaxation time observed for different ice creams of various chemical compositions has been directly related to the protein type (casein vs. whey protein) added to the mixture [44]. Moreover, changes in water relaxation during ice cream storage show that the aqueous phase, although in small proportion in ice cream, nevertheless appears to evolve during storage [44]. Although the ice proton relaxation cannot be distinguished from crystallized fat protons by T_2 measurements, this can be achieved using measurement of T_1 relaxation time [43]. Indeed, for ice cream the spin–spin lattice relaxation of the solid phase has been described by a bi-exponential model. The two relaxation components were attributed to fat and water in the crystallized state, respectively. In addition to this result, it has also been reported for the first time that the spin–lattice relaxation time of the crystallized water in the ice cream varies between 2000 and 4000 ms, depending on the formulation of the ice cream [44]. This significant effect was mainly explained by the protein type and concentration in the ice cream. The ice relaxation was higher when skim milk powder was used in place of whey protein powder. A change in the ice crystal structure was assumed to explain this wide variation.

Nevertheless, interpretation of NMR relaxation of complex products such as cheese requires careful quantitative analysis of the NMR signal in order to avoid confusion between water and liquid fat relaxation, for example. Indeed, in many cases water and fat relaxation cannot be separated and interpretation of T_2 or T_1 in terms of water mobility becomes questionable [45–48]. Depending on the water relaxation time value of the product under study, the temperature of measurement should be fixed in order to provide a way to separate the water relaxation from the fat relaxation. Another solution is to perform two-dimensional spin-relaxation and diffusion experiments. Fat and water relaxation can be distinguished [49] from T_2 vs. T_1, and changes during maturation have been observed from the D vs. T_2 and T_2 vs. T_1 maps [50,51].

Water Retention

The mono-exponential behavior for water relaxation is only observed when the water molecules in different microscopic compartments are averaged by diffusive exchange [52]. If the diffusion coefficient is slow compared to the relaxation rate or if the distance between two water compartments is large, the averaging is no longer effective and bi-exponential water relaxation behavior is observed. The change from mono to bi-exponential relaxation is a powerful way to quantify curd syneresis. Gels formed from milk by renneting may subsequently show syneresis, i.e expel liquid, because the gel contracts. During syneresis, water relaxation is described by a bi-modal distribution of the transverse relaxation time [53,54]. The two water peaks are related to the location of water in the sample. The long T_2-relaxation time reflects the water expelled from the curd and its value is constant over the period of syneresis. The short-relaxation time is attributed to the water protons and macromolecule exchangeable protons entrapped in the gel. Three kinds of information are provided by the NMR method: curd volume-decreased kinetics, curd moisture-decreased kinetics and the curd relaxation rate [37,55]. The NMR method can also be used to monitor the kinetic effect of lactic fermentation on the water retention properties of yogurts [56] and cheese [57]. A water-holding capacity NMR method based on washing out of water by heavy water was recently proposed [48]. The T_2-experiments were performed before and after washing with D_20. The reduction in the NMR signal is therefore proportional to the amount of water replaced and related to the water-holding capacity of the sample, assuming that the NMR signal for liquid fat protons is negligible.

The rehydration capacity of dairy powders is a crucial quality criterion for dairy companies. Nevertheless, the standard methods are crude and dedicated to milk powder and not suitable for other dairy powders. Davenel *et al.* (1997) have proposed an NMR method for rehydration monitoring [58]. The advantage of the NMR method is that measurement is performed under stirring at a controlled temperature. Consequently, the NMR method provide complete kinetics of the rehydration process and can be used whatever the composition of the powder [59].

Water Diffusion

An alternative way to study water states in macromolecular solutions and gels is self-diffusion measurement of water mobility. This can be achieved by means of the Pulsed Gradient NMR technique (PFG NMR). In comparison with the NMR relaxation technique the interpretation of PFG findings is more straightforward. Moreover, the technique can be applied to most samples and provides structural information about the system being investigated [60–63]. The technique has been used to study water mobility in casein solutions and gels [64], and in cheese [65], and the effect of casein and fat content in model cheese on water diffusion [66]. When water diffusion is restricted within droplets, the droplet size distribution can be determined [67]. This method has been applied to butter [68].

Fat Relaxation

The most widespread NMR application for dairy products is the SFC method [1,67]. Since this method became an international standard [69], certain improvements have been made. Some have involved measurement of the solid-fat ratio in aqueous products such as emulsions [70] and others have focused on the development of more sophisticated curve-fitting methods for the relaxation curve [71]. Compared to calorimetric methods, NMR allows the determination of the SFC both in isothermal conditions and as a function of temperature. Many studies have therefore been published on the crystallization behavior of milk fat. For example, the effects of fractionation [72], high pressure [73], and cooling rate have been studied, and chemical effects such as blending [74–76] and interesterification [77] on crystallization have also been investigated.

The general determination of the SFC is based on the sampling of two points from the NMR signal, one after the dead time of the probe (11 μs) and the next at 70 μs. This method supposes that the relaxation time of the solid part is temperature independent and also independent of fat composition when using an external reference. These assumptions are not always verified. For example, precise analysis of the free induction signal of milk fat at 5 °C, showed that an intermediate phase characterized by relaxation T_2^* (varying from 50 to 250 μs) range could be detected [78,79]. This intermediate phase represents about 4% of the whole fat and thus should be considered when absolute SFC is required. One solution to overcome the choice of sampling time is to fit the complete NMR signal. This solution provides a precise determination of the relaxation time of the solid phase and moreover signal intensity is deduced without the need of correction factor because of the dead time. This method has been successfully applied to fat blends [71], model food emulsion [80] and ice cream mix [81]. The only limitation of this method in cases of emulsion is that the amount of fat should be known or the relaxation time of water and liquid fat should be sufficiently different to allow quantification of the signal intensity of liquid fat and water separately.

The relaxation time of fat has also been studied. When the fat is liquid the relaxation time T_2 is related to the carbon chain length and to the degree of unsaturation [82]. Since much fat in foods is a complex mixture of triglycerides, the NMR signal time is described as a broad distribution of relaxation times [38] and interpretation of such behavior in food becomes difficult. On the other hand, wide changes in the longitudinal relaxation time of solid fat according to polymorphic state have been observed with triglycerides [83]. The longitudinal relaxation time is 12 s at 25 °C for the polymorph β form and decreases to 0.6 when a polymorphic α is obtained. Measurement of T_1 therefore provides a method of following the time course of polymorphic transformation when aging for example. Such variations have also been observed between fat in bulk and in emulsion for model food emulsions [4] or for real food products such as ice cream mix [81]. However, because of the complexity of fat composition the interpretation in terms of changes in polymorphism has not been possible.

Finally, as previously mentioned for w/o emulsion, the droplet size of fat can be determined in o/w emulsion from pulsed field gradient NMR measurements. However, the method has mainly been applied to non-dairy fat-containing products, because of the effect of the crystalline fat. High amounts of solid fat may affect the apparent droplet size because the fat crystal network may introduce a second mechanism to hinder diffusion within the droplet [84]. For dairy products, it was assumed that droplet size measurement with PFG NMR can only be performed at temperatures above 15 °C, in view of the SFC for butterfat according to temperature [84]. For example, the droplet size of fat in cheese has been determined at 37 °C [65].

Conclusion

Despite the complexity of the interpretation of NMR relaxation time parameters, this technique can provide much information that is useful for quality control and for the development of new products based on improved knowledge of molecular and microscopic structure. A new, dedicated, low field spectrometer has recently been proposed (Mouse NMR [85,86]). We are sure that these technical improvements will contribute significantly to the development of NMR relaxation in dairy science and dairy companies.

References

1. Wahlgren M, Drakenberg T. In: GA Webb, P Belton, MJ Mc Carthy (Eds). Annual Reports on NMR Spectroscopy. Academic Press: London, 1995, p 275.
2. Belloque J, Ramos M. Trends Food Sci. Technol. 1999;10:313.
3. Duce SL, Amin MHG, Horsfield MA, Tyszka M, Hall LD. Int. Dairy J. 1995;5(4):311.
4. Mariette F. In: A Webb, PS Belton, AM Gill, DN Rutledge (Eds). Magnetic Resonance in Food Science: Latest Developments. Royal Society of Chemistry: Cambridge, 2003, p 209.
5. Hester RE, Quine DEC. J. Dairy Res. 1977;44:125.
6. Van Beresteyn E. Neth. Milk. Dairy. J. 1972;26:117.
7. Hills BP, Takacs SF, Belton PS. Food Chem. 1990;37:95.
8. Kumosinski TF, Pessen H, Prestrelski SJ, Farrell HMJ. Arch. Biochem. Biophys. 1987;257:259.
9. Venu K, Denisov VP, Halle B. J. Am. Chem. Soc. 1997;119:3122.
10. Halle B, Denisov VP. Biophys. J. 1995;69:242.
11. Belton PS. Comments Agric. Food Chem. 1990;2(3):179.
12. Belton PS. Food Rev. Int. 1993;9(4):551.
13. Mariette F, Tellier C, Brule G, Marchal P. J. Dairy Res. 1993;60(2):175.
14. Brosio E, Altobelli G, Yun Yu S, Di Nola A. J. Food. Technol. 1983;18:219.
15. Roefs SPFM, Van As H, Van Vliet T. J. Food Sci. 1989;54:704.
16. Famelart MH, Gaucheron F, Mariette F, Le Graet Y, Raulot K, Boyaval E. Int. Dairy J. 1997;7(5):325.
17. Padua GW. Water state associated with skim milk components quantitated by NMR, PhD Thesis, University of Illinois, 1989.
18. Lai HM, Schmidt SJ. Food Chem. 1993;46(1):55.
19. Schuck P, Davenel A, Mariette F, Briard V, Mejean S, Piot M. Int. Dairy J. 2002;12(1):51.
20. Le Dean A, Mariette F, Lucas T, Marin M. Lebensm.-Wiss. u.-Technol. 2001;34:299.
21. Farrell HMJ, Pessen H, Kumosinski TF. J. Dairy Sci. 1989;72:562.
22. Brosio E, Altobelli G, Di Nola A. J. Food. Technol. 1984;19:103.
23. Mora-Gutierrez A, Farrell HM, Kumosinski TF, J Agric. Food Chem. 1995;43(10):2574.
24. Mora-Gutierrez A, Farrell HM, Kumosinski TF. J. Agric. Food Chem. 1996;44(1):48.
25. Mora-Gutierrez A, Farrell HM, Kumosinski TF. J. Agric. Food Chem. 1996;44(3):796.
26. Mora-Guttierez A, Kumosinski F, Farrell HMJ. J. Agric. Food Chem. 1997;45:4545.
27. Mora-Gutierrez A, Farrell HM. J. Agric. Food Chem. 2000;48(8):3245.
28. Szuminska K, Gutsze A, Kowalczyk A, Z. Naturforsch (C). 2001;56(11–12):1075.
29. Kimmich R, Nusser W, Gneiting T. Coll. Surf. 1990;45: 283.
30. Kimmich R, Klammer F, Skirda VD, Serebrennikova IA, Maklakov AI, Fatkullin N. Appl. Magn. Reson. 1993;4:425.
31. Hills BP, Takacs SF, Belton PS. Molec. Phys. 1989; 67(4):903.
32. Hills BP, Takacs SF, Belton PS. Molec. Phys. 1989; 67(4):919.
33. Kimmich R, Gneiting T, Kotitschke K, Schnur G. Biophys. J. 1990;58:1183.
34. Lambelet P, Berrocal R, Ducret F. J. Dairy. Sci. 1989;56:211.
35. Lambelet P, Berrocal R, Renevey F. J. Dairy Res. 1992;59(4):517.
36. Pessen H, Purcell JM, Farell HM. Biochim. Biophys. Acta. 1985;828:1.
37. Mariette F, Marchal P. J. Magn. Reson. Anal. 1996; 2(4):290.
38. Chaland B, Mariette F, Marchal P, de Certaines J. J. Dairy Res. 2000;67:609.
39. Chaland B. Ripening mechanisms of soft cheese : A low field MRI study (in french), PhD Thesis, University of Rennes, 1999.
40. Budiman M, Stroshine RL, Cornillon P. J. Dairy Res. 2002;69(4):619.
41. Budiman M, Stroshine RL, Campanella OH. J. Texture Stud. 2000;31(5):477.
42. Godefroy S, Korb JP, Creamer K, Watkinson P, Callaghan PT. J. Coll. Int. Sci. 2003;267:337.
43. Mariette F, Lucas T. J. Agric. Food. Chem. 2005;53:1317–1327.
44. Lucas T, Wagener M, Barey P, Mariette F. Int. Dairy J. 2005;15:1064–1073.
45. Kuo MI, Gunasekaran S, Johnson M, Chen C. Dairy J Sci. 2001;84(9):1950.
46. Schlesser JE, Schmidt SJ, Speckman R. Dairy J. Sci. 1992;75:1753.
47. Hori T. Food J. Sci. 1982;47:1811.
48. Hinrichs R, Gotz J, Noll M, Wolfschoon A, Eibel H, Weisser H. Food Res. Int. 2004;37(7):667.
49. Puaud M, Mariette F, Marchal P. The Third International Conference on Applications of Magnetic Resonance in Food Science, Nantes, France, 1996.
50. Godefroy S, Creamer LK, Watkinson P, Callaghan PT. In: PS Belton, AM Gil, GA Webb, DN Rutledge (Eds). Magnetic Resonance in Food science, Latest Developments. The Royal Society of Chemistry, Cambridge, 2002, p 85.
51. Godefroy S, Callaghan PT. Magn. Reson. Imaging. 2003;21 (3–4):381.
52. Belton PS, Hills BP. Molec. Phys. 1987;61(4):999.
53. Tellier C, Mariette F, Guillement JP, Marchal P. Agric. J. Food Chem. 1993;41(12):2259.

54. Lelievre J, Creamer K. Milchwissenschaft. 1978;33:73.
55. Le Dean A. Water assessment in dairy products: study of dispersions and gels under syneresis, freezing and thawing (in French), PhD Thesis, Institut National Agronomique Paris-Grignon, 2000.
56. Laligant A, Famelart MH, Paquet D, Brule G, Lait. 2003;83(4):307.
57. Metais A, Cambert M, Riaublanc A, Mariette F. Int. Dairy J. 2006;16(4):344–353.
58. Davenel A, Schuck P, Marchal P. Milchwissenschaft. 1997;52(1):35.
59. Davenel A, Schuck P, Mariette F, Brule G. Lait. 2002;82(4):465.
60. Price WS. Concept. Magn. Res. 1997;9:299.
61. Price WS. Concept. Magn. Res. 1998;10:197.
62. Karger J, Pfeiffer H, Heink W. Adv. Mag. Res. 1988;12:1.
63. Callaghan PT. Principles of Nuclear Magnetic Resonance Microscopy. Oxford Science Publications: Oxford, 1991.
64. Mariette F, Colsenet R, Le Garff C, Cambert M. International Congress of Engineering and Food, ICEF 9. Montpellier: France, 2004.
65. Callaghan PT, Jolley KW, Humphrey RS. Colloid. J. Interface Sci. 1983;93:521.
66. Metais A, Cambert M, Riaublanc A, Mariette F. Agric J. Food. Chem. 2004;52(12):3988.
67. Balinov B, Mariette F, Soderman O. In: SE Friberg, K Larsson, J Sjoblom (Eds). Food Emulsions, Marcel Dekker: New York, 2003, p 356.
68. Fourel I, Guillement JP, Le Botlan D. Coll J. Int. Sci. 1995;169:119.
69. ISO 8292:1991 Animal and vegetable fats and oils—Determination of solid fat content—Pulsed nuclear magnetic resonance method, 1991.
70. Van Boekel MAJJ. S Am. Oil Chem. Soc. 1974;51:316.
71. van Duynhoven J, Dubourg I, Goudappel GJ, Roijers E. Am J. Oil Chem. Soc. 2002;79(4):383.
72. Vanhoutte B, Dewettinck K, Vanlerberghe B, Huyghebaert A. Am J. Oil Chem. Soc. 2003;80(3):213.
73. Schutt M, Frede E, Buchheim W. Kieler Milchwirtsch. Forschber. 1995;47(3):209.
74. Hayati IN, Aminah A, Mamot S, Aini IN, Lida HMN, Sabariah S. J. Food Lipids. 2000;7(3):175.
75. Shen Z, Birkett A, Augustin MA, Dungey S, Versteeg C. J Am. Oil Chem. Soc. 2001;78(4):387.
76. Hayati IN, Aminah A, Mamot S, Aini IN, Lida HMInt N. Food J. Sci. Nutr. 2002;53(1):43.
77. Rousseau D, Forestiere K, Hill AR, Marangoni AG, J. Am. Oil Chem. Soc. 1996;73(8):963.
78. Le Botlan D, Helie I. Anal. Chim. Acta. 1995;311(2):217.
79. Le Botlan D, Ouguerram L, Smart L, Pugh L. J. Am. Oil Chem. Soc. 1999;76(2):255.
80. Mariette F, Querangal S, Cambert M, Lopez CC, Riaublanc A. The fifth International Conference on Applications of Magnetic Resonance in Food Science, Aveiro, Portugal, 2000, p 84.
81. Lucas T, Le Ray D, Barey P, Mariette F. Int. Dairy J. 2005;15:1225–1233.
82. Le Botlan DJ, Helie I, Analusis. 1994;22:108.
83. Colquhoun IJ, Grant A. Eurofood Chem V. Versailles, France, 1989, 668.
84. Kiokias S, Reiffers-Magnani CK, Bot A. J. Agric. Food Chem. 2004;52(12):3823.
85. Eymael R, Blumich B. Tech. Mess. 2002;69(7–8):340.
86. Kuhn H, Klein M, Wiesmath A, Demco DE, Blumich B, Kelm J, Gold PW. Magn. Reson. Imaging. 2001;19(3–4):497.

Characterization of Molecular Mobility in Carbohydrate Food Systems by NMR

Pavinee Chinachoti[1], Elena Vittadini[2], Pathama Chatakanonda[3], and Yael Vodovotz[4]
[1]*Hill's Pet Nutrition, Inc. and Subsidiaries, Topeka, KS 66617, USA;*
[2]*Università degli Studi di Parma, Dipartimento di Ingegneria Industriale, 43100 Parma, Italy;*
[3]*Cassava and Starch Technology Research Unit, Kasetsart Agricultural and Agro-Industrial Product Improvement Institute (KAPI), Kasetsart University, Bangkok 10900, Thailand; and*
[4]*Department of Food Science and Technology, The Ohio State University, Columbus, OH 43210, USA*

Introduction

Characterization of molecular mobility in complex systems can provide much useful information that helps scientists understand various biological, chemical, and physical phenomena of a complex system. In this chapter, we will explore the applications of nuclear magnetic resonance (NMR) to determine molecular mobility of primarily cereal systems using multinuclei (proton, deuteron, and oxygen-17), carbon-13 solid-state NMR, proton cross relaxation (CR), and some application use in relation to microbial activity.

Nuclear magnetic resonance spectroscopy has been used to non-invasively measure the mobility of water in complex and heterogeneous systems. Water molecular mobility can be analyzed by NMR spectroscopy [1,2] using proton (^{1}H), deuterium (^{2}H), and oxygen-17 (^{17}O) nuclei much of which have been covered in various books and review articles [3–8].

Water Molecular Mobility by NMR

NMR spectroscopy application in food is primarily based on the ability of NMR to detect water. NMR spectroscopic technique for water is based on a measure of resonant radio frequency adsorption by nuclear spins in presence of applied magnetic field. Depending on the spin quantum number, several energy levels of the resonance is collected which reflects the nature in which the nuclei interact with the applied magnetic field.

The proton (^{1}H) nucleus is the most abundant NMR detectable species and with the spin quantum number (I) of 1, its signal acquisition is relatively easy. However, interpretation of proton relaxation data is complicated by chemical exchange and CR phenomena. Protons associated with different molecules can exchange their position and are subject to CR phenomena between neighboring locations [8–12]. These phenomena can significantly influence the relaxation process [13–15].

Deuterium (^{2}H) is less abundant than proton and its relaxation signal is strongly affected by quadrupolar interactions (because of its quadrupolar moment with spin quantum number (I) of 1). ^{2}H NMR, however, does not escape the contribution from the chemical exchange with other exchangeable deuterons or protons on the solids [8,16].

Oxygen-17 (^{17}O) NMR data are free from the effect of CR and ^{17}O does not likely exhibit a significant oxygen exchange [8,17–20]. Therefore, ^{17}O NMR data are more easily interpreted, but the low ^{17}O abundance (0.037%), accompanied with a strong quadrupolar moment ($I = 5/2$), makes ^{17}O signal acquisition quite difficult. The application of ^{17}O NMR to the study of water mobility is mainly limited to a high moisture environment where bulk water is present. In solid and semisolid systems, water mobility information can be more easily acquired (but more complex to interpret) using ^{1}H and ^{2}H NMR. Enrichment with $H_2^{17}O$ and/or $^{2}H_2O$ can further improve signal acquisition.

Water mobility is characterized by the resonance frequency, spin–lattice and spin–spin relaxation times (T_1 and T_2, respectively). Because possible rapid exchange within the NMR time frame, signals observed are time averaged. Unfortunately, some water molecules may be trapped or associated (chemically or physically) with other molecules. If the water molecule is a distance away in another domain, it may be less efficient in exchanging with other distant water molecules and hence exhibits as a separate population.

On a local level, the physical nature of the tested material plays an important role. In a non-viscous liquid, $T_1 \sim T_2$ and its correlation time (tc is short (Figure 1). As a material becomes more solid at $\tau_c < 10^{-6}$ s, $T_2 \ll T_1$.

At a given physical condition and state, a water molecule exhibits a dynamic processes which may include reorientation (τ_r), translation or diffusion (τ_D), proton or deuteron exchange with neighboring protons or deuterons (τ_e), and (if associated with a macromolecule) tumbling, anisotropic motion [20–22].

Graham A. Webb (ed.), Modern Magnetic Resonance, 1703–1712.
© 2008 *Springer.*

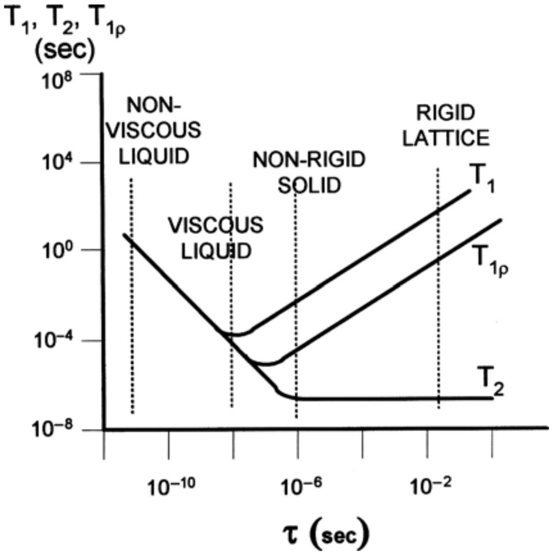

Fig. 1. A typical relationship between T_1, T_2, and $T_{1\rho}$ and τ [2].

NMR to Determine Various Populations of Water

The heterogeneous chemical nature of food components is a known fact but yet least investigated. Molecular diversity of compounds can be characterized according to polarity, ionic property, surface activity, molecular weight, isoelectric point, and so on. Within a molecule (such as protein), heterogeneity in side groups can greatly influence the conformation as well as how the molecular domains interact with the surrounding solvent. For this very reason, it is important to regard water as being different among these different regions. In common terms, water resides around various solid surfaces at residence times short or long depending on the chemical forces between them. The rotational motion (normally described as rotational correlation time τ_r) is one of the properties experimentally described by methods such as NMR using, for instance, typical spin echo experiment.

On a macroscopic and a microscopic scale, food and food ingredients are highly heterogeneous in a variety of length scales. NMR experiments can be performed to detect heterogeneous domains [23]. Relaxometry, by which a time average frequency is measured, determines chemical heterogeneity based on the variation in signal intensity at different frequencies such as amino acid composition of a protein. A time dependence frequency type of experiment is related to time dependence fluctuations of local frequencies, which can be used to determine spatial heterogeneity such as spatial distribution of water or other solvent molecules [23].

In a heterogeneous system, spins exist in a wide variety of environments resulting in a spectrum of relaxation times. Spins are also influenced by chemical and diffusive exchange. Therefore, the measured relaxation decay is a sum of the contributions from all spins, which may have sampled many different environments or exchanged with other spins at different rates within NMR timescale [24].

Spatial distribution of molecules in heterogeneous domains can greatly influence the NMR relaxation signals. Diffusive exchange occurring within the NMR relaxation time has been demonstrated to have a considerable impact on the interpretation of NMR data for biological heterogeneous systems [25]. Diffusive exchange of molecules from spatially separated regions involves random jumps between many different volume elements along the spatial dimensions, whereas chemical exchange between two different chemical species only involves jumping between two types of magnetization density vectors [26]. When the exchange process is fast compared to relaxation rates, only a single average process is observed. On the other hand, if the exchange is relatively slow, two or more processes may be observed depending on the exchange mechanism. In such situation, proton NMR relaxation data can be used to describe some degree of spatial heterogeneity of the system, such as freeze-thawed agarose gel [27] and Sephadex beads [28].

Polymer network depending on cross-linking density may swell in the presence of water trapping the water molecules. The molecules of water, are free to diffuse between the inside and outside of a domain. Spatial dimension can be related to the particle size, and also to the internal cross-linking density of the structural components. These factors affect diffusion distance between water in different internal compartments as well as inside versus outside the particle. This time-dependent diffusive exchange affects the proton relaxation decay observed dependently on CPMG pulse spacing. Hence, pronounced multiple-exponential decay can effectively arise from diffusive exchange.

If inter-pulse spacing (τ) is very short compared to the proton exchange rate (chemical exchange slow), there is less dephasing effect by continually refocusing the transverse magnetization (becoming single exponential). This results in a decrease in the transverse relaxation rate (longer observed T_2). On the other hand, when the pulse spacing is very long compared to the proton exchange rate produces an increased dephasing between refocusing pulses and gives an increased relaxation rate (decreased T_2). As the pulse spacing increases another dispersion becomes noticeable, this arises from water outside diffusing into the particle and then exchanging with other protons. As a result, experiments performed with multiple τ can lead to different number of exponential components some of which are not linked to existence of different sites but rather a reflection of the s spatial morphology of manifestation of the material.

Since the discrete model can be limited to a condition that favors a fast exchange within the NMR time frame, a continuous model has been developed and applied to study heterogeneity of food systems. In the continuous distribution relaxation time model, the discrete character of the basic least squares solution is altered to generate continuous distributions [29].

This model was used to construct a non-negative least squares (NNLS) discrete and continuous spectra for a western red cedar sapwood sample using the data collected with the CPMG experiment [30]. The discrete model shows four to five isolate T_2 values, while the continuous model results in three peaks. The presence of peaks in the continuous spectrum suggests that there were three dominant environments within the wood. The integral area under each peak represents the amount of the fraction of water molecules that have the T_2 values covered by the peak. It is found that the continuous model is the preferred one because it fits the nature of wood in that the lumen water in wood produces a continuous distribution of T_2 values corresponding to the continuous distribution of lumen diameters.

A Fortran computer program called "CONTIN" based on the NNLS approach was developed [31,32]; CONTIN uses a general purpose constrained regularization method and finds the simplest solution that is consistent with prior knowledge and experimental data. More recently, the software program such as RI WinDXP program (Oxford Instruments, Ltd., Abingdon, UK), has been developed to perform the continuous distribution analysis based on the non-negative constraints and optimal smoothing. A continuous distribution of exponentials for FID and CPMG experiments may be defined by the following equation:

$$g_i = \sum_{j=1}^{m} f_j \mathrm{e}^{-t_i/T_j},$$

where g_i is the unknown amplitude of the spectral component at time t_i, f_j the pre-exponential multipliers of the distribution, and T_j the exponential time constants (the T_2 values).

T_2 Distribution of Water in Starch

Multiexponential models are commonly used to analyze NMR relaxation data of food systems. As mentioned earlier, spins exist in a wide variety spectrum of relaxation times, which are influenced by chemical and diffusive exchange within the heterogeneous system [25,33,34]. It is, thus, reasonable to assume that a continuum of relaxation times would arise from a continuum of different environments in which spins exist with different exchange rates. Lillford *et al*. [34] reported that the continuous distribution of relaxation times resulted in an improved representation of what?. Some other researchers have used continuum models to follow the relaxation behavior in various systems [24,30,35–38].

T_2 spectra can be regarded as a probability distribution of spins at various relaxation times. There are often several peaks on a T_2 spectrum. Larger number of peaks (or broader ones) would be expected for heterogeneous samples, whereas fewer but stronger peaks would be expected of more homogeneous samples. The number and degree of variation of the peaks, therefore, can be used to indicate the degree of heterogeneity of the sample being analyzed.

To take this one step further, the relationship between water distribution and starch granule heterogeneity was studied using proton and deuterium NMR techniques [39]. In this work, water proton transverse relaxation times for a packed bed of raw potato starch granules were identified with three distinct water populations. The effect of acid hydrolysis (lintnerization) and the thermal gelatinization of the dynamic state of starch and the microscopic distribution of water within native potato starch granules were also studied [40].

Relative proton CPMG T_2 distribution of cassava starch undergoing stepwise heating exhibited T_2 peaks at 200 and 400 μs (at −62 and −43 °C), respectively (Figure 2). As the temperature was raised, the peak splitted into two peaks (200 μs and 2 ms) before the ice melting temperature above which an appearance of more mobile protons (20 ms) was observed [41]. A significant change in proton CPMG T_2 distribution was also observed upon gelatinization. At the onset of the gelatinization, merging of the two peaks into a broader peak was observed.

In order to assess starch chain mobility, H_2O could be replaced with D_2O (so that only the starch protons would be observed). For cassava starch, a 10-μs T_2 peak component represents the rigid amylopectin and a 800-μs T_2 peak represents the less rigid components (Figure 3). Gelatinization led to a decrease in the rigid chain population and an increase in the mobile chain population [41].

Solid-State Nuclear Magnetic Resonance

^{13}C Cross Polarization and Magic Angle Spinning

Solid-state NMR is a useful tool to probe the molecular structure in the crystalline solids and glassy states. This powerful technique has been used to probe the structure dynamics and mobility of biopolymers [42–45]. Prior to the implementation of this technique, NMR was limited

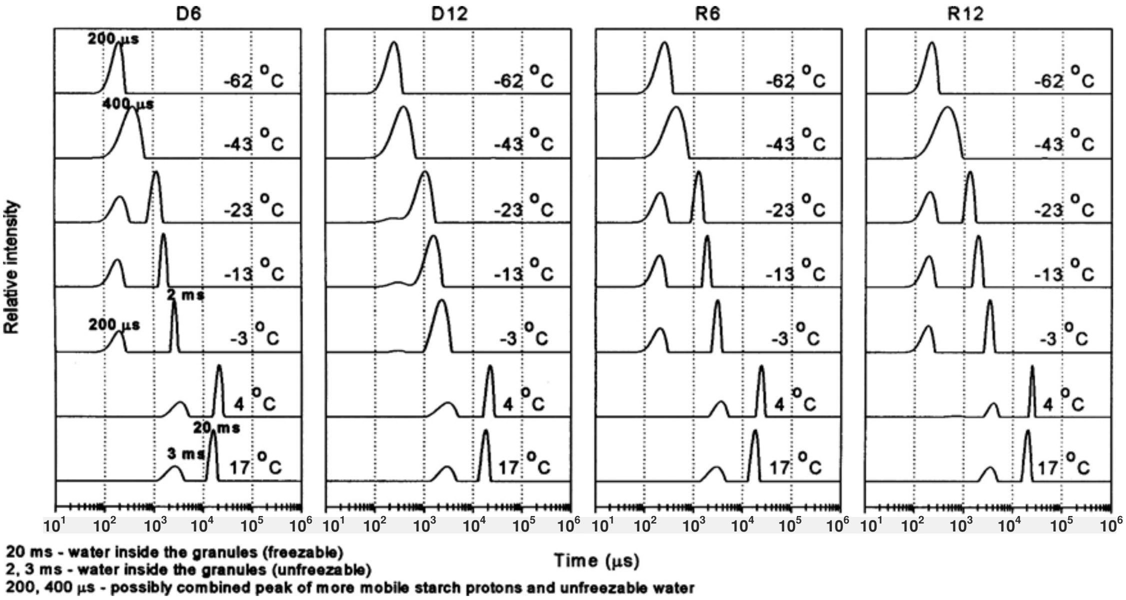

20 ms - water inside the granules (freezable)
2, 3 ms - water inside the granules (unfreezable)
200, 400 μs - possibly combined peak of more mobile starch protons and unfreezable water

Fig. 2. Transverse relaxation time (T_2) distribution of protons for cassava starches (planted in drought season, "D" and rainy season, "R" and harvested at 6 and 12 months) saturated in water as measured from the CPMG sequence [41].

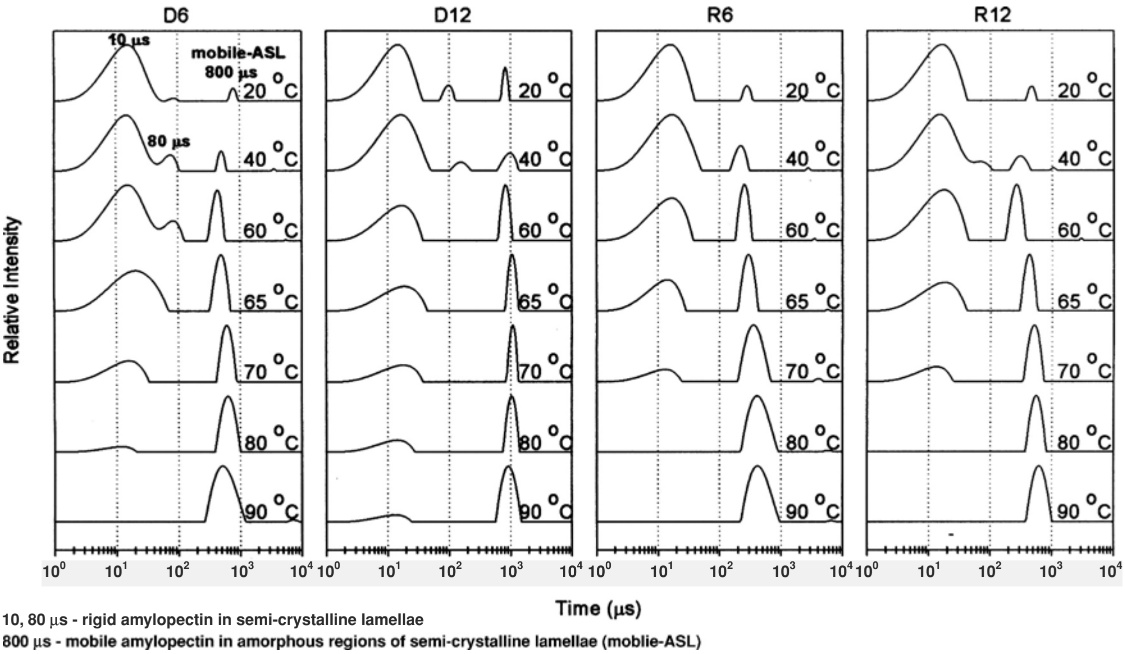

10, 80 μs - rigid amylopectin in semi-crystalline lamellae
800 μs - mobile amylopectin in amorphous regions of semi-crystalline lamellae (moblie-ASL)

Fig. 3. Transverse relaxation time (T_2) distribution of protons for cassava starches (planted in drought season "D" and rainy season, "R" and harvested at 6 and 12 months) saturated in water D_2O as measured from the FID.

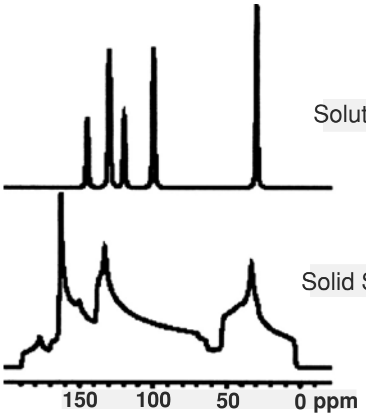

Fig. 4. Comparison of solution and solid-state ^{13}C spectra showing the broadening due to anisotropic chemical shift and dipolar broadening.

to the study of solutions, since solid spectra is generally broad and contains very little specific information (Figure 4) due to anisotropic or orientation-dependent chemical shift and dipolar broadening. The magnetic field experienced by the nucleus varies as a function of the orientation of the molecule in the magnetic field and in a non-viscous liquid, the fields at the various orientations average out due to the tumbling of the molecule. Dipolar interactions averaged to zero in solutions due to rapid rotational and translational motion [46].

Two techniques, namely magic angle spinning (MAS) and cross polarization (CP), are commonly used in conjunction to overcome the anisotropy and dipolar broadening. If a sample is spun rapidly at an angle of 54.74° to the applied magnetic field, the dipolar interactions are reduced. At this magic angle, the chemical shift tensor (s) is equal to the isotropic chemical shift (s_i), which is the one found in solutions when dipolar interactions are not seen. MAS, therefore, reduces the broad chemical shift powder pattern to the isotropic sharp pattern found in liquids [48]. In solid-state NMR, samples are placed in a special sample tube and the tube is placed inside a rotor. The rotor, and hence the sample, are oriented at the magic angle and the sample is then spun at a rate of thousands of revolutions per second. The spinning rate must be comparable to the solid-state line width. CP involves the transfer of polarization from abundant spins to dilute spins in order to enhance signal to noise and reduce waiting time between successive experiments.

For nuclei with low natural abundance (such as ^{13}C), the average of many signals (scans) need to be accumulated to obtain a spectrum when using Fourier Transform, pulsed techniques. The repetition rate is dictated by T_1 (spin–lattice relaxation time) and for ^{13}C, the T_1 values are very long in solids and, therefore, the accumulation of the data required would take a prohibitively long time. Consequently, CP is used in which the polarization of the abundant ^{1}H nuclear spin with short T_1 is transferred to that of the ^{13}C nuclei. After CP, the repetition rate is determined by the short ^{1}H T_1s [46,48]. Therefore, by utilizing CP–MAS NMR, both the resolution and experimental time frames have been improved.

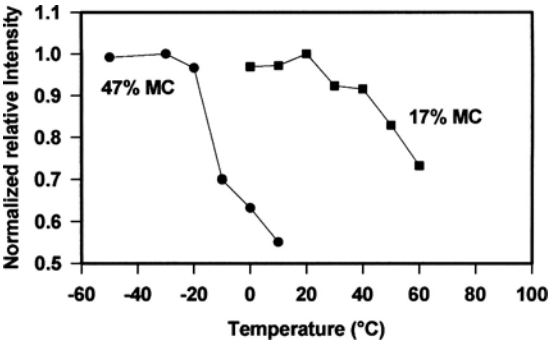

Fig. 5. The change in intensity of carbon 1 of 17 and 47% moisture wheat starch gels at decreasing temperature obtained from ^{13}C CP–MAS measurements [47].

^{13}C CP–MAS NMR can be used to monitor the development of rigid components in starch [49]. This method was applied to the study of different crystalline (A and B pattern [50]) and amorphous [51] structures of starch as well as the effect of hydration [52]. For example, Figure 5 shows the differences in the changes in carbon 1 of a 17 and 47% moisture starch gels upon heating [47]. Carbon 1 has been used to describe the molecular motions of amorphous starch [53]. The increase in mobility (decrease in intensity) at temperatures above 20 °C for 17% vs. above −20 °C for 47% gels was attributed to the glass-rubber transition [47].

Relaxation Time in the Rotating Frame ($T_{1\rho}$)

The relaxation times (which in reality describe the decay of energy) may be used to ascertain the mobility of the probed nuclei in the solid state (the correlation time of motion). The time frame for each of the relaxation times in the solid state range from seconds for T_1 to ms for $T_{1\rho}$ (rotating-frame relaxation time). $T_{1\rho}$ can be used to measure molecular motions in glassy, rubbery, and crystalline solids, since it is sensitive to motions associated with frequencies in the 10–100 kHz range [54]. $T_{1\rho}$ (^{1}H) is performed by monitoring the intensity of ^{13}C NMR signals as a function of the duration of a ^{1}H spin-lock field. The $T_{1\rho}$ (^{1}H) values are obtained by spin locking the proton

Fig. 6. Typical ^{1}H cross-relaxation NMR Z-spectra curves constructed from water resonance saturation as a function of offset frequency [59].

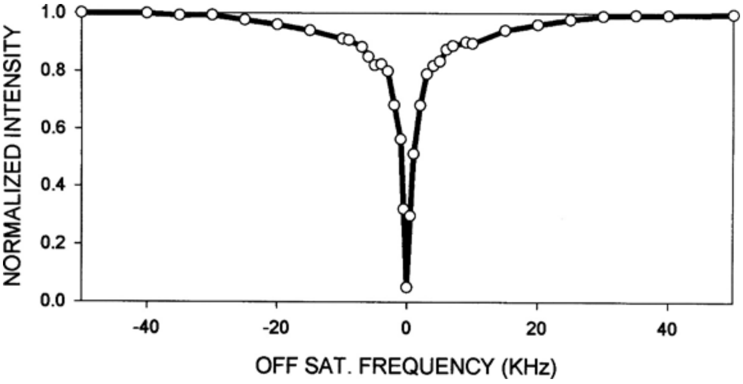

spins in the rotating frame for a variable delay (spin-lock time) prior to CP. The plot of different relaxation times vs. the correlation time at a fixed frequency would theoretically yield U-shaped curves. The minimum observed occurs when the frequency of the molecular motion is comparable to the measured frequency of the spectrometer [55]. Temperature is used to measure correlation time since the two parameters are related with the following equation $\tau = \tau_0 e^{\Delta E/kT}$, where τ is the correlation time, k Boltzman's constant, E the activation energy, and T the temperature.

$T_{1\rho}$ (^{1}H) has been found to decrease in heated starch compared with native starch [44] most likely due to the presence of amorphous domains. Li and co-workers [44] found the $T_{1\rho}$ (^{1}H) minimum (mobility) for wheat gluten depended on moisture content with 2% showing a minimum at -13 °C and at 20% moisture the minimum was shifted to below -30 °C. However, the observed ^{1}H $T_{1\rho}$ is influenced by a number of factors including the molecular motions of each domain, domain size, spin diffusion, cross relaxation, and dipole–dipole interactions between water and starch [44]. $T_{1\rho}$ (^{13}C), on the other hand, provides information of the carbon mobility more directly and therefore changes in the polymer molecular dynamics can be monitored and related to phase transitions [54].

Solid Mobility by Cross Relaxation

Cross relaxation NMR spectroscopy is a high-resolution proton (^{1}H) method for determining the information on the relaxation of the solid component via the observable liquid spin system [56]. The ^{1}H CR NMR method has been shown to be a beneficial tool for probing solid components in gels using a simple and economical NMR spectrometer, without the need for a solid-state instrument [57]. A sample is irradiated with a radio frequency pulse that is off-resonance from the liquid signal. Due to the dipolar coupling between the liquid and solid protons, the amplitude of the liquid spectrum will change with the offset frequency, and a Z-spectrum is obtained [56–58].

Figure 6 shows a typical Z-spectrum generated using the amplitude of the liquid spectrum (water resonance saturation) as a function of offset frequency. At sufficiently large offset frequencies, solid protons are not saturated and no CR occurs between the solid and liquid protons after a 90° pulse. As the frequency offset difference decreased (small offset frequencies, Figure 6), the excited solid protons transfer magnetization to liquid protons. This results in a decrease of NMR liquid signal due to the CR between the spins of restricted mobility and those of the mobile bulk-water pool [59]. The Z-spectrum thus contains information of the internal mobility of the solid components in the sample [58]. An inverted plot of the same data (the y-axis being $1 - M^{z}/M^{z0}$) would closely resemble a typical solids ^{1}H spectrum.

CR NMR has been used to study a variety of physicochemical phenomenon in carbohydrate systems, such as molecular mobility around glass transition region in 50% starch gels [57]. In this starch study, an increase in the relative quantity of rigid protons was observed between 0 and -10 °C that was attributed to the glass transition and/or to ice formation. Inulin and maltodextrin gel aging exhibited immobile fraction due to the re-crystallization as detected by CR NMR [60]. Wu and Eads [61] also found an increase in the area and width of the Z-spectral line shape for waxy starch gels during aging. The complex Z-spectra have been decomposed into a Lorentzian (more mobile, solid protons) and a Gaussian (more rigid, solid protons) component. Assignment of the latter was supported by DSC data [61].

In bread, Vodovotz and co-workers [62] reported no change observed in the Z-spectrum of a bread sample (Figure 7), whereas those for gelatinized waxy starch (GX), gelatinized wheat starch (GW), and heated gluten (HG) increased in the width at half height of the

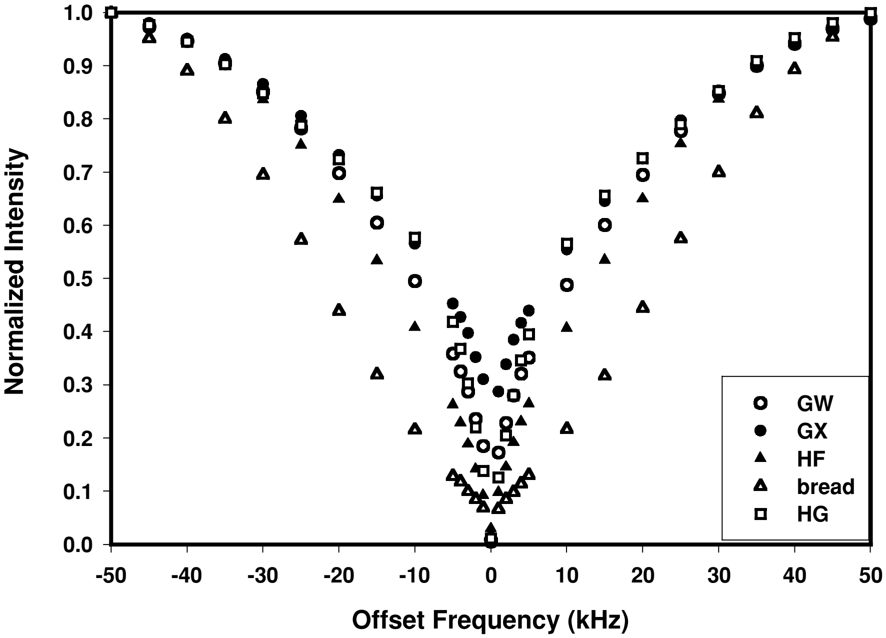

Fig. 7. Results of cross-relaxation ^{1}H NMR experiments for bread and its components at day 0 storage. Abbreviations are for wheat starch (GW), gelatinized waxy starch (GX), heated gluten (HG), and heated flour (HF) [62].

decomposed broad component (presumably an increased rigidity). Since this was not related to amylopectin retrogradation (DSC result), the difference in molecular mobility was attributed to the role of gluten and/or redistribution of water in the amorphous regions of the samples.

NMR Mobility and Microbial Activity

NMR relaxometry can be useful for investigation of water mobility and how it may influence microbial growth and survival. Investigative studies have been focused both on mold germination and growth in semi-solid and solid media and on survival and growth of *Staphylococcus aureus* in liquid media [63–70]. In addition, some reports include the impact of microstructure and water distribution [71,72].

A first investigation about water mobility and microbial response was reported by Chinachoti [73] where an addition of sucrose to a hydrated starch system induced both a reduction in a_{w} and promoted mold germination was proposed to be related to the presence of mobile water as depicted from some ^{17}O NMR results. Evidently because of the redistribution of water from trapped in the hydrated starch granules to extragranular water dissolving sucrose, the water became more rapidly exchanging in bulk solution outside of the granules. Although the short-range rotational mobility was high in both the cases, the extragranular water was able to rapidly exchange and free to diffuse, hence promoting mold spore germination. The presence of this freely exchanging water was earlier assigned to "solute" water and was reported to promote mold germination [63,74].

Because it could be argued that sucrose also served as a carbon nutrient, there was a need to repeat experiments with a more carefully designed system where nutritive contents were the same in all treatments. A media containing only non-nutritive, non-toxic carbohydrates (L-sorbose and cellulose) was used to grow a mutant strain of *Aspergillus nidulans* spores ruling out any possible influence of sucrose acting as nutrient to the cells [66,67]. The composition of the media was designed to alter not only its physical state but also its water molecular dynamics by changing the L-sorbose:cellulose ratio. A substantial increase in water mobility as measured by ^{2}H and ^{17}O NMR T_2 relaxation time was measured when sorbose solubilized. Mold spore germination time and growth rate were both highly dependent on both ^{2}H and ^{17}O NMR T_2 relaxation times irrespectively of system solid composition (sorbose:cellulose ratio) as shown in Figure 8. Mold spore germination time, therefore, correlated closely to the mobile water associated with dissolved sorbose. This experimental evidence indicates that in these solid-semisolid

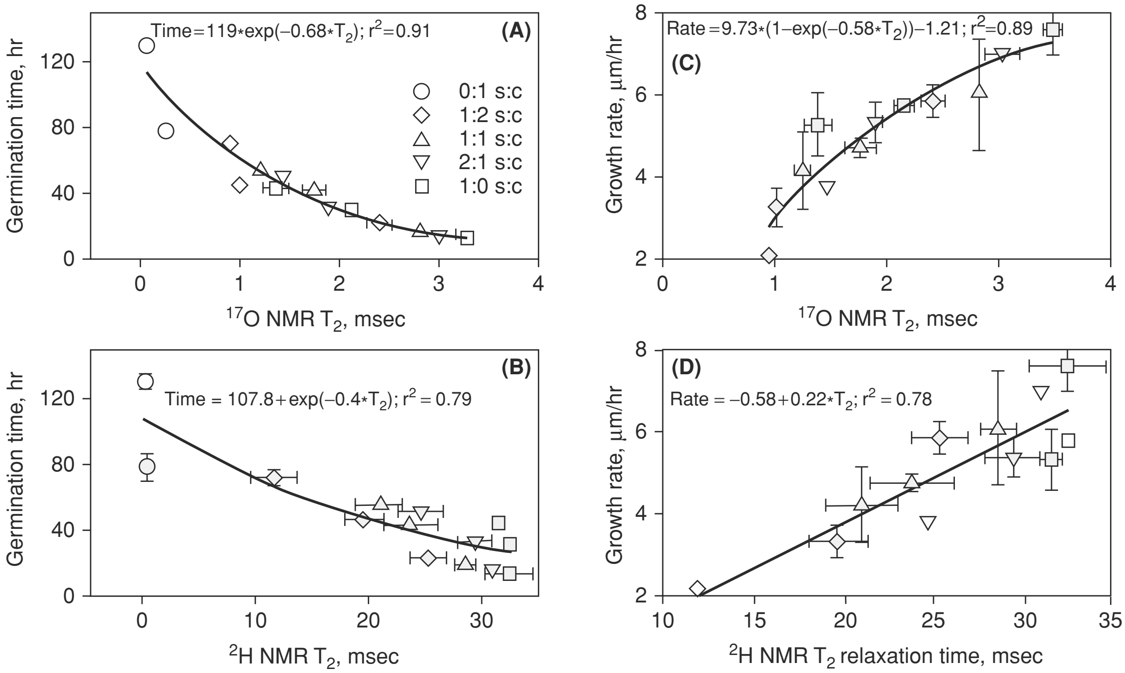

Fig. 8. Aspergillus nidulans (biA-1 sorA-2) germination time and hyphae growth rate as a function of ^{2}H NMR and ^{17}O NMR T_2 relaxation times of cellulose (c), sorbose (s), and orange serum broth solids with different s:c ratios at 25 °C [67].

systems water NMR mobility as described by T_2 relaxation time is key indicator to describe mold spore germination (both lag time and hyphae growth rate). More data and discussion can be found elsewhere [75].

In a liquid media system, growth of *S. aureus* was studied in brain heart infusion media. ^{17}O and ^{2}H NMR were applied to describe a model media with a presence of humectants such as NaCl, raffinose, and glycerol [64,65]. In relatively diluted, liquid media (over 0.90–0.99 a_w range with T_2 in ms range), the most "bound" water exhibited correlation time in ∼10 ps range (highly mobile and free), hence the bacterial growth was found to be far less dependent on the water mobility but rather on the quantity of bound water (10–30% of the water was considered perturbed or bound) [70]. Using a model assuming two-state, fast exchange with anisotropic, two correlation time for bound water [76–79]. In this case, a_w has been consistently shown to be a describing parameter governing the bacterial activity not because of the presence of bound water but rather an osmotic effect. More on this topic has been described [75].

This model assumes the existence of different water populations (anisotropically and isotropically reorienting) and calculates more specific dynamic molecular mobility parameters such as correlation time (^{17}O τ^{s}_{bw}) of the different water populations and the amount of bound water (^{17}O P_w). These physicochemical properties of the media can be used to describe the microbial media activity [70,75].

A few promising studies address microbial response in relation to translational water mobility parameters [80–82]. Moreover, ^{1}H solid-state NMR has been applied to microbial survival study in solid (glassy) systems [64,69]. This is described in more details elsewhere [75].

In summary, it has been suggested that microbial response depends highly on the dynamic properties of the water present in the environment. The study on the molecular dynamic properties of water in culture media for microorganisms could provide additional descriptor of water availability that may potentially become a tool to understand, predict, and modulate the microbial response. This may lead to an innovative means to better control microbial food safety and microbial food biotechnological developments.

Concluding Remarks

Advanced knowledge in Food Science in the future can be accomplished from fundamental understanding of food components and their interactions. The challenge of understanding molecular origins of complex systems, such as food, requires more sophisticated approaches. Applications of advanced methods such as NMR to study and solve Food Science problems can lead to better understanding at a molecular level in areas, such as encapsulation, mechanical strength, phase transition, diffusion, and non-invasive imaging. With new development in NMR together with many other rapidly emerging analytical advances, future discovery in food science can be indeed quite exciting.

References

1. Belton PS. In: GA Web, PS Belton, MJ McCarthy (Eds). Annual Reports on NMR Spectroscopy, Vol. 31. Academic Press: London, 1995, p 1.
2. Cornejo F, Chinachoti P. In: PS Belton, AM Gil, GA Webb, D Rutledge (Eds). Magnetic Resonance in Food Science: Latest Development. The Royal Society of Chemistry: Cambridge, 2003, p 25.
3. Finley JW, Schmidt SJ, Serianni AS (Eds). NMR Applications in Biopolymers. Plenum Press: New York, 1990.
4. Belton PS, Delgadillo I, Gill AM, Webb GA (Eds). Magnetic Resonance in Food Science. The Royal Society of Chemistry: Cambridge, 1995.
5. Belton PS, Hills BP, Webb GA (Eds). Advances in Magnetic Resonance in Food Science. The Royal Society of Chemistry: Cambridge, 1999.
6. Belton PS, Gil AM, Webb GA, Rutledge D (Eds). Magnetic Resonance in Food Science: Latest Development. The Royal Society of Chemistry: Cambridge, 2003.
7. Hills B. Magnetic Resonance Imaging in Food Science. John Wiley & Sons: New York, 1998.
8. Richardson SJ, Steinberg MP. In: LB Rockland, LR Beuchat (Eds). Water Activity: Theory and Applications to Food. Marcel Dekker: New York, 1987, p 235.
9. Belton P. Comments Agric. Food Chem. 1990;2:179.
10. Hills B. Mol. Phys. 1992;76:509.
11. Koening S, Bryant R, Hallenga K, Jacob G. Biochemistry 1978;17:4348.
12. Shirley W, Bryant R. J. Amer. Chem. Soc. 1982;104:2910.
13. Halle B, Wennestrom H. J. Phys. Chem. 1981;75:1928.
14. Schmidt SJ, Lai HM. In: H Levine, L Slade (Eds). Water Relationships in Foods. Plenum Press: New York, 1991, p 405.
15. Colquhoun IJ, Goodfellow BJ. In: RH Wilson (Ed). Spectroscopic Techniques for Food Analysis. VCH Publishers: New York, 1994, p 87.
16. Smith ICP, Mantsch HH. In: GC Levy (Ed). NMR Spectroscopy: New Methods and Applications, Vol. 19. Syracuse University: Syracuse, NY, 1981, p 97.
17. Richardson SJ, Baianu IC, Steinberg MP. Starke 1987;39:302.
18. Richardson SJ, Baianu IC, Steinberg MP. J. Agric. Food Chem. 1986;34:17.
19. Richardson SJ, Baianu IC, Steinberg MP. J. Food Sci. 1987;52:806.
20. Belton PS, Ring SG, Botham RL, Hills BP. Mol. Phys. 1991;72:1123.
21. Packer K. Phil. Trans. R. Soc. 1977;278:59.
22. Hills BP. Mol. Phys. 1991;72:1099.
23. Belton PS. J. Phys. Chem. 1995;99:17061.
24. Kroeker RM, Henkelman RM. J. Magn. Reson. 1986;69:218.
25. Belton PS, Hills BP. Mol. Phys. 1987;61:999.
26. Hills BP, Takasc SC, Belton PS. Mol. Phys. 1989;67:1309.
27. Belton PS, Hills BP, Raimbaud ER. Mol. Phys. 1988;63:725.
28. Hills BP, Takacs SF, Belton PS. Mol. Phys. 1989;67:919.
29. Ruan RR, Chen PL. Water in Foods and Biological Materials: A Nuclear Magnetic Resonance Approach. Technomic Publishing Company, Inc.: Lancaster, PA, 1999.
30. Whittall KP, MacKay AL,.J. Food Technol. 1989;5:65.
31. Provencher SW. Comput. Phys. Comm. 1982;27:213.
32. Provencher SW. Comput. Phys. Comm. 1982;27:229.
33. Zimmerman JR, Brittin WE. J. Phys. Chem. 1957;61:1328.
34. Lillford PJ, Clark AH, Jones DV. In: SP Rowland (Ed). Water in Polymers. American Chemical Society: Washington, DC, 1980, p 177.
35. Newcomb CH, Graham SJ, Bronskill MJ. J. Magn. Reson. 1990;90:279.
36. Menon RS, Allen PS. J. Magn. Reson. 1991;86:214.
37. Araujo CD, MacKay AL, Hailey JRT, Whittall KP, Le H. Wood Sci. Technol. 1992;26:101.
38. Tellier C, Mariette F, Guillement J, Marchal P. J. Agric. Food Chem. 1993;41:2259.
39. Tang HR, Goddward J,Hills BP. Carbohydr. Polym. 2000;43:375.
40. Tang HR, Brun A, Hills BP. Carbohydr. Polym. 2001;46:7.
41. Chatakanonda P. Water and Strach Chain Mobility in Cassava Starch as Monitored by NMR-Effects of Heat-Moisture Treatments, Growth Conditions and Harvest Time. Doctoral dissertation. Department of Food Science, University of Massachusetts, Amherst, MA, 203.
42. Wegmann J, Krucker M, Bachmann S, Fischer G, Zeeb D, Lienau A, Glaser T, Runge F, Lüddecke E, Albert K. J. Agric. Food Chem. 2002;50:7510.
43. Calucci L, Forte C, Galleschi L, Geppi M., Ghiringhelli S. ^{13}C and ^{1}H solid state NMR investigation of hydration effects on gluten dynamics. Int. J. Biol. Macromol. 2003;32:179.
44. Li S, Dickinson LC, Chinachoti P. Cereal Chem. 1996; 73:736.
45. Baik M-Y, Dickinson LC, Chinachoti P. J. Agric. Food Chem. 2003;51:1242.
46. Pines A, Gibby MG, Waugh JS. J. Chem. Phys. 1973;59:569.
47. Vodovotz Y. Aging of starch and bread as studied by DSC, DMA, NMR and confocal microscopy. Doctoral dissertation. University of Massachusetts, Amherst, MA, 1996.
48. Tonelli AE. NMR Spectroscopy and Polymer Microstructure: The Conformational Connection. VCH Publishers, Inc.: New York, 1989.
49. Blanshard JMV, Jaroszkiewicz EM, Gidley MJ. In: JW Finley, SJ Schmidt, AS Serianni (Eds). NMR Applications in Biopolymers. ACS Symposium Series. Plenum Pub. Corp.: New York, 1990, p 155.
50. Veregin RP, Fyfe CA, Marchessault RH, Taylor MG. Macromolecules. 1986;19:1030.
51. Vodovotz Y, Chinachoti P. In: PS Belton, BP Hills, GAWebb (Eds). Applications of Magnetic Resonance to Food Science. The Royal Society of Chemistry: Cambridge, 1999, p 185.
52. Kalichevsky MT, Jaroszkiewicz EM, Ablett S, Blanshard JMV, Lillford PJ. Carbohyd. Polym. 1992;18:77.

53. Gidley MJ, Bociek SM. J. Am. Chem. Soc. 1988;110:3820.
54. Schafer J, Stejskal EO, Buchdahl R. Macromolecules. 1977;10:384.
55. Ablett S, Darke AH, Izzard MJ, Lillford PJ. In: JMV Blanshard, PJ Lillford (Eds). The Glassy State in Foods. University Press: Nottingham, 1993.
56. Grad J, Bryant RG. J. Magn. Reson. 1990;90:1.
57. Vodovotz Y, Dickenson LC, Chinachoti P. J. Agric. Food Chem. 2000;48:4948.
58. Wu JY, Bryant RG, Eads TM. J. Agric. Food Chem. 1992; 40:449.
59. Tessier JJ, Dillon N, Carpenter A, Hall LD. J. Magn. Reson., Series B, 1995;107:138.
60. Van Duynhoven JPM, Kulik AS,Jonker HRA, Haverkamp J. Carbohydr. Polym. 1999;40:211.
61. Wu JY, Eads TM. Carbohydr. Polym. 1993;20:51.
62. Vodovotz Y, Vittadini E, Sachleben JR. Carbohyd. Res. 2002;337:147.
63. Lavoie J, Chinachoti P. In: PS Belton, I Delgadillo, AM Gil, GA Webb (Eds). Magnetic Resonance in Food Science. The Royal Society of Chemistry: Cambridge, 1995, p 33.
64. Lavoie JP. Cellular response of *Staphylococcus aureus* as related to NMR detected water and system mobility, water activity and media formulation. PhD dissertation. Department of Food Science, University of Massachusetts, Amherst, MA, 1998.
65. Lavoie JP, Labbe RG, Chinachoti P. J. Food Sci. 1997;62:861.
66. Pham X. Role of water mobility on germination and growth of *Aspergillus nidulans*. Masters Thesis. Department of Food Science, University of Massachusetts, Amherst, MA, 1998.
67. Pham X, Vittadini E, Levin RE, Chinachoti P. J. Agric. Food Chem. 1999;47:4976.
68. Vittadini E, Chinachoti P. Int. J. Food Sci. Technol. 2003; 38:841.
69. Vittadini E, Dickinson LC, Chinachoti P. Carbohyd. Polym. 2002;49:261.
70. Vittadini E, Schmidt SJ, Chinachoti P. Molecul. Phys. 2001;99:1641.
71. Hills BP, Buff C, Wright KM, Sutcliffe LH, Ridge Y. Int. J. Food Microbiol. 2001;68:187.
72. Hills BP, Arnould L, Bossu C, Ridge YP. Int. J. Food Microbiol. 2001;66:163.
73. Chinachoti P. Food Technol. 1993;1:134.
74. Lang K. Physical, chemical and microbiological characteristics of polymer and solute bound water. PhD dissertation. University of Illinois at Urbana-Champaign, 1980.
75. Chinachoti P, Vittadini E. In: MP Buera, PJ Lillford, J Welti-Chanes, HR Corti (Eds). Water Properties Related to the Technology and Stability of Food, Pharmaceutical and Biological Materials. CRC Press: Boca Raton, FL, 2006.
76. Halle B, Wennestrom H. J. Phys. Chem.1981;75:1928.
77. Belton PS, Ring SG, Botham RL, Hills BP. Mol. Phys. 1991;72:123.
78. Hills BP. Mol. Phys.1991;72:1099.
79. Colquhoun IJ, Goodfellow BJ. In: RH Wilson (Ed). Spectroscopic Techniques for Food Analysis. VCH Publishers: New York, 1994, p 87.
80. Hills BP, Manning CE, Ridge Y, Brocklehurst T. J. Sci. Food Agric. 1996;71:185.
81. Hills BP, Manning CE, Ridge Y, Brocklehurst T. Int. J. of Food Microb. 1997;36:187.
82. Kou Y, Molitor PF, Schmidt SJ. J. Food Sci. 1999;64:950.

Diffusion and Relaxation in Gels

Joachim Götz and Ruth Hinrichs

Lehrstuhl für Lebensmittelverpackungstechnik, Technische Universität München, Weihenstephaner Steig 22, 85350 Freising, Germany

Introduction

Foods are often heterogeneous mixtures of materials with complicated material behavior and structure properties. Redistribution of constituents (water, fat, solvents) and structural changes including phase transitions are induced by many processing operations including storage. Water, especially, acts as a transportation medium, reacting agent, intermolecular link and textural medium. In food process technology, both the integral and local moisture contents, the type of water binding, and the mobility of water molecules (free, retained, adsorbed) are relevant with regard to the yield, sensory evaluation, stability (physical and microbiological), the texture, and flow behavior (diffusive/convective) in many technical applications (e.g. thermal treating, solid–fluid separation, ad-/desorption, de-/mixing, de-/agglomeration). It is, therefore, desirable to obtain deeper insight into the microstructure of food systems in order to forgo time-intensive trial-and-error in food structuring or production like the common practice to apply simple empirical tests. The overall objective of this review is to elucidate the possibilities to characterize the structure of gels with respect to (a) the pore system (generally: solid matrix) probed by the diffusion behavior of the corresponding solvents and (b) the water-binding or, macroscopically, the water-holding capacity (WHC).

Diffusion

Diffusive flow processes in solid systems are mainly influenced by the pore system architecture, chemical composition of the solid surface and resulting solid–fluid interactions. The molecular diffusion of constituents in gels allows one to analyze the transport phenomena of confined fluids [1] [de-/hydration, fat bloom (chocolate), syneresis (dairy products, mustard), and controlled drug –release] and fluid–solid interactions.

Molecular Diffusion in Disperse Systems

NMR PFG techniques allow the determination of self-diffusion coefficients D_S as a function of the effective diffusion time Δ and to calculate the mean distance traveled by the diffusing molecules (pure liquids or fluids confined in gels) during the diffusion time [2–4]. In dilute solutions and gels with low material-specific solid concentration the self-diffusion coefficient D_S is independent of the diffusion time [5,6]. D_S is reduced compared to pure water due to obstruction and hydration of the dissolved molecules (hydrocolloids, proteins) or simply solutes (salts, sugars). This is in agreement with Stokes–Einstein for the Fickian diffusion coefficient D_F

$$D_F = \frac{kT}{6\pi a}\frac{1}{\eta}, \qquad (1)$$

where a is the radius of a spherical particle and η the dynamic viscosity of the solvent. According to the proportionality between D_F and D_S (Equation 1) an increased viscosity of the serum causes a reduction of D_F and D_S (reviews [7,8] of NMR and other methods for self/inter-diffusion). A dependence of $D_S(t)$ on t in diffusion experiments indicates that the diffusion is restricted due to physical barriers, e.g. network systems in gels (collagen [9], gellan gum [10], and starch [11]). NMR PFG allows the observation of diffusion in anisotropic structures or anisotropic diffusion.

Characterization of Pore Systems

In disperse systems the diffusing particles can be used for probing the microstructure with diffusion [6,12,13]. Characteristic lengths inside the solid matrix of a few micrometers are accessible. These spatial resolutions cannot be realized using MRI methods. NMR diffusion experiments provide information concerning fluid saturation or the existence of fluid layers adsorbed at the solid matrix [14]. It can, furthermore, be differentiated between mass transport in the gas phase, the fluid –phase, or through the solid material. A special version of PGSE experiments (diffusion diffraction, q-space microscopy, or imaging [15–18]) has proven its capability to characterize connected porous systems. Porous systems often have fractal properties [19]. Self-diffusion processes are sensitive to the dimensional character of the path of diffusing particles due to the microstructure. For the free diffusion, the

Graham A. Webb (ed.), Modern Magnetic Resonance, 1713–1719.

© 2008 *Springer.*

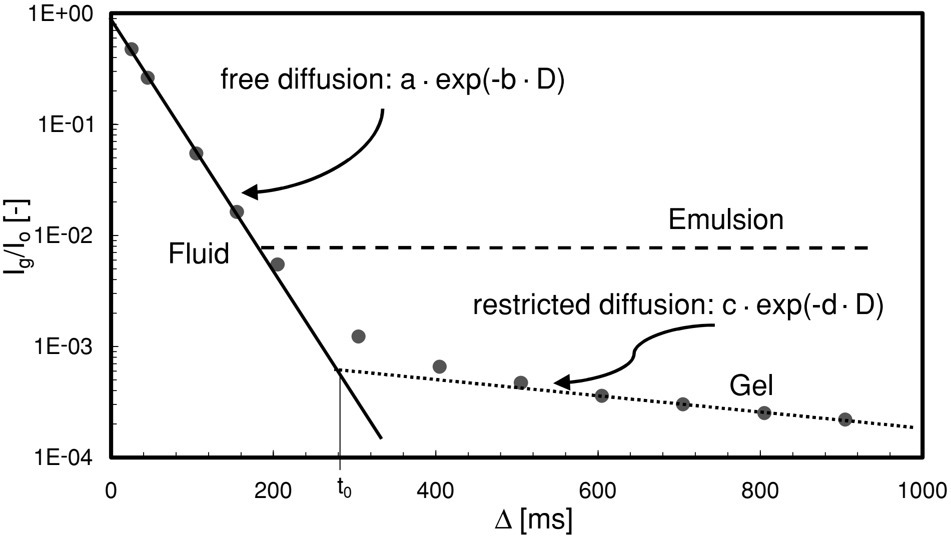

Fig. 1. Schematic presentation of the ratio of the spin-echo amplitudes I_g/I_0 for a fluid with free diffusion, an emulsion with monodisperse drops (matrix signal suppressed) and a network with free ($D_{Sf} \sim b$) diffusion (short Δ) and restricted ($D_{Sr} \sim d$) diffusion (long Δ).

mean square distance from the origin at $t > 0$ is

$$\langle r^2 \rangle \sim D_{Sf} t. \tag{2}$$

For restricted diffusion it holds [20]

$$\langle r^2 \rangle \sim D_{Sf} t^{2/(2+\theta)}. \tag{3}$$

The θ effective dimensionality of the random walk vanishes for Brownian motion [3,14,21]. For sufficiently long times, the mean square distance $\langle r^2 \rangle$ becomes linear as a function of time

$$\langle r^2 \rangle \sim D_{Sr} t. \tag{4}$$

The self-diffusion coefficient D_{Sr} for restricted diffusion is also called effective diffusion coefficient D_{eff} for long times. The time dependence of the self-diffusion coefficient contains information about the structure of porous media [18,21–24]: (a) characteristic dimensions of the gel structure (critical pore radius r_c), (b) free diffusion for short times, dependent on the pore –structure, and the pore fluid, D_{Sf}, and (c), if different from case (b), restricted diffusion behavior for long time D_{Sr}. D_{Sr} is a measure for the macroscopic permeability of the pore structure, D_{Sf} characterizes the viscosity of the serum [8], generally smaller than that of water due to solutes. I_g is the signal (e.g. PGSE or PGTSE), with applied gradient magnetic field $\mathbf{g}$, I_0 is the corresponding signal without gradient. The ratio of the spin-echo amplitude with I_g and without applied gradient field I_0 [2,3] is given by

$$I_g/I_0 = \exp\{-\gamma^2 \delta^2 g^2 [\Delta - (1/3)\delta] D_S\}. \tag{5}$$

Figure 1 shows the ratio of the spin-echo amplitudes with and without gradient, I_g/I_0, (a) for a fluid with free diffusion, (b) an emulsion with monodisperse drops (the signal of the matrix has been suppressed), and (c) a gel-network with free diffusion for short times and restricted diffusion for long times. Figure 1 illustrates the method of how to derive the self-diffusion coefficients at free D_{Sf} (~b: slope for short Δ) and restricted D_{Sr} (~slope d: for long Δ) diffusion and of the critical pore radius r_c of the matrix ($\sim[D_{Sf} t_0]^{0.5}$) with the evolution of I_g/I_0. The intersection point of both straight lines, which are asymptotes for the short- and long-time diffusion behavior, defines the critical time t_0. t_0 depends on the characteristic length scales of the pore system and D_{Sf}. The critical pore radius r_c (spherical cavities) is given by [4,25]

$$r_c = [5 D_{Sf} t_0]^{0.5}. \tag{6}$$

Besides D_{Sf}, D_{Sr}, and r_c, further parameters characterizing the structure the pore system can be derived from D_S as a function of Δ: the tortuosity $T = D_{Sf}/D_{Sr}$ [21] or $[(1-\phi) D_{Sf}/D_{Sr}]^{0.5}$ (ϕ: mean porosity) [26], the surface-to-pore-volume ratio S/V, derived from this, the pore size distribution [23], characteristic lengths r_{ch} [27], and the permeability [28]. Many disperse systems are not only heterogeneous at microscopic, but also at meso-/macroscopic lengths. In some cases, the heterogeneities are caused by phase separation (creaming up) including syneresis (dairy products, mustard), mechanical loading, swelling, the use of fillers/fibers (yoghurts) or process-specific heterogeneities like different morphology of core and shell zones (chocolate, dairy products). Hence, it is desirable to infer structural data (T, S/V), which are spatially resolved by combining MRI and dynamic imaging methods (diffusion/flow, ENMR), especially, if the characteristic lengths are below the spatial resolution of common MRI techniques [29].

PFG NMR allows one to quantify the effect of the composition, the pH value, the concentration of ions and sugars, the denaturation fraction of proteins and the impact of the processing/process conditions on the structure in gels [30,31]. In dairy products, D_{Sf}, D_{Sr}, and r_{c} do not seem to correlate with one another. It is plausible to assume that r_{c}, like the average drop radius of water in w/o emulsions, is relevant for the microbiological stability of the gel. The diffusion coefficient of the serum D_{Sf} and, even to a higher extent, the permeability D_{Sr} presumably correlate with the texture, the sensorial (e.g. sandy), the filtration/washing and syneresis behavior of gels. Furthermore, it is possible to observe structural changes due to sol–gel transitions (hydrocolloids, denaturation), their temporal evolution, dependence on denaturation temperature/duration/fraction or ageing-processes during storage (syneresis) [32]. Combining PFG and T_2 two fractions of water (bound to collagen or retained in channels traversing collagen fibers) were observed in collagen gels [9]. D_{S} of aqueous proteins systems increases with temperature and water content [33]. Analogous experiments have been performed in starch/dextran [32,34,35] or casein systems [36], cheese [37], curdlan [38], and gellan gum [39]. The correlation between D_{Sf}, D_{Sr}, and r_{c} characterizes different sol/gel states. A review of diffusion experiments in disperse media (emulsions, porous foods) is given in Ref. [8].

Relaxation

TD-NMR [40,41] are applied in food technology in order to (a) characterize the food composition, the chemical structure/physical state (solid/liquid, crystalline/amorphous), or molecular dynamics/structural changes caused by processing [42–44] and (b) derive correlations between NMR parameters and macroscopic quality factors applicable as tools for process/quality control (on-line process NMR spectroscopy). Molecular/microscopic (molecular mass [45]) and macroscopic properties (η [45,46], permeability [47]) can be obtained (averaged, partially resolved).

Ad (a): Structural Characterisation

The interpretation of relaxation time data for an unambiguous characterization of different physical states of water or other components present in heterogeneous systems, derived from spectroscopic data [48–50], has not been clarified to its full extent due to chemical [51,52], diffusion [53,54], or spin quantum exchange [55] processes. The relaxation in aqueous systems has been studied by ^{1}H, ^{2}H [56,57], ^{13}C [58], and ^{17}O [59,60] NMR. ^{1}H NMR is applied in the majority of the experiments because of the wide spreading of ^{1}H spectrometers and the possibility to analyze without preparation. ^{2}H and ^{17}O NMR, however, provide many fundamental data on water relaxation mechanisms in heterogeneous media [5,61–63].

T_1 and T_2 allow one to distinguish between free (no interaction with solid particles or dissolved molecules) and immobilized (crystallization, hydration, or other chemically/physically bound) water. Assuming models for exchange processes (chemical, diffusion, spin quantum), the relaxation times and fractions of the corresponding water types can principally be derived. Usually, up to four different groups of spins (two correlated with water, two with the dissolved macromolecules) can be distinguished in protein and polysaccharide solutions [5,64]. Hydroxyl or amino protons can exchange with water protons, other protons are not able to exchange. Combining ^{1}H, ^{23}Na, ^{87}Rb, and ^{133}Cs NMR and adding the corresponding cations three water phases (free bulk, strongly interacting with κ-carrageenan, and weakly bound) were detected in κ-carrageenan gels [65]. For one-phase relaxation the observable T_2 relaxation times $T_{2\mathrm{obs}}$ (analogous T_1) can be used as characteristic T_2. Reviews of empirical or theoretically established models of the correlation between the concentration of dissolved molecules and the observed or the average T_2 of solutions are given by [8,83]. Thus, conclusions concerning the influence of macromolecules and their concentrations on the existence of multiple water phases $T_{2,i}$ and their fractions $d_{2,i}$ can be drawn [5,43,66].

Structural Changes Including Phase Transitions and Denaturation

Many foods and food components are thermally treated (pasteurization, sterilization, rectification, distillation, drying, freezing, freeze drying, and freeze concentrating) [67]. The variation of the temperature generally causes changing NMR parameters (relaxation times, spectra, or D_{S}). For simple fluids like water T_1, T_2 and D_{S} increase with the temperature. High-resolution NMR is an independent method besides X-ray analysis for the characterization of protein structures (denaturation, pH) [68–70]. Investigations concerning the heat treatment of proteins by means of LR-NMR (T_1, T_2, D_{S}) have been performed

[71–76] after and not during the thermal treatment (at temperatures below the denaturation temperature in order to prevent further changes) varying the process temperature, the pH value and the concentrations of protein, ions and sugars. Reversible (increased T_2: higher mobility at higher temperature) and irreversible transformations (decreased T_2: aggregation) can thereby not be differentiated. This procedure provides only reaction kinetic information using a series of tests with different samples. This is a great disadvantage for natural substances due to their compositional variety. In aqueous protein systems generally four phases can be distinguished. There are both proteins whose $T_{2,i}$ of the phases with higher mobility are increased due to the thermal denaturation and proteins with $T_{2,i}$ reduced after the thermal denaturation, whereby only two phases have been detected [72]. The dependence between T_1 or T_2 and the temperature (fixed treatment duration) and the T_2/T_1 ratio indicate structural changes (sol–gel transitions, freezing damage [73]). Online NMR-measurements offer possibility to study denaturation the during the thermal treatment (average time $T_{2\mathrm{m}}$, relaxation times of the single phases $T_{2,i}$, and fractions d_i). The advantage is that several measurements can be performed with the same sample (without interrupting the thermal treatment and/or continuing with another sample), thus achieving higher accuracies of measurements. The reaction orders and rate constant of the participating reactions can be derived. If the relaxation data vary after thermal/pressure treatments, reversible and irreversible structural changes can be distinguished.

WHC Including *Sol–Gel Transitions and Syneresis*

In food technology, the bonding type and mobility of water molecules are relevant with regard to the yield, sensory evaluation, stability, texture, flow behavior, and processing. There are many measuring methods available to characterize the WHC of a mixture [77–80]; many techniques originally developed in practice, provide quick, and easy indications concerning the studied material. Most of the available methods usually provide differing results, which are not absolute values and are, therefore, generally not comparable or transferable to technological processes. These difficulties are due to (i) different measuring principles and experimental conditions and (ii) the frequent destruction/modification of the structure due to the measuring procedure (centrifugation). A precise characterization of the WHC for food constituents like proteins and hydrocolloids is required for a reliable design of products and processes. For different materials, the relationship between the WHC and the other macroscopic (flow/deformation/sensoryl/syneresis behavior) and microscopic properties (fine stranded/particulate network) is not identical, thus complicating a practicable definition of the WHC. Rennet acid gels, for example, have a coarser network with thicker protein strings than pure acid gels [81]. Rennet gels are firmer, with a lower WHC. As mentioned before, the definition of water types depends on the applied measuring technique. The fraction of bound water is defined in rheology as bound physically/chemically at solid surfaces or retained in the interior of solid particles. With regard to NMR water is bound, if it interacts with solid material or if the water molecules are in sufficiently small cavities. For free water it is not of any importance, if fluid molecules are inside or outside of solid particles. Another difficulty is that disperse media usually have different microstructures during rheological (flowing) and NMR experiments (at rest), apart from Rheo-NMR [82] including flow experiments.

In order to differentiate free water, which can be removed through capillaries (non-stirred) or out of the pore system (stirred), from water retained in micelles/agglomerates, the special setup was developed [8,83–85]. The sample is filled into an NMR glass closed at the bottom with a PTFE-thread. T_2 experiments are performed at the original sample and afterward at the sample being washed with D_2O. Between sample and thread is a filter membrane. The mobile free water in the sample is substituted by D_2O non-detectable by ^{1}H NMR. Exchange processes between water and OH/NH/SH groups are neglected. Thus, with the help of the washout test, immobilized, retained free and mobile free water can be distinguished. The fraction of water/serum that contributes to phase-separation phenomena like syneresis possibly correlates with the phase distribution and the amount of the water, which can be washed out. If the water content is known, it is possible to define the WHC (physically/chemically bound plus water retained in pores) with the fraction p_r of washable water

$$\mathrm{WHC}_{\mathrm{NMR}} = \frac{m_{\mathrm{Wnw}}}{m_{\mathrm{S}}} = \frac{m_{\mathrm{Wnw}}}{m_{\mathrm{W}}}\frac{m_{\mathrm{W}}}{m_{\mathrm{S}}} = p_r F, \qquad (7)$$

where m_{Wnw} is the mass of non-washable water, m_{W} the total mass of water, m_{S} the dry mass, p_r the $m_{\mathrm{Wnw}}/m_{\mathrm{W}}$, averaged over all phases, and F the water content of a gel (w/w). It is remarkable that not only water of the phase with the highest mobility, but also of phases with reduced mobility (T_2) is washable. This means that the molecular mobility characterized by T_2 and the washability (Equation 7) are different, but complementary characteristic gel features. The washout test was used to study the influence of the recipe and processing on the evolution of the WHC and p_r of yoghurts (fermented in glasses or cut out) [31].

Hydrocolloids

Hydrocolloids are used (e.g. jellied and dairy products, cocoa, ice-cream, marmalade, sausages, convenience food) as thickeners, gelling agents, or stabilizers. It is to incorporate water into foods (higher yield and lower fat content). Many functional properties of proteins in foods are attributed to interactions with water and other food constituents [79]. Many hydrocolloids exhibit hysteresis of their TD-NMR or rheological parameters for cyclic temperature variations [31,86,87] and a strong pH dependence [88]. Polymer networks are usually thermoreversible due to the H-bridges breaking up at sufficiently high temperatures. The influence of temperature and gelatine concentration on the structure of gelatine solutions was studied with T_1 [89] and T_2 [90]. The water relaxation in biopolymer systems was modeled assuming proton exchange cross-relaxation [91,92]. The mean T_2 relaxation times in gelatine systems increases dramatically at the temperature-induced sol/gel transition. Chemical/diffusive exchange in water/gelatine systems was studied by variation of the CPMG pulse spacing [93]. ^{1}H and ^{23}Na NMR (T_1, T_2) enable one to differentiate up to four water phases in aqueous gelatine gels [94,95]. Properties of starch relevant for food technology are the swelling (temperature, moisture: ^{1}H: T_1, T_2; ^{2}H: T_1, T_2, spectra [96,97]), plastisication/gelatinization (^{1}H T_2, ^{2}H spectra [98]), the degree of polymerization, glass transitions (T_1, T_2, spectra [99]), retrogradation (T_1, T_2 [100]), conformations of dissolved starch molecules like multiple/double-helices or eggbox [86], fraction of crystallinity (CP-MAS [101], ^{13}C [66]), the ratio of amylose/amylopectin [102], water content (T_1, T_2 [89,99,103]), ^{2}H spectra [104], and storage behavior (T_2, MRI [105]). After a heat treatment the carrageenan molecules reveal a disordered coil form. When reducing the temperature, the conformation of κ- and ι-carrageenan changes to ordered helical structure (e.g. double-helices) and aggregates of helices coupled to gelation [87]. Various parameters [concentration, temperature, type (T_1, T_2 [86,89]), molecular mass (^{1}H spectra [105]), composition of carrageenan molecules (κ-, ι-units: ^{1}H, ^{13}C spectra [107]), ionic type/content [87]/composition [108]] have a strong impact on macroscopic (texture, flow/sensorial behavior, sol–gel transition) and microscopic properties (T_1, T_2, spectra). Gelling (hysteresis) and only viscosity-increasing carrageenan types (λ) are differentiable by the temperature dependence of the $T_{2,i}$ and d_i [8,31]. This provides a deeper insight into the microstructure than $T_{2\mathrm{m}}$ alone [86]. $T_{2\mathrm{m}}$ for the solutions correlates with their voluminosity (i.e. immobilized water). The voluminosity in gels is not determinable with rheology yet.

Ad (b): Correlations

The motivation to derive correlations between NMR and material properties is that these correlations are ideal to determine industrially relevant quantities (material process parameters) by partly methodologically/apparatively more comfortable, non-destructive, often less time-consuming and on-line capable NMR methods (no trace analysis). This is a necessary prerequisite for an effective process/quality control [109–112]. Continuous- and stop-flow process NMR spectroscopy are realized [113]. The continuous-flow requires usually premagnetization for a complete polarization of the sample. The sensor is integrated into a pipe, belts, or chutes. Applications are the monitoring of the fermentation (yoghurts) [83], mashing [46], and cooking (rice species, shelling/polishing process: Götz *et al.*, 2004).

Besides D_S determined by PFG NMR, relaxation times are another independent approach to characterize the gel structure and to study the dynamics of de-/hydration of fluids. The relaxation times of fluids in gels (partial/completely saturated) are generally reduced compared to the free and bulk fluid due to interactions between liquid molecules and the liquid–solid interface. In many cases, a simple two-site model is used to interpret the observed enhanced relaxation rates in gels [48,53,114], partly a homogeneous water layer is assumed at the solid surface [24,115]. A practicable approach based on T_1 is the assumption of rapid exchange of liquid molecules between (i) the zone at the solid surface (interactions between the liquid and the solid material), and (ii) the molecules in the bulk. The change of T_1 (porous medium) compared to $T_{1\mathrm{f}}$ in the bulk phase is used to derive the fraction f of the fluid interacting with the solid. In order to characterize the density of reactive surface sites in a fluid-saturated porous system, the influence of ion concentrations from different salts on T_1 was measured [28]. Fluid molecules near solid walls are exposed to relaxation mechanisms different from those in the bulk fluid. Various models have been developed to derive pore size distributions from relaxation measurements. Due to the complex interactions, formalisms generally valid for all porous media have not been developed yet [116]. In spite of these ambiguities, relaxation measurements enable one to characterize individual pore systems. Based on a two-site model, the mean relaxation time T_1 is related to the pore radius $r_\mathrm{p} = 2V/S$. Thus, it is possible to derive the pore size distribution from the T_1 frequency distribution [118–120]. If the gel structures do not significantly alter in the temperature regime above and below the freezing phase transition of the fluid, measurements are performed at temperatures above and below the freezing phase transition. While the bulk fluid is frozen, a non-frozen fluid layer exists at the solid surface due to the different and often incommensurable crystal structures of the fluid adsorbate and the surface structure. The fluid molecules in the adsorbed layer are, even in the frozen state of the bulk fluid, surprisingly mobile (translationally along the surface).

In order to obtain information concerning the size distribution of crystallites in frozen gels the size distribution of pores in freeze-dried starchgels was determined by T_2

relaxometry using acetone (no matrix collapse) instead of water [121,122]. Besides the possibility to calculate the gel permeability (T, S/V) [23,28,123] with empirical models (permeability porosity ϕ) [124], permeabilities by correlating T_1, T_2, $T_{1\rho}$, D_S, and ϕ are derived [125]. Further correlations between macroscopic properties (water activity, microbial stability/shelf-life, solution-rate of spray-dried powders, caking behavior of powders, drug release in proteineous matrices, and sensory texture) or capillary/pressure curves and NMR data are given in Ref. [8].

References

1. Le Bihan D. In: DM Grant, RK Harris (Eds). Encyclopedia of NMR, Vol. 3. Wiley: Chichester, 1996, p 1645.
2. Stejskal EO, Tanner JE. J. Chem. Phys. 1965;41:288.
3. Callaghan PT. Principles of NMR Microscopy. Oxford University Press: Oxford, 1991.
4. Kärger J, Fleischer G. TRAC. 1994;12:145.
5. Colquhoun IJ, Goodfellow BJ. In: RH Wilson (Ed). Spectroscopic Techniques for Food Analysis. John Wiley & Sons: New York, 1994, p 87.
6. Hills BP. Magnetic Resonance Imaging in Food Science. John Wiley & Sons: New York, 1998.
7. Bartusseck I. NMR-Untersuchungen von Diffusionsvorgängen in Mehrkomponentensystemen. RWTH, Diss., Aachen, 2002.
8. Götz J. Applications of NMR to Food and Model Systems in Process Engineering. Habilitation, http://tumb1.biblio.tu-muenchen.de/publ/diss/ww/2004/goetz. html, TUM, 2004.
9. Knauss R, Fleischer G, Gründer W, Kärger J, Werner A. Magn. Reson. Med. 1996;36:241.
10. Ohtsuka A, Watanabe T. Carbohydr. Polym. 1996;30:135.
11. Watanabe H, Fukuoka M. In: TL Barsby, AM Donald, PJ Frazier (Eds). Starch—Advances in Structure and Function. RSC: Cambridge, 2001, p 53.
12. Holz M. Nachr. Chem. Tech. Lab. 1986;34:858.
13. Velan SS, Chandrakumar N. J. Magn. Reson. 1996;123:122.
14. Appel M, Fleischer G, Kärger J, Fujara F, Siegel S. Europhys. Lett. 1996;34:483.
15. Callaghan PT. J. Magn. Reson. Ser. A. 1995;113:53.
16. Packer KJ. In: DM Grant, RK Harris (Eds). Encyclopedia of NMR, Vol. 3. Wiley Press: Chichester, 1996, p 1615.
17. Johnson CS. In: DM Grant, RK Harris (Eds). Encyclopedia of NMR, Vol. 3. Wiley Press: Chichester, 1996, p 1626.
18. Mitra PP. Phys. A. 1997;241:122.
19. Mandelbrot BB. The Fractal Geometry of Nature. Freemann, San Francisco, 1982.
20. Banavar JR, Lipsicas M, Willemsen JF. Phys. Rev. B. 1985;32:6066.
21. Kärger J, Heitjens P, Haberlandt R (Eds). Diffusion in Condensed Matter. Vieweg: Wiesbaden, 1998.
22. Hallmann M, Unger KK, Appel M, Fleischer G, Kärger J. J. Phys. Chem. 1996;100:7729.
23. Latour LL, Kleinberg RL, Mitra PP, Sotak CH. J. Magn. Reson. Ser. A. 1995;112:83.
24. Watson AT, Chang CT. Prog. Nucl. Magn. Reson. Spectrosc. 1997;31:343.
25. Appel M, Fleischer G, Kärger J, Dieng AC, Riess G. Macromolecules. 1995;28:2345.
26. Epstein N. Chem. Eng. Sci. 1989;44:777.
27. Kärger J, Pfeifer H, Heink W. Adv. Magn. Res. 1988;12:1.
28. Frosch GP, Tillich JE, Haselmeier R, Holz M, Althaus E. Geothermics. 2000;29:671.
29. Tillich J. NMR-Methoden zum Studium von Struktur und Transport in porösen Medien. Uni., Diss., Karlsruhe, 2002.
30. Götz J, Zick K, Hinrichs R, Weisser H. Z. Lebensm. Unters. FA. 2004;218:323.
31. Hinrichs R, Götz J, Weisser H. Proc 2nd Int Workshop Eurofood's Water. Reims, 2002, Specif. Food Chem., 2003.
32. Ohtsuka A, Watanabe T, Suzuki T. Carbohydr. Polym. 1994;25:95.
33. Kimmich R, Klammler F, Skirda VD, Serebrennikova IA, Maklakov AI, Fatkulin N, Appl. Magn. Reson. 1993;4:425.
34. Farhat IA, Loisel E, Saez P, Derbyshire W, Blanshard JM. Int. J. Food Sci. Tech. 1997;32:377.
35. Kwak S, Viet MT, Lafleur M. J. Magn. Reson. 2003;162:198.
36. Mariette F, Topgaard D, Jönsson B, Söderman O. J. Agric. Food Chem. 2002;50:4295.
37. Métais A, Mariette F. J. Magn. Reson. 2003;165:265.
38. Kwak S, Lafleur M. Colloid Surface A. 2003;221:231.
39. Watanabe T, Ohtsuka A, Murase N, Barth P, Gersonde K. Magn. Reson. Med. 1996;35:697.
40. Belton PS. In: RH Wilson (Ed). Spectroscopic Techniques for Food Analysis. John Wiley & Sons: New York, 1994.
41. Alberti A, Belton PS, Gil AM. Ann. Rep. NMR Spectrom. 2002;47:111.
42. Belton PS. Prog. Biophys. Mol. Biol. 1994;61:61.
43. Cornillon P. Semin. Food Anal. 1998;3:235.
44. Pedersen HT, Ablett S, Martin DR, Mallett MJ, Engelsen SB. J. Magn. Reson. 2003;165:49.
45. Götz J, Altmann S, Weisser H. Proc. 1st Eur. Silicon Days, München, 2001.
46. Götz J, Schneider J, Först P, Weisser H. J. Am. Soc. Brewing Chem. 2003;61:37.
47. Watson AT, Chang CT. Prog. Nucl. Magn. Reson. Spectrosc. 1997;31:343.
48. Zimmerman JR, Brittin WE. J. Phys. Chem. 1957;61:1328.
49. Hills BP, Takacs S, Belton P. Food Chem. 1990;37:95.
50. Belton PS. Int. J. Biol. Macromol. 1997;21:81.
51. Carver JP, Richards RE. J. Magn. Reson. 1972;6:89.
52. Berliner LJ, Reuben J. Biological Magnetic Resonance. Plenum Press: New York, 1980.
53. Brownstein KR, Tarr CE. Phys. Rev. A. 1979;19:2446.
54. Belton PS, Hills BP. Mol. Phys. 1987;61:999.
55. Edzes H, Samulski E. J. Magn. Reson. 1987;31:202.
56. Hallenga K, Koenig SH. Biochemistry. 1976;15:4255.
57. T. Kumosinski F, Pessen H, Farrell HM. In: H Levine, L Slade (Eds). Water Relationships in Foods, Advances in Experimental Medicine and Biology, Vol. 302. Plenum Press: New York, 1991, p 541.
58. Cassin G, de Costa C, van Duynhoven J, Agterof WG. Langmuir. 1998;14:5757.
59. Halle B, Denisov VP, Venu K. In: LJ Krishna Berliner (Ed). Biological Magnetic Resonance, Vol. 17. Kluwer/Plenum Publishers: New York, 1999.

60. Mora-Gutierrez A, Kumosinski TF, Farrell HM. J. Agric. Food Chem. 1997;45:4545.
61. Ruan RR, Chen PL. Water in Foods and Biological Systems. A Nuclear Magnetic Approach. Technomic Publishing: Lancaster, 1998.
62. Belloque J, Ramos M. Trends Food Sci. Tech. 1999;10:313.
63. Nölting B. Protein Folding Kinetics, Springer, Berlin, 1999.
64. Nusser W. NMR-Untersuchungen zur molekularen Dynamik in Protein-Wasser-Systemen. Uni., Diss., Ulm, 1990.
65. Hikichi K. Polym. Gels Netw. 1993;1:19.
66. Gidley MJ, McArthur AJ, Darke AH, Ablett S. In: E Dickinson (Ed). New Physico-Chemical Techniques for the Characterisation of Complex Food Systems. Blackie Academic Professional: London, 1995, p 296.
67. Harz H-P. Untersuchungen zum Gefrierverhalten flüssiger Lebensmittel. Uni., Diss., Karlsruhe, 1987.
68. Jonas J, Jonas A. Annu. Rev. Biophys. Biomol. Struct. 1994;23:287.
69. Cavanagh J, Fairbrother WJ, Palmer AG, Skelton NJ. Protein NMR Spectroscopy, Principles and Practice. Academic Press: New York, 1996.
70. Hancock TJ, Hsu JT. Biotech. Prog. 1996;12:494.
71. Lambelet P, Berrocal R, Renevey F. J. Dairy Res. 1992;59:517.
72. Lambelet P, Ducret F, Leuba JL, Geoffroy M. J. Agric. Food Chem. 1991;39:287.
73. Lambelet P, Renevey F, Kaabi C, Raemy A. J. Food Sci. 1995;43:1462.
74. Hills BP, Takacs S, Belton P. Mol. Phys. 1989;67:919.
75. Barfod N. Proc. Conference, Rebild, Denmark, 1991.
76. LeDean A, Mariette F, Lucas T, Marin M. Lebensm. Wiss. Technol. 2001;34:299.
77. Kinsella JE. Crit. Rev. Food Sci. 1984;21:197.
78. Kinsella JE, Fox PF. In: Int. Dairy Federation (Ed). IDF Bulletin 209, 1987, p 12.
79. Kneifel W, Paquin P, Abert T, Richard J-P. J. Dairy Sci. 1991;74:2027.
80. Kulicke W-M, Eidam D, Kath F, Kix M, Kull AH. Starch/Stärke. 1996;48:105.
81. Schkoda P. Serumbindung und Rheologie fermentierter Milchprodukte. TU, Diss., München, 1998.
82. Götz J. Rheo-NMR with applications on food. In: G Webb (Ed). Handbook of Modern Magnetic Resonance. Kluwer Academic Publishers, London, 2005.
83. Hinrichs R. NMR-Messungen zum Charakterisieren der Wasserbindung und der Struktur in Systemen aus Milchproteinen und Hydrokolloiden.: TU, Diss., München, 2004.
84. Hinrichs R, Götz J, Noll M, Wolfschoon A, Eibel H, Weisser H. Characterisation of Different Treated Whey Protein Concentrates by Means of Low Resolution Nuclear Magnetic Resonance (LR NMR). To appear in International Dairy Journal, 2006.
85. Hinrichs R, Götz J, Noll M, Wolfschoon A, Eibel H, Weisser H. Characterisation of the Water-Holding Capacity of Fresh Cheese Samples by Means of Low Resolution Nuclear Magnetic Resonance. Food Res. Int. 2004;37:667–676.
86. Suggett A. In: F Franks (Ed). Water, Vol. 4. Plenum Press: New York, 1975, p 550.
87. Lewis GP, Derbyshire W, Ablett S, Lillford PJ, Norton IT. Carbohydr. Res. 1987;160:397.
88. Kerr WL, Wicker L. Carbohydr. Polym. 2000;42:133.
89. Labuza TP, Busk GC. J. Food Sci. 1979;44:1379.
90. Lambelet P, Berrocal R, Desarzens C, Froehlicher I, Ducret F. J. Food Sci. 1988;53:943.
91. Hills BP. Mol. Phys. 1992;76:489/509.
92. Djabourov M. Gèlification Thermorèversible du Système Eau-Gèlatine. Paris: Uni., PhD, 1986.
93. Traoré A, Foucat L, Renou J-P. Eur. Biophys. J. 2000;29:159.
94. Vackier M-C, Hills BP, Rutledge DN, J. Magn. Reson. 1999;138:36.
95. Vackier M-C, Rutledge DN. Food Chem. 1996;57:287.
96. Lechert H, Maiwald W, Köthe R, Basler W-D. J. Food Process. Preserv. 1980;3:275.
97. Lechert H. Proc. 52nd Conference FEI, Hamburg, 1994.
98. Tang H-R, Brun A, Hills BP. Carbohydr. Polym. 2001; 46:7.
99. Kou Y, Dickinson LC, Chinachoti P. J. Agric. Food Chem. 2000;48:5489.
100. Farhat IA, Blanshard JM, Mitchell JR. Biopolymers. 2000;52:411.
101. Blanshard JM, Jarozkiewicz EM, Gidley MJ. In: JW Finley, SJ Schmidt, A Seriani (Eds). NMR Applications in Biopolymers. Plenum: New York, 1990, p 155.
102. Dunn LB, Krueger WJ. In: H Höcker (Ed). Macromolecular Symposia. Wiley-VVH: Weinheim, 1999, p 179.
103. Leung HK, Steinberg MP, Wie LS, Nelson AI. J. Food Sci. 1976;41:297.
104. Yakubu PI, Baianu IC, Orr PH. In: DS Reid (Ed). The Properties of Water in Foods ISOPOW 6. Blackie Academicand International: London, 1998, p 160.
105. Ruan RR, Almaer S, Huang VT, Perkins P, Chen P, Fulcher RG. Cereal Chem. 1996;73:328.
106. van de Velde F, Peppelman HA, Rollema HS, Tromp RH. Carbohydr. Res. 2001;331:271.
107. Borgstrom J, Egermayer M, Sparrman T, Quist PO, Picullell L. Langmuir. 1998;14:4935.
108. McCarthy MJ, McCarthy KL. Magn. Reson. Imaging. 1996;14:799.
109. Hills BP. Trends Food Sci. Tech. 1995;6:111.
110. Rutledge DN. Food Control. 2001;12:437.
111. Cho SI, Chung CH. TASAE. 2001;44:377.
112. Nordon A, McGill CA, Littlejohn D. Analyst. 2001;126: 260.
113. Barrie PJ. Ann. RNMR S. 2000;41:265.
114. Tellier C, Mariette F, Guillement JP, Marchall P. J. Agric. Food Chem. 1993;41:2259.
115. Smith DM, Hua D-W, Earl WL. MRS Bull. 1994;19:44.
116. Chui MM, Philipps RJ, McCarthy MJ. J. Colloid Interface Sci. 1995;174:336.
117. Stapf S, Kimmich R. J. Chem. Phys. 1995;103:2247.
118. Zavada T, Kimmich R. Phys. Rev. E. 1999;59:5848.
119. Hills BP, Snaar JE. Mol. Phys. 1992;76:979.
120. Hills BP, Wright KM, Snaar JE. J. Magn. Reson. Anal. 1996;2:305.
121. Hürlimann MD, Latour LL, Sotak CH. Magn. Reson. Imaging. 1994;12:325.
122. Gupte AR. Widerstandsgesetz der Porenströmung. Uni., Diss., Karlsruhe, 1970.
123. Friedmann TE, Windhab E. Separ. Sci. Technol. 1998;33:2221.

NMR Relaxation and Diffusion Studies of Horticultural Products

B.P. Hills

Institute of Food Research, Norwich Research Park, Colney, Norwich NR4 7UA,UK

Introduction

The importance of the worldwide production of fruit and vegetables both for human health and as an economic force should not be underestimated. In the United States alone, the fruit and vegetable industry generates over $6 billion in income annually. Much research effort is aimed at maximizing production by optimizing the factors affecting growth in the field such as irrigation, nutrients, and harvesting times as well as finding optimum storage conditions, especially for fruit kept in long-term storage for export and/or off-season marketing. It also involves finding the best ways to sort and grade fruit coming out of storage which means developing non-invasive sensors of fruit and vegetable quality.

Because it is non-invasive, NMR has been widely used to research each of these stages. High-resolution NMR spectroscopy and imaging have been used to study physiological changes during plant growth, development, and storage and these aspects have been reviewed [1]. MRI has also been used to monitor water transport during preservation processes such as drying and freezing and examples of this work can be found in Refs. [2–4]. However, the main focus of this chapter will be the correlation between proton NMR relaxometry and diffusometry and fruit and vegetable quality. As we shall see, these NMR techniques are especially sensitive to the (sub)-cellular compartmentation of water and this is affected by physiological changes during ripening and storage and also holds promise for the development of non-invasive NMR sensors during the sorting and grading stage. We therefore begin by reviewing the relationship between NMR water proton relaxometry and diffusometry and cell tissue structure.

NMR Relaxation and Water Compartmentation

In the absence of paramagnetic ions, there are three main phenomena that affect water proton relaxation in plant tissue, namely,

(a) Fast proton exchange on a (sub-)millisecond timescale between water and exchangeable protons on cell metabolites, especially sugars and biopolymers, including the cell wall biopolymers and starch granules.
(b) Dephasing of transverse magnetization by the diffusion of water molecules through internal field gradients created by magnetic susceptibility discontinuities in the tissue, especially across the interface of inter-cellular air gaps. This effect is especially important at high field strengths when gradients are largest.
(c) Diffusion of water between the various subcellular (vacuolar, cytoplasmic) and extra-cellular water compartments which averages the magnetization to an extent that depends on cell morphology and membrane permeability.

The fact that plant cells are compartmentalized means that, in general, the transverse and longitudinal relaxation are multiple exponential. Moreover, if transverse relaxation occurs by the proton exchange and internal field gradient mechanisms then, in general, the observed CPMG transverse relaxation behavior depends on the field strength and the CPMG pulse spacing. However, relating the NMR data to factors such as organelle size and membrane permeability is far from straightforward though a start has been made by combining the proton exchange model [5] with a simplified spherical cell model of a plant cell [6]. This has proved useful in fitting the changing relaxation data during the drying and freezing of apple [7], carrot [8], and potato [9] parenchyma tissue. In principle, the same theoretical approach could be used to model the changes in relaxation behavior observed as plant tissue ripens, though this has yet to be attempted.

The potential of multi-dimensional relaxation experiments for exploring the relationship between water compartmentation and fruit/vegetable quality has only just begun to be explored. Figure 1 shows the T_1–T_2 cross-correlation spectrum for parenchyma tissue of fresh red delicious apple. The dependence of the peak positions and intensities on physiological conditions such as mealiness are being researched in the authors laboratory and hold considerable promise [10].

Given the likelihood that online NMR sensors will be based on low rather than high field strengths it is

Graham A. Webb (ed.), Modern Magnetic Resonance, 1721–1727.
© 2008 *Springer.*

Fig. 1. A typical T_1–T_2 correlation spectrum of parenchyma tissue of red delicious apple acquired at room temperature at 23 MHz with a CPMG pulse spacing of 200 μs. The diagonal line denotes $T_1 = T_2$. The vertical and horizontal dot-dashed lines denote the limits of reliability based on the acquisition parameters.

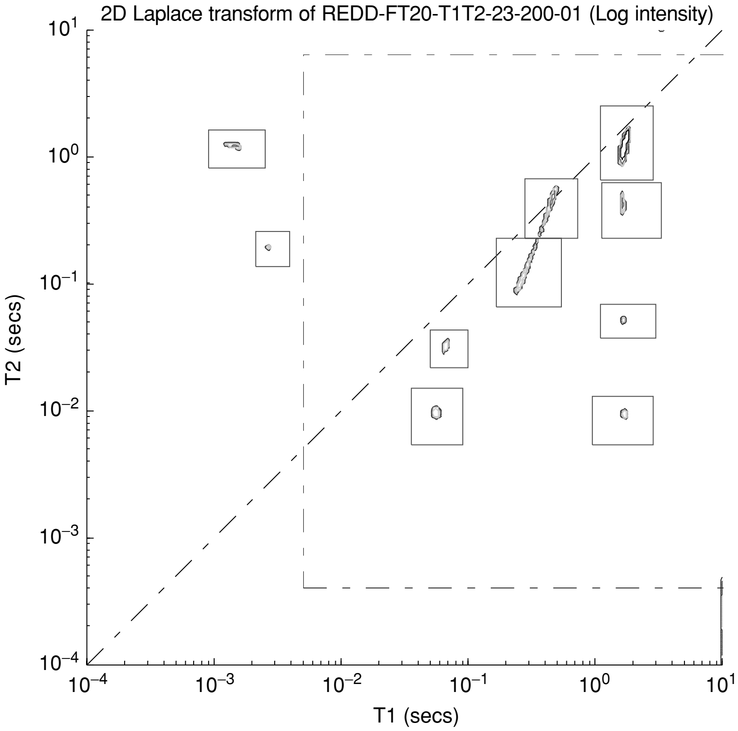

surprising that so little field cycling relaxometry has been reported for plant tissue. The dependence of the longitudinal relaxation time on field strength gives a direct handle on the spectral densities describing molecular mobility in the tissue, data that could provide a useful test of the numerical cell model. It would be especially useful to see how the spectral densities change during tissue breakdown for conditions such as mealiness and chilling injury.

Although correlations between relaxation and quality naturally focus on simple T_2 and T_1 measurements, it should not be forgotten that these are not the only types of relaxation that can be studied. Relaxation in the rotating frame, characterized by $T_{1\rho}$, is another potentially valuable handle on tissue quality and this, in general, depends on the strength of the spin-locking field and the spin-locking angle. Possible correlations between cross-polarization rates and quality factors are an additional aspect that appears to have been overlooked, yet image contrast based on cross relaxation is an important diagnostic tool in clinical imaging and therefore, potentially, in plant imaging. In this context, cross relaxation refers to the transfer of longitudinal proton magnetization between water and more rigid biopolymers in the plant tissue matrix. These rates can be measured by sequences such as those of Goldman and Shen [11].

NMR Diffusometry and Water Compartmentation

In contrast to water proton relaxation, there have been very few attempts to correlate water diffusivity in cellular tissue as measured with PGSE sequences to plant quality factors. An exception is the early work of Keener *et al.* [12] who found a useful correlation between the apparent water diffusion coefficient and apple maturity as measured by the refractometer Brix value. The paucity of work on water diffusivity is surprising because the restriction of water diffusion by cell membrane and cell wall barriers is a useful and sensitive probe of changes in cell morphology. The potential of PGSE studies of cellular tissue was illustrated by Hills and Snaar in their studies of fresh parenchyma apple tissue [6]. In a PGSE, Stejskal–Tanner experiment the echo amplitude, $S(q, \Delta, \tau)$ is a function of both the echo time, 2τ, the diffusion time, Δ, defined as the time between gradient pulses and the wave vector, q, defined as the area of the gradient pulse, $\gamma G\delta/2\pi$. For

Table 1: Comparison of theoretical and experimental p_i and a_i in Equation (1) for apple parenchyma tissue

i	a_i (experimental)	a_i (theory)	p_i (experimental)	p_i (theory)
1	0.292	0.302	0.78	0.80
2	0.032	0.044	0.13	0.10
3	0.007	0.017	0.09	0.10

variation of Δ at fixed τ we can write

$$S(q, \Delta, \tau) = \Sigma_i\, p_i(q, \tau) \exp(-\Delta/a_i(q, \tau)), \qquad (1)$$

where the $a_i(q, \tau)$ are generalized diffusion times and p_i are the associated fractional populations. Both these coefficients depend on the wave vector, q. In principle, these additional coefficients can be analyzed and related to quality factors in an analogous manner to the relaxation times discussed in the previous section, though no one has yet attempted to do this. Table 1 shows a comparison of the experimental coefficients for fresh apple tissue with those calculated with the numerical cell model. The agreement is quite reasonable and supports the general theoretical framework. It would be interesting to apply this approach to mealy apple and to other types of fruit and vegetable.

Quite clearly there remains a great deal of basic NMR and modeling work to be done before we can claim to understand the relaxation and diffusion behavior of horticultural products. The next section surveys the literature up to 2004 with no claim to completeness.

Fruit and Vegetable Quality

The literature to the end of 1999 relating to internal defects and storage disorders has been summarized by Clark *et al.* [1] and Koizumi *et al.* [13]. The more recent literature to 2003 has been reviewed by Hills and Clark [14]. The types of **product studied and the quality disorders investigated are summarized in Table 2. Space does not permit each product in Table 2 to be discussed in detail, so we illustrate the NMR-quality correlations for the most intensively studied examples, namely apple and potato.

Apple Maturity

Up to three peaks have been reported in the distribution of water proton transverse relaxation times in parenchyma apple tissue measured with the CPMG sequence with a short 90–180° pulse spacing at 2.3 T (100 MHz) [7]. These peaks have been assigned to vacuolar water and water associated with cytoplasm and cell wall. The effect of freezing and drying on this relaxation time spectrum has been modeled with a numerical cell model with moderate success.

Keener *et al.* [12] have investigated the relationship between low-field (0.13 T; 5.4 MHz) apparent water proton diffusion coefficients (D_w), the dominant CPMG T_2 measured with a pulse spacing of 2 ms, and degree of ripeness (soluble solids content) as measured by refractometry. The following trends were reported:

(a) In healthy "Golden Delicious" and "Granny Smith" apples, the T_2 decreased with increasing soluble solid content (Brix) in healthy apples.
(b) The water diffusivity decreased with increasing soluble solid content in all samples, both bruised and healthy. This is no doubt a result of the increasing viscosity of more concentrated sugar solutions.
(c) Internal defects caused by bruising, watercore, and internal browning resulted in a decrease in T_2 in all varieties at this low field strength. It remains to be seen whether T_1 also shows useful correlations with soluble solids and internal defects.

Cho *et al.* [15] reported that the amplitude of the sugar proton peak following water suppression with a T_1 null sequence correlated well with the sugar content in apples (as well as banana and muskmelon). This exploited the observation that the T_1 of exchangeable water protons was at least twice as long as that of the non-exchanging sugar protons, so a simple inversion recovery sequence with a delay time chosen to null the water signal, leaves a substantial positive sugar proton signal.

Apple Bruises

A combination of spin-echo and gradient reversed echo imaging in a high field magnet at 1.4 T, showed that the redistribution of intra- and extra-cellular water arising from cell and membrane damage in the bruised region actually results in a decrease in the mean transverse relaxation rate, T_2, as measured by the CPMG sequence [16]. This established that the enhanced image intensity observed for bruised tissue with high-field MRI could not be a result of intrinsic T_2 changes. Instead, the enhanced brightness results from a reduction in the signal attenuation arising from water diffusing through internal magnetic field

Table 2: Summary of references to NMR studies of quality factors in the major types of fruit and vegetables

				Heat and chill injury		
Product	Maturity	Bruises/voids	Tissue breakdown	Heat	Chill	Infections
Fruit						
Apple	12,15,31	12,16,18,31,32	10,12,17,19–21,31,33–39	–	–	–
Avocado	40–42	–	–	–	–	–
Banana	43	–	–	–	–	–
Kiwifruit	44	–	–	–	45,46	–
Mandarin	47	–	–	–	–	48
Mango	49–52	–	–	53,54	–	–
Melon	55,56	55–57	58	–	–	–
Nectarine	41	–	59	–	–	60
Orange	41	–	18	–	–	–
Peach	–	–	59	–	–	–
Pear	49	18	61,62	–	–	–
Pineapple	56	–	18	–	–	–
Tangerine	63	63	63	–	–	–
Berries						
Blueberry	64	–	–	–	64	–
Grape	65–67	–	–	–	–	–
Strawberry	68,69	68,69	–	–	–	68,69
Small, stone fruit (drupes)						Pit detection
Cherry	70	–	–	–	–	71
Olive	–	–	–	–	–	72
Plum/prune	73	–	–	–	–	–
Vegetables						
Potato	74	75	75			76–78
Squash					79–81	56
Tomato	18,51,82–84					

gradients created by the magnetic susceptibility difference between air in extra-cellular spaces and cellular fluid. This is an important observation because the effect of internal gradients on the effective relaxation rate is expected to vary as the square of the applied field as well as on the pulse spacing. Reducing the field strength to say 0.14 T (a proton frequency of ca. 6 MHz) would be expected to reduce the effect of the internal gradients on the relaxation rate by at least two orders of magnitude so that bruises in a low-field imaging system could actually appear with lower rather than higher intensity. This prediction remains to be investigated but highlights the importance of repeating the NMR-internal quality correlations over a range of frequencies, especially the low-field range.

Internal Browning Disorders in Apples

Internal browning disorder manifests itself as light and dark brown patches throughout the cortex and core. The disorder is induced by high CO_2 concentrations, especially during storage in modified atmospheres, but can also appear in unpicked fruit on the tree. As its name implies, the brown patches are not visible from the outside but give contrast in MRI. The light brown regions have a lower signal intensity than normal tissue because of a reduced proton density and a shorter T_2. Dark brown regions have higher intensity than normal tissue because of a longer T_2 [17].

Watercore in Apples

In normal apple tissue, the inter-cellular spaces are ordinarily filled with air. However, in watercore-affected tissue, the air is replaced by a sorbitol solution giving the cut tissue a translucent watery appearance. Watercore is also associated with elevated water content and decreased reducing sugars. The disorder mostly occurs late in the growing season in over-mature unpicked fruit and cannot be visibly detected in the intact fruit. The higher water proton density in the affected tissue gives a higher MRI image intensity, allowing watercore to be readily identified [18].

Mealiness in apples

Mealiness in apples results from a breakdown in adhesion between cells so that chewing the apple tissue results in cell separation rather than cell rupture. Eating a mealy apple is therefore associated with the unpleasant sensory perception of a lack of juiciness, loss of crispness, and hardness. The first significant correlations between NMR measurements and mealiness were reported by Barreiro *et al.* [19,20], who found that the histogram of T_2 values (i.e. the number of pixels having a particular T_2) for mealy apples was skewed to shorter relaxation times with a significant tail located in the maximum T_2 range. In contrast, non-mealy apples had normal, non-skewed T_2 histograms. More recently, increasing mealiness has been shown to cause a systematic reduction in the non-spatially resolved CPMG-T_2 values undertaken at the slightly lower field of 2.32 T [21].

Potato

Most NMR studies of potato have focused on understanding the effects of processes such as boiling, frying, freezing, and drying [9,22,23]. Exceptions are the NMR microimaging of healthy and diseased potato tubers reported by Goodman and co-workers [24–26] and relaxation changes in healthy tubers following induced wounding. Most recently, a number of papers have appeared where NMR relaxometry on raw potato has been used to predict the sensory texture after boiling [27–29]. It is therefore surprising that, despite the importance of potato, there are so few published studies where NMR/MRI has been used to detect internal quality defects in raw tubers. Such internal defects include brown core and hollow heart. Using multi-slice spin-echo imaging, Wang *et al.* [30] have demonstrated that both brown core and hollow heart can be detected by MRI. Brown core, a physiological disorder of potato characterized by medulla tissues in the center of the tuber turning from light- to dark-brown in color, is associated with loss of membrane structures, cytoplasm, and organelles and a thickening of cell walls that results in the affected tissue having a longer T_2 relaxation time. It is therefore recognizable by high signal intensity in scans with long echo times. The "hollow heart" condition results from cells in the pith area of the tuber splitting apart to form star- or lens-shaped air-filled cavities near the center of the tuber. The hollow heart condition is therefore distinguished by the absence of signal in images or one-dimensional profiles.

Another quality defect which is adversely affecting the marketing of potato products has been termed the hardening syndrome. Here, internal lumps form inside the potato during cooking. While a number of biochemical and physiological investigations are underway to try to understand the origins of this syndrome it remains to be seen whether NMR studies on the raw potato can identify regions likely to form internal lumps.

Conclusions

Although Table 2 shows that many diverse quality factors in fruit and vegetables can be detected with NMR it is also clear that a great deal of fundamental NMR remains to be done. Apple is one of the most intensively studied fruit, yet we find no reports on field cycling relaxometry, no attempts to measure cross-relaxation rates or $T_{1\rho}$, and no systematic investigation of water diffusivity in relation to physiological defects such as mealiness. Little work has been done to correlate PGSE measurements of the restriction of water diffusivity to quality factors. The gaps in Table 2 also emphasize the extent of the more applied work that remains to be done before NMR sensors can be applied to all these diverse types of fruit and vegetable.

Very few of the references in Table 2 attempt any quantitative modeling of their NMR data in terms of cell microstructure or composition. Such models would be extremely useful in choosing the optimum acquisition pulse sequences and for rationalizing differences between sample varieties and the effects of harvesting times and storage conditions. The numerical cell model is a first step in this direction but more realistic cell morphologies could be tackled with finite element and Monte Carlo numerical methods.

As mentioned in the introduction, many of the reports cited in this review have been based on measurements made with superconducting magnets at relatively high spectrometer fields. Unless there is a major breakthrough such as high temperature superconductivity, these high field magnets are unlikely to be used in NMR sensors for sorting and grading. There is therefore a need to repeat many of the measurements at much lower fields (<0.5 T) appropriate to permanent and resistive magnet technology.

Acknowledgment

B.P. Hills gratefully acknowledges the financial support of the BBSRC during the preparation of this work.

References

1. Clark CJ, Hockings PD, Joyce DC, Mazucco RA. Postharvest Biol. Technol. 1997;11:1.

2. Hills BP. Magnetic Resonance Imaging in Food Science. Wiley: New York, 1998, p 152.
3. McCarthy MJ. Magnetic Resonance Imaging in Foods. Chapman and Hall: New York, 1994.
4. Ruan RR, Chen PL. Water in Foods and Biological Materials: A Nuclear Magnetic Resonance Approach. Technomic Publishing: Basel, 1998.
5. Hills BP. Mol. Phys. 1992;76:489.
6. Hills BP, Snaar JEM. Mol. Phys. 1992;76:979.
7. Hills BP, Remigereau B. Int. J. Food Sci. Technol. 1997; 32:51
8. Hills BP, Nott KP. Appl. Magn. Reson. 1999;17:521
9. Hills BP, Le Floch G. Food Chem. 1994;51:331.
10. Hills BP, Benamira S, Marigheto N, Wright KM. Appl. Magn. Reson. 2004;26:543.
11. Goldman M, Shen L. Phys. Rev. 1966;144:321.
12. Keener KM, Stroshine RL, Nyenhuis JA. J. Am. Soc. Hortic. Sci. 1999;124:289.
13. Koizumi M, Ishida N, Kano H. Curr. Top. Plant Biol. 2000;2:1.
14. Hills BP, Clark CJ. Annu. Rep. NMR Spectrosc. 2003;50:75.
15. Cho SI, Bellon V, Eads TM, Stroshine RL, Krutz GW. J. Food Sci. 1991;56:1091.
16. McCarthy MJ, Zion B, Chen P, Ablett S, Darke AH, Lillford PJ. J. Sci. Food Agric. 1995;67:13.
17. Gonzalez JJ, Valle RC, Bobroff S, Viasi WV, Mitcham EJ, McCarthy MJ. Postharvest Biol. Technol. 2001;22:179
18. Chen P, McCarthy MJ, Kauten R. Trans. ASAE. 1989;32:1747
19. Barreiro P, Ortiz C, Ruiz-Altisent M, Ruiz-Cabello J, Fernandez-Valle ME, Recasens I, Asensio M. Magn. Reson. Imaging. 2000;18:1175.
20. Barreiro P, Ruiz-Cabello J, Fernandez-Valle ME, Ortiz C, Ruiz-Altisent M. Magn. Reson. Imaging. 1999;17:275.
21. Barreiro P, Moya A, Correa E, Ruis-Altisent M, Fernandez-Valle M, Peirs A, Wright KM, Hills BP. Appl. Magn. Reson. 2002;22:387.
22. Kantt CA, Webb AG, Litchfield JB. J. Food Sci. 1997; 62:1001.
23. Ruan R, Schmidt SJ, Schmidt AR, Litchfield JB. J. Food Process Eng. 1991;14:297.
24. Snijder AJ, Glidewell SM, Goodman BA. Abstracts of the 3rd International Conference of Magnetic Resonance Microscopy, Würzburg, Germany, 1995.
25. Goodman BA, Glidewell SM. Phyton. Annu. Rev. Bot. 1997;37:81.
26. Snijder AJ, Wastie RL, Glidewell SM, Goodman BA. Biochem. Soc. Trans. 1996;24:442.
27. Thybo AK, Andersen HJ, Karlsson AH, Donstrup S, Stodkilde-Jorgensen H. Lebensm. Wiss. Technol. 2003; 36:315.
28. Thybo AK, Bechmann IE, Martens M, Engelsen SB. Lebensm. Wiss. Technol. 2000;33:103.
29. Thygesen LG, Thybo AK, Engelsen SB. Food Sci. Technol. 2001;34:469.
30. Wang PC, Song HF, Yan ZJ. Proceedings of the 35th Experimental NMR Conference (ENC), Pacific Grove, CA, 1994.
31. Keener KM, Stroshine RL, Nyenhuis JA. Trans. ASAE. 1997;40:1633
32. Zion B, Chen P, McCarthy MJ. Comput. Elect. Agric. 1995;13:289.
33. Wang SY, Wang PC, Faust M. Sci. Hortic. 1998;35:227.
34. Clark CJ, Burmeister DM. Hortscience. 1999;34:915.
35. Jung KH, Stroshine R, Cornillon P, Hirst PM. ASAE Conference Paper No. 98-6020, Orlando, FL, 1998.
36. Clark CJ, Richardson CA. N.Z. J. Crop Hortic. Sci. 1999;27:47.
37. Clark CJ, MacFall JS, Bieleski RL. Sci. Hortic. 1998;73:13.
38. Clark CJ, Bieleski RL. Proceeding of the Sensors for Nondestructive Testing Conference, Orlando, FL, p 211, 1997.
39. Golding JB, Sarafis V, Crozier S, Rose SE. Hortscience. 1997;32:112.
40. Chen P, McCarthy MJ, Kauten R, Sarig Y, Han S. J. Agric. Eng. Res. 1993;55:177.
41. Stroshine RL, Wai WK, Krutz GW. ASAE Conference Paper No. 93-6535, Chicago, IL, 1993.
42. Chen P, McCarthy MJ, Kim SM, Zion B. Trans. ASAE. 1996;39:2205.
43. Raffo A, Gianferri R, Barbieri R, Brosio E. Food Chem. 2005;89:149.
44. Clark CJ, Drummond LN, MacFall JS. J. Sci. Food Agric. 1998;78:349.
45. Clark C. N.Z. Kiwifruit. 1993;February:10.
46. Kerr WL, Clark CJ, McCarthy MJ, de Ropp JS. Sci. Hortic. 1997;69:169.
47. Clark CJ, Richardson AC, Marsh KB. Hortscience. 1999;34:1071.
48. Blasco J, Molto E, Alamar MC. Abstracts of the 6th International Conference on Applications of NMR in Food Science, Paris, 2002.
49. Kim SM, McCarthy MJ, Chen P. European Agricultural Engineering Conference Paper 98-F-017, Oslo, 1998.
50. Gil AM, Duarte IF, Delgadillo I, Colquhoun IJ, Casuscelli F, Humpfer E, Spraul M. J. Agric. Food Chem. 2000;48: 1524.
51. Kim SM, McCarthy MJ, Chen P. ASAE Conference Paper No. 94-6519, Atlanta, GA, 1994.
52. Kim SM, Chen P, McCarthy MJ, Zion B. J. Agric. Eng. Res. 1999;74:293.
53. Joyce DC, Hockings PD, Mazucco RA, Shorter AJ, Brereton IM. Postharvest Biol. Technol. 1993;3:305.
54. Joyce DC, Hockings PD, Mazucco RA, Shorter AJ. Funct. Plant Biol. 2002;29:873
55. Saito K, Miki T, Hayashi S, Shimada M, Ikegaya D, Kimura N, Takabatake K. Abstracts of Magnetic Resonance/Spectroscopy in Food Science, International Workshop, Harima, Japan, 1997.
56. Hall LD, Evans SD, Nott KP. Magn. Reson. Imaging. 1998;16:485.
57. Saito K, Miki T, Hayashi S, Kajikawa H, Shimada M, Kawate Y, Nishizawa T, Ikegaya D, Kimura N, Takabatake K, Sugiura N, Suzuki M. Cryogenics. 1996;36:1027.
58. Zion B. personal Communication, 1994.
59. Sonego L, Ben-Arie R, Raynal J, Pech JC. Postharvest Biol. Technol. 1995;5:187.
60. Clark CJ. Hortscience. 1999;27:1291.
61. Wang CY, Wang PC. Hortscience. 1989;24:106.
62. Lammertyn J, Dresselaers T, van Hecke P, Jancsok P, Wevers M, Nicolai BM. Postharvest Biol. Technol. under review.
63. Yantarasri T, Sornsrivichai J. Acta Hortic. 1998;464:494.
64. Gamble GR. J. Food Sci. 1994;59:571.
65. Goodman BA, Williamson B, Chudek JA. Magn. Reson. Imaging. 1993;11:1039.

66. Pope JM, Jonas D, Walker RR. Protoplasma. 1993;173: 177.
67. Cho SI, Stroshine RL, Baianu IC, Krutz GW. Trans. ASAE. 1993;36:1217
68. Maas JL, Line MJ. Acta Hortic. 1995;398:241.
69. Goodman BA, Williamson B, Simpson EJ, Chudek JA, Hunter G, Prior DAM. Magn. Reson. Imaging. 1996;14:187.
70. Cho SI, Stroshine RL, Baianu IC, Krutz GW. Trans. ASAE. 1993;36:1217.
71. Zion B, McCarthy MJ, Chen P. Lebensm. Wiss. Technol. 1994;27:457.
72. Zion B, Kim SM, McCarthy MJ, Chen P. J. Sci. Food Agric. 1997;75:496.
73. Zion B, Chen P, McCarthy MJ. J. Sci. Food Agric. 1995;67:423.
74. Thybo AK, Andersen HJ, Karlsson AH, Donstrup S, Stodkilde-Jorgensen H. Lebensm. Wiss. Technol. under review.
75. Wang PC, Song HF, Yan ZJ. Proceedings of the 35th Experimental NMR Conference (ENC), Pacific Grove, CA, 1994.
76. Snijder AJ, Glidewell SM, Goodman BA. Abstracts of the 3rd International Conference of Magnetic Resonance Microscopy, Würzburg, Germany, 1995.
77. Goodman BA, Glidewell SM. Microscopy and Analysis, 1995;59:7.
78. Snijder AJ, Wastie RL, Glidewell SM, Goodman BA. Biochem. Soc. Trans. 1996;24:442.
79. Wang CY, Wang PC. Environ. Exp. Bot. 1992;32:213.
80. Duce SL, Carpenter TA, Hall LD. J. Food Eng. 1992;16:165.
81. Naruke T, Oshita S, Walton JH, Kuroki S, Deo Y, Kawagoe Y. Abstracts of the Postharvest Unlimited Conference, Leuven, Belgium, 2002.
82. Saltveit ME. Postharvest Biol. Technol. 1991;1:153.
83. Ishida N, Kobayashi T, Koizumi M, Kano H. Agric. Biol. Chem. 1989;53:2363.
84. Ishida N, Koizumi M, Kano H. Sci. Hortic. 1994;57: 335.

Proton NMR Relaxometry in Meat Science

Hanne Christine Bertram and Henrik Jørgen Andersen
Department of Food Science, Danish Institute of Agricultural Sciences, P.O. Box 50, DK-8830 Tjele, Denmark

Introduction

The main constituents of muscle and meat are water, protein, and fats, which represent approximately 75%, 18–20%, and 2–5%, respectively. Lean meat content and water-holding capacity (WHC) are of high interest to the meat industry as these are directly reflected in the payment of meat carcasses and the economic value of the meat during storage and further processing. Moreover, WHC and especially the distribution of the water within the meat are known to affect the sensory properties and the shelf life of meat. Consequently, measurement of lean meat content, WHC and water distribution in meat, and an understanding of intrinsic factors (e.g. species, genotype, muscle type), and technological processes (e.g. slaughter procedure, cooling regime, storage, processing) on water characteristics within the meat are of major importance for the meat industry. Especially non-invasive and non-destructive measuring techniques are demanded by the industry to control these important quality parameters.

^{1}H low-field nuclear magnetic resonance (NMR relaxometry) being a non-invasive and non-destructive measuring technique is a potential technique that might be a future quality control tool in the meat industry, as it has been demonstrated a cheap, robust and rapid method to measure fat content, solid/liquid ratios, and water-holding characteristics in many foods.

In common low-field NMR studies, only the contribution from protons of mobile compounds, i.e. water and fat is "visualized." Both longitudinal relaxation (T_1) and transverse relaxation (T_2) have been used to characterize meats, for reviews see [1,2], with T_1 being most successful in fat determination and T_2 being most successful in characterization of water mobility and distribution. Below is given the most successful applications of ^{1}H NMR relaxometry within meat science together with future perspectives of the methodology within the area.

Determination of Fat Content in Meat and Meat Products Using NMR Relaxometry

NMR relaxometry has been applied for determination of fat content in meat and meat products. Using the inversion recovery method, correlations between the amplitude of a T_1 population and fat content in minced meat and meat emulsions determined by chemical analyses have been demonstrated [3]. Fat content in minced meat has also been determined by a low-field ^{1}H NMR application where pulsed field gradients were included to suppress the water proton signal, which resulted in very high correlations to fat determinations by extraction [4].

T_2 Relaxation in Meat

It was early recognized that the T_2 relaxation in muscle and meat is non-mono-exponential [5–11]. Often the non-mono-exponentiality of the T_2 relaxation in muscle and meat has been solved by decomposing the relaxation decay into two exponential components [12–17]. The two relaxation components (water populations) are characterized by a time constant around 35–50 ms representing approximately 80–95% of the relaxation, and a time constant around 100–250 ms, representing approximately 5–15% of the relaxation, respectively. These two relaxation components have been suggested to reflect slow exchange of water between intra- and extra-cellular water pools, respectively, and were initially ascribed to intra- and extra-cellular water [6,8,9,15], as a correlation between the slowest relaxing time constant and the distance between fiber bundles was demonstrated [15]. However, studies attempting to verify or disprove this intra/extracellular model by characterization of relaxometry characteristics after cell membrane disruption in muscle and meats [18,19] or disruption of the overall structures by homogenization [9,19,20] have all failed to show altered relaxation behavior. This implies that intact cell membranes acting as barriers cannot alone explain the non-mono-exponential T_2 relaxation in muscle tissues. Homogenization of muscle tissue has been found to decrease the fraction of the slowest component together with a minor decrease in the relaxation rate of the fastest component [20] or give rise to a clear shift towards more mono-exponential relaxation with a time constant intermediate between the two relaxation components observed in intact tissue [9,19]. Consequently, the degree of disintegration of the overall structural organization is directly reflected in T_2 characteristics of the major relaxation component around 35–50 ms and the slower relaxing component

Graham A. Webb (ed.), Modern Magnetic Resonance, 1729–1733.
© 2008 *Springer*.

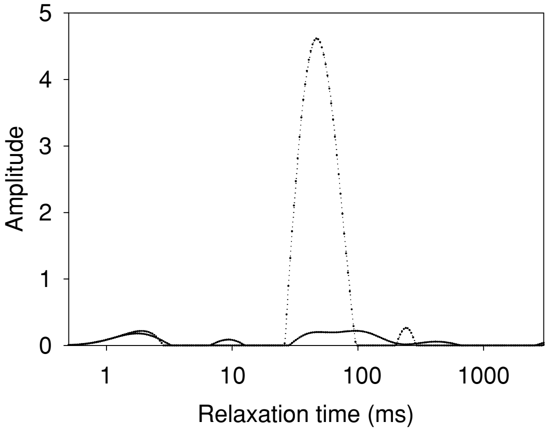

Fig. 1. Distributed T_2 relaxation times measured in a fresh pork sample (dotted line), and upon freeze-drying and rehydration with D_2O (solid line). The T_2 relaxation measurements were performed with a resonance frequency for protons of 23 MHz. The distributed exponential fitting analysis was performed according to the regularization algorithm by Butler *et al.* [45] and carried out in MatLab version 6.5 using in-house scripts.

around 100–250 ms. Thus the major water component, characterized by a time constant of approximately 35–50 ms and accounting for 80–95% of the relaxation, represents water trapped within the protein-dense myofibrillar network, while the slowest water component, characterized by a time constant between 100–250 ms and accounting for 5–15% of the relaxation, represents water located outside the myofibrillar protein network, i.e. extra-myofibrillar water.

Three-exponential decomposition of the T_2 relaxation decay gives rise to an additional fast relaxing component (water population) with a time constant between 0 and 10 ms representing about 5% of the relaxation [6,8]. Introduction of distributed exponential fitting of the T_2 relaxation decay [21] supports the presence of three relaxation components in meats with the fastest component having relaxation times around 2–6 ms [20,22–27]. Figure 1 displays the distributed T_2 relaxation times measured in a pork sample before and after replacement of the myowater with deuterium oxide (D_2O being ^{1}H NMR silent). Noticeably, upon replacement of the myowater with D_2O the major water component and the slower relaxing water component almost disappear while the fast component with relaxation times 2–6 ms is unaffected. This implies that the fast relaxation population represents protons not susceptible to exchange, i.e. hydration water. The existence of the third fast relaxing water component in meat is still a matter of dispute.

Water-Holding Capacity

Traditionally the water characteristics of meat are determined by invasive gravimetric methods [28,29] that not always reflect the water characteristics during storage and processing. Renou *et al.* [12] were the first to report that T_1 and T_2 relaxation characteristics of meat correlated with traditional meat quality traits in pork, and that the proton relaxation contains information about the WHC of meat. Subsequently, several studies have confirmed the findings by Renou *et al.* [12] and revealed that especially T_2 relaxation in meat is highly correlated with WHC measured by traditional gravimetrically methods. Correlation coefficients between WHC determined gravimetrically and T_2 relaxation variables of $r = 0.6$–0.8 have been found [15–17,30]. Considering the relatively poor repeatability of the gravimetric methods, these results must be considered promising in establishing NMR T_2 relaxation as a superior alternative to existing methods for determination of WHC in meat.

The physical rationale for a relationship between the T_2 relaxation in meat and WHC is that water expelled from the meat is directly reflected in a decrease in the amplitude of the slowest relaxing component (extra-myofibrillar water) [22].

Relaxometry Studies During Conversion of Muscle to Meat

Several characteristic physical and biochemical processes are taking place during the conversion of muscles to meat. These processes determine the subsequent meat quality development, and therefore a very great interest attaches to a basic understanding of the underlying mechanisms. The non-destructive nature of NMR relaxometry makes the technique an excellent tool in the investigation of continuous events taking place during conversion of muscle to meat. Thus by combining transverse relaxation, impedance (Py), and muscle contraction measurements during the early post mortem period in porcine *muscle longissimus dorsi* (pork loin) a fundamental understanding of water mobility and distribution, membrane properties, and physical events have been established [27] (Figure 2). The reorganization of water taking place post mortem is closely associated with membrane properties with the changes in the major relaxation component being directly dependent on the structural organization triggered through the *rigor* development, which is in agreement with a relationship between myofilament lattice spacing and transverse relaxation in pork [23]. In summary, a continuous NMR approach has not only been able to establish the reorganization of water in the muscles during conversion to meat, but has also demonstrated how the reorganization of water is related to physical processes taking

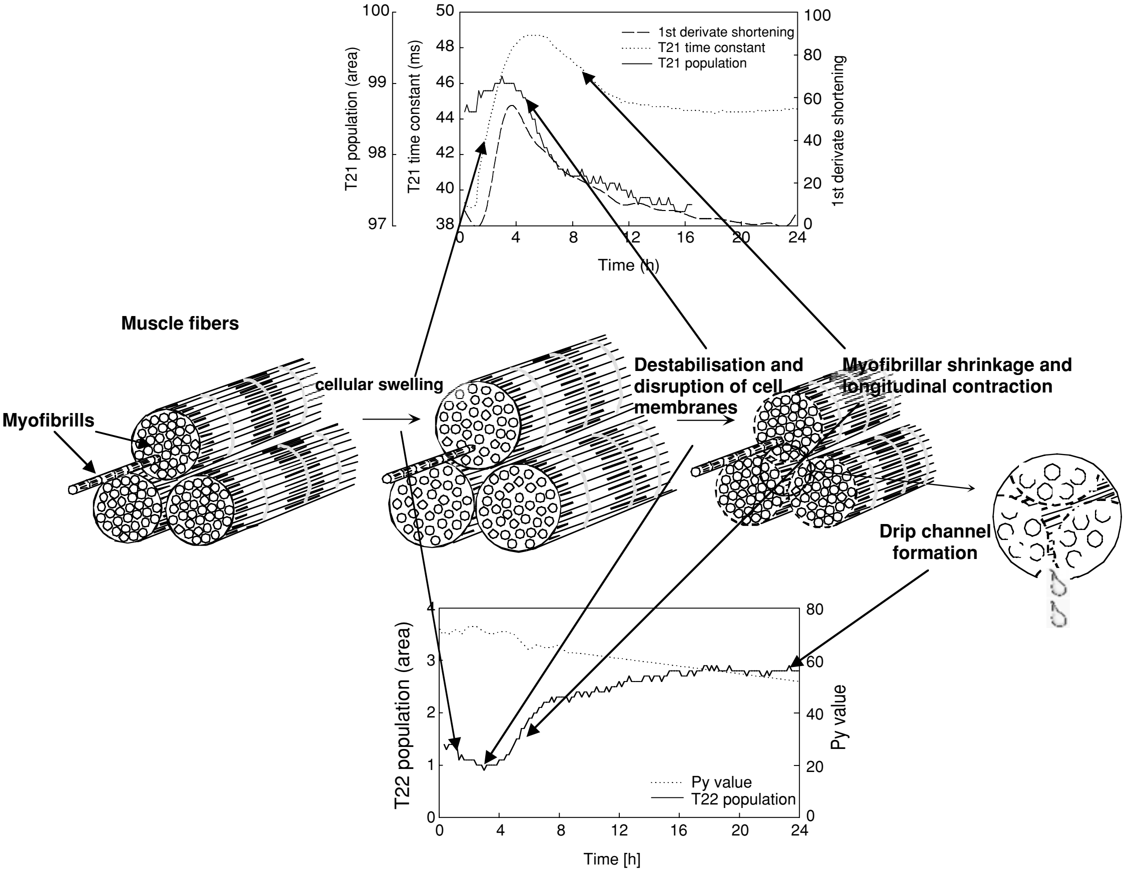

Fig. 2. Illustration of proposed mechanisms in the post mortem reorganization of muscle fluids and its relation to observed changes in the NMR T_{22} population. The initial event is a cellular swelling, caused by the increased intra-cellular osmolarity post mortem. At this stage the membrane structures are rendered almost intact resulting in increased intra-cellular water volume. Subsequent destabilization and disruption of membrane structures is initiated at a stage where the cellular homeostasis begins to debilitate. This initiates the second water redistribution phase where water will be expelled from the myofibrillar matrix by combined longitudinal contraction of the myofilament lattice due to the ongoing rigor process and lateral shrinkage in myofilament spacing due to falling pH, which forces intramyofibrillar water into the extra-cellular space where it becomes potential drip. Reprinted from Meat Science, Vol 66, Bertram, H.C., Schäfer, A., Rosenvold, K. & Andersen, H.J. Physical changes of significance for early post mortem water distribution in porcine M. longissimus, 915–924, 2004, with permission from Elsevier.

place post mortem, i.e. contraction and membrane destabilization, which have brought a novel and more basic understanding of principal mechanisms in the formation of drip from meat.

Transverse relaxation measurements have also made it possible to further elucidate the effects of cooling rates on water characteristics during the conversion of muscle to meat [26] showing that the T_2 populations depend on the structural organization of cellular water post mortem including membrane integrity, which both depend on the cooling rate. Moreover, using T_2 relaxometry on muscle with different energy levels (muscle glycogen and creatine phosphate concentrations) during its conversion to meat has revealed that the progression in the relaxation component reflecting intra-cellular/myofibrillar water is dependent on the pH progress post mortem [31]. Finally, the progress in post mortem pH in meat was by T_2 relaxometry found to influence the extent of the two major relaxation components with a fast pH fall giving rise to broader distributions of relaxation times of the individual water populations. This merges with the more heterogeneous structure found upon protein denaturation and triggered by a rapid pH fall [25].

The Carr-Purcell-Meiboom-Gill pulse sequence [32,33] is most often applied for T_2 relaxation measurements in meats. However, a multi-gradient CPMG pulse sequence where the CPMG sequence is combined with a ramped, external field gradient to include diffusive weighting to each relaxation time component has also been introduced [34,35]. This approach has recently been applied to investigate the significance of diffusive processes on a microscopic scale in muscles during conversion to meat [36]. The obtained data noticeably imply that both diffusion and relaxation contribute to the relaxation of the two water populations in meat. These preliminary data clearly demonstrate that combining NMR relaxometry with NMR diffusion measurements will be of interest to further elucidate the relationship between T_2 relaxation and diffusive motions in meats in the future.

Relaxometry Applied During Meat Processing

NMR relaxation measurements provide the possibility for a continuous study of the influence of cooking temperature on water characteristics within meat [37–40]. Thus applying T_2 measurements continuously over the entire cooking process suggest that the on-set of myosin denaturation taking place at 40–45°C gives rise to either expulsion of water from the myofibrillar lattice or formation of a porous myosin gel [39,40].

The effect of incorporation of additives such as gums or non-meat proteins into processed meats has only been studied by NMR relaxometry to a limited extent [41], and further attention to this area in the future is appreciated as the potential of an improved understanding of optimized water-binding in processed meats and meat batters is of great economic importance for the meat industry. Recently, NMR relaxometry was demonstrated to give information regarding structural changes and reorganization of water during frozen storage [42], which can be used in optimization of storage conditions and cooking procedures of pre-frozen meats.

Finally, NMR relaxometry has also been applied to predict technological parameters such as cooking loss, Napole Yield, and frying loss in meat [12,30,43,44]. Modest correlations have been reported, however, compared with alternative measurements in fresh meat, e.g. pH and WHC, T_2 relaxation has been shown to be superior [44].

Conclusions

Numerous applications of NMR relaxometry have been reported in meat science within recent years. The technique has proven successful in determination of fat content and WHC of meats. Because of the non-destructive character of NMR, the technique has been demonstrated to be an excellent tool for dynamic studies during conversion of muscle and has thereby successfully contributed to improve the basic knowledge about the on-going biochemical and biophysical post mortem processes of significance for subsequent meat quality development. An improved understanding of the origin of the observed relaxation behavior in muscle and meat has further strengthened the potential of NMR relaxometry. In relation to meat processing NMR can be expected to contribute increasingly within this area in future in the elucidation of dynamic changes during processing steps such as cooking, salting, marination, and freezer storage. In conclusion, NMR relaxometry has proven to provide valuable information about substantial meat quality attributes and the expected development within NMR mobile devices upon further development of the hardware will without doubt make on-line NMR relaxometry a reality within the meat industry in the near future.

References

1. Bertram HC, Andersen HJ. Ann. Rep. NMR Spectrosc. 2004;53:157.
2. Renou J-P. Ann. Rep. NMR Spectrosc 1995;31:312.
3. Renou JP, Kopp J, Valin C. J. Food Technol. 1985;20:23.
4. Pedersen HT, Berg H, Lundby F, Engelsen SB. Inn. Food Sci. Emerg. Technol. 2001;2:87.
5. Cope FW. Biophys. J. 1969;9:303.
6. Hazlewood CF, Chang DC, Nichols BL, Woessner DE, Biophys. J. 1974;14:583.
7. Hansen JR, Biochem. Biophys. Acta. 1971;230:482.
8. Belton PS, Jackson RR, Packer KJ. Biochim. Biophys. Acta. 1972;286:16.
9. Pearson RT, Duff ID, Derbyshire W, Blanshard JMV. Biochim. Biophys. Acta. 1974;362:188.
10. Fung BM. Biophys. J. 1977;19:315.
11. Diegel JG, Pintar MM. Biophys. J. 1975;15:855.
12. Renou JP, Monin G, Sellier P. Meat Sci. 1985;15:225.
13. Renou JP, Kopp J, Gatellier P, Monin G, Kozak-Reiss G. Meat Sci. 1989;26:101.
14. Le Rumear E, de Certaines J, Toulouse P, Rochcongar P. Magn. Reson. Imaging, 1987;5:267.
15. Tornberg E, Andersson A, Göransson Å, von Seth G. Pork Quality: Genetic and Metabolic Factors. CAB International: UK, 1993, p 239.
16. Brøndum J, Munck L, Henckel P, Karlsson A, Tornberg E, Engelsen SB. Meat Sci. 2000;55:177.
17. Bertram HC, Karlsson AH, Andersen HJ. Meat Sci. 2001; 57:125.
18. Fung BM, Puon PS. Biophys. J. 1981;3:27.
19. Cole WC, LeBlanC AD, Jhingran SG. Magn. Reson. Med. 1993;29:19.
20. Bertram HC, Karlsson AH, Rasmussen M, Dønstrup S, Petersen OD, Andersen HJ. J. Agric. Food. Chem. 2001; 49:3092.

21. Kroeker RM, Henkelman RM. Analysis of biological NMR relaxation data with continuous distributions of relaxation times. J. Magn. Reson., 1986;69:218.
22. Bertram HC, Dønstrup S, Karlsson AH, Andersen HJ. Meat Sci. 2002;60:279.
23. Bertram HC, Purslow PP, Andersen HJ. J. Agric. Food Chem. 2002;50:824.
24. Bertram HC, Rasmussen M, Busk H,Oksbjerg N, Karlsson AH, Andersen HJ. J. Magn. Reson. 2002;157:267.
25. Bertram HC, Whittaker AK, Karlsson AH, Andersen HJ. J. Agric. Food Chem. 2003;51:4072.
26. Bertram HC, Karlsson AH, Andersen HJ. Meat Sci. 2003;65:1281.
27. Bertram HC, Rosenvold K, Schäfer A, Andersen HJ. Meat Sci. 2004;66:915.
28. Trout GR. Meat Sci. 1988;23:235.
29. Honikel KO. Meat Sci. 1998;49:447.
30. Brown RJS, Capozzi F, Cavani C, Cremonini MA Petracci M, Placucci G. J. Magn. Reson. 2000;147:89.
31. Tornberg E, Wahlgren M, Brøndum J, Engelsen SB. Food Chem. 2000;69:407.
32. Carr HY, Purcell EM. Am. J. Phys. 1954;94:630.
33. Meiboom S, Gill D. Rev. Sci. Instrum. 1958;29:688.
34. Hills BP, Wright KM, Snaar JEM. Magn. Reson. Imaging. 1996;14:715.
35. Hills BP, Wright KM, Snaar JEM. Magn. Reson. Imaging. 1996;14:305.
36. Bertram HC. Magn. Reson. Imaging. 2004;22:557.
37. Tornberg E, Larsson G. Proceedings from 32nd European Meeting of Meat Research Workers, Ghent, Belgien, 1986, p 437.
38. Borisova MA, Oreshkin EF. Meat Sci. 1992;31:257.
39. Micklander E, Peshlov B, Purslow PP, Engelsen SB. Trends Food Sci. Technol. 2002;13:341.
40. Bertram HC, Engelsen SB, Busk H, Karlsson AH, Andersen HJ. Meat Sci. 2004;66:437.
41. Dawkins NL, Gager NL, Cornillon JP, Kim Y, Phelps O. J. Food Sci. 2001;66:1276.
42. Yano S, Tanaka M, Suzuki N, Kanzaki Y. Food Sci. Technol. Res. 2002;8:137.
43. Fjelkner-Modig S, Tornberg E. Meat Sci. 1986;17:213.
44. Bertram HC, Andersen HJ, Karlsson AH, Horn P, Hedegaard J, Nørgaard L, Engelsen SB. Meat Sci. 2003;65: 707.
45. Butler JP, Reeds JA, Dawson SV. SIAM J. Num Analy. 1981;18:381.

Time-Domain NMR in Quality Control: More Advanced Methods

Gisela Guthausen[1], Harald Todt[1], Wolfgang Burk[1], Dieter Schmalbein[1], and Andreas Kamlowski[2]
[1]*Minispec Division, Bruker Optik GmbH; and*
[2]*MicroSpin Division, Bruker Biospin GmbH, Silberstreifen, 76287 Rheinstetten, Germany*

Introduction

The classic application of time-domain (TD-)NMR in food science and industry are devoted to products containing either a dominating amount of water or fat with the aim to determine the concentration or the amount of a specific component. The analysis result is commonly the fat content, in some examples also the moisture content. This is due to the fact that in TD-NMR almost no spectral resolution is available and that the transverse and longitudinal NMR relaxation properties of fat and water molecules are not substantially different. Moreover, the selectivity in commonly known TD-NMR pulse sequences is too small to guarantee a clear separation of signals. The classical approach was to pre-dry the samples either for example by an oven, chemical reagents like $CuSO_4$ or *via* infrared or microwave drying processes. The disadvantage of the pre-drying is clearly that it is a time-consuming method requiring labor time and rendering the TD-NMR application a two-step approach. Therefore, more elaborate experiments have to be examined in order to address these application questions on food products. Due to the technical development of the TD-NMR spectrometer, especially of the electronic part in recent years, also more sophisticated experiments can be implemented and run for quality control in food science and industry. In this paper the physical background and selected examples of new applications will be shown.

Gradient Experiments

Fat and Water Content Determination

In parallel to the already discussed relaxation parameters, diffusion properties can be exploited by pulsed field gradient (PFG) experiments in order to separate signal contributions of different molecules. As an example, the diffusion coefficients of water and oil differ by about a factor of 100. A variety of PFG sequences is available, allowing dedicated approaches to the individual problem. As an example, the conventional Hahn Echo equipped with pulsed gradients and the PFG stimulated echo sequence are shown in Figure 1.

The key application—as discussed—is the determination of the fat/oil content in fresh food in the presence of a high water content. By adjusting the timing of the sequence properly, the contrast of the components to be differentiated can be optimized. In Figure 2 the echo attenuation of a fresh salmon sample is depicted as a function of the square of the gradient strength. The fast and slowly decaying components are due to water and oil on the time scale of this experiment, respectively. Extrapolation of the slowly decaying phase (solid line) to zero gradient strength provides a measure of the oil content. Calibration of the signal against known standards allows the determination of the relative oil or fat concentration. The calibration can be done very quickly and requires only few well-known reference samples for each type of product.

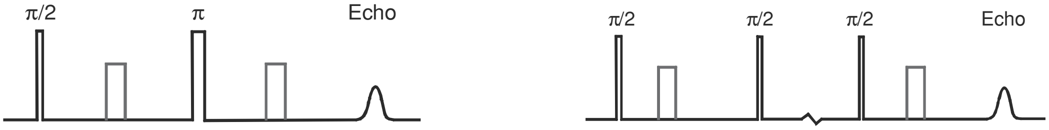

Fig. 1. PFG Hahn-Echo (left) and PFG stimulated echo PFG-STE (right) used in TD-NMR for discriminating components exhibiting different diffusion properties. Whether to use Hahn or stimulated echo depends on the relaxation and diffusion properties of the product to be investigated.

Graham A. Webb (ed.), Modern Magnetic Resonance, 1735–1738.
© 2008 *Springer.*

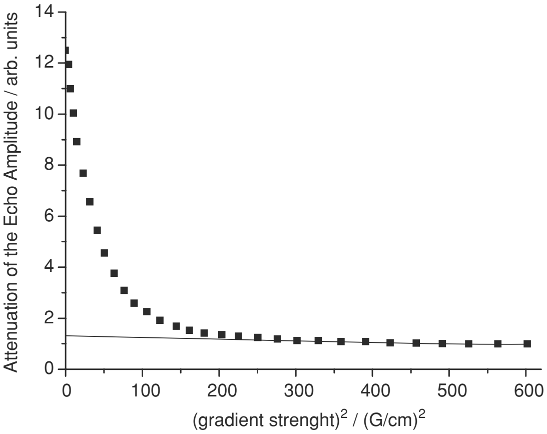

Fig. 2. Echo attenuation as function of the squared gradient strength measured on a fresh salmon sample. The diffusion coefficients of water and oil differ strongly such that at larger gradients only the oil signal is left. By extrapolating the oil signal to zero gradient strength, the oil or fat content can be determined [1].

Clearly, the PFG-NMR approach implies that the sample can be readily investigated without the need of predrying. The method was examined for different products such as sauces, mayonnaises, margarines, and dairy products with fat content in the range of 4–80%.

It should be pointed out that not only the simple Hahn echo pulse sequence with increment of the echo time as in Figure 2 can be applied. More elegant solutions make use of multi-echo sequences such as the CPMG (named after Carr, Purcell, Meiboom, and Gill [2]). In addition, destroying effects of eddy currents at small echo times can be avoided using static gradients.

A disadvantage of the method shown so far is that sample weight is required for determination of fat or oil concentration. This disadvantage can be circumvented by acquiring the FID directly after the dead time of the TD-NMR instrument and back-extrapolating the amplitude to time $t = 0$. This will lead to the total ^{1}H NMR signal that is proportional to weight of the sample. Thus, the overall one-step measurement time can be reduced to several 10 s.

Droplet Size Determination

In emulsions, a very important quantity and QC parameter in food science and industry is the distribution of droplet sizes. The droplet size of the dispersed component determines for example the microbial growth properties, eventually the product's shelf life, and the mouth feeling of the finished product. Examples of common food emulsions are mayonnaise for oil droplets, margarine for water droplets.

The physical background of droplet size distributions measured by PFG-STE NMR can be found in the restricted diffusion phenomenon. It was observed that the δ dependence (duration of the gradient pulses) of the transverse magnetization decay reflects the spatial restriction of the molecules under observation. The decay curves exhibit characteristic curvatures which can be described analytically and analyzed in terms of the geometrical dimensions [3]. Assuming a spherical geometry of the droplets and a log normal distribution of droplet sizes in the samples, an analytical expression can be found. Fitting to the NMR data reveals parameters like mean droplet diameter and width of the droplet size distribution. The analysis can be made volume related or related to the number of droplets.

Of course, either water signal in case of oil droplet or oil signal in case of water droplet has to be suppressed. This can be achieved for example by gradients or by an additional inversion pulse, respectively. In Figure 3, an example of a decay curve measured with a Bruker 20 MHz mq 20 minispec system and the corresponding droplet size distribution are shown.

Combined Relaxation Analysis in Foods with High Water Content

As already indicated, the knowledge of fat or oil and water content of products is of prime importance in food industry. It is well known that the transverse and also the longitudinal relaxation times of water and fat differ. The same is valid for several other ingredients as for example proteins. The relaxation properties of these components are exploited in the application discussed in this section. Clearly, as the differences in relaxation times are relatively small and as magnetization relaxation depends also on other parameters like temperature, salt concentration and the local environment of the molecules, a common measurement of well known relaxation times like T_1 and T_2 is not sufficient for establishing a good correlation to the sample properties. Therefore, a combined relaxation experiment is to be applied, where the magnetization at a given time is determined by both, the longitudinal and the transverse relaxation (Figure 4). There are several approaches to realize this aim. One of them uses a steady state dynamic equilibrium [4], others [5] make use of the longitudinal recovery of magnetization and measure the transverse magnetization at each point of the T_1 curve by CPMG. Using a modified sequence which also acquires the FID in addition to the echoes, "hard" components can also be measured and analyzed. Thus, the relaxation properties $T_1(M(t,T_2), M(t,T_2^*))$, $T_2(M(t,T_1))$, and $T_2^*(M(t,T_1))$ can be measured within one experiment. The information obtained by this experiment is huge and not easily analyzed quantitatively in terms of classic

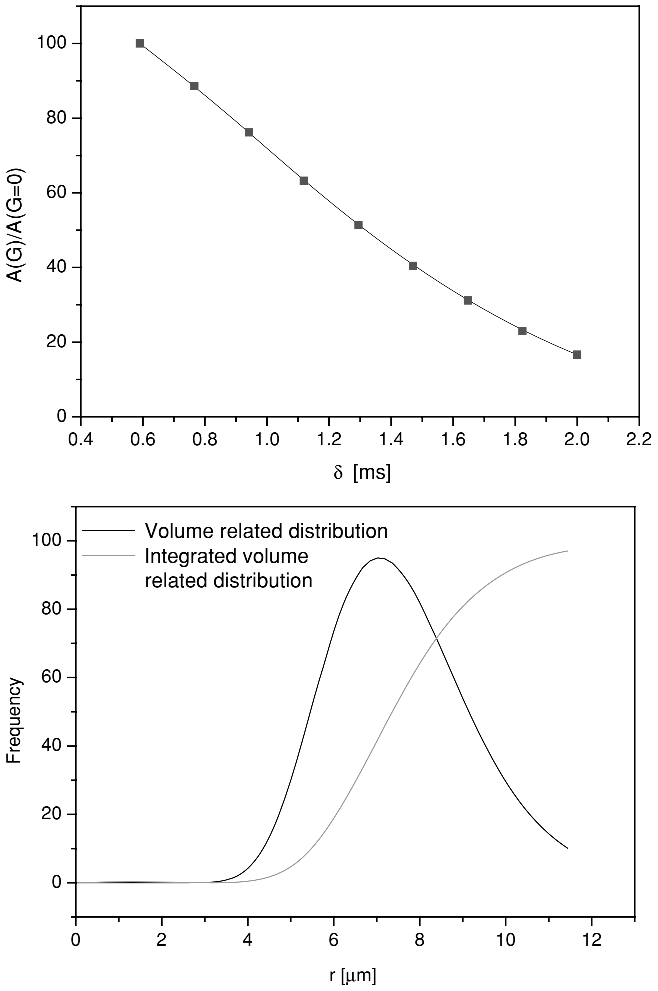

Fig. 3. Decay function A(G)/A(G = 0) and the corresponding droplet size distribution function as measured on an mq 20 minispec and analyzed via the minispec software.

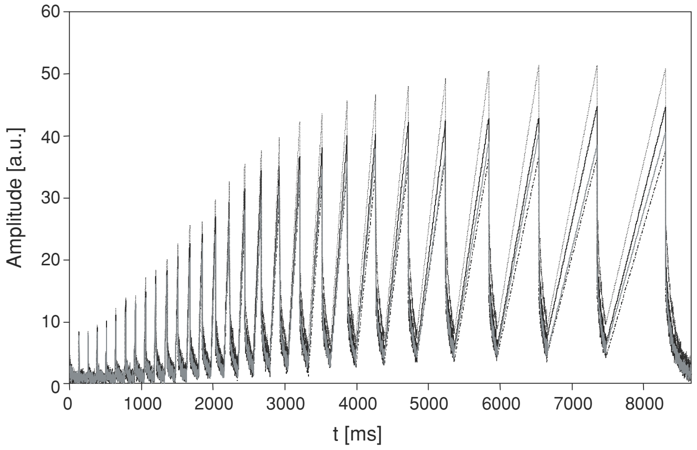

Fig. 4. Time dependence of the NMR signal measured by a combined relaxation time experiment. Four different samples each with a specific composition are shown. The differences in the time dependence due to the specific relaxation times are obvious.

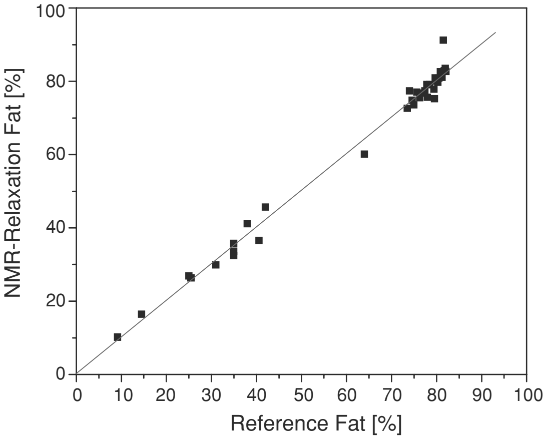

Fig. 5. Fat content as determined by the combined relaxation analysis for margarines, mayonnaises, and sauces. A clear correlation with the reference fat content could be established. The correlation coefficient amounts to 0.994, the statistic F-factor to 2814. The correlation considered 35 different samples with a fat content between 9.2 and 82.1%.

relaxation time analysis. Therefore, another approach was chosen for data processing, using statistical, i.e. chemometric methods [6]. These methods are commonly applied for example in near infrared studies. One of the advantages is, that a correlation with several sample properties can easily be established. As an example in Figure 5 the results of fat analysis on mayonnaises, margarines, and sauces being characterized by wet chemical methods are shown (samples from Unilever Bestfoods, the Netherlands). Please note that the three types of products fall onto the same calibration curve. This implies the possibility to establish a common calibration model which will be valid for several products thus reducing the effort which is usually necessary for chemometric data processing.

Conclusion

Two TD-NMR methods for content determination in wet foods were presented, namely the combined relaxation analysis and the PFG-NMR experiments. The experiments were discussed and typical measurement results were shown. In addition, a typical application of TD-NMR in food industry, the determination of droplet size distribution functions, was outlined. All measurements were performed with Bruker minispec instruments at 20 MHz.

Acknowledgements

We would like to thank S. Sies, Unilever Bestfoods The Netherlands, R&D Baarn, and R. Poser, I. Dederer from BAFF (Bundesanstalt für Fleischforschung in Kulmbach, Germany) for providing us well-characterized samples.

References

1. Todt H, Burk W, Guthausen G, Guthausen A, Kamlowski A, Schmalbein D, Quality control with time-domain NMR. Eur. J. Lipid Sci. Technol. 2001;103(12):835–40.
2. a) Carr HY, Purcell EM. Phys. Rev. 1954;98:630.
   b) Meiboom S, Gill D. Rev. Sci. Instrum. 1958;29:688.
3. Callaghan PT. Principles of NMR Microscopy. Clarendon Press: Oxford, 1993 and references therein.
4. Guthausen A, Zimmer G, Blümler P, Blümich B, J. Magn. Reson. 1998;130:1.
5. Tinsley FC, Taicher GZ, Heiman ML. Obesity Res. 2004;12: 150–160.
6. see http://www.chemometrics.net/.

Time-Domain NMR in Quality Control: Standard Applications in Food

Harald Todt[1], Gisela Guthausen[1], Wolfgang Burk[1], Dieter Schmalbein[1], and Andreas Kamlowski[2]

[1] *Minispec Division, Bruker Optik GmbH; and*

[2] *MicroSpin Division, Bruker Biospin GmbH, Silberstreifen, 76287 Rheinstetten, Germany*

Introduction

Although NMR is ubiquitously applied for chemical analysis and structural research as well as in its clinical adaptation of magnetic resonance imaging (MRI), its use in quality control/quality assurance (QC/QA) is often not very well known. It is this successful application field of NMR, which is dealt with in this contribution.

The field of QC/QA with pulsed NMR has started about 35 years ago in a cooperation of Unilever Research (The Netherlands) and Bruker Physik AG. The idea was raised to build a small table-top time-domain (TD)-NMR analyzer for the solid-to-liquid ratio analysis on fat compositions. The method based on the first TD-NMR analyzers has become an immediate success and was introduced in all major fat facilities world-widely. Nowadays, this method is widely adapted and well known as the so-called Solid Fat Content (SFC) determination [1]. It is recognized as an International Standard Method [2–4].

Presently, the pool of TD-NMR applications in the field of QC/QA summarizes more than 50 different procedures of which more than half are targeted towards food.

In this article, the following application fields will be addressed:

A) Determination of the SFC in fat compositions
B) Simultaneous oil and moisture determination in food (moisture content below approx. 15%)
C) Oil content determination in pre-dried olives

Time-Domain NMR (TD-NMR)

As TD-NMR experiments are either based on relaxometry or diffusiometry, i.e. on differences of the samples in their NMR-related properties, there is no need for highly homogenous magnetic fields or high field strengths as commonly required in FT-NMR. Thus, permanent magnet technology (typically at 10 or 20 MHz proton frequency) is well suited. This significantly reduces overall system costs as well as running costs (no cryogens required as in case of superconducting magnets). Moreover, right from the start, Bruker's TD-NMR instruments have been designed as bench-top systems with small footprint.

Most common TD-NMR applications are based on simple NMR pulse sequences, like the Free Induction Decay (FID) or the Hahn-echo acquisition [5]. TD-NMR systems can, however, also be used to measure relaxation time constants, like T_1, T_2, $T_{1\rho}$, or to perform pulsed field gradient (PFG-)NMR experiments (see also the accompanying article in this book "Time-Domain NMR in Quality Control: More Advanced Methods").

In order to apply the TD-NMR method to QC/QA, the NMR signal of interest (amplitudes or differences in the relaxation time constants) are correlated to the physico-chemical property of interest, i.e. the TD-NMR system is calibrated against reference values. For instance, the liquid and solid fat components differ in their respective relaxation behavior. Therefore, the FID signal of a mixture of both components typically also exhibits two components: a fast (solid fraction) and a slow (liquid fraction) decaying part. Sampling the signal amplitudes directly after pulse excitation and after the decay of the solid fraction provides a measure of the solid (liquid) fat content [6].

A. Determination of the SFC in Fat Compositions

As mentioned in the introduction, the SFC application is widely used. The SFC values of the fat composite are measured as function of temperature of the sample (Figure 1). This way, characteristic melting curves are gathered indicative of the fat composition. These melting curves are critical production parameters for the manufactures of fat compositions.

Different procedures and tempering schemes are described in the International Standard Methods [2–4]. The most important procedures will be introduced in the following.

Direct Method

The direct SFC method relies on a set of three calibration standard samples for instrument calibration. The FID

Graham A. Webb (ed.), Modern Magnetic Resonance, 1739–1743.
© 2008 *Springer.*

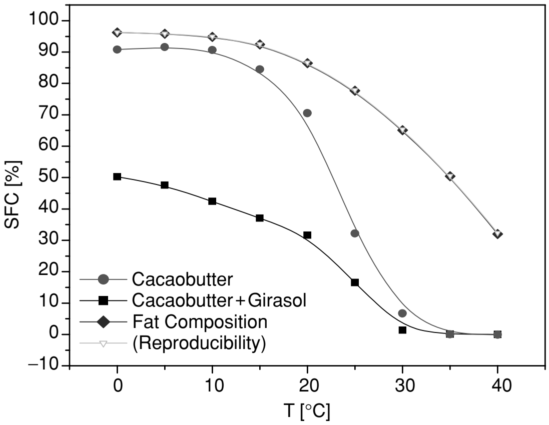

Fig. 1. SFC values determined using the serial method. Different food compositions are shown together with a reproducibility measurement.

pulse sequence is utilized for the acquisition. In order to obtain the SFC value at a particular temperature, correction factors (referred to as F-, K-, and O-factors) need to be applied (cf. Figure 2) which are determined from the calibration standard samples. After the FID acquisition, the amplitudes of two sampling windows are calculated. The so-called F-factor accounts for the instrument dead time (ca. 8 μs), and corrects the amplitude of the solid fraction; the K-factor accounts for the effect of signal decay due to magnet inhomogeneity. Finally, the O-factor accounts for possible signal offsets. In sum, the analysis of unknown samples is carried out by applying one single TD-NMR FID measurement followed by correction using the above described factors.

This method is applied as a QC tool to control the production of the fat compositions according to the desired properties. Regarding the tempering and sample handling procedures, two approaches are adapted (Figure 3), which do not necessarily provide the same SFC values.

Parallel Method

The parallel method uses at least one sample for each temperature. As a matter of fact, it's the fastest method to obtain the SFC values as a function of temperature. All samples are crystallized at once at 0 °C together (typically for 1 h). Subsequently, the tubes are distributed over the different water baths at the different temperatures. The TD-NMR measurement completes this parallel SFC method.

Serial Method

The serial method uses one sample, which encompasses all desired temperatures followed by the TD-NMR measurement. The sample is crystallized again at 0 °C and then inserted into the first water bath. After the tempering time has passed and the first NMR analysis has been

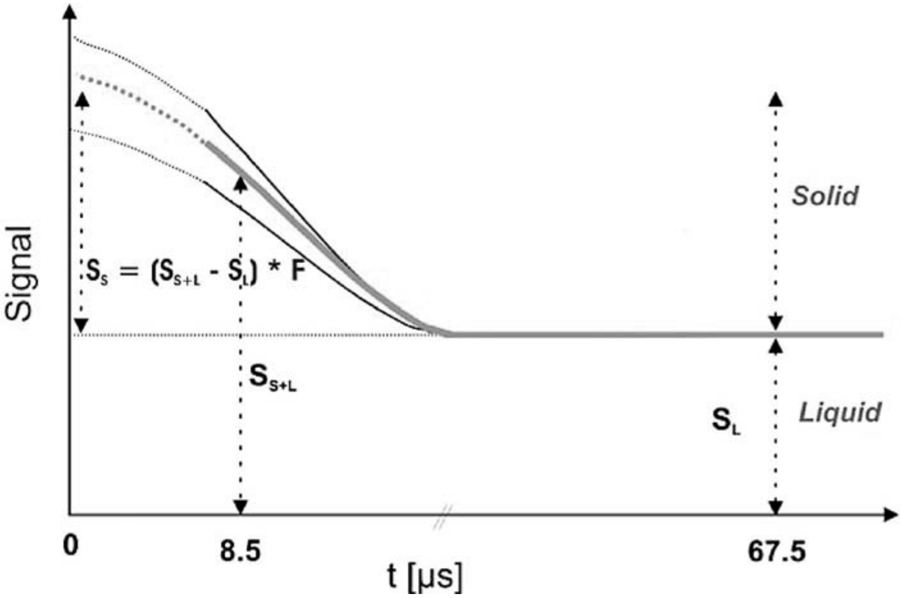

Fig. 2. Time scheme of the FID and its analysis in case of SFC determination.

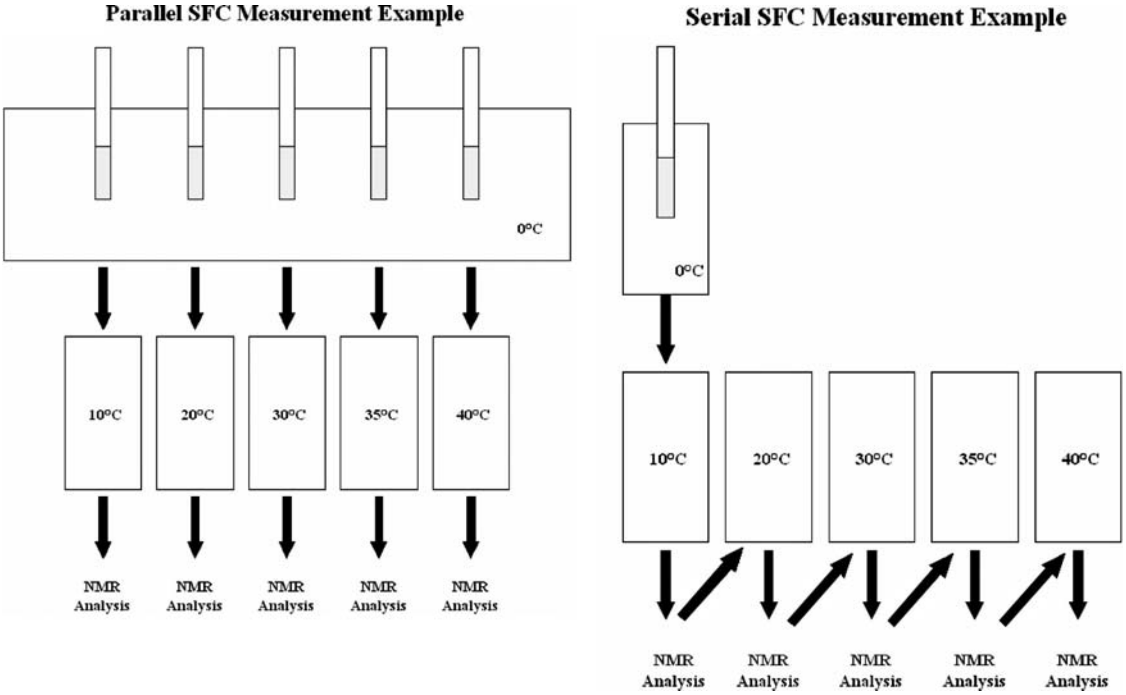

Fig. 3. Sample Handling of parallel (left) and serial SFC method (right).

performed, the same tube is directly inserted into the next bath with next measurement temperature and so on. This method has the advantage that less samples need to be prepared for a complete SFC determination.

Indirect Method

The direct method, which is well suited for QC, assumes that the average F-factor is the same for all samples. This is, strictly speaking, not correct. The so-called indirect SFC method overcomes this limitation, leading to the "correct" SFC values. This is required in research and development (R&D) of new fat compositions. The indirect method is based on a two step TD-NMR measurement: First, at the desired sample temperature, the liquid part of the NMR signal is measured while the sample is placed only within the homogenous region of the RF coil. Secondly, the sample is completely melted (typically at 60 °C) and measured again to obtain the NMR response of the totally melted sample. Both amplitudes are used to calculate the SFC result, taking into account the temperature-dependence of the NMR signal amplitudes. Clearly, no calibration standards are required for this approach.

Solid-Echo Method

Besides the direct and indirect SFC methods, the so-called solid-echo method is used in R&D environment for SFC determination [7]. Due to the nature of the solid-echo pulse sequence, both liquid and solid fractions of the sample contribute to the solid-echo amplitude. However, as in case of the direct method, calibration via calibration standard samples and correction factors is required.

Comparison with Dilatometry/Solid Fat Index

The NMR approach is well-established throughout the world. However, historically dilatometry has been applied, i.e. the change in the sample volume as a function of temperature is measured. The result of which is known as the Solid Fat Index (SFI).

From the TD-NMR SFC perspective, the dilatometry method has considerable drawbacks:

- Sample preparation is more demanding, for instance, the fat (composition) must be de-aerated and an indicator has to added (required for improved visualization).
- Samples containing some ingredients (might) react with indicator—SFI is not applicable for these samples.

- SFI does not work for fats that are higher in solids than about 80%.
- Dilatometry by virtue of the method is a serial method.

Moreover, it has been shown [8] that the TD-NMR/SFC approach is much more accurate. An increased accuracy of a factor of five has been reported. Note, since a chemical indicator is utilized, dilatometry has to be considered as a wet chemical method.

Automation of SFC Analysis

For ultimate accuracy and reproducibility combined with high sample throughout an SFC automation system is required. This is because the time interval for the tempering schemes have to be obeyed. For special fat compositions tempering time errors like few minutes lead to significant changes in the results, as the fat composition might be more or less crystallized. A few robot SFC systems (for instance, at Unilever Research, The Netherlands) with Bruker minispec TD-NMR analyzer are installed in the world.

B. Simultaneous Oil and Moisture Determination in Food (Moisture Content Below Approx. 15%)

Only few years after the introduction of the SFC method with TD-NMR, the application area of TD-NMR has been widened by applying the Hahn-echo NMR pulse sequence (Figure 4) to determined the total oil and moisture content in food samples. Almost all types of food samples could be analyzed providing the water content is minor (typically below 15%) [9], see Table 1. Again, the oil and moisture analyses for seeds and seed residues have become International Standards Methods [10–12]. According to these methods, both the FID signal amplitude, S_1, and the echo amplitude, S_2, are measured (see Figure 4). The amplitudes S_1 (at 50 μs following the 90° pulse) and S_2 (at $\tau = 7$ ms) represent the sum of the oil and moisture signals and the oil content, respectively. Thus, the amplitude difference, $S_1 - S_2$, is due to the moisture content.

The oil and moisture contents can be measured simultaneously with the system after primary calibration. The calibration is performed only once and will be automatically archived.

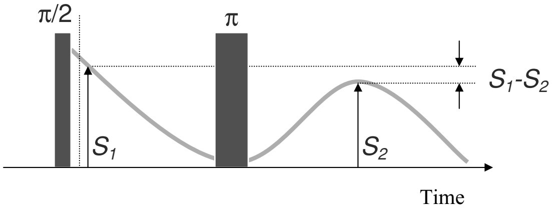

Fig. 4. Hahn-echo sequence and data processing for simultaneous determination of moisture and oil content in seeds.

Table 1: Applications of TD-NMR for determination of moisture and oil.

- Moisture and fat/oil content in (dry) food:
  - Cocoa powder, cocoa beans, and chocolate (mass and liquor)
  - Snacks, cereals, chips, brezel, fischli, bread
  - All types of nuts and almonds, cookies, beans, lentils, linseed
  - Milk Powders, bakery powders, baby food, low moisture cheese, soup powders
  - Flavors, flour, semolina, starch, sugar beet
- Moisture/oil in all types of seeds and residues
- Moisture/fat content in animal feed

Advantages of NMR, compared to other standard methods like chemical oil extraction, are a minimum sample preparation and a quick analysis time which is in the order of seconds. Moreover, chemical solvents are not required lifting the problem of waste disposal. Naturally, the TD-NMR systems are turn-key systems which do not require skilled personnel.

Obviously, different products (e.g. rape seeds/sunflower seeds) require different calibration curves. In Figure 5 a typical calibration curve is depicted. Generally, only a few reference samples typically 3 to 5-are required. The values from reference methods, like Soxhlet extraction and Karl-Fischer Water Determination, are utilized to calibrate the TD-NMR equipment. In seed breeding applications, however, the oil calibration is

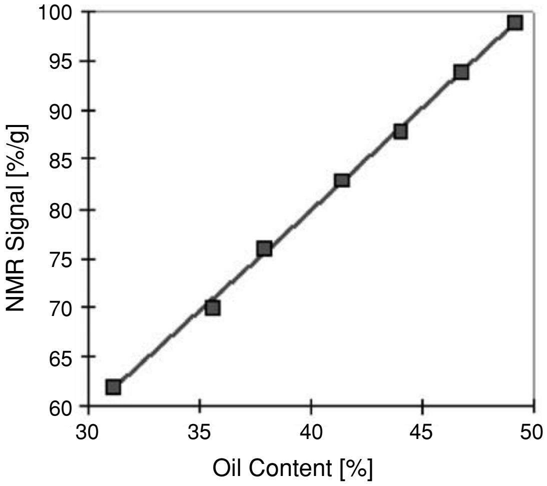

Fig. 5. Calibration Curve for oil determination in seeds. The mass-normalized NMR signal is a function of the oil concentration.

done differently: Pure oil samples are utilized for system calibration. In addition, the oil sample mass is taken into account by weighing. This way, systematic errors and uncertainties from the reference methods are excluded. For inhomogenous samples likes big seeds or nuts, TD-NMR systems with large measurement volumes are available.

Fat Content Determination in Chocolate

Another standard method is the determination of fat content in chocolate, more precisely in chocolate mass and paste as well as in chocolate liquor [13]. As chocolate samples contain a small amount of iron due to the production process, the Hahn-echo pulse sequence is applied with shorter pulse spacing, typically 200 μs only (compared to the 3.5 ms spacing of the seed application). This method also requires that all fat is melted. Whereas pure cocoa butter melts at 38 °C, fat blends containing fats like vegetable oils might required higher pre-tempering temperature, in some cases even up to 50 °C. Calibration of the TD-NMR application can be done conveniently with pure cocoa butter. Alternatively, well-characterized chocolate samples can be used for calibration. Often and unlike the seed application (cf. above) multiple products can be analyzed with one calibration line.

C. Oil Content Determination in Pre-Dried Olives

Oil and moisture determination on food samples containing only bound water can be done easily, though only sample weighing is required. An overview of typical applications is provided in Table 1. However, samples with high amounts of water/free water cannot be handled this way. The NMR signal from water will interfere with that of the oil. This is because the relaxation times of free water and oil are rather similar. Under these circumstances, the samples (like olives, sausages, fish, meet) need to be predried to remove free water from the sample. Following this preparation step, the Hahn-echo sequence is adapted to determine the oil content precisely. This method has found more than a hundred of users only in Spain for the precise oil content determination in olive paste [14]. Experience teaches that the upper limit for moisture and/or water determination without pre-drying is about 15% (see the article in this handbook “Time-Domain NMR in Quality Control: More Advanced Methods” for an alternative approach).

Conclusion

Due to the multiple advantages of the NMR method mentioned above the popularity of TD-NMR in QC/QA is steadily increasing. Especially in food industry more demanding and challenging applications like the analysis of wet food or protein determinations are coming up. Naturally, high-resolution NMR can easily provide the solution to these application. However, like in the early day of TD-NMR (see Introduction) the investment costs for such a system are simply too high. On the other hand, TD-NMR instrumentation seem to be an ideal QC tool to provide answers to these new challenges also because of its relatively low investment costs.

Acknowledgment

As TD-NMR applications in food industry have been often developed in cooperation with Unilever Research / The Netherlands, their input is acknowledged at this occasion.

References

1. Bruker minispec: Food Industry SFC Application Notes Numbers 1, 2, 4, 5 and 6.
2. American Oil Chemist Society AOCS Official Method Cd 16b – 93: SFC by Low Resolution Magnetic Resonance.
3. IUPAC Norm Version 1987: 2.150 (ex 2.323) Solid content determination in fats by NMR (Low resolution nuclear magnetic resonance).
4. ISO 8292: 1991(E)/International Standard: Animal and vegetable fats and oils—Determination of solid fat content—Pulsed nuclear magnetic resonance method/First Edition 1991-12-01.
5. Hahn EL. Spin echos. Phys. Rev. 1950; 80:580–94.
6. van Duynhoven J. Determination of MG and TG phase composition by TD-NMR. J. Am. Oil Chem. Soc. 2002; 79(4).
7. Gribnau MCM. Determination of solid/liquid ratios of fats and oils by low-resolution pulsed NMR. Trends Food Sci. Technol. 1992;3(August/September).
8. Bruker minispec: Food Industry SFC Application Note Number 4.
9. Bruker minispec: Food Industry Application Note Number 7/Food Applications.
10. American Oil Chemist Society AOCS Ak 4-95: Simultaneous Determination of Oil and Moisture Contents of Oilseeds Using Pulsed NMR Spectroscopy (1999).
11. ISO/CD 10632: Oilseed Residues: Simultaneous Determination of Oil and Water Contents: Method using Pulsed NMR/June 1993.
12. ISO 10565: 1995 (E): Oilseeds—Simultaneous determination of oil and water contents—Method using pulsed nuclear magnetic resonance spectrometry.
13. Bruker minispec: Food Industry Application Notes Numbers 14 and 31.
14. Bruker minispec: Information Flyer Food Industry Number 7/Oil Content in Olives.

Nuclear Magnetic Relaxation in Starch Systems

Huiru Tang[1,2] and Yulan Wang[3]
[1]School of Chemical Science, Shaanxi University of Science and Technology, Xianyang, Shaanxi, P.R. China;
[2] State Key Laboratory of Magnetic Resonance and Molecular and Atomic Physics, Wuhan Institute of Physics and Mathematics Academy of Science, Wuhan 430071, P.R. China; and
[3]Biological Chemistry Section, Biomedical Sciences Division, Imperial College London, South Kensington, London SW7 2AZ UK

Introduction

Native starch granules possess some unique microstructures with a distribution of structural domains having different dynamic properties [1–5]. These properties together with the molecular interactions in starch are major factors critically affecting the molecular responses to processing and physical properties of the resultant products. Therefore, in order to understand the starch functionality, such as in adhesives, biodegradable plastics [6] and drug-delivery systems [7], one has to understand the dynamics of the individual components, such as polysaccharides, water, and other additives, and the whole interactive complex. However, the complexity of the starch dynamics are far from fully understood. Few data are available to quantitatively describe the starch dynamics and the effects on starch functionalities. In the literature, starch polysaccharides are still frequently described *only* broadly as “rigid” for the crystalline forms and “mobile” for the amorphous ones.

There are three types of native starch, Type-A, normally found in cereals, Type-B, which are found in tubers, and Type-C, which are from legumes. Two distinct starch polysaccharides are present, namely, amylose that is a polymer of glucose (glucan) with $\alpha(1\rightarrow4)$ linkages and amylopectin, which is an $\alpha(1\rightarrow4)$ glucan with some $\alpha(1\rightarrow6)$ branches. The polysaccharides can either be in the crystalline or amorphous forms. Amongst the crystalline forms, the glucan is present as double helices which are arranged in two distinct fashions [8,9] forming two distinct crystal packings, A-type and B-type.

On the more macroscopic scale, the components of the starch granules, including water, polysaccharides, and some small molecules such as lipids, collectively form the microstructures such as the amorphous growth rings and semicrystalline hard shells. For the hydrated starch, which is arguably one of the simplest starch system, the complexity is expected to include (1) the presence of multiple phases and compartments for the polysaccharides and water, (2) variations in the interactions between the polysaccharides, and (3) the interactions between polysaccharides and other molecules such as water, which often leads to more variations to the polysaccharide properties. When processed, starch structure together with its dynamics and interactions are profoundly altered and the participation of the other molecules such as polyols and proteins, increased the complexity of the starch systems. It is thus not trivial to gain insights into the dynamics of each chemical moiety or the whole systems during the changes. The ideal research methods for these systems ought to (1) be non-invasive and non-destructive to facilitate *in situ* investigations, (2) be able to provide information on molecular structure, dynamics and interactions, (3) be useable for multiphasic and multi-compartmental systems, and (4) to be able to access information at different time and length scales. Undoubtedly, NMR is the method of choice offering a number of nuclei, including C, H, and O, as reporting probes. Water properties have been extensively investigated with NMR in the native starch granules [3,4,10–16] and in the processed starch systems and mixtures [17–20] (e.g. doughs and bread). However, such investigation of molecular dynamics of starch polysaccharides are not comprehensively documented. The proton relaxation times of polysaccharides measured either *via*. ^{13}C signals or directly from ^{1}H under MAS offers an unique opportunity for studies of starch polysaccharides [11,21–23]. Proton relaxation induced spectral-editing techniques provide probability to obtain the structure details for starch polysaccharides in various dynamic states [4,5,21]. ^{13}C NMR properties are also useful for the same purposes. The future of such studies will be increasingly focused on (1) the dynamics of polysaccharides, (2) interactions between the polysaccharides and other molecules, (3) the relationships between the physical properties of starch and the domain distribution and dynamic state of the starch polysaccharides, (4) how these properties are relevant in establishing and determining the response of starch granules to multi-parametric processing treatments, such as acid-hydrolysis and gelatinisation, and ultimately functionality.

This chapter will not attempt to compile the relevant literature exhaustively. Instead, the NMR-relaxation based strategies for studying the molecular dynamics

Graham A. Webb (ed.), Modern Magnetic Resonance, 1745–1754.
© 2008 *Springer.*

of polysaccharides and water in starch systems will be discussed.

General Considerations for NMR of Starch Systems

With modern spectrometers, NMR signals are recorded in the form of free induction decays (FIDs), which are the magnetisation changes as a function of time following a radio-frequency (RF) pulse (Figure 1a) or a pulse sequence (Figure 1). An NMR spectrum is obtained directly from Fourier transformation of such an FID,

$$S(\omega) = \frac{1}{2\pi} \int_{-\infty}^{+\infty} F(t) e^{-i\omega t} \mathrm{d}t \tag{1}$$

In the solid biopolymers such as starch, ^{1}H, and ^{13}C are the most useful nuclei for the purpose of NMR. For ^{1}H in such systems, the scalar couplings are relatively weak (1–200 Hz), the dominant nuclear magnetic interactions include dipole–dipole interactions (up to 100 kHz) and chemical shift anisotropy (CSA) (up to 10 kHz). The typical proton FID of solid starch (Figure 2a) consists of a fast decay part and a slower one [11–14,22–24]. The corresponding ^{1}H NMR spectrum has a broad peak of several tens kHz with a sharp one ($\sim$kHz) superimposed (Figure 2b). The ^{1}H NMR signals of biopolymers can be analysed directly from FID or in the frequency domains, which will be discussed in later sections. Useful information on molecular dynamics can be obtained from the dipole–dipole interactions between protons and that of a pair of protons is given as [25–27]:

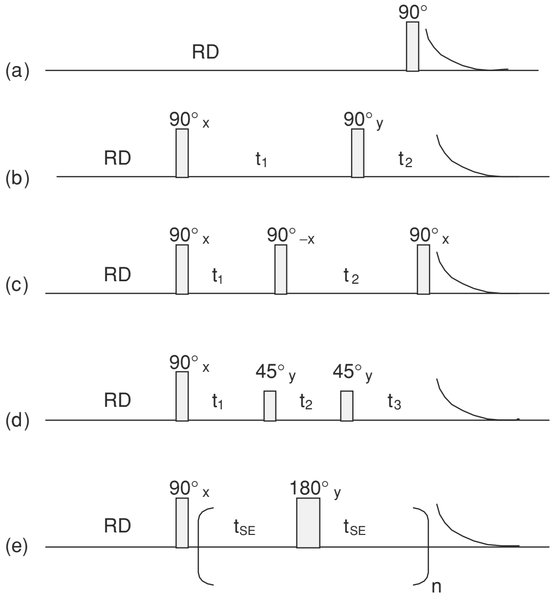

Fig. 1. Some pulse sequences for starch studies. (a) single pulse; (b) solid echo; (c) Goldman-Shen; (d) Jeener-Broaekhart; (e) CPMG sequence.

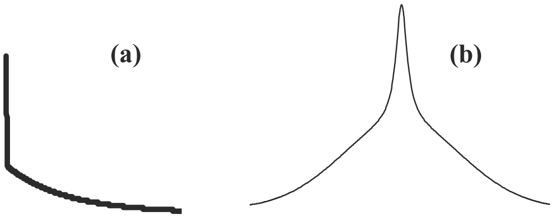

Fig. 2. A typical FID (a) and ^{1}H NMR spectrum (b) for solid biopolymers

$$\langle H_{\mathrm{D}} \rangle = \frac{\gamma^2 \hbar}{r^3} \left(1 - 3\cos^2\theta\right) = \gamma \langle H_{\mathrm{L}} \rangle \tag{2}$$

where γ is the proton magnetogyric ratio, $\hbar$ Planck's constant divided by 2π, $\langle H_{\mathrm{L}} \rangle$ the local dipolar field, r the inter-proton distance and θ the angle between the inter-proton vector and the external magnetic field. It is, thus, apparent that the dipole–dipole interaction is independent on the external magnetic field strength. Chemical shift describes the electronic environment in which spins are situated and is dependent on the dispositions of electronic charge about the nuclear sites. The form of these interactions is generally written as [25–27]

$$H_{\mathrm{CS}} = -\sum_i I_i \sigma_i B_0 \tag{3}$$

where I is the spin quantum number, σ the chemical shielding tensor of nucleus i and B_0 the external magnetic field. In a solution, fast molecular tumbling makes the chemical shift interactions isotropic, resulting in a single value of chemical shift as fingerprints of the spins from different environment. In a solid, however, a single value for chemical shielding is not adequate to describe such interactions since chemical shift varies with the orientation of the magnetic field with respective to the local principal axes.

The CSA has to be used to describe the interactions. This is not necessarily undesirable since CSA bears important structural and dynamic information [28]. Although no results have been reported for starch polysaccharides yet, ^{13}C CSA has already been used to study dynamics of a small sugar [29]. If a sample contains several crystallites with different orientation, the so-called powder spectrum [25–27] will arise (Figure 3), which contains information about the local electronic symmetry of the nuclear site. The CSA of a powdered sample describes the

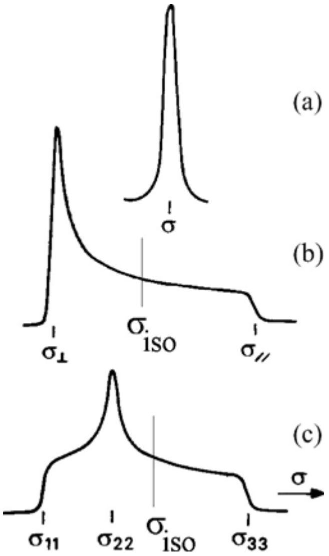

Fig. 3. Powder patterns for (a) spherically symmetric, (b) axially symmetric and (c) asymmetric patterns

three dimensional chemical shielding of the nucleus by the surrounding electrons and is conveniently parameterized with three principal components of the chemical shielding tensor [25–27], σ_{11}, σ_{22}, and σ_{33}, respectively (Figure 3). Three types of powder pattern are normally encountered depending on the principal values. If all three values are the same ($\sigma_{11} = \sigma_{22} = \sigma_{33}$, Figure 3a), it is said the pattern is spherically symmetric [25–27]; if only two of the values are the same ($\sigma_{11} = \sigma_{22}$ or $\sigma_{22} = \sigma_{33}$, Figure 3b), it is said the pattern is axially symmetric [25–27]; if all three values are different from each other ($\sigma_{11} \neq \sigma_{22} \neq \sigma_{33}$, Figure 3c), it is said the pattern is asymmetric [25–27]. The isotropic chemical shift is then given as [25–27]

$$\sigma_{\mathrm{AV}} = \frac{1}{3}(\sigma_{11} + \sigma_{22} + \sigma_{33}) \tag{4}$$

Using the so-called deshielding convention for CSA as shown [25–27] in Equation (5)

$$|\sigma_{33} - \sigma_{\mathrm{AV}}| \geq |\sigma_{11} - \sigma_{\mathrm{AV}}| \geq |\sigma_{22} - \sigma_{\mathrm{AV}}| \tag{5}$$

the shielding anisotropy $\Delta\sigma$ and the asymmetry η are given as

$$\Delta\sigma = \sigma_{33} - \frac{(\sigma_{11} + \sigma_{22})}{2} \tag{6}$$

$$\eta = \frac{|\sigma_{22} - \sigma_{11}|}{\Delta\sigma} \tag{7}$$

Two other functions were suggested to describe the tensor quantities of the chemical shift including the span (Ω), which is the difference between two extreme components, and the skew (κ) [25]:

$$\Omega = |\sigma_{33} - \sigma_{11}| \tag{8}$$

$$\kappa = \frac{3}{\Omega}(\sigma_{22} - \sigma_{\mathrm{AV}}) \tag{9}$$

Care should be taken when analysing the CSA properties since there are several different conventions in use.

In an external magnetic field, spins excited by an RF pulse will eventually relax back to the equilibrium state. Such relaxation processes are informative to molecular dynamics and interactions. Five major relaxation phenomena can be encountered in studying biopolymer systems, spin–lattice relaxation characterized by T_1, $T_{1\rho}$, $T_{1\mathrm{D}}$ and $T_{1\mathrm{Q}}$, and spin–spin relaxation characterized by T_2. These relaxation processes are sensitive to molecular motions with the rotational correction time (τ_{c}) from nanoseconds to milliseconds. Amongst the relaxation processes, the spin–lattice relaxation in the laboratory frame (T_1), is sensitive to the fast motions comparable to the Larmor frequency ($\tau_{\mathrm{c}} \sim 10^{-9}$ s) and the spin–lattice relaxation time in the rotating frame ($T_{1\,\mathrm{\rho}}$) is sensitive to motions comparable to the spin-locking field frequency ($\tau_{\mathrm{c}} \sim 10^{-3}$–$10^{-6}$ s). The spin–lattice relaxation time in the local dipolar field ($T_{1\mathrm{D}}$) is also of great value for studying motions and, in theory, is sensitive to motion frequency comparable to the local dipolar field frequency (10^2–10^5 Hz, $\tau_{\mathrm{c}} \sim 10^{-5}$–$10^{-2}$ s). $T_{1\mathrm{Q}}$ is the spin–lattice relaxation time for the quadrupolar nuclei such as ^{17}O and ^{2}H. When a specific site is labelled with ^{2}H, the line shape analysis for ^{2}H NMR spectra, which is dominated by the quadrupolar interaction, can provide quantitative information about fast dynamic process with a τ_{c} around 10^{-4}–10^{-7} s. Two dimensional ^{2}H exchange NMR experiments [30] allow access of information about slow motions (up to 1 s).

For native and processed starch systems, the nuclei ^{1}H, ^{2}H, ^{13}C, and ^{17}O are suitable for NMR studies to probe the structure and dynamics of the starch systems. Whilst the ^{13}C NMR signals are exclusively from polysaccharides, in the solid starch systems, proton NMR signals consist of those of polysaccharides and of water entangled together. This entangled information is often difficult to interpret unambiguously and the proton signals of the polysaccharides and water are often required to be separated. This can be done conveniently by D_2O exchange. When the polysaccharides are the focus of a study, samples can be suspended repeatedly [3,11,31] in excessive D_2O to remove the water protons in the system although such an exchange process will also remove the exchangeable protons (OHs). Consequently, the ^{1}H NMR signals will be predominantly from ring protons of the polysaccharides [3,11,31]. The natural abundance of ^{2}H and ^{17}O are too low to be sensitive enough for NMR studies of polysaccharides, nevertheless, the ^{2}H and ^{17}O NMR can be extremely useful if water is the focus of studies and the deuterated and ^{17}O labelled water are employed. When ^2H_2O is used, the starch systems will have to be exchanged with sufficient D_2O and the ^{2}H NMR signals will be mostly from water though some will be from exchangeable hydroxyl groups as well [3,4,14,32]. When $H_2{}^{17}O$ is used, on the other hand, the ^{17}O NMR signals will be exclusively from water [20,33–36]. With an appropriate combination of the above, water and polysaccharides signals can be selectively observed. Apart from those two nuclei, other nuclei with natural isotopes can also be employed depending on the purposes of studies. For example, if salts are important, NaCl can be used to provide source of signals for ^{23}Na NMR and NaF can be employed to observe both ^{23}Na [33,37] and ^{19}F NMR signals.

Solid Starch Systems

Starch systems can be either in native granular state, gels, and solubilized forms. For the solublized starch systems, their behavior will be more like polymers in viscous solution, therefore the NMR strategy will be similar to that of the solution state NMR.

All the other forms of starch systems are heterogeneous and contain multiple components in the proton relaxation time measurements [5]. For example, under magic angle spinning (at about 4–5 kHz) at the ambient temperature, wheat starch containing 33% water showed [38] two proton $T_{1\rho}$ components (4 and 7 ms). Another study showed that D_2O exchanged and D_2O saturated starch (Table 1) [5] had single T_1 (2.5–3 s) at 300 MHz and two $T_{1\rho}$ (2–4 ms, ~30 ms) processes. This suggested that the spin-diffusion was efficient on the time scale of a few seconds but not efficient on $T_{1\rho}$ time scale (~30 ms), hence multiple domains are present on the $T_{1\rho}$ time scale. The same system studied with PRISE (Proton relaxation induced spectral-editing) techniques showed [5] that that long $T_{1\rho}$ component (~30 ms) is associated with the polysaccharides in the crystalline lamellae whereas the short $T_{1\rho}$ component (2–4 ms) is associated with amylose in the gaps between amylopectin clusters. T_2 of these wet starch systems is more complex. However, with solid-echo sequence [39,40] (Figure 1B), proton T_2 can be measured for the spins experiencing residual dipolar interactions. Three T_2 components were observed [5] as short (14 μs), intermediate (~300 μs) and long (1–20 ms) components. With PRISE techniques, it has found that the short T_2 component is associated with polysaccharides in the crystalline lamellae whereas the other two components are associated with polysaccharides in the amorphous lamellae and amylose in the gaps between amylopectin clusters [5].

Table 1: Proton relaxation data for D_2O exchanged and saturated starch granules [5]

	T_1/s	T_1/ms	T_2/μs
Corn starch (Type-A) (D_2O ~ 45–55%)	2.64	24.9 (58%) 3.80 (42%)	14 (75%) 354 (12%) 9570 (12%)
Potato starch (Type-B) (D_2O ~ 45–55%)	2.78	29.8(57%) 2.92 (43%)	14 (70%) 296 (20%) 28300 (10%)
Pea starch (Type-C) (D_2O ~ 45–55%)	2.57	28.3(49%) 3.25 (51%)	14 (80%) 372 (10%) 20800 (10%)

Proton Spin–Spin Relaxation and Second Moment of Solid Starch Polysaccharides

For starch polysaccharides, there are two proton T_2 time scales, one that is shorter than 1ms and the other, which lies between millisecond and seconds. In both cases, the observed spin–spin relaxation process can be considered as a sum of the contributions from the dipole–dipole interactions, field inhomogeneity and other mechanisms (Eqution 10). In the dipolar interaction dominated systems, the first term in Equation (10) is so great that the contributions of the other terms are negligible. Therefore, when it is shorter than 1ms, T_2 can be conveniently measured from the time domain NMR signal (FID). However, when T_2 is long (>1m), the contribution of field inhomogeneity and other mechanisms will be significant and measurements from FID are no longer adequate. In such cases, T_2 has to be measured using CPMG method [41], in which the short T_2 component will be "filtered-off" by choosing an appropriate spin-echo delay t_{SE} (Figure 1), leaving only the long T_2 components. Examples of this situation include water in starch systems and amorphous polysaccharides in the water-rich environments, which will be dealt with in later sections. We shall deal with the short T_2 scale first.

$$\left(\frac{1}{T_2}\right)_{obs} = \left(\frac{1}{T_2}\right)_{D} + \left(\frac{1}{T_2}\right)_{IH} + \left(\frac{1}{T_2}\right)_{others} \qquad (10)$$

In solids, the ^{1}H NMR line shape is dominated by the dipole–dipole interactions (H_D) between the neighboring protons. In the absence of molecular motions, the FID of such a system decays rapidly; the corresponding proton NMR spectrum appeared as a broad featureless peak. Whilst many solid polymers featured a Gaussian decay for their proton FIDs, the FID of solid starch as in the cases of most solid sugars can be characterized neither by an exponential function nor by a Gaussian function. Therefore, it is often not practical to analyse the "rigid" starch by the spin–spin relaxation time T_2. Similar to the other carbohydrate systems such as glassy maltose [42], plant cell walls [43–45] and model systems [45–49], however, the proton FIDs can be approximated adequately by a Gaussian decay modified by a sinc function [43–50], from which the second moment of the NMR spectra, M_{2r}, can be evaluated quantitatively.

The rigid lattice second moment of a biopolymer can be calculated with lattice summation described by van der Vleck equation [51] if reasonable structure information is available. Proton positions in X-ray structures are often not accurate and the neutron structures give much more accurate results.

The true second moment, M_2, is independent of molecular motions. However, the measured second moment also known as residual second moment, M_{2r}, can be used to investigate the motions. In general, when the correlation time, τ_c, is greater compared to the inverse of linewidth, i.e. $\tau_c \gg (\gamma\sqrt{M_{2r}})^{-1}$, the hydrogen nuclei (protons) are said to undergo slow motions and give rise to so-called "rigid lattice" NMR spectra. When $\tau_c \approx (\gamma\sqrt{M_{2r}})^{-1}$, the fluctuation of the dipolar interactions becomes fast enough to average H_D to some extent and the M_{2r} is expected to start decreasing. If $\tau_c \ll (\gamma\sqrt{M_{2r}})^{-1}$, the hydrogen nuclei are said to undergo fast motions. The motion modulated reduction of the apparent proton second moment is observed by an amount $\Delta M_2 = M_2 - M_{2r}$.

The FIDs of starch consist of a fast decay and a slow decay parts. After removal of water (and OHs) by exhaustive D_2O exchange, the FID remains as two parts though the slow decay part is often reduced [11] in intensity due to the removal of the contributions of H_2O. The interpretation for such composite line shapes is often simplified as two different structure domains, "rigid" and "mobile" ones. Whilst such interpretation is true in many cases, it can sometimes suffer from oversimplification [52]. In fact, the multiple-decays in T_2 process can also arise in other situations, for example, when there are broad distributions of correlation times [53,54], cross-correlation effects in the anisotropic motion of molecular segments [55], and cross-relaxation between two spin species intermingled at short distances from each other [56]. It is therefore always desirable to ascertain the nature of the multiple-component decays experimentally. This can be achieved by inspecting the shapes of the dipolar echoes and monitoring the behaviour of the magnetisation transfers *via* the Goldman-Shen experiment [56] (Figure 1c).

By using the Jeener-Broekaert sequence [57] (90°_x-t_1-45°_y-t_2-45°_y-t_3-acq, Figure 1d), some Zeeman order can be transferred into the dipolar order, allowing the measurement of spin–lattice relaxation times along local dipolar fields (T_{1D}). For a homogenous solid biopolymer, when $t_1 \approx T_2$, and $t_2 \geq t_3$, a single Jeener echo is expected, whose shape and amplitude depends on the time derivative of the FID [57]. However, if an inhomogeneous distributions of second rank spin interactions are present, three echoes can be observed [58] respectively at $t_3 = t_1$ and $t_3 = t_2 \pm t_1$ and, for long t_1, superposition of echoes are present together with the changes in the shapes of the echoes as a function of t_2 variations [59].

In addition, one can use the Goldman-Shen sequence [56] (90°_x-τ_1-90°_{-x}-τ_2-90°_x-acq, Figure1C) to prepare the spin system in a non-equilibrium state with distinct domains at different spin temperatures. The recovery to a *quasi* equilibrium state can then be monitored as domains achieve a common spin temperature through spin diffusion. When $\tau_1 \geq 5\ T_{2\text{short}}$, where $T_{2\text{short}}$ is the T_2 of the fast decay component, the macroscopic magnetisation of the rigid domain is selectively filtered-off. The residual magnetisation of the slow decay component, characterized by a $T_{2\text{long}}$, is then realigned along the magnetic field and the transfer of the magnetisation between domains (or the changes of spin temperature) *via* spin diffusion can be monitored by varying τ_2. If spin-diffusion or spin translation occurs between some distinct phases of a heterogeneous sample, the return and growth of the fast component of the FID will be observed when $\tau_2 \geq T_{2\text{long}}$. In such cases, the size and dimension of domains can be estimated [60–63] from the diffusion coefficient, D, and relaxation times. This will be described in later sections.

On the other hand, however, in the event of a broad distribution of correlation times or fast spin translation between spins intermingled at short distances or cross-correlation effects of a segment moving anisotropically, only one spin population is expected corresponding to a single homogenous phase. The recovery process of the $T_{2\text{short}}$ component will be rapid ($\tau_2 < T_{2\text{long}}$). In such cases, the domains are absent.

Domains and Spin-Diffusion in the Solid Starch Polysaccharides

Assuming the spin diffusion as a random walk process, the mean diffusion distance $\langle d \rangle$ over the interval T_1 is [60–63]

$$\langle d \rangle = \sqrt{2DT_1} \qquad (11)$$

where D is the diffusion coefficient. For biopolymers in the solid state with a Gaussian line shape, the diffusion coefficient is given [64] approximately by

$$D = \frac{\langle r\rangle^2}{60\pi T_2} \tag{12}$$

where $\langle r\rangle^2$ is the mean-squared inter-nuclear spacing and T_2 is the measured FID decay constant. Since the local dipolar field is given by

$$\langle H_L\rangle = \frac{\Delta H}{\sqrt{12}} \tag{13}$$

where ΔH is the line width (in Gauss) at the half height [65]. By measuring ΔH and working out $\langle H_L\rangle$, an average $\langle r\rangle$ for the proton separation can be obtained from Equation (2). This together with the measured T_1 and T_2 values allows estimation of the domain dimensions according to the Equation (11–12).

However, one has to be aware that in the dipolar coupled systems, spatial inhomogeneity measured by ^{1}H NMR can be achieved *only for a certain range of length scales*. Spatial fluctuations within the correlation length of the local dipolar fields cannot be resolved. This sets a lower bound resolution to a few near neighbour distances, i.e. about 5–10 Å.

Proton Spin–Lattice Relaxation of Solid Starch Polysaccharides in the Laboratory Frame

^{1}H relaxation times are most widely employed for studying the dynamics due to high sensitivity and well-established theories. For biopolymers, the proton T_1 can be conveniently measured using inversion-recovery or saturation-recovery sequences either by directly detecting the ^{1}H NMR signals or indirectly *via* ^{13}C (e.g. CPMAS). In the dipolar interaction dominated system, the proton relaxation time, T_1, obeys the relaxation theory described by Bloembergen, Purcell and Pound [66]. Assuming exponential correlation function and single correlation time, the T_1 can be evaluated quantitatively with the well-known Kubo-Tomita expression (Equation 14) [67–70],

$$R_1 = \frac{1}{T_1} = \sum_{i\geq 1} C_i\left[\frac{\tau_{ci}}{1+\omega_0^2\tau_{ci}^2} + \frac{4\tau_{ci}}{1+4\omega_0^2\tau_{ci}^2}\right] \tag{14}$$

where ω_0 is the proton Larmor frequency and τ_c the rotational correlation time of the motions responsible for the spin–lattice relaxation, which normally follows the Arrhenius activation law

$$\tau_c = \tau_0 \exp\left(\frac{Ea}{RT}\right) \tag{15}$$

where τ_o is the pre-exponential factor corresponding to the rotational correlation time at infinite temperature, E_a the activation energy for the motion and R the gas constant. For a motional process, when $\omega_0\tau_c = 0.6154$, T_1 reaches a minima or R_1 reaches a peak where

$$R_1{}^{\mathrm{Max}} = 1.425C/\omega_0 \tag{16}$$

C in the Equation (14) and (16) is the relaxation constant and is related to the spatial arrangement of protons in the sample, thus, a useful structural parameter. For a powder, C is given by Equation (17)

$$C = \frac{9}{20N}\cdot\gamma^4\hbar^2\left(\sum_j r_{jk}^{-6} + \sum_k\sum_{l\neq j,k} r_{\mathrm{jl}}^{-6}\right), \tag{17}$$

where N is the number of protons to be relaxed and, r_{jk} is the inter-proton distances between a pair of protons j and k, γ is the proton magnetogyric ratio. The first term in parenthesis describes the intra-pair spin properties whereas the second term describes the inter-pair ones. It is thus apparent that, by measuring T_1 as a function of temperature or the Larmor frequency, one can access parameters describing the molecular motions (E_a, τ_o, C) and the geometry of the groups (r) involved in the motions if no phase transition or chemical decompositions were intermingled into the motional processes.

However, even in most of single-phase homopolymer systems, the assumption of a single τ_c is not always valid [71–76]. A distribution of τ_c is more realistic [71–76] although the reasons for such τ_c distribution are not well studied. The distribution of activation energy due to the distribution of molecular conformers is one possibility (P.S. Belton, personal communication). In biopolymer systems such as starch, such distribution is often complex. The dynamics of starch polysaccharides in much slow frequency region (several kHz) is also extremely important especially for the mechanical properties. Such dynamics cannot be easily probed with T_1 but can be investigated by measuring the proton T_2 or M_{2r}, T_{1D} and $T_{1\rho}$ relaxation times.

Proton Spin–Lattice Relaxation of Solid Starch Polysaccharides in the Rotating Frame

To study slow motions in several kHz regions, ^{1}H $T_{1\rho}$ can be conveniently measured by a single pulse followed with a variable spin-lock scheme. $T_{1\rho}$ can also be used to quantitatively analyse the molecular motions by fitting the experimental $R_{1\rho}$ data to an expression similar to that used in R_1 analysis [46,47,49,67–69]:

$$R_{1\rho} = \frac{1}{T_{1\rho}} = \frac{3}{2}\sum_{\mathrm{i}\geq 1} C_i\left[\frac{\tau_{ci}}{1+4\omega_{ei}{}^2\tau_{ci}{}^2} + \frac{5}{3}\times\frac{\tau_{ci}}{1+\omega_o{}^2\tau_{ci}{}^2} + \frac{2}{3}\times\frac{\tau_{ci}}{1+4\omega_o{}^2\tau_{ci}{}^2}\right] \tag{18}$$

where ω_0, τ_c and C have the same meaning as in the case of T_1. ω_e is the effective field for relaxation in frequency units, which is often dependent on both the spin-locking frequency (ω_{SP}) and the local dipolar field (in frequency unit), ω_L.

When $\tau_c < T_2$ and $\omega_{SP} \gg \omega_D$, $T_{1\rho}$ can be interpreted through the theory of Bloembergen, Purcell and Pound [66], therefore, ω_e can be replaced by ω_{SP}. When $\tau_c \gg T_2$, the so-called Slichter-Ailion conditions apply [77]. However, if ω_{SP} and ω_D are in the same order of magnitude and $\tau_c \leq T_2$ stands, the effects of the local dipolar field has to be taken into consideration as follows [78]:

$$\omega_e = \sqrt{\omega_{SP}{}^2 + \omega_L{}^2} \tag{19}$$

In practice, ω_L is temperature dependent and has to be modeled by an empirical relationship, such as the Sigmoid function [43–49,67–69], to give the closest values to that of the experimental ones. For a motional process, when $\omega_e \tau_c = 0.6101$, $T_{1\rho}$ reaches a minimum.

In most of starch systems, multiple components are frequently detected [5,38] for ^{1}H $T_{1\rho}$ of starch systems due to the heterogeneity of such systems. The magnetization transfers between domains *via* spin diffusion over the whole sample can be used to obtain information on the dimension of the domains. In the meantime, the multiple components of relaxation times provide a great opportunity to access information on the structure and interactions of the different domains *via* relaxation-edited spectroscopy. In theory (see Equation 18), $T_{1\rho}$ measurements as a function of temperature or relaxation frequency can also be used to characterize the molecular dynamics quantitatively (E_a, τ_o, C, r) in the similar way to that for T_1. However, in real starch systems, measuring the relaxation time as a function of sample temperature is not always possible without causing samples to undergo physical changes, such as phase transition, and chemical decomposition. The changes often occur "inconveniently" in the temperature range one want to investigate. Nevertheless, such problems can be avoided by measuring T_1 as a function of the frequency [79], ω_o, and analyse the motional processes accordingly. The commercial fast-field cycling spectrometers with field switching speed of 0.1 ms/MHz are now available, covering the frequency range of 10 kHz to 80 MHz. This makes it possible to study molecular motions in the range of several tens of kilohertz to hundred of megahertz at one given temperature [31,79,80].

^{13}C Spin–Lattice Relaxation for Starch Polysaccharides

The T_1 and $T_{1\rho}$ of ^{13}C for starch polysaccharides can be measured directly, providing information on the spectroscopically resolved sites. Using appropriate pulse sequences [81–84], the chemical shift anisotropy (CSA) can also be measured to gain dynamics information. The advantage of using ^{13}C method is that the NMR signals contain only these of polysaccharides and there will be no water signals directly intermingled. So far, there is still a lack of systematic ^{13}C relaxation study of starch though some data have been reported for maltose [85] and starch gels [33,86]. Some early efforts were concentrated on the measurements of ^{13}C T_1 for the prepared crystalline starches [87], which was only possible after the invention of CPMAS experiment. For both A- and B-type dry crystalline amylose [87], ^{13}C T_1 values were about 20 s and 5 s for the C-1 and C-6 respectively. The C-6 has a much shorter ^{13}C T_1 presumably due to the *trans-gauche* conformational motions of CH_2OH group [43–46,88–91]. However, ^{13}C T_1 values are much smaller than these for crystalline cellulose I of cotton [87] (140–210 s), indicating more motional mobility for starch polysaccharides than cellulose.

Full hydration of starch led to only a small decrease [87] of T_1 value for C-1 (13–16 s) and C-6 (3–4 s). Similar observations were made [87] for C-4 (dry$\sim$14, hydrated$\sim$11–13 s). In contrast, glycogen, a similar polysaccharides, showed dramatic decrease of ^{13}C T_1 values upon hydration [92]. It is suggested that the hydration-induced enhancement for molecular dynamics is only limited for the ordered starch polysaccharides. For the V-type amylose as a single helical amylose-lipids complex, T_1 of C-1 showed significant increase upon hydration [87], from 7 s (anhydrous) to 11 s (fully hydrated). Similar observations were made for other pyran ring carbons, indicating that hydration promoted the formation of the ordered structure in this case. The ^{13}C T_1 of amorphous starch are considerably shorter than the crystalline ones. For example, the amorphous wheat starch containing 33% water showed ^{13}C T_1 of 300ms for CH_2OH and 600 ms for the ring carbons [38]. The difference of ^{13}C T_1 has been employed in some spectral editing of ^{13}C NMR spectra, termed as mobility-resolved spectroscopy [93]. It is conceivable that a systematic ^{13}C relaxation studies ought to provide some significant insights into the dynamics of the starch polysaccharides. Nevertheless, for systems as complex as starch polysaccharides, some background knowledge is always helpful on the single-phase starch models such as the crystalline sperulites and short chain amorphous polysaccharides.

Water in Starch Systems

In most starch systems, water is an essential constituent thus plays important roles in starch functionality. NMR techniques have already been employed in studying water molecules in starch systems for decades. The first such

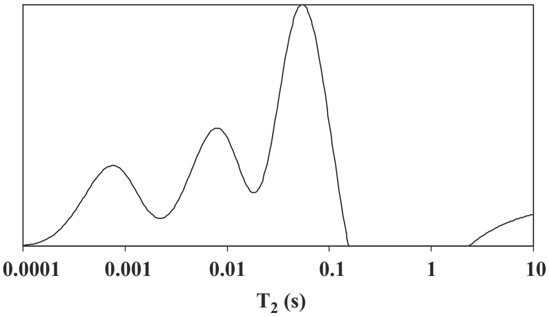

Fig. 4. A TRESY spectrum of water in wet potato starch granules showing four water populations detectable in the system as water in the crystalline region (0.001 s), water in the amorphous region (0.01 s), water trapped between granules (0.1 s) and bulk water (10 s).

study was published in Nature [94] in 1960 on the starch polysaccharide–water interactions, showing the broadening water proton lines in high resolution NMR spectra of starch gels. In 1970s, some low-resolution ^{1}H NMR studies of the "bound water" of corn starch [95] were also published and such studies were continuously reported from 1980s to 2000s [10–15,32,96–98] with the gradual improvement of NMR hardware. Some progress has also been made in understanding of the water dynamics in acid hydrolysis and gelatinisation. This area of research will remain active for sometime.

Since most of water in starch systems is in the long T_2 regime, the CPMG spin echo experiment [41] will be most suitable. The CPMG echo trains are better analysed as a continuous distribution of exponentials, yielding a spectrum [3,4,16,99–103] of T_2 components with distributive T_2 values (Figure 4). This method was called transverse relaxation spectroscopy (TRESY) [3] and has found widespread application especially in the porous systems. The use of TRESY methods has led to new insights into the state of water in starch systems. For example, TRESY methods enabled most populations [3,11,23,104] of water in the native starch granules to be identified in all three types of starch granules; they are bulk water, water trapped between granules, water in the amorphous growth rings, water in the semi-crystalline regions and structural water in the hexagon channels formed by the double helices. Amongst them, the "channel water" in the granules and hydrolysed starch spherulites, which remained unfrozen until temperature reached as low as -50°C [3,4,11], was also observable from the D_2O saturated B-type [3,4,11,14,15] and C-type [3,4,11] starches using ^{2}H NMR as an 1kHz splitting.

^{1}H TRESY methods have also been employed to investigate the effects of acid hydrolysis (Linterization), thermal heating and gelatinisation on the dynamics of starch and microscopic distribution of water within the starch systems [3,11]. By monitoring the changes of proton T_2 spectra of a starch/water system, it has been possible to monitoring the changes of the dynamic behaviour of water such as swelling induced water absorption [4,11]. By replacing H_2O with D_2O, the proton TRESY method were employed to monitor the molecular dynamic changes of starch polysaccharides [3,11], especially near the gelatinisation temperature. Below the gelatinisation temperature, the proton NMR signals are mostly from polysaccharides and ^{1}H NMR signals from FID offers a direct observation of the polysaccharides [3,11]. On the other hand, ^{1}H CPMG signals near and above gelatinisation temperature provide an unambiguous monitoring handle to the mobilized starch [3,11]. To the similar systems, ^{2}H and ^{17}O NMR is useful to monitor the changes of water dynamics in response to the processing such as gelatinisation.

Future Perspective

Although studies of starch using NMR relaxation have extended to various extent to both starch polysaccharides and water, more systematic studies are still in need to understand the systems more comprehensively. Whilst most efforts were devoted to the crystalline starch, limited attentions were paid to the amorphous starches even though most of the processed starch is in the amorphous form and hence is important for the rubbery properties. Furthermore, only few studies have been directed towards the interactions between components in the complex. NMR diffusion is not extensively employed even though it is expected to provide essential information on dynamics and interactions of starch systems. It is thus conceivable that the future studies will be focused more on the dynamics and interactions of polysaccharides. The other important questions, which remain unanswered, include: what are the relationships between the physical properties and the domain distribution and dynamic state of the starch polysaccharides (if any); how are these properties relevant in establishing and determining the response of starch granules to multi-parametric processing and ultimately functionality.

References

1. Gallant DJ, Bouchet B, Baldwin PM, Carbohydr. Polym. 1997;32:177.
2. Buleon A, Colonna P, Planchot V, Ball S. Int. J. Biol. Macromol. 1998;23:85.
3. Tang HR, Godward J, Hills B. Carbohydr. Polym. 2000;43:375.

4. Tang HR, Hills BP. In: GA Webb, PS Belton, AM Gil, I Delgadillo, (Eds). Magnetic Resonance in Food Science—A View to the Future. Royal Society of Chemistry: Cambridge, 2001, p 155.
5. Tang HR, Hills BP. Biomacromol. 2003;4:1269.
6. Shogren RL, Lawton JW, Doane WM, Tiefenbacher KF. Polymer. 1998;39:6649.
7. Simonsen L, Hovgaard L, Mortensen PB, Brondsted H. Euro. J. Pharm. Sci. 1995;3:329.
8. Wu HCH, Sarko A. Carbohydr. Res. 1978;61:7.
9. Wu HCH, Sarko A. Carbohydr. Res. 1978;61:27.
10. Baianu IC. Cereal Foods World. 1986;31:584.
11. Tang HR, Brun A, Hills B. Carbohydr. Polym. 2001;46:7.
12. Tanner SF, Hills BP, Parker R. J. Chem. Soc. Farad. Trans. 1991;87:2613.
13. Kulik AS, Decosta JR, Haverkamp J. J. Agri. Food Chem. 1994;42:2803.
14. Yakubu PI, Ozu EM, Baianu IC, Orr PH. J. Agri. Food Chem. 1993;41:162.
15. Yakubu PI, Baianu IC, Orr PH. J. Food Sci. 1990;55: 458.
16. Chatakanonda P, Chinachoti P, Sriroth K, Piyachomkwan K, Chotineeranat S, Tang HR, Hills B. Carbohydr. Polym. 2003;53:233.
17. Chen PL, Long Z, Ruan R, Labuza TP. Food Sci. Techn. 1997;30:178.
18. Ruan RR, Zou C, Wadhawan C, Martinez B, Chen PL, Addis P. J. Food Proc. Preserv. 1997;21:91.
19. Ruan RR, Long ZZ, Song AJ, Chen PL. Food Sci. Techn. 1998;31:516.
20. Kimshin MS, Mari F, Rao PA, Stengle TR, Chinachoti P. J. Agri. Food Chem. 1991;39:1915.
21. Tang HR, Wang YL, Belton PS. Solid State NMR. 2000;15:239.
22. Li S, Dickinson LC, Chinachoti P. Cereal Chem. 1996;73:736.
23. Kou Y, Dickinson LC, Chinachoti P. J. Agri. Food Chem. 2000;48:5489.
24. Colquhoun IJ, Parker R, Ring SG, Sun L, Tang HR, Carbohydr. Polym. 1995;27:255.
25. Dybowski C, Lichter RL. NMR Spectros. Tech. Dekker: New York, 1987.
26. Mehring M. Principles of High Resolution NMR in Solids. Springer-Verlag: Berlin, 1983.
27. Fyfe CA. Solid Sate NMR for Chemists. C.F.C. ress: Guelph, Ontario, Canada, 1983
28. Spiess HW. Chem. Rev. 1991;91:1321.
29. Tang HR, Belton PS, Davies SC, Hughes DL. Carbohydr. Res. 2001;330:391.
30. Schmidtrohr K, Spiess HW. Multidimensional solid state NMR and Polymers. Academic Press: London, 1994.
31. Hills BP, Wang YL, Tang HR. Mol. Phys. 2001;99:1679.
32. Baianu IC, Yakubu PH, Ozu E. Abstr. Papers Am. Chem. Soc. 215, 239-OLY (1998).
33. Chinachoti P, White VA, Lo L, Stengle TR. Cereal Chem. 1991;68:238.
34. Chinachoti P, Kimshin MS, Mari F, Lo L. Cereal Chem. 1991;68:245.
35. Lim H, Setser CS, Paukstelis JV, Sobczynska D. Cereal Chem. 1992;69:382.
36. Cheetham NH, Tao LP. Carbohydr. Polym. 1998;35:279.
37. Kojima T, Sekine M, Sugiyama J, Ishida N, Nagata T. J. Jap. Soc. Food Sci. Technol.– Nippon Shokuhin Kagaku Kogaku Kaishi. 1996;43:1098.
38. Morgan KR, Furneaux RH, Larsen NG. Carbohydr. Res. 1995;276:387.
39. Powles JG, Mansfield P. Phys. Lett. 1962;2:58.
40. Mansfield P. Phys. Revi. 1965;137:a961–a974.
41. Meiboom S, Gill D. Rev. Sci. Instrum. 1958;29:688.
42. Hills BP, Pardoe K. J. Mol. Liq. 1995;63:229.
43. Tang HR, Belton PS, Ng A, Waldron KW, Ryden P. Spectrochim. Acta. Pt. A. 1999;55:883.
44. Tang HR, Zhao BL, Belton PS, Sutcliffe LH, Ng A. Magn. Reson. Chem. 2000;38:765.
45. Tang HR, Belton PS. In: PS Belton, BP Hills, GA Webb (Eds). Advances of Magnetic Resonance in Food Science. Royal Society of Chemistry: Cambridge, 1999, p 166.
46. Tang HR, Belton PS. Solid State NMR. 2002;21:117.
47. Wang YL, Tang HR, Belton PS. J. Phys. Chem. B.0 2002;106:12834.
48. Tang HR, Wang YL, Belton PS. Phys. Chem. Chem. Phys. 2004;6:3694.
49. Tang HR, Belton PS. Solid State NMR. 1998;12:21.
50. Abragam A. The Principles of Nuclear Magnetism. Oxford University Press: Oxford, 1961.
51. van Vleck JH. Phys. Rev. 1948;74:1168.
52. Lacelle S, Gerstein BC. Biopolymers. 1987;26:849.
53. Resing HA. Adv. Mol. Relaxation Processes. 1972;3:199.
54. Resing HA. J. Chem. Phys. 1967;43:669.
55. Werbelow LG, Marshall AG. J. Magn. Reson. 1973;11:299.
56. Goldman M, Shen L. Phys. Rev. 1966;144:321.
57. Jeener J, Broekaert P. Phys. Rev. 1967;157:232.
58. Bloom M, Burnell EE, Roeder SBW, Valic MI. J. Chem. Phys. 1977;66:3012.
59. Cheung TTP. Phys. Rev. B. 1981;23:1404.
60. Cheung TTP. J. Chem. Phys. 1982;76:1248.
61. Cheung TTP. Appl. Spectr. 1997;51:1703.
62. Cheung TTP. Gerstein BC. J. Appl. Phys. 1981;52:5517.
63. Goldman M. Spin Temperature and Nuclear Magnetic Resonance in Solids. Clarendon Press: Oxford, 1970.
64. Cheung TTP, Yaris R. Carbohydr. Polym. 1980;72:3604–16.
65. Bloembergen N, Purcell EM, Pound RV. Phys. Rev. 1948;73:679.
66. Belton P, Wang YL. Mol. Phys. 1997;90:119.
67. Wang YL, Belton PS, Tang HR. Chem. Phys. Letts. 1997;268:387.
68. Wang YL, Belton PS, Tang HR. Solid State NMR. 1999;14:19.
69. Kubo R, Tomita K. J. Phys. Soc. Jpn. 1954;9:888.
70. Andrew ER, Gaspar R, Vennart W. Biopolymers. 1978;17:1913.
71. Andrew ER, Bryant DJ, Cashell EM, Gaspar R, Meng QA. Polymer. 1981;22:715.
72. Andrew ER, Bryant DJ, Cashell EM, Meng QA. Febs Letters. 1981;126:208.
73. Andrew ER, Bryant DJ, Cashell EM, Meng QA, Phys. Lett. A. 1982;88:487.
74. Andrew ER, Bone DN, Bryant DJ, Cashell EM, Gaspar R, Meng QA. Pure. Appl. Chem. 1982;54:585.
75. Andrew ER. Polymer. 1985;26:190.
76. Slichter CP, Ailion D. Phys. Rev. 1964;135:A1099–A1100.

77. Mccall DW, Douglass DC. Appl. Phys. Lett. 1965;7:12.
78. Belton PS, Wang Y. Magnetic Resonance in Food Science—A View to the Future. 2001;262:145.
79. Wang YL, Belton PS. Chem. Phys. Letts. 2000;325: 33.
80. Gan ZH. J. Am. Chem. Soc. 1992;114:8307.
81. Gan ZH, Ernst RR. J. Magn. Reson. A. 1996;123:140.
82. Gan ZH, Grant DM, Ernst RR. Chem. Phys. Letts. 1996;254:349.
83. Hu JZ, Wang W, Liu F, Solum MS, Alderman DW, Pugmire RJ, Grant DM. J. Magn. Reson. A. 1995;113:210.
84. Tromp RH, vanDusschoten D, Parker R, Ring SG. Phys. Chem. Chem. Phys. 1999;1:1927.
85. Vodovotz Y, Chinachoti P. In: Belton PS, Hills BP, Webb GA (eds). Advances of Magnetic Resonances in Food Science. Royal Society of Chemistry: Cambridge, 1999, p. 185.
86. Horii F, Yamamoto H, Hirai A, Kitamaru R. Carbohydr. Res. 1987;160:29.
87. Reynhardt EC. Mol. Phys. 1990;69:1083.
88. Latanowicz L, Reynhardt EC. Ber. Bunsen Gesell. Phys. Chem. Int. J. Phys. Chem. 1994;98:818.
89. Latanowicz L, Reynhardt EC, Utrecht R, Medycki W. Ber. Bunsen-Gesell. Phys. Chem. Chem. Phys. 1995;99:152.
90. Reynhardt EC, Latanowicz L. Chem. Phys. Letts. 1996;251:235.
91. Jackson CL, Bryant RG, Biochem. 1989;28:5024.
92. Foster TJ, Ablett S, Mccann MC, Gidley MJ. Biopolymers. 1996;39:51.
93. Collison R, McDonald MP. Nature. 1960;186:548.
94. Mousseri J, Steinberg JMP, Nelson AI, Wei LS. J. Food Sci. 1974;39:114.
95. Kuhn K, Kruschak W, Lechert H. Starch-Starke. 1987;39:1.
96. Rugraff YL, Desbois P, LeBotlan DJ. Carbohydr. Res. 1996;295:185.
97. Chinachoti P, Stengle TR. J. Food Sci. 1990;55:1732.
98. Hills BP, Lefloch G. Food Chem. 1994;51:331.
99. Hills BP, Wright KM, Snaar JM. Magn. Reson. Imag. 1996;14:715.
100. Hills BP, Wright KM, Snaar JM. Magn. Reson. Imag. 1996;14:305.
101. Hills BP, Remigereau B. Int. J. Food Sci. Technol. 1997;32:51.
102. Hills BP, Godward J, Manning CE, Biechlin JL, Wright KM. Magn. Reson. Imag. 1998;16:557.
103. Li S, Dickinson LC, Chinachoti P. J. Agri. Food Chem. 1998;46:62.

High Resolution Solid State Methods

Magic Angle Spinning NMR of Flours and Doughs

Maria Antonietta Brescia and Antonio Sacco
Dipartimento di Chimica, Università di Bari, via Orabona 4, 70126 Bari, Italy

Introduction

The study of the properties of wheat flours is necessary to understand the mechanical and rheological properties of the resulting dough and therefore of the finished baked products. In the specific case of bread, recent works have concerned low resolution NMR for studying water and lipid mobility [1–3]. The mobility of water in dough is an important parameter being related to the quality of gluten network. To gain more insight in the structural characteristics of dough and of its principal components, gluten and starch, solid-state Magic Angle Spinning (MAS) NMR was applied. The interactions of each dough component with water and effects of heating during bread making were also studied. MAS methods improve resolution by averaging dipolar interactions, along with chemical shift anisotropy and magnetic susceptibility. This permits to detect easily and quantify signals due to various components of dough and flours.

In this chapter applications of ^{13}C and ^{1}H MAS NMR spectroscopy to flours and dough and to their major components, starch and proteins, will be reviewed and the potential of these techniques in exploring the correlation between molecular level information and macroscopic properties of dough and flours will be examined.

^{13}C Cross Polarization MAS NMR of Flours

The first ^{13}C cross polarization (CP-MAS) NMR study of flours was performed by Baianu and Förster [4]. They found that the broad features of spectra of wheat grains were similar to those of the corresponding flours. The subtle differences were supposed to be due to starch damage and mechanical breaking of protein chains. The major signals present in the CP-MAS ^{13}C NMR spectrum of flour are due to sugar carbons in the starch components of the flours, resonating at 96–102 ppm (C_1), 70–73 ppm (C_2, C_3, and C_5), 77–83 ppm (C_4), and 59–62 ppm (C_6). The tail of the 62 ppm starch resonance obscures signals due to Cα's of the proteins, while signals due to protein side-chain aliphatic carbon resonate at 20–35 ppm, and do not overlap with other signals. The relative intensities of the protein and starch resonances allow calculating the protein content of durum and tender wheat flours.

The resolution of the signals permitted the application of relaxation experiments and to determine the average rotating-frame proton relaxation time $T_{1\rho}$(H) of each carbon [5]. From these measurements it emerged that all the starch protons have a similar $T_{1\rho}$(H) while for proteins $T_{1\rho}$(H) is 30% lower indicating that starch and proteins are separated into distinct domains.

^{1}H High Resolution MAS NMR of Flours

Even if ^{13}C CP-MAS NMR has the advantage of avoiding sample manipulation, the information that can be inferred from these spectra is strongly limited by the low resolution due to the presence of very broad signals generated by high molecular weight (HMW) components.

^{1}H High Resolution (HR-MAS) NMR technique permitted to overcome these difficulties combining the typical advantages of solid- and liquid-state NMR techniques. Samples for ^{1}H HR-MAS measurements were prepared in the rotors mixing 33 mg of D_2O with 40 mg of flour to obtain homogeneous samples with similar degrees of swelling. A typical ^{1}H HR-MAS spectrum of durum wheat flour, obtained using a presaturation sequence for water suppression, is reported in Figure 1. More than 80 peaks can be distinguished resulting mainly from lipids and polysaccharides. Lipids assignment was performed [6] on the basis of correlations observed in TOCSY and ^{1}H-^{13}C HMQC spectra (Table 1). A detailed assignment of saccharide moieties was not possible due to overlap among TOCSY correlations. The heights of the resonances showing neither overlapping nor correlation with other signals were evaluated in the ^{1}H HR-MAS spectra of 12 durum wheat flours coming from southern Italy to be used as variables for Principal Component Analysis. The results permitted to detect differences among the samples mainly due to their geographical origin. This procedure demonstrated its reliability also when it was applied on an enlarged data set formed by 26 samples of two cultivars at 13 different locations in Italy [7] and was able to differentiate samples coming from North, Central, and South Italy according to the geographical origin and cultivar.

^{1}H HR-MAS was also employed to study the kinetic release of oligosaccharides due to hydrolases in the amylolytic starch degradation of wheat flours [8]. The increasing intensities of β-glucose and anomeric protons of the

Graham A. Webb (ed.), Modern Magnetic Resonance, 1757–1763.
© 2008 *Springer.*

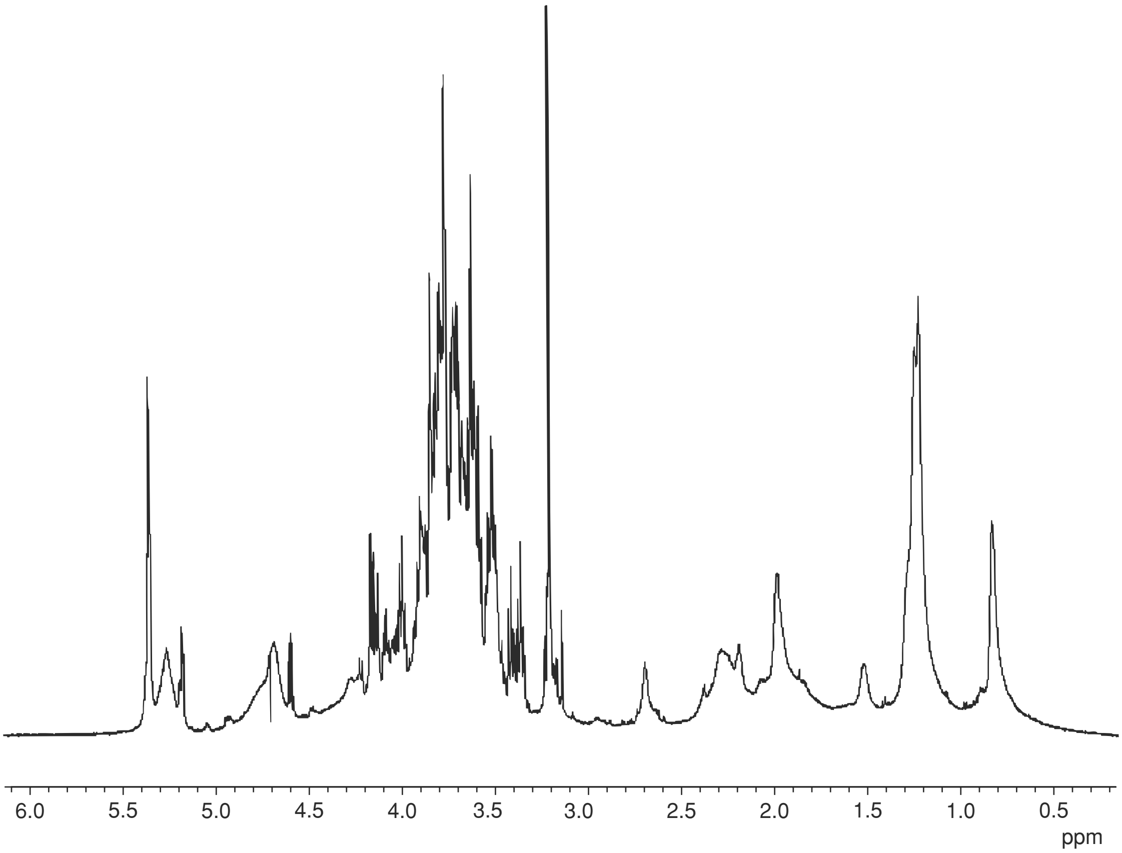

Fig. 1. ^{1}H HR-MAS spectrum of a durum wheat flour (From Ref. [7]).

reducing ends of β-maltose were determined as function of time for several durum and soft wheat samples and were fit with a Michaelis Menten kinetic equation to obtain kinetic parameters that are associated to the transformation of starch into maltose and maltose into glucose. A relationship between the kinetic degradation of starch and the botanical origin of the flour was suggested.

^{1}H and ^{13}C MAS NMR of Doughs

The hydration of flour is an important step in the baking process. Differences in the mechanical properties of dough are related to the interactions of water and flour.

Hydrated durum and tender wheat flours were analyzed with CP-MAS and showed a decreased intensity of signals due to protein carbons in comparison with the spectra of the dry flours, being nearly absent in the spectrum of the tender wheat flours [5] (Figure 2). This was explained supposing a reduced effect of water on protein components in durum wheat flours, because proteins are linked to starch–protein particles and remain solid-like. Hydration of the tender flour proteins generates a liquid-like component that can act like a compatibilizer rendering tender flour more processable than durum wheat flour.

Some properties of the flours were investigated, in order to assess its suitability for technological purposes. In particular, the peculiar viscosity and elasticity of hydrated flours are associated to the quantity and quality of gluten. These properties were extensively investigated [9] to understand their origin at a molecular level and the behavior of specific groups or protein moieties on the formation of the hydrated network. These studies were firstly performed on molecules that could be used as simple models [10]. For this reason, the major constituents of gluten, gliadins, and glutenins, were separately analyzed. In particular, it was interesting to gain information about the water-insoluble network obtained by hydration of these proteins to low water content, since this is closer to the protein during dough making.

Table 1: Proton assignment of durum wheat flour lipid moieties (From ref. [6]).

δ (ppm)	Moiety	Assignment
0.83	$\mathbf{CH_3}$–$(CH_2)n$–CH_2–	Lipids
1.22	–$(\mathbf{CH_2})n$–CH_2–	Lipids
1.50	–$(\mathbf{CH_2})$–CH_2–CO–O–	Lipids
1.98	–$\mathbf{CH_2}$–CH=CH–	Lipids
2.18	–CH_2–$\mathbf{CH_2}$–CO—O–	Lipids
2.69	–CH=CH–$\mathbf{CH_2}$–CH=CH–	Lipids
3.26	C2	β-glucose
3.40	C4	β-glucose
3.41	C4	α-glucose
4.64	C1	β-glucose
4.65	C1 reducing end	β-maltose
5.23	C1	α-glucose
5.23	C1 reducing end	α-maltose
5.24	–**CH**=CH–	Lipids
5.41	C1 non reducing end	α-maltose
5.41	C1 non reducing end	β-maltose
5.35–5.50	Non reducing ends	carbohydrates

Gliadins

The first ^{13}C CP-MAS NMR studies on gliadins were performed by Baianu [11]. The wheat proteins ω-gliadins, that are associated with dough viscosity, have a relatively simple structure; therefore they were used as a model to study hydration with ^{13}C CP-MAS NMR [12,13]. The changes in resolution and intensity of the signals present in the spectrum were analyzed at different hydration percentages and were correlated with the protein conformational changes (Figure 3). An improvement of spectral resolution with hydration reflected a change in the protein conformation. Moreover, the loss of the proline Cδ signal was detected, indicating an increased mobility of this group. These observations were enriched with results obtained with the T_2 relaxation time measurements, and were consistent with the formation of mobile protein loops together with residual regions of strong interprotein interactions with hydration. These evidences support the "loop and train" model, common in some polymers, in which "loops" of solvated mobile polymer coexist with "trains" polymer bonded to the surface [9].

The effect of hydration was also studied by ^{1}H HR-MAS NMR on ω-gliadins. Proton T_1 measurements were made under MAS conditions for 19% hydrated samples showing that the most mobile protons were leucine methyl groups [12]. Anyway, great care was required to interpret T_1 relaxation times, since they were found to be dependent on the sample spinning rates [13]. In the spectra of 48% hydrated ω-gliadins, it was possible to observe resonances of backbone NH groups (8.2 ppm), arising from glutamine and phenylalanine residues, as well as side-chains NH groups (6.9 ppm) and aromatic protons (7.3 ppm), indicating that mobility is not restricted to protein side-chains, but includes also protein backbone regions [12].

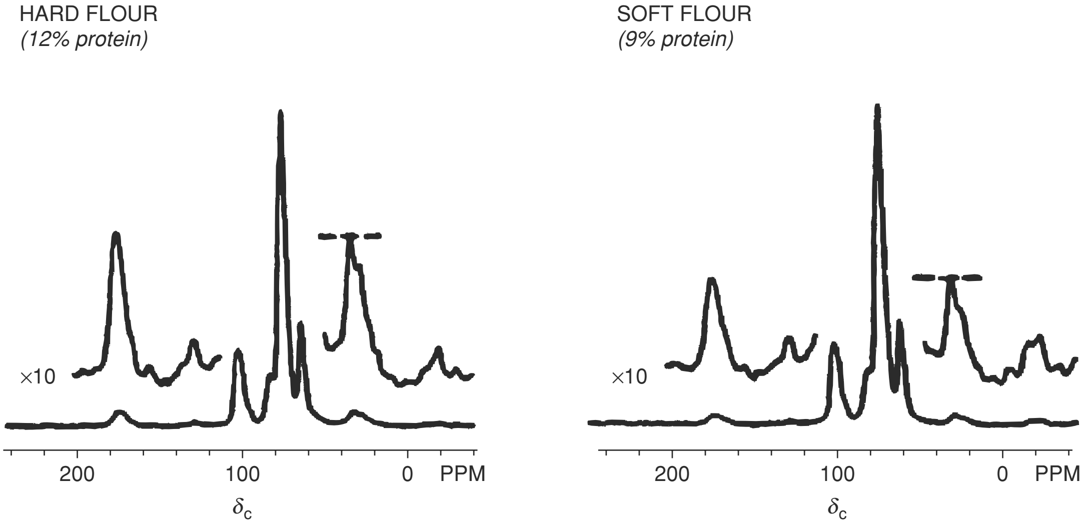

Fig. 2. ^{13}C CP-MAS NMR spectrum of a wheat flours: (left) durum wheat flour, (right) soft wheat flour (From Ref. [5]).

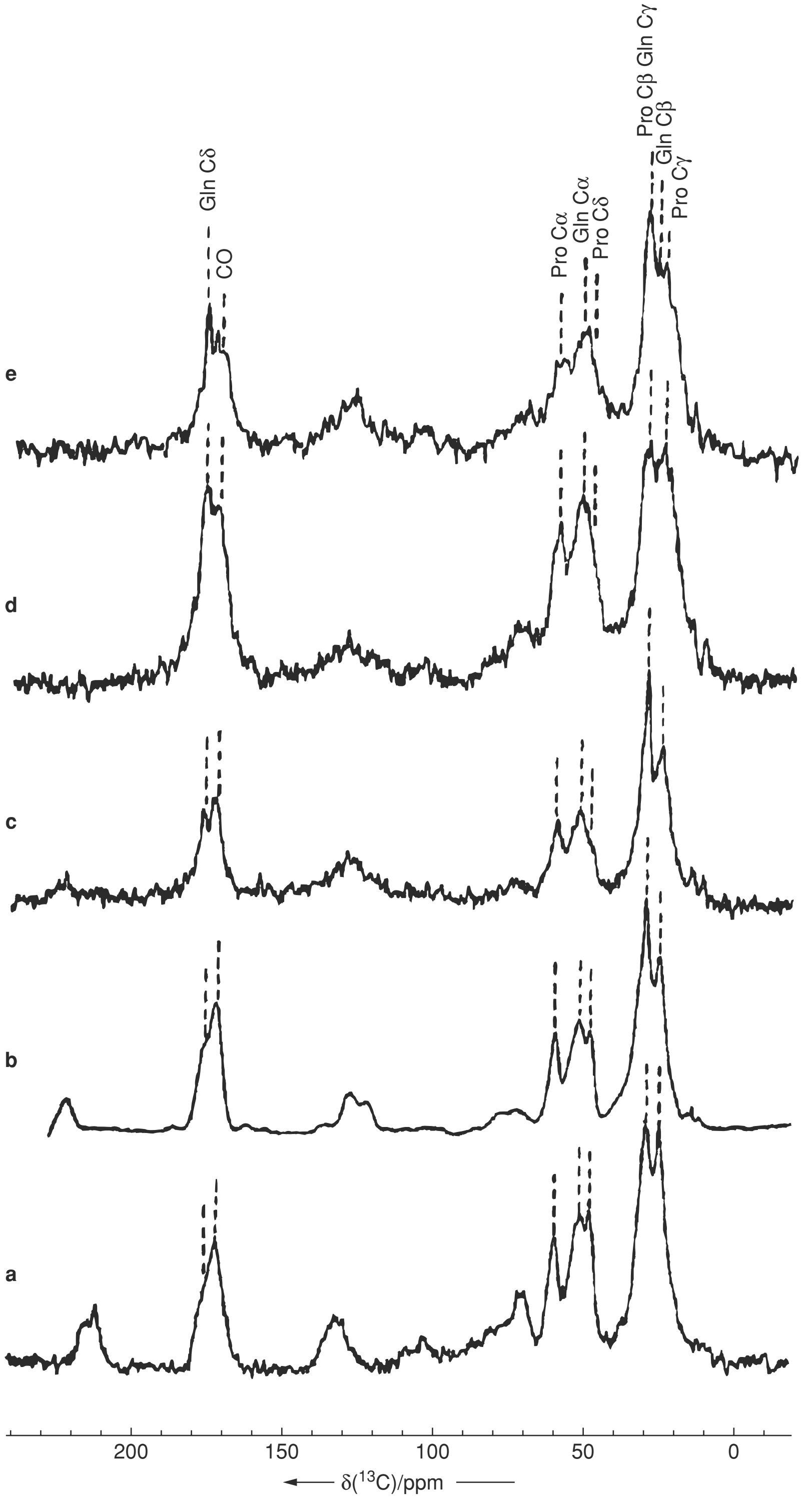

Fig. 3. ^{13}C CP-MAS spectra of ω-gliadins at different hydrations: (a) 0% water, 464 scans; (b) 7% water, 11,720 scans; (c) 19% water, 32,305 scans; (d) 35% water, 5500 scans; (e) 50% water, 17,732 scans (From Ref. [13]).

^{13}C CP-MAS NMR was also employed to the conformational and dynamical study of the hydration of the barley storage protein, C-hordein that is structurally homologous to ω-gliadins [14]. It was found that two types of domains with different mobility were present. It appeared that the relative proportion of rigid and mobile domains was related to the extent of hydration, which was dependent on the proportion of hydrophilic amino acid residues.

High Molecular Weight Fractions

The gluten HMW fraction has been extensively studied due to its high contribution in determining the viscoelastic properties of gluten. HMW subunits are most important in the structure of the wheat proteins glutenins, since they form the backbone of glutenin being linked together by means of disulphide bonds. ^{13}C CP-MAS studies performed on the hydrated proteins helped to individuate some relationships between structural properties and the characteristics of the hydrated network [15]. The decreasing of the signal to noise ratio with hydration, due to higher protein mobility, was analyzed in order to find those structural characteristics that were related to higher or lower mobility. In particular, it was demonstrated that the presence of disulphide bonds was responsible of higher mobility, while the irregular sequences present in chain ends cause hindrance of the network due to the formation of interchain bonds. In absence of irregular chain ends long chain peptides are insoluble in water and form a rather mobile network. The influence of the protein primary structure on the type of network formed was also studied on model systems [16].

^{13}C and ^{1}H MAS studies on HMW subunits helped the elucidation of the structure of the protein segments involved in the loops and trains sections. Trains sections contain glutamine residues close to hydrophobic residues forming hydrogen bonds that hold protein segments together, while loops involve hydrophilic glutamine-rich segments that may also contain glycine. The network formed by the hydrated protein could be further hindered by hydrophobic interactions established by proteins terminal domains [17].

^{1}H MAS spectroscopy was a suitable method to study the effect of hydration on wheat proteins, since the weakened dipolar interactions that characterize these systems enable the acquisition of well-resolved ^{1}H NMR spectra. The resolution of protein spectra was significantly improved using HR-MAS spectroscopy [18] that allowed the application of 2D experiments to obtain the assignment of the protein structures. Considerable shifts were observed for some resonances, relative to the chemical shifts of amino acids in solution, indicating that specific interactions occur in the hydrated protein network. Moreover, evidences were found about the existence of two main environments for glutamine residues: one situated in protein segments adopting the β-sheet conformation, remaining relatively hindered, and the other associated to a more mobile section, possibly adopting a β-turn configuration.

Gluten

Dry and hydrated gluten was directly analyzed by ^{13}C CP-MAS NMR and Single Pulse Excitation (SPE)-MAS experiment [19,20]. While cross polarization detects the solid-like parts of the samples, because the present signals are due to carbon nuclei strongly coupled to protons via dipolar interactions, only mobile nuclei generate signal in SPE experiment (Figure 4). Therefore these two approaches are different and give complementary information about local chemical environments and mobility. It was shown that resonances of residual starch and protein backbone carbons are enhanced in CP spectra of dry gluten, suggesting that they are located in rigid domains. Lipid carbons and glutamine side-chain carbonyl groups are clearly visible only in SPE spectra, indicating that they are present in a more mobile environment. With hydration, starch and proteins gave signals with a lower signal to noise ratio, due to a higher mobility of these fractions, more pronounced for proteins than for starch. The $T_{1\rho}$(H)values of the hydrated gluten were similar for all the carbon resonances. This result is indicative of a mixing among the different domains of the samples (protein backbone, side-chains and starch), induced by hydration.

^{13}C CP-MAS NMR gluten spectra did not differ when various baking quality wheat samples were compared; therefore no correlation was found between protein environment sampled by the technique and the baking quality [19].

^{1}H MAS spectra of hydrated gluten contain well-resolved signals due to lipids, while protein aliphatic chains give broad resonances. As in the spectra of hydrated ω-gliadins, resonances of backbone and side-chain NH groups were observed, supporting the loop and train model.

The variations of gluten due to heating/cooling processes were checked to understand its behavior, at a molecular level, during the baking process. From the study of the relaxation times it was shown that gluten protein aliphatic peaks have an increase of T_2 with heating and a decrease with cooling, which indicates the reversibility of the dynamic changes. The increase of line width at half height of water in gluten samples during heating and cooling was interpreted as reflecting an increasing hindrance of the system.

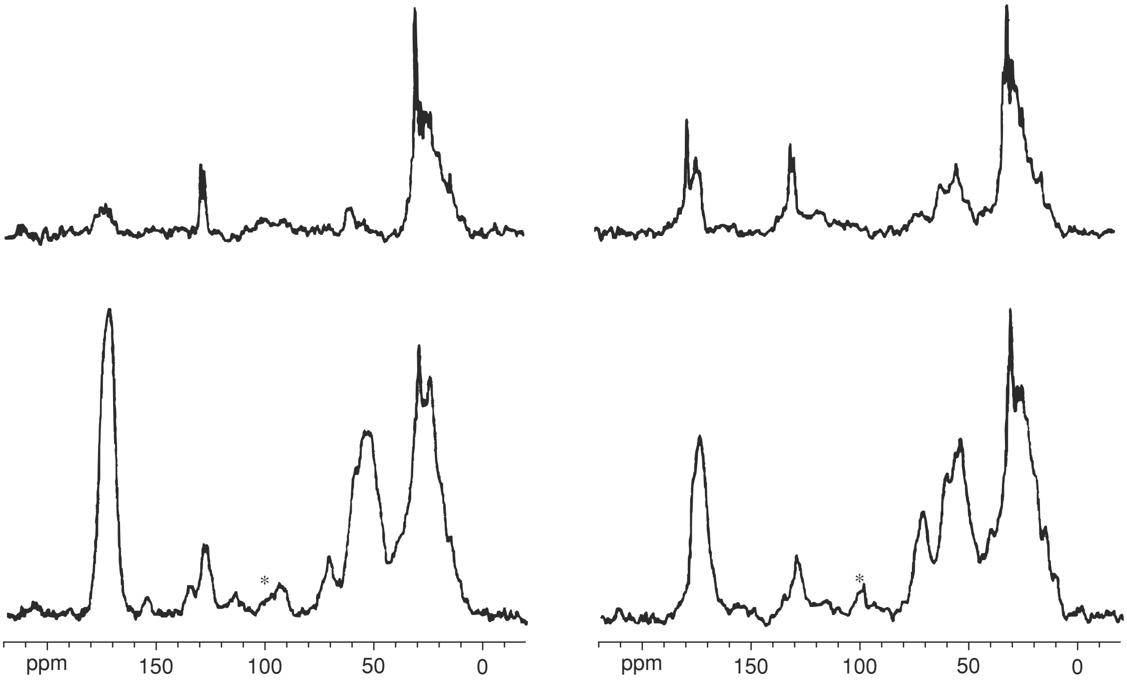

Fig. 4. ^{13}C NMR spectra recorded by means of SPE and CP experiments on dry (sample A, left) and H_2O hydrated (sample B, right) gluten: (top) SPE; (bottom) CP. All experiments were performed under MAS conditions at a spinning rate of 6 kHz; asterisks denote spinning sidebands (Adapted from Ref. [20]).

Starch

The behavior of starch upon heating was investigated in order to understand the processes that occur to this dough component during baking. Starch contains both crystalline and amorphous structures. Its crystalline nature is revealed by the pattern shown by the C_1 glucose peak, resonating at 101 ppm. In particular, in the A-type crystalline form, typical of cereal starches, it appears as a triplet, while in B form, typical of tuber starches, it is a doublet. The existence of a distinct amorphous region was suggested [21] by the presence of peaks resonating at 103.3 and 82.0 ppm having different rotating-frame relaxation rates compared to peaks of others starch protons. These peaks were assigned to random single helices present in the (1→6) linked branching regions.

The major noticeable change in the ^{13}C CP-MAS NMRspectra of heated starch was the loss of signal intensity due to the increased mobility associated to its gelatinization. Anyway, the increase in relative intensity of peaks originated from the amorphous region was also observed. This means that upon gel formation the amorphous form of starch is the dominant component.

The effect of heating and cooling process was studied on starch fractions extracted by wheat flours [22]. From relaxation measurement it emerged that T_2 of water decreases during heating, due to the formation of a starch gel at high temperatures. This parameter decreases during cooling, probably for separation of water from starch, due to starch precipitation. This explanation is consistent with the broadening of starch peak upon cooling and from T_2 values. The addition of the flour oligosaccharides pentosans to the isolated starch resulted in a more mobile network and in a starch higher organization upon cooling.

Bread

Spectra of bread are similar to those obtained for starch gels. During storage of some breads, an increase of C_1 signal intensity revealed a decreased molecular mobility due to starch crystallization or retrogradation. Traces of B-type configuration were revealed in aged breads through the inspection of C_1 resonance patterns. These observations were supported by X-ray diffraction data [23].

Some authors studied the effect of glycerol addition on starch rigidity of bread samples stored with and without crust [23]. The addition of glycerol determined the lowering of signal intensities, revealing a decrease in the rigidity of starch. Breads stored with crust gave higher signal intensities, probably due to higher level of rigid domains.

^{1}H HR-MAS NMR spectroscopy was applied to the analysis of typical bread samples of southern Italy [24]. Apart from the difference in the total lipid content (higher in flours than in bread) substantial differences between the ^{1}H HR-MAS NMR spectra of a bread crumb and of the relative flour were noticed. Two considerably intense signals appear in the crumb spectrum (respectively at 1.91 and at 2.43 ppm). Their assignment was made on the basis of the HSQC ^{1}H-^{13}C spectrum (with ^{13}C signals resonating respectively at 23.12 and 33.09 ppm) and the aid of chemical shifts found in literature [25]. The observed signals were assigned to acetic and succinic acids, formed as a consequence of secondary fermentation processes. These compounds were determined in other analyzed crumb samples and were also detected in the dough before cooking. Nevertheless the amount of these acids was variable in different crumb samples and, in some cases, succinic acid could not be easily detected. The dependence of these differences on the type of yeast, fermentation, and cooking conditions is under investigation. In the sugar region (3–5.5 ppm) of the crumb spectrum it was possible to point out the absence of some peaks present in the flour spectrum. This was due to the scission of some polysaccharides into simple sugars that undergo fermentation. In the crumb TOCSY spectrum a correlation peak was found between resonances at 4.15 and 1.39 ppm, which was absent in the flour spectrum. Neither of these proton resonances could be identified in the monodimensional spectrum due to overlapping with more intense signals. This peak was attributed to lactic acid, formed during fermentation processes, according to the ^{13}C chemical shift values in the heterocorrelated spectrum.

There were no salient differences between the crumb and the crust spectrum of the same bread except for the 3–5.5 ppm range of the latter due to the effects of partial crust carbonization.

References

1. Chen PL, Long Z, Ruan R, Labuza TP. Food Sci. Technol. 1997;30:178.
2. Roudaut G, van Dusschoten D, Van Has H, Hemminga MA, Le Meste M. J. Cereal Sci. 1998;28:147.
3. Roudaut G, Maglione M, van Dusschoten D, Le Meste M. Cereal Chem. 1999;76:70.
4. Baianu IC, Förster H. J. Appl. Biochem. 1980;2:347.
5. Garbow JR, Schaefer J. J. Agric. Food. Chem. 1991;39:877.
6. Sacco A, Bolsi IN, Massini R, Spraul M, Humpfer E, Ghelli S. J. Agric. Food. Chem. 1998;46:4242.
7. Brescia MA, Di Martino G, Fares C, Di Fonzo N, Platani C, Ghelli S, Reniero F, Sacco A. Cereal Chem. 2002;79:238.
8. Amato ME, Ansanelli G, Fisichella S, Lamanna R, Scarlata G, Sobolev AP, Segre A. J. Agric. Food. Chem. 2004;52:823.
9. Belton PS. J. Cereal Sci. 1999;29:103.
10. Gil AM, Masui K, Naito A, Tatham AS, Belton PS, Saitô H. Biopolymers. 1997;41:289.
11. Baianu IC. J. Sci. Food Agric. 1981;32:309.
12. Belton PS, Gil AM, Grant A, Alberti E, Tatham AS. Spectrochim. Acta A. 1998;54:955.
13. Gil AM, Alberti E, Tatham AS, Belton PS, Humpfer E, Spraul M. Magn. Reson. Chem. 1997;35:S101.
14. Gil AM, Masui K, Naito A, Tatham AS, Belton PS, Saitô H. Biopolymers. 1996;41:289.
15. Gil AM, Alberti E, Naitô A, Okuda K, Saitô H, Tatham AS, Gilbert S In: PS Belton, BP Hills, GA Webb (Eds). Advances in Magnetic Resonance in Food Science. The Royal Society of Chemistry: Cambridge, 1999, p 126.
16. Alberti E, Gilbert SM, Tatham AS, Shewry PR, Naito A, Okuda K, Saitô H, Gil AM. Biopolymers. 2002;65:158.
17. Alberti E, Gilbert SM, Tatham AS, Shewry PS, Gil AM. Biopolymers. 2002;67:487.
18. Alberti E, Humpfer E, Spraul M, Gilbert SM, Tatham AS, Shewry PS, Gil AM. Biopolymers. 2001;58:33.
19. Belton PS, Duce SL, Tatham AS. Int. J. Biol. Macromol. 1987;9:357.
20. Calucci L, Forte C, Galleschi L, Geppi M, Ghiringhelli S. Int. J. Biol. Macromol. 2003;32:179.
21. Morgan KR, Furneaux RH, Stanley RA. Carbohydr. Res. 1992;235:15.
22. Gil AM, Alberti E, Santos D. In: GA Webb, PS Belton, AM Gil, I Delgadillo (Eds). Magnetic Resonance in Food Science—A View to the Next Century. The Royal Society of Chemistry: Cambridge, 2001, p 43.
23. Baik M, Dickinson LC, Chinachoti P. J. Agric. Food. Chem. 2003;51:1242.
24. Brescia MA, Sgaramella A, Ghelli S, Sacco A. J. Sci. Food Agric. 2003;83:1463.
25. Fan TWM. Prog. Magn. Reson. Spectrosc. 1996;2:161.

High-Resolution Magic Angle Spinning NMR Spectroscopy of Fruits and Vegetables

Ana M. Gil and Iola F. Duarte
Department of Chemistry, CICECO, University of Aveiro, 3810-193 Aveiro, Portugal

Nuclear magnetic resonance (NMR) spectroscopy has long been applied to the detection and quantification of plant and fruit extracts, often after some kind of separation/purification treatment for simplification and concentration of the system. The challenge remaining regards the application of NMR to heterogeneous and intact systems, so that full use of the non-invasiveness of NMR is made. Tackling physically inhomogeneous materials such as intact fruits and vegetables or some of their components (e.g. skin, pulp, pips) must take into account that different physical phases are characterized by distinct magnetic susceptibilities and that anisotropic effects such as chemical shift anisotropy and internuclear dipolar interactions play increasingly important roles in semisolid and solid materials. The NMR lines in the spectrum are broadened to an extent related to the strength of the effect. Magnetic susceptibility effects may lead to hundreds of Hz to kHz line broadening, depending on the nature of the phases, whereas dipolar interactions may broaden NMR signals up to tens or even hundreds of kHz, in the extreme case of rigid solids. In order to recover spectral resolution, magic angle spinning (MAS) is employed. This consists of spinning the rotor containing the sample around an axis making an angle of $54^\circ 44'$ with the direction of the external magnetic field B_0. Detailed descriptions of this procedure and its principles may be found elsewhere [1,2]. A necessary condition for MAS to result in satisfactory line narrowing is, however, that the spinning speed is at least of the same order of magnitude as the line broadening interaction. In the case of intact fruits, resolved spectra of tissues are typically achievable at spinning rates <1–2 kHz, whereas harder parts or components will require faster rates. In some cases, plasticization or swelling of the materials may be required to enable a resolved spectrum to be obtained, using technically achievable spinning rates, without risking mechanical damage of the sample (usually maximum rates used are 4–6 kHz). The designation of high-resolution (HR) MAS has typically been applied to the observation of the ^1H nucleus under specific conditions (described below) that allow resolution improvement relative to the standard MAS method. However, due to the very limited applications of ^1H HR-MAS to fruits and vegetables, the present text will also review the applications of standard ^1H and ^{13}C MAS to those samples.

MAS NMR was for the first time applied to intact fruit tissue for the observation of ^{13}C [3]. ^{13}C MAS spectra of intact grape, peach, persimmon, banana, and apple tissues were obtained. Low spinning speeds (300–1000 Hz) were found sufficient to reduce susceptibility broadening and obtain suitably resolved spectra. Assignment was aided by observing ^1H–^{13}C scalar couplings in spectra recorded with no proton decoupling. Fructose, glucose and sucrose could be quantified by integration of the corresponding signals in the ^{13}C MAS spectra. Measurement of nuclear Overhauser effect and carbon spin–lattice relaxation times (T_1) allowed the dynamic characterization of the sugars, found to undergo isotropic tumbling at rates close to those found in pure sugar solutions. ^1H MAS NMR was, very shortly after, applied to the fruit tissues of grape, banana, and apple [4]. In the absence of MAS, the spectra were line broadened mainly by magnetic susceptibility heterogeneity. The use of standard MAS enabled the detection of components at levels as low as 0.01% of fresh sample weight. Water, glucose, fructose, sucrose, organic acids (malic, citric, and tartaric), and total fatty acyl lipids were quantified by integration. The potential use of the method for non-destructive food analysis is stressed by the authors. Further work clearly showed that MAS NMR only provides information on the less rigid phase(s) of the system. The chosen example was banana tissue [5], for which the solid phase (dominated by starch) was characterized by cross-relaxation NMR and the liquid phase by ^1H MAS NMR. Quantification was achieved in both solid and liquid phases over the duration of ripening and, whereas starch decreased from 20 to 2% of fresh weight, the three main sugars were found to increase, partially due to the conversion of starch.

In recent years, MAS NMR of fruits has been performed making use of the increasing magnetic fields available and the technical development of HR-MAS. HR-MAS involves the use of a high-resolution probe usually optimized for the observation of ^1H in liquids and semisolids, with the possibility of employing MAS for the latter. In addition, the use of MAS rotors with bottom and (optional) top inserts reduces phase separation

Graham A. Webb (ed.), Modern Magnetic Resonance, 1765–1768.
© 2008 *Springer.*

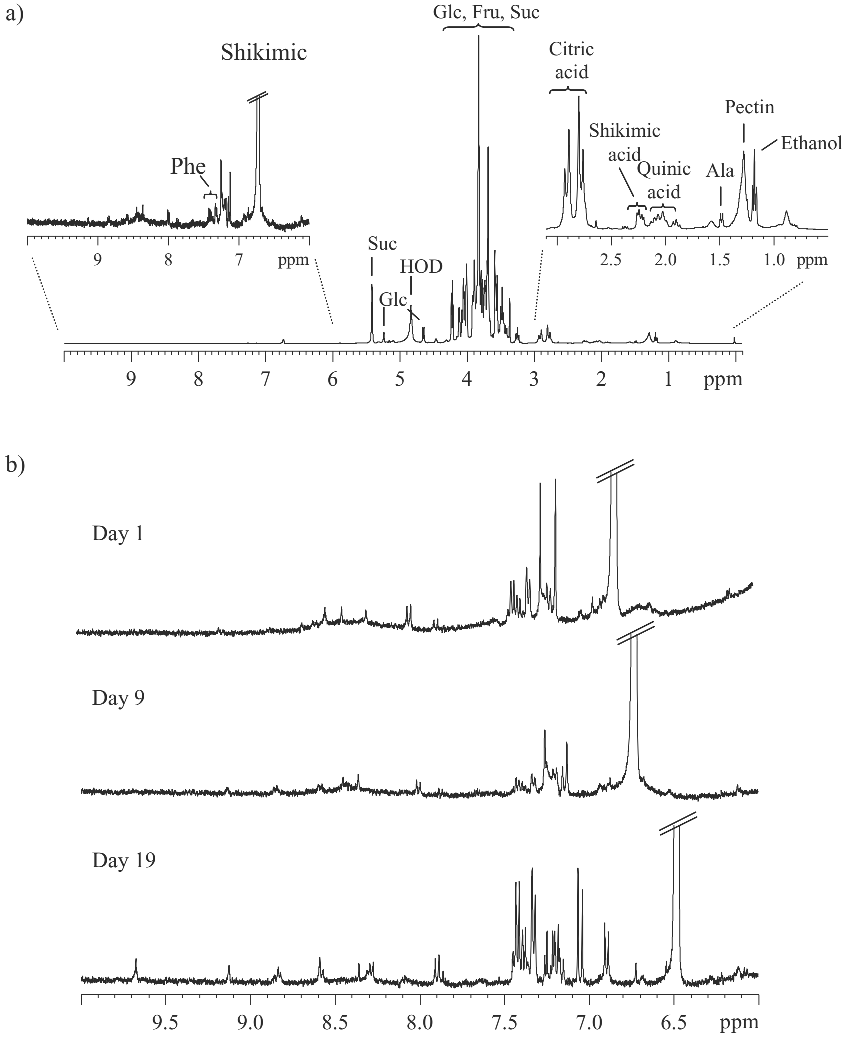

Fig. 1. (a) Full ^{1}H HR-MAS spectrum of mango pulp and (b) changes in the aromatic regions of mango ^{1}H HR-MAS spectra as a function of ripening; Day 1 = unripe fruit; day 9 = fruit ready to eat; day 19 = over ripened fruit.

and solvent evaporation, as well as reducing magnetic susceptibility effects, thus leading to improved resolution. HR-MAS of mango fruit tissue was carried out as a function of ripening enabling compositional changes to be followed in high molecular weight components, e.g. pectins, lipids and polyphenolics, as well as in small compounds mostly present in the liquid phase [6]. Figure 1a shows the full 400 MHz ^{1}H HR-MAS spectrum of mango pulp and Figure 1b shows the changes taking place in the aromatic region of spectra. *J*-resolved, total correlation spectroscopy (TOCSY; Figure 2) and ^{1}H–^{13}C correlation experiments were performed, thus allowing detailed assignments to be made. A list of compounds found in mango was reported and differences between pulp and juice compositions discussed. More recently, 600 MHz HR-MAS was used to determine the detailed composition of tomato pulp of different cultivars [7]. This work describes the comprehensive use of a combination of high-resolution experiments [*J*-resolved, correlation spectroscopy, TOCSY, diffusion ordered spectroscopy, heteronuclear single-quantum coherence (HSQC), and heteronuclear multiple-bond correlation (HMBC)] to

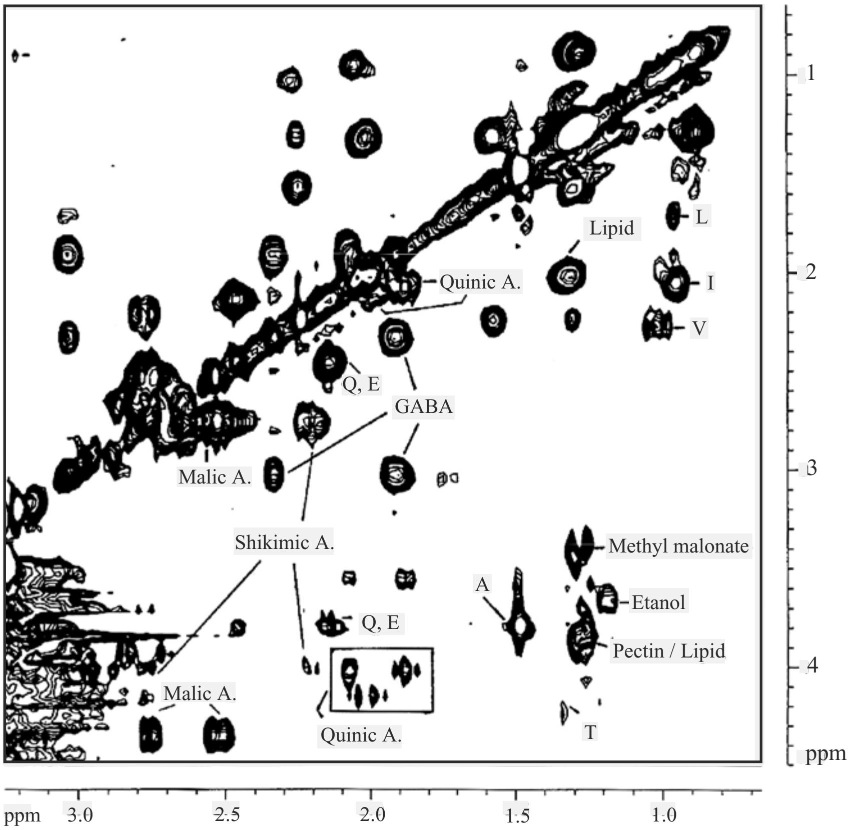

Fig. 2. Expansion of the aliphatic region of the TOCSY spectrum obtained for ripe mango pulp. Reprinted with permission from Ref. [6]. © 2000 American Chemical Society.

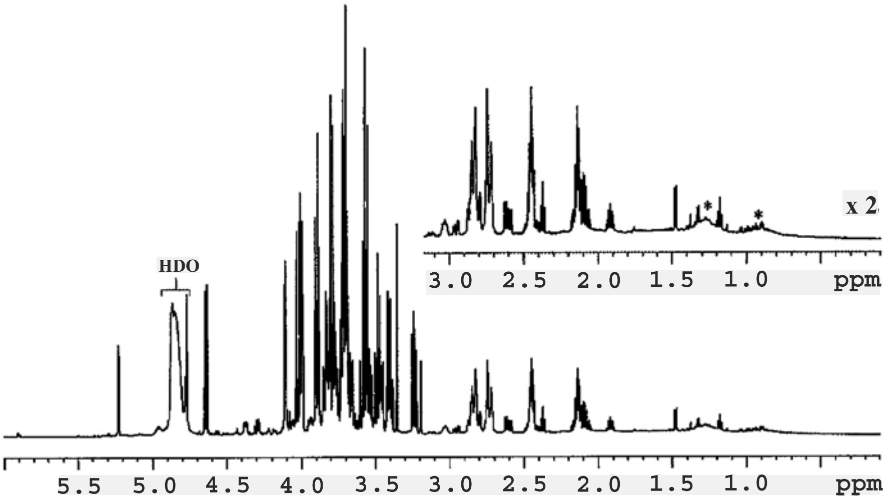

Fig. 3. ^{1}H HR-MAS NMR spectrum of Red Setter tomato pulp. The inset represents a vertical expansion of the high-field region. The positions of the broad resonances due to fatty acids are labeled with asterisks. Reprinted with permission from Ref. [7]. Copyright 2003 © John Wiley & Sons Limited.

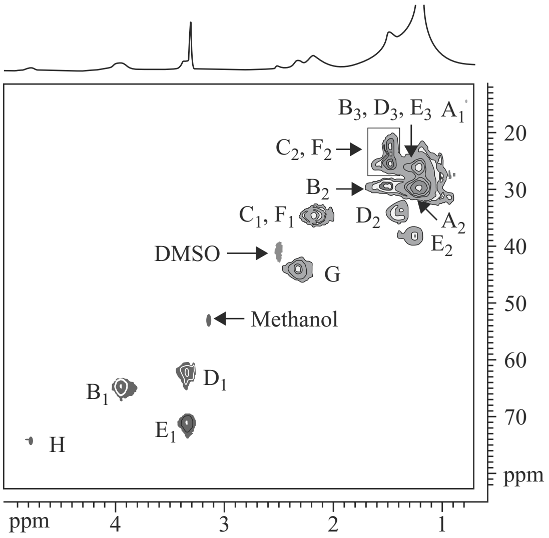

Fig. 4. 600 MHz ^{1}H–^{13}C HR-MAS NMR HSQC spectrum of tomato cutin swollen in DMSO-d_6 while spinning at 9 kHz. Reprinted with permission from Ref. [10]. © 2003 Elsevier.

establish the composition of tomato pulp and differences between two selected cultivars. Figure 3 demonstrates the high quality of the 1D spectra registered under HR-MAS conditions. Differences between pulp and juice compositions were discussed and the potential of the technique, in tandem with statistical analysis, for the rapid characterization of tomatoes is advanced.

Applications of ^{1}H HR-MAS to fruits are still limited, no studies having been reported on intact vegetable samples. However, applications of HR-MAS to selected fruit and vegetable components, rather than to the intact products, are also worth mentioning. The study of plant cutin, one of the main polymeric lipid components found in plant cuticles, has attracted particular attention [8–10]. The knowledge of cutin molecular architecture has been hindered by its insolubility and it was found that ^{1}H MAS and ^{1}H HR-MAS of cutin swelled in DMSO gives valuable information on cutin structure [8–10]. Solvent swelling enhances molecular mobility and this enabled well-resolved 600 MHz ^{1}H HR-MAS spectra to be obtained for lime cutin as well as for potato suberin [8]. Analysis of the corresponding ^{1}H–^{13}C HMBC spectra enabled valuable structural information to be obtained. More recently, a detailed account of HR-MAS of tomato cutin has been reported [10], with information added from solid-state ^{13}C NMR methods. The use of 1D and 2D TOCSY and HSQC (Figure 4) experiments under HR-MAS conditions enabled detailed through-bond connectivities and assignments to be made for tomato cutin. Structural findings indicative of the existence of cutin cross-linking were reported for the first time.

References

1. Harris RK. Nuclear Magnetic Resonance Spectroscopy. A Physicochemical View. Longman Scientific and Technical: London, 1991.
2. Stejskal EO, Memory JD. High Resolution NMR in the Solid State. Fundamentals of CP/MAS. Oxford University Press: New York, 1994.
3. Ni QW, Eads TM. J. Agric. Food Chem. 1992;40(9):1507.
4. Ni QW, Eads TM. J. Agric. Food Chem. 1993;41(7):1026.
5. Ni QW, Eads TM. J. Agric. Food Chem. 1993;41(7):1035.
6. Gil AM, Duarte IF, Delgadillo ID, Colquhoun IJ, Casuscelli F, Humpfer E, Spraul M. J. Agric. Food Chem. 2000;48(5):1524.
7. Sobolev AP, Segre A, Lamanna R. Magn. Reson. Chem. 2003;41(4):237.
8. Stark RE, Yan B, Ray AK, Chen Z, Fang X, Garbow JR. Solid State Nucl. Mag. 2000;16(1–2):37.
9. Fang XH, Qiu F, Yan B, Wang H, Mort AJ, Stark RE. Phytochemistry. 2001;57(6):1035.
10. Deshmukh AP, Simpson AJ, Hatcher PG. Phytochemistry. 2003;64(6):1163.

High-Resolution Solid-State NMR of Gluten and Dough

Lucia Calucci[1] and Marco Geppi[2]
[1]*Istituto per i Processi Chimico-Fisici del CNR, 56124 Pisa, Italy; and*
[2]*Dipartimento di Chimica e Chimica Industriale, Università degli Studi di Pisa, 56126 Pisa, Italy*

Introduction

Wheat flour is the most important ingredient in baked food products. Rheological properties of dough, which are recognized to be central to the successful manufacturing of cooking products, are governed by the interactions of water, which represents 40–46 wt% of the mixture, with the main components of flour, namely, starch (65–75 wt%) and proteins (8–18 wt%). The water-insoluble fraction of flour, obtained as a rubbery mass with peculiar viscoelastic properties by gently washing a dough in an excess of water or dilute salt solution, is called gluten. Gluten is composed by a heterogeneous mixture of proteins (75–85 wt%), classified into the two main groups of glutenins and gliadins on the basis of solubility, residual carbohydrates (10–15 wt%, mainly starch), and lipids (5–10 wt%). During the kneading process, gluten interacts with water forming a cross-linked network filled with starch granules allowing the formation of viscoelastic doughs, capable of trapping gases produced during fermentation processes in the preparation of baking products. Therefore, the microscopic origin of dough properties, and thus the structural and dynamic changes induced on flour components upon hydration at a molecular level, is of great practical interest.

Among the techniques allowing flour and gluten to be studied in the solid state, either dry or hydrated, solid-state NMR (SS-NMR) spectroscopy has proved to be particularly successful in investigating molecular structure, conformational order and dynamics. In the last three decades, SS-NMR has been increasingly applied to characterize the main components of flour: particular emphasis has been given to the investigation of amorphous and crystalline states of starch, properties of gluten proteins, water organization and mobility, average size of domains with different composition, as well as influence of hydration on the structural and dynamic properties of flour components. To this aim, several high and low-resolution SS-NMR techniques, including the measurement of relaxation times, have been used.

In this section, a survey of high-resolution SS-NMR applications to dough and gluten is presented; the reader can refer to other sections of this handbook for high-resolution SS-NMR applications to starch (high-resolution solid state NMR of starch) and for relaxation studies (relaxation time measurements in water/seed proteins, relaxation time measurements in dough and gluten, relaxation time measurements in water/starch granules and gels). The nuclei investigated in high-resolution SS-NMR studies of flour and gluten are ^{1}H and ^{13}C. Wideline (static) ^{1}H spectra of flour and gluten exhibit no chemical shift resolution, but reveal the presence of components with different mobility which can be quantified by means of suitable free induction decay (FID) analysis techniques. By magic angle spinning (MAS) spectral resolution can be recovered only for the mobile components of the samples, the faster spinning frequencies currently available on most solid-state spectrometers (15–35 kHz) being less than the rigid component line width. The chemical composition of mobile and soluble fractions can be also characterized by high-resolution MAS (HR-MAS) techniques, which allow a liquid-like spectral resolution to be obtained on solvent-added semi-solid samples thanks to a special probe and rotor design [1].

High-resolution ^{13}C spectra can be recorded on solid samples by combining MAS and high power decoupling (HPD) techniques; chemical shifts are determined not only by the chemical structure, as in liquids, but also by molecular conformations and/or crystalline packing. In the case of dough and gluten, this allows different crystalline and amorphous phases to be distinguished directly from chemical shift, but line broadening due to the heterogeneous composition and conformational distribution present in these samples often limits the spectral resolution. Two kinds of ^{13}C MAS NMR experiments, namely single pulse excitation (SPE) [2] and cross-polarization (CP), are usually carried out on flour and gluten samples and their comparison is exploited to highlight differences in carbons chemical environment and mobility. In fact, while the SPE experiment is in principle quantitative, provided a recycle time is used long enough to allow complete relaxation of all ^{13}C nuclei, the CP experiment enhances signals of carbon nuclei strongly coupled to protons via dipolar interactions, i.e. in proton-rich and rigid environments. Signals from carbons in mobile domains can be usually highlighted in SPE spectra with short recycle times (e.g. 2 s) because of their fast spin–lattice relaxation.

Graham A. Webb (ed.), Modern Magnetic Resonance, 1769–1776.
© 2008 *Springer.*

Further discriminations among ^{13}C nuclei belonging to domains with different mobility can be performed on the basis of the relaxation behavior of protons which have dipolar couplings to them by using modified-CP pulse sequences. For instance, delayed-CP experiments allow signals arising from rigid phases to be suppressed, due to their short (about 10–20 μs) ^{1}H spin–spin relaxation time (T_2), while ^{13}C spectra of the sole rigid domains can be obtained by short contact time (<100 μs) CP experiments, where only the signals of carbons experiencing strong dipolar C–H couplings appear. Moreover, variable spin-lock time CP experiments may discriminate among carbon nuclei coupled to protons having remarkably different spin–lattice relaxation times in the rotating frame ($T_{1\rho}$) [3].

Gluten

^{13}C MAS

^{13}C CP- and SPE-MAS spectra have been acquired on gluten samples from wheat of different hardness and cultivar, as well as on storage proteins, in either dry or hydrated states; examples of such spectra are shown in Figure 1. In general, the following groups of resonances

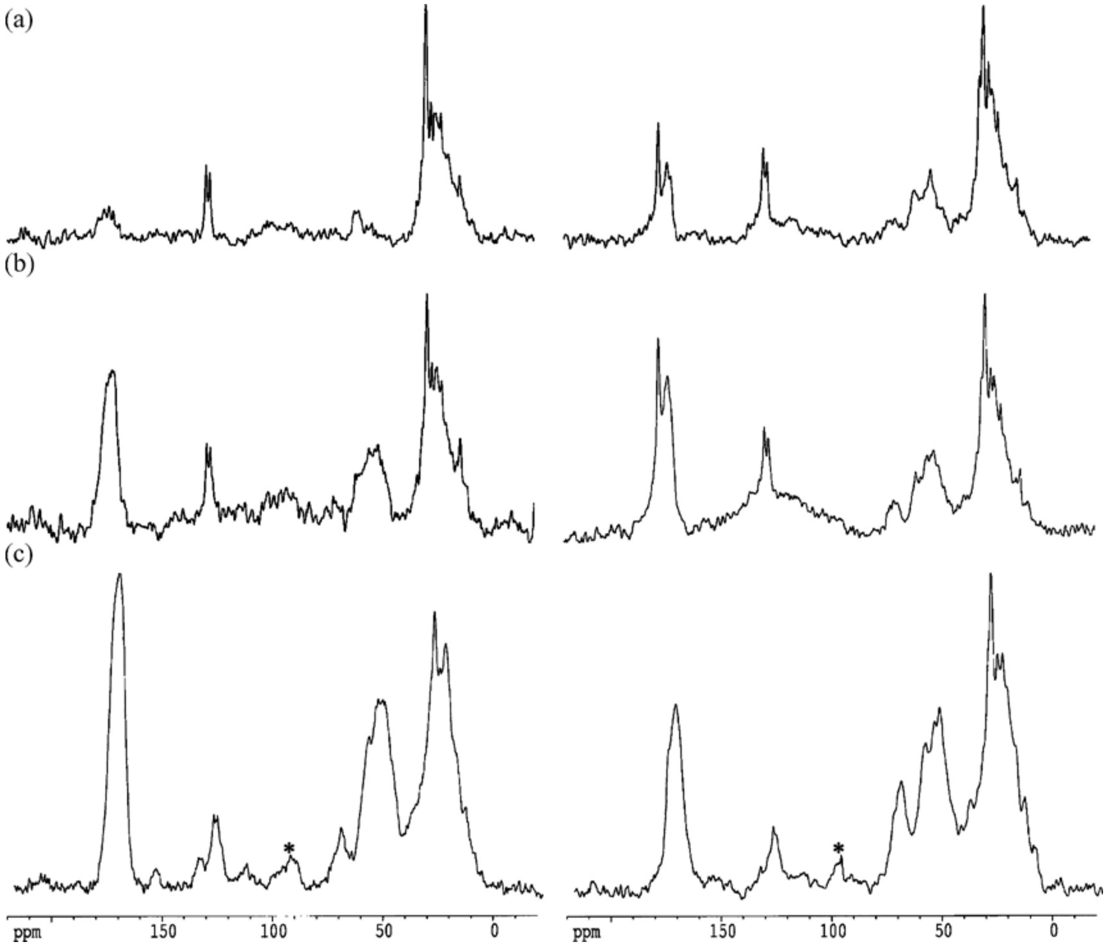

Fig. 1. ^{13}C spectra recorded by means of SPE and CP experiments on dry (left) and hydrated (right) gluten: (a) SPE with a recycle time of 1 s; (b) SPE with a recycle time of 60 s; (c) CP. All experiments were performed under HPD and MAS conditions at a spinning rate of 6 kHz. Asterisks denote spinning sidebands. Reprinted with permission from Ref. [4]. © 2003 Elsevier.

can be distinguished in the spectra and collectively assigned to gluten components: 0–40 ppm (alkyl groups in protein side chains and lipids), 40–65 ppm (alkyl groups in protein main chains), 65–80 ppm (starch), 125–135 ppm (protein aromatic moieties and lipid olefinic carbons), 165–185 ppm (carbonyl groups in proteins and lipids) [4]. Individual contributions of some amino acid residues are recognized within each group of protein resonances. A more detailed interpretation of the spectra in terms of conformations and/or molecular packing can be performed for isolated gluten proteins (for instance ω-gliadins and high molecular weight glutenin subunits), allowing β-sheet, α-helix and β-turns structures to be identified [5,6]. Such detailed attributions are prevented in the case of whole gluten by its heterogeneous character, bringing to a superposition of a considerable number of resonances with slightly different chemical shift values in several regions of the spectrum.

The CP- and SPE-MAS spectra of dry gluten (Figure 1) are somewhat different and their comparison can qualitatively highlight differences in the local structure and dynamics of carbon environments. Signals from starch and protein backbone carbons are enhanced in the CP spectra, indicating that most of these nuclei are located in rigid domains. The mobile fraction of gluten is constituted by lipids (narrow peaks in the 125–135 ppm and, in part, 0–40 ppm spectral regions) and protein side chains (0–40 ppm), as observed from SPE spectra acquired with a short recycle time. Spectra of components with different mobility can be also selectively recorded by resorting to modified-CP techniques, exploiting differences in ^{1}H T_2 and $T_{1\rho}$ relaxation times, as well as on CP times T_{CH}. In particular, it has been observed that protein side chain signals only contribute to a delayed-CP spectrum recorded with a delay of 40 μs and a contact time of 1–2 ms [4], while a CP spectrum recorded with a very long contact time (20 ms) shows signals from lipids only [7]. Upon hydration with a water amount suitable to obtain a cohesive elastic mass (60–100 g of water per 100 g of dry gluten), plasticization of gluten proteins occurs, as clearly indicated by the presence of signals from protein main chain carbons in SPE spectra acquired with short recycle times; however, considerable protein and, especially, starch fractions remain quite rigid as it can be inferred from the comparison between CP spectra of dry and hydrated gluten (Figure 1c). Changes in the dynamics of proline and glutamine residues upon hydration have been highlighted on either whole gluten or its isolated proteins: the side chain carbonyl carbon of glutamine surrounded by water molecules gives rise to a well distinct sharp peak at 177 ppm, strongly enhanced in SPE spectra (Figure 1a and b); proline Cδ (48.6 ppm) and Cγ (25.5 ppm) peaks have been observed to decrease in intensity in CP spectra by increasing the water content because of the speeding up of ring puckering [5,6]. The high-resolution of the ^{13}C spectra also allows the indirect measurement of ^{1}H spin–lattice relaxation times, that, being affected by the spin diffusion process, contain important information on the average dimensions of the different domains present in gluten. For instance, it has been shown [4] that hydration causes an intimate mixing between protein and residual starch domains, otherwise separated on a 200 Å spatial scale in dry gluten. ^{13}C MAS experiments are useful in unraveling dynamic rather than structural differences in gluten; in fact, while ^{13}C CP-MAS spectra of different protein fractions do not show significant differences, mainly because of their similar amino acid compositions, suitable sets of selective experiments allow domains with different dynamic behavior (lipids, storage proteins with different solubility properties, protein backbone, and side chains) to be singled out without requiring sample pre-treatments which could alter the physicochemical properties of the sample. Therefore, any attempt to correlate ^{13}C CP-MAS spectral features of dry gluten or protein fractions with wheat hardness, cultivar, and breadmaking quality has failed so far [7–9]. On the other hand, ^{13}C high-resolution SS-NMR experiments, in combination with ^{1}H high and low-resolution NMR techniques, revealed particularly successful in understanding properties of hydrated gluten, such as average domain size, interactions among components and plasticization effects on different components, thus contributing to the formulation of the “loop and train” model [10,11].

^{1}H MAS

The static ^{1}H spectrum of dry gluten shows at least two unresolved signals with half-height widths of a few and a few tens of kHz, respectively, while a more complex superposition of lines is present in the spectra of the hydrated samples, where the broadest component can still be observed, even though with a lower relative intensity, and a narrower signal with a line width of less than 1 kHz is present. Nevertheless, peaks with line widths of the order of a few Hz are never revealed, thus indicating the absence of liquid-like water domains. A much bigger proportion of rigid domains is present in dry than in hydrated samples, indicating a plasticization of gluten upon hydration. On spinning at the magic angle, some fine structure is observable in the spectra recorded on both dry and hydrated samples even at very low spinning rates, indicating the presence of a fraction of nuclei belonging to very mobile groups. However, the broadest line of the static spectrum remains substantially unchanged under MAS conditions up to a spinning rate of about 6 kHz, while at much higher spinning rates (12–15 kHz) it is split into a central band, with a line width of a few kHz, and a series of sidebands. In the spectra of dry gluten resolved signals are mainly due

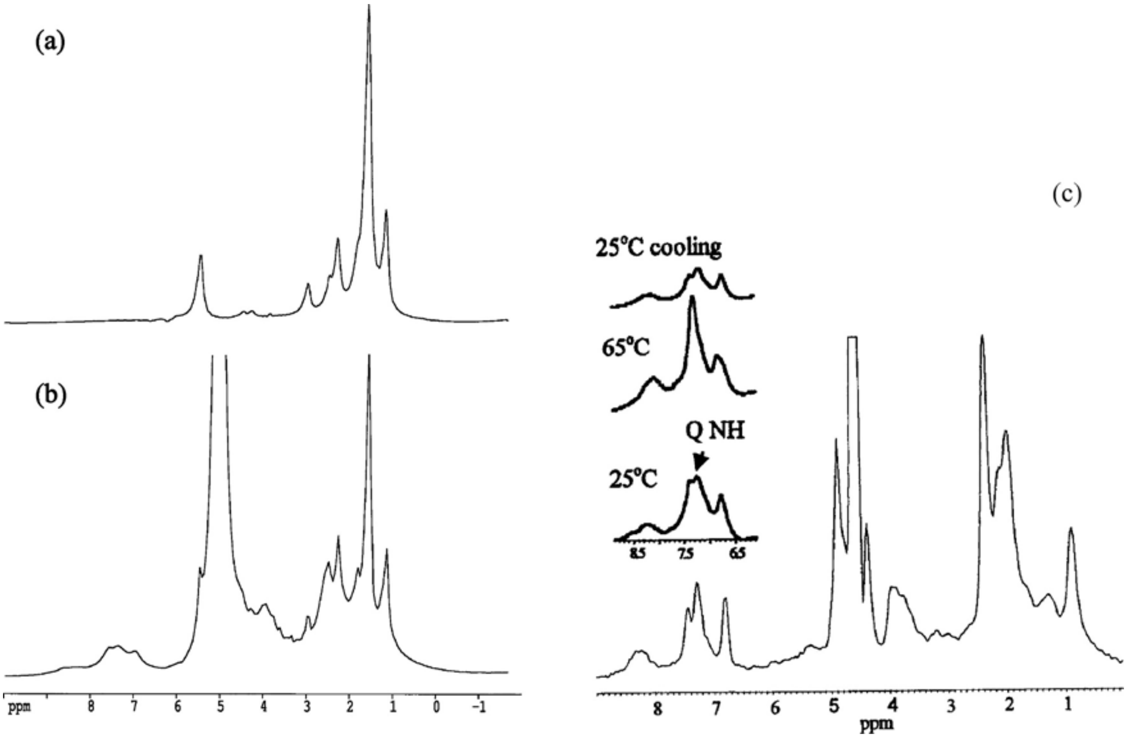

Fig. 2. Expansions of ^{1}H MAS spectra of gluten: (a) dry gluten; (b) D_2O hydrated gluten; (c) D_2O hydrated delipidated gluten. Insets of (c) show NH and aromatic resonances in a sample subjected to heating and successive cooling. Spectra (a) and (b) were recorded with a MAS rate of 12 kHz, while 15 kHz were used in (c). Spectrum (c) was obtained by Gaussian resolution enhancement. (a) and (b) reprinted with permission from Ref. [4]. © 2003 Elsevier. (c) Reprinted from Alberti E. Magnetic resonance studies of cereal proteins and some solid model systems. Ph.D. Thesis. Universitade de Aveiro, Portugal, 2000 and Ref. [12].

to lipid protons (Figure 2a); in those of hydrated gluten several resolved signals ascribable to protons belonging to mobile protein groups are also present (Figure 2b), in agreement with the plasticization effect observed in ^{13}C MAS experiments.

The protein signals have been selectively observed on delipidated gluten samples and a detailed assignment in terms of different amino acid residues has been performed by resorting to resolution enhancement techniques in FID processing (Figure 2c). An assignment of the main resolved peaks present in dry and hydrated gluten spectra is reported in Table 1. The signal due to glutamine side chain NH protons (7.2 ppm) can be exploited to obtain information on the dependence of microscopic phenomena, such as hydrogen bond interactions, on gluten heating and cooling [12].

^{1}H HR-MAS experiments have been performed on ω-gliadins [5] and HMW glutenin subunits [11] (Figure 3a and b). Well resolved spectra have been obtained and 2D techniques typical of solution-state NMR (NOESY, HETCOR, TOCSY) have been employed to perform a detailed assignment of signals.

Flour and Dough

^{13}C MAS

^{13}C CP-MAS spectra of flour [12,13–16](Figure 4c) are dominated by the peaks of starch: resonances from C-1 (96–102 ppm), C-4 (77–83 ppm), and C-6 (59–62 ppm) carbons of α-D-glucose can be easily distinguished, while C-2, C-3, and C-5 carbons all contribute to a signal centered at 70–73 ppm. Line width, multiplicity, and chemical shift of these resonances allow the state of starch to be identified (see “Solid-state high-resolution NMR of starch”); usually broad lines (6–8 ppm line width) are observed, arising from conformational distributions

Table 1: Resonances commonly resolved in proton MAS spectra of gluten, flour, and dough

Chemical shift (ppm)	Assignment
0.9	Lipid CH_3, Leuδ, Valγ
1.2–1.4	Lipid chain CH_2, Thrγ, Alaβ
1.5	Lipid –$\mathbf{CH_2}$–CH_2–COO–
1.7	Leuγ, Argγ
2.0–2.2	Lipid –$\mathbf{CH_2}$–CH=CH–, lipid –CH_2–$\mathbf{CH_2}$–COO–, Proβ, Proγ
2.4	Glnγ, Argβ
2.7	Lipid –CH=CH–$\mathbf{CH_2}$–CH=CH–
3.5–4.0	Starch H2, H6
4.0–4.5	Proδ, protein backbone protons
4.6–4.8	Water
5.2	Starch H1
5.3	Lipid olefinic protons
6.8	Tyrε
7.1	Tyrδ
6.8–7.7	Glnδ
8.0–8.3	Protein backbone–NH

of glucose moieties in amorphous starch. Weak peaks from aliphatic (10–40 ppm) and aromatic (∼130 ppm) side chain carbons and from main chain peptide carbonyl carbons (∼175 ppm) of gluten proteins are also present in the ^{13}C CP-MAS spectrum of flour.

In the ^{13}C SPE-MAS spectrum of flour, recorded with a very short recycle delay (1–2 s) (Figure 4a) [16], the olefin and alkyl carbon signals from lipids, resonating at about 130 ppm and in the range 10–40 ppm, respectively, are clearly observed, because of the mobile nature of lipids in cereal seeds. Signals from starch are also present in SPE-MAS spectra, but the ratio between the intensity of the C-6 peak and that of the other starch peaks is much higher than in the corresponding CP spectra; this feature is ascribable to the shorter ^{13}C T_1 of C-6, due to the interconformational motions of the CH_2OH groups [17].

The ^{13}C CP- and SPE-MAS spectra of dough essentially show the same signals of the corresponding spectra of dry flour (Figure 4) [14,16], but with a different intensity, as a result of the plasticizing effect of water on flour components. For instance, the much lower signal-to-noise ratio for starch resonances in the CP-MAS spectra of dough clearly indicates the presence of less rigid starch domains; however, these domains do not reach a very mobile regime, since they do not give rise to remarkable changes in the SPE spectra recorded with a short recycle delay. On the other hand, SPE spectra of dough clearly show the presence of signals peculiar to hydrated gluten, already pointed out in the Gluten—^{13}C MAS section, thus indicating that gluten, experiencing a dramatic increase of mobility upon hydration, is the component of flour mainly interacting with water. Evidences of different interactions between water and gluten proteins from hard and soft wheat have also been reported [14].

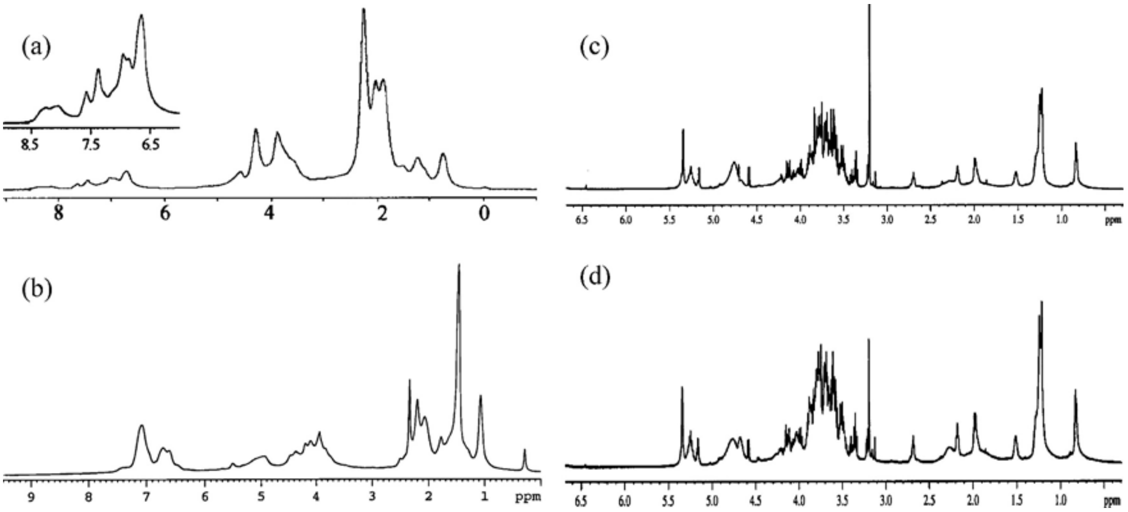

Fig. 3. ^{1}H HR-MAS spectra of (a) alkylated 1D×5 high molecular weight glutenin, (b) ω-gliadin, (c) durum wheat flour, and (d) soft wheat flour. (a) Reprinted with permission from Ref. [11]. © 2001 John Wiley and Sons Ltd. (b) Reprinted with permission from Ref. [5]. © 1997 John Wiley and Sons Ltd. (c) and (d) reprinted from Ref. [20]. © 2003 Society of Chemical Industry (permission granted by John Wiley and Sons Ltd.)

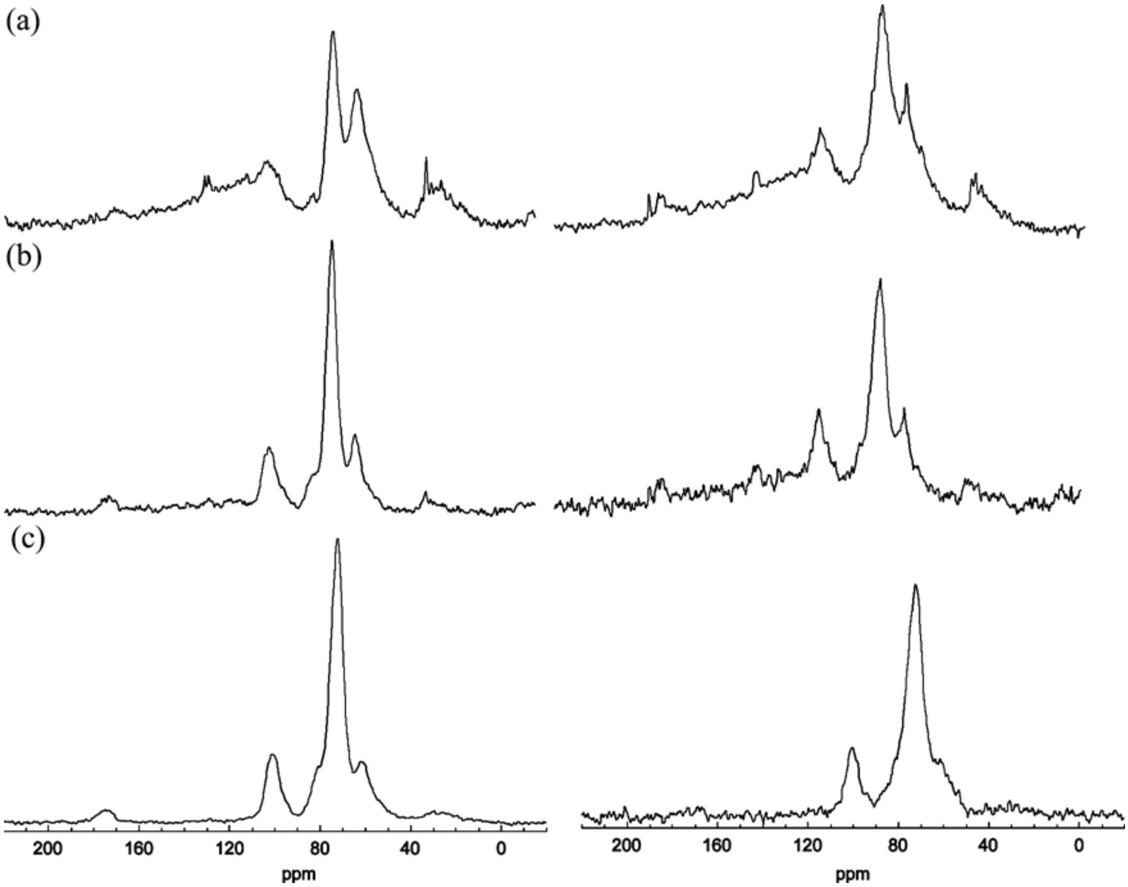

Fig. 4. ^{13}C spectra recorded by means of SPE and CP experiments on flour (left) and dough (right): (a) SPE with a recycle time of 2 s; (b) SPE with a recycle time of 60 s; (c) CP with contact time of 1 ms and recycle time of 5 s. Spectra (a), (b), and (c) were recorded with 10,000, 1000, and 2000 scans, respectively, at a Larmor frequency of 75.47 MHz. All experiments were performed under HPD and MAS conditions at a spinning rate of 7 kHz.

^{1}H MAS

At room temperature, the static ^{1}H spectra of dry flour samples consist of at least two unresolved signals with half-height widths of about 2 and 50 kHz (Figure 5b), corresponding to two main components with high and low mobility, respectively [16]. In the spectra recorded under MAS conditions (Figure 5a and d), some fine structure is observed even at very low spinning rates (500 Hz), arising from the resolution of the narrower line; this resolution improves up to spinning rates of 1.5–2 kHz, but no significant changes are observed increasing the spinning rate further. Resolved signals can be ascribed to lipids, which therefore represent the most mobile fraction of flour, in agreement with what observed in ^{13}C SPE-MAS spectra, and, to a lesser extent, to proteins (Table 1) [4,18]. At high spinning rates (above 6 kHz) a partial splitting of the broader resonance into large spinning sidebands is observed, due to the inhomogeneous component of the homonuclear dipolar interaction, which, however, is not particularly informative.

In the room temperature static spectra of dough, two unresolved signals are present as in those of dry flour, but with approximately halved line widths and a much bigger proportion of the narrower signal (Figure 5c). As in the case of hydrated gluten, no liquid-like water can be detected. In the high-resolution spectra of the mobile fraction of dough, obtained by MAS (Figure 5f), signals due to protons of bound water (about 4.7 ppm), starch (about 3.8 ppm), as well as aromatic (6.8–7.3 ppm) and

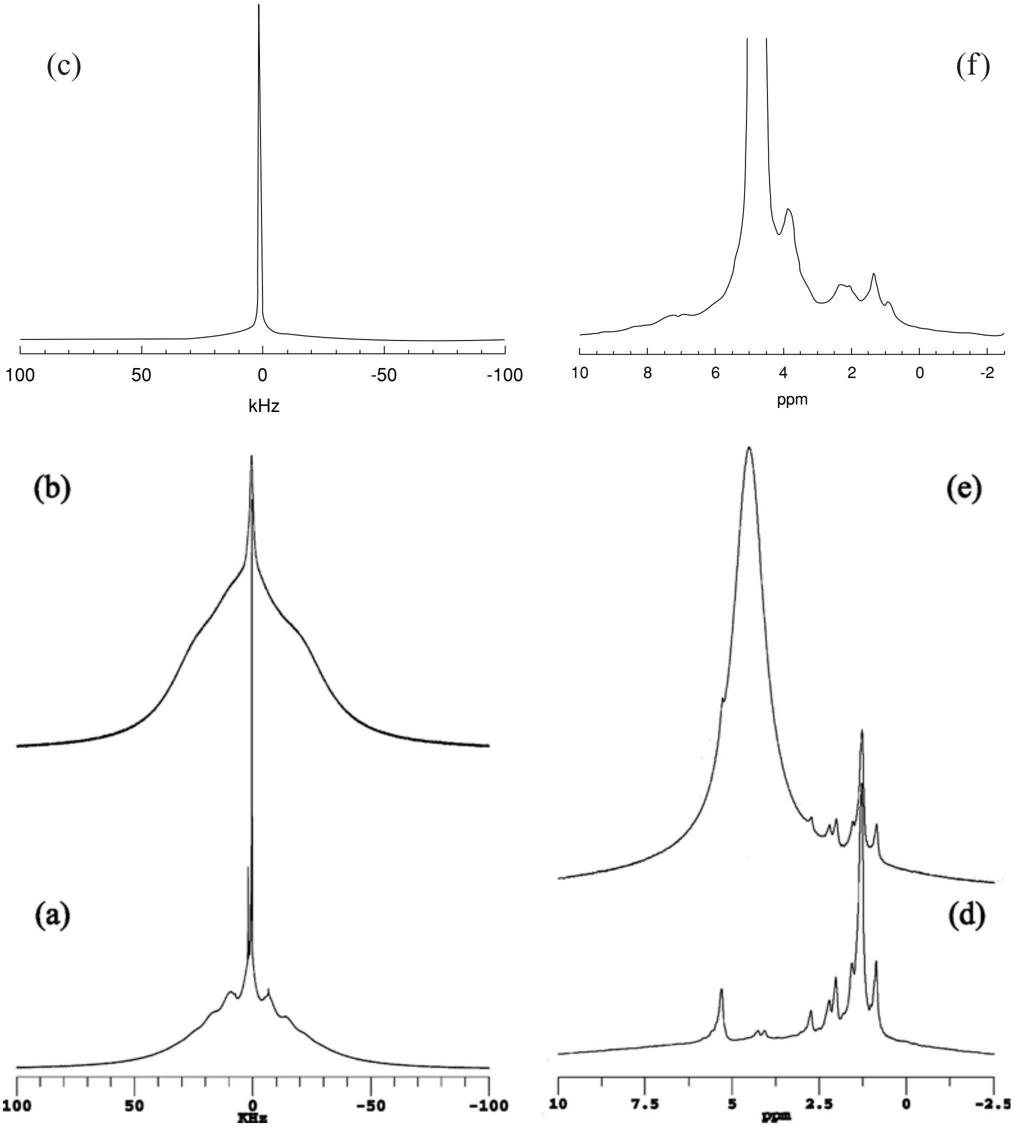

Fig. 5. (a) ^{1}H MAS spectrum of dry flour; (b) ^{1}H static spectrum of dry flour; (c) ^{1}H static spectrum of dough (45 wt% of water); (d) expansion of (a); (e) expansion of the ^{1}H MAS spectrum of naturally hydrated flour (∼14 wt% of water); (f) expansion of the ^{1}H MAS spectrum of dough (45 wt% of water). MAS spectra were recorded with a spinning rate of 7 kHz. (a), (b), (d), and (e) reprinted with permission from Ref. [16]. © 2004 American Chemical Society.

NH (8.0–8.3 ppm) protein groups are present in addition to those observed for dry flour. ^{1}H HR-MAS NMR spectroscopy has been recently applied to hydrated flour samples [18–20]. Spectra with more than 80 signals (Figure 3c and d) are obtained, where sharp resonances are mainly due to simple saccharides, whereas broader signals are ascribed to lipids (signals in the 0.8–2.7 ppm range) and polysaccharides (signals in the central spectral region). A quite accurate peak assignment has been performed [18] taking advantage of the fact that HR-MAS NMR spectroscopy allows the application of high-resolution 1D (CPMG, NOESY) and 2D (TOCSY, HMQC, HSQC) techniques. If combined with a suitable multivariate statistical analysis, ^{1}H HR-MAS can be considered a promising technique for assessing the geographical and varietal origin of wheat flour, avoiding the drawbacks connected with the pre-treatment of the samples and requiring a reasonably short time for the analysis.

References

1. Fitch WL, Detre G, Holmes CP, Shoolery JN, Keifer PA. J. Org. Chem. 1994;59:7955.
2. SPE is the simplest direct excitation pulse sequence; sometimes more complex sequences, for instance using “depth” pulses, can be used in order to suppress background signals.
3. McBrierty VJ, Packer KJ. Nuclear Magnetic Resonance in Solid Polymers. Cambridge University Press: Cambridge, 1993.
4. Calucci L, Forte C, Galleschi L, Geppi M, Ghiringhelli S. Int. J. Biol. Macromol. 2003;32:179.
5. Gil AM, Alberti E, Tatham AS, Belton PS, Humpfer E, Spraul M. Magn. Reson. Chem. 1997;35:S101.
6. Alberti E, Gilbert SM, Tatham AS, Shewry PR, Gil AM. Biopolymers. 2002;67:487.
7. Belton PS, Duce SL, Colquhoun IJ, Tatham AS. Magn. Reson. Chem. 1988;26:245.
8. Moonen JHE, Hemminga MA, Graveland A. J. Cereal Sci. 1985;3:319.
9. Belton PS, Duce SL, Tatham AS. Int. J. Biol. Macromol. 1987;9:357.
10. Belton PS. J. Cereal Sci. 1999;29:103; Shewry PR, Popineau Y, Lafiandra D, Belton P. Trends Food Sci. Technol. 2001;11:433.
11. Alberti E, Humpfer E, Spraul M, Gilbert SM, Tatham AS, Shewry PR, Gil AM, Biopolymers. 2001;58:33.
12. Gil AM, Alberti E, Santos D. An insight into the structure of foods using ^{13}C and ^{1}H MAS NMR: application to wheat dough. In: GA Webb, PS Belton, AM Gil, I Delgadillo (Eds). Magnetic Resonance in Food Science—A View to the Future. The Royal Society of Chemistry: Cambridge, 2001, p 43.
13. O’Donnell DJ, Ackerman JJH, Maciel GE. J. Agric. Food Chem. 1981;29:514.
14. Garbow JR, Schaefer J. J. Agric. Food Chem. 1991;39:877.
15. Baik M-Y, Dickinson LC, Chinachoti P. J. Agric. Food Chem. 2003;51:1242.
16. Calucci L, Galleschi L, Geppi M, Mollica G. Biomacromolecules. 2004;5:1536.
17. Tang H, Hills BP. Biomacromolecules. 2003;4:1269.
18. Sacco A, Neri Bolsi I, Massini R, Spraul M, Humpfer E, Ghelli S. J. Agric. Food Chem. 1998;46:4242.
19. Brescia MA, Di Martino G, Fares C, Di Fonzo N, Platani C, Ghelli S, Reniero F, Sacco A. Cereal Chem. 2002;79:238.
20. Brescia MA, Sgaramella A, Ghelli S, Sacco A. J. Sci. Food Agric. 2003;83:1463.

High-Resolution Solid-State NMR as an Analytical Tool to Study Plant Seeds

Michel Bardet, Marie Françoise Foray, and Armel Guillermo
Service de Chimie Inorganique et Biologique, Département de Recherche Fondamentale sur la Matière Condensée,
CEA-Grenoble, 38054 Grenoble, Cedex 9, France

Introduction

High-resolution solid-state NMR has found widespread applications in various fields of agricultural and food sciences [1–6]. The technical improvements of high-resolution solid-state NMR have been tremendous for the last 10 years; the sensitivity and the design of probes, the setting and the control of spinning rates at the magic-angle spinning (MAS), the decoupling power strength, the decoupling schemes, and the large number of available pulse sequences are certainly among the most significant technical improvements [7,8].

In that respect seeds are valuable biological materials to be studied with high-resolution solid-state NMR. The initial interest of high-resolution solid-state NMR studies on seeds appeared undoubted in the possibility of a rapid and non-invasive *in situ* characterization of the lipid moiety of seeds with ^{13}C or ^{1}H NMR [9–14]. The large number of studies concerning the oil compositions of seeds gives a clear illustration of this assertion. Lipids can be one of the most abundant constituents of seeds, in oleaginous crops for instance [15–17]. Lipids are very important components not only on a biochemical point of view but also for economical aspects. Indeed, they are a major source of renewable energy and they do not participate to CO_2 enrichment of atmosphere.

An important aspect that has to be taken into account is that the mature seeds are, in most of cases dormant organisms, therefore the gas exchanges are very low [18]. Therefore, seeds can be kept in non-biological environments such as those met inside the rotors, tight cylinder containers, required in CP/MAS probes. Recording NMR spectra of dormant seeds under MAS does not require specific equipments to maintain aerobic conditions such as those required for *in vivo* NMR studies that are performed on cell suspensions or living tissues [19]. Up to now the CP/MAS experiments have not appeared to damage seeds using spinning rates up to 12,000 Hz. This point can be easily demonstrated by performing germination tests on the seeds that were used for NMR experiments. Nevertheless, very high spinning rates, such as 32,000 Hz, have to use with care since roughly a 60 °C temperature increase can be recorded for the samples if no cooling is employed.

Spectral Edition Inside the Seeds

For NMR methodology development, seeds represent an interesting example of a complex biological material. The complexity arises both from their heterogeneous chemical composition and from their specific organization at a cellular scale and at a macroscopic level, that is to say teguments, cotyledons and embryonic axes. The food reserves that are required during the germination are mainly fats (oils), carbohydrates, and proteins. According to the nature and biological origins of seeds, their relative amounts are extremely variable.

Generally, triacyglycerols (TAG) are the form of fat or oil storage and are contained in small subcellular droplets called oil bodies [20]. The natural biological variation found in the types of food reserves is a property that has been fully used by seed producers to select or modify seeds in order to improve the quality or the quantity of these reserves. As a result, from the point of view of NMR spectroscopy, liquid and solid properties of dormant seeds are expected. These behaviors can be defined by NMR through the consequences of the molecular mobility on the more or less complete averaging to zero of the proton–carbon dipolar interactions.

Solid-Like Domains

With the commonly used CP/MAS experiments that combines proton to carbons cross-polarization (CP) transfer and MAS. This sequence is therefore devoted to observe carbons with strong dipolar interactions with the surrounding protons, because of that all the carbons belonging to rigid domains can be observed as shown in Figure 1A.

Liquid-Like Domains

The carbons spectra of mobile compounds can be selectively observed by direct polarization with single-pulse

Graham A. Webb (ed.), Modern Magnetic Resonance, 1777–1781.
© 2008 *Springer.*

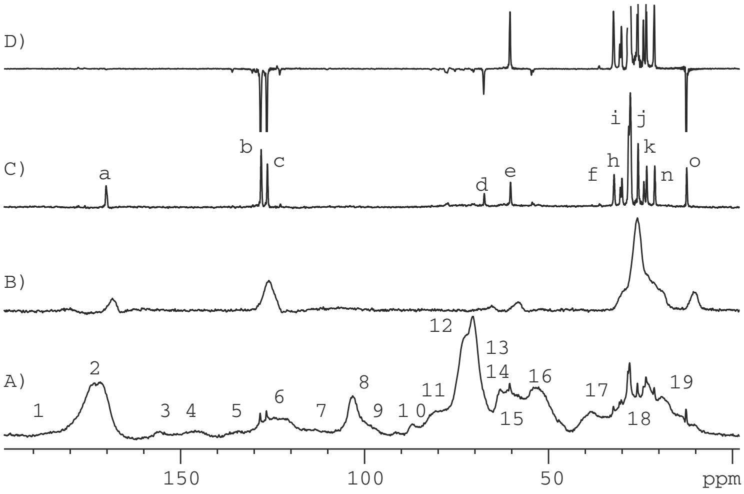

Fig. 1. 100 MHz ^{13}C high-resolution solid-state NMR spectra of *Lactuca sativa* seeds recorded with: CP/MAS experiment (A), SP experiment without sample spinning (B), and SP/MAS experiment (B), SP/MAS experiment (C), and DEPT experiment with a $3\pi/4$ polarization transfer pulse without sample spinning (D).

excitation (SP), proton decoupling being applied during signal acquisition. Nevertheless, this simple sequence has to be combined with rotation (3000 up to 10,000 Hz) of the sample at the magic angle (54.74°) related to the vertical magnetic field) in order to record high-resolution spectra. Otherwise the signals that are recorded in the liquid domains remain broad. The broadening of the signals is easily explained by the magnetic susceptibility anisotropy arising from the strong difference between the susceptibility of seeds and the air filling the space available between seeds. Moreover, the microscopic magnetic susceptibility gradients inherent in seed tissues also contribute to line broadening. These different aspects are exemplified with spectra B and C in Figure 1, that shows typical ^{13}C spectra of liquid-like domains of *Lactuca sativa* seeds recorded with direct polarization of carbons either under static or MAS conditions.

It is worth noting that once the dipolar interactions are averaged by Brownian motions, all the sequences devoted to liquid NMR can be directly applied even on such heterogeneous material.

For instance, the polarization transfer from proton to carbon through their indirect coupling is efficient for the products belonging to liquid domains inside seeds. Thus, the robust DEPT experiment [21] is fully operant, as illustrated in Figure 1D, and allows us to assign the different signals in relation to the number of protons they are bound to, that is to say CH_3, CH_2, CH, and quaternary carbons. Figure 2 gives a 2D example of such sequences with the proton–carbon correlation map recorded with the appropriate 2D heteronuclear experiment. The quality of the correlation map is excellent and illustrates that the use of such sequences appears promising for direct studies of metabolites inside seeds.

Liquid-Like Domains with Residual Dipolar Interactions

Recently we also have shown that it was also possible to detect in the liquid domain [22], the signals of molecules that present residual proton–proton dipolar couplings by using spin echo experiment with proton–proton dipolar decoupling during one of the echo delays. For instance, in the case of *Pisum sativum* seeds broad ^{13}C signals assigned to sugars were shown to present such features.

Assignments of the NMR Signals

Due to the chemical nature of seeds most of the analytical studies carried with solid-state ^{13}C NMR have been performed on lipids and sugar components and a few works have also been reported on proteins of seeds so far [1,23,24]. For the products that present a liquid-like behavior inside the seeds, such as lipids, the amount of available works concerning the assignments of such compounds carried out with liquid-state NMR studies is very important [25–29] and can be used almost directly to identify these compounds and assign their NMR spectra in the whole seeds. In order to help the assignment of spectra recorded on whole seeds, it can be very useful to start analyzes of the different parts of dissected seeds when it is possible, namely teguments, cotyledons, and embryonic axes [2,30]. The assignment of the spectra relies on classical strategies used in NMR, such as analyses of model compounds of the different expected biopolymers combined with analyses of products that can be extracted [31]. Finally, the assignments reported in Tables 1 and 2 give some information on the most common ^{13}C NMR

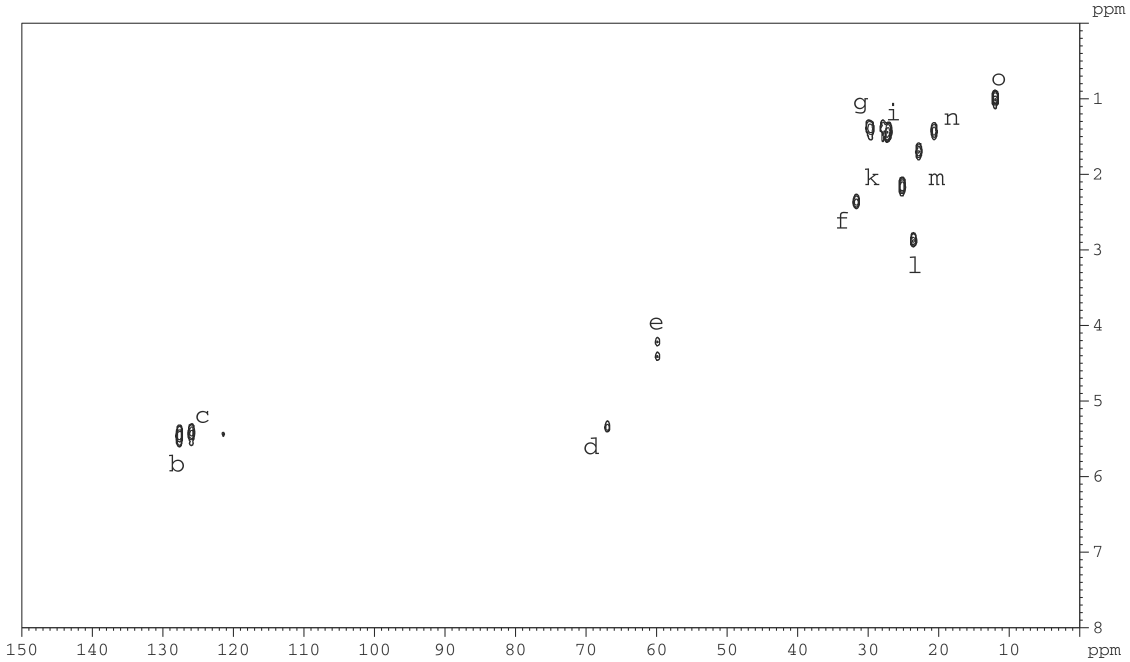

Fig. 2. ^{1}H–^{13}C correlation spectrum of *Lactuca sativa* recorded under MAS.

assignments that can generally proposed for the seeds and can be helpful as a starting point to attribute NMR spectra of seeds. Solid-state NMR has been successfully applied to study physiological processes such as those occurring during the first steps of germination [14]. The assignment of the large number of metabolites that are formed during this process represents certainly the main challenge for this kind of studies. Figure 3 illustrates an example of changes appearing in the spectra of conifer seeds during germination. It can be recalled that provided that some cares are taken, spectra can be recorded under quantitative conditions. Therefore, it is possible to follow kinetic and related experiments.

Solid-State Proton NMR

Proton NMR studies have not been very important so far, several reasons first due to chemical complexity of seeds the proton spectra can appear very broad and featureless as long as the liquid domains of seeds are concerned. If the solid domains are concerned, their proton spectra remain very large even under MAS conditions mainly due to the strong proton–proton dipolar interactions that cannot be averaged to zero. As for classical solid material, CRAMPS multipulse can be used to record high-resolution proton spectra. Generally such studies have concerned relaxation parameter measurements of the seed constituents and of water that are correlated with changes in the biological states of seeds and physiological processes. However, the interpretation of these measurements is not straightforward. The work made by Ridenour *et al.* [32] gives an example of proton NMR of study in the solid state that described the experimental conditions and led to correlate the changes in relaxation parameters with aging of seeds.

Conclusion and Prospects

All these different NMR experiments that have been reported herein can be performed on classical and commercial CP/MAS probes devoted to solid materials. They allow one to edit spectra of solid and liquid domains of seeds. These experiments are easily implemented on modern commercial spectrometers and can be readily carried out either for routine controls of seed sets or for more fundamental researches. The strategy of combining these different experiments is certainly a first step to molecular imaging when working on biological materials. All the modern solid-state NMR experiments that have been appearing for the last 10 years that correlate homo- or heteronuclear chemical shifts should of great interest. They have been already successfully applied to characterize wood or cellulose itself [33,34] but not yet applied, to our

Table 1: Assignment of ^{13}C NMR SP/MAS spectrum of *Pisum sativum*

Region or pic numbers	Chemical shift (ppm)	Signal type*	Assignment
a	172	Quaternary	Oleic/linoleic (C=O)
b	130	CH	Oleic/linoleic
c	128	CH	Linoleic
d	69	CH	Glycerol (C-β)
e	62	CH_2	Glycerol (C-α)
f	34	CH_2	Oleic (C-2)
g	32	CH_2	Oleic (C-16)
h	31.5	CH_2	Linoleic (C-16)
i	30	CH_2	Oleic/linoleic (C-18)
j	29.2	CH_2	Oleic/linoleic (C-18)
k	27	CH_2	Linoleic (C-8, C-14), oleic (C-8, C-11)
l	25.6	CH_2	Linoleic (C-11)
m	25	CH_2	Oleic/linoleic (C-3)
n	22.6	CH_2	Oleic/linoleic (C-17)
o	14	CH_3	Oleic/linoleic (C-18)

*Based on DEPT experiment.

knowledge, to whole seeds. In a near future, the perspective of combining high-resolution solid-state NMR with pulse-field gradient experiments should be a promising development in order to reach localized information about the dynamic of mobile molecules and the size of the subcellular objects on intact biological samples. Other nuclei such as phosphorus or nitrogen should also provide interesting information on these systems.

Table 2: Assignment of ^{13}C CP/MAS spectrum of *Pisum sativum*

Region or pic numbers	Chemical shift (ppm)	Signal type*	Assignment
1	195–190	Quaternary	C=O in lignins
2	180–160	Quaternary	C=O (in esters, acids) of lignins, hemicelluloses and proteins
3	160–140	Quaternary	C-1/C-3 in etherified and non-etherified syringyl units in lignins
4	139–130	Quaternary	C-1/C-4 of aromatic units in lignins
5	130–120	CH	CH of aromatic units in lignins
6	130–115	CH	carbons of phenylalamine in proteins
7	108–100	CH	C-2/C-5 of aromatic units in lignins
8	105	CH	C-1 of celluloses and hemicelluloses
9	100	CH	C-1 of starch
10	89	CH	C-4 in celluloses
11	84	CH	C-4 in celluloses
12	75	CH	C-2 in celluloses
13	72	CH	C-3/C-5 in celluloses; C-2/C-3 in hemicelluloses
14	65	CH_2	C-6 in celluloses
15	63	CH_2	C-5 in hemicelluloses
16	55.5	CH_3	CH/CH_2 in proteins; OCH_3 in lignins
17	40	CH_2	Proteins
18	30	CH_2	Proteins
19	21.5	CH_3	CH_3COO– in hemicelluloses

*Based on dipolar dephasing experiment.

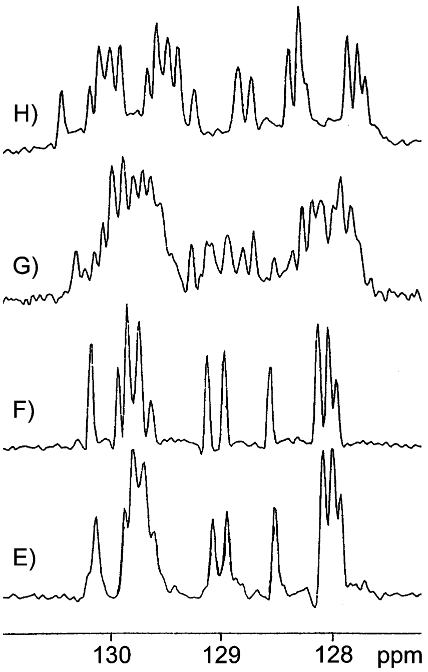

Fig. 3. 125.76 MHz ^{13}C SP/MAS spectra of the olefinic region of *Picea sitchensis* seeds: after stratification (E); after 1 day germination (F); after 2 days germination (G); after 3 days germination (H). Reproduced with permission from Sayer *et al.* [14].

References

1. O'Donnell DJ, Ackerman JJH, Maciel GE. J. Agric. Food Chem. 1981;29:514.
2. Bardet M, Foray MF, Bourguignon J, Krajewski P. Magn. Reson. Chem. 2001;39:733.
3. Jarvis MC, Apperley DC. Plant Physiol. 1990;92:61.
4. Gil AM, Neto CP. Annu. Rep. Spectrosc. 1999;75.
5. Paris M, Bizot H, Emery J, Buzaré JY, Buléon A. Carbohydr. Polym. 2000;39:327.
6. Jarvis MC. Carbohydr. Res. 1990;201:327.
7. Voelkel R. Angew. Chem. Int. Ed. 1988;27:1468.
8. Laws DL, Marcus HML, Jerschow A. Angew. Chem. Int. Ed. 2002;41:3096.
9. Haw JF, Maciel GE. J. Am. Chem. Soc. Anal. Chem. 1983;55(8):1262.
10. Rutar V. J. Agric. Food Chem. 1989;37:67.
11. Wollenberg K. J. Am. Oil Chem. Soc. 1991;68(6):391.
12. Rutar V, Kovac M, Lahajnar G. J. Am. Oil Chem. Soc. 1989;66(7):961.
13. Hutton WC, Garbow JR, Hayes TR. Lipids 1999;34(12):1339.
14. Sayer BG, Preston CM. Seed Sci. Technol. 1996;24:321.
15. Sinclair TW, Dewis CT. Sciences 1975;189:565.
16. Berrie AMM. In: MB Wilkings (Ed). Advanced Plant Physiology. John Wiley and Sons: New York, 1990, p 440.
17. Kramer PJ, Kozlowski TT. Physiology of Woody Plants. Academic Press: New York, San Francisco, London, 1979, p 494.
18. Footitt S, Vargas D, Cohn MA. Physiol. Plant 1995;94:667.
19. Loughman BC, Ratcliffe RG. Adv. Plant Nutr. 1984;1:241.
20. Huang AHC. Oil bodies and oleosins in seeds. Annu. Rev. Plant Physiol. Plant. Mol. Biol. 1992:43:177.
21. Doddrell DM, Pegg DT, Bendall MR. J. Magn. Reson. 1982;48:323.
22. Bardet M, Foray MF. J. Magn. Reson. 2003;160:157.
23. Gil AM, Albertini E, Tatham AS, Belton PS, Humpfer E, Spraul M. Magn. Reson. Chem. 1997;35:S101.
24. Gil AM, Masui K, Naito A, Tatham AS, Belton PS, Saitô H. Biopolymers 1997;41:289.
25. Wenkert E, Buckwalter BL, Burfitt IR, GašiÊ MJ, Gottlieb HE, Hagaman EW, Schell FM, Wovkulich PM, Zheleva A. In: GC Levy (Ed). Topics in Carbons-13 NMR Spectroscopy. Wiley: New York, London, Sidney, Toronto, 1976.
26. Seidl PR, do Nascimento RS, Spectros. Int. J. 1990;8:183.
27. Gambir PN. Proc. India Acad. Sci. (Chem. Sci.) 1994;107(7):1583.
28. Mavromoustakos T, Zervou M, Theodoropoulou E, Panagiotopoulos D, Bona G, Day M, Helmis A. Magn. Reson. Chem. 1997;35:S3.
29. Sacchi R, Addeo F, Paolillo L. Magn. Reson. Chem. 1997;35:S133.
30. Ribas de Oliveira CM, Iacomini M, Alquini Y, Gorin PAJ. New Phytologist 2001;152:501.
31. Bardet M, Gagnaire D, Nardin R, Vincendon M. Holzforchung 1986;40:17.
32. Ridenour CF, Xiong J, Maciel GE. Biophys. J. 1996;70:511.
33. Bardet M, Emsley L, Vincendon M. Solid State NMR 2000;8:25.
34. Lesage A, Bardet M, Emsley L. J. Am. Chem. Soc. 1999;121:10987.

High-Resolution Solid-State NMR Spectroscopy of Starch Polysaccharides

Huiru Tang[1,2] and Yulan Wang[3]

[1]School of Chemical Science, Shaanxi University of Science and Technology, Xianyang, Shaanxi, P. R. China;
[2] State Key Laboratory of Magnetic Resonance and Molecular and Atomic Physics, Wuhan Institute of Physics and Mathematics, the Chinese Academy of Sciences, Wuhan 430071, P.R. China; and
[3]Biological Chemistry Section, Biomedical Sciences Division, Imperial College London, South Kensington, London SW7 2AZ, UK

Introduction

Starch is synthesized from carbon dioxide and water via the plant photosynthesis and is one of the largest storage form of the solar energy. As one of the most abundant biopolymers in nature, starch accounts for up to 90% of cereal seeds based on the dry weight. Apart from being one of important nutrients for mankind and animals, starch has become an important raw material in many applications such as adhesives, biodegradable materials [1], and drug-delivery systems [2]. For the environmental consideration, starch is also important since it is renewable, biocompatible, biodegradable, and synthesized via a pollution-free process. "Complete combustion" of starch returns the same amount of carbon dioxide that plants consumed in synthesizing the polysaccharides, creating no new load to the overall carbon dioxide pool. Therefore, consumption of starch is carbon dioxide balanced for the overall atmosphere.

In industrial applications of starch, it is generally believed that the molecular structure, dynamics, and interactions of the starch polysaccharides are key factors determining starch functionality [3–5]. Elucidation of such properties is, therefore, fundamentally important to understand the mode of actions of starch as the energy storage for plant cells and the starch functionality in applications. For this reason, intensive research has already been carried out on the native starch granules and processed starch using a variety of techniques such as NMR [5–21], X-ray diffraction [20,22–25], microscopy [26,27], and neutron scattering [28,29]. Consequently, substantial progress has been made in understanding the starch structure, which has already been reviewed comprehensively [30–32].

It is now common knowledge that there are two structurally distinct starch polysaccharides [30–32], amylose, and amylopectin. Amylose is a linear $\alpha(1 \rightarrow 4)$-linked glucan (i.e. polymer of glucose) with small amount of $\alpha(1 \rightarrow 6)$ branches having a molecular mass ranging from a few thousand to a few million Daltons. In contrast, amylopectin is the $\alpha(1 \rightarrow 4)$-linked glucan having more $\alpha(1 \rightarrow 6)$ branches with molecular mass ranging from 10^6 to 10^9 Da [30–32]. Both polysaccharides can be in either the amorphous or crystalline forms. In the native starch, these polysaccharides assembled together to form granules with a diameter of 1–100 μm, consisting of layers of the semi-crystalline shells and amorphous growth shells in an alternating fashion [30–32] (Figure 1). The crystallinity of native starch is normally about 15–50% depending on the sources.

The semi-crystalline shells are about 120–400 nm in thickness, almost three times as thick as the amorphous ones, and are formed by so-called "large blocklets" in the "olive shape." The "blocklets," in turn, are formed by some crystalline stacks [30–32]. Within each crystalline stack, there are arrays of amylopectin clusters (Figure 1) arranged in the form of crystalline lamellae (C, Figure 1) or double helices zone (∼5–6 nm) and amorphous lamellae (A, Figure 1) or branching zone (∼4 nm). The gaps between these clusters, as shown in Figure 1, are filled with (∼5 nm) amylose and, in some cases, amylose–lipid complexes [30–32] (V, Figure 1). The X-ray diffraction results showed that there are two types of crystal packings [22–25] for these double helices, types A and B (Figure 1). Type B crystals consist of six double helices arranged in a hexagonal fashion with the middle (channel) filled with some water of crystallization, whereas the type A crystals have another double helix filled the channel of the hexagonal packing [22–25]. Therefore, there are fewer water molecules in type A crystals than type B crystals. Based on the crystal packing, starch granules were classified into three types, A, B, and C, which are found, respectively, in cereal, tuber, and legume.The A- and B-type starches are composed of type A and type B crystal structures, respectively, and C-type starch is a composite of both [21,33–35]. Another type of starch known as V type is the amylose–lipid complex in the form of single helix [17,18,36].

Among many physical techniques, high-resolution solid-state NMR has been employed in studying starch polysaccharides since the first successful combination of

Graham A. Webb (ed.), Modern Magnetic Resonance, 1783–1791.
© 2008 *Springer.*

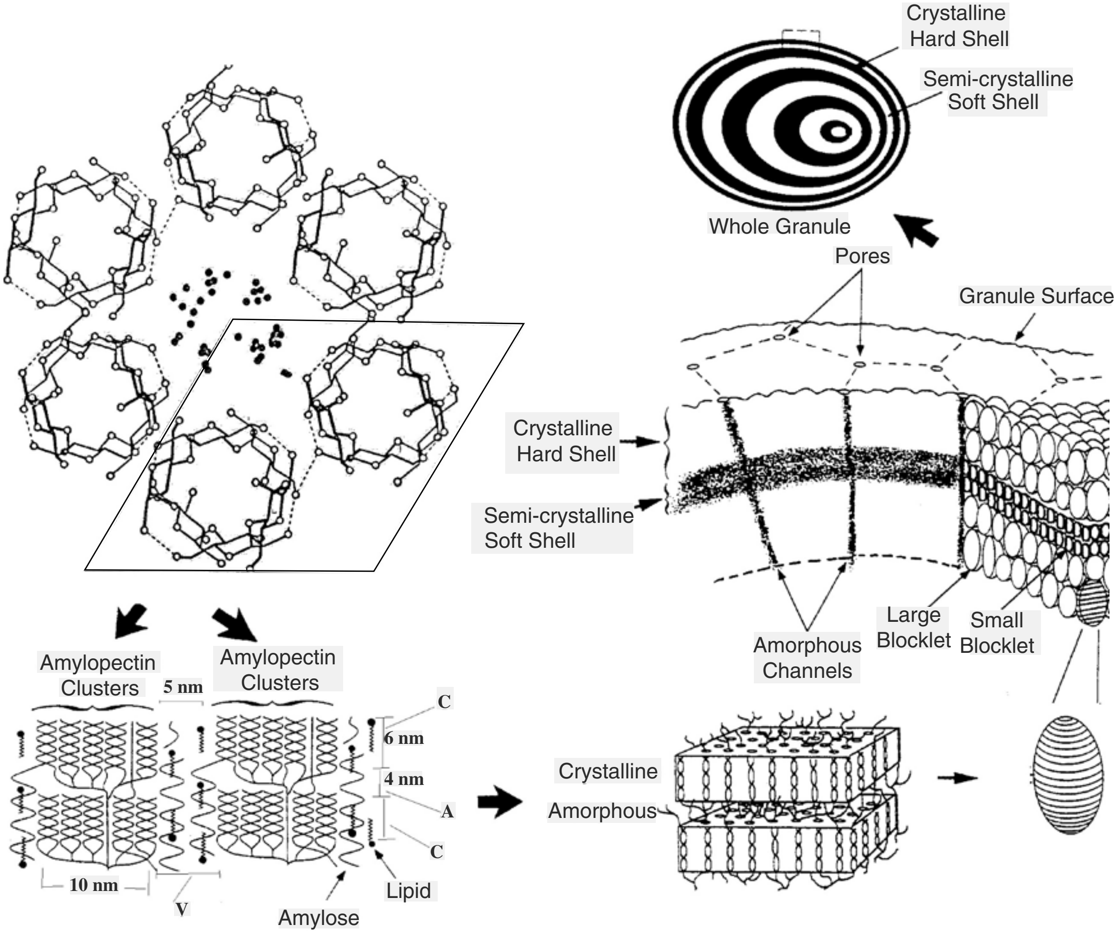
Crystalline
Hard Shell
Semi-crystalline
Soft Shell
Whole Granule
Pores
Granule Surface
Crystalline
Hard Shell
Semi-crystalline
Soft Shell
Amorphous
Channels
Large
Blocklet
Small
Blocklet
Amylopectin
Clusters
5 nm
Amylopectin
Clusters
C
6 nm
4 nm
A
C
10 nm
V
Amylose
Lipid
Crystalline
Amorphous

Fig. 1. Schematic presentation of the structural features of the native starch granules [1–3].

cross-polarization (CP) with magic angle spinning (MAS) [37] in 1976. The detection of starch resonances was initially reported in the ^{13}C CPMAS NMR spectra of flour [38] and seeds [10]. Since then, ^{13}C CPMAS NMR studies of starch have expanded with a breathtaking pace, which is based on a number of important foundation work [13–15,17] in the mid of 1980s. ^{13}C CPMAS NMR results showed unique C-1 resonance patterns for the crystalline polysaccharides in three different types of starch. For crystalline A-type or cereal starch, C-1 showed a distinct three-peak pattern [13–15,17], whereas for the B-type or tuber starch, a two-peak pattern [13–15,17] is observed. C-1 of C-type starch shows a mixed pattern of both A and B types [21]. The V-type amylose [16–19] shows a single resonance for C-1. The C-1 resonances of all these types of starch have been assigned and well-documented in literature [13–19]. So far, however, the resonances of C-2, C-3, C-4, and C-5 for starch have not yet been assigned ambiguously.

Based on the success of CPMAS NMR, the ^{13}C relaxation times were measured to obtain information about the dynamics of starch polysaccharides. The results showed that, generally, the crystalline starch is motionally restricted. For the crystalline starches [17], the values of ^{13}C relaxation time (T_1) are about 14–20 s for C-1 and 4–6 s for C-6. In contrast, T_1 values for the amorphous starch [18] were about 600 ms for the ring carbons and 100 ms for C-6. In both the cases, however, T_1 for C-6 was shorter than the ring carbons probably due to the conformational motions of the CH_2OH group as observed in other carbohydrate systems [39–42]. For both crystalline A- and B-type starches, full hydration leads to only a small decrease of T_1 of C-1. On the contrary, the T_1 value for C-1 in V-type amylose [17] (i.e. amylose–lipid complex) increased from 7 to 11 s upon hydration. This change of dynamics probably results from the hydration induced conformational changes to more ordered structure. Recently, some more ^{13}C CPMAS NMR results have also been reported on the polysaccharides in the amorphous starch [43,44]. Local range heterogeneity has been investigated in terms of both structure and dynamics. In these studies, a resonance at about 94 ppm, which appeared in almost all ^{13}C CPMAS NMR spectra in the literature, was also discussed for the first time [4,44].

Spectral editing techniques have shown great potential in starch research, including the "mobility-resolved" ^{13}C NMR spectroscopy [45] and the proton-relaxation-induced spectral editing (PRISE) [4,5,46] techniques. The former takes advantages of differences in ^{13}C properties to detect starch polysaccharides having different mobility, whereas the latter takes advantages of differences in the proton relaxation times to disentangle the ^{13}C resonances of different fraction of starch polysaccharides. Potentially, both methods can be combined to probe the heterogeneity and dynamics of starch systems. The recently developed 2D high-resolution solid-state NMR spectroscopic techniques are expected to play an important role in studies of starch polysaccharides [47–50].

In this article, we are not attempted to provide an exhaustive review on the high-resolution solid-state NMR techniques available nor on the results for starch in the literature. Instated, it is aimed to highlight the problems related to such systems and to discuss possible strategies for the high-resolution solid-state NMR studies of the starch polysaccharides. Therefore, only a brief theoretic account of relevant NMR is given.

NMR Techniques

Nuclear–Spin Interactions in Starch

Starch consists of three elements, carbon, hydrogen, and oxygen. Among them the NMR active oxygen isotope, ^{17}O, has a spin quantum number I of 5/2 and extremely low natural abundance (0.037%). Consequently, ^{17}O NMR is deemed not so useful for studying starch polysaccharides unless such samples were enriched with ^{17}O. However, the combination of the sensitivity enhancement by CP with the multiple-quantum MAS [51,52] may lead to useful information from the ^{17}O NMR. For hydrogen, on the other hand, ^{1}H has a spin quantum number of 1/2, high natural abundance (99.985%) and is the most NMR-sensitive nucleus in nature. For carbon, the NMR active isotope, ^{13}C, has a spin quantum number of 1/2 with relatively low natural abundance (1.108%), even though it is still much higher than ^{17}O. So far, therefore, ^{1}H and ^{13}C have been the choices of spin probes, in particular, in the high-resolution NMR studies of starches.

For ^{1}H and ^{13}C in solids, the nuclear–spin interactions relevant to NMR include Zeeman interactions, dipole–dipole (DD) interactions, chemical shift (CS) interactions, scalar interactions, and spin—rotation (SR) interactions. The Zeeman interactions are between nuclear spins and applied external magnetic field, providing possibility for spin transitions from different energy levels thus NMR signals. The magnitude of the Zeeman interactions are generally in the order of a few hundreds of megahertz (MHz) and that of the other nuclear–spin interactions is in the order of hundred kilohertz (kHz) at most (see Table 1), producing only a relatively small perturbations to the Zeeman interactions. In the solid state, both scalar and SR interactions are relatively weak compared with DD interactions and CS interactions, thus often neglected. The scalar coupling information, however, can be obtained using the two dimensional high-resolution solid-state NMR techniques [49,50] when necessary. The DD and CS interactions contain some extremely important information in both structure and dynamic aspects, although they are the major line-broadening factors. For high-resolution NMR spectroscopy, the DD interactions and chemical shift anisotropy (CSA) can be eliminated with the combination of high power decoupling and magic angle sample spinning.

Magic Angle Spinning

In as early as 1958, Andrew *et al*. started to use rapid sample rotation to narrow the lines broadened by the dipolar interactions [53]. A year later, Andrew's group [54]

Table 1: Nuclear–spin interactions for ^{1}H and ^{13}C in a 9.4 T magnetic field

	Nuclear–spin interactions			
	Zeeman (MHz)	Dipole–dipole (kHz)	Chemical shift (kHz)	Scalar
^{1}H Magnitude in solution	400.0	~0	Isotropic	<0.2 kHz
Magnitude in solids	400.0	<100	~5(CSA)	<0.2 kHz
^{13}C Magnitude in solution	100.6	~0	Isotropic	<0.2 kHz
Magnitude in solids	100.6	~100(^{1}H–^{13}C)	~20(CSA)	<0.2 kHz

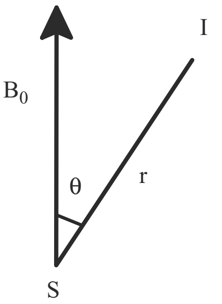

Fig. 2. Co-ordinate system for describing dipolar interactions between two spins, I and S, with a distance of r.

and Lowe [55] independently recognized the magic of the MAS for eliminating the line-broadening effects of the dipolar interactions. Later in 1962, Andrew's group also realized the magic power of spinning sample at the magic angle for removing the line-broadening effects of CSA [56].

In theory, the DD interaction between a pair of nuclei S and I is independent on the strength of external magnetic field. However, it is dependent on the orientation of the inter-nuclear vector relative to the magnetic field and is proportional to the inverse cube of the inter-nuclear distance, $1/r_{\mathrm{IS}}^3$, as given [57–59]:

$$H_D^{\mathrm{IS}} = \frac{\hbar\gamma_{\mathrm{I}}\gamma_{\mathrm{S}}}{r_{\mathrm{IS}}^3}(1 - 3\cos^2\theta)\mathrm{I}_Z\mathrm{S}_Z, \tag{1}$$

where θ is the angle between inter-nuclear vector and the magnetic field B_0 (see Figure 2); γ_{I} and γ_{S} are the magnetogyric ratio for nuclei I and S, $\hbar$ is Planck's constant divided by 2π; I_Z and S_Z are spin operators for nuclei I and S. When $\theta = 54.7^\circ$, the angular dependence term $(1 - 3\cos^2\theta)$ equals zero and the DD interaction vanishes magically! In liquids where molecules tumble rapidly and isotropically, the angular dependence term $(1 - 3\cos^2\theta)$ has to be integrated over a sphere since all angles are sampled. Such integration is zero, thus the DD interactions are said motionally averaged to zero. For a solid containing many spins with restricted motions, the DD interactions can be expressed as a statistical property as the mean squared dipolar field also known as the second moment. In such a case, if a sample is mechanically spun about an axis having the magic angle, 54.7°, relative to the external magnetic field, the dipolar interactions will be eliminated if the sample-spinning rate is fast compared to the magnitude of dipolar interactions.

The CS interaction can be expressed collectively as [57–59]

$$H_{\mathrm{CS}} = \gamma\hbar\sigma_{ZZ}S_Z B_0 \tag{2}$$

and

$$\sigma_{ZZ} = \lambda_{11}^2\sigma_{11} + \lambda_{22}^2\sigma_{22} + \lambda_{33}^2\sigma_{33}, \tag{3}$$

where σ_{11}, σ_{22}, and σ_{33} are the principal values of the chemical shift tensor, which are the values along a set of axes fixed in the molecule; λ_{11}, λ_{22} and λ_{33} are the direction cosines of the molecule's fixed axes with respect to the external field B_0. It is therefore apparent that, for a single crystal, the observed chemical shifts are dependent on the strength of the external magnetic field and the orientation of the principal axis systems with respect to the external magnetic field. If all three values of σ_{11}, σ_{22}, and σ_{33} are not the same, then CS interactions are anisotropic. For a powder sample, the crystals are distributed randomly in every orientation so that a broad spectrum known as "powder pattern" is observed due to the CSA. Mechanical spinning of a sample causes the direction cosines (λ_{11}, λ_{22} and λ_{33}) to become time dependent and such dependence is give as [59]

$$\lambda_Q = \cos\beta\cos\chi_Q + \sin\beta\sin\chi_Q\cos(\omega_r t + \phi_Q), \tag{4}$$

where β is the angle that rotating axis makes with external magnetic field, χ_Q the angle that rotation axis makes with the Qth principal axis of the chemical shift tensor, and ϕ_Q the azimuthal angle of the Qth principal axis at time $t = 0$. If a sample is undergoing so-called the rigid body rotation about an axis making an angle β with the external magnetic field, the CS interaction can be expressed as [59]

$$\sigma_{\mathrm{zz}} = \frac{1}{2}\sin^2\beta(\sigma_{\mathrm{iso}}) + \frac{1}{2}(3\cos^2\beta - 1) \times \sum_Q \sigma_Q\cos^2\chi_Q + f(t) \tag{5}$$

where σ_{iso} is the isotropic chemical shift and $f(t)$ collectively describes the time-dependent terms. When $\beta = 54.7^\circ$ the term, $(3\cos^2\beta - 1)$ is zeroed and the CSA is magically eliminated. Therefore, the axis making an angle of 54.7° with the external magnetic field is called magic angle for the magical effects of eliminating the line-broadening factors such as the dipolar interactions and CSA. With modern spectrometers, the magic angle can be set conveniently with an accuracy of 0.1° by observing ^{79}Br NMR signal (spin-side bands) of a rotating potassium bromide (KBr) sample.

High-Resolution ^{1}H NMR Spectroscopy

For an organic solid such as starch, the ^{1}H homonuclear DD interactions can be as strong as up to several tens of kilohertz (~100 kHz), while its CSA is in the order of

10 ppm or several kilohertz. To obtain the high-resolution ^{1}H NMR spectra of such systems, measures have to be taken to overcome the line-broadening interactions such as DD and CSA. The proton CSA is relatively small and can be averaged by MAS with a rate of several kilohertz, whereas the proton DD interactions cannot be averaged easily with MAS alone.

In reality, starch systems are heterogeneous and contain fractions of polysaccharides with considerable molecular mobility, such as amorphous part, and the motionally restricted fractions such as these in the crystalline phase. For the starch polysaccharides having substantial motions, only weak line-broadening effects are experienced from residual dipolar interactions, CSA and magnetic susceptibility. A good quality high-resolution ^{1}H NMR (HRMAS NMR) spectrum can be obtained with MAS alone at a moderate spin rate (a few kilohertz). On the other hand, for the crystalline polysaccharides, strong dipolar interactions are expected, MAS alone is no longer sufficient to overcome the DD interactions. Therefore, more efficient dipolar decoupling techniques are required to achieve high resolution.

Efficient dipolar decoupling can be achieved by employing multiple-pulse sequences such as WAHUHA-4 [60], MREV-8 [61], BR-24 [62], TREV [63], and BLEW-12 [64]. With modern spectrometers, it is reasonably easy to set up these pulse sequences in conjunction with MAS to obtain high-resolution spectrum for the high natural abundance nuclei, such as ^{19}F and ^{1}H, in the ordered polymer systems. Such combined technique is called combined rotation and multiple-pulse spectroscopy (CRAMPS) [65]. However, these pulse sequences were originally designed for the static samples and therefore are limited to the slow MAS conditions (<3 kHz). Physical rotation of the sample by fast MAS (>15 kHz) impairs the efficiency of the multiple-pulse sequences [48,66]. Over the last decade, nevertheless, a new generation of improved pulse sequences has been reported such as frequency-switched Lee–Goldburg [67–71] (FSLG), phase-modulated Lee–Goldburg [72–74] (PMLG), the MSHOT sequence [75,76]. Most of these sequences work well at moderate to fast MAS conditions (10–15 kHz) with a line narrowing efficiency comparable to the conventional CRAMPS and are robust to experimental imperfections [48,66]. With the constant time CRAMPS experiment [77] ($\omega_r = 12.5$ kHz), the line width of methyl group for solid L-alanine has been narrowed down to 60 Hz (or 0.12 ppm at 500 MHz). More recently, the DUMBO-1 sequence has been developed [78] and vigorously explored [66,78]. Such resolution of ^{1}H dimension also enabled a number of 2D NMR experiments to be performed in similar way to that for solution state NMR such as HMQC [66,79,80], HSQC [80], and INADEQUATE [81]. Undoubtedly, ^{1}H CRAMPS NMR spectroscopy will be improved further and should be extremely useful to provide information for all the starch polysaccharides. The difference between ^{1}H CRAMPS and HRMAS NMR spectroscopy will provide information about the polysaccharides only in the rigid phase. Although ^{1}H has high sensitivity, its small chemical shift dispersion range (<20 ppm) poses a limit to its resolution. ^{13}C has a much greater span of chemical shift range and is expect to provide the higher resolution to obtain information on different structural sites.

High-Resolution ^{13}C NMR Spectroscopy

In solids, the low sensitivity of ^{13}C due to its low natural abundance imposes a huge problem for acquiring ^{13}C spectrum. This problem is further amplified by the lengthy T_1 of ^{13}C due to its low abundance and magnetic moment. For example, ^{13}C T_1 of the crystalline starch can be as long [17] as 20 s, even though it is considerable shorter than that of crystalline cellulose (140–210 s) [17]. Consequently, some prohibitively lengthy repetition time is required for the FT experiments. To solve the problem, the Hartmann–Hahn double resonance experiment [82,83] has been employed as a CP scheme. Under so-called Hartmann–Hahn [82–84] matching condition

$$\gamma_{\mathrm{H}} B_{1\mathrm{H}} = \gamma_{\mathrm{C}} B_{1\mathrm{C}} \tag{6}$$

thermal contact between ^{13}C and ^{1}H spin systems is established. The ^{1}H magnetization is transferred to the ^{13}C to establish a common spin temperature for both spin systems. Since γ_{H} is about four times of γ_C, such magnetization transfer will enable ^{13}C to enhance the sensitivity of by about fourfolds. Furthermore, with such Hartmann–Hahn match, the repetition of the ^{13}C NMR experiments will become dependent on the proton T_1, which is only a few seconds. To eliminate the H–C dipolar interactions, the employment of high-power (~60 kHz) proton decoupling (HPDEC) technique is often necessary. With a combination of CP, MAS, and HPDEC, the high-resolution solid-state ^{13}C CPMAS NMR spectra of starch can be readily obtained to take the advantage of (1) the sensitivity of ^{1}H (fourfold enhancement), (2) shorter ^{1}H T_1 (than the ^{13}C T_1) enabling shorter experimental repetition time, and (3) greater dispersion of ^{13}C chemical shift (than ^{1}H), thus provides excellent opportunities for higher resolution. With efficient proton decoupling schemes, ^{1}H–^{13}C 2D NMR methods in the solid state will undoubtedly offer some powerful tools for studies of the starch polysaccharides in the near future. It is also apparent that the proton relaxation times become potential tools for spectral editing.

Spectral Editing Techniques

Two types of spectral editing methods have been applied in starch studies so far, so-called "mobility-resolved spectroscopy" [45] and PRISE [4,5,46]. These two methods are based on either the differences in the strength of ^{1}H–^{13}C dipolar interactions or the differences in the proton relaxation times (T_1, $T_{1\rho}$, $T_{1\mathrm{D}}$, and T_2) of the starch polysaccharides. The combination of the ^{1}H CRAMPS and ^{1}H HR-NMR spectroscopy can also be regarded as spectral editing tools similar to so-called "mobility-resolved" spectroscopy.

Mobility-Resolved NMR Spectroscopy

The mobility-resolved NMR spectroscopy was used to separate the ^{13}C resonances of polysaccharides having different mobility by exploiting their differences in ability to cross-polarize and their ^{13}C spin–lattice relaxation behavior [45,46,85,86]. A number of situations may arise. In the most mobile extreme, the molecules undergo rapid and isotropic motions, both the ^{1}H–^{1}H and the ^{1}H–^{13}C dipolar interactions are completely averaged; a ^{13}C NMR spectrum can be obtained using the typical solution state NMR techniques. If the residual dipolar interactions of the polysaccharides are not zero but weaker relative to the rate of MAS, then, a high-resolution MAS ^{13}C NMR spectrum is obtainable. Such a MAS spectrum will also contain the resonances of polysaccharides appeared in the above solution state NMR spectrum. Moreover, the rate of MAS and proton decoupling power can be varied in a systematic fashion to differentiate slightly different polysaccharides experiencing various levels of the ^{1}H–^{1}H and ^{1}H–^{13}C dipolar interactions, respectively.

These experiments can be easily performed with a single-pulse excitation (SPE) combined with MAS and proton decoupling [4,5,45,46,85,87] (non-spinning experiments can be considered as a special case of MAS). Such experiments were collectively referred to as ^{13}C SPEMAS NMR. In the SPEMAS experiments, a single-pulse excites all carbons; therefore, in principle, all carbon signals are observable. However, because ^{13}C spin–lattice relaxation times in solids are relatively long (>5 s), the choice of a short repetition time (which ought to be as short as duty cycle allows and is normally shorter than 1s) to selectively observe only the ^{13}C signals with short T_1 and to speed up experiments. The short ^{13}C T_1 component can be simplistically regarded as being diagnostic for the mobile carbon sites in polysaccharides. This simplification, while it is often valid, should be treated with some care when used in different systems [4,5,46,85,87]. This is because that the product of the relevant local dipolar field and the spectra densities at the ^{13}C Larmor frequency, the sum and difference of the ^{13}C Larmor frequency and those of the neighboring dipoles are sufficiently large to cause efficient relaxation. For example, in the case of a methyl group in crystalline samples, its short ^{13}C T_1 does not imply rapid isotropic tumbling but merely that rotations about one axis is rapid. In certain cases, significant levels of paramagnetic species present in dry solid samples also act as a potent source of relaxation, dramatically shortening ^{13}C T_1 even when the spectral densities at the appropriate frequency are quite low.

On the other hand, the observation of a ^{13}C CPMAS signals may be interpreted as the present of carbon sites experiencing a static local dipolar field under MAS conditions. This implies that at least some motions are in the rigid lattice regime, even though as in the case of methyl groups this does not preclude highly anisotropic motions involving some motions in the rigid lattice and motional narrowing regimes. Therefore, care has to be taken to interpret polysaccharide mobility using this "mobility-resolved" spectroscopy simply because there are some overlapping regions of dynamics which SPEMAS and CP-MAS experiments cannot distinguish. A combination of proton relaxation and ^{13}C NMR spectroscopy may offer an alternative strategy to relate polysaccharide structure with dynamics.

Proton Relaxation Induced Spectral Editing Techniques

It is well known that the measurements of proton relaxation times (T_1, $T_{1\rho}$, $T_{1\mathrm{D}}$, and T_2) are extremely useful to probe molecular dynamics of carbohydrates [39–42,88–96]. The spin–lattice relaxation times (T_1, $T_{1\rho}$, and $T_{1\mathrm{D}}$) are sensitive to motions, respectively, in the proton Larmor frequency, effective field frequency for the spin–lattice relaxation in the rotating frame, and the local dipolar field frequency. When heterogeneity is present as in the case of many starch systems, some of these relaxation processes will be observed as multiple components depending on the relativity of the spin diffusion efficiency and length of the relaxation time. If spin diffusion is efficient on a given relaxation time scale, spins in question will have a common spin temperature [97]; relaxation time will be a single process. On the other hand, if the spin diffusion is not efficient enough on a given relaxation time scale, the whole spin pool will show some domains (heterogeneity) and this relaxation will show a multiple-component features [97]. Detection of the multiple components for the proton spin–lattice relaxation times enables one to estimate the dimension of domains [98–100]. The structural features (spectral characteristics) of these domains can also be obtained by PRISE methods, which can be conveniently implemented by preparing the proton magnetization before CP as shown [46] in Figure 3.

In Figure 3A, proton magnetization is prepared with an inversion-recovery "relaxation filter" to separate the

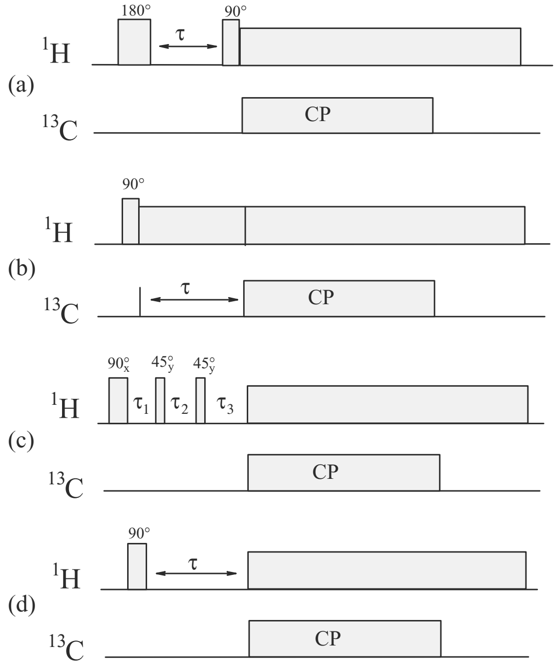

Fig. 3. Pulse sequences for the PRISE experiments with (A) ^{1}HT_1, (B) $T_{1\rho}$, (C) $T_{1\mathrm{D}}$, and (D) T_2 editing.

domains with different proton T_1. In a simple case of two components, the values of relaxation delay τ can be chosen such that the NMR signals in the final spectrum have intensities depending upon the length of τ relative to T_1. For example, one can conveniently choose τ to enable the relevant signals to have a positive peak $(\tau > T_1^* \ln 2)$, negative peak $(\tau < T_1^* \ln 2)$ or no peak at all $(\tau = T_1^* \ln 2)$.

As shown in Figure 3B, the proton magnetization can also be prepared using a spin-locking sequence $(90^\circ_x - \tau_{\mathrm{SPy}})$ such that components with different $T_{1\rho}$ can be separated by choosing an appropriate spin-lock time, τ_{SP}, and spin-lock power. Moreover, The Jeener–Broekaert sequence [101] $(90^\circ{}_{x-}\tau_1 - 45^\circ{}_{y-}\tau_2 - 45^\circ{}_{y-}\tau_3-)$ can be used to transfer some Zeeman order into the dipolar order. For a homogenous solid biopolymer, when $\tau_1 \approx T_2$, and $\tau_2 \geq \tau_3$, a single Jeener echo is expected, whose shape and amplitude are dependent on the time derivative of the FID [101]. The decay of the echo amplitude as a function of τ_2 is characterized by the relaxation time $T_{1\mathrm{D}}$. Therefore, by selecting appropriate τ_2 in the proton preparation part of sequence shown in Figure 3C, the ^{13}C signals of the components with different $T_{1\mathrm{D}}$ can also be selectively observed. In the case of proton T_2 editing, the magnetization can be prepared using a simple pulse-delay preparation as illustrated in Figure 3D. Such an experiment is essentially a slice in so-called 2D WISE experiment [102,103].

The proton relaxation times can be measured either directly by observing protons or indirectly via CPMAS experiments. Direct proton observation offers excellent experimental sensitivity and simplicity. However, it is extremely important to measure the proton relaxation times under identical conditions to that PRISE experiments are performed. This is because (1) sample spinning lead to some degree of sample heating and (2) more seriously, all proton relaxation processes are affected by the sample spinning [46,104–109] at the magic angle.

Under MAS conditions at the room temperature, the fully hydrated granules of all three types starch showed a single proton T_1, two $T_{1\rho}$ components and at least three T_2 components [4]. PRISE experiments have revealed that the long $T_{1\rho}$ component (~30 ms) in the native starch granules is associated with the crystalline polysaccharides, whereas the short $T_{1\rho}$ component (2~4 ms) is associated with amylose in the gaps between amylopectin clusters. For the proton T_2 components, the short one (~14 µs) is associated with polysaccharides in the crystalline lamellae, whereas the long one (10–20 ms), accounting for about 10%, is associated with polysaccharides with molecular mobility so high that CP was not efficient. The intermediate component (T_2 ~ 300–400 µs) is associated with polysaccharides in the amorphous lamellae. Similar multiple (^{1}H) $T_1\rho$ components have also been related to the domain structures for polysaccharides in the moisten starch granules (33% water) [18] and bread [110]. However, little has been reported with $T_{1\mathrm{D}}$ editing though that should be useful.

Future Perspectives

So far, most of the high-resolution solid-state NMR work has been concentrated on the crystalline (or ordered) polysaccharides in starch. Relatively fewer reports focused their attention on the less ordered or amorphous starch polysaccharides, which are more relevant to the functionality in applications. With the catalogue of methods available, it is probably the right time to take the challenge to focus the attention to the structural, dynamics and interactions of amorphous starch. Furthermore, a number of aspects of starch structure remain inadequately understood. For example, the presence of "small blocklets" in "the growth rings" and "large blocklets" in the semi-crystalline shells remains to be fully established, although the concept of "blocklets" emerged [111] as early as in 1858. The relationships between the starch functionality and the domain distribution, dynamic state of the starch polysaccharides in the native and processed starch are not well understood even though these properties are important in establishing and determining the response of starch granules to multi-parametric processing treatments, such as acid-hydrolysis and gelatinization, and ultimately functionality.

From NMR technique point of view, although high-resolution ^{13}C NMR spectroscopy has been extensively exploited in starch studies, few high-resolution ^{1}H NMR results have been reported so far. Furthermore, with some recent developments in the two dimensional NMR in the solid states, heteronuclear correlation spectroscopic techniques such as HETERCOR, HMQC [66,79,80], HSQC [80] and INADEQUATE [81] have already been demonstrated in the solid states. Measurements of H-C scalar coupling have been reported using so-called MAS-J-HMQC [66,79,80] and MAS-J-HSQC [80] methods. Hydrogen bonding interactions in the organic solids have been studied [49,50]. The solid-state INADEQUATE experiment [81] has also been developed to establish the C–C connectivity [81,112]. This together with the 2D NMR exchange experiments has shown particular usefulness in unambiguously assigning the ^{13}C spectrum of cellulose [113]. Although most of these high-resolution 2D NMR methods were developed for studying peptides and proteins, it is conceivable that similar strategies should be extremely valuable for studying the starch polysaccharides.

References

1. Shogren RL, Lawton JW, Doane WM, Tiefenbacher KF. Polymer. 1998;39:6649.
2. Simonsen L, Hovgaard L, Mortensen PB, Brondsted H. Euro. J. Pharm. Sci. 1995;3:329.
3. Tang HR, Brun A, Hills B. Carbohydr. Polym. 2001;46:7.
4. Tang HR, Hills BP. Biomacromolecules. 2003;4:1269.
5. Tang HR, Hills BP. In: GA Webb, PS Belton, AM Gil, I Delgadillo (Eds). Magnetic Resonance in Food Science—A View to the Future. Royal Society of Chemistry: Cambridge, 2001, p 155.
6. Tang HR, Godward J, Hills B. Carbohydr. Polym. 2000;43:375.
7. Mousseri J, Steinberg JMP, Nelson AI, Wei LS. J. Food Sci. 1974;39:114.
8. Baianu IC, Forster H. J. Appl. Biochem. 1980;2:347.
9. Garbow JR, Schaefer J. J. Agric. Food Chem. 1991;39:877.
10. O'Donnell DJ, Ackerman JJ, Maciel GE. J. Agric. Food Chem. 1981;29:514.
11. Li S, Dickinson LC, Chinachoti P. J. Agric. Food Chem. 1998;46:62.
12. Kou Y, Dickinson LC, Chinachoti P. J. Agric. Food Chem. 2000;48:5489.
13. Gidley MJ, Bociek SM. J. Am. Chem. Soc. 1985;107:7040.
14. Gidley MJ, Bociek SM. J. Am. Chem. Soc. 1988;110:3820.
15. Veregin RP, Fyfe CA, Marchessault RH, Taylor MG. Macromolecules 1986;19:1030.
16. Hewitt JM, Linder M, Perez S, Buleon A. Carbohydr. Res. 1986;154:1.
17. Horii F, Yamamoto H, Hirai A, Kitamaru R. Carbohydr. Res. 1987;160:29.
18. Morgan KR, Furneaux RH, Larsen NG. Carbohydr. Res. 1995;276:387.
19. Snape CE, Morrison WR, MarotoValer MM, Karkalas J, Pethrick RA. Carbohydr. Polym. 1998;36:225.
20. Shefer A, Shefer S, Kost J, Langer R. Macromolecules. 1992;25:6756.
21. Bogracheva TY, Wang YL, Hedley CL. Biopolymers. 2001;58:247.
22. Wu HCH, Sarko A. Carbohydr. Res. 1978;61:7.
23. Wu HCH, Sarko A. Carbohydr. Res. 1978;61:27.
24. Imberty A, Chanzy H, Perez S, Buleon A, Tran V. J. Mol. Biol. 1988;201:365.
25. Imberty A, Perez S. Biopolymers. 1988;27:1205.
26. Baldwin PM, Adler J, Davies MC, Melia CD. J. Cereal Sci. 1998;27:255.
27. Rani MS, Bhattacharya KR. Starch-Starke. 1995;47:334.
28. Blanshard JV, Bates DR, Muhr AH, Worcester DL, Higgins JS. Carbohydr. Polym. 1984;4:427.
29. Jenkins PJ, Donald AM. Polymer. 1996;37:5559.
30. Gallant DJ, Bouchet B, Baldwin PM. Carbohydr. Polym. 1997;32:177.
31. Imberty A, Buleon A, Tran V, Perez S. Starch-Starke. 1991;43:375.
32. Buleon A, Colonna P, Planchot V, Ball S. Int. J. Biol. Macromol. 1998;23:85.
33. Bogracheva TY, Morris VJ, Ring SG, Hedley CL. Biopolymers. 1998;45:323.
34. Bogracheva TY, Wang YL, Wang TL, Hedley CL. Biopolymers. 2002;64:268.
35. Wang TL, Bogracheva TY, Hedley CL. J. Exp. Bot. 1998;49:481.
36. Buleon A, Duprat F, Booy FP, Chanzy H. Carbohydr. Polym. 1984;4:161.
37. Schaefer J, Stejskal EO. J. Am. Chem. Soc. 1976;98:1031.
38. Baianu IC, Forster HJ. J. Appl. Biochem. 1980;2:347.
39. Tang HR, Belton PS. Solid State NMR. 2002;21:117.
40. Latanowicz L, Reynhardt EC. Ber. Bunsen-Gesell. Phys. Chem.-Int. J. Phys. Chem. 1994;98:818.
41. Latanowicz L, Reynhardt EC, Utrecht R, Medycki W. Ber. Bunsen-Gesell. Phys. Chem.-Chem. Phys. 1995;99:152.
42. Reynhardt EC, Latanowicz L. Chem. Phys. Lett. 1996;251:235.
43. Paris M, Bizot H, Emery J, Buzare JY, Buleon A. Carbohydr. Polym. 1999;39:327.
44. Paris M, Bizot H, Emery J, Buzare JY, Buleon A. Int. J. Biol. Macromol. 2001;29:127.
45. Foster TJ, Ablett S, Mccann MC, Gidley MJ. Biopolymers. 1996;39:51.
46. Tang HR, Wang YL, Belton PS, Solid State NMR. 2000;15:239.
47. Sakellariou D, Brown SP, Lesage A, Hediger S, Bardet M, Meriles CA, Pines A, Emsley L. J. Am. Chem. Soc. 2003;125:4376.
48. Brown SP, Spiess HW. Chem. Rev. 2001;101:4125.
49. Brown SP, Perez-Torralba M, Sanz D, Claramunt RM, Emsley L. Chem. Commun. 2002:1852.
50. Brown SP, Perez-Torralba M, Sanz D, Claramunt RM, Emsley L. J. Am. Chem. Soc. 2002;124:1152.

51. Goldbourt A, Madhu PK. Monat. Chem. 2002;133:1497.
52. Rovnyak D, Filip C, Itin B, Stern AS, WAGNER G, Griffin RG, Hoch JC. J. Magn. Reson. 2003;161:43.
53. Andrew ER, Bradbury A, Eades RG. Nature. 1958;182:1659.
54. Andrew ER, Bradbury A. Nature. 1959;183:1802.
55. Lowe IJ. Phys. Rev. Lett. 1959;2:285.
56. Andrew ER, Eades RG. Disc. Farad. Soc. 1962;34:38.
57. Mehring M. Principles of High Resolution NMR in Solids. Springer-Verlag: Berlin, 1983.
58. Fyfe CA. Solid Sate NMR for Chemists. C.F.C. Press: Guelph, ON, 1983.
59. Dybowski C, Lichter RL. NMR Spectroscopy Techniques. Dekker: New York, 1987.
60. Waugh JS, Huber L, Haeberlen U. Phys. Rev. Lett. 1968;20:180.
61. Rhim WK, Elleman DD, Vaughan RW. J. Chem. Phys. 1973;59:3740.
62. Burum DP, Rhim WK. J. Chem. Phys. 1979;71:944.
63. Takegoshi K, Mcdowell CA. Chem. Phys. Lett. 1985;116:100.
64. Burum DP, Linder M, Ernst RR. J. Magn. Reson. 1981;44:173.
65. Scheler G, Haubenreisser U, Rosenberger H. J. Magn. Reson. 1981;44:134.
66. Lesage A, Sakellariou D, Hediger S, Elena B, Charmont P, Steuernagel S, Emsley L. J. Magn. Reson. 2003;163:105.
67. Lee M, Goldburg W. Phys. Rev. 1965;140:A1261–71.
68. Levitt MH, Kolbert AC, Bielecki A, Ruben DJ. Solid State NMR. 1993;2:151.
69. Bielecki A, Kolbert AC, Levitt MH. Chem. Phys. Lett. 1989;155:341.
70. Lesage A, Steuernagel S, Emsley L. J. Am. Chem. Soc. 1998;120:7095.
71. Charmont P, Lesage A, Steuernagel S, Engelke F, Emsley L. J. Magn. Reson. 2000;145:334.
72. Vinogradov E, Madhu PK, Vega S. Chem. Phys. Lett. 1999;314:443.
73. Vinogradov E, Madhu PK, Vega S. Chem. Phys. Lett. 2000;329:207.
74. Vinogradov E, Madhu PK, Vega S. J. Chem. Phys. 2001;115:8983.
75. Hohwy M, Bower PV, Jakobsen HJ, Nielsen NC. Chem. Phys. Lett. 1997;273:297.
76. Hohwy M, Rasmussen JT, Bower PV, Jakobsen HJ, Nielsen NC. J. Magn. Reson. 1998;133:374.
77. Lesage A, Duma L, Sakellariou D, Emsley L. J. Am. Chem. Soc. 2001;123:5747.
78. Sakellariou D, Lesage A, Hodgkinson P, Emsley L. Chem. Phys. Lett. 2000;319:253.
79. Lesage A, Sakellariou D, Steuernagel S, Emsley L. J. Am. Chem. Soc. 1998;120:13194.
80. Lesage A, Emsley L. J. Magn. Reson. 2001;148:449.
81. Lesage A, Bardet M, Emsley L. J. Am. Chem. Soc. 1999;121:10987.
82. Pines A, Gibby MG, Waugh JS. Chem. Phys. Lett. 1972;15:373.
83. Pines A, Gibby MG, Waugh JS. J. Chem. Phys. 1973;59:569.
84. Hartmann SR, Hahn EL. Phys. Rev. 1962;128:2042.
85. Tang HR, Belton PS, Ng A, Ryden P. J. Agric. Food Chem. 1999;47:510.
86. Tang HR, Hills BP. Biomacromolecules. 2003;4:1269.
87. Colquhoun IJ, Parker R, Ring SG, Sun L, Tang HR. Carbohydr. Polym. 1995;27:255.
88. Tang HR, Belton PS. Solid State NMR. 1998;12:21.
89. Froneman S, Reynhardt EC. J. Appl. Phys. D. 1991;24:387.
90. Reynhardt EC. Mol. Phys. 1990;69:1083.
91. Tromp RH, van Dusschoten D, Parker R, Ring SG. Phys. Chem. Chem. Phys. 1999;1:1927.
92. Tang HR, Belton PS. In: PS Belton, BP Hills, GA Webb (Eds). Advances of Magnetic Resonance in Food Science. Royal Society of Chemistry: Cambridge, 1999, p 166.
93. Tang HR, Belton PS, Ng A, Waldron KW, Ryden P. Spectrochim. Acta Pt. A. 1999;55:883.
94. Tang HR, Zhao BL, Belton PS, Sutcliffe LH, Ng A. Magn. Reson. Chem. 2000;38:765.
95. Wang YL, Tang HR, Belton PS. J. Phys. Chem. B. 2002;106:12834.
96. Tang HR, Wang YL, Belton PS. Phys. Chem. Chem. Phys. 2004;6:3694.
97. Goldman M. Spin Temperature and Nuclear Magnetic Resonance in Solids. Clarendon Press: Oxford, 1970.
98. Cheung TTP. Phys. Rev. B. 1981;23:1404.
99. Cheung TTP. J. Chem. Phys. 1982;76:1248.
100. Cheung TTP. Appl. Spectr. 1997;51:1703.
101. Jeener J, Broekaert P. Phys. Rev. 1967;157:232.
102. Schmidtrohr K, Clauss J, Spiess HW. Macromolecules. 1992;25:3273.
103. Clauss J, Schmidtrohr K, Adam A, Boeffel C, Spiess HW. Macromolecules. 1992;25:5208.
104. Wind RA, Emid S. Phys. Rev. Lett. 1974;33:1422.
105. Hayashi S. Solid State NMR. 1994;3:323.
106. Gil AM, Alberti E. Solid State NMR. 1998;11:203.
107. Garroway AN. J. Magn. Res. 1979;34:283.
108. Vanderhart DL, Garroway AN. J. Chem. Phys. 1979;71:2773.
109. Emid S, Smidt J, Pines A. J. Magn. Reson. 1981;45:94.
110. Morgan KR, Furneaux RH, Stanley RA. Carbohydr. Res. 1992;235:15.
111. Nageli CW. Starkekorner Pflanzenphysiologische Untersuchungen. F. Schultess: Zurich, 1858.
112. Lesage A, Auger C, Caldarelli S, Emsley L. J. Am. Chem. Soc. 1997;119:7867.
113. Bardet M, Emsley L, Vincendon M. Solid State NMR. 1997;8:25.

Imaging and Related Techniques

NMR Imaging of Bread and Biscuit

Lucas Tiphaine, M. Wagner, S. Quellec, and A. Davenel
Cemagref, Food Process Engineering Research Unit, 17 avenue de Cucillé, F-35044 Rennes Cdx

Introduction

Bread making is a process consisting of four basic steps, mixing, kneading, proofing, and baking. Although each step contributes to the set up of the aerated structure of bread, the baking process of the dough foam is the ultimate and more impressive part of the bread making process. The final open sponge structure with interconnected cells results from more or less simultaneous physical, chemical, and biochemical changes during baking such as volume expansion, evaporation of water, protein denaturation, starch gelatinization, and formation of a open network of pores.

Significant increase in computing power authorized the construction of complex dynamic models for the heat and mass transfer and physical and chemical changes during baking of dough. Due to the lack of precise experimental data, none of the numerous theoretical approaches of the baking process [1] could be fully validated. The assessment of both water transport and local expansion is especially required. This made the control of the baking operation incomplete at the industrial scale. The chilling step is also poorly controlled as it is often neglected relatively to the preceding baking step. Nevertheless, some changes of particular interest at the industrial scale still occur in the cooling product, among them, weight losses and collapses in the porous structure.

Non invasive and dynamic monitoring by using X-ray tomography or MRI may provide insights into how porosity, humidity, gelatinization evolve during these particular steps in the bread making process. A first challenge is to monitoring porosity by the MRI technique (see chapter on NMR imaging of dough) during the slow dough proving process, not significantly affected by moisture, temperature, and macromolecular structure variations, but resulting in a drastic MRI signal loss due to a primary volume expansion. A bigger challenge is to monitoring the fast baking process with a further volume expansion and spatially dependent moisture losses and starch gelatinization resulting from the large temperature increase.

The codification of the MRI images based on the application of magnetic gradients in each space direction only confined the technique to the partial observation of the more mobile protons by scanning spin-echoes. Additionally, MRI parameters of the food matrix, i.e. transverse T_2 and longitudinal T_1 relaxation times and apparent proton densities, drastically evolve during baking. The evolution of the gray levels in MRI images during the baking process cannot be simply fitted by the two monotonous conjugated effects of the increase of the relaxation times related to the increase of the molecular mobility (Arrhenius' law) and of the decrease of the MRI sensitivity with temperature (Curie's law). This evolution is largely affected by the growing interactions between water and starch during gelatinization and the loss of water at the periphery of the food matrix (Figure 1). It must be emphasized that MRI differs from X-ray by its sensitivity to temperature and molecular structure.

This review presents the state of the investigations to characterize the bread crumb and to identify the contributions of the different phenomena, porosity, moisture, and molecular structure, to the MRI signal in the view of quantifying their kinetics in every part of the matrix.

Monitoring the Baking Process

Conception of an MRI Oven

The first challenge in monitoring the baking process is the construction of an oven compatible with the MRI system. At least two devices of this kind have been described in literature [2,3]. Among all the constraints, the first one is the insulation from heat as air temperatures to be reproduced from the industrial scale range from 160 to 250 °C. Good insulation can be performed with traditional insulator, but often requires large thicknesses. This may impair in turn the quality of acquisition, as a receiver antenna with a much larger size than the product and consequently with a lower signal-to-noise performance, must be chosen. Second, the usual and cheapest heating system includes electric resistances and hence must be set outside the Faraday cage. A system dedicated to the air circulation from the heating system to the product is then required. Third, the use of metal in the construction of the oven part surrounding the product is obviously forbidden. A particularity of the metallic walls in conventional ovens is the generation of a heating source by radiation; to our knowledge, such levels of radiation will be hardly obtained with other

Graham A. Webb (ed.), Modern Magnetic Resonance, 1795–1799.
© 2008 *Springer.*

Fig. 1. Evolution with temperature of gray level in dough/crumb at two different levels of water content (Open Siemens 0.2 T, spin-echo sequence, $T_E = 8$ ms, $T_R = 420$ ms, slice thickness = 10 mm, FOV = 64 × 128, matrix = 128 × 128, number of scans = 2) (From Ref. [3]).

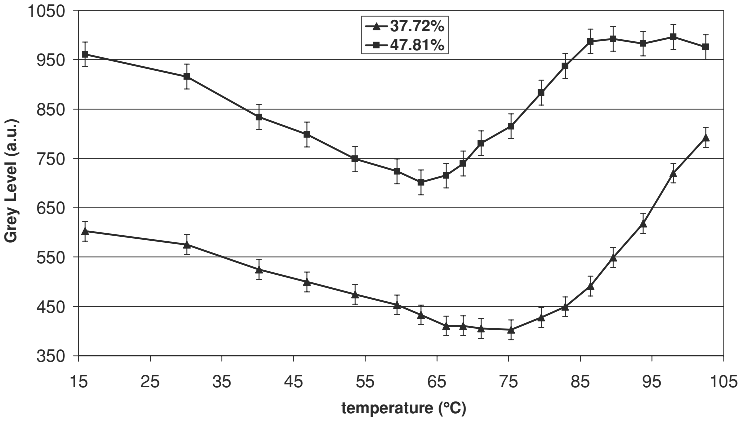

material. In fact, very few matter (only Teflon and glass to our knowledge) are compatible with both MRI and high temperatures. At last, the oven surrounding the product should reproduce a thermal environment, if not identical, at least approaching the industrial one. For instance an adequate heating of the base-plate on which the product lies must be ensured. The small volume available around the product is often a severe constraint to complete with this objective.

Factors Influencing the MRI Signal During Baking

The MRI signal is sensitive to several sources of variation during baking: temperature, water content, macromolecular structure, and porosity. Thus MRI could be a tool relevant for characterizing during the process: heat and water transport, protein denaturation and starch gelatinization, and volume expansion. But these modifications are concomitant (Figure 1) and all affect the MRI signal during baking to a certain extent. This will be illustrated in Figure 2 with MRI images acquired during the baking of bread [3].

The volume expansion is exhausted by the superimposition of the outlines of the first image on the image acquired at 5 min. In parallel, the MRI signal progressively reduced from top and bottom surfaces, passing from warm to cold colors. An analysis of sensitivity showed that in areas where temperature did not overpass 38 °C within this period (e.g. at core), more than 80% of the signal decrease could be explained by the increase of porosity. Anywhere else in the bread section, none of the contributions to the signal variations can be negliged and a general method should be developed in order to decouple or isolate the different contributions.

Beyond 7 min i.e. after externally visible expansion was complete, few variations in MRI signal were observed at the exception of the appearance of local brightnesses (warm colors in the last five images from Figure 2). It must be emphasized that these bright areas were observed even after bread temperature had stabilized at 100 °C—with a supposingly stable molecular structure. Hence this increase in the MRI signal could be interpreted by a local increase either in density or in water content. Observations made on the final bread slices (2 mm thick) cut at the same location as the MRI slice, tend to attribute the brightness to zones of higher densities. Indeed it is highly probable that at this stage of baking, the volume expansion of the core was not fully realized and its expansion would have exerted compression forces on the regions surrounding the whole core; if their mechanical properties

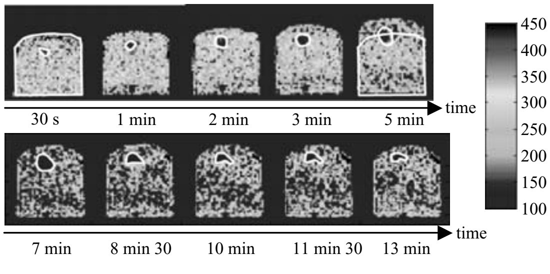

Fig. 2. MRI images of bread baking (air temperature 185°C, air velocity 2 m/s, insulated side walls of the mould). Bread composition: wheat flour: 300 g, water: 225 g, sucrose: 6 g, salt: 6 g, compressed yeast: 9 g, rape oil: 6 g. Same imager and sequence parameters as for Figure 1 except the number of scans (only one) so that images were taken at 30-s intervals (From Ref. [3]). The range of variation is given by the gray level scale located on the right of the figure. (See also Plate 132 on page XXIV in the Color Plate Section.)

were not resistant enough, these regions may in turn have densified.

The preceding analysis emphasizes not only the rich-character of MRI images during baking, but also the difficulties in interpreting the MRI signal variations and the need for developing an MRI method, which would decouple the different sources of variation of the MRI signal during baking. Again it would be dangerous in the view of producing mechanistic interpretations of baking, to directly convert the lowest GL in terms of high porosity, or to relate the variations from the MRI signal of crumb directly with changes in water content, without taking into account the effects of temperature and of structural changes at the molecular scale.

At last it is worth underlying that the development of quantitative methods should be accompanied by an experimental strategy for calibration and validation. In this view, the overall approach proposed by Heil *et al*. merits full consideration [4]—although one may find the experimental procedures not enough detailed. Sagittal 2D T_1-weighted images were acquired and segmented to estimate the variations in porosity during baking. The calculated porosity showed high correlation with displacement although unavoidable loss of moisture was not taken into account. Water–oil ratios were estimated by MRI spectrometry localized by a planar pulse sequence in six experimental volumes (4 mm^3) in the dough during baking. The authors confronted water concentrations deduced from MRI and from gravimetric measurements. The linear correlation was not excellent (large data dispersion with $R^2 = 0.84$). Nevertheless the method can still be improved, for instance by correcting the signal inhomogeneities produced by the non uniform magnetic field [4], or by taking into account the effect of temperature on the proton signal.

Specific Interests of MRI in Better Characterizing the Mechanisms Underlying the Baking Process

Surprisingly, very few MRI results referring to the baking process and its interpretation have been published so far [2–5]. This may be partially due to an unrealistic reproduction of the baking process within the MRI magnet (see the first sub-section) and to the difficulty in interpreting the MRI signal (see the preceding sub-section).

However, already published results are quite promising. They mainly refer to the spatial and temporal changes in moisture content during baking. Heil *et al*. produced kinetics of water concentration at different locations in biscuit; however the baking conditions do not allow full confidence in the set of data (baking was interrupted for the MRI acquisition and then continued on). Increase in water concentration at the center of biscuits was reported but unfortunately no evidence of it was given in the paper [4]. Although geometrical changes (external diameter and height in biscuit [2]) could be monitored in a quantitative way, data of local porosity were rarely found [3,4] and with no real quantitative analysis.

Monitoring the Post-Chilling and Freezing Steps

The variations of the MRI signal during the chilling step will be detailed below in the case of part-baked breads (partially baked before chilling and freezing), but the conclusions to be drawn will be of broader application. An echo-gradient sequence was selected for this purpose as it revealed to be very little sensitive to differences in susceptibility between air and crumb when implemented on a low magnetic field imager (0.2 T), with small echo time values [6].

Variations of the MRI Signal During Chilling and Freezing of Part-Baked Breads

In the crumb at core, the MRI signal remained constant for a while and then decreased steeply to the signal intensity in the image background (Figure 3A). The latter decrease was relevant of the freezing process [7]. Hence no variation was observed during the pre-chilling step. Some voxels in crumb, located in particular just beneath the upper crust of the loaf, may exhibit a specific behavior during the pre-chilling step, with a primary increase in signal—up to 30% (Figure 3A).

During the chilling step, the MRI signal may vary under different mechanisms. Temperature decreases locally. Water concentration in crumb may locally decrease as vapor still escapes from the product surface or locally increase since the vapor filling the bread pores is expected to condensate under cooling. The changing structures of starch or proteins in crumb accompany both the retrogradation and gelling processes. At last, under gas compression and/or active retraction of the network under cooling, collapses of the porous structure are often observed hence producing variations in the local gas fraction. A preliminary study permitted to rank these different sources [7]. Molecular structure and temperature effects could be neglected with respect to the level of noise in the images. And the 30% of increase in the MRI signal could be explained by either a 9% decrease in porosity or a 24–37% increase in water concentration, or a combined effect. Sampling in the thawed loaf for dry matter measurements gave no evidence of a significant water concentration gradient in the crumb under concern. At this stage, the increase in the MRI signal was thus mainly attributed to the collapse of the loaf structure [8].

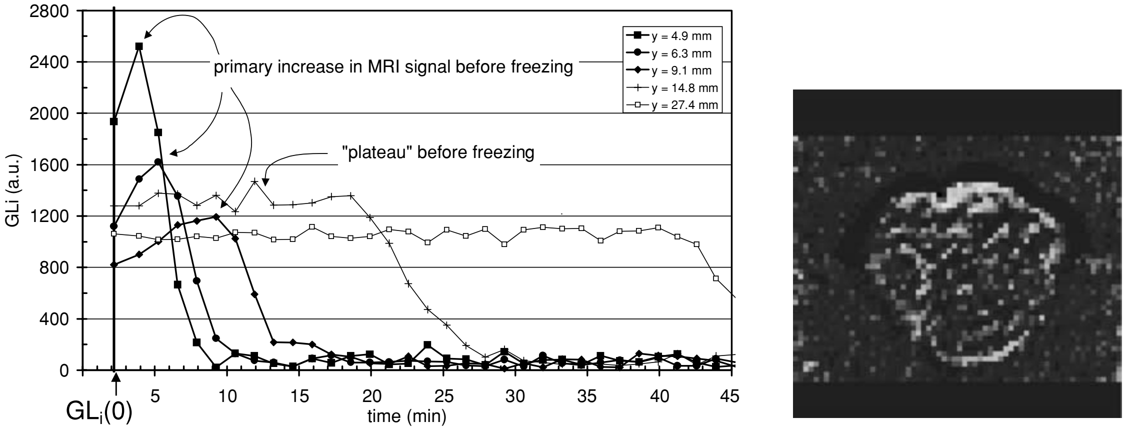

Fig. 3. MRI signal during freezing of part-breads (Open Siemens 0.2 T, gradient echo sequence, $T_E = 4$ms, $T_R = 200$ ms, slice thickness = 12 mm, FOV = 66 × 88, matrix = 48 × 64, number of scans = 2) (From Ref. [8]). Left: y refers to the position along a vertical profile, with $y = 0$ for the upper crust and $y = 27.4$ mm for the approximate geometrical center of the loaf section. Right: differences of gray level between the start of acquisition and the start of freezing (decrease in the signal). Red and dark blue represent respectively the highest and lowest values of increase. (See also Plate 133 on page XXV in the Color Plate Section.)

This conclusion may change with other configurations. No effect of temperature or porous structure was assumed during the chilling of wheat flake biscuits, and the MRI variations were converted into cartographies of water content directly using a calibration curve obtained from final products at different levels of humidity and measured at ambient temperature [5].

MRI for Better Controlling the Final Product Quality: A Theory for Explaining the Occurrence of Crust Flaking

Crust flaking is a well-known default of frozen part-baked breads. It was initially believed that sub-structures of different mechanical properties (e.g. crust/crumb) could be weakened by the bread collapse and that mechanical chocks during transportation or hydro-thermal chocks during final baking could then participate to the splitting up of crust pieces.

Practically, the chilling and freezing processes were monitored by MRI [8] in breads producing either low or high flaking [9]. The bread with low flaking presented the highest increase in the MRI signal and revealed to be able to respond to constraints by a relatively high extent of deformation. At the contrary, the bread with high flaking deformed to a lesser extent. As a consequence, higher tensile forces could have been generated within the loaf structure, especially on its flanks where most flakes are formed [9]. It is noteworthy that collapse was observed by MRI from the early step of pre-chilling and was continued during the freezing step, with a higher intensity and a higher rate [8]. This last point is coherent with the industrials' experience, which considers the freezing step as a necessary step for observing flaking.

Assessing the Bread Crumb Structure

The final bread crumb structure is a criterion, at least easily accessible with the view of all the difficulties in instrumenting the bread in the process of baking. It can serve the evaluation of the effects of the formulation and of the bread making process. The different techniques for examining the bread crumb structure have been recently reviewed with their major limits [10]; among them: the lack of 3-D information (most give 2D images of a 3-D reality), the complicated process of preparation or the limited size of samples. An easy-to-use MRI method for depicturing the 3D architecture of breads or for reducing to the extreme the slice thickness (0.3 mm) has been recently proposed [10,11] (Figure 4).

Though baked breads contain approximately 40% of water, it is difficult to obtain clear images of grain structure with conventional (spin-echo) sequences (see the Introduction section). The originality of the method lies on the pre-soaking of the bread pieces in an organic solvent; the bread structure thus appears as a "shadow" in the solvent image. Among the tested solvents, acetone was selected because of its single peak that prevented chemical

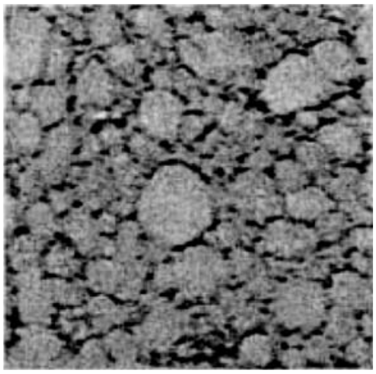

Fig. 4. MRI microscopy of bread (Bruker DRX300 7T, $T_E = 4$ ms, $T_R = 1$ s, matrix = 256 × 256 × 256 with a corresponding 100 μm voxel resolution) (reprinted from Ref. [10] copyright, with permission from Elsevier).

shift effect on images and of the retention of the bread structure. The addition of heavy metals, especially a 8 mM concentration of Fe^{3+}, shortened the overly long relaxation times of acetone to practical lengths for imaging. Two types of NMR imagers and sequences have been tested (refer to the legend of Figure 4).

Under such operating conditions, the histogram of pixel frequency against gray level was bimodal and allowed to handle the MRI images as binary ones. The distribution in the cell sizes could then be estimated after a simple thresholding method has been applied to the images.

References

1. Sablani SS, Marcotte M, Baik OD, Castaigne F. Lebensmittel-Wissenschaft und-Technologie. 1998;31:201.
2. Hong SW, Yan ZY, Otterburn MS, McCarthy MJ. Magn. Reson. Imaging. 1996;14(7/8):923.
3. Wagner W, Lucas T, Davenel A, Broyart B, Collewet G,Trystram G. Study of bread baking process: MRI experimental data. Proceedings ICEF9, Montpellier, Fr, 2003, p 496.
4. Heil JR, Ozilgen M, Mc Carthy MJ. In: G Barbosa-Canosava, M Okos (Eds). AIChE Symposium Series. American Chemical Society: Washington, DC, 1993, p 39.
5. Duce SL, Ablett S, Darke AH, Pickles J, Hart C. Cereal Chem. 1995;72(1):105.
6. Grenier A, Lucas T, Davenel A, Collewet G, Le Bail A. In: PS Belton, AM Gil, GA Webb, D Rutledge (Eds). Magnetic Resonance in Food Science, The Royal Society of London, London, 2003, p 136.
7. Lucas T, Le Ray D, Davenel A. J. Food Eng. 2005;70(2):139–149.
8. Lucas T, Quellec S, Le Bail A, Davenel A.J. Food Eng. 2005;70(2):151–164.
9. Le Bail A, Monteau JY, Lucas T, Chargelegue A, Reverdy Y. J. Food Eng. 2005;69(4):503–509.
10. Ishida N, Takano H, Naito S, Isobe S, Uemura K, Haishi T, Kose K, Koizumi M, Kano H. Magn. Reson. Imaging. 2001;19:867.
11. Naito S, Ishida N, Takano H, Koizumi M, Kano H. Food Sci. Technol. Res., 2003;9(2):155.

NMR Imaging of Dairy Products

F. Mariette
CEMAGREF, Food Engineering research unit, 17 avenue de Cucillé, CS64427, 35044 Rennes Cedex, France

Introduction

Most MRI applications to dairy products are based on the sensitivity of relaxation time to chemical composition and changes in structure. It should therefore be borne in mind that for many dairy products the NMR relaxation signal is multi-exponential. This behavior is mainly explained by the chemical composition, since protons from water, fat, and protein contribute to the signal. Moreover, two phases can be observed according to the measurement temperature, i.e the liquid and solid fat. All these aspects complicate the interpretation of NMR relaxation time parameters and contrast in the MR image. Nevertheless, as the spin–spin relaxation time of protein protons and crystallized fat protons are very short, the image intensity is only dependent on the relaxation of the liquid phase, i.e the liquid fat proton and the water protons. Of course, if MRI acquisitions are performed at low temperatures where most of the fat is crystallized, the gray level intensity will describe only the water protons. This explains why most work has been done on low fat products or at low temperatures, or in high fat products such as cream and cheese, although some methods have been proposed to suppress water and fat signals selectively.

Our intention in this chapter is to present a wide range of MRI applications in dairy science. It will be broken into four parts: determination of water distribution, the macroscopic information that can be obtained from MR images, molecular and micro-structural information and temperature, and flow measurements.

Water and Fat Content and Distribution

Using MRI to obtain water and fat content distribution is one of the applications that is widely represented in the literature about food. Two reasons can be proposed. Firstly the gravimetic technique for water determination and the chemical extraction method for fat determination are known to be time consuming, and this limits their use for the determination of spatial distribution in the food matrix. Secondly, water content is one of the most relevant factors to the quality of food [1] and its distribution is rarely uniform in a product. This therefore explains why considerable efforts have been made to devise effective techniques to quantify the spatial distribution of fat and water non-destructively.

Two NMR parameters are used to determine water content: proton density and spin–spin relaxation time T_2. The spin–lattice relaxation time T_1 can also be used but because its sensitivity to water content is lower than T_2, the latter is preferred. When using proton density image, the water content is given by:

$$W(x) = K\rho(x)(1 - \mathrm{e}^{-T_\mathrm{R}/(T_1(x))})\mathrm{e}^{-T_\mathrm{E}/(T_2(x))} \qquad (1)$$

with K a constant which depends on the scanner and $\rho(x)$ the proton density, T_2, T_1 the spin–spin and spin–lattice relaxation time for each voxel x, respectively and T_R and T_E the repetition time and echo time, respectively. It is important to recognize that the signal strength, constant proportionality, and relaxation time will all vary with position and within the sample. Variations in the relaxation time are induced by changes in the concentration and also by changes in temperature, as generally observed in the case of drying. As a consequence, specific methods for the correction of variations in relaxation time and inhomogeneity of the scanner are required [2]. When the inhomogeneity in the image intensity induced by the scanner is high, the water content can be assessed from a T_2 map. As the gray level inhomogeneity is independent of the relaxation time, the inhomogeneity is the same for the whole image for a multi-echo sequence, whatever the echo time. The computation of T_2 therefore provides a simple way to correct the images. This method has been successfully used for the determination of water distribution during the draining of curd (Figure 1) [3,4]. With this specific application, other information can be extracted from MR images such as the size of the curd, the location of whey, and the amount of whey in the container [5,6], and modeling of the drainage can be performed [7,8]. The same approach has been used to study the effects of freeze-thawing on the macroscopic structure and water distribution in the curd [9].

Equation 1 is only valid when the NMR signal is mono-exponential. When the relaxation is not exponential, multi-exponential fitting has to be performed in order to extract the fraction of each relaxation component. This requires a more sophisticated acquisition sequence and the complexity of the model between the gray level intensity and the water content increases. This situation if

Graham A. Webb (ed.), Modern Magnetic Resonance, 1801–1806.
© 2008 *Springer.*

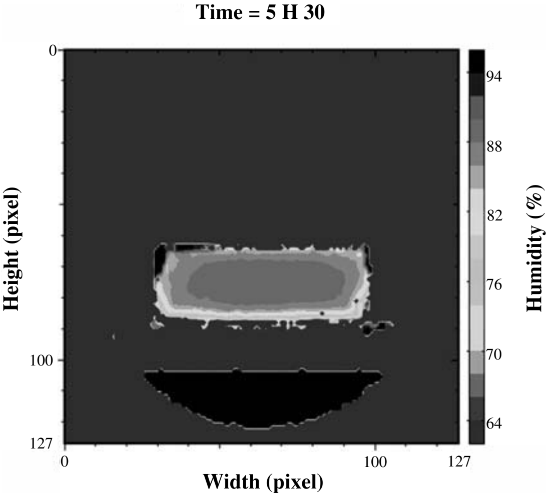

Fig. 1. Water distribution in curd according to draining time (From Mariette *et al*. [4] with permission). (See also Plate 134 on page XXV in the Color Plate Section.)

often observed for fatty products and the best solution is to implement a specific MRI sequence to suppress one of the components in order to apply the simple case defined by Equation 1. This approach has been used to quantify separately the water and fat distribution in cheese [10] and in cream [11]. Two approaches have been proposed, the first uses difference in the relaxation time between fat and water protons, and the second uses the difference in resonance frequency. For dairy products, the chemical shift based methods are preferred as the fat relaxation time is widely dispersed and fat suppression is then difficult to achieve. For example, the chemical shift Dixon imaging sequence was used to study the movement of lipids in cream to the top of a vial of milk [11], and the chemical shift selective (CHESS) suppression technique was used to obtain water only and fat only MR images of cheddar cheese [10].

Macrostructure Information

Dairy products, especially cheeses, are inhomogeneous products at a macroscopic length scale. For example, the size, number and shapes of the holes are modified according to the manufacturing process, and contribute to the overall quality of the product. Regular sphere-shaped holes are the result of the production of CO_2 from the biochemical activity of the bacteria, but non-regular shaped holes are explained by mechanical constraints during the manipulation of the curd. Moreover, the thickness of the rind increases and morphological defects can be observed during the ripening of cheese, which have an effect on the overall appearance of the product and on consumer perception. Many attempts have therefore been made to quantify the macroscopic structure or organization of cheese and to relate the feature to quality criteria. This approach was first applied to Swiss cheese for quantification of the morphology of holes [12–14]. A standard spin-echo sequence was used, and the MR images were analyzed. The number of holes was determined, the thinness ratio, cross-sectional area, and hole center locations were calculated. The mean gray level, angular moment, and contrast of gray scale images were calculated to define the internal texture of Swiss cheese. Using these parameters a classification procedure was devised. This approach was also used for the classification of soft cheese according to the processing condition, and also to predict the sensory textural properties of the cheese [15,16]. For this application, several images were acquired for each cheese with different experimental conditions: spin-echo sequences with different T_E, and T_R, for T_2-weighted and T_1-weighted images, respectively, and gradient echo sequence for magnetic susceptibility-weighted images. Textural features were computed using the co-occurrence matrix method on each image. Classification was performed directly according to the textural features, allowing the complete discrimination of the cheese according to the processing conditions. A predictive model of the sensory parameters was also obtained from stepwise linear regression. Although the texture analysis methods to quantify the structure of MR images are very powerful for food applications and for medical applications, attention should paid to the sensitivity of these methods to normalization procedures of the images which can significantly affect the significance of the results [17]. Other examples have dealt with the determination of rind thickness [18] and analysis of the structure of blue-veined cheeses [19].

Micro-Structure and Molecular Structure

The micro- and molecular structures of dairy products can be ideally investigated by T_2 water relaxation time. Numerous NMR studies have demonstrated the sensitivity of water relaxation to the casein micellar structure [6,20–22]. As a consequence, any modification of the structure of the casein gel can potentially be demonstrated by MRI. Moreover, since relaxation time parameters are sensitive to micro-heterogeneity when the diffusive exchange between the water compartments becomes slow, information about the water holding capacity can be obtained. This has been well illustrated in experiments involving the ripening of soft cheeses [23]. After enzymatic coagulation of the milk, the gel is drained and salted and then all the biochemical changes that occur during

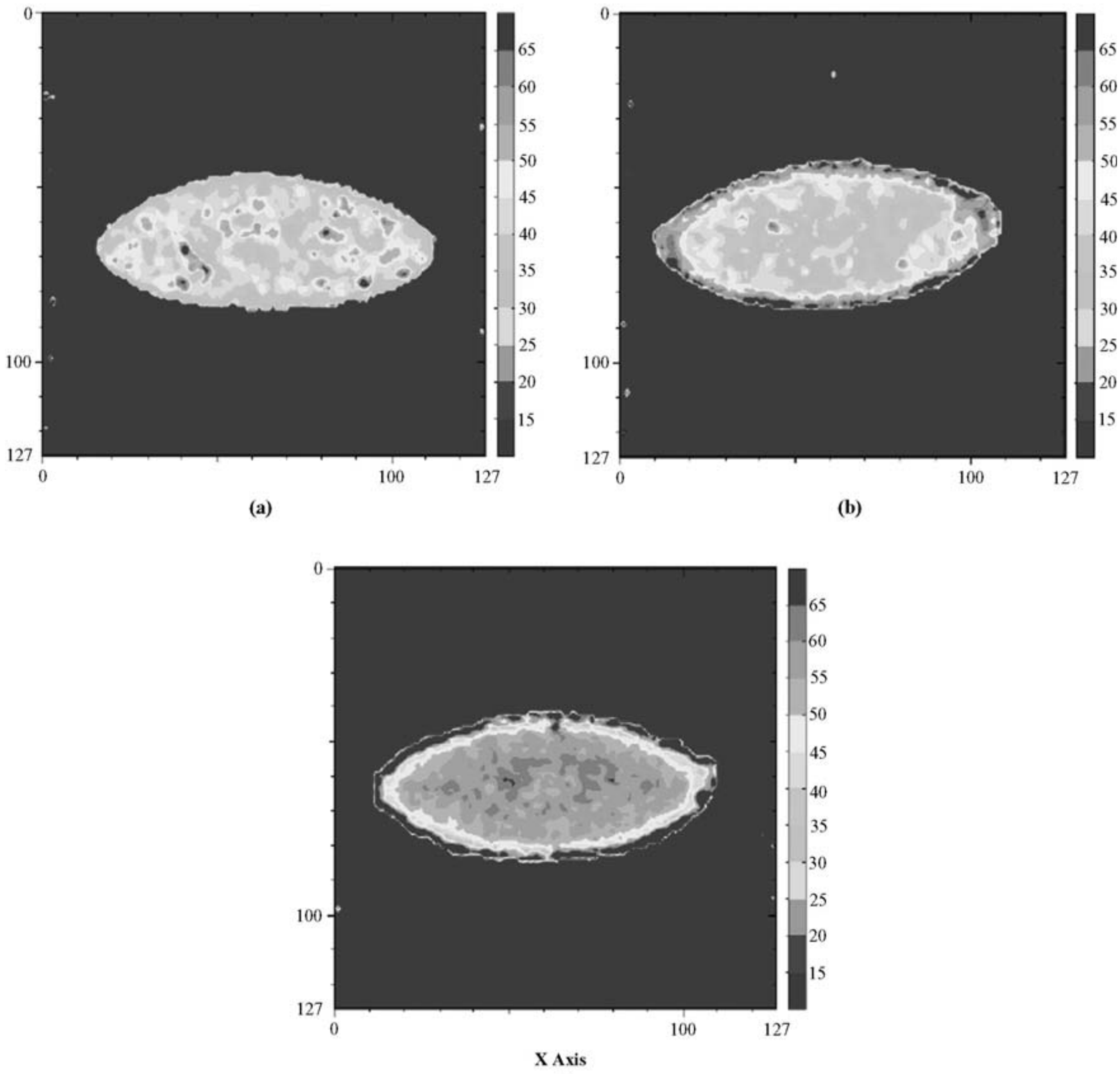

(a)

(b)

(c)

Fig. 2. T_2 map of soft cheeses according to ripening time. D + 9 (a), D + 14 (b) and D + 44 (c) (From Chaland [23] with permission). (See also Plate 135 on page XXVI in the Color Plate Section.)

ripening begin. The lactate produced by the lactic bacteria during the acidification period is oxidized during ripening. This metabolism of lactate causes an increase in pH. The combined action of pH and salt precipitation (especially calcium) changes the protein gel structure and softens the cheese. These modifications in turn induce an increase in the water relaxation time. For example, the transverse relaxation time of the water phase is 35 ms for a commercial non-mature soft cheese and reaches 60 ms when the cheese is mature. This variation in relaxation depends on the dry matter in the cheese: the lower the level of dry matter, the greater the variation. However, the sensitivity of the relaxation time to ripening is enough to use the relaxation time as a parameter for application of MRI. Figure 2 represents the T_2 map of soft cheeses according to time of ripening. The T_2 map was calculated from a relaxation decay curve measured with a 2D Fourier transform multi-echo sequence [23]. After 9 days the relaxation time of the cheese was low and little heterogeneity was observed. After 14 days an increase in T_2 was observed on the periphery of the cheese. Moreover, there was a gradient from the center to the cheese surface. The high T_2 value voxel number increased over time, to the detriment of the low T_2 value voxel number. After 44 days, all the voxels reached the same T_2 values and the cheese was totally mature. The variation in T_2 observed during ripening was in close agreement with the expected ripening mechanism. The MRI technique could therefore be applied to different ripening conditions, and the ripening kinetics could be followed.

The effects of freezing on mozzarella according to the T_2 distribution in the T_2 map have been studied [24]. Differences were noted in the T_2 histogram between unfrozen pasta filata and non-pasta filata. Moreover, after a freezing-thawing process the T_2 histogram was modified and this effect was dependent on the initial structure of the cheese and also on the storage time. The differences are explained by the micro-structure of the gel and by the damage to the protein structure induced by the freezing-thawing process.

Relaxation time distribution is highly sensitive to the formation of small water compartments inside the gel and this situation is encountered in young cheeses. The water distribution is non-uniform after draining and salting. Moreover, because of cutting of the curd before draining, small numbers of residual water pockets are entrapped between the curd pieces. These water compartments lead to increased T_2 distribution if studied by NMR but can also be detected by MRI [18,25]. The water pockets characterized by longer T_2 values appears in white in the MRI image presented. The water pocket can be quantified according to ripening time after the threshold of the image (Figure 3).

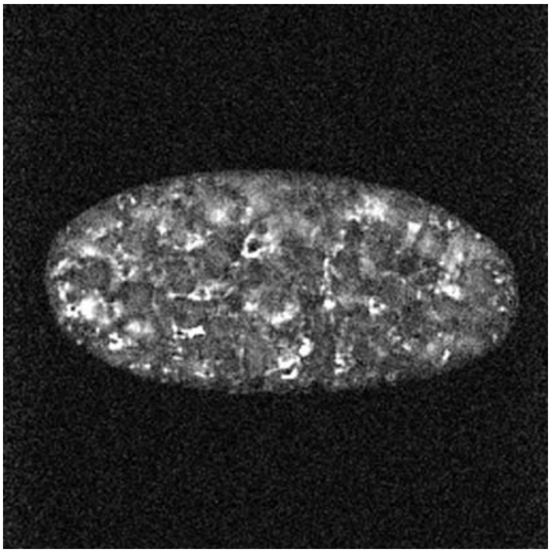

Fig. 3. T_2-weighted MR images of a young soft cheese (From Chaland [23] with permission).

Temperature and Flow

Many NMR parameters are sensitive to temperature and can be used as tracers for the non-invasive measurement of temperature. Among all the NMR parameters sensitive to temperature such as T_1, T_2relaxation times, diffusion coefficient, and chemical shift, the latter has been found to be the most effective as it does not suffer from dependency on any physical structure. Some examples have been reported study heat transfer in cheese [26,27].

Using MRI, flow can be measured with appropriate experimental protocols. These techniques are referred to as NMR velocimetry. The advantage of this technique is that a velocimetry profile or map can be obtained without assumptions concerning the uniformity of the shear rate. For example, the behavior of processed cheese melts during pipe flow [28] and the effects of temperature on the rheology of butter fat and margarine have been studied [29,30]. Measurements were performed with a 7 T NMR spectrometer equipped with a micro-imaging probehead. A pulse field gradient spin-echo sequence was applied. A Couette cell consisting of two concentric glass tubes filled with the sample of interest was inserted into the probehead. Figure 4 shows an example of an MRI image for water in the Couette cell. The right part corresponds to the water in the annulus space and the left part to the water in the central space. Note that the fluid in the inner tube is used as a marker to find the velocity of the outer surface. A velocity profile can be computed (Figure 5) from these images. A power law fluid model was therefore used to fit the velocity profile and to describe the shear thinning and thickening. The velocity profiles

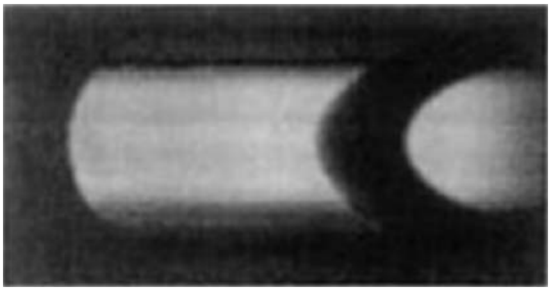

Fig. 4. MR Image of water in the cylindrical Couette cell (From Britton *et al*. [30] with permission).

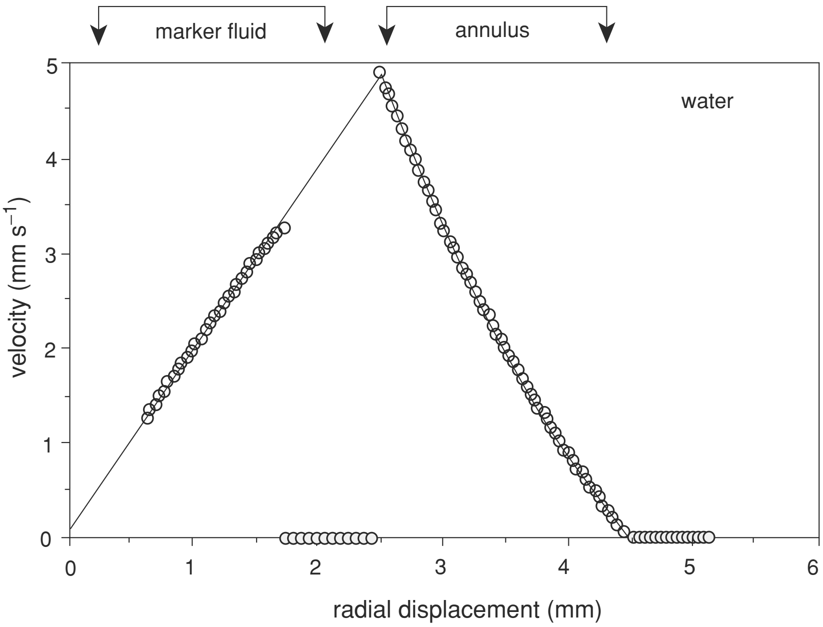

Fig. 5. Radial velocity profile taken across the cylindrical Couette cell in the case of water (From Britton *et al.* [30] with permission).

for butter between 25 and 42°C exhibited a yield stress transition around 35°C. Below this value, the shear rate was heterogeneous. This method appears very promising to investigate the particulate and molecular origins of complex rheological properties of dairy materials.

Conclusion

The MRI applications illustrated in these examples demonstrate the potential for non-invasive characterization of dairy processing and how information about composition and internal structure of the product can assist understanding about dairy engineering. New developments in NMR and MRI methods will enable new applications with improved image quality to be proposed in the future.

References

1. Isengard HD. Food Control. 2001;12(7):395.
2. Mc Carthy MJ. Magnetic Resonance Imaging in Foods. Chapman & Hall: New York, 1994.
3. Mariette F, Sauzeau O, Franconi JM, Marchal P. The Fourth International Conference on Applications of Magnetic Resonance in Food Science, Norwich, UK 1998.
4. Mariette F, Cambert M, Franconi F, Marchal P. Les produits alimentaires et l'eau, Agoral 99, Nantes, 1999, p 405.
5. Ozilgen M, Kauten RJ, Process Biochem. 1994;29(5):373.
6. Mariette F. In: A Webb, PS Belton, AM Gill, DN Rutledge (Eds). Magnetic Resonance in Food Science: Latest Developments. Royal Society of Chemistry: Cambridge, 2003, p 209.
7. Kamalaki MS, Mc Carthy MJ, Mc Carthy KL. IFT Annual Meeting, Chicago, USA, 2003.
8. Tijskens E, De Baerdemaeker J. Math. Comput. Simul. 2004;65(1–2):165.
9. Le Dean A. Water assessment in dairy products: study of dispersions and gels under syneresis, freezing and thawing (in French). PhD Thesis. Institut National Agronomique Paris-Grignon, 2000.
10. Ruan R, Chang K, Chen PL, Fulcher RG, Bastian ED. J. Dairy Sci. 1998;80:9.
11. Duce SL, Amin MHG, Horsfield MA, Tyszka M, Hall LD. Int. Dairy J. 1995;5(4):311.
12. Rosenberg M, McCarthy MJ, Kauten R. Food Struct. 1991;10:185.
13. Rosenberg M, McCarthy MJ, Kauten R. J. Dairy Sci. 1992;75:2083.
14. Kim SM, Mc Carthy MJ, Chen P. J. Magn. Reson. Anal. 1996;2(4):281.
15. Mariette F, Collewet G, Marchal P, Franconi JM. In: P Belton, B Hills, GA Webb (Eds). Advances in Magnetic Resonance in Food Science. The Royal Society of Chemistry, Cambridge, 1999, p 24.
16. Mariette F, Collewet G, Fortier P, Soulie JM. In: GA Webb, P Belton, AM Gil, I Delgadillo (Eds). Magnetic Resonance

in Food Science. A View to the Future, The Royal Society of Chemistry, Cambridge, 2001, p 67.

17. Collewet G, Strzelecki M, Mariette F. Magn. Reson. Imaging 2004;22(1):81.
18. Chaland B, Mariette F, Marchal P, de Certaines J. The Fifth International Conference on Applications of Magnetic Resonance in Food Science, Aveiro, Portugal, 2000, p 90.
19. Onea A, Collewet G, Fernandez C, Vartan C, Richard N, Mariette F. SPIE, The International Society for Optical Engineering, 2003.
20. Mariette F, Tellier C, Brule G, Marchal P. J. Dairy Res. 1993;60(2):175.
21. Famelart MH, Gaucheron F, Mariette F, Le Graet Y, Raulot K, Boyaval E. Int. Dairy J. 1997;7(5):325.
22. Le Dean A, Mariette F, Marin M. J. Agric. Food Chem. 2004;52(17):5449.
23. Chaland B. Ripening mechanisms of soft cheese : a low field MRI study (in French), PhD Thesis, University of Rennes, 1999.
24. Kuo MI, Anderson ME, Gunasekaran S. J. Dairy Sci. 2003; 86(8):2525.
25. Fortier P, Mariette F, Soulie JM. Food Factory of the Future. Gothenburg, Sweden, 2001, p 13.
26. Ruan RR, Chang K, Chen PL, Ning A. Drying Technol. 1998;16(7):1459.
27. Chang K, Ruan R, Chen PL, Ye X. International Meeting of the Society of Agricultural Engineers, Toronto, Ontario, Canada, 1999.
28. Yoon WB, McCarthy KL. J. Food Process Eng. 2003;26(6): 559.
29. Britton MM, Callaghan PT. J. Texture Stud. 2000;31(3):245.
30. Britton MM, Callaghan PT. Magn. Reson. Chem. 35, S37 (1997).

NMR Imaging of Dough

Lucas Tiphaine, A. Grenier, G. Collewet, and A. Davenel
Cemagref, Food Process Engineering Research Unit, 17 avenue de Cucillé, 35044 Rennes Cedex, France

Introduction

The flavor and the structure of crumb are the main factors in consumer acceptance of bakery products. The final structure depends to a significant extent on the creation and control of gas bubble structures in the unbaked matrix, and the retention of these gas bubbles in a suitable form until the matrix becomes set or baked. Bread making may be viewed as a series of aeration stages: bubbles are incorporated during mixing, the bubbles are inflated with carbon dioxide during proving, and the aerated structure is modified and set by baking. For greater convenience to craft bakers and greater compliance in logistics management, the immemorial continued process of proving and baking, has been sophisticated by introducing intermediary steps such as retarding techniques by cooling yeasted doughs, deep freezing of unproven fermented doughs, or part-baked bread in centralized production plants (Figure 1). The new steps have contributed to make more complex the physical and chemical changes that occur inside the dough during processing. Bread making quality of frozen green dough is affected by the degradation of both yeast activity and dough rheology. The water crystallization process plays a major role in such degradations. The rate at which ice forms with lowering temperature, the microscopic structure of ice crystals as well as its evolution during cold storage are known as parameters of importance. As invasive measurements may provoke dough collapse, the characterization of the expansion process has been reduced to a number of global volumetric parameters. In the last decades, sophisticated measurements and macroscopic invasive techniques have allowed a better understanding of these changes. If the resolution of confocal microscopy is efficient to yield the number of bubbles and the porosity of dough, only bubbles close to the dough surface can be observed. If the X-ray tomography and the MRI technique both have the potential to investigate the porosity in all parts of the dough, only MRI offers the possibility to measure simultaneously porosity and to localize ice gradients during the thawing–proving process. Actually MRI parameters characteristic of the dough, i.e. transversal T_2 and longitudinal T_1 relaxation times, and apparent proton densities, are sensitive to structural changes such as water crystallization, but also moisture modifications, expansion process, and temperature changes in the matrix. The codification of the MRI images based on the application of magnetic gradients in each space direction before spin or gradient echo scanning, combined to the rapid relaxation of water protons in dough (e.g. T_2 is comprised between 0.5 and 35 ms depending on temperature) confined the technique to the partial observation of the more mobile protons: a more or less important fraction of the protons of liquid water and a fraction of the hydroxyl protons of macromolecules in interaction with water. Large reduction in the MRI signal is associated, on the one hand, to the crystallization from up to 50–60% of the water during freezing of green dough and, on the other hand, to the expansion during proving with the incorporation of up to 60–70% of gas in bubbles. This involves to pay attention to maintain exploitable signal-to-noise ratio all along the processes, by finding the best compromise in the choice of the spatial resolution, the echo time and the number of excitations for signal averaging. After that, the complex relationship between gray levels in the dough images and physical state of the different parts of the dough requires large investigations to quantify the precise contribution of each phenomenon. This review presents the state of art of the performances of the MRI technique to visualize and quantify the phenomena occurring during the making of dough (freezing and proving) and to help their complex modeling.

Assessment of Ice Fraction Cartographies During Freezing, Storage, and Thawing of Raw Dough

Factors Influencing the MRI Signal of Frozen Dough

As only liquid protons give the MRI signal, the increasing ice fraction in the voxel volume results in a decreasing intensity of the MRI signal. The MRI signal in the voxel i is thus proportional to:

$$\mathrm{GL}(i,t) \propto (1-\varepsilon(i))\left(1-\frac{\rho_{\mathrm{dough}}}{\rho_{\mathrm{ice}}}\omega_{\mathrm{ice}}(i,t)\right) \times \mathrm{GL}_{\mathrm{remain\ liq}}(i,t), \qquad (1)$$

where ω_{ice} is the ice fraction (kg of ice per kg of dough), ρ_{ice} and ρ_{dough}, the densities of ice and dough (kg m^{-3}),

Graham A. Webb (ed.), Modern Magnetic Resonance, 1807–1812.
© 2008 *Springer.*

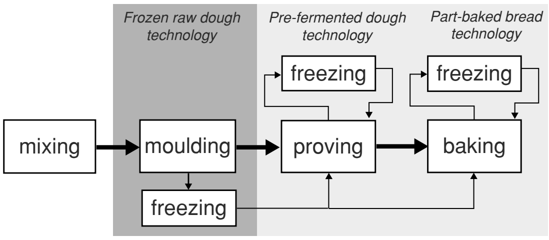
Frozen raw dough technology
Pre-fermented dough technology
Part-baked bread technology
mixing
moulding
freezing
proving
freezing
baking
freezing

Fig. 1. Schematic diagram of the bread-making process and the retarding (usually freezing) steps induced by its industrialization. Each retarding step induces a change of companies, e.g. producer/retailer.

ε, the volume fraction occupied by air bubbles—incorporated at the mixing step, $GL_{\text{remain liq}}$, the MRI signal from a voxel that would be full of the remaining liquid phase, and t, the processing time. The porosity of raw dough is often considered constant—no gas compression at cooling nor collapse of bubbles during storage. $GL_{\text{remain liq}}$ takes into account the changes in the NMR relaxation times, resulting from temperature decrease and freeze-concentration. It is tempting to directly relate the ice fraction to the intensity of the MRI signal, but from Equation (1) it is clearly not the sole factor affecting the MRI signal during the phase change of water. Despite these combined effects, the gray level in frozen dough is (surprisingly) *linearly* correlated to the ice fraction (Figure 2). This makes MRI a quite perfect ice sensor. The non-negligible effect of the changing NMR relaxation times during freezing [1–3] is evident from the disappearance of the MRI signal at high levels of unfrozen water contents. For the operating conditions of Figure 2, the MRI intensity in dough is hardly distinguished from the signal of the image background at −10.8°C although at such temperature, the ice fraction is only 57 g per 100 g of total water. Sensitivity of the MRI sensor to lower temperatures can be achieved through shorter echo time values [1] or using other sequences [2].

MRI for the Characterization of Heterogeneities in Frozen/Thawed Dough

As the high deformability of dough does not permit an accurate positioning of intrusive sensors, like thermocouples, the non-invasive character of MRI is obviously advantageous for assessing heat transfer. As an ice sensor, MRI will provide information about non-equilibrium states which was not available up to now and which will complement the usual temperature information. Additionally, it is a unique technique to assess the typical multidimensionality of heat transfer in dough [1,2]. As the dough stick is placed on a baking net for freezing, its top surface is in free contact with air, whereas on its flanks the space for air circulation (and consequently the heat transfer exchange) is reduced due to the proximity of the net wall. Hence heat transfer is 2D proceeding along the dough radius, but differing with the angle (Figure 3). Such data will obviously allow a more extensive validation of numerical models in the case of complex product geometries or thermal boundary conditions and help the design of equipments.

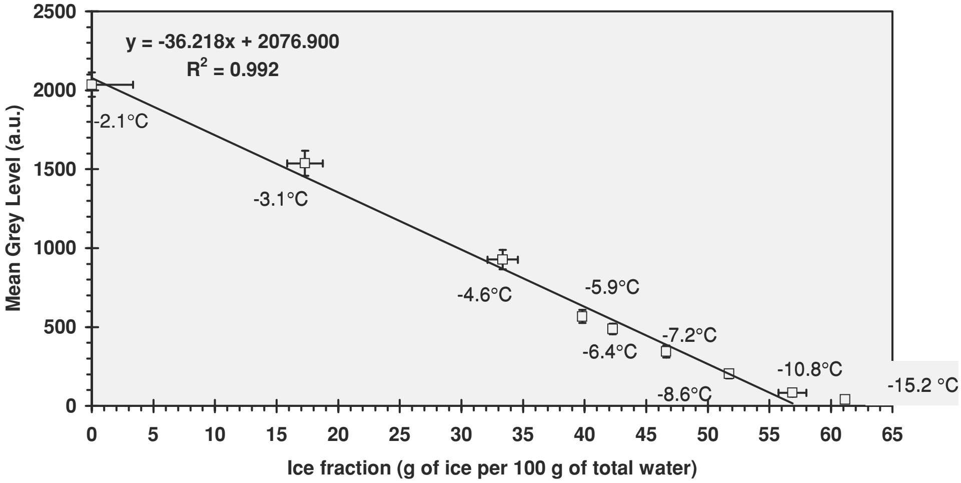

Fig. 2. Mean gray level (Siemens 0.2 T, echo-gradient sequence, TE = 4 ms, TR = 300 ms, slice thickness = 12 mm, FOV = 175 × 175, matrix = 96 × 128, number of scans = 3) as function of ice fraction as measured by NMR. From Ref. [1].

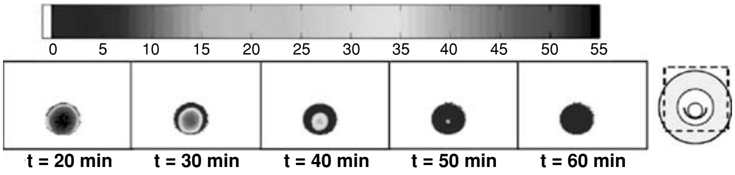

Fig. 3. MRI ice fraction (g of ice per 100 g of total water) maps during the thawing of a dough stick (water content 46.1%, 5 cm in diameter, 30 cm long, initial freezing temperature: –2.1 °C, initial temperature: –27 °C, air temperature: +31.5°C, air velocity: 10 m s^{-1}). Same acquisition conditions as in Figure 2. From Ref. [6]. (See also Plate 136 on page XXVI in the Color Plate Section.)

Changes may also occur under temperature fluctuations during cold storage, leading to micro- and macroscopic redistribution of water. From M_0 maps performed with a 4.7 T SISCO system on dough just after thawing, Esselink *et al.* observed beneath the dough surface, the replacement of low signal levels, attributed to void cells, by high levels attributed to a higher water density and concluded to ice recrystallization in void cells during dough storage [4].

Assessment of Porosity During the Proving Process

Factors Influencing the MRI Signal of Proofed Dough

In a given voxel i, the MRI signal from dough is proportional to:

$$\mathrm{GL}(i,t) \propto (1-\varepsilon(i,t))\mathrm{GL}_{\mathrm{dough}}(i,t), \tag{2}$$

where $\mathrm{GL}_{\mathrm{dough}}$ is the gray level expected from a voxel that would be full of dough (no air bubbles) and t, the processing time. As proving proceeds, dissolved carbon dioxide, ethanol, and water will vaporize into bubbles resulting in increasing bubble size and dough porosity. As only liquid protons give the MRI signal, the increasing gas volume fraction at the voxel scale results in a decreasing intensity of signal. $\mathrm{GL}_{\mathrm{dough}}$ takes into account the variation in the NMR properties of dough (proton density, transversal, and longitudinal relaxation times) resulting from changes in temperature (water), concentration, or composition (enzymatic reaction), which may possibly occur during proving.

Equation (2) assumes the absence of interaction between the gas and the MRI signal, especially no magnetic susceptibility between air and dough (H1), as well as a centered Gaussian distribution of the electronic noise (H2) [5]. It must be emphasized that if the voxel is smaller than a given bubble size (ranging from 100 μm to a few millimeters at the end of proving), its GL will reach the one observed in the image background and "black" holes will be distinguished in the MRI dough object as a result of the presence of gas bubbles. The same applies to cell walls (about 50 μm thickness). Such specific cases will be further detailed in the last sub-section.

The following developments assume that $\mathrm{GL}_{\mathrm{dough}}$ from Equation (2) is constant during proving—no changes in temperature, water concentration, or composition (H3). Under these hypotheses, the local porosity can be deduced from the gray level, provided that the two parameters are known in a reference condition [5]:

$$\frac{\mathrm{GL}(i,t)}{\mathrm{GL}(i,t_{\mathrm{ref}})} = \frac{1-\varepsilon(i,t)}{1-\varepsilon(i,t_{\mathrm{ref}})}, \tag{3}$$

As the dough matter is perpetually moving, Equation (2) cannot be validated easily, if ever, and a volume balance can be applied only at the entire dough scale:

$$\overline{\varepsilon}(t) = \frac{V(t) - V(t_{\mathrm{ref}})[1-\varepsilon(t_{\mathrm{ref}})]}{V(t)}, \tag{4}$$

where $V(t)$ is the total dough volume and $\overline{\varepsilon}(t)$, the mean porosity in dough. The latter can be compared to the mean porosity deduced from the MRI mean gray level ($\overline{GL}$), after generalizing Equation (3) and assuming an uniform initial distribution of porosity (H4) [5]:

$$\overline{\varepsilon}(t) = 1 - (1-\varepsilon(t_{\mathrm{ref}}))\frac{\overline{GL}(t)}{\overline{GL}(t_{\mathrm{ref}})}. \tag{5}$$

For the validation purpose, it was first checked by NMR that changes in composition under enzymatic reactions had no effect on the relaxation signal [5]; this partially validated hypothesis H3. In order to fully verify hypothesis H3, very low water exchange and heat exchange were performed, thanks to the optimization of the experimental device and procedure for proving [5]. The mean porosity calculated from the mean MRI gray level—deduced from Equation (5), was in good agreement with the mean porosity calculated from total dough volume—Equation (4), as illustrated in Figure 4. As heat and mass transfer often take place concomitantly to fermentation at the industrial scale, the estimation of porosity—Equation (2) from MRI images acquired under realistic process conditions should be preceded by a pre-correction step [6].

Fig. 4. Mean porosity estimated from volumetric and MRI measurements during proving (26 °C). (Siemens 0.2 T, spin echo sequence, TE = 11 ms, TR = 300 ms, slice thickness = 12 mm, FOV = 175 × 175, matrix = 96 × 128, number of scans = 2.) From Ref. [5].

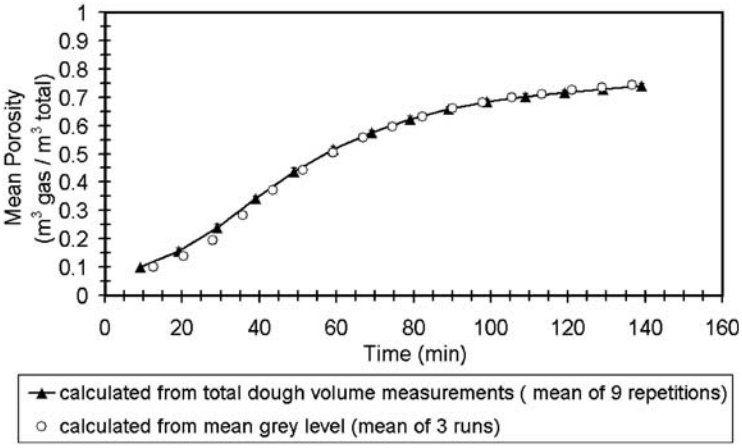

The present analysis can be of far-reaching use as it can serve as a validation procedure when testing new MRI sequences or new algorithms for image processing. For instance, echo-gradient sequences are known to be sensitive to the magnetic susceptibility between air and dough, and hypothesis H1 is no longer verified in such case. Applying Equation (2) will then result in overestimated local porosity or bubble size. Such artefact is expected especially at high magnetic field [7], but is also encountered at low magnetic field for long echo times [8]. It would be worth developing test objects dedicated to the same validation purposes, but at the local scale.

Large-Scale Information (Dough Scale)

At any processing time, the specific volume of the dough can be deduced from the area occupied by the dough object in the 2D MRI image [5,9,10]. Such parameter is usually obtained from volumetric measurements—using transparent, graduated containers, or monitoring the displacement of a liquid in a graduated column. However, by inducing additional pressure or frictions to the walls, these methods may be source of bias (e.g. use of a cover disposed on the top of the dough or weight of the liquid column). MRI does not present such inconvenient. Thanks to the possible positioning of multiple slices or even the use of a 3D sequence, it also offers the unique opportunity of dealing with geometries presenting strong anisotropy, e.g. French baguette or croissant compared to sandwich bread. The MRI volume accuracy obviously depends on the facility to detect the dough outlines from the image background. In other words, it relies on the signal-to-noise ratio, the spatial resolution—affecting the partial volume effect, and the type of algorithm retained for image processing.

Intermediate-Scale Information

Dough proving is often thought as a homogeneous process. However, areas of lower or higher densities can be observed from loaf slices [4,9]. Anisotropy may even be evident from the deformed external shape of the proofed dough [10]. These intermediate-scale heterogeneities are likely to happen under stresses. They may be of mechanical nature like the ones induced between sheets or within the roll at moulding [10] or by the outer surface—restraining the expansion [9]. Heat treatments producing intense thermal gradients within dough during previous processing steps [6] may also generate stress on the yeasts or the gluten network.

The scale under concern, ranging from one to a few millimeters, is much larger than the average cell size and parameters like local porosity (ε) or local displacement are more adequate to characterize such heterogeneities. As an illustration, Figure 5 presents the local porosity in dough sticks that have been previously frozen at different rates (at –30 or –40 °C) stored during 2 weeks at –20 °C and thawed before proving at 30 °C [6]. The dough frozen at –40 °C needed longer proving times to produce similar final volume. Additionally, it exhibited a core with porosity lower than the outer layers, even after long proving times whereas the dough frozen at –30 °C had a quite homogeneous porous structure (at a 1-mm scale). In fact, due to the cylindrical geometry of dough, the core freezes at a higher rate and it was found that over a certain threshold—which is over passed in the case of −40 °C at core, the expansion rate—through the survival of yeasts probably, is affected by the freezing rate.

Monitoring preferentially orientated motions of matter is a complementary, rather dynamic, way to characterize

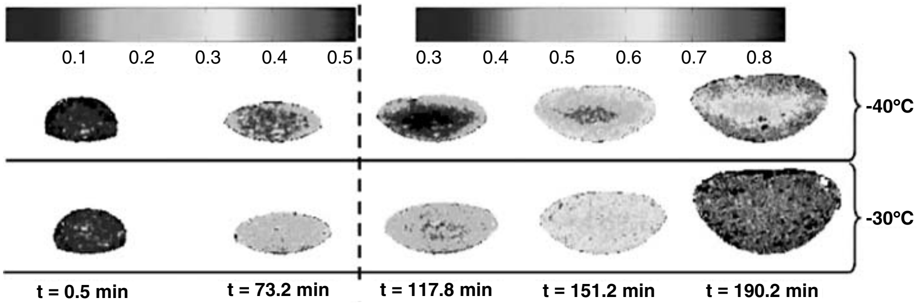

Fig. 5. MRI porosity maps (Siemens 0.2 T, spin echo sequence, TE = 15 ms, TR = 300 ms, slice thickness = 12 mm, FOV = 175 × 175, matrix = 96 × 128, number of scans = 2) of dough sticks previously frozen at −30 and −40 °C. From Ref. [6]. (See also Plate 137 on page XXVII in the Color Plate Section.)

the heterogeneous features of the dough expansion. Surprisingly, this point has received little attention so far [10]. Future investigations in this field would require the development of methods, either at the acquisition step—for instance to "trace" the matter in motion, or at the image processing step, with the adaptation of softwares developed for other applications, e.g. the use of optical flow [10].

Small-Scale Information (Bubble Scale)

Lastly, the distribution in size of cells and of cell walls can be assessed by MRI microscopy. Spatial resolutions that have already been tested [7,10–12] range from 100 to 270 μm, with slice thickness between 0.5 and 3 mm. Optical and electron microscopy [13,14] are more classically used, but these techniques are invasive and less suitable for monitoring dynamic processes in dough during proving. Additionally, the large-sized cells are often omitted because of the small sample slice. The X-ray tomography also offers non-invasive, dynamic monitoring of expansion and may compare with MRI [15–16].

The main challenge with developing MRI microscopy lies on the compromise between spatial and temporal resolutions. Especially, the number of scans (and thus the acquisition time) will tend to increase so to counter-balance the low signal-to-noise ratio resulting from higher spatial resolution. The acquisition durations of the previously tested sequences range from 2 to 8.5 min. Ideally, it should be small relatively to the (linear) period of major expansion (about 20 min), otherwise fast movements of the dough will cause blurring in the images.

The final objective is to get quantitative parameters descriptive of the dough cellular structure. Both the MRI sequence and the algorithm for image processing should be carefully chosen so to avoid bias in the way of quantification. The use of sequences sensitive to local inhomogeneities should be avoided, as already mentioned. Methods for estimating the size of holes have already been developed and tested on similar camera images of dough or bread, obtained from either loaf or microscope slices. Only apparent gas cell distributions (estimated from the 2D image of a 3D reality) have been assessed so far with no reconstruction of the true gas cell distribution by mathematical means [17]. With the same idea, MRI data recorded in 3D mode, combined with a time-resolved analysis will be interesting to track the behavior of individual gas bubbles.

Nevertheless, results obtained with 2D microscopy are already promising. Especially, the gas cell distribution observed by MRI on proofed dough is preserved in the crumb structure of the bread after baking [10]. These results confirmed that the crumb structure is already defined at an early stage of the bread-making process and baking is not the sole determining step. Other effects on the dough cellular structure have also been studied, such as: the freeze-sensitivity of yeast [11], the dough formulation [7], a pre-fermentation step before freezing [11], moulding with fast or slow deformations [10], the kneading temperature [10].

References

1. Lucas T, Grenier A, Quellec S, Le Bail A, Davenel A. J. Food Eng. 2005;70(2):151.
2. Lee S, Cornillon P, Kim YR. J. Food Sci. 2002;67(6):2251.
3. Grenier A, Lucas T, Davenel A, Cambert M, Le Bail A, Mariette F. J. Cereal Sci. In press.
4. Esselink EFJ, van Aalst H, Maliepaard M, van Duynhoven JPM. Cereal Chem. 2003;80(4):396.
5. Grenier A, Lucas T, Collewet G, Le Bail A. MRI. 2003;21(9):1071.
6. Grenier A. Ph.D. Thesis. University of Nantes, France, 2003, p 115.
7. Bonny JM, Rouillé J, Della Valle G, Devaux MF, Doubliez JP, Renou JP. MRI. 2003;22:395.

8. Grenier A, Lucas T, Davenel A, Collewet G, Le Bail A. In: Belton PS, Gil AM, Webb GA, Rutledge D (Eds). Magnetic Resonance in Food Science. The Royal Society of London, London, 2003, p 136.
9. Goetz J, Grob D, Koehler P. Eur. Food Res. Technol. 2003;217(6):504.
10. van Duynhoven JPM, van Kempen GMP, van Sluis R, Rieger B, Weegels P, van Vliet L J, Nicolay K. Cereal Chem. 2003;80(4):390.
11. Takano H, Naito S, Ishida N, Koizumi M, Kano H. J. Food Sci. 2002;67(7):2725.
12. Takano H, Ishida N, Koizumi M, Kano H. J. Food Sci. 2002;67(1):244.
13. Campbell GM, Rielly CD, Fryer PJ, Sadd PA. Trans. I. Chem. E. (Part C) 1991;69:67.
14. Whitworth MB, Alava JM. In: Campbell GM, Webb C, Pandiella SS, Niranjan K (Eds). Bubbles in Food. Eagan Press, St. Paul, 1999, p 221.
15. Falcone, PM, Baiano, A, Zanini, F, Mancini, L, Tromba, G, Montanari, F, Del Nobile, MA. J. Food Sci. 2004;69(1):E38–E43.
16. Babin, P, Della Valle, G, Dendieval, R, Lassoued, N, Salvo, L. Journal of Material Science. in press.
17. Campbell GM, Rielly CD, Fryer PJ, Sadd PA. In: Campbell GM, Webb C, Pandiella SS, Niranjan K (Eds). Bubbles in Food. Eagan Press, St. Paul, 1999, p 207.

MRI in Food Process Engineering

Joachim Götz
Fraunhofer-Institut Chemische Technologie, 76327 Pfinztal, Germany

Introduction

Most foods (initial/final) and food components are disperse multiphase systems (suspensions, foams, emulsions, porous/dry/wet bulk solids). Aspects of the material properties essential for both consumer and producer are the structure (different length-scales) and flow behavior. The flow behavior is important for the design of *process unit operations* and *sensory behavior* of the final food product. The structure is correlated with various macroscopic properties like the storage/ageing behavior, phase separation (syneresis, sedimentation) [1,2], and the filtration/deformation/flow/sensorial behavior. Correlations between the evolution of the stress and porosity, agglomeration, and flow-type are established for flowing foods (starch solutions [3], wheat dough [4]). It is, therefore, plausible to assume that the correlation between the structure and the rheology is generally valid. Materials with volume fractions of the disperse phase higher than 5 vol.% are usually opaque [5]. MRI offers the possibility to perform measurements non-invasively, non-destructively, and highly selective (*in situ*, online) in order to study the structure or trace structural changes or inner transport processes in different phases/states of aggregation (without preparations) during production, storage, transportation, and consumption (temporal, spatial, chemical resolved). Samples may be studied several times under identical or changed conditions, which is a great advantage (time saving, higher accuracy, interior surface) compared to preparative microscopy. The objective of MRI in food process engineering is to develop and check appropriate models and describe the system for a reliable process design, quality control, and process control, in order to forgo time-intensive trial and -error. Foods have often to be built up step by step from simple ingredients to complex systems in order (i) to study effects of single constituents and (ii) to quantify interactions between constituents. On the basis of the knowledge of the involved phenomena, new products/apparatus with improved process conditions can be developed economically [6].

Structure and Changes

The pore structure of solid matrices (spatially resolved volume concentrations of constituents) and the composition have obviously a strong impact on convective/diffusive transport phenomena. In order to model or simulate transport processes in disperse media detailed geometrical data of the matrix are necessary for the discretisation of the region in question and the generation of the grids. Therefore, the analysis of the pore structure is an important prerequisite for a better understanding of transport processes in or of flowing foods [7]. The MRI applications to foods and food components are focused on the analysis of their structure/composition and detection of structural modifications due to processing/conditions. The local intensity $I(\mathbf{r})$ is due to various contrast techniques [8] generally a complex function of the applied method, sequence parameters (T_E, T_R), spin-density, material properties (relaxation, chemical shift, D_S), and velocity. There are sequences available for the quantification of specific material parameters mentioned above. In many investigations, the used sequences and sequence parameters are optimized with regard to maximal contrast. Applications in food technology are

(a) to determine the local fluid/solid concentration (products or apparatus) [7],
(b) to analyze the structure of heterogeneous foods (differentiation of components): fruit [9], vegetables [10,11], cheese [12] (ripening, spoilage), chocolate products [7], pasta [13], ham, meat products [14,15], dough [16,17], crackers [18], bones [19], filter cakes [20,21], and foams [7], and
(c) to quantify spatially resolved structural changes/reactions caused by process unit operations, storage/ageing, transportation [22–24].

The determination of the local concentration of detectable spins (a) and the structure analysis (b) are often different aspects of the same study.

Distribution of Concentration

The structure, quality, and sensorial behavior of many foods depend on the state and distribution of food components (water, oil, hydrocolloids, proteins). The components are often distinguished by CSI or relaxation times weighted imaging [8,25–30]. NMR provides an approach to characterize the food structure, interactions between

Graham A. Webb (ed.), Modern Magnetic Resonance, 1813–1818.
© 2008 *Springer.*

food components, possible induced structural changes, and monitors the spreading of water and oil. Hydrocolloids are used for the production of many food products in order to modify the textural properties (thickening, gelling, stabilizing). It is possible to determine the local hydrocolloid concentration by T_2 [31,32].

The comparison of extruded pastes shows that the moisture distribution changes dramatically using cellulose [33]. The regions with the highest moisture are without cellulose at the surface. After adding cellulose the maximum of the moisture is in the middle. MRI allows one to optimize the extrusion varying composition, pretreatment, die-geometry, and process parameters. By studying the processes in the interior of the extruder (including die) evolving cracks are observable. Analogous experiments are imaginable to determine the local moisture in extruded pasta (macaroni) for optimization of the production. The flow of pastes around an installed stick in the die leads to increased moisture in volume elements having passed internal fittings [33]. Depending on the local moisture these regions may tend toward spoilage.

Analysis of the Structure

There are principally two possibilities to study the pore system/structure of porous materials:

- direct imaging of the matrix, and
- indirect imaging of the pore system, when it is/has been saturated with a fluid which contains protons, revealing the inverse inner structure.

Direct Imaging

MRI provides 3D representations of foams [34], whereas SEM is only capable of monitoring the surface structure. In order to study the interior of foams by SEM the sample has to be destroyed. MRI allows to image the foam again after or even during the deformation. Thus, the evolution of the pore system [possible breaking of matrices (bars, cells)] can be monitored online. Direct imaging was applied to aerated countlines [7] with a dense layer at the surface and an inhomogeneous poresize distribution. This causes spatial varying firmness and, therefore, sensorial behavior. Two zones can be differentiated in chocolate bars [7]: the inner zone (peanuts: mobile oil) and the outer with pure chocolate (low signal). Nuts and fat fillings produce good contrast, whereas dried fruit and biscuit can hardly be observed [35]. MRI can, furthermore, be used to determine the distribution of fat concentration and polymorphic states of cocoa-butter [36]. This allows one to quantify the influence of heat treatments on the composition/conformations of fat phases and detect water/fat migration during storing, like the migration of triacylglycerol in composite confectionary [37,38]. The evolution of the profiles depend on the storage temperature [39]. Thus, fat bloom can be detected before its visible recrystallization at the surface. MRI provides a rapid test for studying fat bloom (process, recipe, storage conditions). It is also conceivable to use MRI indicators for measuring pH and redox [40]. In several cheese types holes, cracks, and seams of mould were localized (production, storage) and the local grade of ripening was differentiated [12,41]. Short relaxation times in solids cause problems for MRI with echo times longer than 1 ms. The signal decays, before it can be detected. With the help of SPI a signal can already be recorded at 50 μs [19]. A great disadvantage of SPI is the long measuring times (several hours: spatial resolution) [42].

MRI was also applied to study packaging materials or foods in packages (structure, composition, delamination [43]). Commercial food products are online characterized concerning spoilage without removal of the packages [44–46] (correlation of the degree of bacterial spoilage and T_2). The patterns in T_2-weighted MRI of the same matrix are characteristic for bacteria contaminating the sample [44]. The content in plastic-, paper-, or glass-packages and polypropylene cartons with an aluminum foil-top are imaged without any significant artifact [47]. Papers with aluminum foil and ferrous metal-tops (shielded RF, modified B_0) cause problems.

Indirect Imaging

A prerequisite for the indirect method is that (i) all pores can be filled with the proton containing fluid [48] and (ii) the pore system is not changed due to the hydration (swelling). MRI is used to characterize the porosity distribution in water saturated bulk solids/filter cakes and their evolution during mechanical thermic dewatering (filtration, expression) [49–54] and in salt-water ice-systems using decane as pore fluid [55,56]. Indirect MRI was used for tablets filled with Gd-doped oil [57]. The structure was studied for optimizing the agglomeration (parameters, recipe) with regard to the tablet design (coating) and the release of ingredients. MRI enables one to determine the density/porosity of tablets, characterize the homogeneity (±3%), and detect cracks. The structure determines the kinetics of dissolving and drug release (c). The indirect MRI can essentially be improved by hyperpolarized gases (^{3}He, ^{129}Xe) [58–59] due to an enhanced saturation. Ceramics in the green state can often be studied directly [33]. After sintering, ceramics have to be impregnated with detectable fluids/gases. This method is presumably appropriate for porous foods with low content of detectable spins.

Structural Changes and Reactions

Dynamic processes (changes slow compared to the measuring time) can be studied by serial MRI. Presently, the measuring time of one image (64×32 pixels) cannot be decreased below 60 ms/image despite newly developed hardware and sequences (Snapshot-FLASH [60,61], EPI [62], Turbo-RARE [63]). MRI was used to characterize the texture of foods due to storage/ageing (ripening, pathogen infection), damage (bruising), and processing, without peeling [64,65]. Water- and oil-distribution were studied in emulsions (phase separation: creaming) [25,66,67]. The stability of foams (cream, egg-white, beer) was analyzed [68]. Drainage and collapse were observed without process disturbation/preparation. Reviews of MRI applied to foods in mechanical (flow, separation), thermal (drying/baking, heating [69], freezing [70], melting/thawing/solidifying/crystallization, extraction/distillation), and chemical processing (kinetics) are given in Refs. [10,18,71–77].

Serial MRI was used in order to track solvent-diffusion phenomena (water, fat, solutes, solids) in heterogeneous materials [78]. Most of the applied methods for analyzing transport processes are based on integral experiments [79] (total weight). These techniques enable, in many cases, an effective process control. Integral data are not sufficient for modeling and deriving product/process parameters necessary for an effective process design. MRI allows one to observe the solvent concentration, detect heterogeneities (defects, cracks, voids) [80,81] and determine D_S or further NMR quantities [78] (spatial/temporally resolved). Inhomogeneities are observed directly by MRI or indirectly by serial MRI mapping the penetrant-uptake [82]. Assuming a material law for the diffusion the corresponding material parameters (D_S as a function of solvent concentration) can be derived from the monitored profiles. The knowledge of the network and modifications of the network dependent on the local concentration of the diffusing substances are used to improve the modeling. MRI of dewatering/filtration processes reveals the evolution of the structure of filter cakes [20,21,49,50]. Serial MRI could, furthermore, be applied to study the evolution of filter cakes or sediments (centrifugation) and the structure effect of mechanical deformation (shear, ultrasonic) or additives (flocculating/dispersing). The determined porosity profiles are required for an appropriate modeling and design of solid/liquid separation [7,83].

MRI of freezing/thawing of carrageenan gels revealed two-phase changes and at least three phases [67]. A rapid MRI method to study the freezing of raw potatoes did not show a sharply defined processing front, but a region with several water/ice-phases [84]. The extension of this region increases faster than linearly with time. The effect of freezing/thawing and storing of pork can be authenticated by MRI of T_1, T_2, and D_S [85]. Especially T_2 is sensitive to damaging effects of thermal cycles. Drying processes are studied with MRI: corn and cellulose/agar gels (contact-drying) [86], model gel [10,87], and carrots or apples (microwaves) [88,89]. The moisture distribution is homogeneous in gels during drying [86], in corn inhomogeneous (corn morphology). The decreasing integral moisture is usually combined with shrinkage. The extension of cracks correlates with the moisture gradients [90]. The distribution of the moisture and temperature is determined in a model gel [91]. The pore structure strongly influences the drying process. Aim was to characterize the pore system and structure changes, discriminate drying mechanisms (moisture mobility), and analyze the crack behavior during drying. Further applications could be the drying of multicomponent systems (evolution of swelling [92], shrinkage, crack formation). The effect of freeze–thawing on the structure (moisture distribution) of meat, poultry, fish [93], or vegetables [94] is quantified by MRI. The change of relaxation times after thermal treatments is caused by protein denaturation, aggregation, or cross-linking [93]. The signal patterns in vegetables alter dramatically after freezing. The changes of the tissue morphology are caused by the rupture of cell walls, subsequent decreasing turgor, and decreasing firmness. MRI reveals the kinetics of melting/crystallization of fat (liquid-to-solid ratio) [95].

Textural structural changes in lasagne for various cooking/holding-times were recorded [96]. With the cooking time, the moisture increases inducing swelling. The firmness decreases caused by moisture redistribution during holding. MRI allows one to determine the optimal holding conditions (temperature, relative humidity) and modify the composition and process for lengthened holding with constant properties. In boiled grains a front of moisture progresses toward the center, steamed grains show a homogeneous moisture distribution [97]. The understanding and hence the design of baking processes (plus fermentation) is rather difficult due to combined heat/mass transfer (water, gas, fat), chemical/biological reactions, and changing pore structures (shrinkage/expansion). The final pore structure is related to the sensorial behavior of the baked product. Therefore, a deeper insight into the processes during fermentation/baking are required in order to optimize the production process (sensory/ageing behavior, energy demand, production costs, output) [29,66]. Localized spectroscopy was combined with MRI to study void formation, lipid/water migration/loss during baking [98,99]. MRI was also used to characterize the architecture of baked breads [100]. The baked samples were acetone saturated. The fermentation in yeasted wheat doughs was monitored by serial MRI (effect of handling on dough properties) [101]. The increase of the loaf volume was clearly demonstrated, but an exact measurement was not carried out. In order to monitor the fermentation without preparations/interruptions online, dough samples were placed in PTFE tubes (decreased wall friction) [17]. The MRI results correlate well with non-NMR volumetric measurements. MRI clearly reveals slices of higher mass density and, therefore, lower gas permeability at the surface during the fermentation [17]. Dough with baking powder was observed during baking [16].

During the gelation of Na-alginate (Ca^{2+}-induced) a sol/gel-boundary migrates through the sample [31,32,97,102]. The Ca^{2+} progress depends on the initial ion concentration, ionic strength of the sol, and the developing pore system. The data correlate in the short-time behavior with known reaction diffusion models. Deviations for long times are probably caused by syneresis, which describes the progress of phase separation in disperse foods (cheese, yoghurt). For syneresis, serum was detected at the outside of the skim-milk samples, using CSI [29]. The molecular processes causing syneresis are not completely clarified [7].

Many dried food products (pasta, legumes, puree powder, milk powder) are rehydrated before consuming. The rehydration is possibly combined with dissolution, swelling or gelling after mixing, homogenization, and heating or cooling [66]. As mentioned above (b), the structure of a tablet determines the kinetics of dissolving [103] and drug release [7,104–106]. Liquid diffuses into the tablet matrix, polymers hydrate, and build up a gel layer (barrier for liquid ingress and drug release).

Diffusive processes are the migration of brine into meat (^{23}Na [107]), water diffusion into polyamide (O_2-barrier in dry plastic-packages) [108], and water imbibition in cork [109]. A reliable prediction of the evolution of the drying is still impossible. In order to find suitable dryers, practical drying experiments still cannot be forgone. The main reason is that the distribution of water or other fluids and the character of the mass/heat transport cannot be derived from the total vaporized amount of fluid [110]. Examples of combinations between NMR data and modeling are given for freezing [111], rehydration [112], and drying. Characteristic parameters for pore systems (fractal dimension, correlation length, percolation probability [113]) can be derived by conventional MRI (saturated pore system). MRI can be used as a basis for the generation of grids for simulations, e.g. to model the microscopic deformation behavior of disperse foods. The comparison of simulation and MRI results might help to verify and improve the understanding of microstructures and microprocesses in disperse foods undergoing a macroscopic deformation. Structural changes due to transport processes and the possibility of NMR to characterize transport processes are reviewed in Ref. [7].

References

1. Lelievre J, Creamer L. Milchwissenschaft. 1978;33:73.
2. Gerhards C. Untersuchungen zur Synärese von Tafelsenf. Uni. Diss., Karlsruhe, 1994.
3. Dolan KD, Steffe JL. J. Texture Stud. 1990;21:265.
4. Schluentz EJ, Steffe JF, Ng PK. J. Texture Stud. 2000;31:41.
5. Roco G. Particulate Two-Phase Flow. Butterworth Heinemann: Boston, 1992.
6. Kretschmer T, Kohlhof J. Neue Werkstoffe. Springer: Berlin, 1995.
7. Götz J. Applications of NMR to Food and Model Systems in Process Engineering. Habilitation, http://tumb1.biblio.tu-muenchen.de/publ/diss/ww/2004/goetz.html, TUM.
8. Callaghan PT. Principles of NMR Microscopy. Oxford University Press: Oxford, 1991.
9. Galed G, Fernández-Valle ME, Martínez A, Heras A. Magn. Reson. Imaging. 2004;22:127.
10. Schrader GW, Litchfield JB, Schmidt SJ. Food Technol. 1992;46:77–83.
11. Hall LD, Evans SD, Nott KP. Magn. Reson. Imaging. 1998;16:5.
12. Rosenberg M, McCarthy MJ, Kauten R. Food Struct. 1991;10:185.
13. Kojima TI, Horigane AK, Yoshida M, Nagata T, Nagasawa A. J. Food Sci. 2001;66:1361.
14. Guiheneuf TM, Parker AD, Tessier JJ, Hall LD. Magn. Reson. Chem. 1997;35:112.
15. Guiheneuf TM, Tessier J-J, Herrod NJ, Hall LD. J. Sci. Food Agric. 1996;71:163.
16. Götz J, Geißler E, Köhler P, Groß D, Lehmann V. Food Res. Int. submitted.
17. Götz J, Groß D, Köhler P. Eur. Food Res. Technol. 2003;217:504.
18. Yan ZY, McCarthy MJ, Klemann L, Otterburn MS, Finley J. Magn. Reson. Imaging. 1996;14:979.
19. Oerther T. Kernspintomographische Untersuchungen an trabekulären Knochen. Uni. Diss., Heidelberg/Mannheim, 2002.
20. Wandelt B. Analyse de la Formation des Dépôts des Particles Lors d'un Procédé d'Ultrafiltration Tangentielle. Thèse INP, Toulouse, 1993.
21. Kaulisch E-M. Untersuchungen zur selektiven Partikelablagerung bei der Querstrom-Mikrofiltration. Uni. Diss., Karlsruhe, 1995.
22. Gladden LF. Chem. Eng. Sci. 1994;49:3339.
23. Gladden LF. AIChE J. 2003;49:2.
24. Gladden LF, Alexander P. Meas. Sci. Technol. 1996;7:423.
25. Winkler M, McCarthy MJ, German JB. J. Food Sci. 1992;56:811.
26. Duce SL, Ablett S, Darke AH, Pickles J, Hart C, Hall LD. Anal. Tech. Instrum. 1995;72:105.
27. Ruan RR, Chang K, Chen PL, Fulcher RG, Bastian ED. J. Dairy Sci. 1998;81:9.
28. Ruan RR, Chen PL. Water in Foods and Biological Systems. A Nuclear Magnetic Approach. Technomic Publishing: Lancaster, 1998.
29. McCarthy MJ, Kauten RJ. Trends Food Sci. Technol. 1990;56:134.
30. Horigane AK, Motoi H, Irie K, Yoshida M. J. Food Sci. 2003;68(6):2034.
31. Potter K, Balcom BJ, Carpenter TA, Hall LD. Carbohyd. Res. 1994;257:117.
32. Potter K, Carpenter TA, Hall LD. Carbohyd. Res. 1993;246:43.
33. Götz J. Möglichkeiten der Kernspintomographie zur Diagnose von Strömungsvorgängen und Strukturänderungen in Pasten. Uni. Diss. Karlsruhe, 1994.
34. Szayna M, Völkel R. Solid State Nucl. Magn. 1999;15:99.

35. Miquel ME, Hall LD. Lebensm. Wiss. Technol. 1998;31:93.
36. Duce SL, Carpenter TA, Hall LD. Lebensm. Wiss. Technol. 1990;23:545.
37. Guiheneuf TM, Couzens PJ, Wille H-J, Hall LD. J. Sci. Food Agric. 1997;73:265.
38. Guiheneuf TM, Gibbs SJ, Hall LD. J. Food Eng. 1997;31:457.
39. Jana AH, Thakar PN. Indian Food Ind. 1993;12:33.
40. Evans SD, Hall LD. SPECIRsc 2001;262:22.
41. Duce SL, Amin MHG, Horsfield A, Hall LD. Int. Dairy J. 1995;31:311.
42. Nauerth A, Gewiese B. Bruker Appl. Note. 1993.
43. Segre AL, Capitani D, Malinconico M, Martuscelli E, Groß D, Lehmann V. J. Materials Sci. Lett. 1993;12: 728.
44. Schenz TW, Dauber B, Nicholls C, Gardner C, Scott VA, Roberts SP, Hennesy MJ. Food Sci. Technol. Today. 1999;13:92.
45. Mermelstein NH. Food Technol. 1999;53:94.
46. Schenz TW, Courtney KL, Israel BR, Reaves LA. US Patent 5, 270.650, 1993.
47. Wright JJ, Hall LD. In: M Mathlouthi (Ed). Food Packaging and Preservation. Blackie Academic and Professional: London, 1994, p 197.
48. Kose K. J. Magn. Reson. A. 1996;118:195.
49. Fordham EJ, Gibbs SJ, Hall LD. Magn. Reson. Imaging. 1994;12:279.
50. Korger V. Dampfdruckentwässerung. Uni. Diss., Karlsruhe, 1994.
51. Yao S, Costello M, Fane AG, Pope JM. J. Membrane Sci. 1995;99:207.
52. Yao S, Pope JM, Fane AG. Bull Magn. Reson. 1995;17:220.
53. Pope JM, Yao S, Fane AG. J. Membrane Sci. 1996;118:247.
54. Yao S, Fane AG, Pope JM. Magn. Reson. Imaging. 1997;15:235.
55. Menzel M, Han S, Stapf S, Blümich B. J. Magn. Reson. 2000;143:376.
56. Eicken H, Bock C, Wittig R, Miller H, Poertner H-O. Cold Reg. Sci. Technol. 2000;31:207.
57. Nebgen G, Groß D, Lehmann V, Müller F. J. Pharm. Sci. 1995;84:283.
58. Wittig F, Kauczor H-U. Spektrumder Wiss. 1997;5:16.
59. Moudrakovski I, Lang S, Ratcliffe C, Simard B, Gilesand S, Ripmeester J. J. Magn. Reson. 2000;144:372.
60. Haase A. Magn. Reson. Med. 1990;13:77.
61. Haase A, Frahm J, Matthaei D, Hänicke W, Merboldt KD. J. Magn. Reson. 1986;67:258.
62. Mansfield P. C Solid State Phys. 1977;10:L55.
63. Hennig J, Nauerth A, Friedburg H. Magn. Reson. Med. 1986;3:823.
64. Ishida N, Kobayashi T, Koizuma M, Kano H. Agric. Biol. Chem. 1989;53:2363.
65. Hall LD, Evans SD, Nott KP. Magn. Reson. Imaging. 1998;16:5.
66. Duce SL, Hall LD. J. Food Eng. 1995;26:251.
67. Gibbs SJ, Hall LD. Meas. Sci. Technol. 1996;7:827.
68. German JB, McCarthy MJ. J. Agric. Food Chem. 1989;37:1321.
69. Ye X, Ruan R, Chen P, Doona C, Taub IA. J. Food Sci. 2003;68:1341.
70. Lee S, Cornillon P, Kim YR. J. Food Sci. 2002;67:2251.
71. McCarthy MJ. Magnetic Resonance Imaging in Foods. Chapman & Hall: New York, 1994.
72. McCarthy MJ, McCarthy KL. J. Sci. Food Agric. 1994;65:257.
73. Corbett AM, Phillips RJ, Kauten RJ, McCarthy KL. J. Rheol. 1995;35:907.
74. Watanabe H, Fukuoka M, Watanabe T. In A Gaonkar (Ed). Characterization of Food: Emerging Methods. Elsevier: Amsterdam, 1995, p 117.
75. Belton PS, Hills BP, Webb GA (Eds). Proceedings of the IV International Conference on Applications of Magnetic Resonance in Food Science, Norwich, UK, RSC, Cambridge, 1998.
76. Hills BP. Magnetic Resonance Imaging in Food Science. John Wiley & Sons: New York, 1998.
77. Webb GA, Belton PS, Gil AM, Delgadillo I (Eds). Proceedings of the II International Conference on Applications of Magnetic Resonance in Food Science, Aveiro, RSC, Cambridge, 2000.
78. Watson AT, Chang CT. Prog. Nucl. Magn. Reson. Spectrosc. 1997;31:343.
79. McCarthy MJ, Lasseux D, Maneval JE. J. Food Eng. 1994; 22:211.
80. Rothwell WP, Holecek DR, Kershaw JA. J. Polym. Sci. Polym. Lett. Ed. 1984;22:241.
81. Koenig JL. In: B Blümich, W Kuhn (Eds). Magnetic Resonance Microscopy, VCH, Weinheim, 1992, p 187.
82. Webb AG, Hall LD. Polym. Commun. 1990;31:422.
83. Rembor H-J. Das Verhalten von Tiefenfiltern bei zunehmender Staubbelastung.Uni. Diss., Karlsruhe 2001.
84. Hills BP, Goncalves O, Harrison M, Godward J. Magn. Reson. Chem. 1997;35:29.
85. Guiheneuf TM, Parker AD, Tesser JJ, Hall LD. Magn. Reson. Chem. 1997;35:122.
86. Song H, Litchfield JB. AIChE Sym. Ser. 1993;297(89)55.
87. Bows JR, Patrick ML, Nott KP, Hall LD. Int. J. Food Sci. Technol. 2001;36:243.
88. Regier M, Erle U, Schubert H. CIT. 2000;72:935.
89. Regier M, Guthausen G, Schubert H. CIT. 2002;74:601.
90. Leisen J, Hou L, Beckham HW, Carr WW. In: P Blümler, B Blümich, R Botto, E Fukushima (Eds). Spatially Resolved Magnetic Resonance. Wiley-VHC: Weinheim, 1998, p 265.
91. Nott KP, Bows JR, Patrick ML. Int. J. Food Sci. Technol. 1999;34:305.
92. Douglas JF. Phys. Rev. E. 1996;54:2677.
93. Hall LD, Evans SD, Nott KP. Magn. Reson. Imaging. 1998;16:5–6.
94. Duce SL, Carpenter TA, Hall LD. J. Food Eng. 1992;16:165.
95. Simoneau C, Carthy MJ, Reid DS, German JB. Trends Food Sci. Technol. 1992;3:208.
96. Gonzalez JJ, McCarthy KL, McCarthy MJ. J. Texture Stud. 2000;31:93.
97. Stapley AG, Hyde TM, Gladden LF, Fryer PJ. Int. J. Food Sci. Technol. 1997;32:355.
98. Heil JR, Ozilgen M, McCarthy MJ. Am. Instrum. Chem. Eng. Symp. Ser. 1993;297:39.
99. Ruan RR, Almaer S, Huang VT, Perkins P, Chen P, Fulcher RG. Cereal Chem. 1996;73:328.
100. Ishida N, Takano H, Naito S, Isobe S, Uemura K, Haishi T, Kose K, Koizumi M, Kano H. Magn. Reson. Imaging. 2001;19:867.

101. Takano H, Ishida N, Koizumi M, Kano H. J. Food Sci. 2002;67:244.
102. Duez J-M, Mestdagh M, Demeure R, Goudemant J-F, Hills BP, Godward J. Magn. Reson. Chem. 2000;38:324.
103. Snaar JE, Hardy IJ, Bowtell R, Melia CD, Cook W. Magn. Reson. Imaging. 2001;19:583.
104. Rajabi-Siahboomi AR, Bowtell RW, Mansfield P, Henderson A, Davies MC, Melia CD. J. Control Release. 1994;31: 121.
105. Black S. In: P Blümler, B Blümich, R Botto, E Fukushima (Eds). Spatially Resolved Magnetic Resonance. Wiley-VHC: Weinheim, 1998, p 259.
106. Fahie BJ, Nangia A, Chopra SK, Fyfe CA, Grondey H, Blazek A. J. Control Release. 1998;51:179.
107. Guiheneuf TM, Gibbs SJ, Hall LD. J. Food Eng. 1997;31:457.
108. Blackband S, Mansfield P. J. Phys. C Solid State Phys. 1986;19:49.
109. Gil AM, Lopes MH, Pascoal Neto C, Callaghan PT. J. Materials Sci. 2000;35:1891.
110. Harding SG, Johns ML, Pugh SR, Fryers PJ, Gladden LF. Food Addit. Contam. 1997;14:583.
111. Kerr WL, Kauten RJ, Ozilgen M, McCarthy MJ, Reid DS. J. Food Process. Eng. 1996;19:363.
112. Hills BP, Babonneau F, Quantin VM, Gaudet F, Belton PS. J. Food Eng. 1996;27:71.
113. Stauffer D, Aharony A. Introduction to Percolation Theory. Taylor & Francis: London, 1985.

Rheo-NMR: Applications to Food

Joachim Götz[1] and Klaus Zick[2]
[1]Fraunhofer-Institut Chemische Technologie, 76327 Pfinztal, Germany; and
[2]Bruker BioSpin GmbH, Am Silberstreifen, 76287 Rheinstetten, Germany

Introduction

In food process engineering, the handling, pumping, extrusion, or mixing of highly concentrated disperse systems is of importance for initial, intermediate, or final products. Examples are suspensions (beer mashes, chocolate, dough), foams (protein-, carbohydrate-based), emulsions, porous solids (baked products), and dry/wet bulk solids (malt, sugar). Although plenty of information concerning the rheology of multiphase system is available, the modeling of the flow behavior, structure of the produced system, and its stability cannot be considered as totally completed. In spite of its great importance, the determination of viscosities of disperse systems is difficult in principle [1,2]. Defined velocity profiles in rheometers (so-called viscometric flows), the homogeneity of the sample during the experiment, and applicability of continuous mechanics are usually prerequisites for rheometric studies. In disperse multiphase systems, demixing (phase separation: sedimentation, creaming, wall layers), scale effects [3], preparation, time effects (crushing, de-/agglomeration), tearing apart (fat, ointments), and wall slip cause problems when studying the flow behavior and determining flow functions of disperse systems with conventional rheometric methods.

Materials with volume fractions of the disperse phase higher than 5 vol.% are usually opaque [4]. NMR offers the possibility to perform measurements non-invasively, non-destructively, and highly selective (*in situ*, *online*) in order to study the structure, structural changes, or inner transport processes (without preparations) in flowing materials. The objective of this contribution is to demonstrate the potential of various NMR techniques in monitoring flow processes and the structure of disperse systems. The relevance of NMR for engineering is based on the following possibilities and applications of non-invasive and non-destructive spectroscopic/tomographic sequences with possible temporal, spatial, and chemical resolution:

- The *composition* and *inner structure* of static and dynamic systems and processes are accessible for quantitative characterization.
- *Process and quality control* can be realized without preparing or disturbing the corresponding product or process.
- *Micromodels* and *physically established, phenomenological constitutive laws* may be derived from the microscopic data. These models are required for the professional design of industrial processing units and products. The corresponding material functions can be derived by fitting the experimental data.
- By means of the microscopic non-destructive and non-invasive access, the development and *validation of models* concerning the flow behavior, boundary/initial conditions, and the critical *verification of predictions* for technical solutions is possible by comparison with NMR results.

The flow behavior is specially important in process engineering: (i) it can be used for process and quality control, (ii) it is required for the design of production plants, and (iii) it has an obvious impact on the structure of materials (sensory behavior). According to the definition used for the scope of this contribution, Rheo-NMR encloses all NMR applications dealing with the combination of flow behavior, flow induced structural changes, and NMR data. Thus, it is possible:

(a) to realize *flow experiments* [5,6] (*viscometric* flows: tube flow, Couette flow, plane shear flow, plate/plate, cone/plate) in NMR devices in order to determine the corresponding velocity profiles. By means of additional information (tube flow: pressure drop, Couette: tormentum) assuming constitutive laws it is possible to derive the corresponding *viscosity*- and *wall slip functions*.
(b) to study and quantify *flow induced structural changes* by means of appropriate NMR experiments [7–9].
(c) to derive *correlations* between microscopic NMR data and macroscopic rheological material parameters. These correlations could be very helpful for an effective process and quality control by an online determination of practice relevant quantities (viscosity, molar mass) [1,10] in order to control the assumed

Graham A. Webb (ed.), Modern Magnetic Resonance, 1819–1824.
© 2008 *Springer.*

or required process conditions and increase the efficiency of production units.

(d) to realize experimental conditions (concentration/velocity fields) which simulate the *practice relevant test conditions* in apparatus or processes in food technology. The corresponding materials or phenomena evolve differently without mixing. Therefore, it is impossible to perform these experiments using conventional NMR techniques.

NMR applications analyzing the impact of structure of solid systems on the convective/diffusive flow processes [1] are not taken into consideration.

Applications of Rheo-NMR

Flow of Disperse Multiphase/Complex Materials

In contrast to most other techniques even the flow inside of complex structures and disperse, opaque materials can be analyzed. For a homogeneous sample its velocity profile can be obtained. For specific samples with several phases the velocity profiles of the single components can be determined [11–14]. Flow experiments provide model-free velocity data, especially phase encoding methods, in arbitrary directions. Flow experiments with disperse multiphase materials or of other complex liquid systems [15,16] in viscometric flows [plate/plate, cone/plate, tube flow, extruder (capillary rheometer), Couette] offer the possibility to characterize (quantitatively) the flow behavior or the mixing/demixing behavior (with the help of the evolution of the volume concentrations or the corresponding dispersion coefficient [11]) of the present phases in the tested material. The application of MRI to determine material functions, i.e. flow- and wall slip- functions, was proposed and described in Refs. [17–19]. For this application, NMR flow experiments are combined with further measurements like the differential pressure (tube flow, capillary rheometry) or the torque (Couette flow). Advantages of flow experiments are the possibility to detect possible separation processes (homogeneity with regard to the moisture, hollow spaces or cracks), to control the supposed flow pattern, e.g. shear flow [6,20], or the degree of filling in the test device [21]. For heterogeneous multiphase systems it does not seem to make sense to realize viscometric flows in rheometers where the homogeneity of the material is assumed for the evaluation without any control [21]. Flow- and wall slip functions of homogeneous and quasi-homogeneous materials, i.e. one-phase fluids in good approximation can be determined in one single experiment [14]. Flow experiments have already been applied to study the flow in several set ups. Not only suspensions or pastes have been studied, but also water and solutions of sugars, polysaccharides and hydrocolloids [22–28], tomato juice [29], butter and margarine [30], egg-white and polymer solutions [31–33], suspensions [26,34–37], fibrous suspensions [38,39], blood [40], and wet bulk solids [41,42].

Tube Flow

Assuming appropriate material laws the corresponding material functions can be derived from the velocity profiles in a tube flow determined with MRI. The flow of polymer solutions, particle dispersions, and aqueous polysaccharide solutions was already analyzed with MRI velocimetry [13,14,26,36,43–47] in order to characterize the flow behavior and detect apparent wall slip for these materials in Poiseuille flow. MRI was used to study the flow of PSPB-water pastes (polystyrene–polybutadiene copolymer) in steady state flows [17]. The velocity profiles and volume concentrations of free water and the solid matrix of flowing pastes could be mutually independently determined via MRI flow experiments. This supplies direct proof of the relative displacement of free water in flowing pastes. It was possible to measure the wall slip of the two phases and, therefore, to differentiate between the shear and slip shares of the total volumetric flow. The flow in tubes with various geometric structures, e.g. a tube with constant circular cross-section [48], tubes with contraction and expansion [48], a tube with one or more cylinders [11], or with a U-bend [14] were studied. The measurement of the time-averaged velocity offers, in a technological view, the possibility to study the influence of material characteristics (ratio of the fluid and solid, type and concentration of additives, general formulation) and process parameter (pretreatment of the sample, process and store temperature, convey distance) on the flow behavior and structure of dispersions.

Couette

Ultrafast MRI techniques were presented to visualize steady and unsteady Couette flows of water [49–51]. In several papers [29,52–55], the velocity profiles of the Couette flow for homogeneous Newtonian and Non-Newtonian fluids were visualized by MRI and, thus, shear rate distributions could be derived. The aim was to evaluate standard rheometric methods for one-phase fluids by means of MRI. Like in the case of the tube flow, viscosity functions can be derived from the velocity profiles determined with MRI [21]. The shear induced diffusion and structure in concentrated density matched suspensions undergoing Couette flow was monitored [41,42]. MRI reveals that PMMA suspensions demix during the shear experiment. The fluid fraction increases at the rotating inner cylinder and decreases monotonously from the inner shaft to the outer cylinder. The flow behavior of PTFE pastes and other highly viscous fluids was analyzed in a new Couette shear device, developed especially for pastes [21]. The results prove that Couette shear experiments are generally not suitable for all pastes or concentrated suspensions. It cannot be guaranteed, without additional experiments, that the assumed constitutive law and corresponding viscosity functions can be transferred to model the velocity profile in any 3D problem. Flow experiments in extruders or other test devices are described in [1,56,57].

Analysis of Flow Induced Structural Changes

Nakatani *et al*. proposed the so-called Rheo-NMR to record the microscopic structural changes (e.g. shear-induced phase transitions) in polymer melts and solutions as a function of the shear rate, time (energy input), and temperature both in transient and steady state flow [7]. Conventional rheometer designs (e.g. cone/plate, plate/plate, Couette) are integrated into standard NMR probes. The use of isotopic labeling enables one to differentiate the "mechanical" behavior of chain ends from internal segments of the sheared molecules. Applications to polymeric systems and food systems in shear and extensional flow are given in Refs. [8,9,15,54,58–63]. Carrageenan sol and gels can be distinguished by means of flow experiments [16]. If a flowing sol is cooled down slowly beneath the sol–gel temperature, which holds for materials at rest, only partial gelation can be observed. The sol state (65°C), the gel state (30°C), and the shear induced sol state (30°C) exhibit clearly distinguishable spectra. (i) Polymer sites with reduced segmental mobility (junction zones) caused by intermolecular interactions and (ii) molecules or molecule groups, which are not or less influenced by these interactions and thus reveal higher T_2, can be observed by means of T_2 distributions. Shearing causes a reduction of junction zones [see (i)]. Shear flow and extension flow induced structural changes were studied in dough and its components [65].

Correlation Between Flow Behavior and T_1- or T_2-Relaxation Times

For pure fluids (e.g. water, glycerine, ethyl alcohol, acetic acid), which are rheologically simple Newtonian fluids, theoretically and experimentally a correlation between the NMR relaxation times T_1 and T_2, respectively, and the dynamic viscosity η was found, which is valid independently of temperature and pressure [68,69]. This correlation also holds for aqueous solutions like aqueous sugar solutions, fruit juices, beer, and wine [70]. Further studies on silicone oil/glass sphere suspensions and beer mashes demonstrated that the T_2–η correlation which was originally exclusively derived for Newtonian fluids can also be applied to suspensions [2,71]. In contrast to aqueous sugar solutions, there is not a simple potential dependence in suspensions between the viscosity and the corresponding relaxation times. The correlation between characteristic viscosities such as the zero-shear rate viscosity η_0 or the viscosity at high shear rates κ η_∞ can, nevertheless, be used to determine viscosities by means of the corresponding T_1 or T_2. In other words, the viscosities η are a function of the relaxation times T_1 and T_2: $\eta = \eta(T_1, T_2)$. For the modified four-parameter Carreau model holds [72]

$$\eta(\kappa) = \frac{\eta_0 - \eta_\infty}{[1 + (\kappa/\kappa_1)^a]^{0.5}} + \eta_\infty \qquad (1)$$

κ:shear rate, η_0: zero-shear rate viscosity, η_∞: viscosity at high shear rates, a, κ_1: parameters.

Only finely ground malt can be tested in conventional rheometers, as due to scale effects [3] with respect to the maximum particle size suspensions containing particles with diameters in the order of the characteristic dimensions of the rheometer do not fulfill the prerequisites of continuum mechanics. Continuum mechanics is, however, one of the main prerequisites of conventional rheometry. For silicone oils with different molecular weights, it is possible to determine the viscosity and molecular mass by using a correlation with the corresponding T_2 [10]. Similar correlations between T_1 or T_2 and η have been found for *cis*-polyisoprene solutions [73], solutions and suspensions of carbohydrates and sugars of corn [74], milk during acidification with yoghurt culture with and without stabilizers (storage and loss moduli G' and G'' [75]), paper pulps [76], industrial sauces containing starch with different cooking time (G', G'' [77]), model cheese samples (compression and stress relaxation measurements [78]), emulsions (phase diagrams, shear flow [79]), and chocolate masses (microscopy, shear flow [80]). Besides scale effects, homogeneity is another prerequisite for simple rheological constitutive laws. This is a crucial aspect in process engineering, as many products are multiphase systems. Phenomena causing heterogeneity (phase separation: sedimentation, creaming) and tearing apart (fats, ointments) are usually difficult to detect and quantify in conventional rheometry. Flow experiments combined with spatially resolved spectroscopy or possibly MRI will allow to observe heterogeneity causing flow induced effects and wall slip. Appropriate spectroscopic methods enable to characterize flow induced time effects caused by the energy input or due to special preparation techniques like de-/agglomeration or crushing [66].

Due to the great importance of the viscosity, especially for process and quality control, viscometric methods were developed which allow an online determination of the viscosity [81]. Besides the possibility of combining velocity or, furthermore, concentration profiles with the corresponding stress distribution (assuming constitutive laws) [see (a)] flow- and wall slip-functions can be derived by fitting the velocity frequency distributions [35,82]: (i) direct 2D imaging of the tube cross-section and subsequent determination of the velocity frequency distribution, (ii) radial velocity profiles from 1D projections and subsequent determination of the velocity frequency distribution, and (iii) velocity spectra [38]. Principally, it is possible to derive the flow functions (assuming constitutive laws) and information concerning the pore radius distribution from the velocity frequency distribution and an additional single-point measurement of the shear stress [38].

Realization of Practice Simulating Test Conditions

Rheo-NMR probes enable one, as shown above, to monitor flow induced structural changes in complex fluids undergoing well-defined flow types and mechanical treatments (stress, deformation, deformation velocity tensor and derivatives). They could, furthermore, be used to guarantee homogeneity as mixing devices with known shear rate distributions during arbitrary NMR experiments. Mixtures of substances are (i) miscible on molecular level or (ii) only miscible on a non-molecular level [83]. In many industrial disperse mixtures, constituents are present which dissolve partially during the processing. Furthermore, the system may tend to phase separation. Thus, the mixture is not stabile and separates, if the mixing process has been stopped. Examples for this combination of mixture (i) and (ii) behavior (dissolving and sedimentation/ascending) are beer mashes or starch/water mixtures. In order to develop reliable online process and quality controls and analyze efficiently the evolution of possible concentration dependent reactions in food systems [protein denaturation, starch plasticization or gelling, degradation of polysaccharides (beer: β-glucan)] at practice similar conditions, homogenize composition patterns have to be realized during processing and simultaneous NMR experiments.

The corresponding materials or phenomena evolve differently without mixing. As a consequence the corresponding processes achieve a minor efficiency and quality. The same holds for ceramic masses which require sufficient mechanical energy input by shearing or kneading [66] or ultra-sonification [67] in order to obtain and maintain structural homogeneity for time periods sufficient for a reliable handling during processing. Comparable materials are problematic to study by non-localized NMR spectroscopy without continuous mixing. Thus Rheo-NMR probes enable one to characterize online reacting, eventually phase separating disperse systems, to identify occurring processes, and to derive relevant kinetic parameters.

NMR studies of reacting or non-reacting disperse food systems can be performed in adapted Rheo-NMR devices. Besides the thermally or enzymically induced reactions/structural changes the corresponding velocity profiles have been derived in beer mashes, starch solutions, and water as reference. Thus, using triggered NMR sequences it is possible to detect sediments (possibly causing fouling, spoilage, undesired reactions due to overheating at the vessel walls) and, at the same time, evaluate the mixing potential of stirring vessel and stirrers in combination with the applied process conditions for a given material [84].

Relevance of NMR for Process Engineering

If a material in a specific production process (extrusion, pumping, or mixing) has certain advantages and disadavantages, it naturally to enhance the advantages and simultaneously reduce the disadvantages by a simple treatment. Therefore, measuring techniques (empirical plus advanced, if necessary) are required to identify the relevant microprocesses and microstructures in the flowing material. If the microprocesses are known, the material can be modified by an appropriate adaption process (additives, coating, ultrasonification [67], kneading [66]), to meet the requirements of the customers. To summarize the findings, NMR enables one to study many food products and processes in food processing which are often inaccessible by other measuring techniques. The flow behavior is especially important in process engineering: (i) it can be used for process and quality control, (ii) it is required for the design of production plants, and (iii) it has an obvious impact on the structure of foods (sensory behavior). Reviews on spectroscopic/tomographic methods applied in process engineering are given in Refs. [1,85–87]. The advantages of NMR applications in engineering in order to study combined flow- and NMR-phenomena are

- None or only minor preparation (dilution for optical techniques) is necessary.
- Tracers do not have to be added in general. Detectable spins themselves can act as tracers.
- NMR measurements are non-destructive and non-invasive.
- Processes can be studied completely by means of NMR using one single sample, thus reducing systematic measuring errors resulting from compositional/experimental variations.
- Using other techniques without spatial resolution, effects are averaged, e.g. in systems tending to phase separating, and might be misinterpreted or added possibly to measuring errors.
- An online determination of practice relevant quantities (viscosity, water-holding capacity, denaturation fraction) is possible in order to control the assumed or required process conditions (temperature, concentration, velocity distributions).
- Demixing can be prevented (ultra-sonification or Rheo-NMR probe).

References

1. Götz J. Applications of NMR to Food and Model Systems in Process Engineering. Habilitation, http://tumb1.biblio.tu-muenchen.de/publ/diss/ww/2004/goetz.html, TUM.
2. Götz J, Schneider J, Först P, Weisser H. J. Am. Soc. Brewing Chem. 2003;61:37.
3. Becker E, Bürger W. Kontinuumsmechanik. Teubner: Stuttgart, 1975.
4. Roco G. Particulate Two-Phase Flow. Butterworth Heinemann: Boston, 1992.
5. Pope JM, Yao S. Concepts Magn. Reson. 1993;5:281.
6. Götz J, Müller D, Buggisch H, Tasche-Lara C. Chem. Eng. Process. 1994;33:385.
7. Nakatani AI, Poliks MD, Samulski ET. Macromolecules. 1990;23:2686.
8. Callaghan PT. Rep. Prog. Phys. 1999;62:599.
9. Callaghan PT, Fischer E. Bruker Rep. 2001;149:34.
10. Götz J, Altmann S, Weisser H. In: Proc. 1st Eur. Silicon Days, München, 2001.
11. Götz J, Zick K, Heinen C, König T. Chem. Eng. Process. 2002;41:611.
12. Laukamper-Ostendorf S, Lemke HD, Blümler P, Blümich B. J. Membrane Sci. 1998;138:287.
13. Götz J, Zick K. Chem. Eng. Technol. 2003;26:59.
14. Götz J, Zick K, Kreibich W. Chem. Eng. Process. 2003;42:515.
15. Callaghan PT, Gil AM. Rheol. Acta. 1999;38:528.
16. Callaghan PT, Gil AM. SpeciRSC 2001;262:29.
17. Götz J. Möglichkeiten der Kernspintomographie zur Diagnose von Strömungsvorgängen und Strukturänderungen in Pasten. Uni. Diss., Karlsruhe, 1994.
18. Gibbs SJ, Haycock DE, Hall LD. J. Magn. Reson. 1997;125:43.
19. Cheung MK, Powell RL, McCarthy MJ. AIChE J. 1997;43:10.
20. Kuethe DO, Herfkens RJ. Magn. Reson. Med. 1989;10:57.
21. Götz J, Kreibich W, Peciar M, Buggisch H. J. Non-Newton Fluid. 2001;98:117.
22. McCarthy KL, Kauten RJ, McCarthy MJ, Steffe JF. J. Food Eng. 1992;16:109.
23. McCarthy MJ, Kauten RJ, Agemura CK. Trends Food Sci. Technol. 1992;58:215.
24. McCarthy MJ. Magnetic Resonance Imaging in Foods. Chapman & Hall: New York, 1994.
25. McCarthy KL, Kerr WL. J. Food Eng. 1998;37:11.
26. Gibbs SJ, Xing D, Ablett S, Evans ID, Frith W, Haycock DE, Carpenter TA, Hall LD. J. Rheol. 1994;3:1757.
27. Manz B, Seymour JD, Callaghan PT. J. Magn. Reson. 1997;125:153.
28. Yeow YL, Taylor JW. J. Rheol. 2002;46:351.
29. Britton MM, Callaghan PT. Magn. Res. Chem. 1997;35:37.
30. Britton MM, Callaghan PT. J. Texture Stud. 2000;31:245.
31. Rofe CF, Lambert RK, Callaghan PT. J. Rheol. 1994(38);4:875.
32. Rofe CJ, DeVargas L, Perez-Gonzalez J, Lambert RK, Callaghan PT. J. Rheol. 1996;40:1115.
33. Xia Y, Callaghan PT. Macromolecules. 1991;24:4777.
34. Ding J, Lyczkowski RW, Sha WT, Altobelli SA, Fukushima E. Powder Technol. 1993;77:301.
35. Gibbs SJ, Haycock DE, Frith WJ, Ablett S, Hall LD. J. Magn. Reson. 1997;125:43.
36. Gibbs SJ, James KL, Hall LD, Haycock DE, Frith W, Ablett S. J. Rheol. 1996;40:425.
37. Han M, Kim C, Kim M, Lee S. J. Rheol. 1999;43:1157.
38. Seymour JD, Maneval JE, McCarthy KL, Powell RL, McCarthy MJ. J. Texture Stud. 1995;26:89.
39. Seymour JD, Maneval LE, McCarthy KL, McCarthy MJ, Powell RL. Phys. Fluids A. 1993;5:3010.
40. Han S, Marseille O, Chwatinski C, Blümich B. J. Magn. Reson. 2001;152:87.
41. Abbott J, Tetlow N, Graham AL, Altobelli SA, Fukushima E, Mondy LA, Stevens TS. J. Rheol. 1991;35:773.
42. Graham AL, Altobelli SA, Fukushima E, Mondy LA, Stephens TS. J. Rheol. 1991;35:191.
43. Altobelli SA, Fukushima E, Mondy LA. J. Rheol. 1991;41:1105.
44. Altobelli SA, Givler RC, Fukushima E. J. Rheol. 1991;35:721.
45. Sinton SW, Chow AW. J. Rheol. 1991;35:735.
46. Arola D, Powell RL, Barrall GA, McCarthy MJ. J. Rheol. 1999;43:9.
47. Corbett AM, Phillips RJ, Kauten RJ, McCarthy KL. J. Rheol. 1995;35:907.
48. Arola D, Powell RL, McCarthy MJ, Li T-Q, Oedberg L. AIChE. 1998;44:2597.
49. Kose K, Satoh K, Inouye T, Yasuoka H. J. Phys. Soc. Jpn. 1985;54:81.
50. Kose K. Phys. Rev. Lett. 1994;72:1467.
51. Kose K. Phys. Fluids. 1994;6:S4.
52. Chingas GC, Frydman L, Barrall GA, Harwood JS. In: B Blümich, W Kuhn (Eds). Magnetic Resonance Microscopy. VCH: Weinheim, 1992, p 373.
53. Mair RW, Callaghan PT. J. Rheol. 1997;41:901.
54. Britton MM, Callaghan PT, Kilfoil ML, Mair RW, Owens KM. Appl. Magn. Reson. 1998;15:287.
55. Britton MM, Mair RW, Lambert RK, Callaghan PT. J. Rheol. 1999;43:897.
56. Lee Y, McCarthy MJ, McCarthy KL. J. Food Eng. 2001;50:167.
57. Cheung MK, Powell RL, McCarthy MJ. AIChE J. 1997;43:10.
58. Grabowski DA, Schmidt C. Macromolecules. 1994;27:2632.
59. Lukaschek M, Grabowski DA, Schmidt C. Langmuir. 1995;11:3590.
60. Fischer E, Callaghan PT, Heatley F, Scott JE. J. Mol. Struct. 2002;602:303.
61. Orian L, Feio G, Veron A, Farinha Martins A, Polimeno A. Mol. Crystallogr. Liquid Crystallogr. 2003;394:63.
62. Siebert H, Grabowski DA, Schmidt C. Rheol. Acta. 1997;36:618.
63. Badiger MV, Rajamohanan PR, Suryavanshi PM, Ganapathy S, Mashelkar RA. Macromolecules. 2002;35:126.
64. Gil AM, Alberti E, Santos D. SpeciRSC 2001;262:13.
65. Götz J, Zimehl R. J. Colloids Polym. 2002;280:389.
66. Götz J, Garrecht H, Geißler A, Peciar M. DE10024762.8, Patent-application, 2000.
67. Bloembergen N, Purcell EM, Pound RV. Nature. 1947;160:475.
68. Bloembergen N, Purcell EM, Pound RV. Phys. Rev. 1948;73:679.
69. Harz H-P. Untersuchungen zum Gefrierverhalten flüssiger Lebensmittel. Uni. Diss., Karlsruhe, 1987.
70. Götz J, Schneider J, Weisser H. CIT. 2000;72:1074.

71. Carreau PJ, Lavoie P-A, Bagassi MH. Macromol. Symp. 1996;108:111.
72. Charlesby A, Bridges BJ. Eur. Polym. J. 1981;17:645.
73. Mora-Gutierrez A, Baianu IC. J. Agric. Food Chem. 1989;37:796.
74. Barfod N. In: Proc. Conference, Rebild, Denmark, 1991.
75. Draheim EJ, Ragauskas AJ. J. Wood Chem. Technol. 1997;17:287.
76. Thebaudin J-Y, Lefebre A-C, Davenel A. Sci. Aliment. 1998;18:283.
77. Budiman M, Stroshine RI, Campanella OH. J. Texture. Stud. 2000;31:477.
78. Yaghmur A, Aserin A, Antalek B, Garti N. Langmuir. 2003;19:1063.
79. Götz J, Balzer H, Hinrichs R, Weisser H. Appl. Rheol. Characterisation of the Structure and the Flow Behaviour of Suspensions Used as Model Chocolate Systems by Means of NMR and Rheology. Appl. Rheol. 2005;15(2):98–111.
80. Cullen PJ, Duffy AP, O'Donnell CP, O'Callaghan DJ. Trends Food Sci. Technol. 2000;11:451.
81. Heinen C. MRI-Untersuchungen zur Strömung newtonscher/nicht-newtonscher Fluide in porösen Strukturen. Uni. Diss., Karlsruhe, 2004.
82. Löffler F, Raasch J. Grundlagen der Mechanischen Verfahrenstechnik. Vieweg: Wiesbaden, 1991.
83. Götz J, Zick K, Lehmann V, Groß D, Peciar M. Analysis of the Mixing and Flow Behaviour of Beer Mashes in a Stirring Vessel by Means of NMR Flow Experiments. To be submitted.
84. Williams RA, Beck MS (Eds). Process-Tomography. Butterworth Heinemann: Oxford, 1995.
85. Nordon A, McGill CA, Littlejohn D. Analyst. Camb. 2001;126:260.
86. Smith EG, Kohli R, Martin PA, Instone T, Roberts N, Edwards RHT. In: DM Scott, RA Williams (Eds). Frontiers in Industrial Process Tomography. Engineering Foundation: New York, 1995, p 223.

Temperature Measurements by Magnetic Resonance

Kevin P. Nott and Laurance D. Hall
University of Cambridge School of Clinical Medicine, Robinson Way, Cambridge, CB2 2PZ, UK

Introduction

Most of the Magnetic Resonance (MR) parameters of water are temperature dependent, and each has their own advantages and disadvantages as the basis for specific applications in terms of the interplay between spatial- and temporal-resolution, as well as the accuracy of the temperatures measured. Although by far the most widely used application for *MR thermometry* is for interventional thermal therapy procedures on muscles in the human body [1,2] such measurements are increasingly being applied to thermal processing of foods. Although temperature is an important variable for such studies, its role is often complicated by interrelated heat- and mass-transfer processes, as well as the structural-changes that accompany cooking; this poses an array of problems owing to the wide variety of foodstuffs. Nevertheless, the unique power of Magnetic Resonance Imaging (MRI) is not only that it can be used to measure temperature distributions non-invasively in three dimensions, but also other relevant parameters including thermal-convection, moisture-loss, and -redistribution, starch-gelatinization, protein-denaturation, and other phase transitions which can occur either during, or after, the heating process.

Although, much research has involved Computational Fluid Dynamics (CFD) modeling of the often interrelated heat- and mass-transfer processes associated with thermal processing [3], as well as the moving boundaries associated with structural- and phase-changes [4], the limited processing power of computers often requires simplifying assumptions to decrease otherwise excessive calculation times. Therefore, there is a need for measurement techniques that can acquire data for processes that are too complicated to model, as well as to validate the models themselves. This article will describe the MR parameters and protocols that have been used to rapidly map temperature in a variety of model and real foodstuffs (Table 1).

T_1 and T_2 Relaxation Times

Although both the spin-lattice (T_1) and spin-spin (T_2) relaxation times of the protons of water are dependent on water mobility and, as a consequence, are sensitive to temperature, quantitation of both parameters using spin echo imaging can be time consuming. Also T_2 relaxation is very sensitive to structure hence has not been used to measure temperature of foods; however, it has been used on solid polymers which are homogeneous and have very short relaxation times [5]. In contrast, T_1-weighted spin echo images are acquired more rapidly by shortening the time allowed for recovery of the magnetization between the initial 180° pulse and the next phase encoding step, and then calibrating the resultant images against temperature. Hulbert *et al.* quantified the temperature sensitivity of T_1, then compared T_1-weighted images acquired with different repetition times (acquired in 24 and 33 sec) to map the temperature distribution in a pre-cooked carrot [6]. T_1-weighted images (acquired in 12 sec) were subsequently used to map temperature across a carrot piece heated in a stream of hot water; a trial and error modeling procedure was used to calculate the fluid-to-particle convective heat transfer coefficient [7].

Ruan *et al.* used a Turbo FLASH gradient echo sequence with an inversion recovery preparation [8] to acquire in 25 sec a set of seven images used to calculate a T_1 map, which in turn was calibrated to temperature [9]; the MRI results compared favorably with numerical simulations of heat transfer during cooling of cheese [10]. Whereas the acquisition time is similar to that of a T_1-weighted spin echo image, it is faster than acquiring a T_1 image from a set of spin echo images, which can take 10–20 min. In addition, the advantage of acquiring more than one image in order to calculate T_1 is thatthe system error is reduced and therefore the accuracy is believed to be higher. Ruan *et al.* used similar methodology to map temperature during an ohmic heating process [11]; the T_1 relaxation data (acquired in 14 sec) was subsequently fitted to a bi-exponential model, the longer component of which was used to map temperature across potato, beef, and carrot particles in a starch carrier medium.

Diffusion Coefficient

The effect of molecular diffusion in the presence of a magnetic field gradient on MR signals was first described in some of the classical NMR papers [12,13]. Diffusion causes an attenuation of the amplitude of the MR signal due to a loss of phase coherence between precessing spins that move randomly along the direction of a magnetic field gradient; the extent of the amplitude attenuation depends

Graham A. Webb (ed.), Modern Magnetic Resonance, 1825–1830.
© 2008 *Springer.*

Table 1: Sensitivity and accuracy of the MRI parameters of water used to measure temperature in real and model food systems (Taken from 2D slice images unless otherwise stated)

Sample	Measurement	Temperature range (°C)	Spatial-resolution	Temporal-resolution	Sensitivity	Error	Reference
Model food gel	Diffusion*	18–42	1.5 mm^2	30 s	13%/°C	<1.26°C	[15]
Potato	Diffusion*	20–50	0.75 mm^2	10 s	13.5%/°C	0.5 °C	[16]
Carrot	T_1	19–80	Bulk	—	3 %/°C	—	[6]
Potato	$T_1^{\dagger}$	22–95	—	14 s	1.9%/°C	—	[11]
Beef					1.2%/°C		
Carrot					1.0%/°C		
Water	Chemical shift	0–100	Bulk	—	0.01 ppm/°C	—	[17]
1% NaCl solution	Chemical shift	35–51	0.36 mm^2	15 s	0.0098 ppm/°C	1 °C	[19]
Agar gel					0.0103 ppm/°C		
Boiled egg white					0.0091 ppm/°C		
Chicken muscle					0.0114 ppm/°C		
Gel	Chemical shift	20–60	0.88 mm^2	8 s	0.0098 ppm/°C	<5°C	[20]
Raw potato					0.0104 ppm/°C		
Cooked potato					0.0107 ppm/°C		
0.01% NaCl solution	Chemical shift	—	0.88 mm^2	0.64 s	0.0096 ppm/°C	2 °C	(Ruan *et al.*, 2003)
0.3% NaCl solution					0.0102 ppm/°C	2 °C	
Gel + 1.5% NaCl					0.0098 ppm/°C	1 °C	

*Pseudo self-diffusion coefficient.
†Long component of bi-exponential fit.

on the values of the diffusion coefficient and the gradient. The diffusion coefficient can be measured by varying the gradient strengths during a Pulsed Gradient Spin Echo (PGSE) experiment [14]. Molecular transport in liquids is governed by the temperature dependence of their viscosity. Using the Stokes–Einstein relationship between viscosity and the translational self-diffusion coefficient, the temperature dependence can be described by the relation

$$D \propto \exp(-E_a/kT) \tag{1}$$

Sun *et al.* acquired an "effective" self-diffusion coefficient in 30 sec to produce 2D temperature maps of a model food gel [15]; subsequent experiments on potato used a half Fourier transform technique to shorten the acquisition time to 10 sec[16].

Chemical Shift

Background

Theory

Chemical shift refers to the variations in resonance frequency caused by different chemical environments; for example, that between protons of water (–OH) and fat (–CH). It is known that the chemical shift of water protons has a linear dependence with temperature from 0° to 100°C, with a sensitivity of 0.01 ppm/°C [17]. The major advantage of chemical shift is that it is the only parameter which has the potential to be independent of changes which accompany cooking, since its temperature sensitivity is based on the changing fraction and nature of hydrogen bonds with vicinal water molecules, rather than the mobility of water in the food matrix. In contrast, since the T_1, T_2, and diffusion coefficient methods are based on the magnitude of the NMR signal they are dependent on moisture content, which frequently changes during thermal processing.

Chemical shift resolved imaging has been used to separate regions with different temperatures [18]; however, it is time consuming to acquire information for a range of temperatures. Instead, phase mapping is employed which is sensitive to changes in the local magnetic field (B_{loc}) and, as a consequence, chemical shift to which it is related by the equation,

$$B_{\mathrm{loc}} = (1 - \sigma_{\mathrm{tot}})B_0 \tag{2}$$

Since the phase image is also sensitive to magnetic field inhomogeneity, changes of phase have to be measured relative to a reference phase image at a known temperature.

Hence, the temperature dependence of phase (ϕ) in a gradient echo sequence is related to both the field strength and the echo time by the equation,

$$\Delta\phi = C\gamma T_{\mathrm{E}} B_0 \Delta T \qquad (3)$$

where $\Delta\phi$ is the phase shift over a corresponding temperature change ΔT; γ is the magnetogyric ratio of the hydrogen nucleus; T_{E} is the echo time; B_0 is the macroscopic magnetic induction; and C is the proportionality constant. Figure 1 is a schematic diagram which shows the procedure for processing of the temperature maps (in 2D, and 3D volume rendered), in this example induced by microwave heating a jar containing a starch sauce with mushroom particulates.

Temporal changes in the magnetic field need to be accounted for by measuring the phase-changes in a model system at a known, preferably constant, temperature within the same field-of-view as the heated sample. Since the temperature measurement depends on the value of B_{loc}, the accuracy of the temperature measurement will also be affected by the magnetic field homogeneity, particularly at higher temperatures.

In Practice

It is known that for water in a range of foodstuffs, the temperature sensitivity of the phase of its MR signal is close to that of pure water [19,20]. However, although it is possible that chemical shift is insensitive to structural-changes, the phase images will be sensitive to changes of magnetic susceptibility, i.e. the effect that the material has on the magnetic field. Most food materials are diamagnetic; however, large differences in susceptibility, such as at an air/water interface, lead to distortions in the magnetic field that cannot be corrected for. This is particularly problematic for foods which contain air bubbles that change location between acquisition of the reference- and heated-images.

The chemical shift of fat does not change significantly with temperature; hence, unless its contribution is removed from the measured MRI signal, it will introduce error into temperatures measured by phase-changes. Fortuitously, the magnetic susceptibility changes in fat are similar to those of water; hence the phase difference between the water and fat contributions remains constant, leaving the phase-changes due to the temperature dependent chemical shift of water as the unique dependency [21–23]. Unfortunately, since the signal-to-noise and sensitivity of the fat signal is poor, its use as an internal reference is frequently impossible and in most cases it is only feasible to provide a bulk temperature measurement by that method [24].

As with all MRI methods, the accuracy of temperature measurement is a function of water content, and thus is best for water-rich foods; however, the accuracy may be impaired by volume susceptibility changes caused by thermal expansion, and motion associated with liquid flow or convection. Bows *et al*. showed that it was feasible to map temperature across mushroom and meat particulates in a starch-based sauce [25,26], the high viscosity of which ensured there were no visible convection or particulate movement during heating.

Applications

Convective Heating

Kantt *et al*. used phase mapping to measure the temperature distribution across potato particles during an aseptic process [27]; their approach was to syphon off the flow of a starch carrier containing potatoes pieces (1.1–6.9 cm^3) into the MR scanner, then stop the flow for imaging (1.2 mm^2 resolution with a 3mm slice). The MRI temperature maps were used in combination with ANSYS (Canonsburg, PA, USA.) finite element modeling software to calculate the fluid-to-particle convective heat transfer coefficient during aseptic processing of food particulates [7,27]. Since flow can produce artifacts in an MRI image unless it is coherent (or non-turbulent) the fluid has to be either stopped during, or siphoned off for, acquisition.

Sun *et al*. developed a thermostatted glass tube rheometer (essentially a simple heat exchanger) which was optimized for use in an MRI scanner [28]; it allowed flow- and temperature-equilibria to be established in the complete system before the tube was inserted in the scanner without disruption of the fluid flow. Since the fluid flow was coherent, temperature maps could be calculated using the isothermal flowing fluid for the reference phase image. Thus, the phase of the MRI signal was used for measurement of both temperature and velocity through the tube [29], and both those compared well with CFD modeling by FIDAP (Fluent Inc., East Hartford, USA). Such combined measurements are industrially important since determination of residence time, as well as temperature, is important for optimizing thermal processing of fluids flowing through heat exchangers.

Microwave Heating

Phase mapping has also been used to capture with scan times of less than 1 min the 3D heating patterns induced by microwave heating before their dissipation through thermal conduction [30]. Most domestic and industrial food applications involve microwave cavities made of metal which cannot be studied inside a MRI magnet. As a consequence, it is necessary to place the sample in the magnet for acquisition of a “constant temperature” reference phase image, remove it for heating, and then return it to

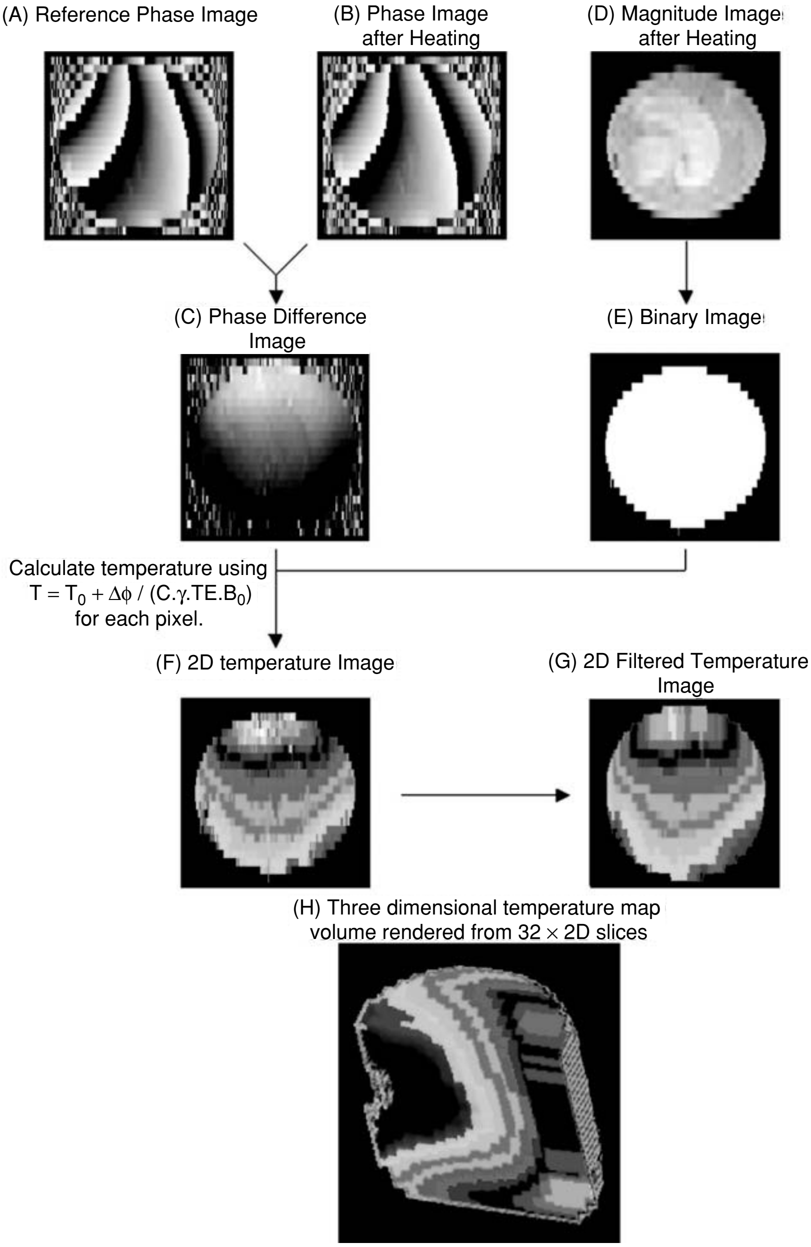
(A) Reference Phase Image
(B) Phase Image after Heating
(D) Magnitude Image after Heating
(C) Phase Difference Image
(E) Binary Image
Calculate temperature using T = T0 + Δϕ / (C.γ.TE.B0) for each pixel.
(F) 2D temperature Image
(G) 2D Filtered Temperature Image
(H) Three dimensional temperature map volume rendered from 32 × 2D slices

Fig. 1. Schematic diagram showing the calculation and processing of the temperature maps from the raw phase data. The "wrapping" of the phase in the reference image of the sample measured at a known temperature (A) represents the magnetic field inhomogeneity across the sample; this is subtracted from the phase of the co-registered image (B) of the heated sample to give the temperature dependent phase change (C). The spatially co-registered magnitude image (D) is thresholded to provide a binary image (E) used "cut out" the phase data from the phase noise, and the temperature for each pixel (T) calculated using the known linear temperature sensitivity of phase ($1/(\mathrm{C}.\gamma.T\mathrm{E}.B_0)$) and temperature of the sample when the reference image was acquired (T_0). A 16-bit scale is applied (F) and the data median filtered to provide contour plots (G) which enable comparisons to be made with CFD. The experimental data shown are taken from a jar containing 100 cm^3 of a mushroom sauce that had been heated without rotation using a prototype industrial microwave applicator (see Ref. [30] for details). The 3D volume rendered image (H) shows not only that the heating is mainly from one side but also that there is a hot spot at the bottom where the curvature of the jar allows the radiation to penetrate from more than one direction. (See also Plate 138 on page XXVII in the Color Plate Section.)

the magnet for acquisition of the heated phase image. This is feasible for objects with a defined geometry, such as a jar, which can be relocated accurately without altering the magnetic field homogeneity to ensure that all measured phase-changes are due to changes in temperature [31]. However, this method cannot be used be foods that shrink due to moisture-loss, such as a potato [32].

Although phase mapping has advantages in terms of signal-to-noise (especially for high temperatures), and of the achievable spatial- and temporal-resolution, its major disadvantage is the necessity for a reference phase image taken at a known temperature and which is spatially co-registered with the heated image.

Ohmic Heating

Phase mapping has been used to map temperature of an ohmically heated whey gel in brine solution [33] to provide better temporal-resolution than for T_1-weighted images [11]. Salt was added to both the gel and fluid to alter their electrical conductivities without significantly changing the temperature sensitivities of water proton chemical shift (Table 1). The heating and cooling regressions were found to be the same indicating the reversibility of the chemical shift method; the electric current was turned off during measurements to avoid interference.

The same protocol was used to map temperature across an ohmically heated potato cylinder immersed in an aqueous solution of NaCl and sodium carboxymethylcellulose (CMC) in order to calculate the time-dependent interface heat transfer coefficients [34]. The images in that study were acquired with the electrical current on as it was found that the stripe artifacts it induced were removed by the phase mapping method; since that approach calculates the relative temperature from the phase difference, the artifacts were cancelled by subtracting the subsequent phase image. The same potato/CMC system was simulated in three dimensions using FEMLAB (Comsol Inc., Burlington, MA, USA) and the temperature maps compared against those obtained by MRI [35]; although there was good overall agreement between them, there were obvious discrepancies due to the heterogeneity of the real foods, to bubble formation and to fluid leakage, all of which are difficult to model.

Summary

MRI temperature mapping has already been applied to a wide variety of foods and thermal processes and, although there are individual complications associated with each specific application, there is no alternative to the acquisition by MRI of temperature data in one, two, or three dimensions. Those same data can also be used either to validate existing CFD models which would otherwise have to be based on assumptions, or to aid the development of new computer models.

References

1. Lewa CJ, de Certaines JD. Spectrosc. Lett. 1994;27: 1369.
2. RB Lufkin (Ed) Interventional MRI, Mosby: London 1999.
3. Wang LJ, Sun DW. Trends Food Sci. Technol. 2003;14: 408.
4. Singh RP. Food Technol. 2000;54:44.
5. Jezzard P, Carpenter TA, Hall LD, Claydon NJ. J. Polymer Sci. B 1992;30:1423.
6. Hulbert GJ, Litchfield JB, SJ Schmidt. J. Food Sci. 1995;60:780.
7. Hulbert GJ, Litchfield JB, Schmidt SJ. J. Food Eng. 1997;34:193.
8. Haase A. Magn. Reson. Med. 1990;13:77.
9. Ruan RR, Chang K, Chen PL, Ning A. Drying Technol. 1998;16:1459.
10. Chang K, Ruan RR, Chen PL. Drying Technol. 1998;16: 1447.
11. Ruan R, Chen P, Chang K, Kim HJ, Taub IA. J. Food Sci. 1999;64:1024.
12. Hahn EL. Phys. Rev. 1950;80:580.
13. Carr HY, Purcell EM. Phys. Rev. 1954;94:630.
14. Stejskal EO, Tanner JE. J. Chem. Phys. 1965;42:288.
15. Sun XZ, Litchfield JB, Schmidt SJ. J. Food Sci. 1993;58:168.
16. Sun XZ, Schmidt SJ, Litchfield JB. J. Food Process Eng. 1994;17:423.
17. Hindman JC. J. Chem. Phys. 1966;44:4582.
18. Hall LD, Talagala SL. J. Magn. Reson. 1985;65:501.
19. Ishihara Y, Calderon A, Watanabe H, Okamoto K, Suzuki Y, Kuroda K, Suzuki Y. Magn. Reson. Med. 1995;34:814.
20. Kantt, CA, Webb AG, Litchfield JB. J. Food Sci. 1997;62:1011.
21. Kuroda K, Suzuki Y, Ishihara Y, Okamoto K, Suzuki Y. Magn. Reson. Med. 1995;35:20.
22. Kuroda K, Oshio K, Chung AH, Hynynen K, Jolesz FA. Magn. Reson. Med. 1997;38:845.
23. Kuroda K, Mulkern RV, Oshio K, Panych LP, Nakai T, Moriya T, Okuda S, Hynynen K, Jolesz FA. Magn. Reson. Med. 2000;43:220.
24. Walton JH, McCarthy MJ. J. Food Process Eng. 1999;22:319.
25. Bows JR, Patrick ML, Nott KP, Hall LD. Int. J. Food Sci. Technol. 2001;36:243.
26. Bows JR, Patrick ML, Hale M, Nott KP, Hall LD. 7th Microwave and High Frequency Heating Conference, Valencia. Servicio de Publicaciones: Valencia, Spain, 1999, p 89.
27. Kantt CA, Schmidt SJ, Sizer CE, Palaniappan S, Litchfield JB. J. Food Sci. 1998;63:305.
28. Sun L, Amin MHG, Hall LD, Wolf B, Frith WJ, Ablett S. Meas. Sci. Technol. 1999;10:1272.
29. Sun L, Hall LD. Int. Comms. Heat Mass Transf. 2001;28:461.
30. Nott KP, Hall LD, Bows JR, Hale M, Patrick ML. Int. J. Food Sci. Technol. 1999;34:305.

31. Nott KP, Hall LD, Bows JR, Hale M, Patrick ML. Magn. Reson. Imaging. 2000;18:69.
32. Nott, KP, Shaarani SM, Hall LD. In: PS Belton, AM Gil, GA Webb, D Rutledge (Eds). Magnetic Resonance in Food Science: Latest Developments, Royal Society of Chemistry, Cambridge, 2003, p 38.
33. Ye X, Ruan R, Chen P, Chang K, Ning K, Taub IA, Doona C. J. Food Eng. 2003;59:143.
34. Ye X, Ruan R, Chen P, Doona C, Taub IA. J. Food Sci. 2003;68:1341.
35. Ye XF, Ruan R, Chen P, Doona C. Lebens. Wiss. U.-Technol. 2004;37:49.

Statistical Methods

Part III

Chemometric Analysis of NMR Data

Nanna Viereck, Lars Nørgaard, Rasmus Bro, and Søren B. Engelsen
Quality & Technology, Department of Food Science, The Royal Veterinary and Agricultural University,
Rolighedsvej 30, DK-1958 Frederiksberg C, DK

Introduction

NMR is one of the most successful and versatile analytical techniques of our time, and it is directly applicable to amorphous, heterogeneous, and opaque systems such as food and foodstuffs. NMR is capable of probing both physical and chemical phenomena which allow food engineers and scientists to obtain a unique fingerprint of the protons (nuclei) in a sample. Sometimes the NMR fingerprint of a complicated food matrix is much too complex for simple interpretation for which reason pattern recognition techniques are required for full evaluation of the data.

The quantitative aspect of NMR data analysis has been and still is suffering from oversimplified data analysis, mainly because the complexity of the data is too great for a deterministic approach and because it is conceptually difficult to cope with a high number of variables. This simplifying tradition has resulted in the widespread normative use of NMR: If you keep only the part of the data that you think is relevant, you will confirm what you already know is important and thus reduce your chances of innovation.

There is no doubt that NMR scientists in industry and academia can learn from the successful progress of near-infrared (NIR) spectroscopy, which in the last decade has revolutionized quality control in practically all areas of primary food and feed production. NIR spectroscopy has been implemented for monitoring quality of millions of samples of cereals, milk, and meat with unprecedented precision and speed. The key to this success is the extraordinary synergy that lies in the merging of a rapid non-invasive NIR spectroscopic sensor and the data technology called chemometrics.

Generally speaking, NMR data comes in two forms: time domain relaxation data probing the physical information and frequency domain chemical shift data primarily probing the chemical information (Figure 1). In general, frequency domain data are obtained from high-resolution spectrometers with superconducting magnets, while time domain data are obtained from low-resolution relaxometers using permanent magnets.

Frequency domain chemical shift data are normally characterized by the fact that molecules, even conformations, give individual chemical shift fingerprints and that the intensity at a given band is proportional to the concentration of the substance giving rise to the band. That concentration is proportional to signal intensity and that signals from a given substance remain stable on the frequency axis are exactly the requirements of bilinear multivariate quantifications. A number of exceptions to this rule exist, including molecular size (i.e. more intense peaks from smaller polymeric molecules than from larger polymeric molecules due to their longer T_1 times), chemical shift changes according to pH, temperature, etc.

Time domain relaxation data are characterized by lack of structure and selectivity, normally being composite exponential decay functions. In contrast to frequency domain chemical shift data, time domain data are direct functions of the mobility of the molecular systems under study. Time domain relaxation data have the property that all measured substances contribute to the intensity at all times but with different exponential weights. At a given time the NMR relaxation signal intensity is proportional to the contributions from the measured substances that are exponentially weighted, i.e. a slow relaxing component contributes relatively more than a fast relaxing component. If we assume that we can extrapolate to time zero, the concentrations of the measured compounds are linearly proportional to signal intensity, which is why univariate NMR relaxation measurements can probe proton density (or mass). Difference or ratio calculations, curve fitting or multivariate data analysis is required to extract more detailed quantitative information from such data. Time domain relaxation data have an additional property, namely, that if the time axis is shifted there will remain a linear relation between the individual relaxation components which is actively utilized in the so-called direct exponential curve resolution method (see chapter on “slicing”).

Perhaps because NMR was developed by physicists and chemists, it has primarily been used for identification, authenticity determination, and simple quantification purposes. Its exploratory and quantitative potential has largely remained unexploited. The first report on the use of chemometrics on NMR data appeared in 1983 by Johnels *et al.* [1], but it was not before the early nineties that new developments of applying chemometric data analysis to high-resolution NMR signals occurred, with the impetus being the analysis of complex 1D and 2D

Graham A. Webb (ed.), Modern Magnetic Resonance, 1833–1843.
© 2008 *Springer.*

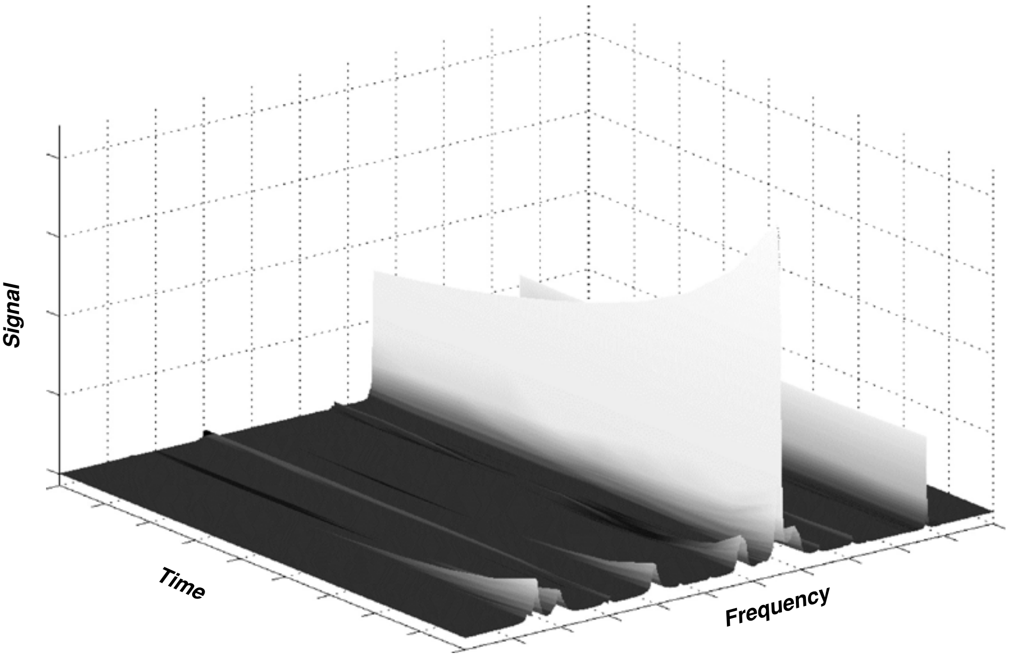

Fig. 1. NMR data comes in two forms: time domain relaxation data and frequency domain chemical shift data.

NMR structures of complex biological and pharmaceutical/therapeutic matrices [2,3]. The use of chemometric data analysis for frequency domain data has now become well-established thanks to the so-called metabonomics approach defined as "Metabolic processes studied by NMR spectroscopy of biofluids" [4], whereas the use of chemometric data analysis for time domain relaxation data is still in its infancy and was first adapted in the late nineties [5–7]. It has been and still is common practice in time domain NMR to design calibration models from univariate signals collected from intrinsically multivariate signals. The most prominent examples are solid-fat determination based on the ratio between the signal at 11 μs and the signal at 70 μs and fat determinations based, for example, on the amplitude of a single gradient-stimulated echo. Such calibrations are, from a data technological point of view, suboptimal approaches.

What is Chemometrics?

The essence of most chemometric methods lies in their construction of common latent factors (or principal components) from underlying latent structures in the original data.

One of the main advantages of chemometric data analysis is the possibility of projecting multivariate data into a few dimensions that can be displayed in a simple graphical representation. Chemometrics is also called "statistics without tears", because it makes it possible to handle large data sets and deal efficiently with real-world multivariate data, taking advantage of the co-linearity of spectral data. In this chapter we will illustrate the application of chemometric data analysis to two different food systems and through them evaluate the current status of the use of two-way chemometrics for the analysis of NMR data.

When using spectroscopic techniques for chemical quantification, traditionally univariate data analytical methods have been used, in which a single response variable is measured or selected from the whole spectrum and only this variable is analyzed. Statistical methods can then be applied for classification, or linear regression can be performed and a regression line can be calculated, indicating how well the measured variables describe the dependent variable in question. However, there are a few problems that should be considered when using univariate methods (Figure 2).

1. *Waste of data.* From a large number of measured variables only one or a few variables are selected for the analysis. Especially for complex samples there is a huge loss of information in using only a few variables from a whole spectrum.

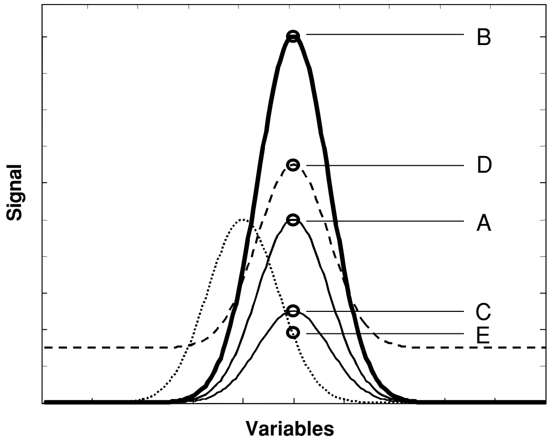

Fig. 2. Examples of problems that arise when univariate analysis is applied to spectral data. Quantitative spectral response of a given analyte in three levels is indicated by spectrum A, B, and C. Spectrum D corresponds to spectrum A with an offset and spectrum E corresponds to spectrum A with a variable shift. The circles indicate readouts in a univariate approach.

2. *A priori knowledge.* Extensive a priori knowledge is required about the sample spectrum in order to choose the right variable and thus a hypothesis about the results to be found is required, which in turn will reduce chances for innovation.
3. *Interference.* Another problem occurs if different components in the sample give signals in the same region as the analyte. In cases of overlapping signals these will be inseparable when only a single variable is measured and the content will be estimated too high due to the several components adding to the signal intensity.
4. *Baseline offset.* From Figure 2 it is seen that if only the variable marked with a dot is recorded, spectrum D will be estimated to have a higher content of the compound in question than spectrum A, even though the two responses have equal amplitude relative to the signal baseline. If the whole spectrum is recorded, the baseline offset of spectrum D is easily detected and the necessary action can be taken to correct for this offset.
5. *Abnormal signals.* Outliers are samples whose spectra do not conform to the majority of samples in a data set and they might have a detrimental effect on the calculated model. An example of this is shown in Figure 2 where one sample has a different spectral signal (spectrum E) than the others. In univariate analysis there is no data analytical way to determine that something is wrong with the sample.

Chemometric data analysis effectively deals with these problems, including handling covariate spectra of complex samples such as foods or biological samples in which the signals are so complex that the signal of a single chemical component cannot be identified, or the property of interest cannot be described by a single peak. The disadvantage of using two-way chemometric models is that it requires data from several samples to be analyzed simultaneously and the qualitative information (e.g. time constants) is lost due to the common practice of extracting orthogonal latent factors.

Several properties are essential for the successful application of chemometrics to spectral data. Firstly, for quantitative spectral analysis, the *intensity axis* must be the same for all samples, as a basic assumption is that the signal intensity is proportional with the concentration and that the signal intensities are additive, analogous to the obedience of Lambert-Beer law in optical spectroscopy. Secondly, chemometric data analysis is based on the extraction of latent components or underlying *common structures* which means that the data should be low-rank bilinear. A practical explanation of the concept of bilinearity is that a given chemical compound gives one and only one spectral signal; hence, this compound will have the same spectral shape in all samples and only vary in intensity from sample to sample. The bilinear chemometric model provides a set of scores and a set of loadings. The loadings describe the spectral shapes needed to describe all the profiles and the scores provide the quantitative information on how much of each loading is present in each sample. In an abstract sense, the loadings can be interpreted as pure spectra and the scores as concentrations. Due to orthogonality constraints, however, the loadings are merely mathematical constructs and therefore, the bilinear components (one loadings vector and its associated scores) are referred to as *latent variables*.

Preparation of Data

While most other types of spectroscopic data can be subjected to chemometric analysis directly from the spectrometer, NMR data often need to be preprocessed in several ways in order to conform to the prerequisites for chemometric data analysis.

1. *Intensity scale.* The data need to have the same intensity scale, which is trivial for most other spectroscopic techniques, but in NMR measurements the data are often scaled in the spectrometer, and this scaling must be removed before chemometric analysis. Secondly, it is often difficult to obtain reproducible shim and sample filling conditions between samples, for which reason normalization is required. This can either be done in the time domain by division by mass or by normalization to the first point (assuming the same proton density and approximately the same proton mobility) or in the

frequency domain by normalization to an internal standard.

2. *Phase errors.* A difficult problem encountered with NMR data is the existence of phase errors. Manual phase correction is usually implemented in the instrument software, but this process is very time consuming, especially for the large data sets that are often analyzed using chemometrics. More importantly, manually phase-correcting a series of spectra will lead to suboptimal results due to the subjective evaluation of the correction necessary for individual spectra. In time domain NMR automatic phase correction is a reality [8], including an algorithm which is built on chemometric grounds [9]. With respect to frequency domain NMR spectroscopy, several methods for automatic phase correction have been suggested; however, none appear to be generally applicable to all types of NMR spectra.
3. *Fourier transformation.* In NMR spectroscopy a Fourier transformation is required to convert the time domain data (free induction decay) to the frequency domain (NMR spectrum). Naturally, quantitative methods require that parameter settings for the Fourier transform (choice of zero-filling and apodization function) are equal for all samples to be evaluated, as they may influence the finer details in the spectra.
4. *Chemical shift variations.* The last preprocessing problem to be mentioned here and which occurs only in high-resolution frequency domain NMR spectroscopy is the chemical shift variations that may occur from sample to sample or even from peak to peak. The overall sample-to-sample variations are due to small variations in spectrometer frequency and the solution is straightforward, as it is a general translation of the entire spectrum either by pattern recognition or by an internal reference peak such as 3-trimethylsilyl-1-[2,2,3,3-$^2H_4$] propionate (TSP). The peak to peak chemical shift variations due to variations in, for example, pH (encountered when analyzing samples such as urine) are much more difficult to handle. Smoothing and/or data reduction in the form called bucketing is a pragmatic solution to the problem, but other more general and elegant methods have been proposed, including Partial Linear Fit [10] and genetic algorithm peak alignment [11]. The so-called warping techniques that have been developed for correction of peak shifts in difficult chromatographic elution profile data [12,13] are also very promising.

Unsupervised Data Exploration by PCA

The basis of most chemometric algorithms is Principal Component Analysis (PCA) which has already celebrated its 100-year anniversary [14] and is still in splendid shape. PCA can be considered as the first amendment in exploratory analysis due to its extraordinarily robust data reduction and data presentation capabilities. In PCA the multivariate (spectral) data set is decomposed into orthogonal components whose linear combinations approximate the original data set in a least squares sense [15]. Common to bilinear models is that an entire matrix, with each row being the measurements on one sample, must be acquired. The model works on this entire data set, instead of on one sample at a time.

The mathematical structure of the PCA model can be described as

$$\mathbf{X} = \mathbf{1} \times \bar{\mathbf{x}}^{\mathrm{T}} + \mathbf{T} \cdot \mathbf{P}^{\mathrm{T}} + \mathbf{E} \tag{1}$$

where $\mathbf{X}$ is the NMR data matrix ($I \times J$; one NMR spectrum/relaxation profile per row), $\mathbf{1}$ is a vector of ones ($Ix1$), $\bar{\mathbf{x}}^{\mathrm{T}}$ is the mean vector of all samples, $\mathbf{P}$ contains underlying profiles ($J \times N$; loadings) and $\mathbf{T}$ is the contributing amplitudes ($I \times N$; scores). The scalar N is the number of factors resolved and $\mathbf{E}$ ($I \times J$) holds residual unexplained variation. For a given N, the mean, scores and loadings are determined in a least square sense. The loadings hold information on which variables are important and which are correlated, and the scores provide information on which samples are grouped, which are extreme etc.

PCA remains the primary tool for initial investigations of large bilinear data structures for the study of trends, grouping and outliers (see below).

Supervised Data Exploration

PLS Regression

Partial Least Squares (PLS) regression [16], essentially based on the PCA concept is its counterpart for regression analysis. While PCA can be compared to shopping (in the data) without a shopping list (i.e. the data analysis is performed without the use of *a priori* knowledge), PLS regression is like shopping *with* a specific shopping list. PLS regression is a predictive two-block regression method based on estimated latent variables and applies to the simultaneous analysis of two data sets for the same objects (e.g. spectra and physical/chemical tests). The latent variables of the spectral data, however, are determined in such a way that only the information needed to predict the physical/chemical data is extracted. The purpose of PLS regression is to build a linear regression model that enables prediction of a desired characteristic from a measured multivariate signal.

Validation

In order to avoid overfit (fitting the noise) in the highly empirical chemometric modeling a suitable validation scheme has to be used. The most optimal situation is to have an independent data set upon which the developed models can be tested to show the true predictive performance of the models. Since this is not always possible due to practical or economical limitations, the method of cross validation [17] can be useful. By excluding some of the samples, modeling the remaining samples and testing the models on the left-out samples, it is possible to obtain a realistic estimate of the significant number of components and the expected prediction error [reported as the root mean square error of cross validation (RMSECV)] [18].

Outlier Detection

An important aspect of chemometric data analysis is the possibility to detect outliers. An outlier is a deviating sample which influences the model incorrectly. The reason can be one of many, such as wrong sample preparation or erroneous handling of the sample, but it can also be due to instrumental artifacts or merely that the sample does not follow the stipulated model. It is important to make an effort to find out why a sample is an outlier before removing it from the data set. Once a sample has been shown to be an outlier, it should be removed from the data set and the calibration model must be recalculated [19].

Variable Selection

There are "fifty ways to leave your lover" and the same statement goes for variable elimination. A multitude of methods exist for the elimination of variables in order to obtain better predictive performance as well as a clearer interpretation of the data. The method of interval PLS (iPLS) [20], based on a simple split of the variables into a number of intervals, is introduced to give an overview of relevant spectral regions in a data set with respect to a given dependent variable. In some cases iPLS also gives rise to models with a better predictive performance compared to the full-spectrum model.

Example I. Chemometric Analysis of NMR Spectra of Apple Juice

As an example of how PLS and PCA can be used to calibrate and classify ^{1}H NMR data, the methods will be demonstrated on ^{1}H NMR spectra of different apple juices with different amounts of added ethanol. Four commercial apple juices (A, B, C, and D) were selected. Apple juices A and B were produced by the same company. Apple juices A, B, and D were produced as an apple concentrate with water added, while C contained pure apple juice. Apple juices A and C contained unfiltered juice, and B contained pure juice from the sort Jonagold. The pH in the four apple juices (A, B, C, and D) was measured to 3.67, 3.62, 3.39, and 3.90, respectively. The NMR data set consists of 48 ^{1}H NMR spectra of the apple juices each with ethanol added in 12 levels [between 0.05 and 10.0% (w/w)] together with four spectra of the pure apple juices. The samples were measured at 293 K on a 400 MHz Bruker Avance NMR spectrometer equipped with an automatic sample changer. Presaturation was applied during the 4 s relaxation delay to suppress the signal from water protons. The spectra were collected into 32K complex data points and 128 scans were acquired for each sample. A spectral window of 8278 Hz was accumulated in an acquisition time of 1.98 s.

The full ^{1}H NMR spectra of the pure apple juices and one of the samples with 0.05% ethanol added are shown in Figure 3. The sugar region between 2.5 and 5.5 ppm contains signals from the major components found in apple juices [21]: glucose (glc), sucrose (suc), fructose (fru), and malic acid (MA). As was also observed by Belton *et al.* [21], the chemical shifts of the methylene protons in MA depend highly on pH within the sample. The region between 1 and 2.5 ppm contains signals from the minor components in apple juice (quinic, lactic, and acetic acids). Noteworthy is the increased region between 1.12 and 1.22 ppm which contains the triplet signal from the CH_3 group of ethanol. Low levels of ethanol can be seen in three of the pure apple juices (A, B, and C). The quartet signal of the CH_2 group of ethanol at 3.6 ppm is hidden below the many signals from the sugars. The other increased region between 6 and 9 ppm contains signals from aromatic compounds which have not been further assigned.

Prior to chemometric data analysis the NMR spectra of the apple juices were aligned spectrally by the dynamic time warping algorithm (DTW) [13]. To investigate the quantitative performance of 400 MHz ^{1}H NMR spectra for measuring ethanol a full-spectrum five-component mean centered PLS model between the spectral data and the ethanol concentration of the juice samples was calculated. The calculations yielded a correlation coefficient of 0.996 and an RMSECV of 0.31 (Figure 4A).

By applying iPLS to these data (Figure 4B) the spectral regions where ethanol gives rise to signals have low RMSECVs when PLS models are calculated on only these intervals. No single interval performs significantly better than the full-spectrum model, but some intervals (44, 60–63) give rise to the same RMSECV as a full-spectrum model.

In order to discriminate between the four apple juices (thirteen) samples of each) an iPLS with a dummy matrix containing the dependent variables was calculated. The dummy matrix consists of four columns, one for each manufacturer, designated by 1s if the juice is from the given manufacturer and 0s if not. A global discriminant

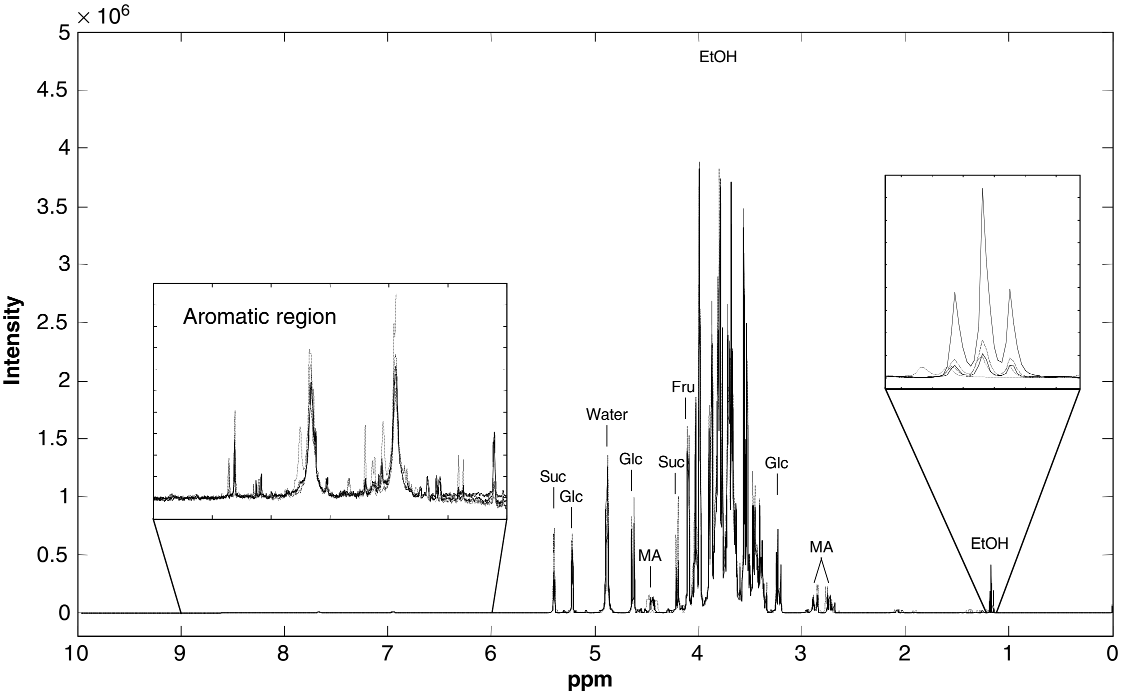

Fig. 3. NMR spectra of the four original apple juice samples (A, B, C, D) and juice sample A spiked with 0.05% ethanol.

PLS model on autoscaled data performs very well on these data and 100% separation is possible using eight PLS components. Thus, using the NMR fingerprint only, it is possible to classify which manufacturer the juice is from. To investigate if specific spectral regions contain the same discriminative ability an iPLS was calculated with the dummy matrix as the dependent matrix. The iPLS plot is shown in Figure 4C and several intervals seem to have discriminative ability. Interval 39 (4.47–4.33 ppm) performs the best and a PCA on this spectral range gives a perfect separation of the juice samples, as seen in Figure 4D. For comparison, a PCA on the full spectrum did not show full separation in any of the score plots (not shown). Furthermore, a mean centered discriminant PLS model on the full spectrum data does not perform well since the ethanol peaks in the spectra dominate the analysis.

Example II. Chemometric Analysis of NMR Relaxation Curves of Minced Meat

Fats are important food constituents and are measured in a number of foodstuffs to assure product quality. Time domain NMR data is sensitive to proton mobility, which is why the technique is useful for solid-fat determinations in the edible oils industry and for swift and accurate measurement of total fat content in dry foods. The established standard NMR approach to measuring total fat in dried food (including meat) is a univariate approach where only one point is acquired from each sample, namely the top-point of a spin-echo [22]. Simple linear regression is used for calibration. This procedure requires that the samples must be dried prior to analysis in order to remove the interfering signal contribution from water protons. Furthermore, the samples are heated to ensure that the entire fat phase is liquid upon NMR analysis to obtain the total fat signal. The second evolution in total fat determination of foods by time domain NMR occurred when pulsed field gradients [23,24] were introduced to suppress the water proton signal, leaving mainly the fat signal and thus rendering the drying step superfluous. In this method normally only one point is acquired, as in the spin-echo experiment, namely the top-point of the gradient-stimulated echo. However it would appear natural to extend the pulse method with an appended CPMG pulse train. In this example we aim to demonstrate how such a simple multivariate upgrade of the gradient-stimulated echo experiment combined with chemometrics can enhance calibration performance for total fat determination in 51 minced meat samples [25].

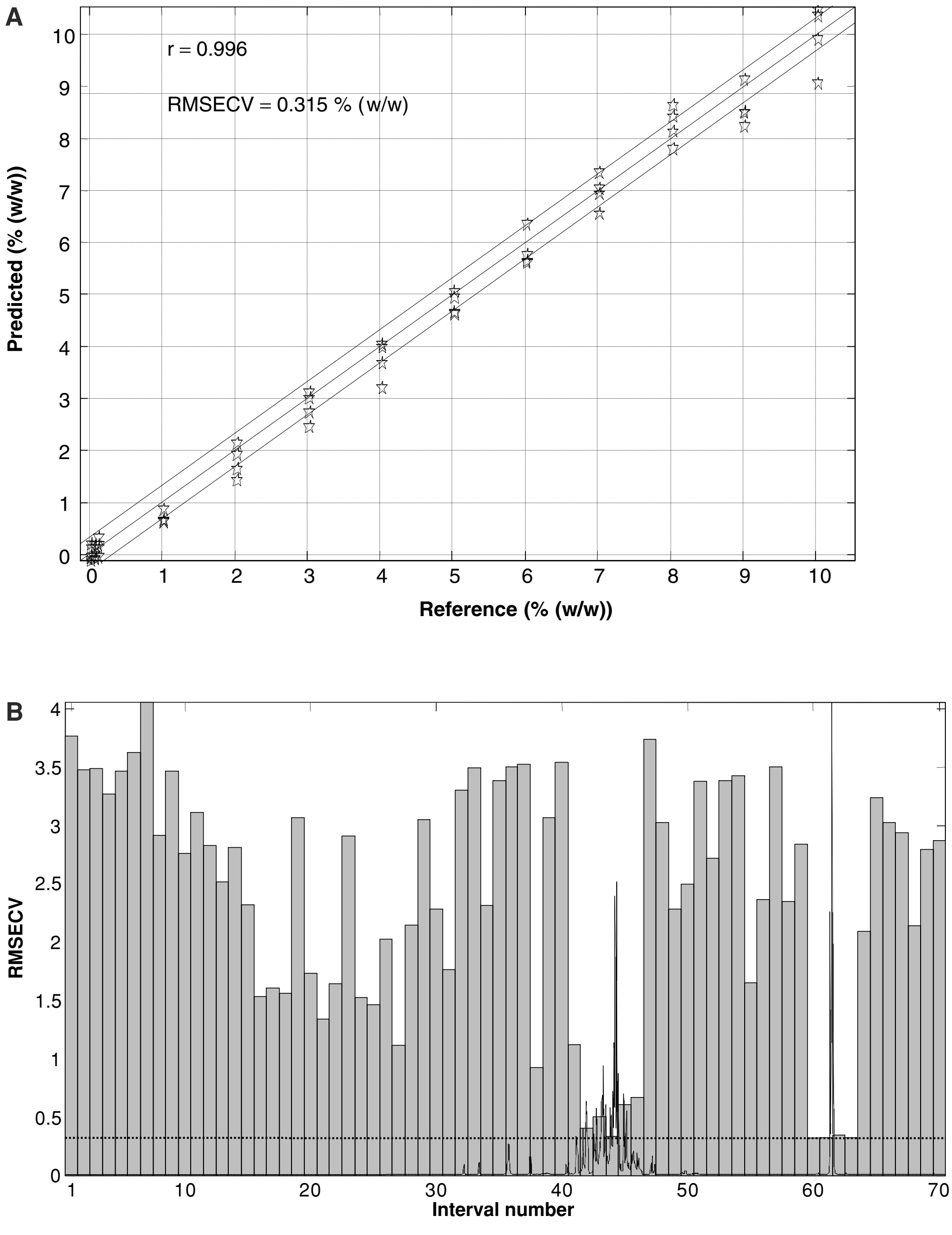

Fig. 4. (A) Predicted vs. measured plot for the ethanol full spectrum model with five PLS components. The middle diagonal line is the model target and the two parallel offset lines indicate limits for +/− RMSECV. (B) Interval PLS plot with 70 intervals and ethanol as the dependent variable. The dotted line is the average error (RMSECV) obtained from a full spectrum model. (C) Interval PLS plot with 70 intervals with a dummy matrix (manufacturer) as the dependent matrix. The dotted line is the RMSECV obtained from a full spectrum model. (D) Score plot from a PCA on interval 39 in the iPLS model (4.47–4.33 ppm). A clear grouping according to the manufacturer is observed.

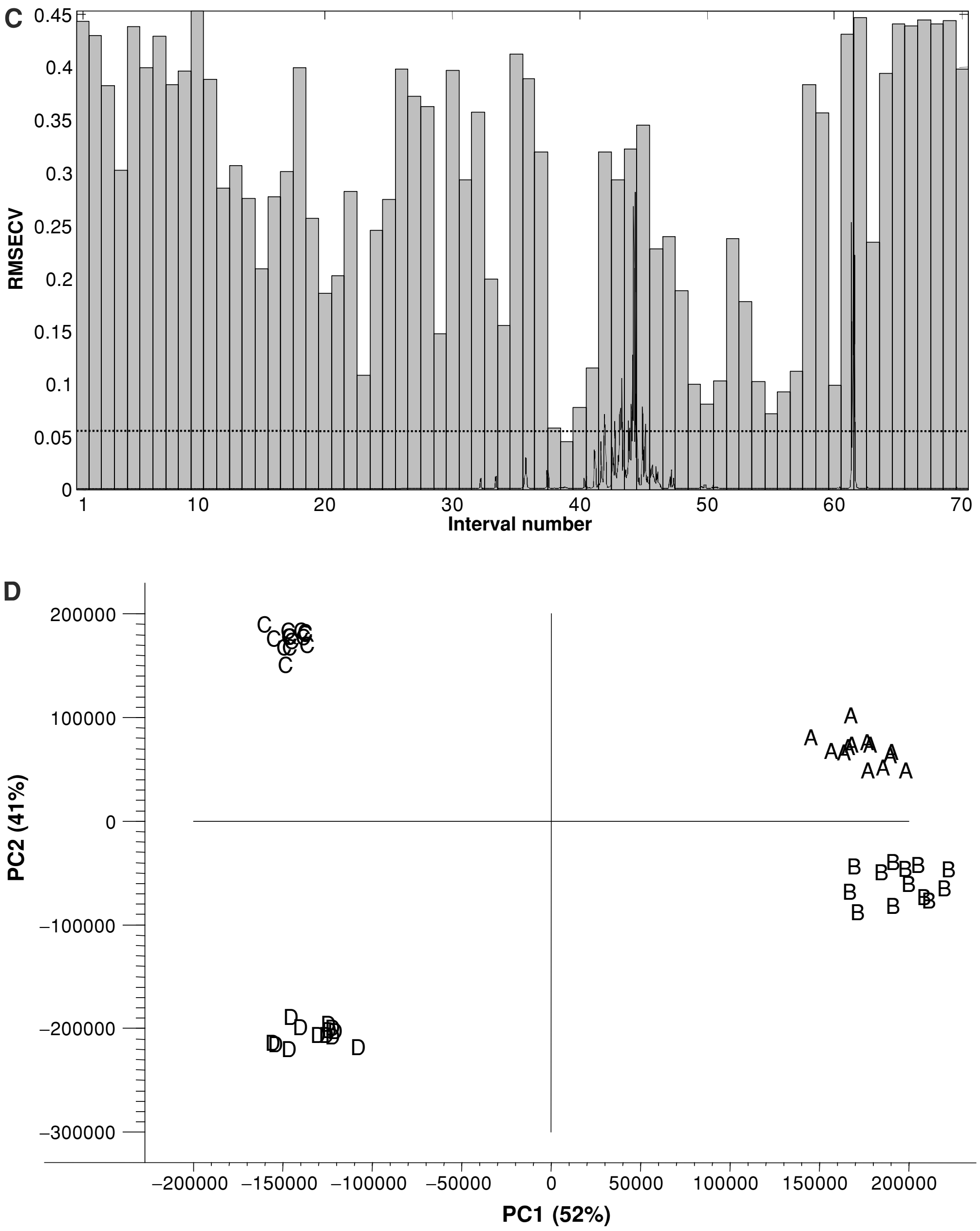

Fig. 4. (*Continued*)

Despite the fact that TD-NMR data rarely satisfies the bilinear condition (underlying latent structures have a tendency to change with concentration), PCA and PLS have proven very robust to this type of data [7]. Figure 5 demonstrates the advantage of the multivariate approach. The relaxation curves of 51 meat samples are given in Figure 5A. In Figure 5B the results of a univariate calibration of the gradient-stimulated echo amplitude of 51 fresh meat samples regressed on the conventional SBR (Schmid, Bondzynski, and Ratzlaff) solvent extraction

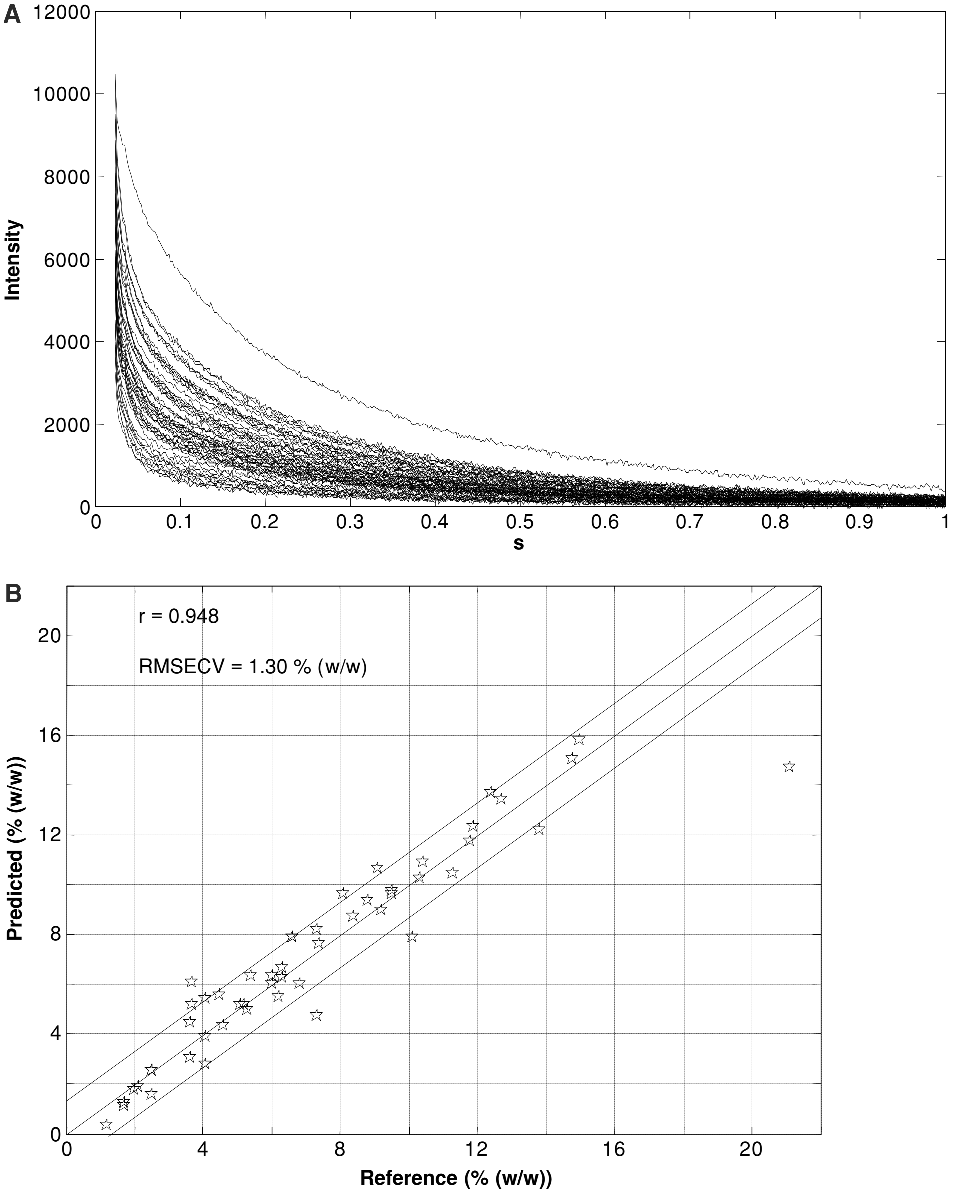

Fig. 5. (A) NMR relaxation spectra of 51 minced meat samples. (B) Predicted vs. measured for a univariate regression model. (C) Regression coefficients from a PLS model with fat as the dependent variable and the NMR relaxation curves as the independent variables. (D) Predicted vs. measured for a multivariate PLS regression model. The middle diagonal line in B and D is the model target and the two parallel offset lines indicate limits for +/− RMSECV.

method is shown. The cross-validated calibration results in a correlation of $r = 0.948$ and an RMSECV (average prediction error) of 1.30% (w/w) fat, and it demonstrates that the linear relationship between the echo amplitude and the SBR fat determination is broken above 20% (w/w) fat. In Figure 5C (regression coefficients) and Figure 5D (predicted vs. measured) the corresponding multivariate calibration results are shown for a multivariate upgrade of the gradient-stimulated echo pulse experiment in which the gradient echo is simply followed by a 180° pulse

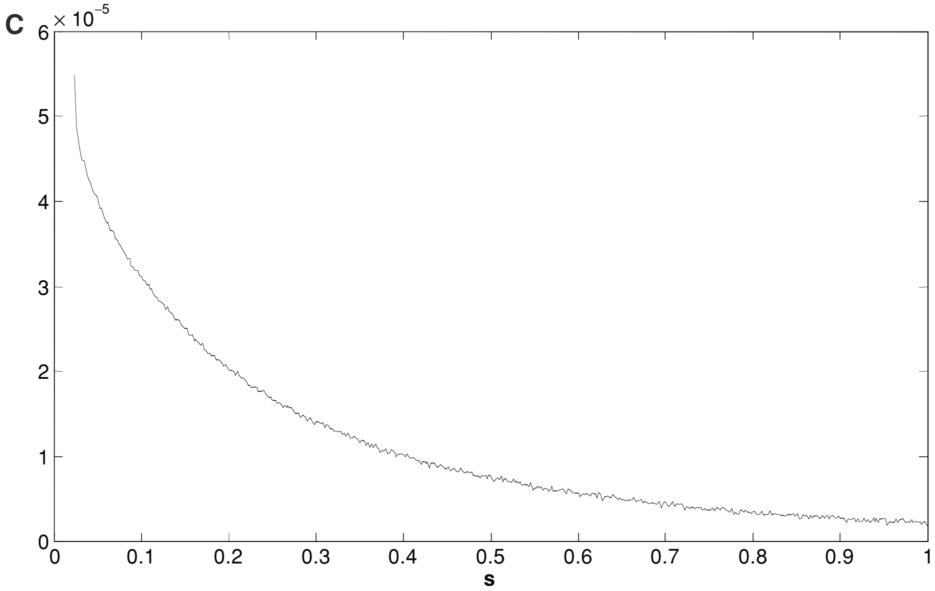

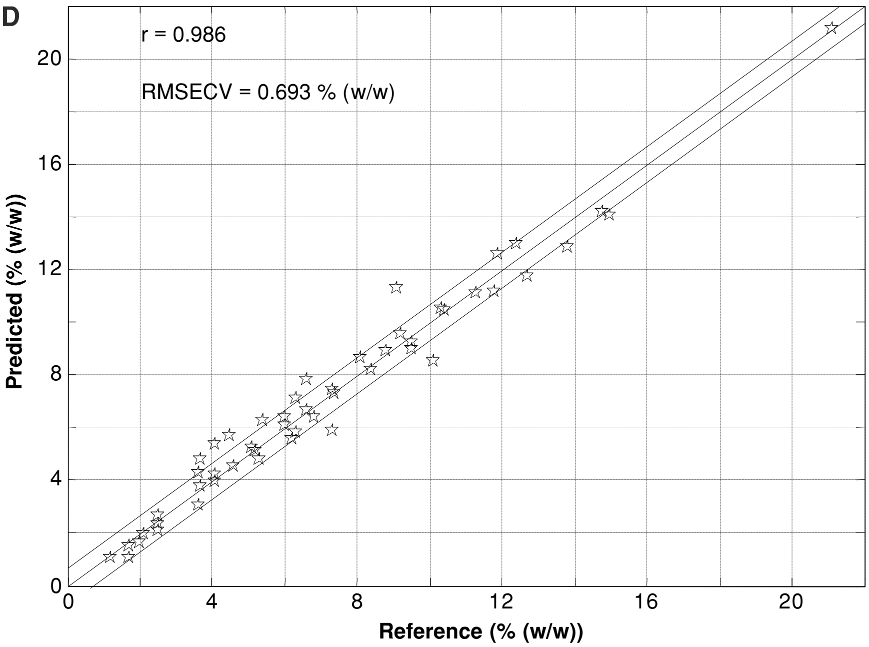

Fig. 5. (*Continued*)

train. The cross-validated calibration based on only one PLS component has now improved the calibration performance to half the error of the traditional approach with $r = 0.986$ and RMSECV = 0.69% (w/w) fat. Moreover, this simple PLS regression model is now able to linearly extrapolate measurements above 20% (w/w) fat. This type of performance enhancement is the rule rather than the exception when comparing univariate or oligovariate approaches with multivariate approaches. For this reason it is intriguing that official standard methods for fat determination are still based on univariate reasoning—we can predict that these dinosaurs soon will be overtaken by new improved company standards, as has been the case with NIR models.

Conclusion

Quantitative NMR spectroscopy has recently been promoted by the metabonomics community. With tremendous challenges and potential for applying quantitative NMR for measuring functional factors in complex food systems, this area of research is still in its infancy.

The challenges, problems, and advantages of extracting quantitative information from NMR data by chemometric methods have been demonstrated. It has been shown that NMR data in both time domain and frequency domain have to be preprocessed in order to comply with chemometric methods. Two examples including time domain NMR data (fat in minced meat) and frequency NMR (ethanol in apple juice) data are given and it has been illustrated that the combination of NMR and chemometrics outperforms univariate approaches with respect to quantitative performance.

References

1. Johnels D, Edlund U, Grahn H, Hellberg S, Sjostrom M, Wold S, Clementi S, Dunn WJ. J. Chem. Soc. Perkin Trans. 1983; 2:863.
2. Grahn H, Delaglio F, Delsuc MA, Levy GC. J. Magn. Reson. 1988;77:294.
3. Hoffman RE, Levy GC. Progr. NMR Spectros. 1991;23: 211.
4. Lindon JC, Nicholson JK, Holmes E, Everett JR. Concepts Magn. Reson. 2000;12:289.
5. Thygesen LG. Holzforschung. 1996;50:434.
6. Gerbanowski A, Rutledge DN, Feinberg MH, Ducauze CJ. Sci. Aliment. 1997;17:309.
7. Bechmann IE, Pedersen HT, N Lørgaard, Engelsen SB. Comparative chemometric analysis of transverse low-field ^{1}H NMR relaxation data. In Advances in Magnetic Resonance in Food Science. Edited by Belton PS, Hills BP, Webb GA. Cambridge, UK. 1999. p. 217.
8. van der Weerd L, Vergeldt FJ, de Jager PA, Van As H. Magn. Reson. Imaging. 2000;18:1151.
9. Pedersen HT, Bro R, Engelsen SB. J. Magn. Reson. 2002;157:141.
10. Vogels JTWE, Tas AC, Venekamp J, van der Greef J. J. Chemom. 1996;10:425.
11. Forshed J, Schuppe-Koistinen I, Jacobsson SP. Anal. Chim. Acta. 2003;487:189.
12. Nielsen NPV, Carstensen JM, Smedsgaard J. J. Chrom. 1998;805:17.
13. Tomasi G, van den Berg F, Andersson CA. J. Chemom. 2004;18:1.
14. Pearson K. Phil. Mag. 1901;2:559.
15. Jackson JE. J. Qual. Technol. 1980;12:201.
16. Wold S, Martens H, Wold H. Lect. Notes Math. 1983;973:286.
17. Wold S. Technometrics 1978;20:397.
18. Stone M. J. Royal Stat. Soc. Series B-Methodol. 1974;36:111.
19. N Tæs, Isaksson T. NIR News 1992;3:8.
20. N Lørgaard, Saudland A, Wagner J, Nielsen JP, Munck L, Engelsen SB. Appl. Spectros. 2000;54:413.
21. Belton PS, Colquhoun IJ, Kemsley EK, Delgadillo I, Roma P, Dennis MJ, Sharman M, Holmes E, Nicholson JK, Spraul M. Food Chem. 1998;61:207.
22. Hahn EL. Phys. Rev. 1950;80:580.
23. Stejskal EO Tanner JE. J. Chem. Phys. 1965;42:288.
24. Tanner JE, Stejskal EO. J. Chem. Phys. 1968;49:1768.
25. Pedersen HT, Berg H, Lundby F, Engelsen SB. Innov. Food Sci. Emerg. Tech. 2001;2:87.

Direct Exponential Curve Resolution by SLICING

Søren B. Engelsen[1], Henrik T. Pedersen[2], and Rasmus Bro[1]
[1] *Quality & Technology, Department of Food Science, The Royal Veterinary and Agricultural University, Rolighedsvej 30, 1958 Frederiksberg C, Denmark; and*
[2] *Protein Structure and Biophysics, Novo Nordisk A/S, 2760 Måløv, Denmark*

Several types of NMR experiments result in data that may be described as a sum of exponential functions (T_1 weighted signals, T_2 weighted signals, and gradient weighted signals). In order to be able to understand and interpret these data, it is imperative to be able to model these with a robust and precise method which is why the numerical scientists have worked for centuries with iterative non-linear least squares curve fitting methods for resolving underlying mono-exponential functions. Recently, a new non-iterative method was proposed by Windig and Antalek [1] called direct exponential curve resolution algorithm (DECRA). The new method has several potential advantages, but first of all it is non-iterative, accurate, and rapid. In this chapter, a more general version of the DECRA method called SLICING is outlined and applied to a simple test case measuring fat in meat by NMR relaxometry.

T_2 weighted low-field pulsed NMR (LF-NMR) is a useful and direct technology for probing proton mobility in, for example, food and feed. The physical state of the two major proton-carrying components in food—fat and water—has fundamental impact on the quality and LF-NMR is therefore an important probe for food quality. The overall water compartmentalization and mobility will often mirror the basic food structure and thus indirectly or directly reflect rheological and sensory quality attributes, as well as many oxidation processes. LF-NMR has the potential not only to measure all of these important food quality attributes but also to perform the task as a non-invasive volumetric measure that potentially holds the promise of being able to facilitate real time process control with product control for 100% of the batch. LF-NMR suffers from a crude resolution and is normally only analyzed in the time domain. The most commonly recorded data is the transverse LF-NMR relaxation data (CPMG) which normally is described as a sum of decaying exponentials:

$$M(t) = \sum_{n=1}^{N} M_{0n} \cdot \exp\left(\frac{-t}{T_{2n}}\right) + \mathrm{e}(t), \tag{1}$$

where $M(t)$ is the intensity of the magnetization in the transverse plane at time t, N is the number of (discrete) exponential functions or components in the sample, M_{0n} is the initial equilibrium magnetization of the nth exponentials, and T_{2n} is the corresponding relaxation time constants. While the T_2 values provide a qualitative description of the spin–spin relaxation, the M_{0n} holds the quantitative description. There exists a number of physical sample effects as described by Diegel and Pintar [2] as well as instrumental effects that may give rise to non-exponential line shapes, but normally exponentiality is assumed and the resulting relaxation decay curves are analyzed by *discrete exponential curve fitting*. In this approach, a relaxation profile is decomposed into a limited number of pure mono-exponential curves (typically less than 4). This is the classical approach which scientists working in the numerical field have been struggling with and refining for more than 200 years [3]. More recent numerical approaches include quasi-Newton least squares fitting using soft line search and factorization. Despite the ill-conditioning property of the exponential-sum fitting problem, in practice numerical methods have become fairly robust, but unfortunately the iterative methods are rather time- and memory-consuming. More importantly, the final results are often strongly dependent on the number of exponential components extracted for which reason an efficient tool for selecting the right number of exponentials is required. An example of a traditional sequential curve fitting is shown in Figure 1. It is characteristic of numerical multi-exponential curve fitting that the interpretation (T_2 values—vertical lines) is drastically influenced by the number of extracted components.

The new DECRA principle in multi-exponential curve resolution is based on three premises:

(1) That there exists a linear relationship between exponentials:

$$\exp\left(\frac{-t}{T_{2n}}\right) \propto \exp\left(\frac{-t+\Delta t}{T_{2n}}\right). \tag{2}$$

(2) By exploiting the linear relationship, multi-exponential decay function can, by a simple pre-operation which we have termed slicing [4], be upgraded from a simple multi-exponential decay curve to a double decaying exponential landscape.

Graham A. Webb (ed.), Modern Magnetic Resonance, 1845–1852.
© 2008 *Springer.*

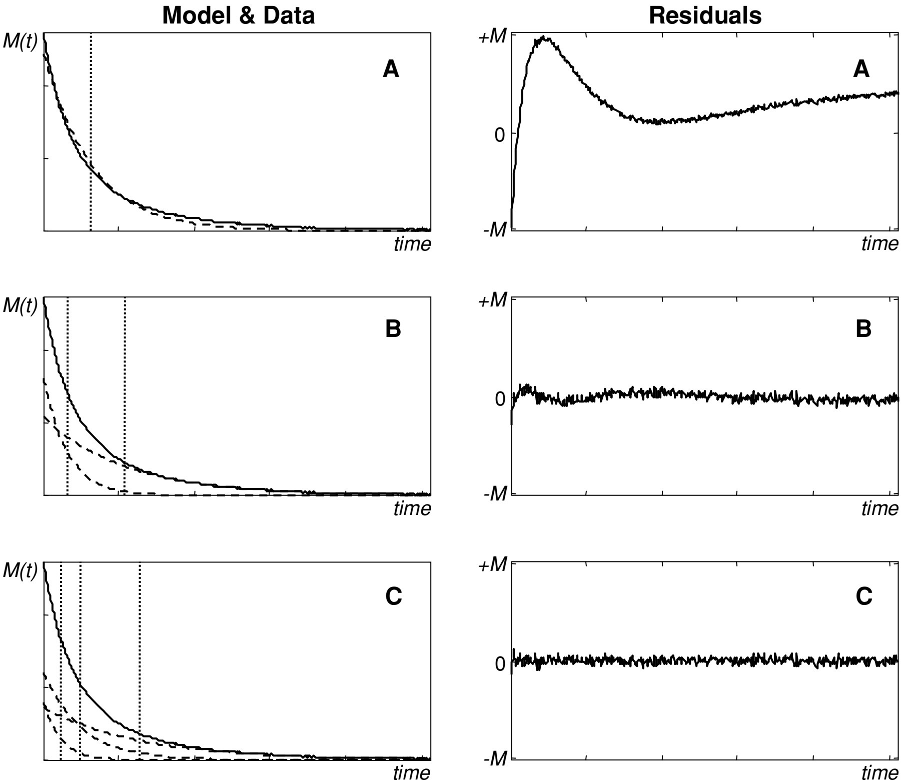

Fig. 1. Numerical curve fitting of a single NMR relaxation profile. (A) The result of fitting a single exponential function. The vertical line indicates the extracted characteristic T_2 time, (B) the result of fitting two exponential functions, and (C) the result of fitting three exponentials.

(3) By the use of a so-called two-dimensional data strategy where several samples are analyzed simultaneously for common underlying phenomena, the sliced data fulfill the criteria of the powerful multi-way algorithms [5] of the general form:

$$x_{ijk} = \sum_{n=1}^{N} a_{in} b_{jn} c_{kn} + e_{ijk}, \quad i = 1, \dots, I; j = 1, \dots, J; \ k = 1, \dots, K. \tag{3}$$

Thus, by rearranging each profile appropriately to a matrix and stacking several such matrices into a three-way data array, the rearranged data can be fitted by a tri-linear model which provides the quantitative (M_0) and qualitative information (T_2).

The principle is applicable in all cases where a sum of exponential functions is analyzed. This also includes spectral time series of chemical reactions displaying simple exponential behavior (first-order kinetics, radioactive decay, etc.). The method is basically built on the fact that a simple translation of a given exponential decay curve leads to a new multi-exponential decay curve that consists of the same underlying features (*quality*: characteristic decay times), but in a new combination of amounts (*quantity*: concentrations or magnitudes), and that the two slices together facilitate the unique advantages offered by tri-linear models. In their first application, Windig and Antalek [1] applied the method to perform exponential curve resolution of first-order reaction kinetics ($C = C_0 e^{-kt}$) monitored by high-resolution NMR at the process line at KODAK (US). Since then, several authors have applied the algorithm in different applications such as multivariate image analysis based on magnetic resonance images [6–9], short-wavelength near infrared analysis [10], UV–VIS [11,12] and solid-state NMR, and mid-infrared [13]. In this chapter, we will describe the technique and illustrate its use on a theoretical data example and an experimental data set.

Tri-Linear Models

While bi-linear chemometric models provide a tremendous advantage to univariate models (see Chemometrics chapter), tri-linear models, Equation (3), offer the additional advantage of unique resolution of underlying components [14]. The "only" assumptions for these multi-order advantages are that several spectra must be analyzed simultaneously, that they share common underlying mono-exponential features (low rank) and that they have tri-linear structure. Several different algorithms are available for tri-linear modeling including *generalized rank annihilation method* (GRAM) [15], *direct tri-linear decomposition* (DTLD) [16], which is a generalization of GRAM, and *parallel factor analysis* (PARAFAC) [17], all essentially fitting Equation (3). With respect to the SLICING problem, we have shown [18] that it is most efficient and adequate to use an algorithm based on the solution of a single generalized eigenvalue problem. While the eigen-based algorithms GRAM and DTLD do not give the least squares solution, they provide fast analytical solutions, and for large data sets with high signal-to-noise ratio and little model error the difference to the least squares solution is often insignificant. As opposed to alternative methods for fitting exponentials, the SLICING algorithm does not require any initial estimates.

Data Slicing

By a simple data pre-transformation, slicing, multi-exponential decay profiles can be upgraded to become bi-linear data structures suitable for tri-linear curve resolution techniques. Different data slicing transformation strategies exist and the simplest possible slicing transformation is as proposed in the original DECRA technique. In this approach, the multi-exponential decay function is copied and then shifted (translated in time) by one variable (see Figure 2A). To keep equal length of the two parts of the multi-exponential decays, the original is shortened by one variable at the end and the copy is shortened by one variable at the beginning. This DECRA-type slicing transformation can be denoted as [1,2]-slicing referring to the indices of the starting variables of each decay curve (slab). The result is a new data structure, a matrix, for each sample/measurement with the dimension $M(t) \times M''(t)$, where the last decay function has the dimension two. Although exponential fitting cannot be performed on two points, it is interesting to note that the underlying time constants for the second decay function $M''(t)$ are identical with those of $M(t)$ since they share the same origin. Furthermore, it is important to remember that the two curves being generated from the same relaxation profile, $M(t)$, share the same underlying time constants according to Equation (2).

It is possible to create more copies (slabs) by shifting the profiles more times. This will make the algorithm more robust, but also requires that the GRAM multi-way algorithm is replaced by either DTLD or PARAFAC. One simple example of such a slicing scheme could be the equally spaced [1,2,3,4,5,6,7,8,9,10]-slicing (Figure 2B) or even better $\log_{10}$-spaced [1,10,100]-slicing (Figure 2C). In our original SLICING method [19], we also investigated a technique to select and optimize slicing parameters (the spacing between slabs and the number of equally spaced slabs). While this technique proved to be very robust, it also meant loss of the speed advantage. An interesting solution to the problem of selecting optimally without prior knowledge of the underlying T_2 values is to select shifts (start variables for new slabs of the three-way array) that are spaced according to the power function 2^x for $x = 0, 1, \ldots, X$ where 2×2^X must be less than or equal to the original number of variables. The algorithm of this slicing scheme is accordingly named as POWERSLICING [18]. In accordance with the transformation terminology above, POWERSLICING gives [1,2,4,8,16,32,64, . . .]-slicing and an example is displayed in Figure 2D (for a sample with 510 time points, i.e. eight slabs). In two dimensions, the resulting landscape of the POWERSLICING transformation in Figure 2D is displayed in Figure 3. This approach, in which the new copies or slabs have exponentially increasing spacing has proven to be a fundamentally feasible strategy for the slicing transformation both in theory and in practice. The shifting scheme is the key to having accurate estimates of the underlying profiles. If the profiles have very fast decays, then small shifts will be beneficial in order to generate adequate variation across the shifting dimension. Small shifts, however, will not provide any accurate variation for more slowly decaying exponential profiles. The POWERSLICING scheme is characterized by providing diverse shifts for both fast, medium, and slow decaying profiles, resulting in a robust and extremely competitive algorithm with respect to speed of calculation.

To test the POWERSLICING technique we applied it to a simulated NMR data set of 30 samples with 2,048 data points containing four underlying exponential components interspaced with a factor of 2. Random noise (0.5% of total sum of squares of the data) was added to the data. This was repeated 3,000 times using different realizations (recalculations) of the noise. Figure 4 compares the performance of (C) POWERSLICING to a traditional two-dimensional numerical approach (D) MatrixFit [19], the previously introduced optimized (B) SLICING [19] and (A) DECRA [1]. From the figure, it is observed that the dispersion of the calculated T_2 estimates by POWERSLICING is comparable and even somewhat narrower than the results from the optimized SLICING; however, POWERSLICING remains a little less accurate in the T_2 estimates compared to the MatrixFit approach. When examining the average

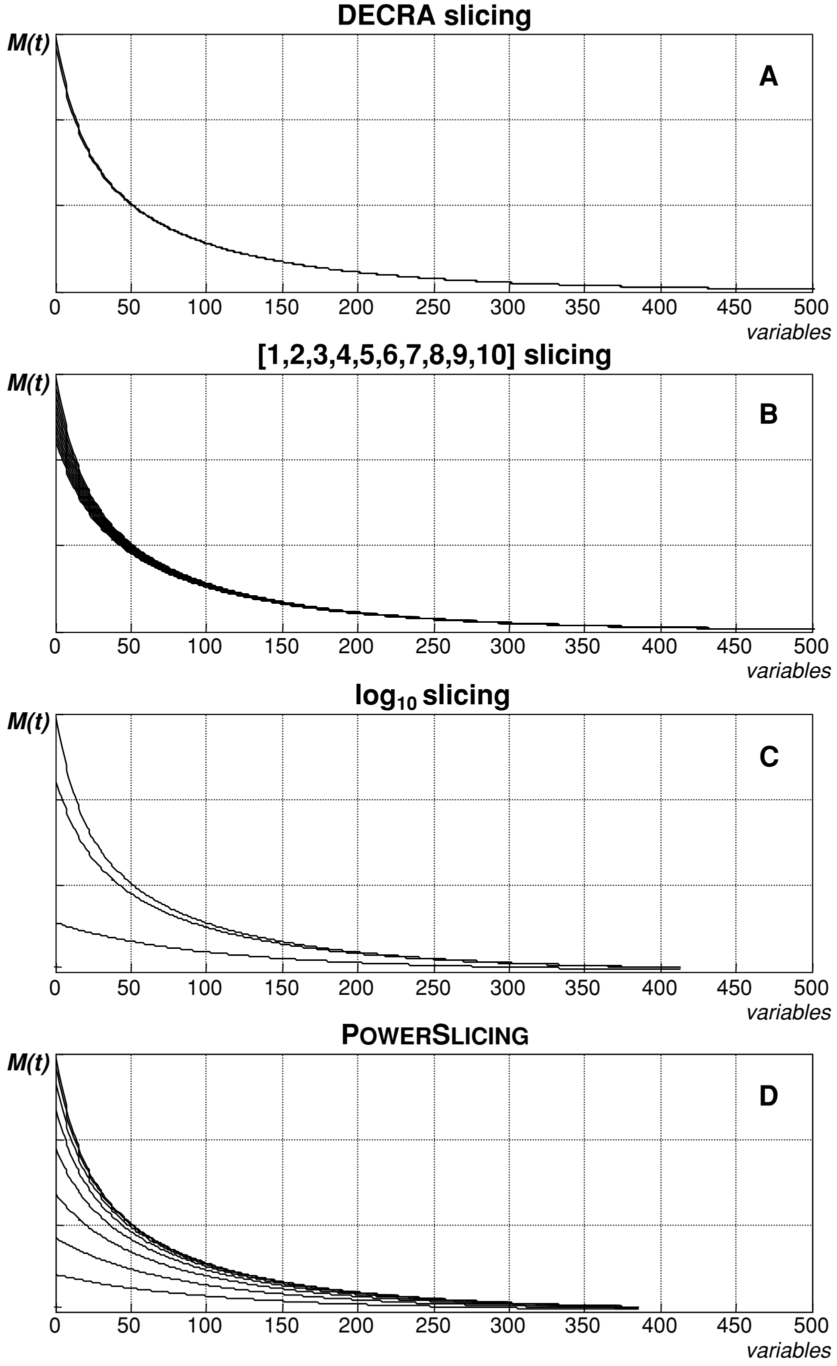

Fig. 2. Examples of different slicing transformations on a single multi-exponential relaxation curve. (A) DECRA or [1,2]-slicing, (B) equidistant [1,2,3,4,5,6,7,8,9,10]-slicing, (C) $\log_{10}$ [1,10,100]-slicing, and (D) PowerSlicing ([1,2,4,8,16,32,64,128]).

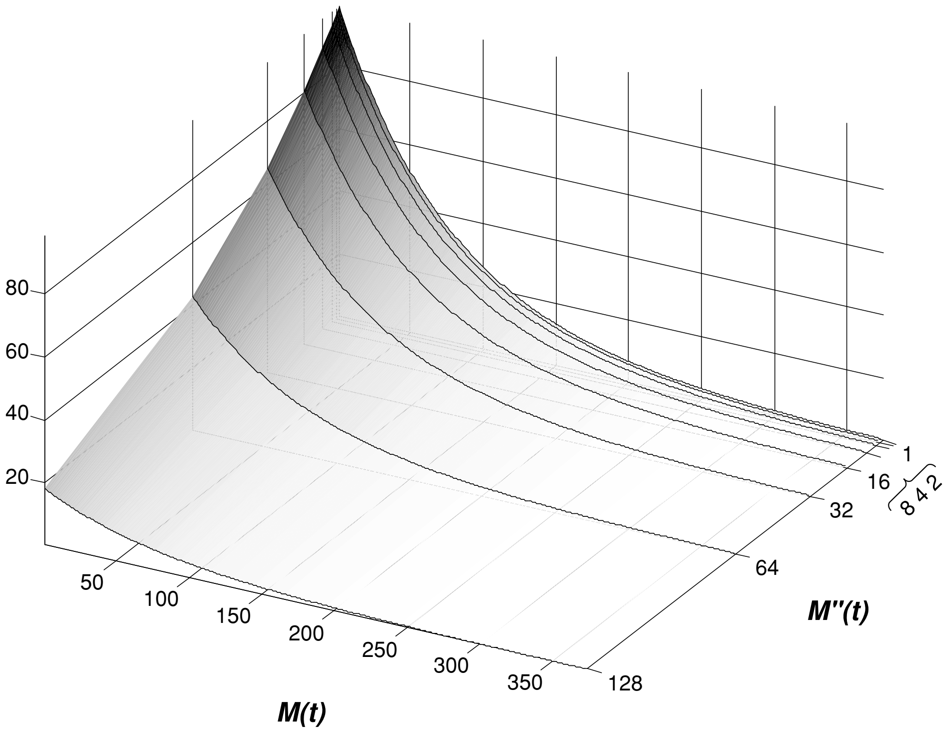

Fig. 3. A double exponential decaying landscape of a single NMR relaxation measurement.

algorithmic speed, PowerSlicing outperforms the optimized Slicing by a factor of approximately 300 and MatrixFit approach by a factor of 8. In terms of resolution, PowerSlicing is substantially better than DECRA which by far offers the poorest resolution, and algorithmic speed is approximately identical.

NMR Relaxometry: An Example

The utility of the Slicing approach will be demonstrated on NMR relaxometry measurements on meat. The data set consists of 47 measurements on minced meat with a total fat content between 1.2 and 15.0% (w/w). The samples were measured at 55 °C to ensure liquid lipid phase and 2,048 even echoes were recorded from a gradient stimulated echo CPMG pulse-sequence with a τ value of 500 μs [20]. A very important aspect of handling LF-NMR data is how the phase correction of the raw quadrature data is performed. Numerical curve fitting algorithms including the new Slicing methods are sensitive to non-optimal phase correction and in particular magnitude transformations should be avoided since this will introduce an artificial (potentially non-constant) offset in data. We have shown that non-optimal phase correction is detrimental to the following analysis and have suggested a simple solution called principal phase correction (PPC) [19] that is able to phase correct without introducing systematic or spurious errors in the corrected data.

Figure 5 shows how the 47 relaxation decays (A) via a two-component Slicing analysis simultaneously is decomposed into two underlying relaxation decays with characteristic T_2 times of 31 and 323 ms, respectively (B). One of the advantages with the underlying tri-linear decomposition of Slicing is that the related scores or concentrations need not to be calibrated to a reference parameter, but only scaled to a single reference. This is possible because the components intrinsically describe physical phenomena directly. Figure 5C shows a scatter plot with the estimated “concentrations” of the slowest relaxing component (323 ms) against a reference analysis of the total fat content in the meat samples (Schmid–Bondzynski–Ratzlaff method). As is observed from the plot, a direct correlation is obtained with a correlation coefficient of $r = 0.988$ (C). It is noteworthy that the high-fat sample apparently is well modeled by the PowerSlicing model in contrast to the simple spin-echo univariate model presented in chapter (see Chemometrics Analysis of NMR Data, page xxx).

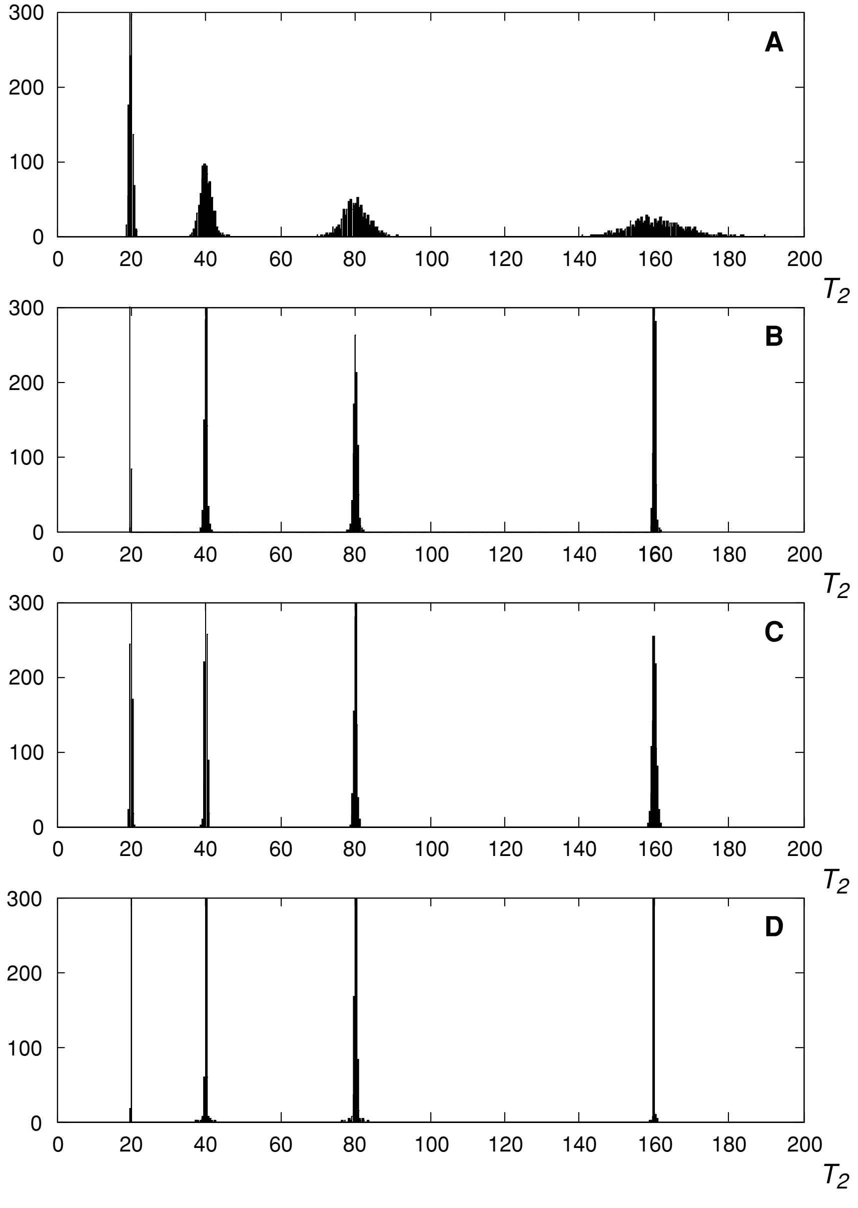

Fig. 4. Dispersion of T_2 values found by (A) DECRA, (B) SlicingOpt, (C) PowerSlicing, and (D) MatrixFit.

Conclusion

By a simple data pre-transformation, slicing, it is possible to upgrade transverse relaxation data to become bilinear. When more samples are available, data can be arranged in a multi-way array to become tri-linear and the slicing pre-transformation facilitates the use of powerful tri-linear mathematical models. When combined, this Slicing method is much faster than traditional methods in extracting characteristic relaxation times and the method has, for example, great potential for mathematical contrasting of MRI images. In an application to NMR

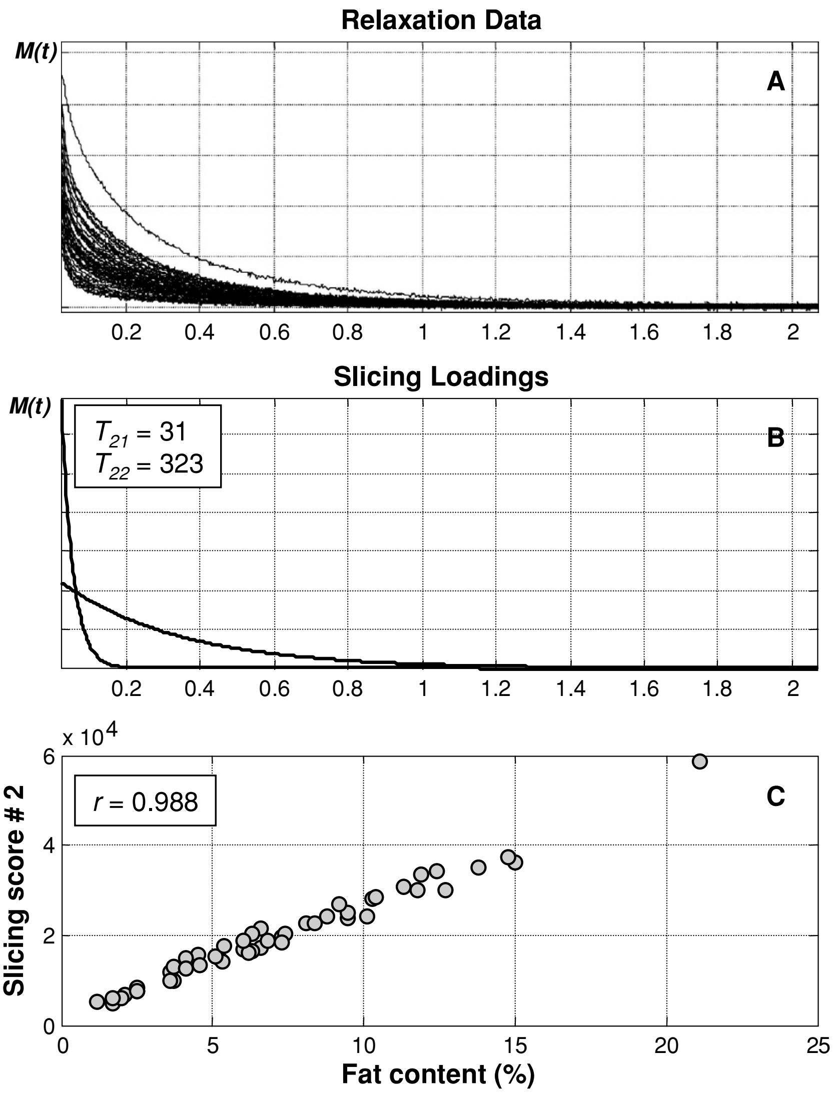

Fig. 5. The PowerSlicing solution to fat-in-meat. (A) Raw data, (B) PowerSlicing loadings, and (C) scatter plot of PowerSlicing score 2 (the slow component) vs. reference value.

relaxometry, we have demonstrated that Slicing provides unique estimates of the underlying profiles.

However, it should be stressed that the result of this procedure will be similar to those of discrete exponential fitting algorithms, fitting common characteristic time constants to a series of samples [19]. Extensive simulations of LF-NMR data revealed that the Slicing approach was comparable, but not superior to a robust classical numerical approach. In practice, it is the dramatically improved speed (largely independent of number of components extracted) and somewhat improved diagnostics of this algorithm, which are attractive. The tremendous speed of the Slicing approach makes it also most qualified for use as pre-processing (super-qualified initial guesses) to traditional numerical curve resolution algorithms.

The consequences of using common characteristic relaxation times in a wider range of quality attribute determinations (i.e. slightly varying time constants from sample to sample) by time domain low-field NMR remain to be investigated. However, it is possible to perform the SLICING pre-transformation twice (or more) and thus from only *a single* relaxation curve generate a tri-linear data cube [21]. This data pre-processing strategy called DOUBLESLICING provides a means to take advantage of tri-linear models when decomposing a single LF-NMR relaxation decay and was rediscovered by Manetti *et al.* [22]. The introduction of DOUBLESLICING leaves one independent of measuring more samples following the same underlying exponential decay functions. In this approach, the number of *slabs* (*pseudo*-samples) must be equal to or larger than the number of components one wishes to extract. This *pseudo*-sample matrix is then sliced again using the SLICING pre-transformation to obtain a *pseudo* tri-linear upgrade of the *pseudo*-sample matrix. Granted, it may appear to be an unnecessary complication to create a three-way data matrix with highly redundant information from a single relaxation curve to solve the simple discrete exponential fitting problem. However, with suitable resampling DOUBLESLICING produces practically the same results as traditional exponential fitting, but with significantly shorter computation times, especially when more than two components are extracted.

References

1. Windig W, Antalek B. Chemom. Intell. Lab. Syst. 1997;37: 241.
2. Diegel JG, Pintar MM. Biophys. J. 1975;15:855.
3. Prony R. J. de l'Ecole Polytechnique. 1795;1:24.
4. Pedersen HT, Bro R, Engelsen SB. Slicing—a novel approach for unique deconvolution of NMR relaxation decays. In: Webb GA, Belton PS, Gil AM, Delgadillo I (Eds). Magnetic Resonance in Food Science: A View to the Future. The Royal Society of Chemistry, Cambridge, UK, 2001, p 202.
5. Bro R. Chemom. Intell. Lab. Syst. 1997;38:149.
6. Windig W, Hornak JP, Antalek B. J. Magn. Reson. 1998;132: 298.
7. Antalek B, Hornak JP, Windig W. J. Magn. Reson. 1998;132: 307.
8. Windig W, Antalek B, Sorriero LJ, Bijlsma S, Louwerse DJ, Smilde AK. J. Chemom. 1999;13:95.
9. Windig W, Antalek B. Chemom. Intell. Lab. Syst. 1999;46: 207.
10. Bijlsma S, Louwerse DJ, Windig W, Smilde AK. Anal. Chim. Acta. 1998;376:339.
11. Bijlsma S, Louwerse DJ, Smilde AK. J. Chemom. 1999;13: 311.
12. Bijlsma S, Smilde AK. J. Chemom. 2000;14:541.
13. Windig W, Antalek B, Robbins MJ, Zumbulyadis N, Heckler CE. J. Chemom. 2000;14:213.
14. Sidiropoulos ND, Bro R. J. Chemom. 2000;14:229.
15. Sánchez E, Kowalski BR. Anal. Chem. 1986;58:499.
16. Sánchez E, Kowalski BR. J. Chemom. 1990;4:29.
17. Harshman RA. UCLA Working Papers Phonetics. 1970; 16:1.
18. Engelsen SB, Bro R. J. Magn. Reson. 2003;163:192.
19. Pedersen HT, Bro R, Engelsen SB. J. Magn. Reson. 2002;157: 141.
20. Pedersen HT, Berg H, Lundby F, Engelsen SB. Innov. Food Sci. Emerg. Tech. 2001;2:87.
21. Micklander E, Thygesen LG, Pedersen HT, van den Berg F, Bro R, Engelsen SB. Multivariate analysis of time domain NMR signals in relation to food quality. In: Webb GA, Belton PS, Rutledge DN (Eds). Magnetic Resonance in Food Science: Latest Developments. The Royal Society of Chemistry, Cambridge, UK, 2003, p 239.
22. Manetti C, Castro C, Zbilut JP. J. Magn. Reson. 2004;168: 273.

ESR Methods

Part III

ESR as a Technique for Food Irradiation Detection

Eric Marchioni

Faculté de Pharmacie, Laboratoire de Chimie Analytique et Sciences de l'Aliment (UMR 7512), Université Louis Pasteur (Strasbourg 1), F-67400 Illkirch, France

Introduction

Known pathogens account for an estimated 14 million cases of food-borne illnesses, resulting in more than 60,000 hospitalizations and 1800 deaths annually in the United States [1]. Important sources of food-borne pathogens include contaminated produce and improperly cooked, handled, or stored food products. Despite important efforts of the food industry, preventable illnesses, and related deaths resulting from the consumption of contaminated foods are still on the rise. Food irradiation is gaining interest in light of this increasing incidence of food-borne diseases in the last decades, as it efficiently reduces the populations of pathogens such as *Salmonella*, *Listeria*, *Campylobacter, E. coli* 0157:H7, and others, but also of parasites and insects [2–4]. The process has been endorsed by the World Health Organization (WHO), the Food and Agriculture Organization (FAO), the Codex Alimentarius Commission, the US Food and Drug Administration (FDA), the US Department of Agriculture (USDA), the American Medical Association, the American Dietetic Association, the American Institute of Food Technologists, and health authorities of approximately 50 countries [5–7]. The list of irradiated products allowed for irradiation varies from one country to another but is often limited to spices, herbs, seasonings, some fresh or dried fruits and vegetables, seafoods, ground beef meat, and poultry [6].

Definition of the Absorbed Dose (kGy)

Ionizing radiations are energy transmitted through space in the form of electromagnetic waves or electrons beams. Food irradiation involves the use of gamma rays generated by radionuclides either ^{60}Co [1.17 and 1.33 MeV ($1\ \text{MeV} = 1.6\times 10^{-13}$ J)] or ^{137}Cs (0.66 MeV), electron beams generated from electric machine sources operated at or below an energy level of 10 MeV or X-rays generated by striking electron beams (energy level at 5 MeV or below) on a metal target of high electronic density [7–10].

The dose of irradiation is measured in units of grays (Gy) or kilograys (kGy). One gray equals the absorption of 1 J of energy in 1 kg of water equivalent food.

Three dose ranges have been defined in food processing according to the effects achieved: between 0.1 and 1.0 kGy (sterilization of insects, destruction of parasites, inhibition of the germination of bulbs and tubers); between 1.0 and 10 kGy (elimination of pathogenic bacteria and increase in the shelf life of food by reduction of the spoilage flora); and more than 10 kGy (sterilization of spices and aromatic herbs) [7]. Doses above 10 kGy are needed for sterilization of generally "ready to eat" foods which require a guaranteed absence of microbes and/or have to sustain long-term unrefrigerated storage [11], e.g. hospital meals, foods for immunocompromised patients, astronauts, soldiers, mountain climbers, or campers.

Labeling

A European Directive, as well as regulations in most countries where food irradiation has been adopted, states that the words "*irradiated*" or "*treated with ionizing radiations*" shall appear on the label of any product sold as items [9]. A specificity of this European Directive is that food products containing irradiated ingredients shall be labeled accordingly. Moreover, the same words shall be required in order to indicate any irradiated ingredients, in whatever amount, used in components of a foodstuff. Labeling legislation and consumers' freedom of choice require that official food control laboratories have at their disposal effective analytical methods enabling them to prove if a food has been subjected to an irradiation treatment or not. This requirement is now fulfilled since the publication of ten standardized protocols, six official methods [12–17], and four screening methods [18–21] for the detection of irradiated foods by the European Committee for Standardization (CEN).

Interactions of Radiation with Matter

While penetrating a food product, high energy electrons, either directly introduced (electrons beams) or induced *in situ* from gamma or X-rays by photoelectric or Compton effect, will lose their energy through electrostatic interactions with atomic valence or molecular binding electrons. Such interactions are not specific and the absorbed dose is distributed according to the relative proportions of

Graham A. Webb (ed.), Modern Magnetic Resonance, 1855–1860.

© 2008 *Springer.*

the various components (water, proteins, lipids, carbohydrates, minerals, etc.) of the irradiated food. The interactions through which primary electrons lose their energy consist in ionization, ejection of one of the electrons out of the target atom or molecule, and formation of a radical cation, but also in excitation and the subsequent passage of an electron of the atom or molecule target in higher energy orbital levels. Ionization and excitation processes occur during very short lapses of time (10^{-18}–10^{-15} s) and lead to a lowering of the energy distribution of the electrons progressing in the food substrate. These electrons of lower energy can better interact with the target atomic or molecular electrons. They can thus lose a very major part of their energy, which makes the interaction very effective, in spite of the observed energy degradation. Then, after 10^{-15}–10^{-13} s, when the energy of the electrons becomes lower than the ionization potential of the food components, the remaining degradations are ascribed only to excitations. If this reduction in energy is such that only excitation of components having a very low excitation energy level is still possible (because of the presence of a ∂ orbital in their electronic structure), these components could be more affected by the radiation treatment than would be expected according to their concentrations in food. After 10^{-13} s, electrons with a much degraded energy will, in the presence of water, lead to the formation of hydrated electrons. The primary and secondary processes of interaction lead to the formation of highly reactive radicals. A great number of them recombine in food, leading to the formation of more or less stable radiolytic products. However, some radicals remain stable for many hours, days, months, and some for probably hundreds of years, according to the degree of mineralization and the relative humidity of the sample. Such very stable radicals can thus be recovered in bones, eggshells, shellfish cuticles, fish scales and teeth, fruit achenes and hulls, dried spices and aromatic herbs, and certain fruits, mostly over the whole commercial storage life of the food.

Food Irradiation Detection

ESR is a spectroscopic method allowing the detection of unpaired electrons, originating from radicals (including those induced by irradiation), or from paramagnetic ions (such as Mn^{2+}). Radicals in food are therefore not specific to irradiation. Nevertheless, ESR can be used as a detection test if the radicals induced by irradiation are stable during the commercial storage life of the food and the corresponding signals are clearly distinguishable from those of the unirradiated material. These radicals occur in the solid and dry components of the food, where the rigid structure of the matrix keeps radicals from reacting with each other or with food components present in the wet portion of the food. The intensity of the signals increases with the concentration of the paramagnetic compounds and thus with the applied dose. Today, particularly three kinds of food components are known to induce stable and specific ESR signals upon irradiation: hydroxyapatite, cellulose, and crystalline mono- and disaccharides.

Hydroxyapatite

Bone tissue is composed of approximately 60% hydroxyapatite [$Ca_{10}(PO_4)_6(OH)_2$] with most of the remaining fraction as collagen. The characteristic ESR spectrum of irradiated bones corresponds to the $CO^{-\bullet}$ radical [22]. When trapped in the hydroxyapatite lattices, this is an extremely stable radical which is used as an indicator of exposure to ionizing radiations. Measurements of ESR signals induced in animal bones are not really new, having been used for accidental post-irradiation dosimetry [23–25] and for dating bones and

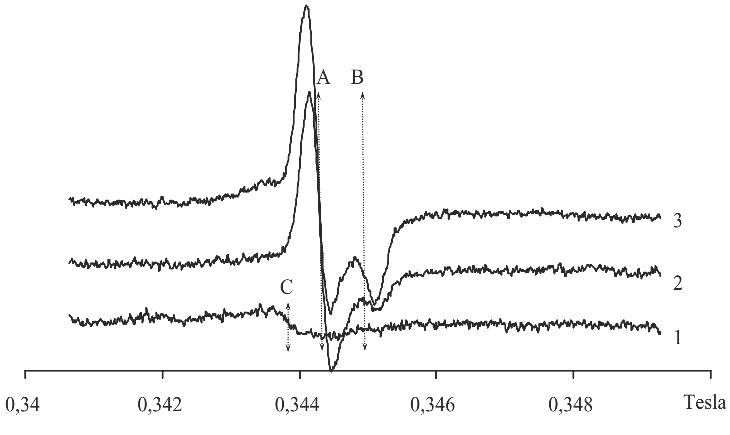

Fig. 1. ESR spectra of chicken bones unirradiated (1) and irradiated at 5 kGy (2 and 3). Dry excised piece of bone (2), bones fragments extracted from MRM (3). Letters A, B, and C show the position of the major ESR lines.

shells [26–28]. As hydroxyapatite is present in bones, scales, teeth, or shells, applications for the detection of irradiated foods containing these items have been widely reported [29–32]. In non-irradiated samples, there is a symmetric absorption with a g-factor $\approx$2.005 and a peak-to-peak line width (ΔH) of $\approx$0.6 mT (Figure 1, spectrum 1, signal C). An asymmetric absorption which is characterized by g-factors $\approx$2.002 and $\approx$1.998 (Figure 1, spectra 2 and 3, signal A and B, respectively) is only observed in irradiated samples containing $CO_2^{-\bullet}$ trapped in hydroxyapatite lattices. Since the signal height for particular bone types can be related to the dose (linearly proportional up to 14 kGy in the case of frog legs), it is possible to obtain a very rough estimate of the dose absorbed by bones using a "standard addition" technique, the ESR signal being recorded after each of several successive re-irradiations [33–35]. Nevertheless, it should be noted that ESR signal strengths depend on several parameters such as irradiation temperature, degree of bone mineralization (age of the animal, type of bone analyzed, etc.), pre- or post-irradiation treatments (cooking or freezing), and preparation of the sample (grinding and drying) [36–38]. In addition, irradiation of whole pieces of meat including bones may yield higher ESR signals than irradiation of dried excised bones alone [39]. It seems therefore very difficult to get, by this method, an accurate estimation of the dose absorbed by the food.

Detection of irradiated fish and meat samples is generally possible above a minimal detectable dose of 0.5 kGy, lower than those used for commercial applications concerning this kind of food product. Moreover, for highly mineralized bones, identification remains possible for lower absorbed doses and is not affected by heating or storage time up to 12 months [14]. For cuticle of crustacea, the ESR signal is much less stable. It may disappear if sample desiccation prior to ESR analysis is performed at temperatures above 40 °C and the intensity of the signals decreases between 44% (claws) and 17% (tail) within 28 days storage at 1 °C depending on the component analyzed [31]. The ESR method was successfully used for the analysis of bones to detect irradiated duck, frog, goose, chicken, rabbit, lamb, turkey, and pork, and in case of fish bones to detect irradiated eel, trout, whiting, sardine, shark, halibut, herring, cod, salmon, and mackerel [14]. Irradiation treatment could also be detected in eggshells [40] and mussel shells [41].

It should be noted that some irradiated food ingredients (mechanically recovered meat) used in the food industry contain very small bone fragments. The use of a specific extraction and purification procedure allows the recovery of these bone fragments and their subsequent ESR analysis for the detection of irradiated ingredients included in culinary preparations (Figure 1, spectrum 3) [42,43].

Cellulose

ESR proved to be one of the techniques that can be used for the identification of irradiated products of plant origin using the paramagnetic species (free radicals) in the cellulose fraction [44,45]. These radicals, first reported by Raffi *et al.* [46] on achenes of irradiated strawberries, were detected by many other authors analyzing the very dry part of most of the irradiated plant products [47–49]. Their ESR spectrum seems to be a hyperfine triplet centered at $g = 2.004$ (Figure 2, signal C). It appears superimposed

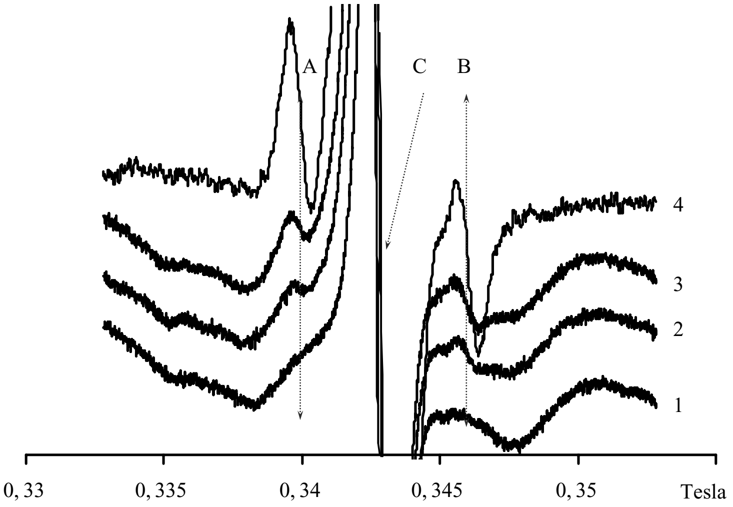

Fig. 2. ESR spectra of dried achenes extracted from unirradiated strawberries (1) and irradiated at 1.5 kGy (2) and 3 kGy (3), and paper irradiated at 5 kGy (4). Letters A, B, and C show the position of the major ESR lines.

on a non-irradiated signal belonging to lignin [50], with a similar g-factor and which is sensitive to radiation, but also to drying processes [51]. From the triplet ESR lines that are induced by irradiation, only the two outermost peaks ($g = 2.020$ and $g = 1.985$, $\Delta H \approx 6$ mT) (Figure 2, signals A and B) can be used in the case of very dry plant products such as paprika powder or dry fruit components, such as achenes, pips, shells, stalks, or stones [47,48,52,53].

In most fruits, the water content is relatively high (80%) and the radicals induced in the pulp were believed unstable and were not observed (in the soft part). Nevertheless, most of the water is free and does not participate in the chemical processes that occur within the cell wall. The active water is about 20–30% which allows radicals induced by radiation to be stable for a period compatible with the shelf life of the product. For the first time, Tabner [54] measured them at doses higher than 2 kGy in the flesh of citrus fruit. After 14 days storage, only the samples irradiated at 10 kGy remained detectable. It has been shown later that the radicals induced by radiation in the pulp of fruits are stable enough to be used as a proof of the irradiation process in the dose interval of 0.1–1 kGy [55–57] even after 3 weeks of storage if the sample dessication, prior to ESR analysis, is performed appropriately [56,57]. One of the benefits of using pulp is its low lignin content which yields much clearer triplet signals than those observed with stalks, skins, or seeds. This also allows a higher signal-to-dose sensitivity that is compatible with dose ranges used in commercial irradiation.

Detection limits and stability are influenced by the crystalline cellulose content and the moisture content of the samples. It is, therefore, important that samples desiccated prior to ESR analysis have not been re-hydrated. As the outermost peaks of the ESR triplet are of very low amplitude compared to the central one, it may be very convenient to use an irradiated sample of paper (cellulose) to get a reference signal for the location of the signals A and B (Figure 2, spectrum 4). Positive identification of the cellulose radicals is evidence of irradiation but the absence of this signal does not constitute evidence that the sample is unirradiated. The minimal detectable dose is about 2 kGy for pistachio nuts (shells) even stored up to 1 year, 5 kGy for paprika powder (live time of the signal depends on the moisture content of the test sample) [15], 1.5 kGy for fresh strawberries (achenes or pulp) stored up to 3 weeks at 1 °C, and 1.0 kGy for fresh papaya (pulp) stored up to 3 weeks at 15 °C [57].

Sugars

Irradiation of pure crystalline sugars induces stable radicals whose ESR spectra may be recorded. When sufficient amounts of crystalline sugars are present in irradiated dried fruits, as figs (Figure 3), mangoes (Figure 4), or raisins, a multicomponent ESR signal may be observed [39]. As different mono- and disaccharides may dominate in fruit samples, different ESR spectra, centered at $g = 2.0035$, may be produced after irradiation (mangoes and papaya $\Delta H = 7.4 - 7.8$ mT, raisins and dehydrated figs $\Delta H = 8.7 - 9.1$ mT) [17]. Irradiated fruits are easily distinguishable from the non-irradiated ones simply because there is no ESR signal (or a little single resonance at $g = 2.004$) in the unirradiated samples (Figures 3 and 4, spectra 1). Nevertheless, if no sugar crystals are present in the sample, irradiation will not produce any specific sugar ESR signals. That is why some irradiated fruits, as have been observed for samples of apricot or prune, do not exhibit any multicomponent ESR signal, even when irradiated at a high dose (10 kGy). On the other hand, as

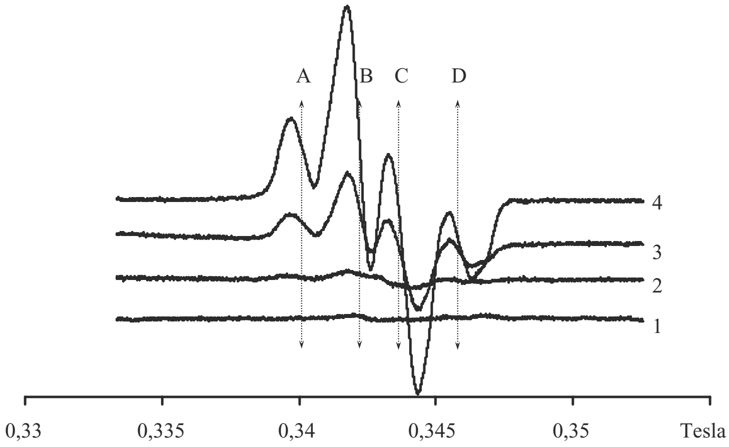

Fig. 3. ESR spectra of dried figs unirradiated (1) and irradiated at 1 kGy (2), 3 kGy (3), and 5 kGy (4). Letters A, B, C, and D show the position of the major multiplet ESR lines.

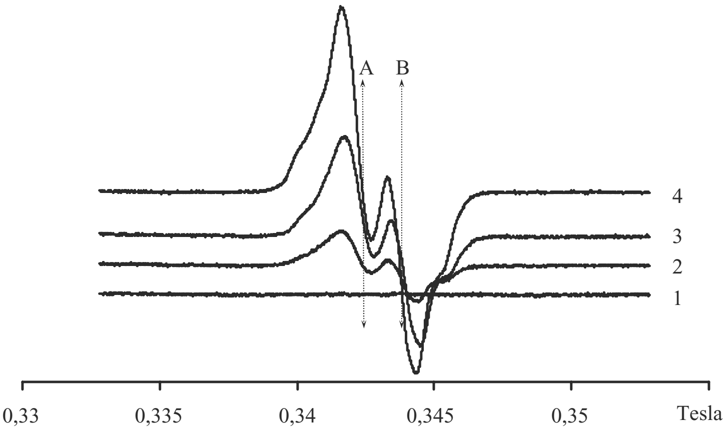

Fig. 4. ESR spectra of dried mangoes unirradiated (1) and irradiated at 1 kGy (2), 3 kGy (3), and 5 kGy (4). Letters A and B show the position of the major multiplet ESR lines.

discussed above for food of plant origin, irradiation can also give rise to the ESR spectrum of the cellulosic material [49]. Multicomponent ESR spectra prove prior irradiation, but the absence of such spectra does not constitute evidence that the sample is unirradiated. The applicability of this method depends on the presence of sufficient quantities of crystalline sugar in the sample at all stages of handling between irradiation and testing. As for the cellulose, radicals are moisture sensitive and it is important that dried samples have not been re-hydrated prior to testing. The minimal detectable dose is of about 1 kGy for dried mangoes, figs, raisins, and papayas.

Conclusion

The complete analytical protocols, including sample preparations and spectrometer settings for the analysis of radicals induced by irradiation in hydroxyapatite, cellulose, and mono- and disaccharides, are described in the official CEN protocols for the detection of irradiated foods [14,15,17]. Using these standard protocols, interlaboratory studies have been successfully carried out with beef bones, trout bones and chicken bones [14], pistachio nut shells, paprika powder and fresh strawberries achenes [15], raisins, dried figs, mangoes, and papayas [17].

Food irradiation detection remains one of the few applications of ESR spectrometry in the field of food analysis. One of its assets is its simplicity which also makes it an inexpensive method compared to other irradiated food detection tests. The realization of such analyses in the food laboratories is now possible since the recent marketing of small, automated, and easy to use benchtop ESR spectrometers at an affordable price. Approximately 1000 analyses of irradiated foods by ESR spectroscopy were carried out in 2002 in the European Union [58].

References

1. Mead PS, Slutsker L, Dietz V, McCaig LF, Bresee JS, Shapiro C, Griffin PM, Tauxe RV. Emerg. Infect. Dis. 1999;5(5):607.
2. Lutter R. Science. 1999;286(5448):2275.
3. Molins RA. Food Irradiation: Principles and Applications. Wiley-Interscience: New York, 2001.
4. Steele JH. Clin. Infect. Dis. 2001;33(3):376.
5. Diehl JF. Safety of Irradiated Foods. Marcel Dekker: New York, 1995.
6. Anonymous. IAEA Database of Clearances, www.iaea.org/icgfi, 2003.
7. Anonymous. Wholesomeness of Irradiated Food: Report of a Joint FAO/IAEA/WHO Expert Committee, WHO Tech. Rep. Ser. 659, Geneva, 1981, p 34.
8. Gregoire O, Cleland MR, Mittendorfer J, Dababneh S, Ehlermann DAE, Fan X, Kappeler F, Logar J, Meissner J, Mullier B, Stichelbaut F, Thayer DW. Radiat. Phys. Chem. 2003;67(2):169.
9. Anonymous, EU. Official J. Eur. Commun., Bruxelles. 1999; L66:16.
10. Anonymous, FAO. Draft Revised Codex General Standard for Irradiated Foods, Alinorm 03/12A, Rome, 2003, p 3.
11. Anonymous, WHO. High Dose Irradiation: Wholesomeness of Food Irradiated at Doses Above 10 kGy: Report of a Joint FAO/IAEA/WHO Expert Committee, WHO Tech. Rep. Ser. 890, Geneva, 1999, p 197.
12. Anonymous, European Committee for Standardization. EN 1784, Bruxelles, 1996, revised 2003.
13. Anonymous, European Committee for Standardization. EN 1785, Bruxelles, 1996, revised 2003.
14. Anonymous, European Committee for Standardization. EN 1786, Bruxelles, 1996.
15. Anonymous, European Committee for Standardization. EN 1787, Bruxelles, 1996, revised 2000.
16. Anonymous, European Committee for Standardization. EN 1788, Bruxelles, 1996, revised 2001.
17. Anonymous, European Committee for Standardization. EN 13708, Bruxelles, 2001.

18. Anonymous, European Committee for Standardization. EN 13751, Bruxelles, 2002.
19. Anonymous, European Committee for Standardization. EN 13783, Bruxelles, 2001.
20. Anonymous, European Committee for Standardization. EN 13784, Bruxelles, 2001.
21. Anonymous, European Committee for Standardization. EN 14569, Bruxelles, 2004.
22. Bacquet G, Truong VQ, Vignoles M, Trombe JC, Bonel G. Calcif. Tissue Int. 1981;33(2):105.
23. Rossi AM, Wafcheck CC, de Jesus EF, Pelegrini F. Appl. Radiat. Isot. 2000;52:1297.
24. Ishii H, Ikeya M, Okano M. Nucl. Sci. Technol. 1990;27:1153.
25. Ikeya M, Miyajima J, Okajima S. Jap. J. Appl. Phys. 1984;23:697.
26. Ikeya M, Miki T. Sciences. 1980;207:977.
27. Ikeya M, Ohmura K. Geochem. J. 1984;18(1):11.
28. Takano M, Fukao Y. Appl. Radiat. Isot. 1994;45(1):49.
29. Desrosiers M, Simic M. J. Agric. Food Chem. 1988;36(3):601.
30. Dodd NJ, Lea JS, Swallow AJ. Nature. 1988;334(6181):387.
31. Stewart EM, Stevenson MH, Gray R. Appl. Radiat. Isot. 1993;44(1–2):433.
32. Stewart EM, Gray R. Appl. Radiat. Isot. 1996;47(11–12):1629.
33. Desrosiers MF, McLaughlin WL, Sheahen LA, Dodd NJF, Lea JS, Evans JC, Rowlands CC, Raffi JJ, Agnel JPL. Int. J. Food Sci. Technol. 1990;25:682.
34. Desrosiers MF, Wilson GL, Hunter CR, Hutton DR. Appl. Radiat. Isot. 1991;42(7):613.
35. Desrosiers MF. Appl. Radiat. Isot. 1991;42(7):617.
36. Lea JS, Dodd NJF, Swallow AJ. Int. J. Food Sci. Technol. 1988;23:625.
37. Chawla SP, Thomas P, Bongirwar DR. Food Res. Int. 2002;35:467.
38. Gray R, Stevenson MH. Int. J. Food Sci. Technol. 1989;24:447.
39. Raffi J, Stevenson MH, Kent M, Thiery JM, Belliardo JJ. Int. J. Food Sci. Technol. 1992;27:111.
40. Regulla DF, Göksu HY, Vogenauer A, Wieser A. Appl. Radiat. Isot. 1994;45(3):371.
41. Desrosiers MF. J. Agric. Food Chem. 1989;37:96.
42. Gray R, Stevenson MH. Radiat. Phys. Chem. 1989;34(6):899.
43. Marchioni E, Horvatovich P, Ndiaye B, Miesch M, Hasselmann C. Radiat. Phys. Chem. 2002;63:447.
44. Desrosiers MF. Appl. Radiat. Isot. 1996;47:1621.
45. Desrosiers M, McLaughlin W. Radiat. Phys. Chem. 1989;34:895.
46. Raffi J, Agnel JP, Buscarlet LA, Martin C. J. Chem. Soc. Faraday Trans. I. 1988;84:3359.
47. Raffi J, Agnel JP. Radiat. Phys. Chem. 1989;34:891.
48. Tabner BJ, Tabner VA. Int. J. Food Sci. Technol. 1994;29:143.
49. Maloney DR, Tabner BJ, Tabner VA. Radiat. Phys. Chem. 1992;39:309.
50. Deighton N, Glidewell SM, Goodmann BA, Morisson IM. Int. J. Food Sci. Technol. 1993;28:45.
51. de Jesus EFO, Rossi AM, Lopes RT. Appl. Radiat. Isot. 1996;47(11–12):1647.
52. Dodd N, Swallow AJ, Ley F. Radiat. Phys. Chem. 1985;26:451.
53. Goodmann BA, McPhail DB, Duthie D. Int. J. Food Sci. Technol. 1989;47:101.
54. Tabner BJ, Tabner VA. Radiat. Phys. Chem. 1996;47:601.
55. de Jesus EFO, Rossi AM, Lopes RT. Appl. Radiat. Isot. 1999;34:173.
56. de Jesus EFO, Rossi AM, Lopes RT. Appl. Radiat. Isot. 2000;52:1375.
57. Delincée H, Soika C. Radiat. Phys. Chem. 2002;63:437.
58. Anonymous. http://europa.eu.int/eur-lex/fr/com/rpt/2004/com2004_0069fr01.pdf.

ESR Spectroscopy for the Study of Oxidative Processes in Food and Beverages

Mogens L. Andersen and Leif H. Skibsted
Food Chemistry, Department of Food Science, The Royal Veterinary and Agricultural University,
Rolighedsvej 30, DK-1958 Frederiksberg C, Denmark

Introduction

Oxidative reactions in food that involve lipids are, together with microbial growth, among the most important causes of spoilage of food and affect both shelf life and the quality of foods. The oxidation of unsaturated lipids in foods is observed as rancidity, while oxidation of proteins may result in other off-flavors and in some cases as a change in texture. The oxidation of vitamins and polyunsaturated fatty acids reduce the nutritional value and form potentially toxic oxidation products, while oxidation of food pigments leads to discoloration. Radicals are intermediates in many of these reactions, and the detection of radicals by electron spin resonance, ESR, provides therefore an excellent way to study early stages of these destructive reactions [1–3]. The study of radicals by ESR can moreover give important mechanistic information, which is useful for designing protective measures against oxidation in food. The detection of radicals by ESR has also recently also been used to predict the oxidative stability of foods, and further to quantify important quality aspects of food.

ESR [also commonly known as electron paramagnetic resonance (EPR) or electron magnetic resonance (EMR)] detects unpaired electrons in atoms and radicals. ESR spectra are characterized by the g-factor that is associated with Zeeman splitting, and which is determined by Equation 1, where h is the Planck constant ($6.6260755 \cdot 10^{-34}$ $\mathrm{J \cdot s}$), ν is the frequency of the applied microwave irradiation, β is the Bohr magneton ($9.2740154 \cdot 10^{-24}$ $\mathrm{J \cdot T^{-1}}$) and B is the magnetic field[4].

$$h\nu = g\beta B \tag{1}$$

Paramagnetic nuclei in radicals can often interact with the unpaired electron causing hyperfine splitting of the ESR lines, which can give useful structural information that allow identification of radicals [4]. Most commercial ESR instruments operate with microwave frequencies around 10 GHz (X-band). Solids and liquids can be studied over a wide temperature range by ESR and samples does not need to be transparent, which makes the technique useful for studies of foods. The very high sensitivity makes the technique useful for detection of radicals at early stages of oxidation in foods. Often ESR is used to compare the relative concentration of radicals in several food samples. In this case it is extremely important that the samples are as similar as possible [5]. It is therefore also important to use reference samples of stable radicals with a known concentration that are as identical as possible to the samples when absolute concentrations of radicals have to be calculated [6].

ESR Detection of Radicals in Foods

Radicals that are formed during oxidative processes in foods are often highly reactive species and are therefore in most cases only encountered as short-lived intermediates with very low steady state concentrations that make direct ESR detection impossible. The lifetime of radicals are often increased dramatically in solid samples, such as dry or frozen foods, where the molecular components are physically trapped, which prevent or slow down chemical reactions that would otherwise quench the radicals rapidly. The direct detection of persistent radicals at room temperature by ESR is therefore often possible in dry foods, where ESR detectable concentrations of physically trapped radicals can accumulate during production and storage. Often only a single line with a g-value in the range 2.003–2.006 and a peak-to-peak line width between 4 and 12 Gauss (Figure 1) is observed in the ESR spectrum of dry foods. However, in many cases also a sextet of lines is observed due to the presence of Mn^{2+}, which is frequently seen in ESR spectra of biological tissues (Figure 1) [7].

The persistence of radicals in dried foods or foods containing solid materials such as bones or shells make it also possible to use ESR for detection and quantification (dosimetry) of irradiation treatments where stable radicals with characteristic ESR spectra are often formed [8].

The origin of the stable radicals in dry foods is unknown and several sources have been suggested including reactions resulting from heat treatment of carbohydrates [9], or oxidation of polyphenols [10] and proteins [2], or formation of Maillard products [11]. However, the stable

Graham A. Webb (ed.), Modern Magnetic Resonance, 1861–1866.
© 2008 *Springer.*

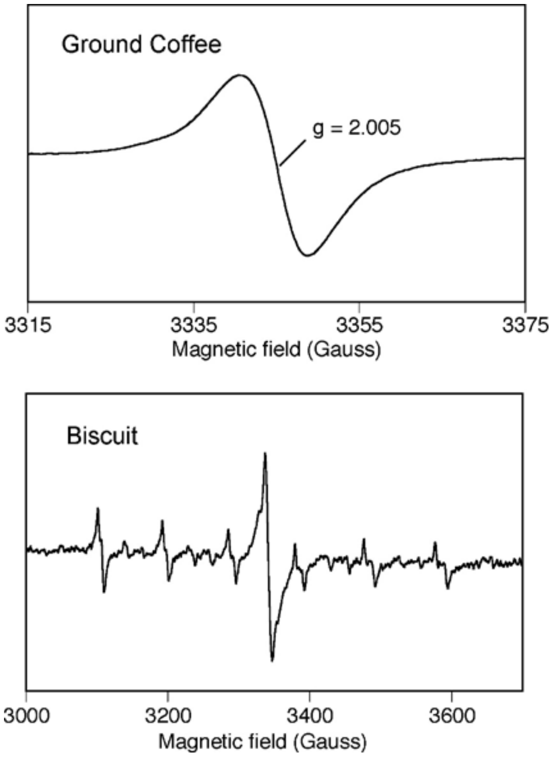

Fig. 1. Typical ESR spectra of persistent radicals detected in dry foods. A single broad signal with g ≈ 2 (presumably due to organic radicals) is often observed. A sextet of lines due to Mn^{2+} is also often observed.

radicals in dry foods have been shown to be good markers of the oxidative status of dry products and several studies have demonstrated that the level of radicals correlate with the extent of lipid oxidation or with external factors such as heat, light and storage time that are likely to induce oxidation (Table 1).

Trapping of radicals in frozen samples has been used together with direct ESR detection for studies of radicals involved in autoxidation of lipids and of light induced formation of lipid radicals in frozen triglycerides at 77 K [24,25]. Radicals that are derived from phenolic compounds have been detected in frozen samples of wine [26].

Spin Trapping

Most foods contain water, which allow the components to diffuse. Radicals in most foods are therefore very short lived with steady state concentrations that are too low to be detected directly by ESR. However, the indirect detection of radicals can under these conditions be carried out by using the spin trapping technique, where a stable radical (called a spin adduct) is formed by the addition of reactive radicals to a spin trap (Figures 2 and 3) [27]. The stability of spin adducts allow the accumulation of ESR detectable concentrations. The spin trapping technique has been used to characterize radicals formed in beverages such as coffee [28] and during oxidative processes in beer [29] (Figure 4).

Spin trapping has also been used to examine the tendency of formation of radicals in mayonnaise and for evaluation of methods for protection of unsaturated lipids in the mayonnaise against oxidation [30,31]. The spin trap PBN was mixed into mayonnaise and the samples were mildly heated at 37 °C for 24–36 h before the amount of radicals were measured by ESR. The amount of radicals could be quantified by comparison with the nitroxyl radical 12-doxylstearic acid that was found to be stable in mayonnaise [32].

Prediction of Oxidative Stability of Foods

Accelerated aging of foods has often been used to predict the long-term stability of foods. Usually the level of oxidation has been followed by measuring the formation of primary or secondary oxidation products. With ESR it is possible to study the radicals that are involved in the oxidative reactions directly, which makes it possible to determine the level of oxidation more directly during forced ageing experiments. The method has been used with great success in the brewing industry to predict the flavor stability of lager beer [33–36]. A spin trap (PBN) is added to the beer after dissolved CO_2 has been removed, and the beer is then heated (50–60 °C) with access to atmospheric oxygen. The presence of antioxidants in the beer will initially inhibit the formation of radicals resulting in a low level of spin adducts in the beginning of the experiment. The antioxidants are consumed as a consequence of their actions, and unhindered formation of radicals will eventually take place when all the active antioxidants are consumed, resulting in a steady increase in the level of spin adducts (Figure 5). The length of the initial lag phase (also called induction period or lag time) is mainly determined by the competition between actions of antioxidants and pro-oxidants, which are also likely to be crucial factors for the oxidative stability under conventional storage of beer. The lag time determined for fresh lager beer has been shown to correlate with the storage stability, making the method suitable for early prediction of the shelf life [34]. The ESR lag time method has also been used for testing the effect of potential antioxidants present in beer on the oxidative stability of beer [37].

The ESR lag time method has been adopted for the prediction of the stability of bulk lipids, although it should

Table 1: ESR detection of radicals in dry foods

Dry product	Observations related to stable radicals detected in foods by ESR	Reference
Plant derived foods		
Coffee-beans	Roasting, water content, and storage affect level of radicals	[12]
Wheat flour and starch	Extrusion, heat, and the presence of oxidizing methyl linoleate increase the level of radicals	[13]
Licorice	Radicals detected in licorice products before and after oral administration	[10]
Dried potato flakes	Level of radicals marker of early oxidation	[14]
Walnut kernels	Heat and air increase level of radicals	[15]
Bread	Heat increase level of radicals	[16]
Peanuts	Light irradiation increase level of radicals	[17]
Oatmeal	Light irradiation increase level of radicals	[17]
Muesli	Light irradiation increase level of radicals	[17]
Dairy products		
Milk powder	Thiobarbituric acid reactive substances and sensory scores of reconstituted milk correlate with level of radicals	[18]
Freeze dried raw milk	α-Tocopherol content correlate with level of radicals	[19]
Freeze dried processed cheese	Thiobarbituric acid reactive substances correlate with level of radicals	[20]
Freeze dried cheese	Results of sensory evaluation correlate with level of radicals	[21]
Infant formula	Water activity and storage affect level of radicals	[22]
Animal derived foods		
Dried chicken meat	Hexanal in headspace and results of sensory evaluation correlate with level of radicals	[23]
Pork scratchings	Presence of oxygen increase level of radicals	[17]

in principle also be possible to use it for lipids present in more complex systems [3,28]. The lag times determined by the ESR method for lipid oxidation in vegetable oils have been shown to correlate with conventional methods for quantification of lipid stability [39].

The tendency to formation of radicals measured by spin trapping radicals during heat treatment has also been used to evaluate the oxidative stability of raw milk [40], sugar-cane spirits [41], processed pork [42] and dry-cured ham [43]. The meat samples were homogenized in buffer

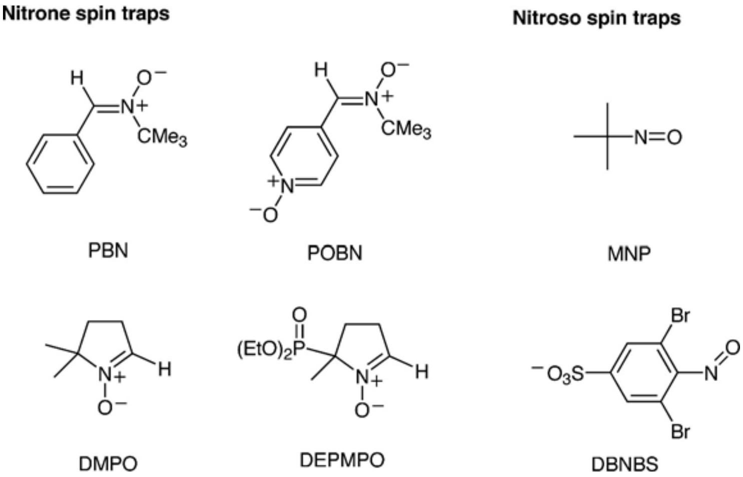

Fig. 2. Common spin traps used in foods to trap radicals.

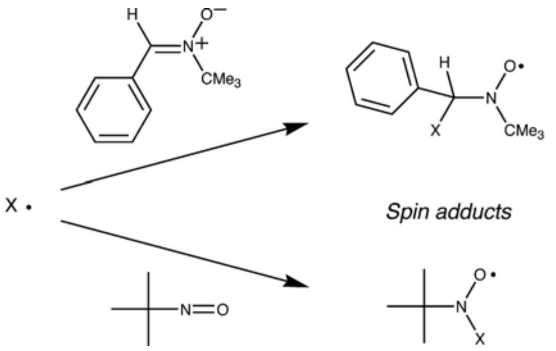

Fig. 3. Spin adducts formed by addition of radicals to spin traps.

containing the spin trap POBN, and the slurry was then heated. Samples were taken from the slurry, filtered and subsequently analyzed by ESR.

Other Uses of ESR for Studies of Food Oxidation

ESR has also been used to detect generation of singlet oxygen, $^1O_2$, which can induce lipid oxidation without the involvement of radicals [44,45]. Singlet oxygen can oxidise 2,2,6,6-tetramethyl-4-piperidone to a stable nitroxyl radical, which can be detected by ESR. The technique has been used to study the photogeneration of singlet oxygen by pigments such as chlorophyll and myoglobin. ESR and spin trapping have been used to characterize the role of riboflavin in light induced formation of radicals in beer [46], and to identify intermediates that are formed upon oxidation of isohumulones that are the principle bittering agents in beer [47], while the direct photodegradation of isohumulones has been studied by time resolved ESR (TREPR) [48].

The presence of antioxidants is an important factor that affects the oxidative stability of foods. Many assays for testing the efficiency of antioxidants in foods are based on measuring the ability to quench stable radicals. This approach called spin scavenging has been used with ESR detection of stable radicals such as potassium nitrosodisulfonate, Fremy's salt [49], 1,1-diphenyl-2-picrylhydrazyl radical, DPPH [50], galvinoxyl radical [49,51], and 2,2,6,6-tetramethylpiperidine-1-oxyl radical, TEMPO [20]. ESR spectroscopy has proved to be useful for such studies, since the level of very low concentrations of radicals can be studied in samples that are not optically transparent.

The line widths of ESR lines are dependent on the presence of paramagnetic substances by Heisenberg spin exchange. The concentration of oxygen, which is a very common paramagnetic compound, affects the line width. By recording the line width of a stable radical (a socalled spin probe) one can measure the oxygen concentration. This approach has been used to measure the concentration of oxygen in oil encapsulated in a glassy carbohydrate/protein matrix, and thus to study the ability of oxygen to penetrate barriers of glassy food components at different temperatures [52].

Perspective and Future Developments

ESR is a relatively new analytical method in food science and routine methods needs to be developed further. New generations of low-cost and user-friendly ESR instruments are however becoming available for

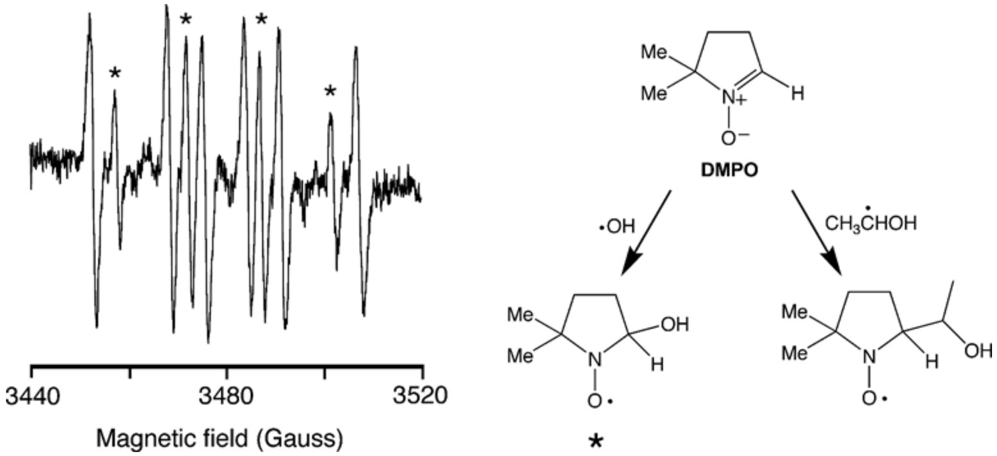

Fig. 4. Spin adducts formed in lager beer by using the spin trap DMPO and generating radicals by the Fenton reaction [29].

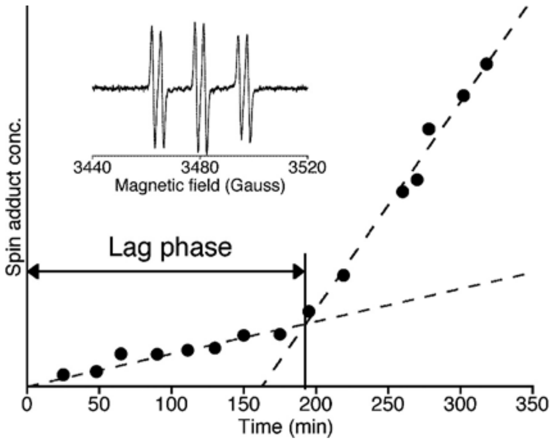

Fig. 5. The formation of PBN spin adducts in lager beer during aerobic heating. The concentration of spin adducts are measured as the amplitude of the central lines of the ESR spectrum (insert).

introduction in quality control laboratories. Another perspective is development of field gradient ESR-spectroscopy for imaging of radical processes in food systems. Using such techniques, spatial propagation of oxidative processes could be studied in multiphase and cellular systems and prooxidative structures be identified and antioxidant application optimized.

References

1. Andersen ML, Skibsted LH. Eur. J. Lipid Sci. Technol. 2002;104:65.
2. Schaich KM. In: MJ Morello, F Shahidi, C-T Ho (Eds). Free Radicals in Food. Chemistry, Nutrition and Health Effects. ACS Symposium Series 807. American Chemical Society, Washington, 2002, p 12.
3. Andersen ML, Velasco J, Skibsted LH. In: A Kamal-Eldin, J Pokorny (Eds). Analysis of Lipid Oxidation. AOCS Press, Champaign, 2005, p 127.
4. Weil JA, Bolton JR, Wertz JE. Electron Paramagnetic Resonance. Wiley-Interscience: New York, 1994.
5. Eaton SS, Eaton GR. In: GW Ewing (Ed). Analytical Instrumentation Handbook, 2nd ed. Marcel Dekker, Inc.: New York, 1997. p 767.
6. Blakley RL, Henry DD, Morgan WT, Clapp WL, Smith CJ, Barr D. Appl. Spectrosc. 2001;55:1375.
7. Saifutdinov RG, Larina LI, Vakul'skaya TI, Voronkov MG. Electron Paramagnetic Resonance in Biochemistry and Medicine. Kluwer Academic/Plenum Publishers: New York, 2001.
8. Rosenthal I. In: MM Mossoba (Ed.). Spectral Methods in Food Analysis. Instrumentation and Applications. Marcel Dekker, Inc.: New York, 1999. p 125.
9. Gonis J, Hewitt DG, Troup G, Hutton DR, Hunter CR. Free Rad. Res. 1995;23:393.
10. Gallez G, Baudelet C, Debuyst R. J. Nutr. 2000;130:1831.
11. Hofman T, Bors W, Stettmaier K. In: MJ Morello, F Shahidi, C-T Ho (Eds). Free Radicals in Food. Chemistry, Nutrition and Health Effects. ACS Symposium Series 807. American Chemical Society, Washington, 2002, p 49.
12. Santanilla JD, Fritsch G, Müller-Warmuth W. Lebensm Z. Unters. Forsch. 1981;172:81.
13. Schaich KM, Rebello CA. Cereal Chem. 1999;76:748.
14. Nissen LR, Huynh-Ba T, Petersen MA, Bertelsen G, Skibsted LH. Food Chem. 2002;79:387.
15. Szöcs F. J. Food. Sci. 2002;67:953.
16. Yordanov ND, Mladenova R. Spectrochim. Acta. Part A. 2004;60:1395.
17. Jensen PN, Danielsen B, Bertelsen G, Skibsted LH, Andersen ML. Food Chem. 2005;91:25.
18. Stapelfeldt H, Nielsen BR, Skibsted LH. Int. Dairy J. 1997;7:331.
19. Stapelfeldt H, Nielsen KN, Jensen SK, Skibsted LH. J. Dairy Res. 1999;66:461.
20. Kristensen D, Skibsted LH. J. Agric. Food Chem. 1999;47:3099.
21. Kristensen D, Orlien V, Mortensen G, Brockhoff P, Skibsted LH. Int. Dairy J. 2000;10:95.
22. Thomsen MK, Knudsen JC, Risbo J, Skibsted LH. Milchwissenschaft 2003;58:406.
23. Nissen LR, Månsson L, Bertelsen G, Huynh-Ba T, Skibsted LH. J. Agric. Food Chem. 2000;48:5548.
24. Yanez J, Sevilla CL, Becker D, Sevilla MD. J. Phys. Chem. 1987;91:487.
25. Geoffrey M, Lambelet P, Richert P. J. Agric. Food Chem. 2000;48:974.
26. Troup GJ, Hutton DR, Hewitt DG, Hunter CR. Free Rad. Res. 1994;20:63.
27. Rosen GM, Britigan BE, Halpern HJ, Pou S. Free Radicals. Biology and Detection by Spin Trapping. Oxford University Press: New York, 1999.
28. Pascual EC, Goodman BA, Yeretzian C. J. Agric. Food Chem. 2002;50:6114.
29. Andersen ML, Skibsted LH. J. Agric. Food Chem. 1998;46:1272.
30. Thomsen MK, Jacobsen C, Skibsted LH. Eur. Food Res. Technol. 2000;211:381.
31. Jacobsen C, Hartvigsen K, Thomsen MK, Hansen LF, Lund P, Skibsted LH, Hølmer G. Adler-Nissen J, Meyer AS. J. Agric. Food Chem. 2001;49:1009.
32. Thomsen MK, Vedstesen H, Skibsted LH. J. Food Lipids 1999;6:149.
33. Uchida M, Ono M. J. Am. Soc. Brew. Chem. 1996;54:198.
34. Uchida M, Suga S, Ono M. J. Am. Soc. Brew. Chem. 1996;54:205.
35. Takaoka S, Kondo H, Uchida M, Kawasaki Y. MBAA Tech. Quart. 1998;35:157.
36. Franz O, Back W. Monatsschrift für Brauwissenschaft 2002;55:8.
37. Andersen ML, Outtrup H, Skibsted LH. J. Agric. Food Chem. 2000;48:3106.
38. Thomsen MK, Kristensen D, Skibsted LH. J. Am. Oil Chem. Soc. 2000;77:725.
39. Velasco J, Andersen ML, Skibsted LH. Food Chem. 2004;85:623.

40. Kristensen D, Andersen ML, Skibsted LH, Milchwissenschaft. 2002;57:255.
41. Bettin SM, Isique WD, Franco DW, Andersen ML, Knudsen S, Skibsted LH. Eur. Food Res. Technol. 2002;215:169.
42. Carlsen CU, Andersen ML, Skibsted LH. Eur. Food Res. Technol. 2001;213:170.
43. Andrés AI, Møller JKS, Adamsen CE, Skibsted LH. Eur. Food Res. Technol. 2004;219:205.
44. Whang K, Peng IC. J. Food Sci. 1988;53:1863.
45. Whang K, Peng IC. J. Food Sci. 1988;53:1918.
46. Laane C, de Roo G, van den Ban E, Sjauw-En-Wa M-W, Duyvis MG, Hagen WA, van Berkel WJH, Hilhorst R, Schmedding DJM, Evans DJ. J. Inst. Brew. 1999;105: 392.
47. Huvaere K, Andersen ML, Olsen K, Skibsted LH, Heyerick A, de Keukeleire D. Chem. Eur. J. 2003;9: 4693.
48. Burns CS, Heyerick A, de Keukeleire D, Forbes MDE. Chem. Eur. J. 2001;7:4554.
49. Gardner PT, McPhail DB, Duthie GG. J. Sci. Food Agric. 1998;76:257.
50. Chen C, Tang H-R, Sutcliffe LH, Belton PS. J. Agric. Food Chem. 2000;48:5710.
51. Quiles JL, Ramírez-Tortosa MC, Gómez JA, Huertas JR, Mataix J. Food Chem. 2002;76:461.
52. Andersen AB, Risbo J, Andersen ML, Skibsted LH. Food Chem. 2000; 70:499.

Part III

Applications to Food Systems

Magnetic Resonance Studies of Food Freezing

William L. Kerr
Department of Food Science and Technology, University of Georgia, Athens, Georgia 30602, USA

Introduction

Freezing is one of the fundamental operations used for food preservation, as the reduction in temperature reduces the rate of deleterious chemical reactions and microbial growth. In some cases, as with ice cream and sherbet, freezing imparts desirable coolness and texture. Many foods are frozen including fruits, vegetables, muscle foods, eggs, dairy products, and dough, as well as an assortment of frozen entrees.

Freezing is a complex physicochemical process involving the development of crystalline, liquid, and glassy states. Some damage may occur as ice develops and causes migration of water out of cells, or from one region to another. Several questions regarding freezing are of interest to food engineers: How long does it take an item to freeze? What size are the ice crystals that develop? What is the nature of unfrozen water in foods? What effect does freezing have on quality? How are food constituents affected by freezing? How does freezing influence post-thawing processes?

A variety of tools have emerged to study frozen foods, including X-ray diffraction, calorimetry, microscopy, and mechanical spectroscopy. As most foods contain water or oil, the use of ^{1}H NMR seems a natural approach for studying the quantity and dynamics of these components. Proton NMR has also proven useful for studying food structure. Other magnetic nuclei, including ^{31}P, ^{23}Na, and ^{13}C have been monitored to better understand the chemistry of food molecules and biopolymers during freezing.

The study of materials containing ice can prove problematic to NMR spectroscopists. Whereas liquid water has magnetic spin relaxation times up to 1–2 s, or in the millisecond range when inside foods, ice has a spin relaxation time of tens of microseconds. In addition, obtaining field homogeneity can be difficult. This article reviews the several NMR methods for studying frozen systems, and is categorized into relaxometry techniques, pulsed field gradient diffusion techniques, magnetic resonance imaging (MRI), chemical spectroscopy, and solid-state NMR.

Spin Relaxometry

One of the first reports on the use of NMR in frozen biological material was by Wikefeldt in 1971 [1]. Using continuous wave ^{1}H NMR, he tested the hypothesis that the rate of ice growth in small blood-drops was controlled by the translational mobility of water. He used the line width $\Delta\nu_{1/2} = 1/\pi T_2^*$ as the measure of mobility, but recognized that mobility might be influenced, and even dominated by rotational motion in addition to translation. In more recent times, Ablett *et al.* found that recrystallization in frozen sugar solutions is correlated with molecular mobility as measured by time domain NMR. In addition, they found that the glass transition temperature (T_g), and the temperature difference ($T - T_g$), are correlated with ice recrystallization rates [2].

Ice, Unfrozen Water, and Glassy States

The quantity of ice that exists in a frozen food at a given temperature is of great interest to food scientists. Traditionally, this has been determined by adiabatic calorimetry, differential scanning calorimetry (DSC), or differential thermal analysis (DTA). ^{1}H NMR has been investigated as a means for quantifying liquid and solid states in frozen materials, as the solid ice protons have a much shorter decay than the liquid water protons [3,4]. Studies have been conducted on sucrose solutions [4], sucrose–protein solutions [5], NaCl solutions [6], water and oil emulsions [7], porous media [8], food gels [9,10], orange juice [11], and wheat dough [12,13]. Free induction decay (FID) experiments following a 90° pulse have been most useful, as measurement time is short and dynamics in the microsecond range can be captured. The initial post dead time signal, at around 10 μs, is proportional to the number of liquid water, ice, and food constituent protons, while the signal at 70 μs is proportional to the liquid state protons. In some cases, fitting with a series of Gaussian curves has been used to extrapolate to the zero time amplitude [13]. The dependence of the magnetization magnitude on temperature must be accounted for, and

Graham A. Webb (ed.), Modern Magnetic Resonance, 1869–1878.
© 2008 *Springer.*

is described by Curie's law:

$$M_0 = \frac{B_o N \gamma^2 h^2 I(I+1)}{3kT} \tag{1}$$

For sucrose solutions, the proportion of protons in the solid phase was given as[4]

$$F = 1 - \frac{M_{0,F} T_F}{M_{0,L} T_L} \tag{2}$$

where M_0 is the initial signal amplitude, and T is the temperature of the frozen (F) and control liquid (L) samples. For a few sugar solutions, the phase diagrams determined by NMR have been compared with those determined calorimetrically, and these are typically in agreement [4].

FID experiments using both H_2O and D_2O have been used to study the effects of cryoprotectants on the eutectic crystallization of NaCl in frozen solutions [6]. As the temperature of frozen NaCl solutions was increased, a sharp increase in the number of liquid-phase protons occurred, which corresponded with the eutectic temperature as measured by DSC. When cryoprotectant sugars were added to NaCl solutions, the number of liquid protons increased, with no apparent change at the expected eutectic temperature. As a result, they concluded that the addition of sugar inhibits eutectic crystallization of NaCl through formation of an amorphous mixture of NaCl, sugar, and water between ice crystals.

Few NMR measurements of the ice content in semisolid frozen foods have been reported, and there are even fewer cases where concurrent calorimetric data is present. The solid and liquid phases of frozen bread dough have been studied using single pulse techniques. Typically, the FID relaxation curves can be resolved into a single fast component (< 20 μs), and one or two slower components [12,13]. In a previous study, the most dramatic decrease in liquid water occurred between 0 and $-10\,^\circ$C. At $-30\,^\circ$C, a precipitous increase in the solid component, and decrease in the liquid component, was observed and attributed to a glass transition. These results were consistent with CPMG experiments, and were highly correlated with dynamic mechanical thermal analysis (DMTA) and dielectric thermal analysis (DETA) measurements. These authors also found that the liquid signal may increase during frozen storage, which they attributed to the growth of ice crystals and redistribution of water.

Cornillon *et al.* used FID experiments to measure the amount of water in different states of various food gels between -40 and $20\,^\circ$C, then used the data to more accurately predict thermophysical properties of the materials [14]. At $-40\,^\circ$C, they observed some liquid-like signal, and attributed this to unfreezable, or bound, water. The amount of unfreezable water ranged from 0.05 to 0.66 g/g dry matter, depending on the gel type and whether sucrose was incorporated in the gel. They also found that 90% of the water was frozen between 0 and $-10\,^\circ$C. Kim *et al.* [15] studied cornstarch gels prepared with 10 or 30% various sugars and sugar alcohols. They found that for non-sugar gels, the onset of melting (T'_m) occurred at $-10\,^\circ$C, while the addition of sugars decreased the onset of melting to lower temperatures. They also found evidence of the occurrence of non-equilibrium freezing. In particular, sugar addition and rapid cooling promoted the formation of a glassy state, with a concomitant reduction in the amount of ice formed. At high cooling rates, the temperature may decrease such that the water is incorporated in a glassy matrix and prevented from further crystallization [16]. Indeed, many measurements of glass transitions in frozen foods incorporate an annealing process in which the sample is held just above the glass transition temperature (T'_g), thereby allowing the maximum amount of ice to be formed.

In addition to quantifying the amount of unfreezable water, NMR has been used to better understand the glassy state of frozen foods. Glassy materials are amorphous solids with little mobility on everyday time scales. As the temperature of a glassy material is increased, one or more glass transitions occur at characteristic temperatures, corresponding to the onset of coordinated molecular motions in the polymer chains [17]. Such transitions in foods, and particularly in frozen foods, are much more complex. First, foods are usually comprised of a variety of biopolymer carbohydrates, proteins, and a myriad of small and medium molecular weight substances. In addition, ice readily forms in high moisture foods; however, a glassy phase may coexist at temperatures below a characteristic temperature (T'_g). A noticeable change in the spin–spin relaxation time, T_2, often occurs at the glass transition temperature [13]. Several studies have suggested that some mobile water remains, even at very low temperatures. For example, Ullmann *et al.* used spin–spin relaxation to study the effects of freeze-concentration on proteinase-catalyzed peptide synthesis, and found that some mobile water existed even at $-70\,^\circ$C [18]. In a series of malto-oligomer solutions, Ablett *et al.* observed a fast (low mobility) and slow (high mobility) relaxing component of the spin–spin relaxation [19]. As the slow relaxing component disappeared when the experiment was conducted with D_2O, they associated this with water. They found that, upon freezing, there was a significant reduction in the intensity of the slow component down to $-10\,^\circ$C, at which point maximum ice was assumed to have formed. These authors were quick to note, however, that signal intensity was not completely due to mobile water, as chemical exchange with labile protons enhances the apparent signal. At lower temperatures, some portion of the water signal still persists, suggesting that there are mobile water protons in the glassy state. Strictly speaking, this indicates only that proton rotational motion persists, and this was better quantified with spin–lattice (T_1) measurements. They also conducted pulsed field gradient experiments, which suggested that some translational motion of water occurs in the glassy state.

NMR studies have also been conducted to determine the ice and unfrozen water states in model systems. Le Botlan *et al.* measured T_2^* and T_1 relaxation in water-in-oil and oil-in-water emulsions [20]. In emulsions held in the frozen state, up to four phases may be present. At $-13\,^\circ$C, at least 99% of the water existed in the solid state. Several researchers have also studied ice formation in porous media. Rault *et al.* used ^{2}H FID to examine ice formation in porous glass with a variety of pore sizes [21]. They showed that only part of the confined water froze, and that a non-frozen interfacial layer approximately 0.5 nm in thickness existed, which explained why water confined to regions less than 1 nm did not freeze. Morishige and Kawano showed that hysteresis occurred between freezing and melting curves in cylindrical pores, becoming more pronounced in larger pores. They attributed this to size-dependent supercooling of water confined in mesopores [22]. In addition, the melting point of water in small spaces, and with high curvature, is expected to be lower than that for bulk water [23]. Watanabe and Mizoguchi also studied porous media, including glass powder, silty soil, and clay saturated with salt solutions. They found that the amount of unfrozen water increased with increasing solute concentration, in the order $\mathrm{NaCl} = \mathrm{KCl} < \mathrm{MgCl_2}$. In addition, Valiullin and Furo used nuclear magnetic resonance magnetization transfer and NMR cryoporometry to study coexisting liquid and frozen phases in porous glasses [24].

Structural Studies

NMR relaxometry has been used to study a variety of structural features in frozen materials, including ice crystal size, ice and water distribution, pore size, and aspects of cellular structure. Most of these studies rely on the effect of relaxation "sinks" on the apparent relaxation time, and are most often described by the Brownstein–Tarr theory [25]. The sinks may be paramagnetic surface impurities, mechanisms that limit molecular tumbling near the surface, or opportunities for chemical exchange. The rate of change of the magnetic moment per unit volume (ρ) is given by

$$\frac{\partial \rho}{\partial t} = D\nabla^2 \rho - \vartheta \rho \tag{3}$$

where D is the self-diffusion coefficient of water, and ϑ is the volume sink parameter. It can be shown that the measured magnetization is given by

$$M(t) = \int_V \rho(\mathbf{r}, t)\,\mathrm{d}V \tag{4}$$

In general, $M(t)$ is related to a sum of exponential terms that include the relaxation time (T_n). If the diffusion of water is sufficiently rapid, and the size of the pores is relatively small, then water in the pore can diffuse to a surface and interact with a sink in a time much smaller than that characteristic of the relaxation processes. In this case, $M(t)$ is a single-exponential process, with an averaged T_2 (or T_1) less than that of bulk water and dependent upon the size of the pore. Equations relating T_n to pore size depend upon the particular geometry assumed for the system. In general, porous systems are heterogeneous in size; therefore, one expects a distribution in T_n characteristic of the distribution of pore sizes. In general, magnetization relaxation data can be deconvolved into a distribution of exponential decay processes. One common approach is through the CONTIN program of Provencher [26].

The size of ice crystals in frozen materials is a key determinant to the quality of the food. However, *in situ* measurement of ice crystal size is problematic. Conventional microscopy requires fixing, thin-sectioning, and a well-controlled temperature stage or the ability to place the microscope in a cold environment. Indirect spin–spin relaxation techniques have been developed to give a bulk measurement of ice crystal size distribution in some products [27,28]. In frozen starch gels, ice crystals were sublimated by freeze-drying, leaving an intact structure containing spaces where ice crystals once existed. These spaces were filled with acetone, presumably leaving the gel structure unaffected. The starch surface acts as a strong relaxation sink for acetone proton transverse magnetization. Pore sizes were determined by the Brownstein–Tarr theory.

A multitude of NMR studies have been conducted on the structure of porous materials. Much fewer, however, have been conducted on frozen porous materials. Hills and Le Floc'h studied transverse relaxation time distributions in randomly packed beds of Sephadex beads [29]. As these included beads of differing radius and cross-link density, this allowed investigation of a broad range of pore size distributions similar to those that might be found in foods. In addition, the dextran matrix provided hydroxyl groups with substantial proton exchange with water. They found that unfrozen Sephadex contained two water-filled compartments consisting of a region inside the beads characterized by $T_{2\mathrm{in}}$ as well as a bulk water region outside the beads. Furthermore, diffusion of water between the compartments was sufficiently rapid so that an averaged T_2

was observed, which depended on the bead pore size. Ice crystals were found to form inside the Sephadex beads, and with sizes less than the bead diameter. In a series of controlled experiments, they examined the temperature dependence of T_2, and found the existence of two phases, that is, ice surrounded by a concentrated dextran gel.

An interesting twist on the theme is the study of porous materials through cryogenic NMR [30]. This approach relies on the fact that water in small pores has a lower equilibrium freezing point. Prepared samples are frozen, raised stepwise to a variety of subfreezing temperatures, and the FID signal intensity determined after the solid signal has decayed. The pore size (R) distribution is derived from the Gibbs–Thompson relationship. The advantage of the cryogenic NMR approach to pore size distribution is that complex properties such as the magnetization sink strength do not need to be measured or assumed. However, materials that are readily deformed or fractured by the formation of ice would give rise to artifacts using this approach.

States of Water

Although many studies exist on the use of NMR relaxometry to examine water states in solutions of protein, carbohydrates, or other solutes, few exist on the properties of frozen solutions. Lucas *et al.* characterized both spin–spin and spin–lattice relaxations of water in frozen sucrose–protein solutions between -13 and 20 °C [31]. At -13 °C, three relaxation components could be distinguished. A short T_2 (16.2 μs) component was associated with ice, while two longer ones, 8–18 ms and 103–110 ms, were associated with non-exchangeable sucrose protons and cryo-concentrated water protons, respectively. These authors were able to calculate the fraction of ice at each temperature. They also noted that T_1 measurements, as opposed to T_2 measurements, gave more information on the ice molecular structure. For example, they determined that the ice phase in sucrose or casein solutions contained pure water, and speculated that incorporation of ions or small molecules could be detected.

A substantial number of NMR relaxometry studies have focused on the effect of freezing and thawing on structural aspects of cellular materials. Most of these have relied on the observation of distinct multiple relaxation phenomena, which can be associated with magnetic nuclei in different states or regions. As with porous systems, these distinctions cannot be made if molecules of interest rapidly diffuse amongst regions. Cameron *et al.* investigated the use of T_1 as a measure of ice crystal size in rat tissue, tendons, and lens material [32]. They found that the average ice crystal size, as determined by microscopy, had a significant positive correlation with T_1.

When maize was dried at temperatures between -30 and 25 °C, two T_1 components were observed, with minimum values at -20 °C [33]. They concluded that water mobility decreased with temperature. Hills and Le Floc'h [29] used spin–spin relaxation to study non-freezing water in potato tissue. In isolated starch granules, distributed exponential analysis showed two water domains, a slower relaxing one outside the granules and a fast relaxing one inside the granules. The relaxation time of the shorter component decreased with temperature, and it was concluded that most unfreezable water was associated with the granules and cell wall material. In whole tissue at -15 °C, they identified three peaks, and tentatively associated them with non-freezing water in cytoplasmic macromolecules (∼1 ms), water in partly frozen starch granules and cell wall material (3–4 ms), and extracellular or cytoplasmic water or water in vacuoles (10 ms). They also reinforced the idea that unfreezable water protons are still mobile, even when the material is in the glassy state ($T < T_g'$).

Hills and Remigereau used NMR to monitor the subcellular and intercellular redistribution of water in apple tissue during drying and freezing [34]. During freezing at -3 °C, ice first formed in the vacuoles, while the cytoplasmic and cell wall compartments froze at much lower temperatures (<-10 °C). Similar relaxation time distributions were observed upon thawing as were seen upon freezing. However, upon complete thawing, T_2 of vacuole water was 250 ms, as compared to 650 ms of the fresh tissue. In addition, the cell wall and cytoplasmic compartments were less well resolved. These authors concluded that NMR relaxometry is a more useful tool for studying subcellular water distributions than are spatially resolved imaging techniques. Similar observations were found during freezing and thawing of carrot parenchyma cells [35].

In seaweed shoots at -10 °C, two fractions of water were observed [36]. The slow ($T_2 \sim 50$ ms) fraction was attributed to protoplasmic water and cell wall polysaccharides, and was completely frozen at -25 °C. The fast ($T_2 < 10$ ms) fraction was attributed to water-soluble proteins. Freezing of the slow component occurred more rapidly than that of the fast component. Interestingly, some water (∼2%) related to the fast component remained unfrozen at temperatures as low as -40 °C.

Muscle foods have also been studied using NMR relaxometry. Heated, pressure treated, and frozen stored cod was studied using spin–spin relaxation [37]. In this case, however, T_2 data were collected over time for samples held at $-$ 20 and -10 °C, but thawed before analysis. In fresh cod, a single exponential decay was observed, with $T_2 = 65$ ms. In addition, by plotting the relaxation rate ($1/T_2$) vs. the $90^\circ - 180^\circ$ pulse spacing, a dispersion in the relaxation rate was seen. This suggested that, in fact, there was a second short relaxation ($T_2 \sim 1$ ms) process present. After freezing and thawing, an additional longer

T_2 component appeared, and was attributed to the appearance of thaw exudates. Steen and Lambelet investigated NMR as a tool to study the texture of cod mince [38]. The longest T_2 of three components increased with temperature and duration of frozen storage. Changes in this component were correlated with degradation of fish texture, as measured by instrumental and sensory techniques.

Farouk and Swan used spin–lattice (T_1) relaxation to study the combined effects of rigor temperature, electrical stimulation, and frozen storage (1 month at −20 °C) on hot-boned beef [39]. They reaffirmed that most of the water in the muscle cell exists between the thick and thin filaments. They found that T_1 values were shorter for frozen/thawed vs. 24 h *post mortem* beef, which they attributed to changes in muscle proteins as a result of denaturation or aggregation. They also found that T_1 after freezing decreased with initial rigor temperature, and argued that this was related to increased protein denaturation and decreased water holding capacity.

PFGSE Diffusion Measurements

While spin–spin and spin–lattice relaxation are sensitive to rotational movement of paramagnetic nuclei, pulsed field gradient stimulated echo-NMR (PFGSE-NMR) techniques can determine translational motion of nuclei. Only a few studies exist of PFGSE-NMR in frozen systems. Callaghan *et al.* designed an NMR spectrometer that uses the Earth's magnetic field to study restricted diffusion in extracted sea ice cores [40]. At −6 °C, they found diffusion rates greater than that in pure water. For samples oriented with the sea ice axis parallel to the gradient, the echo attenuation was independent of the diffusion time Δ, indicating brine pockets with dimensions along the axis sufficiently large to allow unrestricted diffusion. For samples oriented perpendicular to the gradient, diffusion was restricted at $\Delta = 200$ ms, suggesting pores on the order of 40 μm in the perpendicular direction. These authors concluded that water moves tortuously between connected pores with narrow throats. In order to limit artifacts caused by core extraction, a probe was developed that could be inserted directly into the ice sheet [41]. They confirmed the existence of two diffusive elements, and found that water diffusivity was strongly anisotropic, and on short time scales its rapid motion suggested convective transport. Menzel *et al.* studied salt water ice formed by shock freezing or by slow freezing over several hours [42]. For shock frozen ice, the ice structure contained streak-like porous channels with diameters up to 300 μm, and had unrestricted diffusion along one axis. For slowly grown ice, restricted diffusion was observed on the scale of 30 μm.

NMR diffusion studies have also helped characterize the structure of frozen/thawed gels. Polyvinyl alcohol cryogels, containing bovine serum albumen, were formed by freezing at −20 °C, followed by warming to 20 °C [43]. They found that diffusion of PVA sidechains was higher for the gels compared to PVA solutions, and increased with temperature up to 45 °C, but decreased at higher temperature. In contrast, diffusion of water in the gels increased with temperature but did not show a maximum point. Dimensions of the cryogel were analyzed through the effects on restricted diffusion. The authors determined that the compartmental spaces were determined largely by ice and polymer microcrystallites formed during freezing.

Magnetic Resonance Imaging

While spin relaxation and PFGSE measurements give important information on physical states and structural aspects of frozen systems, they do not provide spatial discrimination of properties. MRI allows the measurement of magnetization intensity, typically at a resolution of 100–500 μm, but in the case of microimaging in the 10–100 μm range. Contrast may be provided by differences in ^{1}H density, spin relaxation rates, diffusion rates, or even chemical shift. MRI is subject to similar constraints as found in other NMR techniques, and in particular the fact proton relaxation in ice is quite rapid, thus making it invisible to imaging. Thus, experiments are conducted on thawed materials, or rely on signals emanating from unfrozen water during freezing, or unfrozen liquid in equilibrium with ice after the material is frozen.

Freeze/Thaw Effects

Gamble used MRI to study the effects of freezing on thawed blueberries [44]. The distribution of "unmodified" water ($T_2 \sim 14$ ms) in fresh and frozen/thawed blueberries was obtained using a slice-selective spin-echo technique. The distribution of sugar and "motion-modified" water ($T_2 \sim 6.6$ ms) was also attained, by including an additional hard 180° pulse to invert the ^{1}H magnetization, then collecting signal at the null point of water. By constructing difference images of blueberries before and after freeze/thawing, Gamble showed that freeze/thaw results in the rupture of water-containing membranes in particular locations in the berry.

Several MRI studies have been done on muscle foods. Guiheneuf *et al.* investigated MRI as a means of authenticating fresh vs. frozen pork [45]. They found that the magnetization transfer (MT) rate increased after freezing/thawing of muscle from the same animal, and attributed this to a decrease in moisture content and denaturation of myofibrillar proteins. Evans *et al.* looked at the effects of freezing and thawing on beef, lamb, and pork placed on 6 × 6 multi-well plates [46]. By this approach, they could simultaneously measure six NMR parameters on 168 meat samples. They found that freeze-thawing caused significant changes in moisture content, MT, and T_1. However, they did note that interanimal variation would make it difficult to use MRI for authentication. Similar experiments were also conducted on trout [47], cod, and mackerel [48]. They were able to clearly resolve anatomical features of the fish, and using a three-point Dixon technique, they were able to highlight either high-water or high-fat containing regions. They found no significant changes in NMR parameters when samples were fast-frozen in liquid nitrogen, then thawed, but did observe differences in MT, T_1, and $T_{1,\mathrm{sat}}$ when slow freezing was used. As repeated freeze-thaw cycles produced less change, the authors felt this could be an avenue to authentication. That is, a sample with unknown history could be subjected to a short freeze-thaw cycle. Changes observed from a "fresh" sample would be greater than those found for a previously frozen sample.

Several studies have used MRI to study changes in the structure of frozen/thawed bread dough. Takano *et al.* prepared dough with freeze-sensitive and freeze-tolerant yeast [49]. Images were collected during fermentation following thawing, with each set of images taking 5 min to measure, with a resolution of 100 μm and a slice thickness of 1 mm. They observed that small gas cells formed during mixing without yeast, and that larger nonuniform pores formed during fermentation. They found that prefermentation before freezing increased bread loaf 10–110% for baked breads made with freeze-tolerant yeast, but decreased bread volume when bread was made with freeze-sensitive yeast. Esselink *et al.* used both MRI and cryoSEM to study structural damage incurred during freezing of bread dough [50]. Time-domain NMR showed two T_2 regions, one they associated with water bound to starch and one associated with water rapidly sampling hydration sites in gluten.They surmised that during freezing, ice crystallization causes separation of water, and that this does not return to its original state upon thawing. T_1 and T_2-weighted MR images showed that water is not equally distributed over the dough slice. After frozen storage, the water-rich regions became thicker, consistent with migration of water.

Transient Freezing

Magnetic resonance imaging has also been used to follow the formation of ice during transient freezing. As the T_2 of ice is quite short, ice is relatively invisible to the spin-echo pulse sequences used in imaging. However, the unfrozen phase absent of ice still provides sufficient signal. Kerr *et al.* mimicked commercial freezing by directing the air from an air-blast freezer into a PVC pipe leading through the bore of the MR imaging system, and which contained the sample [51]. They studied potatoes freezing at − 42 and − 11 °C, at air speeds between 2–10 m/s. Images showed the advance of the asymmetric freezing interface and loss of signal intensity as water turned to ice. Temperature profiles were simultaneously monitored with thermocouples, and the amount of heat removed over time was measured by a differential calorimeter. A numerical model was used to predict temperature profiles and freezing interface over time, and was verified using the temperature, calorimetry, and image data. This approach was patented as a means for on-line prediction of enthalpy changes during food freezing [52].

The dynamics of freezing were also studied in immature kiwifruit [53]. With the conventional spin-echo sequence, images took approximately 4.25 min. Thus, a FLASH sequence was attempted, which gave no significant difference in image quality, and allowed image formation within 25 s. Ice formation commenced at the epidermis and gradually progressed to the core. Freezing was asymmetric, and in some cases ice moved rapidly through the core. Spin–spin relaxation was faster, and translational diffusion coefficients greater, in freeze-thawed compared to fresh fruit. Kerr *et al.* also studied a variety of other foods during freezing, including potatoes, carrots, peas, corn, and chicken legs [54]. Internal structures were distinguished based on water and fat. The ice interface advanced uniformly, but asymmetrically, in all samples except for corn. Freezing in corn seemed to be governed by nucleation, as kernels froze individually. The time required for the total signal to disappear corresponded to the time to reach steady-state enthalpy. Kuo *et al.* studied the effects of freezing on mozzarella cheeses [55]. In addition to monitoring the formation of ice in the product, they found that there was a significant change in T_2 and the water self-diffusion coefficient following freeze-thawing that could be used to determine areas of freeze-damage.

In order to achieve even shorter imaging times, Lee *et al.* applied a single-point ramp imaging with T_1 enhancement (SPRITE) imaging to produce 1- and 2-D images of orange juice, lean ground beef, and bread dough [56]. For samples held between 20 and −40 °C, distribution of the liquid-like components was well resolved. The authors noted that SPRITE images are able to show unfrozen water intermingled with ice, while spin-echo images do not.

While traditional MRI has a resolution on the order of 100 μm, it is possible to acquire MR images at the microscopic level. In theory, this should allow the observation of how freezing proceeds into microscopic entities such as cells and cell organelles. Samples of potato 8 mm in length were studied using fast radial microimaging [57]. They captured cross-sectional projections every 30 s for samples placed at −20 °C. The apparently noisy freezing interface was attributed to heterogeneity in the size and structure of cells. Higher resolution imaging has been used to study non-food systems including wintering leaf buds of Momi fir and Japanese red pine [58], and both leaf and flower buds of fool-moon maple [59]. In-plane resolution of 39 µm was attained with a slice thickness of 0.5 mm. MG images clearly showed internal structures including bark, crown tissue, pith, resin canals, leaf bud scales, vascular tissue, and xylem. Bud scales of Momi fir froze quickly at −7 °C, but supercooling down to −21 °C was found in shoot primordial of March buds. In maple, scales and stem barked froze at −7 °C, primordial inflorescence and terminal primordial shoots remained supercooled to −14 °C, and lateral primordial shoots remained unfrozen at −21 °C.

Liquid Phase Chemical Spectroscopy

Chemical shift spectroscopy has been used to study a variety of frozen materials, with the aim of understanding basic chemical, structural and dynamics features as influenced by freezing. Though few studies have dealt directly with foods, much of the results have direct application to food systems. As frozen foods are not readily studied by conventional NMR spectroscopy, studies have focused on the effects of freezing. Direct studies on frozen materials by solid-state NMR will be discussed in a subsequent section.

Phospholipid Membranes

As all foods of a cellular nature, including meat, fruit, and vegetables, contain phospholipid membranes, the study of the effects of freezing on membranes is of interest. Hsieh and Wu used both ^{2}H and ^{31}P NMR to study six phospholipid bilayers at temperatures between −20 and −70 °C [60]. Three types of interbilayer water were observed: supercooled water in two of the bilayer systems at temperatures between −20 and −35 °C which spontaneously nucleates at −35 °C; "perturbed" water at −20 to −70 °C; and bound water. ^{31}P NMR suggested that rotational motion of phospholipids groups was frozen at −40 °C.

Cellular and Tissue Systems

NMR spectroscopy has also been used to study the state of water and cellular metabolism in plant and animal tissue. Haranczyl *et al.* used ^{1}H NMR spectroscopy to study freezing of lichen thallus at temperatures down to −45 °C [61]. They observed a narrow line, which they associated with "bound" water, and a broader peak associated with free water. A broadening line width and decrease in peak area below 0 °C was associated with freezing. At −20 °C, a rapid decrease in area for low moisture samples occurred and was attributed to freezing of loosely bound water. They also postulated that there was a transfer of water from loosely bound to tightly bound states.

Lockett *et al.* used lactate-edited ^{1}H NMR difference spectra to study lactate production in isolated rat liver held on ice [62]. Water suppressed spectra were observed by an interleaved binomial sequence optimized for lactate. In addition, a spin-echo double resonance technique was used in which the lactate group was decoupled by low-power RF energy on alternate scans. An initial peak at 1.26 ppm was assigned to lactate, and steadily increased in the liver tissue over a 24 h period. An additional peak, assigned to alanine, also increased with time.

Both ^{1}H NMR and ^{31}P NMR were used to measure high energy phosphates in wood frogs frozen at −1.5 °C for 7 days. Decreases in the water peaks were used to assess freezing. While most frogs survived slow freezing, no frogs survived the entire rapid freeze. Frogs maintained ATP and creatine phosphate (CP) levels during slow freeze, while rapidly frozen frogs had up to 80% reductions in ATP and CP. Changes in pH were monitored by slight shifts in ATP spectra. Intracellular pH remained between 7.2 and 7.6 for slowly frozen frogs, but decreased to 6.57 during fast freezing.

NMR spectroscopy has also been used to assess cryopreservation of cells and tissues. Hubel *et al.* examined the influence of preculture on the prefreeze and postthaw characteristics of hepatocytes [63]. Cells were processed in a cryopreservation medium containing 10% DMSO, and frozen in a complicated protocol to a final temperature of −100 °C. NMR spectroscopy of lipids showed that *in vitro* cultivation increased the relative levels of cholesterol as compared to membrane phospholipids, as well as phospholipid interconversion. ^{31}P NMR showed an increase in the net energy charge during culturing. Eugene *et al.* monitored the kinetics of permeation of a variety of cryoprotective agents used to preserve human arteries. They found that equilibration was achieved within 120 mins for DMSO, 2,3-butanediol, and glycerol, while polyethyleneglycol (MW 20,000) reached concentrations between 40 and 50% in extracellular spaces.

Solid-State NMR

As frozen systems contain a high degree of solids, it would seem logical to apply solid-state NMR for their study.

Frozen Solutions

A variety of solutes and biomolecules have been studied by solid-state NMR. Appleyard and Evans used ^{13}C NMR with magic angle sample-spinning to study solutions of glycine under a variety of freezing conditions. To avoid crystallization of water, some samples were fired through a fine nozzle into liquid propane to form an amorphous solid state. Others were subject to slow freezing rates. Although they predicted that the distribution of ice I_h and glycine would become more dispersive as the freezing rate increased, they did not observe differences in the NH_3^+ group rotations between fast and slow frozen samples. They felt that these results were encouraging, in that any formation of ice I_h in rapidly frozen samples should not be detrimental to the solute. In addition, they felt this was a good approach to trapping chemical intermediates from enzymatic reactions.

Volke *et al.* studied solutions of α-chymotrypsin frozen during magic angle spinning at 4000 Hz [64]. A very broad ice peak was observed, spanning a region of 160 ppm. To improve resolution, a sine-bell window function was applied to the FID, but this allowed only a qualitative interpretation of the resulting spectrum. However, resonances from protons of the mobile polypeptide chains could be observed. From the T_2^* values they estimated a non-frozen water content of 0.15 to 0.24 g H_2O/g protein.

Dynamic nuclear polarization (DNP) techniques have proven useful to improving the sensitivity of spectra from frozen aqueous solutions. Here, the high-spin polarization of unpaired electrons is coupled to the nuclear spins through microwave irradiation near the electron paramagnetic resonance frequency, using a nitroxide radical as the paramagnetic polarizing agent. Gerfen *et al.* used this approach to study frozen solutions of water and glycerol [65]. The ^1H and ^{13}C NMR signal strengths were improved by a factor of 185. Hall *et al.* used this approach to study arginine and T4 lysozyme in frozen glycerol-water solutions [66].

Smith *et al.* extended the idea of studying biomolecules trapped in low-energy states by freezing them in a glassy matrix [67], using rotational-echo double resonance (REDOR) spectroscopy. Samples of 2-^{13}C,^{15}N-glycine and ^{13}C-methyl β-D-^{15}N-acetylglucosamine were frozen at −80 °C, and spun at 4.5 kHz. Low energy conformation states were developed for both molecules and corroborated with molecular dynamics computational methods.

Whole Foods

In food systems, Li *et al.* used ^2H and ^1H solid-state NMR to study the mobility of unfreezable and freezable water in waxy corn starch [68]. They found that a large percentage of the unfreezable water was relatively mobile even at −32 °C. Bertram *et al.* used ^{13}C cross-polarization MAS NMR to examine differences in pre-slaughter treatments on rapidly frozen pork longissimus muscle [69]. Resonance peaks from fatty acids, carboxylic groups, and carbons in lactate and glycogen were identified. They found a significant difference in methylene carbons attributed to membrane lipids, suggesting altered membrane properties in the muscles of stressed and electrically stunned animals, as compared to control CO_2-stunned animals.

Antifreeze Glycoproteins

Antifreeze proteins and glycoproteins are found in a variety of fish and insects subject to freezing conditions, and help protect the organisms from freezing. There have been some hopes that these could be used in food systems, particularly as they may affect ice nucleation processes. NMR has been used to study the dynamics of antifreeze glycoproteins (AFGP) in the presence of ice [70]. Solid-state ^{13}C NMR indicated that AFGP adopted similar three-dimensional folding in the presence of ice and in the freeze-dried state. A high number of conformers existed, indicative of a very flexible molecule. AFGP-ice interactions were dominated by fast motions on the nano- to picosecond time scale.

Conclusion

A variety of NMR techniques are available to study frozen foods and food components. These include relatively simple relaxation techniques for measuring solid/liquid ratios, imaging approaches to monitor food during freezing, and chemical spectroscopy to measure unfreezable water and conformations of molecules.

References

1. Wikefeld P. Growth of an Ice Phase in Frozen Tissue Studied by Proton Nmr-Spectroscopy. Cryobiology. 1971;8(6):589–93.
2. Ablett S, Clarke CJ *et al.* Relationship between ice recrystallisation rates and the glass transition in frozen sugar solutions. J. Sci. Food Agric. 2002;82(15):1855–9.
3. Harz HP, Loncin M. *et al.* Studies on freezing behavior of liquid foods relating to frozen storage, freeze-drying, and freeze concentration. Chem. Ing. Tech. 1989;61(2):155–7.
4. Weisser H, Harz HP. NMR studies of foods at sub-freezing temperatures. Eng. Food/Proc. Third Int. Congr. Eng. Food. B. M. McKenna. Dublin, Ireland, Elsevier Applied Science. 1984;1:445–54.
5. Lucas T, Mariette F. *et al.* Water, ice and sucrose behavior in frozen sucrose-protein solutions as studied by H-1 NMR. Food Chem. 2004;84(1):77–89.
6. Izutsu K, Yoshioka S. *et al.* Effect of Cryoprotectants on the Eutectic Crystallization of Nacl in Frozen-Solutions Studied by Differential Scanning Calorimetry (Dsc) and Broad-Line Pulsed Nmr. Chem. Pharm. Bull. 1995;43(10):1804–6.
7. Le Botlan D, Wennington J. *et al.* Study of the state of water and oil in frozen emulsions using time domain NMR. J. Colloid Interface Sci. 2000;226(1):16–21.

8. Watanabe K. Mizoguchi M. Amount of unfrozen water in frozen porous media saturated with solution. Cold Regions Sci. Tech. 2002;34(2):103–10.
9. Cornillon P, Andrieu J. *et al.* Use of Nuclear-Magnetic-Resonance to Model Thermophysical Properties of Frozen and Unfrozen Model Food Gels. J. Food Eng. 1995;25(1):1–19.
10. Kim YR, Yoo BS. *et al.* Effect of sugars and sugar alcohols on freezing behavior of corn starch gel as monitored by time domain H-1 NMR spectroscopy. Carbohydr. Polym. 2004;55(1):27–36.
11. Lee S, Pyrak-Nolte LJ. *et al.* Characterisation of frozen orange juice by ultrasound and wavelet analysis. J. Sci. Food Agric. 2004;84(5):405–10.
12. Rasanen J, Blanshard JMV. *et al.* Water distribution in frozen lean wheat doughs. Cereal Chem. 1997;74(6):806–13.
13. Rasanen J, Blanshard JMV. *et al.* Properties of frozen wheat doughs at subzero temperatures. J. Cereal Sci. 1998;28(1):1–14.
14. Cornillon P, Andrieu J. *et al.* Use of Nuclear-Magnetic-Resonance to Model Thermophysical Properties of Frozen and Unfrozen Model Food Gels. J. Food Eng. 1995;25(1):1–19.
15. Kim YR, Yoo BS. *et al.* Effect of sugars and sugar alcohols on freezing behavior of corn starch gel as monitored by time domain H-1 NMR spectroscopy. Carbohydr. Polym. 2004;55(1):27–36.
16. Roos YH, Karel M, Kokini JL. Glass transitions in low moisture and frozen foods: effects on shelf life and quality. Food Tech. 1996;50(11):95–108.
17. Sperling LH. Introduction to polymer science. Ch 1 In: Introd. Phys. Polym. Sci. John Wiley & Sons, Inc.: New York, 1992.
18. Ullmann G, Haensler M. *et al.* Influence of freeze-concentration effect on proteinase-catalysed peptide synthesis in frozen aqueous systems. Biochimi. Et Biophys. Acta-Protein Struct. Mol. Enzymol. 1997;1338(2): 253–8.
19. Ablett S, Darke AH, Izzard MJ, Lillford PJ. Studies of the glass transition in malto-oligomers. In: JMV Blanshard, PJ Lillford (Ed.). The Glassy State in Foods. Loughborough, Nottingham University Press 1993. p 189–200.
20. Le Botlan D, Wennington J. *et al.* Study of the state of water and oil in frozen emulsions using time domain NMR. J. Colloid Interface Sci. 2000;226(1):16–21.
21. Rault J, Neffati R, Juden-Stein P. Melting of ice in porous glass: why water and solvents confined in small pores do not crystallize? Eur. Phys. J. B 2003;36(4):627–37.
22. Morishige K, Kawano K. Freezing and melting of water in a single cylindrical pore: The pore-size dependence of freezing and melting behavior. J. Chem. Phys. 1999;110(10):4867–72.
23. Watanabe K, Mizoguchi M. Amount of unfrozen water in frozen porous media saturated with solution. Cold Regions Sci. Tech. 2002;34(2):103–10.
24. Valiullin R, Furo I. The morphology of coexisting liquid and frozen phases in porous materials as revealed by exchange of nuclear spin magnetization followed by H-1 nuclear magnetic resonance. J. Chem. Phys. 2002;117(5):2307–16.
25. Brownstein KR, Tarr CE. Importance of Classical Diffusion in Nmr-Studies of Water in Biological Cells. Phys. Rev. A 1979;19(6):2446–53.
26. Provencher SW. A constrained egularization method of inverting data represented by linear algebraic or integral equations. Comp. Phys. Commun. 1982;27:213–27.
27. Godward J, Gunning P, Hills BP. An NMR protocol for determining ice crystal size distributions during freezing and pore size distributions during freeze-drying. Appl. Magn. Reson. 1999;17(4):537–56.
28. Cornillon P, McCarthy MJ, Reid DS. Study of restructed diffusion by NMR in freeze-dried starch gels. J. Texture Studies 1997;28(4):421–34.
29. Hills BP, Lefloch G. Nmr-Studies of Non-Freezing Water in Randomly Packed-Beds of Porous Particles. Mol. Phys. 1994;82(4):751–63.
30. Hansen EW, Simon C. *et al.* Probing pore size distribution by cryogenic- and relaxation H-2-NMR. J. Phys. Chem. B 2002;106(48):12396–406.
31. Lucas T, Mariette F, Dominiawsyk S, Le Ray D. Water, ice and sucrose behavior in frozen sucrose-protein solutions as studied by ^{1}H NMR. Food Chem. 2004;84:77–89.
32. Cameron IL, Hunter KE, Ord VA, Fullerton GD. Relationships between ice crystal size, water content and proton NMR relaxation times in cells. Physiol. Chem. Phys. Med. NMR 1985;17:371–86.
33. Borompichaichartkul C, Moran G, Srzednicki GS, Driscoll RH. Studies of physical state of water in maize from North-east China during drying at subzero temperatures. Drying Technol. 2004;22(1/2):295–305.
34. Hills BP, Remigereau B. NMR studies of changes in subcellular water compartmentation in parenchyma apple tissue during drying and freezing. Int. J. Food Sci. Tech. 1997;32:51–61.
35. Hills BP, Nott KP. NMR studies of water compartmentation in carrot parenchyma tissue during drying and freezing. Appl. Magn. Reson. 1999;17(4):521–35.
36. Nikolaev GM, Tropin IV, Goryachev SN, Water status changes in shoots of a seaweed *Ascophyllum nodosum* at subzero temperatures. Russian J. Plant Physiol. 2002;49 (2):242–49.
37. Lambelet P, Renevey F, Kaabi C, Raemy A. Low-field nuclear magnetic resonance relaxation study of stored or processed cod. J. Agric. Food Chem. 1995;43:1462–6.
38. Steen C, Lambelet P. Texture changes in frozen cod mince measured by low-field nuclear magnetic resonance spectroscopy. J. Sci. Food Agric. 1997;75:268–72.
39. Farouk MM, Swan JE. Effect of rigor temperature and frozen storage on functional properties of hot-boned manufacturing beef. Meat Sci. 1998;49(2):233–47.
40. Callaghan PT, Eccles CD, Haskell TG, Langhorne PJ, Seymour J. Earth's field NMR in Antarctica: a pulsed gradient spin echo NMR study of restricted diffusion in sea ice. J. Magn. Reson. 1998;133:148–54.
41. Callaghan PT. Dykstra R, Eccles CD, Haskell TG. Seymour J. A nuclear magnetic resonance study of Antarctic sea ice brine diffusivity. Cold Regions Sci. Technol. 1999;29:153–71.
42. Menzel MI, Han SI, Stapf S, Blumich B. NMR characterization of the pore structure and anisotropic self-diffusion in salt water ice. J. Magn. Reson. 2000;143:376–81.

43. Shapiro Y. Compartmentation in the poly(vinyl alcohol) cryogels. ^{1}H NMR self-diffusion study. Colloids Surf. A: Physicochem. Eng. Aspects 2000;164:71–83.
44. Gamble GR. Non-invasive determination of freezing effects in blueberry fruittissue by magnetic resonance imaging. J. Food Sci. 1994;59:571–73.
45. Guiheneuf TM, Parker AD, Tessier JJ, Hall LD. Authentication of the effect of freezing/thawing of pork by quantitative magnetic resonance imaging. Magn. Reson. Chem. 1997;35:S112–S118.
46. Evans SD, Nott KP, Kshirsagar AA, Hall LD. The effect of freezing and thawing on the magnetic resonance imaging parameters of water in beef, lamb, and pork meat. Int. J. Food Sci. Technol. 1998;33:317–28.
47. Nott KP, Evans DE, Hall LD. Quantitative magnetic resonance imaging of fresh and frozen-thawed trout. Magn. Reson. Imaging.1999;17(3):445–55.
48. Nott KP, Evans DE, Hall LD. The effect of freeze-thawing on the magnetic resonance imaging parameters of cod and mackerel. Lebensmittel Wissenschaft und Technologie 1999;32:261–8.
49. Takano H, Naito S, Ishida N, Koizumi M, Kano H . Fermentation process and grain structure of baked breads from frozen dough using freeze-tolerant yeasts. J. Food Sci. 2002;67(6):2725–33.
50. Esselink EFJ, Aailst Hv, Maliepaard M, van Duynhoven JPM. Long-term storage effect in frozen dough by spectroscopy and microscopy. Cereal Chem. 2003;8(4):396–403.
51. Kerr WL, Kauten RJ, Ozilgen M, McCarthy MJ, Reid DS. NMR imaging, calorimetric, and mathematical modeling studies of food freezing. J. Food Process Eng. 1996;19:363–84.
52. McCarthy MJ, Reid DS. (1997). Nuclear magnetic freezing sensor. U.S. Patent number 5,602,477.
53. Kerr WL, Clark CJ, McCarthy MJ, de Ropp JS. Freezing effects in fruit tissue of kiwifruit observed by magnetic resonance imaging. Scientia Horticulturae 1997;69:169–79.
54. Kerr WL, Reid DS, Kauten RJ, McCarthy MJ. Monitoring the formation of ice during food freezing by magnetic resonance imaging. Lebensmittel Wissenschaft und Technologie 1998;31:215–20.
55. Kuo MI, Anderson ME, Gunasekaran S. Determining effects of freezing on pasta filata and non-pasta filata mozzarella chesses by nuclear magnetic resonance imaging. J. Dairy Sci. 2003;86: 2525–36.
56. Lee S, Cornillon P, Kim YR. Spatial investigation of the non-frozen water distribution in frozen foods. J. Food Sci. 2002;67(6):2251–5.
57. Hills BP, Goncalves O, Harrison M, Godward J. Real time investigation of the freezing of raw potato by NMR microimaging. Magn. Reson. Chem. 1997;35:S29–S36.
58. Ide H, Price WS, Arata Y, Ishikawa M. Freezing behaviors in leaf buds of cold-hardy conifers visualized by NMR microscopy. Tree Physiol. 1998;18:451–8.
59. Ishikawa M, Price WS, Ide H, Arata Y. Visualization of freezing behaviors in leaf and flower buds of fool-moon maple by nuclear magnetic resonance microscopy. Plant Physiol. 1997;115:1515–24.
60. Hsieh CH, Wu WG. Three distinct types of unfrozen water in fully hydrated phospholipids bilayers: A combined ^{2}H- and ^{31}P-NMR study. Chem. Phys. Lipids 1995;78:37–455.
61. Haranczyk H, Gransdjean J, Olech M. Freezing of water bound in lichen thallus as observed by ^{1}H-NMR. I. Freezing of loosely bound water in Cladonia mitis at different hydration levels. Colloids and Surf. B: Biointerfaces. 2003;28:239–49.
62. Lockett CJ, Busza AL, Proctor E, Churchill TA, Williams SR, Fuller BJ. Proton nuclear magnetic resonance spectroscopy of lactate production in isolated rat liver during cold preservation. Cryobiology. 1996;33:271–5.
63. Hubel A, Conroy M, Darr TB. Influence of preculture on the prefreeze and postthaw characteristics of hepatocytes. Biotechnol. Bioeng. 2001;71:173–83.
64. Volke F, Pampel A, Haensler M, Ullmann G. Proton MAS NMR of a protein in a frozen aqueous solution. Chem. Phys. Lett. 1996;262:374–8.
65. Gerfen GJ, Becerra LR, Hall DA, Griffin RG. High frequency dynamic nucler polarization: Polarization transfer to a solute in frozen aqueous solution. J. Chem. Phys. 1995;102(24):9494–97.
66. Hall DA, Maus DC, Gerfen GJ, Inati SJ, Becerra LR, Dahlquist FW, Griffin RG. Polarization-enhanced NMR spectroscopy of biomolecules in frozen solution. Science. 1997;276:930–32.
67. Smit LJ, Boulineau FP, Raftery D, Wei A. Frozen solution conformational analysis by REDOR spectroscopy. J. Amer. Chem. Soc. 2003;125:14958–9.
68. Li S, Dickinson LC, Chinachoti P. Mobility of unfreezable and freezable water in waxy corn starch by 2H and 1H NMR. J. Agric. Food Chem. 1998;46:62–71.
69. Bertram HC, Jakobsen HJ, Karlsson AH, Engelsen SB. Post-mortem changes in porcine M. longissium studied by solid-state 13 C cross-polarization magic-angle spinning nuclear magnetic resonance spectroscopy. J. Agric. Food Chem. 2003;51:2064–9.
70. Tsvetkova NM, Phillips BL, Krishnan VV. *et al.* Dynamics of antifreeze glycoproteins in the presence of ice. Biophys. J. 2002;82:464–73.

Nuclear Magnetic Resonance Studies on the Glass Transition and Crystallization in Low Moisture Sugars

Bill MacNaughtan
Division of Food Sciences, School of Biological Sciences, University of Nottingham, Sutton Bonington Campus,
Loughborough, LEICS, LE12 5RD, UK

Introduction

Sugar glasses are suitable materials for mobility studies due to changes in mobility of many orders of magnitude occurring at the glass transition. In addition, these glasses will often crystallize. The idea behind crystallization from a glassy matrix can be summed up very simply, albeit incompletely. A rigid immobile non-equilibrium glass gives way to a mobile material above the glass transition temperature and allows the material to attain equilibrium by crystallizing. The most common method of studying glassy behavior in carbohydrate [1,2,3] as well as inorganic glasses [4], is to use a thermal technique such as differential scanning calorimetry (DSC). A common trace found in polymer, pharmaceutical and food texts is shown on Figure 1. Of course not all materials will exhibit cold crystallization with resultant melting as shown here. When considering experiments designed to investigate motion in such samples, the simplest approach is to carry out measurements in the obvious regions of the trace i.e. "below the glass transition," "above the glass transition but below crystallization," "above crystallization" etc., and ignore all aspects of the temporal component of the respective events. For example, we know that the dynamic glass transition has a frequency dependence [5] and that the glass transition temperature relevant to a storage trial will probably not be the same as that recorded using DSC at 10 K/min. Additionally, crystallization is a kinetic process [6] whose peak temperature on a DSC trace will change with scanning rate, whereas melting, at least for a small molecule such as sucrose, is an equilibrium event.

Line Width and Shape Studies

A free induction decay (FID) signal recorded on a typical low-resolution time domain spectrometer is shown on Figure 2. The rapidly decaying signal is due to the "solid" or immobile component of the sample, whereas the slowly decaying component is due to the "liquid" or mobile component. There are many bench top NMR spectrometers [7,8], which will produce such traces. Other machines have been produced [9] which will give a direct recording of the spectral peak corresponding with these decays. If we think in terms of Fourier transform pairs, the line widths of solids tend to be wide (frequency domain) with corresponding short decay times (time domain). For protons in a solid, line widths can be greater than 50 kHz and the decay times of the order of 10's of microseconds. Sharp lines and long decays are the rule for liquids. For very wide solid lines, the true line width can be often limited by the excitation bandwidth of the pulse.

Often a beat will be observed in the decay. This is not to be confused with a signal which is off resonance in a machine recording both in phase and out of phase signals, and is present after combination of such signals, for instance when the magnitude is taken. There is some discussion as to how to treat such a decay. The interaction between two protons can be treated rigorously and produces the well-known Pake pattern [10]. For interactions between many spins, this problem was originally approached by performing summations in crystals such as fluorite [11]. It was found that a flattened top Gaussian curve was a good description of the line width, with a Sinc function multiplied by a Gaussian being a good approximation to the FID decay, however the decay in the time domain corresponding to the Pake pattern also has an oscillating character (Figure 3). We are left with the complexity of having at least four possible fits to the solid component if we include simple Gaussian or even a Sinc function multiplied by an exponential [12]. See reference [13] for more details.

Fitting using the sinc/Gaussian function is often known as moments analysis because of the description of solid lines in terms of an infinite series of moments [14]. In practice only the 2nd and 4th moments tend to be significant. The moments expansion of lineshape is

$$G_1^{(4)} = 1 + M_2t^2/2! + M_4t^4/4! +$$

Graham A. Webb (ed.), Modern Magnetic Resonance, 1879–1888.
© 2008 *Springer.*

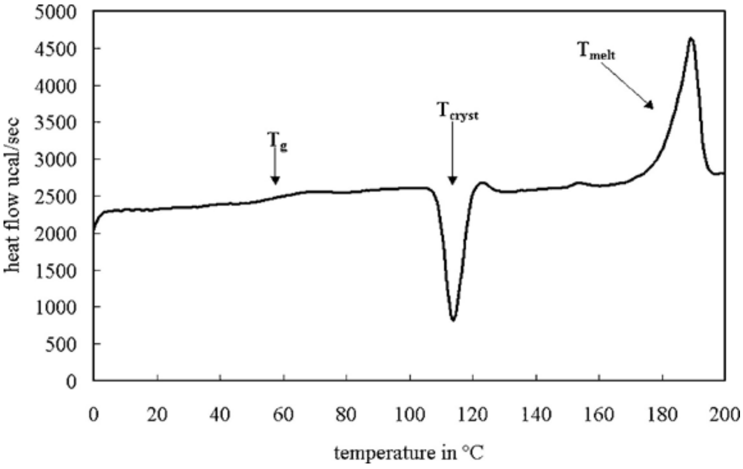

Fig. 1. A DSC thermogram at a scanning rate of 10 K/min, showing glassy, crystallization and melting behavior of amorphous sucrose at a moisture content of 1–2%.

and the series expansion of the function

$$F(t) = \exp(-a^2t^2/2) * \sin \beta t/\beta t$$

$$\text{is } 1 - (a^2 + b^2/3)t^2/2! + (3a^4 + 2a^2b^2 + b^2/5) \times t^4/4! - \text{etc}$$

Therefore the 2nd moment $M_2 = (a^2 + b^2/3)$, and the 4th moment $M_4 = (3a^4 + 2a^2b^2 + b^2/5)$.

It is useful to bear in mind that we are simply describing residual order in the material. In a glassy, apparently totally disordered, material there is still order in the sense that a random mixture of glass balls has nearest, and shells of progressively more disordered, neighbors. Pronounced beats are often observed in glasses (and crystals), which progressively disappear as the material goes through the glass transition. It is an interesting question as to whether amorphous materials and crystals can be distinguished easily solely on the basis of solid line shape. On Figure 4, we can see the results of fitting the solid decay obtained from frozen maltose solutions. It is possible to adjust the recycle delay time so that any signal from the ice, which has a very long T_1, is suppressed. We are effectively examining a maximally freeze concentrated sugar solution, or maltose glass. In the region above 240 K, the approximate T_g' for a maximally concentrated solution of maltose, the fitting using the sinc/Gaussian and Pake functions (both simple and multiple) becomes less good due to motional averaging of the residual order. With increasing temperature the signal is ultimately better fitted to simple functions such as Gaussian and exponentials [15]. However it is interesting to note that the best fit to a solid decay in a

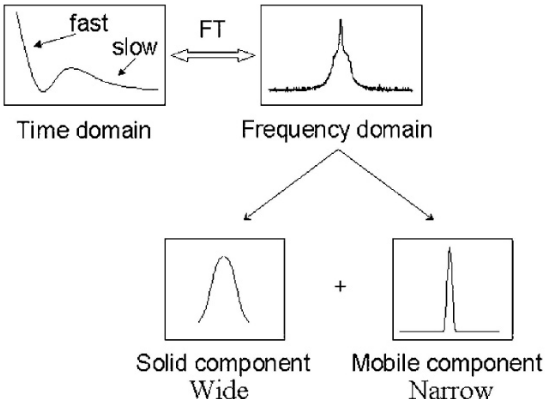

Fig. 2. Typical proton Free Induction Decays (FIDs) and corresponding line widths [13].

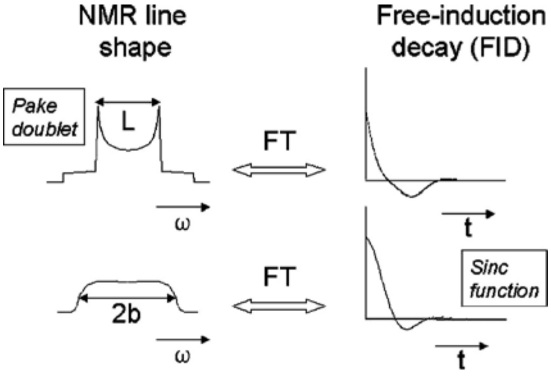

Fig. 3. Two different lineshapes, which will produce similar free induction decays [13].

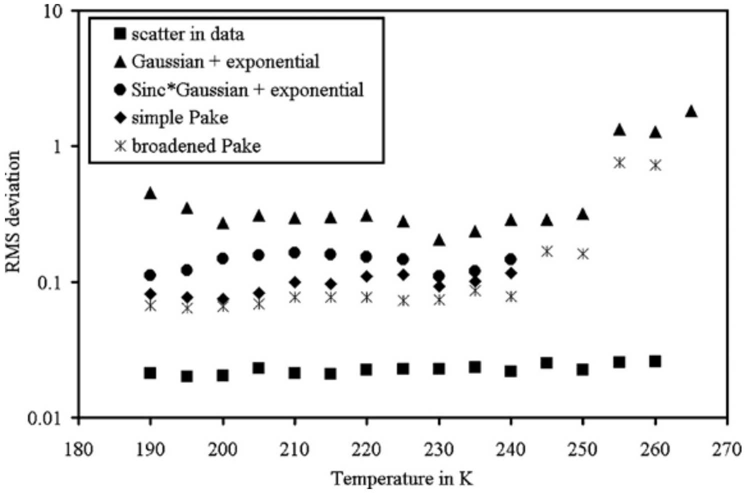

Fig. 4. A series of fits to the free induction decay of a frozen 40% maltose solution.

maltose glass is a decay corresponding to the interactions of a distribution of proton-proton pairs of slightly different separations.

Deuterium Line Shape Studies

That a deuterium powder profile looks similar to the interaction between two proton spins is a consequence of the interaction of a spin 1 particle with an electric field gradient being similar to the interaction between two spin 1/2 particles. The characteristic features of the lineshape will be averaged as the mobility is increased and will ultimately become a single isotropic line. The motion of deuterated glucose was studied in reference [16] where it was found that even above the glass transition temperature, the sample was sufficiently viscous to appear solid-like on the time scale of the measurement and so produce a Pake powder pattern (Figure 5). Interestingly the signature of D_2O in a glass, as opposed to ice, was proposed to be a flat-topped Gaussian, due to a distribution of quadrupolar coupling constants as well as orientations.

Residual orientation of deuterium in say D_2O trapped in interlamellar layers, for example in vanadium pentoxide hydrate, results in incomplete averaging and produces a similar powder pattern with a much reduced spectral width [17]. Hills [12] has used a quadrupolar solid echo measurement to show that D_2O is insensitive to the glass transition in 10% D_2O maltose glasses and is still highly mobile at temperatures well below the glass transition.

Deuterium can of course exchange with exchangeable protons on sugars and can so provide direct information on the state of the sugar [18,19].

Relaxation Studies

In food related work, Relaxation is usually concerned with the mobility of protons and here we will mainly deal with spin-spin or T_2 relaxation. A simple signal has already been shown in the form of the time domain signal of Figure 2. The instrument dead time limits the signal acquisition at short times; the very times where crucial information on the solid is available. This can be overcome by pulse sequences producing solid echoes [20], however information in this region tends to be line shape based rather than the simple decay time. Changes in motion through the glass to rubber transition are typically described by changes in intensity of the solid component and by intensity and time constant of the mobile fraction. Additionally it is difficult to distinguish between a rigid amorphous fraction and any crystals produced by "cold" crystallization above the glass transition, by simple measurements of the solid decay. Information tends to be restricted to indirect changes monitored by the mobile fraction, for example due to a transfer of protons caused by water exclusion from the material which is crystallizing. If this is the case then techniques more suited to the measurement of mobile species, such as the Carr Purcell Meiboom Gill (CPMG) sequence, can be used.

For example, in the case of a commercial product from which sucrose is crystallizing (Figure 6), there is a transfer of water from the sucrose, which contains no water in the unit cell, to the remaining amorphous material, which progressively becomes more mobile. Consequently the immobile to mobile ratio falls. There is an apparent paradox, in that the material appears more mobile with time as an almost completely rigid material is produced. A continuous distribution of T_2 values in the FID shows

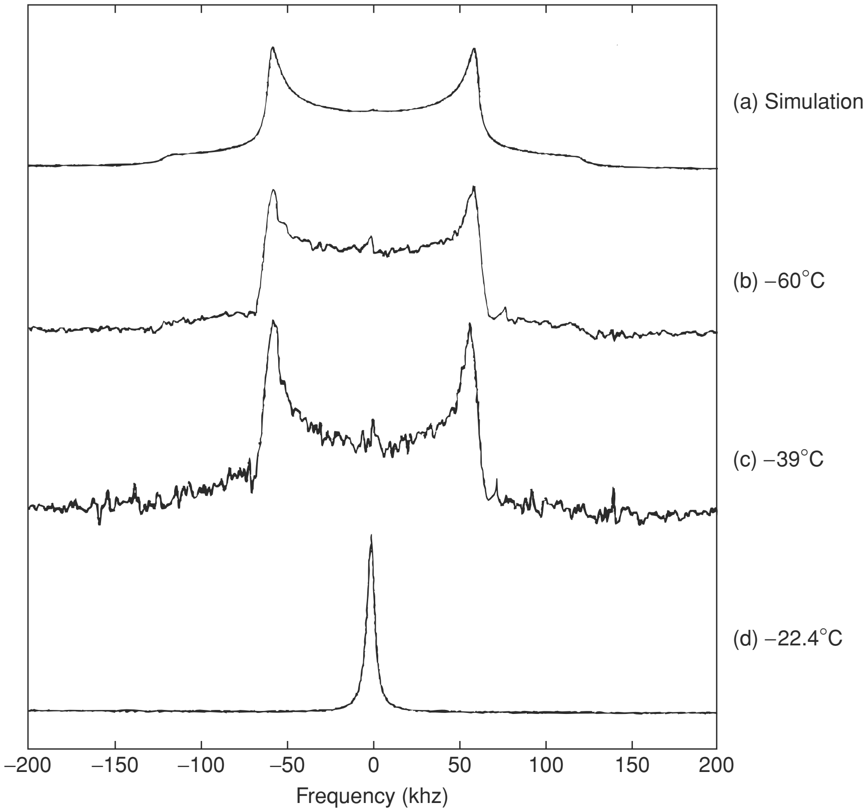

Fig. 5. A series of deuterium lineshapes for deuterated glucose at specified temperatures.

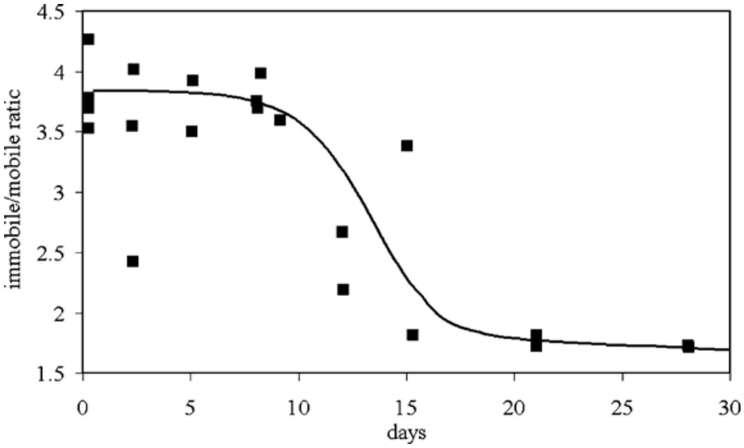

Fig. 6. The change in immobile to mobile ratio as defined by the ratio of the amplitudes of a fitted gaussian (immobile) to exponential (mobile) upon crystallization of sucrose. Notice the significant induction time i.e. time lag at the start of the trace. This is a commercial product with a complex list of ingredients.

these changes clearly, as well as dramatic differences in mobility when the glassy phase is taken above the glass transition temperature. We would see still more complex behavior if a sugar such as lactose, which retains water in the unit cell had crystallized. Changes in the simple decay time of the solid fraction are however small.

Van den Dries *et al.* [18] in a comprehensively argued study of low moisture maltose glasses, demonstrated that the DSC determined glass transition temperature was very close to the temperature of discontinuities in both the mobile T_2 relaxation time and the immobile second moment M_2. By comparison with deuterated samples, where the discontinuity in the second moment was slightly below the T_g, it was concluded that the increased reduction in the second moment above T_g in the protonated sample was due to motion in the exchangeable protons on the maltose. Several other important deductions were convincingly argued. By contrasting Goldman Shen results, which placed an upper limit on chemical exchange, with the transverse relaxation rates which were approximately 2 orders of magnitude greater, it was concluded that chemical exchange could not account for the amplitudes of the mobile and immobile components as the temperature was varied. Rather, below the glass transition there was a contribution of immobilized water protons to the solid maltose proton signal, whereas above T_g there was a contribution of mobile maltose protons to the water signal. Hills [12] has however suggested that increases in the lateral degrees of freedom may be relevant to the observed discontinuity in the mobile fraction.

In addition, by comparing the magnitude of the decrease in viscosity on the formation of a solution from a glass (10^{13}) with the measured reductions in correlation times (10^5) [18], water did not appear to fully sense the glass transition, but was decoupled to a degree dependent on the water content. The lower the water content, the more pronounced was the break (Figure 7). This agreed qualitatively with Ablett *et al.* [21] who observed similar discontinuities in the solid at T_g, however none in the mobile signal. Of particular interest was the observation that the M_2 for crystalline maltose [22] was larger than the glassy value. This may provide an answer to the question in the previous section concerning a way to reliably distinguish between amorphous and crystalline phases by measurements in the solid region. Tang *et al.* [23] have also calculated the second moment for crystalline rhamnose and methyl rhamnose by lattice summation and have carefully argued the contributions to M_2, based on the results of other relaxation measurements, which progressively disappeared as the samples were heated. The absence of a clear structure for glasses meant that rigid lattice M_2's were calculated indirectly.

The arguments in [18] and [23] provide a good rationale for the explanation of many observations in other systems. For instance Farhat *et al.* [24] and Derbyshire [15] have observed discontinuities in the M_2 and the solid T_2 fitted using a Gaussian, of amylose and glucose close to the predicted glass transitions. Kumagai [25] observed discontinuities in M_2close to the predicted glass transition in low moisture sugars containing 1% carrageenan.

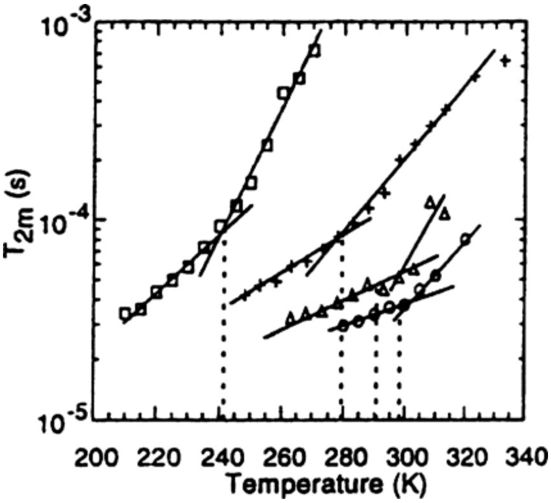

Fig. 7. Typical breaks in the value of the decay time of the mobile component for maltose glasses. Moisture content ○, 5%; △, 7%; +, 10%; □, 20% [18].

Apparent discontinuous behavior in T_1 or longitudinal relaxation has been observed in other materials. Mansfield and Powles [26] carried out some early work on glycerol, measuring T_1 over a wide range of temperature. A dramatic drop in T_1 was observed as the material transformed from a glass to a more mobile state. The estimations of correlation times [27] also proved interesting and this will be returned to in the next section. T_1 discontinuities have also been observed in toluene [28], a molecule not too dissimilar in size to sugars, although glass formation is through Van der Waals bonds rather than H bonding.

Multiple breaks observed in M_2 [25,29] have also raised the interesting possibility of additional "events" above the glass transition. This has been associated with "ball in a cage" or mode-coupling theories of the glass transition [30], where there is an additional breakdown of postulated aggregates at a temperature approximately 20% above T_g. The lateral and orientational time constants are also proposed to separate in this region with the lateral attaining a larger value.

In much of the work presented so far there is the tacit assumption that the T_g determined by rheological and thermal methods and the NMR determined T_g should fall at the same temperature despite the massive difference in frequency of measurement. This is a complex issue. T_1 measurements tend to reflect behavior at high frequencies, whereas T_2 measures contain contributions from both static and high frequencies. $T_{1\rho}$ measurements tend to lie somewhere in between depending on power level used. Clearly there is evidence here that T_1 measurements nevertheless do correspond to low frequency measurements of T_g such as DSC values. This may depend on the degree of coupling between different parts of the molecules. However, work remains to be done on importing ideas from the areas of calorimetry and polymers on the scanning rate and frequency dependence of the glass transition.

High-Resolution Solid-State ^{13}C NMR

Whilst low-resolution relaxation data provide a wealth of information concerning the mobility of entire proton fractions, detailed information on specific protons is obtained indirectly, normally by clever choice of molecules containing for example off-ring methyl or hydroxymethyl groups [23] or deuterium substitution [18]. High-resolution solid-state ^{13}C NMR has the ability to identify, and in addition measure, the relaxation of particular carbons in a molecule. As previously stated, the proton NMR spectrum of a solid often consists of a single wide line as indeed does the carbon spectrum. The main reasons for line broadening in solids are firstly strong dipole–dipole interactions. Each nucleus experiences a different local magnetic field depending on the orientation and distance of the neighboring nuclei. Secondly, Chemical Shift Anisotropy, which reflects the difference in chemical shift according to the orientation of the molecule in the magnetic field, will produce a range of resonance frequencies. This produces inhomogeneous lines which means that each region of the line is distinct from the other regions and can be affected independently, such as by specific irradiation which can "burn" holes in the line [31]. There is a third problem associated with the observation of NMR in solids, namely the long T_1's associated with very immobile samples. A cross polarization stage with high power decoupling whilst spinning at the magic angle (CPMAS NMR), ameliorates all of these problems and in addition provides a rather neat way of distinguishing between mobile and immobile species. Cross polarization relies on species maintaining "magnetic contact" at low frequencies for efficient transfer of magnetic polarization—too much motion—no transfer. Solids are therefore observed. A conventional NMR experiment using a simple 90° pulse will measure all species, however the solid lines will be wide, depending on the decoupling power used, and so only the mobile fraction will be seen. This is often known as a Fourier transform magic angle spinning (FTMAS) or single pulse excitation (SPE) experiment. It is a remarkable fact that using the tricks of the CPMAS method the spectrum of crystalline sucrose, effectively broad and featureless, can be turned into a spectrum with detail comparable to spectra obtained in solution (Figure 8).

The glass in Figure 8 was prepared using a freeze drying method; melt quenching tending to produce colored glasses which, depending on the degree of heating above the melting point, can be upwards of 50% degraded and interestingly exhibit broader peaks. If we have clear chemical shift information available, i.e. we can identify specific carbons in the molecule, we can carry out a series of relaxation measurements, each of which has an associated frequency [32], on individual carbons of the molecule composing the glass.

We therefore have the ability from the experiments shown on Table 1 to construct primitive spectral density maps, from the values of the decay times, i.e. measure the intensity of magnetic fluctuations present at particular frequencies. This is similar to the procedure carried out by Schaefer and Stejskal [33] (see Table 2).

The glass has lower T_1 values, which have less of a spread across the different regions of the molecule compared with the crystal. The hydroxymethyl groups in the sucrose crystal are not completely hydrogen bonded [34] which leaves a certain degree of freedom to rotate. This

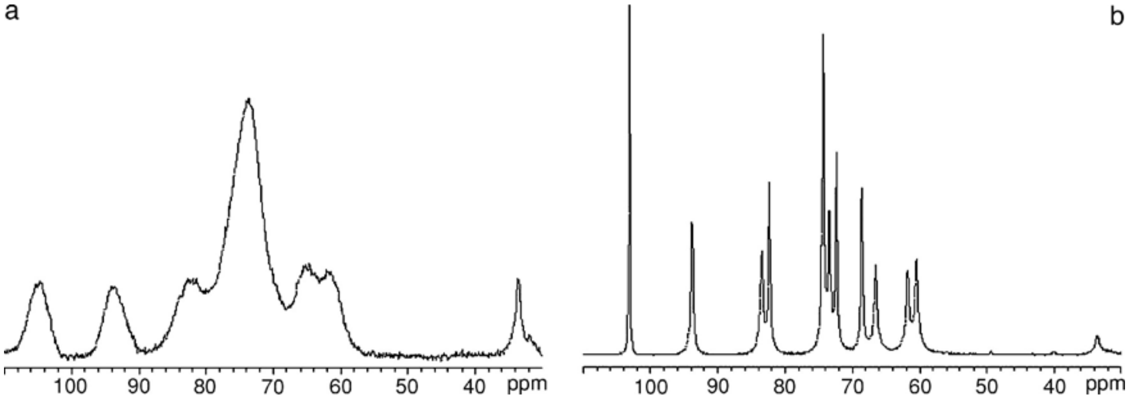

Fig. 8. Typical ^{13}C CPMAS spectra for glassy (left) and crystalline sucrose. The peak at 33 ppm is a polyethylene reference.

Table 1: The frequency of perturbation associated with each experiment

Experiment	Effective motional frequency range
T_1 spin-lattice	Larmor frequency (e.g. 75 MHz for ^{13}C in a > tesla field)
$T_{1\rho}$ spin-lattice	10–50 kHz
T_2 spin-spin	Static to mid-kHz
Cross polarization T_{C-H}	near static

accounts for the large differences in the relaxation parameters, particularly the T_1 values, for these carbons. T_1 was determined here using the sequence described in reference [35]. Similarly the anomeric carbon of the fructose moiety has no directly bound protons, leading to long T_{C-H} time constants.

A simple temperature sweep spanning the DSC determined glass transition, while recording CPMAS spectra can be instructive (Figure 9). A change in T_1 value is seen at the glass transition. Of particular interest is that the discontinuity for the off-ring group is at a lower temperature than the main ring and anomeric groupings. Apparent discontinuities in T_1 and other relaxation parameters have been observed in many systems as outlined in the previous section.

It is interesting to speculate as to the fundamental cause of this type of feature. Connor [36] has generated curves showing the type of T_1 profiles expected for distributions of correlation times based on equations containing terms of the type [37]

$$A\{[\tau/1+\omega_0^2\tau^2]+[4\tau/1+4{\omega_0}^2\tau^2]\}$$

In general a distribution of times leads to a flattened base of the T_1 profile [38]. It is tempting to generate T_1 profiles based on distributions of correlation times for isotropic motion and view these as an explanation for the variation in relaxation parameters with temperature (see Figure 10); apparent linear regions may simply be part of a curve in the distribution if the temperature range is not wide enough. However, increasingly sophisticated techniques, capable of measuring non-isotropic motion, suggest that motion can be fundamentally different in the glassy state and in addition there can be switchovers in particular temperature regions from one form of motion to another [23]. Although strictly belonging to the previous section on relaxation NMR, reference [23] is probably the most thorough approach to correlation times in this area. By careful choice of molecules with off-ring methyl and hydroxymethyl groups the minima in T_1 and $T_{1\rho}$ measurements were fitted accurately by discrete correlation times without recourse to complex distributions.

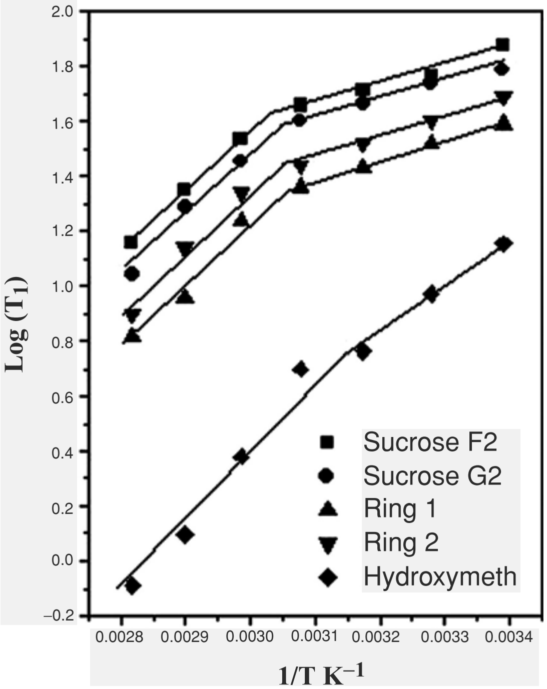

Fig. 9. The Arrhenius variation of the ^{13}C CPMAS determined T_1 in freeze dried sucrose.

Although essentially the same features are observed it we plot other relaxation parameters such as proton or carbon $T_{1\rho,}$ the changes do not approximate two linear regions so closely, at least not in sucrose. This is possibly because there is a more complex spread of correlation

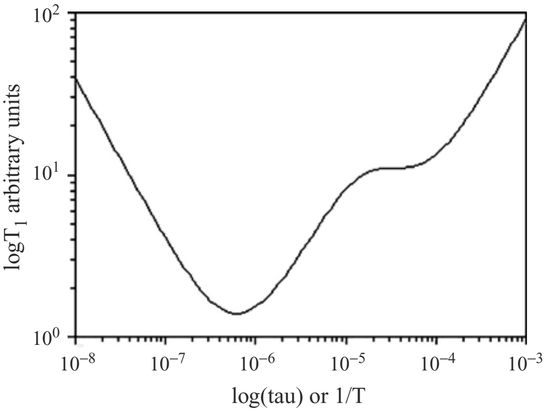

Fig. 10. A theoretical plot showing the effect on T_1 of two distinct correlation times.

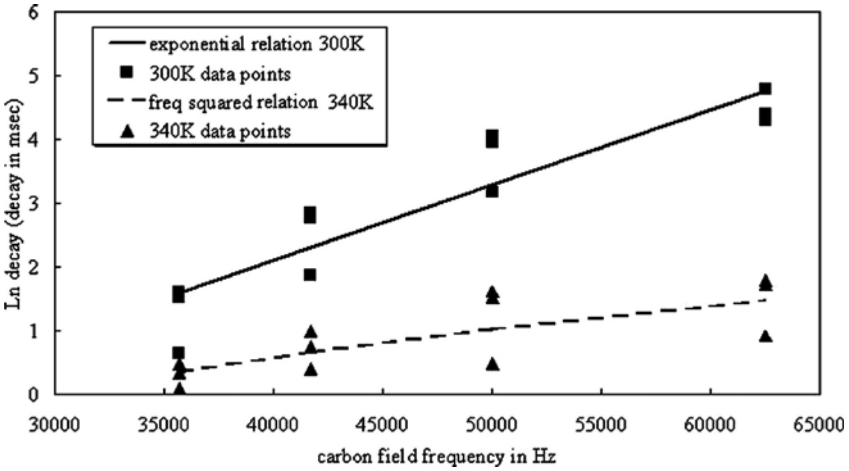

Fig. 11. ^{13}C $T_{1\rho}$ for the ring grouping in freeze dried maltose as a function of the frequency of the spin locking magnetic field.

times at the lower frequency end of the spectrum. Changes in moisture content can also blur apparent sharp features in the graphs. Similar observations have been made in the case of maltose [39] However here at low temperatures there appeared to be an additional reduction in T_1, apparently in disagreement with theory. It was proposed that this was not related to mobility, but may have reflected enhanced spin diffusion in these very rigid systems to efficient relaxation sinks. It has also been proposed that relaxation can be affected by the physical vibrational characteristics of the rotor in CPMAS NMR.

Of great interest both in Figure 9 and in reference [39] is the apparent lower transition temperature of the off-ring hydroxymethyl, when compared with the ring carbons. Moreover the absolute value of T_1 does not reflect the attached number of protons, i.e. is half the value for twice the number of protons, as might be expected. This implies the uncoupling of the motion of certain parts of the molecule from the main glass transition. As in the previous section where water was used as a solvent, the idea of uncoupling was further reinforced by examination of the motion of methanol in maltose methanol solutions [39]. Once again, while the increase in viscosity is of the order 10^{13}, on going from a solution to a glass, the rotational diffusion was only slowed by 4–5 orders of magnitude. This contrasts with other organic glasses measured using deuterium NMR [30], which showed that rotational motion of all components of the mixture tended to the same value as the temperature approached the glass transition. This may reflect the degree of compatibility of the solvent with the glass former.

^{13}C $T_{1\rho}$ measurements have often been cited as particularly relevant to glassy behavior, due to their being sensitive to motions in the mid-kHz region [40,41]. However the unambiguous assignment of ^{13}C $T_{1\rho}$ values to a measure of motion depends on the absence of efficient coupling of the carbon to the proton fraction, which would effectively shunt the magnetization to the lattice. It has been suggested that the variation of ^{13}C $T_{1\rho}$ as a function of frequency of the carbon irradiation is a test of this. If the ^{13}C $T_{1\rho}$ values have an exponential dependence then the $T_{1\rho}$ is tending away from a measure of motion. A squared dependence suggests a closer measure to true motion. This experiment was carried out (Figure 11) on freeze dried maltose and the result obtained, that below the glass transition there was a tight coupling between protons and carbons, whereas above T_g motion began to decouple the carbon/proton transfer of magnetization and $T_{1\rho}$ was a useful motional parameter . This is yet another example of a mobility experiment sensitive to the glass transition.

CPMAS NMR and Crystallization

The experiment described on Figure 9 was terminated at a temperature of 350 K due to the crystallization of the sucrose. As is seen on Table 2 the relaxation parameters for the glass and crystal are quite different. If the glass were to be caught in the act of crystallizing then we would expect a dramatic shift in value of the particular relaxation parameter. Figure 12 shows exactly such an experiment. These experiments can be difficult to reproduce as crystallization parameters such as induction time and rate are affected by shear when the sample is introduced to the CPMAS rotor and subsequently spun at 3–5 kHz.

Table 2: Relaxation times for different carbons in the sucrose molecule, crystal (anhydrous) and glass (1–2% moisture), at ambient temperature (295–305 K). Anomeric data are for the F_2 carbon of sucrose with no attached protons. The G_1 anomeric carbon, having one attached proton, exhibits ring values. Typical or averaged values are shown where several carbons belong to one class. T_1's in seconds, $T_{1\rho}$'s in milliseconds, T_{C-H} in microseconds

Sugar carbon	Anomeric				Ring				Off ring			
experiment	^{13}C T_1	^{13}C $T_{1\rho}$	^{1}H $T_{1\rho}$	T_{C-H}	^{13}C T_1	^{13}C $T_{1\rho}$	^{1}H $T_{1\rho}$	T_{C-H}	^{13}C T_1	^{13}C $T_{1\rho}$	^{1}H $T_{1\rho}$	T_{C-H}
glass	75	70	5	174	44	28	5	42	14	9	5	28
crystal	281	196	>300	248	264	110	>300	46	10	44	>300	26

One can also simply examine CPMAS spectra with time and under suitable conditions of temperature and moisture, observe the emergence of sharp peaks corresponding to crystalline species [42]. A corresponding reduction in the FTMAS trace, which measures the mobile fraction, can also often be seen. The latter depends to a certain extent on the proton decoupling power used in the FTMAS experiment. Large powers enable the rigid amorphous fraction to be seen whilst low powers render visible only the most mobile of species.

In conclusion, the CPMAS method detects glass transitions via a variety of relaxation methods and can measure the rate of crystallization and identify crystallizing species. This latter property distinguishes it from other relaxation methods.

Other NMR Techniques As Monitors of the Glass Transition

Two-dimensional exchange spectroscopy and its time domain echo decay equivalent are capable of providing a more detailed view of motion in glasses than has been presented thus far. In an adaptation of deuterium stimulated echo methods [43,44] which examined reorientation in ortho-terphenyl and glycerol, van Dusschoten *et al.* [45] used glucose, enriched in the 1 and 6 positions with ^{13}C, and examined the motion of the complete molecule and the off-ring hydroxymethyl.

Essentially, the orientation of a nucleus in the external magnetic field determines the frequency of evolution during the first time period. The magnetization is then stored in the *z* direction for a second time period during which rotational motions of the molecule, which change the orientation, will cause evolution at a different frequency in a third time period. Motion will therefore tend to decrease the subsequent echo. A ^{13}C cross polarization stage was incorporated to enhance sensitivity. Deuterium NMR could not be used here because of the relaxation properties in this system. It was found by comparison of experiment with computer simulation that echo decays were well described by a bimodal distribution of jump angles (75% 1–2° and 25% 7–8°) with the off-ring group having a higher value for the larger jump angle. However the motion of the ring and the off-ring group were strongly correlated, with no evidence for substantial rotational freedom. This has also been observed in glucose

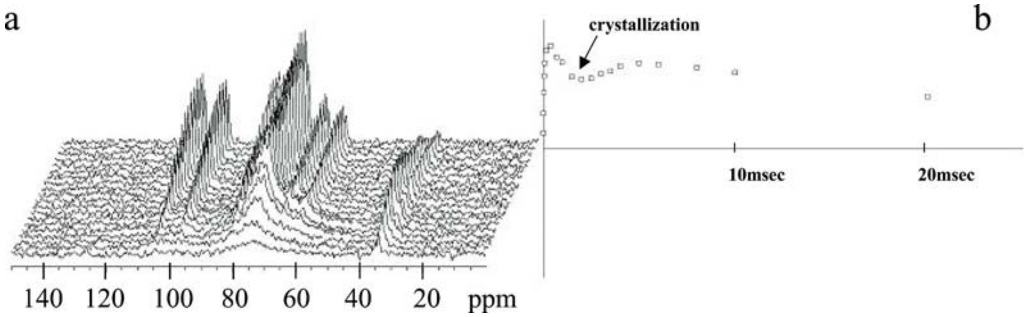

Fig. 12. A variable contact time experiment for freeze-dried 3/1 maltose pullulan at a moisture content of 11%. The emergence of sharp features (back) from the broad amorphous peaks (front) shows the progressive crystallization of maltose. Each trace took approximately 20 min to record. Figure 12b shows the integrated ring peak (75–85 ppm) in Figure 12A as a function of contact time. The normally smooth decay at times greater than about 1 msec is punctuated by a sudden increase in intensity corresponding to the shift in the value of the ^{1}H $T_{1\rho}$.

using CPMAS NMR, however, there are substantial differences in the freedom of off-ring groups amongst sugars. These studies suggest that in the glass and glassy region, isotropic motion or continuous rotational diffusion is no longer a good description of mobility.

Imaging in the Study of Glasses

The use of conventional NMR imaging is usually restricted to mobile systems with the sensitivity and noise being limited by the interplay between T_1 and T_2 values [46]. However the advent of pulse sequences designed specifically for more solid like materials, such as single point or constant time imaging [47], may provide macroscopic and functional information on glassy carbohydrate matrices including sugars, such as the ingress of moisture, although they would appear unlikely ever to give the detailed motional information provided by the previously considered methods.

References

1. Noel TR, Parker R, Ring SM, Ring SG. Carbohydr. Res. 1999;319:166.
2. Borde B, Bizot H, Vigier G, Buleon A. Carbohydr. Polym. 2002;48:111.
3. Simatos D, Blond G, Roudaut G, Champion D, Perez J, Faivre AL. J. Thermal Anal. 1996;47:1419.
4. Moynihan CT, Macedo PB, Montrose CJ, Gupta PK, DeBolt MA, Dill JF, Dom BE, Drake PW, Easteal AJ, Elterman PB, Moeller RP, Sasabe H, Wilder JA. Ann. NY Acad. Sci. 1976;279:15.
5. Weyer S, Merzlyakov M, Schick C. Thermochim. Acta. 2001;377:85.
6. Kedward CJ, MacNaughtan W, Mitchell JR. Carbohydr. Res. 2000;329:423.
7. Bruker Biospin Ltd. Coventry.
8. Resonance Instruments Ltd. Witney: Oxford.
9. Oxford instruments superconductivity [Newport analyser /4000] Witney: Oxford.
10. Pake GE, Purcell EM. Phys. Rev. 1948;74:1184.
11. Lowe IJ, Norberg RE. Phys. Rev. 1957;107:46.
12. Hills BP, Pardoe K. J. Mol. Liq. 1995;63:229.
13. Derbyshire W, van den Bosch M, van Dusschoten D, MacNaughtan W, Farhat IA, Hemminga MA, Mitchell JR. J. Mag. Res. 2004;168:278.
14. Van Vleck JH. Phys. Rev. 1948;74:1168.
15. W. Derbyshire European Project; Molecular Mobility in Foods, supported by European Union Contract ERB-FAIRCT961085.
16. Moran GR, Jeffrey KR. J. Chem. Phys. 1999;110, 3472.
17. Takeda S, Gotoh Y, Maruta G, Takahara S, Kittaka S. Z. Naturforsch. 2002;57:419.
18. Van den Dries IJ, Van Dusschoten D, Hemminga MA. J. Phys. Chem. B. 1998;102:10483.
19. Martin DR (1996) D phil thesis entitled solid state deuterium NMR of some disaccharides univ. of York.
20. Experimental Pulse NMR, Fukushima E, Roeder SBW. Addison Wesley Publishing Company, 1981, p 251.
21. Ablett S, Darke AH, Izzard MJ, Lillford PJ. The Glassy State in Foods. Nottingham University Press, Nottinghom 1993, p 189.
22. Reynhardt EC. Mol. Phys. 1990;69:1083.
23. Tang HR, Wang YL, Belton PS. Phys. Chem. Chem. Phys. 2004;6:3694.
24. Partanen R, Marie V, MacNaughtan W, Forssell P, Farhat IA. Carbohydr. Polym. 2004;56:147.
25. Kumagai H, MacNaughtan W, Fahrat IA, Mitchell JR. Carbohydr. Polym. 2002;48:341.
26. Mansfield P, Powles JG. 1962 Proc. 11th colloque ampère (Amsterdam: North Holland) p 194.
27. Luszczynski K, Kail JAE, Powles JG. Proc. Physic. Soc. 1960;75:243.
28. Hinze G, Sillescu H, Fujara F. Chem. Phys. Lett. 1995; 232:154.
29. Buitink J, van den Dries IJ, Hoekstra FA, Alberda M, Hemminga MA. Biophys. J. 2000;79:1119.
30. Roessler E, Tauchert J, Eiermann P. J. Phys. Chem. 1994;98:8173.
31. Kuhns PL, Conradi MS. J. Chem. Phys. 1982;77:1771.
32. McBrierty VJ, Packer KJ. Nuclear Magnetic Resonance in Solid Polymers. Cambridge University Press: Cambridge, 1995.
33. Schaefer J, Stejskal EO, Buchdahl R. Macromolecules. 1977;10:384.
34. Brown GM, Levy HA, Acta Cryst. B. 1973;29:790.
35. Torchia DA, J. Mag. Res. 1978;30:613.
36. Connor TM, Trans Faraday Soc. 1964;60:1574.
37. Kubo R, Tomita K. J Physic. Soc. Japan, 1954;9,888.
38. Schaefer J. Macromolecules. 1973;6:882.
39. Tromp RH, van Dusschoten D, Parker R, Ring SG. Phys. Chem. Chem. Phys. 1999;1:1927.
40. Schaefer J, Stejskal EO, Steger TR, Sefcik MD, Mckay RA. Macromolecules. 1980;13:1121.
41. vanderhart DL, Garroway AN. J. Chem. Phys. 1979;71: 2773.
42. MAFF Food Link Program, project no FQS06 High sugar polysaccharide systems (1999–2002).
43. Geil B, Fujara F, Sillescu H. J. Mag. Res. 1998;130:18.
44. Bohmer R, Hinze G. J. Chem. Phys. 1998;109:241.
45. van Dusschoten D, Tracht U, Heuer A, Spiess HW. J. Phys. Chem. A. 1999;103:8359.
46. Hills B. Magnetic Resonance Imaging in Food Science. John Wiley & sons, New York 1998.
47. Axelson DE, Kantzas A, Nauerth A. Solid State Nucl. Magn. Reson. 1996;6:309.

Probing the Sensory Properties of Food Materials with Nuclear Magnetic Resonance Spectroscopy and Imaging

Youngsoo Lee, Soo-Yeun Lee, and Shelly J. Schmidt
Department of Food Science and Human Nutrition, University of Illinois at Urbana-Champaign, Urbana, IL 61801, USA

Introduction

Consumers are becoming increasingly interested in the nutrition, science, and safety of the foods they consume. They want high quality, economically priced, healthy, and convenient food that satisfies their sensory expectations. To meet the consumers' needs and expectations, a thorough understanding of the chemical, biological, physical, and sensory aspects of foods is essential. The most innate consumer need and expectation is for the food to provide an acceptable (e.g. a quick lunch) to grand (e.g. Belgium chocolate) sensory experience. If the food possesses several desirable attributes (i.e. low cost, nutritious, and convenient), yet does not "taste good," the consumer will not likely purchase the food again [1]. The five major sensory properties of food materials—appearance, texture, aroma,[1] taste,[1] and irritation—are perceived by the primary human senses—visual (sight), tactile (touch), olfactory (smell), gustatory (taste), auditory (hearing), and chemesthesis[2] (common chemical sense). Figure 1 illustrates the connection between how these six primary human senses (left column) can be used to probe the five major sensory properties of food materials (center column)—the visual system for appearance, tactile, and auditory systems for texture, the olfactory system for aroma, the gustatory system for taste, and the chemethesis system for irritation.

Sensory scientists use well-designed and controlled objective sensory tests with trained human subjects to measure, analyze, and interpret reactions to food materials, as they are perceived by the senses, with the intention of formulating food products with desirable sensory properties. In addition to sensory methods, various instrumental methods have been used to investigate the sensory properties of foods. For example, gas- and liquid-chromatography have been developed to characterize numerous flavor compounds, such as the flavor compounds in roasted coffee beans [5]; texture analysis methods have been used to measure firmness in processed diced tomatoes [6]; and viscometer methods have been used to investigate mouthfeel attributes of beer [7]. Instrumental methods can provide rapid, reproducible, on-line, data that complements and correlates with sensory data. Instrumental methods can evaluate discrete sensory properties of foods and probe their underlying chemical and/or physical causes, however, they lack the integrative powers and sensitivity of the human sensing system. Thus, sensory and instrumental methods can be used in a complementary fashion to both assess the sensory properties of foods and to design foods with desirable sensory properties.

Nuclear magnetic resonance (NMR) spectroscopy and magnetic resonance imaging (MRI) are very versatile, non-invasive, non-destructive molecular level techniques that have been applied to investigate the sensory properties of food materials [8,9,10,11], as well as the activity of the brain while engaged in sensory evaluation [12,13,14,15]. In order to use NMR and MRI to probe the sensory properties of food materials (or brain activity) a relationship (either direct or indirect) between the NMR or MRI observables [16] and the sensory property of interest must be established. The association between the NMR or MRI observable and sensory property is based on a series of connections between fundamental spectroscopic events and molecular, microscopic, and macroscopic properties of the food sample. Figure 1 gives four examples of how various NMR and MRI observables and their associated molecular, sample, or brain activity properties (right column) can be used to probe the five major sensory properties of food materials (center column). In example one, the NMR observables of relaxation time [longitudinal (T_1, sec) and transverse (T_2, sec)] and spin diffusion coefficient (D, m^2/sec) can be used to measure rotational and translational molecular mobility, respectively, which in turn can be correlated to texture (e.g. firmness and crunchiness) and taste (e.g. sweetness

---

[1] "Flavor" is an attribute of foods that is a composite of the smell and taste sensations.

[2] Chemesthesis is defined as the sense mediating irritation aroused by the action of noxious chemicals on exposed or semi exposed mucosal membranes [2,3]. Examples of chemical sensibility humans possess toward irritant compounds are capsaicin in red chili pepper, piperine in black pepper, zingerone in ginger, isothiocyanate in mustard and horse radish and 1-propenyl sulfenic acid in onion and garlic [4].

Graham A. Webb (ed.), Modern Magnetic Resonance, 1889–1894.
© 2008 *Springer.*

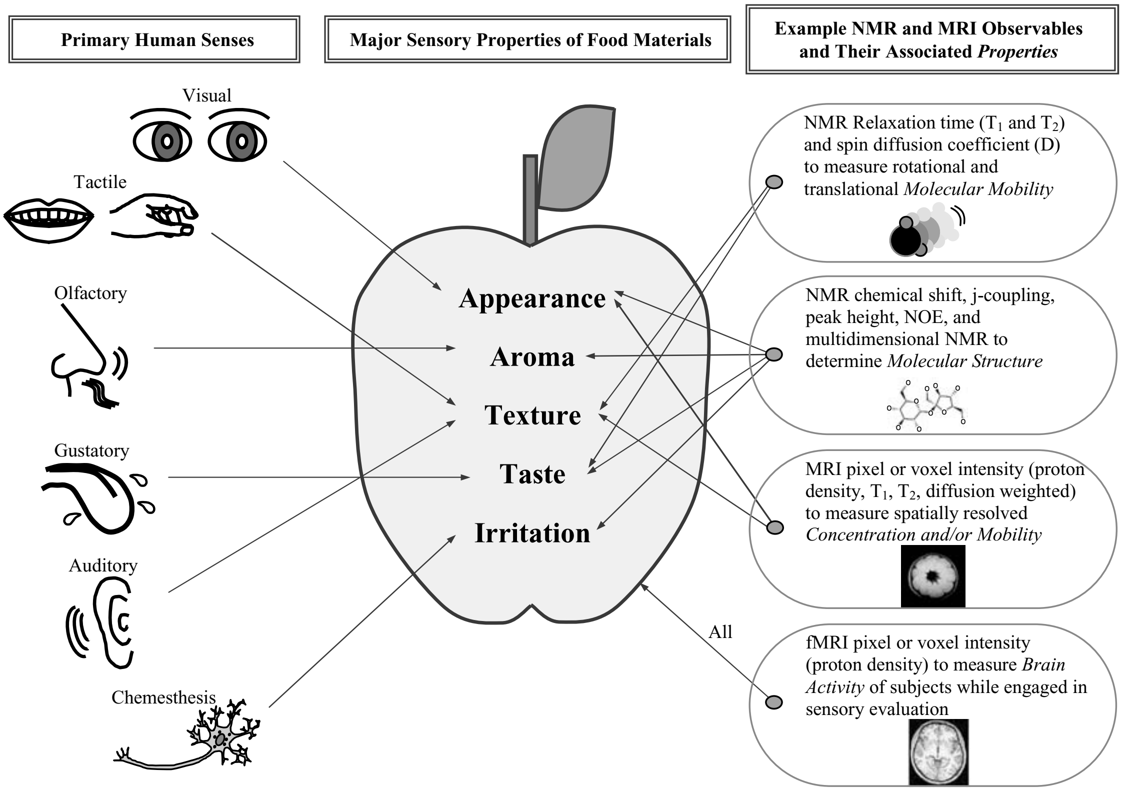
Primary Human Senses
Major Sensory Properties of Food Materials
Example NMR and MRI Observables and Their Associated *Properties*
Visual
Tactile
Olfactory
Gustatory
Auditory
Chemesthesis
Appearance
Aroma
Texture
Taste
Irritation
All
NMR Relaxation time (T_1 and T_2) and spin diffusion coefficient (D) to measure rotational and translational *Molecular Mobility*
NMR chemical shift, j-coupling, peak height, NOE, and multidimensional NMR to determine *Molecular Structure*
MRI pixel or voxel intensity (proton density, T_1, T_2, diffusion weighted) to measure spatially resolved *Concentration and/or Mobility*
fMRI pixel or voxel intensity (proton density) to measure *Brain Activity* of subjects while engaged in sensory evaluation

Fig. 1. Schematic illustration of how the five major sensory properties of food materials (center column) are probed by the six primary human senses (left column) and by various NMR and MRI observables and their associated properties (right column).

and saltiness). In example two, the NMR observables of chemical shift, j-coupling, peak intensity, Nuclear Overhauser Enhancement (NOE), and multidimensional NMR can be used to determine the molecular structure of various color additives (appearance), aroma compounds, taste compounds, and irritants. In example three, the MRI observables of pixel (2-D) or voxel (3-D) intensity can be used to measure spatially resolved sample concentration and/or component molecular mobility, which in turn can be correlated to internal sample appearance and texture sensory properties. In example four, the functional MRI (fMRI) observables of pixel or voxel intensity (typically proton density for measuring changes in blood flow over time) can be used to measure brain activity of a subject while engaged in sensory evaluation. These examples were designed to illustrate the general usefulness of NMR and MRI for probing the five major sensory properties of food materials. The remaining of this article is devoted to the use of magnetic resonance techniques for specifically probing texture and taste properties of food materials.

Texture

The texture of food, in most cases, is measured and expressed by its rheological and structural characteristics [17]. When the texture of food is perceived, one or more of the visual, tactile, and auditory senses are engaged. When a consumer is in the process of choosing a food product, the first level of textural evaluation usually involves the visual and tactile (hand) assessment of the product, especially in the case of fresh produce, meat, fish, and poultry. Subsequent post-purchase textural evaluation of the product involves mastication, also known as chewing, which directly involves the tactile (mouth) and auditory senses, and may be indirectly influenced by the simultaneous activities of the olfactory and gustatory senses. The perception of texture in the mouth is often a critical quality factor for many types of foods, such as the crunchiness of snack foods, the creaminess of puddings and mousses, and the astringency of red wines.[3] Magnetic resonance techniques have been employed to evaluate food texture, along with other instrumental methods, such as texture analysis and viscosity measurements [22]. Food texture studies using magnetic resonance can be categorized into three main types: water mobility, image analysis (MRI), and functional brain imaging (fMRI). Recent research studies that have been done to better understand and evaluate food texture using magnetic resonance are discussed below.

Water Mobility

Water mobility as measured by NMR has been related to the texture of solid and semi-solid food systems [23,24,25,26,27,28,29]. For solid and semi-solid foods, the mobility of water, as measured by free induction decay (FID), longitudinal relaxation time (T_1), or transverse relaxation time (T_2) of the water, has been correlated to instrumental and/or sensory texture measurements. In general, decreasing water mobility (i.e. shorter FID, T_1, and T_2 values) is linked to increasing food texture parameters, such as crispness, firmness, hardness, and elasticity. For example, Chen *et al.* (1997) studied the NMR mobility of water [20 MHz ^{1}H NMR T_1 saturation recovery sequence and T_2 Carr-Purcel-Meiboom-Gill (CPMG)] in bread during storage (5 and 22 °C) and found that several NMR parameters correlated with the firming process in the bread crumb (staling) as measured by the TA.XT2 Texture Analyzer [23]. In another study, Thygesen *et al.* (2001) explored the correlation of low-field ^{1}H NMR parameters extracted from CPMG relaxation curves of raw potatoes and the chemical and sensory analysis of cooked potatoes [28]. The purpose of their study was to understand the underlying chemical connection between the sensory predictive NMR parameters and sensory texture. They tested several potato varieties and two growing methods (organic and non-organic). Overall, it was found that predication of sensory texture quality of boiled potatoes from relaxation curves of raw potatoes is possibly because NMR relaxation curves contain information on water content, which, in turn, is inversely correlated to starch content. It was also reported that NMR is able to probe adhesiveness and springiness mouthfeel attributes slightly better than chemical descriptors due to its sensitivity to the state of the water (bulk or associated with solids) in the sample, a parameter that is uniquely determined by NMR. These studies illustrate the utility and the potential of using NMR for examining the texture of food materials.

Image Analysis

While NMR can measure the spatially averaged water content and mobility of a sample, MRI can measure the spatial distribution of water content and mobility across the sample. In turn, this spatial information has been correlated to the internal textural properties of the sample [30,31,32]. For example, Gonzalez *et al.* (2000) studied the effects of cooking time (9.5, 11, and 15 min) and holding time of lasagna pasta after cooking (4–185 min) on sample textural properties (mechanical testing using the texture analyzer) and internal moisture distribution (*via* MRI at 300 MHz using a spin-echo based imaging sequence) [30]. They reported that changes in MRI moisture distribution correlated well with changes in textural properties. For example, migration of water, as measured by MRI, to the sample center coincided with a significant decrease in peak force required to cut the lasagna pasta during both cooking and holding times.

Functional Brain Imaging

Functional MRI can be used to understand how the human brain responds to the presence of different tactile stimuli [14,15,33]. For example, de Araujo *et al.* (2004) used fMRI (3T Vaian/Siemans whole body scanner) to investigate the representation of food texture and oral fat in the human brain, using carboxymethyl cellulose (CMC) and vegetable oil [33]. The choice of fluid foods minimized the movement of the subjects during imaging, since no chewing was required. It was found that viscosity of tasteless and odorless CMC was represented in the (primary) taste cortex in the anterior insular and that the level of activation was proportional to the log of the CMC viscosity. The ventral anterior cingulated cortex was activated by oral fat independently of its viscosity, and was also activated by sucrose. This study is the first investigation of the oral sensory representation of food texture and fat in the human brain. The results begin to reveal brain mechanisms that may be important in texture-related sensory properties of food that make them palatable, and in turn may be related to the control of food intake and obesity. Even though fMRI is complicated by the problem of movement during chewing, it has great potential for understanding the perception of food texture by the human brain.

---

[3] Astringency is a chemically induced multifaceted oral tactile sensation that is described as a puckering or drying sensation in the mouth. Astringency is thought to result from the interaction between polyphenols and proline-rich salivary proteins, which form a complex that precipitates, and in turn reduces the lubrication effect of saliva on the tongue and the surface of the oral cavity [18]. NMR has been used to characterize the structure and dynamics of the tannin-saliva protein complex [19,20,21].

Taste

The gustatory sense is one of the most common and fundamental senses in life. It is the direct detection of a relatively few specific chemical compounds (compared to the sense of olfaction) on the sensory organs called taste buds or gustatory calyculi, which are concentrated on the upper surface of the tongue [34]. There are currently thought to be five basic tastes: (1) salty, mainly produced by the presence of sodium chloride and to a lesser degree by other salts, such as potassium chloride, (2) sweet, produced by simple carbohydrates, such as sucrose and fructose, as well as high intensity sweeteners, such aspartame and sucralose, (3) bitter, produced by alkaloids and other chemicals, (4) sour, produced by acids, and (5) umami or savory, produced by the salts of glutamic acid, such as monosodium glutamate (MSG), a flavor enhancer. Taste transduction for salty and sour stimuli is thought to be *via* the ion channel mechanism, while sweet, bitter, and umami stimuli are thought to be induced *via* the receptor protein binding mechanism [35,36]. NMR spectroscopy has been used to identify the chemical structure, conformation, and dynamics of the molecules responsible for these taste sensations (taste stimuli or tastants), as well as tastant–receptor interactions. The NMR methods used to investigate the five tastes described above are discussed below by taste category.

Salty

Interest in better understanding the molecular level role of table salt (NaCl), as well as the salt substitute potassium chloride (KCl), in the processability, stability, and salty taste perception of food systems has led to using NMR techniques [37,38,39,40,41]. Ayya (1988) and Rosett *et al.* (1994) used sodium-23 (^{23}Na) NMR to investigate the relationship between perceived saltiness and the binding of Na^+ in aqueous ionic and non-ionic gum systems. In both studies it was observed that ionic gum solutions (carboxymethylcellulose, xanthan, and carrageenan) received lower saltiness intensity ratings compared to non-ionic gum solutions (methylcellulose, guar, and locust bean) with equivalent added Na^+ contents. The lower intensity ratings of the ionic gum solutions were attributed to the interaction of Na^+ and the negatively charged groups of the ionic gums. The Na^+–gum interaction was investigated by measuring the ^{23}Na NMR transverse relaxation rate (R_2*) of the gum systems. Again, in both studies, the ionic gum solutions had higher R_2* values (lower rotational mobility) compared to the non-ionic gum solutions, in the same Na^+ concentration range, indicating that the Na^+ in the ionic gum solutions was slowed down by interacting with the negatively charged groups of the ionic gums.

Rosett *et al.* (1995) examined the competitive binding between K^+ and Na^+ ions to elucidate a mechanism by which the addition of other cations may enhance saltiness perception of processed foods using ^{23}Na NMR relaxation measurements [40]. They reported that the ^{23}Na NMR R_2* values increased with the addition of K^+ to the NaCl ionic xanthan gum system, corresponding to an increase in the average Na^+ mobility. Correspondingly, they found that salty taste increased with the addition of KCl to the NaCl ionic xanthan gum system, as determined by Decision Boundary modeling of subject identification data. They concluded that enhancement of the salty taste of a food system containing NaCl by KCl can be explained, at least in part, by competitive binding of Na^+ and K^+. The K^+ displaces the Na^+ on large negatively charges macromolecules, allowing more Na^+ to remain free for saltiness perception.

Nagata *et al.* (2000) used ^{23}Na and chloride-35 (^{35}Cl) NMR to study the mobility of Na^+ and Cl^- in crab meats cooked by traditional boiling in salt water for 10 min at 100 °C in the case of fresh crab meat and autoclaving with salt water for 90 min at 110 °C in the case of canned crab meat [41]. It was known that traditional boiling produced better tasting crab meat, but the question was why. The researchers measured T_1 by inversion recovery and found that both Na^+ and Cl^- mobility in the crab meat decreased significantly with autoclaving. They hypothesized that the poorer taste of canned crab meat compared to fresh meat was due to the observed reduction in Na^+ and Cl^- mobility.

Sweet

Two areas of sweet taste that have been readily explored using NMR are, (1) the chemical structure of sweet molecules and their solid and solution conformation and, (2) the role of sweet molecule–water interactions and physical properties on sweet taste perception. An example of the first area is the recent research aimed at elucidating the structure-taste relationships of sweet proteins (e.g. brazzein, monellin, and thaumatin) [42,43]. Kohmura *et al.* (2002) used a suite of NMR techniques, including two-dimensional nuclear Overhauser enhancement spectroscopy (NOESY), total correlation spectroscopy (COSY), and double quantum filtered correlation spectroscopy (DQF-COSY), to study the relationship between structure and taste of the sweet protein monellin (4000 times as sweet as sucrose) and thirty-seven synthesized monellin analogs [42]. The results suggest that it is the free β-caroxyl group of the Asp^{B7} residue that binds to the receptor site through ionic bonding and triggers the sensation of intense sweet taste.

In the second area, researchers have enlisted a number of techniques and physical parameters, including NMR, to examine the role of water in sweet taste perception [35,44,45,46,47,48,49]. For example, Aroulmoji *et al.* (2001) investigated the effects of sucrose, caffeine and their mixture on water mobility using both physicochemical properties (intrinsic viscosity, apparent specific volume, and surface tension) and ^{1}H NMR relaxation rate (R_1 and R_2) measurements [35]. NMR data together with physicochemical properties data helped explain the role of water in sweet and bitter taste perception.

Recently, Mahawanich and Schmidt (2004) explored the relationship between the molecular mobility of water and the perceived sweetness of three simple sugars, sucrose, fructose, and glucose solutions (0.15 mol/l to saturation) [49]. The rotational mobility of water was measured by ^{1}H-decoupled oxygen-17 (^{17}O) NMR 500 MHz R_1 (inversion recovery), R_2 (CPMG), and R_2* (line width at half-height). The translational mobility of water was measured using ^{1}H NMR pulse-field spin-echo (PGSE) method. The rotational and translational mobility of the sugar molecules were measured using ^{1}H NMR 500 MHz R_1 (inversion recovery) and translational mobility (PGSE), respectively. In general, as sugar concentration increased the rotational and translational mobility of both the water and sugar molecules decreased, while the maximum sweetness intensity increased. However, the researchers concluded that there appeared to be no direct correlation between the perceived sweetness and the NMR molecular mobility parameters measured in the study. The lack of direct correlation between the perceived sweetness and the NMR molecular mobility parameters was attributed to the complex nature of sweet taste perception and the challenges associated with correlating molecular level parameters with macroscopic sensory data.

Bitter

Bitterness in some foods and beverages are tolerable or to some even desirable, like the bitterness imparted to beer by alpha-acids, or the bitterness imparted to broccoli by glucosinolates, or the bitterness imparted to coffee by caffeine. However, there are a number of bitter compounds found in raw foods or produced by processing or senescence that are undesirable in foods. Hofmann and his lab group, for example, have used NMR techniques to aid in the structural determination of bitter off-tasting compounds in cold-stored and commercial carrot puree and those formed during thermal food processing from Maillard-type reactions [50,51].

Sour

The structure of sour tastants has been determined using NMR. For example, Shima *et al.* (1998) used mass spectrometry, ^{1}H NMR, and ^{13}C NMR to identify the structure of a novel compound [N-(1-methyl-4-hydroxy-3-imidazolin-2,2-ylidene) alanine] that is thought to be responsible for the sour taste aspect of beef broth [52].

Umami

An example of the use of magnetic resonance to explore the relatively new taste of umami is the research by de Araujo *et al.* (2003), which used fMRI (3T Varian/Siemens whole body scanner) to determine the representation of umami in the human brain [36]. The regions in the brain activated by MSG were found to be very similar to the regions activated by glucose. The authors concluded that this similarity in brain activation provides additional evidence that umami is indeed a "fifth taste."

Summary and Future Applications

Sensory evaluation and magnetic resonance are complementary techniques for probing the fundamental nature of the sensory properties of food materials. Their combined use is leading to a deeper understand of the basis of food material properties, with sensory science contributing an integrated macroscopic perspective and magnetic resonance providing a physical-chemical molecular viewpoint. As far as future applications of magnetic resonance, NMR will continue to be used as the method of choice for uncovering the molecular structure, conformation, and dynamics of molecules of importance to sensory science. MRI could be used for monitoring deformation of foods using an artificial mouth to simulate the mastication process, opening up the door for a new generation of texture and flavor release studies. fMRI could be used to develop a map of sensory perceptions in the human brain, which could provide critical information necessary for the development of foods with optimal sensory attributes, functional properties, and nutritional benefits. The future is bright for innovate uses of NMR and MRI in sensory science.

References

1. Karel M, Food Technol., 54(6), 56(2000).
2. Keele CA, Archives Internationales de Pharmacodynami et de Therapie, 1962;139:547.
3. Green BG, Mason JR, Kare MR, eds. Chemical Senses. Volume 2: Irritation. Marcel Dekker, v-vi, New York, 1990, p. 361.
4. Silver WL, Finger TE, The Trigeminal System. In: Smell and Taste in Health and Disease. Getchell TV, others, eds. Raven Press, New York, 1991, p.97–108.

5. Deibler K, Delwiche J, Handbook of Flavor Characterization: Sensory Analysis, Chemistry, and Physiology, Marecel Dekker, Inc., New York, 2003, p 384.
6. Lee SY, Luna I-Guzmán, Chang S, Barret DM, and Guinard JX, Food Qual. Prefer. 1999;10:447.
7. Langstaff SA, Guinard JX, and Lewis MJ, J. Inst. Brew. 1991;97:427.
8. Schmidt SJ, and Ayya N, Characterization of sodium binding in polysaccharides using sodium23 NMR. In "Frontiers in Carbohydrate Research-1: Food Application." Elsevier Applied Science Co., New York, 1989.
9. Robertson T, Schmidt SJ, and Klein BP, Trends Food Sci. Technol., 1992;3:236.
10. Schmidt SJ, and Rosett TR, Use of ^{23}Na NMR to study sodium-macromolecule interactions. In "Ingredient Interactions: Effects on Food Quality," Gaonkar, A.G. (Ed.), Marcel Dekker, Inc., New York, 1995.
11. Schmidt SJ, Advances in Magnetic Resonance in Food Science, The Royal Society of Chemistry, Cambridge, 1999, p 79.
12. Rouby C, Schaal B, Dubois D, Gervais R, and Holley A, Olfaction, Taste, and Cognition, Cambridge University Press, Cambridge, 2002, p 484.
13. de Araujo IET, Rolls ET, Kringelbach ML, McGlone F, and Phillips N, Eur. J Neurosci., 2003;18:2059.
14. Rolls ET, Verhagen JV, and Kadohisa M, J Neurophysiol., 2003;90:3711.
15. Rolls ET, Brain Cognition, 2004;55:11.
16. Eads T, Spectral methods in food analysis. Ed. MM Mossoba, Chapter 1. Principles for Nuclear Magnetic Resonance analysis of intact food materials. Marcel Dekker, New York, 1999.
17. Lawless HT, Heymann H, Sensory Evaluation of Food; Principle and Practices, Kluwer Academy/Plenum Publishers, New York, 1998.
18. Kallithraka S, Bakker J, Clifford MN, J Sens. Stud., 13(1), 29(1998).
19. Baxter NJ, Lilley TH, Haslam E, and Williamson MP, Biochem., 1997;36:5566.
20. Charlton AJ, Baxter NJ, Khan ML, Moir AJG, Haslam E, Davies AP, and Williamson MP, J Agric. Food Chem., 2002;50:1593.
21. Simon C, Barathieu K, Lanuerre M, Schitter JM, Fouquet E, Painet I, and Dufourc EJ, Biochem., 2003;42:10385.
22. Thybo AK, Karlsson AH, Bertram HC, Andersen HJ, Szczypinski P, and Donstrup S, Aarhus, Nuclear magnetic resonance (NMR) and magnetic resonance imaging (MRI) in texture measurement, Chapter 8. In: Texture in Food, Volume 2: Solid foods, D Kilcast (Ed.), Woodhead Publishing Limited, Cambridge, 2004.
23. Chen PL, Long Z, Ruan R, and Labuza TP, Lebensm.-Wiss. u.-Technol., 1997;30:178.
24. Ruan Roger R, Zou C, Wadhawan C, Martinez B, Chen PL, and Addis P, J Food Process. Pres., 1997;21:91.
25. Steen C, Lambelet P, J Sci. Food Agric., 1997;75:268.
26. Brøndum J, Byrne DV, Bak LS, Bertelsen G, and Engelsen SB, Meat Sci., 2000;54:83.
27. Engelsen SB, Jensen MK, Pedersen HT, Nøgaard L, and Munck L, J Cereal Sci., 2001;33:59.
28. Thygesen LG, Thybo AK, and Engelsen SB, Lebensm.-Wiss. u.-Technol., 2001;34:469.
29. Choi SG, Kerr WL, Carbohyd. Polym., 2003;51:1.
30. Gonzalez JJ, McCarthy KJ, McCarthy MJ, J Texture Stud., 2000;31:93.
31. Jétal L, Jirák D, Šuderlová L, and Hájek M, Lebensm.-Wiss. u.-Technol., 2003;36:719.
32. Thybo AK, Szczypinski PM, Karlsson AH, Dønstrup S, Stødkilde-Jørgensen HS, and Andersen HJ, J Food Engi., 2004;61:91.
33. de Araujo IE, and Rolls ET, J Neurosci., 24(12), 3086 (2004).
34. Wikipedia. Basic tastes. <http://en.wikipedia.org/wiki/Basic taste> 2004 (Accessed 20 November 2004)
35. Aroulmoji V, Hutteau F, Mathlouthi M, and Rutledge DN, J Agirc. Food Chem., 2001;49:4039.
36. de Araujo IET, Kringelbach ML, Rolls ET, and Hobden P, J Neurophysol., 90, 313 (2003).
37. Ayya N, 1988. Physiochemical and Sensory Characterization of Interaction in NaCl-Hydrocolliod Systems. Ph.D. Thesis, University of Illinois at Urbana-Champaign, IL.
38. Schmidt SJ, Ayya N, and Shirley L, Lebensm.-Wiss. U.-Technol., 1992;25:540.
39. Rosett TR, Shirley L, Schmidt SJ, and Klein BP, J Food Sci., 59(1), 206(1994).
40. Rosett TR, Wu Z, Schmidt SJ, Ennis DM, and Klein BP, J Food Sci., 60(4), 849(1995).
41. Nagata T, Chuda Y, Yan X, Suzuki M, and Kawasaki K, J Sci. Food Agric., 2000;80:1151.
42. M Kohmura, Mizukoshi T, Nio N, Suzuki E, and Ariyoshi Y, Pure Appl. Chem., 74(7), 1235(2002).
43. Tancredi T, Pastore A, Salvadori S, Esposito V, and Temussi PA, Eur. J Biochem., 2004;271:2231.
44. Mathlouthi M, Food Chem., 1984;13:1.
45. Mathlouthi M, Seuvre AM, J Chem. Soc.-Faraday Trans. I, 1988;84:2641.
46. Mathlouthi M, Hutteau F, and Angiboust JF, Food Chem., 56(3), 215(1996).
47. Birch GG, Karim R, J Sci. Food Agric., 58(4), 563 (1992).
48. Birch GG, Pure Appl. Chem., 2002;7:1103.
49. Mahawanich T, Schmidt SJ, Food Chem., 84,169(2004).
50. Czepa D, Hofmann T, J Agric. Food Chem., 51(13), 3865(2003).
51. Frank O, Jezussek M, and Hofmann T, J Agric. Food Chem., 51(9), 2693(2003).
52. Shima K, Yamada N, Suzuki E, and Harada T, J Agric. Food Chem., 46(4), 1465(1998).

Single-Sided NMR in Foods

Gisela Guthausen[1], Harald Todt[1], Wolfgang Burk[1], Dieter Schmalbein[1], Andreas Guthausen[2,*],
and Andreas Kamlowski[2]
[1] *Minispec Division, Bruker Optik GmbH; and*
[2] *MicroSpin Division, Bruker Biospin GmbH, Silberstreifen, 76287 Rheinstetten*

Introduction

A relatively new approach in NMR is the relaxing of restrictions on the magnetic field homogeneity for the static field B_0 as well as for the radio frequency field B_1, known as single-sided or unilateral NMR. This realization of an NMR device implies cost reduction of the equipment as well as the possibility to non-destructively apply NMR techniques to samples larger than the probe. However, this approach has also physical consequences. The magnetic field gradients are in an order of magnitude where almost every pulse becomes selective thus leading to spatial selectivity which is given by the Larmor frequency and the bandwidth of the tank circuit. In addition, these single-sided NMR devices have an inherent sensitivity to diffusive or convective processes as the field gradients are large. For example, the device used for the measurements presented here exhibits B_0 field gradients in the order of 10–20 T/m, leading to an full width at half maximum, FWHM slice thickness of about 2 mm with a quality factor of the circuit of about 70. The $B_1(r)$ can be constructed such that shape and size of the sensitive volume corresponds to the sample to be measured and is therefore to be tailored to the desired properties. In case of homogeneous food samples, the sensitive volume should be chosen as large as possible, whereas small and sharp volumes are preferred in examinations of local properties. Examples are the investigations of skin cancer and of fat content in living salmon [1].

The Bruker Single-Sided NMR Device

Starting from the NMR-MOUSE® [2–5], a trademark of the RWTH Aachen, a single-sided NMR device was constructed especially for the needs in an industrial environment. The device is small and equipped with exchangeable rf parts for allowing fast and easy change of measurement depth (Figure 1), i.e. tailoring to the application problem. Currently, three measurement depth are available, which are surface, 3 mm, and 5 mm. Moreover, the probe design was chosen such that detuning due to the dielectric constant of the sample was minimized. This lead to an increased reproducibility without any re-tuning of the circuit. Furthermore, the dead time of the probes was reduced to about 11 μs which opened application of the Bruker single-sided NMR device to hard materials like plastics. As the measurements take place in the stray fields of B_0 and B_1, the inherent sensitivity is smaller compared to a conventional NMR spectrometer using homogeneous magnetic fields. Therefore, special attention was given to an optimized signal to noise (S/N) ratio under these circumstances.

Experimental Approaches in Fat and Water Determination

As already discussed in part B (Time-Domain NMR in Quality Control: Advanced Applications in Food), the determination of fat and water content in food is an important application in food analysis. Using Time-Domain (TD-) NMR or even single-sided NMR implies that the chemical shift resolution is usually not high enough to allow a reliable determination of both contents. Therefore the physical parameters NMR relaxation and diffusion have to be exploited. These approaches work for the single-sided NMR devices also.

Diffusion Weighted Approach

As the single-sided NMR devices exhibit strong B_0 and B_1 gradients, it is quite natural to think about the use of the B_0 gradient for selective suppression of the water signal. The difference in the diffusion coefficient, D, can be exploited to create sufficient contrast between water and fat compartments. Several NMR methods are known: (1) The conventional Hahn echo sequence exhibits a dependence on D proportional to $\exp(-D\tau^3)$, where τ is the echo time. Consequently, at large echo times the influence of diffusion is more pronounced. (2) In contrast to the Hahn echo sequence, in multi echo sequences [6] the dependence on the decay time t is proportional to

---

[*] In memoriam

Graham A. Webb (ed.), Modern Magnetic Resonance, 1895–1897.
© 2008 *Springer.*

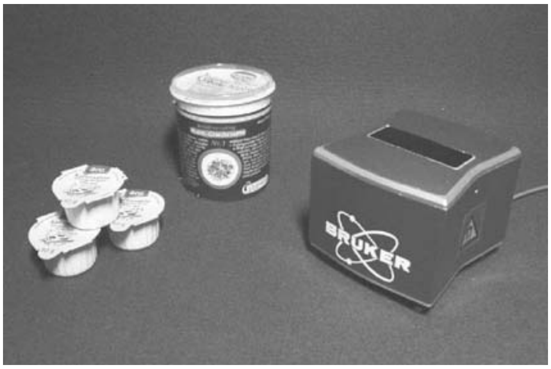

Fig. 1. The Bruker single-sided NMR device, specially constructed for industrial needs. The cream samples are shown for reference. (See also Plate 139 on page XXVIII in the Color Plate Section.)

exp(-*Dt*). However, the decay can be measured within one scan leading to a measurement time advantage over the Hahn echo method. (3) In addition to echoes exploiting mainly transverse magnetization, stimulated echo sequences are known, often being used in restricted diffusion experiments, where only the slower longitudinal relaxation time allows measurements at longer time delays. The disadvantage is again a longer measurement time.

Taking into account the specific prerequisites on experiments using single-sided NMR, the multi echo approach seems to be the most promising in an industrial environment. In Figure 2, the pulse sequence is shown, which was developed for the special needs of fat and water differentiation in quality control [7]: In the first few echoes using small echo times τ_1 the total magnetization of the sample in the sensitive volume is observed except for magnetization contributions due to components with $T_2 < 100$ µs, which are essentially solid like materials as for example packing materials. Several echoes are averaged in order to improve the S/N ratio. In the second interval the diffusion filter is applied such, that at the end only the signal of the fat component remains. In a third part several echoes are averaged for improvement of the S/N ratio of the fat signal. The ratio of the fat signal and the total signal results in the fat content which can be calibrated against reference values in order to provide absolute numbers and to correct for inherent systematic errors. Finally, in the case of $k = n = 0$ (see Figure 2), the case of the CPMG [6] sequence, the complete echo decay is correlated with the fat content, rather than just the calculated ratios of echoes at particular times. This method can also be applied in fat content measurements in fat and water mixtures [8]. As an example, the correlation diagram of fat content of coffee creams determined by this single-sided NMR method with the reference values given by the manufacturer is shown in Figure 3. The surface probe was used for achieving the best possible S/N ratio. The packing material is not influencing the ratio much, because it is relatively thin and the polymer material exhibits a short T_2 relaxation time. The measurement time was about 1 min. The correlation coefficient was determined to 0.996, which allows a reasonable prediction of the fat content through the packaging! It is obvious that

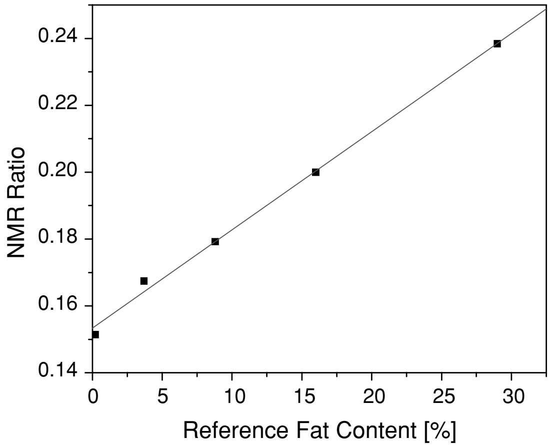

Fig. 3. Correlation diagram of the NMR ratio with the fat content of some coffee creams. The correlation coefficient is 0.996. The sequence used for this experiment is the diffusion weighted ratio method shown in Figure 2. The measurements were performed using the surface insert. (See also Plate 140 on page XXVIII in the Color Plate Section.)

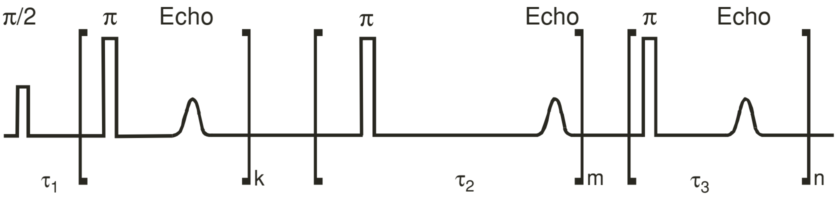

Fig. 2. Pulse sequence for measuring transverse magnetization decays, which are influenced by relaxation processes and diffusion with single-sided NMR.

the S/N of the measurement directly influences the quality of the calibration curve, i.e. the precision of the measurement. The S/N can be improved by increasing the number of repetitions of the experiment, however, leading to longer measurement times. Obviously, the accuracy also depends strongly on the quality of the reference values, which were taken from the nutrition facts on the labels.

Relaxation Time Approach

As discussed in Part B: Time-Domain NMR in Quality Control: Advanced Applications in Food, the relaxation time differences of fat and water protons can be exploited to generate sufficient contrast to allow the contents determination. The same is true in case of single-sided NMR. For a more detailed description we refer to Part B: Time-Domain NMR in Quality Control: Advanced Applications in Food. Again, both NMR relaxation parameters are considered, thus increasing the contrast. In [8], only the transverse relaxation was considered which already leads to reasonable results together with the chemometric data processing. It is essential for the method presented here that the sensitive volume is covered completely and filling factors can be neglected thus circumventing the need of weight of that part of sample contributing to the NMR signal. Again the data processing is performed using a chemometric approach in order to facilitate the analysis of hundreds of data points. A correlation coefficient R of 0.991 was obtained, slightly less than R of the surface measurements using the diffusion weighted ratio method in Figure 3. The measurements were performed in a depth of 3 mm, leading to an inherent decrease of the S/N by a factor of about 3–4. This means that the measurement time should be increased by a factor of 9 for obtaining the same S/N. Here, the measurement time was limited to 5 min due to tempering issues. Of course, an rf insert could be constructed with less pronounced depth selectivity releasing the S/N restriction.

In order to compare the overall analysis time, measurements in homogeneous fields (TD-NMR 20 MHz system) were conducted on the same samples. The measurement time could be reduced to about 1 min. However, the sample preparation time has to be taken into account as well, leading to only small differences in the overall analysis time. The correlation coefficient established with the measurements in the homogeneous field was determined to be slightly higher (0.997 compared to 0.991), which could be due to the mentioned inherent S/N disadvantage of the single-sided NMR devices.

Conclusion

The single-sided NMR can be used for measuring the fat content in packaged products as well as *in vivo*. Two NMR methods were discussed, which may also be applied in other fields when dealing with substances of different relaxation or diffusion properties. The S/N critically determines the quality of the measurement and the correlation, as long as the temperature stability is guaranteed. Improvements of the S/N, i.e. the correlation, or reduction of the measurement time can be achieved by increasing the resonance frequency and by increasing the measurement volume. The major advantage of single-sided NMR measurements is that sample preparation is not required. Products can be examined "as is," even through the packaging in finished dairy products. It should be pointed out that the same measurements can be performed *in vivo* in order to exploit different tissues in surface near regions.

As the single-sided NMR devices use only stray fields, the relatively low S/N is an inherent feature. Several research activities are in progress regarding this issue.

Acknowledgment

We would like to thank S. Sies, Unilever Bestfoods The Netherlands, R&D Baarn, for providing us well-characterized samples.

References

1. Veliyulin E, van der Zwaag C, Erikson U, Burk W, Daaland J-E, to be published.
2. Eidmann G, Savelsberg R, Blümler P, Blümich B. J. Magn. Reson. A 1996;122:104–109.
3. Guthausen A, Zimmer G, Blümler P, Blümich B. J. Magn. Reson. 1998;130:1–7.
4. Balibanu F, Hailu K, Eymael R, Demco DE, Blümich B. J. Magn. Reson. 2000;145:246–258.
5. Guthausen G, Guthausen A, Balibanu F, Eymael R, Hailu K, Schmitz U, Blümich B. Macromol. Mater. Eng. 2000;267/277:25–37.
6. a) Carr HY, Purcell EM. Phys. Rev. 1954;98:630.
   b) Meiboom S, Gill D. Rev. Sci. Instrum. 1958;29:688.
7. a) Guthausen A, Guthausen G, Kamlowski A, Schmalbein D. Lecture on the 2nd Colloquium of Mobile NMR, Vaals, 2002.
   b) Guthausen A, Guthausen G, Kamlowski A, Todt H, Burk W, Schmalbein D. JAOCS 2004;81:727–731.
8. Pedersen HT, Ablett S, Martin DR, Mallett MJD, Engelsen SB. J. Magn. Reson. 2003;165:49–58.

Applications of NMR in the Studies of Starch Systems

Imad A. Farhat
Division of Food Sciences, University of Nottingham, Loughborough, LE12 5RD, UK

Introduction

This chapter reviews the main contributions of NMR spectroscopy to the understanding of the biosynthesis, structure, processing, and performance of starch. The chapter is written from an "NMR user"/Food Science perspective rather from an "NMR specialist"/Spectroscopy one. Because of the context, i.e. a magnetic resonance handbook, a relatively detailed introduction of starch as a material is included for the benefit of readers who may not be familiar with starch.

Starch

Starch is one of the most widely present natural polymers, second only to another glucose polymer, cellulose. It is of major economical importance. The world market size for 2000 was estimated at ~48.5 million tons [1]. While starch constitutes the major proportion of most human and animal diets, the majority of its consumption (~70%) is related to non-food applications such as paper and board manufacturing, textiles, adhesives, pharmaceuticals, etc. [2].

Starch is found mainly in the storage organs of plants in the form of granules. Regardless of their botanical source, starch granules are primarily composed of two glucose polymers, the mainly linear poly $\alpha(1\text{–}4)$ D-glucopyranosyl, amylose, and the highly branched amylopectin with branching from the linear poly $\alpha(1\text{–}4)$ D-glucopyranosyl chains through $\alpha(1\text{–}6)$ bonds [3,4]. The degree of polymerization (DP) of amylose ranges typically between 570 and 4920 depending on the botanical source [3] while amylopectin is a much larger macromolecule with DPs ranging between 3×10^5 – 3×10^6 g/mol [3]. Native starch granules have a concentric alternating amorphous and semi-crystalline growth rings structure (Figure 1). The size, shape, and composition of the granule are strongly dependent on its botanical source. For example, rice starch contains 14–32% amylose depending on variety and growth conditions, its granules are polyhedral and irregular with particle size in the 3–8 μm range while wheat starch (26–31% amylose) granules range between 2 and 38 μm with two granules populations called A and B according to their size. Potato starch contains typically typically ~23% amylose and its granules are smooth ellipsoidal and can be up to 75 μm (Figure 1a) [4,5].

Starch Processing and Storage

Starch is extracted from grains, tubers, and other plant materials through milling/shredding followed by a series of consecutive washing procedures owing to the lack of solubility of the native granules in water at ambient temperature. During processing and subsequent use, starch undergoes a range of physical and chemical modifications.

Starch gelatinization, which results from the input of heat in the presence of water, is by far the most common transformation of starch (pasting, baking, cereal processing, etc.). During gelatinization, water enters the granule and plasticises its amorphous component, which undergoes a glass to rubber transition. The increased mobility of the amorphous phase and the continuing heat input enables the disruption/melting of the dispersed crystallites leading to a loss of molecular order and the swelling of the granule [6,7]. Both the extent of swelling and the temperature at which gelatinization occurs depend strongly on many parameters including botanical source, concentration and the presence and amount of co-solutes such as sugars, salts, etc. Gelatinization leads to dramatic changes of many functional properties, e.g. viscosity, solubility, digestibility, etc.

Post-gelatinization and if the starch polymers retain sufficient molecular mobility i.e. in the rubbery state, retrogradation occurs. Retrogradation is essentially a gelation process involving a disorder to order transition of amylose, a rapid process occurring mostly during cooling and early storage and amylopectin, a slower process occurring over hours–months depending on storage conditions [8]. Retrogradation leads to significant changes to mechanical (e.g. staling of baked foods) and digestibility of starch systems [8–10].

A range of other physical and chemical modifications can be applied to starch to change its functional proprieties such as gelatinization temperature, viscosity, freeze-thaw stability, retrogradation, solubility, surface properties, etc. A reviewing of all existing modified starches is beyond the scope of this chapter. The most common ones include: cross-linking for example using phosphorous oxychloride, sodium trimetaphosphate or adipic anhydride to

Graham A. Webb (ed.), Modern Magnetic Resonance, 1899–1907.
© 2008 *Springer.*

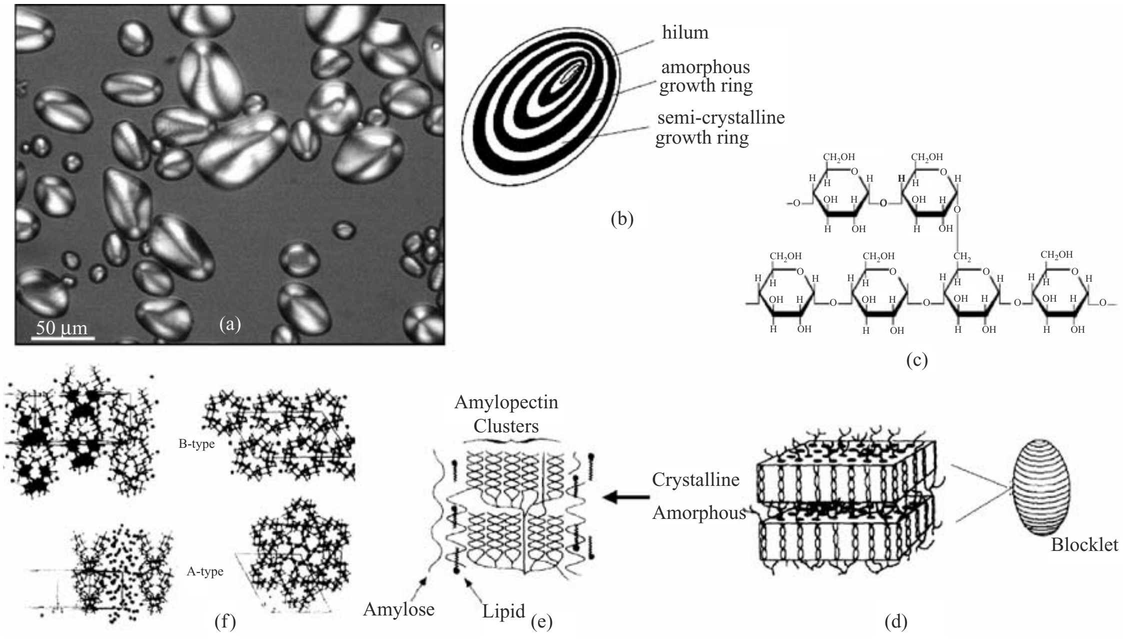

Fig. 1. Overview of the structure of the starch granule. (a) Example of native potato starch granules viewed under polarized light showing typical "maltese-cross" birefringence pattern. (b) Schematic representation of the starch granule with alternating semi-crystalline and amorphous growth rings. (c) The basic chemical structure of amylopectin. (d) The semi-crystalline growth rings are made of blocklets which contain a large number of repeats of crystalline (2D arrays of amylopectin double helices) and amorphous lamellae (double helices junction zones) [11]. The thickness of a crystalline and an amorphous lamellae is ~9 nm. (e) The relationship between amylopectin, amylose, and endogenous lipids (typically phospholipids; potato starch contains negligible amounts of lipids) [12]. (f) The crystalline structure of A (typically from cereals) and B type (typically from tubers) starches [13].

control swelling and improve shear stability, "stabilization" through the grafting of acetates, phosphates, and hydroxypropyl to limit retrogradation or a combination of modifications [2].

NMR Studies of Starch Systems

NMR is widely used to study starch and starch-based foods. In the following, some of these studies will be reviewed under four headings, which roughly map on four classes of NMR methods. This review cannot be exhaustive due to the broadness of the topic.

Chemical Structure and Composition Using Solution State High-Resolution NMR

The extremely high molecular weight of both amylopectin and amylose hinders their characterization by solution state high-resolution NMR. Such studies are often performed using solid-state techniques as discussed later in this chapter.

The main contributions of solution state high-resolution techniques falls into three categories.

Understanding Starch Biosynthesis

Nearly 25 years ago, Meredith and co-workers [14] analyzed the saccharide composition of 80% ethanol extracts of wheat grains sampled periodically during development using ^{13}C NMR. Studies of plant metabolites during growth using NMR, principally by monitoring labeled metabolites (typically glucose, fructose, or sucrose) using HPLC-^{13}C NMR [15–17] or subsequent starch hydrolysates using ^{13}C-^{1}H 2D techniques [18] are widely reported.

Hyphenated HPLC-^{13}C NMR led to useful information on the changes to starch in potato tubers during storage [19]. More recently, the technique was employed to assess genetically modified potato lines where starch biosynthesis was one of the modifications [20]. The results, however, did not detect conclusive effects of the genetic modifications.

In a somehow related context (reverse process), Amato *et al.* [21] studied starch amylosis (hydrolysis by amylase enzymes) in hydrated wheat flours using a combination of High-Resolution Magic Angle Spinning (HR-MAS) (for the flour) and standard high-resolution ^{1}H-NMR spectroscopy (for the liquid extracts). This elegant approach, coupled with multivariate data analysis enabled the authors to study the kinetics of amylosis and detect differences in starch susceptibility to degradation depending on the type of wheat flour.

Characterization of Starch Structure

Only limited number of studies used solutions state NMR to characterize the structure of starch itself. Nilsson *et al.* [22] used ^{1}H-NMR, ^{1}H-^{13}C, and 2D NMR (COSY) to study the degree of branching of amylopectin in normal and genetically modified potatoes. These authors also obtained good agreement between estimates of molecular weight of hydrolyzed starch using NMR and those measured with the more traditional method of size exclusion chromatography.

^{31}P NMR proved to be a very powerful tool in characterizing the phosphorus associated with the starch granule. In starch, organic phosphorus can be broadly divided into two types: phospholipids and phosphate monoesters on the glucosyl units of the starch polysaccharides [23,24]. Cereal starches tend to have higher amounts of phospholipids and less phosphate monoesters on the glucosyl units while tuber starches and in particular potato (~0.9% phosphate monoesters), show the opposite pattern. Phosphate monoesters for most starches tend to be preferentially located on the primary carbon C6 rather than on C3 of the glucosyl unit [23]. Phosphorus content is an important parameter as both phospholipids and phosphate-monoesters affect greatly the functional properties of the starch in terms of swelling, retrogradation, etc. [25].

Characterization of Chemically Modified Starches

The technology of chemically modifying starches is extensively developed and productions are often at industrial scales. The structure of chemically modified starches is often assessed by NMR. In this section, we will limit the review to typical examples of such studies. de Graaf *et al.* [26] described simple (1D ^{1}H-NMR) and rapid (32 scans) methods for the determination of the molar substitution of acetylated and hydroxypropylated potato starches which showed excellent correlation with traditional, time-consuming chemical methods. Not surprisingly, NMR is proving particularly useful in the efforts to selectively derivatise starch [27].

Molecular and Supramolecular Structures Using Solid-State High-Field NMR

High-resolution Magic Angle Spinning and in particular Cross Polarization (CP) MAS techniques have seen extensive applications in studies of starch. The pioneering work of Gidley and co-workers [28–30] and Veregin *et al.* [31,32] laid the foundation for the use of ^{13}C CP-MAS NMR for the study of the organization of amylopectin and amylose at a molecular level. Solid-state NMR is discussed in more details elsewhere in the book, and will only be highlighted in this chapter in the interest of completeness of this review. The main areas of application of the technique in the study of starch systems are,

(i) Polymorphism of crystalline or semi-crystalline starch polysaccharides, particularly through the lineshape of the C1 chemical shift (~102 ppm) which yields a singlet in amorphous systems, a doublet in the case of the B-polymorph and a triplet in the case of the A-polymorph [13,33].
(ii) Consolidation of the concept of short-range molecular order vs. long-range crystalline order, this was particularly important in addressing inconsistencies between two of the most widely established methods in starch characterization, wide-angle X-ray diffraction (crystallinity) and differential scanning calorimetry (melting/molecular order dissociation enthalpy), and improving the understanding of important processes such as gelatinization, retrogradation, digestibility, etc. [4,7,30,34].
(iii) The study of starch–ligand interaction, in particular the formation of complex between amylose (and its derivatives) and hydrophobic ligands such as fatty acids, monoacylglycerides, saturated alcohols, ketones, etc. [29,33,35].
(iv) Molecular dynamics of starch polysaccharides, typically through the behavior of ^{1}H T_1, $T_{1\rho}$, and T_2 and through relaxation edited ^{13}C spectra acquired as a function of variables such as starch botanical source, water content, and temperature [36–38].

Molecular Dynamics Using Time Domain NMR

The characterization of the dynamics of starch biopolymers and water is one of the most established and prolific areas of the application of NMR to starch-based foods. Early reports from Lechert and co-workers [39–41] and Caplin and Blanshard [42] on the dynamics of starch and water protons in starch systems including potato and wheat starches and bread were very detailed and made significant progress in assigning the different ^{1}H populations according to their mobility. These studies also discussed several of the still current issues in the field, such as ^{1}H exchange between starch and water OH groups, using D_2O exchange.

NMR studies of molecular dynamics in starch systems fall into one of the following categories.

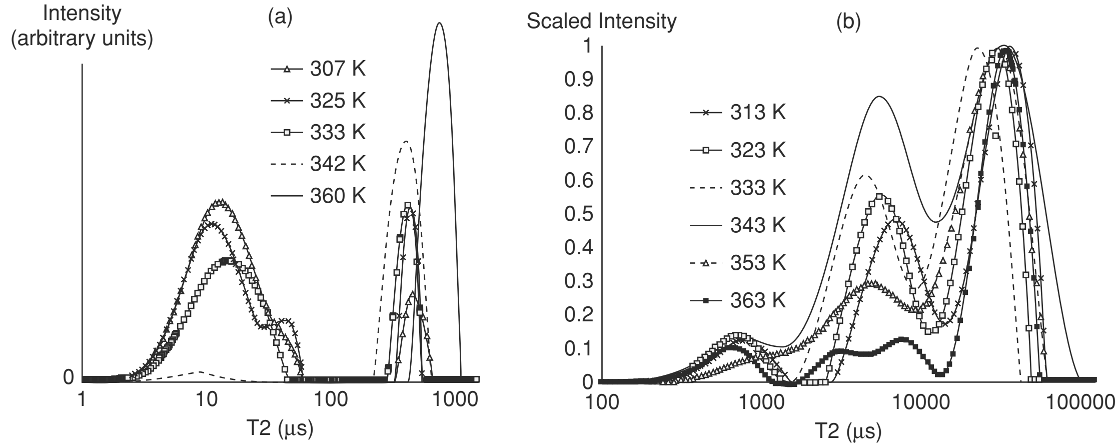

Fig. 2. ^{1}H spin–spin relaxation distributions of potato starch granules (adapted from [43]) at different temperatures. (a) "Non-exchangeable" ^{1}H analysis from FID acquired after D_2O exchange. (b) Water ^{1}H relaxation from CPMG acquired in H_2O. Typically, gelatinization of potato starch occurs in the range ~333–343 K when measured by DSC in excess water conditions [55].

Effect of Temperature (and Water+Temperature) on Starch Properties

Starch gelatinization where, under the effect of increasing temperature and in the presence of water, the amorphous components of starch undergo a glass–rubber transition followed by the melting of the crystalline fraction [6] is one of the most important aspects of this material. Surprisingly, starch gelatinization has received limited attention from an NMR viewpoint despite the fact this was one of the early applications of NMR in that field. As early as 1976, Henning *et al.* [40] studied the gelatinization of potato starch in D_2O through the CPMG decay of the CH protons. More recently, Tang *et al.* [43] reported a comprehensive study of the topic where they fitted FID and CPMG decays of potato starch granules acquired at different temperatures in the presence of either H_2O or D_2O to continuous distributions of exponentials. The "non-exchangeable" protons, i.e. those of CH groups, were monitored through the T_2distributions of the FID and CPMG decays acquired after D_2O exchange of the native granules. The authors assigned the two FID relaxation distributions observed (at ~10 and ~700 μs) (Figure 2a) to CHs of crystalline amylopectin in the semi-crystalline lamellae and to amorphous amylopectin in the amorphous growth rings respectively. They also assigned a CPMG component decaying at ~80ms to amylose CHs. This interpretation suffers from two main weaknesses. First, it assigns the FID signals to amylopectin because a similar pattern was observed for waxy maize starch (a starch containing more than 98% amylopectin). However the mobility of amylopectin and amylose protons in the native granule is unlikely to be significantly different and hence resolved by the technique. This is indirectly alluded to by the same authors in a previous study [44]. Secondly, the exchange of some OH protons in the native granule is unlikely to happen readily as some of these protons are involved in the H-bonded network of the double helical/crystal structures and hence will contribute to the rigid components of the FID below gelatinization but can exchange with water after gelatinization complicating the assignment. Furthermore, it is difficult to imagine such a high mobility of amylose in the native granule, even in the presence of high amounts of water, as it is a high molecular weight polymer ($>10^5$ g/mol in the case of potato), which is known to entangle and possibly co-crystallize with amylopectin in the native granule. The FID component with a T_2 centred at ~10 μs disappeared at temperatures above 342 K, i.e. as gelatinization occurred. This is compatible with the expected increase in mobility as amylopectin crystallites undergo a solid-liquid transition. The CPMG relaxation distributions for the granules in H_2O are often used to study the behavior of water (Figure 2b). It is important to remember that fast ^{1}H exchange between water and starch O–H inevitably makes CPMG decays sensitive to the molecular dynamics of the starch biopolymers. Three main relaxation times were observed; the shortest T_2 distribution was assigned to water in the semi-crystalline lamellae, the intermediate T_2 distribution to water inside the granule, most probably in the amorphous parts of the granule and the longest T_2 distribution to free water outside the granule. As gelatinization proceeds, water enters first the amorphous regions of the granule, hence the increase in the magnitude of the middle distribution. Gelatinization leads to the unfolding of amylopectin

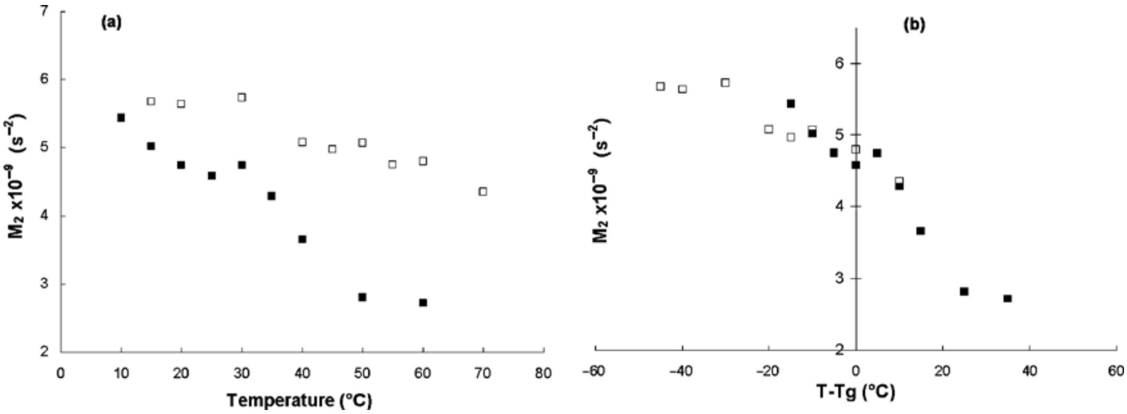

Fig. 3. Effect of temperature on the second moment of milled amylose films containing ~17% (□) and 21% (■) water (wwb) (A). The same data plotted as a function of the "shifted temperature" $T - T_g$ where T_g is the glass transition temperature measured by differential scanning calorimetry (Partanen and Farhat, unpublished).

and the leaching of amylose outside the granule, both of events would contribute to the decreased water mobility through increasing local viscosity and subsequently the shortening of the T_2 of the slowest decaying component (Figure 2b). It is worth noting that the authors were able to extend this approach to monitor the linterization process, i.e. the acid hydrolysis of native starch granules.

Other approaches using multivariate analysis of the CPMG decay [45] led to comparable findings regarding changes in water mobility during gelatinization.

Another aspect of the use of NMR relaxometry to monitor starch molecular dynamics is the ability of relaxation parameters such as the FID second moment (M_2), and the relaxation times T_2 and T_1 to sense changes in molecular mobility at or around the glass-rubber transition in processed fully or partly amorphous systems [46–48]. This is particularly important as the concept of glass-transition and the measurement of the temperature at which it occurs is now widely used by scientists and technologists in the food and pharmaceutical fields to predict processing and stability performance.

Starch–Water Interactions

NMR studies of the interaction of water with starch can be divided broadly into two types depending on whether they dealt with native or processed starch granules.

Hills and co-workers [43,44,49,50] have reported a series of extensive studies of the behavior of water in native and processed starch systems from different botanical sources. Their main findings in terms of assignments of time-domain NMR signals and the dynamics of water were discussed in the previous section. The relaxometry studies were supported by pulsed field gradient studies of self-diffusion of water and q-space imaging [44,49].

Several other studies utilized the self-diffusion coefficient of water in starch systems, measured using a variety of pulsed field gradient techniques, to study stability [51, 52], probe gel structure [53] and impact of co-solutes such sugars [54].

The effect of hydration on the properties of low water content processed starch systems, i.e. typically in the glassy state, is often studied using NMR relaxometry [46–48]. The ability of water to plasticize starch biopolymers leads to effects on NMR relaxation parameters of the polymer, e.g. the second moment (M_2) of the solid component of the FID (Figure 3), similar to those obtained when temperature is increased, with pronounced effect at conditions (temperature, water, and other plasticizers content) where the glass-rubber transition occurs.

Ageing of Intermediate Water Content Starch Systems, Starch Retrogradation

When stored in the rubbery state, i.e. for room temperature conditions, at water contents greater than ~25%, amylose and amylopectin undergo (at different rates) a reordering transition, also known as gelation. This gelation, can ultimately lead to a recrystallization and is one of the processes occurring during the staling, for example, of baked goods and cooked grains [9,56]. A range of NMR techniques have been applied to study starch retrogradation and its impact on the molecular dynamics of starch and water [9,25,45,56–59]. In terms of NMR relaxation parameters, starch retrogradation is reflected typically by:

(i) Increased rigidity of the polymer leading to shorter T_2 of the solid-like component of the FID, an increase of T_1 and an increase of the relative contribution of the solid-like component to the NMR signal.

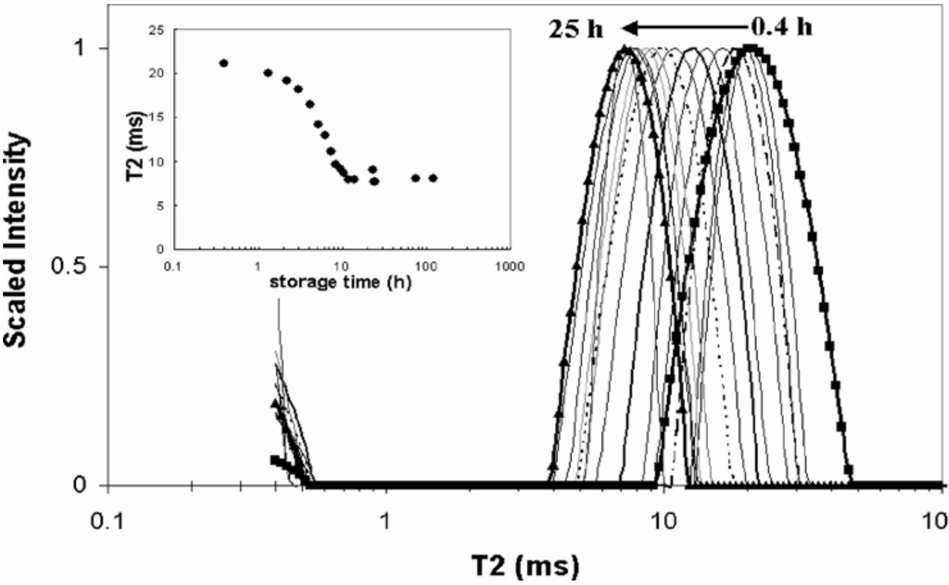

Fig. 4. Effect of amylopectin retrogradation on the relaxation spectrum. Insert, T_2 of main relaxation distribution (adapted from [56]).

(ii) Decreased mobility of water reflected by a decrease in its T_2 often measured using the CPMG pulse sequence (Figure 4). This decrease is believed to reflect the impact of the gelation of the biopolymer matrix and the effect of proton exchange between water and the hydroxyl groups of a less mobile retrograded network of amylopectin and amylose.

(iii) In fully retrograded systems at the low end of the water content range, a beat pattern becomes noticeable in the FID [48] reflecting a solid-like behavior with significant dipolar interactions.

It is interesting to note that these effects, which are very pronounced in starch systems, are much less significant in bread (Farhat *et al.*, unpublished) [59] for similar levels of starch retrogradation. The origin of this observation is not fully understood and it was suggested that it maybe linked to concurrent processes affecting water mobility: strach retrogradation changes to gluten structure, redistribution of water [59].

Imaging

Magnetic resonance imaging has seen numerous applications in food science and has been the subject of many reviews [60,61]. The main applications of the technique in starch systems, involved the study of water migration from or into starch systems during drying or rehydration processes, for example the boiling of grains in water [62,63] compared to steam processing [64] and the drying/hydration of extruded pasta systems [65,66].

Hopkinson *et al.* [67] used Stray Field NMR Imaging (STRAFI) to image water ingress inside amylose pellets and concluded that water migration from vapour followed a Fickian or Case I diffusion process while when the pellet was in contact with liquid water, the diffusion was non-Fickian or Case II. These findings are in-line with those of Stapley *et al.* [63,64]. Comparable findings on high-amylose starch tablets were also reported by Baille and co-workers [68]. STRAFI and other single-point imaging techniques [69] should provide a better handle on water migration inside glassy starch systems where fast water relaxation rarely allows for spin-echo type imaging studies. The main limitation with such studies is that only a minor and somehow superficial links are made to phase/state transitions (e.g. glass-rubber transition) and other molecular relaxation processes occurring during heating and water addition or removal.

The development of flow-imaging techniques [70,71] and the so-called rheo-NMR [72] could offer valuable insights into the behavior of starch dispersion and solutions. Of particular interest would be the behavior of starch granules and subsequent melts in the shear fields of extruders. Attempts have been made by various groups (e.g. McCarthy M.J, unpublished, [73]) where single screw extruders, for example made of polyetheretherketone (PEEK) were used. However, these devices remain rare and unrepresentative of the operational conditions of typical process extruders.

Conclusion

It is clear from this review and the other contributions on the subject of NMR studies of starch systems that the technique in its multiple facets has, like in many other fields, provided valuable and often unique insights to the various aspects of starch and its products, from biosynthesis to structure, processing, and stability. Several areas remain however not fully explored and NMR could lead to significant progress in many of them. Potential areas from a starch technology perspective, could include

- Understanding starch self-assembly during biosynthesis using solid-state techniques.
- Probing molecular dynamics in real-time during thermal/shear/pressure processing.
- Probing the dynamics of "structural water" in native and recrystallized starch systems.
- Monitoring changes in water mobility and redistribution during staling of intermediate water content starch foods in relations with sensory perception.
- Capitalising on the use of 2D techniques relaxation–relaxation, relaxation–diffusion and diffusion–diffusion techniques.

References

1. Commission of the European Community: Evaluation of the Community Policy for Starch and Starch Products. http://europa.eu.int/comm/agriculture/eval/reports/amidon/index_en.htm, 2002.
2. Lillford PJ, Morrison A. Structure/function relationship of starches in food. In: PJ Frazier, P Richmond, AM Donald (Eds). Starch: Structure and Functionality. Royal Society of Chemistry: Cambridge, 1997, p 1–8.
3. Buleon A. *et al.* Starch granules: Structure and biosynthesis. Int. J. Biol. Macromol. 1998;23(2):85–112.
4. Tester RF, Karkalas J, Qi X. Starch—composition, fine structure and architecture. J. Cereal Sci. 2004;39(2):151–65.
5. Jane JL. *et al.* Anthology of Starch Granule Morphology by Scanning Electron-Microscopy. Starch-Starke. 1994;46(4): 121–9.
6. Slade L, Levine H. Water Relationships in Starch Transitions. Carbohydr. Polym. 1993;21(2–3):105–131.
7. Waigh TA. *et al.* The phase transformations in starch during gelatinisation: A liquid crystalline approach. Carbohydr. Res. 2000;328(2):165–76.
8. Miles MJ. *et al.* The roles of amylose and amylopectin in the gelation and retrogradation of starch. Carbohydr. Res. 1985;135(2):271–81.
9. Farhat IA, Blanshard JMV, Mitchell JR. The retrogradation of waxy maize starch extrudates: Effects of storage temperature and water content. Biopolymers. 2000;53(5): 411–22.
10. Farhat IA. *et al.* Effect of the extent of conversion and retrogradation on the digestibility of potato starch. Starch-Starke, 2001;53(9):431–6.
11. Gallant DJ, Bouchet B, PBaldwin M. Microscopy of starch: Evidence of a new level of granule organization. Carbohydr. Polym. 1997;32(3–4):177–91.
12. Blanshard JMV. Starch granule structure and function: A physicochemical approach. In: T Galliard (Ed). Starch: Properties and Potentials, Critical Reports on Applied Chemistry. John Wiley and Sons: Chichester, UK 1987, 13. p 1654.
13. Imberty A. *et al.* Recent Advances in Knowledge of Starch Structure. Starch-Starke, 1991;43(10):375–84.
14. Meredith P. *et al.* The Developing Starch Granule .9. Saccharides of Developing Wheat-Grain Determined by C-13-Nmr Spectroscopy. Starke, 1980;32(6):198–205.
15. Kosegarten H, Kalinowski HO, Mengel K. Long-Term C-13 Labeling of Starch and Sucrose During the Course of Amyloplast Development in Intact Suspension-Cultured Storage-Cells of Potato (Solanum-Tuberosum). J. Plant Physiol. 1995;146(4):405–10.
16. Krook J. *et al.* Sucrose and starch metabolism in carrot (Daucus carota L.) cell suspensions analysed by C-13-labelling: Indications for a cytosol and a plastid-localized oxidative pentose phosphate pathway. J. Exp. Bot. 1998;49(329):1917–24.
17. Komor E. Source physiology and assimilate transport: The interaction of sucrose metabolism, starch storage and phloem export in source leaves and the effects on sugar status in phloem. Austr. J. Plant Physiol. 2000;27(6):497–505.
18. Sriram G. *et al.* Quantification of compartmented metabolic fluxes in developing soybean embryos by employing Biosynthetic ally directed fractional C-13 labeling, C-13, H-1 two-dimensional nuclear magnetic resonance, and comprehensive isotopomer balancing. Plant Physiol. 2004;136(2): 3043–57.
19. Viola R, Davies HV. Effect of Temperature on Pathways of Carbohydrate-Metabolism in Tubers of Potato (Solanum-Tuberosum L). Plant Sci. 1994;103(2):135–43.
20. Defernez M. *et al.* NMR and HPLC-UV profiling of potatoes with genetic modifications to metabolic pathways. J. Agric. Food Chem. 2004;52(20):6075–85.
21. Amato M.E. *et al.* Wheat flour enzymatic amylolysis monitored by in situ H-1 NMR spectroscopy. J. Agric. Food Chem. 2004;52(4):823–31.
22. Nilsson GS. *et al.* Determination of the degree of branching in normal and amylopectin type potato starch with H-1-NMR spectroscopy—Improved resolution and two-dimensional spectroscopy. Starch-Starke 1996;48(10): 352–7.
23. Lim ST. Kasemsuwan T, Jane JL. Characterization of Phosphorus in Starch by P-31-Nuclear Magnetic-Resonance Spectroscopy. Cereal Chem. 1994;71(5):488–93.
24. Kasemsuwan T, Jane JL. Quantitative method for the survey of starch phosphate derivatives and starch phospholipids by P-31 nuclear magnetic resonance spectroscopy. Cereal Chem. 1996;73(6):702–7.
25. Lin PY, Czuchajowska Z. Role of phosphorus in viscosity, gelatinization, and retrogradation of starch. Cereal Chem. 1998;75(5):705–9.
26. deGraaf RA. *et al.* Quantitative analysis of chemically modified starches by H-1- NMR spectroscopy. Starch-Starke 1995;47(12):469–75.

27. Breitinger HG. Synthesis and characterization of 2,3-di-O-akylated amyloses: Hydrophobic substitution destabilizes helical conformation. Biopolymers. 2003;69(3):301–10.
28. Gidley MJ. Quantification of the Structural Features of Starch Polysaccharides by Nmr-Spectroscopy. Carbohydr. Res. 1985;139(JUN):85–93.
29. Gidley MJ, Bociek SM. C-13 Cp/Mas Nmr-Studies of Amylose Inclusion Complexes, Cyclodextrins, and the Amorphous Phase of Starch Granules—Relationships between Glycosidic Linkage Conformation and Solid-State C-13 Chemical-Shifts. J. Amer. Chem. Soc. 1988;110(12):3820–9.
30. Cooke D, Gidley MJ. Loss of Crystalline and Molecular Order During Starch Gelatinization - Origin of the Enthalpic Transition. Carbohydr. Res. 1992;227:103–12.
31. Veregin RP, Fyfe CA, Marchessault RH. Investigation of the Crystalline V Amylose Complexes by High- Resolution C-13 Cp Mas Nmr-Spectroscopy. Macromolecules. 1987;20(12):3007–12.
32. Veregin RP. *et al.* Characterization of the Crystalline-a and Crystalline-B Starch Polymorphs and Investigation of Starch Crystallization by High- Resolution C-13 Cp/Mas Nmr. Macromolecules. 1986;19(4):1030–4.
33. Morgan KR, Furneaux RH, Larsen NG. Solid-State Nmr-Studies on the Structure of Starch Granules. Carbohydr. Res. 1995;276(2):387–99.
34. Paris M. *et al.* NMR local range investigations in amorphous starchy substrates I. Structural heterogeneity probed by C-13 CP-MAS NMR. Int. J. Biol. Macromol. 2001;29(2):127–36.
35. Snape CE. *et al.* Solid state C-13 NMR investigation of lipid ligands in V- amylose inclusion complexes. Carbohydr. Polym. 1998;36(2–3):225–37.
36. Chinachoti P. *et al.* Application of High-Resolution C-13, O-17, and Na-23 Nuclear-Magnetic-Resonance to Study the Influences of Water, Sucrose, and Sodium-Chloride on Starch Gelatinization. Cereal Chem. 1991;68(3):238–44.
37. Tang HR, Hills BP. Use of C-13 MAS NMR to study domain structure and dynamics of polysaccharides in the native starch granules. Biomacromolecules. 2003;4(5):1269–76.
38. Paris M. *et al.* NMR local range investigations in amorphous starchy substrates: II-Dynamical heterogeneity probed by H-1/C-13 magnetization transfer and 2D WISE solid state NMR. Int. J. Biol. Macromol. 2001;29(2):137–43.
39. Lechert H. Possibilities and Limits of Pulsed Nmr-Spectroscopy for Investigation of Problems of Starch-Research and Starch Technology. Starke 1976;28(11):369–73.
40. Hennig HJ, Lechert H, Goemann W. Examination of Swelling Mechanism of Starch by Pulsed Nmr- Method. Starke 1976;28(1):10–13.
41. Hennig HJ. Nmr-Investigations of Role of Water for Structure of Native Starch Granules. Starke 1977;29(1):1–4.
42. Capelin SC, Blanshard JMV. Pulsed Nmr-Studies of Interaction of Water with Gluten and Starch in Bread. Cereal Foods World. 1977;22(9):471–476.
43. Tang HR, Brun A, Hills B. A proton NMR relaxation study of the gelatinisation and acid hydrolysis of native potato starch. Carbohydr. Polym. 2001;46(1):7–18.
44. Tang HR, Godward J, Hills B. The distribution of water in native starch granules—a multinuclear NMR study. Carbohydr. Polym. 2000;43(4):375–87.
45. Engelsen SB. *et al.* NMR-baking and multivariate prediction of instrumental texture parameters in bread. J. Cereal Sci. 2001;33(1):59–69.
46. Kalichevsky MT. *et al.* The Glass-Transition of Amylopectin Measured by Dsc, Dmta and Nmr. Carbohydr. Polym. 1992;18(2):77–88.
47. Roudaut GL. *et al.* Molecular mobility in glassy bread: A multispectroscopy approach. Cereal Chem. 1999;76(1):70–77.
48. Partanen R. *et al.* H-1 NMR study of amylose films plasticised by glycerol and water. Carbohydr. Polym. 2004; 56(2):147–55.
49. Hills BP. *et al.* Microstructural characterization of starch systems by NMR relaxation and Q-SPACE microscopy. Magn. Reson. Imaging. 1998;16(5–6):557–64.
50. Hills BP, Lefloch G. Nmr-Studies of Non-Freezing Water in Cellular Plant-Tissue. Food Chem. 1994;51(3): 331–6.
51. Kou Y, Molitor PF, Schmidt SJ. Mobility and stability characterization of model food systems using NMR, DSC, and conidia germination techniques. J. Food Sci. 1999;64(6): 950–9.
52. Baik MY, Chinachoti P. Water self-diffusion coefficient and staling of white bread as affected by glycerol. Cereal Chem. 2003;80(6):740–4.
53. Ohtsuka A, Watanabe T, Suzuki T. Gel Structure and Water Diffusion Phenomena in Starch Gels Studied by Pulsed-Field Gradient Stimulated Echo Nmr. Carbohydr. Polym. 1994;25(2):95–100.
54. Farhat IA. *et al.* The effect of sugars on the diffusion of water in starch gels: A pulsed field gradient NMR study. Int. J. Food Sci. Tech. 1997;32(5):377–87.
55. Farhat IA. Oguntona T, Neale RJ. Characterisation of starches from West African yams. J. Sci. Food Agric. 1999;79(15):2105–112.
56. Farhat I.A. *et al.* 1H NMR relaxation study of amylopectin retrogradation. In: PS Belton, AM Gil, GA Webb, Rutledge D. (Eds). Advances in Magnetic Resonance in Foods. The Royal Society of Chemistry, 2003:172–79.
57. Lebotlan D, Desbois P. Starch Retrogradation Study in Presence of Sucrose by Low- Resolution Nuclear-Magnetic-Resonance. Cereal Chem. 1995;72(2):191–93.
58. Teo CH, Seow CC. A Pulsed Nmr Method for the Study of Starch Retrogradation. Starch-Starke 1992;44(8): 288–92.
59. Vodovotz Y, Vittadini E, Sachleben JR. Use of H-1 cross-relaxation nuclear magnetic resonance spectroscopy to probe the changes in bread and its components during aging. Carbohydr. Res. 2002;337(2):147–53.
60. McCarthy MJ, McCarthy KL. Applications of magnetic resonance imaging to food research. Magn. Reson. Imaging 1996;14(7–8):799–802.
61. Schmidt SJ, Sun XZ, Litchfield JB. Applications of magnetic resonance imaging in food science. Crit. Rev. Food Sci. Nutr. 1996;36(4):357–85.
62. Takeuchi S. *et al.* The change of moisture distribution in a rice grain during boiling as observed by NMR imaging. J. Food Eng. 1997;33(3–4):281–97.
63. Stapley AGF, Fryer PJ, Gladden LF. Diffusion and reaction in whole wheat grains during boiling. Aiche J. 1998;44(8):1777–89.

64. Stapley AGF. *et al.* Modelling the steaming of whole wheat grains. Chem. Eng. Sci. 1999;54(8):965–75.
65. Hills BP. *et al.* Radial NMR microimaging studies of the rehydration of extruded pasta. J. Food Eng. 1996;27(1): 71–86.
66. Hills BP, Godward J, Wright KM. Fast radial NMR microimaging studies of pasta drying. J. Food Eng. 1997;33 (3–4):321–35.
67. Hopkinson I. *et al.* Fickian and Case II diffusion of water into amylose: A stray field NMR study. Carbohydr. Polym. 1997;34(1–2):39–47.
68. Baille WE. *et al.* NMR imaging of high-amylose starch tablets. 1. Swelling and water uptake. Biomacromolecules. 2002;3(1):214–18.
69. Axelson DE, Kantzas A, Eads T. Single-Point H-1 Magnetic-Resonance-Imaging of Rigid Solids. Can. J. App. Spectros. 1995;40(1):16–26.
70. McCarthy KL. *et al.* Flow Profiles in a Tube Rheometer Using Magnetic-Resonance-Imaging. J. Food Eng. 1992;16 (1–2):109–125.
71. Hall LD. *et al.* Magnetic resonance imaging for industrial process tomography. J. Electron. Imaging 2001;10(3): 601–7.
72. Callaghan PT. Rheo-NMR: Nuclear magnetic resonance and the rheology of complex fluids. Rep. Prog. Phys. 1999;62(4):599–670.
73. Amin MHG. *et al.* A versatile single-screw-extruder system designed for magnetic resonance imaging measurements. Meas. Sci. Technol. 2003;14(10):1760–8.

Author Index

Akoka, S., 1651
Andersen, H.J., 1729
Andersen, M.L., 1861
Anoardo, E., 1439
Ardelean, I., 1471
Ashbrook, S.E., 1551

Bardet, M., 1777
Beaulieu, L., 1569
Beek, van, J.D., 1569
Belloque, J., 1623
Bertram, H.C., 1729
Blümich, B., 1455, 1523, 1581
Böhmer, R., 1487
Bonetto, F., 1439
Brescia, M.A., 1637, 1645, 1757
Bro, R., 1833, 1845
Burk, W., 1739
Buttry, D.A., 1547

Calucci, L., 1769
Casanova, F., 1523
Chatakanonda, P., 1703
Chinachoti, P., 1703
Clark, T.M., 1563
Collewet, G., 1805

Davenel, A., 1795, 1805
Diezemanm, G., 1487
Duarte, I.F., 1617, 1689, 1765

Engelsen, S.B., 1811, 1845
Farhat, I.A., 1899
Farrher, G., 1471
Foray, M.F., 1777

Geppi, A., 1769
Gil, A.M., 1617, 1689, 1765
Götz, J., 1713, 1813, 1819
Grandinetti, P.J., 1563
Grenier, A., 1905
Grinberg, F., 1455
Guichard, E., 1611
Guillermo, A., 1777
Guthausen, A., 1895
Guthausen, G., 1735, 1739, 1895

Heine, C., 1581
Hills, B.P., 1721
Hinderberger, D., 1529
Hinrichs, R., 1713
Hinze, G, 1487
Holland, G.P., 1547

Jamin, E., 1681
Jeffrey, K.R., 1487
Jeschke, G., 1529

Kamlowski, A., 1735, 1739
Kariyo, S., 1455
Kerr, W.L., 1869
Khrapitchev, A., 1581
Kidrič, J., 1597
Kimmich, R., 1471
Košir, I.J., 1597

Lee, Y., 1889
Lee. S.-Y., 1889

MacNaughtan, B., 1879
Marchioni, E., 1855
Mariette, F., 1697, 1801
Martin, G.J., 1651, 1659, 1669, 1681
Martin, M.L., 1651, 1659, 1669
Mathai, M., 1539
Mattea, C., 1471
Meier, B.H., 1569
Mény, C., 1493
Moreau, C., 1611

Nandagopal, M., 1463, 1539
Nørgaard, L., 1833
Nott, K.P., 1825

Panissod, P., 1493
Papadimitrakopoulos, F., 1539
Pedersen, H.T., 1845
Perlo, J., 1523
Pietraß, T., 1479

Quellec, S., 1795

Remaud, G., 1669
Rollema, H.S., 1605

Sacco, A., 1637, 1645, 1757
Schmalbein, D., 1735, 1739, 1895
Schmidt, C., 1515
Schmidt, S.J., 1889
Schnell, I., 1499
Skibsted, L.H., 1861
Spiess, H.W., 1499
Stapf, S., 1455, 1581

Tang, H., 1623, 1745, 1783
Tiphaine, L., 1795, 1805
Todt, H., 1735, 1739, 1895

Utz, M., 1463, 1539

Velde, van de, F., 1605
Viereck, N., 1833
Vittadini, E., 1703
Vodovotz, Y., 1703

Wagner, M., 1795
Wang, Y., 1623, 1745, 1783
Wimperis, S., 1507
Winterlich, M., 1487

Yarger, J.L., 1547

Zhang, B., 1659
Zick, K., 1819

Subject Index

A

α-lactalbumin (ALA), 1634
β-lactoglobulin (BLG), 1614
1D ^{1}HNMR
  fruit juices, 1617
1D NMR
  flavor–food compound interactions, 1611, 1612
2D NOE NMR
  flavor–food compound interactions, 1611
3D imaging imaging with single-sided sensor, 1523
absorbed dose, 1855
acoustically stimulated NMR relaxometry, 1439
additives (carrageenans), 1605
adsorption, gas. *See* gas adsorption
adulteration detection
  exogeneous minor components detection, 1686
  fruit juices, 1704
  isotope strategiesfor, 1707
  wines, 1684
affiliation coefficients, 1662
agar, 1603
alcoholic beverages, 1587. *See also* nonalcoholic beverages
  beer, 1599
  coffee, 1600
  fruit juices, 1601
  wine, 1594
aldehydes compounds analysis
  NMR study of, 1648
Alq$_3$, 1540
  characterizing isomers of, 1542
  ligand dynamics in, 1540
amorphous solids
  quadrupolar NMR of, 1507
anisotropy
  local magnetic, 1497
anthocyanins, 1597
antifreeze glycoproteins, 1876
  solid-state NMR, 1875
apple bruises, 1723
apple juice
  chemometrics, 1833
apple maturity, 1722
apples
  internal browning disorders in, 1723
  mealiness in, 1725
  watercore in, 1724
assignments
  plant seeds, 1777
atomic structure
  NMR and, 1493

B

baking process, 1795
  factors influencing MRI signal during, 1796
  MRI oven and, 1795
  post-chilling and freezing steps monitoring, 1797
  specific interests of MRI in better characterizing, 1797
beer, 1599. *See also* beverages, wines, spirits
  high resolution NMR analysis of, 1689
  HPLC-NMR, 1599
  NMR and, 1599
benzoxazines
  packing structures in, 1503
beverages. *See also* food process engineering
  alcoholic, 1597
  beer, 1599
  chemical composition characterization by NMR, 1597
  coffee, 1600
  nonalcoholic, 1600
  oxidative processes in, 1861
  wine, 1597
bilirubin
  hydrogen bonds in, 1502
binding activities, DNA. *See* DNA-binding activities (hTRF1 and hTRF2 with hTRF2 mutants)
biological NMR
  spectral editing in, 1625
biosynthesis
  starch, 1900
biscuit. *See also* bread
  baking process monitoring, 1795
  MRI oven, 1795
  NMR imaging of, 1795
bitter, 1892
bread, 1762. *See also* biscuit; dairy products
  ^{1}H HR-MAS NMR, 1757
  baking process monitoring, 1795
  crumb structure assessing, 1798
  crust flaking, 1798
  MRI oven, 1795
  MRI signal variation during chilling and freezing, 1797
  MR imaging of, 1795
  post-chilling and freezing steps monitoring, 1797
Brix, 1685
Bruker single-sided NMR device, 1895
butadiene rubber (BR), 1456

C

^{13}C CPMAS NMR
  gliadins, 1759
  gluten, 1761
  starch analysis, 1762
  starch polysaccharides, 1783
^{13}C cross polarization MAS NMR
  of flours, 1757
^{13}CMAS
  flour and dough, 1769
  gluten, 1770
^{13}C NMR
  carbohydrate food systems, 1703
  carbon nanotubes and, 1479
  carrageenans, 1605, 1607
  fatty acids analysis, 1637
  fatty acids positional distribution analysis, 1639
  glycerol esters analysis, 1639
  low moisture sugars, 1879
  minor oil components analysis, 1641
  of doughs, 1757
  oils, 1637
  olive oils analysis, 1642
  starch polysaccharides, 1783
  vegetable oils analysis, 1637
  wine, 1597
^{13}C spin–lattice relaxation(starch systems), 1751
^{13}C SSNMR
  sensitivity enhancement, 1485
carbohydrate food systems
^{13}C NMR, 1705
  cross polarization aspects, 1705, 1707
  MAS, 1705, 1707
  molecular mobility in, 1703
  NMR mobility and microbial activity, 1709
  relaxation time in rotating frame, 1709
  solid mobility by cross relaxation, 1708

- solid-state NMR, 1705
  - T_2 distribution of water, 1705
  - water molecular mobility by, 1703
  - water populations determination, 1704
- carbohydrates. *See also* proteins
  - SNIF-NMR, 1664
  - to ethanol (SNIF-NMR), 1686
  - to glycerol (SNIF-NMR), 1687
- carbon nanotubes
  - ESR and, 1479, 1480
  - gas adsorption on, 1479, 1483
  - multiwalled (MWNT), 1479
  - NMR spectroscopy of, 1479
  - single-walled (SWNT), 1479
- carbon SNIF-NMR, 1657
- carrageenans, 1605
  - ^{13}C NMR analysis, 1605, 1607
  - ^{1}H NMR, 1605, 1606
  - additives, 1608
  - analysis of minor components, 1607
  - carrageenan substituents, 1608
  - contaminants, 1609
  - experimental setup, 1605
  - high resolution NMR of, 1605
  - internal standards and, 1605
  - methodology, 1605
  - sample preparation, 1605
  - structure, 1605
- casein micelles, 1631
- caseins, 1631
- catechins, 1600
- CCPPA. *See* coupled-cluster polarization propagator
- cellular and tissue systems
  - liquid phase chemical spectroscopy, 1875
- cellulose, 1856
- chemical shift
  - temperature measurements, 1825
- chemical shift variations (chemometrics), 1836
- chemically exchanging systems
  - isotope effects in, 1660
- chemically modified starches, 1901
- chemometric analysis
  - of NMR, 1833
- chemometrics
  - apple juice, 1837
  - chemical shift variations, 1836
  - data preparation, 1835
  - defined, 1834
  - Fourier transformation, 1836
  - intensity scale, 1835
  - outlier detection, 1837
  - partial least squares (PLS) regression, 1836
  - phase errors, 1836
  - supervised data exploration by PCA, 1836
  - unsupervised data exploration by PCA, 1836
  - validation, 1836
  - variable selection, 1837
- CHF. *See* coupled Hartree–Fock approximation
- chilling and freezing
  - and MRI signal variation during baking, 1797
  - post-chilling and freezing monitoring during baking, 1797
- chocolate
  - fat content determination in, 1743
- *Clavivlonium ovatum*, 1608
- CML. *See* canine milk lysozyme
- CMR. *See* cardiovascular magnetic resonance
- CNTs. *See* carbon nanotubes
- coffee. *See also* beverages
  - NMR and, 1601
- columnar stacking of discotics, 1505
- complex materials
  - broad distance distributions, 1530
  - concatenated macrocycles in frozen solution, 1531
  - polyelectrolytes, 1534
  - probing polyion-counterion interaction in fluid and frozen solution, 1534
  - site-specific characterization by EPR spin probes, 1529
  - spin labeling principles, 1520
  - spin probes
    - and spin labels, specific-site addressing by, 1529
    - as tracers, 1529
  - structure and dynamics, 1529
- computational fluid dynamics (CFD), 1825
- concatenated macrocycles in frozen solution, 1529
- concentrated juices, 1685
- conjugate orthogonal function, 1463
  - organic semiconductors, 1539
- contaminants (carrageenans), 1607
- CONTIN, 1705
- convective heating, 1827
- correlation
  - NMR and material properties, 1717
- COSY
  - for wines study, 1689
- couette, 1582, 1819
- CP MAS
  - starch systems, 1899
- CP MAS NMR
  - ^{13}C, 1757
  - and crystallization, 1885
  - of flours, 1757
- CPMG, 1881
- cross polarization, 1437
  - carbohydrate food systems, 1703, 1705
  - MAS NMR. *See* CP MAS NMR
- cross relaxation. *See also* relaxation
  - solid mobility (carbohydrate food systems) by, 1708
- cross-link density (elastomers), 1446
- crust flaking, 1798
- crystallization
  - CPMAS NMR and, 1886
  - low moisture sugars, 1879
- CSA
  - distribution functions and, 1463
- CSA–CSA correlation
  - silk, local structure of, 1571
- cutin, 1768
- cytoplasm, 1721

D

- dairy products. *See also* foods
  - fat
    - content and distribution, 1801
    - relaxation aspects, 1699
  - imaging of, 1801
  - macrostructure information, 1802
  - micro-structure, 1802
  - molecular structure, 1802
  - NMR relaxation of, 1697
  - temperature and flow, 1804
  - water
    - content and distribution, 1801
    - diffusion aspects, 1699
    - retention aspects, 1698
- data preparation
  - chemometrics, 1833
- DCE
  - imaging on the basis, 1451
  - in elastomers, 1447
- DECRA
  - LF-NMR, 1845
- denaturation, 1715
- dense silicate phases
  - STMAS NMR, 1556
- deuterium
  - line shape studies (low moisture sugars), 1881
  - quadrupolar splitting, 1466
- DHAP, 1665
- differential scanning calorimetry (DSC), 1879
- diffusion. *See also* diffusometry, NMR
  - fluid, 1471
  - horticultural products, 1721
  - in gels, 1699
  - molecular diffusion, 1713
  - spin-diffusion in starch systems, 1748
  - translational, 1476
  - water, 1698
- diffusion coefficient
  - temperature measurements, 1825
- diffusion filter, 1624
- diffusion measurements
  - PFGSE, 1875

diffusion weighted approach
  single-sided NMR in foods, 1895
diffusometry
  field-gradient NMR, 1471
  horticultural products, 1721
  NMR, 1721
diffusometry, NMR,1471
  Einstein diffusion, 1472
  experimental aspects, 1474
  fast liquid/vapor exchange limit, 1473
  Knudsen diffusion, 1472
  liquid/vapor exchange limit, 1473
  samples and instrumentation, 1474
  slow liquid/vapor exchange limit, 1474
  translational diffusion, 1476
  two-phase exchange model in, 1471
diglycerides analysis
dilatometry, 1741
dipolar correlation effect (DCE), 1445
  background of, 1446
  RDCand, 1446
dipolar correlations
  ultraslow, 1445
dipolar coupling
  elastomers, 1451
dipolar recoupling schemes, supramolecular systems, 1499
direct exponential curve resolution algorithm (DECRA)
  by SLICING, 1845
direct SFC method, 1739. *See also* indirect SFC method
direct tri-linear decomposition (DTLD), 1847
discotics
  columnar stacking of, 1499
disordered materials
  freezing in glassy crystals, 1487
  heterogeneous transport in ionic conductors, 1488
  MRS and, 1487
  NMR and, 1487
  probing secondary relaxations, 1490
  rotational dynamics, 1487
  rotational dynamics near vitrification transition, 1488
  single-molecule spectroscopy, 1491
  translational dynamics, 1487
disordered solids
  quadrupolar NMR of, 1511
disperse systems
  molecular diffusion in, 1713
distance distributions, complex materials and, 1529
distribution functions, 1463
  conjugate orthogonal functions, 1463
  CSA and, 1466
  MAS and, 1466
  NMR and, 1463
  orientational order, 1465
DMAPP, 1670
domains
  starch systems, 1745
DOQSY
  silk, local structure of, 1570, 1571
double quantum (DQ) filtered spectrum (elastomers), 1459
double quantum experiments (elastomers), 1459
dough, 1769
  ^{13}C MAS NMR of, 1758, 1772
  ^{1}H MAS NMR of, 1758
  freezing, storage, and thawing, 1807
  frozen, factors influencing MRI signal, 1807
  frozen/thawed, characterization of heterogeneities in, 1808
  HR solid-state NMR, 1769
  ice fraction cartographies, 1807
  intermediate-scale information, 1810
  large-scale information, 1810
  NMR imaging, 1817
  porosity assessment, 1819
  proofed, factors influencing MRI signal, 1819
  small-scale information, 1821
DQ coherences (DQC), 1501
droplet size determination
  quality control (TD-NMR), 1736
DRYCLEAN method, 1624
durum, 1757
DWI. *See* diffusion-weighted imaging
dynamic angle spinning (DAS), 1507
  high-pressure silicates, 1551
dynamic electrostatic attachment, 1535

E

EC directive 2001/112/EC, 1682
Einstein diffusion, 1472
elastomers
  averaging of dipolar couplings, 1459
  correlating molecular and macroscopic properties of, 1455
  cross-link density, 1457
  DCE in, 1445
  dipolar relaxation, 1456
  double quantum (DQ)
    experiments, 1458
    filtered spectrum, 1458
  relaxation times, 1456
  relaxometry
    and multi-pulse NMR techniques, 1455
    experiments, 1456
elastomers characterization
  spectra and relaxation times, 1455
  ultraslow dipolar correlations monitoring by NMR and, 1445
electron spin resonance. *See* ESR
electronical referencing, 1656
enantiotopic hydrogen sites, 1665
epicatechin, 1613
EPR
  broad distance distributions and, 1529
  supramolecular interactions and, 1529
EPR spin probes. *See also* probes
  for site-specific characterization of complex materials, 1529
ERETIC, 1656
Eri silkworm, 1569
ESEEM, 1535
ESR
  carbon nanotubes and, 1480, 1481
  detection of radicals in foods, 1861
  for food irradiation detection, 1856
  for oxidative processes
    in food and beverages, 1861
esters, glycerol, 1639
ethanol
  isotopic NMR probe for characterizing wines, spirits, and juices, 1681
  SNIF-NMR, 1651
  SNIF-NMR (economic applications), 1681
exogeneous minor components detection
  SNIF-NMR (economic applications), 1686
extrusion, 1814

F

FAIR. *See* flow-sensitive alternating inversion recovery
fast liquid/vapor exchange limit, 1473
fast MAS
  supramolecular systems, 1499
fast-field-cycling (FFC), 1439
fast-MAS NMR
  supramolecular systems, 1480
fat compositions, SFC in
  dilatometry/solid fat index,
    comparison with, 1741
  direct method, 1739
  indirect method, 1741
  SFC analysis automation, 1742
  solid-echo method, 1741
fat content determination
  dairy products, 1801
  in chocolate, 1743
  in meat, 1729
  quality control (TD-NMR), 1725
fat determination
  dairy products, 1801
  single-sided NMR in foods, 1895
fat relaxation, 1699
  NMR study of, 1637
fatty acids positional distribution analysis
  NMR study of, 1639

- fermentation
  - SNIF-NMR and, 1664
- ferromagnetic materials
  - hyperfine field, 1493
  - in field NMR, 1495
  - local magnetic
    - anisotropy, 1495
    - moments, 1493
  - local restoring field, 1493
  - magnetic
    - magnetization profiles, 1493
    - phase separation, 1494
    - stiffness, 1493
  - NMR and atomic structure, 1492
  - structural and magnetic properties, 1492
  - zero-field NMR, 1493
- ferromagnetic multilayers and nanocomposites
  - NMR and, 1492
- FID. *See* free induction decays
- field gradient NMR
  - diffusometry, 1471
- field-cycling experiment, 1456
  - elastomers, 1456
  - in liquid crystals, 1439
- flaking, crust, 1798
- flavonoid, 1600
- flavor–food compound interactions
  - 1D NMR, 1612
  - ^{1}H 1D NMR, 1613
- flavor–food compound interactions by NMR, 1611
- flour. *See also* dough
  - ^{13}C MAS, 1758
  - ^{1}H MAS, 1760
  - ^{13}CCP-MAS NMR, 1757, 1759
  - ^{1}H high resolution MAS NMR of, 1757
- flow
  - aspects of dairy products, 1814
  - characterization with single-sided NMR, 1523
- flow behavior and T_1- or T_2-relaxation times, 1821
- flow experiments couette, 1820
  - food, rheo-NMR and, 1819
  - tube flow, 1820
  - with disperse multiphase/complex materials, 1820
- flow induced structural changes
  - rheo-NMR, 1821
- fluid diffusion
  - NMR and, 1471
  - partially filled nanoscopic and microscopic porous materials, 1471
- fMRI. *See* functional MRI
- food freezing, 1869
  - antifreeze glycoproteins, 1876
  - freeze/thaw effects, 1873
  - frozen solutions, 1875
  - ice, unfrozen water, and glassy states,1869
  - liquid phase chemical spectroscopy, 1875
  - MRI for, 1869, 1873
  - PFGSE diffusion measurements and, 1873
  - solid-state NMR, 1875
  - states of water, 1872
  - structural studies, 1871
  - transient freezing, 1874
  - whole foods, 1876
- food irradiation detection
  - absorbed dose definition, 1855
  - cellulose, 1857
  - ESR for, 1855
  - hydroxyapatite, 1856
  - interactions of radiation with matter, 1855
  - labeling, 1855
  - sugars, 1858
- food process engineering
  - direct imaging (MRI), 1814
  - distribution of concentration, 1813
  - indirect imaging (MRI), 1814
  - MRI in, 1813
  - structural changes and reactions, 1804
  - structure analysis, 1804
  - structure and changes, 1813
- food quality control. *See* quality control (TD-NMR)
- food, rheo-NMR and, 1819
  - flow experiments, 1819
- foods
  - ESR
    - detection of radicals in, 1861
    - for food oxidation study, 1864
  - oxidation
    - ESR for, 1864
    - oxidative processes in, 1861
    - oxidative stability of, 1862
  - sensory properties of, 1889
  - single-sided NMR in, 1895
  - spin trapping aspects in, 1862
- foods with high water content
  - quality control (TD-NMR) aspects,1735
  - relaxation analysis, 1736
- forsterite, 1551. *See also* high-pressure silicates
- Fourier transformation (chemometrics), 1836
- fractionation
  - isotopic, 1652, 1653
  - liquid–vapor, 1659
  - site-specific hydrogen, 1652
- free induction decay (FID), 1746
  - sugars, low moisture, 1879
  - starch systems and, 1746, 1747, 1748
- freeze/thaw effects, food freezing and, 1873
- freezing. *See also* food process engineering
  - and MRI signal variation during baking, 1796
  - ice, unfrozen water, and glassy states, 1869
  - liquid phase chemical spectroscopy, 1875
  - post-chilling and freezing monitoring during baking, 1797
  - states of water, 1872
  - transient freezing, 1874
  - whole foods, 1876
- freezing in glassy crystals, 1487
- frozen dough, 1807, 1808
- frozen solution, 1529, 1531, 1870
  - solid-state NMR, 1875
- fruit juices, 1597. *See also* beverages
  - 1D ^{1}H NMR, 1617
  - adulteration detection, 1685
  - exogeneous minor components detection, 1686
  - high resolution NMR of, 1617
  - LC-NMR/MS, 1617
  - SNIF-NMR (economic applications), 1681
- fruits and vegetables
  - HR MAS NMR, 1765
  - quality, 1721
- functional brain imaging, 1891

G

- galactomannans, 1607
- gas adsorption
  - on carbon nanotubes, 1479
  - on MWNTs, 1480
  - on SWNTs, 1483
- gas-fluidized bed, 1582
- gellan gum, 1713
- gels
  - diffusion and relaxation, 1713
  - diffusion in, 1713
  - relaxation in, 1715
- generalized rank annihilation method (GRAM), 1847
- genetically modified organisms (GMO), 1610
- genomics, structural. *See* structural genomics, NMR and
- glass transition
  - low moisture sugars, 1879, 1883
- glasses, 1880
  - oxide glasses structure, 1563
- glassy crystals
  - freezing, 1488
- gliadins, 1758, 1759. *See also* gluten
  - ^{13}C CP-MAS NMR, 1759
  - ^{1}H HR MAS, 1759
- glucose, isotopic parameters of, 1664
- gluten, 1708, 1709. *See also* gliadins

  ^{1}H MAS, 1771
  high molecular weight fractions, 1761
  HR solid-state NMR, 1769
glycerol
  SNIF-NMR, 1664, 1665
glycerol esters
  NMR study of, 1639
glycoproteins
  antifreeze, 1876
GPP, 1669
granular materials, velocity imaging of, 1581
  gas-fluidized bed, 1582
  NMR and, 1581
  rotating drum, 1585

H

^{1}H high resolution MAS NMR
  bread, 1762
  of flours, 1757
^{1}HHR MAS
  gliadins, 1759
^{1}H MAS
  flour, 1772
  gluten, 1769
^{1}H MAS NMR
  of doughs, 1758
^{1}H NMR
  aldehydes compounds analysis, 1648
  based metabolism and metabonomics, 1623
  carrageenans, 1605, 1606
  diglycerides analysis, 1648
  oils analysis, 1645
  olive oil geographical origin analysis, 1649
  phenolic compounds analysis, 1647
  starch polysaccharides, 1783
  sterols analysis, 1648
  triglycerides analysis, 1645
  volatile compounds analysis, 1648
  wine, 1575
^{1}H solid-state NMR
  supramolecular systems, 1499
^{1}H–^{1}H DQ NMR
  supramolecular systems, 1501
HCV NS3 helicase, 1426
heating
  convective, 1805
  microwave, 1805
  ohmic, 1807
hemicelluloses, 1758
heterogeneous rotational and translational dynamics, disordered materials, 1487
heterogeneous transport in ionic conductors, 1489
hexagonal and lamellar lyomesophases
  rheo-NMR spectroscopy, 1518
hexagonal lyomesophases, 1518
hexa-peri-hexabenzocoronenes (HBCs), 1505
high molecular weight (HMW) subunits, 1610
high molecular weight fractions, 1739
  gluten, 1739
high-pressure silicates, 1551
  DAS, 1531
  dense silicate phases, 1556
  humite minerals, 1556
  hydrous magnesium silicates, 1556
  MAS, 1551
  MQMAS, 1551
  MQMAS NMR, 1552
  oxygen NMR and, 1552
  sample preparation, 1552
  solid-state NMR, 1551
  STMAS NMR, 1556
  upper mantle silicates, 1552
high-resolution^{13}C NMR
  starch polysaccharides, 1762
high-resolution ^{1}H NMR
  oils analysis, 1615
  starch polysaccharides, 1761
high-resolution MAS
  metabolism and metabonomics, NMR-based, 1603
high-resolution MAS NMR
  ^{1}H, 1743
  fruits and vegetables, 1743
  of flours,1743
high-resolution NMR
  based metabonomics, 1623
  beer, 1691
  carrageenans, 1605
  fish oils, fatty acid composition and human metabolism and, 1623
  of fruit juices, 1617
  of milk and milk proteins, 1631
  oil analysis, 1637
  spirits, 1691
  starch systems and, 1899
  wine, 1691
high-resolution solid-state NMR
  dough, 1759
  gluten, 1759
  low moisture sugars, 1884
  plant seeds, 1777
  starch polysaccharides, 1783
  supramolecular systems, 1501
HMBC
  for wines study, 1689
homonuclear dipolar couplings (elastomers), 1455
homonuclear DQ NMR
  supramolecular systems, 1499
Hordeum vulgare, 1320
horticultural products, 1721
  apple
    bruises, 1723
    maturity, 1723
  diffusion study, 1721
  fruit and vegetable quality, 1723
  internal browning disorders in apples, 1724
  mealiness in apples, 1725
  NMR
    diffusometry and water compartmentation, 1722
    relaxation and water compartmentation, 1721
  potato, 1725
  relaxation study, 1721
  water compartmentation and NMR relaxation, 1721
  watercore in apples, 1724
HPIC, 1690
HPICE, 1690
HPLC-NMR
  beer, 1599
HR MAS NMR. *See* high-resolution MAS NMR
HR solid state NMR. *See* high-resolution solid-state NMR
HRMAS. *See* high-resolution MAS
HSQC
  for wines study, 1689
humite minerals
  MAS NMR, 1556
  MQMAS, 1556
  NMR, 1555
  STMAS, 1557
hydrocolloids, 1713
hydrogen bonds
  in bilirubin, 1502
hydrogen isotope redistribution, 1664
hydrous magnesium silicates NMR, 1556
hydroxyapatite, 1856
hydroxytyrosol (OHTy), 1641
hyperfine field (HF), 1493, 1494

I

ice fraction cartographies, 1807
ICP-OES, 1690
IGAIM. *See* individual gauges for atoms in molecules
image analysis. *See also* NMR imaging of food, 1891
iMRI. *See* intraoperative MRI
in field NMR
  ferromagnetic materials, 1497
inhomogeneously broadened NMR, 1463
inorganic materials, quadrupolar NMR of, 1507
  disordered and amorphous solids, 1512
  MQ MAS, 1507
  multiple-quantum MAS, 1507
  pulse sequences for MQMAS, 1509
  spectral analysis, 1511

intensity scale (chemometrics), 1835
ionic conductors, heterogeneous transport in, 1487
IRMS, 1656
isomers of Alq_3, 1542
isotope effects
  and affiliation coefficients, 1662
  in chemically exchanging systems, 1660
  kinetic, 1661
  thermodynamic, in tautomeric equilibria, 1661
isotope ratio mass spectrometry, 1656
isotope ratios, 1651
  as tracers of mechanistic pathways, 1659
  SNIF-NMR principles, 1651
isotope strategies
  for adulterations detection, 1685
isotopic abundances, 1651
  SNIF-NMR principles, 1651
isotopic balance, mass and (SNIF-NMR principles), 1652
isotopic characterization
  of concentrated juices, 1685
isotopic fractionation
  SNIF-NMR principles, 16352, 1653
isotopic NMR probe
  ethanol-based, for characterizing wines, spirits, and juices, 1682
isotopic parameters
  of glucose, 1664
  phase transitions influence on, 1659
  referencing (SNIF-NMR principles), 1654
  transport phenomena effect on, 1659
isotopic redistribution coefficients, 1662

J

juices
  concentrated, 1685
  isotopic characterization of concentrated, 1685
  isotopic NMR probe for characterizing, ethanol-based, 1682
  SNIF-NMR (economic applications), 1681, 1682

K

kaempferol, 1600
Kappaphycus alvarezii, 1608
kinetic isotope effects, 1661
Knudsen diffusion, 1472
Kuhn segment, 1456

L

labeling
  food irradiation detection, 1856
  spin labeling, 1529
lamellar lyomesophases, 1518
Larmor frequency, 1439
LC-NMR
  wine, 1591
LDA. *See* local density approximation
LDBS. *See* locally dense basis set
LF-NMR
  DECRA and, 1845
ligand dynamics in Alq_3, 1540
lignins, 1589
liquid crystalline materials
  molecular dynamics in, 1439
liquid crystals
  field-cycling experiments in, 1439
  molecular reorientations, 1441
  nematic, 1515
  nematic phase, 1439
  order director fluctuations (ODF), 1440
  proton FC relaxometry in, 1441
  self diffusion, 1441
  smectic phase, 1439
  ultrasound induced relaxometry, 1442
liquid phase chemical spectroscopy
  cellular and tissue systems, 1875
  food freezing and, 1875
  phospholipid membranes, 1875
liquid/vapor exchange limit, 1473, 1474
liquid/vapor exchange limit, fast, 1473
liquid-like domains, 1777
  with residual dipolar interactions, 1777
liquid–vapor fractionation effects, 1660
local magnetic anisotropy
  ferromagnetic materials, 1497
local magnetic moments, 1494
local restoring field
  ferromagnetic materials, 1494
LORG. *See* localized orbitals local origin
low moisture sugars, 1879
lyomesophases, hexagonal and lamellar, 1518

M

macrostructure
  dairy products, 1802
magnetic anisotropy, local, 1497
magnetic phase separation, 1496
magnetic resonance
  temperature measurements by, 1825
magnetic resonance imaging. *See* MRI
magnetic resonance spectroscopy. *See* MRS
magnetic stiffness
  ferromagnetic materials, 1493
magnetization profiles
  ferromagnetic materials, 1493
Maillard reaction, 1631
MAS
  carbohydrate food systems, 1705,1707
  distribution functions and, 1463
  flour, 1772
  flour and dough, 1764
  fruits and vegetables, 1765
  gluten, 1770, 1771
  high-pressure silicates, 1551
  inorganic materials, quadrupolar NMR of, 1507
  multiple-quantum, 1507
  starch
    polysaccharides, 1785
    systems, 1901
  supramolecular systems, 1499
MAS NMR
  ^{13}C, 1758
  ^{1}H, 1758
  humite minerals, 1556
  of doughs, 1757
  of flours and doughs, 1756
  xerogels, 1547
mass and isotopic balance (SNIF-NMR principles), 1652
material characterization via relaxometry, 1523
mealiness in apples, 1725
meat
  chemometric analysis,1838
  fat content determination, 1729
  muscle to meat, conversion, 1730
  processing, relaxometry applied during, 1732
  T_2 relaxation in, 1729
  water-holding capacity, 1730
meat science
  proton NMR relaxometry in, 1729
mechanistic pathways
  chemical and biochemical, 1659
metabolism
  ^{1}H NMR,1624
  high reoslution NMR based, 1623
metabolism and tabonomics, NMR-based
  DRYCLEAN method, 1624
  HRMAS, 1626
  metabolite resonances assignments, 1625
  solid-phase extraction method, 1627
  spectral editing, 1625
  water suppression, 1624
  WATERGATE, 1625
metabolite resonances
  assignments of, 1625
metabonomics
  future prospects, 1627
  high resoultion NMR, 1623
micellar calcium phosphate (MCP), 1633
microbial activity
  carbohydrate food systems, 1709
microscopic porous materials, 1471

micro-structure
  dairy products, 1802
microwave heating, 1827
milk and milk proteins
  ^{31}P-NMR, 1632
  casein micelles, 1633
  caseins, 1633
  high-resolution NMR of, 1631
  NMR,1631, 1633
  peptides, 1634
  protein structural changes, 1634
  whey proteins, 1626, 1634
minced meat, chemometric analysis, 1838
minor oil components analysis
  NMR study of, 1641
MIONs. *See* magnetic iron oxide nanoparticles
mobility
  carbohydrate food systems, 1709
mobility and microbial activity, NMR (carbohydrate food systems), 1701, 1709
mobility-resolved NMR
  starch polysaccharides, 1788
moisture determination, quality control (TD-NMR), 1739
molecular diffusion
  in disperse systems, 1713
molecular dynamics
  liquid crystalline materials, 1439
molecular dynamics using time domain NMR (starch systems), 1901
molecular mobility
  in carbohydrate food systems, 1703
  water (carbohydrate food systems), 1703
molecular properties
  elastomers, 1455
molecular reorientations (liquid crystals), 1441
molecular structure
  dairy products, 1802
  starch systems, 1901
MQMAS
  disordered and amorphous solids, 1511
  high-pressure silicates, 1551
  humite minerals, 1556
  inorganic materials, quadrupolar NMR of, 1507
  pulse sequences for, 1509
  spectral analysis, 1511
MQMAS NMR
  high-pressure silicates, 1552
  upper mantle silicates, 1552
MRI
  characterization of heterogeneities in frozen/thawed dough, 1808
  crust flaking and, 1808
  direct imaging (food process engineering), 1814
  factors influencing MRI signal
    of frozen dough, 1807
    of proofed dough, 1809
  food freezing and, 1873
  for food freezing, 1869
  in food process engineering, 1813
  indirect imaging (food process engineering), 1814
  post-chilling and freezing steps monitoring (bread processing), 1797
  sensory properties of food, 1889
  signal variation during chilling and freezing (bread processing), 1787
  specific interests of MRI in better characterizing baking processes, 1797
MRI oven, 1795
  bread and biscuit, 1795
  factors influencing MRI signal during baking, 1796
MRS
  disordered materials and, 1487
MSDF maps, 1451
multi-component and multi-isotope strategies for adulterations detection, 1682
multilayers
  ferromagnetic, 1493
    disperse, 1820
multiple-quantum MAS, 1507
multi-pulse NMR techniques, 1455
multiwalled carbon nanotubes (MWNT), 1471, 1479
muscle to meat, conversion of, 1730
MWNT, 1479
  ESR and, 1460
  gas adsorption on, 1480
  NMR and, 1479
myofibrill, 1600
myricetin, 1600

N

nanocomposites
  ferromagnetic, 1493
nanoscopic porous materials, 1471
nanotubes, carbon, 1479
natural rubber (NR), 1446
nematic liquid crystals, 1516
nematic phase, 1439
NMR
  ^{1}H solid-state, 1499
  acoustically stimulated NMR relaxometry, 1439
  aldehydes compounds analysis, 1648
  and crystallization, 1886
  antifreeze glycoproteins, 1876
  application to food, 1819
  atomic structure and, 1493
  based metabonomics, 1623
  based metabonomics techniques, 1627
  beer, 1689
  beer characterization by, 1599
  beverages' chemical composition characterization and, 1597
  biological, 1625
  carbohydrate food systems, 1705
    molecular mobility characterization, 1703
  carrageenans, 1605
  casein micelles, 1631
  caseins analysis, 1631
  chemometric analysis of, 1833
  CNTs and, 1479
  coffee and, 1601
  diffusometry, 1471
  diglycerides analysis, 1647
  disordered materials and, 1487
  distribution functions and, 1463
  dough, 1769
  fatty acids
    analysis, 1637
    positional distribution analysis, 1639
  ferromagnetic multilayers and nanocomposites and, 1493
  flavor–food compound interactions by, 1611, 1612
  fluid diffusion and, 1471
  food freezing, 1875
  for process engineering, 1813
  for ultraslow dipolar correlations monitoring, 1445
  fruit juices and, 1601
  fruits and vegetables, 1765
  gluten, 1769
  glycerol esters analysis, 1639
  granular materials velocity imaging, 1581
  high resolution solid-state, 1499
  high-pressure silicates, 1551
  horticultural products and, 1721
  humite minerals, 1556
  hydrous magnesium silicates, 1556
  imaging of biscuit, 1795
  imaging of bread, 1795
  in quality control, 1735
  inhomogeneously broadened, 1463
  isotope ratios as tracers of mechanistic pathways and, 1659
  isotopic NMR profile, 1659
  low moisture sugars analysis by, 1879, 1883
  milk and milk proteins, 1631, 1633
  minor oil components analysis, 1641
  mobile. *See* mobile NMR
  multi-pulse NMR techniques, 1455
  MWNTs and, 1479
  NMR-MOUSE, 1523
  of flours and doughs, 1757

- NMR (*cont.*)
  - of fruit juices, 1617
  - of milk and milk proteins, 1631
  - of organic semiconductors, 1539
  - oil analysis, 1637
  - oils analysis, 1645
  - olive oil geographical origin analysis, 1649
  - olive oils analysis, 1642
  - oxide glasses structure and, 1563
  - oxygen NMR, 1551
  - phenolic compounds analysis, 1647
  - plant seeds, 1777, 1779
  - quadrupolar NMR of inorganic materials, 1507
  - quantitative deuterium-NMR, 1653
  - relaxation
    - in starch systems, 1745
    - of dairy products, 1697
  - relaxometry, 1455
  - relaxometry in meat science, 1729
  - rheo-NMR, 1515
  - sensory properties of food, 1889
  - silk
    - local structure of, 1569
  - single-sided, 1523
  - single-sided NMR in foods, 1895
  - SNIF-NMR principles, 1651, 1653, 1669
  - SNIF-NMR (economic applications), 1681
  - solid starch systems, 1748
  - spirits, 1689, 1692
  - standard applications in food, 1739
  - starch polysaccharides, 1783
  - starch systems and, 1900, 1901
  - starch systems applications in, 1899
  - sterols analysis, 1648
  - supramolecular systems and, 1499
  - SWNTs and, 1479
  - TD-NMR, 1735
  - tea, 1600
  - ternary complexes identification and characterization, 1349
  - triglycerides analysis, 1645
  - upper mantle silicates, 1552
  - various water population determination, 1704
  - vegetable oils analysis, 1637
  - volatile compounds analysis, 1648
  - water molecular mobility by, 1703
  - whey proteins, 1631
  - whole foods freezing, 1876
  - wine, 1689
  - wine and, 1598
  - xerogels, 1547
- NMR diffusometry water compartmentation and, 1721
- NMR imaging
  - of dairy products, 1801
  - of dough, 1807
- NMR PFG techniques, 1713
- NMR relaxation
  - minced meat analysis, 1838
- NMR relaxometry
  - SLICING, 1845
- NMR, solid-state. *See* soild-state NMR
- NMRD, 1697
- NMR-MOUSE, 1523, 1895
- NNLS, 1705
- nonalcoholic beverages, 1597. *See also* alcoholic beverages
  - tea, 1597
- nuclear gyromagnetic ratio, 1437
- nuclear–spin interactions in starch polysaccharides, 1785
- nutrigenomics, 1628

O

- ^{17}O NMR
  - high-pressure silicates, 1551
  - oxide glasses structure, 1563
- ohmic heating applications, 1829
- oil and moisture determination, quality control (TD-NMR), 1739
- oil content determination in pre-dried olives, 1740
- oils
  - ^{1}H NMR, 1645
  - aldehydes compounds analysis by ^{1}H NMR, 1648
  - diglycerides analysis by ^{1}H NMR, 1648
  - fatty acids
  - determination by NMR, 1637
  - positional distribution analysis by NMR, 1639
  - glycerol esters determination by NMR, 1639
  - high-resolution ^{13}C NMR study of, 1637
  - minor oil components analysis by NMR, 1641
  - olive oil geographical origin analysis by ^{1}H NMR, 1649
  - olive oils analysis by NMR, 1642
  - phenolic compounds analysis by ^{1}H NMR, 1647
  - sterols analysis by ^{1}H NMR, 1648
  - triglycerides analysis by ^{1}H NMR, 1645
  - vegetable oils analysis by NMR, 1642
  - volatile compounds analysis by ^{1}H NMR, 1648
- oleaginous, 1589
- OLED devices, 1539
- olive oil geographical origin analysis NMR study of, 1649
- olive oils analysis NMR study of, 1642
- olives, oil content determination in, 1743
- order concept (elastomers), 1455
- order director fluctuations, 1439
- order director fluctuations (ODF), 1439, 1440
- organic semiconductors
  - characterizing isomers of Alq$_3$, 1542
  - ligand dynamics in Alq$_3$, 1540
  - NMR of, 1539
  - variable deposition rate studies, 1543
- organoleptic, 1597
- orientational order, 1465
- orthogonal functions, conjugate, 1463
- oxidative processes
  - ESR for study of, 1861
  - in beverages, 1861
  - in food, 1861
- oxidative stability
  - of foods, 1862
- oxide glasses structure, 1563
  - ^{17}O NMR, 1563
- oxygen NMR, 1551

P

- ^{31}P NMR
  - milk and milk proteins, 1631
- packing structures in benzoxazines, 1503
- PANI, 1549
- parallel method
  - quality control (TD-NMR), 1740
- partial least squares (PLS) regression, 1836
- pathways
  - photosynthetic pathways, 1664
- PCA
  - supervised data exploration by (chemometrics), 1836
  - unsupervised data exploration by (chemometrics), 1836
- PDMS, 1599
- pectin, 1569
- peptides
  - NMR analysis of, 1631
- PFGSE diffusion measurements
  - food freezing and, 1873
- PFG-STE NMR, 1736
- PGSE. *See* pulsed gradient spin-echo method
- phase errors (chemometrics), 1836
- phase separation
  - magnetic, 1496
- phase transitions
  - relaxation aspects, 1713
  - shear-induced, 1518
- phenolic compounds analysis
  - NMR study of, 1647
- phloretin, 1601
- phospholipid membranes
  - liquid phase chemical spectroscopy, 1875
- phosphorus MRS. *See* ^{31}P MRS
- photosynthetic pathways, 1664
- plant precursors, 1674

- plant seeds
  - HR solid state NMR, 1777
  - liquid-like domains, 1777
  - liquid-like domains with residual dipolar interactions, 1778
  - NMR signal assignments, 1778
  - residual dipolar interactions, 1778
  - solid-like domains, 1777
  - solid-state NMR, 1779
  - spectral edition inside, 1777
- point-resolved spectroscopy. *See* PRESS
- polyelectrolytes, 1534
  - probing polyion-counterion interaction in fluid and frozen solution, 1534
- polyion-counterion interaction, 1530
- polyphenols, 1597
- polysaccharides
  - solid starch, 1748, 1750
  - starch, 1751
- polyunsaturated fatty acid. *See* PUFA
- pore systems characterization, 1713
- porosity
  - dough, 1807
- porous materials
  - fluid diffusion in, 1471
  - microscopic, 1471
  - nanoscopic, 1471
- potato, NMR study, 1683
- PowerSlicing technique, 1847
- PPV films, 1539
- principal component analysis (PCA)
  - wines analysis, 1689
- PRISE, 1785
- probe dynamics
  - supramolecular interactions detection and, 1520
- probes
  - SNIF-NMR, 1659
- probing secondary relaxations, 1490
- process engineering
  - NMR for, 1819
- proofed dough, 1819
- prostate
  - HRMAS MAS of, 1966
- protein structure
  - milk protein, 1631
- proteins. *See also* membrane proteins milk, 1631
- proton FC relaxometry in liquid crystals, 1441
- proton NMR relaxometry
  - in meat science, 1729
- proton relaxation induced spectral editing (starch polysaccharides), 1788
- proton spin–lattice relaxation
  - starch systems in laboratory frame, 1750
  - starch systems in rotating frame, 1750
- proton spin–spin relaxation (starch systems), 1748
- proton-driven spin-diffusion (PDSD), 1570
- PSPAN, 1549
- pulse sequences
  - for MQMAS, 1507
- pulsed field gradients (PFGs), 1583
  - NMR, 1697
  - quality control (TD-NMR), 1735

Q

- quadrupolar NMR of inorganic materials, 1507
- quadrupolar nuclei, 1437
- quality control (TD-NMR), 1729
  - dilatometry, 1741
  - direct SFC method, 1739
  - droplet size determination, 1736
  - fat
    - and water content determination, 1735
    - content determination in chocolate, 1743
  - gradient experiments, 1735
  - indirect SFC method, 1741
  - oil
    - and moisture determination, 1743
    - content determination in pre-dried olives, 1741, 1743
  - parallel method, 1740
  - relaxation analysis in foods with high water content, 1736
  - serial method, 1735
  - SFC
    - analysis automation, 1742
    - in fat compositions, 1739
  - solid fat index, 1741
  - solid-echo method SFC method, 1741
  - standard applications in food, 1739
- quality control/quality assurance (QC/QA), 1739
- quantitative deuterium-NMR (SNIF-NMR principles), 1653
- quantitative L(omgekeerd)method, 1797
- quercetin, 1600

R

- recoupling
  - dipolar, 1499
- referencing
  - by combined use of SNIF-NMR and isotope ratio mass spectrometry, 1656
  - by means of owrking standard (SNIF-NMR principles), 1657
  - electronical referencing, 1656
  - isotopic parameters, 1653
- regional cerebral blood flow. *See* rCBF
- regional cerebral blood volume. See rCRV
- relaxation
  - ^{13}C spin–lattice, 1751
  - horticultural products, 1721
  - in gels, 1708
  - in meat (T_2), 1721
  - in starch systems, 1745
  - NMR, 1689
  - proton spin–lattice, 1750
  - proton spin–spin, 1748
  - secondary, 1487
  - sol–gel transitions, 1715
  - structural
    - changes including phase transitions and denaturation, 1712
    - characterisation, 1715
  - water relaxation, 1687
- relaxation analysis
  - in foods with high water content, 1736
- relaxation of dairy products, NMR, 1697
  - fat relaxation, 1698
  - water
    - diffusion, 1689
    - relaxation, 1697
    - retention, 1698
- relaxation spectrum, elastomers and, 1447
- relaxation studies (low moisture sugars), 1881
- relaxation time approach
  - single-sided NMR in foods, 1895
- relaxation times
  - elastomers, 1448
  - flow behavior and, 1813
  - in rotating frame (carbohydrate food systems), 1699
  - temperature measurements and, 1825
- relaxation weighted spin density (RWSD), 1451
- relaxometry
  - acoustically stimulated NMR, 1439
  - applied during meat processing, 1724
  - conversion of muscle to meat, 1730
  - food freezing and spin, 1869
  - for fat content determination in meat, 1729
  - in meat science, 1729
  - NMR, 1451, 1841
  - proton FC, 1441
  - ultrasound induced, 1442
- relaxometry experiments
  - elastomers, 1448
- renneting, 1698
- residual dipolar interactions, 1787
  - liquid-like domains with, 1778
- resonances
  - metabolite, 1617
- resveratrol, 1599
- rheo-NMR
  - application to food, 1819
  - flow behavior and T1- or T2 –relaxation times, 1821

rheo-NMR (*cont.*)
  realization of practice simulating test conditions, 1802
rheo-NMR applications, 1820
  couette, 1820
  flow of disperse multiphase/complex materials, 1820
  tube flow, 1820
rheo-NMR spectroscopy, 1515
  experimental aspects, 1515
  hexagonal and lamellar lyomesophases, 1518
  nematic liquid crystals, 1516
  shear-induced phase transitions, 1520
robotics
  rotating drum, 1585
  rotational dynamics
    disordered materials (near vitrification transition), 1487
rotational dynamics, disordered materials, 1487
rotor encoding
  supramolecular systems, 1499

S

Samia cynthia ricini, 1569. *See also* *Bombyx mori*
secondary relaxations
  probing, 1487
SEDOR. *See* spin-echo double resonance
seeds. *See* plant seeds
self diffusion, in liquid crystals, 1439
semiconductors, organic. *See* organic semiconductors
sensor
  single-sided, 1523
sensory properties of food, 1889
  functional brain imaging and, 1891
  image analysis, 1891
  itter, 1892
  salty, 1892
  sour, 1892
  sweet, 1892
  taste, 1892
  texture, 1893
  umami, 1893
  water mobility, 1891
serial method
  quality control (TD-NMR), 1735
SFC, 1697
  automation of, 1742
  fat relaxation aspects, 1698
SFC in fat compositions, 1739
  direct method, 1739
  indirect method, 1741
  quality control (TD-NMR), 1735, 1737
  solid-echo method, 1741
SFC method
  indirect method, 1741
shear-induced phase transitions, 1520
sideband patterns
  supramolecular systems, 1499
signal processing
  SNIF-NMR principles, 1653
signal-to-noise. *See* SNR
silicates
  dense silicate phases, 1558
  high-pressure, 1551
  hydrous magnesium silicates, 1556
  upper mantle silicates, 1544
silk, local structure of, 1563
  CSA–CSA correlation, 1570
  DOQSY, 1570
  molecular-to-nanometer information, 1570
  NMR measurements of torsion angles, 1569
  PDSD, 1570, 1571
  quasi-equilibrium limit, 1570
  SMAS-PDSD experiment, 1571, 1572
  solid-state NMR, 1569
Single Pulse Excitation (SPE), 1761
single-molecule spectroscopy, 1487
single-sided NMR, 1523
  3D imaging with single-sided sensor, 1524
  flow characterization with single-sided sensor, 1525
  in foods, 1893
  material characterization via relaxometry, 1523
  NMR-MOUSE and, 1523
single-sided NMR in foods
  Bruker single-sided NMR, 1895
  diffusion weighted approach, 1895
  fat and water determination, 1895
  relaxation time approach, 1895
single-sided sensor
  3D imaging with, 1524
  flow characterization with, 1525
single-walled carbon nanotubes (SWNT), 1479
site-specific
  characterization of complex materials,
  EPR spin probes for, 1529
  hydrogen fractionation, 1652
  thermodynamic isotope effects, 1659
slice timing correction
  direct exponential curve resolution, 1845
  NMR relaxometry, 1845
  tri-linear models, 1846
slow liquid/vapor exchange limit, 1474
SMAS-PDSD experiment (silk local structure), 1571, 1572
smectic phase, 1439
SNIF-NMR, 1651
  and carbohydrates, 1664
  and ethanol, 1652
  and glycerol, 1657
  chemical and biochemical mechanistic pathways analysis, 1659
  chemical processes characterization, 1675
  climatic effects and geographical origin, 1675
  economic applications, 1673
  enantiotopic hydrogen sites, 1665
  experimental strategies for origin, 1673
  fermentation, 1664
  from carbohydrates to
    ethanol, 1664
    glycerol, 1657
  from mechanistic affiliation to origin inference, 1669
  general methodology, 1674
  hydrogen isotope redistribution, 1664
  identification of starting materials, 1673
  inference of products, 1673
  isotope
    ratios as tracers of mechanistic pathways, 1659
    parameters of glucose, 1664
    redistribution coefficients, 1653
  isotope effects
    and affiliation coefficients, 1662
    in chemically exchanging systems, 1660
  kinetic isotope effects, 1653
  liquid–vapor fractionation effects, 1660
  mechanistic routes of atoms and, 1669
  natural or synthetic origin of products, 1674
  nature laboratory, 1673
  photosynthetic pathways, 1664
  plant precursors identification, 1674
  probes, 1664
  site-specific thermodynamic isotope effects, 1660
  SNIF paramerters of of reactants and products, 1662
  statistical treatments, 1674
  thermodynamic isotope effects in tautomeric equilibria, 1661
SNIF-NMR (economic applications)
  concentrated juices, isotopic characterization of, 1664
  ethanol, 1664
  exogeneous minor components detection, 1686
  fruit juice, 1677
  illegal enrichments, determination of, 1684
  juices, 1677, 1681
  multi-component and multi-isotope strategies for adulterations detection, 1685
  NMR methodologies in, 1684
  origin authentication and data banks for wines, 1683

  regulations about wines and juices, 1681
  spirits, 1681
  wines, 1681
SNIF-NMR principles, 1653
  carbon SNIF-NMR, 1657
  electronical referencing, 1656
  isotope ratio mass spectrometry, 1656
  isotopic abundances, 1651
  isotopic fractionation, 1652, 1653
  isotopic parameters referencing, 1653
  isotopic ratios, 1651
  mass and isotopic balance, 1651
  quantitative deuterium-NMR, 1653
  referencing by combined use of SNIF-NMR and isotope ratio mass spectrometry, 1656
  referencing by means of working standard, 1654
  signal processing, 1654
  site-specific hydrogen fractionation, 1652
sol-gel transitions and syneresis, 1716
solid fat content (SFC), 1739
solid fat index, 1741
solid mobility
  by cross relaxation (carbohydrate food systems), 1708
solid starch polysaccharides, 1748, 1749
  domains and spin-diffusion, 1749
  in laboratory frame, 1747
  spin–lattice relaxation, 1747
    in roatating frame, 1747
  spin–spin relaxation, 1747
solid starch systems, 1747
solid state NMR
  plant seeds, 1777
solid-echo method, 1741
solid-phase extraction method
  metabolism and metabonomics, NMR-based, 1623
solid-state high-field NMR
  starch systems, 1899
solid-state NMR
  ^{1}H, 1499
  antifreeze glycoproteins, 1876
  carbohydrate food systems, 1703
  dough, 1757
  food freezing, 1869
  frozen solutions, 1870
  gluten, 1761
  high-pressure silicates, 1551
  low moisture sugars, 1879
  plant seeds, 1777
  protein misfolding disease, 1389
  silk, local structure of, 1563
  starch polysaccharides, 1783
  supramolecular systems, 1499
  whole foods, 1876
  xerogels, 1547
solid-state proton NMR
  plant seeds and, 1777
solution state high-resolution NMR
  starch systems and, 1899
SOPPA. *See* second order polarization propagator approximation
SOS-DFPT. *See* sum-over-states-density functional perturbation theory
sour
  sensory properties of food, 1889
specific-site addressing by, 1529
spectral analysis
  MQMAS, 1509
spectral editing in biological NMR, 1625
spectral editing techniques
  starch polysaccharides, 1783
spectral editing, proton relaxation-induced, 1784
spin labeling principles, 1529
spin probes
  as tracers, 1529
  EPR, 1529
  supramolecular structures
  starch systems, 1899
  supramolecular systems
  ^{1}H solid-state NMR of, 149
  ^{1}H–1H DQ NMR, 1504
  columnar stacking of discotics, 1505
  dipolar recoupling schemes, 1499
  DQ coherences, 1501
  fast MAS, 1499
  fast-MAS NMR, 1499
  high resolution solid-state NMR, 1499
  homonuclear DQ NMR, 1501
  hydrogen bonds in bilirubin, 1502
  MAS and, 1499
  packing structures in benzoxazines, 1503
  rotor encoding and sideband patterns, 1501
spin relaxometry, 1869
  food freezing and, 1869
spin trapping, 1862
spin-diffusion
  starch systems, 1745
spirits
  high resolution NMR analysis of, 1689
  isotopic NMR probe for characterizing, ethanol-based, 1677
  NMR, 1684
  SNIF-NMR (economic applications), 1673
SSNMR. *See* solid-state NMR
starch
  ^{13}C CP-MAS, 1757
starch, 1757
starch biosynthesis, 1900
starch polysaccharides, 1783
  ^{13}C CPMAS NMR, 1784
  ^{13}C spin–lattice relaxation, 1751
  ^{1}H NMR, 1786
  future perspectives, 1789
  high-resolution13C NMR, 1787
  high-resolution^{1}H NMR, 1786
  HR solid-state NMR, 1775
  MAS, 1775
  mobility-resolved NMR, 1788
  nuclear–spin interactions in, 1785
  proton relaxation induced spectral editing, 1785
  spectral editing techniques, 1785
starch retrogradation, 1903
starch systems
  ^{13}C spin–lattice relaxation, 1751
  ageing of intermediate water content, 1903
  chemical structure and composition, 1900
  chemically modified, 1901
  CP MAS, 1901
  domains and spin-diffusion in, 1749
  FID, 1740, 1741, 1742
  future perspectives, 1789
  general considerations for NMR, 1746
  imaging, 1889
  molecular and supramolecular structures, 1901
  molecular dynamics using time domain NMR, 1895
  MRI, 1889
  NMR applications in, 1879
  NMR relaxation in, 1735
  processing and storage, 1899
  proton spin–lattice relaxation
    in laboratory frame, 1747
    in rotating frame, 1747
  proton spin–spin relaxation, 1748
  solid, 1739
  solid starch polysaccharides, 1748
    in laboratory frame, 1747
    in roatating frame, 1747
  starch
    biosynthesis, 1899
    polysaccharides, 1745
    retrogradation, 1899
  starch–water interactions, 1903
  structure characterization, 1893
  temperature effect on, 1897
  water in, 1746
starch, T_2 distribution of water, 1705
starch–water interactions, 1903
statistical treatments
  SNIF-NMR, 1669
sterols analysis
  NMR study of, 1639
STMAS
  humite minerals, 1556
STMAS NMR
  dense silicate phases, 1556
structural and dynamic distribution functions, 1463

sugars, 1858
sugars, low moisture, 1875
  CPMAS NMR and crystallization, 1886
  deuterium line shape studies, 1881
  glass transition and, 1879
  glass transition and crystallization in, 1879
  HR SS ^{13}C NMR, 1876
  line width and shape studies, 1879
  NMR analysis of, 1869
  relaxation studies, 1881
supramolecular interactions
  detection by changing probe dynamics, 1529
  EPR and, 1529
supramolecular structures
  spin probes and spin labels, 1529
sweet
  sensory properties of food, 1889
SWNT, 1479
  ESR and, 1479
  gas adsorption on, 1479
  NMR and, 1471
syneresis, 1591
synthetic poly-(styrene-butadiene) (SBR) networks, 1447

T

T_1- or T_2 -relaxation times
  flow behavior and, 1821
T_2 distribution of water in starch, 1705
T_2 relaxation in meat, 1729
taste, 1889
  bitter, 1890
  salty, 1889
  sour, 1890
  sweet, 1889
  umami, 1890
tautomeric equilibria, thermodynamic isotope effects in, 1660
TD-NMR
  in quality control, 1735
  standard applications in food, 1739
  tea
    NMR and, 1600
temperature
  aspects of dairy products, 1801
temperature effect on starch systems, 1899
temperature measurements
  by magnetic resonance, 1825
  chemical shift, 1826
  convective heating applications, 1827
  diffusion coefficient, 1825
  microwave heating applications, 1827
  MRI applications, 1827
  ohmic heating applications, 1829
  T_1 and T_2 relaxation times, 1825
territorially bound probes, 1537
texture, food, 1889
thawed dough, 1808
theaflavins, 1600
thearubigins, 1600
theophylline, 1600
thermodynamic isotope effects, 1659
  in tautomeric equilibria, 1660
  site-specific, 1659
time domain NMR
  in quality control, 1735
  starch systems, 1899
time resolved ESR, 1864
torsion angles
  measurement (silk local structure), 1569
  NMR measurements of (silk structure), 1569
tracers of mechanistic pathways, isotope ratios as, 1659
transient freezing, 1874
translational diffusion, 1476
translational dynamics, disordered materials, 1487
TREPR, 1864
triacyglycerols (TAG), 1777
triglycerides analysis
  NMR study of, 1645
trigonelline, 1600
tri-linear models, 1846
tube flow, 1819
turgor, 1592
two-phase exchange model, 1471

U

ultraslow dipolar correlations monitoring by NMR, 1445
ultrasound induced relaxometry, 1442
umami
  sensory properties of food, 1889
upper mantle silicates
  MQMAS NMR, 1552

V

vacuole, 1590
vanillin, 1590
vegetable oils analysis
  NMR study of, 1639
vegetables
  HR MAS NMR of, 1765
  quality, 1724
velocity imaging of granular materials, 1581
vitrification transition
  rotational dynamics of disordered materials, 1487
volatile compounds analysis
  NMR study of, 1649

W

water compartmentation
  NMR diffusion (horticultural products), 1721
  NMR relaxation and (horticultural products), 1720
water content
  foods with high (quality control aspects), 1735
water content and distribution
  dairy products, 1793
water content determination
  quality control (TD-NMR), 1734
water content starch systems, 1903
water determination
  single-sided NMR in foods, 1895
water in starch systems, 1748
water interactions
  starch–water interactions (starch systems), 1903
water mobility food, 1891
water molecular mobility by NMR (carbohydrate food systems), 1703
water relaxation
  dairy products, 1697
water retention, 168
water suppression, 1624
watercore in apples, 1724
WATERGATE, 1625
water-holding capacity, 1698
  in meat, 1729
WHC, 1713
whey proteins, 1634
  ALA, 1634
  BLG, 1634
  NMR analysis of, 1634
whole foods
  solid-state NMR, 1876
wine, 1597
  ^{13}C NMR, 1598
  ^{1}H NMR, 1598
  adulteration detection, 1685
  high resolution NMR analysis of, 1689
  illegal enrichments, determination of 1684
  isotopic NMR probe for characterizing, ethanol-based, 1682
  LC-NMR, 1598
  NMR and, 1678
  origin authentication and data banks, 1683
  principal component analysis, 1691
  SNIF-NMR (economic applications), 1681

X

xerogels
  MAS NMR, 1545
  solid-state NMR of, 1547